Time-resolved structures of electrical discharges in gases: experiment and stochastic model

A.D.O. Bawagan, L. Fell, and J. Logan

Abstract: The time-resolved discharge patterns generated in a gaseous dielectric breakdown (DB) are imaged using a fast optical imaging system (≈40 ns exposure time). The discharge patterns from various gases (He, air, and SF_6) show general features consistent with their known dielectric strength. A new stochastic pattern-forming model that explicitly includes time is presented and is shown to produce theoretical DB patterns in qualitative agreement with the present experimental discharge patterns for air (N_2). The stochastic DB model (with time) also provides an approximation to the discharge current, which is in good agreement with published current wave forms.

Key words: gas discharge, electron scattering, fractal.

Résumé : Faisant appel à un système rapide d'imagerie optique (≈40 ns de temps d'exposition), on a enregistré des images des patrons de décharge résolus en fonction du temps obtenus lors d'une prédissociation gazeuse diélectrique (DB). Les patrons de décharge de divers gaz (He, air, SF_6) présentent des caractéristiques générales qui sont en accord avec les valeurs connues de leur force diélectrique. On présente un nouveau modèle stochastique de la formation des patrons qui inclut explicitement le temps et on montre qu'il conduit à des patrons théoriques de DB qui sont qualitativement en accord avec les données expérimentales pour les patrons de décharge de l'air (N_2). Le modèle stochastique de DB (incluant le temps) permet aussi d'obtenir une approximation du courant de décharge qui est en bon accord avec les formes de vague qui publiées actuellement.

Mots clés : décharge gazeuse, diffraction des électrons, fractal.

[Traduit par la rédaction]

1. Introduction

The recent discovery (1) that electrical discharges in air can be a very energy-efficient method for decomposing volatile organic compounds (VOCs) has focussed attention to the long-established field of gaseous dielectric breakdown or, more generally, the field of nonthermal plasma chemistry. The term "gaseous dielectric breakdown" simply reflects the origins of the field and the predominance of its application in high-voltage insulation for power generation systems (2). The ubiquitous use of VOCs in the manufacturing and use of everyday consumer products (e.g., trichloroethylene for cleaning, carbon tetrachloride as solvent, etc.) and the recognition that these chlorinated VOCs are extremely toxic has led to a global search for cost-effective VOC abatement procedures. Nonthermal plasma techniques, such as electrical discharges and high-energy electron beams, are extremely efficient because most of the electrical energy goes into the production of energetic electrons (that lead to degradation of VOCs) rather than into gas heating. This new development has therefore led to a deeper understanding of the physico-chemical mechanisms (3–8) underlying electrical discharges in air or, more generally, gaseous dielectric breakdown.

In 1987 Dhali and Williams (3) presented a two-dimensional mathematical simulation of the gaseous dielectric breakdown problem in air, which captured the essential physico-chemical processes. They considered the simplest set of dynamical equations, which included the deterministic continuity equations for electrons and for positive ions, plus Poisson's law of electrostatics, which couples the electric field to the charges. Other theoretical methods, such as Monte Carlo methods (2), can also be used for simulating these nonstationary processes observed in gas discharges. It is now understood that the initial processes that lead to dielectric breakdown or to the formation of discharges are the so-called streamers or streamer leaders (9). The term "streamers" simply reflects the general shape of the transient phenomenon prior to discharges that have been observed using streak camera methods.[2]

Received June 23, 1997.

A.D.O. Bawagan,[1] **L. Fell, and J. Logan.** Ottawa–Carleton Chemistry Institute, Carleton University, Ottawa, ON K1S 5B6, Canada.

[1] Author to whom correspondence may be addressed. Telephone: (613) 520-3841. Fax: (613) 520–3830. E-mail: abawagan@ccs.carleton.ca

[2] The microscopic processes involved in a gas discharge are called streamers and leaders (8, 9). The initial process involves the formation of streamers, which have very low optical luminosity, followed by the leader discharge, which has a higher luminosity. The final stage is referred to as the "spark-over," which is characterized by extreme brightness and sometimes a "sonic boom." The present experiments are concerned only with the streamer and leader processes (i.e., breakdown).

© 1998 NRC Canada

Fig. 1. Basic schematic for the generation of a streamer–leader discharge. A positive high voltage is effectively introduced to the electrode by "grounding" the electrode. As the thyratron (see Fig. 2) switches on, the normally grounded ring becomes negative. This produces a potential between the electrode and the ring, which is of *positive* polarity.

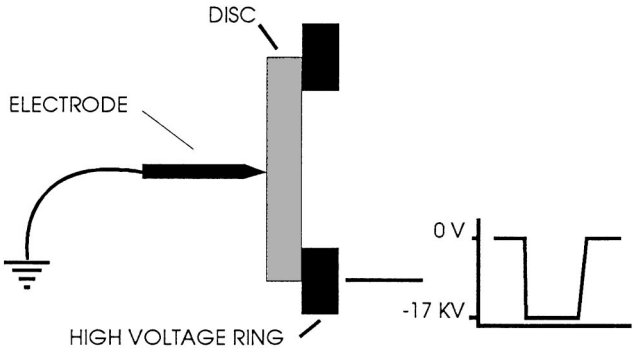

Recently, Vitello et al. (4) performed a more accurate numerical simulation (2-D) of the dynamical evolution of streamers using the Dhali–Williams equations, and this revealed, for the first time, a realistic microscopic picture of the streamer morphology. In particular, Vitello et al. (4) showed that there are distinct phases in the time development of streamers, and that this development is driven by a very narrow streamer front (≈10 μm), also called a thin ionization wave. The separation of the length scale between the typical width of the streamer front (μm) and the length of the body of the streamer (mm) has led Ebert et al. (5) into an elegant analysis of the pattern-forming problem as an example of what they refer to as "front propagation into unstable states." These new numerical results (3, 4), coupled with more detailed experimental studies of the dynamics of streamer development (10–13), are leading to a convergent understanding of gaseous dielectric breakdown at the microscopic level.

On a larger scale, it is well known that a high-voltage discharge generates a "tree-like" branched pattern, also known as a Lichtenberg figure. Niemeyer and co-workers (6, 10) have shown that these tree-like structures can be described as a fractal or self-similar pattern (14). For a fractal structure in two dimensions, the total length $N(r)$ of all branches inside a circle of radius r is related as follows:

$$[1] \quad N(r) \approx r^D$$

A plot of log N versus log r will yield a linear relationship characterized by a slope equal to D, or what is referred to as the fractal dimension (14).

We have recently extended the Niemeyer-type (point-circle geometry) dielectric-breakdown experiment by incorporating a fast optical imaging system (15). A significant advantage of the present experiment is the capability to produce time-resolved images of the dielectric breakdown in the nanosecond range, compared to that conducted by Niemeyer et al. (6), which yields time-integrated photographs in the microsecond range. We showed (15) that the time development of the dielectric breakdown in air is also a fractal, as revealed by an analysis of each single frame from a single discharge.

In the present work, we extend the previous work and report the time-resolved dielectric-breakdown images in He, air (N_2), and SF_6, thus providing a broad cross section of chemical systems. We also present a new stochastic model of dielectric breakdown, which incorporates explicitly the dimension of time. This allows us to make direct (but still qualitative) comparisons with our time-resolved DB images, as well as other traditional experimental measurements such as discharge current.

This work therefore paves the way for our more distant goal of providing a "phenomenological link" between the microscopic gas-phase information (e.g., photo-ionization and electron-impact cross sections, reaction rates, thermal relaxation rates, etc.) and the macroscopic structures generated in a streamer–leader discharge. The recognition and acceptance of the important length and time scales relevant to the dynamic development of streamers in discharges in air (5) indicate that the resolution of the macroscopic pattern-forming problem in dielectric breakdown from first principles may be closer at hand.

2. Experimental details

The experimental apparatus has been reported earlier (15), and only a brief discussion is presented along with minor modifications. The gaseous dielectric breakdown experiment is shown schematically in Fig. 1. A positive high-voltage pulse (+22 kV max, 1 μs width) is introduced to a sharp stainless-steel electrode that is located in the center of a sapphire disc (2 mm in thickness, dielectric constant $\epsilon_r = 10.2$). The positive input voltage is referenced relative to a stainless-steel ring (20 mm inner radius) situated at the rim of the sapphire disc. The streamer–leader discharge that results is observed from the backside of the sapphire disc. The arrangement is very similar to the arrangement introduced by Niemeyer et al. (6), except that the present experiments are conducted at moderate pressures of He, air (N_2), and SF_6, as opposed to high-pressure SF_6. To a good approximation, this arrangement produces an equipotential channel system growing in a plane. The growth is therefore *two-dimensional,* even though the electric field lines are three-dimensional (6).

The fast high-voltage pulse is generated using a stable high-voltage DC supply (Brandenburg 25-P), a storage capacitor (1300 pF), and a grounded grid thyratron (EG&G HY-1102). The low impedance and stable switching ability of the thyratron allow the reproducible production of fast high-voltage pulses ($t_{rise} \approx 30$ ns). The fast optical imaging system is composed of several optical devices coupled together to achieve the maximum possible gain (Fig. 2). Because of the small exposure times necessary to observe the streamer–leader discharge and the low visible photon flux generated during the breakdown period, a total gain of $\geq 10^5$ was necessary. A macro lens (Canon) views the back end of the disc (Fig. 1), and then an image intensifier (Star-Tron MK 303ABN) operated at maximum gain (≈60 000) is used. The image generated by the Star-Tron MK 303ABN is then photographed using a streak camera (IMACON 790 with IMACON 50/40 intensifier) operated in framing mode with an exposure time of 40 ns per frame. The thyratron and the IMACON camera are both triggered by a pulse–delay generator (SRS DG535) with a 16.45 μs delay as shown in Fig. 2. This allows precise timing such that the leading edge of the high-voltage pulse is coincident with frame 1. A total of 6–8 frames are generated for each single discharge and are permanently recorded on Polaroid 612 film (20 000 ASA). The interframe time difference is ~160 ns, thus giving a total time record of 1600 ns for eight frames (i.e., for each discharge).

© 1998 NRC Canada

Fig. 2. Schematic of the dielectric breakdown apparatus (Carleton University) and the optical imaging system (Ontario Hydro Technologies). See text for details.

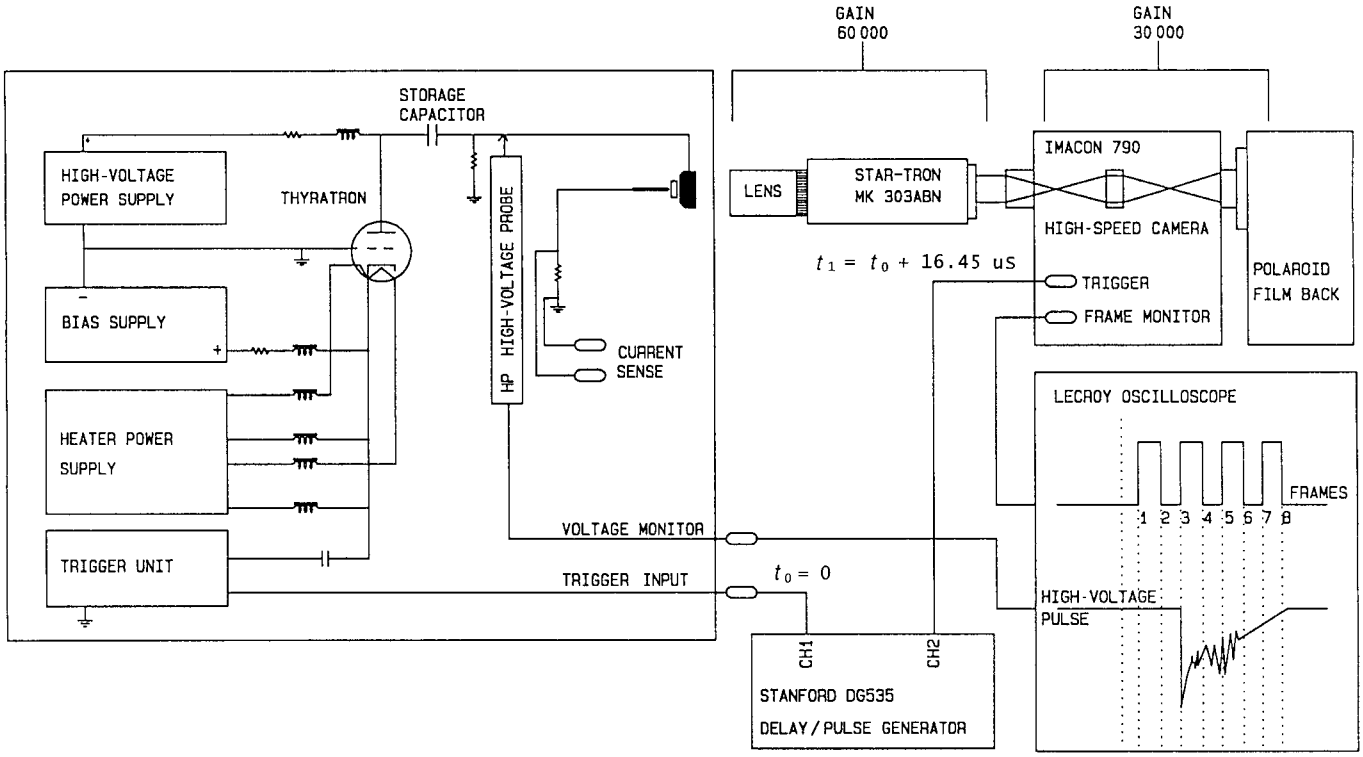

Nonlinear distortions of the optical system were studied using a fine-ruled grating and a He–Ne laser light source. Optical distortions were limited to the edges of the viewing field and were never greater than 10%. These distortions therefore do not affect any of the reported DB images.

3. Results and discussion

3.1 Experimental dielectric breakdown (DB) patterns

The IMACON images of the dielectric breakdown patterns of He, air (N_2), and SF_6 are shown in Fig. 3. The framed images obtained in the present experiment have an exposure time of 40 ns each, in stark contrast to the images obtained by Niemeyer et al. (6), which are *time-integrated* and are equivalent to ≈1 μs exposure time. Each frame captures an image of the dielectric breakdown as it progresses such that there are eight frames per dielectric breakdown. The frames are numbered consecutively (frames 1–8), as shown in Fig. 3*d,* against a backdrop of the full view of the imaging system. This full view was obtained by taking an image of the breakdown return spark or spark-over, which is extremely bright and illuminates the whole image intensifier. Frame 7 is missing because of a slight electronic misalignment in the IMACON camera.

The dielectric breakdown patterns for He, air (N_2), and SF_6 were obtained at 8.5 kV, 17.0 kV, and 21.7 kV, respectively. The DB patterns were not observed below these voltages. For a comparable value, the breakdown voltage value for SF_6 should actually be higher than 21.7 kV, since the DB image (Fig. 3*c*) is barely visible. We were unable to increase the voltage further because our experimental apparatus is currently limited to a maximum voltage of +22 kV. The present breakdown voltage values can be compared with the breakdown voltages reported in the literature under nonuniform field conditions (13, 16), scaled to the same pressure and gap distance (*Pd*) in Table 1. For reference, the breakdown voltages under uniform field conditions (17) are also shown. It should be noted that the general phenomenon of gaseous dielectric breakdown is extremely complex, and the reported breakdown voltages are very sensitive to the details of, for example, the voltage pulse, voltage polarity, conductor geometry, gas pressure, and insulator surface condition, etc. (2, 13, 16, 17). Thus detailed comparisons of the present experiment with other results should take these into consideration. Furthermore, the voltages we report are breakdown voltages, i.e., voltages just prior to breakdown. The comparison presented in Table 1 is therefore only used for *qualitative* purposes and illustrates that the relative order of dielectric strength of the various gases is reproduced. The order of dielectric strength (i.e., increasing breakdown voltage) for a nonuniform field (point-to-circle) as obtained from Fig. 3 is

[2] He << air (N_2) << SF_6

which is in good agreement with previous studies (13, 16, 17). The above order also indicates that the observed images are predominantly a result of the direct breakdown of the gas, as opposed to surface flashover, which is an alternative phenomenon discussed later.

It is not the goal of this study to obtain precise breakdown voltages (which is an important goal in itself) but rather to investigate the temporal characteristics of the DB patterns. The relation of the observed DB patterns to actual physico-chemical processes is our main interest, and it is hoped that the temporal characteristics of the DB patterns will provide support for the

© 1998 NRC Canada

Fig. 3. Time-resolved IMACON images generated by a fast HV pulse with exposure time ≈40 ns per frame for (*a*) helium at 8.5 kV, (*b*) air (N_2) at 17.0 kV, and (*c*) sulfur hexafluoride at 21.7 kV. Some faint structures in the original Polaroid film may not appear in the reproductions. (*d*) Sequence order (1–8) of IMACON frames for each discharge.

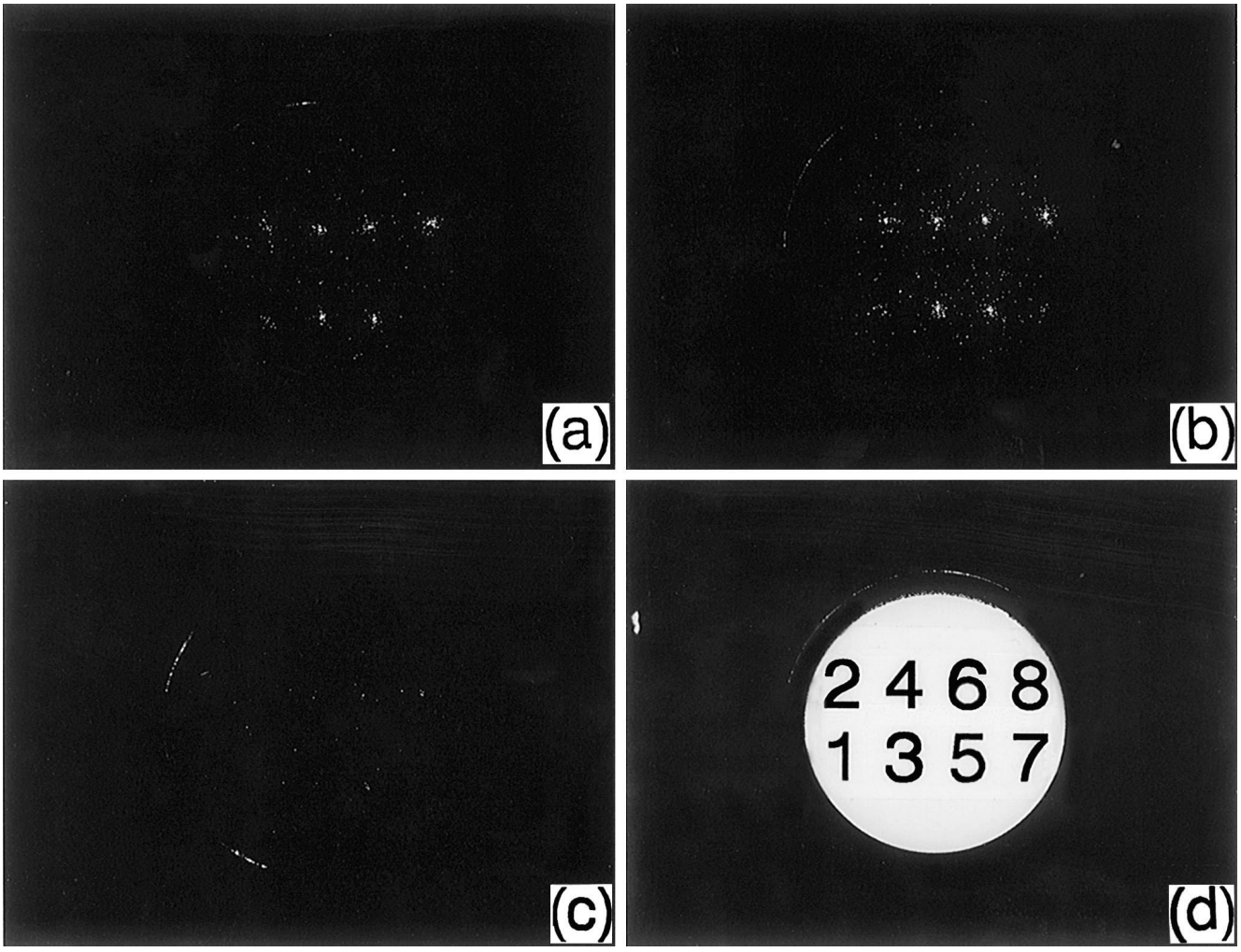

development of suitable models of gaseous dielectric breakdown. In the next section, we provide a brief background of the relevant chemistry and physics of gaseous dielectric breakdown.

3.2 Streamer–leader theory

The possible scattering events involved in the avalanche generation observed in transient phenomena in the breakdown of gases are indicated below for a neutral molecule, M^0 :

[3] $e^- + M^0 \rightarrow e^- + e^- + M^+$

[4] $e^- + M^0 \rightarrow M^-$

[5] $e^- + M^0 \rightarrow e^- + M^0$

Gallimberti (9) has outlined the relevant chemical reactions in the dynamical development of streamers, which is now referred to as the streamer–leader theory (8, 9). The streamer–leader theory of breakdown is a response to the failure of the Townsend theory (18) to predict the relevant breakdown parameters in gases at atmospheric pressures or higher.[3] It is now recognized that breakdown in air (long gaps) involves a multi-step process whose elementary step is the so-called streamer. The existence of streamers was postulated by Raether (19) in 1939 and is basically a propagating thin channel of ionization. Although electrically neutral because of the equal number of positive and negative charges, under an external field (which may be weak) thin layers of charge or space charge develop at the tips of this thin filament, as shown in Fig. 4. The field developed by the space charges at the tip of the streamer can be quite significant and adds to the applied field yielding a *much-enhanced* total electric field. It is only recently (4, 5) that the precise magnitude of these fields has been determined.

[3] Townsend theory (18) is the first physical theory successfully developed for gas electrical breakdown. It postulates the electron impact ionization of free gas molecules and subsequent multiplication of electrons through a nonlocal, secondary electron mechanism. Townsend theory predicts the increase of electron density (n_e) to follow $dn_e/dt = \alpha(E)v_e n_e$, where $\alpha(E)$ is the Townsend or ionization coefficient, E is the local field, and v_e is the electron drift velocity. From the above equation, the theoretical breakdown voltage can be derived and is generally in agreement with experimental results at low gas pressures and uniform field conditions (16).

© 1998 NRC Canada

Table 1. Comparison of electrical breakdown voltages (V) of gases at same pressure–distances (Pd).

Sample	Breakdown voltage (+kV)	Pressure (atm)	V/P (kV/atm)	$V/(Pd)$ (kV atm^{-1} cm^{-1})
He (this work)	8.5	4.5	1.9	0.95[a]
He (ref. 13)				2.0[b]
He (ref. 17)				2.0[c]
Air (this work)	17.0	1.0	17.0	8.5[a]
Air (ref. 13)				10[b, d]
N_2 (ref. 13)				10[b, d]
N_2 (ref. 16)				7.9[e]
Air (ref. 17)				25[c, d]
N_2 (ref. 17)				25[c, d]
SF_6 (this work)	21.7	0.8	27.1	13.6[a]
SF_6 (ref. 16)				39.4[e]
SF_6 (ref. 17)				150[c]

[a] Nonuniform field conditions; d = 2.0 cm with sapphire spacer.
[b] Nonuniform field conditions; data from Fig. 2 (1 atm, 1.5 cm) in ref. 13 (1 atm = 101.3 kPa).
[c] Uniform field conditions; data from Fig. 2 (20 bar mm) in ref. 17 (1 bar = 100 kPa).
[d] Breakdown voltages of air and N_2 are essentially the same under atmospheric conditions.
[e] Nonuniform field conditions; data from Fig. 5.22 (1 atm, 2.54 cm) in ref. 16.

It is suggested that the quenching of the positive space charge at the tip (see Fig. 4) leads to photoemission, which subsequently photo-ionizes the gas molecules just ahead of the tip — the so-called active region (9). The photo-generated electrons are quite energetic and lead to an avalanche of electron–molecule reactions (see eq. [3]) (20). In fact, spectroscopic studies by Gallimberti (9) have revealed that the brightest (in the visible range) region of the streamer–leader is the *tip* of the growing streamer–leader formation. The enhanced electric field will generate considerable ionization of neighboring gases, which would then electronically relax, releasing the observed photons. The streamer tip also serves as the growth point for new streamers and, therefore, may be considered a *branch point*. The number of branch points $b(r)$ at large enough values of r is proportional to the number of branches, which in turn is related to $N(r)$ (6, 15),

$$[6] \qquad b(r) \approx \frac{\mathrm{d}N(r)}{\mathrm{d}r} \approx r^{D_f-1}$$

The slope of log b versus log r would then be equal to $D_f - 1$. As previously shown in our earlier work (15), these DB patterns can be characterized as fractal images with a fractal parameter, $D_f = 1.8$, which is in agreement with earlier measurements (6, 10) and extensive theoretical simulations (21). Our present understanding assumes that the observed "dots" in the DB images (Fig. 3) are the branch points of the growing streamer–leader of gaseous DB. We have explored alternative explanations (see below), but none provide as consistent an explanation as that presented above. Further support for our assumption is provided by a new stochastic DB model, which is presented in section 3.3.

Another possible explanation for the observed images in Fig. 3 is the phenomenon of surface flashover (22–24). Surface flashover refers to the observation of surface field emission of

Fig. 4. Schematic of growing streamer with enhanced total electric field at tips. The tip dimensions are exaggerated to highlight the space-charge effect.

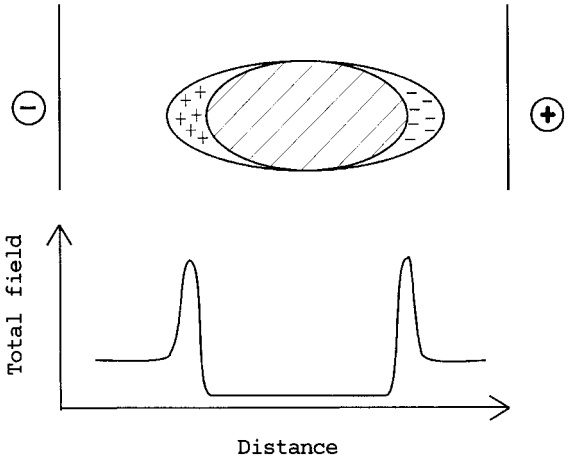

electrons, followed by the conduction of a small current across the insulator, which is sandwiched by two electrodes that are at sufficiently high voltage. Thus, surface flashover can be initiated at any part of the insulator surface. Although surface flashover is generally observed only under vacuum conditions (22, 24), it can also occur at atmospheric pressure (23); however, it is quite difficult to separate the gas-mediated processes in this case. For example, surface flashover in sapphire has been observed and characterized only under high-vacuum conditions (lower than 10^{-6} torr) (1 torr = 133.3 Pa) (22, 24). Thus, at the pressures presently studied, surface flashover is not the major reason for the observed images; the images refer to breakdown of the respective gases (Fig. 3). This is also consistent with the observed trend in the breakdown voltages (see Table 1), which would have stayed fairly constant if surface flashover was the dominant mechanism responsible for the observed images.

3.3 Stochastic model of gaseous dielectric breakdown

The present model is an extension of an earlier DB model reported by Niemeyer et al. (6), also known as the NPW model. We assume the following assumptions:

(*a*) The DB pattern grows stepwise from an initial single seed at the center.

(*b*) At each step one bond is added to the pattern, linking a point of the pattern to a new point.

(*c*) To each of these dashed bonds a growth probability at site i, j (p_{ij}) is associated, which is a linear function of the local electric field (i.e., potential difference between the existing structure and the growth site).

$$[7] \qquad p_{ij} = \frac{\Phi_{ij}}{\Sigma\Phi_{ij}}$$

Since the potential is zero, $\Phi = 0$, in the existing structure, the potential difference is simply the local potential, Φ_{ij}.

(*d*) To each recently grown bond there is an elapsed time associated, given by

$$[8] \qquad \tau_{ij} = \frac{c}{\Phi_{ij}}$$

© 1998 NRC Canada

Fig. 5. (*a*) Computer simulation of the dielectric breakdown images using the present stochastic DB model with the explicit inclusion of time. Simulation of dielectric breakdown using a square 501 × 501 grid generates 20 350 bonds. The fractal dimension is 1.69 ± 0.01, which is very close to the accepted value of 1.70 (21). Quoted error refers only to the statistical error of the linear fit and does not include errors due to the grid (lattice) type. **(***b*) Time development of growing fractal. Absolute time scale was obtained from eq. [8].

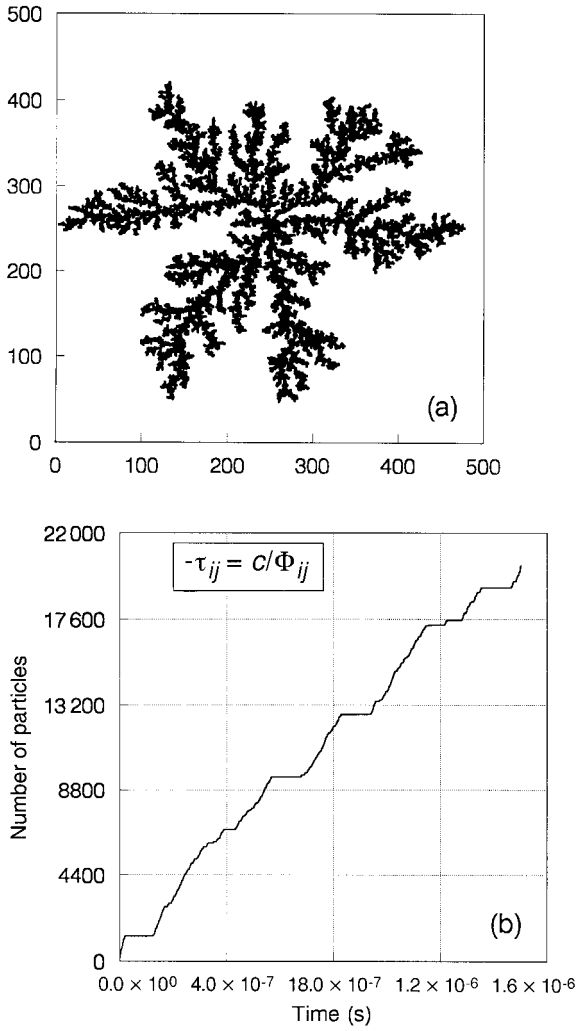

Fig. 6. Simulated discharge current as a function of time using (*a*) 501 × 501 and (*b*) 401 × 401 grids. Breakdown occurs at 1.5 μs. Approximate current is obtained from the derivative of the charge vs. time curve (Fig. 5*b*). Gaps in the time axis indicate the stochastic nature of the discharge, but the overall shape of the predicted current wave form is independent of the simulation grid dimensions. The parameters are chosen to be consistent for N_2 breakdown under nonuniform conditions. See text for details.

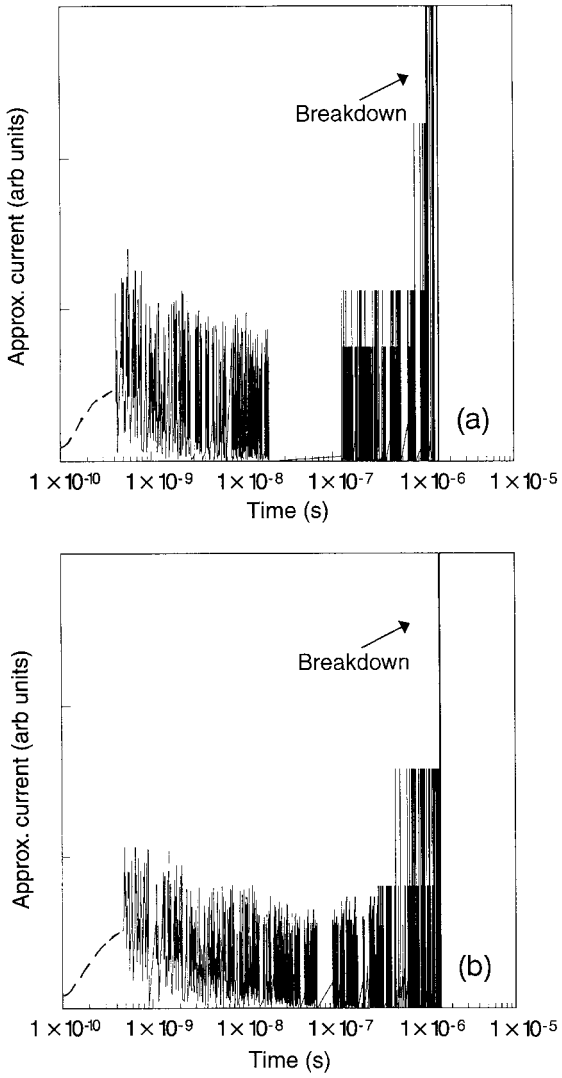

where Φ_{ij} is the potential at the point chosen and c is a defined constant.

(*e*) DB growth ends when one of the bonds reaches the edge of the circle.

The discharge pattern indicated by the dots (bonds) is considered equipotential ($\Phi = 0$), whereas $\Phi = 1$ outside the external circle, defined by the radius of the stainless steel ring (see Fig. 1). At each step (*b*), the Laplace equation,

$$[9] \quad \nabla^2 \Phi = 0$$

is solved using the finite-difference method. This step is the most CPU time-consuming aspect of the simulation.

Assumption (*d*) is a modification of the NPW model (6) and takes into account the temporal development of the DB pattern. The simplest, and perhaps most natural, expression for the elapsed time for each step in the simulation is that given in eq. [8], which can be derived from classical arguments. In the present work, the elapsed time for the growth of the bond is assumed to be consistent with the time scales predicted by the recent, highly accurate 2-D numerical simulations of Vitello et al. (4) as well as the mathematical analysis of Ebert et al. (5). We choose a time scale, $t_0 = (\alpha v_e E)^{-1} = 3$ ps, which is obtained for a voltage difference of 25 kV across a 0.5 cm gap in N_2, used in both published simulations (3, 4) and is reasonably similar to the DB experiments with air reported in the present study. The time scale refers to the amount of time an electron traverses the length scale ($\alpha_o^{-1} = 2.3$ μm) for a given drift velocity (v_e) and local field (E). Here, α_0 refers to the ionization constant, defined by the phenomenological Townsend ionization coefficient, $\alpha(E) = \alpha_0 e^{-E_0/E}$ (18). The time scale (t_0)

© 1998 NRC Canada

will naturally vary with the gaseous sample, but is ignored at present so as to focus on the general features brought about by the introduction of assumption (*d*). From this time scale, the constant *c* in eq. [8] can be estimated given the total time (t_{tot}) from inception to discharge, which is well described by Martin's semiempirical equation (25). The total time (in seconds) is given by,

$$[10] \quad t_{tot} = k\rho^{0.25}\left(\frac{d}{\Delta V}\right)^{3.5}$$

where $k = 1.1 \times 10^5$, ρ is the gas density (g/cm^3), *d* is the gap distance (cm), and ΔV is the gap voltage (kV) (25). For consistency we use the parameters appropriate for N_2 and our geometry, and we arrive at a total time of approximately 1.5 μs. Thus, to properly model the dielectric breakdown in air we would need at most 5×10^5 bonds (number of bonds = 1.5 μs/3 ps) on a 1001×1001 grid. This assumes that *on average* each bond is formed within the time scale prescribed by Ebert et al. (5). This requires a very huge numerical simulation beyond the capabilities of our present computer, thus a scaling study is performed at different grid sizes (and therefore total bonds). From the scaling study of grids of side lengths of 101, 201, 301, 401, and 501, we can find the appropriate constant that renders the time scale absolute as well as the maximum grid size that is physically meaningful within the context of the given time scale.

The predicted structure from the present DB stochastic model is shown in Fig. 5*a*, and the temporal characteristics of the corresponding structure is shown in Fig. 5*b*. The DB pattern is grown on a square 501×501 grid and is composed of about 20 000 bonds. The present numerical simulation took approximately 150 h in computing time on a Pentium workstation (133 MHz, 32 Mb RAM), using a custom-built Fortran program compiled with Lahey Fortran (LF90B). The calculated fractal (Hausdorff) dimension for this 2-D structure is 1.69 ± 0.01 and is very close to the generally accepted numerical simulation value of 1.70 (21). There is currently no analytical method that successfully predicts the fractal (Hausdorff) dimension for this 2-D structure although several attempts toward an analytical solution have been presented in literature (26). It is precisely the absence of an analytical solution to this "simple-looking" problem that makes pattern formation in dielectric breakdown particularly interesting.

The time development of the DB model pattern shown in Fig. 5*b* can also be interpreted in terms of the time development of charge, as suggested by Biller (27) and Kukhta et al. (28) who both used different algorithms for calculating physical time. Kukhta et al. (28) assumed time to be inversely proportional to an "average" potential of the growing fractal, and further assumed a variable dielectric constant for the growing structure. The model developed by Kukhta et al. (28) therefore has significantly more parameters than the original NPW model and the model we have presented. On the other hand, Biller (27) assumed a Poisson-like distribution for the probability that a bond grows at time τ (27). Each bond is then chosen and grown on the basis of the shortest growth time. Furthermore, Biller (27) presented his simulation results on a relative time scale and thus cannot be directly compared with any experimental result. It is important to note, however, that Biller's result (27) is in qualitative agreement with Fig. 5*b*.

To provide an approximation to the discharge current, which is a well-defined experimental quantity, the derivative of the charge vs. time curve (Fig. 5*b*) is obtained using the method of differences and is shown in Fig. 6. Two simulations (501×501 grid and 401×401 grid) are shown to illustrate features of the predicted discharge current in order to determine whether the current is dependent on the simulation grid dimensions. Clearly, the overall shape or profile of the predicted discharge current is independent of the details of the simulation. Several experimental current wave forms have been published (see Figs. 5 and 6 in ref. 11, Fig. 3.46 in ref. 16, Fig. 1 in ref. 29, Fig. 3.6 in ref. 30, and Fig. 2 in ref. 31), and all are in qualitative agreement with the present simulation in terms of the overall shape and the absolute decay times. The present simulation (Fig. 6) indicates the initial formation of a small current that decays slowly within the first 100 ns, in semiquantitative agreement with the recent, highly accurate simulation reported by Morrow and Lowke (see Figs. 1 and 2 in ref. 32) and the detailed experiments of Marode (Figs. 5 and 6 in ref. 11). The predicted circuit current then stays essentially flat until the explosive onset of breakdown at 1.5 μs. It is also quite interesting to note that the current wave forms and DB structures obtained by Yamada et al. (29) in a point-plane discharge in *liquid* carbon tetrachloride is strikingly similar to Fig. 6 and Fig. 5*a*, respectively. This is not surprising, since it has been suggested that these experiments in "liquid media are of a gaseous nature" (7) similar in some respect to the present gaseous DB experiments. To properly simulate the circuit current the flow of all positive and negative charges have to be considered. Nevertheless, the present approximation, which includes only the negative charges (i.e., the growing DB structure), is quite reasonable and captures the essential features of the discharge current.

In Fig. 7 we show simulated DB images extracted from the new stochastic DB model, which explicitly includes time, and

Fig. 7. Simulated time-resolved DB images on a 501×501 grid, based on the stochastic DB model with time. The first few branch points are assumed to be continuously active. Frames 2–7 are shown, corresponding to 40 ns each and 160 ns interframe separation. Frame 4 is not erroneous. The parameters are chosen to be consistent for N_2 breakdown under nonuniform conditions. See text for details.

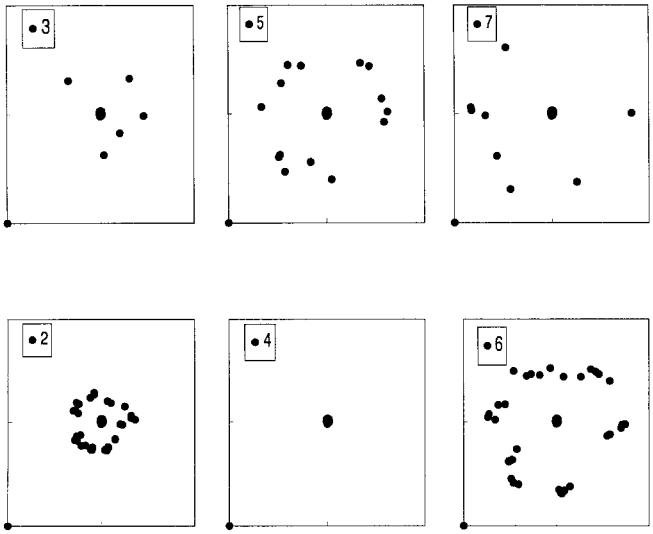

© 1998 NRC Canada

thus can be reasonably compared with the present experiments (Fig. 3). Six time slices of the total simulation are taken, corresponding to 40 ns for each slice. The first few branch points of the simulation are kept, maintaining the assumption that the positive electrode at the center of the ring is "always active." Note that all the simulated photos display only the branch points, where we define a branch point as any point in the simulation with at least three bonds connected to the point. The qualitative agreement between the simulated DB images (Fig. 7) and the experimental DB images in air (Fig. 3*b*) is quite surprising, considering the approximations involved. Frame 4 in Fig. 7 may appear anomalous, but this simply reflects the stochastic nature of the predicted discharge. At some point in time the predicted discharge becomes "quiet" (see Fig. 6), and it is simply accidental that frame 4 falls into this quiet phase. Factors that are not considered in the present simulation include (*i*) the finite lifetimes of the excited neutral and ionic states responsible for most of the fluorescence, which can be larger than the IMACON exposure time, and (*ii*) the response function of the optical system. Further details of the simulation will be published elsewhere (33).

The case for SF_6 (Fig. 3*c*) is quite complicated and is understood to be due to the very different chemical processes involved in the breakdown of SF_6 molecules (34). It is well known that electron attachment (35) (see eq. [4]) becomes a dominant mechanism in the electrical breakdown of SF_6. Electron-attachment processes are not considered in the models reported by Dhali and Williams (3) and Vitello et al. (4).

4. Conclusions

In summary, we have presented time-resolved discharge patterns generated in a gaseous dielectric breakdown (DB). The discharge patterns from various gases (He, air, and SF_6) show general features consistent with their known dielectric strength. A new stochastic pattern-forming model that explicitly includes time is presented and is shown to produce theoretical DB patterns in qualitative agreement with the present experimental discharge pattern for air (N_2). The stochastic DB model (with time) also provides an approximation to the discharge current, which is in good agreement with published current wave forms. This level of agreement was made possible by the use of recent accurate numerical solutions of 2-D continuity equations for streamer growth (3, 4) which indicated the proper time scales. These new developments would seem to indicate that the macroscopic structures (i.e., tree-like structures) observed in dielectric breakdown may be understood from the microscopic mechanisms of streamer growth. For example, it would be interesting to see whether the stochastic DB model we have presented can be combined with the 2-D simulations of Dhali and Williams (3) and Vitello et al. (4). The introduction of a stochastic element to the Dhali–Williams equations (as suggested above) would produce fluctuations, which could lead to a global description of dielectric breakdown patterns from the micrometre scale all the way up to the centimetre scale.

Acknowledgements

We would like to thank S. Rizzetto and J.M. Braun of Ontario Hydro Technologies for valuable assistance in the imaging experiments. We also acknowledge the assistance of J. Treurniet and M. Kono in developing the branch-point programs. We especially thank Frazer Williams for helpful discussions. This work was funded by the Natural Sciences and Engineering Research Council (NSERC) of Canada.

References

1. B.M. Penetrante, M.C. Hsiao, J.N. Bardsley, B.T. Merritt, G.E. Vogtlin, P.H. Wallman, A. Kuthi, C.P. Burkhart, and J.R. Bayless. Phys. Lett. A, **209**, 69 (1995); B.M. Penetrante and S.E. Schultheis (*Editors*). Nonthermal plasma techniques for pollution control: part B — electron beam and electrical discharge processing. Springer-Verlag, Heidelberg. 1993; S. Masuda. Pure Appl. Chem. **60**, 727 (1988).
2. L. Niemeyer. IEEE Trans. Dielectr. Electr. Insul. **2**, 510 (1995); G.R. Govinda Raju and J. Liu. IEEE Trans. Dielectr. Electr. Insul. **2**, 1004 (1995).
3. S.K. Dhali and P.F. Williams. Phys. Rev. A: At. Mol. Opt. Phys. **31**, 4696 (1987).
4. P.A. Vitello, B.M. Penetrante, and J.N. Bardsley. Phys. Rev. E: Stat. Phys. Plasmas, Fluids, Relat. Interdiscip. Top. **49**, 5574 (1994).
5. U. Ebert, W. van Saarloos, and C. Caroli. Phys. Rev. Lett. **77**, 4178 (1996); Phys. Rev. E: Stat. Phys. Plasmas, Fluids, Relat. Interdiscip. Top. **55**, 1530 (1997).
6. L. Niemeyer, L. Pietronero, and H.J. Wiesman. Phys. Rev. Lett. **52**, 1033 (1984); **57**, 650 (1986).
7. M.I. Dyakonov and V.Y. Kachorovskii. Sov. Phys. JETP, **68,** 1070 (1989); N.L. Aleksandrov and E.M. Bazelyan. J. Phys. D: Appl. Phys. **29**, 740 (1996).
8. L. Pietronero and H.J. Wiesman. Z. Phys. B: Condens. Matter, **70**, 87 (1988).
9. I. Gallimberti. J. Phys. (Paris), **40**, C7 (1979); I. Gallimberti, J.K. Hepworth, and R.C. Klewe. J. Phys. D: Appl. Phys. **7**, 880 (1974); I. Gallimberti. J. Phys. D: Appl. Phys. **5**, 2179 (1972).
10. N. Femia, L. Niemeyer, and V. Tucci. J. Phys. D: Appl. Phys. **26**, 619 (1993).
11. E. Marode. J. Appl. Phys. **46**, 2005 (1975).
12. W.J. Yi, B.J. Hankla, and P.F. Williams. IEEE Trans. Plasma Sci. **24**, 93 (1996).
13. N. Hayakawa, M. Fujimori, M. Hikita, and H. Okubo. *In* Proc. IEEE Int. Symp. Elect. Insul. Pittsburg, Pa. 1994. p. 241.
14. B. Mandelbrot. Fractals: form, chance and dimension. Freeman, San Francisco. 1977; F. Hausdorff. Math. Ann. **79**, 157 (1919); H.E. Stanley. J. Phys. A: Math. Nucl. Gen. **10**, L211 (1977).
15. J. Logan, J. Treurniet, A.D.O. Bawagan, S. Rizzetto, J.M. Braun, and B.D. Aguda. Can. J. Chem. **71**, 2079 (1993).
16. J.M. Meek and J.D. Craggs. Electrical breakdown of gases. John Wiley and Sons, New York. 1983.
17. J.H. Mason. IEEE Trans. Electr. Insul. **13**, 211 (1978).
18. J.S. Townsend. Electricity in gases. Clarendon, Oxford. 1915.
19. H. Raether. Z. Phys. B: Condens. Matter, **112**, 464 (1939); L.B. Loeb and J.M. Meek. J. Appl. Phys. **11**, 438 (1940).
20. K.T. Leung. J. Electron Spectrosc. Relat. Phenom. **35**, 327 (1985); A.D.O. Bawagan. Colloq. Phys. C6, **3**, 175 (1993).
21. P. Meakin. Phys. Rev. A: At. Mol. Opt. Phys. **27**, 604 (1983); 1495 (1983).
22. B.M. Coaker, N.S. Xu, R.V. Latham, and F.J. Jones. IEEE Trans. Dielectr. Electr. Insul. **2**, 210 (1995).
23. S.Y. Li, K.D. Srivastava, and G.D. Theophilus. IEEE Trans. Dielectr. Electr. Insul. **2**, 114 (1995).
24. S. Kobayashi, K. Kiyokawa, Y. Saito, and N. Sato. Proc. 15th Int. Symp. Discharges Elect. Insul. Vacuum. Darmstadt, Germany. 1992. p. 217.
25. T.H. Martin. *In* Proc. 5th IEEE Pulsed Power Conf. *Edited by*

© 1998 NRC Canada

P.J. Turchi and M.F. Rose. IEEE, New York, U.S.A. 1985. p. 74.
26. L. Pietronero, A. Erzan, and C. Evertsz. Phys. Rev. Lett. **61**, 861 (1988).
27. P. Biller. *In* IEEE Proc. 11th ICDL. *Edited by* J. Fuhr and P. Biller. Baden-Dattwil, Germany. 1993. p. 199.
28. V.R. Kukhta, V.V. Lopatin, and M.D. Noskov. Tech. Phys. **40**, 150 (1995); M.D. Noskov, V.R. Kukhta, and V.V. Lopatin. J. Phys. D: Appl. Phys. **28**, 1187 (1995).
29. H. Yamada, K. Tamada, R. Takeishi, Y. Oshi, and T. Fujiwara. *In* IEEE Proc. 11th ICDL. *Edited by* J. Fuhr and P. Biller. Baden-Dattwil, Germany. 1993. p. 294.
30. P.F. Williams. EPRI Technical Report TR–101794. EPRI, Palo Alto, Calif. 1993.
31. E.H.R. Gaxiola and J.M. Wetzer. IEE Conf. Publ. No. 430. 1996. p.116.
32. R. Morrow and J.J. Lowke. J. Phys. D: Appl. Phys. **30**, 614 (1997); Pure Appl. Chem. **66**, 1287 (1994).
33. A.D.O. Bawagan. Chem. Phys. Lett. In press.
34. R. Morrow. Nucl. Instrum. Methods Phys. Res. Sect. A, **382**, 57 (1996).
35. L. Sanche. IEEE Trans. Electr. Insul. **28**, 789 (1993).

© 1998 NRC Canada

Polyacrylic acid pore-filled microporous membranes and their use in membrane-mediated synthesis of nanocrystalline ferrihydrite

Françoise M. Winnik, André Morneau, Alicja M. Mika, Ronald F. Childs, Anna Roig, Elies Molins, and Ronald F. Ziolo

Abstract: A series of cation-exchange membranes were obtained by photoinitiated grafting of acrylic acid onto a polypropylene microporous support having 0.2 μm diameter pores. The poly(acrylic acid) was shown to be contained within the pores of the membrane. The ion-exchange capacities of these "pore-filled" membranes ranged from 65 to 80% of the theoretical values calculated on the basis of their measured graft yields, with water contents ranging from 72 to 77%. The membranes exhibited a chemical valve effect of flux as a function of pH. Treatment of a poly(acrylic acid) grafted membrane with a solution containing ferrous ions resulted in a large uptake of iron (>24% by weight of iron with a membrane containing 152% graft yield of poly(acrylic acid)). Subsequent alkaline (pH 14) oxidation at 70°C with either oxygen or hydrogen peroxide led to the formation of a superparamagnetic nanocrystalline form of ferrihydrite, $5Fe_2O_3 \cdot 9H_2O$. The oxide was identified by temperature-dependent Mössbauer spectroscopy recorded from 300 K to 4.2 K. TEM micrographs of sectioned membranes that were treated with H_2O_2 revealed the presence of two iron oxide morphologies, disk-shaped particles 3–4 nm in diameter and needle-like particles about 4 nm wide and 50 nm long. Only disk-shaped particles were observed in membranes treated with O_2. Magnetization measurements indicate that the membranes are superparamagnetic above 50 K with a room temperature magnetization of 3.3 emu g^{-1} at 20 kOe.

Key words: membrane, poly(acrylic acid); iron oxide, magnetic, Mössbauer spectroscopy; magnetization, photografting.

Résumé : On a obtenu une série de membranes échangeuses de cations en procédant à une greffe photoinitiée de l'acide acrylique sur un support microporeux de polypropylène comportant des pores de 0,2 μm de diamètre. On a montré que l'acide polyacrylique est inséré dans les pores de la membrane. Les capacités de ces membranes «à pores remplies» à agir comme échangeuses d'ion varient de 65 à 80% des valeurs théoriques calculées sur la base des rendements de greffe, avec des contenus en eau allant de 72 à 77%. Les membranes présentent un effet de valve chimique de flux en fonction du pH. Le traitement d'une membrane greffée avec de l'acide polyacrylique par une solution contenant des ions ferreux provoque une forte absorption de fer (>24% de fer, en poids, par une membrane contenant un rendement de greffe d'acide polyacrylique de 152%). Une oxydation alcaline (pH de 14) subséquente, à 70°C avec de l'oxygène ou du peroxyde d'hydrogène, conduit à la formation d'une forme nanocristalline supermagnétique de la ferrihydride, $5Fe_2O_3 \cdot 9H_2O$. On a identifié l'oxyde par spectroscopie de Mössbauer en fonction de la température, enregistrée de 4,2 à 300 K. Des micrographes «TEM» de membranes sectionnées traitées à l'aide de H_2O_2 ont permis de révéler la présence de deux morphologies d'oxyde de fer, des particules en forme de disque de 3 à 4 nm de diamètres et d'autres en forme d'aiguilles de 4 nm de largeur et 50 nm de longueur. On n'observe que les particules en forme de disque dans les membranes traitées avec de l' oxygène. Des mesures de magnétisation indiquent que les membranes sont superparamagnétiques au-dessus de 50 K; à la température ambiante, la magnétisation est de 3,3 emu g^{-1}, à 20 kOe.

Mots clés : membrane, acide polyacrylique; oxyde de fer, magnétique, spectroscopie Mössbauer; magnétisation; photogreffage.

[Traduit par la rédaction]

Received July 21, 1997.

F.M. Winnik,[1] A. Morneau, A.M. Mika, and R.F. Childs.[1] Department of Chemistry, McMaster University, 1280 Main St. W, Hamilton, ON L8S 4M1, Canada.
A. Roig and E. Molins. Instituto de Ciència de Materiales de Barcelona, Campus UAB, 08193 Bellaterra Barcelona, Spain.
R.F. Ziolo. Wilson Center for Research and Technology, Xerox Corporation, Webster, NY 14580, U.S.A.

[1] Authors to whom correspodence may be addressed. Telephone: (905) 525-9140, ext. 23497. Fax: (905) 540-1310. E-mail: winnikf@mcmaster.ca

Introduction

Polymer templates have proven to be extremely versatile hosts in the controlled synthesis of organic–inorganic nanocomposites. As hosts, they provide functionalities and structured frameworks for the synthesis and confinement of molecular clusters and nanoscale particulates. Over the past decade several research groups have examined the synthesis and properties of ultrafine iron-containing particles precipitated in the micropores of perfluorinated ion-exchange membranes such as Nafion7 (1–4). In these membranes, sulfonic acid groups can bind ions such as Fe^{2+} and Fe^{3+}, which upon further

© 1998 NRC Canada

treatment can be reacted to form precipitates of small inorganic particles within the membrane pores.

Recently, Mika et al. (5) reported a new type of anion-exchange membrane composed of a neutral porous substrate with grafted poly(4-vinylpyridine) filling the pores. Such membranes combine a high charge density with the mechanical strength, chemical inertness, and dimensional stability of a porous support. A key feature of these membranes is that the filling polyelectrolyte is flexible and can change its conformation. However, swelling of the polyelectrolyte in the presence of water is restricted by the microporous support. As a result, these membranes exhibit an outstanding pH valve effect of more than three orders of magnitude.

This pore-filling or "gel in shell" (6) construct of ion-exchange membranes can in principle be extended to cation-exchange materials by the incorporation of a negatively charged polyelectrolyte into the pores of a microporous substrate. In this paper we describe the preparation and characterization of cation-exchange membranes in which poly(acrylic) acid is anchored within the pores of a microporous polypropylene support. There are several reports of poly(acrylic) and poly(methacrylic) acid (7) being grafted onto the surface of microporous membranes and partial filling of the pores would appear to be occurring with some of these membranes (8). With the membranes described here we show that the anchored poly(acrylic) acid is located within the pores and not on the surface of the substrate.

In the present study, we demonstrate that these novel membranes can be used as templates for the in-situ preparation of nanoscale magnetic oxides. The incorporation of magnetic nanoparticulates in membranes provides new potential for the management and control of the membrane performance. Iron oxides were precipitated within the modified membranes by a two-step process comprising (*i*) an ion-exchange step to transfer ferrous ions into the grafted polyelectrolyte network and (*ii*) the oxidation of the ferrous ions by either oxygen or hydrogen peroxide in alkaline medium. This method has been demonstrated to yield superparamagnetic forms of iron oxides and (or) iron hydroxyoxides in a variety of polymeric templates (9, 10). The preparation and chemical, morphological, and magnetic properties of the new composite membranes are reported herein.

Experimental section

Materials

The porous membrane was a polypropylene (PP) microfiltration membrane supplied by the 3M Company (average pore diameter: 0.197 μm, porosity: 61.1% by volume, thickness: 51.1 μm). Acrylic acid (Aldrich Chemical Co.) was purified by vacuum distillation. Benzoin ethyl ether (Aldrich Chemical Co.) was used as a photoinitiator. Ferrous chloride ($FeCl_2 \cdot 4H_2O$) was purchased from Fisher Scientific. Sodium hydroxide and hydrogen peroxide (30% v/v) were obtained from BDH Inc. Water was deionized with a Barnstead NANOpure water purification system.

Instrumentation

UV spectra were recorded on a Hewlett Packard 8452A diode array spectrometer. Scanning electron microscopy (SEM) was carried out using an ISI DS130 instrument. Carbon coatings were used. Transmission electron microscopy (TEM) was performed with a Phillips CM-12 microscope, operated at 120 kV, equipped with an energy-dispersive X-ray spectroscopy (EDS) microanalysis system (McMaster University, Brockhouse Institute for Materials Research). For TEM analysis, membranes were solvent-exchanged with ethanol and embedded in a Spurr resin that was cured at 70°C overnight. Ultrathin sectioning (70 nm in thickness) of the resulting blocks was performed with an RMC MT-7 ultramicrotome equipped with a diamond knife. The sections were mounted on copper grids. Some sections were coated with carbon before observation. A superconducting quantum interference device (SQUID) Quantum Design magnetometer (McMaster University, Department of Physics and Astronomy) was used for determination of the magnetic properties. The sample (approximately 5 mg) was placed in a no. 3 gelatin capsule. This was inserted into a cylindrical sample holder (ca. 6 mm in diameter) placed in the sample compartment of the magnetometer. Mössbauer spectra were obtained using a constant acceleration Mössbauer spectrometer (Instituto de Ciència de Materiales de Barcelona) with a 10 mCi $^{57}Co/Rh$ source. The source was moved via a triangular velocity wave form and γ-ray counts were collected in a 512 multichannel analyzer. The data were folded, plotted, and fitted by a computer procedure. Velocity calibration was done using a 25 mm thick metallic Fe foil, and the Mössbauer spectral parameters are given relative to this standard at room temperature. The membrane samples, approximately 50 μm thick and with 24.4% by weight of Fe, were placed in the spectrometer as obtained.

Photografting of the membranes

The reactions were carried out in a photoreactor as has been described elsewhere (5). The substrate membrane (11.0 × 12.8 cm^2) was soaked in acetone for 16 h, dried in vacuum at room temperature, and weighed. It was placed against the inner wall of the reactor vessel. A solution of benzoin ethyl ether (1.0–1.5% by weight) in acrylic acid (3.0 mL) was poured into the reactor vessel. The reactor and its content were degassed by freeze-thawing. Subsequently the reactor vessel was rotated manually in order to wet the membrane with the monomer/initiator solution. The wet membrane was irradiated for 30 min in a Rayonet-type photoreactor equipped with 10 lamps, 5 lamps emitting at 300 nm and 5 lamps emitting at 350 nm. The irradiated membrane was removed from the reactor vessel and placed in a Soxhlet extractor. It was extracted with boiling water for 92 h. The water in the membrane was exchanged with ethanol. The membrane was dried in vacuum at room temperature and weighed in order to determine the grafting yield, which was taken as the percentage of mass increase of the substrate membrane(s). Membranes were conditioned by repeated treatments with 1 M HCl, water, and 1 M NaOH.

Determination of the membrane properties

Ion-exchange capacity

A conditioned membrane was washed thoroughly with deionized water. It was kept in contact with aqueous NaOH (100.0 mL, 0.0500 M) for 16 h. It was removed from the solution and rinsed carefully with water while held above the NaOH solution. The excess NaOH in solution was titrated with HCl in the presence of methyl red in order to determine the number of OH^- equivalents neutralized by the poly(acrylic

© 1998 NRC Canada

acid). The ion exchange capacity was calculated by taking the ratio of the membrane-neutralized OH^- equivalents to the mass of the dry grafted membrane.

Water uptake

The conditioned water-swollen membrane was placed between two sheets of wet filter paper and pressed gently to remove surface water. The water content (WU) was determined from the difference between the mass of the water-swollen and that of the dry membrane, using the following equation:

$$WU(\%) = 100\% \ (m_w - m_d)/m_w$$

where m_w is the mass of a water-swollen membrane sample and m_d the mass of the dry sample.

Permeability

Permeability of the grafted and nascent membranes was measured using a stirred ultrafiltration cell (Nuclepore, S76-400) with an active membrane area of 38.50 cm^2. The pressure applied was 100 kPa. The test solutions were stirred at a rate of 250–300 rpm. The pH of the feed solution was adjusted by addition of HCl or NaOH. Prior to each measurement, the membranes were equilibrated with the test solution under pressure until a stable flux was achieved, with the difference between two subsequent readings being less than 5%. The transmembrane flux (kg m^{-2} s^{-1}) was calculated as the mass of permeate collected from the unit of membrane surface area (m^2) over the unit of time (s). The flux was corrected to 25°C by using an experimental temperature correction factor (11). The membrane permeability was calculated by dividing the flux by the applied pressure.

Preparation of iron oxide containing membranes

The poly(acrylic acid) grafted membrane (ca. 10 × 10 cm) was placed in a solution of ferrous chloride, $FeCl_2 \cdot 4H_2O$ (5.0 g, 0.025 mol), in water (500 mL) and purged with nitrogen for 16 h. The membrane was removed from this solution and washed with water until the eluent was iron-free, as determined by the thiocyanate test (12). The membrane was then cut in two. Each piece was immersed in aqueous NaOH (200 mL, 1 N) and heated to 70°C. A constant stream of air was then bubbled through one of the solutions while heating for 4 h to oxidize Fe^{2+}. The solution was cooled to room temperature, whereupon the membrane was removed and washed with water until the pH of the eluent was neutral. The membrane, designated membrane A, was dried at room temperature under vacuum. A solution of hydrogen peroxide (12 mL, 30% by volume) in water (25 mL) was added dropwise to the solution containing the other half of the membrane, to oxidize Fe^{2+} more directly. At the end of the peroxide addition the mixture was kept at 70°C for 4 h. The membrane, designated membrane B, was removed from the cooled solution, washed with water until the pH of the eluent was neutral, and dried.

Spectrophotometric determination of the iron incorporated within the membranes

A known amount of the dry iron-containing membrane (ca. 10 mg) was treated with concentrated HCl (2 mL) for 30 min at room temperature. The mixture was filtered on a medium fritted glass funnel and washed with about 2 mL of water. The eluent was brought to 10 mL by addition of water. The amount of iron in this solution was determined spectrophotochemically using the tris(1,10-phenanthroline) iron(II) complex test (13).

Results and discussion

Preparation and characterization of the membranes

Photografting

The membranes used in this work were formed by grafting acrylic acid into the pores of a microporous polypropylene (PP) support membrane. The support membrane, which is prepared by a thermally induced phase separation process (14), has a highly porous structure (porosity 61.1% by volume) consisting of a series of fine fibrils linked together by nodules. The average pore diameter of the membrane is close to 0.2 μm.

The photochemical grafting of vinyl monomers onto polyolefin films was pioneered by Ang et al. (15) and by Ogiwara et al. (16). It has been used to functionalize porous materials such as cellulose filters (17). A number of monomers and monomer mixtures have been employed, including acrylic acid (18). In this work the photochemical method used was based on the techniques developed in these laboratories for grafting 4-vinylpyridine onto a range of microporous PP membranes (5). In this procedure the photoinitiator, benzoin ethyl ether, is dissolved in the neat monomer, acrylic acid. During the irradiation the membrane is supported on the walls of a glass vessel. Under these conditions ungrafted homopolymer, poly(acrylic acid) (PAA), is also formed. The homopolymer was removed by extraction from the PAA-grafted membrane using water at 100°C.

Various levels of PA grafting yields can be achieved depending on the intensity of the light used and the length of irradiation. The membranes were physically robust with incorporation levels below 200%. At higher graft yields, the membranes were fragile and broke readily when subjected to the extraction step. This fragility is likely the result of the large swelling pressures generated on hydration of the membranes with high graft yields.

The grafted membranes were characterized by measurement of their ion-exchange capacities and water content as well as by electron microscopy. Typically, the ion-exchange capacities were found to be in the range of 65–80% of the theoretical values calculated on the basis of their measured graft yield. In contrast to the hydrophobic polypropylene substrate, the grafted membranes are hydrophilic. The water content in the hydrated samples amounted to 72–77% of their weight.

SEM micrographs of the front and back surfaces (front being defined as the side of the membrane exposed to the light source) were indistinguishable from those of the nascent membrane. This finding parallels our previous work with poly(4-vinylpyridine) pore-filled membranes where SEMs of the freeze-substituted membranes similarly showed no discernible change in the membranes as compared to the starting base material (19). In the anhydrous conditions used in the SEM examination, presumably the poly(acrylic acid) tightly covers the surfaces of the polypropylene substrate.

Evidence for the distribution of poly(acrylic acid) incorporated in the membranes was obtained using SEM and TEM

© 1998 NRC Canada

Table 1. The pH valves of poly(acrylic acid) and poly(4-vinylpyridine)-grafted membranes.

		Flux (kg m^{-2} s^{-1}) at pH			
Grafted polyelectrolyte	Graft yield %	2.6 ± 0.1	Valve position	7.0 ± 0.1	Valve position
None	0	—	—	0.32	—
Poly(acrylic acid)	56.0	0.0132	Open	0.0015	Closed
Poly(4-vinylpyridine)	35.9	0.00097	Closed	0.106	Open

Fig. 1. Flux vs. pH: the pH-valve effect recorded for a polypropylene membrane grafted with 56.0% of poly(acrylic acid). Applied pressure: 100 kPa.

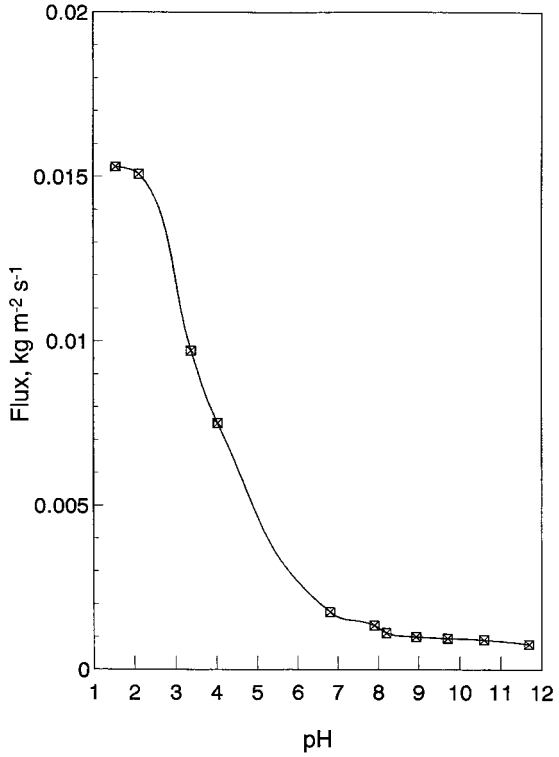

(vide infra) and EDX analyses. For EDX analyses the poly(acrylic acid) was converted to its potassium salt and analyses for potassium of the front and back surfaces were carried out. Potassium was readily detected on both surfaces. However, there was a marked asymmetry in the loading of potassium on the front and back surfaces with there being four times more potassium present on the front surface. As with poly(4-vinylpyridine) based membranes of this type, this asymmetry probably results from evaporation of the monomer from the back surface during the photopolymerization (5).

The pH-dependent water permeability of the PAA-grafted membranes under pressure was measured at various pH values. The flux–pH relationship obtained with a 56%-grafted membrane at 100 kPa pressure is presented in Fig. 1. The curve representing this relationship has a characteristic shape indicating that the membrane is functioning as a chemical valve (3). There is one order of magnitude change in flux in the pH range of 3–6. Surface grafting of poly(methacrylic acid) or poly(acrylic acid) on the surface of microporous supports has also been shown to give pH-sensitive membranes (7).

Anchoring of poly(4-vinylpyridine) inside the pores of polypropylene or polyethylene microfiltration membranes produces membranes with a very large pH valve behaviour (5). Comparison of the membranes obtained by grafting poly-(4-vinylpyridine) and poly(acrylic acid) into pores of the same polypropylene substrate (Table 1) shows not only the expected difference in the point of closure of these two valves on the pH scale but also a very large difference in the magnitude of the valve effect. While the permeabilities (or fluxes at the same pressure) of these two types of membranes are similar when the valves are closed, they differ substantially when the valves are open. Poly(4-vinylpyridine) in the free base form is a hydrophobic polymer and adopts a tightly coiled conformation affecting the membrane permeability to a small extent as compared to the starting base membrane. However, in the case of poly(acrylic acid) the polymer is expected to form a hydrogel, even when in its un-ionized form. As a result, the open-valve flux with the poly(acrylic acid) membrane is substantially reduced from that of the ungrafted membrane. The valve effect seen with poly(acrylic acid) would seem to be due to ionization of the carboxylic acid functions at higher pH rather than the result of conformational changes occurring upon ionization of poly(4-vinylpyridine) grafted membranes.

Binding of Fe(II) by the grafted membrane

A membrane with a high degree of grafting, 152% graft yield, was selected for this study, in order to provide a high density of binding sites for the ferrous ions. The measured ion-exchange capacity of the dry membrane was 5.39 mequiv. g^{-1}, a value that is far higher than that normally encountered in ion-exchange membranes. It is, however, lower than the theoretical ion-exchange capacity of the membrane (8.38 mequiv. g^{-1}) calculated on the basis of the mass of incorporated poly(acrylic acid). Despite the incorporation of a large amount of poly(acrylic acid) into the base membrane, the water content of the grafted membrane (in Na^+ form) was 72% by weight, a value that exceeds the measured porosity of the base membrane.

The membrane (152% graft yield) was treated with an Fe(II) solution and then washed with deionized water until no further iron could be detected in the washings. The total concentration of iron taken up by the membrane, measured after the oxidation step (outlined below), was found to be 24.4% by weight, or 5.8 mmol g^{-1} of the dry grafted membrane. The amount of iron absorbed is essentially the same as the ion-exchange capacity of the membrane, indicating that one iron atom is absorbed per ionizable carboxylic group present in the membrane. Curiously, and unlike the parent membrane or the PAA-grafted membrane, the Fe(II) loaded membrane was brittle and had to be handled with care to prevent breaking. Presumably the brittleness results from a high level of "cross-linking"

© 1998 NRC Canada

Table 2. Magnetic properties of the membranes.

	T(K)	Membrane A	Membrane B
Saturation magnetization J_s (emu g^{-1})	5	8.8 ± 0.2	8.3 ± 0.2
	300	3.4 ± 0.2	3.3 ± 0.2
Remanent magnetization (emu g^{-1})	5	1.2 ± 0.1	1.2 ± 0.1
	300	0	0
Coercivity H_c (Oe)	5	914 ± 5	1000 ± 5
	300	10 ± 2	10 ± 2
Magnetic susceptibility χ_g (emu g^{-1} Oe^{-1})	300	0.21 ± 0.05	0.20 ± 0.05

Fig. 2. Schematic representation of the process employed in the preparation of the iron oxide containing materials. Note: the intermediate formation of $Fe(OH)_2$ is postulated on mechanistic grounds and from the appearance of a green color in the substrate.

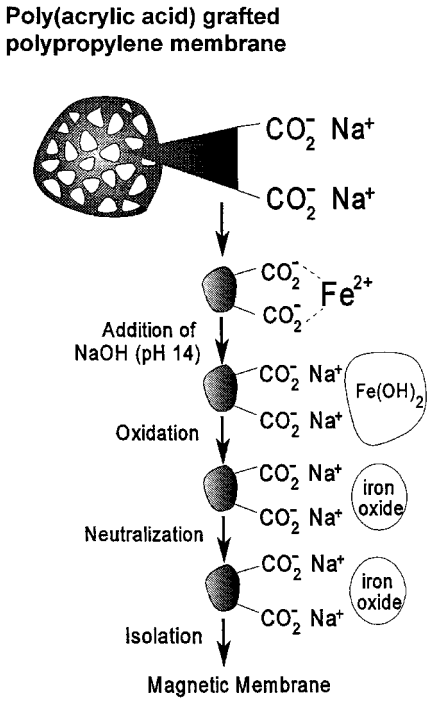

throughout the membrane (20) between carboxylic acid groups on the grafted chains and the bridging iron(II) ions.

The adsorption of metal ions such as Cu^{2+}, Co^{2+}, and Cr^{3+} by poly(acrylic acid) plasma-grafted onto polyethylene films has been reported by Osada and Iriyama (21). However, it is interesting that the amount of metal absorbed by their films ranged between 0.01 and 0.04 mol per repeat unit of PAA. This value is nearly two orders of magnitude lower than the amount of iron adsorbed by the pore-filled membrane used in this study and presumably reflects the different nature of the plasma-surface-grafted poly(acrylic acid) as compared to the pore-filled materials described here.

Oxidation of the membrane-bound Fe(II)

The Fe(II) loaded membranes were oxidized under the conditions outlined in Fig. 2. The iron content of each membrane was essentially identical (approximately 24% w/w Fe, based on the dry membrane). We note that, after oxidation, the membranes recovered their original mechanical properties and were no longer brittle. This observation further supports our hypothesis that Fe^{2+} serves as a cross-linking species in the preoxidized membranes.

Fig. 3. Magnetization curves of the membrane A. Top: zero-field cooled magnetic hysteresis loop at room temperature; bottom: at 5 K.

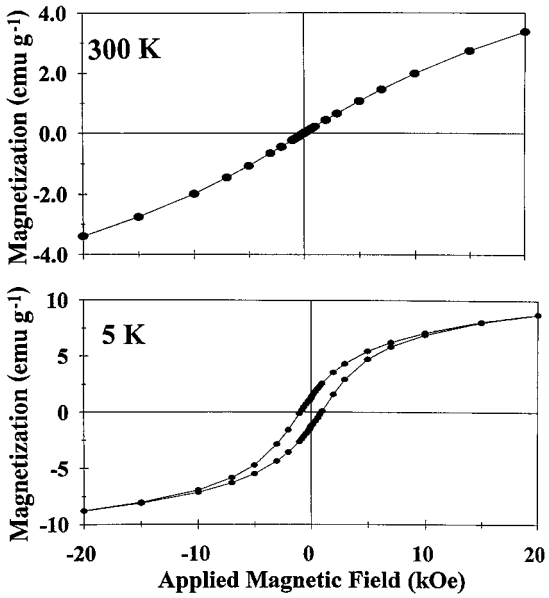

Magnetic properties of the membranes

Magnetic properties of the membranes are listed in Table 2. A plot of the room temperature magnetization as a function of magnetic field for the two membranes showed no hysteresis. At 5 K, the plots of magnetization versus magnetic field exhibited a hysteresis loop with coercivity values of 914 and 1000 Oe for membranes A and B, respectively. Figure 3 presents the curves recorded at 300 K (top) and 5 K (bottom) in the case of membrane A, with those for membrane B being nearly identical. These data suggest superparamagnetic rather than paramagnetic behavior of the membranes, consistent with the ultrasmall crystalline size of the precipitated oxide and with the Mössbauer data (vide infra).

Morphology of the membranes and iron oxide characterization

Morphology

Transmission electron micrographs (TEMs) of the membranes that were embedded in a Spurr resin prior to examination are shown in Figs. 4 and 5. They reveal clusters of iron oxide

© 1998 NRC Canada

Fig. 4. TEM micrographs of sections of membrane A at two different magnifications: (*a*) 17 000, bright field; (*b*) 260 000, dark field.

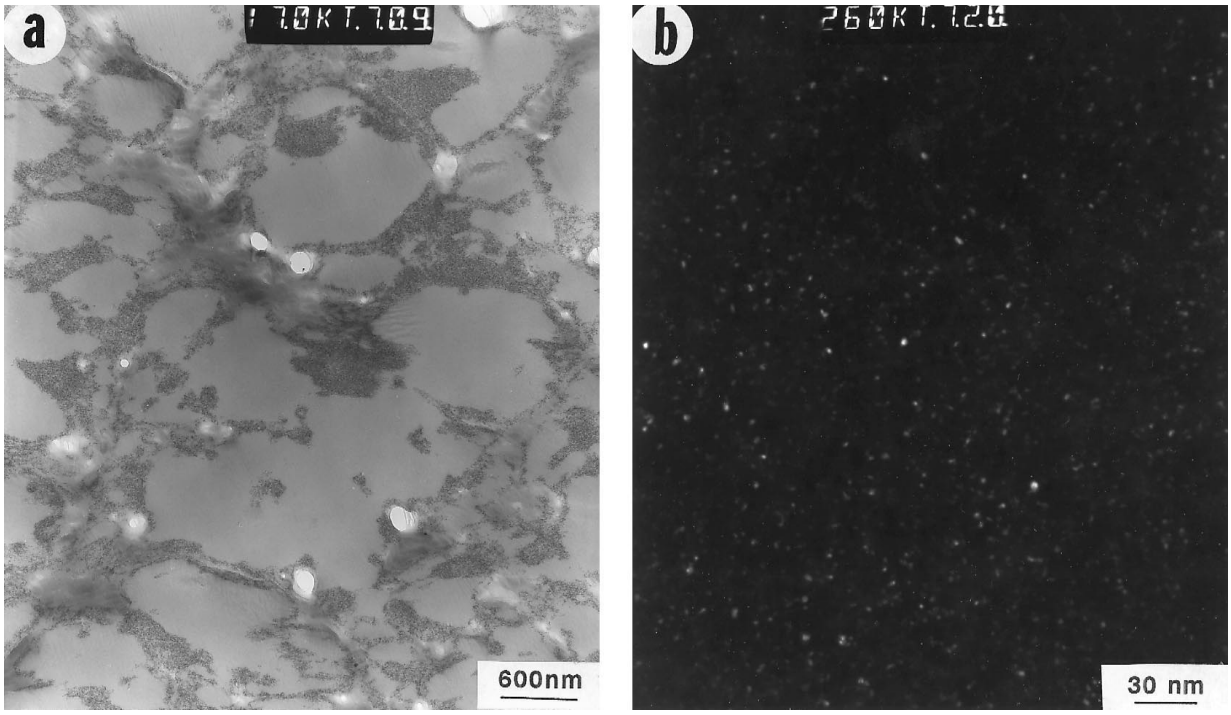

particles located in an interconnected network. It would appear that the clusters are giving an image of the poly(acrylic acid) filled pores of the microporous membrane. The area occupied by the clusters, however, is smaller than expected from the high porosity of the substrate membranes and may indicate a deformation of the membrane due to TEM sample preparation. The particles in membrane A (Fig. 4), which were formed by O_2 oxidation of Fe^{2+}, are disk-shaped and range in size from 3 to 4 nm. In membrane B, which had been treated with H_2O_2, similar particles were present along with needle-like particles about 50 nm long and 4 nm wide. The disk-shaped particles in both membranes were too small to yield resolvable diffraction patterns. Selected area electron diffraction of the needle-like particles (Fig. 5, inset), however, suggested the possibilities of ferrihydrite, $5Fe_2O_3 \cdot 9H_2O$, and ferroxyhyte, δ′-FeOOH, a poorly ordered form of δ-FeOOH. Electron energy loss spectra of the nanocrystalline particles in membrane B showed hexagonal crystal symmetry consistent with both forms of iron oxide.

Iron oxide characterization

To establish the identity of the nanoparticulate iron oxide, a Mössbauer study of both membranes was conducted. Table 3 shows the Mössbauer spectral parameters from 300 K to 4.2 K. The temperature variations of the spectra for each membrane are shown in Figs. 6 and 7. From 300 K to 69 K, the Mössbauer spectra consist of a paramagnetic component due to the fast superparamagnetic relaxation of the magnetic moments of the particles. Field-dependent magnetization data at 300 K for both membranes (Fig. 3) show the absence of hysteresis, consistent with superparamagnetic behavior. For membrane B, there is a magnetically split component that amounts to 10% of the total resonant area, consistent with the TEM results that show two types of particles of different size and morphology.

Fig. 5. TEM micrograph of a section of membrane B; inset: electron diffraction pattern obtained from several needle-like oxide particles.

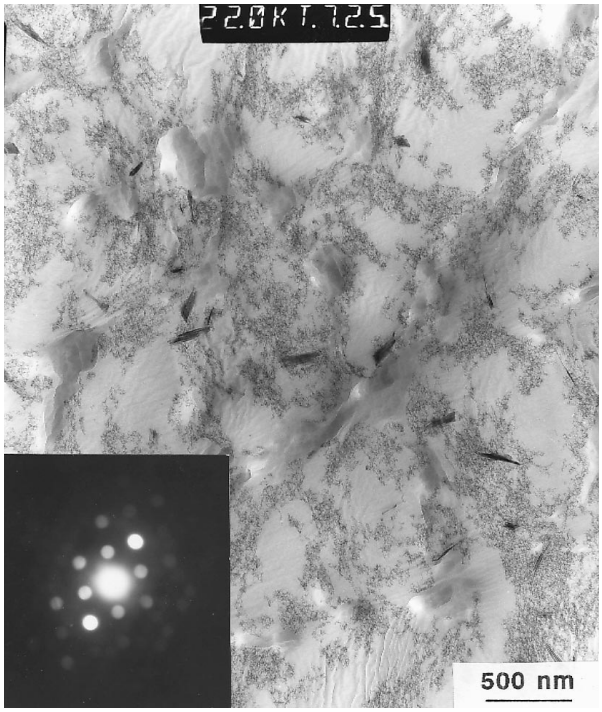

At 4.2 K, the spectra for both membranes were completely split magnetically.

The superparamagnetic components of the spectra were fitted with two doublets. It was observed that this procedure improved the quality of the fit by lowering the χ^2 values. In the case of

© 1998 NRC Canada

Table. 3. Hyperfine parameters of the fittings of the Mössbauer spectra at different temperatures.[a]

Sample	T (K)	δ/Fe (mm s^{-1})	ΔE_q (mm s^{-1})	Γ (mm s^{-1})	$<B_{hf}>_{av}$ (tesla)	σ_{Bhf} (tesla)	Area (%)	χ^2
A								
	300	0.33 (0.03)	0.54 (0.02)	0.36 (0.02)	—	—	62	1.0
		0.35 (0.03)	0.87 (0.04)	0.39 (0.04)			38	
	69	0.44 (0.03)	0.70 (0.02)	0.89 (0.06)	—	—	57	0.9
		0.46 (0.05)	1.80 (0.09)	3.70 (0.06)			43	
	30	0.45 (0.04)	0.04 (0.06)	—	45.0 (0.4)	3.9 (0.9)	100	1.2
	4.2	0.45 (0.04)	–0.02 (0.04)	—	50.4 (0.2)	2.4 (0.2)	100	2.9
B								
	300	0.34 (0.02)	0.51 (0.01)	0.39 (0.2)	—	—	41	5.5
		0.35 (0.02)	0.89 (0.09)	0.39 (0.2)			59	
	69	0.46 (0.02)	0.74 (0.02)	0.85 (0.2)			60	1.4
		0.51 (0.06)	1.40 (0.09)	4.3 (0.8)			31	
		0.49 (0.02)	–0.20 (0.04)		48.3 (0.8)	1.9 (0.9)	9	
	4.2	0.46 (0.04)	–0.03 (0.02)	—	50.2 (0.2)	2.5 (0.2)	100	2.5

[a] B_{hf} is the hyperfine field in tesla and corresponds to the average field of the distribution, and the standard deviation of the distribution, σ_{Bhf}, is given. ΔE_q, δ/Fe, and Γ are the quadrupolar splitting, the isomer shift (relative to α-Fe), and the full width at half maximum, respectively, all given in mm s^{-1}. The area of each subspectrum is given as a relative percentage. The χ^2 parameter is also given. The numbers in parentheses represent the errors in the given values.

Fig. 6. Temperature variation of the Mössbauer spectra between 300 K and 4.2 K for membrane A. Dots are experimental data; solid lines are computer-fitted spectra. The hyperfine parameters of the subspectra are given in Table 2.

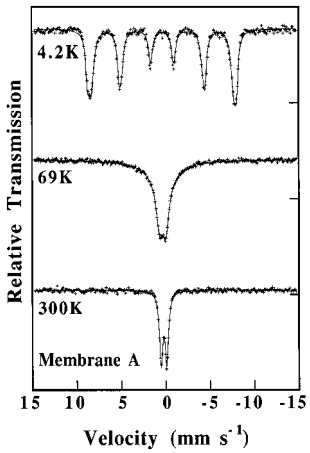

Fig. 7. Temperature variation of the Mössbauer spectra between 300 K and 4.2 K for membrane B (see caption of Fig. 5).

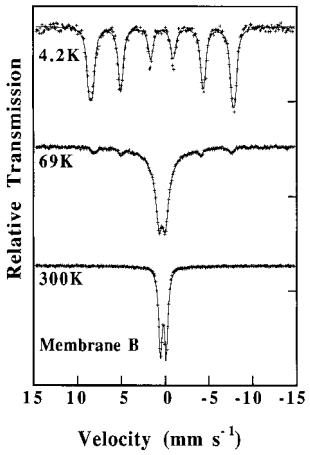

membrane B at 300 K, the χ^2 was 15.7 for one doublet and 5.5 for two doublets; this improvement is not as large in the other spectra. At the same time, this method was also used for comparing our results to previously reported data. The spectral values of the two doublets fitting for each membrane were found to be in agreement with those reported earlier for isometric nanocrystalline particles of ferrihydrite, $5Fe_2O_3 \cdot 9H_2O$, 2–6 nm in diameter (22, 23). This assignment is also consistent with the TEM data, which showed the main components of membranes A and B to be isometric particles 3–4 nm in diameter. In the absence of a matrix, ferrihydrite may be formed from the rapid hydrolysis of Fe(III) solutions (24). Ferrihydrite is a common biogenic mineral formed in matrix-mediated processes and it is known to exist in both a crystalline and an amorphous form (25).

The magnetically split spectra at 4.2 K were fitted with a distribution of hyperfine fields. At 4.2 K, the observed spectral parameters also coincide with those of ferrihydrite in a well-crystallized form, or so-called six-line ferrihydrite (16, 17, 26). The presence of a certain amount of feroxyhyte, δ′-FeOOH, can not be ruled out on the basis of the Mössbauer data (27). This is particularly true for membrane B, which, as shown by TEM, contains some larger needle-like particles. We assume that they are responsible for the magnetic split component of membrane B (approximately 10%) at 69 K. It is only visible at this temperature because at higher or lower temperatures it gets blurred by the main component, namely, the isometric particles of 3–4 nm in diameter. We note that reasonably well characterized δ′-FeOOH was prepared under similar conditions in solution (28).

We used the data obtained from the membrane A to evaluate the effective anisotropy constant, K_{eff}, since in this case, as shown by TEM, there is only one kind of particle morphology with an average diameter of 4 nm. The Mössbauer blocking temperature, defined as the temperature at which the spectra show 50% of unsplit component and 50% of split component, was evaluated to be 50 ± 10 K, within the error range previously reported (29). Using an Arrhenius law $\tau_m = \tau_0 \exp(K_{eff} V / k_B T_B)$,

© 1998 NRC Canada

where $\tau_0 = 10^{-10}$ s is a constant, and $\tau_m = 5 \times 10^{-9}$ s is the Mössbauer characteristic time, we obtain $K_{eff} = 8 \times 10^4$ J m^{-3}, a value that coincides with the previously reported value for ferrihydrite (30).

We note that the alkaline oxidation of ferrous ions, performed under similar conditions to those reported here but bound to different templates, resulted in the formation of different magnetic oxides. In the case of sulfonated macroporous polymeric microspheres having pore sizes from 50 to 200 nm, the major iron oxide was a superparamagnetic form of goethite, α-FeOOH (31). When the ferrous ions were confined within the pores of mesoporous sulfonated polymeric microspheres having pore sizes from 10 to 100 nm, the alkaline oxidation led to the formation of γ-Fe_2O_3 (maghemite) in addition to goethite (32). In the presence of sulfated latex particles, the reaction yielded predominantly $Fe(OH)_3$ (31). In the case of sulfonated, lightly cross-linked polystyrene, the alkaline oxidation of Fe(II) led exclusively to the formation of maghemite (9). These observations demonstrate, not unexpectedly, that the template, in addition to the macroscopically imposed reaction conditions, plays a critical role in controlling the phase, size, and shape of the precipitated iron oxide. We note that when carboxylated resins were used in place of the sulfonated polystyrenes in ref. 9, only non- or weakly magnetic forms of iron oxide resulted, as in the present case. Ferrihydrite, a weakly magnetic material, which forms the core component of the iron storage protein ferritin in numerous animal classes, enjoys a large abundance and a wide phyletic distribution in nature (25). It is apparently synthesized by matrix- and membrane-mediated mineralization processes.

Conclusions

In this work we have shown that a pore-filled cation-exchange membrane can be readily prepared by photografting acrylic acid into the pores of a microporous polypropylene support. The poly(acrylic acid) contained within the pores is flexible and this, combined with the very high ion-exchange capacities and water contents of the membranes, allows the facile loading of large amounts of a transition metal such as Fe(II). As such, these membranes form ideal hosts for the formation of nano-particles.

Acknowledgements

We thank Professor C. Stager (Department of Physics and Astronomy, McMaster University) for use of the SQUID magnetometer and for helpful discussions. TEM analysis was performed by Dr. A. Perovic (Department of Materials Science and Engineering, McMaster University). The work was supported in part by grants from the Ontario Center for Materials Research (F.M.W and A.M.), the Natural Sciences and Engineering Research Council of Canada (R.F.C., F.M.W., and A.M.M.), and 3M Canada, Inc. (R.F.C. and A.M.M.).

References

1. M. Pineri, J.C. Jesior, and J.M. D. Coey. J. Membr. Sci. **24**, 325 (1985).
2. J.M. Zen, G. Chen, F.-R.F. Fan, and A.J. Bard. Chem. Phys. Lett. **169**, 23 (1990).
3. E.Y.Tsymbal, F.K. Chibirova, and I.G. Kostyuchenko. J. Magnet. Magnet. Mater. **136**, 197 (1994).
4. B. Rodmacq. J. Phys. Chem. Solids, **45**, 1119 (1984).
5. A.M. Mika, R.F. Childs, J.M. Dickson, B.E. McCarry, and D.R. Gagnon. J. Membr. Sci. **108**, 37 (1995).
6. J.T. Kim and J.L. Anderson. Ind. Eng. Chem. Res. **30**, 1008 (1991); E. Boschetti. J. Chromatog. **A, 658**, 207 (1994).
7. Y. Osada and Y. Iriyama. Thin Solid Films, **118**, 197 (1984); M. Ulbricht. React. Funct. Polym. **31**, 165 (1966); F. Poncin-Epaillard, B. Chevot, and J. Brosse. J. Appl. Polym. Sci. **53**, 1291 (1994); Y. Lee, S. Ihm, J. Shim, J. Kim, C. Cho, and Y. Sung. Polymer, **36**, 81 (1995).
8. T. Yamaguchi, S. Nakao, and S. Kimura. Macromolecules, **24**, 5522 (1991); Ind. Eng. Chem. Res. **32**, 848 (1993); J. Membr. Sci. **95**, 39 (1994).
9. R.F. Ziolo, E.P. Giannelis, B.A. Weinstein, M.P. O'Horo, B.N. Ganguly, V. Mehrotra, M.W. Russell, and D.R. Huffman. Science, **257**, 219 (1992).
10. L. Raymond, J.-F. Revol, D.H. Ryan, and R.H. Marchessault. Chem. Mater. **224**, 133 (1994).
11. S. Sourirajan. Reverse osmosis. Academic Press, New York. 1970. Chap. 3.
12. Reagent chemicals, American Chemical Society, specifications. 6th ed. American Chemical Society, Washington, D.C. 1981. pp. 25–26.
13. L.G. Saywell and B.B. Cunningham. Ind. Eng. Chem. **9**, 67 (1937); M.G. Mellon. Ind. Eng. Chem. **10**, 60 (1938).
14. D.R. Lloyd, K.E. Kinzer, and H.S. Tseng. J. Membr. Sci. **52**, 239 (1990).
15. C.H. Ang, J.L. Garnett, R. Levot, M.A. Long, and N.T. Yen. J. Polym. Sci., Polym. Lett. Ed. **18**, 471 (1980).
16. T.M. Ogiwara, K. Kanda, M. Takumi, and H. Kubota. J. Polym. Sci., Polym. Lett. Ed. **19**, 457 (1981).
17. I.R. Bellobono, F. Muffato, C. Ermondi, E. Selli, and L. Righetto. J. Membr. Sci. **55**, 273 (1991).
18. Y. Ogiwara, K. Torikoshi, and H. Kubota. J. Polym. Sci., Polym. Lett. Ed. **20**, 17 (1982).
19. A.M. Mika, R.F. Childs, M. West, and J.N.A. Lott. J. Membr. Sci. **136**, 221 (1997).
20. J.R. MacCallum and C.A. Vincent (*Editors*). *In* Polymer electrolyte reviews–1. Elsevier Applied Science, London. 1987. p. 23.
21. Y. Osada and Y. Iriyama. Thin Solid Films, **118**, 197 (1984).
22. E. Murad and U. Schwertmann. Am. Mineral. **65**, 1044 (1980)
23. E. Murad. *In* Magnetic properties of fine particles. *Edited by* J.L. Dormann and D. Fiorani. Elsevier Science Publishers, London.1992. pp. 339–349.
24. U. Schwermann and R.M. Cornell.Iron oxides in the laboratory. Preparation and characterisation. VCH, Weinheim. 1991.
25. H.A. Lowenstam and J.L. Kirschvink. *In* Magnetite biomineralization and magnetoreception in organisms. *Edited by* J.L. Kirschvink, D.S. Jones, and B.J. MacFadden. Plenum, New York. 1985. pp. 3–15.
26. E. Murad, L.H. Bowen, G.L. Long, and T.G. Quin. Clay Miner. **23**, 161 (1988).
27. C. Bender Koch, C.A. Oxborrow, S. Mørup, M.B. Madsen, A.J. Quinn, and J.M.D. Coey. Phys. Chem. Miner. **22**, 333 (1995).
28. W.Z. Feitknecht. Electrochemistry, **63**, 34 (1959).
29. L. Cianchi, M. Maucini, G. Spina, and H. Tang. J. Phys.: Condens. Matter, **4**, 2073 (1992).
30. R.E. Vandenberghe, E. De Grave, C. Landuydt, and L.H. Bowen. Hyperfine Interact. **53**, 175 (1990).
31. F.M. Winnik, A.Morneau, R.F. Ziolo, H.D.H. Stöver, W.-H. Li. Langmuir, **11**, 3660 (1994).
32. F.M. Winnik, A. Morneau, R.F. Ziolo, K. Schäfer, H.D.H. Stöver, and W.-H. Li. Manuscript in preparation.

© 1998 NRC Canada

Energétique des liaisons inter- et intramoléculaires dans les trois isomères de l'aminopyridine

Raphaël Sabbah et Maria Ermelinda da Silva Eusébio

Résumé: Le présent travail porte sur l'étude thermodynamique des trois isomères de l'aminopyridine (AP) de formule générale : $C_5H_6N_2$. Il a été réalisé en utilisant trois techniques : la calorimétrie de combustion de faibles quantités de substance (quelques milligrammes par essai), la calorimétrie de sublimation et l'analyse thermique différentielle. Cette étude nous a permis : de déterminer les enthalpies de combustion, de sublimation et de fusion de ces composés ainsi que la température de leur point triple; de préciser la stabilité relative des trois isomères; de déterminer les énergies de conjugaison expérimentales et de les comparer aux valeurs théoriques; de déterminer les enthalpies d'atomisation des trois composés et de vérifier qu'elles sont compatibles aux valeurs calculées à partir des contributions énergétiques précédemment déterminées au laboratoire; de déterminer qualitativement et quantitativement les interactions intermoléculaires.

Mots clés : isomères de l'aminopyridine; enthalpie de combustion, de sublimation, de fusion, des liaisons inter- et intramoléculaires.

Abstract: The present work is concerned with a thermodynamic study of the three aminopyridine (AP) isomers (general formula: $C_5H_6N_2$). It was achieved using three techniques: combustion calorimetry of small amounts of substance (a few milligrams), sublimation calorimetry, and differential thermal analysis. From this study, it was possible to determine the enthalpies of combustion, sublimation, and fusion of these compounds and their triple point temperatures; to discuss the relative stability of the three molecules; to determine the experimental resonance energies and compare them with the theoretical values; to determine the atomization enthalpies and compare them with the values calculated from the energetical contributions previously determined in our laboratory; to determine the enthalpy of the intermolecular bonds.

Key words: aminopyridine isomers; enthalpy of combustion, of sublimation, of fusion, of inter- and intramolecular bonds.

1. Introduction

L'analyse des coupes lourdes du pétrole et des produits issus de la liquéfaction des charbons révèle l'existence dans ceux-ci à côté de molécules aromatiques, généralement polynuclées, d'hétérocycles contenant de l'oxygène, du soufre et de l'azote.

Diverses actions, entreprises depuis quelques années, ont eu pour but de valoriser ces coupes et produits. C'est le cas de l'opération d'hydrodénitrogénation (HDN) qui cherche à transformer les molécules renfermant de l'azote en hydrocarbures aromatiques correspondants afin d'obtenir des combustibles non polluants possédant un indice d'octane élevé.

Le calcul d'une chaleur de réaction, quelquefois difficile à déterminer directement à l'aide d'un calorimètre, d'un bilan énergétique, se heurte souvent au manque de données thermodynamiques précises concernant ce type de molécules.

Reçu le 28 juillet 1997.

R. Sabbah[1] **et M.E. da Silva Eusébio.**[2] Centre de thermodynamique et de microcalorimétrie du Centre national de la recherche scientifique, 26, rue du 141ème RIA, 13331 - Marseille, Cedex 03, France.

1. Auteur auquel la correspondance doit être adressée. Tél. : 33 4 91 28 20 62. Téléc. : 33 4 91 50 38 29. Mél. : raphael.sabbah @ ctm.cnrs-mrs.fr
2. Professeur auxiliaire au Département de chimie de l'Université de Coimbra (Portugal) en stage postdoctoral au laboratoire.

Possédant au laboratoire les moyens de déterminer certaines grandeurs thermodynamiques telles que l'enthalpie de formation à l'état condensé ou gazeux, l'enthalpie de sublimation/vaporisation, avec une exactitude suffisamment élevée tout en n'utilisant que peu de substance (une étude complète nécessite 200 mg environ de substance pure), nous avons, dans le présent travail, étudié les trois isomères de l'aminopyridine. Ce travail s'inscrit bien dans le cadre de notre thème de recherche «Energétique des liaisons inter- et intramoléculaires dans les substances organiques» et vise la mise en évidence du lien existant entre grandeurs énergétiques et structure. Cette étude a été réalisée par calorimétrie de combustion de faibles quantités de substance, de sublimation et par analyse thermique différentielle : mesure du degré de pureté de l'échantillon soumis à l'étude, de son enthalpie de fusion ainsi que de la température de son point triple.

De par la simplicité de leur structure, les aminopyridines, molécules conjuguées, sont souvent étudiées en vue d'utiliser les résultats dans la réalisation de modèles pouvant être appliqués à l'étude de molécules plus complexes.

Enfin, précisons que les aminopyridines sont des intermédiaires de synthèse, qu'elles sont aussi utilisées comme complexants en chimie organique et inorganique et que leurs dérivés sont utilisés en teinturerie et en biologie comme stimulants du système nerveux (1).

Les données thermodynamiques relatives aux aminopyridines et consignées dans la littérature sont très peu nombreuses (2, 3). Nous en reparlerons avec les résultats expérimentaux.

© 1998 NRC Canada

Il en est de même des informations relatant la structure cristalline de ces composés (4–6).

2. Partie expérimentale

2.1. Produits utilisés

Les trois substances étudiées sont des produits Aldrich de pureté supérieure ou égale à 99%. L'analyse thermique différentielle ayant confirmé ce résultat pour les deux isomères *ortho* et *para* (tableau 2), nous n'avons repurifié que l'isomère *méta* trois fois successivement par sublimation à 327 K et sous une pression résiduelle de 1,3 Pa.

Signalons, au passage, que ces trois substances sont nocives par inhalation, ingestion et contact avec la peau. Leur manipulation, réalisée sous hotte aspirante, a donc nécessité quelques précautions telles que le port de lunettes, masque et gants appropriés.

Afin d'éviter toute action de la lumière et de l'humidité sur les substances étudiées, celles-ci ont été stockées dans un dessiccateur en verre brun renfermant de la potasse.

2.2. Appareillages, techniques et modes opératoires

2.2.1. Analyse thermique différentielle

Nous avons utilisé la version moyenne température de l'analyseur thermique différentiel et les cellules expérimentales en verre décrites dans la référence 7.

Dans toutes nos expériences : (*i*) la vitesse de montée en température du four a été de 0,2 K min–1; (*ii*) la masse de substance utilisée a été d'environ 100 mg, déterminée par double pesée à l'aide d'une balance Mettler, type M5, sensible au μg et dont l'exactitude des pesées est de ±2 μg; (*iii*) la préparation des échantillons et leur mise en container ont été conduites de la façon décrite dans la référence 7.

La mesure des températures a été faite à l'aide de deux thermocouples (thermocoax, type 2ABI 15), l'un est solidaire de l'échantillon, l'autre de la référence (alumine-α). La différence entre les f.e.m. délivrées par ces deux thermocouples est amplifiée par un microvoltmètre AOIP, type EVA, sensibilité 100 μV pleine échelle. Le signal ainsi amplifié est envoyé simultanément à un enregistreur Sefram, type Gépérac, pour le visualiser, et à un multimètre Keithley, modèle 175, pour le digitaliser. Un autre multimètre Keithley, modèle 196, sensibilité 300 mV (résolution 100 nV) est utilisé pour mesurer la f.e.m correspondant à la température de l'échantillon. Les données issues de ces deux multimètres sont envoyées vers un ordinateur en vue de leur traitement à l'aide d'un programme écrit et mis au point au laboratoire. En appliquant l'équation de Clausius–Clapeyron et la loi de Raoult, ce programme permet de déterminer la pureté de l'échantillon, son enthalpie de fusion ainsi que la température de son point triple.

Comme indiqué dans la référence 7, l'étalonnage (*i*) en température, de notre analyseur thermique, a été réalisé à partir d'échantillons rigoureusement purs de naphtalène, de fluorène, d'acides benzoïque, diphénylacétique et anisique, de carbazole et d'anthraquinone, dont la température de leur point triple est bien connue dans la littérature; et (*ii*) en énergie, a été réalisé à partir d'échantillons rigoureusement purs de naphtalène, de fluorène, d'acides benzoïque et diphénylacétique, dont l'enthalpie de fusion est bien connue dans la littérature.

2.2.2. Calorimétrie de combustion

Les enthalpies de combustion de nos composés ont été déterminées en utilisant un calorimètre isotherme, à flux thermique, monopile, basculant, CRMT (sensibilité : 0,0623 V W^{-1}) équipé d'une microbombe en acier inoxydable (Superimphy 625) de volume interne égal à 43 cm^3 à la température ambiante.

Le signal issu du calorimètre est amplifié par un microvoltmètre électronique AOIP, modèle EVA, sensibilité 100 mV pleine échelle, avant son envoi simultané sur un intégrateur électronique, conçu, réalisé et mis au point au laboratoire, qui détermine l'aire des thermogrammes $dQ/dt = f(t)$, et sur un enregistreur potentiométrique Sefram, modèle Servotrace, qui le visualise.

La rotation du calorimètre suivant plusieurs plans permet à toutes les génératrices de la bombe d'être lavées par l'eau déminéralisée placée en son fond (1 cm^3).

Comme indiqué dans la référence 8, les substances à étudier sont mises sous forme de pastilles. À cet effet, nous avons utilisé un ensemble piston-moule façonné dans un acier trempé, ce qui a pour effet d'éviter l'entraînement dans les pastilles de traces de métal et d'augmenter ainsi la qualité des résultats. Compte tenu de la volatilité de l'isomère *ortho* et d'une éventuelle oxydation des substances par l'oxygène sous 3,04 MPa en présence de vapeur d'eau (2), nous avons scellé nos pastilles dans des petits sachets en polyéthène confectionnés par nos soins à partir d'un film de 50 μm d'épaisseur.

Les pesées ont été effectuées sur une microbalance Mettler, modèle UM3, équipée d'un jeu de poids étalonnés par le N.I.S.T. Sa portée est de 3 g et sa sensibilité de 0,1 μg. L'erreur commise avec cette balance sur une pesée de quelques milligrammes est de l'ordre de ±0,2 μg. Dans toutes nos pesées, nous avons tenu compte des corrections de poussée de l'air pour calculer les masses réelles.

Une fois garnie, la bombe est remplie d'oxygène sous une pression de 3,04 MPa. L'oxygène N45, utilisé à cet effet, provient de l'Air Liquide et son degré de pureté est supérieur à 99,995% (fraction molaire d'azote $<10^{-5}$). La durée d'une expérience a toujours été de 90 min à partir du moment de la mise de feu.

Après chaque expérience, nous avons déterminé, dans la phase aqueuse, la concentration d'acide nitrique par titrage acido-basique en présence de phénolphtaléine avec une solution de soude préalablement titrée à l'aide de solutions d'acide oxalique de concentrations connues, et avons vérifié, à l'aide des tubes de Dräger, l'absence d'oxyde de carbone et d'oxydes d'azote (NO, NO_2) dans la phase gazeuse (sensibilité des tubes <1 ppm pour CO et <0,1 ppm pour NO et NO_2).

2.2.3. Calorimétrie de sublimation

Nous avons utilisé un calorimètre Tian–Calvet (sensibilité 0,0621 V W^{-1}) associé à un montage différentiel doté de cellules d'effusion de Knudsen pour déterminer les enthalpies de sublimation de nos composés. L'étalonnage de notre système calorimétrique a été réalisé par effet Joule avant et après chaque série d'expériences. Le mode opératoire a été décrit dans la référence 9. Précisons que :

(*i*) le signal issu du calorimètre est amplifié par un nanovoltmètre Keithley modèle 147, sensibilité 100 μV pleine échelle, puis digitalisé par un multimètre numérique Keithley

© 1998 NRC Canada

Tableau 1. Grandeurs physiques des substances utilisées à 298,15 K.

Substance	Formule	M[a] (g mol^{-1})	ρ (g cm^{-3})	$-(\partial U/\partial P)_T$ (J g^{-1} MPa^{-1})
Acide benzoïque	$C_7H_6O_2$	122,1234	1,32 (10)	0,12 (10)
Coton	$CH_{1,791}O_{0,850}$	27,4157	1,50 (10)	0,29 (10)
Polyéthène	$(CH_2)_n$	$(14,0269)_n$	0,92 (11)	0,055 (11)
2-AP	$C_5H_6N_2$	94,11612	1,24 (4)	0,13[b]
3-AP	$C_5H_6N_2$	94,11612	1,24 (5)	0,13[b]
4-AP	$C_5H_6N_2$	94,11612	1,28 (6)	0,13[b]

[a] Calculée à partir du tableau des masses atomiques de 1993 (12).
[b] Valeurs estimées.

Tableau 2. Analyse thermique différentielle des trois isomères de l'aminopyridine.

Substance	Pureté ce travail (mol %)	Pureté littérature (mol %)	T_{pt}[a] ce travail (K)	T_{pt} littérature (K)	$\Delta_{fus}H_m$ ce travail (kJ mol^{-1})	$\Delta_{fus}H_m$ littérature (kJ mol^{-1})
2-AP	99,91±0,01		331,53±0,03	330–331 (13)	15,3±0,1	
3-AP	99,91±0,01		335,52±0,02	337–338 (13) 429,94 (14)	14,4±0,4	
4-AP	99,92±0,01	99,3 (14)	432,13±0,01	431–432 (13)	19,3±0,3	20,07(14)

[a] Températures du point triple définies par rapport à l'EIT-90.

modèle 175 et enregistré sur un enregistreur potentiométrique Sefram, modèle Servotrace;

(*ii*) les trois isomères ont été étudiés à 298,15 K. Compte tenu de la faible pression de vapeur saturante des substances étudiées (4,7, 0,76 et 0,0071 Pa à 298,15 K respectivement pour les isomères *ortho*, *méta* et *para*), nous avons admis l'identité $\Delta_{sub}H_m(T) \equiv \Delta_{sub}H^\circ_m(T)$;

(*iii*) le diamètre des trous d'effusion pratiqués dans des joints en laiton de 0,1 mm d'épaisseur est de 0,2, 0,5 et 3 mm respectivement dans le cas de la 2-, 3- et 4-aminopyridine;

(*iv*) l'ouverture et la fermeture de l'orifice d'effusion des cellules sont pilotées par l'ordinateur;

(*v*) toutes les pesées ont été effectuées à l'aide d'une balance Mettler, type UM3.

L'acquisition et le traitement des données sont réalisés à l'aide d'un ordinateur et d'un programme conçu et mis au point au laboratoire. Il permet, entre autres, de déterminer l'aire des thermogrammes et, à partir du coefficient d'étalonnage, l'enthalpie de sublimation de nos composés à la température de l'expérience $\Delta_{sub}H^\circ_m(T)$.

Les différents calorimètres et analyseur thermique, leurs périphériques ainsi que les balances sont placés dans des salles thermorégulées à (19,0 ± 0,2)°C.

3. Résultats

Les constantes physiques de nos composés sont résumées dans le tableau 1.

3.1. Analyse thermique différentielle

Les résultats obtenus ainsi que ceux qui sont empruntés à la littérature sont rassemblés dans le tableau 2. Notons qu'aucune des trois substances ne semble se décomposer de façon appréciable entre la température ambiante et son point de fusion.

Les résultats de l'enthalpie de fusion, consignés dans la littérature, sont très peu nombreux et concernent l'isomère *para*. Notre valeur diffère de 4% de celle de Donnelly et al. (14). Signalons, au passage, que ces auteurs opèrent sur des échantillons de pureté 99,3% dont la masse est comprise entre 1,5 et 2 mg (exactitude ±0,2 mg) placés dans des godets en aluminium non scellés. De plus, leur calorimètre à balayage a été étalonné à partir d'un seul échantillon : l'indium, métal dont les propriétés de transfert thermique sont différentes de celles d'une substance organique.

Quant aux températures du point triple des trois isomères étudiés, celles-ci sont compatibles avec les résultats de la littérature (13, 14).

3.2. Calorimétrie de combustion

L'équivalent énergétique du système calorimétrique (U_{calor}) a été déterminé à partir de 14 combustions d'acide benzoïque échantillon 39 i du N.I.S.T. pour lequel $\Delta_c u^\circ$(cr, 298,15 K) = (–26 414 ± 3) J g^{-1} (15). Dans chaque expérience, nous avons utilisé de 7 à 16 mg d'acide et environ 0,2 mg de coton (dont l'énergie de combustion, préalablement déterminée au laboratoire, a pour valeur $\Delta_c u^\circ$(cd, 298,15 K) = (–16 399 ± 23) J g^{-1} (16)). Afin de mettre en évidence l'influence du polyéthène sur les résultats, neuf de ces expériences ont été réalisées avec des pastilles scellées dans des sachets confectionnés avec ce matériau ($\Delta_c u^\circ$(cd, 298,15 K) = (–46 347 ± 7) J g^{-1} (17). À l'issue de ces expériences nous n'avons noté aucune différence dans les résultats des combustions effectuées en présence de polyéthène. Nous avons trouvé U_{calor} = (15,465 ± 0,004) J V^{-1} s^{-1}.

Les enthalpies standard de combustion de nos composés concernent la réaction suivante :

$$C_5H_6N_2(cr) + \frac{13}{2}\,O_2\,(g) \rightarrow 5\,CO_2\,(g) + 3\,H_2O\,(l) + N_2\,(g)$$

et sont calculées, à l'aide de l' ordinateur et d'un programme écrit et mis au point au laboratoire, à partir de nos valeurs

© 1998 NRC Canada

Tableau 3. Combustion de la 2-aminopyridine à 298,15 K.

$m_{subst.}$ (mg)	$m_{polyéthène}$ (mg)	m_{coton} (mg)	n (HNO_3) (10^{-6} mol)	A (V s)	$-\Delta U$ (J)	$-W_1$ (J)	W_2 (J)	$-\Delta_c U^\circ_m$ (kJ mol^{-1})
4,7020	2,9728	0,2278	10,4	18,420 93	284,878	141,521	0,818	2853,07
6,0871	3,4518	0,2418	14,2	22,639 37	350,117	163,946	1,083	2861,60
4,9254	3,4824	0,2475	13,6	20,431 90	315,977	165,458	1,026	2856,56
6,8870	4,1316	0,2385	20,3	26,225 96	405,582	195,399	1,495	2851,88
6,0234	3,4941	0,2368	24,5	22,615 38	349,745	165,825	1,697	2847,24
5,9229	2,9651	0,2307	15,8	20,800 18	321,673	141,207	1,172	2849,01
4,0997	2,7226	0,2938	10,5	16,561 97	256,129	131,003	0,805	2854,01
5,4033	2,8518	0,2629	14,2	19,530 14	302,032	136,484	1,062	2865,04
12,7430	5,3754	0,2138	34,0	41,460 24	641,179	252,640	2,489	2851,25
11,8584	4,2977	0,1761	29,5	36,497 36	564,428	202,074	2,171	2858,65
				$-\Delta_c U^\circ_m$(cr, 298,15 K)/kJ mol^{-1} = 2854,8 ± 1,8				
				$-\Delta_c H^\circ_m$(cr, 298,15 K)/kJ mol^{-1} = 2856,1 ± 1,8				
				$\Delta_f H^\circ_m$(cr, 298,15 K)/kJ mol^{-1} = 31,0 ± 1,8				

A = aire des thermogrammes,
ΔU = variation de l'énergie interne de la bombe et de son contenu,
W_1 = énergie de combustion du coton et du polyéthène,
W_2 = corrections pour passer à l'état de référence.

Tableau 4. Combustion de la 3-aminopyridine à 298,15 K.

$m_{subst.}$ (mg)	$m_{polyéthène}$ (mg)	m_{coton} (mg)	n (HNO_3) (10^{-6} mol)	A (Vs)	$-\Delta U$ (J)	$-W_1$ (J)	W_2 (J)	$-\Delta_c U^\circ_m$ (kJ mol^{-1})
9,1444	4,4488	0,2184	24,9	31,755 49	491,096	209,771	1,831	2876,61
11,0617	4,2725	0,2760	29,8	35,142 20	543,471	202,544	2,167	2882,26
11,1580	4,6358	0,1900	29,4	36,356 99	562,226	217,972	2,158	2885,80
8,6389	4,5240	0,2265	24,4	31,080 70	480,660	213,389	1,789	2892,23
12,3500	4,9252	0,2497	34,4	40,862 84	631,940	232,364	2,508	2889,10
10,4135	4,6447	0,2390	27,6	34,959 45	540,644	219,188	2,029	2886,95
12,7695	4,8550	0,2481	32,7	40,196 46	621,634	229,084	2,401	2875,55
11,5256	5,3148	0,2742	31,3	39,257 29	607,110	250,822	2,299	2890,61
8,7899	4,8293	0,2013	23,0	32,178 00	497,630	227,125	1,721	2877,95
7,6329	4,3243	0,2471	20,5	28,437 25	439,779	204,471	1,528	2885,26
12,0730	4,5972	0,1354	30,3	38,01250	587,860	215,287	2,234	2887,00
12,7561	4,6914	0,2056	31,9	39,73405	614,483	220,804	2,348	2887,29
				$-\Delta_c U^\circ_m$(cr, 298,15 K)/kJ mol^{-1} = 2884,5 ± 1,6				
				$-\Delta_c H^\circ_m$(cr, 298,15 K)/kJ mol^{-1} = 2885,7 ± 1,6				
				$\Delta_f H^\circ_m$(cr, 298,15 K)/kJ mol^{-1} = 60,7 ± 1,6				

A = aire des thermogrammes,
ΔU = variation de l'énergie interne de la bombe et de son contenu,
W_1 = énergie de combustion du coton et du polyéthène,
W_2 = corrections pour passer à l'état de référence.

expérimentales en tenant compte des corrections dites de Washburn.

La combustion des trois isomères s'est révélée complète, aucune trace de cendre ne subsistant dans le corps de la bombe et dans le creuset une fois l'expérience terminée et les dosages par tubes colorimétriques de Dräger n'ayant révélé aucune présence de CO et d'oxydes d'azote dans la phase gazeuse.

Les résultats relatifs à ces manipulations sont rassemblés dans les tableaux 3–5.

Nous avons remarqué qu'environ 12% de l'azote contenu dans nos composés se trouvaient, à l'issue de la combustion, sous forme d'acide nitrique. L'expérience a montré que la quantité d'acide nitreux formé est excessivement faible et peut être négligée.

Comparée aux seules valeurs de la littérature, obtenues par calorimétrie de combustion classique et reportées dans la référence 2, notre valeur expérimentale de l'enthalpie de combustion est compatible dans le cas de l'isomère *méta* (–2885,2 ± 0,5) kJ mol^{-1}; elle s'en écarte de 0,3% et de 0,1% respectivement dans celui de l'isomère *ortho* (–2864,4 ± 0,5) kJ mol^{-1} et *para* (–2866,8 ± 0,5) kJ mol^{-1}.

3.3. Calorimétrie de sublimation

Les enthalpies de sublimation de nos substances à 298,15 K sont consignées dans le tableau 6. Comparés aux seules valeurs de la littérature consignées dans la référence 2 (*ortho* : (78,7 ± 0,8) kJ mol^{-1}, *méta* : (84,0 ± 1,4) kJ mol^{-1}, *para* : (88,1 ± 1,1) kJ mol^{-1}), nos résultats présentent des écarts

© 1998 NRC Canada

Tableau 5. Combustion de la 4-aminopyridine à 298,15 K.

$m_{subst.}$ (mg)	$m_{polyéthène}$ (mg)	m_{coton} (mg)	n (HNO_3) (10^{-6} mol)	A (V s)	$-U$ (J)	$-W_1$ (J)	W_2 (J)	$-\Delta_c U^\circ_m$ (kJ mol^{-1})
6,1837	4,0918	0,2419	18,6	24,757 37	382,870	193,610	1,374	2859,63
5,2456	3,6310	0,2760	15,5	21,591 17	333,905	172,813	1,151	2869,66
6,8191	3,4007	0,1717	18,7	23,863 63	369,049	160,428	1,377	2860,34
4,0641	3,0097	0,2760	13,4	17,365 53	268,556	144,017	0,979	2861,38
8,5953	3,0681	0,2035	22,7	26,423 30	408,634	286,278	1,651	2862,78
8,4264	3,7100	0,2725	22,3	28,105 01	434,641	176,417	1,639	2865,86
11,9728	3,2938	0,3055	28,8	33,844 62	523,404	157,668	2,111	2858,40

$-\Delta_c U^\circ_m$(cr, 298,15 K)/kJ mol^{-1} = 2862,6 ± 1,5

$-\Delta_c H^\circ_m$(cr, 298,15 K)/kJ mol^{-1} = 2863,8 ± 1,5

$\Delta_f H^\circ_m$(cr, 298,15 K)/kJ mol^{-1} = 38,8 ± 1,5

A = aire des thermogrammes,
U = variation de l'énergie interne de la bombe et de son contenu,
W_1 = énergie de combustion du coton et du polyéthène,
W_2 = corrections pour passer à l'état de référence.

Tableau 6. Sublimation des trois isomères de l'aminopyridine à 298,15 K.

2-AP									
m/mg	15,2008	13,3654	13,7964	16,2440	15,7003	16,1186	14,7526	14,1843	16,7759
$\Delta_{sub}H^\circ_m$ / kJ mol^{-1}	76,90	76,09	77,33	75,68	74,61	76,59	75,54	77,87	77,59
$\Delta_{sub}H^\circ_m$(298,15 K) = (76,47 ± 0,36) kJ mol^{-1}									
3-AP									
m/mg	16,7631	10,0684	12,3723	12,6024	14,8885	12,7737	11,4600	22,2749	18,1783
$\Delta_{sub}H^\circ_m$ / kJ mol^{-1}	81,11	81,61	79,65	79,53	79,49	80,72	80,95	80,66	82,10
$\Delta_{sub}H^\circ_m$(298,15 K) = (80,65 ± 0,31) kJ mol^{-1}									
4-AP									
m/mg	4,7887	3,7433	5,0099	3,6016	4,1351	4,9336	3,6091		
$\Delta_{sub}H^\circ_m$ / kJ mol^{-1}	87,34	85,81	86,48	86,63	89,01	87,37	87,02		
$\Delta_{sub}H^\circ_m$(298,15 K) = (87,09 ± 0,38) kJ mol^{-1}									

compris entre 1,3 et 4,1%. Toutefois, signalons qu'à notre avis, la procédure expérimentale utilisée par Bickerton et al.(2) ne conduit pas à la mesure d'une enthalpie de sublimation.

3.4. Enthalpie de formation à l'état gazeux

En utilisant les résultats expérimentaux obtenus par calorimétrie de combustion et de sublimation, nous avons calculé l'enthalpie molaire standard de formation à l'état gazeux de chacun des trois isomères. Celle-ci est égale à (107,5 ± 1,8) kJ mol^{-1}, (141,4 ± 1,6) kJ mol^{-1} et (125,9 ± 1,6) kJ mol^{-1} respectivement pour les isomères *ortho*, *méta* et *para*.

3.5. Enthalpie d'atomisation

À une température donnée, la réaction d'atomisation des aminopyridines s'écrit :

$$C_5H_6N_2\ (g) \rightarrow 5\ C(g) + 6\ H(g) + 2\ N(g)$$

En conséquence, à 298,15 K, l'enthalpie liée à cette réaction est égale à :

$$\Delta_{a,exp}H^\circ_m = 5\Delta_f H^\circ_m\ [C(g)] + 6\ \Delta_f H^\circ_m\ [H(g)] + 2\ \Delta_f H^\circ_m\ [N(g)] - \Delta_f H^\circ_m\ [C_5H_6N_2\ (g)]$$

Les valeurs de $\Delta_{a,exp}H^\circ_m$(298,15 K) de nos substances (tableau 7) ont été calculées en utilisant les valeurs de $\Delta_f H^\circ_m$(g,298,15 K) de C, H et N consignées dans la référence 18 et qui valent respectivement (716,67 ± 0,44), (217,997 ± 0,006) et (472,68 ± 0,40) kJ mol^{-1}.

Dans le présent travail, l'incertitude qui accompagne les résultats expérimentaux représente l'écart moyen, $\sigma_m = \{\Sigma(x - x_0)^2 \pm n(n-1)\}^{1/2}$, x étant chacune des n valeurs entrant dans le calcul de la moyenne x_0. Lorsque la valeur expérimentale est fonction de plusieurs variables, l'incertitude calculée tient compte de l'erreur sur chacune de ces variables.

4. Discussion

4.1. Energie de conjugaison

L'énergie de conjugaison est la différence entre l'énergie réelle de la molécule et l'énergie qu'elle aurait si les divers systèmes insaturés qu'elle comporte étaient indépendants. Sur le plan pratique, pour la déterminer, il suffit d'utiliser les enthalpies standard de combustion à l'état gazeux de la molécule réelle et de la molécule fictive non conjuguée. La première de ces grandeurs s'obtient expérimentalement et la seconde nécessite le recours aux systématiques. En ce qui nous concerne, nous avons utilisé celle de Klages qui est consignée dans la référence 19.

Nous avons également calculé l'énergie de conjugaison théorique à l'aide de la méthode de calcul indiquée dans la référence 20 et ce, en utilisant les paramètres suivants : α_N (pyridine) = α + 0,250 β_0; α_N (aniline) = α + 2,250 β_0; β_{CN} (pyridine) = 1,315 β_0; β_{CN} (aniline) = 0,750 β_0; β_0 est l'intégrale de recouvrement de la molécule de benzène; elle est égale à131,7 kJ mol^{-1}.

© 1998 NRC Canada

Tableau 7. Enthalpies d'atomisation expérimentales et calculées des trois isomères de l'aminopyridine.

Isomère	$\Delta_{a,exp}H^{\circ}_{m}$ (298,15 K) (kJ mol^{-1})	$\Delta_{a,calc}H^{\circ}_{m}$ (298,15 K) (kJ mol^{-1})
2-AP	5729,2 ± 2,2	5688,0
3-AP	5695,3 ± 2,0	5688,0
4-AP	5710,8 ± 2,0	5688,0

Tableau 8. Energies de conjugaison expérimentales et théoriques des trois isomères de l'aminopyridine.

Isomère	$E_{conj,exp}$ (kJ mol^{-1})	$E_{conj,théor}$ (kJ mol^{-1})
2-AP	182,6	174,0
3-AP	168,2	175,3
4-AP	182,9	174,2

Comme nous pouvons le constater, les valeurs de l'énergie de conjugaison expérimentale et théorique (tableau 8) ainsi obtenues sont compatibles.

4.2. Liaisons intramoléculaires dans les aminopyridines

Par définition, l'enthalpie d'atomisation d'une molécule est égale à la somme des liaisons intramoléculaires compte tenu des facteurs de stabilisation et de déstabilisation. Pour retrouver, par le calcul, l'enthalpie d'atomisation de nos composés, nous avons tenu compte du principe de la transférabilité et avons utilisé, entre autres, les valeurs énergétiques des liaisons intramoléculaires préalablement déterminées au laboratoire (21) : H ($C_b - C_b$) = 504,97 kJ mol^{-1}, H ($C_b - H$) = 415,88 kJ mol^{-1}, H (C – N = C) = 902,18 kJ mol^{-1}, H (C_b–NH_2) = 1102,37 kJ mol^{-1}).

Les valeurs ainsi calculées sont consignées dans le tableau 7 et sont en très bon accord avec les valeurs expérimentales (différence : 0,7%, 0,1% et 0,4% respectivement dans le cas des isomères *ortho*, *méta* et *para*).

4.3. Liaisons intermoléculaires dans les aminopyridines

L'enthalpie de sublimation d'une substance est liée aux interactions intermoléculaires. Dans le cas des aminopyridines, ces interactions sont du type van der Waals et concernent les forces de dispersion et d'interactions dipolaires. À côté de ces interactions, il existe aussi des liaisons hydrogène intermoléculaires (4–6). L'analyse des trois références 4 – 6 nous apporte les renseignements suivants :

1. Les molécules d'isomères *ortho* sont liés deux par deux par des liaisons hydrogènes intermoléculaires (4). Compte tenu que des trois valeurs d'enthalpie de sublimation, celle de l'isomère *ortho* est la plus faible, il est permis de penser qu'un certain nombre de molécules partent sous forme de dimères en phase gazeuse.

2. La distance N—H···N étant respectivement égale à 3,123 et 3,007 Å dans les cristaux d'isomère *méta* et *para* (5, 6), les liaisons hydrogène intermoléculaires sont plus faibles dans le cristal d'isomère *méta* qu'elles ne le sont dans celui d'isomère *para*. Ce résultat permet d'expliquer la raison pour laquelle la valeur de l'enthalpie de sublimation de l'isomère *méta* est plus faible que celle de l'isomère *para*.

Pour déterminer la part énergétique des forces de dispersion (London), nous avons considéré qu'elle est, en première approximation, égale à l'enthalpie de sublimation du méthylbenzène, composé isoélectronique des aminopyridines. Le méthylbenzène étant liquide à 298,15 K, pour déterminer son enthalpie de sublimation à cette température, nous avons, en première approximation, appliqué la relation :

$$\Delta_{sub}H^{\circ}_{m}(298{,}15\ \text{K}) = \Delta_{vap}H^{\circ}_{m}(298{,}15\ \text{K}) + \Delta_{fus}H_{m}(298{,}15\ \text{K})$$

Les valeurs de $\Delta_{vap}H^{\circ}_{m}(298{,}15\ \text{K})$ et de $\Delta_{fus}H_{m}(178{,}15\ \text{K})$ sont respectivement égales à 38,06 kJ mol^{-1} (22) et 6,64 kJ mol^{-1} (23). Nous avons calculé la valeur de $\Delta_{fus}H_{m}$ (298,15 K) en appliquant la règle de Sidgwich (24) :

$$\Delta_{fus}H_{m}(298{,}15\ \text{K}) = \Delta_{fus}H_{m}(T_{fus}) - 0{,}055\ (T_{fus} - 298{,}15)$$

Il s'en suit que $\Delta_{sub}H^{\circ}_{m}(298{,}15\ \text{K})$ pour la molécule de méthylbenzène est égale à 51,3 kJ mol^{-1}.

En considérant qu'en phase gazeuse les molécules d'isomères *méta* et *para* sont à l'état de monomère, à une température donnée (ici 298,15 K), la différence Δ_1 entre la valeur de l'enthalpie de sublimation de ces molécules et celle du méthylbenzène représente la part énergétique d'interaction dipolaire et de liaisons hydrogène intermoléculaires. Dans le cas présent, cette part est respectivement égale à 29,4 et 35,8 kJ mol^{-1}. Afin de déterminer la contribution énergétique des interactions dipolaires Δ_2, nous avons, après l'avoir calculée de la même façon que pour le méthylbenzène en utilisant les données consignées dans les références 22 et 25, comparé l'enthalpie de sublimation du chlorobenzène (composé isoélectronique du méthylbenzène et des aminopyridines, liquide à 298,15 K, qui présente un moment dipolaire mais ne forme pas de liaisons hydrogène intermoléculaires) à celle du méthylbenzène. La valeur obtenue est faible et égale à 3,1 kJ mol^{-1}. La différence $\Delta_1 - \Delta_2$, soit 26,3 et 32,7 kJ mol^{-1} respectivement dans le cas des isomères *méta* et *para*, représente la part énergétique pouvant être attribuée aux liaisons hydrogènes intermoléculaires mises en évidence par des études cristallographiques (4–6). Étant donné qu'il ne se forme que deux ponts hydrogène par molécule d'isomère 3- ou 4-aminopyridine, l'enthalpie d'une liaison hydrogène peut être estimée à 15 kJ mol^{-1}. Cette valeur est compatible avec toutes celles qui ont été précédemment déterminées au laboratoire (26–31).

Remerciements

L'un de nous (M.E.S.E.) remercie la Junta Nacional de Investigação Científica e Tecnológica ainsi que la Fundação Calouste Gulbenkian pour l'aide matérielle lui ayant permis d'effectuer un stage postdoctoral au Centre de thermodynamique et de microcalorimétrie du CNRS à Marseille. Ce travail a été réalisé au cours de ce stage.

Bibliographie

1. S.Wagaw et S.L.Buchwald. J. Org. Chem. **61**, 7240 (1996).
2. J. Bickerton, G. Pilcher et G. Al-Takhin. J. Chem. Thermodyn. **16**, 373 (1984).
3. J.A. Draeger. J. Chem. Thermodyn. **16**, 1075 (1984).
4. M. Chao, E. Schempp et R.D. Rosenstein. Acta Crystallogr. Sect. B : Struct. Crystallogr. Cryst. Chem. **B31**, 2922 (1975).

© 1998 NRC Canada

5. M. Chao, E. Schempp et R.D. Rosenstein. Acta Crystallogr. Sect. B : Struct. Crystallogr. Cryst. Chem. **B31**, 2924 (1975).
6. M. Chao et E. Schempp. Acta Crystallogr. Sect. B : Struct. Crystallogr. Cryst. Chem. **B33**, 1557 (1977).
7. (*a*) R. Sabbah et L. El Watik. J. Therm. Anal. **36**, 2291 (1990); (*b*) R. Sabbah et I. Antipine. J. Therm. Anal. **32**, 1929 (1987).
8. R. Sabbah et I. Antipine. Bull. Soc. Chim. Fr. **3**, 392 (1987).
9. R. Sabbah, I. Antipine, M. Coten et L. Davy. Thermochim. Acta, **115**, 153 (1987).
10. W.D. Good et N.K. Smith. J. Chem. Eng. Data, **14**, 102 (1969).
11. J.D. Cox, H.A. Gundry et A.J. Head. Trans. Faraday Soc. **60**, 653 (1964).
12. Atomic weights of the elements. Pure Appl. Chem. **66**, 2423 (1994).
13. D.L. Lide (*Éditeur*). Handbook of chemistry and physics. 71^{e} éd. CRC Press, Boca Raton, Fla. 1990–1991.
14. J.R. Donnelly, L.A. Drewes, R.L. Johnson, W.D. Munslow, K.K. Knapp et G.W. Sovocool. Thermochim. Acta, **167**, 155 (1990).
15. J.D. Cox et G. Pilcher. Thermochemistry of organic and orgametallic compounds. Academic Press, London. 1970.
16. R. Sabbah et M. Coten. Thermochim. Acta, **49**, 307 (1981).
17. C. Minadakis et R. Sabbah. Thermochim. Acta, **55**, 147 (1982).
18. Report of the codata task group on key values of thermodynamics. J. Chem. Thermodyn. **10**, 903 (1978).
19. G.W. Wheland. Resonance in organic chemistry. Wiley, New-York. 1955. Chap. 3.
20. R. Sabbah, M. Gilbert et A. Julg. Thermochim. Acta, **10**, 345 (1974).
21. R. Sabbah et M. Laffitte. Thermochim. Acta, **25**, 376 (1978).
22. Y. Majer, V. Svoboda et H.V. Kehiaian. Enthalpies of vaporization of organic compounds: a critical review and data compilation. IUPAC Chem. Data Ser. N^{o} **32**. 1985.
23. D.W. Scott, G.B. Guthrie, J.F. Messerly, S.S. Todd, W.T. Berg, I.A. Hossenlopp et J.P. McCullough. J. Phys. Chem. **66**, 911 (1962).
24. T.L. Cottrell. The strengths of chemical bonds. 2^{e} éd. Butterworths, London. 1958.
25. D.R. Stull, E.F. Westrum, Jr. et G.C. Sinke. The chemical thermodynamics of organic compounds. Wiley, New York. 1969.
26. R. Sabbah et E.N.L.E. Buluku. Can. J. Chem. **69**, 481 (1991).
27. R. Sabbah et M. Gouali. Can. J. Chem. **74**, 500 (1996).
28. R. Sabbah et L. Perez. Can. J. Chem. **75**, 357 (1997).
29. R. Sabbah et M. Gouali. Aust. J. Chem. **47**, 1651 (1994).
30. (*a*) P. Knauth et R. Sabbah. Can. J. Chem. **68**, 731 (1990); (*b*) Bull Soc. Chim. Fr. **5**, 834 (1988).
31. S. Skoulika et R. Sabbah. Thermochim. Acta, **61**, 203 (1983).

© 1998 NRC Canada

A ^{1}H NMR study of cyclodextrin – hydrocarbon surfactant inclusion complexes in aqueous solutions

Lee D. Wilson and Ronald E. Verrall

Abstract: A ^{1}H NMR chemical shift (δ) study of a homologous series of hydrocarbon (hc) ($C_xH_{2x+1}CO_2Na$, x = 5, 7, 9, 11, 13) surfactants (S) has been carried out in water and in binary solvent (D_2O + cyclodextrin (CD)) systems at 22°C. Complementary ^{1}H NMR chemical shift (δ) data of the cyclodextrins in binary (D_2O + S) systems containing hc surfactants have also been obtained. Complex induced shift (CIS) values for selected host or guest protons were found to increase as the alkyl chain (C_x) length of the surfactant increased. The CIS values are found to depend on the following factors: (*i*) the magnitude of the binding constant (K_i, i = 1:1, 2:1), (*ii*) the chain length of the surfactant, (*iii*) the mole ratio of the host to guest species, (*iv*) the host–guest stoichiometry, and (*v*) the host–guest inclusion geometry. The CIS values of the CD–S systems have been analyzed using equilibrium models in which 1:1 complexes, 1:1 plus 2:1 complexes, and uncomplexed species are present. Differences in the binding affinity, stoichiometry, and inclusion geometry of the complexes formed between a given hc surfactant and the various cyclodextrins were observed.

Key words: cyclodextrin, surfactant, NMR, chemical shift, complex, binding constant.

Résumé : Opérant à 22°C, dans des solutions aqueuses et dans des systèmes de solvants binaires (D_2O + cyclodextrine (CD)), on a effectué une étude des déplacements chimiques (δ) en RMN du ^{1}H d'une série homologue d'agents de surface (S) hydrocarbonés (hc) ($C_xH_{2x+1}CO_2Na$, x = 5, 7, 9, 11, 13). On a aussi réalisé une étude complémentaire sur les déplacements chimiques (δ) en RMN du ^{1}H de cyclodextrines dans des systèmes binaires (D_2O + S) contenant des agents de surface hc. On a observé que les valeurs des déplacements induits par des complexes («CIS») de protons hôtes ou invités choisis augmentent avec une augmentation de la longueur de la chaîne alkyle (C_x) de l'agent de surface. On a observé que les valeurs de «CIS» dépendent des facteurs suivants: (*i*) la valeur de la constante d'association (K_i, i = 1:1, 2:1), (*ii*) la longueur de la chaîne de l'agent de surface, (*iii*) le rapport molaire des espèces hôtes et invitées, (*iv*) la stoechiométrie hôte–invité et (*v*) la géométrie d'inclusion hôte–invité. On a analysé les valeurs «CIS» des systèmes CD–S à l'aide de modèles en équilibre dans lesquels on retrouve des espèces qui ne sont pas complexées ainsi que des complexes 1:1 et 1:1 en présence de complexes 2:1. On a observé des différences d'affinités d'association, de stoechiométrie, et de géométrie d'inclusion des complexes formé entre un agent de surface hc donné et les diverses des cyclodextrines.

Mots clés : cyclodextrine, agent de surface, RMN, déplacement chimique, complexe, constante d'association.
[Traduit par la rédaction]

Introduction

Cyclodextrin (CD) hosts, because of their ability to form non-covalent complexes with inorganic and organic molecules in aqueous solution (1, 2), are an important class of oligosaccharide complexing agents that can be used in a wide range of technical applications. Alkyl derivatives of β-CD are particularly promising as pharmaceutical excipients because of their low toxicity and their greater solubility in water and organic solvents (3, 4). In comparison to β-CD, there have been relatively few studies carried out on the binding properties of the alkyl β-CD derivatives. Varying the structure of the host and guest species in a systematic manner is a useful approach to enable correlation of the chemical structure of the species with the binding affinity between the host and guest (5, 6). This information is a critical requirement if one is to obtain a better understanding of the key intermolecular interactions, leading to the stability of the complex.

In previous studies, we have used spectral displacement and apparent molar volume measurements to investigate the binding affinity (7–9) of β-CD and its alkyl derivatives with homologous series of both hc and fluorocarbon (fc) sodium alkyl carboxylate salts. NMR spectroscopy has also been shown (10–13) to be a useful technique to study these systems, since the ^{1}H NMR chemical shifts (δ) of both the interior protons of β-CD (14) and the guest nuclei (15) can be analyzed to provide information about the inclusion mode, stoichiometry, and binding affinity of the inclusion complexes. While there have been numerous reports of ^{1}H NMR studies (16–18) of CD – aromatic guest systems, primarily because of the anisotropic properties of the arene ring and the good spectral dispersion of the aromatic protons, there have been comparatively fewer studies employing aliphatic guest systems (19–22). There is a

Received August 25, 1997.

L.D. Wilson and R.E. Verrall.[1] Department of Chemistry, Thorvaldson Building, University of Saskatchewan, 110 Science Place, Saskatoon, SK S7N 5C9, Canada.

[1] Author to whom correspondence may be addressed. Telephone: (306) 966–4669. Fax: (306) 966–4730. E-mail: verrallr@sask.usask.ca

© 1998 NRC Canada

Scheme 1. Types of host–guest stoichiometry, where CD = cyclodextrin and S = surfactant.

$$\beta\text{-CD} + S \overset{K_{1:1}}{\rightleftharpoons} \beta\text{-CD–S}$$

$$\beta\text{-CD} + 2\,S \overset{K_{1:2}}{\rightleftharpoons} \beta\text{-CD–S}_2$$

$$2\,\beta\text{-CD} + S \overset{K_{2:1}}{\rightleftharpoons} \beta\text{-CD}_2\text{–S}$$

need to carry out a comprehensive and complementary NMR study of such aliphatic guest systems in order to further investigate their complexation behavior with cyclodextrins. To this end, and to complement our previous studies of CD – sodium alkyl carboxylate systems, we have used the NMR technique to determine the binding affinities of various complexes formed between these host–guest systems.

We report the analysis of NMR chemical shift measurements of ^{1}H nuclei of hc surfactants and cyclodextrin compounds determined in both D_2O and in ternary (D_2O + CD + S) aqueous solutions in order to establish the self-consistency between the binding constants derived from the host and guest NMR data. The study of a homologous series of surfactants of increasing alkyl chain length (C_x) provides an opportunity to analyze the degree of alkyl chain coiling that occurs in the complexes as the number of carbon atoms in the chain increases. On the other hand, a study of β-CD and its alkyl derivatives provides an opportunity to investigate the effect of structural changes in the annulus region of the CD on the overall binding affinity of the complexes that are formed with a common guest surfactant. The alkyl β-CD derivatives used include 6-*O*-2 hydroxypropyl (HP-β-CD), 2,6-di-*O*-methyl (DM-β-CD), and 2, 3, 6-tri-*O*-methyl (TM-β-CD). Finally, the use of modeling techniques to account for the various types of CD–S stoichiometry (cf. Scheme 1), such as 1:1, 2:1, etc., can be quantitatively assessed.

Experimental

Instrumentation

NMR measurements were carried out using a Bruker AM-300 300 MHz spectrometer operating at 295 ± 0.1 K, with temperature regulated by means of a Haake temperature control system. Proton chemical shifts of the guest or host were referenced with respect to the protons of an external solution of 5×10^{-3} M DSS (4,4-dimethyl 4-silapentane sodium sulphonate) in D_2O (Aldrich, 99.9%) taken as 0 ppm. The precision in the chemical shift measurements is estimated to be $\pm 1 \times 10^{-3}$ ppm or better. In the case of the ROESY experiments (18), the standard pulse program provided by Bruker was utilized with a 250 ms spinlock time and a 600 μs relaxation delay.

Materials

DM-β-CD (Cyclolab, lot no. CY-2004.0, relative molar mass (M) = 1331 g mol^{-1}, degree of substitution (DS) = 14, purity >70% as 2,6-DM-β-CD regioisomer), HP-β-CD (Cyclolab, lot no. CY-2005.2, M = 1384 g mol^{-1}, DS = 4.6, purity ~95%), TM-β-CD (Am. Maize, research sample, M = 1429.6 g mol^{-1}, DS = 21, purity ~95%), β-CD (Aldrich, >99%), and α-CD (Aldrich, >99%) were used as received. The water content of the cyclodextrin compounds was determined using a Karl Fischer titration procedure, and it was taken into account in the calculation of concentration. To simplify the spectrum, β-CD was twice lyophilized from D_2O to effect an exchange of the hydroxyl protons with deuterium. The hc surfactants ($C_xH_{2x+1}CO_2Na$, x = 5, 7, 9, 11, 13) (Sigma, 99%) were purified as outlined previously (8). The p(H + D) was adjusted to 10.5, with the use of NaOD to minimize protonation of the carboxylate anion ($pK_b \approx 9$) and dissociation of the β-CD hydroxyl protons ($pK_a \approx 12$) (1).

In the study of the ^{1}H nuclei of β-CD, the concentration of the cyclodextrin (C_{CD}) was fixed, and the concentration of surfactant (C_S) was varied, where $C_S \leq$ CMC. In the case of the surfactant nuclei, C_S was fixed such that $C_S \leq$ CMC and C_{CD} was varied. All stock solutions were freshly prepared by volume and serially diluted.

Models and calculations

The chemical shift contributions of complexes having different stoichiometries were weighted according to their mole fraction content in solution, as shown in the following expressions:

$$[1] \quad \delta_{obs} = X_f\,\delta_f + X_{1:1}\delta_{1:1}$$

$$[2] \quad \delta_{obs} = X_f\,\delta_f + X_{1:1}\delta_{1:1} + X_{2:1}\delta_{2:1}$$

where X_f, $X_{1:1}$, and $X_{2:1}$ are the mole fractions of the unbound component (surfactant or CD), 1:1 complex, and 2:1 complex, respectively, and δ_f, $\delta_{1:1}$, and $\delta_{2:1}$ are the chemical shifts of the unbound species, 1:1 complex, and 2:1 complex, respectively. δ_{obs} is the observed chemical shift signal and it is a weighted average, comprised of bound and unbound species, due to fast exchange on the NMR time scale. Equations [1] and [2] can be expressed in terms of either host or guest ^{1}H NMR data. The equilibrium binding constants (K_i) are related to the mole fractions (X_i) of the unbound and bound species through the equilibrium relations describing the different complexes. The simulation of experimental NMR chemical shifts for solutions containing host and guest species was performed by using a nonlinear least-squares (NLLS) fitting program employing a Marquardt–Levenberg algorithm. K_i and δ_i were used as adjustable parameters whereas δ_f was obtained from the δ data for the host or guest in D_2O in the absence of a third component. In eq. [2], the Newton–Raphson method was employed to obtain the concentration of unbound species (23). The "best fit" to the experimental data was obtained by minimizing the sums of the squares of the residuals (SSR), $SSR = \sum (\delta_{obs,i} - \delta_{calc,i})^2$, where δ_{calc} and δ_{obs} are the calculated (according to eqs. [1] and [2]) and experimental values, respectively. The chemical shift data for the guest and host are presented graphically as a difference (Δδ), defined by eqs. [3] and [4], respectively.

$$[3] \quad \Delta\delta = \delta_{obs} - \delta_f$$

$$[4] \quad \Delta\delta = \delta_f - \delta_{obs}$$

where δ_{obs} and δ_f were previously defined. Positive Δδ values

© 1998 NRC Canada

Scheme 2. Molecular structure and numbering scheme for the ^{1}H nuclei of β-cyclodextrin (β-CD; where R = H) and for alkyl-substituted β-CD (R-β-CD) host systems.

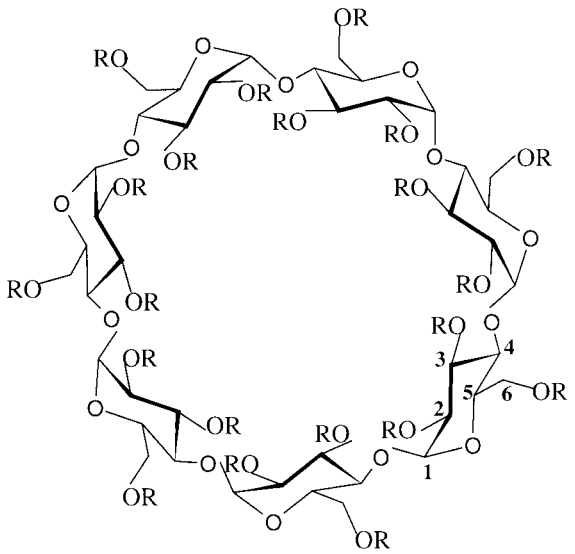

R = -H, -CH_3, -$CH_2CH(OH)CH_3$

for the surfactant nuclei refer to downfield (away from DSS) shifts, due to the lower resonance frequency of δ_f relative to δ_{obs}. Positive $\Delta\delta$ values for the host nuclei refer to upfield (towards DSS) shifts, due to the higher resonance frequency of δ_f relative to δ_{obs}. Chemical shift differences ($\Delta\delta$) are plotted as a function of mole ratio (R), where $R = C_S/C_{CD}$ or C_{CD}/C_S, for host and guest NMR data, respectively.

Results and discussion

Schemes 2 and 3 depict the molecular structure and numbering schemes utilized to identify the various host and guest ^{1}H nuclei for the compounds investigated in this study. Estimates of the binding constants (K_i) obtained from the NLLS analysis of the host (H(3) and H(5)) and guest (CH_3) ^{1}H nuclei for β-CD–S complexes are listed in Table 1. In most instances, the ^{1}H NMR data for C(1)H_2 and C(2)H_2 of the guest were not used to calculate K_i, because of the small magnitude of the complex induced shift (CIS) values. The collection of methylene ($(CH_2)_n$) protons (cf. Scheme 3) exhibits changes in chemical shift similar to that of the CH_3 group, however, the individual CH_2 groups were not well resolved and, therefore, they were not used in the calculation of K_i. The apolar cavity protons (H(3) and H(5)) of β-CD and those of the terminal CH_3 group of the surfactant displayed the largest CIS values, suggesting that the complex formed is one of inclusion and that the interactions occur primarily between the lipophilic regions of the host and guest, as expected for binding processes enhanced by hydrophobic effects (24, 25). In general, the CIS values for the guest nuclei are approximately 30–50% smaller than those for the host. Notwithstanding the differences in sensitivity of the host and guest nuclei to medium effects, the values of K_i estimated from these different data sets are consistent, as seen in Table 1. Generally, the magnitude of K_i increases as C_x increases, and the values are in reasonable agreement with those

Scheme 3. Molecular structure and numbering scheme for the guest protons of the surfactants examined in this work.

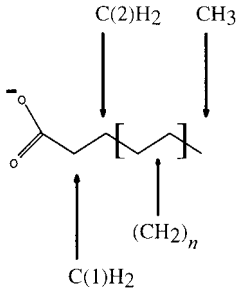

previously reported (7). β-CD – sodium tetradecanoate (ST) and β-CD – sodium dodecanoate (SDodec) formed both 1:1 and 2:1 complexes, whereas all of the other β-CD–S systems formed 1:1 complexes at the concentrations investigated in this study. Previous reports (26, 27) have also indicated that anionic and cationic surfactants of alkyl chain length comparable to SDodec and ST form 2:1 complexes with β-CD, and the values of $K_{1:1}$ exceed $K_{2:1}$ by one to two orders of magnitude, in agreement with the results given in Table 1.

Table 2 lists the values of K_i for complexes formed between different cyclodextrin compounds and the hc surfactants. They were obtained from the NLLS analysis of ^{1}H NMR data of the guest only (cf. Scheme 3). Spectral overlap of the H(3) and H(5) proton resonance spectra of the modified CDs with those of other ^{1}H host nuclei precluded their quantitative analysis to obtain estimates of K_i of the complexes. The magnitude of K_i increases as C_x increases for α-CD and the modified CDs in a manner similar to that observed for β-CD (Table 1). Differences in binding affinities are observed among the modified CDs, depending on the degree of alkyl substitution of the hydroxyl groups in the annulus of the CD. As well, the smaller cavity diameter of α-CD (4.5 Å), compared to β-CD (6.3 Å) (28), is expected to bind the hc surfactants more tightly due to the comparable van der Waals diameter of the methyl group (4 Å) (29) of the surfactant. Indeed, the magnitude of $K_{1:1}$ is greatest for α-CD when $x = 5$, however, β-CD binds more strongly for surfactants with longer chain length because of its increased cavity size. α-CD includes surfactants such that they adopt an all-*trans* conformation for the reason noted above. However, the larger diameter of the β-CD cavity enables the surfactant chain to coil by adopting gauche conformations. Park and Song (30) estimate that approximately eight methylene groups can be accommodated within β-CD if allowance is made for chain coiling. Correspondingly fewer groups can be included if the alkyl chain assumes an all-*trans* conformation (cf. Fig. 3, ref. 25), as is the case of inclusion within α-CD. Thus, the onset of the formation of 2:1 complexes for α-CD ($x = 9$) and β-CD ($x = 11$) is consistent with these facts. The greater binding affinity between β-CD and *n*-alkyl chain surfactants is consistent with the transfer of more alkyl groups from water to the apolar cavity and implicates the importance of the hydrophobic effect (24).

Alkyl substituted β-CD (R-β-CD) derivatives show similar features, however, there are specific differences in binding affinity that can be attributed to the nature of the substituted alkyl groups in the annular regions of R-β-CD. In contrast to α- and

© 1998 NRC Canada

Table 1. Binding constants (K_i, i = 1:1, 2:1)[a] obtained from ^{1}H NMR chemical shift measurements of the guest (CH_3) and host (H(3) and H(5)) protons of various β-CD–surfactant complexes at 295 K.

Surfactant	H(3)	H(5)	CH_3	Lit. (ref. 7)[b]
$C_6H_{11}O_2Na$ Shex	1.0×10^2 (1.0×10^1)[b,d]	1.3×10^2 (2.3×10^1)[b,d]	6.0×10^1 (1.2×10^1)[b,d]	$5.5 \pm 0.7 \times 10^1$
$C_8H_{16}O_2Na$ SO	7.7×10^2 (3.7×10^1)[b]	6.5×10^2 (6.6×10^1)[b]	7.0×10^2 (2.9×10^2)[b]	$6.6 \pm 0.8 \times 10^2$
$C_{10}H_{19}O_2Na$ Sdec	8.0×10^3 (1.5×10^3)[b]	5.2×10^3 (7.0×10^2)[b]	8.0×10^3 (1.7×10^1)[b]	$5.1 \pm 0.6 \times 10^3$
$C_{12}H_{23}O_2Na$ Sdodec	5.0×10^4 (2.5×10^4)[b]	5.0×10^4 (2.5×10^4)[b]	3.3×10^4 (1.7×10^4)[b]	$1.6 \pm 0.2 \times 10^4$
	4.0×10^2 (2.0×10^2)[c]	4.0×10^2 (2.0×10^2)[c]	4.3×10^2 (2.2×10^2)[c]	
$C_{14}H_{27}O_2Na$ ST	1.0×10^5 (5.0×10^4)[b]	1.1×10^5 (5.3×10^4)[b]	6.3×10^4 (3.2×10^4)[b]	$4.8 \pm 0.6 \times 10^4$
	1.0×10^3 (0.5×10^3)[c]	2.0×10^3 (1.0×10^3)[c]	1.6×10^3 (8.0×10^2)[c]	

[a] Other resolvable resonance lines such as C(1)H_2 and C(2)H_2 were not utilized to calculate K_i due to the small magnitude of the CIS values.
[b] $K_{1:1}$ (M^{-1}).
[c] $K_{2:1}$ (M^{-2}).
[d] Standard error for K_i is given in parentheses.

Table 2. Binding constants (K_i, i = 1:1, 2:1) obtained from ^{1}H NMR chemical shift measurements of the guest protons of various CD–surfactant complexes at 295 K.

Surfactant	α-CD	β-CD	DM-β-CD	TM-β-CD	HP-β-CD
$C_6H_{11}O_2Na$	3.3×10^2 (1.3×10^1)[a,b]	6.0×10^1 (1.2×10^1)[a,b]	1.3×10^2 (3.0×10^1)[a,b]	2.6×10^1 (1.1×10^1)[a,b]	2.0×10^1 (4.0×10^0)[a,b]
	211 ± 12[d]	67.6 ± 1.8[d]; 34[f]			
$C_8H_{16}O_2Na$	4.7×10^2 (7.1×10^1)[a]	7.0×10^2 (2.9×10^2)[a]	3.4×10^2 (3.1×10^1)[a]	1.0×10^2 (1.8×10^2)[a]	7.64×10^2 (1.6×10^1)[a]
	622 ± 26[d]; 2100 ± 12[e]	683 ± 8[d]; 420[e]; 370[f]			
$C_{10}H_{19}O_2Na$	5.6×10^3 (2.8×10^3)[a]	8.0×10^3 (1.7×10^1)[a]	4.8×10^3 (3.8×10^2)[a]	4.6×10^2 (5.7×10^1)[a]	2.0×10^3 (2.6×10^2)[a]
	6.5×10^2 (3.3×10^2)[c]	7500 ± 900[d]; 740[f]			
	1.8×10^3 [d]				
$C_{12}H_{23}O_2Na$	2.1×10^4 (1.1×10^4)[a]	3.3×10^4 (1.7×10^4)[a]	1.0×10^4 (4.5×10^3)[a]	4.3×10^3 (1.3×10^3)[a]	3.8×10^3 (1.1×10^3)[a]
	1.2×10^3 (6.0×10^2)[c]	4.3×10^2 (2.2×10^2)[c]			
		1600 [f]			
$C_{14}H_{27}O_2Na$	4.0×10^4 (2.0×10^4)[a]	6.3×10^4 (3.2×10^4)[a]	5.0×10^4 (2.5×10^4)[a]	2.3×10^4 (3.8×10^3)[a]	1.6×10^4 (8.2×10^3)[a]
	6.2×10^3 (3.1×10^3)[c]	1.6×10^3 (8.0×10^2)[c]			

[a] $K_{1:1}$ (M^{-1}).
[b] Standard error for K_i is given in parentheses.
[c] $K_{2:1}$ (M^{-2}).
[d] Values for $K_{1:1}$(M^{-1}) from ref. 39.
[e] Values for $K_{1:1}$(M^{-1}) from ref. 40.
[f] Values for $K_{1:1}$(M^{-1}) from ref. 41.

β-CD, the R-β-CD derivatives form 1:1 complexes under the same conditions, due to their extended cavity length created by the alkyl groups in the annular regions. In previous work (9), differences in binding affinity between β-CD and R-β-CD were attributed to steric effects created by the close proximity of the carboxylate head group of the surfactant and the annular hydroxyl groups. The relative binding affinity of hc surfactants with the various CDs follows the order: β-CD > α-CD > DM-β-CD > TM-β-CD > HP-β-CD. The relative ordering of the R-β-CDs are consistent with steric effects imposed by the increasing degree of substitution (DS) of methyl groups from DM- to TM-β-CD. While HP-β-CD has a lower DS than DM-β-CD, the hydroxypropyl group is much larger than a methyl group. As well, the greater hydrophilicity of the hydroxypropyl group may create an additional steric effect due to hydration, and this effect would be absent in the case of the methyl substituted CDs. Thus, as the size of the alkyl group and the DS of cyclodextrin increase, greater steric hindrance impedes complex formation between the host and guest.

Figure 1 shows a plot of Δδ vs. mole ratio (R) for the β-CD–sodium octanoate (SO) system. This figure represents typical CIS values for the host and guest nuclei of a weakly bound β-CD–S complex. The CIS values for the host and guest increase as R increases and follow the order: Δδ H(5) > Δδ H(3) > Δδ CH_3. The CIS values of the host protons increase nonlinearly and become approximately constant at $R > 3$, which indicates that this is a weakly bound 1:1 CD–S complex, since an excess of either host or guest must be present in order to reach a saturation level of bound species ($X_{1:1}$) (13). The broken lines through the data points represent the best-fit line according to eq. [1].

Figure 2 is a plot of Δδ vs. mole ratio (R) for the β-CD – sodium dodecanoate (SDodec) system. This figure represents typical CIS values for the host and guest nuclei of a strongly bound β-CD–S complex. There is a marked leveling-off of the CIS values at $R \approx 1$, which is typical of complexes possessing large values of K_i (13). The CIS values for the nuclei of the host and guest increase linearly with increasing R and follow

© 1998 NRC Canada

Fig. 1. Δδ vs. mole ratio (R), where $R = C_S/C_{\beta\text{-CD}}$ for hosts (H(3) and H(5)) and $R = C_{\beta\text{-CD}}/C_S$ for guest (CH_3); ^{1}H NMR data of the β-CD–$C_7H_{15}CO_2Na$ system at $T = 295$ K.

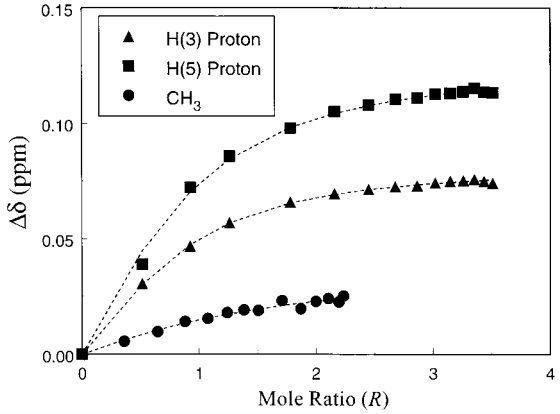

Fig. 2. Δδ vs. mole ratio (R), where $R = C_S/C_{\beta\text{-CD}}$ for hosts (H(3) and H(5)) and $R = C_{\beta\text{-CD}}/C_S$ for guest (CH_3); ^{1}H NMR data of the β-CD–$C_{11}H_{23}CO_2Na$ system at $T = 295$ K.

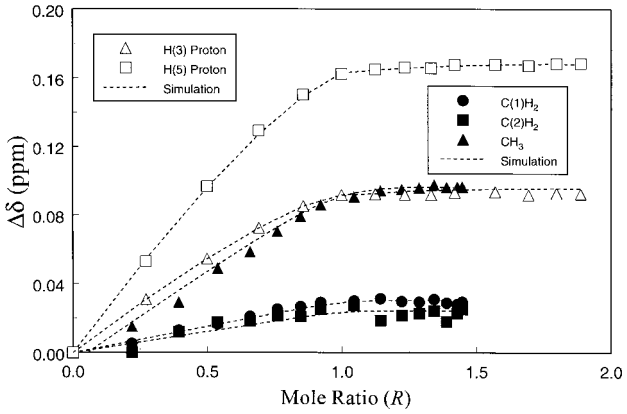

Fig. 3. Δδ vs. mole ratio (R), where $R = C_{\alpha\text{-CD}}/C_S$ for guests ($C(1)H_2$, $C(2)H_2$, and CH_3); ^{1}H NMR data of the α-CD–$C_{11}H_{23}CO_2Na$ system at $T = 295$ K.

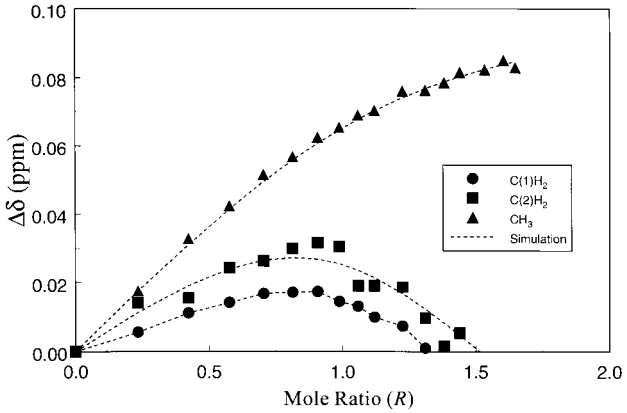

Fig. 4. Δδ vs. mole ratio (R), where $R = C_{DM\text{-}\beta\text{-CD}}/C_S$ for guests ($C(1)H_2$, $C(2)H_2$, and CH_3); ^{1}H NMR data of the DM-β-CD–$C_{11}H_{23}CO_2Na$ system at $T = 295$ K.

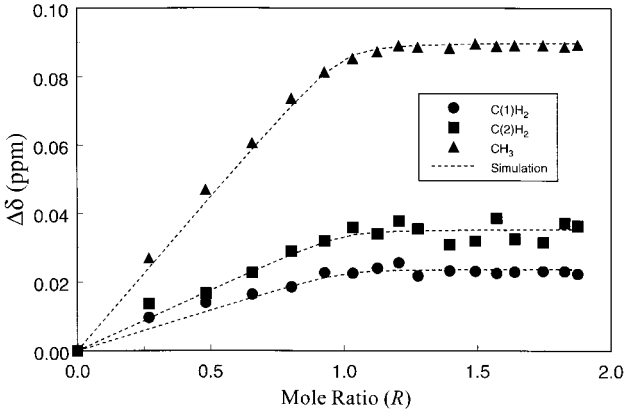

the order: Δδ H(5) > Δδ H(3) > Δδ CH_3 > Δδ $C(1)H_2$ ≈ Δδ $C(2)H_2$. The broken lines through the data points represent the best fit according to eq. [2]. Equation [1] provides a satisfactory fit up to $R = 1$; however, a poorer fit is observed for $R > 1$, suggesting that the stoichiometry is not simply 1:1 but a combination of 1:1 and 2:1 complexes. In general, $K_{1:1} >> K_{2:1}$ and, as is the case of the β-CD–SDodec system, the formation of 2:1 CD–S complexes is favored when $C_{CD} > C_S$, i.e., $R > 1$. This is in agreement with our previous results (8).

Figures 3–6 illustrate plots of Δδ vs. mole ratio (R) for the guest nuclei of various CD–SDodec complexes. Comparison of these diagrams with Fig. 2 shows how variation of the alkyl substitution of the hydroxyl groups of β-CD affects the binding affinity with a common guest. Figure 3 shows the α-CD–SDodec system, and the CIS values for $C(1)H_2$ and $C(2)H_2$ of the guest display a positive increase up to $R \approx 1$ and a sharp decrease when $R > 1$. The deshielding of these nuclei beyond $R \approx 1$ can be attributed to type (*c*) interactions, described below, due to the formation of a 2:1 "channel-type" complex (27), since the carboxylate head group becomes desolvated as it is drawn closer toward the annular hydroxyl region. Indirect support for changes in the solvation of the carboxylate head group has also been concluded from an emf study (31) of the β-CD–SDec system. It was rationalized as being due to an increase in the degree of sodium counterion binding to the surfactant head group when the head group is complexed. The importance of solvation of the carboxylate head group has also been alluded to in an earlier NMR study (32). However, a recent attempt to quantify the solvation component of polar functional groups through the Gibbs energy change of complex formation revealed that the relative contributions of solute–solute vs. solute–solvent interactions are difficult to model in host–guest binding phenomena (5, 6). The lower rate of increase of Δδ CH_3 vs. R beyond $R > 1$ can also be attributed to the role of type (*b*) interactions in the binding process. The magnitude of the CIS values for the guest nuclei follow the order: Δδ CH_3 > Δδ $C(2)H_2$ > Δδ $C(1)H_2$. The broken lines through the data points represent the best fit according to eq. [2]. Application of eq. [1] did not provide a suitable fit to the experimental data, which further corroborates that the stoichiometry is not simply 1:1 but a combination of 1:1 and 2:1 complexes. Castronuovo et al. (33) have reported that the formation of 2:1 α-CD–S complexes are unlikely for alkyl carboxylate salts having C_x, $x = 2$–11 due to the solvation

© 1998 NRC Canada

Fig. 5. Δδ vs. mole ratio (R), where $R = C_{TM\text{-}\beta\text{-}CD}/C_S$ for guests ($C(1)H_2$, $C(2)H_2$, and CH_3); ^1H NMR data of the TM-β-CD–$C_{11}H_{23}CO_2Na$ system at $T = 295$ K.

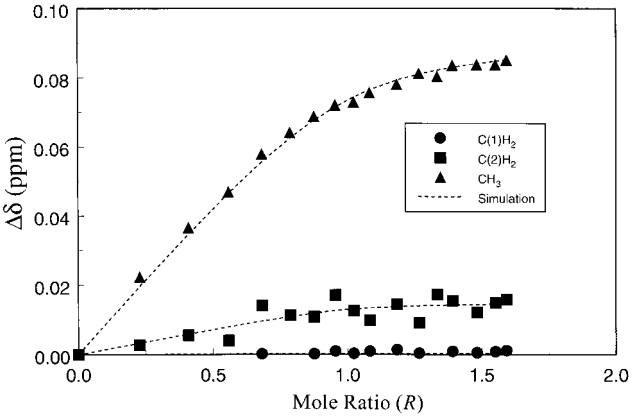

Fig. 6. Δδ vs. mole ratio (R), where $R = C_{HP\text{-}\beta\text{-}CD}/C_S$ for guests ($C(1)H_2$, $C(2)H_2$, and CH_3); ^1H NMR data of the HP-β-CD–$C_{11}H_{23}CO_2Na$ system at $T = 295$ K.

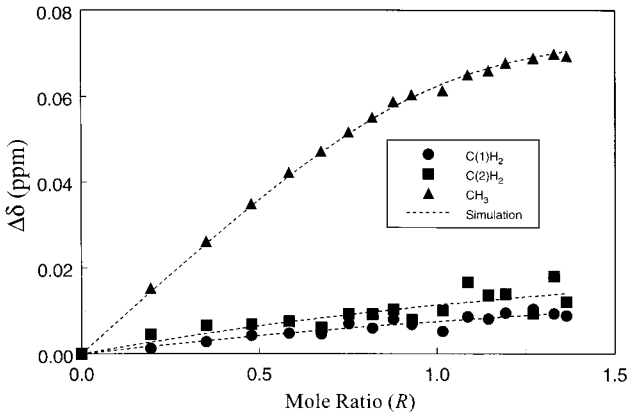

requirements of the carboxylate group. However, our results clearly show that 2:1 α-CD–S complexes are favored for systems with C_x, $x \geq 9$ and that such a stoichiometry optimizes apolar–apolar and minimizes apolar–polar interactions (24). This energy minimization is partly driven by the host system, α-CD, since its smaller cavity diameter and ability to adopt an "induced-fit" (34) favors an all-*trans* conformation of the alkyl chain, thereby requiring a second CD to include the surfactants when C_x, $x > 8$.

Figures 4 and 5 illustrate plots of Δδ vs. mole ratio (R) for DM- and TM-β-CD with SDodec, respectively. These figures show the effect of increasing the number of methyl groups in the host macrocycle on the binding affinity with SDodec. A comparison of these figures reveals that the DM-β-CD–SDodec system has larger CIS values for the guest protons and sharper breaks at the $R = 1$ mole ratio. As well, the CIS values for these protons level off beyond $R = 1$, whereas the CIS values of the $C(2)H_2$ and CH_3 groups of the guest in the TM-β-CD–SDodec system (Fig. 5) increase slightly beyond $R = 1$. These results are consistent with the formation of 1:1 complexes and the greater binding affinity of DM-β-CD, relative to TM-β-CD, with SDodec. The weaker binding affinity of TM-β-CD is probably due to greater steric hindrance in its annular region because of the increased degree of substitution. The broken lines in these figures represent the best fit of the experimental data according to eq. [1].

In previous work (8), it was determined that methyl derivatives of β-CD formed 1:2 CD–S complexes (cf. Scheme 1) with longer chain length surfactant systems. It is possible to fit the experimental data using a model that accounts for 1:2 complexes, using an expression analogous to eq. [2]. However, the molecular environment of a CH_3 group in a 1:1 or a 1:2 complex is anticipated to be similar ($\delta_{1:1} \approx \delta_{1:2}$), and it is difficult to justify the use of a four-parameter equation when eq. [1] seems to provide a suitable fit. In the case of the β-CD–SDodec system, a reasonable fit to eq. [1] was obtained up to $R = 1$, whereas eq. [2] provided a more suitable fit over the entire range of experimental data. For the β-CD–SDodec system ($K_{1:1} >> K_{2:1}$), 1:1 complexes are favored when $R \leq 1$ and 2:1 complexes are favored when $R > 1$, which is consistent with the excess of host at the latter condition. The above results indicate that it is possible to overlook additional complexation equilibria when obtaining experimental data in a limited concentration range, particularly when several complexes, having stability constants of vastly different magnitudes, are formed. It is also important to recognize that various experimental techniques are more or less sensitive to the bulk property being measured. The techniques can be divided into two categories: (*i*) those that measure, directly or indirectly, the concentration of bound or unbound species, and (*ii*) those that measure a physical property that is proportional to the concentration of bound or unbound species. The distinction between these two categories is the reason that there is a lack of agreement amongst K_i values for a given system, and this issue has been discussed elsewhere (7).

Figure 6 is a plot of Δδ vs. mole ratio (R) for HP-β-CD with SDodec. The magnitude of Δδ increases as R increases, and the CIS values at $R = 1$ follow the order: $\Delta\delta\ CH_3 > \Delta\delta\ C(2)H_2 > \Delta\delta\ C(1)H_2$. Figures 5 and 6 shows similar features; however, the CIS values for the host protons in Fig. 6 display a moderate increase beyond $R = 1$ and their magnitudes do not exceed those in Fig. 5, indicating that HP-β-CD has a lower binding affinity than TM-β-CD with SDodec. This can be attributed to steric effects, as mentioned in the discussion of results in Table 2. The broken lines through the experimental data represent the best-fit curves according to eq. [1].

Table 3 lists the CIS values of the guest nuclei at a 1:1 CD–S mole ratio ($R = 1$). The extensive overlap of the individual $(CH_2)_n$ protons, as shown by the appearance of a broad singlet in the NMR resonance, precluded a quantitative investigation of their component CIS values. An analysis of the Δδ data for the $C(1)H_2$, $C(2)H_2$, and CH_3 protons can provide insight into the geometry of the CD–S complex, since $C(1)H_2$ and $C(2)H_2$ are adjacent to the hydrophilic carboxylate group whereas the CH_3 group is located in a lipophilic environment. However, a thorough quantitative analysis of the CIS values is complicated by numerous antagonistic shielding and deshielding effects (35). For example: (*a*) H-bonding between the CD hydroxyl groups and the carboxylate head group is expected to reduce the intramolecular shielding on the $C(1)H_2$ and $C(2)H_2$ protons and result in positive CIS values; (*b*) the goodness of fit between the alkyl chain of the surfactant and host systems possessing narrower cavities, such as α-CD and TM-β-CD, may induce an all-*trans* conformation of the alkyl

© 1998 NRC Canada

Table 3. ^{1}H NMR complex induced shift (CIS) values[a] of various guest nuclei[b] at the 1:1 mole ratio for various CD–surfactant complexes at 295 K.

Surfactant	α-CD	β-CD	DM-β-CD	TM-β-CD	HP-β-CD
$C_6H_{11}O_2Na$	0.033; 0.067; 0.045	0.002; 0.004; 0.005	–0.003; ≈0; 0.001	–0.001; –0.001; 0.002	–0.020; 0.002; 0.028
$C_8H_{16}O_2Na$	0.024; 0.049; 0.053	0.008; 0.019; 0.015	–0.007; –0.003; 0.021	–0.005; 0.005; 0.022	–0.001; 0.009; 0.040
$C_{10}H_{19}O_2Na$	0.002; 0.026; 0.054	0.007; 0.003; 0.058	0.006; 0.004; 0.055	–0.015; –0.002; 0.059	–0.003; ≈0; 0.055
$C_{12}H_{23}O_2Na$	–0.052; –0.035; 0.083	0.028; 0.023; 0.089	0.022; 0.032; 0.085	≈0; 0.013; 0.073	0.007; 0.011; 0.062
$C_{14}H_{27}O_2Na$	0.016; 0.023; 0.057	0.036; 0.044; 0.105	0.025; 0.027; 0.079	–0.003; 0.014; 0.064	0.016; 0.016; 0.060

[a] CIS value (ppm) = $\delta_{obs} - \delta_f$, where all δ values are measured relative to the external standard DSS.
[b] First value corresponds to C(1)H_2; second value corresponds to C(2)H_2; third value corresponds to CH_3.

chain. This maximizes the distance between adjacent CH_2 groups and decreases the intramolecular shielding within the alkyl chain, resulting in positive CIS values; and (*c*) the apolar environment of the CD interior and (or) alkyl substituents in the annular hydroxyl region results in shielding of the alkyl chain and contributes to negative CIS values. In Table 3, the CIS values of the CH_3 group protons increase as C_x increases, indicating the prominence of type (*b*) effects. However, for x = 13, this parameter shows a small decrease relative to x = 11 for α-CD and TM-β-CD. This may be due to the methyl group extending beyond the CD cavity and into the interfacial region, resulting in a decrease of type (*b*) effects (36). The prominence of type (*b*) interactions can be seen in a comparison of the CIS values for C(1)H_2 and C(2)H_2 groups for SHex, SO, and SDec, respectively. For the α-CD system, the CIS values decrease as C_x increases, whereas for β-CD, minimal changes in this parameter are observed. The decrease observed for α-CD–S systems can be attributed to the extension of the carboxylate head group further into the bulk phase as C_x increases thereby decreasing the magnitude of type (*b*) effects. In contrast to α-CD, the larger cavity diameter of β-CD does not induce an all-*trans* conformation of the alkyl chain of the surfactant, as seen by the similar CIS values for the C(1)H_2 and C(2)H_2 groups. Hence, as C_x increases for the β-CD–S systems, smaller CIS values are expected for C(1)H_2 and C(2)H_2 protons, due to smaller perturbations to the conformation of the surfactant alkyl chain (36) upon inclusion into the host cavity. These results are also consistent with previous conclusions that only weak interactions occur between an *n*-alkyl carboxylate anion and the annular hydroxyl groups of CD (7). Similar values of Δδ at R = 1 were found previously for the C(1)H_2, C(2)H_2, and CH_3 protons of a series of *n*-alkyl amine and *n*-alkyl carboxylic acid guests (22). As well, values of the change in heat capacity, ΔC_p°, for complexes formed between β-CD and a homologous series of *n*-alkylammonium and *n*-carboxylate ions were found to be similar. Thus, there is substantive evidence that suggests there is minimal solvent reorganization of highly hydrated groups of a guest species and of the hydroxyl groups of the cyclodextrin host upon complex formation (37). A comparison of CIS values for β-CD–S and R-β-CD–S systems indicates that alkyl substitution effects are not readily discernible because of the similarity in the magnitudes of the CIS values for the C(1)H_2 and C(2)H_2 groups of the guest. However, some evidence can be derived regarding the location of the CH_3 group in the host. These results indicate the primary importance of apolar–apolar interactions between the alkyl chain of the surfactant and the CD interior and the secondary importance of interactions between the head group of the surfactant and hydroxyl groups in the CD annular regions.

The C(1)H_2 and C(2)H_2 groups in the 2:1 α-CD–S ($x \geq 9$) and 2:1 β-CD–S ($x \geq 11$) complexes reflect type (*c*) effects, as seen by the decrease in the CIS values beyond R = 1. The effect is amplified for surfactants with longer chain length as the CIS values exhibit a decrease at R = 2 (not shown). The absence of 2:1 complexes for the R-β-CD hosts is consistent with their increased cavity depth (2). These few results illustrate that it is difficult to ascribe changes in CIS values unequivocally to one specific effect, since there are marked differences in stoichiometry, inclusion geometry, and binding affinity among these host–guest systems.

The CIS values for the ^{1}H nuclei of β-CD have not been listed, however, the trends for Δδ H(5) and Δδ H(3) of the host parallel those for Δδ CH_3 of the guest. The positive CIS values for the host nuclei reflect an increase in shielding during complex formation as C_x increases. This is a result of expulsion of water from the CD interior and its replacement by an apolar alkyl chain. The magnitudes of Δδ for H(5) and H(3) range from two to ten times that for a typical CH_3 group and may be attributed to the anisotropic properties of the CD cavity (14). At the 1:1 mole ratio, Δδ H(5) > Δδ H(3) for all β-CD–S systems, since the H(5) nuclei is located at the narrower end of the torus and experiences closer intermolecular contacts with the alkyl chain of the surfactant. The concentration dependence of the CIS values for H(3) and H(5) protons provide support for the existence of 2:1 complexes and corroborate the guest data for the β-CD–ST and β-CD–SDodec complexes. The inclusion mode for the 2:1 complexes appears to be a capping arrangement of a second β-CD onto the protruding apolar alkyl chain of the guest in the 1:1 complex. It is difficult to unequivocally ascertain whether it is the primary or the secondary hydroxyl end of the second CD that preferentially associates with the surfactant because of the similar trends in the CIS values for H(3) and H(5) protons of the host beyond the R = 1 mole ratio. This is somewhat surprising, since the primary hydroxyl end of β-CD is reported to be more lipophilic than the secondary hydroxyl end (28). The former is more dipolar in nature due to the less extensive participation of the hydroxyl groups in intramolecular H-bonding.

Figure 7 is a ROESY spectrum of the β-CD–SDodec system. It is difficult to ascertain for this complex whether the carboxylate head group is located at the wide or narrow end of the torus, due to the small CIS values for the C(1)H_2 and C(2)H_2 protons. As well, the absence of cross peaks for intermolecular interactions between these groups and other nuclei of β-CD in the ROESY spectrum may be due to weak interactions with the highly hydrated head group and (or) to inclusion of the surfactant within the CD interior in a random fashion. These reasons are consistent with the similar CIS values for

© 1998 NRC Canada

Fig. 7. ROESY spectrum for β-CD–$C_{11}H_{23}CO_2Na$ system at 293 K with spinlock time of 250 ms and a relaxation delay of 600 μs.

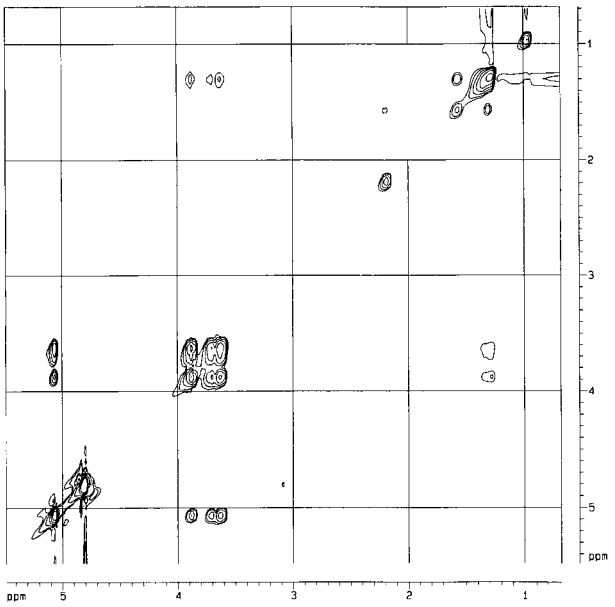

the C(1)H_2 and C(2)H_2 protons of the alkyl carboxylates in complexes with β-CD and R-β-CD hosts systems**.** Guest molecules possessing charged groups, such as the *p*-nitrophenolate anion, locate the charged group at the wider end annular region of β-CD(16). Tee et al. (38) have also proposed that the ester functional group locates at the same end, based on kinetic studies. The most intense cross peaks observed in the ROESY spectrum are for the protons of the methylene ($(CH_2)_n$) groups located toward the center of the alkyl chain of the guest and for the H(3) and H(5) host protons. The intensity of these peaks increases as the alkyl chain length of the surfactant increases. The correlations between the CH_3 group of the surfactant and host protons are negligible or absent, indicating that either there are weak interactions between the host and guest, due to rapidly changing inclusion geometries, and (or) there are competitive intramolecular relaxation pathways. The absence of any correlation between protons of the CH_3 group of the surfactant and those of the host are surprising, given the magnitude of the CIS values in Table 3 and the fact that, usually, there is a correlation between the magnitude of a CIS value and the extent of intermolecular contacts (18).

Scheme 4 illustrates the predicted structures of a 2:1 CD–S complex based on CIS values, ROESY data, and an analysis of the spectral lines of the collective methylene ($(CH_2)_n$) groups. The structure of a 1:1 CD–S complex is not shown, however, the alkyl chain of the surfactant is included in the CD interior and the carboxylate head group is located near either the primary or secondary annular hydroxyl groups. The stacking of a second CD onto the 1:1 complex, forming a 2:1 complex, likely occurs in a random fashion, based on the similar CIS values for the H(3) and H(5) host protons beyond $R = 1$, as shown by the two possible inclusion geometries. Figure 8 illustrates the resonance lines for the $(CH_2)_n$ protons for SDec, SDodec, and ST in the presence of α- and β-CD, respectively, at the $R = 2$ mole ratio. Recall that the signal for

Scheme 4. Proposed inclusion geometries for a 2:1 CD–S complex, as determined from ^{1}H NMR data.

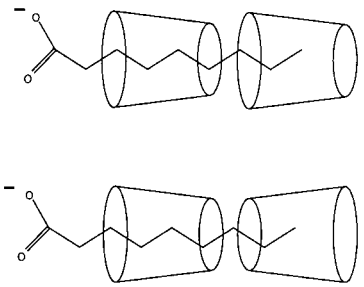

the $(CH_2)_n$ protons appears as a broad singlet in the absence of any added CD. The appearance of asymmetry in this signal, in the presence of CD at $R = 2$, reflects nonequivalent molecular environments attributable to the formation of 1:1 and 2:1 complexes. The CIS values for the $(CH_2)_n$ groups are greater for α-CD ($\Delta\delta_{max} \approx 0.11$ ppm) and lower in β-CD ($\Delta\delta_{max} \approx 0.03$ ppm), which can be attributed to conformational changes of type (*b*), discussed above, between the uncomplexed and complexed guest. The asymmetry begins to appear for surfactants with $C_x \geq 9$ for α-CD and β-CD, respectively. The apparent lack of broadening and asymmetry in the signal for SDec with α-CD may indicate that the 2:1 complex is either weakly bound (cf. Table 2) and (or) interacting with the terminus of the protruding alkyl chain. The β-CD–SDec system forms 1:1 complexes, exclusively, and serves as a useful benchmark for analyzing line shapes of the 2:1 complexes. In Fig. 8*a*, the extreme upfield signal (closest to DSS) for SDodec and ST is due to unbound CH_2 groups residing in the bulk, since the CIS values are similar to a surfactant in D_2O alone, whereas the lower field component of the signal is due to 1:1 and 2:1 complexes. In Fig. 8*b*, the low field shoulder appearing in SDodec and ST is due to the 2:1 complex, whereas the high field components are assigned to the 1:1 complex. The integrated area of the low field component of the asymmetric peak (shown above the peak) and its CIS value are consistent with the end-capping of a second CD onto the 1:1 complex. Clearly, as C_x increases, the broadening of the line increases and the downfield resonance lines increase in intensity, indicating that additional CH_2 groups are bound in a 2:1 complex. From these results it appears that five CH_2 groups can be included within α-CD and seven or eight CH_2 groups within β-CD. The former values are in reasonable agreement with estimates derived from calorimetry (33), and the latter are in agreement with previous estimates (8, 30).

Conclusions

An investigation of the ^{1}H NMR chemical shifts (δ) of a homologous series of hydrocarbon (hc) ($C_xH_{2x+1}CO_2Na$, $x = 5$, 7, 9, 11, 13) surfactants (S) has been determined in water and in aqueous solutions containing various cyclodextrin compounds at 295 K. The chemical shifts of the ^{1}H nuclei of both the surfactants and cyclodextrin compounds were studied. The magnitudes of the complex induced shift (CIS) values of the ^{1}H nuclei of the surfactants and cyclodextrins were found to increase as the alkyl chain length (C_x) increased, irrespective

© 1998 NRC Canada

Fig. 8. Comparison of ^{1}H NMR signals of methylene $(CH_2)_n$ protons (cf. Scheme 3) for the surfactants (*i*) SDec, (*ii*) SDodec, and (*iii*) ST, complexed with (*A*) α-CD and (*B*) β-CD, at mole ratio $R = 2$ and $T = 293$ K.

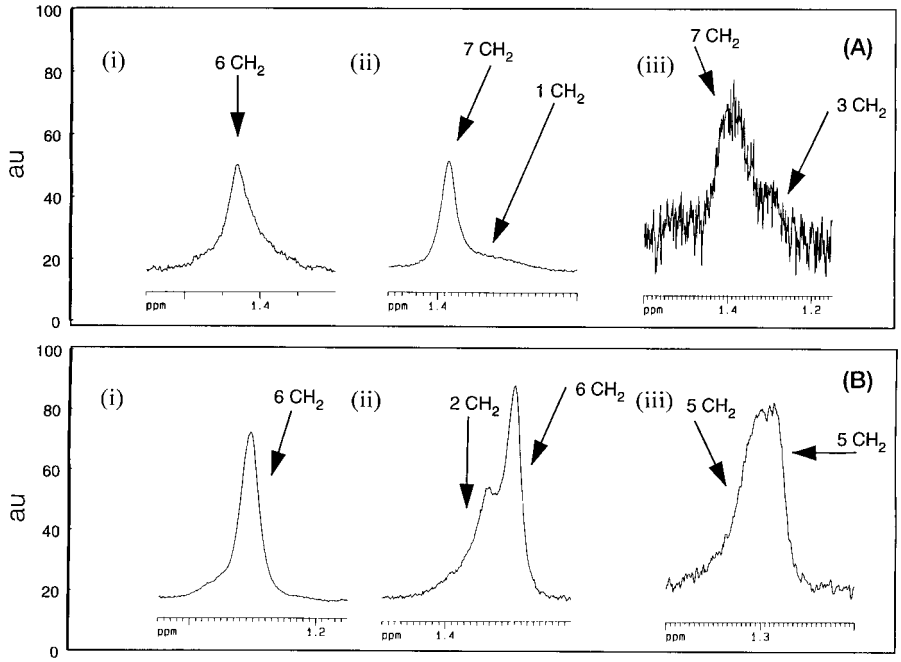

of the type of CD. The CIS values were found to depend on the following factors: (*i*) the magnitude of the binding constant (K_i), (*ii*) the chain length of surfactant, (*iii*) the mole ratio of the host to guest species, (*iv*) the stoichiometry of the host–guest, and (*v*) the host–guest inclusion geometry.

The CIS values for the cyclodextrins and the surfactants have been analyzed in terms of the complexed and uncomplexed species using models that account for different types of host–guest complexes having 1:1 stoichiometry and 1:1 plus 2:1 stoichiometry. Binding constants have been obtained for the various CD–S systems and the magnitude of K_i was found to increase as C_x increases. As well, differences in the binding affinity, stoichiometry, and inclusion geometry of complexes formed between the hc surfactants and α-CD, β-CD, and modified CDs were observed. Most of the host systems formed 1:1 complexes except for α-CD and β-CD, which formed 2:1 complexes with surfactants when $x = 9$, 11, 13 and $x = 11$, 13, respectively. The binding affinity of the host systems with the hc surfactants follows the order: β-CD > α-CD > DM-β-CD > TM-β-CD > HP-β-CD.

The NMR data obtained in this study have provided quantitative and structural information about the nature of the complexes formed in the various CD–S systems. There is evidence that the binding constants of complexes formed between modified cyclodextrins and surfactants are affected by hydration and steric hindrance in the annular region of the macrocycle.

Acknowledgements

Financial assistance provided by the Natural Sciences and Engineering Research Council of Canada (NSERC) is acknowledged. L.D.W. is grateful for the award of a Graduate Teaching Fellowship from the University of Saskatchewan and would like to thank Dr. Gong Zhang of the Department of Chemical Engineering, University of Saskatchewan, for helpful discussions concerning the analysis programs. The authors thank American Maize, Inc., for providing a complimentary research sample of TM-β-CD.

References

1. W.J. Shieh and A.R. Hedges. J.M.S. Pure Appl. Chem. A, **33**, 673 (1996), and refs. cited therein.
2. G. Wenz. Angew. Chem. Int. Ed. Engl. **33**, 803 (1994), and refs. cited therein.
3. T. Loftsson and M.E. Brewster. J. Pharm. Sci. **85**, 1017 (1996), and refs. cited therein.
4. E. Leray, F. Leroy-Lechat, H. Parrot-Lopez, and D. Duchêne. Supramol. Chem. **5**, 149 (1995).
5. A. Gadre, V. Rudïger, H.-J. Schneider, and K.A. Connors. J. Pharm. Sci. **86**, 236 (1997).
6. K.A. Connors. J. Pharm Sci. **85**, 796 (1996).
7. L.D. Wilson, S.R. Siddall, and R.E. Verrall. Can. J. Chem. **75**, 927 (1997).
8. L.D. Wilson and R.E. Verrall. J. Phys. Chem. B **101**, 9270 (1997), and refs. cited therein.
9. L.D. Wilson and R.E. Verrall. J. Phys. Chem. B. (1998). In press.
10. H.-J. Schneider and H. Dürr *(Editors)*. *In* Frontiers in supramolecular chemistry and photochemistry. VCH, Weinheim, Germany. 1991. pp. 29–56, 123–143.
11. B. Perly, F. Djedaïni, and P. Berthault. *In* New trends in cyclodextrins and derivatives. *Edited by* D. Duchêne. Editions de Santé, Paris. 1991. Chap. 5.
12. A.M. Claire Myles, D.J. Barlow, G. France, and M.J. Lawrence. Biochim. Biophys. Acta, **1199**, 27 (1994).
13. T. Wang, J.S. Bradshaw, and R.M. Izatt. J. Heterocycl. Chem. **31**, 1097 (1994).
14. Y. Inoue. Ann. Rep. NMR Spectrosc. **27**, 59 (1993).
15. Z.J. Tan, X.X. Zhu, and G.R. Brown. Langmuir, **10**, 1034 (1994).
16. R.J. Bergeron. *In* Inclusion compounds: physical properties and applications. Vol. 3. *Edited by* J. L. Atwood, J.E.D. Davies, D.D. MacNicol. Academic Press, London. 1984. pp. 391–443.

© 1998 NRC Canada

17. D.J. Wood, F.E. Hruska, and W. Saenger. J. Am. Chem. Soc. **99**, 1735 (1977).
18. H.-J. Schneider. Recl. Trav. Chim. Pays-Bas Belg. **112**, 412 (1993).
19. G. Qing-Xiang, L. Zi-Zhang, R. Tan, Z. Xiao-Qing, and L. You-Cheng. J. Inclusion Phenom. Mol. Recognit. Chem. **17**, 149 (1994).
20. B. Casu, A. Grenni, A. Naggi, G.T. Torri, M. Virtuani, and B. Focher. Carbohydr. Res. **200**, 101 (1990).
21. M. Watanabe, H. Nakamura, and T. Matsuo. Bull. Chem. Soc. Jpn. **65**, 164 (1992).
22. M.V. Rekharsky, M.P. Mayhew, R.N. Goldberg, P.D. Ross, Y. Yamashoji, and Y. Inoue. J. Phys. Chem. B, **101**, 87 (1997).
23. N. Funasaki, H. Yodo, S. Hada, and S. Neya. Bull. Chem. Soc. Jpn. **65**, 1323 (1992).
24. W. Blokzijl, and J.F.B.N. Engberts. Angew. Chem. Int. Ed. Engl. **32**, 1545 (1993).
25. F.W. Lichtenthaler and S. Immel. Starch/Staerke, **48**, 145 (1996).
26. U.R. Dharmawardana, S.D. Christian, E.E. Tucker, R.W. Taylor, and J.F. Scamehorn. Langmuir, **9**, 2258 (1993).
27. W.M.Z. Wan Yunus, J. Taylor, D.M. Bloor, D.G. Hall, and E. Wyn-Jones. J. Phys. Chem. **96**, 8979 (1992).
28. F.W. Lichtenthaler and S. Immel. Liebigs Ann.Chem. 27 (1996).
29. J.E. Huheey. *In* Inorganic chemistry: principles of structure and reactivity. 3rd ed. Harper and Row, New York. 1983. p. 259.
30. J.W. Park and H.J. Song. J. Phys. Chem. **93**, 6454 (1989).
31. Y.E. MacPherson, R. Palepu, and V.C. Reinsborough. J. Inclusion Phenom. Mol. Recognit. Chem. **9**, 137 (1990).
32. R.J. Bergeron, M.A. Channing, K.A. McGovern, and W.P. Roberts. Bioorg. Chem. **8**, 263 (1979).
33. G. Castronuovo, V. Elia, D. Fessas, F. Velleca, and G. Viscardi. Carbohydr. Res. **287**, 127 (1996).
34. W. Saenger, M. Noltmeyer, P.C. Manor, B. Hingerty, and B. Klar. Bioorg. Chem. **5**, 187 (1976).
35. J.B. Lambert, H.F. Shurvell, D. Lightner, and R.G. Cooks. *In* Introduction to organic spectroscopy. Macmillan Pub. Co., New York. 1987. Chap. 3.
36. P.B. Miranda, V. Saijo, and Y.R. Shen. Chem. Phys. Lett. **264**, 387 (1997).
37. P.D. Ross, and M.V. Rekharsky. Biophys. J. **71**, 2144 (1996).
38. O.S. Tee, T.A. Gadosy, and J.B. Giorgi. J. Chem. Soc. Perkin Trans. 2, 1705 (1993).
39. R.I. Gelb and L.M. Schwartz. J. Inclusion Phenom. Mol. Recognit. Chem. **7**, 465 (1989).
40. E. Saint Aman and D. Serve. J. Colloid Interface Sci. **138**, 365 (1990).
41. R. Palepu and J.E. Richardson. Langmuir, **5**, 218 (1989).

© 1998 NRC Canada

Facial selectivity in the addition of nucleophiles to the radical cations of substituted 2-methyleneadamantanes

Susan Swansburg, Kristin Janz, Gloria Jocys, Alexandra Pincock, and James Pincock

Abstract: The diphenylmethylenecyclohexane, **2**, and the substituted 2-methyleneadamantanes, **3**–**7**, have been prepared. The radical cation of each was generated by photochemical oxidation using 1,4-dicyanobenzene as the sensitizer, and their reactivity was examined in methanol–acetonitrile mixtures with added tetraethylammonium cyanide. Although compound **2** reacted only by tautomerization, the other compounds all gave addition products. For the monoaryl alkenes **3**, **4,** and **5**, comparable yields of both methanol and HCN addition products were obtained, resulting from nucleophilic attack at either end of the alkene radical cation. For the diphenylalkenes **6** and **7**, the regioselectivity favored nucleophilic attack at the adamantyl carbon, and the addition products were predominantly those of HCN addition. For the 5-methoxy compound **7**, HCN addition was facially selective with a *syn:anti* ratio of 58:42.

Key words: methyleneadamantanes, facial selectivity, radical cations.

Résumé : On a préparé le diphénylméthylènecyclohexane, **2**, ainsi que les 2-méthylèneadamantanes substitués **3**–**7**. On en a ensuite préparé les cations radicaux par une oxydation photochimique impliquant le 1,4-dicyanobenzène comme sensibilisateur et on a étudié leur réactivité dans des mélanges de méthanol–acétonitrile dans lesquels on a ajouté du cyanure de tétraméthylammonium. Même si le composé **2** ne réagit que par tautomérisation, tous les autres composés conduisent à des produits d'addition. Pour les monoarylalcènes **3**, **4** et **5**, on a obtenu des rendements comparables de produits d'addition de méthanol et de HCN provenant d'une attaque nucléophile à l'une des deux extrémités du cation radical de l'alcène. Pour les diphénylalcènes **6** et **7**, la régiosélectivité favorise l'attaque nucléophile sur le carbone adamantyle; les produits d'addition proviennent alors en prédominance d'une addition de HCN. Pour le composé 5-méthoxy **7**, l'addition du HCN se fait sélectivement sur une face et le rapport *syn : anti* est égal à 58 : 42.

Mots clés : méthylèneadamantanes, sélectivité faciale, cations radicaux.

[Traduit par la rédaction]

Introduction

The factors that control diastereoselectivity in additions to planar carbon atoms continue to attract considerable experimental (1–4) and theoretical (5) interest. In a pioneering study (6), le Noble and co-workers showed that substituted 5-X-2-adamantyl systems,[2] **1**, are particularly useful probes in these studies. Steric differences between the *syn* and *anti*[3] faces are minimized, there is none of the conformational ambiguity inherent in more flexible systems, and only two products can be formed. Therefore, the long-range electronic effect between the substituent and the reaction center at C2 can be assessed by the ratio of *syn* to *anti* products. With very few exceptions, *syn* attack is preferred. Because most of the X groups studied have been inductively electron withdrawing (relative to H at C7), *syn* represents attack on the same side as the electron-deficient σ bonds (C1—C9 and C3—C4) but antiperiplanar to the electron-rich σ bonds (C1—C8 and C3—C10). Current debate focuses mainly on whether the observed diastereoselectivities are controlled by hyperconjugative or electrostatic field effects.

Examples of the types of reactions that have been studied include nucleophilic additions to 2-adamantanones (1, 3), electrophilic additions to 2-methyleneadamantenes (3), solvolysis of 2-adamantyl compounds (6–8), radical trapping

Received July 30, 1997.

S. Swansburg, K. Janz, G. Jocys, A. Pincock, and J. Pincock.[1] Department of Chemistry, Dalhousie University, Halifax, NS B3H 4J3, Canada.

[1] Author to whom correspondence may be addressed. Telephone: (902) 494-3324. Fax: (902) 494-1310. E-mail: pincock@chem1.chem.dal.ca

[2] These numbers, depending on substituents, may or may not correspond to IUPAC numbering. They have been adopted by chemists studying the effect of substituents in adamantyl chemistry so that C2 is the site of interest and C5 is the position of the substituent.

[3] A variety of stereochemical designations have been used: *syn* = *zu* and *anti* = *en*. In reactions such as hydride or organometallic addition to 5-X-2-adamantanones, the carbonyl oxygen that becomes the alcohol of the product takes stereochemical nomenclature priority. Therefore, *syn* hydride reduction gives the *anti* or *E* product and *anti* attack gives the *syn* or *Z* product.

© 1998 NRC Canada

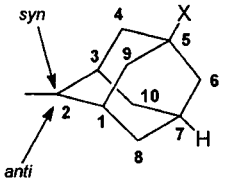

1

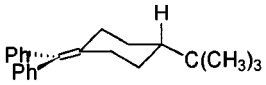

2

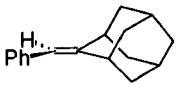

3

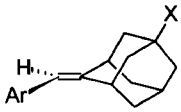

4: Ar = Anisyl, X = H

5: Ar = Ph; X = 4-OCH_3

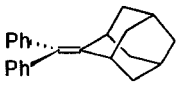

6

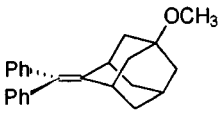

7

(9), sigmatropic rearrangements (Claisen) (10), and photochemical [2 + 2] cycloadditions of alkenes to 2-adamantanones (11, 12). Facial selectivity in the reactions of 5-aza (13), 5-azoxy (14), and perfluoro (15) adamantane derivatives have also been reported. To our knowledge, the reactivity of radical ions has not been studied. We now report on the syntheses of the derivatives **2**–**7** and the products obtained from their radical cations. These cations were generated by photochemical electron transfer using 1,4-dicyanobenzene (DCB) as the electron acceptor; the cations were then trapped by nucleophiles (methanol, cyanide ion) according to the well-established procedures developed by Arnold and Maroulis (16). The choice of substrates was made on the basis that aryl-substituted alkenes are readily oxidized by the excited singlet state of DCB, and that **5** and **7**, containing the 5-methoxy group, can both be prepared from commercially available 5-hydroxy-2-adamantanone.

[1]

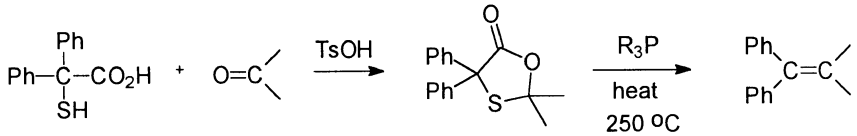

2a, 6a, 7a

[2]

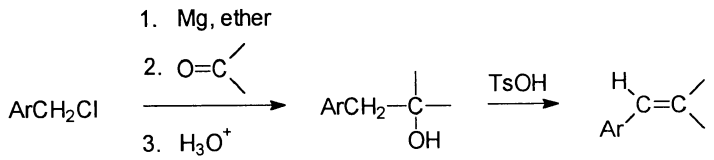

3a, 4a, 5a

Results and discussion

Syntheses of diphenyl alkenes 2, 6, and 7

The diphenylalkenes were synthesized from the corresponding 1,3-oxathiolan-5-ones **2a, 6a**, and **7a**, eq. [1], by pyrolysis at 250°C, in the presence of tris(diethylamino)phosphine. This twofold extrusion process, developed by Barton and Willis (17), provides a convenient route to these highly hindered alkenes. The 1,3-oxathiolan-5-ones were prepared by condensation of the appropriate ketone with thiobenzilic acid (*p*-toluenesulfonic acid catalysis) in benzene with azeotropic removal of water. For **2a** and **7a,** a mixture of diastereomers resulted; the ratio for both cases was close to 60:40. Separation of these isomers was possible by column chromatography but no attempt was made to assign the individual structures for **2a**. For **7a**, in the major isomer the sulfur was *syn* to the 5-methoxy group as determined by X-ray crystallography (Fig. 1).[4] We do not know if this represents a kinetic preference. Separation of the mixtures of **2a** and **7a** was not necessary for the next step as the stereochemical distinction is lost in the conversion to the alkene.

Syntheses of monophenyl alkenes 3, 4, and 5

Grignard reaction of 2-adamantanone or 5-methoxy-2-adamatanone with either benzyl chloride or 4-methoxybenzyl chloride gave alcohol products **3a**, **4a,** and **5a,** which were dehydrated in benzene (*p*-toluenesulfonic acid catalysis),

[4] T.S. Cameron and W. Kwiatkowski. Department of Chemistry, Dalhousie University, unpublished results, 1996.

© 1998 NRC Canada

eq. [2]. The alcohol **3a** has been prepared previously by the same procedure but was converted to **3** by dehydration using phosphoric acid (18).

Photochemistry of 2

Although alkene **2** was prepared primarily to develop the synthetic and photochemical methodology required for the adamantyl systems, the reactivity of its radical cation is also of interest. The presence of the *tert*-butyl group at C4 locks the cyclohexane ring in a fixed conformation, making the approach of a nucleophile to the two faces of the carbon–carbon double bond very different for steric reasons. However, irradiation of alkene **2** with DCB as the sensitizer, in 3:1 acetonitrile:methanol, did not result in the formation of nucleophile addition products. Rather, the sole product observed was the tautomer of the starting material, **8** (eq. [3]), in which the carbon–carbon double bond is now endocyclic. In retrospect, this deconjugation reaction is not unexpected. Arnold and Mines (19) have reported several examples of photochemical tautomerization of alkenes, including diphenylmethylenecyclohexane, analogous to **2** but without the *tert*-butyl group. In their studies, 2,6-lutidine was added to facilitate the isomerization reaction but for alkene **2** no base was required.

The mechanism proposed (19) for these tautomerizations begins with photoinduced electron transfer to form the alkene radical cation (and the radical anion of DCB), followed by deprotonation at the allylic position. The acidity of these hydrogens is known to be enhanced in the radical cation. Reduction of the allylic radical by the radical anion of DCB gives the allylic anion, which on reprotonation by methanol results in either the starting alkene or its tautomer. The position of the equilibrium between the two isomers is controlled by their relative oxidation potentials. Between **2** and **8**, **2** has a considerably lower oxidation potential and is therefore photochemically converted to **8**, whereas **8**, with the higher oxidation potential, is not converted back to **2**. The efficiency of this conversion for **2**, relative to that of the other alkenes studied previously (19), is probably a result of the fact that the axial allylic carbon–hydrogen bond is fixed in an appropriate geometry for effective overlap with the singly occupied molecular orbital (SOMO) of the initially formed radical cation. Therefore, tautomerization occurs in preference to addition of methanol across the double bond. Even in the presence of

Fig. 1. ORTEP representation from the X-ray crystal structure of **7a**, isomer 1.

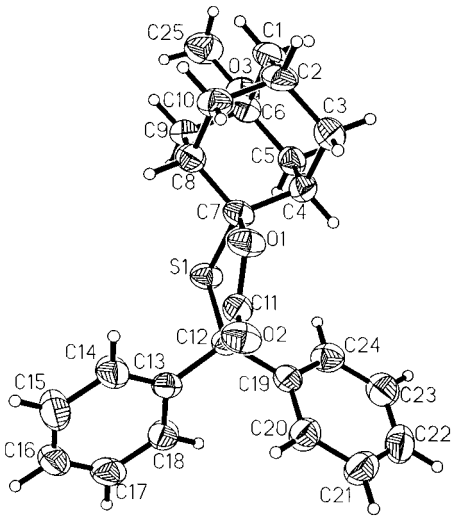

[3]

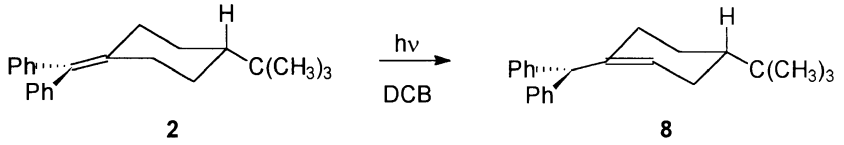

2 **8**

[4]

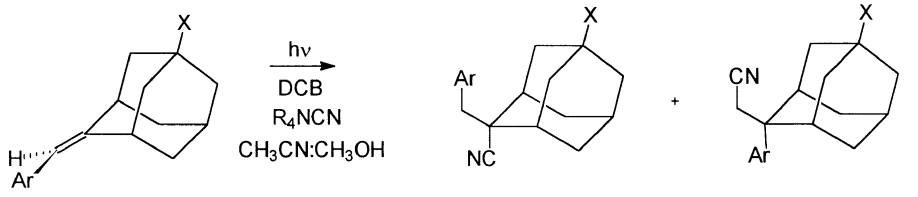

3: Ar = Ph; X = H
4: Ar = Anisyl; X = H

9: Ar = Ph; X = H
13: Ar = Anisyl; X = H

10: Ar = Ph; X = H
14: Ar = Anisyl; X = H

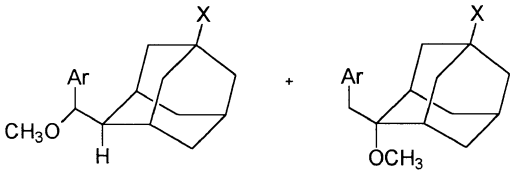

11: Ar = Ph; X = H
15: Ar = Anisyl; X = H

12: Ar = Ph; X = H
16: Ar = Anisyl; X = H

© 1998 NRC Canada

Fig. 2. ORTEP representation from the X-ray crystal structure of **9**.

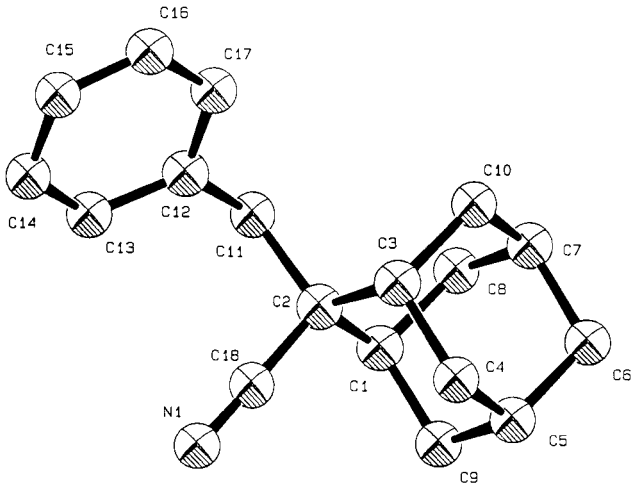

Fig. 3. ORTEP representation from the X-ray crystal structure of **10**.

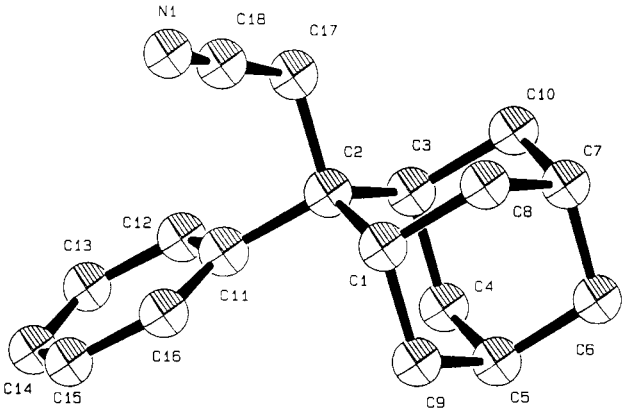

tetraethylammonium cyanide, addition products were not formed in detectable yield; again, only **8** was observed.

Photochemistry of 3

In the adamantyl analogues, the tautomerization reaction is unlikely, because of the high strain associated with placing double bonds in adamantane rings (thermodynamic rationale) and also because the allylic hydrogens are not oriented appropriately for favourable overlap with the SOMO of the radical cation (kinetic rationale).

Irradiation of alkene **3** with DCB and added tetraethylammonium cyanide (4.5 mM) in 9:1 (by volume) acetonitrile:methanol gave the four addition products shown in eq. [4]. These products were identified, in a preliminary way, by their mass spectra (GC–MS). In all cases, the spectra are simple, showing a few prominent ions that are easily assigned to fragments of the molecules. For instance, the base peaks have *m/z* values corresponding to the following fragments: **9** (91, $PhCH_2$+), **10** (211, 2-Ph-Ad^+), **11** (121, $PhCH\text{-}OCH_3$+), **12** (225, 2-CH_3O-Ad^+). The four products were separated by preparative-scale column chromatography on silica gel. Detailed ^1H and ^{13}C NMR spectral analyses support the proposed structures. In addition, the structures of the HCN addition products, **9** and **10**, were confirmed by X-ray crystallography (Figs. 2 and 3).[4] The cyano group is directly bonded to C2 of the adamantane ring in **9**, but is on the exocyclic carbon in **10**. In the latter structure, the phenyl group has migrated to the adamantyl carbon, C2. Ether **11** was not isolated from the reaction mixture but a synthetic sample was prepared by hydroboration of alkene **3** followed by conversion to the methyl ether by treatment with sodium hydride and methyl iodide. Integration of the ^1H NMR signals of the crude reaction mixture for the hydrogens α to the phenyl ring indicated that **11/12** are formed in a ratio of one to three.

The yields for the reaction of **3**, by calibrated GC–FID analysis (corrected for unreacted starting material at 50% conversion of **3**), are as follows: **9** (34%), **10** (24%), **11** plus **12** (25%); the mass balance is 81%. The yield of the two products resulting from addition of cyanide ion is greater than that of those resulting from addition of methanol, as expected based on the relative reactivities of the two nucleophiles. Johnston and Schepp (20, 21) have measured second-order rate constants for the addition of nucleophiles to a series of substituted styrene radical cations generated directly from the parent alkene by laser flash photolysis. For each radical cation studied, the rate constant for methanol addition was orders of magnitude slower than for any other nucleophile studied. For instance, the rate constant for reaction of the 4-methoxystyrene radical cation in 4:1 water:acetonitrile is 3×10^4 M^{-1} s^{-1} for methanol and 1.0×10^8 M^{-1} s^{-1} for cyanide ion.

The established mechanism for these addition reactions involves product-determining attack of the nucleophile on the radical cation. To confirm that the radical cation of **3** is formed efficiently, the quenching of DCB fluorescence by **3** was examined. The Stern–Volmer slope gave $k_q\tau_{DCB} = 17$ M^{-1}. Using 9.7 ns as the singlet lifetime of DCB (16), the calculated quenching rate constant is 1.8×10^{10} M^{-1} s^{-1}, comparable to the diffusional limits (22) in acetonitrile (1.9×10^{10} M^{-1} s^{-1}) and methanol (1.2×10^{10} M^{-1} s^{-1}), suggesting that formation of the radical cation will occur readily. As predicted by the Weller equation (23), oxidation of **3** by the excited singlet state of DCB should be exothermic if the oxidation potential of the alkene is below 2.2 V; the measured value for **3** is 1.37 V (CH_3CN versus SCE).

The cyano adducts **9** and **10** are formed in a ratio of 1.4:1, invariant with percent conversion. This ratio is, at least in part, a reflection of the relative stabilities of the benzyl and tertiary radicals formed by attack of cyanide ion at the two ends of the double bond of the radical cation of **3**. For addition to diphenylethylene, the nucleophile adds exclusively to the radical cation at the terminal carbon to give the more stable diphenylmethyl radical intermediate. Therefore, the result is anti-Markovnikov addition (16). For **3**, the two possible radical intermediates are of comparable stability. The benzylic radical is formed in slight preference to the tertiary one, and **9** is therefore the expected product. Cyanide ion attacks the radical cation at the 2-adamantyl position, and this is followed by reduction (by the radical anion of DCB) of the radical to the anion, and subsequent protonation of the anion by the solvent, methanol. In contrast, product **10** was unexpected. The phenyl group has migrated to C2 of the adamantane ring. A reasonable pathway for formation of this product requires several steps: attack of the cyanide ion on the radical cation to form the tertiary 2-adamantyl radical, 1,2-migration of the phenyl group to give the α-cyano radical, reduction of this radical to the

© 1998 NRC Canada

corresponding anion, and finally protonation of the anion by the solvent.

Several facts support this mechanism. First, the tertiary radical would be relatively long-lived. Oxidation potentials indicate that it will not be reduced by the radical anion of DCB, because the oxidation potential of the radical anion of DCB (1.6 V) (24) is lower than that of the *tert*-butyl anion (greater than 2.0 V) (25). Second, although radical rearrangements are uncommon, examples of 1,2-phenyl migrations are well known (26). For instance, this so-called neophyl rearrangement for the 2-phenyl-2-methylpropyl radical is shown in eq. [5]; Franz et al. (27) determined the rate constant for this 1,2-phenyl migration to be 764 s^{-1} at 298 K. A similar 1,2-phenyl shift can be proposed in the formation of **10**. Although the rearrangement should be slower, since the precursor radical

[5] 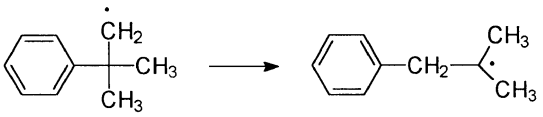

is tertiary, the low concentration of the radical would allow this relatively slow unimolecular process to compete with bimolecular processes. Third, once formed, the α-cyano radical would be easily reduced to the corresponding cyano-stabilized anion. None of the possible product resulting from trapping of the initially formed tertiary radical in this sequence was detected.

Similar 1,2-phenyl migrations have been observed for the radical cation induced epoxidation of both **3** (28) and **6** (28, 29) but the rearrangements proceed by a secondary reaction of the radical cation of the first formed epoxide.

Another mechanism for cyanide addition to **3** is possible. As mentioned above, the reactions of the radical cations of a variety of substituted styrenes with nucleophiles have been studied by laser flash photolysis (20, 21). In some cases, the mechanism has been shown to involve initial electron transfer to regenerate the original alkene along with the oxidized nucleophile. Combination of these two species could give the same radical as is formed in the above mechanism. However, this possibility can probably be excluded. It was not observed in the laser flash experiments with cyanide ion as the nucleophile. Moreover, for this pathway to be efficient, the oxidation potential of **3** (1.37 V, CH_3CN versus SCE) must be higher than that of cyanide ion. The latter oxidation potential is quite solvent dependent (30), with a value of 1.3 V in acetonitrile and 1.7 V in the protic solvent, water. Because of the methanol used in the 9:1 acetonitrile:methanol medium in these photolysis reactions, the oxidation potential of cyanide ion is likely to be closer to the value for water. Therefore, reaction by electron transfer of the radical cation of **3** with cyanide ion is probably endergonic, making this second mechanistic possibility unlikely.

The two ether products, **11** and **12**, were not separated by GC and were therefore quantified together. As mentioned above, they were formed in a ratio of one to three as determined by ^{1}H NMR integration. These ethers are the two regioisomers resulting from reaction of methanol with either end of the carbon–carbon double bond of the radical cation of **3**. Again, addition favours formation of the benzylic radical over the tertiary one although the degree of selectivity differs somewhat for the two nucleophiles. Methanol (3:1) is more selective than cyanide ion (1.4:1). There is still no firm mechanistic rationale for the regioselectivity of methanol addition to the radical cations of phenyl-substituted alkenes (31). In the current proposals, methanol initially adds to the radical cation to give a distonic radical cation and this addition may proceed through an encounter complex. Until the two possible distonic radicals are deprotonated to give radicals, this addition process may be reversible. The observed regiochemistry may then result, in a complex way, from a combination of both the rates of formation and the thermodynamic stability of these intermediates.

A product analogous to **10**, resulting from migration of the phenyl group, was not detected in the methanol addition products. One possible explanation is that a methoxy substituent should not stabilize a radical centre to as great an extent as would a cyano substituent (32). Therefore, the neophyl rearrangement may not be energetically favorable.

As in the cyano case, the tertiary radical intermediate from methanol addition is not reduced by the radical anion of DCB. Therefore, ether **11** probably results from hydrogen abstraction by this radical rather than from protonation of the corresponding anion. To test this conclusion, the photoreaction was repeated using CH_3OD in the presence of added cyanide ion in 9:1 acetonitrile:methanol. The amount of deuterium incorporated into each of the four products was determined from single ion monitoring mass spectrometry (SIMS), using the intensities of the M, M + 1, and M + 2 peaks. As expected from the above mechanistic proposal, both cyano adducts, **9** and **10**, contained deuterium in 90% excess relative to natural abundance samples. The molecular ion of ether **12** was not intense enough to give reliable results, as it readily fragmented in the mass spectrometer, with the base peak corresponding to the 2-methoxy-2-adamantyl cation. However, SIMS analysis of the C_7H_7 fragment ions at *m*/*z* 91, 92, and 93 gave only 30% of deuterium in excess of natural abundance. This result must be interpreted with caution, as more than one mass spectral fragmentation pathway may lead to ions at these masses. However, the enhanced percentage of deuterium found for this fragment ion suggests that, at least part of the time, the precursor radical to **12** is reduced and protonated by the solvent. Ether **11** showed only 5% deuterium in excess of natural abundance, which is consistent with hydrogen atom abstraction as the major pathway from tertiary radical to product.

Photochemistry of 4 and 5

Because the product mixtures obtained from **3** were fairly complex, alkene **4** was also studied, with the hope that the added 4-methoxy group would improve the regioselectivity of the attack at C2 of the adamantane ring.

Photoreaction of alkene **4**, under the same conditions as used for **3**, gave the products **13**–**16**, also shown in eq. [4]. The ratio of (**13** + **14**) to (**15** + **16**) was 3.8:1. These products are structurally parallel to those formed upon reaction of alkene **3**, but the relative yields are quite different. The yield of cyano adduct **14**, involving migration of a phenyl group, was extremely low; integration of the ^{1}H NMR signals for the methylene protons suggested a ratio for **13**/**14** of approximately 10:1. In fact, **14** was detected mainly because its presence was expected based on the products from the reaction of **3**.

© 1998 NRC Canada

Fig. 4. ORTEP representation from the X-ray crystal structure of **17**.

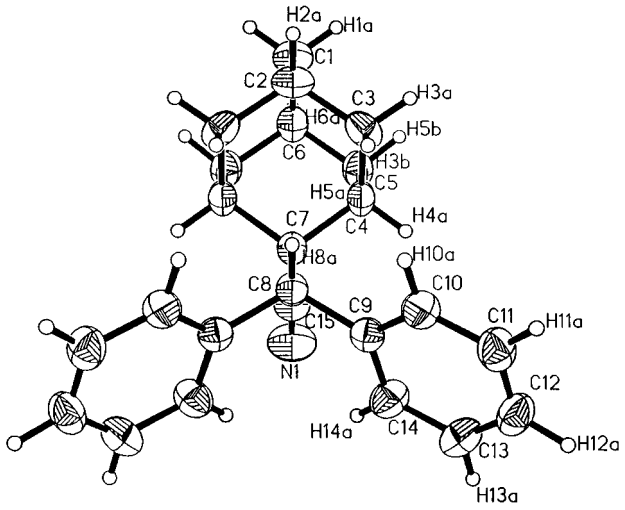

As was the case with **3**, an HCN addition product derived from the unrearranged tertiary radical intermediate was not detected. These results demonstrate that cyanide ion addition to the radical cation of **4** is highly regioselective. Presumably, the presence of a 4-methoxy substituent on the phenyl ring stabilizes the benzyl radical, favouring its formation relative to the unsubstituted case. As with alkene **3**, the regioselectivity of addition is much less pronounced when methanol is the nucleophile as compared to cyanide ion. Integration of characteristic ^{1}H NMR signals from a spectrum of the product mixture gave a ratio of the ether products, **15:16**, equal to 1.5:1.

Some initial experiments towards studying facial selectivity in reactions of **5** were undertaken. The alkene was prepared, in low yield, but the product mixtures obtained in the photochemistry were complex and separations were difficult. These experiments were abandoned when the photochemistry of **6** indicated that **7** would be an easier probe to use than **5**.

Photochemistry of 6

Photolysis of **6** in 9:1 CH_3CN:CH_3OH with 9.8 mM tetraethylammonium cyanide gave one major product, **17**, and a minor one, **18**, eq. [6]. The ratio, by GC integration, was greater than 20:1. The structure of **17** was unambiguously established by X-ray crystallography, Fig. 4.[4] The minor product was not isolated and its structure was assigned only on the basis of its fragmentation in the GC–MS, where the base peak (*m/z*, 211) agreed with expected fragmentation of **18** to the 2-phenyl-2-adamantyl cation. The base peak for **17** (*m/z*, 177) corresponded to the diphenylmethyl cation. Evidence for low yields of methanol addition products was obtained by GC–MS, but these were not isolated either. By calibrated GC–FID analysis, a 61% yield of **17** was obtained after 85% conversion of **5**. These experiments show that the photochemistry of **5** is simpler than that of **3**. First, the regioselectivity of the addition reaction now greatly favors cyanide attack at the adamantyl tertiary carbon to give the diphenylmethyl radical. Second, the radical cation of the diphenyl alkene **6** is much more selective in its reaction with nucleophiles, cyanide ion reacting in preference to methanol. This is probably a result of its greater stability relative to the other radical cations studied and its consequent lower reactivity.

To confirm that photoinduced electron transfer was also efficient for this diphenyl derivative, fluorescence quenching experiments were again conducted. Stern–Volmer plots of the quenching of both DCB and 1,4-dicyanonaphthalene (DCN) by **6** were linear and gave $k_{eq}\tau$ values of 120 M^{-1} and 66 M^{-1}, respectively. Using the singlet lifetimes of 9.7 ns for DCB (16) and 10.1 ns for DCN (33) gives quenching rate constants of 1.3×10^{10} M^{-1} s^{-1} and 0.66×10^{10} M^{-1} s^{-1}, both values close to the diffusional limit, in agreement with expectations based on the Weller (23) equation and the oxidation potential of **6**,

[6]

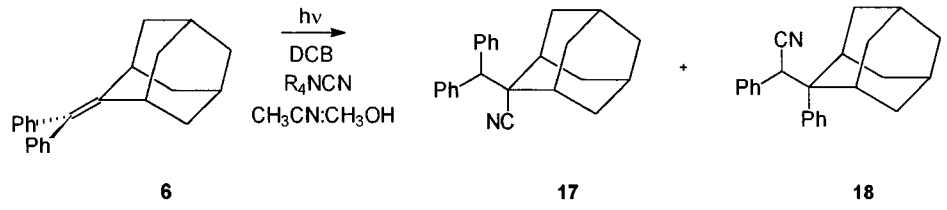

6 **17** **18**

[7]

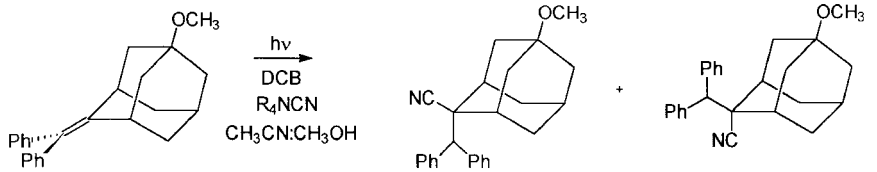

7 **19** (51%) **20** (37%) **21** (12%)

© 1998 NRC Canada

Fig. 5. ORTEP representation from the X-ray crystal structure of **19**.

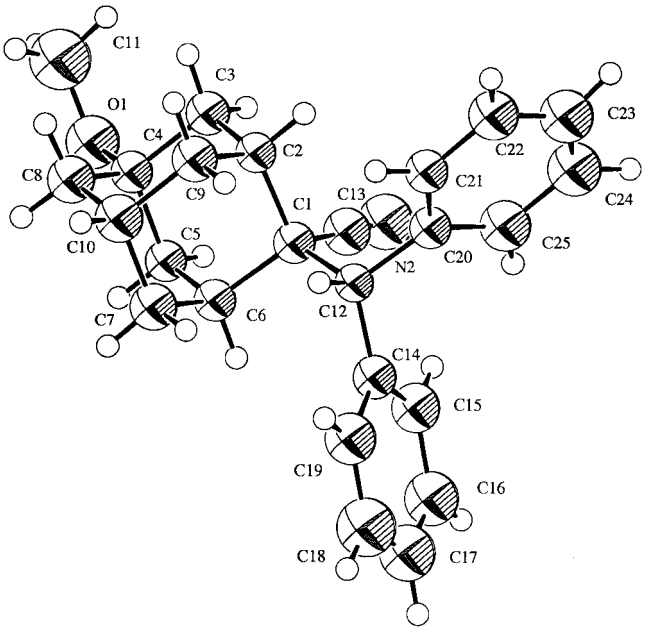

1.58 V (CH_3CN, vs. SCE); a value of 1.56 V (CH_2Cl_2, vs. SCE) has been reported (29).

Photochemistry of 7

The above results for the alkenes **2**–**6** suggested that the 5-methoxy substituted diphenyl derivative, **7**, would be the best choice for studying the facial selectivity of addition to these radical cations. In the presence of cyanide ion, irradiation of **6** gives only one major product; with the added methoxy substituent in **7**, the two major products should be the diastereomers resulting from nucleophilic attack at the two faces, and analysis of their ratio should be simple.

This assumption proved to be correct. Photolysis of **7** (240 mg) in 9:1 CH_3CN:CH_3OH with 4.6 mM tetraethylammonium cyanide resulted in over 90% conversion in only 2 h. The products formed, with yields by calibrated GC–FID at 78% conversion of **7**, are shown in eq. [7]; mass balance for these three products is 81%. The gross structures of the two major products, **19** and **20**, were again easily assigned by GC–MS since the base peak in both at *m/z* 167 corresponded to the diphenylmethyl cation; the minor isomer, **21**, resulting from migration of phenyl group by the same mechanism as for the other adamantane derivatives, had a base peak at *m*/*z* 241 corresponding to the 5-methoxy–2-phenyladamantyl cation.

Pure samples of **19** and **20** were obtained by column chromatography and recrystallization. An X-ray structure for **19**, Fig. 5,[4] unambiguously assigns it to the *syn* isomer. This same assignment had been tentatively made by ^{13}C NMR spectra using both the chemical shifts for the unsubstituted HCN addition product, **17**, and the expected chemical shift effect of the added 5-methoxy group (34). The observed (calculated) δ values for the two compounds are, for **19**: C1,C3, 34.4 (34.2); C4,C9, 29.9 (29.8); C5, 28.6 (28.8); C6, 41.8 (41.6); C7, 70.5 (70.0); C8,C10, 38.2 (38.5) and for **20**: C1,C3, 34.9 (34.2); C4,C9, 35.1 (34.3); C5, 70.7 (70.0); C6, 40.7 (41.6); C7, 28.8 (28.8); C8, C10, 34.1 (34.1). The excellent agreement obtained is in accord with the assignments of the stereochemistry of **19** (and hence **20**) demonstrated by the crystal structure.

The ratio of the *syn* to *anti* isomers was obtained both by GC–FID (58:42) and by integration of the methoxy signals in the ^1H NMR spectrum (58:42) of the crude photolysis mixture. This ratio (GC–FID) remained constant as a function of percentage conversion of **7** because, as expected, the nitrile products are photochemically inert under the reaction conditions for their formation. Therefore the ratio obtained is a primary product ratio reflecting the facial selectivity in the nucleophilic attack of cyanide ion on the radical cation of **7**.

Previously reported literature values of *syn:anti* isomer ratios for a variety of reactions with very different mechanisms will put the value obtained for **7** in context. For instance (substrate, substituent, conditions, *syn:anti*): 2-adamantanone, 5-OCH_3, $NaBH_4/H_2O$/0°C, 64:36 (3); 2-adamantanone, 5-OCH_3, MeLi/ether/0°C, 63:37 (3); 2-adamantane carboxylic acid, 5-Ph, Br_2/CCl_4/40°C (Hunsdiecker reaction), 58:42 (9); 2-adamantanone, 5-F, hν, NC-CH═CH-CN, CH_3CN (Paterno–Büchi reaction), 57:43 (12). Trapping of 2-adamantyl cations gives higher *syn:anti* ratios: 2-methyleneadamantane, 5-OCH_3, HCl/CH_3NO_2/0°C, 85:14 (3); 2-methyleneadamantane, 5-F, HCl/CH_3NO_2/0°C, 100:0 (3); 2-methyladamantanol, 5-F, HCl/CH_2Cl_2/0°C, 83:13 (6).

The first observation is the relatively low variation in the *syn:anti* ratio with reaction type. For instance, in the Paterno–Büchi reaction, the product-determining step is the quenching of the excited singlet state of 2-adamantanone by the alkene; the rate constant is known to be diffusional (i.e., rate constant approaching 10^{10} M^{-1} s^{-1}). The rate is also very fast for trapping of the 2-adamantyl radical in the Hunsdiecker reaction. In contrast to these two reactions where the product ratio reflects the trapping of a reactive intermediate, the $NaBH_4$ reduction of 2-adamantanone is a relatively slow process; the product-determining step is now expressed in minutes (i.e., rate constant approximately 10^{-2} M^{-1} s^{-1}). Therefore reactions differing in rate constant by at least 10^{12} show similar facial selectivity! The reactivity/selectivity principle predicts that the photochemical reaction occurring at the diffusional limit might be expected to show considerably less selectivity and perhaps none at all.

A possible explanation for these observations is that the facial selectivity observed for the transient intermediates is a consequence of a nonplanar geometry at C2 of the adamantane ring. This is a reasonable possibility because the *n*–π* excited

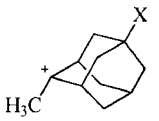

22

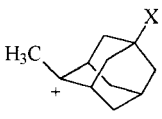

23

singlet state of ketones (35) is, and tertiary radicals (ref. 35, pp. 264–267) may be, pyramidal. In fact, the interpretation for the very high facial selectivity observed for 2-adamantyl cations is that the substituent at C5 controls the equilibration between two diastereomeric pyramidal cations (free or intimate ion pairs), **22** and **23** (3). Because carbocations, unless they are highly stabilized, are known to be quenched by nucleophiles at the diffusional rate (36), the facial selectivity is determined

© 1998 NRC Canada

by the ratio of the concentration of **22** to that of **23** and not by their relative reactivity. The substituent exhibits a large effect because the equilibrium favors **22** over **23** as a result of the hyperconjugative interaction between the substituent and the full positive charge at the electrophilic center.

Because of these possibilities, the geometry of the radical cation of **7** is clearly an important factor to consider. MO calculations at both the AM1 level and STO–3G level[5] gave a planar geometry at C2 but this level of theory is probably not adequate to make a reliable prediction. The AM1 calculations gave spin densities of 0.50 and 0.22 at the adamantane C2 and the diphenylmethylene carbon, respectively; in contrast, the charge densities (0.08 and 0.09) are both very low. Thus, the radical cation of **7** might be expected to show the low facial selectivity characteristic of a radical reaction rather than that of a cation. This is indeed the case, the 58:42 *syn*:*anti* ratio being the same as that observed in the trapping of the 2-adamantyl radical by Br_2 (9). The regioselectivity for the addition of cyanide ion to the radical cations of both **6** and **7** highly favors nucleophilic attack at the endocyclic carbon. Because the charge density is essentially identical at these two carbons, this observation may reflect the higher stability of the product diphenylmethyl radical over the other possibility, the tertiary 2-adamantyl radical. For 1,1-diphenylethylene, the radical cation reacts exclusively at the C2 but, in this case, the calculated charge density is considerably higher at that carbon (0.21 versus 0.12 at the diphenylmethyl carbon) (37).

Experimental

General experimental

Proton (^{1}H) and carbon (^{13}C) nuclear magnetic resonance (NMR) spectra were obtained in deuterated chloroform ($CDCl_3$) on either a Bruker AC 250F NMR spectrometer in automation mode or, as indicated, on an AMX 400 wide-bore NMR spectrometer. Proton chemical shifts are reported in parts per million (δ) relative to tetramethylsilane (0.00) as an internal standard. Reported coupling constants are experimental values. In many cases, coupling between ring protons in the adamantyl systems was unresolved, and the chemical shifts were reported as singlets. Carbon chemical shifts are reported relative to deuterated chloroform (triplet centred at δ 77.07). Multiplicities are abbreviated as follows: s = singlet, d = doublet, t = triplet, q = quartet, m = multiplet. Carbon multiplicities were assigned from either DEPT with multiplicity analysis (DEM) or J modulation (JMOD) experiments.

Electron-impact mass spectra (MS) were run at 70 eV ionizing energy, either on a CEC 21-104 single focussing or a CEC 21-110B double focussing mass spectrometer. Ionizing energies are reported in parentheses for spectra not run at 70 eV. Samples were introduced directly into the mass spectrometer source using a glass or quartz probe and were heated until an adequate ion current was observed. Masses are reported as mass/charge (*m*/*z*) ratios. Ion intensities are given in parentheses relative to the base peak intensity (100). The molecular ion is indicated by M. Accurate mass determinations were made on the CEC 21-110B spectrometer with perfluorokerosene (PFK) as an internal standard at a resolution of approximately 10 000. Chemical ionization mass spectra (CIMS) were run on a Fisons/VG Quattro triple quadrupole mass spectrometer, using isobutane as the ionizing gas. Spectra are reported in the normal manner.

Ultraviolet (UV) spectra were obtained in acetonitrile–methanol on a Varian Cary 219 spectrometer using a 1 cm quartz cuvette. Wavelength maxima (λ_{max}) are reported in nanometres. Infrared (IR) spectra were obtained on a Nicolet 205 FT-IR spectrometer. Samples were run either neat or as a Nujol mull on sodium chloride plates. Frequencies are reported in wave numbers (cm^{-1}). Melting points were determined on a Fisher–Johns melting point apparatus and are uncorrected. Combustion analyses were carried out by Canadian Microanalytical Services Ltd., Delta, B.C., Canada.

GC–MS analyses were done on a Hewlett–Packard 5890A GC and a 5970 mass selective detector. The column used was 5% phenyl methyl silicon on fused silica with a film thickness of 0.25 μm and column dimensions of 25 m × 0.2 mm. Masses are reported in the same manner as described above. GC–FID analyses were carried out on a Perkin–Elmer Autosystem gas chromatograph using either a DB-5 column, 15 m × 0.53 mm, with a film thickness of 1.5 μm, or a BT-1 100% polymethylsilicone column, 12 m × 0.22 mm, with a film thickness of 0.25 μm. Data were analyzed using computer software written in-house. HPLC analyses were done using a Waters 6000 solvent delivery system and a Waters U6K injector under isocratic conditions with a flow rate of 2 mL/min using a Brownlee Lab Spheri-10 10 μL reverse-phase column (25 × 0.46 cm) with a Waters model 450 variable wavelength detector. UV detection was at either 254 or 280 nm.

Column chromatography was carried out using silica gel (60 Å, 70–230 mesh) from the Aldrich Chemical Company. Column solvents, hexane and ethyl acetate, were distilled prior to use. Fractions were monitored by either GC–FID or thin-layer chromatography (tlc) using silica-coated polyester plates, purchased from the Aldrich Chemical Company.

The following compounds were purchased from the Aldrich Chemical Company: benzilic acid, phenyl isothiocyanate, 4-*tert*-butylcyclohexanone, *p*-toluenesulfonic acid, 2-adamantanone, tris(diethylamino)phosphine, magnesium turnings, benzyl chloride, 4-methoxybenzyl chloride, 5-hydroxy-2-adamantanone, methyl iodide, sodium hydride (56–58% suspension in oil), 1.0 M borane – tetrahydrofuran complex, tetraethylammonium cyanide. These chemicals were used without further purification unless otherwise noted.

Synthesis of alkenes 2, 6, and 7

Thiobenzylic acid

The following procedure was adapted from that reported by Becker and Bistrzycki (38). Benzilic acid was recrystallized from water prior to use. Benzilic acid (8.88 g, 0.039 mol) and phenyl isothiocyanate (7.49 g, 0.055 mol) were combined, and were ground to a slurry using a mortar and pestle. After the slurry was transferred to an Erlenmeyer flask, glacial acetic acid (10 mL) was added as solvent and the mixture was stirred and cooled to 0°C in an ice–water bath. Concentrated sulfuric acid (5 mL) was added dropwise, and the resulting red slurry stirred at 0°C for 2 h, then at room temperature for 2 h longer. Stirring was stopped, and the mixture was left to sit overnight. The resulting pink paste was poured into a beaker of crushed

[5] M.S.W. Chan, Department of Chemistry, Dalhousie University, unpublished results, 1997.

© 1998 NRC Canada

ice, and the solid collected by suction filtration. Recrystallization from methanol–water gave the intermediate product, $PhN(H)C(O)SC(Ph)_2CO_2H$, as colourless crystals (8.80 g, 62% yield); mp 144–146°C (lit. (38) mp 140.5°C).

The product from above (8.80 g, 0.024 mol) was refluxed in 10% KOH (300 mL) for 5 h. After cooling, the solution was gravity filtered to remove a white solid. The filtrate was then acidified with aqueous hydrochloric acid and the resulting solid was collected by suction filtration. Recrystallization from 50% acetic acid gave thiobenzilic acid as white needles (5.17 g, 87% yield); mp 149–151°C (lit. (40) 147.5–149°C).

5-Methoxy-2-adamantanone

Sodium hydride (15 mol% excess), was washed with hexanes, then added to a stirred solution of 5 hydroxy-2-adamantanone (1.0 g, 0.060 mol) in dimethyl sulfoxide (DMSO, 15 mL). The solution became cloudy, and vigorous bubbling was observed. After 30 min methyl iodide (15 mol% excess) was added dropwise and the solution left to stir until clear (overnight). The reaction was quenched with water and extracted three times with dichloromethane. The combined organic layers were washed three times with water and twice with brine to remove the DMSO, then dried over anhydrous magnesium sulfate, and the solvent was removed under vacuum. The crude ether (81%) was purified by column chromatography (10:90 ethyl acetate:hexane). ^{13}C NMR data of the isolated oil agreed with literature values (34).

1,3-Oxathiolan-5-ones

This procedure was developed by Barton and Willis (17). Thiobenzilic acid (4.1 mmol), *p*-toluenesulfonic acid (1.5 mmol), and the appropriate ketone (4.1 mmol) were combined in a round-bottom flask fitted with a Dean–Stark trap and condenser. Benzene (70 mL) was added as solvent. The mixture was refluxed (5–8 h) under nitrogen with azeotropic removal of water. The resulting solution was cooled, washed four times with saturated sodium bicarbonate, then with water until the aqueous layer was neutral to pH paper. The organic layer was then dried over anhydrous magnesium sulfate and the solvent was removed under vacuum. The 1,3-oxathiolan-5-ones were purified by column chromatography to give colourless solids.

4-tert-*Butylcyclohexanespiro-2'-(4',4'-diphenyl-1',3'-oxathiolan-5'-one),* **2a**

4-*tert*-Butylcyclohexanone was recrystallized from low-boiling petroleum ether prior to use. The two product diastereomers (overall yield 96%) were separated once for characterization purposes, but otherwise the mixture was used for the next step.

Isomer 1: mp 156–158°C; ^{1}H NMR (400 MHz) δ: 7.48–7.27 (m, 10H), 2.14 (d, 2H, J = 13.4 Hz), 1.72 (td, 2H, J = 14 Hz, 4 Hz), 1.65 (d, 2H, J = 13.4 Hz), 1.45 (q, 2H, J = 14 Hz), 1.01 (tt, 1H, J = 12.6 Hz, 4 Hz), 0.83 (s, 9H); ^{13}C NMR δ: 173.81, 141.09, 128.57, 128.35, 127.93, 87.63, 67.67, 46.53, 40.88, 32.35, 27.47, 24.39;

Isomer 2: mp 102–105°C; ^{1}H NMR (400 MHz) δ: 7.5–7.2 (m, 10H), 1.98 (d, 2H, J = 12.9 Hz), 1.88 (td, 2H, J = 12.9 Hz, 3.1 Hz), 1.77 (d, 2H, J = 13.1 Hz,), 1.25 (qd, 2H, J = 13.1 Hz, 3.1 Hz), 0.98 (tt, 1H, J = 12.2 Hz, 3.1 Hz), 0.86 (s, 9H); ^{13}C NMR δ: 173.46 (s), 140.93 (s), 128.33 (d), 128.24 (d), 127.803, 90.66 (s), 66.88 (s), 46.11 (d), 39.53 (t), 32.08 (s), 27.43 (q), 24.37 (t); MS *m/z*: 381 (M + 1, 11), 380 (M, 37), 337 (26), 336 (100), 335 (25), 237 (11), 199 (22), 198 (94), 170 (18), 167 (37), 166 (28), 165 (76), 121 (28), 57 (37), 54 (12), 40 (22).

Tricyclo[3.3.1.1^{3,7}]decane-2-spiro-2'-(4',4'-diphenyl-1',3'-oxathiolan-5'-one), ***6a*** *(84% yield):* mp 120–120.5°C; ^{1}H NMR (400 MHz) δ: 7.57–7.54 (m, 4H), 7.32–7.23 (m, 6H), 2.23 (d, 2H, J = 12.2 Hz), 2.02 (d, 2H, J = 12.2 Hz), 1.89 (s, 2H), 1.87 (s, 1H), 1.81 (s, 1H), 1.68 (s, 6H); ^{13}C NMR δ: 173.78 (s), 141.26 (s), 128.52 (d), 128.37 (d), 127.91 (d), 94.89 (s), 67.35 (s), 40.22 (d), 37.17 (t), 35.09 (t), 33.97 (t), 26.22 (d), 26.13 (d); MS *m/z*: 376 (M, 16), 333 (20), 332 (100), 331 (20), 256 (13), 212 (33), 211 (28), 198 (54), 167 (16), 166 (30), 165 (98), 131 (23), 121 (26), 105 (21).

5-Methoxy-tricyclo[3.3.1.1^{3,7}]decane-2-spiro-2'-(4',4'-diphenyl-1',3'-oxathiolan-5'-one), **7a** *(32% yield, as a mixture of diastereoisomers)*

Isomer 1: mp 157–158°C; ^{1}H NMR δ: 7.5–7.4 (m, 4H), 7.4–7.2 (m, 6H), 3.19 (s, 3H), 2.2–2.05 (m, 5H), 2.05–1.99 (d, 2H), 1.8–1.6 (m, 4H), 1.6–1.4 (d, 2H); ^{13}C NMR δ: 173.05, 140.75, 128.20, 128.19, 127.80, 93.21, 70.06, 67.15, 48.23, 41.70, 40.23, 37.83, 32.72, 27.95; MS *m/z*: 406 (M, 22), 363 (25), 362 (100), 361 (27), 198 (74), 167 (30), 166 (26), 165 (64), 120 (18), 109 (54).

Isomer 2: mp 138–139°C; ^{1}H NMR δ: 7.6–7.4 (m, 4H), 7.4–7.2 (m, 6H), 3.16 (s, 3H), 2.3–2.1 (m, 5H), 1.9–1.8 (d, 2H), 1.8–1.6 (m, 4H), 1.6–1.5 (d, 2H); ^{13}C NMR δ: 172.98, 140.68, 128.20, 128.18, 127.80, 92.69, 69.71, 67.11, 48.07, 42.00, 40.73, 36.68, 33.78, 27.98; MS *m/z*: 406 (38), 363 (34), 362 (100), 361 (37), 199 (17), 198 (67), 167 (31), 166 (26), 165 (77), 120 (30), 109 (18); X-ray structure, Fig. 1.[4]

Pyrolysis of 1,3-oxathiolan-5-ones

Tris(diethylamino)phosphine (greater than 15% mol excess) and the appropriate 1,3-oxathiolan–5-one were heated in an oil bath (240–260°C) under nitrogen for 8 h. Purification of the crude reaction mixture by column chromatography (100% hexane) gave the desired alkene as a colourless solid.

4-tert-*Butyl-2-diphenylmethylenecyclohexane,* ***2****:* Recrystallized from ethanol (67% yield), mp 105–107°C; UV (3:1 CH_3CN:CH_3OH): λ_{max} 240 nm, ε 1.1 × 10^4 M^{-1} cm^{-1}; ^{1}H NMR (400 MHz) δ: 7.24–7.10 (m, 10H), 2.66 (d, 2H, J = 13.2 Hz), 1.91 (dd, 2H, J = 13.2 Hz, 3.77 Hz), 1.83 (d, 2H, J = 13.4 Hz), 1.24–1.21 (m, 1H), 1.16–1.10 (m, 2H), 0.85 (s, 9H); ^{13}C NMR δ: 143.18 (s), 139.15 (s), 134.23 (s), 129.94 (d), 127.90 (d), 126.08 (d), 48.36 (d), 32.54 (s), 32.31 (t), 29.38 (t), 27.71 (q); MS *m/z*: 305 (M + 1, 26), 304 (M, 100), 206 (11), 205 (12), 180 (33), 167 (25), 91 (19), 57 (15); HRMS calcd. for $C_{23}H_{28}$: 304.219; found: 304.218.

2-Diphenylmethylenetricyclo[3.3.1.1^{3,7}]decane, **6***:* Recrystallized from ethanol (73% yield), mp 109.5–111°C (lit. (19) mp 107–109°C); UV (3:1 CH_3CN:CH_3OH): λ_{max} 244 nm, ε 1.31 × 10^4 M^{-1} cm^{-1}; ^{1}H NMR δ: 7.28–7.11 (m, 10H), 2.77 (s, 2H),

© 1998 NRC Canada

1.99 (s, 2H), 1.86 (s, 10H); ^{13}C NMR δ: 146.65 (s), 143.03 (s), 130.73 (s), 129.59 (d), 127.97 (d), 126.00 (d), 39.63 (t, C4, C8, C9, C10), 37.17 (t, C6), 34.42 (d, C1, C3), 28.22 (d, C5, C7); MS *m/z*: 301 (M + 1, 24), 300 (M, 100). Anal. calcd. for $C_{23}H_{24}$: C 91.95, H 8.05; found: C 91.98, H 8.07.

5-Methoxy-2-diphenylmethylenetricyclo[3.3.1.1^{3,7}]decane, ***7****:* 41% yield, UV: λ_{max} 240 nm, ε 1.10×10^4 M^{-1} cm^{-1}; ^{1}H NMR δ: 7.3–7.2 (m, 4H), 7.2–7.1 (m, 6H), 3.28 (s, 3H), 2.93 (s, 2H), 2.0–1.6 (m, 11H); ^{13}C NMR δ: 144.08 (s), 142.65 (s), 131.91 (s), 129.39 (d), 128.06 (d), 126.25 (d), 71.85 (s, C5), 48.19 (s), 42.12 (t, C4, C9), 40.56 (t, C6), 38.54 (t, C8, C10), 35.74 (d, C1, C3), 30.51 (d, C7); MS *m/z*: 331 (M + 1, 24), 330 (M, 100); HRMS calcd. for $C_{24}H_{26}O$: 330.198; found: 330.198.

Synthesis of alkenes 3, 4, and 5

Preparation of alcohols

2-Phenylmethyl-2-tricyclo[3.3.1.1^{3,7}]decanol, ***3a***
Magnesium turnings (0.33 g, 0.014 mol) and anhydrous ether (5 mL) were combined under nitrogen in an oven-dried three-neck flask equipped with a reflux condenser. A few drops of a solution of benzyl chloride (1.4 mL, 0.012 mol) in anhydrous ether (10 mL) were added via a dropping funnel. When no signs of reaction were observed, the flask was immersed in a warm water bath, a single crystal of iodine was added, and the magnesium turnings were broken into smaller pieces with a spatula, until the solution turned cloudy. The resulting solution was cooled to 0°C in an ice–water bath, and the remaining benzyl chloride was added over a period of half an hour, followed by 15 min of reflux. The solution was then cooled to 0°C followed by dropwise addition of 2-adamantanone (1.67 g, 0.011 mol) in anhydrous ether (20 mL). After the addition was complete, the resulting solution was refluxed for an additional 15 min, and cooled to room temperature. The ethereal solution was transferred to a separatory funnel containing cold, saturated ammonium chloride. The ether layer was removed, and the aqueous layer was extracted with ether. The combined ether layers were washed with water, dried over anhydrous magnesium sulfate, and the solvent removed by rotary evaporation. The crude oil was purified by column chromatography (10:90 ethyl acetate:hexane) to give the desired alcohol as a white solid (59% yield); ^{1}H NMR δ: 7.19 (s, 5H), 2.91 (s, 2H), 2.15 (d, 2H, J = 12.2 Hz), 2.04 (d, 2H, J = 12.8 Hz), 1.86 (s, 1H), 1.75–1.62 (m, 6H), 1.48 (s, 2H), 1.42 (s, 1H); ^{13}C NMR δ: 137.06, 130.35, 127.80, 126.01, 74.24, 43.59, 38.17, 36.50, 34.29, 32.66, 27.28, 27.14. The ^{1}H NMR spectrum of this alcohol agrees with that previously reported (18).

2-(4-Methoxyphenylmethyl)-2-tricyclo[3.3.1.1^{3,7}]decanol, ***4a***
Magnesium turnings (0.55 g, 0.023 mol) were activated by vigorous stirring under nitrogen for 3 days prior to reaction (39). Sufficient anhydrous ether (5 mL) was added to just cover the magnesium, and the mixture was cooled to 0°C. A few drops of a solution of 4-methoxybenzyl chloride (3.0 g, 0.019 mol) in anhydrous ether (20 mL) were added. Once the solution turned cloudy, signalling formation of the Grignard reagent, the remaining 4-methoxybenzyl chloride solution was added over a half-hour period. The resulting solution was stirred for an additional 15 min. A solution of 2-adamantanone (1.0 g, 0.007 mol) in anhydrous ether (20 mL) was added dropwise over a 1 h period. Stirring was continued overnight at room temperature, and the resulting solution worked up in the same manner as above for **3a**: ^{1}H NMR δ: 7.14 (d, 2H, J = 8.5 Hz), 6.84 (d, 2H, J = 8.5 Hz), 3.79 (s, 3H), 2.93 (s, 2H), 2.06–1.92 (m, 8H), 1.77 (d, 2H, J = 11.3 Hz), 1.68 (d, 2H, J = 11.3 Hz), 1.52 (d, 2H, J = 12.2 Hz); ^{13}C NMR δ: 158.33, 131.53, 129.16, 113.7, 74.54, 55.23,42.90, 39.27, 38.45, 36.83, 34.62, 33.02, 27.55.

5-Methoxy-2-phenylmethyl-2-tricyclo[3.3.1.1^{3,7}]decanol ***5a***
The method was the same as that used for **3a**, except that THF was used in place of ether as the solvent and, instead of heating at reflux, the solution was stirred overnight at room temperature prior to work-up. Two isomers, the (*E*) and the (*Z*) alcohol, were obtained. Spectral data were assigned based on literature data for (*E*)- and (*Z*)-5-methoxy-2-adamantanol.

(E)-Alcohol: 1H NMR δ: 7.32–7.21 (m, 5H), 3.28 (s, 3H), 3.01 (s, 2H), 2.12–2.08 (m, 5H), 1.85–1.74 (m, 6H), 1.39–1.34 (m, 3H); ^{13}C NMR δ: 136.79, 130.57, 128.46, 126.74, 74.00, 71.92, 48.40, 43.84, 41.10, 38.56, 37.85, 31.91, 29.30.

(Z)-Alcohol: ^{1}H NMR δ: 7.34–7.20 (m, 5H), 3.21 (s, 3H), 2.97 (s, 2H), 2.26–2.21 (m, 3H), 2.04–1.99 (m, 3H), 1.89 (s, 2H), 1.72–1.62 (m, 4H), 1.47–1.42 (m, 2H); ^{13}C NMR δ: 137.03, 130.54, 128.42, 126.70, 73.49, 71.51, 48.10, 43.13, 41.66, 38.94, 35.98, 33.44, 29.34.

Dehydration of alcohols
The alcohols **3a**, **4a,** and **5a** were dehydrated in benzene, in the presence of *p*-toluenesulfonic acid (10 mol%) as catalyst, using the same apparatus and procedure as for the preparation of 1,3-oxathiolan-5-ones.

2-Phenylmethylenetricyclo[3.3.1.1^{3,7}]decane, ***3****:* UV (9:1 CH_3CN:CH_3OH): λ_{max} 246 nm, ε 1.5×10^4 M^{-1} cm^{-1}; ^{1}H NMR δ: 7.26–7.16 (m, 5H), 6.18 (s, 1H), 3.16 (s, 1H), 2.49 (s, 1H), 1.99 (s, 2H), 1.93 (s, 4H), 1.86 (s, 6H); ^{13}C NMR δ: 151.26 (s, C2), 138.34 (s), 128.77 (d), 128.08 (d), 125.68 (d), 117.10 (d), 41.06 (d, C3), 39.91 (t, C4,C10), 37.28 (t, C8, C9), 32.32 (d, C1), 28.49 (d, C5, C7); MS *m/z:* 225 (M + 1, 14), 224 (M, 100), 167 (10), 129 (12), 128 (12), 91 (22). Exact Mass calcd. for $C_{17}H_{20}$: 224.156; found: 224.158. The ^{1}H NMR spectrum agrees with that reported previously (18).

2-(4-Methoxyphenylmethylene)tricyclo[3.3.1.1^{3,7}]decane, ***4****:* IR (Nujol):1609, 15.09, 1449, 1299, 1247, 1176, 1040, 867, 822, 714; UV (3:1 CH_3CN:CH_3OH): λ_{max} 250 nm, ε 2.0×10^4 M^{-1} cm^{-1}; ^{1}H NMR δ: 7.13 (d, 2H, J = 8.7 Hz), 6.84 (d, 2H, J = 8.7 Hz), 6.12 (s, 1H), 3.80 (s, 3H), 3.13 (s, 1H), 2.47 (s, 1H), 1.98 (s, 2H), 1.92 (s, 4H), 1.85 (s, 6H); ^{13}C NMR δ: 157.66 (C2), 150.27, 131.01, 129.81, 116.43, 113.51, 55.28, 40.97 (C3), 39.98 (C4, C10), 39.07 (C8, C9), 37.30 (C6), 32.26 (C1), 28.52 (C5, C7); MS *m/z*: 255 (M + 1, 22), 254 (M, 100), 121 (19). Anal. calcd. for $C_{18}H_{22}O$: C 84.99, H 8.72; found: C 84.68, H 8.63.

5-Methoxy-2-phenylmethylenetricyclo[3.3.1.1^{3,7}]decane ***5****:* UV (9:1 CH_3CN:CH_3OH): λ_{max} 243 nm, ε 1.47×10^4 M^{-1} cm^{-1};

© 1998 NRC Canada

^{1}H NMR δ: 7.29–7.16 (m, 5H), 6.20 (s, 1H), 3.32 (s, 3H), 2.69 (s, 1H), 2.27 (s, 1H), 1.89–1.72 (m, 10H); ^{13}C NMR δ: 148.59 (s), 137.94 (s), 128.61 (d), 128.05 (d), 125.90 (d), 118.37 (C11, d), 71.80 (C5, s), 48.07 (q), 42.23 (C6, t), 41.99 (C3, d), 41.45 (C9, t), 40.65 (C4, t), 38.80 (C8, t), 37.92 (C10, t), 33.23 (C7, d), 30.53 (C1, d); MS *m/z*: 255 (M + 1, 19), 254 (M, 100), 167 (13), 162 (12), 134 (12), 119 (26), 109 (20), 105 (11), 91 (14), 86 (34), 84 (50), 71 (11), 56 (19), 46 (10), 40 (10). Anal. calcd. for $C_{18}H_{22}O$: C 84.99, H 8.72; found: C 84.79, H 8.54.

Photochemistry

Either a 200 or 450 W Hanovia medium-pressure mercury lamp was used as the light source for photoreactions. Mixtures of acetonitrile and methanol were used as solvent in every case. Acetonitrile was purified by a four-step procedure: distillation from sodium hydride, distillation from phosphorus pentoxide, passage through basic alumina, and distillation from calcium hydride after 24 h reflux under nitrogen. Methanol was distilled from sodium prior to use. Dicyanobenzene (DCB) and 1,4-dicyanonaphthalene were available in our laboratory. DCB and the desired alkene were dissolved in acetonitrile–methanol in an immersion well (300 or 420 mL) equipped with a Pyrex filter. The solution was purged with nitrogen for 15 min prior to the irradiation. A positive pressure of nitrogen and magnetic stirring were maintained for the duration of the reaction. After the photolysis the solvent was removed under vacuum and the photoproducts were separated by column chromatography on silica gel and identified by spectroscopic methods.

Photoproducts

4-tert-*Butyl-1-diphenylmethylcyclohexene,* ***8****:* ^{1}H NMR δ: 7.29–7.13 (m, 10H), 5.21 (s, 1H), 4.64 (s, 1H), 2.01–1.98 (m, 2H), 1.87–1.76 (m, 2H), 1.31–.122 (m, 2H), 1.04–0.99 (m, 1H), 0.85 (s, 9H); ^{13}C NMR δ: 143.05 (s), 143.02 (s), 139.70 (s), 129.35 (d), 129.29 (d), 128.17 (d), 128.14 (d), 126.14 (d), 126.08 (d), 125.74 (d), 58.48 (s), 44.18 (s), 32.26, 30.38, 27.27 (q), 27.11, 24.51; GC–MS *m/z*: 305 (15, M + 1), 304 (M, 61), 206 (13), 205 (14), 180 (31), 168 (15), 167 (100), 166 (13), 165 (31), 141 (10), 129 (19), 128 (13), 117 (11), 115 (15), 91 (51), 57 (47).

2-Phenylmethyl-2-tricyclo[3.3.1.1^{3,7}]decanenitrile, ***9****:* Recrystallized from ethanol–water, mp 105–106.5°C; ^{1}H NMR δ: 7.32–7.24 (m, 5H), 3.08 (s, 3H), 2.24 (d, 2H, *J* = 13.4 Hz), 2.16 (d, 2H, *J* = 14.0 Hz), 1.92 (s, 4H), 1.83 (s, 1H), 1.76 (s, 4H), 1.70 (s, 1H); ^{13}C NMR δ: 135.80, 130.20, 128.26, 127.14, 123.81, 46.31, 40.09, 38.05, 35.35, 33.15, 31.05, 26.96, 26.81; MS *m/z*: 252 (M + 1, 11), 251 (M, 67), 91 (100). Anal. calcd. for $C_{18}H_{21}N$: C 86.01, H 8.42; found: C 86.14, H 8.42. X-ray structure, Fig. 2.[4]

2-Phenyl-2-(2-tricyclo[3.3.1.1^{3,7}]decanyl)ethanenitrile, ***10****:* Recrystallized from ethanol–water, mp 140.5–142°C; ^{1}H NMR δ: 7.44–7.21 (m, 5H), 3.73 (s, 2H), 2.58 (s, 2H), 2.10 (s, 1H), 2.05 (s, 2H), 1.98 (s, 1H), 1.90 (s, 2H), 1.86 (s, 2H), 1.72 (s, 4H), 1.64 (s, 2H); ^{13}C NMR δ: 144.23 (s), 128.72 (d), 126.59 (d), 126.11 (d), 117.88 (s), 44.91 (s), 38.32 (t), 32.84 (t), 30.50 (t), 27.55 (d), 26.95 (d); MS *m/z*: 251 (M, 6), 212 (17), 211 (100, M – CH_2CN), 91 (11); HRMS calcd. for $C_{18}H_{21}N$: 251.167; found: 251.66. X-ray structure, Fig. 3.[4]

Methyl 1-phenyl-2-(2-tricyclo[3.3.1.1^{3,7}]decanyl)ethyl ether, ***11***

This ether was not isolated from the photoreaction of **3** but was prepared as follows.

1-Phenyl-2-(2-tricyclo[3.3.1.1^{3,7}]decanyl)ethanol

A solution of alkene **22** (0.10 g, 4.46×10^{-4} mol) in THF (15 mL) was cooled to 0°C in an ice–water bath with stirring. Borane (1.0 M solution in THF, 2.5 mL, 0.0025 mol) was added dropwise and the resulting solution was warmed to room temperature and stirred for several hours. The reaction was then opened to the air, and water (1 mL), followed by aqueous sodium hydroxide (3 M, 2 mL), was added dropwise. Vigorous bubbling was observed. Hydrogen peroxide (30% solution, 2 mL) was added dropwise, after which the solution was left to stir for 5 min at 0°C, then for 20 min at room temperature. Water (10 mL) and ether (20 mL) were added to the reaction flask and the resulting mixture was left to stir for several minutes. The solution was transferred to a separatory funnel leaving a white solid behind, and was extracted three times with ether. The combined ether extracts were dried over anhydrous magnesium sulfate and the solvent removed under vacuum. Purification by column chromatography (95:5 hexane:ethyl acetate) gave the desired alcohol (0.10 g, 91% yield); ^{1}H NMR δ: 7.41–7.22 (m, 5H), 4.84 (d, 1H, *J* = 10.4 Hz), 2.32 (s, 1H), 2.08 (d, 1H, *J* = 12.8 Hz), 1.93–1.49 (m, 11H), 1.44 (d, 1H, *J* = 10.7 Hz), 1.20 (s, 1H); ^{13}C NMR δ: 144.05, 128.45, 127.67, 126.73, 74.69, 51.43, 39.06, 38.81, 38.25, 32.24, 31.66, 28.89, 28.19, 28.01, 27.84.

The ether **11** was prepared from the above alcohol by the same procedure as 5-methoxy-2-adamantone, above: ^{1}H NMR δ: 7.34–7.25 (m, 5H), 4.31 (d, 1H, *J* = 10.4 Hz), 3.16 (s, 3H), 2.35 (s, 1H), 2.05 (d, 1H, *J* = 12.8 Hz), 1.94–1.53 (m, 11H), 1.44 (d, 1H, *J* = 10.4 Hz); ^{13}C NMR δ: 141.49, 128.27, 127.55, 127.47, 84.26, 56.76, 50.88, 39.14, 38.82, 38.34, 31.96, 30.09, 29.42, 28.32, 28.16, 27.95; GC–MS *m/z*: 122 (16), 121 (100), 91 (23), 79 (12), 77 (24).

Methyl 2-phenylmethyl-2-tricyclo[3.3.1.1^{3,7}]decanyl ether, ***12****:* Recrystallized from ethanol, mp 101–103°C; ^{1}H NMR δ: 7.31–7.19 (m, 5H), 3.34 (s, 3H), 3.00 (s, 2H), 2.12–2.00 (m, 4H), 1.91–1.69 (m, 8H), 1.46 (d, 2H); ^{13}C NMR δ: 137.92, 130.19, 128.02, 125.97, 79.57, 47.34 (C2), 38.42 (C6), 35.21 (C4,C9), 34.53 (C1,C3), 33.63 (C8,C10), 32.80 (C11), 27.70 (C7), 27.29 (C5); MS (70 eV) *m/z*: 165 (100, M – C_7H_7), 91 (19); MS (20 eV) *m*/z: 256 (M, 1), 166 (12), 165 (100), 91 (19), 81 (10), 79 (11); CIMS (iso-C_4H_{10}) *m/z*: 257 (4), 226 (18), 225 (100), 185 (10), 165 (37).

2-(4-Methoxyphenylmethyl)-2-tricyclo[3.3.1.1^{3,7}]decanenitrile, ***13****:* mp 96–98°C; ^{1}H NMR δ: 7.27 (d, 2H, *J* = 8.5 Hz), 6.86 (d, 2H, *J* = 8.5 Hz), 3.79 (s, 3H), 3.03 (s, 2H), 2.24 (d, 2H, *J* = 12.8 Hz), 2.15 (s, 2H, *J* = 13.4 Hz), 1.92 (s, 4H), 1.83 (s, 1H), 1.76 (s, 4H), 1.69 (s, 1H); ^{13}C NMR δ: 158.72, 131.18, 127.80, 123.98, 113.66, 55.19, 46.51, 39.24, 38.07, 35.39, 33.09, 31.04, 27.00, 26.85; MS *m/z*: 281 (M, 100), 121 (100); HRMS calcd. for $C_{19}H_{23}NO$: 281.178; found: 281.180.

© 1998 NRC Canada

2-(4-Methoxyphenyl)-2-(2-tricyclo[3.3.1.1^{3,7}]decanyl)ethanenitrile, ***14****:* ^{1}H NMR δ: 7.32 (d, 2H, *J* = 8.7 Hz), 6.92 (d, 2H, *J* = 8.7 Hz), 3.81 (s, 3H), 2.73 (s, 2H), 2.74 (s, 2H), 2.06 (d, 2H, *J* = 14.6 Hz), 1.98 (s, 1H), 1.88 (d, 2H, *J* = 11.6 Hz), 1.73 (s, 2H), 1.63 (s, 1H), 1.57 (s, 4H); MS *m/z*: 281 (M, 10), 242 (22), 241 (100, M – CH_2CN), 130 (34), 128 (23), 121 (20), 102 (15), 85 (19), 56 (39), 55 (11), 54 (26), 42 (42), 40 (43), 38 (15), 29 (28), 38 (24); HRMS calcd. for $C_{19}H_{23}NO$: 281.178;found: 281.176.

Methyl 2-(4-methoxyphenylmethyl)-2-tricyclo[3.3.1.1^{3,7}]-decanyl ether, ***15****:* mp 81–82.5°C; IR (Nujol): 2227, 1611, 1511, 1444, 1251, 1177, 1030; ^{1}H NMR δ: 7.15 (d, 2H, *J* = 8.5 Hz), 6.82 (d, 2H, *J* = 8.5 Hz), 3.78 (s, 3H), 3.33 (s, 3H), 2.94 (s, 2H), 2.10 (d, 2H, *J* = 12.2 Hz), 2.00 (d, 2H, *J* = 12.2 Hz), 1.90 (s, 1H), 1.76 (s, 4H), 1.68 (s, 2H), 1.57 (s, 1H), 1.45 (d, 2H, *J* = 11.9 Hz); ^{13}C NMR δ: 157.85, 131.00, 129.88, 113.49, 79.52, 55.24, 47.30, 38.42, 34.51, 34.30, 22.56, 32.81, 27.72, 27.32; MS *m/z*: 254 (M, 28),166 (10), 165 (100), 121 (10); HRMS calcd. for $C_{19}H_{26}O_2$: 286.193; found: 286.192.

Methyl 1-(4-methoxyphenyl)-2-(2-tricyclo[3.3.1.1^{3,7}]decanyl)-ethyl ether, ***16****:* ^{1}H NMR δ: 7.21 (d, 2H, *J* = 8.7 Hz), 6.88 (d, 2H, *J* = 8.7 Hz), 4.26 (d, 1H, *J* = 10.4 Hz), 3.81 (s, 3H), 3.13 (s, 3H), 2.31–1.56 (m, 14H); ^{13}C NMR δ: 159.05, 133.42, 128.56, 113.65, 83.74, 56.59, 55.25, 50.83, 39.18, 38.84, 38.37, 32.27, 31.97, 28.80, 28.37, 28.18, 27.97; MS *m/z*: 286 (M, 5), 152 (10), 151 (100).

2-(Diphenylmethyl)-2-tricyclo[3,3,1,1^{3,7}]decanitrile, ***17****:* mp 256–257.5°C; ^{1}H NMR δ: 7.7–7.6 (m, 4H), 7.4–7.2 (m, 6H), 4.61 (s, 1H), 2.35–2.15 (m, 4H), 1.94 (bs, 4H), 1.9–1.7 (m, 4H), 1.7–1.6 (d, 2H); ^{13}C NMR (250 MHz) δ: 139.40 (s), 129.37 (d), 128.59 (d), 127.19 (d), 123.95 (s, CN), 52.40 (d, Ph_2CH), 48.01 (s, C2), 38.22 (t, C6), 35.15 (t, C8,C10), 32.02 (d, C1, C3), 30.86 (t, C4,C9), 26.61 (d, C5 or C7), 26.58 (d, C5 or C7). Assignments in the ^{13}C spectrum were based on an NOE experiment; irradiation of the diphenylmethyl C-H gave enhancements only for the *ortho* aromatic hydrogens and a doublet at δ 2.19. An ^{1}H/^{13}C correlated spectrum demonstrated that the proton was attched to C4 at δ 30.86. MS *m/z:* 327 (M, 7), 210 (12), 168 (16), 167 (100), 108 (14), 105 (27), 91 (16), 77 (10); HRMS calcd. for $C_{24}H_{25}N$: 327.199; found: 327.198. The X-ray structure is shown in Fig. 4.[4]

1,2-Diphenyl-2-(2-tricyclo[3.3.1.1^{3,7}]ethanenitrile, ***18****:* GC–MS *m/z*: 212 (13), 211 (100), 167 (20), 129 (10), 91 (38).

syn-*5-Methoxy-2-(diphenylmethyl)-2-tricyclo[3.3.1.1^{3,7}]-decanenitrile,* ***19****:* mp 176–178°C; ^{1}H NMR δ: 7.7–7.6 (m, 4H), 7.5–7.2 (m, 6H), 4.51 (s,1H), 3.23 (s, 3H), 2.4–2.1 (m, 6H), 1.8–1.6 (m, 7H); ^{13}C NMR (250 MHz) δ: 138.95 (s), 129.30 (d), 128.70 (d), 127.38 (d), 123.50 (CN), 70.66 (s, C5), 52.43 (d, Ph_2CH), 48.17 (q), 47.45 (s, C2), 40.73 (t, C6), 35.06 (t, C4,C9), 34.87 (d, C1,C3), 34.08 (t, C8,C10), 28.78 (d, C7); MS *m/z:* 357 (M, 2), 168 (28), 167 (100), 165 (22); HRMS calcd. for $C_{25}H_{27}NO$: 357.209; found: 357.210. The X-ray structure is shown in Fig. 5.[4]

anti-*5-Methoxy-2-(diphenylmethyl)-2-tricyclo[3.3.1.1^{3,7}]-decanenitrile,* ***20****:* mp 148–149°C; ^{1}H NMR δ: 7.7–7.6 (d, 4H), 7.4–7.2 (m, 6H), 4.52 (s, 1H), 3.28 (s, 3H), 2.3–2.1 (m, 6H), 1.8–1.6 (m, 7H); ^{13}C NMR (250 MHz) δ: 138.95 (s), 129.30 (d), 128.70 (d), 127.39 (d), 123.34 (CN), 70.66 (s, C5), 52.43 (d, Ph_2CH), 48.17 (q, CH_3O), 47.45 (s, C2), 40.72 (d, C6), 35.06 (t, C4, C9), 34.88 (d, C1, C3), 34.08 (t, C8, C10), 28.78 (d, C7); MS *m/z:* 357 (M, 2), 168 (19), 167 (100), 165 (19); HRMS calcd. for $C_{25}H_{27}NO$: 357.209; found: 357.209.

1,2-Diphenyl-2-(5-methoxy-2-tricyclo[3.3.1.1^{3,7}]ethanenitrile, ***21****: GC–MS m/z:* 242 (19), 241 (100, 2-phenyl-5-methoxy-2-adamantyl$^+$), 167 (10), 109 (22), 91 (19).

Photolysis of 3 in methanol-OD

The photoreaction of alkene **3** in the presence of added cyanide ion was repeated on 0.10 g of the alkene using deuterated methanol, CH_3OD. The reaction was stopped at low percentage conversion, and the photoproducts were not separated. The percentage deuterium in the products was obtained using the Single Ion Monitoring (SIMS) program on the GC–MS and software developed in-house.

Fluorescence quenching studies

A Perkin–Elmer MFP 66 fluorescence spectrometer at 25°C was used for fluorescence measurements. Samples were prepared with constant concentration of the sensitizer, either DCB or 1,4-dicyanonaphthalene, and varying concentration of alkene in either 9:1 or 3:1 acetonitrile:methanol. All samples were degassed by three freeze–pump–thaw cycles.

Cyclic voltametric measurements

Cylic voltammetry at a sweep rate of 100 mV/s was used to obtain the oxidation potentials of the alkenes. The apparatus has been described previously (40). The working electrode was a platinum sphere (1 mm diameter) and the counter electrode was a platinum wire. The reference electrode was saturated calomel (SCE), which was connected to the solution (0.1 M TEAP, acetonitrile) through a Luggin capillary. The alkene concentration was ca. 0.005 M. Because the anodic wave was irreversible, the half-wave potential was taken as 0.028 V before the peak potential (41).

Acknowledgements

We thank the Natural Sciences and Engineering Research Council of Canada (NSERC) for the financial support that made this work possible. S.S. thanks the Dalhousie Faculty of Graduate Studies for the award of a graduate fellowship. We also thank Dr. Peter de Lijser for the measurement of oxidation potentials and Professor D.R. Arnold for helpful discussions.

References

1. B.W. Gung. Tetrahedron, **52**, 5263 (1996).
2. M. Kaselj, J.L. Adcock, H. Luo, H. Zhang, H. Li, and W.J. le Noble. J. Am. Chem. Soc. **117**, 7088 (1995), and refs. therein.
3. W. Adcock, J. Cotton, and N.A. Trout. J. Org. Chem. **59**, 1867 (1994).
4. G. Mehta, F.A. Khan, N. Mohal, I.N. Narayan Namboothiri, P. Kalyanaraman, and J. Chandrasekhar. J. Chem. Soc. Perkin Trans.1, 2665 (1996).
5. J.M. Coxon, K.N. Houk, and R.T. Luibrand. J. Org. Chem. **60**, 418 (1995).

© 1998 NRC Canada

6. C.K. Cheung, L.T. Tseng, M.-H. Lin, S. Srivastava, and W.J. le Noble. J. Am. Chem. Soc. **108**, 1598 (1986).
7. M. Xie and W.J. le Noble. J. Org. Chem. **54**, 3839 (1989).
8. I.H. Song and W.J le Noble. J. Org. Chem. **59**, 58 (1994).
9. V.R. Bodepudi and W.J. le Noble. J. Org. Chem. **56**, 2001 (1991).
10. A. Mukherjee, Q. Wu, and W.J. le Noble. J. Org. Chem. **59**, 3270 (1994).
11. W.-S. Chung, Y.-D. Liu, and N.-J. Wang. J. Chem. Soc. Perkin Trans. 2, 581 (1995).
12. W.-S. Chung, N.J. Turro, S. Srivastava, and W.J. le Noble. J. Org. Chem. **56**, 5020 (1991).
13. J. Lau, E.M. Gonikberg, J. Hung, and W.J. le Noble. J. Am. Chem. Soc. **117**, 11421 (1995).
14. J.M. Hahn and W.J. le Noble. J. Am. Chem. Soc. **114**, 1916 (1992).
15. M. Kaselj, J.L. Adcock, H. Luo, H. Zhang, H. Li, and W.J. le Noble. J. Am. Chem. Soc. **117**, 7088 (1995).
16. D.R. Arnold and A.J. Maroulis. J. Am. Chem. Soc. **98**, 5931 (1976).
17. D.H.R. Barton and B.J. Willis. J. Chem. Soc. Perkin Trans.1, 305 (1972).
18. H. Kreul. Chem. Ber. **108**, 1198 (1975).
19. D.R. Arnold and S.A. Mines. Can. J. Chem. **65**, 2312 (1987).
20. L.J. Johnston and N.P Schepp. J. Am. Chem. Soc. **115**, 6564 (1993).
21. L.J. Johnston and N.P. Schepp. Adv. Electron Transfer Chem. **5**, 41 (1996).
22. S.L. Murov, I. Carmichael, and G.L. Hug. Handbook of photochemistry. 2nd ed. Marcel Dekker, New York. 1993. p. 207.
23. D. Rehm and A. Weller. Isr. J. Chem. **8**, 259 (1970).
24. D.D. Wayner. CRC Handbook of organic photochemistry. Vol.II. *Edited by* J.C. Scaiano. CRC Press, Boca Raton, Fla. 1989. Chap. 18.
25. D.D.M. Wayner, D.J. McPhee, and D. Griller. J. Am. Chem. Soc. **110**, 132 (1988).
26. J.W. Wilt. Free radicals. Vol. I. *Edited by* T.K. Kochi. John Wiley & Sons, New York. 1973. p. 346.
27. J.A. Franz, R.D. Barrows, and D.M. Camaioni. J. Am. Chem. Soc. **106**, 3964 (1984).
28. L. Lopez, L. Troisi, and G. Mele. Tetrahedron Lett. **32**, 117 (1991).
29. E. Bosch and J.K. Kochi. J. Am. Chem. Soc. **118**, 1319 (1996).
30. L. Ebberson. Electron transfer reactions in organic chemistry. Springer-Verlag, New York. 1987. p. 47.
31. D.R. Arnold, M.S.W. Chan, and K.A. McManus. Can. J. Chem. **74**, 2143 (1996).
32. G. Leroy, D. Peeters, M. Sana, and C. Wilante. Substituent effects in radical chemistry. *Edited by* H.G. Viehe, Z. Janousek, and R. Merenyi. D. Reidel, Dordrecht. 1986. p.1.
33. R.A. Neunteufel and D.R. Arnold. J. Am. Chem. Soc. **95**, 4080 (1973).
34. H. Duddeck, F. Hollowood, A. Karim, and M.A. McKervey. J. Chem. Soc. Perkin Trans. 2, 360 (1979).
35. F.A. Carroll. Perspectives in structure and mechanism in organic chemistry. Brooks/Cole, Pacific Grove, Calif. 1998. p. 828.
36. R.A. McClelland. Tetrahedron, **52**, 6823 (1996).
37. D.R. Arnold, X. Du, and J. Chen. Can. J. Chem. **73**, 307 (1995).
38. H. Becker and A. Bistrzycki. Ber. Dtsch. Chem. Ges. **47**, 3145 (1917).
39. K.V. Baker, J.M. Brown, N. Hughes, A.J. Skarnulis, and A. Sexton. J. Org. Chem. **56**, 698 (1991).
40. D.R. Arnold and D.D.M. Wayner. Can. J. Chem. **64**, 100 (1986).
41. (*a*) R.S. Nicholson and I. Shain. Anal. Chem. **36**, 706 (1964); (*b*) Anal. Chem. **37**, 178 (1965).

© 1998 NRC Canada

Molecular modelling and NMR studies of the caffeine dimer[1]

Michael Falk, Warren Chew, John A. Walter, Witold Kwiatkowski, Katherine D. Barclay, and Gerald A. Klassen

Abstract: A survey of crystal structures containing the xanthine ring shows that caffeine-like molecules tend to stack in parallel in a variety of stacking geometries, suggesting that a stacked pair of caffeine molecules has many conformations of comparable energy. Molecular modelling suggests that the caffeine dimer, the major associated species in aqueous solution, may occur in nine distinct conformations. In agreement with the crystal survey and the modelling results, NMR spectra of caffeine solutions exhibit intermolecular nuclear Overhauser enhancements (NOEs), consistent with a dynamic equilibrium of several conformations of the dimer of comparable energies.

Key words: caffeine, dimer, self-association, molecular modelling, intermolecular nuclear Overhauser enhancements (NOEs).

Résumé : Une revue des structures cristallines comportant un noyau xanthine montre que les molécules qui ressemblent à la caféine ont tendance à se superposer de façon parallèle en adoptant diverses géométries; ces données suggèrent qu'une paire de molécules de caféine peut adopter plusieurs conformations d'énergies comparables. La modélisation moléculaire suggère que le dimère de la caféine, l'espèce associée principale en solution aqueuse, peut adopter neuf conformations distinctes. En accord avec la revue des structures cristallines et des études de modélisation moléculaire, les spectres de RMN de la caféine en solution présentent des effets Overhauser nucléaires (EON) intermoléculaires qui correspondent avec un équilibre dynamique de plusieurs conformations du dimère d'énergies comparables.

Mots clés : caféine, dimère, autoassociation, modélisation moléculaire, effets Overhauser nucléaire (EON) intermoléculaires.

[Traduit par la rédaction]

Introduction

Caffeine (Fig. 1), or 1,3,7-trimethylxanthine, is the most widely ingested mood-altering substance (1). Its mode of action is within the central nervous system where it acts as a stimulant, perhaps by competitive blockade of endogenous adenosine at A_1 and A_2 receptors (2). In this context, the self-association of caffeine molecules in aqueous solution, which has been demonstrated by many different physical and spectroscopic methods (3–9), might have physiological significance. It is known that caffeine associates to form dimers, and to some extent also trimers and higher aggregates (9). That these aggregates involve the stacking of caffeine molecules is clearly shown by the existence of ring current shifts of ^{1}H resonances to high field, with increasing solution concentration (10). However, the actual geometry of the dimer has not been clarified (11–16). Even more uncertain is the geometry of the higher aggregates and their proportions. The commonly assumed isodesmic model assumes that the sequential equilibrium constants K_2, K_3, K_4, etc. are equal (7, 8, 17, 18), but infrared results (9) suggest that the dimerization constant K_2 is substantially larger than K_3.

In the present work we have addressed these problems in several ways. We have studied the caffeine–caffeine geometry by molecular modelling methods and by a survey of caffeine-like molecules in crystals. We have measured the intermolecular nuclear Overhauser enhancements (NOEs) of caffeine in aqueous solution, which do not appear to have been previously observed. The combination of these NOE results with molecular modelling and crystal data affords new insight into the structure of caffeine dimers, the preponderant species in solution. Our findings also apply to the stacking interactions of other aromatic molecules implicated in physiological phenomena (19).

Possible geometries of stacked caffeine molecules

To discuss the geometry of a pair of caffeine molecules stacked with their rings in parallel, we use a coordinate system (Fig. 1) such that the centroid of the *bottom* molecule is at the origin, its C_8—H_8 bond points in the *x* direction, its purine ring lies in

Received July 29, 1997.

M. Falk,[2] W. Chew,[3] and J.A. Walter. Institute for Marine Biosciences, National Research Council of Canada, Halifax, NS B3H 3Z1, Canada.

W. Kwiatkowski. Department of Chemistry, Dalhousie University, Halifax, NS B3H 4J3, Canada.

K.D. Barclay[4] and G.A. Klassen. Maritime Heart Centre, Victoria General Hospital, Halifax, NS B3H 2Y9, Canada.

[1] NRCC No. 39768.

[2] Author to whom correspondence may be addressed. Institute for Marine Biosciences, National Research Council of Canada, 1411 Oxford Street, Halifax, NS B3H 3Z1, Canada. Telephone: (902) 426-8265. Fax: (902) 426-9413. E-mail: michael.falk@nrc.ca

[3] Present address: Wyeth Ayerst Canada Ltd., 1025 Marcel-Laurin Blvd., St. Laurent, QC H4R 1J6, Canada.

[4] Present address: School of Health and Human Performance, Dalhousie University, Halifax, NS B3H 3J5, Canada.

© 1998 NRC Canada

Fig. 1. Caffeine molecule showing the numbering of atoms and the coordinate system.

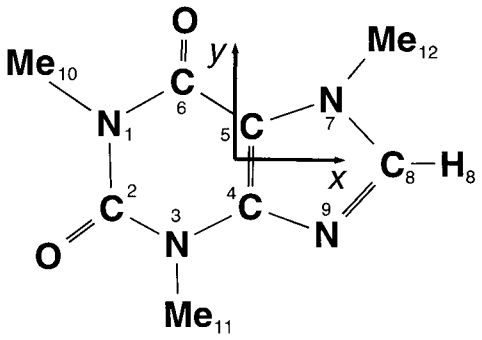

Table 1. Previously suggested dimer geometries.

Reference	Method	Dimer	Angle *R*
Thakkar et al. (11, 12)	^{1}H NMR	**B**	0°
Kikkert et al. (13)	UV spectra	**B**	0°
Fritzsche et al. (14)	^{1}H NMR	**A or B**	90° or 270°
Kan et al. (15)	^{1}H and ^{13}C NMR	**A**	90°
Yanuka et al. (16)	^{1}H NMR	**A**	0°

the *x*–*y* plane, and the top molecule is displaced from the bottom one in the positive *z* direction. There are two distinct ways in which a pair of caffeine molecules can stack (Fig. 2). In structure **A** ("top-to-bottom"), the two caffeines are related by a simple translation along the *z*-axis, followed by a rotation by an arbitrary angle about the *z*-axis, and a glide in the *x*–*y* plane. In structure **B** ("top-to-top"), the two caffeines are related by a translation along the *z*-axis, followed by a rotation of *either* the top molecule *or* the bottom molecule by 180° about the *x*-axis (again, followed by a rotation by an arbitrary angle about the *z*-axis, and a glide in the *x*–*y* plane). The two ways of generating **B** result in enantiomers.

Stacked caffeine pairs **A** and **B** possess four degrees of freedom for which we have employed the following four parameters: *R* (angle of clockwise rotation in the *x*–*y* plane of the top molecule with respect to the bottom molecule), *X* (translation of the top molecule along *x*-axis), *Y* (translation of the top molecule along *y*-axis), and *Z* (spacing between the two molecular planes).

It should be noted that **A** possesses mirror–plane symmetry (point group C_s) when $R = 0°$, and a centre of symmetry (point group C_i) when $R = 180°$, but becomes dissymmetric (point group C_1) for other values of *R*, so that pairs of structures corresponding to *R* and $360° - R$ are enantiomeric. Structure **B** possesses a two-fold symmetry axis (symmetry point group C_2) preserved for all values of *R* and is always dissymmetric, occurring as "right-handed" or "left-handed" enantiomers. The enantiomers cannot be distinguished by NMR spectra, or most other physical measurements, however, their occurrence and the symmetry of **A** and **B** play an important part in determining the relative weights of different conformational structures.

Earlier authors assumed that a caffeine dimer occurs in one preferred conformation, but have about equally favoured the two possible structures, **A** and **B,** with the angle *R* of either 0° or 90° (Table 1). Their conclusions have been based largely on NMR phenomena such as ring current effects, which, while

Fig. 2. Dimers **A** and **B,** after Kikkert et al. (13).

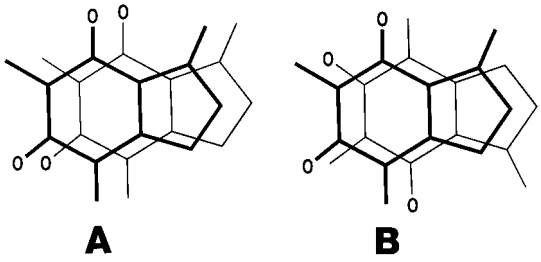

indicating that the rings are parallel and in close proximity, are not very sensitive to the relative orientation and displacement of the two component molecules. The earlier results, therefore, provide no secure basis for deciding in favour of a particular dimer geometry. The possibility that the dimer may exist as a dynamic mixture of energetically similar conformers does not appear to have been considered.

Geometries of caffeine-like molecules in crystals

Aromatic molecules in crystals tend to organize themselves in one of two different ways: face-to-face parallel stacking, with a characteristic spacing of about 3.4 Å, and edge-to-face or T-shape arrangement in which the rings approach at highly inclined angles, often perpendicular (20, 21). C···C interactions dominate in the parallel stacking, while H···C interactions dominate in the T-shape arrangement.

Crystalline benzene adopts the T-shape arrangement (20) but increasing molecular area, increasing ratio of carbons to hydrogens, heterosubstitution, and presence of carbonyl groups all favour parallel stacking over T-shape (20, 22, 23). Therefore, caffeine-like molecules may be expected to exhibit stacking strongly. This expectation is, indeed, confirmed by a survey of crystalline structures.

We have surveyed the Cambridge Structural Database (24) for crystal structures containing the xanthine skeleton, without bulky side groups, and containing no other structural elements except for water of hydration. Eleven such structures were found (25–35), involving 14 distinct stacking geometries, listed in Table 2. Every one of these structures involves parallel stacking of molecules with the characteristic 3.4 Å spacing. The T-shape approach was only encountered in two structures (**3** and **4** in Table 2) in which the stacking was particularly loose, as shown by the unusually large values of the offset parameter *X*. While all of the eleven structures involve stacking, there is a wide spread of geometries: the interplane spacing parameter *Z* varies from 3.25 to 3.57 Å, while the offset parameters *X* and *Y* vary from 0.11 to 4.44 Å, averaging 1.7 Å for *X* and 0.7 Å for *Y*. An offset of 1–2 Å is very common for stacked aromatic rings in crystals (20), and offset geometry has been said to correspond to the lowest energy of a pair of stacked rings (23).

The stacked molecules in these crystals adopt two arrangements. In the *infinite stack*, the more common arrangement, each molecule has two parallel neighbours, above and below. In the somewhat less common *stacked-pair* arrangement, each molecule has only one parallel neighbour. In seven crystals the arrangement of near-neighbours is "top-to-bottom,"

© 1998 NRC Canada

Table 2. Geometry of stacked caffeine analogues in crystals.

Crystal structure (ref.)	Arrangement		*R* (°)	*X* (Å)	*Y* (Å)	*Z* (Å)
1. Caffeine monohydrate (25)	Stack	**A**	0	1.93	0.80	3.37
2. 3-Methyl xanthine (26)	Stack	**A**	0	1.11	1.19	3.37
3. 1-Methyl-9-amino xanthine (27)	Loose pair	**B**	180	–4.44	–0.22	3.23
4. 1,7,9-Trimethyl-2,6-purinedione (28)	Loose stack	**A**	0	–4.07	0.97	3.34
5. 3-Hydroxyxanthine dihydrate (29)	Pair	**B**	180	0.84	1.04	3.32
6. Isocoffeine (30)	Stack ***a***	**A**	180	0.29	1.34	3.37
	b	**A**	180	–2.80	0.31	3.40
7. Monosodium urate monohydrate (31)	Stack	**A**	0	1.23	–0.71	3.27
8. 7-Butyl–1,3-dimethylxanthine (32)	Stack ***a***	**B**	–6	0.11	0.13	3.42
	b	**B**	+3	–0.22	–1.81	3.57
9. Theophylline monohydrate (33)	Stack	**A**	0	2.93	0.21	3.39
10. 1,3,7,9-Tetramethyluric acid (34)	Stack ***a***	**A**	180	0.67	–0.27	3.40
	b	**A**	180	–0.52	–0.57	3.34
11. Uric acid (35)	Pair	**B**	180	–2.36	1.14	3.25
Mean values:				±1.7	±0.7	3.37

corresponding to structure **A**, while in four crystals it is "top-to-top," corresponding to structure **B**.

The relative orientation of the stacking molecules, given by the angle *R*, depends on their symmetry relation. If these molecules are crystallographically related by lattice translation, *R* is 0° (structures **1**, **2**, **4**, **7**, and **9**). If they are related by inversion, *R* is 180° (structures **3**, **5**, **6**, **10**, and **11**). In the latter case, the *second-nearest* neighbours are related by a lattice translation, and the values of parameters *X*, *Y*, and *Z* alternate along the stack (***a*** and ***b*** in Table 2). In structure **8** the stacking molecules are related by a screw axis, and the parameter *R* takes alternating non-zero values along the stack.

The survey of crystal data demonstrates a strong tendency of caffeine-like molecules to stack either as pairs or as infinite chains of parallel molecules, adopting either the top-to-bottom or the top-to-top arrangement. The wide spread of observed pair geometries is consistent with the existence of many possible interpair arrangements of comparable energy. The incidence of the T-shape geometry is low, suggesting that it is energetically less favourable than parallel stacking.

Molecular modelling

The method

A conformational study of the caffeine dimer was carried out by molecular modelling, using SYBYL software (SYBYL version 6.2, Tripos, Inc., St. Louis, Mo.) running on a Personal Iris 4D/35 TurboGraphic workstation (Silicon Graphics, Inc., Mountain View, Calif.) under the IRIX 5.2 operating system. The conformational search was carried out under the Tripos force field (36), including electrostatic terms based on atomic charges computed by the Gasteiger–Marsili algorithm (37, 38). The calculations were first carried out under the condition $\varepsilon = R_{ij}$, i.e., the dielectric constant ε set to equal the interatomic distance R_{ij} in Å, simulating the screening effect of a water-like solvent on the electrostatic charges (39). To assess the effect of the water medium on the relative energies of the dimer conformers, the calculations were repeated with ε = 1 corresponding to vacuum, then with ε = 80 corresponding to liquid water, and finally with ε = 1 but with a small cluster of water molecules surrounding the caffeine dimer. The water cluster was formed using the SYBYL solvent algorithm, which adds solvent molecules one at a time, with an energy minimization at each step. For hydrate clusters of up to five H_2O molecules, this procedure led to a unique minimized energy for all nine conformers. For larger clusters, however, repeated runs produced several alternative structures, so that a large computational effort would be needed to ensure that the structure of lowest energy had been identified. The energies of the dimer conformers were also calculated using the alternative force fields AMBER (39) (available within the SYBYL software) and MM+ (used with the Hyperchem software package supplied by Hypercube Inc., Waterloo, Ont.) The force field MM+ is an extended version of the MM2 force field developed by Allinger (40).

Preliminary survey of dimer stability

In a preliminary survey, we have repeatedly minimized the energy of a pair of caffeine molecules, starting from many arbitrary geometries. Energy minimization nearly always led to a parallel-stacked orientation. On rare occasions the molecular pair became "stuck" in a nonparallel orientation, which was invariably of much higher energy by at least 6 kcal/mol. Minimizations that started with the prepared T-shaped geometry, known to be stable for benzene dimers (20), also led to a parallel-stacked geometry. This geometry clearly corresponds to the stable form of caffeine dimer under the force fields used. Therefore, especially in view of the results of the crystal survey (previous section) and the recent report of Kollman and coworkers (41) on the greater relative stability of the parallel-stacked geometry of toluene dimers compared to benzene dimers, we have henceforth concentrated our conformation study on the parallel-stacked pairs of molecules.

Survey of energy as a function of parameters R, X, Y, *and* Z

To survey the shape of the potential of a pair of parallel-stacked caffeine molecules as a function of *R*, *X*, *Y*, and *Z*, we varied each of these parameters in turn, keeping the others constant. In this survey, we used the macro DIMER, written in SYBYL programming language by Chris van Dyke of Tripos Inc. and modified by Peter Spierenburg. In the DIMER procedure, one caffeine molecule is placed in the *x*–*y* plane at $z = 0$, its centre of mass being at (0, 0, 0). The second caffeine molecule is placed at height *Z* above the first one, either without

© 1998 NRC Canada

Fig. 3. Plot of energy as a function of rotation R about the z-axis for dimers **A** and **B**. Parameters $X = Y = 0$ Å, $Z = 3.4$ Å; Tripos force field; $\varepsilon = R_{ij}$.

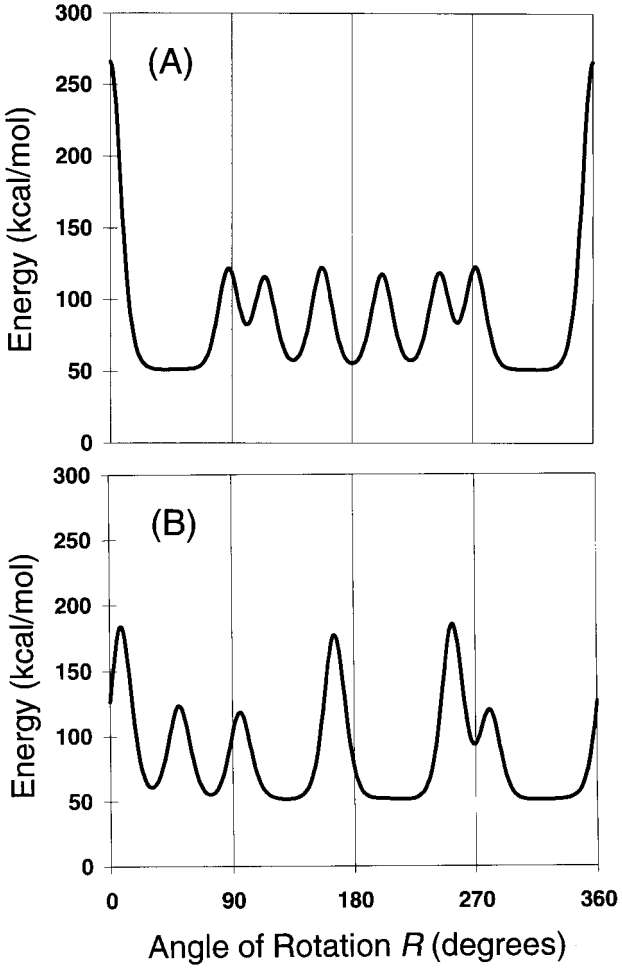

Fig. 4. Plot of energy as a function of the lateral movement (along X and Y) of the caffeine molecules in dimer **B**. (*a*) Near the global minimum; $R = 318°$, $Z = 3.4$ Å. (*b*) Near a local maximum; $R = 245°$, $Z = 3.4$ Å. The isocontour lines shown correspond to 51–57 kcal/mol. Tripos force field; $\varepsilon = R_{ij}$.

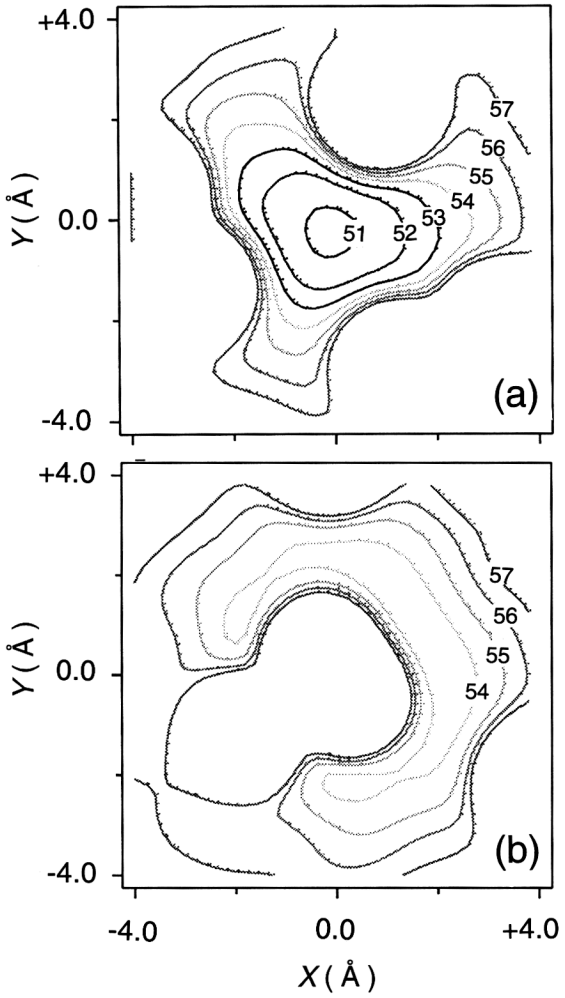

rotation (dimer **A**) or with 180° rotation about x (dimer **B**). The macro creates dimer structures for the specified ranges and intervals of parameters R, X, Y, and Z, computes their energy, and stores the structures in a database.

The dependence of the energy on the rotation angle R is shown in Fig. 3. To generate this plot, parameter R was varied in steps of 1°, the other parameters being kept constant: $Z = 3.4$ Å, $X = Y = 0$ Å. A series of energy minima are observed for each dimer, seven for **A** (six of them forming three equivalent pairs, due to symmetry) and six for **B**. Some of the minima are relatively flat. The minima are separated by relatively sharp energy maxima due to repulsive methyl contacts. The energy minima can be identified with regions of R where the three methyl groups of one caffeine avoid those of the other caffeine.

The dependence of energy on X and Y is shown in Fig. 4. Two distinct situations arise. For R values corresponding to conformations of relatively low energy, avoiding repulsive methyl contacts, the minimum is near $X = 0$, $Y = 0$, corresponding to maximum overlap of the two aromatic-ring systems. The potential well is then a centrally located circle, as in Fig. 4*a*. For R values corresponding to conformations of higher energy, methyl repulsions are avoided by moving the aromatic rings apart laterally. The potential well in these cases forms a circular or crescent-shaped valley surrounding an energy maximum near $X = 0$, $Y = 0$, as in Fig. 4*b*.

The dependence of energy on the interplanar spacing Z is shown in Fig. 5. It is qualitatively the same for all values of R, X, and Y, being governed by the van der Waals energy terms. There is one minimum, with a steep increase toward smaller separations and a less steep increase toward greater separations. However, the position and depth of the minimum depend strongly on the values of R, X, and Y. For combinations of these parameters that correspond to conformations of relatively low energy, the minimum occurs near $Z = 3.25$ Å as in Fig. 5*a*. For conformations of high energy, the minimum occurs at values of Z greater than 4 Å as in Fig. 5*b*.

Search for stable conformations

Figures 3–5 demonstrate the shape of the dimer potential with respect to the parameters R, X, Y, and Z. Keeping in mind this general shape, we searched for stable conformations of dimer **A** and **B**, using the macro DIMER as follows. For each of 72

© 1998 NRC Canada

Fig. 5. Plot of energy as a function of the spacing Z between the planes of the two caffeine molecules in dimer **B**. $X = Y = 0$ Å, $R =$ 318° (case *a*), $R = 245°$ (case *b*). Tripos force field; $\varepsilon = R_{ij}$.

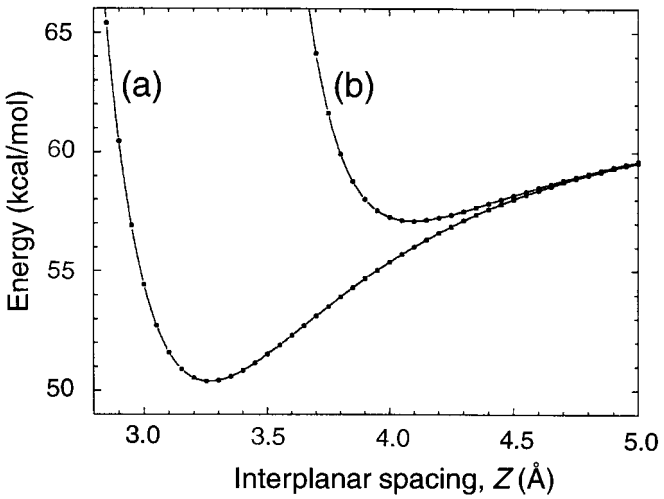

values of the angle R (range 0–360°, interval 5°), we generated $41 \times 41 = 1681$ structures with X and Y varying from –4 to +4 Å in steps of 0.2 Å, the value of Z being kept constant at 3.4 Å. Of each such set of 1681 structures we retained only the one of lowest energy. This led to 72 candidate structures, whose energies we then minimized. In these minimizations the two caffeine molecules were not constrained to parallel planes, and all atom coordinates were allowed to vary freely. Nevertheless, in agreement with our preliminary observations, all minimized structures ended up with the two caffeine molecules in parallel planes.

For dimer **A**, four distinct minima were found, **A1**–**A4**, corresponding roughly to the minima in Fig. 3*a*. Minimum **A4** occurs once, while **A1**, **A2**, and **A3** occur twice due to symmetry. For dimer **B**, five distinct minima were found, **B1**–**B5**, corresponding to the five deeper minima in Fig. 3*b*. The energies and geometric parameters of these nine minima are listed in Table 3. A thorough examination of the local conformation space confirmed that the nine minima correspond to distinct conformers with energies that are within 1.3 kcal/mol of one another. Conformer **A1** has a double energy minimum and all the other conformers a single energy minimum. When all geometric parameters are allowed to vary, energy barriers that separate the various minima are only of the order of 1–3 kcal/mol, much lower than those for rigid rotation (shown in Fig. 3), which amount to 50–100 kcal/mol. The reason for this difference is that for a given value of the angle R the repulsive methyl contacts can be very much diminished by the two molecules sliding laterally (increasing X and Y) and by spreading farther apart (increasing Z).

Four of the nine dimer conformations correspond to pair geometries found in crystals of caffeine-like molecules: **A1** corresponds to structures **1**, **2**, **4**, **7**, and **9**; **A4** corresponds to **6*a***, **6*b***, **10*a***, and **10*b***; **B3** corresponds to **3**, **5,** and **11**; and **B5** corresponds to **8*a*** and **8*b***. These correspondences are based on the A–B classification and the rough values of the angles R and R' (defined below). The values of the offset parameters X and Y generally do not match.

The nine conformers

The picture that emerges from molecular modelling is that of a caffeine dimer with many possible conformations of similar energy, likely to exist as a mixture. This mixture can be approximately represented as composed of the nine conformers **A1**–**A4** and **B1**–**B5**, with relative populations that can be determined from Boltzmann factors corrected for the multiplicity factors shown in Table 3 in which symmetry and the doublet structure of the potential well of dimer **A1** are taken into account. Table 3 records the energies and the calculated populations for the nine energy-minimized conformers, the parameters R', X, Y, and Z, which define dimer geometry, and the average intermolecular H···H approaches ($1/r^3$ averaging) for comparison with the observed NOE data. For the energy-minimized conformers, the parameter R' is the dihedral angle H_8'-C_8'-C_8''-H_8'' (where the primed and double-primed atoms refer to the two caffeine molecules), closely related to the z-rotation angle, R. The two quantities R' and R are equal when there is no lateral displacement of the two molecules, i.e., when $X = Y = 0$, but differ by as much as 40° when X or Y are large. The fully energy-minimized dimer conformers have the interplanar spacing Z about 3.1 Å (3.25–3.57 Å in crystals) and the lateral displacements X and Y in the range 0–1.8 Å, (0.1–4.4 Å in crystals).

The above results were obtained using the Tripos force field and distance-dependent dielectric constant $\varepsilon = R_{ij}$, which qualitatively simulates the water medium in which electrostatic interactions should die off more rapidly with distance than in vacuum (39). We have also re-minimized the dimer conformers under two alternate settings of the dielectric constant within the Tripos force field as well as under two other force fields, AMBER and MM+. As could be expected, the *absolute energies* of caffeine dimers, obtained in these alternative calculations, were considerably different. The *relative energies*, however, were similar (Table 4). The conformer with lowest energy was in every case the same, **B5**, and the total spread of energies of the conformers was 1.3 kcal/mol.

To further assess the applicability of our results to caffeine dimers in aqueous medium, we have re-minimized the nine conformers **A1**–**B5**, surrounded by water clusters consisting of one to five H_2O molecules. In these results (columns 5–7, Table 4), again **B5** remained the conformer with lowest energy, and the total spread of energies of the conformers was 2.9 kcal/mol. Since all these calculations, including those with explicit water molecules, have yielded comparable results, we conclude that our main finding that the dimer has nine conformers of comparable energies and hence of appreciable populations holds for caffeine in aqueous medium. The apparent insensitivity of the *relative energies* of the dimer conformers to the presence of water molecules implies that the hydrophobic forces stabilize the various stacked arrangements almost equally well.

Measurement of intermolecular NOE

The detection of intermolecular nuclear Overhauser enhancements (NOEs) offers the potential to distinguish between different models for the caffeine dimer. We undertook such measurements using the one-dimensional NOE-difference technique on caffeine solutions at four different concentrations, reasoning that intermolecular NOEs should appear to

© 1998 NRC Canada

Table 3. Stable conformations of caffeine dimer, their geometry, and average intermolecular H···H approaches.

				Dimer geometry							
Conformer	Multiplicity	Relative energy[a] (kcal/mol)	Population (%)	R' (deg)	X (Å)	Y (Å)	Z (Å)	H_8'-H_{10}'' (Å)	H_8'-H_{11}'' (Å)	H_{10}'-H_{12}'' (Å)	H_{11}'-H_{12}'' (Å)
A1	4	0.727	28.1	41.1	–0.46	+0.11	3.06	7.29	4.58	5.43	6.57
A2	2	0.987	9.0	115.0	–0.92	+0.20	3.08	4.34	4.04	4.15	3.87
A3	2	1.220	6.1	152.4	–1.01	+0.01	3.08	3.67	4.25	4.79	3.61
A4	1	0.864	5.5	180.0	–1.75	+0.13	3.05	3.59	6.17	5.29	3.96
B1	1	1.333	2.5	75.1	+0.26	+0.33	3.07	5.16	7.19	7.55	7.18
B2	1	0.885	5.4	87.0	–0.96	+1.30	3.11	3.61	7.95	5.14	8.08
B3	1	0.299	14.5	200.8	+0.20	–0.12	3.05	3.56	4.47	3.43	6.67
B4	1	0.938	4.9	290.6	–0.47	–0.34	3.10	6.61	3.15	4.15	4.13
B5	1	0.000	24.0	9.7	–0.19	+0.14	3.05	7.81	6.51	7.92	4.17
Population-weighted average over conformers:								4.73	4.71	4.78	4.74

[a] Tripos force field; $\varepsilon = R_{ij}$. The energies are relative to that of the conformer with lowest energy.

Table 4. Energies[a] of the nine conformers of caffeine dimer hydrated by N molecules of H_2O, calculated under different force fields and different values of dielectric constant.

Force field	Tripos						AMBER	MM+
Dielec. const.	$\varepsilon = R_{ij}$	$\varepsilon = 80$	$\varepsilon = 1$	$\varepsilon = 1$	$\varepsilon = 1$	$\varepsilon = 1$	$\varepsilon = R_{ij}$	$\varepsilon = 1$
N	0	0	0	1	3	5	0	0
A1	0.72	0.65	0.70	0.50	1.37	0.93	0.24	0.42
A2	0.99	0.70	0.97	0.53	1.65	1.62	0.50	0.70
A3	1.22	1.33	1.15	0.80	2.27	2.95	0.70	0.71
A4	0.86	1.02	0.74	0.49	1.34	1.36	0.34	0.70
B1	1.33	1.36	1.25	0.94	1.12	2.56	0.70	0.79
B2	0.89	0.89	0.82	0.68	1.52	1.80	0.76	0.69
B3	0.30	0.01	0.30	0.26	0.78	0.35	0.45	0.29
B4	0.94	1.10	0.94	0.74	1.27	2.34	0.57	0.50
B5	0.00	0.00	0.00	0.00	0.00	0.00	0.00	0.00

[a] The energies (kcal/mol) are relative to that of the conformer with lowest energy.

increase with concentration due to the greater proportion of dimer in solution, whereas intramolecular NOEs should remain constant. Preliminary experiments indicated that other techniques for detecting NOE, such as NOESY, were not sufficiently sensitive with our instrument to measure very small intermolecular effects.

Experimental

All experiments were performed with a Bruker AMX–500 spectrometer at 500.13 MHz with spectral width 4504 Hz, acquisition time 1.82 s, excitation pulse 6 μs (45°), temperature 20.0°C, and continuous irradiation for 5 s between data-acquisition periods. The power setting was 40–50 dB, sufficient to produce ca. 90% saturation of a single resonance. To ensure uniformity of conditions and to minimize drift, a cycle of interspersed on-resonance and off-resonance irradiations was repeated 12 or more times, with 16 scans added and 4 dummy scans at each repetition. Total transients added to each spectrum varied from 192 for the highest caffeine concentration to 944 for the lowest concentration. Solutions of caffeine (Sigma cat. no. C–0750) were made up by weight in "100%" D_2O (MSD Isotopes cat. no. MD–1743) to 0.001, 0.005, 0.010, 0.051, and 0.10 M, placed in Wilmad 535pp NMR tubes, and degassed by three to four successive freeze–pump–thaw cycles after which N_2 was injected over the solutions. Samples were not spun during acquisition. Spectra were processed under identical conditions of exponential weighting (LB (line broadening) 0.2 and 3.0 Hz) and phasing, and those corresponding to on-resonance irradiation were subtracted, without alteration of intensity scales, from the off-resonance spectra. NOEs (%) were measured from the difference spectra by integrating each resonance after calibrating the integral of the irradiated peak to 100 units for the H_8 resonance or 300 units for the methyl resonance and correcting for the number of protons represented by each peak. Linear base-line corrections were applied if necessary over ca. 0.1 ppm regions on either side of the peaks. As all ^1H resonances of caffeine are singlets, NOEs were detectable to very low levels (ca. 0.03% at 0.1 M, 0.10% at 0.001 M caffeine). Errors were estimated from the noise levels of integrals, and separate off-resonance spectra were subtracted from each other to check for exactness of cancellation. Results from a series of irradiations were discarded if separate off-resonance spectra, when subtracted, left residual integrals greater than the noise level. The chemical shift of the HOD peak was set to 4.67 ppm.

Results

The ^1H NMR spectrum of caffeine consists of four sharp singlet resonances, assigned as δ: 7.70 (H_8), 3.71 (H_{12}), 3.23 (H_{11}), 3.06 (H_{10}) (42). Figure 6 shows a series of NOE-difference

© 1998 NRC Canada

Fig. 6. One-dimensional NOE-difference spectra of caffeine at 0.1 M in D_2O, with irradiation of *(a)* H_8, (*b*) H_{12}, (*c*) H_{10}, and (*d*) H_{11}.

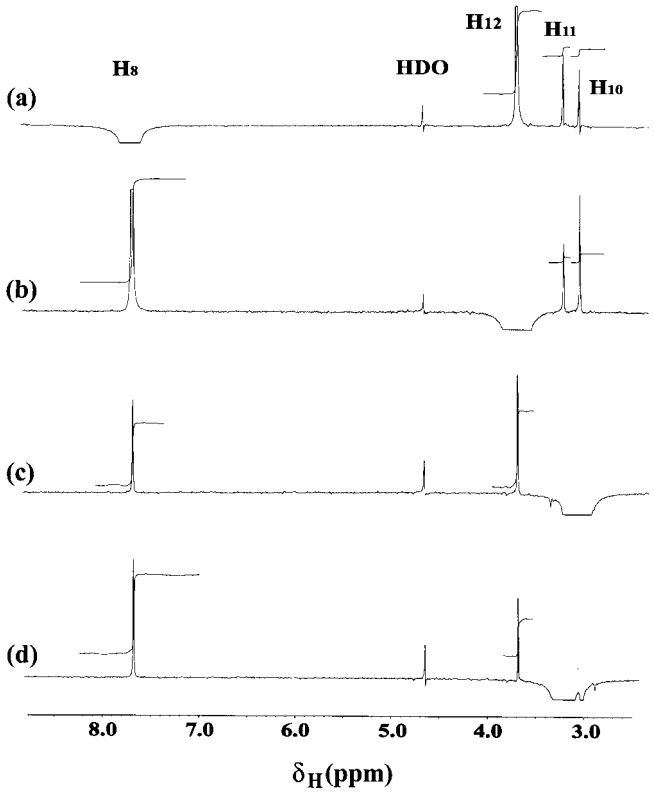

spectra, obtained from 0.1 M caffeine, in which NOEs are clearly detectable between all proton pairs except those for which partial saturation (ps) precludes observation. Similar results were obtained at the lower concentrations, the results of the complete series of NOE-difference experiments being summarized in Table 5.

A large positive NOE η_C was observed as expected between H_8 and H_{12}. The magnitude remained virtually constant with concentration, indicating that the intermolecular component was negligible compared to the intramolecular: ca. 2.3% NOE observed at H_{12} when H_8 was irradiated; ca. 14.9% for the reverse NOE. The NOEs in different directions between protons at a pair of positions are not expected to be identical, due to likely differences in relaxation pathways. Thus spin–rotation contributions to relaxation of unhindered methyl groups result in a lower NOE when H_8 is irradiated than when H_{12} is irradiated. All the other observable NOEs were also positive, and decreased as concentration was lowered, showing that these NOEs were predominantly intermolecular, without contributions from relayed NOE or exchange phenomena.

Approximate calculations of the contributions of intramolecular NOEs to total NOEs, and of the average intermolecular H—H distances from the remaining intermolecular NOEs, were based on the two-spin approximation (43).

All *intra*molecular H—H distances r_A other than H_8—H_{12} are in the range 5.24–7.40 Å, if calculated using molecular modeling. Assuming that the steady-state NOE is proportional to $\langle r^3 \rangle^{-2}$, appropriate for rapidly rotating methyl groups (43), and taking the averaged $\langle r^3 \rangle$ intramolecular H_8—H_{12} distance r_C (= 3.05 Å) as a calibration, the intramolecular NOE contribution η_A to the total NOE η_T for each proton pair was estimated from $\eta_A = \eta_C [r_C / r_A]^6$, yielding the numbers in Table 5.

The intermolecular contributions $\eta_E = (\eta_T - \eta_A)/(1 - p_M)$ were in turn used in calculations of average intermolecular H—H distances r_E, from $r_E = r_C [\eta_C / \eta_E]^{1/6}$. As intermolecular NOEs could occur only within dimers or higher oligomers, the mole fraction p_M of monomer calculated from isodesmic (18) or monomer–dimer–polymer (9) descriptions of caffeine equilibria was used as above to correct each intermolecular NOE contribution. This method of estimation of distance is supported by a recent study of solutions of trinitrotoluene complexes with aromatic hydrocarbons (44) in which good agreement was found between internuclear distances calculated from one-dimensional NOE difference experiments (as above) or from selective one-dimensional NOE build-up rates, with X-ray measurements of the solid complexes.

Intermolecular NOEs (Table 5) were clearly detected in at least one direction between the proton pairs H_8'-H_{10}'', H_8'-H_{11}'', H_{10}'-H_{12}'', H_{11}'-H_{12}'', where the single and double primes distinguish atoms of the two caffeine molecules of the dimer. For H_8'-H_{12}'' any intermolecular NOE was overwhelmed by the intramolecular effect. Certain NOEs denoted "ps" in Table 5, such as H_{10}'-H_{11}'', were not detectable even if they had been present, due to partial saturation resulting from closely-spaced resonances. For each pair, the total NOE is averaged over equivalent methyl protons and over dimers having the top and bottom caffeine molecules reversed.

Discussion

Analysis of NOE and modelling results

Table 3 records the average intermolecular H—H distances obtained from modelling for each conformer **A1**–**B5**, averaged over all contributing protons. It also gives the overall values of these distances, averaged over the nine conformers. The averaging was carried out in proportion to the inverse third power of the distance (43), according to eqs. [1]–[3] in Appendix.

Seven of the nine conformers have one or more interproton distances in the range of 6–8 Å, clearly too long to produce measurable internuclear NOEs. The other two conformers (**A2** and **A3**) yield no such long distances, but are of relatively high energy (under all force fields and dielectric constant settings investigated) and must be presumed to have low populations. Therefore, modelling implies that the observed NOE signals must originate in a mixture of conformers. Indeed, the four H—H distances averaged over all conformers (bottom line in Table 3) are about 4.7 Å, in excellent agreement with the average internuclear distance (4.6 ± 0.2 Å) calculated from the NOEs using the monomer–dimer–polymer model for caffeine equilibria. The same measured average based on the isodesmic model is lower (4.0 ± 0.2 Å), as this model predicts a smaller proportion of caffeine oligomers at a given concentration, and therefore a higher average intermolecular NOE per oligomer.

In view of the approximations used in deriving the intermolecular distances from the NOE data, and uncertainties in equilibrium constants, these observations do not decisively favour the monomer–dimer–polymer model over the isodesmic model, although in principle the models could be distinguished by sufficiently accurate measurements of this type. However,

© 1998 NRC Canada

Table 5. NOEs between ^{1}H resonances of caffeine and the derived H—H distance estimates at varying caffeine concentrations.[a]

		Resonance where NOE observed											
		H8			H10			H11			H12		
Caffeine conc. (M)	Irradiated resonance	% NOE Total	% NOE Intramol.	Dist. (Å)	% NOE Total	% NOE Intramol.	Dist. (Å)	% NOE Total	% NOE Intramol.	Dist. (Å)	% NOE Total	% NOE Intramol.	Dist. (Å)
0.100	H8	—			0.15(3)	0.01	4.7(2)	0.23(3)	0.09	4.7(2)	2.26(11)		
	H10	1.15(3)	0.07	4.6(2)	—			ps			0.46(3)	0.04	4.0(2)
	H11	1.73(11)	0.56	4.5(2)	ps			—			0.26(5)	0.02	4.3(2)
	H12	14.54(14)			0.42(8)	0.04	4.0(2)	0.21(3)	0.02	4.5(2)	—		
0.050	H8	—			0.11(3)	0.01	5.0(3)	0.21(3)	0.09	4.5(2)	2.39(6)		
	H10	1.02(27)	0.07	4.7(2)	—			ps			0.25(4)	0.04	4.4(2)
	H11	1.75(27)	0.56	4.5(2)	ps			—			nm		
	H12	15.77(21)			0.45(15)	0.04	4.0(2)	0.16(3)	0.02	4.7(2)	—		
0.010	H8	—			0.16(18)	0.01	4.4(5)	0.18(2)	0.09	4.5(2)	2.26(12)		
	H10	0.75(38)	0.07	4.7(3)	—			ps			0.10(3)	0.04	5.1(3)
	H11	1.06(70)	0.56	5.0(7)	ps			—			nm		
	H12	15.42(45)			0.23(19)	0.04	4.2(5)	<0.1	0.02	>4.9	—		
0.001	H8	—			<0.1			<0.15			2.12		
	H10	<0.30			—			ps			<0.20		
	H11	0.80(25)			ps			—			nm		
	H12	14.00(6)			<0.15			<0.20			—		

[a] Each NOE-difference spectrum was independently processed and integrated three times. For each proton pair, the table shows the average total % NOE, with errors in parentheses, then the estimated intramolecular NOE contribution. NOEs that could not be measured due to partial saturation are marked "ps," and those that could not be measured due to other experimental causes are marked "nm." The average intermolecular distances, with errors in parentheses, calculated from the residual intermolecular NOE, after subtraction of the intramolecular component and correction for oligomers, is based on the monomer–dimer–polymer model (see text). The entries for 0.001 M caffeine are total NOEs, or upper limits; errors precluded intermolecular distance estimates at this concentration.

the conclusion that the most consistent description of caffeine dimerization is a dynamic exchange among nine dimer conformers of comparable energy is strongly supported, because intermolecular NOEs are observed between all proton pairs for which measurement was possible.

Conformations of higher caffeine aggregates

In the first approximation, the interactions between the molecules of the larger aggregates should closely correspond to those of the dimer. For example, formally the trimer can be of four possible types, **A-A**, **A-B**, **B-A**, or **B-B**, and further distinctions can be made between conformers such as **A1-A1**, **A1-A2**, . . . **B5-B5**, yielding a total of $9 \times 9 = 81$ possible trimer conformers. However, their energies are unlikely to be the exact sums of dimer energies, and it is possible that the higher aggregates are generally less capable of variation than the dimer. There is evidence from infrared spectroscopy that the C=O groups are accessible to water in the caffeine dimer but not in the higher aggregates (9), which may imply greater uniformity of the latter. Greater uniformity of the higher aggregates agrees with the equilibrium constant for their formation, which is much smaller than the constant for the dimerization, presumably due to entropic factors.

Possible physiological consequences

The mode of action of mood-altering drugs upon the central nervous system involves binding to tissue receptors in the agonist or antagonist mode (45). The stacking association of caffeine with itself and with other small molecules, such as adenosine, is likely to lead to a dynamic equilibrium between many complexes. This would affect the availability of caffeine and adenosine to bind with receptors.

Hirsh (46) has reviewed many of the anomalous responses of caffeine in the central nervous system, such as increasing locomotor activity in animals. If the dose is increased progressively, a maximum occurs and then further increases cause a progressive decrease in activity. As these effects are presumed to be related to caffeine's competitive binding to adenosine receptors in the brain (47), stacking may contribute to an anomalous dose–response curve. Preliminary work in our laboratory (G.A.K. and K.D.B.) has demonstrated that adenosine's dose–response curve as a vasodilator also has anomalies. For example, when adenosine was given with peptides such as angiotensin II or oxytocin, the physiological responses to the peptide were altered (19). Studies of the binding of caffeine, adenosine, and vasoactive peptides to solubilized adenosine receptors, with concurrent monitoring of the degree of self- and hetero-stacking, might elucidate these phenomena and help determine if the reported anomalies in caffeine responses are in fact connected with stacking interactions occurring under physiological conditions.

Acknowledgements

We wish to acknowledge financial support from Merck Frosst Canada and the Heart and Stroke Foundation of Nova Scotia and valuable technical help from Chris van Dyke and Peter Spierenburg (programming), Ian W. Burton (use of Hypercube software), and Debora A. Arden (averaging calculations). We thank Prof. T. Bruce Grindley for a critical reading of the manuscript.

© 1998 NRC Canada

References

1. G.L. Clementz and J.W. Dailey. Am. Fam. Physician, **37**, 167 (1988).
2. S.H. Snyder, J.J. Katims, Z. Annau, R.F. Bruns, and J.W. Daly. Proc. Natl. Acad. Sci. U.S.A. **78**, 3260 (1981).
3. P.O.P. Ts'o, J.S. Melvin, and A.S. Olson. J. Am. Chem. Soc. **85**, 1289 (1963).
4. A.A. Maevsky and B.I. Sukhorukov. Nucl. Acids Res. **8**, 3029 (1980).
5. H. Bothe and H.K. Cammenga. Thermochim. Acta, **69**, 235 (1983).
6. H. Hoiland, A. Skauge, and I. Stokkeland. J. Phys. Chem. **88**, 6350 (1984).
7. R. Rymdén and P. Stilbs. Biophys. Chem. **21**, 145 (1985).
8. N. Iza, M. Gil, J.L. Montero, and J. Morcillo. J. Mol. Struct. **175**, 25 (1988).
9. M. Falk, M. Gil, and N. Iza. Can. J. Chem. **68**, 1293 (1990).
10. S.J. Perkins. Biol. Magn. Reson. **4**, 193 (1982).
11. A.L. Thakkar, L.G. Tensmeyer, R.B. Hermann, and W.L. Wilham. J. Chem. Soc. Chem. Commun. **9**, 524 (1970).
12. A.L. Thakkar, L.G. Tensmeyer, and W.L. Wilham. J. Pharm. Sci. **60**, 1267 (1971).
13. J.N. Kikkert, G.R. Kelly, and T. Kurucsev. Biopolymers, **12**, 1459 (1973).
14. H. Fritzsche, I. Petri, H. Schultz, K. Weller, P. Sedmera, and H. Lang. Biophys. Chem. **11**, 109 (1980).
15. L.S. Kan, P.N. Borer, D.R. Cheng, and P.O.P. Ts'o. Biopolymers, **19**, 1641 (1980).
16. Y. Yanuka, J. Zahalka, and M. Donbrow. J. Chem. Soc. Perkin Trans. 2, 911 (1986).
17. W.E. Price, K.A. Trickett, and K.R. Harris. J. Chem. Soc. Faraday Trans. 1, **85**, 3281 (1989).
18. T.H. Lilley, H. Lindsell, and A. Maestre. J. Chem. Soc. Faraday Trans. **88**, 2865 (1992).
19. G.A. Klassen. Coron. Artery Dis. **1**, 707 (1990).
20. G.R. Desiraju. *In* Crystal engineering, the design of organic solids. Elsevier, Amsterdam. 1989. pp. 92–102.
21. G.R. Desiraju and A. Gavezzotti. J. Chem. Soc. Chem. Commun. 621 (1989).
22. J.A.R.P. Sarma and G.R. Desiraju. Acc. Chem. Res. **19**, 222 (1986).
23. C.A. Hunter. J. Mol. Biol. **230**, 1025 (1993).
24. F.H. Allen, O. Kennard, and R. Taylor. Acc. Chem. Res. **16**, 146 (1983).
25. D.J. Sutor. Acta Crystallogr. **11**, 453 (1958).
26. J.N. Low, P. Tollin, E. Brand, and C. Wilson. Acta Crystallogr. **42**, 1447 (1986).
27. V.V. Kuz'menko, T.A. Kuz'menko, G.G. Aleksandrov, A.F. Pozharskii, and A.V. Gulevskaya. Khim. Geterotsikl. Soedin. SSSR, 836 (1987).
28. M. Parvez and G. Ferguson. Acta Crystallogr. Sect. C: Cryst. Struct. Commun. **C50**, 1303 (1994).
29. W.E. Thiessen, H.A. Levy, and B.D. Flaig. Acta Crystallogr. Sect. B: Struct. Crystallogr. Cryst. Chem. **B34**, 2495 (1978).
30. H. Rasmussen and E. Sletten. Acta Chem. Scand. **27**, 2757 (1973).
31. N.S. Mandel and G.S. Mandel. J. Am. Chem. Soc. **98**, 2319 (1976).
32. O. Agostini, G. Bonacchi, P. Dapporto, P. Paoli, L. Pogliani, and E. Toja. J. Chem. Soc. Perkin Trans. 2, 1061 (1994).
33. D.J. Sutor. Acta Crystallogr. **11**, 83 (1958).
34. D.J. Sutor. Acta Crystallogr. **16**, 97 (1963).
35. H. Ringertz. Acta Crystallogr. **20**, 397 (1966).
36. M. Clark, R.D. Cramer III, and N. Van Opdenbosch. J. Comput. Chem. **10**, 982 (1989).
37. J. Gasteiger and M. Marsili. Tetrahedron, **36**, 3219 (1980).
38. J. Gasteiger and M. Marsili. Org. Magn. Reson. **15**, 353 (1981).
39. S.J. Weiner, P.A. Kollman, D.A. Case, U.C. Singh, C. Ghio, G. Alagona, S. Profeta, Jr., and P. Weiner. J. Am. Chem. Soc. **106**, 765 (1984).
40. N.A. Allinger. J. Am. Chem. Soc. **99**, 8127 (1977).
41. C. Chipot, R. Jaffe, B. Maigret, D.A. Pearlman, and P.A. Kollman. J. Am. Chem. Soc. **118**, 11217 (1996).
42. T.G. Alexander and M. Maienthal. J. Pharm. Sci. **53**, 962 (1964).
43. D. Neuhaus and M.P. Williamson. The nuclear overhauser effect in structural and conformational analysis. VCH Publishers, New York. 1989.
44. R.E. Hoffman and M. Rabinovitz. Magn. Reson. Chem. **31**, 1031 (1993).
45. S.S. Wijmenga, M.M.W. Mooren, and C.W. Hilbers. *In* NMR of macromolecules: a practical approach. *Edited by* G.C.K. Roberts. Oxford University Press, Oxford. 1993. p. 217.
46. K. Hirsh. *In* The methylxanthine beverages and foods: chemistry, consumptions and health effects. *Edited by* G.A. Spiller. Alan R. Liss, Inc., New York. 1984. p. 235.
47. B.B. Fredholm. NIPS, **10**, 122 (1995).

Appendix: averaging the H···H distances

The averaging of the H···H distances in each conformer was done proportionately to the inverse third power of the distance. Averaging over the n equivalent proton distances R_{ij} for the *i*th equivalent proton pair in conformer *j* was done as follows:

$$[1] \quad (1/R_{j,\mathrm{av}}) = [(1/n)\ \Sigma_i\ (1/R_{ij})^3]^{1/3}$$

Six proton pairs had to be thus averaged in the case of H_8'-H_{10}'' and H_8'-H_{11}'' (for example, in the latter case the pairs H_8'-H_{11a}'', H_8'-H_{11b}'', H_8'-H_{11c}'', H_8''-H_{11a}', H_8''-H_{11b}', and H_8''-$H11_c'$). Eighteen proton pairs had to be averaged in the case of H_{10}'-H_{12}'' and H_{11}'-H_{12}''.

Final averaging over the equivalent proton pairs and over the nine conformers was done as follows,

$$[2] \quad (1/R_{\mathrm{av}}) = \{\Sigma_j\ P_j\ [(1/n)\ \Sigma_j\ (1/R_{ij})^3]\}^{1/3}$$

where P_j is the population factor for conformer *j*. The population factors at temperature $T = 300$ K were calculated from the energies E_j and multiplicities M_j of the individual conformers by assuming a Boltzmann distribution:

$$[3] \quad P_j = M_j \exp(-E_j/RT) \,/\, \Sigma_j\ M_j \exp(-E_j/RT)$$

© 1998 NRC Canada

Coriolis coupling constants and inertial defect of B_2F_4 by ab initio calculations and the iterative method

Marcos Loroño, J.R. Anacona, and Anibal Sierralta

Abstract: Structural parameters, harmonic frequencies, and force constants of B_2F_4 were obtained in internal coordinates from ab initio RHF calculations with the 6-311G* basis set. The results obtained are used to calculate the Coriolis coupling constants and the inertial defect for $^{10}B_2F_4$ and $^{11}B_2F_4$ and to compare these values with those obtained by using the autoconsistency method. Both the ab initio and the iterative force fields, despite some significant differences, reproduce the vibrational wave numbers equally well and yield nearly the same Coriolis coupling constants and inertial defects. The calculated inertial defects for $^{10}B_2F_4$ and $^{11}B_2F_4$ are –0.942 and –0.919 amu Å^2, respectively.

Key words: Coriolis coupling constants, inertial defect, B_2F_4, harmonic frequencies, force constants.

Résumé : Faisant appel à des calculs ab initio RHF avec l'ensemble de base 6-311G*, on a déterminé les paramètres structuraux, les fréquences harmoniques et les constantes de force du B_2F_4 dans des coordonnées internes. On a utilisé ces résultats pour calculer les constantes de couplage de Coriolis et le défaut d'inertie du $^{10}B_2F_4$ et du $^{11}B_2F_4$ et on a comparé ces valeurs à celles obtenues en faisant appel à la méthode autocohérente. Les méthodes ab initio et d'itération des champs de force, malgré des différences importantes, permettent toutes les deux de reproduire aussi bien les nombres d'onde vibrationnels et elles conduisent pratiquement aux même constantes de couplage de Coriolis et aux même défauts d'inertie. Les défauts d'inertie du $^{10}B_2F_4$ et du $^{11}B_2F_4$ sont respectivement –0,942 et –0,919 amu Å^2.

Mots clés : constantes de couplage de Coriolis, défaut d'inertie, B_2F_4, fréquences harmoniques, constantes de force.

[Traduit par la rédaction]

Introduction

Diboron tetrafluoride, B_2F_4, has been shown (1) by X-ray diffraction to be planar in the crystalline state at –120°C with molecular symmetry D_{2h}. Gayles and Self (2) reported the infrared spectra of the gaseous and solid states and, by a comparison of these data, suggested that the spectral difference could be attributed to a structural change from D_{2h} in the solid to D_{2d} in the gaseous state.

Further spectroscopic data have been gathered for B_2F_4 in both gas (3, 4) and solid phases (4) as well as in matrix isolation (5). Interpretations of data from the earlier studies (2–4) as well as results of theoretical calculations (6–8) are in disagreement concerning the molecular conformation; however, the later infrared and Raman work (4) revealed no violation of the mutual exclusion rule, suggesting D_{2h} symmetry for the molecule in both gas and solid phases. The latest study of gaseous B_2F_4 by electron diffraction (9) confirms that the molecule has a planar equilibrium conformation.

Received May 1, 1997.

M. Loroño and J.R. Anacona.[1] Departamento de Química, Universidad de Oriente, Apartado Postal 208, Cumaná, Venezuela.
A. Sierralta. Centro de Química, Instituto Venezolana de Investigaciones Científicos, Apartado 21827, Caracas, Venezuela.

[1] Author to whom correspondence may be addressed. Fax: 58-93-514023. E-mail: janacona@sucre.udo.edu.ve

No experimental information regarding Coriolis coupling constants for B_2F_4 has been published before and the precise calculation of these quantities can be extremely useful for the analysis of rotational structure and prediction of rovibrational band shapes. New methodologies have been proposed (10–12) to describe the classical dynamics of two vibrational modes of a polyatomic molecule coupled by Coriolis interaction to overall molecular rotation; however, in order to appreciate the influence of the force field on Coriolis coupling constant values we have used traditional methods (13) that are still applicable today. Thus, we carried out normal coordinate calculations to obtain force constants and vibrational wave numbers, utilizing the 6-311G* basis set. The iterative autoconsistency method was also applied in order to compare the results with those obtained from ab initio calculations. The results of these studies are reported herein.

Ab initio calculations

The HONDO-8 program from the MOTECC-90 (TM) package was used to carry out the LCAO-MO-SCF restricted Hartree–Fock calculations for diboron tetrafluoride in order to predict the molecular structures and also to provide the force constants and vibrational wave numbers. The energy minimum with respect to nuclear coordinates (–447.54 a.u.) was obtained by simultaneous relaxation of all geometric parameters using the gradient method of Pulay (14, 15). The 6-311G* basis set was utilized to carry out the calculations assuming a planar conformation (D_{2h} symmetry). The optimized geometric parameters do not differ

© 1998 NRC Canada

Table 1. Definition of the coordinates for B_2F_4.

Ab initio	Iterative method
In plane	
St B–B	$A_{1g} = D$
St B_1–F_4	$= 1/2\,(Q_1 + Q_2 + Q_3 + Q_4)$
St B_1–F_5	$= 1/\sqrt{3}\,(\alpha_1 + \alpha_2) - 1/(2\sqrt{3})(\beta_1 + \beta_2 + \beta_3 + \beta_4)$
St B_2–F_6	$B_{1g} = 1/2(Q_2 - Q_1 + Q_4 - Q_3)$
St B_2–F_3	$= 1/2(\beta_3 - \beta_1 + \beta_4 - \beta_2)$
Def BFF = $1/\sqrt{6}\,(2\alpha_1 - \beta_1 - \beta_3)$	$B_{2u} = 1/2(Q_1 - Q_2 - Q_3 + Q_4)$
Rock BFF = $1/\sqrt{2}\,(\beta_1 - \beta_3)$	$= 1/2(\beta_1 - \beta_3 - \beta_2 + \beta_4)$
Def' BFF = $1/\sqrt{6}\,(2\alpha_2 - \beta_2 - \beta_4)$	$B_{3u} = 1/2(Q_3 + Q_4 - Q_1 - Q_2)$
Rock' BFF = $1/\sqrt{2}\,(\beta_2 - \beta_4)$	$= 1/\sqrt{3}\,(\alpha_1 - \alpha_2) + 1/(2\sqrt{3})(\beta_2 + \beta_4 - \beta_1 - \beta_3)$
Out of plane	
Tor = $1/2(\tau_1 + \tau_2 + \tau_3 + \tau_4)$	$A_{1u} = \tau$
Wag = $1/\sqrt{2}\,(\theta_1 + \theta_2)$	$B_{1u} = 1/\sqrt{2}\,(\theta_1 + \theta_2)$
Wag' = $1/\sqrt{2}\,(\theta_1 - \theta_2)$	$B_{2g} = 1/\sqrt{2}\,(\theta_1 - \theta_2)$

$\tau_1 = \tau_{4123}$, $\tau_2 = \tau_{5126}$, $\tau_3 = \tau_{4126}$, and $\tau_4 = \tau_{5123}$.

Fig. 1. The in-plane and out-of-plane internal coordinates of the B_2F_4 molecule. τ, torsional angle; θ_1 and θ_2, waggings.

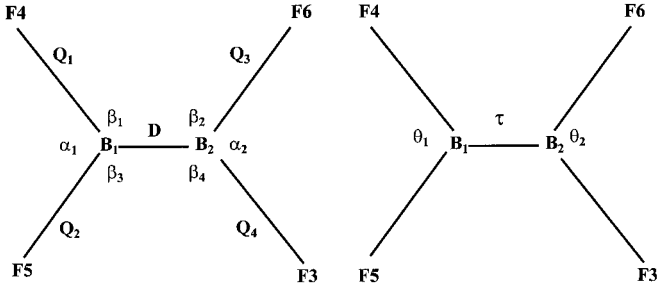

significantly from the experimental values determined from the electron diffraction study (9). There is excellent agreement between the calculated value of 1.31 Å for the B—F bond distance and the experimental value of 1.317(2) Å. Similar agreement is also noted between the calculated value of 1.74 Å for the B—B bond distance and the experimental value of 1.720(4) Å. The calculated value for the F-B-B angle (121.28°) also agrees well with the experimental value of 121.4(1)°. Interestingly, these results were the same when the smaller MIDI-3 basis set was used and they agree well with the reported values of ab initio optimized geometries for B_2F_4 with the 6-31G* basis set (16, 17).

A normal coordinate analysis was carried out in order to obtain a more complete description of the molecular motions involved in the fundamental vibrations as well as to provide a more definitive basis for the vibrational assignment. These analyses were performed utilizing ab initio calculations and Wilson's approach (18) to the force field problem of partitioning the secular equation determining the vibrational wave numbers into *F* and *G* matrices. Twelve symmetry coordinates constructed from fourteen internal coordinates (Table 1), along with the Cartesian coordinates obtained for the optimized structures, were used to calculate the *G* and *B* matrices. The internal coordinates are shown in Fig. 1 and they are the same as those defined previously for ethylene (19).

Table 2. Comparison of observed and calculated vibrational wave numbers of $^{11}B_2F_4$.

	ν	ν_{obs}[a]	Ab initio	Scaled	Iterative	Intensity[b]
A_{1g}	ν_1	1398	1464	1385	1398	0
	ν_2	672	695	662	672	0
	ν_3	319	335	319	319	0
A_{1u}	ν_4	21	64	60	21	0
B_{1g}	ν_5	1298	1454	1357	1298	0
	ν_6	326	423	407	326	0
B_{2g}	ν_8	646	759	724	646	0
B_{1u}	ν_7	392	400	346	392	2.10
B_{2u}	ν_9	1335	1455	1370	1335	19.00
	ν_{10}	149	170	160	149	0.10
B_{3u}	ν_{11}	1133	1214	1149	1133	11.00
	ν_{12}	538	570	540	538	1.75

[a] Observed wave numbers from ref. 4.
[b] Calculated IR intensities in km/mol.

Unscaled 6-311G* vibrational wave numbers are listed in Table 2 in the columns labelled ab initio. It can be observed that the calculated wave numbers are significantly higher than those observed experimentally. Therefore, the force fields calculated with the 6-311G* basis set were subsequently scaled by using factors of 0.9 for all diagonal force constants. For the interaction force constants no geometric average of the scaling factors was used. With this procedure the calculated frequencies are in much better agreement with the observed frequencies. Table 2 also contains the predicted vibrational wave numbers with a different set of force constants obtained by the iterative method. The calculated dipole moment derivatives were used to evaluate the theoretical absolute infrared intensities for the ungerade motions of B_{1u}, B_{2u}, and B_{3u}, which are only IR active. The calculated values in km/mol are included in Table 2; the experimental values are not given, as no accurate measurements seem to have been carried out for B_2F_4. The scaled force fields in internal coordinates calculated by the HONDO-8 program with the 6-311G* basis set are shown in Table 3.

© 1998 NRC Canada

Table 3. Scaled ab initio force field (mdyn Å^{-1}) for B_2F_4.

In-plane force constants									
St B–B	2.655	0.099	0.099	0.099	0.099	–0.122	–0.122	0.000	0.000
St B–F		6.896	0.906	0.144	0.112	0.242	–0.066	0.229	–0.110
St B–F			6.896	0.112	0.144	0.242	–0.066	–0.229	0.110
St B–F				6.896	0.906	–0.066	0.242	–0.110	0.229
St B–F					6.896	–0.066	0.242	0.110	–0.229
Def BF2						0.899	0.052	0.000	0.000
Def' BF2							0.899	0.000	0.000
Roc BF2								0.521	–0.139
Roc' BF2									0.521
Out-of-plane force constants									
Tor	0.013	0.000	0.000						
Wag		0.391	0.063						
Wag'			0.391						

Iterative method (20)

To calculate the wave numbers of the normal molecular vibrations in the harmonic approximation, the following secular equations were used:

$$[1] \quad G_{^{10}B} F_{^{11}B} L^{cal}_{^{10}B} = L_{^{10}B} \Lambda_{^{11}B} \; ; \; G_{^{11}B} F_{^{10}B} L^{cal}_{^{11}B} = L_{^{11}B} \Lambda_{^{11}B}$$

where $G_{^{10}B}$and $G_{^{11}B}$ are the matrices of kinetic coefficients of isotopically substituted molecules containing ^{10}B or ^{11}B isotopes. F characterizes the molecular force field and the columns of the matrix L are the coefficients of the normal coordinates. The elements of the diagonal matrix Λ are vibrational frequency parameters. Under suitable conditions of normalization the experimental set of vibrational frequency parameters Λ^{exp} is reproduced exactly by the matrix F.

$$[2] \quad F_{^{10}B} = \tilde{L}^{-1}_{^{10}B} \Lambda^{exp}_{^{10}B} L^{-1}_{^{10}B} \quad ; \quad F_{^{11}B} = \tilde{L}^{-1}_{^{11}B} \Lambda^{exp}_{^{11}B} L^{-1}_{^{11}B}$$

Using eq. [2], with a starting F_0 matrix and $\Lambda^{exp}_{^{10}B}$ and $\Lambda^{exp}_{^{11}B}$ matrices, the secular equations of eq. [1] are solved iteratively until the following criteria are satisfied: the difference between $F_{^{10}B}$ and $F_{^{11}B}$ is minimized (<0.01%), the change in force field from one iteration to another is minimal, and the goodness of the fit between the experimental (4) and calculated values of the vibrational wave numbers. The in-plane and out-of-plane internal coordinates considered in the iterative method are similar to those considered in the ab initio calculations. The bond lengths and interbond angles used in the calculations are the experimental values (9). The vibrational representations of the planar configurations of B_2F_4 of D_{2h} symmetry are:

$$\Gamma = 3A_{1g} + A_{1u} + 2B_{1g} + B_{1u} + B_{2g} + 2B_{2u} + 2B_{3u}$$

The matrix G in internal coordinates is reduced by symmetry through the use of a U transformation matrix determined by molecular symmetry and, in order to have all force constants in mdyn Å^{-1}, the angle bending coordinates were scaled with the B—F bond distance. The symmetry coordinates used in the iterative method are listed in Table 1, whereas in Table 2 it can be observed that the calculated frequencies are concordant with the experimental values.

Coriolis coupling constants

To calculate the 23 nonvanishing elements of the Coriolis coupling constants the well-known matrix equation proposed by Meal and Polo (21) was used.

$$[3] \quad \zeta^{\alpha} = L^{-1} \, \tilde{C}^{\alpha} L^{-1}$$

where

$$C^{\alpha} = B \, M^{1/2} \, T^{\alpha} \, M^{1/2} \, \tilde{B}, \quad \alpha = x, y, z$$

T^{α} are matrices of dimension $3N \times 3N$ formed by N identical 3×3 blocks along the diagonal, M is a diagonal matrix whose elements are the atomic masses, B is the transformation matrix between internal and Cartesian coordinates, and L is the symmetrized transformation matrix between internal and normal coordinates. For $^{10}B_2F_4$ and $^{11}B_2F_4$ molecules the y-axis was taken to be perpendicular to the molecular plane and the z-axis to run along the B—B bond. Two L matrices of eigenvectors were used to solve eq. [3], one obtained from ab initio calculations and the other from application of the iterative method. The calculated Coriolis coupling constants are given in Table 4. Both sets of Coriolis coupling constants fulfill the sum rules derived by Meal and Polo (21) and Kuchitsu et al. (22) and were used to evaluate the inertial defect in the ground vibrational state.

Inertial defects

The general formula for the inertial defect of a planar molecule is

$$[4] \quad \Delta_{total} = \Delta_{vib} + \Delta_{cent} + \Delta_{elect}$$

where Δ_{vib} is the contribution to the inertial defect of the vibrational motion in the ground state and Δ_{cent} is a minor contribution due to centrifugal distortion. Δ_{elect}, the electronic contribution due to π-electrons, was not considered because, as can be seen in Table 3, the B–B stretching force constant has a value of 2.635 mdyn Å^{-1}, suggesting that there is no π-donation from halogen atom to boron, with some subsequent $p\pi$–$p\pi$ overlap between the two boron orbitals. Δ_{vib} is the major contribution to the total inertial defect and in the present case it was the only contribution calculated according to the formalism of Jeyapandian and Savari Raj (23).

© 1998 NRC Canada

Table 4. Coriolis coupling constants of B_2F_4.[a]

	$^{10}B_2F_4$				$^{11}B_2F_4$			
	ν_A	ν_B	$\zeta_{ab\ initio}$	$\zeta_{Iterative}$	ν_A	ν_B	$\zeta_{ab\ initio}$	$\zeta_{Iterative}$
				***x*-axis**				
(B_{1g},B_{1u})	1308	392	–0.963	–0.957	1298	392	–0.962	–0.953
	326	392	–0.269	–0.291	326	392	–0.275	–0.303
(B_{2u},B_{2g})	1358	646	0.965	0.969	1335	646	0.960	0.966
	149	646	–0.262	–0.249	149	646	–0.279	–0.258
(B_{3u},A_{1u})	1148	21	0.503	0.525	1133	21	0.524	0.547
	540	21	0.865	0.851	538	21	0.852	0.837
				***y*-axis**				
(A_{1g},B_{1u})	1404	392	0.945	0.975	1398	392	0.937	0.973
	673	392	–0.065	–0.031	672	392	–0.066	–0.030
	320	392	–0.321	–0.221	319	392	–0.342	–0.231
(B_{2u},A_{1u})	1358	21	–0.269	–0.249	1335	21	–0.279	–0.258
	149	21	–0.963	–0.969	149	21	–0.960	–0.966
(B_{3u},B_{2g})	1148	646	–0.865	–0.851	1133	646	–0.852	–0.837
	540	646	0.503	0.525	538	646	0.524	0.547
				***z*-axis**				
(A_{1g},B_{1g})	1404	1308	–0.846	–0.878	1398	1298	–0.828	–0.867
	673	1308	–0.265	–0.091	672	1298	–0.275	–0.098
	320	1308	0.463	0.470	319	1298	0.489	0.489
	1404	326	–0.491	–0.464	1398	326	–0.514	–0.484
	673	326	0.482	0.408	672	326	0.466	0.406
	320	326	–0.726	–0.787	319	326	–0.720	–0.775
(B_{2u},B_{3u})	1358	1148	0.697	0.694	1335	1133	0.671	0.668
	149	1148	–0.717	–0.720	149	1133	–0.741	–0.744
	1358	540	–0.697	–0.720	1335	538	–0.671	–0.745
	149	540	–0.717	–0.694	149	538	–0.741	–0.668

[a] ν_A and ν_B represent vibrational wave numbers.

Table 5. The calculated inertial defects (amu Å^2) for B_2F_4.

	Ab initio			Iterative method		
Molecule	$\Delta_{in\ plane}$	$\Delta_{out\ of\ plane}$	Δ_{total}	$\Delta_{in\ plane}$	$\Delta_{out\ of\ plane}$	Δ_{total}
$^{10}B_2F_4$	0.972	–1.914	–0.942	0.950	–1.902	–0.952
$^{11}B_2F_4$	1.001	–1.920	–0.919	0.955	–1.909	–0.954

$$[5]\qquad \Delta_{vib,\ in\ plane} = \frac{h}{2\pi^2 c}\left\{\sum_S\sum_{S'}(\zeta^y_{SS'})^2\left[\frac{1}{\nu s}+\frac{1}{\nu s'}-\frac{1}{\nu s+\nu s'}\right]\right\}$$

$$[6]\qquad \Delta_{vib,\ out\ plane} = -\frac{h}{2\pi^2 c}\left\{\sum_S\sum_t[(\zeta^x_{St})^2+(\zeta^z_{St})^2]\left[\frac{1}{\nu s}-\frac{1}{\nu s+\nu t}\right]+\frac{1}{2}\sum_t\frac{1}{\nu t}\right\}$$

The in-plane and out-of-plane contributions to Δ_{vib} are given in Table 5.

Discussion

We have calculated two different sets of force constants; one of them was obtained by using the iterative method, which is an empirical method of carrying out a simultaneous fit for a pair of isotopically substituted molecules. The iterative procedure has the advantage that rather high variations in the matrix F_0 lead to little or no change in the final matrix F. The other set of force constants was obtained by ab initio Hartree–Fock calculations using the TZP basis, which provides harmonic force constants to a much better accuracy. The diagonal harmonic terms in internal coordinates are obtained within the reasonable accuracy of typically 10–30% and, more importantly, the deviations are very systematic in a qualitative sense.

© 1998 NRC Canada

Table 6. Comparison of force constants (mdyn Å^{-1}) for B_2F_4.

	Ab initio	Iterative
Stretch		
B–B (*D*)	2.655	6.739
B–F (*Q*)	6.896	6.011
Bend		
FBF (α)	0.899	0.485
BBF (β)	0.521	0.290
Stretch–stretch		
BB/BF	0.099	0.775
BF_4/BF_5	0.906	0.510
BF_4/BF_6	0.144	–0.587
BF_4/BF_3	0.112	–0.630
Stretch–bend		
BB/BBF	0.000	0.168
BB/FBF	–0.122	–0.337
BF/FBF (α_1)	0.242	0.146
BF/FBF (α_2)	–0.066	–0.121
BF/BBF (β_3)	0.229	0.150
BF/BBF (β_4)	–0.110	–0.183
Bend–bend		
F_4BF_5/F_3BF_6	0.052	–0.052
F_5BB/BBF_3	–0.139	–0.026
F_5BB/F_4BF_5	0.000	–0.242
F_3BB/BBF_6	0.000	0.026

The scaled ab initio force constants are listed in Table 6, along with those given by the iterative method, and there are some significant differences that should be noted. For example, the ab initio B–B stretch and the B–B/B–F interaction constants are significantly smaller than those obtained by the iterative method. The ab initio values for the BF_4/BF_6 and BF_4/BF_5 stretch–stretch and the F_4BF_5/F_3BF_6 bend–bend interaction constants are found to be positive, with values 0.144, 0.112, and 0.052 mdyn Å^{-1}, respectively, whereas negative values of –0.587, –0.630, and –0.052 mdyn Å^{-1}, respectively, were obtained through the iterative method. Finally, the iterative FBF and BBF bends and the BF_4/BF_5 interaction constant are about five-ninths of the scaled ab initio values.

The scaled ab initio force constant matrices show a large number of off-diagonal elements close to zero. However, there is only one unusually large value, the bond–bond interaction constant with values of $f_{B\text{-}F/B\text{-}F} = 0.906$. The scaled ab initio bond stretching force constants increase in the order $f_{B\text{-}B} < f_{B\text{-}F}$ with values 2.655 and 6.896 mdyn Å^{-1}, respectively, and they follow the reverse order of the stretching force constant values obtained by using empirical methods (3, 24). In general, the iterative force constants are not very close to those obtained from the scaled ab initio values; however, the differences in the force fields do not lead to large differences in the normal modes. In consequence, the Coriolis coupling constants show themselves to be only slightly sensitive to variations in the force constants. The largest zeta values are the (ν_1, ν_2) and (ν_8, ν_9) interactions along the *x*-axis, the (ν_1, ν_3) interaction along the *y*-axis, and the (ν_6, ν_{10}) interaction along the *z*-axis in all molecules. The Coriolis coupling constants follow sum rules with an average deviation of less than 0.02%. The calculated inertial defects follow the order $^{10}B_2F_4 < {}^{11}B_2F_4$, in agreement with the presence of heavier atoms in the molecule.

Acknowledgement

The authors would like to thank Dr. Y. Aray (Centro de Química, IVIC) for his help and useful suggestions.

References

1. L. Trefanos and W.N. Lipscomb. J. Chem. Phys. **28**, 54 (1958).
2. J.N. Gayles and J. Self. J. Chem. Phys. **40**, 3530 (1964).
3. L.A. Nimon, K.S. Seshadri, R.C. Taylor, and D. White. J. Chem. Phys. **53**, 2416 (1970).
4. J.R. Durig, J.W. Thompson, J.D. Witt, and J.D. Odom. J. Chem. Phys. **58**, 5339 (1973).
5. M. Atoji, P.J. Weatley, and W.N. Lipscomb. J. Chem. Phys. **27**, 196 (1957).
6. D.E. Mann and L. Fano. J. Chem. Phys. **26**, 1665 (1957).
7. K. Hedberg and R. Ryan. J. Chem. Phys. **41**, 2214 (1964).
8. R. Ryan and K. Hedberg. J. Chem. Phys. **50**, 4986 (1969).
9. D.D. Danielson, J.V. Patton, and K. Hedberg. J. Am. Chem. Soc. **90**, 6484 (1977).
10. C.C. Martens. J. Chem. Phys. **94**, 3594 (1991).
11. M.S. Krishnan and T. Carrington, Jr. J. Chem. Phys. **95**, 1884 (1991).
12. D.C. Burleigh, R.C. Mayrhofer, and E.L. Sibert III. J. Chem. Phys. **89**, 7201 (1988).
13. A.G. Ozkabak and L. Goodman. J. Chem. Phys. **87**, 2564 (1987).
14. P. Pulay. Mol. Phys. **17**, 197(1969).
15. P. Pulay. *In* Modern theoretical chemistry. Vol. 4. *Edited by* H.F Schaefer III. Plenum, New York. 1977. pp 153–185.
16. M. Bühl, J. Gauss, M. Hofmann, and P. Schleyer. J. Am. Chem. Soc. **115**, 12385 (1993).
17. J. Demachy and F. Volatron. J. Phys. Chem. **98**, 10728 (1994).
18. E.B. Wilson, J.C. Decius, and P.C. Cross. *In* Molecular vibrations. McGraw–Hill, New York. 1975.
19. P. Pulay, G. Fogarasi, G. Pongor, J.E. Boggs, and A. Vargha. J. Am. Chem. Soc. **105**, 7037 (1983).
20. R. Aroca, E.A. Robinson, Yu N. Panchenko, and V.Y. Pupyshev. Chem. Phys. Lett. **43**, 387 (1976).
21. J.H. Meal and S.R. Polo. J. Chem. Phys. **24**, 1119 (1956).
22. K. Kuchitsu, T. Oka, and Y. Morino. J. Mol. Spectrosc. **15**, 51 (1965).
23. S. Jeyapandian and G.A. Savari Raj. J. Mol. Struct. **14**, 17 (1971).
24. J.R. Anacona and M. Loroño. J. Mol. Struct. (THEOCHEM), **304**, 279 (1994).

© 1998 NRC Canada

A kinetic study of the reactions of dimethyl sulfide bridged tetramethylplatinum(II) and octamethylplatinum(IV) complexes with dimethyl sulfide and bidentate ligands

Katsuyuki Nakayama, Yuichi Kondo, and Koji Ishihara

Abstract: Kinetics for the reactions of

[1] $[Pt^{IV}_2Me_8\ (\mu\text{-}SMe_2)_2] + 2\ Me_2S \underset{k_d}{\overset{k_f}{\rightleftharpoons}} 2\ [Pt^{IV}Me_4(SMe_2)_2]$

[2] $[Pt^{II}_2Me_4\ (\mu\text{-}SMe_2)_2] + 2\ Me_2S \overset{k_r}{\rightarrow} 2\ [Pt^{II}Me_2(SMe_2)_2]$

and

[3] $[Pt^{IV}_2Me_8\ (\mu\text{-}SMe_2)_2] + 2NN \rightarrow 2\ [Pt^{IV}Me_4(NN)] + 2\ Me_2S$

where NN = bipy or 4,4′-Me_2-bipy, have been studied at various temperatures and pressures. Reaction [3] was shown to consist of the rapid conversion of the dimer to a monomer and the much slower subsequent substitution of the dimethyl sulfide with bidentate ligand NN:

$[Pt^{IV}_2Me_8(\mu\text{-}SMe_2)_2] + 2\ Me_2S \rightleftharpoons 2\ [Pt^{IV}Me_4(SMe_2)_2]$

and

$[Pt^{IV}Me_4(SMe_2)_2] + NN \rightarrow [Pt^{IV}Me_4(NN)] + 2\ Me_2S$

The rate constants and activation parameters for the reactions are as follows: $k_f = 3.16 \pm 0.06\ M^{-1}\ s^{-1}$ (25°C), $\Delta H^{\neq}_f = 51.8 \pm 1.7$ kJ mol^{-1}, $\Delta S^{\neq}_f = -61.0 \pm 5.8$ J mol^{-1} K^{-1}, $k_d = 1.18 \pm 0.22\ M^{-1}\ s^{-1}$ (25°C), $\Delta H^{\neq}_d = 65 \pm 22$ kJ mol^{-1}, $\Delta S^{\neq}_d = -26 \pm 73$ J mol^{-1} K^{-1} for reaction [1] in *n*-hexane; $k_f = 6.68 \pm 0.06\ M^{-1}\ s^{-1}$ (25°C), $\Delta H^{\neq}_f = 58.0 \pm 3.1$ kJ mol^{-1}, $\Delta S^{\neq}_f = -34.5 \pm 10.5$ J mol^{-1} K^{-1}, $\Delta V^{\neq}_f = -10.7 \pm 1.3$ cm^3 mol^{-1} for reaction [2] in dichloromethane; $k_2 = (7.09 \pm 1.89) \times 10^{-4}\ M^{-1}\ s^{-1}$, $\Delta H^{\neq}_2 = 95 \pm 21$ kJ mol^{-1}, and $\Delta S^{\neq}_2 = 18 \pm 70$ J mol^{-1} K^{-1}, $\Delta V^{\neq}_2 = 9 \pm 9$ cm^3 mol^{-1} for reaction [3] with bipy, and $k_1 = (1.10 \pm 0.10) \times 10^{-2}\ s^{-1}$, $k_3/k_{-1} = (4.33 \pm 0.30) \times 10^{-2}$, and $k_2 = (6.09 \pm 1.35) \times 10^{-4}\ M^{-1}\ s^{-1}$ for reaction [3] with 4,4′-Me_2-bipy. It was shown that reactions [1] and [2] proceed nucleophilically without any intermediates, and reaction [3] proceeds through a mainly k_2 path for NN = bipy and through both k_1 and k_2 paths for NN = 4,4′-Me_2-bipy, without appreciable participation of the direct reaction between the dimer and NN as shown by the following reaction scheme.

Key words: octamethylplatinum(IV) dimer, tetramethylplatinum(II) dimer, reaction mechanism, high-pressure kinetics.

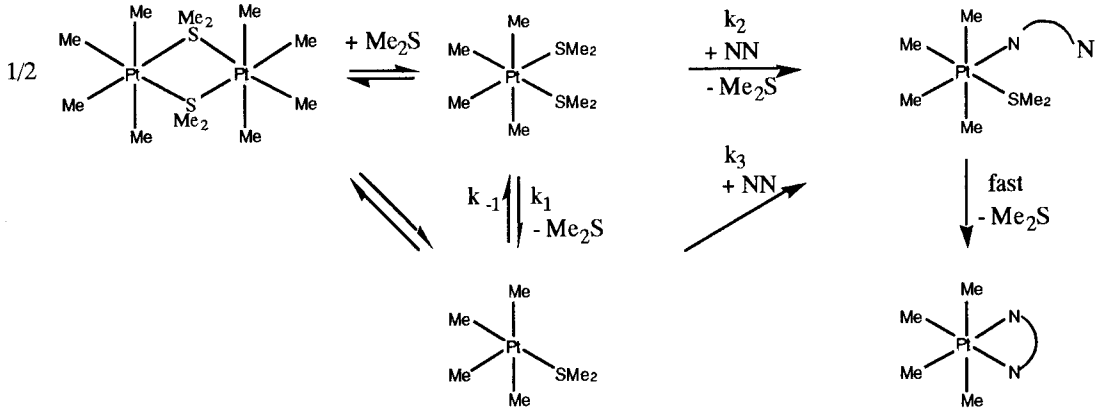

Received June 27, 1997.

K. Nakayama, Y. Kondo, and K. Ishihara.[1] Department of Chemistry, School of Science and Engineering, Waseda University, Okubo, Shinjuku-ku, Tokyo 169, Japan.

[1] Author to whom correspondence may be addressed. Telephone: (03) 5286-3241. Fax: (03)3208-2735. E-mail: ishi3719@mn.waseda.ac.jp

© 1998 NRC Canada

Résumé : Opérant à diverses températures et à diverses pressions, on a examiné la cinétique des réactions :

[1] $[Pt^{IV}_2Me_8\ (\mu\text{-}SMe_2)_2] + 2\ Me_2S \underset{k_d}{\overset{k_f}{\rightleftharpoons}} 2\ [Pt^{IV}Me_4(SMe_2)_2]$

[2] $[Pt^{II}_2Me_4\ (\mu\text{-}SMe_2)_2] + 2\ Me_2S \overset{k_f}{\rightarrow} 2\ [Pt^{II}Me_2(SMe_2)_2]$

et

[3] $[Pt^{IV}_2Me_8\ (\mu\text{-}SMe_2)_2] + 2NN \rightarrow 2\ [Pt^{IV}Me_4(NN)] + 2\ Me_2S$

dans laquelle NN = bipy ou 4,4′-Me_2-bipy. On a montré que la réaction [3] comporte une conversion rapide du dimère en un monomère et en une substitution subséquente beaucoup plus lente du sulfure de diméthyle par le coordinat bidentate NN :

$[Pt^{IV}_2Me_8(\mu\text{-}SMe_2)_2] + 2\ Me_2S \rightleftharpoons 2\ [Pt^{IV}Me_4(SMe_2)_2]$

et

$[Pt^{IV}Me_4(SMe_2)_2] + NN \rightarrow [Pt^{IV}Me_4(NN)] + 2\ Me_2S$

Les constantes de vitesse et les paramètres d'activation des réactions sont les suivants : $k_f = 3{,}16 \pm 0{,}06\ M^{-1}\ s^{-1}$ (25°C), $\Delta H^{\neq}_f = 51{,}8 \pm 1{,}7$ kJ mol^{-1}, $\Delta S^{\neq}_f = -61{,}0 \pm 5{,}8$ J mol^{-1} K^{-1}, $k_d = 1{,}18 \pm 0{,}22\ M^{-1}\ s^{-1}$ (25°C), $\Delta H^{\neq}_d = 65 \pm 22$ kJ mol^{-1}, $\Delta S^{\neq}_d = -26 \pm 73$ J mol^{-1} K^{-1} pour la réaction [1] dans l'hexane; $k_f = 6{,}68 \pm 0{,}06\ M^{-1}\ s^{-1}$ (25°C), $\Delta H^{\neq}_f = 58{,}0 \pm 3{,}1$ kJ mol^{-1}, $\Delta S^{\neq}_f = -34{,}5 \pm 10{,}5$ J mol^{-1} K^{-1}, $\Delta V^{\neq}_f = -10{,}7 \pm 1{,}3$ cm^3 mol^{-1} pour la réaction [2] dans le dichlorométhane; $k_2 = (7{,}09 \pm 1{,}89) \times 10^{-4}\ M^{-1}\ s^{-1}$ (25°C), $\Delta H^{\neq}_2 = 95 \pm 21$ kJ mol^{-1}, $\Delta S^{\neq}_2 = 18 \pm 70$ J mol^{-1} K^{-1}, $\Delta V^{\neq}_2 = 9 \pm 9$ cm^3 mol^{-1} pour la réaction [3] avec la bipy et $k_1 = (1{,}10 \pm 0{,}10) \times 10^{-2}\ M^{-1}\ s^{-1}$ (25°C), $k_3/k_{-1} = (4{,}33 \pm 0{,}30) \times 10^{-2}$, et $k_2 = (6{,}09 \pm 1{,}35) \times 10^{-4}\ M^{-1}\ s^{-1}$ (25°C) pour la réaction [3] avec la 4,4′-Me_2-bipy. On a démontré que les réactions [1] et [2] sont nucléophiles, sans intermédiaires, et que la réaction [3] se produit principalement par une voie k_2 lorsque NN = bipy et par des voies tant k_1 que k_2 lorsque NN = 4,4′-Me_2-bipy, sans participation importante de la réaction directe entre le dimère et NN représentée par le schéma réactionnel précédent.

Mots clés : dimère de l'octaméthylplatine(IV), dimère du tétraméthylplatine(II), mécanisme réactionnel, cinétique à pression élevée.

[Traduit par la rédaction]

Introduction

The ligand substitution mechanism of platinum(II) complexes, including organoplatinum(II) complexes such as *cis*-$[PtR_2X_2]$ (where R is an alkyl or aryl group), has been well exemplified by a number of studies (1–5). However, little is known about the substitution mechanism on inert platinum(IV) complexes, despite the fact that Pt(IV) complexes are perhaps no less common. Thus, it is well known that $PtCl_6^{2-}$ is easily produced in solution when platinum metal is dissolved in aqua regia. This gap in our understanding of Pt(IV) complexes is due mainly to the fact that substitution reactions on Werner complexes of Pt(IV) are always accompanied by redox catalysis (6, 7). On the other hand, substitution on comparatively labile methylplatinum(IV) complexes occurs straightforwardly without any side reactions, because of the strong electron-donating property of coordinated methyl groups. In addition, it is of interest mechanistically, because it would proceed electrophilically as well as nucleophilically.

Many mechanistically interesting reactions of methylplatinum(IV) complexes have been reported by Puddephatt et al. (8, 9), some of which are illustrated in Scheme 1. In this scheme, we have already studied kinetically reaction [4], the reaction of $[Pt^{IV}Me_4(NN)]$ (NN = 1,10-phenanthroline or 2,2′-bipyridine) with HA (HA = formic, acetic, benzoic, or salicylic acid), and have shown that it proceeds with an S_E2 mechanism (10). We report here on the ligand substitution mechanism for reactions [1] and [3], and the reaction of $[Pt^{II}_2Me_4(\mu\text{-}SMe_2)_2]$ with dimethyl sulfide as well.

Scheme 1

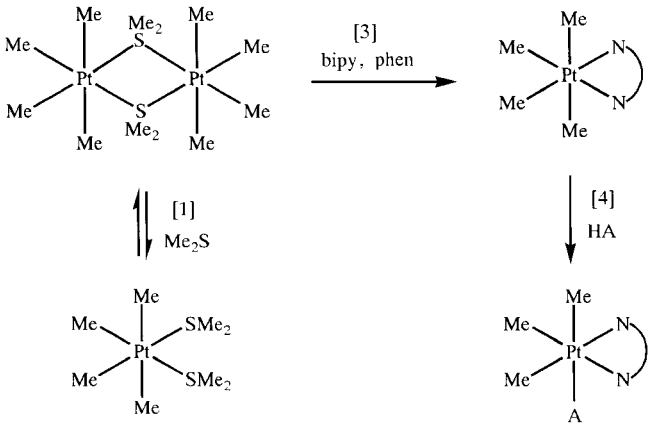

Experimental

Materials

$[Pt^{IV}_2Me_8(\mu\text{-}SMe_2)_2]$ and $[Pt^{II}_2Me_4(\mu\text{-}SMe_2)_2]$ were synthesized and recrystallized according to the literature (2, 8). Deuterated solvents (E. Merck), dehydrated solvents (Kanto Chemical Co. Inc., Tokyo), and the other reagent grade chemicals (Kanto) were used as received. Sample solutions were prepared just before use.

Measurements

Measurements were carried out in a similar manner to the

© 1998 NRC Canada

Fig. 1. UV spectra for the reactions of $[Pt^{IV}_2Me_8(\mu\text{-}SMe_2)_2]$ in *n*-hexane (*a*) and of $[Pt^{II}_2Me_4(\mu\text{-}SMe_2)_2]$ in dichloromethane (*b*) with dimethyl sulfide at 25°C. (*a*) At every 2 min, $C_{Pt2} = 6.14 \times 10^{-5}$ M, and $C_{Me2S} = 1.34 \times 10^{-3}$ M; (*b*) at every 60 s, $C_{Pt2} = 6.20 \times 10^{-5}$ M and $C_{Me2S} = 3.16 \times 10^{-3}$ M.

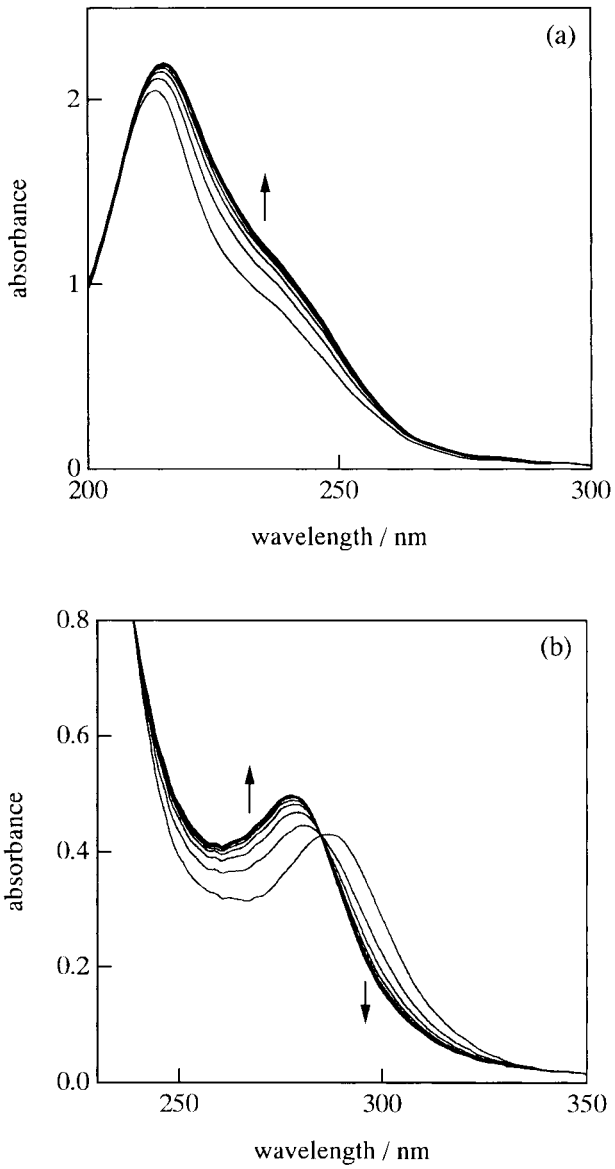

previous study (9). The reactions of $[Pt^{IV}_2Me_8(\mu\text{-}SMe_2)_2]$ and $[Pt^{II}_2Me_4(\mu\text{-}SMe_2)_2]$ with dimethyl sulfide, and $[Pt^{IV}_2Me_8(\mu\text{-}SMe_2)_2]$ with 2,2′-bipyridine (bipy) and 4,4′-dimethyl-2,2′-bipyridine (4,4′-Me_2-bipy) were followed at 230, 290, 465, and 440 nm, respectively, under pseudo-first-order conditions. The first-mentioned reaction could not be followed at elevated pressures because of the nontransparency of a pair of sapphire optical windows mounted in a high-pressure vessel, which absorbs UV light shorter than 250 nm (11). The second reaction was started by mixing the equilibrated solution of $[Pt^{IV}_2Me_8(\mu\text{-}SMe_2)_2]$ and dimethyl sulfide with the ligand solution. In the kinetic experiments, the total concentrations of the complex, C_{Pt2} ($Pt_2 = [Pt^{IV}_2Me_8(\mu\text{-}SMe_2)_2]$ or $[Pt^{II}_2Me_4(\mu\text{-}SMe_2)_2]$) and dimethyl sulfide, C_{Me2S}, were as follows: $C_{Pt2} = (6.30–7.88) \times 10^{-5}$ M and $C_{Me2S} = (0.928–2.45) \times 10^{-3}$ M for the reaction of $[Pt^{IV}_2Me_8(\mu\text{-}SMe_2)_2]$ with Me_2S; $C_{Pt2} = (5.50–13.9) \times 10^{-5}$ M and $C_{Me2S} = (1.89–8.20) \times 10^{-3}$ M for the reaction of $[Pt^{II}_2Me_4(\mu\text{-}SMe_2)_2]$ with Me_2S; $C_{Pt2} = (6.38–6.95) \times 10^{-5}$ M and $C_{Me2S} = (0.984–2.25) \times 10^{-3}$ M for the reaction of $[Pt^{IV}_2Me_8(\mu\text{-}SMe_2)_2]$ with NN (NN = bipy or 4,4′-Me_2-bipy) (see supplementary material, Tables S1–S4[2]). First-order plots were perfectly linear. The same spectrophotometers as those used in the previous study (10) were employed for acquiring data. Each ^{1}H NMR peak was assigned according to the literature (2, 8, 9, 12).

Results and discussion

Kinetics for dimer ⇌ monomer

$$[1] \quad [Pt^{IV}_2Me_8(\mu\text{-}SMe_2)_2] + 2\,Me_2S \underset{k_d}{\overset{k_f}{\rightleftharpoons}} 2\,[Pt^{IV}Me_4(SMe_2)_2]$$

$$[2] \quad [Pt^{II}_2Me_4(\mu\text{-}SMe_2)_2] + 2\,Me_2S \overset{k_f}{\rightarrow} 2\,[Pt^{II}Me_2(SMe_2)_2]$$

Figures 1*a* and 1*b* show the spectral change with time for reactions [1] and [2], respectively. Changes in the ^{1}H NMR spectra with time for reactions [1] and [2], shown in Figs. 2*a* and 2*b,* respectively, were consistent with those in spectrophotometry, i.e., the peaks of methyl protons of the dimers diminished with time, while those of methyl protons of the monomers grew. Figures 2*a* and 2*b* also show that reaction [2] proceeds to completion under the present conditions, since the peaks due to the Pt(II) dimer disappear completely, while reaction [1] reaches an equilibrium.

Reactions [1] and [2] were first order with respect to the concentration of the unreacted Pt(IV) or Pt(II) dimer, $[Pt_2]$, thus the rate equation is expressed by eq. [3], where k_{obs} is the conditional pseudo-first-order rate constant.

$$[3] \quad -d[Pt_2] / dt = k_{obs}[Pt_2]$$

For reaction [1], k_{obs} depends not only on the total concentration of the ligand (C_{Me2S}) but also on that of the complex, C_{Pt2}, as is evident in Figs. 3*a* and 3*b*. However, for reaction [2], k_{obs} depends only upon the ligand concentration, i.e., k_{obs} is independent of C_{Pt2} (see Figs. 4*a* and 4*b*), and the plot of k_{obs} vs. C_{Me2S} is linear with zero intercept. Thus, k_{obs} for reaction [2] is simply represented by eq. [4], albeit the expression of k_{obs} for reaction [1] is rather complicated because of the contribution of the reverse reaction.

$$[4] \quad k_{obs} = k_f C_{Me2S}$$

Under the present experimental conditions, $C_{Me2S} >> C_{Pt2}$, reaction [1] can be regarded as a simple equilibrium between a dimer and a monomer such as $A_2 = 2A$. Then, the equation used for the ultrasonic relaxation may be applicable to the present system (13). Thus, k_{obs} for reaction [1] is given by eq. [5] (vide Appendix).

[2] Tables S1–S4, showing numerical values of rate constants for the reactions of $[Pt^{IV}_2Me_8(\mu\text{-}SMe_2)_2]$ with Me_2S and NN, and of $[Pt^{II}_2Me_4(\mu\text{-}SMe_2)_2]$ with Me_2S at various temperatures and pressures (5 pages), have been deposited as supplementary material and can be purchased from: The Depository of Unpublished Data, Document Delivery, CISTI, National Research Council Canada, Ottawa, Canada K1A 0S2.

© 1998 NRC Canada

Fig. 2. ^{1}H NMR spectra for the reactions of $[Pt^{IV}_2Me_8(\mu\text{-}SMe_2)_2]$ (*a*) and $[Pt^{II}_2Me_4(\mu\text{-}SMe_2)_2]$ (*b*) in $CDCl_3$ at room temperature. (*a*) $C_{Pt2} = 2.00 \times 10^{-3}$ M and $C_{Me2S} = 1.02 \times 10^{-2}$ M: (*i*) 1, (*ii*) 15, (*iii*) 30 min after the reaction started; (*b*) $C_{Pt2} = 1.29 \times 10^{-3}$ M and $C_{Me2S} = 6.47 \times 10^{-3}$ M at –20°C: (*i*) 1, (*ii*) 10, (*iii*) 160 min after the reaction started.

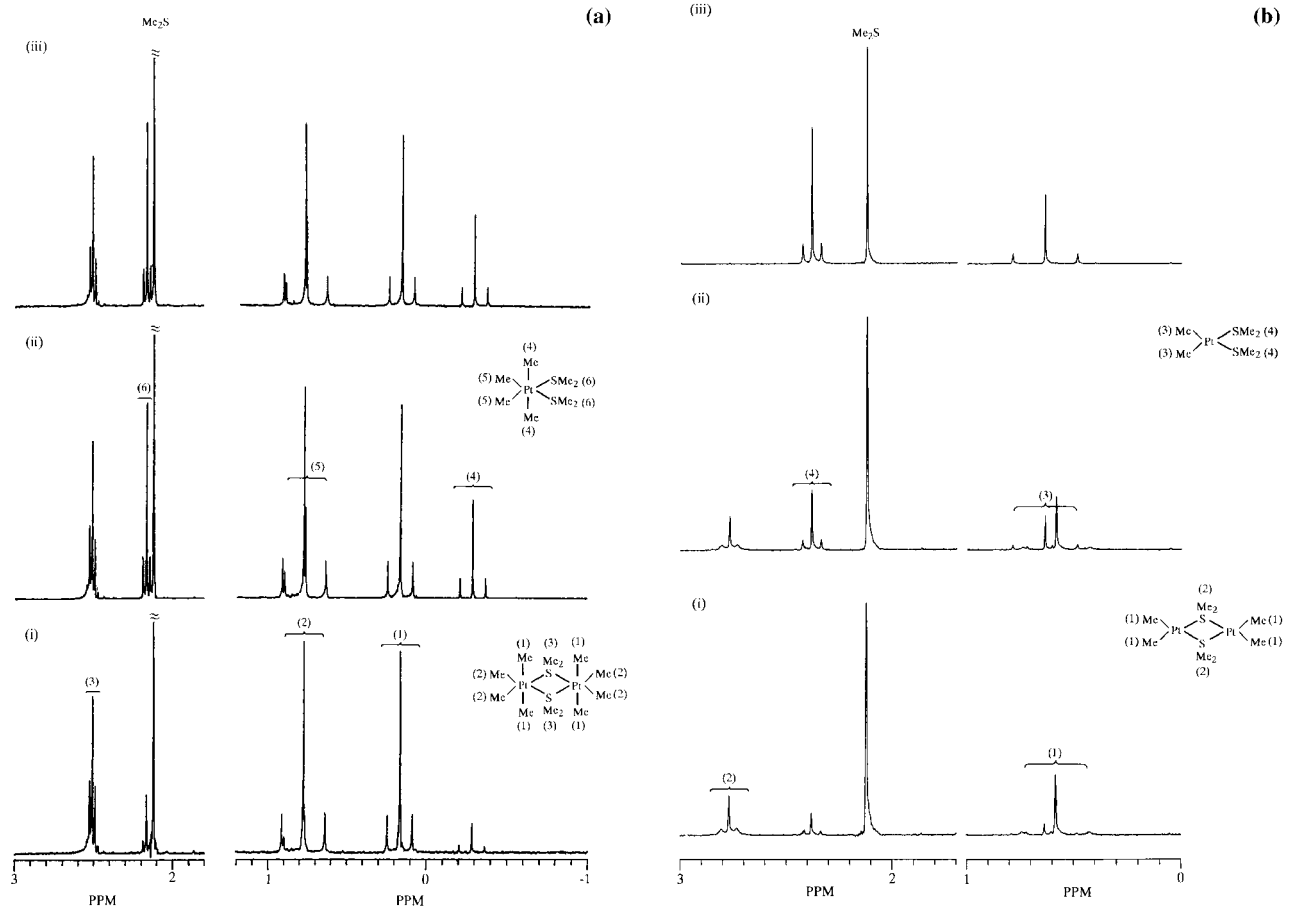

Scheme 2

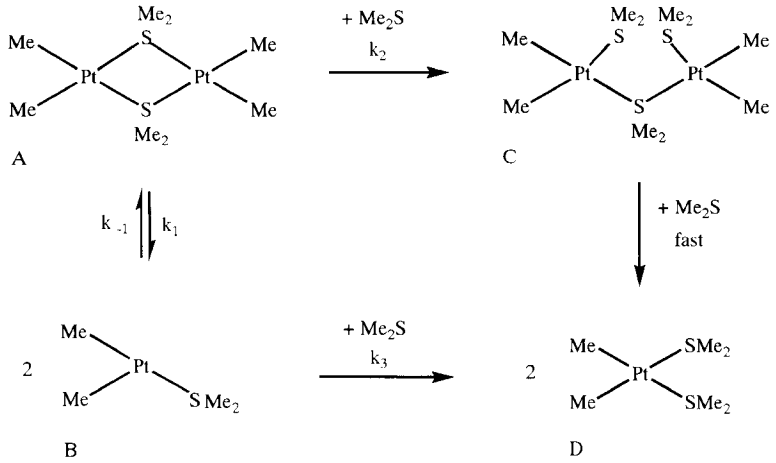

[5] $$k_{obs}^2 / (C_{Pt2}\, C_{Me2S}) = k_f^2\, C_{Me2S} / C_{Pt2} + 16\, k_f\, k_d$$

This equation explains well the experimental results as shown in Fig. 5. The activation parameters obtained are listed in Table 1.

The reaction of the Pt(II) dimer with Me_2S is expressed by Scheme 2, which consists of two reaction paths, k_2 and k_3, followed by a much faster step from intermediate C to final product D. Path k_2 involves no detectable intermediates, while path k_3 presumably involves intermediate B with reduced coordination number. When the steady-state approximation is applied to intermediate B, k_{obs} is given by eq. [6].

[6] $$k_{obs} = k_2[Me_2S] + \frac{k_1 k_3\, [Me_2S]}{k_{-1} + k_3[Me_2S]}$$

© 1998 NRC Canada

Fig. 3. Dependence of k_{obs} on C_{Me2S} (*a*) and on C_{Pt2} (*b*) for the reaction of $[Pt^{IV}{}_2Me_8(\mu\text{-}SMe_2)_2]$ with Me_2S in *n*-hexane at various temperatures. (*a*) $C_{Pt2} = (6.30–6.93) \times 10^{-5}$ M, $\lambda = 230$ nm; (*b*) $C_{Me2S} = 1.21 \times 10^{-3}$ M, $\lambda = 230$ nm, $T = 25°C$. Solid lines are the best-fit lines drawn by applying a nonlinear least-squares fitting to eq. [5].

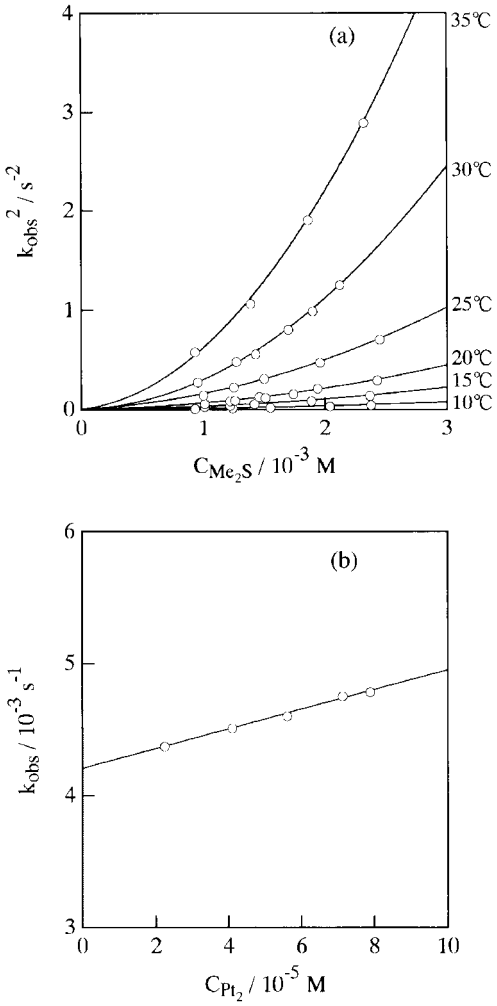

The first and second terms on the right-hand side in eq. [6] refer to the k_2 and k_3 paths, respectively. Obviously, the plot of k_{obs} vs. C_{Me2S} ($C_{Me2S} \sim [Me_2S]$, since $C_{Pt2} << C_{Me2S}$) will become linear at higher C_{Me2S}, when the second term contributes significantly to $k_{obs,}$ and k_{-1} is comparable to $k_3[Me_2S]$ at lower C_{Me2S}, which is inconsistent with the present results (see eq. [4] and Fig. 4*a*). However, when $k_{-1} >> k_3[Me_2S]$, which seems to be the present case, the plot will always be linear. That is, the k_2 and k_3 paths are kinetically indistinguishable, though all the spectrophotometric analyses mentioned so far favor simple conversion of the Pt(II) dimer to the product, without an appreciable amount of intermediates.

The same is true for the reaction of the Pt(IV) dimer with Me_2S, namely, it is also kinetically indistinguishable whether or not the k_3 path coexists with the k_2 path in Scheme 3. Then, the same conclusion can be drawn for the Pt(IV) reaction as for the Pt(II) dimer. It is more likely that the observed reactions of the Pt(IV) and Pt(II) dimers proceed mainly through path k_2, because the negative entropies and volumes of activation

Fig. 4. Dependence of k_{obs} on C_{Me2S} (*a*) and on C_{Pt2} (*b*) for the reaction of $[Pt^{II}{}_2Me_4(\mu\text{-}SMe_2)_2]$ with Me_2S in dichloromethane at various temperatures. (*a*) $C_{Pt2} = 8.10 \times 10^{-5}$ M, $\lambda = 290$ nm; (*b*) $C_{Me2S} = 3.47 \times 10^{-3}$ M, $\lambda = 290$ nm, $T = 25°C$.

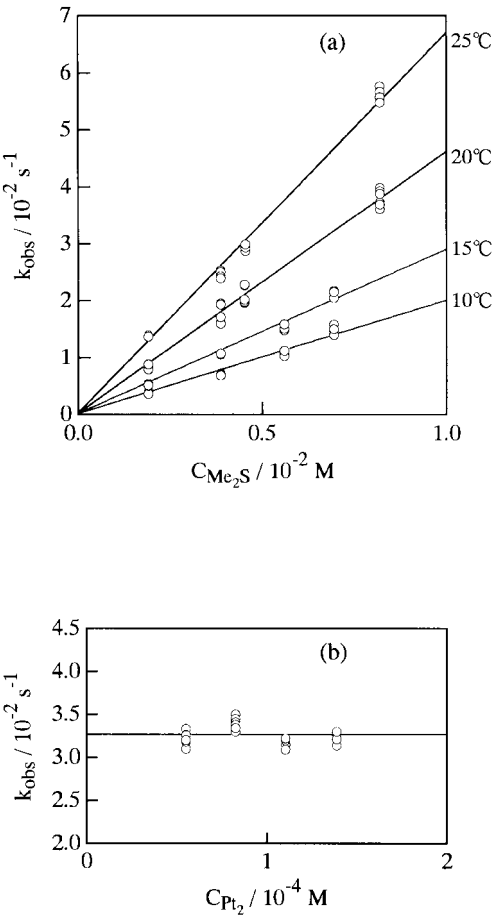

for these reactions in Table 1 are consistent with the associative interchange mechanism.

Substitution on $[Pt^{IV}{}_2Me_8(\mu\text{-}SMe_2)_2]$ for bidentate ligands

[7] $1/2\ [Pt^{IV}{}_2Me_8(\mu\text{-}SMe_2)_2] + NN \rightarrow [Pt^{IV}Me_4(NN)] + 2\ Me_2S$

(Nn = bipy or 4,4′-Me_2-bipy)

The change in spectra with time for reaction [7] was followed spectrophotometrically in the absence and in the presence, respectively, of excess Me_2S,when a much higher concentration of NN (C_{NN}) than C_{Pt2} was used to ensure pseudo-first-order conditions. In the absence of excess Me_2S, the first-order plots $\ln(A_\infty - A_t)$ vs. t (A_t and A_∞ are the absorbance at time t and at equilibrium, respectively) were curved; however, in the presence of added Me_2S they were entirely linear, which allows us to calculate k_{obs} in eq. [8].

[8] $d[Pt^{IV}Me_4(NN)] / dt = k_{obs}[Pt^{IV}Me_4(NN)]$

^{1}H NMR spectra for reaction [7] are shown in Fig. 6, and changes in peak height of the lines recorded at lower temperature are plotted against time in Fig. 7. The methyl protons of the dimer decrease towards zero with time; however, the methyl protons of both the free Me_2S and of the product complex keep increasing to a finite height even after the methyl

© 1998 NRC Canada

Table 1. Rate constants at 25°C and activation parameters for reactions [1] in *n*-hexane and [2] in dichloromethane.

Reaction	Path	k/M^{-1} s^{-1}	$\Delta H^{\neq}$/kJ mol^{-1}	$\Delta S^{\neq}$/J mol^{-1} K^{-1}	$\Delta V^{\neq}$/cm^3 mol^{-1}
[1]	k_f	3.16 ± 0.66	51.8 ± 1.7	–61.0 ± 5.9	—
[2]	k_d	1.18 ± 0.22	65.2 ± 22.1	–26.3 ±73.2	—
[3]	k_f	6.68 ± 0.06	58.0 ± 3.1	–34.5 ±10.5	–10.7 ± 1.3

Scheme 3

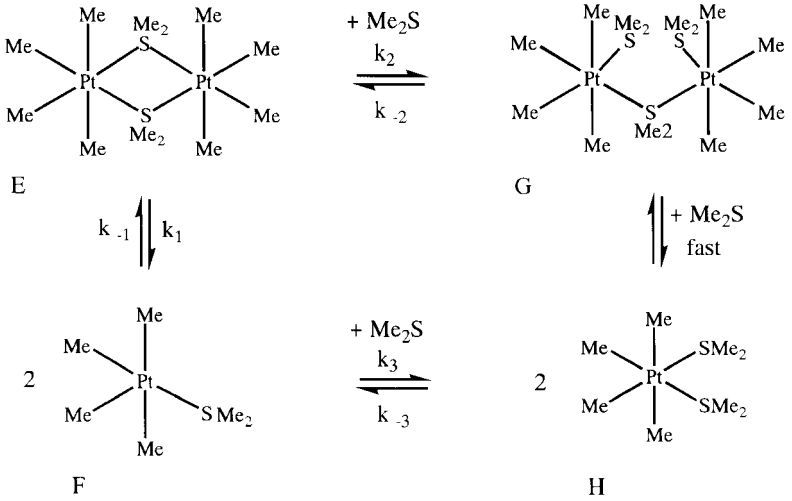

Fig. 5. Dependence of $k_{obs}{}^2C_{Me2S}{}^{-1}C_{Pt2}{}^{-1}$ on $C_{Me2S}C_{Pt2}{}^{-1}$ for the reaction of $[Pt^{IV}{}_2Me_8(\mu\text{-}SMe_2)_2]$ with Me_2S in *n*-hexane at various temperatures. $C_{Pt2} = (6.30–7.88) \times 10^{-5}$ M, $\lambda = 230$ nm. Solid lines are the best-fit lines drawn by applying a nonlinear least-squares fitting to eq. [5].

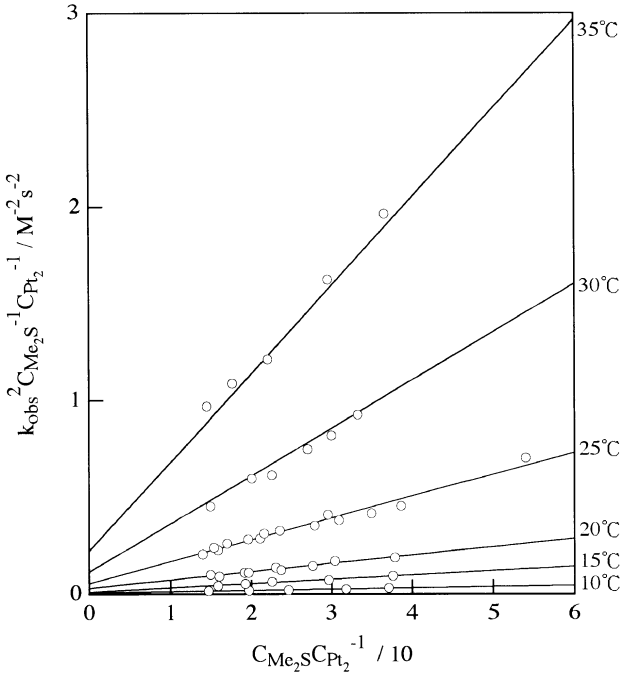

Fig. 6. ^{1}H NMR spectra for the reaction of $[Pt^{IV}{}_2Me_8(\mu\text{-}SMe_2)_2]$ with bipy in $CDCl_3$ at room temperature. $C_{Pt2} = 4.24 \times 10^{-3}$ M, $C_{Me2S} = 9.15 \times 10^{-3}$ M, $C_{bipy} = 3.02 \times 10^{-2}$ M: (*i*) 3, (*ii*) 5, (*iii*) 13, (*iv*) 40, (*v*) 150 min after the reaction started.

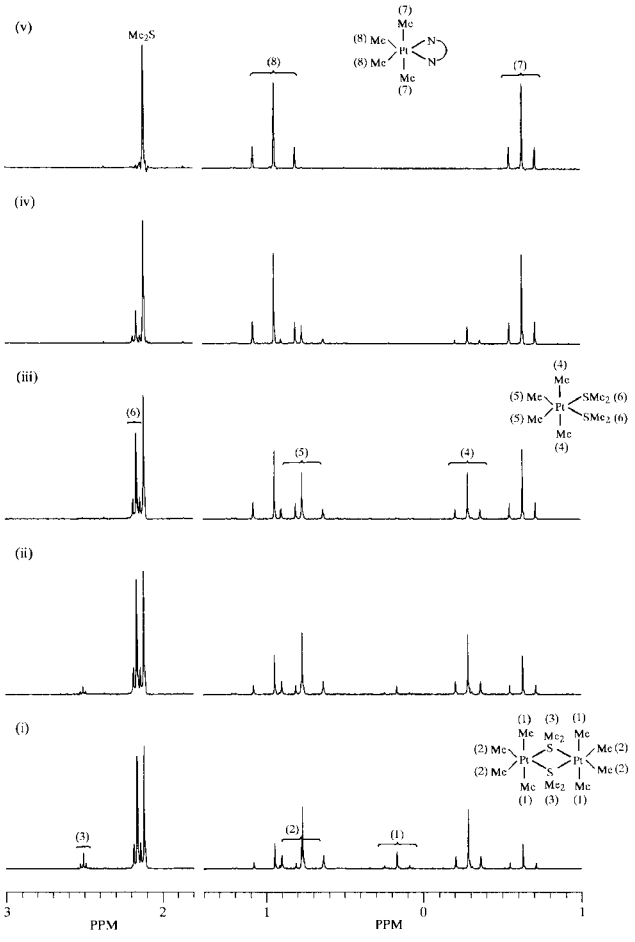

protons of the dimer have vanished. It is worth noting that the product increases exponentially from zero after an induction period (Fig. 7). On the other hand, it can also be seen from Fig. 7 that the protons of the methyl group bound to Pt in $[Pt^{IV}Me_4(SMe_2)_2]$ first increase, then decrease exponentially to zero. Rate constants were estimated from the curves in

© 1998 NRC Canada

Fig. 7. Change in peak height with time after the Me_2S + bipy solution was mixed with the $[Pt^{IV}{}_2Me_8(\mu\text{-}SMe_2)_2]$ solution in $CDCl_3$ at –20°C. $C_{Pt2} = 2.60 \times 10^{-3}$ M, $C_{Me2S} = 1.20 \times 10^{-2}$ M, $C_{bipy} = 5.20 \times 10^{-2}$ M. (○) at 0.18 ppm; (Δ) at –0.29 ppm; (□) at –0.62 ppm.

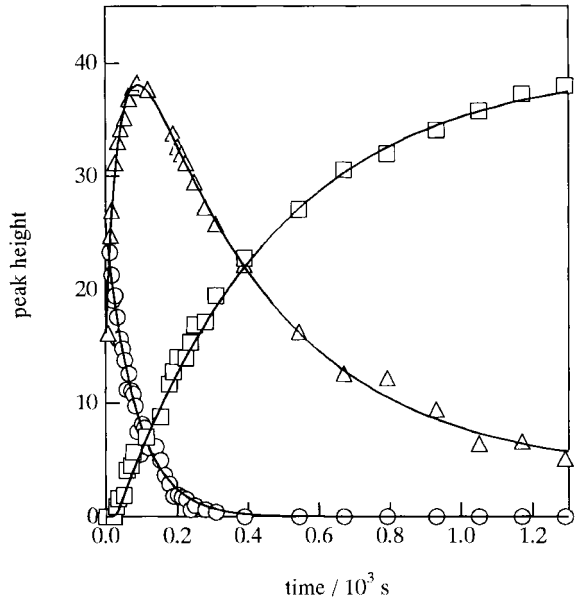

Scheme 4

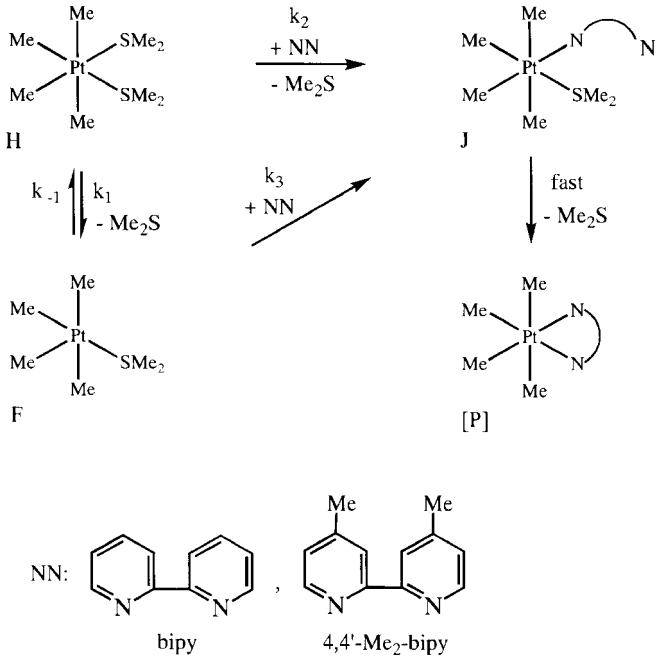

Fig. 7: the values $(1.19 \pm 0.04) \times 10^{-3}$ s^{-1} and $(2.22 \pm 0.09) \times 10^{-4}$ s^{-1} were calculated from the disappearance of the dimer and the appearance of the product, respectively. And the values $(2.39 \pm 0.74) \times 10^{-3}$ s^{-1} and $(2.14 \pm 0.12) \times 10^{-4}$ s^{-1} were estimated from the increase and decrease, respectively, of $[Pt^{IV}Me_4(SMe_2)_2]$. The rate constants for the faster reaction ($(1.19 \pm 0.04) \times 10^{-3}$ s^{-1} and $(2.39 \pm 0.74) \times 10^{-3}$ s^{-1}) indicate

Fig. 8. Dependence of k_{obs} on C_{NN} for the reaction of $[Pt^{IV}{}_2Me_8(\mu\text{-}SMe_2)_2]$ with NN in dichloromethane at 25°C. (*a*) $C_{Pt2} = 1.43 \times 10^{-4}$ M, λ = 465 nm, $C_{Me2S} = 1.29 \times 10^{-2}$ M (1), 1.95×10^{-2} M (2), 5.60×10^{-2} M (3); 7.95×10^{-2} M (4) for NN = bipy; (*b*) $C_{Pt2} = 1.40 \times 10^{-4}$ M, λ = 440 nm, $C_{Me2S} = 1.05 \times 10^{-2}$ M for NN = 4,4′-Me_2-bipy.

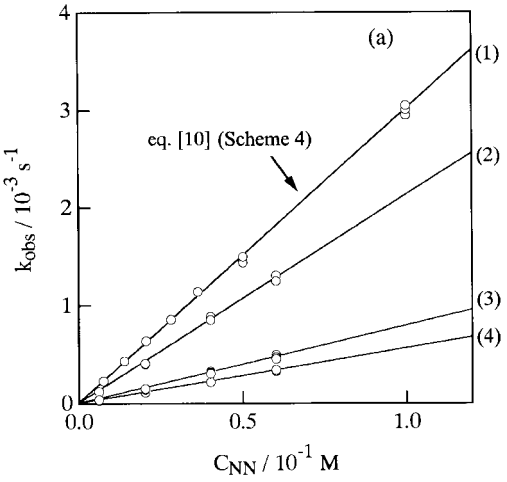

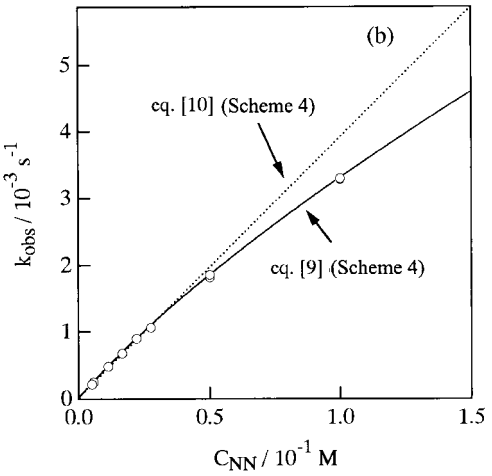

that $-d[dimer]/dt = (1/2) \times d[Pt^{IV}Me_4(SMe_2)_2]/dt$ holds, as is required for reaction [1]. For the slower reaction, the rate constants ($(2.22 \pm 0.09) \times 10^{-4}$ s^{-1} and $(2.14 \pm 0.12) \times 10^{-4}$ s^{-1}) agree with each other within the experimental error. These results indicate that the dimer would be unreactive with NN and would be consumed mainly through the reaction of the more reactive $[Pt^{IV}Me_4(SMe_2)_2]$ with NN to form final product $[Pt^{IV}Me_4(NN)]$ without a reverse reaction. That is, the reaction would be stepwise: $[Pt^{IV}{}_2Me_8(\mu\text{-}SMe_2)_2] + 2Me_2S \rightleftharpoons 2[Pt^{IV}Me_4(SMe_2)_2]$ and $[Pt^{IV}Me_4(SMe_2)_2] + NN \rightarrow [Pt^{IV}Me_4(NN)] + 2Me_2S$, and the change in the UV–VIS spectra would correspond to the second step, i.e., from $[Pt^{IV}Me_4(SMe_2)_2]$ to final product $[Pt^{IV}Me_4(NN)]$ via an intermediate with an open chelate ring, because a much higher concentration of Me_2S was employed in the spectrophotometric measurements, which considerably shifts the equilibrium of reaction [1] towards the right-hand side.

© 1998 NRC Canada

Table 2. Rate constants for reaction [3] at 25°C in dichloromethane.

	k_1/s^{-1}	k_3/k_{-1}	$k_2/M^{-1}\ s^{-1}$	$k_1\ k_3/k_{-1}$
bipy		$(3.51 \pm 0.35) \times 10^{-2}$ [a]	$(7.09 \pm 1.89) \times 10^{-4}$	
			$\Delta H_2^{\neq} = 94.7 \pm 20.6$ kJ mol^{-1}	$\Delta H_0^{\neq} = 99.7 \pm 3.1$ kJ mol^{-1}
			$\Delta S_2^{\neq} = 17.7 \pm 69.1$ J mol^{-1} K^{-1}	$\Delta S_0^{\neq} = 23.5 \pm 10.3$ J mol^{-1} K^{-1}
			$\Delta V_2^{\neq} = -9.3 \pm 9.1$ cm^3 mol^{-1}	$\Delta V_0^{\neq} = 9.7 \pm 0.5$ cm^3 mol^{-1}
4,4′-Me_2-bipy	$(1.10 \pm 0.10) \times 10^{-2}$	$(4.33 \pm 0.30) \times 10^{-2}$	$(6.09 \pm 1.35) \times 10^{-4}$	

[a] Calculated by using the value of k_1 (= 1.10×10^{-2}) for the 4,4′-Me_2-bipy system.

Scheme 5

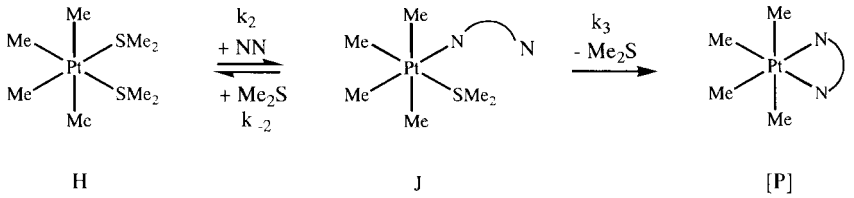

Fig. 9. Dependence of k_{obs} on C_{Me2S} for the reaction of $[Pt^{IV}_2Me_8(\mu\text{-}SMe_2)_2]$ with NN in dichloromethane at 25°C. (*a*) $C_{Pt2} = 1.43 \times 10^{-4}$ M, $C_{NN} = 2.00 \times 10^{-2}$ M, λ = 465 nm for NN = bipy; (*b*) $C_{Pt2} = 1.40 \times 10^{-4}$ M, $C_{NN} = 2.20 \times 10^{-2}$ M, λ = 440 nm for NN = 4,4′-Me_2-bipy.

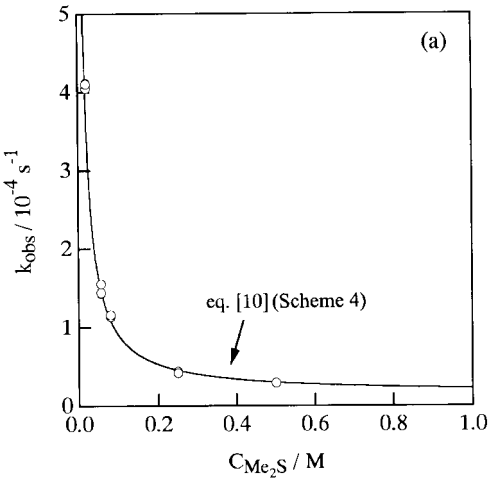

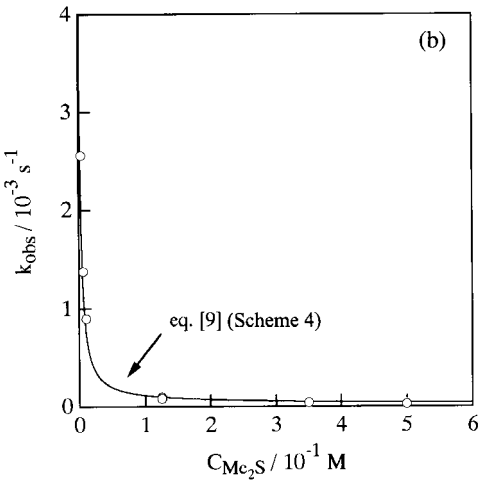

Fig. 10. Dependence of C_{NN}/k_{obs} on C_{Me2S} in dichloromethane at 25°C. (*a*) $C_{Pt2} = 1.40 \times 10^{-4}$ M for NN = bipy; (*b*) $C_{Pt2} = 1.40 \times 10^{-4}$ M for NN = 4,4′-Me_2-bipy.

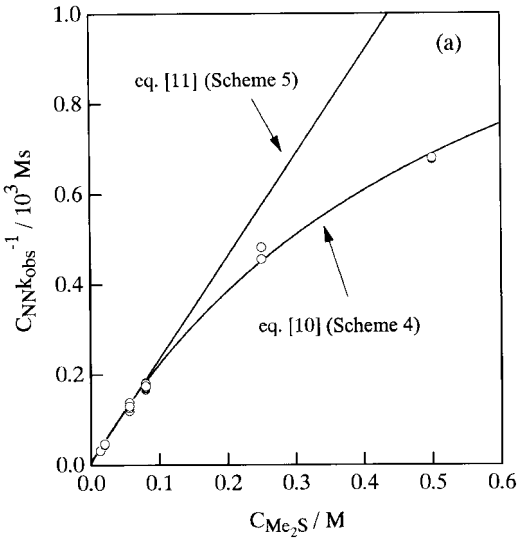

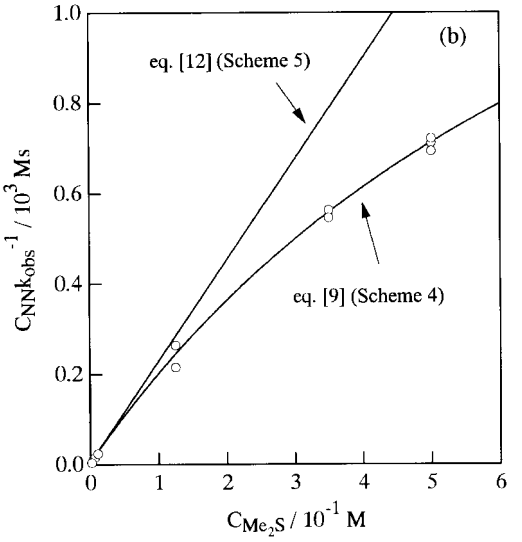

© 1998 NRC Canada

The pseudo-first-order rate constant k_{obs} for the reaction with bipy depends linearly on C_{bipy}, although the reaction with 4,4′-Me_2-bipy deviates from a straight line at higher C_{NN}, as shown in Figs. 8*a* and 8*b*, respectively. In contrast, k_{obs} decreases drastically with increasing C_{Me2S} for the reactions of both bipy and 4,4′-Me_2-bipy, as shown in Fig. 9.

Reaction [7] is represented by Scheme 4. Application of the steady-state approximation to coordinatively unsaturated intermediate F gives eq. [9].

$$[9] \quad k_{obs} = k_2[NN] + \frac{k_1k_3[NN]}{k_{-1}[Me_2S] + k_3[NN]} = k_2[NN] + \frac{k_1[NN]}{(k_{-1}/k_3)[Me_2S] + [NN]}$$

In the case of NN = bipy, if $k_{-1}[Me_2S] >> k_3[NN]$ in the second term in eq. [9], then eq. [9] is reduced to eq. [10]. It can be seen from Fig. 9 that the second term in eq. [10] contributes significantly to k_{obs}. The results in Figs. 8*a* and 9 are explained well by eq. [10].

$$[10] \quad k_{obs} = k_2[NN] + \frac{k_1k_3[NN]}{k_{-1}[Me_2S]}$$

On the other hand, when NN = 4,4′-Me_2-bipy, the k_3[NN] term is not negligible compared to $k_{-1}[Me_2S]$, i.e., these two terms are comparable, which makes the plots in Fig. 8*b* curved at higher C_{NN}.

Alternatively, Scheme 5 may explain the results in Figs. 8 and 9, although the rate-determining chelate-ring closure seems to be less plausible in view of the strong *trans* effect of the methyl group (14). In this scheme, when the steady-state approximation is applied to intermediate J with an open chelate ring, and when the fast equilibrium between H and J is followed by rate-determining chelate-ring closure, eqs. [11] and [12] are obtained, respectively.

$$[11] \quad k_{obs} = \frac{k_2k_3[NN]}{k_{-2}[Me_2S] + k_3}$$

$$[12] \quad k_{obs} = \frac{k_2k_3[NN]}{k_{-2}[Me_2S] + k_2[NN]}$$

Equations [11] and [12] fit the experimental results well at $[Me_2S] < 0.1$ M in the case of NN = bipy, and at $[Me_2S] < 0.05$ M in the case of NN = 4,4′-Me_2-bipy, while eqs. [9] and [10] fit the results very well over the concentration range examined, as shown in Fig. 10. Thus, the experimental results agree with the mechanism presented in Scheme 4.

The values of the rate constants and activation parameters obtained are listed in Table 2. In this table, the values of k_1, k_2, and k_3/k_{-1} for the 4,4′-Me_2-bipy system were obtained from eq. [9]. For the bipy system, only the values of k_2 and k_1k_3/k_{-1} are obtainable from eq. [10]. The k_3/k_{-1} value was calculated with the values of k_1k_3/k_{-1} and k_1 for the 4,4′-Me_2-bipy system, which is common to both systems. The k_3/k_{-1} value reflects the reactivity of NN because k_{-1} is common to any NN. Thus, k_3 for the bipy system is slightly smaller than that for 4,4′-Me_2-bipy with higher basicity, which is in accordance with normal nucleophilic substitution. For path k_2, the large errors in the rate constants and activation parameters, which come from intercepts that are often not precisely determinable, make detailed discussion impossible. However, such kinetic parameters still suggest that the reaction of intermediate H with bipy would proceed with a Ia mechanism.

References

1. R.J. Puddephatt and P.J. Thompson. J. Chem. Soc. Dalton Trans. 1219 (1977).
2. J.D. Scott and R.J. Puddephatt. Organometallics, **2**, 1643 (1983).
3. D. Minniti, G. Alibrandi, M.L. Tobe, and R. Romeo. Inorg. Chem. **26**, 3956 (1987).
4. R. Romeo. Inorg. Chem. **11**, 21 (1990).
5. S. Lanza, G. Alibrandi, L.M. Scolaro, and S. Sergi. Inorg. Chim. Acta, **201**, 137 (1992).
6. A. Peloso. Coord. Chem. Rev. **10**, 165 (1973).
7. C.H. Langford and V.S. Sastri. MTP Int. Rev. Sci.: Inorg. Chem. Ser. One, 9 (1972).
8. M. Lashanizadehgan, M. Rashidi, J.E. Hux, R.J. Puddephatt, and S.S.M. Ling. J. Organomet. Chem. **269**, 317 (1984).
9. J.E. Hux and R.J. Puddephatt. Inorg. Chim. Acta, **100**, 1 (1985).
10. Y. Kondo, M. Ishikawa, and K. Ishihara. Inorg. Chim. Acta, **241**, 81 (1996).
11. K. Ishihara and M. Takagi. Rev. Sci. Instrum. **65**, 513 (1994).
12. D.E. Clegg, J.R. Hall and G.A. Swile. J. Organomet. Chem. **38**, 403 (1972).
13. M. Eigen and L. DeMaeyer. *In* Technique of organic chemistry. Vol. VIII. 2nd ed. *Edited by* A. Weissberger. Interscience Publishers, New York. 1963.
14. D.E. Clegg and J.R. Hall. Aust. J. Chem. **20**, 2025 (1967).

Appendix

$$Pt_2Me_8(\mu\text{-}SMe_2)_2 + 2\ Me_2S \underset{k_d}{\overset{k_f}{\rightleftharpoons}} 2\ Pt\ Me_4(SMe_2)_2$$

$[Pt_2Me_8(\mu\text{-}SMe_2)_2] = C_1$, $[PtMe_4(SMe_2)_2] = C_2$, $[Me_2S] = C_{Me2S}$ (C_1, $C_2 << C_{Me2S}$)

$$\underset{C_1}{Pt_2Me_8(\mu\text{–}SMe_2)_2} \underset{k_d}{\overset{k_f'}{\rightleftharpoons}} \underset{C_2}{2\ PtMe_4(SMe_2)_2}$$

$K = k_f' / k_d = C_2^2 / C_1$

$k_{obs} = 4\ k_d\ C_2 + k_f' = k_d\ (4\ C_2 + K)$, which is from ref. 13.

$C_{Pt2} = C_2 / 2 + C_1$

$C_1 = C_{Pt2} - C_2 / 2$

$K = C_2^2 / C_1 = C_2^2 / (C_{Pt2} - C_2 / 2)$

$C_2 = (-K + (K^2 + 16\ C_{Pt2}\ K)^{1/2})/4$

$k_{obs} = k_d(-K + (K_2 + 16\ C_{Pt2}\ K)^{1/2} + K) = k_d\ (K_2 + 16\ C_{Pt2}\ K)^{1/2}$

$k_{obs}^2 = k_d^2\ K^2 + 16\ k_d^2\ C_{Pt2}\ K = k_f'^2 + 16\ k_f'\ k_d\ C_{Pt2}$

$k_{obs}^2 = k_f^2\ C_{Me2S}^2 + 16\ k_f\ k_d\ C_{Pt2}\ C_{Me2S}$

$k_{obs}^2\ C_{Me2S}^{-1}\ C_{Pt2}^{-1} = k_f^2\ C_{Me2S}\ C_{Pt}^{-1} + 16\ k_f\ k_d$

© 1998 NRC Canada

Salt effect on the solubility of *mer*-(+)-tris(L-alaninato)cobalt(III)

Yasuki Yoshimura

Abstract: The effect of NaF, NaCl, NaBr, NaI, $NaNO_3$, CH_3COONH_4, NaH_2PO_4, and $(NH_4)_2SO_4$ on *mer*-(+)-tris(L-alaninato)cobalt(III) (*mer*-(+)-[Co(L-ala)$_3$]) was examined by determining the solubility of the chelate. While the solubility of *mer*-(+)-[Co(L-ala)$_3$] (salting-in effect) increased with the addition of NaCl, NaBr, NaI, and $NaNO_3$, the solubility (salting-out effect) decreased with the addition of NaF, CH_3COONH_4, and NaH_2PO_4. In low salt concentration $(NH_4)_2SO_4$ caused slight salting-in, but in salt concentration >0.5 mol dm^{-3} $(NH_4)_2SO_4$ brought about salting-out. The magnitude of the salting-in effect increased in the order of NaCl < $NaNO_3$ < NaBr < NaI. The standard enthalpy (ΔH_s°) and entropy (ΔS_s°) of dissolution for *mer*-(+)-[Co(L-ala)$_3$] were estimated from the temperature dependence of the solubility. When ΔH_s° was plotted against $T\Delta S_s^\circ$, a single-correlation straight line was obtained for the salts that brought about the salting-in effect. On the basis of these findings, the origin of the salting-in effect was discussed. Furthermore, while NaF, NaCl, and NaBr showed larger salting-in effect on *fac*-tris(glycinato)cobalt(III) (*fac*-[Co(gly)$_3$]) than on *mer*-(+)-[Co(L-ala)$_3$], NaI greatly decreased the solubility of *fac*-[Co(gly)$_3$]. At the present stage, an explanation for this anomalous salting-out effect of NaI cannot be presented.

Key words: salt effect, solubility, thermodynamic parameters of dissolution, *mer*-tris(L-alaninato)cobalt(III), *fac*-tris(glycinato)cobalt(III).

Résumé : En se basant sur la solubilité du chélate, on a déterminé l'effet de NaF, NaCl, NaBr, NaI, $NaNO_3$, CH_3COONH_4, NaH_2PO_4 et $(NH_4)_2SO_4$ sur le *mer*(+)-tris(L-alaninato)cobalt(III) (*mer*-(+)-[Co(L-ala)$_3$]). Alors que le NaCl, le NaBr, le NaI et le $NaNO_3$ augmentent la solubilité du *mer*-(+)-[Co(L-ala)$_3$] (effet de relargage inversé), le NaF, le CH_3COONH_4 et la NaH_2PO_4 diminuent sa solubilité (effet de relargage). Le $(NH_4)_2SO_4$ provoque un relargage à des concentrations supérieures à 0,5 mol dm^{-3}; aux concentrations inférieures, il provoque un faible effet contraire. L'effet de relargage inversé augmente dans l'ordre NaCl < $NaNO_3$ < NaBr < NaI. Utilisant la relation entre la solubilité et la température, on a évalué l'enthalpie standard (ΔH_s°) ainsi que l'entropie de dissolution (ΔS_s°) du *mer*-(+)-[Co(L-ala)$_3$]. Quand on trace un graphique du ΔH_s° en fonction du $T\Delta S_s^\circ$, on obtient une seule ligne droite de corrélation pour les sels qui provoquent un effet de relargage inversé. Sur la base de ces constatations, on discute de l'origine de cet effet. De plus, même si le NaF, le NaCl et le NaBr provoquent un plus grand effet de relargage inversé sur le *fac*-tris(glycinato)cobalt(III) (*fac*-[Co(gly)$_3$]) que sur le *mer*-(+)-[Co(L-ala)$_3$], le NaI diminue fortement la solubilité du *fac*-[Co(gly)$_3$]. Sur la base des données actuelles, il n'est pas possible de présenter une explication pour cet effet anormal de relargage du NaI.

Mots clés : effet de sel, solubilité, paramètres thermodynamiques de dissolution, *mer*(+)-tris(L-alaninato)cobalt(III), *fac*-tris(glycinato)cobalt(III).

[Traduit par la rédaction]

Introduction

It has been extensively reported that the solubilities of nonelectrolytes in water decrease upon the addition of various inorganic salts (salting-out effect) (1–3). Long and McDevit (2) attributed the salting-out effect to an increase in the internal pressure, resulting from an ion–water interaction (2, 4). This theory predicts that many of the inorganic salts result in the salting-out effect on nonpolar nonelectrolytes. However, Sugunan (5) and Sugunan and Thomas (5) have reported that K_2SO_4 and KF markedly increase the solubilities of substituted benzoic acids (salting-in effect) and attributed the salting-in effect to hydrogen bond formation between the benzoic acids and SO_4^{2-} or F^-.

The author has also found that NaCl and Na_2SO_4 result in the salting-out effect on tris(2,4-pentanedionato)cobalt(III) ([Co(acac)$_3$]) but exhibit the salting-in effect on *fac*-(–)-tris(D-prolinato)cobalt(III) (*fac*-(–)-[Co(D-pro)$_3$]) (6). In this paper, (+) and (–) represent dextrorotatory and levorotatory at 589 nm, respectively. Especially, it is worthwhile to notice that $(NH_4)_2SO_4$, which is a well-known salting-out agent for protein, also exhibits a large salting-in effect on *fac*-(–)-[Co(D-pro)$_3$], with salt concentration less than 1 mol dm^{-3}. To elucidate the origin of the specific salting-in effect on *fac*-(–)-[Co(D-pro)$_3$], various experimental attempts are needed, but considerably low solubility of this chelate makes these attempts difficult.

In connection with the above-mentioned experimental

Received June 5, 1997.

Y. Yoshimura.[1] Laboratory of Chemistry, Faculty of Humanities and Social Sciences, Iwate University, Ueda, Morioka, 020 Japan.

[1] Telephone: (019) 621–6824. Fax: (019) 621–6824. E-mail: yasumura@iwate-u.ac.jp

© 1998 NRC Canada

restriction, the salt effect on the solubility of *mer*-tris(amino acidato)cobalt(III) (*mer*-[Co(amino acidato)$_3$]), which is more soluble than the corresponding *fac*-isomer, can be examined more systematically by using a wide variety of salts. Such examination may be expected to provide helpful information concerning the explanation for the above salting-in effect on *fac*-(–)-[Co(D-pro)$_3$].

Amino acid residue in the peptide chain of proteins forms the peptide bonding between the amino group of one amino acid and the carboxyl group of another amino acid. On the other hand, the amino acid in *fac*- and *mer*-[Co(amino acidato)$_3$] binds to the cobalt ion through both the amino nitrogen and the carboxylato oxygen, and resembles the amino acid residue in the peptide chain in terms of the loss of amphoteric character. Thus, the elucidation of the salting-in effect on *fac*- and *mer*-[Co(amino acidato)$_3$] may be expected to present a new approach to the salt effect on proteins.

Furthermore, the solubilities of four isomers of tris(L- or D-amino acidato)cobalt(III) (*fac*-(+)-, *fac*-(–)-, *mer*-(+)-, and *mer*-(–)-isomers) considerably differ from one another (7), and at the present stage this difference seems not to be explained clearly (8). In connection with this problem, it is worthwhile to examine the difference in some properties between *fac*- and *mer*-isomers, such as the salt effect on their solubilities.

Thus, in this study the solubility of *mer*-(+)-tris(L-alaninato)cobalt(III) (*mer*-(+)-[Co(L-ala)$_3$]) in aqueous solutions of NaF, NaCl, NaBr, NaI, $NaNO_3$, $(NH_4)_2SO_4$, CH_3COONH_4, and NaH_2PO_4 is determined over the temperature range of 5–35°C, and the salt effect on *mer*-(+)-[Co(L-ala)$_3$] is compared with that on *fac*-(–)-[Co(D-pro)$_3$] and *fac*-tris(glycinato)cobalt(III) (*fac*-[Co(gly)$_3$]).

Experimental

The synthesis and separation of *mer*-(+)-[Co(L-ala)$_3$] were carried out in a manner reported in the literature (9), and the preparation of *fac*-[Co(gly)$_3$] was previously reported (10). The solubilities of *mer*-(+)-[Co(L-ala)$_3$] and *fac*-[Co(gly)$_3$] were accomplished by using the same procedure as previously reported (11).

The solubility in mol kg^{-1} (S_m) is defined as the moles of chelate molecules in 1 kg of an aqueous salt mixture, and the solubility in mol dm^{-3} (S_c) at 25°C is also obtained as previously reported (6). The chelate concentration used to calculate the solubility was determined spectrophotometrically by measuring the absorbances at 542 nm for *mer*-(+)-[Co(L-ala)$_3$] and at 520 nm for *fac*-[Co(gly)$_3$], except for the experiment in aqueous NaF solutions for *fac*-[Co(gly)$_3$] where the absorbance at 217 nm was measured. In the experiment in aqueous NaI solutions, the apparatus for solubility determination was covered with black cloth to prevent the formation of I_3^- species.

Commercial NaF, NaCl, NaBr, NaI, $NaNO_3$, NaH_2PO_4, CH_3COONH_4, and $(NH_4)_2SO_4$ (reagent grade, Wako Chemical Industries Ltd.) were used without further purification. NaF, NaCl, NaBr, NaI, $NaNO_3$, and NaH_2PO_4 were dried for 3 h at 120°C and stored in a silica-gel desiccator. CH_3COONH_4 and $(NH_4)_2SO_4$ were dried in a vacuum desiccator over concentrated H_2SO_4 for several days. For the solubility measurement, the salt concentration in the working solution of each salt was calculated in both mol kg^{-1} and mol dm^{-3} (m_s and c_s, respectively). Redistilled water was used.

Results

The S_m values in aqueous salt solutions are listed in Table 1 for *mer*-(+)-[Co(L-ala)$_3$] and in Table 2 for *fac*-[Co(gly)$_3$]. The S_c values at 25°C of these chelates are tabulated in Table 3.

The solubility measurement was repeated at least four times at each temperature in all cases. The solubilities given in these tables are the mean values of the individual experimental values. The errors given in parentheses denote the deviations at 95% confidence levels and are less than 2%, except for the solubility measurement for *fac*-[Co(gly)$_3$] in aqueous NaI solutions.

In the spectrophotometric determination of *fac*-[Co(gly)$_3$] in the aqueous NaI solutions, the absorbance at 520 nm became extremely small because of the large salting-out effect of NaI. In addition, the absorption of NaI at about 250 nm inhibited the spectrophotometric determination using the absorbance at 217 nm. For these reasons, the errors for the solubility measurement of *fac*-[Co(gly)$_3$] in the aqueous NaI solutions became considerably large. Furthermore, in the region of NaI concentration of 0.5–3.0 mol dm^{-3}, the absorbance at 520 nm was too small to determine the solubility of *fac*-[Co(gly)$_3$].

In the determination of solubility in the aqueous NaI solutions, an absorbance at about 365 nm became progressively large during the course of equilibration because of the formation of I_3^- species. However, since the formation of I_3^- was reduced by covering the apparatus with black cloth, the absorbances of *mer*-(+)-[Co(L-ala)$_3$] at 543 nm and of *fac*-[Co(gly)$_3$] at 520 nm were not affected.

To demonstrate the effect of salts on the solubilities of *mer*-(+)-[Co(L-ala)$_3$] and *fac*-[Co(gly)$_3$], the values of $\log(S_c^\circ/S_c)$ at 25°C are plotted against c_s in Figs. 1 and 2, respectively. S_c° is the solubility in mol dm^{-3} in water. The solubility of *mer*-(+)-[Co(L-ala)$_3$] decreased in the presence of NaH_2PO_4, CH_3COONH_4, and NaF (salting-out) and increased with the addition of NaCl, $NaNO_3$, NaBr, and NaI (salting-in). $(NH_4)_2SO_4$ showed the slight salting-in effect at low c_s values but resulted in the salting-out effect at c_s values >0.5 mol dm^{-3}. For *fac*-[Co(gly)$_3$], on the other hand, while the addition of NaF, NaCl, and NaBr resulted in the salting-in effect, the addition of NaI exhibited an extremely large salting-out effect.

Since the solubility values for *mer*-(+)-[Co(L-ala)$_3$] and *fac*-[Co(gly)$_3$] tabulated in Tables 1–3 are fairly small, these saturated solutions may be regarded as being ideal dilute solutions with respect to the chelates. Thus, without an activity correction the standard enthalpy (ΔH_s°) and entropy (ΔS_s°) of dissolution at 25°C for these chelates were estimated, based on the temperature dependence of ln S_m in the same manner as previously reported (12). The standard state for the chelate in solution is 1 mol kg^{-1}.

Discussion

To compare the magnitude of the salt effect on *mer*-(+)-[Co(L-ala)$_3$] with that on *fac*-[Co(gly)$_3$], the experimental data for $\log(S_c^\circ/S_c)$ illustrated in Figs. 1 and 2 were fitted to the following power series for the c_s values

$$[1] \quad \log (S_c^\circ/S_c) = A + k_s c_s + k_s' c_s 2 + \cdots\cdots$$

where k_s and k_s' are the salting coefficients, which indicate the

© 1998 NRC Canada

Table 1. Solubility (S_m, 10^{-3} mol kg^{-1}) of mer-(+)-[Co(L-ala)$_3$] in water and in aqueous salt solutions.[a]

		In NaCl					In $NaNO_3$				
		NaCl concentration, m_s (mol kg^{-1})					$NaNO_3$ concentration, m_s (mol kg^{-1})				
T (°C)	In water	0.208	0.723	1.542	3.208	5.461	0.171	0.524	1.257	2.718	4.654
5	3.13 (0.03)	3.38 (0.04)	3.98 (0.03)	4.46 (0.03)	5.01 (0.03)	5.68 (0.03)	3.48 (0.02)	4.02 (0.03)	4.83 (0.02)	5.51 (0.03)	5.71 (0.03)
10	3.34 (0.03)	3.58 (0.02)	4.12 (0.02)	4.61 (0.02)	5.11 (0.01)	5.68 (0.02)	3.65 (0.01)	4.18 (0.02)	4.97 (0.02)	5.59 (0.03)	5.75 (0.02)
15	3.51 (0.02)	3.76 (0.03)	4.30 (0.03)	4.77 (0.03)	5.21 (0.02)	5.80 (0.04)	3.83 (0.01)	4.34 (0.02)	5.11 (0.03)	5.74 (0.04)	5.89 (0.04)
20	3.76 (0.02)	3.99 (0.02)	4.53 (0.02)	4.98 (0.01)	5.39 (0.04)	5.91 (0.06)	4.03 (0.02)	4.54 (0.01)	5.31 (0.02)	5.89 (0.02)	6.04 (0.02)
25	3.97 (0.01)	4.22 (0.03)	4.74 (0.02)	5.20 (0.03)	5.56 (0.02)	6.11 (0.03)	4.30 (0.02)	4.76 (0.01)	5.56 (0.03)	6.12 (0.06)	6.25 (0.03)
30	4.25 (0.03)	4.51 (0.03)	5.05 (0.01)	5.46 (0.03)	5.85 (0.03)	6.37 (0.03)	4.54 (0.04)	5.08 (0.03)	5.79 (0.03)	6.41 (0.06)	6.51 (0.03)
35	4.53 (0.04)	4.86 (0.01)	5.40 (0.03)	5.80 (0.04)	6.13 (0.03)	6.64 (0.06)	4.88 (0.02)	5.36 (0.02)	6.17 (0.02)	6.75 (0.02)	6.83 (0.04)
40	4.85 (0.02)										
45	5.27 (0.03)										
50	5.71 (0.02)										

	In NaBr					In $(NH_4)_2SO_4$				
	NaBr concentration, m_s (mol kg^{-1})					$(NH_4)_2SO_4$ concentration, m_s (mol kg^{-1})				
T (°C)	0.156	0.572	1.574	3.286	5.169	0.152	0.518	1.292	2.264	3.770
5	3.34 (0.03)	4.12 (0.02)	5.81 (0.04)	8.46 (0.04)	12.7 (0.1)	3.21 (0.02)	3.07 (0.03)	2.10 (0.02)	1.29 (0.02)	0.623 (0.003)
10	3.52 (0.02)	4.31 (0.04)	5.92 (0.03)	8.40 (0.04)	12.4 (0.1)	3.40 (0.01)	3.19 (0.02)	2.18 (0.02)	1.34 (0.01)	0.658 (0.005)
15	3.71 (0.03)	4.46 (0.02)	6.02 (0.03)	8.41 (0.03)	12.2 (0.1)	3.58 (0.04)	3.37 (0.03)	2.30 (0.02)	1.42 (0.01)	0.697 (0.012)
20	3.94 (0.04)	4.68 (0.02)	6.20 (0.04)	8.48 (0.04)	12.2 (0.1)	3.82 (0.04)	3.55 (0.02)	2.42 (0.02)	1.50 (0.01)	0.747 (0.012)
25	4.20 (0.01)	4.92 (0.04)	6.42 (0.03)	8.68 (0.04)	12.4 (0.1)	4.06 (0.01)	3.75 (0.02)	2.58 (0.03)	1.61 (0.01)	0.806 (0.012)
30	4.46 (0.05)	5.20 (0.04)	6.73 (0.05)	8.95 (0.07)	12.7 (0.1)	4.33 (0.03)	4.01 (0.02)	2.69 (0.02)	1.69 (0.01)	0.875 (0.010)
35	4.76 (0.03)	5.54 (0.02)	7.09 (0.02)	9.30 (0.06)	13.2 (0.1)	4.64 (0.03)	4.25 (0.03)	2.88 (0.02)	1.79 (0.01)	0.916 (0.010)

	In CH_3COONH_4					In NaH_2PO_4			
	CH_3COONH_4 concentration, m_s (mol kg^{-1})					NaH_2PO_4 concentration, m_s (mol kg^{-1})			
T (°C)	0.161	0.553	1.482	3.461	5.434	0.104	0.511	1.260	1.797
5	3.05 (0.03)	2.88 (0.01)	2.47 (0.01)	1.87 (0.02)	1.48 (0.01)	3.05 (0.02)	2.60 (0.01)	1.80 (0.02)	1.43 (0.01)
10	3.23 (0.01)	3.06 (0.02)	2.61 (0.01)	1.97 (0.02)	1.56 (0.01)	3.18 (0.01)	2.72 (0.03)	1.90 (0.02)	1.53 (0.01)
15	3.44 (0.03)	3.24 (0.01)	2.78 (0.03)	2.11 (0.03)	1.67 (0.01)	3.37 (0.03)	2.89 (0.01)	2.02 (0.01)	1.63 (0.01)
20	3.66 (0.02)	3.48 (0.02)	2.96 (0.03)	2.27 (0.03)	1.81 (0.01)	3.60 (0.04)	3.05 (0.02)	2.16 (0.02)	1.75 (0.01)
25	3.90 (0.02)	3.71 (0.01)	3.21 (0.02)	2.46 (0.01)	1.95 (0.01)	3.81 (0.02)	3.28 (0.02)	2.31 (0.01)	1.89 (0.03)
30	4.19 (0.02)	3.99 (0.03)	3.44 (0.02)	2.65 (0.02)	2.13 (0.02)	4.11 (0.01)	3.49 (0.02)	2.49 (0.03)	2.03 (0.01)
35	4.44 (0.02)	4.27 (0.03)	3.68 (0.01)	2.87 (0.02)	2.30 (0.01)	4.43 (0.01)	3.77 (0.02)	2.67 (0.01)	2.22 (0.02)

	In NaF			In NaI					
	NaF concentration, m_s (mol kg^{-1})			NaI concentration, m_s (mol kg^{-1})					
T (°C)	0.115	0.400	0.766	0.198	0.468	1.113	2.541	4.314	5.293
5	2.93 (0.02)	2.69 (0.03)	2.34 (0.04)	3.62 (0.02)	5.69 (0.03)	7.80 (0.04)	10.4 (0.1)	21.3 (0.1)	32.6 (0.2)
10	3.12 (0.03)	2.82 (0.04)	2.46 (0.02)	3.76 (0.04)	5.79 (0.02)	7.80 (0.02)	10.3 (0.1)	20.8 (0.1)	31.1 (0.1)
15	3.26 (0.02)	3.00 (0.02)	2.62 (0.02)	3.96 (0.02)	5.94 (0.02)	7.82 (0.03)	10.3 (0.1)	20.2 (0.1)	30.0 (0.2)
20	3.46 (0.05)	3.19 (0.02)	2.80 (0.03)	4.16 (0.02)	6.11 (0.02)	7.96 (0.04)	10.3 (0.1)	19.8 (0.1)	29.4 (0.4)
25	3.75 (0.04)	3.41 (0.04)	2.97 (0.04)	4.40 (0.05)	6.33 (0.04)	8.09 (0.04)	10.5 (0.1)	19.8 (0.1)	29.0 (0.1)
30	3.98 (0.05)	3.66 (0.02)	3.20 (0.03)	4.68 (0.02)	6.60 (0.03)	8.42 (0.02)	10.7 (0.1)	20.1 (0.2)	29.1 (0.1)
35	4.33 (0.07)	3.95 (0.02)	3.47 (0.02)	5.02 (0.03)	6.92 (0.03)	8.72 (0.04)	11.2 (0.1)	20.5 (0.3)	29.7 (0.5)

[a] Errors denoting 95% confidence levels are given in parentheses.

© 1998 NRC Canada

Table 2. Solubility (S_m, 10^{-4} mol kg) of *fac*-[Co(gly)$_3$] in aqueous salt solutions.[a]

	In NaF			In NaI			In NaBr				
	NaF concentration, m_s (mol kg^{-1})			NaI concentration, m_s (mol kg^{-1})			NaBr concentration, m_s (mol kg^{-1})				
T (°C)	0.115	0.418	0.734	0.158	0.497	3.480	0.163	0.551	1.249	3.055	4.987
5	3.17 (0.05)	4.15 (0.06)	4.43 (0.04)						16.3 (0.1)	66.9 (0.5)	222 (3)
10	3.84 (0.05)	4.85 (0.06)	5.40 (0.03)						18.6 (0.1)	72.4 (0.3)	231 (1)
15	4.64 (0.06)	5.86 (0.05)	6.50 (0.08)				6.02 (0.03)	10.7 (0.1)	21.4 (0.1)	78.8 (0.2)	242 (1)
20	5.73 (0.04)	7.00 (0.09)	7.85 (0.09)	1.68 (0.04)	1.01 (0.06)	1.43 (0.05)	7.21 (0.11)	12.5 (0.1)	24.7 (0.2)	86.6 (0.4)	255 (1)
25	6.70 (0.06)	8.37 (0.13)	9.33 (0.09)	2.14 (0.04)	1.32 (0.06)	1.64 (0.06)	8.64 (0.11)	14.6 (0.1)	28.4 (0.2)	95.3 (0.6)	271 (1)
30	7.94 (0.03)	9.82 (0.08)	11.2 (0.1)	2.78 (0.05)	1.71 (0.02)	1.85 (0.06)	10.5 (0.1)	17.2 (0.2)	32.7 (0.3)	106 (1)	295 (1)
35	9.54 (0.08)	11.7 (0.1)	13.2 (0.1)	3.51 (0.08)	2.20 (0.03)	2.09 (0.04)	12.4 (0.1)	20.3 (0.2)	38.0 (0.3)	118 (1)	320 (2)

[a] Errors denoting 95% confidence levels are given in parentheses.

Table 3. Solubilities (S_c) of *mer*-(+)-[Co(L-ala)$_3$] and *fac*-[Co(gly)$_3$] in aqueous salt solutions at 25°C.[a]

(*a*) *mer*-(+)-[Co(L-ala)$_3$][b]

NaCl		$NaNO_3$		NaBr		NaI	
c_s/mol dm^{-3}	$S_c \times 10^3$/mol dm^{-3}	c_s/mol dm^{-3}	$S_c \times 10^3$/mol dm^{-3}	c_s/mol dm^{-3}	$S_c \times 10^3$/mol dm^{-3}	c_s/mol dm^{-3}	$S_c \times 10^3$/mol dm^{-3}
0.207	4.34 (0.03)	0.170	4.41 (0.02)	0.155	4.32 (0.02)	0.196	4.57 (0.05)
0.710	4.97 (0.02)	0.515	4.98 (0.02)	0.562	5.23 (0.03)	0.459	7.22 (0.04)
1.493	5.61 (0.04)	1.206	6.03 (0.04)	1.507	7.30 (0.04)	1.065	9.88 (0.07)
3.001	6.32 (0.02)	2.492	7.08 (0.07)	3.007	10.9 (0.1)	2.307	13.5 (0.1)
4.878	7.36 (0.02)	4.020	7.73 (0.04)	4.503	17.0 (0.1)	3.693	28.5 (0.2)
						4.377	44.0 (0.2)

$(NH_4)_2SO_4$		CH_3COONH_4		NaH_2PO_4		NaF	
c_s/mol dm^{-3}	$S_c \times 10^3$/mol dm^{-3}	c_s/mol dm^{-3}	$S_c \times 10^3$/mol dm^{-3}	c_s/mol dm^{-3}	$S_c \times 10^3$/mol dm^{-3}	c_s/mol dm^{-3}	$S_c \times 10^3$/mol dm^{-3}
0.150	4.18 (0.01)	0.159	3.98 (0.02)	0.103	3.91 (0.01)	0.101	3.84 (0.03)
0.501	3.96 (0.02)	0.533	3.81 (0.01)	0.501	3.48 (0.02)	0.399	3.54 (0.04)
1.190	2.85 (0.04)	1.354	3.31 (0.01)	1.201	2.58 (0.01)	0.762	3.13 (0.04)
1.963	1.84 (0.01)	2.838	2.58 (0.01)	1.678	2.17 (0.04)		
2.979	0.971 (0.014)	4.030	2.09 (0.02)				

(*b*) *fac*-[Co(gly)$_3$][c]

NaF		NaBr		NaI	
c_s/mol dm^{-3}	$S_c \times 10^4$/mol dm^{-3}	c_s/mol dm^{-3}	$S_c \times 10^3$/mol dm^{-3}	c_s/mol dm^{-3}	$S_c \times 10^4$/mol dm^{-3}
0.115	6.90 (0.04)	0.162	0.886 (0.011)	0.157	2.20 (0.04)
0.417	8.72 (0.14)	0.542	1.53 (0.01)	0.487	1.41 (0.06)
0.730	9.87 (0.10)	1.205	3.16 (0.03)	3.061	2.23 (0.08)
		2.812	11.9 (0.1)		
		4.364	36.8 (0.1)		

[a] Errors denoting 95% confidence levels are given in parentheses.
[b] $S_c^\circ = 4.05\ (0.01) \times 10^{-3}$ mol dm^{-3}.
[c] $S_c^\circ = 6.78\ (0.07) \times 10^{-4}$ mol dm^{-3}.

magnitude of the salt effect. The k_s values, which may be estimated as limiting slopes of the curves in Figs. 1 and 2 at $c_s = 0$ mol dm^{-3} (2), are listed in Table 4 where the k_s values for *fac*-(–)-[Co(D-pro)$_3$] reported in the preceding paper (6) are also tabulated. The k_s values of NaI for *fac*-[Co(gly)$_3$] could not be obtained due to the lack of solubility data for NaI concentrations of 0.5–3.0 mol dm^{-3}. A positive value for k_s represents the salting-out effect, and a negative value represents the salting-in effect.

In the preceding paper (6), it was postulated that hydrogen bond formation between the proton of the amino group in *fac*-[Co(amino acidato)$_3$] and SO_4^{2-} or Cl^- brings about the salting-in phenomenon. As shown in Table 4, the order of the magnitude of the salting-in effect on *mer*-(+)-[Co(L-ala)$_3$] is $NaCl < NaNO_3 < NaBr < NaI$, and NaF exhibits the salting-out effect. On the other hand, the tendency for hydrogen bond formation with F^- is greater than that with Cl^-. The hydrogen bond formation with Br^- and I^- seems to be improbable. In addition, the salts of SO_4^{2-}, $H_2PO_4^-$, and CH_3COO^-, which can form the hydrogen-bond, exhibit the salting-out effect. These results indicate that the hydrogen bond formation is not the origin of the salting-in phenomenon.

As an attempt to consider the salt effect using the thermodynamic parameters of dissolution, ΔH_s° is plotted against $T\Delta S_s^\circ$ in Fig. 3 for *mer*-(+)-[Co(L-ala)$_3$] and in Fig. 4 for *fac*-[Co(gly)$_3$]. For the salts that bring about the salting-in effect on *mer*-(+)-[Co(L-ala)$_3$], a single linear correlation between ΔH_s° and $T\Delta S_s^\circ$ is observed. The correlation can be expressed by

© 1998 NRC Canada

Fig. 1. Plot of $\log(S_c^\circ/S_c)$ against c_s for *mer*-(+)-[Co(L-ala)$_3$].

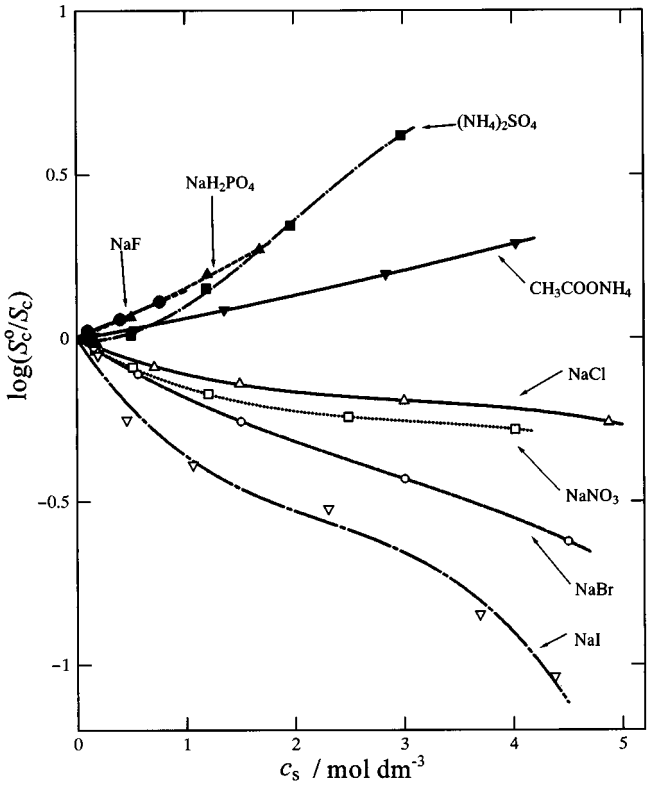

[2] $\Delta H_s^\circ = 1.7T\Delta S_s^\circ + 17.1, \quad \gamma = 0.981$

where γ is the correlation coefficient and the straight line passes through the data for water. The data for the salts that exhibit the salting-out effect deviate from the straight line with increasing salt concentration. As a typical example, the data in $(NH_4)_2SO_4$ solutions are plotted in Fig. 3. These findings indicate that the salting-in effect on *mer*-(+)-[Co(L-ala)$_3$] is caused by a decrease in ΔH_s°, and that the origin of the effect is common to NaCl, $NaNO_3$, NaBr, and NaI.

In the case of the salt effect on *fac*-[Co(gly)$_3$], linear correlation between ΔH_s° and $T\Delta S_s^\circ$ is found only for NaBr (solid line in Fig. 4) and is expressed by

[3] $\Delta H_s^\circ = 2.1T\Delta S_s^\circ + 7.5, \quad \gamma = 0.990$

While eq. [3] does not pass through the data for water, the data for water and for salt solutions with the lowest c_s give a separate correlation line (broken line in Fig. 4) expressed by

[4] $\Delta H_s^\circ = 1.3T\Delta S_s^\circ + 15.4, \quad \gamma = 0.992$

These results may suggest that the origin of the salting-in effect on *fac*-[Co(gly)$_3$] with high c_s values differs from that with low c_s values.

In the case of the salt effect on [Co(acac)$_3$], NaCl exhibits the salting-out effect in agreement with the prediction of the McDevit and Long (4) theory (k_s = 0.41 dm^3 mol^{-1}), and the salting-out effect is caused by an increase in ΔH_s° (6). It is well known that k_s of a more polar nonelectrolyte is smaller than k_s of a less polar one (2). It is not accurate to state that *mer*-(+)-[Co(L-ala)$_3$] and *fac*-[Co(gly)$_3$] are polar enough to make k_s negative for NaCl.

Sugunan (5) has found that the magnitude of the salting-in effect on 2-, 3-, and 4-nitrobenzoic acids decreases in the order $I^- > Br^- > NO_3^- > Cl^-$ and explained that hydrogen bond formation between carboxyl groups and water molecules liberated by structure-breaking action of the anions (the structure-breaking action also decreases in the order $I^- > Br^- > NO_3^- > Cl^-$) increases the solubilities of these benzoic acids (5). The above order of the salting-in effect on the substituted benzoic acids agrees with the order for *mer*-(+)-[Co(L-ala)$_3$] (see Table 4). The k_s values for *mer*-(+)-[Co(L-ala)$_3$] are comparable to those for nitrobenzoic acid. For example, k_s of NaCl for the latter is –0.19 dm^3 mol^{-1} (5). These findings may suggest that the origin of the salting-in effect on *mer*-(+)-[Co(L-ala)$_3$] is also the structure-breaking action of anions. The increasing hydrogen bond formation between the chelate and water molecules results in a decrease in both ΔH_s° and ΔS_s°.

Fig. 2. Plot of $\log(S_c^\circ/S_c)$ against c_s for *fac*-[Co(gly)$_3$]. Data for NaCl solutions were taken from ref. 6; data for NaI solutions over the c_s range of 0.5–3.0 mol dm^{-1} were not available (see text).

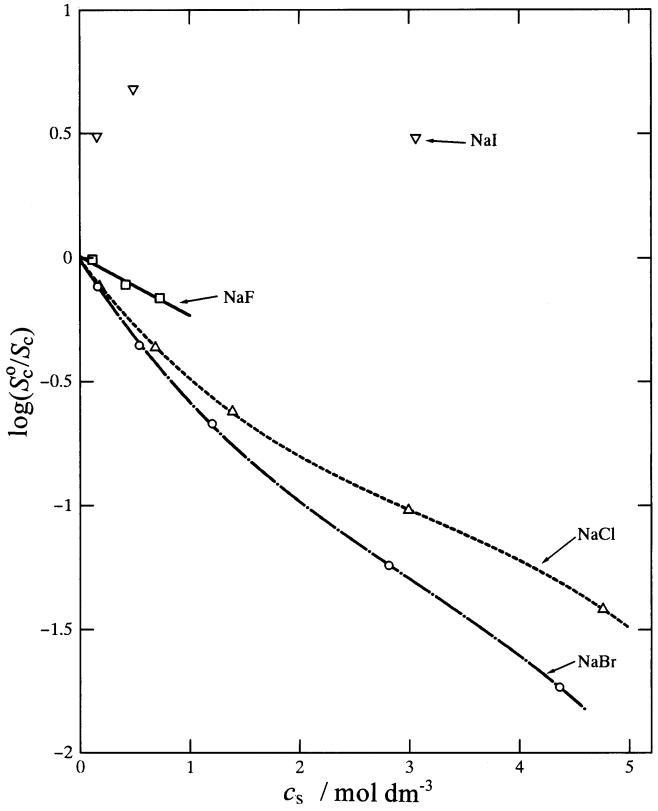

It has been reported that the α-carbon atom proton in α-amino acid is activated upon chelation (13). The possibility that the activated α-carbon atom proton plays a part in the salting-in phenomenon may be also pointed out, because the amino acid itself is subject to the salting-out effect of NaCl (6). In this connection, it is noteworthy to examine the effect of salts on the chelates of Co(III) with β- alanine and 2-aminoisobutylic acid. In any event, more extensive data on the salt effect for [Co(amino acidato)$_3$] is needed to clearly explain the salting-in phenomenon.

For all the salts studied other than NaI, k_s for *fac*-[Co(gly)$_3$] and *fac*-(–)-[Co(D-pro)$_3$] is smaller than k_s for *mer*-(+)-[Co(L-ala)$_3$]. While the origin of the salting-in effect on

© 1998 NRC Canada

Table 4. Limiting salting coefficients (k_s) for mer-(+)-[Co(L-ala)$_3$], *fac*-[Co(gly)$_3$], and *fac*-(–)-[Co(D-pro)$_3$].[a]

	k_s/dm^3 mol^{-1}		
Salt	mer-(+)-[Co(L-ala)$_3$]	*fac*-[Co(gly)$_3$]	*fac*-(–)-[Co(D-pro)$_3$][b]
NaF	0.142 (0.017)	–0.239 (0.060)	
NaCl	–0.146 (0.018)	–0.594 (0.027) [b]	–0.649 (0.067)
$NaNO_3$	–0.202 (0.058)		
NaBr	–0.221 (0.007)	–0.693 (0.048)	
NaI	–0.506 (0.135)		
NaH_2P0_4	0.144 (0.043)		
CH_3COONH_4	0.062 (0.005)		
$(NH_4)_2SO_4$	–0.019 (0.092)		–1.459 (0.414)

[a] Errors denoting 95% confidence levels are given in parentheses.
[b] Calculated from the data given in ref. 6.

Fig. 3. Correlation between ΔH_s° and $T\Delta S_s^\circ$ for the salt effect on the solubility of *mer*-(+)-[Co(L-ala)$_3$]. Solid line is drawn by applying the least-squares method to the data for the salts that exhibit the salting-in effect.

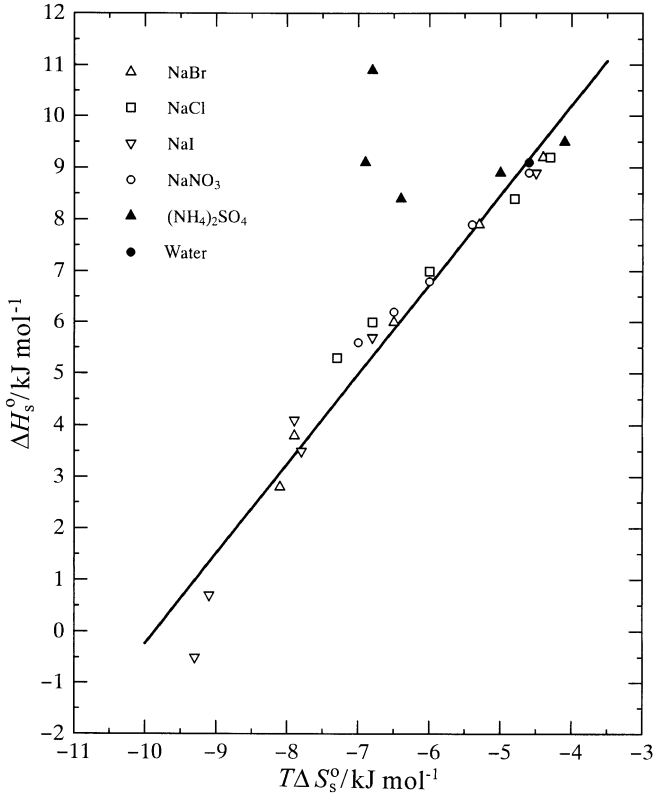

Fig. 4. Correlation between ΔH_s° and $T\Delta S_s^\circ$ for the salt effect on the solubility of *fac*-[Co(gly)$_3$]. Solid and broken lines are drawn by applying the least-squares method to the data for NaBr solutions and for the solutions with lowest c_s values, respectively.

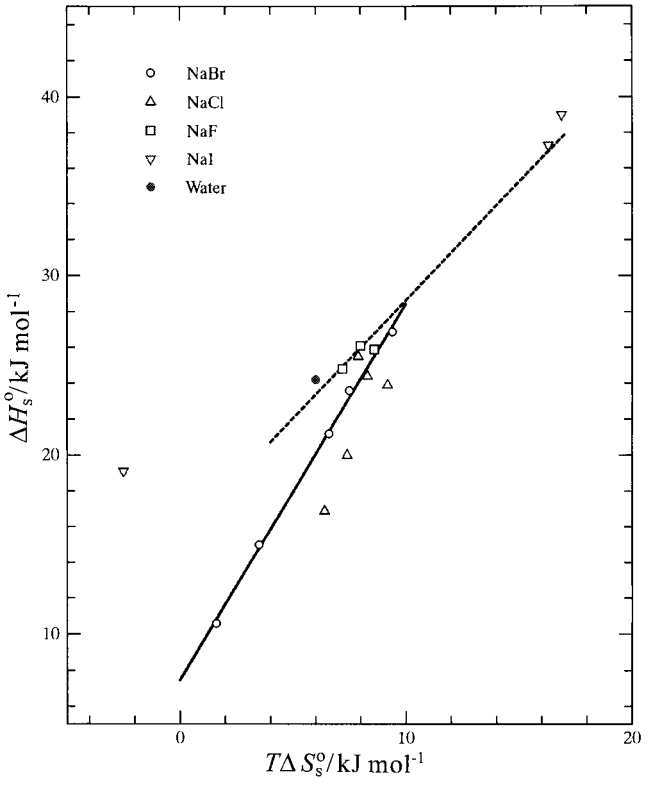

fac-[Co(amino acidato)$_3$] seems to be complicated, as shown in Fig. 4, the above finding may be attributed in part to the postulation that *fac*-[Co(amino acidato)$_3$] is more polar than *mer*-[Co(amino acidato)$_3$]. This postulation is reasonable on the basis of the geometric feature that in the *fac*-isomer three amino and carboxylato groups are mutually *cis*, but in the *mer*-isomer a set of amino and carboxylato groups are *trans*.

The marked salting-out effect of NaI on *fac*-[Co(gly)$_3$] (see Fig. 2) is particularly surprising in comparison with the fact that the salting-in effect of NaI on *mer*-(+)-[Co(L-ala)$_3$] is largest among sodium halides. At the present stage, this anomalous salting-out phenomenon of NaI cannot be explained because of the lack of available data.

References

1. P.M. Gross. Chem. Rev. (Washington, D.C.) **13**, 91 (1933).
2. F.A. Long and W.F. McDevit. Chem. Rev. (Washington, D.C.) **51**, 119 (1952).
3. R. Aveyard and R. Heselden. J. Chem. Soc. Faraday Trans. 1, **71**, 312 (1975).
4. W.F. McDevit and F.A. Long. J. Am. Chem. Soc. **74**, 1773 (1952).

© 1998 NRC Canada

5. S. Sugunan. Indian J. Chem. Sect. A: Inorg. Bio-inorg. Phys. Theor. Anal. Chem. **22A**, 150 (1983); **23A**, 763 (1984); S. Sugunan and B. Thomas. J. Solution Chem. **23**, 81 (1994).
6. Y. Yoshimura. Bull. Chem. Soc. Jpn. **69**, 2565 (1996).
7. B.E. Douglas and S. Yamada. Inorg. Chem. **4**, 1561 (1965).
8. R. Herak, B. Prelesnik, and I. Krstanovic. Acta Crystallogr. Sect. B: Struct. Crystallogr. Cryst. Chem. **B34**, 91 (1978).
9. R.G. Denning and T.S. Piper. Inorg. Chem. **5**, 1056 (1966).
10. Y. Yoshimura. Can. J. Chem. **69**, 1388 (1991).
11. Y. Yoshimura, N. Sato, and M. Kikuchi. Bull. Chem. Soc. Jpn. **59**, 2135 (1986).
12. Y. Yoshimura. Can. J. Chem. **67**, 2108 (1989).
13. R.D. Gillard, S.H. Laurie, D.C. Price, D.A. Phipps, and C.F. Weick. J. Chem. Soc. Dalton Trans. 1217, (1974).

© 1998 NRC Canada

Carbocation-like reactivity patterns in X′-substituted-4-biphenylylnitrenium ions

Daniel Ren and Robert A. McClelland

Abstract: 4-Azido-X′-substituted biphenyls (X′ = 4′-MeO, 4′-Me, 4′-F, 3′-Me, 4′-Cl, H, 3′-MeO, 3′-Cl, 4′-CF_3) have been prepared and subjected to 248 nm flash photolysis irradiation in 20:80 acetonitrile:water. Transient X′-substituted 4-biphenylylnitrenium ions **10** (Ar-C_6H_4-N^+H) are observed, with lifetimes ranging from 0.6 ms (4′-MeO) to 26 ns (4′-CF_3). These cations are quenched by azide ion, with values of k_{az} ranging from 6 to 10×10^9 M^{-1} s^{-1}, with the majority in the range $(9–10) \times 10^9$. This near constant k_{az} provides further evidence that arylnitrenium ions are quenched by azide ion at the diffusion limit. The solvent reactivities, plotted in a single-parameter Hammett plot against σ^+(X), exhibit a poor correlation, with the points for the *para* π-electron donors deviating from the correlation line based on the other substituents in the direction of requiring a more negative substituent parameter. The data are more satisfactorily fit to the two-parameter Yukawa–Tsuno equation; the parameter r^+ obtained in this fit is 2.8. Thus the resonance interaction of the *para* π-donor X′-substituents with the positive charge of the cation is underestimated by σ^+, a situation that has previously been observed with benzylic-type carbenium ions. The conclusion is made that, in their reaction with water, 4-biphenylylnitrenium ions behave like benzyl cations bearing two additional stabilizing vinyl groups, i.e., as if they had the structure Ar-C^+(C═C)$_2$. The inherent reactivity and the pattern of the aryl substituent effects are in fact similar to those in the carbocation series Ar-C^+(Ph)$_2$.

Key words: nitrenium, nitrene, aryl azide, photochemistry, lifetime.

Résumé : On a préparé des 4-azidobiphényles substitués par des groupes X′ (X′ = 4′-MeO, 4′-Me, 4′-F, 3′-M3, 4′-Cl, H, 3′-MeO, 3′-Cl, 4′CF_3) et on les a soumis à une irradiation de photolyse éclair à 248 nm, en solution dans un mélange 20 : 80 d'acétonitrile : eau. On a observé la présence des ions 4-biphénylylnitrénium substitués par les groupes X′ (**10**) (Ar-C_6H_4-N^+H) dont les temps de vie varient de 0,6 ms (4′-MeO) à 26 ns (4′-CF_3). On a piégé ces cations par l'ion azoture, avec des valeurs de k_{az} allant de 6 à 10×10^9 M^{-1} s^{-1} alors que la majorité se trouve entre 9 et 10×10^9 M^{-1} s^{-1}. Cette valeur pratiquement constante de k_{az} suggère une fois de plus que les ions arylnitrénium sont piégés par l'ion azoture à la limite de la diffusion. La courbe des réactivités de solvant avec un seul paramètre de Hammett σ^+(X) donne une mauvaise corrélation alors que les points pour les substituants *para* donneurs d'électrons π dévient de la droite de corrélation établie à l'aide des autres substituants; le sens de cette déviation suggère l'utilisation d'un paramètre de substituant plus négatif. Les données conduisent à une meilleure corrélation avec l'équation à deux paramètres de Yukawa–Tsuno; le paramètre r^+ ainsi obtenu est de 2,8. L'interaction de résonance entre les substituants X′ *para* donneurs d'électrons π et la charge positive du cation est donc sous-évaluée par σ^+; cette situation avait été observée antérieurement avec des ions carbénium de type benzylique. On en conclut donc que, lors de leur réaction avec l'eau, les ions 4-biphénylnitrénium se comportent comme des cations benzyliques portant deux groupes vinyliques additionnels, comme s'ils avaient une structure du type Ar-C^+(C═C)$_2$. L'activité inhérente et le patron des effets des substituants aryles sont en fait semblables à ceux observés dans la série des carbocations Ar-C^+(Ph)$_2$.

Mots clés : nitrénium, nitrène, azidobenzènes, photochimie, temps de vie.

[Traduit par la rédaction]

We recently reported the direct observation of the 4-biphenylylnitrenium ion (**1**, R = H) (1) and its N-acetyl analog (**1**, R = Ac) (2) in water using the technique of laser flash photolysis. The N-acetyl derivative was obtained upon photolysis of N-chloro and N-sulfatoxy precursors **2**, and the N-H derivative upon irradiation of the azide **3**, the cation forming via rapid solvent protonation of the singlet nitrene **4** formed by nitrogen extrusion (3).

Received June 13, 1997.

D. Ren and R.A. McClelland.[1] Department of Chemistry, University of Toronto, Toronto, ON M5A 3H6, Canada.

[1] Author to whom correspondence may be addressed. Telephone: (416) 978-3592. Fax: (416) 978-3592. E-mail: rmcclell@alchemy.chem.utoronto.ca

Excellent evidence exists pointing to these nitrenium ions as the reactive electrophiles responsible for DNA binding of the carcinogens 4-aminobiphenyl and 4-(acetylamino) biphenyl (4, 5). The flash photolysis experiments have provided direct information regarding their lifetimes in water, and their reactivities with added nucleophiles (6).

Like benzyl cations, additional resonance contributors for **1** can be written with the positive charge at the *ortho* and *para* positions, the latter as illustrated in Scheme 1 by structure **1a**. There is in fact experimental evidence that these carbenium ion contributors do indeed make a significant contribution.

(*i*) The cations **1** react with water at the ring carbon *para* to the nitrogen (1, 2, 7) to form as the initial product the cyclohexadienone imine **5**. In the case of the parent nitrenium ion (R = H) the imine is simply hydrolyzed to give the ketone **5a** (1, 7), while with the N-acyl derivative there are also

 © 1998 NRC Canada

Scheme 1.

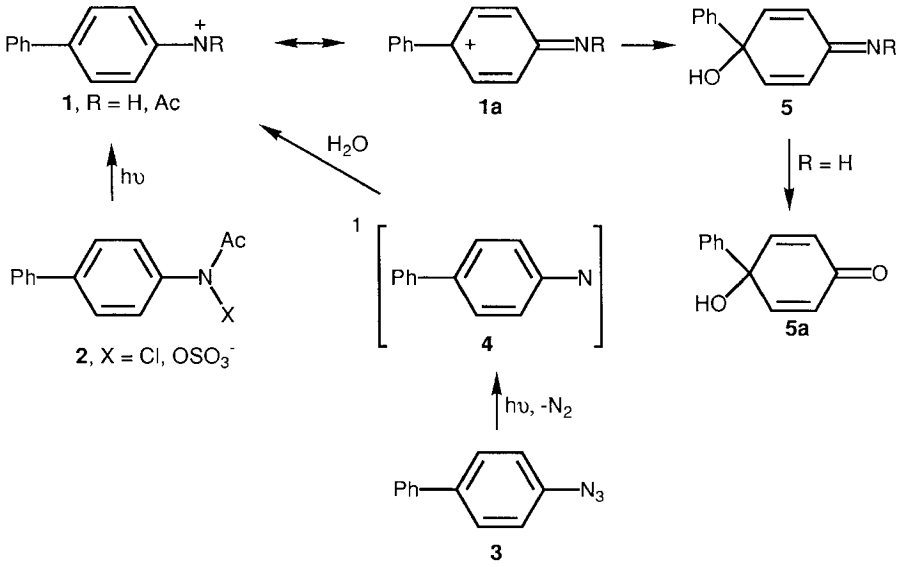

rearrangements to restore aromaticity (7). Also indicative of the delocalization of the positive charge to the ring is the very small difference in reactivity between the NH and N-acetyl cations, a factor of only three ((1, 7, 8). In other words, substituting the nitrogen with an electronegative group has little effect on reactivity, as if there was little positive charge localized on this nitrogen.

(*ii*) Novak et al. obtained aqueous lifetimes of a series of *p*-substituted phenylnitrenium ions **6** using the "azide-clock" approach (9). These lifetimes were found to correlate very poorly with the σ^+ constant of the *para* substituent. This lack of correlation is seen also with carbenium ions (see later). However, the plots for the nitrenium ions are highly scattered, indicating that the *para* substituents interact with the positive charge in a way that is very different from the interaction in an arylcarbenium ion.

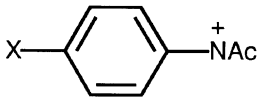

6, X = H, Cl, Me, MeO, Ph

(*iii*) The kinetic data for the decay of **1**, R = H, in acid solutions show that the cation equilibrates with a conjugate acid, presumably the dication **7**. The acidity constant K_a for **7** calculated from the kinetics is 0.8 (2). This is not inconsistent with a structure for the cation such as **1a**, an imine whose basicity is reduced because of a nearby positive charge.

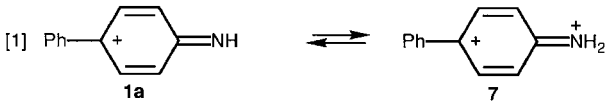

(*iv*) Williams and co-workers (10) reached similar conclusions about the importance of carbenium resonance contributors through the comparison of the rate constants for formation of nitrenium ions from hydroxylamines **8** under acidic conditions. They found little difference between the parent system (**8**, R_1 = H = R_2) and the system with an N-alkyl substituent (**8**, R_1 = Et, R_2 = H). Substitution at the *para* carbon (**8**, R_1 = H, R_2 = Me) resulted in a pronounced rate acceleration.

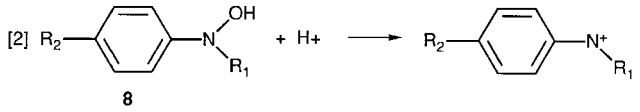

8

We present in this paper an examination of the lifetimes of 4-biphenylylnitrenium ions **10** bearing substituents in the phenyl ring distant from the formal nitrenium ion center. These cations can be generated from the appropriate azide precursor, in the same manner as the parent (1). Pronounced substituent effects are observed. Our analysis suggests that the substituents in this ring interact with the positive charge much as they do in benzylic carbocations, in other words, as if the positive charge was placed at the *para* carbon as in structure **10a**.

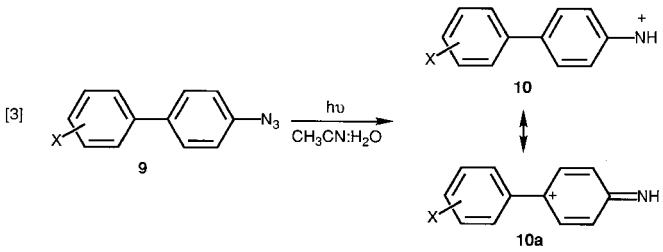

Results and discussion

Preparation of precursors

The substituents X chosen for this study are given in Table 1. The precursor azides **9** were prepared as shown in Scheme 2. The key step, the formation of the biphenyl skeleton, was achieved by palladium-catalyzed cross-coupling of *p*-bromoaniline and an appropriately substituted phenylboronic acid (11). The latter was prepared by the reaction of the appropriate

© 1998 NRC Canada

Scheme 2.

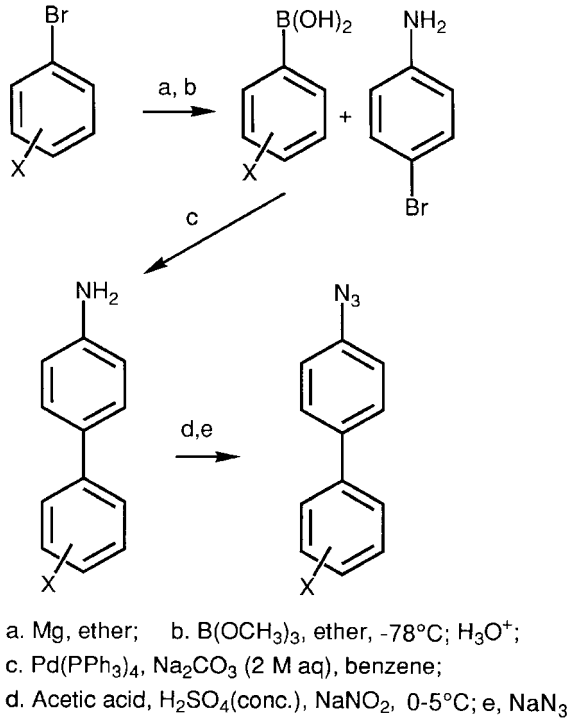

a. Mg, ether; b. $B(OCH_3)_3$, ether, -78°C; H_3O^+;
c. $Pd(PPh_3)_4$, Na_2CO_3 (2 M aq), benzene;
d. Acetic acid, H_2SO_4(conc.), $NaNO_2$, 0-5°C; e, NaN_3

Grignard reagent with trimethyl borate, followed by hydrolysis (12). The 4-aminobiaryls were converted to the azides **9** by diazotization, followed by the addition of sodium azide (13).

Flash photolysis experiments

Flash photolysis experiments were carried out with laser irradiation at 248 nm in an aqueous solution containing 20% acetonitrile. As illustrated by the four representative spectra in Fig. 1, the substituted biphenyl azides show behaviour qualitatively similar to that previously seen with the parent 4-azidobiphenyl (1). This consists of a relatively intense transient with λ_{max} in the region from 460 to 500 nm. This decays with first-order kinetics, with rate constants given in Table 1. At the end of the decay there is little residual absorbance above 400 nm. Also present is a second peak in the region 300–350 nm that does not decay over 100 μs.

Based upon the similarity with the parent, the transient above 400 nm can be attributed to the appropriate arylnitrenium ion **10**. This assignment is corroborated by the demonstration that these transients are effectively quenched by azide ion, indeed with second-order rate constants similar to the value obtained for the parent (Table 1). Quenching by azide ion is one criterion that points to a cationic intermediate (14). In fact, in the case of the parent 4-biphenylylnitrenium ion, there is excellent agreement between the k_{az}:k_w ratio obtained with flash photolysis and the value determined by product analysis for a ground state solvolysis reaction (7).

The identity of the non-decaying transient below 400 nm is uncertain. This absorbance is also seen with the parent system, where product analysis reveals that there is not a 100% yield of nitrenium ion on irradiation in 20% acetonitrile (1). The latter observation indicates that the protonation forming the nitrenium ion (as shown in Scheme 1) is not the only fate of the singlet nitrene. We assume that the absorbance below 400 nm represents some species forming in the competing reaction (or reactions), possibly a triplet nitrene or a ring-expanded 1,2-didehydroazepine **13** (15).

Table 1. Rate constants at 20°C and absorption maxima for X′-substituted 4-biphenylylnitrenium ions in 20% acetonitrile:water.

Substituent	k_w (s^{-1})[a]	k_{az}(M^{-1} s^{-1})[b]	λ_{max}(nm)
4′-Methoxy	1.58×10^3	6.1×10^9	500
4′-Methyl	2.74×10^5	9.2×10^9	490
4′-Fluoro	1.32×10^6	9.4×10^9	470
3′-Methyl	1.50×10^6	9.2×10^9	470
3′-Methoxy	2.46×10^6	7.9×10^9	475
4′-Chloro	2.53×10^6	10.0×10^9	480
None	2.70×10^6 [c]	9.6×10^9	465
3′-Chloro	1.30×10^7	10.2×10^9	475
4′-Trifluoromethyl	3.8×10^7	Not measured[d]	Not measured[d]

[a] First-order rate constant for decay in the solvent alone.
[b] Second-order rate constant for quenching by sodium azide.
[c] 2.84×10^6 s^{-1} (ref. 2).
[d] Because of very rapid decay in solvent alone.

Absorption maxima

As seen in Table 1, the substituents do have a small effect on the λ_{max} of the nitrenium ions **10**, λ_{max} in general increasing with greater electron donation. This trend is similar to that observed in benzylic-type cations. Thus, for example, the λ_{max} (in acetonitrile) for diarylmethyl cations 4-X-$C_6H_4C^+$HPh are 425 nm (X = CF_3), 435 (H), 436 (F), 456 (Cl), 450 (Me), and 455 (MeO) (16). Similarly, cumyl cations (4-X-$C_6H_4C^+(CH_3)_2$) in $(CF_3)_2$CHOH have λ_{max} at 325 nm (X = H), 340 (4-Me), and 360 (4-MeO) (17). While it is risky to base structural conclusions on absorption maxima, the similar behaviour with **10** is at least consistent with the idea that there is a significant benzylic-type interaction between the ring bearing the substituent and the positive charge.

Also worth noting is the λ_{max} at 502 nm of the persistent biphenylylnitrenium ion **11** obtained by anodic oxidation of the corresponding aniline derivative in acetonitrile (18). This cation is obviously analogous to **10** except for the additional *tert*-butyl groups *ortho* to the formal nitrenium ion center. While the effect of these groups is unknown, the λ_{max} for **11** clearly falls within the same pattern that we observe with **10**. One interesting feature with **11** is that the *tert*-butyl groups exhibit nonequivalent signals in the ^{1}H NMR spectrum (18).

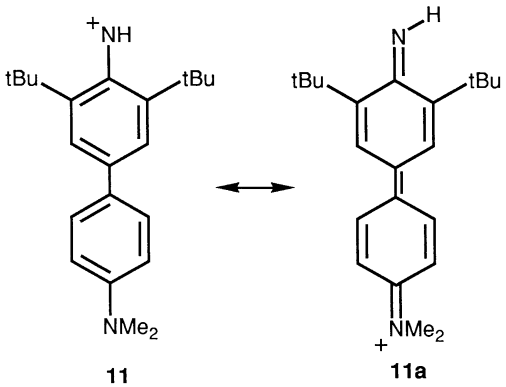

11 **11a**

© 1998 NRC Canada

Fig. 1. Transient spectra following 248 nm irradiation of 50 μM solutions of 3′- or 4′-substituted 4-azidobiphenyls **10** in 20% acetonitrile. Spectra were obtained from the optical density change immediately after completion of the laser pulse.

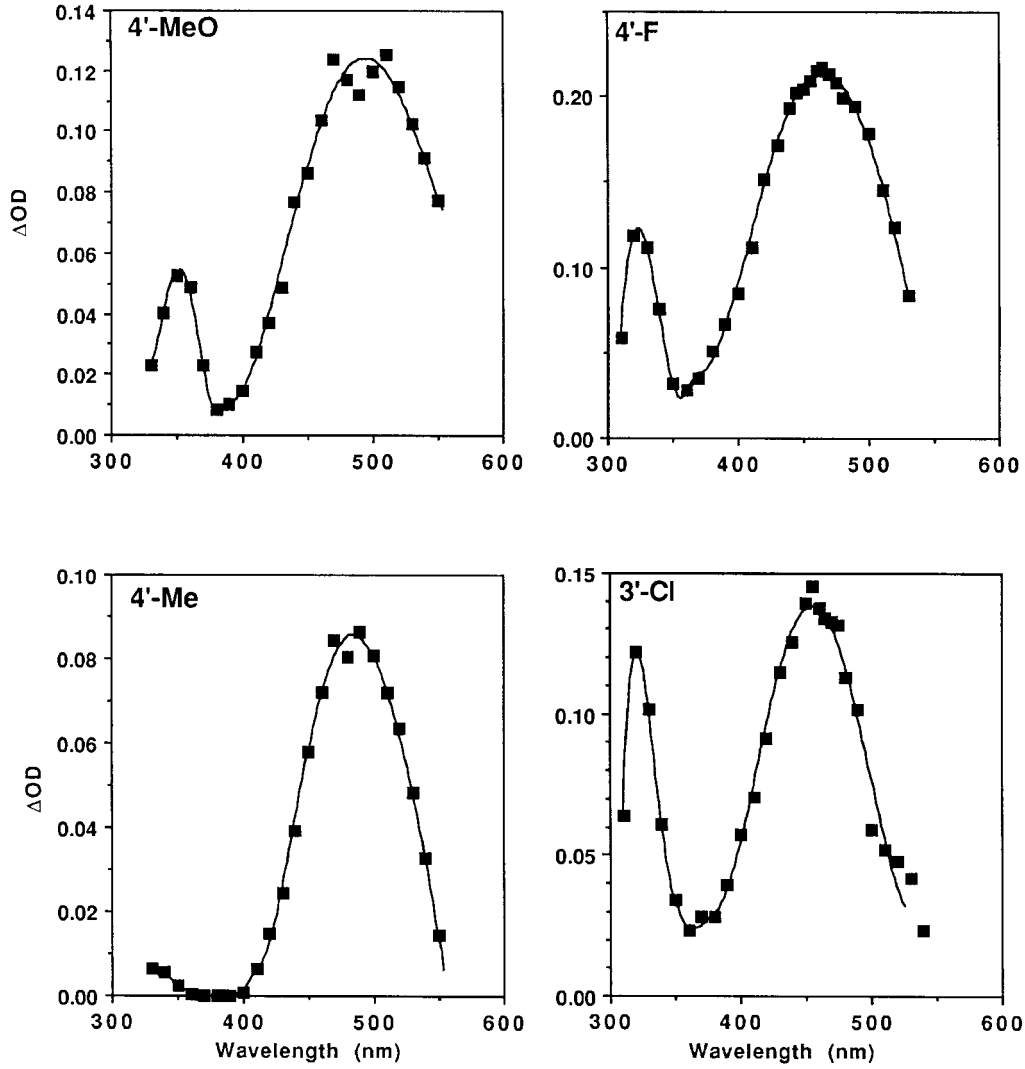

This clearly points to a nonlinear -N^+-H moiety, whose geometry is fixed on the NMR time scale by extensive charge delocalization, such as shown in structure **11a**.

Rate constants for azide trapping

Azide ion has seen extensive use as a "clock" for obtaining absolute rate constants from selectivities measured by competition kinetics. The assumption is made that this nucleophile reacts with short-lived cations at a constant, diffusion-limited, rate constant, with assignment of a value of 5×10^9 M^{-1} s^{-1} for that limit. This approach was originally applied to reactivities of carbenium ions (19, 20), and still sees considerable use in this regard (21). Laser flash photolysis has provided direct evidence that the assumption is valid, through the observation that rate constants k_{az} for series of structurally related carbocations become independent of substituent (22). The limits are typical of encounter-controlled reactions, although in a given solvent there is a slight dependence on structural type. Thus, diarylmethyl cations in 20% acetonitrile have a limiting k_{az} of ~7×10^9 M^{-1} s^{-1}, while with triarylmethyl cations the limit would be ~5×10^9 M^{-1} s^{-1} (22).

Azide has also been employed to "clock" reactivities of arylnitrenium ions (6–9, 23). On the basis of the absolute k_{az} values for 4-biphenylyl- and 2-fluorenylnitrenium ions, the reaction with azide has indeed been suggested to be diffusion-limited (1, 2). The data in Table 1 now show that this is the case. Despite a change of over four orders of magnitude in the solvent rate constants, the values of k_{az} all lie within the range $6–10 \times 10^9$ M^{-1} s^{-1}, with the majority in the range $9–10 \times 10^9$ M^{-1} s^{-1}. The limit, ~1×10^{10} M^{-1} s^{-1}, is slightly higher than those of the di- and triarylmethyl cations. The rate constant calculated from the Debye–Smoluchowski equation for a diffusion-controlled cation–anion encounter in this solvent is ~1.5×10^{10} M^{-1} s^{-1} (22). The smaller observed limits can be explained through a model where there are nonproductive encounters in which the anion and cation cannot actually combine (22). The slightly higher limit with the arylnitrenium ion would suggest that there are fewer of these nonproductive encounters with this system.

It can be noted that the limit of 1×10^{10} M^{-1} s^{-1} obtained from the data in Table 1 refers to solutions that have effectively zero ionic strength. Addition of salts can have significant

© 1998 NRC Canada

Table 2. Parameters from two-parameter analysis of rate constants for solvent addition to benzylic-type cations **12–14**[a] and to biphenylylnitrenium ions **10**.

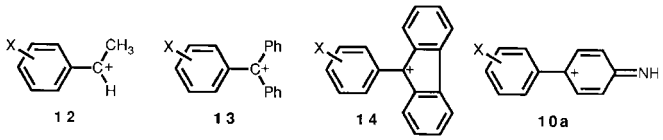

ρ	+2.7	+1.3	+1.3	+1.8
$\rho^+ = r^+ \rho$	+6.1	+4.7	+2.8	+5.0
r^+	2.3	3.6	2.2	2.8
k_s(X = H) (s^{-1})	$\sim 1 \times 10^{11}$ [b]	1.5×10^5	1.5×10^7	2.7×10^6

[a]Data for **12** refer to 50:50 2,2,2-trifluoroethanol:water and are from ref. 20, using a value for X = 4-Me_2N from ref. 28. Data for **13** refer to 1:2 acetonitrile:water and are from ref. 27. Data for **14** refer to 1:4 acetonitrile:water and are from ref. 28.

[b]Estimate (ref. 20).

effects on the azide reactivity (24). In 20% acetonitrile containing 0.5 M $NaClO_4$, the limiting rate for the biphenylylnitrenium ions is $\sim 5 \times 10^9$ M^{-1} s^{-1} (1).

Solvent reactivities

Despite the fact that the change is taking place in the phenyl ring remote from the formal N^+ center, substituents have a pronounced effect on the lifetime of **10**. From the least reactive, 4′-methoxy, to the most reactive, 4′-trifluoromethyl, there is a change of over four orders of magnitude. In attempting a quantitative correlation, we initially constructed a single-parameter Hammett plot, employing σ^+ as the substituent constant. As shown in Fig. 2*a*, this correlation is poor, with the points for the *para* π-electron donors, especially 4′-methoxy, deviating significantly from the correlation line based on the other substituents. Moreover, the deviation of these points is in the unusual direction of requiring a more negative substituent parameter in order for the point to fit on the line. In other words, the σ^+ constant is underestimating the effect of the substituent.

This type of behaviour has previously been observed (20, 27, 28) for benzylic-type cations **12**–**14** (see Table 2). The data are more satisfactorily fit to the two-parameter Yukawa–Tsuno equation (eq. [4]),

$$[4] \quad \log(k_w/k_w^\circ) = \rho\,[\,\sigma + r^+(\,\sigma^+ - \sigma)]$$

where k_w° is the rate constant for the unsubstituted compound, ρ has its normal meaning, and r^+ is a scaling parameter that effectively provides substituent parameters other than σ^+ and σ. The r^+ parameter was intended to lie between zero and one, representing substituent interactions intermediate between those described by σ and σ^+. As shown in Table 2, values significantly greater than one are required for the cation water reactivities. This is also true for **10**, where $r^+ = 2.8$ provides the best fit for the experimental data. This fit is illustrated in Fig. 2*b*; as shown in this figure, the methoxy substituent in **10** behaves as if it has a "σ" substituent constant of –1.7.

Table 2 provides a comparison of the ρ and r^+ parameters obtained with **10** and those previously found with **12**–**14**. Also listed is the ρ^+ parameter, the product of ρ and r^+, which is

Fig. 2. Linear free energy correlations. (*a*) A single-parameter correlation of log k_w versus the Hammett σ^+ substituent constant. The line drawn in this figure (slope = 2.0) is the least-squares line calculated for the solid squares, representing the 4′-CF_3, 3′-Cl, 3′-MeO, 3′-Me, and unsubstituted cations. (*b*) Plots log k_w versus $\sigma + r^+(\sigma^+ - \sigma)$, where the value of $r^+ = 2.8$ has been obtained from application of the two-parameter Yukawa–Tsuno equation (25). The line drawn in this figure (slope = 1.8) is the least-squares line for all the points. Values of σ and σ^+ are taken from ref. 26.

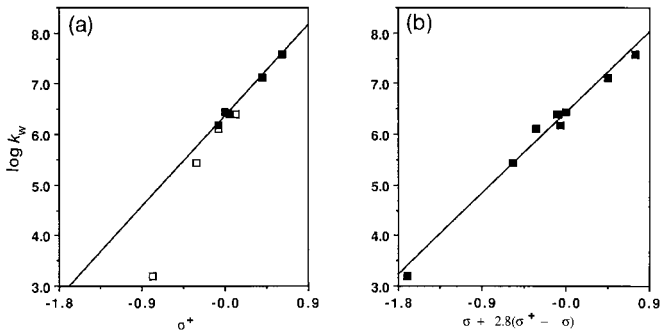

effectively a measure of the resonance effect of the substituents on the reaction (20). This comparison shows very clearly that substituents in **10** interact with the positive charge very much as if this cation were a benzylic cation, i.e., as if the structure were **10a**. This conclusion is particularly evident when the "inherent" reactivities, the rate constant for the derivative with X = H, are considered. The least stable and most reactive cation is phenethyl, which has only one other stabilizing substituent, a methyl group, on the C^+ center. This system has the largest values of ρ and ρ^+ , indicating the greatest interaction with the aryl ring. The most stable and least reactive cation is triphenylmethyl, where there are two additional stabilizing phenyl groups on the C^+ center. As expected, the series ArC^+Ph_2 has smaller values of ρ and ρ^+ since there is less demand for stabilization by substituents in the one ring. The biphenylylnitrenium ions, written as **10a**, can be viewed as benzylic cations with two stabilizing vinyl substituents. The reactivity of this system lies intermediate between phenethyl and triphenylmethyl, albeit closer to the latter. The substituent effects are also intermediate, again closer to triphenylmethyl.

The fluorenyl cations **13** are not considered in these comparisons, since the aryl ring is significantly twisted from coplanarity (28), attenuating the substituent effects. In this respect it is interesting that the biphenylylnitrenium ions do show such a strong resonance interaction with the substituents in the distal ring. Biphenyls would normally be regarded as being significantly twisted but this clearly is not the case for the nitrenium ions. For a substituent such as 4′-methoxy to have such a strong stabilizing effect, the two rings must be fairly close to being coplanar. This is obviously part of the reason that 4-biphenylylnitrenium ions can be formed so readily both thermally and photochemically.

Conclusions

The qualitative observation of very significant substituent effects on the lifetime and the quantitative comparisons just discussed provide further experimental support for the idea that

© 1998 NRC Canada

arylnitrenium ions are better regarded as carbocations, with a significant portion of the positive charge at the ring carbons. The 4-biphenylylnitrenium ions, in their reaction with water, behave very much like benzyl cations bearing two additional stabilizing vinyl groups, i.e., Ar-C^+(C═C)$_2$. Their inherent reactivity and the pattern of their aryl substituent effects are very similar to those in the carbocation series Ar-C^+(Ph)$_2$.

Experimental section

Flash photolysis experiments were carried out in the normal manner with ca. 20 ns pulses at 248 nm (ca. 60 mJ per pulse) from a Lumonics excimer laser (KrF emission). Solutions of the 4-azidobiphenyl precursors in 20% acetonitrile were 20–50 μM, and the experiments were carried out under air. The rate constants k_{az} were calculated as the slope of the plot of k_{decay} versus [NaN_3], for five or six concentrations of sodium azide over the range 0–1 mM. Rate constants for the 4′-methoxy compound were determined with both the laser flash photolysis apparatus where the rate is at about the longest time limit possible, and with a conventional flash photolysis apparatus (29). Excellent agreement was observed between the two.

Synthesis. General coupling procedure

A 50 mL flask was charged under argon with 0.35 g of $Pd(PPh_3)_4$ (0.3 mmol), 20 mL of benzene, 1.72 g of *p*-bromoaniline (10 mmol), and 10 mL of 2 M aqueous Na_2CO_3 solution, and then 10 mmol of arylboronic acid in a minimum amount of 95% ethanol was added. The mixture was refluxed overnight under vigorous stirring. After the reaction was completed, the product was extracted with ether, washed with a saturated NaCl solution, dried over $NaSO_4$, and the solvent was removed. The crude product was further purified by column chromatography on silica gel, eluting with ethyl acetate – hexanes, and was recrystallized in aqueous ethanol.

General procedure for the syntheses of biaryl azides

The 4-aminobiphenyl (10 mmol) was dissolved in 40 mL of glacial acetic acid containing 10 mL of concentrated sulfuric acid. The solution was cooled to below 5°C in an ice bath and diazotized with a solution of 0.76 g of $NaNO_2$ (11 mmol) in 7 mL of distilled water. After 1 h of stirring, 100 mL of ice-water was added. Enough urea was added to destroy the excess nitrous acid, and 0.5 g of Norite was then added. The cold suspension was stirred for 15 min and was then rapidly filtered into a flask immersed in an ice bath. The clear, yellow filtrate was treated with 1.34 g of NaN_3 (20 mmol) in 10 mL of water at 0°C. Nitrogen was immediately evolved, the solution became turbid, and a light tan precipitate formed in a few minutes. The mixture was kept in the ice-bath and stirred for 1 h after the addition of NaN_3 was completed, and was then allowed to warm up to room temperature and stand overnight. The precipitate was filtered off, and washed first with 10% Na_2CO_3 and then with water. The crude product was purified by column chromatography on silica gel eluted with ethyl acetate – hexanes and was recrystallized in hexanes.

The following azides were prepared by the procedure described above.

4-Azido-4′-methoxybiphenyl: ^{1}H NMR (500 MHz, $CDCl_3$), δ: 7.51 (2H, d, J = 8.5 Hz), 7.47 (2H, d, J = 8.5 Hz), 7.05 (2H, d, J = 8.5 Hz), 6.95 (2H, d, J = 8.5 Hz), 3.83 (3H, s); HRMS *m*/*z*, calcd. for $C_{13}H_{11}N_3O$: 225.0902; found: 225.0891; calcd. for $C_{13}H_{11}NO$ (M –N_2): 197.0841; found: 197.0837.

4-Azido-4-methylbiphenyl: ^{1}H NMR (500 MHz, $CDCl_3$), δ: 7.54 (2H, d, J = 8.5 Hz), 7.44 (2H, d, J = 8.5 Hz), 7.23 (2H, d, J = 8.5 Hz), 7.06 (2H, d, J = 8.5 Hz), 2.37 (3H, s); HRMS *m*/*z*, calcd. for $C_{13}H_{11}N_3$: 209.0953; found: 209.0951.

4-Azido-4′-fluorobiphenyl: ^{1}H NMR (500 MHz, $CDCl_3$), δ: 7.51–7.47 (4H, m), 7.12–7.06 (4H, m); HRMS *m*/*z*, calcd. for $C_{12}H_8N_3F$: 213.0702; found: 213.0694.

4-Azido-4′-chlorobiphenyl: ^{1}H NMR (500 MHz, $CDCl_3$), δ: 7.52 (2H, d, J = 8.5 Hz), 7.46 (2H, d, J = 8.5 Hz), 7.38 (2H, d, J = 8.5 Hz), 7.08 (2H, d, J = 8.5 Hz); HRMS *m*/*z*, calcd. for $C_{12}H_8N_3Cl$: 229.0407; found: 229.0409.

4-Azido-4′-trifluoromethylbiphenyl: ^{1}H NMR (500 MHz, $CDCl_3$), δ: 7.67 (2H, d, J = 8.5 Hz), 7.64 (2H, d, J = 8.5 Hz), 7.57 (2H, d, J = 8.5 Hz), 7.11 (2H, d, J = 8.5 Hz); HRMS *m*/*z*, calcd. for $C_{13}H_8N_3F_3$: 263.0670; found: 263.0668.

4-Azido-3′-chlorobiphenyl: ^{1}H NMR (500 MHz, $CDCl_3$), δ: 7.54–7.52 (3H, m), 7.42–7.4 (1H, m), 7.334 (1H, t, J = 8.0 Hz), 7.31–7.29 (1H, m), 7.08 (2H, d, J = 8.5 Hz); HRMS *m*/*z*, calcd. for $C_{12}H_8N_3Cl$: 229.0407; found: 229.0411.

4-Azido-3′-methylbiphenyl: ^{1}H NMR (500 MHz, $CDCl_3$), δ: 7.55 (2H, d, J = 8.5 Hz), 7.36–7.3 (3H, m), 7.16–7.14 (1H, m), 7.07 (2H, d, J = 8.5 Hz); HRMS *m*/*z*, calcd. for $C_{12}H_8N_3Cl$: 209.0953; found: 209.0957.

4-Azido-3′-methoxybiphenyl: ^{1}H NMR (500 MHz, $CDCl_3$), δ: 7.59 (2H, d, J = 8.5 Hz), 7.37 (1H, t, J = 8.0 Hz), 7.18–7.08 (3H, m), 6.94–6.90 (1H, m), 3.88 (3H, s); HRMS *m*/*z*, calcd. for $C_{13}H_{11}N_3O$: 225.0902; found: 225.0891; calcd. for $C_{13}H_{11}NO$ (M–N_2): 197.0841; found:197.0897.

Acknowledgement

Financial support from the Natural Sciences and Engineering Research Council of Canada is gratefully acknowledged.

References

1. R.A. McClelland, M.J. Kahley, P.A. Davidse, and G. Hadzialic. J. Am. Chem. Soc. **118**, 4794 (1996).
2. P.A. Davidse, M.J. Kahley, R.A. McClelland, and M. Novak. J. Am. Chem. Soc. **116**, 4513 (1994).
3. G.B. Schuster and M.S. Platz. Adv. Photochem. **17**, 143 (1992).
4. A. Dipple. Carcinogenesis, **16**, 437 (1995).
5. M. Novak and S. Kennedy. J. Am. Chem. Soc. **117**, 574 (1995).
6. R.A. McClelland, M.J. Kahley, and P.A. Davidse. J. Phys. Org. Chem. **9**, 355 (1996).
7. M. Novak, M.J. Kahley, E. Eiger, J.S. Helmick, and H.E. Peters. J. Am. Chem. Soc. **115**, 9453 (1993).
8. M. Novak, M.J. Kahley, J. Lin, S.A. Kennedy, and T.G. James. J. Org. Chem. **60**, 8294 (1995).
9. M. Novak, M.J. Kahley, J. Lin, S.A. Kennedy, and L.A. Swanegan. J. Am. Chem. Soc. **116**, 11626 (1994).

© 1998 NRC Canada

10. G. Kohnstam, W.A. Petch, and D.L.H. Williams. J. Chem. Soc. Perkin Trans 2, 423 (1984).
11. R.B. Millar and S. Dugar. Organometallics, **3**, 1261 (1984).
12. R.M. Washburn, E. Levens, C.F. Albright, F.A. Billing, and E.S. Cernak. Adv. Chem. Ser. **23**, 102 (1959).
13. P.A.S. Smith and B.B. Brown. J. Am. Chem. Soc. **73**, 2438 (1951).
14. R.A. McClelland. Tetrahedron, **52**, 6823 (1996).
15. G.B. Schuster and M.S. Platz. Adv. Photochem. **17**, 143 (1992).
16. J. Bartl, S. Steenken, H. Mayr, and R.A. McClelland. J. Am. Chem. Soc. **112**, 6918 (1990).
17. R.A. McClelland, C. Chan, F. Cozens, A. Modro, and S. Steenken. Angew. Chem. Int. Ed. Engl. **30**, 1337 (1991).
18. A. Riecker and B. Speiser. Tetrahedron Lett. **31**, 5013 (1990).
19. J.P. Richard and W.P. Jencks. J. Am. Chem. Soc. **104**, 4689 (1982).
20. J.P. Richard, M.E. Rothenberg, and W.P. Jencks. J. Am. Chem. Soc. **106**, 1361 (1984).
21. J.P. Richard, S.-S. Lin, J.M. Buccigros, and T.L. Amyes. J. Am. Chem. Soc. **51**, 12603 (1996).
22. R.A. McClelland, V.M. Kanagasabapathy, N. Banait, and S. Steenken. J. Am. Chem. Soc. **113**, 1009 (1991).
23. J.C. Fishbein and R.A. McClelland. J. Am. Chem. Soc. **109**, 2824 (1987).
24. E.O. Alonso, L.J. Johnston, J.S. Scaiano, and V.G. Toscano. J. Am. Chem. Soc. **112**, 1270 (1990).
25. Y. Yukawa, Y. Tsuno, and M. Sawada. Bull. Chem. Soc. Jpn. **39**, 2274 (1966).
26. H.C. Brown, D.P. Kelley, and M. Periasamy. Proc. Natl. Acad. Sci. U.S.A. **77**, 6956 (1980).
27. R.A. McClelland, V.M. Kanagasabapathy, N. Banait, and S. Steenken. J. Am. Chem. Soc. **111**, 3966 (1989).
28. F.L. Cozens, N. Mathivanan, R.A. McClelland, and S. Steenken. J. Chem. Soc. Perkin Trans. 2, 2083 (1992).
29. A.A. Allen, A.J. Kresge, N.P. Schepp, and T.T. Tidwell. Can. J. Chem. **65**, 1719 (1987).

© 1998 NRC Canada

Synthesis, electrochemistry, structure, and magnetic susceptibility of 5-*tert*-butyl-1,3-bis-(1,2,3,5-dithiadiazolyl)benzene. Structural effect of the bulky substituent[1]

Richard A. Beekman, René T. Boeré, Klaus H. Moock, and Masood Parvez

Abstract: The crystal structure of the title compound was determined at 250 K in space group $I\bar{4}2m$, $a = 20.661(5)$ Å, $c = 6.764(7)$ Å, $Z = 8$. The individual dithiadiazole rings form two sets of contrarotatory 4-member pinwheels clustered around a 4-fold rotation–inversion axis located halfway along the unit cell edges, describing an infinite channel lined with sulfur atoms but in which there are short intra-stack contacts through only one S atom of each CN_2S_2 group. The double-layer stacking occurs in order to accommodate the bulk of the ^{t}Bu group, and the spacing between layers is very regular, with short and long S···S contacts of 3.48(2) and 3.61(2) Å and considerable thermal motion in the *c* direction. The title compound and its SbF_6^- salt are oxidized at +0.81 V (in CH_2Cl_2) and at +0.61 V (in CH_3CN), while a reduction process is observed only in CH_2Cl_2 at –0.73 V vs. SCE. Magnetic susceptibility data between 5 and 400 K demonstrate at very low temperature that the sample follows the Curie–Weiss law, $\theta = 0$ K, and $\chi_0 = -156$ ppm emu mol^{-1}. The free-spin concentration at $T = 0$ K is ≈1.3%, due to paramagnetic defects in an essentially diamagnetic structure. The diamagnetism starts to lift above 210 K; above 260 K, a strong antiferromagnetic exchange is operative. These results are consistent with the lifting of the Peierls distortion in this structure, starting above ≈200 K. The crystal structure of the parent diamidine 5-*tert*-butyl-1,3-$[(Me_3Si)_2NCNSiMe_3]_2C_6H_3$ was determined in $C2/c$ with $a = 10.0788(3)$, $b = 21.328(5)$, $c = 20.876(5)$ Å, $\beta = 99.41(2)°$, $Z = 4$. The two amidine functional groups are equivalent by crystal symmetry.

Key words: dithiadiazole, diradical, magnetic susceptibility, crystal structure, bulky substituent.

Résumé : On a déterminé la structure cristalline du composé mentionné dans le titre à 250 K; il cristallise dans le groupe d'espace $I\bar{4}2m$ avec $a = 20{,}661(5)$ Å, $c = 6{,}754(7)$ Å et $Z = 8$. Les noyaux dithiadiazoles individuels forment deux ensembles à sens contraire, en forme de moulinet à quatre membres, regroupés autour d'un axe de rotation–inversion quaternaire situé à mi-chemin le long des arêtes du motif élémentaire et décrivant un canal infini bordé d'atomes de soufre; on n'y observe toutefois qu'un seul point de contact court entre les empilements et il se produit entre un atome de soufre de chaque groupe CN_2S_2. L'empilement à deux couches se produit de façon à accommoder l'encombrement du groupe *tert*-butyle et la distance entre les couches est très régulière alors que les distances S···S courtes et longues sont respectivement de 3,48(2) et 3,61(2) Å et qu'on observe beaucoup de mouvement thermique dans la direction *c*. Le composé mentionné dans le titre et son sel de SbF_6^- sont oxydés à +0,81 V (dans le CH_2Cl_2) et à +0,61 V (dans le CH_3CN) alors que l'on n'observe le processus de réduction que dans le CH_2Cl_2, à –0,73 V vs. SCE. Les données de susceptibilité magnétique entre 5 et 400 K démontrent que, à température très basse, l'échantillon obéit à la loi de Curie–Weiss, $\theta = 0$ K et $\chi_0 = -156$ ppm emu mol^{-1}. La concentration libre de spin à $T = 0$ K est égale à 1,3% à cause de défauts paramagnétiques dans une structure essentiellement diamagnétique. Le diamagnétisme commence à s'éliminer et, au-dessus de 260 K, un important échange antiferromagnétique est en action. Ces résultats sont en accord avec l'élimination progressive de la distorsion de Peierls dans cette structure à partir d'environ 200 K. On a déterminé la structure cristalline de la diamine parent, 5-*tert*-butyl-1,3-$[(Me_3Si)_2NCNSiMe_3]_2C_6H_3$, qui cristallise dans le groupe d'espace $C2/c$, avec $a = 10{,}0788(3)$, $b = 21{,}328(5)$ et $c = 20{,}876(5)$ Å, $\beta = 99{,}41(2)°$ et $Z = 4$. Les deux groupes fonctionnels amidines sont équivalents par symétrie cristalline.

Mots clés : dithiadiazole, diradical, susceptibilité magnétique, structure cristalline, substituant encombrant.

[Traduit par la rédaction]

Received July 8, 1997.

R.A. Beekman and R.T. Boeré.[2] Department of Chemistry, University of Lethbridge, Lethbridge, AB T1K 3M4, Canada.

K.H. Moock. Research School of Chemistry, Australian National University, Canberra, ACT 0200, Australia.

M. Parvez. Department of Chemistry, University of Calgary, Calgary, AB T2N 1N4, Canada.

[1] Presented in part at the 80th Canadian Society for Chemistry Conference, Windsor, Ontario, July 1–4, 1997.

[2] Author to whom correspondence may be addressed. Telephone: (403) 329-2045. Fax: (403) 329-2057. E-mail: boere@uleth.ca

© 1998 NRC Canada

Introduction

1,2,3,5-Dithia- and diselena-diazoles, **1**, have been extensively investigated as potential single-component molecular conductors (1). Early examples formed isolated dimer pairs, as in the first structurally characterized compound, 4-phenyl-1,2,3,5-dithiadiazole (2). Molecular engineering has focused on obtaining solids in which the heterocycles are stacked into infinite arrays in the solid, yet in all cases where stacking is observed for neutral systems, the *spacing* of the layers alternates between short and long separation. This has been interpreted as the result of a Peierls distortion (3). There is evidence from magnetic measurements that this distortion may be overcome at a higher temperature for the neutral derivatives, and it

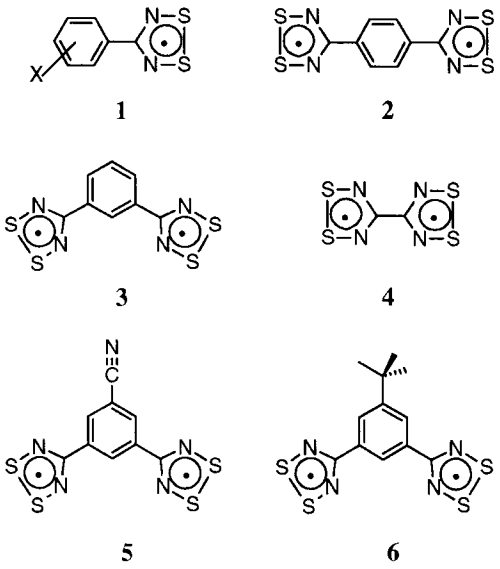

is overcome in some systems by partial oxidation (4). Up till now the main strategies used to overcome this inherent tendency to distortion have been (*i*) to minimize the bulk of the R-group, e.g., **1**, but with the aromatic ring replaced only by an H atom (5), or by increasing the nuclearity of the dithiadiazole centres to include bi- and tri-functional species such as **2** (6), **3** (7), or **4** (8); and (*ii*) through the inclusion of ancillary donor sites (e.g., nitrile on (9–11) or nitrogen *within* (12) the aryl backbone), as in **5** (9). Recently, the latter strategy applied to 4-$NCC_6F_4CN_2S_2$ resulted, due to strong interaction with the nitrile groups, in a sheet structure that, while evenly spaced, has no vertical stacks at all; consistently this material behaves as a bulk paramagnet (13). A second phase of this material undergoes a phase transition to a "canted antiferromagnetic" state at 36 K (14).

Bulky substituents have, on the other hand, not been employed before. We report here the synthesis and characterization of **6** in which a *tert*-butyl (^{t}Bu) group is located in the 5-position of the aromatic backbone. The effect of the bulky substituent on the structure is profound. Whereas **3** and **5** form stacked structures in which the molecules overlay directly, **6** has a stacked structure with every second layer reversed in order to accommodate the *tert*-butyl groups. It is the first example of a dithiadiazole that forms such *double-layer* stacks. Spacing within the stacks is much more regular than in

Scheme 1

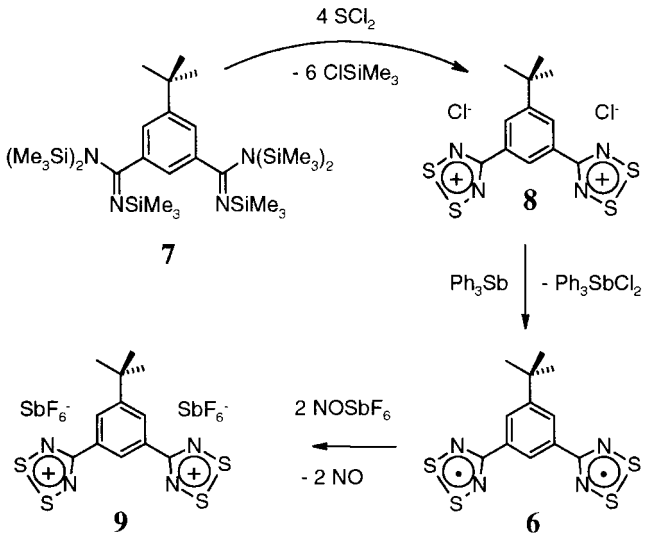

2, **3,** or **5**. The observed structure is consistent with a material that is stabilized *above* the Peierls distortion at room temperature, a conclusion substantiated by the magnetic susceptibility profile measured between 5 and 400 K.

In addition to a strong structural influence, the ^{t}Bu group has a solubilizing effect that has allowed measurements of the solution electrochemistry of **6**. Previously, **2** had been the only bifunctional dithiadiazole characterized by solution electrochemistry (15). The electrochemical behaviour of **6** supports previous conclusions that the two CN_2S_2 groups act as independent redox centres.

Results and discussion

Synthesis

Starting from the known 5-*tert*-butyl-1,3-dicyanobenzene (16), the persilylated amidine **7** was prepared using methods we have recently described in detail (17). Amidine **7** was fully characterized by chemical methods and by X-ray crystallography. In particular, it was important to be certain that both nitrile groups were derivatized to the amidine. Results of the structure determination are discussed below, while the spectroscopic properties are listed in the experimental section. Scheme 1 indicates the sequence of synthetic reactions used to prepare the title compound. **7** was condensed with sulfur dichloride (excess), and the resulting orange bisdithiadiazolium dichloride **8**, which was not further characterized, was reduced to the neutral diradical **6** using triphenylantimony. Purification of the crude diradical was performed by repetitive vacuum sublimation in a three-zone tube furnace at 10^{-2} Torr (1 Torr = 133.3 Pa), and crystals suitable for a diffraction study were grown in a furnace gradient of 50/100/180°C.

Oxidation of the diradical using nitrosyl hexafluoroantimonate afforded the SbF_6^- salt of the dication, **9**, which could be recrystallized as an orange solid containing solvent of crystallization. Compound **9** was used in the electrochemical studies described next.

© 1998 NRC Canada

Fig. 1. A typical steady-state cyclic voltammogram of **6** obtained in CH_2Cl_2 solution with 0.5 M NBu_4PF_6 electrolyte and containing the ferrocene internal voltammetric reference compound.

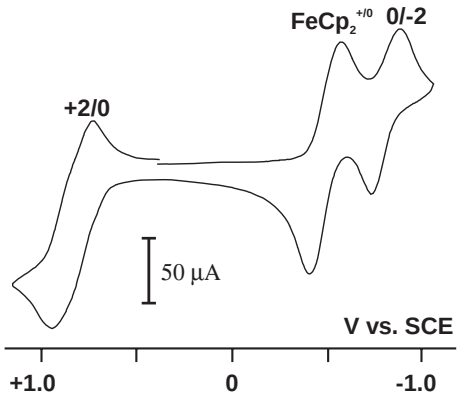

Table 1. Voltammetric data for the compounds.[a]

	$E_{1/2}$ / V			
	CH_3CN [b]		CH_2Cl_2 [c]	
Compound	Oxidation	Reduction	Oxidation	Reduction
6 (diradical)	Insoluble	Insoluble	+0.81	–0.79
9 (SbF_6^- salt)	+0.61 [d]	Not observed	Insoluble	Insoluble
2 (diradical) [e]	Insoluble	Insoluble	+0.78	–0.72
2 (SbF_6^- salt) [e]	+0.61 [f]	–0.80	Insoluble	Insoluble

[a] All potentials measured in *both* alternating current (a.c.) and cyclic voltammetry (cv) techniques.
[b] At a platinum electrode in CH_3CN containing 0.2 mol L^{-1} NBu_4PF_6 electrolyte, referenced to SCE such that $E_{1/2}$ = +0.38 for $[FeCp_2]^{+/-}$.
[c] At a platinum electrode in CH_2Cl_2 containing 0.5 mol L^{-1} NBu_4PF_6 electrolyte, referenced to SCE such that $E_{1/2}$ = +0.48 for $[FeCp_2]^{+/-}$.
[d] Separation between anodic and cathodic peak of 40 mV.
[e] Reference 15.
[f] Separation between anodic and cathodic peak of 30 mV.

Voltammetry and ESR spectroscopy

A combination of cyclic and a.c. voltammetry in typical organic solvents (CH_2Cl_2 and CH_3CN) was employed in an evacuated cell (18). We had previously investigated the electrochemical behaviour in solution of substituted aryl dithiadiazole radicals **1** as a function of substituent **X**, in a very rigorous procedure in which we obtained data in *both* solvents starting from either the free radical or a salt of a non-interacting anion (15, 19). We were also able to obtain acceptable cyclic voltammograms for the bifunctional diradical **2**, but only from CH_2Cl_2 solutions; similarly a salt of its dication could only be measured in CH_3CN. However, the isomeric **3** proved to be too insoluble for such studies. The ^{t}Bu group in **6** has a solubilizing effect, so that we were able to obtain reversible redox potentials for this compound in dichloromethane, and for the salt **9** in acetonitrile. For **6** in CH_2Cl_2 the oxidation process occurs at +0.81 V and the reduction at –0.79 V (vs. SCE). For the SbF_6^- salt, soluble only in CH_3CN, the 2-electron oxidation is observed at +0.61 V.

Voltammetric data for **6**, **9,** and **2** are compiled in Table 1. The redox potentials measured for the $2^+/2\cdot$ ("oxidation") and the $2\cdot/2^-$ ("reduction") processes are remarkably similar for the two forms **6** and **9** and the analogous versions (diradical and dication) of **2**. This confirms that the substituent effect of one dithiadiazole group attached to an aromatic ring on another similarly attached group is extremely small, and is independent of *meta* or *para* geometry. The two CN_2S_2 rings seem to behave independently. The 0.2 V difference between the potentials in acetonitrile and dichloromethane are typical for this ring system (15). The cell potentials, i.e., $\Delta E_{1/2}$, are also comparable to other dithiadiazole systems, and are larger than those observed for diselenadiazoles (15).

A typical steady-state cyclic voltammogram for the diradical measured in CH_2Cl_2 is presented in Fig. 1. There is a large separation between the anodic and cathodic peaks for both waves, with 250 mV for the oxidative and 190 mV for the reductive process. This is most likely due to the extremely low solubility of **6** in dichloromethane. (Thus a solution prepared by adding crystals of **6** to highly purified CH_2Cl_2 remains colourless, but has detectable ESR signals and voltammetric waves. However, the bulk solubility is negligible.) Similarly, with its concentration adjusted to that of the compound being studied, the reference compound, ferrocene, is almost equally broadened with a separation of 180 mV. The solubility of the cation from the salt **7** is considerably greater in acetonitrile, a solvent whose dielectric properties generally favour more "ideal" voltammograms. Only the oxidation process is reversible for this compound, a situation noted previously for monofunctional dithiadiazole cations. The absence of a reversible "reduction" wave, technically the second reduction starting from the dication, was attributed to a rapid comproportionation reaction between the small amount of anion formed and the large excess of cation (20).

There has been some discussion in the literature regarding the nature of the electron transfer processes in bifunctional dithiadiazoles (8, 21). Are the two groups on a single ring *simultaneously* oxidized or reduced? Can a radical cation or a radical anion be formed? These effects normally show up in the shapes of the cyclic voltammograms and size of the anodic–cathodic peak separations. We believe that a verdict has not been reached on this question. The data obtained for the "oxidation" process in acetonitrile (first reduction of the dication from **9**) are indicative of a two-electron step in which ΔE = 0, producing single peaks with a separation between anodic and cathodic peak of 40 mV, intermediate between those of a single (58 mV) and a two-electron (29 mV) process (22). However, the solubility of all bifunctional compounds prepared thus far is simply too low to draw authoritative conclusions.

ESR measurements show that there is a weak intramolecular exchange between the two radical centers on a single molecule at room temperature; intermolecular effects can be ruled out at the extremely low concentrations involved. Figure 2 shows limiting spectra in dichloromethane. At 250 K, a simple 5-line pattern due to hyperfine interaction to two equivalent ^{14}N nuclei is observed, with a_N = 0.51 mT. On warming, a more complex pattern develops, consistent with an intramolecular exchange coupling J_{ex} between radical centres that has probably not yet reached its limit at 340 K; at higher temperatures, the solvent boiled out of the resonant cavity. Exchange effects have been noted previously for diradicals, and the magnitude of the exchange process for **6** is intermediate between that of **2** and **3** (6, 7). The apparent absence of exchange phenomena in the electrochemistry may simply reflect

© 1998 NRC Canada

Fig. 2. X-Band ESR spectra of **6** at (*a*) 250 K and (*b*) 340 K measured in CH_2Cl_2 solution using 4 mm cylindrical quartz tubes.

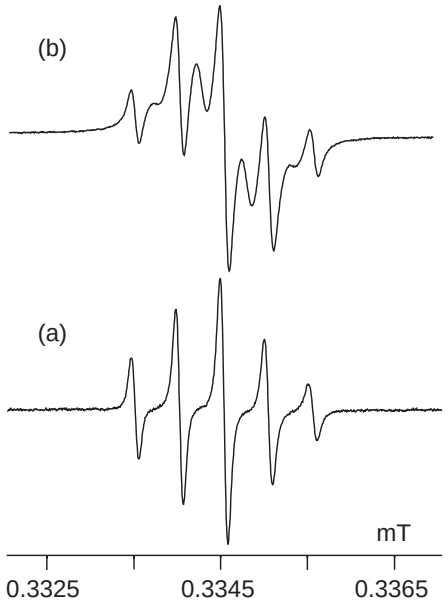

differences in the time scales of the cyclic voltammetry and ESR experiments.

In summary, the *tert*-butyl group is responsible for a marginal increase in solubility for the 1,3-bisdithiadiazole ring system, allowing the measurement of solution redox potentials for the first time. However, the solubility is still too low either for definitive electrochemical work on any cooperative effects between the two CN_2S_2 rings on a single molecule, or for detailed study of the intramolecular spin exchange mechanism by ESR. The preparation of more soluble derivatives is underway.

Table 2. Crystallographic data.

Compound	**6**	**7**
Formula	$C_{12}H_{12}N_4S_4$	$C_{30}H_{66}N_4Si_6$
fw	340.49	651.39
Crystal system	Tetragonal	Monoclinic
Space group	$I\bar{4}2m$ (No. 121)	$C2/c$ (No. 15)
a, Å	20.661(5)	10.078(3)
b, Å		21.328(5)
c, Å	6.764(7)	20.876(5)
β, deg		99.41(2)
V, Å^3	2887(1)	4426(1)
Z	8	4
ρ_{calc}, g cm^{-3}	1.566	0.977
F(000)	1408.00	1432.00
μ, cm^{-1}	6.51	2.10
Crystal size, mm	0.50 × 0.40 × 0.30	0.40 × 0.39 × 0.13
Temperature, K	250	200
Scan speed, deg min^{-1}	8.0 (in ω)	4.0 (in ω)
Scan range, deg	1.68 + 0.34 tan θ	1.47 + 0.34 tan θ
$2\theta_{max}$, deg	55.1	50.1
Crystal decay,%	0.99	0.11
Absorption correction	Empirical	Empirical
Absorption range	0.8510–1.0000	0.9624–1.0000
Total reflections	989	4276
Unique reflections	989	4026
R for merge		0.019
Data with $I \geq 3.00\sigma(I)$	499	1848
Solution method	Direct methods	Direct methods
Parameters refined	97	182
R	0.043	0.059
R_w	0.042	0.060
gof	2.07	2.0
Largest Δ/σ	0.52	0.001
Final difference map, e Å^{-3}	0.27	0.70

Rigaku AFC6S, MoK_α radiation (λ = 0.71069 Å); graphite monochromator, takeoff angle 6.0°, aperture 6 × 13 mm (horizontal × vertical) at a distance of 400 mm from the crystal, stationary background counts (scan/background time ratio 2:1), ω–2θ scans, empirical absorption correction applied based on azimuthal scans of several reflections, data corrected for Lorentz and polarization effects, solution by direct methods (SAPI91), refined by full-matrix least squares (DIRDIF94), function minimized $\sum w(|F_o| - |F_c|)^2$ where $w = 4F_o2/\sigma^2(F_o2)$, $R = \sum||F_o| - |F_c||/\sum|F_o|$, $R_w = (\sum w(|F_o| - |F_c|)^2/\sum|F_o|^2)^{1/2}$, and gof = $[\sum w(|F_o| - |F_c|)^2/(m - n)]^{1/2}$. Values given for R, R_w, and gof are based on those reflections with $I \geq 3.00\sigma(I)$.

Crystal and molecular structure of 7

A suitable single crystal of **7** was obtained by slow sublimation in a large round-bottomed sublimer, data crystals forming on the outside, air-cooled, region of the device. Data collection at low temperature helped to limit thermal motion of the many methyl groups in the molecule, and an *R*-factor of 6% was obtained with a data to parameter ratio of 10:1. Details of the structure determination and metric parameters are found in Tables 2–5. An ORTEP representation of the structure is presented in Fig. 3. The structure was refined in space group $C2/c$ with four molecules per unit cell. The molecule consistently occupies a special position, with C12, C14, and C15 all lying on a twofold rotation axis. This requires disorder in the positions of the three ^{t}Bu methyl groups. The disorder was modeled using two sets of methyl groups at half-occupancy with bond lengths constrained to 1.50 Å and isotropic temperature factors. The two amidine functional groups are crystallographically identical. The C10—N1 and C10—N2 distances are 1.410(5) and 1.264(5) Å, consistent with a C—N single and C═N double bond, respectively. For comparison, the distances in hexakis(trimethylsilyl)-1,4-benzdiamidine are 1.413(3) and 1.271(3) Å (23). All other molecular distances are unexceptional.

Crystal and molecular structure of 6

Several attempts to obtain data sets at lower temperatures did not lead to a satisfactory solution, but the data set collected at 250 K solved successfully. Details of the structure determination and metric parameters are found in Tables 2–5. An ORTEP representation of a single molecule is given in Fig. 4, which provides the atomic numbering scheme. In the molecular structure, the S—S, S—N, and N—C bond lengths agree closely with the experimental and calculated (square bracketed) values found for the $(HCN_2S_2)_2$ dimer: 2.07(3) [2.071]; 1.64(6) [1.635]; 1.32(8) [1.323] (24). They also compare closely with those found in **3**, which also crystallizes in a tetragonal space group, $I4_1/a$, and possesses a different layered structure, with pinwheel arrangement within the layers (6).

Much more interesting is the intermolecular structure. Two views of the crystal structure are presented in Figs. 5 and 6.

© 1998 NRC Canada

Table 3. Final atomic coordinates (fractional) and B_{eq}[a] (Å^2) for **6** and **7** ($\times 10^4$).

Atom	*x*	*y*	*z*	B_{iso}/B_{eq}
		6		
S(1)	0.70414(8)	0.02541(7)	0.255(1)	4.26(5)
S(2)	0.60713(8)	0.05153(8)	0.251(1)	4.95(5)
N(1)	0.7306(2)	0.0995(2)	0.263(3)	3.1(2)
N(2)	0.6213(2)	0.1294(2)	0.246(4)	4.0(1)
C(1)	0.6845(3)	0.1445(3)	0.247(4)	3.0(2)
C(2)	0.7043(3)	0.2140(3)	0.249(3)	2.4(1)
C(3)	0.7690(3)	0.2310	0.232(4)	2.1(1)
C(4)	0.6565(3)	0.2618(3)	0.233(3)	2.0(2)
C(5)	0.6734(3)	0.3266	0.252(5)	2.6(1)
C(6)	0.6204(3)	0.3796	0.226(5)	2.3(2)
C(7)	0.6422(5)	0.4411(5)	0.311(4)	13.7(7)
C(8)	0.6051(5)	0.3949	0.021(3)	8.5(4)
		7		
Si(1)	7516(2)	1383(1)	1656(1)	36(1)
Si(2)	5139(2)	2091(1)	793(1)	38(1)
Si(3)	2605(2)	414(1)	565(1)	38(1)
N(1)	5814(4)	1461(2)	1301(2)	29(1)
N(2)	4021(4)	860(2)	790(2)	32(1)
C(1)	8014(6)	555(3)	1816(3)	51(2)
C(2)	8606(6)	1683(3)	1076(3)	55(2)
C(3)	7892(6)	1826(3)	2429(3)	55(2)
C(4)	3424(6)	2284(3)	939(3)	51(2)
C(5)	6146(7)	2808(3)	1054(4)	71(2)
C(6)	5167(7)	1950(3)	–86(3)	58(2)
C(7)	1469(7)	882(4)	–55(4)	74(2)
C(8)	3067(7)	–316(3)	185(4)	69(2)
C(9)	1648(6)	230(3)	1233(3)	63(2)
C(10)	4895(5)	959(3)	1291(3)	28(1)
C(11)	4966(5)	610(1)	1922(2)	25(1)
C(12)	5000	932	2500	23(2)
C(13)	4938(6)	–41(2)	1929(3)	32(1)
C(14)	5000	–397(3)	2500	40(2)
C(15)	5000	–1075(3)	2500	73(3)
C(16)	5081	–1389	3148	56(4)
C(17)	3959	–1366	1991	58(4)
C(18)	6299	–1257	2288	133(7)

[a] $B_{eq} = 8/3\pi^2(U_{11}(aa^*)^2 + U_{22}(bb^*)^2 + U_{33}(cc^*)^2 + 2U_{12}aa^*bb^* \cos\gamma + 2U_{13}aa^*cc^* \cos\beta + 2U_{23}bb^*cc^* \cos\alpha)$

Table 4. Selected interatomic distances (Å) for **6** and **7**.

Atoms	Distance	Atoms	Distance
	6		
S(1)—S(2)	2.076(2)	S(1)—N(1)	1.627(4)
S(2)—N(2)	1.636(5)	N(1)—C(1)	1.335(7)
N(2)—C(1)	1.342(7)	C(1)—C(2)	1.494(7)
C(2)—C(3)	1.387(7)	C(2)—C(4)	1.402(8)
C(4)—C(5)	1.390(8)	C(5)—C(6)	1.56(1)
C(6)—C(7)	1.47(2)	C(6)—C(7)	1.47(2)
C(6)—C(8)	1.46(4)		
	7		
N(1)—Si(1)	1.762(4)	C(1)—Si(1)	1.853(6)
C(2)—Si(1)	1.874(6)	C(3)—Si(1)	1.856(6)
N(1)—Si(2)	1.776(4)	C(4)—Si(2)	1.851(6)
C(5)—Si(2)	1.867(6)	C(6)—Si(2)	1.863(6)
C(8)—Si(3)	1.841(7)	C(9)—Si(3)	1.862(7)
C(10)—N(1)	1.414(6)	C(10)—N(2)	1.270(6)
C(11)—C(10)	1.503(7)	C(12)—C(11)	1.384(2)
C(15)—C(14)	1.446(7)		

Table 5. Selected bond angles (°) for **6** and **7**.

Atoms	Angle	Atoms	Angle
	6		
S(2)S(1)-N(1)	94.6(2)	S(1)-S(2)-N(2)	94.8(2)
S(1)-N(1)-C(1)	114.3(4)	S(2)-N(2)-C(1)	113.7(4)
N(1)-C(1)-N(2)	122.2(5)	N(1)-C(1)-C(2)	118.2(5)
N(2)-C(1)-C(2)	119.3(5)	C(1)-C(2)-C(3)	120.5(6)
C(1)-C(2)-C(4)	118.9(5)	C(3)-C(2)-C(4)	119.6(7)
C(2)-C(3)-C(2)	118.8(8)	C(2)-C(4)-C(5)	119.6(6)
C(4)-C(5)-C(4)	118.5(g)	C(4)-C(5)-C(6)	119.3(7)
C(4)-C(5)-C(6)	119.3(7)	C(5)-C(6)-C(7)	110(1)
C(5)-C(6)-C(7)	110(1)	C(5)-C(6)-C(8)	114(2)
C(7)-C(6)-C(7)	112(2)	C(7)-C(6)-C(8)	104(1)
C(7)-C(6)-C(8)	104(1)		
	7		
Si(2)-N(1)-Si(1)	125.0(3)	C(10)-N(1)-Si(1)	121.6(4)
C(10)-N(1)-Si(2)	112.2(3)	C(10)-N(2)-Si(3)	138.7(4)
N(2)-C(10)-N(1)	120.1(5)	C(11)-C(10)-N(1)	115.2(4)
C(11)-C(10)-N(2)	124.5(5)	C(12)-C(11)-C(10)	120.6(3)
C(11)-C(12)-C(11)	120.6(4)	C(14)-C(13)-C(11)	123.5(5)
C(13)-C(14)-C(13)	114.5(6)	C(15)-C(14)-C(13)	122.8(3)

There are eight molecules per unit cell. At the center of the cell is located a $\bar{4}$ symmetry axis, perpendicular to the plane shown in Fig. 5, and passing through the point {1/2,1/2,0}. This axis defines the packing of the ^{t}Bu groups: diagonally opposed groups are at the same level; neighbouring groups are half a *c* translation apart, resulting in a double helical staircase of ^{t}Bu groups surrounding an infinite channel lined by hydrogen atoms. A more complex channel is located at the other $\bar{4}$ axis perpendicular to *c*, which passes through the family of points {1/2,0,0}. To depict this channel more accurately, four additional molecules have been added to the unit cell in the *–b* direction in Fig. 5.[3] In all, eight CN_2S_2 rings contribute to the two layers of the depicted channel. Consistent with the $\bar{4}$ symmetry, the pinwheel geometry of four CN_2S_2 rings is *reversed* every second layer, so that the infinite channel lined by sulfur atoms is defined by two *contrarotating* pinwheel groups of dithiadiazole rings. Whereas the pinwheel motif has been seen in numerous dithiadiazole structures, this is the first example of contrarotating double layers of pinwheels.

Each molecule of **6** is centred on a 2_1 screw axis parallel to *c* and passing through the point {1/4,1/4,0}, defining a forward–backward packing motif for each subsequent molecule of **6** in an infinite stack. That this motif is adopted in order to accommodate the bulky ^{t}Bu groups while maintaining as many intermolecular S···S and S···N contacts as possible seems almost certain, since both **3** and **5** have structures in which the

[3] The channel is quite narrow, having a diameter of only 1.3 Å when the van der Waals' radius of sulfur is taken as 1.80 Å.

© 1998 NRC Canada

Fig. 3. ORTEP representation, showing the atom numbering scheme, of a single molecule of **7** as it is found in the crystal structure. The molecule lies on a twofold rotation axis, and the *t*Bu group is disordered. In the refinement two constrained groups (half-occupancy) with isotropic temperature factors were allowed; only a single group has been drawn in the picture.

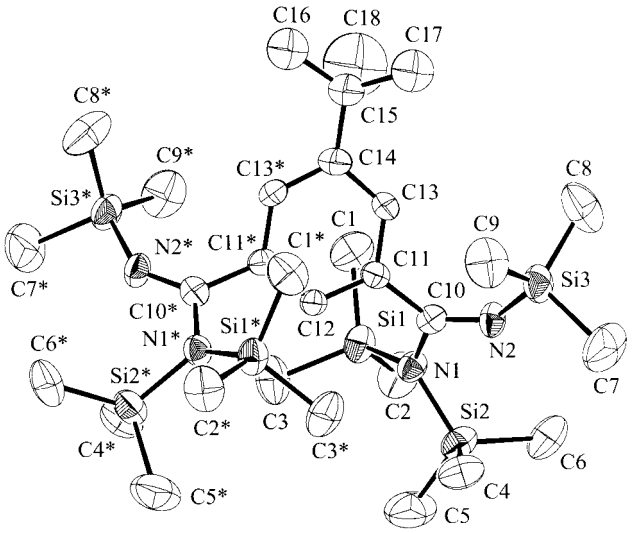

Fig. 4. ORTEP representation, showing the atom numbering scheme, of a single molecule of **6** as it is found in the crystal structure.

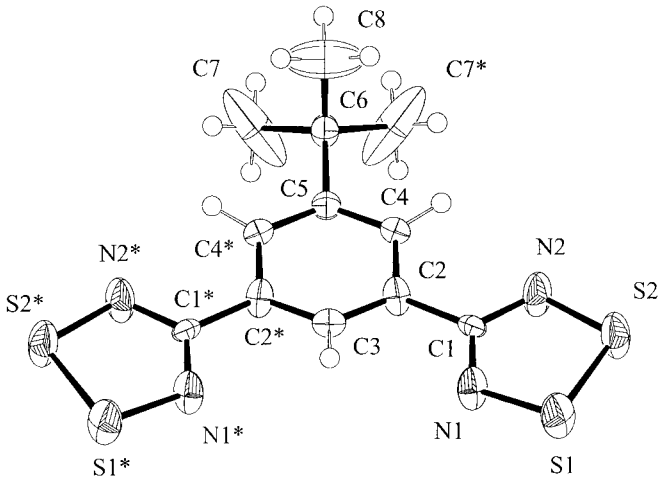

bent 1,3-$(S_2N_2C)C_6H_3$ units lie directly above one another in a superimposed infinite stack. Spacing between the layers in **6** is much more even than in either **3** or **5**. This is shown very clearly in Fig. 6, which is a view perpendicular to the *a* axis depicting only the CN_2S_2 units of a single sulfur channel. The unit cell diagonals are mirror planes; consistently, the two halves of each molecule of **6** are identical by symmetry and the *t*Bu groups are ordered. The crystal symmetry does not require planarity of the molecules. Consistently, the CN_2S_2 rings are both canted and cupped slightly at the equilibrium distance of the structure determined at 250 K. However, the thermal ellipsoids (Fig. 4) are elongated in the perpendicular direction, so that we expect there to be considerable rocking vibration. At the equilibrium distances determined in the structure, each layer is separated by two slightly longer and two slightly shorter interstack S···S distances, at 3.48(2) and 3.61(2) Å. These distances should be compared to the mean short and long distances in **3** (3.140 and 3.966 Å) and in **5** (3.12 and 3.89 Å). The mean distances are much more comparable: 3.55 in **3** and **6**, 3.51 in **5**. However, since the S···S contacts in **6** are at an angle to the perpendicular, it follows that the ring centroid-to-centroid distance in **6** at 3.382 Å is considerably

Fig. 5. PLUTO representation of the crystal packing observed in the solid-state structure of **6**. The view is down the *c* axis, and the range of indices plotted is *a*: 0–1; *b*: –1/2–1; *c*: 0–1. Heavy solid and broken lines represent the intermolecular sulfur–sulfur contacts at S2 on the upper (black) and lower (gray) layers, as well as between layers at S1.

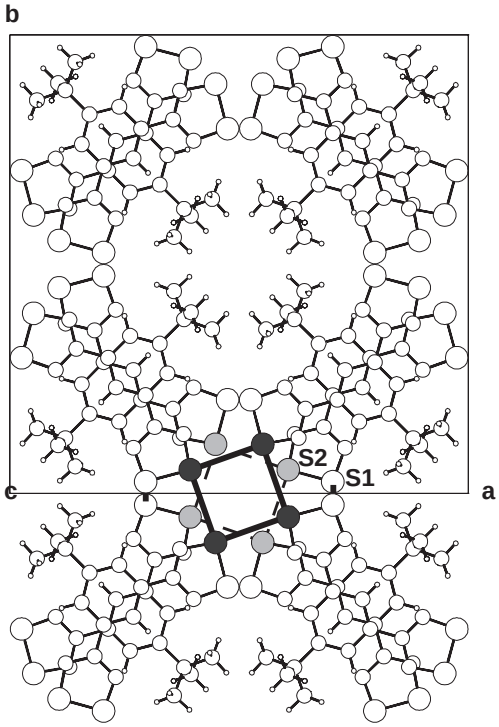

Fig. 6. Side view of portion of a single infinite sulfur-lined channel centred on a $\bar{4}$ axis. Only the CN_2S_2 rings are drawn in this PLUTO representation. The larger diameter spheres are the sulfur atoms.

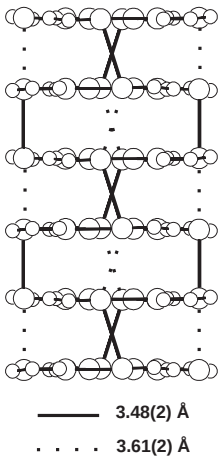

© 1998 NRC Canada

shorter than that in **3** (3.631) and **5** (3.52 Å). Indeed in **6** the separation approaches that in graphite (3.35 Å) (25). The offset packing of the benzene rings in **6** is highly reminiscent of the ground-state structure of graphite, while in **3** and **5** the C_6 rings are directly superimposed.

The pinwheels in each layer are identical except for the direction of rotation. The cross-ring contacts are all 3.474(2) Å between the S2 atoms on adjacent rings. These contacts are noticeably *longer* than in **3** (3.140 and 3.284 Å), which has a pinwheel structure (6), but shorter than the interactions in the lower-symmetry structure of **5** (9). It may be that despite the central $\bar{4}$ symmetry, the ^{t}Bu groups generate considerable steric hindrance and that this prevents the S1 atoms from lining up into a truly vertical column. The calculated density of the structure is consistently the lowest of any bifunctional neutral dithiadiazole (1.57 g cm^{-3}, vs. a range of 1.61– 2.26 for a variety of bifunctional species (6–8)).

In summary, the crystal structure of **6** is a unique double-layered stacking type. This structure is adopted to accommodate the bulk of the ^{t}Bu groups while still maintaining interlayer contacts among the sulfur atoms. Contrary to previous belief, bulky substituents can be useful molecular engineering tools for the development of stacking dithiadiazole radicals. There are no secondary S–X interactions since there are no other donor sites in the molecules. However, steric repulsion among the bulky substituents may be hindering an even more efficient packing, as reflected in the long cross-stack distances. It may be that modification of the substituents while maintaining bulk (^{i}Pr, CF_3, CCl_3), with or without symmetry lowering, may lead to other double-layer stacked structures with tighter packing within the stacks.

Magnetism and conductivity

The magnetic susceptibility of the title compound was measured as a function of temperature and the results are presented in Fig. 7.[4] The response of the sample to magnetization is complex, typical of bifunctional dithiadiazole systems (4, 6, 7). At very low temperature the sample obeys the Curie–Weiss Law, with $\theta = 0$ K and $\chi_0 = -156$ ppm emu mol^{-1}. The free-spin concentration at absolute zero is estimated to be 1.3%, reflecting paramagnetic defects in an essentially diamagnetic structure. The diamagnetism starts to lift above 210 K, and there is a distinct kink in the susceptibility v*s. T* response at 260 K. A plot of χT vs. *T* (Fig. 7*b*) is linear for the points recorded above 260 K, indicative of an antiferromagnetic exchange interaction in this temperature range. At room temperature, the magnetization corresponds to approximately 0.30 unpaired electrons *per molecule*. The susceptibility data bear remarkable similarity to those of **3** and **5**, *except that the onset of paramagnetism is found 200 K lower in the title compound*. The room temperature pressed-pellet conductivity of the material is less than 10^{-7} S cm^{-1}; this absence of conductivity, given a rich source of carriers, is often observed for neutral dithiadiazoles, leading to the conclusion that their bandwidths are narrow (4). In effect they are Mott insulators (26). The observed structure, consistent with the magnetic behaviour, suggests that the orientation imposed on the title compound by the bulky ^{t}Bu group has stabilized it *above* the Peierls distortion at room temperature, the first stacking neutral dithiadiazole for which this has been achieved. The crystal symmetry of the 250 K structure allows a range of structures from alternating long–short–long S1···S1 distances to completely even spacing. It is possible that below 210 K a greater distortion sets in to produce a fully diamagnetic structure, and in support of this hypothesis several X-ray data sets collected between 150 and 250 K did not lead to satisfactory solutions.

In summary, the novel "double-layer" geometry adopted by the title compound is a consequence of having to pack the large ^{t}Bu group efficiently while preserving intermolecular S···S and S···N contacts. This leads to the unusual dithiadiazole stacking pattern in which a *single* sulfur atom chain maintains contacts down the stack, but with weak interstack interactions. The most dramatic effect of the structure adopted by **6** is on the magnetic behaviour, with the onset of paramagnetism 200 K lower in temperature than in **3** or **5**. Recently some distorted bifunctional dithiadiazoles with biphenyl spacers have shown a slight lowering of the onset temperature (ca. 50 K),[5] but nothing as dramatic as in **6**. Optimization of the spacing substituent may finally allow the preparation of densely stacked neutral dithiadiazoles with equal spacing at room temperature and a sufficiently high bandwidth to achieve a conducting state. Alternatively, bulky groups may find great utility in designing molecular magnets from isolated dithiadiazole groups, a goal recently advanced by others (14). Efforts in both of these directions are underway.

Experimental section

Starting materials and general procedures

5-*tert*-Butylisophthalic acid, sulfur dichloride, 1,1,1,3,3,3-hexamethyldisilazane, *n*-butyllithium, thionyl chloride, ammonium hydroxide, chlorotrimethylsilane, nitrosonium hexafluoroantimonate, and triphenylantimony were all obtained commercially (Aldrich). Sulfur dichloride was distilled before use. Lithium bis(trimethylsilyl)amide diethyl etherate was prepared as described previously (17). Acetonitrile (Fisher HPLC grade) was distilled from phosphorus pentoxide, and toluene from sodium metal. All reactions were performed under an atmosphere of dry nitrogen. NMR spectra were acquired at 250.13 (^{1}H) and 62.90 (^{13}C) MHz on a Bruker AC250-F spectrometer, and ESR spectra on a Bruker EMX instrument. Infrared spectra were obtained as Nujol mulls or KBr pellets on a Bomen MB102 instrument. Elemental analyses were performed by MHW Laboratories, Phoenix, Ariz., and mass spectra were recorded by the Mass Spectrometry Center, University of Alberta, Edmonton.

Preparation of 5-*tert*-butyl-1,3-[$(Me_3Si)_2NCNSiMe_3]_2C_6H_3$, (5-^{t}Bu-1,3-DIBADS)

Solid 5-*tert*-butylisophthalonitrile (46.06 g, 250 mmol) (16) was added to a slurry of lithium bis(trimethylsilyl)amide diethyl etherate (120.75 g, 500 mmol) in 1500 mL of toluene and the mixture was then stirred overnight at 50–70°C. Chlorotrimethylsilane (96 mL, 750 mmol) was added and the mixture

[4] The measurement was performed by R.C. Haddon and T.T.M. Palstra at Bell Laboratories (Lucent Technologies, Murray Hill, N.J.) using a SQUID magnetometer operating at 1 tesla.

[5] T.M. Barclay, A.W. Cordes, N.A. George, R.T. Oakley, and R.C. Haddon, 80th Canadian Society for Chemistry Conference, Windsor, Ontario, July 1–4, 1997. Abstract No. 335.

© 1998 NRC Canada

heated to a gentle reflux for an additional 48 h. The mixture was then cooled and filtered (LiCl) and the solvent removed in vacuo. The residual oil was dissolved in 30 mL of hot toluene and 20 mL of acetonitrile was added while the solution was still hot. After cooling to room temperature an additional 20 mL acetonitrile was added to the solution after which it was cooled to –30°C overnight to give crystalline 5-^{t}Bu-1,3-DIBADS (56.89 g, 0.0873 mol, 35%), mp 118–120°C. IR (KBr pellet): 2972 (vs), 2905 (sh), 1638 (br), 1481 (m), 1362 (m), 1310 (m), 1252 (vs), 1215 (vs), 1148 (s), 1119 (m), 1036 (m), 1011 (m), 907 (vs), 841 (br), 747 (s), 724 (s), 694 (s), 658 (m), 629 (m), 585 (w), 555 (w), 497 (w), 424 (m), 379 (w), 345 (m). ^{1}H NMR (δ, $CDCl_3$): 0.066 (s, 54 H, $SiMe_3$), 1.32 (s, 9 H, ^{t}Bu), 7.17 (t, 1.55 Hz, 1 H, phenylene), 7.33 (d, 1.55 Hz, 2 H, phenylene). ^{13}C NMR: 2.66, 31.2, 34.8, 124.9, 126.9, 142.6, 149.7, 167.0. Mass spectrum, *m/z:* 651 ($C_4H_9C_6H_3[CN_2Si(CH_3)_3]_2^+$, 42%), 635 ($C_3H_6C_6H_3[CN_2(Si(CH_3)_3]_2^+$, 12%), 547 ($C_4H_8C_6H_3CN_2$-$(Si(CH_3)_3)_3CN_2(Si(CH_3)_3)_2^+$, 13%), 506 ($C_4H_7C_6H_3[CN_2$-$(Si(CH_3)_3]_2^+$, 6%), 490 ($C_3H_3C_6H_3[CN_2(Si(CH_3)_3)_2]_2^+$, 12%), 390 ($C_4H_7C_6H_3CN_2(Si(CH_3)_3)_3^+$, 13%), 259 ($CN_2(Si(CH_3)_3)_2^+$, 14%), 73 ($Si(CH_3)_3^+$, 100%). Anal. calcd. for $C_{30}H_{66}N_4Si_6$: C 55.32, H 10.21, N 8.60%; found: C 55.32, H 9.96, N 8.60%.

Preparation of 5-*tert*-butyl-1,3-$(S_2N_2C)_2C_6H_3$

Sulfur dichloride (7.5 mL, 120 mmol) was added, while stirring, to a slurry of 5-^{t}Bu-1,3-DIBADS (6.1 g, 9.36 mmol) in 150 mL of acetonitrile. The resulting mixture was heated to a gentle reflux for 3 h and then filtered to afford crude 5-^{t}Bu-1,3-$[(S_2N_2C)_2C_6H_3]^{2+}(Cl^-)_2$ (2.56 g, 6.22 mmol, 80%) as an orange solid that was dried in vacuo overnight. Ph_3Sb (2.42 g, 6.84 mmol) was added to a stirring slurry of the orange solid in 65 mL of degassed CH_3CN and the mixture was refluxed for 2 h. The crude product (2.01g, 5.9 mmol, 95%), which is both oxygen and moisture sensitive, was then slowly sublimed in a three-zone (50/100/170–180°C) tube furnace over 4 days at 1×10^{-2} Torr to produce large black crystals, collected in the 170°C range (0.589 g, 1.73 mmol, 28%), that are much less air sensitive than the crude product. This was resublimed to produce analytical samples of product, mp 258–262°C. IR (1700–250 cm^{-1}): 1678 (w), 1603 (w), 1551 (w), 1339 (vs), 1273 (m), 1217 (w), 1103 (br), 993 (m), 951 (w), 910 (w), 891 (w), 837 (w), 799 (vs), 706 (w), 691 (vs), 679 (sh), 577 (w), 511 (m). Mass spectrum, *m/z:* 340 ($C_4H_9C_6H_6(CN_2S_2)_2^+$, 100%), 325 ($C_3H_6C_6H_3(CN_2S_2)_2^+$, 18%), 294 ($C_4H_9C_6H_3$-$CN_2S_2CNS^+$, 16%), 262 ($C_4H_9C_6H_3CN_2S_2CN^+$, 67%), 247 ($C_3H_6C_6H_3CN_2S_2CN^+$, 14%), 169 ($C_3H_6C_6H_3(CN)_2^+$, 23%), 141 ($C_3H_6C_6H_3C_2^+$, 31%), 78 ($S_2N^+$, 55%). Anal. calcd. for $C_{12}H_{12}N_4S_4$: C 42.33, H 3.55, N 16.45%; found: C 42.44, H 3.40, N 16.51%.

Preparation of 5-*tert*-butyl-1,3$[(S_2N_2C)_2C_6H_3]^{2+}$ $(SbF_6^-)_2$

5-^{t}Bu-1,3$[C_6H_3(CN_2S_2)_2]^{2+}$ $(Cl^-)_2$ (1.0 g, 2.43 mmol) and nitrosonium hexafluoroantimonate (1.29 g, 4.86 mmol) were added to a 250 mL side-arm flask followed by 5 mL acetonitrile. After gentle reflux for 1 h, the solvent was evaporated in a stream of N_2 (g). The crude product was dissolved in 60 mL of dichloromethane and a minimum amount of acetonitrile (15–20 mL). After cooling to –30°C, crystalline **9** was collected by cold filtration. Yield 0.71 g, 0.874 mmol, 36%, mp (dec.) 205–211°C. IR (1700–250 cm^{-1}): 1689 (w), 1603 (w), 1418 (m), 1356 (vs), 1271 (m), 1211 (w), 1123 (br), 1038 (w), 1017 (w), 968 (w), 899 (m), 837 (sh), 720 (m), 662 (vs), 552 (w), 289 (s). Anal. calcd. for $C_{12}H_{12}N_4S_4Sb_2F_{12}$: C 17.75, H 1.49, N 6.90%; found: C 17.65, H 1.44, N 6.78%. The solid was insufficiently volatile to yield a mass spectrum.

Fig. 7. Plots of (*a*) the magnetic susceptibility of **6** as a function of temperature, and (*b*) the fraction of Curie spins per molecule, determined from the susceptibility data, as a function of temperature.

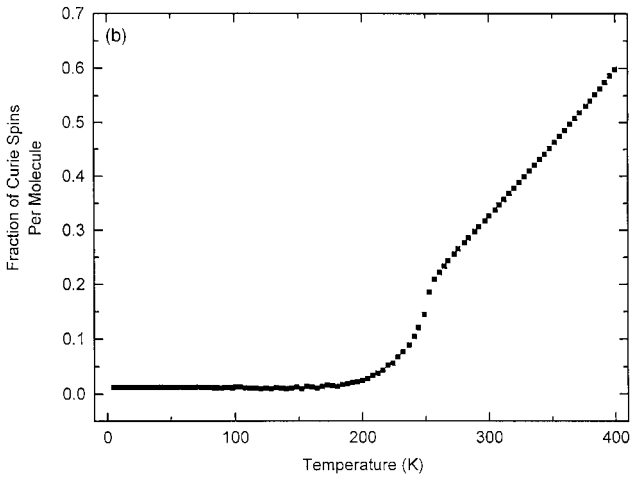

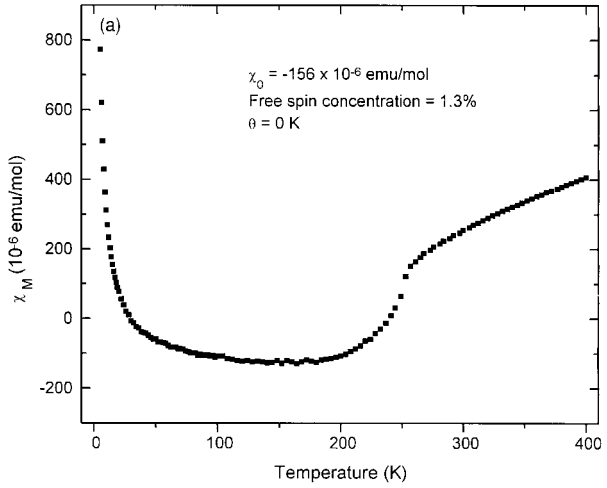

Crystal structure determination.

Crystallographic data appear in Table 2. The final unit-cell parameters were obtained by least squares on the setting angles for 25 reflections with 2θ = 20.2°–30.0° for **7** and for 14 reflections with 2θ = 18.5°–21.5° for **6**. Hydrogen atoms were included at geometrically idealized positions (C—H 0.95 Å), but were not refined. All non-hydrogen atoms were refined anisotropically. Scattering factors were those of Cromer and Waber (27), and allowance was made for anomalous dispersion (28). Computer programs used at Calgary include SAPI91 (29), DIRDIF94 (30), and teXsan (31); and, at Lethbridge, NRC386, a PC version of NRCVAX (31). Final fractional coordinates and B_{eq} appear in Table 3, selected interatomic distances in Table 4, and selected bond angles in Table 5. ORTEP diagrams showing the atomic numbering scheme are presented in

© 1998 NRC Canada

Fig. 3 (**7**) and Fig. 4 (**6**). Crystal structure reports, and additional tables of final positional parameters, bond lengths and angles, hydrogen atom coordinates, and anisotropic displacement parameters for both **6** and **7** have been deposited as supplementary material.[6]

Electrochemistry

For the voltammetric experiments the vacuum-tight all-glass cell with Pt electrodes that has been described previously (18) was employed. The cell was charged with electrolyte ($N^nBu_4PF_6$) and the solvent, dry degassed CH_3CN or CH_2Cl_2, was transferred on a vacuum line. Samples and ferrocene as an internal reference were added to the cell using break-seal techniques. The ferricenium/ferrocene couple is observed in this system at +0.38 V (CH_3CN) and +0.48 V (CH_2Cl_2) vs. SCE at 25°C. Cyclic voltammetric (scan rates $\nu = 20–500$ mV s^{-1}) and phase-sensitive alternating current experiments ($\omega = 610$ Hz, $\nu = 10$ mV s^{-1}) were carried out with a PAR 170 electrochemical system.

Acknowledgments

We thank Prof. Robert Thompson, University of British Columbia, for a preliminary magnetic susceptibility measurement at room temperature, and Dr. Robert Haddon, Bell Labs, for the VT measurements. Dr. Ralph Weber of Bruker, U.S.A., provided time on the EMX spectrometer, and we thank the staff at Bruker for their assistance. The Natural Sciences and Engineering Research Council of Canada and the University of Lethbridge Research Fund provided financial support.

References

1. (*a*) R.T. Oakley. Can. J. Chem. **71**, 1775 (1993); (*b*) A.W. Cordes, R.C. Haddon, and R.T. Oakley. *In* The chemistry of inorganic ring systems. *Edited by* R. Steudel. Elsevier, Amsterdam. 1992. p. 295; (*c*) A.J. Banister and J.M. Rawson. *In* The chemistry of inorganic ring systems. *Edited by* R. Steudel. Elsevier, Amsterdam. 1992. p. 323; (*d*) J.M. Rawson, A.J. Banister, and I. Lavender. Adv. Heterocycl. Chem. **62**, 137 (1995).
2. A. Vegas, A. Pérez-Salazar, A.J. Banister, and R.G. Hey. J. Chem. Soc. Dalton Trans. 1812 (1980).
3. A.W. Cordes, R.C. Haddon, and R.T. Oakley. Adv. Mater. **6**, 798 (1994).
4. C.D. Bryan, A.W. Cordes, R.M. Fleming, N.A. George, S.H. Glarum, R.C. Haddon, C.D. MacKinnon, R.T. Oakley, T.T.M. Palstra, and A.S. Perel. J. Am. Chem. Soc. **117**, 6880 (1995).
5. C.D. Bryan, A.W. Cordes, R.C. Haddon, R.G. Hicks, D.K. Kennepohl, C.D. MacKinnon, R.T. Oakley, T.T.M. Palstra, A.S. Perel, S.R. Scott, L.F. Schneemeyer, and J.V. Waszczak. J. Am. Chem. Soc. **116**, 1205 (1994).
6. M.P. Andrews, A.W. Cordes, D.C. Douglass, R.M. Fleming, S.H. Glarum, R.C. Haddon, P. Marsh, R.T. Oakley, T.T.M. Palstra, L.F. Schneemeyer, G.W. Trucks, R. Tycko, J.V. Waszczak, K.M. Young, and N.M. Zimmerman. J. Am. Chem. Soc. **113**, 3559 (1991).
7. A.W. Cordes, R.C. Haddon, R.T. Oakley, L.F. Schneemeyer, J.V. Waszczak, K.M. Young, and N.M. Zimmerman. J. Am. Chem. Soc. **113**, 582 (1991).
8. C.D. Bryan, A.W. Cordes, J.D. Goddard, R.C Haddon, R.G. Hicks, C.D. MacKinnon, R.C. Mawhinney, R.T. Oakley, T.T.M. Palstra, and A.S. Perel. J. Am. Chem. Soc. **118**, 330 (1996).
9. A.W. Cordes, R.C. Haddon, R.G. Hicks, D.K. Kennepohl, R.T. Oakley, T.T.M. Palstra, L.F. Schneemeyer, S.R. Scott, and J.V. Waszczak. Chem. Mater. **5**, 820 (1993).
10. W.M. Davis, R.G. Hicks, R.T. Oakley, B. Zhao, and N.J. Taylor. Can. J. Chem. **71**, 180 (1993).
11. A.W. Cordes, R.C. Haddon, R.G. Hicks, R.T. Oakley, and T.T.M. Palstra. Inorg. Chem. **31**, 1802 (1992).
12. A.W. Cordes, R.C. Haddon, R.G. Hicks, D.K. Kennepohl, R.T. Oakley, L.F. Schneemeyer, and J.V. Waszczak. Inorg. Chem. **32**, 1554 (1993).
13. A.J. Banister, N. Bricklebank, W. Clegg, M.R.J. Elsegood, C.I. Gregory, I. Lavender, J.M. Rawson, and B.K. Tanner. J. Chem. Soc. Chem. Commun. 679 (1995).
14. A.J. Banister, N. Bricklebank, I. Lavender, J.M. Rawson, C.I. Gregory, B.K. Tanner, W. Clegg, M.R.J. Elsegood, and F. Palacio. Angew. Chem. Int. Ed. Engl. **35**, 2533 (1996).
15. R.T. Boeré and K.H. Moock. J. Am. Chem. Soc. **117**, 4775 (1995).
16. M.A. McCall, J.R. Caldwell, H.G. Moore, and H.M. Beard. J. Macromol. Sci. Chem. **A3**, 911 (1969).
17. R.T. Boeré, R.G. Hicks, and R.T. Oakley. Inorg. Synth. **21**, 94 (1997).
18. K.H. Moock and M.H. Rock. J. Chem. Soc. Dalton Trans. 2459 (1993).
19. R.T. Boeré, K.H. Moock, and M.Z. Parvez. Z. Anorg. Allg. Chem. **520**, 1589 (1994).
20. C.M. Aherne, A.J. Banister, I.B. Gorrell, M.I. Hansford, Z.V. Hauptman, A.W. Luke, and J.M. Rawson. J. Chem. Soc. Dalton Trans. 967 (1993).
21. P. Del Bel Belluz, A.W. Cordes, E.M. Kristof, P.V. Kristof, S.W. Liblong, and R.T. Oakley. J. Am. Chem. Soc. **111**, 9276 (1989).
22. J.B. Flanagan, S. Margel, A.J. Bard, and F.C. Anson. J. Am. Chem. Soc. **100**, 4248 (1978).
23. F. Weller, F. Schmock, and K. Dehnicke. Z. Naturforsch. B: Chem. Sci. **44**, 548 (1989).
24. A.W. Cordes, C.D. Bryan, W.M. Davis, R.H. de Laat, S.H. Glarum, J.D. Goddard, R.C. Haddon, R.G. Hicks, D.K. Kennepohl, R.T.Oakley, S.R. Scott, and N.P.C. Westwood. J. Am. Chem. Soc. **115**, 7232 (1993).
25. F.A. Cotton and G. Wilkinson. Advanced inorganic chemistry. 3rd ed. Wiley, New York. 1972. p. 288.
26. P.A. Cox. Electronic structure and chemistry of solids. Oxford University Press, Oxford. 1987. p. 134.
27. D.T. Cromer and J.T. Waber. International tables for X-ray crystallography. Vol. IV. The Kynoch Press, Birmingham, England. 1974. Table 2.2 A.
28. D.C. Creagh and W.J. McAuley. International tables for crystallography. Vol C. *Edited by* A.J.C. Wilson. Kluwer Academic Publishers, Boston. 1992. Table 4.2.6.8, pp. 219–222.
29. H.-F. Fan. Structure analysis programs with intelligent control. Rigaku Corporation, Tokyo. 1991.
30. P.T. Beurskens, G. Admiraal, G. Beurskens, W.P. Bosman, R. de Gelder, R. Israel, and J.M.M. Smits. The DIRDIF-94 program system. Technical Report of the Crystallography Laboratory, University of Nijmegen, The Netherlands. 1992.
31. TEXSAN. Single-crystal structure analysis software. Molecular Structure Corporation, The Woodlands, Texas. 1994.
32. E.J. Gabe, Y. LePage, J.P. Charland, F.L. Lee, and P.S. White. J. Appl. Crystallogr. **22**, 348 (1989).

[6] This material may be purchased from: The Depository of Unpublished Data, Document Delivery, CISTI, National Research Council Canada, Ottawa, Canada K1A 0S2. The crystal structure reports, including tables of bond lengths, bond angles, and atomic coordinates, have also been deposited with the Cambridge Crystallographic Data Centre, and can be obtained on request from The Director, Cambridge Crystallographic Data Centre, University Chemical Laboratory, 12 Union Road, Cambridge, CB2 1EZ, U.K.

© 1998 NRC Canada

Total synthesis of (±)-9-deoxygoniopypyrone. Application of the iodocyclofunctionalization reaction of α-allenic alcohol derivatives

Richard W. Friesen and Suzanne Bissada

Can. J. Chem. Downloaded from www.nrcresearchpress.com by Peking University on 09/05/12
For personal use only.

Abstract: The synthesis of (±)-9-deoxygoniopypyrone (**1**) from the α-allenic alcohol **5** is described. Iodocyclofunctionaliztion of the *N*-tosyl carbamate derivative of **5** using I_2 and Ag_2CO_3 provided, in a highly diastereoselective and regioselective fashion, the vinyl iodo *syn*-vicinal diol **4**. Two routes were explored in order to introduce the third stereogenic centre in the molecule. Reductive deiodination of the vinyl iodide and diastereoselective epoxidation of the derived acetonide **14** using mCPBA provided a mixture of epoxides **15** and **16** (2:1) in which the desired *threo* diastereomer predominated. Alternatively, dihydroxylation of acetonide **14** (OsO_4, NMO) yielded a mixture of diols **21** and **22** (2:3) which were separated after monosilylation (TBDMSCl) of the primary alcohol. The major silyl ether *erythro* diastereomer **24** was converted to the desired epoxide **15** by mesylation (MsCl, Et_3N) and epoxide formation (TBAF) with inversion of stereochemistry. The minor *threo* diastereomer **23** was also converted to the desired epoxide **15** (TBAF; $ArSO_2Cl$; NaOMe). Epoxide opening was effected with lithium acetylide and the resulting alkyne **27** was carbonylated (MeLi, $ClCO_2Me$) to afford the α,β-acetylenic ester **28**. Semi hydrogenation over Lindlar's catalyst followed by protecting- group removal under acidic conditions provided (±)-8-epigoniodiol **30**. Finally, conversion of **30** to (±)-9-deoxygoniopypyrone **1** was effected under basic conditions (DBU).

Key words: (±)-9-deoxygoniopypyrone, α-allenic alcohol, iodocyclofunctionalization, *syn*-diol.

Résumé : On décrit la synthèse de la (±)-9-désoxygoniopyrone (**1**) à partir de l'alcool α-allénique **5**. L'iodocyclofonctionnalisation du dérivé *N*-tosylcarbamate du produit **5** à l'aide de I_2 et de Ag_2CO_3 a conduit au vinyl iodo diol *syn*-vicinal **4** avec une diastéréosélectivité et une régiosélectivité élevées. Dans le but d'introduire le troisième centre stéréogénique de la molécule, on a exploré deux voies. D'une part, la déiodation réductrice de l'iodure de vinyle et l'époxydation diastéréosélective du dérivé acétonide **14** à l'aide de l'acide *m*-chloroperbenzoïque (AmCPB) conduisent à un mélange d'époxydes **15** et **16** (2 : 1) dans lequel le diastéréomère *thréo* recherché prédomine. D'autre part, la dihydroxylation de l'acétonide **14** (OsO_4, NMO) fournit un mélange des diols **21** et **22** (2 : 3) qui ont pu être séparés après monosilylation («TBDMSCl») de l'alcool primaire. On a transformé l'éther silylé du diastéréomère *érythro* (**24**) prépondérant en époxyde **15** recherché en procédant à une mésylation («MsCl», Et_3N) suivie de la formation d'un époxyde («TBAF») avec inversion de stéréochimie. Le diastéréomère *thréo* (**23**) minoritaire a aussi été transformé en époxyde **15** recherché («TBAF»; $ArSO_2Cl$; NaOMe). On a effectué l'ouverture de l'époxyde à l'aide d'acétylure de lithium et on a effectué une décarbonylation de l'alcyne **27** qui en résulte (MeLi, $ClCO_2Me$) pour conduire à l'ester α,β-acétylénique **28** qui, par semihydrogénation sur du catalyseur de Lindlar suivie de l'élimination des groupes protecteurs dans des conditions acides, fournit le (±)-8-épigoniodiol **30**. Enfin, on a effectué la conversion du composé **30** en (±)-9-désoxygoniopyrone (**1**) dans des conditions basiques («DBU»).

Mots clés : (±)-9-désoxygoniopyrone, alcool α-allénique, iodocyclofonctionnalisation, *syn*-diol.

[Traduit par la rédaction]

Introduction

The cytotoxic (ED_{50} 7.4 μg/mL against HT-29 cells) bicyclic styryl lactone (+)-9-deoxygoniopypyrone (**1**) was isolated in 1990 from the stem bark of *Goniothalamus giganteus* Hook. f. & Thomas (Annonaceae) (1). (+)-9-Deoxygoniopypyrone (**1**) possesses several interesting structural features, including the novel 2,6-dioxabicyclo[3.3.1]nonan-3-one molecular scaffold, that make it attractive as a synthetic target. Within this framework, the key substructure in terms of synthesis is the triol

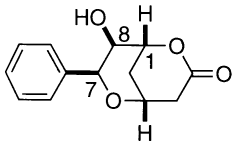

1

moiety in which the three contiguous oxygen-bearing stereocentres (C7/C8/C1) are in a *syn*,*syn* relationship (see **2**).

We have been interested in the synthesis of natural products using our recently described method for the highly diastereoselective conversion of the *N*-tosyl carbamate derivatives of secondary α-allenic alcohols such as **5** into vinyl iodo *syn*-vicinal diols **4** (2–6). We felt that the implementation of

Received August 18, 1997.

R.W. Friesen[1] and S. Bissada. Department of Medicinal Chemistry, Merck Frosst Centre for Therapeutic Research, P.O. Box 1005, Pointe Claire – Dorval, QC H9R 4P8, Canada.

[1]Author to whom correspondence may be addressed. Telephone: (514) 428–3164. Fax: (514) 695–0693. E-mail: rick_friesen@merck.com

© 1998 NRC Canada

Can. J. Chem. Downloaded from www.nrcresearchpress.com by Peking University on 09/05/12
For personal use only.

Scheme 1.

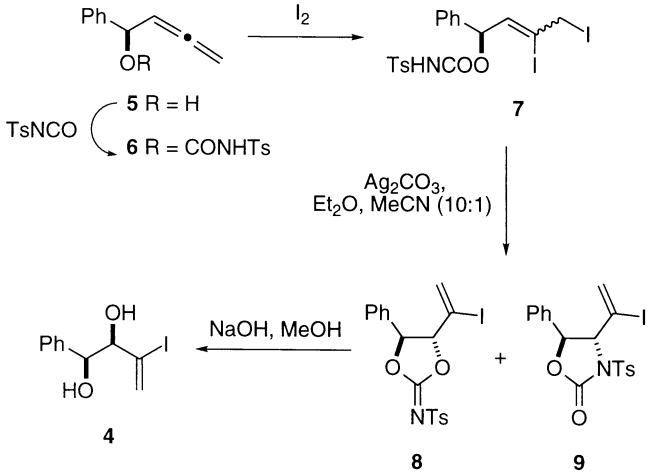

this iodocyclofunctionalization strategy would allow us to address the structurally interesting features in **1**. According to our retrosynthetic plan, the relative stereochemistry between the C7/C8 hydroxy moieties in **1** (natural product numbering used throughout) would be readily established using this method. Following reductive deiodination of the vinyl iodide moiety in **4**, diastereoselective oxidation (epoxidation or dihydroxylation) of the resulting olefin would introduce the third stereocentre and provide the epoxide **3**. Homologation of **3** would afford the α,β-unsaturated ester **2**, the immediate precursor to **1**. Herein, we describe the full details of the synthesis of (±)-**1** (Schemes 1–3) according to this strategy.[2]

Two syntheses of (+)-**1** have been reported in the literature. The first synthesis by Honda and co-workers (7), which utilized 2,3-*O*-isopropylidene-D-glyceraldehyde as the chiral

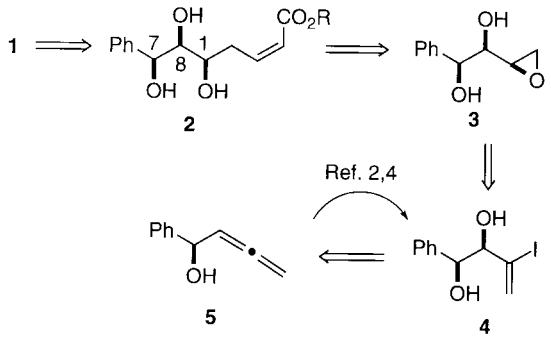

starting material, demonstrated that the absolute configuration of the natural product (+)-**1** is as depicted. Subsequent to our published synthesis of (±)-**1**,[2] Yang and Zhou described the synthesis of (+)-**1** from methyl cinnamate using Sharpless asymmetric dihydroxylation technology (8). In contrast to our synthesis, both of these groups introduced one of the three contiguous hydroxy-bearing stereocentres by the nucleophilic addition of a metalated aromatic to an α-alkoxy aldehyde.

Results and discussion

The vinyl iodo *syn*-diol **4** was prepared from the racemic α-allenic alcohol **5**,[3] using our previously reported

[2] For a preliminary account of this work, see ref. 3.

[3] Although **5** is racemic, only a single enantiomer has been drawn throughout.

Scheme 2.

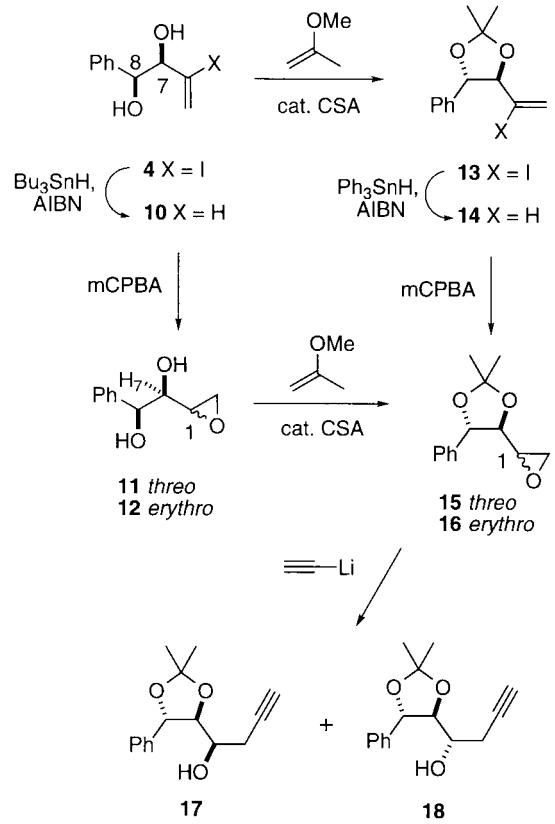

iodocyclofunctionalization procedure (2, 4) (Scheme 1). Thus, alcohol **5** was treated sequentially with TsNCO and I_2 to provide an *E/Z* mixture of diiodides **7** (5) that was cyclized by treatment with Ag_2CO_3 in ether–MeCN (10:1). Filtration of the silver salts and concentration of the reaction mixture provided the crude cyclization products. In accord with our earlier observations (2, 4), inspection of the ^{1}H NMR spectrum of the crude reaction mixture revealed that the imino carbonate **8** was obtained in a highly diastereoselective fashion (diastereoselectivity >50:1) together with minor amounts (<5%) of the related carbamate **9** (9). From a practical point of view, it is important to point out that it is essential to wash the solid silver salt cake extensively with ethyl acetate and methanol in order to achieve optimum recovery of the initial cyclization products. Hydrolysis of the crude mixture with methanolic sodium hydroxide yielded the desired vinyl iodo *syn*-diol **4** in 66% overall yield after chromatography. Reductive deiodination of **4** using *n*-Bu_3SnH–AIBN provided the unsaturated diol **10** in 81% yield (Scheme 2).

The strategy for the synthesis of **1** from *syn*-diol **10** required that the installation of the C1 oxygen occur with *threo* diastereoselectivity relative to the hydroxy moieties at C7 and C8. In keeping with the plan that chain extension to an intermediate such as **2** would be required, epoxidation of **10** appeared to be an obvious strategy. The directed diastereoselective epoxidation reactions of allylic and homoallylic alcohols or diols are well documented (10–15). Typically, transition metal (Ti, V) mediated epoxidations of such olefins, including monosubstituted alkenes, afford the *erythro* diastereomers with good to excellent stereoselectivity. Conversely, epoxidations of both

© 1998 NRC Canada

Can. J. Chem. Downloaded from www.nrcresearchpress.com by Peking University on 09/05/12
For personal use only.

allylic and homoallylic alcohols with mCPBA are marginally diastereoselective in favour of the *threo* epoxides. For example, upon treatment of 3-buten-2-ol or 4-penten-2-ol with mCPBA, the corresponding *threo* epoxide isomers are obtained in ratios of 3:2 and 1.2:1, respectively (10–12). Not surprisingly, exposure of ene diol **10** to mCPBA at room temperature provided a mixture of epoxides **11**/**12** in a ratio of 2:1 (51%) (Scheme 2).

The stereochemical assignments of the epoxy diol diastereomers **11**/**12** are based on comparison of their ^{1}H NMR spectral data with those of structurally similar epoxy alcohols (13–15). The characteristic proton resonance in these spectra is that of H7. Typically, the resonance frequency of this proton is observed at higher field in the *threo* isomer than in the *erythro* isomer. In the case of epoxy diols **11**/**12**, the chemical shift of H7 in the major isomer (δ 3.68) is 0.25 ppm upfield relative to the corresponding resonance in the minor isomer (δ 3.93). This observation is consistent with the reported literature data (13–15) and suggests that the major isomer is in fact the *threo* epoxy diol **11**.

A variety of methods, including metal-catalyzed directed epoxidation (Ti, V) (10–12), were attempted in an effort to increase the *threo* diastereoselectivity in the epoxidation of **10** but without any improvement in selectivity. In addition, several monoprotected alcohol derivatives of **10** (MOM, TBDMS) (6) were also oxidized using mCPBA or the VO(acac)$_2$–*t*-BuOOH epoxidation system (10–12). All of these reactions were unsatisfying since they resulted in low diastereoselectivity and were also plagued by low conversion or competing side reactions such as benzylic oxidation. As far as we are aware, the general *threo* diastereoselective epoxidation of this class of monosubstituted olefinic alcohols (or diols) remains an unsolved problem in organic synthesis.[4]

We then turned our attention to the epoxidation of a protected diol, the acetonide **14** (Scheme 2). Thus, treatment of **14** with mCPBA at room temperature for 3 days provided the epoxides **15** and **16** as an inseparable 2:1 mixture in a combined isolated yield of 96%. Although in this reaction the diastereoselectivity was no better than that observed in the epoxidation of diol **10**, the yield was substantially better. Furthermore, it was anticipated that the stereocentre at C1 in isomer **16** could be inverted at a later stage in the synthesis and thus the epoxide mixture **15**/**16** was carried forward. The assignment of the relative stereochemistry in the major epoxide diastereomer **15** was only tentative and was made primarily by correlation with the products derived from the epoxidation of **10** described earlier. The epoxide mixture **11**/**12** derived from **10** was converted into the corresponding mixture of acetonides **15**/**16** (2:1) and the major isomer from this mixture was identical with the major epoxide **15** obtained upon epoxidation of **14**. The eventual conversion of **15** to **1** (vide infra) confirmed this stereochemical assignment.

The epoxide mixture **15**/**16** was treated with the dianion of propiolic acid according to the conditions of Carlson and Oyler (17). This reaction was extremely capricious and we were never able to find conditions that would bring about the epoxide opening of **15**/**16** in a reproducible fashion on a quantity of material. However, treatment of the epoxide mixture **15**/**16** with lithium acetylide – EDA complex in THF–HMPA at

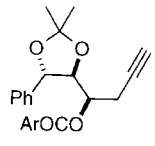

19

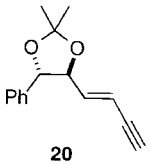

20

room temperature afforded the readily separable acetylenic alcohols **17** and **18** in isolated yields of 55% and 26%, respectively. Omission of the HMPA from this reaction mixture resulted in only low (<10%) conversion. The inversion of the C1 alcohol stereocentre in **18** was attempted using Mitsunobu chemistry. The conditions described by Martin and Dodge (18) using *p*-nitrobenzoic acid and DEAD in PhMe provided predominantly the *E*-enyne **20** (76%) along with only 7% of the desired benzoate **19,** which was subsequently hydrolyzed to the alcohol **17**. Other related methods that were attempted for the inversion of the C1 stereocentre in **18**, including a two-step oxidation–reduction sequence, were also unsatisfactory.

Due to our inability to invert the C1 (natural product numbering) stereocentre in the acetylenic alcohol **18**, we then considered the possibility of carrying out a dihydroxylation of olefin **14** in order to introduce the desired oxygenation pattern. It was anticipated, based on Kishi's rules (19) and additional literature precedent (20), that the bishydroxylation of monosubstituted olefin **14** would not be highly diastereoselective and that the major diastereomer would possess the undesired *erythro* relative stereochemistry at C1. However, it was expected that *both* diol diastereomers resulting from dihydroxylation could be efficiently converted into the desired epoxide **15**. Although this route would be more lengthy than direct epoxidation of the olefin, it would ultimately provide a single epoxide with the correct relative stereochemistry at C1.

In the event, olefin **14** was treated with catalytic OsO_4 and NMO to provide a 2:3 (by inspection of the integrated ^{1}H NMR spectrum) mixture of diols **21** and **22**, respectively (Scheme 3). The major diastereomer **22** was assigned the *erythro* configuration based upon literature precedent (19, 20). The crude diol mixture was silylated using TBDMSCl at 0°C and the readily separable monosilylated diols **23** and **24** were obtained in overall isolated yields of 37 and 57%, respectively, from olefin **14**. A two-step reaction sequence, involving formation of the mesylate **26** (MsCl, Et_3N, 0°C) followed by intramolecular displacement using TBAF at room temperature, effected the transformation of the major diastereomer **24** into the desired epoxide **15** in 86% overall yield. Desilylation (TBAF) of silyl ether **23** followed by conversion of the primary alcohol to the aryl sulfonate **25** using 2-mesitylenesulfonyl chloride (0°C to room temperature) was accomplished in 92% yield. Treatment of **25** with K_2CO_3 in MeOH provided epoxide **15** in 97% yield. Therefore, the overall conversion from **14** to **15** via the dihydroxylation strategy illustrated in Scheme 3 is an acceptable 82%.

With pure epoxide **15** now in hand, alkylation with lithium

[4] Roush and Michaelides have reported that a MOM monoprotected *syn*-diol related to **10** is epoxidized with exceptionally high *threo* diastereoselectivity usingVO(acac)$_2$–*t*-BuOOH (16). However, in this literature example, the unprotected non-benzylic homoallylic alcohol is flanked by a group that is much more sterically bulky than the phenyl group of **10**.

© 1998 NRC Canada

Can. J. Chem. Downloaded from www.nrcresearchpress.com by Peking University on 09/05/12
For personal use only.

Scheme 3.

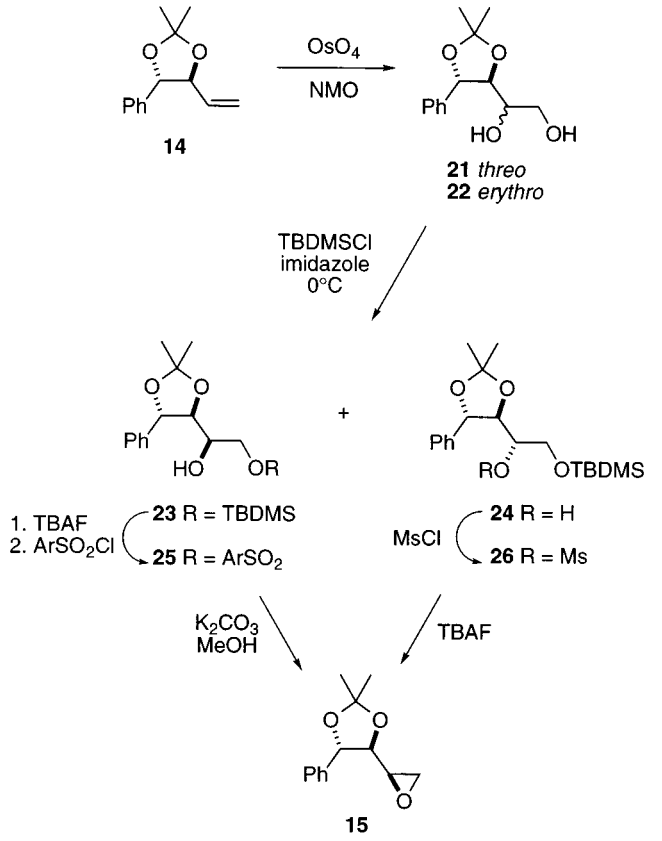

Scheme 4.

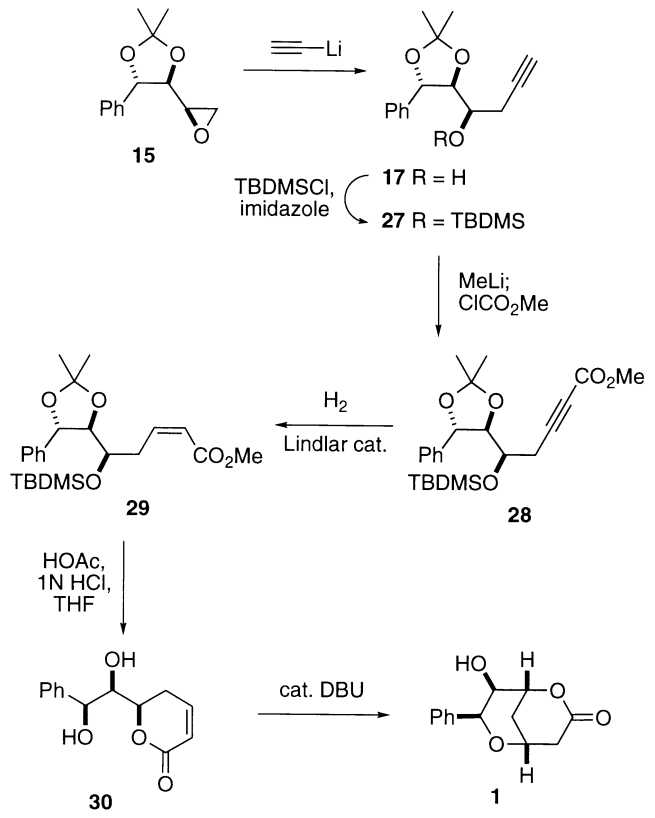

acetylide – EDA complex in THF–HMPA at room temperature as described previously led to the acetylenic alcohol **17** (88%) (Scheme 4). Protection of the alcohol **17** (TBDMSOTf, Et_3N; 96%) followed by methoxycarbonylation (MeLi; $ClCO_2Me$; 91%) provided the α,β-acetylenic ester **28**. The three-step sequence from **15** to **28** (alkylation, silylation, methoxycarbonylation), while somewhat more lengthy than the originally anticipated reaction with propiolic acid dianion (vide supra), proceeds in excellent overall yield.

The conversion of the α,β-acetylenic ester **28** to the dihydropyran-2-one **30**, the immediate precursor to **1**, followed the strategy described by Carlson et al. for the synthesis of simple dihydropyran-2-ones (17). Thus, semi hydrogenation of the alkyne **28** over Lindlar's catalyst (5% Pd on Ca_2CO_3) cleanly provided the *Z* olefin **29**. The ^1H NMR spectrum of the crude material indicated the clean conversion of **28** to **29** without competing over-reduction or olefin *E*/*Z* isomerization. The crude reaction mixture was treated with a mixture of HOAc, 1 N HCl, and THF (1:1:1 v/v/v) at 65°C, resulting in the complete deprotection of the triol and subsequent cyclization to the lactone **30** (8-epigoniodiol) (7). Again, analysis of the crude reaction mixture (^1H NMR) revealed that a small amount of **30** had undergone cyclization to **1** under these reaction conditions. Thus, once again, the crude reaction mixture was used and the cyclization was completed using conditions that had been described by Honda and co-workers (1% DBU in THF) (7). Synthetic (±)-9-deoxygoniopypyrone (**1**) (mp 185–186°C, EtOH) was isolated in 60% yield for the three steps from **28** and exhibited spectral data (^1H and ^{13}C NMR, IR) identical to the data reported (1) for the natural product.

Experimental

General information

^1H NMR spectra were recorded at 300, 400, or 500 MHz in acetone-d_6 or $CDCl_3$ as specified. Broad-band proton-decoupled ^{13}C NMR spectra were recorded at 100 or 125 MHz in $CDCl_3$. IR spectra were recorded on neat samples unless stated otherwise. Solvents were anhydrous and were transferred via syringes under an atmosphere of argon or nitrogen. Work-up procedures involving the drying of organics were carried out with $MgSO_4$. Flash column chromatography (referred to as chromatography) was performed with 230–400 mesh silica gel, eluting with the solvents indicated (v/v). Elemental analyses were performed by Oneida Research Services, Inc., Whitesboro, N.Y., or the Laboratoire d'analyse élémentaire, Université de Montréal. Compounds for which high-resolution mass measurements are given were homogeneous by TLC analysis and gave satisfactory spectroscopic data indicative of their purity.

3,4-Dihydroxy-2-iodo-phenyl-1-butene ***4***

To a solution of 1-phenyl-2,3-butadien-1-ol **5** (10.5 g, 71.8 mmol) in ether (350 mL) at room temperature was slowly added *p*-TsNCO (12.0 mL, 1.1 equiv.). The mixture was stirred at room temperature for 30 min and then solid I_2 (18.2 g, 1.0 equiv.) was added in several portions over 1 h. Ag_2CO_3 (29.7 g, 1.5 equiv.) and MeCN (35 mL) were added sequentially and the resulting mixture was stirred at room temperature for 15 h. The reaction mixture was filtered through Celite, and the filter pad was washed extensively with ethyl acetate

© 1998 NRC Canada

Can. J. Chem. Downloaded from www.nrcresearchpress.com by Peking University on 09/05/12
For personal use only.

(approximately 2 L) followed by methanol (approximately 500 mL). The filtrate was concentrated, the crude mixture was dissolved in methanol – 1 N NaOH (3:1 v/v, 320 mL) and stirred at room temperature for 15 h. The methanol was evaporated and the solution was neutralized to ~pH 7 by the addition of 1 N HCl. The mixture was extracted with CH_2Cl_2 (3 × 500 mL) and the combined organics were dried and concentrated. Chromatography (toluene–acetone, 6:1 to 5:1) of the residual material provided the diol **4** (13.7 g, 66%) as a white solid, mp 68.5–69.5°C. IR ($CHCl_3$): 3590, 1630, 1275 cm^{-1}; ^1H NMR (300 MHz, $CDCl_3$) δ: 3.09 (br s, 1H), 3.23 (br s, 1H), 3.72 (br d, 1H, J = 6.0 Hz), 4.77 (d, 1H, J = 6.5 Hz), 5.80 (d, 1H, J = 1.8 Hz), 6.10 (dd, 1H, J = 1.0, 1.8 Hz), 7.26–7.39 (m, 5H); ^{13}C NMR δ: 75.8, 81.5, 111.6, 126.7, 128.2, 128.3, 128.6, 139.5. Anal. calcd. for $C_{10}H_{11}IO_2$: C 41.40, H 3.82; found: C 41.24, H 3.69.

3,4-Dihydroxy-4-phenyl-1-butene ***10***

To a solution of vinyl iodide **4** (8.0 g, 27.6 mmol) in refluxing benzene (333 mL) was added *n*-Bu_3SnH (8.2 mL, 1.1 equiv.) and AIBN (100 mg) and the solution was refluxed for 15 h. The solution was cooled to room temperature and then 10% KF (300 mL) and EtOAc (300 mL) were added. After 45 min, the white precipitate was filtered off and the filtrate was extracted with EtOAc (2×). The combined organics were washed with 10% KF and with brine, dried, and concentrated. Chromatography (hexane followed by hexane–EtOAc, 3:2) of the residue provided the diol **10** (3.66 g, 81%) as a colourless oil. IR: 3300, 1050 cm^{-1}; ^1H NMR (300 MHz, $CDCl_3$) δ: 2.50 (br s, 2H), 4.21 (ddt, 1H, J = 5.5, 6.9, 1.5 Hz), 4.48 (d, 1H, J = 6.9 Hz), 5.13 (dt, 1H, J = 10.6, 1.5 Hz), 5.23 (dt, 1H, J = 17.3, 1.5 Hz), 5.71 (ddd, 1H, J = 5.5, 10.6, 17.3 Hz), 7.25–7.44 (m, 5H); ^{13}C NMR δ: 76.9, 77.6, 117.0, 127.0, 128.1, 128.4, 136.3, 140.2. Anal. calcd. for $C_{10}H_{12}O_2$: C 73.15, H 7.37; found: C 73.27, H 7.66.

Epoxidation of 3,4-dihydroxy-4-phenyl-1-butene ***10*** *(epoxides* ***11*** *and* ***12****)*

To a solution of diol **10** (116 mg, 0.71 mmol) in CH_2Cl_2 (3 mL) at room temperature was added mCPBA (458 mg, 3.0 equiv.) and the mixture was stirred for 16 h. Saturated sodium carbonate was added and the mixture was extracted with EtOAc (2×). The combined organics were washed with 1 N NaOH and brine, dried, and concentrated. Inspection of this crude reaction mixture by ^1H NMR spectroscopy indicated a 2:1 mixture of isomers. Chromatography (hexane–EtOAc, 1:2) of the residue provided a mixture of the epoxy diols **11** and **12** (65 mg, 51%) as a colourless oil. Major isomer **11:** ^1H NMR (500 MHz, $CDCl_3$) δ: 2.55 (dd, 1H, J = 2.8, 4.9 Hz), 2.65 (dd, 1H, J = 4.2, 4.9 Hz), 2.97 (ddd, 1H, J = 2.8, 3.8, 4.2 Hz), 3.68 (dd, 1H, J = 3.8, 7.4 Hz), 4.73 (d, 1H, J = 7.4 Hz), 7.35 (m, 5H). Minor isomer **12:** ^1H NMR (500 MHz, $CDCl_3$) δ: 2.77 (dd, 1H, J = 4.0, 5.0 Hz), 2.86 (dd, 1H, J = 2.8, 5.0 Hz), 2.94 (ddd, 1H, J = 2.8, 3.6, 4.0 Hz), 3.93 (dd, 1H, J = 3.6, 5.9 Hz), 4.70 (d, 1H, J = 5.9 Hz), 7.35 (m, 5H).

Acetonide ***13***

A solution of diol **4** (1.8 g, 6.2 mmol), 2-methoxypropene (0.9 mL, 1.5 equiv.), and camphorsulfonic acid (25 mg) in DMF (10 mL) was stirred at room temperature for 2 h. The mixture was poured into ammonium acetate buffer and extracted with ether (4×). The combined organics were washed with water and brine, dried, and concentrated. Chromatography (hexane–ether, 10:1) of the residue provided the acetonide **13** (1.89 g, 92%) as a colourless oil. IR: 1050 cm^{-1}; ^1H NMR (300 MHz, $CDCl_3$) δ: 1.59 (s, 3H), 1.63 (s, 3H), 3.63 (dd, 1H, J = 0.8, 8.0 Hz), 4.83 (d, 1H, J = 8.0 Hz), 5.99 (d, 1H, J = 1.5 Hz), 6.28 (dd, 1H, J = 0.8, 1.5 Hz), 7.28–7.38 (m, 5H); ^{13}C NMR δ: 27.4, 27.5, 82.8, 88.0, 109.0, 110.3, 126.5, 128.36, 128.42, 130.0, 136.7. Anal. calcd. for $C_{13}H_{15}IO_2$: C 47.29, H 4.58; found: C 46.88, H 4.50.

Olefin ***14***

A mixture of vinyl iodide **13** (1.8 g, 6.2 mmol), triphenyltin hydride (2.6 g, 1.2 equiv.), and AIBN (20 mg) in benzene (40 mL) was heated at reflux for 90 min. The solution was cooled to room temperature and then 10% KF (100 mL) and EtOAc (100 mL) were added. After 15 min, the white precipitate was filtered off and the filtrate was extracted with EtOAc (2×). The combined organics were washed with 10% KF and brine, dried, and concentrated. Chromatography (hexane–ether, 15:1) of the residue provided the olefin **14** (1.09 g, 87%) as a colourless oil. IR: 2980, 1365, 1230, 1050 cm^{-1}; ^1H NMR: (300 MHz, $CDCl_3$) δ: 1.53 (s, 3H), 1.57 (s, 3H), 4.17 (app t, 1H, J = 8.4 Hz), 4.64 (d, 1H, J = 8.4 Hz), 5.20–5.27 (m, 2H), 5.87 (m, 1H), 7.26–7.58 (m, 5H); ^{13}C NMR δ: 27.0, 27.1, 82.9, 84.7, 109.3, 119.3, 126.4, 128.2, 128.4, 133.9, 137.2. Exact Mass calcd. for $C_{13}H_{17}O_2$ $(M+H)^+$: 205.1229; found: 205.1228.

Epoxidation of olefin ***14*** *(epoxides* ***15*** *and* ***16****)*

To a solution of olefin **14** (950 mg, 4.65 mmol) in dichloromethane (50 mL) at 0°C was added mCPBA (3.0 g, 3 equiv.). After 30 min, the cold bath was removed and the mixture was stirred at room temperature for 72 h. Saturated $NaHCO_3$ (100 mL) was added and the mixture was extracted with dichloromethane (2×). The combined organics were washed with saturated $NaHCO_3$ (2×), water, and brine, then dried and concentrated. Chromatography (hexane–EtOAc, 9:1) of the residue provided an inseparable mixture of the epoxides **15** and **16** (983 mg, 96%) as a colourless oil. Inspection of this mixture by ^1H NMR spectroscopy indicated a 2:1 mixture of isomers. Major isomer **15:** ^1H NMR (300 MHz, $CDCl_3$) δ: 1.50 (s, 3H), 1.55 (s, 3H), 2.48 (dd, 1H, J = 2.6, 5.3 Hz), 2.75 (dd, 1H, J = 4.2, 5.3 Hz), 3.06 (ddd, 1H, J = 2.6, 4.2, 5.0 Hz), 3.62 (dd, 1H, J = 5.0, 8.7 Hz), 4.91 (d, 1H, J = 8.7 Hz), 7.35 (m, 5H). Minor isomer **16:** ^1H NMR (300 MHz, $CDCl_3$) δ: 1.52 (s, 3H), 1.54 (s, 3H), 2.67 (dd, 1H, J = 2.6, 5.0 Hz), 2.81 (dd, 1H, J = 4.0, 5.0 Hz), 3.14 (ddd, 1H, J = 2.6, 4.0, 5.1 Hz), 3.73 (dd, 1H, J = 5.1, 8.1 Hz), 4.94 (d, 1H, J = 8.1 Hz), 7.35 (m, 5H).

Alkynes ***17*** *and* ***18***

Lithium acetylide – EDA complex (540 mg, 1.3 equiv.) was added portionwise over 2 min to a solution of the epoxide mixture **15**/**16** (887 mg, 4.03 mmol) in THF (10 mL) and HMPA (4 mL). The resulting mixture was stirred at room temperature for 15 h and then water was carefully added. The mixture was extracted with EtOAc (3×), and the combined organics were washed with 10% HCl (3×), water, and brine, then dried and concentrated. Chromatography (toluene–EtOAc, 10:1) of the residue provided the alkynes **17** and **18**. The first compound to

© 1998 NRC Canada

Can. J. Chem. Downloaded from www.nrcresearchpress.com by Peking University on 09/05/12
For personal use only.

be eluted was the minor isomer **18** (260 mg, 26%), a colourless oil**.** IR: 3450, 3300, 2115, 1240, 1055 cm^{-1}; ^1H NMR (300 MHz, $CDCl_3$) δ: 1.47 (s, 3H), 1.53 (s, 3H), 1.97 (t, 1H, J = 2.7 Hz), 2.15 (br s, 1H), 2.41–2.44 (m, 2H), 3.92–3.99 (m, 2H), 4.98 (AB q, 1H, J = 3.8, 11.2 Hz), 7.26–7.37 (m, 3H), 7.41–7.45 (m, 2H); ^{13}C NMR δ: 23.7, 27.0, 27.2, 70.4, 71.1, 79.9, 80.3, 84.0, 109.5, 127.4, 128.3, 128.5, 138.4. Anal. calcd. for $C_{15}H_{18}O_3$: C 73.15, H 7.37; found: C 73.27, H 7.46. Further elution provided the major isomer **17** (535 mg, 55%) as a white solid, mp 101.5–102.5°C. IR (KBr): 3460, 3300, 2120, 1240, 1060 cm^{-1}; ^1H NMR (300 MHz, $CDCl_3$) δ: 1.51 (s, 3H), 1.56 (s, 3H), 1.95 (t, 1H, J = 2.7 Hz), 2.36 (ddd, 1H, J = 2.7, 6.5, 16.7 Hz), 2.37 (br s, 1H), 2.47 (ddd, 1H, J = 2.7, 7.3, 16.7 Hz), 3.74 (br m, 1H), 3.91 (dd, 1H, J = 2.0, 8.6 Hz), 4.91 (d, 1H, J = 8.6 Hz), 7.30–7.41 (m, 5H); ^{13}C NMR δ: 25.3, 26.9, 27.2, 67.3, 70.5, 79.1, 80.2, 83.8, 109.5, 126.8, 128.4, 128.7, 137.3. Anal. calcd. for $C_{15}H_{18}O_3$: C 73.15, H 7.37; found: C 73.19, H 7.38.

*Enyne **20** and benzoate **19***

To a solution of alcohol **18** (144 mg, 0.58 mmol) in toluene (12 mL) at room temperature was added sequentially Ph_3P (307 mg, 2 equiv.), DEAD (0.18 mL, 2 equiv.), and *p*-nitrobenzoic acid (195 mg, 2 equiv.). The resulting mixture was stirred for 2 h and then hexane (30 mL) was added. The white preciptate was filtered through Celite and to the filtrate was added EtOAc. The combined organics were washed with saturated $NaHCO_3$ (3×), dried, and concentrated. Chromatography (hexane–EtOAc, 9:1 to 4:1) of the residue first provided the enyne **20** (101 mg, 76%) as a white solid, mp 52–53°C. IR ($CHCl_3$): 3300, 1490, 1450, 1380, 1050, 690 cm^{-1}; ^1H NMR (300 MHz, $CDCl_3$) δ: 1.52 (s, 3H), 1.57 (s, 3H), 2.90 (d, 1H, J = 2.3 Hz), 4.20 (ddd, 1H, J = 1.3, 6.4, 8.4 Hz), 4.65 (d, 1H, J = 8.4 Hz), 5.68 (ddd, 1H, J = 1.3, 2.3, 15.9 Hz), 6.21 (ddd, 1H, J = 0.5, 6.4, 15.9 Hz), 7.27–7.37 (m, 5H); ^{13}C NMR δ: 26.9, 27.0, 78.7, 81.2, 82.8, 83.3, 109.7, 112.1, 126.4, 128.4, 128.6, 136.7, 140.0. Anal. calcd. for $C_{15}H_{16}O_2$: C 78.92, H 7.06; found: C 79.30, H 7.15. Further elution provided the benzoate **19** (17 mg, 7%), which was obtained as a white solid. Benzoate **19** was dissolved in MeOH (2 mL) and water (0.1 mL) and treated with K_2CO_3 (2 mg). After 24 h, the mixture was concentrated and subjected to chromatography (9:1 toluene–EtOAc). The alkynol **17** was obtained as a white solid (4 mg, 95%).

*Silyl ethers **23** and **24***

To a solution of alkene **14** (1.0 g, 4.9 mmol) and $NMO{\cdot}H_2O$ (1.4 g, 2.1 equiv.) in acetone (20 mL) and water (2 mL) at room temperature was added a solution of OsO_4 (1 mL of a 4% solution in water) and the mixture was stirred for 15 h. A saturated solution of Na_2SO_3 (30 mL) was added and the resulting mixture was stirred for 1 h. The mixture was extracted with EtOAc (2×) and the organics were washed successively with saturated Na_2SO_3, water, and brine and then dried and concentrated. The residual oil so obtained (analysis by ^1H NMR spectroscopy indicated it to be a 3:2 mixture of diastereomers) and imidazole (790 mg, 2.4 equiv.) were dissolved in CH_2Cl_2 (18 mL) and cooled to 0°C. TBDMSCl (875 mg, 1.2 equiv.) was added as a solid and the resulting mixture was stirred at 0°C for 2 h. Water (50 mL) was added and extracted with EtOAc (2×). The organics were washed with brine and concentrated. The residual oil was subjected to chromatography (hexane–EtOAc, 10:1). The major diastereomer, silyl ether **24** (985 mg, 57%), was eluted first and was obtained as a colourless oil. IR: 3480, 840 cm^{-1}; ^1H NMR (500 MHz, $CDCl_3$) δ: 0.02 (s, 3H), 0.03 (s, 3H), 0.86 (s, 9H), 1.48 (s, 3H), 1.53 (s, 3H), 2.48 (d, 1H, J = 4.8 Hz), 3.61 (dd, 1H, J = 6.5, 10.1 Hz), 3.71 (dd, 1H, J = 3.9, 10.1 Hz), 3.83 (m, 1H), 3.92 (dd, 1H, J = 6.8, 7.7 Hz), 5.03 (d, 1H, J = 7.7 Hz), 7.26–7.47 (m, 5H); ^{13}C NMR (125 MHz) δ: –5.6, –5.5, 18.2, 25.7, 27.0, 27.1, 64.0, 72.9, 81.1, 82.3, 109.3, 127.2, 128.0, 128.3, 138.9. Anal. calcd. for $C_{19}H_{32}O_4Si$: C 64.73, H 9.15; found: C 64.89, H 9.42. Further elution provided the minor diastereomer, silyl ether **23** (648 mg, 37%), as a colourless oil. IR: 3480, 830 cm^{-1}; ^1H NMR (500 MHz, $CDCl_3$) δ: –0.04 (s, 3H), –0.01 (s, 3H), 0.81 (s, 9H), 1.51 (s, 3H), 1.55 (s, 3H), 2.45 (d, 1H, J = 7.3 Hz), 3.54 (m, 1H), 3.59–3.64 (m, 2H), 3.87 (dd, 1H, J = 1.8, 8.7 Hz), 4.99 (d, 1H, J = 8.7 Hz), 7.27–7.41 (m, 5H); ^{13}C NMR (125 MHz) δ: –5.6, –5.5, 18.1, 25.7, 26.9, 27.2, 64.7, 68.7, 79.0, 82.2, 109.3, 126.8, 128.3, 128.5, 137.5. Anal. calcd. for $C_{19}H_{32}O_4Si$: C 64.73, H 9.15; found: C 64.48, H 9.06.

*Epoxide **15** from the major silyl ether diastereomer **24***

To a solution of alcohol **24** (885 mg, 2.51 mmol) and Et_3N (1.05 mL, 3 equiv.) in CH_2Cl_2 (10 mL) at 0°C was added methanesulfonyl chloride (0.29 mL, 1.5 equiv.). After 15 min, water was added and the resulting mixture was stirred at room temperature for 15 min. The mixture was extracted with EtOAc (2×) and the organics were washed with water, dried, and concentrated. The colourless residue was dissolved in THF (10 mL) and TBAF (5.0 mL, 2 equiv.) was added. The reaction mixture was stirred at room temperature for 15 h and then water was added. The mixture was extracted with EtOAc (2×) and the organics were washed with water and brine, dried, and concentrated. Chromatography (hexane–EtOAc, 6:1) of the residual oil provided epoxide **15** (477 mg, 86%) as a colourless oil. IR: 1235 cm^{-1}. ^1H NMR (300 MHz, $CDCl_3$) δ: 1.50 (s, 3H), 1.55 (s, 3H), 2.48 (dd, 1H, J = 2.6, 5.3 Hz), 2.75 (dd, 1H, J = 4.2, 5.3 Hz), 3.06 (ddd, 1H, J = 2.6, 4.2, 5.0 Hz), 3.62 (dd, 1H, J = 5.0, 8.7 Hz), 4.91 (d, 1H, J = 8.7 Hz), 7.35 (m, 5H); ^{13}C NMR (125 MHz) δ: 26.6, 26.9, 43.7, 50.2, 80.0, 83.2, 109.8, 126.3, 128.3, 128.6, 137.4. Anal. calcd. for $C_{13}H_{16}O_3$: C 70.89, H 7.32; found: C 70.54, H 7.34.

*Aryl sulfonate **25***

To a solution of silyl ether **23** (741 mg, 2.10 mmol) in THF (10 mL) was added TBAF (2.3 mL, 1.1 equiv.) and, after 1 h, water was added. The mixture was extracted with EtOAc (3×) and the organics were washed with water and brine, dried, and concentrated. The residual white solid was dissolved in pyridine (10 mL) and cooled to 0°C. 2-Mesitylenesulfonyl chloride (520 mg, 1.1 equiv.) was added as a solid and the resulting mixture was stirred at 0°C for 1 h and then gradually warmed to room temperature over 6 h. After stirring at room temperature for 16 h, 1 N HCl was added and the resulting mixture was extracted with EtOAc (2×). The organics were washed with 1 N HCl and brine, dried, and concentrated. Chromatography (hexane–EtOAc, 3:1) of the residual oil provided the aryl sulfonate **25** (813 mg, 92%) as a colourless glass. IR: 3500, 1380 cm^{-1}; ^1H NMR (500 MHz, $CDCl_3$) δ: 1.47 (s, 3H), 1.51 (s, 3H), 2.28 (s, 3H), 2.43 (d, 1H, J = 8.9 Hz), 2.54 (s, 6H), 3.72 (dd, 1H, J = 1.5, 8.6 Hz), 3.77 (m, 1H), 3.94 (dd, 1H, J = 5.3, 10.4 Hz), 3.98 (dd, 1H, J = 7.1, 10.4 Hz), 4.96 (d, 1H,

© 1998 NRC Canada

Can. J. Chem. Downloaded from www.nrcresearchpress.com by Peking University on 09/05/12
For personal use only.

J = 8.6 Hz), 6.92 (s, 2H), 7.30–7.38 (m, 5H); ^{13}C NMR (125 MHz) δ: 21.0, 22.4, 26.8, 27.1, 66.0, 70.3, 78.7, 81.9, 109.8, 126.6, 128.6, 128.7, 130.3, 131.7, 136.8, 139.9, 143.4. Anal. calcd. for $C_{22}H_{28}O_6S$: C 62.84, H 6.71; found: C 62.45, H 6.77.

*Epoxide **15** from the aryl sulfonate **25***

A mixture of aryl sulfonate **25** (761 mg, 1.81 mmol) and solid K_2CO_3 (500 mg, 2 equiv.) in MeOH (20 mL) was stirred at room temperature for 90 min and then saturated NH_4Cl was added. The mixture was extracted with EtOAc (2×) and the combined organics were washed with water and brine, dried, and concentrated. Chromatography (hexane–EtOAc, 7:1) of the residual oil provided epoxide **15** (387 mg, 97%) as a colourless oil.

*Alkyne **17***

Following the procedure described above for the alkynylation of the epoxide mixture **15**/**16**, the pure epoxide **15** (853 mg, 3.87 mmol) was converted to alkyne **17** (839 mg, 88%).

*Silyl ether **27***

To a solution of alcohol **17** (450 mg, 1.83 mmol) and Et_3N (0.6 mL, 2.4 equiv.) in dichloromethane (15 mL) at 0°C was added TBDMSOTf (0.5 mL, 1.2 equiv.). The mixture was stirred at 0°C for 30 min and then at room temperature for 2 h. Ammonium acetate buffer was added and the mixture was extracted with dichloromethane (3×). The combined organics were dried and concentrated. Chromatography (hexane–ether, 20:1) of the residue provided the silyl ether **27** (633 mg, 96%) as a white solid, mp 60.5–61.5°C. IR ($CHCl_3$): 3310, 1250, 1065, 830 cm^{-1}; ^{1}H NMR (300 MHz, $CDCl_3$) δ: 0.07 (s, 3H), 0.12 (s, 3H), 0.89 (s, 9H), 1.50 (s, 3H), 1.55 (s, 3H), 1.93 (t, 1H, J = 2.7 Hz), 2.39 (ddd, 1H, J = 2.7, 6.0, 16.6 Hz), 2.58 (ddd, 1H, J = 2.7, 7.1, 16.6 Hz), 3.90 (ddd, 1H, J = 3.0, 6.0, 7.1 Hz), 4.07 (dd, 1H, J = 3.0, 8.4 Hz), 4.97 (d, 1H, J = 8.4 Hz), 7.34 (m, 5H); ^{13}C NMR δ: –4.5, –4.2, 18.1, 24.2, 25.8, 27.0, 27.4, 69.6, 70.4, 78.6, 81.1, 84.2, 109.1, 127.2, 128.2, 128.5, 138.3. Anal. calcd. for $C_{21}H_{32}O_3Si$: C 69.96, H 8.94; found: C 70.23, H 9.12.

*Ester **28***

To a solution of alkyne **27** (543 mg, 1.51 mmol) in THF (15 mL) at –78°C was added MeLi (1.6 mL of a 1.4 M solution in ether, 1.5 equiv.) and the resulting mixture was stirred at –78°C for 5 min, and at 0°C for 30 min. Methyl chloroformate (0.2 mL, 1.5 equiv.) was then added and the mixture was stirred for a further 30 min at 0°C. Ammonium acetate buffer was added and the mixture was extracted with EtOAc (3×). The combined organics were dried and concentrated. Chromatography (hexane–ether, 9:1) of the residue provided the ester **28** (576 mg, 91%) as a white solid, mp 50.5–51.5°C. IR ($CHCl_3$): 2220, 1710, 1250, 1065, 835 cm^{-1}; ^{1}H NMR (300 MHz, $CDCl_3$) δ: 0.02 (s, 3H), 0.11 (s, 3H), 0.84 (s, 9H), 1.47 (s, 3H), 1.52 (s, 3H), 2.49 (dd, 1H, J = 6.2, 17.0 Hz), 2.69 (dd, 1H, J = 5.7, 17.0 Hz), 3.71 (s, 3H), 3.96–4.08 (m, 2H), 4.91 (d, 1H, J = 8.0 Hz), 7.25–7.40 (m, 5H); ^{13}C NMR δ: –4.6, 18.0, 24.3, 25.7, 26.9, 27.3, 52.4, 69.3, 74.4, 78.6, 84.3, 86.3, 109.2, 127.2, 128.3, 128.5, 138.0, 153.8. Anal. calcd. for $C_{23}H_{34}O_5Si$: C 66.00, H 8.18; found: C 66.34, H 8.40.

*Pyranone **30** ((±)-8-epigoniodiol)*

A mixture of ester **28** (330 mg, 0.79 mmol) and Lindlar's catalyst (33 mg) in THF (60 mL) was stirred under an atmosphere of hydrogen gas (1 atm (101.3 kPa)) for 1 h. The mixture was filtered through Celite, washing with EtOAc. The filtrate was concentrated and inspection by ^{1}H NMR spectroscopy indicated the absence of starting material and the presence of one olefin isomer (**29**). ^{1}H NMR (300 MHz, $CDCl_3$) δ: 0.01 (s, 3H), 0.05 (s, 3H), 0.82 (s, 9H), 1.48 (s, 3H), 1.51 (s, 3H), 2.89 (m, 2H), 3.66 (s, 3H), 3.85–3.96 (m, 2H), 4.90 (d, 1H, J = 8.2 Hz), 5.74 (td, 1H, J = 1.8, 11.5 Hz), 6.30 (td, 1H, J = 7.3, 11.5 Hz), 7.25–7.40 (m, 5H). The crude mixture was stirred in a mixture of THF (2 mL), 1 N HCl (1 mL), and glacial HOAc (1 mL) at 65°C for 3 h. The solution was cooled to room temperature and then co-evaporated with toluene (3×). Ammonium acetate buffer was poured into the residue and the mixture was extracted with EtOAc (4×). The combined organics were dried and concentrated. A small portion of this material was purified by chromatography (toluene–EtOAc, 4:1) to provide the pyranone **30** as a white solid, mp 99–100°C. IR (KBr): 3400, 1710, 1250 cm^{-1}; ^{1}H NMR (300 MHz, $CDCl_3$) δ: 2.11 (dddd, 1H, J = 0.7, 3.8, 6.3, 18.6 Hz), 2.81 (tdd, 1H, J = 2.4, 12.6, 18.6 Hz), 3.31 (br s, 1H), 3.44 (br s, 1H), 3.63 (br m, 1H), 4.18 (ddd, 1H, J = 2.2, 3.8, 12.6 Hz), 4.95 (d, 1H, J = 7.3 Hz), 5.92 (ddd, 1H, J = 0.7, 2.4, 9.8 Hz), 6.84 (ddd, 1H, J = 2.4, 6.3, 9.8 Hz), 7.33 (m, 5H). Exact Mass calcd. for $C_{13}H_{15}O_4$ $(M+H)^+$: 235.0971; found: 235.0970. The remainder of the material was used directly in the subsequent reaction.

*(±)-9-Deoxygoniopypyrone (**1**)*

The crude material containing the pyranone **30** was stirred in a solution of 1% DBU in THF (3 mL) at room temperature for 15 h. The mixture was concentrated and the residual material was subjected to chromatography (toluene–EtOAc, 17:3). (±)-9-Deoxygoniopypyrone (**1**) (111 mg, 60% from **28**) was obtained as a white solid, mp 183–184°C. IR (KBr): 3450, 1740, 1720, 1270 cm^{-1}; ^{1}H NMR (500 MHz, $CDCl_3$) δ: 1.55 (br s, 1H), 1.83 (dd, 1H, J = 4.0, 14.1 Hz), 2.58 (d quintet, 1H, J = 14.1, 2.1 Hz), 2.85 (dd, 1H, J = 5.1, 19.3 Hz), 2.96 (dm, 1H, J = 19.3 Hz), 3.94 (m, 1H), 4.51 (m, 1H), 4.86 (app septet, 1H, J = 1.8 Hz), 4.95 (d, 1H, J = 1.6 Hz), 7.30–7.42 (m, 5H); ^{13}C NMR δ: 24.1, 36.4, 66.2, 68.4, 70.6, 74.7, 126.2, 128.4, 129.0, 136.8, 169.3. Anal. calcd. for $C_{13}H_{14}O_4$: C 66.46, H 6.02; found: C 66.20, H 6.19.

References

1. (*a*) X. Fang, J.E. Anderson, C. Chang, P.E. Fanwick, and J.L. McLaughlin. J. Chem. Soc. Perkin Trans. 1, 1655 (1990); (*b*) X. Fang, J.E. Anderson, C. Chang, and J.L. McLaughlin. J. Nat. Prod. **54**, 1034 (1991).
2. R.W. Friesen and A. Giroux. Tetrahedron Lett. **34**, 119 (1993).
3. R.W. Friesen and S. Bissada. Tetrahedron Lett. **35**, 5615 (1994).
4. R.W. Friesen and A. Giroux. Can. J. Chem. **72**, 1857 (1994).
5. R.W. Friesen, C.I. Bayly, and J.A. Fogg. J. Org. Chem. **60**, 448 (1995).
6. R.W. Friesen and C. Vanderwal. J. Org. Chem. **61**, 9103 (1996).
7. M. Tsubuki, K. Kanai, and T. Honda. J. Chem. Soc. Chem. Commun. 1640 (1992).
8. Z.-C. Yang and W.-S. Zhou. Chin. J. Chem. **14**, 152 (1996).
9. R.W. Friesen and A.E. Kolaczewska. J. Org. Chem. **56**, 4888 (1991).

© 1998 NRC Canada

10. K.B. Sharpless and T.R. Verhoeven. Aldrichimica Acta, **12**, 63 (1979).
11. R.A. Johnson and K.B. Sharpless. *In* Catalytic asymmetric synthesis. *Edited by* I. Ojima. VCH Publishers, Inc., New York. 1993. pp. 101–158.
12. A.H. Hoveyda, D.A. Evans, and G.C. Fu. Chem. Rev. **93**, 1307 (1993).
13. E.D. Mihelich. Tetrahedron Lett. 4729 (1979).
14. W. Adam and B. Nestler. J. Am. Chem. Soc. **115**, 7226 (1993).
15. W. Adam, K. Peters, and M. Renz. J. Org. Chem. **62**, 3183 (1997).
16. W.R. Roush and M.R. Michaelides. Tetrahedron Lett. **27**, 3353 (1986).
17. (*a*) R.M. Carlson and A.R. Oyler. Tetrahedron Lett. 2615 (1974); (*b*) R.M. Carlson, A.R. Oyler, and J.R. Peterson. J. Org. Chem. **40**, 1610 (1975).
18. S.F. Martin and J.A. Dodge. Tetrahedron Lett. **32**, 3017 (1991).
19. J.K. Cha, W.J. Christ, and Y. Kishi. Tetrahedron, **40**, 2247 (1984).
20. J.K. Cha and N.-S. Kim. Chem. Rev. **95**, 1761 (1995).

List of abbreviations

mCPBA: *m*-chloroperoxybenzoic acid
NMO: *N*-methylmorpholine *N*-oxide
TBDMSCI: *tert*-butyldimethylsilyl chloride
TBDMSOTf: *tert*-butyldimethylsilyl trifluoromethanesulfonate
TBAF: tetrabutylammonium fluoride
DBU: 1,8-diazabicyclo[5.4.0]undec-7-ene
AIBN: 2,2′-azobisisobutyronitrile
MOM: methoxymethyl
TBDMS: *tert*-butyldimethylsilyl
HMPA: hexamethylphosphoramide
DEAD: diethyl azodicarboxylate

Can. J. Chem. Downloaded from www.nrcresearchpress.com by Peking University on 09/05/12
For personal use only.

© 1998 NRC Canada

Transverse compression and the secondary H/D isotope effects in intramolecular S_N2 methyl- transfer reactions

Saul Wolfe, Chan-Kyung Kim, Kiyull Yang, Noham Weinberg, and Zheng Shi

Abstract: Using ab initio molecular orbital theory mainly at the 3-21+G level, intramolecular S_N2 methyl transfer between two oxygens confined within a rigid template is found to proceed exclusively by a high energy retention mechanism when the oxygens are separated by three or four bonds, and by a high energy inversion mechanism when the oxygens are separated by six bonds. Both mechanisms exist when the oxygens are separated by five bonds. The CH_3/CD_3 kinetic isotope effects are normal (1.21–1.34) in the retention processes and inverse (0.66–0.81) in the inversion reactions. In the case of inversion, compression of C—H bonds of the transition state by structural effects in the plane perpendicular to the O-C-O plane increases the inverse isotope effect. The retention barriers are high because retention is inherently unfavorable, even when pericyclic stabilization of the transition state is possible. The inversion barriers are high because a rigid template cannot accommodate a linear O-CH_3-O structure, and the O-C-O bending vibration is stiff (the Eschenmoser effect). Using a novel design strategy, a nonrigid template has been found in which the barrier and the CH_3/CD_3 kinetic isotope effect are the same as in an intermolecular reaction.

Key words: Eschenmoser effect, isotope effect, compression, S_N2, sigmatropic rearrangement.

Résumé : En se basant sur des calculs ab initio d'orbitales moléculaires au niveau 3-21+G, on peut conclure que le transfert intramoléculaire S_N2 d'un groupe méthyle entre deux oxygènes maintenus de façon rigide dans une matrice rigide se fait avec un mécanisme de rétention de haute énergie lorsque les oxygènes sont séparés par trois ou quatre liaisons et par un mécanisme d'inversion de haute énergie lorsque les oxygènes sont séparés par six liaisons. Les deux mécanismes existent lorsque les oxygènes sont séparés par cinq liaisons. Les effets isotopiques cinétiques CH_3/CD_3 sont normaux (1,21–1,34) dans le processus avec rétention et inversés (0,66–0,81) dans les réactions de rétention. Dans le cas de l'inversion, une compression des liaisons C—H de l'état de transition résultant d'effets structuraux dans le plan perpendiculaire au plan O-C-O provoque une augmentation de l'effet isotopique inverse. Les barrières à la rétention sont élevées parce que la rétention est intrinsèquement défavorisée même quand la stabilisation péricyclique de l'état de transition est possible. Les barrières d'inversion sont élevées parce qu'une matrice rigide ne peut accommoder une structure linéaire O-CH_3-O et que la vibration de déformation O-C-O est importante (effet Eschenmoser). Utilisant une nouvelle stratégie de conception, on a développé une matrice non rigide dans laquelle la barrière ainsi que l'effet isotopique cinétique CH_3/CD_3 sont les mêmes que dans la réaction intermoléculaire.

Mots clés : effet Eschenmoser, effets isotopiques, compression, S_N2, réarrangement sigmatropique.

[Traduit par la rédaction]

Introduction

Steric compression and the S_N2 transition state

Over half a century elapsed between Baeyer's postulate of *Spannung* (1), Kehrmann's discussion of *Raumerfüllung* (2), Meyer's *Gesetze der sterischen Behinderungen* (3), and the first attempts to quantify the concept of steric compression. Following a suggestion that the low reactivities of neopentyl halides in bimolecular substitution reactions are caused by compression of their S_N2 transition states (4), Dostrovsky, Hughes, and Ingold (5) developed a rudimentary force field to calculate this compression and to pattern reactivity trends in a series of identity reactions (eq. [1])

[1] $$X^- + R\text{-}X \rightarrow X\text{-}R + X$$

with R = methyl, ethyl, *n*-propyl, isopropyl, isobutyl, *t*-butyl, and neopentyl. Because the information needed to treat bond stretching and bending at the reactive carbon was not yet very accurate or complete, an idealized transition state model was assumed in which the reactive carbon atom and the entering and leaving groups were collinear, with C—X bond lengths that remained constant throughout the series. Compression

Received July 14, 1997.

S. Wolfe,[1] C-K. Kim,[2] K. Yang,[3] N. Weinberg, and Z. Shi. Department of Chemistry, Simon Fraser University, Burnaby, BC V5A 1S6, Canada.

[1] Author to whom correspondence may be addressed. Telephone: (604) 291–5972. Fax: (604) 291–5973. E-mail: swolfe@sfu.ca

[2] Present address: Department of Chemistry, Inha University, Inchon 402–751, Republic of Korea.

[3] Present address: Department of Chemical Education, Gyeongsang National University, Chinju 660–701, Republic of Korea.

© 1998 NRC Canada

was then calculated by the assumption of an appropriate functional form for the van der Waals repulsions between nonbonded atoms. Although the specific choices made by these authors could be criticized (6), and later workers found the calculations to be "so cumbersome that few...have felt able to discuss the method...in any detail" (7), this daring intellectual exercise, together with an important contemporaneous

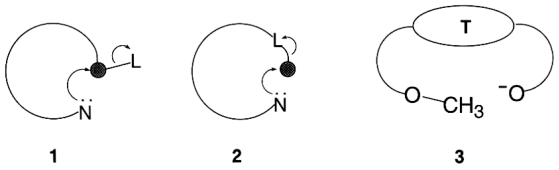

suggestion by T.L. Hill (8) and Westheimer's treatment of biphenyl atropisomerism (9), are the foundations of today's sophisticated molecular mechanics procedures (10).

The force field treatment of S_N2 transition states was refined by the Ingold school (11) and then by Abraham et al. (7) and de Tar et al. (12). In the latter work, for the series X = Br and R = *n*-propyl, isobutyl, and neopentyl, increasing steric compression in the transition states was seen in a gradual increase in the C—Br bond lengths (2.22, 2.23, 2.28 Å) and a systematic decrease in the Br-C-Br bond angles (161.4, 155.3, 143.2°). These geometric trends reflect the use of a bending force constant (3×10^{-5} mdyn Å deg^{-2} molecule^{-1}) (1 dyn = 10 μN) that allows compression in the β-series to be more easily relieved by bending than by stretching (force constant 6.6×10^{-2} mdyn Å^{-1} molecule^{-1}). It is noteworthy that AM1 calculations (13, present work, 14) reproduce the force-field trends in the C—Br bond lengths (2.29, 2.30, and 2.31 Å, respectively), and the Br-C-Br bond angles (159.4, 155.5, and 145.3°) of the transition structures.

Longitudinal compression of the S_N2 transition state

There is an obvious relationship between the classical alkyl halide reactivity sequence (ethyl > propyl > isobutyl > neopentyl) (3, 4) and the calculated *longitudinal* compression of their S_N2 transition structures, by which we mean the compression of these structures in the X–C–X plane. Eschenmoser and co-workers (15) were the first to recognize and prove that although the formation of five- and six-membered rings by exocyclic S_N2 ring closure, i.e., **1**, is highly favored over competing intermolecular reactions (16, 17), the deceptively enticing methyl transfer depicted in **2** is so inhibited by longitudinal compression in a five- or six-membered cyclic *transition state* that only intermolecular reactions are observed. Subsequent work by King and McGarrity (18) confirmed that the "failure to observe the endocyclic reaction arises not because the intermolecular reaction is inordinately fast but simply because the intramolecular reaction is slow" and undetectable when the endocyclic transition state contains fewer than nine atoms. There are now many examples of endocyclic restriction of the S_N2 mechanism (19), and the synthetic implications of this effect have been the subject of much interest (20).

Fig. 1. Upper: optimized 3-21+G inversion transition structure for the reaction CH_3O^- + CH_3-OCH_3. Lower: optimized 3-21+G retention transition structure for the reaction CH_3O^- + CH_3-OCH_3.

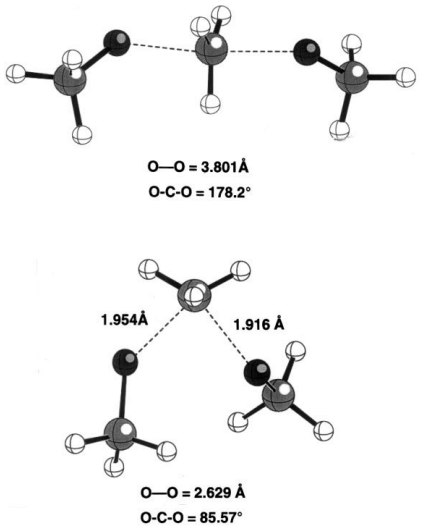

Longitudinal compression and secondary H/D isotope effects

We have recently discussed the effect of longitudinal compression on the barriers and secondary kinetic CH_3/CD_3 isotope effects (k_H/k_D) of intermolecular methyl-transfer reactions (21). The isotope effects are inverse ($k_H/k_D < 1$), primarily as a result of the increase in C-H (C-D) stretching frequencies that accompanies the tetrahedral to trigonal change in geometry of the methyl group (22).[4] Because the X-C-Y bond angles of the transition structures of such reactions are close to 180°, compression has implied a tightening (23) of C—X and C—Y bond lengths in the transition state. In both identity (X = Y) and nonidentity (X ≠ Y) reactions, this kind of compression is found to be associated with a decrease in the barrier and an increase in k_H/k_D. We have noted that these findings create a problem for the contention (24) that k_H/k_D decreases in enzymic methyl transfer because of specific compression of the enzymic transition state and that this compression may represent the source of the enzymatic catalysis.[5]

Transverse compression

The present work was undertaken to explore the consequences of both longitudinal and transverse compression on the barriers and secondary isotope effects of intramolecular methyl-transfer reactions. By transverse compression we mean compression in the plane perpendicular to the X–C–Y plane and, specifically, compression of C—H bonds in the transition

[4] Some recent discussions of this subject, referring specifically to nonidentity methyl-transfer reactions (22*a*, *b*), are flawed (*i*) by a failure to recognize that the isotope effects in such reactions are determined, inter alia, by the isotope effects of the two identity reactions and the reaction enthalpy (21*b*); (*ii*) by the contention that ion–molecule complexes do not have to be taken into account. Further discussion of this latter point can be found in footnote 81 of ref. 22*c*.

[5] See ref. 24*e* for more recent work on this subject, leading to the conclusion that the enzymatic and nonenzymatic transition structures are very similar.

© 1998 NRC Canada

Fig. 2. Left: transition structure, barrier, and CH_3/CD_3 kinetic isotope effect for intramolecular methyl transfer in **4**. Center: transition structure, barrier, and CH_3/CD_3 kinetic isotope effect for intramolecular methyl transfer in the reaction **5** ⇌ **6**. Right, transition structure, barrier, and CH_3/CD_3 for intramolecular methyl transfer in **7**.

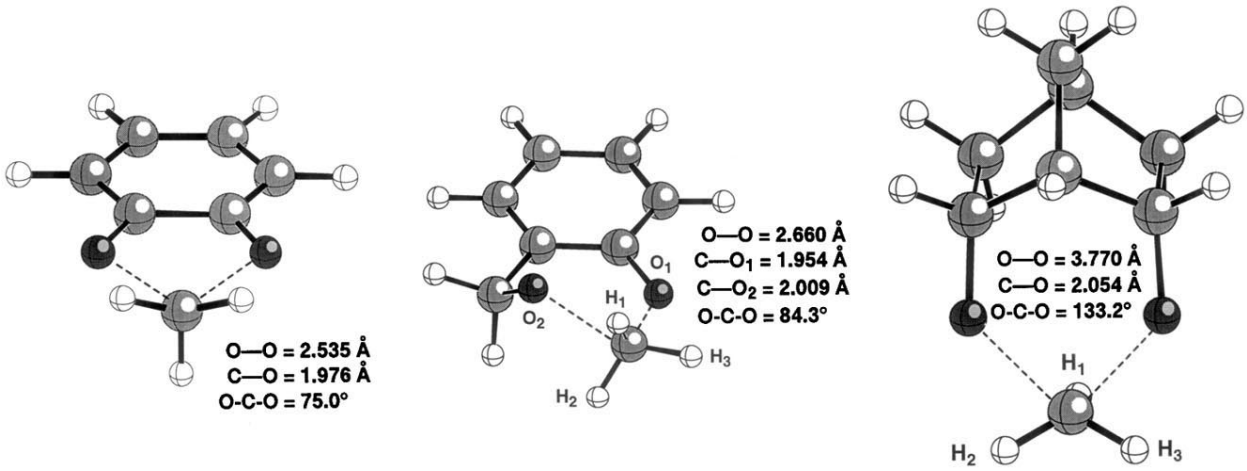

Fig. 3. Left: intramolecular methyl transfer in **8** with retention of configuration. Right: intramolecular methyl transfer in **8** with inversion of configuration.

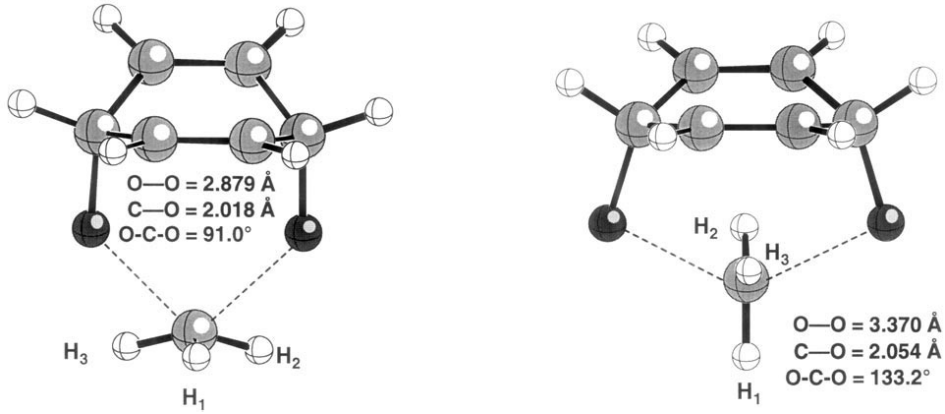

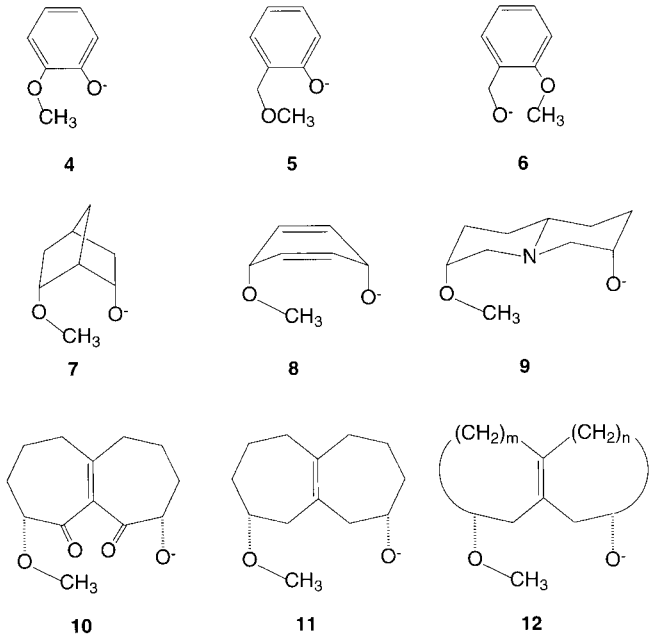

structure. It was reasoned that because the change in these bond lengths had already been found to be primarily responsible for the inverse isotope effect, any structural factor that causes additional compression of these bonds should lead to a more inverse isotope effect, and that this might be achieved with a reactant such as **3** in which **T** is a template whose dimensions are to be determined. Ideally, **T** would provide both compression of the transition structure and catalysis of the reaction.

Results and discussion

Anionic intermolecular methyl transfer between two oxygens. The optimized retention and inversion transition structures

The problem was approached in stages. In the first stage, the compression effects encountered during methyl transfer between two oxygens were examined using, as a benchmark, 3-21+G calculations[6] (25) on the reaction of eq. [2]. The calculated barrier for

[6] All ab initio calculations were performed using Gaussian 92 (25*c*).

© 1998 NRC Canada

Fig. 4. Upper left: intramolecular methyl transfer in **9**. Lower left: a side view of the transition structure, with definitions of H_1, H_2, and H_3, and the contributions of these hydrons to the CH_3/CD_3 isotope effect. Upper center: intramolecular methyl transfer in **10**. Lower center: a side view of the transition structure.Upper right: intramolecular methyl transfer in **11**. Lower right: a side view of the transition structure.

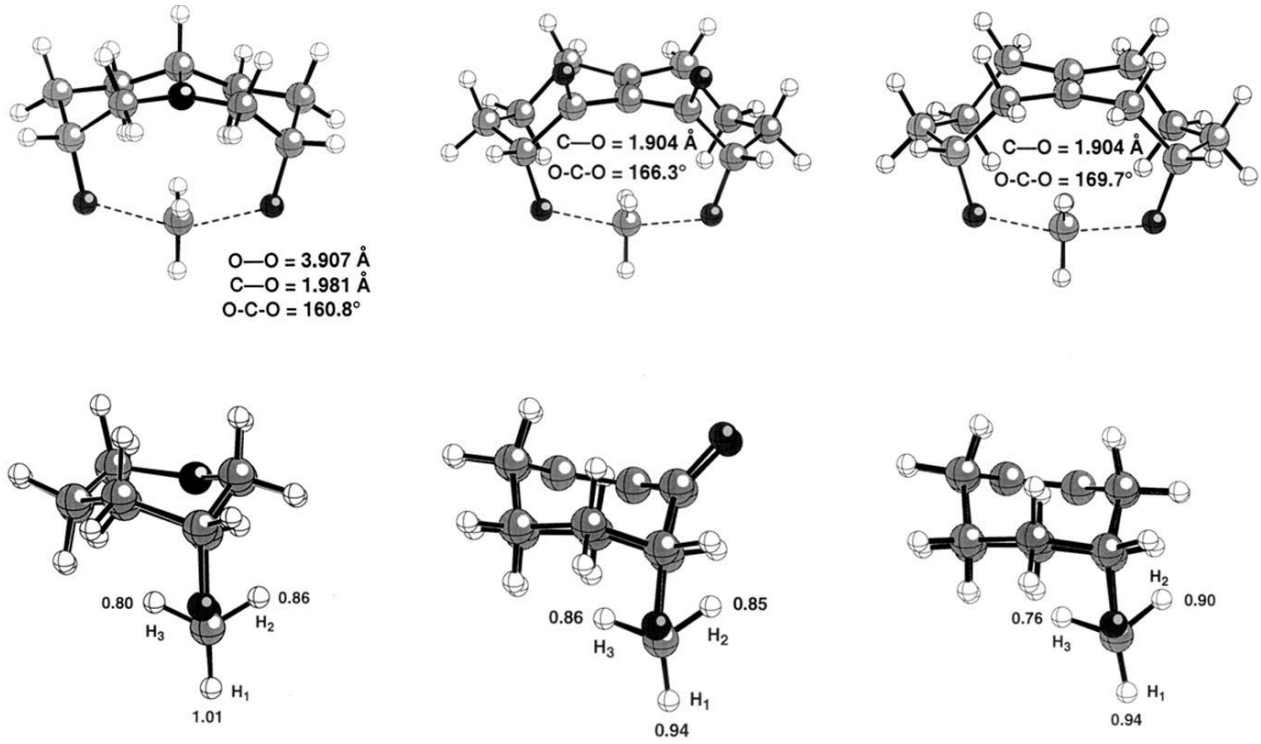

[2] $CH_3O^- + CH_3\text{-}OCH_3 \rightarrow CH_3O\text{-}CH_3 + {}^-OCH_3$

intermolecular methyl transfer with inversion of configuration is 25.4 kcal/mol, and the transition structure (Fig. 1, upper) has C—O bond lengths of 1.90 Å, an O—O distance of 3.8 Å, and an O-C-O angle of 178.2°. The transition structure for intermolecular methyl transfer with retention of configuration was also found. This structure (Fig. 1, lower) has C—O bond lengths of 1.95 and 1.92 Å, an O—O distance of 2.63 Å, an O-C-O angle of 85.6°, and it is 51.2 kcal/mol less stable than the structure of Fig. 1 (upper). This energy difference is so large (26) that nucleophilic displacement at carbon with apparent retention of configuration must be regarded as definitive evidence of a multistep process that includes an even number of inversion steps (27).

In the second stage, the effect of longitudinal compression on the energetics of intramolecular methyl transfer was estimated from the O–C–O bending force constant of the inversion transition structure of Fig. 1.[7] This 3-21+G force constant is part of the Gaussian output and is calculated to be 0.2634 hartree/bohr^2 (0.0503 kcal mol^{-1} deg^{-2}). Using the harmonic approximation ΔE (kcal/mol) = $k\theta^2/2$, where θ (degrees) is the deviation of the O-C-O angle from linearity, leads to ΔE = 2.52 and 5.66 kcal/mol for θ = 10° and θ = 15°, respectively. Since two competing reactions whose activation energies differ by 2.52 and 5.66 kcal/mol will differ in reactivity by factors of 70 and 14 000, respectively, at 298 K, a compression of as little as 10° in the O-C-O angle of an inversion transition structure would be sufficient to make intramolecular methyl transfer with inversion of configuration difficult to detect with respect to a competing unconstrained intermolecular inversion process.

CH_3/CD_3 isotope effects in intramolecular methyl transfer between oxygens separated by three, four, five, and six bonds. The retention and inversion mechanisms exhibit different isotope effects

Figures 2–4 show the results of 3-21+G calculations of intramolecular methyl transfer in the β, γ, δ, and ε-methoxyalkoxides **4**–**11**. These substrates have oxygens separated by three, four, five, or six bonds, and the relative positions of the oxygens are constrained by the templates. With the exception of **5** ⇌ **6**, all of the reactions are identity methyl transfers. Table 1 gives the enthalpies of activation calculated at MP2(= FC)/6–31+G*//3-21+G, the C—H bond lengths of the transition structures, the H/D isotope effect for each hydron, and the CH_3/CD_3 isotope effects.[8]

Only the retention mechanism was found in the cases of **4**–**7**, and only inversion was found for **9**–**11**. Both mechanisms were seen in the case of **8**.

The isotope effects in the inversion reactions constitute evidence for the postulated transverse compression of the S_N2 transition state. As noted in several studies (21, 30), C—H bond lengths in the transition structures of intermolecular methyl-transfer reactions do not depend strongly upon the nature of the entering and leaving groups. In the inversion transition structure of Fig. 1, the average C—H bond length is 1.064 Å. In the inversion transition structure of Fig. 3, one

[7] For related studies, see ref. 28.

[8] Isotope effects were calculated with the Bigeleisen equation (29*a*), using methods described in refs. 29*b* and *c*.

© 1998 NRC Canada

Table 1. Transition structure, C—H_i bond lengths, CH_i/CD_i isotope effects, CH_3/CD_3 isotope effects, and barriers[a] of intramolecular methyl-transfer reactions.

	Hydron	Bond length (Å)	k_H/k_D	k_{CH_3}/k_{CD_3}	Barrier
4	H_1	1.068	1.09		
	H_2	1.074	1.07		
	H_3	1.074	1.03	1.21	52.4
5	H_1	1.068	1.03		
	H_2	1.071	1.06		
	H_3	1.075	1.16	1.27[b]	75.6[b]
6				1.28[c]	44.2[c]
7	H_1	1.069	0.96		
	H_2	1.077	1.18		
	H_3	1.077	1.05	1.21	57.8
$\mathbf{8}_{ret}$	H_1	1.066	1.06		
	H_2	1.072	1.12		
	H_3	1.072	1.11	1.34	72.9
$\mathbf{8}_{inv}$	H_1	1.076	1.15		
	H_2	1.046	0.83		
	H_3	1.046	0.83	0.81	61.4
9	H_1	1.069	1.01		
	H_2	1.051	0.86		
	H_3	1.041	0.80	0.70	47.0
10	H_1	1.066	0.94		
	H_2	1.051	0.85		
	H_3	1.049	0.86	0.69	35.6
11	H_1	1.065	0.94		
	H_2	1.054	0.90		
	H_3	1.051	0.76	0.66	32.6

[a]Refers to $\Delta H^{\neq}$ in kcal/mol.
[b]Refers to **5** → **6**.
[c]Refers to **6** → **5**.

methyl hydron (H_1) is antiperiplanar to the π-system of the cyclohexadiene template, and its C—H bond is lengthened slightly (1.076 Å). The other hydrons (H_2 and H_3) are imbedded in the π-system, and their bond lengths are compressed to 1.046 Å. The isotope effect for H_1 is normal (1.15), but for H_2 and H_3 it is inverse (0.83). The stretching and bending contributions to the overall CH_3/CD_3 isotope effect of 0.81 are 0.69 and 1.17, respectively.

In the transition structure of **9** (Fig. 4, left), one methyl hydron (H_1) is antiperiplanar to the azadecalin skeleton, and its C—H bond length (1.069 Å) is normal. The isotope effect is also normal (1.01). The side view of this transition structure shows that a second methyl hydron (H_2) is compressed, by interaction with the equatorial hydrogens adjacent to nitrogen, to a bond length of 1.051 Å. Its isotope effect is 0.86. The third methyl hydron (H_3) lies under the nitrogen lone pair, and it is compressed to a bond length of 1.041 Å. Its isotope effect is 0.80. The CH_3/CD_3 isotope effect is 0.70.

In the transition structure of **10** (Fig. 4, center), H_1 is antiperiplanar to the bicyclic template, and it has the longest bond length (1.066 Å). A second hydron, H_3, is *endo* to the bicyclic system, and it has the shortest bond length (1.049 Å). The *exo* hydron, H_2, is *syn* to the carbonyl groups, and it has a bond length of 1.059 Å. The CH_3/CD_3 isotope effect is 0.69.

In the transition structure of **11** (Fig. 4, right), H_1 is antiperiplanar to the bicyclic template, and it has the longest bond length (1.065 Å) and highest k_H/k_D (0.94). The CH_3/CD_3 isotope effect is 0.66.

There is a significant difference in the isotope effects of the retention and inversion processes. The origin of this difference is best seen by examination of the retention and inversion transition structures of Fig. 3, which have (unscaled) imaginary frequencies of 834*i* and 860*i*, respectively. In the inversion structure, the imaginary frequency is the O–C–O antisymmetric stretch. In the retention structure, the imaginary frequency is a rocking motion about the C—H_1 bond as a pivot. The isotope effects are 1.06 for H_1 and 1.12 for H_2 and H_3. The CH_3/CD_3 isotope effect of 1.34 contains a stretching component of 1.07, a bending component of 1.34, and a stretch–bend component of 0.90. The principal contribution to the bending component of the isotope effect (k_{CH_3}/k_{CD_3} = 1.22) is made by a vibration, similar to that of the imaginary frequency, which has a frequency (uncorrected) of 958 cm^{-1}. This is shown as a series of instant structures at the left of Fig. 5,[9] together with the corresponding vibration in the inversion structure, which has a frequency (unscaled) of 1159 cm^{-1}, and contributes 0.97 to the overall 0.81 CH_3/CD_3 isotope effect.

The retention mechanisms found for **4** (Fig. 2, left) and **7** (Fig. 2, right) also exhibit normal isotope effects, 1.21 in each case. For **5** ⇌ **6** (Fig. 2, center), the isotope effects are 1.29 in the exoergic direction, and 1.27 in the endoergic direction.

The difference in the retention and inversion isotope effects appears to be large enough to offer an alternative to the chiral methyl group (32) for the determination of the stereochemical course of methyl transfer (33). More importantly (34), the difference in isotope effects can allow retention and double inversion mechanisms to be distinguished.

Barriers to methyl transfer in the rigid templates 4–11

All of the activation enthalpies shown in Table 1 are much larger than the barrier for intermolecular methyl transfer with inversion of configuration (25.4 kcal/mol). This is the expected result in the case of the retention mechanisms (26). In the case of the inversion mechanism for **8**, most of the excess energy of the transition structure originates in the longitudinal compression associated with an O-C-O angle of 133°.

In the case of **9**, the barrier is more than 20 kcal/mol higher than that of an intermolecular methyl transfer. Approximately half of this increase (9 kcal/mol) can be attributed to the longitudinal compression associated with the O-C-O angle of 161°. The remainder is caused by the compression of the template itself in the formation of the transition structure. For example, as summarized in Fig. 6, reoptimization of the reactant **9r** as **9r(t)**, with the azadecalin skeleton constrained to the geometry of the transition structure **9t**, destabilizes the structure by 18.2 kcal/mol. Replacement of the oxygen atoms of **9r** and **9t** by hydrogens (**9r(H)** and **9t(H)**) and reoptimization with all other geometrical parameters constrained to those of **9r** and **9t**, reveals that the distortion of the azadecalin backbone amounts to 10 kcal/mol. The energy difference between **9t** and **9r(t)** is 28.8 kcal/mol, close to the 28.4 kcal/mol calculated when the carbon atoms geminal to oxygen in **9r** and **9t** are replaced by hydrogens, and the resulting structures **9rc** and **9ts** are reoptimized.

It is evident that the azadecalin backbone is too rigid, and

[9] These structures were generated using the programme XMol (31).

© 1998 NRC Canada

Fig. 5. A series of instant structures (top to bottom) showing the vibration that leads to the 958 cm^{-1} frequency in $\mathbf{10}_{ret}$ (left); secondary H/D isotope effects, 1.22; total, 1.34. The corresponding vibration in $\mathbf{10}_{inv}$ (right) has a frequency of 1159 cm^{-1}.

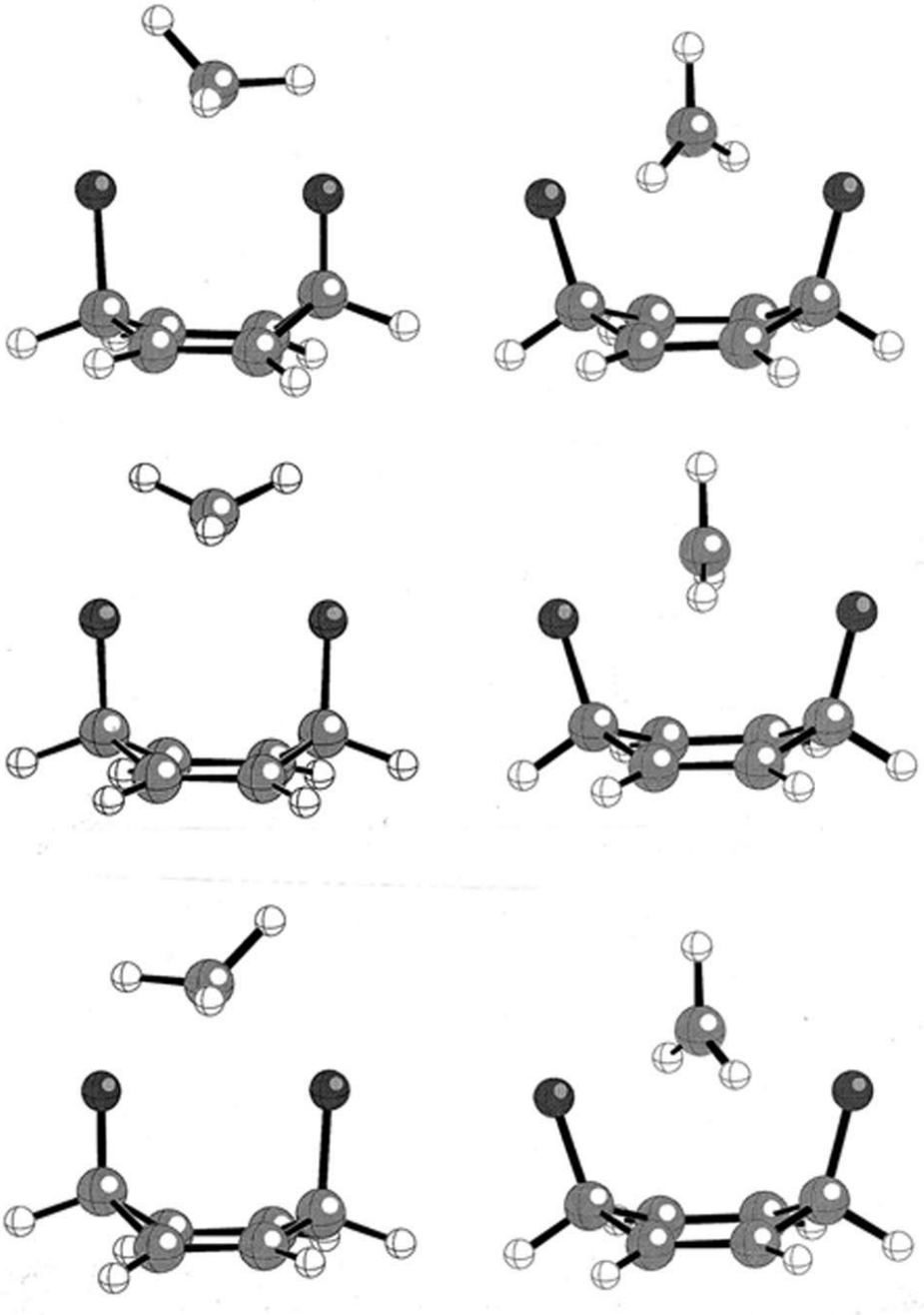

that the geometry of **9** does not permit a linear methyl transfer. The sum of the angles at nitrogen in the transition structure **9t** is 359.1°, and in **9r** it is 344.8°. Inspection of **9r(H)** and **9t(H)** in Fig. 6 suggests that the planar configuration at nitrogen in the transition structure contributes 10 kcal/mol to the destabilization of the structure. This potential for distortion is avoided in **10** and **11**, because the bridgehead atoms are planar in both the reactant and the transition structure. Using AM1, the geometry of **12** was optimized for (n, m) = (1, 1), (1, 2), (2, 2), (2, 3), and (3, 3), and the O—O distances, O-C-O angles, and methyl-transfer barriers were examined in each case. This strategy led to the (3, 3) systems seen in **10** and **11**, in which the methyl-transfer barriers are reduced to 35.6 and 32.6 kcal/mol, respectively. However, although the longitudinal compression associated with the 170° O-C-O angle in the transition structure of **11** is estimated to be only 2.5 kcal/mol, the template is not entirely free of compression, and the barrier is still 7 kcal/mol higher than that of the parent intermolecular methyl-transfer reaction.

Design of a flexible template for intramolecular methyl transfer

Although transverse compression of the methyl-transfer transition state has thus been found to produce a more inverse

© 1998 NRC Canada

Fig. 6. Analysis of the factors that contribute to the destabilization of the template in the transition structure of **9**.

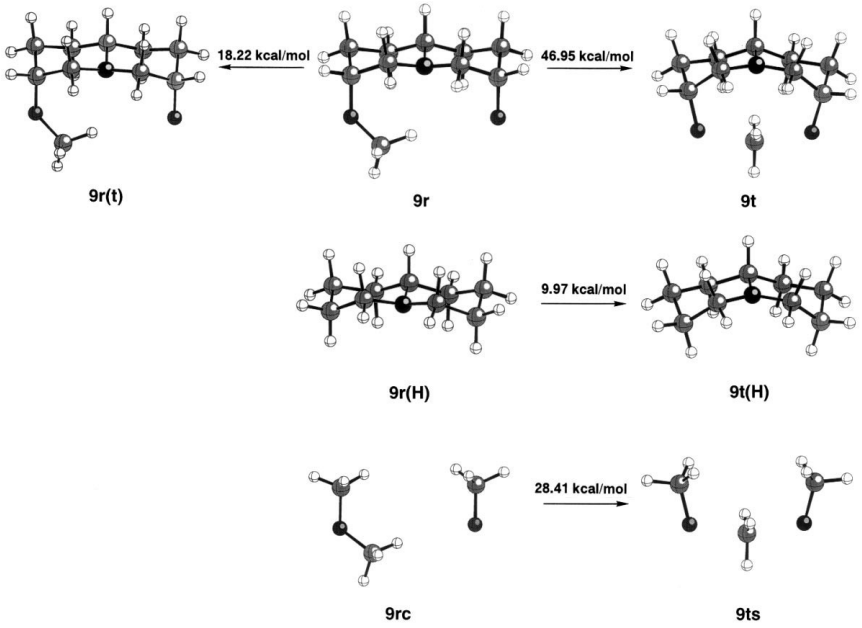

Fig. 7. Design of a flexible template for intramolecular methyl transfer.

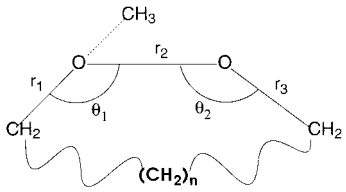

secondary isotope effect, the additional compression introduced by the use of a rigid template overcomes any potential for catalysis of the process. It was, therefore, necessary to design an acyclic, flexible structure.

We have recently reported a novel stochastic search strategy for the conformational analysis of cyclic structures (35). Since the reactant (RC) and transition state (TS) of an intramolecular methyl transfer are pseudocyclic structures, it was possible to adapt this stochastic strategy to the search for superimposable RC and TS templates. The system was treated as an $(n + 4)$-membered ring (Fig. 7) containing an O···O "bond," with the bond lengths r_1, r_2, and r_3, and the bond angles θ_1 and θ_2 constrained to the values seen in the transition state and reactant of the intermolecular reaction. All other bond lengths and bond angles were found by MM3 minimization (36). The torsion angles of the $(CH_2)_n$ chain were obtained by random variation, as described previously (35). Using a 30° torsional increment, a total of 3733 RC rings and 3860 TS rings were produced from 10 000 randomly generated structures. Two thousand each of RC and TS rings were then minimized using MM3, with the bond lengths and bond angles at the reaction center frozen. This was achieved by the definition of atom types having $k_{stretch} = 100$ mdyn/Å (cf. $k_{CC} = 4.5$ mdyn/Å) and $k_{bend} = 10$ mdyn Å rad^{-2} (cf. $k_{CCC} = 0.67$ mdyn Å rad^{-2}). All other parameters of these atoms were taken from the values employed in MM3.

For the case of a 12-membered ring ($n = 8$), this strategy afforded 255 RC minima and 208 TS minima. These were then matched to identify structurally similar (RC, TS) pairs using the rms deviations of the torsion angles of the $(CH_2)_8$ chain as a criterion. The lowest energy pair was found to be the second lowest RC minimum (0.38 kcal/mol above the lowest minimum) and the second lowest TS minimum (0.34 kcal/mol above the lowest minimum). To complete the design process, the methyl group to be transferred was added.

Both of these structures were then subjected to 3-21+G minimization, and were optimized successfully. The results are summarized in structures **13-RC** and **13-TS** of Fig. 8, which also includes an optimized RC[10] and TS (cf. Fig. 1, left) of the intermolecular methyl-transfer reaction.

It can be seen that the reactive centers of the two reactants and the two transition structures are virtually superimposable. The CH_3/CD_3 kinetic isotope effects calculated for RC → TS are also the same, and the free energies of activation differ by only 1.2 kcal/mol. The strategy employed to discover **13** thus appears to lead to a template for efficient intramolecular methyl transfer in the gas phase. Moreover, close examination of the CH_3 bond lengths included in Fig. 8 indicates that the methyl hydrogen that points towards the concave face of **13-TS** exhibits transverse compression. It should be possible to alter the properties of such templates by incorporation of substituents on the concave face of the chain, and initial studies in this direction suggest that structures having $n > 8$ will be of interest.

The inversion barriers, geometrical parameters, and CH_3/CD_3 isotope effects of intramolecular methyl transfer are coupled

Figure 9 applies the Walsh–Gimarc rules (37) to the internal geometries of methyl groups having D_{3h} (**14**) and C_{2v} (**15**)

[10] This structure is not the global minimum at 3-21+G (29*b*), but it is a genuine stationary point having no imaginary frequencies.

© 1998 NRC Canada

Fig. 8. Intramolecular methyl transfer with inversion of configuration in the parent system (upper) and in the flexible template **13** (lower).

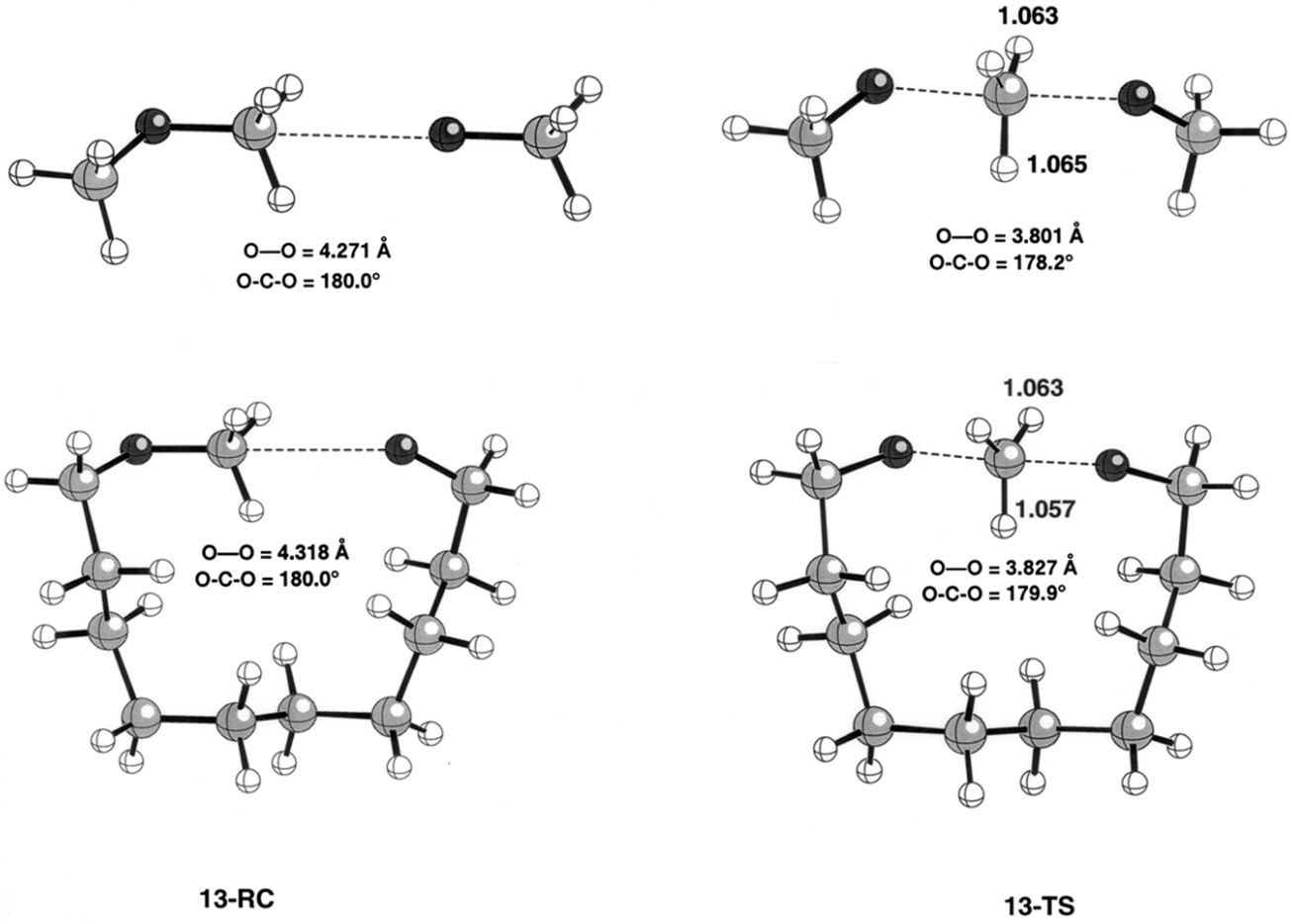

symmetry. In **14**, the π-type *e* orbitals are degenerate. In **15**, the orbitals are nondegenerate; an increase in the H_b-C-H_b angle stabilizes the b_2 orbital and destabilizes the a_1 orbital. The destabilization is caused by the increased out-of-phase interaction between the 1*s* coefficients of H_b and the 1*s* coefficient of H_a, which is relieved by an increase in the C—H_a bond length.[11]

As we have seen, there is a systematic decrease in the methyl-transfer barriers in the series **8** (Fig. 3), **9**, **10**, **11** (Fig. 4), and **13** (Fig. 8), mainly because the O-C-O angles of the transition structures increase from 133.2 to 179.8°. The decrease in the barriers is accompanied by a decrease in the H_2-C-H_3 angles, from 128.5° in **8** to 119.9° in **13-TS**, leading to an inverse relationship between the O-C-O and H_2-C-H_3 angles. This is shown in Fig. 10*a*, and is undoubtedly steric in origin. In accord with the Walsh–Gimarc rules, the decrease in the H_2-C-H_3 angle is accompanied by a decrease in the C—H_1 bond length (Fig. 10*b*), and the C—H_1 bond length therefore decreases as the barrier decreases (Fig. 10*c*). As a result, the contribution of H_1 to the secondary CH_3/CD_3 isotope effect changes from normal to inverse as the barrier decreases (Fig. 10*d*).

[11] These predictions have been confirmed by calculations on $CH_aH_bH_b^+$: as the H_b-C-H_b angle is increased, the C—H_a bond length is increased, the b_2 orbital is stabilized, and the a_1 orbital is destabilized.

Fig. 9. Application of the Walsh–Gimarc rules to the frontier orbitals of methyl groups having D_{3h} (**14**) and C_{2v} (**15**) symmetries.

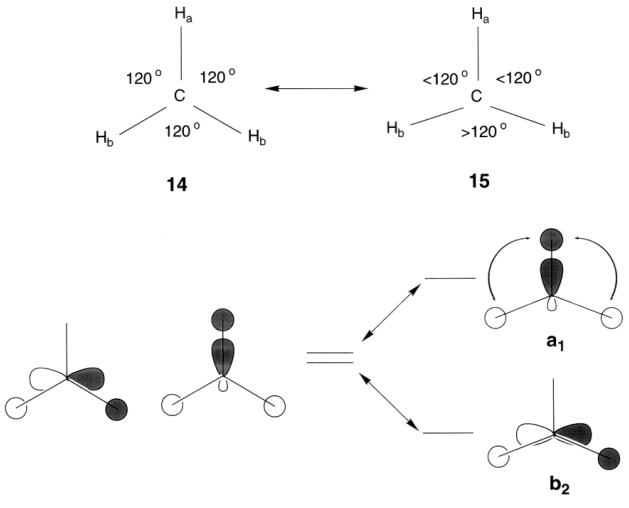

The overall CH_3/CD_3 isotope effect also becomes more inverse as the barrier decreases (Fig. 11), but in the case of this property, **13** does not correlate with **8**–**11**. The reason for this is that intramolecular methyl transfer in **13** proceeds without longitudinal compression, and therefore resembles

© 1998 NRC Canada

Fig. 10. (*a*) Relationship between the H_2-C-H_3 and O-C-O bond angles in the transition structures of **8**, **9**, **10**, **11,** and **13**. (*b*) Relationship between the H_2-C-H_3 bond angles and C—H_1 bond lengths in the transition structures of **8**, **9**, **10**, **11**, and **13**. (*c*) The C—H_1 bond lengths of the transition structures correlate with the barriers of methyl transfer in **8**, **9**, **10**, **11,** and **13**. (*d*) The contribution of H_1 to the CH_3/CD_3 isotope effect in templates **8**, **9**, **10**, **11**, and **13** depends on the methyl-transfer barrier.

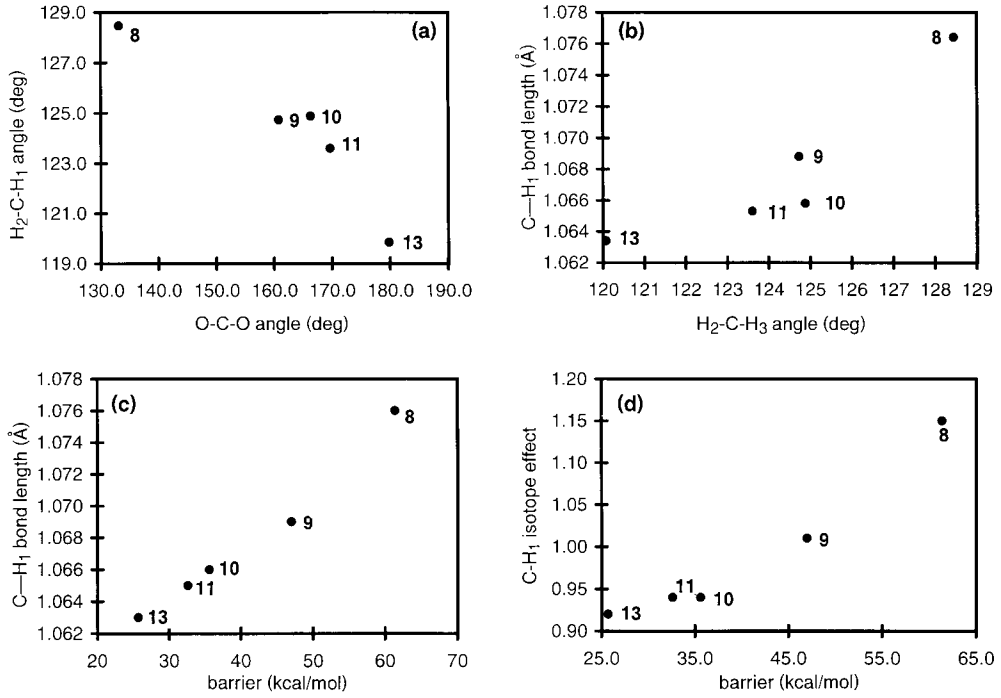

intermolecular methyl transfer, but the transverse compression of H_2 and H_3 in the transition structures of **8**–**11** causes the isotope effects to become more inverse.

Methyl transfer with retention of configuration. Can a [1*s*,4*s*] sigmatropic rearrangement be observed?

In the intramolecular methyl-transfer reactions of **4**–**8** (Figs. 2 and 3), the barrier is never less than 20 kcal/mol higher than that of an unconstrained inversion process and, in each case, the imaginary frequency of the retention transition structure is the rocking vibration discussed in Fig. 5. It is noteworthy that the transition structure of **4** (Fig. 2) exhibits no particular stabilization, because retention of configuration and a barrier less than 20 kcal/mol in the related reaction, the thermal rearrangement of 2-alkoxypyridine-1-oxides to 1-alkoxy-2-pyridones (**16** → **17**) have been thought to be consistent with a [1*s*,4*s*] sigmatropic rearrangement mechanism (38, 39). This interpretation is based on the orbital analysis shown at the top of Fig. 12, which suggests that a 1,4-suprafacial migration of a methyl group is thermally allowed. Although the HOMO of **4**, also shown in Fig. 12, seems to support this interpretation, the argument does not take into account the repulsive, out-of-phase relationship between the orbital of the migrating group and the orbitals at the 2- and 3-positions, which will force this group towards the nodal plane of the π-system. The situation is analogous to that encountered in the frontier molecular orbital treatment of nucleophilic addition to a carbonyl group (Fig. 12, bottom). In the latter case, the well-known (40) nonperpendicular attack of the nucleophile can be rationalized as the result of the out-of-phase relationship between the orbital of the attacking nucleophile and the *p*-orbital on oxygen (41).

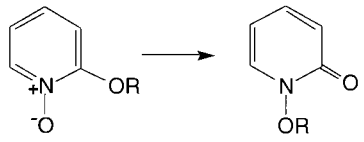

16 **17**

Examination of a side view of the intramolecular methyl-transfer transition structure of **4** (Fig. 13, top) shows that the migrating carbon is only 6° out of the plane of the aromatic system. To check whether this is a basis set effect, the reactant and transition structure of **4** were reoptimized at MP2/6–31+G*. The out-of-plane angle of the migrating methyl group increased to 29° (Fig. 13, bottom), but the barrier remained high (51.5 kcal/mol). Thus, although the 3-21+G basis set overemphasizes the nonperpendicular character of the transition structure of an intramolecular [1*s*,4*s*] sigmatropic methyl rearrangement, it is clear that competing, intermolecular reactions will make an intramolecular reaction experimentally unobservable. The work of Hoppe and Schöllkopf (38) therefore requires reexamination and reinterpretation (34).

Theoretical procedures

Transition structures were located by the reaction coordinate method. The C···O bonds of the entering and leaving groups were fixed at several values near 1.9 Å, all other geometrical parameters were optimized, and the magnitudes and signs of the gradients of the two reaction coordinates were used to improve the trial values. When a structure close to the saddle point was reached, a final refinement was usually achieved using the OPT = CALCALL option of Gaussian 92 (25*c*) in

© 1998 NRC Canada

Fig. 11. Transverse compression leads to a correlation between the CH_3/CD_3 isotope effects and barriers in the rigid templates **8–11**. The flexible template **13** exhibits different behavior.

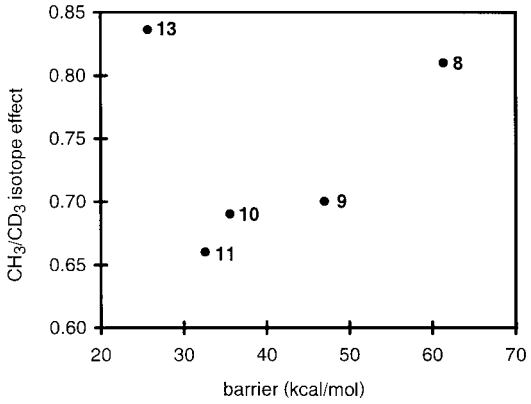

Fig. 12. Top left: orbital interaction between the HOMO of a 4π system and the LUMO of a methyl group; the phase relationship is correct for [1,4] sigmatropic rearrangement with retention of configuration, if the out-of-phase interactions (double-headed arrows) are ignored. Top right: the HOMO of **4**. Bottom: orbital interaction diagram proposed to explain nonperpendicular attack of a nucleophile on a carbonyl group.

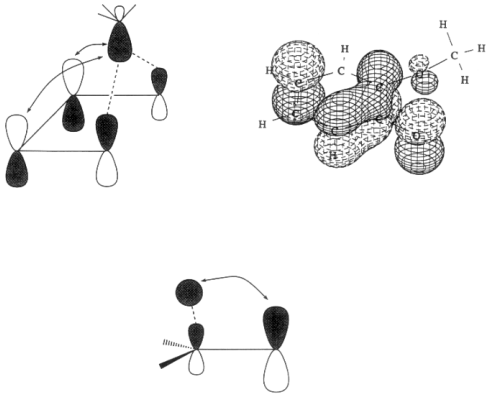

which force constants are calculated in every iteration. For calculations of isotope effects, the frequencies employed as input to the Bigeleisen equation were obtained by scaling of the computed values by 0.9 (29).[12]

Summary and conclusions

Using ab initio molecular orbital theory mainly at the 3-21+G level, the CH_3/CD_3 kinetic isotope effects in intramolecular S_N2 methyl transfer between two oxygens have been found to be normal (1.21–1.34) for retention and inverse (0.66–0.81) for inversion of configuration. It is suggested that the difference in the retention and inversion isotope effects is large enough to constitute an alternative to the chiral methyl group for the determination of the stereochemical course of displacement at methyl, and to allow a genuine retention process to be distinguished from an even number of inversions.

[12] The structures calculated in this work are available as supplementary material, which may be purchased from: the Depository of Unpublished Data, Document Delivery, CISTI, National Research Council of Canada, Ottawa, Canada K1A 0S2.

Fig. 13. Side view of the transition structure for intramolecular methyl transfer in **4**; the methyl carbon is not perpendicular to the aromatic ring. Upper: 3-21+G optimization. Lower: MP2/6–31+G* optimization.

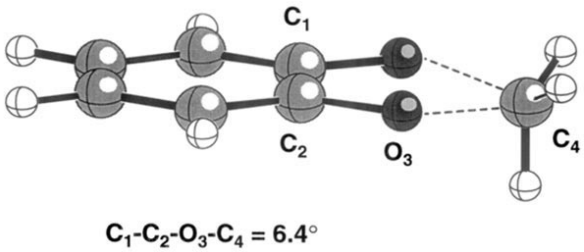

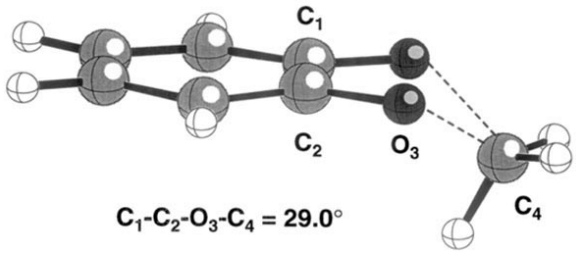

The normal isotope effect in the retention mechanism is the result of a torsional motion about one of the C—H bonds as the methyl carbon rocks between the two oxygens. In the case of inversion, compression of C—H bonds by structural effects in the transition state, here termed transverse compression, increases the inverse isotope effect. The geometry of the methyl group is coupled to the O-C-O angle of the transition structure, so that the methyl C—H bond lengths, the O-C-O angle, the barrier, and the CH_3/CD_3 kinetic isotope effect are all coupled. A 10° deviation from linearity of the O-C-O angle of the inversion transition structure is sufficient to make an intramolecular reaction kinetically noncompetitive with respect to intermolecular processes.

For intramolecular methyl transfer within a rigid template, only a high energy retention mechanism can be found when the oxygens are separated by three or four bonds, and only inversion is seen when the oxygens are separated by six bonds. Both mechanisms exist when the oxygens are separated by five bonds. Since nonlinear methyl transfer occurs within all of the rigid templates examined so far, none of these provides catalysis of the inversion mechanism. However, treatment of the reactant and transition structure of an intramolecular methyl transfer as pseudocyclic structures, and extension to such structures of a recently described stochastic approach to conformational analysis, has led to the discovery of a nonrigid template that permits linear methyl transfer to take place. This template has two oxygens separated by 10 carbons, and the intramolecular methyl-transfer barrier and CH_3/CD_3 isotope effect are the same as in the intermolecular reaction.

There is no evidence for pericyclic stabilization of a [1*s*,4*s*] intramolecular sigmatropic retention process in the degenerate rearrangement of the anion of *o*-catechol *O*-methyl ether. The

© 1998 NRC Canada

reason for this is that the out-of-phase interaction between the *p*-orbital of the migrating group and *p*-orbitals of the aromatic ring forces the methyl group towards the nodal plane of the π-system.

Acknowledgements

The authors thank Dr. Inga Hoppe for kindly providing a copy of her 1971 Göttingen dissertation and the Natural Sciences and Engineering Research Council of Canada for financial support.

References

1. A. Baeyer. Chem. Ber. **18**, 2269 (1885).
2. F. Kehrmann. Chem. Ber. **23**, 130 (1890).
3. V. Meyer. Chem. Ber. **27**, 510 (1894).
4. E.D. Hughes. Trans. Faraday Soc. **37**, 603 (1941).
5. I. Dostrovsky, E.D. Hughes, and C.K. Ingold. J. Chem. Soc. 173 (1946).
6. A.G. Evans, M.G. Evans, and M. Polanyi. J. Chem. Soc. 558 (1947).
7. M.H. Abraham, P.L. Grellier, and M.J. Hogarth. J. Chem. Soc. Perkin Trans. 2, 1365 (1975).
8. T.L. Hill. J. Chem. Phys. **14**, 465 (1946).
9. F.H. Westheimer and J.E. Mayer. J. Chem. Phys. **14**, 733 (1946); F.H. Westheimer. J. Chem. Phys. **15**, 252 (1947); *In* Steric effects in organic chemistry. *Edited by* M.S. Newman. John Wiley, New York. 1956.
10. D.H.R. Barton. J. Chem. Soc. 340 (1948); J.B. Hendrickson. J. Am. Chem. Soc. **83**, 4537 (1961); K.B. Wiberg. J. Am. Chem. Soc. **87**, 1070 (1965); J.D. Dunitz and H.-B. Bürgi. *In* Chemical crystallography. MTP International Review of Science, Physical Chemistry. Ser. 2. Vol. 11. *Edited by* J.M. Robertson. Butterworths, London. 1975. p. 81; A. Warshel. *In* Modern theoretical chemistry. Vol. 7. *Edited by* G.A. Segal. Plenum Press, New York. 1977. p. 133; U. Burkert and N.L. Allinger. Molecular mechanics. ACS Monograph 177. American Chemical Society, Washington, D.C. 1982; E. Osawa and H. Musso. Top. Stereochem. **13**, 117 (1982); N.L. Allinger. *In* Accurate molecular structures. Their determination and importance. *Edited by* A. Domenicano and I. Hargittai. Oxford University Press, Oxford. 1992. p. 336.
11. P.B.D. De la Mare, L. Fowden, E.D. Hughes, C.K. Ingold, and J.D.H. Mackie. J. Chem. Soc. 3200 (1955).
12. D.F. de Tar, D.F. McMullen, and N.P. Luthra. J. Am. Chem. Soc. **100**, 2484 (1978).
13. M.J.S. Dewar, E.G. Zoebisch, E.F. Healy, and J.J.P. Stewart. J. Am. Chem. Soc. **107**, 3902 (1985).
14. N.T. Anh, F. Maurel, B.T. Thanh, H.H. Thao, and Y.T. N'Guessan. New J. Chem. **18**, 473 (1994); N.T. Anh, B.T. Thanh, H.H. Thao, and Y.T. N'Guessan. New J. Chem. **18**, 489 (1994); F.R. Jensen. Chem. Phys. Lett. **196**, 368 (1992).
15. L. Tenud, S. Farook, J. Seibl, and A. Eschenmoser. Helv. Chim. Acta, **53**, 2059 (1970).
16. L. Ruzicka, W. Brugger, M. Pfeiffer, H. Schinz, and M. Stoll. Helv. Chim. Acta, **9**, 499 (1926).
17. C. Galli, G. Illuminati, L. Mandolini, and P. Tamborra. J. Am. Chem. Soc. **99**, 2591 (1977); L. Mandolini. J. Am. Chem. Soc. **100**, 499 (1978); D.F. DeTar and N.P. Luthra. J. Am. Chem. Soc. **102**, 4505 (1980).
18. J.F. King and M.J. McGarrity. J. Chem. Soc. Chem. Commun. 1140 (1979); J. Chem. Soc. Chem. Commun. 175 (1982); M.J. McGarrity, J.F. King, and J.B. Stothers. Tetrahedron Lett. **23**, 4465 (1982).
19. P. Beak. Acc. Chem. Res. **25**, 209 (1992); V.I. Minkin, L.P. Olekhanovich, and Yu. A. Zhdanov. Molecular design of tautomeric compounds. Reidel Publishing Company, Dordrecht, The Netherlands. 1988.
20. G. Stork and J.F. Cohen. J. Am. Chem. Soc. **96**, 5270 (1974); F.M. Menger. Tetrahedron, **39**, 1013 (1983); S. Danishevsky. Science, **259**, 469 (1993).
21. (*a*) S. Wolfe and C.-K. Kim. J. Am. Chem. Soc. **113**, 8056 (1991); (*b*) R.J. Boyd, C.-K. Kim, Z. Shi, N. Weinberg, and S. Wolfe. J. Am. Chem. Soc. **115**, 10147 (1993).
22. (*a*) R.A. Poirier, Y. Wang, and K.C. Westaway. J. Am. Chem. Soc. **116**, 2526 (1994); (*b*) I. Lee. Chem. Soc. Rev. **24**, 223 (1995); (*c*) M.N. Glukhovtsev, A. Pross, and L. Radom. J. Am. Chem. Soc. **118**, 6273 (1996); S. Glad and F. Jensen. J. Am. Chem. Soc. **119**, 227 (1997).
23. S.S. Shaik, H.B. Schlegel, and S. Wolfe. Theoretical aspects of physical organic chemistry. The S_N2 mechanism. Wiley-Interscience, New York. 1992.
24. (*a*) I. Mihel, J.O. Knipe, J.K. Coward, and R.L. Schowen. J. Am. Chem. Soc. **101**, 4349 (1979); (*b*) C.H. Gray, J.K. Coward, K.B. Schowen, and R.L. Schowen. J. Am. Chem. Soc. **101**, 4351 (1979); (*c*) M.F. Hegazi, R.T. Borchardt, and R.L. Schowen. J. Am. Chem. Soc. **101**, 4359 (1979); (*d*) J. Rodgers, D.A. Femec, and R.L. Schowen. J. Am. Chem. Soc. **104**, 3263 (1982); (*e*) Y.-J. Zheng and T.C. Bruice. J. Am. Chem. Soc. **119**, 8137 (1997).
25. (*a*) T. Clark, J. Chandrasekhar, G.W. Spitznagel, and P.v.R. Schleyer. J. Comput. Chem. **4**, 294 (1983); (*b*) W.J. Hehre, L. Radom, P.v.R. Schleyer, and J.A. Pople. Ab initio molecular orbital theory. Wiley-Interscience, New York. 1985; (*c*) M.J. Frisch, G.W. Trucks, M. Head-Gordon, P.M.W. Gill, M.W. Wong, J.B. Foresman, B.G. Johnson, H.B. Schlegel, M.A. Robb, E.S. Replogle, S. Gomperts, J.L. Andres, K. Raghavachari, J.S. Binkley, C. Gonzalez, R.L. Martin, D.J. Fox, D.J. DeFrees, J. Baker, J.J.P. Stewart, and J.A. Pople. Gaussian 92, Revision B. Gaussian, Inc., Pittsburgh, Pa. 1992.
26. L. Deng, V. Branchadell, and T. Ziegler. J. Am. Chem. Soc. **116**, 10645 (1994); S. Harder, A. Streitwieser, J.T. Petty, and P.v.R. Schleyer. J. Am. Chem. Soc. **117**, 3253 (1995); M.N. Glukhovtsev, A. Pross, H.B. Schlegel, R.D. Bach, and L. Radom. J. Am. Chem. Soc. **118**, 11258 (1996).
27. H.G. Floss and S. Lee. Acc. Chem. Res. **26**, 116 (1993); D.R. Houck, K. Kobayashi, J.M. Williamson, and H.G. Floss. J. Am. Chem. Soc. **108**, 5365 (1986); T. Frenzel, P. Zhou, and H.G. Floss. Arch. Biochem. Biophys. **278**, 35 (1990).
28. V.I. Minkin, M.E. Kletskii, R.M. Minyaev, B. Ya. Simkin, and V.A. Pichko. Zh. Org. Khim. **19**, 9 (1983); C.H. Heathcock, T.W. von Geldern, C.B. Lebrilla, and W.F. Maier. J. Org. Chem. **50**, 968 (1985).
29. (*a*) J. Bigeleisen. J. Chem. Phys. **17**, 675 (1949); (*b*) S. Wolfe, S. Hoz, C.-K. Kim, and K. Yang. J. Am. Chem. Soc. **112**, 4186 (1990); (*c*) S. Wolfe and C.-K. Kim. J. Am. Chem. Soc. **113**, 8056 (1991).
30. M.N. Glukhovtsev, A. Pross, and L. Radom. J. Am. Chem. Soc. **117**, 2024 (1995).
31. XMol: Version 1.3.1. Minnesota Supercomputer Center, Inc., Minneapolis, Minn. 1993.
32. J.W. Cornforth, J.W. Redmond, H. Eggerer, W. Buckel,and C. Gutschow. Nature, **221**, 1212 (1969); J. Lüthy, J. Rétey, and D. Arigoni. Nature, **221**, 1213 (1969).
33. T.R. Griffin, D.B. Cook, A. Haynes, J.M. Pearson, D. Monti, and G.E. Morris. J. Am. Chem. Soc. **118**, 3029 (1996).
34. S. Wolfe, K. Yang, N. Weinberg, Z. Shi, Y.-H. Hsieh, S. Ro, and R.D. Sharma. Chem. Eur. J. 1998. In press.
35. N. Weinberg and S. Wolfe. J. Am. Chem. Soc. **116**, 9860 (1994).
36. N.L. Allinger, Y.H. Yuh, and J.-H. Lii. J. Am. Chem. Soc. **111**, 8551 (1989).
37. A.D. Walsh. J. Chem. Soc. 2260 (1952), et seq.; B.M. Gimarc.

© 1998 NRC Canada

Acc. Chem. Res. **7**, 384 (1974); B.M. Gimarc. Molecular structure and bonding. The qualitative molecular orbital approach. Academic Press, New York. 1979.
38. I. Hoppe. Doctoral dissertation. Göttingen, Germany. 1971; U. Schöllkopf and I. Hoppe. Tetrahedron Lett. **27**, 4527 (1971); Ann. Chem. **765**, 153 (1972).
39. R.B. Woodward and R. Hoffmann. Angew. Chem. Int. Ed. Engl. **8**, 781 (1969).
40. H.-B. Bürgi, J.D. Dunitz, and E. Shefter. J. Am. Chem. Soc. **95**, 5065 (1973); H.-B. Bürgi, J.D. Dunitz, J.-M. Lehn, and G. Wipff. Tetrahedron, **30**, 1563 (1974); H.-B. Bürgi, J.-M. Lehn, and G. Wipff. J. Am. Chem. Soc. **96**, 1956 (1974).
41. N.T. Anh and O. Eisenstein. Nouv. J. Chim. **1**, 61 (1977); N.T. Anh. Orbitales frontières. CNRS Éditions, Paris. 1995. pp. 123, 124.

© 1998 NRC Canada

Hydration of the carbonyl group. Further evidence for a cooperative mechanism from experimental and theoretical studies of the hydrations of formaldehyde, acetaldehyde, acetone, and cyclohexanone

Saul Wolfe, Zheng Shi, Kiyull Yang, Stephen Ro, Noham Weinberg, and Chan-Kyung Kim

Abstract: The experimental pseudo-first-order rate constant for the neutral hydration of acetone by $H_2{}^{18}O$ has been determined by taking advantage of the ^{18}O isotope shift in the ^{13}C NMR spectrum of 2-^{13}C-labelled acetone. With the inclusion of this result, a previously reported computational procedure has been extended, with some refinements, to the neutral hydrations of formaldehyde, acetaldehyde, acetone, and cyclohexanone by different-sized water clusters in water solvent. Excellent agreement has been achieved between the experimental free energies of activation and the free energies of activation calculated for a cyclic mechanism in which the principal reaction channel contains four nonspectator water molecules. The computational procedure predicts that the cyclic water tetramer and the cubic water octamer are the principal constituents of bulk water, in agreement with Benson's tetramer–octamer model.

Key words: isotope shift, basis set superposition error (BSSE), self-consistent reaction field (SCRF), water clusters, hydration.

Résumé : On a déterminé la constante de vitesse expérimentale du pseudo-premier ordre pour la réaction d'hydratation neutre de l'acétone par le $H_2{}^{18}O$ en tirant profit du déplacement isotopique du ^{18}O dans le spectre RMN du ^{13}C de l'acétone marquée au ^{13}C en position 2. Après l'inclusion de ce résultat et en y apportant quelques améliorations, la méthode de calcul rapporté précédemment a éte étendu aux hydratations neutres du formaldéhyde, de l'acétaldéhyde, de l'acétone et de la cyclohexanone par des agrégats d'eau de diverses grosseurs dans l'eau comme solvant. On a obtenu d'excellents accords entre les énergies libres d'activation expérimentales et les valeurs correspondantes calculées pour un mécanisme cyclique dans lequel la voie de réaction principale comporte quatre molécules d'eau comme non spectateurs. La méthode de calcul permet de prédire que le tétramère cyclique et l'octamère cubique de l'eau sont les constituants principaux de l'eau dans son ensemble, en accord avec le modéle tétramère–octamère de Benson.

Mots clés : déplacement isotopique, erreur dérivée de la superposition d'ensemble de fonctions de base (« BSSE »), champ réactionnel autocohérent (« SCRF »), agrégats d'eau, hydratation.

[Traduit par la rédaction]

Introduction

The stepwise neutral hydration of a carbonyl group, e.g., eqs. [1]–[3], proceeds via

[1] $RR'C{=}O + H_2O \rightleftarrows RR'C{=}OH^+ + OH^-$

[2] $H_2O + RR'C{=}OH^+ \rightleftarrows H_2O^+\text{-}CRR'\text{-}OH$

[3] $H_2O + H_2O^+\text{-}CRR'\text{-}OH \rightleftarrows H_3O^+ + HO\text{-}CRR'\text{-}OH$

charged intermediates. If these intermediates were formed in water solvent, they would undergo continuous solvation and desolvation as they appeared and disappeared. Eigen (1) pointed out in 1965 that this sequence of events might be disfavored with respect to a cyclic, "cooperative" mechanism, and the subsequent experimental work of Bell et al. (2) quickly lent support to this idea. However, apart from numerous computational studies of the gas-phase hydration of formaldehyde by one or two water molecules (3), the cooperative mechanism has received only limited consideration (4), and the possibility

Received July 22, 1997.

This paper is dedicated to our longtime friend and colleague, Erwin Buncel, on the occasion of the beginning of his latest career.

S. Wolfe,[1] Z. Shi, K. Yang,[2] S. Ro, and C-K. Kim.[3] Department of Chemistry, Simon Fraser University, Burnaby, BC V5A 1S6, Canada. **N. Weinberg.** Department of Chemistry, Simon Fraser University, Burnaby, BC V5A 1S6, and Department of Chemistry, University College of the Fraser Valley, Abbotsford, BC V2S 7M9, Canada.

[1] Author to whom correspondence may be addressed. Telephone: (604) 291–5972. Fax: (604) 291–5973. E-mail: swolfe@sfu.ca.
[2] Present address: Department of Chemical Education, Gyeongsang National University, Chinju 660–701, Republic of Korea.
[3] Present address: Department of Chemistry, Inha University, Inchon 402–751, Republic of Korea.

 © 1998 NRC Canada

Fig. 1. A summary of the processes that describe the hydration of formaldehyde by $(H_2O)_n$.

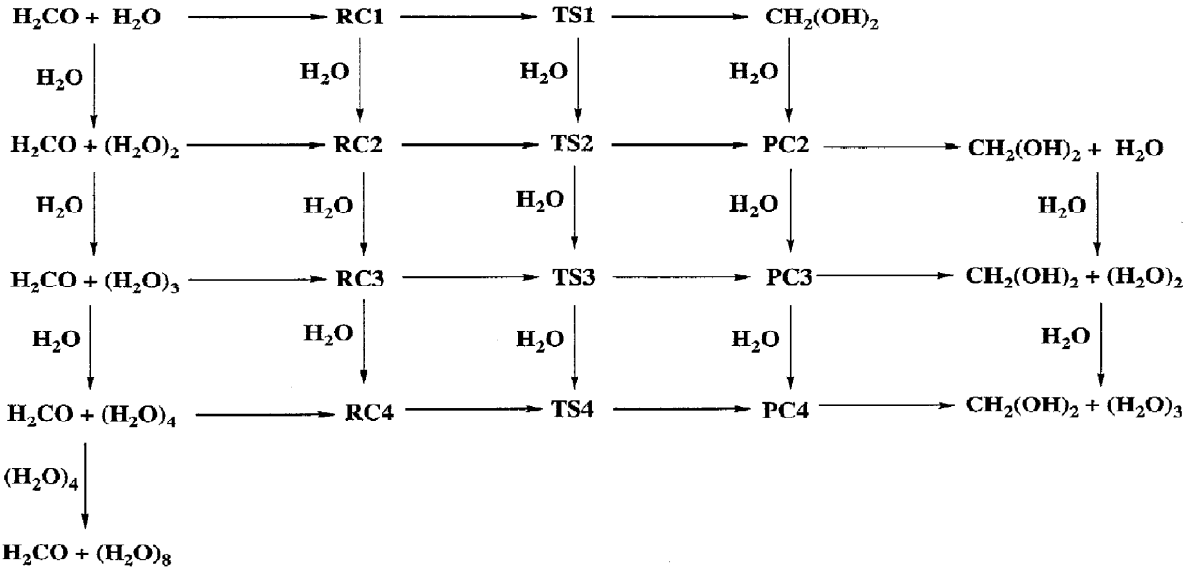

Fig. 2. The carbonyl carbon region of the ^{13}C NMR spectrum of a solution of 2-^{13}C-labelled acetone in $H_2{}^{18}O$ at various times.

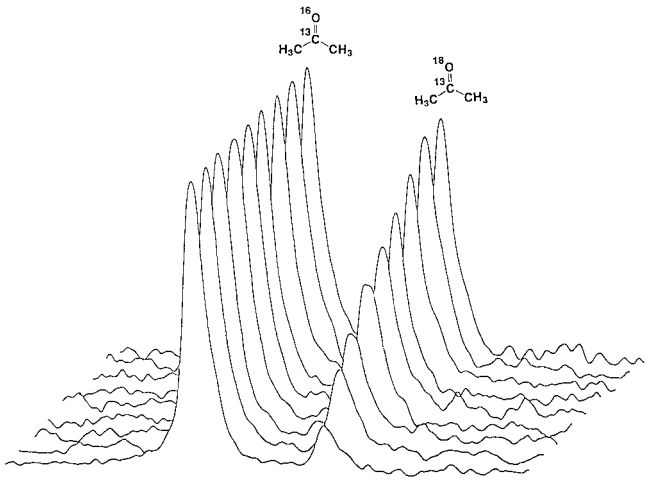

Fig. 3. Pseudo-first-order plot of the neutral hydration of acetone-2-^{13}C; $k_1 = 8.5 \times 10^{-6}$ s^{-1}; $r = 0.995$.

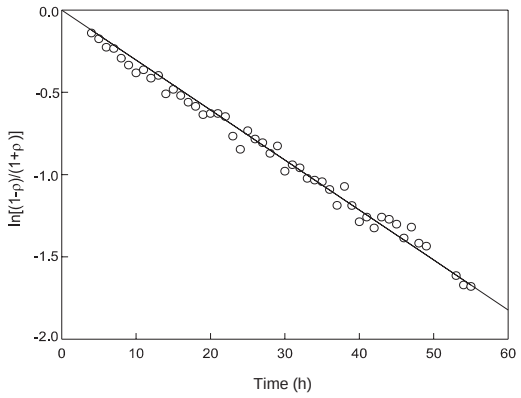

that nonionic pathways contribute significantly to hydrolytic processes in water solvent is usually disregarded.

We have suggested (5, 6) that penicillin-recognizing enzymes react via a cooperative mechanism. This proposal was advanced initially because of the presence of a small number of conserved water molecules in these enzymes, whose locations in the active sites are compatible with their participation in cyclic processes. A first test of the proposal, which employed gas-phase ab initio molecular orbital calculations to study the effect of one or two water molecules on the neutral alcoholysis of β-lactam rings (6–8), gave encouraging results and led to a more detailed theoretical examination of the cooperative mechanism, including quantitative connections to real experiments conducted in solution (9).

To treat the hydration of formaldehyde in water solvent, the self-consistent reaction field (SCRF) method (10) was first used to calculate the standard Gibbs free energies of the stationary structures summarized by the network of reactions depicted in Fig. 1, where RC*n* is a reactant complex of the type cyclo-CH_2O-$[H_2O]_n$ that proceeds over a transition state TS*n* to a product complex cyclo-$[HO\text{-}CH_2\text{-}OH][H_2O]_{n-1}$. The free energies were then corrected for basis set superposition error (BSSE) (11) and entropic effects associated with the loss of translational and rotational motion in solution. This provided the rate and equilibrium constants of the elementary steps of the reaction network, and the overall rate of hydration of formaldehyde was calculated as the sum of the contributions from reaction channels that involve one, two, three, or four water molecules. The final theoretical pseudo-first-order rate constant of 11.2 s^{-1} at 298 K agreed well with the estimated experimental value of 9.2 s^{-1} (12), and over 99% of the reaction was calculated to proceed via the cyclic complex **1** in which $n = 3$. This prediction is consistent with the experimental results of Bell et al. (2*a*), who concluded that the neutral hydration of a carbonyl group in dioxane solvent is catalyzed by two

© 1998 NRC Canada

Table 1. Calculated electronic energies E, vibrational energies E_v^{298}, and entropies S^{298} of the species that participate in the hydration of formaldehyde, acetaldehyde, acetone, and cyclohexanone.[a]

	Gas phase (HF/3–21G)			Water (HF/3–21G)		
Molecule	E (au)[b]	E_v^{298} (kcal/mol)	S^{298} (cal mol^{-1} K^{-1})	E (au)[b]	E_v^{298} (kcal/mol)	S^{298} (cal mol^{-1} K^{-1})
H_2O	–75.58596	13.668	45.087	–75.59046	13.674	45.104
$(H_2O)_2$	–151.18940	31.914	67.179	–151.20184	31.959	65.441
$(H_2O)_3$	–226.81434	51.255	73.868	–226.81870	51.228	72.732
$(H_2O)_4$	–302.44126	69.574	84.772	–302.44126	69.264	86.034
$(H_2O)_8$	–604.94305	145.439	114.356	–604.94305	145.088	144.688
CH_2O	–113.22182	18.195	52.139	–113.22558	18.220	52.146
CH_3CHO	–152.05525	38.128	62.381	–152.05867	38.121	62.286
$(CH_3)_2CO$	–190.88722	57.854	71.091	–190.89012	57.842	69.556
$(CH_2)_5CO$	–306.19162	103.916	77.949	–306.19395	103.914	77.938
			$CH_2O + (H_2O)_n$			
RC1	–188.82234	36.350	69.785	–188.83030	36.175	74.073
TS1	–188.75680	34.544	61.261	–188.76396	34.644	61.177
RC2	–264.43402	54.819	83.545	–264.43431	54.691	84.549
TS2	–264.41306	52.848	69.868	–264.41606	52.611	71.441
RC3	–340.05542	73.696	92.590	–340.05549	73.464	94.130
TS3	–340.04587	70.602	80.526	–340.04881	70.845	81.967
RC4	–415.67082	91.923	107.857	–415.67295	91.611	108.372
TS4	–415.66461	88.156	94.217	–415.66849	90.045	97.937
			$CH_3CHO + (H_2O)_n$			
$RC1_h$[c]	–227.65648	56.258	78.339	–227.66383	56.024	83.225
$TS1_h$	–227.58877	53.984	68.150	–227.59379	54.020	68.044
$RC2_h$	–303.27015	74.697	90.089	–303.27047	74.578	90.903
$TS2_h$	–303.24375	72.276	76.360	–303.24561	72.062	76.942
$RC3_h$	–378.88897	93.271	102.571	–378.88908	93.067	104.121
$TS3_h$	–378.87536	89.877	87.093	–378.87720	89.957	87.966
$RC4_h$	–454.50502	111.576	116.100	–454.50789	111.257	117.923
$TS4_h$	–454.49390	107.385	100.667	–454.49698	108.545	102.808
$RC1_m$[d]	–227.65985	56.398	76.698	–227.66403	56.424	76.604
$TS1_m$	–227.58887	53.952	68.399	–227.59336	54.000	68.300
$RC2_m$	–303.27386	74.826	90.875	–303.27577	74.775	91.274
$TS2_m$	–303.24329	72.192	76.076	–303.24537	71.985	76.908
$RC3_m$	–378.88906	93.427	99.395	–378.88995	93.150	102.704
$TS3_m$	–378.87573	89.817	85.809	–378.87767	89.839	86.797
$RC4_m$	–454.50467	111.678	114.731	–454.50760	111.403	114.651
$TS4_m$	–454.49442	107.234	98.741	–454.49805	108.007	99.924
			$(CH_3)_2CO + (H_2O)_n$			
RC1	–266.48508	75.619	88.641	–266.49369	75.693	87.111
TS1	–266.41920	73.254	74.645	–266.42268	73.261	74.545
RC2	–342.10466	94.427	97.267	–342.10504	94.275	100.124
TS2	–342.07275	91.465	81.562	–342.07419	91.275	81.880
RC3	–417.72280	112.888	110.877	–417.72379	112.775	109.547
TS3	–417.70424	108.924	91.453	–417.70551	108.852	92.140
RC4	–493.33978	131.286	121.045	–493.34230	131.111	122.257
TS4	–493.32265	126.267	104.300	–493.32534	126.904	105.801
			$(CH_2)_5CO + (H_2O)_n$			
$RC1_{ax}$[e]	–381.79411	121.926	95.783	–381.79468	121.945	94.205
$TS1_{ax}$	–381.72680	119.054	82.544	–381.72931	119.052	82.504
$RC2_{ax}$	–457.41108	140.620	105.137	–454.41122	140.541	105.931
$TS2_{ax}$	–457.37969	137.318	89.364	–457.38079	137.307	89.610
$RC3_{ax}$	–533.02680	158.909	115.788	–533.03027	159.261	115.055
$TS3_{ax}$	–533.01097	154.824	99.340	–533.01192	154.766	99.847
$RC4_{ax}$	–608.64425	177.299	128.014	–608.64764	177.563	127.824

© 1998 NRC Canada

Table 1 (*continued*).

$TS4_{ax}$	–608.62969	171.796	112.071	–608.63203	172.275	112.084
$RC1_{eq}$ [f]	–381.78944	121.577	96.343	–381.79027	121.507	97.492
$TS1_{eq}$	–381.72540	119.203	83.195	–381.72758	119.195	83.212
$RC2_{eq}$	–457.40892	140.363	106.324	–457.40922	140.265	107.451
$TS2_{eq}$	–457.37966	137.501	90.292	–457.38056	137.364	90.555
$RC3_{eq}$	–533.02695	158.864	120.819	–533.02743	158.771	120.141
$TS3_{eq}$	–533.01132	155.232	99.954	–533.01224	155.293	100.543
$RC4_{eq}$	–608.64197	177.056	132.963	–608.64687	177.207	130.276
$TS4_{eq}$	–608.63018	172.441	112.314	–608.63236	173.128	114.152

[a] Vibrational energies and entropies at 298 K. Entropies calculated by the Gaussian program, at 298 K in cal mol^{-1} K^{-1}; in the gas phase, $E^{298} = E + E_v^{298} 3RT$; $H^{298} = E^{298} + (PV)^{298}$.
[b] 1 au = 627.5 kcal/mol.
[c] h refers to attack *syn* to H (see structure **2**).
[d] m refers to attack *syn* to the methyl group (see structure **3**).
[e] ax refers to axial attack.
[f] eq refers to equatorial attack.

Table 2. Pseudo-first-order rate constants k and free energies of activation $\Delta G^{\neq}$ of uncatalyzed hydration of carbonyl groups at 298 K.

	Experimental		Calculated [a]		Calculated [b]	
Molecule	k (s^{-1})	$\Delta G^{\neq}$ (kcal/mol)	k (s^{-1})	$\Delta G^{\neq}$ (kcal/mol)	k (s^{-1})	$\Delta G^{\neq}$ (kcal/mol)
Formaldehyde	9.3 [c]	16.1	11.1	16.02	1.3	17.29
Acetaldehyde	4.3×10^{-3} [d]	20.7	4.0×10^{-2}	19.36	3.0×10^{-3}	20.89
Acetone	8.9×10^{-6} [e]	24.3	4.9×10^{-4}	21.97	19.6×10^{-6}	23.87
Cyclohexanone	0.7×10^{-4} [f]	23.1	3.6×10^{-2}	19.41	1.36×10^{-4}	22.72

[a] Using the strategy of ref. 9.
[b] Using the strategy of the present work.
[c] Reference 12.
[d] Reference 20.
[e] Present work.
[f] Reference 21.

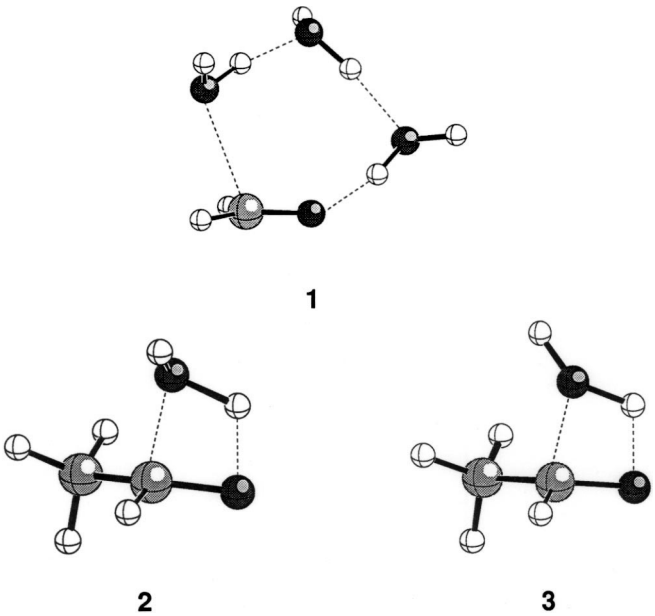

additional water molecules. The calculations also predicted that water dimer is a major constituent of bulk water. This does not agree with the Benson and Siebert (13) tetramer–octamer model.

The foregoing strategy has now been extended, with some refinements, to the neutral hydrations of acetaldehyde, acetone, and cyclohexanone in water solvent at 298 K. In the case of acetone, the experimental pseudo-first-order rate constant for the neutral hydration at 298 K, previously available as an estimate (14), was redetermined. In the case of acetaldehyde, two directions of attack are possible in each of the reaction channels, since addition may occur *syn* to hydrogen or *syn* to methyl, as shown in **2** and **3** for the one-water mechanism. In the case of cyclohexanone, there is axial and equatorial attack in each of the reaction channels. All of these pathways were examined.

Theory

Computations were performed using the Gaussian 92 (15) and Gaussian 94 (16) programmes, with the 3–21G basis set (17). This choice was dictated by the sizes of the systems to be treated, and is validated by the earlier finding (9) that, in the case of formaldehyde, HF/3–21G and MP2/6–31G(d) (18) calculations produce very similar results. The gas-phase reaction networks were calculated first, to obtain estimates of the radii of the spherical cavities needed for the application of the SCRF procedure with a dielectric constant of 78.5 (9, 10). All stationary points were verified by frequency calculations.

© 1998 NRC Canada

Fig. 4. A comparison of the experimental free energies of activation for the neutral hydrations of formaldehyde, acetaldehyde, acetone, and cyclohexanone, and the free energies of activation calculated using the strategy of ref. 9.

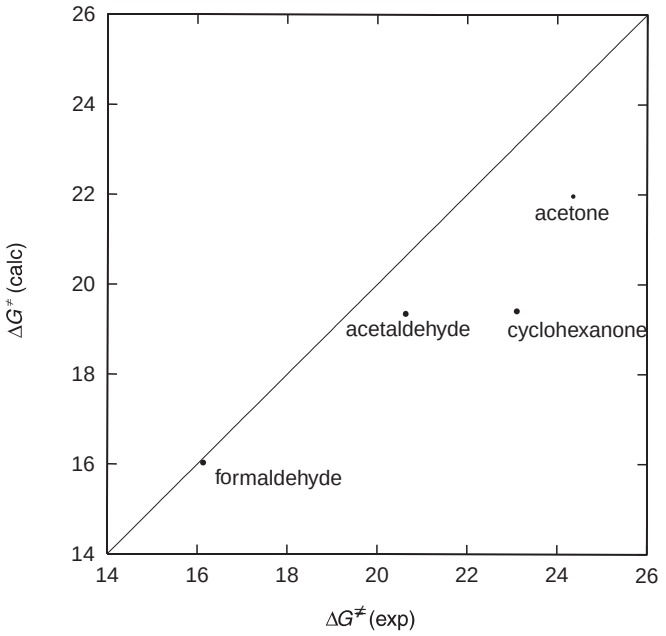

Fig. 6. Modification of Fig. 4, with theoretical free energies of activation calculated using the new BSSE procedure.

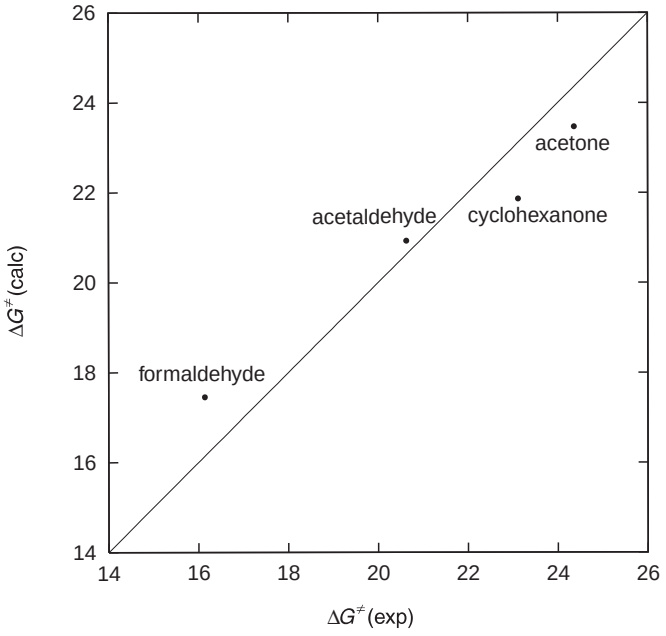

Experimental

A 2 mL vial was washed, dried for 24 h at 140°C, cooled under nitrogen, and charged successively with 98.5% enriched $H_2{}^{18}O$ (51 μL) (Aldrich) and $H_2{}^{16}O$ (49 μL), obtained from a MilliQ Plus ultrapure water system. The mixture was transferred immediately to a micro NMR tube maintained at 298 ± 0.1°C in the probe of a Bruker 600 AMX spectrometer

Fig. 5. Schematic representation of the strategy for the computation of basis set superposition error in ref. 9.

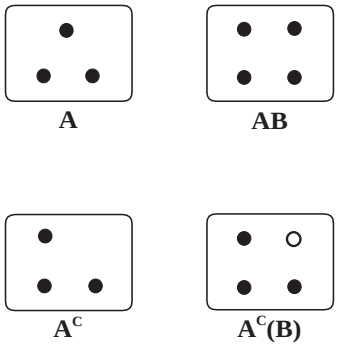

operating at a frequency of 150.03 MHz. Temperature control was achieved with a Euroterm VT temperature regulator. The hydration of acetone was initiated by injection of 12.5 μL of 99% atom-enriched 2 -^{13}C-acetone to produce a 1.7 M solution and a molar ratio of water to acetone of 35:1. The proton-decoupled ^{13}C NMR spectrum was recorded as a single scan every 60 min to obtain the peaks of $(Me)_2{}^{13}C{=}{}^{16}O[^{16}O]$ and $(Me)_2{}^{13}C{=}{}^{18}O[^{18}O]$, whose chemical shifts differ by 0.05 ppm (19). Figure 2 shows a typical set of spectra. These spectra were integrated to obtain the $[^{18}O]/[^{16}O]$ ratio (ρ) as a function of time.

The data were analyzed in terms of the equilibria shown in eq. [4]. The assumptions

$$[4] \qquad [^{16}O] \underset{k_2}{\overset{k_1}{\rightleftharpoons}} [diol]^* \underset{k_1}{\overset{k_2}{\rightleftharpoons}} [^{18}O]$$

of steady-state kinetics, a constant concentration of solvent, and a kinetic isotope effect of unity lead to eq. [5], where k_1 is the pseudo-first-order rate constant of interest.

$$[5] \qquad \ln\left(\frac{1-\rho}{1+\rho}\right) = -k_1 t$$

Results

Neutral hydration of acetone

Figure 3 is a plot of eq. [5] for the experiment described in the experimental section. The pseudo-first-order rate constant (average of two experiments) is $(8.9 \pm 0.4) \times 10^{-6}$ s^{-1}.

Application of the theoretical procedure of ref. 9 to the hydrations of acetaldehyde, acetone, and cyclohexanone

Table 1 summarizes the primary computational data. Full details of all stationary structures are available as supplementary data.[5] Table 2 gives the experimental pseudo-first-order rate constants at 298 K, the theoretical pseudo-first-order rate constants calculated using the strategy of ref. 9, and the experimental and theoretical Gibbs free energies of activation for the neutral hydrations of the four compounds. As can be seen in Fig. 4, only formaldehyde exhibits acceptable agreement between the experimental and theoretical activation barriers.

[5] Copies of material on deposit can be purchased from: The Depository of Unpublished Data, Document Delivery, CISTI, National Research Council Canada, Ottawa, Canada K1A 0S2.

© 1998 NRC Canada

Table 3. Basis set superposition error (BSSE) for the formation of $(H_2O)_n$ from nH_2O, and the formation of RCn from the interaction of $(H_2O)_n$ with a carbonyl compound in water.

Species	BSSE (kcal/mol)	Species	BSSE (kcal/mol)	Species	BSSE (kcal/mol)
Water clusters		Formaldehyde		Acetone	
$(H_2O)_2$	4.92	RC1	3.47	RC1	6.62
$(H_2O)_3$	18.59	RC2	8.70	RC2	10.72
$(H_2O)_4$	25.14	RC3	11.24	RC3	14.64
$(H_2O)_8$	74.05	RC4	13.45	RC4	16.83
Acetaldehyde *syn* to H		Acetaldehyde *syn* to Me			
$RC1_h$[a]	3.69	$RC1_m$[b]	8.01		
$RC2_h$	9.59	$RC2_m$	10.11		
$RC3_h$	11.36	$RC3_m$	14.36		
$RC4_h$	14.41	$RC4_m$	16.84		
Cyclohexanone axial		Cyclohexanone equatorial			
$RC1_{ax}$[c]	8.63	$RC1_{eq}$[d]	8.93		
$RC2_{ax}$	11.64	$RC2_{eq}$	10.86		
$RC3_{ax}$	18.86	$RC3_{eq}$	14.19		
$RC4_{ax}$	20.88	$RC4_{eq}$	17.88		

[a] h refers to attack *syn* to H (see structure **2**).
[b] m refers to attack *syn* to the methyl group (see structure **3**).
[c] ax refers to axial attack.
[d] eq refers to equatorial attack.

Table 4. Corrected enthalpy and entropy changes in water solvent at 298 K.

Reaction	ΔH (kcal/mol)	ΔS (cal mol^{-1} K^{-1})	ΔG (kcal/mol)
Water			
$2H_2O \rightarrow (H_2O)_2$	–5.16	–7.12	–3.03
$3H_2O \rightarrow (H_2O)_3$	–4.12	–21.67	2.34
$4H_2O \rightarrow (H_2O)_4$	–15.03	–28.49	–6.53
$8H_2O \rightarrow (H_2O)_8$	–39.49	–77.66	–16.33
Formaldehyde			
$CH_2O + (H_2O) \rightarrow$ RC1	–2.88	–2.98	
$CH_2O + (H_2O)_2 \rightarrow$ RC2	7.10	–6.18	
$CH_2O + (H_2O)_3 \rightarrow$ RC3	6.44	–2.09	
$CH_2O + (H_2O)_4 \rightarrow$ RC4	11.96	–0.97	
RC1 → TS1	40.10	–12.90	
RC2 → TS2	9.37	–13.11	
RC3 → TS3	1.57	–12.16	
RC4 → TS4	1.24	–10.44	
Acetaldehyde *syn* to H			
$CH_3CHO + (H_2O) \rightarrow$ RC1	–2.97	–0.37	
$CH_3CHO + (H_2O)_2 \rightarrow$ RC2	6.06	–6.03	
$CH_3CHO + (H_2O)_3 \rightarrow$ RC3	5.95	1.77	
$CH_3CHO + (H_2O)_4 \rightarrow$ RC4	11.26	2.39	
RC1 → TS1	41.95	–15.18	
RC2 → TS2	13.09	–13.96	
RC3 → TS3	4.35	–16.16	
RC4 → TS4	4.13	–15.12	
Acetaldehyde *syn* to Me			
$CH_3CHO + (H_2O) \rightarrow$ RC1	1.61	–7.50	
$CH_3CHO + (H_2O)_2 \rightarrow$ RC2	3.45	–6.07	
$CH_3CHO + (H_2O)_3 \rightarrow$ RC3	8.49	0.71	
$CH_3CHO + (H_2O)_4 \rightarrow$ RC4	14.27	–0.40	
RC1 → TS1	41.92	–8.30	
RC2 → TS2	16.29	–14.37	
RC3 → TS3	4.39	–15.91	
RC4 → TS4	2.60	–14.73	
Acetone			
$(CH_3)_2CO + (H_2O) \rightarrow$ RC1	0.90	–4.84	
$(CH_3)_2CO + (H_2O)_2 \rightarrow$ RC2	5.21	–4.13	
$(CH_3)_2CO + (H_2O)_3 \rightarrow$ RC3	7.17	0.01	
$(CH_3)_2CO + (H_2O)_4 \rightarrow$ RC4	12.20	–0.28	
RC1 → TS1	42.13	–12.57	
RC2 → TS2	16.36	–18.24	
RC3 → TS3	7.55	–17.41	
RC4 → TS4	6.44	–16.46	
Cyclohexanone axial			
$(CH_2)_5CO + (H_2O) \rightarrow$ RC1	4.87	–3.59	
$(CH_2)_5CO + (H_2O)_2 \rightarrow$ RC2	4.85	–4.56	
$(CH_2)_5CO + (H_2O)_3 \rightarrow$ RC3	10.14	–0.29	
$(CH_2)_5CO + (H_2O)_4 \rightarrow$ RC4	15.69	–0.31	
RC1 → TS1	38.13	–11.70	
RC2 → TS2	15.86	–16.32	
RC3 → TS3	7.02	–15.21	
RC4 → TS4	4.51	–15.74	
Cyclohexanone equatorial			
$(CH_2)_5CO + (H_2O) \rightarrow$ RC1	7.51	–0.47	
$(CH_2)_5CO + (H_2O)_2 \rightarrow$ RC2	5.05	–3.10	
$(CH_2)_5CO + (H_2O)_3 \rightarrow$ RC3	6.77	4.51	
$(CH_2)_5CO + (H_2O)_4 \rightarrow$ RC4	12.82	1.89	
RC1 → TS1	37.03	–14.28	
RC2 → TS2	15.08	–16.90	
RC3 → TS3	6.05	–19.60	
RC4 → TS4	5.02	–16.12	

© 1998 NRC Canada

Fig. 7. Modification of Fig. 4, with theoretical free energies of activation calculated using mass-weighted corrections to entropies.

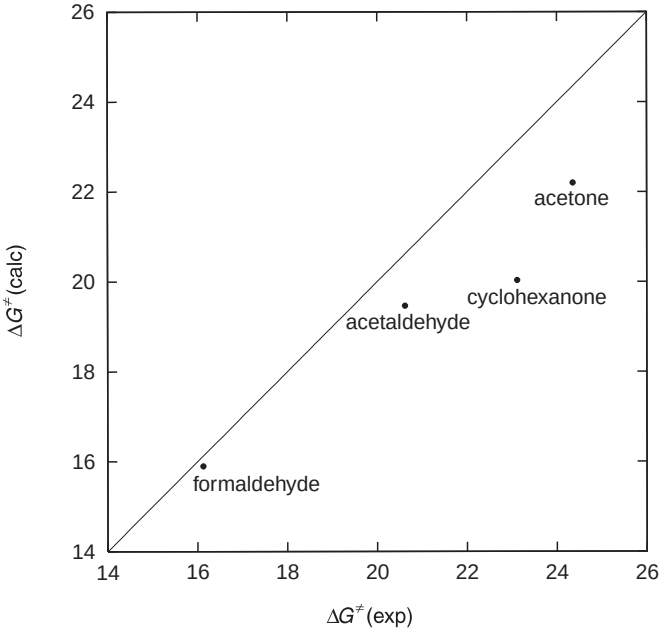

Fig. 8. Corrected free-energy changes (kcal/mol) in the network of reactions that describe the neutral hydration of formaldehyde. The transition structure of the principal reaction channel is shown.

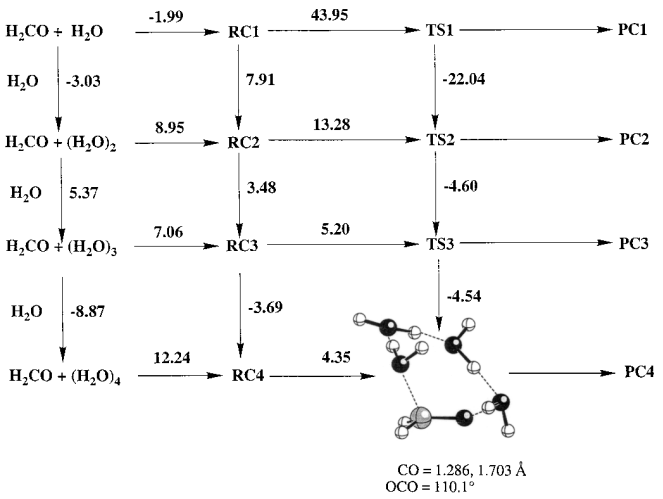

Fig. 9. Corrected free-energy changes (kcal/mol) in the network of reactions that describe the neutral hydration of acetaldehyde, with attack from the direction *syn* to hydrogen. The transition structure of the principal reaction channel is shown.

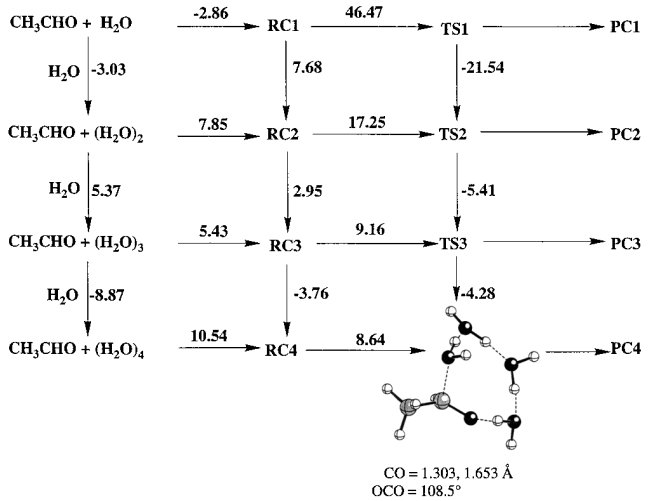

Fig. 10. Corrected free-energy changes (kcal/mol) in the network of reactions that describe the neutral hydration of acetaldehyde, with attack from the direction *syn* to the methyl group. The transition structure of the principal reaction channel is shown.

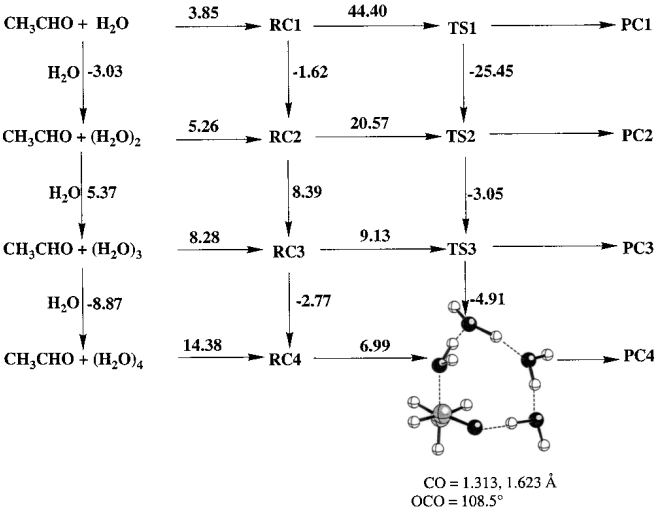

Over the complete data set, the rms deviation from the line of unit slope is 2.29 kcal/mol.

A consideration of possible origins of this deviation led to a re-examination and refinement of the BSSE and low-frequency corrections employed in ref. 9 and in the theoretical kinetic analysis of Fig. 4. These comprised a potential source of error, because the concentrations of $(H_2O)_n$ and RC*n* that are employed in the kinetic analysis are determined by their free energies, which depend upon the magnitudes of the BSSE corrections to the enthalpies, and the low-frequency corrections to the entropies calculated by Gaussian 94.

Re-examination and refinement of BSSE corrections to enthalpies

In our earlier study (9), a stepwise approach was used in which a BSSE correction was calculated for each elementary step (A + B → AB) of the overall process using eq. [6],

$$[6] \qquad E^{\mathrm{BSSE}} = (E^{\mathrm{C}}_{\mathrm{A}} - E^{\mathrm{C}}_{\mathrm{A(B)}}) + (E^{\mathrm{C}}_{\mathrm{B}} - E^{\mathrm{C}}_{\mathrm{B(A)}})$$

in which $E^{\mathrm{C}}_{\mathrm{A(B)}}$ and $E^{\mathrm{C}}_{\mathrm{A}}$ ($E^{\mathrm{C}}_{\mathrm{B(A)}}$ and $E^{\mathrm{C}}_{\mathrm{B}}$) are the energies of A(B) at the geometry of A(B) in AB, in the presence and absence of the ghost orbitals of B(A). The strategy is depicted schematically in Fig. 5. If A is water trimer and AB is water tetramer, the structures of A^C and $A^C(B)$ are as shown, where the open circle represents the ghost molecule B.

When defined in this way, the BSSE correction takes into account the energy difference between A and A^C (a deformation energy), and it is thought to be applicable when the geometry of an isolated species A differs significantly from the geometry of A in AB. However, this approximation makes the

© 1998 NRC Canada

Fig. 11. Corrected free-energy changes (kcal/mol) in the network of reactions that describe the neutral hydration of acetone. The transition structure of the principal reaction channel is shown.

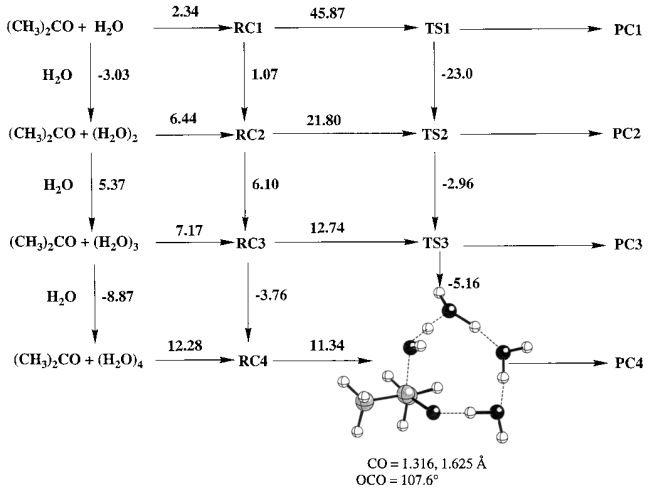

Fig. 12. Corrected free-energy changes in the network of reactions that describe the neutral hydration of cyclohexanone, with attack from the equatorial direction. The transition structure of the principal reaction channel is shown.

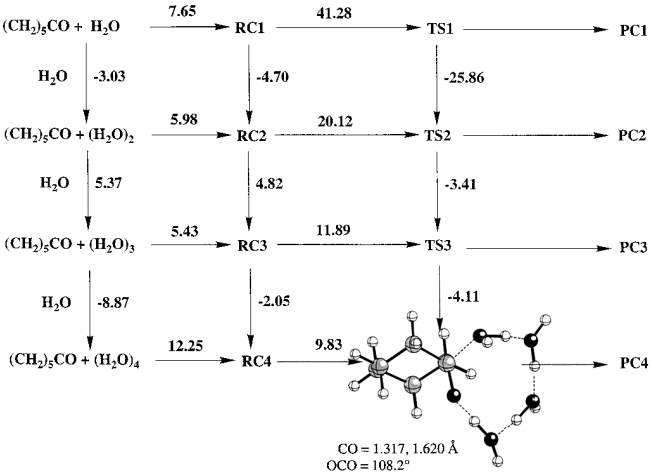

unjustifiable assumption that the BSSE is the same for A and A^C. If the variations in the geometries of the participating species are significant in each step, different BSSE corrections will be calculated for the different pathways of a two-step process A + B + C → ABC, i.e., A + B + C → AB + C → ABC and A + B + C → A + BC → ABC may have different BSSE corrections.

One way to avoid such problems is to recognize that each node of a reaction network comprises a thermodynamic state that is characterized by a unique set of thermodynamic parameters, and the values of these parameters do not depend on how this state is reached. Consequently, if a parameter can be reliably determined for one of the paths, its value can be used to calculate the variation over other paths. For example, for the process A + B + C → ABC, there is no ambiguity regarding the deformation energies of the monomers. The BSSE correction to the energy change will, therefore, take the simple form shown in eq. [7]. This strategy allows a BSSE-corrected energy to be assigned, without ambiguity, to

$$[7]\quad E^{\mathrm{BSSE}} = (E^{\mathrm{C}}_{\mathrm{A}} - E^{\mathrm{C}}_{\mathrm{A(BC)}}) + (E^{\mathrm{C}}_{\mathrm{B}} - E^{\mathrm{C}}_{\mathrm{B(AC)}}) + (E^{\mathrm{C}}_{\mathrm{C}} - E^{\mathrm{C}}_{\mathrm{C(AB)}})$$

each component of the reaction network.

For the water complexes w_n and the reactant complexes w_nc, the new BSSE corrections are now introduced through eqs. [8] and [9]. Table 3 summarizes the new BSSE

Fig. 13. Corrected free-energy changes (kcal/mol) in the network of reactions that describe the neutral hydration of cyclohexanone, with attack from the axial direction. The transition structure of the principal reaction channel is shown.

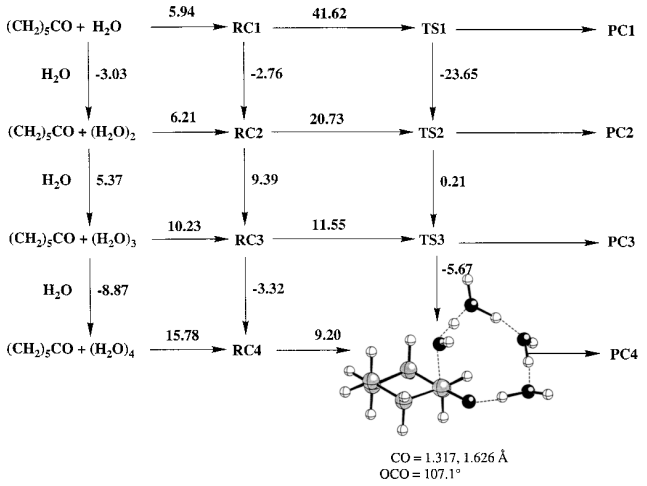

Fig. 14. Comparison of the experimental free energies of activation for the neutral hydrations of formaldehyde, acetaldehyde, acetone, and cyclohexanone, and the theoretical free energies of activation calculated for a cooperative mechanism with refinements of the treatment of BSSE and low-frequency vibrations.

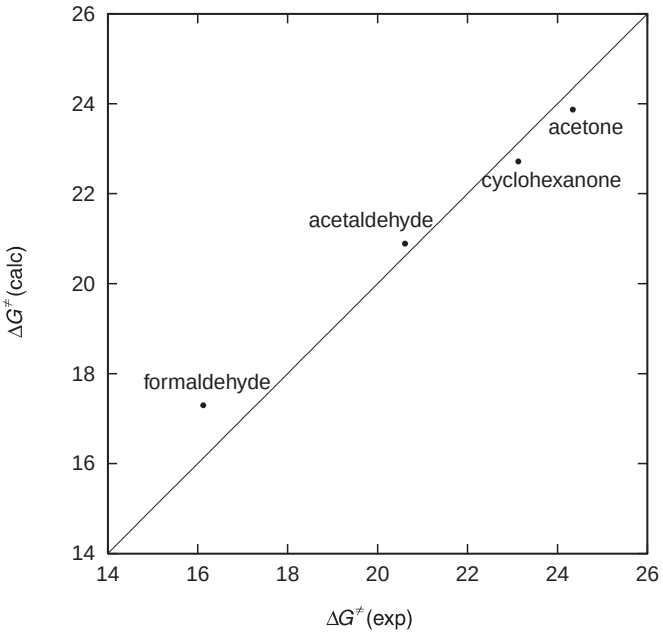

© 1998 NRC Canada

Table 5. Concentrations (M) of RR′C═O, $(H_2O)_n$, and RC*n*, contributions of the different reaction channels, pseudo-first-order rate constants k (s^{-1}), and free energies of activation (kcal/mol) for the uncatalyzed hydration of 1 M solutions of aldehydes and ketones.

Substrate (Reaction channel)	Species	Concentration	Contribution to reaction
Formaldehyde	$(H_2O)_1$	0.0404	
	$(H_2O)_2$	0.2738	
	$(H_2O)_3$	0.1267×10^{-5}	
	$(H_2O)_4$	0.1644	
	$(H_2O)_8$	0.6715×10^{1}	
	CH_2O	0.4632	
	RC1	0.5368	0.000
	RC2	0.3497×10^{-7}	0.000
	RC3	0.3913×10^{-11}	0.012
	RC4	0.8000×10^{-10}	0.988
$k_{calc} = 1.30$; $k_{exp}{}^a = 9.2$			
$\Delta G^{\neq}_{calc} = 17.29$; $\Delta G^{\neq}_{exp} = 16.13$			
Acetaldehyde	$(H_2O)_1$	0.0404	
	$(H_2O)_2$	0.2735	
	$(H_2O)_3$	0.1267×10^{-5}	
	$(H_2O)_4$	0.1640	
	$(H_2O)_8$	0.6678×10^{1}	
	CH_3CHO	0.1647	
(*syn* to H)	RC1	0.8353	0.000
	RC2	0.7865×10^{-7}	0.000
	RC3	0.2192×10^{-10}	0.017
	RC4	0.5020×10^{-9}	0.959
(*syn* to Me)	RC1	0.1004×10^{-4}	0.000
	RC2	0.6272×10^{-5}	0.000
	RC3	0.1778×10^{-12}	0.000
	RC4	0.7697×10^{-12}	0.024
$k_{calc} = 3.02 \times 10^{-3}$; $k_{exp}{}^a = 4.3 \times 10^{-3}$			
$\Delta G^{\neq}_{calc} = 20.89$; $\Delta G^{\neq}_{exp} = 20.67^a$			

Substrate (Reaction channel)	Species	Concentration	Contribution to reaction
Acetone	$(H_2O)_1$	0.0405	
	$(H_2O)_2$	0.2745	
	$(H_2O)_3$	0.1271×10^{-5}	
	$(H_2O)_4$	0.1652	
	$(H_2O)_8$	0.6781×10^{1}	
	$(CH_3)_2CO$	0.9992	
	RC1	0.7738×10^{-3}	0.000
	RC2	0.5210×10^{-5}	0.001
	RC3	0.7037×10^{-10}	0.004
	RC4	0.1629×10^{-9}	0.995
$k_{calc} = 19.6 \times 10^{-6}$; $k_{exp}{}^a = 8.9 \times 10^{-6}$			
$\Delta G^{\neq}_{calc} = 23.87$; $\Delta G^{\neq}_{exp} = 24.34$			
Cyclohexanone	$(H_2O)_1$	0.0405	
	$(H_2O)_2$	0.2745	
	$(H_2O)_3$	0.1271×10^{-5}	
	$(H_2O)_4$	0.1652	
	$(H_2O)_8$	0.6781×10^{1}	
	$(CH_2)_5CO$	0.1000×10^{1}	
(axial)	RC1	0.1772×10^{-5}	0.000
	RC2	0.7714×10^{-5}	0.000
	RC3	0.3998×10^{-13}	0.000
	RC4	0.4441×10^{-12}	0.007
(equatorial)	RC1	0.9980×10^{-7}	0.000
	RC2	0.1137×10^{-4}	0.002
	RC3	0.1336×10^{-9}	0.023
	RC4	0.1715×10^{-9}	0.967
$k_{ax} = 1.05 \times 10^{-6}$; $k_{eq} = 1.35 \times 10^{-4}$; $k_{calc} = 1.36 \times 10^{-4}$; $k_{exp}{}^a = 0.7 \times 10^{-4}$			
$\Delta G^{\neq}_{ax} = 25.60$; $\Delta G^{\neq}_{eq} = 22.72$; $\Delta G^{\neq}_{calc} = 22.72$; $\Delta G^{\neq}_{exp} = 23.11$			

[a] Data from Table 2.

[8] $n\mathrm{w} \rightarrow \mathrm{w}_n$,
$E(\mathrm{w}_n) = \Delta E_{\mathrm{uncorr}} + E^{\mathrm{BSSE}} + nE(\mathrm{w})$

[9] $n\mathrm{w} + \mathrm{c} \rightarrow \mathrm{w}_n\mathrm{c}$,
$E(\mathrm{w}_n\mathrm{c}) = \Delta E_{\mathrm{uncorr}} + E^{\mathrm{BSSE}} + nE(\mathrm{w}) + E(\mathrm{c})$

corrections, and the resulting refined values of ΔH are given in Table 4. These lead to the modification of Fig. 4 to Fig. 6. With an rms deviation of 1.02 kcal/mol from the line of unit slope, this represents a significant improvement.

Re-examination of low-frequency vibrations and corrections to entropies in solution

The ideal-gas statistical mechanical procedure is used in Gaussian 92 and Gaussian 94 to calculate thermodynamic parameters, not only in the gas phase but also in the SCRF treatment. This approximation is reasonable for the description of the enthalpy of a reaction in solution, but entropic effects are greatly overestimated. The reason for this is that, in the gas phase, the major contribution to the entropy change calculated for an association reaction A + B → AB arises from the loss of six degrees of freedom, representing free translations and rotations of A and B, and the conversion of these into six vibrational modes of AB. In solution, rotational and translational motions are restricted and are better described by a set of low-frequency vibrations (22), which can be represented by a single effective frequency ν (9, 23). The assumption that ν is approximately the same for A, B, and AB then leads to eq. [10] for a free-energy change in

$$[10] \quad \Delta G_{\mathrm{liq}} = \Delta H_{\mathrm{gas}} + T\Delta S_{\mathrm{v}} - 6RT\left[\frac{h\nu/\kappa T}{\exp(h\nu/\kappa T) - 1} - \ln[1 - \exp(-h\nu/kT)]\right]$$

solution, where ΔH_{gas} and ΔS_{v} are, respectively, the BSSE-corrected SCRF enthalpy change and the contribution of intramolecular vibrations to the entropy change calculated by the Gaussian programme.

© 1998 NRC Canada

In ref. 9, an effective frequency $\nu = 115$ cm was obtained, using eq. [11],

$$[11] \quad v = \frac{1}{2\pi}(k/m)^{1/2}$$

from calculations on water, which yielded an effective force constant $k = 1.7 \times 10^4$ dyn cm^{-1} (1 dyn = 10 μN). This effective frequency was used in eq. [44] of ref. 9 (≡ eq. [10]) for the final calculation of all free-energy changes. A refinement of this approach is to employ different effective frequencies for the stationary structures of the reaction network by taking the different masses of these structures into account, i.e., $\nu_i = (m_j/m_i)^{1/2}\nu_j$. The resulting corrected entropies are included in Table 4 and, with this refinement and the original treatment of BSSE, Fig. 4 is modified to Fig. 7, which exhibits an rms deviation of 1.96 kcal/mol from the line of unit slope.

Combining the refined BSSE and low-frequency corrections

The free-energy changes shown for the different water clusters in Table 4 lead to the important conclusion that the formation of $(H_2O)_{2n}$ from $(H_2O)_n$ is exoergic for each of $n = 1$, 2, and 4. Consequently, in terms of the equilibria examined in the present work, the "'cubic-shaped octamer' and 'two cyclic tetramers' appear to be the principal species present in liquid water" (13).The corrected free-energy changes in the hydration reactions are shown in Figs. 8–13, and the kinetic analyses, based on these free-energy changes, are summarized in Table 5. The final results are included in Table 2 and plotted in Fig. 14, which show that the rms deviation from the line of unit slope has been reduced to 0.67 kcal/mol. The success of the overall correlation validates Eigen's original proposal (1) regarding the neutral hydration of a carbonyl group.

Inspection of the final column of Table 5 leads to the following additional conclusions: (*i*) *the four-water molecule channel predominates*. The transition structures of these channels are included in Figs. 8–13, and they have the expected (24) nonperpendicular attack angle; (*ii*) *hydration of acetaldehyde proceeds from the direction* syn *to hydrogen*; (*iii*) *equatorial hydration of cyclohexanone is two orders of magnitude faster than axial hydration*. The stereoelectronic implications of (*iii*) and the application of the strategy of the present work to compounds of the type XCH_2CHO will be discussed in a forthcoming paper. Extensions of the approach to carboxylic acid-catalyzed hydration, and neutral, carboxylic acid-catalyzed and enzyme-catalyzed ester and amide hydrolysis have also been completed and will soon be submitted for publication.

Acknowledgements

The authors thank Professor J.P. Guthrie for a helpful suggestion, and the Natural Sciences and Engineering Research Council of Canada for financial support.

References

1. M. Eigen. Discuss. Faraday Soc. **39**, 7 (1965).
2. (*a*) R.P. Bell, J.P. Millington, and J.M. Pink. Proc. R. Soc. London Ser. A, **303**, 1 (1968); (*b*) R.P. Bell and J.E. Critchlow. Proc. R. Soc. London Ser. A, **325**, 35 (1971); (*c*) R.P. Bell and P.E. Sörensen. J. Chem. Soc. Perkin Trans. 2, 1740 (1972).
3. J.M. Madura and W.L. Jorgensen. J. Am. Chem. Soc. **108**, 2517 (1986); O.N. Ventura, E.L. Coitiño, K. Irving, and A. Iglesias. J. Mol. Struct. (THEOCHEM), **210**, 427 (1990); D. Peeters and G. Leroy. Can. J. Chem. **69**, 1376 (1991); A. Tachibana, H. Fueno, M. Yamato, and T. Yamabe. Int. J. Quantum Chem. **40**, 435 (1991); O.N. Ventura and E.S. Apostolova. J. Org. Chem. U.S.S.R. **27**, 573 (1991); E.L. Coitiño, A. Lledós, and J. Bertran. J. Comput. Chem. **13**, 1037 (1992); I.H. Williams. J. Am. Chem. Soc. **109**, 6299 (1987); C. Kozmutza, Zs. Ozoróczy, and E. Kapuy. J. Mol. Struct. (THEOCHEM), **204**, 101 (1990).
4. R.A. Cox and K. Yates. Can. J. Chem. **59**, 2853 (1981); R.A. Cox. Can. J. Chem. **74**, 1779 (1996).
5. S. Wolfe. Can. J. Chem. **72**, 1014 (1994).
6. S. Wolfe, C.-K. Kim, and K. Yang. Can. J. Chem. **72**, 1033 (1994).
7. S. Wolfe, H. Jin, K. Yang, C.-K. Kim, and E. McEachern. Can. J. Chem. **72**, 1051 (1994).
8. J. Pitarch, M.F. Ruiz-López, J.-L. Pascal-Ahuir, E. Silla, and I. Tuñón. J. Phys. Chem. B, **101**, 3581 (1997).
9. S. Wolfe, C.-K. Kim, K. Yang, N. Weinberg, and Z. Shi. J. Am. Chem. Soc. **117**, 4240 (1995).
10. O. Tapia and O. Goscinski. Mol. Phys. **29**, 1653 (1975); S. Miertuš, E. Scrocco, and J. Tomasi. J. Chem. Phys. **55**, 117 (1981); J.L. Pascual-Ahuir, E. Silla, J. Tomasi, and R. Bonaccorsi. J. Comput. Chem. **8**, 778 (1987); R. Bianco, S. Miertuš, M. Persico, and J. Tomasi. J. Chem. Phys. **168**, 281 (1992); G.W.A. Milne, M.C. Nicklaus, and M. Hodošek. J. Mol. Struct. **291**, 89 (1993); F.J. Olivares del Valle, M.A. Aguilar, and J.C. Contador. Chem. Phys. **170**, 161 (1993); M. Aguilar, R. Bianco, S. Miertuš, M. Persico, and J. Tomasi. J. Chem. Phys. **174**, 397 (1993); D.M.P. Mingos, A.L. Rohl, and J. Burgess. J. Chem. Soc. Dalton Trans. 423 (1993); B. Honig, K. Sharp, and A.-S. Yang. J. Phys. Chem. **97**, 1101 (1993); H.J. Kim, R. Bianco, B.J. Gertner, and J.T. Hynes. J. Phys. Chem. **97**, 1723 (1993); M. Bachs, F.J. Luque, and M. Orozco. J. Comput. Chem. **15**, 446 (1994); M.W. Wong, K.B. Wiberg, and M.J. Frisch. J. Chem. Phys. **95**, 8991 (1991); J. Am. Chem. Soc. **113**, 4776 (1991); **114**, 1645 (1992); A.S. Cieplak and K.B. Wiberg. J. Am. Chem. Soc. **114**, 9226 (1992); O.G. Parchment, I.H. Hillier, D.V.S. Green, N.A. Burton, J.O. Morley, and H.F. Schaefer III. J. Chem. Soc. Perkin Trans. 2, 1681 (1992); J.J.W. McDouall. J. Org. Chem. **57**, 2861 (1992); K.B. Wiberg and M.W. Wong. J. Am. Chem. Soc. **115**, 1078 (1993); I. Tuñón, E. Silla, and J. Tomasi. J. Phys. Chem. **96**, 9043 (1992); O.G. Parchment, D.V.S. Green, P.J. Taylor, and I.H. Hillier. J. Am. Chem. Soc. **115**, 2352 (1993); M.W. Wong, R. Leung-Toung, and C. Wentrup. J. Am. Chem. Soc. **115**, 2465 (1993); F.J. Luque. J. Phys. Chem. **97**, 9380 (1993); F.J. Olivares del Valle, M.A. Aguilar, and S. Tolosa. J. Mol. Struct. (THEOCHEM), **279**, 223 (1993); P.E. Young and I.H. Hillier. Chem. Phys. Lett. **215**, 405 (1993); I.R. Gould and I.H. Hillier. J. Chem. Soc. Perkin Trans. 2, 1771 (1993); F.R. Tortonda, J.-L. Pascual-Ahuir, E. Silla, and I. Tuñón. J. Phys. Chem. **97**, 11087 (1993); M. Orozco, W.L. Jorgensen, and F.J. Luque. J. Comput. Chem. **14**, 1498 (1993); K.B. Wiberg and M. Marquez. J. Am. Chem. Soc. **116**, 2197 (1994).
11. S.F. Boys and F. Bernardi. Mol. Phys. **19**, 553 (1970); O.N. Ventura, E.L. Coitiño, K. Irving, A. Iglesias, and A. LLedós. J. Mol. Struct. (THEOCHEM), **210**, 427 (1990); D.B. Cook, T.L. Sordo, and J.A. Sordo. J. Chem. Soc. Chem. Commun. 185 (1990); P. Valiron, Á. Vibók, and I. Mayer. J. Comput. Chem. **14**, 401 (1993); L. Turi and J.J. Dannenberg. J. Phys. Chem. **97**, 2488 (1993); J.A. Dobado and J.M. Molina. J. Phys. Chem. **97**, 7499 (1993); E.R. Davidson and S.J. Chakravorty. Chem. Phys. Lett. **217**, 48 (1993); I. Mayer, Á. Vibók, and P. Valiron. Chem. Phys. Lett. **224**, 166 (1994); P. Wind and J.-L. Heully. Chem. Phys. Lett. **230**, 35 (1994); T. Neuhauser, B.A. Hess, C. Reutel, and E. Weber. J. Phys. Chem. **98**, 6459 (1994); M. Kieninger, S.

© 1998 NRC Canada

Suhai, and I. Mayer. Chem. Phys. Lett. **230**, 485 (1994); F.M. Muguet and G.W. Robinson. J. Chem. Phys. **102**, 3648 (1995); H.L. Williams, E.M. Mas, K. Szalewicz, and B. Jeziorski. J. Chem. Phys. **103**, 7374 (1995); I. Alkorta, J. Elguero, and C. Foces-Foces. J. Chem. Soc. Chem. Commun. 1633 (1996); M. Gutowski, M.M. Szesniak, and G. Chalasinski. Chem. Phys. Lett. **241**, 140 (1995); J.J. Novoa, M. Planas, and M.C Rovira. Chem. Phys. Lett. **251**, 33 (1996); M. Planas, C. Lee, and J.J. Novoa. J. Phys. Chem. **100**, 16495 (1996); F. Jensen. Chem. Phys. Lett. **261**, 633 (1996).

12. R.P. Bell and P.G. Evans. Proc. R. Soc. London Ser. A, **291**, 297 (1966); I.H. Williams, D. Spangler, D.A. Femec, G.M. Maggiora, and R.L. Schowen. J. Am. Chem. Soc. **105**, 31 (1983).
13. S.W. Benson and E.D. Siebert. J. Am. Chem. Soc. **114**, 4269 (1992).
14. P. Greenzaid, Z. Luz, and D. Samuel. Trans. Faraday Soc. **64**, 2780 (1968).
15. M.J. Frisch, G.W. Trucks, M. Head-Gordon, P.M.W. Gill, M.W. Wong, J.B. Foresman, B.G. Johnson, H.B. Schlegel, M.A. Robb, E.S. Replogle, S. Gomperts, J.L. Andres, K. Raghavacharan, J.S. Binkley, C. Gonzalez, R.L. Martin, D.J. Fox, D.J. DeFrees, J. Baker, J.J.P. Stewart, and J.A. Pople. Gaussian 92, Revision B. Gaussian, Inc., Pittsburgh, Pa. 1992.
16. M.J. Frisch, G.W. Trucks, H.B. Schlegel, P.M.W. Gill, B.G. Johnson, M.A. Robb, J.R. Cheeseman, T. Keith, G.A. Petersson, J.A. Montgomery, K. Raghavachari, M.A. Al-Laham, V.G. Zakrzewski, J.V. Ortiz, J.B. Foresman, J. Cioslowski, B.B. Stefanov, A. Nanayakkara, M. Challacombe, C.Y. Peng, P.Y. Ayala, W. Chen, M.W. Wong, J.L. Andres, E.S. Replogle, R. Gomperts, R.L. Martin, D.J. Fox, J.S. Binkley, D.J. DeFrees, J. Baker, J.P. Stewart, M. Head-Gordon, C. Gonzales, and J.A. Pople. Gaussian 94, Revision D.1. Gaussian, Inc., Pittsburgh, Pa. 1995.
17. J.S. Binkley, J.A. Pople, and W.J. Hehre. J. Am. Chem. Soc. **102**, 939 (1980).
18. W.J. Hehre, L. Radom, P.v.R. Schleyer, and J.A. Pople. Ab initio molecular orbital theory. Wiley-Interscience, New York. 1986.
19. J.M. Risley and R.L. Van Etten. J. Am. Chem. Soc. **102**, 4609 (1980).
20. R.P. Bell, M.H. Rand, and K.M.A. Wynne-Jones. Trans. Faraday Soc. **52**, 1093 (1956); J.E. Critchlow. J. Chem. Soc. Faraday Trans. 1, **68**, 1774 (1972).
21. P. Greenzaid, Z. Luz, and D. Samuel. Trans. Faraday Soc. **64**, 2787 (1968).
22. J.O. Hirschfelder, C.F. Curtis, and R.B. Bird. Molecular theory of gases and liquids. Wiley, New York. 1954.
23. R. Kubo. Statistical mechanics. North Holland Publishers, Amsterdam. 1965.
24. H.B. Bürgi, J.D. Dunitz, and E. Shefter. J. Am. Chem. Soc. **95**, 5065 (1973); N.T. Anh. Orbitales frontieres. CNRS Éditions, Paris. 1995. pp. 123, 124.

© 1998 NRC Canada

1,2-Bis(1-aryl-3-alkyltriazen-3-yl)ethanes and related compounds

Donald L. Hooper, Ian R. Pottie, Marc Vacheresse, and Keith Vaughan

Abstract: A series of novel bistriazenes, the 1,2-bis(1-aryl-3-methyltriazen-3-yl)ethanes, Ar-N═N-NMe-CH_2CH_2-NMe-N═N-Ar, have been synthesized by diazonium coupling with *N,N′*-dimethylethylenediamine. These bistriazenes are stable crystalline compounds and have been unequivocally characterized by IR and NMR spectroscopy (^{1}H and ^{13}C), and elemental analysis. The structures of two compounds in the series have been confirmed by X-ray crystallography. The ^{1}H NMR spectra show significant line broadening of the N-methyl resonances arising from the restricted rotation around the N2—N3 bond of the triazene units. The presence of strongly electron-withdrawing groups on the aryl ring restricts the rotation to the point where the N-methyl signals of the rotamers are distinct even at room temperature; four resonances of the N-methyl signal are clearly evident and these can be assigned to the *anti–anti*, *syn–syn,* and *syn–anti* conformations of the bistriazene. Diazonium coupling with *N,N′*-diethylethylenediamine affords the N,N′-diethyl homologues of the bistriazenes, which have been similarly characterized. As model compounds to assist in spectroscopic analysis, a series of related triazenes, the 1-(1-aryl-3-methyltriazen-3-yl)-*N,N*-dimethyl-2-ethanamines, were prepared by diazonium coupling with *N,N,N′*-trimethylethylenediamine. These dialkyltriazenes exist mainly as oils, but characterization was achieved by IR, ^{1}H NMR, and ^{13}C NMR spectroscopy, also showing the presence of two rotamers in solution when strongly electron-withdrawing substituents are bonded to the aryl moiety.

Key words: triazene, bistriazene, diazonium, ethylenediamine, molecular dynamics, NMR.

Résumé : On a synthétisé une série de nouveaux bistriazènes, les 1,2-bis(1-aryl-3-méthyltrizén-3-yl)éthanes Ar-N═N-NMe-C_2-C_2-NMe-N═N-Ar, par couplage de diazonium avec la *N,N′*-diméthyléthylènediamine. Ces bistriazènes sont des composés cristallins stables et on les a caractérisés sans équivoque par leurs analyses élémentaires et par spectroscopies IR et RMN (du ^{1}H et du ^{13}C). On a confirmé les structures de deux composés de la série par diffraction des rayons X. Dans les spectres de RMN du ^{1}H, on observe un élargissement important des raies dues aux résonances des groupes N-méthyles résultant d'une rotation empêchée autour de la liaison N2—N3 des unités triazènes. La présence de groupes fortement électroaffinitaires sur le noyau aryle provoque une restriction de la rotation telle qu'elle que l'on peut observer des signaux distincts pour les groupes N-méthyles, même à la température ambiante; on peut facilement observer quatre raies de résonance comme signal du N-méthyle et celles-ci peuvent être attribuées aux conformations *anti–anti, syn–syn* et *syn–anti* du bistriazène. Le couplage de diazonium avec la *N,N′*-diéthyléthylènediamine conduit aux analogues N,N′-diéthylés des bistriazènes qui ont été caractérisés de la même manière. Dans le but d'avoir des composés modèles permettant d'aider dans les analyses spectroscopiques, on a préparé une série de triazènes apparentés, les 1-(1-aryl-3-méthyltraizén-3-yl)-*N,N*-diméthyl-2-éthanamines, par couplage de diazonium avec la *N,N,N′*-triméthyléthylènediamine. Ces dialkyltriazènes existent principalement sous la forme d'huiles qui ont été caractérisées par spectroscopies IR et RMN du ^{1}H et du ^{13}C; quand la portion aryle comporte des substituants fortement électroaffinitaires, on y détecte aussi la présence de deux rotamères en solution.

Mots clés : triazène, bistriazène, diazonium, éthylènediamine, dynamique moléculaire, RMN.

[Traduit par la rédaction]

Introduction

The trivial name "bistriazene" has been used to describe a number of organic molecules that contain more than one triazene unit (N═N-N). The synthesis of 1,2-bis(alkyltriazeno)ethanes (**1**) was reported by Blumenstein and Michejda (1) from the reaction of an alkyllithium reagent with the diazide, $N_3CH_2CH_2N_3$; these triazenes are potently cytotoxic and are believed to have the ability to cross-link DNA. The hydroxymethyltriazenes, Ar-N═N-NR-CH_2OH, another class of cytotoxic triazene, are produced in the coupling reaction of a formaldehyde–methylamine mixture with a series of diazonium ions (2). A bistriazene by-product of this reaction, the *N,N*-bis(1-aryl-3-methyltriazen-3-ylmethyl)methylamine (**2**), is formed when there is an absence of M groups within the aryl ring and a low formaldehyde/methylamine ratio is used (3).

Recently we reported the synthesis of a different type of bistriazene; the 1,2-bis[4′-(triazenyl)phenyl]ethanes (**3**) were

Received July 29, 1997.

D.L. Hooper. Department of Chemistry, Dalhousie University, Halifax, NS B3H 4J3, Canada.

I.R. Pottie, M. Vacheresse, and K. Vaughan.[1] Department of Chemistry, Saint Mary's University, Halifax, NS B3H 3C3, Canada.

[1] Author to whom correspondence may be addressed. Telephone: (902) 420-5650. Fax: (902) 496-8104. E-mail: keith.vaughan@stmarys.ca

© 1998 NRC Canada

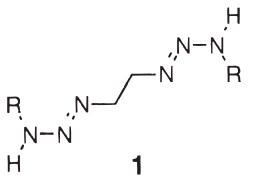

1

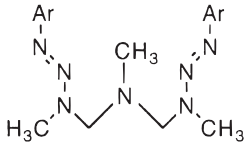

2

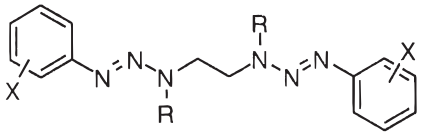

4 R = Me

5 R = Et

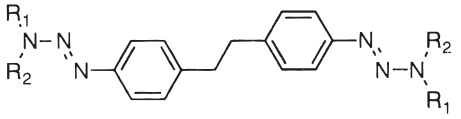

3

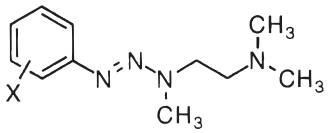

6

Table 1. Physical data for 1,2-bis(1-aryl-3-methyltriazen-3-yl)ethanes **4**.

Compound	X	Yield (%)	Melting point (°C)	IR (cm^{-1})	Recryst. solvent
4a	H	88	68–70	750, 690	Hexanes
4b	*p*-CN	95	167–168	2180 (CN)	Ethanol
4c	*p*-CO_2Me	98	128–129	1680 (C═O), 1250, 1135 (C-O)	Ethanol
4d	*p*-CO_2Et	87	99–100	1680 (C═O), 1240, 1125 (C-O)	Hexanes
4e	*p*-CH_3	96	99–101	800 (OOP *p*-sub)	Hexanes
4f	*p*-NO_2	98	219–222	1320, 1490 (NO_2)	Toluene
4g	*p*-OCH_3	76	104–106	1225, 1100 (C-O)	Hexanes
4h	*p*-$COCH_3$	92	159–161	1650 (C═O)	Ethanol
4i	*p*-Br	82	114–116	1050 (Ar-Br)	Hexanes
4j	*o*-CN	50	111–112.5	2180 (CN)	Hexanes – ethyl acetate
4k	*o*-CO_2Me	63	75–80	1710 (C═O), 1050, 1225 (C-O)	Hexanes –ethyl acetate
4l	*o*-CO_2Et	79	Oil	1690 (C═O)	Column
4m	*o*-CH_3	78	Oil	730 (OOP *o*-sub)	Column
4n	*o*-NO_2	57	101.5–103	1500, 1360 (NO_2)	Hexanes
4o	*o*-OCH_3	50	79.5–82	1210, 1040 (C-O)	Hexanes –ethyl acetate
4p	*o*-$COCH_3$	69	Oil	1710 (C═O)	Column

synthesized by bis-diazotization of 4,4′-ethylenedianiline and coupling of the resulting bisdiazonium salt with the appropriate alkylamine (4). This paper reports the synthesis of a new type of bistriazene, the 1,2-bis(1-aryl-3-methyltriazen-3-yl)ethanes (**4**) and the N-ethyl homologues (**5**), by the reaction of the appropriate diazonium salt with the *N,N*′-dialkylethylenediamine. We also report here the synthesis of novel dialkyltriazenes, the 1-(1-aryl-3-methyltriazen-3-yl)-*N,N*-dimethyl-2-ethaneamines (**6**), by the reaction of the appropriate diazonium salt with *N,N,N*′-trimethylethylenediamine. It is anticipated that triazenes of series **4** and **6** will have antitumour activity of the same order as that reported (5) for the 1-aryl-3,3-dimethyltriazenes, Ar-N═N-NMe_2.

Experimental

All reagents were reagent grade materials purchased from Aldrich Chemical Co. Ltd. and were used without further purification. Melting points were determined on a Reichert hot-stage microscope and are uncorrected. Infrared spectra were obtained using Nujol mulls, unless otherwise stated, on a Perkin–Elmer 299 spectrophotometer. ^1H and ^{13}C NMR spectra were obtained on a Bruker 250 MHz spectrophotometer at the Atlantic Regional Magnetic Resonance Center at Dalhousie University in Halifax, Nova Scotia. Chemical shifts were recorded in $CDCl_3$ solutions at 20°C, and are relative to TMS as internal standard. Crystal structures were determined on an Enraf–Nonius CAD-4 diffractometer. Elemental analyses were performed by the Canadian Microanalytical Service Ltd., Delta, B.C.

1,2-Bis(1-aryl-3-alkyltriazen-3-yl)ethanes 4 and 5

General procedure

The arylamine $ArNH_2$ (0.01 mol) was dissolved in 2 N hydrochloric acid (25 mL) and gently heated if necessary to obtain a clear solution. (Arylamines with *ortho* substituents were dissolved in 3 N HCl to prevent precipitation during diazotization.) The solution was cooled in ice–salt and kept at 0–5°C while being diazotized with a solution of sodium nitrite (0.011 mol) in deionized water (10 mL). The diazonium salt solution was stirred for a further 0.5 h and any insoluble impurities were removed by vacuum filtration. The *N,N*′-dialkyl-1,2-ethanediamine (0.005 mol) was dissolved in deionized water (5 mL) and then added to the cold diazonium salt solution, keeping the temperature at 0–5°C. The resulting mixture

© 1998 NRC Canada

Table 2. ^{1}H NMR data for 1,2-bis(1-aryl-3-methyltriazen-3-yl)ethanes (**4**); chemical shifts in ppm relative to TMS (1%) at 22°C in $CDCl_3$.

Compound	X	N-Me	Aromatic	-CH_2-	X
4a	H	3.24 (br)	7.11–7.37	4.02	N/A
4b	*p*-CN	3.53, 3.25	7.56, 7.53, 7.36, 7.33	4.14	N/A
4c	*p*-CO_2Me	3.24 (br)	8.00, 7.97, 7.40, 7.37	4.10	3.90
4d	*p*-CO_2Et	3.24 (br)	8.01, 7.98, 7.40, 7.37	4.10	4.36 (q) 1.39 (t)
4e	*p*-CH_3	3.23	7.31, 7.28, 7.13, 7.10	4.00	2.32
4f	*p*-NO_2	3.23, 3.33	8.19, 8.16, 8.14, 8.10, 7.54, 7.50, 7.43, 7.39	4.35	—
4g	*p*-OCH_3	3.22	7.36, 7.33, 6.87, 6.84	4.00	3.80
4h	*p*-$COCH_3$	3.25	7.92, 7.89, 7.40, 7.38	4.12	2.58
4i	*p*-Br	3.23	7.42, 7.39, 7.25, 7.24	4.03	N/A
4j	*o*-CN	3.32, 3.37 3.55, 3.65	7.09–7.63	4.16, 4.22	N/A
4k	*o*-CO_2Me	3.27 (br)	7.06–7.76	4.08 (br)	3.85
4l	*o*-CO_2Et	3.26 (br)	7.15–7.67	4.07 (br), 1.31 (t)	4.32 (q)
4m	*o*-CH_3	3.24 (br)	7.01–7.18	4.03	2.37
4n	*o*-NO_2	3.24, 3.54, 3.57	7.15–7.74	4.11, 4.01	N/A
4o	*o*-OCH_3	3.32	6.86–7.29	4.07	3.86
4p	*o*-$COCH_3$	3.22 (br)	7.16–7.52	4.10	2.46

Table 3. ^{13}C NMR data for 1,2-bis(1-aryl-3-methyltriazen-3-yl)ethanes (**4**); chemical shifts in ppm relative to TMS(1%) at 22°C in $CDCl_3$.

Compound	X	N-Me	Aromatic	-CH_2-	X
4a	H	Not obsd.	150.7, 128.9 125.7, 120.7	Not obsd.	N/A
4b	*p*-CN	35.4	153.6, 133.0, 121.1, 119.4	54.4	108.3
4c	*p*-CO_2Me	35.4	154.1, 130.6, 126.9, 120.4	54.5	167.1, 52.0
4d	*p*-CO_2Et	Not obsd.	154.0, 130.5, 127.3, 120.3	Not obsd.	166.6, 14.4, 60.8
4e	*p*-CH_3	36.3	148.5, 135.3, 129.4, 120.5	52.13	21.06
4g	*p*-OCH_3	36.5	157.8, 144.6, 121.6, 114.02	51.75	55.46
4h	*p*-$COCH_3$	35.4	154.1, 134.2, 129.4, 120.5	54.3	197.4, 26.55
4i	*p*-Br	Not obsd.	149.6, 131.8, 122.2, 118.8	Not obsd.	N/A
4j	*o*-CN	42.9, 42.8 36.3, 35.7	117.9–153.05	54.4, 51.1, 48.1, 43.9	107.5
4k	*o*-CO_2Me	34.9	149.8, 131.8, 129.6, 126.15, 125.1, 119.5	54.2	52.0, 168.6
4l	*o*-CO_2Et	Not obsd	149.6, 131.6, 129.5, 126.6, 125.1, 119.4	Not obsd.	60.9, 14.4
4m	*o*-CH_3	35.5	148.5, 132.7, 130.6, 126.2, 125.5, 116.6	52.7	17.7
4o	*o*-OCH_3	35.6	152.3, 139.8, 126.85, 121.1, 119.2, 110.7	54.2	56.1
4p	*o*-$COCH_3$	32.1, 35.6	148.5, 135.1, 131.6, 128.3, 125.6, 118.2	54.2	203.4, 21.1, 14.2

was stirred for 0.5 h and then the pH was adjusted to the alkaline region (approx. pH = 8) using saturated $NaHCO_3$. The product then precipitated from solution as an oil or as a solid.

Solid precipitates were isolated by vacuum filtration and purified by recrystallization from an appropriate solvent (see Table 1). Oils were recovered by extraction into dichloromethane (3 15-mL aliquots), and the extract was dried over anhydrous sodium sulphate. The extract was filtered and rotoevaporated under vacuum to remove the solvent. The residual oil was purified by either (*a*) column chromatography using Hi-Flosil (60–200 mesh) with 10:1 hexanes/ethyl acetate as eluent, or (*b*) by dissolving the oil (e.g., compound **5f**) in hot hexane – ethyl acetate and cooling to afford an oil of greater purity. The crude oils usually showed two or three dots on TLC; when the crude oil was purified by method (*b*), the TLC became much cleaner — the two impurities would usually disappear from the TLC plate and the NMR spectra were also much cleaner.

Physical data for compounds **4a–4p** are reported in Table 1 and NMR data can be found in Tables 2 and 3. The data collected for compounds **5a–5g** can be found in Tables 4–6. The identities of compounds **4b**, **4e**, **4h**, **4j**, **4o**, and **5a** were confirmed by elemental analysis (Table 7).

1-(1-Aryl-3-methyltriazen-3-yl)-*N,N*-dimethyl-2-ethanamine 6

General procedure

The general procedure for the synthesis of series **4** and **5**, above, was reproduced using *N,N,N′*-trimethyl-1,2-ethylenediamine to couple with one equivalent of the diazonium salt. However, with series **6** it was found necessary to use saturated aqueous KOH to adjust the alkalinity to approximately pH = 12, in order to precipitate these triazenes. The products were mainly oils or solids (Table 8). Solids were purified by crystallization. Oils were purified as described above. None of the products formed as oils showed impurities in the

© 1998 NRC Canada

Table 4. Physical data for 1,2-bis(1-aryl-3-ethyltriazen-3-yl)ethanes (**5**).

Compound	X	Yield (%)	Melting point (°C)	IR (cm^{-1})	Recryst. solvent
5a	*p*-CN	67	122–124	2215 (CN)	Ethanol
5b	*p*-CO_2Me	65	94–96	1715 (C═O), 1282, 1101 (C-O)	Ethanol
5c	*p*-CO_2Et	53	106.5–108	1713 (C═O), 1278, 1094 (C-O)	Ethanol
5d	*p*-CH_3	87	49.5–51.5	823 (OOP *p*-sub)	Hexanes
5e	*p*-NO_2	56	149–150	1320, 1490 (NO_2)	Ethanol
5f	*p*-OCH_3	67	Oil	1237, 1068 (C-O)	Hexane – ethyl acetate
5g	*p*-$COCH_3$	87	116–118	1671 (C═O)	Ethanol

Table 5. ^{1}H NMR data for 1,2-bis(1-aryl-3-ethyltriazen-3-yl)ethanes (**5**); chemical shifts in ppm relative to TMS (1%) at 22°C in $CDCl_3$.

Compound	X	N-CH_2-CH_3	Aromatic	CH_2	X
5a	*p*-CN	3.83 (q), 1.36 (br)	7.62, 7.59, 7.49, 7.27	4.05	—
5b	*p*-CO_2Me	3.81 (q), 1.31 (br)	8.04, 8.01, 7.48, 7.44	4.02	3.90 (O-CH_3)
5c	*p*-CO_2Et	3.82 (q), 1.32 (br)	8.05, 8.01, 7.47, 7.44	4.03	4.37 (CH_2), 1.40 (CH_3)
5d	*p*-CH_3	3.74 (q), 1.26 (t)	7.35, 7.32, 7.15, 7.11	3.94	2.33
5e	*p*-NO_2	3.87 (q), 1.40 (t), 1.24 (t)	8.23, 8.19, 7.53, 7.49	4.08 (br)	—
5f	*p*-OCH_3	3.74 (q), 1.26 (t)	7.41, 7.37, 6.89, 6.86	3.93	3.79
5g	*p*-$COCH_3$	3.84 (q), 1.33 (br)	7.97, 7.94, 7.49, 7.46	4.05	2.60

Table 6. ^{13}C NMR data for 1,2-bis(1-aryl-3-ethyltriazen-3-yl)ethanes (**5**); chemical shifts in ppm relative to TMS (1%) at 22°C in $CDCl_3$.

Compound	X	N-CH_2-CH_3	Aromatic	CH_2	X
5a	*p*-CN	43.5, 14.3	153.9, 133.1, 121.1, 119.4	50.85	108.2
5b	*p*-CO_2Me	Not obsd.	154.3, 130.6, 126.8, 120.3	50.6	167.05 (C═O), 51.9 (CH_3)
5c	*p*-CO_2Et	Not obsd.	154.2, 130.6, 127.2, 120.25	Not obsd.	60.8 (CH_2), 14.4 (CH_3), 166.6 (C═O)
5d	*p*-CH_3	45.8, 13.7	148.7, 135.2, 129.5, 120.4	Not obsd.	21.1
5e	*p*-NO_2	43.6, 14.3	155.6, 144.9, 124.9, 120.7	51.1	—
5f	*p*-OCH_3	46.2, 13.5	157.7, 144.7, 121.4, 114.1	Not obsd.	55.4
5g	*p*-$COCH_3$	43.5, 14.4	154.4, 134.1, 129.6, 120.4	50.7	197.3 (C═O), 26.5 (CH_3)

NMR spectra and they show one spot on TLC. NMR spectroscopic data are shown in Tables 9 and 10.

Discussion

Synthesis

The 1,2-bis(1-aryl-3-methyltriazen-3-yl)ethanes (**4**) were synthesized in excellent yields by diazonium coupling with *N,N′*-dimethyl-1,2-ethylenediamine; yields are in the range 50–98% depending on the substituent in the aryl group. Likewise, diazonium coupling with *N,N′*-diethyl-1,2-ethylenediamine afforded the homologous ethyl bistriazenes (**5**). Most of the compounds in series **4** and **5** are crystalline solids. The 1-(1-aryl-3-methyltriazen-3-yl)-*N,N*-dimethyl-2-ethanamines (**6**), which were required as model compounds for spectroscopic analysis, were obtained in good yield (65–99%) by diazonium coupling with *N,N,N′*-trimethyl-1,2-ethylenediamine. However, these dialkyltriazenes (**6**) did not come out of solution when neutralization with sodium bicarbonate, our usual procedure, was attempted; it was found necessary to use potassium hydroxide as the base to get these triazenes to separate from solution and most of the products were oils. Only compounds **6b** and **6f** were obtained as crystalline solids.

Table 7. Elemental analysis for selected compounds.

	Calculated			Found		
Compound	%C	%H	%N	%C	%H	%N
4b	62.41	5.24	32.35	62.32	5.35	32.29
4e	66.64	7.46	25.90	66.47	7.52	26.11
4h	63.14	6.36	22.10	63.04	6.23	22.08
4j	62.41	5.24	32.35	62.22	5.23	32.59
4o	60.66	6.79	23.58	60.63	6.85	23.40
5a	64.17	5.88	29.95	64.15	5.92	29.98
6f	52.58	6.82	27.87	52.83	6.80	27.88

Infrared spectra

The IR spectra of compounds in all three series, **4**, **5,** and **6**, are in accord with the assigned structures. The out-of-plane bending vibrations are consistent with the position of substitution: *ortho*-substituted compounds give a single band in the range 720–740 cm^{-1} and *para*-substituted compounds give a single band at ca. 800 cm^{-1} Diagnostic functional group bands are consistent with the substituent in the aryl ring. For example, the ester substituents of compounds **4c**, **4d**, **4k**, **4l**, **5b**, **5c**, **6c**, **6d**, **6k,** and **6l** show carbonyl group stretching vibrations between 1680 and 1715 cm^{-1} A nitrile group band at 2180 cm^{-1}

© 1998 NRC Canada

Table 8. Physical data for 1-(1-aryl-3-methyltriazen-3-yl)-*N,N*-dimethyl–2-ethanamines (**6**).

Compound	X	Yield (%)	Melting point (°C)	IR (cm^{-1})	Recryst. solvent
6a	H	77	Oil	740, 670	Hexanes – ethyl acetate
6b	*p*-CN	87	52–53	2160 (CN)	Hexanes
6c	*p*-CO_2Me	99	Oil	1680 (C═O), 1250, 1080 (C-O)	Hexanes – ethyl acetate
6d	*p*-CO_2Et	79	Oil	1690 (C═O), 1250, 1080 (C-O)	Hexanes – ethyl acetate
6e	*p*-CH_3	89	Oil	800 (OOP *p*-sub)	Hexanes – ethyl acetate
6f	*p*-NO_2	82	58.5–60	1350, 1480 (NO_2)	Hexanes
6g	*p*-OCH_3	81	Oil	1220, 1010 (C-O)	Hexanes – ethyl acetate
6h	*p*-$COCH_3$	97	Oil	1640 (C═O)	Column
6i	*p*-Br	79	Oil	1040 (Ar-Br)	Hexanes – ethyl acetate
6j	*o*-CN	72	Oil	2180 (CN)	Hexanes – ethyl acetate
6k	*o*-CO_2Me	79	Oil	1700 (C═O), 1050, 1220 (C-O)	Hexanes – ethyl acetate
6l	*o*-CO_2Et	65	Oil	1690 (C═O), 1050, 1220 (C-O)	Hexanes – ethyl acetate
6m	*o*-CH_3	87	Oil	740 (OOP *o*-sub)	Hexanes – ethyl acetate
6n	*o*-NO_2	84	Oil	1500, 1320 (NO_2)	Toluene
6o	*o*-OCH_3	93	Oil	1220, 1050 (C-O)	Hexanes – ethyl acetate
6p	*o*-$COCH_3$	81	Oil	1650 (C═O)	Column

Table 9. ^1H NMR data for 1-(1-aryl-3-methyltriazen-3-yl)-*N,N*-dimethyl–2-ethanamines (**6**); chemical shifts in ppm relative to TMS (1%) at 22°C in $CDCl_3$.

Compound	X	N-Me	N-Me_2	Aromatic	CH_2	X
6a	H	3.25 (br)	2.28	7.1–7.4	3.85 (t), 2.57 (t)	—
6b	*p*-CN	3.57, 3.25	2.29	7.61, 7.57, 7.49, 7.45	3.91 (t), 2.61 (t)	—
6c	*p*-CO_2Me	3.25 (br)	2.29	7.99, 8.02, 7.47, 7.44	3.90 (t), 2.60 (t)	3.89
6d	*p*-CO_2Et	3.26 (br)	2.29	8.03, 8.00, 7.47, 7.44	3.90 (t), 2.60 (t)	4.33(q), 1.39(t)
6e	*p*-CH_3	3.23	2.28	7.34, 7.30, 7.13, 7.10	3.83 (t), 2.56 (t)	2.32
6f	*p*-NO_2	3.29, 3.60	2.30	8.20, 8.17, 7.51, 7.48	3.94 (t), 2.63 (t)	—
6g	*p*-OCH_3	3.21	2.28	7.39, 7.37, 6.87, 6.85	3.82 (t), 2.56 (t)	3.78
6h	*p*-$COCH_3$	3.26 (br)	2.29	7.95, 7.93, 7.49, 7.45	3.91 (t), 2.61 (t)	2.58
6i	*p*-Br	3.23 (br)	2.27	7.43, 7.40, 7.31, 7.27	3.84 (t), 2.56 (t)	—
6j	*o*-CN	3.32, 3.58	2.29, 2.31	7.12–7.60	3.92 (t) ,2.63 (t)	—
6k	*o*-CO_2Me	3.23 (br)	2.27	7.12–7.63	3.85 (t), 2.58 (t)	3.86
6l	*o*-CO_2Et	3.23	2.27	7.12–7.63	3.83 (t), 2.58 (t)	1.35 (t), 4.33 (q)
6m	*o*-CH_3	3.25 (br)	2.28	7.01–7.35	3.85 (t), 2.57 (t)	2.26
6n	*o*-NO_2	3.13, 3.23	2.29	7.14–7.66	3.89 (t), 2.52 (t)	—
6o	*o*-OCH_3	3.29	2.28	6.88–7.15	3.87 (t), 2.59 (t)	3.88
6p	*o*-$COCH_3$	3.23 (br)	2.28	7.46–7.13	3.89 (t), 2.57 (t)	2.61

Table 10. ^{13}C NMR data for 1-(1-aryl-3-methyltriazen-3-yl)-*N,N*-dimethyl–2-ethanamines (**6**); chemical shifts in ppm relative to TMS (1%) at 22°C in $CDCl_3$.

Compound	X	N-Me	N-Me_2	Aromatic	CH_2	X
6a	H	Not obsd.	45.7	151.0, 128.8, 125.3, 120.6	57.4	—
6b	*p*-CN	35.2	45.6	154.3, 133.0, 121.1, 119.6	54.5, 57.9	107.7
6c	*p*-CO_2Me	34.9	45.6	154.5, 130.5, 126.4, 120.2	54.2, 57.8	51.8, 167.0
6d	*p*-CO_2Et	35.0	45.6	154.5, 130.5, 126.8, 120.2	54.3, 57.9	60.7, 166.7
6e	*p*-CH_3	35.8	45.6	148.6, 134.9, 129.3, 120.3	52.7, 57.3	21.0
6f	*p*-NO_2	35.3	45.6	156.0, 144.6, 124.8, 120.6	54.6, 57.8	—
6g	*p*-OCH_3	35.7	45.5	158.2, 144.7, 121.4, 113.9	52.1, 57.25	55.3
6h	*p*-$COCH_3$	35.0	45.6	154.6, 133,7, 129.5, 120.3	54.3, 57.8	26.5, 197.4
6i	*p*-Br	35.1	45.7	149.9, 131.8, 122.2, 118.3	53.95, 57.7	—
6j	*o*-CN	35.3	45.6	153, 133, 125, 118, 117.5, 117.1	54.25, 57.7	107.3
6k	*o*-CO_2Me	34.7	45.45	150, 131, 129, 126, 125, 119	53.8, 57.7	51.7, 168.8
6l	*o*-CO_2Et	34.75	45.45	150, 131, 129, 127, 125, 119	53.7, 57.7	60.6, 168.4
6m	*o*-CH_3	Not obsd.	45.7	149, 133, 131, 126, 125, 117	Not obsd.	17.7
6n	*o*-NO_2	35.25	45.5	144, 132, 125, 124, 120, 114	54.3, 57.8	—
6o	*o*-OCH_3	Not obsd.	45.7	153, 141, 126, 121, 119, 112	57.5	56.1
6p	*o*-$COCH_3$	35.4	45.6	149, 135, 132, 128, 125, 118	54.0, 57.8	32.2, 203.7

© 1998 NRC Canada

is present in the spectra of compounds **4b**, **4j,** and **6j**. The spectra of **4f**, **4n**, and **5e** contain the symmetric and assymmetric vibrations of the nitro group at 1320/1490, 1360/1500, and 1320/1490 cm^{-1}, respectively. Compounds **4i** and **6i** show strong bands at 1040 and 1050 cm^{-1}, respectively, which may be assigned to the aryl bromide.

NMR spectra

^1H NMR

Proton NMR spectra provided unequivocal evidence for the structures of the bistriazene series, **4** and **5**, and the triazenes, **6**. For example, the aromatic signals of the *para*-substituted bistriazenes **4b**–**4i** were found between 6.84 and 8.01 ppm and exhibited the general splitting pattern of an AA′BB′ system (Table 2). Compounds **4j**–**4p** showed complex aromatic splitting patterns at 6.86–7.76 ppm due to the *ortho* substituent. O-Methyl protons in the ester substituents of **4c** and **4k** and the alkoxy substituents of **4g** and **4o** gave signals in the range 3.80–3.90 ppm; the acetyl Me groups in **4h** and **4p** resonated at 2.58 and 2.46 ppm, respectively. The chemical shift of the N-CH_2 protons in the ethylene link was typically in the range 4.0–4.2 ppm, and the N-CH_3 protons were generally found between 3.22 and 3.32 ppm.

A number of the compounds of type **4** show significant broadening of the N-methyl and N-methylene signals in the ^1H NMR spectra. The spectra of 1-aryl-3,3-dialkyltriazenes, Ar-N═N-NMe_2, frequently show broadening of the NMR N-alkyl signals; this has been attributed to restricted rotation around the N2—N3 bond and the equilibrium between rotamers **7A** and **7B** (6):

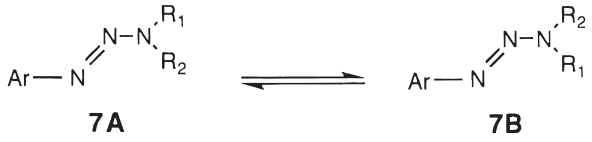

7A **7B**

Indeed, some of the compounds of series **4** have NMR spectra in which the signals of the N-methyl protons of the rotamers are resolved at room temperature, e.g., bistriazene **4j**. Further examination of this phenomenon has been investigated by a variable temperature (VT) NMR study (see later discussion).

Proton NMR spectra also confirmed the structures of the series of N-ethyl bistriazenes **5a–5g**; all compounds had a characteristic AA′BB′ pattern in the range 6.86–8.05 ppm. The spectra exhibit the appropriate signals of the *para* substituents. The N-CH_2 protons of the ethylene link give rise to a slightly broadened singlet at 3.93–4.08 ppm. The N-ethyl moiety exhibits, as expected, two sets of protons with an integral ratio 2:3. The two-proton signal of the N-methylene group appears as a quartet in the range 3.74–3.87 ppm, while the appearance of the methyl protons of the ethyl groups depends on the nature of the aryl substituent. When the substituent on the aryl ring is electron donating, as in **5d** and **5f**, the methyl protons are resolved as a clear triplet at 1.26 ppm. However, when the substituent is electron withdrawing, as in **5a**, **5b**, **5c**, and **5g**, the methyl protons appear as a broad singlet. In one case, that of the *para*-nitro bistriazene **5e**, the methyl protons of the N-ethyl group resolve into two slightly broadened triplets at 1.24 and 1.40 ppm.

Scheme 1.

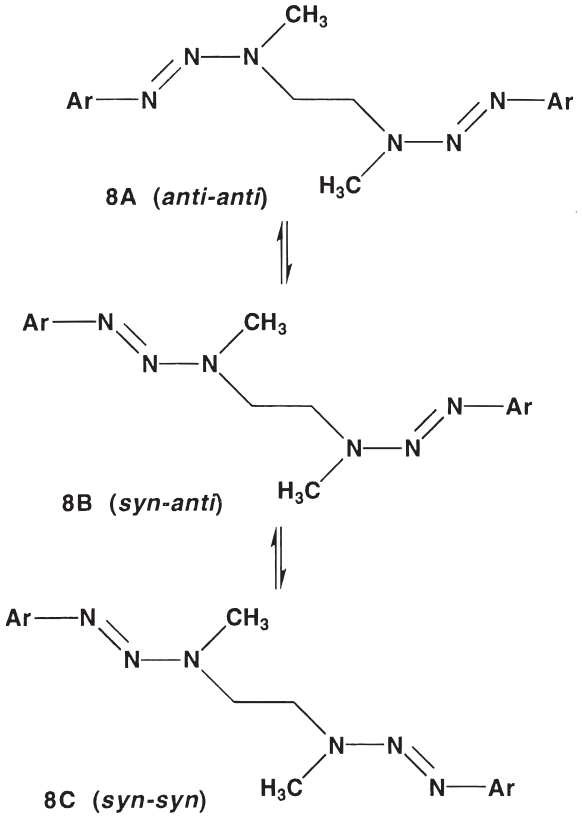

The lineshapes of these signals from the N-ethyl groups in the compounds of series 5 would logically have something to do with the restricted rotation around the N2—N3 bond in the triazene units. However, there is no immediate explanation for the anomalous observation that the line-broadening is only observed for the more distant methyl protons of the N-ethyl groups.

The ^1H NMR spectra of the triazenes **6a–6p** corroborate the assigned structures and show features consistent with restricted rotation around the N2—N3 bond in the triazene unit. The signals of the aromatic protons and the protons of the aryl substituents are all as expected. The methylene groups of the ethylene moiety are not equivalent and appear as two triplets integrating for two protons each. The methylene group adjacent to the triazene unit is deshielded by the triazene moiety and resonates as a sharp signal at δ 3.82–3.94; the other methylene group is more shielded, appearing at δ 2.52–2.63, and in some cases (when the aryl substituent is strongly electron withdrawing) is significantly broadened. The protons of the N-dimethyl groups give rise to a sharp signal in the range δ 2.27–2.30, with the exception of the *ortho*-cyano derivative **6j**, which has two signals resolved at δ 2.29 and 2.31. The triazene N-methyl protons give rise to a distinctly broadened singlet in the range δ 3.21–3.29; when there is a strongly electron withdrawing nitro or cyano group in the *ortho* or *para* position of the aryl ring, these N-methyl signals are resolved into two signals at δ 3.23–3.32 and δ 3.57–3.60. These observations are indicative of an equilibrium between the *syn* and *anti* forms of the triazene (**6A** and **6B**) due to the restricted rotation around the N2—N3 bond of the triazene:

© 1998 NRC Canada

Fig. 1. Variable temperature NMR spectra of the bistriazene **4k** in the N-alkyl resonance region at the following temperatures: (*A*) 295 K; (*B*) 283 K; (*C*) 273 K; (*D*) 253 K; (*E*) 243 K; (*F*) 233 K.

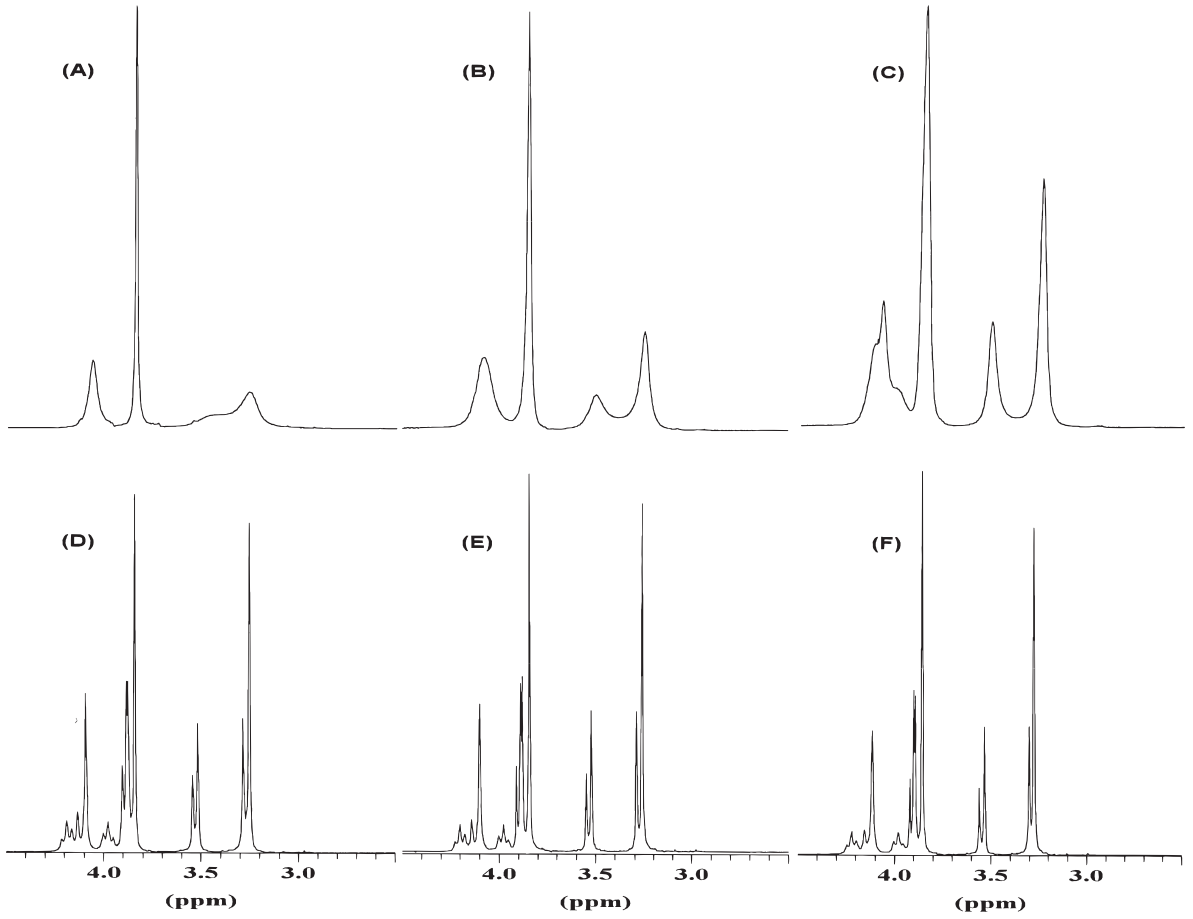

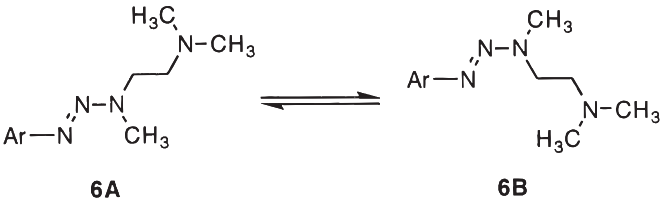

6A **6B**

Compounds of series **6** proved to be good model compounds for prediction of chemical shifts of comparable protons in the bistriazenes **4**. In **6**, the N-methyl group adjacent to the triazene unit occurs in the range 3.21–3.32 ppm, compared to the range 3.22–3.32 ppm for the N-methyl protons in **4**. The N-methylene protons adjacent to the triazene in **6** resonate in the range 3.82–3.94 ppm; the N-methylene protons in **4** are slightly more deshielded by the presence of the second triazene unit and occur in the range 4.00–4.30 ppm.

^{13}C *NMR*

The structures of the bistriazenes in series **4** were corroborated by ^{13}C NMR spectroscopy (Table 3). The aromatic resonances of compounds **4a**–**4i** were observed as four signals in the range 114.0–157.8 ppm, whereas the *ortho*-substituted compounds **4j**–**4p** showed six aromatic resonances between 110.7 and 153.05 ppm. A greater number of aromatic signals were resolved in the spectrum of compound **4j** due to the dynamic equilibrium of the rotamers. O-Methyl carbons in the esters (**4c**, **4k**) and alkoxy (**4g**, **4o**) substituents had signals in the range δ 52–56. These signals were very close to the N-methylene carbon signals within the spectrum, but the N-methylene signals were weak and easily distinguished from the stronger methyl carbon resonances. Confirmation of the assignments was obtained from DEPT experiments. The N-methyl carbons give rise to weak signals (not always observed) at δ 35–36, and the N-methylene carbons, when observed, are also weak in the range δ 52–54. The weak signals may be due to the low nuclear Overhauser enhancement of the signals. The spectrum of the *ortho*-cyano compound **4j** is unique in that the resonances of four distinct N-methyl carbons are observed, along with four different N-methylene signals; these observations can be accounted for by the presence of three rotamers in solution (see later discussion of VT-NMR and Scheme 1).

^{13}C NMR spectra of the bistriazenes of series **5** follow a similar pattern to those above (Table 6), and the ^{13}C NMR spectra of the triazene series **6** are consistent (Table 10). The signal from the methyl carbons of the N-Me_2 unit are strong, with resonance in the range 45.45–45.73 ppm, whereas the triazene N-methyl group gives a weak carbon signal in the range 34–35 ppm. Two weak signals are observed for the N-methylene carbons in **6** at δ 52–54 and δ ca. 57.

© 1998 NRC Canada

Fig. 2. Variable temperature NMR spectra of the bistriazene **4k** in the N-alkyl resonance region at the following temperatures: (*A*) 295 K; (*B*) 303 K; (*C*) 313 K.

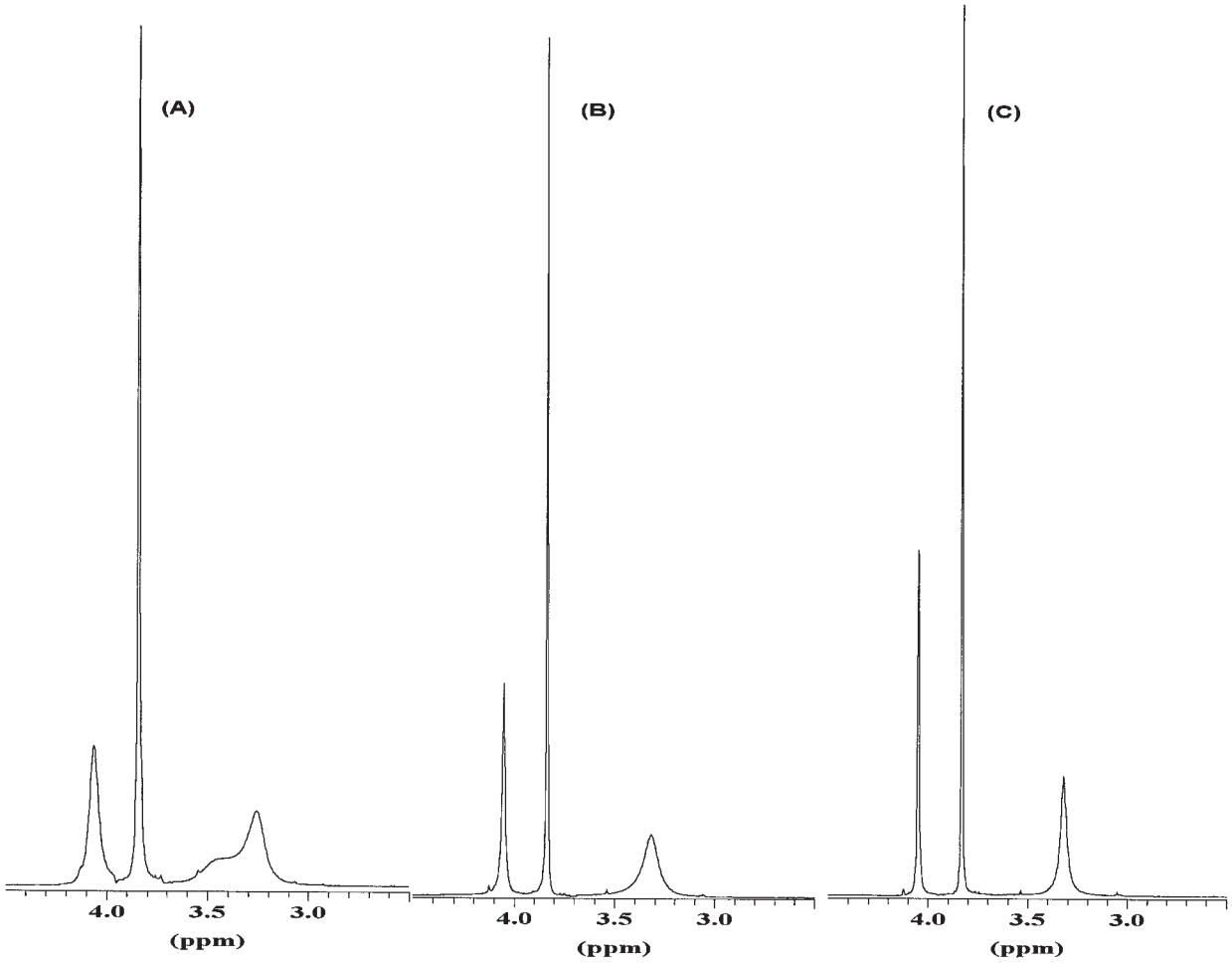

Variable temperature ^1H NMR spectroscopy

Variable temperature ^{1}H NMR experiments were conducted on two *ortho*-substituted compounds in the bistriazene series, namely, the ester **4k** and the nitrile **4j**. The results for the ester **4k** are shown in Figs. 1 and 2. In the room temperature spectrum, Fig. 1*A*, the N-methyl signals are broadened considerably. When the temperature is raised, Fig. 2, the N-methyl signals become sharper and, at 313 K (Fig. 2*C)*, a single, averaged-out, N-methyl signal is observed at δ 3.35 ppm. When the temperature of a solution of **4k** is lowered (Fig. 1 *A–F*), the signals sharpen and resolve at 253 K into four distinct N-Me signals, which can be assigned to the three rotamers, **8A**, **8B,** and **8*C*** (Scheme 1). The strongest signal of the group at δ 3.25 ppm is assigned to the equivalent N-methyl groups of the predictably predominant *anti–anti* rotamer (**8A**) and the weakest signal at δ 3.54 is assigned to the equivalent N-methyl groups of the *syn–syn* rotamer (**8C**). The two equal-intensity signals at δ 3.28/3.51 ppm are assigned to the nonequivalent N-methyl groups of the *syn–anti* rotamer (**8B**); the percent population of the three rotamers can be estimated from the relative heights of these N-methyl signals to be 50% **8A**, 40% **8B**, and 10% **8C**.

Evaluation of the temperature dependence of the NMR spectra of **4k** by the line-width method described by Akhtar et al. (6) afforded useful information about the dynamics of the rotation around the N2—N3 bond in this molecule. The free energy of activation ($\Delta G^{\ddagger}$) at 295 K was calculated to be 14.6 kcal/mol with a rate constant $k = 92.4$ s^{-1}. It is interesting

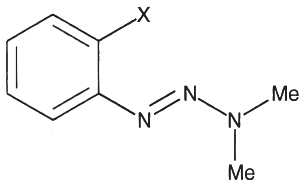

9 (a) X = CO_2Me
(b) X = CN

to compare these kinetic data with the unpublished data[2] for the analogous 1-aryl-3,3-dimethyltriazene **9a** containing the same aryl substituent, *ortho*-CO_2Me, as compound **4k**. For compound **9a** the $\Delta G^{\ddagger}$ was found to be 14.5 kcal/mol at 297 K; thus the barrier to rotation around the N2—N3 bond in the triazene moiety of the bistriazene is virtually identical to that in a simple 1-aryl-3,3-dialkyltriazene.

[2] W.D. Bullerwell, M.P. Merrin, D.L. Hooper, and K. Vaughan. Unpublished results.

© 1998 NRC Canada

Fig. 3. Variable temperature NMR spectra of the bistriazene **4j** in the N-alkyl resonance region at the following temperatures: (*A*) 295 K; (*B*) 303 K; (*C*) 313 K; (*D*) 323 K.

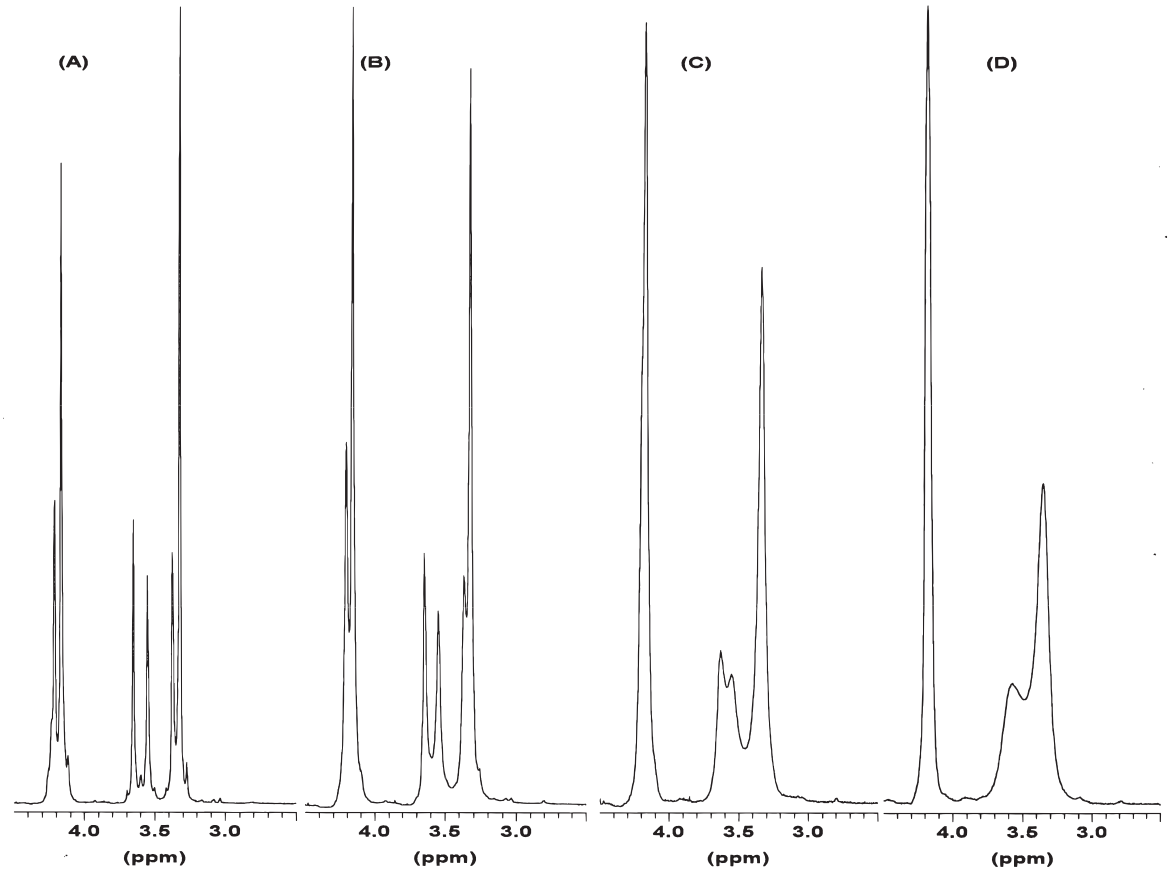

Scheme 2. The resonance structures of compound **10** (cf. **4j**) arising from through-conjugation with the nitrile group; the repulsion between the positively charged nitrogen atoms causes the molecule to adopt the staggered conformation.

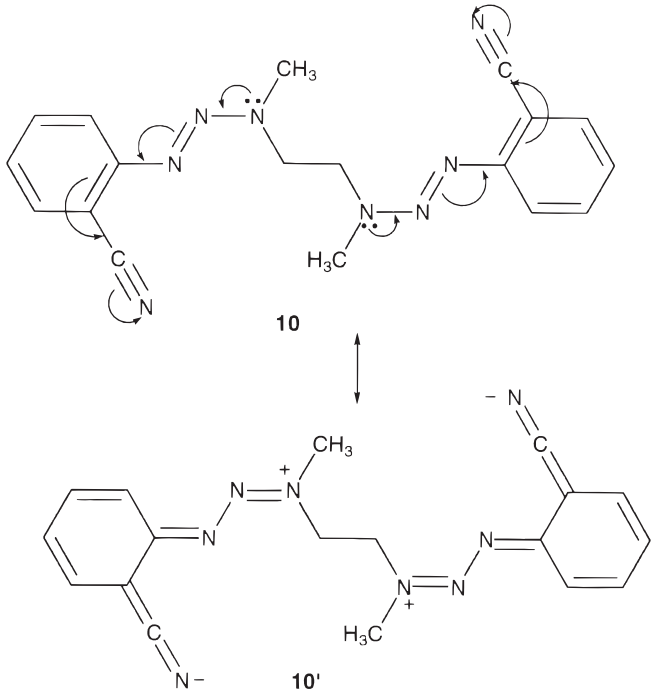

In the NMR spectrum of the *ortho*-cyano bistriazene **4j**, the N-methyl signals of the three rotamers are resolved in the room temperature spectrum, which has the exact same appearance as the 253 K spectrum of **4k**. Figure 3 shows the effect of raising the temperature on the NMR spectrum of **4j**; the peaks broaden and begin to coalesce. Analysis of the spectra in Fig. 3 by the line-width method affords a free energy of activation of 16.0 kcal/mol at 297 K, corresponding to a rate constant k = 10.1 s^{-1}. This value compares closely with the observed barrier to rotation in the analogous 1-aryl-3,3-dimethyltriazene **9b**, which has a $\Delta G^{\ddagger}$ value of 15.3 kcal/mol at 283 K.[2] When we compare the k values for the two bistriazenes, it appears that the rotation in the *ortho*-cyano compound **4j** is about 10 times slower than the rotation in the ester **4k**, indicating that the bond order of the N2—N3 bond is greater in **4j** than in **4k**. The greater double bond character of the N2—N3 bond in **4j** may be attributed to the contribution of the resonance delocalization to the overall structure as depicted in Scheme 2; it is significant to this argument that the two cyano-substituted triazenes **4b** and **4j** have IR absorptions at 2180 cm^{-1}, lower than the normal frequency for an aryl nitrile (>2200 cm^{-1}). Analogous changes are observed in the N-methylene region of the NMR spectrum of **4j** when the temperature is raised. At room temperature there are two distinct resonances, at δ 4.15 and 4.22, for the protons of the N-CH_2CH_2-N moiety. When the temperature is raised, these signals coalesce (Fig. 3).

© 1998 NRC Canada

Fig. 4. ORTEP diagram of the *ortho*-cyano-substituted bistriazene **4j**.

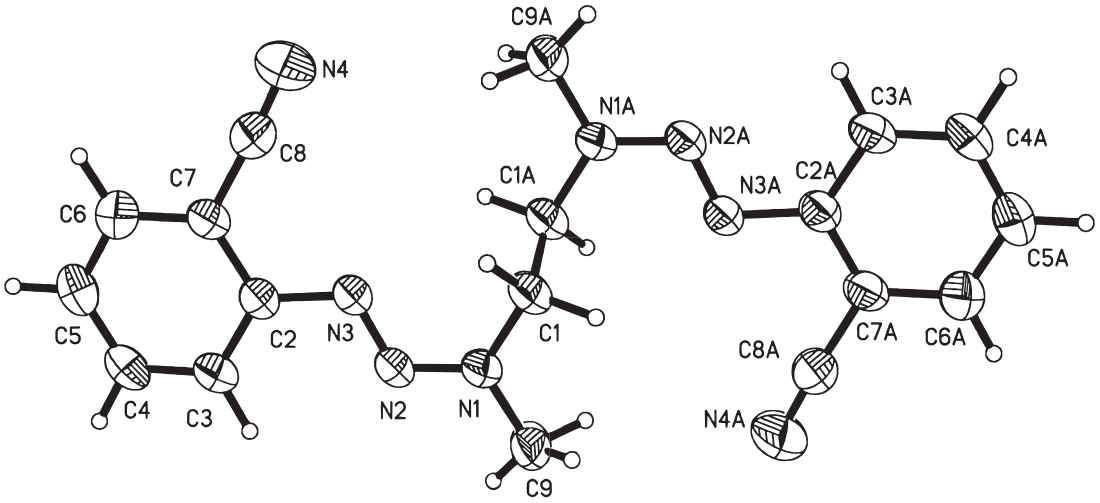

Fig. 5. ORTEP diagram of the *ortho*-methoxy-substituted bistriazene **4o**.

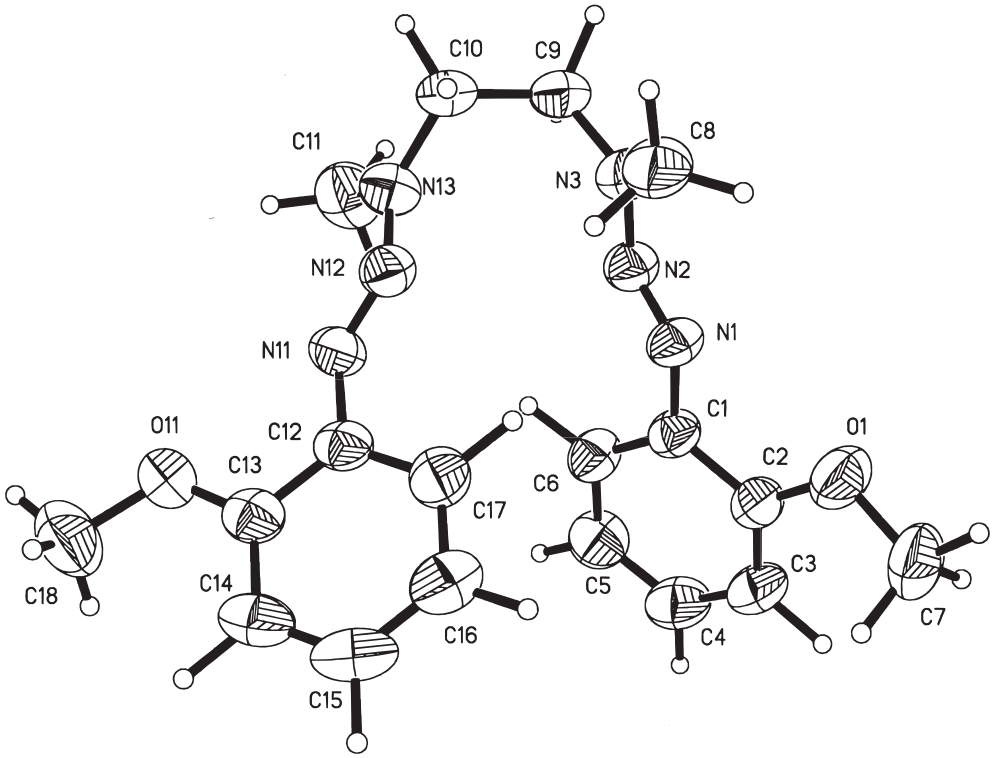

X-ray crystallography

The structures of the *ortho*-cyano-substituted bistriazene **4j** and of the *ortho*-methoxy analogue **4o** have been determined by X-ray crystallography (7). In the solid state (Fig. 4), the *o*-cyano compound **4j** adopts the *anti–anti* structure (**10**; the analogue of structure **8A** in Scheme 1), consistent with the NMR data of this compound. The solid state structure is the same as the preferred rotamer seen in a solution of this compound by NMR. Predictably, **4j** assumes the "staggered" conformation with respect to the orientation around the C—C bond of the ethane link. In contrast, the *o*-methoxy analogue **4o** exists in the solid state (Fig. 5) with the "*gauche*" conformation around the C—C bond of the ethane unit and adopts the *syn–syn* configuration around the N2—N3 bonds of the triazene units. The electron-donating capabilities of the *ortho*-methoxy group would not be expected to increase the bond

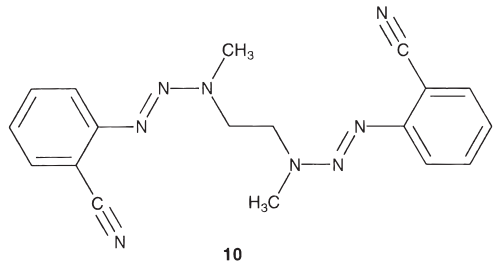

10

© 1998 NRC Canada

order of the N2—N3 bonds. Thus there is free rotation around the N2—N3 bond in compound **4o**, which enables the molecule to fold over onto itself. Full details of these X-ray crystal structures will be published elsewhere (7).

Conclusions

This paper has shown that 1,2-bis(1-aryl-3-alkyltriazen-3-yl)ethanes **4** and **5** can be readily synthesized; the bistriazenes have been fully characterized by spectroscopic methods, and the rotational properties of the molecules around the N2—N3 bond of the triazene have been explored by variable temperature NMR spectroscopy. X-ray crystallography has confirmed

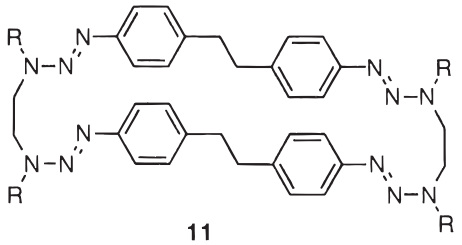

11

the structure of two examples of the bistriazene series. The synthesis and identification of these bistriazenes opens up the possibility of the design and synthesis of macrocyclic triazene-containing molecules. By combining the structural elements of the bistriazenes of types **3** and **4** into one unit, it should be possible to isolate macrocyclic tetrakistriazenes represented by structure **11**. These macrocyclic molecules could have a multitude of applications, especially in host–guest chemistry. The abundance of hydrogen bond acceptors could make it possible to place hydrogen bond donors or cationic metals within the cavity of the tetrakistriazene. Such a macrocycle may also have useful biological activity due to the presence of four potentially cytotoxic triazene units within the same molecule.

Acknowledgements

Financial assistance for this project was provided by the Saint Mary's University Senate Research Committee. We gratefully acknowledge the assistance of the Atlantic Regional Magnetic Resonance Centre at Dalhousie University in providing the NMR spectra. The X-ray crystallographic data were obtained with the assistance of Dr. M.J. Zaworotko of the Chemistry Department at Saint Mary's University.

References

1. J.J. Blumenstein and C.J. Michejda. Tetrahedron Lett. **32**, 183 (1991).
2. (*a*) A. Gescher, J.A. Hickman, R.J. Simmonds, M.F.G. Stevens, and K. Vaughan. Tetrahedron Lett. 5041 (1978); (*b*) C.M. Hemens, H.W. Manning, K.Vaughan, R.J. LaFrance, and Y. Tang. Can. J. Chem. **62**, 741 (1984).
3. H.W. Manning, C.M. Hemens, R.J. LaFrance, Y. Tang, and K. Vaughan. Can. J. Chem. **62**, 749 (1984).
4. D.S. Brown, M.P. Merrin, and K. Vaughan. Proc. N. S. Inst. Sci. **40**, 67 (1995).
5. T.A. Connors, P.M. Goddard, K. Merai, W.C.J. Ross, and D.E.V. Wilman. Biochem. Pharmacol. **25**, 241 (1976).
6. M.H. Akhtar, R.S. McDaniel, M. Feser, and A.C. Oehlschlager. Tetrahedron, **34**, 3899 (1968).
7. I.R. Pottie, K. Vaughan, M. Sharma, and M.J. Zaworotko. J. Chem. Crystallogr. In press.

© 1998 NRC Canada

ADDITIONS AND CORRECTIONS / AJOUTS ET CORRECTIONS

Chemistry of cyclic aminooxycarbenes

Philippe Couture and John Warkentin

Ref.: Can. J. Chem. **75**, 1281 (1997).

On page 1283, the caption for Fig. 2 should read: ···**3***e*,··· (i.e., change **3***c* to **3***e*, leaving all else the same).
The formulae should be replaced with the following. The spectra and the temperatures stay as they are.

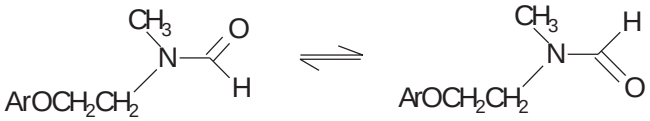

(Ar = 4-$C_6H_4CH_3$)

Received December 22, 1997.

P. Couture and J. Warkentin.[1] Department of Chemistry, McMaster University, Hamilton, ON L8S 4M1, Canada.

[2] Author to whom correspondence may be addressed. Telephone: (905) 525-9140. Fax: (905) 522-2509. E-mail: warkentt@mcmaster.ca

© 1998 NRC Canada

Frondoside C, a new nonholostane triterpene glycoside from the sea cucumber *Cucumaria frondosa*: structure and cytotoxicity of its desulfated derivative

Sergey A. Avilov, Olga A. Drozdova, Vladimir I. Kalinin, Anatoly I. Kalinovsky, Valentin A. Stonik, Elena N. Gudimova, Ricardo Riguera, and Carlos JimØnez

Abstract: Frondoside C (**1**) is a new sulfated nonholostane triterpene glycoside obtained (with the glycosides closed by aglycone structure as impurities) from the sea cucumber *Cucumaria frondosa*. Its structure has been elucidated on the basis of spectral data (NMR and MS) of compound **1** and of its desulfated derivative (**2**) obtained by solvolysis. Frondoside C (**1**) is just the seventh glycoside reported from sea cucumbers, having a lanostane-type aglycone devoid of the typical 18(20)-lactone ring.

Key words: *Cucumaria frondosa*, sea cucumbers, frondosides, triterepene glycosides, antitumor activity.

Résumé : On a isolé un nouveau glycoside sulfaté du triterpène nonholostane, le frondoside C (**1**) (comportant des glycosides de la structure aglycone comme impuretés), à partir du concombre de mer *Cucumaria frondosa*. On a déterminé sa structure en se basant sur des données spectrales (RMN et SM) du composé **1** et de son dérivé désulfaté (**2**) obtenu par solvolyse. Le frondoside C (**1**) n'est que le septième glycoside à avoir été observé dans les concombres de mer, avec un aglycone de type lanostane ne comportant pas de cycle lactone typique en 18(20).

Mots clés : *Cucumaria frondosa*, concombres de mer, frondosides, glycosides de triterpène, activité antitumorale.

[Traduit par la rédaction]

The sea cucumber *Cucumaria frondosa* Gunnerus (*Cucumariidae*) is a widespread benthic animal inhabiting the North Atlantic and western Arctic seas. Previous studies of this sea cucumber have yielded two new holostane pentaglycosides, the monosulfated frondoside A (1) and the disulfated frondoside B (2). More recently, we have isolated a new minor monosulfated tetraoside frondoside A_1, along with frondoside A, from specimens of *C. frondosa* collected in Barents Sea (3).

Continuing with our investigations on bioactive secondary metabolites of marine origin, we report here our results on the study of the more polar triterpene glycosides from *C. frondosa,* with the isolation of a new saponin that we named frondoside C. Column chromatography on polychrom-1 (powdered Teflon) of the ethanolic extract of *C. frondosa* gave a mixture of glycosides that was separated by column chromatography on silica gel, affording frondoside C (**1**) accompanied by very small amounts of other polar glycosides with identical carbohydrate chain. Attempts to purify **1** by HPLC were unsuccessful. To establish wholly its structure, we resorted to spectroscopic analysis of impure **1** and the pure compound **2** that resulted from solvolysis of **1**. Thus, solvolysis of **1** with pyridine–dioxane mixture afforded, after HPLC purification, the pure desulfated derivative **2**.

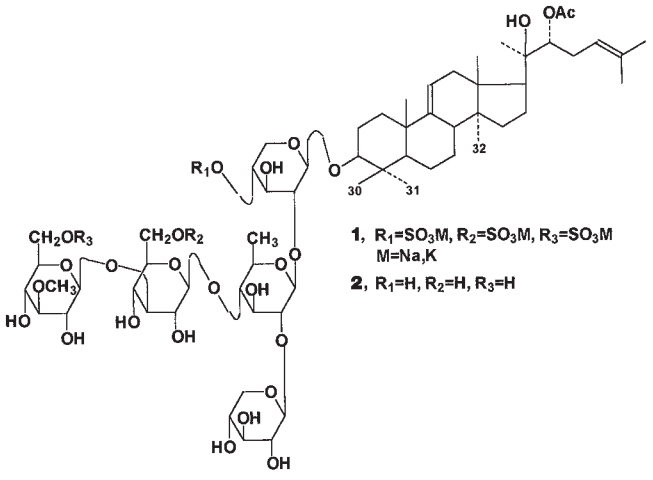

Received July 9, 1997.

S.A. Avilov,[1] O.A. Drozdova, V.I. Kalinin, A.I. Kalinovsky, and V.A. Stonik. Pacific Institute of Bioorganic Chemistry, Far East Division of the Russian Academy of Sciences, Vladivostok 690022, Russia.
E.N. Gudimova. Murmansk Marine Biological Institute of Kolsky Scientific Center of the Russian Academy of Sciences, Dalnije Zelentsy, Murmansk District 184631, Russia.
R. Riguera. Departamento de Quimica Organica, Facultad de Quimica and Instituto de Acuicultura, Universidad de Santiago de Compostela, Santiago de Compostela 15706, Spain.
C. Jiménez. Departamento de Quimica Fundamental e Industrial, Facultad de Ciencias, Universidad de La Coruña, La Coruña 15071, Spain.

[1] Author to whom correspondence may be addressed. Telephone: +7–(4232)–31–11–68. Fax: +7–(4232)–31–40–50. E-mail: kav@piboc.marine.su

© 1998 NRC Canada

The presence of five doublets in the ^{1}H NMR of **2** (J = 7.1–7.5 Hz) at δ 4.75, 4.86, 5.05, 5.12, and 5.20 ppm, produced by the anomeric protons correlated by HMQC (heteronuclear multiple quantum correlation) to the corresponding anomeric carbons (Table 1), were indicative of a pentaglycoside chain. The characteristic proton resonances of the methyl groups at δ 1.59 ppm (d, J = 6.4 Hz) and δ 3.79 (s) indicated the presence of a quinovose and 3-*O*-methyl glucose residues in the oligosaccharide chain. Comparison of the carbon resonances due to the carbohydrate chain of **1** and **2** (Table 1) showed complete coincidence with those of the trisulfated pentaoside cucumarioside A_7-1, isolated from *Cucumaria japonica* (4), and those of the desulfated derivative of cucumarioside A_7-1, respectively. Therefore we assume that compound **1** and cucumarioside A_7-1 share identical carbohydrate chains. The location of sulfate groups of **1** at C-4 of internal xylose (Xyl_1) and at C-6 of glucose and 3-*O*-methyl glucose units was confirmed by the comparison of the carbon resonances of **1** with those of its desulfated derivative **2** (Table 1) and other holostane and nonholostane sea-cucumber glycosides (4–6).

Comparison of the spectral data of the aglycone part of **2** with those published for the desulfated penaustrosides A and B from *Pentacta australis* (5) suggested the same Δ^9 lanostane skeleton for **1** and **2**, featuring a 20-hydroxy group but bearing a different side chain. In fact, the carbon chemical shifts corresponding to C-1 through C-16, C-18, C-19, and C-30 through C-32 of **2** are practically identical to those of desulfated penaustrosides A and B. The 9(11)- double bond was corroborated by chemical shifts at δ 149.9 (s, C-9) and 115.2 (d, C-11) that correlated by HMQC with the olefinic proton at δ 5.17 (m, H-11), while the carbon signal at δ 76.4 (s, C-20) indicated the presence of a tertiary carbon bonded to a hydroxyl group.

The remaining proton and carbon resonances allowed us the elucidation of the side-chain moiety. The presence of a terminal isopropylidene group in the side chain of **2** was deduced by the carbon chemical shifts at δ 133.3 (s, C-25) and 121.7 (d, C-24) (correlated to the olefinic proton δ 5.21 (1H, brt, H-24)) and the vinyl methyl signals at δ 26.0 (q, C-26) and 18.1 (q, C-27) (correlated to δ 1.61 and 1.62 (each 3H, s) by HMQC). Lastly, an acetoxy group (δ 170.8 (s) and 21.7 (q)/ 2.12 (3H, s)) was located at C-22 by comparison of the carbon resonances of **2** with those of desulfated penaustroside A (5). The shifts to higher field observed for C-20 (δ 76.4; Δ = 2.2 ppm) and to lower field for C-21 (δ 21.3; Δ = –5.0 ppm) and C-17 (δ 50.6; Δ = –2.7 ppm) correspond to the β- and γ-shift effects of acetate groups (7) predicted for that position in **2**. On the other hand, the carbon chemical shifts of the side chain of **2** are very similar to those of protoreasteroside, isolated from the starfish *Protoreaster nodosus*, containing a 5α-cholesta-9(11),24(25)-diene-3β,6α,20,22-tetraol as aglycone (8). Furthermore, this structure was supported by HMQC, ^{1}H-^{1}H COSY, and selective homonuclear decouplings of **2**, thus irradiation of the signals at δ 5.20 (1H, m, H-22) and δ 5.21 (1H, brt, H-24) produced the collapse of the allylic methylene at δ 2.00–2.40 (2H, brm, H-23).

The 20*R*,22*R* configurations for the hydroxy group at C-20 and the acetoxy group at C-22 in **2** were suggested by the almost coincidence of the corresponding carbon chemical shifts of **2** and the known 2β,3β,22(*R*)-triacetoxy-14α,20(*R*),25-trihydroxy-5β-cholest-7(8)-en-6-one (9). This hypothesis was supported by the comparison of spectral data of **2** with those of the four stereoisomers of 5α-cholestane-3β,20,22-triol with respect to C-20 and C-22, synthesized by Hikino et al. (10), taking into consideration shifted effects of an acetoxy group at C-22. Thus, the higher field of the methyl group C-21 at δ 21.3 for **2** was indicative of a 20(*R*) configuration.[2] In the same way, the value of the C-21 methyl protons at δ 1.50 (3H, s) in the ^{1}H NMR (C_5D_5N) of **2** suggested a 22*R* configuration.[3]

The structure proposed (Fig. 1) was confirmed by MS. Thus, the positive FABMS of desulfated frondoside C (**2**) shows the pseudomolecular ions at m/z 1271 $[M + Na]^+$ and 1287 $[M + K]^+$ (molecular formula $C_{61}H_{100}O_{26}$), and a significant fragment ion at m/z 507 [aglycone + Na + H]$^+$ due to the loss of the carbohydrate chain from the pseudomolecular ion. Other ions confirmed the presence of the acetoxy group in the side chain of **2** (m/z 1129, 1130, 163, 164, and 165) and the sequence of the monosaccharide units in the oligosacharide

Table 1. ^{13}C NMR chemical shifts of the sugar moieties of frondoside C (**1**) and its desulfated derivative (**2**).[a, b]

Carbon	**1**	**2**	Carbon	**1**	**2**
Xyl_1 (1→C-3)			MeGlc (1→3Glu)		
1	104.6 d	105.3 d	1	105.3 d	105.8 d
2	83.0[b] d	83.1[b] d	2	75.0 d	75.1 d
3	75.5 d	78.0 d	3	87.0 d	88.1 d
4	76.0[c] d	70.6 d	4	70.9 d	71.1 d
5	64.6 t	66.7 t	5	77.2 d	78.5 d
			6	68.3[c] t	62.7 t
			Ome	61.3 q	60.8 q
Qui (1→2Xyl_1)			Xyl_2 (1→2Qui)		
1	103.3 d	103.3 d	1	105.8 d	106.2 d
2	83.4 d	83.6 d	2	75.6 d	75.8 d
3	75.5 d	76.0 d	3	77.2 d	77.3 d
4	87.0[b] d	86.9[b] d	4	70.8 d	70.8 d
5	72.0 d	71.4 d	5	67.2 t	67.2 t
6	18.7 q	18.4 q			
Glc (1→4Qui)					
1	105.2 d	104.9 d			
2	74.4 d	73.9 d			
3	87.3[b] d	88.5[b] d			
4	70.0 d	70.1 d			
5	76.0 d	77.9 d			
6	68.5[c] t	62.5 t			

[a] Recorded at 62.7 MHz in C_5D_5N:D_2O (4:1). Xyl, β-*D*-xylopyranose; Glc, β-*D*-glucopyranose; Qui, β-*D*-quinovopyranose; MeGlc, β-*D*-3-OMe-glucopyranose.
[b] Interglycosidic positions.
[c] Sulfate positions.

[2] The carbon chemical shift of the methyl group C-21 in (20*R*, 22*R*) and (20*R*, 22*S*) 5α-cholestane–3β,20,22-triol occurs at higher field (δ 21.1 and 21.9) than those of the (20*S*, 22*R*) and (20*S*, 22*S*) derivatives (δ 23.8 and 24.2). (See refs. 8–10.)

[3] The (20*R*, 22*R*) 5α-cholestane–3β,20,22-triol display the C-21 methyl protons at δ 1.51, while the (20*R*, 22*S*), (20*S*,22*R*), and (20*S*, 22*S*) derivatives shows those protons at δ 1.60, 1.44, and 1.32, respectively. (See refs. 8–10.)

© 1998 NRC Canada

Fig. 1. Fragmentation of **2** in the positive FABMS.

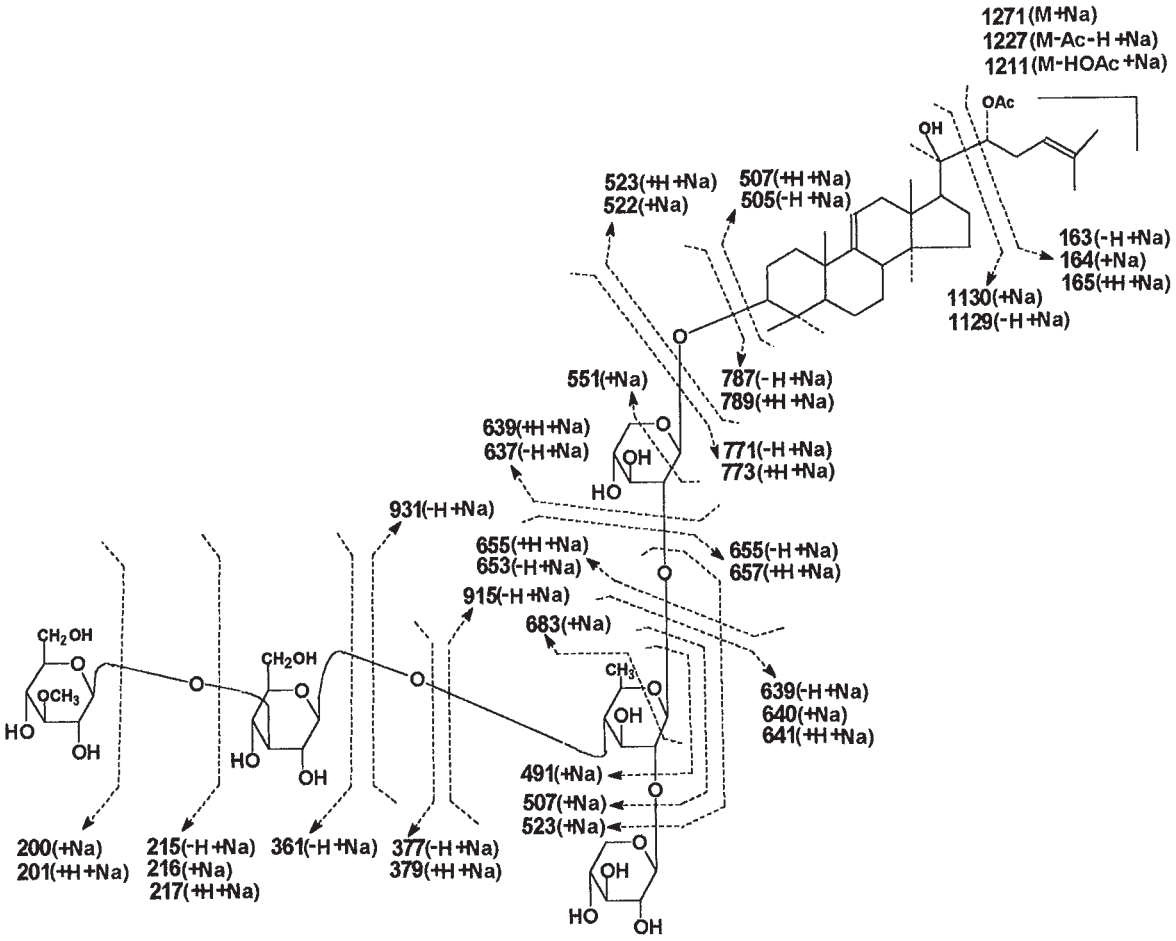

chain as depicted in Fig. 1. Assuming that the sugars belong to the *D*-configuration family and the ions at sulfate groups are sodium and potassium, as is the case in related sea-cucumber glycosides (1, 2), we conclude that frondoside C (**1**) has the structure 20(*R*)-hydroxy,22(*R*)-acetoxy-3β-*O*-{[3-*O*-methyl-β-*D*-6-sulfonato-glucopyranosyl-(1→3)-*O*-β-*D*-6-sulfonato-glucopyranosyl-(1→4)]-*O*-[β-*D*-xylopyranosyl-(1→2)]-*O*-β-*D*-quinovopyranosyl-(1→2)-*O*-β-*D*-4-sulfonatoxylopyranosyl}-lanosta-9(11), 24(25)-diene sodium (or potassium) salt.

Most of sea-cucumber triterpene glycosides reported so far in the literature (more than 70) belong to the so-called holostane series, characterized by the presence of an 18(20)-lactone ring in the aglycone moiety (11–13). Sea-cucumber lanostane glycosides devoid of the 18(20)-lactone are rare and, in fact, only six have been published. These are kurilosides A and C from *Duasmodactyla kurilensis* (14), psolusoside B from *Psolus fabricii* (15), Ds-penaustrosides A and B from *Pentacta australis* (5), cucumarioside G_2 from *Eupentacta fraudatrix* (16), and koreoside A from *Cucumaria koraiensis* (17). Frondoside C (**1**) reported in this paper is the seventh lanostane glycoside without the 18(20)-lactone found in sea cucumbers.

The desulfated frondoside C (**2**) was found to present intense cytotoxic activity (IC_{50} = 1 μg/mL) when tested in vitro against several standard mice and human tumoral cell lines (P-388, Schabel, A-549, HT-29, and Mel-28).

Experimental section

General experimental procedures

All melting points were determined with a Kofler thermogenerate apparatus. Specific rotation was measured on a Perkin–Elmer 141 polarimeter. One- and two-dimensional NMR spectra were obtained on a Bruker WM-250 spectrometer at 250 MHz (^{1}H), 500 MHz (^{1}H), and 62.7 MHz (^{13}C) in C_5D_5N:D_2O (4:1) with TMS as an internal reference. The FABMS (positive ion mode) was performed on a Fission VG-Quattro spectrometer and obtained with Cs atoms at 7–9 keV and a matrix of glycerol–thioglycerol + NaCl. HPLC was performed with a Dupont 8800 chromatograph equipped with a RIDK–102 differential refractometer (Laboratorni Pristroje, Prague).

Animal material

The sea cucumber *Cucumaria frondosa* (family *Cucumariidae*; order *Dendrochirotida*) was collected in Dalnezelenetskaya Bay (Kolsky Peninsula, Barents Sea) in August 1988. The collection was carried out with scuba divers at 10–15 m in depth. A voucher specimen is on deposit in the collection of Murmansk Marine Biological Institute of Kolsky Scientific Center of the Russian Academy of Sciences, Dalnyje Zelentsy, Murmansk District, Russia. The specimens were kept in EtOH.

© 1998 NRC Canada

Extraction and isolation of 1

The specimens (30 kg) were cut into pieces and extracted twice with hot ethanol. The combined extracts were concentrated to dryness under low pressure, and the residue was chromatographed on a polychrom-1 column (powdered Teflon, Biolar, Latvia) previously filled with EtOH. Inorganic salts and polar impurities were washed out with H_2O, and the fraction containing the glycosides was then eluted with 50% ethanol. This fraction was further chromatographed on a silica-gel column, eluting with a $CHCl_3$–EtOH–H_2O (100:100:17) system and affording two main fractions, the first one composed by monosulfated glycosides (4.1 g) and the second one by the most polar glycosides (2.4 g). This last fraction was repeatedly chromatographed on a silica-gel column, with the $CHCl_3$–MeOH–H_2O (650:300:54) system, affording impure frondoside C (**1**) (323 mg) and also containing the glycosides closed by aglycone structure as impurities, which were directly converted into **2** by solvolysis. See Table 1 for ^{13}C NMR data.

Solvolysis of frondoside C

To a solution of 323 mg of **1** (with impurities) in 10 mL of H_2O, 50 mg of resin DOWEX (H^+) was added (rt, 20 min). The resin was filtered off, washed with H_2O (35 mL) and EtOH (25 mL). The combined filtrates were evaporated to dryness under low pressure, and the residue dissolved in 10 mL of dioxane–pyridine (1:1) was refluxed for 1 h. The reaction mixture was concentrated under low pressure and repeatedly chromatographed on a silica-gel column, eluting with the $CHCl_3$–MeOH–H_2O (650:150:22) system. The residue (270 mg) was submitted for HPLC on a Silasorb C-18 column (80% MeOH, 20% water), producing 50 mg of pure desulfated derivative **2**.

Desulfated frondoside C (2)

$[\alpha]_D^{20}$ –21 (*c* 0,1, pyridine), mp 262–264°C, ^1H NMR (δ, ppm): 5.20 (1H, $J = 7.5$ Hz, H1-Xyl_1), 5.12 (1H, $J = 7.1$ Hz, H1-Xyl_2), 5.05 (1H, $J = 7.1$ Hz, H1-Qui), 4.86 (1H, $J = 7.5$ Hz, H1-Glc), 4.75 (1H, $J = 7.1$ Hz, H1-MeGlc), 3.79 (3H, s, OMe of MeGlc), 1.59 (3H, d, $J = 6.4$ Hz, Me6-Qui). See Tables 1 and 2 for ^{13}C NMR data and Table 2 for aglycone moiety data. FABMS (positive ion mode) *m*/*z* (rel. intensity): 1287 ($C_{61}H_{100}O_{26}S_2K$, $[M + K]^+$, 3.5), 1271 ($[M + Na]^+$, 1.9), 1227 ($[M - Ac - H + Na]^+$, 2.2), 1211 ($[M - HOAc + Na]^+$, 1.5), 1129 (2.7), 1130 (1.5), 931 ($[M–177–162–H + Na]^+$, 1.6), 639 ($[M–177–162–H + Na]^+$, 4.6), 507 ([aglycone + Na + H]$^+$, 7), 523 (12), 491 (23), 173 (100), 165 (78), 164 (8), 163 (28).

Antitumor activity

Antitumor activity was determined in the cell lines P-388 (mouse lymphoma ATCC:CCL 46), Schabel (mouse lymphoma MDR), A-549 (human lung carcinoma ATCC: CCL 35), HT-29 (human colon carcinoma ATCC: HTB 38), and Mel-28 (human melanoma ATCC: HTB 72).

Acknowledgment

R.R. acknowledges financial support from XUGA 20901B95 and MAR95–1933 CO2-O2.

Table 2. ^{13}C NMR and selected ^1H NMR chemical shifts of the aglycone moiety of desulfated frondoside C (**2**).

Carbon	δ_C mult.[a]	δ_H mult.[b]
1	37.0 d	
2	27.4 t	
3	89.1 d	3.13 brt
4	39.8 s	
5	53.6 d	
6	21.9 t	
7	28.8 t	
8	41.9 d	
9	149.9 s	
10	40.3 s	
11	115.2 d	5.17 m
12	38.5 t	
13	46.2 s	
14	47.6 s	
15	34.3 t	
16	22.6 t	
17	50.6 d	
18	17.2 q	0.99 s
19	22.8 q	0.96 s
20	76.4 s	
21	21.3 q	1.50 s
22	79.9 d	5.20 m
23	30.6 t	2.00–2.40 brm
24	121.7 d	5.21 brt
25	133.3 s	
26	26.0 q	1.61[c] s
27	18.1 q	1.62[c] s
30	16.9 q	1.02 s
31	28.6 q	1.15 s
32	19.2 q	0.74 s
OAc	170.8 s	
	21.7 q	2.12 s

[a] Recorded at 62.9 MHz in C_5D_5N:D_2O (4:1).
[b] Recorded at 500 MHz in C_5D_5N:D_2O (4:1).
[c] Interchangeable.

References

1. M. Girard, J. Belanger, J.W. ApSimon, F.X. Garneau, C. Harvey, and J.-R. Brisson. Can. J. Chem. **68**, 11 (1990).
2. J.A. Findley, N. Yayli, and L. Radics. J. Nat. Prod. **55**, 93 (1992).
3. S.A. Avilov, V.I. Kalinin, O.A. Drozdova, A.I. Kalinovsky, V.A. Stonik, and E. N. Gudimova. Khim. Prir. Soedin. 260 (1993).
4. O.A. Drozdova, S.A. Avilov, A.I. Kalinovsky, V.A. Stonik, Y.M. Milgrom, and Y.W. Rashkes. Khim. Prir. Soedin. 369 (1993).
5. T. Miamoto, K. Togawa, R. Higuchi, T. Komori, and T. Sasaki. J. Nat. Prod. **55**, 940 (1992).
6. A.S. Shashkov and O.S. Chizhov. Bioorg. Khim. **2**, 437 (1976).
7. F.W. Wehrli and T. Nishida. *In* Fortschr. chem. org. naturst. (Prog. chem. org. nat. prod.) Vol. 36. *Edited by* L. Lechmeister. Springer, New York. 1979. pp. 1–229.
8. R. Riccio, F. Zollo, E. Finamore, L. Minale, D. Laurent, G. Bargibant, and J. Pusset. J. Nat. Prod. **48**, 266 (1985).
9. H. Hikino, T. Okuyama, C. Konno, and T. Takemoto. Chem. Pharm. Bull. **23**, 125 (1975).
10. H. Hikino, T. Okuyama, S. Arihara, Y. Hikino, T. Takemoto, H. Mori, and K. Shibata. Chem. Pharm. Bull. **23**, 1458 (1975).
11. G.G. Habermehl and H.C. Krebs. *In* Studies in natural products

© 1998 NRC Canada

chemistry. Vol. 7. *Edited by* Atta-ur-Rahman. Elsevier Science Publishers B.V, Amsterdam. 1990. pp. 265–316.
12. V.A. Stonik, G.B. Elyakov. *In* Bioorganic marine chemistry. Vol. 2. *Edited by* P.J. Scheuer. Springer, Berlin, New York, Tokyo. 1988. pp. 43–86.
13. V.I. Kalinin, V.S. Levin, and V.A. Stonik. The chemical morphology: Triterpene glycosides of sea cucumbers (Holothurioidea, Echinodermata). Dalnauka, Vladivostok, U.S.S.R. 1994.
14. S.A. Avilov, A.I. Kalinovsky, and V.A. Stonik. Khim. Prir. Soedin. 221 (1991).
15. V.I. Kalinin, A.I. Kalinovsky, V.A. Stonik, P.S. Dmitrenok, and Y.N. Elkin. Khim. Prir. Soedin. 361 (1989).
16. S.A. Avilov, V.I. Kalinin, T.N. Makarieva, V.A. Stonik, A.I. Kalinovsky, Y.W. Rashkes, and Y.M. Milgrom. J. Nat. Prod. **57**, 1166 (1994).
17. S.A. Avilov, A.I. Kalinovsky, V.I. Kalinin, V.A. Stonik, R. Riguera, and C. Jimenez. J. Nat. Prod. **60**, 808 (1997).

© 1998 NRC Canada

Synthesis of *cis*-*p*-dioxano-12-crown-4 and X-ray crystallography of the (1:1) complex with lithium thiocyanate

Alex B. Driega, Gerald W. Buchanan, and Corinne Bensimon

Abstract: The synthesis of a novel 12-crown-4 analogue (*cis*-*p*-dioxano-12-crown-4 or *cis*-3,6,9,13,15-pentaoxabicyclo[9.3.1]pentadecane) is described. The (1:1) LiNCS complex crystallizes in the monoclinic *Cc* space group; $a = 8.4973(2)$ Å, $b = 18.0659(4)$ Å, $c = 8.9168(1)$ Å, and $\beta = 90.713(1)°$ with $Z = 4$. The crown adopts C_1 symmetry to which the Li^+ is coordinated in a rectangular pyramid with an apical $^-$NCS.

Key words: crown ethers, structure, complexation.

Résumé : On décrit la synthèse d'un nouvel analogue d'une 12-couronne-4 (*cis*-*p*-dioxano-12-couronne-4 ou *cis*-3,6,9,13,15-pentaoxabicyclo[9.3.1]pentadécane). Le complexe (1:1) avec le LiNCS cristallise dans le groupe d'espace monoclinique *Cc*, avec $a = 8{,}4973(2)$ Å, $b = 18{,}0659(4)$ Å et $c = 8{,}9168(1)$ Å, $\beta = 90{,}713(1)°$ et $Z = 4$. La couronne adopte une symétrie C_1 dans laquelle la coordination du Li^+ est s'effectue dans une pyramide rectangulaire avec un $^-$NCS apical.

Mots clés : éthers couronnes, structure, complexation.

[Traduit par la rédaction]

Introduction

The known solid-state conformations of 12-crown-4 ether (12C4) or 1,4,7,10-tetraoxadodecane fall into three symmetry classes C_i, C_4, and C_s. The free ligand adopts C_i symmetry (1), while in non-tetradentate complexes all three classes are encountered (C_i symmetry in ref. 2, C_4 symmetry in refs. 2*c* and 3, C_s symmetry in ref. 4). In complexes where the four oxygens are coordinated to a metal cation, the crown adopts C_4 symmetry (5–7), with the exception of one C_s transition-metal complex (8). However the *cis*-*syn*-*cis*-dicyclohexano-12C4 analogue, upon (1:1) complexation with LiNCS, crystallizes with an asymmetric geometry (9).

Force-field calculations on 12C4 utilizing AMBER (10), MM2 (11), MM3 (12), and WBFF (13) each report anywhere from 4 to 55 low energy conformations, designated by *gauche*/*anti* torsion angle codes, with no shared global minimum. These studies consistently locate the C_i, C_4, and C_s conformers amongst the lowest in energy. To date, the C_i conformer has not been located as a global minimum,[2] which indicates that the solid-state geometry may be dominated by crystal packing forces (14, 15).

Herein is presented the stereospecific synthesis of *cis*-*p*-dioxano-12C4 (*cis*-3,6,9,13,15-pentaoxabicyclo[9.3.1]pentadecane) **1** and **1**·LiNCS. The crown nature of **1**, with a diequatorial dioxane chair, is that of 12C4 in which C_i and C_4 symmetry are forbidden. Hence X-ray crystallographic studies on **1** have the potential to complement those on 12C4 itself. Conversely, with a flattened diaxial dioxane chair, or a diequatorial boat, **1** can adopt a 14C4 nature. In this light, complexation with Li^+ is of particular interest, owing to the high affinity of this metal ion to 14C4 moieties (16). The morpholino analogue of **1** is known (mixture of *cis* and *trans* stereoisomers), but no structural information is available (17).

Results and discussion

Crystallographic data for **1**·LiNCS are presented in Table l*a*. Atomic bond lengths are in Table l*b*, while bond angles are in Table 1*c*. Torsion angles for networks not involving H atoms are collected in Table 1*d*. Atomic parameters and anisotropic temperature factors are available as supplementary data.[3]

Structure of 1·LiNCS

In the ORTEP diagram of **1**·LiNCS, the substituents bonded to C1 and C11 of the dioxane chair are equatorial (Fig. 1), hence the C2-C1-O15-C11-C10 unit is *anti*-*anti*. All oxygen lone pairs are oriented to one side of the crown cavity, therefore three 12C4 conformations are possible: conformation **A** with

Received June 27, 1997.

A.B. Driega,[1] G.W. Buchanan, and C. Bensimon.
Ottawa–Carleton Chemistry Institute, Dept. of Chemistry, Carleton University, 1125 Colonel By Drive, Ottawa, ON K1S SB6, Canada.

[1] Author to whom correspondence may be addressed.

[2] As pointed out by the authors in ref. 12, the global minimum conformation **IIb** in ref. 10 corresponds to C_s and not C_i symmetry.

[3] Copies of supplementary material may be purchased from: The Depository of Unpublished Data, Document Delivery, CISTI, National Research Council Canada, Ottawa, Canada K1A 0S2. Atomic parameters have also been deposited at the Cambridge Crystallographic Data Centre and can be obtained on request from The Director, Cambridge Crystallographic Data Centre, University Chemical Laboratory, 12 Union Road, Cambridge, CB2 1EZ, United Kingdom. Structure factors are no longer being deposited and can be obtained on request from the author.

© 1998 NRC Canada

Table l. *(a)* Crystallographic data.

Formula	$C_{11}H_{18}LiNO_5S$
fw	283.27
Crystal system	Monoclinic
Space group	*Cc*
a (Å)	8.4973 (2)
b (Å)	18.0659 (1)
c (Å)	8.9168 (1)
β	90.713 (1)
V (Å)^3	1368.72 (5)
Z (molecules/unit cell)	4
D_{calc} (g/cm^3)	1.374
μ (mm^{-1})	0.21
Crystal dimensions (mm^3)	0.20 × 0.20 × 0.20
Radiation, λ (Å)	Mo*K*α (0.7093)
Octants measured	*h*(–11 to 8), *k*(–24 to 24), *l*(–11 to 8)
2Θ (max.)	57.0
No. of reflections with $I_{net} > 2.5\sigma I_{net}$	2733
No. of unique reflections	2816
No. of measured reflections	4769
R merge	2.2%
R_f (sig. reflections)	0.052
R_w (sig. reflections)	0.079
Maximum shift/σ ratio	0.083
Goodness of fit	2.78
Last D-map (e/Å^3)	
Deepest hole	–0.420
Highest peak	0.520

Table 1. (*b*) Atomic bond distances.

Bond	Length (Å)
Nl–C16	1.165(6)
Nl–Li	1.966(9)
S1–C16	1.638(4)
O3–C2	1.449(5)
O3–C4	1.439(5)
O3–Li	2.195(9)
O6–C5	1.434(5)
O6–C7	1.441(6)
O6–Li	2.026(8)
O9–C8	1.443(5)
O9–C10	1.431(6)
O9–Li	2.157(9)
O13–C12	1.445(5)
O13–C14	1.428(6)
O15–C1	1.455(5)
O15–C11	1.438(5)
O15–Li	1.982(8)
C1–C2	1.525(6)
C1–C14	1.500(6)
C4–C5	1.500(7)
C7–C8	1.509(7)
C10–C11	1.538(6)
C11–C12	1.512(6)

Table l. (*c*) Atomic bond angles.

Bond	Angle (deg)	Bond	Angle (deg)
C16-Nl-Li	172.8(5)	C2-O3-C4	117.0(3)
C2-O3-Li	107.9(3)	C4-O3-Li	105.0(3)
C5-O6-C7	114.4(4)	C5-O6-Li	104.9(3)
C7-O6-Li	109.6(3)	C8-O9-C10	114.1(4)
C8-O9-Li	106.0(3)	C10-O9-Li	106.1(3)
C12-O13-C14	111.9(3)	C1-O15-C11	111.9(3)
Cl-O15-Li	121.4(3)	C11-Ol5-Li	121.2(3)
O15-C1-C2	105.9(3)	O15-Cl-C14	108.1(3)
C2-Cl-C14	112.4(4)	O3-C2-C1	112.5(4)
O3-C4-C5	112.4(4)	O6-C5-C4	107.6(4)
O6-C7-C8	111.9(3)	O9-C8-C7	107.5(4)
O9-C10-C11	110.0(3)	O15-C11-C10	103.9(3)
O15-C11-C12	108.2(3)	C10-C11-C12	116.1(4)
O13-C12-C11	109.4(3)	O13-C14-C1	110.0(3)
N1-C16-S1	178.6(4)	N1-Li-O3	108.1(4)
N1-Li-O6	125.5(4)	N1-Li-O9	106.9(4)
N1-Li-O15	124.2(4)	O3-Li-O6	81.9(3)
O3-Li-O9	144.5(4)	O3-Li-O15	78.0(3)
O6-Li-O9	82.7(3)	O6-Li-O15	110.2(4)
O9-Li-O15	77.7(3)		

Table 1. (*d*) Torsion angles.

Bond	Angle (deg)	Bond	Angle (deg)
Li-Nl-C16-S1	–50.0(5)	C16-Nl-Li-O3	–39.6(6)
C16-Nl-Li-O6	–129.8(11)	Cl6-Nl-Li-O9	137.2(11)
C16-Nl-Li-O15	50.8(7)	C4-O3-C2-C1	–79.7(6)
Li-O3-C2-C1	38.4(5)	C2-O3-C4-C5	96.4(7)
Li-O3-C4-C5	–23.2(5)	C2-O3-Li-N1	104.1(9)
C9-O3-Li-O6	–131.0(10)	C2-O3-Li-O9	–66.0(6)
C2-O3-Li-O15	–18.3(4)	C4-O3-Li-N1	–130.4(10)
C4-O3-Li-O6	–5.5(4)	C4-O3-Li-O9	59.5(6)
C4-O3-Li-O15	107.2(9)	C7-O6-C5-C4	–175.7(9)
Li-O6-C5-C4	–55.6(6)	C5-O6-C7-C8	81.9(7)
Li-O6-C7-C8	–35.6(5)	C5-O6-Li-N1	139.9(10)
C5-O6-Li-O3	33.4(5)	C5-O6-Li-O9	–114.6(9)
C5-O6-Li-O15	–40.6(5)	C7-O6-Li-N1	–96.9(8)
C7-O6-Li-O3	156.7(10)	C7-O6-Li-O9	8.7(4)
C7-O6-Li-O15	82.7(8)	C10-O9-C8-C7	–158.4(9)
Li-O9-C8-C7	–42.1(5)	C8-O9-C10-C11	67.6(6)
Li-O9-C10-C11	–48.6(5)	C8-O9-Li-N1	144.4(10)
C8-O9-Li-O3	–45.4(5)	C8-O9-Li-O6	19.4(4)
C8-O9-Li-O15	–93.2(8)	C10-O9-Li-N1	–94.0(8)
C10-O9-Li-O3	76.2(7)	C10-O9-Li-O6	141.0(10)
Cl0-O9-Li-O15	28.4(5)	C14-O13-C12-C11	59.2(6)
Cl2-O13-C14-C1	–58.2(5)	C11-O15-C1-C2	–179.8(8)
C11-O15-C1-C14	–59.5(5)	Li-O15-C1-C2	26.0(5)
Li-O15-C1-C14	146.3(7)	C1-O15-C11-C10	–175.1(8)
Cl-O15-C11-C12	60.8(5)	Li-O15-C11-C10	–20.9(5)
Li-O15-C11-C12	–144.9(8)	Cl-O15-Li-N1	–109.1(9)
Cl-O15-Li-O3	–5.2(4)	C1-O15-Li-O6	71.4(7)
C1-O15-Li-O9,	148.7(10)	Cll-O15-Li-N1	99.1(8)
C11-O15-Li-O3	–157.0(10)	C11-O15-Li-O6	–80.4(7)
C11-O15-Li-O9	–3.1(4)	O15-C1-C2-O3	41.4(4)
C14-C1-C2-O3	–158.9(9)	O15-C1-C14-O13	56.6(5)
C2-C1-C14-O13	172.3(9)	O3-C4-C5-O6	54.1(5)
O6-C7-C8-O9	53.6(5)	O9-C10-C11-O15	45.5(5)
O9-C10-C11-C12	164.2(9)	O15-C11-C12-O13	–58.7(5)

© 1998 NRC Canada

Fig. 1. (*a*) ORTEP plot of **1**·LiNCS showing ligand conformation only. (*b*) ORTEP plot of **1**·LiNCS, perpendicular view, showing Li complexation.

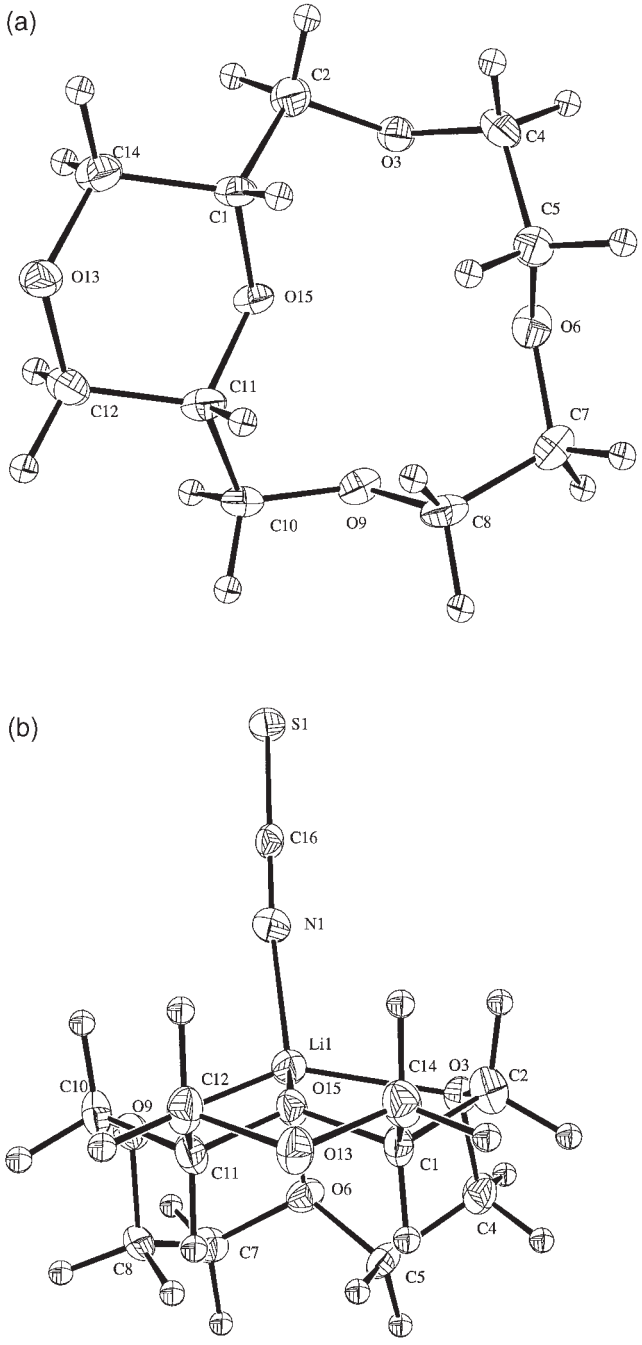

C_2 symmetry (*a*+*g*+*g* –*g*–*ga* *a*+*g*+*g* –*g*–*ga*)[4] superimposable on the diamond lattice, and a rectangular [2,4,2,4] [5] crown cavity (11); conformation **B** with C_2 symmetry (*a*+*g*+*g* *a*+*g*+*g* –*g*–*ga* –*g*–*ga*) and a square [2,3,4,3] crown cavity; or conformation **C** with C_1 symmetry (*a*+*g*+*g* *a*+*g*+*g* *a*+*g*+*g* –*g*–*ga*) possessing traits intermediate [2,3,3,4] between the previous two.

[4] The first torsion angle is defined by a C-O-C-C network where +*g*(0°→120°), –*g*(0°→ –120°), *a*(120°→ –120°).

[5] Denotes corners, i.e., the number of bonds between *a*+*g*+*g* or *a*–*g*–*g* segments.

Note that the *cis-syn-cis*-dicyclohexano-12C4 analogue, which lacks an *anti-anti* constraint (9), adopts conformation **C** upon (1:1) complexation with LiNCS.

The crown cavity of **1**·LiNCS is somewhat rectangular with diagonal 0···0 distances of 3.3 and 4.1 Å. The mean deviation of the least-squares plane defined by the binding oxygens is 0.24 Å, and the Li^+ is situated 0.90 Å from this plane, capped by the nitrogen of the anion. The mean Li···0 distance is 2.09 Å which, considering the known 12C4·Li^+ complexes, compares favourably with 12C4·LiNCS (2.08 Å) (5) and *cis-syn-cis*-dicyclohexano-12C4·LiNCS (2.11 Å) (9), but is considerably shorter than 12C4·$LiNPh_2$ (2.20 Å) and 12C4·$LiN(SiMe_3)_2$ (2.23 Å) (6). These trends reflect the degree of conformational freedom of the macrocycle within the lattice, since all Li···N distances remain nearly constant (1.97–2.00 Å). A similar observation is made by Kamitori et al. (7) for a $(12C4)_2$·Li^+ species included in a γ-cyclodextrin framework, where the mean Li···0 distance is about 0.16 Å longer than usual (6).

Inspection of the macrocyclic torsion angles (Table 2) reveals that **l**·LiNCS adopts conformation **C**. Note that the lower half of the macrocycle (Fig. 1*a*) has the extended boat geometry of conformation **B**, while the upper half has the geometry of conformation **A**.There are two small O-C-C-O torsion angles in the range of 40–50°, in keeping with other 12C4·Li^+ complexes (5, 6, 9), which provide focused C-O dipoles for optimal directional coordination. In 12C4 sandwich complexes (4*a*, 6, 7), the metal resides further out of the crown cavity, and the O-C-C-O angles are similar to those in the dioxane ring of **l**·LiNCS (Table l*d*) (18). Differential scanning calorimetry measurements on **1**·LiNCS show no phase transitions between –100°C and the decomposition point at 218–222°C.

Conformational analysis

Of the three possible 12C4 tetradentate complexation geometries, the results of AMBER (10), MM2 (11), and MM3 (12) force-field calculations all favour conformation **C**. Indeed, the AMBER study locates this geometry (conformer **IIc**) as the third lowest overall in energy (10).[2] The detailed torsion angles reported in the MM2 study (conformer **19**) (11) are in excellent agreement with the experimental **1**·LiNCS geometry, the largest difference being 10° with a mean deviation of 5° (Table 2). Our MM2 minimization of **1** in the X-ray geometry keeps all torsion angles to within 15° of the experimental geometry, with a mean deviation of 6°. Evidently the dioxane ring contributes little strain[6] to the macrocycle in conformation **C**.

Our MM2 minimization of **1** in conformation **B** reveals that, although the cavity dimensions are appropriate for (1:1) Li^+ complexation with diagonal O···O distances of 3.8 and 4.1 Å, the lone pairs on O3 and O9 face too far outward. However, by flattening the extended boat into a geometry suitable for

[6] When correlating theory to experiment between parent compounds and their analogues based on torsion angle codes, caution must be exercised. An illustrative example is that *cis-syn-cis*-dicyclohexano-12C4 crystallizes with the crown in C_4 symmetry (*a*+*g*+*g* *a*+*g*+*g* *a*+*g*+*g* *a*+*g*+*g*), but the (1:1) LiNCS complex does not (9). Here pseudorotation into a C_4 complexation geometry results in severe compression of the ethylene glycol O-C-C-O networks due to the relatively inflexible cyclohexane moieties.

© 1998 NRC Canada

Table 2. Experimental and calculated macrocyclic torsion angles of **1**·LiNCS and related compounds.

Network	**1**·LiNCS	DC12C4·LiNCS[a]	MM2 on **1**[b]	MM2 on 12C4[c]
C1-C2-O3-C4	–79.7	–84.6	–65.6	–70.7
C2-O3-C4-C5	96.4	104.1	86.0	98.6
O3-C4-C5-O6	54.1	50.0	64.1	53.0
C4-C5-O6-C7	–175.7	–176.3	177.3	–176.8
C5-O6-C7-C8	81.9	76.8	67.7	71.5
O6-C7-C8-O9	53.6	54.3	58.1	56.2
C7-C8-O9-C10	–158.4	–161.9	–158.3	–154.6
C8-O9-C10-C11	67.6	80.7	68.5	73.2
O9-C10-C11-O15	45.5	46.6	44.2	44.4
C10-C11-O15-C1	–175.1	–157.7	–178.2	–168.6
C11-O15-C1-C2	–179.8	166.8	–178.3	173.0
O15-C1-C2-C3	–41.4	–49.2	–43.4	–48.5

[a] *Cis-syn-cis*-dicyclohexano-12-crown-4 (see ref. 9).
[b] In the X-ray geometry of **1**·LiNCS.
[c] Conformation **19** (see ref. 11).

complexation, the bridge O-C-C-O networks become seriously compressed to <40° due to the inflexible dioxane ring. Finally, for conformation **A**, tetradentate complexation is deemed unlikely due to the oblong dimensions of the crown cavity as reflected in the diagonal O···O distances of 2.7 and 4.1 Å.

It is noteworthy that the (1:1) LiNCS complexes of two structurally diverse 12C4 analogues crystallize with the same asymmetric [2,3,3,4] conformation (Table 2). This behaviour is anticipated to be of importance in the design of Li^+ selective complexing agents. Investigation into the preferred conformation of **1** in solution at low temperature (15, 19) is in progress. In this regard the C_s conformation of 12C4, which contains a plane of symmetry, is a likely candidate (8, 10–13, 14).

Experimental

Materials

cis-*3,6,9,13,15-pentaoxabicyclo[9.3.1]pentadecane (**1**)*
A mixture of *cis*-2,6-bis(iodomethyl)-*p*-dioxane (20) (2.00 g, 5.4 mmol), $NaHCO_3$ (1.00 g, 12.0 mmol), 4 mL H_2O, and 20 mL DMF was stirred at 110°C for 17 h. The solution was then filtered, the solvents removed in vacuo, and the residue pyrolyzed in a Kugelrohr distillation apparatus at 135–140°C (0.6 mm) to obtain *cis*-2,6-bis(hydroxymethyl)-*p*-dioxane (95% pure by ^{13}C NMR) as an oil; 60% yield. To a stirred mixture of *t*BuOLi (648 mg, 10.8 mmol) in 20 mL *t*BuOH was added dropwise the diol (400 mg, 2.7 mmol) in 5 mL *t*BuOH, and then the nonhomogeneous solution refluxed at 80°C in an oil bath for 4 h with a $CaCl_2$ drying tube connected to the top of the condenser. Then bis-2-chloroethoxy ether (386 mg, 2.7 mmol) was added, followed by LiBr (234 mg, 2.7 mmol), and the gentle reflux continued for 2 weeks. The solution (blue to litmus) was then neutralized with 6 M HCl, and the solvent removed in vacuo. The residue was taken up in 20 mL of H_2O, acidified with HCl, and then extracted with $CHCl_3$ (3 × 20 mL). The combined organic phases were dried over anhydrous Na_2SO_4, and the solvent removed by rotary evaporation. The residue was eluted with $CHCl_3$:MeOH 15:2 on a preparative silica TLC plate, 1 mm thickness, $R_f = 0.65$, with detection by phosphomolybdic acid in EtOH (20% w/w), to give **1** as a colourless oil; 14% yield. ^1H NMR ($CDCl_3$) δ: 3.34–3.56 (m, 2H), 3.59–3.91 (m, 7H); ^{13}C NMR ($CDCl_3$) δ: 66.9 (t, $^1J_{C\text{-}H}$ = 141 Hz), 68.6 (t, $^1J_{C\text{-}H}$ = 138 Hz), 69.8 (t, $^1J_{C\text{-}H}$ = 140 Hz), 71.2 (t, $^1J_{C\text{-}H}$ = 142 Hz), 74.7 (d,$^1J_{C\text{-}H}$ = 143 Hz).

cis-*3,6,9,13,15-pentaoxabicyclo[9.3.1]pentadecane·LiNCS (**1**·LiNCS)*
To **1** (30 mg, 0.14 mmol) in 1 mL of Me_2CO was added LiNCS (25% H_2O w/w, 15 mg, 0.17 mmol), and after 30 min crystallization commenced. The solvent was allowed to slowly evaporate to about 0.5 mL in volume whereupon X-ray grade crystals in the form of hexagonal plates were collected; mp 218–222°C (d).

X-ray crystallographic measurements and structure solution

A summary of the crystallographic data is given in Table 1*a*. Diffraction intensities were collected on a Rigaku diffractometer using Mo*K*α radiation at –100°C. The Θ/2Θ scan technique was used to a maximum 2Θ value of 57.0°.

The systematic absences gave a choice of two space groups, namely *Cc* and *C*2/*c*. The structure was solved in the lowest symmetry *Cc* and then was checked for missing symmetry. No missing symmetry was found, thus confirming that *Cc* was the correct space group. Unit cell parameters were obtained from least-squares refinement using the setting angles of 4632 reflections in the range $3 < 2\Theta < 57°$.The data were corrected for Lorentz and polarization effects. No absorption correction was made. The structure was solved by direct methods plus Fourier maps and was refined by full-matrix least-squares analysis with weights based on counting statistics. The non-hydrogen atoms were refined anisotropically, and H atoms were calculated. No crystal decay was noted during data collection. All calculations were performed using the NRC VAX crystal structure programs (21). Structure factor tables and anisotropic temperature factors are available as supplementary data.[3]

© 1998 NRC Canada

References

1. P. Groth. Acta Chem. Scand. Ser. A, **A32**, 279 (1978).
2. (*a*) R.D. Rogers, A.H. Bond, W.G. Hipple, A.N. Rollins, and R.F. Henry. Inorg. Chem. **30**, 2671 (1991); (*b*) E.A. Babaian, M. Huff, F.A. Tibbals, and D.C. Hrncir. J. Chem. Soc. Chem. Comm. 306 (1990); (*c*) R.D. Rogers. J. Coord. Chem. **16**, 415 (1988); (*d*) M.A. Neuman, E.C. Steiner, F.P. van Remoortere, and F.P. Boer. Inorg Chem. **14**, 734 (1975).
3. S. Kamitori, K. Hirotsu, and T. Higuchi. J. Chem. Soc. Chem. Comm. 690 (1986).
4. (*a*) R.D. Rogers, A.N. Rollins, R.D. Etzenhouser, and R.F. Henry. J. Inclusion Phenom. Mol. Recognit. Chem. **8**, 375 (1990); (*b*) R.D. Rogers, M.M. Benning, R. D. Etzenhouser, and A.N. Rollins. J. Chem. Soc. Chem. Comm. 1586 (1989).
5. P. Groth. Acta Chem. Scand. Ser. A, **A35**, 463 (1981).
6. R.A. Bartlett, H.V. Rasika Dias, H. Hope, B.D. Murray, M.M. Olmstead, and P.P. Power. J. Am. Chem. Soc. **108**, 6921 (1986); P.P. Power. Acc. Chem. Res. **21**, 147 (1988), and refs. cited therein.
7. S. Kamitori, K. Hirotsu, and T. Higuchi. J. Am. Chem. Soc. **109**, 2409 (1987); P.G. Jones, T. Gries, H. Grutzmacher, H.W. Roesky, J. Schimkowiak, and G.M. Sheldrick. Angew. Chem. Int. Ed. Engl. **23**, 376 (1984); E. Mason and H.A. Eick. Acta Crystallogr. Sect. B, **B38**, 1821 (1982); N. Armagan. Acta Crystallogr. Sect. B, **B33**, 2281 (1977); P.P. North, E.C. Steiner, F.P. van Remoortere, and F.P. Boer. Acta Crystallogr. Sect. B, **B32**, 370 (1974); F.P. Boer, M.A. Neuman, F.P. van Remoortere, and E.C. Steiner. Inorg Chem. **13**, 2826 (1974); F.P. van Remoortere and F.P. Boer. Inorg. Chem. **13**, 2071 (1974).
8. F.P. van Remoortere, F.P. Boer, and E.C. Steiner. Acta Crystallogr. Sect. B, **B31**, 1420 (1975).
9. G.W. Buchanan, R.A. Kirby, J.P. Charland, and C.I. Ratcliffe. J. Org. Chem. **56**, 203 (1991).
10. A.E. Howard, U.C. Singh, M. Billeter, and P.A. Kollman. J. Am. Chem. Soc. **110**, 6984 (1988).
11. J. Kostrowicki and J.P. Biernat. J. Inclusion Phenom. Mol. Recognit. Chem. **11**, 205 (1991).
12. B.P. Hay, J.R. Rustad, J.P. Zipperer, and D.W. Wester. J. Mol. Struct. **337**, 39 (1995).
13. M.J. Bovill, D.J. Chadwick, and I.O. Sutherland. J. Chem. Soc. Perkin Trans. 2, 1529 (1980).
14. E.T. Seidl and H.F. Schaefer III. J. Phys. Chem. **95**, 3589 (1991).
15. M. Gerzain, G.W. Buchanan, A.B. Driega, G.A. Facey, G. Enright, and R.A. Kirby. J. Chem. Soc. Perkin Trans. 2, 2687 (1996).
16. Y. Liu, Y. Inoue, and T. Hakushi. Bull. Chem. Soc. Jpn. **63**, 3044 (1990); A.S. Attiyat, Y.A. Ibrahim, A.M. Kadry, R.Y. Xie, and G.D. Christian. Fresenius' Z. Anal. Chem. **329**, 12 (1987).
17. I. Ikeda, K. Kohmoto, Y. Ozawa, H. Kurosawa, and M. Okahara. J. Org. Chem. **53**, 5964 (1988).
18. N.W. Alcock and J.F. Sawyer. J. Chem. Soc. Dalton Trans. 115 (1980); J.C. Barnes and T.J.R. Weakley. Acta Crystallogr. Sect. B, **B34**, 1984 (1978); M. Davis and O. Hassel. Acta Chem. Scand. **17**, 1181 (1963).
19. G.W. Buchanan, A.B. Driega, A. Moghimi, C. Bensimon, and K. Bourque. Can. J. Chem. **71**, 951 (1993).
20. R.K. Summerbell, G. Lestina, and H. Waite. J. Am. Chem. Soc. **79**, 234 (1957).
21. E.J. Gabe, Y. LePage, J.P. Charland, F.L. Lee, and P.S. White. J. Appl. Crystallogr. **22**, 384 (1989).

© 1998 NRC Canada

The stereochemistry of hippurate alkylation

John M. McIntosh, E. Jay Kiser, and Zhigang Tian

Abstract: Alkylation of the hippurate esters of *trans* 2-(*p*-substituted phenyl)cyclohexanol with benzyl bromide affords phenylalanine derivatives in high chemical yield. The reaction stereoselectivity varies from 20 to >98% depending on the aromatic group in the cyclohexyl auxiliary. A model that correctly predicts the sense of the induction is proposed.

Key words: enolate conformation, π-stacking, 2-phenylcyclohexanol, chiral auxiliary.

Résumé : L'alkylation des hippurates du *trans* 2-(phényl *p*-substitué) cyclohexanol avec le bromure de benzyle conduit à des dérivés de la phénylalanine, avec un rendement chimique élevé. La stéréosélectivité de la réaction varie de 20 à >98% dépendant du groupe aromatique fixé sur l'auxiliaire cyclohexyle. On propose un modèle qui prédit correctement le sens de l'induction.

Mots clés : conformation de l'énolate, empilement π, 2-phénylcyclohexanol, auxiliaire chiral.

[Traduit par la rédaction]

Introduction

Significant success in controlling stereochemical aspects of reactions has traditionally been limited to using steric effects as the control elements. Results of enolate reactions that have well-understood, rigid, transition state structures enforced by cyclic and intermolecular coordination (e.g., the aldol condensation and Lewis acid catalyzed Diels–Alder reactions) are relatively easily interpreted. Conversely, reactions that do not normally have these coordinations (e.g., enolate alkylations) are much less well understood and predictable. However, there are increasingly frequent reports of the alteration of a stereochemical result by the presence of an aromatic residue that appears to be remote from the reacting center. Perhaps the first specific observations of this effect were made by Corey et al. (1) in the chiral reduction of a ketone in the prostaglandin series and by Posner and Lentz (2) in the alkylation of a cyclopentanone derivative. The apparent influence of π-systems has been noted in many other instances where 8-phenylmenthol has been used in place of menthol (see refs. 3–12) and, in particular, in the use of *trans* 2-phenylcyclohexanol as a chiral auxiliary (4, 13–15). The concept of π-stacking has been promulgated as a major contributor to these effects (16–18) and this aspect has been summarized in a review (19).

For some time we have been examining the factors underlying this effect in alkylation reactions and we have uncovered some interesting electronic effects (20, 21). Those experiments, which involved imine **1** as the alkylation substrate, were relatively easily interpreted since imine **1** is relatively rigid and the enolate is monoanionic. We have also reported that benzylation of **2a** gave modest stereoselectivity (56% de) whereas **2b** provided much improved results (85% de) (22), again emphasizing the significance of π-unsaturation in inducing asymmetry.

Ester enolates can exist in two configurations (*cis* and *trans* (23)). Incorporation of chirality with its associated conformational mobility into an ester enolate, in combination with the configurational questions, makes prediction of the stereochemical outcome of a reaction of such species much more difficult. It has been noted that nucleophilic reactions of ester enolates derived from cyclohexane-based auxiliaries do not provide the high levels of stereochemical control seen with electrophilic reactions (14). Further complicating the picture when hippurate esters are used is the dianionic nature of the enolates.

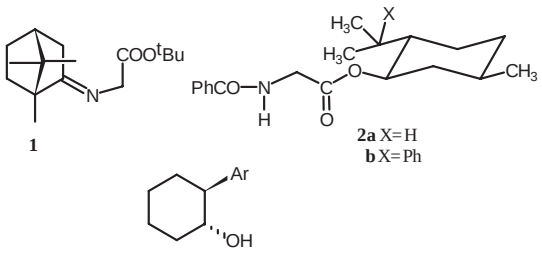

1

2a X = H
b X = Ph

3a Ar = Ph
b Ar = *p*-F-phenyl
c Ar = *p*-CF_3-phenyl
d Ar = *p*-MeO-phenyl
e Ar = *p*-CH_3-phenyl
f Ar = 1-naphthalenyl
g Ar = *p*-^{t}Bu-phenyl

The typical approach to selecting an effective chiral auxiliary is to determine which gives the best level of induction and then choose the enantiomer that gives the desired product stereoisomer. The associations that lead to effective chirality transfer are very complicated and an empirical model that predicts the stereochemical outcome of alkylation reactions would be a valuable tool. In an attempt to construct such a predictive model for cyclohexane-based auxiliaries (14) and to determine whether a relationship between π-electron density and stereoselectivity exists in this system, we prepared a series

Received August 28, 1997.

J.M. McIntosh,[1] E.J. Kiser, and Z. Tian. Department of Chemistry and Biochemistry, University of Windsor, Windsor, ON N9B 3P4, Canada.

[1] Author to whom correspondence may be addressed. Telephone: (519) 253-4232, ext. 3531. Fax: (519) 973-7098. E-Mail: jmci@uwindsor.ca

© 1998 NRC Canada

Table 1. NMR assignments of diastereomers of **5a**.

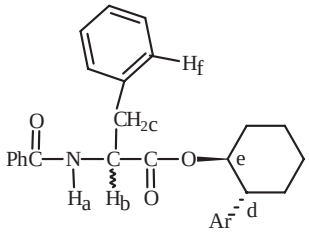

	Major diastereomer			Minor diastereomer		
Proton no.	Shift (ppm)	Mult.	*J* (Hz)	Shift (ppm)	Mult.	*J* (Hz)
a	6.29	d	7.3	6.25	d	7.7
b	4.72	q	6	4.88	m[a]	
c	3.18–3.05	½ ABq	13.8, 6.0	2.91–2.88	½ ABq	13.9, 5.6
	3.04–2.96	½ ABq	13.8, 5.0	2.60–2.56	½ ABq	13.9, 5.1
d	2.73–2.60	dt	12.2, 3.2	2.77	dt	12.2, 3.6
e	4.98	m		4.97	m[a]	
f				6.43	d	6.9

[a] Overlapping.

of alcohols (**3a–g**) and their hippurate esters **4** and benzylated the esters under the previously established (22) conditions (eq. [1]).

[1]

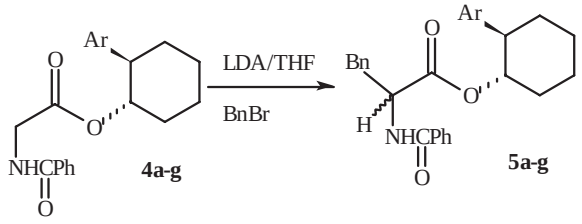

The alcohols **3a**–**e** were prepared either by opening cyclohexene oxide with the appropriate organometallic reagent (24) or, less desirably, by hydroboration–oxidation of the corresponding alkene. Acid-catalyzed condensation with hippuric acid routinely afforded the hippurate esters **4**. The two protons of the glycine methylene in **4** were highly diastereotopic as evidenced by their NMR absorptions, a fact that augured well for good diastereoselection (13). Alkylation of **4** with benzyl bromide afforded the corresponding phenylalanine derivatives **5** in generally excellent yield (>85%). Separation of unreacted starting material without separation of the diastereomers of **5** was easily achieved by column chromatography.

HPLC analysis of the mixture of diastereomers was difficult. The separations were small at best and were strongly dependent on the aromatic substituent, necessitating the development of new separation parameters for each derivative. This difficulty was overcome by the serendipitous observation that the minor diastereomer (see Table 1) formed in the alkylation reaction exhibited a unique NMR signal at δ 6.45. Extensive decoupling and 2D NMR experiments identified this signal as arising from the two *ortho* protons of the aromatic residue of the benzyl group. This was further confirmed by performing the alkylation with benzyl bromide-d_7 (25) and noting the absence of the δ 6.45 signal. Preparation of an authentic sample of each diastereomer of **5a** from optically pure (1*R*,2*S*)-**3a** and *N*-benzoyl-(*S*)-phenylalanine and *N*-benzoyl-(*R*)-phenylalanine revealed that this signal was absent in the NMR spectrum of the former. Therefore, the major diastereomer formed in the alkylation reaction (see Table 1) must have the (*S**, 1*R**,2*S**) configuration. Although the signal for the amino acid methine proton (b, Table 1) in the minor diastereomer was partially merged with that of the carbinol protons (e) on the auxiliary at 300 MHz, the corresponding signal of the **major** diastereomer was well separated from all other signals. Integration of the NMR absorptions for the *ortho* protons (f) of the minor diastereomer and the absorption for the amino acid methine proton (b) in the major diastereomer allowed direct assessment of the reaction stereoselectivity. The doublet of AB quartets due to the benzylic protons (c) in each diastereomer were well resolved from each other, but in some cases the benzylic proton (d) on the auxiliary obscured one of these signals. In every case, however, there were sufficient resolved signals to be able to measure the de as accurately as the NMR technique would inherently allow. Where more than one set of signals could be used, the agreement between the calculations was excellent. A listing of the relevant NMR signals and their assignments in **5a**, which are representative of all **5,** is shown in Table 1.

The stereochemical results of the alkylation reactions are shown in Table 2 along with the results from the menthyl and 8-phenylmenthyl esters previously reported.

Conclusions

Both the size and sense of the stereochemical induction require comment. It is clear from comparison with authentic ester **5a** that esters derived from (1*R**,2*S**)-**3** afford the *S** configuration at the alkylation center as the major product in every case. The predictive model we proposed previously (22) can also be applied here. The preferred conformation of acetals and dialkoxycarbenium ions is *anti–gauche* ("anomeric effect") (26). This conformation minimizes the repulsion between the oxygen lone pairs of electrons. If the cyclohexane ring is constrained to the all-equatorial form and a cyclic coordination between the lithium cation, the enolate oxygen atom, and the nitrogen atom is invoked (*trans* enolate), the *anti–gauche*

© 1998 NRC Canada

Table 2. Diastereomeric excesses observed.

Compound	2-Substituent	de%	Compound	2-Substituent	de%
Menthyl	Isopropyl	56[a]	**5d**	2-MeO-phenyl	55
8-Phenylmenthyl	Dimethylphenylmethyl	85[a]	**5e**	*p*-Tolyl	58
5a	Phenyl	80	**5f**	1-Naphthalenyl	>98
5b	4-F-phenyl	75	**5g**	4-^{t}Bu-phenyl	~20
5c	4-CF_3-phenyl	84			

[a] See ref. 22.

conformation **6a** uniquely predicts the correct stereochemical result, whereas the *anti–anti* conformation **6b** predicts the opposite result. It is interesting to note that Berkowitz and coworkers have suggested (4, 27) the same model for alanine alkylation but they base their arguments on an extended enolate (**6a**) vs. a folded one (**6b**). The argument advanced in that case, based on the steric effect, relied on the interaction of a methyl substituent on the nucleophilic carbon (**6**, R = Me) with a hydrogen at C-1 of the auxiliary that destabilizes conformer **6b**. In our case, this interaction is missing, but the model still obtains. Further, Berkowitz finds the stereoselectivity to be much higher with 8-phenylmenthol than with **3a** as the auxiliary, a result that does not apply in our examples. In any event, the model is useful in a predictive sense but, in the absence of more

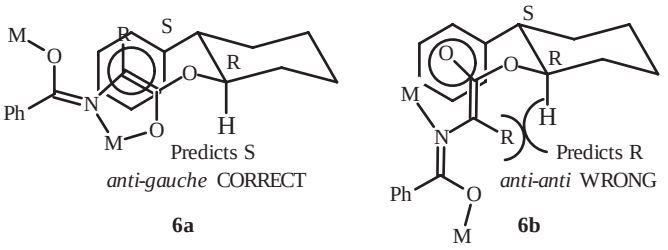

information, cannot be considered theoretically meaningful.

In contrast to the results reported for the alkylation of imine **1**, there appears to be no correlation of the stereoselectivity with the electron density in the aromatic ring. The substituent clearly has an effect but further work is required to define this. The dianionic form of the enolate is a major difference, which must be taken into consideration. Nevertheless, compared to the purely aliphatic substituents (menthol), the presence of a simple phenyl group enhances dramatically the stereochemical control and the naphthalenyl substituent appears to impart a level of control that, if general, may have some practical applications. We are currently investigating the effect of changing the electronic character of the alkylation agent in this system and will report these results in the near future.

Experimental

Unless otherwise noted, all ^{1}H NMR data were obtained at 300 MHz on Bruker AC300 or DPX300 instruments in $CDCl_3$; the ^{13}C NMR spectra were obtained on the same instruments at 75 MHz in the same solvent.

(±) *trans* 2-(4-Fluorophenyl)cyclohexanol (3b). Example of preparation of alcohols from the alkene

To 6.6 g (0.0375 mol) of 1-(4-fluorophenyl)cyclohexene (29, 30) in 50 mL THF was added 50 mL of borane–THF solution (1.0 M). The reaction was stirred for 1 h at ambient temperature, water was added very slowly via syringe until gas evolution ceased, and then 4 mL of 3 M NaOH solution was added. 30% Hydrogen peroxide (4 mL) was added slowly; the reaction was stirred for 1 h at ambient temperature, poured into water, and extracted with ether. The extracts were dried and evaporated to afford 7.06 g (97%) of **3b** (28) as a clear oil; ^{1}H NMR: 7.18 (dd, 2H, J = 5.7, 8.4 Hz), 6.99 (t, 2H, J = 8.7 Hz), 3.58 (m, 1H), 2.39 (t, 1H, J = 12.9 Hz), 2.25–0.8 (m, 9H); ^{13}C NMR: 161.7 (d, J = 242 Hz), 139.9, 129.2 (d, J = 9.5 Hz), 115.4 (d, J = 22 Hz), 74.4, 52.4, 34.6, 33.5, 26.0, 25.0; *m/z*: 194, 148, 135, 122, 109.

All alcohols were also prepared from copper-catalyzed reaction of the appropriately substituted phenylmagnesium halide with cyclohexene oxide using the method of Whitesell as modified by Basavaiah and Rao (24). The products were identical in every respect with those prepared from the alkenes.

In the same manner alcohols **3d** (28), **3e** (31), **3f** (28, 32, 33), and **3g** (28) were prepared.

(±) trans *2-(4-Trifluoromethyl)cyclohexanol (**3c**):* from 1-(4-trifluoromethylphenyl)cyclohexene (31): oil; ^{1}H NMR: 7.58 and 7.30 (ABq, 4H, J = 8.3 Hz), 3.63 (m, 1H), 2.47 (dt, 1H, J = 8.5, 2.1 Hz), 2.11 (m, 1H), 1.95–1.00 (m, 8H); ^{13}C NMR: 147.9, 128.3, 128.1, 125.1, 74.3, 51.1, 35.0, 33.4, 26.0, 25.1, 22.1; *m/z:* 244, 201, 159, 129, 57. Anal. calcd. for $C_{13}H_{15}F_3O$: C 63.92, H 6.19; found: C 63.88, H 5.95.

(±) trans *2-(4-*tert*-Butylphenyl)cyclohexanol (**3g**) (28):* mp 51–54°C; ^{1}H NMR: 7.33 (½ABq, 2H, J = 8.2 Hz), 7.17 (½ABq, 2H, J = 8.2 Hz), 32.62 (dt, 1H, J = 4.4, 9.9 Hz), 2.38 (dt, 1H, J = 3.8, 13.2 Hz), 2.2–1.2 (m, 18H); ^{13}C NMR: 149.7, 140.1, 127.6, 123.8, 74.6, 52.8, 38.9, 34.5, 33.3, 31.5, 26.3, 25.2; *m/z*: 232, 217, 131, 83.

(±) *trans* 2-Phenylcyclohexyl hippurate (4a). Example of preparation of hippurate esters

A mixture of 5.7 mmol of alcohol, 6 mmol of hippuric acid, and 0.5 mmol tosic acid was dissolved in 25 mL of toluene and refluxed for 12 h under a Dean–Stark water trap. After cooling to ambient temperature, 1 mL of saturated aqueous $NaHCO_3$ was added and the mixture was stirred vigorously for 5 min and transferred to a separatory funnel with the aid of 25 mL of ethyl acetate. The layers were separated and the aqueous layer extracted with 3 × 10 mL of EtOAc. The combined organic layers were washed successively with 5 mL of water and 5 mL of saturated brine, and dried over magnesium sulfate. Evaporation afforded the crude ester, which was recrystallized from

© 1998 NRC Canada

4:1 hexane:EtOAc. Typical yields of the pure esters ranged from 75 to 90%.

*For **4a**:* mp 100–102°C; ^{1}H NMR: 7.69 (d, 2H, J = 6.9 Hz), 7.60–7.05 (m, 9H), 6.43 (br s, 1H), 5.02 (m, 1H), 4.06 (d, ½ABq, 1H, J = 5.1, 18.3 Hz), 3.75 (d, ½ABq, 1H, J = 4.5, 18.3 Hz), 2.69 (m, 1H), 2.30–0.80 (m, 8H); ^{13}C NMR: 169.3, 167.2, 142.8, 133.9, 131.8, 128.6, 128.5, 127.6, 127.1, 126.8, 76.7, 49.8, 41.9, 33.6, 32.3, 25.8, 24.8; *m/z:* 338 (M+1), 180, 158, 105, 91, 77. Anal. calcd. for $C_{21}H_{23}NO_3$: C 74.75, H 6.87, N 4.15; found: C 74.23, H 6.87, N 4.47.

(±) trans *2-(4-Fluorophenyl)cyclohexyl hippurate (**4b**):* mp 104–106°C; ^{1}H NMR: 7.70 (d, 2H, J = 6.9 Hz), 7.42 (m, 3H), 7.11 (m, 2H), 6.92 (t, 2H, J = 8.7 Hz), 6.42 (br s, 1H), 4.96 (m, 1H), 4.09 (d, ½ABq, 1H, J = 5.4, 18.6 Hz), 3.76 (d, ½ABq, 1H, J = 4.5, 18.6 Hz), 2.65 (m, 1H), 1.96–1.00 (m, 8H); ^{13}C NMR: 169.3, 167.3, 161.6 (d, J = 242 Hz), 138.4, 133.8, 131.8, 129.0, 128.9, 128.7, 127.1, 115.2 (d, J = 21 Hz), 76.7, 49.0, 41.9, 33.8, 32.3, 25.7, 24.8; *m/z*: 356 (M+1), 180, 177, 176, 162, 148, 134, 109, 105. Anal. calcd. for $C_{21}H_{22}FNO_3$: C 70.97, H 6.24; found: C 70.89, H 6.18.

(±) trans *2-(4-Trifluoromethylphenyl)cyclohexyl hippurate (**4c**):* mp 128–129°C; ^{1}H NMR: 7.70 (d, 2H, J = 7.2 Hz), 7.53–7.21 (m, 7H), 6.41 (br s, 1H), 5.03 (m, 1H), 4.10 (d, ½ABq, 1H, J = 5.4, 18.6 Hz), 3.76 (d, ½ABq, 1H, J = 4.5, 18.6 Hz), 2.76 (dt, 1H, J = 8.7, 12.3 Hz), 2.40–1.15 (m, 9H); ^{13}C NMR: 169.2, 167.2, 146.8, 133.6, 131.7, 128.6, 127.8, 127.0, 125.4, 76.6, 49.4, 41.7, 33.5, 32.1, 25.5, 24.6; *m/z*: 406 (M+1), 226, 180, 149, 134, 105. Anal. calcd. for $C_{22}H_{22}F_3NO_3$: C 65.18, H 5.47, N 3.46; found: C 65.03, H 5.67, N 3.62.

(±) trans *2-(4-Methoxyphenyl)cyclohexyl hippurate (**4d**):* mp 121–123°C; ^{1}H NMR: 7.71 (d, 2H, J = 7.1 Hz), 7.16 (m, 3H), 7.08 (d, 2H, J = 7.1 Hz), 6.71 (d, 2H, J = 10.0 Hz), 6.45 (br s, 1H), 4.08 (d, ½ABq, 1H, J = 4.9, 18.2 Hz), 3.80 (d, ½ABq, 1H, J = 4.4, 18.2 Hz), 3.75 (s, 3H), 2.62 (m, 1H), 2.13–1.20 (m, 9H); ^{13}C NMR: 169.3, 167.2, 158.3, 134.8, 133.9, 131.8, 128.6, 128.5, 127.1, 113.9, 78.2, 55.2, 48.9, 41.9, 33.6, 32.3, 25.8, 24.8; *m/z*: 367, 188, 160, 121, 105. Anal. calcd. for $C_{22}H_{25}NO_4$: C 71.91, H 6.86, N 3.81; found: C 72.06, H 6.95, N 4.10.

(±) trans *2-(4-Methylphenyl)cyclohexyl hippurate **(4e)**:* mp 136–137°C; ^{1}H NMR: 7.85–7.25 (m, 5H), 7.05 (s, 4H), 6.45 (m, 1H), 5.05 (m, 1H), 4.07 (d, ½ABq, 1H, J = 5.5, 18.7 Hz), 3.79 (d, ½ABq, 1H, J = 5.0, 18.7 Hz), 2.64 (m, 1H), 2.26 (3H, s), 2.4–1.8 (m, 8H); ^{13}C NMR: 169.3, 139.7, 136.2, 133.9, 131.8, 129.2, 128.6, 127.4, 127.1, 78.1, 49.3, 42.0, 33.7, 32.3, 25.8, 25.0, 21.1. Anal. calcd. for $C_{22}H_{25}NO_3$: C 75.19, H 7.17; found: C 74.93, H 7.25.

(±) trans *2-(1-Naphthalenylcyclohexyl) hippurate **(4f)**:* mp 142–143°C; ^{1}H NMR: 8.13 (d, 1H, J = 8.1 Hz), 7.82 (d, 1H, J = 7.5 Hz), 7.68 (d, 1H, J = 8.7 Hz), 7.60–7.29 (m, 9H), 6.19 (br s, 1H), 5.26 (m, 1H), 3.91 (d, ½ABq, 1H, J = 5.4, 18.6 Hz), 3.62 (m, 1H), 3.42 (d, ½ABq, 1H, J = 4.5, 18.6 Hz), 2.35–1.30 (m, 8H); ^{13}C NMR: 169.3, 167.1, 138.9, 134.0, 132.1, 131.7, 129.1, 128.6, 127.1, 125.9, 125.7, 125.6, 123.1, 122.9, 76.7, 43.5, 41.7, 33.9, 32.7, 26.1, 24.9; *m/z*: 387, 208, 141, 105. Anal. calcd. for $C_{25}H_{25}NO_3$: C 77.49, H 6.50; found: C 77.39, H 6.12.

(±) trans *2-(4-*tert*-Butylphenyl)cyclohexyl hippurate **(4g)**:* mp 164–165°C; ^{1}H NMR: 7.69 (d, 2H, J = 7.1 Hz), 7.38 (m, 3H), 7.25 (d, 2H, J = 8.2 Hz), 7.08 (d, 2H, J = 8.2 Hz), 6.41 (br s, 1H), 4.95 (m, 1H), 4.06 (d, ½ABq, 1H, J = 4.9, 18.7 Hz), 3.82 (d, ½ABq, 1H, J = 4.4, 18.7 Hz), 2.66 (m, 1H), 2.22–1.00 (m, 17H); ^{13}C NMR: 169.4, 167.2, 149.5, 139.6, 133.9, 131.8, 128.8, 128.6, 127.1, 125.3, 78.1, 49.1, 46.9, 42.0, 33.6, 32.3, 31.4, 25.8, 24.8; *m/z*: 394, 214, 199, 147, 105. Anal. calcd. for $C_{25}H_{31}NO_3$: C 76.30, H 7.94, N 3.56; found: C 76.46, H 7.69, N 4.19.

Preparation of authentic *trans* 2-phenylcyclohexyl *N*-benzoylphenylalaninate diastereomers (5a)

*(a) (1*R*,2*S*)-2-Phenylcyclohexyl* N*-benzoyl-(*S*)-phenylalaninate*
A mixture of 200 mg (1.13 mmol) of (–)-(1*R*,2*S*)-*trans*-2-phenylcyclohexanol (Aldrich), 350 mg (1.36 mmol) *N*-benzoyl-(*S*)-phenylalanine, and 25 mg of tosic acid was refluxed in 25 mL of benzene under a Dean–Stark water separator for 20 h. The solution was cooled to room temperature, treated with 2 mL of saturated aqueous $NaHCO_3$ solution with vigorous stirring, and diluted with 25 mL of EtOAc. The layers were separated; the organic layer was washed with water and brine, dried ($MgSO_4$), and evaporated to give 420 mg of crude ester. ^{1}H NMR indicated 76% de. The crude material was recrystallized from EtOAc at –15°C. The ^{1}H NMR of the product showed only the major diastereomer of **5a**; mp 158°C, $[\alpha]_D$ +24.4 (*c* 1.0, $CHCl_3$); ^{1}H NMR: 7.63–7.06 (m, 15H), 6.29 (d, 1H, J = 7.3 Hz), 4.98 (m, 1H), 4.72 (q, 1H, J = 6.0 Hz), 3.10 (d, ½ ABq, 1H, J = 13.8, 6.0 Hz), 3.00 (d, ½ABq, 1H, J = 13.8, 5.0 Hz), 2.70 (dt, 1H, J = 12.2, 3.2 Hz), 2.15 (m, 1H), 2.10–1.25 (m, 7H); ^{13}C NMR: 171.02, 166.87, 142.91, 136.45, 132.02, 129.94, 128.93, 128.81, 128.76, 127.79, 127.33, 127.07, 78.38, 53.81, 50.08, 37.83, 33.89, 32.55, 26.09, 25.14; HRMS, *m/z* calcd. for $C_{28}H_{29}NO_3$: 427.21474; found: 427.21388.

*(b) (1*R*,2*S*)-2-Phenylcyclohexyl* N*-benzoyl-(*R*)-phenylalaninate*
In exactly the same way as described above, but using *N*-benzoyl-(*R*)-phenylalanine, an authentic sample of the minor diastereomer obtained from the alkylation reaction was prepared; mp 155–157°C, $[\alpha]_D$ –30.0 (*c* 1.0, $CHCl_3$); ^{1}H NMR (500 MHz): 7.63–7.09 (m, 13H), 6.44 (d, 1H, J = 6.9 Hz), 6.29 (d, 1H, J = 7.3 Hz), 4.98 (m, 1H), 4.89 (m, 1H), 2.88 (d, ½ ABq, 1H, J = 14.3, 5.5 Hz), 2.55 (d, ½ABq, 1H, J = 14.3, 5.1 Hz), 2.78 (dt, 1H, J = 12.2, 3.6,Hz), 2.15 (m, 1H), 2.10–1.25 (m, 7H); ^{13}C NMR (125 MHz): 170.93, 166.76, 135.62, 134.17, 131.65, 129.44, 128.71, 128.57, 128.33, 127.86, 127.10, 127.00, 126.83, 78.57, 53.27, 49.73, 37.19, 33.84, 32.33, 25.79, 24.74; HRMS, *m/z* calcd. for $C_{28}H_{29}NO_3$: 427.21474; found: 427.21295.

Alkylation of hippurate esters 4: preparation of phenylalaninates 5

A solution of 120 µL (0.8 mmol) of diisopropylamine in 3 mL dry THF was cooled to 0°C under N_2. nBuLi (0.8 mmol, 2.32 M in hexanes) was added and the mixture was stirred at 0°C for 30 min. The solution was cooled to –78°C and 0.4 mmol of

© 1998 NRC Canada

hippurate **4** in 2 mL of THF was added slowly. A bright yellow color formed immediately that turned to dark orange. The solution was stirred for 90 min at –78°C and then 0.40 mmol of benzyl bromide in 2 mL of THF was added dropwise. After stirring for another 90 min at –78°C, the color reverted to light yellow; 1 mL of 3 M HCl was added and the solution was allowed to warm to room temperature while vigorous stirring was continued. The solution was diluted with 5 mL of ether, the layers were separated, and the aqueous layer was extracted with 3 × 5 mL of $CHCl_3$. The combined organic phases were dried ($MgSO_4$) and evaporated to afford the crude product. Purification without separation of the diastereomers was achieved by column chromatography on silica gel (3:1 petroleum ether:EtOAc). The chemical yields were in excess of 80%. The ratio of stereoisomers present was determined using ^{1}H NMR as described in the text. In all cases, except that of the naphthalenyl derivative **5f**, mixtures of diastereomers were obtained. In the case of **5f**, the product was obtained diastereomerically pure, mp 180–181°C; ^{1}H NMR: 8.13 (m, 1H), 7.75 (m, 1H), 7.70 (d, 1H, J = 7.2 Hz), 7.51–7.18 (m, 12H), 6.93 (m, 2H), 5.99 (d, 1H, J = 7.2 Hz), 5.21 (m, 1H), 4.50 (ABq, 1H, J = 7.3, 6.1 Hz), 3.66 (m, 1H), 2.87 (d, ½Abq, 1H, J = 6.0, 13.9 Hz), 2.55 (d, ½Abq, 1H, J = 8.0, 13.9 Hz), 2.26 (m, 1H), 2.15–1.25 (m, 7H); ^{13}C NMR:170.9, 166.8, 139.2, 136.4, 134.4, 134.3, 132.5, 131.9, 129.8, 129.5, 128.9, 128.7, 127.4, 127.2, 126.2, 126.1, 125.8, 123.4, 78.6, 53.8, 37.6, 34.0, 32.9, 26.4, 25.2; HRMS, *m/z* calcd. for $C_{32}H_{31}NO_3$: 477.23039; found: 477.23144.

Preparation and use of benzyl bromide-d_7

Toluene-d_8 was reacted with *N*-bromosuccinimide according to the method of Greenwood et al. (34). The solid was removed by filtration and the solvent removed under vacuum. The residue was used in the alkylation reaction as described above. The NMR of the product gave no indication of an absorption between δ 6.3 and 7.0 and the absorption at δ 4.72 was a clean doublet.

Acknowledgements

This work was supported by the Natural Sciences and Engineering Research Council of Canada through operating grants to J.M.M. and grants for the purchase of the NMR spectrometers. The assistance of M. Fuerth, V. Lazarescu, and H. Ganjavi in obtaining some of the data is gratefully acknowledged.

References

1. E.J. Corey, K.B. Becker, and R.K. Varma. J. Am. Chem. Soc. **94**, 8616 (1972).
2. G.H. Posner and C.M. Lentz. Tetrahedron Lett. 3215 (1977).
3. J. Barluenga, J.M. Montserrat, J. Florez, S. Garcia-Granda, and E. Martin. Angew. Chem. **106**, 1451 (1994).
4. D.B. Berkowitz and M.K. Smith. J. Org. Chem. **60**, 1233 (1995).
5. D.S. Brown, M.J. Earle, M.T. El Gihani, and H. Heaney. Synlett, 269 (1995).
6. D.L. Comins and D.H. LaMunyon. Tetrahedron Lett. **35**, 7343 (1994).
7. S.E. Denmark and B.D. Griedel. J. Org. Chem. **59**, 5136 (1994).
8. I. Fleming and N.D. Kindon. J. Chem. Soc. Perkin Trans. 1, 303 (1995).
9. T. Mandai, Y. Kaihara, and J. Tsuji. J. Org. Chem. **59**, 5847 (1994).
10. M. Nishida, H. Hayashi, Y. Yamaura, E. Yanaginuma, O. Yonemitsu, A. Nishida, and N. Kawahara. Tetrahedron Lett. **36**, 269 (1995).
11. K. Nordstroem and C. Moberg. Tetrahedron Lett. **35**, 7267 (1994).
12. T. Tsunoda, Y. Yamamiya, Y. Kawamura, and S. Ito. Tetrahedron Lett. **36**, 2529 (1995).
13. J.K. Whitesell, R.M. Lawrence, and H.-H. Chen. J. Org. Chem. **51**, 4779 (1986).
14. J.K. Whitesell. Chem. Rev. **92**, 953 (1992).
15. F. De Angelis, M.L. Forcellese, A. Gambacortra, and R. Nicoletti. Org. Mass Spectrom. **12**, 313 (1977).
16. A.S. Cieplak, B.D. Tait, and C.R. Johnson. J. Am. Chem. Soc. **111**, 8447 (1989).
17. J.F. Maddaluno, N. Gresh, and C. Giessner-Prettre. J. Org. Chem. **59**, 793 (1994).
18. G.B. Jones and B.J. Chapman. SynLett, **5**, 439 (1997).
19. G.B. Jones and B.J. Chapman. Synthesis, 475 (1995).
20. J.M. McIntosh, R.K. Leavitt, P. Mishra, K.C. Cassidy, J.E. Drake, and R. Chadha. J. Org. Chem. **53**, 1947 (1988).
21. J.M. McIntosh and P. Mishra. Can. J. Chem. **64**, 726 (1986).
22. J.M. McIntosh, R. Thangarasa, N.K. Foley, D.J. Ager, D.E. Froen, and R.C. Klix. Tetrahedron, **50**, 1967 (1994).
23. C.H. Heathcock, C.T. Buse, W.A. Kleschick, M.C. Pirrung, J.E. Sohn, and J. Lampe. J. Org. Chem. **45**, 1066 (1980).
24. D. Basavaiah and P.D. Rao. Tetrahedron: Asymmetry, **5**, 223 (1994).
25. M. Moreno-Manas, J. Bassa, N. Llado, and R. Pleixats. J. Heterocycl. Chem. **27**, 673 (1990).
26. P. Deslongchamps. Stereoelectronic effects in organic chemistry. Pergamon, New York. 1983.
27. M.L. Pederson and D.B. Berkowitz. J. Org. Chem. **58**, 6966 (1993).
28. H. Buschmann, N. Hoffmann, and H.D. Scharf. Tetrahedron: Asymmetry, **2**, 1429 (1991).
29. A. Balsamo, C. Battistini, P. Crotti, and B. Macchia. Gazz. Chim. Ital. **106**, 77 (1976).
30. P. Beak and K.R. Berger. J. Am. Chem. Soc. **102**, 3848 (1980).
31. D. Potin, F. Dumas, and J. D'Angelo. J. Am. Chem. Soc. **112**, 3483 (1990).
32. P.H. Dussault, K.R. Woller, and M.C. Hillier. Tetrahedron, **50**, 8929 (1994).
33. D. Basavaiah and P.R. Krishna. Indian J. Chem. Sect. B **1**. 131 (1993).
34. F.L. Greenwood, M.D. Kellert, and J. Sedlak. Org. Synth. Coll. Vol. **IV**, 108 (1963).

© 1998 NRC Canada

Rate enhancement of nickel(II) complexation in dilute anionic surfactant solutions

Catherine E. Drennan, Rachelle J. Hughes, Vincent C. Reinsborough, and Oladega O. Soriyan

Abstract: Kinetic studies through stopped-flow spectroscopy were undertaken in the dilute solution range of anionic surfactants where pronounced rate enhancement or inhibition of Ni^{2+}–ligand complexations is often observed at surfactant concentrations much below the critical micelle concentration (CMC). The results are interpreted in terms of Ni–surfactant micelles as the agents responsible for the rate changes in dilute surfactant solution. At higher surfactant concentrations these micelles are transformed into mixed micelles (counterion and size changes), eventually becoming normal surfactant micelles close to the CMC. Surface tension, dye solubility, conductivity, and fluorescent probe investigations support this interpretation.

Key words: micellar catalysis, sodium dodecyl sulfate, micelles, critical micelle concentration, premicelles, Ni^{2+}–ligand complexations.

Résumé : On a réalisé des études cinétiques par spectroscopie à flux stoppé sur des solutions diluées d'agents de surface anioniques, à des concentrations très inférieures à la concentration micellaire critique (CMC) auxquelles on observe souvent des effets importants d'accélération ou d'inhibition des vitesses de complexations Ni^{2+}–ligand. On interprète les résultats en fonction de micelles Ni – agent de surface qui agissent comme agents responsables pour les changements de vitesse en solutions diluées d'agent de surface. À des concentrations supérieures d'agent de surface, ces micelles se transforment en micelles mixtes (changements de contre-ion et de grosseur) qui deviennent éventuellement des micelles normales d'agent de surface lorsqu'on approche de la CMC. Les données relatives à la tension superficielle, la solubilité des colorants et la conductivité ainsi que les études à l'aide de sondes fluorescentes sont en accord avec cette interprétation.

Mots clés : catalyse micellaire, dodécylsulfate de sodium, micelles, concentration micellaire critique, prémicelle, complexations Ni^{2+}–ligand.

[Traduit par la rédaction]

Introduction

In surfactant solutions, anomalies in phyiscochemical properties occurring below the generally accepted value of the critical micelle concentration (CMC) are usually ascribed to premicellar aggregates. The latter are thought to adopt various forms, e.g., surfactant dimers (1), oligomers (2), dye surfactant enwrapments (3, 4), surfactant clusters centered by a metal ion (5), substrate–surfactant complexes (6), depending upon the solutes accompanying the surfactant in solution. Since the characterization of the aggregates is not an easy problem, and is usually peripheral to the main thrust of the surfactant investigation at hand, little effort has been made to investigate the phenomenon more generally. We report here on a surfactant solution situation where premicellar aggregation has been speculated: supposedly micelle-mediated rate changes of a probe reaction commencing well below the reported CMC of the surfactant. In an effort to understand surfactant catalysis more completely, we set out to uncover the solution aggregates promoting rate enhancement below the CMC in these systems. A critical look at the situation leads us to discount premicelles as the responsible species.

In our kinetic studies over the past two decades, in which the complexation of $Ni^{2+}_{(aq)}$ with the neutral bidentate ligand pyridine-2-azo-*p*-dimethylaniline (PADA) has been commonly used as a probe reaction in anionic surfactant solutions to test for micellar catalysis, rate enhancements were noted at surfactant concentrations well below the literature values of the CMC (7, 8). A model that has enjoyed considerable success in the post-CMC region ascribes the rate promotion to the favourable partitioning from bulk solution of both reactants into or onto the anionic micelles. Micelles of constant size and composition are critical to the discussion. This modelling has been so refined that variations in parameters can confidently be attributed to changes in the structure of the underlying micelle (9). Early work with this particular catalysis effect noted that it commenced in the premicellar range and speculated that the aggregates below the CMC were probably complexes consisting of a few surfactant molecules and a solubilized PADA molecule (10). There have been no further attempts to characterize these premicellar complexes. The focus of all studies undertaken in this system has been the concentration range well above the CMC where the micelles are

Received September 22, 1997.

C.E. Drennan, R.J. Hughes, V.C. Reinsborough,[1] and O.O. Soriyan. Department of Chemistry, Mount Allison University, Sackville, NB E4L 1G8, Canada.

[1] Author to whom correspondence may be addressed. Telephone: (506) 364-3362 (office); (506) 364-2361 (dept sec); (506) 536-0592 (home). Fax: (506) 364-2313. E-mail: vcreinsb@mta.ca

© 1998 NRC Canada

Fig. 1. Rate enhancements (R) of Ni^{2+}–PADA complexation in SDS solutions with 0.50 mM Ni^{2+}.

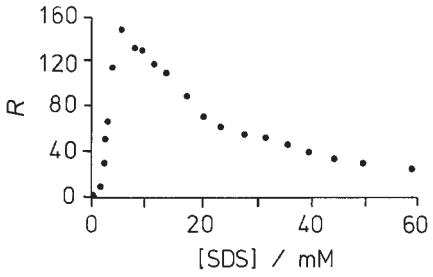

presumably better behaved and premicellar aggregates do not exist.

It is somewhat intriguing and, at the same time, disconcerting that the successful model does not allow for any premicellar activity. Yet, the maximum rate enhancement is usually attained in the vicinity of the literature value of the CMC. In a similar reactive situation, in the electron transfer between substituted and unsubstituted Fe^{2+} and Fe^{3+}, Pelizzetti and Pramauro (11) observed that in sodium dodecyl sulfate solutions the rate increase phenomenon was almost entirely confined to the pre-CMC concentration region as defined by the reported value of the CMC for that surfactant. Ionic additives normally depress the CMC but not to the extent that has been noted in these studies. The aim of the present study was to identify, if possible, the solution aggregates responsible for the dilute solution or pre-CMC rate enhancements observed in metal ion complexations in anionic surfactant solutions and to relate these to the micelles that are present in more concentrated solutions.

The kinetics of the formation of the Ni^{2+}–murexide complex was also investigated as a complementary study to the Ni^{2+}–PADA complexation reaction. In contrast to the neutral PADA molecule, the murexide ion is negatively charged in the pH region studied and thus the formation of anionic micelles inhibits rather than promotes Ni^{2+}–murexide complexation. The positively charged metal ions are attracted to the micelles whereas the negatively charged ligands remain predominantly in solution. This means that the CMC should be revealed by a sudden decrease in the observed rate coefficient for the murexide complexation.

Sodium and nickel dodecyl sulfates were the chief surfactants used but other anionic and cationic surfactants were also investigated in solution to provide corroborative evidence and further insight. Conductivity, dye solubility, dye fluorescence, and surface tension measurements furnished independent assessments of the CMC values.

Experimental

The stopped-flow technique as described previously (7, 12) was used to obtain rate coefficients for the Ni^{2+}–PADA and Ni^{2+}–murexide complexation reactions. Pseudo-first-order conditions (the metal ion was typically millimolar in concentration while the ligand was 10^{-5} M) pertained at 25.0°C for the formation of the Ni^{2+}–PADA and the Ni^{2+}–murexide complexes at pH 8.0 and pH 4.5 (no buffers), respectively.

Independent measurements of the CMC were obtained directly from solution conductivities and surface tensions and, indirectly, from fluorescence spectroscopy. The latter technique used the fluorophore, trisbipyridyl Ru^{2+} ion, which fluoresces more intensely in a micellar environment than in water. The CMC was taken to be the break in the fluorescence vs. surfactant concentration curve but, because the fluorophore itself may be involved in the micellization process (3), the results were not given the same weight as the other two methods. Conductivity measurements were obtained with a Radiometer CDM83 bridge with the solutions thermostatted at 25.0°C. Plots of specific conductivity against surfactant concentration were used to determine the CMC as the intersection of the straight-line portions of the curve. A du Nouy tensiometer was used to detect the CMC by the break in the surface tension vs. log[surfactant] curve.

All chemicals were the best available commercially and were not further treated. The purity of the sodium dodecyl sulfate used in the surface tension measurements was >99% and deemed acceptable as it showed only a small minimium in the solution surface tension (<1 dyne cm^{-1}). Nickel dodecyl sulfate ($Ni(DS)_2$) was prepared by crystallization from aqueous solution containing SDS and a slight stoichiometric excess of $NiCl_2$. Recrystallizations were effected in aqueous ethanol and deionized water. Analysis by Desert Analytics (Tucson, Arizona) showed that the pale green crystals contained 8.80% Ni (9.96% expected), 8.79% H (8.55% expected), 0.02% Na, and less than 0.05% Cl. Water of crystallization had likely been incorporated into the solid $Ni(DS)_2$, which could account for the low Ni and high H contents. The important point is that this ion replacement process had eliminated Na as a possible counterion in aqueous solutions of the prepared $Ni(DS)_2$.

Results and discussion

For the Ni^{2+}–PADA reaction in dilute sodium dodecyl sulfate (SDS) solutions, the observed rate coefficient (k_{obs}) did not change from the no-SDS-in-solution value ($k°_{obs}$) until a specific SDS concentration was reached. Beyond this concentration, k_{obs} rose sharply to a maximum followed by a more gradual decrease with increasing SDS concentration to kinetic values approaching $k°_{obs}$. With $[Ni^{2+}] = 0.50$ mM, the maximum in k_{obs} was approximately 160 times the $k°_{obs}$ value (cf. Fig. 1 where R is the ratio of k_{obs} to $k°_{obs}$). The initial point of departure of the k_{obs} value from the $k°_{obs}$ or the "specific SDS concentration" alluded to above should be where micelles first form in solution, i.e., it should locate the critical micelle concentration or CMC of SDS. However, these apparent CMC values or ACMCs are found in the 1–4 mM SDS range whereas the CMC of SDS is well known to be 8.1 mM at 25.0°C (13).

Figure 2 reveals that the ACMC for SDS is markedly dependent on the Ni^{2+} ion concentration used in the complexation reaction. One possibility that this Ni^{2+} dependence suggests is that an Atherton–Dymond type of cluster consisting of a Ni^{2+} ion surrounded by a number of surfactant monomers (5) is formed at the ACMC and provides the preferred reaction site for the complexation. The PADA molecule may also be attracted hydrophobically or by some other mechanism to the cluster, resulting in the complexation rate being promoted below the CMC. For SDS concentrations greater than the CMC, these clusters will presumably be less stable than SDS micelles and "micellar" catalysis can then properly be

© 1998 NRC Canada

Fig. 2. Rate enhancements (R) of Ni^{2+}–PADA complexation in the pre-CMC range in SDS solutions (CMC, 8.1 mM SDS) at various Ni^{2+} concentrations: ●, 0.30 mM Ni^{2+}; o, 0.50 mM Ni^{2+}; ■, 1.00 mM Ni^{2+}; ✚, 2.00 mM Ni^{2+}; ×, 3.00 mM Ni^{2+}.

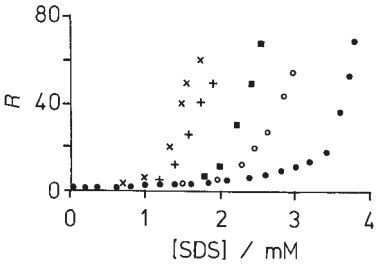

Fig. 3. Surface tension (ST) of SDS solutions containing 1.00 mM Ni^{2+}.

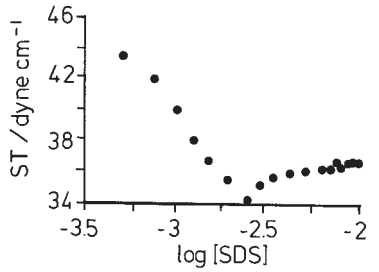

said to occur. The argument against premicellar clusters of this type is that there are no obvious discontinuities in solution properties where clusters may be said to have become micelles and, in the surfactant concentration from the ACMC to the CMC, solution characteristics are those typical of micellar behaviour. A demonstration of the latter is the surface tension of Ni^{2+} ion doped solutions of SDS where the ACMC is indicated by the beginning of the plateau in the surface tension vs. log[SDS] curve in standard micellar fashion (Fig. 3). Clusters of the type described above would not depress the surface tension as radically and, moreover, in yielding to micelles in more concentrated solutions, should cause the surface tension to experience a further decrease instead of the observed constancy in value.

But what type of micelle could be present in these Ni^{2+} ion doped, dilute surfactant solutions? Normal SDS micelles would not be expected to be present at concentrations almost an order of magnitude less than the CMC for SDS. From the observation that the ACMC is influenced by the amount of Ni^{2+} in solution, the formation of Ni dodecyl sulfate or $Ni(DS)_2$ micelles at the apparent CMC is a possibility. The literature value for the CMC of $Ni(DS)_2$ at 30°C is 1.2 mM $Ni(DS)_2$ (14) and, at the highest concentrations of Ni^{2+} used, the ACMC is approaching this value (Fig. 2). Since this evaluation was important to the argument, the CMC of $Ni(DS)_2$ was redetermined from surface tension and conductivity data (Fig. 4) and found to agree with the literature value. Thus, it is conceivable that, in a 2 mM SDS solution containing 1 mM Ni^{2+}, $Ni(DS)_2$ micelles may initially be formed. On further addition of SDS, a mixed micelle will appear, with the Ni^{2+} ions being eventually displaced by Na^+ ions as counterions. When the CMC for SDS is achieved, Na^+ ions are about 10 times more numerous in solution than Ni^{2+} ions in 1 mM Ni^{2+} and the micelles are essentially SDS micelles, with a smooth transition having

Fig. 4. Specific conductivity (C) (●) and surface tension (ST) (o) of $Ni(DS)_2$ solutions.

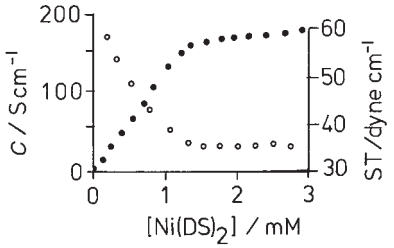

Fig. 5. Rate enhancements (R) of Ni^{2+}–PADA complexation in sodium octyl sulfate (SOS) solutions at various Ni^{2+} concentrations: ×, 0.50 mM Ni^{2+}; ✚, 1.00 mM Ni^{2+}; ●, 2.00 mM Ni^{2+}; o, 3.00 mM Ni^{2+}. The triangle indicates the CMC value for SOS.

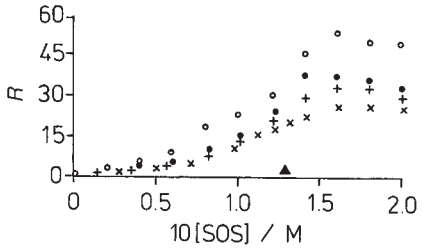

Fig. 6. Rate enhancements (R) of Ni^{2+}–PADA complexation in sodium perfluorooctanoate (SPFO) at various Ni^{2+} concentrations: o, 0.50 mM Ni^{2+}; ●, 1.00 mM Ni^{2+}; ×, 2.00 mM Ni^{2+}; ✚, 3.00 mM Ni^{2+}. The triangle indicates the CMC value for SPFO.

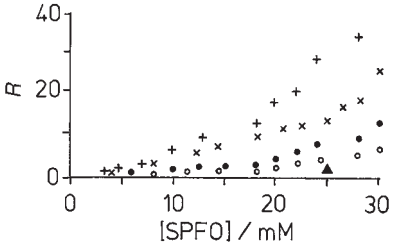

occurred from almost pure $Ni(DS)_2$ micelles to almost pure SDS micelles.

Kinetic studies were conducted in several anionic surfactant systems to test the universality of the dependence of the ACMC on Ni^{2+} concentration. For shorter chained alkyl sulfates than SDS, the catalytic effect was less pronounced but again an apparent CMC appeared and its dependence on the Ni^{2+} concentration consistently occurred. Figure 5 displays the kinetic data for the Ni^{2+}–PADA reaction in sodium octyl sulfate (SOS) at various Ni^{2+} concentrations. Figure 6 shows that fluorocarbon anionic surfactants such as sodium perfluorooctanoate (SPFO) exhibit similar kinetic behaviour towards Ni^{2+} when it is a constituent of the solution background. The CMC value for SOS at 25.0°C is 0.12 M (13, 15) but ACMC values were as low as 0.02 M SOS. Similarly, SPFO has a CMC of 25 mM (16, 17), which is much higher than the first appearance of catalytic activity in this system. The tendency of increasing [Ni^{2+}] bringing about a decrease in the apparent CMC appears to be independent of the length or nature of the tail of the anionic surfactant. Once again, Ni^{2+} ion is implicated

© 1998 NRC Canada

Fig. 7. Rate coefficients (k_{obs}) of Ni^{2+}–PADA complexation in dodecyltrimethylammonium bromide (DTAB) solutions.

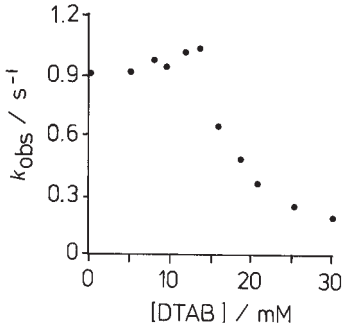

Fig. 8. Rate coeficients (k_{obs}) for Ni^{2+}–murexide complexation in SDS solutions at various Ni^{2+} concentrations: ■, 0.30 mM Ni^{2+}; □, 0.50 mM Ni^{2+}; ●, 1.00 mM Ni^{2+}; ○, 2.00 mM Ni2+.

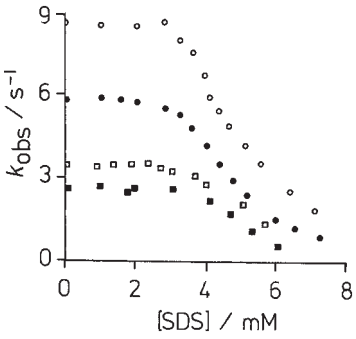

as playing a major role in the solution aggregate responsible for the rate enhancements.

Another way to confirm the essential role of the Ni^{2+} ion in this phenomenon is to carry out the Ni^{2+}–PADA reaction in the presence of a cationic surfactant such as dodecyltrimethylammonium chloride or DTAB. Micellar inhibition occurs because only PADA and not Ni^{2+} ion is preferentially partitioned into the positively charged micelle. As a result, k_{obs}values do not change until the CMC is reached on DTAB addition and above this concentration they decrease (Fig. 7). As opposed to the kinetic studies in anionic surfactant micellar systems reported above, no anomalous lowering of the CMC (15 mM DTAB (13)) was detected for any background Ni^{2+} concentrations. This supports the contention that Ni^{2+} and not PADA is essential to the composition of the solution aggregate that gives rise to the CMC decreases noted in anionic surfactant systems.

Still another variation on the Ni^{2+} complexation theme is available and that is to change the ligand from neutral PADA to a negatively charged species such as murexide ion, and to return to SDS solutions to observe complex formation (Fig. 8). Now the roles of the reactants, Ni^{2+} and ligand, are switched as it is the latter rather than the former that remains in solution at SDS concentrations greater than the CMC. The end result (Fig. 8) is a curve similar to Fig. 7 except that the breakpoint is lower than the reported CMC and is dependent upon the Ni^{2+} concentration in similar fashion to the ACMC values for the Ni^{2+}–PADA complexation reaction. The similarity of the breakpoints or ACMC values for the two Ni^{2+} complexations

Fig. 9. Solubility of PADA in SDS solutions at 25.0°C.

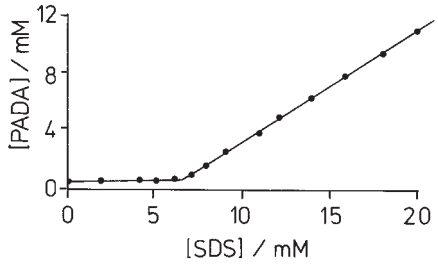

Table 1. Apparent CMC values (mM) of SDS solutions in Ni^{2+} environments.

	Ni^{2+} concentrations (mM)					
Method	0.00	0.30	0.50	1.00	2.00	3.00
Ni^{2+}–PADA kinetics	—	3.4	2.3	1.8	1.3	1.0
Ni^{2+}–murexide kinetics	—	3.5	2.5	2	2	—
Conductivity	8.0	3.8	2.8	2.1	—	—
		8.9[a]	9.1[a]	11.7[a]		
Surface tension	8.0	—	2.7	2	—	—
PADA solubility	6.8	—	—	—	—	—
Fluorophore	8.8	—	6.2	4.8	4.2	3.8

[a] Second breakpoint.

is remarkable given the opposite directions in which the kinetic rates are affected in SDS solutions. This implies that the same solution species is responsible for the departure from normality in both reactive systems despite the use of two different ligands, i.e., the ligand is not incorporated into the "premicellar" aggregate. Reinforcing this conclusion is that a Ni^{2+}-containing solution aggregate into which the neutral PADA molecule and the negatively charged murexide ion are indiscriminately included is problematic. The dependence of ACMC upon [Ni^{2+}] reiterates that Ni^{2+} is an important constituent of the responsible solution aggregate.

Corroborative evidence that the ligand does not play a major role, if any, in the solution aggregation process is found in the relationship between PADA solubility and SDS concentration (Fig. 9). The breakpoint in the solubility curve corresponds approximately to the literature value of the CMC for SDS (Table 1; dye solubility and fluorophore detection methods for the CMC are approximate because the "foreign" probes must impact upon the micellization process at the probe concentrations used). The lack of anomalous behaviour in the PADA solubility data close to the CMC implies that the ligand is not associating with the surfactant except in micelle solubilization.

That the CMC in ionic surfactant solutions is depressed by salts is well known. A concomitant observation is that the micellar size also increases with increasing salt background. The reason commonly given for this is that the ionic atmosphere lessens the repulsion between the polar head groups, allowing the hydrophobic attraction between the surfactant tails to dominate at an earlier surfactant concentration and resulting in "premature" micelle formation (18). Although in this picture there are no premicellar aggregates but only micelles that form at the ACMC, the micelle structure is unspecified and the implication is that the extra ions are essentially

© 1998 NRC Canada

Fig. 10. ACMC values for SDS in divalent metal nitrate solutions determined with a fluorescent probe: ○, Zn^{2+}; ●, Mn^{2+}; ■, Ni^{2+}.

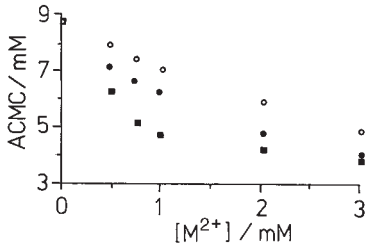

spectators to the micelle formation process. Values of the ACMC for SDS in various salt backgrounds were determined by conventional methods to ascertain whether they corresponded to the breakpoints seen kinetically in the present study. Spectrofluorometrically determined CMC values in SDS solutions with $Ni(NO_3)_2$ as additive decreased with increasing $[Ni^{2+}]$ (Fig. 10) but not to the same extent as indicated by the onset of catalytic activity for the Ni^{2+}–PADA reaction (Fig. 2 and Table 1). Parenthetically, other divalent ions such as Zn^{2+} and Mn^{2+} were found to be less effective than Ni^{2+} ion in lowering the CMC, which suggests an ion specificity not considered in the usual explanation for CMC lowering through electrolyte addition. On the other hand, because the fluorescence technique is an indirect method (see Experimental) and, as explained above, "interferes" with the micelle formation process, these results can be given only qualitative significance. Oftentimes, dyes such as the trisbipyridyl probe are directly involved in premicellar association (3, 4). The PADA solubility method of detecting the CMC can be faulted on similar grounds and the slightly low value of the CMC for SDS as determined from Fig. 9 is likely a result of some interaction between SDS and PADA.

CMC determinations can be made more confidently through the direct methods of surface tension and conductivity. The CMC determinations from the breaks in the surface tension plots in Ni^{2+}-doped SDS solutions agree with the catalytic activity results although the minimum in the surface tension plot normally seen when surface-active additives and impurities are present tends to blur the exact location of the CMC (Fig. 3). The dependence of the solution conductivity on surfactant concentration is often used to obtain micellar parameters in an experimentally and theoretically straightforward manner (19). The CMC is revealed as the intersection of two straight lines. In Ni^{2+}-doped SDS solution systems, since the Ni^{2+} ion contributes much more to solution conductivity than does the SDS ion, the background Ni^{2+} ion concentration must be kept low (less than 2 mM Ni^{2+}) to detect any appreciable conductivity change on micellization. When this is done, two breaks in the conductivity curve are discernible and they consistently occur with linear portions between them (Fig. 11). The first point of intersection decreases with increasing Ni^{2+} ion concentration while the second one approximates the expected CMC value for SDS and increases slightly with Ni^{2+} concentration (Fig. 11 and Table 1). The reasonable agreement between the first conductivity breakpoints and the SDS concentrations at which micellar catalysis begins in earnest in the Ni^{2+}–PADA reaction suggests that the same phenomenon is responsible. Thus, the conclusion drawn from the CMC lowerings of Table 1 is that the fluorescence, conductivity, surface

Fig. 11. Specific conductivity (*C*) of SDS solutions for three representative Ni^{2+} backgrounds: curve 1, in 0.00 mM Ni^{2+}; curve 2, in 0.50 mM Ni^{2+}; curve 3, in 1.00 mM Ni^{2+}. Carets indicate the breakpoints. Data for 0.30 mM Ni^{2+} omitted for clarity (cf. Table 1).

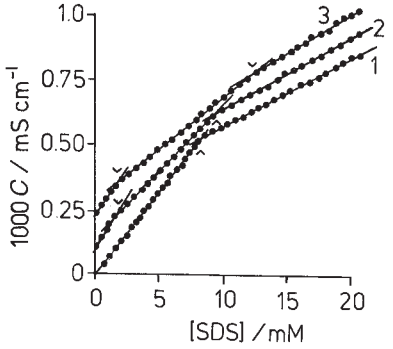

tension, and the two kinetic techniques are sensing the same associative process at the ACMC but the first-mentioned method is susceptible to more error.

Conclusion

With this agreement in ACMC values among the different techniques and the kinetic findings, the conclusion is that micelles with Ni^{2+} as the predominant counterion form at the ACMC. These micelles are probably twice the size of the "normal" micelles of the system. Magnesium dodecyl sulfate micelles are known to be roughly twice the size of SDS micelles (20). As the surfactant concentration is increased beyond the ACMC, the surfactant cation gradually replaces Ni^{2+} ion as the micellar counterion to form mixed micelles. This micelle transformation is essentially completed in the vicinity of the CMC value of the pure surfactant and is signalled by a change in slope of the conductivity curve (Fig. 11). The conversion from mixed to normal micelles is raised to greater surfactant concentrations for greater Ni^{2+} backgrounds. Corkill and Goodman (21), from conductivity measurements, have postulated similar mixed micelles for the $Ca(DS)_2$ + SDS system.

Carlsson et al. (22) have pointed out that the competition between divalent counterions with monovalent counterions in the micellar situation can have far-reaching effects. These considerations must be borne in mind when modelling the kinetic behaviour of probe reactions in the mixed micelle region, which, as this study suggests, exists between the ACMC and the CMC. Only beyond this latter surfactant concentration can micelles totally characteristic of the surfactant be expected to exist. This explains in part why the micellar catalysis modelling of this portion of the surfactant concentration range has been successful. Experimentalists have simply avoided this region and worked in the range of 1.5 to 5 times the CMC where it can reasonably be assumed that the micelles are more representative of the surfactant and are constant in size.

It remains to be seen whether this explanation is more widely applicable to surfactant systems containing ions other than Ni^{2+}. The widely different ACMCs for Ni^{2+} as compared with those for other divalent ions suggests that this may be the case (Fig. 10); i.e., more than just the charge on the added ion

© 1998 NRC Canada

must be taken into account. Mixed micelle theory should be of assistance here in clarifying the picture.

Acknowledgements

We are grateful to the National Universities Commission (Nigeria) for a research fellowship to O.O.S. and to the Natural Sciences and Engineering Research Council of Canada for financial aid. Andrew Rodenhiser is thanked for valuable discussions and Karen Berberich for experimental work.

References

1. M.J. Vold. J. Colloid Interface Sci. **116**, 129 (1987).
2. P. Wängnerud and B. Jönsson. Langmuir, **10**, 3542 (1994).
3. S. Niu, K.R. Gopidas, and N.J. Turro. Langmuir, **8**, 1271 (1992).
4. M. Katsumata, K. Kasatani, M. Kawasaki, and H. Sato. Bull. Chem. Soc. Jpn. **55**, 717 (1982).
5. S.J. Atherton and C.M.G. Dymond. J. Phys. Chem. **93**, 6809 (1989).
6. G. Cerichelli, G. Mancini, L. Luchetti, G. Savelli, and C.A. Bunton. Langmuir, **10**, 10 (1994); **10**, 3982 (1994).
7. V.C. Reinsborough and B.H. Robinson. J. Chem. Soc. Faraday Trans. 1, **75**, 2395 (1979).
8. Y.L. Favaro and V.C. Reinsborough. Can. J. Chem. **72**, 2443 (1994).
9. T.J. Connolly and V.C. Reinsborough. Can. J. Chem. **70**, 1581 (1992).
10. J. Holzwarth, W. Knoche, and B.H. Robinson. Ber. Bunsen-ges. Phys. Chem. **82**, 1001 (1978).
11. E. Pelizzetti and E. Pramauro. Inorg. Chem. **19**, 1407 (1980).
12. J.R. Hicks and V.C. Reinsborough. Can. J. Chem. **62**, 990 (1984).
13. N.M. van Os, J.R. Haak, and L.A.M. Rupert. *In* Physico-chemical properties of selected anionic, cationic and nonionic surfactants. Elsevier Science Publishers, Amsterdam. 1993.
14. P. Mukerjee and K.J. Mysels. *In* Critical micelle concentrations of aqueous surfactant systems. NSRDS–NBS 36. U.S. Government Printing Office, Washington. 1971.
15. P.D.I. Fletcher and V.C. Reinsborough. Can. J. Chem. **59**, 1361 (1981).
16. W. Guo, T.A. Brown, and B.M. Fung. J. Phys. Chem. **95**, 1829 (1991).
17. T.J. Connolly, V.C.Reinsborough, and X. Xiang. Aust. J. Chem. **45**, 769 (1992).
18. D. Attwood and A.T. Florence. *In* Surfactant systems: their chemistry, pharmacy and biology. Chapman and Hall, London. 1983. p. 92.
19. Y. Moroi and N. Yoshida. Langmuir, **13**, 3909 (1997).
20. S. Borbély, S. Vass, and L. Cser. Physica B (Amsterdam): **213&214**, 600 (1995).
21. J.M. Corkill and J.F. Goodman. J. Chem Soc. 206 (1962).
22. I. Carlsson, H. Edlund, G. Persson, and B. Lindström. J. Colloid Interface Sci. **180**, 598 (1996).

© 1998 NRC Canada

Pressure-tuning infrared and Raman spectroscopic study of (2,2′-bipyridine)tetracarbonylchromium(0)

Steven M. Barnett, Anton n Vlček, Jr., and Ian S. Butler

Abstract: Pressure-tuning infrared and Raman spectroscopic studies were performed on (2,2′-bipyridine)tetracarbonylchromium(0), $Cr(CO)_4(bpy)$. Previous bpy ring mode assignments were confirmed with new assignments offered by examination of the pressure-induced alterations in the vibrational spectra. The electron-density distribution of the bipyridyl ligand (and consequently, the electron-donating ability to the central metal) is modulated by the application of pressure. The pressure dependence of the carbonyl moieties reveals that the bipyridyl ligand can accommodate a significant portion of the molecular compressibility at higher pressures.

Key words: infrared, Raman, pressure, $Cr(CO)_4(bpy)$, metal carbonyl.

Résumé : On a réalisé des études spectroscopiques, Raman et infrarouge sous pression, sur le (2,2′-bipyridine)chrome(0)-tétracarbonyle, $Cr(CO)_4(bpy)$. On a ainsi pu confirmer les attributions antérieures faites à l'aide du bpy en utilisant les nouvelles possibilités d'attribution offertes par l'étude des déformations induites sous pression dans les spectres de vibration. La distribution de la densité électronique du ligand bipyridyle (et conséquemment la capacité du centre métallique à donner des électrons) est modulée par l'application de la pression. L'effet de la pression sur les unités carbonyles révèle que le ligand bipyridyle joue un rôle important dans la compressibilité moléculaire à des pressions plus élevées.

Mots clés : infrarouge, Raman, pression, $Cr(CO)_4(bpy)$, carbonyle metallique.

[Traduit par la rédaction]

Introduction

The photochemical, electrochemical, and physical properties of species with the general structure $M(CO)_4(bpy)$ (M = Cr, Mo, W; bpy = 2,2′-bipyridine) have been extensively studied (1–16). The weak luminescence observed on photoexcitation of $M(CO)_4(bpy)$ (M = Cr, Mo, W) complexes (17) has been explained by an energetically low metal-to-ligand change-transfer (MLCT) excited state. The presence of a low-lying unoccupied π^* orbital on the bpy ligand permits the reduction of $Cr(CO)_4(bpy)$ without loss of a carbonyl (18, 19). Recent studies have described the energy and character of the lowest MLCT transition (20, 21) as well as the mechanism for ^{1}MLCT and ^{3}MLCT relaxation to the ground state and for CO photodissociation (22).

Pressure-tuning spectroscopic studies can be extremely powerful in elucidating structural features of complicated organic and organometallic systems (23–27). While pressure-tuning infrared spectroscopic studies using diamond anvil cells (DAC) are relatively simple with the increased speed and sensitivity of Fourier transform (FT) spectrometers and the use of infrared microscopes which greatly facilitate sample alignment, information on the structural changes characterized by low-frequency vibrations (such as metal–ligand vibrations) cannot be studied (28, 29). Furthermore, the strong diamond absorbance of the DAC in the 2400–1800 cm^{-1} region does not permit the direct observation of many functional groups such as metal carbonyls, nitriles, and alkynes. Pressure-tuning Raman spectroscopic studies provide information on these excluded regions of the infrared spectra. However, weak features cannot be observed in conventional pressure-tuning Raman experiments using visible laser excitation due to the intense fluorescent background of the type IIA diamonds in the DAC, as well as decomposition and fluorescence observed in many organometallic complexes, resulting in poor spectra and spectral artifacts which may be difficult to interpret.

For organic molecules, an increase in the energy of most vibrational modes is observed with increasing pressure (i.e., a positive pressure dependence) accompanied by a decrease in the interatomic distances. However, in metal carbonyls, the application of pressure increases the π-backbonding between the central metal atom and the carbonyl ligands, which forces

Received March 26, 1997.

S.M. Barnett[1] and I.S. Butler.[2] Department of Chemistry, McGill University, 801 Sherbrooke Street West, Montreal, QC H3A 2K6, Canada.

A. Vlček, Jr.[3] J. Heyrovský Institute of Physical Chemistry, Academy of Sciences of the Czech Republic, Dolejskova 3, 182 23 Prague, Czech Republic.

[1] Current address: Laboratory of Chemical Physics, National Institute of Diabetes, Digestive, and Kidney Diseases, National Institutes of Health, Building 5, Room B1-38, 9000 Rockville Pike, Bethesda, Maryland 20892-0510, U.S.A.

[2] Author to whom correspondence may be addressed. Telephone: (514) 398–6940. Fax: (514) 398–3797. E-mail: butler@omc.lan.mcgill.ca.

[3] Current address: Department of Chemistry, Queen Mary and Westfield College (University of London), Mile End Road, London E1 4NS, United Kingdom.

© 1998 NRC Canada

more electron density into the CO π^* orbitals, leading to decreased (30) or negative (31) pressure dependences for many carbonyl ligands in organometallic complexes, especially with an electron-donating ligand bound to the metal atom.

Spectroscopic studies of bipyridine and organometallic complexes containing bipyridyl ligands have been performed using infrared (32, 33), Raman (34, 35), and resonance Raman (36–38) spectroscopies as well as studies incorporating the effect of pressure in conjunction with these techniques (39–43) and with surface enhanced Raman spectroscopy (SERS) (44). Normal mode analyses for the assignment of vibrationally active bands have been performed on free 2,2′-bipyridine (45, 46), and a normal coordinate analysis (NCA) has been performed on tris(bipyridine)ruthenium(II) (47). The study of complexes such as $Cr(CO)_4$(bpy) and $W(CO)_4$(phen) provide an excellent opportunity to evaluate the electronic structure of bipyridyl ligand binding in organometallic systems (20, 48).

In an attempt to combine the large spectral range available in pressure-tuning Raman spectroscopic studies with the lack of sample decomposition using near-infrared excitation, the pressure-tuning Raman experiment was recently adapted to a FT–Raman spectrometer using near-IR (1064 nm) laser illumination (49, 50). In this work, pressure-tuning infrared and Raman spectroscopic studies were performed on $Cr(CO)_4$(bpy) to investigate the bonding and electronic structure of organometallic complexes containing bipyridyl ligands.

Experimental

Materials

(2,2′-Bipyridine)tetracarbonylchromium(0), $Cr(CO)_4$(bpy), was synthesized, as described previously (22), by refluxing a toluene solution containing $Cr(CO)_6$ and bipyridine (1:1 molar ratio) for 2 h under an Ar atmosphere. The crude product precipitated after cooling was purified by crystallization from a CH_2Cl_2–isooctane mixture after most of the CH_2Cl_2 was distilled off. The purity was verified by infrared and UV-vis absorption spectroscopy.

Instrumentation

Infrared and Raman spectroscopy

Infrared spectra were obtained at 1 cm^{-1} resolution on a Bruker IFS-48 spectrometer equipped with an A-590 infrared microscope, a Sony color video system, and a mercury cadmium telluride (MCT) detector cooled by liquid N_2. Near-IR FT–Raman measurements were obtained at 2 cm^{-1} resolution on a Bruker IFS-88 spectrometer equipped with a Bruker FRA-106 Raman attachment coupled to a Nikon Optiphot-2 microscope by two 1.0 m fiber-optic cables. Sample illumination and collection of the scattered light were performed through a Nikon 20X objective with a working distance of 10 cm. The typical laser power was 100 mW from a Nd:YAG laser operating at 1064.1 nm. Rejection of the intense Raman scattering of diamond from the DAC was performed by placing a holographic notch filter between the DAC and the interferometer in the optical train. The filter had its maximum rejection at 1240.0 nm which corresponds to a 1332 cm^{-1} shift from the 1064.1 nm wavelength of the Nd:YAG laser.

Fig. 1. Near-infrared FT–Raman spectrum from 2200 to 50 cm^{-1} of $Cr(CO)_4$(bpy) in the solid state (spectrum ratio based on the instrument response function).

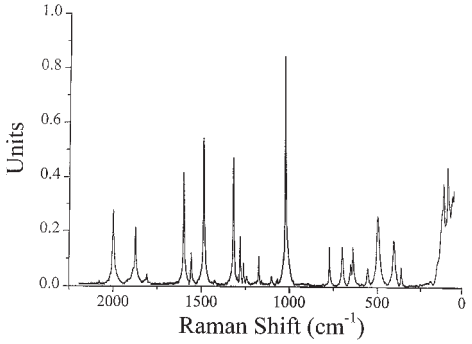

Diamond anvil cell (DAC)

The DAC for pressure-tuning infrared and Raman spectroscopic measurements was obtained from High-Pressure Diamond Optics (Tucson, Ariz.) A 300-mm hole drilled in the center of a stainless-steel gasket 370 mm in thickness was used to hold the sample between the parallel faces of two type IIA diamonds. Infrared and Raman spectra were obtained up to 25 kbar with pressure calibration performed by the sodium nitrate method. The shift in frequency of the intense, antisymmetric stretching mode of the NO_3– anion at 1401.3 cm^{-1} was used to calibrate the pressure according to the equation (51):

$$P = 1.775\Delta\nu - (0.795\Delta\nu e^{-\Delta\nu/78})$$

where $\Delta\nu$ is the difference (in wave numbers) between the peak position at pressure P (in kbar) and at atmospheric pressure.

Results and discussion

The near-IR FT–Raman spectrum of $Cr(CO)_4$(bpy) is shown in Fig. 1. The frequency of each vibrationally active feature was obtained by constructing a plot relating the frequency of the vibrational mode as a function of pressure and subsequently calculating the frequency at 1 bar (atmospheric pressure) (1 bar = 100 kPa). The pressure dependences ($d\nu\, dP^{-1}$) of the infrared and Raman active modes in $Cr(CO)_4$(bpy) are listed in Table 1 with comments that describe the atomic motions constituting the potential energy distribution (PED) from the NCA of $[Ru(bpy)_3]^{3+}$, listed in descending order of their contribution (47). For example, the infrared and Raman active vibrations at ~1071 cm^{-1} are composed of ν(CC), δ(CCH), and ν(CN) atomic motions in decreasing order of importance.

Vibrational assignments

Most of the assignments in Table 1 for the bpy ligand are based on the NCA (47) analysis of $[Ru(bpy)_3]^{3+}$, since most bipyridyl ring modes should not appreciably change in frequency for $Cr(CO)_4$(bpy). Vibrational modes involving the central metal could show a change in frequency arising from a decrease in the mass of the metal (which would increase the frequency relative to $[Ru(bpy)_3]^{3+}$) as well as changes in both the metal–bpy force constant and in the PED for that mode (which could increase or decrease the observed frequency).

© 1998 NRC Canada

Table 1. Infrared and Raman pressure behavior of $Cr(CO)_4(bpy)$.[a]

IR (cm^{-1})	$d\nu/dP$ (cm^{-1} $kbar^{-1}$)	Raman (cm^{-1})	$d\nu/dP$ (cm^{-1} $kbar^{-1}$)	Assignment	Comments[c]
		87	(*i*)[b]	δ(A–Cr–B)	
		113	(*i*)[b]	δ(A–Cr–B)	
		156	0.66		
		366	0.41	ν_{18}	ν(CrN), ν(C_2C_2'), α(CCC)
411	(*i*)[b]	407	0.79	ν(Cr–C)[*cis*]	
452	(*i*)[b]				
470	(*i*)[b]				
		496	0.04	δ(CrCO)	
553	(*i*)[b]	555	0.56	ν(Cr–C)[*trans*]	
637	(*i*)[b]	638	0.29	ν_{17}	α(CCC), ν(CrN), δ(CrN)
648	0.10	650	0.14	ν_{37}	α(CCC), α(NC_2C_3)
698	0.40	700	0.35	δ(CrCO)	
735	0.05			γ(CH)	
761	0.18			γ(CH)	
		772	0.24	ν_{16}	α(CCC), δ(CCH), ν(C_iC_{i+1})
808	0.10			γ(CH)	
887	0.18			γ(CH)	
965	0.12			γ(CH)	
995	0.12			γ(CH)	
1020	0.40	1021	0.39	ν_{15}	ν(C_iC_{i+1})
1032	0.50			ν_{35}	ν(C_iC_{i+1}), ν(CN)
1046	0.17			C–H bend	
		1067	0.80	$\nu_{36} + \nu_{38}$	
1072	0.28	1074	(*i*)[b]	ν_{34}	ν(C_iC_{i+1}), δ(CCH), ν(CN)
1101	0.27	1102	(*i*)[b]	ν_{14}	δ(CCH), ν(C_iC_{i+1}), α(CCC)
1119	0.19			ν_{33}	δ(CCH), ν(C_iC_{i+1}), α(CCC)
1158	0.15	1158	(*i*)[b]	ν_{32}	α(CCC), δ(CCH), α(CNC), ν(C_iC_{i+1})
1173	0.18	1174	(*i*)[b]	ν_{12}	δ(CCH)
1201	0.13			ν_{31}	δ(CCH)
1231	0.30				
1245	0.49	1244	(*ii*)[b]	ν_{30}	ν(CN), δ(CCH)
1262	0.56	1263	(*ii*)[b]	ν_{11}	δ(CCH), ν(CN)
1281	0.38	1281	(*ii*)[b]	ν_{10}	ν(C_iC_{i+1}), ν(CN)
1298	0.29	1298	(*ii*)[b]	$2 \times \nu_{37}$	
1318	0.25	1319	(*ii*)[b]	ν_9	δ(CCH), ν(C_2C_2')
1425	0.12	1428	(*ii*)[b]	ν_{28}	δ(CCH), ν(C_iC_{i+1})
1442	0.23			ν_8	δ(CCH), ν(C_iC_{i+1}), ν(CN)
1472	0.23			ν_{27}	δ(CCH), ν(C_iC_{i+1}), ν(CN)
		1488	0.37	ν_7	δ(CCH), ν(C_iC_{i+1}), ν(CN)
1569	0.29	1561	0.25	ν_6	ν(C_iC_{i+1}), ν(CN), δ(CCH)
1601	0.38	1602	0.40	ν_5	ν(C_iC_{i+1}), ν(C_2C_2'), ν(CN)
1813	(*iii*)[b]	1812	0.15	ν_{as}(CO)[*trans*]	b_2
1871	(*iii*)[b]	1877	0.37	ν_s(CO)	a_1 (1)
		1889	(*i*)[b]		
1908	(*iii*)[b]			ν_{as}(CO)[*cis*]	b_1
2002	(*iii*)[b]	2002	0.31	ν_s(CO)	a_1 (2)
2767	0.73				
2848	0.61			$2 \times \nu_{28}$	
		2858	(*i*)[b]		
2921	1.20			$2 \times \nu_{27}$	
2975	0.02			$\nu_{26} + \nu_{28}$	
3020	0.62			ν(CH)	
		3072	(*i*)[b]	ν(CH)	
3087	0.84	3085	(*i*)[b]	ν(CH)	

© 1998 NRC Canada

Table 1 (*concluded*).

IR (cm^{-1})	dν/dP (cm^{-1} $kbar^{-1}$)	Raman (cm^{-1})	dν/dP (cm^{-1} $kbar^{-1}$)	Assignment	Comments[c]
		3100	(*i*)[b]	ν(CH)	
3119	0.91			$2 \times \nu_6/\nu_{26}$	
3141	0.75				

[a] Infrared and Raman frequencies accurate to ±1 cm^{-1}.

[b] Modes observed in the infrared or Raman spectra but (*i*) signal too weak to see in DAC, (*ii*) signal blocked by absorption of diamonds in the infrared spectrum, or (*iii*) signal blocked in the Raman spectrum by FT–Raman Supernotch filter.

[c] PED of bipyridyl ring modes from ref. 47 or assignment of ν(CO) modes.

Bipyridyl ring modes

The bipyridyl ring modes observed in $Cr(CO)_4$(bpy) correlate well with those observed in previous works and in the NCA analysis of $[Ru(bpy)_3]^{3+}$. Some modes with a metal–nitrogen stretching or bending component in their PED did shift in frequency but, in general, there is excellent correlation between the frequencies observed here and in previous investigations.

The low pressure sensitivities (0.05–0.18 cm^{-1} $kbar^{-1}$) of the infrared spectroscopic features between 700 and 1000 cm^{-1} (i.e., 995, 965, 887, 808, 761, and 735 cm^{-1}) verify the γ(CH) mode assignment made from experiments on $[Ru(bpy)_3]^{3+}$ (47). The frequency of these γ(CH) modes also correlates well with pressure-insensitive bands observed in the Raman spectra of other systems containing bipyridyl ligands, and their weak Raman activity is typical for C–H bending modes. The feature at 1045 cm^{-1} in the infrared spectrum was not assigned in the $[Ru(bpy)_3]^{3+}$ study (47), but the low pressure dependence (0.17 cm^{-1} $kbar^{-1}$) confirms the assignment of a C–H bend for $Eu(bpy)_2Cl_3$, as proposed by Bayer and Ferraro (39). The low pressure sensitivity (0.13 cm^{-1} $kbar^{-1}$) of the band assigned to ν_{31} (1201 cm^{-1} in the infrared), which was predicted at 1185 cm^{-1} in NCA calculations (47), corresponds well with a δ(CCH) mode in the bipyridyl ring. It has previously been observed between 1227 and 1210 cm^{-1} in studies on $Pd(bpy)Cl_2$ (32), $Ni(py)_4Cl_2$ (py = pyridine) (43), and $[Ru(bpy)_3]^{3+}$ (47).

The infrared-active arene mode assigned to ν_{15} (1020 cm^{-1}) corresponds with a prominent 1020 cm^{-1} resonance Raman band[1] and was calculated to appear at 1036 cm^{-1} in $[Ru(bpy)_3]^{3+}$ (47). This feature has a pressure dependence of 0.40 cm^{-1} $kbar^{-1}$ and corresponds well with features observed in the spectra of complexes containing bipyridyl ligands bound to Eu, Ni, and Co (39); with the pressure dependence of this mode exhibited by pyridine coordinated to Zn and Ni (0.43 cm^{-1} $kbar^{-1}$) (43), and with the pressure dependence exhibited in the SERS spectrum of pyridine on silver (0.30 cm^{-1} $kbar^{-1}$) (44).

The feature at 1066 cm^{-1} has been observed in other organometallic complexes containing bipyridyl ligands (32) and has an extremely high pressure dependence (0.80 cm^{-1} $kbar^{-1}$). Large shifts in the frequency of vibrational features with pressure, such as for the 1066 cm^{-1} feature, are typically observed in inorganic systems or as overtones and combinations of organic vibrational modes. It has tentatively been assigned to a combination of two or more modes since no mode involving metal–ligand vibrations would be expected to appear at this frequency in $Cr(CO)_4$(bpy). The most likely assignment for this band is a combination of the ν_{36} and ν_{38} modes. The ν_{38} mode, comprised of ring twisting motions, is calculated to be near 460 cm^{-1} in $[Ru(bpy)_3]^{3+}$ (47). However, it has not been observed in this study and the fundamental probably has very weak Raman activity. This combination is likely responsible for the 1060 cm^{-1} feature, since the PED of both the ν_{36} and ν_{38} features is comprised of approximately 50% bipyridyl ring twisting motion.

Pressure dependence of modes involving Cr–N vibrations

The vibrations modes which include Cr–N stretching or bending provide insight into the metal–ligand binding in $Cr(CO)_4$(bpy). While some similarities would be expected from previous studies on $[Ru(bpy)_3]^{3+}$, many of these modes are difficult to assign, since the ligands and central metal atoms are different, leading to different PEDs and vibrational frequencies for the normal modes.

The feature at 637 cm^{-1} is assigned to ν_{17} which consists of bipyridyl ring twisting and Ru–N stretching motions in $[Ru(bpy)_3]^{3+}$; its behavior under pressure (~0.29 cm^{-1} $kbar^{-1}$) reflects the metal–ligand stretching components more than the α(CCC) component, providing further evidence for the small contribution from ν(Cr–CO) or δ(CrCO) motions attributed in resonance Raman studies of ^{13}C-labeled $Cr(CO)_4$(bpy) (ref.). This mode is sensitive to the presence of the central metal, since it shifted 40–50 cm^{-1} up in frequency (compared with free pyridine) and was insensitive to pressure on binding to Zn (43). In pressure-tuning studies of $Eu(bpy)_2Cl_3$, this mode absorbed at 710 cm^{-1} with a pressure sensitivity of 0.2 cm^{-1} $kbar^{-1}$ (39). However, the pressure sensitivity of ν_{17} here (0.35–0.40 cm^{-1} $kbar^{-1}$) indicates that in $Cr(CO)_4$(bpy) the PED has a higher degree of ν(M–N) component than in $[Ru(bpy)_3]^{3+}$ or $Eu(bpy)_2Cl_2$, revealing that the bipyridyl electronic structure is sensitive to the size of the metal.

Pressure dependence of carbonyl stretching and bending modes

There are four C–O stretching modes of $Cr(CO)_4$(bpy) with symmetry b_2, a_1, b_1, and a_1 in increasing energy (11, 52). Two of these features have been assigned to the asymmetric vibrations involving the carbonyls *trans* and *cis* to bipyridine (i.e., $\nu_{as}(CO)^{trans}$ and $\nu_{as}(CO)^{cis}$) (30, 53). The bipyridyl ligand is a four-electron donor which increases the electron density at the metal and the π-backbonding to the carbonyl ligands, lowering the ν(CO) frequencies in the *trans* carbonyls relative to the *cis* carbonyls, as shown in Table 1. There is strong mixing of the two symmetric ν(CO) bands which do not permit the carbonyls to be distinguished as purely *cis* or *trans*.[4]

[4] A. Vlček, Jr., F.-W. Grevels, T.L. Snoeck, and D.J. Stufkens. Unpublished data.

© 1998 NRC Canada

In a previous pressure-tuning infrared spectroscopic study of *cis*-$Cr(CO)_4(CNBut\text{-}t)_2$ (30), two ν(Cr–CO) bands were assigned at 409 and 490 cm^{-1}. However, the low pressure dependence of the $Cr(CO)_4(bpy)$ feature at 496 cm^{-1} (0.04 $cm^{-1}\,kbar^{-1}$) excludes any prominent metal–ligand stretching component; this feature has recently been assigned to a δ(CrCO) mode in resonance Raman studies of ^{13}C-labeled $Cr(CO)_4(bpy)$ (ref.). For $Cr(CO)_4(bpy)$, the two ν(Cr–CO) modes are assigned to the bands at 407 and 555 cm^{-1} in the Raman spectra (assigned from the pressure dependences of these two modes).

Electronic structure of organometallic complexes containing bipyridyl ligands

In using the metal carbonyl vibrational modes as probes of bipyridyl electronic structure, the results presented in this study provide an interesting examination of metal–ligand binding in organometallic complexes containing bipyridyl ligands. The presence of bpy affects the frequencies of the ν(CO) and ν(Cr–CO) modes for the *trans* carbonyls, as would be expected by the donation of electron density from the bipyridyl ligand to the metal center, resulting in a decrease in the frequency of the $\nu(CO)^{trans}$ modes and an increase in the $\nu(Cr–CO)^{trans}$ frequency. The effect of the *trans* ligands was also observed in similar pressure-tuning infrared and Raman spectroscopic studies on $Cr(CO)_4(CNBut\text{-}t)_2$ where the frequency of the $\nu(CO)^{trans}$ modes was lower than the frequency of the $\nu(CO)^{cis}$ mode, and the pressure dependence of the *trans* carbonyls was markedly lower than for the *cis* carbonyls due to increased backbonding at higher pressures (e.g., $d\nu_s[CO]^{cis}\,dP^{-1} = 0.99\ cm^{-1}\,kbar^{-1}$; $d\nu_s[CO]^{trans}\,dP^{-1} = 0.21\ cm^{-1}\,kbar^{-1}$) (30). In $Cr(CO)_4(bpy)$, the pressure dependence of the *cis* carbonyl modes was much lower than that observed in $Cr(CO)_4(CNBut\text{-}t)_2$ (cf. Table 1). Some of the decreased pressure dependence may be attributed to the bipyridyl ligand accommodating a greater portion of the molecular compressibility at higher pressures, since it is larger (and more pressure sensitive) than the CNBut-*t* ligands in $Cr(CO)_4(CNBut\text{-}t)_2$.

The electron density distribution of the bipyridyl ligand (and consequently, the electron-donating ability to the central metal) appears to be modulated by the application of pressure. This variability in electron density within the bipyridyl ligand is likely related to the great diversity of MLCT states which are exhibited by the series of organometallic complexes with bipyridine or bipyrazine ligands. Further pressure-tuning studies of organometallic complexes involving bipyridine and bipyrazine will reveal the nature of the vibrational systems in these complexes and ultimately aid in elucidating the complex photochemistry of these diverse systems.

References

1. L.E. Orgel. Inorg. Chem. **1**, 25 (1962).
2. D.M. Adams. J. Chem. Soc. A, 88 (1969).
3. B. Hutchison and K. Nakamoto. Inorg. Chim. Acta, **3**, 591 (1969).
4. R.T. Jernigan, R.A. Brown, and G.R. Dobson. J. Coord. Chem. **2**, 47 (1972).
5. C.L. Hyde and D.J. Darensbourg. Inorg. Chem. **12**, 1075 (1973).
6. M.S. Wrighton and D.L. Morse. J. Organomet. Chem. **97**, 405 (1975).
7. R.W. Balk, T. Snoeck, D.J. Stufkens, and A. Oskam. Inorg. Chem. **19**, 3015 (1980).
8. J.A. Connor and C. J. Overton. J. Organomet. Chem. **249**, 165 (1983).
9. J.A. Connor and C. J. Overton. J. Organomet. Chem. **282**, 349 (1983).
10. P.C. Servaas, H.K. van Dijk, T.L. Snoeck, D.J. Stufkens, and A. Oskam. Inorg. Chem. **24**, 4494 (1985).
11. D.M. Manuta and A.J. Lees. Inorg. Chem. **25**, 1354 (1986).
12. D. Miholova, B. Gas, S. Zalis, J. Klima, and A.A. Vlček. J. Organomet. Chem. **330**, 75 (1987).
13. D.J. Stufkens. Coord. Chem. Rev. **104**, 39 (1990).
14. J.-H. Perng and J.I. Zink. Inorg. Chem. **29**, 1158 (1990).
15. A.Vlček, Jr., J. Víchová, and F. Hartl. Coord. Chem. Rev. **132**, 166 (1994).
16. I.G. Virrels, M.W. George, J.J. Turner, J. Peters, and A. Vlček, Jr. Organometallics, **15**, 4089 (1996).
17. Y. Kaizu, I. Fujita, and H.Z. Kobayashi. Phys. Chem. **79**, 298 (1972).
18. Y. Kaizu and H. Kobayashi. Bull. Chem. Soc. Jpn. **43**, 2492 (1970).
19. Y. Kaizu and H. Kobayashi. Bull. Chem. Soc. Jpn. **45**, 470 (1970).
20. H. Kobayashi, Y. Kaizu, H. Kimura, H. Matsuzawa, and H. Adachi. Mol. Phys. **64**, 1009 (1988).
21. D. Guillaumont, C. Daniel, and A. Vlček, Jr. Inorg. Chem. In press.
22. J. Víchová, F. Hartl, and A. Vlček, Jr. J. Am. Chem. Soc. **114**, 10 903 (1992).
23. J.R. Ferraro. Vibrational spectroscopy at high external pressures. Academic Press Inc., Orlando. 1984.
24. D.M. Adams, P.D. Hatton, and A.C. Shaw. J. Chem. Soc. Chem. Commun. 226 (1981).
25. Y. Huang, I.S. Butler, D.F.R. Gilson, and D. Lafleur. Inorg. Chem. **30**, 117 (1991).
26. Y. Huang, I.S. Butler, and D.F.R. Gilson. Inorg. Chem. **30**, 1098 (1991).
27. Y. Huang, I.S. Butler, and D.F.R. Gilson. Spectrochim. Acta Part A, **47A**, 909 (1991).
28. K. Aoki, Y. Kakudate, M. Yoshida, S. Usuba, and S. Fujiwara. J. Chem. Phys. **91**, 2814 (1989).
29. H. Yamawaki, K. Aoki, Y. Kakudate, M. Yoshida, S. Usuba, and S. Fujiwara. Chem. Phys. Lett. **198**, 183 (1992).
30. H. Li and I.S. Butler. Inorg. Chem. **34**, 1193 (1995).
31. D.M. Adams and I.O.C. Ekejiuba. J. Chem. Phys. **77**, 4793 (1982).
32. J.R. Durig, B.R. Mitchell, D.W. Sink, J.N. Willis, Jr., and A.D. Wilson. Spectrochim. Acta Part A, **23A**, 1121 (1967).
33. E.D. McKenzie. Coord. Chem. Rev. **6**, 187 (1971).
34. J.S. Strukl and J.L. Walter. Spectrochim. Acta Part A, **27A**, 209 (1971).
35. J.S. Strukl and J.L. Walter. Spectrochim. Acta Part A, **27A**, 223 (1971).
36. D.J. Barker, R.P. Cooney, and L.A. Summers. J. Raman Spectrosc. **16**, 265 (1985).
37. P.A. Mabrouk and M.S. Wrighton. Inorg. Chem. **25**, 526 (1986).
38. V.R.L. Constantino, H.E. Toma, L.F.C. de Oliveira, and P.S. Santos. J. Raman Spectrosc. **22**, 629 (1992).
39. R. Bayer and J.R. Ferraro. Inorg. Chem. **8**, 1654 (1969).
40. J.R. Ferraro and J. Takemoto. Appl. Spectrosc. **28**, 66 (1974).
41. A.M. Heyns and M.W. Venter. J. Phys. Chem. **89**, 4546 (1985).
42. H.-B. Kim, T. Hiraga, T. Uchida, N. Kitamura, and S. Tazuke. Coord. Chem. Rev. **97**, 81 (1990).
43. A.M. Heyns and M.W. Venter. J. Chem. Phys. **93**, 7581 (1990).
44. C.J. Sandroff, H.E. King, Jr., and D.R. Herschbach. J. Phys. Chem. **88**, 5647 (1984).

© 1998 NRC Canada

45. N. Neto, M. Muniz-Miranda, L. Angeloni, and E. Castellucci. Spectrochim. Acta Part A, **39A**, 97 (1983).
46. N. Neto, M. Muniz-Miranda, L. Angeloni, and E. Castellucci. Spectrochim. Acta Part A, **39A**, 107 (1983).
47. P.K. Mallick, G.D. Danzer, D.P. Strommen, and J.R. Kincaid. J. Phys. Chem. **92**, 5628 (1988).
48. E. Lindsay, A. Vlček, Jr., and C.H. Langford. Inorg. Chem. **32**, 2269 (1993).
49. N.L. Ross. Spectrochim. Acta Part A, **49A**, 681 (1993).
50. S.M. Barnett, R.D. Markwell, S.H.R. Brienne, I.S. Butler, D.F.R. Gilson, N.T. Kawai, and A. Vlček, Jr. J. Raman Spectrosc. **24**, 471 (1993).
51. D.D. Klug and E. Whalley. Rev. Sci. Instrum. **54**, 1205 (1983).
52. D.M. Adams. J. Chem. Soc. A, 88 (1969).
53. C.S. Kraihanzel and F.A. Cotton. Inorg. Chem. **2**, 533 (1963).

© 1998 NRC Canada

Stereoelectronic effects in sulfonyl compounds: axial orientation of an *N*-methyl group in a six-membered sultam[1,2]

James Frederick King, Gay Yuyitung, Manjinder Singh Gill, Jeffrey Charles Stewart, and Nicholas Charles Payne

Abstract: The *trans* form of octahydro-1-methyl-1*H*-2,1-benzothiazine 2,2-dioxide, in which a six-membered sultam unit is *trans*-fused to cyclohexane, has been synthesized. The single-crystal X-ray structure shows the molecule to have the *N*-methyl group in the *axial* orientation. The generalized anomeric effect believed to be responsible for the axial preference is estimated at ≥2 kcal mol^{-1}.

Key words: generalized anomeric effect, negative hyperconjugation, sulfonamides, sultams, X-ray crystallography.

Résumé : On a synthétisé la forme *trans* du 2,2-dioxyde de l'octahydro-1-méthyl-1*H*-2,1-benzothiazine dans laquelle une unité sultame à six chaînons est liée de façon *trans* à un cyclohexane. Une détermination de structure par diffraction des rayons X par un cristal unique montre que le groupe *N*-méthyle occupe une orientation *axiale*. On évalue que l'effet anomère généralisé qui serait responsable de la préférence axiale est de l'ordre de 2 kcal mol^{-1}.

Mots clés : effet anomère généralisé, hyperconjugaison négative, sulfonamides, sultames, diffraction des rayons X.

[Traduit par la rédaction]

Introduction

There is good evidence for the existence in sulfonyl compounds of the general formula $-SO_2-\ddot{X}$, where X = OR, NR_2, C^-R^2, etc., of delocalization as indicated by $-SO_2-\ddot{X} \leftrightarrow -\overline{S}O_2 \equiv X^+$, and that this delocalization depends on the orientation of the free

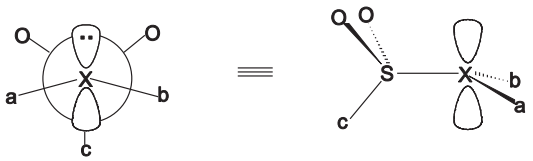

1

electron pair, i.e., that it is a stereoelectronic effect which may be included under the heading of a "generalized anomeric effect" (2) or "negative (or anionic) hyperconjugation"(3). Much of the support for this picture derives from the extensive experimental and theoretical studies on α-sulfonyl carbanions (for summaries see refs. 4 and 5 and sources cited). Theoretical studies currently concur in favouring depiction of the delocalization as involving, primarily, not *d*-orbitals as had been earlier proposed (see, for example, refs. 6 and 7), but rather $n \rightarrow \sigma^*$ donation (8–10). The more limited studies on sulfonamides and related species (11–16) and on sulfonic esters (14–16) point to a similar, if smaller, delocalization in these species. Structure **1** shows the lowest energy conformation about the S—X bond as indicated by a variety of procedures (11–15). Note that the typical projected *a*–X–*b* angle is neither 120° (as expected for sp^3 hybridization) nor 180° (for sp^2 hybridization), but is rather something in between, ranging from 130° to 175° with sulfonamides.

Among the various estimates for the energy barrier to rotation around the S—X bond we note Bors and Streitwieser's calculated value of about 14 kcal mol^{-1} for CH_2—SO_2CH_3 (9)

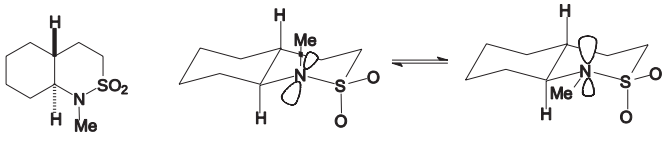

2 2a 2b

and Jennings and Spratt's determination by ^{1}H NMR spectrometry of 11.5 kcal mol^{-1} assigned to rotation around the S—N bond in Et_2NSO_2Cl (12); the latter method was not applicable to other sulfonamides (e.g., Et_2NSO_2Me), and it was surmised that the rotational barrier in such species is lower.

Received June 6, 1997.

J.F. King,[3] G. Yuyitung, M.S. Gill, J.C. Stewart, and N.C. Payne.[4] Department of Chemistry, The University of Western Ontario, London, ON N6A 5B7, Canada.

[1] Part 41 in the series Organic Sulfur Mechanisms. For part 40 see ref. 1.

[2] Taken in part from the Honors B.Sc. theses of G. Yuyitung (1992) and J.C. Stewart (1995).

[3] Author to whom correspondence on the organic chemistry may be addressed. Telephone: (519) 679–2111, ext. 6348. E-mail: scijfk@uwoadmin.uwo.ca.

[4] Author to whom correspondence on X-ray crystallography may be addressed. Telephone: (519) 661–3793. E-mail: noggin@julian.uwo.ca.

© 1998 NRC Canada

Scheme 1.

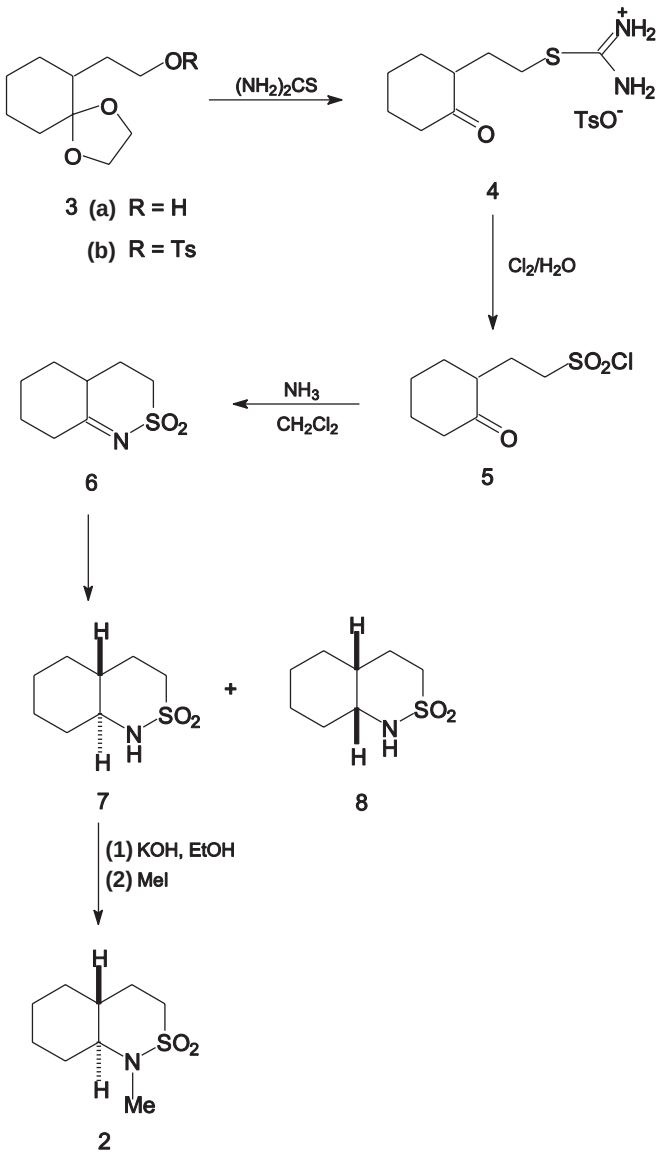

In the present study we have sought information on the energetics and chemical effects of the generalized anomeric effect in sulfonamides by synthesizing a sulfonamide in which the steric and stereoelectronic effects must compete. The specific example chosen was the sulfonamide **2**, in which the favourable "anomeric effect geometry" shown in **1** may be achieved only at the expense of placing the methyl group in an axial conformation. The competition is illustrated in structures **2a** ⇌ **2b**; **2a** has the stereoelectronically preferred arrangement as in **1**, but **2b** has the sterically preferred equatorial orientation of the methyl group. The question we sought to answer is, which orientation is favoured, or, perhaps rather optimistically, what is $\Delta G°$ for the equilibrium **2a** ⇌ **2b**?

Results and discussion

Scheme 1 shows the synthesis of the bicyclic sultam **2**. The ultimate starting materials, cyclohexanone and ethyl bromoacetate were converted to the hydroxyacetal **3a** as described by Segre et al. (17). The sulfonyl chloride (**5**) was obtained from **3a** by tosylation to **3b**, S_N2 displacement with thiourea with accompanying hydrolysis of the acetal to form **4**, followed by aqueous chlorination. Reaction of **5** with ammonia gave, presumably by way of the keto-sulfonamide, the sulfonimine **6**. Reduction of **6** with $LiAlH_4$ in THF gave a 60:40 mixture of stereoisomers (mp 123–125°C and 134–135°C, respectively) separable by thick-layer chromatography. The stereochemistry of the products was tentatively assigned from the ^{1}H NMR spectra. In the lower melting isomer the methine attached to the nitrogen gave a triplet of doublets (each peak slightly broadened) at ~3.0 ppm, consistent with an axial hydrogen split by two axial neighbours and one equatorial neighbour as in the *trans* isomer **7**. In the higher melting isomer the methine hydrogen showed a relatively narrow signal at 3.8 ppm, indicating a hydrogen with only small coupling constants with neighbours, as would be the case for the conformer of **8** with the methine C-H equatorial to the cyclohexane ring. This assignment was confirmed by a single-crystal X-ray structure

Fig. 1. A view of **7**. Thermal ellipsoids are drawn at the 50% probability level.

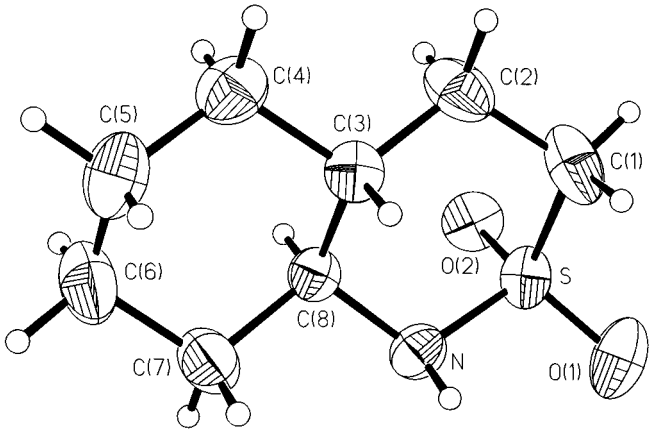

Fig. 2. A view of **2**. Thermal ellipsoids are drawn at the 50% probability level.

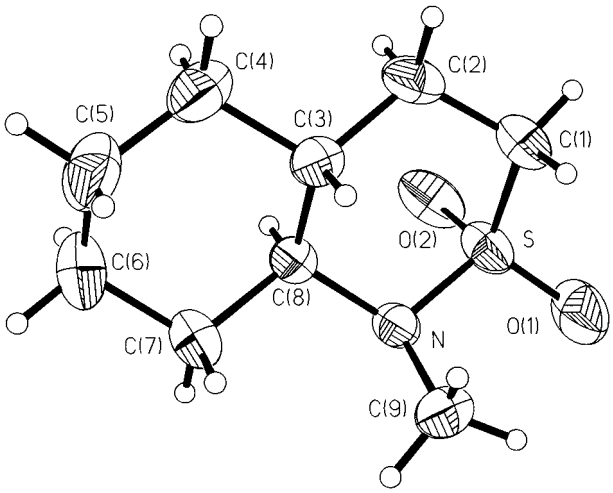

© 1998 NRC Canada

determination of the low-melting isomer (Fig. 1) that showed it to be the *trans* isomer **7**.

Methylation of **7** with methyl iodide in the presence of base gave the *N*-methyl sultam **2** as a crystalline solid melting at 58–60°C. The single crystal X-ray structure (Fig. 2) is in full accord with the assigned structure and clearly shows the methyl group to be in the *axial* position.

If we may assume that the structure of **2** given by the X-ray diffraction analysis is, in fact, that of the lowest energy conformation, then this result accords well with the view that the generalized anomeric effect in sulfonamides leads to a substantial stabilization of the conformation that maximizes this effect. In this instance it is sufficient to overcome completely the usual preference for the equatorial orientation of a substituent on a six-membered ring. In methylcyclohexane itself, $\Delta G°$ for the conformational change axial $\rightleftharpoons$ equatorial is –1.74 kcal mol^{-1} (18). Obviously there are important points of difference between **2** and methylcyclohexane, notably: (*a*) the partial flattening of the nitrogen atom (from increased *p* character, as discussed above) accompanying delocalization of the electrons into the sulfonyl group, (*b*) the longer bond lengths associated with the sulfur atom, and (*c*) the presence of oxygen atoms on the sulfur. We note, however, that the H–H non-

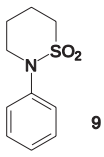

9

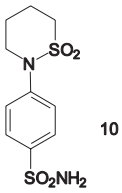

10

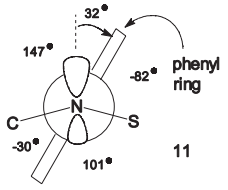

11

bonding distance between the hydrogens on C-3 and the hydrogens on C-9 (see Fig. 2 for numbering), i.e., the axial ring juncture hydrogen and the nearest hydrogen of the axial methyl group, is 2.36 Å, a number close to the 2.34 Å found by MMX (PC Model) calculations for the analogous hydrogen–hydrogen interactions in methylcyclohexane. This suggests that the axial *N*-Me group in **2** is indeed subject to nonbonding repulsions of comparable or perhaps slightly diminished magnitude with respect to those on axial methylcyclohexane. If we take a conservative estimate of the steric energy of the axial methyl group in **2** as –1 kcal mol^{-1} (i.e., distinctly less than the 1.74 kcal mol^{-1} in axial methylcyclohexane), and if, indeed, the axial conformation of **2** is the substantially favoured form as suggested by the X-ray result, then, keeping in mind the reservations noted above, we may suggest a value of ≥2 kcal mol^{-1} for the anomeric effect in **2**.

This result is to be contrasted with that observed with *N*-phenyl six-membered sultams **9** and **10**, both of which were found in X-ray crystallographic studies to have the phenyl group in the *equatorial* position (19, 20). The phenyl group is distinctly larger than the methyl group (the *A* value for phenyl is 2.8 vs. 1.74 kcal mol^{-1} for methyl) (21). If this is the only factor, these results could be interpreted as indicating that the anomeric effect is simply not large enough to counter the larger "size" of the phenyl group (and hence must be assigned a value of less than, say, 2.5 kcal mol^{-1}). Such an interpretation must be viewed with caution, however, because the electrons in *N*-alkyl and *N*-aryl sulfonamides may well show different intrinsic anomeric effects, because of the greater electronegativity of aryl (vs. alkyl) groups and (or) partial delocalization of the *N*-aryl free electron pair into the aromatic ring, thereby making it less available for delocalization into the sulfonyl group. The latter factor would not appear to be particularly important with **9** or **10**, however, because the free electron pair and the phenyl ring do not seem to be well oriented for effective delocalization. As may be seen from the Newman projection (**11**) of the N-aryl bond in **9**, the orbital of the free electron pair makes an angle of only 32° with the phenyl ring, rather than the optimal 90° (the other numbers are the observed torsional angles (18)).

Table 1. Bond lengths (Å) and angles (deg).

Bond(s)	**7**	**2**
S—O(1)	1.428(2)	1.430(2)
S—O(2)	1.4384(14)	1.439(2)
S—N	1.633(2)	1.638(2)
S—C(1)	1.759(2)	1.764(2)
N—C(8)	1.484(2)	1.490(2)
N—C(9)		1.474(3)
C(1)—C(2)	1.527(3)	1.519(3)
C(2)—C(3)	1.526(3)	1.536(3)
C(3)—C(4)	1.528(3)	1.528(3)
C(3)—C(8)	1.533(2)	1.534(3)
C(4)—C(5)	1.515(3)	1.520(4)
C(5)—C(6)	1.518(3)	1.513(4)
C(6)—C(7)	1.523(3)	1.519(3)
C(7)—C(8)	1.523(2)	1.518(3)
O(1)-S-O(2)	117.87(9)	118.42(13)
O(1)-S-N	107.82(9)	108.48(10)
O(2)-S-N	106.79(8)	106.89(10)
O(1)-S-C(1)	111.15(11)	110.60(13)
O(2)-S-C(1)	107.90(11)	108.03(12)
N-S-C(1)	104.39(9)	103.30(10)
C(8)-N-S	115.03(12)	112.05(12)
C(9)-N-C(8)		116.5(2)
C(9)-N-S		115.05(14)
C(2)-C(1)-S	110.03(13)	109.8(2)
C(3)-C(2)-C(1)	113.1(2)	113.9(2)
C(2)-C(3)-C(4)	112.1(2)	110.8(2)
C(2)-C(3)-C(8)	112.1(2)	112.3(2)
C(4)-C(3)-C(8)	109.22(14)	110.0(2)
C(5)-C(4)-C(3)	112.2(2)	112.8(2)
C(4)-C(5)-C(6)	110.9(2)	111.1(2)
C(5)-C(6)-C(7)	111.2(2)	110.7(2)
C(8)-C(7)-C(6)	110.9(2)	110.9(2)
N-C(8)-C(7)	108.7(2)	111.0(2)
N-C(8)-C(3)	112.86(13)	113.2(2)
C(7)-C(8)-C(3)	111.8(2)	111.4(2)

Further structure descriptions

The crystal structure of **7** is built up from molecules linked by hydrogen bonds N—H...O(2) at (x, $-½ - y$, $z - ½$) (N—H 0.90, H...O(2) 2.10 Å, N—H...O(2) 174°). The closest nonbonding

© 1998 NRC Canada

approach is H(8)...H(4A) at (x, ½ – y, ½ + z) 2.55 Å. All distances and angles within the molecule are normal, and the H atom on the nitrogen clearly occupies an axial position. The crystal structure of **2** is built up from separate molecules. The closest nonbonding approach is H(1B)...O(2) at (1 – x, 1 – y, –z) 2.45 Å. Selected interatomic distances and angles for both compounds are given in Table 1. Distances and angles within molecule **2** are normal, and agree well with those in **7**. The projected C-N-C angle in **7** (136.0(3)°), which is obtained from the difference of the C1-S-N-C9 and C1-S-N-C8 torsional angles (respectively, –78.0(2)° and 58.0(2)°), is in the low end of the range (130°–175°) quoted above.

There is a significant difference between the S—O bond lengths in each compound. Thus the S—O(equatorial) distance is significantly shorter than the S—O(axial) distance (λ = 4.3 in **7** and 3.2 in **2**).

Comparison with published ab initio calculations

Katzenellenbogen and co-workers (16) have reported ab initio calculations on *N*-methyl methanesulfonamide and methyl methanesulfonate. Because their conclusions are in some important ways at variance with both our present and our earlier results (15) (which they do not appear to have noticed), a comment at this stage would appear to be in order. Their MO calculations lead them to conclude that the lowest energy conformation of methyl methanesulfonate has a C-S-O-C torsion angle of 179.9°. They also reported an X-ray single-crystal structure determination of a sulfonic ester, which showed a C-S-O-C torsion angle of 173.1°. With the sulfonamide, two energy minima were calculated; the higher energy form (by 1.5–1.9 kcal mol^{-1}) showed a C-S-N-C torsion angle of 72° (much like **1**), but in the lower energy conformation the C-S-N-C angle was 98.7°, with the major lobe of the orbital containing the free electron pair eclipsed with the S—C bond and the N—H bond eclipsed with S—O bond. They compared the sulfonamide MO calculation results with a previously published X-ray structure of methanesulfonanilide (CH_3SO_2NHPh).

In our earlier study (15) of crystal structures of sulfonic esters reported in the Cambridge Datafile (for 1986), we found a total of 106 "hits" (compounds) giving 121 dihedral angles; of these 101 were in the range 60°–120°, and 5 in the range 160°–180°. Evidently neither Katzenellenbogen's MO calculations nor his single compound determined by X-ray crystallography adequately represent the structures of sulfonic esters, at least in the solid phase.

In the earlier paper (15) we also looked at the structures of *N,N*-disubstituted sulfonamides and found that 124 of 140 C-S-N-C torsion angles were in the range 60°–120°, and only one example, N-phenylsulfonyl-2,2,6,6-tetramethyl-4-oxopiperidine (22), had the free electron pair eclipsed with the S—C bond, corresponding to the lower energy minimum in the calculations of Katzenellenbogen. It should also be noted that the X-ray structure of methanesulfonanilide mentioned by Katzenellenbogen and co-workers has C-S-N-C and C-S-N-H angles of –62.2° and 70.4°, respectively, i.e., in the same range as most of the corresponding disubstituted sulfonamides in our earlier study described above. Katzenellenbogen and co-workers suggested that "crystal lattice forces and the presence of functional groups which might be involved in interactions (e.g., hydrogen bonding) can play a significant role in determining torsional angles." In the disubstituted sulfonamides there is no N—H bond and such hydrogen bonding cannot be a factor; in addition, it seems extremely improbable to us that crystal lattice forces would provide such a clear trend favouring the 60°–120° torsional angle if it were opposed to a significant factor in favour of another conformation, e.g., that corresponding to Katzenellenbogen's minimum energy conformation.

Another way of looking at these results emerges from MO calculations done on methanesulfonamide ($CH_3SO_2NH_2$) in this department (D.F. Klassen and N.C. Baird, personal communication); the calculations were carried out with the GAUSSIAN 86 package using the 6-31G* basis set with *d*-orbitals on the sulfur atom only. The minimum energy structure showed *both* N—H bonds eclipsed with the S—O bonds. The X-ray crystal structure of $CH_3SO_2NH_2$, on the other hand (ref. 23 and also N.C. Payne, unpublished results), shows each sulfonyl oxygen to be hydrogen-bonded to the hydrogen on the nitrogen of an adjacent molecule, which is then associated with the first molecule by the complementary N—H—O—S hydrogen bond; thus each molecule is attached by two hydrogen bonds to two other methanesulfonamide molecules. These results are consistent with two notions: (*a*) that the N—H—O—S hydrogen bond (whether inter- or intramolecular) is strong, and (*b*) that the synperiplanar anomeric effect, in which the (electron pair)-N-S-C torsion angle in sulfonyl compounds is ~0°, may well be of comparable energy with the more usual antiperiplanar (with (electron pair)-X-S-C angle ~180°) conformation; evidence for the synperiplanar effect in acetal reactions (24) and α-sulfonyl carbanion formation (25) has been described. For the *N,N*-disubstituted sulfonamides of our previous study, the observed preference for the C-S-N-C torsion angle of 90 ± 30° (i.e., the antiperiplanar conformation) over the synperiplanar conformation is probably due primarily to the extra energy of the eclipsing interactions between the sulfonyl oxygen atoms and the substituents on the nitrogen atom. When the N-substituent is a hydrogen atom the nonbonding interaction is small and may well be more than compensated by the hydrogen bonding discussed above. With most other groups, and certainly with simple alkyl and aryl groups, these eclipsing interactions may be expected to be destabilizing, and hence the antiperiplanar conformation to be the more stable conformation except perhaps with mono-*N*-substituted sulfonamides with a small substituent, or conceivably, very cluttered *N,N*-disubstituted sulfonamides; the exception noted above, *N*-phenylsulfonyl-2,2,6,6-tetramethyl-4-oxopiperidine, which shows the synperiplanar form (and a twist-boat six-membered ring) in the crystal (22), may be an example of this.

The MO calculations of Katzenellenbogen and co-workers and of Klassen and Baird agree in assigning a low energy barrier (~2 kcal mol^{-1}) to inversion at the nitrogen; it seems highly likely that we are dealing with products of complete equilibration (as implied by **2a** ⇌ **2b**, above) in all cases.

Finally we point to the similarity in geometry between **2** and **7**. The fact that the N-H is axial is of course in good agreement with the operation of the anomeric effect (negative hyperconjugation). This N-H is also, however, hydrogen bonded to the sulfonyl oxygen of the neighbouring molecule (see above) and for the reasons discussed in the above paragraphs it would seem imprudent to ascribe the axial orientation of the hydrogen on nitrogen exclusively to the anomeric effect.

© 1998 NRC Canada

Experimental

Instruments and general procedures

^1H and ^{13}C NMR data were obtained using Varian Gemini 200, XL200, and XL300 instruments and are normally of solutions in $CDCl_3$; chemical shifts were determined relative to TMS. IR spectra were obtained on $CHCl_3$ solutions (0.1 mm) using an IFS/32 FTIR Bruker or a Perkin Elmer 2000 FT-IR spectrometer. Melting points were determined using either a Fisher-Johns melting point apparatus or a Kofler Hot Stage and are uncorrected. Kiesel Gel, silica gel for TLC (containing 5% $CaSO_4$, from InterScience, Markham, Ontario), was used for thin-layer chromatography and thick-layer preparative plates. Reagent grade chemicals and solvents were used, unless otherwise noted. Work-up refers to (*a*) partitioning of reaction mixture between water and an organic solvent, (*b*) making the aqueous phase acidic with 1 M H_2SO_4, (*c*) extraction with organic solvent, and (*d*) drying of the organic layer with anhydrous magnesium sulfate and evaporation of the organic solvent using a Büchi rotary evaporator attached to a water aspirator. Mass spectra were determined with a Finnigan MAT-311A spectrometer (at 70 eV).

Ethylene ketal of 2-[2 hydroxyethyl]cyclohexanone (3a)

The procedure of Segre et al. (17) gave **3a** as a clear liquid. ^1H NMR δ: 1.08–2.05 (m, 11H), 2.83 (s, 1H), 3.37–3.80 (m, 2H), 3.87–4.12 (s, 4H); ^{13}C NMR δ: 23.6, 24.4, 30.2, 32.0, 34.2, 41.6, 61.2, 64.2, 64.5, 110.5.

6-[2-(4-Methylphenylsulfonyloxy)ethyl]-1,4-dioxospiro-[6,5]decane (3b)

p-Toluenesulfonyl chloride (14.63 g, 76.8 mmol), freshly recrystallized from petroleum ether (bp 35–60°C), was added to a solution of **3a** (11.95 g, 64 mmol) in dry pyridine. After 23 h in the refrigerator, the reaction mixture was hydrolysed with ice, acidified with 2 M HCl, then extracted with dichloromethane. Evaporation of the solvent gave **3b** (16.86 g, 78%) as a light brown liquid. ^1H NMR δ: 0.97–2.15 (m, 11H), 2.45 (s, 3H), 3.78–3.99 (m, 4H), 4.12 (t, 2H), 7.21–7.92 (dd, 4H). ^{13}C NMR δ: 21.6, 23.5, 24.4, 28.1, 29.3, 34.3, 40.7, 64.4, 64.6, 69.7, 110.0, 127.8, 129.6, 133.1, 144.5.

S-[2-(2-Oxocyclohexyl)]ethylthiouronium *p*-toluenesulfonate (4)

A solution of **3b** (16.5 g, 49 mmol) and thiourea (4.2 g, 55 mmol) was refluxed in absolute ethanol (75 mL) for 15 h; the solvent was removed in vacuo, to give a yellowish liquid. Recrystallization from water gave **4** as a white crystalline solid (12 g, 60%), mp 160–162°C; ^1H NMR (CD_3OD) δ: 1.3–2.20 (m, 8H), 2.37 (s, 3H), 2.30–2.68 (m, 2H), 2.90–3.28 (m, 2H), 3.30 (m, 1H), 7.21–7.73 (dd, 4H); ^{13}C NMR (CD_3OD) δ: 21.3, 26.2, 29.1, 29.2, 30.8, 35.4, 42.9, 50.2, 126.9, 129.9, 141.8, 143.4, 173.1, 215.8.

2-(2-Chlorosulfonylethyl) cyclohexanone (5)

A solution of **4** (5 g, 12 mmol) in water was added quickly to an ice-cooled saturated solution of chlorine in water. The reaction mixture was stirred vigorously for 1 min with a constant flow of chlorine. Extraction with dichloromethane was quickly followed by brief washings with a small amount of aqueous sodium bisulfite. Evaporation of the solvent gave **5** as a colourless liquid (2.27 g, 84%). IR ν_{max}: 2939 (m), 2864 (m), 1709 (s), 1375 (s), 1169 (s) cm^{-1}; ^1H NMR δ: 1.33–2.45 (m, 10H), 2.48–2.67 (m, 1H), 3.64–3.99 (m, 2H); ^{13}C NMR δ: 24.7, 24.9, 27.7, 34.3, 41.9, 48.1, 63.3, 211.4.

3,4,4a,5,6,7,8-Hexahydro-1*H*-2,1-benzothiazine 2,2-dioxide (6)

Anhydrous ammonia was bubbled into dichloromethane and **5** (224 mg, 1 mmol) was added quickly. The reaction mixture was stirred for 1 h with a constant flow of ammonia. Work-up gave **6** as a light yellow liquid (166 mg, 88%). IR ν_{max}: 3256–3277 (br, m), 2938 (s), 2864 (s), 1620 (s), 1323 (s), 1155 (s) cm^{-1}; ^1H NMR δ: 1.11–2.72 (m, 11H), 2.96–3.46 (m, 2H); ^{13}C NMR δ: 24.9, 25.5, 26.8, 33.9, 39.0, 39.7, 44.5, 188.5.

trans- and *cis*-Octahydro-1*H*-2,1-benzothiazine 2,2-dioxide (7 and 8)

$LiAlH_4$ (0.5 g, 13 mmol) was added to a solution of **6** (2 g, 10 mmol) in dry THF and the reaction mixture was stirred for 1 h at room temperature. Work-up gave a mixture of the *trans* and *cis* isomers (**7** and **8**) in a 60:40 ratio as judged from the ^1H NMR of the reaction mixture, as an oil (1.7 g, 85%). The reaction mixture was separated on thick-layer preparative plates; eluting three times with 1:3 ethyl acetate:petroleum ether (bp 35–60°C) gave **7** (*trans* isomer) as the upper band and **8** (*cis* isomer) as the lower band, both as white solids; **7**: recrystallized from ether; mp 123–125°C, IR ν_{max}: 3364 (br, w), 2936 (m), 1451 (w), 1402 (m), 1339 (s), 1281 (w), 1153 (s), 1113 (w) cm^{-1}; ^1H NMR δ: 0.98–1.40 (m, 5H), 1.67–2.10 (m, 6H), 2.95–3.06 (m, 1H), 3.12 (td, 1H, J = 11 Hz, J = 3.5 Hz), 3.25 (dt, 1H, J = 13 Hz, J = 3.5 Hz), 4.1 (d, 1H); ^{13}C NMR δ: 24.7, 25.4, 30.4, 30.9 32.5, 41.1, 50.3, 59.6; Exact Mass calcd. for $C_8H_{15}NO_2S$: 189.0823; found: 189.0819; **8**: recrystallized from ether; mp 134–135°C, IR ν_{max}: 3380 (br, w), 2935 (m), 1450 (w), 1404 (w), 1323 (s), 1288 (w), 1176 (s), 1148 (s) cm^{-1}; ^1H NMR δ: 1.22–2.05 (m, 10H), 2.28–2.45 (m, 1H), 2.96–3.10 (m, 2H), 3.77 (s, 1H), 4.72 (s, NH, 1H); ^{13}C NMR δ: 19.8, 23.8, 25.0, 28.8, 30.2, 32.6, 44.5, 54.5; Exact Mass calcd. for $C_8H_{15}NO_2S$: 189.0823; found: 189.0817.

trans-Octahydro-1-methyl-1*H*-2,1-benzothiazine 2,2-dioxide (2)

Compound **7** (99 mg, 0.52 mg) was added to a solution of KOH (70 mg) in ethanol (5 mL); the reaction mixture was stirred for 20 min, after which methyl iodide (5 mL, large excess) was added. The above reaction mixture was stirred for 23 h at room temperature. The ethanol was removed on the rotary evaporator and then worked up to give **2** as a white solid (91 mg, 85%), which was recrystallized from ether:petroleum ether (bp 35-60°C), mp 58-60°C; IR ν_{max}: 2940 (m), 1337 (s), 1288 (w), 1153 (s), 1128 (m), 907 (m) cm^{-1}; ^1H NMR δ: 1.0–1.56 (m, 5H), 1.67–2.05 (m, 6H), 2.75 (s, 3H), 2.92–3.15 (m, 2H), 3.40 (td, J = 11 Hz, J = 3.7 Hz); ^{13}C NMR δ: 25.0, 25.3, 29.4, 30.5, 30.6, 31.8, 34.0, 45.5, 63.0; Exact Mass calcd. for $C_9H_{17}NO_2S$: 203.0980; found: 203.0980. ^1H and ^{13}C NMR spectra (Gemini 300) of **2** in CD_2Cl_2 or in CD_2Cl_2:$CFCl_3$ (1:1) from room temperature to –90°C showed only broadening of peaks assignable to the low solubility of **2** at low temperature, and no sign of additional signals.

© 1998 NRC Canada

Table 2. Crystal data and structure refinement details.

Compound	**7**	**2**
Empirical formula	$C_8H_{15}NO_2S$	$C_9H_{17}NO_2S$
Formula weight	189.27	203.30
Temperature (K)	297(2)	296(2)
Wavelength (Å)	Mo Kα, λ = 0.71073	
Crystal system	Monoclinic	
Space group	$P2_1/c$ (No. 14)	
Unit cell dimensions	a = 14.835(3)	a = 9.410(4)
	b = 6.8870(10)	b = 10.179(2)
	c = 9.286(2)	c = 11.271(2)
	β = 92.85(3)	β = 102.10(2)
Volume (Å^3)	947.6(3)	1055.6(5)
Z	4	
Density (calculated)	1.327 Mg m^{-3}	1.279 Mg m^{-3}
Absorption coefficient	0.303 mm^{-1}	0.277 mm^{-1}
F(000) electrons	408	440
Crystal size (mm)	0.19 × 0.27 × 0.34	0.18 × 0.17 × 0.35
θ range for data (deg)	2.75–25.00	2.21–29.96
Index ranges	$-17 \le h \le 17$	$0 \le h \le 13$
	$-8 \le k \le 1$	$0 \le k \le 14$
	$-1 \le l \le 11$	$-15 \le l \le 15$
Reflections collected	2336	3248
Independent reflections	1660 [R(int) = 0.0147]	3080 [R(int) = 0.0171]
Refinement method	Full-matrix least squares on F^2	
Data / parameters	1659 / 110	3078 / 119
Goodness-of-fit on F^2	1.053	1.008
Final R indices [I>2σ(I)]	R = 0.0324, wR_2 = 0.0824	R = 0.0465, wR_2 = 0.1183
R indices (all data)	R = 0.0408, wR_2 = 0.0901	R = 0.1192, wR_2 = 0.1548
Largest peak and hole	0.269 and –0.222 e Å^{-3}	0.276 and –0.245 e Å^{-3}

X-ray crystallography

Structure solution and refinement

Crystals of *trans*-octahydro-1*H*-2,1-benzothiazine-2,2-dioxide (**7**) are colorless transparent prisms. A preliminary examination carried out on a Siemens P4 diffractometer, using the XSCANS software (26) running on a PC, established the space group and cell dimensions. The crystal density was measured by the neutral buoyancy method in aqueous zinc chloride solution. Data collection of one quadrant was carried out in the ω–2θ scan mode at variable scan speeds within a maximum time per datum of 60 s. Stationary background estimates were made at scan limits. Standard reflections were monitored every 180 min of X-ray exposure time and showed no change. Lorentz, polarization, and decay corrections were applied using the Siemens XSCANS program, but no absorption correction was made. In all there were 1660 unique data for structure solution and refinement.

Crystals of *trans*-octahydro-1-methyl-2,1-benzothiazine-2,2-dioxide (**2**) are colorless transparent prisms. A preliminary examination carried out on an Enraf–Nonius CAD4 diffractometer using the EXPRESS software (27) running on a Microvax II established the space group and cell dimensions. The crystal density was measured by the neutral buoyancy method in aqueous zinc chloride solution. Data collection of one quadrant was performed in the ω–2θ scan mode at variable scan speeds within a maximum time per datum of 60 s. Background estimates were made at 25% scan extensions on each side. Standard reflections were monitored every 180 min of X-ray exposure time, and did not vary. Lorentz, polarization, and decay corrections were applied, but no absorption correction. There was a total of 3080 unique data for structure solution and refinement. Crystal and experimental data for both compounds are summarized in Table 2.

The structures were solved by direct methods (SHELXS) (28) and refined by full-matrix least-squares techniques on F^2 (SHELX93) (29). All but H atoms were assigned anisotropic thermal parameters. All hydrogen atoms were located successfully by difference Fourier methods, placed in calculated positions (C—H = 0.95 Å), and included in the structure factor calculations in riding mode (29). The H atom positions of the methyl group in compound **2** were optimized through a rotating group refinement. The H(N) atom in compound **7** was clearly axial in a difference Fourier synthesis. No secondary extinction corrections were required. Analyses of variance suggested that the weighting schemes were appropriate. Refinement on F^2 converged, for compound **7** at agreement factors R = 0.0324 and R_2 = 0.0824 for 110 variables and 1659 data, and for compound **2** at values of R = 0.0465 and R_2 = 0.1183 for 119 variables and 3078 data. Total difference Fourier syntheses contained no unusual features.

Final positional parameters are given in Table 3 for both compounds, while anisotropic thermal parameters and

© 1998 NRC Canada

Table 3. Atomic coordinates ($\times 10^4$) and equivalent isotropic displacement parameters ($Å^2 \times 10^3$).

Atom	*x*	*y*	*z*	*U*(eq)
Compound 7				
S	1247(1)	–1659(1)	9217(1)	40(1)
O(1)	620(1)	–3228(3)	9262(2)	63(1)
O(2)	1567(1)	–814(2)	10564(1)	47(1)
N	2135(1)	–2438(2)	8419(2)	38(1)
C(1)	822(1)	226(4)	8099(2)	56(1)
C(2)	1575(1)	1658(3)	7794(2)	51(1)
C(3)	2381(1)	703(3)	7118(2)	38(1)
C(4)	3112(1)	2176(3)	6786(2)	50(1)
C(5)	3906(1)	1237(4)	6093(2)	59(1)
C(6)	4306(1)	–378(4)	7036(3)	62(1)
C(7)	3594(1)	–1875(3)	7384(2)	52(1)
C(8)	2796(1)	–914(3)	8071(2)	34(1)
Compound 2				
S	4076(1)	2862(1)	101(1)	55(1)
O(1)	5179(2)	2008(2)	–159(2)	87(1)
O(2)	3537(2)	3891(2)	–749(2)	72(1)
N	2673(2)	1969(2)	242(2)	43(1)
C(1)	4636(2)	3579(3)	1548(2)	57(1)
C(2)	3369(3)	4302(2)	1892(2)	56(1)
C(3)	2016(2)	3443(2)	1847(2)	45(1)
C(4)	774(3)	4251(3)	2155(3)	69(1)
C(5)	–609(3)	3455(3)	2081(3)	80(1)
C(6)	–1069(3)	2805(3)	853(3)	74(1)
C(7)	151(2)	1960(2)	574(2)	53(1)
C(8)	1514(2)	2771(2)	612(2)	39(1)
C(9)	3031(3)	710(2)	881(3)	62(1)

U(eq) is defined as one third of the trace of the orthogonalized U_{ij} tensor.

hydrogen atom parameters have been deposited as Tables S1 and S2.[5]

Acknowledgements

This work was supported by the Natural Sciences and Engineering Research Council of Canada.

References

1. J.F. King and M.S. Gill. J. Org. Chem. **61**, 7250 (1996).
2. R.U. Lemieux. Pure Appl. Chem. **25**, 527 (1971).
3. P.v.R. Schleyer and A.J. Kos. Tetrahedron, **39**, 1141 (1983).
4. G. Boche. Angew. Chem. Int. Ed. Engl. **28**, 277 (1989).
5. J.S. Grossert, J. Hoyle, T.S. Cameron, S.P. Roe, and B.R. Vincent. Can. J. Chem. **65**, 1407 (1987).
6. W.v.E. Doering and L.K. Levy. J. Am. Chem. Soc. **77**, 509 (1955).
7. D.W.J. Cruickshank. J. Chem. Soc. 5486 (1961).
8. S. Wolfe, A. Stolow, and L.A. LaJohn. Tetrahedron Lett. **24**, 4071 (1983).
9. D.A. Bors and A. Streitwieser, Jr. J. Am. Chem. Soc. **108**, 1397 (1986).
10. R. Koch and E. Anders. J. Org. Chem. 59, 4529 (1994).
11. T. Jordan, H.W. Smith, L.L. Lohr, Jr., and W.N. Lipscomb. J. Am. Chem. Soc. **85**, 846 (1963).
12. W.B. Jennings and R. Spratt. Chem. Commun. 1418 (1970).
13. J.F. King, K.C. Khemani, S. Skonieczny, and N.C. Payne. J. Chem. Soc. Chem. Commun. 415 (1988).
14. A.C. Hazell. Acta Crystallogr. Sect. B: Struct. Crystallogr. Cryst. Chem. **B30**, 2724 (1974).
15. J.F. King, K.C. Khemani, S. Skonieczny, and N.C. Payne. Rev. Heteroat. Chem. **1**, 80 (1988).
16. R.D. Bindal, J.T. Golab, and J.A. Katzenellenbogen. J. Am. Chem. Soc. **112**, 7861 (1990).
17. A. Segre, R. Viterbo, and G. Parisi. J. Am. Chem. Soc. **79**, 3503 (1957).
18. H. Booth and J.R. Everett. J. Chem. Soc. Perkin Trans. 2, 255 (1980).
19. A. McIntosh. B.Sc. Thesis, University of Western Ontario. 1990.
20. A Camerman and N. Camerman. Can. J. Chem. **53**, 2194 (1975).
21. E.L. Eliel and S. Wilen. *In* Stereochemistry of organic compounds. John Wiley & Sons, New York. 1994. p. 697.
22. S. Sato, T. Yoshioka, and C. Tamura. Acta Crystallogr. Sect. B: Struct. Crystallogr. Cryst. Chem. **B31**, 1385 (1975).
23. L.G. Vorontsova. Zh. Strukt. Khim. **7**, 280 (1966); Chem. Abstr. **65**, 4761a (1966).
24. S. Li, A.J. Kirby, and P. Deslongchamps. Tetrahedron Lett. **34**, 7757 (1993); S. Li and P. Deslongchamps. Tetrahedron Lett. **34**, 7759 (1993).
25. Z.R. Guo. Ph.D. Thesis. University of Western Ontario. 1993; J.F. King. M. Li, and Z.R. Guo. 79th Canadian Society of Chemistry Conference, St John's, Nfld., June 1996. Abstract 77.
26. XSCANS users manual, Version 2.1. Siemens X-ray Analytical, Madison, Wis. 1994.
27. Enraf–Nonius EXPRESS users manual, Enraf–Nonius, Delft, The Netherlands. 1990.
28. G.M. Sheldrick. SHELXS. Program for solution of crystal structures. University of Göttingen, Germany. 1986.
29. G.M. Sheldrick. SHELX93. Program for refinement of crystal structures. University of Göttingen, Germany. 1993

[5] Tables of hydrogen atom parameters and anisotropic thermal parameters may be purchased from: The Depository of Unpublished Data, Document Delivery, CISTI, National Research Council Canada, Ottawa, Canada K1A 0S2. The tables of hydrogen atom parameters have also been deposited with the Cambridge Crystallographic Data Centre, and can be obtained on request from The Director, Cambridge Crystallographic Data Centre, University Chemical Laboratory, 12 Union Road, Cambridge, CB2 1EZ, U.K. Tables of structure amplitudes are no longer being deposited, but are available directly from the author.

© 1998 NRC Canada

Cooperative antioxidant effects of ascorbate and thiols with di-*tert*-butylcatechol during inhibited peroxidation in solution and in sodium dodecyl sulfate (SDS) micelles

Fengde Xi and L. Ross C. Barclay

Abstract: The antioxidant activities, k_{inh}, of catechol, **1**, 4-*tert*-butylcatechol, **2**, and 3,5-di-*tert*-butylcatechol (DTBC), **3**, determined by the inhibited oxygen-uptake method during peroxidation of styrene initiated by AIBN are 55.0×10^4, 88.4×10^4, and 149×10^4 $M^{-1}s^{-1}$, respectively, and the stoichiometric factors (n) were 2.1–2.3. A decrease by 50-fold in k_{inh} for **3** and a drop of 1.1–1.4 in n observed during inhibited peroxidation of methyl linoleate in aqueous sodium dodecyl sulfate (SDS) initiated by di-*tert*-butylhyponitrile (DBHN) is attributed to hydrogen bonding by water on the antioxidant and on the intermediate di-*tert*-butylsemiquinone radical, **5**, formed in the inhibition step. Combinations of ascorbyl palmitate with **3** exhibited cooperative (not synergistic) antioxidant effects during inhibited peroxidation of styrene in solution. Combinations of ascorbic acid with **3** exhibited synergistic effects during inhibited peroxidation of methyl linoleate initiated by DBHN in SDS micelles. A profile of the effect of concentration of ascorbate on this synergism indicates a mole of **3** is regenerated per mole of ascorbate. The thiols, homocysteine, and polyethylene glycol thiol (polythiol) also exhibited synergistic effects with DTBC in this inhibition. Either ascorbate or polythiol rapidly reduces di-*tert*-butyl-*ortho*-quinone (DTBQ), **4**, to **3** in methanol or in SDS micelles, and the combination of **3** + ascorbate acted as an efficient inhibitor in this medium. The esr studies indicate the semiquinone radical, **5**, produced photochemically from **3** or spontaneously from **3** + **4** in solution, to be very persistent at room temperature. A pathway, mediated by **5**, is proposed to account for the cooperative and synergistic effects observed and for the additional combination effect discovered when the three inhibitors: **3**, ascorbate, and a thiol are used in the SDS medium. Combinations of such antioxidants are expected to be useful for inhibition of yellowing of pulps and paper with high lignin content, and to be significant in the in vivo reductions of *ortho*-quinones and semiquinone radicals formed during oxidations of various biomolecules.

Key words: catechols, ascorbate, thiols, radicals, antioxidants.

Résumé : Les activités antioxydantes, k_{inh}, du catéchol, **1**, du 4-*tert*-butylcathécol, **2**, et du 3,5-di-*tert*-butylcathécol (DTBC), **3**, déterminées par la méthode d'absorption d'oxygène inhibé pendant la peroxydation du styrène initiée par le AIBN sont respectivement de 55.0×10^4, 88.4×10^4 et 149×10^4 $M^{-1}s^{-1}$ et les facteurs stoechiométriques (n) vont 2.1–2.3. On observe une diminution de 50 fois de la valeur k_{inh} pour le composé **3** et une diminution de la valeur de n jusqu'à 1.1–1.4 lors de la peroxydation inhibée du linoléate de méthyle, dans une solution aqueuse de dodécyl sulfate de sodium (DSS), initiée par le di-*tert*-butylhyponitrile (DBHN). On attribue ces diminutions aux liaisons hydrogènes de l'eau sur l'antioxydant et sur le radical intermédiaire di-*tert*-butylsemiquinone, **5**, formé pendant l'étape d'inhibition. La combinaison du palmitate d'ascorbyle avec le radical **3** a un effet antioxydant coopératif (pas synergique) lors de la peroxydation inhibée du styrène en solution. La combinaison de l'acide ascorbique avec le radical **3** provoque un effet synergique pendant la peroxydation inhibée du linoléate de méthyle initiée par le DBHN dans des micelles de DSS. Un profil de l'effet de la concentration de l'ascorbate sur cet effet synergique indique qu'une mole du radical **3** est régénérée par mole d'ascorbate. Les thiols, l'homocystéine et un polyéthylène glycol thiol (polythiol) ont également des effets synergiques avec le DTBC lors de cette inhibition. L'ascorbate ou le polythiol réduit rapidement la di-*tert*-butyl-*ortho*-quinone (DTBQ), **4**, en **3** dans le méthanol ou dans des micelles de DSS, et la combinaison de **3** + l'ascorbate agit comme un inhibiteur efficace dans ce milieu. Les études de rpe indiquent que le radical semiquinone, **5**, produit photochimiquement à partir de **3** ou spontanément à partir du mélange de **3** + **4** en solution, est très persistant à la température ambiante. On propose un mécanisme impliquant le radical **5** pour tenir compte des effets coopératif et synergique observés et de l'effet de combinaison additionnelle découvert lorsque les trois inhibiteurs : le composé **3**, l'ascorbate et un thiol sont utilisés dans une solution aqueuse de DSS. On s'attend à ce que les combinaisons de tels antioxydants soient utiles pour l'inhibition du jaunissement des pulpes et du papier riches en lignine, et soient importantes dans les réductions in vivo des radicaux *ortho*-quinones et semiquinones formés pendant l'oxydation de diverses biomolécules.

Mots clés : catéchols, ascorbate, thiols, radicaux, antioxydants.

[Traduit par la rédaction]

Received August 25, 1997.

F. Xi and L.R.C. Barclay.[1] Department of Chemistry, Mount Allison University, Sackville, NB E4L 1G8, Canada.

[1]Author to whom correspondence may be addressed. Telephone: (506) 364–2369. Fax: (506) 364–2313. E-mail: rbarclay@mta.ca

© 1998 NRC Canada

Introduction

The formation of coloured *ortho*-quinonoid structures, from intermediate substituted aryloxyl radicals, in lignin is known to be responsible for the major portion of the undesirable yellowing that develops when mechanical pulps are exposed to light and oxygen (1–3). However, both polymeric thiols and ascorbate are able to readily reduce *ortho*-quinones to colourless hydroquinones (4, 5), and the natural thiol amino acid, homocysteine, is known to rapidly regenerate ascorbate from its oxidation product, dehydroascorbic acid (6). Consequently, a combination of ascorbate with thiols is expected to be a possible strategy to inhibit the yellowing of mechanical pulps and paper with high lignin content. In this study we used catechol, **1**, 4-*tert*-butylcatechol, **2**, 3,5-di-*tert*-butylcatechol, (DTBC) **3**, as antioxidants. 3,5-Di-*tert*-butyl-*ortho*-quinone (DTBQ), **4**, derived from **3** is used as a model for the *thermal* oxidative yellowing. This study employs free-radical chain peroxidation under controlled conditions using azo initiators so that the antioxidant activities of **1**–**3** are determined. In addition, these quantitative kinetic studies permit evaluations of the effect of combinations of antioxidants. Ascorbate, thiols, and combinations of these with **3** are used as inhibitors to evaluate cooperative or synergistic antioxidation and to study the reductive regeneration of **3** from **4**.

The quantitative kinetic method of autoxidation is a very useful method to determine the activities of antioxidants and to examine the effects of combinations of antioxidants for possible cooperative or synergistic action. Uninhibited autoxidation of organic substrates follows the free-radical mechanism shown in eqs. [1]–[4] when oxidation is initiated by an azo initiator.

Initiation:

[1] $\text{R-N=N-R} \xrightarrow{k_i} 2\text{R}\cdot + \text{N}_2$, rate $= R_i$

Propagation:

[2] $\text{R}\cdot + \text{O}_2 \xrightarrow{\text{fast}} \text{ROO}\cdot$

[3] $\text{ROO} + \text{RH (substrate)} \xrightarrow{k_p} \text{ROOH} + \text{R}\cdot$

Termination:

[4] $\text{ROO}\cdot + \text{ROO}\cdot \xrightarrow{2k_t}$ nonradical products $+ \text{O}_2$

The rate law for this mechanism is given in eq. [5], where k_p is the propagation rate constant, $2k_t$, the termination rate constant, [RH], the substrate concentration, and R_i, the rate of chain initiation.

[5] $$-\text{d}[\text{O}_2]/\text{d}t = k_p/2k_t^{1/2}[\text{RH}]R_i^{1/2}$$

The quantitative kinetic method employs azo initiators with known rate constants of decomposition, k_i, and efficiency, e, of initiation, so that R_i is controlled, as shown in eq. [6].

[6] $$R_i = 2ek_i\,[\text{R-N=N-R}]$$

During inhibited oxidation by a phenolic antioxidant (ArOH), efficient antioxidants can trap two peroxyl radicals, as represented by eqs. [7] and [8].

[7] $\text{ArOH} + \text{ROO}\cdot \xrightarrow{k_{inh}} \text{ArO}\cdot + \text{ROOH}$

[8] $\text{ArO}\cdot + \text{ROO}\cdot \rightarrow \text{ArOROO}$

During this inhibition, oxygen uptake is suppressed until the antioxidant is consumed. The inhibition period, τ, has a simple relationship to R_i, which can be measured using eq. [9] where n is the stoichiometric factor, the number of peroxyl radicals trapped per antioxidant molecule.

[9] $$R_i = n\,[\text{ArOH}]/\tau$$

Using a steady stable approximation, the rate law during suppressed oxidation can be expressed in terms of R_i, the concentrations of substrate and antioxidant, and the rate constants for propagation, k_p, and inhibition, k_{inh}, according to eq. [10]:

[10] $$-\text{d}[\text{O}_2]/\text{d}t = (k_p/k_{inh}\,[\text{RH}]R_i)/n[\text{ArOH}]$$

These quantitative kinetic methods have been applied as models of biological systems to determine activities of antioxidants in heterogeneous systems such as lipids in aqueous micelles (6–13). In this paper we report on (*i*) the antioxidant activities (k_{inh} of eq. [7]) of catechols **1**, **2**, and **3** during inhibited peroxidation of styrene in solution and of methyl linoleate and in 0.50 M sodium dodecyl sulphate (SDS), (*ii*) direct and azo-initiated oxidation of **3**, and (*iii*) the effect of ascorbate, ascorbyl palmitate, homocysteine, and a polythiol[2] both alone and in combinations of ascorbate + thiol as inhibitors of azo-initiated thermal peroxidation. Reactions in styrene solution were initiated by azobisisobutyrylnitrile (AIBN) where R_i is measured using 2,2,5,7,8-pentamethyl-4-hydroxylchroman (PMHC). Reactions in aqueous SDS micelles are initiated by di-*tert*-butylhyponitrite (DBHN) or azobis(amidinopropane hydrochloride) (ABAP), and the R_i is measured using 2-carboxy-2,5,7,8-tetramethyl-4-hyroxychroman (Trolox).

Results

1. The antioxidant activities of catechols 1–3 and their stoichiometric factors (*n*)

The antioxidant activities of **1**, **2**, and **3** were determined by measurements of the oxygen uptake during the course of the inhibition period, referred to herein as the IOU method. The integrated form of the equation for inhibition, eq. [11], was used as before (7), and k_{inh} was obtained from a plot of the linear equation, $\Delta[\text{O}_2]_t$ versus $-\ln(1 - t/\tau)$, where the slope is equal to $k_p[\text{RH}]/k_{inh.}$

[11] $$\Delta[\text{O}_2]_t = (-k_p/k_{inh}) \times [\text{RH}]\ln(1 - t/\tau)$$

Values of k_p determined separately in styrene (41.0 M s^{-1}) (14) and for linoleate in 0.50 M SDS (37.0 M s^{-1}) (15) under these conditions were used in the calculations.

The stoichiometric factor, n, was determined relative to the value of $n = 2$, which we used for the model compound PMHC (16),[3] by determination of R_i employing PMHC (eq. [9]) and measurements of the induction periods for known amounts of **1**, **2**, and **3** under the same conditions. The n factor for **1**, **2**, and **3** are then calculated using eq. [12].

[2] Polythiol prepared from polyethylene glycol and thiolactic acid, referred to as PEG 3400, was kindly provided by Dr. J.K.S. Wan of the Department of Chemistry, Queen's University, Kingston, Ont.

[3] The actual value for PMHC under these conditions was found to be $n = 1.89$, relative to $n = 2.00$ for α-tocopherol (16).

© 1998 NRC Canada

Fig. 1. Autoxidation of styrene (4.37 M) in chlorobenzene initiated by AIBN (1.85×10^{-2} M) at 30°C. (*a*) *A*, uninhibited reaction; *B*, inhibited by catechol (5.16×10^{-6} M); *C*, inhibited by 4-*tert*-butylcatechol (5.70×10^{-6} M); *D*, inhibited by 3,5-di-*tert*-butylcatechol (5.16×10^{-6} M); $R_i = 2.27 \times 10^{-9}$ M s^{-1}. (*b*) Plots of oxygen consumed versus $-\ln(1 - t/\tau)$ for peroxidation of styrene in chlorobenzene initiated by AIBN; ∇, inhibited by catechol; ○, inhibited by 4-*tert*-butylcatechol; Δ, inhibited by 3,5-di-*tert*-butylcatechol. Amounts are given in Table 1. The antioxidant activities, k_{inh}, are obtained from the slopes which equal $k_p/k_{inh} \times$ [R-H] (see text).

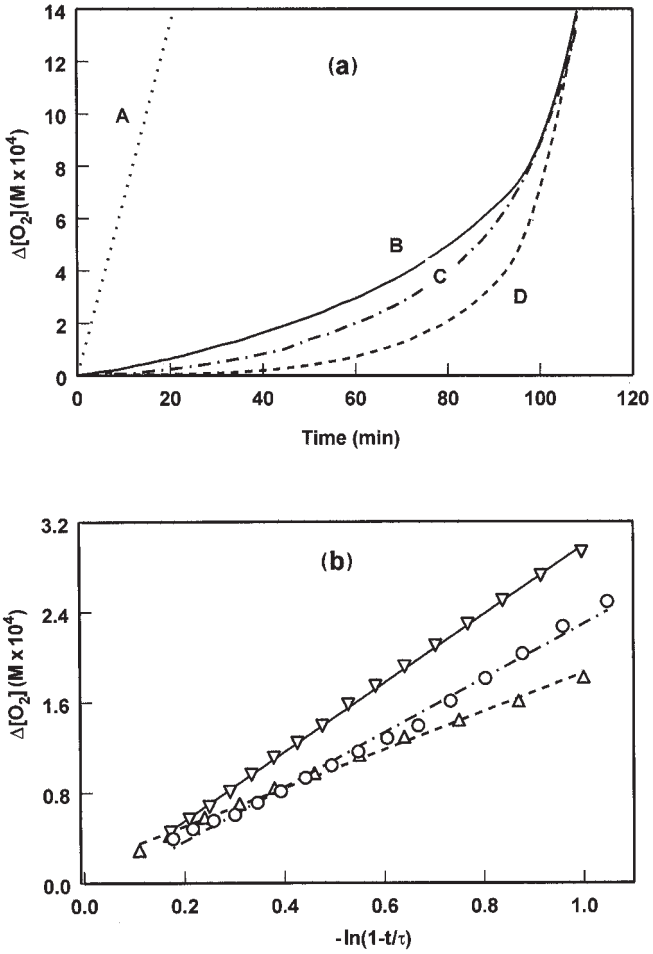

[12] $n = R_i \times \tau/[\text{ArOH}]$

(a) Antioxidant activities in homogeneous solution

Initial experiments on the effects of catechols were conducted in homogeneous solution during inhibited oxidative polymerization of styrene initiated by AIBN, since reliable data on various phenolic antioxidants are available in the literature (16, 17). The experimental profiles of inhibition by **1**, **2**, and **3** (shown in Fig. 1*a*) indicate that they possess antioxidant properties. Their antioxidant activities k_{inh} are determined by the plot of oxygen uptake during inhibition periods versus $-\ln(1 - t/\tau)$ (Fig. 1*b*). The values are in the order **3** > **2** > **1** (Table 1). The disubstituted catechol **3** exhibits significant antioxidant activity, since its $k_{inh} = 149 \times 10^4$ M^{-1} s^{-1} is approximately half that of α-tocopherol (vitamin E), one of the most active natural chain-breaking antioxidants (17).

Fig. 2. Autoxidation of methyl linoleate (see Table 2 for amount) in 3.00 mL 0.50 M SDS – phosphate buffer (pH 7) at 37°C. (a) *A*, initiated by DBHN (2.38×10^{-5} mol), uninhibited reaction; *B*, initiated by DBHN (3.14×10^{-5} mol), inhibited by 3,5-di-*tert*-butylcatechol (2.40×10^{-8} mol), $R_i = 3.47 \times 10^{-7}$ M s^{-1}; *C*, initiated by ABAP (2.5×10^{-5} mol), inhibited by 3,5-di-*tert*-butylcatechol (3.16×10^{-8} mol), $R_i = 3.90 \times 10^{-9}$ M s^{-1}. (*b*) Plots of oxygen consumed versus $\ln(1 - t/\tau)$ for peroxidation of methyl linoleate in SDS micelles, inhibited by 3,5 di-*tert*-butylcatechol; ∇, initiated by DBHN; Δ, initiated by ABAP. Amounts are given in Table 2. The antioxidant activities, k_{inh}, are obtained from the slopes which equal $k_p/k_{inh} \times$ [R-H] (see text).

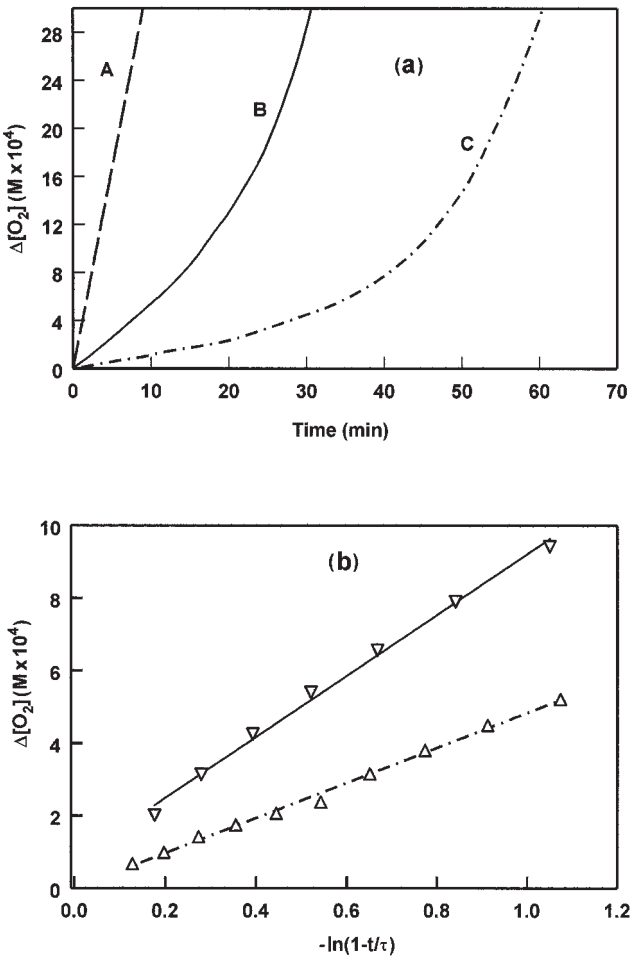

(b) In aqueous SDS micelles

The typical profiles of DBHN- and ABAP-initiated peroxidations of methyl linoleate in aqueous micelles showing the effect of **3** are illustrated in Fig. 2*a*. Linear plots for the integrated expression obtained for **3** are given in Fig. 2*b*. The data of measurements are given in Table 2. The antioxidant activity of **3**, $k_{inh} = (3.31–2.32) \times 10^4$ M^{-1} s^{-1}, dropped 45- to 64-fold in micelles, compared with k_{inh} in homogeneous solution (see Table 1).

Solutions of DTBC in 0.50 M SDS were found to undergo oxidation directly at 37°C. After 2 h, which is the average time for most inhibition periods for azo-initiated experiments, approximately 3% of **3** was consumed according to oxygen-uptake studies and measurement of the amount of quinone, **4**, formed by determination of the absorbance at 412 nm.

© 1998 NRC Canada

Table 1. Antioxidant activities of catechols during AIBN thermally initiated peroxidation of styrene [a] at 30°C.

No.	Initiator AIBN ($M \times 10^2$)	Antioxidant ($M \times 10^6$)	Inhibition period ($s \times 10^{-3}$)	R_i[b] ($M\ s^{-1} \times 10^9$)	Chain-length range	k_{inh}[c] ($M^{-1}\ s^{-1} \times 10^{-4}$)	n[d]
		1					
1	1.85	6.20	6.12	2.27	38–77	55.6	2.24
2	1.84	5.16	5.58	2.17	37–83	53.2	2.35
3	1.84	5.16	5.70	2.09	35–79	56.1	2.31
						55.0 ± 1.8	2.30 ± 0.06
		2					
1	1.83	5.70	5.54	2.27	16–37	87.0	2.21
2	1.83	5.73	5.49	2.16	15–35	92.6	2.07
3	1.75	5.62	5.45	2.09	17–34	85.7	2.03
						88.4 ± 4.2	2.11 ± 0.10
		3					
1	5.09	9.05	3.42	6.07	16–30	142	2.30
2	5.09	9.07	3.46	6.07	17–31	155	2.31
3	4.98	9.05	3.60	5.94	18–42	150.8	2.36
						149 ± 7	2.32 ± 0.04

[a] 1.00 mL styrene in 1.00 mL chlorobenzene was used in measurements of antioxidant activities of catechol **1** and 4-TBC **2**; 1.50 mL styrene in 0.5 mL chlorobenzene was used for measurements using DTBC **3**.

[b] The rate of chain initiation was measured with PMHC; see eq. [9] in text.

[c] Inhibition rate constants were determined from the slope of the plot of $\Delta[O_2]_t$ versus $-\ln(1 - t/\tau)$; see text.

[d] The stoichiometric factor was determined relative to $n = 2$ for PMHC using the relationship $n = R_i \times \tau/[ArOH]$.

Table 2. Antioxidant activity of DTBC during DBHN thermally initiated peroxidation of methyl linoleate[a] in SDS micelles and in phosphate buffer (pH 7) at 37°C.

No.	Initiator[b] ($M \times 10^2$)	Antioxidant DTBC **3**[b] ($M \times 10^4$)	Inhibition period ($s \times 10^{-3}$)	R_i[b,c] ($M\ s^{-1} \times 10^9$)	Chain-length range	k_{inh}[d] ($M^{-1}s^{-1} \times 10^{-4}$)	n[c]
	DBHN						
1	6.34	5.67	2.25	347	5–7	2.25	1.42
2	6.36	5.67	2.10	389	4–8	2.29	1.44
3	6.36	4.54	1.62	389	3–7	2.44	1.38
						2.32 ± 0.12	1.41 ± 0.03
	ABAP						
1	0.837	1.01	2.55	3.90	4–10	3.39	1.06
2	0.826	1.01	2.82	3.71	4–10	3.32	1.05
3	0.826	1.01	3.00	3.71	4–10	3.24	1.11
						3.31 ± 0.08	1.07 ± 0.04

[a] 70 μL methyl linoleate in 3 mL 0.50 M SDS micelles was used in DBHN-initiated peroxidation; 50 μL methyl linoleate in 3.00 mL 0.5 M SDS micelles was used in ABAP-initiated peroxidation.

[b] Concentrations of DBHN and DTBC are mol/L of micelles, using a calculated volume of 3.75×10^{-4} L for 3.00 mL of 0.50 M SDS (see ref. 11); amounts of DBHN were measured spectrally; concentration of ABAP is mol/L of the bulk phase, 2.00 mL.

[c] The rate of chain initiation was measured with Trolox; see eq. [9] in text.

[d] Inhibition rate constants were determined from the slope of the plot of $\Delta[O_2]_t$ versus $-\ln(1 - t/\tau)$; see text.

2. Cooperative effects of ascorbate and thiols on the inhibited peroxidation by DTBC

(a) In homogenous solution

A number of experiments were carried out to determine the cooperative inhibiting effects of ascorbyl palmitate and polythiol with DTBC on peroxidation of styrene, a phenomenon observed previously with ascorbate and α-tocopherol and its analogues (11, 18–23). The results show that induction periods for combinations of ascorbyl palmitate with DTBC are longer than that for DTBC alone, as illustrated in Fig. 3, although the induction periods for the combination ($\tau_{DTBC+AP}$) are less than the sum of separate induction periods ($\tau_{DTBC} + \tau_{AP}$) by DTBC and ascorbyl palmitate. The combination of polythiol with DTBC resulted in the same effect (not shown). The data of cooperative inhibiting activities are given in Table 3. The extensions of induction periods are indicative of regeneration of DTBC from its phenoxyl free radical by ascorbyl palmitate and polythiol. The product of the extension, τ_{ext}, and the rate of chain initiation, R_i, is a measure of the stoichiometric factor for regeneration of DTBC by ascorbyl palmitate or polythiol as shown in eq. [13].

© 1998 NRC Canada

Fig. 3. Autoxidation of styrene (7.77 M) in tetrachloroethane (2.25 mL), thermally initiated by AIBN (3.71×10^{-2} M) at 30 °C. *A*, uninhibited reaction; *B*, inhibited by ascorbyl palmitate (5.01×10^{-6} M); *C*, inhibited by 3,5-di-*tert*-butylcatechol (5.01×10^{-6} M); *D*, inhibited by 3,5-di-*tert*-butylcatechol (5.01×10^{-6} M) and ascorbyl palmitate (5.01×10^{-6} M); $R_i = 4.17 \times 10^{-9}$ M s^{-1}.

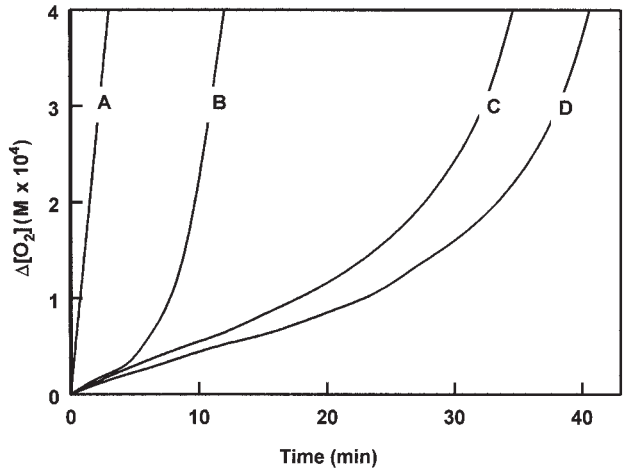

[13] $n = R_i\,[\tau_{DTBC+AP(thiol)} - \tau_{DTBC}]/AP(thiol)$

The value of *n* obtained under these conditions is 0.22 for ascorbyl palmitate and 0.19 for polythiol, assuming that both of the -SH groups of polythiol are involved. The stoichiometric factor is very low. This is probably due to autoxidation of ascorbyl palmitate and polythiol in the presence of oxygen under these conditions.

(b) In aqueous SDS micelles

The relative cooperative antioxidant effects of ascorbate, homocysteine, and polythiol with DTBC during peroxidation of methyl linoleate initiated by DBHN were determined by experiments conducted in 0.50 M SDS. Some typical profiles of oxygen uptake are illustrated in Fig. 4 to show the effect of ascorbate and DTBC, separately and in combination. The data are summarized in Tables 4 and 5. As can be seen in Fig. 4*a*, ascorbate when used alone was a rather poor inhibitor of autoxidation of methyl linoleate in SDS micelles. These results are in agreement with those of earlier studies (8). The combination of ascorbate with DTBC alone was found to greatly extend the inhibition period. The data in Table 4 show that the lengths of induction periods obtained by combinations of ascorbate and DTBC ($\tau_{(C+DTBC)}$) are longer than the sum of the separate induction periods using the same amounts of ascorbate and DTBC. The amount of synergism observed varies from 23 to 57%, depending on the ratio of ascorbate/DTBC. The quantitative studies on the effects of different ratios of ascorbate/DTBC on the length of induction periods give further insight into the efficiency with which ascorbate in the aqueous phase regenerates DTBC in the micellar phase. The extension $\tau_{(C+DTBC)} - \tau_{DTBC}$ (see column 6 in Table 5) can be taken as an indication of the amount of DTBC regenerated for a particular rate of chain initiation, R_i. Thus, the product $R_i \times (\tau_{(C+DTBC)} - \tau_{DTBC})$ is a measure of the amount of radicals trapped by ascorbate, and the product is divided by the number of moles of ascorbate to obtain the stoichiometric factor (*n*) of ascorbate, i.e., the amount of DTBC regenerated per mole of

Fig. 4. Autoxidation of methyl linoleate (5.43×10^{-5} mol) in 2.00 mL 0.50 M SDS – phosphate buffer (pH 7), initiated by DBHN (5.75×10^{-6} mol) at 37°C. (*a*) *A*, uninhibited reaction; *B*, inhibited by ascorbic acid (4.54×10^{-8} mol); *C*, inhibited by 3,5-di-*tert*-butylcatechol (4.54×10^{-8} mol); *D*, inhibited by 3,5-di-*tert*-butylcatechol (4.54×10^{-8} mol) and ascorbic acid (4.54×10^{-8} mol); $R_i = 1.08 \times 10^{-11}$ mol s^{-1}. (*b*) Plot of extension of the induction period $\times R_i$ versus moles of ascorbate (see text and Table 5).

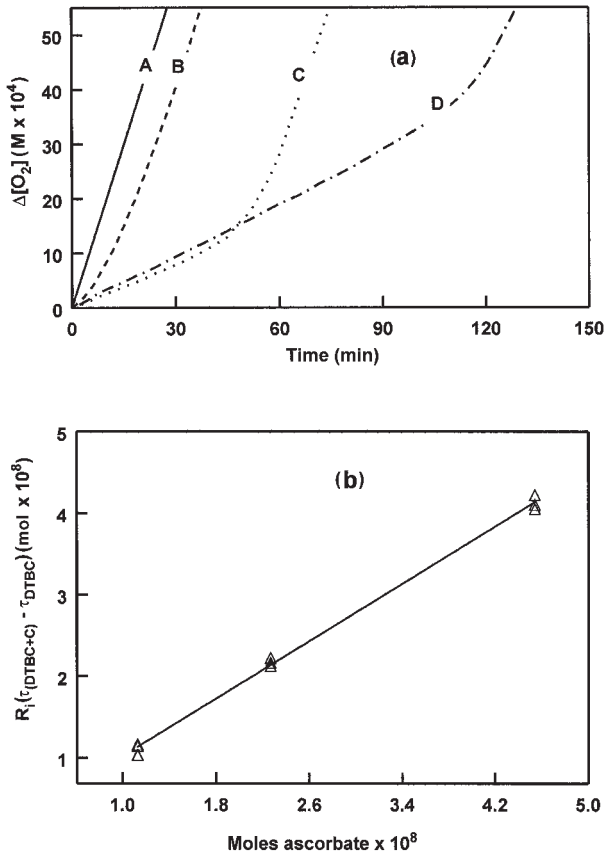

ascorbate. The stoichiometric factor for this interaction was found to drop as the ratio of ascorbate/DTBC was varied from 0.25 to 2. At low concentrations of added ascorbate, the value of *n* was found to be approximately 1, while at higher combination ratio the value dropped to 0.68, probably due to significant loss of ascorbate via its own autoxidation. A plot of the product $R_i \times (\tau_{(C+DTBC)} - \tau_{DTBC})$ versus the moles of ascorbate added to the reaction system is drawn as shown in Fig. 4*b*. The slope of the plot gives a value of $n = 0.71$ up to 9.08×10^{-8} mol ascorbate. Similar synergetic inhibiting effects on peroxidation of methyl linoleate resulted from combinations of DTBC with homocysteine and polythiol, as shown in Figs. 5*a* and *b*. The data are summarized in Table 6. Again, the induction periods for the combinations are longer than the sum of induction periods by DTBC, homocysteine, and polythiol, separately. The value of the stoichiometric factor is 0.46 for homocysteine, 0.51 for polythiol. The degradation of polythiol was determined under the experimental conditions described above. Figure 5*b* shows that in the case of the combination of DTBC and polythiol (curve C) the rate of uptake does not return to the uninhibited rate at the end of the induction period. We find by

© 1998 NRC Canada

Table 3. Cooperative inhibiting effect of ascorbyl palmitate (AP) and polythiol with di-*tert*-butylcatechol on the thermally initiated autoxidation of styrene[a] in solution at 30°C.

Initiator AIBN ($M \times 10^2$)	Substrate styrene (M)	Inhibitors ($M \times 10^6$) DTBC	AP	Inhibition period ($s \times 10^{-3}$) τ_{DTBC}	$\tau_{(DTBC+AP)}$	Extension τ_{ext} ($s \times 10^{-3}$)	R_i ($M\ s^{-1} \times 10^9$)	$R_i \times \tau_{ext}$ ($M \times 10^6$)	$R_i \times \tau_{ext}$/AP
3.71	7.768	5.01	5.01	1.74	2.04	0.30	4.17	1.26	0.25
3.64	7.768	5.01	5.01	1.89	2.17	0.28	4.15	1.19	0.24
3.64	7.768	5.01	9.98	1.97	2.47	0.50	4.02	2.03	0.20
3.69	7.768	4.97	9.95	1.85	2.34	0.48	3.96	1.94	0.20
									0.22 ± 0.03
			Thiol		$\tau_{(DTBC+Thiol)}$				$R_i \times \tau_{ext}$/2 thiol[b]
5.30	7.768	4.62	4.56	1.12	1.43	0.32	5.85	1.91	0.209
5.30	7.768	4.62	9.09	1.20	1.67	0.47	5.99	2.84	0.156
									0.37 ± 0.05

[a] 1.5 mL styrene in 0.5 mL tetrachloroethane were used in each experiment.
[b] Each polythiol molecule contains two effective groups, SH.

Table 4. Inhibiting effects of C and DTBC, separately and in combination, on DBHN-initiated peroxidation of linoleate[a] in micelles at 37°C.

Initiator DBHN ($mol \times 10^6$)	Inhibitors ($mol \times 10^8$) C	DTBC	Inhibition period ($s \times 10^{-3}$) τ_C	τ_{DTBC}	τ_{C+DTBC}	$\tau_{(C+DTBC)} - (\tau_C + \tau_{DTBC})$ ($s \times 10^{-3}$)	R_i ($mol\ s^{-1} \times 10^{11}$)
5.75	1.13		0.23				1.21
		4.52		2.90			
	1.13	4.52			3.86	0.73	
5.58	2.27		0.41				1.24
		4.52		3.05			
	2.27	4.52			4.61	1.15	
5.18	4.54		0.90				1.08
		4.52		3.67			
	4.54	4.52			6.35	1.78	
4.58	9.08		1.40				1.02
		4.52		3.75			
	9.08	4.52			8.10	2.95	

[a] 5.43×10^{-5} mol methyl linoleate used in each experiment. In experiments using both water-soluble inhibitors (C, ascorbate) and DTBC, amounts are given in moles.

thiol analysis that this is due to residual polythiol after the break in the inhibition period. This polythiol alone does not give a definite inhibition period but only causes a reduction in the rate of oxygen uptake.

Experiments were carried out to determine if combinations of homocysteine and polythiol further enhance cooperative inhibition effects of DTBC and ascorbate on DBHN-initiated peroxidation of linoleate in micelles. A typical trace shown in Fig. 6 indicates that a thiol does afford additional cooperative antioxidation activities when used with DTBC and ascorbate. The results are summarized in Table 7.

3. Regeneration of DTBC, 3, by ascorbates and thiols and of ascorbate by homocysteine and polythiol

*(a) Regeneration of DTBC, **3**, from di-*tert*-butyl-ortho-quinone (DTBQ) with ascorbate and thiols in organic solvent or in SDS micelles*

Experiments were carried out by uv measurement to determine the effects of ascorbate, homocysteine, and polythiol on the oxidation product, DTBQ, of DTBC. Results of these experiments are illustrated in Fig. 7. Ascorbyl palmitate took 2 h to regenerate 43% of DTBC when a ratio of ascorbyl palmitate/DTBQ of 1 in tetrachloroethane was used. On the other hand, either ascorbyl palmitate or ascorbate regenerated DTBC *rapidly* in SDS micelles. Homocysteine and polythiol are somewhat slower to regenerate DTBC in SDS micelles than ascorbate, however, they regenerate 87% and 93% DTBC, respectively, within 60 min.

(b) Regeneration of ascorbate from dehydroascorbic acid with homocysteine or polythiol in SDS micelles

It is reported that homocysteine is able to regenerate ascorbate from its oxidation product, dehydroascorbic acid, in aqueous buffer. In this study, we find that either homocysteine or polythiol acts on dehydroascorbic acid to regenerate ascorbic acid, as previously mentioned (6), measured by analysis using potassium ferricyanide.

© 1998 NRC Canada

Table 5. Inhibiting effect of DTBC and combination of DTBC with C on peroxidation of linoleate[a] in micelles at 37°C.

Initiator DBHN ($mol \times 10^6$)	Inhibitors ($mol \times 10^8$)		Inhibition period ($s \times 10^{-3}$)		Extension τ_{ext} ($s \times 10^{-3}$)	R_i ($mol\ s^{-1} \times 10^{11}$)	$R_i \times \tau_{ext}$ ($mol \times 10^8$)	$R_i \times \tau_{ext}$/C
	DTBC	C	τ_{DTBC}	$\tau_{(C+DTBC)}$				
5.75	4.52	1.16	2.73	3.60	0.87	1.48	1.15	1.0
	4.52	1.36	2.90	3.86	0.95	1.21	1.16	1.0
	4.52	1.36	3.13	3.97	0.84	1.21	1.03	0.91
5.58	4.52	2.27	2.83	4.63	1.80	1.20	2.16	0.95
	4.52	2.27	3.05	4.76	1.71	1.24	2.12	0.94
	4.52	2.27	3.15	4.84	1.68	1.32	2.22	0.98
5.18	4.52	4.54	3.58	6.85	3.27	1.29	4.22	0.93
	4.52	4.54	3.67	7.42	3.75	1.08	4.05	0.89
	4.52	4.54	4.22	7.95	3.73	1.10	4.10	0.90
4.58	4.52	9.08	3.60	8.12	4.51	1.41	6.37	0.65
	4.52	9.08	3.75	8.10	4.35	1.42	6.18	0.68
	4.52	9.08	3.95	8.21	4.25	1.39	5.92	0.65

[a] 5.43×10^{-5} mol methyl linoleate used in each experiment. In experiments using both water-soluble inhibitors (C, ascorbate; homo, homocysteine; poly, polythiol) and DTBC, amounts are given in moles.

Table 6. Cooperative inhibiting effect of combination of thiols with DTBC on DBHN-initiated peroxidation of linoleate[a] in micelles at 37°C.

Initiator DBHN ($mol \times 10^6$)	Inhibitors ($mol \times 10^8$)		Inhibition period ($s \times 10^{-3}$)			Extension τ_{ext} ($s \times 10^{-3}$)	R_i ($mol\ s^{-1} \times 10^{11}$)	$R_i \times \tau_{ext}$ ($mol \times 10^8$)	$R_i \times \tau_{ext}$/homo
	DTBC	homo	τ_{DTBC}	τ_{homo}	$\tau_{(DTBC+homo)}$				
8.68	5.01	12.04	1.73	0.31	3.60	1.86	3.24	6.04	0.50
8.68	5.01	12.04	1.83		3.91	2.08	3.15	6.57	0.55
8.68	5.01	25.08	1.66	0.49	4.73	3.06	3.18	9.75	0.39
8.68	5.01	25.08	1.69		4.58	2.89	3.39	9.80	0.39
									0.46 ± 0.07
		poly			$\tau_{(DTBC+poly)}$				$R_i \times \tau_{ext}$/poly[b]
8.07	4.85	12.50	1.94		6.16	4.22	3.56	15.02	0.60
8.07	4.85	12.50	1.69		3.90	3.90	3.55	13.84	0.56
8.61	4.85	25.00	1.67		8.17	6.50	3.27	21.25	0.43
									0.51 ± 0.08

[a] 5.43×10^{-5} mol methyl linoleate used in run. In experiments using both water-soluble inhibitors (C, ascorbate; homo, homocysteine; poly, polythiol) and DTBC, amounts are given in moles.
[b] Each polythiol molecule contains two effective groups, SH.

(c) Regeneration of DTBC, ***3,*** *from DTBQ during peroxidation in organic solvent or in SDS micelles*

To determine the effect of ascorbate on DTBQ during peroxidations of styrene and of methyl linoleate, experiments were conducted on regeneration of DTBC by ascorbyl palmitate, under conditions of AIBN-initiated peroxidation, using styrene as a substrate in 1,1,2,2-tetrachloroethane (TEC), and by ascorbate during DBHN-initiated or ABAP-initiated peroxidation of methyl linoleate in SDS micelles. The results are illustrated in Figs. 8*a* and *b*. As can be seen, the inhibition periods ($\tau_{AP+DTBQ}$), when ascorbyl palmitate is used along with 3,5-di-*tert*-butyl-*ortho*-quinone (DTBQ), are longer than those (τ_{AP}) when ascorbyl palmitate is used alone. The extended inhibition periods ($\tau_{AP+DTBQ} - \tau_{AP}$), which are attributed to regenerated DTBC, were divided by the inhibition periods by the same amounts of DTBC to give the percentage of regeneration of DTBC from DTBQ. The results show that ascorbyl palmitate does not efficiently regenerate DTBC in a nonprotic solvent. A combination of DTBQ and ascorbyl palmitate at ratio of 1 only regenerated 9% DTBC. In micelles, however, a ratio of ascorbate/DTBQ of 1 regenerated 100% DTBC during either DBHN-initiated or ABAP-initiated peroxidation as shown in Fig. 8*b* during initiation by DBHN.

4. Observation on the di-*tert*-butylsemiquinone radical (5)

The di-*tert*-butylsemiquinone radical (**5**) was observed in pulse radiolysis studies (5), but there are no reports that we are aware of on its esr spectra. Because **5** appears to be an important intermediate in our inhibition studies (vide infra), we conducted a few esr experiments on its formation and quenching by ascorbate and the polythiol. The esr spectra of other *ortho*-semiquinone radicals have been studied in some detail by different groups (24–27). The spectra can be complicated due to intramolecular and intermolecular chemical exchanges which in turn are subject to solvent effects (26). Nevertheless, we can assign a 16-line spectrum formed during photolysis with

© 1998 NRC Canada

Fig. 5. Autoxidation of methyl linoleate (5.43×10^{-5} mol) in 2.00 mL 0.50 M SDS – phosphate buffer (pH 7), initiated by DBHN (8.68×10^{-6} mol) at 37°C. (*a*) *A*, uninhibited reaction; *B*, inhibited by 3,5-di-*tert*-butylcatechol (5.01×10^{-8} mol); *C*, inhibited by 3,5-di-*tert*- butylcatechol (5.01×10^{-8} mol) and homocysteine (12.04×10^{-8} mol); $R_i = 1.08 \times 10^{-11}$ mol s^{-1}. (*b*) *A*, uninhibited reaction; *B*, inhibited by 3,5-di-*tert*-butylcatechol (4.85×10^{-8} mol); *C*, inhibited by 3,5-di-*tert*-butylcatechol (4.85×10^{-8} mol) and polythiol (12.50×10^{-6} mol); $R_i = 1.21\text{x } 10^{-11}$ mol s^{-1}.

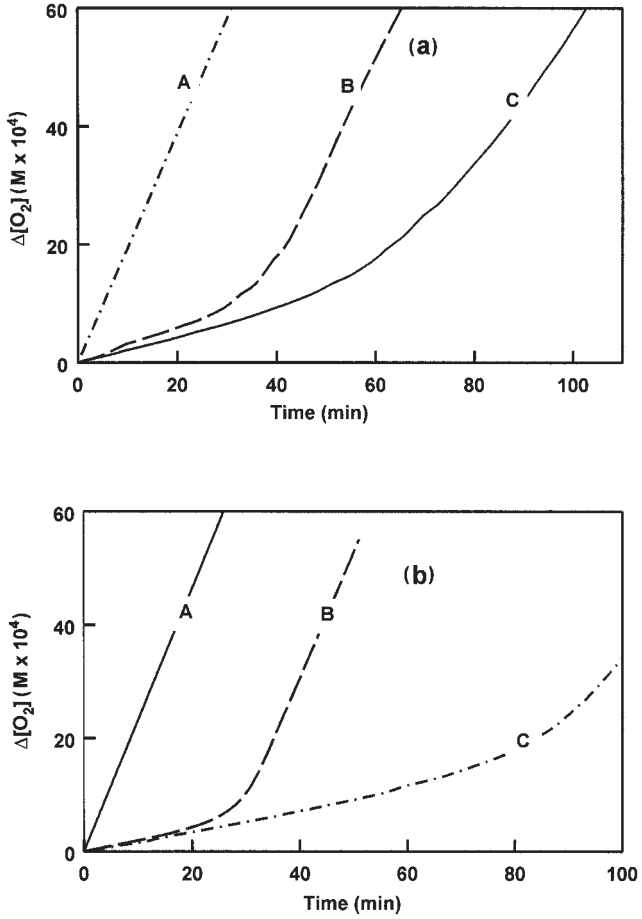

di-*tert*-butylperoxide in hexane to the di-*tert*-butylsemiquinone radical, **5** (Fig. 9*a*). This radical was remarkably persistent and the signal remained strong after several hours at room temperature. The signals were rapidly quenched on addition of polythiol (Fig. 9*b*). It was interesting to discover that this persistent spectrum was also observed (not shown) on mixing equimolar amounts of DTBC (**3**) and the DTBQ (**4**) in hexane; that is, the same semiquinone radical forms on spontaneous hydrogen abstraction from the catechol by *ortho*-quinone in laboratory light. The photolysis of **3** in methanol and di-*tert*-butylperoxide followed by the addition of ascorbic acid in methanol quenched the signal of the semiquinone radical, and there remains a doublet, $a_H = 1.86$ G, assigned to the ascorbyl radical (28) (Fig. 9*c*). On the other hand, we did not observe the semiquinone radical during the rapid reduction of DTBQ by ascorbic acid directly in the esr probe. Evidently, the conversion of DTBQ to DTBC is rapid under these conditions such that the intermediate radical is not observed.

Fig. 6. Autoxidation of methyl linoleate (5.43×10^{-5} mol) in 2.00 mL 0.50 M SDS – phosphate buffer (pH 7), initiated by DBHN (9.14×10^{-6} mol) at 37°C. *A*, uninhibited reaction; *B*, inhibited by 3,5-di-*tert*-butylcatechol (4.06×10^{-8} mol); *C*, inhibited by 3,5-di-*tert*-butylcatechol (4.06×10^{-8} mol) and ascorbic acid (4.06×10^{-8} mol); *D*, inhibited by 3,5-di-*tert*-butylcatechol (4.06×10^{-8} mol), ascorbic acid (4.06×10^{-8} mol), and polythiol (12.04×10^{-6} mol); $R_i = 2.14 \times 10^{-11}$ mol s^{-1}.

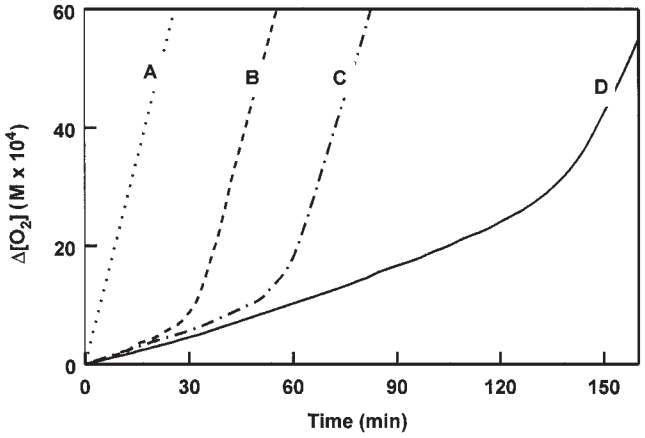

Discussion

1. The antioxidant activities of catechols

The catechol structural unit appears in nature in a wide variety of sources and has attracted a remarkable interest because of the antioxidant property it imparts to the more complex structure containing this simple system. For example, polyphenolic compounds known as flavonoids and caffeic acid, which are commonly found in fruits and vegetables, were reported frequently to possess antioxidant activity (29–33). In animals the catechol structure appears in arylethylamines (catechol amines) and in steroidal compounds (e.g., catechol estrogens), and both classes of compounds have been reported to be antioxidants. For example, L-dopa and dopamine were reported to have both toxic and antioxidant effects on animal cell cultures (34, 35), and such effects of these compounds may be significant in neural diseases (36). Catechol steroids such as 2-hydroxyestradiol and 2-hydroxyestrone were reported earlier to possess high antioxidant activity in liposomes even compared to vitamin E (37), and these compounds were reported more recently to be effective antioxidants during peroxidation of lipoproteins (38, 39) and rat liver microsomes (40, 41).

Unfortunately, these studies on antioxidant effects of natural compounds containing the catechol unit involved initiation in the presence of heavy-metal ions. Consequently, catechols could act both as *preventative* antioxidants by complexation of the metal ions as well as *chain-breaking* antioxidants. Under these conditions, it is difficult to evaluate their activities as peroxyl radical chain-breaking antioxidants.

We believe that the present inhibited oxygen-uptake procedure provides the best method to evaluate antioxidant activities of various catechols. Our results provide the first unambiguous determinations of the peroxyl-radical trapping activities of simple catechols. Two main factors appear to account for the activities of catechols **1**, **2**, and **3**: (*i*) intramolecular hydrogen bonding in the aryloxyl radical semiquinone formed in the

© 1998 NRC Canada

Table 7. Cooperative inhibiting effects of combination of thiols with C and DTBC on DBHN-initiated peroxidation of linoleate[a] in micelles at 37°C.

Initiator ($mol \times 10^6$)	Inhibitors ($mol \times 10^8$)			Inhibition period	R_i	$R_i \times \tau_{ext}$	$R_i \times$
DBHN	DTBC	C	homo	($s \times 10^{-3}$)	($mol\ s^{-1} \times 10^{11}$)	($mol \times 10^8$)	τ_{ext}/homo
8.01	5.02			1.96	2.74		
	5.02	4.85		3.63			
	5.02	4.85	12.54	6.34		7.40	0.60
8.01	5.02	4.85			3.10		
	5.02	4.85					0.48
	5.02	4.85	25.08			12.10	0.54 ± 0.06
			poly				$R_i \times \tau_{ext}$/poly[b]
8.64	4.98			2.12	3.17		
	4.98	5.01		4.87			
	4.98	5.01	12.02	9.08		13.36	0.56
8.64	4.98			2.27	3.01		
	4.98	5.01		5.09			0.44
	4.98	5.01	25.04	12.31		21.76	0.50 ± 0.06

[a] 5.43×10^{-5} mol methyl linoleate used in each experiment. In experiments using both water-soluble inhibitors (C, ascorbate; homo, homocysteine; poly, polythiol) and DTBC, amounts are given in moles.
[b] Each polythiol molecule contains two effective groups, SH.

rate-determining inhibition step (eq. [7]), and (*ii*) stabilization of the radical by the inductive effects of the *tert*-butyl group(s). Hydrogen bonding of the intermediate semiquinone radical is probably the more significant effect because we find that **3** is nearly 50 times more active than propylguaiacol, where this factor is blocked by the *ortho*-methoxyl group (42). In this regard, it is interesting to note that even the unsubstituted catechol, **1**, is more active than the simple polyalkyl phenols (17). Additional activity is attributed to the inductive effect of a *tert*-butyl operating *para* (17) or *meta* to the incipient phenoxyl radical, so that the relative ratios of the k_{inh} values of **2**/**1** and **3**/**2** are 1.60 and 1.64, respectively. The stoichiometric factors, *n*, of the three catechols in homogeneous nonprotic solvent were in the range of 2.1–2.3. Details of the partial peroxyl-radical trapping by catechols is under study to clarify the factors determining *n* values. These could involve contributions of both the phenolic hydroxyls and the recombination step (eq. [8]).

The antioxidant activity of **3** dropped dramatically in the aqueous SDS micelles system by an average of approximately 50-fold. Effects of aqueous media on antioxidant activities of phenols have been the subject of considerable interest and debate (10, 15, 43, 44). In these catechols we interpret the decrease of activity in terms of a combination of H-bonding effects by water, namely, (*i*) the effect of H-bonding by water on the catechol antioxidant, which hinders abstraction of a phenolic hydrogen by peroxyl radicals, and (*ii*) *intermolecular* H-bonding between the phenolic hydroxyl in the semiquinone radical and water. The latter effect is expected to inhibit the main factor that controls the activity of **3**, i.e., *intramolecular* H-bonding in the semiquinone radical at least in nonprotic solvents.

The drop in the stoichiometric factor for **3** found in aqueous SDS micelles, by a factor of 1.7 during initiation by DBHN or by 2.2 during initiation by ABAP (Table 2), when compared to results in chlorobenzene–styrene (Table 1) contrasts with earlier results for some monohydroxyphenols, where about the same values for *n* were found in 0.50 M SDS as in solution (7). This overall decreased efficiency in the antioxidant effect of **3** in aqueous SDS is in part attributed to oxidation of **3** in this medium. Solutions in SDS were found to become yellow whereas they are stable for days in an organic solvent. Hydrogen bonding by water of the semiquinone radical may also contribute to lowering the *n* factor by inhibiting the second hydrogen from effective reaction with peroxyl radicals.

Fig. 7. Plots of regeneration of 3,5-di-*tert*-butylcatechol from 3,5-di-*tert*-butylquinone (2.03×10^{-5} M); ∇, by equimolar AP in tetrachloroethane; Δ , by equimolar AP or C in 0.50 M SDS micelles; ○, by equimolar polythiol in SDS micelles; ◇, by equimolar homocysteine in 0.50 M SDS micelles.

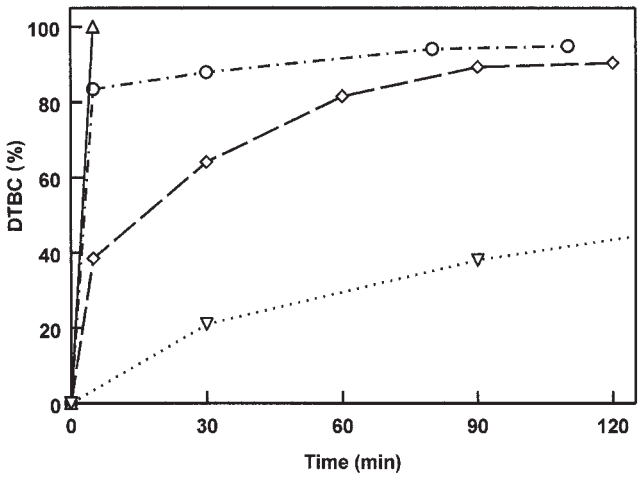

2. Cooperative antioxidant effects of ascorbate and thiols with di-*tert*-butylcatechol: the di-*tert* -butylsemiquinone radical

The results on cooperative effects between antioxidants in these experiments illustrate the very significant control that a

© 1998 NRC Canada

Fig. 8. (*a*) Autoxidation of styrene (6.46 M) initiated by AIBN (4.04×10^{-2} mol) in tetrachloroethane. *A*, uninhibited reaction; *B*, inhibited by ascorbyl palmitate (1.01×10^{-5} M); *C*, inhibited by 3,5-di-*tert*-butylquinone (1.02×10^{-5} M) and ascorbyl palmitate (1.01×10^{-5} M); *D*, inhibited by 3,5-di-*tert*-butylcatechol (1.02×10^{-5} M). (*b*) Autoxidation of methyl linoleate (5.43×10^{-5} mol), initiated by DBHN (5.86×10^{-5} mol) in 0.50 M SDS – phosphate buffer (pH 7). *A*, uninhibited reaction; *B*, inhibited by ascorbic acid (8.78×10^{-8} mol); *C*, inhibited by 3,5-di-*tert*-butylquinone (8.78×10^{-8} mol) and ascorbyl palmitate (8.78×10^{-8} mol); *D*, inhibited by 3,5-di-*tert*- butylcatechol (8.78×10^{-8} mol).

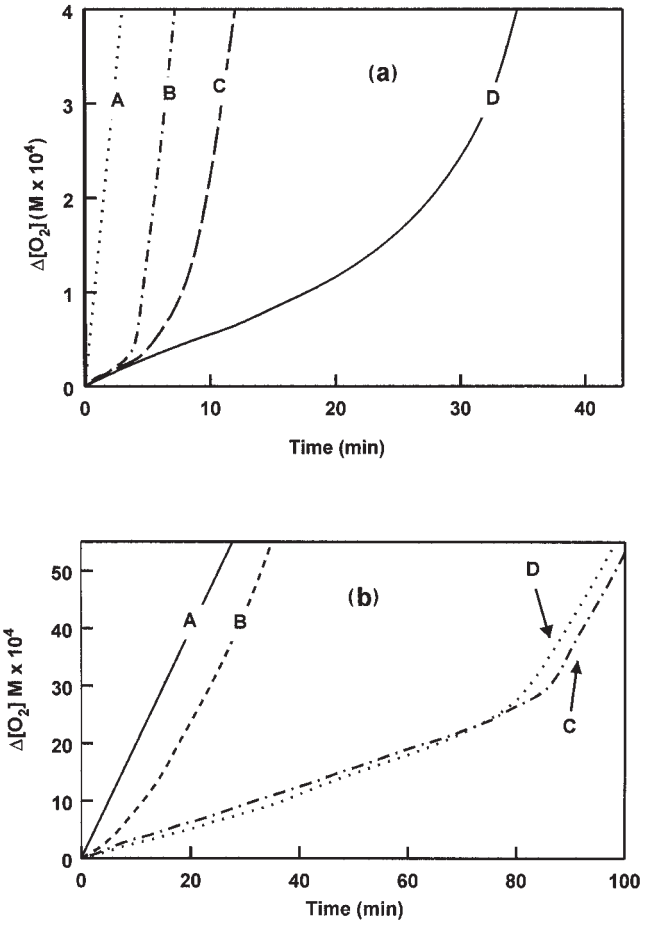

biphasic system like SDS micelles exerts on interaction between water- and lipid-soluble antioxidants. In homogeneous solution, combinations of ascorbyl palmitate or of polythiol with DTBC gave additive effects whereby the induction periods of DTBC were extended. In contrast, such combinations of vitamin C or polythiol with DTBC in 0.50 M SDS resulted in synergistic interactions. The amount of synergism, represented by the difference $\tau_{(C+DTBC)} - (\tau_{DTBC} + \tau_C)$ in Table 4 was in the range of 23–57%. The results are complicated by the oxidation of vitamin C, which is well known to occur readily in water (6), however, a detailed study employing various concentrations of ascorbate (e.g., Fig. 4*b*) shows that it can regenerate a mole of DTBC per mole of ascorbate. These results employing micelles resemble synergistic effects observed for the interaction of vitamin C with α-tocopherol or of Trolox reported earlier in micelles (11) and in phospholipid bilayers (18).

The observed cooperative antioxidant effects for

Fig. 9. The esr spectra. (*a*) Di-*tert*-butylsemiquinone radical, **5**, formed by photolysis of di-*tert*-butylcatechol, **3**, with di-*tert*-butyl peroxide in hexane. (*b*) Scan from (*a*) immediately after addition of polythiol in hexane. (*c*) Spectrum assigned to ascorbyl radical after quenching of **5** by addition of ascorbic acid in methanol. Concentrations are in the range of 10–50 mM.

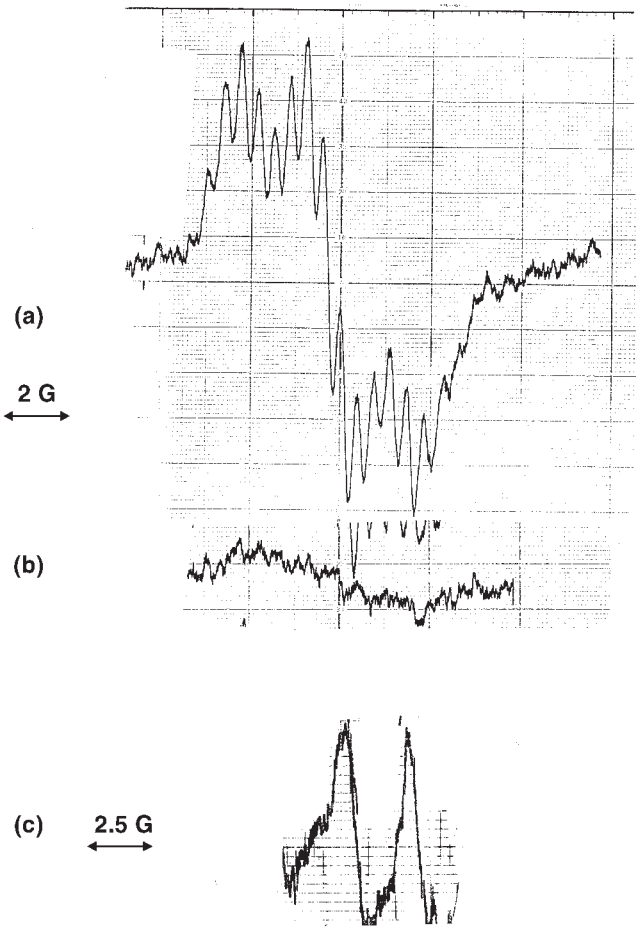

combinations of homocysteine or of polythiol with the catechol DTBC (Table 6) imply regeneration of DTBC from the intermediate semiquinone radical (**5**) by hydrogen transfer from the thiols. This mechanism is supported by the observed rapid quenching of the otherwise persistent radical upon addition of polythiol in solution (Figs. 9*a*, *b*). While this appears to be a novel thiol mediated regeneration of a catechol from its semiquinone radical, regenerations of phenols from phenoxyl radicals by thiols are known to be facile (45–47), including repair of the galvinoxyl (48) and Trolox C radical (49) by thiols and of the vitamin E radical during inhibition of free-radical peroxidation of phosphatidylcholine liposomes by combinations of vitamin E and cysteine (50).

It is of particular interest to find that *combinations* of three inhibitors, DTBC, vitamin C, and a thiol provided additional cooperative inhibition effects. As shown in Table 7, homocysteine or polythiol gave additional *cooperative extensions* of induction periods provided by the cooperative effects of DTBC + ascorbate. A typical trace of such effects is shown in Fig. 6. The mechanism of such "combination effects" is a matter of some speculation. Nevertheless, it is probable that the

© 1998 NRC Canada

thiols act to regenerate the vitamin C from the ascorbyl radical and (or) from dehydroascorbate. The latter regeneration was observed earlier to be facile in aqueous SDS micelles (6), and the thiols and ascorbate are in the same (aqueous) phase in these current studies.

The quinone, **4**, was shown earlier (5) to convert to the catechol **3** by reduction with ascorbate in aqueous methanol. Our results using the quinone combined with ascorbate added to peroxidizing methyl linoleate in SDS micelles demonstrate that this reduction occurs efficiently in the presence of a radical chain reaction. This result, together with the rapid reduction of the quinone to the catechol in SDS micelles at pH 7, indicates that rapid electron transfer from ionized ascorbate ($pK_1 = 4.2$) (28) is probably the initial step in this reduction. The much faster conversion of DTBQ to DTBC in aqueous SDS (pH 7) by ascorbate compared to the conversion in a nonprotic solvent (tetrachloroethane) is expected, considering the known effects of polar protic solvents on electron transfer reactions (51).

The relationships between compounds **3**, **4**, and intermediate **5** are outlined in Scheme 1. The observations on the cooperative and synergistic effects involving regeneration of DTBC by ascorbate and the combination effect with a thiol and ascorbate are accounted for by indicating that the processes are mediated via the intermediate semiquinone radical, **5**. Our results on the significant antioxidant activity of catechols, the persistent semiquinone radical, facile reduction of the quinone (**4**) to the catechol (**3**), and synergistic interactions of ascorbate and thiols with the catechol in an aqueous system have significant implications for the antioxidant activity of various natural antioxidants and their interactions in natural systems. For example, the antioxidant activity of the polyhydroxy flavonoids, currently receiving considerable attention, is probably due to the catechol group, as suggested in recent calculations (24). Persistent semiquinone radicals could be responsible for the persistent "residual phenoxy structures formed" in CTMP and TMP papers (4), which are significant in the yellowing process. In this regard, the combination effects of inhibitors we found is expected to play an important role in the prevention of yellowing. In human systems, it now seems probable that ascorbate and natural thiols play very important roles to maintain molecules such as catechol amines and steroidal catechols in their reduced forms (34–41).

Scheme 1

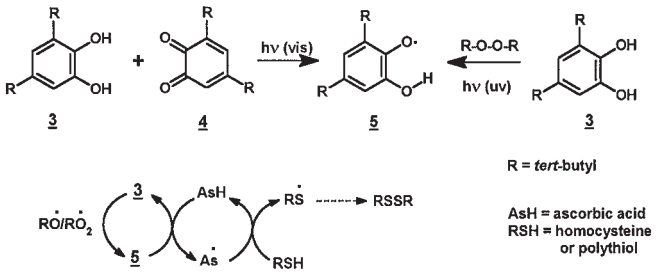

Experimental

Materials and preparations

The solvents used, chlorobenzene, 1,1,2,2-tetrachloroethane (TCE), methanol, and water, were of HPLC grade. Styrene was purchased from the Aldrich Chemical Co. and was passed through a packed column prior to using to remove the inhibitor. Methyl linoleate was purchased from Nuchek Prep, Inc. AIBN and ABAP were obtained from Polysciences Inc. DBHN was prepared by a known method (52). Catechol, 4-*tert*-butylcatechol, DTBC, ascorbic acid, and 5-5'-dithiobis(2-nitrobenzoic acid) (DTNB) were purchased from Aldrich Chemical Co., and dehydroascorbic acid from Pfaltz and Bauer, Inc. Polythiol was a gift from Dr. J.K.S. Wan from Queen's University, Kingston, Ont., and Trolox, a gift from Hoffman–LaRoche, Nutley, New Jersey. Di-*tert*-butyl-*ortho*-quinone (DTBQ) was prepared using a known method (53). Potassium ferricyanide was obtained from Fisher Scientific Co. Phosphate buffer (pH 7) was prepared from 0.05 M each of NaH_2PO_4 and Na_2HPO_4 in glass-distilled water containing 1×10^{-4} M EDTA and adjusted to the desired pH with NaOH. Immediately before use, this solution was passed through a Chelex-100 column (Bio-Rad 50–100 mesh) to remove traces of heavy metals. Electrophoresis pure sodium dodecyl sulfate (SDS) was purchased from Bio-Rad Laboratories. Stock solutions of 0.50 M SDS were prepared in the 0.10 M phosphate buffer (pH 7) described above.

Autoxidation procedure

Autoxidations and inhibition studies of oxygen uptake were carried out at 30 or 37°C (760 Torr) (1 Torr = 133.3 Pa) under oxygen in a sensitive dual-channel calibrated pressure transducer system that is described elsewhere (54, 55). For AIBN-initiated autoxidations, a known amount of styrene diluted to 2 mL with chlorobenzene or tetrachloroethane was shaken in a calibrated cell on the pressure transducer until a steady base line on a recorder was established. After constant oxygen uptake started by injecting a known amount of AIBN, the uninhibited autoxidation was measured, followed by injection of a known amount of inhibitor to measure induction periods and determine its antioxidant activity. The R_i was determined by injecting a known amount of PMHC and measuring the time until the rate returned to the uninhibited rate of oxygen uptake. For DBHN-initiated autoxidation, a 2.00 mL sample of DBHN in 0.50 M SDS was added to a sample cell, followed by a known amount of methyl linoleate; the rate of constant oxygen uptake was measured, followed by injection of the antioxidants in buffered SDS and determination of the inhibition periods. For ABAP-initiated autoxidation, typically 50 μL of methyl linoleate was added to 2.00 mL of 0.50 M SDS in a calibrated cell. This mixture was shaken to establish a steady base line followed by injection of 100 μL of 0.50 M ABAP in buffer to start the reaction. Known amounts of the antioxidants in SDS were then injected into the cell and inhibition periods were measured as before.

Analyses

Thiol analysis was performed by the Ellman method (56) using the reaction with DTNB and measuring the absorption of the reaction mixture at 412 nm. Ascorbic acid was determined by its reaction of potassium ferricyanide, the latter forming a bright-yellow solution in phosphate buffer that absorbs at 420 nm (6). DTBC and DTBQ were analysed by measuring the absorption at 281 and 412 nm, respectively.

Electron-spin resonance measurements were made directly

© 1998 NRC Canada

in the probe of a Varian E–3 bench-top spectrometer at room temperature. Photolysis experiments using an Oriel 200 W super pressure Hg arc on DTBC in hexane containing di-*tert*-butylperoxide (Pfaltz and Bauer) or experiments on combinations of DTBC and DTBQ were conducted in quartz tubes under argon. Due to solubility limits, experiments using ascorbic acid were carried out in methanol under argon in flat esr tubes or capillaries. Concentations of compounds used were generally in the range of 10–50 mM.

Acknowledgements

Support of this research by the Mechanical and Chemimechanical Wood-Pulps Network, part of Canada's Network of Centres of Excellence, is gratefully acknowledged. We thank Roger Smith and Allister MacDonald for construction of the sensitive pressure – transducer – oxygen-uptake apparatus required for this research and Krista McLeod for prepartion of di-*tert*-butylhyponitrite.

References

1. J.A. Schmidt and C. Heitner. J. Wood Chem. Technol. **15**, 223 (1995).
2. D.S. Argyropoulos, C. Heitner, and F.G. Morin. Holzforschung, **46**, 211 (1992).
3. S.E. Lebo, W.F.W. Lonsky, T.J. McDonough, P.J. Meduecz, and D.R. Dimmel. J. Pulp Pap. Sci. **16**, J 139 (1990).
4. J.K.S. Wan and M.C. Depew. Res. Chem. Intermed. **22**, 241 (1996).
5. S.V. Jovanovic, K. Konya, and J.C. Scaiano. Can. J. Chem. **73**, 1803 (1995).
6. L.R.C. Barclay, K.A. Dakin, and J.A.Y. Khor. Res. Chem. Intermed. **21**, 467 (1995).
7. L.R.C. Barclay, C.D. Edwards, K. Mukai, Y. Egawa, and T. Nishi. J. Org. Chem. **60**, 2739 (1995).
8. W.A. Pryor, J.A. Cornicelli, L.J. Devau, B. Tait, B.K. Trivedi, D.T. Witiak, and M. Wu. J. Org. Chem. **58**, 3521 (1993).
9. L. Castle and M.J. Perkins. J. Am. Chem. Soc. **108**, 6382 (1980).
10. L.R.C. Barclay, K.A. Baskin, S.J. Locke, and T.D. Schaefer. Can. J. Chem. **65**, 2529 (1987).
11. L.R.C. Barclay, S.J. Locke, and J.M. MacNeil. Can. J. Chem. **63**, 366 (1985).
12. L.R.C. Barclay, S.J. Locke, J.M. MacNeil, J. VanKessel, G.W. Burton, and K.U.Ingold. J. Am. Chem. Soc. **104**, 2479 (1984).
13. Y. Yamamoto, S. Haga, E. Niki, and Y. Kamiya. Bull. Chem. Soc. Jpn. **57**, 1260 (1984).
14. J.A. Howard and K.U. Ingold. Can. J. Chem. **43**, 2729 (1965).
15. W.A. Pryor, T. Strickland, and D.F. Church. J. Am. Chem. Soc. **110**, 2224 (1986).
16. G.W. Burton and K.U. Ingold. J. Am. Chem. Soc. **103**, 6472, (1981).
17. G.W. Burton, T. Doba, E.J. Gabe, L. Hughes, F.L. Lee, L. Prasad, and K.U. Ingold. J. Am. Chem. Soc. **107**, 7053 (1985).
18. T. Doba, G.W. Burton, and K.U. Ingold. Biochim. Biophys. Acta, **835**, 298 (1985).
19. M. Scarpa, A. Rigo, M. Maiorino, F. Ursini, and C. Gregolin. Biochim. Biophys. Acta, **801**, 215 (1984).
20. E. Niki, T. Saito, A. Kawakami, and Y. Kamiya. J. Biol. Chem. **259**, 4177 (1984).
21. H.-W. Leung, M.J. Vang, and R.D. Mavis. Biochim. Biophys. Acta, **664**, 266 (1981).
22. E. Niki, A. Kawakami, Y. Yamamoto, and Y. Kamiya. Bull. Chem. Soc. Jpn. **58**, 1971 (1985).
23. C. Rousseau, C. Richard, and R. Martin. J. Chim. Phys. Phys.-Chim. Biol. **81**, 137 (1984).
24. S.A.B.E. van Acker, M.J. de Groot, D.-J. van den Berg, M.N.J.L. Thromp, G.D-O. den Kelder, W.J.F. van der Vijgh, and A. Bast. Chem. Res. Toxicol. **9**, 1305 (1996).
25. M. Geoffroy, P. Lambelet, and P. Richert. Free Radical Res. Commun. **21**, 247 (1994).
26. K. Loth and F. Graf. Helv. Chim. Acta, **64**, 1910 (1981).
27. W.T. Dixon and D. Murphy. J. Chem. Soc. Faraday Trans. 2, **72**, 135 (1976).
28. G.R. Buettner and B.A. Jurkiewicz. *In* Analysis of free radicals in biological systems. *Edited by* A.E. Favier, J. Cadet, B. Kalyanaraman, M. Fontecave, and J.L. Pierre. Birhauser Verlag, Basel, Switzerland. 1995. pp. 145–164.
29. S. Kitagawa, T. Sakuma, and S. Yonemura. Chem. Pharm. Bull. **43**, 1263 (1995).
30. S.V. Jovanovic, S. Steenken, M. Tosic, B. Marjanovig, and M.G. Simic. J. Am. Chem Soc. **116**, 4846 (1994).
31. J. Terao, M. Piskula, and Q. Yao. Arch. Biochem. Biophys. **308**, 278 (1994).
32. L. Benov and N. Georgiev. Phytother. Res. **8**, 92 (1993).
33. J.T. Terao, H. Karasawa, H. Arai, A. Nagao, T. Suzuki, and K. Takama. Biosci. Biotechnol. Biochem. **57**, 1204 (1993).
34. T.G. Hastings, D.A. Lewis, and M.J. Zigmond. Proc. Natl. Acad. Sci. U.S.A. **93**, 1956 (1996).
35. C. Mytilineou, S.K. Han, and G. Cohen. J. Neurochem. **61**, 1470 (1993).
36. J. Liu and A. Mori. Arch. Biochem. Biophys. **302**, 118 (1993).
37. M. Nakano, K. Sugioka, I. Naito, S. Takekoshi, and E. Niki. Biochem. Biophys. Res. Commun. **142**, 919 (1987).
38. M. Tang, W. Abplanalp, S. Ayres, and M.T.R. Subbiah. Metabolism, **45**, 411 (1996).
39. S. Taniguchi, T. Yanase, K. Kobayashi, R. Takayanagi, M. Haji, F. Umeda, and H. Nawata. Endocrinol. Jpn. **41**, 605 (1994).
40. M. Lacort, A.M. Leal, M. Liza, C. Martin, R. Martinez, and M.B. Ruiz-Larrea. Lipids, **30**, 141 (1995).
41. K. Takanashi, K. Watanabe, and I. Yoshizawa. Biol. Pharm. Bull. **18**, 1120 (1995).
42. L.R.C. Barclay, F. Xi, and J.Q. Norris. J. Wood Chem Technol. **17**, 73 (1997).
43. L. Valgimigli, K.U. Ingold, and J. Lusztyk. J. Chem. Soc. **118**, 3545 (1996).
44. M. Iwatsaki, J. Tsuchiya, E. Komuro, Y. Yamamoto, and E. Niki. Biochim. Biophys. Acta, **1200**, 19 (1994).
45. R. Goldman, W. Bors, C. Michel, B.W. Day, and V.E. Kagan. Environ. Nutr. Interact. **1**, 97 (1997).
46. D.A. Stoyanovsky, R. Goldman, H.G. Claycamp, and V.E. Kagan. Arch. Biochem. Biophys. **317**, 315 (1995).
47. K. Stolze and H. Nohl. Free Radical Res. Commun. **16**, 159 (1992).
48. J. Tsuchiya, T. Yamada, E. Niki, and Y. Kamiya. Bull. Chem. Soc. Jpn. **58**, 326 (1985).
49. M.J. Davies, L.G. Forni, and R.L. Willson. Biochem. J. **255**, 513 (1988).
50. T. Motoyama, M. Miki, M. Mino, M. Takahashi, and E. Niki. Arch. Biochem. Biophys. **270**, 635, (1989).
51. M.J. Weaver. Chem. Rev. **92**, 463 (1992).
52. D.G. Mendenhall. Tetrahedron Lett. **24**, 451 (1983).
53. W. Flaig and H. Bieergans, Ann. Chem. **597**, 196 (1955).
54. L.R.C. Barclay, K.A. Baskin, K.A. Dakin, S.J. Locke, and M.R. Vinquist. Can. J. Chem. **68**, 2258 (1990).
55. D.D.M. Wayner and G.W. Burton. *In* Handbook of free radicals and antioxidants in biomedicine. Vol 3. CRC Press, Boco Raton, Fla. 1989. pp. 223–232.
56. G.L. Ellman. Arch. Biochem. Biophys. **82**, 70 (1959).

© 1998 NRC Canada

Dynamics of silicate exchange in highly alkaline potassium silicate solutions

Eva Vallazza, Alex D. Bain, and Thomas W. Swaddle

Abstract: The problem of measuring the kinetics of Si exchange between aqueous silicate species by ^{29}Si NMR has been revisited, using highly alkaline KOH solutions (2.8 mol Si^{IV} per kg solvent, $[Si^{IV}]/K_2O = 0.43$) at 60–90°C to minimize the number of silicate species present. Longitudinal ^{29}Si relaxation times T_1 and apparent rate constants estimated from line-shape analysis (LSA) varied markedly with the degree of purity of the KOH used, but rate constants k obtained by selective inversion–recovery (SIR) using the CIFIT data-fitting program were independent of the source of KOH and were smaller than those obtained from LSA by at least an order of magnitude. Although only four kinetically significant silicate anions (monomer M, dimer D, linear trimer L, and cyclic trimer C) were present, overlap of the D and L resonances prevented complete analysis of the SIR data. True rate constants could therefore be obtained only for the M–D exchange (for formation of D, k_1 (90°C) = 0.13 ± 0.01 kg mol $^{-1}$ s^{-1}, $\Delta H_1^{\ddagger}$ = 67.4 kJ mol^{-1}, $\Delta S_1^{\ddagger}$ = –78 J K^{-1} mol^{-1}; for dissociation of D, k_{-1} (90°C) = 1.4 ± 0.1 s^{-1}, $\Delta H_{-1}^{\ddagger}$ = 64.7 kJ mol^{-1}, and $\Delta S_1^{\ddagger}$ = –66 J K^{-1} mol^{-1}). Models that included L as the precursor of C (MDLC mechanism) showed, within the limitations imposed by D–L band overlap, that the reactivities of M, D, L, and C in Si-O-Si link formation or dissociation were all roughly comparable. Good fits of the experimental data, however, and equally reliable rate constants for the M–D exchange, could be obtained with models that ignored the presence of L entirely (MDC mechanism). The simple MDC model also provides consistent apparent rate constants k_C and k_{-C} for the *overall* formation of C from M + D and the reverse process, respectively, by SIR of either M or C ($\Delta H_C^{\ddagger}$ = 76.5 kJ mol^{-1}, $\Delta S_C^{\ddagger}$ = –57 J K^{-1} mol^{-1}; $\Delta H_{-C}^{\ddagger}$ = 88.6 kJ mol^{-1}, and $\Delta S_{-C}^{\ddagger}$ = –7 J K^{-1} mol^{-1}).

Key words: kinetics, silicates, ^{29}Si NMR.

Résumé : On a réexaminé le problème associé à la mesure de la cinétique de l'échange du Si entre des espèces silicates aqueuses à l'aide de la RMN du ^{29}Si; à cette fin, opérant à des températures allant de 60 à 90°C, on a utilisé des solutions extrêmement alcalines de KOH (contenant 2,8 mol Si^{IV} par kg de solvant, $[Si^{IV}]/K_2O = 0,43$) afin de minimiser le nombre d'espèces de silicate. Les temps de relaxation longitudinale du ^{29}Si, T_1, ainsi que les constantes apparentes de vitesse évaluées sur la base d'une analyse de la forme de la raie («LSA») varient beaucoup avec le degré de pureté du KOH utilisé; toutefois, les constantes de vitesse k, obtenues par une récupération sélective de l'inversion («SIR») en utilisant le programme «CIFIT» d'ajustement des données, sont indépendantes de la source de KOH et elles sont au moins 10 fois plus faibles que celles obtenues par la méthode de «LSA». Même si seulement quatre anions silicates (monomère, M; dimère, D; trimère linéaire, L; trimère cyclique, C) cinétiquement significatifs sont présents, le recouvrement des résonances des entités D et L rend impossible l'analyse complète des données «SIR». On n'a donc pu obtenir les vraies constantes de vitesse que pour l'échange M–D (pour la formation de D, k_1 (90°C) = 0,013 ± 0,01 kg mol^{-1} s^{-1}, $\Delta H_1^{\ddagger}$ = 67,4 kJ mol^{-1} et $\Delta S_1^{\ddagger}$ = –78 J K^{-1} mol^{-1}; pour la dissociation de D, k_{-1} (90°C) = 1,3 ± 0,1 s^{-1}, $\Delta H_{-1}^{\ddagger}$ = 64,7 kJ mol^{-1} et $\Delta S_{-1}^{\ddagger}$ = –66 J K^{-1} mol^{-1}). Les modèles qui incluent L comme précurseur de C (mécanisme MDLC) démontrent, sujet aux limitations imposées par le recouvrement des bandes D–L, que les réactivités de M, D, L et C sont assez semblables pour la formation et la dissociation de la liaison Si-O-Si. Toutefois, de bons accords avec les données expérimentales et des constantes de vitesse également fiables pour l'échange M–D pourraient aussi être obtenus à l'aide de modèles qui ignoreraient complètement la présence de L (mécanisme MDC). Le modèle MDC simple fournit aussi des constantes de vitesse apparentes k_C et k_{-C} cohérentes respectivement pour la formation *globale* de C à partir des entités M + D ainsi que pour le processus inverse, par «SIR» des entités soit M ou C ($\Delta H_C^{\ddagger}$ = 76,5 kJ mol^{-1} et $\Delta S_C^{\ddagger}$ = –57 J K^{-1} mol^{-1}; $\Delta H_{-C}^{\ddagger}$ = 88,6 kJ mol^{-1} et $\Delta S_{-C}^{\ddagger}$ = –7 J K^{-1} mol^{-1}).

Mots clés : cinétique, silicates, RMN du ^{29}Si.

[Traduit par la rédaction]

Received August 20, 1997.

E. Vallazza and T.W. Swaddle.[1] Department of Chemistry, The University of Calgary, Calgary, AB T2N 1N4, Canada.
A.D. Bain. Department of Chemistry, McMaster University, Hamilton, ON L8S 4M1, Canada.

[1] Author to whom correspondence may be addressed. Telephone: (403) 220-5358. Fax: (403) 289-9488. E-mail: swaddle@chem.ucalgary.ca

© 1998 NRC Canada

Introduction

Aqueous solutions of silicates and aluminosilicates are important in a wide variety of technological, geological, and biomedical contexts, as noted in a recent review (1). Silicate anions occur in alkaline aqueous solution in at least 25 oligomeric forms, in addition to the orthosilicate monomer $(HO)_{4-z}SiO_z^{z-}$. In their pioneering studies, Harris et al. (2–5) identified most of these oligomers by ^{29}Si NMR spectroscopy, a technique that, along with ^{17}O NMR, also reveals that the oligomers (other than special cases such as the cubic cage species $Si_8O_{20}^{8-}$ (6)) undergo rapid intermolecular Si–Si site exchange (7–13).

It has proved difficult, however, to obtain reliable rate constants for exchange between specific silicate species in typical solutions with pH around 11, where the average charge per Si atom is about –1, because of the excessive number of species present. The number of detectable oligomeric species diminishes as the pH and temperature are raised (14), whereas the rates of Si site exchange increase with rising temperature but decrease with rising pH (10). Thus, the most favorable conditions for the quantitative study of Si–Si exchange kinetics by NMR are high pH and elevated temperatures — conditions that have some intrinsic technological interest in relation to the synthesis of zeolite catalysts and the carryover of silicate in the Bayer process for bauxite refining (1). An added complication, however, is that traditional NMR line-shape analysis (LSA) methods of determining exchange rates are subject to error because of nonkinetic contributions to the line widths, particularly line broadening by adventitious paramagnetic contaminants (8, 10), and this problem can be expected to worsen with the addition of high concentrations of alkalis that inevitably contain traces of paramagnetic substances (15).

Fortunately, the kinetics of Si–Si chemical exchange can be studied without these complications by the technique of *selective inversion–recovery* (SIR) (8, 10, 12), in which the magnetization of the population of one exchanging species is inverted and the propagation of the magnetic perturbation to the other species through chemical exchange is monitored. The rate of disappearance of the imposed perturbation of magnetization is then a function of the chemical exchange rates and nuclear spin-lattice relaxation times T_1 of the species involved in exchange, and numerical analysis can, in principle, separate these parameters to yield unambiguous chemical exchange rate constants. Rigorous analysis of the evolution of the observed spectral changes with time t is not trivial, particularly for intermolecular processes such as silicate–silicate exchange, and was not attempted in our previous report on this topic (10). The original ^{29}Si SIR study by Harris and co-workers (8) gave rate constants only for the dimerization of orthosilicate (0.21 and 1.06 kg mol^{-1} s^{-1} at 83 and 107°C, respectively) in a solution of 2.8 mol kg^{-1} SiO_2 in aqueous KOH (K:Si = 3.8:1). Bell and co-workers (12) considered the interconversion of the monomer M, the dimer D, and the cyclic trimer C (Fig. 1) in SIR experiments on solutions of 3 mol% SiO_2 in 10 mol% aqueous KOH, but only for a single unspecified temperature, and the possible involvement of other oligomers was not taken into account. Thus, there is need for a reexamination of the problem of silicate exchange kinetics.

The present article describes an attempt to extract reliable rate constants k by the SIR and LSA methods for silicate exchange at 60–90°C in highly alkaline potassium silicate solutions, in which the only detectable silicate species present were the monomer $(HO)_{4-z}SiO_z^{z-}$ (M), the dimer $(HO)_{6-z}(Si_2O)O_z^{z-}$ (D), the "linear" or acyclic trimer $(HO)_{8-z}(Si_3O_2)O_z^{z-}$ (L), the cyclic trimer $(HO)_{6-z}(Si_3O_3)O_z^{z-}$ (C), and the branched tetramer $(HO)_{8-z}(Si_4O_4)O_z^{z-}$ (B) (Fig. 1). We focus upon results from two particular samples, called I and II, that were almost identical except for the source of the KOH used. Numerical analysis of SIR data was carried out using the CIFIT program (16–18), which is based on Muhandiram and McClung's SIFIT procedure (19). The rate constants so obtained are subject to uncertainties arising from the irreducible chemical complexity of the exchanging silicate system, but nevertheless the results present a more complete picture than previously published studies (8, 10, 12). Comparison is made with rate constants estimated from complete line-shape analyses. In particular, it is shown that trace impurities in the alkali lead to substantially shortened longitudinal relaxation times T_1 and to apparent rate constants for Si–Si exchange from LSA that are too large.

Fig. 1. Schematic representation of structures of silicate species detectable in this study. Each black dot represents a silicon atom, tetrahedrally surrounded by oxygens; the lines represent Si-O-Si links.

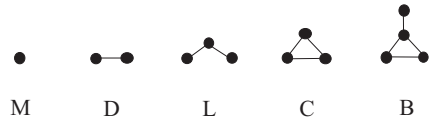

Experimental

Materials

All alkaline solutions were prepared in Teflon–FEP containers, which were soaked successively in dilute solutions of HCl, HNO_3, and Na_2H_2EDTA prior to use. Amorphous silica was prepared by dropwise hydrolysis of freshly distilled silicon tetrachloride (Fisher, technical grade) in water. The resulting gel was dried, crushed, and washed with water. Potassium hydroxide solutions were prepared by dissolving solid KOH (BDH ACS grade for sample I, or Alfa Aesar, 99.995% pure on the basis of metals content, for sample II) in freshly boiled solvent consisting of approximately 75% D_2O (Aldrich, 99.9 at.% D) and 25% deionized distilled H_2O.

Sample preparation

Samples were prepared directly in Teflon–FEP NMR tube liners by dissolving a known quantity of silica (dried at 250°C) in a weighed portion of KOH solution that had been standardized with potassium hydrogen phthalate. Dissolved oxygen was purged from the sample with N_2, then the tube was closed with a Teflon stopper and sealed with Parafilm. The compositions of samples I and II are given in Table 1 in various ways to facilitate comparison with other published work.

NMR measurements

Silicon-29 spectra were obtained at 59.624 MHz on a Bruker AMX2-300 spectrometer using a 10 mm probehead with spin rate of 10 Hz. The glass coil supports of the probe and the NMR glass tube gave rise to a broad signal centered around –40 ppm relative to the orthosilicate resonance. Spectra were

© 1998 NRC Canada

Table 1. Composition of solutions.

	Sample I	Sample II
$[Si^{IV}]$/mol (kg solvent)$^{-1}$	2.80	2.79
$[Si^{IV}]$/mol%	4.17	4.17
$[K^+]$/mol (kg solvent)$^{-1}$	13.0	12.9
$[K^+]$/mol%	9.67	9.63
K/Si	4.64	4.62
$R = [Si]/[K_2O]$	0.431	0.433
Source of KOH	BDH, ACS grade	Alfa Aesar, 99.995%
[M]/mol kg^{-1} (60°C)	2.134	2.127
[D]/mol kg^{-1} (60°C)	0.401	0.399
[L]/mol kg^{-1} (60°C)	0.1002	0.0998
[C]/mol kg^{-1} (60°C)	0.1646	0.1640
[M]/mol kg^{-1} (90°C)	2.140	2.133
[D]/mol kg^{-1} (90°C)	0.438	0.436
[L]/mol kg^{-1} (90°C)	0.0962	0.0958
[C]/mol kg^{-1} (90°C)	0.1255	0.1250

recorded over a temperature range from 4.5 to 90°C. Temperature calibration was carried out using the proton spectra of neat ethylene glycol (Fisher, ACS Certified) (20).

The ^{29}Si 90° pulse width was determined for each temperature and was between 22 μs (at 4.5°C) and 45 μs (at 90°C). Longitudinal relaxation times T_1 (Table 2) were estimated by nonselective inversion–recovery measurements (180°–τ–90°–FID–t_d), and pulse intervals were chosen to be greater than 5 times the maximum measured T_1, i.e., intervals of 30–75 s for sample I and 75–300 s for sample II. Selective inversion–recovery (SIR) experiments were conducted as described by Morris and Freeman (21). A DANTE sequence of 18 pulses of 5 μs with 0.4–0.7 ms interpulse delay was used to invert selectively the Q^0 Si spins[2] of the monomeric silicate anion M, the Q^1 spins of Si of the dimer D and linear trimer L (overlapping bands), or the Q^2 Si spins in three-membered rings of cyclic trimer C and branched tetramer B (overlapping bands). Results of M-, (D + L)-, and C-SIR experiments on sample I at 90°C, and sample II at 60 and 90°C, have been deposited as supplementary material.[3]

Calculations

Complete line-shape analyses (LSA) were carried out using the Fortran program GNMR derived from the exchange-modified Bloch equations (10). For each sample, the low-temperature (4.5°C) unbroadened spectrum was simulated manually by iterating the positions, line widths, and areas of five computer-generated Lorentzian peaks. Reaction models were tested to find appropriate sets of rate equations (kinetic matrices (22)) that would replicate the observed line broadening.

SIR curves were calculated using the C program CIFIT (16, 17), designed to fit data from SIR experiments of systems undergoing slow chemical exchange. CIFIT searches for the set of parameters (rate constants k, relaxation times T_1, and initial and equilibrium band intensities M_0 and M_∞) that best fits the experimental data. Since the three observed peaks have different line widths, peak areas were used to describe changes in z-magnetizations. They were calculated by integrating the simulated peaks obtained by deconvoluting spectra processed with an artificial line broadening of 1 Hz using the Bruker WINFIT program. For each SIR experiment the normalized peak areas were fitted optimally using the CIFIT program with various mechanistic models. Since the number of parameters was large, it was generally necessary to allow only the M_0 and M_∞ values and limited sets of k and T_1 to vary in a given computation; the best-fit values of k and T_1 and the associated uncertainties were then determined by manual iteration (18). In cases where the propagated SIR effect on a particular peak was weak, k and T_1 values determined for that peak by its direct inversion were inserted as fixed parameters.

[2] The connectivity n of a silicon center is denoted as Q^n ; thus, the connectivity of a terminal SiO_4 unit is Q^1, and that of the Si centers in the cubic octamer $Si_8O_{20}^{8-}$ is Q^3.

[3] Tables S1–S9 (10 pages), giving integrated signal intensities as functions of delay time for M-, (D + L)-, and C-SIR experiments on sample I at 90°C, and on sample II at 60 and 90°C, may be purchased from: the Depository of Unpublished Data, Document Delivery, CISTI, National Research Council Canada, Ottawa, Canada K1A 0S2.

Table 2. Longitudinal ^{29}Si relaxation times from nonselective inversion–recovery.

Sample	Temp./°C	Longitudinal relaxation times T_1/s		
		M peak	Combined D/L band	Combined C/B band
I	90	7	6	6
II	90	20	21	17
II	60	16	9	13

Results

It can be inferred immediately from the experimental spectra shown in Figs. 2 and 3 that there is a much larger intrinsic line broadening for sample I (that with the less pure KOH) than for sample II, and hence that line-shape analysis for sample I is likely to overestimate the chemical exchange rates. Furthermore, although the spectra at 90°C (the optimum temperature for SIR experiments on the samples used in this study) for both samples show a single band at chemical shift $\delta \approx -7.0$ ppm, it is clear from the low-temperature spectra that this feature includes intensity from the minor but not negligible band at $\delta \approx -6.9$ ppm due to the Q^2 silicons of the linear trimer L, as well as from the dimer D. Extrapolation from spectra run at lower temperatures indicated that the band comprised 80% D with 20% L at 60°C, and 82% D with 18% L at 90°C. These and other relative integrated band intensities allowed calculation of the actual concentrations of M, D, L, and C in the two samples at 60 and 90°C (Table 1).

On the other hand, the resonance expected for the Q^2 silicon of L at $\delta \approx -16.6$ ppm (14) was not observable (probably because of strong kinetic line broadening) and was of necessity neglected. The small feature discernible at $\delta \approx -9.5$ ppm, attributable to the branched tetramer B, remained distinct from 4.5 to 90°C for sample II at least, and therefore corresponded to exchange processes slow enough to be disregarded in calculating the integrated C signal intensity.

Longitudinal ^{29}Si relaxation times T_1 calculated from nonselective inversion experiments are listed in Table 2. Values of T_1 obtained at 90°C may be partly averaged by chemical exchange (23); Kinrade et al. (15) report that onset of averaging of T_1 occurred above 50°C for a sample containing 2.2 mol kg^{-1} of each of NaOH and SiO_2 but, in the present study

© 1998 NRC Canada

Fig. 2. Comparison of experimental (dotted lines) and simulated (solid lines) spectra for sample I at various temperatures. The simulations are based on the assumption that the spectrum at 4.5°C shows no chemical exchange. Small variations in resonance frequencies caused by phenomena other than spin–site exchange, as well as shifts in population equilibria, were corrected manually. The branched tetramer peak at about –9.5 ppm was neglected in line-shape analyses and in the interpretation of selective inversion–recovery experiments.

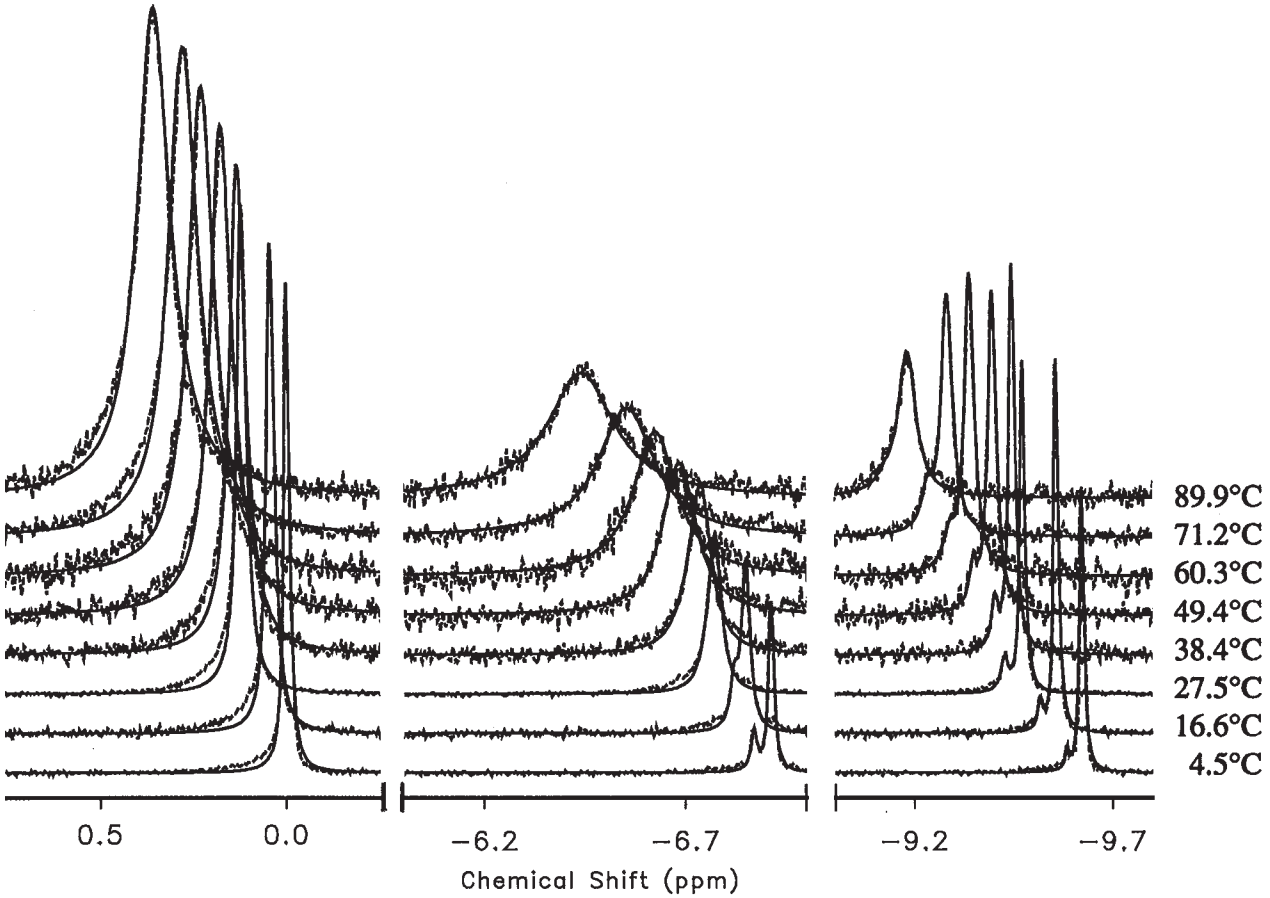

with higher alkalinity and consequently slower chemical exchange, T_1 data obtained at 60°C should be reasonably close to the values for independent silicate centers.

When fitting the data in both line-shape analysis and selective inversion–recovery, two main mechanisms were considered:

MDC mechanism:

[1] $M + M \underset{k_{-D}}{\overset{k_D}{\rightleftharpoons}} D$

$k_D' = k_D[M] = k_{-D}[D]/[M]$; $K_D = k_D/k_{-D} = [D]/[M]^2$

[2] $M + D \underset{k_{-C}}{\overset{k_C}{\rightleftharpoons}} C$

$k_C' = k_C[D] = k_{-C}[C]/[M]$; $K_C = k_C/k_{-C} = [C]/[D][M]$

MDLC mechanism:

[3] $M + M \underset{k_{-1}}{\overset{k_1}{\rightleftharpoons}} D$

$k_1' = k_1[M] = k_{-1}[D]/[M]$; $K_1 = k_1/k_{-1} = [D]/[M]^2 = K_D$

[4] $M + D \underset{k_{-2}}{\overset{k_2}{\rightleftharpoons}} L$

$k_2' = k_2[D] = k_{-2}[L]/[M]$; $K_2 = k_2/k_{-2} = [L]/[D][M]$

Table 3. Equilibrium constants, and associated enthalpies and entropies of reaction, for the MDLC reaction scheme under the

Parameter	$i = 1$	$i = 2$	$i = 3$
K_i (60°C)	0.088[a]	0.117[a]	1.64
K_i (90°C)	0.096[a]	0.103[a]	1.30_5
ΔH_i/kJ mol^{-1}	+2.7	–4.4	–7.7
ΔS_i/J K^{-1} mol^{-1}	–12	–31	–19

[a] Units: kg mol^{-1}.

[5] $L \underset{k_{-3}}{\overset{k_3}{\rightleftharpoons}} C$

$k_3 = k_{-3}[C]/[L]$; $K_3 = k_3/k_{-3} = [C]/[L]$; $K_2K_3 = K_C$.

Here, the various k_i are rate constants and the K_i are equilibrium constants. Values of K_i and the associated enthalpies (ΔH_i) and entropies (ΔS_i) estimated from the data of Table 1 and cognate data for lower temperatures are given in Table 3. The MDC mechanism differs from the MDLC mechanism in that participation of the linear trimer L in the exchange processes is discounted, i.e., either addition of monomer to dimer and subsequent ring closure to form the trimer can be

© 1998 NRC Canada

Fig. 3. Comparison of experimental (dotted lines) and simulated (solid lines) spectra for sample II at various temperatures. Details as for Fig. 2.

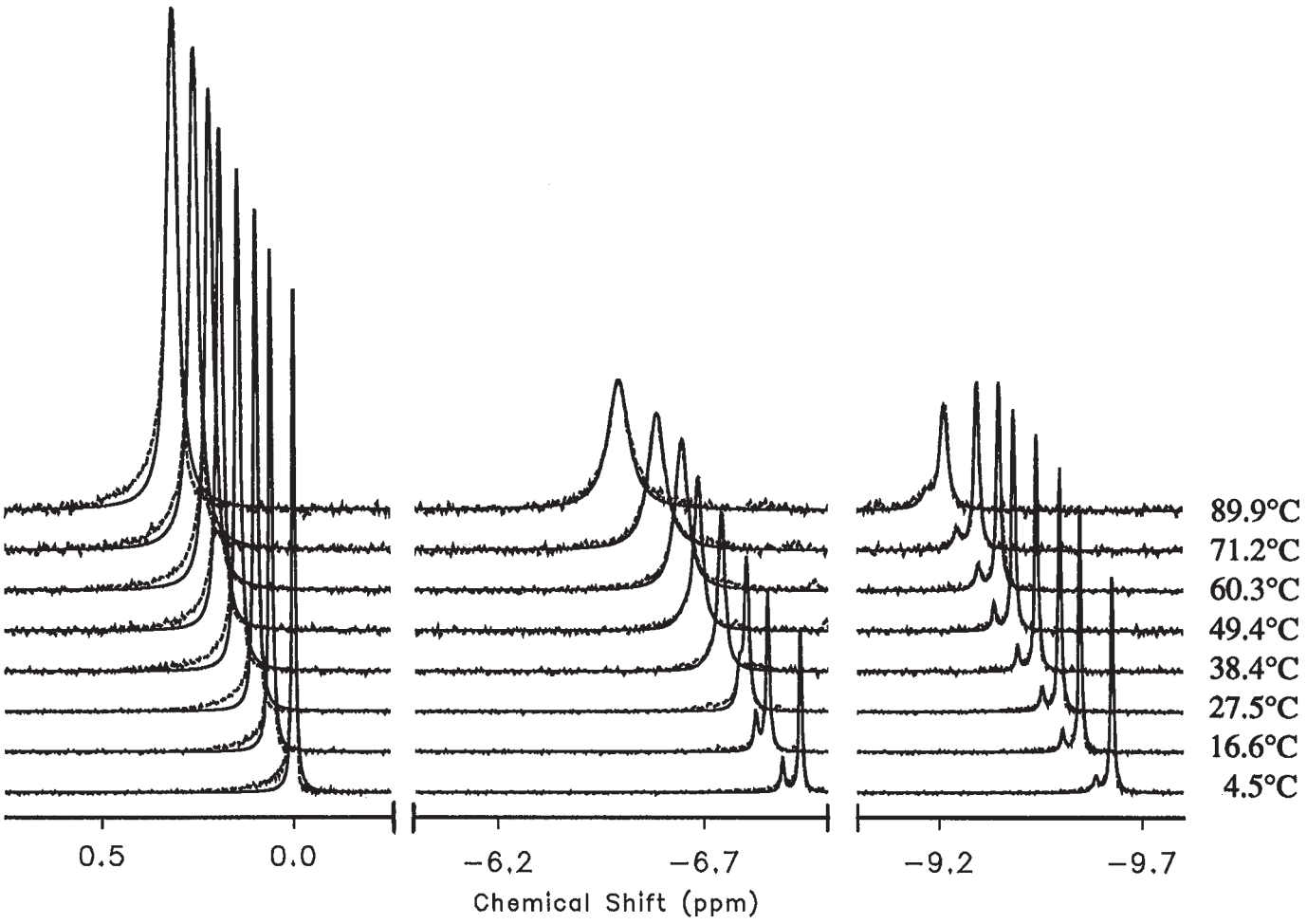

represented by a single rate constant k_C or, contrary to chemical intuition, L is not an intermediate in the D–C exchange process.

Selective inversion–recovery analysis

As is shown in the Appendix, the kinetic equation for the MDC mechanism is

$$[6]\quad \frac{\mathrm{d}}{\mathrm{d}t}\begin{bmatrix} M \\ D \\ C \end{bmatrix} = k_D'\begin{bmatrix} -1 & \frac{M_\infty}{D_\infty} \\ 1 & -\frac{M_\infty}{D_\infty} \end{bmatrix}\begin{bmatrix} M \\ D \end{bmatrix} + k_C'\begin{bmatrix} -1 & 0 & \frac{M_\infty}{C_\infty} \\ 0 & -2\frac{M_\infty}{D_\infty} & 2\frac{M_\infty}{C_\infty} \\ 1 & 2\frac{M_\infty}{D_\infty} & -3\frac{M_\infty}{C_\infty} \end{bmatrix}\begin{bmatrix} M \\ D \\ C \end{bmatrix}$$

where the italicized quantities M, D, and C are the magnetizations of the monomer M, dimer D, and cyclic trimer C, respectively. The subscripts ∞ indicate equilibrium values, and these are proportional to the corresponding concentrations multiplied by the number of nuclei per molecule of the particular kind observed. The branched tetramer was excluded and the area of the peak at –9.7 ppm was attributed to the cyclic trimer alone. If the participation of the linear trimer as the precursor of the cyclic trimer in the exchange processes is included (MDLC mechanism), and it is assumed that all three Si nuclei in L were represented in the (D + L) band, the kinetic equation becomes

© 1998 NRC Canada

$$[7]\quad \frac{\mathrm{d}}{\mathrm{d}t}\begin{bmatrix} M \\ D \\ L \\ C \end{bmatrix} = k_1'\begin{bmatrix} -1 & \frac{M_\infty}{D_\infty} \\ 1 & -\frac{M_\infty}{D_\infty} \end{bmatrix}\begin{bmatrix} M \\ D \end{bmatrix} + k_2'\begin{bmatrix} -1 & 0 & \frac{M_\infty}{L_\infty} \\ 0 & -2\frac{M_\infty}{D_\infty} & 2\frac{M_\infty}{L_\infty} \\ 1 & 2\frac{M_\infty}{D_\infty} & -3\frac{M_\infty}{L_\infty} \end{bmatrix}\begin{bmatrix} -1 & \frac{L_\infty}{C_\infty} \\ 1 & -\frac{L_\infty}{C_\infty} \end{bmatrix}\begin{bmatrix} L \\ C \end{bmatrix}$$

In fact, only the two Q^1 nuclei in L are expected to contribute to the intensity of the (D + L) band, but for computational purposes the signal of the unobservable third (Q^2) nucleus had to be assumed to be included to conserve the number of NMR-active sites in eqs. [4] and [5]. It should be noted that, while reaction [5] involves three NMR-active nuclei, it is also mechanistically triply degenerate, i.e., any of the three Si-O-Si links in C may be broken to form L.

Because the overlap of the D and L resonances prevents rigorous numerical analysis of the SIR data, several approximate approaches with more or less faulty assumptions were tried with the object of producing consistent, accurate fits of the experimental results in terms of a mechanistic picture, as well as meaningful rate constants for those reaction steps for which these could be defined.

Model (i)

The (D + L) band was assumed to represent the major component D alone, and the MDC model was applied; that is, we feigned ignorance of the composite character of this band for expediency in computation (the true concentrations of D and L were, however, used in calculating K_C, K_D, k_{-C}, and k_{-D}). Separate experiments involving, respectively, selective inversion of the M, (D + L), and C bands can be accommodated by the CIFIT program for the MDC mechanism (Figs. 4–7).

Model (ii)

The minor component L of the (D + L) band was assumed to be inactive in Si exchange on the time scale of the M–D and D–C exchanges; the MDC model was then applied to data sets in which the integrated ($D + L$) signal intensities were uniformly reduced by an amount L_∞ corresponding to the stoichiometric concentration of Q^1 L nuclei. The M-SIR data of sample I are well represented by this approach, but the assumption that L is inactive cannot be correct since no sharp resonance corresponding to the Q^2 nucleus of L was detectable and no inverted signal corresponding to the L component persisted in SIR of the combined (D + L) band.

Model (iii)

As a variant of (*ii*), the MDC mechanism was applied with all ($D + L$) signal intensities reduced by a factor of $L_\infty/(D_\infty + L_\infty)$. This implies that the time dependence of L follows that of D, as could happen if equilibration of L with D + M were rapid on a time scale on which the formation of C is slow.

Model (iv)

D–C exchange was assumed to proceed through L as an intermediate, and the MDLC mechanism was invoked. To achieve this in an approximate way, the integrated ($D + L$) band intensity was divided proportionally into magnetizations D and L, as in model (*iii*), on the basis of the *known* equilibrium concentrations of D and L (Table 1). This dissection is exact for the equilibrium magnetizations D_∞ and L_∞ that appear in the CIFIT matrices of eq. [7] and is accurate enough for the zero-time magnetizations required by the CIFIT program, but it is unlikely to reflect accurately the evolutions of D and L over time during spin inversion–recovery unless they are fortuitously similar. This assumption is reasonable, however, since the pseudo-first-order reactions of M with another M and with D are likely to be mechanistically similar and, besides, the change in the intensity of the L signal with time will be small relative to the concurrent changes in M, D, and C. Since the CIFIT program cannot handle SIR of the (D + L) band if it is divided into two contributions, only M-SIR and C-SIR data can be analyzed with this model. To reduce the number of parameters, a reasonable approximation, viz., that T_1 values for the Q^1 silicons of D and L are the same, was made. Typical results of this approach are shown in Figs. 8 (sample II) and 9 (sample I, with scales expanded to show detail).

Model (v)

The fraction of the (D + L) band allocated to L as in model *(iv)* was augmented by 50% to represent a contribution from the missing Q^2 resonance of L, and the MDLC mechanism was applied. The kinetic and NMR parameters so obtained for a given sample and temperature were essentially the same as those obtained in model (*iv*); thus, the numerical analysis of the SIR results was insensitive to the number of active nuclei assigned to the L resonance when preparing the data files.

The numerical results of the various SIR analyses are collected in Tables 4 and 5. Adopted (in most cases, averaged) values of the kinetic parameters are listed in Table 6. The inconsistency of rate constants derived from D-SIR reflects the composite nature of the (D + L) band.

Line-shape simulations

Line-shape simulations were carried out for spectra acquired from 4.5 to 90°C, with the assumption that there was no observable chemical exchange at 4.5°C and therefore the line widths at this low temperature represent natural line widths. Line positions, populations, and rate constants were adjusted manually to describe the experimental spectra. It became evident that the apparent rate constants for LSA were much greater than for SIR, but also that no self-consistent set of rate constants corresponding to the MDC or MDLC mechanisms could be derived. The monomer and dimer peaks could not both be accurately reproduced simultaneously unless an additional line- broadening factor for the monomer was arbitrarily included. This excess broadening of the M signal was more evident in sample I than in sample II, and experiments with samples not described in Table 1 showed that the broadening

© 1998 NRC Canada

Fig. 4. M-SIR of sample I at 90°C, MDC model. (●): M signal; (▼): (D + L) signal; (▲): C signal. Fitted curves yield T_1^{-1} =0.101, 0.25, and 0.14 s^{-1} for M, (D + L), and C, respectively; $k_D' = 0.282$ s^{-1}, and $k_C' = 0.037$ s^{-1}.

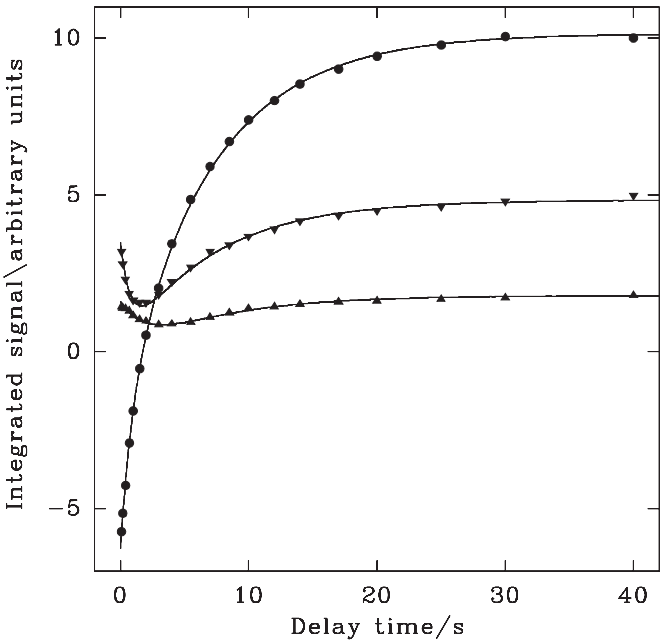

Fig. 5. M-SIR of sample II at 90°C, MDC model. Legend as for Fig. 4. Fitted curves yield T_1^{-1} = 0.035, 0.080, and 0.024 s^{-1} for M, (D + L), and C, respectively; $k_D' = 0.31$ s^{-1}, and $k_C' = 0.029$ s^{-1}.

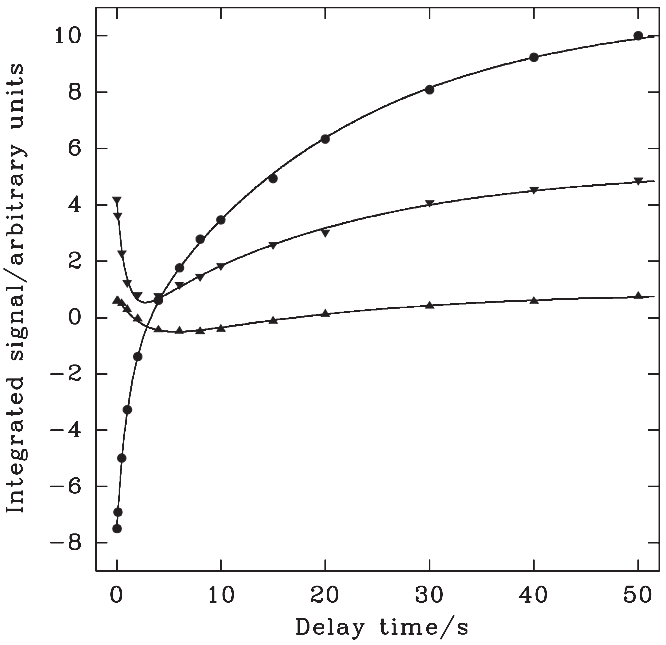

was greater the more ACS Reagent-grade alkali that was present, despite the fact that increasing [OH^-] is known to retard the Si–Si exchange rate (10). The excess broadening was arbitrarily expressed as an apparent rate constant k_{corr}, which may represent a process, other than simple silicate–silicate exchange, in which the monomer interacts preferentially with

Fig. 6. D-SIR of sample II at 90°C, MDC model. Legend as for Fig. 4. Fitted curves correspond to T_1^{-1} = 0.037, 0.080, and 0.035 s^{-1} for M, (D + L), and C, respectively; $k_D' = 0.28$ s^{-1}, and $k_C' = 0.25$ s^{-1}.

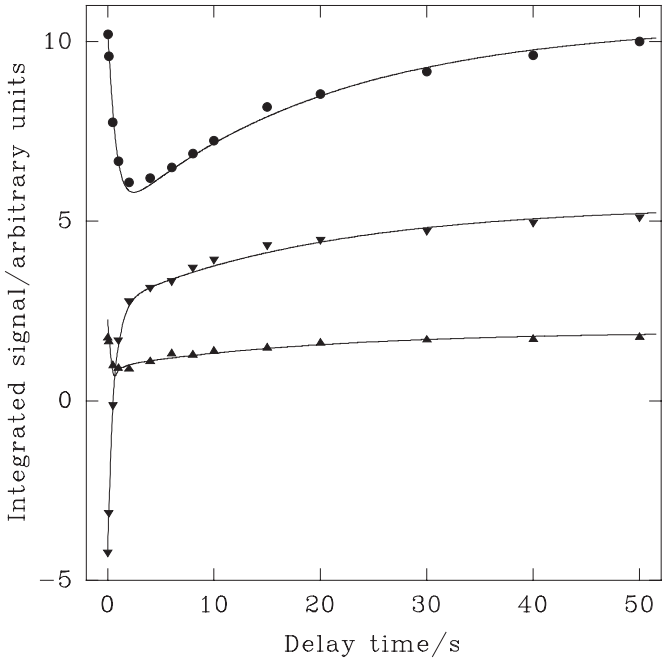

Fig. 7. C-SIR of sample II at 90°C, MDC model. Legend as for Fig. 4. The broken curves represent best fits and yield T_1^{-1} = 0.016, 0.084, and 0.044 s^{-1} for M, (D + L), and C, respectively, k_D' 0.034 s^{-1}, and $k_C' = 0.044$ s^{-1}. The solid curves are constructed with fixed parameters derived in other calculations: T_1^{-1} = 0.037, 0.080, and 0.044 s^{-1} for M, (D + L), and C, respectively, and $k_D' = 0.28$ s^{-1}; these give $k_C' = 0.040$ s^{-1}.

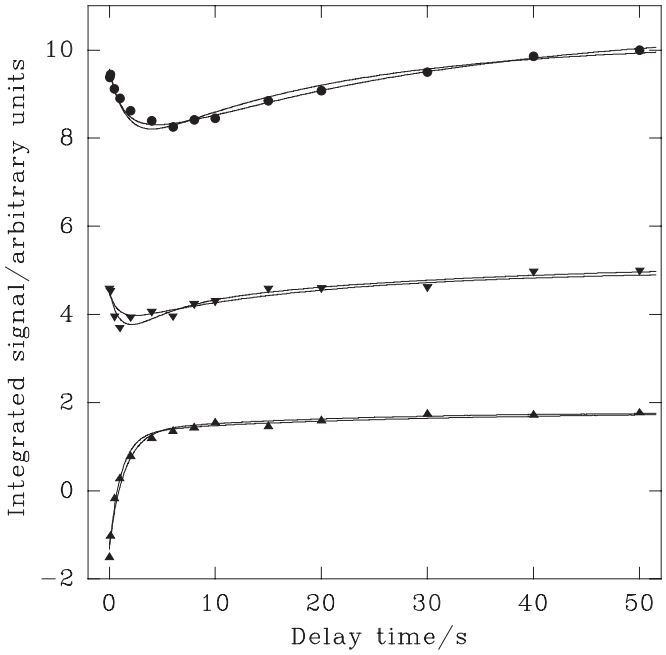

paramagnetic impurities brought in with the alkali. To facilitate LSA simulations based on the MDLC mechanism for the

© 1998 NRC Canada

Fig. 8. M-SIR of sample II at 90°C, MDLC model (*iv*). (●): M signal; (▼): estimated D signal; (■), estimated L signal; (▲): C signal. Fitted curves correspond to $T_1^{-1} = 0.036$, 0.070, 0.070, and 0.053 s^{-1} for M, D, L, and C, respectively; $k_1' = 0.26$ s^{-1}, $k_2' = 0.089$ s^{-1}, and $k_3' = 1.4$ s^{-1}. The dimer signal intensities have been increased by 1.0 unit for clarity.

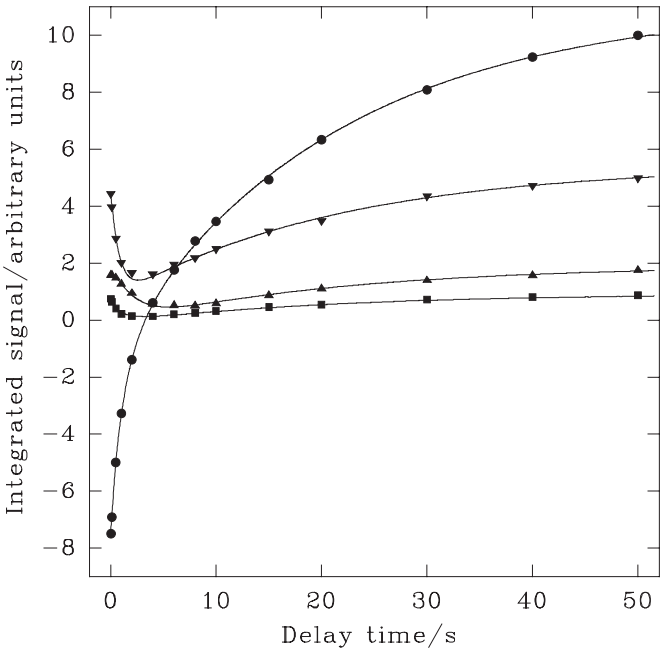

Fig. 9. Early stages of M-SIR for sample I at 90°C, MDLC model (*iv*). Legend as for Fig. 8. Fitted curves correspond to $T_1^{-1} = 0.101$, 0.29, 0.29, and 0.084 s^{-1} for M, D, L, and C, respectively; $k_1' = 0.24$ s^{-1}, $k_2' = 0.097$ s^{-1}, and $k_3' = 1.5$ s^{-1}.

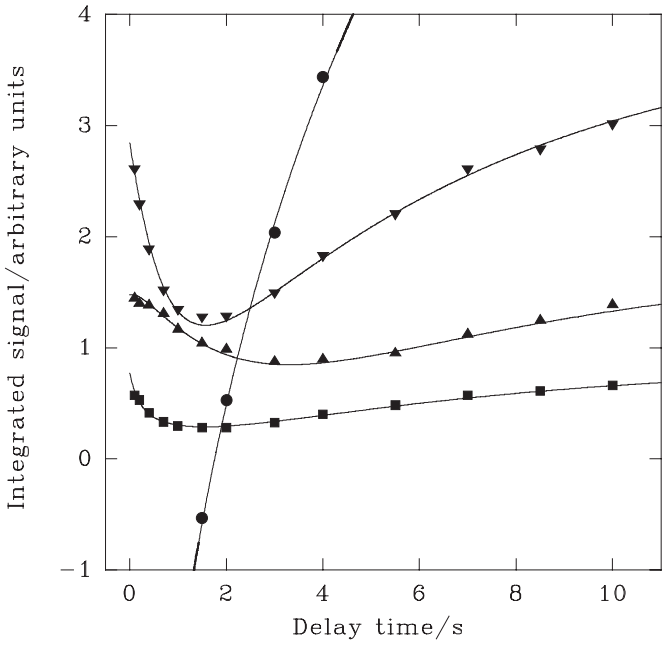

sake of order-of-magnitude comparison with the SIR results, $k_1'$was set equal to k_2', giving the approximate data of Table 7.

Discussion

The conditional ΔH_i values of Table 3 illustrate the general observation (14) that, at a given [OH^-], higher temperatures disfavor the larger oligomers; the monomer–dimer equilibrium, however, is almost thermoneutral. It is not possible at present to apportion contributions to the thermodynamic parameters between proton ionization of Si-O-H groups (relatively few of which should remain in the highly alkaline solutions used in this study) and Si-O-Si bonding changes.

A salient feature of the SIR results is that T_1 values for the various ^{29}Si nuclei are in reasonable agreement between different experiments for a particular sample and temperature but are about three times as long for sample II as for sample I, as may be seen in the nonselective inversion results of Table 2 as well as in the SIR data of Tables 4 and 5 and by visual inspection of Figs. 4 and 5 (noting the different time scales). Since samples I and II differ significantly only in the source of KOH used, we may conclude that paramagnetic contaminants are present in sufficiently high levels in typical concentrated aqueous KOH solutions to exert important influences on the ^{29}Si NMR spectra of silicates. These observations are consistent with those of Creswell et al. (8) and Kinrade et al. (15).

Consequently, rate constants for Si exchange in alkaline solution estimated by line-shape analyses will almost inevitably be too large. This is borne out by the SIR results, which gave rate constants an order of magnitude lower than did LSA even for sample II (that with the purer KOH). Furthermore, it proved impossible to obtain accurate LSA fits for all the major bands simultaneously on the basis of silicate–silicate exchange alone; excess broadening of the monomer band may represent a preferentially rapid interaction of the monomer with some impurity.

In the SIR analyses, selective inversion of the strong M band gave much more reliable SIR data than did inversion of the (D + L) band (which is composite as well as much weaker than the M signal) or of the C band (the weakest; the C-SIR spectra of sample I were of especially poor quality, and those of sample II could not be analyzed unambiguously, as shown in Fig. 7). Unfortunately, complications due to the overlap of the D and L signals could not be avoided, and the results of the computations, summarized in Tables 4–6, are therefore necessarily tentative. Furthermore, our failure to observe the Q^2 center of L serves as a warning that other undetected Si centers could have contributed to the dynamics of a network of Si–Si exchanges. Nevertheless, there is encouraging consistency in the rate constants for M–D exchange (±10% of the average in Table 6) for the two samples and different modes of analysis. Clearly, k_D and k_{-D} are identical with k_1 and k_{-1}, respectively, and are the true reaction rate constants governing monomer–dimer exchange under the given conditions. Thus, at 90°C, $k_1 = 0.13 \pm 0.01$ kg mol s^{-1} and $k_{-1} = 1.4 \pm 0.1$ s^{-1}, with corresponding activation parameters $\Delta H_1^{\ddagger} = 67.4$ kJ mol^{-1}, $\Delta S_1^{\ddagger} = -78$ J K^{-1} mol^{-1}, $\Delta H_{-1}^{\ddagger} = 64.7$ kJ mol^{-1}, and $\Delta S_{-1}^{\ddagger} = -66$ J K^{-1} mol^{-1}.

Creswell et al. (8) reported first-order rate constants k_D of 0.21 and 1.06 kg mol^{-1} s^{-1} at 83 and 107°C, respectively, obtained with an MDC model for a solution containing 2.8 mol kg^{-1} SiO_2 with K/Si = 3.8. These values are 2.6–2.9 times faster than calculated for these temperatures from our activation parameters, in accordance with the general observation that Si exchange rates become slower with rising alkalinity. If each Si center is associated with two negative charges, as is

© 1998 NRC Canada

Table 4. Interpretation of SIR data via the MDC (three-site) mechanism.[a]

Sample	Temp./°C	SIR	T_1^{-1}/s^{-1} M	T_1^{-1}/s^{-1} D	T_1^{-1}/s^{-1} C	k_D'/s^{-1}	k_C'/s^{-1}
I	90	M	0.104	0.27	0.10	0.298	0.035
		M[b]	(0.15)	(0.12)	0.14	0.280	0.026
		M[c]	0.12	0.26	0.083	0.256	0.033
		D	0.094	0.21	0.13	0.278	0.08
		C	*0.104*	*0.21*	0.102	*0.28*	0.038
II	90	M	0.034	0.080	0.024	0.312	0.032
		M[c]	0.043	0.077	0.034	0.280	0.034
		D	0.042	0.086	0.067	0.300	0.07
		C	(0.016)	0.084	0.043	(0.034)	0.044
		C	*0.037*	*0.080*	0.043	*0.28*	0.034
II	60	M	0.063	0.20	—[d]	0.039	—[d]
		D	0.069	0.20	0.103	0.039	0.006
		C	*0.067* [d]	*0.20* [d]	0.105	*0.039* [d]	0.0030

[a] Model (*i*), except as indicated; parentheses denote an unreliable result, excluded from final averaging; italicized data are fixed parameters taken from other experiments.
[b] Model (*ii*).
[c] Model (*iii*).
[d] SIR effect too small.

Table 5. Interpretation of SIR data via the MDLC (four-site) mechanism.[a]

Sample	Temp /°C	SIR	T_1/s M	T_1/s D[b]	T_1/s L[b]	T_1/s C	k_1'/s^{-1}	k_2'/s^{-1}	k_3 /s^{-1}
I	90	M	9.9	3.4	3.4	12	0.243	0.097	1.5
		C	*9.9*	*3.4*	*3.4*	*12*	*0.29*	*0.097*	1.6
II	90	M	28	14	14	19	0.261	0.089	1.4
		C	*28*	*14*	*14*	*29*	*0.261*	*0.089*	2.1
II	60	M	16	4.5	4.5	(22)[c]	0.030	0.009	(0.06)[c]
		C	*16*[c]	*4.5*[c]	*4.5*[c]	*10.8*	*0.030*[c]	*0.009*[c]	0.11

[a] Model (*iv*); parentheses denote an unreliable result, excluded from final averaging; italicized data are fixed parameters taken from other analyses.
[b] T_1 for D and L were taken as equal to reduce the number of parameters.
[c] SIR effect too small.

likely at such high pH, then the concentration of free OH^- was about 5.4 mol kg^{-1} in our samples I and II, as compared with 3.0 mol kg^{-1} in the solutions of Creswell et al. (8), but no simple relationship between k_1 and stoichiometric [OH^-] can be expected in these highly concentrated solutions in which interionic interactions will be strong and the activity of solvent water will be far removed from unity. McCormick et al. (12) used an MDC model to obtain $k_D = 0.05–0.1$ L mol^{-1} s^{-1} and $k_C = 0.1–0.2$ L mol^{-1} s^{-1} (see Appendix) for a solution containing 3 mol% SiO_2 with $SiO_2/K_2O = 0.6$, but the temperature was not reported; very short (<1 s) T_1 values suggest the presence of substantial concentrations of paramagnetic solutes in their solutions.

The agreement between values of the overall rate constant k_C for the formation of the cyclic trimer from D and M obtained by C-SIR (Table 6) and those from M-SIR is good, considering the roughness of the C-SIR data and the oversimplification inherent in the MDC model. Values of k_C are reproduced by $\Delta H_C^{\ddagger} = 76.5$ kJ mol^{-1} and $\Delta S_C^{\ddagger} = -57$ J K^{-1} mol^{-1}, and k_{-C} by $\Delta H_{-C}^{\ddagger} = 88.6$ kJ mol^{-1} and $\Delta S_{-C}^{\ddagger} = -7$ J K^{-1} mol^{-1}.

The rate constants k_2, k_3, and their reverse counterparts from the MDLC model (Table 6) are in some measure fictitious because of the arbitrariness of the assumptions about the role of L. The quality of fits of the data using model (*iv*), however, suggests that the implicit scenario of the formation of D from 2M and of L from M + D followed by a ring-closure step to form C, all at comparable rates, is realistic. Values of k_2 are less than twice k_1, implying similar reactivities of M and D toward attack by M, although this may be an artifact of the assumptions of model (*iv*). Close scrutiny of the early stages of M-SIR (see Figs. 4–8 and especially Fig. 9) suggests that transfer of magnetization from D and L into C is somewhat slower, particularly in the first few hundred milliseconds. This effect is not easy to quantify, since k_2 and k_3 are of different kinetic orders and therefore not directly comparable, but clearly (and perhaps contrary to naive expectations) ring closure of L to form C is not significantly faster than other Si-O-Si link-forming processes. As for the reverse processes, the pseudo-first-order reverse rate constants k_{-D}, k_{-C}, k_{-1}, k_{-2}, and k_{-3}, all of which refer to the breaking of a Si-O-Si link, span only a narrow range. This suggests that Si-O-Si bond cleavage rates are not strongly affected by the intramolecular environment in small silicate oligomers.

In conclusion, this study shows that rate constants for sili-

© 1998 NRC Canada

Table 6. Adopted values of kinetic parameters from SIR analyses.[a]

Model	Parameter	SIR	Value at 60°C	Value at 90°C
MDC	k_D'/s^{-1}	M,D,C	**0.039 ± 0.004**	**0.286 ± 0.018**
	k_C'/s^{-1}	M,C	0.0030 ± 0.0007	0.035 ± 0.005
	k_D/kg mol^{-1} s^{-1}	M,D,C	**0.018 ± 0.002**	**0.134 ± 0.008**
	k_{-D}/s^{-1}	M,D,C	**0.21 ± 0.02**	**1.40 ± 0.08**
	k_C/kg mol^{-1} s^{-1}	C	0.0075 ± 0.0013	0.080 ± 0.013
	k_{-C}/s^{-1}	C	0.039 ± 0.008	0.60 ± 0.05
MDLC	k_1'/s^{-1}	M	**0.030 ± 0.003**	**0.26 ± 0.02**
	k_2'/s^{-1}	M	0.009 ± 0.001	0.093 ± 0.004
	k_3/s^{-1}	C	0.11 ± 0.01	1.6 ± 0.3
	k_1/kg mol^{-1} s^{-1}	M	**0.014 ± 0.002**	**0.124 ± 0.010**
	k_2/kg mol^{-1} s^{-1}	M	0.023 ± 0.003	0.21 ± 0.02
	k_{-1}/s^{-1}	M	**0.16 ± 0.01**	**1.3 ± 0.1**
	k_{-2}/s^{-1}	M	0.19 ± 0.02	2.0 ± 0.2
	k_{-3}/s^{-1}	C	0.067 ± 0.007	1.2 ± 0.3

[a] Values in **bold type** are true rate constants; others are dependent upon the models used.

Table 7. Approximate apparent rate constants at 90°C from line-shape analysis according to the MDLC mechanism.

Sample	k_1'/s^{-1} [a]	k_{corr}/s^{-1}	k_3/s^{-1}
I	7	1.5	17
II	2.1	0.1	4.4

[a] Assumed ≈ k_2'.

cate monomer–dimer exchange in aqueous alkaline solution can be obtained with a reproducibility of better than ±10% from selective inversion–recovery ^{29}Si NMR by use of the CIFIT program. Furthermore, these SIR rate constants are unaffected by trace (presumably paramagnetic) contaminants, inevitably introduced with the alkali, that accelerate both longitudinal and transverse magnetic relaxation and invalidate rate constants estimated from NMR line-shape analysis; in the very highly alkaline solutions of this study, such rate constants were too large by an order of magnitude even when the purest commercial KOH was used, although apparent rate constants reported in other LSA studies in which the alkalinity was relatively low should still be at least qualitatively useful. Unfortunately, the overlapping of NMR resonances, particularly those of the centrally important dimer and linear trimer, invalidate the use of SIR of those resonances and prohibit a full quantitative analysis of the exchange kinetics of silicate oligomers, even when the number of such oligomers is minimized by use of elevated temperatures and very high alkalinity. Models that attempt to recognize the mechanistic participation of the linear trimer can represent the experimental data well, but the simple MDC model (*i*) based on eqs. [1] and [2] suffices to describe the experimental data from M-, D-, or C-SIR consistently and accurately, and to give meaningful values of the rate constants for monomer–dimer and overall dimer – cyclic trimer exchanges. Definitive rate constants for the D–L and L–C steps of the MDLC model cannot be obtained, but the reactivities of Si centers in formation and cleavage of Si-O-Si links, including the cyclization of L, are evidently rather similar for the silicate species considered in this study under the conditions of high pH and [Si].

Acknowledgements

We thank Ms. Qiao Wu for assistance in running some of the NMR spectra, and the Natural Sciences and Engineering Research Council of Canada for equipment and research grants.

References

1. T.W. Swaddle, J. Salerno, and P.A. Tregloan. Chem. Soc. Rev. **23**, 319 (1994).
2. R.K. Harris and R.H. Newman. J. Chem. Soc. Faraday Trans. 2, **73**, 1204 (1977).
3. R.K. Harris, C.T.G. Knight, and W.E. Hull. J. Am. Chem. Soc. **103**, 1577 (1981).
4. R.K. Harris and C.T.G. Knight. J. Chem. Soc. Faraday Trans. 2, **79**, 1525, 1539 (1983).
5. R.K. Harris, E.K.F. Bahlmann, K. Metcalfe, and E.G. Smith. Magn. Reson. Chem. **31**, 743 (1993); R.K. Harris, J. Parkinson, and A. Samadi-Maybodi. J. Chem. Soc. Dalton Trans. 2533 (1997).
6. C.T.G. Knight, R.J. Kirkpatrick, and E. Oldfield. J. Chem. Soc. Chem. Commun. 66 (1986).
7. R.K. Harris, J. Jones, C.T.G. Knight, and R.H. Newman. J. Mol. Liq. **29**, 63 (1984).
8. C.J. Creswell, R.K. Harris, and P.T. Jageland. J. Chem. Soc. Chem. Commun. 1261 (1984).
9. C.T.G. Knight, R.J. Kirkpatrick, and E. Oldfield. J. Magn. Reson. **78**, 31 (1988).
10. S.D. Kinrade and T.W. Swaddle. Inorg. Chem. **27**, 4259 (1988).
11. S.D. Kinrade and T.W. Swaddle. Inorg. Chem. **28**, 1952 (1989).
12. A.V. McCormick, A.T. Bell, and C.J. Radke. J. Phys. Chem. **93**, 1737 (1989).
13. S.D. Kinrade. J. Phys. Chem. **100**, 4760 (1996).
14. S.D. Kinrade and T.W. Swaddle. Inorg. Chem. **27**, 4253 (1988).
15. S.D. Kinrade, K. Marat, and C.T.G. Knight. J. Phys. Chem. **100**, 18351 (1996).
16. A.D. Bain and J.A. Cramer. J. Magn. Reson. Ser. A. **103**, 217 (1993).
17. A.D. Bain and J.A. Cramer. J. Phys. Chem. **97**, 2884 (1993).

© 1998 NRC Canada

18. A.D. Bain and J.A. Cramer. J. Magn. Reson. Ser. A. **118**, 21 (1996).
19. D.R. Muhandiram and R.E.D. McClung. J. Magn. Reson. **71**, 187 (1987).
20. C. Ammann, P. Meier, and A.E. Merbach. J. Magn. Reson. **46**, 319 (1982).
21. G.A. Morris and R. Freeman. J. Magn. Reson. **29**, 433 (1978).
22. R.A. Sack. Mol. Phys. **1**, 163 (1958).
23. S.D. Kinrade and T.W. Swaddle. J. Am. Chem. Soc. **108**, 7159 (1986).

Appendix: Derivation of eqs. [6] and [7]

Since the NMR-active ^{29}Si isotope is present only at natural (i.e., low) abundance, we may consider the exchange of a single spin-inverted ^{29}Si center (a) between monomer (A), dimer (AA), and cyclic trimer (*c*-AAA) sites, as in eqs. [8]–[11]. In the derivation of eq. [6], the possible intermediacy of the linear trimer in eqs. [9]–[11] is ignored (MDC model). We may also disregard degenerate exchange processes such as [12], since such processes may be assumed to occur through intermediates of increased or reduced connectivity (reactions [8]–[11]). All three pathways [9]–[11] must be included, even though the products *c*-aAA, *c*-AAa, and *c*-AaA are indistinguishable.

[8] $\mathrm{a + A} \underset{k_{-D}}{\overset{k_D}{\rightleftharpoons}} \mathrm{aA}$

[9] $\mathrm{a + AA} \underset{k_{-C}}{\overset{k_C}{\rightleftharpoons}} \mathit{c}\text{–aAA}$

[10] $\mathrm{A + Aa} \underset{k_{-C}}{\overset{k_C}{\rightleftharpoons}} \mathit{c}\text{–AAa}$

[11] $\mathrm{Aa + A} \underset{k_{-C}}{\overset{k_C}{\rightleftharpoons}} \mathit{c}\text{–AaA}$

[12] $\mathrm{a + AA} \rightleftharpoons \mathrm{aA + A}$

The kinetic equations for the chemical exchange processes [8]–[11] are then as follows.

[13] $\mathrm{d[a]}/dt = -k_D\mathrm{[a][A]} - k_C\mathrm{[a][AA]} + k_{-D}\mathrm{[aA]} + k_{-C}[c\text{-aAA}]$

[14] $\mathrm{d[aA]}/dt = k_D\mathrm{[a][A]} + 2k_{-C}[c\text{-aAA}] - k_{-D}\mathrm{[aA]} - 2k_C\mathrm{[A][aA]}$

[15] $\mathrm{d[aAA]}/dt = k_C\mathrm{[a][AA]} + k_C\mathrm{[aA][A]} - 2k_{-C}[c\text{-aAA}]$

The *observed* time-dependent magnetizations M, D, and C and their equilibrium values M_∞, D_∞, and C_∞, however, arise from all nuclei at sites of a given kind, and so we have:

$[\mathrm{a}] \propto M; [\mathrm{aA}] \propto D/2; [c\text{-aAA}] \propto C/3$

$[\mathrm{A}] = [\mathrm{M}] \propto M_\infty; [\mathrm{AA}] = [\mathrm{D}] \propto D_\infty/2; [c\text{-AAA}] = [\mathrm{C}] \propto C_\infty/3$

The kinetic equation is then

$$[15]\quad \frac{\mathrm{d}}{\mathrm{d}t}\begin{bmatrix} M \\ D \\ C \end{bmatrix} = \begin{bmatrix} -k_D\mathrm{[M]} - k_C\mathrm{[D]} & k_{-D}/2 & k_{-C}/3 \\ k_D\mathrm{[M]} & -(k_{-D}/2) - k_C\mathrm{[M]} & 2k_{-C}/3 \\ k_C\mathrm{[D]} & k_C\mathrm{[M]}/2 & -k_{-C} \end{bmatrix}\begin{bmatrix} M \\ D \\ C \end{bmatrix}$$

Incorporating the equilibrium relationships given with eqs. [1] and [2], we obtain:

$$[16]\quad \frac{\mathrm{d}}{\mathrm{d}t}\begin{bmatrix} M \\ D \\ C \end{bmatrix} = \begin{bmatrix} -k_D\mathrm{[M]} - k_C\mathrm{[D]} & k_D\dfrac{\mathrm{[M]^2}}{2\mathrm{[D]}} & k_C\dfrac{\mathrm{[M][D]}}{3\mathrm{[C]}} \\ k_D\mathrm{[M]} & -k_D\dfrac{\mathrm{[M]^2}}{2\mathrm{[D]}} - k_c\mathrm{[M]} & 2k_C\dfrac{\mathrm{[M][D]}}{3\mathrm{[C]}} \\ k_C\mathrm{[D]} & k_C\mathrm{[M]} & -k_{-C}\dfrac{\mathrm{[M][D]}}{\mathrm{[C]}} \end{bmatrix}\begin{bmatrix} M \\ D \\ C \end{bmatrix}$$

$$= k_D\mathrm{[M]}\begin{bmatrix} -1 & \dfrac{M_\infty}{D_\infty} \\ 1 & -\dfrac{M_\infty}{D_\infty} \end{bmatrix}\begin{bmatrix} M \\ D \end{bmatrix} + k_C\mathrm{[D]}\begin{bmatrix} -1 & 0 & \dfrac{M_\infty}{C_\infty} \\ 0 & -2\dfrac{M_\infty}{D_\infty} & 2\dfrac{M_\infty}{C_\infty} \\ 1 & 2\dfrac{M_\infty}{D_\infty} & -3\dfrac{M_\infty}{C_\infty} \end{bmatrix}\begin{bmatrix} M \\ D \\ C \end{bmatrix}$$

On writing $k_D\mathrm{[M]} = k_D'$ and $k_C\mathrm{[D]} = k_C'$, this becomes eq. [6]. Equation [16] is essentially that used by McCormick et al. (12) except that the k_1 defined by them corresponds to $k_D/2$ (as a result of counting path [8] twice). Equation [7] may be derived in a similar fashion, with the assumption that the magnetizations L^t and L^c of the terminal and central Si sites in the species L (aAA and AaA; $L^c = L^t/2 = L/3$) can be taken in combination. In practice, neither L^t nor L^c can be independently observed at temperatures at which chemical exchange rates can be reliably measured by ^{29}Si NMR. For the same reason, the full 5×5 kinetic matrix that includes L^t and L^c was not considered in this work.

© 1998 NRC Canada

Control of relative migration of small inorganic and organic anions with cyclodextrins in capillary electrophoresis (CE)

Costas Stathakis and Richard M. Cassidy

Abstract: The capillary electrophoretic separation of iodide, nitrate, perchlorate, thiocyanate, bromate, iodate, and ethane-, butane-, pentane-, and octanesulphonate was examined in sodium chromate or potassium hydrogen phthalate electrolytes and in the presence of α-, γ-, (0–40 mmol/L) and β-cyclodextrin (0–10 mmol/L). Largest decreases in electrophoretic mobility were observed for iodide, perchlorate, and thiocyanate, probably due to inclusion of these anions in the cyclodextrin (CD) cavity. Changes in migration patterns and electroosmotic flow were observed, which depended on cyclodextrin type and concentration and on electrolyte–cyclodextrin interactions. Thus for larger cavity cyclodextrins (β- or γ- cyclodextrin) or in the presence of chromate, relatively small decreases in electrophoretic mobilities for all the anions were observed, indicating that a good match between analyte and cavity size and minimal cyclodextrin affinity for electrolyte ions are essential for different migration patterns. Separation efficiencies were between 50 000 and 400 000 theoretical plates, and calibration plots for iodide and octanesulphonate were linear; $R^2 = 0.998$ and 0.9999, respectively, in the concentration range (5×10^{-5})–(5×10^{-3}) mol/L.

Key words: capillary electrophoresis, inorganic and organic anions, cyclodextrins, inclusion complex, electroosmotic flow control.

Résumé : Opérant dans des électrolytes de chromate de sodium ou de phtalate acide de potassium, en présence d'α-, γ- (0–40 mmol/L) et β-cyclodextrines (0–10 mmol/L), on a étudié la séparation par électrophorèse capillaire des ions iodure, nitrate, perchlorate, thiocyanate, bromate, iodate et éthane-, butane-, pentane- et octanesulfonate. Les diminutions les plus importantes dans la mobilité électrophorétique ont été observées avec les ions iodure, perchlorate et thiocyanate, probablement à cause d'une inclusion de ces anions dans la cavité de la cyclodextrine (CD). Des changements dans les patrons de migration et dans l'écoulement électroosmotique ont été observés; ils dépendent du type de cyclodextrine, de la concentration et des interactions électrolyte–cyclodextrine. Ainsi, avec tous les anions et les cyclodextrines de cavité plus grande (β- ou γ-cyclodextrine) ou en présence de chromate, on a observé des diminutions relativement faibles des mobilités électrophorétiques; ces résultats indiquent qu'une bonne correspondance entre les analytes et la taille de la cavité ainsi qu'une affinité minimale de la cyclodextrine pour les ions électrolytes sont essentiels pour différents patrons de migration. Les efficacités de séparation s'établissent entre 50 000 et 400 000 plateaux théoriques et les courbes de calibration pour les ions iodure et octanesulfonate sont linéaires; $R^2 = 0{,}998$ et 0,9999 respectivement pour la plage de concentration allant de (5×10^{-5}) à (5×10^{-3}) mol/L.

Mots clés : électrophorèse capillaire, anions inorganiques et organiques, cyclodextrines, complexe d'inclusion, contrôle de l'écoulement électroosmotique.

[Traduit par la rédaction]

Introduction

In recent years capillary electrophoresis (CE) has emerged as a viable alternative to ion chromatography for the separation and quantitation of small inorganic and organic ions (1–5). Optimization of CE separations requires control of electroosmotic flow (EOF) and of analyte relative migration, which can be accomplished via incorporation of additives (e.g., cationic surfactants (1), polyelectrolytes (6), complexing agents (3)) capable of wall and analyte interactions. However, with surfactant additives a number of difficulties have been reported for the analysis of hydrophobic ("structure breaking") inorganic anions (e.g., iodide, perchlorate, and thiocyanate) and with some surfactant species. Weakly hydrated inorganic anions form strong ion pairs with cationic surfactants, resulting in decreased efficiencies (2), whereas alkyl sulphonate species with chain lengths greater than C_5 interact strongly with surfactant additives and co-migrate with the neutral marker (3). Although some of these difficulties are circumvented with polyelectrolytes, alternative means for controlling analyte migration may be desirable in some analytical situations. One alternative may be hydrophobic inclusion of small inorganic and organic anions with cyclodextrins (CDs). CDs have been

Received February 27, 1997.

C. Stathakis[1] and R.M. Cassidy. University of Saskatchewan, Chemistry Department, 110 Science Place, Saskatoon, SK S7N 5C9, Canada.

[1] Author to whom correspondence may be addressed. Current address: University of Alberta, Chemistry Dept., Edmonton, AB T6G 2G2, Canada. Telephone: (403) 492–9251. Fax: (403) 492–8231. E-mail: costas.stathakis@ualberta.ca

© 1998 NRC Canada

used for control of relative migration in the separation of neutral (7, 8) or charged (9–11) aromatic species, and such interactions have also been modelled theoretically (12–15). CD affinity for inorganic anions has not been explored for optimization of CE separations, although physicochemical studies (16–18) indicate that interactions of CDs with anions such as iodide, thiocyanate, and perchlorate are possible and the extent of CD–analyte interaction correlates with the relative hydrophobicities of these anions. It should be possible to control analyte–CD interactions, and thus analyte relative migration patterns, via choice of CD concentration, cavity size, and the nature of the electrolyte anion. In addition, native CDs are neutral, a feature that should allow for changes in CD concentration without compromising efficiency and resolution because of Joule heating.

This paper examines the potential of cyclodextrins for control of relative migration of small anion separations in CE. The analytes examined included iodide, nitrate, thiocyanate, perchlorate, and ethane-, butane-, pentane-, and octanesulphonate. The choice of these anions was based on their differing hydrophobicities (and presumably their CD affinities), and because of the difficulties associated with the CE separation of some of these ions (e.g., octanesulphonate) in the presence of cationic surfactants. Chromate and phthalate electrolytes were chosen because they are expected to interact to a different extent with the cyclodextrins, and these interactions should have different effects on CD–analyte complexation and thus analyte migration.

Materials and methods

Instrumentation

The capillary electrophoretic (CE) instrument used was a Quanta 4000 (Waters, Milford, Mass.) equipped with a pen-ray lamp-detector cell assembly and forced-air cooling. Detection was indirect at 254 nm (Hg lamp). The CE unit was interfaced to a NEC APC IV personal computer (DX286, 12 MHz). Data acquisition was done via a Maxima 820 chromatography workstation (version 3.30, Dynamic Solutions, Sykesville, Md.) at data acquisition rates ranging from 1 to 25 Hz. All pH measurements were done with a model 805 MP Accumet pH meter (Fisher Scientific, Edmonton, Alta.) equipped with a Ag/AgCl reference electrode. An AE163 digital balance (Mettler Instrument, Greifensee, Switzerland) was used to weigh out all stock solutions used to prepare standards and separation electrolytes.

Capillary preparation

Fused silica capillaries (Polymicro Technologies, Phoenix, Ariz.) had an inner diameter (i.d. = 75 μm) and an outside diameter (o.d. = 365 μm). Capillary end-to-end length was 60 cm and end-to-detection window was 52 cm. Prior to the first run the capillary was conditioned with the separation medium for periods ranging from 15 to 30 min. In between runs, the capillary was rinsed with the separation medium for about 2 min using a vacuum (15 mm Hg) (1 mm Hg = 133.3 Pa) or a syringe. When separation electrolytes were changed, the capillary was purged with deionized distilled water (DDW) then 0.1 mol/L NaOH, followed by a purge with DDW. Overnight conditioning of capillaries was done by rinsing with DDW using gravity flow.

Reagents and analyte standards

All standard, sample, and separation electrolyte stock solutions were prepared in distilled deionized water (Corning, Mega-Pure, MP-6A & D2, Elmira, N.Y.) and were introduced into the capillary via hydrostatic injection for 15 s (10^{-4} mol/L) from a height of 10 cm. Reagents, such as separation electrolytes, polymers, and analyte standards, were used as obtained from the manufacturer without further purification. Separation electrolytes were filtered by passing through a Nylon filter (0.2 μm pore, Cole-Palmer,Chicago, Ill.) to remove any particulate matter. The cationic polyelectrolyte, poly(1,1-dimethyl-3,5-dimethylenepiperidinium chloride) (PDDPiCl, MW 200 000 g/mol), available as 20% solids in water, was purchased from Polysciences Inc. (Warrington, Pa.) and converted to the chromate and phthalate form as outlined elsewhere (6). The cyclodextrins were purchased from Aldrich (Milwaukee, Wis.) Sodium chromate tetrahydrate (99+%) was purchased from Aldrich, and potassium hydrogen phthalate was acquired from BDH Chemicals (Toronto, Ont.) All analyte standards were analytical grade and were prepared in deionized distilled water as 0.02 mol/L stock solutions. Adjustment of pH was done with chromium(VI) oxide (chromic acid; 99.9%; Aldrich) and phthalic acid (BDH).

Calculations

The rate of electroosmosis was monitored via measurement of the neutral marker (water) migration time at the tip of the peak. Electroosmotic mobility (μ_{eo}) was calculated from

$$[1] \quad \mu_{eo} = \frac{l \times L}{V \times t_{eo}}$$

where V is the separation voltage (V), L is the capillary length (cm), l is the injection-to-detection window length (cm), and t_{eo} is the migration time of the neutral marker (s). Observed migration mobility (μ) for analyte species was calculated from

$$[2] \quad \mu = \frac{l \times L}{V \times t}$$

where t is the analyte migration time (s). Analyte electrophoretic mobility (μ_{ep}) was calculated from

$$[3] \quad \mu_{ep} = \mu - \mu_{eo}$$

Points of μ_{ep} or μ_{eo} versus polyelectrolyte concentration on the various plots are connected with lines for clarity only, and regions in between points do not represent data measured. The error associated with each point is <1% (RSD).

The number of theoretical plates (N) was calculated from

$$[4] \quad N = 5.54 \times \left(\frac{t}{w_{0.5}} \right)^2$$

where t is the zone *net* migration time (s) and $w_{0.5}$ is the width (in time units) at 50% of the peak height. Efficiencies were calculated from electropherograms sampled at 10 points/s.

© 1998 NRC Canada

Fig. 1. Plot of electroosmotic mobility versus concentration of cyclodextrin. **1**, α-CD; **2**, β-CD; **3**, γ-CD. Experimental conditions: 5 mmol/L sodium chromate plus 0.002% (w/v) PDDPiCr at pH 8; neutral marker, water peak; direction of electroosmotic flow is towards the anode; field strength, 333 V/cm.

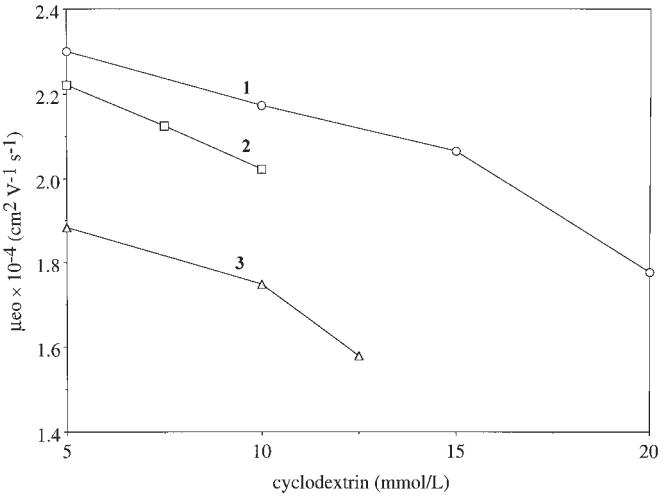

Fig. 2. Plot of electrophoretic mobility versus concentration of α-CD (mmol/L). **1**, nitrate; **2**, iodide; **3**, bromate; **4**, thiocyanate; **5**, perchlorate; **6**, iodate; **7**, ethanesulphonate; **8**, butanesulphonate; **9**, pentanesulphonate; **10**, octanesulphonate. Experimental conditions: 5 mmol/L sodium chromate plus 0.002% (w/v) PDDPiCr at pH 8; field strength, 333 V/cm.

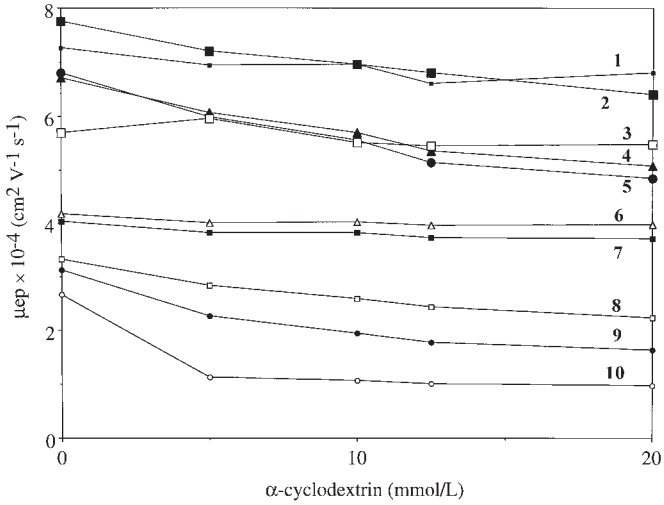

Results and discussion

Electroosmotic flow studies

A small amount of polyelectrolyte PDDPiCr or PDDPiPh (0.002% w/v) was incorporated to assure stable and anodal EOF, based on our previous studies with cationic polymers (6). A study was then conducted on the effects of cyclodextrin type and concentration in 5 mmol/L sodium chromate plus 0.002% (w/v) PDDPiCr at pH 8 and in 5 mmol/L potassium hydrogen phthalate (KHP) plus 0.002% (w/v) PDDPiPh at pH 6.4. The difference in pH for the two separation media does not influence analyte or CD speciation to any significant extent. Polyelectrolyte–CD interactions are generally weak and not expected to influence EOF magnitude. This is in contrast to surfactant–CD interactions where the surfactant tail has a high affinity for the CD cavity, a process that may compete not only with surfactant wall adsorption (and thus EOF reversal) but also with analyte inclusion. However, as indicated in Fig. 1 for the chromate system, small decreases in EOF were observed as a function of cyclodextrin type and concentration. Decreasing EOF rates were observed along the series γ- > β- > α-, which are in the same order as increasing viscosity values for separation electrolyte in the presence of equimolar amounts of the three different CDs (15, 19). EOF reproducibility was 0.96–2.6% (RSD) over a 2.5 h period.

Selectivity control studies

Migration patterns were found to depend on CD type and concentration and on the electrolyte co-ion. As indicated in Fig. 2 for the chromate system, the largest decreases in electrophoretic mobility were observed for the more hydrophobic anions iodide, perchlorate, and thiocyanate. The ability to preferentially slow down perchlorate and thiocyanate via CD complexation is useful in changing analyte migration order. Over the concentration range 0–20 mmol/L there were several changes in migration order of the inorganic anions, but the sulphonate surfactants migrated in order of increasing chain length. Typical electropherograms demonstrating migration-order dependence on CD type for the inorganic anions are shown in Fig. 3 (20 mmol/L α-CD) and Fig. 4 (12 mmol/L γ-CD). For the surfactant species, improved resolution was observed, especially between ethane- and butanesulfonate; the results in Fig. 2 suggest that ethanesulfonate does not interact appreciably with α-CD. With β-CD (Fig. 5), decreasing electrophoretic mobilities were also observed, but were relatively small likely due to the fact that β-CD has a larger cavity than α-cyclodextrin (by a factor of 1.25 (20)), which does not allow for strong inclusion of the anions. As a result, the anions migrate close to their free-zone electrophoretic mobilities, and incomplete resolution between thiocyanate and perchlorate was observed. With γ-CD, which has an even larger cavity, fairly constant electrophoretic mobility versus CD concentration profiles where observed for all anions including the alkyl sulphonates. Although it has been reported that a number of long-chain surfactants (e.g., sodium dodecyl sulfate) have a high affinity for the CD cavity (21), such an effect is presumably smaller for these lower chain surfactants. Inclusion of chromate by the CDs is not expected to influence CD–analyte interactions significantly, since isotachophoretic data indicates that chromate interacts weakly with α-, β-, and γ-CD, compared to perchlorate or thiocyanate (22).

With a phthalate electrolyte (Fig. 6), changes in mobility were larger compared to chromate electrolytes. This indicates that chromate probably interacts with the CD cavity to a larger extent than phthalate. This observation is in agreement with data indicating that *charged* aromatic species have CD association constants that are smaller by a factor of 10–20 compared to their neutral counterparts (23). In both chromate and phthalate electrolytes and in the case of β-CD, analyte electrophoretic mobilities were constant to within a few percent, presumably due to an analyte size – CD cavity mismatch, which does not favour analyte inclusion. Separation efficiencies in chromate and phthalate electrolytes were between 50 000 and

© 1998 NRC Canada

Fig. 3. Electropherogram showing the separation of a series of inorganic anions in 5 mmol/L sodium chromate plus 12 mmol/L γ-CD at pH 8. **1**, nitrate; **2**, iodide; **3**, bromate; **4**, thiocyanate; **5**, perchlorate; hydrostatic injection for 10 s (10^{-4} mol/L) from a height of 10 cm; field strength, 333 V/cm.

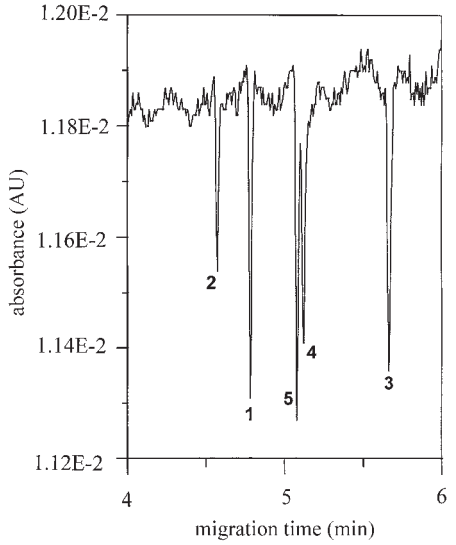

Fig. 4. Electropherogram showing the separation of a series of inorganic anions in 5 mmol/L sodium chromate plus 20 mmol/L α-CD at pH 8. **1**, nitrate; **2**, iodide; **3**, bromate; **4**, thiocyanate; **5**, perchlorate; hydrostatic injection for 15 s (10^{-4} mol/L) from a height of 10 cm; field strength, 333 V/cm.

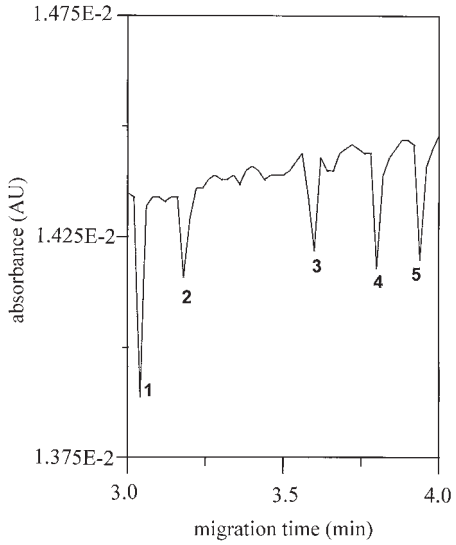

Fig. 5. Plot of electrophoretic mobility versus concentration of β-CD (mmol/L). **1**, nitrate; **2**, iodide; **3**, bromate; **4**, thiocyanate; **5**, perchlorate; **6**, iodate; **7**, ethanesulphonate; **8**, butanesulphonate; **9**, pentanesulphonate; **10**, octanesulphonate. Experimental conditions: 5 mmol/L sodium chromate plus 0.002% (w/v) PDDPiCr at pH 8; field strength, 333 V/cm.

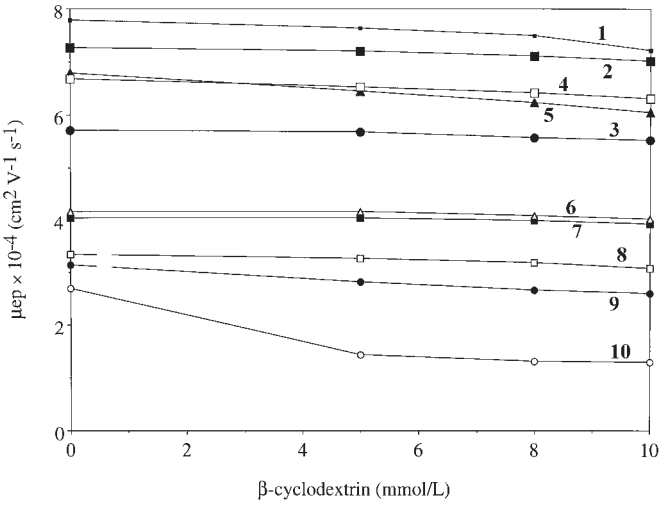

Fig. 6. Plot of electrophoretic mobility versus concentration of α-CD (mmol/L). **1**, nitrate; **2**, iodide; **3**, bromate; **4**, thiocyanate; **5**, perchlorate; **6**, iodate; **7**, ethanesulphonate; **8**, butanesulphonate; **9**, pentanesulphonate; **10**, octanesulphonate. Experimental conditions: 5 mmol/L potassium hydrogen phthalate plus 0.002% PDDPiPh (w/v) at pH 6; field strength, 333 V/cm.

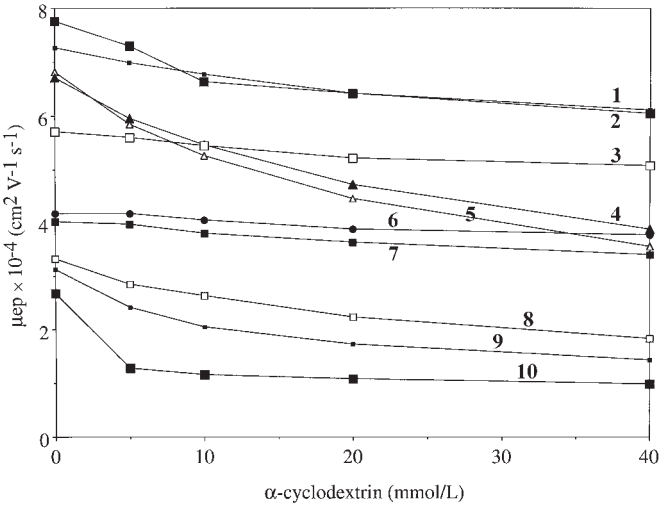

400 000 theoretical plates, which indicate rapid and reversible analyte inclusion in the CD cavity.

The migration orders observed for the inorganic anions in the presence of CDs are different to the orders seen for a number of surfactants and other electrolyte systems. Kaneta et al. (24) studied the separation of iodide, nitrate, bromate, and iodate in 0.2–25 mmol/L cetyltrimethylammonium chloride (CTAC). Selectivities reflected the relative affinity of these anions for the micellar core, and the orders of migration for the anions were nitrate, bromate, iodate, and iodide (1.0 mmol/L CTAC) and iodate, bromate, nitrate, and iodide (25 mmol/L CTAC). In the presence of cyclodextrins, the order of migration was either iodide, nitrate, bromate, and iodate or nitrate, iodide, bromate, and iodate. Jimidard and Massart (25) studied the separation of a series of inorganic anions in 0.45 mmol/L CTAB. The order of migration they observed was nitrate, iodide, and iodate. Separation efficiency for iodide, however, was quite low (12 000 theoretical plates), possibly due to strong ion-pairing interactions with CTAB. Similarly, Jones and Jandik (26) reported the separation of iodide, nitrate, and perchlorate in 0.3 mmol/L OFM, with the migration order iodide, nitrate, and perchlorate. In their

© 1998 NRC Canada

Fig. 7. Electropherogram of 1×10^{-4} mol/L chloride plus 4×10^{-3} mol/L iodide in 5 mmol/L sodium chromate at pH 7.9 with no α-CD (*a*) and with 17 mmol/L α-CD (*b*). **1**, chloride; **2**, iodide; hydrostatic injection for 10 s from a height of 10 cm; field strength, 333 V/cm.

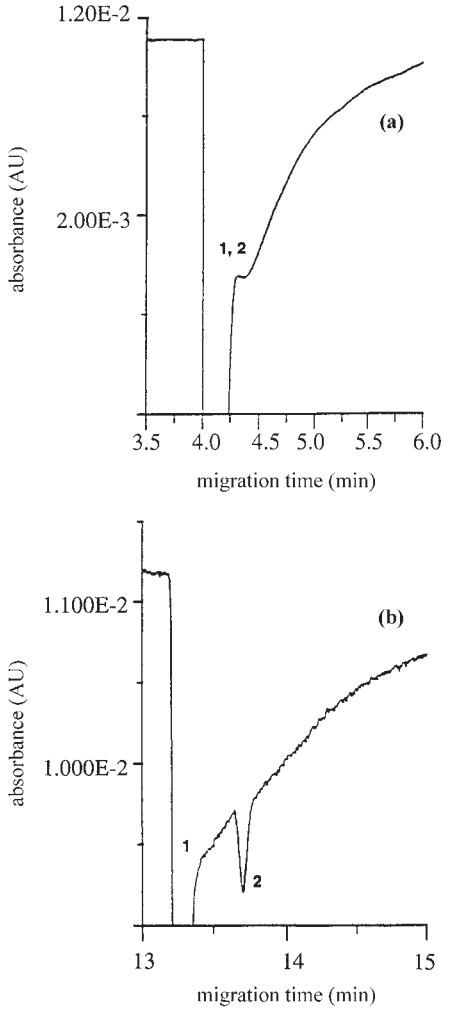

electropherograms, chloride was only partially resolved from iodide; Fig. 7 shows the improvement in resolution of chloride in the presence of a 40-fold excess of iodide when α-CD is used. Similarly, Buchberger and Haddad (27) reported co-migration of iodide and bromide in 0.5 mmol/L OFM plus 30% v/v methanol. Both these anions were well resolved in 10 mmol/L β-CD (data not shown in Fig. 5). Hauser et al. (28) described the separation of nitrate, iodide, and perchlorate in 10 mmol/L acetic acid and sodium acetate buffer (pH 5.0) under counter-electroosmotic conditions. Although all anions are well resolved, analysis times are relatively long (11 min) and peaks for perchlorate and iodide exhibit tailing. Thus for some analytical situations the application of CD additives may prove useful in controlling relative migration.

Application of this separation methodology was briefly examined for the determination of iodide and octanesulphonate ((1×10^{-5})–(1×10^{-3}) mol/L; five concentration points) in a series of simulated samples. Analysis of iodide is of interest to the food and fertilizer industries, whereas the determination of octanesulphonate is important to detergent and emulsifier manufacturers. Calibration plots for iodide and octanesulphonate were linear; $R^2 = 0.998$ and 0.9999, respectively, with sensitivity plots constant to ±8%, only in the range (1×10^{-4})–(1×10^{-3}) mol/L, and to ±20% for iodide in the concentration range (5×10^{-5})–(1×10^{-3}) mol/L.

Acknowledgments

The authors acknowledge the financial support of the Natural Sciences and Engineering Research Council of Canada (NSERC) and the Waters Corporation (Milford, Mass.).

References

1. F. Foret, S. Fanali, A. Nardi, and P. Bocek. Electrophoresis, **11**, 780 (1990).
2. W.R. Jones and P. Jandik. J. Chromatogr. **546**, 445 (1991).
3. J. Romano, P. Jandik, W.R. Jones, and P.E. Jackson. J. Chromatogr. **546**, 411 (1991).
4. A. Weston, P.R. Brown, P. Jandik, W.R. Jones, and A.L. Heckenberg. J. Chromatogr. **593**, 289 (1992).
5. A. Weston, P.R. Brown, A.L. Heckenberg, P. Jandik, and W.R. Jones. J. Chromatogr. **602**, 249 (1992).
6. C. Stathakis and R.M. Cassidy. Anal. Chem. **66**, 2110 (1994).
7. S. Terabe, H. Ozaki, K. Otsuka, and T. Ando. J. Chromatogr. **332**, 211 (1985).
8. H. Nishi and M. Matsuo. J. Liq. Chromatogr. **14**, 973 (1991).
9. B. Koppenhoefer, U. Epperlein, B. Christian, J. Yibing, C. Yuying, and L. Bingcheng. J. Chromatogr. A, **717**, 181 (1995).
10. S. Razee, A. Tamura, and T. Masujima. J. Chromatogr. A, **715**, 179 (1995).
11. M. Heuermann and G. Blaschke. J. Chromatogr. **648**, 267 (1993).
12. S.A.C. Wren and R.C. Rowe. J. Chromatogr. **603**, 235 (1992).
13. S.A.C. Wren. J. Chromatogr. **636**, 57 (1993).
14. C.A. Lucy, R. Brown, and K.K.-C. Yeung. J. Chromatogr. A, **745**, 9 (1996).
15. X. Peng, M.T. Bowser, P. Britz-McKibbin, G.M. Bebault, J.R. Morris, and D.D.Y. Chen. Electrophoresis, **18**, 706 (1997).
16. R.P. Rohrbach, L.J. Rodriguez, E.M. Eyring, and J.F. Wojcik. J. Phys. Chem. **81**, 944 (1977).
17. Y. Matsui, E. Tanemura, and T. Nonomura. Bull. Chem. Soc. Jpn. **66**, 2827 (1993).
18. Y. Yamashoji, M. Fujiwara, T. Matsushita, and M. Tanaka. Chem. Lett. 1029 (1993).
19. A. Shibukawa, D.K. Lloyd, and I.W. Warner. Chromatographia, **35**, 419 (1993).
20. J. Snopek, I. Jelinek, and E. Smolkova-Keulemansova. J. Chromatogr. **452**, 571 (1988).
21. S. Terabe, Y. Miyashita, O. Shibata, E.R. Barnhart, L.R. Aleaxander, D.G. Patterson, B.L. Karger, K. Hosoya, and N. Tanaka. J. Chromatogr. **516**, 23 (1990).
22. K. Fukushi and K. Hiiro. J. Chromatogr. A, **684**, 343 (1994).
23. K.A. Connors. *In* Proceedings of the first international symposium on cyclodextrins. *Edited by* J. Szejtli. Kluwer Boston, Budapest, Hungary. 1981. p. 166.
24. T. Kaneta, S. Tanaka, M. Taga, and H. Yoshida. Anal. Chem. **64**, 798 (1992).
25. M. Jimidar amd D.L. Massart. Anal. Chim. Acta, **294**, 165 (1994).
26. W.R. Jones and P. Jandik. J. Chromatogr. **608**, 385 (1992).
27. W. Buchberger and P.R. Haddad. J. Chromatogr. **608**, 59 (1992).
28. P.C. Hauser, N.D. Renner, and A.P.C. Hong. Anal. Chim. Acta, **295**, 181 (1994).

© 1998 NRC Canada

Synthesis of *trans*-2,3-dimethoxy-3-(phenylamino)flavanones and related compounds[1]

Surya K. De, Mrinal G. Dhara, and Asok K. Mallik

Abstract: *trans*-2,3-Dimethoxy-3-(phenylamino)flavanones **(2)**, a new type of flavanone derivatives, are synthesized from flavanones or 2′-hydroxychalcones in two steps, the first one being a condensation with nitrosobenzenes (Ehrlich–Sachs reaction) and the second an oxidation with (diacetoxyiodo)benzene in methanol. Nitrone formation, an important side reaction of the Ehrlich–Sachs reaction, has also been exploited to synthesize **2** simply by use of an excess of nitrosobenzene in aqueous methanol. Syntheses of several analogues of **2** are also reported.

Key words: *trans*-2,3-dimethoxy-3-(phenylamino)flavanones, 2′-hydroxychalcones, nitrosobenzenes, 3-(phenylamino)flavones, (diacetoxyiodo)benzene.

Résumé : On a réalisé la synthèse de *trans*-2,3-diméthoxy-3-(phénylamino)flavones (**2**), un nouveau type de dérivés des flavones; cette synthèse fait appel à l'utilisation des flavanones ou 2'-hydroxychalcones comme produits de départ et elle implique deux étapes, la première étant une condensation avec des nitrosobenzènes (réaction d'Ehrlich–Sachs) et la deuxième une oxydation à l'aide de (diacétoxyiodo)benzène dans le méthanol. On a aussi exploité la formation de nitrone, une réaction secondaire importante dans la réaction d'Ehrlich–Sachs, pour réaliser une synthèse simple du composé **2** en utilisant un excès de nitrosobenzène dans du méthanol aqueux. On rapporte aussi les synthèses de plusieurs analogues du composé **2.**

Mots clés : *trans*-2,3-diméthoxy-3-(phénylamino)flavones, 2'-hydroxychalcones, nitrosobenzènes, 3-(phénylamino)flavones, (diacétoxyiodo)benzène.

[Traduit par la rédaction]

Introduction

Recently, we reported (1) the formation of *trans*-2,3-dimethoxy-3-(*p*-formylphenylamino)-4′-nitroflavanones **(1)** during the alkali-catalysed condensation of *o*-hydroxyacetophenones with *p*-nitrobenzaldehyde. This is a novel reaction and the products are a new type of flavanone derivatives. Subjecting equimolar mixtures of 2′-hydroxy-4-nitrochalcones and *p*-nitrobenzaldehyde to similar reaction conditions, **1** could be obtained in 45–52% yield. However, attempted general synthesis of *trans*-2,3-dimethoxy-3-(phenylamino)flavanones **(2)** by variation of one or both of the 2′-hydroxychalcone and nitroarene components did not meet with success (1). From a consideration of potential biological activities (2, 3) of this new class of compounds we undertook a general synthesis of **2**. In this study we could develop two synthetic methods; one involves condensation of flavanones **(4)** or 2′-hydroxychalcones **(5)** with nitrosobenzenes followed by hypervalent iodine oxidation of the condensates (3-(phenylamino)flavones **(3)**) in methanol, and the other involves reaction of **4** or **5** with excess nitrosobenzenes in aqueous methanolic alkali. Several analogues of **2** have also been synthesized. An account of these studies is presented herein.

Received September 16, 1996.[2]

S.K. De, M.G. Dhara, and A.K. Mallik.[3] Department of Chemistry, Jadavpur University, Calcutta, 700 032, India.

[1] The major part of this work was presented at the 10th International Conference on Organic Synthesis held at the Indian Institute of Science, Bangalore-560 012, India, December 11–16, 1994.

[2] Revision received October 15, 1997.

[3] Author to whom correspondence may be addressed. Telephone: 91-33-473-4044. Fax: 91-33-473-1484. E-mail: probir. bose @ gems. vsnl. net. in

Results and discussion

The target compounds **(2)** have structural similarity with 2,3-dimethoxy-3 hydroxyflavanones **(6)**. A number of methods for the synthesis of **6** involve oxidation of flavonols **(7)** in methanol (4–10). This prompted us to start from 3-(phenylamino)flavones **(3)** for synthesis of **2**. The hypervalent iodine reagent (diacetoxyiodo)benzene (DAIB), recently applied by us for some other reactions (11, 12), was chosen to effect the oxidation. Thus, six 3-(phenylamino)flavones **(3a–f)** prepared by condensing flavanones **(4)** or 2′-hydroxychalcones **(5)** with nitrosobenzenes (equimolar amount, Method I) (13, 14) were first reacted with DAIB in methanol. For **3a–e** the desired products **(2a–e)** were obtained in good yields (Table 1) (plausible mechanism given in Scheme 1). However, in the case of **3f**, the methanolic solution turned violet immediately on addition of DAIB and neither a crystalline product nor the starting material could be obtained from the reaction mixture. This is possibly due to formation of a radical through homolysis of the N—I bond of **8** (15, 16), and its subsequent reactions. The products **2a–e** were characterized by their spectral data. The

© 1998 NRC Canada

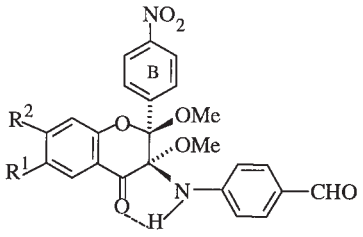

1a : $R^1 = R^2 = H$
b : $R^1 = H$, $R^2 = OMe$
c : $R^1 = OMe$, $R^2 = H$

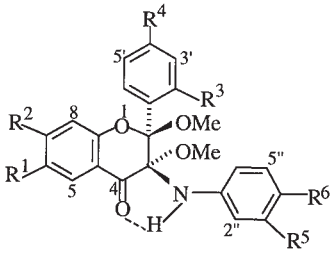

2

a : $R^1 = R^2 = R^3 = R^4 = R^5 = R^6 = H$
c : $R^1 = R^2 = R^3 = R^5 = R^6 = H$, $R^4 = OMe$
e : $R^1 = R^3 = R^5 = R^6 = H$, $R^2 = OMe$, $R^4 = Cl$
g : $R^1 = R^2 = R^3 = R^5 = R^6 = H$, $R^4 = Cl$
i : $R^1 = R^2 = R^3 = R^4 = R^5 = H$, $R^6 = Me$
k : $R^1 = R^2 = R^4 = R^6 = H$, $R^3 = OMe$, $R^5 = Me$

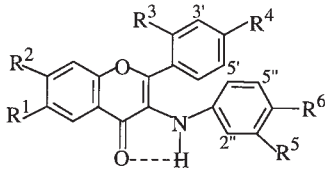

3

b : $R^1 = R^2 = R^3 = R^4 = R^5 = H$, $R^6 = Cl$
d : $R^1 = R^2 = R^3 = R^5 = R^6 = H$, $R^4 = NO_2$
f : $R^1 = R^2 = R^3 = R^4 = R^5 = H$, $R^6 = NMe_2$
h : $R^1 = R^2 = R^3 = R^4 = R^6 = H$ $R^5 = Me$
j : $R^1 = OMe$, $R^2 = R^3 = R^4 = R^5 = R^6 = H$

Table 1. Results of DAIB/MeOH oxidation of **3**.

Starting material	**3a**	**3b**	**3c**	**3d**	**3e**
Product	**2a**	**2b**	**2c**	**2d**	**2e**
Yield (%)	65	67	58	59	62

Scheme 1.

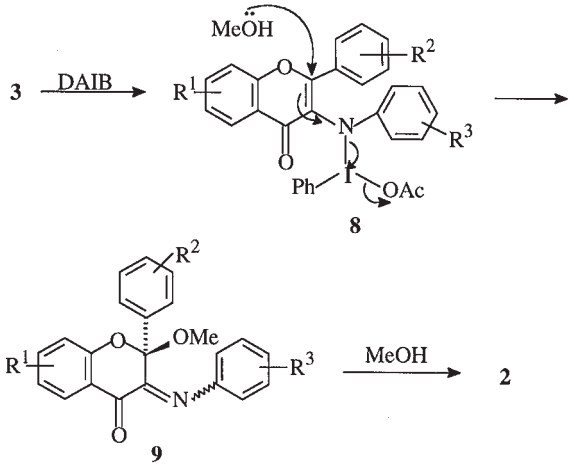

most conspicuous feature in the ^1H NMR spectra of **1a**–**c** (appearance of broad signal for the B-ring protons (1) owing to slow rotation of this ring at ambient temperature) was also present in those of **2a–e**. The positions of the ^1H NMR signals for 2-OMe and 3-OMe in **2a–e** (one at δ 2.90–2.99 and the other at δ 3.09–3.10) were very close to those in **1a–c** (1). Moreover, the last step in the proposed mechanism for formation of **2a–e** (Scheme 1) is similar to that in the case of **1a–c**. Based on these similarities, the *trans* configuration has been assigned.

The only previously known 3-(phenylamino)flavone **3f** was reported (13, 14) to be formed by alkali-catalysed condensation of flavanone and *p*-nitroso-*N,N*-dimethylaniline in aqueous ethanol. But in neither of the two reports of its synthesis was the yield mentioned. Applying the same method, we could obtain **3a–f** in only moderate (30–47%) yield. A study of the Ehrlich–Sachs reaction (17, 18) revealed that nitrone formation (through oxidation of the intermediate **10** with a second molecule of nitrosobenzene) is an important side reaction (Scheme 2). Moreover, the reacting nitrosobenzene can undergo reduction with alcoholic alkali (ref. 17, p. 261). We suggested the intermediacy of nitrones (1) in the formation of **1**. Thus, we envisaged that if nitrones of type **11** are generated in an alkaline reaction medium containing methanol then there is scope for formation of the target compounds in the same step. Although the factors determining the relative amounts of imines and nitrones are not well understood (17, 18), in considering the requirements of the reaction leading to nitrones we decided to use excess nitrosobenzene. Moreover, since 2′-

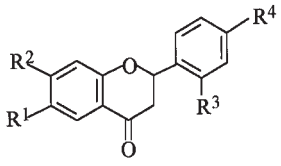

4

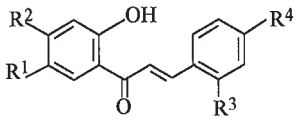

5

a : $R^1 = R^2 = R^3 = R^4 = H$
b : $R^1 = R^2 = R^3 = H$, $R^4 = OMe$
c : $R^1 = R^2 = R^3 = H$, $R^4 = NO_2$
d : $R^1 = R^3 = H$, $R^2 = OMe$, $R^4 = Cl$
e : $R^1 = R^2 = R^3 = H$, $R^4 = Cl$
f : $R^1 = OMe$, $R^2 = R^3 = R^4 = H$
g : $R^1 = R^2 = R^4 = H$, $R^3 = OMe$

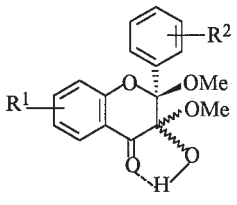

6

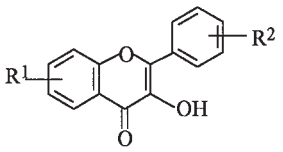

7

hydroxychalcones (**5**) are known to equilibriate with flavanones (**4**) in alkali, we simplified our methodology further by starting from **5**. Thus, we carried out reactions of flavanones or 2′-hydroxychalcones with excess nitrosobenzene (2.5 mol) in aqueous methanolic alkali (Method II) and obtained the

© 1998 NRC Canada

Table 2. Results of the reactions of flavanones (**4**)/2′-hydrocychalcones (**5**) with excess nitrosobenzenes (2.5 mol).

Reactants		
Flavanones (**4**)/ 2′-hydrocychalcones (**5**)	Nitrosobenzenes	Product(s) (yield, %)
4a	PhNO	**2a** (44) + **3a** (trace)
5a	PhNO	**2a** (39) + **3a** (5)
4a	*p*-ClC_6H_4NO	**2b** (23) + **3b** (10)
5b	PhNO	**2c** (32) + **3c** (trace)
5c	PhNO	**2d** (32) + **3d** (4)
5d	PhNO	**2e** (41)
5e	PhNO	**2g** (46) + **3g** (trace)
4a	*m*-MeC_6H_4NO	**2h** (41) + **3h** (trace)
5a	*p*-MeC_6H_4NO	**2i** (36)
5f	PhNO	**2j** (46)
5g	*m*-MeC_6H_4NO	**2k** (21) + **3k** (trace)

desired compounds in moderate yields (Table 2) along with 3-(phenylamino)flavones (yield: 0–10%). Further increase of the amount of nitrosobenzene did not give **2** in significantly greater yield, but in some cases made product purification more difficult owing to formation of greater amounts of azo- and azoxy-benzenes through reduction (ref. 17, p. 261). On the other hand, several samples of **2** could be obtained even by using a molar proportion of nitrosobenzene.

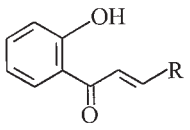

12 : R = 2-Furyl

13 : R = 2-Thienyl

14 : R = -CH $\overset{E}{=}$ CHPh

15 : R = 9-Anthryl

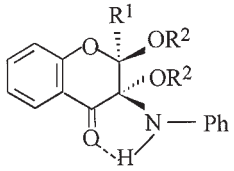

16 : R^1 = 2-Furyl, R^2 = Me

17 : R^1 = 2-Thienyl, R^2 = Me

18 : R^1 = -CH$\overset{E}{=}$CHPh, R^2 = Me

19 : R^1 =Ph, R^2 = Et

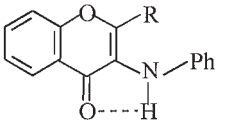

20 : R = -CH $\overset{E}{=}$ CHPh

21 : R = 9-Anthryl

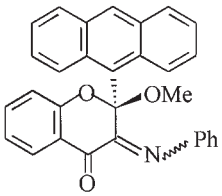

22

Thus, we could develop two methodologies for general synthesis of **2**, of which the latter appears more attractive because of its simplicity. However, its main drawback is that the reaction is not very reproducible under similar conditions. This is not at all unexpected (17, 18). Each of the yields recorded in Table 2 is the best result obtained from a group of three analogous experiments.

Effort was then given to synthesis of some analogues of **2**. The heterocyclic analogues **16** and **17** were synthesized by Method II simply by starting from **12** and **13**, respectively

Scheme 2.

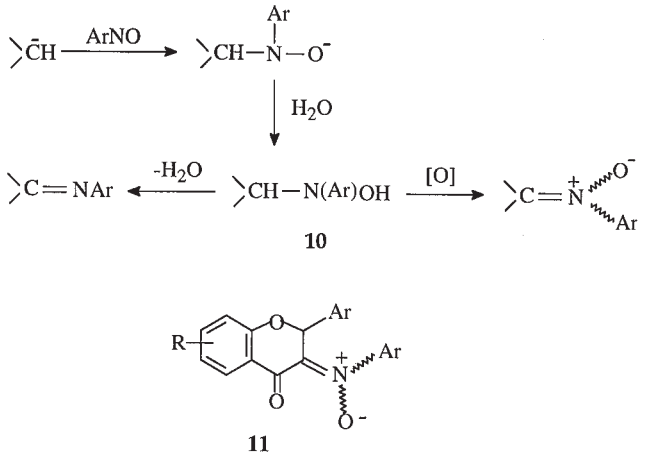

10

11

(yields: 39 and 34%). When compounds **14** and **15** were subjected to such reaction conditions, **20** and **21** (yields : 45 and 42%), respectively, were obtained, but no trace of analogues of **2**. DAIB oxidation of **20** in methanol afforded **18** (yield: 74%). It may be noted that the styryl double bond of **20** remains unattacked. DAIB oxidation of **21** in methanol yielded **22** (62%), but not an analogue of **2**, possibly due to inhibition of methanol addition to the imino moiety by an unfavourable steric effect. The ethoxy analogue of **2a**, not formed by treatment of **4a** with excess nitrosobenzene in aqueous ethanolic alkali, was obtained by oxidation of **3a** with DAIB in ethanol. Here, at room temperature the reaction was very slow (yield: 15%, after 60 h) while at reflux temperature no **19** could be isolated from the resulting black gummy material obtained after disappearance of **3a**.

Experimental

Melting points (mps) were recorded in a Köfler block and are uncorrected. IR spectra were recorded in Nujol on a Perkin–Elmer 297 spectrophotometer. ^{1}H NMR spectra were recorded in $CDCl_3$ on Varian EM 360 (60 MHz), Hitachi R-600 (60 MHz), JEOL FX 100 (100 MHz), Bruker AC-200 (200 MHz), Bruker AM-300L (300 MHz), and Bruker AMX-500 (500 MHz) spectrometers. The ^{13}C NMR spectrum was recorded in $CDCl_3$ on a Bruker AMX-500 (125 MHz) spectrometer. Mass spectra were recorded on a Shimadju QP-1000 spectrometer.

Analytical samples were routinely dried in vacuo at room temperature. Column and thin-layer chromatographies were carried out using neutral alumina (S.D. Fine Chem.) and alumina for TLC (SRL), respectively.

p-Nitroso-*N,N*-dimethylaniline was prepared through nitrosation of *N,N*-dimethylaniline while the other nitrosobenzenes were prepared from the corresponding nitrobenzene through Zn–NH_4Cl reduction followed by $Na_2Cr_2O_7$–H_2SO_4 oxidation (19). The 2′-hydroxychalcones (**5**) and flavanones (**4**) used were known compounds (20).

General procedure for reaction of flavanones (4) or 2′-hydroxychalcones (5) with nitrosobenzenes

(a) By using equimolar amounts of the reactants

To a mixture of **4** or **5** (1 mmol) and nitrosobenzene (1 mmol)

© 1998 NRC Canada

in ethanol or methanol (10 mL) was added potassium hydroxide solution (20%, 2 mL) and the solution was stirred at room temperature for 10 h. The reaction mixture was then diluted with water and extracted with ether (4 × 25 mL). The ether extract was concentrated and the residue was chromatographed. Pure 3-(phenylamino)flavone (**3**) thus obtained (yellow to red solid) was crystallized from chloroform–petrol. Yield (%): **3a**, 47; **3b**, 38; **3c**, 45; **3d**, 39; **3e**, 42; **3f**, 30.

(b) By using excess nitrosobenzene in aqueous methanolic solution

A mixture of **4** or **5** (1 mmol) and nitrosobenzene (2.5 mmol) in methanol was treated with potassium hydroxide solution by the aforesaid procedure. After the usual work-up, the resulting material was chromatographed. *trans*-2,3-Dimethoxy-3-(phenylamino)flavanone (**2**) (colourless solid) was eluted first and then 3-(phenylamino)flavone (**3**), if any. Finally **2** was crystallized from chloroform–petrol.

General procedure for DAIB oxidation of 3-(phenylamino)flavones (3) in methanol

DAIB (1 mmol) was added in four portions at 5 min intervals to a solution of **3** (1 mmol) in dry methanol (10 mL) and the mixture was stirred at room temperature. After disappearance of the starting material (within ca. 6 h) the solvent was removed from the reaction mixture and the concentrate was chromatographed. Pure **2** thus obtained was crystallized.

Syntheses of **16–19** and **22** were achieved by following experimental procedures analogous to those mentioned above. The melting points and analytical and spectral data of the different compounds were as follows.

3a: mp 166–167°C; IR: 3335 (N-H) and 1620 (C=O) cm^{-1}; ^1H NMR (100 MHz) δ: 6.24 (1H, br s, N-H), 6.60–6.82 (3H, m, H-2″, 4″, 6″), 6.94–7.14 (2H, m, H-3″, 5″), 7.30–7.84 (5H, m, H-6, 8, 3′, 4′, 5′), 7.74 (1H, ddd, J = 8.5, 7, and 1.8 Hz, H-7), 7.90–8.08 (2H, m, H-2′, 6′), and 8.32 (1H, dd, J = 8.5 and 1.8 Hz, H-5). Anal. calcd. for $C_{21}H_{15}NO_2$: C 80.49, H 4.82, N 4.47%; found: C 80.12, H 4.94, N 4.10%.

3b: mp 155–156°C; IR: 3340 (N-H) and 1615 (C=O) cm^{-1}; ^1H NMR (100 MHz) δ: 6.22 (1H, br s, N-H), 6.58 (2H, m,[4] H-2″, 6″), 7.00 (2H, m,[4] H-3″, 5″), 7.30–7.86 (6H, m, H-6, 7, 8, 3′, 4′, 5′), 7.87–8.02 (2H, m, H-2′, 6′), and 8.30 (1H, dd, J = 8 and 2 Hz, H-5). Anal. calcd. for $C_{21}H_{14}ClNO_2$: C 72.50, H 4.02%; found: C 71.89, H 4.24%.

3c: mp 144–145°C; IR: 3320 (N-H) and 1615 (C=O) cm^{-1}; ^1H NMR (60 MHz) δ: 3.80 (3H, s, OCH_3), 6.26 (1H, br s, N-H), 6.50–7.76 (9H, m, Ar-H), 7.98 (1H, dt, J = 8 and 2 Hz, H-7), 8.03 (2H, d, J = 8 Hz, H-2′, 6′), and 8.30 (1H, dd, J = 8 and 2 Hz, H-5). Anal. calcd. for $C_{22}H_{17}NO_3$: C 76.95, H 4.99%; found: C 76.63, H 4.78%.

3d: mp 191–192°C; IR: 3320 (N-H), 1640 (C=O), and 1530 (arom. NO_2) cm^{-1}; ^1H NMR (100 MHz) δ: 6.40–6.84 (4H, m, N-H, H-2″,4″,6″), 6.92–7.12 (2H, m, H-3″, 5″), 7.38–7.88 (3H, m, H-6, 7, 8), 8.08 and 8.18 (each 2H, d, J = 9 Hz, H-2′, 6′ and H-3′, 5′), and 8.32 (1H, dd, J = 8 and 1.5 Hz, H-5). Anal. calcd. for $C_{21}H_{14}N_2O_4$: C 70.39, H 3.94, N 7.82%; found: C 70.05, H 3.91, N 7.34%.

3e: mp 235–236°C; IR: 3320 (N-H) and 1630 (C=O) cm^{-1}; ^1H NMR (300 MHz) δ: 3.95 (3H, s, OCH_3), 6.33 (1H, br s, N-H), 6.63 (2H, d, J = 8 Hz, H-2″, 6″), 6.75 (1H, t, J = 7.4 Hz, H-4″), 6.94 (1H, d, J = 2.4 Hz, H-8), 6.98–7.06 (3H, m, H-6, 3″, 5″), 7.34 (2H, m,[4] H-3′, 5′), 7.89 (2H, m,[4] H-2′, 6′), and 8.15 (1H, d, J = 9 Hz, H-5). Anal. calcd. for $C_{22}H_{16}ClNO_3$: C 69.93, H 4.23%; found: C 69.10, H 4.44%.

3f: mp 152–153°C (lit. (14) mp 153°C).

2a: mp 135–136°C; IR: 3400 (N-H) and 1710 (C=O) cm^{-1}; ^1H NMR (500 MHz) δ: 2.92 and 3.09 (each 3H, s, 2 × OCH_3), 5.36 (1H, br s, N-H), 6.10 (2H, dd, J = 7.7 and 1 Hz, H-2″, 6″), 6.48 (1H, dt, J = 7.1 and 1 Hz, H-4″), 6.72 (2H, dd, J = 7.7 and 7.1 Hz, H-3″, 5″), 7.07–7.36 and 7.48–7.74 (each 2H, br, H-2′, 3′, 5′, 6′), 7.11–7.15 (2H, m, H-6, 8), 7.29 (1H, br t, J ≈7.5 Hz, H-4′), 7.59 (1H, ddd, J = 8.9, 7.5, and 1.7 Hz, H-7), and 7.93 (1H, dd, J = 8 and 1.7 Hz, H-5); ^{13}C NMR δ: 50.65 (OCH_3), 51.19 (OCH_3), 88.16 (C-3), 107.08 (C-2), 115.52 (C-2″, 6″), 117.65 (C-8), 117.78 (C-4″), 118.84 (C-4a), 121.95 (C-6), 127.46 (C-5), 127.95 (C-2′, 6′), 128.06 (C-3″, 5″), 129.30 (C-3′, 4′, 5′), 134.23 (C-1′), 136.34 (C-7), 143.65 (C-1″), 156.39 (C-8a), and 190.85 (C-4); EIMS *m/z:* 375 (M^+, 98.5%), 360 (M^+–Me, 24.6), 224 (54.5), 212 (78.5), 211 (26.2), 196 (14.2), 181 (17.8), 180 (18.2), 163 (39.2), 152 (14.3), 151 (13.2), 134 (35.7), 121 (45.4), 120 (32.1), 119 (44.8), 105 ($PhCO^+$, 100), 92 (35.7), 91 (21.4), and 77 (Ph^+, 99.2). Anal. calcd. for $C_{23}H_{21}NO_4$: C 73.58, H 5.64, N 3.73%; found: C 72.89, H 5.66, N 3.52%.

2b: mp 181–182°C; IR: 3405 (N-H) and 1705 (C=O) cm^{-1}; ^1H NMR (60 MHz) δ: 2.90 and 3.10 (each 3H, s, 2 × OCH_3), 5.40 (1H, br s, N-H), 6.04 (2H, m,[4] H-2″, 6″), 6.70 (2H, m,[4] H-3″, 5″), 7.00–7.78 (8H, m, Ar-H), and 7.97 (1H, dd, J = 8 and 2 Hz, H-5). Anal. calcd. for $C_{23}H_{20}ClNO_4$: C 67.39, H 4.88%; found: C 66.72; H 4.78%.

2c: mp 151–152°C; IR: 3410 (N-H) and 1708 (C=O) cm^{-1}; ^1H NMR (60 MHz) δ: 2.95, 3.10, and 3.80 (each 3H, s, 3 × OCH_3), 5.36 (1H, br s, N-H), 6.16 (2H, dd, J = 8 and 1.5 Hz, H-2″, 6″), 6.47–7.62 (10H, m, Ar-H), and 7.93 (1H, dd, J = 8 and 2 Hz, H-5). Anal. calcd. for $C_{24}H_{23}NO_5$: C 71.10, H 5.72%; found: C 70.45, H 5.81%.

2d: mp 183–184°C; IR: 3400 (N-H), 1708 (C=O), and 1530 (arom. NO_2) cm^{-1}; ^1H NMR (100 MHz) δ: 2.99 and 3.09 (each 3H, s, 2 × OCH_3), 5.28 (1H, br s, N-H), 6.17 (2H, dd, J = 8 and 1.5 Hz, H-2″, 6″), 6.42–6.88 (3H, m, H-3″, 4″, 5″), 7.06–7.32 (2H, m, H-6, 8), and 7.56–8.28 (6H, m, H-5, 7, 2′, 3′, 5′, 6′). Anal. calcd. for $C_{23}H_{20}N_2O_6$: C 65.71, H 4.79, N 6.66%; found: C 65.04, H 4.36, N 6.12%.

2e: mp 125–126°C; IR: 3395 (N-H) and 1705 (C=O) cm^{-1}; ^1H NMR (60 MHz) δ: 2.95, 3.09, and 3.87 (each 3H, s, 3 × OCH_3), 5.29 (1H, br s, N-H), 6.15 (2H, dd, J = 8 and 1.5 Hz, H-2″, 6″), 6.45–6.94 (5H, m, H-6, 8, 3″, 4″, 5″), 7.15 and 7.54 (each 2H, br d, J = 8 Hz, H-2′, 3′, 5′, 6′), and 7.85 (1H, dd, J = 8 and 2 Hz, H-5). Anal. calcd. for $C_{24}H_{22}ClNO_5$: C 65.52, H 5.06%; found: C 64.89, H 5.31%.

2g: mp 166–167°C; IR: 3400 (N-H) and 1705 (C=O) cm^{-1}; ^1H NMR (60 MHz) δ: 2.93 and 3.07 (each 3H, s, 2 × OCH_3), 5.28 (1H, br s, N-H), 6.12 (2H, dd, J = 8 and 1.5 Hz, H-2″, 6″), 6.50–6.80 (3H, m, H-3″, 4″, 5″), 6.97–7.27 (4H, m, H-6, 8, 2′, 6′), 7.38–7.75 (3H, m, H-7, 3′, 5′), and 7.91 (1H, dd, J = 8 and 2 Hz, H-5). Anal. calcd. for $C_{23}H_{20}ClNO_4$: C 67.39, H 4.88%; found: C 66.83, H 4.78%.

2h: mp 141–142°C; IR: 3390 (N-H) and 1710 (C=O) cm^{-1}; ^1H NMR (200 MHz) δ: 1.95 (3H, s, 3″-CH_3), 2.92 and 3.10

[4] Pattern resembled a pair of triplets, AA′BB′ system, $J_{AB} = J_{A'B'} \approx$ 8.5 Hz, $J_{AA'} \approx$ 2.5 or 3 Hz, $J_{BB''} \approx$ 3 or 2.5 Hz (21).

© 1998 NRC Canada

(each 3H, s, 2 × OCH_3), 5.34 (1H, br s, N-H), 5.85 (1H, br s, H-2″), 6.01 (1H, dd, *J* = 8 and 2 Hz, H-6″), 6.32 (1H, d, *J* = 8 Hz, H-4″), 6.67 (1H, t, *J* = 8 Hz, H-5″), 7.10–7.90 (8H, m, Ar-H), and 7.94 (1H, dd, *J* = 8 and 1.8 Hz, H-5). Anal. calcd. for $C_{24}H_{23}NO_4$: C 74.02, H 5.95%; found: C 74.15, H 6.16%.

2i: mp 183–184°C; IR: 3400 (N-H) and 1710 (C=O) cm^{-1}; ^1H NMR (100 MHz) δ: 2.08 (3H, s, 4″-CH_3), 2.90 and 3.10 (each 3H, s, 2 × OCH_3), 5.31 (1H, br s, N-H), 6.03 (2H, m,[4] H-2″, 6″), 6.57 (2H, m,[4] H-3″, 5″), 7.00–7.84 (8H, m, Ar-H), and 7.97 (1H, dd, *J* = 8 and 2 Hz, H-5). Anal. calcd. for $C_{24}H_{23}NO_4$: C 74.02, H 5.95%; found: C 73.57, H 5.91%.

2j: mp 176–177°C; IR: 3400 (N-H) and 1710 (C=O) cm^{-1}; ^1H NMR (60 MHz) δ: 2.93, 3.07, and 3.83 (each 3H, s, 3 × OCH_3), 5.33 (1H, br s, N-H), 6.10 (2H, dd, *J* = 8 and 1.5 Hz, H-2″, 6″), 6.40–6.80 (3H, m, H-3″, 4″, 5″), and 7.04–7.70 (8H, m, Ar-H). Anal. calcd. for $C_{24}H_{23}NO_5$: C 71.10, H 5.72%; found: C 70.33, H 6.01%.

2k: mp 185–187°C; IR: 3390 (N-H) and 1710 (C=O) cm^{-1}; ^1H NMR (300 MHz) δ: 1.94 (3H, s, 3″-CH_3), 2.98 and 3.15 (each 3H, s, 2 × OCH_3), 3.24 (3H, br s, 2′-OCH_3), 5.41 (1H, s, N-H), 6.03 (1H, br s, H-2″), 6.23 (1H, dd, *J* = 8 and 1.5 Hz, H-6″), 6.33 (1H, d, *J* = 7.3 Hz, H-4″), 6.49 (1H, br d, *J*≈ 8.3 Hz, H-3′), 6.70 (1H, t, *J* = 7.8 Hz, H-5″), 7.08 (1H, br t, *J* ≈7.4 Hz, H-5′), 7.09–7.13 (2H, m, H-6, 8), 7.31 (1H, dt, *J* = 8.7 and 1.7 Hz, H-4′), 7.58 (1H, ddd, *J* = 8.8, 7.4, and 1.6 Hz, H-7), 7.92 (1H, dd, *J* = 7.9 and 1.6 Hz, H-5), and 8.0 (1H, br d, *J* ≈ 6.8 Hz, H-6′). Anal. calcd. for $C_{25}H_{25}NO_5$: C 71.58, H 6.01%; found: C 70.87, H 6.26%.

16: mp 126–127°C; IR: 3395 (N-H) and 1715 (C=O) cm^{-1}; ^1H NMR (100 MHz) δ: 2.98 and 3.16 (each 3H, s, 2 × OCH_3), 5.44 (1H, br s, N-H), 6.32–6.44 (3H, m, H-4′, 2″, 6″), 6.56–6.80 (3H, m, H-3″, 4″, 5″), 6.88–7.25 (4H, m, H-6, 8, 3′, 5′), 7.64 (1H, ddd, *J* = 8, 7.4, and 2 Hz, H-7), and 7.96 (1H, dd, *J* = 8 and 2 Hz, H-5). Anal. calcd. for $C_{21}H_{19}NO_5$: C 69.03, H 5.24, N 3.83%; found: C 68.41, H 5.56, N 3.71%.

17: mp 161–162°C; IR: 3390 (N-H) and 1710 (C=O) cm^{-1}; ^1H NMR (300 MHz) δ: 2.97 and 3.20 (each 3H, s, 2 × OCH_3), 5.42 (1H, br s, N-H), 6.29 (2H, dd, *J* = 7.8 and 1.5 Hz, H-2″, 6″), 6.58 (1H, t, *J* = 7.5 Hz, H-4″), 6.84–6.90 (3H, m, H-4′, 3″, 5″), 7.11–7.17 (3H, m, H-6, 8, 3′), 7.35 (1H, dd, *J* = 4.9 and 1.1 Hz, H-5′), 7.61 (1H, dt, *J* = 8.8 and 1.7 Hz, H-7), and 7.92 (1H, dd, *J* = 8 and 1.7 Hz, H-5). Anal. calcd. for $C_{21}H_{19}NO_4S$: C 66.14, H 4.98%; found: C 66.01, H 5.26%.

20: mp 174–175°C; IR: 3320 (N-H) and 1630 (C=O) cm^{-1}; ^1H NMR (60 MHz) δ: 6.10 (1H, br s, N-H), 6.72–7.80 (15H, Ar-H and olefinic H), and 8.25 (1H, dd, *J* = 8 and 2 Hz, H-5). Anal. calcd. for $C_{23}H_{17}NO_2$: C 81.40, H 5.05%; found: C 81.13, H 4.89%.

18: mp 161–162°C; IR: 3400 (N-H) and 1710 (C=O) cm^{-1}; ^1H NMR (100 MHz) δ: 3.06 and 3.13 (each 3H, s, 2 × OCH_3), 5.41 (1H, br s, N-H), 5.98 (1H, d, *J* = 16 Hz, H-β), 6.68–7.48 (13H, m, Ar-H and H-α), 7.65 (1H, dt, *J* = 8 and 2 Hz, H-7), and 7.96 (1H, dd, *J* = 8 and 2 Hz, H-5); EIMS *m/z:* 401 (M^+, 10.8%), 386 (M^+–Me, 13.4), 280 (32.1), 238 (10.2), 224 (15.5), 161 (12.3), 131 (PhCH=CHCO$^+$, 100), 120 (22.5), 103 (PhCH=CH$^+$, 44), 92 (22.5), and 77 (45). Anal. calcd. for $C_{25}H_{23}NO_4$: C 74.80, H 5.77%; found: C 74.21, H 5.85%.

21: mp 228–230°C; IR: 3340 (N-H) and 1645 (C=O) cm^{-1}; ^1H NMR (100 MHz) δ: 5.88 (1H, br s, N-H), 6.20–6.60 (5H, m, H-2″, 6″), 7.40–7.60 (6H, m, H-6, 8, 2′, 3′,6′, 7′), 7.64 (1H, dt, *J* = 8 and 2 Hz, H-7), 7.84–8.06 (4H, m, H-1′, 4′, 5′, 8′), 8.45 (1H, s, H-10′), and 8.53 (1H, dd, *J* = 8 and 2 Hz, H-5). Anal. calcd. for $C_{29}H_{19}NO_2$: C 84.24, H 4.63%; found: C 83.92, H 4.45%.

22: mp 233–234°C (yellow needles); IR: 1661(C=O) and 1628 (C=N) cm^{-1}; ^1H NMR (300 MHz) δ: 3.06 (3H, s, OCH_3), 6.66 (2H, d, *J* = 7.6 Hz, H-2″, 6″), 7.01 (1H, t, *J* = 7.3 Hz, H-4″), 7.14–7.25 (3H, m), 7.42–7.46 (3H, m), 7.60 (1H, dt, *J* = 7.1 and 1.5 Hz, H-7),7.80–7.83 (1H, m), 7.95–8.03 (3H, m), 8.31–8.34 (1H, m), 8.54 (1H, s, H-10′), and 8.67–8.71 (2H, m); EIMS *m/z:* 443 (M^+, 95.1%), 428 (M^+–Me, 8.2), 412 (8.6), 336 (17.3), 309 (20.1), 308 (36.9), 281 (42.5), 253 (42.7), 252 (30.7), 205 (9-Anthr.–CO$^+$, 100), 177 (9-Anthr.$^+$, 100), 176 (70.8), 151(21.1), 120 (23.4), 104 (10.8), 103 (14.4), 92 (47.5), and 77 (31.7). Anal. calcd. for $C_{30}H_{21}NO_3$: C 81.25, H 4.77%; found: C 80.78, H 4.67%.

19: mp 143–144°C; IR: 3395 (N-H) and 1718 (C=O) cm^{-1}; ^1H NMR (300 MHz) δ: 0.82 and 0.91 (each 3H, t, *J* = 7 Hz, 2 × CH_3), 2.90–2.99 (1H, m), 3.14–3.26 (2H, m) and 3.43–3.49 (1H, m) (2 × -OCH_2-), 5.33 (1H, br s, N-H), 6.06 (2H, dd, *J* = 7.8 and 1.5 Hz, H-2″, 6″), 6.45 (1H, t, *J* = 7.8 Hz, H-4″), 6.71 (2H, t, *J* = 7.8 Hz, H-3″, 5″), 6.94–7.81 (4H, br, H-2′, 3′, 5′, 6′), 7.06–7.12 (2H, m, H-6, 8), 7.31(1H, br t, *J* ≈7.5 Hz, H-4′), 7.57 (1H, dt, *J* = 8.2 and 1.7 Hz, H-7), and 7.89 (1H, dd, *J* = 7.8 and 1.7 Hz, H-5). Anal. calcd. for $C_{25}H_{25}NO_4$: C 74.42, H 6.25%; found: C 74.16, H 6.03%.

Acknowledgements

The authors are grateful to Dr. B.C. Ranu (Indian Association for Cultivation of Science, Calcutta), Dr. A. Patra (University of Calcutta), Mr. S.K. Bhattacharya (University of Pennsylvania), and the authorities of Indian Institute of Chemical Biology (Calcutta), Indian Institute of Technology (Kharagpur), and Regional Sophisticated Instrumentation Centre (Bose Institute, Calcutta) for NMR and mass spectral measurements. Financial assistance from the University Grants Commission, New Delhi, and the authorities of Jadavpur University is gratefully acknowledged.

References

1. A.K. Mallik, M.M. Saha, U.K. Mallik, S. Goswami, D.R. McPhail, and A.T. McPhail. J. Chem. Soc. Chem. Commun. 130 (1992).
2. M.K. Buening, J.G. Fortner, A. Kappas, and A.H. Conney. Biochem. Biophys. Res. Commun. **8**, 348 (1978).
3. M.K. Buening, R.L. Chang, M.-T. Huang, J.G. Fortner, A.W. Wood, and A.H. Conney. Cancer Res. **41**, 67 (1981).
4. H.-D. Becker. J. Org. Chem. **30**, 989 (1965).
5. M.A. Smith, R.A. Webb, and L.J. Cline. J. Org. Chem. **30**, 995 (1965).
6. M. Utaka and A. Takeda. J. Chem. Soc. Chem. Commun. 1824 (1985).
7. O.V. Singh, M.S. Khanna, M.P. Tanwar, C.P. Garg, and R.P. Kapoor. Synth. Commun. **20**, 2401 (1990).
8. R.M. Moriarty, O. Prakash, H.A. Musallam, and V.K. Mahesh. Heterocycles, **24**, 1641 (1986).
9. M. Khanna, (Km) Sangeeta, C.P. Garg, and R.P. Kapoor. Synth. Commun. **22**, 893 (1992).
10. D. Kumar and O.V. Singh. Synth. Commun. **22**, 1333 (1992).
11. U.K. Mallik and A.K. Mallik. Indian J. Chem. **30B**, 611 (1991).
12. U.K. Mallik and A.K. Mallik. Indian J. Chem. **31B**, 696 (1992).
13. D. Evans and I.M. Lockhart. J. Chem. Soc. (C), 711 (1966).

© 1998 NRC Canada

14. P. Pfeiffer and T. Hesse. J. Prakt. Chem. **158**, 315 (1941); Chem. Abstr. **36**, 764 (1942).
15. N. Lewis and P. Wallbank. Synthesis, 1103 (1987).
16. H.G. Viehe, Z. Janousek, R. Merenyi, and L. Stelle. Acc. Chem. Res. **18**, 148 (1985).
17. J.H. Boyer. *In* The chemistry of nitro and nitroso groups. Part I. *Edited by* S. Patai. Interscience Publishers, New York. 1969. p. 277.
18. R.G. Coombers. *In* Comprehensive organic chemistry. Vol. 2. *Edited by* D.H.R. Barton and W.D. Ollis. Pergamon Press, Oxford. 1979. p. 321.
19. Vogel's textbook of practical organic chemistry. ELBS/Longman, Essex. 1978. p.722.
20. U.K. Mallik, M.M. Saha, and A.K. Mallik. (*a*) Indian J. Chem. **28B**, 970 (1989); (*b*) J. Indian Chem. Soc. **67**, 478 (1990).
21. J.R. Dyer. Applications of absorption spectroscopy of organic compounds. Prentice–Hall of India Pvt. Ltd., New Delhi. 1984. p. 110.

© 1998 NRC Canada

Crystal structure, spectroscopic and magnetic studies, and antioxidative properties of catena-[diaqua(dihydro-orotato)manganese(II)]

Paule Castan, Christine Viala, Paul-Louis Fabre, Françoise Nepveu, Jean-Pierre Souchard, and Gérald Bernardinelli

Abstract: The polynuclear manganese(II) complex of L-dihydroorotic acid has been synthesized and characterized by X-ray crystallography, UV–visible spectroscopy, and magnetic susceptibility measurements. Crystal data: triclinic, space group $P\bar{1}$, $a = 4.7239(5)$ Å, $b = 7.902(1)$ Å, $c = 10.552(2)$ Å, $\alpha = 105.80(1)°$, $\beta = 98.864(7)°$, $\gamma = 104.69(1)°$, $V = 355.9(1)$ Å^3, $Z = 1$, $R = 0.035$, $Rw = 0.028$. This complex consists of polymer chains of manganese atoms that are bound together via carboxylate bridges with a Mn···Mn distance in the chain of 4.724 Å. The radical scavenging properties of the complex have been evaluated by ESR spectroscopy and cyclic voltammetry methods and compared to those of vitamin E and BHT (2,6-di-*tert*-butyl-4-methylphenol).

Key words: orotic acid, L-dihydroorotic acid, manganese(II) complex, antioxidative properties.

Résumé : Le complexe du manganèse(II) et de l'acide L-dihydroorotique a été synthétisé et caractérisé par spectroscopie UV–visible, susceptibilité magnétique et par diffraction des rayons X. Données cristallographiques : triclinique, groupe d'espace $P\bar{1}$, $a = 4.7239(5)$ Å, $b = 7.902(1)$ Å, $c = 10.552(2)$ Å, $\alpha = 105.80(1)°$, $\beta = 98.864(7)°$, $\gamma = 104.69(1)°$, $V = 355.9(1)$ Å^3, $Z = 1$, $R = 0.035$, $Rw = 0.028$. Ce complexe se présente comme une chaine polymérique d'atomes de manganèse liés entre eux par des ponts carboxylate, la distance Mn···Mn étant de 4.724 Å. Les propriétés antioxydantes de ce composé ont été évaluées par RPE et voltammétrie cyclique et comparées à celles de la vitamine E et du BHT (2,6-di-*tert*-butyl-4-methylphenol).

Mots clés : acide orotique, acide L-dihydroorotique, complexe du manganèse(II), propriétés antioxydantes.

Introduction

Orotic acid[2] (6-carboxyuracil, 1,2,3,6-tetrahydro-2,6-dioxo-4-pyrimidinecarboxylic acid, $OrotH_3$), being closely related to the biologically important pyrimidine bases, plays a significant role in many biological processes (1, 2). Moreover, it has been extensively used in medicine in the form of metal complexes, its therapeutical action depending on the nature of the complexed metal (3). We recently obtained the complex of 3-methylorotate with palladium(II), which displays a significant antitumor activity comparable to *cisplatin* (4, 5).In addition to its biological importance, orotic acid and its substituted derivatives (which may be viewed as substituted uracils) are also interesting ligands since they are potentially multidentate (the coordination may occur through the two N atoms of the pyrimidine ring, the two carbonyl oxygens, and the carboxylic group) and the metal complexes of orotic (4, 6–13) and isoorotic (14–16) acids have been the subject of a number of solution, spectral, and structural studies. However, studies on its coordination properties in solution and in the solid state show that orotic acid coordinates mainly via N1 and one oxygen atom of the carboxylato group. The only exceptions known so far are the copper(II) complex of 5-nitroorotic acid, which coordinates via the N1 and N3 nitrogen atoms (9), and the uranium complex of orotic acid, which coordinates only by one oxygen of the carboxylato group (17). Orotic acid does not enter the inner coordination sphere of the metal in zinc and magnesium compounds (18, 19).

As part of a program aimed at evaluating the antioxidative properties of small molecular weight metal complexes and in accordance with the reported superoxide radical scavenging activity of the Mn^{2+} ion in a number of in vitro and in vivo systems (20, 21), we studied the variation of this activity in manganese complexes with weak ligands such as carboxylic acids (22, 23). We recently described the quantitative analysis of such properties by ESR spectroscopy (24). Both the biological role and the nature of these substituted carboxylic acids prompted us to investigate the radical scavenging properties of Mn(lI) complexes of orotic acid and of some of its derivatives. Preliminary steps in this program have been to investigate the molecular structures and the physical properties of orotato complexes with manganese and we have recently reported on polynuclear manganese(II) complexes of orotic acid and of some of its derivatives (25).

Received July 18, 1997.

P. Castan,[1] C. Viala, and P.-L. Fabre. Laboratoire de chimie inorganique, Université Paul Sabatier; 118 route de Narbonne, 31062 Toulouse Cedex 04, France.
F. Nepveu and J.-P. Souchard. Laboratoire de synthèse, physico-chimie et radiobiologie, Université Paul Sabatier, 118 route de Narbonne, 31062 Toulouse Cedex 04, France.
G. Bernardinelli. Laboratoire de cristallographie, 24 Quai E. Ansermet, CH-1211 Geneva 4, Switzerland.

[1] Author to whom correspondence may be addressed. Telephone: (33) 05-61-55-61-00. Fax: (33) 05-61-55-61-18.

[2] The nomenclature and numbering scheme of uracils and substituted uracils are shown in Fig. 1.

© 1998 NRC Canada

Fig. 1. Numbering scheme of dihydroorotic acid ($R_1 = R_2 = H$).

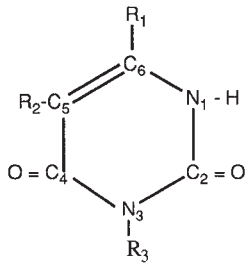

$R^1 = R^2 = R^3 = H$, Uracil

$R^1 = COOH$, $R^2 = R^3 = H$, Orotic acid

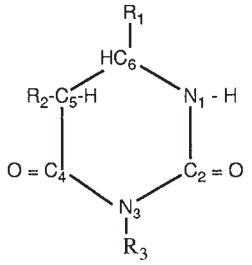

$R^1 = COOH$, $R^2 = R^3 = H$, Dihydroorotic acid

The present work reports the structural, spectral, and magnetic properties of the manganese(II) complex with dihydroorotic acid together with its SOD (superoxide dismutase)-like activities evaluated by ESR spectroscopy and cyclic voltammetry methods. This ligand, unlike orotic acid, presents a nonaromatic pyrimidine ring. The aim of this work was to study a possible modification of the coordinating and antioxidative properties of the resulting manganese(II) complex, associated with the structural difference arising from this loss of aromaticity.

Experimental

Materials

L-Dihydroorotic acid, 5,5-dimethyl-1-pyrroline *N*-oxide (DMPO), diethylenetriaminepentaacetic acid (DTPA), and dimethylaminoethylamine (DMAEA) were purchased from Aldrich Chemical Co. All other chemicals and solvents were of reagent grade.

Synthesis of $[Mn(C_5H_6N_2O_4)_2 \cdot (H_2O)_2]_n$

An aqueous solution of manganese(II) acetate (1 mmol, 5 mL) is added to a solution of L-dihydroorotic acid (1 mmol) in water–acetonitrile (80/20). The pH is adjusted to 7 by adding an ammoniacal solution and, after stirring for 2 h, the mixture is filtered off. After the filtrate has been allowed to stand for 3 weeks in a closed flask, at room temperature, pale tan crystals are formed. Anal. calcd. for $C_{10}H_{l4}MnN_4O_{10}$: Mn 13.56, C 29.64, H 3.48, N 13.82; found: Mn 13.3, C 29.25, H 3.4, N 13.7.

Physical measurements

Elemental analyses were carried out at Service Interuniversitaire de Microanalyse, Toulouse. UV spectra were recorded on a SECOMAM S 1000 spectrometer in aqueous solutions. IR spectra were recorded on a Perkin–Elmer 983 G spectrometer coupled with a Perkin–Elmer infrared data station. Samples were run in the solid state (KBr pellets).

Variable-temperature magnetic susceptibility data were collected on powdered samples of the title compound with the use of a SQUID-based sample magnetometer on a Quantum Design model MPMS instrument. All data were corrected for diamagnetism of the ligand estimated from Pascal's constants (26). ESR spectra in the solid state (300 and 120 K) and as water or water – ethylene glycol glasses at 100 K were recorded on a Bruker ESP 300E spectrometer. Acidity constants were determined through acid–base titrations by means of a METHROM autoburette.

Antioxidative properties

To study the superoxide scavenging properties, the ESR spectra were recorded on a Bruker ER 200 D spectrometer at room temperature by starting a 3 min scan after adding acetaldehyde (AC). Recording conditions were as follows: central field, 3500 G; scan range field, 200 G; microwave frequency, 9.71 GHz; frequency modulation, 70 kHz; field modulation intensity, 1 G; time constant, 0.5 s; scan speed, 24 G min^{-1}. A 1 mL sample of solution was prepared in a glass tube by adding the reagents in the following order: DMPO (50 mmol L^{-1}), xanthine oxidase (XOD) (0.018 U mL^{-1}), tested compound (x mmol L^{-1}), and acetaldehyde (60 mmol L^{-1}) in phosphate or DMAEA buffers (pH 7.4) containing 15 mM DTPA. For each concentration of compound tested, the percentage of inhibition of the ESR signal compared to the signal of the blank was calculated by adding the height of the sextet peaks of the $O_2^{\bullet -}$ dependent AC–XOD carbon-centered signal (the AC–XOD system with DMPO in phosphate or DMAEA buffers produced a sextet ESR signal resulting from the presence of the $O_2^{\bullet -}$ anion in the medium (27)). The $O_2^{\bullet -}$ scavenging activity was quantified by the compound concentration inducing a 50% decrease in the control ESR signal intensity (IC50).

Electrochemical measurements were carried out by cyclic voltammetry with a homemade potentiostat driven by a PC computer. The electrochemical cell was a conventional three-electrode configuration: working electrode, gold disk (diameter l mm); reference electrode, SCE; counter electrode, Pt wire. Experiments were carried out at room temperature in oxygenated dimethylformamide (DMF) with Bu_4NClO_4 as supporting electrolyte. The cyclic voltammetry method is based on the electrochemical properties of the redox couple, which appears to be quasi-reversible at a gold electrode in DMF. When an $O_2^{\bullet -}$ scavenger is added, the cyclic voltammogram is modified according to the kinetics of the $O_2^{\bullet -}$ deactivation. On the backward sweep, the anodic peak current, Ip_{ox}, which corresponds to $O_2^{\bullet -}$ oxidation, is lower than the initial cathodic peak current Ip_{red} of the reduction of O_2 into $O_2^{\bullet -}$ during the forward sweep. The analysis of the peak current ratio RIp (= Ip_{OX}/Ip_{red}) as a function of the potential scan speed and of the concentration of the drug tested allows the determination of the kinetic constants. The method has been standardized with vitamin E and BHT (2,6-di-*tert*-butyl-4-methylphenol).

© 1998 NRC Canada

To compare the results obtained from the two methods, radical scavenging activities are expressed as vitamin E equivalents.

X-ray crystal structure determination

Crystal data, measurement of intensities, and structure refinement are summarized in Table 1. Unit cell parameters and diffracted intensities were measured at room temperature on a STOE-STADI 4 diffractometer using graphite monochromated MoKα radiation. Data were corrected for Lorentz and polarization effects and for absorption. The structure was solved by direct methods (MULTRAN87) (28) and refined by the XTAL 3.2 program (29). Atomic scattering factors and anomalous dispersion terms are taken from ref. 30. All H-atom coordinates were observed and refined. Selected positional and isotropic displacement parameters for non-hydrogen atoms are listed in Table 2, and interatomic distances and angles in Table 3. Complete crystal data and final fractional atomic coordinates with estimated standard deviations have been deposited as supplementary material.[3]

Results and discussion

Description of the structure

Bearing in mind the number of potential coordination sites of L-dihydroorotic acid, polymeric chains may be expected. However, very few polymeric complexes have been observed with orotic acid itself. In polymeric Co(III) and Ni(II) complexes of orotic acid, metal atoms are hexacoordinated to one orotato anion at the N1 ring nitrogen and at the adjacent carboxylate oxygen and to another orotato anion at the exocyclic keto oxygen O4. Thus in these complexes orotic acid acts as a tridentate ligand and bridges metal ions, forming polymer chains.

The Mn(II) complexes of orotic acid, 5-nitroorotic acid, and 3-methylorotic acid that we recently reported (25) consist of polymer chains in which the manganese atom is bonded to the orotato anion at the ring nitrogen N1 and at the adjacent carboxylate group. The anions are associated to form chains, the carboxylato group acting as a bridge between the metal ions, and thus the orotato group is tridentate (N1 and two oxygens of the carboxylate group). By contrast, in the isoorotic acid Mn(II) complex (15), the metal is bonded to the isoorotato anion at one oxygen of the carboxylate group and at the adjacent oxygen atom of the ring.

An ORTEP drawing of the diaqua(dihydroorotato)manganese(II) complex along with the labelling scheme is shown in Fig. 2. Selected interatomic distances and angles are listed in Table 3. This complex consists of polymer chains of manganese that are bound together via carboxylate bridges. The manganese(II) ion is situated at an inversion center (1/2, 1/2, 0) and is involved in a hexa coordination, which is the most common coordination of manganese(II). Each dihydroorotato anion is bidentate by the two oxygen atoms of the carboxylate group and thus bridges two metal ions, which are bound in the chain by two -O-C-O- bridges. Four types of carboxylate bridges have been identified in the literature; only the *syn–syn* configuration brings the metal atoms close enough to form a clustered structure. In this structure two carboxylates of two ligand molecules bridge the metal atoms by two *anti–syn* types

Table 1. Summary of crystal data, measurement of intensities, and structure refinement.

Empirical formula	$C_{10}H_{14}MnN_4O_{10}$
Molecular weight	405.2
Crystal system	Triclinic
Space group	$P\bar{1}$
a/Å	4.7239(5)
b/Å	7.902(1)
c/Å	10.552(2)
α/deg	105.80(1)
γ/deg	104.69(1)
V/Å^3	355.9(1)
Z	1
D_c/g cm^{-1}	1.89
F_{ooo}	207
μ(MoKα)/mm^{-1}	0.997
2θ range (deg)	6–50
No of measured reflections	2682
No of independent reflections	1266
No of observed reflections	1190
No of parameters	144
Weighting scheme	$[\sigma^2 (F_o)]^{-1}$
Criterion for observed reflections	$\|F_o\| < 4\sigma(F_o)$
Goodness of fit *S*	2.90
R, *Rw*	0.035, 0.028

Table 2. Non-hydrogen atoms positional and isotropic displacement parameters.

Atom	*x*/*a*	*y*/*b*	*z*/*c*	*U*eq
Mn	1/2	1/2	0	0.0213(2)
O1	0.2570(3)	0.3952(3)	0.1314(2)	0.0321(7)
O2	–0.2196(3)	0.3139(2)	0.0155(2)	0.0274(7)
O3	–0.6438(4)	–0.0459(3)	0.3271(2)	0.0368(7)
O4	0.2790(3)	0.3376(3)	0.5658(2)	0.0319(7)
N1	–0.1908(4)	0.1545(3)	0.4445(2)	0.0305(9)
N2	0.1182(4)	0.3420(3)	0.3534(2)	0.0274(8)
C1	–0.1326(5)	0.3048(4)	0.2394(3)	0.031(1)
C2	–0.3375(6)	0.1093(4)	0.2045(3)	0.031(1)
C3	–0.4095(5)	0.0651(3)	0.3271(3)	0.0257(9)
C4	0.0850(5)	0.2852(3)	0.4590(2)	0.0250(9)
C5	–0.0215(5)	0.3369(3)	0.1171(2)	0.0237(9)
O01	0.7961(4)	0.7040(3)	0.1854(2)	0.0338(8)

[3] Tables of experimental data and refinement conditions, bond distances and angles, atomic coordinates and equivalent isotropic displacement parameters, as well as an experimental EPR spectrum obtained from frozen glass (water – ethylene glycol) have been deposited as supplementary material and can be purchased from: The Depository of Unpublished Data, Document Delivery, CISTI, National Research Council Canada, Ottawa, Canada K1A 0S2. The tables of atomic parameters and bond distances and angles have also been deposited with the Cambridge Crystallographic Data Centre, and can be obtained on request from The Director, Cambridge Crystallographic Data Centre, University Chemical Laboratory, 12 Union Road, Cambridge, CB2 1EZ, U.K.

© 1998 NRC Canada

Table 3. Interatomic distances (Å) and angles (deg) for complex, with e.s.d's in parentheses.

Mn environment			
Mn—O1	2.135(2)	Mn—O2	2.235(2)
Mn—O01	2.163(2)		
Ol-Mn-O01	84.85(7)	Ol-Mn-O'01	95.15(7)
Ol-Mn-O2	88.65(7)	Ol-Mn-O'2	92.35(7)
O0l-Mn-O2	89.29(7)	O0l-Mn-O'2	90.71(7)
Ligand			
O1—C5	1.249(3)	O2—C5	1.247(3)
O3—C3	1.226(3)	O4—C4	1.231(3)
N1—C3	1.364(3)	N1—C4	1.399(3)
N2—C4	1.326(4)	C1—C2	1.511(4)
C1—C5	1.524(4)	C2—C3	1.493(4)
N2—C1	1.459(3)		
C3-N1-C4	125.4(2)	C1-N2-C4	123.0(2)
N2-C1-C2	109.2(3)	N2-C1-C5	111.4(2)
C2-C1-C5	111.3(2)	C1-C2-C3	112.3(2)
O3-C3-N1	119.7(3)	O3-C3-C2	124.6(2)
N1-C3-C2	115.7(2)	O4-C4-N1	119.0(3)
O4-C4-N2	124.7(2)	N1-C4-N2	116.3(2)
O1-C5-O2	126.5(3)	O1-C5-C1	117.1(2)
O2-C5-C1	116.2(2)		
Dihedral angles			
C4-N1-C3-O3	–179.4(3)	N2-C1-C2-C3	47.3(3)
C4-N1-C3-C2	2.0(4)	C5-C1-C2-C3	170.8(2)
C3-N1-C4-O4	–170.5(3)	N2-Cl-C5-O1	–2.6(4)
C3-N1-C4-N2	8.7(4)	N2-C1-C5-O2	–178.0(2)
C4-N2-C1-C2	–40.6(3)	C2-Cl-C5-O1	–124.8(3)
C4-N2-C1-C5	–164.0(2)	C2-C1-C5-O2	59.8(3)
C1-N2-C4-O4	–168.0(3)	C1-C2-C3-O3	150.5(3)
Cl-N2-C4-N1	12.8(4)	Cl-C2-C3-N1	–30.9(4)

of carboxylate bridges forming a polymeric stack parallel to the (011) plane. Carboxylate bridging between transition-metal atoms such as copper(II) acetate hydrate (31, 32) and its analogues with other metal ions is well known. The hexa coordination around a metal atom is provided by four oxygens of four orotato anions and two water molecules (O1, O2, O′1, O′2, O01, and O′01). The octahedron has deviated from D_3 symmetry and four shorter and two longer metal–ligand bond lengths are observed. The Mn—O distances of 2.135(2), 2.163(2), and 2.235(2) Å (for Mn—O2) plainly indicate this distortion. However, the two carboxylate bond lengths are almost identical, i.e., C5—O1 = 1.249(3) and C5—O2 = 1.247(3) Å. In all structures known to date where the orotate is complexed to a metal, it acts as a dianionic ligand (13), the only exception being a uranium(VI) complex where the ligand is mono-deprotonated at the carboxylic function and monodentate (17). In the present structure both nitrogens are protonated and the dihydroorotato entity is only deprotonated at the carboxylate function.

Since the crystal structure of the dihydroorotic acid itself has not been determined, structural parameters for the dihydroorotato anion may be tentatively compared to those of orotic acid monohydrate (33). The deviation of the ring from planarity is very important; it is correlated with loss of the aromatic properties of the pyrimidine ring by addition of two hydrogen atoms on the C1—C2 bond. The dihedral angles C4-N2-C1-C2 and C2-C1-C5-O2 are 40.6(3)º and 59.8(3)°, respectively. As expected, the N2—C4, C4—N1, and N1—C3 bond lengths are slightly different than those observed for orotic acid but the bond lengths C2—C3 (1.493(4) Å), C1—C2 (1.511(4) Å), and C1—C5 (1.524(4) Å) are longer according to their single bond character. In the same way the bond distance C1—N2 (1.459(3) Å) is significantly longer than in orotic acid complexes (mean value 1.36 Å). The two carbonyl bond lengths, C3—O3 and C4—O4 at 1.226(3) and 1.231(3) Å, respectively, are in good agreement with those found in orotic acid itself (33).

Magnetic susceptibility

The magnetic susceptibility for the complex has been measured from 290 K to 5 K. At room temperature, the complex has an effective magnetic moment per manganese(II) ion of 5.83 BM, indicating the high-spin nature of the manganese ion.

The effective magnetic moment per manganese(II) decreases slowly from 5.93 to 5.02 until 20 K. The decrease is more pronounced below 20 K and the magnetic moment reaches 3.17 BM/Mn at 5 K. The results of the X-ray crystal structure determination indicate a chain structure with an *anti–syn* configuration and a Mn···Mn distance of 4.723 Å inside the chain. This distance suggests that spin–spin magnetic interactions are unlikely to occur between the manganese ions of neighbouring chains or inside the chain, since to achieve

© 1998 NRC Canada

Fig. 2. Structure of $[Mn(C_5H_6N_2O_4)_2 \cdot (H_2O)_2]$. Ellipsoids are represented at 50% probability level.

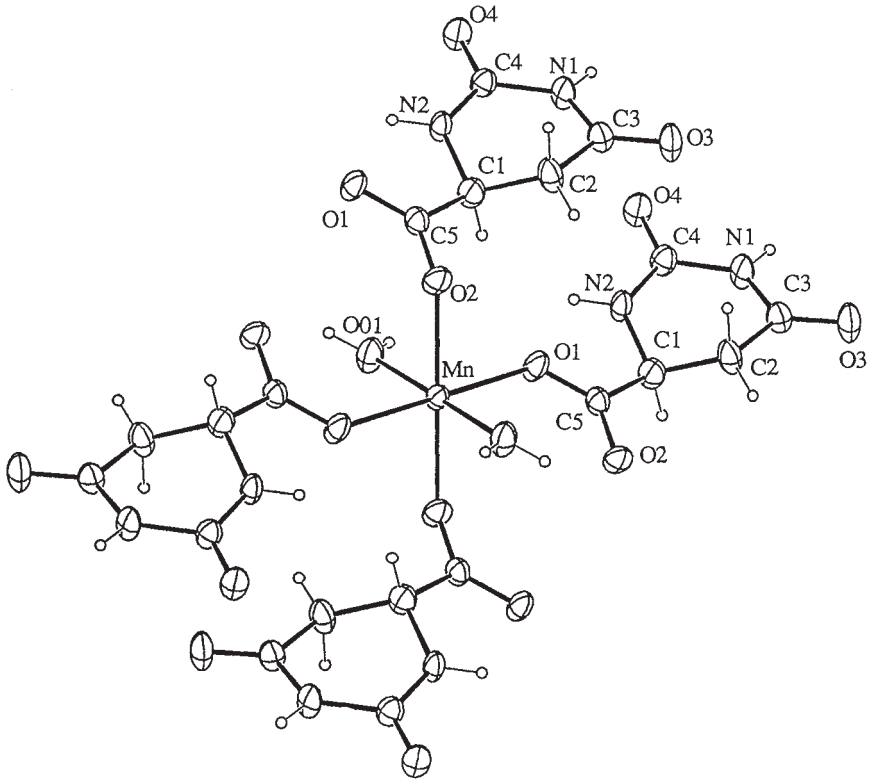

Fig. 3. Representation of the polymeric structure: $[Mn(C_5H_6NO_4)_2 \cdot (H_2O)_2]_n$.

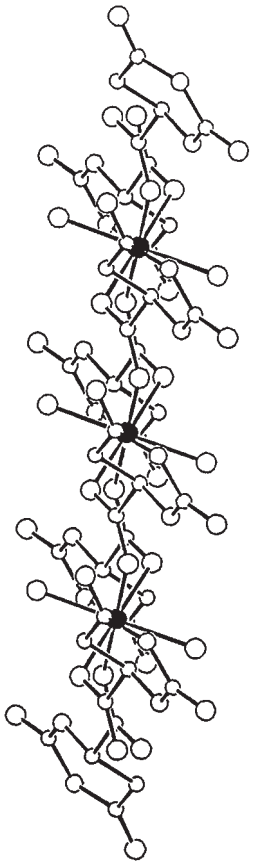

substantial cooperative effects in physical properties, metal ions must be brought close together by bridging in the *syn–syn* configuration. However, the distortion of the manganese coordination octahedron is large enough to result in a zero-field splitting of the manganese(II) ground state and to afford a small lowering of the magnetic moment at low temperature as was previously observed for some manganese(II) complexes (34).

The complex exhibits powder X-band EPR spectra characterized by a broad resonance near $g \approx 2$ that does not show appreciable temperature dependence. However, frozen solution spectra obtained from water – ethylene glycol glasses at 95 K exhibit a central allowed hyperfine sextet typical for a Mn^{2+} ion with a fine-structure pattern similar to those observed for electronically isolated manganese species. This indicates that no interactions between the manganese atoms are involved.

Solution studies

Linear free energy relationships for proton dissociation and metal complexation have been evidenced for the pyrimidine–acid systems (35) and have also been reported in the literature for various aromatic or aliphatic systems. In water, the acidity constants of orotic acid are $pK_1 = 2.07$ and $pK_2 = 9.45$ with pK_1 corresponding to COOH and pK_2 to NH deprotonations. The acidity constants of 5-nitroorotic acid are $pK_1 = 1.5$ and $pK_2 = 4.94$, proton dissociation being considerably enhanced by the electron withdrawal groups. For L-dihydroorotic acid, only the first acid dissociation constant ($pK_1 = 3$) can be determined in H_2O (in this case, NH is less acid than H_2O). The second proton dissociation constant, which may occur from a

© 1998 NRC Canada

Table 4. Distances (Å) and angles (deg) of hydrogen bonds D—H···A for the complex; D = donor atom, A = acceptor atom.

D	H	A	D—A	D—H·· ·A
Intra				
N2	H02	O1	2.639(3)	98(2)
Inter				
N1	H01	O3[a]	2.920(4)	174(3)
N2	H02	O4[b]	3.109(2)	169(2)
O01	H012	O4[b]	2.798(3)	161(4)

[a] –*x*–1, –*y*, 1–*z*
[b] 1–*x*, 1–y, 1–*z*

Fig. 4. Cyclic voltammograms of the dioxygen system at a gold electrode in 10 mL of DMF with increasing concentrations of the complex $[Mn(C_5H_6N_2O_4)_2\cdot(H_2O)_2]_n$ (scan rate 0.1 V/s).

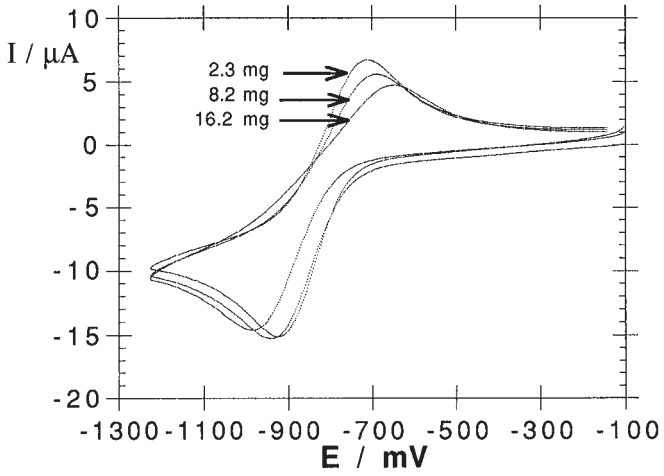

Fig. 5. Comparative antioxidative properties of Mn complexes with reference to vitamin E: (**A**) cyclic voltammetry (CV) and (**B**) electron spin resonance (ESR). Ligand: **a** orotic; **b** 3-methylorotic; **c** 5-nitroorotic; **d** dihydroorotic; **e** $MnCl_2$.

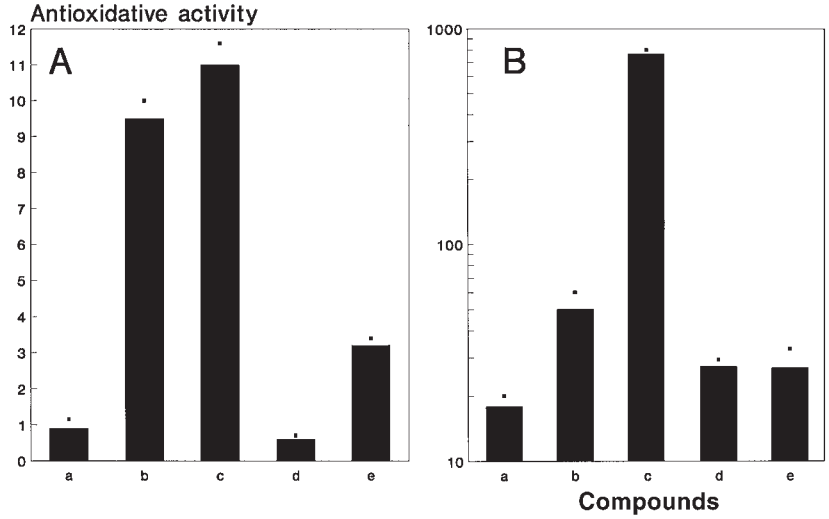

NH dissociation, was observed to occur in a pH region greater than 12. Taking into account these results, one might expect that, even in the presence of a metal atom, the deprotonation at one of the nitrogen atoms does not occur and that the metal atom may only coordinate to the carboxylic function.

In the same way, perturbation of the π system, which was found to have a pronounced effect on the dissociation constants determined potentiometrically, also induces considerable modification of the UV spectra. Thus, at the same acidic pH (pH = 3), the orotic acid exhibits a band at 285 nm, while L-dihydroorotic acid shows two bands at 198 and 216 nm. These two bands may be attributed to the two independent π systems, the carboxylic group (216 nm) and the ring (198 nm). Moreover, no shift is observed when the pH is increased to 12. This may be related to the fact that even at high pH values only the carboxylic function is deprotonated.

Relationships between complexation sites of pyrimidine derivatives and UV data have been reported in the past and one may note that the UV spectra predict the sites of deprotonation and then those of coordination (35–37); this was the case with copper and nickel complexes of orotic acid (38) for which the complexation induced a significant bathochromic shift of the ligand absorption band (λ_{max} = 316 nm versus 285 nm for the free ligand) correlated to complexation at the carboxylic group and adjacent endocyclic nitrogen atom.

In an attempt to elucidate the metal–ligand binding mode of manganese(II) towards L-dihydroorotic acid, UV absorption spectra of the free ligand, of the isolated Mn(II) complex, and of ligand–Mn(II) salt mixtures in different ratios were recorded and compared. For the isolated complex, any shift in the maximum absorbance wavelength (λ_{max} = 216 nm) with respect to the free anion was observed in aqueous solution. Moreover, addition of manganese(II) salt to a solution of L-dihydroorotic acid does not induce a significant bathochromic shift even with a large metal salt excess (1:50). These results indicate that the complex dissociates in aqueous solution and has a low stability since no complexation is observed even in the presence of a large excess of metal salt. We have already remarked upon (25) a quite similar behaviour for orotic acid itself in the presence of manganese salt.

© 1998 NRC Canada

Antioxidative properties

The antioxidative properties of this compound have been evaluated and compared to those of known antioxidants (vitamin E, BHT) and to those of manganese complexes of orotic acid derivatives that we have already described (39). The results are expressed with reference to vitamin E used as standard. A logarithmic scale is used to present ESR results.

Figure 4 shows cyclic voltammograms of the dioxygen system in DMF at a gold electrode. When no Mn complex is added, the electrochemical system of dioxygen is quasi-reversible (40, 41): the backward peak current is equal to the forward one. When the complex is added, the backward peak current decreases as for an EC process. The decrease of the backward peak current is enhanced when the complex concentration is increased. This can be schematized by:

$$O_2 + e \rightleftharpoons O_2^{\bullet -}$$

$$O_2^{\bullet -} + X \rightarrow \text{products } O_2^{\bullet -} + X \rightarrow \text{products}$$

By comparison of the peak ratio (backward peak current/forward peak current) for the complex with that of BHT or vitamin E, the radical scavenging activity is given in terms of a BHT or vitamin E equivalent. The complex presents a superoxide scavenging activity of 0.6 mol vitamin E/mol. Figure 5A represents the radical scavenging activities of the different Mn complexes. The activity observed for the complex of dihydroorotic acid is of the same order of magnitude as those of the Mn(orotate) complex or of the Mn(II) ion in the same buffer. However, this activity is far below that of the Mn(5-nitroorotate) complex. This low activity can be attributed to their low stability, as was the case for the complex of orotic acid.

ESR measurements give similar results, except that a logarithmic scale was used (Fig. 5B). This difference is because of the solvents used for the measurements, DMF for cyclic voltammetry and water for ESR. As the superoxide radical scavenging goes through an acid–base reaction that allows superoxide disproportionation, the radical scavenging activities (by ESR) appear higher in water than in DMF and have to be related to the acidic properties.

Conclusion

In a recent paper we emphasized that the major binding mode of the Mn(II) ion with orotic acid and some of its derivatives (where the aromatic structure of the pyrimidine ring is preserved) remains the N1 and carboxylate sites in the solid state as well as in solution. This is not the case for dihydroorotic acid, for which only the carboxylate group is involved in the metal coordination. Moreover, UV absorption spectra offer a good indication of the behaviour of these complexes in solution. In the course of our studies concerning the antioxidative properties of manganese(II) complexes of orotic acid derivatives, three types of behaviour have been found: unstable and labile complexes such as those of orotic (**a**) or dihydroorotic (**d**) acids for which no antioxidative properties were found (the activity lies in the same range that of $MnCl_2$ itself); the unstable but inert complex of 3-methylorotic acid (**b**) for which antioxidative properties are significant; and the stable and inert complex of 5-nitroorotic acid (**c**) for which very high antioxidative properties was found.

References

1. J. Leberman, A. Kornberg, and E.S. Simms. J. Biol. Chem. **215**, 403 (1955).
2. A. Lehninger. Biochemistry. Worth Publishers Inc., New York.1970. p. 661.
3. N.K. Davidenko and N.N. Zinich. Russ. J. Chem. **24**, 891 (1979).
4. P. Castan, E. Colacio-Rodriguez, A.L. Beauchamp, S. Cros, and S. Wimmer. J. Inorg. Biochem. **36**, 225 (1990).
5. J.L. Butour, S. Wimmer, F. Wimmer, and P. Castan. Chem.-Biol. Interact. **104**, 165 (1997).
6. M. Sabat, D. Zlinska, and B. Jezowska-Trzebiatowska. Acta Crystallogr. Sect. B: Struct. Crystallogr. Cryst. Chem. **B36**, 1187 (1980).
7. I. Mutikainen and P. Lumme. Acta Crystallogr. Sect. B: Struct. Crystallogr. Cryst. Chem. **B36**, 2233 (1980).
8. T. Solin, K. Matsumoto, and K. Fuwa. Bull. Soc. Chim. Jpn. **54**, 3731 (1981).
9. P. Arrizabalaga, P. Castan, and F. Dahan. Inorg. Chem. **22**, 2245 (1983).
10. I. Mutikainen. Finn. Chem. Lett. 193 (1985).
11. M. Kubiac and B. Thomas. Acta Crystallogr. Sect. C: Cryst. Struct. Commun. **C42**, 1705 (1986).
12. I. Mutikainen. Inorg. Chim. Acta, **136**, 155 (1987).
13. I. Mutikainen. Ann. Acad. Sci. Fenn. **217**, 1 (1988), and refs. therein.
14. F. Hueso-Urena, M.N. Moreno-Carretero, J.M. Salas-Peregrin, C. Valenzuela-Calahorro, and G. Alvarez de Cienfuegos-Lopez. Thermochim. Acta, **133**, 341 (1988); F. Hueso-Urena, M.N. Moreno-Carretero, M. Quiros-Olozabal, J.M. Salas-Peregrin, R. Faure, and G. Alvarez de Cienfuegos-Lopez. Inorg. Chim. Acta, **241**, 61 (1996).
15. G. Maistralis, N. Katsaros, D. Mentzafos, and A. Terzis. Acta Crystallogr. Sect. C: Cryst. Struct. Commun. **C47**, 740 (1991).
16. F. Hueso-Urena, M.N. Moreno-Carretero, J.M. Salas-Peregrin, and G. Alvarez de Cienfuegos-Lopez. J. Inorg. Biochem. **43**, 17 (1991).
17. D. Menitzafos, N. Katsaros, and A. Terzis. Acta Crystallogr. Sect. C: Cryst. Struct. Commun. **C43**, 1905 (1987).
18. I. Bach, O. Kumberger, and H. Schmidbaur. Chem. Ber. **123**, 2267 (1990).
19. O. Kumberger, J. Riede, and H. Schmidbaur. Z. Naturforsch. B: Chem. Sci. **48**, 961 (1993).
20. Y. Kono, M. Takahashi, and K. Asada. Arch. Biochem. Biophys. **174**, 454 (1976).
21. F.S. Archibald and I. Fridovich. Arch. Biochem. Biophys. **214**, 452 (1982).
22. F.J. Arnais Garcia, C. Capul, P. Castan, D. Deguenon, P. Derache, and F. Nepveu. *In* Metal ions in biology and medicine. *Edited by* P. Collery, L.A. Poirier, M. Manfait, and J.C. Etienne. John Libbey Eurotext, Paris. 1990 p. 21.
23. S. Rivomanana, M. Massol, P. Derache, and F. Nepveu. *In* Electron spin resonance (ESR), applications in organic and bioorganic materials. *Edited by* B. Catoire. Springer Verlag, Berlin. 1992. p. 105.
24. M. Berkaoui, J.P. Souchard, M. Massol, and F. Nepveu. J. Chim. Phys. **91**, 1799 (1994).
25. F. Nepveu, N. Gaultier, N. Korber, J. Jaud, and P. Castan. J. Chem. Soc. Dalton Trans. 4005 (1995).
26. P. Pascal. Ann. Chim. Phys. (Paris), **19**, 5 (1910).
27. J.P. Souchard and F. Nepveu. J. Chim. Phys. In press.
28. P. Main, S.J. Fiske, S.E. Hull, L. Lessinger, G. Germain, J.P. Declercq, and M.M. Woolfson. A system of computer programs for the automatic solution of crystal structures from X-ray diffraction Data. University of York, England, and Louvain-la Neuve, Belgium. 1987.

© 1998 NRC Canada

29. S.R. Hall and J.M. Steward (*Editors*). XTAL3.2 users manual. Universities of Western Australia and Maryland. 1992.
30. International tables for X-ray crystallography. Vol. IV. Kynoch Press, Birmingham. 1974.
31. J.H. Van Niekerk and F.R.L. Schoenig. Acta Crystallogr. **6**, 227 (1953).
32. P. De Meester, S.R. Flecher, and A.C. Skapski. J. Chem. Soc. Dalton Trans. 2575 (1973).
33. F. Takusagawa and A. Shimada. Bull. Chem. Soc. Jpn. **46**, 2011 (1973).
34. B. Mabad, P. Cassoux, J.-P. Tuchagues, and D.N. Hendrickson. Inorg. Chem. **35**, 1420 (1986).
35. E.R. Tucci, C.H. Ke, and N.C. Li. J. Inorg. Nucl. Chem. **29**, 1657 (1967).
36. E.R. Tucci and N.C. Li. J. Inorg. Nucl. Chem. **25**, 17 (1963).
37. J.J. Fox, N. Yung, and I. Wenpen. Biochim. Biophys. Acta, **23**, 295 (1957).
38. D. Lalart, G. Guillerez, G. Dodin, and J.-E. Dubois. J. Chem. Soc. Perkin Trans. 2, 1057 (1981).
39. J.P. Souchard, P.L. Fabre, J.P. Patau, M. Massol, P. Castan, and F. Nepveu. *In* Therapeutic uses of trace elements. *Edited by* J. Neve, P. Chapuis, and M. Lamand. Plenum Press, New York. 1996. p. 247.
40. P. Coffre and D.T Sawyer. Anal. Chem. **58**, 1057 (1986).
41. C.P Andrieux, P. Hapiot, and J.M. Savéant. J. Am. Chem. Soc. **109**, 3768 (1987).

© 1998 NRC Canada

The reactions of a 1-alkenesulfenate anion with TMS-X reagents; a variable temperature NMR study

Mitchell D. Refvik and Adrian L. Schwan

Abstract: Lithium (*E*)-1-hexenesulfenate (**5a**) was treated with a number of TMS-X (TMS = trimethylsilyl) reagents to afford *N,N*-bis(trimethylsilyl)-(*E*)-1-hexenesulfenamide (**7a**) and (or) di((*E*)-1 hexenyl) disulfide (**8**), usually in low yield. The cleanest reactions, those from use of TMS-Cl (to afford **7a**) and TMS-CN (which yields **8**) were analyzed by variable temperature NMR. It was found that the low-temperature silylation reaction using TMS-Cl affords **7a** and thiosulfinate **12** as initial products. Warming the mixture coerces the decomposition of **12**. Treatment of **5a** with TMS-CN also yields thiosulfinate **12** which is reduced to disulfide **8** as the temperature warms, possibly by action of cyanide ion. Evidence is presented that allows a confident structural assignment of the transient thiosulfinate **12**, and mechanisms are suggested for the formation of **12**. The study also led to the NMR observation of (*E*)-1-hexenesulfenate (**5a**).

Key words: sulfenate, thiosulfinate, variable temperature NMR (VT NMR), silylation.

Résumé : Le traitement du (*E*)-1-hexènesulfénate de lithium (**5a**) avec un certain nombre de réactifs du type TMS-X (TMS = triméthylsilyle) conduit au *N,N*-bis(triméthylsilyl)-(*E*)-1-hexènesulfénamide (**7a**) et (ou) au disulfure de di((*E*)-1-hexényle) (**8**), généralement avec de faibles rendements. Les réactions les plus propres, celles impliquant le TMS-Cl (conduisant au produit **7a**) et le TMS-CN (conduisant au produit **8**), ont été analysées par RMN à température variable. On a observé que la silylation à basse température, à l'aide de TMS-Cl, conduit initialement au produit **7a** et au thiosulfinate **12**. Par réchauffement du mélange, il s'opère une décomposition du produit **12**. Le traitement du produit **5a** par du TMS-CN conduit aussi au thiosulfinate **12** qui, par élévation de la température, est réduit en disulfure **8** possiblement par l'action de l'ion cyanure. On présente des données qui permettent d'attribuer avec confiance une structure au thiosulfinate transitoire **12** et on suggère des mécanismes pour la formation du produit **12**. L'étude a aussi permis d'observer le (*E*)-1-hexènesulfénate (**5a**) par RMN.

Mots clés : sulfénate, thiosulfinate, RMN à température variable (RMN TV), silylation.

[Traduit par la rédaction]

There is persistent interest in the chemistry of sulfenic acids and their derivatives for a variety of reasons (1–4). Sulfenic acids (**1**) themselves are recognized primarily for their role in biological processes (2, 5). Despite their notorious instability (1), some sulfenic acids can be isolated and characterized, but only when they are generated in atypical steric (6) or electronic environments (7). Sulfenic acid amides (**2**), considerably more stable than their corresponding acids, often demonstrate chiroptical properties about the S—N bond (8).

Unsaturated sulfenic acid derivatives are the most important contributors to the flavour and lachrymatory properties of onions, garlic, and related *Allium* plants (2). Specifically, 1-propenesulfenic acid (**3**) has been shown to be the precursor of (*Z*)- and (*E*)-propanethial *S*-oxides (**4**), the familiar lachrymatory factor of onions (9). Unsaturated sulfenic acid amides have demonstrated usefulness in synthesis (10–12).

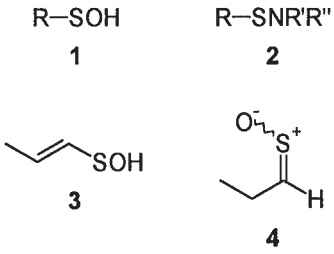

1-Alkenesulfenate anions (**5**) can be generated through the regiospecific deprotonation and stereoselective ring opening of thiirane *S*-oxides (**6**) (13) and are captured with reactive alkyl halides; the overall result is a useful preparation of *E*-1-alkenyl sulfoxides. Treatment of the 1-alkenesulfenates with trimethylsilyl chloride (TMS-Cl) resulted in the recovery of *N,N*-bis(trimethylsilyl)-1-alkenesulfenamides (**7**) which have served as a general source of other 1-alkenesulfenamides and also 1-alkenesulfonamides (14, 15).

The mechanism for the conversion of the sulfenate, nucleophilic at sulfur, to the sulfenamide, which is electrophilic at

Received August 8, 1997.

M.D. Refvik[1] and A.L. Schwan.[2] Guelph–Waterloo Centre for Graduate Work in Chemistry and Biochemistry, Department of Chemistry and Biochemistry, University of Guelph, Guelph, ON N1G 2W1, Canada.

[1] Current address: Phillips Petroleum, Bartlesville, OK, U.S.A.
[2] Author to whom correspondence may be addressed. Telephone: (519)-824-4120. Fax: (519)-766-1499. E-mail: schwan@chembio.uoguelph.ca

© 1998 NRC Canada

Table 1. The reaction of **5a** with TMS-X reagents.

	% yield of [a]	
Electrophile	**7a**	**8**
TMS-Cl	25[b]	0
TMS-Br	22	17[c]
TMS-I [d]	29	7[c]
TMS-N_3	16	16[c]
$(TMSO)_2SO_2$	7	14[c]
TMS-CN	0	48[b]

[a] Yields were determined by GC quantitation against naphthalene, which was added as an internal standard.
[b] Yield of crude but pure material.
[c] Mixture of (*E*,*E*) and (*E*,*Z*) isomers; the (*E*,*Z*) isomer was identified through analysis of its GC/MS mass spectrum and by retention time relative to the (*E*,*E*) isomer.
[d] TMS-I was introduced in CH_2Cl_2.

sulfur, is not well understood. Hence a study of the reactions of 1-alkenesulfenate anions with a collection of TMS-X reagents was undertaken, and in this paper, we report a number of variable temperature NMR (VT NMR) experiments that provide insight into some of the transformations taking place.

Results and discussion

As part of our investigation into the role played by the TMS-Cl during the conversion of sulfenate to sulfenamide, (*E*)-1-hexenesulfenate (**5a**) was treated with a number of different TMS-X reagents. The products are shown in reaction [1], and

[1]

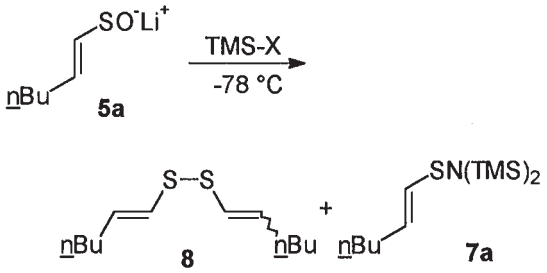

the quantitation of those products is outlined in Table 1. Since early experiments in the area were associated with the silylation reaction presented in Scheme 1 (15), recovery of sulfenamide **7a** as the major product was predicted. Surprisingly, disulfide **8** was a significant component of several of the reaction mixtures, and it was the lone product in the reaction of the TMS-CN with sulfenate **5a**. Further analysis of the mixtures revealed significant nonvolatile oligomeric material that would not pass through a GC or flash-chromatography column (silica gel). Its presence could be confirmed by conglomerations of peaks in the ^{1}H NMR spectrum at δ 0.9–1.2 ppm and in the ^{13}C NMR spectrum at δ 20–30 ppm. Other TMS-X reagents were employed, but TMS-OAc, TMS-$OC(O)CF_3$, TMS-OTf, and TMS-OSO_2Ph afforded negligible isolable products.

Any mechanism put forth to account for the formation of the products obtained must address the following facets of Table 1. Most important is that identity of the leaving group in the silylation reactions plays a key role in the chemistry perhaps by influencing the initial point of silylation and (or) by participating directly in subsequent chemistry. The proposed mechanism must also account for the fact that the hexenyl portion of **8** is prone to isomerization, while the (*E*)-hexenyl geometry of **7a** is preserved. The ensuing discussion focuses primarily on the chemistry induced by TMS-Cl and TMS-CN, since their reactions represent each extreme of the observed reactivity modes.

Scheme 2 offers a series of reactions that could account for the observed products, based on precedented or generally accepted chemistry (16–21). Variable temperature NMR was utilized to analyze some of the reactions of Scheme 2, with the hope of determining the exact processes occurring. To maintain consistency with prior preparative sulfenate chemistry (13), THF-d_8 was utilized as the solvent for the NMR experiments. LiHMDS·Et_2O (22), a white solid, was used instead of the commercially available THF solution of LiHMDS in order to reduce solvent interference in the NMR spectra. Control experiments indicated that the etherate behaved in a manner comparable to the commercial THF solutions of LiHMDS. The olefinic region of the VT NMR spectrum was our principal focus. Indeed, it proved to be the least cluttered and the most diagnostic region. Little information could be gleaned in the upfield portion of the spectrum.

A logical starting point for the study was the ^{1}H NMR spectrum of 1-alkenesulfenate anion **5a** in solution. This species was generated on a small scale in THF-d_8, and the solution was transferred to an NMR tube while maintaining a cold solution (23). The ^{1}H NMR spectrum obtained (Fig. 1*a*) shows a doublet at δ 6.30 ppm corresponding to the vinyl proton adjacent to the sulfur, and a doublet of triplets at δ 4.94 assigned as the vinyl proton β to the sulfur, each consistent with the electron distribution within **5a**. Another set of peaks present in this spectrum was tentatively assigned to be thiosulfinate **12**; further evidence for this assignment was found later in this study (vide infra). The small doublet at δ 6.06 ppm and the doublet of triplets at δ 5.88 ppm are due to disulfide **8**.

Prior to introduction into the NMR tube, the mixture had been spiked with a known amount of benzene, which allowed for calculation of approximate yields of identifiable compounds.[3] It must be noted that the amounts utilized were small, and consequently an inescapable margin of error accompanies the quantitation of this and other mixtures. Alkenesulfenate **5a** was present in approximately 70% yield, while thiosulfinate **12** was present in approximately 20% yield. When preparative sulfenate mixtures are quenched with a reactive alkyl halide, vinyl sulfoxide is obtained usually in ca. 70% yield, in accord with the sulfenate concentration in the NMR tube mixture.

Sulfenate **5a** was regenerated under identical circumstances, and the new sample was treated with TMS-Cl. The ^{1}H NMR spectrum recorded at –60°C (Fig. 1*b*) shows resonances consistent with sulfenamide **7a** and another major product. The vinyl hydrogens of **7a** exhibit a doublet at δ 6.36 ppm for the hydrogen adjacent to the sulfur, and a doublet of triplets at 5.29 ppm for the other vinyl hydrogen. These peaks persist in the ^{1}H NMR spectrum up to room temperature and indefinitely thereafter, as would be expected for a stable compound. The other product possesses a doublet at 6.64 ppm and may be responsible for other peaks in the spectrum, all of which are noticeably similar to those already tentatively assigned to **12**.

[3] Integration was employed for quantitation, but it has been left off of the NMR spectra presented herein.

© 1998 NRC Canada

Scheme 1.

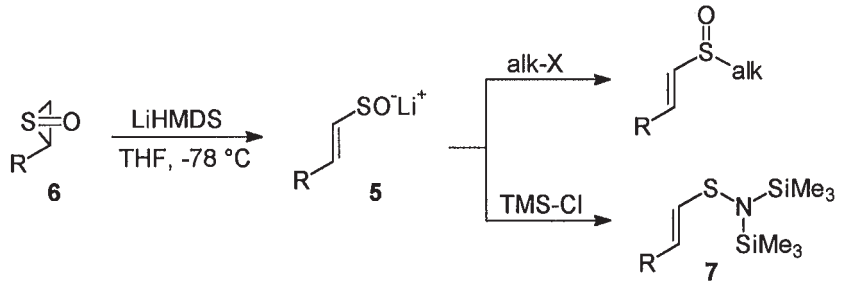

Scheme 2.

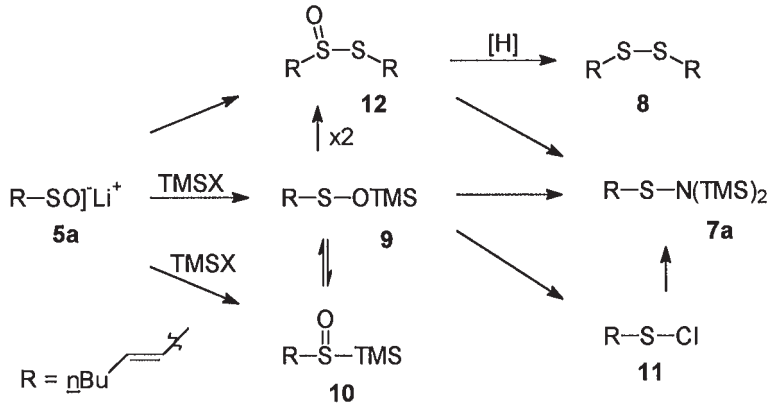

Given this assignment, a **12**:**7a** ratio of 1:1 can be measured in the mixture. Hence, for every molecule of sulfenate that proceeds to sulfenamide, two molecules combine to form thiosulfinate.

To confirm that the unknown was indeed thiosulfinate **12** an attempt was made to prepare it independently through oxidation of the corresponding disulfide **8**. The literature suggested that such a conversion to the thiosulfinate would be a facile process (24). Indeed, thiosulfinate **12** could be generated by the *m*-CPBA oxidation of **8** in $CDCl_3$ at –60°C. The ^{1}H NMR spectrum was recorded after introduction of the precooled (to –60°C) sample into the probe (Fig. 1*d*). The vinyl hydrogens of **12** form a conglomeration of peaks at δ 6.34–6.62. This data compares favourably with the ^{1}H NMR spectrum of (*E*)-1-propenyl (*E*)-1-propenethiosulfinate (**13**), which exhibits vinyl hydrogens at δ 6.30–6.65 (24). Furthermore, the remainder of the ^{1}H NMR spectrum of **12** exhibited the predicted multiplets.

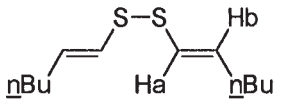

8

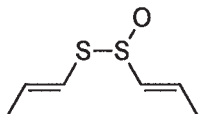

13

The ^{1}H NMR spectrum of **12** in $CDCl_3$ bears little resemblance to the ^{1}H NMR spectrum of **12** in THF-d_8. To overcome this difficulty, the two NMR solutions were mixed, and the ^{1}H NMR of the mixture was rapidly recorded at 0°C (Fig. 1*c*). The resulting spectrum indicates the presence of **7a** and a more intense, different, but not additional collection of new peaks now representing the spectrum of **12** in the $CDCl_3$–THF-d_8 solvent system. The ratio of **12** to **7a** is much higher than in the original solution, providing evidence that thiosulfinate **12** was present in each solution. Allowing the solution to warm to room temperature resulted in the disappearance of the signals from **12**, characterizing it as a species only stable up to approximately 0°C. Furthermore, the decomposition of **12** is consistent with the low yields of recoverable material obtained from other silicon electrophile quenching reactions (Table 1) (24, 25).[4]

The most convincing evidence for the presence of **12** in these mixtures came when another reaction of **5a** with TMS-Cl was conducted, and both the ^{1}H NMR and ^{13}C NMR spectra were recorded at –78°C (Figs. 2 and 3). As expected, sulfenamide **7a** (ca. 35%) and **12** (ca. 46%) were present. The ^{13}C NMR spectrum showed seven lines in the vinylic region: one for the benzene additive, two for sulfenamide **7a**, and four lines that were assigned to **12**. After warming to room temperature and the concomitant decomposition of **12**, each of the spectra were recorded again (Figs. 2*b* and 3*b*). Four lines in the vinylic region of the ^{13}C NMR disappeared, thereby designating the peaks attributable to **12**. Of the four resonances that were lost, two are particularly supportive of the structure **12**. A peak at δ 148.7 ppm is characteristic of a vinylic carbon beside a sulfinyl functionality, while the 116.6 ppm line can be assigned to a vinylic carbon β to a divalent sulfur. All four of these vinylic ^{13}C NMR resonances (148.7, 140.4, 132.7, 116.6) are consistent with those exhibited for **13** (145.4, 136.4, 130.7, 115.6) (24).

In the context of chemistry, the information gained on

[4] Compound **13** and its geometric relatives rearrange to bicyclic compounds (24); we were unable to find any evidence for a similar transformation of **12**. Highly substituted 1-alkenyl 1-alkenethiosulfinates are stable at ambient temperature and can be fully characterized (25).

© 1998 NRC Canada

Fig. 1. [1]H NMR spectra of (*a*) sulfenate **5a** at –78°C; (*b*) sulfenate **5a** after addition of TMS-Cl at –60°C; mixture contains sulfenamide **7a** and thiosulfinate **12**; (*c*) sulfenate–TMS-Cl mixture after addition of independently prepared **12** at 0°C; (*d*) independently prepared **12** at –60°C.

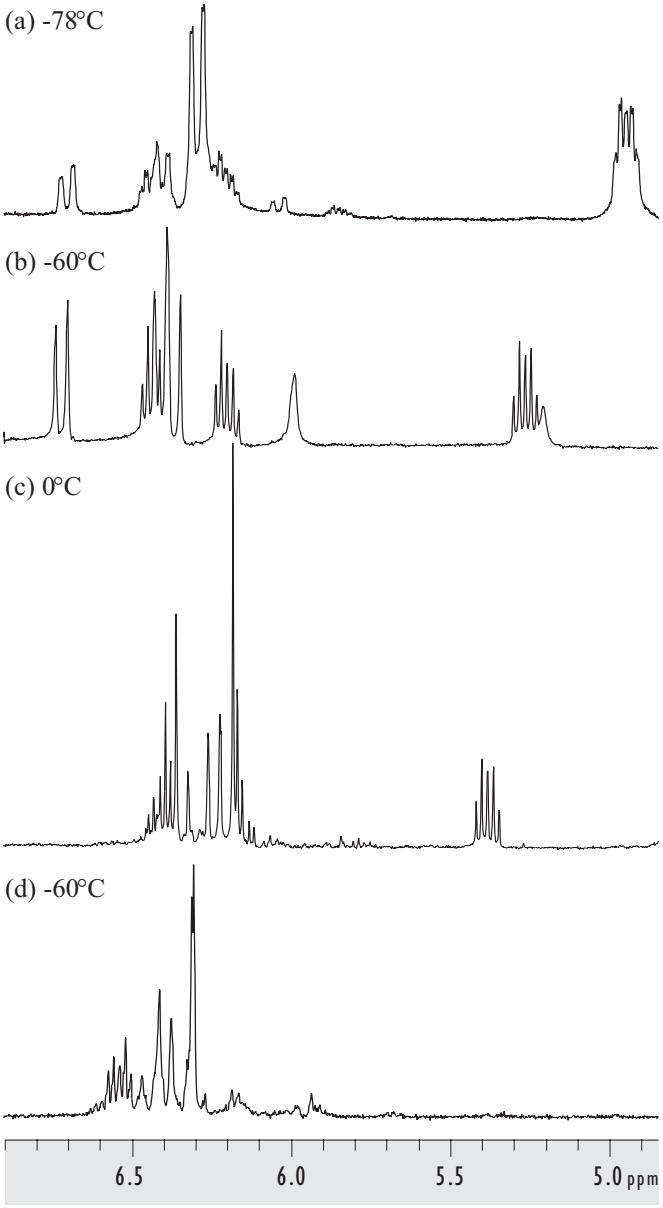

Fig. 2. [1]H NMR spectra of reaction mixture of **5a** and TMS-Cl at (*a*) –78°C; (*b*) 15°C.

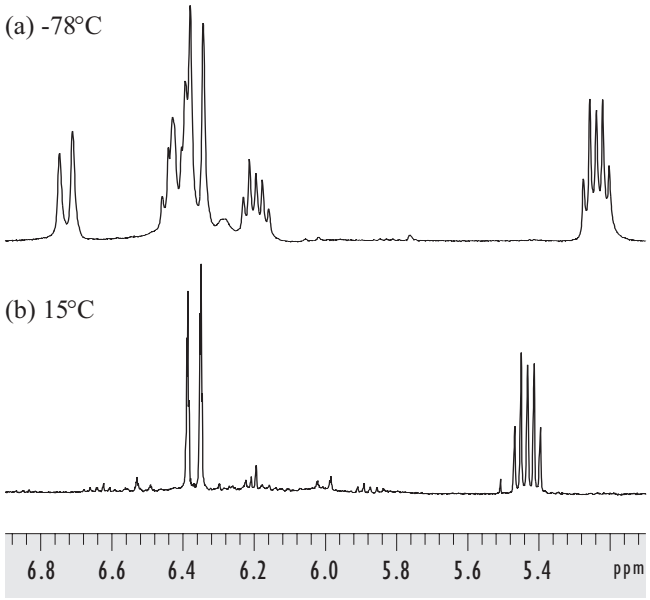

Fig. 3. [13]C NMR spectra of reaction mixture of **5a** and TMS-Cl at (*a*) –78°C; (*b*) 15°C.

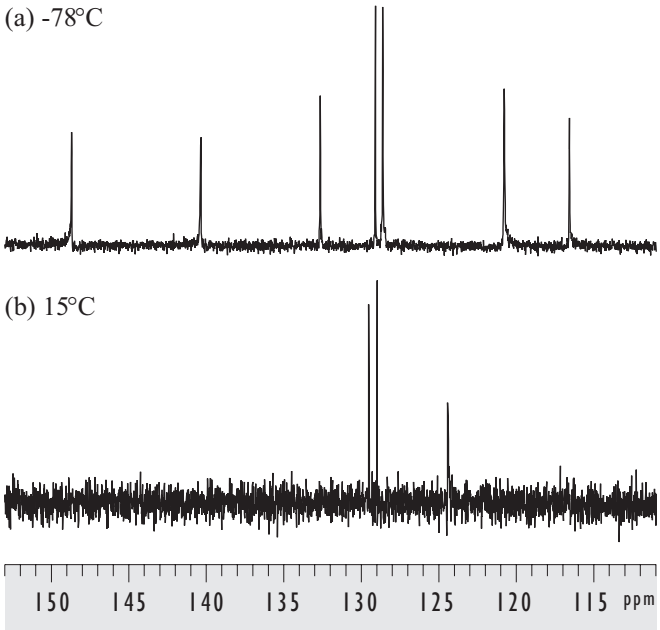

warming the solution was also quite informative. Sulfenamide was determined to still be present in 35% yield, pointing out that thiosulfinate **12** *does not* suffer the fate of a nucleophilic substitution reaction with hexamethyldisilazane to produce sulfenamide **7a** under these conditions. Otherwise the yield of sulfenamide **7a** should have increased as **12** was depleting.

Examination of the mechanism proposed in Scheme 2 suggests that **7a** must be formed through the nucleophilic reaction of hexamethyldisilazane on some species. It follows that increasing the nucleophilicity of the amine may result in an improved yield of **7a**. Towards this end, sulfenate **5a** was generated using 2 equiv. of LiHMDS. The result, as analyzed by [1]H NMR, was the formation of sulfenamide **7a** in approximately 50% yield, thiosulfinate **12** (ca. 7%) and disulfide **8** (10%). The high yield of **7a** has significant ramifications for the synthetic utility of this procedure. Indeed, the published procedure for the preparation of sulfenamides **7** utilizes 2 equiv. of hexamethyldisilazide. The observation of increased amounts of **8** is also in accord with previous preparative chemistry (15).

The observation of thiosulfinate **12** accompanying **7a** is worthy of further discussion. The usual fate of sulfenic acids (2, 17, 26) is dimerization with loss of H_2O (Fig. 4(*i*)), and this process could create some **12** through the presence of adventitious water. In the TMS-Cl quenched reaction, a similar

© 1998 NRC Canada

Fig. 4. Possible modes of thiosulfinate formation from (*i*) sulfenic acids as proposed earlier, G = H; (*ii*) from silyl sulfenate esters, G = Me_3Si.

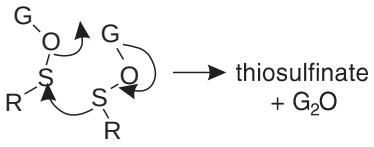

mechanism can be proposed whereby trimethylsilyl group replaces the H (Fig. 4(*ii*)). Hence some of the silyl sulfenates **9** are captured by hexamethyldisilazane to afford sulfenamide while dimerization of **9** with loss of TMS-O-TMS competes. The experiment employing 2 equiv. of LiHMDS supports this hypothesis: a stronger nucleophile, present in a greater concentration would be expected to capture **9** more readily and other fates of **9** are reduced. Accordingly, sulfenamide **7a** was obtained in higher yield in that experiment.

Having completed an investigation of the reaction of TMS-Cl with **5a** the focus became the reaction involving TMS-CN. The techniques utilized previously were also applicable to the study of the reaction of TMS-CN. Thus 0.8 equiv. of TMS-CN was added to a THF-d_8 solution of **5a**, and a ^{1}H NMR spectrum was obtained (Fig. 5*a*). At –78°C the solution was found to contain **12** in about 35% yield and unreacted **5a** (35%). The probe was then allowed to warm, and spectra were recorded at approximately 10° intervals. At –30°C disulfide **8** was present in about 15% yield (Fig. 5*b*) while thiosulfinate (**12**) concentration fell to about 15% yield. Hence formation of **8** was probably occurring at the expense of **12** as proposed in Scheme 2. Finally in the room temperature sample, **8** was quantitated to be about 38% yield while **12** had disappeared entirely (Fig. 5*c*). This is strong evidence for the formation of **8** through deoxygenation of **12** by some mechanism, possibly that proposed by Oae and co-workers (19).[5] (*E*)-1-Hexenesulfenate (**5a**) concentration was determined to be steady at 35% throughout the temperature range.

The proposed mechanisms also accommodate an explanation for the observation of some (*E,Z*)-dihexenyl disulfide. In an attempted synthesis of certain geometrically pure 1-alkenyl thiosulfinates (24), it was observed that both *E* and *Z* isomers were always present. It has been submitted that compounds such as **12**, possessing an RCH═CHSS(O)- unit, have the opportunity to undergo a 2,3-sigmatropic shift, similar to that observed for allylic sulfoxides (i.e., a sulfenate–sulfoxide rearrangement), and upon reversion of such a shift, either geometric isomer may result.[6] The general mechanism demands that other counterions of the TMS-X reagents (e.g., Br^-, I^-, N_3^-) also possess the ability to effect deoxygenation, albeit with significantly less efficiency. Hence some of **12** has the opportunity to rearrange before its reduction to **8** or to an isomer of **8** (before its decomposition).

A final set of experiments were performed in order to examine the possibility of *S*-silylation of the sulfenates, which may occur upon sulfenate quench with TMS-CN. To probe the possibility of this particular reaction, sulfinyl silane **10** became

[5] Addition of commercial LiCN–DMF to mixtures containing **12** afforded small amounts of disulfide **8** upon warming.

[6] For a suitable reaction scheme the reader is referred to refs. 2 and (or) 24.

Fig. 5. ^{1}H NMR spectra of reaction mixture of **5a** and TMS-CN at (*a*) –78°C; (*b*) –30°C; (*c*) 20°C. Note appearance of vinylic peaks (Ha, Hb) of **8** in spectra (*b*) and (*c*).

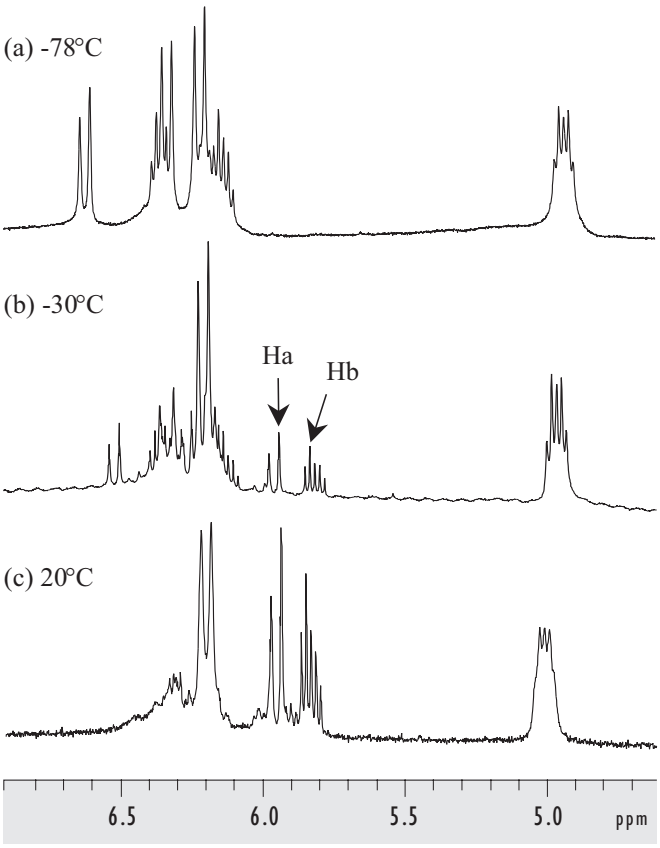

a target for an independent preparation. One could conceive of the synthesis of **10** through simple oxidation of the corresponding thioether **14** (27). The oxidation of **14** with 1 equiv. of MCPBA in an NMR tube ($CDCl_3$) provided a 50:50 mixture of starting material and a product assigned to be trimethylsilyl 1-hexenesulfinate (**15**) (see reaction [2]). Complete isolation

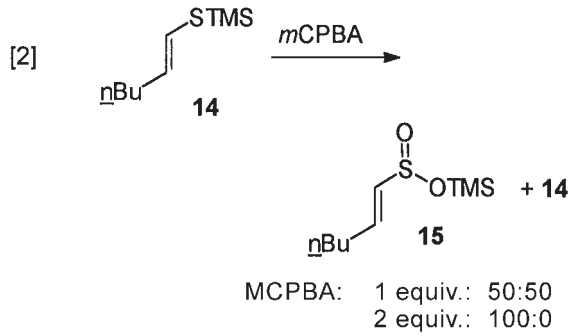

and characterization of sulfinate **15** was not feasible due its decomposition and the presence of an accompanying by-product, *m*-chlorobenzoic acid. Nevertheless, GC/MS and ^{1}H NMR data were consistent with the assigned structure. The use of 2 equiv. of oxidant under similar conditions resulted in the complete conversion to **15** with no detectable **14**. These results are in agreement with those of Davis et al. (18) who found that the oxidation of silyl thioethers with oxaziridines afforded trialkylsilyl benzenesulfinates in good yields.

© 1998 NRC Canada

The oxidation probably occurs by initial formation of sulfoxide **10**, which rapidly tautomerizes to **9**. Compared to silyl thioether **14**, sulfenate **9** is then more susceptible to oxidation, due to the α-effect (18). This chemistry lends support to the proposal that **9** and **10** are in equilibrium (Scheme 2), with sulfenate **9** as the preferred tautomer. Hence, any evidence in support of the direct formation of **10** as shown in Scheme 2 would be fleeting. Likewise, if **10** were formed, its participation in any other chemistry is unlikely, due to its propensity to convert to **9**.

It would appear that our inability to gain any spectral evidence for **9** in the sulfenate quenching mixtures is due to the reactive nucleophiles (sulfenate and amine[7]) present under the conditions for its generation. However, of the stable trimethylsilyl alkane- and arenesulfenates known (18, 28), the arenesulfenates were prepared in the presence of hexamethyldisilazane (18). Our lab has already demonstrated that *N*-(1-alkenylthio)phthalimides, a family of unsaturated sulfenic acid amides, are more electrophilic at sulfur than their saturated counterparts. It follows here that sulfenates such as **9** are also more electrophilic at sulfur compared to the known stable analogs. In accord with our results, it has recently been communicated that trimethylsilyl 1,2-di(4-methoxyphenyl)-ethenesulfenate also has limited stability and readily reacts with amines and nucleophilic sulfur compounds (29).

An unresolved question remains: why is there significant sulfenamide formation when TMS-Cl is the quenching electrophile and virtually no formation when TMS-CN is employed? *S*-Silylation is not the solution to this problem. However, a feasible explanation may be based on the relative rates of reaction of **5a** with TMS-Cl and TMS-CN. Based on HSAB theory, one may expect the *O*-silylation of sulfenate **5a** with TMS-Cl to be rapid and complete upon addition of the chloride. Then sulfenate **9** is available for subsequent (slower) reaction with disilazane. On the other hand, based on HSAB, the *O*-silylation of **5a** with TMS-CN is predicted to be slower. As that substitution proceeds at its sluggish pace, the remaining unreacted **5a** may effect a substitution on newly created **9**, a reaction that is not possible when TMS-Cl is the electrophile, since it will rapidly functionalize *all* of the sulfenate (**5a**). The by-product of the reaction of **5a** and **9** is $^{-}$OTMS, which would probably be converted to TMS-O-TMS by reaction with TMS-CN. The resulting cyanide would then be available for the deoxygenation reaction. Support for this particular proposal was found when a model reaction was performed between $TMSO^{-}Li^{+}$ and TMS-CN in THF. Upon warming the solution from –78°C to rt, TMS-O-TMS was definitely formed in >90% yield (by NMR and GC analysis). Finally, since the sulfenate and the $^{-}$OTMS are both contributing to the consumption of the TMS-CN reagent, a rationale has been found for the observation of unreacted **5a** in Fig. 5.

Experimental

General

The *m*-CPBA was purchased from Aldrich Chemical Co. and was standardized by oxidation of benzyl sulfide prior to use. Where necessary, flasks were predried by vacuum flame drying, and syringes were dried by oven storage at 110 ºC followed by cooling in a desiccator. Air-sensitive reactions were performed under a positive pressure of dry nitrogen.

The VT NMR experiments were performed on the Varian Unity spectrometer operating at 400 MHz for ^{1}H NMR spectra and at 100.6 MHz for ^{13}C NMR spectra. The ^{1}H NMR spectra recorded in THF-d_8 were referenced to the residual protons on the carbons adjacent to the oxygen in THF-d_8 (δ = 3.58 ppm) while ^{13}C spectra were referenced to the quintet at δ = 67.4 ppm, due to the carbons adjacent to the oxygen in THF. The THF-d_8 was purchased from Aldrich Chemical Co. and was stored under nitrogen over oven-activated 4 Å molecular sieves at 3°C. Glassware utilized for the transfer of solutions in the VT NMR experiments was oven dried at 110°C, cooled in a desiccator, and stored on dry ice prior to use. The characterization of **7a** has been presented elsewhere (15).

Reactions of 1-alkenesulfenate 5a with TMS-X reagents

*Reaction of **5a** with TMS-Cl*

Compound **6a** (50.0 mg, 0.378 mmol) in cold dry THF (2 mL) was added to a solution of LiHMDS (0.42 mL, 0.42 mmol) in dry THF (10 mL) at –78°C. After 0.5 h cyclohexene (1 mL) was added followed by TMS-Cl (41.0 mg, 0.378 mmol). The mixture was allowed to warm to room temperature over 2 h and was then stirred for 16 h at ambient temperature. The solution was combined with saturated ammonium chloride (50 mL) and was extracted with ethyl acetate (3 × 15 mL). Extracts were washed with water (3 × 25 mL), brine (1 × 25 mL), then dried over anhydrous sodium sulfate and concentrated to yield crude **7a** (26.3 mg, 0.0954 mmol, 25%).

*Reaction of **5a** with TMS-CN*

Compound **6a** (50.0 mg, 0.378 mmol) was reacted as above with LiHMDS (0.42 mL, 0.42 mmol) in dry THF (12 mL) at –78°C. After 0.5 h cyclohexene (1 mL) was added followed by TMS-CN (38.0 mg, 0.378 mmol). The mixture was allowed to stir and was worked up as above. Concentration followed by chromatography yielded pure bis((*E*)-1-hexenyl) disulfide **8** (20.9 mg, 0.0902 mmol, 48%) as a colourless oil. Spectral data for **8**: ^{1}H NMR (200 MHz) δ: 6.08–5.92 (m, 4H), 2.11 (q, J = 6.0 Hz, 2H), 1.54–1.25 (m, 6H), 0.89 (t, J = 7.0 Hz, 3H); ^{13}C NMR (50.3 MHz) δ: 136.02, 123.35, 32.20, 30.98, 21.92, 13.65; IR (neat) cm^{-1}: 3018, 2927, 2856, 1638, 1445, 1433, 1333, 1135, 1013, 916; MS *m*/*z* (%): 230 (M^{+}, 100), 154 (34), 116 (27), 115 (59), 112 (20), 111 (47), 97 (29), 85 (32), 83 (25), 81 (54), 73 (94), 60 (20), 55 (54); HRMS (*m*/*z*): calcd. for $C_{12}H_{22}S_2$: 230.1163; found: 230.1160.

*General procedure for the reaction of **5a** with TMS-X reagents*

(*E*)-1-Alkenesulfenate **5a** was generated at a concentration of 0.1 M in dry THF at –78°C using the methodology outlined above. After 0.5 h the TMS-X reagent was introduced in dry THF or dry dichloromethane (0.5 mL). The mixture was allowed to warm to room temperature over 2 h and was then stirred at ambient temperature for 16 h. The mixture was then diluted with water (25 mL) and extracted into ethyl acetate (3 × 10 mL). The extracts were washed with water (3 × 10 mL), brine (1 × 10 mL),

[7] Use of a carbon base rather than an amide would preclude the presence of the amine after sulfenate formation. However, our experiments and those of others (see ref. 13 and citations therein) have shown that desulfurization of the thiirane *S*-oxide is the dominating reaction when carbon bases are employed.

© 1998 NRC Canada

and dried over anhydrous Na_2SO_4. Naphthalene (15–20 mg, 0.12–0.16 mmol) was added to the solution, and a sample was introduced into the gas chromatograph. Comparison of the peak areas resulted in the yields listed in Table 1.

Variable temperature NMR experiments

*General procedure for the formation and reactions of **5a***
Solid LiHMDS etherate (94.4–218 mg, 0.391–0.905 mmol) was introduced into a flame-dried flask (10 mL) followed by purging with nitrogen. THF-d_8 (0.40–0.60 mL) and benzene (2.0–3.0 μL), if used, was introduced, and the solution was cooled to –78°C. Compound **6a** (46.9–59.8 mg, 0.355–0.452 mmol) in THF-d_8 (0.20–0.30 mL) was introduced and the mixture was allowed to stir for 0.5 h. If utilized, the TMS-X reagent was introduced neat, and the solution was allowed to stir a further 5 min followed by transfer to a precooled NMR tube and temporary storage at –78°C.

*Synthesis and observation of **5a***
Following the above procedure, LiHMDS etherate (105 mg, 0.433 mmol), **6a** (52.1 mg, 0.394 mmol), and benzene (2.0 μL) were combined. The spectrum (Fig. 1*a*) was recorded at –78°C, and comparison of the integration indicated the presence of **5a** (70%) and **12** (20%) as well as some **8**.

*Reaction of **5a** with TMS-Cl and combination with **12***
Following the above procedure, LiHMDS etherate (94.4 mg, 0.433 mmol) and **6a** (46.9 mg, 0.355 mmol) were combined followed by the addition of TMS-Cl (30.9 mg, 0.284 mmol). The ^{1}H NMR spectrum (Fig. 1*b*) was recorded at –60°C and indicated the presence of **7a** and **12**. This solution was combined with the $CDCl_3$ solution of **12** produced as described below and the ^{1}H NMR spectrum was recorded at 0°C (Fig. 1*c*).

*Oxidation of **8** with* m-*CPBA*
To a solution of **8** (35.2 mg, 0.153 mmol) in $CDCl_3$ (1.5 mL) at –60°C was added *m*-CPBA (38.0 mg, 0.153 mmol). The reaction was stirred for 10 min at –60°C and was then suction-filtered through three grams of crushed anhydrous potassium carbonate into a flask maintained at –60°C. A sample of the solution was transferred to an NMR tube, and the ^{1}H NMR spectrum was obtained. δ (ppm): 6.64–6.32 (m, 2H), 2.30 (m, 1H), 2.21 (m, 1H), 1.47–1.21 (m, 4H), 0.85 (m, 3H); see also Fig. 1*d*.

*Reaction of **5a** with TMS-Cl*
Following the above procedure, LiHMDS etherate (115 mg, 0.477 mmol), **6a** (57.3 mg, 0.433 mmol), and benzene (3.0 μL) were combined followed by the addition of TMS-Cl (37.7 mg, 0.347 mmol). The ^{1}H NMR spectra was recorded at –78°C to show **7a** (35%) and **12** (46%). The spectra were then recorded at ambient temperature to show only **7a** (35%).

*Reaction of **5a** with TMS-Cl and LiHMDS*
Following the above procedure, LiHMDS etherate (218 mg, 0.905 mmol), **6a** (59.8 mg, 0.452 mmol), and benzene (3.0 μL) were combined followed by the addition of TMS-Cl (39.3 mg, 0.362 mmol). The ^{1}H NMR spectrum was recorded at –78°C to show **7a** (50%), **12** (7%), and **8** (10%). A second spectrum, recorded at ambient temperature, showed **7a** (58%) and **8** (10%).

*Reaction of **5a** with TMS-CN*
Following the above procedure, LiHMDS etherate (115 mg, 0.475 mmol), **6a** (59.8 mg, 0.452 mmol), and benzene (3.0 μL) were combined followed by the addition of TMS-CN (36.0 mg, 0.362 mmol). The spectrum (Fig. 5*a*) was recorded at –78°C to show **5a** (35%) and **12** (35%). A second spectrum, recorded at –30°C, showed **8** (15%), **12** (15%), and **5a** (35%) (Fig. 5*b*). A final spectrum recorded at ambient temperature showed **8** (38%) and **5a** (35%) (Fig. 5*c*).

*Reaction of **14** with 1 equiv. of* m-*CPBA*
Utilizing the procedure adopted for the oxidation of **8** above, **14** (68.4 mg, 0.363 mmol) and *m*-CPBA (89.5 mg, 0.363 mmol) were combined in $CDCl_3$ (1.5 mL) at –60°C. After suction filtration, a sample of the solution was transferred to an NMR tube, and the ^{1}H NMR spectrum was obtained. Examination of the crude spectrum showed **14** and **15** in a 1:1 ratio and *m*-chlorobenzoic acid. Crude spectral data for compound **15**: ^{1}H NMR (400 MHz) δ: 6.29–6.15 (m, 2H), 2.03 (q, J = 7.0 Hz, 2H), 1.32–1.08 (m, 4H), 0.80 (t, J = 7.1 Hz, 3H), 0.07 (s, 9H); GC/MS *m*/*z* (%): 220 (M^+, 18), 157 (15), 141 (17), 129 (24), 122 (16), 75 (27), 73 (100), 59 (14), 55 (21).

*Reaction of **14** with 2 equiv. of* m-*CPBA*
The above procedure was followed utilizing **14** (129 mg, 0.689 mmol) in $CDCl_3$ (1.5 mL) and *m*-CPBA (339 mg, 1.37 mmol) in $CDCl_3$ (1.5 mL). Examination of the crude spectrum indicated the presence of **15** and *m*-chlorobenzoic acid.

Acknowledgements

The authors wish to thank the Natural Sciences and Engineering Research Council (NSERC) of Canada for generously supporting this research and Prof. R.T. Oakley for alerting us to the usefulness of LiHMDS etherate and for donating a sample of it. The valuable technical assistance of Dr. Yvonne Lear and Ms. Laura McConachie is gratefully acknowledged. The Schwan group also thanks Dr. Sriram Naganathan for kindly providing a copy of his PhD thesis and for his helpful comments pertaining to this manuscript.

References

1. S. Patai *(Editor)*. The chemistry of sulfenic acids and their derivatives. Wiley–Interscience, New York. 1990.
2. E. Block. Angew. Chem. Int. Ed. Engl. **31**, 1135 (1992).
3. (*a*) M.C. Aversa, A. Barattucci, P. Bonaccorsi, P. Giannetto, and D.N. Jones. J. Org. Chem. **62**, 4376 (1997); (*b*) D.N. Jones, T.P. Kogan, P. Murray-Rust, J. Murray-Rust, and R.F. Newton. J. Chem. Soc. Perkin Trans. 1, 1325 (1982).
4. G. Mazzanti, E. van Helvoirt, L.A. van Vliet, R. Ruinaard, S. Masiero, B.F. Bonini, and B. Zwanenburg. J. Chem. Soc. Perkin Trans. 1, 3299 (1994).
5. (*a*) L.A.G.M. van den Broek, L.P.C. Delbressine, and H.C.J. Ottenheijm. *In* The chemistry of sulfenic acids and their derivatives. *Edited by* S. Patai. Wiley–Interscience, New York. 1990. pp. 701–721; (*b*) W.S. Allison. Acc. Chem. Res. **9**, 293 (1976).
6. (*a*) A. Ishii, K. Komiya, and J. Nakayama. J. Am. Chem. Soc. **118**, 12 836 (1996); (*b*) T. Yoshimura, E. Tsukurimichi, S.

© 1998 NRC Canada

Yamazaki, S. Soga, C. Shimasaki, and K. Hasegawa. J. Chem. Soc. Chem. Commun. 1337 (1992); (*c*) T. Saiki, K. Goto, N. Tokitoh, and R. Okazaki. J. Org. Chem. **61**, 2924 (1996).
7. D.R. Hogg. *In* The chemistry of sulfenic acids and their derivatives. *Edited by* S. Patai. Wiley–Interscience, New York. 1990. pp. 361–367.
8. D. Kost and M. Raban. *In* The chemistry of sulfenic acids and their derivatives. *Edited by* S. Patai. Wiley–Interscience, New York. 1990. pp. 23–82.
9. E. Block, J.Z. Gillies, C.W. Gillies, A.A. Bazzi, D. Putman, L.K. Revelle, D. Wang, and X. Zhang. J. Am. Chem. Soc. **118**, 7492 (1996).
10. G. Capozzi, F. De Sio, S. Menichetti, C. Nativi, and P.L. Pacini. Synthesis, 521 (1994).
11. J.-B. Baudin, S.A. Julia, and O. Ruel. Tetrahedron, **43**, 881 (1987).
12. E. Busi, G. Capozzi, S. Menichetti, and C. Nativi. Synthesis, 643 (1992).
13. M.D. Refvik, R.D.J. Froese, J.D. Goddard, H.H. Pham, M.F. Pippert, and A.L. Schwan. J. Am. Chem. Soc. **117**, 184 (1995).
14. M.D. Refvik and A.L. Schwan. J. Org. Chem. **61**, 4232 (1996).
15. M.D. Refvik and A.L. Schwan. Tetrahedron, **52**, 8387 (1996).
16. (*a*) D.R. Hogg and A. Robertson. Tetrahedron Lett. 3783 (1974); (*b*) J. Chem. Soc. Perkin Trans. 1, 1125 (1979).
17. T. Yoshimura, K. Hamada, S. Yamazaki, C. Shimasaki, S. Ono, and E. Tsukurimichi. Bull. Chem. Soc. Jpn. **68**, 211 (1995).
18. F.A. Davis, S.Q.A. Rizvi, R. Ardecky, D.J. Gosciniak, A.J. Friedman, and S.G. Yocklovich. J. Org. Chem. **45**, 1650 (1980).
19. S. Tamagaki, H. Hirota, and S. Oae. Bull. Chem. Soc. Jpn. **47**, 2075 (1974).
20. (*a*) D. Landini, A. Maia, and F. Montanari. J. Am. Chem. Soc. **100**, 2796 (1978); (*b*) R. Alexander, E.C.F. Ko, A.J. Parker, and T.J. Broxton. J. Am. Chem. Soc. **90**, 5049 (1968).
21. J.L. Kice and C.-C.A. Liu. J. Org. Chem. **44**, 1918 (1979).
22. R.T. Boeré, R.G. Hicks, and R.T. Oakley. Inorg. Synth. **31**, 94 (1997).
23. G. Derbesy and D.N. Harpp. J. Org. Chem. **60**, 1044 (1995).
24. (*a*) S. Naganathan. Ph.D. thesis, The State University of New York at Albany. Albany, N.Y. 1992; (*b*) E. Block, T. Bayer, S. Naganathan, and S.-H. Zhao. J. Am. Chem. Soc. **118**, 2799 (1996).
25. B.F. Bonini, E. Foresti, R. Leardini, G. Maccagnani, and G. Mazzanti. Tetrahedron Lett. **25**, 445 (1984).
26. E. Block and J. O'Conner. J. Am. Chem. Soc. **96**, 3929 (1974).
27. A.L. Schwan and M.D. Refvik. Synlett. 96 (1998).
28. T.S. Chou. Tetrahedron Lett. 725 (1974).
29. D.W. Hoard, W.D. Luke, and R.A. Johnson. Abstracts of the 214th ACS national meeting. No. ORGN 326. American Chemical Society, Washington. 1997.

© 1998 NRC Canada

A search for an inexpensive calculational method for the reliable prediction of the first adiabatic and vertical ionization potentials of carbenes. Photoelectron spectra of two stable carbenes

Heidi M. Muchall, Nick H. Werstiuk, and Biswajit Choudhury

Abstract: Photoelectron (PE) spectra of two stable carbenes **7** and **8** have been recorded and the spectra have been interpreted with the aid of eigenvalues and eigenvectors taken from Becke3LYP calculations. For the carbene series **6**–**8**, the lone pair on the carbene carbon atom is the HOMO. The first adiabatic ionization potential (IP) of eight electronically quite different carbenes has been calculated using semiempirical PM3 and ab initio HF, Becke3LYP, and Becke3PW91 methods (3-21G(*) and 6-31+G* basis sets) as well as the CBS-4 model. For the first vertical IP, the HAM/3, Becke3LYP, and Becke3PW91 methods have been employed. CBS-4 and DFT calculations show excellent agreement with experimental values. Considering both accuracy and speed, the method of choice for the prediction of first ionization potentials of carbenes seems to be Becke3LYP/6-31+G*//Becke3LYP/3-21G(*).

Key words: carbenes, electronic structure, first ionization potential, photoelectron spectroscopy, quantum chemical calculations.

Résumé : On a déterminé les spectres photoélectroniques (PE) des deux carbènes stables **7** et **8** et on en a fait l'interprétation à l'aide des valeurs et des vecteurs propres obtenus à partir de calculs Becke3LYP. Pour les séries de carbènes **6**–**8**, la paire d'électron non partagée qui se trouve sur l'atome de carbone du carbène est la HOMO. En utilisant des calculs semi-empiriques PM3 et ab initio HF, les méthodes Becke3LYP et Becke3PW91 (ensembles de base 3-21G(*) et 6-31+G*) ainsi le modèle CBS-4, on a calculé le premier potentiel d'ionisation adiabatique (PI) de huit carbènes assez différents d'un point de vue électronique. Pour le premier PI vertical, on a utilisé les méthodes HAM/3, Becke3LYP et Becke3PW91. Les résultats des calculs CBS-4 et DFT présentent un excellent accord avec les valeurs expérimentales. Considérant l'exactitude et la vitesse, la méthode de choix pour prédire les premiers potentiels d'ionisation de carbène semble être la méthode Becke3LYP/6-31+G*//Becke3LYP/3-21G(*).

Mots clés : carbènes, structure électronique, premier potentiel d'ionisation, spectroscopie photoélectronique, calculs de chimie quantique.

[Traduit par la rédaction]

Introduction

Photoelectron (PE) spectroscopy gives information on electronic structure and binding that can be obtained by no other technique. For PE spectroscopic studies, carbenes have been generated in the gas phase from suitable precursors by techniques such as pyrolysis (1, 2) and microwave discharge (3).[2] Usually, carbenes are more or less short-lived reactive intermediates. To be detected, they must be sufficiently long lived to be ionized. Both the precursor and the lifetime of a carbene can present difficulties to a PE spectroscopic study. First, if the conversion of the precursor is not complete, ionization bands of the starting compound will still be present in the PE spectrum and possibly overlap with those of the carbene in crucial regions. And, as the carbene is not the only product formed from the starting compound, possible overlap with bands from the other primary products must be taken into account. Second, even if the carbene is generated close to the ionization beam of the spectrometer, rearrangement, fragmentation, and dimerization of the carbene can lead to secondary products whose bands can further complicate the PE spectrum.

When a carbene is to be generated explicitly, at least problems arising from the precursor can be overcome by simply choosing the most suitable one. When, on the other hand, the carbene is one possible product in a pyrolysis study, all of the items mentioned above are likely to produce a complex PE spectrum. In this case, and especially when the PE spectrum of the carbene is unknown, it is imperative to have a procedure that allows easy, accurate prediction of the first ionization of the carbene, as this is the most likely not to be covered by other ionizations.

Received Aug 25, 1997.

H.M. Muchall,[1] N.H. Werstiuk,[1] and B. Choudhury.
Department of Chemistry, McMaster University, Hamilton, ON L8S 4M1, Canada.

[1] Authors to whom correspondence may be addressed. Telephone: (905) 525-9140. Fax: (905) 522-2509. E-mail: muchall@mcmaster.ca, werstiuk@mcmaster.ca

[2] An overview of methods for generating reactive intermediates in PE spectroscopic studies was recently given by Chen (4).

© 1998 NRC Canada

Fig. 1. UV photoelectron spectra of carbenes (*a*) **7** and (*b*) **8**.

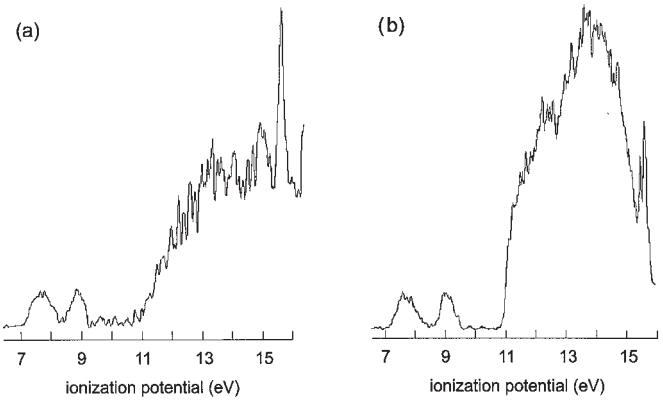

Interpretation of the PE spectrum of a molecule is usually achieved via Koopmans' theorem (5), which equates the ionization potential (IP) in question with the negative orbital energy of the respective molecular orbital taken from quantum chemical calculations. While this method often works well when several ionizations can be attributed to one molecule and relative energy differences can be taken as additional information, absolute orbital energies are usually systematically off, sometimes by as much as several electron volts, depending on the calculational method used. This approach is therefore not particularly suited for the prediction of the first ionization.

Yet the first ionization potential is easily accessible by computing the energy difference between the neutral molecule (*N* electrons) and its radical cation (*N*–1 electrons). The geometry of the radical cation can be quite different from that of the neutral, which leads to an energetic separation between the adiabatic and vertical IPs. While the energy difference based on a full geometry optimization of both species gives the adiabatic (IP_a), ignoring the geometry change upon ionization (which is achieved through a single-point energy calculation on the geometrical structure of the neutral for (*N*–1) electrons) gives the vertical (IP_v) ionization potential. These calculated values are compared to those taken from the PE spectra to evaluate their quality. In recent years, models have been developed that give accurate energies and are therefore well suited to predict IPs (6). These models, like the G2 (7) and CBS (8) series, are very costly in terms of computational resources and can only be applied to molecules having a small number of heavy atoms (8).

Our goal was to find a method that can provide us with good predictions for first IPs of even relatively large carbenes in a reasonably short time. For future work, such a method could then be applied to the detection of unstable carbenes in our pyrolytic studies. In this paper, we present semiempirical and ab initio calculations of the first IP_a and IP_v of carbenes **1**–**5** as well as of "stable" carbenes **6**–**8**. Experimental values for **1**–**6** are taken from the literature (1–3, 9–11); He(I) PE spectra of **7** and **8** are presented here for the first time.

Experimental

HF (12), CBS-4 (8), Becke3LYP (13*a*,13*b*), and Becke3PW91 (13*b*, 13*c*) calculations were carried out on IBM RS/6000 model 39H, 350, and 530 computers with GAUSSIAN 94 (14). Semiempirical PM3 (15) calculations were performed with the MOPAC (16) program package (version 6.00) on an IBM RS/6000 model 320H computer. All semiempirical geometry optimizations used the keyword PRECISE to tighten the convergence criteria. The equilibrium geometries obtained with PM3 were used in the HAM/3 (17) calculations on the IBM RS/6000 model 320H computer. Graphical representations of the calculationally determined eigenvectors (PM3//Becke3LYP/6-31+G*; these were checked against Becke3LYP/6-31+G*// Becke3LYP/6-31+G* eigenvectors and were found to compare well) were plotted from HyperChem 5.[3]

PE spectra were measured with a locally built instrument (18) by signal averaging 12 scans with nitrogen (15.6 eV) as the calibrant. Linearity of the scale was ensured through calibrations with methyl iodide (9.54 and 10.16 eV) and O_2 (12.30 eV) performed prior to the experiments.

1,3-Diethyl-4,5-dimethylimidazol-2-ylidene (**7**) and 1,3-diisopropyl-4,5-dimethylimidazol-2-ylidene (**8**) were prepared according to the literature (19).

Table 1. Experimental and calculated (HAM/3) vertical ionization potentials IP (eV) and Becke3LYP/6-31+G*// Becke3LYP/3-21G orbital energies ε (eV) of carbenes **6**–**8**.

6			**7**			**8**		
IP			IP			IP		
Exp.[a]	Calcd.	–ε	Exp.	Calcd.	–ε	Exp.	Calcd.	–ε
7.68	7.97	5.69	7.71	7.87	5.72	7.56	7.81	5.64
8.22	8.17	6.16	7.71	7.92	5.77	7.56	7.84	5.65
9.24	9.31	7.16	9.06	9.19	7.03	8.89	9.08	6.95
11.21	11.27	8.98	11.4	11.33	9.43	11.1	11.10	9.08

[a]Taken from ref. 9.

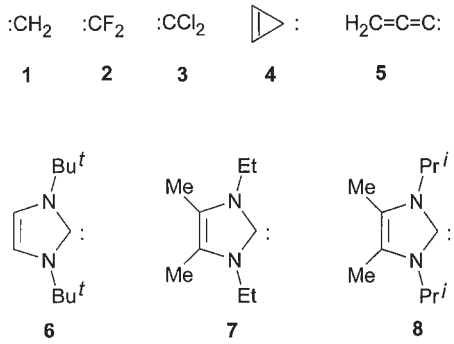

Results and discussion

Photoelectron spectra of stable carbenes 6–8

Ultraviolet PE spectra of carbenes **7** and **8** are depicted in Fig. 1. The spectra show great similarity with the He(I) PE spectrum of **6** (9): all three spectra exhibit two low-energy bands well separated from the main group of σ bands, which has a shoulder on the low-energy side, and the first band in each of the spectra is made up of two ionizations. The first four ionizations of **7** and **8** ($IP_{exp.}$) are listed in Table 1 along with those reported for **6** (9). While for the *tert*-butyl substituted carbene **6** the separation of the first two ionizations is large

[3] Hypercube, Inc., Waterloo, Ont. 1996.

© 1998 NRC Canada

Fig. 2. Most stable conformations for carbenes **7** (Becke3LYP/6-31+G*) and **8** (Becke3LYP/3-21G*).

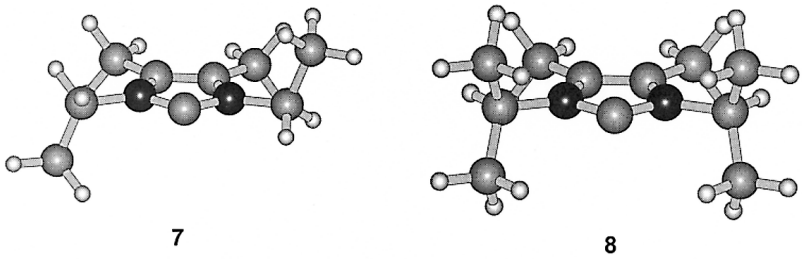

enough to give rise to two discrete maxima, for the ethyl and isopropyl analogues **7** and **8**, respectively, this difference is smaller and thus leads to one broad band for which only one maximum can be given. As can be seen in Table 1, Becke3LYP/6-31+G*//Becke3LYP/3-21G orbital energies ε for **6**–**8** (the lowest energy conformation for **7** and **8** is given in Fig. 2) mirror the experimental relative energy differences perfectly (the absolute deviation between –ε and $IP_{exp.}$ is about 2 eV, a value not unusual for Becke3LYP calculations). While on going from **6** to **7** there is little change in the HOMO energy, HOMO-1 is destabilized by 0.4 eV. This fact confirms the character of HOMO and HOMO-1 of carbene **6** as given by Arduengo et al. (9). The HOMO is the in-plane lone pair on the carbene carbon n_C rather than a ring π orbital (as suggested for the unsubstituted parent carbene (20)): in the sequence **6**–**7**, a π orbital would exhibit a destabilization due to methyl substitution on the ring, a behavior that is observed for HOMO-1 (π_3). Methyl substitution affects HOMO-2 (π_2) in the same way as HOMO-1 whereas HOMO-3 (mostly σ-type electron density on nitrogen substituents) is stabilized when *tert*-butyl groups are exchanged for ethyl groups. So the orbital sequence in carbenes **6**–**8**, in accord with Arduengo et al. (9), is $n_C > \pi_3 > \pi_2 > \sigma$, which is confirmed by the PE spectra.

The semiempirical HAM/3 method gives ionization potentials directly. In Table 1 IP_v's are given for PM3 optimized geometries. For **6** and **7** these geometries do not differ significantly from those obtained with ab initio methods; for **8** the methine hydrogens are twisted 47° out of the plane with PM3 (the in-plane ab initio conformation for **8** is shown in Fig. 2, yet this does not much affect the calculated ionization potentials). HAM/3 IPs show a very good correlation with the experimental data.

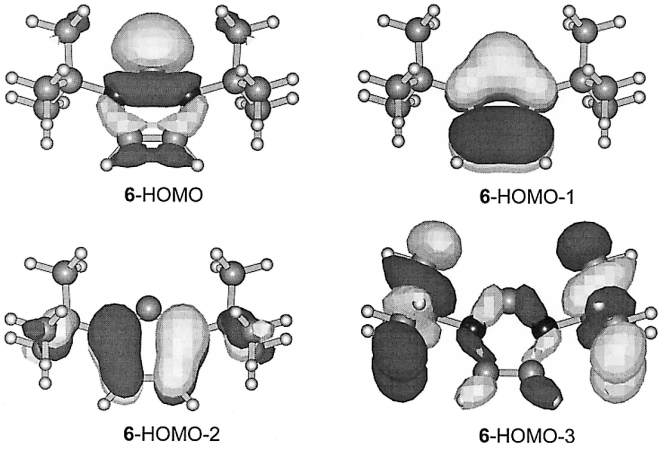

Calculation of the first adiabatic ionization potential

The limitation for the number of carbenes studied in this work is the number of carbene PE spectra available. We took PE spectroscopic literature values for the first adiabatic ionization potentials of singlet (21) carbenes **2**–**5** (1–3). To include a triplet carbene, the IP_a of the parent methylene (**1**) determined from a mass spectrometric experiment (10.35 eV) (11) as well as from the Rydberg series in its VUV spectrum (10.40 eV) (10) was also considered. For these carbenes, we performed calculations for first IP_a's using the compound computational model CBS-4. While being the smallest — and fastest — model in the CBS/PNO (complete basis set/pair natural orbitals) series, this model still gives accurate molecular energies on a UHF/3-21G(*) optimized geometry (the mean absolute deviation from experimental IPs for the G2 test set (22) is 2.2 kcal mol^{-1} or 0.1 eV; the maximum error is 6.1 kcal mol^{-1} or 0.3 eV for hydrogen fluoride) (8). Total energies from which IP_a's are computed are listed in Table 2. As can be seen in Table 3, CBS-4 values for carbenes **1**–**3** and **5** differ from experiment by less than 0.2 eV; the difference for **4** is only slightly larger. The mean absolute deviation is 0.13 eV, a figure against which other calculational methods can be evaluated.

There have been previous attempts at calculating first adiabatic IPs of carbenes in the literature. Using an electron propagator method (MCSTEP), Nichols et al. (23) in 1994 applied adiabatic corrections to calculated vertical ionization potentials of **1**. Rodriquez, Bohme, and Hopkinson (24) in 1996 employed fourth-order Møller–Plesset theory and QCISD(T) to obtain enthalpies of formation for **1** and **3** and from these deduce IP_a's. In 1989, Wong and Radom (25) used the CISD/6-31G* level of theory to predict the, at that time unknown, IP_a of **4** to be 8.8 eV, a value that is still 0.35 eV off. Russo, Sicilia, and Toscano (26) in 1992 used a density functional approach (LCGTO-LSD/NLC) to the IP_a's of **1**–**3**. They report 10.69 eV for **1**, 11.56 eV for **2**, and 9.55 eV for **3**, which, compared to the experimental data stated in this paper, give differences of 0.29, 0.14, and 0.28 eV, respectively. These values seem to suggest that density functional theory is suitable for our purpose.

Tables 2 and 3 give results from semiempirical PM3 and ab initio HF, Becke3LYP, and Becke3PW91 methods. PM3 IP_a's (Table 3) for difluoro carbene (**2**), dichloro carbene (**3**), and propadienylidene (**5**) are unacceptably low and even though those of methylene (**1**) and cyclopropenylidene (**4**) are very close to the experimental values, PM3 cannot be used for our

© 1998 NRC Canada

Table 2. Ab initio total energies (hartrees) and PM3 heats of formation (kcal mol^{-1}) for optimized geometries for carbenes **1**–**5** with *N* and *N*–1 electrons.

	Number of electrons	**1**	**2**	**3**	**4**	**5**
CBS-4	*N*	–39.077 579	–237.487 215	–957.413 803	–115.158 279	–115.132 313
	N–1	–38.693 913	–237.064 719	–957.079 771	–114.814 424	–114.753 286
PM3	*N*	71.64	–49.09	57.45	136.17	139.37
	N–1	310.58	201.15	212.80	350.76	362.70
HF/6-31+G*	*N*	–38.923 719	–236.671 751	–956.715 811	–114.627 381	–114.599 271
	N–1	–38.566 493	–236.289 448	–956.408 058	–114.335 510	–114.272 080
B3LYP/3-21G	*N*	–38.936 055	–236.393 390	–953.755 592[a]	–114.690 050	–114.694 755
	N–1	–38.555 452	–235.977 747	–953.386 355[b]	–114.359 722	–114.319 198
B3LYP/6-31+G*	*N*	–39.154 890	–237.711 308	–958.388 918	–115.361 684	–115.342 591
	N–1	–38.772 761	–237.289 913	–958.050 779	–115.027 242	–114.957 802
(+ZPVE)[c]	*N*	–39.137 542	–237.704 573	–958.384 919	–115.329 432	–115.311 348
	N–1	–38.756 218	–237.281 601	–958.045 505	–114.994 425	–114.926 986
B3LYP/6-31+G*//	*N*	–39.154 864	–237.709 291	–958.377 853	–115.359 662	–115.342 492
B3LYP/3-21G(*)	*N*–1	–38.772 757	–237.286 859	–958.044 394	–115.026 737	–114.957 752
B3PW91/3-21G(*)	*N*	–38.922 924	–236.307 901	–953.864 982	–114.641 021	–114.640 063
	N–1	–38.535 457	–235.891 058	–953.528 919	–114.309 362	–114.260 035
B3PW91/6-31+G*	*N*	–39.140 743	–237.618 323	–958.264 337	–115.312 328	–115.286 037
	N–1	–38.753 605	–237.202 117	–957.928 944	–114.979 628	–114.907 511
B3PW91/6-31+G*//	*N*	–39.140 721	–237.616 022	–958.263 159	–115.310 130	–115.285 950
B3PW91/3-21G(*)	*N*–1	–38.753 603	–237.198 761	–957.928 933	–114.979 004	–114.907 381

[a]B3LYP/3-21G* value is –953.991 570.
[b]B3LYP/3-21G* value is –953.655 543.
[c]ZPVE (not scaled) corrected B3LYP/6-31+G* total energies.

Table 3. Observed and calculated first adiabatic ionization potentials (eV) of carbenes **1**–**8**.

	1	**2**	**3**	**4**	**5**	**6**	**7**	**8**
$IP_{a,obs}$	10.4[a]	11.42[b]	9.27[c]	9.15[d]	10.43[d]	7.2[e]	7.1[f]	7.0[f]
CBS-4	10.44	11.50	9.09	9.36	10.31			
PM3	10.36	10.85	6.74	9.31	9.68	7.88	8.14	8.07
HF/6-31+G*	9.72	10.40	8.37	7.94	8.90			
B3LYP/3-21G	10.36	11.31	10.05[g]	8.99	10.22	6.84	6.91	6.81
B3LYP/6-31+G*	10.40	11.47	9.20	9.10	10.47	7.14	7.26	
(+ZPVE)[h]	10.38	11.51	9.24	9.12	10.46			
B3LYP/6-31+G*//	10.40	11.50	9.18	9.06	10.47	7.12	7.24	7.06
B3LYP/3-21G(*)								
B3PW91/3-21G(*)	10.54	11.34	9.14	9.02	10.34	6.85	6.92	6.83
B3PW91/6-31+G*	10.53	11.32	9.13	9.05	10.30			
B3PW91/6-31+G*//	10.53	11.35	9.09	9.01	10.30	7.32	7.57	7.00
B3PW91/3-21G(*)								

[a]References 10, 11.
[b]Reference 3.
[c]Reference 1.
[d]Reference 2.
[e]Estimated from ref. 9.
[f]This work.
[g]B3LYP/3-21G* value is 9.14 eV.
[h]ZPVE (not scaled) corrected B3LYP/6-31+G* total energies.

purpose. HF with a 6-31+G* basis set performs much worse; all IP_a's are prohibitively low. Becke3LYP, on the other hand, with as small a basis set as 3-21G, gives very good agreement with experiment, the only exception being for dichloro carbene (**3**). This is obviously due to the presence of third-row chlorine atoms and is corrected by including polarization functions in the basis set (Table 3). The resulting mean absolute deviation is an amazing 0.13 eV, the same value that we obtained using CBS-4. With the 6-31+G* basis set it even drops to 0.04 eV for this set of five carbenes, which is considerably better than the CBS-4 value.

For Becke3LYP calculations we omitted corrections for zero-point vibrational energies (ZPVEs) as we expected their influence to be small. A check with unscaled ZPVEs (the

© 1998 NRC Canada

Table 4. Ab initio total energies (hartrees) and PM3 heats of formation (kcal mol^{-1}) for optimized geometries for carbenes **6**–**8** with *N* and *N*–1 electrons.

	Number of electrons	**6**	**7**	**8**
PM3	*N*	14.99	16.93	6.67
	N–1	196.64	204.70	192.83
B3LYP/3-21G	*N*	–537.742 612	–459.541 260	–537.751 035
	N–1	–537.491 300	–459.287 465	–537.500 666
B3LYP/6-31+G*	*N*	–540.701 937	–462.082 812	
	N–1	–540.439 654	–461.816 130	
B3LYP/6-31+G*// B3LYP/3-21G(*)	*N*	–540.699 913	–462.080 961	–540.711 260
	N–1	–540.438 104	–461.814 873	–540.451 716
B3PW91/3-21G(*)	*N*	–537.552 549	–459.375 795	–537.559 916
	N–1	–537.300 717	–459.121 491	–537.308 901
B3PW91/6-31+G*// B3PW91/3-21G(*)	*N*	–540.499 975	–461.908 494	–540.511 437
	N–1	–540.240 705	–461.645 146	–540.254 247

Table 5. Observed and calculated first vertical ionization potentials (eV) of carbenes **1**–**8**.

	1	**2**	**3**	**4**	**5**	**6**	**7**	**8**
$IP_{v,obs}$	—[a]	12.27[b]	9.8[c]	9.4[d]	10.43[d]	7.68[e]	7.71[f]	7.56[f]
HAM/3[g]	9.11	12.31	—[h]	10.06	10.00	7.97	7.88	7.81
B3LYP/6-31+G*	10.42	12.33	10.18	9.42	10.43	7.56	7.66	—[i]
B3LYP/6-31+G*// B3LYP/3-21G(*)	10.43	12.60	10.43	9.61	10.41	7.69	7.82	7.59
B3PW91/6-31+G*	10.56	12.21	10.12	9.37	10.42	—[i]	—[i]	—[i]
B3PW91/6-31+G*// B3PW91/3-21G(*)	10.56	12.49	10.38	9.57	10.39	7.63	7.65	7.51

[a]Not known.
[b]Reference 3.
[c]Estimated from ref. 1.
[d]Estimated from ref. 2.
[e]Reference 9.
[f]This work.
[g]On PM3 optimized geometries.
[h]HAM/3 is not parameterized for chlorine.
[i]The carbene was not optimized at this level of theory.

factor for Becke3LYP/6-31G* is 0.98 (6), which is close enough to 1.0; we assumed the same to be true for the 6-31+G* basis) on Becke3LYP/6-31+G* total energies confirmed this (Tables 2 and 3).

Although the number of carbenes studied is small, electronically **1**–**5** are quite different. That Becke3LYP did an excellent job of predicting all first IP_a's was promising for an extension of the study to the so-called "stable" carbenes **6**–**8**. Carbenes **6**–**8** have considerably more heavy atoms than carbenes **1**–**5** and obtaining optimized geometries of their radical cations using Becke3LYP/6-31+G* is still computationally demanding. We therefore checked the possibility of doing single-point energy calculations at this level of theory using the Becke3LYP/3-21G(*) optimized geometries. The result is a mean absolute deviation of 0.06 eV; calculated IP_a's can be seen in Table 3. So this is probably the method of choice for calculating the first IP_a of carbenes of all sizes.

For a further comparison,[4] we repeated the above DFT calculations using the PW91 correlation functional (Tables 2 and 3). While Becke3PW91 performs slightly better than Becke3LYP with the 3-21G(*) basis set, it is definitely worse when the 6-31+G* basis set is employed.

Experimental IP_a's of carbenes **6**–**8** as given in Table 3 were estimated from their PE spectra (onset of the first band). The calculational data (Tables 3 and 4) for these stable carbenes confirm the previous findings for the ordinary carbenes: Becke3LYP/6-31+G*//Becke3LYP/3-21G(*) gives excellent results.

Calculation of the first vertical ionization potential

Experimental first vertical IPs of carbenes **2**–**8** are listed in Table 5. As there are no reported IP_v's for carbenes **3**–**5**, we estimated them from their PE spectra (maximum of the band) (1, 2). For carbenes **6**–**8** we have shown that IP_v's calculated with the semiempirical HAM/3 method are in very good agreement with experiment (see above). This statement was based on a total of 12 IPs for the three compounds. Yet, if only the first IP_v of a carbene is considered, deviations from the experimental value can be rather large (Table 5).

A calculation of the first IP_v differs from a calculation of the first IP_a: while the IP_a requires optimized geometries for both the carbene *and* its radical cation (relaxation), for the IP_v

[4] We thank A.D. Becke for suggesting this comparison.

© 1998 NRC Canada

Table 6. Ab initio total energies (hartrees) for single-point energy calculations for N–1 electrons on carbene optimized geometries for carbenes **1**–**8**.

	B3LYP/6-31+G*	B3LYP/6-31+G*// B3LYP/3-21G(*)	B3PW91/6-31+G*	B3PW91/6-31+G*// B3PW91/3-21G(*)
1	–38.771 923	–38.771 678	–38.752 788	–38.752 607
2	–237.258 112	–237.246 377	–237.169 708	–237.156 819
3	–958.014 792	–958.004 503	–957.892 397	–957.881 649
4	–115.015 580	–115.006 556	–114.967 917	–114.958 579
5	–114.959 358	–114.960 061	–114.903 182	–114.904 021
6	–540.424 084	–540.417 214	—[a]	–540.219 579
7	–461.801 290	–461.793 751	—[a]	–461.627 432
8	—[a]	–540.432 303	—[a]	–540.235 277

[a]The carbene was not optimized at this level of theory.

the energy of the radical cation is calculated on the geometry of the neutral carbene (no relaxation). As for the first IP_a, there have been attempts at calculating first vertical IPs of carbenes. In 1985, Nguyen et al. (27) performed HF, MP2, MP3, and MP4SDQ (6-31G** basis) single-point energy calculations on the HF/3-21G* geometry for **3** and obtained IP_v's of 9.45, 9.73, 9.86, and 9.75 eV, respectively, which shows the level of theory necessary to get close to the estimated value of 9.8 eV given in Table 5. Bauschlicher and Taylor (28) in 1987 published full CI benchmark calculations for IP_v's of **1** to which other high-level calculations were compared (X.-C. Wang and K.F. Freed in 1989 (29), Nichols et al. (23)). The work of Wong and Radom (25) includes the predicted IP_v of **4**. The reported value of 9.0 eV using CISD/6-31G* differs from the value in Table 5 by 0.4 eV. Russo, Sicilia, and Toscano (26) give LCGTO-LSD/NLC IP_v's for **1** (10.73 eV), **2** (12.09 eV), and **3** (10.30 eV).

Table 5 shows the Becke3LYP/6-31+G* IP_v's (total energies for the radical cations are given in Table 6) from this work for carbenes **1**–**7**. For **1**, there is no IP_v available, but our calculations suggest that it should be close to its IP_a of 10.4 eV. IP_v's for **2** and **4**–**7** are very close to the experimental values with the largest difference of 0.12 eV for **6**. The difference for **3** with 0.38 eV is somewhat large; this might be partially due to an uncertainty in our estimation of the experimental first IP_v. As can be seen in Table 5, good results are obtained with Becke3LYP/6-31+G*//Becke3LYP/3-21G(*) for **1**–**8**, especially for carbenes with more heavy atoms. Except for dihalo carbenes **2** and **3** with a difference of 0.33 and 0.63 eV (the latter value could be smaller, see above), respectively, IP_v's differ by less than 0.22 eV. Becke3PW91 values for the first vertical IP, in contrast to values obtained for the first adiabatic IP, are comparable to those obtained with Becke3LYP (Table 5).

Conclusions

Recorded PE spectra of stable carbenes **7** and **8** resemble that of the *tert*-butyl substituted carbene **6**. An interpretation of the change in ionization potentials on going from **6** to **7** together with orbital energies taken from Becke3LYP/6-31+G* calculations and the effect of methyl substitution on the ring gave the character of the four highest occupied molecular orbitals for **6**–**8** as $n_C > \pi_3 > \pi_2 > \sigma$.

The Becke3LYP method was employed in the calculation of first adiabatic and vertical ionization potentials of carbenes **1**–**8**. For the IP_a's of the small carbenes **1**–**5**, a mean absolute deviation of 0.04 eV was achieved with Becke3LYP/6-31+G*; this was found to be substantially better than even the CBS-4 performance (mean absolute deviation of 0.13 eV) for this set of molecules. The Becke3LYP/6-31+G*//Becke3LYP/3-21G(*) level of theory was also tested and found to be sufficiently accurate (the largest absolute error was 0.14 eV for **7**, which could be due to an uncertainty in our location of the experimental IP_a). While semiempirical PM3 and ab initio HF/6-31+G* calculations gave unsatisfactory values for the adiabatic IP, those obtained with the Becke3PW91 method were found to be only slightly worse than Becke3LYP results.

Calculated Becke3LYP/6-31+G* first IP_v's of carbenes **2**–**7** are very close to the experimental values (less than 0.13 eV difference) with the exception of dichloro carbene (**3**) (the difference of 0.38 eV could again be attributed to an error in our prediction of the experimental IP_v). Becke3LYP/6-31+G*//Becke3LYP/3-21G(*) gave similar results with a slight loss of accuracy. For IP_v's, Becke3PW91 performs about as well as Becke3LYP.

This study has provided us with a calculational method, Becke3LYP/6-31+G*, that gives accurate first adiabatic and vertical ionization potentials for carbenes without being computationally too demanding. Depending on the size of the carbene, 3-21G(*) or 6-31+G* basis sets can be employed in geometry optimizations. In future gas phase pyrolysis studies, this can aid in the interpretation of PE spectra with regard to the possible presence of carbenes.

Acknowledgments

We gratefully acknowledge the use of the IBM SP2 computer at Queen's University granted under the auspices of an IBM Canada – Queen's University collaborative project. We thank Ms. O. Donini for assistance with operational aspects of parallel GAUSSIAN 94, and the Natural Sciences and Engineering Research Council of Canada (NSERC) for financial support. We also gratefully acknowledge the usage of the SGI computing installation in the Geochemistry Labs at McMaster funded by NSERC.

References

1. D.W. Kohn, E.S.J. Robles, C.F. Logan, and P. Chen. J. Phys. Chem. **97**, 4936 (1993).
2. H. Clauberg, D.W. Minsek, and P. Chen. J. Am. Chem. Soc. **114**, 99 (1992).

© 1998 NRC Canada

3. J.M. Dyke, L. Golob, N. Jonathan, A. Morris, and M. Okuda. J. Chem. Soc. Faraday Trans. 2, **70**, 1828 (1974).
4. P. Chen. Unimol. Bimol. Ion–Mol. React. Dyn. 371 (1994).
5. T. Koopmans. Physica, **1**, 104 (1933).
6. J.B. Foresman and A. Frisch. Exploring chemistry with electronic structure methods. 2nd ed. Gaussian, Inc., Pittsburgh, Pa. 1996.
7. L.A. Curtiss, K. Raghavachari, G.W. Trucks, and J.A. Pople. J. Chem. Phys. **94**, 7221 (1991); J. Chem. Phys. **98**, 1293 (1993).
8. J.W. Ochterski, G.A. Petersson, and J.A. Montgomery, Jr. J. Chem. Phys. **104**, 2598 (1996).
9. A.J. Arduengo III, H. Bock, H. Chen, M. Denk, D.A. Dixon, J.C. Green, W.A. Herrmann, N.L. Jones, M. Wagner, and R. West. J. Am. Chem. Soc. **116**, 6641 (1994).
10. G. Herzberg. Can. J. Phys. **39**, 1511 (1961).
11. W. Reineke and K. Strein. Ber. Bunsen-Ges. Phys. Chem. **80**, 343 (1976).
12. W.J. Hehre, L. Radom, P.v.R. Schleyer, and J.A. Pople. Ab initio molecular orbital theory. John Wiley & Sons, New York. 1986.
13. (*a*) A.D. Becke. J. Chem. Phys. **98**, 5648 (1993); (*b*) C. Lee, W. Yang, and R.G. Parr. Phys. Rev. B: Condens. Matter, **37**, 785 (1988); (*c*) J.P. Perdew and Y. Wang. Phys. Rev. B: Condens. Matter, **45**, 13244 (1992).
14. M.J. Frisch, G.W. Trucks, H.B. Schlegel, P.M.W. Gill, B.G. Johnson, M.A. Robb, J.R. Cheeseman, T. Keith, G.A. Petersson, J.A. Montgomery, K. Raghavachari, M.A. Al-Laham, V.G. Zakrzewski, J.V. Ortiz, J.B. Foresman, C.Y. Peng, P.Y. Ayala, W. Chen, M.W. Wong, J.L. Andres, E.S. Replogle, R. Gomperts, R.L. Martin, D.J. Fox, J.S. Binkley, D.J. Defrees, J. Baker, J.P. Stewart, M. Head-Gordon, C. Gonzalez, and J.A. Pople. Gaussian 94, Revision B.3. Gaussian, Inc., Pittsburgh, Pa. 1995.
15. J.J.P. Stewart. J. Comput. Chem. **10**, 209 (1989).
16. J.J.P. Stewart. QCPE, 455, (1983).
17. L. Åsbrink, C. Fridh, and E. Lindholm. HAM/3, QCPE Bull. **13**, 393 (1981).
18. N.H. Werstiuk, D.N. Butler, and E. Shahid. Can. J. Chem. **65**, 760 (1986).
19. N. Kuhn and T. Kratz. Synthesis, 561 (1993).
20. C. Heinemann and W. Thiel. Chem. Phys. Lett. **217**, 11 (1994).
21. O.M. Nefedov, M.P. Egorov, A.I. Ioffe, L.G. Menchikov, P.S. Zuev, V.I. Minkin, B.Ya. Simkin, and M.N. Glukhovtsev. Pure Appl. Chem. **64**, 265 (1992).
22. L.A. Curtis, K. Raghavachari, G.W. Trucks, and J.A. Pople. J. Chem. Phys. **94**, 7221 (1991).
23. J.A. Nichols, D. Heryadi, D.L. Yeager, and J.T. Golab. J. Chem. Phys. **100**, 2947 (1994).
24. C.F. Rodriquez, D.K. Bohme, and A.C. Hopkinson. J. Phys. Chem. **100**, 2942 (1996).
25. M.W. Wong and L. Radom. Org. Mass Spectrom. **24**, 539 (1989).
26. N. Russo, E. Sicilia, and M. Toscano. J. Chem. Phys. **97**, 5031 (1992).
27. M.T. Nguyen, M.C. Kerins, A.F. Hegarty, and N.J. Fitzpatrick. Chem. Phys. Lett. **117**, 295 (1985).
28. C.W. Bauschlicher, Jr. and P.R. Taylor. J. Chem. Phys. **86**, 2844 (1987).
29. X.-C. Wang and K.F. Freed. J. Chem. Phys. **91**, 1142 (1989).

© 1998 NRC Canada

Photochemical reduction of CO_2 using Cu-loaded silicate rock powder suspended in water

Kiyohisa Ohta, Youko Ueda, Satoshi Nakaguchi, and Takayuki Mizuno

Abstract: The photocatalytic reduction of CO_2 using copper-loaded silicate rocks has been reported. The Cu–silicate rock powders suspended in the solution were illuminated with sunlight. Amphibolite, gneiss, granite, granodiorite, phyllite, quartzdiorite, and shale, which are quite ordinary rocks, were tested as substrates (silicate rock) of the catalyst. These catalysts were specific for the formation of formic acid. The effects of amounts of copper, illumination time, and temperature were investigated on photoreduction of CO_2. The 30% Cu-loaded quartzdiorite (0.3 g/g) in these Cu rocks was the best catalyst. The formation of formic acid on the Cu–silicate rock increased with time up to 10 h after which the formation decreased, and then became constant. The formic acid formation decreased with temperature for 10 h sunlight illumination. For the photochemical reduction of CO_2, a relatively low temperature was suitable. With photochemical reduction, the maximum yield of formic acid was 54 nmol/g under optimum experimental conditions. The carbon dioxide reduction system developed might well become of practical interest for the photochemical production of raw materials for the photochemical industry.

Key words: photocatalytic reduction of carbon dioxide, formic acid, copper-loaded silicate rocks, temperature effect, illumination time.

Résumé : On a réalisé la réduction photocatalytique du CO_2 à l'aide de roches de silicate enduites de cuivre. Les roches de silicate enduites de cuivre, réduites en poudre, ont été mises en suspension dans des solvants et irradiés par de la lumière solaire. Des roches ordinaires d'amphibolite, gneiss, granit, granodiorite, phyllite, quartzdiorite et de schiste ont été évaluées comme substrats (roches de silicate) pour le catalyseur. Ces catalyseurs sont spécifiques pour la formation d'acide formique. On a étudié l'influence des quantités de cuivre, des temps d'illumination et de la température sur la photoréduction du CO_2. La quartzdiorite portant 30% de cuivre (0,3 g/g) est le meilleur catalyseur. La formation d'acide formique sur des roches de silicate enduites de cuivre augmente avec le temps, jusqu'à 10 h; toutefois, au-delà de ce temps, la formation diminue et devient constante. Jusqu'à 10 h d'illumination, la formation d'acide formique diminue avec la température. Pour la réduction photochimique du CO_2, des températures relativement faibles. Dans des conditions expérimentales optimales, le rendement maximal d'acide formique par réduction photochimique est de 54 nmol/g. Le système de réduction du dioxyde de carbone qui a été développé pourrait avoir un intérêt pratique pour la production photochimique de produits de base pour l'industrie photochimique.

Mots clés : réduction photocatalytique du dioxyde de carbone, acide formique, roches enduites de cuivre, effet de la température, temps d'illumination.

[Traduit par la rédaction]

The establishment of techniques for the removal of CO_2 and its conversion into organic raw materials is of interest because of the approaching exhaustion of petroleum deposits and the greenhouse effect of the increase of CO_2 in the atmosphere. Therefore, many methods for the fixation and removal of CO_2 have been reported (1–7). In these studies, photocatalytic reduction of CO_2 (1, 3, 5, 6, 8–12) is drawing worldwide attention because of simplicity and easy control of the system, specificity for the formations of fuel and organic raw materials, and low cost. Fujishima and co-workers (8) showed that CO_2 in water was reduced to formic acid, formaldehyde, and methanol, using photosensitive semiconductor powders such as WO_3, TiO_2, ZnO, CdS, GaP, and SiC. Halmann (5) and Halmann and Aurian-Blajeni (9) have reported CO_2 reduction of aqueous suspensions of WO_3, TiO_2, ZnO, Fe_2O_3, or nontronite by irradiation with sunlight or an Hg lamp. Thampi et al. (10) examined methanation and photomethanation of CO_2 at room temperature and atmospheric pressure, using TiO_2-loaded Ru/RuO_x. Rophael and Malati (11) described photocatalyzed reduction of aqueous sodium carbonate to carbon using platinized titania. Hirano et al. (12) studied photocatalyzed reduction of CO_2 to methanol, formaldehyde, and formic acid in aqueous TiO_2 suspension mixed with copper powder. However, these catalysts are artificial and expensive. To develop a low cost catalyst for CO_2 reduction, quite ordinary rocks need to be investigated. In a previous study (13), it was found that

Received July 25, 1997.

K. Ohta,[1] Y. Ueda, S. Nakaguchi, and T. Mizuno. Department of Chemistry for Materials, Faculty of Engineering, Mie University, Mie, Tsu 514, Japan.

[1] Author to whom correspondence may be addressed. Telephone: –81–59–231–9427. Fax: –81–59–231–9427; –81–59–231–9442; –81–59–231–9478. E-mail: ohta@chem.mie-u.ac.jp

© 1998 NRC Canada

Fig. 1. Effect of amounts of Cu on photoreduction of CO_2 at ambient temperature; ○, amphibolite; □, gneiss; ●, granite; substrate, 30 mesh, 1 g; illumination time, 10 h.

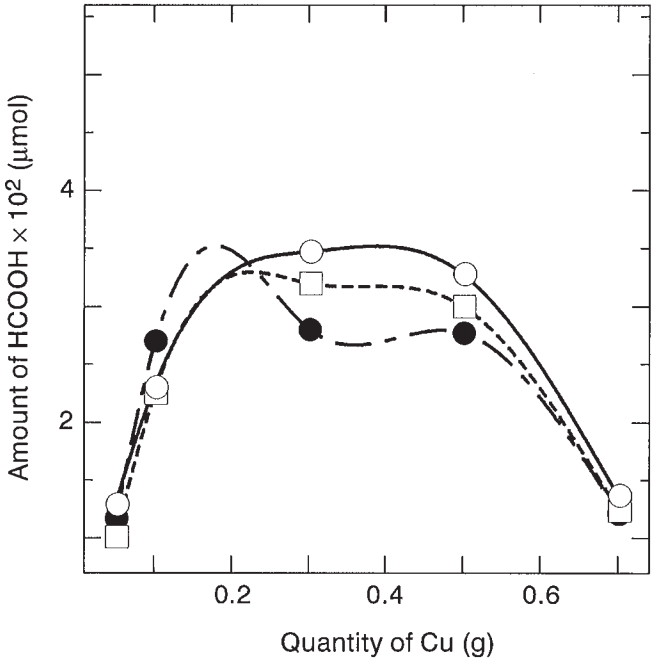

Fig. 2. Effect of amounts of Cu on photoreduction of CO_2 at ambient temperature; Δ, granodiorite; ○, phyllite; □, quartzdiorite; ●, shale; substrate, 30 mesh, 1 g; illumination time, 10 h.

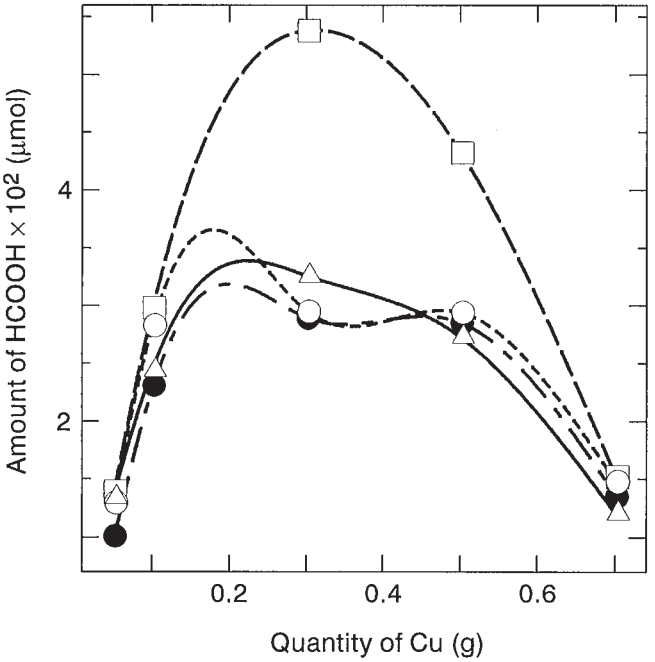

water decomposed to hydrogen and oxygen on silicate rock powders under sunlight illumination. Furthermore, since copper was useful for the photoreduction, as Hirano et al. (12) reported, copper-loaded rocks were prepared as the catalysts. However, there is little information on the photoreduction of CO_2 using copper-loaded silicate rock powders under sunlight.

In this report, a photocatalytic reduction of CO_2 using copper-loaded silicate rock powders at ambient temperature is described. The Cu–silicate rock powders suspended in the solution were illuminated with sunlight.

Experimental

Preparation of Cu-loaded silicate rock powders

The substrates of the photocatalyst used were silicate rocks. The rocks were amphibolite, gneiss, granite, granodiorite, phyllite, quartzdiorite, and shale. These are quite ordinary rocks that were collected from a river beach and a mountain of middle Japan.

The rocks were pulverized in an iron mortar and then were sieved by 30-mesh stainless sieves. The diameter of the powder particulates was about 0.85 mm, and the surface area was 0.25–0.30 m^2/g by BET adsorption method. After washing with 1 M nitric acid and distilled deionized water to wash down metals from the surface of the rock powders, the sample was prepared by heating to dry for 8 h at 150°C in an oven to sterilize microorganisms. After drying, the powders were placed in copper chloride solution with optional concentration (0.11–1.4 g/mL) and stirred sufficiently. The silicate rock powders were dried, after recovery by filtration, at 150°C for 4 h in an oven and heated in a hydrogen gas stream at 400°C for 2 h to reduce $CuCl_2$ to metallic copper. After being cooled in nitrogen atmosphere, the powders were weighed to calculate the amount of Cu loaded.

Procedures

The Cu–silicate rock powders were accurately weighed (about 5 g) and placed in a Pyrex glass photocell reported in a previous paper (13). After the addition of fresh water (5 mL), highly purified carbon dioxide gas (99.9999% purity) was bubbled for 10 min at a rate of 2 mL/s. The pH of the solution was 4.96. The vessel was stopped with a silicon rubber stopper to prevent loss of carbon dioxide and evaporation of water. The powders in the vessel were illuminated by sunlight (about 31 600 lux, corresponding to 284 W/m^2). In this case, the short ultraviolet radiation ($\lambda < 310$ nm) was removed by the vessel wall. The intensity of sunlight was measured by a Koito radiometer (IKS-35) and a lumeter (Tokyo Photoelectric, Type ANA-500). For X-ray analysis of the catalyst, a Rigaku L114-1 X-ray diffraction apparatus equipped with a Cu anode and a proportional detector was used. Scanning electron micrographs (SEM) were measured with a Hitachi HHS-2X scanning electron microscope.

Product analysis

Gaseous products by the photocatalytic reduction of carbon dioxide were analyzed by gas chromatography (Porapak Q and molecular sieve 5A columns) using high-purity helium gas as carrier gas. However, gaseous product such as methane was not detected. The products dissolved in water were analyzed by liquid chromatography (Hitachi L600) with an Ionpak KC-811 and KC-810P. The identification of formic acid was performed by analysis of standard high-purity formic acid.

© 1998 NRC Canada

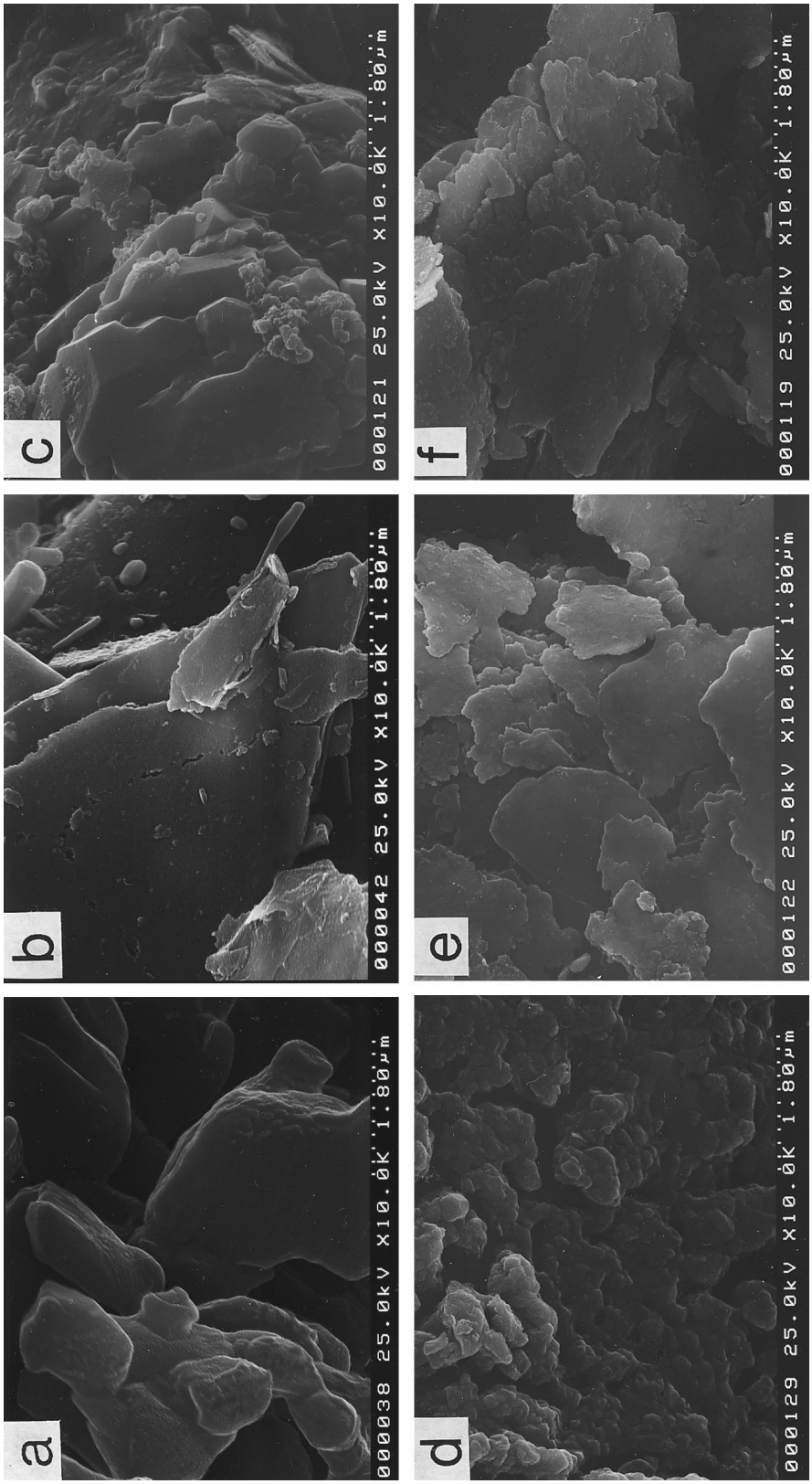

Fig. 3. Scanning electron micrographs of quartz diorite (× 10 000); (*a*) Cu (30%) rock before hydrogen reduction; (*b*) Cu (30%) rock after hydrogen reduction; (*c*) Cu (30%) rock after illumination; (*d*) Cu (70%) rock before hydrogen reduction; (*e*) Cu (70%) rock after hydrogen reduction; (*f*) Cu (70%) rock after illumination.

© 1998 NRC Canada

Fig. 4. A relationship between FeO contents in rocks and formic acid formation; Cu (30%) rock powders.

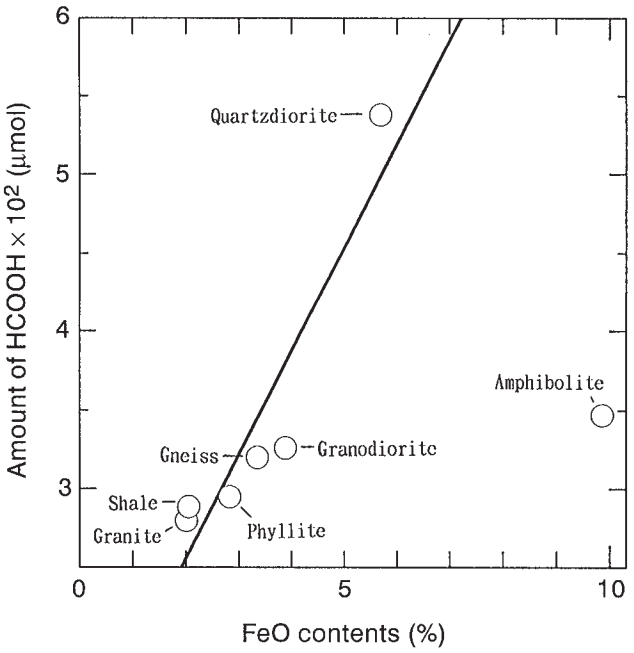

Fig. 5. Effect of illumination time on formic acid formation at ambient temperature; Cu (30%) – quartzdiorite; 30 mesh, 1 g.

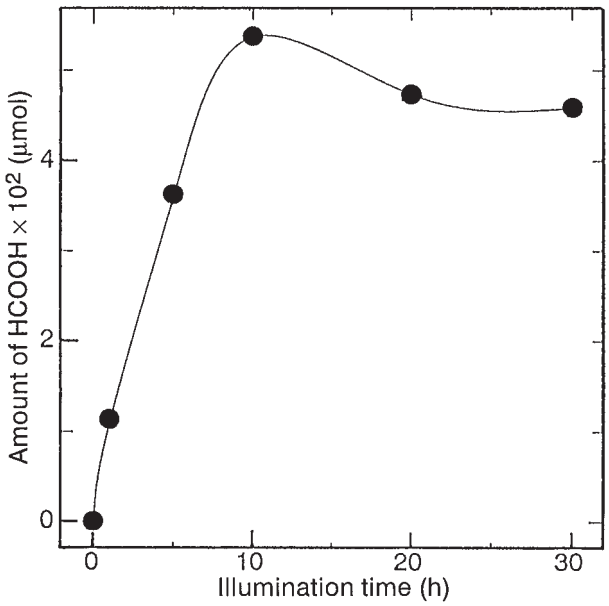

Fig. 6. Effect of temperature on formic acid formation for 10 h illumination; Cu (30%) – quartzdiorite; 30 mesh, 1 g.

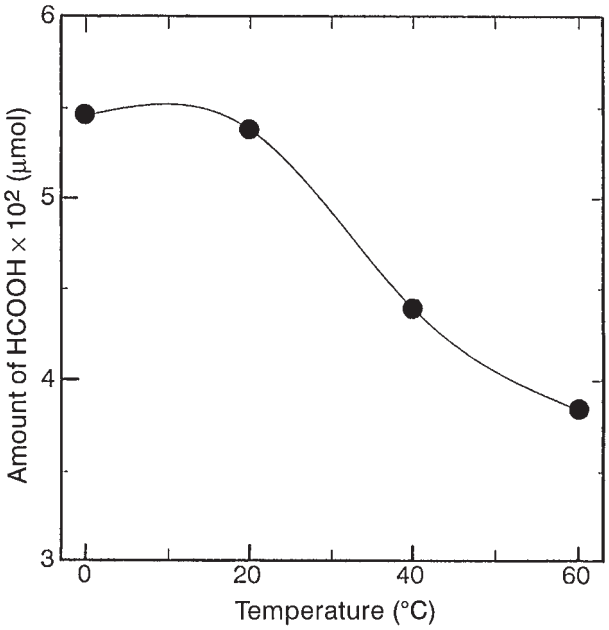

Results and discussion

A Cu electrode has been used for electrochemical reduction of CO_2 to hydrocarbons (2, 4). Hirano et al. (12) reported that methanol, formaldehyde, methane, and carbon monoxide were formed in CO_2-saturated aqueous solution containing powdered suspensions of TiO_2 and Cu. Therefore, a photocatalytic effect of Cu-loaded silicate rock powders on the reduction of CO_2 was examined.

Effect of amounts of Cu on photoreduction of CO_2

The effect of amounts of loaded Cu on photoreduction of CO_2 at ambient temperature was evaluated under 10 h illuminations. The amounts of Cu loaded were 0.05, 0.1, 0.3, 0.5, and 0.7 g per 1 g rock powders (5, 10, 30, 50, and 70 wt.%). In the present work, the main product formed on the Cu rocks was formic acid. Methane, ethylene, ethane, hydrogen, methanol, and formaldehyde were not detected. No product was formed from carbon dioxide by photocatalytic reduction in the dark. The formic acid formations for the amounts of loaded Cu are shown in Figs. 1 and 2. Formic acid formations on Cu: amphibolite (Fig. 1), gneiss (Fig. 1), granodiorite (Fig. 2), quartzdiorite (Fig. 2), and shale (Fig. 2) increased with an increase of Cu up to 0.3 g/g of Cu; and the maximum amounts of formic acid were 35, 32, 33, 54, and 29 nmol/g, respectively. The formation amounts on Cu rocks over 0.4 g/g of Cu decreased dramatically. The formic acid formations on Cu–granite and Cu–phyllite were maximum at 0.1–0.5 g/g of Cu, as shown in Figs. 1 and 2. The largest quantity of formic acid was obtained on Cu (30%) – quartzdiorite. Since the amount of formic acids formed on the Cu–silicate rock powders was larger than that obtained with only silicate rock powders (13), it was found that Cu loading was useful to formic acid production. However, the reason for maximum formation of formic acid on Cu 30 wt.% rocks is not clear.

Surfaces of Cu–silicates were observed by a scanning electron microscope. Typical scanning electron micrographs of Cu–silicate rock (quartzdiorite) are shown in Fig. 3. Before hydrogen reduction, small anisotropic crystals of copper chloride can be visually observed on Cu (30%) – silicate rock (Fig. 3*a*), and surfaces of Cu (70%) – silicate rock are covered with the crystals (Fig. 3*d*). Metal copper (0.3–0.7 mm) on Cu (5–30%) – silicate rock substrates becomes apparent in the SEM photographs of Cu (5–30%) – silicate rocks after hydrogen reduction (Fig. 3*b*). The Cu (70%) – silicate rock is coated

© 1998 NRC Canada

Fig. 7. X-ray diffraction pattern for quartz diorite.

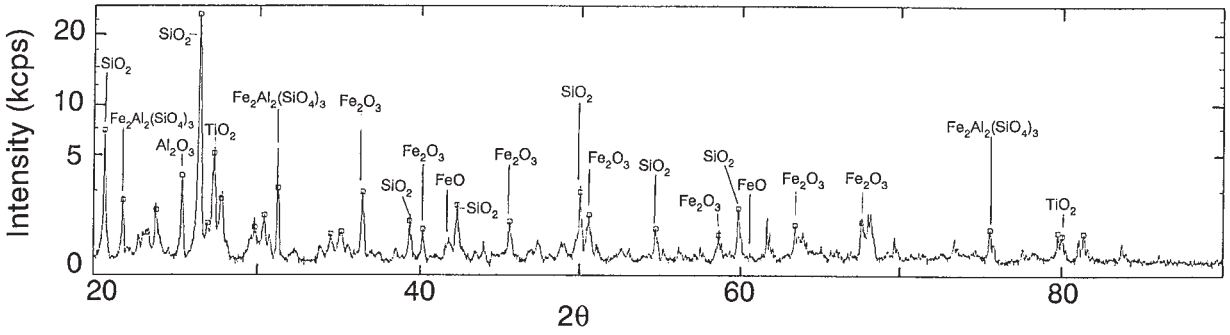

with flakes (plate copper metals) produced by hydrogen reduction, as shown in Fig. 3*e*. After sunlight illumination, the crystals of rock substrate in Cu (30%) – rock catalysts changed to rounding crystals (Fig. 3*c*), but the surface of Cu (70%) – silicate rock did not change compared with that of the rock after hydrogen reduction (Fig. 3*f*). The phenomenon of Cu (30%) – silicate rocks is probably due to the higher yield of formic acid.

Since TiO_2 and Fe^{2+} salts in tested rocks are well known as a photocatalyst and an electron carrier (14, 15), respectively, a relationship between the composition of these compounds and the maximum amount of formic acid obtained on Cu (30%) rock powders was investigated. A graph of FeO content vs. the maximum amount of formic acid produced was examined because these rocks contained similar amounts of $Ti0_2$ (0.34–0.94%). Formic acid formation is significant for FeO contents of <6% in these rocks, as shown in Fig. 4.

Effect of illumination time

The effect of illumination time on photoreduction of CO_2 was investigated by use of a Cu-loaded quartzdiorite catalyst (0.3 g/g of Cu), which was the best catalyst in the Cu rocks. The results at ambient temperature are shown in Fig. 5. Formic acid on the Cu-loaded quartzdiorite increased with time up to 10 h, but over the time the formations of formic acid decreased, and then became constant. The phenomenon may be due to the decomposition of formic acid. Consequently, the maximum yield of formic acid was 54 nmol/g on Cu–quartzdiorite powders over 10 h.

Effect of temperature

The effect of temperature on the photochemical reduction of CO_2 was evaluated by use of Cu–quartzdiorite powders. The results under 10 h sunlight illumination are shown in Fig. 6. The formic acid formation decreased with temperature. A reason for the phenomenon seems to be the lower solubility of CO_2 in higher temperature water. For the photochemical reduction of CO_2, lower temperature was suitable.

Reduction process

To reveal the reduction process, X-ray diffraction patterns were measured for silicate rocks used as a catalyst. The typical pattern is shown in Fig. 7. All of these rocks contained small amounts of TiO_2 (0.34–0.94%) and Fe^{2+} salts (2.0–9.84%), which are known as a photocatalyst and an electron carrier (14, 15), respectively. From the results, the detection of oxygen emission in the present study, and the literature cited above (8, 10, 12, 13), the formic acid formation process by CO_2 reduction on Cu–silicate rocks is suggested to be as follows:

$$\text{Cu rock} + h\nu \rightarrow \text{Cu rock}^{*}(\, e^{-}_{cond} + h^{+}_{val}\,)$$

For an oxidation:

$$H_2O \xrightarrow[\text{Cu / } TiO_2\text{, Fe salts / } SiO_2]{h\nu} 2H^{+} + 1/2\ O_2$$

For a reduction:

$$CO_2 \xrightarrow[\text{Cu / } TiO_2\text{, Fe salts / } SiO_2]{e^{-},\ h\nu} \cdot CO_2^{-} \xrightarrow[\text{Cu / } TiO_2\text{, Fe salts / } SiO_2]{H^{+} + e^{-}} HCOO^{-}$$

In conclusion, formic acid was specifically produced on the photocatalyst Cu (30 wt.%) – silicate rock powders in the present work. The amounts of formic acids formed with the Cu–silicate rock powders were larger than that obtained with only silicate rock powders (13). Since the Cu-loaded silicate rock powders catalysts are relatively easy to make and inexpensive, the CO_2 reduction system developed may be economically feasible in large-scale formic acid productions. In other words, the system might well become of practical interest for photochemical fuel production, storage of solar energy, and organic raw material production. However, it has some disadvantages: low yield and necessity of large area for the plant.

Acknowledgments

This work was supported financially by the Ministry of Education, Science, Sports and Culture of Japan, and the Research Foundation for the Electrotechnology of Chubu.

References

1. W.M. Ayers (*Editor*). *In* Catalytic activation of carbon dioxide. ACS Symp. Ser. **363**, 102 (1988).
2. K. Ito (*Editor*). Proc. Int. Symp. Chem. Fixation Carbon Dioxide (ISCF-CO_2–91). Nagoya, Japan. 1991. pp. 1–426.
3. G.L. Haller and D.E. Resasco. Adv. Catal. **36**, 173 (1989).
4. I. Taniguchi. *In* Modern aspects of electrochemistry. Vol. 20. *Edited by* J.O'M. Bockris, R.E. White, and B.E. Conway. Plenum Press, New York. 1989. pp. 327–400.
5. M. Halmann. *In* Energy resources through photochemistry and catalysis. Chap.15. *Edited by* M. Gratzel. Academic Press, New York. 1983.
6. M. Kirch, J.M. Lehn, and J.P. Sauvage. Helv. Chim. Acta, **62**, 1345 (1979).
7. J.P. Collin and J.P. Sauvage. Coord. Chem. Rev. **93**, 245 (1989).

© 1998 NRC Canada

8. T. Inoue, A. Fujishima, S. Konishi, and K. Honda. Nature (London), **227**, 637 (1979).
9. M. Halmann and B. Aurian-Blajeni. Proc. 2nd European Commun. Photovolt. Sol. Energ. Conf. 682 (1979). M. Halmann and B. Aurian-Blajeni. Sol. Energy Mat. **10**, 85 (1984).
10. K.R. Thampi, J. Kiwi, and M. Gratzel. Nature (London), **327**, 506 (1987).
11. M.W. Rophael and M.A. Malati. J. Chem. Soc. Chem. Commun. 1418 (1987).
12. K. Hirano, K. Inoue, and T. Yatsu. J. Photochem. Photobiol. A, **64**, 255 (1992).
13. K. Ohta, T. Kawamura, S. Kuroda, and T. Mizuno. Proc. Symp. Environ. Aspects Electrochem. Photoelectrochem. 85 (1994).
14. T. Inoue, A. Fujishima, S. Konishi, and K. Honda. Nature (London), **227**, 637 (1979); A. Fujishima and K. Honda. Nature (London), **238**, 37 (1972).
15. N. Getoff. Z. Naturforsch. B: Anorg. Chem. Org. Chem. **17B**, 87 (1962).

© 1998 NRC Canada

Influence des ultrasons sur la diastéréosélectivité. Synthèse d'imidazolidine-4-one chirales

Cathy Hubert et Bernard Garrigues

Résumé : La synthèse d'imidazolidine-4-one a pu être réalisée en trois étapes. Lors de la dernière étape de réduction d'une fonction cétonique, le dithionite de sodium s'est révélé un excellent agent réducteur. La réaction est lente sous chauffage classique et conduit à une faible diastéréosélectivité. Sous irradiation ultrasonore, nous avons pu observer une importante sélectivité avec un bon rendement. Le dithionite de sodium permet de travailler dans l'eau et évite l'utilisation d'agent réducteur comme les hydrures.

Mots clés : dithionite de sodium, ultrasons, imidazolidine-4-one.

Abstract: A three-step synthesis of imidazolidine-4-one has been realized. Sodium dithionite was a very efficient reagent for the last step, the reduction of a ketone. The reaction is slow under the normal conditions of heating and its diastereoselectivity is poor. Under the influence of ultrasound, the selectivity and the yield are very good. The use of sodium dithionite makes it possible to work in water and to avoid the use of hydrides.

Key words: sodium dithionite, ultrasound, imidazolidine-4-one.

[Journal translation]

Introduction

Devant certaines difficultés expérimentales les chimistes ont été incités à rechercher des méthodes d'activation susceptibles d'augmenter d'une part la vitesse et le rendement, d'autre part la régio- et la stéréosélectivité. Parmi ces méthodes, les ultrasons jouent un rôle important.

Il existe à ce jour peu d'exemples dans lesquels les ultrasons ont pu modifier la stéréochimie et la sélectivité de certaines réactions.

Une isomérisation *Z*/*E* a pu être mise en évidence, sous ultrasons, dans le cas de maléate (1), de cinnamonitrile (2), d'hydantoines (3) et de phosphines vinyliques (4).

D'autre part Ando et al. (5) a observé que la sonication permet d'éviter l'utilisation de la catalyse par transfert de phase dans l'oxydation des alcools avec le permanganate de potassium. Cette méthode est très sélective car une double liaison reste intacte sous ultrasons en milieu apolaire, et seule la fonction alcool est oxydée, ce qui n'est pas le cas en milieu polaire.

Dans le cas de la réaction de Diels–Alder entre des styrènes et des 1,4-benzoquinones sous ultrasons, les dérivés phénanthréniques sont obtenus avec une régiosélectivité importante (6).

Nous nous proposons dans ce travail d'étudier l'influence des ultrasons sur la diastéréosélectivité lors de la synthèse d'imidazolidinones chirales, obtenues par réduction sonochimique de cétones en alcool.

Les exemples de réduction sonochimique de cétones sont peu nombreux. On citera la réduction de cétones aromatiques en alcool par le lithium, en présence de 4,4′-di-(*tert*-butyl) biphényl (7–9), la réduction de la cyclohexanone en présence d'halogénures d'alkyle et de lithium (10, 11) et de benzophénone avec l'aluminium dans NH_3 à 25°C sous ultrasons (12). Dans aucune des trois méthodes une modification de la sélectivité n'a été observée.

Partie experimentale

Généralités

Ultrasons : les réactions que nous avons décrites ont été réalisées avec un générateur Bioblock Scientific et une sonde de 13 mm de diamètre dans un réacteur thermostaté double paroi.

Spectres RMN ^{1}H : déplacements chimiques en ppm par rapport au TMS; constantes de couplage en Hz; appareil Bruker AC 80.

Spectres RMN ^{13}C : déplacements chimiques en ppm par rapport au TMS; appareil Bruker AC 250.

Spectres IR : entre lames KBr; enregistrés sur un spectromètre Perkin–Elmer 257.

Les analyses élémentaires ont été effectuées par le service de Microanalyse de l'École nationale supérieure de chimie de Toulouse. Tous les produits nouveaux donnent des analyses satisfaisantes C ± 0,48, H ± 0,4, N ± 0,53. La purification des produits sur colonne est effectuée avec de la silice (230–400 mesh).

Points de fusion, non corrigés en capillaires appareil (Tottoli, Büchi).

Reçu le 11 juillet 1997.

C. Hubert et B. Garrigues.[1] Hétérochimie fondamentale et appliquée (Enseignement Supérieur Associé 5069 du Centre national de la recherche scientifique), Université Paul Sabatier, 118 Route de Narbonne, 31062 Toulouse Cedex, France.

1. Auteur à qui adresser toute correspondance. Tél. : 33(0)5 61-55-63-54. Téléc. : 33(0)5 61-55-82-45.

© 1997 NRC Canada

*Méthode générale (5*S*) :* ***1a–1d***
À 0,01 mole de N-méthyl amide de *S*-(α) amino-acide préparé d'après la littérature (13), on ajoute 30 mL d'acétone et 30 mL de DMF. On chauffe 24 h au reflux. Après élimination complète du DMF le résidu est purifié sur colonne de silice, éluant : $CHCl_3/CH_3CO_2Et$ (9/1).

*(5*S*) :* ***1a*** : huile, Rdt = 79%. IR : 3315 (NH), 1692 (C=O) cm^{-1}. RMN ^1H ($CDCl_3$) : 3,05 (q, 1H, ^3J = 6,8, C_5H), 2,30 (s, 3H, NCH_3), 0,95 (d, 3H, ^3J = 6,8, CH_3), 0,83 (s, 6H, CH_3). RMN ^{13}C ($CDCl_3$) : 174,4 (C_1), 74,9 (C_3), 53,9 (C_5), 28,1 (CH_3), 25,1 (CH_3), 24,7 (CH_3), 16,2 (CH_3).

*(5*S*) :* ***1b*** : huile, Rdt = 78%. IR : 3324 (NH), 1681 (C=O) cm^{-1}. RMN ^1H ($CDCl_3$) : 3,32 (dd, 1H, ^3J = 7,0, ^3J = 3,0, C_5H), 2,60 (s, 3H, NCH_3), 2,25 (s, 1H, NH), 1,69–1,52 (m, 3H, CH_2CH), 1,40 (s, 3H, CH_3), 1,29 (s, 3H, CH_3), 0,79 (d, 3H, J = 5,9, CH_3), 0,76 (d, 3H, J = 5,9, CH_3). RMN ^{13}C ($CDCl_3$) : 174,9 (C_1), 75,5 (C_3), 58,4 (C_5), 41,6 (CH_2), 27,3 (CH_3), 25,1 (CH_3), 24,6 (CH), 23,2 (CH_3), 21,3 (CH_3), 20,9 (CH_3).

*(5*S*) :* ***1c*** : huile, Rdt = 85%. IR : 3321 (NH), 1681 (C=O) cm^{-1}. RMN ^1H ($CDCl_3$) : 7,46–7,25 (m, 5H, arom.), 4,63 (m, 1H, C_5H), 2,85 (s, 3H, NCH_3), 1,49 (s, 3H, CH_3), 1,41 (s, 3H, CH_3). RMN ^{13}C ($CDCl_3$) : 172,5 (C_1), 138,4 (arom.), 128,2 (arom.), 127,9 (arom.), 127,6 (arom.), 75,6 (C_3), 62,1 (C_5), 27,7 (NCH_3), 25,5 (CH_3), 25,4 (CH_3).

*(5*S*) :* ***1d*** : huile, Rdt = 80%. IR et RMN ^1H comparables à la littérature (14). RMN ^{13}C ($CDCl_3$) : 173,4 (C_1), 137,2 (arom.), 130,3 (arom.), 128,5 (arom.), 126,6 (arom.), 75,5 (C_3), 59,2 (C_5), 37,2 (CH_2), 27,2 (CH_3), 25,3 (CH_3), 25,2 (CH_3).

*Méthode générale (5*S*) :* ***2a–2d***
À un mélange de 0,01 mole de (5*S*) : **1a–2a** et 0,01 mole de NEt_3 en solution dans le toluène (20 mL), on ajoute goutte à goutte 0,01 mole de PhCOCOCl à 0°C dans le toluène (20 mL). On laisse sous agitation pendant 12 h. La phase organique est lavée avec une solution saturée d'acide oxalique (3 × 20 mL). Le produit recherché est obtenu après séparation sur colonne, éluant : $CHCl_3/CH_3CO_2Et$ (9/1).

*(5*S*) :* ***2a*** : huile, Rdt = 49%. IR : 1710 (C=O), 1650 (C=O) cm^{-1}. RMN ^1H ($CDCl_3$) : 7,89–7,38 (m, 5H, arom.), 4,29 (q, 1H, ^3J = 6,8 C_5H), 2,79 (s, 3H, NCH_3), 1,55 (s, 3H, CH_3), 1,53 (s, 3H, CH_3), 1,17 (d, 1H, ^2J = 6,8, CH_3). RMN ^{13}C ($CDCl_3$) : 188,8 (C=O), 168,3 (C=O), 164,1 (C=O), 134,8 (arom.), 132,8 (arom.), 129,9 (arom.), 129,1 (arom.), 79,5 (C_3), 54,1 (C_5), 24,8 (CH_3), 24,6 (CH_3), 23,2 (CH_3), 20,6 (CH_3).

*(5*S*) :* ***2b*** : solide (*F* = 75°C), Rdt = 83%. IR : 1696 (C=O), 1675 (C=O), 1643 (C=O) cm^{-1}. RMN ^1H ($CDCl_3$) : 7,99–7,26 (m, 5H, arom.), 4,37 (dd, ^3J = 2,6, ^3J = 9,6 C_5H), 2,65 (s, NCH_3), 1,81 (s, 6H, CH_3), 1,56–1,29 (m, 3H, CH_2CH), 0,80 (d, 3H, ^3J = 6,5, CH_3), 0,57 (d, 3H, J = 6,7, CH_3). RMN ^{13}C ($CDCl_3$) : 166,6 (C=O), 166,2 (C=O), 164,1 (C=O), 134,9 (arom.), 132,7 (arom.), 130,0 (arom.), 129,1 (arom.), 79,2 (C_3), 56,4 (C_5), 43,5 (CH_2), 27,2 (CH_3), 24,6 (CH), 24,3 (CH_3), 24,2 (CH_3), 23,3 (CH_3), 23,1 (CH_3).

*(5*S*) :* ***2c*** : solide (*F* = 152°C), Rdt = 65%. IR : 1705 (C=O), 1675 (C=O), 1644 (C=O) cm^{-1}. RMN ^1H ($CDCl_3$) : 7,53–6,9 (m, 10H, arom.), 5,38 (m, 1H, C_5H), 2,94 (s, 3H, NCH_3), 2,09 (s, 3H, CH_3), 1,80 (s, 3H, CH_3). RMN ^{13}C ($CDCl_3$) : 189,2 (C=O), 166,5 (C=O), 164,8 (C=O), 135,8 (arom.), 133,9 (arom.), 132,2 (arom.), 129,6 (arom.), 128,6 (arom.), 128,3 (arom.), 128,2 (arom.), 128,1 (arom.), 79,4 (C_3), 62,6 (C_5), 24,7 (CH_3), 24,5 (CH_3), 23,5 (CH_3).

*(5*S*) :* ***2d*** : Rdt = 63%. IR et RMN ^1H comparables à la littérature (14). RMN ^{13}C ($CDCl_3$) : 189,0 (C=O), 166,8 (C=O),163,9 (C=O), 135,1 (arom.), 134,9 (arom.), 132,5 (arom.), 130,3 (arom.), 130,1 (arom.), 129,1 (arom.), 128,1 (arom.), 127,4 (arom.), 79,9 (C_3), 59,9 (C_5), 37,7 (CH_2), 24,2 (CH_3), 23,8 (CH_3), 22,1 (CH_3).

*Méthode générale (5*S*, 2′*R*) :* ***3a–3d*** *et (5*S*–2′*S*) :* ***4a–4d***
À 1/100 de mole de (5*S*) : **2a–2d** en solution dans 35 mL de dioxanne, à 85°C, on ajoute 35 mL d'eau à 85°C contenant 5,5 g de $NaHCO_3$, dans un récipient thermostaté à 85°C sous argon. On rajoute ensuite 2,5 g de dithionite de sodium (Merck, LAB, réf. 6507). Trois autres additions successives de 2,5 g de $Na_2S_2O_4$ sont effectuées au bout de 5, 10, 15 min. La réaction est arrêtée, soit après 30 min d'irradiation ultrasonore à 85°C, soit au bout de 4 h de chauffage dans le réacteur à 85°C. On ajoute de l'eau jusqu'à ce que la solution devienne claire, puis on extrait à l'éther (3 × 50 mL). La phase organique est séchée sur $MgSO_4$. Le produit recherché est isolé après séparation sur colonne de silice (éluant : acétate d'éthyle). Les rendements et le rapport entre les diastéréoisomères **3**/**4** sont indiqués dans le tableau 1. La reproductibilité de la méthode a été vérifiée.

*(5*S*, 2′*R*) :* ***3a*** : IR : 3420 (OH), 1703 (C=O), 1650 (C=O) cm^{-1}. RMN ^1H ($CDCl_3$) : 7,34–7,25 (m, 5H, arom.), 5,10 (d, 1H, ^3J = 6,6, C′$_2$H), 4,58 (d, 1H, ^3J = 6,6, OH), 3,79 (q, 1H, ^3J = 6,6, C_5H), 2,77 (s, 3H, NCH_3), 1,72 (s, 3H, CH_3), 1,63 (s, 3H, CH_3), 1,56 (d, 3H, ^3J = 6,6, CH_3). RMN ^{13}C ($CDCl_3$) : 170,7 (C=O), 166,4 (C=O), 137,9 (arom.), 129,3 (arom.), 129,1 (arom.), 127,2 (arom.), 79,9 (C_3), 72,4 (C_2), 53,4 (C_5), 24,9 (CH_3), 24,5 (CH_3), 22,9 (CH_3), 20,2 (CH_3).

*(5*S*, 2′*S*) :* ***4a*** : IR : 3278 (OH), 1693 (C=O), 1686 (C=O) cm^{-1}. RMN ^1H ($CDCl_3$) : 7,39–7,26 (m, 5H, arom.), 5,08 (s, 1H, C′$_2$H), 4,33 (q, 1H, ^3J = 6,8, C_5H), 2,86 (s, 3H, NCH_3), 1,80 (s, 3H, CH_3), 1,64 (s, 3H, CH_3), 0,97 (d, 3H, ^3J = 6,8, CH_3). RMN ^{13}C ($CDCl_3$) : 170,8 (C=O), 166,7 (C=O), 139,6 (arom.), 129,4 (arom.), 128,1 (arom.), 125,3 (arom.), 80,1 (C_3), 72,4 (C′$_2$), 54,5 (C_5), 24,9 (CH_3), 24,7 (CH_3), 24,2 (CH_3), 20,8 (CH_3).

*(5*S*, 2′*R*) :* ***3b*** : IR : 3422 (OH), 1708 (C=O), 1654 (C=O) cm^{-1}. RMN ^1H ($CDCl_3$) : 7,33–7,24 (m, 5H, arom.), 5,07 (d, 1H, ^3J = 6,9, C′$_2$H), 4,51 (d, 1H, ^3J = 6,9, OH), 3,78 (m, 1H, C_5H), 2,73 (s, 3H, NCH_3), 2,1–1,7 (m, 3 H, CH_2CH), 1,72 (s, 3H, CH_3), 1,60 (s, 3H, CH_3), 1,01 (d, 3H, ^3J = 7,0, CH_3), 0,92 (d, 1H, ^3J = 7,0, CH_3). RMN ^{13}C ($CDCl_3$) : 170,6 (C=O), 167,9 (C=O), 136,1 (arom.), 129,3 (arom.), 129,1 (arom.), 127,2 (arom.), 79,3 (C_3), 72,5 (C′$_2$), 55,5 (C_5), 44,2 (CH_2), 24,5 (CH_3), 24,3 (CH), 24,1 (CH_3), 23,8 (CH_3), 22,9 (CH_3), 20,8 (CH_3).

*(5*S*, 2′*S*) :* ***4b*** : IR : 3405 (OH), 1693 (C=O), 1649 (C=O)

© 1997 NRC Canada

Tableau 1. Influence des substituants sur le rendement et la sélectivité.

	Ultrasons			Chauffage classique		
R	Rdt (%)	Temps (h)	% **3**/**4**	Rdt (%)	Temps (h)	% **3**/**4**
CH_3	76	0,5	90/10	36	4	70/30
$CH_2CH(CH_3)_2$	91	0,5	98/2	42	4	82/18
Ph	94	0,5	93/7	27	4	85/15
CH_2Ph	85	0,5	95/5	31	4	79/21

Température 85°C

cm^{-1}. RMN ^1H ($CDCl_3$) : 7,47–7,26 (m, 5H, arom.), 5,07 (s, 1H, C′$_2$H), 4,35 (m, 1H, C_5H), 2,64 (s, 3H, NCH_3), 1,74 (s, 6H, CH_3), 1,56–1,30 (m, 3H, CH_2CH), 0,76 (d, 3H, ^3J = 6,6, CH_3), 0,38 (d, 3H, ^3J = 6,5, CH_3). RMN ^{13}C ($CDCl_3$) : 170,8 (C=O), 166,0 (C=O), 139,3 (arom.), 129,1 (arom.), 127,9 (arom.), 126,9 (arom.), 72,2 (C′$_2$), 57,0 (C_5), 42,2 (CH_2), 24,5 (CH_3), 24,1 (CH), 23,9 (CH_3), 23,7 (CH_3), 23,4 (CH_3), 20,9 (CH_3).

*(5*S*, 2′*R*) :* ***3c*** : IR : 3421 (OH), 1715 (C=O), 1657 (C=O) cm^{-1}. RMN ^1H ($CDCl_3$) : 7,45–6,20 (m, 10H, arom.), 5,58 (m, 2H, C′$_2$H et C_5H), 4,36 (d, 1H, *J* = 6,0, OH), 2,77 (s, 3H, NCH_3), 1,98 (s, 3H, CH_3), 1,74 (s, 3H, CH_3). RMN ^{13}C ($CDCl_3$) : 171,8 (C=O), 165,8 (C=O), 137,4 (arom.), 135,8 (arom.), 129,4 (arom.), 129,3 (arom.), 129,2 (arom.), 128,9 (arom.), 127,5 (arom.), 125,9 (arom.), 79,8 (C_3), 72,5 (C'$_2$), 61,8 (C_5), 24,7 (CH_3), 24,4 (CH_3), 23,2 (CH_3).

*5*S*, 2′*S*) :* ***4c*** : RMN ^1H ($CDCl_3$) : 7,40–6,36 (m, 10H, arom.), 5,75 (d, 1H, ^3J = 6,7, C′$_2$H), 5,71 (s, 1H, C_5H), 2,80 (s, 3H, NCH_3), 2,00 (s, 3H, CH_3), 1,75 (s, 3H, CH_3).

*5*S*, 2′*S*) :* ***3d*** ; IR et RMN ^1H comparables à la littérature (14). RMN ^{13}C ($CDCl_3$) : 170,9 (C=O), 166,8 (C=O), 137,8 (arom.), 134,9 (arom.), 130,1 (arom.), 129,3 (arom.), 129,2 (arom.), 127,7 (arom.), 127,6 (arom.), 126,7 (arom.), 80,1 (C_3), 72,7 (C′$_2$), 59,3 (C_5), 37,1 (CH_2), 24,3 (CH_3), 23,2 (CH_3), 22,2 (CH_3).

*(5*S*, 2′*S*) :* ***4d*** : IR et RMN ^1H comparables à la littérature (14). RMN ^{13}C ($CDCl_3$) : 170,9 (C=O), 166,8 (C=O), 137,7 (arom.), 134,6 (arom.), 130,1 (arom.), 129,4 (arom.), 129,3 (arom.), 127,6 (arom.), 126,7 (arom.), 126,6 (arom.), 80,2 (C_3), 72,7 (C′$_2$), 59,3 (C_5). 37,1 (CH_2), 24,2 (CH_3), 23,2 (CH_3), 22,3 (CH_3).

RØsultats et discussion

Nous avons étudié la réduction d'α-oxo amide (5*S*) : **2a–2d** dérivant d'acide phényl-glyoxilique contenant un auxiliaire chiral : (5*S*)-5-alkyl-2,2,3 triméthylimidazolidine-4-one ((5*S*) : **1a–1d**). Cet auxiliaire chiral a été utilisé pour la première fois lors de la réduction d'α-oxo amides avec le $NaBH_4$ dans le cas du composé **2d** (14).

Les imidazolidines-4-one (5*S*) : **1a–1d** ont été préparées en faisant réagir les N-méthyl amides d'amino-acides dans l'acétone 24 h au reflux (14) (schéma 1).

L'étape suivante consiste en une N-acylation de **1a–1d** à partir de PhCOCOCl; elle conduit aux α-oxo-amides chirales **2a–2d**, de configuration *S*.

Nous avons choisi lors de la dernière étape comme agent réducteur le dithionite de sodium ($Na_2S_2O_4$) car d'une part, il ne réduit pas les amides et d'autre part, il a été montré dans la littérature que les réactions mettant en jeu un transfert monoélectronique sont accélérées sous ultrasons (15–19). Deux hypothèses ont été avancées pour expliquer le mécanisme de la réduction de la fonction carbonyle par la dithionite de sodium (20). La première met en jeu un transfert d'électrons. Le radical anion sulfoxylate formé au cours de l'homolyse de la liaison S—S est à l'origine de ce transfert d'électron (21, 22) :

Schéma 1.

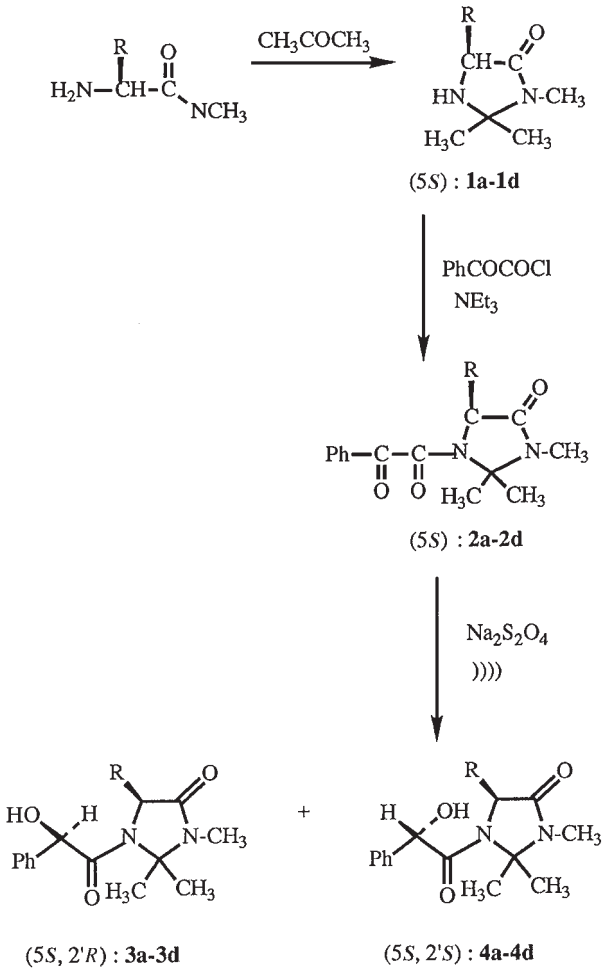

a : R = CH_3
b : R = $CH_2CH(CH_3)_2$
c : R = Ph
d : R = CH_2Ph

© 1997 NRC Canada

$S_2O_4^{2-} \leftrightharpoons 2SO_2^-$. Ce radical a pu être détecté par RPE (23–25). La deuxième hypothèse fait appel à une addition nucléophile sur le groupement carbonyle (20).

Enfin, dans un cas, il a été mis en évidence lors d'une réduction de la fonction carbonyle, que l'addition nucléophile peut être éliminée au profit d'un seul mécanisme faisant appel à un transfert d'électron (26).

Nous avons comparé dans les mêmes conditions expérimentales la réduction par chauffage classique et sous irradiation ultrasonore à l'aide d'une sonde plongeante à 85°C dans un réacteur thermostaté. Nous avons vérifié qu'en dessous de cette température, on n'observe pas de réaction (27). On opère dans un mélange eau–dioxanne (50/50) pour augmenter la solubilité du produit organique **2a–2d**. On doit d'une part opérer sous argon pour éviter l'oxydation du dithionite de sodium (28), d'autre part ajouter $Na_2S_2O_4$ en petites quantités pour éviter une décomposition spontanée en solution aqueuse en thiosulfate et sulfite (29, 30) et enfin travailler en milieu basique ($NaHCO_3$) pour éviter la rapide décomposition de $Na_2S_2O_4$.

Comme on peut le voir dans le tableau 1, la réaction, par chauffage classique, conduit au bout de 4 h à un rendement compris entre seulement 27% (pour R = Ph) et 42% (pour $R = CH_2CH(CH_3)_2$). Le rapport entre les deux diastéréoisomères (5*S*, 2'*R*) : **3a** et (5*S*-2'*S*) : **4a** est compris entre 70/30 ($R = CH_3$) et 85/15 (R = Ph). Dans les mêmes conditions de concentration et de température (85°C), sous irradiation ultrasonore au bout de seulement 30 min, le rendement est compris entre 76% ($R = CH_3$) et 94% (R = Ph). Cette réaction sous ultrasons conduit à une importante diastéréosélectivité : le diastéréoisomère (5*S*, 2'*R*) : **3** est très majoritaire, son pourcentage varie entre 90% ($R = CH_3$) et 98% $R = CH(CH_3)_2$.

Les deux diastéréoisomères ont été séparés sur colonne de silice. Pour déterminer la configuration absolue de **3a–3d**, nous avons utilisé la méthode déjà utilisée dans la littérature (14) qui consiste à préparer un échantillon authentique de (5*S*, 2'*R*) : **3a–3d** en deux étapes. Dans la première, (R)-$PhCH(OH)CO_2H$ (1 équiv.) réagit avec $(COCl)_2$ (1 équiv.) dans CH_2Cl_2 1 h à 25°C; on rajoute ensuite (5*S*) : **1a–1d** (1 équiv.) et de la triéthylamine (2 équiv.) dans CH_2Cl_2 à 0°C. L'échantillon observé correspond au diastéréoisomère majoritaire (5*S*, 2'*R*) : **3a–3d** obtenu lors de la réduction par le dithionite de sodium.

En conclusion, la synthèse d'imidazolidine-4-one a pu être réalisée en trois étapes. Lors de la dernière étape de réduction d'une fonction cétonique, le dithionite de sodium s'est révélé un excellent agent réducteur. La réaction est lente sous chauffage classique et conduit à une faible diastéréosélectivité. Sous irradiation ultrasonore, nous avons pu observer une importante sélectivité avec un bon rendement. Le dithionite de sodium permet de travailler dans l'eau et évite l'utilisation d'agent réducteur comme les hydrures.

Remerciements

Nous remercions Madame A. Colomer pour l'enregistrement des spectres IR.

Bibliographie

1. J. Reiss. Ultrasonics, **30**, 397 (1992).
2. B.A. Feit, E. Ishai et A. Levy. J. Chem. Res. (S), 247 (1993).
3. S.F. Tan, P.L. Au-Yong et L.T. Lee. J. Phys. Org. Chem. **5**, 795 (1992) ; Chem. Abstr. **118**, 212183 (1993).
4. D. Semenzin, G. Etemad-Moghadam, D. Albouy et M. Koenig. Tetrahedron Lett. **35**, 3297 (1994).
5. T. Ando, S. Sumi, T. Kawate, J. Ishihara et T. Hanafusa. J. Chem. Soc. Chem. Commun. 439 (1984).
6. F. Matloubi Moghaddam, P. Rüedi, Z.R. Zhang et F. Flachsmann. Tetrahedron Lett. **35**, 2153 (1994).
7. I.T. Badejo, R. Karaman, N.W. Lee, E.C. Lutz, M.T. Mamanta et J.L. Fry. J. Chem. Soc. Chem. Commun. 566 (1989).
8. I.T. Badejo, R. Karaman et J.L. Fry. J. Org. Chem. **54**, 4591 (1989).
9. R. Karaman, D.T. Kohlamn et J.L. Fry. Tetrahedron Lett. **31**, 6155 (1990).
10. J.C. De Souza Barboza, C. Petrier et J.L. Luche. Tetrahedron Lett. **28**, 2013 (1987).
11. A. Moyano, M.A. Pericàs, A. Riera et J.L. Luche. Tetrahedron Lett. **31**, 7619 (1990).
12. R. Sato, T. Nagaoka, T. Goto et M. Saito. Bull. Chem. Soc. Jpn. **63**, 290 (1990).
13. V. Santi et P.V. Danenberg. Biochemistry, **10**, 4813 (1971).
14. I. Solodin, Y. Goldberg, G. Zelcans et E. Lukevics. J. Chem. Soc. Chem. Commun. 1321 (1990).
15. J.L. Luche, C. Petrier, C. Einhorn, J. Einhorn, J.C. De Souza Barboza, C. Dupuy, P. Delair, C. Allavena et T. Tuschl. Ultrasonics, **28**, 316 (1990).
16. J.L. Luche, C. Einhorn, J. Einhorn et J.V. Sinisterra-Gago. Tetrahedron Lett. **31**, 4125 (1990).
17. J.L. Luche. Ultrasonics, **30**, 156 (1992).
18. B. Oussaid, O. Diallo, M. Soufiaoui et B. Garrigues. Bull. Soc. Chim. Fr. **132**, 461 (1995).
19. C. Hubert, A. Munoz, B. Garrigues et J.L. Luche. J. Org. Chem. **60**, 1488 (1995).
20. O. Louis-André et G. Gelbard. Bull. Soc. Chim. Fr. 565 (1986).
21. R.G. Rinker, D.M. Masson et W.H. Corcoran. J. Phys. Chim. **63**, 302 (1959).
22. S. Lynn, R.G. Rinker et W.H. Corcoran. J. Phys. Chim. **68**, 2363 (1964).
23. W.G. Hodgson, A. Neaves et C.A. Parker. Nature (London), **178**, 489 (1956).
24. B. Milicevic et G. Eignmann. Helv. Chim. Acta, **46**, 192 (1963).
25. L. Burlamacchi, G. Guarini et E. Tiezzi. Trans. Faraday Soc. **65**, 496 (1969).
26. S.M. Heilmann, J.K. Rasmussen et H.K. Smith. J. Org. Chem. **48**, 987 (1983).
27. J.G. De Vries et R.M. Kellogg. J. Org. Chem. **45**, 4126 (1980).
28. C. Creutz et N. Sutin. Inorg. Chem. **13**, 2041 (1974).
29. M.W. Lister et R.C. Garvie. Can. J. Chem. **37**, 1567 (1959).
30. M. Wayman et W.J. Lem. Can. J. Chem. **48**, 782 (1970).

© 1997 NRC Canada

COMMUNICATION

Thermolysis of 2,2-dimethoxy-5,5-dimethyl-Δ^3-1,3,4-oxadiazoline studied with photoelectron spectroscopy. He(I) photoelectron spectrum of dimethoxycarbene

H.M. Muchall, N.H. Werstiuk, B. Choudhury, J. Ma, J. Warkentin, and J.P. Pezacki

Abstract: Gas phase thermolysis of 2,2-dimethoxy-5,5-dimethyl-Δ^3-1,3,4-oxadiazoline (**1**) in an ultraviolet photoelectron spectrometer by means of a CW CO_2 laser as directed heat source at 26 W gave a complex PE spectrum that included ionization bands belonging to acetone, tetramethoxyethylene (**3**), and dimethyl oxalate (**4**). Subtraction of the spectra of acetone, **3**, and **4** from the pyrolysis spectrum of **1** left a simple PE spectrum that is attributed to dimethoxycarbene (**2**) along with some ethane. Becke3LYP/6-31+G* calculations gave first adiabatic and vertical ionization potentials of **2** as well as orbital energies that are in perfect agreement with experimental values. From the available experimental and calculational data, **2** is assumed to adopt a *w* conformation.

Key words: dimethoxycarbene, 2,2-dimethoxy-Δ^3-1,3,4-oxadiazoline, tetramethoxyethylene, He(I) photoelectron spectroscopy, thermolysis.

Résumé : La thermolyse en phase gazeuse de la 2,2-diméthoxy-5,5-diméthyl-Δ^3-1,3,4-oxadiazoline (**1**) dans un spectromètre photoélectronique ultraviolet, à l'aide d'un laser à CO_2 CW utilisé comme source dirigée de chaleur à 26 W, conduit à un spectre PE complexe comportant des bandes d'ionisation appartenant à l'acétone, au tétraméthoxyéthylène (**3**) et à l'oxalate de diméthyle (**4**). Si l'on soustrait les spectres de l'acétone et ceux des composés **3** et **4** du spectre de pyrolyse du composé **1**, on obtient un spectre PE résiduel qui a été attribué au diméthoxycarbène (**2**) en présence de faibles quantités d'éthane. Des calculs de Becke3LYP/6-31+G* ont permis d'obtenir les premiers potentiels d'ionisation adiabatique et verticale de l'entité **2** ainsi que des énergies d'orbitales qui sont en parfait accord avec les valeurs expérimentales. Sur la base des données expérimentales et résultats des calculs, on peut faire l'hypothèse que l'entité **2** adopte une conformation *w*.

Mots clés : diméthoxycarbène, 2,2-diméthoxy-Δ^3-1,3,4-oxadiazoline, tétraméthoxyéthylène, spectroscopie photoélectronique He(I), thermolyse.

[Traduit par la rédaction]

The combination of photoelectron (PE) spectroscopy with quantum chemical calculations of molecular orbital eigenvalues and eigenvectors gives information about the electronic structure and bonding of stable as well as transient species that is provided by no other technique. PE spectra of transient carbenes are very rare (1) due to the high reactivity of these species, which requires special instrumentation. Usually, reactive intermediates are generated pyrolytically from thermally labile precursors using electrically heated furnaces that are several centimeters in length (2). Yet carbenes have to be generated close to the ionization beam to minimize the incursion of reactions like rearrangement, fragmentation, or dimerization. Our unique ultraviolet PE spectrometer – CW CO_2 laser apparatus (3) allows us to use the laser as a directed heat source to produce a hot zone as short as 1 mm in length on the tip of a quartz tube positioned at about 1 cm from the point of intersection with the ionization beam. We used this setup successfully to obtain PE spectra of short-lived reactive species such as benzazete and *o*-benzyne (4), 1,2-cyclohexadiene (5), 1-(2-thiaindane)ketene and benzocyclobutenethione (6), as well as *p*-substituted phenylketenes (7) through pyrolyses of suitable precursors (Scheme 1).

We decided to study the thermal gas phase decomposition of 2,2-dimethoxy-5,5-dimethyl-Δ^3-1,3,4-oxadiazoline (**1**) (8), because thermolysis in solution had shown formation of

Received September 25, 1997.

H.M. Muchall,[1] N.H. Werstiuk,[1] B. Choudhury, J. Ma, J. Warkentin, and J.P. Pezacki. Department of Chemistry, McMaster University, Hamilton, ON L8S 4M1, Canada.

[1] Authors to whom correspondence may be addressed. Telephone: (905) 525-9140. Fax: (905) 522-2509. E-mail: muchall@mcmaster.ca, werstiuk@mcmaster.ca

© 1998 NRC Canada

Scheme 1.

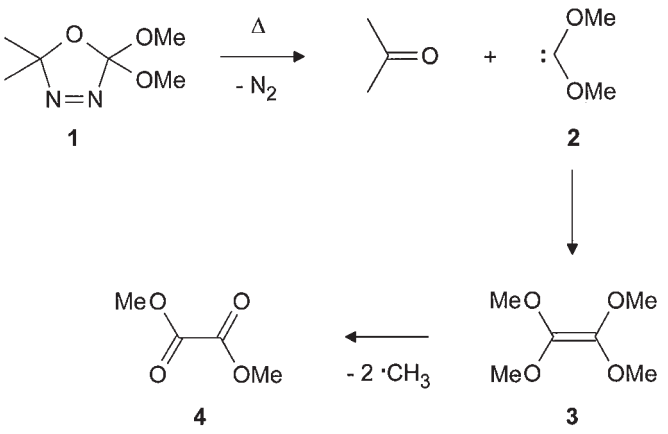

Fig. 1. He(I) photoelectron spectra of (*a*) 2,2-dimethoxy-5,5-dimethyl-Δ^3-1,3,4-oxadiazoline (**1**); (*b*) the pyrolysate of **1** obtained at a laser power level of 26 W; (*c*) tetramethoxyethylene (**3**); (*d*) dimethoxycarbene (**2**) after subtraction (the hatched bands are due to ethane). Uniformly shifted calculated eigenvalues (Becke3LYP/6-31+G*) are given as vertical bars in (*a*) and (*d*).

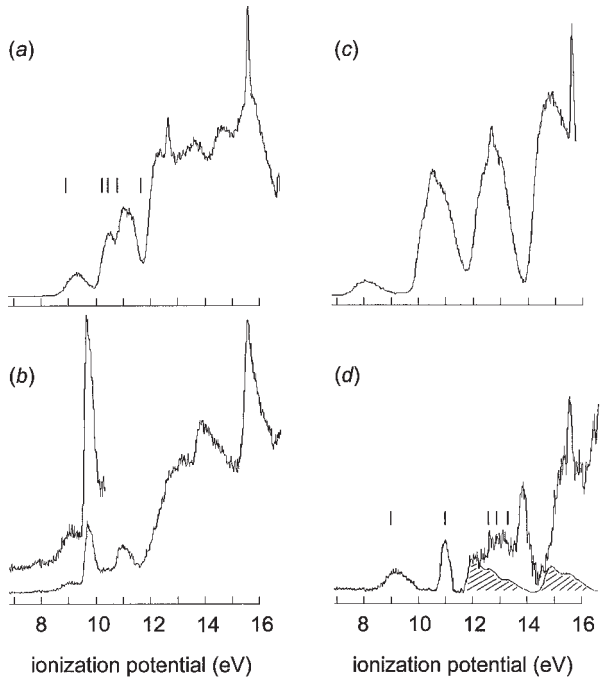

tetramethoxyethylene (**3**) (9) and preliminary flash vacuum pyrolysis experiments on **1** gave dimethyl oxalate (**4**), both of which could arise from a common precursor, dimethoxycarbene (**2**). Our recent computational study on the first adiabatic and vertical ionization potentials of carbenes (10) provided us with a calculational method (Becke3LYP/6-31+G* (11)) for the reliable prediction of these values. Applying these calculations to dimethoxycarbene (**2**), we expected to identify **2** through its ionization potentials if its spectrum actually was present in the pyrolysis spectrum of **1**, and possibly to establish its conformation. The particular choice of oxadiazoline **1** for this study was made because (*a*) it is a source of **2**; (*b*) it gave

Fig. 2. Preferred conformation (Becke3LYP/6-31+G*) of (*a*) oxadiazoline **1** and (*b*) conformers **2***w* and **2***sk* of dimethoxycarbene.

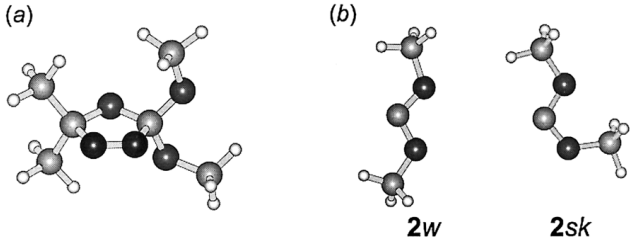

Table 1. Total energies E_T (hartrees) and calculated ionization potentials IP (eV) of optimized geometries of **1**–**3** (N electrons) and their radical cations (N–1 electrons) according to Becke3LYP/6-31+G*.

	Number of electrons	E_T	IP
1	N	–571.004 434	
	N–1 [a]	–570.677 705	8.89
2*w*	N	–268.309 870 [b]	
	N–1 [c]	–268.011 517	8.29
	N–1 [a]	–267.978 827	9.01
2*sk*	N	–268.306 911 [d]	
	N–1 [c]	–268.008 806	8.11
	N–1 [a]	–267.975 877	9.01
3	N	–536.693 043 [e]	
	N–1 [c]	–536.445 198	6.68
	N–1 [a]	–536.403 737	7.87

[a] Single-point energy calculation on the molecule's optimized geometry for IP_v.
[b] E_T corrected for zero-point vibrational energy is –268.220 668.
[c] The geometry of the radical cation was optimized for IP_a.
[d] E_T corrected for zero-point vibrational energy is –268.217 754.
[e] For the all-*anti* conformer.

us the additional opportunity to compare the mode of its decomposition (on a different path **1** can also yield nitrogen, dimethylcarbene, and dimethyl carbonate) in the gas phase to that in solution (9); and (*c*) it is the first member in a series of similar oxadiazolines that could be used as possible precursors of O,S- and O,N-substituted carbenes in the gas phase. In this communication, we report the results of a He(I) PE spectroscopic study of the thermolysis of oxadiazoline **1** along with ab initio (Gaussian 94 (12)) calculational data on **1** and two of its pyrolysis products, dimethoxycarbene (**2**) and tetramethoxyethylene (**3**). PE spectra for **2** and **3** are presented for the first time.

The PE spectrum of **1** is shown in Fig. 1*a*. Three bands belonging to four ionizations (at 9.30, 10.49, 11.00, and 11.22 eV) are separated from the main group of bands with its first band at about 12.1 eV. The sharp peak at 12.63 eV belongs to traces of water. Vertical bars in Fig. 1*a* give negative Becke3LYP/6-31+G* orbital energies (–ε 6.81, 8.11, 8.33, 8.74, and 9.49 eV), which are shifted so that the HOMO energy equals that of the calculated first vertical ionization potential IP_v (8.89 eV; total energies are given in Table 1). Support for applying a Koopmans' Theorem-like interpretation of orbital energies at the DFT level of theory in PE spectroscopic studies has been provided by Arduengo et al. (1*d*). The most stable conformation of **1**, with methoxy groups "sickle" as shown in Fig. 2*a*, was used in these calculations.

© 1998 NRC Canada

The PE spectrum of the pyrolysate of **1** taken at a laser power level of 26 W, which corresponds to a temperature of 500 ± 50°C (3), is given in Fig. 1*b*. Besides nitrogen (sharp peak at 15.60 eV), the complex spectrum shows the prominent band of acetone (9.70 eV) (13). On its low-energy side, two bands of low intensity with maxima at 8.0 and 9.0 eV can be attributed to further pyrolysis products. One path of decomposition of oxadiazoline **1** is given in Scheme 1. If nitrogen and acetone are two products, the remaining PE spectrum must be partially due to dimethoxycarbene (**2**) or to products arising from **2**. When tetramethoxyethylene (**3**), the product of dimerization of **2**, was prepared (14) and its PE spectrum (Fig. 1*c*) recorded, the first low-intensity band in the pyrolysis spectrum of **1** could be assigned to **3** (first IP at 8.0, shoulder at 10.1, and maximum of the second band at 10.5 eV). Interesting is the very broad first band of **3**: its IP_a (first adiabatic ionization potential) is at 7.1 eV. Calculated Becke3LYP/6-31+G* first adiabatic and vertical IPs (Table 1) of the all-*anti* conformer, which is the global minimum according to HF/3-21G calculations, match experimental values and confirm the energy difference between IP_a and IP_v found in the spectrum. Upon opening the fast-pumping valve on the spectrometer in the thermolysis of **1**, the band at 8.0 eV disappeared, which is proof that **3** is formed through dimerization of **2**. To know whether **3** is stable at the thermolysis temperature (its thermal decomposition has been reported (15)), it was pyrolyzed in an independent experiment. The PE spectrum of the pyrolysate of **3** (not given) obtained at a laser power level of 26 W seems to be exclusively that of dimethyl oxalate (**4**) (16): IPs of bands are the same as those in a spectrum of an authentic sample of **4** taken with our spectrometer. The peak for the methyl radical (the literature value (17) is 9.84 eV) cannot be identified with certainty; it might be present on the low-energy side of the first band of **4**.

When the PE spectra of acetone, tetramethoxyethylene (**3**), and dimethyl oxalate (**4**) were subtracted from the pyrolysis spectrum of **1**, a simple spectrum remained. There are two bands of comparable intensity at 9.0 (onset at 8.4 eV) and 11.0 eV, followed by an unstructured region with its first band at 12.0 eV and a further maximum at 13.8 eV. These ionizations, except for the band at 12.0 eV, are reproduced nicely by Becke3LYP/6-31+G* calculations on dimethoxycarbene (**2**): for the *w* conformer given in Fig. 2(*b*), which is more stable than the *sk* conformer by 7.67 kJ mol^{-1} (or 7.64 kJ mol^{-1} when zero-point vibrational energies are included), IP_a and IP_v are 8.29 and 9.01 eV, respectively, and if orbital energies (–ε 6.36, 8.39, 9.97, and 10.34 eV) are shifted uniformly as explained above, the correlation is ideal (Fig. 1*d*). While data for the *sk* conformer are not too different, IP_a 8.11 eV, IP_v 9.01 eV, –ε 6.36, 8.71, 9.80, and 10.30 eV, a distinction between **2***w* and **2***sk* is possible by means of the second IP. The additional band at 12.0 eV is the only obvious ionization not arising from **2**. The facts that there are no bands unaccounted for in the low-energy region of the spectrum and that methyl radicals are being formed in the thermolysis of **3** led us to assign this band to ethane (literature (13) IP is 11.99 eV). Additional support for this is supplied by subtraction of the PE spectrum of **4** from the pyrolysis spectrum of **3**, which leaves a spectrum that has the features of that of ethane (13).

Neither were the products of a second possible path of decomposition of **1**, dimethylcarbene (and from it propene) and dimethyl carbonate, detected in the pyrolysis PE spectrum, in agreement with results reported for the thermolysis of **1** in solution (9).

Acknowledgment

We gratefully acknowledge the usage of the IBM SP2 computer at Queen's University granted under the auspices of an IBM Canada – Queen's University collaborative project. We thank Ms. O. Donini for assistance with operational aspects of parallel Gaussian 94, and the Natural Sciences and Engineering Research Council of Canada (NSERC) for financial support. We also gratefully acknowledge the usage of the SGI computing installation in the Geochemistry Labs at McMaster funded by NSERC.

References

1. (*a*) D.W. Kohn, E.S.J. Robles, C.F. Logan, and P. Chen. J. Phys. Chem. **97**, 4936 (1993); (*b*) H. Clauberg, D.W. Minsek, and P. Chen. J. Am. Chem. Soc. **114**, 99 (1992); *(c)* J.M. Dyke, L. Golob, N. Jonathan, A. Morris, and M. Okuda. J. Chem. Soc. Faraday Trans. 2, **70**, 1828 (1974); *(d)* A.J. Arduengo III, H. Bock, H. Chen, M. Denk, D.A. Dixon, J.C. Green, W.A. Herrmann, N.L. Jones, M. Wagner, and R. West. J. Am. Chem. Soc. **116**, 6641 (1994).
2. R. Schulz and R. Schweig. *In* Structure and reactivity. *Edited by* J.F. Liebman and A. Greenberg. VCH Publishers Inc., New York. 1988. Chap. 8; N.P.C. Westwood. Chem. Soc. Rev. **18**, 317 (1989); P. Chen. Unimol. Bimol. Ion–Mol. React. Dyn. 371 (1994).
3. N.H. Werstiuk, C.D. Roy, and J. Ma. Can. J. Chem. **72**, 2537 (1994).
4. N.H. Werstiuk, C.D. Roy, and J. Ma. Can. J. Chem. **73**, 146 (1995).
5. N.H. Werstiuk, J. Ma, and C.D. Roy. Can. J. Chem. **74**, 1903 (1996).
6. N.H. Werstiuk, J. Ma, C.D. Roy, A.J. Kresge, and E.A. Jefferson. Can. J. Chem. **74**, 2536 (1996).
7. N.H. Werstiuk, H.M. Muchall, J. Ma, and M.T.H. Liu. Can. J. Chem. Submitted.
8. K. Kassam, D.L. Pole, M. El-Saidi, and J. Warkentin. J. Am. Chem. Soc. **116**, 1161 (1994).
9. M. El-Saidi, K. Kassam, D.L. Pole, T. Tadey, and J. Warkentin. J. Am. Chem. Soc. **114**, 8751 (1992).
10. H.M. Muchall, N.H. Werstiuk, and B. Choudhury. Can. J. Chem. In press.
11. A.D. Becke. J. Chem. Phys. **98**, 5648 (1993); C. Lee, W. Yang, and R.G. Parr. Phys. Rev. B: Condens. Matter, **37**, 785 (1988).
12. M.J. Frisch, G.W. Trucks, H.B. Schlegel, P.M.W. Gill, B.G. Johnson, M.A. Robb, J.R. Cheeseman, T. Keith, G.A. Petersson, J.A. Montgomery, K. Raghavachari, M.A. Al-Laham, V.G. Zakrzewski, J.V. Ortiz, J.B. Foresman, C.Y. Peng, P.Y. Ayala, W. Chen, M.W. Wong, J.L. Andres, E.S. Replogle, R. Gomperts, R.L. Martin, D.J. Fox, J.S. Binkley, D.J. Defrees, J. Baker, J.P. Stewart, M. Head-Gordon, C. Gonzalez, and J.A. Pople. Gaussian 94, Revision B.3. Gaussian, Inc., Pittsburgh, Pa. 1995.
13. K. Kimura, K. Katsumata, Y. Achiba, T. Yamazaki, and S. Iwata. Handbook of HeI photoelectron spectra of fundamental organic molecules. Japan Scientific Societies Press, Tokyo, and Halsted Press, New York. 1981.
14. D. Belluš, H. Fischer, H. Greuter, and P. Martin. Helv. Chim. Acta, **61**, 1784 (1978).
15. R.W. Hoffmann, J. Schneider, and H. Häuser. Chem. Ber. **99**, 1892 (1966).
16. S.P. McGlynn and J.L. Meeks. J. Electron Spectrosc. Relat. Phenom. **8**, 85 (1976).
17. L. Golob, N. Jonathan, A. Morris, M. Okuda, and K.J. Ross. J. Electron Spectrosc. Relat. Phenom. **1**, 506 (1972–73).

© 1998 NRC Canada

A benzo-fused oxapenem from a β-lactam-4-ylidene

Philippe Couture and John Warkentin

Abstract: Spiro-fused β-lactam oxadiazoline **2a** was prepared from acetone semicarbazone in five steps. Thermolysis of **2a** at 100°C in benzene led to carbene **3a**, which cyclized to the benzo-fused oxapenem derivative **4** via intramolecular OH insertion. Compound **10**, with a β-lactam ring linked to an azetidinedione ring, was a minor product.

Key words: benzoxapenem, carbene, β-lactam-4-ylidene, OH insertion.

Résumé : Utilisant la semicarbazone de l'acétone comme produit de départ, on a préparé l'oxadiazoline **2a**, une spiro β-lactame, en cinq étapes. La thermolyse du produit **2a** à 100°C, dans le benzène, conduit au carbène **3a** qui, par cyclisation par le biais d'une insertion intramoléculaire, donne le dérivé benzooxapénème **4**. On retrouve aussi le composé **10**, comportant un cycle β-lactame lié à un cycle azétidinedione, comme produit mineur.

Mots clés : benzoxapénème, carbène, β-lactam-4-ylidène, insertion de OH.

[Traduit par la rédaction]

Studies of the chemistry of β-lactam-4-ylidenes, generated by thermolysis of spiro-fused β-lactam oxadiazolines (**1**) (1), have recently been reported. This work demonstrated that those carbenes undergo both inter- and intramolecular reactions in fair to excellent yields, including cyclopropanation with styrene, insertion into the OH bond of methanol, and insertion into a tethered OH group (1*a*) to afford the oxapenam nucleus, Scheme 1.[2] β-Lactams have been prepared by a large number of methods[3] including a carbene-based approach to the four-membered ring from a diazoamide (3). Oxapenams, oxapenems, and other bicyclic β-lactam systems are also well known (4) and a carbene approach to the oxapenam ring, by CH insertion into a CH_2 group of the five-membered ring system, was successful, Scheme 2 (5). Benzo-fused oxapenems appear to be unreported, possibly because they are not expected to be biologically active. Many β-lactams that have well-established antibiotic activity bear acetic acid functionality at N (6). Nevertheless the synthesis of a simple benzo-fused oxapenem was of interest as a test of the β-lactam-4-ylidene approach, which could become useful for compounds bearing other functionality.

Results and discussion

Benzoxapenem **4**, from the ylidene **3a**, required oxadiazoline precursor **2a** (Scheme 3), which had been reported (1*a*), but without the phenolic OH group. That group could be incorporated by introducing the protection/deprotection methods shown in Scheme 4.[4] Semicarbazone **5** was prepared by transamination of acetone semicarbazone with 2-aminophenol in refluxing toluene. Protection of the phenol as the TBDMS ether was followed by oxidative cyclization with $PhI(OAc)_2$, which afforded imino oxadiazoline **6**. The β-lactam ring of **7** was then constructed by means of the ketene-plus-imine approach (2*d*, 7), by treating **6** with diphenylacetyl chloride (1.2 equiv.) in the presence of triethylamine (2.5 equiv.) at –23°C. Subsequent deprotection of the phenolic group with nBu_4NF (8) gave the desired **2a**.

Thermolysis (100°C, 24 h) of **2a** as a 14 mM solution in benzene generated β-lactam-4-ylidene **3a**, which, as anticipated on the basis of analogy (9), underwent intramolecular O-H insertion to yield benzoxapenem **4** in 53% yield (Scheme 3). The mechanism may involve attack of the hydroxyl oxygen at the carbene carbon (ylide formation), rather than proton transfer to that carbon, because a β-lactam-4-ylidene is appreciably electrophilic, as implied from its cyclopropanation reaction with 4-bromo-1-butene (1*e*). Compound **10** was also formed, as a minor product isolated in 7% yield,[5] as well as several very minor products that were not identified. One possible multistep mechanism that could account for **10** is illustrated in Scheme 5. It involves, as a competing pathway, 1,3-dipolar cycloreversion of the oxadiazoline ring to 2-diazopropane and a 2,4-azetidinedione (**8**). The 2-diazopropane thus generated reacts with the starting material, phenol **2a**, to give ether **2c**. Predominant 1,3-dipolar cycloreversion of the latter generates carbene **3c**, which undergoes an intermolecular C-H insertion reaction with **2a** to give **9**. Finally, fragmentation of the oxadiazoline moiety of **9** by the competing pathway (loss of 2-diazopropane) yields **10**. This sequence, involving the "minor" cycloreversion twice, requires that the process should occur in ca. 30% yield ($0.3 \times 0.3 = 0.09$; 7% found), assuming

Received November 17, 1997.

P. Couture and J. Warkentin.[1] Department of Chemistry, McMaster University, Hamilton, ON L8S 4M1, Canada.

[1] Author to whom correspondence may be addressed. Telephone: (905) 525-9140. Fax: (905) 522-2509. E-mail: warkent@mcmail.cis.mcmaster.ca

[2] Carbonyl ylides (not shown in Scheme 1) and N_2 are probably formed first, by 1,3-dipolar cycloreversion.

[3] For reviews see refs. 2a–2*d*.

[4] Yields are not optimized

[5] The structure was firmly established by means of single-crystal X-ray diffraction.

© 1998 NRC Canada

Scheme 1.

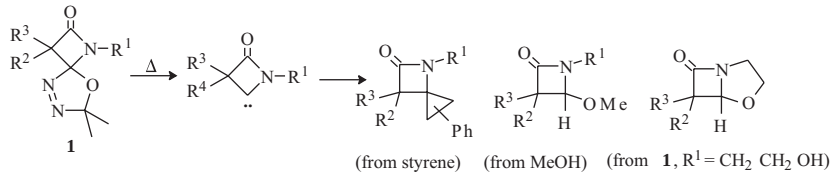

Scheme 2.

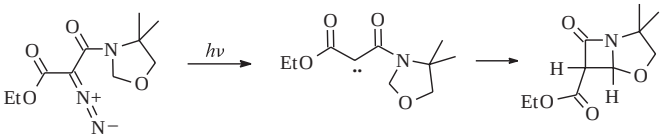

Scheme 3.

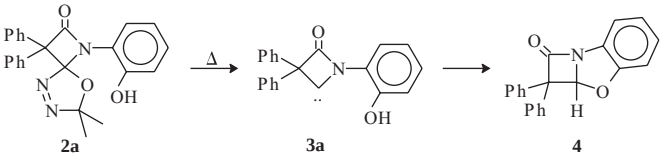

Scheme 4.

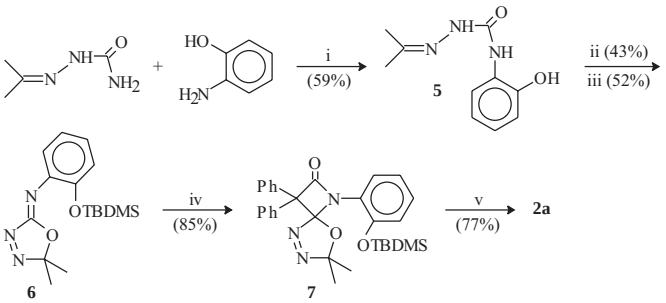

Reagents and conditions: i. toluene, reflux; ii. NEt_3, TBDMSCl, CH_2Cl_2, 0°C; iii. $PhI(OAc)_2$, CH_2Cl_2, 0°C to rt; iv. NEt_3, $Ph_2CHCOCl$, CH_2Cl_2, –23°C; v. nBu_4NF, THF, –23°C to rt.

that cycloreversion to diazopropane is equally likely in **2a** and **9**. Formation of **12** from **11** is a precedent for such a cycloreversion, Scheme 6 (10). Another way of generating the azetidinedione would involve fragmentation of a carbonyl ylide intermediate (11) to that dione and propylidene as shown in Scheme 7 for the known case **13**→**14** (12). Although 2-propylidene also could isopropylate the phenolic OH group, the known fast 1,2 H-migration in that carbene (13) makes that pathway unlikely.

In summary, β-lactam-4-ylidene **3a** inserts effectively into the tethered phenolic OH group, as expected, to afford the apparently new, tricyclic, benzo-fused oxapenem system **4**, 2,3-benz-6,6-diphenyl-4-oxa-1-azabicyclo[3.2.0]hept-2-en-7-one.

Experimental

Preparation of 5

A solution of acetone semicarbazone (2.88 g, 25 mmol) and 2-aminophenol (2.88 g, 26 mmol) in toluene (9 mL) was heated to reflux for 8.5 h. The product, precipitated from the

Scheme 5.

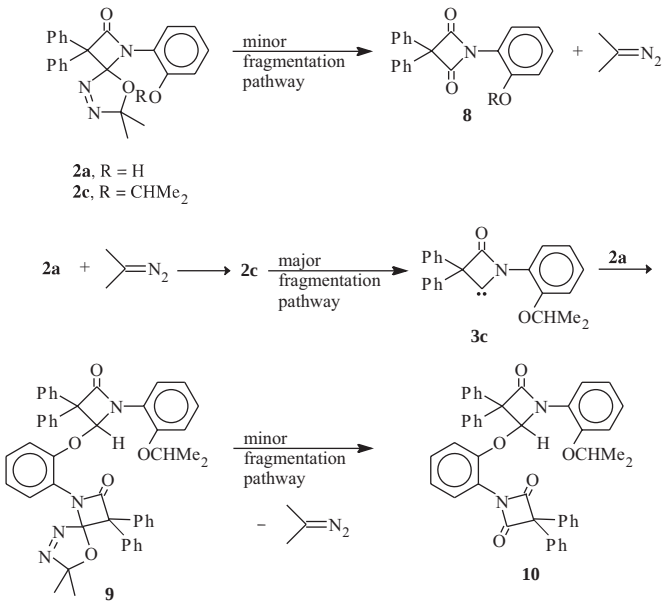

Scheme 6.

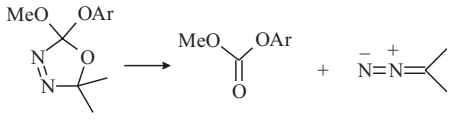

Scheme 7.

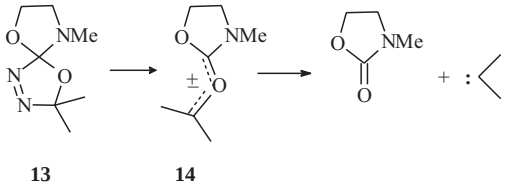

cooled solution, was triturated with diethyl ether and obtained as a white solid in 59% yield. It could be recrystallized from ethanol–ether, but with some decomposition; mp 165–166°C (turns orange at ca. 140°C); IR (KBr) cm^{-1}: 3500–2500 (OH, NH), 1654 (C═O), 1558; ^1H NMR (300 MHz, $CDCl_3$): 1.91 (s, 3H), 2.05 (s, 3H), 6.60–7.20 (m, 4H), 8.27 (br s, 1H), 8.61 (br s, 1H), 9.57 (br s, 1H); ^{13}C NMR (75 MHz, C_6D_6): 16.14, 24.66, 120.18, 120.22, 122.40, 126.03, 126.39, ca. 128 (overlap with solvent signal), 149.72, 156.06; MS (EI) *m/z*: 207 (M^+, 21%), 135 (6), 109 (100), 99 (23), 79 (23), 72 (35); MS (CI, NH_3) *m/z*: 208 $(M+H)^+$; HRMS *m/z* calcd. for $C_{10}H_{13}N_3O_2$ (M^+): 207.1008; found: 207.1008.

© 1998 NRC Canada

Protection of the OH group of 5

Semicarbazone **5** (3.40 g, 16 mmol) was dissolved in CH_2Cl_2 (100 mL) to which triethylamine (3.00 g, 30 mmol) was added. A solution of *tert*-$BuSiMe_2Cl$ (3.71 g, 25 mmol, in 35 mL of CH_2Cl_2) was then added dropwise to the ice-cold semicarbazone solution. The solution was kept at 0°C for a further 5 h before it was allowed to warm to room temperature overnight. The solid recovered after evaporation of the solvent was washed with water (to remove $Et_3NH^+Cl^-$) and recrystallized from toluene. Beige solid (43% yield), mp 170–171°C; IR (CCl_4) cm^{-1}: 3387 (NH), 3207 (NH), 1688 (C═O), 1534; ^1H NMR (300 MHz, $CDCl_3$): 0.29 (s, 6H), 1.05 (s, 9H), 1.92 (s, 3H), 2.03 (s, 3H), 6.80–7.00 (m, 3H), 8.10 (br s, 1H), 8.28 (dd, ^4J = 1.8 Hz, ^3J = 7.8 Hz), 8.69 (br s, 1H); ^{13}C NMR (75 MHz, C_6D_6): –4.28, 16.54, 18.22, 24.98, 25.85, 117.52, 119.35, 121.47, 122.17, 130.09, 144.14, 147.31, 153.54; MS (EI) *m/z*: 321 (M^+, 8%), 264 (M – ^{t}Bu, 100), 208 (10), 166 (57), 150 (46), 135 (26), 99 (22), 73 (61), 56 (29); MS (CI, NH_3) *m/z*: 322 $(M+H)^+$; HRMS *m/z* calcd. for $C_{16}H_{27}N_3O_2Si$ (M^+): 321.1873; found: 321.1868.

Preparation of 6

A solution of $PhI(OAc)_2$ (3.75 g, 12 mmol, in 75 mL of CH_2Cl_2) was added over 1 h to the protected semicarbazone (3.00 g, 9.3 mmol, in 75 mL of CH_2Cl_2) at 0°C under N_2. The solution was allowed to warm to room temperature overnight. After washing with aqueous $NaHCO_3$ (5%) and water, the organic phase was dried ($MgSO_4$), and the solvent was evaporated in vacuo. Separation of the product mixture by column chromatography on silica, eluting first with hexane and then with 5% ethyl acetate in hexane, gave 1.55 g (52%) of **6** (*Z* isomer assumed to be the major component) as a dark yellow solid that melted over the range ca. 52–60°C; IR (KBr) cm^{-1}: 1717 (C═N), 1481, 1265, 1107, 927, 842; ^1H NMR (200 MHz, $CDCl_3$): 0.21 (s, 6H), 0.99 (s, 9H), 1.63 (s, 6H), 6.88–7.02 (m, 2H), 7.02–7.14 (m, 1H), 7.23–7.33 (m, 1H); ^{13}C NMR (50 MHz, $CDCl_3$): –4.35, 18.34, 23.54, 25.70, 121.11, 121.32, 121.72, 122.86, 126.76, 135.21, 149.04, 159.63; MS (EI) *m/z*: 262 (M – ^{t}Bu, 14%), 206 (16), 192 (81), 176 (68), 164 (23), 150 (6), 135 (6), 100 (14), 84 (39), 74 (18), 47 (100); MS (CI, NH_3) *m/z*: 320 $(M+H)^+$.

Preparation of 7

This was carried out essentially as described by Zoghbi and Warkentin (1*d*) for related compounds. To a solution of **6** (0.82 g, 2.6 mmol) and triethylamine (0.66 g, 6.5 mmol) in CH_2Cl_2 (25 mL) at –23°C, diphenylacetyl chloride (0.74 g, 3.2 mmol, in 13 mL of CH_2Cl_2) was added over about 30 min. The solution was kept in the cold bath for an additional 1 h, and was then allowed to warm to room temperature overnight. After washing with aqueous $NaHCO_3$ (5%) and brine, and drying over $MgSO_4$, the solvent was evaporated. The product was obtained as a white solid in 85% yield following purification by radial chromatography (5–10% ethyl acetate in hexane); mp ca. 118–120°C (dec.); IR (CCl_4) cm^{-1}: 1786 (C═O), 1501; ^1H NMR (200 MHz, $CDCl_3$): 0.16 (s, 3H), 0.17 (s, 3H), 0.83 (s, 9H), 1.14 (s, 3H), 1.58 (s, 3H), 6.79–6.93 (m, 2H), 7.08–7.60 (m, 12H); ^{13}C NMR (50 MHz, $CDCl_3$): –4.16, 18.21, 24.26, 24.73, 25.57, 74.42, 119.49, 120.69, 122.20, 122.64, 125.43, 127.44, 127.90, 128.17, 128.29, 128.38, 130.19, 135.99, 137.21, 153.01, 166.87; MS (EI) *m/z*: 514 (M^+, 3%), 457 (M – ^{t}Bu, 10), 444 (M – diazopropane, 9), 428 (M – N_2–Me_2CO, 34), 400 (100), 387 (14), 358 (26), 342 (96), 265 (16), 249 (43), 234 (23), 194 ($[Ph_2C{=}C{=}O]^+$, 70), 165 (69), 117 (13), 73 (47); MS (CI, NH_3) *m/z*: 514 $(M+H)^+$.

Preparation of 2a

A solution of the protected oxadiazoline (0.66 g, 1.3 mmol) in dry THF (3.0 mL) was placed in a flask fitted with a septum. After flushing with dry N_2, the flask was immersed in an ice bath for several minutes, before adding 1.75 mL of nBu_4NF (1.0 M in THF, 1.75 mmol) by syringe, over about 15 min. The sample was kept in ice for an additional 20–30 min, and was then left to reach room temperature during 2 h. After evaporation of the solvent, a mixture of 15 mL of CH_2Cl_2 + 6 mL of 0.1 N HCl was added to the crude product mixture. After separation of the two layers, the aqueous phase was extracted with CH_2Cl_2, and the combined organic fractions were washed with aqueous $NaHCO_3$ (5%) and water. Slightly impure **2a**, obtained after chromatography on silica using 10–40% ethyl acetate in hexane as elution solvent, was recrystallized from ethyl acetate – hexane to afford a white solid in 77% yield; mp ca. 120–150°C (dec.); IR (CCl_4) cm^{-1}: 3600–3000 br (OH), 1745 (C═O), 1497; ^1H NMR (300 MHz, $CDCl_3$): 1.43 (s, 3H), 1.49 (s, 3H), 6.79–6.93 (m, 2H), 7.01–7.12 (m, 2H), 7.17–7.26 (m, 1H), 7.28–7.50 (m, 10H); ^{13}C NMR (75 MHz, $CDCl_3$, some signals overlap): 24.17, 24.22, 74.77, 119.07, 120.72, 120.95, 123.36, 124.52, 128.07, 128.39, 128.44, 128.67, 129.98, 133.97, 135.74, 151.29, 163.53; MS (EI) *m/z*: 285 (13%), 254 (4), 208 (5), 194 ($[Ph_2C{=}C{=}O]^+$, 89), 177 (9), 165 (100), 152 (7), 135 (23), 115 (7), 84 (10), 77 (7), 63 (10), 45 (46); MS (CI, NH_3) *m/z*: 417 $(M+NH_4)^+$, 400 $(M+H)^+$. Anal. calcd. for $C_{24}H_{21}N_3O_3$: C 72.17, H 5.30, N 10.52; found: C 72.45, H 5.00, N 10.55.

Preparation of 4 and 10

A sample of **2a** (285 mg, 0.71 mmol), dissolved in benzene (50 mL), was heated at 100°C for 24 h. The thermolysis products were separated by radial chromatography with solutions of ethyl acetate and hexane in various proportions.

Compound **4** was obtained as a white solid, mp 157–158°C (sample recrystallized from ethyl acetate – hexane); IR (CCl_4) cm^{-1}: 1801 (C═O), 1473, 1274; ^1H NMR (200 MHz, $CDCl_3$): 6.46 (s, 1H), 6.77–7.12 (m, 3H), 7.20–7.50 (m, 11H); ^{13}C NMR (50 MHz, $CDCl_3$): 76.59, 97.08, 109.73, 117.49, 121.76, 126.49, 126.87, 127.68, 128.00, 128.06, 128.41, 129.11, 130.31, 135.06, 138.20, 155.71, 177.19; MS (EI) *m/z*: 194 ($[Ph_2C{=}C{=}O]^+$, 32%), 165 (100), 139 (11), 115 (4), 86 (6), 74 (4), 63 (6), 51 (6); MS (CI, NH_3) *m/z*: 331 $(M+NH_4)^+$, 314 $(M+H)^+$. Anal. calcd. for $C_{21}H_{15}NO_2$: C 80.49, H 4.82, N 4.47; found: C 80.59, H 4.87, N 4.39.

Product **10** was also a white solid, mp 176–177°C (from ethyl acetate – hexane); IR (CCl_4) cm^{-1}: 1771 (C═O), 1754 (C═O), 1501, 1382; ^1H NMR (200 MHz, $CDCl_3$): 1.01 (d, ^3J = 6.0 Hz, 3H), 1.24 (d, ^3J = 6.0 Hz, 3H), 4.54 (septet, ^3J = 6.0 Hz, 1H), 6.7–7.7 (m, 29H); ^{13}C NMR (50 MHz, $CDCl_3$): 21.63, 22.01, 70.00, 73.25, 74.51, 89.80, 112.93, 114.21, 119.63, 120.30, 121.85, 123.46, 125.26, 126.78, 127.28, 127.51, 127.66, 127.79, 127.91, 128.24, 128.78, 128.92, 130.09, 134.84, 135.19, 138.10, 150.07, 150.87, 167.02, 168.08; MS (EI) *m/z*: 684 (M^+, 2%), 507 (12), 490 (6), 356 (41), 328 (100), 314 (20), 286 (91), 194 ($[Ph_2C{=}C{=}O]^+$, 65),

© 1998 NRC Canada

180 (15), 165 (65), 120 (21). The structure of **10** was established by means of single-crystal X-ray diffraction.

Acknowledgement

We thank Dr. J. Britten for the X-ray crystallography, and Dr. R. Smith and Mr. F. Ramelan for the mass spectrometry. Financial support from the Natural Sciences and Engineering Research Council of Canada (NSERC) is also gratefully acknowledged.

References

1. (*a*) M. Zoghbi and J. Warkentin. J. Org. Chem. **56**, 3214 (1991); (*b*) Can. J. Chem. **70**, 2792 (1992); (*c*) Can. J. Chem. **71**, 907 (1993); (*d*) Can. J. Chem. **71**, 912 (1993); (*e*) M. Zoghbi, S.E. Horne, and J. Warkentin. J. Org. Chem. **59**, 4090 (1994).
2. (*a*) R.B. Sykes, C.M. Cimarusti, D.P. Bonner, K. Bush, D.M. Floyd, N.H. Geodopapadakakou, W.H. Koster, W.C. Lin, W.L. Parker, P.A. Principle, M.L. Rathnum, W.A. Sluusarchyk, W.H. Treo, and J.S. Wells. Nature, **291**, 489 (1981); (*b*) P.C. Cherry and C.W. Newell. *In* Chemistry and biology of β-lactam antibiotics. Vol. 2. *Edited by* R.B. Morin and M. Gorman. Academic Press, New York. 1982. pp. 361–408; (*c*) A.G. Brown and S.M. Roberts (*Editors*). Recent advances in the chemistry of β-lactam antibiotics. The Royal Society of Chemistry, Burlington House, London. 1984; (*d*) T. Kametani. Heterocycles, **25**, 729 (1987).
3. M.P. Doyle, R.J. Pieters, J. Taunton, and H.Q. Pho. J. Org. Chem. **56**, 820 (1991).
4. W. Nagata, M. Narisada, and T. Yoshida. *In* Chemistry and biology of β-lactam antibiotics. *Edited by* R.B. Morin and M. Gorman. Vol. 2. Academic Press, New York. 1982. pp. 1–98.
5. T.B. Goldberg and D.R. Hall. J. Chem. Soc. Perkin Trans. 1, 1517 (1975).
6. K.B. Holden. *In* Chemistry and biology of β-lactam antibiotics. *Edited by* R.B. Morin and M. Gorman. Vol. 2. Academic Press, New York. 1982. pp. 99–131.
7. K.B. Holden. *In* Chemistry and biology of β-lactam antibiotics. *Edited by* R.B. Morin and M. Gorman. Vol. 2. Academic Press, New York. 1982. pp. 114–131.
8. E.J. Corey and B.B. Snider. J. Am. Chem. Soc. **94**, 2549 (1972).
9. (*a*) W. Kirmse. *In* Advances in carbene chemistry. *Edited by* U.H. Brinker. JAI Press, Greenwich, Conn. 1994. pp. 1–57; (*b*) G. Homberger, W. Kirmse, and R. Lelgemann. Chem. Ber. **124**, 1867 (1991). (*c*) W. Kimse, T. Meinert, D.A. Modarelli, and M.S. Platz. J. Am. Chem. Soc. **115**, 8918 (1993).
10. P. Couture, M. El-Saidi, and J. Warkentin. Can. J. Chem. **75**, 326 (1997).
11. P. Couture, J.K. Terlouw, and J. Warkentin. J. Am. Chem. Soc. **118**, 4214 (1996).
12. P. Couture and J. Warkentin. Can. J. Chem. **75**, 1264 (1997).
13. J.P. Pezacki, P. Couture, J.A. Dunn, J. Warkentin, P. Wood, J. Lusztyk, T. Chen, F. Ford, J. Toscano, and M.S. Platz. J. Am. Chem. Soc. Submitted.

© 1998 NRC Canada

Synthesis, spectroscopy, and structures of the seven-coordinate complexes $(CH_3)_2AsC(CF_3)$═$C(CF_3)As(CH_3)_2W(CO)_2I_2P(OC_6H_5)_3$ and $[(CH_3)_2AsC(CF_3)$═$C(CF_3)As(CH_3)_2]_2W(CO)Br_2$ and spectroscopy of related seven-coordinate complexes

Richard J. Barton, Sushil K. Manocha, Beverly E. Robertson, and Lynn M. Mihichuk

Abstract: (L-L)$W(CO)_3I_2$ (L-L = $(CH_3)_2AsC(CF_3)$═$C(CF_3)As(CH_3)_2$) reacts with the monodentate phosphite $P(OC_6H_5)_3$ and (L-L)$W(CO)_3Br_2$ reacts with L-L to form new seven-coordinate complexes (L-L)$W(CO)_2I_2P(OC_6H_5)_3$ and (L-L)$_2W(CO)Br_2$. Low-temperature X-ray diffraction analyses show the tungsten atom to be seven coordinate in both complexes, with the geometry most closely approximated by a monocapped octahedral environment, the capping group being a carbonyl in the dicarbonyl complex; the geometry is most closely approximated by a pentagonal bipyramidal environment in the monocarbonyl complex. The ^1H, ^{13}C, and ^{19}F NMR data indicate that the dicarbonyl complex is stereochemically nonrigid at 298 K and rigid at lower temperatures, while the monocarbonyl is nonrigid both at 298 K and at lower temperatures. $\Delta G^{\neq}$ values calculated at coalescence temperatures are consistent with an intramolecular rearrangement process for both complexes. The ^{13}C chemical shifts and $^2J(^{13}C\text{-}^{31}P)$ values provide important structural considerations in the assignment of a seven-coordinate geometry. Spectroscopic properties for the related seven-coordinate dicarbonyl complexes (L-L)$W(CO)_2PX_2$ (P = $P(OC_6H_5)_3$; X = Br; P = $P(OCH_3)_3$, $P(C_6H_5)_3$; X = Br, I) and monocarbonyl complexes (L-L)$_2W(CO)I_2$ and (L-L)$W(CO)X_2[P(OCH_3)_3]_2$ (X = Br, I) are presented and compared to those of the two title complexes.

Key words: seven-coordination, X-ray, NMR analysis.

Résumé : Le (L-L)$W(CO)_3I_2$ (L-L = $(CH_3)_2AsC(CF_3)$═$C(CF_3)As(CH_3)_2$) réagit avec le phosphite monodentate $P(OC_6H_5)_3$ alors que (L-L)$W(CO_3)Br_2$ réagit avec L-L pour former respectivement les nouveaux complexes heptacoordinés (L-L)$W(CO)_2I_2P(OC_6H_5)_3$ et (L-L)$_2W(CO)Br_2$. Des analyses de diffraction des rayons X à basse température ont permis de montrer que l'atome de tungstène est heptacoordiné dans les deux complexes: dans le complexe dicarbonyle, sa géométrie peut être décrite approximativement par un environnement octaédrique à cap unique qui est le dicarbonyle; dans le complexe monocarbonyle, la géométrie peut être décrite approximativement par un environnement bipyramidal pentagonal. Les données de RMN du ^1H, du ^{13}C et du ^{19}F indiquent que le complexe dicarbonyle est stéréochimiquement non rigide à 298 K mais qu'il est rigide à des températures inférieures; par ailleurs, le complexe monocarbonyle n'est pas rigide ni à 298 K ni à des températures inférieures. Pour chacun de ces complexes, les valeurs de $\Delta G^{\neq}$ calculées à partir des températures de coalescence sont en accord avec un processus de réarrangement intramoléculaire. Les valeurs des déplacements chimiques en ^{13}C ainsi que celles des $^2J(^{13}C\text{-}^{31}P)$ fournissent des considérations structurales importantes dans l'attribution de la géométrie heptacoordinée. On rapporte les propriétés spectroscopiques des complexes dicarbonyles heptacoordinés apparentés (L-L)$W(CO)_2PX_2$ (P = $P(OC_6H_5)_3$; X = Br; P = $P(OCH_3)_3$ ou $P(C_6H_5)_3$; X = Br, I) et des complexes monocarbonyles (L-L)$_2W(CO)I_2$ et (L-L)$W(CO)X_2[P(OCH_3)_3]_2$ (X = Br, I) et on les compare à celles des deux complexes mentionnés dans le titre.

Mots clés : heptacoordination, rayons X, analyse par RMN.

[Traduit par la rédaction]

Introduction

In the area of seven coordination the relevant polytopal polyhedra are the pentagonal bipyramid, the monocapped octahedron, and the quadrilaterally monocapped trigonal prism. X-ray crystallographic studies of seven-coordinate transition metal carbonyl complexes have shown the latter two types of geometry to predominate (1–12). However, the actual structures seldom match the ideal polyhedral arrangements, and

Received August 12, 1997.

R.J. Barton, S.K. Manocha, B.E. Robertson, and L.M. Mihichuk.[1] Department of Chemistry, University of Regina, Regina, SK S4S 0A2, Canada.

[1] Author to whom correspondence may be addressed. Telephone: (306) 585-4793. Fax: (306) 585-4894. E-mail: mihichuk@meena.cc.uregina.ca

© 1998 NRC Canada

various criteria have been proposed to aid in the assignment of the most appropriate description to an experimentally determined polyhedron (13–15).

We have been interested in the seven-coordinate chemistry of group six metal (Mo, W) carbonyl complexes from the point of view of structure and dynamic behaviour (10–12, 16). Structural studies have been restricted to the tungsten analogues because the corresponding molybdenum complexes decompose in the X-ray beam during X-ray analysis, preventing the collection of useful structural data. In addition the 14.4% spin one-half ^{183}W atom provides important coupling parameters not present in the molybdenum series. The molybdenum and tungsten complexes nevertheless show similar properties and are assumed to behave in a similar manner with regard to fluxionality and reactivity. Our present study, which includes a detailed spectroscopic investigation of tungsten complexes containing one bidentate ligand and extends into a study of corresponding complexes incorporating two bidentate ligands, allows for a greater understanding of structural features in terms of a predominant geometry and fluxional behaviour.

Seven-coordinate carbonyl complexes also exhibit fluxionality in solution, resulting in room-temperature NMR spectra often not being consistent with the X-ray crystal structure. The reason for this behaviour is thought to be due to the small energy barriers between stereochemical isomers. To explain the mechanisms of these dynamic processes both intramolecular and (or) intermolecular pathways are possible (14, 16–18), and no typical mechanism is responsible for these processes although most are described as intramolecular rearrangements. We are compiling structural and solution NMR data in order to better understand the dynamic behaviour and elucidate the mechanism of the ligand motion.

In this paper we describe the synthesis, X-ray structure, spectroscopic properties, and fluxional behaviour of the seven-coordinate complexes $(CH_3)_2AsC(CF_3)=C(CF_3)As(CH_3)_2$-$W(CO)_2I_2P(OC_6H_5)_3$ and $[(CH_3)_2AsC(CF_3)=C(CF_3)As(CH_3)_2]_2$-$W(CO)Br_2$ and spectroscopic properties of related seven-coordinate complexes.

Experimental section

General considerations

All reactions were carried out under an argon atmosphere using standard Schlenk tube techniques. Solvents were dried and purified by known procedures and distilled under nitrogen prior to use. The ligand *cis*-2,3-bis(dimethylarsino)-1,1,1,4,4,4-hexafluorobut-2-ene(L-L) (19, 20) and the starting complexes (L-L)$W(CO)_3I_2$ and (L-L)$W(CO)_3Br_2$ were prepared as previously described (16).

All seven-coordinate dicarbonyl complexes for which spectroscopic data are presented were prepared in a similar manner to that of (L-L)$W(CO)_2I_2P(OC_6H_5)_3$, discussed below. Specifically, the preparation of (L-L)$W(CO)_2I_2P(OCH_3)_3$ (11) and (L-L)$W(CO)_2Br_2P(C_6H_5)_3$ (12) have been previously described. The synthesis of the seven-coordinate monocarbonyl complex (L-L)$W(CO)Br_2[P(OCH_3)_3]_2$ has been previously described (10), and the iodo analogue was prepared in a similar manner to that of (L-L)$_2W(CO)Br_2$, discussed below, as was (L-L)$_2W(CO)I_2$.

The ^1H, ^{31}P-{^1H}, ^{19}F-{^1H}, and ^{13}C NMR data were recorded on a Bruker AC 200 QNP NMR spectrometer (^1H, 200.13 MHz; ^{31}P, 81.02 MHz; ^{19}F, 188.31 MHz; ^{13}C, 50.3 MHz). Chemical shifts are expressed in parts per million, downfield from $Si(CH_3)_4$ (^1H, ^{13}C), downfield (positive) or upfield (negative) from 85% H_3PO_4(^{31}P) and upfield (negative) from $CFCl_3$(^{19}F).

Infrared spectra were recorded on a Perkin–Elmer 1600 FT instrument in dichloromethane and are reported in cm^{-1}. Elemental analyses were measured using a Perkin–Elmer 2400 CHN elemental analyzer.

Table 1. Crystallographic data for (L-L)$W(CO)_2I_2P(OC_6H_5)_3$ and (L-L)$_2W(CO)Br_2$.

	(L-L)$W(CO)_2I_2P(OC_6H_5)_3$	(L-L)$_2W(CO)Br_2$
Mol. formula	$C_{28}H_{27}As_2F_6I_2O_5PW$	$C_{17}H_{24}As_4Br_2F_{12}OW$
Mol. wt.	1175.91	1115.58
Cryst. syst.	Monoclinic	Monoclinic
Space group	*C*2/*c*	$P2_1/c$
a, Å	24.444(2)	14.073(2)
b, Å	15.704(1)	14.523(2)
c, Å	19.038(1)	29.434(4)
β, deg	97.12(1)	105.08(2)
V, Å^3	7252	5808
Z	8	8
D_{calcd}, g cm^{-3}	2.15	2.55
D_{measd}, g cm^{-3}	2.20	2.48
F(0,0,0)	4400	4144
μ(Mo Kα), cm^{-1}	69.06	120.25
R^a	0.047	0.073
wR^b	0.063	0.100

^{a} $R = \Sigma||F_o| - |F_c||/\Sigma|F_o|$.
^{b} $wR = [\Sigma w(|F_o| - |F_c|)^2/\Sigma w|F_o|^2]^{1/2}$.

Preparation of (L-L)$W(CO)_2I_2P(OC_6H_5)_3$

The (L-L)$W(CO)_3I_2$ (0.25 g, 0.28 mmol) and $P(OC_6H_5)_3$ (0.12 g, 0.32 mmol) were refluxed in 50 mL of benzene for 17 h. The infrared spectra indicated complete conversion of the tricarbonyl complex to the dicarbonyl complex. The solvent was removed in vacuo, and the resulting yellow solid was washed with *n*-hexane to remove any unreacted $P(OC_6H_5)_3$ and was then recrystallized from a dichloromethane hexane mixture at –20°C to give 0.25 g (75%) of (L-L)$W(CO)_2I_2P(OC_6H_5)_3$. ^1H NMR ($CDCl_3$): 2.01 (s, 12H, $As(CH_3)_2$), 7.27 (m, 15H, $P(OC_6H_5)_3$); ^{31}P-{^1H}NMR ($CDCl_3$): 90.7 (s, W-P, $J(^{183}W$-$^{31}P) = 403$ Hz); ^{19}F-{^1H}NMR ($CDCl_3$): –53.1 (s, CF_3). Anal. calcd. for $C_{28}H_{27}As_2F_6I_2O_5PW$: C 28.57, H 2.30, I 21.60; found: C 28.90, H 2.29, I 21.77.

Preparation of (L-L)$_2W(CO)Br_2$

The (L-L)$W(CO)_3Br_2$ (0.25 g, 0.31 mmol) and (L-L) (0.25 g, 0.67 mmol) were refluxed in 50 mL of toluene for 22 h. The colour of the reaction mixture changed from yellow to orange to dark brown. Infrared spectroscopy indicated complete conversion of the tricarbonyl complex to the monocarbonyl complex. The solvent was removed in vacuo, and the resulting brown–black solid was recrystallized from a toluene–hexane mixture at –20°C to give 0.23 g (65%) of (L-L)$_2W(CO)Br_2$. ^1H NMR (CD_2Cl_2): 2.05 (s, $As(CH_3)_2$); ^{19}F-{^1H}NMR ($CDCl_3$): –50.6 (s, CF_3). Anal. calcd. for $C_{17}H_{24}As_4Br_2F_{12}OW$: C 18.29, H 2.15, Br 14.34; found: C 17.93, H 2.08, Br 14.81.

© 1998 NRC Canada

Table 2. Selected bond distances (Å) and angles (deg) for (L-L)W(CO)$_2$I$_2$P(OC$_6$H$_5$)$_3$.

Bond	Distance (Å)	Bond	Distance (Å)
W—As(1)	2.5603(7)	W—C(1)	1.942(7)
W—As(2)	2.6004(7)	W—C(2)	1.957(8)
W—I(1)	2.8684(6)	C(1)—O(1)	1.16(1)
W—I(2)	2.8698(7)	C(2)—O(2)	1.17(1)
W—P	2.457(2)		
Bond	**Angle (deg)**	**Bond**	**Angle (deg)**
As(1)-W-As(2)	76.02(2)	P-W-C(1)	110.7(2)
As(1)-W-I(1)	159.74(2)	P-W-C(2)	77.2(2)
As(1)-W-I(2)	76.88(4)	C(1)-W-C(2)	71.2(3)
As(1)-W-P	110.88(4)	W-C(1)-O(1)	179.1(7)
As(1)-W-C(1)	114.8(2)	W-C(2)-O(2)	176.6(6)
As(1)-W-C(2)	71.9(2)	W-As(1)-C(8)	109.7(2)
As(2)-W-I(1)	89.51(2)	W-As(1)-C(9)	114.9(3)
As(2)-W-I(2)	83.24(2)	W-As(1)-C(10)	120.6(3)
As(2)-W-P	161.67(4)	C(8)-As(1)-C(9)	110.7(4)
As(2)-W-C(1)	79.6(2)	C(8)-As(1)-C(10)	98.9(3)
As(2)-W-C(2)	121.0(2)	C(9)-As(1)-C(10)	100.6(4)
I(1)-W-I(2)	87.54(2)	W-As(2)-C(3)	118.7(3)
I(1)-W-P	79.09(4)	W-As(2)-C(4)	115.4(3)
I(1)-W-C(1)	75.4(2)	W-As(2)-C(5)	110.3(2)
I(1)-W-C(2)	128.2(2)	C(3)-As(2)-C(4)	104.5(5)
I(2)-W-P	82.00(4)	C(3)-As(2)-C(5)	101.8(4)
I(2)-W-C(1)	155.8(2)	C(4)-As(2)-C(5)	104.3(4)
I(2)-W-C(2)	132.7(2)		

Fig. 1. ORTEP diagram for (L-L)W(CO)$_2$I$_2$P(OC$_6$H$_5$)$_3$ showing the atomic labelling scheme with 50% probability thermal ellipsoids.

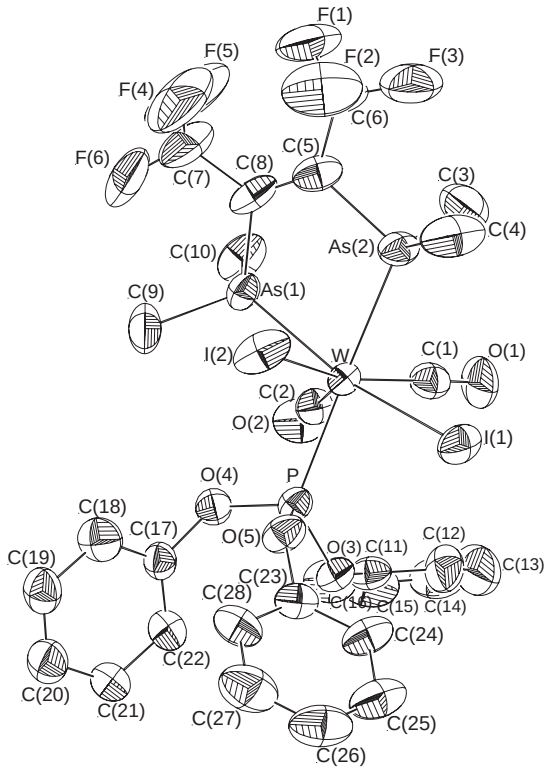

Crystallographic characterization of (L-L)W(CO)$_2$I$_2$P(OC$_6$H$_5$)$_3$

A yellow–orange crystal with approximate dimensions 0.41 × 0.44 × 0.45 mm was selected and coated with collodion. Preliminary investigation of the precession photographs showed symmetry and systematic extinction conditions (*hkl*: $h + k = 2n$; *h*01: h, $l = 2n$; and 0*k*0: $k = 2n$) indicative of the space group *C*2/*c* or *Cc*. The accurate unit cell parameters were obtained from the least-squares refinement of 24 reflections and their Friedel pairs in the 2θ range 35–45°, as observed on a modified Picker FACS-1 four-circle diffractometer. The intensity data were collected at 218 ± 4 K using an Enraf–Nonius Universal low-temperature device. Three standard reflections were measured after every 47 reflections. No significant decay was observed during data collection.

The intensities of 8291 independent reflections were measured for 2θ values between 3° and 55° of which 6663 were considered to be observed with $I \geq 2\sigma(I)$. Absorption corrections were applied using the Gaussian integration method. The crystal data are given in Table 1. The intensity statistics indicated the centrosymmetric space group *C*2/*c*. The structure was solved by combined direct methods and Fourier syntheses. All non-hydrogen atoms were refined anisotropically by the full-matrix least-squares method. Weights were assigned according to the REGWT program with $w = (\sigma_c^2 + \sigma_m^2)^{-1}$, where σ_c^2 is the variance and σ_m^2 is the term calculated by REGWT using iterative methods to remove the systematic trends with respect to *F* and sin θ/λ in the residuals of the structure factors (21). Several cycles of least-squares refinement were performed to achieve a convergence with a conventional *R* value of 0.047 and a weighted *R* value of 0.063. The maximum and average shift/esd of the least-squares parameters were 1.8×10^{-3} and 1.1×10^{-4}, respectively. In the final Fourier difference map a peak corresponding to 1.71 e Å^{-3} was located approximately 1.07 Å from the center of the W atom. The residual density near the heavy transition metal is not unexpected in light of the approximations used in the absorption corrections. All calculations were carried out using the XTAL 2.4 system of programs (22). Important bond lengths and bond angles are given in Table 2.[2] An ORTEP drawing showing the atomic labelling scheme is given in Fig. 1, and a schematic diagram showing the torsional angles in the five-membered ring of the chelate ligand for (L-L)W(CO)$_2$I$_2$P(OC$_6$H$_5$)$_3$ and (L-L)W(CO)$_2$I$_2$P(OCH$_3$)$_3$ is given in Fig. 2.

Crystallographic characterization of (L-L)$_2$W(CO)Br$_2$

Brown–black plates were crystallized from a toluene–hexane

[2] The supplementary material includes tables of atomic coordinates for the non-hydrogen atoms, additional bond distances and angles, anisotropic and isotropic thermal parameters, free energy values, and coalescence temperatures. The complete set of data (11 pages) may be purchased from: The Depository of Unpublished Data, Document Delivery, CISTI, National Research Council of Canada, Ottawa, Canada K1A 0S2. Tables of atomic coordinates for the non-hydrogen atoms and additional bond distances and angles have also been deposited with the Cambridge Crystallographic Data Centre, and can be obtained on request from The Director, Cambridge Crystallographic Data Centre, University Chemical Laboratory, 12 Union Road, Cambridge, CB2 1EZ, U.K. Two tables of observed and calculated structure factors (94 pages) can be obtained from the corresponding author.

© 1998 NRC Canada

Table 3. Selected bond distances (Å) and angles (deg) for $(L\text{-}L)_2W(CO)Br_2$.

Bond	Distance (Å)	Bond	Distance (Å)
W—As(1)	2.573(2)	W′—As(1)′	2.575(2)
W—As(2)	2.626(3)	W′—As(2)′	2.620(2)
W—As(3)	2.578(3)	W′—As(3)′	2.577(2)
W—As(4)	2.585(2)	W′—As(4)′	2.584(2)
W—Br(1)	2.624(3)	W′—Br(1)′	2.624(3)
W—Br(2)	2.647(3)	W—Br(2)′	2.664(3)
W—C(1)	1.78(2)	W′—C(1)′	1.78(2)
C(1)—O(1)	1.22(3)	C(1)′—O(1)′	1.19(3)
Bond	**Angle (deg)**	**Bond**	**Angle (deg)**
As(1)-W-As(2)	80.30(8)	W-As(1)-C(2)	121.0(7)
As(3)-W-As(4)	75.63(8)	W-As(1)-C(3)	116.1(8)
As(1)-W-Br(1)	76.51(9)	W-As(1)-C(4)	110.6(7)
As(1)-W-Br(2)	71.9(9)	C(2)-As(1)-C(3)	100(1)
As(1)-W-As(3)	137.36(8)	C(2)-As(1)-C(4)	100(1)
As(1)-W-As(4)	145.91(9)	C(3)-As(1)-C(4)	106(1)
As(1)-W-C(1)	84.5(7)	W-As(2)-C(5)	106.1(7)
As(2)-W-C(1)	164.8(7)	W-As(2)-C(8)	121.8(8)
As(2)-W-Br(1)	82.30(10)	W-As(2)-C(9)	118.9(7)
As(2)-W-Br(2)	76.51(10)	C(5)-As(2)-C(8)	98.7(9)
As(2)-W-As(3)	106.17(9)	C(5)-As(2)-C(9)	104(1)
As(2)-W-As(4)	100.57(8)	C(8)-As(2)-C(9)	103(1)
As(3)-W-Br(1)	145.51(9)	W-As(3)-C(10)	124.1(7)
As(3)-W-Br(2)	69.00(9)	W-As(3)-C(11)	110.8(8)
As(3)-W-C(1)	85.9(7)	W-As(3)-C(12)	113.9(7)
As(4)-W-C(1)	91.2(7)	C(10)-As(3)-C(11)	103(1)
As(4)-W-Br(1)	69.93(8)	C(10)-As(3)-C(12)	99(1)
As(4)-W-Br(2)	141.77(10)	C(11)-As(3)-C(12)	102(1)
Br(1)-W-C(1)	92.9(7)	W-As(4)-C(13)	114.4(6)
Br(2)-W-C(1)	100.1(7)	W-As(4)-C(16)	120.5(7)
Br(1)-W-Br(2)	144.39(10)	W-As(4)-C(17)	115.6(7)
As(3)-W-As(4)	75.63(8)	C(13)-As(4)-C(16)	103(1)
As(1)′-W′-As(2)′	80.38(8)	C(13)-As(4)-C(17)	97(1)
As(3)′-W′-As(4)′	75.75(8)	C(16)-As(4)-C(17)	102(1)
As(1)′-W′-Br(1)′	77.03(8)	W-C(1)-O(1)	176(1)
As(1)′-W′-Br(2)′	71.72(9)	W′-As(1)′-C(2)′	122.2(6)
As(1)′-W′-As(3)′	136.89(8)	W′-As(1)′-C(3)′	116.1(7)
As(1)′-W′-As(4)′	146.41(9)	W′-As(1)′-C(4)′	110.0(7)
As(1)′-W′-C(1)′	85.3(7)	C(2)′-As(1)′-C(3)′	99(1)
As(2)′-W′-C(1)′	165.7(7)	C(2)′-As(1)′-C(4)′	100(1)
As(2)′-W′-Br(1)′	82.50(10)	C(3)′-As(1)′-C(4)′	106(1)
As(2)′-W′-Br(2)′	77.20(9)	W′-As(2)′-C(5)′	106.9(7)
As(2)′-W′-As(3)′	105.95(9)	W′-As(2)′-C(8)′	121.3(7)
As(2)′-W′-As(4)′	100.07(8)	W′-As(2)′-C(9)′	119.1(7)
As(3)′-W′-Br(1)′	145.50(9)	C(5)′-As(2)′-C(8)′	99(1)
As(3)′-W′-Br(2)′	68.53(8)	C(5)′-As(2)′-C(9)′	103(1)
As(3)′-W′-C(1)′	84.9(7)	C(8)′-As(2)′-C(9)′	103(1)
As(4)′-W′-C(1)′	91.5(6)	W′-As(3)′-C(10)′	123.9(7)
As(4)′-W′-Br(1)′	69.81(8)	W′-As(3)′-C(11)′	110.8(7)
As(4)′-W′-Br(2)′	141.55(10)	W′-As(3)′-C(12)′	113.7(7)
Br(1)′-W′-C(1)′	93.8(7)	C(10)′-As(3)′-C(11)′	104(1)
Br(2)′-W′-C(1)′	98.9(6)	C(10)′-As(3)′-C(12)′	99(1)
Br(1)′-W′-Br(2)′	145.00(10)	C(11)′-As(3)′-C(12)′	102(1)
As(3)′-W′-As(4)′	75.75(8)	W′-As(4)′-C(13)′	114.9(7)
W′-As(4)′-C(16)′	120.0(7)	C(13)′-As(4)′-C(17)′	99(1)
W′-As(4)′-C(17)′	114.4(7)	C(16)′-As(4)′-C(17)′	102(1)
C(13)′-As(4)′-C(16)′	103(1)	W′-C(1)′-O(1)′	175(1)

Fig. 2. Schematic diagram showing the torsional angles in the five-membered ring of the chelate ligand for $(L\text{-}L)W(CO)_2I_2P(OC_6H_5)_3$ (top numbers) and the related complex $(L\text{-}L)W(CO)_2I_2P(OCH_3)_3$ (bottom numbers).

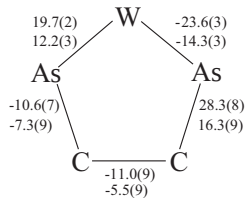

mixture at –20°C under an inert atmosphere. A hexagonal plate with approximate dimensions 0.39 × 0.22 × 0.19 mm was selected and coated with collodion. Precession photographs showed systematic extinction conditions ($h0l$: $l = 2n$; $0k0$: $k = 2n$) and symmetry indicative of the space group $P2_1/c$. The accurate unit cell parameters were obtained from the least-squares refinement of 36 reflections in the 2θ range 25–45°, observed as for the previous compound. The data were collected at 203 ± 4 K. The intensities of three standard reflections, measured after every 47 data points, showed an average decay of 20% over the period of the data collection.

The intensities of 7611 reflections were measured (hkl, $hk\bar{l}$ for 2θ values in the range 3–45°) of which 5364 were considered to be observed with $I \geq 2\sigma(I)$. The data were corrected for the decay in the standard reflections, and absorption corrections were applied as for the previous compound. Faces of the crystal were not well defined and were approximated. The crystal data are given in Table 1. The structure has two independent molecules in the unit cell. The structure was solved by the heavy-atom method, using direct methods to confirm the positions of the two tungsten atoms. The remaining non-hydrogen atoms were found from successive Fourier maps. The positions of the hydrogen atoms were not apparent on the difference maps. The structure was refined by full-matrix least squares, treating the tungsten, arsenic, bromine, and fluorine atoms anisotropically and the carbon and oxygen atoms isotropically. Weights were assigned as $w = \sigma_c^{-2}$, where σ_c^2 is the variance in F as calculated from counting statistics and the instability factor.

The refinement converged to a conventional R value of 0.073 and a weighted R value of 0.10. These high values reflect the decay of the sample during data collection and the poor quality of the sample as manifested by a large number of weak reflections. The maximum and average shift/esd were 1.2×10^{-3} and 3.1×10^{-5}, respectively, at the end of refinement. The coordinates of the two independent molecules were approximately related by the operator $1/2 + x$, $1/2 - y$, z. If this relation were exact, reflections $h0l$ would be absent. The data showed that these reflections were weak but not absent. Further examination showed that they were not due to multiple scattering. Therefore, the apparent symmetry is only approximate. Pairs of residual electron-density peaks, with a maximum height of 3.6 e Å^{-3}, were observed near each of the tungsten, bromine, and arsenic atoms, reflecting the limitations in the approximate absorption corrections.

All calculations were carried out using the XTAL 2.4 system of programs (22). Important bond lengths and angles are given in Table 3. The labelling for the two molecules are

© 1998 NRC Canada

Fig. 3. ORTEP diagram for $(L\text{-}L)_2W(CO)Br_2$ showing the atomic labelling scheme for the unprimed molecule with 50% probability thermal ellipsoids.

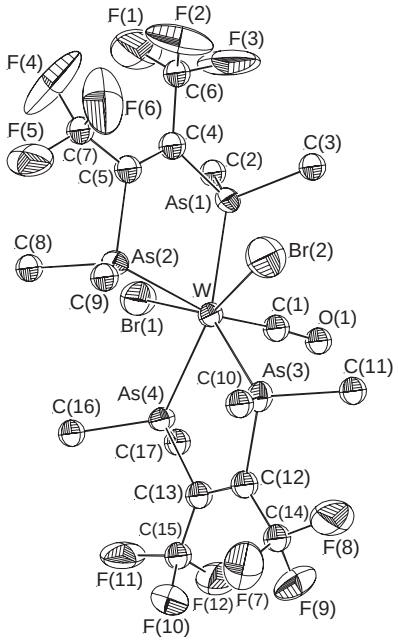

identical except that the chemical symbols for one are primed. An ORTEP drawing showing the labelling scheme for the unprimed molecule is given in Fig. 3.

Results and discussion

Synthesis of the seven-coordinate complexes

The dicarbonyl complexes containing a monodentate phosphine or phosphite ligand were readily synthesized from the corresponding tricarbonyl complexes in refluxing benzene. More vigorous conditions (refluxing toluene) were necessary to form the monocarbonyl complexes; attempts yielded only $(L\text{-}L)_2W(CO)X_2$ and $(L\text{-}L)W(CO)X_2[P(OCH_3)_3]_2$ (X = Br, I). Presumably there is congestion around the tungsten atom with ligands such as $P(C_6H_5)_3$, $P(OC_6H_5)_3$, $P(OC_2H_5)_3$, and $P(C_4H_9)_3$.

Crystal structure of $(L\text{-}L)W(CO)_2I_2P(OC_6H_5)_3$

The tungsten atom is seven-coordinate with the coordination sphere containing the two arsenic atoms of the L-L ligand, two iodine atoms, two carbon atoms of the carbonyl groups, and the phosphorus atom of the triphenylphosphite group. To determine the stereochemistry of the title compound we have used the δ parameters of Porai–Koshits and Aslanov (23), as calculated by Muetterties and Guggenberger (13). The δ parameter values (21°, 17°, 6°), when compared with the idealized monocapped octahedron (24.2°, 24.2°, 24.2°) and the idealized monocapped trigonal prism (0°, 0°, 41.5°), indicate the geometry to be closer to a monocapped octahedron. For this geometry the capping atom is the C(2) carbonyl group with the capped face containing the As(1), C(1), and P atoms. Kepert (24) has shown that seven-coordinate complexes containing one bidentate ligand with a normalized *bite* (defined as the distance between points representing the donor atoms of the bidentate ligands on a sphere of unit radius and with the same angles subtended at the center as in the real coordination polyhedron) less than 1.11 would be expected to exhibit pentagonal–bipyramidal geometry, and those with a normalized *bite* greater than 1.11 would be expected to exhibit either monocapped octahedral or monocapped trigonal prismatic geometry. The observed geometry of the tungsten complex with a normalized *bite* of 1.24 for the L-L ligand is in accord with Kepert's (24) conclusions. A similar geometry is observed for the related complex $(L\text{-}L)W(CO)_2I_2P(OCH_3)_3$ with an L-L normalized *bite* of 1.23 (11). Both complexes also exhibit other features associated with a monocapped octahedral geometry. The mean $C_c\text{-}W\text{-}A_c$ and $C_c\text{-}W\text{-}A_u$ angles (C_c is a capping atom, A_c is an atom in the capped face, and A_u is an atom in the uncapped face) are 73.4° and 127.3° for the triphenylphosphite compound and 72.7° and 127.8° for the trimethyl phosphite complex (11), respectively, with corresponding angles for an ideal monocapped octahedron being 74.1° and 125.5° (25). The other feature is that the unique capping atom has very close contacts with the three atoms in the capped face. Thus in the triphenylphosphite complex the capping carbon is 2.27, 2.69, and 2.77 Å from the C, As, and P atoms, respectively, in the capped face and in the related trimethyl phosphite complex 2.28, 2.71, and 2.69 Å from these atoms (11).

The five-membered ring of the chelate ligand shows a moderate degree of puckering in both the triphenylphosphite and trimethyl phosphite complexes. The torsional angles for both complexes are shown in Fig. 2. The ring-puckering parameters, according to the method of Cremer and Pople (26) are $q = 0.42$ and $\phi = 14°$ for $(L\text{-}L)W(CO)_2I_2P(OC_6H_5)_3$ and $q = 0.26$ and $\phi = 10.1°$ for $(L\text{-}L)W(CO)_2I_2P(OCH_3)_3$ (11), indicating a moderate degree of puckering, intermediate between a twist and envelope conformation. The greater degree of puckering in the triphenylphosphite complex is primarily due to the presence of the bulky phenyl rings compared to the methyl groups. The tetrahedral coordination of the arsenic atoms is also distorted by the contacts.

The two carbon monoxide ligands are in a *cis* arrangement to each other (71.2°), the arrangement required in order to minimize competition for dπ electron density from the d^4 tungsten atom. The lengths of the two W—As bonds are significantly different from each other at 2.5603(7) and 2.6004(7) Å, which can be explained by a consideration of their respective *trans* ligands. The I(1) atom *trans* to As(1) is not as strong an acceptor as the P atom *trans* to As(2), resulting in greater back donation to As(1). This results in a shortening of the W—As(1) bond compared to the W—As(2) bond, the difference being 0.04(1) Å. The average W—I bond length of 2.87 Å in this complex is close to the average of 2.85 Å reported for similar complexes (27, 28). The W—P bond length of 2.457(2) Å is similar to that in $(L\text{-}L)W(CO)_2I_2P(OCH_3)_2$ (2.466(3) Å) (11) but considerably shorter as compared to $(L\text{-}L)W(CO)_2Br_2P(C_6H_5)_3$ (2.548(2) Å) (12). This difference may reflect both the steric restrictions of the greater bulk of the $P(C_6H_5)_3$ groups and the presence of more double-bond character through back donation from the tungsten in $(L\text{-}L)W(CO)_2I_2P(OC_6H_5)_3$. These results are in accord with differences in the π-acceptor ability of the phosphorus ligands.

Crystal structure of $(L\text{-}L)_2W(CO)Br_2$

The structure contains two crystallographically independent

© 1998 NRC Canada

Fig. 4. Schematic diagram showing the torsional angles in the two five-membered rings of the chelate ligands for $(L\text{-}L)_2W(CO)Br_2$. As(1) and As(2) occupy equatorial and axial positions, respectively; As(3) and As(4), equatorial positions. The top numbers refer to each ring of the unprimed molecule and the bottom numbers to each corresponding ring of the primed molecule.

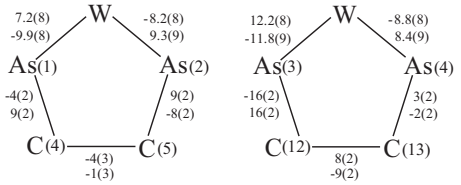

molecules that are related as near enantiomers. They are chemically equivalent; equivalent metal—ligand bond distances differ by less than 0.02 Å, equivalent interligand distances differ by an average of 0.04 Å, and intramolecular bond angles agree within 2.5°. In both molecules the two L-L ligands chelate the metal to form a seven-coordinate tungsten (II) complex with the two bromine atoms and the carbonyl group. The tungsten atom has a slightly distorted pentagonal bipyramidal geometry. The δ parameters of Porai–Koshits and Aslanov (23) are 37° and 52°. In the pentagonal bipyramid the third δ parameter represents an interatomic vector internal to the polyhedron. The δ values for an ideal pentagonal bipyramid with identical ligands are both 54.4°. The equatorial plane of the pyramid is occupied by an L-L ligand, the two bromine atoms, and one arsenic atom of the other L-L ligand, leaving the second arsenic atom and the carbonyl group to fill the apical positions. The tungsten atom is displaced from the average plane of the pentagonal ring by 0.0144(2) Å. Thus this less symmetric pentagonal bipyramid has fewer steric constraints than the more symmetric one with both L-L ligands in the pentagonal plane, with repulsions between the methyl groups on adjacent arsenic atoms.

This type of geometry is rare (29, 30) for seven-coordinate carbonyl complexes of the type $MX_2(CO)_nL_{5-n}$ (M = Mo, W; n = 1–3). The tungsten—carbon bond is unique, being extremely short (1.78(2) Å) compared to a related monocarbonyl complex (10) containing two monodentate $P(OCH_3)_3$ ligands (1.86(3) Å) and the related dicarbonyl complexes (11, 12) (average 1.94 Å). The relative shortness of the tungsten—carbon bond here represents considerable double-bond character arising from back donation of π electrons from tungsten.

The four five-membered rings of the chelate ligands in the two independent molecules of $(L\text{-}L)_2W(CO)Br_2$ show a variation in conformation. Their torsional angles are shown in Fig. 4. One of the two chelates in each independent molecule has a *bite* that spans from the equatorial plane of the pentagonal bipyramid to one of the axial vertices (equatorial–axial), involving the atoms As(1) and As(2). The other chelate in each molecule has a *bite* that forms an edge of the equatorial plane (equatorial–equatorial), involving the atoms As(3) and As(4).

Because of the approximate enantiomorphic relation between the two independent molecules, the torsional angles of their equatorial–equatorial five-membered rings have similar torsional angle magnitudes but with opposite signs. This is further illustrated by the ring-puckering parameters of Cremer and Pople (26), which show similar puckering amplitudes (0.20 for each) and puckering phase angles different by approximately 180° (200° in one molecule and 22° in the other molecule). These phase angles correspond to the twist conformation of a five-membered ring. The equatorial–axial chelates are less similar, with puckering amplitudes of 0.15 and 0.18, and the respective puckering phase angles of 168° and 1°. These phase angles correspond to an intermediate twist-boat conformation and a boat conformation, respectively. In this case, four of the torsional angles show opposite signs, with the fifth small and negative in both cases.

Table 4. The ν(CO) and ^{13}C NMR data (carbonyl region) for seven-coordinate complexes.

Complex	ν(CO) (cm^{-1})[a]	δ (ppm)[b]	$^2J(^{13}C\text{-}^{31}P)$ (Hz)
$(L\text{-}L)W(CO)_2I_2P(OC_6H_5)_3$	1959 (vs)	212.4(d)	9.3
	1875 (s)	240.4(d)	39.9
$(L\text{-}L)W(CO)_2Br_2P(OC_6H_5)_3$	1956 (vs)	217.0(d)	8.3
	1872 (s)	245.8(d)	37.0
$(L\text{-}L)W(CO)_2I_2P(OCH_3)_3$	1948 (vs)	215.0(d)	9.7
	1870 (s)	240.4(d)	42.1
$(L\text{-}L)W(CO)_2Br_2P(OCH_3)_3$	1950 (vs)	220.0(d)	5.8
	1868 (s)	246.1(d)	39.6
$(L\text{-}L)W(CO)_2I_2P(C_6H_5)_3$	1937 (vs)	216.7(d)	5.1
	1855 (s)	246.5(d)	29.0
$(L\text{-}L)W(CO)_2Br_2P(C_6H_5)_3$	1940 (vs)	222.2(d)	5.0
	1854 (s)	250.8(d)	27.3
$(L\text{-}L)W(CO)I_2[P(OCH_3)_3]_2$	1833	254.8(dd)	37.0, 39.6
$(L\text{-}L)W(CO)Br_2[P(OCH_3)_3]_2$	1829	259.0(dd)	34.8, 36.0
$(L\text{-}L)_2W(CO)I_2$	1811	241.5(s)	
$(L\text{-}L)_2W(CO)Br_2$	1809	260.5(s)	

[a] Spectra were recorded in CH_2Cl_2; vs = very strong, s = strong.

[b] Spectra were recorded in CD_2Cl_2 at 200 K in the presence of a trace amount of [Cr(acac)$_3$]; s = singlet, d = doublet, dd = doublet of doublets.

Spectroscopic properties of $(L\text{-}L)W(CO)_2I_2P(OC_6H_5)_3$ and related seven-coordinate dicarbonyl complexes

Table 4 lists carbonyl IR stretching frequencies and ^{13}C NMR data, and Table 5 lists $^{19}F\text{-}\{^1H\}$ and $^{31}P\text{-}\{^1H\}$ NMR data for all the seven-coordinate complexes under study. The observation of a single As–CH_3 resonance in the ^1H NMR spectrum (297 K) and a single CF_3 resonance in the $^{19}F\text{-}\{^1H\}$ NMR spectrum of $(L\text{-}L)W(CO)_2I_2P(OC_6H_5)_3$ are not consistent with the molecule having a static solution structure equivalent to that determined from the X-ray determination. The static structure consistent with the solid-state structure is frozen out at 200 K. Thus, As–CH_3 resonances are found at 1.50, 1.84, 2.51, two CF_3 quartets at –52.2 and –53.8, and two ^{13}C doublets (carbonyl region) at 212.4 and 240.4. It is assumed that accidental degeneracy may have caused the 1:2:1 As–CH_3 triplet, since all other related complexes exhibited four equal-area As–CH_3 resonances. The dicarbonyl complexes are related as shown by the similarity of carbonyl stretching frequencies, chemical shifts, coupling constants, and variable temperature ^1H and $^{19}F\text{-}\{^1H\}$ NMR data. As the temperature is increased, four As–CH_3 peaks (three for the title compound) indicative of the low-temperature slow-exchange limiting spectra coalesce into two peaks. The line broadening continues until an averaged

© 1998 NRC Canada

Table 5. The ^{19}F-{^{1}H} and ^{31}P-{^{1}H} NMR data for seven-coordinate complexes.

Complex	δ(^{19}F) (ppm)[a] 297 K	δ(^{19}F) (ppm)[a] 210 K	$J(^{19}F\text{-}^{19}F)$ (Hz)	δ(^{31}P) (ppm)[b]	$J(^{31}P\text{-}^{183}W)$ (Hz)
(L-L)W(CO)$_2$I$_2$P(OC$_6$H$_5$)$_3$	–53.1 (s)	–52.2 (q, 3F) –53.8 (q, 3F)	14.3	90.7	402.8
(L-L)W(CO)$_2$Br$_2$P(OC$_6$H$_5$)$_3$	–51.4 (s)	–50.7 (q, 3F) –52.3 (q, 3F)	14.1	101.1	406.1
(L-L)W(CO)$_2$I$_2$P(OCH$_3$)$_3$	–51.5 (s)	–51.5 (m, 6F)	—	104.7	364.7
(L-L)W(CO)$_2$Br$_2$P(OCH$_3$)$_3$	–51.3 (s)	–51.4 (m, 6F)	—	112.3	377.1
(L-L)W(CO)$_2$I$_2$P(C$_6$H$_5$)$_3$	–52.2 (s)	–52.3 (m, 6F)	—	–7.1	216.1
(L-L)W(CO)$_2$Br$_2$P(C$_6$H$_5$)$_3$	–51.1 (s)	–51.4 (m, 6F)	—	4.8	222.3
(L-L)W(CO)I$_2$[P(OCH$_3$)$_3$]$_2$	–52.7 (s)	–53.0 (q, 3F) –54.1 (q, 3F)	14.3	104.5 130.2 $^{2}J(^{31}P\text{-}^{31}P)$ = 31.9 Hz	411.9 389.5
(L-L)W(CO)Br$_2$[P(OCH$_3$)$_3$]$_2$	–51.7 (s)	–51.1 (q, 3F) –52.3 (q, 3F)	14.3	113.5 138.3 $^{2}J(^{31}P\text{-}^{31}P)$ = 30.8 Hz	418.1 384.5
(L-L)$_2$W(CO)I$_2$	–50.7 (s)	–51.0 (m)	—	—	—
(L-L)$_2$W(CO)Br$_2$	–50.6 (s)	–51.0 (m)	—	—	—

[a] Spectra were recorded in CD_2Cl_2; s = singlet, q = quartet, m = A_3B_3 multiplet.
[b] Each resonance (297 K) appeared as a singlet with ^{183}W satellites except for (L-L)W(CO)X$_2$[P(OCH$_3$)$_3$]$_2$ (X = Br, I) for which each resonance (210 K) appeared as a doublet with ^{183}W satellites.

single As–CH_3 resonance is observed, indicative of the high-temperature fast-exchange limiting spectra.

The ^{13}C chemical shifts (carbonyl region), carbonyl stretching frequencies, and $J(^{31}P\text{-}^{183}W)$ values are consistent with the electronic differences of the three phosphorus monodentate ligands in which P(C$_6$H$_5$)$_3$ is a better net donor: P(OC$_6$H$_5$)$_3$, P(OCH$_3$)$_3$, P(C$_6$H$_5$)$_3$. An examination of the low-temperature ^{13}C chemical shifts in Table 4 shows two unique resonances for the dicarbonyl complexes, one that is approximately 30 ppm downfield from the other. For the title dicarbonyl complex the downfield resonance is assigned to the unique capping carbonyl group consistent with the work of Colton and Kevekordes (31), where they assigned the low field carbonyl chemical shift absorption to the capping carbon in a structure best described as a monocapped octahedron. Another unique feature of the ^{13}C NMR data is the large differences in $^{2}J(^{13}C\text{-}^{31}P)$ values that are consistent with *cis* coupling. Previous work has shown an average $^{2}J(^{13}C\text{-}^{31}P)$ value of 32 Hz for angles subtended at tungsten by the phosphorus and carbonyl carbon in the range of 72–78° and a $^{2}J(^{13}C\text{-}^{31}P)$ value of 6 Hz for a corresponding angle of 95° (25, 32–34). On this basis the larger $^{2}J(^{13}C\text{-}^{31}P)$ value could be assigned to the carbonyl with a P-W-C angle in the range 70–80° and the lower $^{2}J(^{13}C\text{-}^{31}P)$ value to the carbonyl with a P-W-C angle above 100°. For the title dicarbonyl complex, the capping carbonyl (<P-W-C = 77.2°) is assigned the resonance with $^{2}J(^{13}C\text{-}^{31}P)$ = 39.9 Hz, and the noncapping carbonyl (<P-W-C = 110.7°) the resonance with $^{2}J(^{13}C\text{-}^{31}P)$ = 9.3 Hz. These assignments are compatible with the earlier assignments made for the carbonyl group chemical shift on the basis of the unique capping position.

In view of the difficulty in assigning a configuration for seven-coordinate complexes based on multinuclear NMR data, we believe ^{13}C chemical shifts and $^{2}J(^{13}C\text{-}^{31}P)$ values provide important insights in elucidating structural considerations.

There have been many possible pathways suggested to explain the fluxional behaviour in seven-coordinate compounds involving dissociative processes and intramolecular rearrangements. Dissociative processes such as phosphite or phosphine dissociation or carbonyl dissociation for the dicarbonyl complexes can be eliminated by the fact that the ^{31}P-{^{1}H} fast-exchange limiting NMR spectra exhibited $^{31}P\text{-}^{183}W$ coupling, and ^{13}C fast-exchange limiting NMR spectra exhibited both $^{13}C\text{-}^{183}W$ and $^{13}C\text{-}^{31}P$ coupling. Dissociation of one end of the chelated ligand would probably require a much higher barrier than that which is observed ($\Delta G^{\neq}$ values in the range 45.1–54.0 kJ/mol).

The activation energy barriers $\Delta G^{\neq}$ for methyl group exchange (calculated from the Eyring equation (35) at the coalescence temperature) show an increase, with an increase in the size of the halide and the bulk of the phosphorus ligand, consistent with an intramolecular process (36) in which the tungsten—halide and tungsten—phosphorus bonds are retained throughout the dynamic process.

To explain the dynamic behaviour of the title compound an exchange process can be envisaged, which itself varies over a narrow temperature range. The process might begin with random scrambling of the atoms I(1), C(1), and P, leaving the atom I(2) rigidly held in the "pocket" of the chelate ring. This would equilibrate the atoms C(4) and C(9) as one pair, and the atoms C(3) and C(10) as the other pair. As the temperature is raised further the atom I(2) is gradually added to the random scrambling motion, causing coalescence to a single peak. The $\Delta G^{\neq}$ value associated with the lower temperature part of the process is 51.7(2) kJ/mol and with the higher temperature part of the process is 54.0(2) kJ/mol. The similarity of these two values supports the description of the phenomenon responsible for the coalescence as being one process.

Spectroscopic properties of (L-L)$_2$W(CO)Br$_2$ and related seven-coordinate monocarbonyl complexes

As with the previous complex, the observations of a single As–CH_3 resonance in the ^{1}H NMR spectrum (297 K) and a

© 1998 NRC Canada

Fig. 5. Schematic diagram illustrating a pathway for the dynamic behaviour for $(L\text{-}L)_2W(CO)Br_2$.

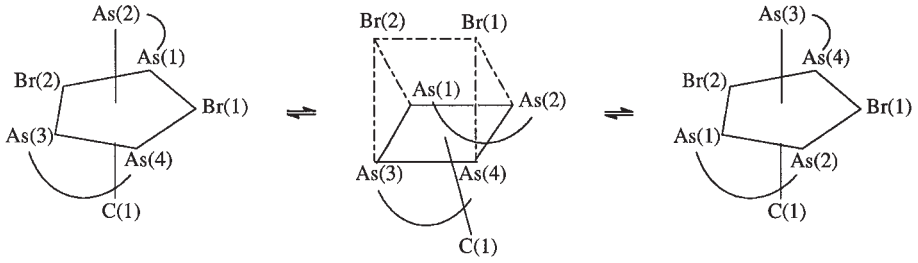

Fig. 6. Schematic diagram illustrating a pathway for the dynamic behaviour for $(L\text{-}L)W(CO)Br_2[P(OCH_3)_3]_2$.

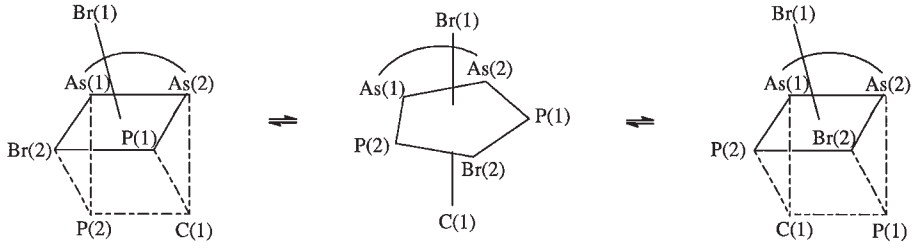

single CF_3 resonance in the $^{19}F\text{-}\{^1H\}$NMR spectrum of $(L\text{-}L)_2W(CO)Br_2$ are not consistent with the X-ray crystal structure, suggesting dynamic behaviour. Lowering the temperature to 180 K produced two As–CH_3 resonances at 1.76 and 2.15 and a complex CF_3 multiplet centred at –51.0. Further lowering of the temperature to 170 K (lowest attainable due to solvent limitations) caused the low field As–CH_3 resonance to broaden. Thus it was not possible to obtain a low-temperature slow-exchange limiting spectrum indicative of the solid-state X-ray crystal structure. The $\Delta G^{\neq}$ value of 43.5 kJ/mol is comparatively low for a complex containing two bidentate ligands relative to the dicarbonyl complexes; perhaps the small *bite* of the two L-L ligands provides extra space around the tungsten centre for other ligands, thus enhancing the possibility for rearrangements.

A nondissociative mechanism consistent with the NMR data could involve a concerted rearrangement in which the roles of the two bidentate L-L ligands are reversed, and the environments of their methyl groups are also equilibrated. An intermediate polyhedron between the two pentagonal bipyramidal geometries is a monocapped trigonal prism, with the carbonyl ligand capping the quadrilateral face formed by the four arsenic atoms as illustrated in Fig. 5. Then the polyhedron found in the crystal can be generated from it by moving any one of the four As atoms through the Br- -Br edge of that polyhedron to become the apical polyhedron of the pentagonal bipyramid, leaving its ligand mate near the pentagonal plane between the two Br atoms.

If the pentagonal symmetry is not fully formed, as is seen in the crystal structure, then there will be a tendency for relaxation back to the monocapped trigonal prism intermediate polyhedron to proceed along the same route as that by which the pentagonal bipyramid was formed. This would then leave two broad peaks, corresponding to the As–CH_3 resonances for the CH_3 on the two sides of the plane of the intermediate. The deviations from the full symmetry of the pentagonal bipyramid are associated with the puckering of the plane of the bidentate ligand. However, if the full symmetry of the pentagonal bipyramid is formed at higher temperature, then relaxation back to the intermediate polyhedron may take place with equal probability for the apical As to arrive back in the monocapped trigonal pyramid sharing an edge with Br(1) or with Br(2). Then all eight As–CH_3 resonances would be equilibrated.

Attempts to produce other related monocarbonyl complexes have only yielded $(L\text{-}L)W(CO)X_2[P(OCH_3)_3]_2$ (X = Br, I). We have previously published the X-ray crystal structure of $(L\text{-}L)W(CO)Br_2[P(OCH_3)_3]_2$ (10) and have included extensive spectroscopic data in the present paper. Low-temperature NMR studies of the trimethylphosphite monocarbonyl complex suggest a static structure consistent with the X-ray crystal structure (best described as a monocapped trigonal prism with a Br in the capping position and two As atoms, a P, and a Br atom in the quadrilateral capped face; four ^1H As-CH_3 singlets; and two $^{31}P\text{-}\{^1H\}$doublets). As the temperature is increased the four As–CH_3 resonances coalesce into two and then into an averaged As–CH_3 resonance. Similarly, the two $^{31}P\text{-}\{^1H\}$doublets coalesce into a single resonance with ^{183}W satellites. The $\Delta G^{\neq}$ values (51.3 and 69.7 kJ/mol) are considerably higher than the previously discussed monocarbonyl containing the two bidentate L-L ligands, reflecting a greater steric hindrance exerted by the bulkier $P(OCH_3)_3$ monodentate ligands. The equilibration of four As–CH_3 resonances into two and two ^{31}P resonances into one can be rationalized by the dynamic behaviour illustrated in Fig. 6, producing a pentagonal bipyramidal intermediate with $As_1As_2Br_2P_1P_2$ in the equatorial plane. This would equilibrate the As–CH_3 groups above the pentagonal plane as one set and As–CH_3 groups below the pentagonal plane as the other set as well as equilibrating the two ^{31}P environments of the trimethylphosphite ligands. The equilibration of two As–CH_3 resonances into one at a coalescence temperature of 348 K occurs with a higher activation energy than that for the first process (69.7 vs. 51.3 kJ/mol), suggesting either a dissociative process or a high-energy random scrambling process. The possibility of phosphorus dissociation can be eliminated on the basis of the retention of $J(^{31}P\text{-}^{183}W)$ coupling in the high-temperature fast-exchange limiting spectra.

Finally, the low-temperature ^{13}C NMR data (carbonyl

© 1998 NRC Canada

region) are consistent with *cis* coupling on the basis of $^2J(^{13}C-^{31}P)$ values (Table 4), and the values of 34.8 and 36.0 Hz for the bromomonocarbonyl are consistent with the angles subtended at tungsten by the phosphorus and carbonyl carbon atoms (71° and 76°) (10), a correlation previously discussed for the dicarbonyl complexes.

To determine the influence of the bidentate ligand and to provide additional ^{31}P NMR parameters that were lacking in this study further work is continuing in the area of seven coordination incorporating the ligands $(C_6H_5)_2PCH_2P(C_6H_5)_2$, $(C_6H_5)_2PCH_2CH_2P(C_6H_5)_2$, and *cis*-$(C_6H_5)_2PCH{=}CHP(C_6H_5)_2$. This work is aimed at the study of monocarbonyl complexes containing two identical bidentate ligands and two different bidentate ligands. In addition the potential use of ^{183}W NMR is being investigated.

Acknowledgment

We thank the Faculty of Science, University of Regina, for financial support and Quinn Major for computing assistance.

References

1. F.A. Cotton, L.R. Falvello, and J.H. Meadows. Inorg. Chem. **24**, 514 (1985).
2. A. Mercer and J. Trotter. Can. J. Chem. **52**, 3331 (1974).
3. A.L. Beauchamp, F. Belanger-Gariepy, and S. Arali. Inorg. Chem. **24**, 1860 (1985).
4. M.G.B. Drew and J.D. Wilkins. J. Chem. Soc. Dalton Trans. 2664 (1973).
5. F.A. Cotton and M. Matusz. Polyhedron, **6**, 261 (1987).
6. A. Blagg, A.T. Hutton, and B.L. Shaw. Polyhedron, **6**, 95 (1987).
7. P.K. Baker, M.B. Hursthouse, A.I. Karaulov, A.J. Lavery, K.M. Abdul Malik, D.J. Muldoon, and A. Shawcross. J. Chem. Soc. Dalton Trans. 3493 (1994).
8. R.P.K. Babu, S.S. Krishnamurthy, and M. Nethaji. Organometallics, **14**, 2047 (1995).
9. P.K. Baker, M.E. Harman, S. Hughes, M.B. Hursthouse, and K.M. Abdul Malik. J.Organomet. Chem. **498**, 257 (1995).
10. L. Mihichuk, M. Pizzey, B. Robertson, and R. Barton. Can. J. Chem. **64**, 991 (1986).
11. L.M. Mihichuk, C.L. Giesinger, B.E. Roberston, and R.J. Barton. Can. J. Chem. **65**, 2634 (1987).
12. S.K. Manocha, L.M. Mihichuk, R.J. Barton, and B.E. Robertson. Acta Crystallogr. Sect. C, **C47**, 722 (1991).
13. E.L. Muetterties and L.J. Guggenberger. J. Am. Chem. Soc. **96**, 1748 (1974).
14. M.G.B. Drew. Prog. Inorg. Chem. **23**, 67 (1977).
15. M.G.B. Drew and C.J. Rix. J. Organomet. Chem. **102**, 467 (1975).
16. W.R. Cullen and L.M. Mihichuk. Can. J. Chem. **54**, 2548 (1976).
17. J.L. Templeton and B.C. Ward. J. Am. Chem. Soc. **103**, 3743 (1981).
18. P.J. Domaille and S.S. Wreford. Inorg. Chem. **19**, 2188 (1980).
19. W.R. Cullen and L.M. Mihichuk. Can. J. Chem. **53**, 3401 (1975).
20. J.P. Crow, W.R. Cullen, F.G. Herring, J.R. Sams, and R.L. Tapping. Inorg. Chem. **10**, 1616 (1971).
21. H. Wang and B.E. Robertson. Structure and statistics in crystallography. Adenine Press, Giilderland, N.Y. 1985.
22. S.R. Hall and J.M. Stewart. Xtal 2.4 users manual. Universities of Western Australia and Maryland. 1988.
23. M.A. Porai-Koshits and L.A. Aslanov. Zh. Strukt. Khim. **13**, 266 (1972).
24. D.L. Kepert. Inorganic stereochemistry. Inorganic chemistry concepts. Vol. 6. Springer-Verlag, New York. 1982.
25. R.O. Day, W.H. Batschelet, and R.A. Archer. Inorg. Chem. **19**, 2113 (1980).
26. D. Cremer and J.A. Pople. J. Am. Chem. Soc. **97**, 1354 (1975).
27. M.G.B. Drew and J.D. Wilkins. J. Chem. Soc. Dalton Trans. 1654 (1974).
28. M.G.B. Drew and J.D. Wilkins. J. Organomet. Chem. **69**, 271 (1974).
29. F.A. Cotton and R. Poli. Inorg. Chem. **25**, 3703 (1986).
30. F.A. Cotton, L.R. Falvello, and R. Poli. Polyhedron, **6**, 1135 (1987).
31. R. Colton and J. Kevekordes. Aust. J. Chem. **35**, 895 (1982).
32. R.S. Herrick and J.L. Templeton. Inorg. Chem. **25**, 1270 (1986).
33. L.S. Van Der Sluys, K.A. Kubat-Martin, G.J. Kubas, and K.G. Caulton. Inorg. Chem. **30**, 306 (1991).
34. L.H. Randall, A.A. Cherkas, and A.J. Carty. Organometallics, **8**, 568 (1989).
35. J. Sandstrom. Dynamic NMR spectroscopy. Academic Press, New York. 1982.
36. L.D. Brown, S. Datta, J.K. Kouba, L.K. Smith, and S.S. Wreford. Inorg. Chem. **17**, 729 (1978), and refs. therein.

© 1998 NRC Canada

Chiral *N*-(*o*-aryl)-thiazolidinediones: synthesis from rhodanines and investigation on rotational enantiomers by NMR spectroscopy

Mehmet Karataş, Serap Koni, and İlknur Doğan

Abstract: Sterically hindered *N*-(*o*-aryl)-rhodanines (**a**) (*N*-(*o*-aryl)-2-thioxo-4-thiazolidinones) have been synthesized and the *N*-(*o*-tolyl) and *N*-(*o*-chlorophenyl) derivatives have been converted to their dioxo analogs (**b**) (*N*-(*o*-aryl)-2,4-thiazolidinediones). The chirality of the compounds in their conformational ground states was proved by detection of the diastereotopic protons or methyl groups at C-5 of the heteroring using ^{1}H and ^{13}C NMR spectroscopy. In the presence of the optically active auxiliary (*S*)-(+)-1-(9-anthryl)-2,2,2-trifluoroethanol the enantiomers of the racemic mixtures formed diastereomeric association complexes via H-bonding.

Key words: chirality, chiral auxiliary, rotational isomerism, *N*-(*o*-aryl)-rhodanines, *N*-(*o*-aryl)-2,4-thiazolidinediones, ^{1}H and ^{13}C NMR.

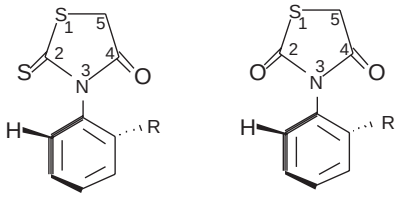

Résumé : On a synthétisé les *N*-(*o*-aryl)-rhodanines (**a**) stériquement empêchées (*N*-(*o*-aryl)-2-thioxo-4-thiazolidinones) et on a transformé les dérivés *N*-(*o*-tolyle) et *N*-(*o*-chlorophényle) en leurs analogues dioxo (**b**) (*N*-(*o*-aryl)-2,4-thiazolidine-2,4-diones). Faisant appel à la RMN du ^{1}H et du ^{13}C, on a déterminé la chiralité des composés dans leurs états conformationnels fondamentaux par détection des protons ou des groupes méthyles diastéréotopiques en C-5 de l'hétérocycle. En présence de l'auxiliaire optiquement actif (*S*)-(+)-1-(9-anthryl)-2,2,2-trifluoroéthanol, les énantiomères présents dans les mélanges racémiques forment des complexes d'association diastéréomères par le biais de liaisons hydrogènes.

Mots clés : chiralité, auxiliaire de chiralité, isomérie rotationnelle, *N*-(*o*-aryl)-rhodanines, *N*-(*o*-aryl)-thiazolidine-2,4-diones, RMN du ^{1}H et du ^{13}C.

[Traduit par la rédaction]

Introduction

Conformational isomerism in *N*-*o*-aryl substituted heterocyclic compounds has attracted considerable attention (1–5) because of their analogy to sterically hindered biphenyls. Experimental (6–12) as well as theoretical (13) studies have been reported concerning the enantiomeric and diastereomeric rotational isomers resulting from restricted internal rotation around the $C_{(aryl)}$—$N_{(heterocyclic)}$ bond. In a previous study, *N*-*o*-aryl substituted 2-thioxo-4-oxazolidinones and rhodanines were synthesized (14), their chirality was proven (14), and their enantiomers were preparatively enriched on cellulose triacetate (15). Barriers to racemization have also been determined experimentally (16–19). The present work is about the synthesis of *N*-*o*-aryl substituted 2,4-thiazolidinediones from rhodanines (Table 1) and (or) from the reaction of isocyanates with ethyl thioglycolate and the study of rotational isomerism in these molecules. Their enantiomers are detected by ^{1}H NMR in the presence of an optically active auxiliary compound.

Results and discussion

Racemic mixtures of *N*-(*o*-aryl)-rhodanines have been synthesized either from the reaction of isothiocyanates with ethyl thioglycolate or from α-halo carboxylic acid salts with

Received November 14, 1996.[1]

M. Karataş, S. Koni, and İ. Doğan.[2] Chemistry Department, Boğaziçi University, Bebek 80815, İstanbul, Turkey.

[1] Revision received September 24, 1997.
[2] Author to whom correspondence may be addressed. Telephone: (90-212) 263 15 40 (1610). Fax: (90-212) 287 24 67. E-mail: dogan@boun.edu.tr

© 1998 NRC Canada

Table 1. ^{1}H NMR data (200 MHz and 60 MHz) of the racemates in the absence and in the presence of (*S*)-(+)-1-(9-anthryl)-2,2,2-trifluoroethanol, ((*S*)-(+)-TFAE).

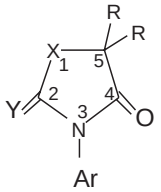

(M) + (P)

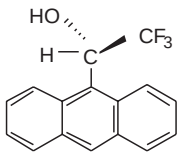

(*S*)-(+)-TFAE

Comp.	X	Y	R	Ar	Medium	δ (ppm) 5-CH_2	δ (ppm) *o*-CH_3	δ (ppm) 5,5-$(CH_3)_2$
1	S	O	H	*o*-Tolyl	$CDCl_3$	4.14 (s)	2.18	—
					C_6D_6	2.96, 2.92 (AB)	1.92	—
					[a]	4.13 (s)	2.16	—
2	S	O	H	*o*-Cl	$CDCl_3$	4.21, 4.14 (AB)	—	—
				Phenyl	C_6D_6	3.07, 2.94 (AB)	—	—
					[a]	4.04, 3.93 (AB)	—	—
						4.03, 3.94 (AB)		
3	S	O	H	α-$C_{10}H_7$	$CDCl_3$	4.29, 4.22 (AB)	—	—
				Naphthyl	C_6D_6	3.05, 2.98 (AB)	—	—
					[b]	4.05, 3.94 (AB)	—	—
					[a]	4.04, 3.96 (AB)	—	—
						4.28, 4.21 (AB)		
						4.26 (s)		
4	S	S	H	*o*-Tolyl	[c]	4.28 (s)	2.2	—
5	NH	S	H	*o*-Tolyl	$CDCl_3$	4.28, 4.25 (AB)	2.2	—
					C_6D_6	2.93, 2.86 (AB)	2.08	—
					[a]	4.16 (s)	2.17,2.15	—
6	S	S	H	*o*-Br	$CDCl_3$	4.28, 4.21 (AB)	—	—
				Phenyl	C_6D_6	3.10, 2.92 (AB)	—	—
					[d]	2.95, 2.89 (AB)	—	—
						2.94, 2.88 (AB)		
7	S	S	H	α-$C_{10}H_7$	$CDCl_3$	4.33, 4.27 (AB)	—	—
				Naphthyl	C_6D_6	3.00, 2.93 (AB)	—	—
					[d]	2.98, 2.90 (AB)	—	—
						2.97, 2.89 (AB)		
8	S	S	CH_3	*o*-Tolyl	[c]	—	2.16 (s)	1.83 (s)
9	S	O	CH_3	*o*-Tolyl	$CDCl_3$	—	2.17 (s)	1.84, 1.83 (s,s)
					C_6D_6	—	1.95 (s)	1.33, 1.32 (s,s)
					[d]	—	1.90 (s)	1.28, 1.27 (s,s)

[a] $CDCl_3$, 4 equivalents of (*S*)-(+)-TFAE.
[b] $CDCl_3$, 8 equivalents of (*S*)-(+)-TFAE.
[c] Spectrum taken at 60 MHz.
[d] C_6D_6, 8 equivalents of (*S*)-(+)-TFAE.

ammonium *o*-aryldithiocarbamate (obtained from carbon disulfide and *ortho*-substituted aniline in 25% ammonia solution (20)). The yields were found to be much higher for the former (61% vs. 5–15%). Conversion of the synthesized rhodanines (Table 1) to the corresponding thiazolidinediones was attempted by the reaction with bromine in acetic acid. *N*-*o*-tolyl- and *N*-*o*-chlorophenyl substituted rhodanines were successfully converted to the diones in 31–56% yield (Scheme 1). However, the reaction failed with sterically more hindered rhodanines such as *N*-(*o*-bromophenyl) and *N*-(α-naphthyl)-rhodanines. The thiazolidinediones were also synthesized independently, from the reaction of aryl isocyanates with ethyl thioglycolate.

The 200 MHz ^{1}H or ^{13}C NMR spectra of the synthesized compounds (Table 1) showed the presence of diastereotopic protons or methyl groups. Thus, in ^{1}H NMR, AB coupling patterns were observed for the protons on C-5 of the heteroring (Fig. 1). The two methyl groups bonded to C-5 were observed as separate singlets in the ^{1}H NMR spectrum and as different signals in the ^{13}C NMR spectrum.

The chemical shift differences of the AB protons ranged from 0.18 to 0.01 ppm, the differences being solvent dependent. The shift differences were found to be largest in hexadeuterobenzene. The coupling constants ranged from 17.5 to 18.3 Hz. The ^{1}H and ^{13}C NMR results are summarized in Tables 1 and 2, respectively. All proton-bearing phenyl and naphthyl carbons were found to resonate in the relatively narrow region between 121 and 134 ppm in the ^{13}C NMR spectra.

© 1998 NRC Canada

Scheme 1.

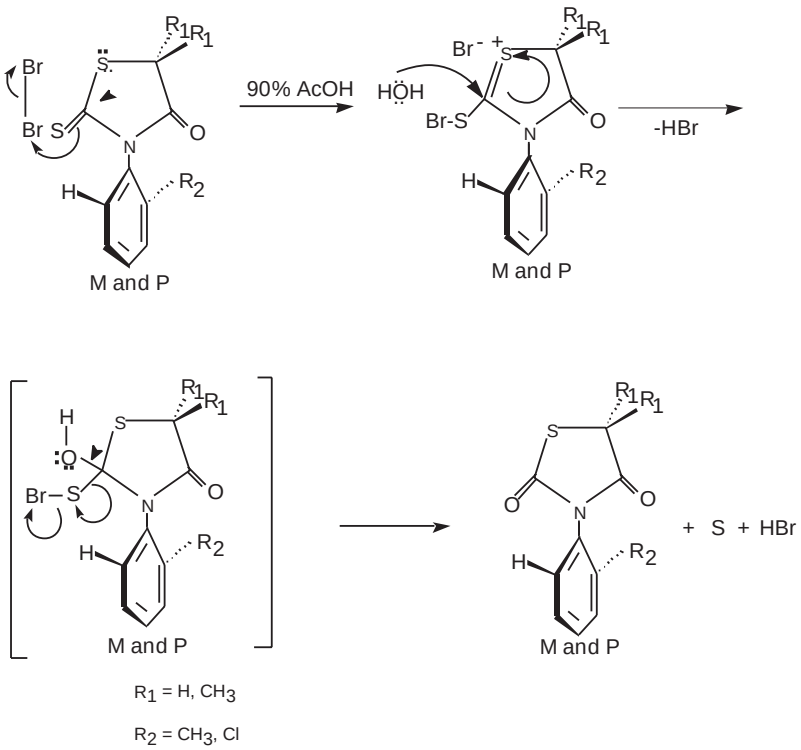

Although unambigious assignments could not be made for some of the carbons on a one-to-one basis, the values for most carbons were assigned based on chemical shift criteria (Table 2).

The presence of the AB quartets and observation of different signals for methyl groups at C-5 showed the presence of a large rotational barrier in the molecules, resulting in a slow conformational interconversion on the NMR time scale. Otherwise, the groups attached to this carbon would have been isochronous. Thus the thiazolidinediones studied here were found to be mixtures of two slowly interconverting enantiomers.This is consistent with the earlier observations (14, 21) that steric interactions within these molecules are caused by the presence of an *o*-aryl substituent and the oxo and (or) thioxo groups on the heteroring. As the *ortho* substituents become bulkier, the barrier to interconversion between the enantiomers should increase. Of the compounds studied, the largest AB splitting was observed for the C-5 protons of *N*-(*o*-bromophenyl)-rhodanine, which is expected to be the sterically most hindered one, namely, to have a lowest energy conformation with the largest dihedral angle. In fact, coalescence of the AB signals of even *N*-(*o*-chlorophenyl)-2,4-thiazolidinedione and *N*-(α-naphthyl)-2,4-thiazolidinedione was not observed by ^{1}H NMR at 90°C in pyridine. This shows that the activation energy for rotation for these molecules should be higher than 100 kJ/mol, which means that they could be resolved at room temperature. Especially if the *o*-bromoaryl derivatives, which are expected to have the largest barriers due to the size of the bromo substituent, were resolved, the chiral enantiomers could be used in further chemical reactions, without being racemized, at suitably chosen temperatures and reaction times determined mainly by the energy barrier. Conversion of the chiral rhodanine to the corresponding chiral thiazolidinedione might have been interesting for the correlation of configurations (12) of the two structurally related compounds. However, attempts to convert the racemic rhodanines to thiazolidinediones at room temperatures failed.

Since both enantiomers of the compounds were found to be separated by a racemization barrier high enough for the process to be slow on the NMR time scale, addition of a chiral auxiliary compound should split some of their signals via formation of diastereomeric association complexes. Pirkle's alcohol, *S*-(+)-2,2,2-trifluoro-1-(9-anthryl)ethanol (*S*-(+)-TFAE), was used for this purpose. The chiral auxiliary is expected to be associated with the compounds studied through H-bonding. π–π Interactions between the aryl or naphthyl groups and the anthryl group of the (*S*)-(+)-TFAE may also be important (14, 21) in forming the diastereomeric complexes. In fact, upfield shifts of 0.01–0.2 ppm for the 5-CH_2 protons accompanied by signal splittings of the AB quartets and 0.03–0.05 ppm upfield shifts for *ortho* CH_3 protons were observed. It turned out that, for these compounds, the 5-CH_2 group is a better probe in studying the hindered rotation than is the *ortho* CH_3 group. The latter split only in the case of compound **5,** by a chemical shift difference of 0.02 ppm. Two signals that had been observed for the diastereotopic methyl groups at C-5 did not split further in the presence of (*S*)-(+)-TFAE. Best results were obtained when 8 equiv. of the chiral auxiliary was used (see Table 1, compound **3**). Proton NMR results in the presence of the chiral auxiliary are given in Table 1.

IR spectra of the compounds were especially useful in following the conversion reactions. The only structural difference between the rhodanines and 2,4-thiazolidinediones is the replacement of the carbonyl group at position 2 by a thiocarbonyl. The C═S group of the rhodanines showed stretching

© 1998 NRC Canada

Table 2. ^{13}C chemical shifts (ppm) of the compounds **6**, **7**, and **9** in hexadeuterobenzene.

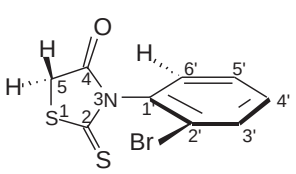

(M) + (P)

6

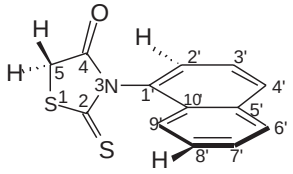

(M) + (P)

7

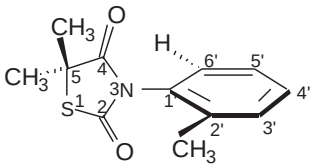

(M) + (P)

9

	Compound		
Carbon	**6**	**7**	**9**
2	171.9	173.8	[a]
4	[a]	[a]	[a]
5-$(CH_3)_2$	—	—	27.52, 28.37[d]
C-5	35.6	36.6	17.3
1’	135.8	134.5	136.2
2’	123.2	121.5	133.2
3’	133.7	130.6[b]	131.2
4’	131.2[b]	126.6[c]	129.7[b]
5’	130.9[b]	129.2	128.9[b]
6’	128.5	127.3[c]	127.1
7’	—	128.9[b]	—
8’	—	125.5[c]	—
9’	—	127.6[b]	—
10’	—	131.2	—

[a]Carbonyl carbon could not be observed due to long relaxation time and low concentration.
[b,c]Arbitrary assignment.
[d]Diastereotopic groups.

vibrations at 1250, 1210, and 1168 cm^{-1} that were found to disappear upon conversion to 2,4-thiazolidinediones.

Experimental

Proton NMR spectra were recorded on a Varian T-60A (60 MHz, $T = 24°C$), or on a Bruker AC-200 (200 MHz, $T = 23°C$) spectrometer. Carbon-13 NMR spectra were recorded on a Bruker AC-200 spectrometer (200 MHz, $T = 23°C$). The IR spectra were recorded on a Perkin Elmer 1600 FT-IR or Mattson 1000 FT-IR spectrometer using KBr discs. Melting points were determined using an Electrothermal 9100 melting point apparatus. Ultraviolet spectra were obtained in ethanol on a Unicam UV2-100 spectrophotometer. Elemental analyses were obtained on a Carlo Erba 1100 instrument.

Materials

Arylisocyanates were prepared from the corresponding commercially available acid chloride derivatives and sodium azide in toluene. α-Naphthyl chloride was synthesized from the corresponding commercially available α-naphthoic acid and thionyl chloride. *N*-(*o*-Tolyl)-isothiocyanate was prepared from *o*-toluidene and carbon disulfide with lead(II) nitrate, as described in the literature (20). *N*-(*o*-Bromophenyl)- and *N*-(α-naphthyl)-isothiocyanates (purity >98%) and (*S*)-(+)-1-(9-anthryl)-2,2,2-trifluoroethanol were purchased from Aldrich.

The synthesis of *N*-(*o*-aryl)-rhodanines

Two different methods of synthesis were undertaken for the preparation of *N*-(*o*-aryl)-rhodanines.

Method A (ref.14)
Arylisothiocyanate (0.025 mol) and ethyl thioglycolate (0.025 mol) were mixed in 25 mL of toluene, and metallic sodium (0.0025 mol) was added in small pieces. The reaction mixture was refluxed for 5 h. Toluene was distilled off and the remaining crude product was purified by recrystallizing twice from ethanol.

Method B (ref.14)
The reaction of ammonium *o*-aryldithiocarbamate (obtained from CS_2 and *ortho*-substituted aniline in 25% ammonia solution (20)) with the α-halo carboxylic acid salt was carried out in aqueous alkaline solution at room temperature. After 1 h stirring, the mixture was acidified with concentrated HCl (pH = 5–5.5) and warmed on a water bath for 2 h. The crude product was extracted from the reaction mixture by a suitable solvent (e.g., benzene or carbon tetrachloride). The white crystals that appeared after awhile were discarded by vacuum filtration and the solvent was distilled off. The remaining crude product was purified by recrystallizing from ethanol.

The synthesis of *N*-(*o*-aryl)-2,4-thiazolidinediones

Two different methods of synthesis were undertaken for the preparation of *N*-(*o*-aryl)-2,4-thiazolidinediones.

Method A′
o-Arylisocyanate (0.02 mol) and ethyl thioglycolate (0.02 mol) were mixed in 15 mL of toluene. Metallic sodium (0.05–0.1 g) was added in small pieces. After the addition of sodium the reaction mixture was heated at 80 °C for 10 h. Then

© 1998 NRC Canada

Fig. 1. The 200 MHz ^{1}H NMR signals of C-5 methylene protons of **2** at room temperature (*a*) in $CDCl_3$, (*b*) in C_6D_6, and (*c*) in $CDCl_3$ in the presence of 4 equiv. of (*S*)-(+)-TFAE.

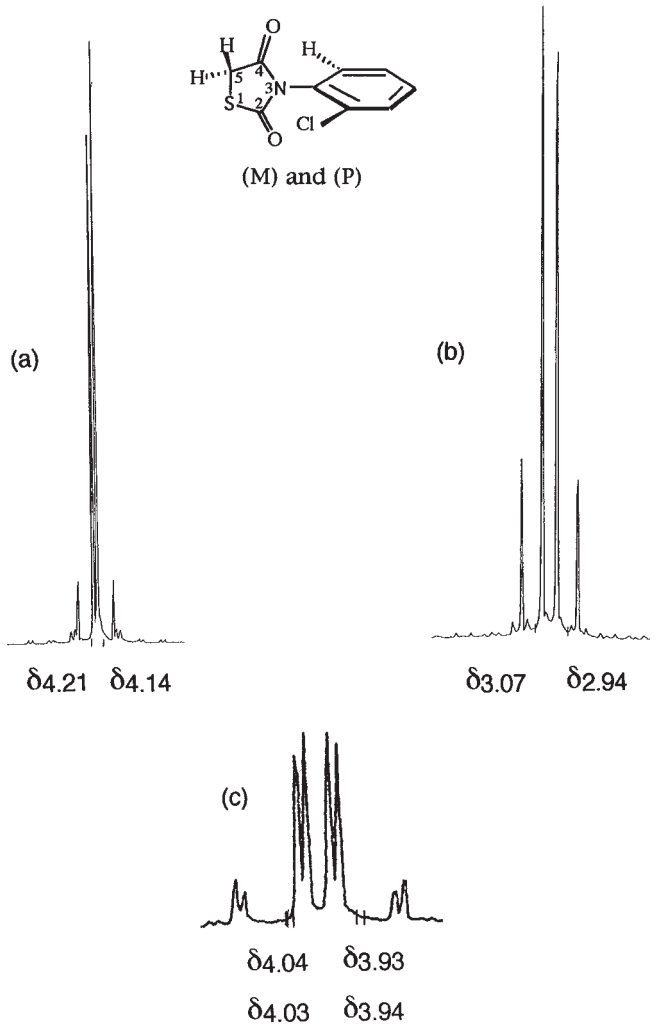

the temperature was raised to 100–110 °C for 1 h. The toluene was distilled off, and the *N*-(*o*-aryl)-2,4-thiazolidinedione left in the flask was purified through recrystallization from ethanol.

Method B′

General procedure for the conversion of *N*-(*o*-aryl)-rhodanine to *N*-(*o*-aryl)-2,4-thiazolidinedione (22): 1 mmol *N*-(*o*-aryl)-rhodanine was dissolved in 90% acetic acid solution at reflux temperature (95°C). Bromine (2 mmol) was introduced dropwise into the flask with stirring. The reaction mixture was heated under reflux and monitored by thin-layer chromatography (TLC) on silica with a chloroform:toluene mixture (15:3) as eluent. When the reaction was completed, the reaction mixture was treated with charcoal and filtered. Acetic acid solution was distilled off by vacuum distillation. The residue was lixiviated with chloroform. After distillation of the chloroform, the remaining crude product was purified by recrystallization (three times) from ethanol.

N-*(*o-*Tolyl)-2,4-thiazolidinedione,* **1**

Synthesized according to the general procedure described in method A′ or method B′. Yields: 19% and 32%, respectively; mp 120–122°C; UV (ethanol), λ_{max}: 221 nm (ε 7.41×10^3 cm^{-1} M^{-1}), 263 nm (ε 5.62×10^2 cm^{-1} M^{-1}), 463 nm(ε 4.17×10^1 cm^{-1} M^{-1}), 530 nm (ε 4.17×10^1 cm^{-1} M^{-1}), 570 nm (ε 3.1×10^1 cm^{-1} M^{-1}); ^{1}H NMR ($CDCl_3$) δ: 2.18 (3H, s), 4.14 (2H, s), 7.10–7.47 (4H, m); ^{1}H NMR (C_6D_6) δ: 1.92 (3H, s), δ_A: 2.96, δ_B: 2.92 (2H, B). Anal. calcd. for $C_{10}H_9NO_2S$: C 57.97, H 4.34, N 6.76%; found: C 57.91, H 4.28, N 6.71%.

N-*(*o-*Chlorophenyl)-2,4-thiazolidinedione,* **2**

Synthesized according to the general procedure described in method A′ or method B′. Yields: 19% and 31%, respectively; mp 137–139°C; UV (ethanol), λ_{max}: 219 nm (ε 8.13×10^3 cm^{-1} M^{-1}), 265 nm (ε 6.17×10^2 cm^{-1} M^{-1}), 463 nm (ε 5.13×10^2 cm^{-1} M^{-1}), 530 nm (ε 5.13×10^2 cm^{-1} M^{-1}), 571 nm (ε 3.39×10^1 cm^{-1} M^{-1}); ^{1}H NMR ($CDCl_3$) δ_A: 4.21, δ_B: 4.14 (2H,B, J_{AB} = 17.5 Hz), δ: 7.59–7.24 (4H, m); ^{1}H NMR (C_6D_6) δ_A: 3.07, δ_B: 2.94 (2H, AB). Anal. calcd. for $C_9H_6NO_2SCl$: C 47.49, H 2.64, N 6.15%; found: C 47.40, H 2.59, N 5.96%.

N-*(*α-*Naphthyl)-2,4-thiazolidinedione,* **3**

Synthesized according to the general procedure described in method A′. Yield: 7%; mp 155–157°C; UV (ethanol), λ_{max}: 222 nm (ε 1.38×10^4 cm^{-1} M^{-1}), 269 nm (ε 1.29×10^3 cm^{-1} M^{-1}), 281 nm (ε 1.35×10^3 cm^{-1} M^{-1}), 463 nm (ε 4.90×10^1 cm^{-1} M^{-1}), 528 nm (ε 4.90×10^1 cm^{-1} M^{-1}), 571 nm (ε 3.63×10^1 cm^{-1} M^{-1}); ^{1}H NMR ($CDCl_3$) δ_A : 4.29, δ_B: 4.22 (2H, AB, J_{AB} = 17.6 Hz), δ: 7.25–8.01 (7H, m); ^{1}H NMR (C_6D_6) δ_A: 3.05, δ_B: 2.98 (2H, AB). Anal. calcd. for $C_{13}H_9NO_2S$: C 64.19, H 3.70, N 5.76%; found: C 63.11, H 3.63, N 5.69%.

N-*(*o-*Tolyl)-rhodanine,* **4**

Synthesized according to the general procedure described in method A or method B. Yields: 61% and 5%, respectively; mp 110°C; UV (ethanol), λ_{max}: 256 nm (ε 1.26×10^4 cm^{-1} M^{-1}), 295 nm (ε 1.41×10^4 cm^{-1} M^{-1}), 388 nm (ε 6.61×10^1 cm^{-1} M^{-1}); ^{1}H NMR ($CDCl_3$) δ: 2.20 (3H, s), 4.28 (2H, s), 7.47–6.87 (4H, m).

N-*(*o-*Tolyl)-thiohydantoin,* **5**

Obtained by the reaction of o-tolyl isothiocyanate and glycine in ethanol. The reaction was carried out in aqueous NaOH solution. After the mixture was heated for 2 h under reflux, excess alcohol was distilled off. Later, dilute HCl was added to the mixture and the mixture was evaporated to dryness. The residue was recrystallized from ethanol. Yield: 30%; mp 145°C; ^{1}H NMR ($CDCl_3$) δ: 2.2 (3H, s), δ_A: 4.28, δ_B: 4.25 (2H, AB, J_{AB} = 24.7 Hz), 7.68–7.13 (4H, m); ^{1}H NMR (C_6D_6) δ: 2.08 (3H, s), δ_A: 2.93, δ_B: 2.86 (2H, AB). Anal. calcd. for $C_{10}H_{10}N_2OS$: C 58.25, H 4.85, N 13.59%; found: C 58.21, H 4.80, N 13.51%.

N-*(*o-*Bromophenyl)-rhodanine,* **6**

Synthesized according to the general procedure described in method A. Yield: 60%; mp 144–145°C; UV (ethanol), λ_{max}: 202 nm (ε 1.55×10^4 cm^{-1} M^{-1}), 253 nm (ε 1.07×10^4 cm^{-1} M^{-1}), 294 nm (ε 1.10×10^4 cm^{-1} M^{-1}), 395 nm (ε 7.94×10^1 cm^{-1} M^{-1}); ^{1}H NMR ($CDCl_3$) δ_A: 4.28, δ_B: 4.21 (2H,,AB, J_{AB} = 18.29 Hz), δ: 7.77–7.22 (4H, m); ^{1}H NMR (C_6D_6) δ_A: 3.10, δ_B: 2.92 (2H, AB, J_{AB} = 18.29 Hz). Anal. calcd. for

© 1998 NRC Canada

$C_9H_6NOS_2Br$: C 37.50, H 2.08, N 4.8%; found: C 37.48, H 1.98, N 4.74%.

N-*(α-Naphthyl)-rhodanine,* **7**
Synthesized according to the general procedure described in method A. Yield: 37%; mp 169.2–171.2°C; UV(ethanol), λ_{max}: 219 nm (ε 4.90×10^3 cm^{-1} M^{-1}), 254 nm (ε 1.15×10^3 cm^{-1} M^{-1}), 292 nm (ε 1.02×10^3 cm^{-1} M^{-1}), 464 nm (ε 6.46×10^1 cm^{-1} M^{-1}), 531 nm (ε 5.75×10^1 cm^{-1} M^{-1}), 571 nm (ε 4.57×10^1 cm^{-1} M^{-1}), 581 nm (ε 4.57×10^1 cm^{-1} M^{-1}); ^1H NMR ($CDCl_3$) δ_A: 4.33, δ_B: 4.27 (2H, AB, J_{AB} = 18.31 Hz), δ: 8.15–7.12 (7H, m); ^1H NMR (C_6D_6) δ_A: 3.00, δ_B: 2.93 (2H, AB, J_{AB} = 18.32 Hz). Anal. calcd. for $C_{13}H_9NOS_2$: C 60.23, H 3.48, N 5.41%; found : C 60.20, H 3.57, N 4.98%.

N-*(*o-*Tolyl)-5,5-dimethylrhodanine,* **8**
Synthesized according to the general procedure described in method B. Yield: 15.2%; mp 72–73°C; UV (ethanol), λ_{max}: 257 nm (ε 1.23×10^4 cm^{-1} M^{-1}), 297 nm (ε 1.51×10^4 cm^{-1} M^{-1}), 393 nm (ε 6.31×10^1 cm^{-1} M^{-1}); ^1H NMR ($CDCl_3$) δ: 1.83 (6H, s), 2.16 (3H,s), 7.17–6.93 (4H, m). Anal. calcd for $C_{12}H_{13}NOS_2$: C 57.34, H 5.21, N, 5.57%; found : C 57.01, H 5.15, N, 5.65%.

N-*(*o-*Tolyl)-5,5-dimethyl-2,4-thiazolidinedione,* **9**
Synthesized according to the general procedure described in method B′. Yield: 56%; mp 67–68°C; UV (ethanol), λ_{max}: 203 nm (ε 1.38×10^4 cm^{-1} M^{-1}), 283 nm (ε 1.66×10^2 cm^{-1} M^{-1}), 308 nm (ε 1.35×10^2 cm^{-1} M^{-1});^1H NMR ($CDCl_3$) δ: 1.84, 1.83 (3H, 3H, s, s), 2.17 (3H, s), 7.38–7.10 (4H, m); ^1H NMR (C_6D_6) δ: 1.33, 1.32 (3H, 3H, s, s), 1.95(3H, s), 7.28–6.76 (4H, m). Anal calcd. for $C_{12}H_{13}NO_2S$: C 61.28, H 5.53, N 5.96%; found: C 61.70, H 4.87, N 5.40%.

Acknowledgement

The authors thank the Boğaziçi University Research Fund for support of the project 94B0546.

References

1. P.H. Bird, L.D. Colebrook, A.R. Fraser, and H.G. Giles. J. Chem. Soc Chem. Commun. 225 (1974).
2. L.D. Colebrook and H.G. Giles. Can. J. Chem. **51**, 3635 (1972).
3. L.D. Colebrook and H.G. Giles. Tetrahedron Lett. 5239 (1972).
4. L.D.Colebrook and H.G. Giles. Can. J. Chem. **53**, 3431(1975).
5. A. Djafri, C. Roussel, and J. Sandström. J. Chem. Soc. Perkin Trans. 2, 273 (1985).
6. W.H. Pirkle. J. Am. Chem. Soc. **88**, 1837 (1966).
7. A. Mannschreck, V. Jonas, and B. Kolb. Angew. Chem. **12**, 583 (1973).
8. C. Kashima, A. Katoh, Y. Omote, and Y. Nakata. Heterocycles, **9**, 469 (1978).
9. M. Mintas, Z. Orhanovic, K. Jakopcic, H. Kohler, G. Stuhler, and A. Mannschreck. Tetrahedron, **41**, 229 (1985).
10. C. Roussel and A. Djafri. New J. Chem. **10**, 399 (1986).
11. C. Roussel and A. Chemlal. J. Chromatogr. **95**, 462 (1989).
12. C. Roussel, J. Stein, and L. Beauvais. New J. Chem. 169 (1990).
13. L.D. Colebrook. Can. J. Chem. **69**, 1957 (1991).
14. İ. Dogan, T. Burgemeister, S. İçli, and A. Mannschreck. Tetrahedron, 48, 7157 (1992).
15. İ. Doğan, N. Pustet, and A. Mannschreck. J. Chem. Soc. Perkin Trans. 2, 1557 (1993).
16. C. Roussel, M. Adjimi, A. Chemlal, and A. Djafri. J. Org. Chem. **53**, 5076 (1988).
17. J. Vorcapic'-Furac', M. Mintas, T. Burgemeister, and A. Mannschreck. J. Chem. Soc. Perkin Trans. 2, 713 (1989).
18. M. Mintas, V. Mihaljevic', H. Koller, D. Schuster, and A. Mannschreck. J. Chem. Soc. Perkin Trans. 2, 619 (1990).
19. R. Sarac-Arneri, M. Mintas, N. Pustet, and A. Mannschreck. Monatsh. Chem. **125**, 457 (1994).
20. I.A. Vogel. *In* Practical organic chemistry. 4th ed. Wiley, New York. 1978. p. 736.
21. L.D. Colebrook, S. İçli, and F.H. Hund. Can. J. Chem. **53**, 1556 (1975).
22. M.T. Omar. Bull. Chem. Soc. Jpn. **64**, 750 (1991).

© 1998 NRC Canada

Oxidation of olefins catalyzed by iron complexes of bleomycin model compounds bearing a hydrophobic or hydrophilic steric factor

Kazuo Shinozuka, Junya Kohda, and Hiroaki Sawai

Abstract: The bleomycin (BLM) model iron complexes bearing either a hydrophobic or hydrophilic steric factor around the sixth coordination sphere exhibited considerable substrate specificity and stereoselectivity in the oxidation of *cis*- and *trans*-olefins in a methanol solution in the presence of H_2O_2. The catalytic efficiency of the complexes was somehow correlated with the nature of the steric factor rather than with their oxygen-activating ability. In a benzene–phosphate buffer (micelle-forming condition), on the other hand, only the complex having micelle-forming ability exhibited the epoxidation of the substrates.

Key words: bleomycin model compound, steric factor, substrate specificity, asymmetric oxidation, oxidation in micelle.

Résumé : Lors de l'oxydation d'oléfines *cis* ou *trans* en solution dans le méthanol, en présence de H_2O_2, les complexes de fer, modèles de la bléomycine, qui portent un facteur stérique hydrophobe ou hydrophile autour de la sixième sphère de coordination présentent une spécificité et une stéréosélectivité importante par rapport au substrat. Il existe une légère corrélation entre l'efficacité catalytique des complexes et la nature du facteur stérique plutôt qu'avec leur habilité à activer l'oxygène. Par ailleurs, dans un tampon de benzène–phosphate (un condition de former une micelle), seul le complexe ayant la possibilité de former une micelle permet d'effectuer l'époxydation des substrats.

Mots clés : composé modèle de la bléomycine, facteur stérique, spécificité par rapport au substrat, oxydation asymétrique, oxydation dans une micelle.

[Traduit par la rédaction]

Introduction

The antitumor antibiotic bleomycin (BLM) is a member of a family of glycopeptides isolated as a Cu(II) complex from a culture of *Streptomyces veticillus* (1). In living tissue, BLM forms an Fe(II) complex and activates molecular oxygen, thereby inducing the oxidative cleavage of DNA (2). It has been shown that the active species responsible for the oxidative reaction is related to the transient BLM–Fe(III)–OOH complex (3). In addition to the DNA cleaving activity, the BLM–Fe complex exhibits catalytic oxidation of olefinic substrates such as stilbene, styrene, and β-methylstyrene in the presence of O_2, H_2O_2, PhIO, or $KHSO_2$ (4, 5*a*, *c*). In the reaction, the BLM–Fe complex was found to oxidize *cis*-olefinic substrates more efficiently than the corresponding *trans*-olefinic substrates (4*a–c*, *e*, 5*a*, *c*). An asymmetric oxidation was, however, observed only in the oxidation of *cis*-β-methylstyrene with the BLM–Fe–H_2O_2 system (5*c*).

Meanwhile, a number of studies have been reported on the synthesis and properties of model compounds, which simplified the metal coordination site of BLM. Thus, the oxidation of *cis*- and *trans*-β-methylstyrene and stilbene by Fe complexes of several BLM model compounds were reported by Ohno and co-workers (5*a*, *c*, *d*) and Mascharak and co-workers (5*e*, *f*). The reaction using these model complexes with H_2O_2 as the oxidant seems to proceed stereoselectively, in general. Some of these complexes also exhibited substrate selectivity between the *cis*- and *trans*-olefinic substrates in the reaction like the BLM–Fe complex (5*a*, *c*, *e*, *f*). However, very limited work has been done on the asymmetric oxidation of the olefinic substrates using the model complexes (5*c, d*). Furthermore, the effect of the steric factor of the BLM model compounds in place of the disaccharide moiety of the BLM on the efficiency and the stereoselectivity of the oxidation remains uncertain.

Previously, we have reported the synthesis of simple BLM model compounds bearing a hydrophobic or hydrophilic steric factor around the sixth coordination sphere in place of the disaccharide moiety of the BLM, namely, the model compound **I** bearing a long alkyl chain (lauryl group), the model compound **II** bearing a *tert*-butyl group, and the model compound **III** bearing a trishydroxymethyl group (Fig. 1) (6, 7). The steric factor in the models is introduced in a chiral-specific manner at the carboxy residue of L-histidine through an amide linkage instead of the position of the hydroxy residue of *erythro*-β-hydroxy-L-histidine through an ether linkage, as in the case of BLM or the models reported by Ohno and co-workers (1, 5*a–d*). The iron complexes of **I**, **II**, and **III** have exhibited significantly high oxygen activation ability (6, 7). The compound **I** has also shown micelle-forming ability (6).

Received August 18, 1997.

Kazuo Shinozuka, Junya Kohda, and Hiroaki Sawai.[1]
Department of Chemistry, Faculty of Engineering, Gunma University, Kiryu City 376, Japan.

[1] Author to whom correspondence may be addressed. Telephone: + 81 (0) 277-30-1222. Fax: + 81 (0) 277-30-1224. E-mail: sawai@chem.gunma-u.ac.jp

© 1998 NRC Canada

Fig. 1. Structure of the model complexes.

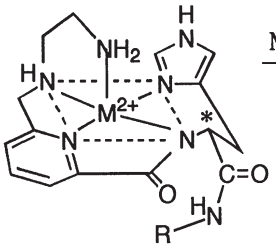

Model	R
I	$-(CH_2)_{11}CH_3$
II	$-C(CH_3)_3$
III	$-C(CH_2OH)_3$

To examine the effects of the steric factor around the sixth coordination sphere and the formation ofa micelle on the oxidation reaction, we carried out the oxidation of olefinic compounds using the iron complexes of **I**, **II** and **III** in a methanol solution and in a micelle-forming condition (benzene buffer).

Results and discussion

Oxidation of olefin in a solution

The oxidation reaction by the Fe(III) complex system of the compound **I**, **II**, or **III** with H_2O_2 in solution was carried out as follows. A solution of the model Fe(III) complex, H_2O_2 (50 equiv. to the complex), and substrate (50 equiv. to the complex) in degassed methanol was stirred under argon atmosphere at room temperature. After the addition of dichloromethane and brine, the mixture was partitioned and the organic layer was isolated. The solution was directly analyzed by gas chromatography. The products were identified by comparing their retention time with those of the authentic racemic samples. The absolute stereochemistry and enantiomeric excess (ee) of the epoxides were determined, based on the ^{1}H NMR measurement (8, 5*d*). The details of these are described in the experimental section.

In methanol solution, the Fe(III)–H_2O_2 systems of **I**, **II**, and **III** exhibited catalytic oxidation of the substrates, giving the corresponding epoxides as the major products as shown in Table 1. The results also clearly demonstrate that the reaction proceeds stereoselectively. Thus, *cis*-olefin afforded *cis*-epoxides and *trans*-olefin gave *trans*-epoxides with concomitant formation of benzaldehyde. Small amounts of *trans*-epoxides were formed with the *cis*-olefin oxidation while the oxidation of *trans*-olefin gave *trans*-epoxides exclusively. The results are in agreement with the previous reports using the BLM–Fe complex and the simplified model complexes of BLM (4, 5*a*, *d–f*).

The extent of the oxidation of *cis*-stilbene was much more pronounced than that of *trans*- stilbene, as observed in the case of BLM–Fe(III) mediated reaction (4*a–c*, *e*, 5*c*). The observed substrate discrimination ability could be derived from the fact that the stereochemical environment around the oxygen coordination site (catalytic site) of the current model complexes is highly crowded to achieve the stereochemical discrimination between the isomers, as was discussed previously in the oxidation by BLM–Fe(III) (5*a*, *c*). Another interesting feature in the current results is that the catalytic efficiency of the complexes was not proportional to their oxygen-activating ability (5*a*) but to the nature of the steric factor. Our previous estimation of oxygen-activating ability based on the EPR spin-trapping experiment for the model Fe complexes **I**, **II**, and **III** is 58, 52, and 74% of that of the BLM standard, respectively (Table 2) (6, 7). The model complex **III**–Fe(III) (7) having a hydrophilic steric factor, however, exhibited the lowest catalytic efficiency among the complexes. A high degree of asymmetric induction was also observed in the oxidation of *cis*-olefins. For example, 1,2-dihydronaphthalene was epoxidized to the corresponding (–)-*cis*-epoxide in about 36 and 49% of enantiomeric excess (ee) with **I–**Fe(III) and **II–**Fe(III), respectively. In general, **II**–Fe(III) exhibited slightly higher enantioselective efficiency to the substrates tested than **I–**Fe(III), as indicated in Table 1.

These results suggest that oxygen is bound tightly to the central iron at the sixth coordination site of the model complexes, and the stereochemical environment around the iron–oxygen center may influence the transition state of the oxidation reaction. Furthermore, the fact that the model complexes bearing hydrophobic steric factor (**I**–Fe and **II**–Fe) exhibited higher degree of catalytic efficiency as well as the asymmetric induction in epoxidation compared with the complex bearing a hydrophilic steric factor (**III–**Fe) suggest that a kind of direct interaction, such as hydrophobic interaction or CH–π interaction (9), between the phenyl group of the substrates and the steric factor of **I**–Fe and **II**–Fe may exist. Such interaction would help to arrange the spatial direction of the interaction between the substrate and the complex more stringently than the simple steric repulsion between the substrates and the steric factor.

Oxidation of olefin in a micelle-forming condition

As was reported previously, the model compound **I** and its metal complex have micelle-forming abilities (6). Thus, we first attempted to determine the critical micelle concentration (cmc) of **I** using a Cu(II) complex of I. Measurement of cmc was performed by the UV turbidity method (Fig. 2) (10). To a solution of **I**–Cu(II) complex (0.01–0.16 mM) in Tris-HCl buffer (100 mM, pH 7.2) was added chloroform. After the sonication of the mixture, the UV transmittance (T'/T) of the resulting mixture was measured (10), where T' is the transmittance of the mixture after the sonication, and T is the transmittance of the corresponding aqueous solution. The value of cmc determined by the method was 0.09 mM.

The oxidation reaction by the Fe(III)–H_2O_2 system of **I** or **II** in a micelle-forming condition was carried out in the same manner as the reaction in solution conditions, except that the solvent methanol was replaced with a benzene–phosphate buffer (1/10, v/v, pH 7.2). Under these conditions, the formation of the micelle was observed for the case of the **I–**Fe(III) complex at the concentration higher than ≈0.075 mM but not for the case of the **II**–Fe(III) complex. Table 3 shows the results of oxidation in the micelle-forming conditions with the model complexes **I**–Fe(III) and **II–**Fe(III). Contrary to the reaction carried out in methanol, only the **I**–Fe(III) complex exhibited the epoxidation of the substrates. The reactions of the **I**–Fe(III) complex with *cis*-β-methylstyrene and 1,2-dihydronaphthalene gave *cis*-β-methylstyrene oxide and 1,2-dihydronaphthalene oxide, respectively. The efficiency of the reaction was, however, found to depend on the concentration of the complex. Thus, the yield of the products was almost zero below 0.05 mM of the complex, and it increased with increasing concentration of the complex, reaching a plateau over the cmc (Fig. 3). The catalytic efficiency was, however, substantially suppressed compared with the solution condition. These

© 1998 NRC Canada

Table 1. Oxidation of *cis*- and *trans*-olefins with Fe(III)–H_2O_2 complex systems of **I**, **II**, and **III** in a

Substrate	Ligand	Products	Yields(%)[b]	Products	Yields(%)[b]	Products	Yields (%)[b]
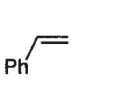	**I**	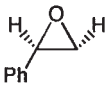	464 (10% ee)				7.1
	II		319 (15% ee)			Ph–CHO	8.2
	III		—[c]				—[c]
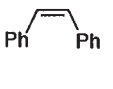	**I**	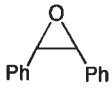	555	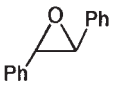	12		22
	II		380		7.2	Ph–CHO	9.9
	III		220		trace		6.0
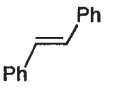	**I**	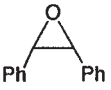	—[d]	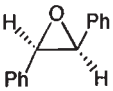	120 (8% ee)		31
	II		—[d]		72 (12% ee)	Ph–CHO	14
	III		—[d]		45 (—)[c]		9.1
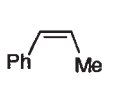	**I**[e]	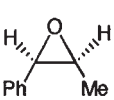	570 (35% ee)	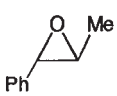	trace		22
	II[e]		390 (47% ee)		trace	Ph–CHO	10
	III[e]		232 (—)[c]		—[d]		6.2
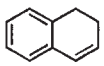	**I**[e]	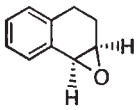	741 (36% ee)				
	II[e]		570 (49% ee)				
	III[e]		126 (—)[c]				

[a] Conditions: iron complex, 0.15 mM; substrate, 50 equiv. to the complex; H_2O_2, 50 equiv. to the complex. The reactions were carried out at room temperature for 30 min, unless otherwise specified.

[b] The yields are based on Fe(III).

[c] The % ee not measured.

[d] Not detected.

[e] Reactions carried out at room temperature for 1 h.

Fig. 2. Measurement of the critical micelle concentration (cmc) for **I**–Cu(II) complex by UV turbidity method.

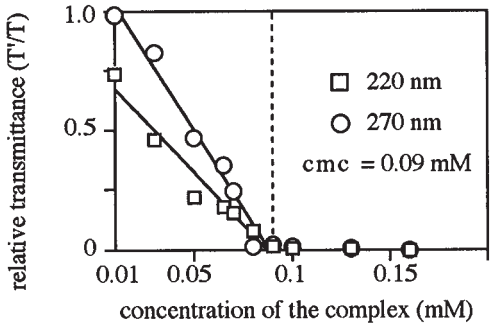

Table 2. Oxygen-activating ability of Fe(II)–O_2 complex systems of BLM and the model compounds.[a]

Ligand	Relative oxygen-activating ability
BLM	100
Model **I**	58
Model **II**	52
Model **III**	74

[a] Oxygen-activating ability was estimated by EPR spin-trapping experiment (5, 6).

results strongly suggest that the oxidation reaction proceeds inside the micelle and, therefore, the resulted epoxides stay inside the micelle.

Interestingly, the enantioselectivity of **I**–Fe(III) in the oxidation of dihydronaphthalene was also substantially decreased compared with that of the reaction in methanol. This may be due to the fact that in the micelle-forming condition, the arrangement of the spatial interaction between the substrate and the complex is rather disturbed compared to homogeneous-solution condition. It should be noted that, although **I**–Fe(III) failed to show high catalytic efficiency and enantioselectivity in the micelle-forming condition, this is the first example of olefin oxidation mediated by BLM model complexes under these conditions.

Concluding remarks

The results presented here demonstrated that iron complexes of simple compounds **I**, **II**, and **III**, mimicking the metal coordination of BLM, exhibit properties that resemble those characteristic of the parent BLM–Fe complex in the oxidation reaction of olefinic substrates in a methanol solution. The complexes showed considerable substrate discrimination ability and stereoselectivity in the reaction, which may reflect the fact that oxygen is bound tightly to the central iron at the sixth coordination site of the model complexes and that the stereochemical environment around the iron–oxygen center is very

© 1998 NRC Canada

Table 3. Oxidation of *cis*- and *trans*-olefins with Fe(III)–H_2O_2 complex systems of **I**, **II**, **III** in a

Substrate	Ligand	Products	Yields (%)[b]	Products	Yields (%)[b]	Products	Yields (%)[b]
Ph, Me	I	O, Ph, Me	35[c]	O, Me, Ph	—[d]	Ph-CHO	8.5
	II		—[d]		—[d]		—[d]
	I	H, O	118 (20% ee)				
	II		<3 (~3% ee)				

[a] Conditions: iron complex, 0.15 mM; substrate, 50 equiv. to the complex; H_2O_2, 50 equiv. to the complex; solvent, phosphate buffer (22 mM, pH 7.2)/benzene, 10/1 (v/v). The reactions were carried out at room temperature for 1 h.

[b] The yields are based on Fe(II).

[c] The % ee not measured.

[d] Not detected.

Fig. 3. Dependence of the oxidation on the concentration of **I**–Fe complex in a micelle-forming condition. Conditions: **I**–Fe complex, 0.02–0.2 mM; substrate, 50 equiv. to the complex; H_2O_2, 50 equiv. to the complex; solvent, phosphate buffer (2–20 mM, pH 7.2)/benzene, 10/1 (v/v). The reactions were carried out at room temperature for 1 h. The yields are based on Fe(III).

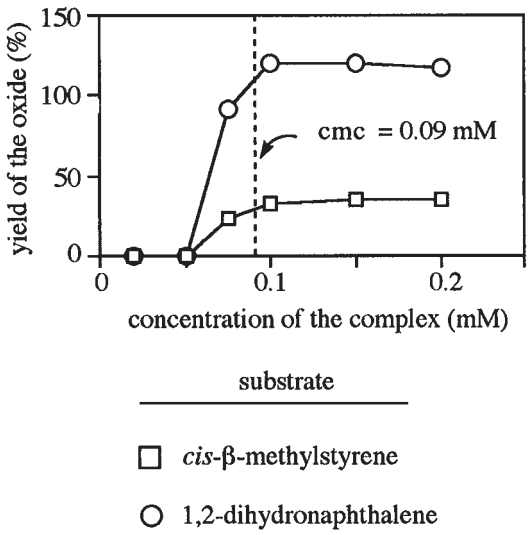

close to that of BLM–Fe. The higher catalytic efficiency and the asymmetric induction in epoxidation observed for the complexes **I** and **II**, both bearing the hydrophobic functional group as the steric factor, seem to suggest that these features are rather correlated with the hydrophobic nature of the steric factor than with their oxygen-activating ability. Thus, the interaction between the steric factor of the complexes and the substrates in addition to the stereochemical environment around the iron–oxygen center of the complex may play an important role in the reaction. Also, we could successfully demonstrate the first example of olefin oxidation mediated by BLM model complex **I** in a micelle-forming condition. Although the catalytic efficiency and the enantioselectivity exhibited by **I**–Fe(III) under these conditions were not very high, the results may provide useful information towards development of a new type of oxidizing agent that is capable of oxidizing substrates in the micelle.

Experimental

General

The synthesis and the physical properties of the model compounds **I**, **II**, and **III** were reported previously (6, 7).

Detection of the oxidation products was done by gas chromatography using a Shimadzu GC-14A equipped with a flame ionization detector (J & W Scientific Fused Silica capillary column, 30 m × 0.25 mm i.d., 0.25 μm film, He as a carrier gas). Identification of the reaction products was performed by injection of the standard materials to compare their retention time. Reagents and solvent were purified by standard procedures. *n*-Octadecane (99.5%) was purchased from Tokyo Kasei and used without further purification. Methanol used for the oxidation reaction was distilled and degassed immediately before use.

Oxidation of olefin using Fe complex of the model compounds I, II, and III and hydrogen peroxide in a methanol solution

The oxidation reaction and the analysis of the products were carried out by a similar procedure reported previously with slight modification (4*b*, 5*d*). The reaction was carried out under argon atmosphere at 25°C. A solution containing 0.48 μmol of an iron complex (formed by admixture of 0.53 μmol of a model ligand and 0.48 μmol of $Fe(ClO_4)_3 \cdot 6H_2O$ in 2.7 mL of MeOH) was combined with a solution containing 24 μmol of olefin in 0.48 mL of methanol. Hydrogen peroxide (1.2 M solution, 20 μL, 24 μmol) was added dropwise. After being stirred for 30 min, CH_2Cl_2 (10 mL) and satd. NaCl (10 mL) was added to the mixture. The mixture was partitioned and the CH_2Cl_2 layer was collected. The aqueous layer was further extracted with CH_2Cl_2. The organic layer was combined, and a small amount of insoluble material was removed by filtration. The volume of the organic layer was standardized to 25 mL by addition of extra CH_2Cl_2 and the internal standard (*n*-octadecane, 0.48 μmol), and the solution was directly analyzed by gas chromatography. Calibration curves were prepared and the products were quantified by area normalization of the peak for the internal standard.

The enantiomeric excess (ee) of the oxide was determined as follows. A solution containing 4.8 μmol of an iron complex (formed by admixture of 5.3 μmol of model ligand and

© 1998 NRC Canada

4.8 μmol of $Fe(ClO_4)_3 \cdot 6H_2O$ in 13 mL of MeOH) was combined with a solution containing 240 μmol of olefin in 2.4 mL of methanol. Hydrogen peroxide (1.2 M solution, 200 μL, 240 μmol) was added dropwise. After being stirred at room temperature for 30 min, the reaction mixture was extracted with CH_2Cl_2, as described above. The obtained organic layer was dried over Na_2SO_4 and concentrated at a temperature below 25°C. Olefin oxide was isolated by applying the residue on a silica-gel column chromatography (eluted with hexane followed by CH_2Cl_2:hexane of 1:10). The ee of the oxide was determined by ^1H NMR measurement using tris[3-(heptafluoropropylhydroxymethylene)-(+)-camphorato] europium(III) as a chiral shift agent (5*d*, 8).

Oxidation of olefin using Fe complex of the model compounds I and II and hydrogen peroxide in a micelle-forming condition

The reaction was carried out in the same manner as above except that the solvent methanol was replaced with a benzene–phosphate buffer (1/10, v/v, pH 7.2). A solution containing 0.48 μmol of iron complex (formed by admixture of 0.53 μmol of model ligand and 0.48 μmol of $Fe(ClO_4)_3 \cdot 6H_2O$ in 2.9 mL of phosphate buffer) was combined with a solution containing 24 μmol of olefin in 0.29 mL of benzene. Hydrogen peroxide (1.2 M solution, 20 μL, 24 μmol) was added dropwise under argon atmosphere. After the mixture was stirred at room temperature for 1 h, a solution obtained by the extractive workup was analyzed by gas chromatography as described above.

The ee of the oxide was determined as follows. A solution containing 4.8 μmol of an iron complex (formed by admixture of 5.3 μmol of model ligand and 4.8 μmol of $Fe(ClO_4)_3 \cdot 6H_2O$ in 13 mL of MeOH) was combined with a solution containing 240 μmol of olefin in 1.3 mL of benzene. Hydrogen peroxide (1.2 M solution, 200 μL, 240 μmol) was added dropwise. After being stirred at room temperature for 1 h, the reaction mixture was extracted with CH_2Cl_2. The obtained organic layer was dried over Na_2SO_4 and concentrated at a temperature below 25°C. Olefin oxide was isolated by silica-gel column chromatography (eluted with hexane followed by CH_2Cl_2:hexane of 1:10) and ee of the oxide was determined as above.

Concentration dependence of the oxidation in a micelle-forming condition using I–Fe complex

The reaction was carried out in the same manner as above except that the concentration of the complex varied from 0.02 to 0.2 mM. Also, the amount of hydrogen peroxide and the substrate used for the reaction was adjusted to 50 equiv. to the complex.

Measurement of the critical micelle concentration (cmc)

The critical concentration was measured according to the published procedure (10) using Cu(II) complex of **I** (6). In brief, to a solution of **I**–Cu(II) complex (0.01–0.16 mM in 100 mM Tris-HCl buffer, pH 7.2, 100 μL) placed in a UV cuvette (1 mm path length) was added chloroform (10 μL), and the mixture was sonicated for 180 s at 25°C. The UV transmittance of the resulted turbid mixture was measured at 220 and 270 nm, which corresponds to the absorption maxima of the complex. Relative transmittance (T'/T), where T' is the transmittance of the aqueous solution after sonication under the presence of chloroform and the T is transmittance of the aqueous solution, is plotted against concentration.

References

1. H. Umezawa, K. Maeda, T. Takeuchi, and Y. Okami. J. Antibiot. (Tokyo) Ser. A. **19A**, 200 (1966).
2. T. Takita, Y. Muraoka, T. Nakatani, A. Fujii, Y. Umezawa, H.Naganara, and H. Umezawa. J. Antibiot. (Tokyo), **31**, 801 (1978).
3. J. Stubbe, J.W. Kozarich, W. Wu, and D.E. Vanderwall. Acc. Chem. Res. **29**, 322 (1996), and refs. cited therein.
4. (*a*) N. Murugesan, G.M. Ehrenfeld, and S.M. Hecht. J. Biol. Chem. **257**, 8600 (1982); (*b*) N. Murugesan and S.M. Hecht. J. Am. Chem. Soc. **107**, 493 (1985); (*c*) R.M. Moriarty, R. Penmasta, and I. Prakash. Tetrahedron Lett. **26**, 4699 (1985); (*d*) M. Girardet and B. Meunier. Tetrahedron Lett. **28**, 2955 (1987); (*e*) E.C. Long and S.M. Hecht. Tetrahedron Lett. **29**, 6413 (1988).
5. (*a*) Y. Sugano, A. Kittaka, M. Ostuka, M. Ohno, Y. Sugiura, and H. Umezawa. Tetrahedron Lett. **27**, 3635 (1986); (*b*) A. Kittaka, Y. Sugano, M. Ostuka, and M.Ohno. Tetrahedron, **44**, 2821 (1988); (*c*) Y. Kaku, M. Otsuka, and M. Ohno. Chem. Lett. 611 (1989); (*d*) A. Suga, T. Sugiyama, M. Ostuka, M. Ohno, Y. Sugiura, and K. Maeda. Tetrahedron, **47**, 1191 (1991); (*e*) D.Y. Dawson, S.E. Hudson, and P.K. Mascharak. J. Inorg. Biochem. **47**, 109 (1992); (*f*) R.J. Guajardo, S.E. Hudson, S.J. Brown, and P.K. Mascharak. J. Am. Chem. Soc. **115**, 7971 (1993).
6. K. Shinozuka, H. Morishita, T. Yamazaki, Y. Sugiura, and H. Sawai. Tetrahedron Lett. **32**, 6869 (1991).
7. J. Kohda, K. Shinozuka, and H. Sawai. Tetrahedron Lett. **36**, 5575 (1995).
8. L. Casted, J.L. Castro, and R. Eiguera. Tetrahedron Lett. **25**, 1205 (1984).
9. M. Nishio, Y. Umezawa, M. Hirota, and Y. Takeuchi. Tetrahedron, **51**, 8665 (1995), and refs. cited therein.
10. M. Yashiro, K. Matsumoto, and S. Yoshikawa. Chem. Lett. 985 (1989).

© 1998 NRC Canada

Surface plasmon resonance sensors using molecularly imprinted polymers for sorbent assay of theophylline, caffeine, and xanthine

Edward P.C. Lai, Ania Fafara, Victoria A. VanderNoot, Mari Kono, and Brandee Polsky

Abstract: A sensor system based on the optical phenomenon of surface plasmon resonance (SPR), which employs either photothermal deflection spectroscopy (PDS) or a photodiode array (PDA) for detection, was developed to use molecularly imprinted (MI) polymethacrylic acid – ethylene glycol dimethacrylates (PMAA–EDMA) as the sensing element. The MI polymers were first processed by Soxhlet extraction to remove the print molecules (theophylline, caffeine, and xanthine), yielding the specific *anti*-polymers. Each *anti*-polymer was layered over a silver film to serve as the analysis surface for the molecularly imprinted sorbent assay (MIA) of one target drug. This surface was exposed for 60 min to an aqueous standard drug solution, dried in air, and the uptake of the print molecule into the *anti*-polymer was monitored by shifts in the SPR angle θ_r (and hence the SPR–PDS signal measured at constant θ). The linear dynamic range of the MIA was found to extend up to 6 mg/mL, with a concentration detection limit estimated at 0.4 mg/mL for theophylline in aqueous solution. A cross-reactivity study of the *anti*-theophylline and *anti*-caffeine polymers, using eight other drugs structurally similar to theophylline and caffeine, showed none or very slight shifts in θ_r. This implies that the *anti*-polymers were selective only for their original print molecules and had no affinity for the other drug molecules. Similar molecular recognition characteristics were observed for the *anti*-xanthine polymer.

Key words: surface plasmon resonance, molecular imprinting, theophylline, caffeine, xanthine, sensor.

Résumé : Dans le but d'utiliser un mélange d'acide polyméthacrylique – diméthylacrylates d'éthylèneglycol (APMA–DMAE) moléculairement imprimés (MI) comme élément senseur, on a développé un système basé sur le phénomène optique de la résonance plasmonique de surface (RPS) et qui fait appel à une détection par spectroscopie de déflexion photothermique (SDP) ou un arrangement de photodiode (APD). Dans une première étape, les polymères MI ont été soumis à une extraction au Soxhlet pour enlever les molécules imprimer (théophylline, caféine et xanthine) afin d'obtenir des anti-polymères spécifiques. On a placé une couche de chacun des anti-polymères sur un film d'argent pour servir de surface d'analyse pour dosage d'un adsorbant moléculairement imprimé (AMI) d'un médicament choisi. On a exposé cette surface à une solution aqueuse de médicament de référence pendant 60 min, on l'a séchée à l'air et on a déterminé l'adsorption de la molécule imprimée dans l'anti-polymère grâce aux déplacements de l'angle θ_r dans la RPS (et, par conséquent, par le biais du signal de RPS–SDP à valeur constante de θ). On a trouvé que la plage dynamique linéaire d'AMI va jusqu'à 6 mg/mL, on évalue que la concentration limite de détection de la théophylline en solution aqueuse est de 0,4 mg/mL. Une étude de réactivité croisée des polymères des *anti*-théophylline et *anti*-caféine, faisant appel à huit autres médicaments structuralement apparentés à la théophylline et à la caféine, a permis de montrer que les déplacements dans la valeur de θ_r sont nuls ou très faibles. Ce résultat implique que les *anti*-polymères ne sont sélectifs que pour les molécules imprimées originales et qu'ils n'ont aucune affinité pour les autres molécules de médicaments. Des caractéristiques de reconnaissance semblables ont aussi été observées avec le polymère de l'*anti*-xanthine.

Mots clés : résonance plasmonique de surface, impression moléculaire, théophylline, caféine, xanthine, senseur.

[Traduit par la rédaction]

Introduction

Sensor devices for the detection of different analytes have great significance in medicine, pharmaceutics, and environmental toxicology. One of the driving forces in chemical-sensing research is for ways to incorporate the inherent specificity of binding and recognition methods to the high sensitivity of instrumental techniques (1). Due to its specificity and high sensitivity, immunoassay is often the method of choice for trace analyses of clinically important compounds contained in complex biological matrices. A wide range of radioisotopic, enzymatic, fluorescent, chemiluminescent, IR-active and redox labels or markers have played an important role in the development of immunoassay in the last two decades. Although these labels certainly have their own specific advantages, they also have characteristics that limit their usefulness

Received Jan 26, 1996.

E.P.C. Lai,[1] A. Fafara, V.A. VanderNoot, M. Kono, and B. Polsky. Ottawa–Carleton Chemistry Institute, Department of Chemistry, Carleton University, Ottawa, ON K1S 5B6, Canada.

[1] Author to whom correspondence may be addressed. Telephone: (613) 520-2600 (ext. 3835). Fax: (613) 520-3749. E-mail: elai@ccs.carleton.ca

© 1998 NRC Canada

in assaying biochemical molecules from both commercial and practical viewpoints (2). Since the success of an immunoassay depends critically on the specific antibody, the making of proprietary antibodies and field analytical test kits based on immunology technology has been monopolized by a handful of manufacturers (e.g., RISc® test kits of EnSys, EnviroGard[7] test kits of Millipore, etc.) Test tubes provided with the kit (package) come precoated with antibodies. However, shelf life is at the maximum extended to three months when stored at room temperature without refrigeration. There is a continuing effort to develop synthetic immunoanalytical reagents that are more stable, particularly utilizing the technique of molecular imprinting.

Two decades ago, Wulff et al. (3) first reported a novel template polymerization called molecular imprinting (MI) by which polymers could be prepared with high selectivity for the template compounds (or print molecules). The MI involves the preparation of a polymer cast by reacting functional monomers in the presence of a print molecule. When the print molecule is removed by extraction, sites are left behind in the polymer that complement the template in shape and positioning of chemical functionality. A stationary phase prepared by template polymerization was applied to the enantio-separation of amino acid derivatives by Mosbach and co-workers (4). Continuous rods of MI polymers were prepared by Matsui et al. (5) for separating positional isomers of diaminonaphthalene and resolving enantiomers of phenylalanine anilide. In 1993, Mosbach and co-workers (6) used the MI technique to create selective recognition sites in polymers that functioned as well as antibodies in ligand-binding assays for two drugs, theophylline and diazepam. This important contribution demonstrated that a completely synthetic approach to the creation of functional binding sites could produce selectivities and binding constants typically in the range from 10^4 to 10^7 M^{-1}, which are comparable to those found in biological systems. Although the molecularly imprinted sorbent assay (MIA) method involved an extra step (extraction) compared with antibody-based methods, the synthetic approach offered several advantages. First, MI is an alternative to the use of laboratory animals to produce receptors, in the form of *anti*-polymers. Second, *anti*-polymers are easier to prepare and cheaper to manufacture than natural antibodies. Third, these polymers are stable enough to be stored in the dry state at ambient temperature for years without loss of recognition capability. Last, it has been confirmed that they are stable in acid, base, organic solvents, high temperatures (e.g., autoclave) and pressure conditions that antibodies could not withstand (7). To date, MI polymers for over 20 classes of compounds have been made (8). Stable MI polymers specific for several nucleotides, amino acids, and herbicides were synthesized for possible use in sensor devices (9). However, they have not extensively been applied on a detector surface to create optical sensors, except the fibre-optic sensing device recently reported for the determination of derivatized amino acids (9), fiber-optic fluorescence of dansyl-L-phenylalanine (10), as well as optical fluorescence of sialic acid (11).

Surface plasmon resonance (SPR) is an optical phenomenon that has been used as a standard approach for the detection of small quantities of organics at a conductive interface. In the Kretschman geometry, incident light is coupled via total internal reflection in a glass prism to the charge density waves (or plasmons) present on the surface of a thin metal film under appropriate conditions of resonance (a simultaneous match of both frequency and wave vector) (12). The SPR has a variety of applications: surface plasmon microscopy (SPM) for high-contrast imaging of thin dielectric films (13), surface-enhanced Raman scattering (SERS), and coherent anti-Stokes Raman scattering (CARS) (14), SPR enhanced laser desorption (15), immunoassay (16), and fibre-optic chemical sensing (17). The SPR chemical sensing depends on the sensitivity of resonance condition to changes in dielectric permittivity very close to the sensor surface. Any changes to the dielectric function of the sample medium in contact with the silver film, during for instance the binding between an immobilized antibody and the antigen, will shift the resonant angle of incidence. Changes in the resonance condition have traditionally been probed by measuring a loss in reflectance (18). Alternatively, Inagaki et al. (19) employed photoacoustic spectrometry to probe the radiationless processes associated with SPR. Our laboratory took advantage of photothermal deflection spectrometry (PDS) to successfully detect SPR (20). The SPR–PDS technique could determine submonolayer quantities (2×10^{-7} g) of anti-human immunoglobulin G (a-IgG). Using a monolayer of a-IgG to act as the sensing surface, a detection limit of 100 parts per billion has been achieved for immunoglobulin G (IgG). These sensor results were linear over concentration ranges encountered in standard immunoassays and therapeutic monitoring. Recently, a SPR biosensor with cavity-enhanced photothermal spectroscopy detection was developed (21), and a sensitivity analysis showed that high signal-to-noise ratios are possible (22). The present work reports the development of both the SPR–PDS sensor system and another SPR system based on a photodiode array (PDA) detector to make use of MI polymers as the sensing surface material. Specifically, three *anti*-polymers that can recognize theophylline, caffeine, and xanthine drug molecules are examined. The *anti*-caffeine and *anti*-xanthine polymers are newly synthesized in our laboratory and reported here for the first time.

Experimental

Molecular imprinting

The MI polymers containing theophylline, caffeine, and xanthine were prepared according to the procedure outlined previously (6). To 25 mL of chloroform contained in a 100 mL flask was added 0.47 g of theophylline, 0.9 g of methacrylic acid (MAA), 9.4 g of ethylene glycol dimethacrylate (EDMA), and 0.12 g of 2,2′-azobis(2-methylproprionitrile) initiator (AIBN). The mixture was degassed in a sonicating bath under vacuum and flushed with nitrogen for 5 min. Polymerization began within 1 h at 60°C inside a thermostatted water jacket and was continued for 24 h. The resultant polymer was ground with a mortar and pestle to produce a fine powder.

Extraction of print molecule

To produce *anti*-theophylline polymer, the print molecule (theophylline) was removed from the polymer powder (0.5 g) by Soxhlet extraction using 150 mL of methanol – acetic acid (9:1 v/v) over 24 h (7). Alternatively, dynamic supercritical fluid extraction (SFE) was carried out on a Suprex SFE/50 supercritical fluid extractor (Pittsburgh, Pa.), using CO_2 at 400

© 1998 NRC Canada

atm (1 atm = 101.3 kPa) and 40°C (density = 0.96–0.99 g mL^{-1}) with a flow rate of 0.5 mL min^{-1} over 60 min. The theophylline extracted from the polymer was collected by passing the supercritical fluid effluent through three glass collection vials, each containing 4 mL of methanol. The SFE was repeated using first CO_2 with 5% (or 9 mL/180 mL) methanol as a modifier under the same conditions as above and next N_2O at 300 atm and 50°C with a flow rate of 0.5 mL min^{-1} over 60 min. In each case, the percent recovery was determined by UV spectrophotometry at 210 and 270 nm, GC-FID (Varian 3400, DB-5 30 m × 0.25 mm column at 150°C, hydrogen gas flow rate = 30 cm/s, retention time = 7.2 min), and HPLC (Varian 9010 solvent delivery system, 100% methanol, Zorbax ODS reverse phase 25 cm × 4.6 mm column, 9050 variable wavelength UV-visible detector set at 270 nm, retention time = 2.5 min).

Anti-polymer overlayer

Silver films for SPR were prepared by Interoptics Ltd. (Ottawa, Ont.) on 1 in. × 1 in. (1 in. = 24.4 mm) glass slides by depositing 57 ± 1 nm of silver at a rate of 1 nm/s on top of a 150 nm in thickness aluminum oxide layer. The aluminum oxide was laid down first to improve adhesion to silver. The silver films on glass slides were wrapped in a special oven-dried paper to prevent contamination of the film surfaces; they were stored under vacuum till needed.

Thin overlayers of *anti*-polymers were coated onto silver films by evaporation, over 60 min, from 100 μL of a 0.1–1.0 mg/mL solution in acetonitrile – acetic acid (99:1 v/v) spotted with a micropipet on approximately 6 cm^2 of silver film surface. The solid *anti*-polymer overlayers were rinsed with water to remove any residual acetic acid and dried in air for 24 h.

MIA

The SPR angular profiles were first recorded for the dry *anti*-polymer overlayers. The overlayers were then exposed to 60 μL of either water or 1–6 mg/mL standard aqueous solutions of theophylline, caffeine, or xanthine, which spread over an area of 1 cm^2. After incubation for 60 min, the *anti*-polymer overlayers were rinsed with water and allowed to dry in air overnight. New SPR angular profiles were measured on the next day either by PDS or with a PDA. Special efforts were made to fix the silver films in exactly the same position on the prism for all SPR analyses.

Cross-reactivity

A set of eight different drugs with similar structures to theophylline and caffeine were obtained from Health Canada (Ottawa, Ont.) for cross-reactivity tests. They included acetaminophen, dyphylline, hydrochlorothiazide, β-hydroxyethyl theophylline, nicotinic acid, phenyl butazone, and theobromine. These drugs were dissolved in water to make up 6 mg/mL solutions, except for hydrochlorothiazide, phenyl butazone, and theobromine, which were hard to dissolve beyond 1–2 mg/mL. After exposure of *anti*-theophylline, *anti*-caffeine, or *anti*-xanthine polymer overlayers to the drug solutions separately, their angular SPR profiles were obtained to determine if any drug had bound to the *anti*-polymers.

The SPR–PDS and SPR–PDA sensor systems

The SPR–PDS sensor system shown in Fig. 1 has been described previously (20). An argon-ion-pumped dye laser provided the excitation beam (λ = 590 nm, irradiated power = 100 mW), which was chopped at 200 Hz and focused through a glass prism (base angle = 45°, refractive index = 1.517 ± 0.001 at 590 nm) on the microscope slide – silver film interface at an angle of incidence θ (analysis area = 0.01–0.04 mm^2). The pump beam was polarized in the plane of incidence, and dibutyl phthalate was used for the optical coupling between the glass prism and the microscope slide. When resonance condition (θ_r) was attained, energy was transferred from the laser beam to excite the surface plasmons on the silver film surface. As the plasmons relaxed nonradiatively, heat was released from the silver film to the surroundings, producing a refractive index gradient in the air medium outside the silver film. A collimated probe beam from a He–Ne laser (output power = 1 mW) passing through this gradient would be deflected. As a result of deflection, the beam intensity at a particular area in space was changed, and a photodiode with a pin hole was used as a detector to generate a PDS signal. The signal amplitude was recorded by a lock-in amplifier, at regular θ intervals over the range of 42–50° to generate an SPR angular profile for θ_r determination.

In the SPR–PDA sensor system, a diode laser (Applied Laser Systems, Grants Pass, Oreg.) with an output power of 10 mW at 670 nm was used as the light source for SPR because of its small dimensions and plane-polarized output (Fig. 2). After the intensity of the laser beam was reduced by a set of neutral density filters of 4.4 OD (optical density), it was focused by a plano-convex lens through the glass prism onto the silver film at the analysis area. The diverging reflected beam was passed through a cylindrical lens and a slit to produce a line image on a PDA (Princeton Instruments, Trenton, N.J.). Each ray of the focused beam had a different angle of incidence θ and would be reflected orderly to fall onto a different photodiode of the array. The PDA was useful for monitoring the angular intensity profile of the line image. Its output signals from 1024 diodes were acquired by a Princeton Instruments model ST120 controller and processed by an ST1000 MSMA computer program for display on the monitor screen. The diode numbers along the *x*-scale corresponded to a range of angles of incidence, which could be calibrated in degree units by placing the arm of a goniometer over the prism at a specified angle and dropping a thin wire from the arm perpendicularly into the incident beam. This thin wire produced a dark line image on the PDA, and hence a sharp dip would be displayed in the angular profile on the screen display. Five different angles of incidence were chosen for the calibration, to cover the entire angular intensity profile of the focused beam. After calibration, any change in SPR angle resulting from a MIA experiment would be observed as a shift to a larger θ value.

Results and discussion

Preparation of *anti*-polymers by MI

Theophylline, caffeine, or xanthine was reacted with MAA and EDMA in the presence of AIBN initiator. Complementary interactions were developed and noncovalent linkages were formed between the print molecule and MAA monomers.

© 1998 NRC Canada

Fig. 1. Schematic diagram of the SPR–PDS sensor system.

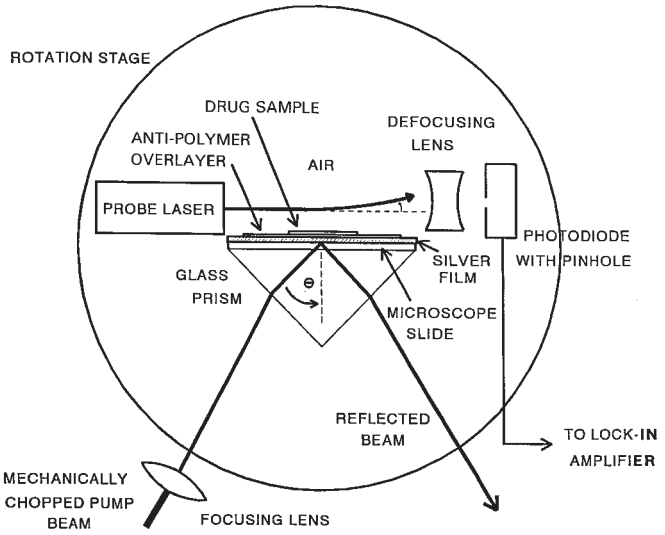

Fig. 2. Schematic diagram of the SPR–PDA sensor system based on a laser diode.

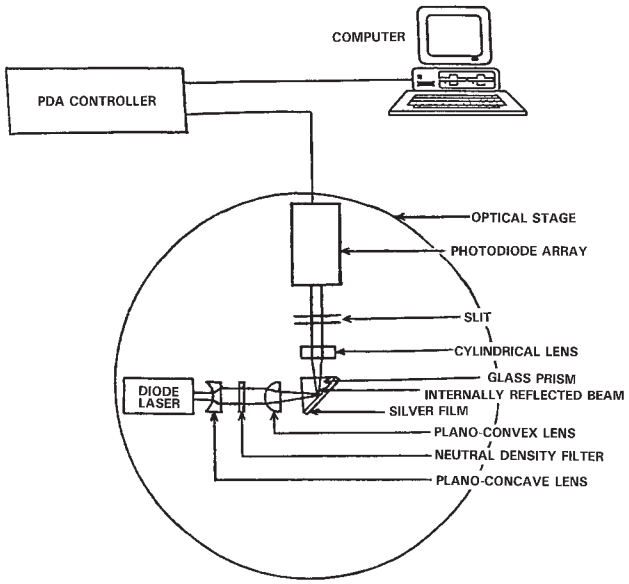

Thermal initiation of the polymerization in the presence of EDMA created a three-dimensional network, cross-linking the MAA monomers to form the MI polymer. After the polymer was isolated and ground, the print molecule could be extracted from the MAA–EDMA matrix as detailed below. This produced an *anti*-polymer with cavities containing sorbent sites that complement the original print molecule in shape and chemical functionality. These sites had an affinity for the print molecule, and molecular recognition would occur when the *anti*-polymer was later exposed to a sample solution containing the print molecule in MIA.

Extraction of print molecule

Soxhlet extraction with methanol – acetic acid (9:1 v/v) over 24 h resulted in near quantitative removal of all three print molecules from their respective MI polymers (see Table 1). Unlike organic networks where open structures from which guest molecules can be removed completely cannot yet be made (23), the cross-linked matrix in MI polymers apparently could engage in dynamic motions that opened up channels for the ready escape of desorbed print molecules.

Although Soxhlet extraction was able to remove nearly all (88–104%) of the theophylline present in the MI polymer powder (at 4.3 wt.%), the process was lengthy and consumed much of the solvent. The SFE was next attempted as a potentially fast, efficient extraction technique. Successful application of SFE to polymers has been reported before. For example, Hirata and Okamato (24) used CO_2 to obtain complete extraction of additives in polyethylene films in under 2 h, compared with 24 h for a Soxhlet extraction. Our use of supercritical CO_2 fluid, however, could recover only 5% of the theophylline from the MI polymer in 1 h. Since theophylline is a polar molecule, the extraction rate might be limited by solubility in the nonpolar supercritical CO_2 fluid. Addition of 5 mol% methanol, which increased the polarity and hence solvent power of CO_2, improved the extraction efficiency to 10%. Further attempt using polar N_2O SFE at 50°C yielded only a modest 9% recovery. The amount of theophylline that could be extracted from PMAA–EDMA by SFE was considerably less than that achieved by Soxhlet extraction. It seems that most of the print molecules were locked into the polymer matrix and not accessible to SFE. For SFE to be successful, the solute must, firstly, be sufficiently soluble in the supercritical fluid and, secondly, be transported sufficiently rapid (by diffusion or otherwise) from the core of the polymeric particles to the surface. Apparently, the rate-determining step was molecular diffusion in the polymer particles when these two SFE experiments were carried out at a temperature of 40–50°C, which was lower than the operating temperature of the Soxhlet extraction. The solvents used for Soxhlet extraction of polymers are normally good swelling agents for the polymer. Since the present MI polymer has an extensive cross-linked matrix structure, its glass transition temperature is ill defined and was experimentally undeterminable by differential scanning calorimetry up to its degradation at 189°C (according to thermogravimetric measurement in our laboratory). It is therefore hard to say whether the SFEs were performed at sufficiently high temperatures so that the polymer was swollen to release the print molecules.

The low proportion of print molecules extractable by SFE is worth some investigation. A hot-ball model has previously been proposed by Bartle et al. (25) for the study of continuous SFE of powdered matrices. Their model assumes that the matrix particles are spheres, that the initial distribution of the solute within the spheres is uniform, and that the flow rate is high enough for the concentration of the solute in the supercritical fluid to be considered effectively zero. Theoretically, 37% of the solute is extracted during an initial period of $0.25t_c$, where t_c is a characteristic time for the extraction defined by $t_c = 4r^2/\pi^2 D$ with D being the diffusion coefficient. The time required to extract 99% of the solute is $4.4t_c$, i.e., 17 times the time needed to extract the first 37%. Thus, it can be calculated how many hours would be required to extract 99% of the solute if the value for D is known. Bartle et al. (25) estimated that, for example, the extraction of 2,6-di-*tert*-butyl-4-methylphenol (BHT) from polypropylene pellets (3 mm in diameter) would take 80 h to obtain a 99% recovery. Temperature is a

© 1998 NRC Canada

Table 1. Extraction of print molecules from MI polymers.

	Recovery (%)		
	Theophylline	Caffeine	Xanthine
Soxhlet extraction (9:1 MeOH/HOAc, 24 h, 150 mL)	88–104	89	>69
Supercritical fluid extraction (CO_2, 40°C, 400 atm,[a] 0.5 mL/min, 1 h)	5	6	—
Supercritical fluid extraction (CO_2 + 5% MeOH, 40°C, 400 atm, 0.5 mL/min, 1 h)	10	—	—
Supercritical fluid extraction (N_20, 50°C, 300 atm, 0.5 mL/min, 1 h)	9	—	—

[a] 1 atm = 101.3 kPa.

very effective parameter for enhancing diffusion and shortening the time required for mass transfer from the core of the polymer particles to the surface. Elevated temperatures will also improve the extraction efficiency by increasing the solubility of the solute in the supercritical fluid. Consequently, significant improvements in SFE of print molecules from MI polymers would only be possible by using higher temperatures, longer extraction times, and supercritical fluids that are both good swelling agents for the polymer and good solvents for the analytes (26).

Anti-polymer overlayer

For a bare silver film 56 nm in thickness, the SPR angular profile was recorded to determine a resonance angle of θ_r = 45.3 ± 0.1° in the prism (see Fig. 3). When an overlayer of the *anti*-polymer was coated on the silver film, θ_r adopted a new value ranging from 45.5 ± 0.2° to 48.6 ± 0.1°. The amount of θ_r shift depends on the thickness of the *anti*-polymer overlayer. From the angular SPR data, the thickness of the *anti*-polymer layer is estimated at 5–10 nm. Note that the depth of penetration for the SPR evanescent field (i.e., the distance at which the light intensity falls to l/e of its initial value) from glass of refractive index n_1 into the medium of lesser refractive index n_2 is given by $dp = \lambda/2\pi(n_1^2\sin^2\theta_1 - n_2^2)^{1/2}$. Typical penetration depths are 100–200 nm (27). Consequently, a thicker *anti*-polymer layer can accommodate more analytes, resulting in a larger SPR response. An optimum thickness, which balances the two effects, exists. It was found that the MIA sensitivity for an *anti*-theophylline polymer overlayer prepared from a 0.04 mg/mL solution was 0.065 normalized unit, which is greater than the sensitivity of 0.055 normalized unit for another overlayer prepared from a 0.10 mg/mL solution. Apparently, the thinner *anti*-polymer overlayer (prepared from the 0.04 mg/mL solution) allowed faster diffusion of theophylline molecules from the external sample solution to the silver–polymer interface where dielectric constant changes were sensed by SPR. Thinner overlayers also generate sharper SPR angular profiles for more sensitive PDS measurements at constant θ. One limitation existed in the preparation of *anti*-polymer overlayers by spotting: the dried overlayer might not be very uniform across the silver film surface. This affected both the position and magnitude of the SPR dip, and reproducibility of results might suffer greatly. The technique of spin coating was attempted, but the problem was not totally resolved. Spraying techniques are being investigated for their usefulness in the preparation of uniform, ultrathin *anti*-polymer overlayers.

Fig. 3. The SPR–PDS angular profiles of bare silver film, silver film with an overlayer of *anti*-theophylline polymer, *anti*-theophylline polymer overlayer after exposure to 6.0 mg/mL of theophylline in water, and *anti*-theophylline polymer overlayer after exposure to 6.0 mg/mL of caffeine in water.

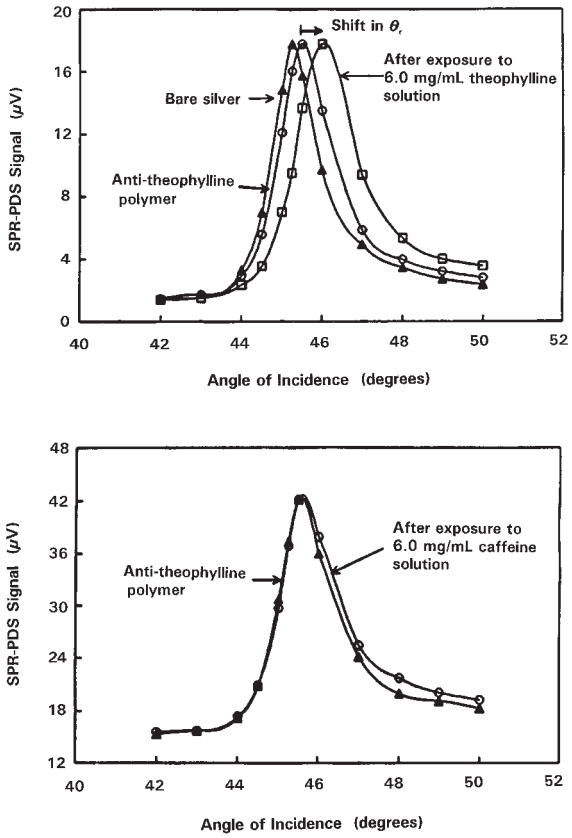

MIA

The capability of the *anti*-theophylline polymer to bind the target molecule selectively was evaluated. Using a bare silver film on the SPR sensor, the PDS signals yielded an angular profile with the peak maximum (or θ_r) at 45.3° as shown in Fig. 3. A thin overlayer of *anti*-theophylline polymer coated onto the silver film from a 0.04 mg/mL polymer solution gave a small θ_r shift of 0.2°. After a 1 h exposure of the *anti*-polymer overlayer to a blank solution containing no theophylline, no

© 1998 NRC Canada

Fig. 4. Standard calibration graph for MIA of theophylline by SPR–PDS.

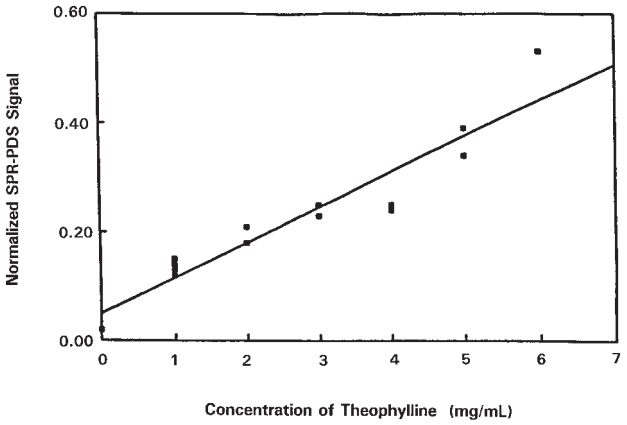

further shift in θ_r was observed. This *anti*-theophylline polymer overlayer was next used as the analysis surface for the MIA of theophylline in water. After the overlayer was exposed to a sample solution of 6.0 mg/mL theophylline for 1 h, the angular SPR profile (or θ_r) shifted further. Clearly, the uptake of theophylline molecules into the sorbent sites of the *anti*-polymer caused sufficient change in the dielectric constant of the overlayer to be monitored via a measurable shift in θ_r. A standard calibration curve was obtained by measuring the SPR–PDS signal amplitudes at a constant $\theta = 46.5°$ for several theophylline concentrations in the range from 0.0 to 6.0 mg/mL. As expected, the higher the concentration of theophylline, the greater the θ_r shift toward larger θ values and hence the stronger the PDS signal amplitude at constant 46.5°. Since the SPR–PDS signal was recorded on a different spot in replicate measurements, and the *anti*-polymer overlayer might not be uniform in thickness, the raw SPR–PDS calibration data were not highly reproducible or perfectly linear. For this reason, the SPR–PDS signals were normalized by calculating the relative deviation of the after-exposure signal from the pre-exposure signal measured at 46.5°. As shown in Fig. 4, the linearity (with a correlation coefficient of 0.97) of standard calibration demonstrates that the SPR–PDS sensor system can be used with MI polymers to determine their complementary print molecules fairly accurately. The signal changes are small enough to assume that the slope of the PDS response is linear. For theophylline in aqueous solution, the concentration detection limit is estimated at 0.4 mg/mL. This analytical sensitivity is modest mainly because the specific recognition of print molecules by their *anti*-polymers is generally most favoured in the same or similar solvent to that originally used for the polymer synthesis (28). Here, theophylline binding to the *anti*-polymer is the most efficient in chloroform. This specific binding can be compromised in aqueous medium where water effectively competes for the hydrogen bonding interactions (29). Similar findings have been evidenced in our recent investigation using the *anti*-polymer as a solid stationary phase in a HPLC column for the separation of theophylline from caffeine and xanthine in chloroform or water as the mobile phase.[2] Extraction of theophyline in blood serum with chloroform can potentially eliminate proteins, increase the analyte concentration,

[2] W.M. Mullet and E.P.C. Lai. Anal. Chem. (1998).Submitted.

Fig. 5. The SPR–PDS angular profiles of bare silver film, silver film with an overlayer of *anti*-caffeine polymer, silver film with an overlayer of *anti*-caffeine polymer after exposure to 3.0 mg/mL of caffeine in water, and after exposure of *anti*-caffeine polymer overlayer to 3.0 mg/mL of theophylline in water.

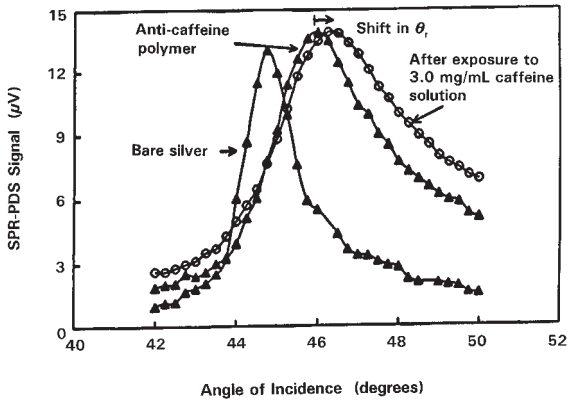

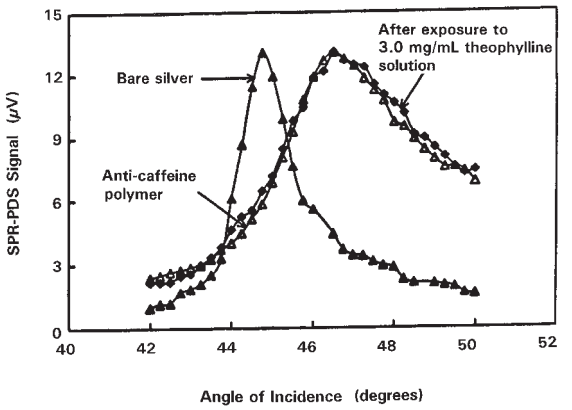

and afford a higher partition coefficient value for better MIA–SPR–PDS sensitivity than measurements in water.

It was proven to be true that print molecules having different shapes can produce cavities of different micro-architectures and functionalities. When our new *anti*-caffeine polymer was exposed to a sample solution of 3.0 mg/mL caffeine, there was a change in θ_r of 0.5° as can be seen in Fig. 5. The same *anti*-caffeine polymer exposed to 3.0 mg/mL theophylline exhibited no change in θ_r and hence showed no significant affinity for this different print molecule at the concentration specified. Thus, it can be concluded that the cavities formed in the caffeine-imprinted PMAA–EDMA during template polymerization possessed a shape and arrangement of functional groups, which corresponded to that of the caffeine molecule mainly. In another study, the print molecule was xanthine, which is the skeleton of theophylline and caffeine. The molecular recognition capability of the *anti*-xanthine polymer was tested by a cross-reaction with theophylline, which has two methyl groups added to the xanthine structure. After exposure of an *anti*-xanthine overlayer to a theophylline sample solution, there was no observable shift in θ_r. It can be concluded again that the *anti*-xanthine polymer had an affinity for its print molecule without the ability to take up theophylline in an amount sufficient to generate a SPR–PDS signal. To the best of our knowledge, this is the first report of *anti*-caffeine

© 1998 NRC Canada

and *anti*-xanthine polymers. Our work has extended and generalized the previous observations by Vlatakis et al. (6) that polymeric matrices formed by the MI technique could recognize their original print molecules. It demonstrates the great potential of MI polymer synthesis as an alternative approach to producing selective receptors for drug immunoassay. Lately, there has been a strong interest in automated analysis (under 6 min per sample) of caffeine and its metabolites (including theophylline and *p*-xanthine) in human plasma using high-performance liquid chromatography with dialysis (30). It would be interesting to see if SPR–PDS using *anti*-polymers could be developed to carry out this specific and other clinically important analyses without the cumbersome deproteination dialysis or plasma heparinization.

Fig. 6. Molecular structures of drugs used to test the selectivity of *anti*-polymers.

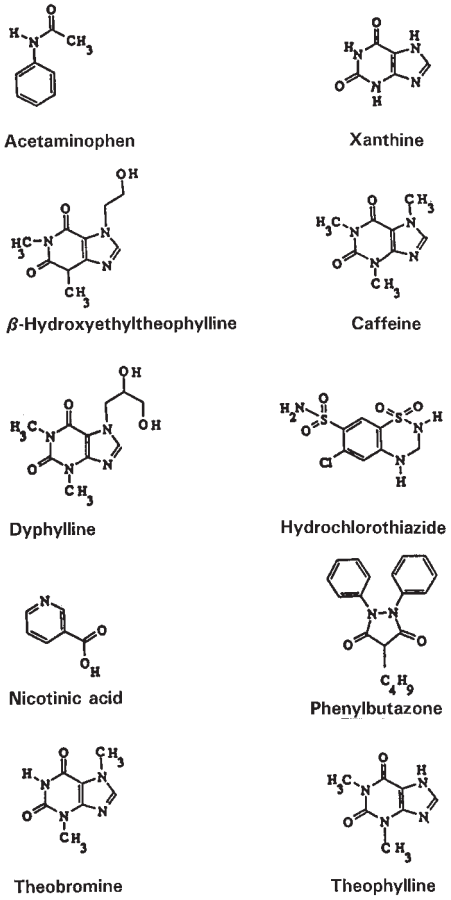

Selectivity of *anti*-polymers

Cross-reactivity of the *anti*-polymers with eight other drugs, several of which are of similar structures to the print molecules (Fig. 6), was studied to test their analytical selectivity. Acetaminophen, dyphylline, hydrochlorothiazide, β-hydroxyethyl theophylline, nicotinic acid, and phenyl butazone all produced no shift in θ_r when their solutions were tested on *anti*-theophylline overlayers. Only theobromine produced a slight shift of 0.2° and would cause minor interferences with the MIA of theophylline if it were present at concentrations above 1 mg/mL. Thus, it can be concluded that the *anti*-theophylline polymer has affinity only for its print molecule theophylline, but not for the other drugs studied in this work. It appears that the print molecule created, during the MI polymerization, a unique PMAA–EDMA architecture of cavities to which only it could recombine to. Although several of these other drugs are similarly shaped and contain many of the same functional groups, MI has shaped a microenvironment (shape and arrangement of functional groups) in those cavities that would not bind them in significant amounts.

Stability

A silver film exposed to the atmosphere was found by SPR analysis to be stable for one day, after which θ_r shifted by approximately 0.10° per day. This was expected, as silver is not stable in the atmosphere. A silver film coated with an *anti*-theophylline polymer overlayer, when exposed to the lab atmosphere, was found to be stable for three days. It generated SPR angular profiles at essentially the same θ_r position. After three days, there was a change in θ_r by 0.15° per day. A similar silver film coated with an *anti*-theophylline polymer overlayer, when kept inside a box, was found to be stable for three days. After that time, θ_r shifted by 0.10° per day. A third silver film coated with an *anti*-theophylline polymer overlayer, when kept under vacuum, was stable for five days. Afterwards only a slight shift in θ_r was observed, by 0.05° per day. Similarly, a silver film coated with an *anti*-xanthine polymer overlayer and kept under vacuum was stable for five days. After that, small shifts in θ_r were observed. These results show that the stability of silver films depends on such factors as room temperature, humidity, etc. If an *anti*-polymer overlayer was applied, it protected the silver film surface and retarded the deterioration. Actual data of use of an *anti*-theophylline polymer column that has been aged over one year in dry storage for the HPLC separation of theophylline from caffeine and xanthine is definitive evidence for the stability of the *anti*-polymer itself.[2]

The practical implication of silver film deterioration is that a differential θ_r measurement must always be made between two regions of the same *anti*-polymer overlayer, one having been exposed to a drug sample solution and the other to a blank only. Nevertheless, accompanying the shifts in θ_r was a broadening of the SPR angular profile, which reduced the steepness of the side slopes and hence decreased the analytical sensitivity in PDS measurements. For future development of SPR–MIA of drugs, it would be greatly beneficial to find a metal that is more stable in the atmosphere. A systematic study of gold films over an extended time period is already under way in order to achieve a longer shelf life for the MIA analysis surface.

The SPR–photodiode array sensor system

While the SPR–PDS sensor system was designed for maximal analytical sensitivity, it is limited to sequential angular measurements. Repeated measurements with increasing θs were required in order to obtain the entire SPR angular profile for a determination of θ_r. This could take some 30 min to complete a range from 42 to 50° if an angular resolution of 0.1° is desirable. A technically simpler and faster SPR sensor system was next developed by using a compact laser diode with convergent light incidence through a glass prism on the silver film and multichannel angular detection of the divergent reflected laser beam with a photodiode array (PDA). The SPR–PDA system

© 1998 NRC Canada

Fig. 7. The SPR–PDA angular intensity profiles for bare silver film, silver film with an overlayer of *anti*-xanthine polymer, *anti*-xanthine polymer overlayer after exposure to 1.0 mg/mL of xanthine in water, and *anti*-xanthine polymer overlayer after exposure to 1.0 mg/mL of theophylline in water.

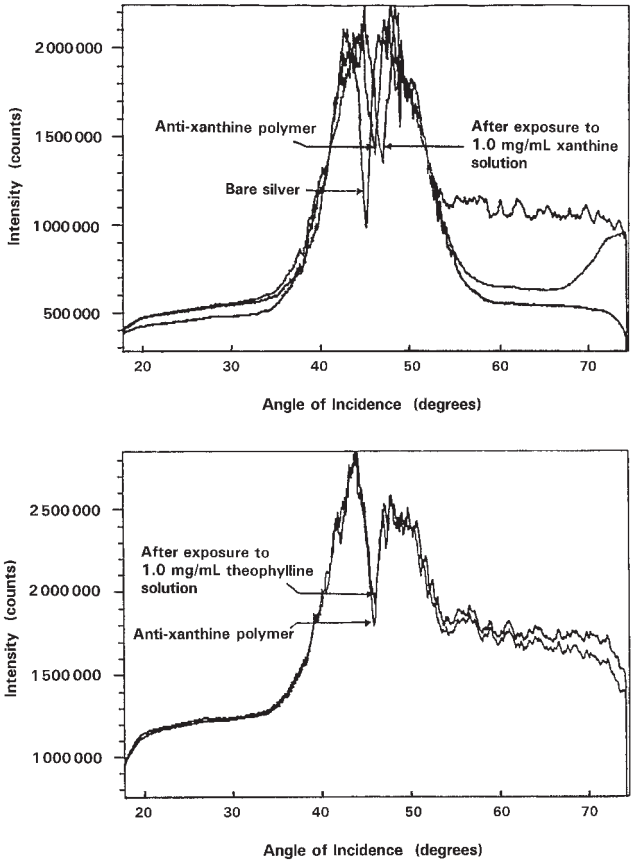

generated a complete angular profile instantly when the reflected beam intensities were monitored simultaneously on many diodes in the array to correspond with various θs at the silver film. Since the incident light was coupled to the surface plasmons, the reflected beam would be diminished in intensity to exhibit a dip in the SPR angular profile. It is obvious from Fig. 7 that the convergent laser beam covered a sufficiently large range of θ to encompass the full width of the SPR dip, with an angular resolution of 0.055°. For a bare silver film, θ_r could be determined as 45.3 ± 0.1° at which the dip minimum occurred. With an *anti*-xanthine polymer overlayer prepared on the silver film from a 0.06 mg/mL solution, θ_r changed to 46.2 ± 0.1°. After the overlayer was exposed to a 1.0 mg/mL xanthine solution, a further shift in θ_r to 47.2 ± 0.1° was observed. Once again, the molecular recognition capability of *anti*-xanthine polymer was proven when the overlayer was exposed to a 1.0 mg/mL theophylline solution, and no shift in θ_r was observed. The faster analysis speeds and good precision of the SPR–PDA sensor system offer several advantages, including shorter method development time and more analyses completed in less time. These could be of great benefits, for example, to the determination of xanthine among nucleosides and bases in biochemical samples.

One drawback of the SPR–PDA sensor system based on a laser diode was the appearance of noise spikes on the angular

Fig. 8. The SPR–PDA angular intensity profiles for a bare silver film, using a planar LED as the light source.

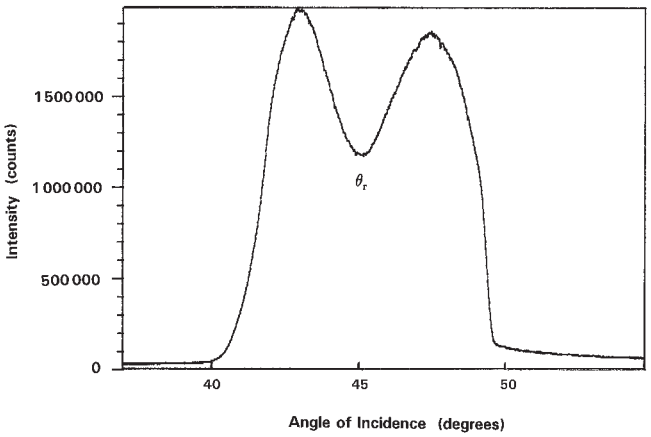

profiles. A better light source would be a planar light-emitting diode (LED) with a spatially uniform output (31). The result in Fig. 8 shows that a very smooth SPR angular profile can be obtained using the LED source, which allows a more precise determination of θ_r. However, curve fitting of a theoretical SPR equation to experimental data is more difficult to perform because of the spatial incoherence and angular divergence of the LED light.

Conclusions

Vlatakis et al. (6) first showed in 1993 that polymeric matrices could be formed by the MI technique to contain cavities that could hold print molecules. Our work has extended their synthetic method to the creation of two new *anti*-polymers with specific binding capacities for caffeine and xanthine. More importantly, an optical sensor system based on SPR has been developed with the use of either PDS or a PDA for the direct determination of drug molecules without prior separation. The PDS offers good sensitivity for the detection of small shifts in θ_r and hence SPR–PDS signal at constant θ during immunoassay. The concentration detection limit is estimated at 0.4 mg/mL of theophylline in aqueous solution. On the other hand, PDA provides a simple and fast acquisition of an entire SPR angular profile for the easy characterization of *anti*-polymers. Results obtained from both SPR–PDS and SPR–PDA have proven that new *anti*-caffeine and *anti*-xanthine polymers can be formed by the MI technique, to hold cavities and sites that have a selective affinity for the original print molecules but do not recognize other structurally similar drugs. Eventually, extension of the MI technique to nucleotide bases such as adenine and guanine (which have similar structures to xanthine) will be of high significance in biochemical analysis. Application of chemically selective *anti*-polymers in SPR sensors has one limitation in terms of the 60 min incubation step. Future work of SPR–MIA based on *anti*-polymers will need to investigate the binding kinetics for rapid sorption of print molecules in different solvents and buffers. The response time and degree of reversibility will determine if thin polymer overlayers can be used as the sensing element of a SPR sensor for continuous monitoring applications in flow injection analysis,

© 1998 NRC Canada

or in electrochromatography for analysis of complex biological samples.

Acknowledgements

This research was partly funded by the Natural Sciences and Engineering Research Council of Canada. Financial support from Dean ApSimon and Dean Gardner, Carleton University, is gratefully acknowledged. M.K. would like to thank the Natural Sciences and Engineering Research Council for an Undergraduate Student Research Award in the summer of 1993. Sincere thanks are extended to Dr. R. Burk for technical SFE instructions and to Dr. J. Yeung, Health Canada, for the drugs tested in the cross-reactivity study.

References

1. M. Vanderlaan, L. Stanker, and B. Watkins (*Editors*). *In* Immunoassays for trace chemical analysis. American Chemical Society, Washington, D.C. 1990.
2. B. Limoges, C. Degrand, P. Brossier, and R.L. Blankespoor. Anal. Chem. **65**, 1054 (1993).
3. (*a*) G. Wulff and A. Sharhan. Angew. Chem. 364 (1972); (*b*) G. Wulff, A. Sharhan, and K. Zabrocki. Tetrahedron Lett. **14**, 4329 (1973); (*c*) G. Wulff, W. Vesper, R. Grobe-Einsler, and A. Sharhan. Makromol. Chem. **178**, 2799 (1977).
4. (*a*) L.I. Anderson, B. Sellergren, and K. Mosbach. Tetrahedron Lett. **25**, 5211 (1984); (*b*) B. Sellergren, B. Ekberg, and K. Mosbach. J. Chromatogr. **347**, 1 (1985).
5. J. Matsui, T. Kato, T. Takeuchi, M. Suzuki, K. Yokoyama, E. Tamiya, and I. Karube. Anal. Chem. **65**, 2223 (1993).
6. G. Vlatakis, L.I. Anderson, R. Muller, and K. Mosbach. Nature (London), **361**, 645 (1993).
7. D. Kriz, O. Ramström, and K. Mosbach. Anal. Chem. **69**, 345A (1997).
8. M.T. Muldoon and L.H. Stanker. Chem. Ind. (London). March 18, 1996. p. 204.
9. S.A. Piletsky, Yu.P. Parhometz, N.V. Lavryk, T.L. Panasyuk, and A.V. El'skaya. Sens. Actuators B, **19**, 629 (1994).
10. D. Kriz, O. Ramström, A. Svensson, and K. Mosbach. Anal. Chem. **67**, 2142 (1995).
11. S.A. Piletsky, E.V. Piletskaya, K. Yano, A. Kugimiya, A.V. Elgersma, R. Levi, U. Kahlow, T. Takeuchi, and I. Karube. Anal. Lett. **29**, 157 (1996).
12. J.J. Cowan. Opt. Commun. **5**, 69 (1972).
13. (*a*) B. Rothenhäusler and W. Knoll. Nature (London), **332**, 615 (1988); (*b*) W. Hickel and W. Knoll. Acta Metall. **37**, 2141 (1989).
14. F.W. Schneider. *In* Non-linear Raman spectroscopy and its applications. *Edited by* W. Kiefer and D.A. Long. Reidel, Dordrecht. 1982. p. 461.
15. I. Lee, T.A. Callcott, and E.T. Arakawa. Anal. Chem. **64**, 476 (1992).
16. (*a*) R.P.H. Kooyman, H. Kolkman, J. Van Gent, and J. Gerve. Anal. Chim. Acta, **213**, 35 (1988); (*b*) B. Liedberg, C. Nylander, and I. Lundström. Sens. Actuators, **4**, 299 (1983).
17. F. Villuendas, J. Tornos, and J. Pelayo. Sens. Actuators A, **37**, 187 (1993).
18. L.T. Flanagan and R.H. Pantell. Electron. Lett. **20**, 968 (1984).
19. T. Inagaki, K. Kagami, and E.T. Arakawa. Phys. Rev. B: Condens. Matter, **24**, 3644 (1981).
20. V.A. VanderNoot and E.P.C. Lai. Spectroscopy, **6**, 28 (1991).
21. H.A. Schuessler, S.H. Chen, Z. Rong, Z.C. Tang, and E.C. Benck. Appl. Opt. **31**, 2669 (1992).
22. A.A. Kolomenskii, P.D. Gershon, and H.A. Schuessler. Prog. Nat. Sci. **6**, S558 (1996).
23. S. Borman. C & EN. Jan. 2, 1995. p. 21.
24. Y. Hirata and Y.J. Okamato. Microcolumn Sep. **1**, 46 (1989).
25. K.D. Bartle, A.A. Clifford, S.B. Hawthorne, J.L. Langenfield, D.J. Miller, and R.J. Robinson. Supercrit. Fluids: Chem. Eng. Princ. Appl. **3**, 143 (1990).
26. X. Lou, H.G. Janssen, and C.A. Cramers. Anal. Chem. **69**, 1598 (1997).
27. J.K. Rice, R.A. Dunbar, and F.V. Bright. Appl. Spectrosc. **48**, 1030 (1994).
28. M. Kempe and K. Mosbach. J. Chromatogr. A, **694**, 3 (1995).
29. J. Mathew and O. Buchardt. Bioconjugate Chem. **6**, 524 (1995).
30. R.E. Major. LC-GC, **13**, 364 (1995).
31. K. Matsubara and S. Kawata. Appl. Opt. **27**, 1160 (1988).

© 1998 NRC Canada

A conformational study of (1*S*, 2*R*, 5*S*)-(+)-menthol using vibrational circular dichroism spectroscopy

Jennifer L. McCann, Arvi Rauk, and Hal Wieser

Abstract: We report the experimental and predicted absorption and vibrational circular dichroism (VCD) spectra of (1*S*, 2*R*, 5*S*)-(+)-menthol. The harmonic force fields and atomic polar tensors (APTs) were obtained for 10 conformers using density functional theory (DFT) with the Becke3LYP functional and the 6-31G** basis set. The atomic axial tensors (AATs) were obtained with restricted Hartree–Fock (RHF) theory and a 6-31G basis set. VCD intensities were predicted from vibronic coupling theory (VCT). The predicted absorption and VCD spectra based on an equilibrium mixture of conformers corresponded well with the experimental spectra, indicating a reasonable geometry and frequency analysis for each of the conformers. The largest contributions towards the equilibrium population derive from conformers in which the cyclohexane ring occupies a chair conformation, the isopropyl group is directed away from the hydroxyl group, and only the hydroxyl group assumes different conformations.

Key words: vibrational circular dichroism (VCD), menthol, conformational analysis.

Résumé : On rapporte les valeurs expérimentales et calculées pour les spectres d'absorption et de dichroïsme circulaire vibrationnel (DCV) du (1*S*,2*R*,5*S*)-(+)-menthol. On a déterminé les champs de force harmonique et les tenseurs atomiques polaires (TAP) de 10 conformères en utilisant la théorie de la densité fonctionnelle (TDF) avec la fonction Becke3LYP et l'ensemble de base 6-31G**. On a obtenu les tenseurs atomiques axiaux (TAA) à l'aide de la théorie de Hartree–Fock restreinte (HFR) et un ensemble de base 6-31G. Les intensités du DCV ont été calculées à partir de la théorie du couplage vibronique (TCV). Les valeurs prédites pour l'absorption et les spectres de DCV, telles que basées sur un mélange à l'équilibre de conformères, correspondent bien aux spectres expérimentaux; ceci indique que la géométrie utilisée et l'analyse de fréquence pour chacun des conformères sont raisonnables. Les contributions les plus importantes à la population à l'équilibre proviennent des conformères dans lesquels le noyau cyclohexane est en conformation chaise, le groupe isopropyle est orienté en direction opposée au groupe hydroxyle et que seul le groupe hydroxyle prend diverses conformations.

Mots clés : dichroïsme circulaire vibrationnel (DCV), menthol, analyse conformationnelle.

[Traduit par la rédaction]

Introduction

Within the framework of structural analysis, vibrational circular dichroism (VCD) spectroscopy (for a general review see ref. 1) has been proven a valuable technique for elucidating the molecular structure of chiral molecules in solution. Even a cursory glance at the VCD spectra of a series of chiral molecules indicates that VCD is remarkably sensitive to small changes in molecular structure, particularly in comparison to conventional absorption spectroscopy. In conjunction with theoretical models, VCD is capable of determining the conformation and absolute configuration of existing or newly discovered chiral molecules. The ability to determine the total molecular structure directly for a wide range of molecules has allowed VCD to create its own niche within the field of conformational analysis and stereochemical determination (for example, see ref. 2).

We have chosen to examine the conformational structure of menthol and its diastereomeric isomers as part of a spectroscopic study on the chiroptical properties of optically active polymers having a chiral substituent, specifically, menthol, isomenthol, or neomenthol (3). Principally, we are interested in the conformation of the menthol moiety and its interaction with the polymer component of the system. The present study was initiated to better understand how the conformation of the menthol moiety is characterized in the VCD spectra, and to relate the VCD spectrum of the menthol pendant to the VCD spectrum of the corresponding polymer.

A second motivation for the current study stems from the fact that menthol plays a central role in many biological and chemical asymmetric reactions, the bulk of which occur in solution. The principle approach in understanding the role of menthol in stereochemical applications involves obtaining explicit knowledge of the molecular structure in solution. The structure of menthol and (or) its derivatives has previously been examined by various techniques including VCD spectroscopy (4), Raman optical activity (ROA) spectroscopy (5), matrix isolation Fourier transform (MI-FT) spectroscopy (6),

Received September 3, 1997.

J.L. McCann, A. Rauk, and H. Wieser.[1] Department of Chemistry, The University of Calgary, Calgary, AB T2N 1N4, Canada.

[1] Author to whom correspondence may be addressed. Telephone: (403) 220-4934. Fax: (403) 289-9488. E-mail: hwieser@acs.ucalgary.ca

© 1998 NRC Canada

Fig. 1. Molecular structure and atom numbering of (1*S*, 2*R*, 5*S*)-(+)-menthol displayed as conformer **1** and conformer **2**.

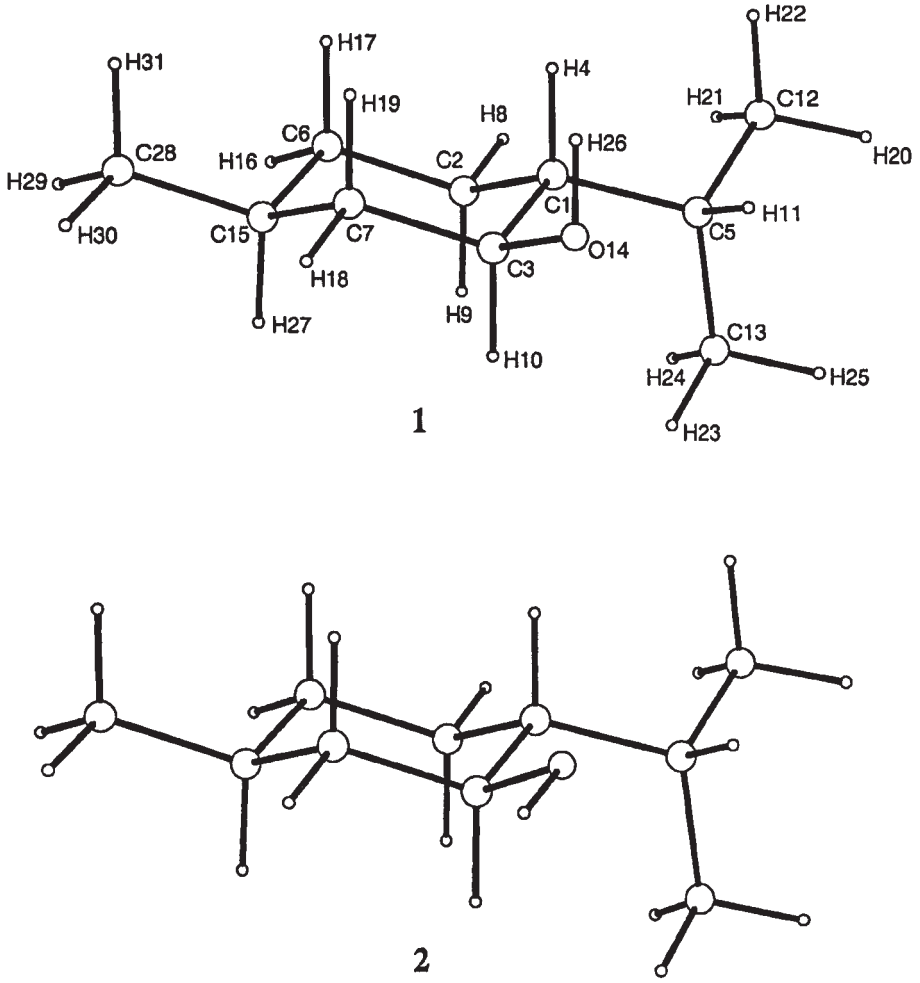

optical rotation (7), as well as common techniques such as X-ray diffraction (for example, ref. 8), NMR (9), and IR spectroscopy (10). However, in none of these cases has it been possible to probe satisfactorily the conformation of the hydroxyl group.

In this paper we present the experimental and predicted IR absorption and VCD spectra of (1*S*, 2*R*, 5*S*)-(+)-menthol. IR and VCD spectra are predicted by ab initio computations. The results from experiment and computation are compared and discussed, with emphasis on the conformation of the hydroxyl and isopropyl groups.

Experimental

(1*S*,2*R*,5*S*)-(+)-Menthol was purchased from Aldrich and was used without further purification. Infrared absorption and VCD spectra were recorded at 4 cm^{-1} resolution on a modified Bomem FT-IR spectrometer (11). The spectra are displayed from 830 to 1550 cm^{-1}. Samples for both IR and VCD spectra were prepared as 0.4 M CCl_4 solutions and measured in a 0.15 mm KBr liquid cell. VCD spectral acquisition involved collecting a block of 500 dc scans, immediately followed by the collection of a block of 5000 ac scans. The raw VCD spectrum was corrected for artifacts by subtracting the VCD spectrum of the opposite enantiomer, and then calibrated in the usual fashion (12). Experimental IR and VCD spectra were analyzed using the Labcalc software (13).[2]

Computations

Computation of the VCD spectra was performed in two stages. In the first stage optimized equilibrium geometries, energies, harmonic force fields, and atomic polar tensors (for absorption intensities) were obtained for 10 conformers via density functional theory (DFT) with the Gaussian94 (14) program using a combination of Becke's three-parameter hybrid method (15) and the correlation functional of Lee, Yang, and Parr (16, 17) (i.e., Becke3LYP), with the 6-31G** basis set. The choice of Becke's hybrid density functional is based on the claim for superior agreement between experiment and theory during the harmonic vibrational analyses of a number of small chiral molecules (18, 19). In the second stage, VCD intensities were calculated with the same equilibrium geometries, harmonic force fields, and atomic polar tensors, and with atomic axial tensors generated at the RHF level and 6-31G basis set in the distributed origin gauge using vibronic coupling theory (VCT) (20–23).

Predicted spectra are displayed as Lorentzian band shapes

[2] Labcalc, Galactic Industries Corp., 395 Main Street, Salem, NH 03079, U.S.A.1992.

© 1998 NRC Canada

Fig. 2. Newman projections of the rotamers of (*a*) the isopropyl group about the C_5—C_1 bond and (*b*) the hydroxyl group about the O_{14}—C_3 bond. Torsion angles (in parentheses) are defined as the angle between H_{11} and H_4 along the C_5—C_1 bond for the isopropyl group, and between H_{26} and H_{10} along the O_{14}—C_3 bond for the hydroxyl group.

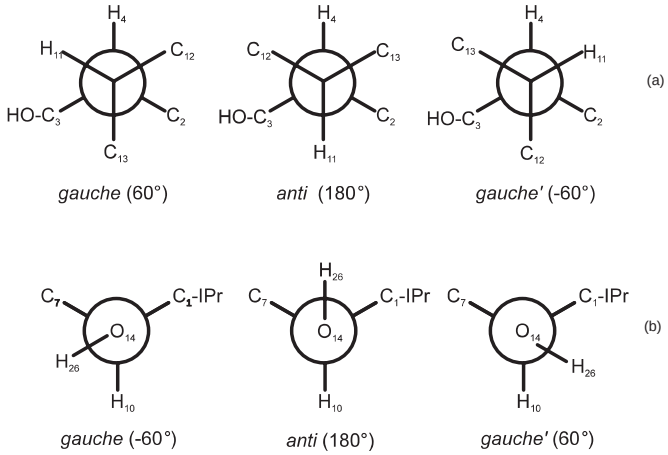

with half-width at half-height of 5 cm^{-1}. Calculated frequencies were uniformly scaled by 0.985 to provide a closer match to experiment. The structural formula and atom numbering used for calculations are given in Fig. 1.

Results and discussion

Conformational and normal mode analyses

Menthol presents a computational challenge as it has a relatively large formula weight and considerable conformational flexibility. The input geometry of menthol used in the present calculations is based on the more stable chair conformation of the cyclohexane ring. The conformational flexibility arises from the possibility of ring inversion and rotation of the isopropyl and hydroxyl groups. For both groups there are 3 possible staggered rotational isomers, comprising a total of 9 rotamers if all substituents are equatorial, or 18 if both equatorial and axial positions are considered for the chair conformation. The energies for 10 of these isomers were calculated, namely, the 9 for which all substituents are equatorial, and 1 conformer in which all substituents are axial. In the conformational and vibrational analyses to follow, the conformation in which all substituents occupy an axial position will not be discussed, other than to obtain the relative energy and molecular populations.

The nomenclature used below to define the conformers is based on the conventional *gauche* (*g*), *anti* (*a*), and *gauche′* (*g′*) designations, which correspond to torsion angles $\tau(H_{11}\text{-}C_1\text{-}C_5\text{-}H_4)$ of 60°, 180°, and –60°, respectively, for the isopropyl group, or torsion angles $\tau(H_{26}\text{-}O_{14}\text{-}C_3\text{-}H_{10})$ of –60°, 180°, and 60°, respectively, for the hydroxyl group (Fig. 2). The nine conformers defined in terms of the torsion angles of the isopropyl and hydroxyl substituents are listed in Table 1, along with the corresponding Becke3LYP/6-31G** energies. In each case the starting geometry was a reasonable structure based on ideal staggered conformations that was then further optimized.

In conformers **1**, **2**, and **4** the isopropyl group occupies an almost perfectly staggered *gauche* conformation, with torsion angles $\tau(H_{11}\text{-}C_5\text{-}C_1\text{-}H_4)$ of 68.85°, 65.53°, and 63.15°, respectively. In the *gauche′* conformation, the isopropyl group is distorted from the perfectly staggered position by ~20°, with torsion angles $\tau(H_{11}\text{-}C_5\text{-}C_1\text{-}H_4)$ of –78.33°, –82.04°, and –81.87° for conformers **3**, **5**, and **7**, respectively. The *anti* conformations of the isopropyl group are also distorted from the perfectly staggered position by ~20°. When the hydroxyl proton is *anti* or *gauche*, the proton of the isopropyl group is directed toward the OH group with torsion angles $\tau(H_{11}\text{-}C_5\text{-}C_1\text{-}H_4)$ corresponding to 163.42° and 154.85°, respectively. When the hydroxyl proton is *gauche′*, i.e., pointing towards the isopropyl group, the environment is more crowded and the proton of the isopropyl group is oriented away from the hydroxyl group with a torsion angle of –160.24°. Rotamers of the hydroxyl group are almost perfectly staggered for the *gauche* and *anti* conformers, with torsion angles, $\tau(H_{26}\text{-}O_{14}\text{-}C_3\text{-}H_{10})$, of –62.24±0.44° and –178.67±1.17° (mean±s.d.), respectively. The more sterically hindered *gauche′* conformation of the hydroxyl group has a more distorted torsion angle of 47.50±2.83°.

Bond distances, angles, and torsion angles averaged over the first nine conformers are listed in Table 2. The average C—C bond distances are reasonable, although more elongated in the crowded environment around C_1. Within the cyclohexane ring, the average C-C-C bond angle is greater than 109° and the average C-C-C-C torsion angle is less than 60°, indicating that the ring is flatter than the normal cyclohexane geometry. The greatest standard deviation of geometrical parameters among the isomers occurs in the vicinity of the isopropyl and hydroxyl groups, while the rest of the ring remains reasonably constant.

The relative energies (including the zero point energy) that were obtained from the Becke3LYP/6-31G** computations were used to estimate the population of conformers from the Boltzmann distribution law. It predicts that only 2 of the 10 isomers will contribute significantly to the population, namely, conformers **1** and **2** (Fig. 1), which account for 37.7% and 24.9%, respectively. In general, the lowest energy conformers are those in which the isopropyl group occupies a *gauche* position, whereas an *anti* position of the isopropyl group is associated with higher energy. The next highest energy conformers are those that have undergone ring inversion, followed by the boat conformations of the cyclohexane ring, the latter of which was calculated using the MM3 force field of Macromodel (24).

A set of non-redundant internal coordinates (local symmetry coordinates, LSCs) was defined following the recommendations of Fogarasi and Pulay (25) (available from the authors). Potential energy distributions (PEDs) calculated at the Becke3LYP/6-31G** level are shown in Table 3 for ν_{67}–ν_{23} for the two lowest energy conformers. PED contributions less than about 10% are not included, with the exception of contributions from O–H bending that have been included for ν_{44}. The vibrations are generally highly coupled, with the descriptions listed in Table 3 accounting for about 11% of a normal mode at worst and 90% at best.

Vibrational analysis

Absorption spectra

The experimental absorption spectra of menthol are displayed

© 1998 NRC Canada

Table 1. Definition and relative energies for the conformers of menthol.[a]

Conformer	Position of hydroxyl group	Isopropyl torsion (°)	Hydroxyl torsion (°)	Isopropyl–hydroxyl torsion notation of conformers	Relative energy [b] (kJ/mol)	Boltzmann distribution [c] (%)
1	eq	68.85 (*g*)	–177.79 (*a*)	*ga*	0.00	37.7
2	eq	65.53 (*g*)	–61.78 (*g*)	*gg*	1.03	24.9
3	eq	–78.33 (*g′*)	–180.0 (*a*)	*g′a*	2.45	14.0
4	eq	63.15 (*g*)	49.64 (*g′*)	*gg′*	2.98	11.3
5	eq	–82.04 (*g′*)	–62.29 (*g*)	*g′g*	3.90	7.8
6	eq	163.42 (*a*)	–178.23 (*a*)	*aa*	7.77	1.6
7	eq	–81.87 (*g′*)	44.29 (*g′*)	*g′g′*	7.80	1.6
8	eq	154.85 (*a*)	–62.65 (*g*)	*ag*	9.57	0.8
9	eq	–160.24 (*a*)	48.57 (*g′*)	*ag′*	13.42	0.2
10	ax	170.07 (*a*)	63.47 (*g′*)	*ag′*	24.34	0.0

[a] From DFT/Becke3LYP/6-31G** calculations.
[b] The energy term includes the sum of electronic and zero point energies.
[c] Calculated at 298 K.

Table 2. Selected average[a] geometrical parameters for the conformers of menthol.[b]

Bond distances / Å				
	C_1—C_2	1.545 ± 0.002	C_1—C_5	1.558 ± 0.004
	C_2—C_6	1.534 ± 0.000	C_5—C_{12}	1.538 ± 0.001
	C_6—C_{15}	1.536 ± 0.001	C_5—C_{13}	1.538 ± 0.001
	C_{15}—C_7	1.536 ± 0.001		
	C_7—C_3	1.534 ± 0.002	C_3—O_{14}	1.431 ± 0.001
	C_3—C_1	1.544 ± 0.004	O_{14}—H_{26}	0.966 ± 0.001
Bond angles /°				
	C_2-C_1-C_3	109.00 ± 0.54		
	C_1-C_2-C_6	112.93 ± 0.68		
	C_2-C_6-C_{15}	112.01 ± 0.28		
	C_6-C_{15}-C_7	109.42 ± 0.38		
	C_{15}-C_7-C_3	113.25 ± 0.58		
	C_7-C_3-C_1	111.81 ± 0.44		
Torsion angles /°				
	C_1-C_2-C_6-C_{15}	–56.22 ± 0.51		
	C_2-C_6-C_{15}-C_7	53.91 ± 0.48		
	C_6-C_{15}-C_7-C_3	–54.50 ± 0.27		
	C_{15}-C_7-C_3-C_1	56.05 ± 1.11		
	C_7-C_3-C_1-C_2	–54.07 ± 1.82		
	C_3-C_1-C_2-C_6	54.84 ± 0.95		

[a] Averages and standard deviations for conformers **1**–**9**.
[b] Geometries are calculated at the DFT/Becke3LYP/6-31G** level.
Atom numbering is shown in Fig. 1

in Fig. 3*a* as a CCl_4 solution and in Fig. 3*b* as a KBr pellet. Figure 3*c* is a composite spectrum that represents the superposition of the predicted spectra of conformers **1**–**9** weighted by Boltzmann distribution (Table 1). Most bands in the composite spectrum arise from the predicted spectrum of one of the two lowest energy conformers (**1** or **2** shown in Fig. 3*d* and 3*e*, respectively), thus permitting the assignment of each band in the composite spectrum to one or more normal modes of **1** or **2**. The analysis performed in this paper involved assigning the experimental bands (numbered 1–32 from low to high frequency, Fig. 3*a*), followed by comparison to bands in the composite spectrum (numbered 1–32 correspondingly, Fig. 3*c*). The experimental bands could then be interpreted in terms of the normal modes of **1** or **2** (numbered 23–67, Fig. 3*d* and 3*e*, respectively). Overall, the theoretical and experimental spectra are in excellent agreement.

Bands 1–9 of the composite spectrum correspond to ν_{23}–ν_{31} for both **1** and **2**, generally agreeing to within a few wave numbers with experiment (Table 3). Although bands 10–15 also tend to agree with experiment, better correspondence could be obtained by small intensity changes and (or) frequency shifts. The larger discrepancies in this region affect bands arising from modes with C–O stretching character, namely bands 10, 11, 12, and 15. In the composite spectrum band 10 is predicted to be too low in intensity, while bands 11 and 12 are predicted to be too high. A slight shift to higher frequency of the calculated band 14, and to lower frequency of band 15, would improve the correspondence with the

© 1998 NRC Canada

Table 3. Experimental and calculated frequencies, dipole strengths, rotational strengths, and PED assignments for two conformers of menthol.

					Calculated[a]							
	Experimental				Conformer **1**				Conformer **2**			
Band	Freq.[b]	D[c]	R[d]	Mode	Freq.[e]	D	R	Assignment from PED[f]	Freq.[e]	D	R	Assignment from PED
1	845	33.0		23	838	17.7	8.5	12.2(C_{15}–C_6 ring stretch) 10.7(C_1–C_3 ring stretch) 10.1(CH_2 rock at C_7)	842	10.5	11.4	11.9(CH_2 rock at C_7) 11.3(C_{15}–C_6 ring stretch) 10.0(CH_2 rock at C_6)
2	876	21.7		24	873	5.0	15.9	25.3(CH_2 rock at C_6) 18.8(Ipr sym stretch)	872	33.1	6.9	23.4(CH_2 rock at C_6) 20.6(Ipr sym stretch)
3	916		–33.1	25	915	3.6	–12.9	16.0(CH_3 rock at C_{28}) 13.3(C_7–C_{15} ring stretch) 10.0(Ipr o/ph rock)	916	1.2	–20.9	19.1(Ipr o/ph rock) 12.1(CH i/p rock at C_5) 10.7(C_7–C_{15} ring stretch)
4	919	45.2		26	919	18.2	–87.2	20.5(CH_2 rock at C_7) 17.8(CH_2 rock at C_2)	921	12.3	99.5	29.1(Ipr o/ph rock) 18.8(CH i/p rock at C_5) 10.8(Ipr o/ph rock')
5	924		173.1	27	923	13.1	93.4	33.0(Ipr o/ph rock) 21.1(CH i/p rock at C_5) 12.5(Ipr o/ph rock')	922	3.3	–64.5	16.2(CH_2 rock at C_7) 14.2(CH_2 rock at C_2) 11.5(CH_3 rock at C_{28})
6	955	6.6	–32.3 (952)[g]	28	953	1.8	–42.9	35.8(Ipr o/ph rock') 16.4(Ipr asym stretch) 11.0(Ipr o/ph rock)	952	1.9	19.6	37.6(Ipr o/ph rock') 17.8(Ipr asym stretch) 11.0(Ipr o/ph rock)
7	966	7.9	106.8	29	963	12.1	53.5	19.1(CH_3 rock at C_{28}) 16.7(CH o/p rock at C_{15})	966	6.3	–1.1	19.7(CH_3 rock at C_{28}) 17.5(CH o/p rock at C_{15})
8	976	20.2	–30.7	30	976	30.9	–63.2	14.6(Ipr i/ph rock') 12.9(C_2–C_1 ring stretch) 11.0(CH_3 rock at C_{28})	976	21.9	–33.4	16.4(Ipr i/ph rock') 12.4(C–Ipr stretch) 11.4(C_6–C_2 ring stretch)
9	992	79.2	300.0	31	987	50.1	29.0	16.5(C–CH_3 stretch) 14.5(C_3–C_7 ring stretch)	994	26.0	86.0	18.7(C_3–C_7 ring stretch) 12.7(C–CH_3 stretch)
10	1024	184.7	–545.5	32	1027	55.3	–136.8	15.3(C_6–C_2 ring stretch) 14.3(C–O stretch)	1026	67.8	–125.3	15.5(C_6–C_2 ring stretch) 9.7(C–O stretch)
11	1044	115.2	264.0 (1042)[g]	33	1044	150	–81.1	18.8(C–O stretch) 13.0(C_6–C_2 ring stretch)	1050	126.9	–53.1	16.2(C_6–C_2 ring stretch) 12.6(C–O stretch) 11.1(C_1–C_3 ring stretch)
12	1056	37.8	411.2	34	1060	57.2	156.7	13.3(CH o/p rock at C_1) 12.7(C–O stretch)	1060	59.7	190.5	20.2(C–O stretch) 13.1(C_3–C_7 ring stretch)
13	1078	30.3	271.8	35	1079	22.8	113.6	11.6(C_1–C_3 ring stretch) 11.3(Ipr asym stretch)	1065	23.4	143.1	10.9(Ipr asym stretch) 10.3(C_1–C_3 ring stretch)
14	1094	34.2		36	1092	108.7	–45.6	18.2(C–CH_3 stretch) 10.1(OH bend) 10.0(OH o/p bend)	1089	5.1	55.9	14.4(CH_2 twist at C_7) 11.0(CH i/p rock at C_1)
15	1103	20.7	–515.0	37	1103	5.7	–40.7	15.3(C_3–C_7 ring stretch) 14.7(CH_2 twist at C_7)	1112	71.7	–167.9	18.6(C–CH_3 stretch) 17.5(C–O stretch) 16.3(Ring trigonal def)
16	1138	12.4	155.6	38	1138	18.0	120.4	10.5(Ipr asym stretch)	1142	32.6	108.7	11.2(C_{15}–C_6 ring stretch) 11.0(CH_3 rock at C_{28}) 10.2(OH bend)
17	1157	1.4	–20.3	39	1161	17.6	–12.5	11.9(Ipr i/ph rock)	1156	4.4	5.2	12.9(OH o/p bend)
18	1174	18.0	44.2	40	1183	16.4	–25.0	10.7(Ipr i/ph rock)	1181	26.6	–5.5	17.2(Ipr i/ph rock)
19	1180	17.9	–20.6	41	1192	18.4	–33.1	26.8(Ipr i/ph rock') 14.8(C–Ipr stretch) 12.0(Ipr sym stretch) 10.5(Ipr i/ph rock)	1191	19.4	1.8	25.7(Ipr i/ph rock') 14.2(C–Ipr stretch) 11.1(Ipr sym stretch)
20	1209	2.4		42	1213	12.8	80.3	17.6(CH o/p rock at C_3)	1220	104.3	–188.0	15.1(OH bend)
21	1223	14.0	–177.7					12.6(OH bend)				12.1(CH o/p rock at C_3)
22	1258	20.7		43	1255	0.7	–11.9	22.3(CH o/p rock at C_1) 17.2(IPr o/p bend) 13.4(CH_2 twist at C_6)	1255	1.8	–6.1	19.1(CH o/p rock at C_1) 15.7(IPr o/p bend) 13.7(CH_2 twist at C_6) 11.7(CH_2 twist at C_7)

© 1998 NRC Canada

Table 3 (*continued*).

	Experimental				Calculated[a]							
					Conformer **1**				Conformer **2**			
Band	Freq.[b]	*D*[c]	*R*[d]	Mode	Freq.[e]	D	*R*	Assignment from PED[f]	Freq.[e]	*D*	*R*	Assignment from PED
23	1271	11.1	582.8	44	1265	31.9	–101.4	16.3(CH_2 twist at C_2) 14.6(CH o/p rock at C_3) 10.7(CH_2 wag at C_6) 6.4(OH bend)	1268	47.2	354.3	15.7(CH_2 twist at C_2) 13.7(CH o/p rock at C_{15}) 12.3(OH bend) 11.4(CH i/p rock at C_3) 10.1(CH_3 o/p bend)
24	1289	16.0	66.8	45	1285	9.4	63.4	27.4(CH o/p rock at C_{15}) 18.1(CH_3 o/p bend) 17.6(CH_2 wag at C_7)	1285	2.3	–11.8	25.5(CH_2 wag at C_7) 17.7(CH o/p rock at C_{15}) 16.0(CH o/p rock at C_3) 11.9(CH_3 o/p bend) 10.7(OH o/p bend)
				46	1307	5.6	–15.7	34.7(CH o/p rock at C_1) 14.1(IPr o/p bend)	1301	24.9	2.2	23.9(CH i/p rock at C_1) 12.2(CH o/p rock at C_5)
26	1308	13.9	–13.5	47	1324	5.8	–44.1	26.8(CH o/p rock at C_{15}) 15.9(CH_2 wag at C_6) 13.2(CH_3 o/p bend) 11.1(CH_2 twist at C_2)	1318	16.5	18.4	33.1(CH o/p rock at C_1) 19.6(CH i/p rock at C_5) 12.9(IPr o/p bend) 10.7(Ipr twist)
				48	1330	10.9	–18.8	17.9(CH o/p rock at C_{15}) 17.8(CH i/p rock at C_5)	1327	6.7	–22.0	28.4(CH o/p rock at C_{15}) 14.5(CH_3 o/p bend) 12.6(CH_2 wag at C_6) 11.3(CH_2 twist at C_2)
				49	1339	11.4	49.2	23.0(CH o/p rock at C_5)	1349	5.4	49.4	26.9(CH_2 wag at C_2) 26.3(CH o/p rock at C_5)
				50	1358	3.6	34.6	37.5(CH i/p rock at C_5) 15.4(Ipr twist) 11.1(CH_2 wag at C_2)	1360	1.7	–56.2	40.7(CH i/p rock at C_5) 16.3(Ipr twist)
27	1345	10.4		51	1367	9.6	–35.4	21.2(CH i/p rock at C_{15}) 11.9(CH i/p rock at C_5)	1362	2.7	–38.0	21.3(CH i/p rock at C_{15}) 15.8(CH o/p rock at C_3) 13.1(CH o/p rock at C_{15}) 10.0(OH o/p bend)
				52	1380	8.3	–81.6	20.5(CH o/p rock at C_5) 19.3 (CH i/p rock at C_1) 10.5 (CH i/p rock at C_3)	1369	30.4	–74.7	23.7(CH o/p rock at C_3) 11.8(OH o/p bend)
				53	1385	0.7	42.8	17.8(CH o/p rock at C_1) 10.6 (CH o/p rock at C_{15}) 10.3 (CH i/p rock at C_5)	1383	2.3	–16.7	18.8(CH o/p rock at C_{15}) 14.0(CH_2 wag at C_6)
				54	1387	5.2	26.0	19.9(CH o/p rock at C_{15}) 16.0(CH o/p rock at C_1)	1386	13.3	–18.9	16.3(CH o/p rock at C_1) 12.4(CH o/p rock at C_3)
28	1369	68.8		55	1398	23.4	21.4	54.1(Ipr o/ph sym def) 11.7(CH i/p rock at C_5)	1397	21.3	–134.9	57.3(Ipr o/ph sym def) 11.9(CH i/p rock at C_5)
				56	1404	24.2	41.9	69.7(CH_3 sym def) 11.1(CH o/p rock at C_3)	1404	2.6	9.1	86.2(CH_3 sym def)
29	1385	35.8		57	1408	119.9	–108.6	49.1(CH o/p rock at C_3) 32.8(OH o/p bend)	1412	14.3	–21.3	82.3(Ipr i/ph sym def)
				58	1417	19.7	12.4	79.2(Ipr i/ph sym def)	1423	15.8	–22.4	25.9(CH o/p rock at C_3) 13.2(OH o/p bend)
				59	1473	0.1	1.2	44.3(CH_2 scissor at C_7) 42.3(CH_2 scissor at C_6)	1474	0.4	–2.0	49.3(CH_2 scissor at C_6) 35.5(CH_2 scissor at C_7)
				60	1478	5.5	–15.9	47.9(Ipr o/ph asym def) 37.9(Ipr o/ph asym def')	1478	4.5	–22.5	53.8(Ipr o/ph asym def) 35.7(Ipr o/ph asym def')
30	1447	47.9		61	1480	8.7	–23.3	54.6(CH_2 scissor at C_2) 21.5(CH_2 scissor at C_7) 10.4(Ipr o/ph asym def)	1481	7.4	–17.8	55.6(CH_2 scissor at C_2) 24.5(CH_2 scissor at C_7)

© 1998 NRC Canada

Table 3 (*concluded*).

	Experimental				Calculated[a]							
					Conformer **1**				Conformer **2**			
Band	Freq.[b]	D[c]	R[d]	Mode	Freq.[e]	D	R	Assignment from PED[f]	Freq.[e]	D	R	Assignment from PED
				62	1486	3.3	–49.9	29.5(CH_2 scissor at C_6) 19.0(CH_3 asym def) 13.7(CH_2 scissor at C_7) 11.4(CH_2 scissor at C_2)	1487	3.2	–61.8	30.2(CH_3 asym def) 18.2(CH_2 scissor at C_6) 12.8(Ipr o/ph asym def')
31	1455	73.3		63	1489	26.6	17.0	60.3(CH_3 asym def) 12.6(Ipr o/ph asym def')	1489	21.2	34.3	38.3(CH_3 asym def) 27.9(Ipr o/ph asym def') 14.1(Ipr o/ph asym def)
				64	1491	7.8	76.9	48.3(CH_3 asym def') 12.8(Ipr o/ph asym def') 10.3(CH_2 scissor at C_6)	1491	8.6	48.1	30.8(CH_3 asym def') 18.4(CH_2 scissor at C_6) 14.6(CH_3 asym def)
				65	1492	0.2	2.4	31.9(CH_3 asym def') 15.9(Ipr o/ph asym def') 14.9(CH_2 scissor at C_2)	1492	1.6	20.5	48.5(CH_3 asym def') 15.2(CH_2 scissor at C_7) 11.0(CH_2 scissor at C_2)
32	1465	57.8		66	1500	13.5	29.6	69.5(Ipr i/ph asym def) 15.0(Ipr i/ph asym def')	1499	16.5	32.7	76.7(Ipr i/ph asym def)
				67	1502	12.1	–1.6	71.0(Ipr i/ph asym def') 11.0 (Ipr i/ph asym def)	1501	11.7	1.4	78.5(Ipr i/ph asym def')

[a]Calculated at the DFT/Becke3LYP/6-31G** level of theory.
[b]Units of frequency are wave number (cm^{-1}).
[c]Units of dipole strength (D) are 10^{-40} (esu·cm)^2.
[d]Units of rotational strength (R) are 10^{-45} (esu cm)^2.
[e]Frequencies are scaled by 0.985.
[f]Only PED with a contribution greater than about ~10% are shown.
[g]Numbers in parentheses correspond to the peak position (cm^{-1}) of the VCD peak.
Symbols: Ipr = isopropyl group; sym = symmetric, asym = asymmetric; i/p = in plane; o/p = out of plane; i/ph = in phase; o/ph = out of phase; def = deformation

experimental spectrum. The bands arising from OH bending, namely 16, 21, and 23, are also closely reproduced in frequency, albeit at a significantly lower intensity. The lower than predicted intensity of these modes is attributed to intermolecular hydrogen bonding. Additional disparities arising from variations in intensity and frequency occur in the regions of methyl symmetric and asymmetric deformations, but are difficult to determine specifically due to the large number of overlapping bands. The most obvious inaccuracy is the failure to predict the characteristic doublet of the isopropyl group that is usually observed at 1385/1370 cm^{-1}. In particular, the in- and out-of-phase asymmetric deformations are predicted to be too close together in frequency.

VCD spectra

The experimental and composite VCD spectra are shown in Fig. 4*a* and 4*b*, respectively. The spectra of the two lowest energy conformers (**1** and **2**) and the corresponding normal modes are shown in Fig. 4*c* and 4*d*. The numbered bands of the experimental and composite spectra correspond to the same transitions observed in absorption. The correspondence between experiment and theory for VCD is even more remarkable than for the absorbance spectra, although the intensities are appreciably underestimated.

Bands 1 and 2 in the composite spectrum are too weak to be observed in the experimental spectrum. Bands 3–9 are reproduced very well in the composite spectrum. Band 10 has a strong negative signal arising from ν_{32} of both **1** and **2**. Band 11 of the composite spectrum is predicted to be negative,

Fig. 3. Absorption spectra of (1*S*, 2*R*, 5*S*)-(+)-menthol from 1550 to 830 cm^{-1}: (*a*) 0.4 M CCl_4 solution; (*b*) KBr pellet; (*c*) a composite of conformers **1**–**9** weighted by Boltzmann distribution; (*d*) conformer **1**; (*e*) conformer **2**. Numbering for (*d*) and (*e*) corresponds to the actual normal modes, and is arbitrary for (*a*) and (*c*).

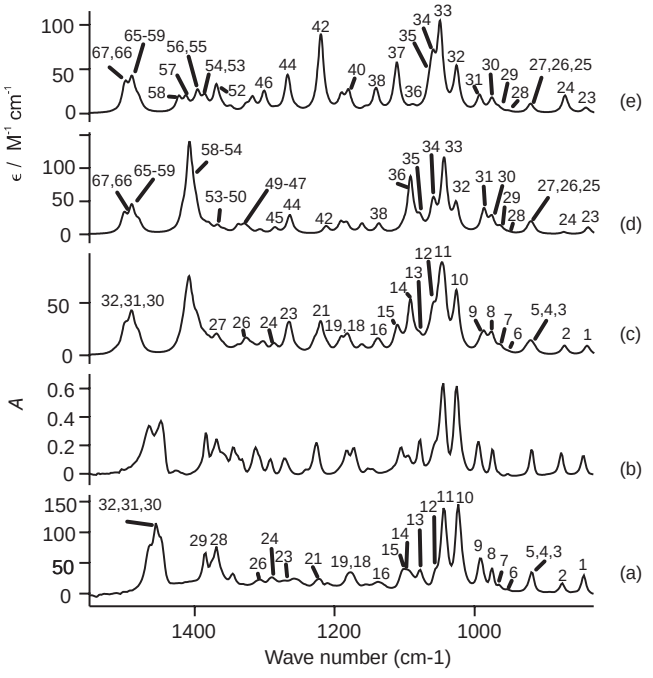

© 1998 NRC Canada

Fig. 4. VCD spectra of (1*S*, 2*R*, 5*S*)-(+)-menthol from 1550 to 830 cm^{-1}: (*a*) 0.4 M CCl_4 solution; (*b*) a composite of conformers **1**–**9** weighted by Boltzmann distribution; (*c*) conformer **1**; (*d*) conformer **2**. Numbering for (*c*) and (*d*) corresponds to the actual normal modes and is arbitrary for (*a*) and (*b*). The arbitrary assignment of numbers in (*a*) and (*b*) corresponds to the numbering used in the absorption spectra (Fig. 3).

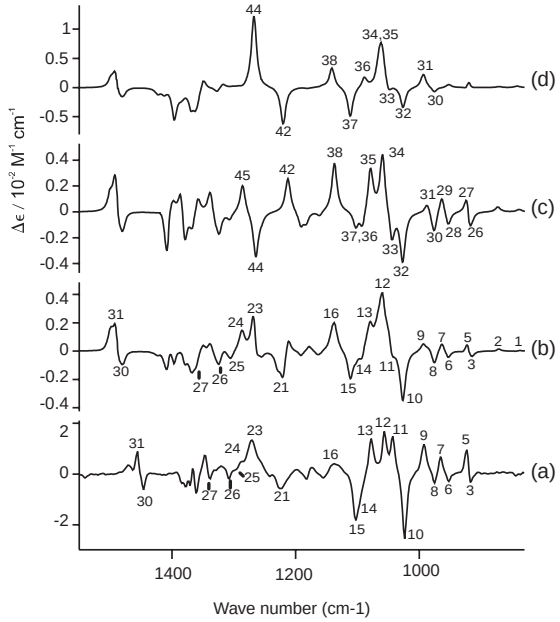

Fig. 5. Simulated absorption spectra of the nine conformers of (+)-menthol listed in Table 1.

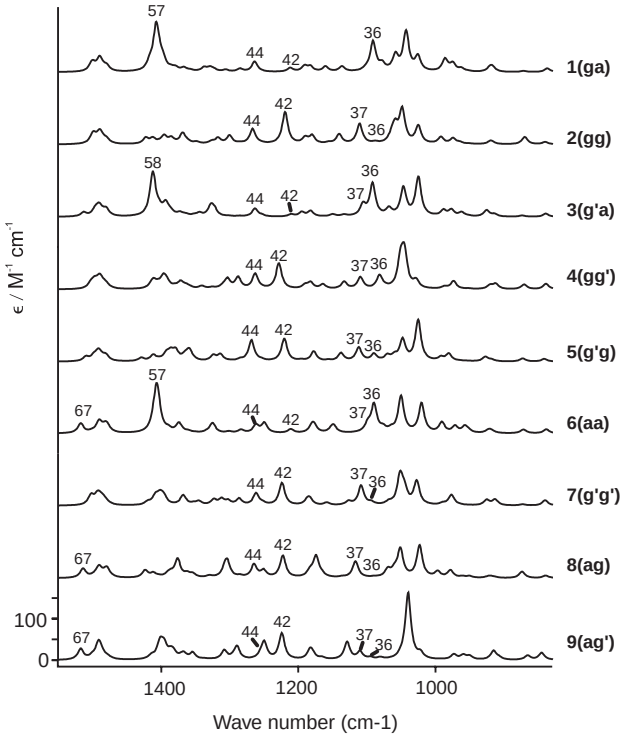

whereas the experimental spectrum exhibits a strong positive feature at the same frequency. Band 12 of the composite spectrum (1062 cm^{-1}) has positive intensity contributions from ν_{34} of **1**, and ν_{34} and ν_{35} of **2**, and is predicted to be too high in intensity. This can be rationalized as follows. If ν_{34} for either **1** and (or) **2** were calculated 10–12 cm^{-1} lower, then the large positive signal for ν_{34} would cancel out the smaller negative signal for ν_{33} occurring at the same frequency, thereby reproducing the characteristic triplet pattern of the experimental spectrum. In the absorption spectrum the intensity of band 12 would be reduced and the peak position of 11 would be shifted to lower frequency while only slightly increasing the intensity of the latter. Accordingly, peak 11 in the experimental VCD spectrum is thought to arise from ν_{34} of **1** and (or) **2**, band 12 is assigned to ν_{35} of **2**, band 13 to ν_{35} of **1**, band 14 to ν_{36} and (or) ν_{37} of **1**, and band 15 to ν_{37} of **2**. Similar to the absorption spectrum, the experimental VCD bands with significant OH bending character are expected to have larger band widths and lower intensities than predicted due to intermolecular hydrogen bonding. The bands arising from OH bending occur at 16, 21, and 23. Band 23 originates from ν_{44} of **2**, while the small negative shoulder at lower frequency originates from the same mode (ν_{44}) of **1**. Similarly, band 21 originates from ν_{42} of **2**, whereas the small positive peak at lower frequency originates from the same mode of **1**. The assignment of band 21 demonstrates the potential of VCD for conformational analysis, where the simple rotation of a ring substituent may change the sign of a signal arising from the same normal mode. In general, the assignment of VCD spectra provides another dimension to spectroscopic analysis, which invariably helps in assigning the vibrational spectra more definitively. Specifically, the analysis of the VCD spectrum has permitted the assignment of a large portion of the experimental absorption spectrum of menthol, a task which would be difficult based on the absorption spectrum alone.

General trends

The computed absorption spectra of the nine conformers of (+)-menthol are displayed in Fig. 5 and the corresponding VCD spectra in Fig. 6. Overall, the absorption and VCD spectra predicted for each rotational isomer are unique, providing a "fingerprint" for each isomer. There are, however, certain trends that can be identified. In particular, the isopropyl and hydroxyl groups have localized vibrations corresponding to the methyl deformations and O–H bending, respectively.

The isopropyl group is characterized by the isopropyl in- or out-of-phase asymmetric deformations coupled with CH_2 scissoring at C_2, C_6, C_7 (1470–1520 cm^{-1}). Thus this region can serve in principle as a conformational probe of the isopropyl group, provided the skeleton of the ring remains the same. The absorption spectrum is noticeably overlapped when the isopropyl group occupies a *gauche* position, more separated for a *gauche´* position, and highly separated for an *anti* position. Specifically, ν_{67}, which consists largely of the isopropyl in-phase asymmetric deformation, is at a much higher frequency for the *anti* conformation. The VCD spectra in Fig. 6 reinforce the generalizations for the absorption spectra. The *gauche* conformers exhibit a very characteristic –/+ bisignate pattern (bands 30/31 from Fig. 4), in contrast to the more sterically hindered *gauche´* or *anti* arrangements where the VCD patterns become more complex and difficult to classify unambiguously. Both the highly overlapped absorption bands and –/+ bisignate VCD signals of the experimental spectra indicate

© 1998 NRC Canada

Fig. 6. Simulated VCD spectra of the nine conformers of (+)-menthol listed in Table 1.

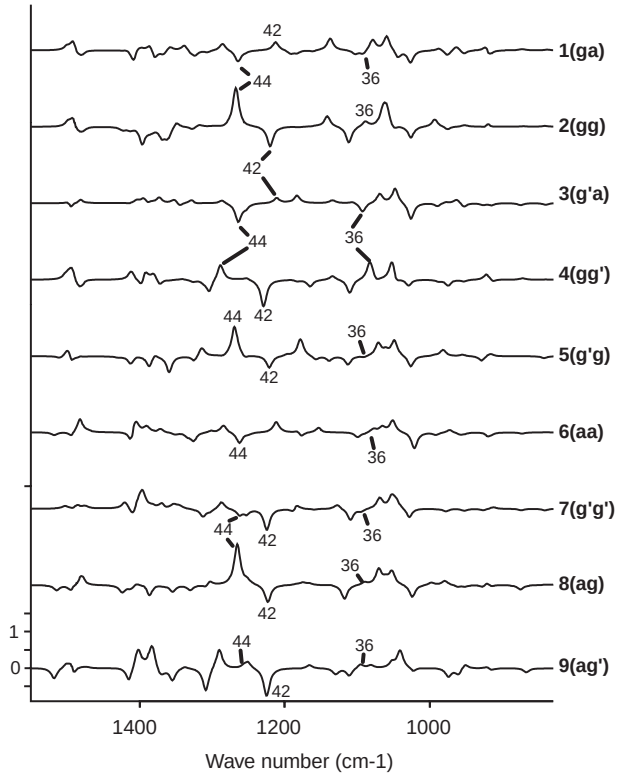

that the dominant conformation of the isopropyl group is *gauche*, in agreement with the predicted populations listed in Table 1.

The bands affected by O–H bending vibrations are similarly characteristic. In absorption, an *anti* position of the hydroxyl group is characterized by a large signal associated with normal modes ν_{57}, ν_{58}, and ν_{36}, and relatively weak signals from modes ν_{37}, ν_{42}, and ν_{44} (Fig. 5). In contrast, the signal arising from ν_{37}, ν_{42}, and ν_{44} is high when the hydroxyl group occupies a *gauche* or *gauche′* position, while that from ν_{57}/ν_{58} and ν_{36} is notably smaller. In the VCD spectra (Fig. 6), the O–H bending patterns are best illustrated by ν_{42} and ν_{44}. For *gauche* conformers of the hydroxyl group, the peaks arising from ν_{42} and ν_{44} are very similar in intensity and sign, displaying strong negative and positive bands for the two modes, respectively. When the hydroxyl group occupies an *anti* conformation the situation is more complex. The largest contribution of O–H bending occurs in ν_{36} and ν_{42}, with a smaller contribution also in ν_{44} (i.e., 6–7%). Modes ν_{42} and ν_{44} appear as strong positive and negative VCD peaks, respectively, the exact opposite of those observed for the *gauche* conformer. Although mode ν_{36} is consistently negative for the *anti* conformer, it is generally lower in intensity and in a more congested region of the spectrum. When the hydroxyl group occupies a *gauche′* position, the O–H bend still contributes significantly to ν_{42} and ν_{44} (although only 4.4% for ν_{44} for conformer 10), giving rise to a strong negative peak for ν_{42} and a weak peak for ν_{44} that is either positive or negative.

The most notable findings here are that the VCD spectra change systematically with the orientation of the hydroxyl and isopropyl groups. These results confirm that VCD spectroscopy can be used as a conformational probe for substituents on the cyclohexane ring, provided the skeleton of the ring remains reasonably the same. Furthermore, if a strong, isolated band exists that is characteristic of a certain conformation, then it may be possible to ascertain the dominant conformation.

Conclusions

Ab initio calculations were performed for 10 conformers of (1*S*, 2*R*, 5*S*)-(+)-menthol. For each conformer, the geometry, force field, and atomic polar tensors necessary for the vibrational frequencies and absorption intensities were calculated at the DFT/B3LYP/6-31G** level using the Gaussian94 program. The atomic axial tensors needed for determining the rotational strengths were calculated at the HF/6-31G level of theory using the VCT90 and Gaussian90 programs, and were combined with the atomic polar tensors and force field calculated at the DFT/B3LYP/6-31G** level to predict the VCD spectra of the 10 conformers. The relative energies calculated for the 10 optimized conformers were used to determine the equilibrium mixture of isomers according to Boltzmann's distribution, from which the composite absorption and VCD spectra were generated. Accordingly, the conformational equilibrium of menthol consists primarily (70%) of contributions from two rotational isomers of the hydroxyl group with the isopropyl group in the *gauche* conformation. The calculated absorption spectrum resulting from the equilibrium mixture of these two isomers is consistent with the experimental observations.

The predicted VCD features also show remarkable agreement with the experimental spectra, despite the lower level of calculations and complexity of the molecule, further demonstrating that it is the quality of the force fields which is important in VCD computations. In fact, the ability to obtain a high correlation for this large terpene demonstrates the potential for VCD spectroscopy in structural analysis of chiral molecules with considerable flexibility and size. The results show that VCD is very sensitive to the conformation of the menthol molecule, including rotational isomers of the substituents on the cyclohexane ring.

Acknowledgements

We would like to thank the Natural Sciences and Engineering Research Council of Canada (NSERC) for financial support. J.L.M. would like to thank the Killam Trust and the University of Calgary for support in the form of graduate scholarships.

References

1. (*a*) L.A. Nafie. Appl. Spectrosc. **50**, 14A (1996); (*b*) P.J. Stephens and M.A. Lowe. Annu. Rev. Phys. Chem. **36**, 213 (1985); (*c*) T.B. Freedman and L.A. Nafie. Top. Stereochem. **17**, 113 (1987).
2. (*a*) J. McCann, A. Rauk, G. Shustov, H. Wieser, and D. Yang. Appl. Spectrosc. **50**, 630 (1996); (*b*) K.J. Jalkanen and S. Suhai. Chem. Phys. **208**, 81 (1996); (*c*) P. Xie and M. Diem. J. Am. Chem. Soc. **117**, 429 (1995).
3. J.L. McCann, A. Rauk, and H. Wieser. J. Mol. Struct. **408**/**409**, 417 (1997).
4. (*a*) L.A. Nafie, T.A. Keiderling, and P.J. Stephens. J. Am. Chem.

© 1998 NRC Canada

Soc. **98**, 2715 (1976); (*b*) R.D. Singh and T.A. Keiderling. J. Am. Chem. Soc. **103**, 2387 (1981); (*c*) L. Laux, V. Pultz, S. Abbate, H.A. Havel, J. Overend, and A. Moscowitz. J. Am. Chem. Soc. **104**, 4276 (1982).

5. (*a*) L.D. Barron and B.P. Clark. J. Chem. Soc. Perkin Trans. 2, 1164 (1979); (*b*) L.D. Barron, L. Hecht, and S.M. Blyth. Spectrochim. Acta, **45A**, 375 (1989).
6. W.M. Coleman III, B.M. Gordon, and B.M. Lawrence. Appl. Spectrosc. **43**, 298 (1989).
7. D. Galisteo, M.E. González-Vadillo, J.A. López Sastre, M.H. Martínez García, and J.F. Rodríguez Amo. J. Mol. Struct. **326**, 239 (1994).
8. (*a*) C. Altona and M. Sundaralingam, Tetrahedron, **26**, 925 (1970); (*b*) A. Heumann. J. Chem. Soc. Chem. Commun. 1113 (1993); (*c*) A. Linden. Acta Crystallogr. Sect. C: Cryst. Struct. Commun. **C51**, 1694 (1995); (*d*) M.R. Caira, V.J. Griffith, L.R. Nassimbeni, and B Van Oudtshoorn. Supramol. Chem. **7**, 119 (1996).
9. (*a*) H. Feltkamp and N.C. Franklin. Tetrahedron, **21**, 1541 (1965); (*b*) C.P. Rader. J. Am. Chem. Soc. **88**, 1713 (1966); (*c*) I. Ohtani, T. Kusumi, M.O. Ishitsuka, and H. Kakisawa. Tetrahedron Lett. **30**, 3147 (1989); (*d*) I. Ohtani, T. Kusumi, Y. Kashman, and H. Kakisawa. J. Am. Chem. Soc. **113**, 4092 (1991); (*e*) T. Pehk, E. Lippmaa, M. Lopp, A. Paju, B.C. Borer, and R.J.K. Taylor. Tetrahedron: Asymmetry, **4**, 1527 (1993); (*f*) A. Heumann and R.J. Faure. J. Org. Chem. **58**, 1276 (1993); (*g*) M. Trujillo, E.Q. Morales, and J.T. Vazquez. J. Org. Chem. **59**, 6637 (1994).
10. (*a*) H.S. Aaron and C.P. Rader. J. Am. Chem. Soc. **85**, 3046 (1963); (*b*) P. Parimoo, A. Bharathi, and D. Mamatha. Asian J. Chem. **8**, 247 (1996).
11. D. Tsankov, T. Eggimann, and H. Wieser. Appl. Spectrosc. **49**, 132 (1994).
12. L.A. Nafie and D.W. Vidrine. *In* Practical Fourier transform infrared spectroscopy. Vol 3. *Edited by* J.R. Ferroaro and L.J. Basile. Academic Press, New York. 1982. p. 83.
13. P. Bour, J. McCann, and H. Wieser. J. Phys. Chem. A. **102**, 102 (1998).
14. M.J. Frisch, G.W. Trucks, H.B. Schlegel, P.M.W. Gill, B.G. Johnson, M.A. Robb, J.R. Cheeseman, T. Keith, G.A. Petersson, J.A. Montgomery, K. Raghavachari, M.A. Al-Laham, V.G. Zakrzewski, J.V. Ortiz, J.B. Foresman, J. Cioslowski, B.B. Stefanov, A. Nanayakkara, M. Challacombe, C.Y. Peng, P.Y. Ayala, W. Chen, M.W. Wong, J.L. Andres, E.S. Replogle, R. Gomperts, R.L. Martin, D.J. Fox, J.S. Binkley, D.J. Defrees, J. Baker, J.P. Stewart, M. Head-Gordon, C. Gonzalez, and J.A. Pople. Gaussian 94, Revision D.2. Gaussian, Inc., Pittsburgh, Pa. 1995.
15. A.D. Becke. J. Chem. Phys. **98**, 5648 (1993).
16. C. Lee, W. Yang, and R.G. Parr. Phys. Rev. B: Condens. Matter, **37**, 785 (1988).
17. B. Miehlich, A. Savin, H. Stoll, and H. Preuss. Chem. Phys. **157**, 200 (1989).
18. P.J. Stephens, F.J. Devlin, C.F. Chabalowski, and M.J. Frisch. J. Phys. Chem. **98**, 11623 (1994).
19. F.J. Devlin, J.W. Finley, P.J. Stephens, and M.J. Frisch. J. Phys. Chem. **99**, 16883 (1995).
20. L.A. Nafie and T.B. Freedman. J. Chem. Phys. **78**, 7108 (1983).
21. M.J. Frisch, M. Head-Gordon, G.W. Trucks, J.B. Foresman, H.B. Schlegel, K. Raghavachari, M. Robb, J.S. Binkley, C. Gonzalez, D.J. Defrees, D.J. Fox, R.A. Whiteside, R. Seeger, C.F. Melius, J. Baker, R.L. Martin, L.R. Kahn, J.J.P. Stewart, S. Topiol, and J.A. Pople. Gaussian 90, Revision I. Gaussian, Inc., Pittsburgh, Pa. 1990.
22. D. Yang and A. Rauk. J. Chem. Phys. **97**, 6517 (1992).
23. D. Yang. Ph.D. Dissertation, University of Calgary, Calgary. 1992.
24. Macromodel V3.5x: F. Mohamadi, N.G.J. Richards, W.C. Guida, R. Liskamp, C. Caufield, G. Chang, T. Hendrickson, and W.C. Still. J. Comput. Chem. **11**, 11 (1990); **11**, 440 (1990).
25. G. Fogarasi and P. Pulay. *In* Vibrational spectra and structure. Vol 13. *Edited by* J.R. Durig. Elsevier, New York. 1985. p. 162.

© 1998 NRC Canada

Interdeterminancy of basin and surface properties of an open system

R.F.W. Bader and F.J. Mart n

Abstract: This paper delineates and illustrates an important physical consequence of the Heisenberg equation of motion governing the expectation value of an observable for a proper open system, one whose basin is bounded by a surface of zero flux in the gradient vector field of the electron density. For a system in a stationary state, this theorem derives from the variation of Schrödinger's energy functional over an open system. The variation demonstrates that the surface of the *open* system, as well as the wave function and energy of the *total* system, are simultaneously stationary with respect to any and all variations $\delta\psi$, corresponding to a stationarity with respect to any and all physical perturbations $-(i\varepsilon/\hbar)\hat{G}\psi$ caused by a generator $\hat{G}$. Thus the properties of a proper open system are dependent upon its surface and vice versa, the theorem equating the expectation value of the commutator of the Hamiltonian and a generator $\hat{G}$ for the open system to the flux in the current density for $\hat{G}$ through its surface. The criticisms of the interdependence of the basin and surface properties of a proper open system that appeared recently in this journal are refuted, including the argument that mutiplication of an electron density by a constant factor yields a density for a different system. The consequences of this interdependence in the construction of a polypeptide through the use of amino acid residues defined as proper open systems is discussed and illustrated through the explicit calculation of the properties of the C|N interatomic surfaces of the amidic bonds. It is demonstrated that the the degree of transferability of a residue is determined by the degree of similarity in the properties of its two bounding amidic surfaces.

Key words: electron density, transferability of density, atoms in molecules, zero flux surface.

Résumé : Dans ce travail on délimite et on illustre une conséquence physique importante de l'équation de mouvement d'Heisenberg relative à la valeur probable d'un phénomène observable d'un système ouvert propre, dont le bassin est fixé par une surface de flux zéro dans le vecteur de gradient du champ de la densité électronique. Pour un système en état stationnaire, ce théorème est dérivé à partir de la variation de la fonction d'énergie de Schrödinger sur le système ouvert. La variation démontre que la surface du système *ouvert*, de même que la fonction d'onde ainsi que l'énergie du système *total*, sont tous stationnaires simultanément par rapport à chacune et à toutes les variations $\delta\psi$; ceci correspond à un état stationnaire par rapport à chacune et à toutes les perturbations physiques $-(i\varepsilon/\hbar)\hat{G}\psi$ provoquées par un générateur $\hat{G}$. Ainsi, les propriétés d'un système ouvert dépendent de sa surface et vice versa puisque, selon le théorème, la valeur probable du commutateur de l'Hamiltonien et d'un générateur $\hat{G}$ d'un système ouvert égale le flux de la densité de courant pour $\hat{G}$ à travers sa surface. On doit donc considérer que les critiques qui ont été publiées récemment dans ce journal au sujet de l'interdépendance du bassin et des propriétés de surface d'un système ouvert propre sont réfutées, y compris l'argument que la multiplication d'une densité électronique par un facteur constant conduit à une densité pour un système différent. On discute des conséquences de cette interdépendance dans la construction d'un polypeptide par l'utilisation de résidus d'acides aminés définis comme des systèmes ouverts propres et on l'illustre par le biais de calculs explicites de propriétés de surfaces interatomiques C|N de liaisons amidiques. On démontre que le degré de transférabilité d'un résidu est déterminé par le degré de similarité dans les propriétés de ses deux surfaces amidiques limitantes.

Mots clés : densité d'électron, transférabilité de la densité, atomes dans des molécules, surface de flux zéro.

[Traduit par la rédaction]

Proper open systems

A proper open system is a region of real space bounded by a surface $S(\mathbf{r})$ through which there is a zero flux in the gradient vector field of the electron density (1–3), the "zero-flux" condition stated in eq [1]:

$$[1] \quad \nabla\rho(\mathbf{r})\cdot\mathbf{n}(\mathbf{r}) = \mathbf{0} \;\forall\; \mathbf{r} \in S(\mathbf{r})$$

Received October 10, 1997.

R.F.W. Bader[1] and F.J. Martín. Department of Chemistry, McMaster University, Hamilton, ON L8S 4M1, Canada.

[1] Author to whom correspondence may be addressed. Telephone: (905) 525-9140, ext 23499. Fax: (905) 522-2509.

where $\mathbf{n}(\mathbf{r})$ is a unit vector normal to $S(\mathbf{r})$. They are termed "proper" because they and their properties are defined by the principle of stationary action, a consequence of the imposition of eq. [1] as a constraint in the variation of the action integral operator for an open system (2–4). The principle of stationary action is a marriage of the principle of least action and Dirac's transformation theory (5). The action integral defines a bounded region of space and time, a space-time volume. The variation of the action over this space-time volume yields the (Schrödinger) equation of motion, just as the corresponding variation does in the classical principle of least action. In the principle of stationary action, however, the mathematical variations in the action at the time end points are retained rather than equated to zero as they are in the principle of least action.

© 1998 NRC Canada

When generalized to an open system, one with finite boundaries, the corresponding variations at the spatial boundaries are retained as well. It is these variations at the time end points and at the system's boundaries that are subsequently identified with the action of temporal and spatial generators of infinitesimal unitary transformations, thereby incorporating Dirac's transformation theory into the action principle (5). Thus, in addition to obtaining Schrödinger's equation describing the temporal development of the total system — the sole result in the principle of least action — one also obtains a variational derivation, unique to a proper open system, of the Heisenberg equation of motion for an observable $\hat{G}$. This operational statement of the principle of stationary action for an open system Ω is expressed as a variation in the Lagrange function operator (2–4), eq. [2*a*]:

$$[2a] \quad \delta\hat{\mathcal{L}}[\hat{\Psi},t,\Omega] = (\varepsilon/2)\{(i/\hbar) < \hat{\Psi}[\hat{H},\hat{G}]\hat{\Psi} >_{\Omega} + cc\}$$

For a proper open system, $\delta\hat{\mathcal{L}}[\hat{\Psi},t,\Omega]$ is given by eq. [2*b*]:

$$[2b] \quad \delta\hat{\mathcal{L}}[\hat{\Psi},t,\Omega] = (\varepsilon/2)\int_{\Omega} d\mathbf{r}\ \{\partial\hat{\rho}_G(\mathbf{r})/\partial t\} + (\varepsilon/2)\oint d\mathbf{S}(\mathbf{r}_S)\cdot\{\hat{\mathbf{j}}_G(\mathbf{r}_S) + cc\}$$

wherein the density operator for generator $\hat{G}$ is denoted by $\hat{\rho}_G(\mathbf{r})$, its current density by $\hat{\mathbf{j}}_G(\mathbf{r})$, and ε denotes an infinitesimal real number.

Interdeterminancy of basin and surface properties

Equation [2] demonstrates that for a system in a stationary state for which $\partial\hat{\rho}_G(\mathbf{r})/\partial t = 0$, the Heisenberg equation of motion equates the expectation value of the commutator to the flux in the associated current density through its surface. A discussion of the stationary state form of this theorem for a proper open system forms the basis of this paper and it is expressed in eq. [3], wherein we have reverted from the language of field theory to the Schrödinger representation in terms of the wave function ψ,

$$[3] \quad (1/2)\{(i/\hbar) < \psi|[\hat{H},\hat{G}(\mathbf{r})]|\psi >_{\Omega} cc\} = (1/2)\oint d\mathbf{S}(\mathbf{r})_S\cdot\{\hat{\mathbf{j}}_G(\mathbf{r}_S) + cc\}$$

where $\mathbf{j}_G(\mathbf{r})$ is the current density for $\hat{G}$

$$[4] \quad \mathbf{j}_G(\mathbf{r}) = (\hbar/2mi)\{\nabla\hat{G}(\mathbf{r}) - \hat{G}(\mathbf{r})\}\Gamma^{(1)}(\mathbf{r},\mathbf{r}')|_{\mathbf{r}=\mathbf{r}'}$$

and $\Gamma^{(1)}(\mathbf{r},\mathbf{r}')$ is the one-electron density matrix. The operator average over the open system Ω denoted by $< \psi|[H,\hat{G}(\mathbf{r})]|\psi >_{\Omega}$ implies a summation over all spins and integration over all spatial coordinates save those denoted by the position vector $\mathbf{r}$ defining the coordinates of the generator, which are integrated over the open system. This mode of integration follows directly from the field theoretic derivation of the principle of stationary action wherein the generator acts on a single field point (3). Equation [3] also applies to an isolated (that is, the total) system in which case the surface integral vanishes, a result sometimes referred to as the hypervirial theorem.

It is useful at this point to introduce the term "basin" from the topological definition of an open system, a basin being the region of space bounded by the union of some number of zero-flux surfaces (3). If the open system contains more than a single attractor (generally a nucleus), then the term basin will be used to refer collectively to the linked set of basins, the surface integrals for each neighbouring pair within the set cancelling in eq. [3].

Equation [3] has an important physical consequence unique to open systems, one that is the subject of this note, since its validity has been questioned in this journal (6). The commutator $(i/\hbar)[\hat{H},\hat{G}]$ in eq. [3] yields some observable whose average over the basin of Ω determines its expectation value for the open system. By eq. [3], this expectation value is equal to the flux in the current density of the observable $\hat{G}$ through the surface bounding the open system. For example, if $\hat{G} = -\mathbf{i}\hbar\nabla$, the electronic momentum operator, the commutator equals $-\nabla\hat{V}$, the operator that determines the force exerted on an electron by all of the remaining particles in the system. Its expectation value yields the Ehrenfest force acting on the electron density contained within the basin of the open system. Equation [3] equates this force to the surface flux in the momentum current density or, equivalently, to the flux in the quantum stress tensor, $\sigma(\mathbf{r})$. The stress tensor has the dimensions of an energy density or pressure and thus the force acting over the basin of an open system is determined in its entirety by the pressure acting on each of its surface elements $d\mathbf{S}$. A similar result is obtained for every observable $\hat{G}$ that is not a constant of the motion.

Thus the properties of an open system are a function of its surface: if the surface of an open system remains unchanged, then so do its average properties and, conversely, a change in the surface necessarily results in changes to the average properties. This property of a proper open system has important consequences in the use of such systems as building blocks in the theoretical construction of large molecules such as polypeptides (7, 8). The use of proper open systems in this manner is a result of their identification with the functional groups of chemistry, since they have been shown to account for all of the characteristic properties associated with this concept (1, 3, 9–15). In particular, atomic and group properties predicted in this manner have been shown to recover the experimentally determined contributions to the volume, energy, polarizability, and magnetic susceptibility in those cases where the group contributions are transferable, as well as additive. While perfect transferability is a theoretical impossibility, it can be approached to within experimental as well as computational accuracy. In those systems that exhibit such near-perfect transferability, the surfaces bounding the functional group in the different molecular environments and their properties are unchanged to the same degree of computational accuracy as are the basin properties, as required by the principle of stationary action. It is this interdependence of the surface and basin properties of an open system that has been challenged (6).

To place this interdependence on a firm mathematical basis, one can step back and replace the action of the infinitesimal generators on ψ with the variation of the state function in the expression for the variation of the action integral. For a

© 1998 NRC Canada

stationary state, this variation becomes a variation in Schrödinger's energy functional $G[\psi,\Omega]$ (2, 3, 16), as employed by him in the derivation of the "wave equation." The principle of stationary action for a proper open system, eq. [2], reduces in this case to

$$[5] \qquad \partial G[\psi,\Omega] = -(i\hbar/2) \oint d\mathbf{S}(\mathbf{r}_S)\cdot\delta_\psi \mathbf{J}(\mathbf{r}) + cc$$

where $\delta_\psi \mathbf{J}(\mathbf{r})$ denotes a variation in the vector current density with respect to a variation in the state vector ψ. Satisfaction of eq. [5] for all variations $\delta\psi$ or, alternatively, for the action of all infinitesimal generators $-(i\varepsilon/\hbar)\hat{G}$ on ψ, and subject to the boundary condition eq. [1], yields Schrödinger's equation $\hat{H}\psi = E\psi$ for the entire system and ensures satisfaction of eq. [3] for all observables $\hat{G}$ for the open system Ω. Equation [5] is in principle a method of minimizing the energy E and obtaining Schrödinger's equation together with all properties for a total system by restricting the variations to the basin of a proper open system interior to the total system and requiring this variation over the basin to equal the flux in the variation of the vector current through its surface. The possibility of employing eq. [5] in this manner was recently reviewed and discussed (17).

The derivation of eq. [2], the atomic statement of the principle of stationary action or its stationary state counterpart, eq. [5], entails both a variation of the surface itself, subject to the constraint expressed in eq. [1], as well as a variation of ψ in the surface (2–4, 16). Thus the generalized variation principle, eq. [5], demonstrates that a proper open system and its zero-flux surface are indeed uniquely interdependent, for it shows that the surface of the open system, as well as the wave function and energy of the total system, are stationary with respect to any and all variations $\delta\psi$, corresponding to a stationarity with respect to any and all physical perturbations $-(i\varepsilon/\hbar)\hat{G}\psi$.

Criticism of the interdeterminancy of basin and surface properties

Stefanov and Cioslowski (6) give two arguments in an attempt to dispute the conclusion that the electron density and the properties of a proper open system are uniquely related to its zero-flux surface. First they argue that this property of a proper open system "corresponds to a noninvertible $R^3 => R^2$ mapping and, therefore, is not bijective." This statement is made without reference to the principle of stationary action and its physical consequences for an open system. Equation [3] maps the properties of the basin onto those of its surface, a mathematical identity obtained from physics via the atomic statement of the principle of stationary action, eq. [5]. This result is hardly novel in physics, classical or quantal. For example, the force acting on an open portion of a system in classical continuum mechanics is determined by the pressure exerted on each of its surface elements with the local pressure being determined by the classical stress tensor, a result that parallels completely the quantum expression for a proper open system (2). It is worth noting that eq. [3] offers the possibility of equating an atomic expectation value to a sum of "bond" contributions in terms of a corresponding sum of surface integrals, there being a separate contribution to the surface integral in eq. [3] from each atom bonded to Ω (3).

In their second argument Stefanov and Cioslowski (6) state that multiplication of a density by a constant factor other than unity, while leaving the form of the gradient vector field and hence the surfaces of zero flux in $\nabla\rho(\mathbf{r})$ unchanged, would change the density within each basin by the constant factor and hence the properties of the open system. The argument is false as follows from the linearity of Schrödinger's equation. Multiplication of the state function or its derived density by a constant simply changes its normalization, but not the physical nature of the system or its properties. The state function ψ and its derived density $\rho(\mathbf{r})$ are uniquely determined by the Hamiltonian and its external potential, regardless of their normalization.

To be explicit and in anticipation of possible counter arguments, consider Schrödinger's equation,

$$[6] \qquad \hat{H}\psi = E\psi$$

which determines ψ to within a constant or a phase factor $\exp(i\phi)$. This remaining degree of freedom is generally determined by requiring that ψ be normalized to unity, thereby enabling Born's probabilistic interpretation of $\psi^*\psi\, d\tau$. The electron density $\rho(\mathbf{r})$ for a normalized ψ is defined to be

$$[7] \qquad \rho(\mathbf{r}) = N \int d\tau'\, \psi^*\psi$$

where the symbol $\int d\tau'$ implies a summation over all spins and integration over all spatial coordinates save those denoted by the position vector $\mathbf{r}$. Multiplication of ψ by a constant $\sqrt{k}$ to give ψ' will yield a density $\rho'(\mathbf{r}) = k\rho(\mathbf{r})$. However, this is not a new density describing a system of kN electrons (assuming k to be integer). It is derived from the same state function ψ, albeit with a new normalization, and determined by the same Hamiltonian. Thus $\rho'(\mathbf{r})$ is simply a density that integrates to kN electrons and its use in the determination of a property entails division by the new normalization factor. That is, for the expectation value of some operator $\hat{o}(\mathbf{r})$ one has

$$[8] \qquad <\hat{o}> = \int \hat{o}(\mathbf{r})\rho'(\mathbf{r})\, d\mathbf{r} / \int d\mathbf{r} \int d\tau'\, \psi'^*\psi'$$

the usual procedure for use of a ψ not normalized to unity.

One might attempt to argue that while the density $\rho'(\mathbf{r})$ is excluded by the linearity of Schrödinger's equation from being a new density for a different Coulombic Hamiltonian, it is a new density for kN electrons determined by some unknown non-Coulombic Hamiltonian. To counter even this argument, we shall appeal to density functional theory and in particular to the use of Levy's functional to suppress the problem of V representability (18). In Levy's functional one searches from among all those ψ which upon reduction yield the given ρ, for that one which yields the minimum value for $<\hat{H}>$. Its use thus extends the domain of variation; the only requirement remaining on $\rho(\mathbf{r})$ is that it be N representable. This latter requirement is met by demanding that the integral of $\rho(\mathbf{r})$ be finite, *but not necessarily equal to N* (19, 20). The density $\rho'(\mathbf{r}) = k\rho$, like ρ itself, must be N representable and since $\rho(\mathbf{r})$ is derivable from ψ (i.e., is N representable with respect to ψ), so is $\rho'(\mathbf{r})$, since it differs from $\rho(\mathbf{r})$ only in its normalization. If this were not the case, there is no demonstrated reason why one could not obtain a density for a non-integer number of electrons through multiplication of an N representable density by a suitable factor. Thus one would have to invoke the existence of Hamiltonians characterized not only by unknown forces but also by fractional numbers of particles. A closely related point is the demonstration that in the variation of

© 1998 NRC Canada

Table 1. Energy additivity and properties of HCH_2-CH_2B.

B	ΔE^a	$\Delta E(HCH_2\|)$	$\Delta E(\|CH_2B)$	$q(HCH_2\|)$	ρ	$\Delta\rho_b$
CH_3	–0.05	–10.8	+10.6	–0.017	0.2588	0.0001
NH_2	–0.09	–8.6	+8.1	+0.008	0.2640	0.0025
OH	–0.33	–2.6	+1.9	+0.047	0.2692	0.0020
F	–1.53	–0.3	–1.4	+0.066	0.2727	0.0028

[a]Energy changes are in kcal/mol, electron densities in atomic units (au). $\Delta E = E(HCH_2CH_2B) - (1/2)\{E(HCH_2CH_2H + E(BCH_2CH_2B)\}$ is calculated from the SCF energies.

Levy's functional the value of the undetermined multiplier μ, which is identified with the chemical potential and associated with the constraint on the normalization of ρ, is, at the point of variation, independent of this normalization (21).

In the same paper Stefanov and Cioslowski (6) compare the "shapes" of carbonyl oxygen atoms in different molecular environments. However, they do not base their study on a comparison of the C|O interatomic surfaces and their properties but rather they define "shape" in terms of a measure obtained from a "similarity index" that involves integration of ρ(**r**) over the common part of the basins of the oxygen atoms in two systems, a measure that is necessarily dominated by the maxima in the core densities that occur at the nuclear positions. Based on this study they conclude that "There is no correlation whatsoever between the shapes and the electronic properties of atoms in molecules." The statement is based on the finding that the properties of the carbonyl oxygen atom exhibit variations in the system R_1R_2CO for a wide range of substituents R_1 and R_2, a result that is in itself unsurprising. The net charges on the oxygen atom, for example, are found to vary between –1.18 e, for R_1 = OH and $R_2 = NH_2$, and –0.94 e for $R_1 = R_2$ = CN, a range of 0.24 e that is subjectively referred to as "broad" (6), but is in fact chemically anticipated.

While their study provides a useful comparison of the variation in the properties of the carbonyl oxygen atom through a series of compounds, it contributes nothing to the understanding of the physics that connects the properties of the surface of an atom to those of its basin. This is obtained through a study of the mechanics that relate the properties of the surface to those of the basin using eq. [3]. It requires the determination of the surface properties, as well as those of the basin (2, 3). The programs SURPROS and PROAIMV (22) enable one to determine the properties of both the interatomic surfaces bounding an atom and those of its basin. SURPROS determines the surface population, surface energy, surface force, and surface tension, for example, and relates each of these properties to the basin average of the associated commutator. It has recently been demonstrated that the quantum definition of pressure is determined by the virial of the force resulting from the electronic momentum flux through the surface of an open system, the surface virial being proportional to the pressure–volume product and equaling $-3pv$ (23). Clearly, the properties of the zero-flux surfaces are as important as those of the basins in determining the mechanics of an atom in a molecule, a point illustrated in the following examples.

Interdeterminancy and transferability of group properties

To illustrate the effect that the interdeterminancy of basin and surface properties required by eq. [3] has on the transferability of a group, consider the series of heteromolecules ACH_2CH_2B with A, B = H, CH_3, NH_2, OH, and F. Their energies are found to equal the arithmetic mean of the energies of the corresponding homomolecules ACH_2CH_2A and BCH_2CH_2B to within a few kcal/mol or less, computationally (see ΔE in Table 1 for the cases A = H) and experimentally. Examples from experiment are provided by A = H in the measured heats of formation of CH_3CH_2B that are found to differ from the arithmetic mean of the heats of formation of ethane and BCH_2CH_2B by +0.32, –0.53, and –0.17 kcal/mol, respectively, for B = OH, Cl, and I (24). The results reported here are obtained using a 6-311++G(3df,2p) basis set in a modified version of GAUSSIAN written by T.A. Keith that incorporates self-consistent virial scaling (SCVS) to ensure satisfaction of the virial theorem.[2] Values of 1×10^{-8} au are obtained for the |2T/V| ratios for the total system. The satisfaction of the atomic statement of the virial theorem is limited only by the accuracy of the numerical integrations, which, when summed over the atoms, yield errors in the total energies of less than 1.0 kcal/mol, as is illustrated below.

The groups $ACH_2|$ and $BCH_2|$ (the vertical bar denoting the defining zero-flux surface of the C—C bond) do undergo small changes in forming the heteromolecule, an amount of charge up to 0.07 e being transferred from one group to the other, Table 1. The electron population is necessarily conserved in forming the heteromolecule, and hence $q(BCH_2|) = -q(HCH_2|)$, but what is perhaps surprising is the extent to which other properties, such as the energy, are nearly similarly conserved. The apparent additivity of their energies is an example of compensatory transferability, the small change in the properties of one group induced by transfer being nullified by a compensatory change in its new neighbour. This behaviour has been illustrated before for the saturated hydrocarbons, which exhibit near-perfect additivity of the energy (10, 12), as exemplified here by the case A = H and B = CH_3 with an associated ΔE value of less than 0.1 kcal/mol. A methyl group $CH_3|$ from ethane withdraws 0.017 e from methylene in the $|CH_2CH_3$ group obtained from butane in their transfer to form propane and the energy of $CH_3|$ undergoes a decrease of 10.8 kcal/mol. However, the energy, as well as the electron population, of the methylene group changes by equal and opposite amounts for each methyl group attached to it, thereby yielding an apparent additivity of the group energies in the normal hydrocarbons in spite of the perturbations induced by their transfer. A methylene group bonded only to one methyl, as in butane, loses electronic charge and increases in energy by half the amount found for the single methylene group in propane. A methylene group bonded only to other methylenes, as first occurs in pentane, possesses a zero net charge and an energy equal to the additive increment for the methylene group. These values for the charge and energy changes are independent of basis set (10, 12).

The ΔE values in Table 1 are calculated from the total SCF energies while the changes in the group energies are obtained from differences of the appropriately summed atomic energies obtained by numerical integration. The small differences between the values of ΔE and the sum of the group energy changes, which have a maximum value of 0.4 kcal/mol, are a

[2] T.A. Keith, private communication.

© 1998 NRC Canada

Table 2. Surface properties of C—C bond in HCH_2-CH_2B.[a]

B	$\mathcal{V}_s(HCH_2\|)$	$\Delta\mathcal{V}_s(H)$	$\mathcal{V}_s(\|CH_2B)$	$\Delta\mathcal{V}_s(B)$	$\Delta\mathcal{V}_s$	$\mathcal{N}_s$	$\Delta\mathcal{N}_s$	$\mathcal{G}_s$	$\Delta\mathcal{G}_s$
CH_3	–0.2063	–0.0279	–0.1690	+0.0267	–0.8	1.2193	0.0003	0.8203	–0.0001
NH_2	–0.2040	–0.0256	–0.1743	+0.0314	+3.6	1.2224	0.0095	0.8322	+0.0104
OH	–0.1906	–0.0122	–0.1852	+0.0065	–3.6	1.2181	0.0110	0.8380	+0.0062
F	–0.1836	–0.0053	–0.1949	–0.0032	–5.3	1.2102	0.0191	0.8348	+0.0130

[a]All quantities in atomic units save $\Delta\mathcal{V}_s$, which is in kcal/mol.

measure of the total error in the integration of the atomic energy contributions.

The changes to the group energies $\Delta E(H\text{-}CH_2|)$ and $\Delta E(|CH_2\text{-}B)$ decrease following B = CH_3, in spite of an increase in the transfer of electronic charge through the series. This occurs because, unlike the case B = CH_3 where almost the entire perturbation is restricted to the two carbon atoms sharing the new surface, the effect of the substitution of a more electronegative atom is increasingly transmitted to the hydrogens as well. Thus the compensatory behaviour is found within each group and dominates the change for B = F. In this case, the near-zero changes in $\Delta E(H\text{-}CH_2|)$ and $\Delta E(|CH_2\text{-}F)$ are the result of nearly equal and opposite changes in the energies of the carbon and hydrogen atoms within each group, in the amounts ±22 and ±13 kcal/mol, respectively, with the carbon being stabilized in methyl and destabilized in CH_2F.

The energy of a group is defined using the atomic statement of the virial theorem obtained from eq. [3] with $G = \mathbf{r}\cdot\mathbf{p}$ (2, 3). This theorem equates the energy of the atom to the negative of its electronic kinetic energy, $E(\Omega) = -T(\Omega)$ or to one-half of the atom's total virial, $E(\Omega) = (1/2)\mathcal{V}(\Omega)$. The total virial $\mathcal{V}(\Omega)$, is composed of two contributions, a basin virial and a surface virial,

$$[9]\qquad \mathcal{V}(\Omega) = \mathcal{V}_b(\Omega) + \mathcal{V}_s(\Omega) = -\int_\Omega \mathbf{r}\cdot\nabla\cdot\sigma(\mathbf{r})\, d\tau + \oint d\mathbf{S}(\mathbf{r}_s)\cdot\mathbf{r}_s\cdot\sigma(\mathbf{r}_s)$$

where $\mathbf{r}$ is referenced to the nucleus. $\mathcal{V}_s(\Omega)$ is the virial of the forces exerted on the surface of the atom or group, the surface energy. For systems in equilibrium geometries as considered here, the sum of the $E(\Omega)$ equals the total energy E of eq. [6]. In these examples of near-perfect additivity, one finds that the surface properties, including the surface energy, exhibit the same compensatory behaviour as do the energy and charge.

The largest perturbations incurred in the formation of ACH_2-CH_2B occur in the vicinity of the new C–C interatomic surface, the density in the surface attaining its largest value at the corresponding bond critical point, a value denoted by ρ_b. Table 1 lists the values of ρ_b for the heteromolecules with A = H, together with $\Delta\rho_b$, the latter quantity providing a measure of the extent to which the values of ρ_b differ from the mean of the homosubstituted values. These differences are small relative to the values of ρ_b and increase with the electronegativity of B. The value of $\Delta\rho_b$ for the formation of propane equals only 0.0001 au, and the new surface closely approximates the average of the two homomolecular surfaces, as reflected in the changes in the surface properties for each fragment, as listed in Table 2.

Among the properties determined in SURPROS is the surface integral of $\nabla\rho\cdot\mathbf{n}$, which should vanish for a proper open system, eq. [1]. The values obtained here are of the order of 1×10^{-4} au. The surface energy of $HCH_2|$ referenced to C, as determined by the surface virial $\mathcal{V}_s(HCH_2|)$, decreases by –0.0279 au (the quantity $\Delta\mathcal{V}_s(H)$ in Table 2) from its value in ethane upon transfer to propane, while the surface energy of $CH_3CH_2|$ referenced to the C of methylene undergoes an increase of +0.0267 au relative to its value in butane. These compensating changes result in a new surface whose energy $\mathcal{V}_s$, obtained by summing the two group contributions, differs by only –0.8 kcal/mol from the mean of the two original surface energies, the quantity $\Delta\mathcal{V}_s$ in Table 2. The addition of the two surface energies to obtain $\mathcal{V}_s$ yields the scalar product of the internuclear vector with the Ehrenfest force acting on the surface, the quantity $\mathbf{R}_{CC}\cdot\mathcal{F}_s$, the contribution of the C–C surface to the total energy of the molecule (3). Other surface properties change in a similar compensatory manner to yield small net displacements from their mean values. The integral of $\rho(\mathbf{r})$ yields $\mathcal{N}_s$, the average number of electrons per unit length, and the integral of the positive definite kinetic energy density $G(\mathbf{r})$ yields $\mathcal{G}_s$, the average electronic kinetic energy per unit length, a "kinetic force." These properties exhibit only small changes from their mean values, as listed under the headings $\Delta\mathcal{N}_s$ and $\Delta\mathcal{G}_s$, the value for $\Delta\mathcal{G}_s$ vanishing for B = CH_3. The ratio $\mathcal{G}_s/\mathcal{N}_s \sim 0.68$ au is the surface average of the kinetic energy per electron.

The data in Table 2 indicate that similar changes are found for the remaining molecules in this series, the magnitudes of $\Delta\mathcal{V}_s$, $\Delta\mathcal{N}_s$, and $\Delta\mathcal{G}_s$ increasing only slightly through the series. Such compensatory behaviour is not restricted to cases of near-perfect additivity. It suggests that a Le Chatelier-like principle underlies the observation of characteristic properties for functional groups, each group changing in response to the presence of another in such a way as to minimize the overall change. Because of the interdeterminancy imposed by eq. [3], this compensatory behaviour is observed in both the basin and surface properties. The same set of molecules, with calculations using the 6-311G** basis set, has been used to demonstrate compensatory behaviour in the source function for the density, the function that determines the contribution from a proper open system to the density at any point in space (25). The magnetic susceptibility and volumes have also been shown to be additive for this series of molecules, their values for the heteromolecule differing from the mean of the values for the homomolecules by 0.3 and 0.7% or less, respectively.

We conclude with a demonstration of how the properties of zero-flux surfaces play an important role in the synthesis of a polypeptide. Figure 1 is an example of an amino acid residue defined by its two amidic surfaces, the alanyl group $|HNC^{\alpha}H(CH_3)C(=O)|$. In general, such a residue will be denoted by |HNAC(=O)|, with A denoting the $C^{\alpha}HR$ group. Defining an amino acid residue in this manner maximizes its transferability from one polypeptide to another. The use of such fragments takes advantage of what we know to be experimentally true, that the geometries and other properties of the

© 1998 NRC Canada

Fig. 1. The alanyl group as an example of an amino acid residue prepared as a proper open system in the glycine mold. The group is represented by the 0.001 au envelope of the electron density and its intersection with the two zero-flux amidic surfaces. The methyl group and the hydrogen atom attached to C^{α} are in the foreground, the |NHA surface is on the left, and the AC(═O)| surface is on the right.

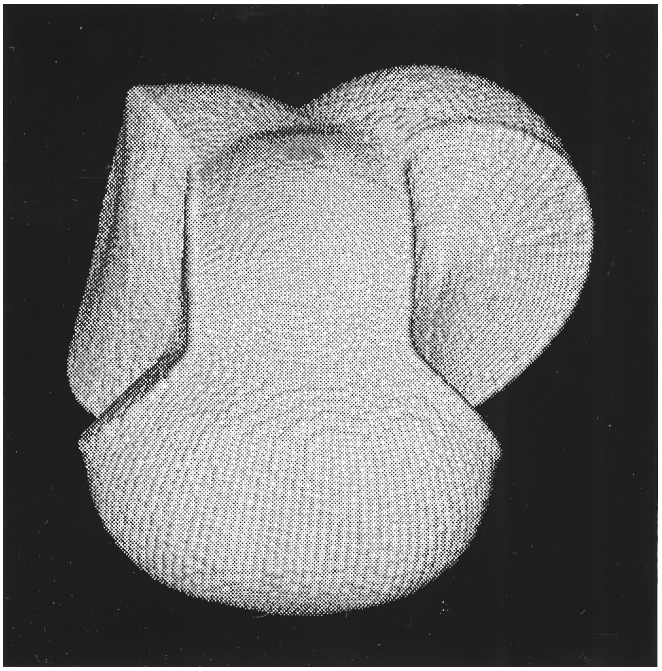

amino acid residues in general exhibit only small variations in different proteins. Knowledge of just how transferable these groups are had to await the theoretical studies (7, 8, 26), studies that demonstrated that the geometries, the electron density, and its related properties of properly defined residues are perhaps even more transferable than one might have hoped for. It was shown that glycyl and alanyl groups defined in one system were transferable without significant change, the lack of change in their properties being reflected in an almost perfect matching of their amidic surfaces in the new molecules, the predicted consequence of the interdeterminancy of basin and surface properties demanded by eq. [3].

Ideally, aside from any charge borne by the R group, an amino acid residue should be neutral if it is to represent a perfectly transferable repeating unit of a polypeptide. This limiting requirement of charge neutrality has an important consequence on the properties of its two bounding zero-flux surfaces, |NHA and AC(═O)|. Poisson's equation for the classical electrostatic potential, upon integration over an open region Ω, states that the net flux in the associated electric field **E**(**r**) through the surface must equal the contained net charge $q(\Omega)$ (27), eq. [10],

$$[10] \quad q(\Omega) = (-1/4\pi) \oint d\mathbf{S}(\mathbf{r}_s)\cdot\mathbf{E}(\mathbf{r}_s)$$

It follows from this result that if a residue possess a zero net charge even though its terminal groups |NH and C(═O)| bear net charges, then the flux of the field out of the residue through the |NHA surface will be equal and opposite to the flux into the residue through the AC(═O)| surface. The most

Fig. 2. A contour diagram of the electron density in triglycine, G′|NHCH$_2$C(═O)|G″ or G|G|G″. The bond paths and the two amidic surfaces are indicated. The symbols A′C(═O)| and *NHA denote the two sides of the amidic surface on the left of the diagram, while AC(═O)| and |NHA″ denote the two sides of the amidic surface on the right. One surface is rotated by 180° with respect to the other. The two surfaces are superimposable when rotated into alignment (as the reader can verify by making a copy and cutting the diagram). The outer contour has the value 0.001 au and the succeeding contours increase in value in the order 2×10^n, 4×10^n, and 8×10^n au with n beginning at –3 and increasing in steps of unity.

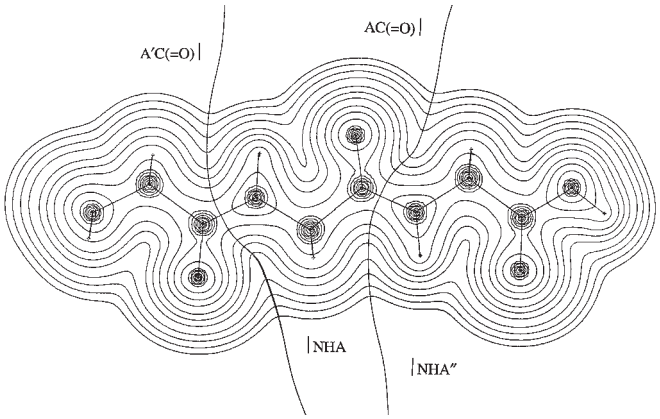

Table 3. Amidic surface properties of central glycyl group in Gly′|Gly|Gly″.[a]

Surface	$\mathcal{N}$	$\mathcal{G}$	$\mathcal{V}_s$	$\mathcal{V}_s$(C(═O)|	$\mathcal{V}_s$(|NH)	**F**(G;S$_i$)
G′|G	1.4668	1.4565	–1.2850	–0.2358	–1.0492	0.5045
G|G″	1.4688	1.4566	–1.2832	–0.2392	–1.0440	0.5051

[a]All quantities in atomic units. Results are from 6-31G*//6-311G** calculations.

direct way of meeting this requirement is for the two surfaces, each viewed with respect to their outwardly directed normal vectors, to be opposite sides of one, identical surface, one side being the template of the other, as illustrated in Fig. 2 for a glycyl residue in triglycyl. This is the very requirement needed to match the |NHA surface with the A′C(═O)| surface of the preceding residue and to match the AC(═O)| surface with the |NHA″ surface of the next residue in the chain. The molecule triglycyl is an example of the use of the "glycine mold," a tripeptide of the general form H$_2$NCH$_2$C(═O)|NHC$^{\alpha}$HRC(═O)|NHCHCO$_2$H and abbreviated to G′|NHC$^{\alpha}$HRC(═O)|G″. This mold is used to define each of the amino acid residues as a proper open system for any required set of dihedral angles ω, ϕ, and ψ (28). Aside from a reversal in the ordering of the N and C atoms sharing the surface, the two amidic surfaces bounding a given residue in the mold should exhibit identical properties if the residue is to match perfectly with its neighbouring residues upon transfer from the tripeptide to a polypeptide environment. (The two surfaces are not identical by symmetry since one faces the NH_2 terminus, while the other faces the CO_2H terminus.)

The data in Table 3 determine how closely the requirement of charge neutrality and its consequences on the amidic

© 1998 NRC Canada

surfaces is met by a glycyl residue defined in the glycine mold, Gly′|Gly|Gly″, for its "planar" minimum energy conformation (7) using a 6-311G** basis set. The net charge on the central glycyl residue, determined by numerical integration of the atoms in the residue, is –0.013 e with an integration error in the total population of the tripepetide yielding a charge of –0.0039 e. The net charge found here appears to be an upper limit for residues defined in the glycine mold, with some residues, the serinyl group for example, yielding net charges of 0.005 e. For the central residue |G| to be neutral and bounded by two identical amidic surfaces would require the two terminal groups G′| and |G″ to bear equal and opposite charges of magnitude 0.5 e. Their actual charges in the tripeptide are +0.506 e and –0.497, respectively.

The values of $\mathcal{N}_s$ for the two amidic surfaces differ by 0.002 au while the values of $\mathcal{G}_s$, the integrals of the kinetic energy density G(**r**), are identical to within the numerical accuracy, Table 3. It appears from a number of examples that the kinetic energy per electron in an amidic surface, the quantity $\mathcal{G}_s/\mathcal{N}_s$, is approximately unity, equal to 0.993 and 0.992 au in the present examples. The quantity $\mathcal{V}_s = \mathbf{R}_{CN} \cdot \mathcal{F}_s$, is a measure of the contribution of the surface energy of an amidic bond to the total energy of the tripeptide, contributions that differ by only 0.0018 au or 1.1 kcal/mol for the two amidic surfaces in triglycine, Table 3. The atomic virial theorem yields a still more stringent condition on the required similarity in the two surfaces if the central group is to be transferable without change. The condition is that the surface energy of the residue G′| referenced to the C atom in the first amidic bond equal the contribution to the surface energy of the central residue |G| referenced to the amidic carbon in the second amidic bond. Similarly, the contribution to the surface energy of the central residue |G| referenced to the N in the first amidic bond should equal the surface energy of the terminal group |G″ referenced to the N atom in the second amidic bond. The calculated differences are found to be 2.1 and –3.2 kcal/mol, Table 3, which sum to the difference in the two surface energies of –1.1 kcal/mol.

The Ehrenfest force exerted on the electron density in an atom is, as discussed above, given by the negative of the surface integral of the stress tensor. The Ehrenfest force exerted on the central residue |G| is the vector sum of the force exerted on each of its amidic surfaces S_i, denoted by $\mathbf{F}(G;S_i)$ in Table 3. Both contributions are not only of nearly equal magnitude, but both are equivalently directed, each lying along the associated C–N internuclear axes and directed into |G|. The similarities in the two amidic surfaces, as determined by a comparison of their properties including one as sensitive as the Ehrenfest force, are indeed remarkable, the differences being within or just above the present thresholds of numerical accuracy in the integrations.

Calculations are currently underway for all 20 of the amino acids clamped in the glycyl mold for conformations with the dihedral angles ψ and ϕ fixed at values characteristic of the α-helix. The determination of the surface properties for each residue determined in this manner will provide an accurate measure of its degree of transferability in terms of a matching of their respective surfaces when linked to form a polypeptide. The study of the ACH_2CH_2B systems demonstrates that the presence of a single methylene group can effectively buffer the effect of a changing substituent, the effect of the buffer being an additivity of properties and a minimization in the perturbation of the new C–C surface. A more enhanced buffering effect is operative for dampening the perturbations of the two amidic surfaces of an amino acid residue arising from changes in the side-chain R through the series of amino acids. Following glycine, the two surfaces are separated from the point of substitution by the group $||C^{\alpha}H\text{-}C^{\beta}H_2|$ in 16 of the amino acids. In two others, C^{β} is bonded to two other carbon atoms while in threonine it is linked to an oxygen. Only in proline and hydroxyproline is C^{α} linked to an atom other than hydrogen or carbon, specifically to nitrogen.

If the pairs of amidic surfaces for each residue exhibit the same degree of similarity as found for the glycyl group, then the residues defined as open systems can be combined without change and all properties of a polypeptide or a portion of it may be obtained with an acceptable accuracy by summation of the properties of each residue. One anticipates that deviations from charge neutrality, as caused by side-chain perturbations or changes in conformation, can in some instances reduce the degree of transferability, a reduction that can be quantitatively monitored by determining the degree of loss in the similarity in the two amidic surfaces. The ability to quantitatively determine this loss of similarity offers the possibility of establishing an empirical correction scheme for the transfer of a residue from the glycyl mold to its polypeptide environment.

Breneman et al. (29) also propose the construction of polyatomic molecules from fragments defined as proper open systems, fragments they label transferable atom equivalents or TAEs. They have developed an empirically based scheme for their assembly, which is done so as to allow each atom to self-consistently adjust to its new zero-flux surface in the polyatomic molecule. In this method, any adjustment of an atom to its new environment is restricted to a shift in its surface and its properties change only as a consequence of the resulting local change in the basin properties, a procedure that takes the interdeterminancy of basin and surface properties to its simplest extreme.

Conclusions

It is the physics of an atom in a molecule that provides the basis for the use of proper open systems in a theoretical synthesis of macromolecules. Stefanov and Cioslowski (6) state "Using the intuitively desirable 'building blocks of chemistry' and thus appealing in its simplicity and elegance, the aforementioned method is nevertheless theoretically flawed, as it invokes the assumption that the shape of an atom uniquely determines the electron density within its basin and consequently all of its electronic properties." This statement is made without reference to the atomic statement of the principle of stationary action, which provides the physics underlying the principle they criticize and whose existence proves their statement to be wrong. The "shape" of a proper open system is not an arbitrary quantity defined in terms of a crude similarity measurement as employed by them, but is instead precisely defined in terms of the zero-flux condition, eq. [1]. When so defined, the physics of the surface and its interrelation with the properties of the open system follows, as demonstrated here. There is nothing in the paper by Stefanov Cioslowski to dispute any of the published results regarding the use of properties of proper open systems in a theoretical synthesis of a macromolecule.

© 1998 NRC Canada

Acknowledgement

We thank Dr. T.A. Keith for bringing to our attention the near additivity of the energy of ACH_2CH_2B relative to the arithmetic mean of the energies of the associated homomolecules. We also thank Dr. J.A. Platts for updating the SURPROS program and for incorporating f basis functions.

References

1. R.F.W. Bader and P.M. Beddall. J. Chem. Phys. **56**, 3320 (1972).
2. R.F.W. Bader and T.T. Nguyen-Dang. Adv. Quantum Chem. **14**, 63 (1981).
3. R.F.W. Bader. Atoms in molecules: a quantum theory. Oxford University Press, Oxford. 1990.
4. R.F.W. Bader. Phys. Rev. B: Condens. Matter, **49**, 13348 (1994).
5. J. Schwinger. Phys. Rev. **82**, 914 (1951).
6. B.B. Stefanov and J. Cioslowski. Can. J. Chem. **74**, 1263 (1996).
7. C. Chang and R.F.W. Bader. J. Phys. Chem. **96**, 1654 (1992).
8. P.L.A. Popelier and R.F.W. Bader. J. Phys. Chem. **98**, 4473 (1994).
9. R.F.W. Bader, P.L.A. Popelier, and T.A. Keith. Angew. Chem. Int. Ed. Engl. **33**, 620 (1994).
10. K.B. Wiberg, R.F.W. Bader, and C.D.H. Lau. J. Am. Chem. Soc. **109**, 1001 1987.
11. R.F.W. Bader, M.T. Carroll, J.R. Cheeseman, and C. Chang. J. Am. Chem. Soc. **109**, 7968 (1987).
12. R.F.W. Bader, K.M. Gough, K.E. Laidig, and T.A. Keith. Mol. Phys. **75**, 1167 (1992).
13. R.F.W. Bader and T.A. Keith, J. Chem. Phys. **99**, 3669 (1993).
14. T.A. Keith and R.F.W. Bader. Can. J. Chem. **74**, 185 (1996).
15. R.F.W. Bader and T.A. Keith. Int. J. Quantum Chem. **60**, 373 (1996).
16. S. Srebrenik and R.F.W. Bader. J. Chem. Phys. **63**, 3945 (1975).
17. R.F.W. Bader. Int. J. Quantum Chem. **56**, 409 (1995).
18. M. Levy. Proc. Natl. Acad. Sci. U.S.A. **76**, 6062 (1979).
19. M. Levy and J.P. Perdew. Int. J. Quantum Chem. **21**, 511 (1982).
20. J. Harriman. Phys. Rev. A: Gen. Phys. **24**, 680 (1981).
21. T.T. Nguyen-Dang, R.F.W. Bader, and H. Essén. Int. J. Quantum Chem. **22**, 1049 (1982).
22. F.W. Biegler-König, R.F.W. Bader, and T.-H. Tang. J. Comput. Chem. **3**, 317 (1982).
23. R.F.W. Bader and M. Austen. J. Chem. Phys. **107**, 4271 (1997).
24. S.W. Benson, F.R. Cruichshank, D.M. Golden, G.R. Haugen, H.E. O'Neal, A.S. Rodgers, R. Shaw, and R. Walsh. Chem. Rev. **69**, 279 (1969).
25. R.F.W. Bader and C. Gatti. Chem. Phys. Lett. In press (1998).
26. R.F.W. Bader, P.A.L. Popelier, and C. Chang. J. Mol. Struct. (Theochem), **255**, 145 (1992).
27. S. Srebenik, R. Pauncz, and H. Weinstein. Chem. Phys. Lett. **32**, 420 (1975).
28. CRC Handbook of biochemistry: selected data for molecular biology. The Chemical Rubber Co., Cleveland, Ohio. 1968. pp. A68–A72.
29. C.M. Breneman, T.R. Thompson, M. Rhem, and M. Dung. Comput. & Chem. **19**, 161 (1995).

© 1998 NRC Canada

A capillary electrophoresis study of the synthesis and stability of 1,2-decanedisulfate, 1-hydroxy-2-decanesulfate, and 2-hydroxy-1-decanesulfate

Richard A. Walker, Aaron C. MacDonald, Tanya MacGillivray, D. Gerrard Marangoni, and Truis Smith-Palmer

Abstract: Capillary zone electrophoresis (CZE) was used to study the preparation of 1,2-decanedisulfate from 1,2-decanediol and determine the stability of the two-headed surfactant and the corresponding hydroxydecanesulfates under both acidic and basic conditions. The optimum buffer for the CZE determination was found to be diethylbarbiturate. Resolution of the hydroxydecanesulfate constitutional isomers was facilitated by the addition of magnesium ions. Decanedisulfate was stable in base but hydrolyzed in acid. The hydroxysulfates hydrolyzed much more rapidly, and in both acid and base. Mechanisms were postulated based on differential rates of formation and hydrolysis of the hydroxydecanesulfate constitutional isomers.

Key words: capillary zone electrophoresis, decanedisulfate, hydroxydecanesulfate, hydrolysis, surfactant.

Résumé : On a utilisé l'électrophorèse en zone de capillarité (EZC) pour étudier la préparation du décane-1,2-disulfate à partir du décane-1,2-diol et pour déterminer la stabilité de cet agent de surface à deux têtes et des hydroxydécanesulfates correspondants tant dans des conditions acides que basiques. On a déterminé que le diéthylbarbiturate est le tampon optimal pour la détermination de l'EZC. La résolution des isomères de constitution de l'hydroxysulfate est facilitée par l'addition d'ions magnésium. Le décanedisulfate est stable en milieu basique, mais il s'hydrolyse en milieu acide. Les hydroxysulfates s'hydrolysent beaucoup plus facilement, tant en milieu acide que basique. On propose des mécanismes qui tiennent compte des différences dans les vitesses de formation et d'hydrolyse des isomères de constitution de l'hydroxydécanesulfate.

Mots clés : électrophorèse en zone de capillarité, décanedisulfate, hydroxydécanesulfate, hydrolyse, agent de surface.

[Traduit par la rédaction]

Introduction

Despite the large numbers of applications of surfactants in the consumer products and petroleum industries, the basic design of the surfactants used (a hydrocarbon tail and a polar head group) has remained relatively constant. The synthesis of novel detergents is important in developing improved technical processes and in academic studies of micelle formation. As part of this initiative, alkanedisulfate surfactants have been synthesized from 1,2-alkane diols (1, 2). The ease of their preparation and subsequent purification is of great interest, as is their stability in acidic and basic media. The latter is especially important in the light of previous studies on the acid hydrolysis of alkanesulfates (3–7) and disulfates (2), and the fact that the resultant alcohols would be highly surface active.

The hydrolyses of alkanesulfates have been followed using a variety of techniques, including colorimetric methods (7, 8), acid–base titrations (6), and the use of radioactively labelled sulfate (4). Recently, alkanesulfates have been analysed using capillary zone electrophoresis (CZE) (9–12). Alkanesulfates do not strongly absorb UV or visible wavelengths of light and so are most conveniently detected during CZE by indirect photometric methods. These methods require that there is an absorbing species in the buffer that can be replaced by the ion of interest. When this occurs, there is a drop in absorbance, which generates a negative peak. Indirect detection is optimum when the mobility of the analyte is close to that of the background ion (13). The electrophoretic mobilities of long-chain alkanesulfates are low because of their size, and thus they are best analysed using a positive power supply (detector at the cathode). They are carried to the detector by the electroosmotic flow, but are separated on the basis of their mobility away from the detector. Nielen (9) used 6 and 12 mM diethylbarbiturate (BARB) buffer at pH 8.6 and a voltage of + 25 kV to separate C2–C12 alkanesulfates. The limits of detection (LODs) were $(1–2) \times 10^{-5}$ M. Gibbons and Hoke quantitatively determined sodium dodecanesulfate (SDS) using 5 mM dihydroxybenzoate (DHB) at pH 8.1 (10). Chen and Pietrzyk used 5 mM salicylate in phosphate buffer at pH 7 to examine mixtures of C6–C14 alkanesulfates (11). Resolution was significantly increased by the addition of magnesium ions. The corresponding alkanesulfonates were found to give responses at similar

Received October 20, 1997.

R.A. Walker, A.C. MacDonald, T. MacGillivray, D.G. Marangoni, and T. Smith-Palmer.[1] Chemistry Department, St Francis Xavier University, Box 5000, Antigonish, NS B2G 2W5, Canada.

[1] Author to whom correspondence may be addressed. Telephone: (902) 867-2270. Fax: (902) 867-2414. E-mail: tsmithpa@stfx.ca

© 1998 NRC Canada

migration times (t_m's), and this suggests that the sodium naphthalenesulfonate – acetonitrile buffer (SNS) (pH 10) used for the separation of alkane sulfonates (14, 15) might also be used for the analysis of alkanesulfates. Nonaqueous buffers (methanol–acetonitrile and methanol–water) have also been used to separate mixtures of alkane sulfates and sulfonates (12). Although the separation times were somewhat higher, so was the separation efficiency.

In this paper, we describe our studies of alkanedisulfate surfactants and the corresponding hydroxysulfate species. CZE was used for the separation of the alkanedisulfates from the corresponding hydroxyalkanesulfates, and from inorganic anions. The constitutional isomers of the hydroxyalkanesulfates were identified by ^{13}C NMR and were separated by CZE after the addition of magnesium ions to the buffer. The stability of the compounds to acid and base hydrolysis was then investigated, as it is of great importance in determining possible future applications. It may also have a bearing on their synthesis and the subsequent work-up.

Experimental

Reagents

Acetonitrile, magnesium chloride, sodium hydroxide, and sodium carbonate were Baker Analysed, J.T. Baker Chemical Co., Phillipsburg, N.J. Sodium 2-naphthalene sulfonate (90%) and 1,2-decanediol were from Aldrich, and diethylbarbituric acid and chlorosulfonic acid were from BDH. Methanol (HPLC grade) and carbon tetrachloride (reagent grade) were from Fisher Scientific, and ethanol (absolute) was from Consolidated Alcohols. All water used was 10 MΩ cm resistivity (Millipore 4000S purification system).

Ethyl sulfate was prepared by adding 6 mL ethanol to 6.5 mL of chlorosulfonic acid, then stirring for 10 min. Additional ethanol was added and the white precipitate of ethyl sulfate was filtered off and dried.

Surfactant preparation

1,2-Decanediol (1 mol) was dissolved in the chosen solvent (usually 50 mL carbon tetrachloride), cooled in an ice bath, and the chosen volume (generally 1.2 mol) of chlorosulfonic acid was added dropwise. The reaction mixture was stirred for 10 min and in some cases an equal volume of 95% cold ethanol was added. The solution was then neutralized with 18 M aqueous sodium hydroxide or saturated aqueous sodium bicarbonate and the precipitated surfactant collected and vacuum dried. Solutions of product were prepared by dissolving 0.083 g in 25 mL water. For analysis by CE, 25 μL of these solutions was added to 0.4 mL water.

Instrumentation

CZE was carried out on a Waters Quanta 4000 capillary electrophoresis system using a 75 μm × 60 cm fused silica capillary (Polymicro Technologies Inc., Phoenix, Ariz.), hydrostatic injection mode for 30 s, a positive power supply, and indirect photometric detection at 254 nm. The data were collected using LabCalc software (Galactic, Salem, N.H.) with 1 V equal to 1 AU, and multiplied by a factor of –1 to invert the peaks. All NMR were run on a Bruker 200 MHz spectrometer. Surfactant samples were analysed using D_2O as the solvent; diol was run in $CDCl_3$.

Analyses

The buffers for the alkanesulfate analyses were prepared as follows. DHB: 2,4-Dihydroxybenzoic acid (0.0771 g) was dissolved in 15 mL methanol, 40 mL water was added, the pH was adjusted to 8.1, and the volume was made up to 100 mL (10). BARB: Diethylbarbituric acid (0.1108 g) was stirred in 60 mL water, the pH was adjusted to pH 8.6, and the volume was made up to 100 mL (9). SNS: 2-Naphthalenesulfonic acid (0.2442 g) was added to 30 mL acetonitrile, the volume was made up to 100 mL with water, and the pH was adjusted to 10 (15). The capillary was rinsed with 0.1 M NaOH (2 min), water (2 min), and buffer (2 min) prior to each run. Mg-BARB: BARB was prepared as above and $MgCl_2$ was added to 50 mL of the buffer. The pH was readjusted and the buffer filtered. The capillary was rinsed with 1 M HCl (0.5 min), water (2 min), 0.1 M NaOH (2 min), water (2 min), then buffer (2 min).

All solutions were passed through a 0.45 μm Millipore filter and sonicated for 5 min before use. LODs were determined using a k value of 3.

Hydrolyses

A 20 mL aliquot of surfactant solution was pipetted into a stoppered flask (a balloon on a syringe needle through the serum cap allowed for expansion due to temperature) in a water bath and the sample was allowed to equilibrate at the chosen temperature. An equal volume of 0.1 M H_2SO_4 or 0.1 M NaOH was added to the surfactant solution. Aliquots (20 μL) were taken and added into 0.5 mL water. These samples were then analysed by CZE using the BARB buffer as described above. All water was carbonate-free.

Results and discussion

Our initial aim was to check the purity of alkanedisulfates, which we had prepared as described in the literature (1, 2) by the reaction of diol with chlorosulfonic acid. We were interested in determining the amounts of chloride and sulfate ions that were present, and if any singly sulfated product (hydroxyalkanesulfate) had been formed. Although methods have been described for determining alkanesulfates using liquid chromatography (ref. 16, and refs. therein) and ion chromatography (17, 18), CZE is now also being used, as described in the introduction. It is much more convenient to set up a new CZE method than a new HPLC method, as the latter method could require a new column and would use much larger quantities of solvent. In addition, the times reported for the CZE analyses tended to be shorter. As an alkanedisulfate has a higher charge to mass ratio than the corresponding hydroxyalkanesulfate and thus a larger electrophoretic mobility, it would be expected that they should be easily separated by CZE. In the systems we examined, choride and sulfate anions were also present. Three different buffers were examined for the separation of 1,2-dodecanedisulfate, and the hydroxydodecanesulfates. Test samples included SDS to facilitate comparison of our results with those previously reported. We assumed that hydroxydodecanesulfate would migrate very close to SDS. Typical electropherograms are shown in Figs. 1–3. Both DHB and BARB

© 1998 NRC Canada

Fig. 1. Electropherogram of 3×10^{-5} M sodium dodecanesulfate (1), 3×10^{-5} M sodium hydroxydodecanesulfate (2), 4×10^{-6} M sodium 1,2-dodecanedisulfate (3), and 20 μg mL^{-1} sulfate (4) in 5 mM 2,4-dihydroxybenzoate in 5% v/v methanol, pH 8.1 in a 60 cm × 75 μm i.d. fused silica capillary, with 30 kV applied giving 11 μA, and indirect detection at 254 nm.

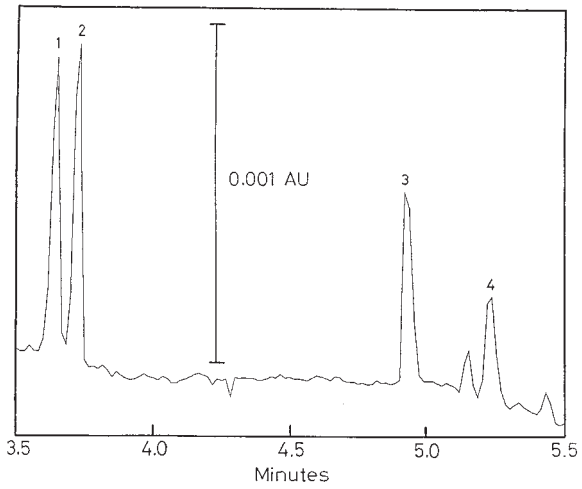

Fig. 2. Electropherogram of 3×10^{-5} M sodium dodecanesulfate (1), 3×10^{-5} M sodium hydroxydodecanesulfate (2), 4×10^{-6} M sodium 1,2-dodecanedisulfate (3), and 20 μg mL^{-1} sulfate (4) in 6 mM diethylbarbiturate, pH 8.6 in a 60 cm × 75 μm i.d. fused silica capillary, with 25 kV applied giving 8 μA, and indirect detection at 254 nm.

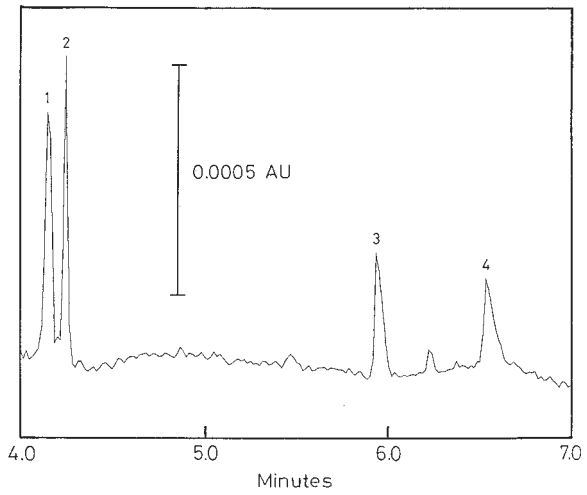

were found to be useful buffers for this separation. These buffers were easy to prepare and, providing the capillary was purged regularly with base (10), the t_m's for the compounds of interest were short and reproducible. The use of BARB as the buffer led to somewhat longer t_m's but the LODs were slightly better (4×10^{-6} M for hydroxydodecanesulfate as compared to 6×10^{-6} M in DHB, and 1×10^{-6} M for dodecanedisulfate as compared to 2×10^{-6} M in DHB). In addition, a peak due to sulfate showed in both these systems, but was cleaner and further removed from the disulfate peak when BARB was used

Fig. 3. Electropherogram of 2.5×10^{-4} M sodium dodecanesulfate (1), 2.5×10^{-4} M sodium hydroxydodecanesulfate (2), and 5×10^{-4} M sodium 1,2-dodecanedisulfate (3) in 10 mM naphthalene sulfonate in 30% v/v acetonitrile, pH 10 in a 60 cm × 75 μm i.d. fused silica capillary, with 20 kV applied giving 11 μA, and indirect detection at 254 nm.

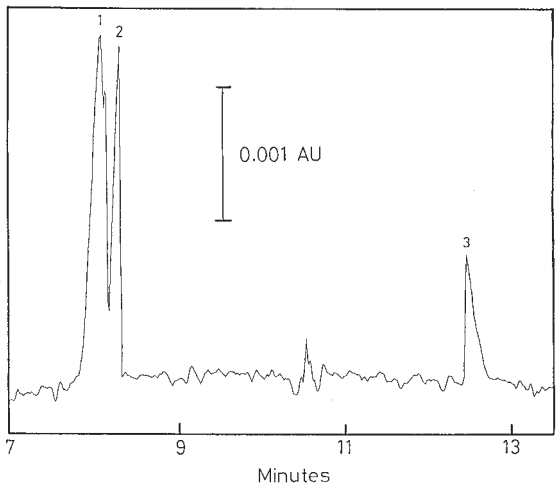

Table 1. ^{13}C NMR shifts (ppm).[a]

	1° OH	2° OH	1° OSO_3	2° OSO_3
Decanediol	66.57	72.34		
1-Hydroxy-2-decanesulfate	66.06			84.19
2-Hydroxy-1-decanesulfate		75.16	72.43	
Decanedisulfate			71.91	80.98
Ethyl sulfate			68.78	

[a] Samples run for 1000 scans

as the buffer (Fig. 2). Chloride was found to have the same migration time as sulfate in these systems. The use of SNS buffer was not as satisfactory. It was much harder to adjust the pH correctly, and the pH was not easily maintained. The t_m's were longer than those for the other two buffers and the LODs were much higher (3×10^{-5} M for hydroxydodecanesulfate and 2×10^{-5} M for dodecanedisulfate). Note that higher concentrations of surfactants were used to obtain Fig. 3 than to obtain Figs. 1 and 2; the higher concentrations were necessary in light of the poorer detection limits, especially that for the disulfate. The use of a 5 mM solution of the buffer was briefly investigated but the base line was considerably more noisy.

Analysis of a series of disulfate surfactant preparations by CZE (BARB buffer) indicated that the purity of our preparations was not consistent. The decanedisulfate (DDS) products in particular were shown to often contain hydroxydecanesulfate (HDS) in significant amounts, and thus it was the preparation of DDS that we chose to investigate further. Standard curves were prepared for DDS (t_m = 6.1 min) and HDS (t_m = 4.6 min) using peak area (A_p) divided by t_m versus concentration as μg/mL. They were fitted with the lines $A_p/t_m = 2.258e^{-4} + 3.339e^{-4}$[DDS] ($R^2$ = 0.986) and $A_p/t_m = -3.663e^{-4} + 1.858e^{-4}$[HDS] ($R^2$ = 0.998), respectively. The fact that the slope of the curve for DDS is about double that for HDS after corrections for t_m's have been made can be attributed to DDS

© 1998 NRC Canada

Fig. 4. Electropherograms of a 0.64 mM mix of sodium 1-hydroxy-2-decanesulfate (1) and sodium 2-hydroxy-1-decanesulfate (2) in BARB buffer with varying concentrations of magnesium chloride as follows: 0.5 mM (*a*) giving 18 μA; 1.0 mM (*b*) giving 22 μA; and 2.8 mM (*c*) giving 30 μA.

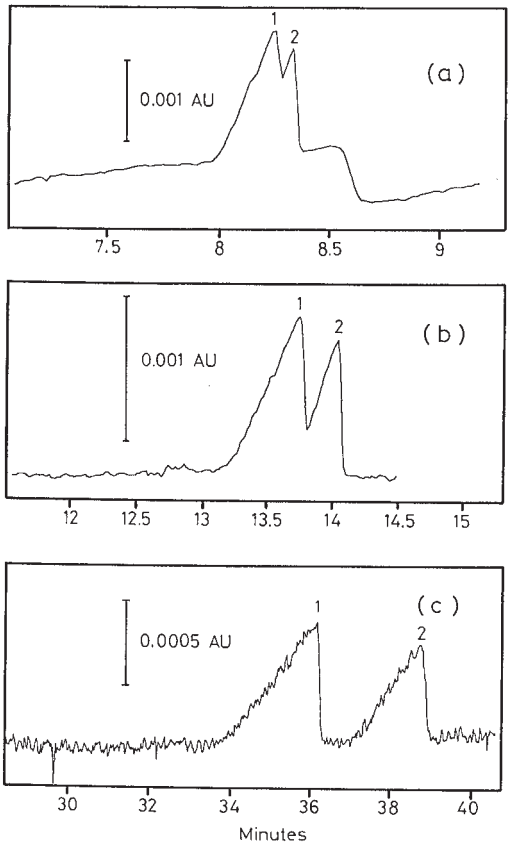

Fig. 5. Plot of migration time versus concentration of magnesium chloride added to BARB buffer for sodium 1-hydroxy-2-decanesulfate (○) and sodium 2-hydroxy-1-decanesulfate (□).

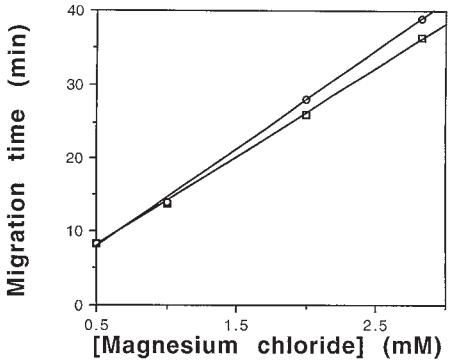

Fig. 6. Newman projections of the conformations of sodium 1-hydroxy-2-decanesulfate (*a*) and sodium 2-hydroxy-1-decanesulfate (*b*) that would lead to epoxide formation.

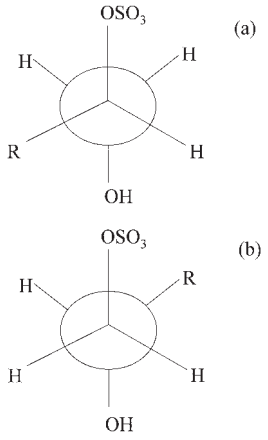

being able to replace twice the number of chromophores because of the second sulfate.

Further syntheses were then carried out under a variety of conditions (changing solvent, stirring time, ratio of chlorosulfonic acid to diol, and work-up procedure). ^{13}C NMR of the product showed the presence of two hydroxydecanesulfates in many cases. Table 1 contains the chemical shifts of the high-frequency carbons of the two isomers compared to those of the diol and the disulfate. By comparison of these shifts, 1-hydroxy-2-decanesulfate (1-OH-2-DS) could easily be distinguished from 2-hydroxy-1-decanesulfate (2-OH-1-DS). These isomers have the same charge and mass, but could be separated by CZE after the addition of magnesium ions to the BARB buffer (Fig. 4). It had been demonstrated previously by Chen and Pietrzyk (11) that addition of cations to a salicylate buffer drastically affects the electroosmotic flow. It is believed that divalent cations have a strong exchange selectivity toward silanol groups. This reduces the negative charge at the capillary wall and prevents the formation of a high concentration of hydrated positive ions at the capillary surface. As a result, the electroosmotic flow is weaker. Separation of isomers is achieved because of small changes in their electrophoretic flow due to differences in their hydrodynamic radii. At low EOF, such differences have more of an effect on a separation. Figure 4 shows three electropherograms with increasing magnesium chloride concentration. As the magnesium concentration was raised, the EOF decreased and resolution of the constitutional isomers of HDS increased. As shown in Fig. 5, there is a linear relationship between the concentration of magnesium chloride used and the migration time of the isomers. For complete resolution, run times as long as 40 min were necessary. Spiking a mixture of the constitutional HDS isomers with 2-OH-1-DS showed that 1-OH-2-DS migrated faster than its isomer. We attribute the different migration rates to differences in their shapes and thus in their hydrodynamic radii. The asymmetry of the peaks can be attributed to the differences in mobilities between the surfactant ions and the diethylbarbiturate ions (19).

© 1998 NRC Canada

In the original preparation described by El Sawy et al. (2), ethanol was used in the reaction work-up before the addition of base. This can lead to the formation of ethyl sulfate, which shows in electropherograms at 5.9 min, coming just before DDS. Ethyl sulfate is easily identified by NMR, with its distinctive downfield peak at 68.78 ppm, and is susceptible to base hydrolysis. We found that stirring a 5 mM solution of ethyl sulfate in 1 M NaOH for 2.5 h at room temperature was enough to destroy all the ethyl sulfate. Stirring in 18 M NaOH led to complete hydrolysis after 20 min.

There was often much more 1-OH-2-DS and 2-OH-1-DS mix present in the product when the ethanol was not added. Ethanol reacts with excess chlorosulfonic acid. Thus acid hydrolysis of the newly formed DDS may be prevented; neutralization with base was usually carried out slowly. In some preparations 1-OH-2-DS and 2-OH-1-DS were formed, but from other preparations we obtained only 2-OH-1-DS. One trend seemed to indicate that two isomers were most often obtained when neutralization was carried out with bicarbonate rather than hydroxide, and we felt that basic hydrolysis might also be involved.

By using CE to follow the reactions, the stability of DDS and HDS to acid and base was further assessed. Attempts to hydrolyze 5.7 mM DDS in 0.1 M NaOH over a 72 h period at 90°C were unsuccessful. This lack of reaction was attributed to the electrostatic repulsion between the charged head groups of the surfactant and the hydroxide anion. However, under the same conditions, 6.5 mM HDS was completely hydrolyzed after 2 h as indicated by the disappearance of its peak in the electropherogram. The hydrolysis of 1-OH-2-DS and 2-OH-1-DS results in the production of diol, which migrates with the water peak. Use of a Mg-BARB buffer to follow the hydrolysis indicated that there was a differential rate of hydrolysis for one isomer over the other. The 1-OH-2-DS isomer was hydrolyzed 20% more rapidly than 2-OH-1-DS. This was explained by invoking an epoxide as the intermediate, as has been done previously in sugar chemistry (20). The conformation from which the 1-OH-2-DS isomer will form an epoxide can be visualized as being more stable than the corresponding conformation of the 2-OH-1-DS isomer (Fig. 6).

Although stable in base, DDS did hydrolyze in acid. However, the hydrolysis does not occur nearly as quickly as was reported by El Sawy et al. (2). Using hours rather than minutes for the times listed by these authors would make them more realistic.

The hydroxydecanesulfates are also unstable to acid. This explains why only a very small peak appears at their characteristic t_m in the electropherograms of samples taken during the acid hydrolysis of DDS. When Mg-BARB is used as the buffer, it can be seen that both 1-OH-2-DS and 2-OH-1-DS are present, but that the 1-OH-2-DS constitutional isomer is present in a higher proportion. We would expect that hydrolysis of the primary sulfate of the DDS would be less hindered, giving 1-OH-2-DS, and for the same reason we would expect 2-OH-1-DS to be hydrolyzed more rapidly than is 1-OH-2-DS.

Conclusions

BARB was demonstrated to be the most useful CZE buffer for analysing the product mixtures. The addition of magnesium ions to the BARB buffer allowed for the separation of 1-OH-2-DS and 2-OH-1-DS, which are constitutional isomers, and thus have the same mass and charge. The amount of magnesium added determined the degree of resolution. Buffer samples containing 1.5 mM magnesium chloride gave base-line resolution.

The preparation of DDS and dodecanedisulfate often led to significant amounts of the corresponding hydroxysulfate side product, depending on the chosen reaction and work-up conditions.DDS was found to be stable in base at 90°C over several hours. However, acid hydrolysis at this temperature produced decanediol and a small amount of 1-OH-2-DS and 2-OH-1-DS, with the former isomer predominating.

1-OH-2-DS and 2-OH-1-DS were unstable in base. The former hydrolyzed more rapidly, and this was attributed to its forming an epoxide intermediate from a less sterically hindered conformation than would the latter.

Control of base in the work-up procedure seems to be a problem in view of the isomer ratios formed. The 1-OH-2-DS isomer would react most quickly and thus be removed first. In some preparations, only the 2-OH-1-DS isomer is present, but never just 1-OH-2-DS. If acid hydrolysis was occuring to any significant extent, we would expect the 1-OH-2-DS isomer to be more significant.

Acknowledgements

The authors thank the Natural Sciences and Engineering Research Council of Canada and St Francis Xavier University Council for Research for funding.

References

1. E.K. Comeau, E.J. Beck, J.F. Caplan, C.V. Howley, and D.G. Marangoni. Can. J. Chem. **73**, 1741 (1995).
2. A.A. El-Sawy, S.A. Essaway, M.M. El-Sukkary, and A.M.F. Eissa. Hung. J. Ind. Chem. **20**, 25 (1992).
3. M. Muramatsu and M. Inoue. J. Colloid Interface Sci. **55**, 80 (1976).
4. H. Nogami, S. Awazu, and Y. Kanakubo. Chem. Pharm. Bull. **11**, 13 (1963).
5. R.R. Reid and W.G. Fredell. TGA Cosmet. J. **30**, 11 (1958).
6. J.L. Kurz. J. Phys. Chem. **66**, 2239 (1962).
7. V.A. Motsavage and H.B. Kostenbauder. J. Colloid Sci. **18**, 603 (1963).
8. G.L. McIntyre. Crit. Rev. Anal. Chem. **21**, 257 (1990).
9. M.W.F. Nielen. J. Chromatogr. **588**, 321 (1991).
10. J.M. Gibbons and S.H. Hoke. J. High Resolut. Chromatog. **17**, 665 (1994).
11. S. Chen and D.J. Pietrzyk. Anal. Chem. **65**, 2770 (1993).
12. H. Salimi-Moosavi and R.M. Cassidy. Anal. Chem. **68**, 293 (1996).
13. F. Foret, S. Fanali, L. Ossicini, and P. Bocek. J. Chromatogr. **470**, 299 (1989).
14. J. Romano, P. Jandik, W.R. Jones, and P.E. Jackson. J. Chromatogr. **546**, 411 (1991).
15. P.G. Heckenberg, B.J. Alden, J. Wildman, J.P. Krol, P.E. Romano, P.E. Jackson, P. Jandik, and W.R. Jones. *In* Waters innovative methods for ion analysis. Waters, Milford, Mass. 1989.
16. D. Zhou and D.J. Pietrzyk. Anal. Chem. **64**, 1003(1992).
17. T. Smith-Palmer, B.R. Wentzell, L.D. Hansen, and C.D. MacPherson. Sci. Total Environ. **83**, 185 (1989).
18. C.E. Hoeft and R.L. Zollars. J. Liquid Chromatogr. **17**, 2691 (1994).
19. P. Gebauer and P. Bocek. Anal.Chem. **69**, 1557 (1997).
20. J.R.Turvey. Adv. Carbohydr. Chem. **20**, 183 (1994).

© 1998 NRC Canada

Competitive study of Meisenheimer rearrangement in a substrate tertiary amine with allylic and propargylic moieties

Krishna C. Majumdar and Gour H. Jana

Abstract: A number of allyl aryl propargyl amines **3a**–**3f** were synthesized in 68–82% yield. These tertiary amines were then treated with one equivalent of *m*-chloroperoxybenzoic acid (*m*-CPBA) to give products **5a–5f** in 79–90% yields arising out of the Meisenheimer rearrangement of the allyl aryl amine moiety accompanying the amine oxide rearrangement of the aryl propargyl amine moiety.

Key words: Meisenheimer rearrangement, [2,3] sigmatropic shift, amine oxide, propargyl amine, allyl amine.

Résumé : On a synthétisé un certain nombre d'allyl aryl propargylamines **3a–3f** avec des rendements allant de 68 à 82%. Par traitement de ces amines tertiaires à l'aide d'un équivalent d'acide *m*-chloroperbenzoïque (*m*-ACPB), on obtient les produits **5a–5f** avec des rendements variant de 79 à 90%; ils résultent d'un réarrangement de Meisenheimer de la portion allyl (aryl) amine qui accompagne la transposition de l'oxyde d'amine de la portion aryl (propargyl) amine.

Mots clés : réarrangement de Meisenheimer, déplacement sigmatropique [2,3], oxyde d'amine, propargylamine, allylamine.

[Traduit par la rédaction]

Introduction

[2,3] Sigmatropic rearrangements are anionic equivalents of the Cope rearrangement and, like [3,3] sigmatropic rearrangements, are not confined to carbon systems but can also involve many hetero systems. The construction of a five-membered pyrrole ring in 2,3-disubstituted indoles through rearrangement of aryl propargyl amine oxides was developed by Thyagarajan and co-workers (1). It was proposed that a [2,3] sigmatropic shift is followed by a unique Claisen rearrangement in which a [3,3] shift takes place through two heteroatoms to give indoles in almost quantitative yields. The formation of indoles occurs readily in one step by simply stirring a solution of aryl propargyl amine with one equivalent of *m*-chloroperoxybenzoic acid (*m*-CPBA) at room temperature without isolation of the labile amine oxide. The initial step in the reorganization of the aryl propargyl amine oxide is also the same [2,3] shift as in the case of the Meisenheimer rearrangement of allyl aryl amine oxides (2). Extensive studies on the Meisenheimer rearrangement have been made and accumulated knowledge suggests that formation of tertiary amine oxides of N-allyl tertiary amines prevails qualitatively in competition with the epoxidation. However, epoxidation occurred with *m*-CPBA in non-allylic systems (3). We have recently observed that the presence of *m*-chlorobenzoic acid in the reaction mixture does not interfere with the Meisenheimer rearrangement. It has also been reported (4) that the amine oxide rearrangement of *N*,*N*-bis(4-aryloxy-2- butynyl)anilines with one equivalent of *m*-CPBA furnishes only one product, 1-(4-aryloxy-2-butynyl)-2-(aryloxymethyl)-3-(*m*-chlorobenzyloxymethyl)indoles, in high yields. This observation indicates that the [2,3] shift is very specific towards one reacting propargyl moiety and the other reacting propargyl moiety is completely unaffected and is appended on the indole nitrogen. A competitive study (5) of the Claisen rearrangement of substrates containing an allyl ether and a propargyl ether moiety in the same molecule was made earlier. However, such a competitive study has not yet been reported for the case of an amine oxide rearrangement. This prompted us to undertake a study of competitive amine oxide rearrangement in a substrate tertiary amine with allylic and propargylic moieties, e.g., N-allyl, N-propargyl anilines (**3a**–**3f**). Here we report of the results of this investigation.

The starting materials (**3a**–**3f**) chosen for this study were prepared by treatment of the appropriate N-propargyl anilines(**1a–1f**) with appropriate allylic halides (**2a–2f**) in refluxing acetone in the presence of anhydrous potassium carbonate in 68–82% yields (Scheme 1). These were characterized by their elemental analyses and various spectral data.

Results and discussion

The amine oxide **4a** was prepared by slow addition of one equivalent of *m*-CPBA in chloroform to a solution of **3a** in same solvent at 0–5°C during 20 min. The formation of a highly polar amine oxide was indicated by thin-layer chromatography (TLC). A new product (a viscous oil) was obtained in 89% yield when the reaction mixture was kept at room

Received December 5, 1996.[1]

This paper is dedicated to Professor A. Chatterjee of the University of Calcutta on the occasion of her 80th birthday.

K.C. Majumdar[2] and G.H. Jana. Department of Chemistry, University of Kalyani, Kalyani - 741 235, West Bengal, India.

[1] Revision received July 1, 1997.

[2] Author to whom correspondence may be addressed. E-mail: kcm@klyuniv.ernet.in

© 1998 NRC Canada

Scheme 1.

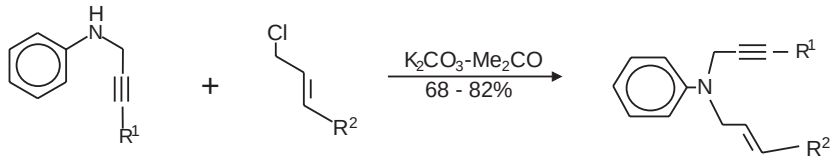

1 **2** **3**

3. a. $R^1 = R^2 = -CH_2O-C_6H_4-Cl$

b $R^1 = R^2 = H$

c $R^1 = R^2 = -CH_2O-C_6H_5$

d $R^1 = R^2 = -CH_2O-C_6H_4-CH_3$

e $R^1 = R^2 = -CH_2O-C_6H_3(CH_3)$

f $R^1 = -CH_2O-C_6H_4-Cl$ $R^2 = H$

Scheme 2.

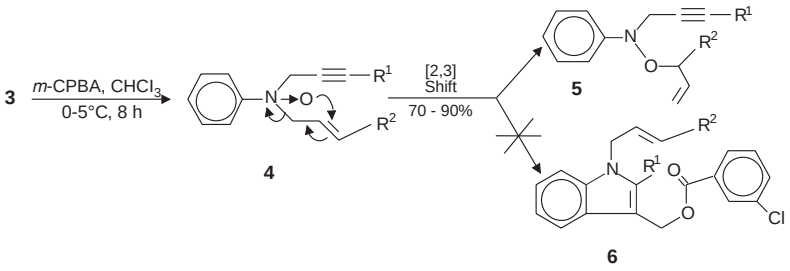

Fig. 1.

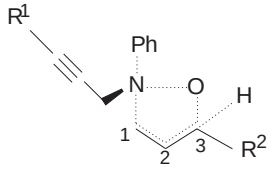

Fig. 2.

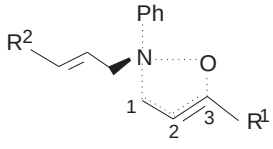

temperature for 8 h. The ^1H NMR spectrum of the product showed a two-proton multiplet at δ 5.20–5.22 and a one-proton multiplet at δ 5.80–6.20 due to the presence of a terminal olefin CH_2═CH function. The IR spectrum clearly indicated the absence of any carbonyl group. No change was observed when this product was refluxed in dry methanol. This product was characterized as **5a** from its elemental analysis and spectral data. It was surprising to note that there was no indication of the formation of an indole derivative such as **6a** that could have been formed by the participation of the propargyl moiety in the rearrangement. Formation of a single product encouraged us to treat each of the substrates **3b–3f** with one equivalent of *m*-CPBA and only the Meisenheimer products **5b–5f** were obtained in 79–90% yields (Scheme 2).

Formation of **5a**–**5f** from **4a**–**4f** is easily explicable by a [2,3] shift in the allyl aryl amine oxide of **4a**–**4f**. Thus, it is seen that the Meisenheimer rearrangement of the allyl aryl amine moiety is preferred over the rearrangement of the allyl propargyl amine oxide moiety. Formation of **5b** and **5f** from **3b** and **3f**, respectively, showed that the course of the reaction is independent of the substituents R^1 and R^2. Suprafacially, a five-membered transition state (6) is more favoured in the allyl system (Fig. 1) than in the propargyl system (Fig. 2) because two consecutive *sp* hybridized carbon atoms are present in the latter. Also, rotation of the C_1—C_2 single bond in the allyl

© 1998 NRC Canada

system decreases the distance between the amine oxide oxygen atom and the C_3 carbon atom, which helps to form a more favourable low-energy five-membered cyclic transition state. Such a competition was reported by Cresson and Atlani (5) for an aliphatic [3,3] sigmatropic rearrangement and the allyl vinyl ether moiety was shown to undergo [3,3] sigmatropic rearrangement in preference to the propargyl vinyl ether moiety.

From this study it is interesting to note that when both N-allyl and N-propargyl moieties are present in the same molecule of an N-alkylaniline-N-oxide, either of which can participate in the [2,3] sigmatropic rearrangement, it is the allyl group that preferentially migrates rather than the propargyl group. Such a system, where an allyl and a propargyl group can compete for the same N-oxide function, has not been studied so far. The preference exhibited by the allyl group is noteworthy. This preference is not restricted only to the [3,3] sigmatropic rearrangement (5) but is also observed in the case of a [2,3] sigmatropic rearrangement.

Experimental section

Methods and materials

UV absorption spectra ware recorded in absolute ethanol. IR spectra were run as thin films. ^{1}H NMR spectra were determined for solutions in $CDCl_3$ with $SiMe_4$ as internal standard at the Indian Institute of Chemical Biology, Calcutta. *J*-Values are given in hertz (Hz). Elemental analyses and mass spectral determinations were carried out by the Regional Sophisticated Instrumentation Centre (Central Drug Research Institute), Lucknow. Pet. ether refers to the petroleum ether of boiling range 60–80°C.

General procedure for the synthesis of tertiary amines 3a–3f

A mixture of N-propargyl anilines **3a–3f** (1.5 mmol), appropriate halides **2a–2g** (1.5 mmol), and anhydrous potassium carbonate (2 g) was refluxed in dry acetone (100 mL) for l0 h. The reaction mixture was then cooled, filtered, and the solvent was removed. The residual liquid was chromatographed over silica gel. Compounds **3a–3f** were obtained when the column was eluted with pet. ether.

Compound **3a:** yield 78%, viscous liquid; UV λ_{max}: 229 (log ε 4.21), 287 (log ε 2.03); IR (thin film): 2900, 1600 cm^{-1}; ^{1}H NMR ($CDCl_3$, 100 MHz) δ: 3.92–4.00 (m, 4H), 4.44–4.60 (m, 4H), 5.80–5.88 (m, 2H), 6.72–7.40 (m, 13H); MS (*m*/*z*): 451, 453, 455 (M^+). Anal. calcd. for $C_{26}H_{23}Cl_2NO_2$: C 69.03, H 5.09, N 3.10%; found: C 69.41, H 5.49, N 3.21%.

Compound **3b:** yield 73%, viscous liquid; UV λ_{max}: 249 (log ε 3.11), 293 (log ε 1.23); IR (thin film): 3280, 1590 cm^{-1}; ^{1}H NMR ($CDCl_3$, 100 MHz) δ: 2.20 (t, *J* = 1.8 Hz, 1H), 3.92–4.12 (m, 4H), 5.16–5.44 (m, 2H), 5.72–6.16 (m, 1H), 6.80–7.08 (m, 3H), 7.20–7.40 (m, 2H); MS (*m*/*z*): 171 (M^+). Anal. calcd. for $C_{12}H_{13}N$: C 84.21, H 7.60, N 8.18%; found: C 84.54, H 7.45, N 7.92%.

Compound **3c:** yield 68%, viscous liquid; UV λ_{max}: 230 (log ε 4.05), 288 (log ε 2.12); IR (thin film): 3900, 1600 cm^{-1}; ^{1}H NMR ($CDCl_3$, 100 MHz) δ: 3.90–4.20 (m, 4H), 4.40–4.70 (m, 4H), 5.80–6.00 (m, 2H), 6.80–7.50 (m, 15H); MS (*m*/*z*): 383 (M^+). Anal. calcd. for $C_{28}H_{25}NO_2$: C 81.46, H 6.53, N 3.66%; found: C 81.08, H 6.31, N 3.98%.

Compound **3d:** Yield 72%, viscous liquid; UV λ_{max}: 230 (log ε 3.94), 288 (log ε 2.23); IR (thin film): 2930 and 1600 cm^{-1}; ^{1}H NMR ($CDCl_3$, 100 MHz) δ: 2.20 (s, 6H), 3.92–4.18 (m, 4H), 4.40–4.72 (m, 4H) 5.80–6.04 (m, 2H), 6.80–7.46 (m,13H); MS (*m*/*z*): 411 (M^+). Anal. calcd. for $C_{28}H_{29}NO_2$: C 81.75, H 7.06, N 3.40%; found: C 82.06, H 7.36, N 3.76%.

Compound **3e:** Yield 82%, viscous liquid; UV λ_{max}: 230 (log ε 4.13), 288 (log ε 2.09); IR (thin film): 2910 and 1600 cm^{-1}; ^{1}H NMR ($CDCl_3$, 100 MHz) δ: 2.22 (s, 6H), 3.92–4.20 (m, 4H), 4.40–4.70 (m, 4H) 5.82–6.00 (m, 2H), 6.80–7.42 (m, 13H); MS (*m*/*z*): 411 (M^+). Anal. calcd. for $C_{28}H_{29}NO_2$: C 81.75, H 7.06, N 3.40%; found: C 81.43, H 6.81, N 3.23%.

Compound **3f:** Yield 76%, viscous liquid; UV λ_{max}: 228 (log ε 3.98), 250 (log ε 1.82); IR (thin film): 2900 and 1600 cm^{-1}; ^{1}H NMR ($CDCl_3$, 100 MHz) δ: 3.80–3.96 (s, 2H), 4.00–4.08 (m, 2H), 4.56–4.68 (m, 2H), 5.04–5.32 (m, 2H), 5.64–6.04 (m, 1H), 6.68–6.96 (m, 5H), 7.08–7.36 (m, 4H); MS (*m*/*z*): 311, 313 (M^+). Anal. calcd. for $C_{19}H_{18}$lNO: C 73.19, H 5.76, N 4.49%; found: C 73.01, H 6.00, N 4.88%.

General procedure for the oxidation and rearrangement of 3a–3f with *m*-CPBA

m-CPBA (1 mmol, 0.38 g, 45%) in chloroform (25 mL) was slowly added to a well-stirred solution of tertiary amines **3a–3f** (1 mmol) dissolved in chloroform (25 mL) at 0–5°C over a period of 20 min. The reaction mixture was stirred at room temperature for an additional 8 h, after which it was washed with a 10% solution of potassium carbonate (3 × 50 mL) and dried (Na_2SO_4). Removal of the solvent gave a crude mass that was purified by column chromatography over silica gel. Compounds **5a–5f** were obtained when the column was eluted with pet. ether.

Compound **5a:** Yield 89%, viscous liquid; UV λ_{max}: 224 (log ε 4.32), 227 (log ε 2.75); IR (thin film): 2940 and 1600 cm^{-1}; ^{1}H NMR ($CDCl_3$, 100 MHz) δ: 4.04–4.16 (m, 4H), 4.48–4.64 (m, 3H), 5.20–5.52 (m, 2H), 5.82–6.20 (m, 1H), 6.72–7.40 (m, 13H); MS (*m*/*z*): 467, 469, 471 (M^+). Anal. calcd. for $C_{26}H_{23}Cl_2NO_3$: C 66.67, H 4.91, N 2.99%; found: C 67.08, H 5.07, N 3.38%.

Compound ***5b:*** Yield 83%, viscous liquid; UV λ_{max}: 235 (log ε 3.72), 288 (log ε 1.83); IR (thin film): 3280 and 1590 cm^{-1}; ^{1}H NMR ($CDCl_3$, 100 MHz) δ: 2.16 (t, *J* = 1.8 Hz, 1H), 4.12 (d, *J* = 1.8 Hz, 2H), 4.40 (d, *J* = 6 Hz, 2H), 5.16–5.44 (m, 2H), 5.88–6.28 (m, 1H), 7.00–7.44 (m, 5H); MS (*m*/*z*) 187 (M^+). Anal. calcd. for $C_{12}H_{13}NO$: C 77.00, H 6.95, N 7.48%; found: C 77.38, H 7.21, N 7.71%.

Compound **5c:** Yield 90%, viscous liquid; UV λ_{max}: 224 (log ε 4.53), 278 (log ε 2.55); IR (thin film): 2920 and 1600 cm^{-1}; ^{1}H NMR ($CDCl_3$, 100 MHz) δ: 4.00–4.20 (m, 4H), 4.44–4.64 (m, 3H), 5.20–5.52 (m, 2H), 5.80–6.20 (m, 1H), 6.80–7.40 (m, 15H); MS (*m*/*z*): 399 (M^+). Anal. calcd. for $C_{26}H_{25}NO_3$: C 78.19, H 6.26, N 3.51%; found: C 78.39, H 6.56, N 3.89%.

© 1998 NRC Canada

Compound **5d:** Yield 88%, viscous liquid; UV λ_{max}: 223 (log ε 4.21), 278 (log ε 2.88); IR (thin film): 2900 and 1600 cm^{-1}; ^1H NMR ($CDCl_3$, 100 MHz) δ: 2.20 (s, 6H), 4.00–4.20 (m, 4H), 4.42–4.64 (m, 3H), 5.20–5.50 (m, 2H), 5.82–6.20 (m, 1H), 6.80–7.36 (m, 13H); MS (*m*/*z*): 427 (M^+). Anal. calcd. for $C_{28}H_{29}NO_3$: C 78.69, H 6.79, N 3.28%; found: C 79.01, H 6.51, N 2.92%.

Compound **5e:** Yield 85%, viscous liquid; UV λ_{max}: 223 (log ε 4.21), 278 (log ε 2.28); IR (thin film): 2900 and 1600 cm^{-1}; ^1H NMR ($CDCl_3$, 100 MHz) δ: 2.20 (s, 6H), 4.02–4.22 (m, 4H), 4.42–4.64 (m, 3H), 5.20–5.50 (m, 2H), 5.80–6.18 (m, 1H), 6.80–7.36 (m, 13H); MS (*m*/*z*): 427 (M^+). Anal. calcd. for $C_{28}H_{29}NO_3$: C 78.69, H 6.79, N 3.28%; found: C 78.39, H 6.71, N 3.51%.

Compound ***5f:*** Yield 79%, viscous liquid; UV λ_{max}: 229 (log ε 4.31); IR (thin film): 3060 and 1600 cm^{-1}; ^1H NMR ($CDCl_3$, 100 MHz) δ: 4.10 (s, 2H), 4.32 (d, J = 6Hz, 2H), 4.60 (s, 2H), 5.12–5.40 (m, 2H), 5.76–6.20 (m, 1H), 6.68–7.40 (m, 9H); MS (*m*/*z*) 327, 329 (M^+). Anal. calcd. for $C_{19}H_{18}ClNO_3$: C 69.62, H 5.49, N 4.27%; found: C 69.29, H 5.29, N 4.02%.

Acknowledgement

We thank the Council of Scientific and Industrial Research (CSIR) (New Delhi) for financial assistance. One of us (G.H.J.) is grateful to CSIR for a fellowship.

References

1. (*a*) B.S. Thyagarajan, J.B. Hillard, K.V. Reddy, and K.C. Majumdar. Tetrahedron Lett. 1999 (1974); (*b*) J.B. Hillard, K.V. Reddy, K.C. Majumdar, and B.S. Thyagarajan. J. Heterocycl. Chem. **11**, 369 (1974); (*c*) K.C. Majumdar and S.K. Chattopadhyay. J. Chem. Soc. Chem. Commun. 524 (1987); (*d*) K.C. Majumdar and S.K. Ghosh. J. Chem. Soc. Perkin Trans. 1, 2889 (1994); (*e*) K.C. Majumdar, G.H. Jana, and U. Das. J. Chem. Soc. Chem. Commun. 517 (1996); (*f*) J. Chem. Soc. Perkin Trans. 1, 1229 (1997).
2. (*a*) J. Meisenheimer. Ber. Dtsch. Chem. Ges. **52**, 1667 (1919); (*b*) R.F. Kleinschmidt and A.C. Cope. J. Am. Chem. Soc. **66**, 1929 (1949).
3. P. Kocovsky. Tetrahedron Lett. **29**, 2475 (1988).
4. B.S.Thyagarajan and K.C. Majumdar. J. Heterocycl. Chem. **12**, 43 (1975).
5. P. Cresson and M. Atlani. C. R. Seances Acad. Sci. Ser. C: **262**, 1433 (1966).
6. M. Moriwaki, Y. Yamamoto, J. Oda, and Y. Inouye. J. Org. Chem. **41**, 300 (1976).

© 1998 NRC Canada

The crystal structure of 3,4,7,8-tetramethylglycoluril

Sengen Sun, James F. Britten, Christopher N. Cow, ChØrif F. Matta, and Paul H.M. Harrison

Abstract: The crystal structure of 3,4,7,8-tetramethylglycoluril (**5**) was determined by X-ray diffraction. The structure reveals a hydrogen-bonding motif in the crystal lattice that differs from that present in related glycolurils. The two sides of each molecule form part of two independent, but parallel, infinite helical chains. These chains are formed by the NH donor and C═O acceptor on one side of a glycoluril molecule, forming H-bonds to two different molecules at adjacent positions within the helix. On the other side of the same molecule, a similar motif generates another helix of opposite helicity to the first. The molecule has a crystallographic plane of symmetry through the two bridgehead carbon atoms and the two bridgehead methyl groups, which are *syn*-periplanar. Thus, **5** is similar to 3,4-dimethylglycoluril (**3**), but differs from some glycolurils, where there is a significant dihedral angle between the two bridgehead-to-bridgehead substituent bonds. Bond lengths and angles in **5** resemble those reported for **3**, but bond lengths around the bridgehead positions are slightly lengthened relative to **3**.

Key words: glycoluril, 1,2,5,8-tetramethyl-2,6,7,8-tetraazabicyclo[3.3.0]octane-3,7-dione, X-ray diffraction, crystal structure, hydrogen-bond array.

Résumé : Faisant appel à la diffraction des rayons X, on a déterminé la structure cristalline du 3,4,7,8-tétraméthylglycolurile (**5**). La structure révèle que le réseau cristallin comporte un motif de liaison hydrogène différent de celui présent dans de glycoluriles apparentés. Les deux côtés de chacune des molécules font partie de deux chaînes hélicoïdales infinies indépendantes, mais parallèles. Ces chaînes sont formées par le NH donneur et un C═O accepteur d'un côté d'une molécule de glycolurile qui créent des liaisons hydrogènes avec deux molécules différentes dans des positions adjacentes à l'intérieur de l'hélice. De l'autre côté de la même molécule, un motif similaire génère une autre hélice dont l'hélicité est inverse de celle de la première. La molécule possède un plan de symétrie cristallographique passant par les deux atomes de carbone en tête de pont et les deux groupes méthyles attachés à la tête de pont qui sont *syn*-périplanaires. Le composé **5** est donc semblable au 3,4-diméthylglycolurile (**3**), mais il diffère de quelques glycoluriles dans lesquels on retrouve un angle dièdre important entre les liaisons portées par les atomes en tête de pont. Les longueurs et les angles des liaisons du composé **5** ressemblent à ceux rapportés pour le composé **3**, mais les longueurs des liaisons autour des positions en tête de pont sont légèrement plus longues que les valeurs correspondantes du composé **3**.

Mots clés : glycolurile, 1,2,5,8-tétraméthyl-2,6,7,8-tétraazabicyclo[3.3.0]octane-3,7-dione, diffraction des rayons X, structure cristalline, arrangement de liaisons hydrogènes.

[Traduit par la rédaction]

Introduction

The glycolurils[2] (e.g., **1**, Fig. 1) have been extensively investigated since their discovery by Schiff (1) in 1877. Interest in these bicyclic molecules has stemmed from the potential use of **1** as a fertilizer (2); the use of nitro derivatives (e.g., **2**) as explosives (3); the psychotropic activity of alkylated glycolurils (e.g., **3**) (4); and the use of 3,4,7,8-tetraacetylglycoluril (**4**) as a bleaching activator (5, 6). A substituted glycoluril forms the basis of the IodoGen method for radio-iodination of biomolecules (7), while other derivatives form molecular clips and cages, which exhibit interesting binding features for organic molecules (8–11) as well as metal ions (9). In some cases these molecular architectures act as catalysts (9, 10), or as models for biological processes, e.g., the photosynthetic reaction centre (12). Cucurbituril provides another example of a synthetic receptor based upon the glycoluril framework (13–15). As a result of the widespread interest in the

Received December 19, 1997.

S. Sun, J.F. Britten, C.N. Cow, C.F. Matta, and P.H.M. Harrison.[1] Department of Chemistry, McMaster University, 1280 Main St. W., Hamilton, ON L8S 4M1, Canada.

[1] Author to whom correspondence may be addressed. Telephone: (905) 525-9140 (ext. 27290). Fax: (905) 522-2509. E-mail: pharriso@mcmail.cis.mcmaster.ca

[2] In IUPAC nomenclature, **1** is 2,4,6,8-tetraazabicyclo[3.3.0]octane-3,7-dione. Glycolurils have also been named as derivatives of perhydroimidazo[4,5-d]imidazol-2,5-dione. We have chosen to use the simpler, trivial name and used the numbering system associated therewith. Compound **5** is thus 1,6,7,8-tetramethylglycoluril, although herein we have chosen the 3,4,7,8-tetramethylglycoluril designation, since this maintains consistency with acyl derivatives of **5**, where the numbering is unambiguous.

© 1998 NRC Canada

Fig. 1. Structures of glycolurils **1**–**5** and **9** and glycoluril core numbering system.

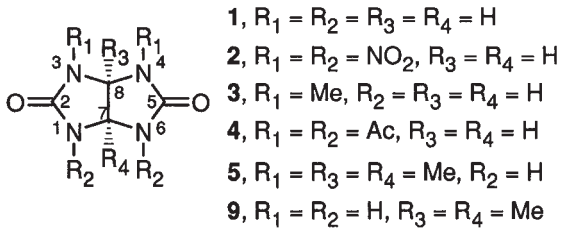

Scheme 1. Use of glycoluril **5** as a template to effect intramolecular Claisen condensations.

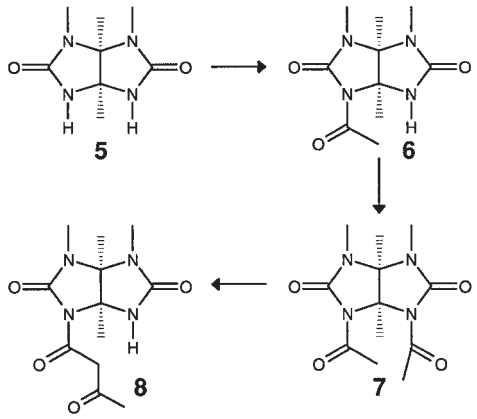

Table 1. Crystal data and structure refinement for **5**.

Empirical formula	$C_8H_{14}N_4O_2$
Formula weight	198.23
Temperature	213(2) K
Wavelength	0.71073 Å
Crystal system	Orthorhombic
Space group	*Pnma*
Unit cell dimensions	a = 10.1297(3) Å, α = 90°
	b = 11.0292(3) Å, β = 90°
	c = 7.9655(2) Å, γ = 90°
Volume, Z	889.93(4) Å^3, 4
Density (calculated)	1.48 Mg/m^3
Absorption coefficient	0.110 mm^{-1}
F(000)	424
Crystal size	0.30 × 0.08 × 0.06 mm
Theta range for data collection	3.15–27.86°
Limiting indices	$-11 \le h \le 13$, $-14 \le k \le 14$, $-10 \le l \le 10$
Reflections collected	7744
Independent reflections	1113 (R(int) = 0.0418)
Refinement method	Full-matrix least squares on F^2
Data / restraints / parameters	1113 / 0 / 114
Goodness-of-fit on F^2	1.088
Final R indices ($I > 2\sigma(I)$)	$R1$ = 0.0430, $wR2$ = 0.0998
R indices (all data)	$R1$ = 0.0535, $wR2$ = 0.1058
Extinction coefficient	0.033(5)
Largest diff. peak and hole	0.417 and –0.169 e Å^{-3}

glycolurils, a variety of crystal structures have been reported for the parent glycoluril (16, 17); for simple alkyl (4, 18–20), nitro (21), and amino (22) derivatives of the bicyclic framework; for several of the synthetic receptors (9, 11, 23); and recently for glycoluril bound to streptavidin (24). In some of these structures, a crystallographic plane of symmetry through C(7), C(8), and the two angular substituents (R_3 and R_4 in Fig. 1) is found, and R_3 and R_4 are thus *syn*-periplanar. In contrast, many other glycolurils exhibit a twist, such that the R_4-C(7)-C(8)-R_3 dihedral angle is non-zero. However, the factors leading to this twist are not entirely clear and are not solely due to the extent of substitution, since 7,8-diaminoglycoluril is twisted (22), while the highly substituted receptors exhibit variable twist (25, 26). Recently, Nolte has shown that two conformations of a synthetic receptor, which vary in their twist, can cocrystallize (27).

We have used 3,4,7,8-tetramethylglycoluril (**5**) as a template to effect intramolecular crossed-Claisen-like condensations between two acyl units (28, 29) in a manner that mimics some of the features of polyketide and fatty acid biosynthesis (Scheme 1). Template **5** can be sequentially acylated twice on the two NH sites to give, for example, acetylglycoluril **6**, then diacetylglycoluril **7**. Compound **7** undergoes an efficient

Table 2. (*a***)** Atomic coordinates (× 10^4) and equivalent isotropic displacement parameters (Å^2 × 10^3) for **5**. $U_{(eq)}$ is defined as one third of the trace of the orthogonalized U_{ij} tensor.

	x	y	z	$U_{(eq)}$
N(1)	8019(1)	3579(1)	–414(2)	30(1)
C(2)	8264(1)	4205(1)	1002(2)	21(1)
N(3)	9134(1)	3582(1)	1924(2)	27(1)
C(7)	8806(2)	2500	–562(2)	21(1)
C(8)	9608(2)	2500	1118(2)	19(1)
C(9)	9598(2)	4028(2)	3504(2)	31(1)
C(11)	11086(2)	2500	956(3)	29(1)
C(12)	9591(3)	2500	–2159(3)	36(1)
O(13)	7774(1)	5171(1)	1402(1)	28(1)
H(1)	7732(19)	3951(19)	–1234(25)	37(5)
H(9A)	8837(37)	4166(36)	4368(43)	39(11)
H(9B)	10234(32)	3507(30)	4056(36)	25(11)
H(9C)	10049(51)	4823(44)	3342(54)	62(14)
H(9D)	9233(49)	3472(49)	4407(57)	23(16)
H(9E)	10570(55)	4199(50)	3492(60)	28(16)
H(9F)	9184(48)	4825(45)	3820(53)	18(15)
H(11A)	11406(20)	3227(18)	368(25)	45(5)
H(11B)	11500(27)	2500	2024(35)	35(7)
H(12A)	10155(22)	3255(18)	–2202(25)	52(6)
H(12B)	8973(29)	2500	–3129(38)	43(8)

Table 2. (*b*) Anisotropic displacement parameters (Å^2 × 10^3) for **5**.[a]

	U_{11}	U_{22}	U_{33}	U_{23}	U_{13}	U_{12}
N(1)	42(1)	27(1)	21(1)	–3(1)	–11(1)	13(1)
C(2)	21(1)	20(1)	21(1)	1(1)	2(1)	–1(1)
N(3)	29(1)	28(1)	23(1)	–1(1)	–9(1)	8(1)
C(7)	26(1)	20(1)	16(1)	0	–2(1)	0
C(8)	21(1)	19(1)	16(1)	0	0(1)	0
C(9)	37(1)	32(1)	25(1)	–9(1)	–11(1)	4(1)
C(11)	22(1)	35(1)	31(1)	0	2(1)	0
C(12)	46(2)	42(1)	19(1)	0	6(1)	0
O(13)	34(1)	22(1)	28(1)	–2(1)	2(1)	6(1)

[a] The anisotropic displacement factor exponent takes the form: $-2\pi^2(h^2a^{*2}U_{11} + \ldots + 2hka^*b^*U_{12})$.

© 1998 NRC Canada

Table 3. Selected bond lengths, angles, and dihedral angles for **5**.[a]

Bond lengths (Å)		Angles (°)		Dihedral angles (°)	
N(1)—C(2)	1.346(2)	C(2)-N(1)-C(7)	113.0(1)	C12 C7 C8 C11	0.0
N(1)—C(7)	1.438(2)	O(13)-C(2)-N(3)	125.1(1)	C7 N1 C2 O13	176.9(1)
C(2)—O(13)	1.218(2)	O(13)-C(2)-N(1)	126.4(1)	C7 N1 C2 N3	–3.8(2)
C(2)—N(3)	1.338(2)	N(3)-C(2)-N(1)	108.6(1)	O13 C2 N3 C9	1.3(2)
N(3)—C(9)	1.431(2)	C(2)-N(3)-C(9)	121.5(1)	N1 C2 N3 C9	179.4(1)
N(3)—C(8)	1.437(2)	C(2)-N(3)-C(8)	113.7(1)	O13 C2 N3 C8	–176.9(1)
C(7)—C(12)	1.500(3)	C(9)-N(3)-C(8)	124.7(1)	N1 C2 N3 C8	3.8(2)
C(7)—C(8)	1.566(3)	N(6)-C(7)-N(1)	111.8(2)	C2 N1 C7 N6	111.5(1)
C(8)—C(11)	1.502(3)	N(1)-C(7)-C(12)	111.3(1)	C2 N1 C7 C12	–123.3(2)
		N(1)-C(7)-C(8)	102.6(1)	C2 N1 C7 C8	2.3(2)
		C(12)-C(7)-C(8)	116.7(2)	C2 N3 C8 N4	–110.7(1)
		N(3)-C(8)-N(4)	112.2(2)	C9 N3 C8 N4	73.8(2)
		N(3)-C(8)-C(11)	111.8(1)	C2 N3 C8 C11	122.8(2)
		N(3)-C(8)-C(7)	102.0(1)	C9 N3 C8 C11	–52.7(2)
		C(11)-C(8)-C(7)	116.4(2)	C2 N3 C8 C7	–2.2(2)
				C9 N3 C8 C7	–177.7(1)
				N1 C7 C8 N4	116.1(1)
				N1 C7 C8 N3	–0.0(2)
				C12 C7 C8 N3	121.9(1)
				N1 C7 C8 C11	–121.9(1)

[a] Symmetry transformation used to generate equivalent atoms: $x, -y + 1/2, z$.

intramolecular rearrangement to give acetoacetylglycoluril **8**, which can be further transformed and cycled through further rounds of acylation and condensation.

To determine whether twisting of the R_4-C(7)-C(8)-R_3 dihedral angle occurs in these derivatives, and to evaluate how this dihedral angle and other molecular features affect the efficiency of the key rearrangement step (**7** to **8**), we undertook a study of the crystal structure of **5** by X-ray diffraction. These results are reported herein; the crystal structures of acetyl derivatives **6** and **7** and other related molecules will be reported shortly.[3]

Results

Glycoluril **5** was prepared, as previously described (30), and crystallized by slow cooling from ethanol. Colourless orthorhombic needles were obtained. The diffraction pattern was obtained on a Siemens SMART CCD/P4/RA diffractometer at –60°C. The structure was solved by direct methods, as implemented in the Siemens SHELXTL program. Table 1 gives crystal data and structure refinement details.

Final atomic coordinates and equivalent isotropic displacement parameters are given in Table 2*a*, while Table 2*b* gives anisotropic displacement parameters. Table 3 provides bond lengths and bond angles for **5**. Figure 2 shows ORTEP drawings of the molecule in three orthogonal views, along with the numbering scheme. A stereoview of the crystal packing is shown in Fig. 3, while Fig. 4 shows two selected views that emphasize the nearest neighbour hydrogen-bond interactions around individual glycoluril molecules.

[3] Supplementary material has been deposited with the Cambridge Crystallographic Data Centre and can be obtained on request from The Director, Cambridge Crystallographic Data Centre, University Chemical Laboratory, 12 Union Road, Cambridge CB2 1EZ, U.K.

Discussion

The presence of multiple NH and C═O sites in glycoluril and its derivatives allows for a variety of different arrays of H-bond donor-acceptor interactions within the crystal lattices. In glycoluril **1** there are four NH donors and two carbonyl acceptors. Each NH site forms a single H-bond to the carbonyl oxygen atom of an adjacent molecule, while each C═O group forms two H-bonds, one to the NH site on *the same* adjacent molecule, thus forming an eight-membered ring comprised of two H-bonds, the other to an NH site on a different neighbour (16, 17). The overall effect is to generate extended two-dimensional nets of molecules with each molecule forming eight hydrogen bonds to four adjacent molecules within the net, although more complex arrays are also possible (16). A similar network exists in 7,8-dimethylglycoluril (**9**) (18). Substitution of alkyl groups onto the nitrogen atoms of glycoluril alters the number of NH donor sites, resulting in different hydrogen-bond arrays: 3,4-dimethylglycoluril (**3**) was cocrystallized with water, which participates in the observed three-dimensional H-bonding network (4). This network no longer involves the cyclic H-bonded structure found in **1**. In contrast, 3,4-diethylglycoluril crystallizes as a dimeric ribbon in a one-dimensional array (19). The eight-membered cyclic structure containing two H-bonds between each pair of molecules is present in 1,4-dinitroglycoluril, which thus also forms a one-dimensional H-bonded array (21). Yet more motifs are found in other disubstituted glycolurils (20), including those where both the glycoluril and the substituents participate in H-bonding (22, 23).

In contrast to the hydrogen-bonding motifs described above, 3,4,7,8-tetramethylglycoluril (**5**) forms extended two-dimensional hydrogen-bonded sheets in the crystal lattice (Fig. 4*a*). The NH of one molecule forms H-bonds to the C═O of another, the adjacent NH of which in turn H-bonds to yet another molecule. Each hydrogen bond exhibits *d*(H···O)

© 1998 NRC Canada

Fig. 2. Three orthogonal views of glycoluril **5**. Atoms 4, 5, 6, 10, and 14 are related by the mirror plane to atoms 3, 2, 1, 9, and 13, respectively (50% thermal ellipsoids).

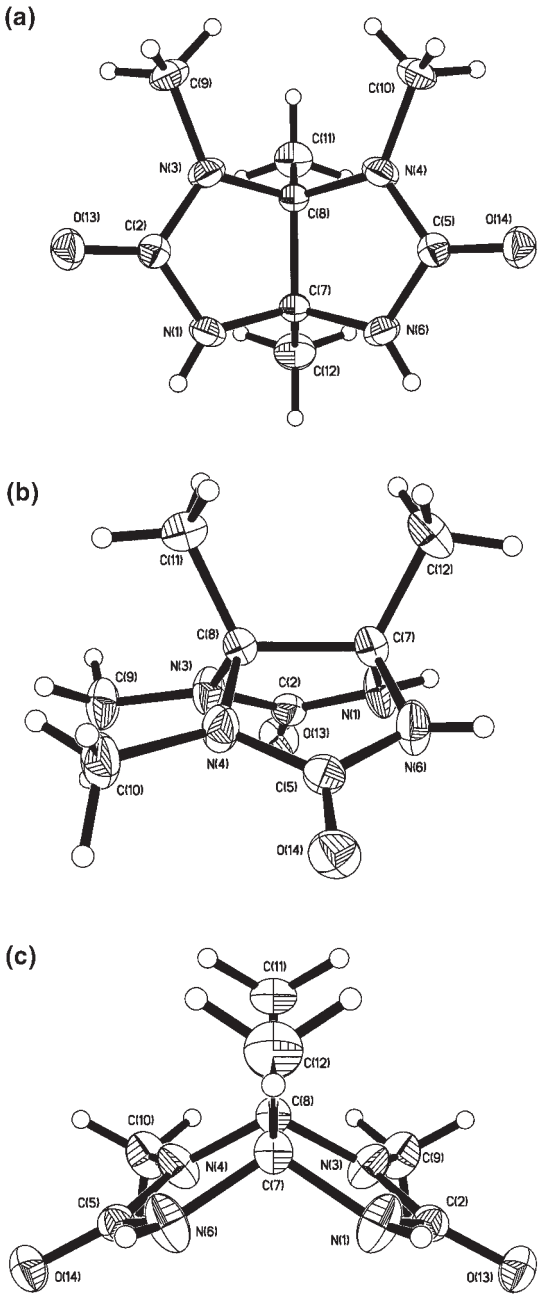

2.18 Å, *d*(H-N) 0.824 Å, angle (N-H···O) 171.5°, and angle (H···O═C(2)) 135.3°. Formation of an eight-membered ring structure with two H-bonds between two molecules does not occur. The NH and C═O groups on the other side of each glycoluril molecule form a similar linear network of H-bonds parallel to the first but of opposite helicity. The net effect is to generate a two-dimensional sheet comprised of an infinite series (along the *b*-axis) of parallel helices (along the *c*-axis), with a helical pitch between molecules of 180°. A view down one such helix is shown in Fig. 4*b*. There are no H-bonding interactions in the third dimension (*a*-axis); rather, there are (probably weak) interactions between the carbonyl oxygen atoms and both the *N*-methyl (*d*(O···H) 2.41 Å) and the bridgehead methyl (*d*(O···H) 2.41 Å) hydrogen atoms. Each sheet is inverted relative to the two adjacent sheets. This structure therefore represents the first example to our knowledge of this hydrogen-bond motif within a member of the glycoluril family.

As with previously reported structures of glycolurils, **5** possesses a *cis*-fused bicyclic structure, with the two *N*-methyl groups on the same side of the molecule, in accord with the structure proposed by Biltz (30) and with our analysis of the NMR spectrum. The N-C-N bond angles are 108.6(1) and 111.8(2)° (cf. ca. 109 and 115° in **3** (4)). The five-membered ring is close to planar (mean and maximum deviations 0.013 and 0.020 Å, respectively) (cf. within 0.014 Å in **9** (18), within 0.030 Å in **3** (4)). Using the RING program (31), the puckering amplitude *Q* (32) was found to be only 0.032 Å. The angle between the mean planes of the two rings is 117.9° (cf. 121.4° in **3** (4) and 115° in **9** (18)). As with glycolurils **3** and **9**, the molecule possesses a mirror plane through the two bridgehead carbons (C(7) and C(8)) and the two attached methyl groups (C(11) and C(12)). The dihedral angle C(11)-C(8)-C(7)-C(12) is thus 0°. Therefore **5** is unlike several of the glycolurils for which X-ray data is available, where this angle reaches values as high as 22–24° (27, 33). It should be noted that all four N atoms, but no ring C atoms, have significant thermal parameters perpendicular to the respective ring planes (Fig. 2*c*). Thus the possibility that the observed structure is the average of two slightly but oppositely twisted conformations cannot be rigorously ruled out.

All the hydrogen atoms within the structure were refined from the experimental data by least-squares fitting. As in 7,8-dimethylglycoluril (**9**) (18), both sets of bridgehead methyl hydrogens are rigidly oriented *anti* and *gauche* to the bridgehead–bridgehead bond, resulting in minimal nonbonded interactions between hydrogens on these two opposing methyl groups (d(H(11A)···H(12A)) 2.41 Å); however, C(12) is relatively free to vibrate along the symmetry plane, as evidenced by the thermal ellipsoids (Fig. 2*b*), unlike C(11), which is locked in place by nonbonded interactions with methyl groups C(9), C(10), and C(12). In contrast, the *N*-methyl hydrogen atoms show disorder, and two major conformations, related by ca. 60° rotation around the N—CH_3 bond, are approximately equally populated (Table 2*a*, H(9)A,B,C where H9B eclipses the N(3)-C(8), and H(9)D,E,F where H9F eclipses the N(3)-C(2) bonds).

The bond lengths and angles for **5** are similar to **3** (4), although the bonds around and between the bridgehead carbon atoms are lengthened by 0.015–0.018 Å (2σ ca. 0.010 Å) compared to **3**. While these small differences are only marginally significant, the observation that *all* these bonds are longer than in **3** is consistent with increased steric bulk imposed by methyl substituents at the bridgehead positions compared to hydrogens. There are corresponding small decreases in the MeN-CO and C═O bond lengths, but the HN—CO bond length is unchanged. Bond angle differences between **3** and **5** correspondingly reflect these effects.

Conclusions

The crystal structure of 3,4,7,8-tetramethylglycoluril (**5**) exhibits a two-dimensional hydrogen-bonded array, which is distinct from previously reported glycoluril structures. The two

© 1998 NRC Canada

Fig. 3. Stereoview of the crystal packing in glycoluril **5**.

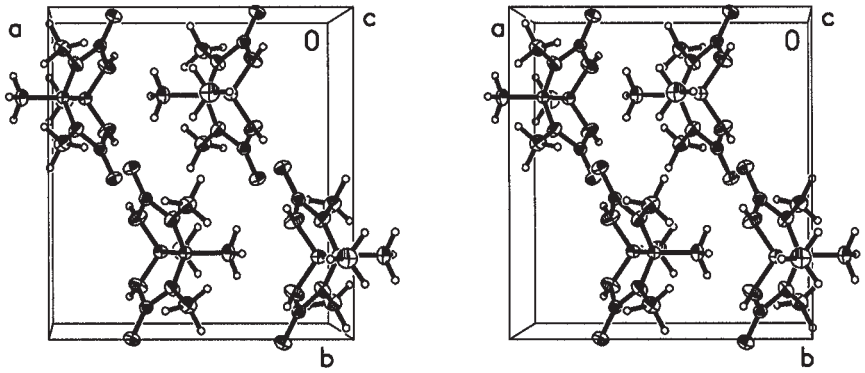

Fig. 4. Intermolecular bonding interactions around molecules of glycoluril **5**. (*a*) Single sheet of molecules. Hydrogen bonds are dashed. The unit cell is shown for reference but actually contains molecules from a second, inverted sheet, which is stacked above and parallel to the sheet shown; (*b*) view down the helix axis, slightly tilted to emphasize helical motif. Symbols: large circles, C; small circles, H; dotted circles, N; hashed circles, O.

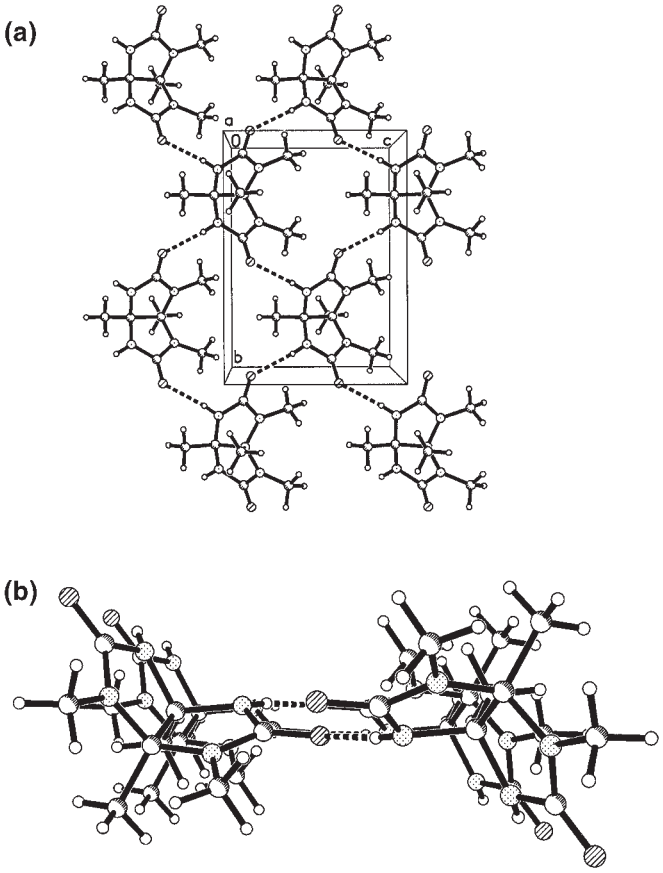

sides of the molecule each form part of two independent infinite helical chains. These chains are formed by the NH donor and C═O acceptor on each side forming H-bonds to two different molecules at adjacent positions within the helix, giving rise to this novel array within the glycolurils. The individual molecules resemble those of 7,8-dimethylglycoluril, with small differences that can be related to the effect of the additional two methyl groups at the bridgehead positions. This system provides a base structure with which to compare acyl derivatives of **5**. These results will be communicated shortly. Crystallographic data have been deposited as supplementary material.

Acknowledgement

This work was supported by the Natural Sciences and Engineering Research Council of Canada (NSERC).

References

1. H. Schiff. Justus Liebigs Ann. Chem. **189**, 157 (1877).
2. T.M. Addiscott and V.H. Thomas. Chem. Ind. (London), 29 (1979).
3. J. Boileau, E. Wimmer, M. Carail, and R. Gallo. Bull. Soc. Chim. Fr. 465 (1986).
4. M.O. Dekaprilevich, L.I. Suvorova, L.I. Khmelnitskii, and Y.T. Struchkov. Acta Cryst. **C50**, 2056 (1994).
5. J. Hofmann, G. Just, D. Moya, S. Ostermann, W. Pritzkow, and M. P. Visothea. J. Prakt. Chem. **332**, 176 (1990).
6. J. Hofmann, G. Just, W. Pritzkow, and H. Schmidt. J. Prakt. Chem. **334**, 293 (1992).
7. P.J. Fraker and J.C. Speck, Jr. Biochem. Biophys. Res. Commun. **80**, 849 (1978).
8. J. Kang and J. Rebek, Jr. Nature (London), **382**, 239 (1996).
9. R.P. Sijbesma and R.J.M. Nolte. Top. Curr. Chem. **175**, 25 (1995).
10. R.J.W. Schuurman, R.F.P. Grimbergen, H.W. Scheeren, and R.J.M. Nolte. Recl. Trav. Chim. Pays-Bas, **115**, 357 (1996).
11. R. Wyler, J. de Mendoza, and J. Rebek, Jr. Angew. Chem. Int. Ed. Engl. **32**, 1699 (1993).
12. J.N.H. Reek, A.E. Rowan, R. de Gelder, P.T. Beurskens, M.J. Crossley, S. De Feyter, F. de Schryver, and R.J.M. Nolte. Angew. Chem. Int. Ed. Engl. **36**, 361 (1997).
13. P. Cintas. J. Inclusion Phenom. Mol. Recognit. Chem. **17**, 205 (1994).
14. W.L. Mock. Top. Curr. Chem. **175**, 1 (1995).
15. D. Whang and K. Kim. J. Am. Chem. Soc. **119**, 451 (1997).
16. N. Li, S. Maluendes, R.H. Blessing, M. Dupuis, G.R. Moss, and G.T. DeTitta. J. Am. Chem. Soc. **116**, 6494 (1994).
17. S. Xu, P.K. Gantzel, and L.B. Clark. Acta Cryst. **C50**, 1988 (1994).
18. V.L. Himes, C.R. Hubbard, A.D. Mighell, and A.J. Fatiadi. Acta Cryst. **B34**, 3102 (1978).
19. E.B. Shamuratov, A.S. Batsanov, Y.T. Struchkov, A.Y. Tsivadze, M.G. Tsintsadze, L.T. Khmel'nitskii, Y.A. Simonov,

© 1998 NRC Canada

A.A. Dvorkin, O.V. Lebedev, and T.B. Markova. Khim. Geterotsikl. Soedin. 937 (1991).
20. N. Modric, M. Poje, I. Vickovic, and M. Bruvo. Acta Cryst. **C46**, 1336 (1990).
21. J. Boileau, E. Wimmer, R. Gilardi, M.M. Stinecipher, R. Gallo, and M. Pierrot. Acta Cryst. **C44**, 696 (1988).
22. N. Modric, M. Poje, and I. Vickovic. Acta Cryst. **C51**, 2594 (1995).
23. X. Garcias, L.M. Toledo, and J. Rebek, Jr. Tetrahedron Lett. **36**, 8535 (1995).
24. B.A. Katz, B. Liu, and R Cass. J. Am. Chem. Soc. **118**, 7914 (1996).
25. R.P. Sijbesma, A.P.M. Kentgens, E.T.G. Lutz, J.H. van der Maas, and R.J.M. Nolte. J. Am. Chem. Soc. **115**, 8999 (1993).
26. W.P. Bosman, P.T. Beurskens, R.P. Sijbesma, and R.J.M. Nolte. Z. Kristallogr. **197**, 305 (1991).
27. G.T.W. Gieling, H.W. Scheeren, R. Israel, and R.J.M. Nolte. J. Chem. Soc. Chem. Commun. 241 (1996).
28. S. Sun and P.H.M. Harrison. Tetrahedron Lett. **33**, 7715 (1992).
29. S. Sun and P. Harrison. J. Chem. Soc. Chem. Commun. 2235 (1994).
30. H. Biltz. Chem. Ber. **40**, 4806 (1907).
31. D. Cremer. RING program. Quantum Chemistry Program Exchange No. QCMP 110. Indiana University, Bloomington, Ind., U.S.A.
32. D. Cremer and J.A. Pople. J. Am. Chem. Soc. **97**, 1354 (1975).
33. H.K.A.C. Coolen, H. Engelkamp, J.N.H. Reek, A.H. Priem, P.W.N.M. van Leeuwen, and R.J.M. Nolte. Recl. Trav. Chim. Pays-Bas, **114**, 65 (1995).

© 1998 NRC Canada

Iodine charge-transfer salts of bis(1,2,3,5-diselenadiazolyl) diradicals; solid-state characterization of the thiophene-bridged derivative $[(Se_2N_2C)C_4H_2S(CN_2Se_2)][I]$

A. Wallace Cordes, Robert C. Haddon, Robin G. Hicks, Richard T. Oakley, and Kristen E. Vajda

Abstract: Electroreduction of the 2,5-thiophene-bridged bis(1,2,3,5-diselenadiazolylium) salt [T-2,5-Se][SbF_6]$_2$ in acetonitrile, at a Pt wire and in the presence of iodine, affords a highly conductive ($\sigma = 10^2$ S cm^{-1} at 293 K) 1:1 charge-transfer (CT) salt [T-2,5-Se][I], the crystal structure of which has been determined by single-crystal X-ray diffraction. The crystals belong to the orthorhombic space group *Fm*2*m*, $a = 3.544(2)$, $b = 10.9808(16)$, $c = 31.464(5)$ Å, $V = 1224.5(7)$ Å^3. The structure consists of perfectly superimposed π-stacks of molecular units bridged by columns of disordered iodines. This packing motif is similar to that of the related 1,3-benzene-bridged derivative [1,3-Se][I], but the lateral intermolecular Se···Se interactions linking adjacent π-stacks are considerably shorter, indicative of a more isotropic electronic structure for [T-2,5-Se][I]. Magnetic susceptibility measurements on [T-2,5-Se][I] nonetheless indicate a phase transition to a diamagnetic state near 200 K, behaviour similar to that observed for [1,3-Se][I]. The electronic structures and transport properties of the two compounds are discussed in the light of extended Hückel band-structure calculations.

Key words: diselenadiazolyl, diradical, charge-transfer salt, magnetic susceptibility, crystal structure.

Résumé : L'électroréduction du sel [T-2,5-Se][SbF_6]$_2$ [bis(1,2,3,5-disélénadiazolylium) avec pont 2,5-thiophène] en solution dans l'acétonitrile, au niveau d'un fil de Pt et en présence d'iode, conduit à un sel de transfert de charge 1:1, [T-2,5-Se][I], de conductivité élevée ($\sigma = 10^2$ S cm^{-1}, à 293 K) dont on a déterminé la structure cristalline par diffraction des rayons X par un cristal unique. Les cristaux sont orthorhombiques, groupe d'espace *Fm*2*m*, avec $a = 3{,}544(2)$ Å, $b = 10{,}9808(16)$ Å, $c = 31{,}464(5)$ Å et $V = 1224{,}5(7)$ Å^3. La structure est formée d'empilements π parfaitement superposés d'unités moléculaires pontées par des colonnes désordonnées d'iodes. Ce motif d'empilement est semblable à celui observé avec le dérivé apparenté [1,3-Se][I] comportant un pont 1,3-benzène; toutefois, les interactions latérales intermoléculaires Se···Se reliant les empilements π adjacents sont beaucoup plus courtes et ceci indique une structure électronique plus isotrope dans le cas du [T-2,5-Se][I]. Des mesures de susceptibilité magnétique effectuées avec le [T-2,5-Se][I] suggèrent toutefois la présence d'une transition de phase vers 200 K qui conduit à un état diamagnétique; ce comportement est semblable à celui observé avec le composé [1,3-Se][I]. On discute des structures électroniques et des propriétés de transport des deux composés à la lumière de calculs étendus de Hückel sur la structure de bande.

Mots clés : disélénadiazolyle, diradical, sel de transfert de charge, susceptibilité magnétique, structure cristalline.

[Traduit par la rédaction]

Introduction

The benzene-bridged bis-(1,2,3,5-dithiadiazolyl) diradicals [1,4-S] **1** and [1,3-S] **2** (E = S, Se) form highly conductive charge-transfer salts with iodine (1, 2). At room temperature the structures of these compounds consist of perfectly superimposed and evenly spaced π-stacks, interspersed by columns of disordered iodines. At lower temperatures charge-density wave (CDW) driven instabilities cause the structures to collapse into diamagnetic, semiconducting states. The susceptibility of these uniformly spaced stacks to anion-assisted (3) CDW distortions was attributed to their relatively one-dimensional electronic structures. In the case of [1,4-S][I] the nature of the charge-density state was characterized by low-temperature X-ray diffraction. From these measurements the degree of bandfilling ($f = 3/8$) was determined, and a simple model of the consequent low-temperature superlattice was proposed (2).

Received August 1, 1997.

A.W. Cordes. Department of Chemistry and Biochemistry, University of Arkansas, Fayetteville, AR 72701, U.S.A.
R.C. Haddon. Department of Chemistry, University of Kentucky, Lexington, KY 40506, U.S.A.
R.G. Hicks, R.T. Oakley,[1] and K.E. Vajda. Department of Chemistry and Biochemistry, University of Guelph, Guelph, ON N1G 2W1, Canada.

[1] Author to whom correspondence may be addressed. Telephone: (519) 823-1929 (ext. 3793). Fax: (519) 766-1499. E-mail: oakley@chembio.uoguelph.ca.

© 1998 NRC Canada

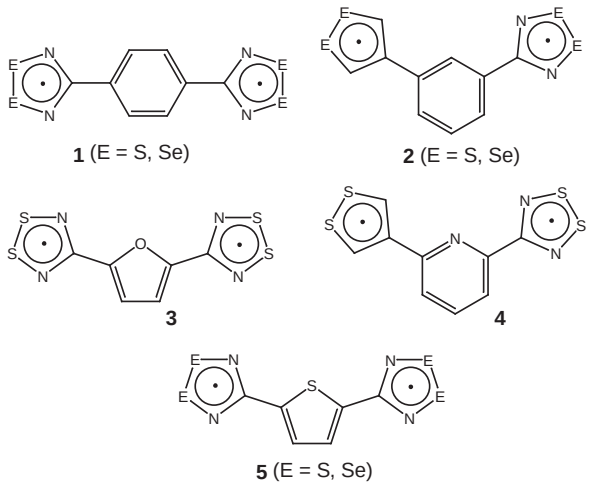

Our attempts to suppress the metal–insulator transition T_{MI} in these π-stacked CT salts has been based on the design of materials with more isotropic electronic structures. Towards this end we have prepared iodine CT salts of the diselenadiazolyl analogues [1,4-Se] and [1,3-Se] (**1** and **2**, E = Se), in the belief that lateral interstack interactions would be enhanced (4). However, although the crystal structures of the sulfur- and selenium-based systems [1,4-E][I] and [1,3-E][I] (E = S, Se), respectively, are similar, the selenium variants actually show *higher* T_{MI} temperatures. We have also pursued sulfur-based diradicals constructed using heterocyclic bridges such as furan **3** and pyridine **4**, but the study of these latter materials is complicated by their tendency to form CT salts with different (notably 2:1) diradical:iodine ratios (5). Herein we extend both these avenues to the thiophene-bridged bis(diselenadiazolyl) [T-2,5-Se] **5** (E = Se). The preparation and solid-state characterization of its 1:1 iodine CT salt is described, and its structure and transport properties compared to those of the closely related 1,3-benzene-bridged CT salt [1,3-Se][I].

The design strategy behind this compound originated from the desire to adjust, but not alter, the "nested spoon" packing pattern exhibited by the π-stacks in [1,3-Se][I]. As illustrated in Scheme 1, the ca. 120° angle subtended between the two CN_2Se_2 rings in each molecule limits intermolecular Se···Se interactions in [1,3-Se][I]; the "bite" angle is too severe. It was hoped that replacement of a benzene ring by a thiophene heterocycle would produce a wider (>120°) "bite" angle, and hence allow for a closer approach of neighbouring CN_2Se_2 rings and enhanced lateral Se···Se contacts. If such a modification of crystal structure could be induced, then its effect on structural stability, i.e., resistance to CDW distortions, could be tested.

Results and discussion

Preparation and crystal growth

We recently reported the synthesis of the thiophene-bridged bis(dithiadiazolyl) [T-2,5-S] **5** (E = S) by the condensation of the bifunctional persilylated carboxamidine **6** with SCl_2, and reduction of the corresponding bis(dithiadiazolylium) dication **7** with triphenylantimony (6). The diradical was purified by fractional sublimation in vacuo (Scheme 2). Like **1** and **2** (E = S), [T-2,5-S] reacts with iodine in hot chlorobenzene to afford a material that, on the basis of mass balance, appears to be

Scheme 1.

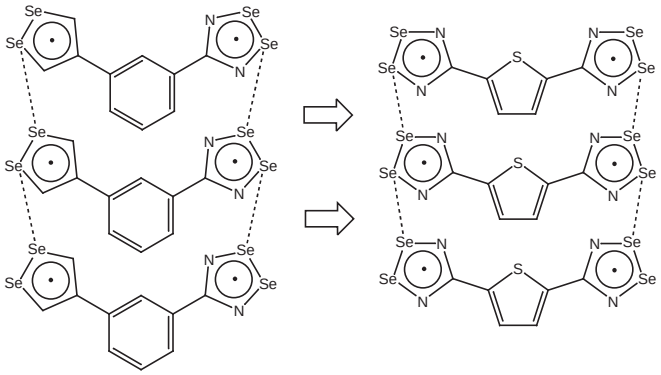

Scheme 2.

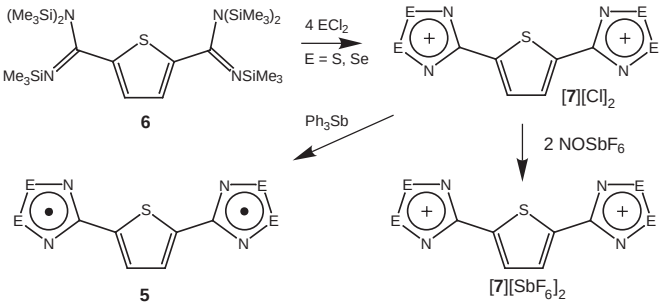

a 1:1 salt, i.e., [T-2,5-S][I]. Proper characterization of this compound was, however, precluded by its thermal decomposition during attempts to sublime it. The selenium analogue [T-2,5-Se] can be prepared in crude form using a similar synthetic sequence, and although the neutral material itself cannot be purified (it decomposes on sublimation), its iodine CT salt can be prepared by electroreduction of the dication [T-2,5-Se]$^{2+}$ (as its hexafluoroantimonate salt) in the presence of (excess) iodine. This technique, which we first developed for the generation of the CT salts [1,4-Se][I] and [1,3-Se][I], requires currents of <5 μA and growth periods of 10–14 days. Under these conditions, along with Pt wire electrodes, acetonitrile as solvent, no supporting electrolyte, and a strictly oxygen-free atmosphere, small needles of [T-2,5-Se][I] can be grown. This material exhibits a pressed pellet conductivity of ca. 10^2 S cm^{-1} at room temperature.

Crystal and molecular structure of [T-2,5-Se][I]

Numerous electrocrystallization experiments were performed, and many crystals of [T-2,5-Se][I] were examined; relatively few, however, were suitable for X-ray work. The structural determination reported here suffers from a paucity of data with significant intensity due to the thin dimensions of the crystals and the face-centered noncentric space group. Four data sets were collected; the data set used measured four octants of data for the face-centered orthorhombic *Fm*2*m* lattice. The nitrogen and carbon atoms were refined with isotropic displacement parameters because of the low reflection:parameter ratio, and the hydrogen atoms were constrained to idealized positions. Atomic coordinates for [T-2,5-Se][I] are listed in Table 1, and pertinent intramolecular bond distances are summarized in Table 2. Figure 1 shows an ORTEP picture of the asymmetric unit with the atom numbering scheme. All of the atoms of the

© 1998 NRC Canada

Table 1. Atomic parameters x, y, z and B_{eq}/B_{iso} in [T-2,5-Se][I] (esd in parentheses).

	x	y	z	B_{eq}/B_{iso} [a]
I[b]	0.3812(22)	0.32573	0.2432(3)	6.1(11)
Se1	0	0.2927(5)	0.14255(16)	6.46(22)
Se2	0	0.0942(5)	0.16677(14)	5.50(17)
S	0	0.1880(11)	0	8.4(10)
N1	0	0.2456(21)	0.0873(8)	4.3(5)
N2	0	0.0361(24)	0.1126(8)	4.0(5)
C1	0	0.125(3)	0.0844(12)	4.8(7)
C2	0	0.082(3)	0.0401(9)	3.9(5)
C3	0	–0.029(3)	0.0205(10)	5.4(8)
H	0	–0.101	0.037	6.2

[a] B_{eq} is the mean of the principal axis of the thermal ellipsoid. [b] Occupancy factor = 0.25.

Table 2. Summary of pertinent intramolecular bond lengths (Å) (mean values, esd, or range in parentheses).

	Se—Se	Se—N
$[1,4\text{-Se}]_2$	2.338(19)	1.79(3)
$[1,3\text{-Se}]_2$	2.35(30)	1.78(11)
$[1,4\text{-Se}][SbF_6]\cdot 3PhCN$	2.259(12)	1.725(19)
[1,4-Se][I]	2.305(1)	1.778(6)
[1,3-Se][I]	2.316(6)	1.76(2)
[T-2,5-Se][I]	2.309(8)	1.82(3)

[T-2,5-Se] molecule lie on a mirror plane, and the thiophene S-atom is on the intersection of two mirror planes. The iodine atom is in a general position with an occupancy of 0.25.

From a purely molecular perspective the structural parameters of the [T-2,5-Se] molecule hold few surprises. The Se—Se distance is very similar to those reported for [1,4-Se][I] and [1,3-Se][I], and intermediate in length between those observed in fully oxidized $[RCN_2Se_2]^+$ cations (7) and reduced $[RCN_2Se_2]_2$ radical dimers (8, 9). The balance favours the neutral state nominally, suggestive of less than a full positive charge on the molecule as a whole (less than one half positive charge per CN_2Se_2 ring). While the space group of [T-2,5-Se][I] differs from that of [1,3-Se][I] (*Ima*2) the packing patterns displayed by the two structures (Fig. 2) are very similar, i.e., perfectly superimposed π-stacks with the same "nested spoon" arrangement of adjacent columns. In both cases the iodine atoms are disordered in columns that bridge neighbouring π-stacks in a head-to-head sense. This mode of ion pairing is very typical of both dithia- and diselenadiazolylium halides (1, 2, 10, 11).

When viewed from a direction perpendicular to the stacking axis (Fig. 3), the differences between the two structures become more apparent. In [T-2,5-Se][I] the molecular units are bisected by two mirror planes, so that the two CN_2Se_2 rings and the thiophene bridge are rigorously coplanar. By contrast the [1,3-Se] molecules in [1,3-Se][I] lie on a single mirror plane that bisects the benzene ring. As a whole the molecule is far from planar; the plane of the two CN_2Se_2 rings makes a dihedral angle of 16.7° with the plane of the benzene ring. Despite this difference, the π-stack repeats in [T-2,5-Se][I] (3.544(2) Å) and [1,3-Se][I] (3.543(2) Å) are virtually identical, both being longer than that found in [1,4-Se][I]

Fig. 1. ORTEP drawing of the asymmetric unit in [T-2,5-Se][I], showing atom numbering.

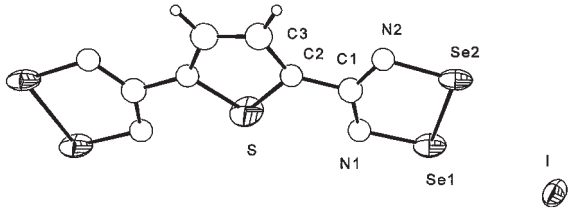

Fig. 2. Packing of [T-2,5-Se][I] (above) and [1,3-Se][I] (below), viewed down the stacking direction. Broken lines indicate lateral intermolecular Se···Se contacts.

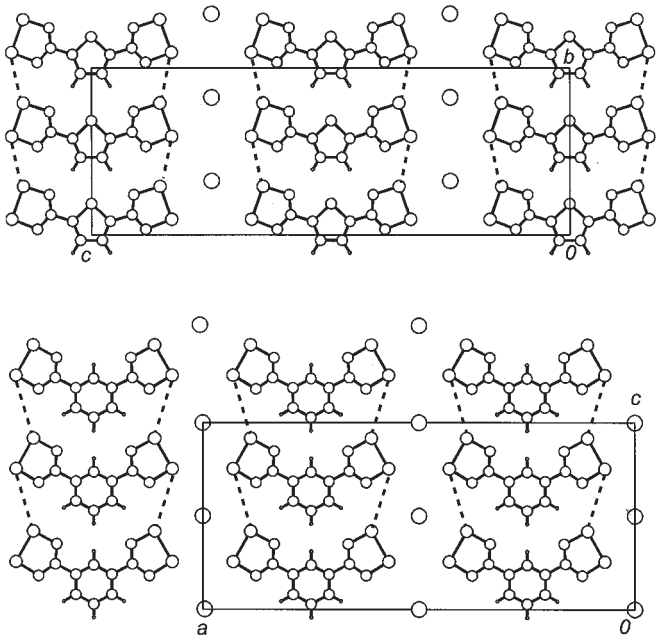

(3.5006(15) Å). Figure 2 also provides a comparison of the registry of the π-stacks. While the molecular units in adjacent columns in [1,3-Se][I] are approximately in register, those in [T-2,5-Se][I] are perfectly out of register. This difference, coupled with the tighter "nested spoon" packing found for [T-2,5-Se][I], affords shorter and more effective intercolumnar Se···Se contacts. In [1,3-Se][I], the closest Se···Se approach (4.323(6) Å), between molecules in the same "layer" of adjacent columns, is well outside of the Se···Se van der Waals separation of 3.8 Å (12). By contrast, in [T-2,5-Se][I], each selenium is laced (Fig. 2) by much shorter (3.832(7) Å) contacts to two neigbouring rings in adjacent stacks.

Magnetic measurements

Figure 4 shows the magnetic susceptibility behaviour of the [T-2,5-Se][I] as a function of temperature. The material is essentially diamagnetic at low temperatures; a Curie fit to the data below 100 K led to a value of $\chi = -249$ cgs ppm mol^{-1} for the diamagnetic term, in good agreement with estimates based on the Pascal scheme, and $\theta = 2$ K. The concentration of unpaired spins was found to be 0.05%. Paramagnetism, which can be associated with the onset of metallic conductivity (1, 2), develops near 200 K, and continues to rise up to 400 K, the limit of the experiment. Qualitatively this behaviour is very

© 1998 NRC Canada

Fig. 3. Packing of [T-2,5-Se][I] (above) and [1,3-Se][I] (below), viewed perpendicular to the stacking direction. Broken lines indicate lateral intermolecular Se···Se contacts.

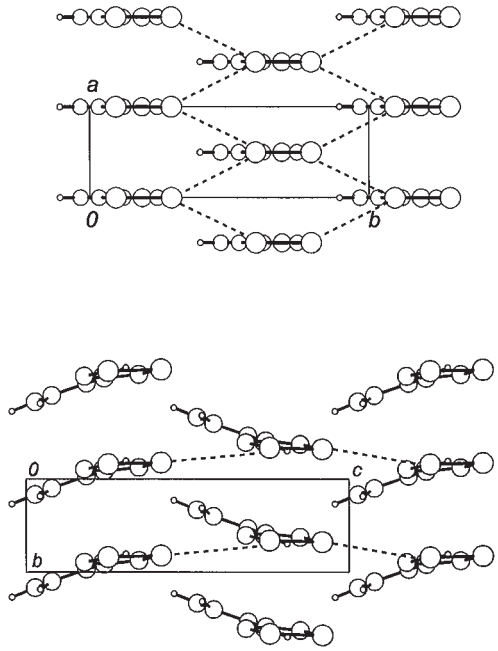

similar to that displayed by [1,3-Se][I]. It also shows a collapse from weakly paramagnetic to a diamagnetic, semiconducting state near 200 K.

Band-structure calculations

To assess the relative magnitude of orbital interactions between the CN_2Se_2 rings along and across the stacks of [T-2,5-Se][I] and [1,3-Se][I], we have carried out a series of extended Hückel band calculations on models related to the two crystal structures. The model focusses on simplified two-dimensional unit cells consisting of two adjacent HCN_2Se_2 radicals located at positions provided by the X-ray data. The consequent crystal orbitals (COs) are accordingly grouped into pairs, the most relevant being those arising from the in-phase and out-of-phase combinations of the singly occupied molecular orbital of the radicals, i.e., $[SOMO]^+$ and $[SOMO]^-$ (Scheme 3), which form the basis for the conduction band of the solid. Figure 5 illustrates the dispersion of these two COs along a^* and b^* for [T-2,5-Se][I], and along b^* and c^* for [1,3-Se][I]. Because both cells are orthorhombic these reciprocal space directions correspond exactly to real space interactions parallel and perpendicular to the π-stacking direction. As expected, given the superimposed nature of the stacking and the nearly identical cell repeats, dispersion along the stacking direction is large, nearly 4 eV for both structures. Lateral dispersion is much smaller for both structures, again as expected, but there are now notable differences in the degree of splitting between the two COs. As a result of the greater packing efficiency found for [T-2,5-Se][I], CO dispersion approaches 0.3 eV, a value similar to that found in many classical organic conductors (13). By contrast, lateral dispersion in [1,3-Se][I] is barely 0.05 eV, reflective of the weak intermolecular interactions apparent from the X-ray structure.

Fig. 4. Magnetic susceptibility of [T-2,5-Se][I], as a function of temperature.

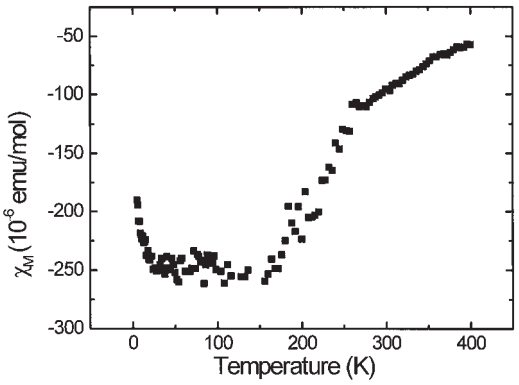

Scheme 3.

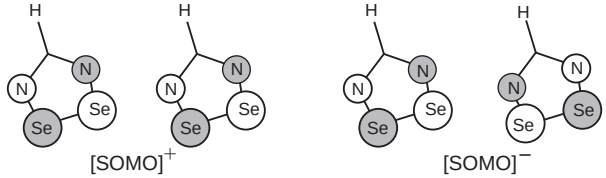

Summary and conclusion

Modification of the shape of the 1,3-benzene-bridged diradical [1,3-Se] by replacement of the bridging benzene ring by thiophene, to generate [T-2,5-Se], has allowed the preparation and comparison of two approximately isostructural iodine charge-transfer salts. The packing efficiency of [T-2,5-Se][I], as indicated by the size of intermolecular Se···Se interactions and the consequent degree of crystal orbital dispersion, is significantly better than that of [1,3-Se][I]. However, while lateral interactions have been improved, the structure of [T-2,5,-Se][I] is still highly one-dimensional; crystal dispersion along the stacking direction is an order of magnitude stronger. Even though a reasonable network of secondary, intercolumnar interactions, one far better than in [1,3-Se][I], has been developed, the overriding factor determining structural stability remains the highly developed interactions along the stack.

Experimental section

General procedures and starting materials

Selenium powder (Aldrich), chlorine gas (Matheson), and $NOSbF_6$ (STREM) were obtained commercially and used as received. Iodine (Fisher) was resublimed before use. The solvents acetonitrile (HPLC grade), benzonitrile, and chlorobenzene were all purified by distillation from P_2O_5. The persilylated thiophene-2,5-bis(carboxamidine) **6** was prepared as previously described (6) by the reaction of $LiN(SiMe_3)_2{\cdot}Et_2O$ (14) with 2,5-dicyanothiophene (15), followed by treatment of the intermediate bis(*N*-lithio amidinate) with chlorotrimethylsilane. Selenium tetrachloride was prepared according to a standard literature method (16). Chemical analyses were performed by MHW Laboratories, Phoenix, Ariz. Infrared spectra of the iodine CT salt could not be obtained because of excessive scattering of the incident radiation by the sample (as a nujol mull).

© 1998 NRC Canada

Fig. 5. Dispersion of the crystal orbitals $[SOMO]^+$ and $[SOMO]^-$ in [T-2,5-Se][I] and [1,3-Se][I], parallel to the stacking direction (above) and perpendicular to the stacking direction (below).

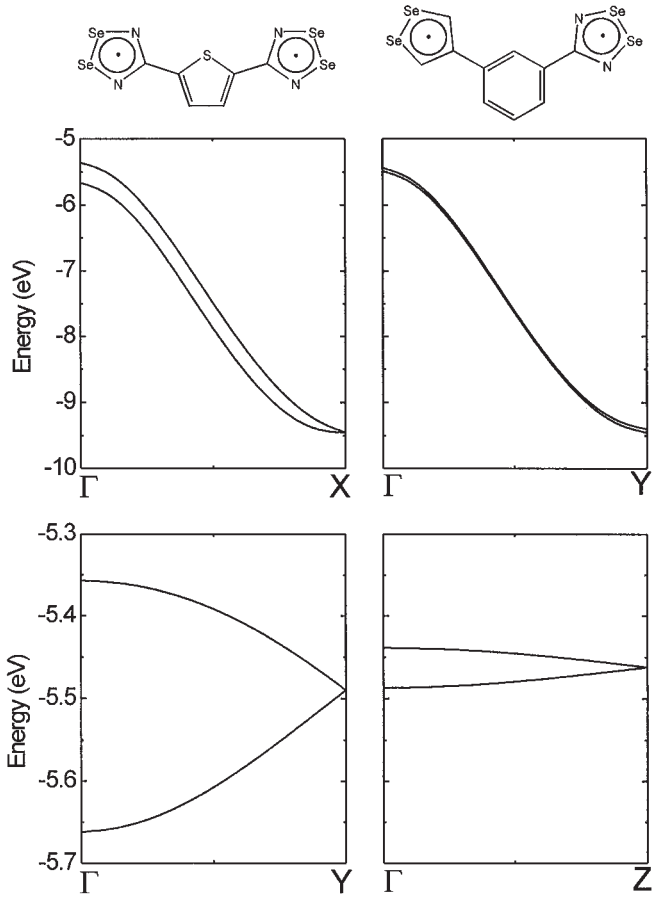

Table 3. Crystal data for [T-2,5-Se][I].

Formula	$Se_4N_4SC_6H_2I$
fw	604.9
a, Å	3.544(2)
b, Å	10.9808(16)
c, Å	31.464(5)
V, Å^3	1224.5(7)
d (calcd.), g cm^{-3}	3.28
Space group	*Fm*2*m*
Z	4
λ, Å	0.7107
Temp., K	293
Linear abs coeff., mm^{-1}	14.5
Data with $I > 3.0\sigma(I)$	245
$R(F)$, $R_w(F)$ [a]	0.056, 0.064

[a] $R = (\Sigma\, ||F_o| - |F_c||)/(\Sigma\, |F_o|)$; $R_w = \{(\Sigma w||F_o| - |F_c||^2)/[\Sigma(w|F_o|^2)]\}^{1/2}$

Preparation of [T-2,5-Se][SbF_6]$_2$

The persilyated thiophene-2,5-bis(carboxamidine) **6** (6.01 g, 10.0 mmol) was added portionwise, as a solid, to a solution of $SeCl_2$ prepared in situ by the reaction of $SeCl_4$ (4.44 g, 20.1 mmol) and elemental selenium (1.59 g, 20.1 mmol) in 100 mL CH_3CN. The resulting dark red slurry was heated under reflux for 16 h. The crude bis(diselenadiazolylium) dichloride salt was filtered off, washed with 3 × 40 mL CH_3CN, and dried in vacuo. Solid $NOSbF_6$ (5.3 g, 20.0 mmol) was added to a slurry of this crude dichloride salt in 30 mL CH_3CN. Immediate gas evolution was observed, and the solid dissolved to give a dark red solution. After 2 h the solvent was removed in vacuo, and the resulting solid mass recrystallized from chlorobenzene–benzonitrile (1:1). The burgundy-coloured crystals were filtered off and redissolved in 50 mL hot chlorobenzene–benzonitrile (1:1). Slow cooling to room temperature of this solution afforded burgundy flakes of the solvate [T-2,5-Se][SbF_6]$_2$·2PhCN (2.9 g, 2.5 mmol, 25%), dec >250°C. Anal. calcd. for $C_{20}H_{12}N_6SSe_4Sb_2F_{12}$: C 20.79, H 1.05, N 7.27; found: C 21.96, H 1.05, N 7.04.

Electrocrystallization of [T-2,5-Se][I]

Crystals of [T-2,5-Se][I] suitable for X-ray work and transport property measurements were prepared by electroreduction of 5 mM solutions of [T-2,5-Se][SbF_6]$_2$·2PhCN in acetonitrile in an H cell (17) fitted with a D porosity frit and Pt wire anode and cathode). Iodine was added to the cathode compartment to a level of 5 mM (10 mM in I). No supporting electrolyte was used. Samples for single crystal X-ray work were typically grown with a current of 3–5 μA over a period of 10–14 days. Material suitable for bulk analysis was grown at a higher current level, e.g., 5–10 μA. The dark, lustrous needles are stable in air. In view of the fact that no supporting electrolyte was used, no attempt was made to run the cells to exhaustion. Indeed, most electrodeposition experiments were halted well before 50% completion. Anal. calcd. for $C_6H_2N_4SSe_4I$: C 11.57, H 0.33, N 9.26, I 20.98; found: C 11.36, H 0.15, N 9.07, I 21.96.[2]

X-ray measurements

All X-ray data were collected on an ENRAF-Nonius CAD-4 diffractometer with monochromated Mo K_α radiation. Crystals were mounted on a glass fiber with silicone rubber. Data were collected using a θ/2θ technique. The structure was solved using direct methods and refined by full-matrix least squares, which minimized $\Sigma w(\Delta F)^2$. A summary of crystallographic data is provided in Table 3. Tables of crystal data, structure solution, and refinement parameters, bond lengths and angles, and anisotropic thermal parameters (five pages) for [T-2,5-Se][I] have been deposited.[3]

Magnetic susceptibility measurements

The magnetic susceptibility of [T-2,5-Se][I] was measured as

[2] As observed for other CT salts of this type, the iodine analysis was variable and irreproducible, as a result of interference from selenium. Repeated and consistent C, H, and N data, plus the iodine occupancy from the X-ray work, confirmed the composition.

[3] Copies of material on deposit may be purchased from: The Depository of Unpublished Data, Document Delivery, CISTI, National Research Council Canada, Ottawa, Canada, K1A 0S2. These data, with the exemption of anisotropic thermal parameters, have also been deposited with the Cambridge Crystallographic Data Centre, and can be obtained on request from The Director, Cambridge Crystallographic Data Centre, University Chemical Laboratory, 12 Union Road, Cambridge, CB2 1EZ, U.K.

© 1998 NRC Canada

a function of temperature on a SQUID magnetometer operating at 1 T.

Band-structure calculations

The band-structure calculations were carried out on a Pentium 166 PC with the EHMACC suite of programs (18) using the parameters discussed previously (9, 19). The off-diagonal elements of the Hamiltonian matrix were calculated with the standard weighting formula (20). In the model two-dimensional calculations, the coordinates of the two HCN_2Se_2 radicals in the unit cell were taken directly from the X-ray data on [T-2,5-Se][I] and [1,3-Se][I].

Acknowledgements

Financial support at Guelph was provided by the Natural Sciences and Engineering Research Council of Canada (NSERC) and at Arkansas by the National Science Foundation (EPSCOR program). R.G.H. acknowledges a NSERC postgraduate scholarship.

References

1. (*a*) C.D. Bryan, A.W. Cordes, R.M. Fleming, N.A. George, S.H. Glarum, R.C. Haddon, R.T. Oakley, T.T.M. Palstra, A.S. Perel, L.F. Schneemeyer, and J.V. Waszczak. Nature, **365**, 821 (1993).
2. C.D. Bryan, A.W. Cordes, R.M. Fleming, N.A. George, S.H. Glarum, R.C. Haddon, C.D. MacKinnon, R.T. Oakley, T.T.M. Palstra, A.S. Perel, L.F. Schneemeyer, and J.V. Waszczak. J. Am. Chem. Soc. **117**, 6880 (1995).
3. M. Kertész and F.Vonderviszt. J. Am. Chem. Soc. **104**, 5889 (1982).
4. C.D. Bryan, A.W. Cordes, N.A. George, R.C. Haddon, C.D. MacKinnon, R.T. Oakley, T.T. M. Palstra, and A.S. Perel. Chem. Mater. **8**, 762 (1996).
5. A.W. Cordes, N.A. George, R.C. Haddon, D.K. Kennepohl, R.T. Oakley, T.T.M. Palstra, and R.W. Reed. Chem. Mater. **8**, 2774 (1996).
6. A.W. Cordes, R.C. Haddon, C.D. MacKinnon, R.T. Oakley, G.W. Patenaude, R.W. Reed, T. Rietveld, and K.E. Vajda. Inorg. Chem. **35**, 7626 (1996).
7. A.W. Cordes and R.T. Oakley. Acta Crystallogr. Sect. C, **C46**, 699 (1990).
8. M.P. Andrews, A.W. Cordes, D.C. Douglass, R.M. Fleming, S.H. Glarum, R.C. Haddon, P. Marsh, R.T. Oakley, T.T.M. Palstra, L.F. Schneemeyer, G.W. Trucks, R.R. Tycko, J.V. Waszczak, W.W. Warren, K.M. Young, and N.M. Zimmerman. J. Am. Chem. Soc. **113**, 3559 (1991).
9. A.W. Cordes, R.C. Haddon, R.T. Oakley, L.F. Schneemeyer, J.V. Waszczak, K.M. Young, and N.M. Zimmerman. J. Am. Chem. Soc. **113**, 582, (1991).
10. C.D. Bryan, A.W. Cordes, J.D. Goddard, R.C. Haddon, R.G. Hicks, C.D. MacKinnon, R.C. Mawhinney, R.T. Oakley, T.T.M. Palstra, and A.S. Perel. J. Am. Chem. Soc. **118**, 330 (1996).
11. C.D. Bryan, A.W. Cordes, R.C. Haddon, R.G. Hicks, R.T. Oakley, T.T.M. Palstra, A.S. Perel, and S.R. Scott. Chem. Mater. **6**, 508 (1994).
12. A. Bondi. J. Phys. Chem. **68**, 441 (1964).
13. J.M. Williams, J.R. Ferraro, R.J. Thorn, K.D. Carlson, U Geiser, H.H. Wang, A.M. Kimi, and M.H. Whangbo. *In* Organic superconductors. Prentice–Hall, Englewood Cliffs, New Jersey. 1992.
14. R.T. Boeré, R.G. Hicks, and R.T. Oakley. Inorg. Synth. **31**, 94 (1997).
15. C. Paulmier, J. Morel, and J. Pastour. Bull. Soc. Chim. Fr. 2511 (1969).
16. G. Brauer. *In* Handbook of preparative chemistry. Vol. 1. Academic Press, New York. 1963. p. 423.
17. (*a*) J.R. Ferraro and J.M Williams. *In* Introduction to synthetic electrical conductors. Academic Press, New York. 1987. p. 25; (*b*) D.A. Stephens, A.E. Rehan, S.J. Compton, R.A. Barkhau, and J.M. Williams. Inorg. Synth. **24**, 135 (1986).
18. Quantum Chemistry Program Exchange, EHMACC. Program no. 571.
19. H. Basch, A. Viste, and H.B. Gray. Theor. Chim. Acta, **3**, 458 (1965).
20. J.H. Ammeter, H.B. Burghi, J.C. Thibeault, and R. Hoffmann. J. Am. Chem. Soc. **100**, 3686 (1978).

© 1998 NRC Canada

N-Glycosyl phosphonamidates: potential transition-state analogue inhibitors of glycopeptidases

Vito Ferro, Larry Weiler, Stephen G. Withers, and Herman Ziltener

Abstract: The synthesis of *N*-glycosyl phosphonamidates has been accomplished via the coupling of peracetylated glycosylamines with an appropriate phosphonochloridate in the presence of pyridine. The resulting glycosyl phosphonamidate esters are dealkylated with bromotrimethylsilane and then deacetylated to give the target compounds, which are potential transition-state analogue inhibitors of glycopeptidases and may prove useful as haptens for generating catalytic antibodies with glycopeptidase activity.

Key words: enzyme inhibition, PNGase, phosphonamidate, amide hydrolysis.

Résumé : On a réalisé la synthèse de phosphonamidates de *N*-glycosyles par le biais du couplage de glycosylamines peracétylées avec un phosphonochloridate approprié effectué en présence de pyridine. On soumet les esters phosphonamides de glycosyles qui en résultent à une désalkylation à l'aide de bromotriméthylsilane, suivie d'une désacétylation qui conduit aux composés recherchés; ceux-ci sont des inhibiteurs d'un analogue potentiel de l'état de transition des glycopeptidases et ils peuvent s'avérer utiles comme haptènes dans la génération catalytique d'anticorps possédant une activité comme glycopeptidase.

Mots clés : inhibition d'enzyme, PNGase, phosphonamidate, hydrolyse d'amide.

[Traduit par la rédaction]

Introduction

Peptide *N*-glycosidases (PNGase) are enzymes that cleave the β-aspartylglucosylamine bond of *N*-linked glycoproteins via an amidase (amidohydrolase) mechanism (1). This family of enzymes is widely distributed in bacteria, plants, and animals, and it is speculated that PNGases may play an important role in the nonlysosomal regulation of various physiological and (or) physicochemical properties of certain target proteins involved in embryonal development (2). The enzyme from the bacterium *Flavobacterium meningosepticum* (PNGase F) (3) is probably the most widely used agent for the deglycosylation of glycoproteins (4) and is thus a valuable biochemical tool for investigating oligosaccharide structure and the biosynthesis of *N*-linked glycoproteins (5). Despite the importance of this enzyme, little is known regarding its mechanism of action and the residues involved in catalysis. The recently determined three-dimensional X-ray crystallographic structure (6) of PNGase F at 2.2 Å resolution does not identify a single active-site area but suggests three possible sites which merit further investigation. Such ambiguity could be removed by determination of the structure of a complex with an inhibitor. However no such inhibitors have been reported, with the exception of the very recently reported C-glycopeptide (7). Increased knowledge of the catalytic mechanism of PNGases should lead to a better understanding of their physiological roles and may facilitate their usage as agents of protein glycosylation by functioning in the reverse mode. Thus it is of great interest to be able to inhibit these enzymes with transition-state analogue inhibitors.

The related amidase aspartylglucosaminidase (AGA) is ubiquitously distributed in mammalian tissues where it plays a central role in the normal ordered catabolism of *N*-linked glycoproteins in lysosomes (8). A genetic deficiency of aspartylglucosaminidase gives rise to aspartylglucosaminuria, a human lysosomal storage disease in which AspNHGlcNAc accumulates (9). Recently its three-dimensional X-ray crystallographic structure has also been determined (10), and as a result a mechanism resembling that of the serine proteases has been proposed for this enzyme.

In this paper we report the first syntheses of *N*-glycosyl phosphonamidates and phosphonamidate esters. We reasoned that compounds of this type should be useful as haptens for generating catalytic antibodies capable of selectively *N*-deglycosylating proteins (or selectively glycosylating them by catalyzing the reverse reaction), an area of great current interest (11, 12). In addition, these compounds are potentially transition-state analogue inhibitors of the enzyme peptide: *N*-glycosidase (PNGase) and the related aspartylglucosaminidase (AGA).

The phosphonamidate functional group is recognized as a stable mimic of the putative transition state of amide bond

Received October 3, 1997.

V. Ferro, L. Weiler, and S.G. Withers.[1] Department of Chemistry, University of British Columbia, 2036 Main Mall, Vancouver, BC V6T 1Z1, Canada.
H. Ziltener. Biomedical Research Centre, University of British Columbia, 2222 Health Sciences Mall, Vancouver, BC V6T 1Z3, Canada.

[1] Author to whom correspondence may be addressed. Telephone: (604) 822-3402. Fax: (604) 822-2847. E-mail: withers@chem.ubc.ca

© 1998 NRC Canada

Scheme 1.

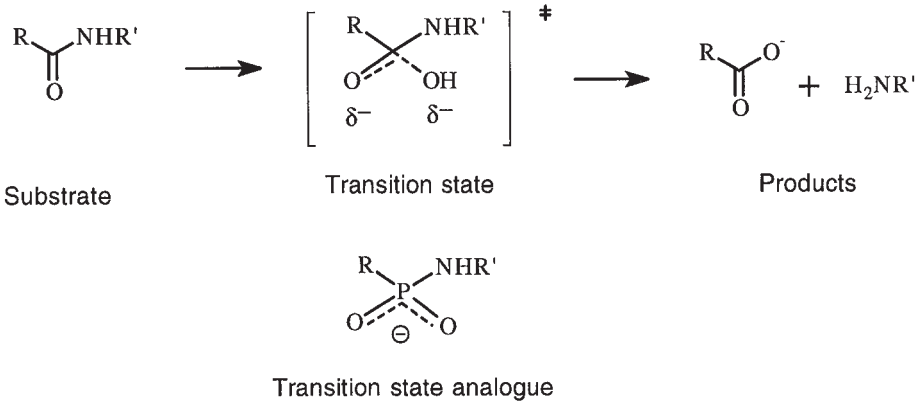

hydrolysis, with close resemblance from both a steric and electronic point of view. It possesses the hydrogen-bonding capacity, the correct overall charge and the correct geometry, shape, and size, as shown in Scheme 1. Phosphonamidates have thus been used successfully as haptens for generating catalytic antibodies with amidase (protease) or esterase activity (13, 14). Antibodies raised to phosphonamidate haptens have also been shown to catalyze the aminolysis of esters to amides (15). In addition, phosphonamidate analogues of natural peptide substrates have found great utility as potent transition-state analogue inhibitors of various proteases (16–23) and ligases (24).

Results and discussion

Phosphonamides are generally prepared by the reaction of amines with phosphonochloridates (25), which are in turn prepared by the reaction of phosphonate diesters with 1 equiv. of phosphorus pentachloride or phosphorus oxychloride. Deprotection then gives the corresponding phosphonamidates. Our approach to simple carbohydrate-derived phosphonamidates was therefore to couple the readily available protected glucosylamines **1** and **2** with an appropriate phosphonochloridate and then to remove the protecting groups.

The glucosylamines **1** and **2** were prepared, respectively, from the corresponding glucosyl azides (26, 27) by catalytic hydrogenation in ethanol with palladium on charcoal and platinum oxide as the respective catalysts. The phosphonochloridate chosen was ethyl benzylphosphonochloridate (**3**), which was readily prepared according to Morise et al. (28) by treatment of diethyl benzylphosphonate with phosphorus oxychloride. It was reacted with the glucosylamines **1** and **2** in pyridine at 0°C for 1 h and was then left overnight at room temperature. The glucosyl phosphonamides **4** and **5** were isolated in yields of 64 and 45%, respectively, following purification by flash chromatography. In the case of **1** (26), the purified (by recrystallization) amine was used in the coupling. Amine **2** (27), however, is known to be rather unstable, giving rise to dimerization products. The crude product formed from the hydrogenation of the azide precursor was therefore used immediately in the coupling step without further purification, leading to a decreased overall yield.

Compounds **4** and **5**, which gave satisfactory combustion analyses and (or) high-resolution mass spectra, were formed as mixtures of two diastereoisomers (about the chiral phosphorus atom) in ratios of approximately 1:1, as clearly evidenced by ^{31}P NMR spectroscopy (δ 26.9, 27.5 and 27.0, 28.0, respectively). Double the number of ^{13}C NMR resonances for **4** and **5** was also observed due to the presence of the additional chiral centre, and these were fully assigned. The ^{1}H NMR spectra, however, were predictably complex.

Dealkylation of the phosphonamidate ester group of **4** was achieved by treatment with bromotrimethylsilane (29) in dichloromethane at reflux followed by aqueous work-up. The product formed upon hydrolysis was the expected phosphonamide **6**, as evidenced by the NMR data of the crude product obtained in deuterochloroform. The ^{31}P NMR spectrum consisted of a singlet at δ 28.7, while the ^{1}H NMR spectrum included a broad, D_2O-exchangeable singlet at δ 6.72 assigned to the hydroxyl group on phosphorus. However, upon purification by flash chromatography, the product obtained in 83% yield as an amorphous solid was no longer compound **6**, but instead a chloroform-insoluble compound assigned the structure **7**, where M^+ is a metal cation presumably picked up from the silica gel. The NMR data, now obtained in deuterated methanol, were completely consistent with this assignment. Of particular note was the ^{31}P NMR spectrum, which showed a marked upfield shift to δ 14.7, indicative of a phosphonamidate (16). In addition, the mass spectrum of **7**, obtained in the negative-ion mode, showed the expected peak at *m/z* 500 (M, 100%). As final confirmation, treatment of **7** with acidic ion-exchange resin (Amberlite IR-120) could readily regenerate **6** (NMR). To complete the deprotection of **4**, compound **7** was treated with sodium methoxide in methanol, neutralized with Amberlite IR-120, and then dissolved in aqueous sodium bicarbonate solution to give the phosphonamidate **8**, as the sodium salt, in 54% overall yield following purification by flash chromatography. The phosphonamidate **9** was similarly obtained from **5** in an overall yield of 30%. Compounds **8** and **9** were fully characterized by ^{1}H, ^{13}C, and ^{31}P NMR spectroscopy and mass spectrometry and were stable in neutral aqueous solution at 25°C for at least two weeks (no change in the ^{31}P NMR spectra).

Phosphonamidate esters (or so called "capped" phosphonamidates) have also been shown to inhibit proteases, with similar but reduced potency to the parent phosphonamidates (19, 21), indicating that the anionic charge of the phosphonamidate may be of lesser importance than its geometry. Therefore, the phosphonamidate esters **10** and **11** were also prepared as potential inhibitors in good yield by simple deprotection of compounds **4** and **5** with ammonia in methanol.

© 1998 NRC Canada

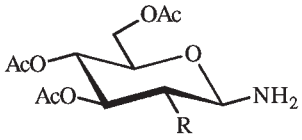

1 R = OAc
2 R = NHAc

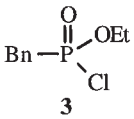

3

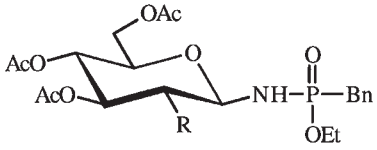

4 R = OAc
5 R = NHAc

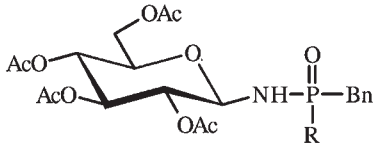

6 R = OH
7 R = O^- M^+

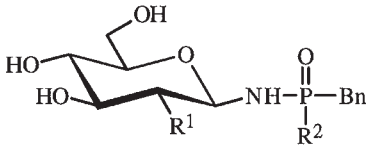

8 R^1 = OH R^2 = O^- Na^+
9 R^1 = NHAc R^2 = O^- Na^+
10 R^1 = OH R^2 = OEt
11 R^1 = NHAc R^2 = OEt

Our attention was next turned to preparing an *N*-glycosyl phosphonamidate hapten (to be conjugated to a carrier protein via a suitable linker) for use in generating catalytic antibodies with PNGase-like activity. To this end we required a suitably functionalized phosphonamidate for introduction of the linker. Phosphonochloridate **14** (13, 30) was therefore prepared according to the literature in good yield from diethyl 4-aminobenzylphosphonate **12**. The amino group of **12** was protected as the trifluoroacetamide by treatment with trifluoroacetic anhydride in pyridine to give the phosphonate **13**. Compound **13** was then heated in chloroform at 50°C with 1 equiv. of phosphorus pentachloride to give **14**, which was used immediately due to its instability. Both **13** and **14** were characterized extensively. The phosphonochloridate **14** was coupled with the amine **2** to give the glucosyl phosphonamide **15** as a mixture of diastereoisomers in 63% yield after flash chromatography. Selective removal of the trifluoroacetamido group of compound **15** should allow for attachment of a suitable linker (either prior to or subsequent to removal of the other protecting groups) and subsequent conjugation to a carrier protein. Details of these studies currently in progress and others directed towards the generation and characterization of catalytic antibodies derived from these haptens will be reported in due course.

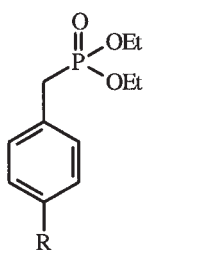

12 R = NH_2
13 R = $NHCOCF_3$

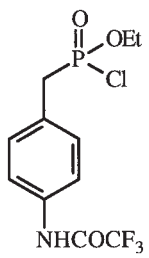

14

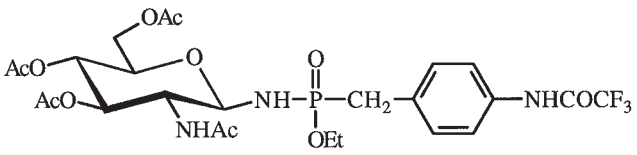

15

Experimental

General

Melting points (mp) were determined on a Laboratory Devices

© 1998 NRC Canada

Mel-Temp II melting point apparatus and are uncorrected. The NMR spectra were recorded on a Bruker AC 200, a Bruker WH 400, or a Varian XL 300 and are referenced to the solvent peak except when run in D_2O where they are referenced to internal acetone (δ_H 2.225, δ_C 31.0). The ^{31}P NMR spectra were recorded at 81 MHz and are referenced to external H_3PO_4 (δ 0.00). Where required, the interpretations were supported by COSY or APT NMR experiments. Mass spectra were obtained by desorption chemical ionization (DCI) on a Delsi Nermag R10-10C mass spectrometer with ammonia as the reactive gas, or by the liquid secondary ion (LSIMS) technique on a Kratos Concept mass spectrometer using thioglycerol–water as the matrix. Microanalyses were performed by Mr. Peter Borda in the microanalytical laboratory of the University of British Columbia. Solvents and reagents used were either reagent grade, certified, or spectral grade and where necessary were dried by standard procedures. Petroleum ether had a boiling range of 35–60°C. Reactions were monitored by thin layer chromatography (TLC) using Merck Kieselgel 60 F_{254} aluminium-backed sheets. Compounds were detected (where possible) under UV light or by charring with 10% sulfuric acid in MeOH or with 10% ammonium molybdate in 2 M sulfuric acid. Flash chromatography was performed on short columns (10–15 cm) of Merck Kieselgel 60 (230–400 mesh) under a positive pressure with specified eluants. Diethyl 4-aminobenzylphosphonate was purchased from Aldrich Chemical Company.

Ethyl *N*-(2,3,4,6-tetra-*O*-acetyl-β-D-glucopyranosyl)-benzylphosphonamide (4)

A solution of ethyl benzylphosphonochloridate **3** (28) (240 mg, 1.10 mmol) in CH_2Cl_2 (1 mL) was added to a solution at 0°C of 2,3,4,6-tetra-*O*-acetyl-β-D-glucopyranosylamine **1** (26) (323 mg, 0.93 mmol) in 1:1 pyridine–CH_2Cl_2 (10 mL). The mixture was stirred at 0°C for 3 h and then at room temperature for 16 h. The mixture was then diluted with EtOAc and poured into water. The organic phase was separated, and the aqueous phase was extracted with EtOAc. The combined organic phases were washed successively with water and brine, dried ($MgSO_4$), filtered, and concentrated. Flash chromatography (4:1 EtOAc – petroleum ether) then gave, as a mixture of diastereoisomers, the phosphonamide **4** (317 mg, 64%) as a colourless oil; ^{31}P NMR ($CDCl_3$) δ: 26.9, 27.5; ^{13}C NMR (75 MHz, $CDCl_3$) δ: 16.1, 16.2 (2 d, J_{CCOP} 6.1 Hz, CH_2CH_3), 20.5–20.6 ($COCH_3$), 36.0, 36.9 (2 d, J_{CP} 128, 123 Hz, $PhCH_2$), 60.3, 60.4 (2 d, J_{COP} 6.7 Hz, CH_2CH_3), 61.9, 62.0 (C-6), 68.4, 68.5 (C-4), 71.3, 71.4 (2 d, J_{CCNP} 9.9, 8.9 Hz, C-2), 72.7, 72.8, 72.9 (C-3, 5), 81.7, 82.5 (C-1), 126.8–131.9 (Ph), 169.5–170.4 (C═O); DCI *m*/*z*: 530 (M + H^+, 100%); HRMS calcd. for $C_{23}H_{32}NO_{11}P$: 530.1791; found: 530.1782.

Ethyl *N*-(2-acetamido-3,4,6-tri-*O*-acetyl-2-deoxy-β-D-glucopyranosyl) benzylphosphonamide (5)

A solution of 2-acetamido-3,4,6-tri-*O*-acetyl-2-deoxy-β-D-glucopyranosyl azide (27) (1.00 g, 2.69 mmol) in EtOH (40 mL) was hydrogenated at room temperature and pressure in the presence of platinum oxide (75 mg) for 5 h. The mixture was then filtered (Celite) and concentrated. The resultant crude 2-acetamido-3,4,6-tri-*O*-acetyl-2-deoxy-β-D-glucopyranosyl amine **2** (27) was dissolved in pyridine (20 mL) and cooled to 0°C. A solution of ethyl benzylphosphonochloridate (0.98 g, 4.5 mmol) in CH_2Cl_2 (5 mL) was then added, and the mixture was stirred at 0°C for 1 h and at room temperature for 16 h. Work-up as described for **4** followed by flash chromatography (1:9 MeOH–EtOAc) then gave, as a mixture of diastereoisomers, the phosphonamide **5** (0.64 g, 45%) as an amorphous solid; ^{31}P NMR ($CDCl_3$) δ: 27.0, 28.0; ^{13}C NMR (75 MHz, $CDCl_3$) δ: 16.1, 16.2 (2 d, J_{CCOP} 6.4 Hz, CH_2CH_3), 20.6–23.1 ($COCH_3$), 35.7, 36.9 (2 d, J_{CP} 128, 124 Hz, $PhCH_2$), 53.9, 54.3 (2 d, J_{CCNP} 8.6, 9.3 Hz, C-2), 60.3, 60.5 (2 d, J_{COP} 7.3, 7.1 Hz, CH_2CH_3), 62.1, 62.3 (C-6), 68.4, 68.6 (C-4), 72.8, 73.0 (C-3, 5), 82.7, 83.9 (C-1), 126.7–132.0 (Ph), 169.4–171.2 (C═O); DCI *m*/*z*: 529 (M + H^+, 90.6%). Anal. calcd. for $C_{23}H_{33}N_2O_{10}P$: C 52.27, H 6.29, N 5.30; found: C 52.11, H 6.27, N 5.14.

N-(β-D-Glucopyranosyl)benzylphosphonamidate sodium salt (8)

A solution of compound **4** (108 mg, 0.20 mmol) and bromotrimethylsilane (153 mg, 132 μL, 1.00 mmol) in CH_2Cl_2 (3 mL) was heated gently at reflux for 2 h. The mixture was concentrated, and the residue was dissolved in aqueous acetonitrile and concentrated to a yellow oil. Flash chromatography (16:4:1 EtOAc–MeOH–H_2O) gave a white amorphous solid (85 mg, 83%), with analytical data consistent with the structure **7**. ^{31}P NMR (MeOH-d_4) δ: 14.7; ^1H NMR (400 MHz, MeOH-d_4) δ: 1.95, 1.96, 1.99, 2.01 (4 s, Me), 3.02 (d, J_{PCH} 20.8 Hz, $PhCH_2$), 3.78–3.85 (bm, H-5), 4.15 (bd, $J_{6A,6B}$ 11.9 Hz, H-6A), 4.25 (bdd, $J_{5,6B}$ 4.9 Hz, H-6B), 4.67 (dd, $J_{1,2} \approx J_{1,P}$ 7.8 Hz, H-1), 4.83 (obscured by H_2O, H-2, NH), 4.99 (dd, $J_{3,4} \approx J_{4,5} = 9.7$ Hz, H-4), 5.26 (dd, $J_{2,3}$ 9.4 Hz, H-3), 7.09–7.42 (m, Ph); ^{13}C NMR (50 MHz, MeOH-d_4) δ: 20.6, 20.7, 20.9 (4 C, Me), 40.4 (d, J_{CP} 120.5 Hz, $PhCH_2$), 63.6 (C-6), 70.3 (C-4), 73.4 (d, J_{CCNP} 8.8 Hz, C-2), 73.8 (C-3), 74.9 (C-5), 84.8 (C-1), 126.6–137.8 (6 C, Ph), 171.4–172.3 (C═O); LSIMS (negative ion mode) *m*/*z*: 500 (M, 100%), 501 (M + 1, 24.7%); HRMS calcd. for $C_{21}H_{27}NO_{11}P$: 500.1322; found: 500.1327.

Treatment of a methanolic solution of **7** with Amberlite IR-120 ion-exchange resin (H^+ form) followed by filtration and concentration could regenerate compound **6** as evidenced by NMR: ^{31}P NMR ($CDCl_3$) δ: 28.7; ^1H NMR (200 MHz, $CDCl_3$) δ: 6.72 (bs, OH). Compound **7** (60 mg) was dissolved in MeOH (3 mL), and a solution of sodium methoxide in MeOH (0.5 mL of 1 M) was added. The mixture was stirred for 20 min, neutralized (Amberlite IR-120, H^+ form), and concentrated. The residue was dissolved in MeOH–H_2O (3:1, 4 mL), and solid $NaHCO_3$ (21 mg, 0.25 mmol) was added. The mixture was stirred at room temperature overnight. The mixture was then concentrated and purified by flash chromatography (7:2:1 EtOAc–MeOH–H_2O) to give a solid that was dissolved in H_2O. Filtration and lyophilization then gave the phosphonamidate **8** (23 mg, 54%) white, amorphous solid. ^{31}P NMR (D_2O) δ: 21.8; ^1H NMR (400 MHz, D_2O) δ: 3.08 (d, J_{PCH} 19.7 Hz, $PhCH_2$), 3.21 (dd, $J_{1,2} \approx J_{2,3} = 9.0$ Hz, H-2), 3.36 (dd, $J_{3,4} \approx J_{4,5}$ 9.0 Hz, H-4), 3.43 (ddd, $J_{5,6A}$ 5.7, $J_{5,6B}$ 2.1 Hz, H-5), 3.50 (dd, H-3), 3.72, 3.92 (2 dd, AB part of an ABX system, $J_{6A,6B}$ 12.2 Hz, H-6A, 6B), 4.31 (dd, J_{PNCH} 8.5 Hz, H-1), 7.23–7.46 (m, Ph); ^{13}C NMR (75 MHz, D_2O) δ: 39.2 (d, J_{CP} 117 Hz, $PhCH_2$), 61.7 (C-6), 70.7 (C-4), 74.5 (d, J_{CCNP} 8 Hz, C-2), 77.3, 77.5 (C-3, 5), 85.3 (C-1), 126.7–136.3 (Ph). LSIMS (negative ion mode) *m*/*z*: 332 (M, 25.9%); HRMS calcd. for $C_{13}H_{19}NO_7P$: 332.0899; found: 332.0900.

© 1998 NRC Canada

_N_-(2-Acetamido-2-deoxy-β-D-glucopyranosyl)benzylphosphonamidate sodium salt (9)

Compound **5** (250 mg, 0.47 mmol) was treated with bromotrimethylsilane and worked up as described for compound **4**. The crude product was subjected to flash chromatography (16:4:1 EtOAc–MeOH–H_2O) to give a pale yellow solid, which was deprotected and treated with $NaHCO_3$ as described for compound **7**. Flash chromatography (5:2:1 EtOAc–MeOH–H_2O) then gave the phosphonamidate **9** (56 mg, 30%) as a white, amorphous solid. ^{31}P NMR (D_2O) δ: 21.2; ^1H NMR (400 MHz, D_2O) δ: 2.04 (s, Me), 3.01 (m, AB part of an ABX system, $J_{A,B}$ 14.3, J_{PCH} 19.8 Hz, PhCH_2), 3.36–3.47 (m, H-4, 5), 3.54 (dd, $J_{2,3} \approx J_{3,4}$ 9.0 Hz, H-3), 3.68 (dd, $J_{1,2}$ 9.4 Hz, H-2), 3.72, 3.92 (2 dd, AB part of an ABX system, $J_{6A,6B}$ 12.0 Hz, $J_{5,6A}$ 5.2 Hz, $J_{5,6B}$ 1.0 Hz, H-6A, 6B), 4.37 (dd, J_{PNCH} 8.8 Hz, H-1), 7.25–7.48 (m, Ph); ^{13}C NMR (75 MHz, D_2O) δ 23.0 (Me), 39.0 (d, J_{CP} 119 Hz, PhCH_2), 56.9 (d, J_{CCNP} 8 Hz, C-2), 61.8 (C-6), 70.9 (C-4), 75.4 (C-3), 77.5 (C-5), 84.3 (C-1), 126.7–136.2 (Ph), 175.6 (C═O). LSIMS (negative ion mode) *m*/*z*: 373 (M, 34.8%); HRMS calcd. for $C_{15}H_{22}N_2O_7P$: 373.1165; found: 373.1160.

Ethyl _N_-(β-D-glucopyranosyl)benzylphosphonamide (10)

Compound **4** (55 mg, 0.10 mmol) was dissolved in MeOH (2 mL), and the solution was cooled to 0°C and saturated with ammonia. It was stirred at 0°C for 1 h and then at room temperature for 16 h. Concentration of the mixture followed by flash chromatography (27:2:1 EtOAc–MeOH–H_2O) gave, as a mixture of diastereoisomers, the phosphonamide **10** (35 mg, 93%) as an amorphous solid; ^{31}P NMR (D_2O) δ: 34.1; ^{13}C NMR (75 MHz, D_2O) δ: 15.8 (d, J_{CCOP} 6.0 Hz, CH_2CH_3), 35.2, 35.7 (2 d, J_{CP} 124.6, 124.2 Hz, PhCH_2), 60.9 (C-6), 62.1, 62.3 (2 d, J_{COP} 7.2 Hz, CH_2CH_3), 69.7 (C-4), 73.6, 73.7 (C-2), 76.7, 76.8, 77.2 (C-3, 5), 83.4, 83.5 (C-1), 127.4–131.8 (Ph); DCI *m*/*z*: 362 (M + H^+, 60.4%), 379 (M + NH_4^+, 100%); HRMS calcd. for $C_{15}H_{24}NO_7P$: 362.1369; found: 362.1353. Anal. calcd. for $C_{15}H_{24}NO_7P \cdot H_2O$: C 47.49, H 6.91, N 3.69; found: C 47.46, H 6.62, N 3.83.

Ethyl _N_-(2-acetamido-2-deoxy-β-D-glucopyranosyl)-benzylphosphonamide (11)

Compound **5** (80 mg, 0.15 mmol) was dissolved in MeOH (3 mL), and the solution was cooled to 0°C and saturated with ammonia. It was stirred at 0°C for 6 h and then concentrated. Flash chromatography (16:4:1 EtOAc–MeOH–H_2O) gave, as a mixture of diastereoisomers, the phosphonamide **11** (53 mg, 87%) as an amorphous solid; ^{31}P NMR (D_2O) δ: 33.7, 33.8; ^{13}C NMR (75 MHz, D_2O) δ: 15.1 (d, J_{CCOP} 5.9 Hz, CH_2CH_3), 21.7, 21.8 ($COCH_3$), 34.1, 35.1 (2 d, J_{CP} 126, 123 Hz, PhCH_2), 55.3, 55.4 (2 d, J_{CCNP} 7.9, 7.4 Hz, C-2), 60.1 (C-6), 61.4, 61.6 (2 d, J_{COP} 7.3, 7.1 Hz, CH_2CH_3), 69.2 (C-4), 74.0, 74.1 (C-3), 76.36, 76.43 (C-5), 81.2, 81.9 (C-1), 126.7–130.9, (Ph), 174.1 (C═O); DCI *m*/*z*: 403 (M + H^+, 28.5%), 420 (M + NH_4^+, 16.2%); HRMS calcd. for $C_{17}H_{27}N_2O_7P$: 403.1634; found: 403.1630. Anal. calcd. for $C_{17}H_{27}N_2O_7P \cdot H_2O$: C 48.57, H 6.95, N 6.66; found: C 48.74, H 7.09, N 6.48.

Diethyl 4-trifluoroacetamidobenzylphosphonate (13)

Trifluoroacetic anhydride (5.19 g, 3.44 mL, 24.7 mmol) was added dropwise over 10 min to a solution at 0°C of diethyl 4-aminobenzylphosphonate **12** (5.00 g, 20.6 mmol) and pyridine (5 mL) in CH_2Cl_2 (40 mL). The mixture was stirred at 0°C for 15 min, allowed to warm to room temperature, stirred at room temperature for 1 h, and then poured into water. The organic phase was separated, and the aqueous phase was extracted with CH_2Cl_2. The combined organic phases were washed successively with 1 M HCl, water, and brine, dried ($MgSO_4$), filtered, and concentrated. The resultant solid was recrystallized from diisopropyl ether to give the phosphonate **13** (13, 30, 31) (5.76 g, 82%) as colourless prisms, mp 149–150°C; ^{31}P NMR ($CDCl_3$) δ: 25.8; ^1H NMR (200 MHz, $CDCl_3$) δ: 1.24 (t, *J* 7.0 Hz, Me), 3.09 (d, *J* 21.5 Hz, PCH_2), 3.86–4.13 (m, 4 H, OCH_2), 7.16 (dd, 2 H, *J* 9.0, 2.5 Hz, ArH), 7.52 (d, 2 H, *J* 8.5 Hz, ArH), 10.22 (bs, NH). Anal. calcd. for $C_{13}H_{17}F_3NO_4P$: C 46.02, H 5.05, N 4.13; found: C 46.06, H 5.16, N 4.18.

Ethyl 4-trifluoroacetamidobenzylphosphonochloridate (14)

A mixture of the phosphonate **13** (339 mg, 1.00 mmol) and PCl_5 (208 mg, 1.00 mmol) in chloroform (10 mL) was heated at 50°C for 16 h. The solvent was evaporated, and petroleum ether (30 mL) was added to the residue. The resultant precipitate was collected and washed with petroleum ether to give the phosphonochloridate **14** (13, 30, 31) (300 mg, 91%) as a white solid, mp 222–224°C (dec), used immediately without further purification; ^{31}P NMR ($CDCl_3$) δ: 38.1; ^1H NMR (200 MHz, $CDCl_3$) δ: 1.37 (t, *J* 7.1 Hz, Me), 3.37–3.63 (m, AB part of an ABX, PCH_2), 4.13–4.41 (m, OCH_2), 7.25 (dd, 2 H, *J* 8.1, 3.2 Hz, ArH), 7.54 (d, 2 H, *J* 7.3 Hz, ArH), 8.99 (bs, NH).

Ethyl _N_-(2′-acetamido-3′,4′,6′-tri-_O_-acetyl-2′-deoxy-β-D-glucopyranosyl)-4-trifluoroacetamidobenzylphosphonamide (15)

2-Acetamido-3,4,6-tri-*O*-acetyl-2-deoxy-β-D-glucopyranosyl azide (372 mg, 1.00 mmol) was hydrogenated as described above, and the resultant crude amine was treated with the phosphonochloridate **14** (460 mg, 1.40 mmol) analogously as described for compound **5**. Flash chromatography (EtOAc→1:9 MeOH–EtOAc) gave, as a mixture of diastereoisomers, the phosphonamide **15** (400 mg, 63%) as an amorphous solid; ^{31}P NMR (DMSO-d_6) δ: 27.0, 27.4; ^{13}C NMR (75 MHz, DMSO-d_6) δ: 16.2 (2 C, d, J_{CCOP} 5.4 Hz, CH_2CH_3), 20.4–20.5 (3 C, $COCH_3$), 22.6, 22.7 ($NHCOCH_3$), 34.6, 35.3 (2 d, J_{CP} 125, 124 Hz, PhCH_2), 53.5, 53.8 (2 d, J_{CCNP} 8.6, 10.4 Hz, C-2), 59.1 (d, J_{COP} 6.7 Hz, CH_2CH_3), 62.0, 62.2 (C-6), 68.6, 68.9 (C-4), 71.6, 71.7, 73.1, 73.2 (C-3, 5), 81.6, 82.4 (C-1), 113.9–134.5 (Ar), 154.1, 154.6 ($COCF_3$), 169.3–170.0 (C═O); DCI *m*/*z* : 640 (M + H^+, 100%). Anal. calcd. for $C_{25}H_{33}F_3N_3O_{11}P$: C 46.95, H 5.20, N 6.57; found: C 46.83, H 5.17, N 6.29.

Acknowledgements

We are grateful to the Natural Sciences and Engineering Research Council of Canada for financial assistance.

References

1. T.H. Plummer, Jr., J.H. Elder, S. Alexander, A.W. Phelan, and A.L. Tarentino. J. Biol. Chem. **259**, 10 700 (1984).
2. T. Suzuki, K. Kitajima, S. Inoue, and Y. Inoue. Glycoconjugate J. **12**, 183 (1995).

© 1998 NRC Canada

3. A.L. Tarentino, C.M.Gómez, and T.H. Plummer, Jr. Biochemistry, **24**, 4665 (1985).
4. A.L. Tarentino and T.H. Plummer, Jr. Methods Enzymol. **230**, 44 (1994).
5. A.L. Tarentino and T.H. Plummer, Jr. Trends Glycosci. Glycotechnol. **5**, 163 (1993).
6. P. Kuhn, A.L. Tarentino, T.H. Plummer, Jr., and P. Van Roey. Biochemistry, **33**, 11 699 (1994).
7. L.-X. Wang, M. Tang, T. Suzuki, K. Kitajima, Y. Inoue, S. Inoue, J.-Q. Fan, and Y.C. Lee. J. Am. Chem. Soc. **119**, 11 137 (1997).
8. E. Ikonen, I. Julkunen, O. Tollersrud, N. Kalkkinen, and L. Peltonen. EMBO (Eur. Mol. Biol. Organ.) J. **12**, 295 (1993).
9. R.J. Pollitt, F.A. Jenner, and H. Merskey. The Lancet, **2**, 253 (1968).
10. C. Oinonen, R. Tikkanen, J. Rouvinen, and L. Peltonen. Nat. Struct. Biol. **2**, 1102 (1995).
11. H. Lis and N. Sharon. Eur. J. Biochem. **218**, 1 (1993).
12. A. Varki. Glycobiology, **3**, 97 (1993).
13. K.D. Janda, D. Schloeder, S.J. Benkovic, and R.A. Lerner. Science (Washington, D.C.), **241**, 1188 (1988).
14. Y.-C.J. Chen, T. Danon, L. Sastry, M. Mubaraki, K.D. Janda, and R.A. Lerner. J. Am. Chem. Soc. **115**, 357 (1993).
15. K.D. Janda, R.A. Lerner, and A. Tramontano. J. Am. Chem. Soc. **110**, 4835 (1988).
16. N.E. Jacobsen and P.A. Bartlett. J. Am. Chem. Soc. **103**, 654 (1981).
17. P.A. Bartlett and C.K. Marlowe. Biochemistry, **22**, 4618 (1983).
18. R.L. Elliott, N. Marko, M.J. Berg, and P.S. Portoghese. J. Med. Chem. **28**, 1208 (1985).
19. K. Yamauchi, S. Ohtsuki, and M. Kinoshita. Biochim. Biophys. Acta, **827**, 275 (1985).
20. K.A. Mookhtiar, C.K. Marlowe, P.A. Bartlett, and H.E. Van Wart. Biochemistry, **26**, 1962 (1987).
21. D.A. McLeod, R.I. Brinkworth, J.A. Ashley, K.D. Janda, and P. Wirsching. Bioorg. Med. Chem. Lett. **1**, 653 (1991).
22. N.P. Camp, P.C. Hawkins, P.B. Hitchcock, and D. Gani. Bioorg. Med. Chem. Lett. **12**, 1047 (1992).
23. S.R. Bertenshaw, R.S. Rogers, M.K. Stern, B.H. Norman, W.M. Moore, G.M. Jerome, L.M. Branson, J.F. McDonald, E.G. McMahon, and M.A. Palomo. J. Med. Chem. **36**, 173 (1993).
24. AM. Lacoste, A.M. Chollet-Gravey, L. Vo Quang, Y. Vo Quang, and F. Le Goffic. Eur. J. Med. Chem. **26**, 255 (1991).
25. R. Hirschmann, K.M. Yager, C. M. Taylor, W. Moore, P.A. Sprengeler, J. Witherington, B.W. Phillips, and A.B. Smith III. J. Am. Chem. Soc. **117**, 6370 (1995).
26. A. Bertho and J. Maier. Justus Liebigs Ann. Chem. **498**, 50 (1932).
27. B. Paul and W. Korytnyk. Carbohydr. Res. **67**, 457 (1978).
28. X. Morise, P. Savignac, J.C. Guillemin, and J.M. Denis. Synth. Commun. **21**, 793 (1991).
29. C.E. McKenna, M.T. Higa, N.H. Cheung, and M.-C. McKenna. Tetrahedron Lett. 155 (1977).
30. A. Tramontano, K.D. Janda, and R.A. Lerner. Proc. Natl. Acad. Sci. U.S.A. **83**, 6736 (1986).

© 1998 NRC Canada

Synthesis, spectroscopic characterization, and structural studies of organogermanium tri- and monothiocarbonates. Crystal structures of $Me_2Ge[S_2CSEt]_2$, $Ph_3Ge[SCO_2Me]$, $Ph_3Ge[SCO_2(i\text{-}Pr)]$, and $Ph_2Ge[SCO_2Me]_2$

John E. Drake and Jincai Yang

Abstract: Two series of *S*-alkyl trithiocarbonate derivatives of dimethylgermane, $Me_2Ge[S_2CSR]_2$, and halodiphenylgermane, $Ph_2GeX[S_2CSR]$, where R = Me, *i*-Pr, *n*-Pr, *n*-Bu and X = Cl, Br, and three series of *O*-alkyl monothiocarbonate derivatives of triphenylgermane, $Ph_3Ge[SCO_2R]$, diphenylgermane, $Ph_2Ge[SCO_2R]$, and trimethylgermane, $Me_3Ge[SCO_2R]$, where R = Me, *i*-Pr, and *n*-Pr, have been prepared in 73–92% yields by the reaction of the potassium or sodium salt of the appropriate tri- or monothiocarbonic acid with dichlorodimethyl-, chlorotriphenyl-, dichlorodiphenyl-, and chlorotrimethylgermane. The compounds were principally characterized by infrared, Raman, and ^1H and ^{13}C NMR spectroscopy, including some variable temperature studies, as well as by mass spectrometry. $Me_2Ge[S_2CSEt]_2$, **1**: $P2_1/m$ (No. 11) with cell parameters $a = 6.647(4)$ Å, $b = 7.423(2)$ Å, $c = 16.290(4)$ Å, $\beta = 91.07(3)°$, $V = 803.6(4)$ Å^3, $Z = 2$, $R = 0.0484$, $R_w = 0.0485$. $Ph_3Ge[SCO_2Me]$, **13**: $P\bar{1}$ (No. 2) with cell parameters $a = 9.970(4)$ Å, $b = 10.660(3)$ Å, $c = 9.853(2)$ Å, $\alpha = 101.78(2)°$, $\beta = 109.98(2)°$, $\gamma = 89.76(3)°$, $V = 961.0(5)$ Å^3, $Z = 2$, $R = 0.0534$, $R_w = 0.0451$. $Ph_3Ge[SCO_2(i\text{-}Pr)]$, **14**: $P\bar{1}$ (No. 2) with cell parameters $a = 14.386(7)$ Å, $b = 18.598(6)$ Å, $c = 9.223(3)$ Å, $\alpha = 102.85(3)°$, $\beta = 94.58(3)°$, $\gamma = 108.13(3)°$, $V = 2256(1)$ Å^3, $Z = 2$, $R = 0.0545$, $R_w = 0.0552$. $Ph_2Ge[SCO_2Me]_2$, **16**: *Cc*, (No. 9) with cell parameters $a = 11.790(4)$ Å, $b = 13.696(5)$ Å, $c = 23.232(6)$ Å, $\beta = 92.26(3)°$, $V = 3748(2)$ Å^3, $Z = 8$, $R = 0.0563$, $R_w = 0.0512$. The immediate environment about Ge is that of tetrahedral but the orientations of the thiocarbonate groups display interesting features.

Key words: structure, germanium, phenyl, methyl, thiocarbonates.

Résumé : On a préparé deux séries de dérivés trithiocarbonates de *S*-alkyle du diméthylgermane, $Me_2Ge[S_2CSR]_2$, et d'halogénodiphénylgermane, $Ph_2GeX[S_2CSR]$, dans lesquels R = Me, *i*-Pr, Pr, Bu et X = Cl, Br et trois séries de dérivés monothiocarbonates de *O*-alkyle du triphénylgermane, $Ph_3Ge[SCO_2R]$, du diphénylgermane, $Ph_2Ge[SCO_2R]$, et du triméthylgermane, $Me_3Ge[SCO_2R]$, dans lesquels R = Me, *i*-Pr et Pr, avec des rendements allant de 73 à 92% en procédant à la réaction du sel de sodium ou de potassium de l'acide tri- ou monothiocarbonique approprié avec le dichlorodiméthyl-, chlorotriphényl-, dichlorodiphényl- et le chlorotriméthylgermane. On a généralement caractérisé les composés par le biais des spectroscopies infrarouge, Raman et RMN du ^1H et du ^{13}C, y compris des études à températures variables, ainsi que par spectrométrie de masse. $Me_2Ge[S_2CSEt]_2$, **1** : $P2_1/m$ (No. 11), avec $a = 6,647(4)$, $b = 7,423(2)$ et $c = 16,290(4)$ Å, $\beta = 91,07(3)°$, $V = 803,6(4)$ Å^3, $Z = 2$, $R = 0,0484$, $R_w = 0,0485$. $Ph_3Ge[SCO_2Me]$, **13** : $P\bar{1}$ (No. 2), avec $a = 9,970(4)$, $b = 10,660(3)$ et $c = 9,853(2)$ Å, $\alpha = 101,78(2)°$, $\beta = 109,98(2)°$ et $\gamma = 89,76(3)°$, $V = 961,0(5)$ Å^3, $Z = 2$, $R = 0,0534$, $R_w = 0,0451$. $Ph_3Ge[SCO_2(i\text{-}Pr)]$, **14** :$P\bar{1}$ (No. 2), avec $a = 14,386(7)$, $b = 18,598(6)$ et $c = 9,223(3)$ Å, $\alpha = 102,85(3)°$, $\beta = 94,58(3)°$ et $\gamma = 108,13(3)°$, $V = 2256(1)$ Å^3, $Z = 2$, $R = 0,0545$, $R_w = 0,0552$. $Ph_2Ge[SCO_2Me]_2$, **16** : *Cc* (No. 9), avec $a = 11,790(4)$, $b = 13,696(5)$ et $c = 23,232(6)$ Å, $\beta = 92,26(3)°$, $V = 3748(2)$ Å^3, $Z = 8$, $R = 0,0563$, $R_w = 0,0512$. L'environnement immédiat du Ge est tétraédrique, mais les orientations des groupes thiocarbonates présentent des caractéristiques intéressantes.

Mots clés : structure, germanium, phényle, méthyle, thiocarbonates.

[Traduit par la rédaction]

Introduction

A wide variety of studies on *O*-alkyl dithiocarbonates (xanthates) have been reported but the analogous trithio- and monothiocarbonates have received considerably less attention. For trithiocarbonates, this can be attributed to the relative ease with which they undergo carbon disulfide elimination (1–3) and most reports relate to transition metal derivatives. As part of our studies on organogermanium dithio carbonates, carbamates, and phosphates (4–14), we have reported on a few

Received October 3, 1997.

J.E. Drake[1] and J. Yang.[2] Department of Chemistry and Biochemistry, University of Windsor, Windsor, ON N9B 3P4, Canada.

[1] Author to whom correspondence may be addressed. Telephone: (519) 253-4232, ext 3551. Fax: (519) 973-7098.

trithiocarbonate derivatives (15), and herein is reported an extension of this work involving *S*-alkyl trithiocarbonate derivatives of dimethylgermane, $Me_2Ge[S_2CSR]_2$, and halodiphenylgermane, $Ph_2GeX[S_2CSR]$, where R = Me, *i*-Pr, *n*-Pr, *n*-Bu and X = Cl, Br. Monothiocarbonate derivatives have received even less attention and again virtually all reports have involved transition metal complexes (16–20). With the exception of those on alkali metal salts (21), only one report on main group element monothiocarbonates, describing some organotellurium derivatives, has appeared (22). Three series of *O*-alkyl monothiocarbonate derivatives of triphenylgermane, $Ph_3Ge[SCO_2R]$, diphenylgermane, $Ph_2Ge[SCO_2R]_2$, and trimethylgermane, $Me_3Ge[SCO_2R]$, where R = Me, *i*-Pr, and *n*-Pr are discussed. All of the compounds described were characterized by NMR, infrared, and Raman spectroscopy, as well as by X-ray crystallography when suitable crystals were obtained.

Experimental

Materials

Me_3GeCl, Me_2GeCl_2, Ph_3GeCl, Ph_2GeCl_2, and Me_3SiBr were obtained from Aldrich and Strem Chemicals, all starting materials being used as supplied. All solvents were dried and distilled prior to use and all reactions were carried out under anhydrous conditions. The salts KS_2CSR, where R = Et, *i*-Pr, *n*-Pr, *n*-Bu, were prepared as described earlier (15) and were further purified by a method based on that described for dithiocarbonates (23). The salts $NaSCO_2R$, where R = Me, *i*-Pr, *n*-Pr, were prepared as follows. Typically, sodium metal (ca. 1.0 g) was added to dry *i*-PrOH (ca. 10 mL) in a flask under N_2 gas and the reaction allowed to proceed for 1 h, before COS gas was bubbled in for 10 min. This was followed by distillation under vacuum and pumping to dryness to give $NaSCO_2$(*i*-Pr); 5.5 g, yield 89%. IR (cm^{-1}), main features: 1550 br s, 1384 mw, 1371 m, 1186 s, 1086 br s, 973 m, 688 m; Raman (cm^{-1}): 830 (100); ^1H NMR (ppm relative to DSS): 4.83 (OC*H*, septet, 6.34 Hz), 1.21 (OCCH_3, d, 6.34 Hz); ^{13}C NMR (ppm relative to DSS): 71.12 (O*C*), 21.98 (OC*C*), 185.86 (S*C*O_2). Similarly were prepared $NaSCO_2Me$; yield 85%. IR (cm^{-1}), main features: 1592 vs, vbr, 1428 m, 1188 m, 1120 vs, br, 1040 m, 965 mw, 695 mw; Raman (cm^{-1}): 825 (100): ^1H NMR (ppm relative to DSS): 3.68 (CH_3), ^{13}C NMR (ppm relative to DSS): 54.36 (*C*H_3), 186.89 (S*C*O_2), and $NaSCO_2$(*n*-Pr); yield 92%. IR (cm^{-1}) main features: 1614 vs, br, 1432 s, 1136 s, 1098 s, 1000 m, 827 m, 668 ms; Raman (cm^{-1}): 841 (100); ^1H NMR (ppm relative to DSS): 4.01 (OCH_2, triplet, 6.6 Hz), 1.65 (OCCH_2, m), 0.94 (CH_3, triplet, 7.4 Hz); ^{13}C NMR (ppm relative to DSS): 69.34 (O*C*), 22.63(OC*C*), 10.66 (OCC*C*), 186.64 (S*C*O_2).

Synthesis of (*S*-organo trithiocarbonato) dimethylgermanes

$Me_2Ge[S_2CSEt]_2$, **1**, *$Me_2Ge[S_2CS(i\text{-}Pr)]_2$,* **2**, *$Me_2Ge[S_2CS($*n*-Pr$)]_2$,* **3**, *and $Me_2Ge[S_2CS($*n*-Bu$)]_2$,* **4**

Typically, Me_2GeCl_2 (0.10 mL, 0.87 mmol) and dried CS_2 (ca. 10 mL) were distilled onto previously degassed KS_2CSEt (0.35 g, 1.99 mmol) in a flask held at –196°C. The contents were stirred for ca. 4 h at 0°C. Unreacted KS_2CSEt and KCl were filtered off and solvent allowed to evaporate under vacuum to produce $Me_2Ge[S_2CSEt]_2$, **1**, a yellow solid (0.30 g, 0.80 mmol, yield 92%). Recrystallization from CS_2 at –15°C gave yellow crystals, mp 35°C. Prepared similarly were $Me_2Ge[S_2CS(i\text{-}Pr)]_2$, **2**, $Me_2Ge[S_2CS(n\text{-}Pr)]_2$, **3**, and $Me_2Ge[S_2CS(n\text{-}Bu)]_2$, **4**, all as yellow oils in yields of 82, 85, and 80%, respectively.

Synthesis of (*S*-organo trithiocarbonato)chloro-dimethylgermanes

$Ph_2GeCl[S_2CSEt]$, **5**, *$Ph_2GeCl[S_2CS(i\text{-}Pr)]$,* **6**, *$Ph_2GeCl[S_2CS($*n*-Pr$)]$,* **7**, *$Ph_2GeCl[S_2CS($*n*-Bu$)]$,* **8**

Typically, Ph_2GeCl_2 (0.30 g, 1.02 mmol), which was contained in a small vial, and dried KS_2CSEt (0.18 g, 1.02 mmol) were placed in a flask, which was then cooled to –196°C, degassed, and dried CS_2 (ca. 8 mL) was distilled in. The mixture was stirred for ca. 2 h at 0°C, KS_2CSEt and KCl filtered off, and the solvent allowed to evaporate under vacuum to produce $Ph_2GeCl[S_2CSEt]$, **5**, a yellow oil (0.32 g, 0.81 mmol, yield 80%). Prepared similarly were $Ph_2GeCl[S_2CS(i\text{-}Pr)]$, **6**, $Ph_2GeCl[S_2CS(n\text{-}Pr)]$, **7**, and $Ph_2GeCl[S_2CS(n\text{-}Bu)]$, **8**, all as yellow oils with yields of 80, 78, and 84%, respectively.

Synthesis of (*S*-organo trithiocarbonato)bromo-dimethylgermanes

$Ph_2GeBr[S_2CSEt]$, **9**, *$Ph_2GeBr[S_2CS(i\text{-}Pr)]$,* **10**, *$Ph_2GeBr[S_2CS($*n*-Pr$)]$,* **11**, *and $Ph_2GeBr[S_2CS($*n*-Bu$)]$,* **12**

Typically, $Ph_2GeCl[S_2CSEt]$ was prepared in situ as above from Ph_2GeCl_2 (0.31 g, 1.05 mmol) and dried KS_2CSEt (0.18 g, 1.05 mmol). The flask was recooled to –196°C, degassed again, Me_3SiBr (ca. 0.3 mL) was distilled in, and then the mixture was stirred for 2 h at 0°C, followed by evaporation under vacuum to remove Me_3SiCl and any unreacted Me_3SiBr, to produce $Ph_2GeBr[S_2CSEt]$, **9**, as a yellow oil (0.39 g, 0.88 mmol, yield 84%). Similarly were prepared $Ph_2GeBr[S_2CS(i\text{-}Pr)]$, **10**, $Ph_2GeBr[S_2CS(n\text{-}Pr)]$, **11**, and $Ph_2GeBr[S_2CS(n\text{-}Bu)]$, **12**, all as yellow oils in yields of 83, 80, and 88%, respectively. Crystallization of **2**–**12** using a variety of solvents and solvent mixtures was not successful, and attempts at obtaining boiling points resulted in the immediate release of CS_2.

Attempted preparations of halodimethylgermanium trithiocarbonates

Efforts to synthesize the species Me_2GeClL and Me_2GeBrL, where L = S_2CSR; R = Et, *i*-Pr, *n*-Pr, *n*-Bu, were not successful. The appropriate stoichiometric reactions were shown by NMR spectroscopy to always give mixtures of Me_2GeXL and Me_2GeL_2. Because of the lack of stability of these compounds, isolation by column chromatography did not give the desired compounds but only decomposition products consistent with CS_2 elimination.

Synthesis of (*O*-organo monothiocarbonato)-triphenylgermanes

$Ph_3Ge[SCO_2Me]$, **13**, *$Ph_3Ge[SCO_2(i\text{-}Pr)]$,* **14**, *and $Ph_3Ge[SCO_2($*n*-Pr$)]$,* **15**

Typically, Ph_3GeCl (0.25 g, 0.74 mmol) and excess, dried $NaSCO_2Me$ (0.09 g, 0.79 mmol) were placed in a previously evacuated flask and CH_2Cl_2 (ca. 15 mL) was distilled in at

© 1998 NRC Canada

–196°C. The mixture was stirred for 4 h at room temperature, followed by filtration and evaporation under vacuum to give $Ph_3Ge[SCO_2Me]$, **13**, a colorless solid (0.26 g, 0.66 mmol, yield 89%). Recrystallization from a CH_2Cl_2–*n*-hexane mixture gave colorless crystals, mp 101–102°C. Peaks corresponding to ^{74}Ge in a typical germanium cluster were seen at *m/z* (relative intensity): 396 ($(M)^+$, 2%), 337 ($(M - CO_2Me)^+$, 3%), 319 ($(M - Ph)^+$, 10%), 305 ($(M - SCO_2Me)^+$, 100%), 259 ($(M - PhCO_2Me)^+$, 30%), 228 ($(M - PhSCO_2Me)^+$, 30%), 183 ($(M - Ph_2CO_2Me)^+$, 5%), and 151 ($(M - Ph_2SCO_2Me)^+$, 50%). Prepared similarly was $Ph_3Ge[SCO_2(i\text{-}Pr)]$, **14**, a colorless solid (0.30 g, 0.71 mmol, yield 86%). Recrystallization from a CH_2Cl_2–*n*-hexane mixture gave colorless crystals, mp 98–99°C. Similarly was prepared $Ph_3Ge[SCO_2(n\text{-}Pr)]$, **15**, a colorless solid (0.29 g, 0.69 mmol, yield 89%), mp 91–93°C. Peaks corresponding to ^{74}Ge were seen at *m/z* (relative intensity): 305 ($(M - SCO_2C_3H_7)^+$, 100%), 287 ($(M - PhSCO)^+$, 15%), 245 ($(M - PhSCOC_3H_6)^+$, 20%), 228 ($(M - PhSCO_2C_3H_7)^+$, 38%), and 151 ($(M - Ph_2SCO_2C_3H_7)^+$, 46%). However, attempts at recrystallization failed to give crystals suitable for X-ray diffraction.

Synthesis of bis(*O*-organo monothiocarbonato)-diphenylgermanes

$Ph_2Ge[SCO_2Me]_2$, **16**, *$Ph_2Ge[SCO_2(i\text{-}Pr)]_2$,* **17**, *and $Ph_2Ge[SCO_2(n\text{-}Pr)]_2$,* **18**

Typically, Ph_2GeCl_2 (0.25 g, 0.85 mmol) in a vial and $NaSCO_2Me$ (0.25 g, 2.19 mmol) were placed in a flask and CH_2Cl_2 (ca. 15 mL) was distilled in at –196°C. Reaction and separation were carried out as for **13** to give $Ph_2Ge[SCO_2Me]_2$, **16**, as a colorless solid (0.30 g, 0.70 mmol, yield 82%). Recrystallization from a CH_2Cl_2–*n*-hexane mixture gave colorless crystals, mp 69°C. Peaks corresponding to ^{74}Ge were seen at *m/z* (relative intensity): 351 ($(M - CO_2Me)^+$, 1%), 319 ($(M - SCO_2Me)^+$, 8%), 259 ($(M - SCO_2Me(CO_2Me))^+$, 80%), 229 ($(M - SCO_2Me(SCO_2CH_2))^+$, 60%), 151 ($(M - Ph(SCO_2Me)_2)^+$, 55%), and 105 ($M - Ph_2SCO_2Me(CO_2Me))^+$, 37%), as well as 60 ($(COS)^+$, 100%). Similarly was prepared $Ph_2Ge[SCO_2(i\text{-}Pr)]_2$, **17**, as a colorless solid (yield 81%). Peaks corresponding to ^{74}Ge were seen at *m/z* (relative intensity): 469 ($(M)^+$ 5%), 347 ($M - SCO_2C_3H_7)^+$, 32%), 287 ($M - SCO_2C_3H_7(COS))^+$, 82%), 229 ($M - SCO_2C_3H_7(SCO_2C_3H_6))^+$, 100%), and 183 ($M - PhSCO_2C_3H_7(CO_2C_3H_7)^+$, 3%). Recrystallization from a CH_2Cl_2–*n*-hexane mixture gave colorless crystals, mp 95–96°C, but they were not of X-ray quality. Similarly was formed $Ph_2Ge[SCO_2(n\text{-}Pr)]_2$, **18**, as a colorless oil (yield 81%). Peaks corresponding to ^{74}Ge were seen at *m/z* (relative intensity): 347 ($(M - SCO_2C_3H_7)^+$, 22%), 304 ($(M - SCO_2C_3H_7(C_3H_7))^+$, 6%), 287 ($(M - SCO_2C_3H_7)(COS)]^+$, 48%), 259 ($(M - SCO_2C_3H_7(CO_2C_3H_7))^+$, 10%), 229 ($(M - SCO_2C_3H_7(SCO_2C_3H_6))^+$, 54%), 183 ($(M - PhSCO_2C_3H_7(CO_2C_3H_7)^+$, 23%), and 151 ($(M - Ph(SCO_2C_3H_7)_2)^+$, 28%), along with 60 ((COS)+, 67%).

Synthesis of (*O*-organo monothiocarbonato)-trimethylgermanes

$Me_3Ge[SCO_2Me]$, **19**, *$Me_3Ge[SCO_2(i\text{-}Pr)]$,* **20,** *and $Me_3Ge[SCO_2(n\text{-}Pr)]$,* **21**

Typically, Me_3GeCl (0.20 mL, 1.62 mmol) and CH_2Cl_2 (ca. 8 mL) were distilled onto $NaSCO_2Me$ (0.22 g, 1.93 mmol) at –196°C. The mixture was stirred for 4 h at room temperature, followed by filtration and evaporation under vacuum to give $Me_3Ge[SCO_2Me]$, **19**, as a colorless liquid (0.25 g, 1.20 mmol, yield 74%), bp 82–84°C. Similarly were formed $Me_3Ge[SCO_2(i\text{-}Pr)]$, **20**, a colorless liquid, yield 76%, bp 92–94°C, and $Me_3Ge[SCO_2(n\text{-}Pr)]$, **21**, a colorless liquid, yield 73%, bp 88–90°C.

Attempted preparation of halodiphenylgermanium monothiocarbonates

Attempts to isolate samples of $Ph_2GeCl[SCO_2R]$ species were not successful. Reactions with 1:1 molar ratios of Ph_2GeCl_2 and $NaSCO_2R$ always gave mixtures of the halo and bis compounds, as was confirmed from the ^1H NMR spectra.

Physical measurements

The infrared spectra were recorded on a Nicolet 5DX FT spectrometer as KBr pellets or oils smeared between KBr windows in the region 4000–400 cm^{-1}, and far infrared spectra on a Bomem DA3 infrared spectrometer between polyethylene films as oils or Nujol mulls. The Raman spectra were recorded on samples in sealed glass capillaries on a JEOL-XY Raman spectrometer using the 5145 Å exciting line of an argon ion laser. The ^1H and ^{13}C {H}NMR spectra were recorded on a Bruker 300 FT/NMR spectrometer at 300.133 and 75.471 MHz, respectively, in $CDCl_3$ using Me_4Si as internal standard. All NMR spectra were run at ambient temperature, with the exception of the routine VT NMR studies, and under standard operating conditions. The melting points were determined on a Fisher–Johns apparatus. The mass spectra were recorded on a Kratos Profile GC–MS spectrometer.

X-ray crystallographic analysis

Crystals of $Me_2Ge[S_2CSEt]_2$, **1**, were grown from carbon disulfide at –15°C and those of $Ph_3Ge[SCO_2Me]$, **13**, $Ph_3Ge[SCO_2(i\text{-}Pr)]$, **14**, and $Ph_2Ge[SCO_2Me]_2$, **16**, from CH_2Cl_2–*n*-hexane mixtures at 5°C. A yellow block crystal of **1** and colorless block crystals of **13, 14**, and **16**, of approximate dimensions $0.38 \times 0.24 \times 0.18$, $0.30 \times 0.30 \times 0.21$, $0.34 \times 0.25 \times 0.20$, and $0.35 \times 0.26 \times 0.23$ mm, respectively, were sealed in thin-walled glass capillaries and mounted on a Rigaku AFC6S diffractometer, with graphite-monochromated Mo Kα radiation.

Data collection was carried out as reported in detail earlier (10) and the important parameters are included in Table 1. Of the 1672 (**1**), 3597 (**13**), 7522 (**14**), and 3645 (**16**) reflections that were collected, 1536 (**1**), 3386 (**13**), 7178 (**14**), and 3645 (**16**) were unique. The intensities of three representative reflections measured after every 150 reflections remained constant throughout data collection, indicating crystal and electronic stability (no decay correction was applied for **1**, **13**, and **16**). However, over the course of data collection the standards decreased by 8.2% for **14**, so a linear correction factor was applied. The linear absorption coefficient for Mo Kα is 26.6 for **1**, 16.8 for **13**, 15.8 for **14**, and 18.7 cm^{-1} for **16**. An empirical absorption correction, based on azimuthal scans of several reflections, was applied that resulted in transmission factors ranging from 0.59 to 1.00 for **1**, 0.81 to 1.00 for **13**, 0.78 to 1.00 for **14**, and 0.77 to 1.00 for **16**. The data were corrected for Lorentz and polarization effects.

The structure was solved by direct methods (24) and all

© 1998 NRC Canada

Table 1. Summary of crystal data, intensity collection, and structural refinement for $Me_2Ge[S_2CSEt]_2$, **1**, $Ph_3Ge[SCO_2Me]$, **13**, $Ph_3Ge[SCO_2(i\text{-}Pr)]$, **14**, and $Ph_2Ge[SCO_2Me]_2$, **16**.

Parameter	1	13	14	16
Cell constants				
a (Å)	6.647(4)	9.970(4)	14.386(7)	11.790(4)
b (Å)	7.423(2)	10.660(3)	18.598(6)	13.696(5)
c (Å)	16.290(4)	9.853(2)	9.223(3)	23.232(6)
α (deg)	90.00	101.78(2)	102.85(3)	90.00
β (deg)	91.07(3)	109.98(2)	94.58(3)	92.26(3)
γ (deg)	90.00	89.76(3)	108.13(3)	90.00
Cell volume (Å^3)	803.6(4)	961.0(5)	2256(1)	3748(2)
Crystal system	monoclinic	triclinic	triclinic	monoclinic
Space group	$P2_1/m$	$P\bar{1}$	$P\bar{1}$	Cc
Mol.wt (g mol^{-1})	377.16	395.01	477.00	409.01
Z	2	2	2	8
Temperature (°C)	–30	23	23	23
ρ_{calcd} (g cm^{-3})	1.56	1.37	1.369	1.45
Absorption coefficient μ (cm^{-1})	26.55	16.8	15.82	18.70
Transmission factors	0.59–1.00	0.81–1.00	0.78–1.00	0.84–1.07
Radiation	MoKα 0.71609 Å			
Monochromater	Highly oriented graphite			
Max 2θ angle	50	50	50	50
Total reflections measured	1672	3597	7522	3645
Unique data used	771	1440	1725	1944
No. of parameters refined (NP)	88	127	214	225
$R = \Sigma\|\|F_o\| - \|F_c\|\|/\Sigma\|F_o\|$	0.0484	0.0534	0.0545	0.0563
$R_w = [(\Sigma w(\|F_o\| - \|F_c\|)^2/ \Sigma wF_o^2)]$	0.0485	0.0451	0.0552	0.0512
Goodness of fit	1.88	1.63	1.50	2.06
Largest shift/esd, final cycle	0.001	0.001	0.001	0.001
Largest resid elect density (e Å^{-3})	0.76	0.43	0.57	0.63

calculations were performed using the TEXSAN (25) crystallographic software package of Molecular Structure Corp. The non-hydrogen atoms were refined anisotropically and the hydrogen atoms were included in their idealized position with C—H set at 0.95 Å and with isotropic thermal parameters set at 1.2 times that of the carbon atom to which they were attached. The final cycle of full-matrix least-squares refinement[3] was based on 771 (**1**), 1440 (**13**), 1725 (**14**), and 1944 (**16**) observed reflections (I 3.00σ(I)) and 88 (**1**), 127 (**13**), 214 (**14**), and 225 (**16**) variable parameters and converged (largest parameter shift was 0.001 times its esd) with unweighted and weighted agreement factors of $R = \Sigma \mid |F_o| - |F_c| \mid / |F_c| =$ 0.0485 (**1**), 0.0534 (**13**), 0.0545 (**14**), and 0.0563 (**16**) and $R_w = [(\Sigma w(|F_o| - |F_c|)^2 / F_o^2)]^{1/2} = 0.0485$ (**1**), 0.0451 (**13**), 0.0552 (**14**), and 0.0512 (**16**). The standard deviation of an observation of unit weight [4] was 1.88 (**1**), 1.63 (**13**), 1.50 (**14**), and 2.06 (**16**). The refinement of **16** was carried out on both enantiomorphs by inverting the structure and the better solution chosen. The maximum and minimum peaks on the final difference Fourier map corresponded to 0.86 and –0.62 e/Å^3, respectively, for **1**; 0.43 and –0.38 e/Å^3, respectively, for **13**; 0.57 and –0.40 e/Å^3, respectively, for **14**; and 0.63 and –0.53 e/Å^3, respectively, for **16**.

Table 2. Final fractional coordinates and B(eq) for non-hydrogen atoms of $Me_2Ge[S_2CSEt]_2$, **1**, with standard deviations in parentheses.

Atom	x	y	z	B(eq)
Ge(1)	0.0127(2)	1/4	0.7452(1)	3.56(7)
S(1)	–0.3109(5)	1/4	0.7920(2)	4.1(2)
S(2)	–0.0433(6)	1/4	0.9427(3)	5.4(2)
S(3)	–0.4925(5)	1/4	0.9481(2)	3.7(2)
S(4)	–0.1083(5)	1/4	0.6123(2)	4.2(2)
S(5)	0.3389(6)	1/4	0.6158(3)	7.8(3)
S(6)	0.0951(6)	1/4	0.4599(3)	5.4(2)
C(1)	–0.266(2)	1/4	0.8998(8)	3.2(6)
C(2)	–0.421(2)	1/4	1.0565(8)	4.1(8)
C(3)	–0.607(3)	1/4	1.104(1)	6(1)
C(4)	0.124(2)	1/4	0.566(1)	5.0(9)
C(5)	0.354(3)	1/4	0.427(1)	8(1)
C(6)	0.366(3)	1/4	0.340(1)	9(1)
C(7)	0.131(1)	0.018(2)	0.7705(6)	5.2(6)

The final atomic coordinates and equivalent isotropic thermal parameters for the non-hydrogen atoms are given in Tables 2–5, important distances and bond angles in Tables 6–9, and ORTEP diagrams in Figs. 1–4. Tables of final anisotropic

[3] Least-squares function minimized: $\Sigma w(|F_o| - |F_c|)^2$, where $w = 4F_o^2(F_o^2)$, $\sigma^2(F_o^2) = [S^2(C + R^2B) + pF_o^2)^2]/(Lp)^2$, S = scan rate, C = total integrated peak count, R = ratio of scan time to background counting time, Lp = Lorentz-polarization factor, and $p = p$ factor.

[4] Standard deviation of an observation of unit weight: $[\Sigma w(|F_o| - |F_c|)^2/N_o - N_v)^{1/2}]$, where N_o = number of observations and N_v = number of variables.

© 1998 NRC Canada

Table 3. Final fractional coordinates and *B*(eq) for non-hydrogen atoms of $Ph_3Ge[SCO_2Me]$, **13**, with standard deviations in parentheses.

Atom	*x*	*y*	*z*	*B*(eq)
Ge(1)	0.8021(1)	0.1505(1)	0.1526(1)	3.68(4)
S(1)	0.6413(3)	0.2207(2)	0.2601(3)	4.9(1)
O(1)	0.6728(8)	0.4161(6)	0.1430(8)	5.4(3)
O(2)	0.5102(7)	0.4219(6)	0.2543(7)	5.2(3)
C(1)	0.612(1)	0.370(1)	0.208(1)	4.1(5)
C(2)	0.469(1)	0.544(1)	0.217(1)	7.2(6)
C(3)	0.730(1)	0.1554(8)	–0.055(1)	3.7(2)
C(4)	0.588(1)	0.1192(9)	–0.143(1)	4.6(2)
C(5)	0.541(1)	0.114(1)	–0.294(1)	5.4(2)
C(6)	0.634(1)	0.147(1)	–0.357(1)	5.2(2)
C(7)	0.773(1)	0.186(1)	–0.272(1)	5.7(3)
C(8)	0.825(1)	0.191(1)	–0.119(1)	4.9(2)
C(9)	0.991(1)	0.2392(9)	0.257(1)	3.9(2)
C(10)	1.009(1)	0.370(1)	0.317(1)	7.8(3)
C(11)	1.151(1)	0.430(1)	0.387(1)	8.3(4)
C(12)	1.261(1)	0.360(1)	0.393(1)	7.0(3)
C(13)	1.248(1)	0.234(1)	0.344(1)	6.9(3)
C(14)	1.107(1)	0.172(1)	0.270(1)	5.6(3)
C(15)	0.809(1)	–0.0272(9)	0.176(1)	4.0(2)
C(16)	0.773(1)	–0.127(1)	0.052(1)	5.1(2)
C(17)	0.781(1)	–0.254(1)	0.071(1)	6.2(3)
C(18)	0.822(1)	–0.277(1)	0.208(1)	6.6(3)
C(19)	0.856(1)	–0.182(1)	0.331(1)	6.5(3)
C(20)	0.851(1)	–0.054(1)	0.317(1)	5.3(2)

thermal parameters of non-hydrogen atoms, and fractional coordinates and thermal parameters of hydrogen atoms have been deposited.[5]

Results and discussion

The synthesis of bis(*S*-alkyl trithiocarbonato)dimethylgermanes, **1**–**4**, chloro(*S*-alkyl trithiocarbonato)diphenylgermanes, **5**–**8**, (*O*-alkyl monothiocarbonato)triphenylgermanes, **13**–**15**, bis(*O*-alkyl monothiocarbonato)diphenylgermanes, **16**–**18**, and (*O*-alkyl monothiocarbonato)trimethylgermanes, **19**–**21**, can be readily achieved in 73–90% yield by the reaction of the salt of the appropriate thiocarbonic acid in dried CS_2, CH_3Cl, or CH_2Cl_2 as solvent, or monothiocarbonic acid in dried CH_2Cl_2 as solvent with chlorotriphenylgermane, dichlorodiphenylgermane, or chlorotrimethylgermane using a standard Schlenk line in accord with eqs. [1]–[5]:

[1] $$Me_2GeCl_2 + 2KS_2CSR \rightarrow Me_2Ge[S_2CSR]_2 + 2KCl$$

[2] $$Ph_2GeCl_2 + KS_2CSR \rightarrow Ph_2GeCl[S_2CSR] + KCl$$
(R = Et, *i*-Pr, *n*-Pr, *n*-Bu)

[5] Copies of material deposited may be purchased from: The Depository of Unpublished Data, Document Delivery, CISTI, National Research Council Canada, Ottawa, ON K1A 0S2, Canada. Tables of atomic coordinates have been deposited with the Cambridge Crystallographic Centre, and can be obtained on request from The Director, Cambridge Crystallographic Centre, University Chemical Laboratory, 12 Union Road, Cambridge CB2 1EZ, U.K. Structure factor amplitudes are no longer being deposited and may be obtained directly from the author.

Table 4. Final fractional coordinates and *B*(eq) for non-hydrogen atoms of $Ph_3Ge[SCO_2(i\text{-}Pr)]$, **14**, with standard deviations in parentheses.

Atom	*x*	*y*	*z*	*B*(eq)
Ge(1)	0.9640(2)	0.8101(1)	0.4295(2)	3.4(1)
Ge(2)	0.4446(1)	0.3182(1)	–0.0880(2)	3.1(1)
Cl(1)	0.6910(6)	0.1257(5)	0.9721(9)	12.2(4)
Cl(2)	0.6209(7)	0.0436(5)	0.665(1)	13.4(5)
S(1)	1.1066(4)	0.8712(3)	0.5929(6)	4.7(3)
S(2)	0.5905(4)	0.3769(3)	0.0696(6)	8(2)
O(1)	1.159(1)	0.7761(9)	0.381(1)	5.7(7)
O(2)	1.258(1)	0.8311(8)	0.605(2)	5.9(7)
O(3)	0.643(1)	0.2956(8)	–0.167(1)	4.7(6)
O(4)	0.761(1)	0.3719(7)	0.032(1)	4.9(6)
C(1)	1.183(1)	0.821(1)	0.508(2)	4(1)
C(2)	1.321(2)	0.784(1)	0.560(2)	6(1)
C(3)	1.281(2)	0.710(2)	0.605(3)	10(2)
C(4)	1.424(2)	0.835(1)	0.640(3)	9(1)
C(5)	0.9335(9)	0.6982(5)	0.395(2)	4.9
C(6)	0.9620(8)	0.6679(7)	0.510(1)	4.9
C(7)	0.9354(9)	0.5870(8)	0.488(1)	4.9
C(8)	0.8803(9)	0.5364(5)	0.352(2)	4.9
C(9)	0.8518(8)	0.5667(7)	0.237(1)	4.9
C(10)	0.8784(9)	0.6476(8)	0.259(1)	4.9
C(11)	0.966(1)	0.8428(7)	0.243(1)	4.8
C(12)	1.0299(8)	0.8267(6)	0.145(1)	4.8
C(13)	1.0312(8)	0.8510(7)	0.012(1)	4.8
C(14)	0.969(1)	0.8914(7)	–0.022(1)	4.8
C(15)	0.9051(8)	0.9075(6)	0.077(1)	4.8
C(16)	0.9037(8)	0.8831(7)	0.210(1)	4.8
C(17)	0.8750(9)	0.8476(8)	0.548(1)	4.6
C(18)	0.794(1)	0.7940(5)	0.584(1)	4.6
C(19)	0.7295(7)	0.8206(7)	0.669(1)	4.6
C(20)	0.7464(8)	0.9008(9)	0.719(1)	4.6
C(21)	0.828(1)	0.9544(5)	0.683(1)	4.6
C(22)	0.8919(7)	0.9278(7)	0.598(1)	4.6
C(23)	0.667(1)	0.338(1)	–0.048(2)	3.2(9)
C(24)	0.835(1)	0.352(1)	–0.049(2)	5(1)
C(25)	0.869(2)	0.404(1)	–0.147(3)	8(1)
C(26)	0.919(2)	0.357(1)	0.068(2)	7.3(6)
C(27)	0.4120(8)	0.2056(5)	–0.125(2)	4.7
C(28)	0.4304(8)	0.1705(7)	–0.012(1)	4.7
C(29)	0.4014(8)	0.0891(8)	–0.043(1)	4.7
C(30)	0.3542(9)	0.0427(5)	–0.187(1)	4.7
C(31)	0.3358(8)	0.0778(7)	–0.300(1)	4.7
C(32)	0.3647(8)	0.1593(8)	–0.269(1)	4.7
C(33)	0.3569(9)	0.3550(8)	0.034(1)	4.4
C(34)	0.272(1)	0.3017(5)	0.061(1)	4.4
C(35)	0.2061(7)	0.3286(7)	0.142(1)	4.4
C(36)	0.2252(8)	0.4090(8)	0.196(1)	4.4
C(37)	0.310(1)	0.4623(5)	0.169(1)	4.4
C(38)	0.3761(7)	0.4354(7)	0.088(1)	4.4
C(39)	0.444(1)	0.3539(7)	–0.270(1)	4.7
C(40)	0.4973(8)	0.3349(6)	–0.384(1)	4.7
C(41)	0.4895(8)	0.3599(7)	–0.515(1)	4.7
C(42)	0.428(1)	0.4039(7)	–0.532(1)	4.7
C(43)	0.3752(8)	0.4228(6)	–0.418(1)	4.7
C(44)	0.3831(8)	0.3978(7)	–0.287(1)	4.7
C(45)	0.634(2)	0.121(1)	0.800(3)	10(1)

© 1998 NRC Canada

Table 5. Final fractional coordinates and *B*(eq) for non-hydrogen atoms of $Ph_2Ge[SCO_2Me]_2$, **16** with standard deviations in parentheses.

Atom	*x*	*y*	*z*	*B*(eq)
Ge(1)	0.2414	0.7159(1)	0.3834	3.31(8)
Ge(2)	–0.0090(2)	0.9707(1)	0.08263(9)	3.38(9)
S(1)	0.2911(5)	0.8261(3)	0.4521(2)	4.9(3)
S(2)	0.2123(5)	0.5951(4)	0.4470(2)	5.0(3)
S(3)	0.0181(5)	0.8536(4)	0.0163(2)	5.2(3)
S(4)	–0.0514(5)	1.0846(4)	0.0145(2)	4.9(3)
O(1)	0.292(1)	0.925(1)	0.3547(6)	5.9(8)
O(2)	0.334(2)	1.0076(9)	0.4359(6)	6.3(8)
O(3)	0.160(1)	0.5159(8)	0.3450(6)	5.4(8)
O(4)	0.142(1)	0.4248(9)	0.4237(5)	5.5(7)
O(5)	0.052(1)	0.764(1)	0.1165(6)	5.8(8)
O(6)	0.090(1)	0.6841(9)	0.0344(6)	6.3(8)
O(7)	–0.050(1)	1.1861(9)	0.1118(7)	5.8(8)
O(8)	–0.103(2)	1.259(1)	0.0293(7)	8(1)
C(1)	0.304(2)	0.928(1)	0.405(1)	5(1)
C(2)	0.353(3)	1.096(2)	0.401(2)	12(2)
C(3)	0.168(2)	0.506(1)	0.396(1)	3.6(9)
C(4)	0.102(2)	0.342(2)	0.387(1)	9(2)
C(5)	0.368(1)	0.684(1)	0.3368(6)	5.9
C(6)	0.454(1)	0.615(1)	0.3490(5)	5.9
C(7)	0.543(1)	0.6047(9)	0.3119(6)	5.9
C(8)	0.547(1)	0.662(1)	0.2625(6)	5.9
C(9)	0.462(1)	0.731(1)	0.2503(5)	5.9
C(10)	0.372(1)	0.7414(9)	0.2874(6)	5.9
C(11)	0.1002(8)	0.753(1)	0.3443(5)	5.3
C(12)	0.024(1)	0.804(1)	0.3777(4)	5.3
C(13)	–0.080(1)	0.8335(8)	0.3536(5)	5.3
C(14)	–0.1091(8)	0.8121(9)	0.2962(5)	5.3
C(15)	–0.033(1)	0.761(1)	0.2628(4)	5.3
C(16)	0.071(1)	0.7312(8)	0.2869(5)	5.3
C(17)	0.056(2)	0.758(1)	0.065(1)	5(1)
C(18)	0.122(2)	0.598(1)	0.070(1)	7(1)
C(19)	–0.069(2)	1.184(1)	0.0609(9)	4(1)
C(20)	–0.126(3)	1.350(2)	0.061(1)	9(2)
C(21)	0.1297(9)	1.004(1)	0.1240(5)	5.3
C(22)	0.211(1)	1.0670(9)	0.1032(4)	5.3
C(23)	0.311(1)	1.0849(8)	0.1356(5)	5.3
C(24)	0.3297(9)	1.039(1)	0.1888(5)	5.3
C(25)	0.248(1)	0.976(1)	0.2096(4)	5.3
C(26)	0.148(1)	0.9578(8)	0.1772(5)	5.3
C(27)	–0.1376(8)	0.9442(9)	0.1294(5)	4.5
C(28)	–0.214(1)	0.8710(8)	0.1116(4)	4.5
C(29)	–0.3113(9)	0.8545(7)	0.1420(5)	4.5
C(30)	–0.3332(8)	0.9111(9)	0.1903(5)	4.5
C(31)	–0.257(1)	0.9842(8)	0.2081(4)	4.5
C(32)	–0.1595(9)	1.0007(8)	0.1776(5)	4.5

[3] $Ph_3GeCl + NaSCO_2R \rightarrow Ph_3Ge[SCO_2R] + NaCl$

[4] $Ph_2GeCl_2 + 2NaSCO_2R \rightarrow Ph_2Ge[SCO_2R]_2 + 2NaCl$

[5] $Me_3GeCl + NaSCO_2R \rightarrow Me_3Ge[SCO_2R] + NaCl$
(R = Me, *i*-Pr, *n*-Pr)

The salts are used in considerable excess relative to the stoichiometric requirements to ensure complete reaction in eqs. [1], [3], [4], and [5] and exact stoichiometric amounts in eq. [2] to favor the formation of the mixed chloro derivatives. It is essential that the trithiocarbonate salts be carefully repurified before use to avoid side reactions leading to polysulfides (23), but monothiocarbonate salts can be used as prepared provided pure dry alcohol was used in their preparation.

Chloro(*S*-alkyl trithiocarbonato)diphenylgermanes react readily in situ with bromotrimethylsilane in CS_2 or CH_2Cl_2 to give bromo(*S*-alkyl trithiocarbonato)diphenylgermanes, **9**–**12**, in accord with eq. [6]. An excess of Me_3SiBr is used as both it and Me_3SiCl are readily volatile and so are easily separated from the products.

[6] $Ph_2GeCl[S_2CSR] + Me_3SiBr \rightarrow Ph_2GeBr[S_2CSR] + Me_3SiCl$
(R = Et, *i*-Pr, *n*-Pr, *n*-Bu)

Table 6. Interatomic distances (Å) and angles (deg) for $Me_2Ge[S_2CSEt]_2$, **1**.

Ge(1)—S(1)	2.296(4)	Ge(1)—S(4)	2.294(4)
Ge(1)—C(7)	1.93(1)		
S(1)—C(1)	1.78(1)	S(4)—C(4)	1.73(1)
S(2)—C(1)	1.62(1)	S(5)—C(4)	1.63(2)
S(3)—C(1)	1.71(1)	S(6)—C(4)	1.74(2)
S(3)—C(2)	1.82(1)	S(6)—C(5)	1.81(2)
C(2)—C(3)	1.48(2)	C(5)—C(6)	1.43(2)
Ge(1)—S(2)	3.246(5)	Ge(1)—S(5)	3.051(5)
Ge(1)—S(3)	4.756(4)	Ge(1)—S(6)	4.688(1)
S(1)-Ge(1)-S(4)	90.0(1)	C(7)-Ge(1)-C(7)[a]	125.8(6)
S(1)-Ge(1)-C(7)	107.9(3)	S(1)-Ge(1)-C(7)[a]	107.9(3)
S(4)-Ge(1)-C(7)	109.6(3)	S(4)-Ge(1)-C(7)[a]	109.6(3)
Ge(1)-S(1)-C(1)	100.8(4)	Ge(1)-S(4)-C(4)	96.3(6)
S(1)-C(1)-S(2)	124.1(8)	S(4)-C(4)-S(5)	125(1)
S(1)-C(1)-S(3)	108.7(7)	S(4)-C(4)-S(6)	110.5(9)
S(2)-C(1)-S(3)	127.2(9)	S(5)-C(4)-S(6)	125.0(9)
C(1)-S(3)-C(2)	103.2(7)	C(4)-S(6)-C(5)	101.7(8)
S(3)-C(2)-C(3)	108(1)	S(6)-C(5)-C(6)	111(2)
S(1)-Ge(1)—S(2)	62.9(1)	S(4)-Ge(1)—S(5)	65.8(1)

[a] *x*, 1/2 – *y*, *z*.

Table 7. Interatomic distances (Å) and angles (deg) for $Ph_3Ge[SCO_2Me]$, **13**.

Ge(1)—S(1)	2.253(3)	Ge(1)—C(3)	1.931(9)
Ge(1)—C(9)	1.946(9)	Ge(1)—C(15)	1.950(9)
S(1)—C(1)	1.77(1)	O(1)—C(1)	1.19(1)
O(2)—C(1)	1.32(1)	O(2)—C(2)	1.45(1)
Ge(1)—O(1)	3.112(7)	Ge(1)—O(2)	4.331(7)
S(1)-Ge(1)-C(3)	110.6(3)	S(1)-Ge(1)-C(9)	112.8(3)
S(1)-Ge(1)-C(15)	100.4(3)	C(3)-Ge(1)-C(15)	110.1(4)
C(3)-Ge(1)-C(9)	112.8(4)	C(9)-Ge(1)-C(15)	109.4(4)
Ge(1)-S(1)-C(1)	99.6(4)	C(1)-O(2)-C(2)	115.1(8)
S(1)-C(1)-O(1)	125.9(8)	S(1)-C(1)-O(2)	107.8(7)
Ge(1)-C(3)-C(4)	121.8(7)	Ge(1)-C(3)-C(8)	119.1(7)
Ge(1)-C(9)-C(10)	122.1(8)	Ge(1)-C(9)-C(14)	119.2(8)
Ge(1)-C(15)-C(16)	119.9(7)	Ge(1)-C(15)-C(20)	120.1(7)
O(1)-C(1)-O(2)	126.0(1)	S(1)-Ge(1)—O(1)	56.4(1)
O(1)—Ge(1)-C(3)	75.4(3)	O(1)—Ge(1)-C(9)	89.0(3)
O(1)—Ge(1)-C(15)	155.5(3)		

© 1998 NRC Canada

Table 8. Interatomic distances (Å) and angles (deg) for $Ph_3Ge[SCO_2(i\text{-}Pr)]$, **14**.

Ge(1)—S(1)	2.251(5)	Ge(2)—S(2)	2.256(5)
Ge(1)—C(5)	1.93(1)	Ge(2)—C(27)	1.940(9)
Ge(1)—C(11)	1.94(1)	Ge(2)—C(33)	1.94(1)
Ge(1)—C(17)	1.94(1)	Ge(2)—C(39)	1.94(1)
S(1)—C(1)	1.78(2)	S(2)—C(23)	1.80(2)
O(1)—C(1)	1.23(2)	O(3)—C(23)	1.16(2)
O(2)—C(1)	1.28(3)	O(4)—C(23)	1.38(2)
O(2)—C(2)	1.48(3)	O(4)—C(24)	1.44(3)
C(2)—C(3)	1.48(4)	C(24)—C(25)	1.47(4)
C(2)—C(4)	1.51(3)	C(24)—C(26)	1.51(3)
Ge(1)—O(1)	3.10(2)	Ge(2)—O(3)	3.13(2)
Ge(1)—O(2)	4.27(2)	Ge(2)—O(4)	4.34(1)
S(1)-Ge(1)-C(5)	108.4(4)	S(2)-Ge(2)-C(27)	108.3(4)
S(1)-Ge(1)-C(11)	113.2(4)	S(2)-Ge(2)-C(33)	100.8(3)
S(1)-Ge(1)-C(17)	99.4(3)	S(2)-Ge(2)-C(39)	112.7(4)
C(5)-Ge(1)-C(11)	112.5(5)	C(27)-Ge(2)-C(33)	111.4(6)
C(5)-Ge(1)-C(17)	112.1(5)	C(27)-Ge(2)-C(39)	113.7(5)
C(11)-Ge(1)-C(17)	110.5(6)	C(11)-Ge(2)-C(39)	109.3(6)
Ge(1)-S(1)-C(1)	100.5(6)	Ge(2)-S(2)-C(23)	98.3(6)
S(1)-C(1)-O(1)	123(2)	S(2)-C(23)-O(3)	128(2)
S(1)-C(1)-O(2)	110(2)	S(2)-C(23)-O(4)	105(1)
O(1)-C(1)-O(2)	127(2)	O(3)-C(23)-O(4)	127(2)
C(1)-O(2)-C(2)	117(2)	C(23)-O(4)-C(24)	114(1)
O(2)-C(2)-C(3)	107(2)	O(4)-C(24)-C(25)	111(2)
O(2)-C(2)-C(4)	105(2)	O(4)-C(24)-C(26)	107(2)
C(3)-C(2)-C(4)	115(2)	C(25)-C(24)-C(26)	112(2)
Ge(1)-C(5)-C(6)	119.8(8)	Ge(2)-C(27)-C(28)	122.2(8)
Ge(1)-C(5)-C(10)	120(1)	Ge(2)-C(27)-C(32)	118(1)
Ge(1)-C(11)-C(12)	121(1)	Ge(2)-C(33)-C(34)	120(1)
Ge(1)-C(11)-C(16)	119.4(9)	Ge(2)-C(33)-C(38)	119.7(9)
Ge(1)-C(17)-C(18)	120(1)	Ge(2)-C(39)-C(40)	124(1)
Ge(1)-C(17)-C(22)	120.3(9)	Ge(2)-C(39)-C(44)	116.4(9)
S(1)-Ge(1)—O1()	56.7(3)	S(2)-Ge(2)—O3()	56.8(3)
O(1)—Ge(1)-C(5)	72.9(5)	O(2)—Ge(2)-C(27)	77.9(5)
O(1)—Ge(1)-C(11)	88.6(5)	O(2)—Ge(2)-C(33)	157.5(4)
O(1)—Ge(1)-C(17)	154.8(4)	O(2)—Ge(2)-C(39)	83.6(5)

Table 9. Interatomic distances (Å) and angles (deg) for $Ph_2Ge[SCO_2Me]_2$, **16**.

Ge(1)—S(1)	2.257(5)	Ge(2)—S(3)	2.255(6)
Ge(1)—S(2)	2.255(5)	Ge(2)—S(4)	2.264(5)
Ge(1)—C(5)	1.93(1)	Ge(2)—C(21)	1.92(1)
Ge(1)—C(11)	1.93(1)	Ge(2)—C(27)	1.93(1)
S(1)—C(1)	1.78(2)	S(3)—C(17)	1.77(2)
S(2)—C(3)	1.77(2)	S(4)—C(19)	1.76(2)
O(1)—C(1)	1.18(3)	O(5)—C(17)	1.20(3)
O(2)—C(1)	1.34(2)	O(6)—C(17)	1.31(3)
O(2)—C(2)	1.47(3)	O(6)—C(18)	1.49(3)
O(3)—C(3)	1.19(3)	O(7)—C(19)	1.20(3)
O(4)—C(3)	1.33(2)	O(8)—C(19)	1.32(2)
O(4)—C(4)	1.48(3)	O(8)—C(20)	1.47(3)
Ge(1)—O(1)	3.00(1)	Ge(2)—O(5)	3.02(1)
Ge(1)—O(2)	4.30(1)	Ge(2)—O(6)	4.26(1)
Ge(1)—O(3)	3.03(1)	Ge(2)—O(7)	3.07(1)
Ge(1)—O(4)	4.27(1)	Ge(2)—O(8)	4.28(2)
S(1)-Ge(1)-S(2)	93.9(2)	S(3)-Ge(2)-S(4)	92.6(2)
S(1)-Ge(1)-C(5)	111.4(4)	S(3)-Ge(2)-C(21)	111.6(4)
S(1)-Ge(1)-C(11)	110.7(4)	S(3)-Ge(2)-C(27)	112.7(4)
S(2)-Ge(1)-C(5)	109.9(5)	S(4)-Ge(2)-C(21)	110.5(4)
S(2)-Ge(1)-C(11)	110.4(4)	S(4)-Ge(2)-C(27)	111.5(4)
C(5)-Ge(1)-C(11)	117.9(5)	C(21)-Ge(2)-C(27)	115.7(5)
Ge(1)-S(1)-C(1)	96.8(7)	Ge(2)-S(3)-C(17)	97.3(7)
S(1)-C(1)-O(1)	124(1)	S(3)-C(17)-O(5)	125(2)
S(1)-C(1)-O(2)	110(2)	S(3)-C(17)-O(6)	107(2)
O(1)-C(1)-O(2)	126(2)	O(5)-C(17)-O(6)	128(2)
C(1)-O(2)-C(2)	115(2)	C(17)-O(6)-C(18)	113(2)
Ge(1)-S(2)-C(3)	96.5(7)	Ge(2)-S(4)-C(19)	97.8(7)
S(2)-C(3)-O(3)	127(1)	S(4)-C(19)-O(7)	127(1)
S(2)-C(3)-O(4)	109(1)	S(4)-C(19)-O(8)	108(1)
O(3)-C(3)-O(4)	124(2)	O(7)-C(19)-O(8)	125(2)
C(3)-O(4)-C(4)	116(2)	C(19)-O(8)-C(20)	116(2)
Ge(1)-C(5)-C(6)	127(1)	Ge(2)-C(21)-C(22)	123.8(9)
Ge(1)-C(5)-C(10)	112.5(9)	Ge(2)-C(21)-C(26)	116.2(8)
Ge(1)-C(11)-C(12)	115.4(9)	Ge(2)-C(27)-C(28)	118.5(8)
Ge(1)-C(11)-C(16)	124.6(9)	Ge(2)-C(27)-C(32)	121.4(8)
S(1)-Ge(1)—O(1)	58.1(1)	S(3)-Ge(2)—O(5)	58.1(3)
S(2)-Ge(1)—O(3)	58.3(1)	S(4)-Ge(2)—O(7)	57.3(3)
S(2)-Ge(1)—O(1)	151.9(3)	S(4)-Ge(2)—O(5)	150.7(3)
S(1)-Ge(1)—O(3)	152.1(3)	S(3)-Ge(2)—O(7)	149.6(3)
O(1)—Ge(1)—O(3)	149.4(4)	O(5)—Ge(2)—O(7)	152.0(4)

In general, all of the compounds are susceptible to moisture and air on exposure to the atmosphere, as was found for the corresponding dithiocarbonates as well as for the related trithiocarbonates reported earlier (15). This appears to be especially true for the bis-diphenyl derivatives, **16**–**18**, where the formation of crystals of $(Ph_2GeO)_3$, the ring trimer of diphenylgermanium oxide, was confirmed by X-ray crystallography (26) when solutions of $Ph_2Ge[SCO_2R]_2$ species in CH_2Cl_2 are evaporated over several days while exposed to moist air. In addition, the trithiocarbonates, **1**–**12**, characteristically readily undergo carbon disulfide elimination at room temperature in accord with eqs. [7]–[9], so that all of the compounds are stored at –15°C in sealed containers.

[7] $Ph_2GeX[S_2CSR] \rightarrow Ph_2GeX[SR] + CS_2$

[8] $Me_2Ge[S_2CSR]_2 \rightarrow Me_2Ge[S_2CSR][SR] + CS_2$

[9] $Me_2Ge[S_2CSR][SR] \rightarrow Me_2Ge[SR]_2 + CS_2$

All compounds were readily dissolved in chloroform, which was therefore used as the preferred solvent for recording NMR spectra.

Carbon disulfide elimination

In all cases, for **2**–**12**, attempts to distill the yellow oils under vacuum or to warm them to obtain their boiling points resulted in the rapid expulsion of CS_2. As found with the $Ph_3Ge[S_2CSR]$ species (15), the ^1H and ^{13}C NMR spectra of sealed samples of solutions of compounds **1**–**12** held at room temperature showed a steady decrease in intensity of the signals attributable to $Me_2Ge[S_2CSR]_2$, **1**–**4**, or $Ph_2XGe[S_2CSR]$, **5**–**12**, species. Typically, in the ^{13}C NMR spectra, a peak at 192.7 ppm, attributable to CS_2, soon appeared and steadily increased in intensity with time as the peak originally observed in the range 225.68–226.70 ppm for **1**–**4** and 217.35–224.86

© 1998 NRC Canada

Table 10. ^{1}H chemical shifts in the NMR spectra of compounds **1**–**4** as well as the decomposition products $Me_2Ge[S_2CSR][SR]$, where R = Et, *i*-Pr, *n*-Pr, and *n*-Bu.[a–c]

Compounds	Ge-CH_3	S-CH_n	SC-CH_n'	SCC-CH_3''
$Me_2Ge[S_2CSEt]_2$, **1**	1.43 (s)	3.06 (4H, q, 7.4)	1.20 (6H, t, 7.4)	
$Me_2Ge[S_2CS(i\text{-}Pr)]_2$, **2**	1.43 (s)	3.68 (2H, sept, 6.9)	1.26 (12H, d, 6.9)	
$Me_2Ge[S_2CS(n\text{-}Pr)]_2$, **3**	1.42 (s)	3.04 (4H, t, 7.4)	1.58 (4H, m, 7.4, 7.3)	0.90 (6H, t, 7.3)
$Me_2Ge[S_2CS(n\text{-}Bu)]_2$, **4**[d]	1.42 (s)	3.08 (4H, t, 7.3)	1.54 (4H, m ,7.3, 7.3)	1.31 (4H, m, 7.3, 7.3)
$Me_2Ge[S_2CSEt]$*[SEt]*	1.11 (s)	3.20 (2H, q, 7.4) *2.65 (2H, q, 7.4)*	1.30 (3H, t, 7.4) *1.28 (3H, t, 7.4)*	
$Me_2Ge[S_2CS(i\text{-}Pr)]$*[S(*i*-Pr)]*	1.12 (s)	3.88 (1H, sept, 6.8) *3.27 (1H, sept, 6.6)*	1.36 (6H, d, 6.8) *1.37 (6H, d, 6.6)*	
$Me_2Ge[S_2CS(n\text{-}Pr)]$*[S(*n*-Pr)]*	1.10 (s)	3.18 (2H, t, 7.3) *2.59 (2H, t, 7.3)*	1.69 (2H, m) *1.61 (2H, m)*	0.98 (3H, t, 7.5) *0.96 (3H, t, 7.5)*
$Me_2Ge[S_2CS(n\text{-}Bu)]$*[S(*n*-Bu)]*[e]	1.08 (s)	3.18 (2H, t, 7.4) *2.58 (2H, t, 7.4)*	1.62 (2H, m) *1.59 (2H, m)*	1.39 (2H, m) *1.37 (2H, m)*

[a] The spectra were recorded in $CDCl_3$ and are reported in ppm from Me_4Si, using $CHCl_3$ as a second standard.
[b] Multiplicities (s = singlet, d = doublet, t = triplet, sept = septet, m = multiplet), and coupling constants in Hz are given in parentheses.
[c] Peaks attributable to [SR] groups are in italics.
[d] Peaks also assigned to SC_3-CH_3" at 0.86 (6H, t, 7.3).
[e] Peaks also assigned to SC_3-CH_3" are seen at 0.89 (3H, t, 7.0) and *0.97 (3H, t, 7.3)*.

Table 11. ^{13}C chemical shifts in the NMR spectra of compounds **1**–**4** as well as the decomposition products $Me_2Ge[S_2CSR][SR]$ where R = Et, *i*-Pr, *n*-Pr, and *n*-Bu.[a]

Compounds	Ge-*C*	S-*C*	SC-*C*	SC_2-*C*	SC_3-*C*	S_2*C*S
$Me_2Ge[S_2CSEt]_2$, **1**	9.83	34.16	12.70			226.11
$Me_2Ge[S_2CS(i\text{-}Pr)]_2$, **2**	9.92	44.96	21.73			225.68
$Me_2Ge[S_2CS(n\text{-}Pr)]_2$, **3**	9.86	41.89	21.29	13.64		226.28
$Me_2Ge[S_2CS(n\text{-}Bu)]_2$, **4**	9.87	39.79	29.74	22.22	13.72	226.26
$Me_2Ge[S_2CSEt]$*[SEt]*	5.82	33.84 *(22.60)*	12.69 *(18.68)*			226.53
$Me_2Ge[S_2CS(i\text{-}Pr)]$*[S(*i*-Pr)]*	6.21	44.45 *(34.35)*	21.73 *(27.82)*			226.12
$Me_2Ge[S_2CS(n\text{-}Pr)]$*[S(*n*-Pr)]*	5.88	41.56 *(30.28)*	21.29 *(26.46)*	13.84 *(13.43)*		226.70
$Me_2Ge[S_2CS(n\text{-}Bu)]$*[S(*n*-Bu)]*	5.83	39.40 *(35.15)*	29.81 *(27.91)*	21.83 *(22.22)*	13.72 *(13.55)*	226.64

[a] The spectra are recorded in $CDCl_3$ and are reported in ppm from Me_4Si.

Table 12. ^{1}H chemical shifts in the NMR spectra of compounds **5**–**12**. [a–c]

Compounds	Ge-C_6H_5	S-CH_n	SC-CH_n'	SCC-CH_3''
$Ph_2GeCl[S_2CSEt]$, **5**	7.88–7.85 (4H) 7.53–7.45 (6H)	3.13 (2H, q, 7.4)	1.28 (3H, t, 7.5)	
$Ph_2GeCl[S_2CS(i\text{-}Pr)]$, **6**	7.86–7.83 (4H) 7.49–7.46 (6H)	3.71 (1H, sept, 6.9)	1.34 (6H, d, 6.9)	
$Ph_2GeCl[S_2CS(n\text{-}Pr)]$, **7**	7.87–7.84 (4H) 7.50–7.45 (6H)	3.10 (2H, t, 7.3)	1.66 (2H, m, 7.3, 7.4)	0.95 (3H, t, 7.4)
$Ph_2GeCl[S_2CS(n\text{-}Bu)]$, **8**	7.86–7.83 (4H) 7.52–7.47 (6H)	3.11 (2H, t, 7.4)	1.60 (2H, m, 7.4, 7.5)	1.35 (2H, m, 7.5, 7.3)
$Ph_2GeBr[S_2CSEt]$, **9**	7.73–7.70 (4H) 7.51–7.47 (6H)	3.26 (2H, q, 7.4)	1.33 (3H, t, 7.4)	
$Ph_2GeBr[S_2CS(i\text{-}Pr)]$, **10**	7.75–7.72 (4H) 7.51–7.49 (6H)	3.92 (1H, sept, 6.9)	1.39 (6H, d, 6.9)	
$Ph_2GeBr[S_2CS(n\text{-}Pr)]$, **11**	7.72–7.69 (4H) 7.49–7.46 (6H)	3.21 (2H, t, 7.3)	1.70 (2H, m, 7.3, 7.3)	0.99 (3H, t, 7.3)
$Ph_2GeBr[S_2CS(n\text{-}Bu)]$, **12**	7.73–7.71 (4H) 7.50–7.49 (6H)	3.25 (2H, t, 7.4)	1.67 (2H, m, 7.4, 7.5)	1.42 (2H, m, 7.5, 7.3)

[a] The spectra were recorded in $CDCl_3$ and are reported in ppm from Me_4Si, using $CHCl_3$ as a second standard.
[b] Number of protons, multiplicities (d = doublet, t = triplet, sept = septet, m = multiplet), and coupling constants in Hz are given in parentheses.
[c] Peaks also assigned to SC_3-CH_3" at 0.87 (3H, t, 7.3) for **8** and at 0.93 (3H, t, 7.3) for **12**.

Table 13. ^{13}C chemical shifts in the NMR spectra of compounds, **5**–**12**.[a,b]

Compounds	Ge-C_6	S-*C*	SC-*C*	SC_2-*C*	S_2*C*S
$Ph_2GeCl[S_2CSEt]$, **5**	135.60, 133.77, 131.17, 128.88	34.51	12.55		224.63
$Ph_2GeCl[S_2CS(i\text{-}Pr)]$, **6**	135.71, 133.73, 131.08, 128.84	45.56	21.64		224.27
$Ph_2GeCl[S_2CS(n\text{-}Pr)]$, **7**	135.60, 133.76, 131.14, 128.88	42.21	21.13	13.58	224.86
$Ph_2GeCl[S_2CS(n\text{-}Bu)]$, **8**	135.59, 133.73, 131.11, 128.84	40.11	29.53	22.18	224.83
$Ph_2GeBr[S_2CSEt]$, **9**	135.38, 132.79, 131.76, 129.04	33.90	12.74		217.64
$Ph_2GeBr[S_2CS(i\text{-}Pr)]$, **10**	135.38, 132.79, 131.62, 129.10	45.02	21.7		217.35
$Ph_2GeBr[S_2CS(n\text{-}Pr)]$, **11**	135.31, 132.75, 131.79, 129.04	41.53	21.3	13.5	217.92
$Ph_2GeBr[S_2CS(n\text{-}Bu)]$, **12**	135.38, 132.79, 131.76, 129.04	39.46	29.77	22.16	217.81

[a] The spectra are recorded in $CDCl_3$ and are reported in ppm from Me_4Si.
[b] Peaks attributable to SC_3-*C* are seen at 13.63 for **8** and at 13.71 for **12**.

© 1998 NRC Canada

Table 14. ^{1}H chemical shifts in the NMR spectra of compounds **13**–**21**.[a,b]

Compounds	Ge-C$_6H_5$/CH_3	O-CH_n	OC-CH_n	OCC-CH_3
$Ph_3Ge[SCO_2Me]$, **13**	7.64–7.61 (6H) 7.44–7.40 (9H)	3.58 (3H, s)		
$Ph_3Ge[SCO_2(i\text{-}Pr)]$, **14**	7.64–7.61 (6H) 7.41–7.36 (9H)	4.86 (1H, sept, 6.4)	0.96 (6H, d, 6.4)	
$Ph_3Ge[SCO_2(n\text{-}Pr)]$, **15**	7.64–7.61 (6H) 7.43–7.39 (9H)	3.93 (2H, t, 6.8)	1.42 (2H, m)	0.73 (3H, t, 7.4)
$Ph_2Ge[SCO_2Me]_2$, **16**	7.79–7.76 (4H) 7.48–7.45 (6H)	3.59 (6H, s)		
$Ph_2Ge[SCO_2(i\text{-}Pr)]_2$, **17**	7.79–7.76 (4H) 7.45–7.43 (6H)	4.85 (2H, sept, 6.2)	0.99 (12H, d, 6.2)	
$Ph_2Ge[SCO_2(n\text{-}Pr)]_2$, **18**	7.79–7.76 (4H) 7.49–7.43 (6H)	3.94 (4H, t, 6.9)	1.45 (4H, m)	0.75 (6H, t, 7.4)
$Me_3Ge[SCO_2Me]$, **19**	0.57 (9H)	3.65 (3H, s)		
$Me_3Ge[SCO_2(i\text{-}Pr)]$, **20**	0.54 (9H)	4.91 (1H, sept, 6.3)	1.17 (6H, d, 6.3)	
$Me_3Ge[SCO_2(n\text{-}Pr)]$, **21**	0.59 (9H)	4.04 (2H, t, 6.6)	1.62 (2H, m)	0.89 (3H, t, 7.4)

[a] The spectra were recorded in $CDCl_3$ and are reported in ppm from Me_4Si, using $CHCl_3$ as a second standard.
[b] Number of protons, multiplicities (d = doublet, t = triplet, sept = septet, m = multiplet), and coupling constants in Hz are given in parentheses.

Table 15. ^{13}C chemical shifts in the NMR spectra of compounds **13**–**21**.[a]

Compounds	Ge-C_6H_5/CH_3	O-*C*	OC-*C*	OC_2-*C*	SCO_2
$Ph_3Ge[SCO_2Me]$, **13**	134.74, 134.51, 130.14, 128.63	54.39			169.32
$Ph_3Ge[SCO_2(i\text{-}Pr)]$, **14**	134.83, 134.71, 130.04, 128.56	72.20	21.48		168.05
$Ph_3Ge[SCO_2(n\text{-}Pr)]$, **15**	134.71, 134.65, 130.07, 128.59	69.51	21.88	10.18	168.80
$Ph_2Ge[SCO_2Me]_2$, **16**	134.30, 133.93, 130.92, 128.70	54.75			168.61
$Ph_2Ge[SCO_2(i\text{-}Pr)]_2$, **17**	134.61, 133.90, 130.76, 128.70	72.97	21.48		167.28
$Ph_2Ge[SCO_2(n\text{-}Pr)]_2$, **18**	134.31, 133.92, 130.82, 128.72	69.97	21.83	10.15	168.08
$Me_3Ge[SCO_2Me]$, **19**	2.06	53.89			170.80
$Me_3Ge[SCO_2(i\text{-}Pr)]$, **20**	2.21	71.23	21.90		169.49
$Me_3Ge[SCO_2(n\text{-}Pr)]$, **21**	2.13	68.90	22.09	10.38	170.35

[a] The spectra were recorded in $CDCl_3$ and reported in ppm from Me_4Si.

Table 16. Selected features and their assignments in the vibrational spectra of compounds **1**–**4.**[a,b]

$Me_2Ge[S_2CSEt]_2$, **1**		$Me_2Ge[S_2CS(i\text{-}Pr)]_2$, **2**		$Me_2Ge[S_2CS(n\text{-}Pr)]_2$, **3**		$Me_2Ge[S_2CS(n\text{-}Bu)]_2$, **4**		
IR	[Raman]	IR	[Raman]	IR	[Raman]	IR	[Raman]	Assignment
1066 s	[1072 (100)]	1067 vs	[1069 (55)]	1077 s	[1078 (60)]	1083 vs	[1082 (50)]	$\nu(S_2CSC)_a$
1033 s	[1026 (67]	1040 vs	[1039 (100)]	1043 vs	[1043 (100)]	1045 vs	[1047 (100)]	$\nu(S_2CSC)_b$
858 vs sh	[n.o.]	880 vs sh	[n.o.]	860 s sh	[n.o.]	860 s	[n.o.]	$\nu(H_3CGe)$
826 s	[827 (50)]	808 vs	[811 (5)]	819 vs	[815 (15)]	811 vs	[802 (25)]	$\nu(S_2CSC)_c$
623 m	[621 (20)]	627 m	[626 (20)]	626 m	[626 (20)]	626 m	[624 (35)]	$\nu(Ge\text{-}C)_{asym}$
569 w	[577 (65)]	616 m	[578 (40)]	580 m	[578 (50)]	578 m	[577 (50)]	$\nu(Ge\text{-}C)_{sym}$
509 w	[512 (65)]	531 w	[530 (70)]	510 w	[511 (80)]	509 m	[512 (75)]	$\nu(S_2CSC)_d$
407 m sh	[407 (54)]	406 m sh	[405 (50)]	416 m	[415 (50)]	406 m	[405 (55)]	$\nu(Ge\text{-}S)_{asym}$
360 m	[365 (35)]	360 w	[364 (30)]	373 m	[365 (40)]	388 s	[384 (20)]	$\nu(Ge\text{-}S)_{sym}$
314 m	[319 (20)]	329 s	[324 (20)]	319 m	[321 (15)]	328 m	[324 (10)]	$\delta(S_2CSC)$
194 w	[190 (50)]	213 m	[195 (50)]	191 w	[191 (75)]	191 s	[189 (75)]	$\rho(S_2CSC)$

[a] Parentheses denote relative intensities in the Raman effect.
[b] s = strong, m = medium, w = weak, sh = shoulder, br = broad, and v = very.

ppm for **5**–**12**, attributable to the S_2CS carbon, decreased in intensity to eventually disappear. As with the $Ph_2Ge[S_2CSR]_2$ series, more complicated spectra were observed between the NMR spectra of the freshly prepared $Me_2Ge[S_2CSR]_2$ species, **1**–**4**, and the final spectra that contained only peaks attributable to CS_2 and $Me_2Ge[SR]_2$. The additional peaks were entirely consistent with the formation of the intermediate $Me_2Ge[S_2CSR][SR]$ compounds, whose relevant ^{1}H and ^{13}C NMR data are also presented in Tables 10 and 11, respectively. For the three derivatives that are oils, **2**–**4**, CS_2 elimination is complete after approximately 5 days. The halodiphenyl derivatives **5**–**12** decompose even more rapidly, the original signals attributable to $Ph_2GeX[S_2CSR]$ being totally lost in 1–2 days to be replaced by peaks attributable to the corresponding $Ph_2GeX[SR]$ compounds.

Nuclear magnetic resonance spectra

For $Me_2Ge[S_2CSR]_2$, **1**–**4**, the ^{1}H NMR chemical shifts (Table 10) of methyl attached to Ge are similar for all trithiocarbonate derivatives, being dependent on the number of groups attached to Ge rather than the alkyl group of the ligand. Thus, the chemical shifts of CH_3-Ge are at 1.42–1.43 ppm for **1**–**4** compared to 0.71–0.73 ppm for $Me_3Ge[S_2CSR]$ (15). The same phenomenon was noted for $Me_2Ge[S_2CNMe_2]_2$ and

© 1998 NRC Canada

$Me_3Ge[S_2CNMe_2]$, suggesting the group electronegativities of trithiocarbonates and dithiocarbamates are similar (6). In general, all alkyl group peaks of the ligands have the fine structure and relative intensities expected for first-order spectra, except of course for the central CH_2 groups in *n*-propyl and *n*-butyl. The phenyl signals in $Ph_2GeCl[S_2CSR]$, **5**–**8**, are very similar in appearance and position to those reported for $Ph_2Ge[S_2CSR]_2$ (15) while those of $Ph_2GeBr[S_2CSR]$, **9**–**12**, are similar to $Ph_3Ge[S_2CSR]$ derivatives (Table 12). The chemical shifts within the ligands of these halo derivatives have values that differ systematically from the bis-diphenyl compounds, the proton shifts being increasingly upfield in the order bis < Cl < Br. The similarity of all spectra suggests the trithiocarbonate groups are in identical environments in all compounds **1**–**12**.

In the ^{13}C NMR spectra (Tables 11 and 13) the chemical shifts of the alkyl groups in the ligand are relatively similar regardless of the nature (methyl or phenyl) or number of groups attached to germanium. Comparison with the corresponding S_2COR derivatives (12, 13) indicates similar values for chemical shifts of all alkyl carbon atoms except for those directly attached to the sulfur atom, the difference in shift being consistently ca. 35 ppm as illustrated by that of CH_2 in $Me_2Ge[S_2CSCH_2CH_3]_2$ (33.84) and $Me_2Ge[S_2COCH_2CH_3]_2$ (71.10 ppm) (12). In contrast, there is an upfield shift of ca. 14 ppm for the central trithiocarbonate carbon atom so that S_2CS has chemical shifts of 225.68–226.28 ppm for **1**–**4** (Table 11) compared to 207.04–212.12 ppm for S_2CO in related dithiocarbonates (12, 13). For **5**–**12** (Table 13), the chemical shifts in ligands are basically the same as in the corresponding bis compounds, while for the S_2CS carbon in $Ph_2GeCl[S_2CSR]$ the shift is downfield relative to $Ph_2Ge[S_2CSR]_2$ (15) by ca. 2 ppm, but is upfield by ca. 5 ppm for $Ph_2GeBr[S_2CSR]$. As noted for the ^1H NMR spectra, the consistencies in the ^{13}C NMR spectra point to similar trithiocarbonate environments in compounds **1**–**12**.

The ^1H and ^{13}C NMR spectral data for monothiocarbonate compounds **13**–**21** are presented in Tables 14 and 15, respectively. The ^1H NMR spectra recorded in $CDCl_3$ confirm that the products are over 98% pure relative to any hydrogen-containing impurities and integration ratios are as expected. The signals due to the phenyl groups in compounds **13**–**18** (two sets of peaks between 7.36 and 7.79 ppm) are very similar in appearance and position to those of the analogous dithiocarbonate and trithiocarbonate series (15) as well as other phenylgermanium derivatives containing Ge—S bonds, so once again the chemical shifts are dependent on the presence of the Ge—S link(s) rather than the nature of the thiocarbonate groups attached to sulfur (4–14). The monothiocarbonate ligands again give first-order spectra when expected, with chemical shifts comparable to those of the corresponding salts. The chemical shifts of hydrogen atoms on the carbon atom attached to oxygen (i.e., $OCH/OCH_2/OCH_3$) are similar for a given monothiocarbonate regardless of the number of phenyl groups attached to germanium, as was observed for the corresponding OCH_n groups in analogous dithiocarbonates and SCH_n groups in trithiocarbonates. The chemical shifts in the O-linked monothiocarbonates lie between those of the O-linked dithiocarbonates and the S-linked trithiocarbonates, suggesting that the electronegativity of the SCO_2 group lies between those of S_2CO and S_2CS. In $Me_3Ge[SCO_2R]$ species **19**–**21**, the CH_3-Ge chemical shifts hardly vary, the values being slightly less than those reported for $Me_3Ge[S_2CNMe_2]$ and the $Me_3Ge[S_2CSR]$ derivatives (15), which is consistent with the group electronegativity of monothiocarbonates being slightly larger than those of dithiocarbamates (6) and trithiocarbonates. The similarity of all of the spectra again indicates that the environments of the monothiocarbonate groups in solution are identical in **13**–**21**.

In the ^{13}C NMR spectra, the chemical shifts of monothiocarbonate alkyl groups are again similar regardless of the number or nature of groups attached to germanium. The chemical shifts for the carbon atom of the SCO_2 groups in **13**–**21** range from 167.28 to 170.80 ppm, compared to 207.04 to 212.12 ppm for a variety of S_2CO groups, and 221.36 to 226.41 ppm for the S_2CS groups in the analogous trithiocarbonates. The $(CH_3)_3Ge$ chemical shifts are similar for **19, 20**, and **21** and are close to those of the analogous dithiocarbonates (11, 12) and trithiocarbonates. The general similarity of the values of the ^{13}C NMR chemical shifts in **13**–**21** is again consistent with the presence of similar monothiocarbonate linkages in solution.

Infrared and Raman spectra

Distinctive features in the infrared and Raman spectra and their assignments are given in Table 16 for $Me_2Ge[S_2CSR]_2$, **1**–**4**, and in Table 17 for $Ph_2GeCl[S_2CSR]$, **5**–**8**, and $Ph_2GeBr[S_2CSR]$, **9**–**12**. The assignments in the tables make use of such factors as the distinctive strong methyl germanium rocking mode at approximately 850 cm^{-1} (11); the pairs of fingerprints of decreasing intensity at ca. 740 and 695 cm^{-1}, 460 and 335 cm^{-1}, and 1435 and 1095 cm^{-1} in the infrared spectra for phenyl germanes and the very intense Raman peak close to 1000 cm^{-1} (12); comparisons with the spectra of previously reported related organogermanium trithiocarbonates; comparisons with the spectra of the starting salts, KS_2CSR; and the decrease in intensity of strong bands in the spectra of all of the compounds **1**–**24** as CS_2 elimination occurs. The labelling of the phenyl modes uses the Wiffen convention (27).

Typical values for C═S and C–S stretching vibrations are 1090 and 700 cm^{-1}, respectively, so assigning four specific stretches as $\nu(S{=}CS_2)$, $\nu(S_2C{-}SR)$, $\nu(S_2CS{-}C)$, and $\nu(GeS{-}CS_2)$ is not reasonable because the average positions of $\nu(S_2CSC)_a$, $\nu(S_2CSC)_b$, $\nu(S_2CSC)_c$, and $\nu(S_2CSC)_d$ are 1069, 1044, 826, and 515 cm^{-1}, respectively. Their similarity in all derivatives suggests that all are strongly coupled in a similar fashion and all have structures similar to those of $Me_2Ge[S_2CSEt]_2$, **1**, and $Ph_2Ge[S_2CS(i\text{-}Pr)]_2$ (15). The assignment of $\nu(S_2CSC)_d$ at ca. 515 cm^{-1} is close to that of the symmetric stretch in CS_3^{2-} (28), while the asymmetric stretch in CS_3^{2-} is typically seen in the range of 900–950 cm^{-1}, which is bracketed by the positions of $\nu(S_2CSC)_b$, and $\nu(S_2CSC)_c$. The asymmetric and symmetric Ge–C stretches are seen at ca. 626 and 580 cm^{-1} in all $Me_2Ge[S_2CSR]_2$, **1**–**4**, these values being similar to those in Me_2GeCl_2. The similarity of the position and separation between the modes indicates that **1**–**4** should have C-Ge-C angles as wide as that of 121(4)° in Me_2GeCl_2 (29). Table 6 confirms that the C-Ge-C angle in $Me_2Ge[S_2CSEt]_2$ is 128.8(6)°.

The Ge–Cl stretching vibration, $\nu(Ge{-}Cl)$, is close to 282 cm^{-1} in all $Ph_2GeCl[S_2CSR]$, **5**–**8**, compared to an average of ca. 400 cm^{-1} in Ph_2GeCl_2. A similar shift was noted for

© 1998 NRC Canada

Table 17. Selected features and their assignments in the vibrational spectra of compounds $Ph_2GeCl[S_2CSR]$ **5**–**8** and $Ph_2GeBr[S_2CSR]$, **9**–**12**, where R = Et, *i*-Pr, *n*-Pr, and *n*-Bu.[a–d]

5		**6**		**7**		**8**		**9**		**10**		**11**		**12**		
IR	[Raman]	IR	[Raman]	IR	[Raman]	IR	[Raman]	IR	[Raman]	IR	[Raman]	IR	[Raman]	IR	[Raman]	Assignment
1581 w	[1585 (25)]	1583 w	[1584 (25)]	1583 w	[1583 (30)]	1583 w	[n.o.]	1583 w	[1583 (30)]	1585 w	[1583 (35)]	15803 w	[1586 (30)]	1583 w	[1584 (20)]	*l*-Phenyl
1432 m		1433 vs		1433 m		1434 s		1434 s		1434 vs		1434 m		1434 s		*n*-Phenyl[d]
1186 w	[1187 (5)]	1184 ms	[n.o.]	1183 m	[1184 (10)]	1183 w	[n.o.]	1184 w	[1187 (5)]	1184 mw	[1187 (5)]	1184 w	[1185 (5)]	1183 w	[1184 (5)]	*a*-Phenyl
1158 w	[1158 (5)]	1157 s	[n.o.]	1159 w	[1155 (5)]	1158 vw	[1159 (5)]	1158 m	[1158 (5)]	1158 m	[1158 (5)]	1154 vw	[1150 (5)]	1160 w	[1161 (5)]	*e*-Phenyl
1088 s sh	[1085 (5)]	1091 vs	[1082 (5)]	1091 s	[1084 (5)]	1090 m	[1086 (10)]	1091 s	[1085 (10)]	1092 s	[1085 (5)]	1091 s	[1084 (5)]	1090 m	[1087 (10)]	*q*-Phenyl[c]
1072 vs	[n.o.]	1070 vs	[1070 (25)]	1058 s	[1070 (10)]	1066 s sh	[1070 (15)]	1067 m	[1063 (5)]	1068 m	[n.o.]	1063 m	[n.o.]	1060 m	[1060 (5)]	$\nu(S_2CSC)_a$
1044 s sh	[n.o.]	1039 vs	[1041 (35)]	1043 s	[1044 (10)]	1048 m	[1048 (25)]	1050 m	[n.o.]	1051 s	[n.o.]	1035 m	[n.o.]	1049 m	[1045 (15)]	$\nu(S_2CSC)_b$
1031 s	[1025 (10)]	1027 vs	[1026 (20)]	1026 s	[1025 (20)]	1026 m	[1026 (20)]	1025 m	[1025 (10)]	1026 m	[1025 (10)]	1025 s	[1027 (15)]	1026 m	[1026 (20)]	*b*-Phenyl
1004 m	[998 (100)]	998 s	[999 (100)]	998 m	[998 (100)]	998 m	[999 (100)]	998 s	[998 (100)]	998 s	[998 (100)]	998 m	[999 (100)]	998 m	[998 (100)]	*p*-Phenyl[c]
849 s		845 vs		840 s br		843 s br		820 s		821 s		819 m		819 m		$\nu(S_2CSC)_c$[d]
737 vs		736 vs		735 vs		735 vs		734 s		734 s		735 s		734 s		*f*-Phenyl[d]
692 s		692 vs		693 vs		692 vs		691 s		692 s		691 s		691 s		*v*-Phenyl[d]
675 s sh	[671 (10)]	669 mw	[668 (60)]	679 s sh	[669 (20)]	680 sh	[670 (30)]	674 m	[671 (15)]	674 m	[671 (15)]	674 w	[673 (15)]	676 m	[671 (10)]	*r*-Phenyl[c]
509 w	[517 (5)]	532 w	[532 (25)]	512 w	[512 (15)]	511 w	[512 (25)]	n.o.	[517 (5)]	524 w	[n.o.]	509 w	[n.o.]	508 w	[501 (25)]	$\nu(S_2CSC)_d$
459 s		459 vs		458 w		458 w		457 s		457 s		457 s		457 s		*y*-Phenyl[c,d]
411 s	[n.o.]	414 m	[429 (15)]	427 m	[428 (8)]	414 m	[420 (5)]	400 w	[n.o.]	403 w	[n.o.]	405 w	[n.o.]	401 m	[408 (5)]	ν(Ge-S)
365 m	[365 (45)]	363 s	[365 (50)]	367 m	[377 (60)]	366 m	[361 (10)]	318 m	[n.o]	315 s	[n.o.]	319 m	[n.o.]	320 s	[n.o.]	$\delta(S_2CSC)$
332 m		335 s		335 m		336 m		318 m		315 s		319 m		320 s		*t*-Phenyl[c,d]
283 s	[282 (10)]	282 m	[282 (10)]	284 s	[286 (50)]	280 m	[n.o.]	225 w	[224 (90)]	225 w[	224 (95)]	226 w	[223 (85)]	226 w	[225 (80)]	ν(Ge-X)
200 w	[196 (35)]	200 w	[196 (40)]	200 w	[204 (80)]	200 m	[200 (5)]	190 m	[193 (35)]	191 w	[193 (20)]	191 w	[198 (5]	195 m	[198 (5)]	$\rho(S_2CSC)$

[a] Parentheses denote relative intensities in the Raman effect.
[b] s = strong, m = medium, w = weak, sh = shoulder, br = broad, and v = very.
[c] X-sensitive modes.
[d] No corresponding modes observed in the Raman effect.

© 1998 NRC Canada

Table 18. Selected features and their assignments in the vibrational spectra of **13**–**15**.[a,b]

$Ph_3Ge[SCO_2Me]$, **13**		$Ph_3Ge[SCO_2(i\text{-}Pr)]$, **14**		$Ph_3Ge[SCO_2(n\text{-}Pr)]$, **15**		
IR	Raman	IR	Raman	IR	Raman	Assignment
1695 vs	n.o.[c]	1695 vs	1700 (2)	1698 s	1696 (5)	$\nu(SCO_2C)_a$
n.o.	1585 (30)	n.o.	1587(20)	n.o.	1587 (30)	*l*-Phenyl
1428 s	1429 (1)	1428 s	n.o.	1435 ms	1435 (1)	*n*-Phenyl
1188 s	1188 (7)	1187 ms	n.o.	1185 m,sh	1184 (10)	*a*-Phenyl
1158 s,sh	1158 (7)	1162 s	n.o.	1164 m,sh	1158 (12)	*e*-Phenyl
1140 s	n.o.	1148 s	n.o.	1118 s	n.o.	$\nu(SCO_2C)_b$
1089 s	n.o.	1089 s	n.o.	1090 s	1089 (3)	$\nu(SC_2OC)_c$
1023 m	1027 (8)	1023 m	1025(10)	1027 s	1026 (20)	*b*-Phenyl
996 m	999 (100)	998 m	1001(100)	999 m	1001 (100)	*p*-Phenyl
815 ms	835 (2)	848 s	849 (1)	830 ms	840 (1)	$\pi(SCO_2)$
736 s	n.o.	737 s	n.o.	738 s	n.o.	*f*-Phenyl
697 s	n.o.	697 s	n.o.	699 s	n.o.	*v*-Phenyl
675 m,sh	668 (8)	675 m,sh	667 (10)	675 m	668 (15)	$\nu(SCO_2C)_d$ + *r*-phenyl
462 s	n.o.	468 s	n.o.	463 s,br	n.o.	*y*-Phenyl
419 m	428 (5)	436 m	430 (2)	424 m	n.o.	ν(Ge-S)

[a] Parentheses denote relative intensities in the Raman effect.
[b] s = strong, m = medium, sh = shoulder, br = broad.
[c] Not observed.

Table 19. Selected features and their assignments in the vibrational spectra of **16**–**18**.[a,b]

$Ph_2Ge[SCO_2Me]_2$, **16**		$Ph_2Ge[SCO_2(i\text{-}Pr)]_2$, **17**		$Ph_2Ge[SCO_2(n\text{-}Pr)]_2$, **18**		
IR	Raman	IR	Raman	IR	Raman	Assignment
1695 s	n.o.[c]	1698 s	1692 (8)	1702 s	1700 (2)	$\nu(SCO_2C)_a$
n.o.	1584 (40)	n.o.	1585 (30)	n.o.[c]	1578 (30)	*l*-Phenyl
1427 s	n.o.	1436 m	n.o.	1434 s	11432 (5)	*n*-Phenyl
1191 s	1187 (5)	1170 s,sh	1170 (5)	1170 s	n.o.	*a*-Phenyl
1134 s	n.o.	1159 s	n.o.	1132 vs	1156 (5)	$\nu(SCO_2C)_b$
1090 s	n.o.	1087 s	1090 (5)	1095 s	1080 (4)	$\nu(SCO_2C)_c$
1025 s	1027 (15)	1025 ms	1027 (20)	1023 s,sh	1026 (20)	*b*-Phenyl
998 m	999 (100)	999 m	1000 (100)	1000 m,sh	996 (100)	*p*-Phenyl
817 s	843 (30)	843 ms	846 (15)	833 m	843 (4)	$\pi(SCO_2)$
736 s	n.o.	738 m	n.o.	737 s	n.o.	*f*-Phenyl
693 s	n.o.	695 m,sh	n.o.	695 s	n.o.	*v*-Phenyl
678 s,br	678 (3)	673 m br	672 (2)	675 s	670 (10)	$\nu(SCO_2C)_d$ + *r*-phenyl
460 s	n.o.	461 m	n.o.	460 s	n.o.	*y*-Phenyl
434 ms	432 (2)	440 s	438 (15)	427 m	427 (3)	$\nu(Ge\text{-}S)_{asym}$
392 m	395 (1)	394 m	n.o.	390 s	392 (2)	$\nu(Ge\text{-}S)_{sym}$

[a] Parentheses denote relative intensities in the Raman effect.
[b] s = strong, m =medium, sh = shoulder, br = broad.
[c] Not observed.

Table 20. Selected features and their assignments in the vibrational spectra of **19**–**21**.[a,b]

$Me_3Ge[SCO_2Me]$, **19**		$Me_3Ge[SCO_2(i\text{-}Pr)]$, **20**		$Me_3Ge[SCO_2(n\text{-}Pr)]$, **21**		
IR	Raman	IR	Raman	IR	Raman	Assignment
1694 vs	1687 (5)	1694 vs	1688 (5)	1691 vs	1688 (2)	$\nu(SCO_2C)_a$
1145 vs	1145 (5)	1134 vs	1140 (3)	1132 vs	n.o.	$\nu(SCO_2C)_b$
1067 s,sh	1097 (5)	1090 s	1091 (2)	1066 s,sh	1088 (3)	$\nu(SCO_2C)_c$
820 s,sh	848 (10)	835 s	840 (5)	832 s	841 (5)	$\pi(SCO_2)$
676 s	n.o.[c]	678 s	n.o.	675 s	n.o.	$\nu(SCO_2C)_d$
627 s	611 (30)	617 ms	612 (40)	613 s	610 (35)	$\nu(Ge\text{-}C)_{asym}$
587 s	569 (100)	575 s	570 (100)	570 ms	569 (100)	$\nu(Ge\text{-}C)_{sym}$
441 s	437 (10)	434 s	437 (2)	419 ms	421 (5)	ν(Ge-S)

[a] Parentheses denote relative intensities in the Raman effect.
[b] s = strong, m = medium, sh = shoulder, br = broad.
[c] Not observed.

© 1998 NRC Canada

$Me_2GeCl[S_2CNEt_2]$ where ν(Ge–Cl) was assigned at 293 cm^{-1} (8). Similarly, ν(Ge–Br), is at ca. 224 cm^{-1} in all $Ph_2GeBr[S_2CSR]$, **9**–**12**, compared to ca. 315 cm^{-1} Ph_2GeBr_2. This weakening of the Ge—X bond by the trithiocarbonate group may contribute to the difficulty of isolating the mixed $Me_2GeX[S_2CSR]$ species. A weak Ge—X bond, accompanied by less stereochemical hindrance to an incoming group with Me rather than Ph groups attached to germanium, could result in partially substituted compounds acting as reactive intermediates that could also undergo rapid exchange to the bis substituted species and dihalodimethylgermane.

Distinctive features in the infrared and Raman spectra and their assignments are given for $Ph_3Ge[SCO_2R]$, **13**–**15**, $Ph_2Ge[SCO_2R]_2$, **16**–**18**, and $Me_3Ge[SCO_2R]$, **19**–**21**, in Tables 18–20. The assignments are based on the same factors described for the trithiocarbonates along with trends involving related dithiocarbonate species. A strong band attributable to the C═O stretching vibration, ν(C═O), which is observed at ca. 1620 cm^{-1} in the $NaSCO_2R$ salts, is shifted to higher wave number (1690–1703 cm^{-1}) in all nine compounds. This supports the presence of an essentially monodentate monothiocarbonate ligand with a very strong terminal C═O bond. The O atoms of the SCO_2C group should give rise to two intense peaks in the infrared spectra, in addition to the one at 1690–1703 cm^{-1}, and two such peaks, which are presumably primarily attributable to ν(SC–O) and ν(SCO–C), are seen in the region 1188–1066 cm^{-1} for **13**–**21,** designated $\nu(SCO_2C)_b$ and $\nu(SCO_2C)_c$, respectively. These assignments are entirely consistent with the X-ray structures of compounds **13, 14**, and **16**. Two distinctive strong peaks are also seen at ca. 840 and 670 cm^{-1}. The former can be assigned to the out-of-plane bend, $\pi(SCO_2)$, which is assigned at 830–873 cm^{-1} for $\pi(CO_3)$ in carbonate salts, suggesting similar π-electron delocalization in these planar groups. The fourth stretching vibration, $\nu(SCO_2C)_d$, presumably primarily ν(GeS–C), is assigned to 670–678 cm^{-1}, which is similar to general assignments of C—S single bonds and to the assignments reported for the corresponding dithiocarbonates.

The Ge–S vibrational modes are readily assigned within 440–400 cm^{-1} for **13**–**21** in similar positions to those in the dithiocarbamates (4–6) and Me_3GeSR (30), but at slightly higher wave number compared to those of the trithiocarbonates. This is consistent with the greater tendency for the trithiocarbonates to form anisobidentate links leading to slightly weaker Ge—S primary bonds. The Ge—S bond lengths in **13, 14**, and **16** are slightly shorter than those of $Me_2Ge[S_2CSEt]_2$, **1**, and $Ph_2Ge[S_2CS(i\text{-}Pr)]_2$.

The crystal structure of $Me_2Ge[S_2CSEt]_2$, 1

Dimethylbis(*S*-ethyl trithiocarbonato)germane, **1**, crystallizes in the space group $P2_1/m$. The ORTEP diagram in Fig. 1(*a*) illustrates, along with Table 6, that the immediate environment about germanium is that of a distorted tetrahedron. The S-Ge-C angles have an average value of 108.8(10)° compared with 111.8(17)° for $Ph_2Ge[S_2CS(i\text{-}Pr)]_2$ (15). By contrast, the C-Ge-C angles are very much larger than the regular tetrahedral angle: 128.8(6)° in **1** compared with 118.1(3)° in $Ph_2Ge[S_2CS(i\text{-}Pr)]_2$. This opening up of the C-Ge-C angle in $Me_2Ge[S_2CSEt]_2$ was predicted from its vibrational spectrum. The average Ge—C bond length of 1.93(1) Å is typical for R_2GeL_2 or R_3GeL species, where L is a sulfur-bonding moiety,

Fig. 1. ORTEP plots of the molecule $Me_2Ge[S_2CSEt]_2$ (**1**) illustrating (*a*) the tetrahedral environment about germanium, (*b*) the pendant sulfur atoms acting as weak donors, and (*c*) the planarity of all non-hydrogen atoms except the carbon atoms of the ethyl groups. The atoms are drawn with 30% probability ellipsoids. Hydrogen atoms omitted for clarity in (*a*) and (*b*).

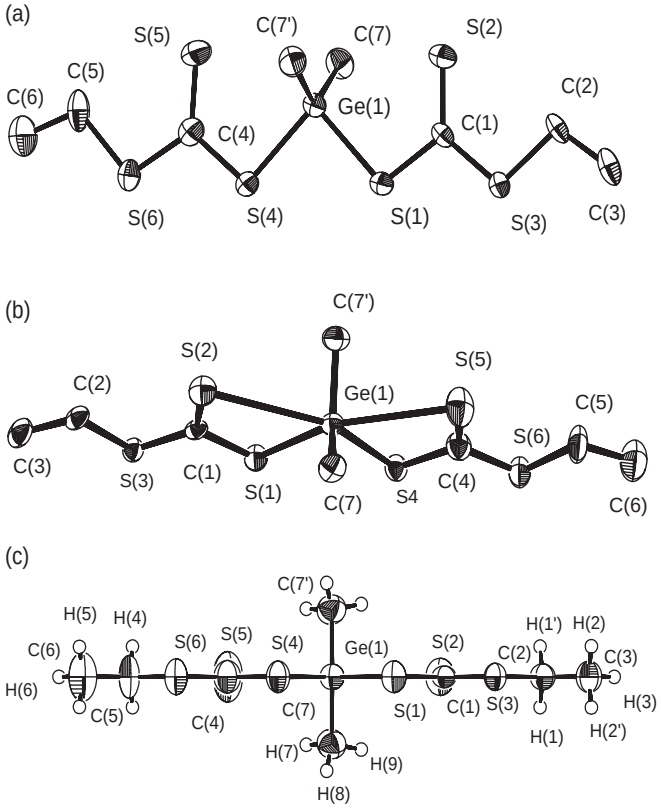

being similar to those in $Ph_2Ge[S_2CS(i\text{-}Pr)]_2$, $Ph_2Ge[S_2CO(i\text{-}Pr)]_2$ (12), $Me_2Ge[S_2CNMe_2]_2$ (6), $Me_2GeCl[S_2CNMe_2]$ (5), and even in $Ph_3GeSC_6H_4(t\text{-}Bu)$ (31).

The closing down of the S-Ge-S angles to 90.0(1)° in **1** is similar to that observed in the dithiocarbamate analogues, $Ph_2Ge[S_2CNEt_2]_2$ and $Me_2Ge[S_2CNMe_2]_2$, where the S-Ge-S angles are 84.4(1)° and 87.0(1)°, respectively. These smaller angles are associated with the fact that a terminal sulfur (C═S) atom is oriented toward the germanium center (see Fig. 1) at Ge—S distances of 3.051(5) and 3.246(5) Å for $Me_2Ge[S_2CSEt]_2$, 3.078(2) and 3.158(2) Å for $Me_2Ge[S_2CNMe_2]_2$, 3.224(5) and 3.304(5) Å for $Ph_2Ge[S_2CS(i\text{-}Pr)]_2$, and 3.183(1) Å for $Ph_2Ge[S_2CNEt_2]_2$. By contrast, in the analogous dithiocarbonate, $Ph_2Ge[S_2CO(i\text{-}Pr)]_2$, where the terminal sulfur atom is oriented away from the germanium center (with Ge—S = 4.753(4) Å), the S-Ge-S angle is much larger at 103.2(1)° (12). Whether distances in the range of 3.05–3.3 Å, which are considerably less than the sum of the van der Waals radii of 3.75 Å, are sufficiently short to be considered as partial bonds may be questioned, but there is a relationship between these Ge—S nonbonding or anisobonding distances and the closing down of the S-Ge-S angle from the regular tetrahedral angle when the sulfur atom is oriented toward, rather than away from, germanium.

The average Ge—S bond length (2.295(1) Å) in **1** is longer than in the analogous dithiocarbonate, $Ph_2Ge[S_2CO(i\text{-}Pr)]_2$

© 1998 NRC Canada

(2.252(3) Å) in which there are no Ge—S secondary interactions (15). However, it is similar to those in $Ph_2Ge[S_2CNEt_2]_2$, $Me_2Ge[S_2CNMe_2]_2$, and other germanium dithiocarbamates where there is the same probability of the presence of secondary bonding (6, 14). In view of the similarities noted in the spectra of the trithiocarbonates, all of these *S*-alkyl trithiocarbonate derivatives probably have the same weak anisobidentate bonding as indicated by the molecular structures of $Me_2Ge[S_2CSEt]_2$, **1**, and $Ph_2Ge[S_2CS(i\text{-}Pr)]_2$ (15). The C═S bonds in **1**, which average 1.63(8) Å, are very slightly longer than those in $Ph_2Ge[S_2CO(i\text{-}Pr)]_2$, 1.61(1) Å, which is again consistent with the presence of weak secondary interactions leading to the orientation of the terminal C═S rather than the CSR moiety toward the germanium centre. The average bite angle of 62.4(7)° in $Ph_2Ge[S_2CS(i\text{-}Pr)]_2$ is essentially the same as that in $Ph_2Ge[S_2CNEt_2]_2$, where anisobidentate linkages appear to give a better overall description of the bonding of dithiocarbamates to germanium (14). There is an even larger bite angle of 65.8(1)° in **1**, which suggests an even stronger anisobidentate bond as implied by the inclusion of Ge(1)—S(2) and Ge(1)—S(4) bonds in Fig. 1(*b*).

The S—CR bonds in the trithiocarbonate groups at 1.82(2) Å are essentially as expected from the sum of the covalent radii of S and C, whereas the average length of C—SGe and C—SR bonds is 1.74(2) Å, and that of the "terminal" C═S bond is 1.63(1) Å, indicating that π-electron density delocalization is not significantly extended beyond the planar groups. Nevertheless, all of the non-hydrogen atoms in both trithiocarbonate groups are coplanar, as required by the mirror plane, and the relationship between the groups is well illustrated by Fig. 1(*c*).

The crystal structures of $Ph_3Ge[SCO_2Me]$, 13, $Ph_3Ge[SCO_2(i\text{-}Pr)].0.5CH_2Cl_2$, 14, and $Ph_2Ge[SCO_2Me]_2$, 16

Triphenyl(*O*-methyl monothiocarbonato)germane, **13**, and triphenyl(*O*-isopropyl monothio-carbonato)germane, **14**, both crystallize in the space group $P\bar{1}$ (No. 2), the latter with dichloromethane in the lattice. The ORTEP diagrams in Figs. 2 and 3 illustrate, along with Tables 7 and 8, that the immediate environment about germanium in both molecules is that of a distorted tetrahedron. The average values of the C-Ge-C angles are 110.8(4)° in **13** and 111.6(16)° for the two independent molecules in **14**, while those of the S-Ge-C angles are 108(6)° in **13** and 107(5)° in **14**. It is immediately obvious that the variation in the S-Ge-C angles is larger than for the C-Ge-C angle, which arises because one S-Ge-C angle is considerably smaller (100.4(3)° in **13** and 99.4(3)° in **14**) than the other two (111.8(15)° in **13** and 110.7(27)° in **14**). All of these values are close to those found for the analogous dithiocarbonates, $Ph_3Ge[S_2COMe]$ and $Ph_3Ge[S_2CO(i\text{-}Pr)]$. The similarity extends to dithiophospates, such as $Ph_3Ge[S_2P(OMe)_2]$, where one S-Ge-C angle is again significantly smaller than the other two (4). In the dithiocarbonates and dithiophosphates, an alkoxy group is oriented towards germanium in preference to a terminal sulfur atom, whereas in **13** and **14** the alkoxy group is oriented away from germanium and the terminal oxygen atom toward germanium. Possibly, the slightly smaller range in the S-Ge-C angles in the monothiocarbonates reflects the fact that the less bulky terminal oxygen atom is more readily accommodated.

The Ge—C distances, which range from 1.931(9) to 1.950(9) Å in **13** and 1.93(1) to 1.94(1) Å in **14**, are comparable with those found in the analogous trithiocarbonates and related species as described above, and cover the same range as in the dithiophosphate, $Ph_3Ge[S_2P(OMe)_2]$, 1.930(5)–1.950(5) Å. The Ge—S bond length of 2.254(3) Å in both **13** and **14** is bracketed by those reported for the dithiocarbonates, $Ph_3Ge[S_2COMe]$ (2.249(4) Å) and $Ph_3Ge[S_2CO(i\text{-}Pr)]$ (2.272(2) Å), and slightly shorter than in the dithiophosphate, $Ph_3Ge[S_2P(OMe)_2]$ (2.285(1) Å).

Fig. 2. ORTEP plot of the molecule $Ph_3Ge[SCO_2Me]$ (**13**). The atoms are drawn with 30% probability ellipsoids. Hydrogen atoms omitted for clarity.

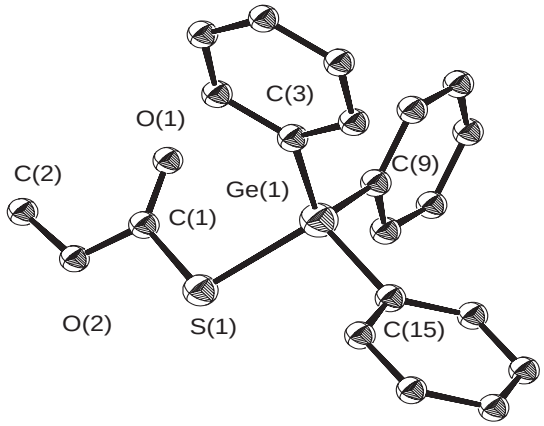

As expected, the terminal C═O bond lengths of 1.19(1) and 1.20(5) Å in **13** and **14**, respectively, are much shorter than the other C—O bonds. They are also close to the expected value for a C═O double bond. The SC—O bonds, in turn, are significantly shorter than the SCO—C bonds, being similar to those reported for the two analogous dithiocarbonates (avg. 1.34(1) and 1.45(1) Å, respectively), which is consistent with the π-bond character not extending significantly beyond the planar SCO_2 core.

The terminal O atom is oriented towards germanium, with the Ge—O distance being 3.112(7) and 3.12(2) Å in **13** and **14**, respectively, which is similar to the Ge—S distances in trithiocarbonates. Thus, the intramolecular interactions, if any, must be extremely weak. However, as mentioned above, the orientations of the ligand in the dithiocarbonates and $Ph_3Ge[S_2P(OMe)_2]$ are both such as to place the (OR) groups, rather than the terminal sulfur atoms, closer to the germanium center and the Ge—OR distances in $Ph_3Ge[S_2COMe]$ (2.98(2) Å) and $Ph_3Ge[S_2CO(i\text{-}Pr)]$ (3.115(4) Å), are similar to the Ge—O(terminal) distances in **13** and **14**.

Diphenylbis(O-methyl monothiocarbonato)germane, $Ph_2Ge[SCO_2Me]_2$, **16**, crystallizes in the space group *Cc* (No. 9). The ORTEP diagram (Fig. 4) and Table 9 confirm that the immediate environment about germanium is again the expected distorted tetrahedron. The S-Ge-S angle of 93.3(7)° and C-Ge-C angle of 117.85(7)° are very close to those in the analogous dithiocarbonates, $Ph_2Ge[S_2COMe]_2$, where the corresponding angles are 93.4(2)° and 117.1(3)°) (11). The distortion from the regular tetrahedral angle is greater than was found for $Ph_2Ge[S_2CO(i\text{-}Pr)]_2$ (12), where the corresponding angles are 103.2(1)° and 115.6(3)°, but less than that found for the trithiocarbonate, $Ph_2Ge[S_2CS(i\text{-}Pr)]_2$, described earlier (15), where the corresponding angles are 87.3(2)° and 118.1(3)° respec-

© 1998 NRC Canada

Fig. 3. ORTEP plot of the molecule $Ph_3Ge[SCO_2(i\text{-}Pr)]$ (**14**) showing both molecules in the asymmetric unit as well as the CH_2Cl_2 trapped in the lattice. The atoms are drawn with 30% probability ellipsoids. Hydrogen atoms omitted for clarity except for those in dichloromethane.

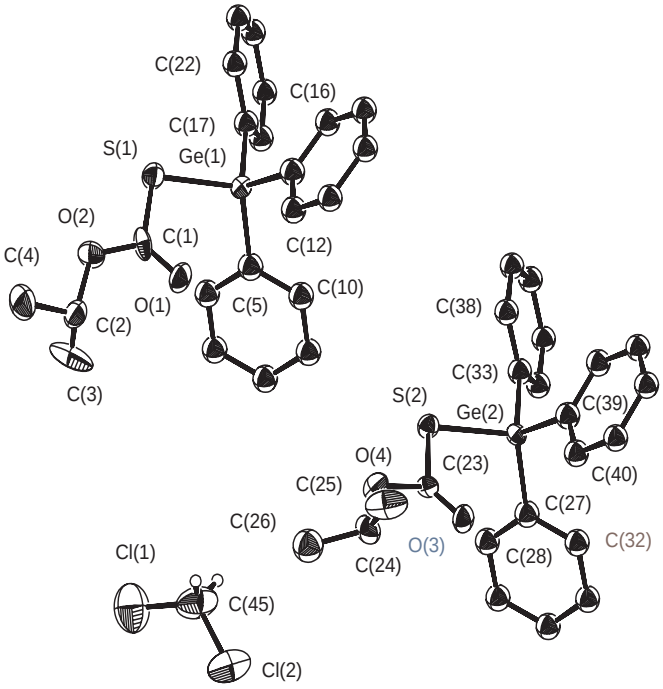

Fig. 4. ORTEP plots of the molecule $Ph_2Ge[SCO_2Me]_2$ (**16**) showing different views of the two molecules in the asymmetric unit. The atoms are drawn with 30% probability ellipsoids. Hydrogen atoms omitted for clarity except for those in dichloromethane.

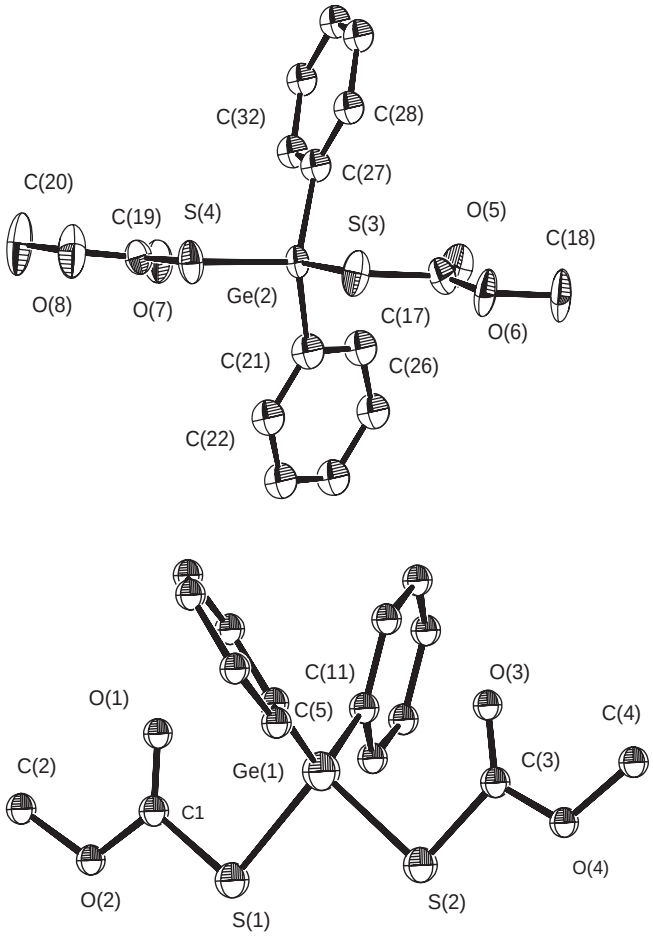

tively, or $Me_2Ge[S_2CSEt]_2$, **1**, with angles of 90.0(1)° and 128.6(6)°, respectively. The S-Ge-S angle in **16** is considerably wider than the 84.4° in $Ph_2Ge[S_2CNEt_2]_2$ (8), where the ligand was assumed to be anisobidentate.

The Ge—C bond length of 1.928(5) Å in **16** is again very similar to those reported for **13** and **14**, as well for trithiocarbonates including **1**, and the other S-linked groups mentioned earlier. The average Ge—S bond length in **16** of 2.258(4) Å brackets those observed in $Ph_2Ge[S_2COMe]_2$ (2.262(3) Å) and $Ph_2Ge[S_2CO(i\text{-}Pr)]_2$ (2.252(1) Å) and is slightly shorter than those found for the dithiocarbamate, $Ph_2Ge[S_2CNEt_2]_2$ (2.277(2) Å) and the trithiocarbonate, $Ph_2Ge[S_2CS(i\text{-}Pr)]_2$ (2.280(5) Å). In general, the bis compounds appear to have slightly longer Ge—S bonds than those containing only one thio ligand as in **13** and **14.**

The GeS—C average bond length in **16** of 1.77(1) Å is not significantly different from those in **13** and **14**, and is typical of values observed in $Ph_2Ge[S_2COMe]_2$, $Ph_2Ge[S_2CO(i\text{-}Pr)]_2$, and $Ph_2Ge[S_2CNEt_2]_2$ (1.76(1) Å), as well as for $Ph_2Ge[S_2CS(i\text{-}Pr)]_2$ (1.745(6) Å). The distances between germanium and the terminal O atom of 3.00(1) and 3.07(1) Å are similar to those in **13** and **14**, as are the S-Ge—O bite angles, which range from 57.3(3)° to 62.9(1)°, again indicating that if there is any secondary interaction between germanium and the terminal O atom, it must be very weak. The bond lengths and angles within the SCO_2C group of **16** are essentially the same as in **13** and **14**. The angles in the planar core do indeed add up to 360°, with average values in **16** being O═C-S (125.8(13)°), O═C-O (125.8(17)°), and S-C-O (108.5(13)°) compared with O═C-S (125.0(14)°), O═C-O (125.7(6)°, and S-C-O (109.3(16)° for **13** and **14**. The much larger angles involving the terminal C═O bond reflect the fact that this is the bond most strongly involved in the delocalized π-bonding. The average value of the C-O-C angle in all three molecules is 116(1)°, which is consistent with much less π-bond character in C—O bonds involved in the C-O-C link than in the SCO_2 core. The Ge-S-C angles, which ranged from 96.5(7)° to 100.5(6)°, are somewhat smaller, but essentially very similar to the corresponding angles in $Ph_2Ge[S_2COMe]_2$, 102.7(5)°, $Ph_2Ge[S_2CO(i\text{-}Pr)]_2$, 105.0(3)°, $Ph_2Ge[S_2CNEt_2]_2$, 102.1(1)°, as well as in $Ph_2Ge[S_2CS(i\text{-}Pr)]_2$, 101(1)°, indicating little or no change in the nature of this link regardless of the thio derivative attached.

Concluding comments

Previous studies of organogermanium dithiocarbonates gave a wide variety of relatively stable derivatives, some of which were tested for suitability as oil additives. Given the paucity of work on any main group monothiocarbonates, it is somewhat surprising that organogermanium monothiocarbonates have proven to be relatively easy to prepare and characterize fully by spectroscopic methods as well as by X-ray crystallography. However, the organogermanium trithiocarbonates all readily

© 1998 NRC Canada

eliminate CS_2 regardless of the nature of the organo groups or the number of groups attached to germanium. By contrast, the only sign of reductive elimination in the monothiocarbonates is the presence of the COS^+ ion in some of their mass spectra. The interpretation of the NMR and vibrational spectra is entirely consistent, with the structures found in the solid state being essentially maintained in solution. Thus, like the dithiocarbonates, there is an essentially monodentate link through sulfur. However, in all cases in the solid state, there is apparently a weak interaction with the "terminal" sulfur atom (for tri- and dithiocarbonates) and possibly even with the "terminal" oxygen atom (for monothiocarbonates) as these atoms are oriented toward the germanium center at distances well inside that of the sum of the van der Waals radii, particularly for Ge—S. In related tellurium species, we found that on occasion, as in $Ph_2Te[SCO_2(i\text{-}Pr)]_2$, one of the OR groups was oriented toward tellurium and the pendant oxygen was possibly involved in a weak link to an adjacent tellurium center, creating a weakly bonded extended structure. There was no indication of similar behavior with germanium.

Acknowledgement

We wish to thank the Natural Sciences and Engineering Research Council of Canada for financial support.

References

1. D. Coucouvanis, S.J. Lippard, and J.A. Zubieta. J. Am. Chem. Soc. **92**, 3342 (1970).
2. J.W. Andrews, D. Coucouvanis, and J.P. Fackler, Jr. Inorg. Chem. **3**, 4932 (1972).
3. D. Coucouvanis. Prog. Inorg. Chem. **26**, 310 (1979).
4. R.K. Chadha, J.E. Drake, and A.B. Sarkar. Inorg. Chem. **24**, 3156 (1985).
5. R.K. Chadha, J.E. Drake, and A.B. Sarkar. Inorg. Chem. **23**, 4769 (1984).
6. R.K. Chadha, J.E. Drake, and A.B. Sarkar. Inorg. Chem. **25**, 2201 (1986).
7. R.K. Chadha, J.E. Drake, and A.B. Sarkar. Inorg. Chem. **26**, 2885 (1987).
8. R.K. Chadha, J.E. Drake, and A.B. Sarkar. Inorg. Chim. Acta, **143**, 31 (1988).
9. J.E. Drake, A.G. Mislankar, and R. Ratnani. Can. J. Chem. **72**, 830 (1994).
10. J.E. Drake, L.N Khasrou, A.G. Mislankar, R. Ratnani, and J. Yang. Can. J. Chem. **73**, 915 (1995).
11. J.E. Drake, A.B. Sarkar, and M.L.Y. Wong. Inorg. Chem. **29**, 785 (1990).
12. J.E. Drake, A.B. Sarkar, and M.L.Y. Wong. Inorg. Chem. **30**, 2174 (1991).
13. J.E. Drake, A.G. Mislankar, and J. Yang. Inorg. Chem. **31**, 5543 (1992).
14. J.E. Drake, A.G. Mislankar, and J. Yang. Inorg. Chim. Acta, **211**, 37 (1993).
15. J.E. Drake and J. Yang. Inorg. Chem. **33**, 854 (1993).
16. K.K. Pandey and H.L. Wingan. Rev. Inorg. Chem. **6**, 71 (1984).
17. S. Datta and H.L. Agarwala. Indian J. Chem. **20A**, 1190 (1981).
18. T.V. Ashworth, M. Nolte, and E.J. Singleton. J. Organomet. Chem. **121**, C57 (1975).
19. T.R. Gaffney and J.A. Ibers. Inorg. Chem. **21**, 2860 (1982).
20. N. Sonoda and T. Tanaja. Inorg. Chim. Acta, **12**, 261 (1975).
21. C. Bender. Bull. Chem. Soc. **12**, 256 (1869).
22. J.E. Drake, A.G. Mislankar, R. Ratnani, and J. Yang. Can. J. Chem. **74**, 1968 (1996).
23. C.C. Dewitt and E.E. Roper. J. Am. Chem. Soc. **54**, 444 (1932).
24. G.M. Sheldrick. Acta Crystallogr. Sect.A: Found. Crystallogr. **A46**, 467 (1990).
25. TEXSAN-TEXRAY structure analysis package. Molecular Structure Corp., The Woodlands, Tex. 1985 and 1992.
26. W. Metlesics and H. Zeiss. J. Am. Chem. Soc. **82**, 3321 (1960).
27. D.H Wiffen. J. Chem. Soc. 3350 (1956).
28. J.D. Ross. Inorganic IR and Raman spectra. McGraw–Hill, London. 1972. p 160.
29. J.E. Griffiths. Spectrochim. Acta, **20**, 1335 (1964).
30. J.E. Drake, H.E. Henderson, and L.N. Khasrou. Spectrochim. Acta, **38A**, 31 (1982).
31. M.E. Cradwick, R.D. Taylor, and J.L. Wardell. J. Organomet. Chem. **66**, 43 (1974).

© 1998 NRC Canada

The decarbonylation of ionized β-hydroxypyruvic acid: the hydrogen-bridged radical cation $[CH_2{=}O{\cdots}H{\cdots}O{=}C\text{-}OH]^{\bullet+}$ studied by experiment and theory

Lorne M. Fell, Peter C. Burgers, Paul J.A. Ruttink, and Johan K. Terlouw

Abstract: The intriguing gas-phase ion chemistry of β-hydroxypyruvic acid (HPA), $HOCH_2C(=O)COOH$, has been investigated using tandem mass spectrometry (metastable ion (MI) and (multiple) collision-induced dissociation (CID) experiments, neutralization–reionization mass spectrometry (NRMS), ^{18}O and D isotopic labelling on both the acid and its methyl ester) in conjunction with computational chemistry (ab initio MO and density functional theories). HPA does not enolize upon evaporation, but it retains its keto structure. When ionized, decarbonylation occurs and, depending on the internal-energy content, this dissociation reaction proceeds via two distinct routes. The source-generated, high-energy ions lose the keto C═O, not via a least-motion extrusion into ionized glycolic acid, $HOCH_2COOH^{\bullet+}$, but via a rearrangement that yields the title H-bridged radical cation $CH_2{=}O{\cdots}H{\cdots}O{=}C\text{-}OH^{\bullet+}$ for which $\Delta H_f^0 = 99 \pm 3$ kcal/mol. The long-lived low-energy ions enolize prior to decarbonylation and lose the carboxyl C═O. Again, this is not a least-motion extrusion (which would produce the most stable isomer, $HOC(H){=}C(OH)_2^{\bullet+}$, $\Delta H_f^0 = 73$ kcal/mol) but a rearrangement yielding the ion–dipole complex $HOC(H)C{\equiv}C{=}O^{\bullet+}/H_2O$. The methyl ester of HPA behaves analogously, yielding $CH_2{=}O{\cdots}H{\cdots}O{=}C\text{-}OCH_3^{\bullet+}$ and $HOC(H)C{\equiv}C{=}O^{\bullet+}/CH_3OH$ upon decarbonylation of the high- and low-energy ions, respectively. Decarboxylation into the ylidion $CH_2OH_2^{\bullet+}$ characterizes the dissociation chemistry of both the title H-bridged ion and its glycolic acid isomer $HOCH_2COOH^{\bullet+}$. A computational analysis of this reaction (which satisfies the experimental observations) leads to the proposal that the decarboxylation of the acid occurs via $CH_2\text{-}O(H){\cdots}H{\cdots}O{=}C{=}O^{\bullet+}$ as the key intermediate, whereas the title H-bridged ion follows a higher energy route that involves ion–dipole rotations leading to the ionized carbene $HO(H_2)CO\text{-}C\text{-}OH^{\bullet+}$ and the distonic ion $H_2O\text{-}C(H_2)\text{-}O\text{-}C{=}O^{\bullet+}$ as key intermediates.

Key words: tandem mass spectrometry, hydrogen-bridged radical cation, hydroxypyruvic acid, ab initio calculations, keto–enol tautomerization, ^{18}O labelling.

Résumé : Faisant appel à la spectrométrie de masse en tandem (ion métastable (IM) et expériences de dissociations induites par des collisions (DIC) (multiples), spectrométrie de masse avec neutralisation et réionisation (SMNR), marquage isotopique à ^{18}O et D tant de l'acide que de l'ester méthylique) en combinaison avec des calculs théoriques (théories de OM ab initio et densité fonctionnelle), on a étudié la chimie ionique en phase gazeuse de l'acide β-hydroxypyruvique (AHP), $HOCH_2C(=O)COOH$, qui présente des caractéristiques intrigantes. L'AHP ne s'énolise pas par évaporation; elle garde sa structure cétonique. Son ionisation provoque une décarbonylation et, suivant le niveau de l'énergie interne, cette réaction se produit par le biais de deux voies distinctes. Les ions d'énergie élevée générés par la source perdent le groupe carbonyle, C═O, non pas par une extrusion de moindre mouvement conduisant à l'acide glycolique ionisé, $HOCH_2COOH^{\bullet+}$, mais par le biais d'un réarrangement conduisant au cation radical à pont hydrogène mentionné dans le titre, $CH_2{=}O{\cdots}H{\cdots}O{=}C\text{-}OH^{\bullet+}$, pour lequel le $\Delta H_f^0 = 99 \pm 3$ kcal mol)[1]. Les ions de faible énergie et de longue vie s'énolisent avant la décarbonylation et ils perdent le C═O du carboxyle. Encore une fois, il ne s'agit pas d'une extrusion par le moindre mouvement (qui produirait l'isomère le plus stable, $HOC(H){=}C(OH)_2^{\bullet+}$, $\Delta H_f^0 = 73$ kcal mol^{-1}), mais d'un réarrangement conduisant au complexe ion–dipôle $HOC(H)C{\equiv}C{=}O^{\bullet+}/H_2O$. L'ester méthylique de l'AHP se comporte de la même manière et les décarbonylations des ions à haute et à basse énergie conduisent respectivement aux ions radicaux $CH_2{=}O{\cdots}H{\cdots}O{=}C\text{-}OCH_3^{\bullet+}$ et $HOC(H)C{\equiv}C{=}O^{\bullet+}/CH_3OH$. La décarboxylation de l'ion ylure $CH_2OH_2^{\bullet+}$ caractérise la chimie de dissociation de l'ion à pont hydrogène mentionné dans le titre ainsi que son isomère de l'acide glycolique, $HOCH_2COOH^{\bullet+}$. Une analyse de cette réaction

Received December 8, 1997.

Cet article est dédié au Docteur Pierre Longevialle à l'occasion de sa retraite, en reconnaissance pour sa contribution à la compréhension de la chimie des ions en phase gazeuse.

L.M. Fell and J.K. Terlouw.[1] Department of Chemistry, McMaster University, 1280 Main Street West, Hamilton, ON L8S 4M1, Canada.
P.C. Burgers. Hercules European Research Center BV, Nijverheidsweg 60, 3771 ME Barneveld, The Netherlands.
P.J.A. Ruttink. Theoretical Chemistry Group, Department of Chemistry, University of Utrecht, Padualaan 14, 3584 CH Utrecht, The Netherlands.

[1] Author to whom correspondence may be addressed. Telephone: (905) 525-9140 (ext. 27111). Fax: (905 522-2509. (E-mail: terlouwj@mcmail.cis.mcmaster.ca

© 1998 NRC Canada

par calculs théoriques (qui satisfait les résultats expérimentaux) permet de proposer que la décarboxylation de l'acide se produit par le biais de CH_2-O(H)O···HO···O═C═O$^{\bullet+}$ comme intermédiaire principal alors que l'ion à pont hydrogène mentionné dans le titre passe par une voie d'énergie plus élevée qui implique des rotations ion–dipôle conduisant au carbène ionisé, HO(H_2)CO-C-OH$^{\bullet+}$, et à l'ion distonique H_2O-C(H_2)-O-C═O$^{\bullet+}$ comme intermédiaires clés.

Mots clés : spectrométrie de masse en tandem, cation radical à pont hydrogène, acide hydroxypyruvique, calculs ab initio, tautomérie céto–énolique, marquage au ^{18}O.

[Traduit par la rédaction]

Introduction

In the context of ionic rearrangements, hydrogen-bridged radical cations (for selected reviews see ref. 1), particularly O···H···O and N···H···O bonded ions, are being proposed with increasing frequency as intermediates to rationalize the dissociation behaviour of low-energy radical cations. This growing realization (2) follows findings from both theory and experiment that such hydrogen-bridged species can be thermodynamically more stable than the nonrearranged reactant, which makes them energetically attractive intermediates. Ab initio calculations on such species do not only attest to their stability, they also confirm the intuitive expectation that the bridging H in these complexes is more closely connected to the moiety of higher proton affinity (PA). In fact, such (necessarily asymmetric) O···H···O bridged radical cations can best be described as H-bridged ion–dipole complexes of the type [M···H-R]$^{\bullet+}$ or [M-H···R]$^{\bullet+}$ (M = molecule, R = radical), where most of the stabilization energy is provided by ion–dipole interactions. As shown in recent studies on ionized ethylene glycol, $HOCH_2CH_2OH^{\bullet+}$ (3), acetol, $CH_3C(=O)CH_2OH^{\bullet+}$(4), and several related molecules (5), the O···H···O intermediates undergo a facile isomerization leading to C-H···O bridged ions, and these are the key intermediates in the low-energy dissociation reactions of the molecular ions. Such C-H···O species are not as stable as their O···H···O bonded counterparts, but calculations indicate that they can be easily formed from O···H···O bonded ions by a dipole-catalyzed proton shift (3, 4), a process that is identical to Böhme's concept of "proton-transfer catalysis" (6).[2] In a recent experimental study (7) it was observed that the isomerization $CH_3OH^{\bullet+} \rightarrow CH_2OH_2^{\bullet+}$, which does not occur unassisted, can be catalyzed by the addition of water; this constitutes a prime example of proton-transport catalysis, which has recently been confirmed and elegantly rationalized by the ab initio computational studies of Radom and co-workers (7*c–e*).

Despite their role as key intermediates in dissociation reactions, only relatively few H-bridged radical cations have been characterized as stable product ions, in part because of the experimental difficulties to differentiate such ions from their distonic counterparts (1*c*). The well characterized species include the vinyl alcohol – water and methanol ions CH_2═C(H)O···H···$OH_2^{\bullet+}$ and CH_2═C(H)O···H···$HOCH_3^{\bullet+}$ (2), the carbonic acid isomer HO···H···O═C═O$^{\bullet+}$(8), CH_3(H)O···H···O═C-H$^{\bullet+}$(9), which is also a key intermediate in the dissociation chemistry of ionized ethylene glycol (3), and most recently H_2O···H···O═C-OH$^{\bullet+}$. The latter ion was shown in a combined experimental and theoretical study to be the stable product ion formed by the consecutive loss of three CO molecules from HOOC(OH)═C(OH)COOH$^{\bullet+}$, ionized dihydroxyfumaric acid (DHF) (10).

In the present study we report on the identification of a related H-bridged radical cation, viz. CH_2═O···H···O═C-OH$^{\bullet+}$, which forms part of the $C_2H_4O_3^{\bullet+}$ (*m/z* 76) system of ions and which inter alia comprises ionized glycolic acid, $HOCH_2COOH^{\bullet+}$, and its enol HOC(H)═C(OH)$_2^{\bullet+}$ (11) as members whose neutral counterpart are molecules of conventional structure. A combination of tandem mass spectrometric techniques (metastable ion (MI), collision-induced dissociation (CID), neutralization–reionization mass spectrometry (NRMS), and MS/MS/MS experiments) and computational chemistry (using ab initio MO and density functional theories) is used to show that the decarbonylation of ionized ß-hydroxypyruvic acid (HPA), **I**$^{\bullet+}$, does *not* lead, via a least-motion extrusion, to ionized glycolic acid, **2**$^{\bullet+}$, nor to its enol, **1**$^{\bullet+}$, but rather to the H-bridged radical cation **3a**$^{\bullet+}$:

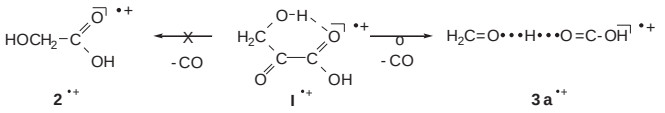

This H-bridged ion has two closely related isomers, viz. CH_2═O···H···O(H)-C═O$^{\bullet+}$, **3b**$^{\bullet+}$, and CH_2O(H)···H···O═C═O$^{\bullet+}$, **3c**$^{\bullet+}$, of which the latter, as shown in the theoretical section below, is by far the most stable. Since formation of $CH_2OH_2^{\bullet+}$ and CO_2 represents the dissociation reaction of lowest energy requirement in **3a**$^{\bullet+}$ and also in **2**$^{\bullet+}$, the participation of **3c**$^{\bullet+}$ in their isomerization cum dissociation reactions will be considered using results of ab initio MO theoretical calculations.

The above scenario refers to the decarbonylation reaction in the ion source, i.e., the loss of CO from high-energy HPA ions. Low-energy (metastable) HPA ions also lose CO but, it will be shown, from molecular ions that have isomerized into their enol counterpart, viz. ionized 1,2-dihydroxyacrylic acid, **II**$^{\bullet+}$:

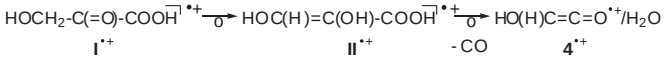

The resulting product ion is not the H-bridged species **3a**$^{\bullet+}$ but the more stable ion–dipole complex **4**$^{\bullet+}$ whose dissociation chemistry is related to that of the enol ion HOC(H)═C(OH)$_2^{\bullet+}$, **1**$^{\bullet+}$, (11).

The principal precursor molecule used in this study, ß-hydroxypyruvic acid, has been the subject of numerous biochemical studies (12, 13) but, unlike pyruvic acid itself, HPA is a thermally labile compound that decomposes vigorously at

[2] For CH_3^+ shuttle see V. Baranov et al. (6).

© 1998 NRC Canada

Scheme 1.

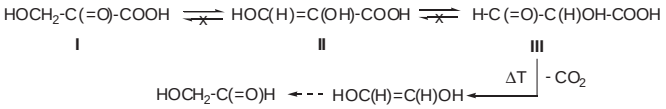

its melting point, 82°C (13*a*). This facile decomposition of the pure solid at elevated temperatures is a decarboxylation that also occurs in aqueous solutions of varying acidity at room temperature where it has been proposed (13*c*, *d*) to yield glycol aldehyde, $HOCH_2CHO$, as the final reaction product. The reaction of HPA in the solid melt may well occur analogously to that established for the decarboxylation of oxalacetic acid (14) i.e., as shown in Scheme 1.

In this context we note that the statement in entry H-0-03641 of the latest edition of *The Dictionary of Organic Compounds* (15) that HPA would consist of an equilibrium mixture of **I** with its enol 1,2-dihydroxyacrylic acid, **II**, is clearly incorrect. The IR spectroscopic findings of Bellamy and Williams (13*b*), the polarographic and UV results of Fleury and Fleury (13*e*), and also the results of our own deuterium incorporation experiments described in the experimental section leave little doubt that at room temperature solid ß-hydroxypyruvic acid and aqueous solutions thereof consist of the keto structure **I**.

Results and discussion

1. Conventional EI mass spectra of ß-hydroxypyruvic acid: thermal decarboxylation vs. electron impact induced decarbonylation

The rather striking differences between the mass spectra displayed in Figs. 1*a* and *b* illustrate how strongly the EI mass spectrum of HPA ($M = 104$) depends upon the method of sample introduction. Figure 1*a* is representative of a typical spectrum obtained from a "bulk" sample introduced at the lowest possible temperature (see Experimental for further details). The overall appearance of the spectrum obtained under these conditions remained fairly constant. The spectrum displays a molecular ion at *m*/*z* 104 and, in the absence of further information, most of the other peaks including the base peak at *m*/*z* 31, CH_2OH^+, can readily be assigned as fragment ions generated from $\mathbf{I}^{\bullet+}$.

Figure 1*b* shows the spectrum obtained from the same sample but now using a much higher source temperature, 170°C. Comparison with Fig. 1*a* shows that the relative intensity of the signals at *m*/*z* 60 and *m*/*z* 44 has greatly increased. The CID spectra of these ions were obtained (spectra not shown), and comparison with reference spectra (16*a*) shows that the *m*/*z* 60 ions are a mixture of $HOCH{=}C(H)OH^{\bullet+}$ and $HOCH_2CHO^{\bullet+}$, whereas the *m*/*z* 44 ions are $CO_2^{\bullet+}$.

Thus at elevated temperatures **I** is prone to decarboxylate, and the structure of the reaction products supports the mechanism presented in Scheme 1 of Introduction.

On the other hand, the decarbonylation responsible for the *m*/*z* 76 ions appears to be a genuine electron impact induced process. This reaction is even more prominent in the EI spectrum of the methyl ester of **I**,[3] which does not suffer from thermal decarboxylation and which is sufficiently volatile to be introduced into the ion source as a vapour at room temperature. As will be shown in detail elsewhere,[3] the molecular ions of the methyl ester decarbonylate via two distinct mechanisms, yielding product ions of a different structure (see Scheme 2): at high internal energies (source-generated ions) the product ion is the

Fig. 1. The EI mass spectrum of β-hydroxypyruvic acid (**I**): (*a*) obtained from a "bulk" sample at an ion source temperature of 110°C (see text); (*b*) obtained from a bulk sample at an ion source temperature of 110°C (see text), using an ion source temperature of 170°C; (*c*) CID mass spectrum [2ffr,O_2] of $\mathbf{I}^+$; (*d*) neutralization–reionization (NR) mass spectrum of $\mathbf{I}^+$ (S denotes the survivor ion).

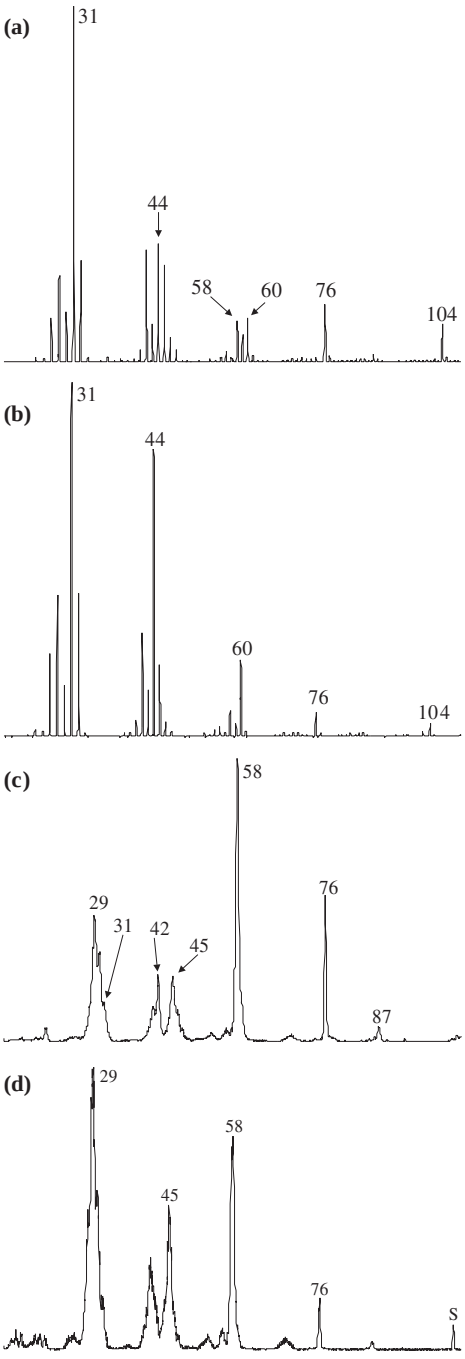

[3] P.C. Burgers, L.M. Fell, P.J.A. Ruttink, and J.K. Terlouw. In preparation.

© 1998 NRC Canada

Scheme 2.

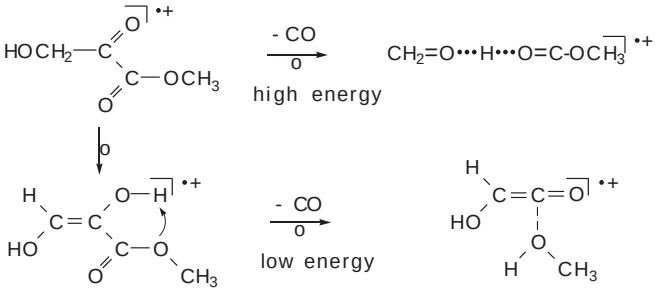

H-bridged radical cation $CH_2{=}O{\cdots}H{\cdots}O{=}C\text{-}OCH_3^{\bullet+}$ (5*a*) whereas the low-energy molecular ions (metastable ions) also produce this ion, but as further discussed in Sect. 5, these ions are produced in admixture with the more stable isomer $HO(H)C{=}C{=}O^{\bullet+}/CH_3OH$ (9). The generation of the latter ion involves a slow isomerization of the keto molecular ion into its enolic counterpart, which then loses CO via a mechanism analogous to that for the decarbonylation of ionized $CH_2{=}C(OH)COOH^{\bullet+}$, which was recently shown (14) to specifically yield $CH_2{=}C{=}O^{\bullet+}/H_2O$ and not the more stable isomer $CH_2{=}C(OH)_2^{\bullet+}$.

A similar situation obtains, we propose, for the parent acid **I**: Fig. 1*c* shows the CID mass spectrum of $\mathbf{I}^{\bullet+}$, and even a cursory inspection indicates that the (majority of the) HPA molecular ions must have lost their parent keto structure, as witnessed by the greatly reduced intensity of the *m/z* 31 CH_2OH^+ ion and the appearance of the prominent peak at *m/z* 58, $HO(H)C{=}C{=}O^{\bullet+}$ (structure identified from a MS/MS experiment and compared with reference spectra (9); result not shown). It will be shown in Sect. 5 that most of these long-lived ions have rearranged to the enol $HOC(H){=}C(OH)COOH^{\bullet+}$, $\mathbf{II}^{\bullet+}$.

Figure 2 shows the CID mass spectra of the source-generated *m/z* 76 $[M - CO]^{\bullet+}$ ions (part *a*) along with that of the *m/z* 76 ions found in the MI spectrum of the molecular ions (part *b*). Also given are the CID mass spectra of the isomeric ions $HOC(H){=}C(OH)_2^{\bullet+}$, $\mathbf{1}^{\bullet+}$, and $HOCH_2COOH^{\bullet+}$, $\mathbf{2}^{\bullet+}$, whose ion chemistry has been discussed in considerable detail in a previous study (11). Comparison of the four spectra shows (*i*) that the source-generated *m/z* 76 ions from HPA are neither $\mathbf{2}^{\bullet+}$ nor its enol nor a mixture thereof and (*ii*) that the structure of the low-energy *m/z* 76 ions from $\mathbf{I}^{\bullet+}$ must be different from that of the source-generated ions, and that it is akin to that of the ionized enol $\mathbf{1}^{\bullet+}$. Thus the source-generated ions and the metastably generated ions (high- and low-energy ions) appear to have different structures (and also different precursor structures), and we will therefore deal with these in different sections.

2. The decarbonylation of high-energy HPA ions: generation of the H-bridged radical cation $CH_2{=}O{\cdots}H{\cdots}O{=}C\text{-}OH^{\bullet+}$, $\mathbf{3a}^{\bullet+}$

The CID mass spectrum of the *m/z* 76 $C_2H_4O_3^{\bullet+}$ ions generated from HPA, $\mathbf{I}^{\bullet+}$, shows a tell-tale peak at *m/z* 46, $C(OH)_2^{\bullet+}$, which differentiates this spectrum from that of the two isomers of conventional structure, viz. ionized glycolic acid, $\mathbf{2}^{\bullet+}$, and its more stable enol $\mathbf{1}^{\bullet+}$. The MI spectrum of the *m/z* 76 ions is dominated by a signal at *m/z* 32 (ion structure established by a MS/MS experiment; result not shown), $CH_2OH_2^{\bullet+}$, and *m/z* 46 is completely absent. Further, the threshold energy for the most

Fig. 2. The CID mass spectra of the $[M - CO]^{\bullet+}$ ions (*m/z* 76) from ionized β-hydroxypyruvic acid, $\mathbf{I}^{\bullet+}$: (*a*) *source*-generated ions; (*b*) *metastably* generated ions; (*c*) and (*d*) represent reference spectra of ionized trihydroxyethylene, $\mathbf{1}^{\bullet+}$, and ionized glycolic acid, $\mathbf{2}^{\bullet+}$, repectively [9].

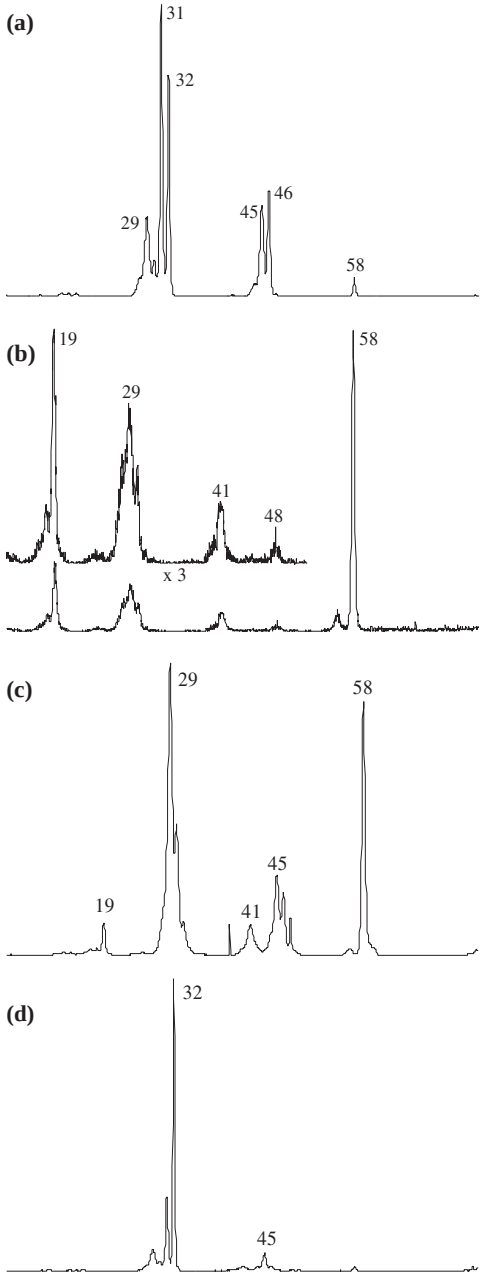

prominent dissociation taking place upon collisional activation, $76^{\bullet+} \rightarrow CH_2OH^+$ (*m/z* 31) + HOCO•, 122 kcal/mol (17), is considerably lower than that for the formation of *m/z* 46, i.e., 149 kcal/mol (17*a*) for $76^{\bullet+} \rightarrow C(OH)_2^{\bullet+} + CH_2{=}O$. That the *m/z* 46 ions are ionized dihydroxycarbene ions and not the isomeric ionized formic acid, $H\text{-}C(=O)OH^{\bullet+}$, follows from a MS/MS experiment (see Fig. 3*a*) and comparison with reference spectra of the two isomeric ions (18). Thus it is reasonable to assume that the formation of *m/z* 46, $C(OH)_2^{\bullet+}$, and $CH_2{=}O$ involves a high-energy direct bond cleavage reaction, and this

© 1998 NRC Canada

Fig. 3. (*a*) Partial CID mass spectrum [3ffr/O_2] of the m/*z* 46 ion in the CID mass spectum of Fig. 2*a*; (*b*) NR mass spectrum of the source-generated m/*z* 76 ions from β-hydroxypyruvic acid.

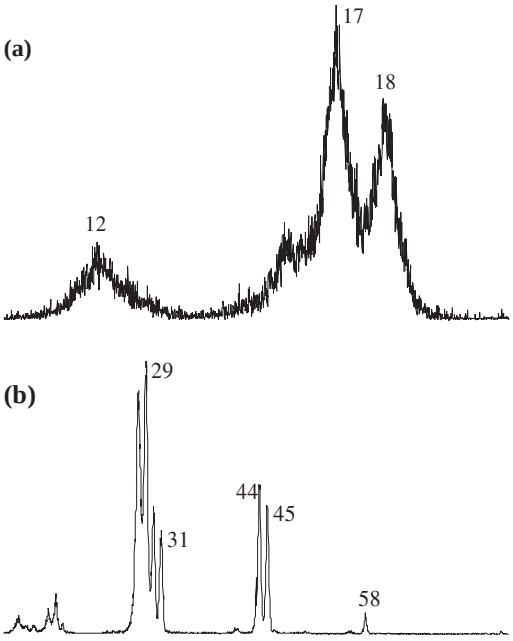

narrows down possible structures for the *m/z* 76 ions to either the H-bridged ion CH_2═O···H···O═C-$OH^{\bullet+}$, **3a**$^{\bullet+}$, or its distonic isomer $CH_2OC(OH)_2^{\bullet+}$, **5**$^{\bullet+}$. Plausible mechanisms for the generation of either ion involve a common 1,5-H transfer and the loss of the carbonyl CO group, as depicted in Scheme 3.

That the ion generated is not the distonic ion **5**$^{\bullet+}$ but rather the H-bridged ion **3a**$^{\bullet+}$ is supported by the following arguments:

(*i*) The first step in the proposed mechanism for the formation of **5**$^{\bullet+}$, an undoubtedly facile 1,5-H shift, leads to a stable intermediate, **V**$^{\bullet+}$ (see Sect. 5), which may be expected to competitively dissociate into $(HO)_2C$═C═O$^{\bullet+}$ (*m/z* 74) + CH_2═O by direct bond cleavage,[4] either in the ion source or upon collisional activation of the long-lived molecular ions. However, neither the EI spectrum of **I** nor the CID mass spectrum of **I**$^{\bullet+}$ shows a signal at *m/z* 74 indicative of this reaction. This also excludes formation of **3a**$^{\bullet+}$ via the H-bridged intermediate CH_2═O···H-O-C(OH)═C═O$^{\bullet}$.

(*ii*) The ionized methyl ester of **I**$^{\bullet+}$ (see above) also shows a prominent decarbonylation, and here the corresponding product ions would be either CH_2═O···H···O═C-$OCH_3^{\bullet+}$ or $CH_2OC(OH)(OCH_3)^{\bullet+}$. The latter ion was independently generated and examined in previous study (5a), and from a comparison of the exchange behaviour of multiple (^{13}C and D) labelled isotopomers, it follows that the methyl ester ion does not generate $CH_2OC(OH)(OCH_3)^{\bullet+}$ but rather

Scheme 3.

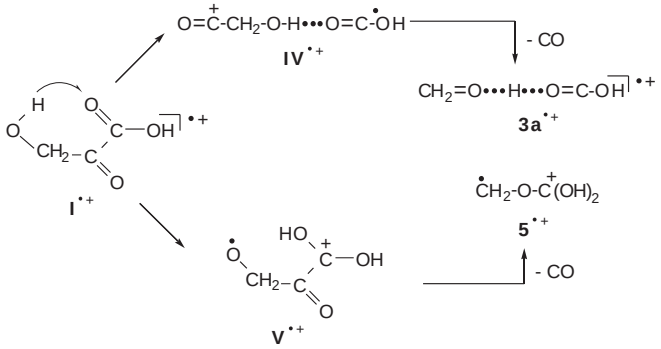

CH_2═O···H···O═C-$OCH_3^{\bullet+}$, and also that the two isomers do not easily communicate.[3]

(*iii*) The $CH_2OC(OH)(OCH_3)^{\bullet+}$ ion undergoes a facile reversible isomerization, via a 1,4-H shift, into $CH_3OC(=O)(OCH_3)^{\bullet+}$ (5*a*) and by analogy ion **5**$^{\bullet+}$, $CH_2OC(OH)_2^{\bullet+}$, may be expected to communicate with $CH_3OC(=O)(OH)^{\bullet+}$. However, this process leads to loss of positional identity of the C- and O-bonded H atoms, and this is not what is observed. Comparison of the CID mass spectrum of the source-generated *m/z* 78 $[M - CO]^{\bullet+}$ ions from the D-labelled HPA isotopomer $DOCH_2C(=O)COOD^{\bullet+}$ with that of the unlabelled *m/z* 76 ion, shown in Fig. 2*a*, showed that the *m/z* 31, 32, 45, and 46 ions are cleanly shifted to *m/z* 32, 34, 46, and 48, respectively, in agreement with the proposed H-bridged structure CH_2═O···D···O═C-$OD^{\bullet+}$, not $CH_2OC(OD)_2^{\bullet+}$.

Thus we propose that the parent acid **I**$^{\bullet+}$ also produces the H-bridged ion, CH_2═O···H···O═C-$OH^{\bullet+}$, **3a**$^{\bullet+}$, and that it is generated by the mechanism depicted above.

Two peaks in the CID mass spectrum of **3a**$^{\bullet+}$ deserve further comment: the signal at *m/z* 32, $CH_2OH_2^{\bullet+}$, which dominates the MI spectrum, and the peak at *m/z* 58. The latter ion, (HO)HC═C═O$^{\bullet+}$ (structure established by a MS/MS experiment; result not shown) is the principal fragment ion in the CID spectrum of the low-energy decarbonylation of **I**$^{\bullet+}$ (see Fig. 2*b*), and its presence in the spectrum of the source-generated *m/z* 76 ions most likely reflects a small contribution of the low-energy decarbonylation product ion **4**$^{\bullet+}$, which will be further discussed in Sect. 5. This may also explain the presence of the weak *m/z* 58 ion in the NR spectrum (for a recent review see ref. 20) of the [**I** – CO]$^{\bullet+}$ source-generated ions (see Fig. 3*b*). The other features of the NR spectrum are readily accommodated by the proposed **3a**$^{\bullet+}$ structure and CIDI (for a recent review see ref. 21) contributions from its metastable dissociation (responsible for the larger part of the peak at *m/z* 44, $CO_2^{\bullet+}$). The neutral counterpart of the hydrogen-bridged ion is not expected to be stable, and indeed the *m/z* 76 survivor signal is of negligible intensity. Neutralized **3a**$^{\bullet+}$ may (formally) dissociate by direct bond cleavage into HOCO$^{\bullet}$ + $CH_2OH^{\bullet}$ and (or) **:**$C(OH)_2$ + CH_2═O, and upon collisional ionization these neutrals would give rise to ions at *m/z* 45 and *m/z* 31 for the first process and *m/z* 46 and *m/z* 30 for the second, and lower mass fragment ions generated therefrom. The fact that *m/z* 46, $C(OH)_2^{\bullet+}$, ions are barely detectable in the NR spectrum is not due to the NR properties of $C(OH)_2^{\bullet+}$ (18) nor to the energetic demands of the **:**$C(OH)_2$ generation

[4] The threshold energy for this reaction is 88.6 kcal/mol, ΔH_f^{298} ($(HO)_2C$═C═O^{+}) is 114.6 kcal/mol (neutral is –76.4 kcal/mol) (G2(MP2) (19*a*, *b*, footnote 5) values, this work), and ΔH_f^{298} (CH_2═O) is –26.0 kcal/mol (18*a*). Note also that $(HO)_2C$═C═O^{+} is a prominent fragment ion in the 70 eV EI mass spectrum of mesoxalic acid, HOOCC(═O)COOH.

[5] For a concise description and evaluation of the various computational methods and strategies see ref. 19*a*.

© 1998 NRC Canada

Scheme 4.

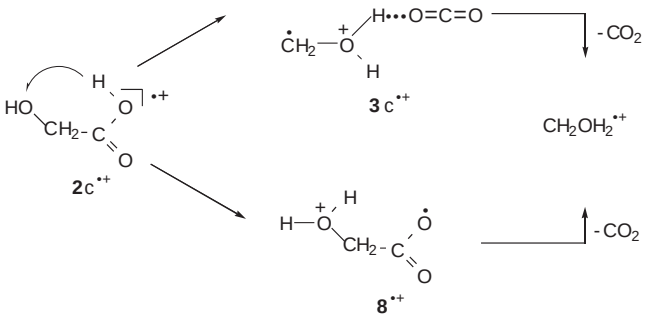

vis-à-vis that of HOCO•, but rather to the charge distribution in **3a**•+, which, as discussed below, is best represented as a CH_2OH^+ *ion* interacting via an H-bridge with a HOCO• dipole. The related H-bridged radical cation $H_2O\cdots H\cdots O{=}C\text{-}OH^{\bullet+}$ shows a similar NR behaviour (10).

The CO_2 loss, which dominates the MI but not the CID spectrum of the source-generated $[\mathbf{I} - CO]^{\bullet+}$ ions, is obviously a rearrangement reaction, since the threshold energy for the generation of $CH_2OH_2^{\bullet+} + CO_2$, 101 kcal/mol, is considerably lower than that associated with the base peak in the CID spectrum: CH_2OH^+ (*m*/*z* 31) + HOCO• = 122 kcal/mol (17). This observation further supports our proposal that the source-generated $[\mathbf{I} - CO]^{\bullet+}$ ions have structure **3a**•+ and not that of the isomeric H-bridged radical cations **3b**•+ or **3c**•+, although the latter may be involved as a stable intermediate en route to the loss of CO_2 from **3a**•+. Loss of CO_2 also dominates the MI spectrum of the isomeric glycolic acid ion **2**•+, and two mechanisms involving a 1,4-H transfer of which one involves the H-bridged ion **3c**•+ can be envisaged (see Scheme 4).

This raises the question: does the H-bridged ion **3a**•+ communicate with **2**•+ prior to the common CO_2 loss, and if not, how then does **3a**•+ isomerize to lose CO_2? Analysis of the metastable peak shapes for the two reactions rules out a facile interconversion, albeit not a communication, between **3a**•+ and **2**•+: the two isomeric ions display Gaussian shaped metastable peaks (21), but that for the loss of CO_2 from **3a**•+, $T_{0.5}$ = 43 meV, is significantly larger than that from **2**•+ whose $T_{0.5}$ value is only 21 meV (0.5 kcal/mol). Unfortunately, another valuable piece of experimental information, i.e., an accurate appearance energy (AE) for the two CO_2 losses is not available: the involatility (glycolic acid) and additional thermal lability (HPA) of the acids precludes AE measurements with the currently accessible instrumentation. In this context we also note that an AE of the *m*/*z* 76 ions from **I**•+ would not lead to an experimental heat of formation of the H-bridged ion **3a**•+ but rather to that of the low-energy isomer **4**•+.

However, the intriguing mechanistic question regarding the loss of CO_2 from **3a**•+ and its relationship with **2**•+ can be addressed computationally. This is done in Sect. 4, but first we will discuss the computational results of the $[\mathbf{I} - CO]^{\bullet+}$ isomers.

3. The structure and stability of $CH_2{=}O\cdots H\cdots O{=}C\text{-}OH^{\bullet+}$ and its principal isomers: ab initio computational results and considerations

The isomers examined are ionized trihydroxyethylene, **1**•+; ionized glycolic acid, **2**•+; the H-bridged radical cations **3a–c**•+; the hydroxyketene•+–water ion–dipole complex **4**•+; the ß-distonic ion **5**•+ of Scheme 3; $HO(H_2)CO\cdots O{=}C\text{-}OH^{\bullet+}$, **6a**•+, an ion–dipole complex derived from **3a**•+ and its carbenic conformer $HO(H_2)C\text{-}O\text{-}C\text{-}OH^{\bullet+}$, **6b**•+; the distonic ions $H_2O\text{-}C(H_2)\text{-}O\text{-}C{=}O^{\bullet+}$, **7**•+, and $H_2O\text{-}C(H_2)\text{-}C(=O)\text{-}O^{\bullet+}$, **8**•+, precursor ions for the direct loss of CO_2 discussed in the next section. Their MP2(full) optimized geometries and CCSD(T) derived relative energies[5] are presented in Fig. 4 and Table 1, respectively, along with the transition states for loss of CO_2, discussed in the next section. Geometries were also optimized using the UHF and B3LYP methodology (using standard basis sets; see theoretical section for further details), and we will refer to those results that are relevant to the discussion.

The optimized geometry for **1**•+ in Fig. 4 represents the lowest energy conformer of the ionized enol (11), which is the most stable of the isomers examined. Its G2(MP2) derived enthalpy of formation, ΔH_f^{298} = 71.6 kcal/mol (11), was chosen as the anchor point because accurate experimental data are not available for any of the isomeric ions. The energy differences between the anchor point and the experimental (thermochemical) values of the dissociation limits $CH_2OH_2^{\bullet+} + CO_2$ and $CH_2OH^+ + HOCO^\bullet$ are 29 and 52 kcal/mol, respectively (see last column of Table 1). These values are gratifyingly close to those derived from our CCSD(T) calculations, 29.8 and 53.4 kcal/mol (note that these refer to 0 K, whereas the estimated energies were evaluated at 298 K). The last column of Table 1 also lists values for those isomeric ions whose ionic enthalpy can be reliably estimated, and here, too, comparison with the calculated energy differences is satisfactory. In particular, the calculated keto ion (**2c**) – enol ion (**1**) energy difference, 35.5 kcal/mol, is close to the estimate, 34 kcal/mol, and also compatible with ionic keto–enol energy differences established in related systems (25). In view of these facts, we propose that the ΔH_f for the key H-bridged ion **3a**•+ equals 99 kcal/mol, with an estimated uncertainty of ±3 kcal/mol.

For ionized glycolic acid, **2**•+, various conformers were examined to determine the most stable conformer and to probe potential routes for the loss of CO_2. The MP2(full) calculations yielded seven stable species, represented by items **2a–e** in Fig. 4. Two of these, **2d**•+ and **2c′**•+, have a greatly elongated C—C bond, whereas optimization starting from the most stable neutral conformer (26) of glycolic acid led to a spontaneous rearrangement via a 1,4-H shift into the energetically favourable distonic ion **2e**•+. No such rearrangement occurs without electron correlation: at the Hartree–Fock (UHF/6-31G*) level of theory, structure **2e**•+ **[UHF]** (see Fig. 4) was obtained with a relative energy (37.5 kcal above ion **1**•+) in reasonable agreement with the keto–enol differences mentioned above.

In view of its stability, the distonic ion **2e**•+ may well be a principal species among the various conformers generated by the EI of glycolic acid. Nevertheless, the CID mass spectrum of **2**•+ in Fig. 2*d* clearly reveals that the structure characteristic high-energy dissociation of **2e**•+ into $C(OH)_2^{\bullet+}$ (*m*/*z* 46) and $CH_2{=}O$ is of only marginal importance, possibly because of a facile interconversion with the various conformers of **2**•+ prior to dissociation.

Ion **2a**•+ is considerably higher in energy (by ~15 kcal/mol) than **2b**•+ and **2c**•+, the other conformers of conventional C—C bond length. This is likely due to differing electronic structures, which is reflected in the geometries shown in Fig. 4. In ion **2a**•+, the charge and the radical are largely located on the

© 1998 NRC Canada

Table 1. The UMP2(full)/6-31G* and CCSD(T)/cc-pVDZ//UMP2(full)/6-31G* energies, zero-point vibrational energies (ZPVEs), and relative energies, E_{rel}, for ionized glycolic acid and its most important isomers.

Ions	UMP2(full)/6-31G* (Hartree, –303)	ZPVE[a] (kcal/mol)	CCSD(T)/cc-pVDZ (Hartree, –303)	E_{rel} MP2 (kcal/mol)	E_{rel} CCSD(T) (kcal/mol)	E_{rel} Estimated (kcal/mol)
1$^{\bullet+}$	–0.14285	41.2	–0.24898	0.0	0.0	0[b]
2a$^{\bullet+}$	–0.05941	38.4	–0.15320	49.6	57.3	
2b$^{\bullet+}$	–0.06414	39.8	–0.17869	48.0	42.7	
2c$^{\bullet+}$	–0.07481	40.5	–0.19122	42.0	35.5	34[c]
2c′$^{\bullet+}$	–0.08404	41.0	–0.19094	36.7	36.2	
2d$^{\bullet+}$	–0.08871	41.2	–0.19387	34.0	34.6	
2e$^{\bullet+}$	–0.09437	40.6	–0.20459	29.8	27.3	
3a$^{\bullet+}$	–0.09607	38.2	–0.19848	26.4	28.7	
3a′$^{\bullet+}$	–0.09484	38.7	–0.20239	27.7	26.8	27[d]
3b$^{\bullet+}$	–0.08637	39.0	–0.19360	33.2	32.6	
3c$^{\bullet+}$	–0.12254	38.5	–0.22138	10.0	14.6	10[d]
4$^{\bullet+}$	–0.10501	39.1	–0.21321	21.7	20.3	
4′$^{\bullet+}$	–0.10692	38.5	–0.21464	19.8	18.8	
4″$^{\bullet+}$	–0.12187	38.3	–0.22888	10.2	9.7	
5$^{\bullet+}$	–0.11518	39.8	–0.21850	16.0	17.7	
6a$^{\bullet+}$	–0.08480	40.0	–0.19108	35.2	35.1	
6b$^{\bullet+}$	–0.07628	41.0	–0.17917	41.6	43.6	
7$^{\bullet+}$	–0.07451	41.2	–0.17439	42.9	46.8	
8$^{\bullet+}$	–0.06511	40.3	–0.17503	47.8	47.3	
TS [**2c′**→**3c**]$^{\bullet+}$	–0.07718	38.6	–0.18148	38.6	39.8	
TS [**2c**→**8**]$^{\bullet+}$	–0.06424	38.5	–0.17589	46.6	51.3	
TS [**6b**→**7**]$^{\bullet+}$	–0.06605	39.0	–0.16979	46.0	49.7	
$CO_2 + CH_2OH_2^{\bullet+}$	–0.09992	36.9	–0.19468	26.2	29.8	29[e]
$CH_2OH^+ + HOCO^{\bullet}$	–0.05112	37.8	–0.15845	54.2	53.4	52[f]
$H(HO)C{=}C{=}O^{\bullet+} + H_2O$	–0.07281	36.7	–0.18163	39.5	37.6	33[g]

[a] Scaled by a factor of 0.9646 (see ref. 23).

[b] Using ΔH_f^{298}(**1**$^{\bullet+}$) = 71.6 kcal/mol and ΔH_f^{0}(**1**$^{\bullet+}$) = 73.4 kcal/mol as the anchor point (G2(MP2) values from ref. 11); ΔH_f^{298}(**1**) values from G2(MP2) (19*a*, *b*) and CBS-4 (19*a*, *c*) are –107.5 and –108.5 kcal/mol, respectively.

[c] Using ΔH_f(**2**) = –139.5 kcal/mol (11) and IE(**2**) = 10.6 eV; the CBS-4 value for the lowest energy conformer of **2** (the neutral counterpart of the UHF structure **2e**$^{\bullet+}$ in Fig. 4) is –137.6 kcal/mol at 298 K (this work).

[d] Using ΔH_f(**3a**$^{\bullet+}$) = 99 kcal/mol and ΔH_f(**3c**$^{\bullet+}$) = 82 kcal/mol; estimates based on the empirical relationship for O/H/O proton bound dimers: SE (kcal/mol) = 30.4 – 0.30ΔPA (23); SE = stabilization energy relative to the dissociation products of lowest combined enthalpy; PA = proton affinity; PA($CH_2{=}O$) = 170.4 kcal/mol (24*a*); PA(CO_2) = 129.4 kcal/mol (24*b*); PA($^{\bullet}CH_2OH \rightarrow CH_2OH_2^{\bullet+}$) = 166 kcal/mol; PA($^{\bullet}COOH \rightarrow C(OH)_2^{\bullet+}$) = 145 kcal/mol; from ΔH_f(COOH) = –46 kcal/mol (17*b*) and $\Delta H_f(C(OH)_2^{\bullet+})$ =175 kcal/mol (17*a*).

[e] Using the following ΔH_f^{298} values: $CH_2OH_2^{\bullet+}$ = 195 kcal/mol and CO_2 = –94 kcal/mol (17*a*).

[f] Using the following ΔH_f^{298} values: CH_2OH^+ = 169 kcal/mol and $^{\bullet}COOH$ = –46 kcal/mol (17*b*).

[g] Using $\Delta H_f^{298}(H_2O)$ = –58 kcal/mol and $\Delta H_f^{298}(HO(H)C{=}C{=}O^{\bullet+})$ = 163 kcal/mol; the latter value was obtained from a G2 calculation (19*a*, *b*) on the isodesmic reaction $HO(H)C{=}C{=}O^{\bullet+} + CH_4 \rightarrow H_2C{=}C{=}O^{\bullet+} + CH_3OH$, using $\Delta H_f^{298}(CH_3OH)$ = –48.2 kcal/mol, $\Delta H_f^{298}(CH_4)$ = –17.8 kcal/mol, and $\Delta H_f^{298}(H_2C{=}C{=}O^{\bullet+})$ = 209 kcal/mol (24*d*).

oxygen atom of the CH_2OH group, since the O—H (1.021 Å) bond is slightly shortened and the C—O (1.379 Å) bond slightly elongated, relative to the corresponding bond length in the neutral, 0.997 and 1.407 Å (26). For **2b**$^{\bullet+}$ and **2c**$^{\bullet+}$, the values are much closer to neutral CH_2OH, and moreover, their carbonyl C═O bond (1.274 and 1.269 Å) is much longer than that in **2a**$^{\bullet+}$ (1.199 Å; the corresponding neutral value is 1.211 Å (26)), indicating that the charge and radical electron are now localized in the carbonyl moiety. These proposals are confirmed by population analysis of these species. Note further that the relative energy of **2a**$^{\bullet+}$ is such that it lies above the direct bond cleavage dissociation into CH_2OH^+ (*m*/*z* 31) and HOCO$^{\bullet}$. Thus, **2a**$^{\bullet+}$ may play a significant role in the high-energy source reactions represented by the conventional 70 eV EI spectrum of **2** (where *m*/*z* 31 is the base peak) but not in the chemistry of the long-lived ions **2**$^{\bullet+}$ sampled by MI and CID experiments.

Conformers **2d**$^{\bullet+}$ and **2c′**$^{\bullet+}$ are so-called long-bonded species (3*a*) having C—C bond lengths of 1.898 and 1.990 Å, respectively (on the DFT surface; values in parentheses in Fig. 4; the effect is less pronounced). Both are low-energy species with geometrical parameters of the HOCO moiety that lie in between that of the HOCO ion and its neutral counterpart, indicating that the charge and the radical are localized in the long C—C bond. Note also that one of these conformers, **2c′**$^{\bullet+}$, along with its short-bonded counterpart, **2c**$^{\bullet+}$, has the correct orientation for a 1,4-H transfer leading to the ultimate loss of CO_2, as depicted in Scheme 4.

The H-bridged radical cations **3a**–**c**$^{\bullet+}$ are among the most stable isomers, and their calculated relative energies agree well

© 1998 NRC Canada

Fig. 4. The MP2(full)/6-31G* optimized geometries of various $C_2H_4O_3^{\cdot+}$ (*m*/*z* 76) isomers; values in parentheses refer to geometries optimized with B3LYP/6-31G*.

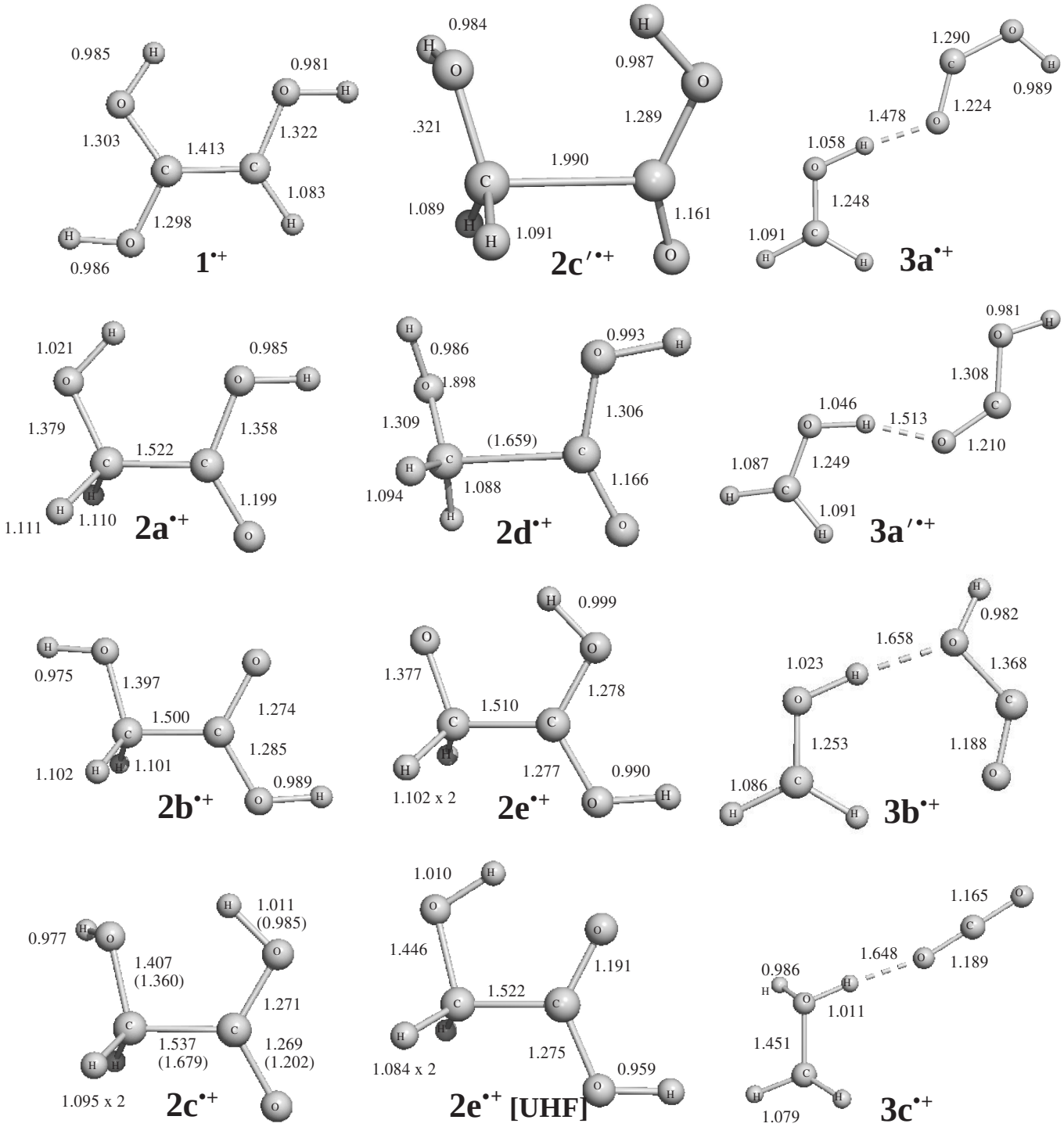

with the estimates. In all these H-bridged structures the moiety with the largest proton affinity (PA) (see footnotes in Table 1 for numerical values) covalently binds the bridging hydrogen. Thus, the best description of ions **3a**$^{\cdot+}$ and **3b**$^{\cdot+}$ is a CH_2OH^+ ion interacting with a HOCO$^{\cdot}$ dipole, that is, **3a**$^{\cdot+}$ and **3b**$^{\cdot+}$ have different connectivities but the same distribution of charge and radical, as confirmed by standard population analysis. Similarly, ion **3c**$^{\cdot+}$ represents the interaction of a CO_2 molecule with

© 1998 NRC Canada

Fig. 4. (*concluded*)

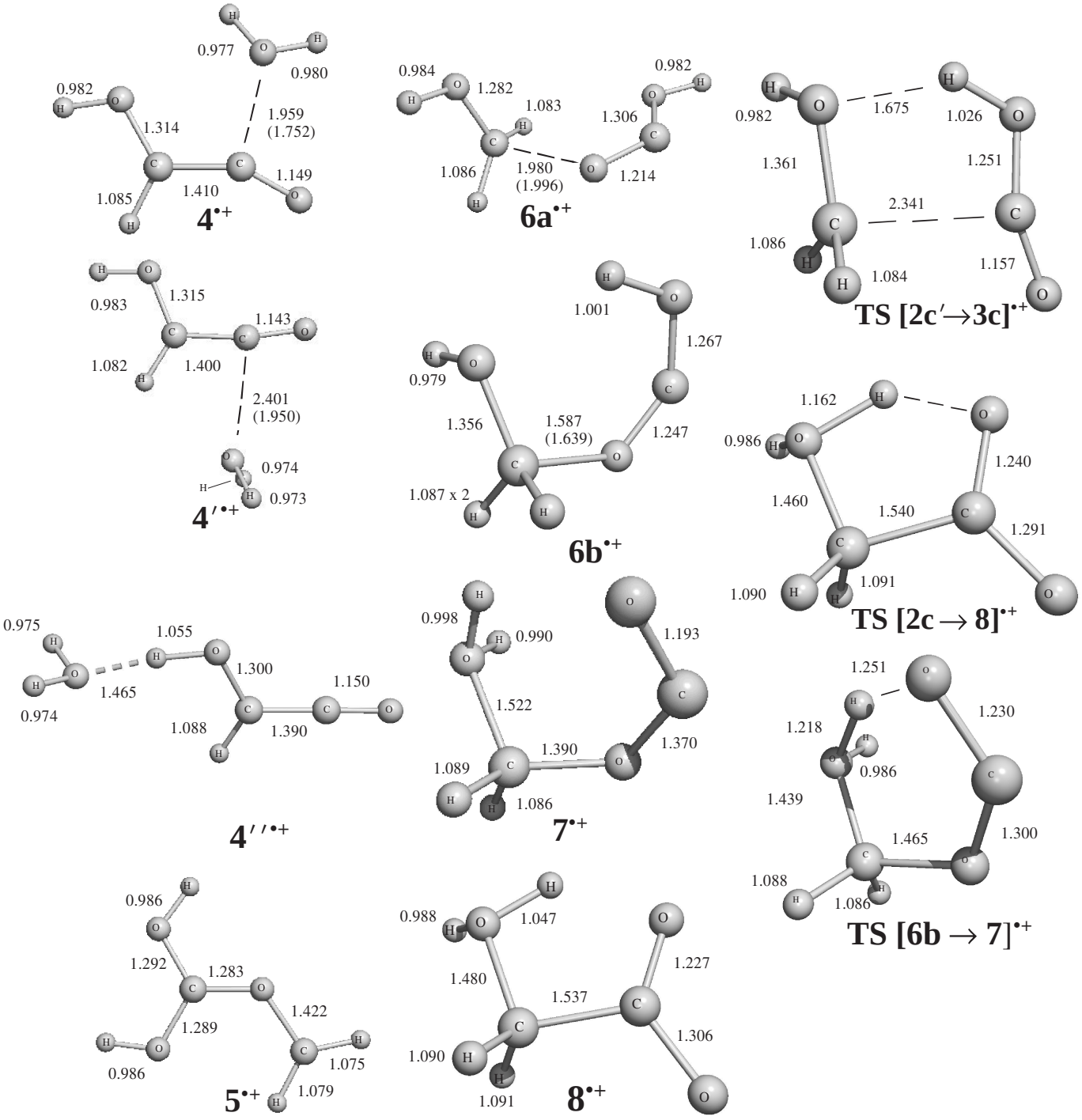

the ylid ion $CH_2OH_2^{\bullet+}$. This ion is the most stable of the H-bridged ions and a prime candidate for the dissociation reaction of lowest energy requirement, viz. loss of CO_2 by separation of the two moieties.

For the ionized hydroxyketene$^{\bullet+}$–water complex, the conformers examined (**4**$^{\bullet+}$, **4′**$^{\bullet+}$, and **4′′**$^{\bullet+}$) were the analogues of the lowest energy conformers in the ketene$^{\bullet+}$–water system (16). Conformers **4**$^{\bullet+}$ and **4′**$^{\bullet+}$ represent "pure" ion–dipole complexes with computationally derived stabilization energies (SE) of 17.3 and 18.8 kcal/mol, respectively. These SE values are in reasonable agreement with those calculated for **4**$^{\bullet+}$ and **4′**$^{\bullet+}$ from SE = 68.8μ/r^2 kcal/mol, using $\mu[H_2O]$ = 1.85 D and

© 1998 NRC Canada

Fig. 5. Energy-level diagram for the decarboxylation of ionized glycolic acid, $\mathbf{2}^{\bullet+}$, versus that of the H-bridged radical cation, $\mathbf{3a'}^{\bullet+}$.

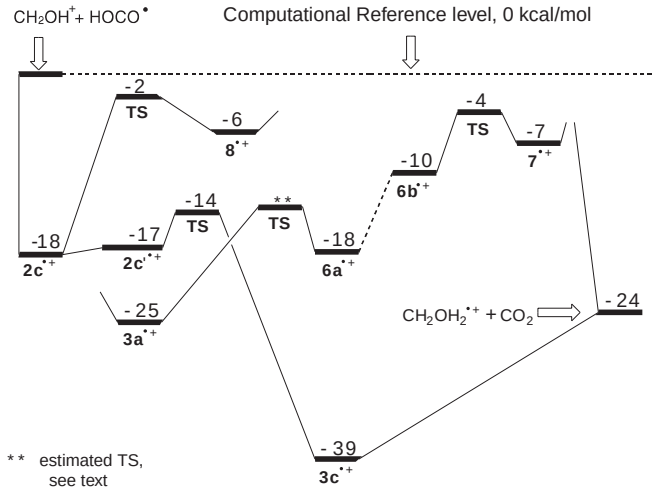

r values of 2.7 and 2.4 Å, derived from the optimized structures in Fig. 4 (17.5 and 22 kcal/mol). Not unexpectedly, conformer $\mathbf{4''}^{\bullet+}$ is considerably lower in energy, by ~10 kcal/mol, because it benefits from the added stabilization of the hydrogen bridge.

The distonic ion $\mathbf{5}^{\bullet+}$ is indeed quite a stable intermediate, as it lies 18 kcal/mol above ion $\mathbf{1}^{\bullet+}$, but as argued above, it is not generated from ionized HPA. Also presented in Table 1 and Fig. 4 are ions $\mathbf{6}^{\bullet+}$–$\mathbf{8}^{\bullet+}$, key intermediates in the decarboxylation of $\mathbf{3a}^{\bullet+}$ and $\mathbf{2}^{\bullet+}$, which will be discussed in the next section along with three strategic transition states.

4. Mechanistic proposals for the loss of CO_2 from $CH_2{=}O{\cdots}H{\cdots}O{=}C{-}OH^{\bullet+}$, $\mathbf{3a}^{\bullet+}$, participation of the stable isomer $CH_2O(H){\cdots}H{\cdots}O{=}C{=}O^{\bullet+}$, $\mathbf{3c}^{\bullet+}$?

First, we will consider how the low-energy glycolic acid ions lose CO_2. Following Scheme 4, one pathway involves isomerization into $\mathbf{3c}^{\bullet+}$, via a 1,4-H transfer and C—C bond cleavage, whereas the alternative route leads to the distonic ions $\mathbf{8}^{\bullet+}$, via a 1,4-H transfer without C—C cleavage. As discussed in the previous section, the long- and short-bonded conformers $\mathbf{2c'}^{\bullet+}$and $\mathbf{2c}^{\bullet+}$ may serve as the immediate precursors. Transition states (TS) could be located for both pathways: TS $[\mathbf{2c}{\rightarrow}\mathbf{8}]^{\bullet+}$ and TS $[\mathbf{2c'}{\rightarrow}\mathbf{3c}]^{\bullet+}$ in Fig. 4. The TS $[\mathbf{2c}{\rightarrow}\mathbf{8}]^{\bullet+}$ lies very high in energy, ca. 16 kcal/mol above $\mathbf{2c}^{\bullet+}$ and only a few kcal/mol below the direct bond cleavage dissociation limit $CH_2OH^+ + HOCO^\bullet$ (see Fig. 5). If this were the principal route by which glycolic acid ions lose CO_2, one would predict the normal mass spectrum to have a sizable molecular ion and the CID spectrum to be dominated by *m*/*z* 31 CH_2OH^+ ions. This is clearly not the case; the normal mass spectrum displays a very weak molecular ion (1 of base peak, *m*/*z* 31), while the CID mass spectrum (Fig. 2*d*) is dominated by loss of CO_2, not $HOCO^\bullet$. Thus, there must be a pathway of much lower energy, and indeed the alternative route $\mathbf{2c'}^{\bullet+} \rightarrow$ TS $[\mathbf{2c'}{\rightarrow}\mathbf{3c}]^{\bullet+} \rightarrow \mathbf{3c}^{\bullet+} \rightarrow CH_2OH_2^{\bullet+} + CO_2$ is calculated to have a critical energy of only a few kcal/mol (see Fig. 5).

Now that we have established that the majority of the low-energy ions $\mathbf{2}^{\bullet+}$ lose CO_2 via the H-bridged ion $\mathbf{3c}^{\bullet+}$, the question arises whether the CO_2 loss from ions $\mathbf{3a}^{\bullet+}$ may follow the same route, via the isomerization $\mathbf{3a}^{\bullet+}{\rightarrow}\mathbf{2}^{\bullet+}$. The one way for this to occur is that the CH_2OH^+ and $HOCO^\bullet$ moieties in $\mathbf{3a}^{\bullet+}$ separate and recombine, carbon to carbon or ion center to radical center, to form glycolic acid ions $\mathbf{2}^{\bullet+}$. However, such a recombination reaction is highly unlikely, since it requires rotation of the dipole of the $HOCO^\bullet$ moiety such that the ion–dipole stabilization is completely lost, and the moieties would fly apart, i.e., dissociation into $CH_2OH^+ + HOCO^\bullet$ would ensue. The same arguments apply to the isomerization $\mathbf{3a}^{\bullet+}{\rightarrow}\mathbf{3c}^{\bullet+}$. That the loss of CO_2 from $\mathbf{2}^{\bullet+}$ and $\mathbf{3a}^{\bullet+}$ would involve a common pathway is therefore unlikely, in agreement with the experimental observations (KER differences) discussed in Sect. 2.

Scheme 5.

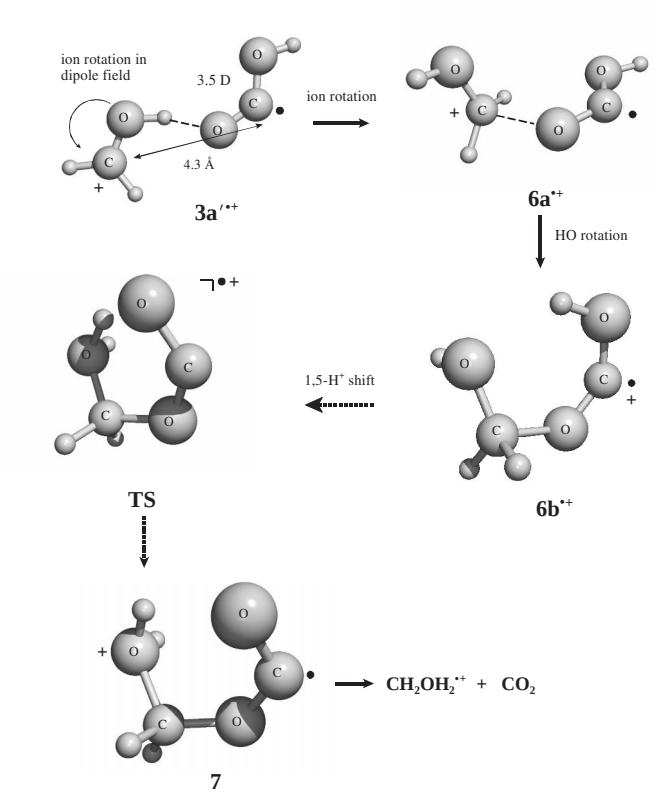

How then does ion $\mathbf{3a}^{\bullet+}$ lose CO_2? Recombination of the separated moieties of $\mathbf{3a}^{\bullet+}$ such that the dipole vector remains pointed to the ionic center would allow the ion to isomerize, and this forms the basis of our mechanistic proposal presented in Scheme 5. The CH_2OH^+ group in $\mathbf{3a}^{\bullet+}$ can freely rotate in the dipole field of $HOCO^\bullet$. Such a motion sacrifices the stabilization energy (SE) of the H-bridge, but it leaves the ion–dipole stabilization intact. The SE of the H-bridged ion $\mathbf{3a'}^{\bullet+}$ is 24 kcal/mol (from data in Table 1), whereas all configurations resulting from the rotation of the CH_2OH^+ moiety about the charged carbon atom at the original ion–dipole distance (4.3 Å) retain a SE of ~13 kcal/mol, still well below the dissociation limit (denoted as ** in Fig. 5). When the rotation is coupled with a shortening of the ion–dipole distance, the SE increases, and this process may eventually lead to the formation of $\mathbf{6a}^{\bullet+}$ whose stability is close to that of ionized glycolic

© 1998 NRC Canada

Fig. 6. The CID mass spectra of the *metastably* generated decarbonylation products from ionized O^{18} labelled methyl β-hydroxypyruvate, $HOCH_2C(=O^{18})COOCH_3$: (*a*) the spectrum of the $[M - CO^{16}]^{\bullet+}$ (*m/z* 92) ions; (*b*) the spectrum of the $[M - CO^{18}]^{\bullet+}$ (*m/z* 90) ions.

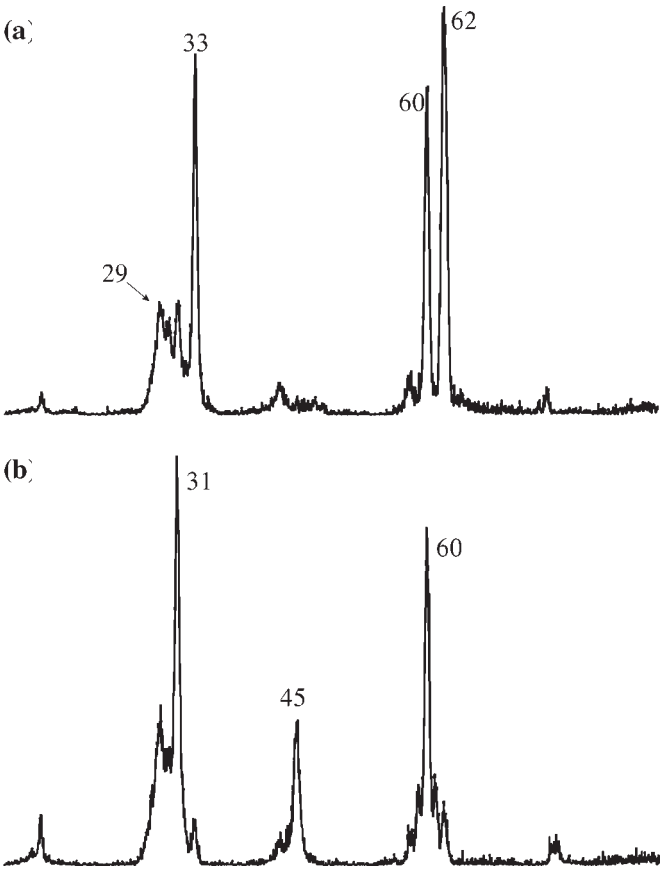

acid (Table 1). Via rotations that are not too energy demanding, **6a**$^{\bullet+}$ may convert into its "conformer" **6b**$^{\bullet+}$ (an ionized carbene). A 1,5-H^+ transfer in this ion would yield the distonic ion **7**$^{\bullet+}$, which by direct bond cleavage exothermically decarboxylates (see Scheme 5 and Fig. 5). We have located (Fig. 4 and Table 1) the key transition state **6b**$^{\bullet+}$→**7**$^{\bullet+}$ in this proposal and, as shown in Fig. 5, it indeed lies below the dissociation limit CH_2OH^+ + HOCO$^{\bullet}$. Note that our calculations predict that ions **3a**$^{\bullet+}$ should dissociate with a significantly larger KER than ions **2c**$^{\bullet+}$.

5. The decarbonylation of low-energy HPA ions I$^{\bullet+}$: isomerization into the enol II$^{\bullet+}$ and generation of the ion–dipole complex HO(H)C═C═O$^{\bullet+}$/H_2O, **4**$^{\bullet+}$ therefrom. Comparison with the behaviour of the ionized methyl ester

We will begin our discussion of the decarbonylation of the metastable HPA ions with a brief analysis of the behaviour of its methyl ester. As was mentioned in Sect. 1 the decarbonylation of the *metastable* molecular ions of the methyl ester occurs via two distinct mechanisms, yielding two different product ions i.e., the methyl(ated) analogue of the H-bridged ion **3a**$^{\bullet+}$, CH_2═O···H···O═C-$OCH_3^{\bullet+}$ (which is the sole product ion generated in the source)[3] in admixture with the more stable isomer HO(H)C═C═O$^{\bullet+}$/CH_3OH (9) (see Scheme 2). A first

Scheme 6.

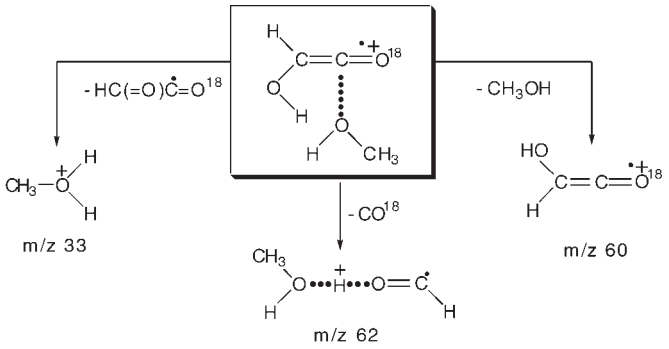

indication that we are dealing with two mechanisms comes from the observation that the metastable peak for the decarbonylation is a Gaussian shaped composite (21) whose $T_{0.5}$ value is 60 meV. Next a sample of the specifically labelled ^{18}O isotopomer $HOCH_2C(=O^{18})COOCH_3$ was prepared, and the MI spectrum of its molecular ion was examined: it displayed two noncomposite Gaussian shaped peaks, at *m/z* 92 (loss of CO^{16}) and *m/z* 90 (loss of CO^{18}) with an intensity ratio of 3:2 and $T_{0.5}$ values of 43 and 96 meV, respectively. Following the proposal in Scheme 2, it is expected that the source-generated ions exclusively lose CO^{18}, and this is substantiated by the EI mass spectrum (not shown) where [*m/z* 92] is less than 5 of I [*m/z* 90]. The CID mass spectra of the metastably generated *m/z* 92 and *m/z* 90 ions are presented in Fig. 6: it is seen that these spectra are entirely different. Loss of CO^{18} yields a spectrum dominated by peaks at *m/z* 60 (CH_3O-C-$OH^{\bullet+}$), 45 (HO-C═O^+), and 31 (CH_2OH^+), which is closely similar to that of the source-generated ions and which is entirely compatible with the formation of the H-bridged ion CH_2═O···H···O═C-$OCH_3^{\bullet+}$ (5a).[3] Loss of CO^{16} yields a spectrum dominated by ions at *m/z* 62, 60, and 33, which we assign to the ion–dipole complex HO(H)C═C═$^{18}O^{\bullet+}$/CH_3OH whose principal dissociation routes are rationalized in Scheme 6.

The proposal in Scheme 6 finds strong support from a previous study (9) on the enol of methyl glycolate ion, HOC(H)═C(OH)$OCH_3^{\bullet+}$, and several D and ^{18}O labelled isotopomers, where it was concluded that part of the low-energy enol ions slowly isomerize into the ion–dipole complex HO(H)C═C═O$^{\bullet+}$/CH_3OH prior to dissociation (see Scheme 1 in ref. 9). In this study it was also established, from an MS/MS/MS/MS experiment, that the *m/z* 62 ion is the H-bridged radical cation $CH_3O(H)$···H···O═C-H$^{\bullet+}$.

Unlike the methyl ester, the metastable peak for the decarbonylation of the low-energy ions of the parent acid, **I**$^{\bullet+}$, is a simple Gaussian ($T_{0.5}$ = 23 meV), and this suggests that we are dealing with a single mechanism. We have already noted (see Sect. 1 and Fig. 2) that the product ions generated are not **3a**$^{\bullet+}$ but rather HO(H)C═C═O$^{\bullet+}$/H_2O, **4**$^{\bullet+}$, a species akin to the enol ion HOC(H)═$C(OH)_2^{\bullet+}$, **1**$^{\bullet+}$, but nevertheless characteristically different. The spectrum of the enol ion features a unique *m/z* 46 ion (HOCOH$^{\bullet+}$ (3*a*)) whereas *m/z* 48 is absent, and the intensity of *m/z* 19 (H_3O^+) is greatly reduced. We also note that the dissociation reactions that characterize HO(H)C═C═O$^{\bullet+}$/CH_3OH (see Scheme 6 and Fig. 6*a*) are also found in the spectrum (Fig. 2*b*) of the putative ion HO(H)C═C═O$^{\bullet+}$/H_2O, **4**$^{\bullet+}$, viz. loss of H_2O yielding HO(H)C═C═O$^{\bullet+}$ (*m/z* 58), loss of CO yielding

Fig. 7. The CID mass spectrum of the molecular ion of the ^{18}O labelled β-hydroxypyruvic acid isotopomer $HOCH_2C(O^{18})COOH$.

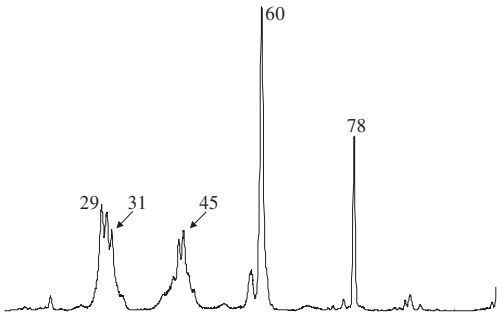

$H_2O(H)O\cdots H\cdots O{=}C\text{-}H^{\bullet+}$(27) (*m*/*z* 48), and loss of $HC(=O)C{=}O^{\bullet}$ yielding H_3O^+ (*m*/*z* 19), albeit that their relative abundances are greatly different.[6]

Analysis of a small sample of $HOCH_2C(=O^{18})COOH$, prepared under carefully controlled conditions (see Experimental) shows that the source-generated ions exclusively lose CO^{18} (providing further support for the high-energy decarbonylation mechanism in Scheme 3), whereas both the MI and the CID spectrum (see Fig. 7) of its molecular ion show a specific loss of CO^{16}. This supports our proposal that the *metastable* ions decarbonylate via a mechanism analogous to that depicted in Scheme 2 for the low-energy methyl ester ions, yielding $HOC(H){=}C{=}O^{\bullet+}/H_2O$, $\mathbf{4}^{\bullet+}$, as the product ion (Scheme 7).

That the majority of the long-lived nondissociating HPA ions have isomerized followed already from a comparison of the CID mass spectrum of $\mathbf{I}^{\bullet+}$ with the EI mass spectrum of the acid (see Sect. 1 and Fig. 1) and also from the observation that the low-energy isomer ($\mathbf{4}^{\bullet+}$ vis à vis $\mathbf{3a}^{\bullet+}$) is not formed at high internal energies.

That it is the enol ion 1,2-dihydroxyacrylic acid, $\mathbf{II}^{\bullet+}$, that is predominantly generated comes from a comparison of the MI, CID, and NR spectra of the independently generated enol: when solid samples of dihydroxyfumaric acid (DHF) are evaporated into the ion source at elevated probe temperatures some thermal decarboxylation takes place, which, analogous to the mechanism for the loss of CO_2 from oxalacetic acid (OAA) (14), may reasonably be expected to yield the gaseous enol **II**:

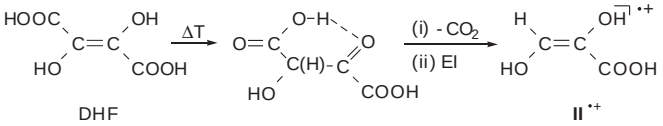

The NR mass spectrum of the *m*/*z* 104 ion generated from DHF appeared to be indistinguishable from that of HPA shown in Fig. 1*d*, whereas its CID mass spectrum was closely similar to that presented in Fig. 1*c*: the only notable difference was the reduced abundance of the *m*/*z* 42 ($CH_2{=}C{=}O^{\bullet+}$) ion. The latter ion is also present in the MI spectrum of the HPA derived ions (10 of base peak at *m*/*z* 76) but not in that of the DHF derived ion, which exclusively decarbonylates yielding *m*/*z* 76 ions whose CID mass spectrum is indistinguishable from that presented in Fig. 2*b* for HPA. Thus, we conclude that the long-lived HPA ions have largely isomerized into their enol counterpart, which may decarbonylate, as shown in Scheme 7, i.e., analogous to the decarbonylation of its lower homologue ionized α-hydroxyacrylic acid, $CH_2{=}C(OH)COOH^{\bullet+}$ (14).

Scheme 7.

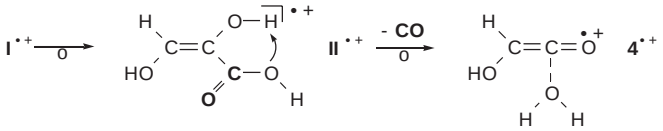

Scheme 8.

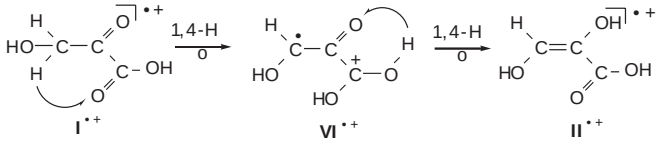

A plausible mechanism for the keto–enol tautomerization of the HPA ions involves two consecutive 1,4-H shifts, with the distonic ion $\mathbf{VI}^{\bullet+}$ as the key intermediate (see Scheme 8).

Considering the size and complexity of the system, a detailed computational treatment of the mechanisms for the high- and low-energy decarbonylation reactions of HPA ions presented in Schemes 3, 7, and 8 would be a formidable task. We have therefore confined ourselves to exploratory calculations at the B3LYP/6-311+G(3df,3pd)//B3LYP/6-31G(d,p) level of theory[5] on the HPA isomers $\mathbf{I}^{\bullet+}$–$\mathbf{VI}^{\bullet+}$ that are proposed in the schemes. Figure 8 shows their optimized geometries, all of which represent stable minima on the $C_3H_4O_4^{\bullet+}$ PES. The enol ion $\mathbf{II}^{\bullet+}$ and the distonic ion $\mathbf{VI}^{\bullet+}$ are found to be considerably more stable than the keto ion $\mathbf{I}^{\bullet+}$, which is in agreement with expectation (25). More importantly, all of the proposed intermediate species are calculated to lie below the dissociation limit for the direct bond cleavage reaction of lowest energy requirement, $\mathbf{I}^{\bullet+} \rightarrow HOCH_2C{=}O^+ + {}^{\bullet}COOH$, calculated to lie 22 kcal/mol above $\mathbf{I}^{\bullet+}$.

Conclusions

Ionized ß-hydroxypyruvic acid (as well as its methyl ester) undergoes decarbonylation, and depending on the internal energy content, fragmentation occurs via two distinct mechanisms, leading to two distinct product structures (see Scheme 9).

(*i*) At high internal energies, specific elimination of the keto C=O is observed; this reaction is not a least-motion extrusion into ionized glycolic acid, $HOCH_2COOH^{\bullet+}$, but a rearrangement that produces the title H-bridged radical cation $CH_2{=}O\cdots H\cdots O{=}C\text{-}OH^{\bullet+}$.

(*ii*) By contrast, at low internal energies, it is the carboxyl C=O that is specifically lost. Comparative collision-induced dissociation experiments show that the long-lived, nondecomposing molecular ions have irreversibly rearranged to the more stable enol structure, $HOCH{=}C(OH)COOH^{\bullet+}$, which serves

[6] The combined product enthalpies for the direct bond cleavage loss of H_2O from $HO(H)C{=}C{=}O^{\bullet+}/H_2O$ and CH_3OH from $HO(H)C{=}C{=}O^{\bullet+}/CH_3OH$ are 105 and 115 kcal/mol, respectively (18*a*, footnote *g* in Table 1). For the rearrangement leading to loss of CO, the corresponding numbers are 111 (27) and 102 (11) kcal/mol. These differences in energy requirement may explain why the loss of CO from $\mathbf{4}^{\bullet+}$ is only a minor reaction, whereas it is prominent in the spectrum of $HO(H)C{=}C{=}O^{\bullet+}/CH_3OH$.

© 1998 NRC Canada

Fig. 8. The B3LYP/6-31G(d,p) optimized geometries for ionized β-hydroxypyruvic acid, $\mathbf{I}^{\bullet+}$, and selected stable isomers thereof. Values in parentheses refer to relative energies (kcal/mol) calculated at the B3LYP/6-311+G(3df,3pd) + ZPVE level of theory.

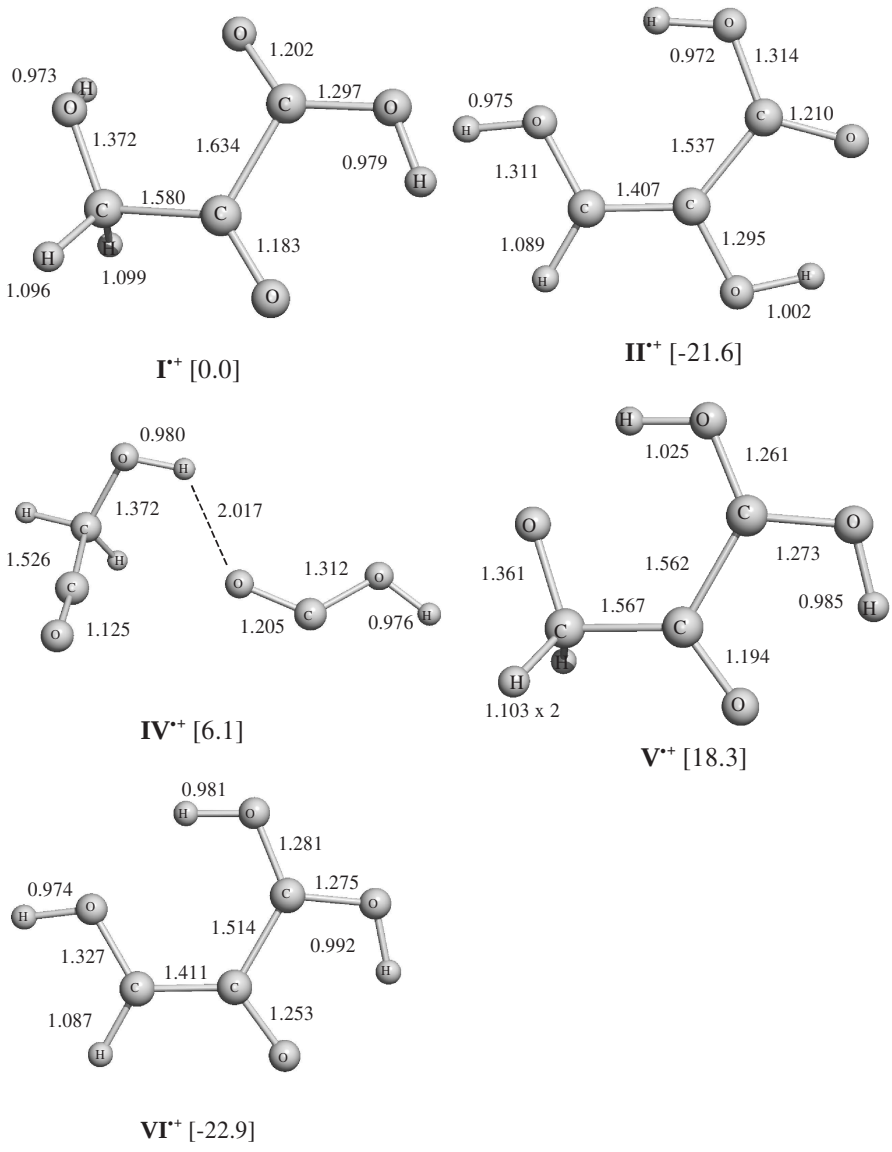

as precursor for CO loss and which contains only one C═O functionality. Again, decarbonylation is not a least-motion extrusion but a rearrangement yielding the ion–dipole complex $HOC(H)C{=}C{=}O^{\bullet+}/H_2O$, which is more stable than the above radical cation.

Hence, the more stable product ions are generated only at low internal energies, i.e., from molecular ions that dissociate slowly, whereas the lesser stable product ions are formed only at elevated energies, i.e., from molecular ions that dissociate rapidly. This is precisely what is expected as the more stable product ion can only be formed after slow isomerization of the molecular ions into the enol structure.

(*iii*) The H-bridged ion and its conventional isomer glycolic acid, $HOCH_2COOH^{\bullet+}$, both undergo decarboxylation into the ylidion $CH_2OH_2^{\bullet+}$. Ab initio calculations indicate that for the acid, stretching of the C—C bond leads eventually to proton transfer to generate the stable H-bridged radical cation CH_2-O(H)···H···O═C═$O^{\bullet+}$, which then sheds CO_2. The titled H-bridged ions dissociate via a higher energy route that involves the ionized carbene $HO(H_2)CO$-C-$OH^{\bullet+}$.

Experimental and theoretical

The ß-hydroxypyruvic acid (HPA) samples used in this study were obtained from Sigma and used without further purification. The EI mass spectrum of HPA shown in Fig. 1*a* was obtained as follows: a probe tube (glass, 15 mm, f = 1 mm) filled with tightly packed sample (~15 mg) was introduced via the direct solids insertion probe into the ion chamber such that the tip of the capillary just protruded into the source, which was kept at 110°C. The bottom part of the sample tube was kept at ambient temperature, and radiative heat transfer from the ion chamber to the sample tube caused the sample to slowly evaporate into the source, yielding a stable ion current for ca.

© 1998 NRC Canada

Scheme 9.

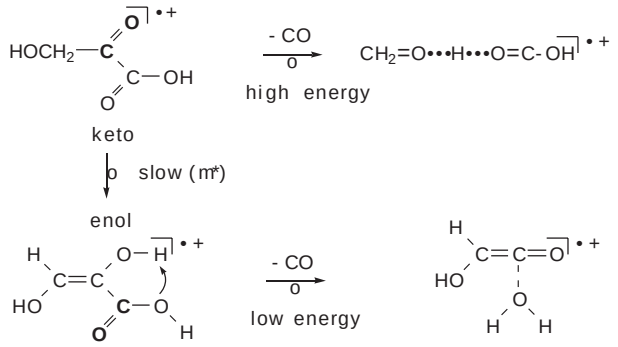

1 h. The spectrum shown in Fig. 1*b* was obtained by increasing the source temperature to 170°C. All other experiments on HPA and the samples described below were performed at a source temperature of 110°C.

Samples of the methyl ester of HPA were prepared on a milligram scale by dissolving ca. 30 mg of the acid in 150 mL of dry methanol and leaving the clear solution at room temperature. A ^{13}C NMR control experiment showed that the esterification of this rather strong acid is essentially complete in 30 min. Next, the alcohol and the water were quickly removed from the reaction mixture using a rotary pump, and the residual viscous liquid was then introduced into the ion chamber of the mass spectrometer using the all-quartz direct liquids insertion probe. The sample reservoir of this probe was kept at ambient temperature, and under these conditions the parent acid does not noticeably evaporate. The ^{18}O labelled isotopomer $HOCH_2C(=O^{18})COOCH_3$ was obtained by first preparing the methyl ester as described above and then adding 20 mL of $H_2{}^{18}O$ (90 ^{18}O, 3.7 ^{17}O) (Ventron GMBH, Karlsruhe) to allow the carbonyl oxygen to exchange (28). The mixture was left at room temperature for 10 min and was then worked up and introduced as described above. The EI mass spectra of the molecular ion region showed that only one ^{18}O atom had been incorporated in the ca. 40 enriched ester. The ^{18}O labelled isotopomer of the acid, $HOCH_2C(=O^{18})COOH$, M = 106, was prepared by dissolving ca. 30 mg of the acid in 200 mL of 3:1 mixture of CH_3OH and $H_2{}^{18}O$ and leaving the clear solution at room temperature for 10 min (at much longer reaction times and when using $H_2{}^{18}O$ only, a noticable exchange of the carboxyl group also takes place). The sample was then worked up and introduced as described above for the acid. The EI mass spectra of the molecular ion region showed that only one ^{18}O atom had been incorporated (m/z 108 is less than 5 of m/z 106) in the ca. 50 enriched ester. The D labelled HPA isotopomer $DOCH_2C(=O)COOD$ was prepared by dissolving ca. 30 mg of the acid in 150 mL of CH_3OD, followed by immediate work up as described above. The EI mass spectra of the sample showed that not more than two D atoms had been incorporated, thus showing that the acid does not equilibrate with its enol form under these conditions (see Introduction). The dihydroxyfumaric acid (DHF) sample came from Aldrich and was used without further purification. The intensity of the m/z 104 ion resulting from EI ionization of its in situ generated thermal decarboxylation product HO(H)C═C(OH)COOH, **II**, was comparable to that of the DHF molecular ion (see Experimental and Table 1 of ref. 10 for further details).

The mass spectrometric experiments were performed with the McMaster University VG Analytical (Manchester, UK) ZAB-R instrument of BE_1E_2 geometry (B, magnet; E, electric sector) (29) using an accelerating voltage of 8 or 10 keV. Metastable ion (MI) mass spectra were recorded in the second field-free region (2ffr). Collision-induced dissociation (CID) mass spectra were recorded in the 2ffr and third field-free region (3ffr), using oxygen as collision gas (transmittance T = 70). The CID mass spectra of the 2ffr metastable or CID peaks (MS/MS experiments) were obtained in the 3ffr, using O_2 as the collision gas. Neutralization–reionization (NR) spectra were recorded in the 2ffr, using , -dimethylaniline as reducing agent and oxygen gas for reionization. All spectra were recorded using a small PC-based data system developed by Mommers Technologies Inc. (Ottawa).

Standard ab initio and density functional MO calculations were performed with the Gaussian 94 suite of programs (30). Key results (transition states) were verified with the GAMESS (30) computational chemistry program using the RHF/DZP methodology (see ref. 3 for details). For the $C_2H_4O_3{}^{\bullet+}$ isomers geometry optimizations and frequency calculations were performed at the UHF/6-31G*, UB3LYP/6-31G* (31), and UMP2(full) /6-31G* levels of theory. The coupled cluster approximation (32) utilizing singles, doubles, and estimated triple excitations (CCSD(T)) was used to obtain our best relative energies on UMP2(full) /6-31G* optimized structures. The CCSD(T) calculations used the double zeta correlation consistent basis set of Dunning, cc-pVDZ (33). Scaling factors for zero-point vibrational energies (ZPVE) were HF = 0.9, B3LYP = unscaled, and MP2(full) = 0.9646 (22). All transition states had the correct number of negative eigenvalues of the corresponding Hessian matrix. The reaction pathways were verified with IRC calculations, at the same level of theory as the geometry optimizations. The HPA isomeric ions (Fig. 8) were optimized with the B3LYP/6-31G(d,p) method. The relative energies reported in Fig. 8 were generated using the same hybrid functional but with a much larger basis set, 6-311+G(3df,3pd), which reproduced typical keto(**I**)–enol(**II**) energy differences. The spin contamination of the UHF wave functions was acceptable for all species investigated, i.e., less than 10 of 0.75. The ray-traced images of the optimized structures in Figs. 4 and 8 were generated from their Gaussian output using a combination of PovChem[7] and POV-Ray.[8] Numerical values for the (dihedral) bond angles in the structures presented are available on request.

Acknowledgements

J.K.T. thanks the Natural Sciences and Engineering Research Council of Canada (NSERC) for financial support and Prof. Ian Spenser for his expert advice in the interpretation of the ^{13}C NMR spectra. P.J.A.R. thanks the Netherlands Organization for Scientific Research (NWO) for making available the Cray-YMP of SARA (Amsterdam) through the Netherlands Foundation for Chemical Research (SON).

[7] P.A. Thiessen. See http://ludwig.scs.uiuc.edu/~paul/PovChem.html.

[8] Rendered images were generated using the copyrighted freeware Persistance of Vision Ray Tracer, POV-Ray Version 3.01, available at http://www.povray.org.

© 1998 NRC Canada

References

1. (*a*) T.H. Morton. Tetrahedron, **38**, 3195 (1982); (*b*) N. Heinrich and H. Schwarz. *n* Ion and cluster ion spectroscopy and structure. *Edited by* J.P. Maier. Elsevier, Amsterdam. 1989. p. 329; (*c*) P.C. Burgers and J.K. Terlouw. *n* Specialist periodical reports: mass spectrometry. Vol. 10. *Edited by* M.E. Rose. The Royal Society of Chemistry, London. 1989. p. 35. (*d*) T.H. Morton. Org. Mass Spectrom. **27**, 353 (1992); (*e*) J.S. Splitter. *n* Applications of mass spectrometry to organic stereochemistry. *Edited by* J.S. Splitter and F. Turecek. VCH, Weinheim. 1994. Chap. 3.
2. (*a*) J.K. Terlouw, W. Heerma, P.C. Burgers, and J.L. Holmes. Can. J. Chem. **62**, 289 (1984); (*b*) R. Postma, P.J.A. Ruttink, F.B. van Duijneveldt, J.K. Terlouw, and J.L. Holmes. Can. J. Chem. **63**, 2798 (1985); (*c*) R. Postma, S.P. van Helden, J.H. van Lenthe, P.J.A. Ruttink, J.K. Terlouw, and J.L. Holmes. Org. Mass Spectrom. **23**, 503 (1988); (*d*) P. George, J.P. Glusker, and C.W. Bock. J. Am. Chem. Soc. **117**,10 131 (1995).
3. (*a*) P.J.A. Ruttink and P.C.Burgers. Org. Mass Spectrom. **28**, 1087 (1993), and refs. cited therein; (*b*) P.C. Burgers, L.M. Fell, A. Milliet, M. Rempp, P.J.A. Ruttink, and J.K. Terlouw. Int. J. Mass Spectrom. Ion Processes, **167/168**, 291 (1997); (*c*) P.J.A. Ruttink, P.C. Burgers, L.M. Fell, and J.K. Terlouw. J. Phys. Chem. In press.
4. P.J.A. Ruttink, P.C. Burgers, and J.K. Terlouw. Can. J. Chem. **74**, 1078 (1996), and refs. cited therein.
5. (*a*) D. Suh, C.A. Kingsmill, P.J.A. Ruttink, P.C. Burgers, and J.K. Terlouw. Int. J.Mass Spectrom. Ion Processes, **146/147**, 305 (1995); (*b*) D. Suh, P.C. Burgers, and J.K. Terlouw. Int. J. Mass Spectrom. Ion Processes, **144**, L1 (1995); (*c*) H. Friedrichs, G.A. McGibbon, and H. Schwarz. Int. J. Mass Spectrom. Ion Processes, **152**, 217 (1996).
6. D.K. Böhme. Int. J. Mass Spectrom. Ion Processes, **115**, 95 (1992); P.J.A. Ruttink. *n* The structure of small radicals and ions. *Edited by* R. Naaman and Z. Vager. Plenum Press, New York. 1989. p. 243; V. Baranov, S. Petrie, and D.K. Böhme. J. Am. Chem. Soc. **118**, 4500 (1996).
7. (*a*) P. Mourges, H.-E. Audier, D. Leblanc, and S. Hammerum. Org. Mass Spectrom. **28**, 1098 (1993); (*b*) H.-E. Audier, D. Leblanc, P. Mourgues, T.B. McMahon, and S. Hammerum. J. Chem. Soc. Chem. Commun. 2329 (1994); (*c*) J.W. Gauld, H.-E. Audier, J. Fossey, and L. Radom. J. Am. Chem. Soc. **118**, 6299 (1996). (*d*) J.W. Gauld and L. Radom. J. Am. Chem. Soc. **119**, 9831 (1997); (*e*) A.J. Chalk and L. Radom. J. Am. Chem. Soc. (1997). In press.
8. D. S lzle, J.K. Terlouw, and H. Schwarz. Angew. Chem. Int. Ed. Engl. **29**, 404 (1990).
9. D. Suh, P.C. Burgers, and J.K. Terlouw. Rapid Commun. Mass Spectrom. **9**, 862 (1995).
10. J. Hrusak, G.A. McGibbon, H. Schwarz, and J.K. Terlouw. Int. J. Mass Spectrom. Ion Processes, **160**, 117 (1997).
11. D. Suh, J.T. Francis, J.K. Terlouw, P.C. Burgers, and R.D. Bowen. Eur. Mass Spectrom. **1**, 545 (1995).
12. J.L. Hedrick and H.J. Sallach. J. Biol. Chem. **236**, 1872 (1961).
13. (*a*) F. Dickens and D.H. Williamson. Biochem. J. **68**, 74 (1958); (*b*) L.J. Bellamy and R.L. Williams. Biochem. J. **68**, 81 (1958); (*c*) F. Dickens and D.H. Williamson. Biochem. J. **68**, 84 (1958); (*d*) C.T. Chow and B. Vennesland. J. Biol. Chem. **233**, 997 (1958); (*e*) M.B. Fleury and D. Fleury. Biological aspects of electrochemistry. Proc. 1st Int. Symp. Experientia Supplementum 18. Rome, Italy. 1971.
14. L.M. Fell, J.T. Francis, J.L. Holmes, and J.K. Terlouw. Int. J. Mass Spectrom. Ion Processes, **165/166b,** 179 (1997).
15. F. Mer. The dictionary of organic compounds. 6th ed. Vol. 4. Chapman Hall, London. 1996. p. 3778.
16. (*a*) J.K. Terlouw, C.G. de Koster, W. Heerma, J.L. Holmes, and P.C. Burgers. Org. Mass Spectrom. **18**, 222 (1983); (*b*) R. Postma, P.J.A. Ruttink, J.K. Terlouw, and J.L. Holmes. J. Chem. Soc. Chem. Commun. 683 (1986).
17. (*a*) S. Lias, J.E. Bartmess, J.F. Liebman, J.L. Holmes, R.D. Levin, and W.G. Mallard. J. Phys. Chem. Ref. Data, **17**, Suppl. 1 (1988); (*b*) J.L. Holmes, F.P. Lossing, and P.M. Mayer. J. Am. Chem. Soc. **113**, 9723 (1991).
18. P.C. Burgers, G.A. McGibbon, and J.K. Terlouw. Chem. Phys. Lett. **224**, 539 (1994).
19. (*a*) J.B. Foresman and A. Frisch. Exploring chemistry with electronic structure methods. Gaussian, Inc., Pittsburgh Pa, 1996. Chap. 7; (*b*) L.A. Curtiss, K. Raghavachari, and J.A. Pople. J. Chem. Phys. **98**, 1293 (1993); (*c*) J.W. Ochterski, G.A. Petersson, and J.A. Montgomery, Jr. J. Chem. Phys. **104**, 2598 (1996), and refs. cited therein.
20. N. Goldberg and H. Schwarz. Acc. Chem. Res. **27**, 34 (1994).
21. J.L. Holmes and J.K. Terlouw. Org. Mass Spectrom. **15**, 383 (1980).
22. J.A. Pople, A.P. Scott, M.W. Wong, and L. Radom. Israel J. Chem. **33**, 345 (1993).
23. M. Meot-Ner (Mautner). J. Am. Chem. Soc. **106**, 1257 (1984).
24. (*a*) B.J. Smith and L. Radom. J. Phys. Chem. **99**, 6468 (1995); (*b*) J.E. Szulejko and T.B. McMahon. J. Am. Chem. Soc. **115**, 7839 (1993); (*c*) H.E. Audier, J. Fossey, P. Mourgues, D. Leblanc, and S. Hammerum. Int. J. Mass Spectrom. Ion Processes, **157/158**, 275 (1996); (*d*) A.P. Scott and L. Radom. Int. J. Mass Spectrom. Ion Processes, **160**, 73 (1997).
25. F. Turecek. *n* The Chemistry of enols. *Edited by* Z. Rappoport. John Wiley Sons, Chichester. 1990. pp. 95–146.
26. K. Iijima, M. Kato, and B. Beagley. J. Mol. Struc. **295**, 289 (1993).
27. (*a*) E. Coitino, A. Lledos, R. Serra, J. Bertran, and O.N. Ventura. J. Am. Chem. Soc. **115**, 9121 (1993); (*b*) E. Coitino, A. Pereira, and O.N. Ventura. J. Chem. Phys. **102**, 2833 (1995).
28. G.W.A. Milne. *n* Mass spectrometry: techniques and applications. Wiley–Interscience, London. 1971. p. 279.
29. H.F. van Garderen, P.J.A. Ruttink, P.C. Burgers, G.A. McGibbon, and J.K. Terlouw. Int. J. Mass Spectrom. Ion Processes, **121**, 159 (1992).
30. (*a*) M. J. Frisch, G.W. Trucks, H.B. Schlegel, P.M.W. Gill, B.G. Johnson, M.A. Robb, J.R. Cheeseman, T.A. Keith, G.A. Peterson, J.A. Montgomery, K. Raghavachari, M.A. Al-Laham, V.G. Zakrevski, J.V. Ortiz, J.B. Foresman, C.Y. Peng, P.Y. Ayala, W. Chen, M.W. Wong, J.L. Andres, E.S. Replogle, R. Gomperts, R.L. Martin, D.J. Fox, J.S. Binkley, D.J. de Frees, J. Baker, J.P. Stewart, M. Head-Gordon, C. Gonzales, and J.A. Pople. Gaussian 94, Revision B.3. Gaussian Inc., Pittsburgh Pa. 1995; (*b*) M.F. Guest and J. Kendrick. GAMESS users manual. SERC Daresbury Laboratory, CCP/86/1, 1986; M. Dupuis, D. Spangler, and J. Wendolowski. NRCC Software Catalog, Vol. 1, Program No. G01 (GAMESS), 1980; M.F. Guest, R.J. Harrison, J.H. van Lenthe, and L.C.H. van Corler. Theor. Chim. Acta, **71** 117 (1987).
31. (*a*) A.D. Becke. J. Chem. Phys. **98**, 5648 (1993); (*b*) C. Lee, W. Yang, and R.G. Parr. Phys. Rev. B: Condens. Matter, **37**, 785 (1988); (*c*) B. Meihlich, A. Savin, H. Stoll, and H. Preuss. Chem. Phys. Lett. **157**, 200 (1989).
32. (*a*) J. Cizek. Adv. Chem. Phys. **14**, 35 (1969); (*b*) J.A. Pople, R. Krishnan, H.B. Schlegel, and J.S. Binkley. Int. J. uant. Chem. **14**, 545 (1978); (*c*) R.J. Bartlett and G.D. Purvis. Int. J. uant. Chem. **14**, 516 (1978).
33. (*a*) T.H. Dunning, Jr. J. Chem. Phys. **90**, 1007 (1989); (*b*) R.A. Kendall, T.H. Dunning, Jr., and R.J. Harrison. J. Chem. Phys. **96**, 6796 (1992).

© 1998 NRC Canada

Kinetics and mechanism of hydroxylamine oxidation by $[Fe_2^{III}(\mu\text{-}O)(phen)_4(H_2O)_2]^{4+}$ in aqueous media[1]

Beauty Chaudhuri and Rupendranath Banerjee

Abstract: Equilibrium studies show that in aqueous solutions containing excess 1,10-phenanthroline (phen) in the range pH 3–9, the complex ion $[Fe_2^{III}(\mu\text{-}O)(phen)_4(H_2O)_2]^{4+}$ (**1**) undergoes rapid but partial hydrolysis and coexists with $[Fe_2^{III}(\mu\text{-}O)(phen)_3(H_2O)_4]^{4+}$ (**1d**), $[Fe_2^{III}(\mu\text{-}O)(phen)_4(H_2O)(OH)]^{3+}$ (**2**), and $[Fe_2^{III}(\mu\text{-}O)(phen)_4(OH)_2]^{2+}$ (**3**). The solution oxidizes hydroxylamine quantitatively to N_2O and is itself reduced to $[Fe(phen)_3]^{2+}$. The reactions in the range pH 3–6 are first-order in concentrations of complex and hydroxylamine but exhibits complex $[H^+]$ dependence, suggesting kinetic contributions from **1**, **1d**, and **2** but not from **3**. Rapid formation of inner-sphere adducts between NH_2OH and different $\{Fe_2O\}^{4+}$ species followed by rate-determining one-electron transfer to produce NHOH and $\{Fe_2O\}^{3+}$ is proposed. All subsequent steps are rapid. Ambient light does not affect kinetics and reaction products.

Key words: kinetics, equilibrium, oxo bridge, iron (III), hydroxylamine.

Résumé : Des études d'équilibre ont montré que, dans des solutions aqueuses contenant un excès de 1,10-phénanthroline (phen), à des pH allant de 3 à 9, l'ion complexe $[Fe_2^{III}(\mu\text{-}O)(phen)_4(H_2O)_2]^{4+}$ (**1**) subit une rapide hydrolyse partielle et qu'il coexiste avec les ions $[Fe_2^{III}(\mu\text{-}O)(phen)_3(H_2O)_4]^{4+}$ (**1d**), $[Fe_2^{III}(\mu\text{-}O)(phen)_4(H_2O)(OH)]^{3+}$ (**2**) et $[Fe_2^{III}(\mu\text{-}O)(phen)_4(OH)_2]^{2+}$ (**3**). Cette solution permet d'oxyder quantitativement l'hydroxylamine en N_2O alors qu'elle est réduite en $[Fe(phen)_3]^{2+}$. Les réactions à des pH allant de 3 à 6 sont du premier ordre en concentrations de complexe et de hydroxylamine, mais la dépendance sur la $[H^+]$ est complexe; ces résultats suggèrent la présence de contributions cinétiques des composés **1**, **1d** et **2**, mais pas du composé **3**. On suggère qu'il y a formation rapide d'adduits dans la sphère interne entre le NH_2OH et diverses espèces de $\{Fe_2O\}^{4+}$ suivie d'un transfert cinétiquement limitant d'un électron conduisant à la formation de NHOH et de $\{Fe_2O\}^{3+}$. Toutes les étapes subséquentes sont rapides. La lumière ambiante n'affecte pas la cinétique et les produits réactionnels.

Mots clés : cinétiques, équilibre, pont oxo, fer(III), hydroxylamine.

[Traduit par la rédaction]

Introduction

The μ-oxo diiron(III) unit, $\{Fe_2O\}^{4+}$, appears conspicuously in iron chemistry, both inside and outside the protein systems. Three reviews (1) emphasized the biological role of this chemical unit and amply represented the interest of inorganic chemists in the synthesis, structural characterization, and spectroscopic and magnetic properties of oxo-bridged diiron(III) complexes. However, reactivity studies appear to be occasional (2), and kinetic and mechanistic studies are extremely rare outside a protein environment (3). The situation appears somewhat surprising when one looks at the rich literature (4) on the substitution and redox kinetics of mononuclear iron(III) species. It might be mentioned at this point that proper interpretation of kinetics of mononuclear species demands detailed knowledge of the solution properties of oxo-bridged binuclear species, which are often difficult to avoid under the kinetic conditions used for mononuclear systems. On the whole, it appeared worthwhile to learn the kinetic and mechanistic features of reactions involving the $\{Fe_2O\}^{4+}$ unit.

The complex salt $[Fe_2(\mu\text{-}O)(phen)_4(H_2O)_2](NO_3)_4{\cdot}5H_2O$ (phen = 1,10-phenanthroline) can be obtained in a highly pure state and was characterized by X-ray crystallography (5). It is a Raman spectroscopic model (5) for the binuclear iron site in ribonucleotide reductase (6*a*) and *met*-hemerythrin, the oxidized form of the oxygen transport protein hemerythrin (6*b*). In solution, the complex oxidizes hydroxylamine at a moderate rate, measurable by conventional spectrophotometry. Oxidation of hydroxylamine in simple inorganic systems has been studied extensively (7–9), but no report is available on the reaction of NH_2OH with any of the different $\{Fe_2O\}^{4+}$ units.

Received June 27, 1997.

B. Chaudhuri and R. Banerjee.[2] Department of Chemistry, Jadavpur University, Calcutta 700 032, India.

[1] This paper is being published without benefit of authors' corrections.

[2] Author to whom correspondence may be addressed. Telephone: 91-33-473-4044. Fax: 91-33-473-1484. E-mail: probir.bose@gems.vsnl.net.in

Experimental

Materials

Crystals of $[Fe_2^{III}(\mu\text{-}O)(phen)_4(H_2O)_2](NO_3)_4{\cdot}5H_2O$ (5) gave satisfactory elemental analyses (calcd. for $C_{48}H_{32}N_{12}O_{13}Fe_2{\cdot}7H_2O$, C 47.15, H 3.8, N 13.75, Fe 9.1; found: C 47.2, H 3.7, N 13.8, Fe 9.1) and electronic spectrum

© 1998 NRC Canada

(5). Hydroxylamine nitrate was prepared in solution by double decomposition of hydroxylamine hydrochloride (A.R., E. Merck) with barium nitrate (A.R., E. Merck) and standardized by oxidation with Fe^{III} in 1 M H_2SO_4 (eq. [1]) (9*a*). The Fe^{II} formed was titrated with standard $(NH_4)_2Ce(NO_3)_6$. We found the solution to be stable (10) for more than a week at room temperature (27°C).

[1] $2NH_2OH + 2\ Fe_2(SO_4)_3 \rightarrow N_2O + 4\ FeSO_4 + 2\ H_2SO_4 + H_2O$

Tris(phenanthroline)iron(III) nitrate (11) and tris(phenanthroline)iron(II) nitrate (12) were prepared according to the literature. The 1,10-phenanthroline was an E. Merck product and was used without further purification. Solution of recrystallized $NaNO_3$ (A.R., B.D.H.) was standardized by ion-exchange technique (13). All other reagents used were of analytical grade. Chromium(II)-scrubbed dinitrogen gas and triply distilled water were used throughout. Reported kinetic and equilibrium data are at 30.0°C and I = 1.0 M.

Physical measurements and kinetics

Equilibrium constants for equilibria [2]–[4] were evaluated spectrophotometrically. Kinetics were monitored mostly at 510 nm, the visible maximum of the reaction product, $[Fe(phen)_3]^{2+}$ (**4**). Large excess of hydroxylamine (c_R = $[NH_3OH^+] + [NH_2OH]$; 5–50 mM) over the total complex (c_{Fe} = 0.05–0.005 mM) was used, and the reactions

[2] $[Fe_2^{III}(\mu\text{-}O)(phen)_4(H_2O)_2]^{4+} + 2H_2O \overset{K_d}{\rightleftharpoons} [Fe_2^{III}(\mu\text{-}O)(phen)_3(H_2O)_4]^{4+} + phen$

[3] $[Fe_2(\mu\text{-}O)(phen)_4(H_2O)_2]^{4+} \overset{K_{a1}}{\rightleftharpoons} [Fe_2^{III}(\mu\text{-}O)(phen)_4(H_2O)(OH)]^{3+} + H^+$

[4] $[Fe_2(\mu\text{-}O)(phen)_4(H_2O)(OH)]^{3+} \overset{K_{a2}}{\rightleftharpoons} [Fe_2^{III}(\mu\text{-}O)(phen)_4(OH)_2]^{2+} + H^+$

were followed in situ in the thermoelectrically controlled (±0.1°C) cell housing (CPS-240A) of a Shimadzu spectrophotometer (UV-1601 PC). For some faster reactions, reactants were mixed in the spectrophotometer cell: 3.0 mL of the reductant solution at the required pH, buffer concentration, and ionic strength (1.0 M) was taken in a cell in the thermostated cell housing and allowed to attain temperature equilibrium. A small volume (<1% of the reductant) of the complex at the same pH, buffer concentration, and ionic strength was rapidly and directly injected into the cell so that the desired complex concentration was achieved after mixing. Recording of absorbance started almost simultaneously in the "kinetic mode" of the spectrophotometer, and the maximum initial absorbance (0.152) indicated that <15% of the initial reaction was missed during mixing. The first-order rate constants, k_o, were obtained from the slope of usual $\log(A_\infty - A_t)$ versus time (t) plots, where A_t and A_∞ are the absorbances at time t and after complete reaction.

We added no external buffer but generally used an excess 1,10-phenanthroline (c_{phen} = $[Hphen^+] + [phen]$) over c_{Fe}. The added phen and hydroxylamine successfully controlled solution pH within ± 0.01 during most of the kinetic studies, and the maximum variation observed was ± 0.03. The pH of experimental solutions were measured with an Orion (710A) pH meter, using a calibrated (13) Orion–Ross combination (model 81-02) electrode. All Y versus X data were analysed using the program package GRAPHER.[3] The reported errors are standard deviations. No attempt was made to estimate the small error propagated from k_o.

Stoichiometry

The UV-vis spectra (14) of product solutions indicate quantitative formation of **4** as a product. The reaction stoichiometry was determined by spectrophotometric titration of the oxidant complex (0.05 mM) with hydroxylamine in the presence of c_{phen} (3.0 mM) at pH 3.5. Different amounts of hydroxylamine were allowed to react with the oxidant solutions. The final absorption, corresponding to consumption of a stoichiometrically equivalent amount of the oxidant, was determined as a function of total hydroxylamine concentration, c_R. The absorbance due to unchanged complex, if any, is negligible (<3%) compared to the absorbance due to **4** formed under the reaction conditions. Stoichiometry was also measured by estimating unchanged hydroxylamine spectrophotometrically. For this purpose, the complex solution (0.02 mM) in excess phen (c_{phen} = 3 mM) was mixed with hydroxylamine (c_R = 0.05 mM). The final optical density at 510 nm indicated the formation of two moles of **4** per mole of **1**. Excess $Fe_2(SO_4)_3$ was then added to the mixture. Two parallel sets were taken. One of them was stored in the dark, the other under the conditions of normal laboratory illumination. The Fe^{2+} ion thus formed produced more of **4**, and absorption at 510 nm increased. The rise in absorption measured after 1 h was used to estimate hydroxylamine.

Since the formation and decay of HNO_2 was observed (15, 16) in some oxidation reactions of NH_2OH, we tested for the presence of any HNO_2 or NO_2^- as by-product. A 25 mL mixture having c_{Fe} = 0.10 mM, c_R = 0.10 mM, and c_{phen} = 5 mM at pH 6.1 was allowed to react completely. The product solution was eluted through a Dowex 50W X-8 cation exchanger in the Na^+ form, made up to 100 mL and subjected to the Griess–Ilsovey reaction for nitrous acid by reaction with sulfanilic acid followed by a coupling reaction with 1-napthyl amine to give an azo dye (λ_{max} = 520 nm, ε (molar extinction coefficient) = $3.3 \times 10^4\ M^{-1}cm^{-1}$). A 1% sulfanilic acid solution was prepared by dissolution of the powder in 25% acetic acid. A 0.6% solution of 1-napthylamine was also prepared in 25% acetic acid.

Results and discussion

Spectral and equilibrium studies

The complex solution is indefinitely stable in the range pH 2–10. However, its spectra change reversibly with changing c_{phen} and media pH. The most prominent spectral change occurs at 440 nm and has been displayed in Fig. 1. The change indicates protic and ligand dissociation equilibria, which can be suppressed almost completely in the presence of excess phen in the range pH 3–4. Under these conditions, **1** is the only absorbing species at λ > 400 nm. Its molar extinction coefficient is $\varepsilon_1 = 1460 \pm 5\ M^{-1}\ cm^{-1}$ at 440 nm.

The absorption versus c_{phen} (≥1.0 mM) data at pH 3.00 yield good fit to eq. [5] for $K_d = (4.97 \pm 0.08) \times 10^{-6}$ M

[3] Grapher. Golden Software Inc. 1988.

© 1998 NRC Canada

and $\varepsilon_{\mathbf{1d}} = (562 \pm 7)\ M^{-1}cm^{-1}$. Equation [5] can be derived for equilibrium [2] provided that $c_{phen} = ([Hphen^+] + [phen]) \approx [Hphen^+]$:

$$[5] \quad \frac{c_{Fe}}{(A_o - A_e)} = \frac{K_{Hphen}\, c_{phen}}{K_d[H^+](\varepsilon_{\mathbf{1}} - \varepsilon_{\mathbf{1d}})} + 1/(\varepsilon_{\mathbf{1}} - \varepsilon_{\mathbf{1d}})$$

where A_e and A_o are absorptions of the equilibrium mixture and of pure **1**, respectively; $\varepsilon_{\mathbf{1d}}$ is the molar extinction coefficient of the species **1d** and K_{Hphen} ($10^{-4.92}$) is the proton dissociation constant (17) for $Hphen^+$. This fit justifies equilibrium [2] and shows that only one phen dissociates under the reaction conditions.

One can safely assume that only equilibrium [3] is responsible for the changes in absorbance of complex solutions containing excess phen in the range pH 3.5–6.0 and thus derive eq. [6].

$$[6] \quad c_{Fe}/(A_o - A_e') = [H^+]/(\varepsilon_{\mathbf{1}} - \varepsilon_{\mathbf{2}})K_{a1} + 1/(\varepsilon_{\mathbf{1}} - \varepsilon_{\mathbf{2}})$$

where A_e' is the equilibrium absorbance in the range pH 3.5–6.0, and $\varepsilon_{\mathbf{2}}$ is the molar absorption coefficient for **2**.

Similarly, in the presence of excess phen, in the range pH 7–9, only equilibrium [4] is assumed to be the cause of change in solution absorbance, with pH in the range 7–9, whereby eq. [7] is valid.

$$[7] \quad c_{Fe}/(A_o' - A_e'') = [H^+]/K_{a2}(\varepsilon_{\mathbf{2}} - \varepsilon_{\mathbf{3}}) + 1/(\varepsilon_{\mathbf{2}} - \varepsilon_{\mathbf{3}})$$

In eq. [7], A_e'' is the equilibrium absorption in the range pH 7–9, $A_o' = \varepsilon_{\mathbf{2}} \times c_{Fe}$, and $\varepsilon_{\mathbf{3}}$ is the molar absorption coefficient for **3**. Absorbance versus pH data in the respective pH ranges were fitted to eqs. [6] and [7] to yield $K_{a1} = (3.84 \pm 0.04) \times 10^{-6}$ M, $K_{a2} = (2.52 \pm 0.08) \times 10^{-8}$ M, $\varepsilon_{\mathbf{2}} = (962 \pm 8)\ M^{-1}\ cm^{-1}$, and $\varepsilon_{\mathbf{3}} = (796 \pm 9)\ M^{-1}cm^{-1}$.

A global fit of absorbance versus $[H^+]$ data in the presence of excess phen was attempted using the $\varepsilon_{\mathbf{2}}$, $\varepsilon_{\mathbf{3}}$ values and eq. [8] for which A is the equilibrium absorption in the range pH 3.5–9.0, $A_2 = \varepsilon_{\mathbf{2}} \times c_{Fe}$, and $A_3 = \varepsilon_{\mathbf{2}} \times c_{Fe}$. A good fit is obtained with $K_{a1} = (4.03 \pm 0.05) \times 10^{-6}$ M and $K_{a2} = (2.54 \pm 0.06) \times 10^{-8}$ M.

$$[8] \quad (A_o - A)[H^+]/(A - A_2) = K_{a1} + (A - A_3)K_{a1}K_{a2}/(A - A_2)[H^+]$$

The pK_{a1} (5.39 ± 0.01) and pK_{a2} (7.59 ± 0.01) values for **1** are smaller than the respective values ($pK_{a1} = 6.36$; $pK_{a2} = 9.84$) for the ruthenium(III) analogue $[Ru^{III}_2(\mu\text{-}O)(bipy)_4(H_2O)_2]^{4+}$ (**5**) (18). Greater acidity of **1** than **5** is due to smaller size of Fe^{III}. The differences ($pK_{a1} - pK_{a2}$) for the binuclear complexes **1** and **5** are comparable to those for the mononuclear Fe^{III} complexes (19) of the type $[ML_4(H_2O)_2]^{3+}$. Prominent electronic interaction of the two M^{III} centres via the oxo bridge in **1** and **5** is thus indicated and is indeed expected from the *anti* ferromagnetic coupling well known (1) in several μ-oxo-bridged complexes of Fe^{III} and Ru^{III}. Binuclear iron(III) complexes with insulating bridging groups cannot enter into such interactions, and they have small differences between pK_{a1} and pK_{a2} (19).

Stoichiometry

No nitrogen(III) product could be detected by the Griess–Ilsovey reaction at pH 6.1. Under our reaction conditions a 2×10^{-6} M $NaNO_2$ solution gave an absorbance of 0.166 per cm at 520 nm. At pH 6.1 the reaction between hydroxylamine and

Fig. 1. Change in absorbance with c_{phen} at fixed pH (3.00) (▲) and change in absorbance with pH at fixed c_{phen} (0.010 M) (●). λ, 440 nm ; c_R, 0.50 mM; I, 1.0 M; path length, 1.00 cm. The solid lines are drawn using calculated values for eqs. [8] and [5], respectively.

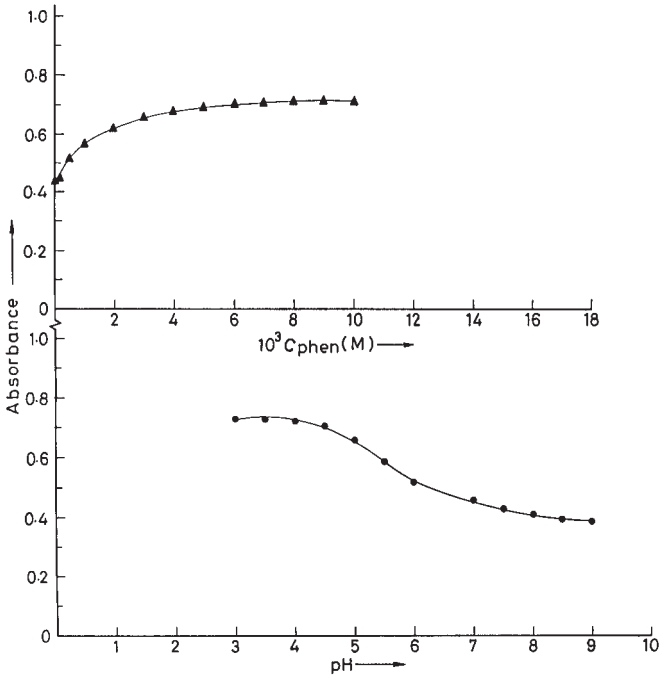

HONO is very slow (20*a*), as is the reaction of HONO with the diiron(III) complexes. Hence, we are confident that HONO did not form at this pH.

Stoichiometric measurements in the presence of excess phenanthroline indicated a 1:1 stoichiometry (eq. [9]) from spectrophotometric titration data and determination of unused hydroxylamine. The measured stoichiometry is independent of whether diffuse light is excluded or not.

$$[9] \quad [Fe_2(\mu\text{-}O)(phen)_4(H_2O)_2]^{4+} + NH_2OH + 2phen = 0.5N_2O + 2[Fe(phen)_3]^+ + 3.5H_2O$$

Different oxidants oxidize hydroxylamine to nitrous oxide, which seems to be the most common oxidation product. Nevertheless, other products like N_2, NO_2^-, NO_3^-, and NO have been reported (8, 20, 21). Gupta and co-workers (9*b*) studied the oxidation of hydroxylamine by iron(III) in acetate buffer, and proposed $[Fe_3O(O_2CMe)_6]^+$ to be the near exclusive iron(III) species along with a small concentration of iron(III) monomers. Complex kinetics and product inhibition by iron(II) were noted, and the initial rate method was used. They reported N_2 as the oxidation product in diffuse light, but ($N_2O + N_2$) in the dark. Butler and Gordon (9*c*) also noticed the effect of light on oxidation products of hydroxylamine with iron(III) in dilute perchloric acid media. The observations are difficult to explain, but two potent sources of complications may be considered: (*a*) auto-oxidation of iron(II) to iron(III), which further consumes hydroxylamine; effectively this implies an additional pathway in which hydroxylamine is oxidized by oxygen (22) under the aerobic conditions used, and (*b*) catalysed oxidation by trace metal ions, which were apparently not excluded. Trace catalysts strongly affect both rate

© 1998 NRC Canada

Fig. 2. Spectral changes with time for a mixture containing c_{Fe} = 0.05 mM, c_R = 0.02 M, and c_{phen} = 3 mM at pH 4.50. (*i*) Spectrum of 0.05 mM complex at the same c_{phen} and pH. Time: (*ii*) 0, (*iii*) 60, (*iv*) 120, (*v*) 270, (*vi*) 360, (*vii*) 480, (*viii*) 660, and (*ix*) 870 s. Cell path length, 1.00 cm.

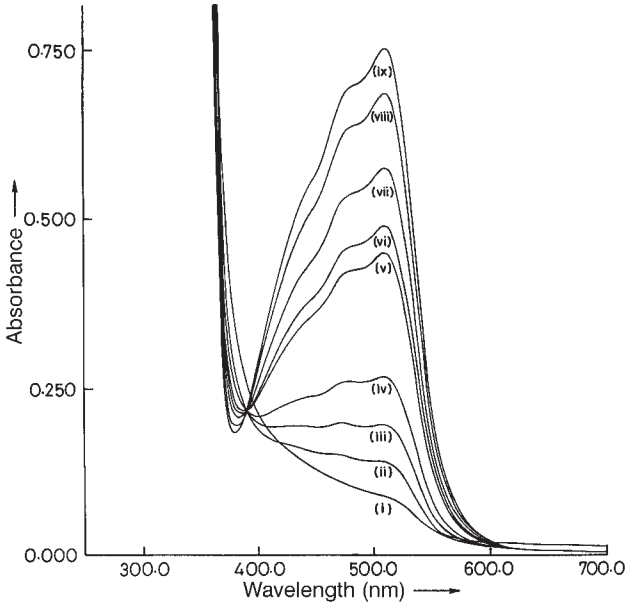

and product of oxidation (23) of NH_2OH and may lead to wrong conclusions about the uncatalyzed process. Light may affect stoichiometry and kinetics by its influence on either (*a*) or (*b*). Moreover, both groups worked with complex mixtures of iron(III) species of different nuclearity, which can oxidize hydroxylamine differently.

We observed no such effect of light in our system, but note that trace metal ions should be sequestered in the presence of added phen. Also, all the oxidant species are well defined and the reaction product, $[Fe(phen)_3]^{2+}$, is stable in air.

Kinetics

During the reaction course, an isosbestic point sets up at 389 nm, and absorption at this point increases with increasing c_R. Some typical values of absorbances are 0.225, 0.246, and 0.274 at c_R = 0.02, 0.04, and 0.06 M, respectively. This strongly suggests incomplete formation of precursor complexes between hydroxylamine and the oxidants. Spectrum of the complex solution, however, does not pass through this point (Fig. 2), and we propose that the isosbestic point sets up between the precursor and the final reaction product. Non-reducing substrates (for example, NCS^-) rapidly form inner-sphere adducts with **1** (24) and analogous complexes (25). Similar adducts seem reasonable with hydroxylamine. The absorbance versus time data at 510 nm obeyed first-order kinetics at least up to 95% reaction. Table 1 shows that k_o decreases with increasing c_{phen} until a constant value is reached for c_{phen} > 1 mM. Qualitatively, the data indicate that **1d** is more reactive than 1 and that [**1d**] decreases with increasing [phen] until [**1d**] becomes kinetically negligible. The value of k_o increases linearly with c_R (≤ 0.05 M), decreases with increase in pH, but does not change (± 5%) with a ten-fold (0.05–0.005 mM) change in concentration of complex. Values of k_o also do not change (± 3%) on changing the monitoring wavelength from 510 to 365 nm, or when the reaction media were purged with dinitrogen, or when stray light was excluded. Scheme 1 seems to be a reasonable explanation for the observed kinetics and equilibria.

Table 1 First-order rate constants.[a]

pH	$c_R \times 10^3$ (M)	$c_{phen} \times 10^3$ (M)	$k_o \times 10^2$ (s^{-1})[b]
3.00	20.0	3.0	0.01 (0.006)
3.50			0.02 (0.015)
4.00			0.04 (0.04)
4.50			0.16 (0.15)
5.00			0.85 (0.88)
5.26			2.17 (2.08)
5.50			4.27 (4.19)
5.70			7.50 (6.9)
5.85			9.61 (9.3)
6.00			13 (12)
4.50	5.0		0.04 (0.037)
	10.0		0.08 (0.074)
	15.0		0.12 (0.11)
	20.0		0.16 (0.15)
	25.0		0.17 (0.18)
	30.0		0.23 (0.22)
	35.0		0.25 (0.26)
	40.0		0.28 (0.30)
4.5	45.0	3.0	0.35 (0.33)
	50.0		0.39 (0.37)
	20.0	0.05	0.81 (0.39)
		0.10	0.34 (0.29)
		0.20	0.23 (0.22)
		0.30	0.17 (0.17)
		0.40	0.18 (0.18)
		0.50	0.155 (0.17)
		0.60	0.155 (0.17)
		1.00	0.15 (0.159)
		2.00	0.145 (0.151)
		4.00	0.150 (0.147)
		6.00	0.145 (0.146)

[a] Temperature, 30.0°C; concentration of complex, 0.05 mM; *I*, 1.0 M ($NaNO_3$).

[b] Average of two or three determinations; standard deviation, 2–4%; parenthetical values are calculated using eq. [10].

Scheme 1

$$\mathbf{1} \rightleftharpoons \mathbf{2} + H^+, \qquad K_{a1} = 4.0 \times 10^{-6}\ M$$

$$\mathbf{1} \rightleftharpoons \mathbf{1d} + \text{phen}, \qquad K_d = 5.0 \times 10^{-6}\ M$$

$$Hphen^+ \rightleftharpoons H^+ + \text{phen}, \qquad K_{Hphen} = 1.2 \times 10^{-5}\ M$$

$$NH_3OH^+ \rightleftharpoons H^+ + NH_2OH, \qquad K_a = 1 \times 10^{-6}\ M \text{ (23)}$$

$$\mathbf{1} + NH_2OH \overset{K_1}{\rightleftharpoons} \mathbf{I_1} \overset{k_1}{\rightarrow} \text{products}$$

$$\mathbf{2} + NH_2OH \overset{K_2}{\rightleftharpoons} \mathbf{I_2} \overset{k_2}{\rightarrow} \text{products}$$

$$\mathbf{1d} + NH_2OH \overset{K_3}{\rightleftharpoons} \mathbf{I_3} \overset{k_3}{\rightarrow} \text{products}$$

In this scheme, $\mathbf{I_1}$ is $[Fe_2(\mu\text{-}O)(phen)_4(H_2O)(NH_2OH)]^{4+}$, $\mathbf{I_2}$ is $[Fe_2(\mu\text{-}O)(phen)_4\text{-}(OH)(NH_2OH)]^{3+}$, $\mathbf{I_3}$ is $[Fe_2(\mu\text{-}O)(phen)_3(H_2O)_3(NH_2OH)]^{4+}$; **1**, **2**, and **1d** are as defined previously.

© 1998 NRC Canada

Provided $K_i[NH_2OH] << 1$ ($i = 1$–4) and $c_R >> c_{Fe}$, the scheme leads to eq. [10].

$$[10] \quad k_o\{([H^+] + K_{a1})[phen] + K_d[H^+]\}/ [NH_2OH] = (k_1K_1[H^+] + k_2K_2K_{a1})[phen] + k_3K_3K_d[H^+] = m_1[phen] + c_1 \text{ (say)}$$

The assumption, $K_i[R] << 1$ seems justified because k_o and the absorbance at the isosbestic point increase linearly with c_R. The maximum value of $[NH_2OH]$ used in kinetics is 0.015 M (pH 4.50, $c_R = 0.05$ M) up to which we observed no indication for rate saturation. Hence, an upper limit for K_i is 5 M^{-1}. Stynes and co-workers (26) noted that weakly basic amines form weak adducts with the oxo-bridged diiron complex $[Fe^{III}(dmgBF_2)_2]_2O$, ($dmgBF_2$ is difluoro(dimethylglyoximato)borate). Hydroxylamine is a weak base and hence expected to form weak adducts with **1** and its derivatives. Hydroxylamine can form O-bonded complexes, but stability constants for such complexes also are very small ($K \leq 0.1$) (21*a*). It is not possible for NH_3OH^+ to coordinate to Fe^{III} without loss of a proton first. Hence, the small values for K_i and the weak acidity of NH_3OH^+ excludes the possibility of NH_3OH^+ to act as an active reducing agent.

The k_o data at fixed pH (4.50) and c_R (0.020 M) but variable c_{phen} yielded a good fit ($r = 0.9989$; $m_1 = 8.29 \times 10^{-5}$; $c_1 = 2.92 \times 10^{-9}$) into eq. [10]. However, a better fit results ($r = 0.9997$; $m_1 = 8.43 \times 10^{-5}$; $c_1 = 1.40 \times 10^{-9}$) if k_o data at the three lowest c_{phen} (0.05, 0.10, 0.20 mM) are excluded (Fig. 3). In the presence of excess phen, [**1d**] is negligible compared to ([**1**] + [**2**]), and (K_{a1} + [H^+])[phen] is >> $K_d[H^+]$. Equation [10] may then be transformed to equation [11].

$$[11] \quad k_o([H^+] + K_{a1})([H^+] + K_a) / c_R = a[H^+]^2 + b[H^+] + c$$

where $a = k_3K_3K_dK_a/K_{Hphen}c_{phen}$, $b = (k_1K_1K_a + k_3K_3K_dK_a/c_{phen})$, and $c = k_2K_2K_{a1}K_a$. Values for k_o at different pH (≥3.5) but fixed c_{phen} and c_R were fitted into eq. [11] and yielded $a = (2.66 \pm 0.01) \times 10^{-3}$ M^{-1} s^{-1}, $b = (2.31 \pm 0.003) \times 10^{-6}$ s^{-1}, and $c = (5.46 \pm 0.03) \times 10^{-11}$ M s^{-1}. From these values, one can extract $k_1K_1 = 0.93 \pm 0.005$ M^{-1} s^{-1}, $k_2K_2 = 13.6 \pm 0.06$ M^{-1} s^{-1}, $k_3K_3 = 19.1 \pm 0.04$ M^{-1} s^{-1}. These parameters and eq. [10] generally reproduce k_o values within ± 10% (see parenthetical values in Table 1). The calculated values also follow the expected trend of variation, but they are considerably smaller than the experimental data when [phen] is very low. Trace-metal ion catalysis may become effective at low [phen] and is a probable cause for the observed deviations.

The second-order rate constants are composite constants (K_ik_i) and both K_i and k_i can control the reactivity of the intermediates. A higher value for K_3 than either K_1 or K_2 seems reasonable, since an iron(III) centre in **1d** should be more electron deficient than that in either **1** or **2**. Moreover, **1d** is structurally less rigid due to the absence of a bulky phen ligand, and can easily accommodate structural changes associated with the electron transfer step,

$$\{Fe^{III}_2O\}^{4+} \rightarrow \{Fe^{III}Fe^{II}O\}^{3+}$$

On this ground, k_3 is likely to be larger than both k_1 and k_2. The higher reactivity of $\mathbf{I_3}$ thus seems justified. It is more difficult to assess the order of reactivity of $\mathbf{I_1}$ with respect to $\mathbf{I_2}$. The water molecule in $\mathbf{I_1}$ is ≈4 times a stronger acid than NH_3OH^+. So internal proton transfer in $\mathbf{I_1}$ may weaken the adduct. This is not possible for $\mathbf{I_2}$. Thus, K_1 should be less than K_2. On the other hand, the smaller charge borne by $\mathbf{I_2}$ should render an intramolecular electron transfer less facile, and k_1 is expected to be greater than k_2. The overall effect of such opposing factors is difficult to predict.

Concentration of the dihydroxo species **3** is very small in the pH range used in kinetics. It does not contain any replaceable water molecule, and all the ligands present are held more tightly than H_2O. It should also be a weak oxidant due to the smaller positive charge on its iron(III) centres. Kinetic activity of **3** is therefore inappreciable in the range pH 3–6.

Conversion of intermediates $\mathbf{I_1}$–$\mathbf{I_3}$ to products must be multistep processes. We propose the rate-determining steps to be one-electron reduction of the intermediates to respective Fe^{II}-O-Fe^{III} dimers, which quickly collapse to Fe^{II} and Fe^{III} monomers. The iron(III) monomer $[Fe(phen)_2(H_2O)_2]^{3+}$ is further reduced to the iron(II) monomer $[Fe(phen)_2(H_2O)_2]^{2+}$, which rapidly forms **4** in the presence of phen. We have verified that $[Fe(phen)_3]^{3+}$ is reduced by hydroxylamine within the time of mixing; $[Fe(phen)_2(H_2O)_2]^{3+}$ is expected to react faster. It is also known that formation of **4** from Fe^{2+} and excess phen is a fast reaction (27) (rate constant ~10^5 s^{-1}). Inner-sphere reduction of $[Fe(phen)_3]^{3+}$ by NH_2OH should be slow since substitution on this iron(III) complex is slow. Such is not the case for the diaqua derivative. Even with $[Fe(phen)_3]^{3+}$ the outer-sphere reaction should be fast. We used simple Marcus relation to calculate the rate constant for outer-sphere oxidation of NH_2OH by $[Fe(phen)_3]^{3+}$ to be 490 $M^{-1}s^{-1}$. Consequently, even at the lowest c_R (= 0.005 M,) used in kinetics, half life for this reaction is only 0.28 s. The parameters used in this calculation are $E^0 = 1.05$ V for the couple $[Fe(phen)_3]^{3+/2+}$, its self-exchange rate constant (≈10^7 M^{-1} s^{-1}) (28), $E^0 = 0.42$ V for the couple NH_2OH^+/ NH_2OH, and its self-exchange rate constant, 5×10^{-13} M^{-1} s^{-1} (8).

Further, the oxo bridge in **1** is stable, and the complex suffers no autodecomposition within the time of kinetic studies. Martell and co-workers (29) explained that the $\{Fe_2O\}^{4+}$ core unit gains stability from superexchange of the d^5 high-spin iron(III) centres across the oxo bridge. But the high-spin Fe^{II} and Fe^{III} are probably less strongly bound to O^{2-}, since both oxidation states have two *anti* bonding electrons directed towards the formal bond axes. This would impart weaker Fe^{II}—O—Fe^{III} and Fe^{II}—O—Fe^{II} bonds, both of which should be rapidly broken by aquation. In fact the oxo bridge in the mixed valence system Fe^{II}-O-Fe^{III} is rare and in general putative outside a protein environment (1*c*). It thus appears that reduction of $\{Fe_2O\}^{4+}$ complexes by hydroxylamine involves several steps, but the rate-determining step is

$$\{Fe_2O\}^{4+} \rightarrow \{Fe_2O\}^{3+}$$

All other steps are either too fast or too slow to qualify as the rate-determining step. The immediate oxidation product of hydroxylamine should be NH_2OH^+. This is known to generate N_2O via HNO (20*a*, 23):

$$NH_2OH \rightarrow H^+ + NHOH + e^- \rightarrow H^+ + HNO + e^- \rightarrow 0.5N_2O + 0.5H_2O$$

The values for K_i could refer to outer-sphere precursor complex formation. However, hydroxylamine has a record low self-exchange rate constant, and outer-sphere reactions occur very rarely with NH_2OH in spite of its moderately low $E°$ value. We observed that **1** does not oxidize $[Fe(CN)_6]^{4-}$,

© 1998 NRC Canada

Fig. 3. Effect of phenanthroline on rate constants at a fixed pH (4.50), c_R (0.05 mM), and I (1.0 M); $p = ([H^+] + K_{a1})[phen] + K_d[H^+]$; $f = K_a c_R/(K_a + [H^+])$. The solid line is drawn using least-squares slope and intercept.

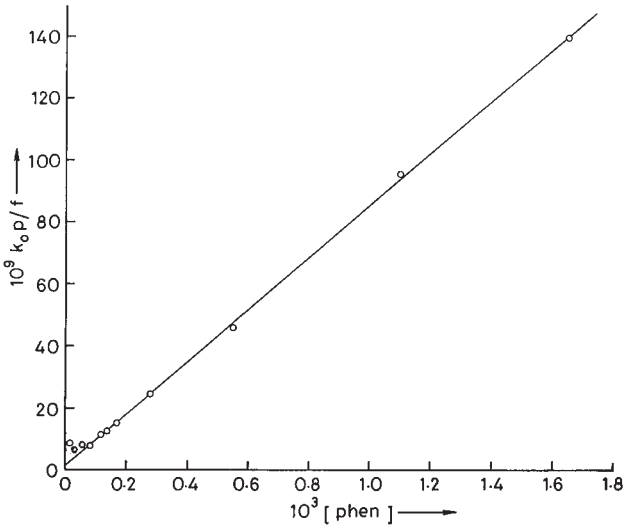

indicating for **1** a reduction potential less than that for the $[Fe(CN)_6]^{4-/3-}$ couple (0.46 V). Calculations using simple Marcus relation ($k_{12} = (k_{11}k_{22}K_{12})^{1/2}$) for outer-sphere reactions with k_iK_i used as k_{12} values imply impossibly high self-exchange rate constants ($k_{11} > 10^{10}$) for the $\{Fe_2O\}^{4+}$ complexes. The calculations refute an outer-sphere mechanism in the present system.

Acknowledgements

Financial assistance for this work from the Department of Science and Technology (New Delhi) and the award of a Senior Research Fellowship to B.C. by the University Grants Commission (New Delhi) are gratefully acknowledged.

References

1. (*a*) J.B. Vincent, G.L Oliver-Lilley, and B.A. Averill. Chem. Rev. **90**, 1447 (1990); (*b*) S.J. Lippard. Angew. Chem. Int. Ed. Engl. **27**, 344 (1988); (*c*) D.M. Kurtz, Jr. Chem. Rev. **90**, 585 (1990).
2. R.M. Buchanan, S. Chem, J.F. Richardson, M. Brossan, L. Forti, A. Morvillo, and R.H. Fish. Inorg. Chem. **33**, 3208 (1994).
3. P.C. Wilkins and R.G. Wilkins. Coord. Chem. Rev. **79**, 195 (1987).
4. (*a*) Z. Zhang and R.B. Jordan. Inorg. Chem. **35**, 1571 (1996); (*b*) E. Bjerghakke, B. Pederson, and G. Nord. J. Am. Chem. Soc. **105**, 1913 (1983).
5. J.E. Plowman, T.M. Loehr, C.K. Schauer, and O.P. Anderson. Inorg. Chem. **23**, 3553 (1984).
6. (*a*) B.M. Sjoberg and A. Grasbend. Adv. Inorg. Biochem. **5**, 87 (1983); (*b*) I.M. Klotz and D.M. Kurtz, Jr. Acc. Chem. Res. **17**, 16 (1984).
7. K. Wieghardt. Adv. Inorg. Bioinorg. Mech. **3**, 213 (1984).
8. M.L. Hung, M.L. Mckee, and D.M. Stanbury. Inorg. Chem. **33**, 5108 (1994).
9. (*a*) W.C. Bray, M.E. Simpson, and A.A. Mackenzie. J. Am. Chem. Soc. **41**, 1363 (1919); (*b*) K. Arora, P. Bhatnagar, A.P. Bhargava, and Y.K. Gupta. J. Chem. Soc. Dalton Trans. 1081 (1991); (*c*) J.H. Butler and L.T. Gordon. Inorg. Chem. **25**, 4573 (1986).
10. F.A. Cotton and G. Wilkinson. Advanced inorganic chemistry. 5th ed. John Wiley and Sons, Singapore. 1988. p. 320.
11. N. Sutin and B.M. Gordon. J. Am. Chem. Soc. **83**, 70 (1961).
12. T.S. Lee, I.M. Kolthoff, and D.L. Leussing. J. Am. Chem. Soc. **70**, 2348 (1948).
13. S. Kundu, A. Bhattacharya, and R. Banerjee. J. Chem. Soc. Dalton Trans. 3951 (1996).
14 I.M. Kolthoff, D.L. Leussing, and T.S. Lee. J. Am. Chem. Soc. **72**, 2173 (1950).
15. J.N. Cooper and D.W. Margerum. Inorg. Chem. **32**, 5905 (1993).
16. R.C. Beckwith, J.N. Cooper, and D.W. Margerum. Inorg. Chem. **33**, 5144 (1994).
17. R.T. Pflaum and W.W. Brandt. J. Am. Chem. Soc. **76**, 6215 (1954).
18. J.A. Gilbert, D.S. Eggleston, W.R. Murphy, Jr., D.A. Geselowitz, S.W. Gersten, D.J. Hodgson, and T.J. Meyer. J. Am. Chem. Soc. **107**, 3855 (1985).
19. M.T. Caudle, C.D. Caldwell, and A.L. Crumbliss. Inorg. Chim. Acta, **240**, 519 (1995).
20. (*a*) R.M. Liu, M.R. McDonaldand, and D.M. Margerum. Inorg. Chem. **34**, 6093 (1995); (*b*) O.P. Strausz, and H.F. Gunning. Trans. Faraday Soc. **60**, 347 (1964); (*c*) D. Beha'r, D. Shapira, and A. Treinin. J. Phys. Chem. **76**, 180 (1972).
21. (*a*) R.A. Scott, G.P. Haight, and J.N. Cooper. J. Am. Chem. Soc. **96**, 4136 (1974); (*b*) W.A. Waters and I.R. Wilson. J. Chem. Soc. A, 534 (1966); (*c*) R. Swaroop and Y.K. Gupta. J. Inorg. Nucl. Chem. **36**, 169 (1974); (*d*) G. Rabai and M.T. Beck. J. Chem. Soc. Dalton Trans. 573 (1982).
22. D.G. Cuisia, C.M. Hwa, J.T. Jacob, and M.L. Salutsky. U.S. Patent 4067690; Chem. Abstr. **88**, 141 457h (1978).
23. G. Bengtson. Acta Chem. Scand. Ser. A, **A37**, 639 (1983).
24. A.F.M. Nazer and C.F. Wells. J. Chem. Soc. Dalton Trans. 1532 (1980).
25. (*a*) T. J. Mizoguchi and S. J. Lippard. Inorg. Chem. **36**, 4526 (1997); (*b*) A.L. Nivorozhkin, E. Anxolabehere-Malbart, P. Mialane, R. Davydou, J. Guilhem, M. Cesario, J.-P. Audiere, J.-J. Girerd, S. Styring, L. Schussler, and J.-L. Seris. Inorg. Chem. **36**, 846 (1997).
26. (*a*) H. Noglik, W. Thompson, and D.V. Stynes. Inorg. Chem. **30**, 4571 (1991); (*b*) E.C. Wilkinson, Y. Dong, and L. Que, Jr. J. Am. Chem. Soc. **116**, 8394 (1994); (*c*) A.A. El-Awady, P.C. Wilkins, and R.G. Wilkins. Inorg. Chem. **24**, 2053 (1985).
27. (*a*) T.S. Lee, I.M. Kolthoff, and D.L. Leussing. J. Am. Chem. Soc. **70**, 3596 (1948); (*b*) J.C. Thompsen and H.A. Mottola. Anal. Chem. **56**, 755 (1984).
28. M. Chan and A.C. Wahl. Abstr. 167th Natl. Meeting, American Chemical Society. INOR 97. Los Angeles, Calif. March, 1974.
29. G. McLendon, R.J. Motekaitis, and A.E. Martell. Inorg. Chem. **15**, 2306 (1976).

© 1998 NRC Canada

COMMUNICATION

Precise measurement of fluorescence from uranium taken up in sodium fluoride

Heather Marshall and Marisa A. Devine

Abstract: The fluorescence signals from replicate samples of uranium taken into fused sodium fluoride beads, read in the prescribed fashion, are not distributed normally. The signal from a single bead shows marked sinusoidal variation as the bead is rotated, and it is the superposition of this sinusoidal variation on the normal variation between beads that gives rise to a widened or even bimodal distribution among replicates. If each bead is read a second time, following a single half rotation, the average of the two readings gives the true signal underlying the sinusoidal variation; the distribution of these true signals represents simply the normal variation between replicate samples, and the precision of results is much improved.

Key words: uranium, fluorescence, fluorometry.

Résumé : Les signaux de fluorescence obtenus de façon prescrite, à partir d'échantillons subdivisés d'uranium prélevés de billes de fluorure de sodium fondues, ne donnent pas une distribution normale. Le signal obtenu à partir d'une seule bille présente une variation sinusoïdale importante lorsqu'on la fait tourner; c'est la superposition de cette variation sinusoïdale sur la variation normale entre les billes qui donne lieu à une distribution élargie ou bimodale entre les échantillons subdivisés. Si l'on effectue une deuxième mesure, après une seule demi-rotation, la moyenne des deux valeurs obtenues conduit à la valeur réelle du signal sous-jacent de la variation sinusoïdale; la distribution de ces valeurs réelles représente simplement la variation normale entre les échantillons subdivisés et il en résulte une amélioration de la précision des résultats.

Mots clés : uranium, fluorescence, fluorométrie.

[Traduit par la rédaction]

Introduction

For the routine determination of uranium, fluorometry of samples taken up in fused sodium fluoride beads is a well established, robust method. The flux of choice (NaF with 2% LiF) and the optimum conditions for bead preparation are well known (1), the fluorescence intensity is proportional to the uranium content over a wide range, and the techniques to correct for possible matrix interference are those generally available for optical methods of quantitative analysis; however, we have found the uncertainty in results to be unpredictable. Close study of the observed signal reveals a corrigible fluctuation, and the precision of determinations can be improved by a simple change in the fluorescence measurement itself.

Consistency in the fusion conditions is clearly a necessity (1). In this laboratory, batches of up to 21 pellets are fused in formed platinum dishes rotating over a ring of propane-fuelled Meker burners; the pellets are heated at 500–600°C, fused at 920–940°C, and annealed at 500–600°C. The beads, in their platinum dishes, are cooled together on a perforated plate of massive aluminum for 30 min before the fluorometric measurement, and that measurement is completed within 1 h.

Although some custom instruments are still in use, most uranium fluorometry is carried out with commercial units such as the Jarrell–Ash Model 27-000 used in this laboratory. In these instruments, fused beads of about 400 mg of flux and containing nanograms of uranium are mounted facing the photomultiplier tube that is to collect the fluorescent light, and exposed to the ultraviolet light from lamps on either side of the tube. The sample holder is a shaped well in a lightproof slide, and mounting a sample bead is simply a matter of placing the bead in the well and closing the slide. The manufacturers and users emphasize the ease and rapidity with which beads can be read, and for routine work high sample throughput can be maintained.

Observations

The simplicity of mounting a bead and reading the fluorescence signal is beguiling; the observed signal is in fact complex, as the fluorescence is apparently anisotropic. If the bead is rotated in the plane of the face displayed to the photomultiplier, the output signal can be observed to have a sinusoidal

Received August 12, 1997.

H. Marshall[1] and M.A. Devine. Radiation Protection Bureau, Health Canada, Postal Locator 6302D1, 775 Brookfield Road, Ottawa, ON K1A 1C1, Canada.

[1] Author to whom correspondence may be addressed. Telephone: (613) 954-6671. Fax: (613) 957-1089. E-mail: Heather_Marshall@hc-sc.gc.ca

© 1998 NRC Canada

Fig. 1. Fluorescence signals from six replicate sample beads. The short horizontal lines mark the characteristic signal intensities, and the sinusoidal traces show the measured signals as the beads are rotated through 360°; the signals are plotted exactly as they were first observed, not shifted to start at zero azimuth.

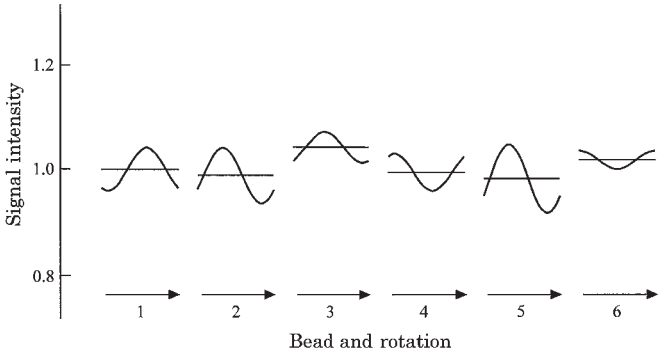

perturbation; the intensity of the signal in any azimuthal orientation can be written as

$$I = C + A \sin \theta$$

where C is the characteristic signal, A is the amplitude of the perturbation, and θ is the angle of rotation from zero azimuth. As there is no visible sign on the bead to define zero azimuth for the sinusoidal perturbation, the beads cannot be mounted immediately in this desirable orientation; the intensity of the signal observed on a single reading includes the term in sin θ, and θ is unknown. The signals from six replicate beads from a single fusion batch, each rotated in this way, are shown in Fig. 1, with the perturbation plotted along a line representing the intensity of the concentration-dependent characteristic signal of each bead; the signals are plotted exactly as they were first observed, with the beads on first mounting proving to have been in orientations of –120, –30, –60, +60, –30, and +90 degrees from zero azimuth.

Discussion

When a bead is slipped into the sample holder, all azimuthal orientations are possible and equally probable. Thus, all signal intensities between $(C - A)$ and $(C + A)$ are possible; however, because sin θ changes more slowly near sin θ = 1, the extreme values are more probable, as shown in Fig. 2. While the mean of this U-shaped distribution is indeed C, a large variance is engendered by the high probability of the extreme values and the otherwise almost flat probability distribution. The superposition of this distribution on the normal distribution of uncertainty in C (the concentration-dependent characteristic signal of the beads) will obviously broaden it, as shown in Fig. 3. It is the large variance of this broadened distribution that made estimates of the precision of the technique, taken from the usual triplicate or quintuplicate measurements, erratic and apparently unrepeatable.

In our experience, the amplitude of the perturbation is about twice the standard deviation of values of C. As shown in Fig. 3*b*, the probability distribution of signal intensity under these circumstances is broad and rather trapezoidal, with an almost constant probability across the midrange. If the amplitude of the sinusoidal perturbation is somewhat larger, the extreme tendency of the perturbation predominates over the central tendency of the normal distribution, and the composite distribution broadens even further and becomes bimodal. When the amplitude of the perturbation is lower, the distribution appears to be simply a broader Gaussian, although it is in fact slightly flattened.

The amplitude of the sinusoidal perturbation is not consistently twice the standard deviation of the characteristic signals but varies, as is apparent in Fig. 1. We did not study this amplitude distribution closely, as we chose to circumvent the problem rather than make allowance for it, but the amplitude appears to be 1.8 ± 0.7 times the underlying standard deviation, which itself is generally 3% of the characteristic intensity.

The final probability distribution of signal intensities from replicate pellets, accumulating the normal distribution of the characteristic signals (which includes the uncertainty in the instrumental reading of the signal), the U-shaped distribution engendered by the azimuthal anisotropy, and the variation in the amplitude of this perturbation, is a broad and roughly normal distribution, as shown in Fig. 3*c*; the standard deviation of this cumulative distribution is about 1.8 times that of the underlying distribution of the characteristic signal. This degradation of precision by a factor of 1.8 could be corrected by taking three times as many replicate pellets, improving the precision again by a factor of $3^{1/2}$, but this would consume time and reagents, and might not even be possible, as handling three times as many pellets in one process run is often awkward with these instruments.

One could avoid dealing with the broadened distribution of signal intensity by correcting or removing the sinusoidal perturbation of the signal from each individual bead, and so dealing with only the true characteristic signals. In mechanical terms, the instrument could be adapted to rotate the bead in its holder while taking a time average of the signal. In arithmetic terms, the signal could be read in the ordinary way with the bead in several orientations, and the data fit to give the best values of the characteristic intensity and the perturbation amplitude. More simply, the signal can be read in the ordinary way, with the bead sitting at whatever the azimuthal angle happens to be, and then read again with the bead turned through exactly 180°. Since

$$\sin(\theta + 180°) = -\sin \theta$$

the average of the two readings is the underlying characteristic intensity, whatever the value of θ. (It is tempting to extend this argument to more closely-spaced readings, and to average four readings taken at 90° intervals, or even twelve readings taken at 30° intervals, but the increased tedium would not be justified; the variance of repeated readings of the signal from one bead in a single orientation is much less than the variance among replicate beads, so the improvement derived from the greater number of readings of each bead would be small.)

Conclusions

The minor added step of reading the signal from each bead a second time completely obviates the azimuthal anisotropy of the fluorescence signals, with almost no increase in analysis time or complexity. The analytical precision is improved, and the advantages of the technique can be exploited with confidence.

© 1998 NRC Canada

Fig. 2. Demonstration of the probability distribution of measured fluorescence signals influenced by a sinusoidal perturbation: (*a*) intensity as a function of azimuth, θ, at 20 equally spaced and equally probable values of θ; (*b*) accumulated values of intensity from these 20 positions; and (*c*) generalized probability distribution of intensity for random azimuthal orientation.

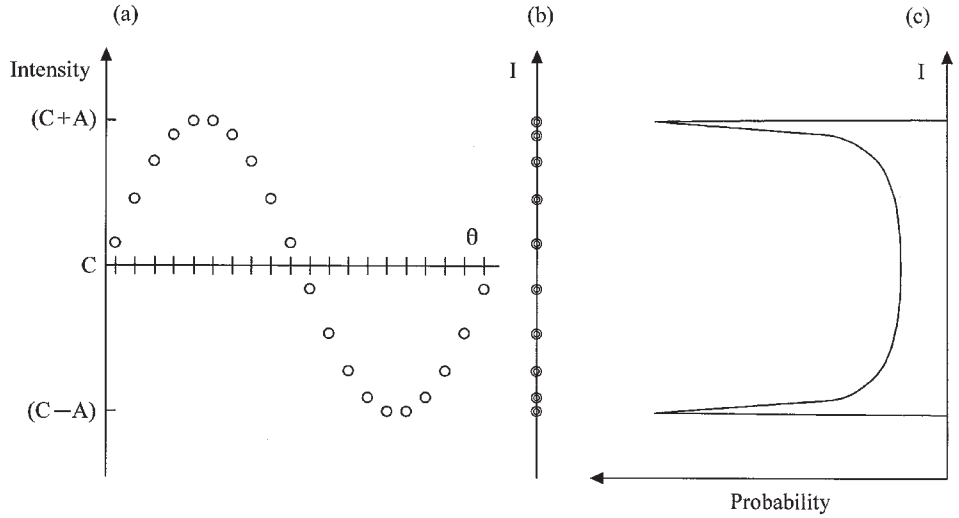

Fig. 3. (*a*) The U-shaped distribution of the sinusoidal perturbation of intensity, of amplitude 2*s*, superimposed on a Gaussian of standard deviation *s*. (*b*) The composite of the Gaussian and perturbation distributions for $A = 3s$, $A = 2s$, and $A = (2/3)s$. (*c*) The final distribution of signal intensity, including a sinusoidal perturbation of $(1.8 \pm 0.7)s$, compared to the underlying Gaussian.

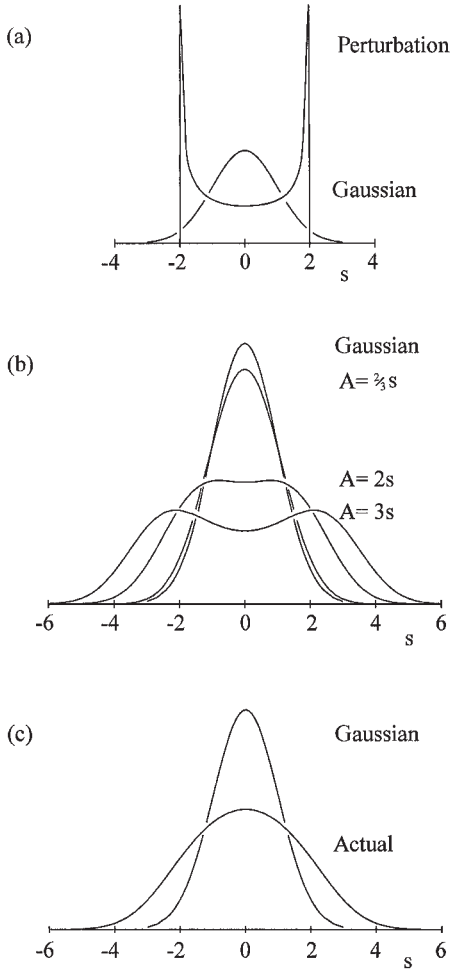

Acknowledgements

Bliss L. Tracy of the Environmental Radiation Hazards Division pored over a great compilation of puzzling readings and results and uncovered the bimodal distribution that was the key to our understanding the problem. Michael Goddard of the Biostatistics Division of the Environmental Health Directorate and Zachary Jacobson of Consulting and Auditing Canada shared their insight into the behaviour of non-Gaussian distributions in many enlightening discussions.

Reference

1. Frederick A. Centanni, Arthur M. Ross, and Michael A. DeSesa. Anal. Chem. **28**, 1651 (1956).

© 1998 NRC Canada

ADDITIONS AND CORRECTIONS / AJOUTS ET CORRECTIONS

Additions and corrections: Transverse compression and the secondary H/D isotope effects in intramolecular S_N2 methyl-transfer reactions

Saul Wolfe, Chan-Kyung Kim, Kiyull Yang, Noham Weinberg, and Zheng Shi

Ref.: Can. J. Chem. **76**, 102–113 (1998).

This article is republished below, as parts of Figs 2–5, 8, and 13 were inadvertently deleted from the original publication. The Publisher regrets this error.

Abstract: Using ab initio molecular orbital theory mainly at the 3-21+G level, intramolecular S_N2 methyl transfer between two oxygens confined within a rigid template is found to proceed exclusively by a high energy retention mechanism when the oxygens are separated by three or four bonds, and by a high energy inversion mechanism when the oxygens are separated by six bonds. Both mechanisms exist when the oxygens are separated by five bonds. The CH_3/CD_3 kinetic isotope effects are normal (1.21–1.34) in the retention processes and inverse (0.66–0.81) in the inversion reactions. In the case of inversion, compression of C—H bonds of the transition state by structural effects in the plane perpendicular to the O-C-O plane increases the inverse isotope effect. The retention barriers are high because retention is inherently unfavorable, even when pericyclic stabilization of the transition state is possible. The inversion barriers are high because a rigid template cannot accommodate a linear O-CH_3-O structure, and the O-C-O bending vibration is stiff (the Eschenmoser effect). Using a novel design strategy, a nonrigid template has been found in which the barrier and the CH_3/CD_3 kinetic isotope effect are the same as in an intermolecular reaction.

Key words: Eschenmoser effect, isotope effect, compression, S_N2, sigmatropic rearrangement.

Résumé : En se basant sur des calculs ab initio d'orbitales moléculaires au niveau 3-21+G, on peut conclure que le transfert intramoléculaire S_N2 d'un groupe méthyle entre deux oxygènes maintenus de façon rigide dans une matrice rigide se fait avec un mécanisme de rétention de haute énergie lorsque les oxygènes sont séparés par trois ou quatre liaisons et par un mécanisme d'inversion de haute énergie lorsque les oxygènes sont séparés par six liaisons. Les deux mécanismes existent lorsque les oxygènes sont séparés par cinq liaisons. Les effets isotopiques cinétiques CH_3/CD_3 sont normaux (1,21–1,34) dans le processus avec rétention et inversés (0,66–0,81) dans les réactions de rétention. Dans le cas de l'inversion, une compression des liaisons C—H de l'état de transition résultant d'effets structuraux dans le plan perpendiculaire au plan O-C-O provoque une augmentation de l'effet isotopique inverse. Les barrières à la rétention sont élevées parce que la rétention est intrinsèquement défavorisée même quand la stabilisation péricyclique de l'état de transition est possible. Les barrières d'inversion sont élevées parce qu'une matrice rigide ne peut accommoder une structure linéaire O-CH_3-O et que la vibration de déformation O-C-O est importante (effet Eschenmoser). Utilisant une nouvelle stratégie de conception, on a développé une matrice non rigide dans laquelle la barrière ainsi que l'effet isotopique cinétique CH_3/CD_3 sont les mêmes que dans la réaction intermoléculaire.

Mots clés : effet Eschenmoser, effets isotopiques, compression, S_N2, réarrangement sigmatropique.

[Traduit par la rédaction]

Received April 21, 1998.

S. Wolfe,[1] C-K. Kim,[2] K. Yang,[3] N. Weinberg, and Z. Shi.
Department of Chemistry, Simon Fraser University, Burnaby, BC V5A 1S6, Canada.

[1] Author to whom correspondence may be addressed.
Telephone: (604) 291–5972. Fax: (604) 291–5973. E-mail:

© 1998 NRC Canada

Introduction

Steric compression and the S_N2 transition state

Over half a century elapsed between Baeyer's postulate of *Spannung* (1), Kehrmann's discussion of *Raumerfüllung* (2), Meyer's *Gesetze der sterischen Behinderungen* (3), and the first attempts to quantify the concept of steric compression. Following a suggestion that the low reactivities of neopentyl halides in bimolecular substitution reactions are caused by compression of their S_N2 transition states (4), Dostrovsky, Hughes, and Ingold (5) developed a rudimentary force field to calculate this compression and to pattern reactivity trends in a series of identity reactions (eq. [1])

[1] $X^- + R\text{-}X \rightarrow X\text{-}R + X$

with R = methyl, ethyl, *n*-propyl, isopropyl, isobutyl, *t*-butyl, and neopentyl. Because the information needed to treat bond stretching and bending at the reactive carbon was not yet very accurate or complete, an idealized transition state model was

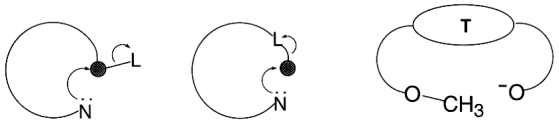

1 2 3

assumed in which the reactive carbon atom and the entering and leaving groups were collinear, with C—X bond lengths that remained constant throughout the series. Compression was then calculated by the assumption of an appropriate functional form for the van der Waals repulsions between nonbonded atoms. Although the specific choices made by these authors could be criticized (6), and later workers found the calculations to be "so cumbersome that few...have felt able to discuss the method...in any detail" (7), this daring intellectual exercise, together with an important contemporaneous suggestion by T.L. Hill (8) and Westheimer's treatment of biphenyl atropisomerism (9), are the foundations of today's sophisticated molecular mechanics procedures (10).

The force field treatment of S_N2 transition states was refined by the Ingold school (11) and then by Abraham et al. (7) and de Tar et al. (12). In the latter work, for the series X = Br and R = *n*-propyl, isobutyl, and neopentyl, increasing steric compression in the transition states was seen in a gradual increase in the C—Br bond lengths (2.22, 2.23, 2.28 Å) and a systematic decrease in the Br-C-Br bond angles (161.4, 155.3, 143.2°). These geometric trends reflect the use of a bending force constant (3×10^{-5} mdyn Å deg^{-2} molecule^{-1}) (1 dyn = 10 μN) that allows compression in the β-series to be more easily relieved by bending than by stretching (force constant 6.6×10^{-2} mdyn Å^{-1} molecule^{-1}). It is noteworthy that AM1 calculations (13, present work) (see also ref. 14) reproduce the force-field trends in the C—Br bond lengths (2.29, 2.30, and 2.31 Å, respectively), and the Br-C-Br bond angles (159.4, 155.5, and 145.3°) of the transition structures.

Longitudinal compression of the S_N2 transition state

There is an obvious relationship between the classical alkyl halide reactivity sequence (ethyl > propyl > isobutyl > neopentyl) (3, 4) and the calculated *longitudinal* compression of their S_N2 transition structures, by which we mean the compression of these structures in the X–C–X plane. Eschenmoser and co-workers (15) were the first to recognize and prove that although the formation of five- and six-membered rings by exocyclic S_N2 ring closure, i.e., **1**, is highly favored over competing intermolecular reactions (16, 17), the deceptively enticing methyl transfer depicted in **2** is so inhibited by longitudinal compression in a five- or six-membered cyclic *transition state* that only intermolecular reactions are observed. Subsequent work by King and McGarrity (18) confirmed that the "failure to observe the endocyclic reaction arises not because the intermolecular reaction is inordinately fast but simply because the intramolecular reaction is slow" and undetectable when the endocyclic transition state contains fewer than nine atoms. There are now many examples of endocyclic restriction of the S_N2 mechanism (19), and the synthetic implications of this effect have been the subject of much interest (20).

Fig. 1. Upper: optimized 3-21+G inversion transition structure for the reaction $CH_3O^- + CH_3\text{-}OCH_3$. Lower: optimized 3-21+G retention transition structure for the reaction $CH_3O^- + CH_3\text{-}OCH_3$.

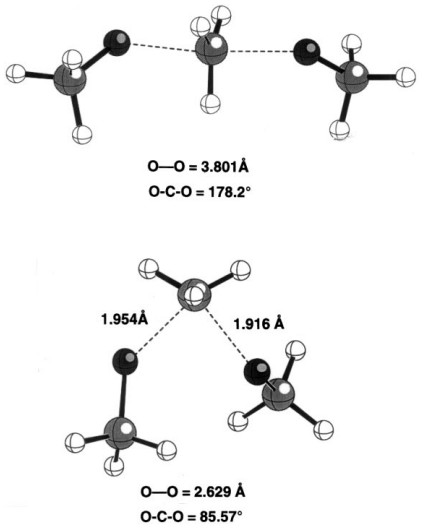

Longitudinal compression and secondary H/D isotope effects

We have recently discussed the effect of longitudinal compression on the barriers and secondary kinetic CH_3/CD_3 isotope effects (k_H/k_D) of intermolecular methyl-transfer reactions (21). The isotope effects are inverse ($k_H/k_D < 1$), primarily as a result of the increase in C-H (C-D) stretching frequencies that accompanies the tetrahedral to trigonal change in geometry of the methyl group (22).[4] Because the X-C-Y bond angles of the transition structures of such reactions are close to 180°, compression has implied a tightening (23) of C—X and C—Y bond lengths in the transition state. In both identity (X = Y) and nonidentity (X ≠ Y) reactions, this kind of compression is found to be associated with a decrease in the barrier and an

[4] Some recent discussions of this subject, referring specifically to nonidentity methyl-transfer reactions (22*a*, *b*), are flawed (*i*) by a failure to recognize that the isotope effects in such reactions are determined, inter alia, by the isotope effects of the two identity reactions and the reaction enthalpy (21*b*); (*ii*) by the contention that ion–molecule complexes do not have to be taken into account. Further discussion of this latter point can be found in footnote 81 of ref. 22*c*.

© 1998 NRC Canada

Fig. 2. Left: transition structure, barrier, and CH_3/CD_3 kinetic isotope effect for intramolecular methyl transfer in **4**. Center: transition structure, barrier, and CH_3/CD_3 kinetic isotope effect for intramolecular methyl transfer in the reaction **5** ⇌ **6**. Right, transition structure, barrier, and CH_3/CD_3 for intramolecular methyl transfer in **7**.

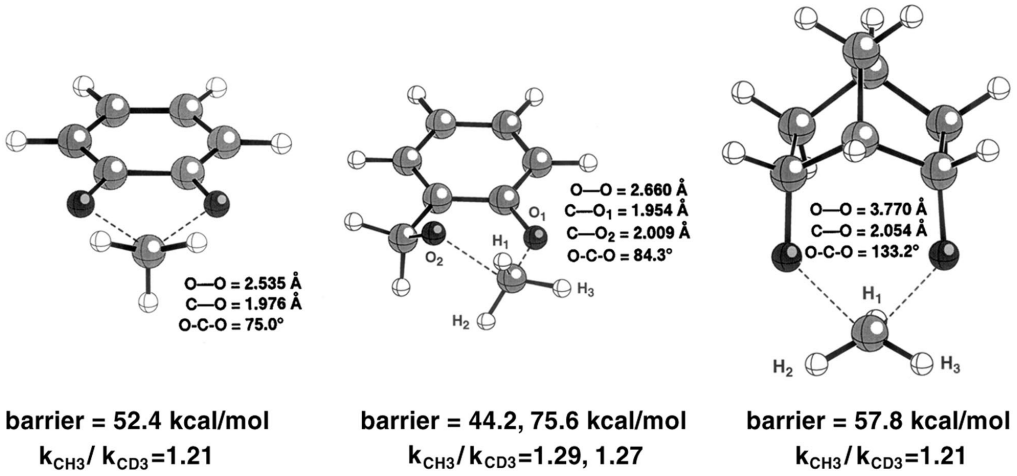

Fig. 3. Left: intramolecular methyl transfer in **8** with retention of configuration. Right: intramolecular methyl transfer in **8** with inversion of configuration.

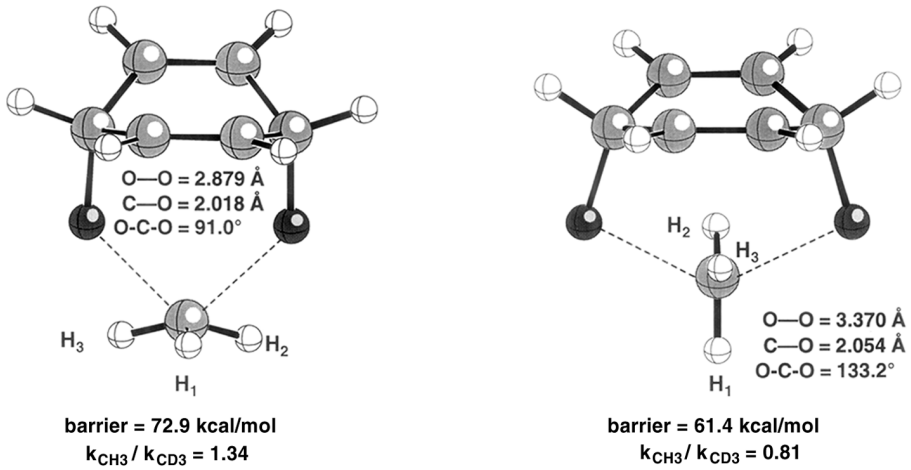

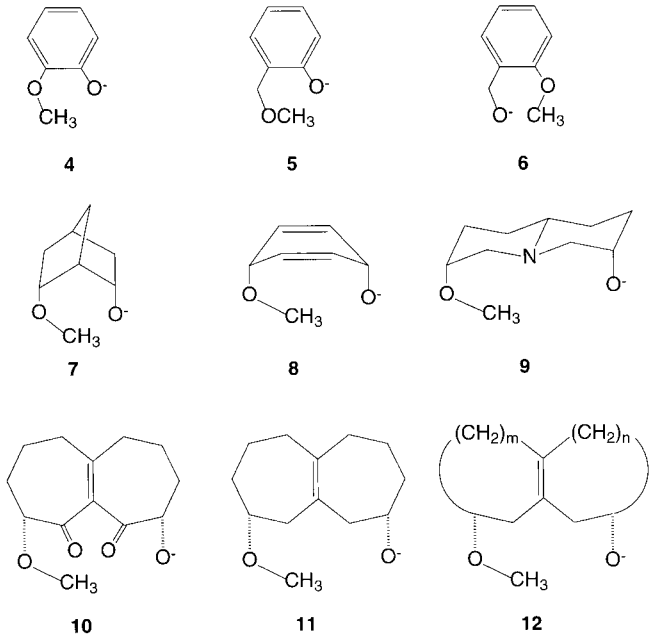

increase in k_H/k_D. We have noted that these findings create a problem for the contention (24) that k_H/k_D decreases in enzymic methyl transfer because of specific compression of the enzymic transition state and that this compression may represent the source of the enzymatic catalysis.[5]

Transverse compression

The present work was undertaken to explore the consequences of both longitudinal and transverse compression on the barriers and secondary isotope effects of intramolecular methyl-transfer reactions. By transverse compression we mean compression in the plane perpendicular to the X–C–Y plane and, specifically, compression of C—H bonds in the transition structure. It was reasoned that because the change in these bond lengths had already been found to be primarily responsible for the inverse isotope effect, any structural factor that causes additional compression of these bonds should lead to a more inverse isotope effect, and that this might be achieved with a

[5] See ref. 24*e* for more recent work on this subject, leading to the conclusion that the enzymatic and nonenzymatic transition structures are very similar.

© 1998 NRC Canada

Fig. 4. Upper left: intramolecular methyl transfer in **9**. Lower left: a side view of the transition structure, with definitions of H_1, H_2, and H_3, and the contributions of these hydrons to the CH_3/CD_3 isotope effect. Upper center: intramolecular methyl transfer in **10**. Lower center: a side view of the transition structure.Upper right: intramolecular methyl transfer in **11**. Lower right: a side view of the transition structure.

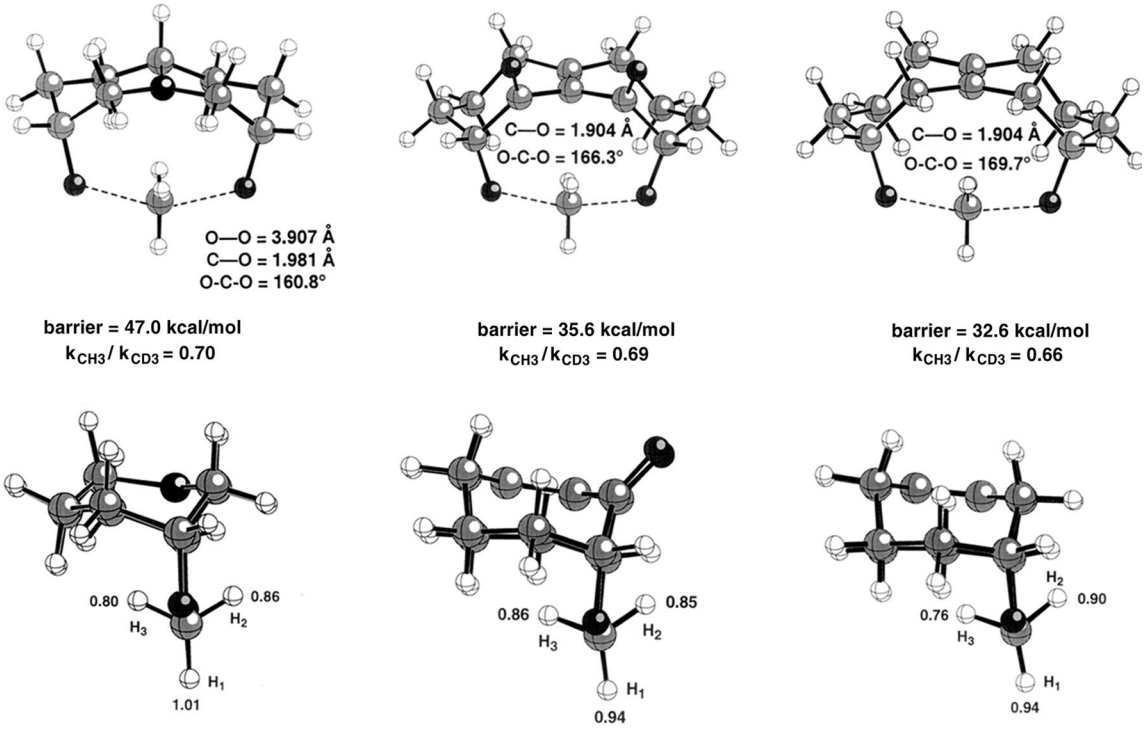

reactant such as **3** in which **T** is a template whose dimensions are to be determined. Ideally, **T** would provide both compression of the transition structure and catalysis of the reaction.

Results and discussion

Anionic intermolecular methyl transfer between two oxygens. The optimized retention and inversion transition structures

The problem was approached in stages. In the first stage, the compression effects encountered during methyl transfer between two oxygens were examined using, as a benchmark, 3-21+G calculations[6] (25) on the reaction of eq. [2]. The calculated barrier for

[2] $CH_3O^- + CH_3\text{-}OCH_3 \rightarrow CH_3O\text{-}CH_3 + {}^-OCH_3$

intermolecular methyl transfer with inversion of configuration is 25.4 kcal/mol, and the transition structure (Fig. 1, upper) has C—O bond lengths of 1.90 Å, an O—O distance of 3.8 Å, and an O-C-O angle of 178.2°. The transition structure for intermolecular methyl transfer with retention of configuration was also found. This structure (Fig. 1, lower) has C—O bond lengths of 1.95 and 1.92 Å, an O—O distance of 2.63 Å, an O-C-O angle of 85.6°, and it is 51.2 kcal/mol less stable than the structure of Fig. 1 (upper). This energy difference is so large (26) that nucleophilic displacement at carbon with apparent retention of configuration must be regarded as definitive evidence of a multistep process that includes an even number of inversion steps (27).

In the second stage, the effect of longitudinal compression on the energetics of intramolecular methyl transfer was estimated from the O–C–O bending force constant of the inversion transition structure of Fig. 1.[7] This 3-21+G force constant is part of the Gaussian output and is calculated to be 0.2634 hartree/bohr^2 (0.0503 kcal mol^{-1} deg^{-2}). Using the harmonic approximation ΔE (kcal/mol) = $k\theta^2/2$, where θ (degrees) is the deviation of the O-C-O angle from linearity, leads to ΔE = 2.52 and 5.66 kcal/mol for θ = 10° and θ = 15°, respectively. Since two competing reactions whose activation energies differ by 2.52 and 5.66 kcal/mol will differ in reactivity by factors of 70 and 14 000, respectively, at 298 K, a compression of as little as 10° in the O-C-O angle of an inversion transition structure would be sufficient to make intramolecular methyl transfer with inversion of configuration difficult to detect with respect to a competing unconstrained intermolecular inversion process.

CH_3/CD_3 isotope effects in intramolecular methyl transfer between oxygens separated by three, four, five, and six bonds. The retention and inversion mechanisms exhibit different isotope effects

Figures 2–4 show the results of 3-21+G calculations of intramolecular methyl transfer in the β, γ, δ, and ε-methoxyalkoxides **4**–**11**. These substrates have oxygens separated by three, four, five, or six bonds, and the relative positions of the oxygens are constrained by the templates. With the exception of **5** ⇌ **6**, all of the reactions are identity methyl transfers. Table 1 gives the enthalpies of activation calculated at MP2(= FC)/6–31+G*//3-21+G, the C—H bond lengths of the transition structures, the H/D isotope effect for each hydron, and the CH_3/CD_3 isotope effects.[8]

Only the retention mechanism was found in the cases of

[6] All ab initio calculations were performed using Gaussian 92 (25*c*).

[7] For related studies, see ref. 28.

[8] Isotope effects were calculated with the Bigeleisen equation (29*a*), using methods described in refs. 29*b* and *c*.

© 1998 NRC Canada

Table 1. Transition structure, C—H_i bond lengths, CH_i/CD_i isotope effects, CH_3/CD_3 isotope effects, and barriers[a] of intramolecular methyl-transfer reactions.

	Hydron	Bond length (Å)	k_H/k_D	k_{CH_3}/k_{CD_3}	Barrier
4	H_1	1.068	1.09		
	H_2	1.074	1.07		
	H_3	1.074	1.03	1.21	52.4
5	H_1	1.068	1.03		
	H_2	1.071	1.06		
	H_3	1.075	1.16	1.27[b]	75.6[b]
6				1.28[c]	44.2[c]
7	H_1	1.069	0.96		
	H_2	1.077	1.18		
	H_3	1.077	1.05	1.21	57.8
$\mathbf{8}_{ret}$	H_1	1.066	1.06		
	H_2	1.072	1.12		
	H_3	1.072	1.11	1.34	72.9
$\mathbf{8}_{inv}$	H_1	1.076	1.15		
	H_2	1.046	0.83		
	H_3	1.046	0.83	0.81	61.4
9	H_1	1.069	1.01		
	H_2	1.051	0.86		
	H_3	1.041	0.80	0.70	47.0
10	H_1	1.066	0.94		
	H_2	1.051	0.85		
	H_3	1.049	0.86	0.69	35.6
11	H_1	1.065	0.94		
	H_2	1.054	0.90		
	H_3	1.051	0.76	0.66	32.6

[a]Refers to $\Delta H^{\neq}$ in kcal/mol.
[b]Refers to **5** → **6**.
[c]Refers to **6** → **5**.

4–**7**, and only inversion was found for **9**–**11**. Both mechanisms were seen in the case of **8**.

The isotope effects in the inversion reactions constitute evidence for the postulated transverse compression of the S_N2 transition state. As noted in several studies (21, 30), C—H bond lengths in the transition structures of intermolecular methyl-transfer reactions do not depend strongly upon the nature of the entering and leaving groups. In the inversion transition structure of Fig. 1, the average C—H bond length is 1.064 Å. In the inversion transition structure of Fig. 3, one methyl hydron (H_1) is antiperiplanar to the π-system of the cyclohexadiene template, and its C—H bond is lengthened slightly (1.076 Å). The other hydrons (H_2 and H_3) are imbedded in the π-system, and their bond lengths are compressed to 1.046 Å. The isotope effect for H_1 is normal (1.15), but for H_2 and H_3 it is inverse (0.83). The stretching and bending contributions to the overall CH_3/CD_3 isotope effect of 0.81 are 0.69 and 1.17, respectively.

In the transition structure of **9** (Fig. 4, left), one methyl hydron (H_1) is antiperiplanar to the azadecalin skeleton, and its C—H bond length (1.069 Å) is normal. The isotope effect is also normal (1.01). The side view of this transition structure shows that a second methyl hydron (H_2) is compressed, by interaction with the equatorial hydrogens adjacent to nitrogen, to a bond length of 1.051 Å. Its isotope effect is 0.86. The third methyl hydron (H_3) lies under the nitrogen lone pair, and it is compressed to a bond length of 1.041 Å. Its isotope effect is 0.80. The CH_3/CD_3 isotope effect is 0.70.

In the transition structure of **10** (Fig. 4, center), H_1 is antiperiplanar to the bicyclic template, and it has the longest bond length (1.066 Å). A second hydron, H_3, is *endo* to the bicyclic system, and it has the shortest bond length (1.049 Å). The *exo* hydron, H_2, is *syn* to the carbonyl groups, and it has a bond length of 1.059 Å. The CH_3/CD_3 isotope effect is 0.69.

In the transition structure of **11** (Fig. 4, right), H_1 is antiperiplanar to the bicyclic template, and it has the longest bond length (1.065 Å) and highest k_H/k_D (0.94). The CH_3/CD_3 isotope effect is 0.66.

There is a significant difference in the isotope effects of the retention and inversion processes. The origin of this difference is best seen by examination of the retention and inversion transition structures of Fig. 3, which have (unscaled) imaginary frequencies of 834*i* and 860*i*, respectively. In the inversion structure, the imaginary frequency is the O–C–O antisymmetric stretch. In the retention structure, the imaginary frequency is a rocking motion about the C—H_1 bond as a pivot. The isotope effects are 1.06 for H_1 and 1.12 for H_2 and H_3. The CH_3/CD_3 isotope effect of 1.34 contains a stretching component of 1.07, a bending component of 1.34, and a stretch–bend component of 0.90. The principal contribution to the bending component of the isotope effect (k_{CH_3}/k_{CD_3} = 1.22) is made by a vibration, similar to that of the imaginary frequency, which has a frequency (uncorrected) of 958 cm^{-1}. This is shown as a series of instant structures at the left of Fig. 5,[9] together with the corresponding vibration in the inversion structure, which has a frequency (unscaled) of 1159 cm^{-1}, and contributes 0.97 to the overall 0.81 CH_3/CD_3 isotope effect.

The retention mechanisms found for **4** (Fig. 2, left) and **7** (Fig. 2, right) also exhibit normal isotope effects, 1.21 in each case. For **5** ⇌ **6** (Fig. 2, center), the isotope effects are 1.29 in the exoergic direction, and 1.27 in the endoergic direction.

The difference in the retention and inversion isotope effects appears to be large enough to offer an alternative to the chiral methyl group (32) for the determination of the stereochemical course of methyl transfer (33). More importantly (34), the difference in isotope effects can allow retention and double inversion mechanisms to be distinguished.

Barriers to methyl transfer in the rigid templates 4–11

All of the activation enthalpies shown in Table 1 are much larger than the barrier for intermolecular methyl transfer with inversion of configuration (25.4 kcal/mol). This is the expected result in the case of the retention mechanisms (26). In the case of the inversion mechanism for **8**, most of the excess energy of the transition structure originates in the longitudinal compression associated with an O-C-O angle of 133°.

In the case of **9**, the barrier is more than 20 kcal/mol higher than that of an intermolecular methyl transfer. Approximately half of this increase (9 kcal/mol) can be attributed to the longitudinal compression associated with the O-C-O angle of 161°. The remainder is caused by the compression of the template itself in the formation of the transition structure. For example, as summarized in Fig. 6, reoptimization of the reactant **9r** as **9r(t)**, with the azadecalin skeleton constrained to the geometry of the transition structure **9t**, destabilizes the

[9] These structures were generated using the programme XMol (31).

© 1998 NRC Canada

Fig. 5. A series of instant structures (top to bottom) showing the vibration that leads to the 958 cm^{-1} frequency in $\mathbf{10}_{ret}$ (left); secondary H/D isotope effects, 1.22; total, 1.34. The corresponding vibration in $\mathbf{10}_{inv}$ (right) has a frequency of 1159 cm^{-1}.

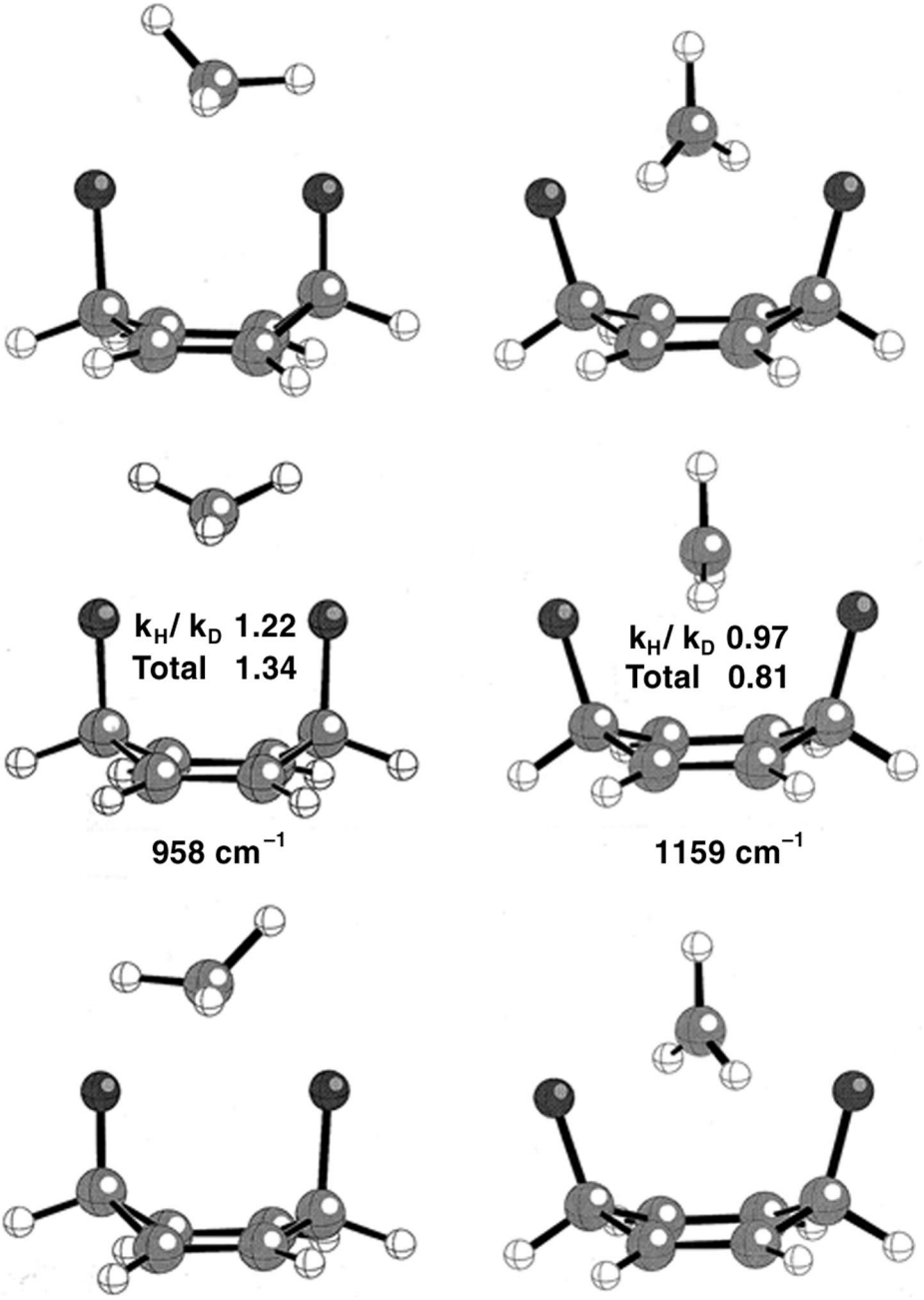

structure by 18.2 kcal/mol. Replacement of the oxygen atoms of **9r** and **9t** by hydrogens (**9r(H)** and **9t(H)**) and reoptimization with all other geometrical parameters constrained to those of **9r** and **9t**, reveals that the distortion of the azadecalin backbone amounts to 10 kcal/mol. The energy difference between **9t** and **9r(t)** is 28.8 kcal/mol, close to the 28.4 kcal/mol calculated when the carbon atoms geminal to oxygen in **9r** and **9t** are replaced by hydrogens, and the resulting structures **9rc** and **9ts** are reoptimized.

It is evident that the azadecalin backbone is too rigid, and that the geometry of **9** does not permit a linear methyl transfer. The sum of the angles at nitrogen in the transition structure **9t** is 359.1°, and in **9r** it is 344.8°. Inspection of **9r(H)** and **9t(H)** in Fig. 6 suggests that the planar configuration at nitrogen in the transition structure contributes 10 kcal/mol to the destabilization of the structure. This potential for distortion is avoided in **10** and **11**, because the bridgehead atoms are planar in both the reactant and the transition structure. Using AM1, the geometry of **12** was optimized for (*n*, *m*) = (1, 1), (1, 2), (2, 2), (2, 3), and (3, 3), and the O—O distances, O-C-O angles, and methyl-transfer barriers were examined in each case. This strategy led to the (3, 3) systems seen in **10** and **11**, in which the methyl-transfer barriers are reduced to 35.6 and 32.6 kcal/mol, respectively. However, although the longitudinal compression associated with the 170° O-C-O angle in the transition structure of **11** is estimated to be only 2.5 kcal/mol, the

© 1998 NRC Canada

Fig. 6. Analysis of the factors that contribute to the destabilization of the template in the transition structure of **9**.

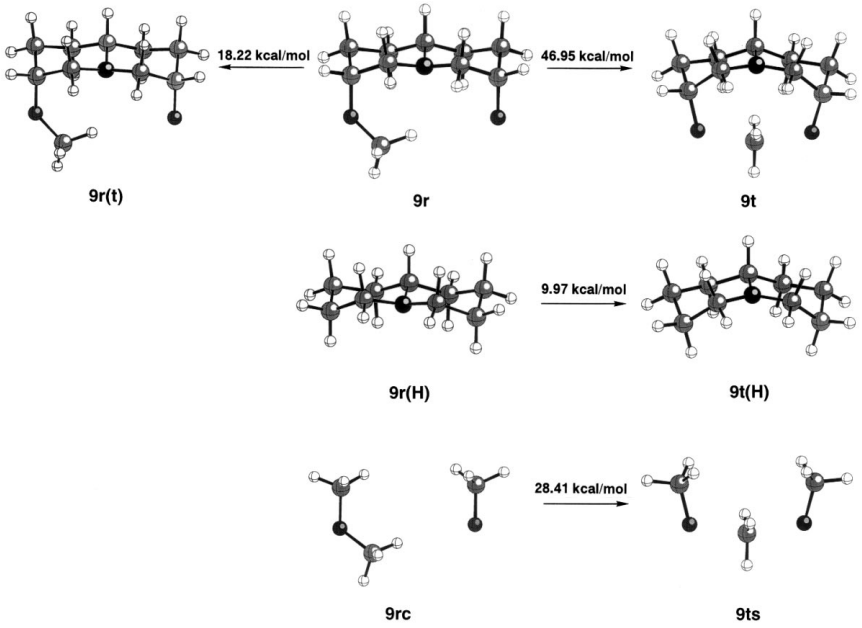

Fig. 7. Design of a flexible template for intramolecular methyl transfer.

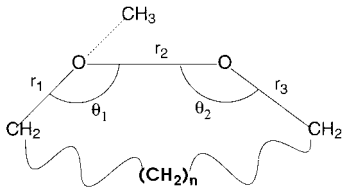

template is not entirely free of compression, and the barrier is still 7 kcal/mol higher than that of the parent intermolecular methyl-transfer reaction.

Design of a flexible template for intramolecular methyl transfer

Although transverse compression of the methyl-transfer transition state has thus been found to produce a more inverse secondary isotope effect, the additional compression introduced by the use of a rigid template overcomes any potential for catalysis of the process. It was, therefore, necessary to design an acyclic, flexible structure.

We have recently reported a novel stochastic search strategy for the conformational analysis of cyclic structures (35). Since the reactant (RC) and transition state (TS) of an intramolecular methyl transfer are pseudocyclic structures, it was possible to adapt this stochastic strategy to the search for superimposable RC and TS templates. The system was treated as an $(n + 4)$-membered ring (Fig. 7) containing an O···O "bond," with the bond lengths r_1, r_2, and r_3, and the bond angles θ_1 and θ_2 constrained to the values seen in the transition state and reactant of the intermolecular reaction. All other bond lengths and bond angles were found by MM3 minimization (36). The torsion angles of the $(CH_2)_n$ chain were obtained by random variation, as described previously (35). Using a 30° torsional increment, a total of 3733 RC rings and 3860 TS rings were produced from 10 000 randomly generated structures. Two thousand each of RC and TS rings were then minimized using MM3, with the bond lengths and bond angles at the reaction center frozen. This was achieved by the definition of atom types having $k_{stretch} = 100$ mdyn/Å (cf. $k_{CC} = 4.5$ mdyn/Å) and $k_{bend} = 10$ mdyn Å rad^{-2} (cf. $k_{CCC} = 0.67$ mdyn Å rad^{-2}). All other parameters of these atoms were taken from the values employed in MM3.

For the case of a 12-membered ring ($n = 8$), this strategy afforded 255 RC minima and 208 TS minima. These were then matched to identify structurally similar (RC, TS) pairs using the rms deviations of the torsion angles of the $(CH_2)_8$ chain as a criterion. The lowest energy pair was found to be the second lowest RC minimum (0.38 kcal/mol above the lowest minimum) and the second lowest TS minimum (0.34 kcal/mol above the lowest minimum). To complete the design process, the methyl group to be transferred was added.

Both of these structures were then subjected to 3-21+G minimization, and were optimized successfully. The results are summarized in structures **13-RC** and **13-TS** of Fig. 8, which also includes an optimized RC[10] and TS (cf. Fig. 1, upper) of the intermolecular methyl-transfer reaction.

It can be seen that the reactive centers of the two reactants and the two transition structures are virtually superimposable. The CH_3/CD_3 kinetic isotope effects calculated for RC → TS are also the same, and the free energies of activation differ by only 1.2 kcal/mol. The strategy employed to discover **13** thus appears to lead to a template for efficient intramolecular methyl transfer in the gas phase. Moreover, close examination of the CH_3 bond lengths included in Fig. 8 indicates that the methyl hydrogen that points towards the concave face of **13-TS** exhibits transverse compression. It should be possible to alter the properties of such templates by incorporation of substituents on the concave face of the chain, and initial studies

[10] This structure is not the global minimum at 3-21+G (29*b*), but it is a genuine stationary point having no imaginary frequencies.

© 1998 NRC Canada

Fig. 8. Intramolecular methyl transfer with inversion of configuration in the parent system (upper) and in the flexible template **13** (lower).

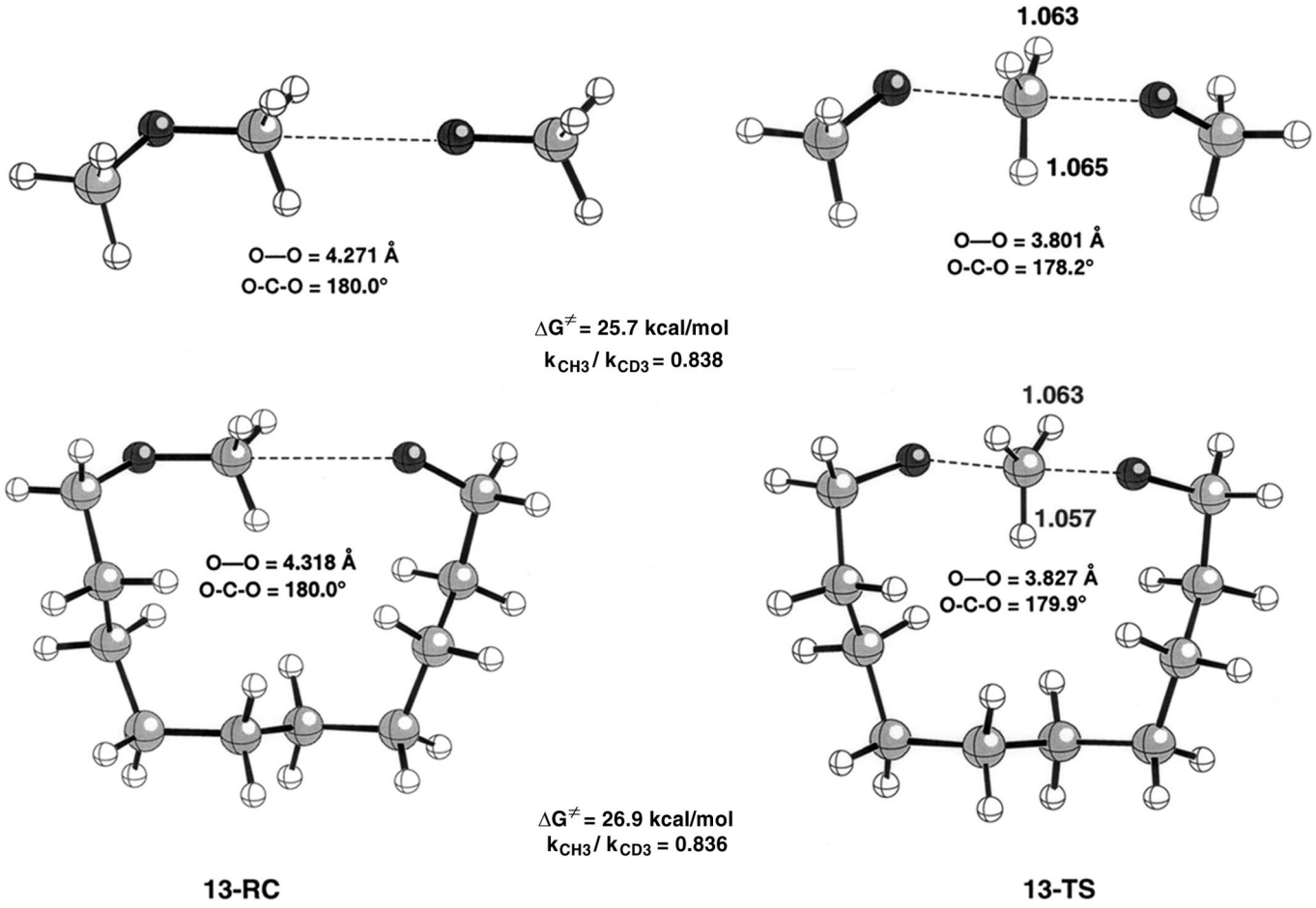

in this direction suggest that structures having $n > 8$ will be of interest.

The inversion barriers, geometrical parameters, and CH_3/CD_3 isotope effects of intramolecular methyl transfer are coupled

Figure 9 applies the Walsh–Gimarc rules (37) to the internal geometries of methyl groups having D_{3h} (**14**) and C_{2v} (**15**) symmetry. In **14**, the π-type *e* orbitals are degenerate. In **15**, the orbitals are nondegenerate; an increase in the H_b-C-H_b angle stabilizes the b_2 orbital and destabilizes the a_1 orbital. The destabilization is caused by the increased out-of-phase interaction between the 1*s* coefficients of H_b and the 1*s* coefficient of H_a, which is relieved by an increase in the C—H_a bond length.[11]

As we have seen, there is a systematic decrease in the methyl-transfer barriers in the series **8** (Fig. 3), **9**, **10**, **11** (Fig. 4), and **13** (Fig. 8), mainly because the O-C-O angles of the transition structures increase from 133.2 to 179.8°. The decrease in the barriers is accompanied by a decrease in the H_2-C-H_3 angles, from 128.5° in **8** to 119.9° in **13-TS**, leading

Fig. 9. Application of the Walsh–Gimarc rules to the frontier orbitals of methyl groups having D_{3h} (**14**) and C_{2v} (**15**) symmetries.

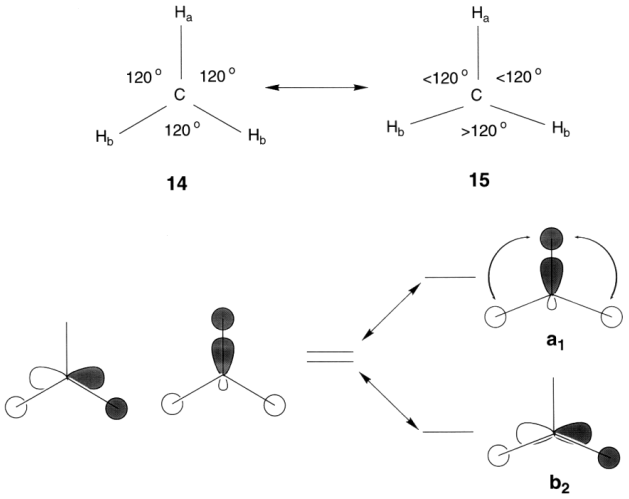

to an inverse relationship between the O-C-O and H_2-C-H_3 angles. This is shown in Fig. 10*a*, and is undoubtedly steric in origin. In accord with the Walsh–Gimarc rules, the decrease in the H_2-C-H_3 angle is accompanied by a decrease in the C—H_1 bond length (Fig. 10*b*), and the C—H_1 bond length

[11] These predictions have been confirmed by calculations on $CH_aH_bH_b^+$: as the H_b-C-H_b angle is increased, the C—H_a bond length is increased, the b_2 orbital is stabilized, and the a_1 orbital is destabilized.

© 1998 NRC Canada

Fig. 10. (*a*) Relationship between the H_2-C-H_3 and O-C-O bond angles in the transition structures of **8**, **9**, **10**, **11,** and **13**. (*b*) Relationship between the H_2-C-H_3 bond angles and C—H_1 bond lengths in the transition structures of **8**, **9**, **10**, **11**, and **13**. (*c*) The C—H_1 bond lengths of the transition structures correlate with the barriers of methyl transfer in **8**, **9**, **10**, **11,** and **13**. (*d*) The contribution of H_1 to the CH_3/CD_3 isotope effect in templates **8**, **9**, **10**, **11**, and **13** depends on the methyl-transfer barrier.

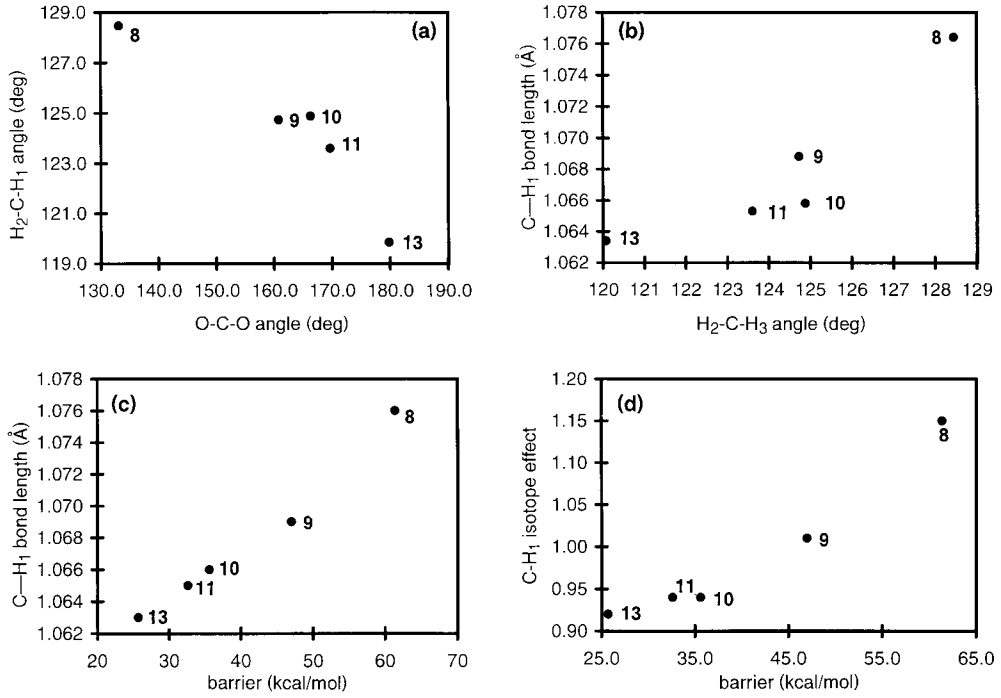

therefore decreases as the barrier decreases (Fig. 10*c*). As a result, the contribution of H_1 to the secondary CH_3/CD_3 isotope effect changes from normal to inverse as the barrier decreases (Fig. 10*d*).

The overall CH_3/CD_3 isotope effect also becomes more inverse as the barrier decreases (Fig. 11), but in the case of this property, **13** does not correlate with **8**–**11**. The reason for this is that intramolecular methyl transfer in **13** proceeds without longitudinal compression, and therefore resembles intermolecular methyl transfer, but the transverse compression of H_2 and H_3 in the transition structures of **8**–**11** causes the isotope effects to become more inverse.

Methyl transfer with retention of configuration. Can a [1*s*,4*s*] sigmatropic rearrangement be observed?

In the intramolecular methyl-transfer reactions of **4**–**8** (Figs. 2 and 3), the barrier is never less than 20 kcal/mol higher than that of an unconstrained inversion process and, in each case, the imaginary frequency of the retention transition structure is the rocking vibration discussed in Fig. 5. It is noteworthy that the transition structure of **4** (Fig. 2) exhibits no particular stabilization, because retention of configuration and a barrier less than 20 kcal/mol in the related reaction, the thermal rearrangement of 2-alkoxypyridine-1-oxides to 1-alkoxy-2-pyridones (**16** → **17**) have been thought to be consistent with a [1*s*,4*s*] sigmatropic rearrangement mechanism (38, 39). This interpretation is based on the orbital analysis shown at the top of Fig. 12, which suggests that a 1,4-suprafacial migration of a methyl group is thermally allowed. Although the HOMO of 4, also shown in Fig. 12, seems to support this interpretation, the argument does not take into account the repulsive, out-of-phase

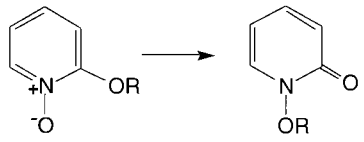

16 **17**

relationship between the orbital of the migrating group and the orbitals at the 2- and 3-positions, which will force this group towards the nodal plane of the π-system. The situation is analogous to that encountered in the frontier molecular orbital treatment of nucleophilic addition to a carbonyl group (Fig. 12, bottom). In the latter case, the well-known (40) nonperpendicular attack of the nucleophile can be rationalized as the result of the out-of-phase relationship between the orbital of the attacking nucleophile and the *p*-orbital on oxygen (41).

Examination of a side view of the intramolecular methyl-transfer transition structure of **4** (Fig. 13, top) shows that the migrating carbon is only 6° out of the plane of the aromatic system. To check whether this is a basis set effect, the reactant and transition structure of **4** were reoptimized at MP2/6–31+G*. The out-of-plane angle of the migrating methyl group increased to 29° (Fig. 13, bottom), but the barrier remained high (51.5 kcal/mol). Thus, although the 3-21+G basis set overemphasizes the nonperpendicular character of the transition structure of an intramolecular [1*s*,4*s*] sigmatropic methyl rearrangement, it is clear that competing, intermolecular reactions will make an intramolecular reaction experimentally unobservable. The work of Hoppe and Schöllkopf (38) therefore requires reexamination and reinterpretation (34).

© 1998 NRC Canada

Fig. 11. Transverse compression leads to a correlation between the CH_3/CD_3 isotope effects and barriers in the rigid templates **8–11**. The flexible template **13** exhibits different behavior.

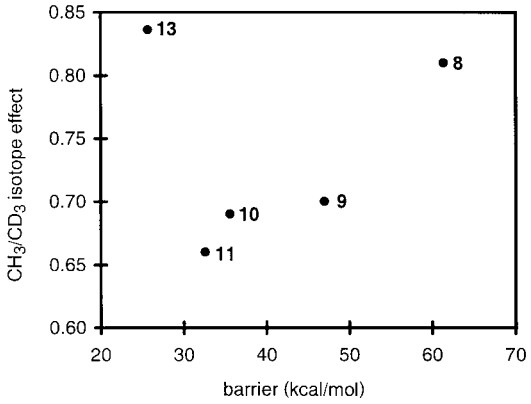

Fig. 12. Top left: orbital interaction between the HOMO of a 4π system and the LUMO of a methyl group; the phase relationship is correct for [1,4] sigmatropic rearrangement with retention of configuration, if the out-of-phase interactions (double-headed arrows) are ignored. Top right: the HOMO of **4**. Bottom: orbital interaction diagram proposed to explain nonperpendicular attack of a nucleophile on a carbonyl group.

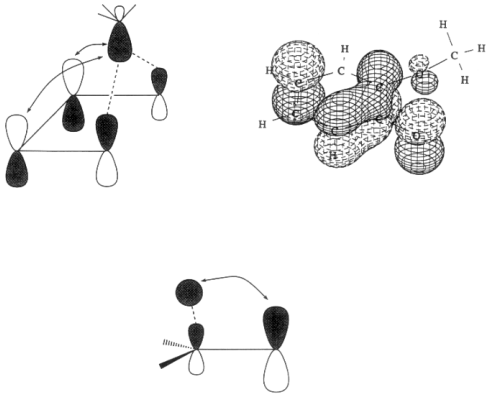

Theoretical procedures

Transition structures were located by the reaction coordinate method. The C···O bonds of the entering and leaving groups were fixed at several values near 1.9 Å, all other geometrical parameters were optimized, and the magnitudes and signs of the gradients of the two reaction coordinates were used to improve the trial values. When a structure close to the saddle point was reached, a final refinement was usually achieved using the OPT = CALCALL option of Gaussian 92 (25*c*) in which force constants are calculated in every iteration. For calculations of isotope effects, the frequencies employed as input to the Bigeleisen equation were obtained by scaling of the computed values by 0.9 (29).[12]

Summary and conclusions

Using ab initio molecular orbital theory mainly at the 3-21+G level, the CH_3/CD_3 kinetic isotope effects in intramolecular S_N2 methyl transfer between two oxygens have been found to be normal (1.21–1.34) for retention and inverse (0.66–0.81) for inversion of configuration. It is suggested that the difference in the retention and inversion isotope effects is large enough to constitute an alternative to the chiral methyl group for the determination of the stereochemical course of displacement at methyl, and to allow a genuine retention process to be distinguished from an even number of inversions.

The normal isotope effect in the retention mechanism is the result of a torsional motion about one of the C—H bonds as the methyl carbon rocks between the two oxygens. In the case of inversion, compression of C—H bonds by structural effects in the transition state, here termed transverse compression, increases the inverse isotope effect. The geometry of the methyl group is coupled to the O-C-O angle of the transition structure, so that the methyl C—H bond lengths, the O-C-O angle, the barrier, and the CH_3/CD_3 kinetic isotope effect are all coupled. A 10° deviation from linearity of the O-C-O angle of the inversion transition structure is sufficient to make an intramolecular reaction kinetically noncompetitive with respect to intermolecular processes.

For intramolecular methyl transfer within a rigid template, only a high energy retention mechanism can be found when the oxygens are separated by three or four bonds, and only inversion is seen when the oxygens are separated by six bonds. Both mechanisms exist when the oxygens are separated by five bonds. Since nonlinear methyl transfer occurs within all of the rigid templates examined so far, none of these provides catalysis of the inversion mechanism. However, treatment of the reactant and transition structure of an intramolecular methyl transfer as pseudocyclic structures, and extension to such

Fig. 13. Side view of the transition structure for intramolecular methyl transfer in **4**; the methyl carbon is not perpendicular to the aromatic ring. Upper: 3-21+G optimization. Lower: MP2/6–31+G* optimization.

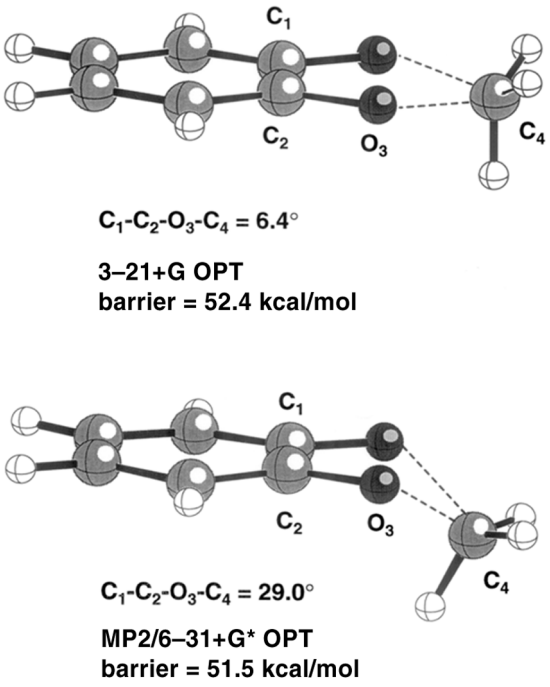

[12] The structures calculated in this work are available as supplementary material, which may be purchased from: the Depository of Unpublished Data, Document Delivery, CISTI, National Research Council of Canada, Ottawa, Canada K1A 0S2.

© 1998 NRC Canada

structures of a recently described stochastic approach to conformational analysis, has led to the discovery of a nonrigid template that permits linear methyl transfer to take place. This template has two oxygens separated by 10 carbons, and the intramolecular methyl-transfer barrier and CH_3/CD_3 isotope effect are the same as in the intermolecular reaction.

There is no evidence for pericyclic stabilization of a [1*s*,4*s*] intramolecular sigmatropic retention process in the degenerate rearrangement of the anion of *o*-catechol *O*-methyl ether. The reason for this is that the out-of-phase interaction between the *p*-orbital of the migrating group and *p*-orbitals of the aromatic ring forces the methyl group towards the nodal plane of the π-system.

Acknowledgements

The authors thank Dr. Inga Hoppe for kindly providing a copy of her 1971 Göttingen dissertation and the Natural Sciences and Engineering Research Council of Canada for financial support.

References

1. A. Baeyer. Chem. Ber. **18**, 2269 (1885).
2. F. Kehrmann. Chem. Ber. **23**, 130 (1890).
3. V. Meyer. Chem. Ber. **27**, 510 (1894).
4. E.D. Hughes. Trans. Faraday Soc. **37**, 603 (1941).
5. I. Dostrovsky, E.D. Hughes, and C.K. Ingold. J. Chem. Soc. 173 (1946).
6. A.G. Evans, M.G. Evans, and M. Polanyi. J. Chem. Soc. 558 (1947).
7. M.H. Abraham, P.L. Grellier, and M.J. Hogarth. J. Chem. Soc. Perkin Trans. 2, 1365 (1975).
8. T.L. Hill. J. Chem. Phys. **14**, 465 (1946).
9. F.H. Westheimer and J.E. Mayer. J. Chem. Phys. **14**, 733 (1946); F.H. Westheimer. J. Chem. Phys. **15**, 252 (1947); *In* Steric effects in organic chemistry. *Edited by* M.S. Newman. John Wiley, New York. 1956.
10. D.H.R. Barton. J. Chem. Soc. 340 (1948); J.B. Hendrickson. J. Am. Chem. Soc. **83**, 4537 (1961); K.B. Wiberg. J. Am. Chem. Soc. **87**, 1070 (1965); J.D. Dunitz and H.-B. Bürgi. *In* Chemical crystallography. MTP International Review of Science, Physical Chemistry. Ser. 2. Vol. 11. *Edited by* J.M. Robertson. Butterworths, London. 1975. p. 81; A. Warshel. *In* Modern theoretical chemistry. Vol. 7. *Edited by* G.A. Segal. Plenum Press, New York. 1977. p. 133; U. Burkert and N.L. Allinger. Molecular mechanics. ACS Monograph 177. American Chemical Society, Washington, D.C. 1982; E. Osawa and H. Musso. Top. Stereochem. **13**, 117 (1982); N.L. Allinger. *In* Accurate molecular structures. Their determination and importance. *Edited by* A. Domenicano and I. Hargittai. Oxford University Press, Oxford. 1992. p. 336.
11. P.B.D. De la Mare, L. Fowden, E.D. Hughes, C.K. Ingold, and J.D.H. Mackie. J. Chem. Soc. 3200 (1955).
12. D.F. de Tar, D.F. McMullen, and N.P. Luthra. J. Am. Chem. Soc. **100**, 2484 (1978).
13. M.J.S. Dewar, E.G. Zoebisch, E.F. Healy, and J.J.P. Stewart. J. Am. Chem. Soc. **107**, 3902 (1985).
14. N.T. Anh, F. Maurel, B.T. Thanh, H.H. Thao, and Y.T. N'Guessan. New J. Chem. **18**, 473 (1994); N.T. Anh, B.T. Thanh, H.H. Thao, and Y.T. N'Guessan. New J. Chem. **18**, 489 (1994); F.R. Jensen. Chem. Phys. Lett. **196**, 368 (1992).
15. L. Tenud, S. Farook, J. Seibl, and A. Eschenmoser. Helv. Chim. Acta, **53**, 2059 (1970).
16. L. Ruzicka, W. Brugger, M. Pfeiffer, H. Schinz, and M. Stoll. Helv. Chim. Acta, **9**, 499 (1926).
17. C. Galli, G. Illuminati, L. Mandolini, and P. Tamborra. J. Am. Chem. Soc. **99**, 2591 (1977); L. Mandolini. J. Am. Chem. Soc. **100**, 499 (1978); D.F. DeTar and N.P. Luthra. J. Am. Chem. Soc. **102**, 4505 (1980).
18. J.F. King and M.J. McGarrity. J. Chem. Soc. Chem. Commun. 1140 (1979); J. Chem. Soc. Chem. Commun. 175 (1982); M.J. McGarrity, J.F. King, and J.B. Stothers. Tetrahedron Lett. **23**, 4465 (1982).
19. P. Beak. Acc. Chem. Res. **25**, 209 (1992); V.I. Minkin, L.P. Olekhanovich, and Yu. A. Zhdanov. Molecular design of tautomeric compounds. Reidel Publishing Company, Dordrecht, The Netherlands. 1988.
20. G. Stork and J.F. Cohen. J. Am. Chem. Soc. **96**, 5270 (1974); F.M. Menger. Tetrahedron, **39**, 1013 (1983); S. Danishevsky. Science, **259**, 469 (1993).
21. (*a*) S. Wolfe and C.-K. Kim. J. Am. Chem. Soc. **113**, 8056 (1991); (*b*) R.J. Boyd, C.-K. Kim, Z. Shi, N. Weinberg, and S. Wolfe. J. Am. Chem. Soc. **115**, 10147 (1993).
22. (*a*) R.A. Poirier, Y. Wang, and K.C. Westaway. J. Am. Chem. Soc. **116**, 2526 (1994); (*b*) I. Lee. Chem. Soc. Rev. **24**, 223 (1995); (*c*) M.N. Glukhovtsev, A. Pross, and L. Radom. J. Am. Chem. Soc. **118**, 6273 (1996); S. Glad and F. Jensen. J. Am. Chem. Soc. **119**, 227 (1997).
23. S.S. Shaik, H.B. Schlegel, and S. Wolfe. Theoretical aspects of physical organic chemistry. The S_N2 mechanism. Wiley-Interscience, New York. 1992.
24. (*a*) I. Mihel, J.O. Knipe, J.K. Coward, and R.L. Schowen. J. Am. Chem. Soc. **101**, 4349 (1979); (*b*) C.H. Gray, J.K. Coward, K.B. Schowen, and R.L. Schowen. J. Am. Chem. Soc. **101**, 4351 (1979); (*c*) M.F. Hegazi, R.T. Borchardt, and R.L. Schowen. J. Am. Chem. Soc. **101**, 4359 (1979); (*d*) J. Rodgers, D.A. Femec, and R.L. Schowen. J. Am. Chem. Soc. **104**, 3263 (1982); (*e*) Y.-J. Zheng and T.C. Bruice. J. Am. Chem. Soc. **119**, 8137 (1997).
25. (*a*) T. Clark, J. Chandrasekhar, G.W. Spitznagel, and P.v.R. Schleyer. J. Comput. Chem. **4**, 294 (1983); (*b*) W.J. Hehre, L. Radom, P.v.R. Schleyer, and J.A. Pople. Ab initio molecular orbital theory. Wiley-Interscience, New York. 1985; (*c*) M.J. Frisch, G.W. Trucks, M. Head-Gordon, P.M.W. Gill, M.W. Wong, J.B. Foresman, B.G. Johnson, H.B. Schlegel, M.A. Robb, E.S. Replogle, S. Gomperts, J.L. Andres, K. Raghavachari, J.S. Binkley, C. Gonzalez, R.L. Martin, D.J. Fox, D.J. DeFrees, J. Baker, J.J.P. Stewart, and J.A. Pople. Gaussian 92, Revision B. Gaussian, Inc., Pittsburgh, Pa. 1992.
26. L. Deng, V. Branchadell, and T. Ziegler. J. Am. Chem. Soc. **116**, 10645 (1994); S. Harder, A. Streitwieser, J.T. Petty, and P.v.R. Schleyer. J. Am. Chem. Soc. **117**, 3253 (1995); M.N. Glukhovtsev, A. Pross, H.B. Schlegel, R.D. Bach, and L. Radom. J. Am. Chem. Soc. **118**, 11258 (1996).
27. H.G. Floss and S. Lee. Acc. Chem. Res. **26**, 116 (1993); D.R. Houck, K. Kobayashi, J.M. Williamson, and H.G. Floss. J. Am. Chem. Soc. **108**, 5365 (1986); T. Frenzel, P. Zhou, and H.G. Floss. Arch. Biochem. Biophys. **278**, 35 (1990).
28. V.I. Minkin, M.E. Kletskii, R.M. Minyaev, B. Ya. Simkin, and V.A. Pichko. Zh. Org. Khim. **19**, 9 (1983); C.H. Heathcock, T.W. von Geldern, C.B. Lebrilla, and W.F. Maier. J. Org. Chem. **50**, 968 (1985).
29. (*a*) J. Bigeleisen. J. Chem. Phys. **17**, 675 (1949); (*b*) S. Wolfe, S. Hoz, C.-K. Kim, and K. Yang. J. Am. Chem. Soc. **112**, 4186 (1990); (*c*) S. Wolfe and C.-K. Kim. J. Am. Chem. Soc. **113**, 8056 (1991).
30. M.N. Glukhovtsev, A. Pross, and L. Radom. J. Am. Chem. Soc. **117**, 2024 (1995).
31. XMol: Version 1.3.1. Minnesota Supercomputer Center, Inc., Minneapolis, Minn. 1993.
32. J.W. Cornforth, J.W. Redmond, H. Eggerer, W. Buckel,and C.

© 1998 NRC Canada

Gutschow. Nature, **221**, 1212 (1969); J. Lüthy, J. Rétey, and D. Arigoni. Nature, **221**, 1213 (1969).
33. T.R. Griffin, D.B. Cook, A. Haynes, J.M. Pearson, D. Monti, and G.E. Morris. J. Am. Chem. Soc. **118**, 3029 (1996).
34. S. Wolfe, K. Yang, N. Weinberg, Z. Shi, Y.-H. Hsieh, S. Ro, and R.D. Sharma. Chem. Eur. J. **4**, 886 (1998).
35. N. Weinberg and S. Wolfe. J. Am. Chem. Soc. **116**, 9860 (1994).
36. N.L. Allinger, Y.H. Yuh, and J.-H. Lii. J. Am. Chem. Soc. **111**, 8551 (1989).
37. A.D. Walsh. J. Chem. Soc. 2260 (1952), et seq.; B.M. Gimarc. Acc. Chem. Res. **7**, 384 (1974); B.M. Gimarc. Molecular structure and bonding. The qualitative molecular orbital approach. Academic Press, New York. 1979.
38. I. Hoppe. Doctoral dissertation. Göttingen, Germany. 1971; U. Schöllkopf and I. Hoppe. Tetrahedron Lett. **27**, 4527 (1971); Ann. Chem. **765**, 153 (1972).
39. R.B. Woodward and R. Hoffmann. Angew. Chem. Int. Ed. Engl. **8**, 781 (1969).
40. H.-B. Bürgi, J.D. Dunitz, and E. Shefter. J. Am. Chem. Soc. **95**, 5065 (1973); H.-B. Bürgi, J.D. Dunitz, J.-M. Lehn, and G. Wipff. Tetrahedron, **30**, 1563 (1974); H.-B. Bürgi, J.-M. Lehn, and G. Wipff. J. Am. Chem. Soc. **96**, 1956 (1974).
41. N.T. Anh and O. Eisenstein. Nouv. J. Chim. **1**, 61 (1977); N.T. Anh. Orbitales frontières. CNRS Éditions, Paris. 1995. pp. 123, 124.

© 1998 NRC Canada

1997 Canadian Society for Chemistry Award Lecture
Ring-opening polymerization (ROP) of strained metallocenophanes: the discovery and development of a new route to high molecular weight poly(metallocenes)[1]

Ian Manners

Abstract: Ring-opening polymerization (ROP) of strained ring-tilted metallocenophanes can be achieved thermally, via anionic or cationic initiation, or by the use of transition-metal catalysts and provides access to a wide range of high molecular weight ($M_w = 10^5$–10^6, $M_n > 10^5$) poly(metallocenes). These materials possess a variety of interesting properties and many are very easy to prepare. This article provides an overview of our work, giving background to and an account of the initial discovery, and discusses work on the synthesis and properties of new poly(metallocenes) and related materials with particular emphasis on recent research directions.

Key words: metallocene, ring-opening polymerization, ferrocenophane, organometallic polymer.

Résumé : La polymérisation par ouverture de cycle (POC) métallocénophanes tendus à cycles inclinés peut être réalisée thermiquement, par initiation anionique ou par utilisation de catalyseurs de métaux de transition; elle donne accès à un éventail important polymétallocènes de poids moléculaires élevés ($M_w = 10^5$–10^6, $M_n > 10^5$). Ces produits possèdent une variété de propriétés intéressantes et un bon nombre peuvent être préparés facilement. Cet article présente une vue d'ensemble de nos travaux préliminaires et de nos découvertes initiales et il permet de discuter de la synthèse et des propriétés de nouveaux polymétallocènes et de produits apparentés en insistant particulièrement des directions de nos travaux récents.

Mots clés : métallocène, polymérisation par ouverture de cycle, ferrocenophane, polymère organométallique.

[Traduit par la rédaction]

Introduction

It is well established that transition-metal complexes and metal-containing solid-state materials possess a diverse array of interesting and useful redox, magnetic, optical, electrical, and catalytic properties. Polymers, on the other hand, are ubiquitous because of their tremendous processing advantages over ceramics and metals. The incorporation of transition metals into a polymer main chain therefore offers unique potential for the preparation of processable materials with properties that differ significantly from those of conventional organic polymers (1, 2). In addition, the diverse range of coordination numbers and geometries that exist for transition elements offer the possibility of accessing polymers with unusual conformational, mechanical, and morphological characteristics. Transition-metal-based polymers might also be expected to function as convenient and processable thermal or photochemical precursors to metal-containing ceramic films, fibers, and coatings with high stability and desirable and useful physical properties. However, the development of the area of transition-metal-based polymer science has been held up by considerable synthetic difficulties (2).

Much of the early work in the field in the 1950s and 1960s targeted poly(metallocenes) (3). Such efforts were encouraged by the remarkable stability and fascinating properties of monomeric and dimeric metallocenes, which were discovered by the fundamental exploratory chemistry conducted during this period. However, most of the attempted polymer syntheses utilized polycondensation reactions where either the difunctional precursors were impure or the coupling chemistry was not clean. For such step-growth processes this guaranteed the generation of low molecular weight materials ($M_n <$ ca. 3000) (4). In addition, the resulting products were often insoluble and poorly characterized. Indeed, at the end of a comprehensive review of the field of metallocene-based polymers in 1970 the authors made the critical analysis that many of the structures assigned to the polymers in the article were "hypothetical and need rigorous analytical verification, and the description of

Received December 23, 1997.

I. Manners.[2] Department of Chemistry, University of Toronto, 80 St. George St., Toronto, ON M5S 3H6, Canada.

[1] This is an invited article based on the 1997 Canadian Society for Chemistry Award for Pure or Applied Inorganic Chemistry.

[2] Telephone: (416) 978-6157. Fax: (416) 978-6157. E-mail: imanners@alchemy.chem.utoronto.ca

© 1998 NRC Canada

experimental procedures and polymer properties more often than not has been superficial or has been lacking altogether" (5).

In the summer of 1990 we initiated a research program in Toronto with a major aim of exploring the use of ring-opening polymerization (ROP) as a route to polymers with metal atoms in the main chain.[3] Generally ROP processes occur via a chain-growth route, which involves a highly reactive intermediate that reacts rapidly with monomer molecules. This allows the facile formation of long polymer chains making high molecular weight polymers easily accessible (2). This is vital as high molecular weights (M_n > ca. 10 000) are required in order to realize the chain entanglement needed to access the advantageous properties of macromolecules such as ease of fabrication into films (2).

At the time we initiated our research program the only reports of the ROP of metal-containing rings involved brief communications on the polymerization of metallaphosphazene rings. In addition, very limited characterization of the resulting poly(metallaphosphazenes) was given (7). Our initial work focussed on the ROP of ferrocenophanes targeting polymers with ferrocene units in the main chain linked by spacers that should permit metal–metal interactions such as organosilane or other σ- or π-conjugated groups.

Previous work on strained [1]ferrocenophanes

The first polymers constructed from ferrocene and organosilane units were briefly described in two patents by Rosenberg and Rausch (8*a*) and Rosenberg (8*b*) in the 1960s. Polycondensation of dilithioferrocene, $fcLi_2$ (fc = $Fe(\eta\text{-}C_5H_4)_2$), with dichloroorganosilanes, R_2SiCl_2, was the reported method (eq. [1]), but the products of assigned structure **1** were black and impure, of low molecular weight (mainly M_n < 2000), and poorly characterized (8).[4]

[1] 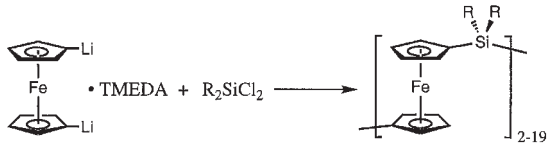

1

At that time [1]ferrocenophanes of any type were unknown, and although their potential presence in the reaction mixtures was considered by Rosenberg et al. (9), it was concluded that such species would be too strained to exist.[5] In 1975 Osborne and Whiteley (10) at the University of Exeter, England, reported the synthesis and characterization of the first [1]ferrocenophane, the $SiPh_2$-bridged species **2**, via the reaction of $fcLi_2$·TMEDA (TMEDA = tetramethylethylenediamine) with Ph_2SiCl_2 in nonpolar solvents (eq. [2]). These researchers showed, using single crystal X-ray diffraction, that **2** possessed a strained structure with a tilt-angle between the planes of the cyclopentadienyl ligands of ca. 19° (11). In contrast, in ferrocene the cyclopentadienyl rings are parallel.

[2] 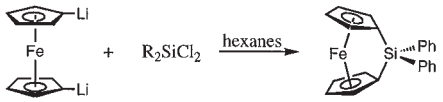

2

The Wrighton group (12) at M.I.T. subsequently synthesized the $SiMe_2$– and $SiCl_2$-bridged analogs in the late 1970s and showed that the methylated species undergoes stoichiometric ring-opening reactions with methanol and other reagents containing reactive -OH functionalities. This chemistry was exploited to allow the controlled derivatization of silica and other materials.

The range of [1]ferrocenophanes was extended in the early 1980s to Ge-, P-, and As-bridged species by the groups of Osborne, Seyferth, and Cullen (13–15). The stoichiometric, anionically induced ring-opening of the phosphorus-bridged [1]ferrocenophane **3** to yield **4** was also described (16) (eq. [3]).

[3] 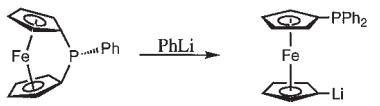

3 **4**

In addition, linear oligomers with between two and five repeat units (mainly the dimer and trimer) were isolated in reactions of **3** with **4** as anionic initiator (17) (eq. [4]). However, attempts to form polymers via anionic ROP of **3** using small quantities of anionic initiator were unsuccessful and afforded unreacted **3** and the same distribution of low molecular weight oligomers $\mathbf{5}_{2-5}$ (mainly $\mathbf{5}_2$ and $\mathbf{5}_3$) (17). This unsuccessful experiment, the sole attempt to polymerize ferrocenophanes via ROP reported in the literature prior to our work, was explained in terms of the propagation step being unfavourable either due to steric effects or insolubility (17).

[4] 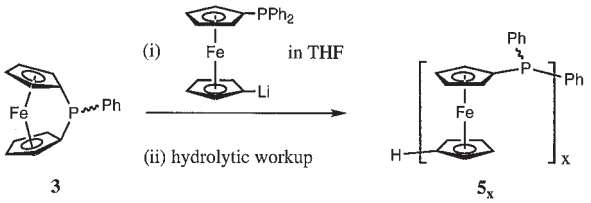

3 $\mathbf{5}_x$

mainly x = 2 or 3

x = 4 or 5 very small amounts

Seyferth et al. (14, 16, 17) also described the production of low molecular weight polymers **6** via the condensation polymerization of $fcLi_2$·TMEDA with $PhPCl_2$ (M_w = 8900) (17) (eq. [5]).

[3] We have also been active in the area of rings and polymers based on main group elements. For a recent review of our work see ref. 6.

[4] In one case involving the use of Ph_2SiCl_2 the resulting black polymer was reported to be only partially soluble, and the soluble fraction was shown by vapour pressure osmometry to possess M_n = ca. 7000. However, based on the insolubility of this material and on our light scattering studies of similar species it is very likely that the molecular weight is overestimated due to aggregation in solution.

[5] It is noteworthy that [2]ferrocenophanes were first prepared in the 1960s, but no studies of their ROP behavior were reported until 1993 (see ref. 52 and refs. cited therein).

© 1998 NRC Canada

[5] 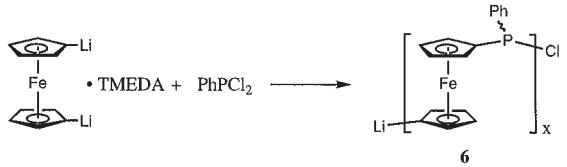

6

Interestingly, under certain conditions (lower temperatures, certain solvents, addition of $fcLi_2$ to $PhPCl_2$ rather than the reverse), the formation of high molecular weight polymers ($M_w > 40\,000$) was also noted (17). This would not be expected in a polycondensation reaction involving $fcLi_2$·TMEDA as a difunctional monomer, as this species is generally too impure to allow the exact stoichiometries necessary for the formation of high molecular weight materials via step-growth processes to be realized (2, 4). Our explanation of this observation was published in 1995 and was based on the advantage of hindsight gathered from our own successful studies of the anionic polymerization behavior of **3** (see below). Thus we suggested that under the specific reaction conditions reported by Seyferth, the phosphorus-bridged [1]ferrocenophane **3** probably forms in situ and then indeed undergoes anionically initiated ROP induced by $fcLi_2$ (18, 19[6]).

The initial discovery of the ROP of [1]ferrocenophanes

The discovery of the ROP of strained metallocenophanes in our group illustrates, once again, the key role that a combination of planned ideas, serendipity, and outstanding, inquisitive students can play in scientific developments. In addition, the crucial role played by the earlier fundamental exploratory chemistry of Osborne (and later Seyferth and Cullen), which led to the synthesis of the structurally interesting molecules that we now refer to as "[1]ferrocenophane monomers" must not be overlooked, particularly in light of the current global trend towards directed research funding.

We identified silicon-bridged [1]ferrocenophanes such as **7** as potential monomers for ROP very early on (indeed, one of the author's proposed areas of research in 1989 that led to the tenure-track position at Toronto was the ROP of organometallic rings, including ferrocenophanes). However, initially we focussed on the ROP behavior of the disilane-bridged [2]ferrocenophane **8** and, unfortunately, found this species to be thermally stable to 350°C and to decompose to uncharacterized products at more elevated temperatures. Nevertheless, this disilane-bridged [2]ferrocenophane was found to exhibit some interesting Pd-catalyzed insertions of alkynes and dienes into the Si—Si bond (20).[7]

Fig. 1. Molecular structure of silicon-bridged [1]ferrocenophane **9** determined by X-ray diffraction. (Reproduced from ref. 20*b* with permission.)

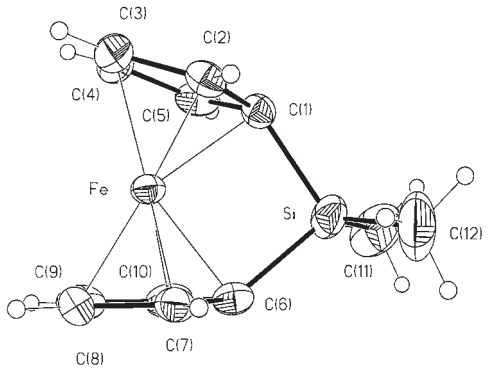

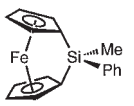

7

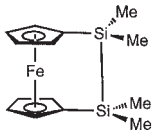

8

Although planned very early on, our work on silicon-bridged [1]ferrocenophanes turned out to be initiated accidentally. Dan Foucher, my first graduate student (and now a scientist at Xerox Research Center of Canada, Mississauga, Ont.) was trying to make the disubstituted ferrocene derivative $fc(SiMe_2Cl)_2$ from the reaction of $fcLi_2$·TMEDA and two equiv. of Me_2SiCl_2 for possible use in Wurtz coupling polymerization reactions. However, on vacuum distillation of the product, rather than the anticipated orange distillate, he obtained an orange polymer in the distillation pot. This he had the curiousity to purify by precipitation with the help of the very able Ben Zhong Tang, a postdoc and now a chemistry professor at Hong Kong University of Science and Technology. Analysis of the polymer by ^1H NMR showed the material to possess a 1:1 rather than the 1:2 ratio of ferrocene units to $SiMe_2$ groups expected from the reaction stoichiometry. Moreover, Dan, as enthusiastic as ever, phoned me at home late at night to inform me that the molecular weight (M_w) of the material had been measured by Gel Permeation Chromatography and was well over 300 000. A discussion of the results in my office with Dan and Ben the next day quickly led us to the conclusion that the polymer could not be formed by step-growth condensation polymerization of $fcLi_2$ with $fc(SiMe_2Cl)_2$, as the molecular weight was far too high. A chain-growth reaction involving the ROP of the [1]silaferrocenophane **9** appeared to be the only logical explanation. Dan Foucher and Ben-Zhong Tang quickly performed the reaction of $fcLi_2$·TMEDA and Me_2SiCl_2 in a 1:1 ratio and isolated the

[6] The discovery that silicon-bridged [1]ferrocenophanes also undergo anionic ROP (19*a*) also led us to speculate (19*b*), again with the advantage of hindsight, that a similar situation might exist for the reported condensation route to low molecular weight poly(ferrocenylsilanes) claimed in patents by Rosenberg and Rausch (8*a*) and Rosenberg (8*b*). Indeed, a recent reinvestigation of the reactions of $fcLi_2$ and R_2SiCl_2, under conditions similar to those described in one of the Rosenberg patents (8*b*), has identified [1]silaferrocenophanes as well as poly(ferrocenylsilanes) (up to 35%) in the reaction mixture in proportions dependent on the experimental conditions. The authors suggest that the polymers reported by Rosenberg were either formed by anionic ROP or, alternatively, were actually decomposition products due to a steam distillation step (19*c*).

[7] Interestingly, [3]trithiaferrocenophanes were also identified as potential monomers for ROP. However, no work was or has been carried out in our group, in particular because of the elegant atom-abstraction polymerization of these species (which gives polymers with a two sulfur atom spacer not three) discovered by Rauchfuss that was reported in early 1992. See ref. 21.

© 1998 NRC Canada

[1]ferrocenophane **9** (Fig. 1). To our great excitement the species thermally polymerized when heated in the melt at 130°C in a sealed tube. The resulting amber, fibrous solid material **10** was readily soluble in organic solvents and possessed a molecular weight (M_w) of over 500 000. This represented the first high molecular weight poly(ferrocenylsilane), the first poly(ferrocene) that had been unequivocally formed via ROP (eq. [6]).

[6] 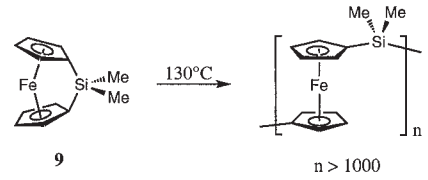

9 n > 1000 **10**

We held off publishing the results for some time as we attempted to get some companies to support a patent application, although some preliminary results were reported at a conference in Vancouver in the Fall of 1991 (22). Finally, after deciding that the first publication in the area would be more useful to a tenure track faculty member and their students than the prospect of a long process of producing examples and exploring applications for a patent, we submitted and published the work in the *Journal of the American Chemical Society* in 1992 (23). Included in this communication were electrochemical studies of the poly(ferrocenylsilane) **10**, which showed that the iron atoms interact with one another. Thus a two-wave cyclic voltammogram was obtained, which was explained in terms of initial oxidation at alternating iron sites and subsequent oxidation, which is more difficult, occurring at the iron atoms in between.

Since those initial discoveries our group has devoted considerable effort towards expanding the scope of the ROP chemistry and exploration of the properties and applications of the resulting poly(ferrocene) materials. Much of the earlier work published between 1992 and 1995 has been reviewed previously (24). In this article an overview of some of our recent work is therefore provided.

Synthesis and properties of poly(ferrocenylsilanes)

Since 1992, a wide range of silicon-bridged [1]ferrocenophanes **11** with either symmetrically or unsymmetrically alkyl or aryl substituted silicon atoms have been prepared and similarly polymerized to high molecular weight ($M_w = 10^5$–10^6, $M_n > 10^5$) poly(ferrocenylsilanes) **12** (eq. [7]). Substituents such as hydrogen, chlorine, trifluoropropyl, norbornenyl, and ferrocenyl groups have also been introduced (2, 24–26).

[7] 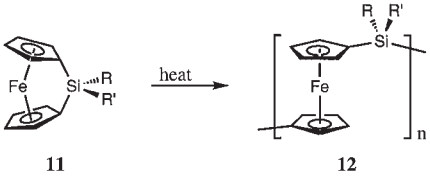

11 **12**

Very recently, we have found a facile route to the first poly(ferrocenylsilanes) **15** and **17** with alkoxy, aryloxy, and amino substituents at silicon (27). These stable materials are accessible via the ROP of similarly substituted [1]silaferrocenophane precursors (**14** and **16**), which can be accessed via nucleophilic substitution reactions on the $SiCl_2$-bridged [1]ferrocenophane **13** (Scheme 1). The latter species is easily prepared in high yield via the reaction of $fcLi_2$·TMEDA with $SiCl_4$.

Scheme 1.

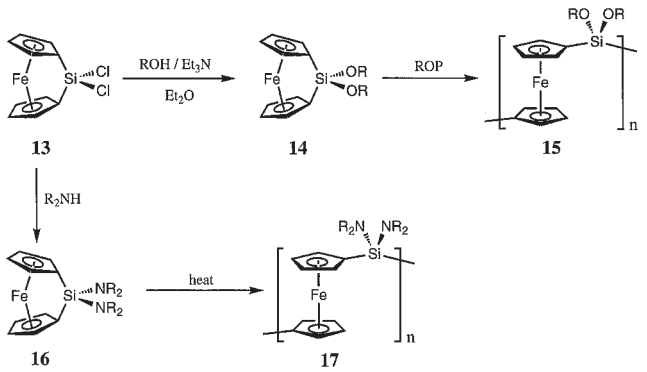

Considerable effort has also been directed towards investigating and understanding the properties of the resulting poly(ferrocenylsilane) materials, the vast majority of which are soluble in organic solvents, despite their very high molecular weights (24).[8] Cyclic voltammetric studies of the high polymers generally show the presence of two reversible oxidation waves in a 1:1 ratio, providing clear evidence for the existence of interactions between the iron atoms (29). The proposal that initial oxidation occurs at alternating iron sites along the main chain has been supported by recent work on model oligomers with between two and nine ferrocene units (30).

The presence of metal–metal interactions has led to studies of the charge transport properties of these materials (24). Oxidative doping of amorphous samples of poly(ferrocenyldimethylsilane) with I_2 have been shown to yield semiconducting materials (σ = ca. 10^{-7} S cm^{-1}), but much higher conductivities (up to $\sigma = 2 \times 10^{-4}$ S cm^{-1}) have recently been reported for more crystalline, oriented samples of **10** and **12** (R = R′ = *n*-Bu) (31). The latter conductivities represent a 10-order of magnitude increase over the undoped materials that are insulating (σ = ca. 10^{-14} S cm^{-1}). Charge transport properties such as hole mobility, which are important for xerography and other device applications, have also been measured and are appreciable (31). Interestingly, several years ago Garnier and co-workers (28*b*) reported that several TCNE-oxidized low molecular weight poly(ferrocenylsilanes) **12** (M_w = ca. 1500) show electron delocalization on the Mössbauer time scale (ca. 10^{-7} s) and also ferromagnetic ordering at low temperatures. However, so far, attempts to detect similar behavior with high molecular weight poly(ferrocenylsilanes) in a collaborative effort with the group of Dermot O'Hare at Oxford have been unsuccessful. Nevertheless, cooperative magnetic behavior has been noted in the case of other polymer systems such as TCNE-oxidized poly(ferrocenylethylenes) (32) (see below).

Poly(ferrocenylsilanes) also exhibit interesting morphology, and several of the symmetrically substituted derivatives will crystallize. For example, the prototypical poly(ferrocenylsilane),

[8] For the work of other groups on poly(ferrocenylsilanes) see ref. 28.

© 1998 NRC Canada

Scheme 2.

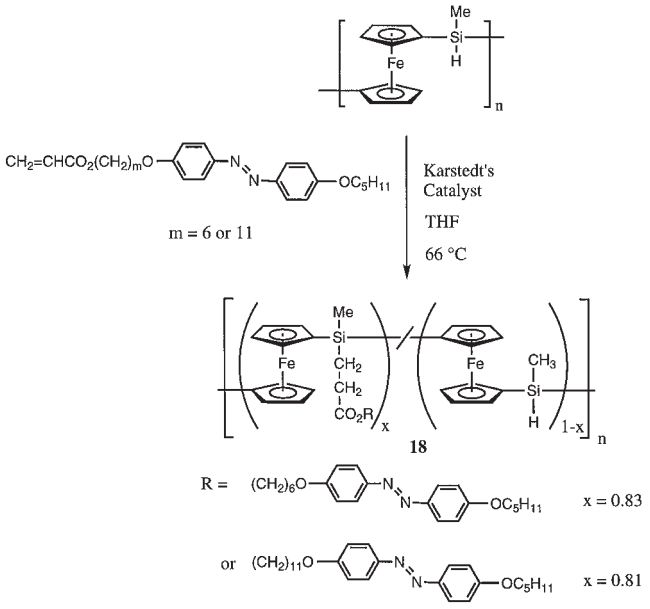

the dimethyl derivative **10**, is an amber, film-forming thermoplastic that possesses melt transitions (T_m) in the range 122–143°C and a glass transition (T_g) at 33°C. In contrast, the *n*-hexyl analogue **12** (R = R′ = *n*-hexyl) is an amber, gummy amorphous material with a T_g of –26°C (24). Alkoxy-substituted poly(ferrocenylsilanes) such as **12** (R = R′ = *n*-hexyloxy) possess T_g values down to –51°C, a remarkable testament to the flexibility of poly(ferrocene) chains, which probably arises from the freely-rotating "molecular ball bearing" nature of the ferrocene unit. It is remarkable that the incorporation of ferrocene units in the side group structure of organic polymers leads to dramatic T_g increases as the steric rigidity of this organometallic unit dominates and the free rotation is irrelevent. Thus, poly(vinylferrocene) possesses a high T_g of 184°C (33).

Recent detailed studies of the dimethyl polymer **10** by a variety of techniques including DSC, Wide Angle X-Ray Scattering (WAXS), and small angle X-ray scattering (SAXS), in collaboration with the group of Julius Vancso (at Toronto and now at U Twente, The Netherlands), suggest that the polymer adopts a similar structure in crystalline regions in the solid state to a crystallized pentamer and that the multiple melt endotherms observed by DSC are a result of the recrystallization of thin lamellae into thicker lamellae (34). The melt temperature of this prototypical poly(ferrocenylsilane) varies from 122–143°C. The equilibrium melting temperature is 143°C, as suggested by studies of a series of well-defined oligomers with between two and nine ferrocene units (30).

Recently, in collaboration with Duncan Bruce at the University of Exeter, England, we have prepared the first liquid crystalline poly(ferrocenylsilanes) **18** via hydrosilylation (35, 36) (Scheme 2). These materials show a nematic mesophase, and the influence of redox state on the liquid crystalline properties is of significant interest.

Many other characteristics of poly(ferrocenylsilanes) have attracted attention. The materials are electrochromic and they change color reversibly from amber to dark blue on oxidation (24, 28*c*, 37). Potential applications as thin films in sensors and

Fig. 2. Molecular structure of the spirocyclic [1]silaferrocenophane **19** determined by X-ray diffraction. (Reproduced from ref. 41 with permission.)

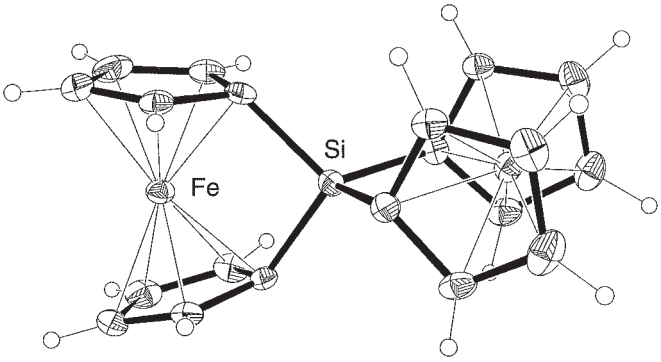

as variable refractive index materials have generated interest (38, 39). In addition, ferromagnetic products which contain α-Fe crystallites are generated by pyrolysis at temperatures above 500°C (40). Very recently, controlled cross-linking of poly(ferrocenylsilanes) has been achieved to yield solvent swellable, redox-active gels (41). The cross-linking can be controlled by using small amounts of the the spirocyclic [1]ferrocenophane **19** (Fig. 2) in the polymerization mixtures. This red, air-stable species is readily accessible from the reaction of $fcLi_2$·TMEDA with $SiCl_4$.

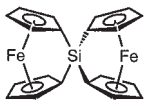

19

Anionic and transition-metal-catalyzed ROP of silicon-bridged [1]ferrocenophanes

Thermal copolymerization can be used to prepare random copolymers from different silicon-bridged [1]ferrocenophanes and also copolymers of ferrocenophanes and other monomers such as cyclic silanes and silicon-bridged bis(benzene)chromium complexes (2, 31). However, thermal ROP of metallocenophanes at elevated temperatures leads to virtually no control over molecular weight, and the molecular weight distribution is broad. We have shown that silicon-bridged [1]ferrocenophanes undergo living anionic ROP at 25°C using initiators such as *n*-BuLi in THF (42). This has permitted the synthesis of poly(ferrocenylsilanes) with controlled molecular weights and narrow polydispersities and has also allowed the preparation of the first block copolymers (e.g., **20**) containing skeletal transition-metal atoms (Scheme 3).

Transition-metal-catalyzed ROP of silicon-bridged [1]ferrocenophanes, which occurs in solution at room temperature, has also been reported using Pt^{II}, Pt^{0}, Rh^{I}, and Pd^{II} catalysts (43, 44). Molecular weight control can also be achieved and materials with novel architectures such as star and graft

© 1998 NRC Canada

Scheme 3.

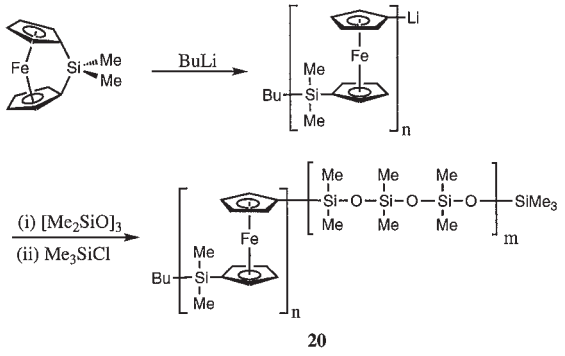

copolymers are accessible (45). Moreover, [1]silaferrocenophanes with different cyclopentadienyl rings (**21**) polymerize to yield the regioregular, crystalline poly(ferrocenylsilane) **22**, whereas thermal ROP affords a regioirregular amorphous material **23** (Scheme 4).

Significant understanding of the mechanism of these transition-metal-catalyzed reactions has also been forthcoming (4). The initial step is believed to be insertion of the transition metal into the strained Cp—Si bond. Indeed, species such as **24** have been prepared from exactly this type of reaction and function as ROP precatalysts, providing that weakly bound coligands (such as 1,5-cyclooctadiene) are present (46) (Fig. 3, eq. [8]). Further studies that aim to permit deeper understanding of the ROP mechanism and that target improved ROP catalysts are underway.

[8]

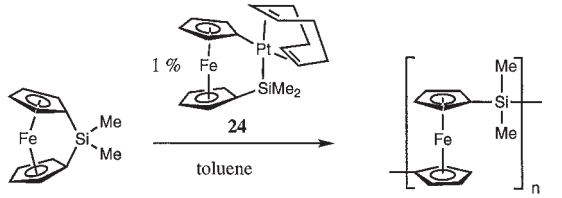

Other poly(metallocenes) via ROP: controlling interactions between metal centers

The ROP route has also been extended to the synthesis of other polymers from [1]ferrocenophane precursors. Poly(ferrocenylgermanes) **25** were first reported in 1993 and possess similar properties to their silicon analogs (47). Recently, after unsuccessful earlier attempts in the 1980s, the first tin-bridged [1]ferrocenophane was prepared. This species undergoes thermal ROP to yield a high molecular weight poly(ferrocenylstannane) **26** (48). Interestingly, this ROP reaction also occurs in solution at room temperature. Studies of this novel ROP process may provide insight into the ROP mechanism for metallocenophanes.

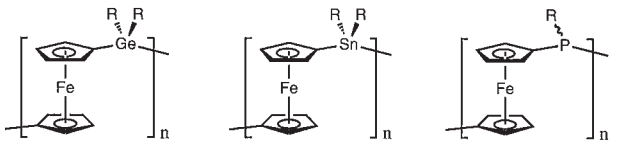

We have also shown that poly(ferrocenylphosphines) **27** are also accessible via the thermal ROP of phosphorus-bridged [1]ferrocenophanes such as **3** (49). In addition, the latter species has also been shown to undergo living anionic ROP to yield high molecular weight materials (e.g., **28**) (eq. [9]), including block copolymers (18*b*). These results contrast with those of the previous studies in the early 1980s (see above) from which it was concluded that ROP of phosphorus-bridged [1]ferrocenophane **3** does not occur and that only the formation of oligomers is possible using ring-opening methods (17).

[9]

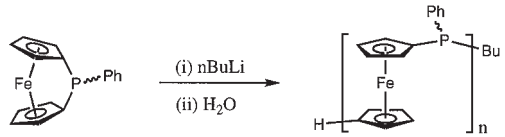

Very recently the first chalcogen-bridged [1]ferrocenophanes have been prepared. The sulfur-bridged [1]ferrocenophane **29** (R = H) is a remarkably strained species with a tilt-angle of 31° (50) (Fig. 4). This compound, and the dimethylated analog, undergo ROP to yield poly(ferrocenylsulfides), **30** (eq. [10]) (51). The iron–iron interactions in the resulting polymers are significantly greater than in the analogous poly(ferrocenylsilanes). For example, the redox coupling on the methylated poly(ferrocenylsulfide) **30** (R = Me) is 0.31–0.33 V, compared to 0.20 V for the analogous poly(dimethylferrocenyldimethylsilane) (51).

[10]

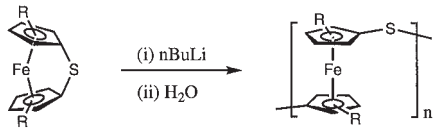

Although disilane-bridged [2]ferrocenophanes (e.g., **8**) possess very small ring-tilt angles (ca. 4–5°) and have been found to be insufficiently strained to undergo thermal ROP, hydrocarbon-bridged [2]ferrocenophanes **31** possess strained ring-tilted structures (tilt-angles = ca. 21°) as a result of the smaller atomic radius of carbon compared to silicon (52). These species have been found to yield poly(ferrocenylethylenes) **32** via ROP at 250–300°C (eq. [11]). As a consequence of the presence of a more insulating bridge, these polymers show much smaller interactions between the iron atoms (redox coupling ca. 0.09 V) compared to poly(ferrocenylsilanes). Nevertheless, in collaboration with the group of Dermot O'Hare at Oxford, we have shown that significant antiferromagnetic interactions are present in TCNE-oxidized samples of these materials (32).

[11]

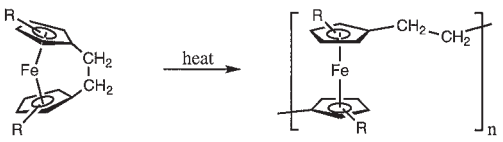

The inclusion of the larger ruthenium atom into a metallocenophane structure gives rise to even more tilted and strained molecules, and hydrocarbon-bridged [2]ruthenocenophanes

© 1998 NRC Canada

Scheme 4.

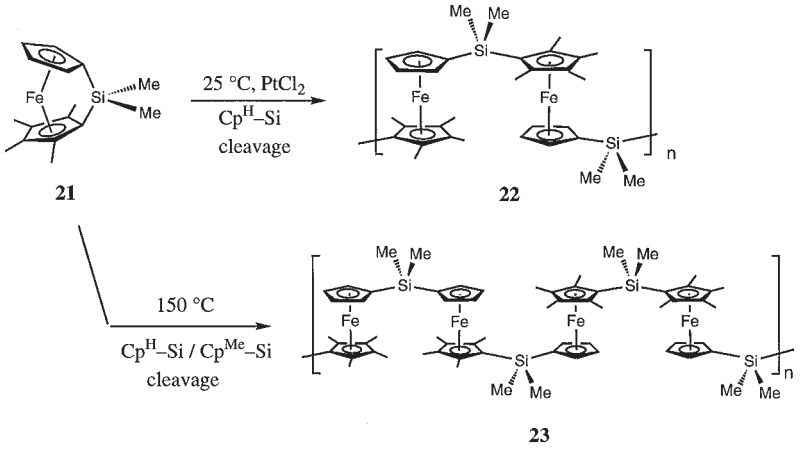

Fig. 3. Molecular structure of the [2]platinasilaferrocenophane **24** determined by X-ray diffraction. (Reproduced from ref. 46 with permission.)

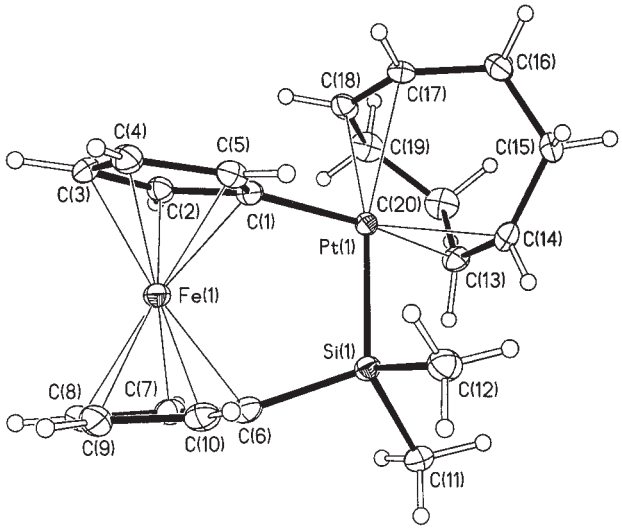

(tilt angles = ca. 29–30°) undergo thermal ROP to yield poly(ruthenocenylethylenes). These materials exhibit significantly different electrochemistry from their iron analogues (53).

Very recently we prepared the first [2]thiacarboferrocenophane **33**, which possess a strained structure with a tilt-angle of ca. 18° (54). This species undergoes the first example of the cationic ROP of a metallocenophane (or any metal containing ring) with initiators such as $MeOSO_2CF_3$ or $BF_3{\cdot}OEt_2$ (eq. [12]). The resulting ring-opened polymers **34** are soluble if $M_n < 6000$ and the synthesis of soluble copolymers is in progress.

[12]

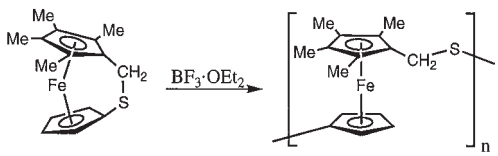

The first [1]ferrocenophane containing a first row element

Fig. 4. Molecular structure of the [1]thiaferrocenophane **29** (R = H) determined by X-ray diffraction. (Reproduced from ref. 51 with permission.)

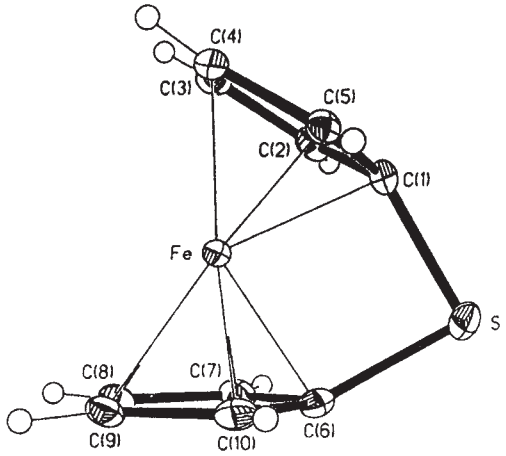

Fig. 5. Molecular structure of the [1]boraferrocenophane **35** determined by X-ray diffraction. (Reproduced from ref. 55 with permission.)

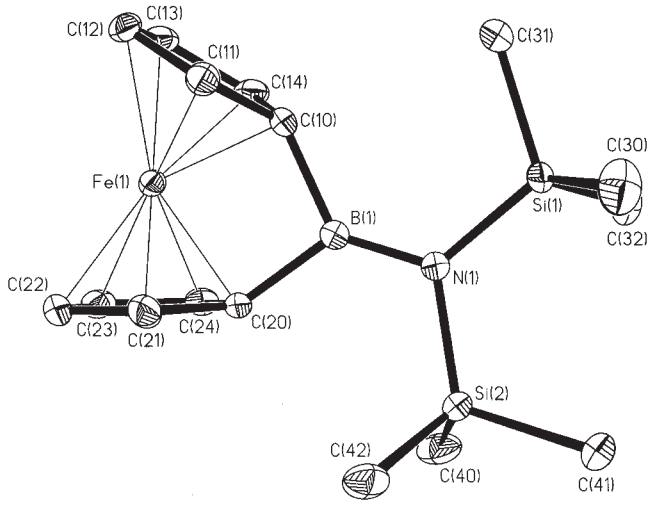

(boron) in the bridge, **35** has also recently been synthesized in collaboration with the group of Holger Braunschweig at the

© 1998 NRC Canada

Fig. 6. Transmission electron micrograph perpendicular to channels of MCM-41 showing the incorporation of ceramics derived from the pyrolysis of poly(ferrocenylsilane) **10** in the mesopores at 900°C. (Reproduced from ref. 56 with permission.)

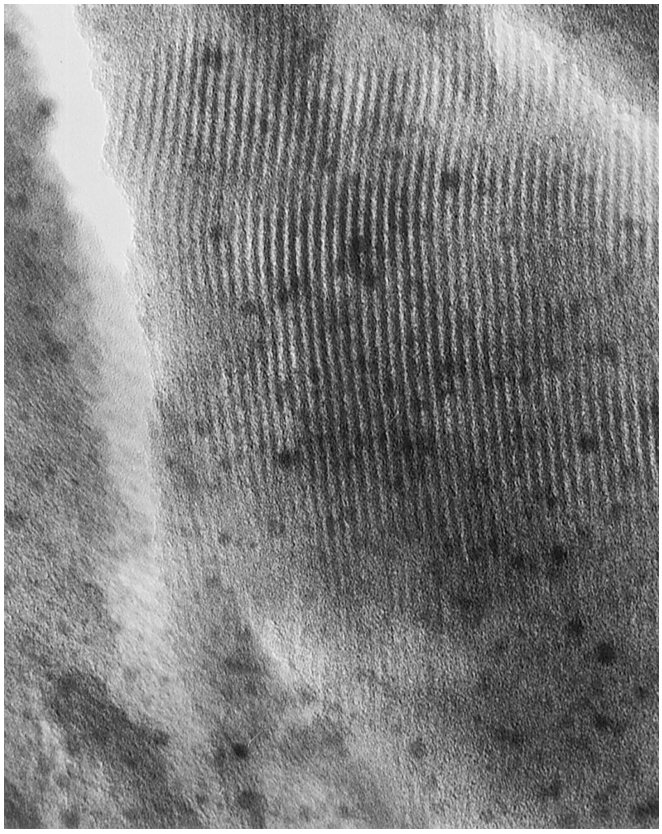

RWTH Aachen (55) (eq. [13]). This highly sensitive species possesses the highest tilt-angle (32°) for an iron group metallocenophane (Fig. 5). Attempts to polymerize this and related species to yield soluble polymers are in progress.

[13] 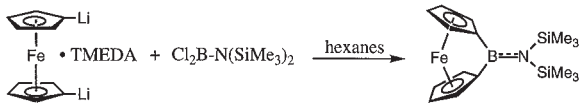

35

Applications of ring-opened poly(ferrocenes) for the preparation of novel materials with nanoscale dimensions

Poly(ferrocenes) function as preceramic polymers and have been shown to yield interesting ferromagnetic Fe-containing ceramic composites at 500–1000°C (40). The use of such involatile but processable polymeric precursors to ceramics is a potentially attractive way of circumventing the difficulty of processing ceramic materials into desired shapes. In collaboration with the group of Geoff Ozin at Toronto (56) we have recently explored the pyrolysis of poly(ferrocenylsilanes) within the channels of the mesoporous silica MCM-41. The monomer **9** can be sublimed into the hexagonal mesopores at room temperature, and ROP can be induced by heating the resulting material at 140°C. Heating to 900°C generates black, nanostructured magnetic ceramic products that can be visualized in the channels by transmission electron microscopy (TEM) (Fig. 6).

Recently, in collaboration with the group of Mitch Winnik at Toronto,[9] we have shown that interesting architectures can be generated via the solution aggregation of poly(ferrocene)-based block copolymers. Thus, block copolymers such as poly(ferrocenyldimethylsilane)-*block*-poly(dimethylsiloxane) **20** (n:m = 1:2) with long polysiloxane blocks have been found to afford cylindrical, wormlike micelles in hexanes. These structures maintain their structural integrity in the solid state and can be readily visualized by tapping-mode Atomic Force Microscopy or by TEM (see Fig. 7). These cylinders consist of a wire-like core of semiconducting poly(ferrocenylsilane), surrounded by a sheath or corona of insulating poly(dimethylsiloxane). Pyrolysis of such structures, particularly if cross-linked, offers the possibility of generating magnetic wire-like structures.

Poly(ferrocene) block copolymers, like organic analogs, phase separate in the solid state. We reported the first studies of the morphology of such materials in 1996 (42). We used TEM, for example, to demonstrate that films of poly(ferrocenylsilane)-polystyrene block copolymers generate cylindrical and (or) lamellar domain structures in the solid state (Fig. 8). Future opportunities exist for the generation of highly ordered structures, which could be selectively oxidized (chemically or electrochemically e.g., by using scanning probe microscope tips) to give materials with interesting properties.[10] For example, the controlled orientation of nanoscale block copolymer spherical, cylindrical, or lamellar redox-active domains (e.g., at surfaces) might allow charge transport in certain directions or the generation of magnetic nanostructures via oxidation or pyrolysis (e.g., using lasers or ion beams). Research work in these and other areas is ongoing, in many cases in collaboration with other groups.

Summary

Ring-opening polymerization of metallocenophanes has allowed facile access to a variety of high molecular weight poly(metallocenes).[11] Much has been accomplished in terms of understanding the properties of these novel and interesting materials. Future work will be directed towards exploring the mechanisms of polymerization, developing new polymers with controlled metal–metal interactions, studying the properties of these materials in more detail and exploring applications in a variety of intriguing areas such as, for example, nanostructured materials, sensors, and charge-transport materials, and redox-active gels.

Acknowledgements

I would like to thank my exceptionally motivated and talented students who have performed most of the research described in this article and whose names are cited in the references. I also thank the Ontario Center for Materials Research (OCMR), the Natural Science and Engineering Research Council of Canada

[9] J.A. Massey, I. Manners, and M.A. Winnik. Unpublished results.
[10] For example, selective oxidation of spatially addressable nanosize redox-active domains might allow information storage.
[11] An experiment designed for undergraduate research laboratories has been devised based on this ROP chemistry (see ref. 57).

© 1998 NRC Canada

Fig. 7. Transmission electron micrograph of the cores of poly(ferrocenyldimethylsilane)-*block*-poly(dimethylsiloxane) micelles aerosol-sprayed from a dilute solution in hexanes onto a thin carbon film supported on mica. No staining agent was used. The micrograph shows regions where the cylinders are starting to pack to form a 2D film as well as isolated cylinders.

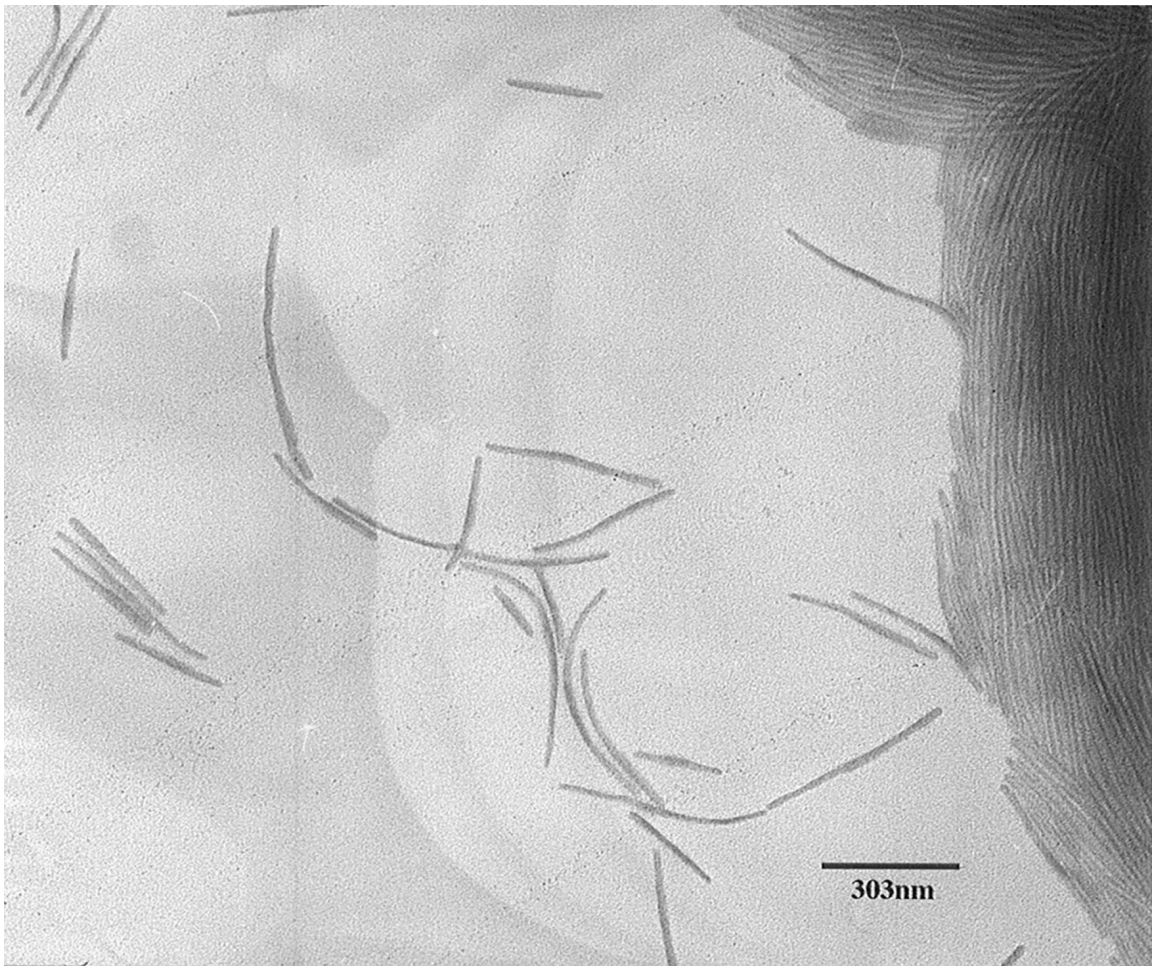

Fig. 8. Transmission electron micrograph of an unannealed film of poly(ferrocenyldimethylsilane)-*block*-polystyrene. No staining agent was used. (Reproduced from ref. 42 with permission.)

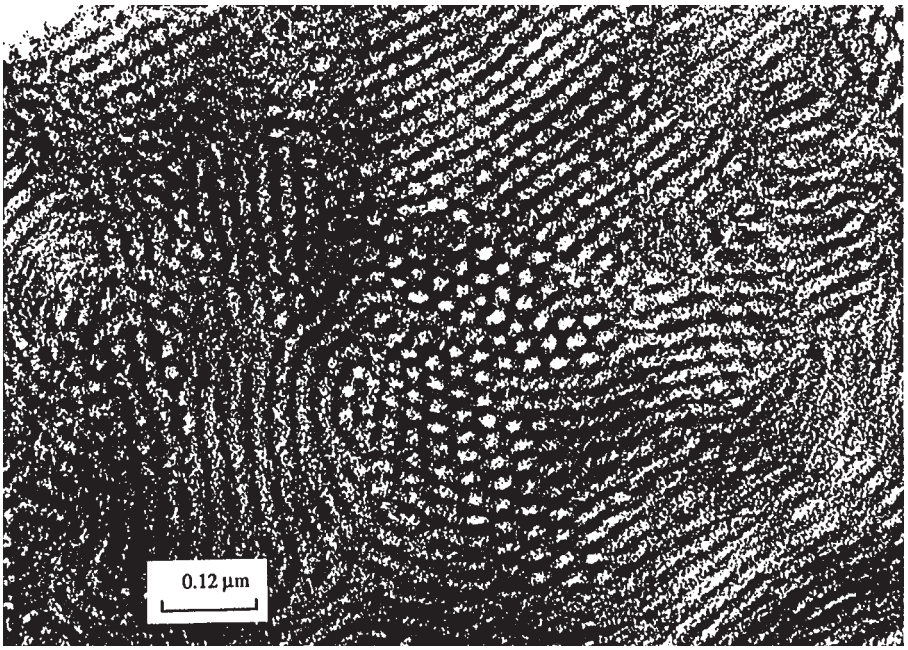

© 1998 NRC Canada

(NSERC), the Petroleum Research Fund (PRF) administered by the American Chemical Society, the Institute for Science and Technology (ICST), Xerox Research Corporation of Canada (XRCC), and the Center for Research in Earth and Space Technology (CRESTech) for funding. I am also very grateful to a number of collaborators whom I have had the pleasure to interact with concerning a variety of projects on poly(metallocenes) of both a synthetic and materials science nature. These include Dermot O'Hare (Oxford, England), Duncan Bruce (Exeter, England), Kris Matyjaszewski (Carnegie–Mellon University), Mark Foster (Akron, U.S.A.), John Greedan (McMaster University), William Geiger (University of Vermont), John Sheridan (Rutgers, Newark, U.S.A.), Keith Balmain (Toronto), Julius Vancso (initially at Toronto and now at Twente, The Netherlands), and Geoffrey Ozin and Mitch Winnik of our Department. I am also extremely grateful to the Alfred P. Sloan Foundation for a Research Fellowship (1994–1998), NSERC for an E.W.R. Steacie Fellowship (1997–1999), and the University of Toronto for a McLean Fellowship (1997–2003).

References

1. C.U Pittman, Jr., C.E. Carraher, and J.R. Reynolds. Organometallic polymers. Encylopedia of polymer science and engineering. Wiley–Interscience, New York. Vol. 10. 1987. p. 541.
2. I. Manners. Angew. Chem. Int. Ed. Engl. **35**, 1602 (1996).
3. E.W. Neuse and H.J. Rosenberg. J. Macromol. Sci. **C4**, 1 (1970).
4. I. Manners. Polyhedron, **15**, 4311 (1996).
5. E.W. Neuse and H.J. Rosenberg. J. Macromol. Sci. **C4**, 130 (1970).
6. D.P. Gates and I. Manners. J. Chem. Soc. Dalton Trans. 2525, (1997).
7. (*a*) H.W. Roesky and M. Lücke. J. Chem. Soc. Chem. Commun. 748 (1989); (*b*) H.W. Roesky and M. Lücke. Angew. Chem. Int. Ed. Engl. **28**, 493 (1989).
8. (*a*) H. Rosenberg and M.D. Rausch. U.S. Patent 3,060,215 (1962); (*b*) H. Rosenberg. U.S. Patent 3,426,053 (1969).
9. E.W. Neuse and H. Rosenberg. J. Macromol. Sci. **C4**, 110 (1970).
10. A.G. Osborne and R.H. Whiteley. J. Organomet. Chem. **101**, C27 (1975).
11. H. Stoeckli-Evans, A.G. Osborne, and R.H. Whiteley. Helv. Chim. Acta, **59**, 2402 (1976).
12. (*a*) M.S. Wrighton, M.C. Palazzotto, A.B. Bocarsly, J.M. Bolts, A.B. Fischer, and L. Nadjo. J. Am. Chem. Soc. **100**, 7264 (1978); (*b*) A.B. Fischer, J.B. Kinney, R.H. Staley, and M.S. Wrighton. J. Am. Chem. Soc. **101**, 6501 (1979).
13. A.G. Osborne, R.H. Whiteley, and R.E. Meads. J. Organomet. Chem. **193**, 345 (1980).
14. D. Seyferth and H.P. Withers, Jr. J. Organomet. Chem. **185**, C1 (1980).
15. I.R. Butler, W.R. Cullen, F.W.B. Einstein, S.J. Rettig, and A.J. Willis. Organometallics, **2**, 128 (1983).
16. D. Seyferth and H.P. Withers, Jr. Organometallics, **1**, 1275 (1982).
17. H.P. Withers, D. Seyferth, J.D. Fellmann, P. Garrou, and S. Martin. Organometallics, **1**, 1283 (1982).
18. (*a*) I. Manners. Adv. Organomet. Chem. **37**, 153 (1995); (*b*) C.H. Honeyman, T.J. Peckham, J.A. Massey, and I. Manners. Chem. Commun. 2589 (1996).
19. (*a*) R. Rulkens, Y. Ni, and I. Manners. J. Am. Chem. Soc. **116**, 12 121 (1994); (*b*) I. Manners. Polyhedron, **15,** 4322 (1996); (*c*) K.H. Pannell and H.K. Sharma. Organometallics, **16**, 3077 (1997).
20. (*a*) W. Finckh, B.Z. Tang, A. Lough, and I. Manners. Organometallics, **11**, 2904 (1992); (*b*) W. Finckh, R. Ziembinski, B.Z. Tang, D.A. Foucher, D.B. Zamble, A. Lough, and I. Manners. Organometallics, **12**, 823 (1993).
21. P.F. Brandt and T.B. Rauchfuss. J. Am. Chem. Soc. **114**, 1926 (1992).
22. I. Manners, M. Liang, C. Waddling, C. Honeyman, D. Foucher, B.Z. Tang, and W. Finckh. New inorganic polymers for specialty applications. Lecture 10-5. 41st Canadian Chemical Engineering Conference, Vancouver, Canada, October 6–9, 1991.
23. D.A. Foucher, B.Z. Tang, and I. Manners. J. Am. Chem. Soc. **114**, 6246 (1992).
24. I. Manners. Adv. Organomet. Chem. **37**, 131 (1995).
25. J.K. Pudelski, R. Rulkens, D.A. Foucher, A.J. Lough, P.M. Macdonald, and I. Manners. Macromolecules, **28**, 7301 (1995).
26. D.L. Zechel, K.C. Hultzsch, R. Rulkens, D. Balaishis, Y. Ni, J.K. Pudelski, A.J. Lough, I. Manners, and D.A. Foucher. Organometallics, **15**, 1972 (1996).
27. P. Nguyen, A.J. Lough, and I. Manners. Macromol. Chem. Rapid. Commun. **18**, 953 (1997).
28. (*a*) M.T. Nguyen, A.F. Diaz, V.V. Dement'ev, and K.H. Pannell. Chem. Mater. **5**, 1389 (1993); (*b*) M. Hmyene, A. Yasser, M. Escorne, A. Percheron-Guegan, and F. Garnier. Adv. Mater. **6**, 564 (1994); (*c*) M.T. Nguyen, A.F. Diaz, V.V. Dement'ev, and K.H. Pannell. Chem. Mater. **6**, 952 (1994); (*d*) S. Barlow, A.L. Rohl, S. Shi, C.M. Freeman, and D. O'Hare. J. Am. Chem. Soc. **118**, 7578 (1996); (*e*) J. Park, Y. Seo, S. Cho, D. Whang, K. Kim, and T. Chang. J. Organomet. Chem. **489**, 23 (1995).
29. D.A. Foucher, C.H. Honeyman, J.M. Nelson, B.-Z. Tang, and I. Manners. Angew. Chem. Int. Ed. Engl. **32**, 1709 (1993).
30. R. Rulkens, A.J. Lough, I. Manners, S.R. Lovelace, C. Grant, and W.E. Geiger. J. Am. Chem. Soc. **118**, 12 683 (1996).
31. R. Rulkens, R. Resendes, A. Verma, I. Manners, K. Murti, E. Fossum, P. Miller, and K. Matyjaszewski. Macromolecules, **30**, 8165 (1997).
32. J.M. Nelson, P. Nguyen, R. Petersen, H. Rengel, P.M. Macdonald, A.J. Lough, I. Manners, N.P. Raju, J.E. Greedan, S. Barlow, and D. O'Hare. Chem. Eur. J. **3**, 573 (1997).
33. P. Nguyen, G. Stojcevic, K. Kulbaba, M. MacLachlan, X.-H. Liu, A.J. Lough, and I. Manners. Macromolecules, (1998). In press.
34. (*a*) J. Rasburn, R. Petersen, T. Jahr, R. Rulkens, I. Manners, and G.J. Vancso. Chem. Mater. **7**, 871 (1995); (*b*) R.G.H. Lammertink, M.A. Hempenius, I. Manners, and G.J. Vancso. Macromolecules, **31**, 795 (1998).
35. X.-H. Liu, D.W. Bruce, and I. Manners. Chem. Commun. 289 (1997).
36. X.-H. Liu, D.W. Bruce, and I. Manners. J. Organomet. Chem. **548**, 49 (1997).
37. D.A. Foucher, R. Ziembinski, R. Rulkens, J.M. Nelson, and I. Manners. *In* Inorganic and organometallic polymers II. ACS Symp. Ser. 572. *Edited by* P. Wisian-Neilson, H.R. Allcock, and K.J. Wynne. American Chemical Society, Washington, D.C. 1994.
38. H. Yim, M.D. Foster, D. Balaishis, and I. Manners. Langmuir (1998). In press.
39. K. Pannell and J. Robillard. U.S. Patent 308856 (1995).
40. R. Petersen, D.A. Foucher, B.-Z. Tang, A.J. Lough, N.P. Raju, J.E. Greedan, and I. Manners. Chem. Mater. **7**, 2045 (1995).
41. M.J. MacLachlan, A.J. Lough, and I. Manners. Macromolecules, **29**, 8562 (1996).
42. Y. Ni, R. Rulkens, and I. Manners. J. Am. Chem. Soc. **118**, 4102 (1996).
43. Y. Ni, R. Rulkens, J.K. Pudelski, and I. Manners. Macromol. Rapid Commun. **16**, 637 (1995).
44. N.P. Reddy, H. Yamashita, and M. Tanaka. Chem. Soc. Chem. Commun. 2263 (1995).
45. P. Gómez-Elipe, P.M. Macdonald, and I. Manners. Angew. Chem. Int. Ed. Engl. **36**, 762 (1997).

© 1998 NRC Canada

46. J.B. Sheridan, K. Temple, A.J. Lough, and I. Manners. J. Chem. Soc. Dalton Trans. 711 (1997).
47. D.A. Foucher and I. Manners. Makromol. Chem. Rapid Commun. **14**, 63 (1993).
48. R. Rulkens, A.J. Lough, and I. Manners. Angew. Chem. Int. Ed. Engl. **35**, 1805 (1996).
49. C.H. Honeyman, D.A. Foucher, F.Y. Dahmen, R. Rulkens, A.J. Lough, and I. Manners. Organometallics, **14**, 5503 (1995).
50. J.K. Pudelski, R. Rulkens, D. Gates, A.J. Lough, and I. Manners. Angew. Chem. Int. Ed. Engl. **34**, 1506 (1995).
51. R. Rulkens, D.P. Gates, J.K. Pudelski, D. Balaishis, D.F. McIntosh, A.J. Lough, and I. Manners. J. Am. Chem. Soc. **119**, 10 976 (1997).
52. J.M. Nelson, H. Rengel, and I. Manners. J. Am. Chem. Soc. **115**, 7035 (1993).
53. J.M. Nelson, A.J. Lough, and I. Manners. Angew. Chem. Int. Ed. Engl. **33**, 989 (1994).
54. R. Resendes, P. Nguyen, A.J. Lough, and I. Manners. Chem. Commun. 1001 (1998).
55. H. Braunschweig, R. Dirk, M. Müller, P. Nguyen, R. Resendes, D.P. Gates, and I. Manners. Angew. Chem. Int. Ed. Engl. **36**, 2338 (1997).
56. M.J. MacLachlan, P. Aroca, N. Coombs, I. Manners, and G.A. Ozin. Adv. Mater. **10**, 144 (1998).
57. Y. Ni, I. Manners, J.B. Sheridan, and R.T.O. Oakley, J. Chem. Ed. 766 (1998).

© 1998 NRC Canada

Friedel Crafts catalysis using supported reagents. Synthesis, characterization, and catalytic application of sol gel-derived silica

Jack M. Miller, David Wails, J. Stephen Hartman, Karla Schebesh, and Jennifer L. Belelie

Abstract: Novel mesoporous silicas have been prepared via a sol–gel route involving fluoride-catalyzed hydrolysis of tetraethylorthosilicate (TEOS). Incorporation of zinc chloride by sol–gel synthesis gives a range of mesoporous materials with significantly higher catalytic activity than the commercially available catalyst, Clayzic, in a model Friedel–Crafts alkylation reaction. The dependence of catalytic activity and physical structure on the amounts of solvent, water, zinc chloride, and potassium fluoride used in the preparation are explored, and the materials have been further characterized by nitrogen adsorption to determine surface areas, total pore volumes, and pore-size distributions and by ^{29}Si and ^{19}F MAS NMR spectroscopy. The most active catalysts generally have the highest total pore volumes, with pore-size distributions larger than 8 nm.

Key words: sol–gel, Friedel–Crafts, Clayzic, silica.

Résumé : On a préparé de nouvelles silices mésoporeuses par le biais d'une voie sol–gel impliquant une hydrolyse, catalysée par le fluorure, de l'orthosilicate de tétraéthyle (OSTE). L'incorporation de chlorure de zinc par la synthèse sol–gel fournit une variété de produits mésoporeux possédant, pour une réaction d'alkylation de Friedel–Crafts modèle, une activité catalytique beaucoup plus élevée que celle du catalyseur Clayzic disponible commercialement. On a étudié la relation entre l'activité catalytique ainsi que la structure physique et les quantités de solvant, d'eau, de chlorure de zinc et de fluorure de potassium utilisés dans la préparation; on a de plus caractérisé les matériaux par spectroscopie RMN du ^{29} Si et du ^{19} F ainsi que par adsorption d'azote pour déterminer les superficies des surfaces, les volumes totaux des pores et les distributions de la taille des pores. Les catalyseurs les plus actifs ont généralement les volumes totaux de pore les plus élevés et la distribution de la taille des pores est généralement supérieure à 8 nm.

Mots clés : sol–gel, Friedel–Crafts, Clayzic, silica.

[Traduit par la rédaction]

Introduction

Supported metal halides, particularly zinc chloride, have been widely investigated as catalysts for Friedel–Crafts reactions in recent years (1). "Clayzic,"[2] zinc chloride supported on Montmorillonite K10 clay, was first reported in 1989 (2) and provides a useful alternative to traditional Friedel–Crafts alkylation catalysts such as $AlCl_3$ and HF, which have environmental drawbacks in addition to often poor selectivity and lack of reusability. Since the original report, this material has been widely investigated (3–10). The activity of the K10 support can be further enhanced by acid treatment, which destroys much of the original support structure and generates mesoporous materials. Pore size is critical, with the optimum diameter being 8–12 nm for maximum catalytic activity of the supported reagent (9, 10). We have recently described the synthesis of related Friedel–Crafts catalysts, based on zinc chloride incorporated into a sol–gel-derived aluminosilicate support (11).

Sol–gel methodologies offer an attractive approach to the synthesis of materials for a number of applications including ceramics, catalysts, and optical devices (12). The low-temperature sol–gel route offers a number of advantages over traditional high-temperature melt processes. Both the chemical composition of the materials and physical properties such as surface area and pore-size distribution can often be precisely controlled. The sol–gel process involves the controlled hydrolysis of suitable precursor molecules, e.g., metal alkoxides in an alcohol solvent, with acid or base catalysis (12). During hydrolysis, partially hydrolyzed metal alkoxides polymerize to give a sol, and further condensation results in gelation. This is followed by aging during which further condensation reactions may occur in the gel and drying to give the final product.

Other supports such as mesoporous silica can also be more effective than montmorillonite K10, and the pore-size characteristics appear to be the most significant factor, rather than the actual chemical nature of the support (9, 10). These studies have, however, been limited to commercially available

Received September 10, 1997.

J.M. Miller,[1] D. Wails, J.S. Hartman, K. Schebesh, and J.L. Belelie. Department of Chemistry, Brock University, St. Catharines, ON L2S 3A1, Canada.

[1] Author to whom correspondence may be addressed. Telephone: (905) 688-5550 (ext. 3402). Fax: (905) 682-9020. E-mail: jmiller@sandcastle.cosc.brocku.ca

[2] Clayzic is a trademark of Contract Catalysts Ltd., Merseyside, U.K.

© 1998 NRC Canada

materials of limited pore-size distribution. In the present work, we describe the application of sol–gel methods to the synthesis of mesoporous silica-based Friedel–Crafts alkylation catalysts.

Experimental

Instrumentation

Gas chromatographic (GC) analysis was carried out using a Perkin–Elmer Sigma 3B gas chromatograph linked to a Hewlett Packard 3396 Series II integrator. Analysis was carried out with the aid of packed columns containing 3% OV-17 on Gas Chrom Q. Products were identified by GC–MS using a Carlo Erba MFC 500 GC interfaced to a Kratos Concept 1S mass spectrometer.

The NMR experiments were carried out on a Bruker DPX-300 multinuclear Fourier Transform spectrometer using a Bruker narrow bore MAS probe with 4 mm zirconia rotors. The ^{29}Si CP–MAS spectra were obtained at 59.62 MHz using cross-polarization with proton decoupling during acquisition and were referenced to external TMS. Samples were spun at 4 KHz in air. A 10 ms contact time was used with a 5 s delay between pulses, and between 5000 and 10 000 FIDs were typically accumulated over a spectral window of 18 000 Hz. The ^{19}F MAS NMR spectra were obtained at 282.88 MHz and referenced to $CFCl_3$ (0 ppm) using powdered Teflon as an external secondary standard (–123.0 ppm). The DEPTH pulse sequence was employed to remove background ^{19}F signals from the probe (13). Samples were spun at 14 KHz with air. The 256 scans were typically accumulated over a 14 KHz spectral width with a 5 s delay between pulses.

Surface area and pore-volume determinations were carried out at 77°K using a Coulter SA3100 instrument with an automated gas volumetric method employing nitrogen as the adsorbate. Surface areas were determined using the BET adsorption method (14) and pore volumes using the BJH method on the desorption branch of the isotherm (15). Samples were outgassed under high vacuum at 200°C for 1 h immediately prior to analysis.

Reagents

Benzene and ethanol were obtained from Caledon Laboratories. All other chemicals were obtained from the Aldrich Chemical Company and used as received.

Typical catalyst preparation

The TEOS (14 mL, 0.06 mol) and ethanol (20 mL) were stirred in a 100 mL teflon beaker, and a mixture of zinc chloride (2.75 g, 0.02 mol) and potassium fluoride (0.21 g, 3.6 mmol) predissolved in distilled water (4.0 mL, 0.22 mol) was added. The beaker was covered with a watch glass and the solution stirred and heated to 70°C until the contents gelled (typically 15 min). Residual solvent was then removed by heating in an oven at 100°C and finally at 225°C overnight. The yield was typically 5.75 g. The amount of TEOS was kept constant for all trials and other variables altered as detailed in the text and in Table 1; the third sample in each series in Table 1 (i.e., samples 3, 8, 13, and 18) corresponds to the basic preparation described above.

Typical catalyst testing procedure

Benzene (22.0 mL, 0.25 mol) was stirred vigorously in a 100 mL round bottomed flask and freshly dried catalyst (typically 0.50 g) added. Benzyl chloride (5.8 mL, 0.05 mol) was then added in one aliquot and the reagents stirred at room temperature for 15 min. The catalyst was filtered and the reaction mixture analyzed by GC. The percent conversion was defined as the total conversion of benzyl chloride (to diphenylmethane and the *ortho*, *meta*, and *para* isomers of dibenzylbenzene). Each series of catalysts described in Table 1 was prepared at least twice. While actual conversions varied slightly between preparations, the relative catalytic activity between each member of a series remained unchanged.

Results and discussion

General

The sol–gel synthesis of silica from tetraalkylsilicates is typically carried out under acidic (such as with HCl or HNO_3) or basic (such as NH_4OH) conditions. However, the resultant materials are ineffective as Friedel–Crafts alkylation catalysts, as tested by alkylation of benzene with benzyl chloride to give diphenylmethane, a standard model reaction with Clayzic and similar systems (2–11). Gelation at extremely low or high pH is known to give materials with microporous structures (16), which do not fit the mesoporous requirement proposed by Rhodes and Brown (9, 10) for active Friedel–Crafts catalysts.

We have recently shown that zinc chloride can be effectively incorporated into an aluminosilicate sol–gel-derived framework during preparation (11), and here we extend this approach to sol–gel-derived silica by adding zinc chloride to the sol–gel system. Although acidic and basic sol–gel synthesis conditions gave materials that were ineffective as Friedel–Crafts catalysts, the presence of fluoride leads to the formation of catalytically active materials, with potassium fluoride giving more active materials than either sodium or ammonium fluoride. Tetraethylorthosilicate was hydrolysed in ethanol with an aqueous solution containing potassium fluoride and zinc chloride. The most active catalyst prepared by this method, dried at 225°C, gave 41% conversion of benzyl chloride, whereas Clayzic (at an optimum 1 mmol g^{-1} $ZnCl_2$ loading) gave only 24% under identical conditions. The catalyst has a type IV nitrogen adsorption–desorption isotherm (Fig. 1) (17). The hysteresis associated with the adsorption–desorption branches of the isotherm suggests that the mesopores associated with the materials are in the form of interparticulate voids rather than framework mesoporosity. The corresponding Barrett–Joyner–Halenda (BJH) plot (15) derived from the desorption branch of the isotherm (Fig. 2) shows a broad, mesoporous structure with a maximum pore volume at 14 nm. The material has a surface area of 168.77 m^2 g^{-1} and a total pore volume of 0.78 cm^3 g^{-1}. Upon heating the material to 500°C, at which temperature zinc chloride is known to volatilize (11), the surface area and pore volume decrease substantially to 25.12 m^2 g^{-1} and 0.17 cm^3 g^{-1} at which point the material loses all catalytic activity.

Effect of solvent

Samples 1–5 in Table 1 detail the effect of varying the amount of ethanol on the physical properties and catalytic ability of

© 1998 NRC Canada

Table 1. Effects of variation in catalyst preparation on benzyl chloride conversion, surface area, and pore volume.

Sample no.	Variable (quantity)	Percent Bz–Cl conversion	Surface area, $m^2\ g^{-1}$	Pore volume, $cm^3\ g^{-1}$
	Solvent volume, mL			
1	10	23	62.9	0.36
2	15	25	70.7	0.41
3[a]	20	33	127.1	0.67
4	25	21	210.5	
5	30	43	245.9	0.58
	Water, mL (moles water:1 mol TEOS)			
6	2 (1.76)	5	76.8	0.19
7	3 (2.64)	19	122.1	0.32
8[a]	4 (3.52)	33	127.1	0.67
9	5 (4.40)	58	118.5	0.57
10	6 (5.28)	28	76.6	0.62
	Zinc chloride, g (loading, mmol g^{-1})[b]			
11	2.25 (5.83)	17	105.4	0.65
12	2.50 (6.48)	31	131.0	0.75
13[a]	2.75 (7.13)	33	127.1	0.67
14	3.00 (7.78)	29	97.9	0.47
15	3.25 (8.34)	42	87.3	0.54
	Potassium fluoride, g (moles:1 mol TEOS)			
16	0.10 (0.03)	0	181.0	0.36
17	0.15 (0.04)	37	126.1	0.82
18[a]	0.20 (0.05)	33	127.1	0.67
19	0.25 (0.07)	23	91.55	0.81
20	0.30 (0.08)	14	94.71	0.54

[a] Reference sample prepared according to the details in the experimental section.
[b] $ZnCl_2$ loading calculation based on the yield of a blank-support preparation.

zinc chloride treated silicas. As the amount of solvent increases, surface areas steadily increase, although pore volumes show a maximum of 0.87 $cm^3\ g^{-1}$ with 20 mL solvent. Catalytic activity shows no clear trend with variation in solvent quantity, although it is noteworthy that highest activities are found with materials having the highest surface area or highest pore volume. Pore-size distributions are shown in Fig. 3, and it can be seen that lower volumes of solvent give materials with significantly broader distributions, whereas higher volumes give more defined structures with the maximum at a diameter of 9.15 nm (sample 5). The ^{29}Si CP–MAS NMR spectra (Fig. 4) of samples 1, 3, and 5 have two broad peaks centered at approximately –102 and –110 ppm, which may be attributed to Q^3 and Q^4 (i.e., $\underline{Si}(OSi)_3OH$ and $\underline{Si}(OSi)_4$) sites, respectively (18, 19). The Q^3 peak shifts from –102.1 ppm (sample 1) to –101.5 (sample 5), while the Q^4 peak shifts from –109.9 (sample 1) to –110.8 (sample 5), suggesting an increase in condensation reactions with an increase in the amount of solvent. The Q^3 ($\underline{Si}(OSi)_3OH$) and Q^4 ($\underline{Si}(OSi)_4$) sites both cover a range of possible environments, since the attached silicas themselves have the possibility of being further condensed to various extents, i.e., $\underline{Si}\text{-O-Si}(OSi)_m(OH)_{3-m}$ (m = 0–3), and average values of m may increase with an increase in the amount of solvent.

The sol–gel process is typically broken down into three different reactions (12):

hydrolysis,

$$\equiv Si\text{-}OC_2H_5 \rightleftharpoons \equiv Si\text{-}OH + C_2H_5OH$$

condensation, and the reverse esterification,

$$\equiv Si\text{-}OC_2H_5 + HO\text{-}Si\equiv \rightleftharpoons \equiv Si\text{-}O\text{-}Si\equiv + C_2H_5OH$$

$$\equiv Si\text{-}OH + HO\text{-}Si\equiv \rightleftharpoons \equiv Si\text{-}O\text{-}Si\equiv + H_2O$$

Since ethanol is involved in these equilibria, its function is not simply that of a solvent but of a reagent, and therefore it is not surprising that changing the amount of solvent has an effect on the silica species formed and the resulting ^{29}Si CP–MAS NMR spectra. In our products following calcination the nonbridging oxygens should be primarily -OH groups, but the presence of some residual -OEt groups has not been ruled out, and their presence could also have some effect on the ^{29}Si chemical shifts.

Effect of amount of water used

Samples 6–10 in Table 1 detail the effect of varying amounts of water on the catalyst performance and the effect on physical

© 1998 NRC Canada

Fig. 1. Catalyst nitrogen adsorption–desorption isotherm.

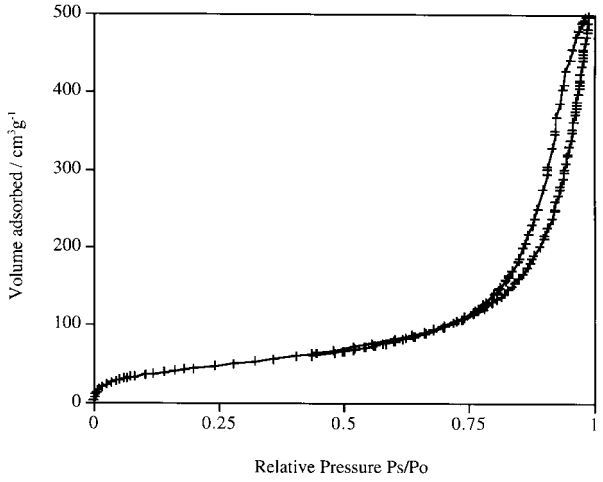

Fig. 2. Catalyst BJH pore distribution.

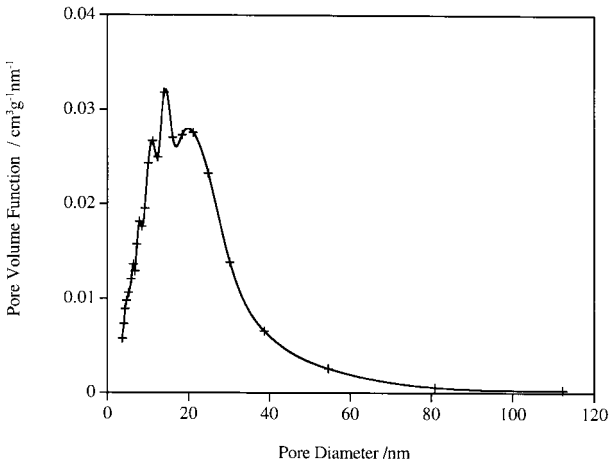

properties. Both surface area and pore volume are at a maximum (127.1 m^2 g^{-1} and 0.67 cm^3 g^{-1}) at a water:TEOS mole ratio of 3.52:1. This material (sample 8 in Table 1) shows a lower catalytic activity than sample 9, which may be anomolous. At other ratios, decreases in catalytic activity correspond to decreases in the surface area or pore volume. In materials with either low surface area or pore volume it is possible that the zinc chloride is overloaded within the pores and is behaving as crystalline zinc chloride rather than the isolated zinc chloride moieties to which the high catalytic activity of this system is attributed (9, 10). The effect on pore-size distribution is shown in Fig. 5. Increasing the amount of water dramatically increases the pore-size distribution, and although sample 7 has the optimum pore distribution as suggested by Rhodes and Brown (9, 10) for mesoporous silicas (8-10 nm), it shows only low catalytic activity. The most active material (sample 9) has an intermediate pore volume and surface area, and has a significant proportion of pore-size distribution above 10 nm. Sample 6, which shows poor activity, has the lowest surface area and pore volume, with the majority of these pores being less than 8 nm in diameter. The ^{29}Si CP–MAS spectra are shown in Fig. 6. Increasing the amount of water results in a

Fig. 3. Effect of amount of solvent on BJH pore distributions; 10 mL, sample 1 (□); 20 mL, sample 3 (◇) ; 30 mL, sample 5 (○).

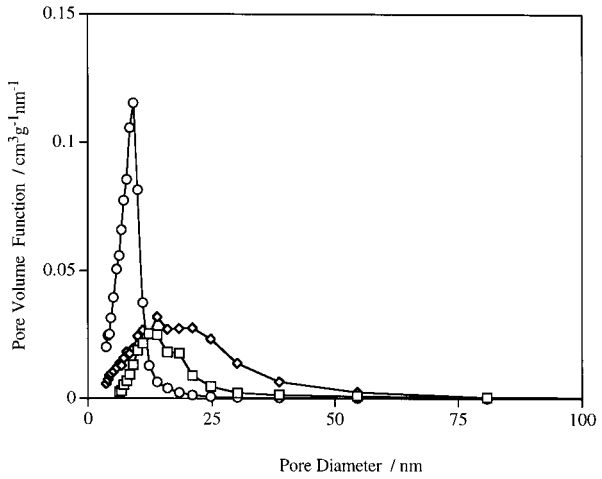

Fig. 4. Effect of amount of solvent on ^{29}Si CP–MAS NMR spectra; (*a*) 10 mL, sample 1; (*b*) 20 mL, sample 3; (*c*) 30 mL, sample 5.

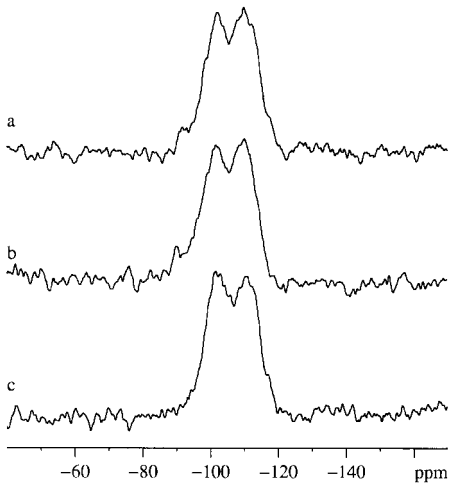

broadening of the +29 Si signal of the Q^3 sites at higher water:TEOS ratios, resulting in a loss of resolution of the Q^3 and Q^4 sites and a small increase in intensity in the region associated with Q^2 (i.e., $Si(OSi)_2(OH)_2$ units) (-75 to -95 ppm), presumably as a result of the increased formation of silanol (Si–OH) groups.

Effect of zinc chloride loading

Samples 11–15 in Table 1 show no clear effect of variation of the amount of zinc chloride on the properties of the catalysts. Increasing the loading should give a steady decrease in both surface area and pore volume as the pores become gradually filled (1). In addition, once the optimum loading has been reached, catalytic activity should drop rapidly as inactive crystalline zinc chloride is formed rather than the catalytically active isolated zinc chloride molecules (9, 10). However, this does not occur here. Although maximum surface area and pore volume are associated with sample 12 (6.48 mmol g^{-1}), and further loading decreases surface area, pore volume does not decrease correspondingly. All of the materials still exhibit a mesoporous structure (Fig. 7), although at lower zinc chloride

© 1998 NRC Canada

Fig. 5. Effect of amount of water on BJH pore distributons; 1.76 mol water /mol TEOS, sample 6 (□); 3.52 mol water/mol TEOS, sample 8 (◇); 5.28 mol water/mol TEOS, sample 10 (○).

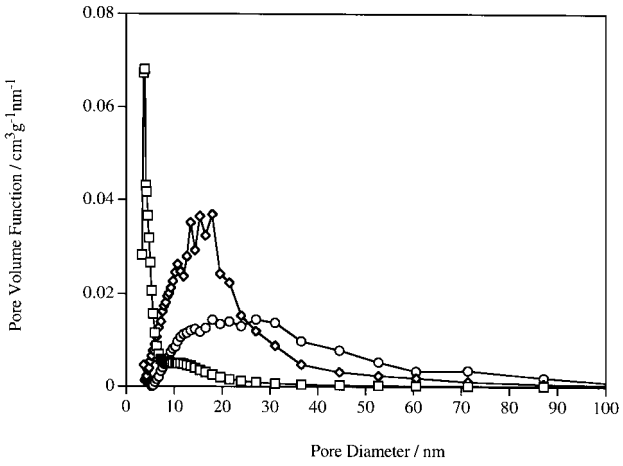

Fig. 6. Effect of amount of water on ^{29}Si CP–MAS NMR spectra; (*a*) 1.76 mol water/mol TEOS, sample 6; (*b*) 3.52 mol water/mol TEOS, sample 8; (*c*) 5.28 mol water/mol TEOS, sample 10.

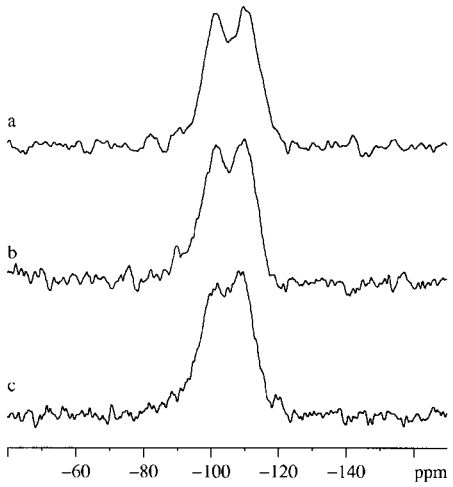

Fig. 7. Effect of zinc chloride loading on BJH pore-volume distributions; 5.83 mmol g^{-1}, sample 11 (□); 7.13 mmol g^{-1}, sample 13 (◇); 8.34 mmol g^{-1}, sample 15 (○).

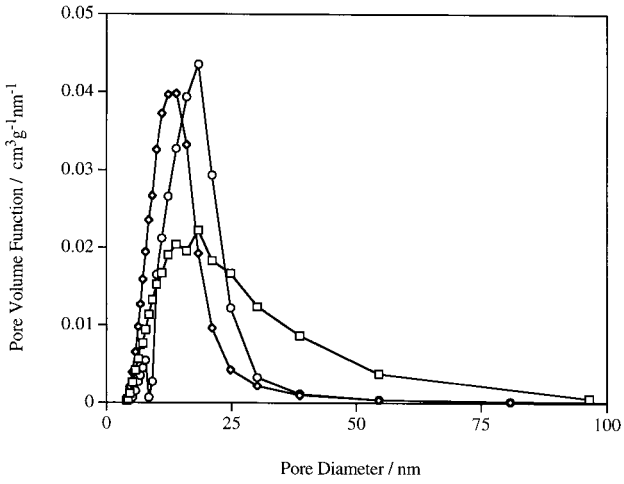

Fig. 8. Effect of zinc chloride loading on ^{29}Si CP–MAS NMR spectra; (*a*) 5.83 mmol g^{-1}, sample11; (*b*) 7.13 mmol g^{-1}, sample 13; (*c*) 8.34 mmol g^{-1}, sample 15.

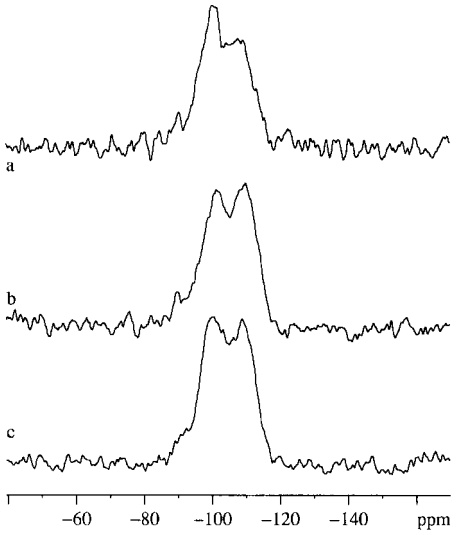

concentrations (sample 11) the distribution is broadened considerably. From the ^{29}Si CP–MAS NMR spectra shown in Fig. 8 it is apparent that the zinc chloride is active during sol–gel synthesis and affects the relative intensities of the Q^3 and Q^4 species, although this effect is less apparent at higher zinc chloride levels. It is possible that reaction of chloride anions with the alkoxysilane gives rise to a Si–Cl group, which is then rapidly hydrolyzed to the silanol. The use of potassium chloride as a catalyst for TEOS polymerization has been reported (20). Since silanol condensation occurs more rapidly than alkoxysilane condensation, systems having more zinc chloride would be expected to show greater degrees of condensation, which would account for increased proportion of Q^4 sites in materials having higher zinc chloride loadings. It is apparent that the zinc chloride as well as the potassium fluoride is acting as a catalyst for condensation reactions in this system.

Effect of potassium fluoride

As detailed for samples 16–20 in Table 1, fluoride concentration has a significant effect on catalyst performance. Fluoride is known to react with an alkoxysilane to give a highly reactive Si—F bond, which is rapidly hydrolyzed in solution (20), although the fluoride-catalyzed TEOS polymerization has previously been reported to give microporous rather than mesoporous materials (21). Sample 16, with the lowest fluoride concentration, was completely ineffective as a catalyst. Although this material has the highest surface area, it has the lowest pore volume, and as shown in Fig. 9, a very sharp distribution centered at 5.79 nm, which is well under the optimum range required for effective Friedel–Crafts catalysis. Higher concentrations of potassium fluoride give much broader pore-size distributions. The effect of fluoride on TEOS polymerization is illustrated by the ^{29}Si CP–MAS NMR spectra (Fig. 10), which show a pronounced increase in the relative intensity of

© 1998 NRC Canada

Fig. 9. Effect of postassium fluoride concentration on BJH pore distributions; 0.03 mol KF/ mol TEOS, sample 16 (□); 0.05 mol KF/mol TEOS, sample 18 (◇); 0.08 mol KF/mol TEOS, sample 20 (○).

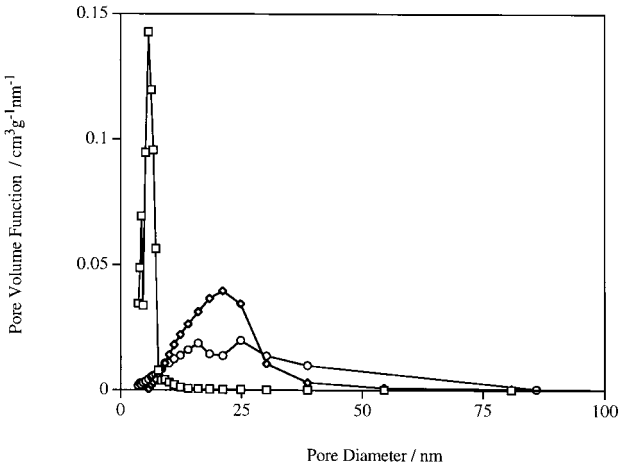

Fig. 10. Effect of potassium fluoride concentration on ^{29}Si CP–MAS NMR spectra; (*a*) 0.03mol/mol TEOS, sample 16; (*b*) 0.05 mol/mol TEOS, sample 18; (*c*) 0.08 mol/mol TEOS,sample 20.

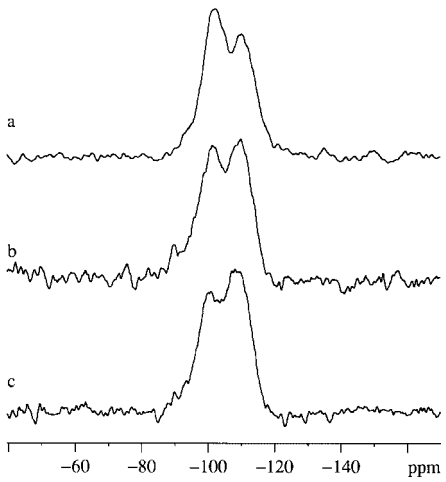

Q^4 sites over Q^3 sites, consistent with a greater degree of condensation reactions occurring at higher fluoride levels in a similar fashion to the effect of zinc chloride previously discussed. The Q^4:Q^3 ratio had recently been observed to increase with increasing amounts of fluoride in the ammonium fluoride catalyzed hydrolysis of tetramethylorthosilicate (22). The ^{19}F MAS NMR spectra (Fig. 11) show a significant broad contribution from residual probe background at low fluoride levels. At low levels, the spectra show two broad peaks centred at -104.3 and -146.4 ppm., which have been attributed to coordinated SiF_4 and SiF_6^{2-} units in a zinc fluoride supported on silica gel system (23). Considering the relative Zn^{2+} and K^+ concentration, the interaction of coordinated SiF_4 and SiF_6^{2-} groups with Zn^{2+} is not unexpected. At increasing KF concentrations, the intensity of the -104.3 ppm band decreases, and the -146.4 ppm peak becomes significantly sharper and

Fig. 11. Effect of potassium fluoride concentration on ^{19}F MAS NMR spectra; (*a*) 0.03 mol/molTEOS, sample 16; (*b*) 0.05 mol/mol TEOS, sample 18; (*c*) 0.08 mol/mol TEOS, sample 20.

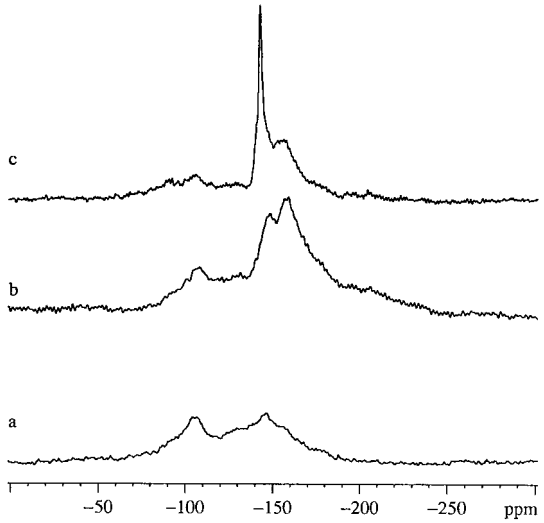

increases in intensity. Increasing levels of fluoride would be expected to further fluorinate the coordinated SiF_4 units to SiF_6^{2-} groups. A third peak at -159.0 ppm, attributed to surface-adsorbed SiF_4/HF in a silica-gel supported KF system (24), also increases in intensity with increasing fluoride concentration, reflecting the increasing role of K^+ in the system.

Conclusions

Sol–gel methods may be applied to the one-step synthesis of a range of silica-based Friedel–Crafts alkylation catalysts, which show greater activity than Clayzic, the commercially available supported reagent. Careful control of preparation conditions is essential for optimum catalytic activity, including the amount of solvent, zinc chloride, potassium fluoride, and water used in the synthesis. Both zinc chloride and potassium fluoride have a catalytic effect on the sol–gel synthesis. As with previous studies, pore-volume distributions have been found to be particularly important. In particular, supported reagents having a significant proportion of pores with diameters less than 8 nm are ineffective in the model reaction. However, large total pore volumes of pores above 8 nm diameter are also an important factor for the most catalytically active materials.

Acknowledgments

We thank the Environmental Science and Technology Alliance of Canada (ESTAC), the Natural Sciences and Engineering Research Council of Canada (NSERC), the Ontario University Industry Incentive Fund (URIF), and Human Resources Development Canada (HRDC) for financial support.

References

1. J.H. Clark, A.P. Kybett, and D.J. Macquarrie. Supported reagents – preparation, analysis and applications. VCH, New York. 1992.
2. J.H. Clark, A.P. Kybett, D.J. Macquarrie, S.J. Barlow, and P. Landon. J. Chem. Soc. Chem. Comm. 1353 (1989).

© 1998 NRC Canada

3. J.H. Clark, S.R. Cullen, S.J. Barlow, and T.W. Bastock. J. Chem. Soc. Perkin Trans. 2, 1117 (1994).
4. S.J. Barlow, T.W. Bastock, J.H. Clark, and S.R. Cullen. Tetrahedron Lett. **34**, 3339 (1993).
5. D.R. Brown, H.G.M. Edwards, D.W. Farwell, and J. Massam. J. Chem. Soc. Faraday Trans. **92**, 1027 (1996).
6. J. Massam and D.R. Brown. Catalysis Lett. **35**, 335 (1995).
7. A. Cornelius, P. Laszlo, and S. Wang. Tetrahedron Lett. **34**, 3849 (1993).
8. S.J. Barlow, J.H. Clark, M.R. Darby, A.P. Kybett, P. Landon, and K. Martin. J. Chem. Res. Synop. 74 (1991).
9. C.N. Rhodes and D.R. Brown. J. Chem. Soc. Faraday Trans. **88**, 2269 (1992).
10. C.N. Rhodes and D.R. Brown. J. Chem. Soc. Faraday Trans. **89**, 1387 (1993).
11. J.M. Miller, D. Wails, J.S. Hartman, and J.L. Belelie. J. Chem. Soc. Faraday Trans. **93**, 2439 (1997).
12. C.J. Brinker and G.W. Scherer. Sol–gel science: the physics and chemistry of sol–gel processing. Academic Press, New York. 1990.
13. J.M. Miller. Prog. Nuc. Mag. Reson. **28**, 255 (1996).
14. S. Brunauer, P.H. Emmett, and E. Teller. J. Am. Chem. Soc. **60**, 309 (1938).
15. E.P. Barrett, L.G. Joyner, and P.H. Halenda. J. Am. Chem. Soc. **73**, 373 (1951).
16. M.K. Titulaer, M.J. den Exter, H. Talsma, J.B.H. Jansen, and J.W. Gues. J. Non-Cryst. Solids, **170**, 113 (1994).
17. International Union of Pure and Applied Chemistry. Pure Appl. Chem. **57**, 604 (1985).
18. G. Engelhardt and D. Michel. High resolution solid state NMR of silicates and zeolites. John Wiley, Chichester. 1987.
19. M. Magi, E. Lippmaa, A. Samoson, G. Engelhardt, and A.R. Grimmer. J. Phys. Chem. **88**, 1518 (1984).
20. E.J.A. Pope and J.D. Mackenzie. J. Non-Cryst. Solids, **87**, 185 (1986).
21. I.C. Tilgner, P. Fischer, F.M. Bohnen, H. Rehage, and W.F. Maier. Microporous Mater. **5**, 77 (1995).
22. A.C. Voegtlin, F. Ruch, J.L. Guth, J. Patarin, and L. Huve. Microporous Mater. **9**, 95 (1997).
23. F.M. Asseid, J.M. Miller, and J.H. Clark. Can. J. Chem. **70**, 2398 (1992).
24. C.V.A. Duke, J.M. Miller, J.H. Clark, and A.P. Kybett. Spectrochim. Acta Part A, **46**, 1381 (1990).

© 1998 NRC Canada

Aromatic aldonitrones of 2-(hydroxyamino)benzyl alcohol and their cyclic isomers. Crystal and molecular structures of a 1-hydroxy-1,2-dihydro-4*H*-3,1-benzoxazine, a boron chelate, and its parent nitrone ligand[1]

Wolfgang Kliegel, J rg Metge, Steven J. Rettig, and James Trotter

Abstract: The synthesis of a series of *C*-aryl-*N*-[2-(hydroxymethyl)phenyl]nitrones, **5** (that can also exist under certain conditions as isomeric 1-hydroxy-2-aryl-1,2-dihydro-4*H*-3,1-benzoxazines, **8**), via 2-(hydroxyamino)benzyl alcohol, **4**, and their subsequent reactions with oxybis(diphenylborane), $(Ph_2B)_2O$, leading to the 5-(arylmethylene)-7,7-diphenyl-6,8-dioxa-5-azonia-7-borata-5*H*-6,7,8,9-tetrahydrobenzocycloheptenes **6** are described. Crystals of 1-hydroxy-2- (4-methoxyphenyl)-1,2-dihydro-4*H*-3,1-benzoxazine, **8***b*, are monoclinic, $a = 9.379(2)$, $b = 10.699(2)$, $c = 12.9392(7)$ Å, $\beta = 99.916(2)°$, $Z = 4$ (two independent molecules), space group *Pa*; those of *C*-[4-(dimethylamino)phenyl]-*N*-[(2-hydroxymethyl)phenyl]nitrone, **5***c,* are monoclinic, $a = 7.687(1)$, $b = 7.891(1)$, $c = 11.5053(9)$ Å, $\beta = 92.781(9)°$, $Z = 2$, space group $P2_1$; and those of 5-[4-(dimethylamino)phenylmethylene]-7,7-diphenyl-6,8-dioxa-5-azonia-7-borata-5*H*-6,7,8,9-tetrahydro-benzocycloheptene, **6***a*, are monoclinic, $a = 10.771(1)$, $b = 13.1057(9)$, $c = 16.8724(7)$ Å, $\beta = 90.005(5)°$, $Z = 4$, space group $P2_1/n$. The structures were solved by direct methods and refined by full-matrix least-squares procedures to $R(F^2) = 0.120$ ($R_w(F^2) = 0.135$) for all 3149 reflections ($R(F) = 0.071$, $R_w(F) = 0.063$ for 1500 reflections with $I \geq 3\sigma(I)$) for **8***b* and $R(F) = 0.035$ and 0.036 ($R_w(F) =$ 0.031 and 0.038) for 1071 and 3594 reflections with $I \geq 3\sigma(I)$, respectively, for **5***c* and **6***a*. Compound **8***b* is the first structurally characterized 1-hydroxy-1,2-dihydro-4*H*-3,1-benzoxazine derivative and **6***a* features a relatively rare seven-membered boron-containing heterocycle.

Key words: *C*-aryl-*N*-[2-(hydroxymethyl)phenyl]nitrones, 1-hydroxy-2-aryl-1,2-dihydro-4*H*-3,1-benzoxazines, organoboron compounds, crystal structures.

Résumé : On décrit la synthèse d'une série de *C*-aryl-*N*-[2-(hydroxyméthyl)phényl]nitrones, **5** (qui peuvent aussi exister dans certaines conditions sous la forme isomère 1-hydroxy-2-aryl-1,2-dihydro-4*H*-3,1-benzoxazines, **8**) par le biais de l'alcool 2-(hydroxyamino)benzylique, **4**, ainsi que leurs réactions subséquentes avec l'oxybis(diphénylborane), $(Ph_2B)_2O$, conduisant à la formation des 5-(arylméthylène)-7,7-diphényl-6,8-dioxa-5-azonia-7-borata-5*H*-6,7,8,9-tétrahydrobenzocycloheptènes, **6**. Les cristaux de la 1-hydroxy-2-(4-méthoxyphényl)-1,2-dihydro-4*H*-3,1-benzoxazine, **8***b*, sont monocliniques, groupe d'espace *Pa*, avec $a = 9,379(2)$, $b = 10,699(2)$ et $c = 12,9392(7)$ Å, $\beta = 99,916(2)°$ et $Z = 4$ (deux molécules indépendantes); ceux de la *C*-[4-(diméthylamino)phényl]-*N*-[(2-hydroxyméthyl)phényl]nitrone, **5***c*, sont monocliniques, groupe d'espace $P2_1$, avec $a = 7,687(1)$, $b = 7,891(1)$ et $c = 11,5053(9)$ Å, $\beta = 92,781(9)°$ et $Z = 2$ et ceux du 5-[4-(diméthylamino)phénylméthylène]-7,7-diphényl-6,8-dioxa-5-azonia-7-borata-5*H*-6,7,8,9-tétrahydrobenzocycloheptène, **6***a*, sont monocliniques, groupe d'espace $P2_1/n$, avec $a = 10,771(1)$, $b = 13,1057(9)$ et $c = 16,8724(7)$ Å, $\beta = 90,005(2)°$ et $Z = 4$. On a résolu les structures par des méthodes directes et on les a affinées par les méthodes des moindres carrés (matrice complète) jusqu'à des valeurs de $R(F^2) =$ 0,120 ($R_w(F^2) = 0,135$) pour l'ensemble des 3149 réflexions ($R(F) = 0,071$ et $R_w(F) = 0,063$ pour 1500 réflexions avec $I \geq 3\sigma(I)$) pour le composé **8***b* et des valeurs de $R(F) = 0,035$ et 0,036 ($R_w(F) = 0,031$ et 0,038) pour 1071 et 3594 réflexions avec $I \geq 3\sigma(I)$ pour respectivement les composés **5***c* et **6***a*. Le composé **8***b* est le premier dérivé de la 1-hydroxy-1,2-dihydro-4*H*-3,1-benzoxazine à être caractérisé et le composé **6***a* comporte un hétérocycle à sept chaînons relativement rare contenant du bore.

Mots clés : *C*-aryl-*N*-[2(-hydroxyméthyl)phénol]nitrones, 1-hydroxy-2-aryl-1,2-dihydro-4*H*-3,1-benzoxazines, composés organoborés, structures cristallines.

[Traduit par la rédaction]

Received December 9, 1997.

W. Kliegel and J. Metge. Institut für Pharmazeutische Chemie der Technischen Universität Braunschweig, Beethovenstrasse 55, 38106 Braunschweig, Germany.

S.J. Rettig and J. Trotter.[2] Department of Chemistry, University of British Columbia, 2036 Main Mall, Vancouver, BC V6T 1Z1, Canada.

[1] Structural studies of organoboron compounds LXVII. Previous paper in this series: ref. 1.

[2] Author to whom correspondence may be addressed. Telephone: (604) 822-4865. Fax: (604) 822-2847. E-mail: jtrt@xray4.chem.ubc.ca

© 1998 NRC Canada

Introduction

As reported in the preceding paper (1), the hitherto unknown *N*-(2-hydroxyphenylmethyl)hydroxylamine **1** (Scheme 1) was trapped as various aromatic aldonitrone derivatives **2**. These nitrones could be applied as bidentate ligands for the formation of seven-membered diphenylboron chelates[3] **3**, provided that the electron density at the *N*-oxide oxygen atom of the nitrone function was sufficiently increased by electron-donating substituents, such as a *p*-dimethylamino group, at the aryl residue.

The question arose whether the nitrones **5** derived from 2-(hydroxyamino)benzyl alcohol, **4** (an isomer of **1**), would be able to serve as chelating ligands enabling the synthesis of the boron chelates **6** and, if so, would there be structural requirements similar to those for **3**? As *N*-aryl derivatives, the hydroxylamine **4** and its nitrone **5** should be weaker bases than the isomeric *N*-alkylhydroxylamine **1** and its nitrone **2**. On the other hand, the alcohol function in **4** and **5** has different ligand properties than does the phenol function in **1** and **2**, considering the higher nucleophilicity of the alcoholate anion relative to that of the phenolate anion. In this report we describe the condensation of the hydroxylamine **4** and aromatic aldehydes to achieve the synthesis of the nitrones **5** and subsequent investigations of the suitability of **5** as bidentate ligands in the formation of the seven-membered boron chelates **6**. The structures of a ring isomer, **8**, an open-chain isomer, **5**, and the product of the reaction of **5** with $(Ph_2B)_2O$, **6**, have been determined by X-ray crystallographic analysis.

Experimental

General procedures

All preparations and reactions were carried out under normal conditions, without protective gas atmosphere. Commercial solvents and reagents were used as supplied. Oxybis(diphenylborane) was prepared according to literature methods (2). Melting points were measured on a Linström SPA-1 apparatus and are uncorrected. Elemental analyses (C, H, N, O): Carlo Erba Elemental Analyzer 1106; (B): oxidative disintegration (Schöninger) and potentiometric titration. Infrared spectra: Phillips PU 9800 FT-IR spectrometer, V 3.00, and Mattson Genesis Series FTIR Rev. I (ATI Unicam). For ^{1}H nmr: Varian EM 390; ^{11}B and ^{13}C nmr: Bruker AC 200. Mass spectra: Finnigan MAT 8430.

2-(Hydroxyamino)-benzyl alcohol, 4

With reference to the method described in the literature (3) 2-nitrobenzyl alcohol (5.10 g, 30.0 mmol) is dissolved in a mixture of 10 mL of methanol and 15 mL of water. After addition of 5 mL of 2 M NH_4Cl solution, zinc dust (8 g) is added in small portions under vigorous stirring. The temperature is kept below 65°C. Stirring is continued after the zinc addition until the temperature falls below 55°C. The warm solution is filtered off and gives small white flakes while cooling down. These crystals are carefully washed with a mimimum amount of water and dried at room temperature. Yield: 0.5 g (11%); mp 106°C (lit. (3) mp 104.2–104.7°C). Infrared (KBr, cm^{-1}): 1588 (C═C); ^{1}H nmr (400 MHz, DMSO-d_6–TMS) δ (ppm): 4.40 (d, J = 5.5 Hz, CH_2), 5.11 (t, J = 5.5 Hz, exchangeable, C-OH), 6.76 (t, J = 7 Hz, 5-H), 7.10 (d, J = 6 Hz, 3-H), 7.13 (d, J = 7 Hz, 4-H), 7.17 (d, J = 7 Hz, 6-H), 7.85 (d, J = 2 Hz, exchangeable, NH), 8.26 (d, J = 2 Hz, exchangeable, C-OH); ^{13}C nmr (100 MHz, DMSO-d_6–TMS) δ (ppm): 59.9 (C-7 "methylene"), 112.1 (C-3), 118.8 (C-5), 126.1 (C-1), 126.3 (C-6), 127.2 (C-4), 148.8 (C-2); assignment of all signals confirmed by C,H-COSY and C,H-COLOC methods; mass spectrum (EI, 70 eV) *m/z* (%): 139 (16) [M$^+$], 121 (100) [M$^+$–H_2O], 120 (85), 105 (21), 104 (23), 93 (66), 92 (61), 77 (45), 66 (58), 65 (64), 51 (24). Anal. calcd. for $C_7H_9NO_2$: C 60.42, H 6.52, N 10.07; found: C 60.53, H 6.62, N 9.88.

N-[2-(Hydroxymethyl)phenyl]-*C*-phenylnitrone, 5*a*,[4] or 1-hydroxy-2-phenyl-1,2-dihydro-4*H*-3,1-benzoxazine, 8*a*

Because of low yields of the pure crystalline 2-(hydroxyamino)-benzyl alcohol, **4**, one third of the warm filtered solution resulting from the Zn dust reduction of 2-nitrobenzyl alcohol (see above), which contains approximately 10 mmol of **4**, is mixed with benzaldehyde (1.06 g, 10.0 mmol). Crystallization commences upon cooling down to room temperature. Yield: 0.80 g (70%) of pale yellow crystals; mp 119°C. Infrared (KBr, cm^{-1}): 3443, 3347 (broadened, O-H), 1608, 1586 (C═N/C═C); ^{1}H nmr (90 MHz, $CDCl_3$–TMS) δ (ppm): 4.55 (s, 10% of 2 H, CH_2), 4.82 and 5.06 (d and d, J = 15 Hz, AB system, 90% of 2 H, CH_2), 5.38 (s, 90% of 1 H, O-CH-N), 5.55 (s, exchangeable, OH), 6.83–7.73 (m, 9 aromatic H and 10% of 1 H, CH═N). Anal. calcd. for $C_{14}H_{13}NO_2$: C 74.00, H 5.77, N 6.16; found: C 74.08, H 5.73, N 6.15.

N-[2-(Hydroxymethyl)phenyl]-*C*-(4-methoxyphenyl)-nitrone, 5*b*,[5] or 1-hydroxy-2-(4-methoxyphenyl)-1,2-dihydro- 4*H*-3,1-benzoxazine, 8*b*

The reaction is carried out as described for **5***a* with 4-methoxybenzaldehyde (1.36 g, 10.0 mmol). Yield: 1.10 g (86%) of colorless crystals; mp 132°C. Infrared (KBr, cm^{-1}): 3474, 3362 (broadened, O-H), 1613, 1590 (C═N/C═C); ^{1}H nmr (90 MHz, $CDCl_3$–TMS) δ (ppm): 3.80 (s, 70% of 3 H, OCH_3), 3.86 (s, 30% of 3 H, OCH_3), 4.56 (s, 30% of 2 H, CH_2), 4.83 and 5.06 (d and d, J = 15 Hz, 70% of 2 H, CH_2), 5.30 (s, 70% of 1 H, O-CH-N), 6.00 (s, exchangeable, OH), 6.80–8.40 (m, 8 aromatic H), 7.60 (s, 30% of 1 H, CH═N). Anal. calcd. for $C_{15}H_{15}NO_3$: C 70.02, H 5.88, N 5.44; found: C 70.15, H 5.86, N 5.49. Crystals suitable for X-ray analysis were obtained by very slow cooling of a solution of **5/8***b* in ethanol after repeated recrystallization.

C-[4-(Dimethylamino)phenyl]-*N*-[2-(hydroxymethyl)phenyl]-nitrone, 5*c*[6]

The reaction is carried out as described for **5***a* with 4-dimethylaminobenzaldehyde (1.49 g, 10.0 mmol). Yield: 1.05 g (78%) of yellow-brown crystals; mp 164°C (from ethanol). Infrared (KBr, cm^{-1}): 3400–2000 (very broad "curtain," peaks at 3385,

[3] Here and elsewhere in this work the term "boron chelate" refers to a nonclassical "chelate" of the Ph_2B^+ moiety. Considering the diphenylborenium moiety as a "pseudometal" explains much of the chemistry of these systems even though the bonding is (necessarily) quite different from that in true metal complexes.

[4] Alternative nomenclature: 2-(phenylmethylenamino)phenylmethanol *N*-oxide.

[5] Alternative nomenclature: 2-(4-methoxyphenylmethylenamino)-phenylmethanol *N*-oxide.

[6] Alternative nomenclature: 2-(4-dimethylamino^1-phenylmethylenamino^2)phenylmethanol N^2-oxide.

© 1998 NRC Canada

Scheme 1.

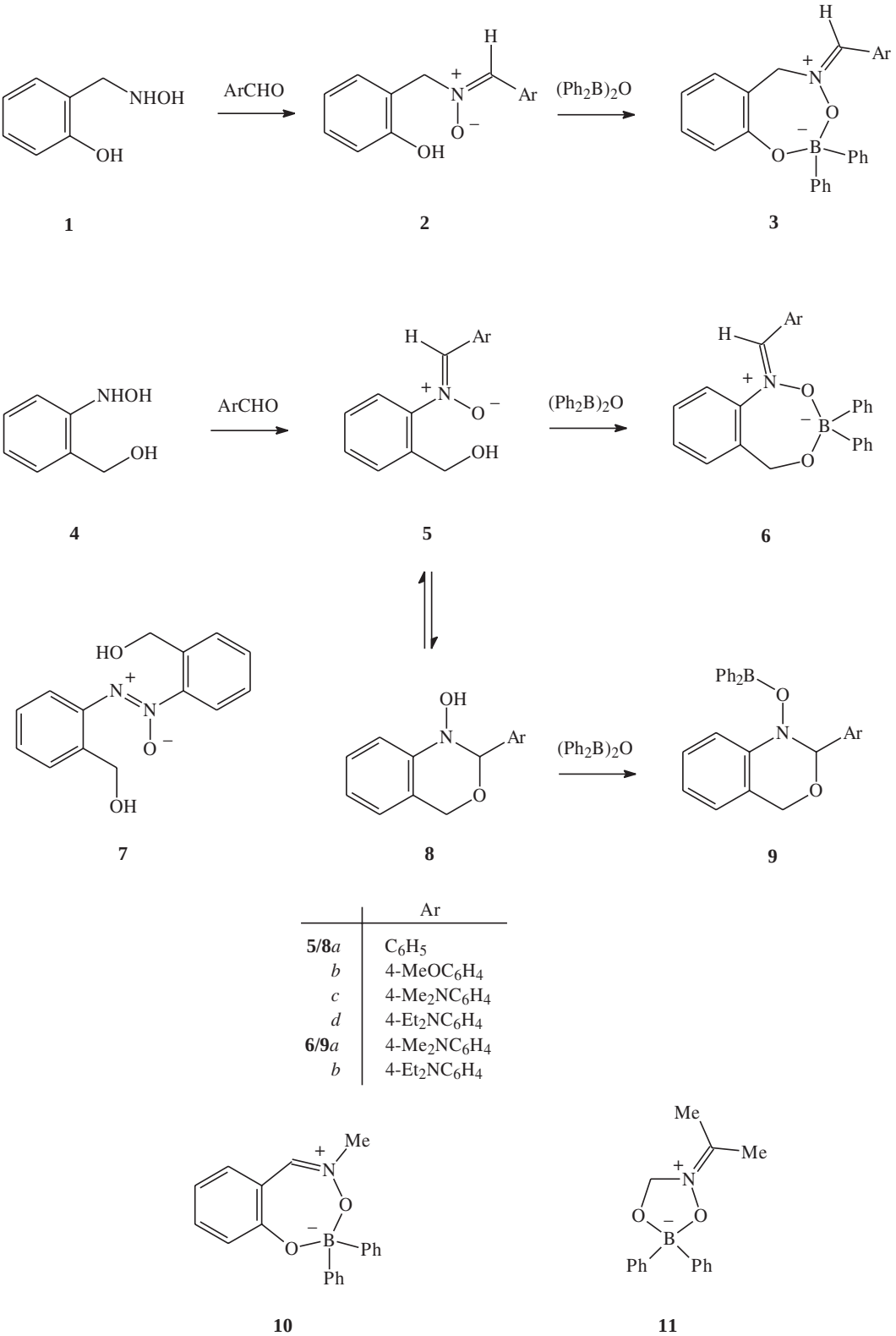

	Ar
5/8*a*	C_6H_5
b	4-$MeOC_6H_4$
c	4-$Me_2NC_6H_4$
d	4-$Et_2NC_6H_4$
6/9*a*	4-$Me_2NC_6H_4$
b	4-$Et_2NC_6H_4$

3266, O-H), 1605, 1578 (C═N/C═C); ^{1}H nmr (90 MHz, $CDCl_3$–TMS) δ (ppm): 3.10 (s, $(CH_3)_2N$), 4.63 (s, CH_2), 5.30 (s, broad, exchangeable, OH), 6.76 and 8.33 (d and d, J = 9 Hz, AA′BB′ system, N-C_6H_4), 7.33–7.50 (m, 4 aromatic H), 7.56 (s, CH═N). Anal. calcd. for $C_{16}H_{18}N_2O_2$: C 71.09, H 6.71, N 10.36; found: C 71.08, H 6.72, N 10.35. Crystals suitable for X-ray analysis were obtained by very slow cooling of a solution of **5***c* in absolute ethanol.

© 1998 NRC Canada

5-[4-(Dimethylamino)phenylmethylene]-7,7-diphenyl-6,8-dioxa-5-azonia-7-borata-5*H*-6,7,8,9-tetrahydrobenzocycloheptene, 6a[7]

5*c* (0.27 g, 1.0 mmol) and oxybis(diphenylborane) (0.17 g, 0.5 mmol) are dissolved in 20 mL of absolute ethanol and refluxed for 10 min. Crystallization commences during cooling to room temperature. Yield: 0.36 g (83%) of orange-colored crystals; mp 156ºC (from ethanol). Infrared (KBr, cm^{-1}): 1617 (C═N), 1603 (C═C); ^{1}H nmr (90 MHz, $CDCl_3$–TMS) δ (ppm): 3.08 (s, $(CH_3)_2N$), 4.98 (m, CH_2), 6.48 and 7.95 (d and d, J = 9 Hz, AA′BB′ system, N-C_6H_4), 6.93–7.73 (m, 14 aromatic H), 7.70 (s, CH═N). Anal. calcd. for $C_{28}H_{27}BN_2O_2$: C 77.43, H 6.27, B 2.49, N 6.45; found: C 77.36, H 6.34, B 2.50, N 6.41. The product gives a blue-colored solution in ethanol upon addition of diphenylcarbazone, indicating the presence of the chelated diphenylborenium (Ph_2B^+) ion (4). Crystals suitable for X-ray analysis were obtained by slow crystallization from absolute ethanol.

5-[4-(Diethylamino)phenylmethylene]-7,7-diphenyl-6,8-dioxa-5-azonia-7-borata-5*H*-6,7,8,9-tetrahydrobenzocycloheptene, 6b[8]

The reaction is carried out as described for **5***a* with 4-diethylaminobenzaldehyde (1.77 g, 10.0 mmol). Since no crystallization could be achieved, the solution of the nitrone (**5***d*) was evaporated. A part of the remaining oily crude product (containing **5***d*) (0.3 g, ca. 1 mmol) and oxybis(diphenylborane) (0.17 g, 0.5 mmol) are dissolved in 20 mL of absolute ethanol and refluxed for 10 min. Cooling the solution yields 0.39 g (84%) of orange-colored crystals; mp 164°C (from ethanol). Infrared (KBr, cm^{-1}): 1617 (C═N), 1603 (C═C); ^{1}H nmr (400 MHz, $CDCl_3$–TMS) δ (ppm): 1.17 (t, J = 7 Hz, 2 CH_3), 3.37 (q, J = 7 Hz, $(CH_2)_2N$), 4.98 (m, OCH_2), 6.26–8.80 (m, 18 aromatic H and CH═N); ^{13}C nmr (100 MHz, $CDCl_3$–TMS) δ (ppm): 12.6 (2 CH_3), 44.9 (2 CH_2), 65.8 (OCH_2), 110.5, 111, 123–126.3 (aromatic C), 133.5 (C═N); ^{11}B nmr (64 MHz, $CDCl_3$–Et_2OBF_3) δ (ppm): 10.8 ($W_{1/2}$ = 364 Hz) and 47.1 ($W_{1/2}$ = 250 Hz), ratio of peak areas 20:1. Anal. calcd. for $C_{30}H_{31}BN_2O_2$: C 77.93, H 6.76, B 2.34, N 6.06; found: C 77.91, H 6.72, B 2.47, N 6.09. **6***b* gives a blue color reaction with diphenylcarbazone as described for **6***a*.

2,2′-Azoxybenzyl alcohol, 7

Pale yellow needles precipitate from the filtered solution (mother liquor) of the synthesis of **4** upon standing in air or upon concentrating the solution. Yield: 0.5 g (12%) of pale yellow needles; mp 121°C (from ethanol–water) (lit. (3) mp 123°C). Infrared (KBr, cm^{-1}): 3270–3070 (broad, OH); ^{1}H nmr (90 MHz, $CDCl_3$–TMS) δ (ppm): 3.03 (s, broad, exchangeable, 2 OH), 4.75 (s, CH_2), 4.78 (s, CH_2), 7.23–7.63 (m, 6 aromatic H), 7.76–7.93 (m, 1 aromatic H), 8.16–8.33 (m, 1 aromatic H). Anal. calcd. for $C_{14}H_{14}N_2O_3$: C 65.11, H 5.46, N 10.85; found: C 65.17, H 5.47, N 10.66. The yield of **7** is raised considerably by bubbling air through the above-mentioned solution of **4**, or by addition of small amounts of oxidants like $K_2Cr_2O_7$ or H_2O_2.

X-ray crystallographic analyses

Crystallographic data appear in Table 1. The final unit-cell parameters were obtained by least squares employing 8737 reflections with 2θ = 4.0°–63.7º for **8***b*, 25 reflections with 2θ = 12.5°–22.3° for **5***c*, and 25 reflections with 2θ = 95.5º–107.5° for **6***a*. The intensities of three standard reflections, measured every 200 reflections throughout the data collections for **5***c* and **6***a*, decayed linearly by 5.6% for **5***c* and by 2.9% for **6***a*. The data were processed,[9] corrected for Lorentz and polarization effects, decay (**5***c* and **6***a*), and absorption (based on analysis of redundant data for **8***b* and azimuthal scans for **5***c* and **6***a*).

The structures were solved by direct methods, the coordinates of the non-hydrogen atoms being determined from *E*-maps or from subsequent difference Fourier syntheses. The solution of the structure of **8***b* was initially attempted (unsuccessfully) in the centrosymmetric space group *P*2/*a* based on the *E*-statistics. Changing to the noncentrosymmetric space group *Pa* gave a solution immediately. The two independent molecules in the asymmetric unit of **8***b* are related by a pseudo-inversion centre, but it should be noted that this cannot be a true center of symmetry since the corresponding chiral carbon atoms, C(8) and C(23), both have the same chirality. The N-OH oxygen atoms of both of the two independent molecules of **8***b* were modeled as (3:1) twofold disordered, representing configurational disorder at the chiral nitrogen atoms. The geometry involving the lower-occupancy NOH oxygen atoms, as well as the anisotropic thermal parameters, in general suggests that the entire molecules of **8***b* are probably disordered with only the components of the NOH oxygen atoms separated enough to be resolved. The resulting structure of **8***b* therefore represents (except for the resolved O atoms and for each of the two independent molecules) a weighted mean of two different stereoisomers having opposite configurations at the nitrogen atom, and the accuracy of the derived parameters is likely less than that indicated by the least-squares standard deviations. For **5***c* the structure analysis was initiated in the noncentrosymmetric space group $P2_1$ on the basis of the *E*-statistics, this choice being validated by subsequent calculations. Twofold disorder (~5:1) of the aromatic -CH_2OH group of **5***c* was modeled by split-atom refinement of the oxygen atom. The site occupancy factors for the disordered oxygen atoms in **8***b* and **5***c* were adjusted as the refinement progressed to result in nearly equal equivalent isotropic thermal parameters for the two components of the disordered models. Low-occupancy oxygen atoms in **8***b* (O(2a)) and **5***c* (O(2a)) were refined with isotropic thermal parameters and all other nonhydrogen atoms were refined with anisotropic thermal parameters. The higher-occupancy NOH hydrogen atoms of **8***b* were placed in difference map positions but were not refined. The major OH hydrogen atom of **5***c* and all hydrogen atoms of **6***a* were refined with isotropic thermal parameters and the carbon-bound hydrogen atoms of **8***b* and **5***c* were fixed in calculated positions

[7] Alternative nomenclature: *N*-(4-dimethylamino[1]-phenylmethylene)-*N*-[2-(diphenylboryloxymethyl)phenyl]amine[2] N^2-oxide (O→B complex).

[8] Alternative nomenclature: *N*-(4-diethylamino[1]-phenylmethylene)-*N*-[2-(diphenylboryloxy-methyl)phenyl]amine[2] N^2-oxide (O→B complex).

[9] *teXsan*: Crystal structure analysis package. Unix version 1.7. Molecular Structure Corporation, The Woodlands, Tex. 1995; *d*TREK*: Area detector software. Molecular Structure Corporation, The Woodlands, Tex. 1997.

© 1998 NRC Canada

Table 1. Crystallographic data.

Compound	**8***b*[a]	**5***c*[b]	**6***a*[b]
Formula	$C_{15}H_{15}NO_3$	$C_{16}H_{18}N_2O_2$	$C_{28}H_{27}BN_2O_2$
fw	257.29	270.33	434.34
Crystal system	Monoclinic	Monoclinic	Monoclinic
Space group	*Pa* (No. 7)	$P2_1$ (No. 4)	$P2_1/n$ (No. 14)
a, Å	9.379(2)	7.687(1)	10.771(1)
b, Å	10.699(2)	7.891(1)	13.1057(9)
c, Å	12.9392(7)	11.5053(9)	16.8724(7)
β, deg	99.916(2)	92.781(9)	90.005(5)
V, Å^3	1279.0(3)	697.0(1)	2381.8(3)
Z	4	2	4
ρ_{calc} , g/cm^3	1.336	1.288	1.211
F(000)	544	288	920
Radiation	Mo	Mo	Cu
μ, cm^{-1}	0.93	0.86	5.59
Crystal size , mm	$0.10 \times 0.35 \times 0.45$	$0.05 \times 0.30 \times 0.35$	$0.22 \times 0.35 \times 0.45$
Transmission factors	0.64–1.03[c]	0.87–1.00	0.88–1.00
Scan type	ω	ω–2θ	ω–2θ
Scan range, deg in ω	0.5	1.10 + 0.35 tan θ	1.00 + 0.20 tan θ
Scan speed, deg/min	—	8 (up to 9 scans)	32 (up to 9 scans)
Data collected	480 frames, 80 s/frame	$+h, +k, \pm l$	$+h, +k, \pm l$
$2\theta_{max}$, deg	60	60	155
Crystal decay,%	—	5.6	2.9
Total reflections	11786	2321	5452
Unique reflections	3149	2176	5170
R_{merge}	0.063	0.021	0.018
No. with $I \geq 3\sigma(I)$	1500	1071	3594
No. of variables	354	189	407
R (F) ($I \geq 3\sigma(I)$)	0.071	0.035	0.036
R_w (F) ($I \geq 3\sigma(I)$)	0.063	0.031	0.038
R (F^2) (all data)	0.120	—	—
R_w (F^2) (all data)	0.135	—	—
gof	2.32	1.80	2.73
Max Δ/σ (final cycle)	0.01	0.004	0.02
Residual density e/Å^3	–0.51 to 0.72	–0.11 to 0.12	–0.11 to 0.14

[a]Temperature 180 K, Rigaku/ADSC CCD diffractometer, Mo K_α ($\lambda = 0.71069$ Å), graphite monochromator, takeoff angle 6.0°, aperture 94.0×94.0 mm at a distance of 39.17 mm from the crystal, $\sigma^2(F^2) = (C + B)/\mathrm{Lp}^2$ (C = scan count, B = background count), function minimized $\sum w(|F_o^2|-|F_c^2|)^2$ where $w = 1/\sigma^2(F_o^2)$, $R = \sum||F_o^2|-|F_c^2||/\sum|F_o^2|$, $R_w = (\sum w(|F_o^2|-|F_c^2|)^2 / \sum w|F_o^2|^2)^{1/2}$, and gof = $[\sum w(|F_o^2|-|F_c^2|)^2/(m-n)]^{1/2}$. Data collected to $2\theta_{max} = 60°$ (full sphere 4–40°, hemisphere 40–60°).
[b]Temperature 294 K, Rigaku AFC6S diffractometer, Mo K_α ($\lambda = 0.71069$ Å) or Cu K_α radiation ($\lambda = 1.54178$ Å), graphite monochromator, takeoff angle 6.0°, aperture 6.0×6.0 mm at a distance of 285 mm from the crystal, stationary background counts at each end of the scan (scan/background time ratio 2:1), $\sigma^2(F^2) = [S^2(C + 4B)]/\mathrm{Lp}^2$ (S = scan rate, C = scan count, B = normalized background count), function minimized $\sum w(|F_o|-|F_c|)^2$ where $w = 4\,F_o^2/\sigma^2(F_o^2)$, $R = \sum||F_o|-|F_c||/\sum|F_o|$, $R_w = (\sum w(|F_o|-|F_c|)^2/\sum w|F_o|^2)^{1/2}$, and gof = $[\sum w(|F_o|-|F_c|)^2/(m-n)]^{1/2}$.
[c]Includes crystal decay, absorption, and scaling corrections

with C—H = 0.98 Å and $B_H = 1.2\ B_{\text{bonded atom}}$. The minor component OH hydrogen atoms of **8***b* and **5***c* could not be located and were excluded from the models. Corrections for secondary extinction were applied (Zachariasen type, isotropic, Gaussian), the final values of the extinction coefficients being $1.5(3) \times 10^{-6}$ for **5***c* and $1.54(2) \times 10^{-5}$ for **6***a* (no extinction correction was necessary for **8***b*). Neutral atom scattering factors for all atoms and anomalous dispersion corrections for the non-hydrogen atoms were taken from the *International Tables for X-Ray Crystallography* (5). No attempts to determine the polarity of **8***b* and the absolute configuration of **5***c* (helical chirality) were made because the data were collected with Mo radiation. Final atomic coordinates and equivalent isotropic thermal parameters, bond lengths, bond angles, and intra-annular torsion angles (for **8***b* and **6***a*) appear in Tables 2–5, respectively. Tables of hydrogen atom parameters, anisotropic thermal parameters, torsion angles, intermolecular contacts, and least-squares planes are available as supplementary material.[10]

[10] These tables may be purchased from: The Depository of Unpublished Data, Document Delivery, CISTI, National Research Council Canada, Ottawa, Canada K1A 0S2. The tables of hydrogen atom coordinates and bond lengths and angles involving hydrogen atoms have also been deposited with the Cambridge Crystallographic Data Centre, University Chemical Laboratory, 12 Union Road, Cambridge CB2 1EZ, U.K.

© 1998 NRC Canada

Table 2. Final atomic coordinates (fractional) and B_{eq} (10^3 Å^2).[a]

Atom	*x*	*y*	*z*	B_{eq}	
			8*b*		
O(1)	0.1655	–0.0360(4)	0.2784	4.3(1)	
O(2)	0.0909(8)	0.2863(5)	0.2750(6)	3.8(2)	0.75
O(2a)	–0.046(2)	0.250(1)	0.315(1)	2.4(3)	0.25
O(3)	0.3923(7)	0.1677(4)	0.7324(5)	3.8(1)	
O(4)	0.5767(5)	0.5101(4)	0.4073(3)	4.4(1)	
O(5)	0.8098(8)	0.2552(4)	0.3699(6)	2.8(1)	0.75
O(5a)	0.675(2)	0.219(1)	0.411(1)	2.4(4)	0.25
O(6)	0.3681(8)	0.3344(4)	–0.0524(5)	4.3(1)	
N(1)	0.0622(8)	0.1609(4)	0.2577(5)	2.7(1)	
N(2)	0.7009(8)	0.3216(5)	0.4207(6)	3.3(1)	
C(1)	0.0129(8)	0.1404(6)	0.1485(6)	3.3(2)	
C(2)	0.0361(8)	0.0261(5)	0.1073(6)	2.6(1)	
C(3)	–0.0244(9)	–0.0010(6)	0.0032(7)	3.8(2)	
C(4)	–0.1097(9)	0.0891(7)	–0.0589(7)	4.5(2)	
C(5)	–0.1285(9)	0.2039(8)	–0.0177(7)	4.7(2)	
C(6)	–0.0678(9)	0.2311(6)	0.0870(6)	3.5(2)	
C(7)	0.130(1)	–0.0697(5)	0.1704(6)	4.0(2)	
C(8)	0.1951(8)	0.0848(5)	0.2938(5)	3.7(1)	
C(9)	0.246(1)	0.1036(6)	0.4108(6)	4.6(2)	
C(10)	0.154(1)	0.0896(6)	0.4795(9)	5.5(2)	
C(11)	0.2003(9)	0.1087(6)	0.5982(7)	4.4(2)	
C(12)	0.3442(8)	0.1468(6)	0.6253(6)	2.9(2)	
C(13)	0.428(1)	0.1640(6)	0.5504(7)	3.9(2)	
C(14)	0.377(1)	0.1457(6)	0.4450(7)	5.3(2)	
C(15)	0.536(1)	0.2166(7)	0.7596(7)	4.6(2)	
C(16)	0.7594(8)	0.3510(5)	0.5279(6)	2.7(2)	
C(17)	0.7351(9)	0.4634(6)	0.5715(7)	3.5(2)	
C(18)	0.793(1)	0.4885(6)	0.6756(7)	4.1(2)	
C(19)	0.873(1)	0.4027(8)	0.7369(7)	4.8(2)	
C(20)	0.8944(9)	0.2872(7)	0.6931(7)	4.4(2)	
C(21)	0.8419(9)	0.2583(5)	0.5905(6)	3.5(2)	
C(22)	0.6424(9)	0.5596(6)	0.5058(7)	3.7(2)	
C(23)	0.6624(8)	0.4321(4)	0.3542(5)	3.3(1)	
C(24)	0.578(1)	0.3993(5)	0.2458(7)	5.2(2)	
C(25)	0.640(1)	0.4208(6)	0.1611(7)	4.5(2)	
C(26)	0.568(1)	0.3967(6)	0.0675(7)	4.7(2)	
C(27)	0.427(1)	0.3526(6)	0.0503(7)	3.8(2)	
C(28)	0.352(1)	0.3306(6)	0.1336(7)	4.1(2)	
C(29)	0.435(1)	0.3582(6)	0.2355(7)	5.2(2)	
C(30)	0.224(1)	0.2846(7)	–0.0759(7)	5.0(2)	
			5*c*		
O(1)	0.0621(3)	0.4122	0.2895(2)	4.53(6)	
O(2)	0.0922(4)	0.1234(6)	0.5510(3)	5.40(9)	0.835
O(2a)	0.088(2)	–0.051(2)	0.372(1)	5.7(3)	0.165
N(1)	–0.0404(3)	0.2996(4)	0.2376(2)	3.35(6)	
N(2)	0.5106(3)	0.3472(5)	–0.1773(2)	4.33(7)	
C(1)	–0.1816(3)	0.2362(5)	0.3069(2)	3.11(7)	
C(2)	–0.1431(4)	0.1346(5)	0.4027(2)	3.39(7)	
C(3)	–0.2832(4)	0.0819(6)	0.4658(2)	4.22(9)	
C(4)	–0.4519(4)	0.1319(6)	0.4367(3)	4.36(9)	
C(5)	–0.4857(4)	0.2346(6)	0.3413(3)	4.36(8)	
C(6)	–0.3486(4)	0.2857(5)	0.2757(3)	3.94(8)	
C(7)	0.0384(4)	0.0738(6)	0.4375(3)	4.54(9)	
C(8)	–0.0242(4)	0.2456(5)	0.1320(3)	3.35(7)	
C(9)	0.1077(3)	0.2918(5)	0.0531(2)	2.91(7)	
C(10)	0.2499(4)	0.3993(5)	0.0792(2)	3.18(7)	
C(11)	0.3794(4)	0.4207(5)	0.0020(3)	3.28(7)	
C(12)	0.3762(4)	0.3359(5)	–0.1055(3)	3.28(8)	
C(13)	0.2277(4)	0.2381(5)	–0.1352(3)	3.68(8)	
C(14)	0.1000(4)	0.2165(5)	–0.0576(3)	3.50(8)	
C(15)	0.6705(4)	0.4338(7)	–0.1402(3)	5.4(1)	
C(16)	0.5115(4)	0.2530(6)	–0.2855(3)	4.97(9)	
			6*a*		
O(1)	0.51323(8)	0.17676(7)	0.23380(6)	3.39(2)	
O(2)	0.38899(9)	0.03591(8)	0.18326(6)	4.09(2)	
N(1)	0.4239(1)	0.24464(9)	0.20906(7)	3.41(2)	
N(2)	0.4496(2)	0.3798(1)	0.58190(9)	6.30(4)	
C(1)	0.4008(1)	0.2474(1)	0.12493(8)	3.64(3)	
C(2)	0.4141(1)	0.1604(1)	0.07878(9)	3.81(3)	
C(3)	0.3901(2)	0.1697(2)	–0.00225(10)	4.69(4)	
C(4)	0.3558(2)	0.2613(2)	–0.0362(1)	5.39(5)	
C(5)	0.3439(2)	0.3459(2)	0.0104(1)	5.63(5)	
C(6)	0.3676(2)	0.3399(1)	0.0907(1)	4.85(4)	
C(7)	0.4488(2)	0.0572(1)	0.11130(10)	4.20(4)	
C(8)	0.3739(2)	0.3082(1)	0.25936(9)	3.95(3)	
C(9)	0.4036(2)	0.3268(1)	0.33939(9)	4.04(3)	
C(10)	0.5109(2)	0.2939(1)	0.3798(1)	4.50(4)	
C(11)	0.5272(2)	0.3142(2)	0.4579(1)	5.04(4)	
C(12)	0.4369(2)	0.3659(1)	0.50298(10)	4.83(4)	
C(13)	0.3331(2)	0.4031(2)	0.4618(1)	6.09(5)	
C(14)	0.3182(2)	0.3843(2)	0.3832(1)	5.73(5)	
C(15)	0.5538(3)	0.3366(4)	0.6239(2)	9.7(1)	
C(16)	0.3567(3)	0.4332(3)	0.6278(2)	8.23(9)	
C(17)	0.5790(1)	0.0004(1)	0.27131(9)	3.96(3)	
C(18)	0.6846(2)	0.0366(2)	0.3102(1)	4.69(4)	
C(19)	0.7853(2)	–0.0260(2)	0.3273(1)	5.82(5)	
C(20)	0.7827(2)	–0.1266(2)	0.3063(1)	6.95(6)	
C(21)	0.6819(3)	–0.1648(2)	0.2669(2)	7.33(7)	
C(22)	0.5809(2)	–0.1018(2)	0.2500(1)	5.97(5)	
C(23)	0.3590(1)	0.0761(1)	0.32620(9)	3.91(3)	
C(24)	0.2344(2)	0.0988(1)	0.3117(1)	4.94(4)	
C(25)	0.1519(2)	0.1204(2)	0.3724(1)	6.20(6)	
C(26)	0.1911(2)	0.1184(2)	0.4497(1)	6.56(6)	
C(27)	0.3114(2)	0.0924(2)	0.4665(1)	5.96(5)	
C(28)	0.3934(2)	0.0714(1)	0.4055(1)	4.84(4)	
B(1)	0.4563(2)	0.0676(1)	0.2537(1)	3.59(4)	

[a] $B_{eq} = (8/3)\pi^2 \sum\sum (U_{ij} a_{i^*} a_{j^*} (\mathbf{a_i} \cdot \mathbf{a_j}))$

Results and discussion

Synthesis and structure of the nitrones 5 and their ring isomers 8

The synthesis of the novel nitrones **5** was achieved by condensation of aromatic aldehydes and the hydroxylamine **4** (prepared as first reported in 1903 (3*a*)). The reduction of 2-nitrobenzyl alcohol with Zn dust and NH_4Cl is, however, not without problems because the isolation of the free hydroxylamine base **4** is only possible with considerable losses, if at all

© 1998 NRC Canada

Table 3. Selected bond lengths (Å) with estimated standard deviations in parentheses.

Bond	Length	Bond	Length
	8*b*		
O(1)—C(7)	1.425(8)	O(1)—C(8)	1.330(6)
O(2)—N(1)	1.378(7)	O(3)—C(12)	1.399(8)
O(3)—C(15)	1.432(8)	N(1)—C(1)	1.426(8)
N(1)—C(8)	1.495(7)	C(1)—C(2)	1.366(9)
C(1)—C(6)	1.392(8)	C(2)—C(3)	1.398(9)
C(2)—C(7)	1.500(8)	C(3)—C(4)	1.41(1)
C(4)—C(5)	1.36(1)	C(5)—C(6)	1.41(1)
C(8)—C(9)	1.521(9)		
	5*c*		
O(1)—N(1)	1.312(3)	N(1)—C(1)	1.466(3)
N(1)—C(8)	1.299(3)	N(2)—C(12)	1.357(4)
N(2)—C(15)	1.452(4)	N(2)—C(16)	1.451(4)
C(8)—C(9)	1.440(4)	C(9)—C(10)	1.405(4)
C(9)—C(14)	1.404(4)	C(10)—C(11)	1.376(4)
C(11)—C(12)	1.406(4)	C(12)—C(13)	1.406(4)
C(13)—C(14)	1.369(4)		
	6*a*		
O(1)—N(1)	1.376(1)	O(1)—B(1)	1.592(2)
O(2)—C(7)	1.402(2)	O(2)—B(1)	1.453(2)
N(1)—C(1)	1.441(2)	N(1)—C(8)	1.306(2)
N(2)—C(12)	1.351(2)	N(2)—C(15)	1.443(4)
N(2)—C(16)	1.446(3)	C(2)—C(7)	1.506(2)
C(8)—C(9)	1.409(2)	C(9)—C(10)	1.410(2)
C(9)—C(14)	1.400(2)	C(10)—C(11)	1.355(2)
C(11)—C(12)	1.408(3)	C(12)—C(13)	1.404(3)
C(13)—C(14)	1.359(3)	C(17)—B(1)	1.616(2)
C(23)—B(1)	1.614(2)		

Table 4. Selected bond angles (deg) with estimated standard deviations in parentheses.

Bonds	Angle (deg)	Bonds	Angle (deg)
	8*b*		
C(7)-O(1)-C(8)	113.6(5)	C(12)-O(3)-C(15)	115.5(5)
O(2)-N(1)-C(1)	109.4(5)	O(2)-N(1)-C(8)	110.5(5)
C(1)-N(1)-C(8)	109.7(5)	O(5)-N(2)-C(16)	110.7(5)
N(1)-C(1)-C(2)	118.5(6)	N(1)-C(1)-C(6)	120.7(6)
C(2)-C(1)-C(6)	120.6(6)	C(1)-C(2)-C(3)	119.7(6)
C(1)-C(2)-C(7)	121.2(6)	C(3)-C(2)-C(7)	119.1(6)
C(2)-C(3)-C(4)	120.2(6)	C(3)-C(4)-C(5)	119.4(7)
C(4)-C(5)-C(6)	120.3(6)	C(1)-C(6)-C(5)	119.7(7)
O(1)-C(7)-C(2)	112.1(5)	O(1)-C(8)-N(1)	109.9(5)
O(1)-C(8)-C(9)	107.4(5)	N(1)-C(8)-C(9)	109.9(5)
	5*c*		
O(1)-N(1)-C(1)	115.3(2)	O(1)-N(1)-C(8)	124.4(2)
C(1)-N(1)-C(8)	120.3(3)	C(12)-N(2)-C(15)	120.7(3)
C(12)-N(2)-C(16)	121.6(3)	C(15)-N(2)-C(16)	117.0(3)
N(1)-C(8)-C(9)	127.5(3)	C(8)-C(9)-C(10)	125.6(3)
C(8)-C(9)-C(14)	117.7(3)	C(10)-C(9)-C(14)	116.6(3)
C(9)-C(10)-C(11)	121.1(3)	C(10)-C(11)-C(12)	121.8(3)
N(2)-C(12)-C(11)	121.5(3)	N(2)-C(12)-C(13)	121.4(3)
C(11)-C(12)-C(13)	117.1(3)	C(12)-C(13)-C(14)	120.6(3)
C(9)-C(14)-C(13)	122.6(3)		
	6*a*		
N(1)-O(1)-B(1)	112.07(10)	C(7)-O(2)-B(1)	115.0(1)
O(1)-N(1)-C(1)	115.8(1)	O(1)-N(1)-C(8)	120.3(1)
C(1)-N(1)-C(8)	123.6(1)	C(12)-N(2)-C(15)	120.7(2)
C(12)-N(2)-C(16)	121.5(2)	C(15)-N(2)-C(16)	117.7(2)
N(1)-C(1)-C(2)	120.9(1)	N(1)-C(1)-C(6)	118.4(1)
C(2)-C(1)-C(6)	120.7(1)	C(1)-C(2)-C(3)	117.2(2)
C(1)-C(2)-C(7)	124.0(1)	C(3)-C(2)-C(7)	118.8(2)
O(2)-C(7)-C(2)	112.3(1)	N(1)-C(8)-C(9)	129.8(1)
C(8)-C(9)-C(10)	126.7(2)	C(8)-C(9)-C(14)	116.7(1)
C(10)-C(9)-C(14)	116.6(2)	C(9)-C(10)-C(11)	121.1(2)
C(10)-C(11)-C(12)	122.0(2)	N(2)-C(12)-C(11)	121.8(2)
N(2)-C(12)-C(13)	121.4(2)	C(11)-C(12)-C(13)	116.8(2)
C(12)-C(13)-C(14)	120.9(2)	C(9)-C(14)-C(13)	122.4(2)
O(1)-B(1)-O(2)	106.0(1)	O(1)-B(1)-C(17)	102.3(1)
O(1)-B(1)-C(23)	110.3(1)	O(2)-B(1)-C(17)	113.7(1)
O(2)-B(1)-C(23)	108.4(1)	C(17)-B(1)-C(23)	115.4(1)

(3*b*). A high solubility in most solvents (including water) as well as the competitive formation of the azoxy compound **7** (via the initially generated nitroso intermediate) reduces the yield of **4**. The yield is improved when **4** is trapped, as its nitrone **5,** directly from the solution resulting from the reduction process. In the literature the hydroxylamine **4** is mentioned only sporadically and without further details or physical data (6). In this work we present some spectroscopic data for **4** that, to the best of our knowledge, have not been previously reported.

The condensation products from **4** and aromatic aldehydes are crystalline compounds with the exception of **5***d*/**8***d*, which could not be crystallized for still unknown reasons. Considerable broadening of the O–H valence stretching bands in the solid state (KBr pellets) infrared spectra of **5**/**8***a–c* (most prominent for the 4-dimethylaminobenzaldehyde derivative) indicates an increased (associative) intra- or intermolecular O—H· · ·O interaction. The 4-dialkylamino substituted aldonitrones **5***c* and **5***d* should possess an increased basicity at the nitrone *N*-oxide function compared to the unsubstituted and 4-methoxy derivatives **5***a* and **5***b* (ref. 1, and refs. therein).

As discussed earlier for the isomeric nitrones of type **2** (1), cycloisomerization of the nitrones **5** leading to the ring tautomers **8** can be expected, at least in solution. No detectable amounts of the cyclotautomers, however, were discovered in the ^{1}H nmr spectra of **2** (1); thus it is surprising that the ^{1}H nmr spectra of **5**/**8***a* and **5**/**8***b* show signals indicating the presence of 90% and 70% of the cyclotautomers **8***a* and **8***b*, respectively, in addition to signals arising from the nitrone forms **5***a* and **5***b* in the respective ratios. In the same solvent ($CDCl_3$) the 4-dimethylaminobenzaldonitrone **5***c* does not give any signals attributable to its cyclic isomer **8***c*. The ^{1}H nmr signals used to discriminate between the isomers and to estimate their relative populations in solution are basically the same as those used for similar ring-chain isomers of nitrones (ref. 1, and refs. therein): the CH═N signal at low field for the open-chain nitrone form **5**, and the middle-field O-CH-N signal for the cyclic acetal form **8**. Additional differences are found between the benzyl-CH_2 signals that appear as a singlet for the open-chain form **5** and as an AB spin coupling pattern (quadruplet) for the cyclic form **8**, indicating the nonequivalence of the CH_2 protons in

© 1998 NRC Canada

Table 5. Intra-annular torsion angles (deg) with standard deviations in parentheses for **8***b* and **6***a*.

Atoms	Value (deg)	Atoms	Value (deg)
		8*b*	
N(1)-C(1)-C(2)-C(7)	–9.1(9)	N(2)-C(16)-C(17)-C(22)	0.8(9)
C(1)-C(2)-C(7)-O(1)	11.1(9)	C(16)-C(17)-C(22)-O(4)	7.5(9)
C(2)-C(7)-O(1)-C(8)	–40.6(7)	C(17)-C(22)-O(4)-C(23)	–41.4(8)
C(7)-O(1)-C(8)-N(1)	66.4(7)	C(22)-O(4)-C(23)-N(2)	63.0(7)
O(1)-C(8)-N(1)-C(1)	–60.4(6)	O(4)-C(23)-N(2)-C(16)	–50.0(6)
C(8)-N(1)-C(1)-C(2)	31.3(7)	C(23)-N(2)-C(16)-C(17)	21.5(8)
		6*a*	
B(1)-O(1)-N(1)-C(1)	–90.0(1)	C(2)-C(7)-O(2)-B(1)	–90.3(2)
O(1)-N(1)-C(1)-C(2)	31.7(2)	C(7)-O(2)-B(1)-O(1)	41.3(2)
N(1)-C(1)-C(2)-C(7)	1.9(2)	O(2)-B(1)-O(1)-N(1)	54.6(1)
C(1)-C(2)-C(7)-O(2)	40.7(2)		

Fig. 1. Stereoview of the two independent molecules of **8***b*; 33% probability thermal ellipsoids are shown for the non-hydrogen atoms. For the sake of clarity, only the major disordered components are shown.

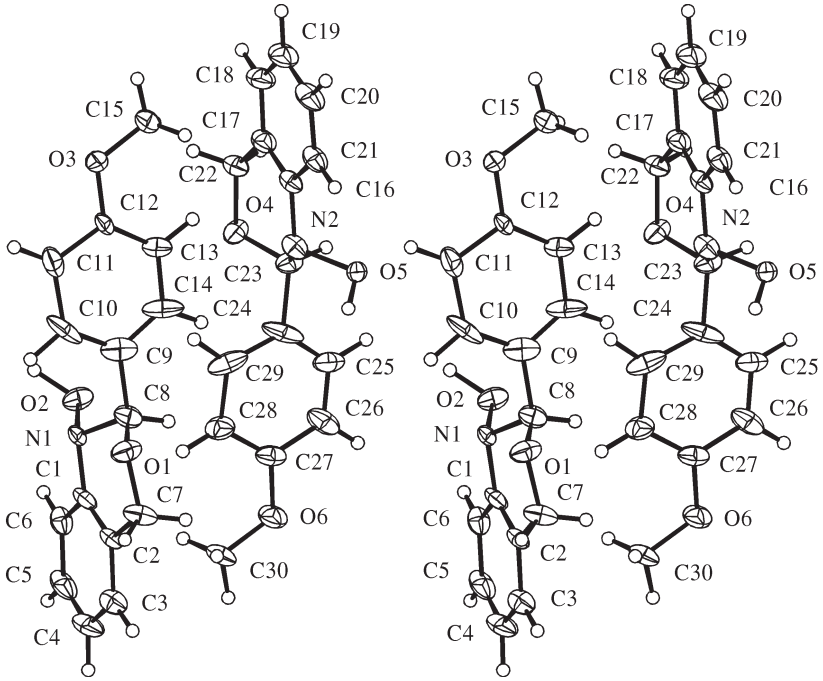

the relatively rigid ring form. In the 4-methoxybenzaldehyde derivative **5/8***b* the 4-methoxy group serves as an additional probe for both of the isomers in that it produces singlets having different chemical shifts for ring and open-chain isomers.

The predominance of the cyclic form **8** in the ^{1}H nmr spectra of **5/8***a* and **5/8***b* induced us to attempt an X-ray crystallographic analysis of one of these derivatives. It was not possible to obtain any suitable crystals of **5/8***a,* while compound **5/8***b* gave weakly diffracting thin plates of poor quality. In spite of the shortcomings of the structure analysis that preclude any detailed discussion of molecular geometry (see Experimental), the X-ray analysis does establish the cyclic structure **8***b,* which, to the best of our knowledge, represents the first example of a 1-hydroxy-1,2-dihydro-4*H*-3,1-benzoxazine. The benzaldehyde derivative **8***a* most likely has the same ring structure. The asymmetric unit of **8***b* consists of two crystallographically independent molecules, related to one another by a pseudoinversion centre. Careful inspection of Fig. 1, however, shows that the corresponding chiral centres (N(1)/N(2) and C(8)/C(23), respectively) have the *same* absolute configurations: *S* at nitrogen and *R* at carbon. The disorder of the NOH groups (see Experimental) further complicates the issue because the minor disorder components have the opposite configuration at the chiral nitrogen atom. The crystal as a whole thus has the composition: *SR*, 37.5%, *RS*, 37.5%, *RR*, 12.5%, and *SS*, 12.5%. The six-membered heterocyclic rings in the two independent molecules of **8***b* have slightly different C(8/23)-envelope conformations (see Table 5) and the 4-methoxyphenyl groups are oriented approximately perpendicular to the mean planes of the fused-ring systems. Bond lengths and angles for **8***b* (Tables 3 and 4) are generally as expected.

An X-ray crystallographic analysis of **5***c* establishes, for the solid state, the open-chain nitrone structure (Fig. 2) indicated by ^{1}H nmr spectroscopy as the sole isomer present in solution. The increased electron density at the nitrone group, induced

© 1998 NRC Canada

Fig. 2. Stereoview of **5***c*; 33% probability thermal ellipsoids are shown for the non-hydrogen atoms. For the sake of clarity, only the major disordered components are shown.

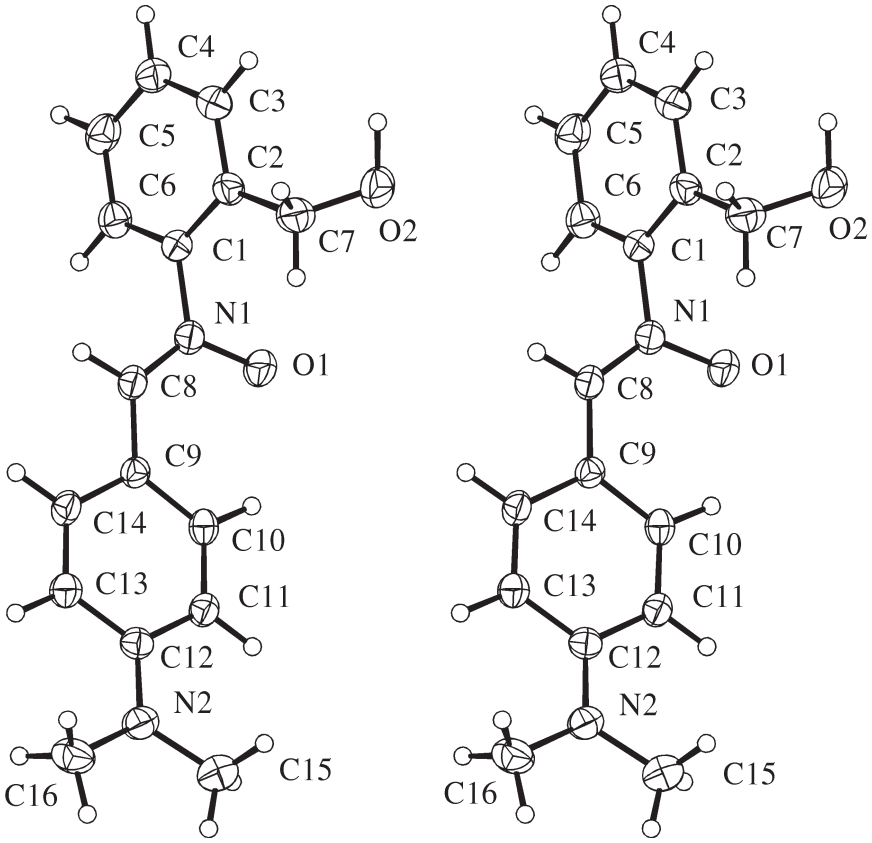

by the 4-dimethylamino substituent at the benzaldehyde moiety, might prevent the cyclotautomerization that affords an electron-poor carbenium ion, and thus stabilizes the open-chain nitrone structure. Unlike the structure of the isomeric nitrone **2** (Ar = 4-$Me_2NC_6H_4$) (1), which possesses a strong intramolecular O—H· · ·O hydrogen bond connecting the phenol and nitrone groups, no such intramolecular interaction between the hydroxymethyl and nitrone groups is present in **5***c*, despite the same ring size of the potential intramolecular seven-membered proton chelate. In **5***c* intermolecular hydrogen bonds between the major component hydroxymethyl groups and the nitrone groups of neighboring molecules form helices about the twofold screw axes (O(2)—H(1)· · ·O(1): O—H = 1.05(5), H· · ·O = 1.74(5), O· · ·O = 2.787(4) Å, O—H· · ·O = 172(4)°). The minor component hydroxymethyl oxygen atom O(2a) is involved in an intermolecular C—H· · ·O interaction having geometrical parameters consistent with hydrogen bonding (7) (C(15)—H(14)· · ·O(2a): C—H = 0.98, H· · ·O = 2.35, C· · ·O = 3.32(1) Å, C—H· · ·O = 170°). The presence of this interaction may be at least partially responsible for the disordering of the hydroxymethyl group. The weaker basicity of the nitrone *N*-oxide group and the weaker acidity of the hydroxymethyl group of **5***c* compared to that of **2** (Ar = 4-$Me_2NC_6H_4$) may, in addition to other crystal packing effects, have some influence in determining whether an *intra*molecular or *inter*molecular hydrogen bond is formed between these functional groups. As noted for **2** (Ar = 4-$Me_2NC_6H_4$) (1), there is an intramolecular C—H· · ·O contact in **5***c* between the nitrone *N*-oxide oxygen atom and an *ortho* hydrogen atom of the aromatic aldehyde moiety (C(10)—H(9)· · ·O(1): H· · ·O = 2.25, C· · ·O = 2.879(3) Å, C—H· · ·O = 121°). Although this interaction does not meet the requirements for a true C—H· · ·O hydrogen bond, it can still be considered as an additional cohesive contribution to the forces determining the molecular conformation (7). As in **2** (Ar = 4-$Me_2NC_6H_4$), this contact might be favored by the approximate coplanarity of the 4-dimethylaminophenyl residue and the nitrone group as a consequence of the resonance effects within the conjugated double bond system extending from the dimethylamino group to the nitrone oxygen atom (1). In accordance with the +M effect of the 4-Me_2N substituent are the relatively short N(2)—C(12), C(10)—C(11), C(13)—C(14), and C(8)—C(9) bonds (1.357(4), 1.376(4), 1.369(4), and 1.440(4) Å, respectively), as well as the relatively longer aromatic bonds C(9)—C(14), C(12)—C(13), C(9)—C(10), and C(11)—C(12) (mean C—C = 1.405 Å). The aromatic ring at N(1), however, deviates from the planar aldonitrone moiety in **5***c*, the angle between normals to the respective mean planes being 70°. The C═N double bond (1.299(3) Å) and the N—O bond (1.312(3) Å) of the nitrone function in **5***c* are as expected for aldonitrones (ref. 1, and refs. therein).

Synthesis and structure of the boron chelates 6

The reaction of **5/8** with diphenylborinic acid anhydride gave crystalline compounds only for the *p*-dialkylaminobenzaldehyde nitrones (**5***c* and **5***d*). The derivatives **5/8***a* and **5/8***b* were recovered unchanged from the reaction mixtures in ethanol, or even in benzene under reflux conditions using a Dean–Stark

© 1998 NRC Canada

Fig. 3. Stereoview of **6***a*; 33% probability thermal ellipsoids are shown for the non-hydrogen atoms.

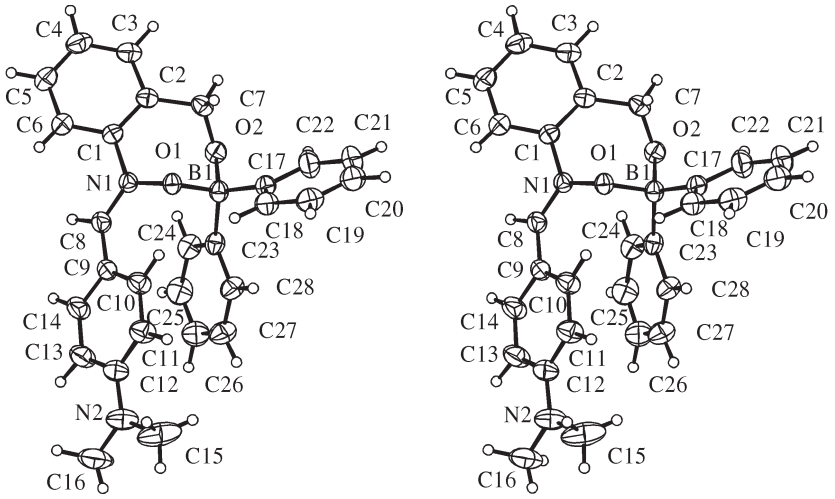

trap for continuous removal of water. The weaker basicity of the nitrone groups and the favored ring structure, deduced from the ^{1}H nmr spectra of **5**/**8***a* and **5**/**8***b* and the crystal structure of **8***b*, might impede the formation of stable boron chelates. The crystalline compounds obtained from **5***c* and **5***d* give elemental analyses, infrared and ^{1}H nmr spectra, and positive color reactions with diphenylcarbazone (4) corresponding to the diphenylboron chelate structure **6**. In the solid state infrared spectra (KBr pellets) of **6** there are no O–H valence stretching bands present, and the C═N absorption band of the nitrone group is found at a somewhat higher frequency (1617 cm^{-1}) than for the free ligands **5**. Similar observations have been made from the infrared spectra of other boron chelates and their nitrone ligands (ref. 1, and refs. therein).

The most striking feature in the ^{1}H nmr spectra of **6** is the signals arising from the benzylic CH_2 protons, which appear as AB quartets pointing to the magnetic inequivalence of the CH_2 protons after the incorporation of the methylene group into the chelate ring of **6**. An AB pattern like this might, however, also indicate the cyclic fixed methylene group in the isomer **9** (or its BONBON dimer). A structure such as **9**, however, can easily be excluded by the conspicuous signal of a nitrone N═CHproton and by the absence of an O-CH-N acetal methine signal in each of the ^{1}H nmr spectra. In addition, the ^{11}B nmr spectrum of **6***b*[11] shows a signal indicating a tetracoordinate boron nucleus at δ (Et_2OBF_3) = 9.2 ppm. A ^{11}B nmr signal with a shift like this cannot be expected from an isomeric compound such as **9***b*, unless it would form BONBON dimers[12] stable enough in solution to give the signals for tetracoordinate (sp^3) boron nuclei. The second ^{11}B nmr signal at 47.1 ppm, although very weak, indicates an uncoordinated Ph_2B-O-R moiety or free diphenylborinic acid, but not necessarily **9***b*. The peak could just as easily appear as a result of solvolytic removal of the coordinating nitrone ligand from the boron nucleus in **6***b,* generating the diphenylborinate of the benzyl alcohol moiety (a trivalent sp^2 boron compound) or free diphenylborinic acid. Similar solvolyses have also been noted for solutions of the diphenylboron chelates **3** (1).

An X-ray analysis of **6***a* establishes the seven-membered chelate structure (Fig. 3). Compound **6***a* is thus an isomer of the diphenylboron chelate **3** (Ar = 4-$Me_2C_6H_4$), which has also been structurally characterized by an X-ray crystallographic analysis (1). The chelate ring formation in **6***a* demonstrates that the hydroxymethyl group, *inter*molecularly hydrogen-bonded in crystalline **5***c*, may be *intra*molecularly hydrogen-bonded in solution, thus allowing the facile replacement of the "chelated" proton by a diphenylborenium (Ph_2B^+) cation.

The intramolecular C—H···O interaction found in the solid state structure of **5***c* is still present in the crystal of **6***a*, the slightly longer C···O distance in **6***a* reflecting the use of the N-oxide group as a ligand for the boron nucleus (C(10)—H(8)···O(1): H···O = 2.27(2), C···O = 2.904(2) Å, C—H···O = 119(1)°). A second weak intramolecular C—H···O interaction between one of the *B*-phenyl residues and the benzyl alcoholate oxygen is probably little more than a consequence of crystal packing forces (C(24)—H(23)···O(2): H···O = 2.47(2), C···O = 2.855(2) Å, C—H···O = 103(1)°). The intermolecular C(14)—H(11)···O(2) (1/2–*x*, 1/2 + *y*, 1/2–*z*) hydrogen bond with an angle of 158(2)° at H, H···O = 2.25(2) Å, and C···O = 3.191(2) Å, however, is most likely an additional cohesive force within the crystal lattice.

The metrical changes, going from the free nitrone ligand **5***c* to the chelate **6***a*, are essentially the same as those observed in the structural study of the ligand **2** and the chelate **3** (Ar = 4-$Me_2C_6H_4$) (1). The nitrone C═N$^+$ double bond remains practically unchanged with only a slight lengthening, whereas the N—O bond is lengthened by 0.06 Å (the corresponding difference between N—O distances in **2** and **3** is 0.05 Å) and shows the reduction of the π-bond order of the N—O bond from 0.34 in the free ligand **5***c* to 0.13 in the chelate **6***a* as estimated from plots of bond lengths vs. HMO–π-bond order (9). The changes at the 4-dimethylaminophenylmethylene moiety are similar to those noted for the isomeric ligand **2** and chelate **3** (1) with the exception of the C(12)—N(2) distance in **5***c*, which is already short compared to the corresponding distance of 1.370(2) Å in **2**. The enhanced double bond

[11] The ^{11}B nmr spectrum of **6***a* could not be obtained because of poor solubility.

[12] For more information on the BONBON dimers of *O*-borinates from hydroxylamine derivatives, see ref. 8 and literature cited therein.

© 1998 NRC Canada

character of the N(2)—C(12), C(10)—C(12), C(13)—C(14), and C(8)—C(9) bonds (1.357(4), 1.376(4), 1.369(4), and 1.440(4) Å, respectively, in **5***c*; 1.351(2), 1.355(2), 1.359(3), and 1.409(2) Å in **6***a*) reflects an increased electron donation from the *p*-dimethylamino group caused by the cooperative electron-pulling effect of the chelated diphenylborenium ion in **6***a*. The (N)O—B bond in **6***a*, coordinating the *N*-oxide group to the boron nucleus, is longer than that in the isomeric boron chelate **3** by about 0.04 Å (1.592(2) vs. 1.549(2) Å), pointing to the weaker nucleophilicity of the *N*-oxide ligand in the nitrone **5***c* and consequently in **6***a*. On the other hand, the (benzyl)O—B bond in **6***a* is about 0.04 Å shorter than the (phenyl)O—B bond in **3** (1.453(2) vs. 1.488(2) Å), indicating the stronger nucleophilicity of the alcoholate ligand in the chelate **6***a* compared to the phenolate ligand in the isomeric chelate **3**.

The (phenyl)C—B bond lengths in **6***a* (mean 1.615(1) Å) are within the range normally observed for tetracoordinate phenylboron compounds and are virtually identical to those in **3** (mean 1.615(2) Å) (1). The mean C—B/mean O—B bond length ratio of 1.060 suggests an only slightly reduced overall ligand binding strength with respect to the diphenylboron nucleus in **6***a* compared to the isomer **3** (mean C—B/mean O—B = 1.063) (1). The sum of bond lengths around the boron atom (6.275 Å) is in accordance with the same parameter in other seven-membered diphenylboron chelates (1) and confirms the observation of an essentially constant value for a given chelate ring size (10). It seems that the chelate ring of **6***a*, having the exocyclic N═C double bond fixed at the anellating benzo moiety, has a little more conformational flexibility than does that of the isomer **3**, allowing somewhat smaller ring angles. The sum of the intracyclic angles of the chelate ring in **6***a* is 806.1°, compared to corresponding values of 811.7° for **3**, and 858.4° for the less flexibile seven-membered chelate ring of the salicylaldonitrone derivative **10** (containing an endocyclic N═C bond) (ref. 1, and refs. therein). Like the seven-membered boron chelate **3**, the isomer **6** may be formally regarded as a "phenylog" (by *o*-phenyl insertion) of the five-membered boron chelate **11** (11), even though the alkylidene substituents at the nitrogen atoms of the nitrone moieties are different. The intracyclic angle in the seven-membered ring at the anellation position at C(1) in **6***a* is close to the expected value of 120° (120.9(1)°), whereas the corresponding angle in the isomer **3** is somewhat compressed (116.8(1)°). This provides evidence for the expected stronger interaction of the (sp^2) nitrogen atom of the nitrone group with the anellated benzene ring in **6***a* relative to the (sp^3) carbon atom of the methylene group at the same ring position in the isomer **3**. As noted for **3**, all of the remaining intracyclic angles in the seven-membered chelate ring of **6***a* are wider than the corresponding ring angles in **11** (11).

Acknowledgments

We thank the Natural Sciences and Engineering Research Council of Canada and the Fonds der Chemischen Industrie, Frankfurt am Main, for financial support. We are grateful to the Chemische Institute der Technischen Universität Braunschweig for the ^{11}B and ^{13}C nmr and mass spectra.

References

1. W. Kliegel, J. Metge, S.J. Rettig, and J. Trotter. Can. J. Chem. **75**, 1830 (1997).
2. (*a*) R. Neu. Chem. Ber. **87**, 802 (1954); (*b*) G.N. Chremos, H. Weidmann, and H.K. Zimmerman. J. Org. Chem. **26**, 1683 (1961).
3. (*a*) E. Bamberger. Ber. Dtsch. Chem. Ges. **36**, 836 (1903); (*b*) A. Reissert and K. Crämer. Ber. Dtsch. Chem. Ges. **61**, 2555 (1928).
4. (*a*) R. Neu. Z. Anal. Chem. **176**, 334 (1960); (*b*) B. Friese and F. Umland. Anal. Chim. Acta, **96**, 303 (1978).
5. (*a*) International tables for X-ray crystallography. Vol. IV. Kynoch Press. Birmingham, U.K. (present distributor Kluwer Academic Publishers: Boston, Mass.). 1974. pp. 99–102; (*b*) International tables for crystallography. Vol. C. Kluwer Academic Publishers. Boston, Mass. 1992. pp. 200–206.
6. (*a*) G.L. Kedderis and D.E. Rickert. Mol. Pharmacol. **28**, 207 (1985); (*b*) J.P. Chism and D.E. Rickert. Chem. Res. Toxicol. **2**, 150 (1989).
7 G.R. Desiraju. Acc. Chem. Res. **29**, 441 (1996).
8. W. Kliegel, J. Nanninga, U Riebe, S.J. Rettig, and J. Trotter. Can. J. Chem. **72**, 1735 (1994).
9. G. Häfelinger. Chem. Ber. **103**, 3370 (1970).
10. C. Orvig, S.J. Rettig, and J. Trotter. Can. J. Chem. **65**, 590 (1987).
11. W. Kliegel, U Riebe, S.J. Rettig, and J. Trotter. Can. J. Chem. **73**, 835 (1995).

© 1998 NRC Canada

The reactivity of the high-energy intermediates formed in the reactions of Group 13 metal atoms and aromatic alkenes

Helen A. Joly, Maria Kepes, Natalie Roy, and Jason Prpic

Abstract: Group 13 metal atoms were reacted with aromatic alkenes in a specialized metal atom reactor known as a "rotating cryostat." The nature of the intermediates formed was deduced from a GC–MS study of their hydrolysis and deuterolysis products. The product studies suggest that 2-phenylaluminacyclopropane, *cis*- and *trans*-3,4-diphenylaluminacyclopentane, and *cis*- and *trans*- 2,4-diphenylaluminacyclopentane are formed when Al atoms react with styrene, and 2-methyl-2-phenylaluminacyclopropane and 3,4-dimethyl-3,4-diphenylaluminacyclopentane are formed when Al atoms react with α-methylstyrene. These findings are consistent with the radicals detected in the EPR spectroscopic studies of Al–alkene reaction mixtures prepared under similar conditions. Mechanisms for the formation of the organoaluminium intermediates are discussed. Analogous organogallium intermediates are formed when gallium atoms react with styrene. The reductive coupling of styrene did not occur when In and Tl atoms were used. Only trace quantities of phenylethane were detected in the hydrolyzed reaction mixture.

Key words: Group 13 metal atoms, aluminium atoms, organoaluminium intermediates, metal atom reactions.

Résumé : On a fait réagir des atomes de métaux du groupe 13 avec des alcènes aromatiques dans le réacteur à atomes de métaux connu sous le nom de « cryostat rotatif ». On a déduit la nature des intermédiaires formés en se basant sur une étude de CG–SM de leurs produits d'hydrolyse et de deutérolyse. Les études sur la nature des produits suggèrent que, lorsqu'on fait réagir des atomes d'aluminium avec le styrène, il se forme du 2-phénylaluminacyclopropane, des *cis*- et *trans*-3,4-diphénylaluminacyclopentanes et des *cis*- et *trans*-2,4-diphénylaluminacyclopentanes; lorsqu'on fait réagir des atomes d'aluminium avec l'α-méthylstyrène, il se forme du 2-méthyl-2-phénylaluminacyclopropane et du 3,4-diméthyl-3,4-diphénylaluminacyclopentane. Ces résultats sont en accord avec les radicaux détectés lors d'études RPE de mélanges provenant de réactions Al–alcènes effectuées dans des conditions semblables. On discute des mécanismes de formation des intermédiaires organoaluminium. Des intermédiaires organogallium semblables se forment lorsqu'on fait réagir des atomes de gallium avec le styrène. Le couplage réducteur du styrène ne se produit pas lorsqu'on utilise des atomes d'In et de Ti. On ne détecte que de très faibles quantités de phényléthane par hydrolyse des mélanges réactionnels.

Mots clés : atomes de métaux du groupe 13, intermédiaires organoaluminium, réactions d'atomes métalliques.

[Traduit par la rédaction]

Introduction

The reactions of metal atoms with organic substrates provide interesting routes to the formation of novel organometallic intermediates. These organometallic intermediates are useful in mediating the modification of organic compounds. The reaction of Group 13 metal atoms with alkenes has been the subject of numerous investigations (1–14, and footnote 3).

Product analysis and (or) electron paramagnetic resonance (EPR) spectroscopy have been used to study the intermediates formed between Al atoms and alkenes at cryogenic temperatures. The product studies usually involve the hydrolysis or deuterolysis of the organometallic adducts formed in the metal atom reaction. The nature of the organometallic intermediate is inferred from the resulting hydrolysis products. For instance, when the organoaluminium adduct resulting from the cocondensation of Al atoms and propene (5, 6) at 77 K was subjected to deuterolysis the major products formed were deuterated propane, 2,3-dimethylbutane, 2-methylpentane, and traces of *n*-hexane. The organoaluminium intermediate most consistent with these products is **1**.

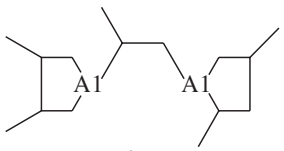

1

The reactive intermediates formed when Al atoms are reacted with propene in an adamantane matrix at 77 K have been studied by EPR spectroscopy (7, 8). Three radical species are

Received November 12, 1996.[1]

H.A. Joly,[2] M. Kepes, N. Roy, and J. Prpic. Department of Chemistry and Biochemistry, Laurentian University, Sudbury, ON P3E 2C6, Canada.

[1] Revision received January 27, 1998.

[2] Author to whom correspondence may be addressed. Telephone: (705) 675-1151, ext. 2333. Fax: (705) 675-4844. E-mail: HJOLY@Nickel.laurentian.ca

[3] J.A. Howard, H.A. Joly, and B. Mile. Unpublished results.

© 1998 NRC Canada

thought to contribute to the overall EPR spectrum, namely, π-allyl aluminium hydride (**2**), the allyl radical (**3**), and a dimethylaluminacyclopentane (**4**), formed upon cyclodimerization of propene.

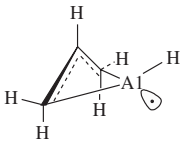

2

3

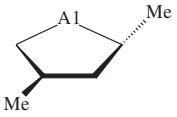

4

In a few cases, Al atoms react with alkenes, e.g., ethene (1–4), $CD_3CH{=}CH_2$ and $CD_3CD{=}CD_2$ (14), to form monoligand π-complexes, Al[alkene].

1,3-Butadiene reacts with Al atoms to form two major paramagnetic species detected by EPR spectroscopy (9), a σ-bonded aluminacyclopentene and aluminium-substituted allyl radicals. It would appear that conjugated systems undergo intramolecular cyclodimerization more easily than intermolecular cyclodimerization, which was observed for the simple alkenes (3, 4, 7, 8) discussed above.

Two groups of workers have investigated the interaction between Al atoms and benzene by EPR spectroscopy (10, 11) and have shown that an Al–benzene molecular complex forms. A good computer simulation of the Al–benzene species in a neon matrix (10) at 4 K was obtained, assuming an interaction between the ground state Al atom ($3s^2$, $3p^1$) and only two of the six protons of the benzene ring. This observation is consistent with the formation of a π-complex, resulting from the dative bonding of the semi-occupied Al $3p_x$ orbital with two antibonding p_π orbitals on two adjacent carbon atoms. In another study (11), the Al–benzene complex isolated in adamantane was warmed to 220 K in the cavity of the EPR spectrometer. The EPR spectrum in this case was best interpreted as the interaction of the Al atom with six equivalent hydrogen nuclei. This led Howard et al. (11) to propose the formation of an η_6-complex in which the Al atom lies along the C_{6v} axis of the benzene ring.

Often reactions of ground-state Ga atoms ($4s^2$, $4p^1$) mimic the reactions of Al atoms. For instance, Ga atoms have also been found to react with alkenes. The Ga–ethylene π-complex is the major paramagnetic species formed when Ga atoms are reacted with ethylene, in both argon (12) at 4 K and adamantane (13) at 77 K. A second paramagnetic species, detected in the Ga–ethylene reaction in adamantane (13), has been tentatively assigned to gallacyclopentane. Ga atoms react with 1,3-butadiene (9, and footnote 3) yielding 1-substituted allyl, $MCH_2CHCHCH_2$. There is no evidence for the cheleotropic addition of Ga leading to the formation of gallacyclopentene as was observed for Al atoms. An EPR study of a Ga atoms matrix isolated in benzene at 77 K (14) indicated that a trapped atom or weak Ga–benzene complex forms that is unlike the $Al[C_6H_6]$ complex found in the Al–benzene reaction. In addition, samples of Ga atoms in benzene, annealed in the cavity of the EPR spectrometer, yielded well-resolved spectra of cyclohexadienyl radicals, $C_6H_7^{\bullet}$.

Based on the studies involving the reaction of Group 13 metal atoms with alkenes, styrene presents two sites for reaction with the metal atoms, the benzene ring and the double bond. We present the results of a product study involving the Group 13 organometallic adducts formed when Group 13 metal atoms are reacted with styrene and α-methylstyrene at cryogenic temperatures.

Experimental

Preparation of the reaction mixtures

A specialized metal atom reactor known as a rotating cryostat (15) was used to prepare the reaction mixtures. The device consisted of a stainless steel drum held in the centre of a reaction chamber that was maintained at ca. 10^{-6} Torr (1 Torr = 133.3 Pa). During operation of the cryostat the liquid nitrogen filled drum rotated at 2000 rpm while the alkene and the metal vapour were introduced through portholes in the outer chamber. The metal atom vapour (generated by resistively heating Al wire, Ga, In, or Tl pellets in a tungsten basket fixed between two electrodes of a furnace), condensed on the cold surface of the rotating drum and was bombarded with the alkene at a pressure of 0.1 Torr. Reaction was believed to occur at the interface of the two reactants. After approximately 8 min, the current supplied to the furnace was decreased to 0 A and the alkene was allowed to condense onto the reaction mixture for an additional 2 min. Next, distilled water or deuterium oxide was introduced through a porthole at a pressure of 1 Torr for 3 min. The above sequence was repeated once. The reaction mixture was transferred at 77 K and under reduced pressure into a sample tube fitted with a rotoflow stopcock. The sample was slowly warmed to room temperature by keeping the sample tube in a Dewar containing liquid N_2 until the coolant had evaporated. Next, approximately 1 mL of distilled water was added to the sample tube. Samples that appeared to contain excess metal were first treated with a few drops of 5% HCl. Dichloromethane (ca. 1 mL) was added to the aqueous phase to extract the organic compounds. Molecular sieves were added to dry the dichloromethane layer, which was subsequently analyzed by gas chromatography – mass spectrometry.

Sample analysis

A Varian Saturn II gas chromatograph – mass spectrometer operating in electron impact mode at 70 eV was used to analyze the hydrolysis products. The gas chromatograph was fitted with a Varian 1093 septum-equipped programmable injector (SPI) and an SPB-1 nonpolar fused silica column (30 m × 0.25 μm film thickness, Supelco). Ultrapur helium was used as the carrier gas with a column head pressure of 12 psi (1 psi = 6.9 kPa). The SPI injector was programmed to hold at 40°C for 0.10 min at which time the temperature was ramped from 40 to 280°C at a rate of 200°C/min. After an initial 2 min hold period the column temperature was increased from 40 to 140°C at 5°C/min, then from 140 to 200°C at 2°C/min with a 5 min final hold period. The transfer line coupling the GC to the MS was maintained at 260°C whereas the temperature of the ion trap manifold was kept at 220°C. The electron impact mass spectral scans were recorded from *m*/*z* 40 to *m*/*z* 350 amu. The hydrolysis products were identified by comparing the retention times and mass spectral data to those of authentic samples.

© 1998 NRC Canada

Table 1. Hydrolysis products of the organoaluminium adducts formed in the reaction of Al atoms with styrene at 77 K.

Entry	Relative amounts of the hydrolysis products[a]			
	EtBz	2,3-DPB *dl*	2,3-DPB *meso*	1,3-DPB
1	26	51	21	2.5
		69[b]	28	3.4
2	43	39	18	0.0
		69[b]	31	0.0
3	[e]	64[b]	26	9.4
4[c]	53	29	14	4.0
		62[b]	30	7.7
5[d]	[e]	70[b]	21	9.9

[a] Based on $AC_i/\Sigma AC_i \times 100$ where AC_i is the area counts for product *i*, obtained from the electronic integration of the peaks in the total ion current chromatogram.

[b] Relative amounts of the isomeric diphenylbutanes.

[c] D_2O was substituted for H_2O in the hydrolysis reaction.

[d] Cyclohexane was deposited as an inert matrix (vapour pressure 1 Torr) along with Al and styrene (vapour pressure 0.1 Torr). No water was added to the reaction mixture until after the mixture had been annealed to room temperature.

[e] EtBz not determined for these cases.

Synthesis of standard samples

Preparation of meso- *and* dl-*2,3-diphenylbutane*

The *meso* and *dl*-2,3-diphenylbutane were synthesized by a method suggested by Kochi (16). Acetone (5 mL) in 50 mL of anhydrous diethyl ether was added dropwise to the Grignard reagent prepared from magnesium turnings (4 g, 0.16 mol) and 1-bromo-1-phenylethane (7.4 mL, 0.057 mol). The reaction mixture was next hydrolyzed and the *meso*- and *dl*-2,3-diphenylbutane recovered by ether extraction. Removal of the ether with the aid of a rotary evaporator resulted in the partial crystallization of a solid. The solid and mother liquor were separated. Recrystallization of the solid from methylcyclohexane – petroleum ether yielded 0.48 g (7%) of *meso*-2,3-diphenylbutane melting from 119 to 121°C (lit. (16) mp 124–126°C). ^{1}H NMR (200 MHz, $CDCl_3$) δ: 7.19–7.35 (m, 10 H), 2.70–2.90 (m, 2 H), 1.08 (d, 6 H). GC–MS: 209 (0.1, $[M - 1]^+$), 133 (2.4, $[M - C_6H_5]^+$), 105 (100, $[C_6H_5CHCH_3]^+$), 104 (30.8), 91 (7.2), 79 (17.5), 77 (16.7), 63 (2.7), 51 (8.5).

The *dl* isomer (0.2 g, 3.5%) was recovered from the mother liquor. ^{1}H NMR (200 MHz, $CDCl_3$) δ: 7.20–7.60 (m, 10 H), 3.05–3.20 (m, 2 H), 1.40 (d, 6 H). GC–MS: 209 (0.12, $[M - 1]^+$), 133 (1.4, $[M - C_6H_5]^+$), 105 (100, $[C_6H_5CHCH_3]^+$), 104 (34.0), 91 (5.1), 79 (19.0), 77 (20.1), 63 (2.9), 51 (8.9).

Preparation of 1,3-diphenylbutane (16, 17)

A mixture containing 6.30 mL (0.054 mol) of acetophenone in diethyl ether was added dropwise to a Grignard reagent prepared by adding 7.38 mL (0.054 mol) of 1-bromo-2-phenylethane in 50 mL of sodium-dried diethyl ether to 3 g (0.25 mol) of magnesium turnings. After hydrolysis with 10% H_2SO_4, 1,3-diphenyl-3-butanol was recovered from the reaction mixture by ether extraction followed by removal of the solvent on a rotary evaporator. Potassium bisulfate (14.7 g, 0.08 mol) was added to the alcohol and the mixture was heated at 160–170°C for 30 min. Distillation of the resulting liquid yielded 1,3-diphenyl-1-butene (bp 126–130°C, 3 Torr). Hydrogenation (17) of the alkene with H_2 and PtO_2 in ethanol resulted in the formation of the desired product. 1,3-Diphenylbutane (2 g, 18% yield) was collected between 115 and 120°C at 2 Torr. ^{1}H NMR (200 MHz, $CDCl_3$) δ: 7.11–7.39 (m, 10 H), 2.60–2.78 (m, 1 H), 2.48–2.59 (m, 2H), 1.86–2.01 (m, 2 H), 1.30 (d, 3H). GC–MS: 210 (30.3, $[M]^+$), 133 (2.9), 119 (11.5), 106 (50.9), 105 (100), 92 (34.6), 91 (75.9), 79 (22.8), 77 (29.6), 51 (18.7).

Results and discussion

Reaction of Al atoms with styrene and α-methylstyrene

Aluminum atoms were reacted with styrene under cryogenic temperatures. The ratio of the metal:styrene was approximately 1:10. Water was added to the reaction mixture. This causes hydrolysis of the C—Al bonds and replacement of Al with a hydrogen atom. The main hydrolysis products detected by GC–MS analysis were phenylethane (EtBz), *dl*-2,3-diphenylbutane (*dl*-2,3-DPB), *meso*-2,3-diphenylbutane (*meso*-2,3-DPB), and 1,3-diphenylbutane (1,3-DPB), Table 1. Confirmation of these assignments was obtained by comparing the mass spectral data and retention times to those obtained for authentic samples.

From the entries 1, 2, and 3 in Table 1 it can be seen that the relative amount of the hydrolysis products formed varied from experiment to experiment, e.g., more phenylethane was formed in the second experiment than in the first (cf. 43% vs. 26%). However, the ratio of *dl*-2,3-, *meso*-2,3-, and 1,3-diphenylbutanes remains relatively constant for the three experiments, i.e., 11.2:4.5:1. In all cases, the relative amount of *dl*-2,3-DPB (69 ± 4%) in the mixture is greater than that of *meso*-2,3-DPB (27 ± 4%), which in turn is greater than the 1,3-DPB (6 ± 4%).

Deuterolysis of the reaction mixture, entry 4, Table 1, resulted in compounds that eluted at retention times similar to those observed for the hydrolysis products. However, in each case, the mass spectral data indicated deuterium incorporation. For instance, the *m*/*z* of the main mass spectral fragments (and the percentage abundance relative to the base peak) observed for phenylethane were 106 (27%), 91 (100%), 77 (9%), 65 (12%), and 51 (25%). The fragment at *m*/*z* 106 is the molecular ion, while the base peak with a *m*/*z* value of 91 corresponds to the $[C_7H_7]^+$ ion obtained from the rupture of the benzylic bond.

In the deuterolysis experiment, the *m*/*z* of the main mass spectral fragments for the compound eluting at a similar retention time as that of phenylethane were 108 (37%), 92 (100%), 77 (2%), 65 (7%), and 51 (4%). This is consistent with the incorporation of two deuterium atoms into the phenylethane molecule because the molecular ion has an *m*/*z* of 108 and the fragment with an *m*/*z* of 92 suggests that the $[C_7H_6D]^+$ ion formed in the fragmentation of the molecule. It has been concluded, therefore, that one of the products formed on deuterolysis of the reaction mixture is phenylethane-1,2-d_2. A similar analysis of the mass spectral data of the remaining deuterolysis products suggests that *dl*-2,3-DPB-1,4-d_2, *meso*-2,3-DPB-1,4-d_2, and 1,3-DPB-1,4-d_2 are formed. The mass spectral data of the isomeric diphenylbutanes and their deuterated analogues are presented in Table 2.

The deuterium atoms in the deuterolysis products mark

© 1998 NRC Canada

Table 2. Mass spectral data for the isomeric diphenylbutanes and their deuterated analogues.

Compound	*m/z* for the main mass spectral fragments[a]
dl-2,3-DPB	133 (1.1, $[M - C_6H_5]^+$), 105 (100, $[C_6H_5CHCH_3]^+$), 104 (33.6, $[C_8H_8]^+$), 91 (4.9, $[C_7H_7]^+$), 79(20.0), 77(22.6)
dl-2,3-DPB-1,4-d_2	135 (0.7, $[M - C_6H_5]^+$), 106 (100, $[C_6H_5CHCH_2D]^+$), 105 (49.0, $[C_8H_7D]^+$), 91 (6.7, $[C_7H_7]^+$), 79(15.0), 77(19.7)
meso-2,3-DPB	105 (100, $[C_6H_5CHCH_3]^+$), 104 (29.8, $[C_8H_8]^+$), 91 (5.6, $[C_7H_7]^+$), 79(19.1), 77(21.1), 63(2.6), 51(9.3)
meso-2,3-DPB-1,4-d_2	106 (100, $[C_6H_5CHCH_2D]^+$), 105 (42.0, $[C_8H_7D]^+$), 91 (8.9, $[C_7H_7]^+$), 79(17.4), 77(20.6), 63(4.6), 51(14.9)
1,3-DPB	210 (25.0, $[M]^+$), 133(1.1, $[M - C_6H_5]^+$), 119 (10.7, $[M - C_7H_7]^+$), 106 (49.5), 105 (100, $[C_8H_9]^+$), 92 (31.8), 91 (74.0, $[C_7H_7]^+$), 79 (27.7), 77 (33.7), 51 (18.1)
1,3-DPB-1,4-d_2	212 (23.0, $[M]^+$), 135 (9.5, $[M - C_6H_5]^+$), 120 (10.5, $[M - C_7H_6D]^+$), 107 (36.8), 106 (100, $[C_8H_9D]^+$), 105 (48.4), 93 (37.9), 92 (57.9), 91 (33.7, $[C_7H_7]^+$), 79 (30.5), 77 (35.8), 51 (20)

[a] The numbers in parentheses represent the relative abundance of the fragment.

Scheme 1.

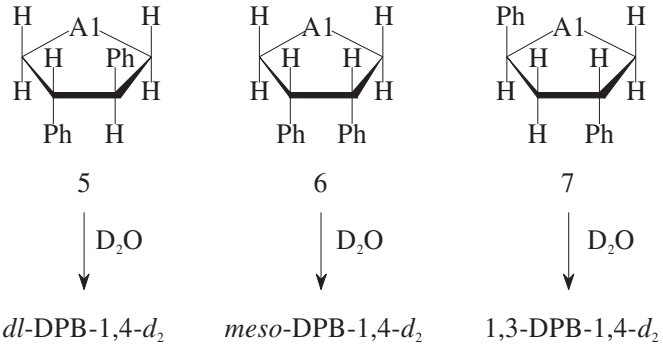

where Al was attached in the original organometallic intermediates. The formation of the dideuteriodiphenylbutanes suggests that two C—Al bonds have been ruptured and replaced in the hydrolysis process by deuterium atoms. The deuterolysis of the aluminacyclopentane intermediates **5**, **6**, and **7** would yield the dideuteriodiphenylbutanes observed in the study, Scheme 1.

Aluminacyclopentanes (3, 4, 7, 8) have been observed spectroscopically in the Al atom reactions of alkenes. In the reaction of Al atoms with ethylene (3, 4), a paramagnetic mononuclear aluminium species with EPR parameters similar to those reported for aluminacyclopentene (9) was detected. In addition, the $M_I = 1/2$ line of the organoaluminium species resolved, upon annealing the Al–ethylene sample, to give a quintet of quintets from the interaction of the unpaired electron with four equivalent hydrogen atoms with a hyperfine interaction (hfi) of 4.0 G, and with four equivalent hydrogen atoms with an hfi of 2.5 G. The two sets of four protons are consistent with aluminacyclopentane where the four protons on the two carbons adjacent to the Al have a 4 G hfi while the four protons on the β carbons have a 2.5 G hfi.

Scheme 2.

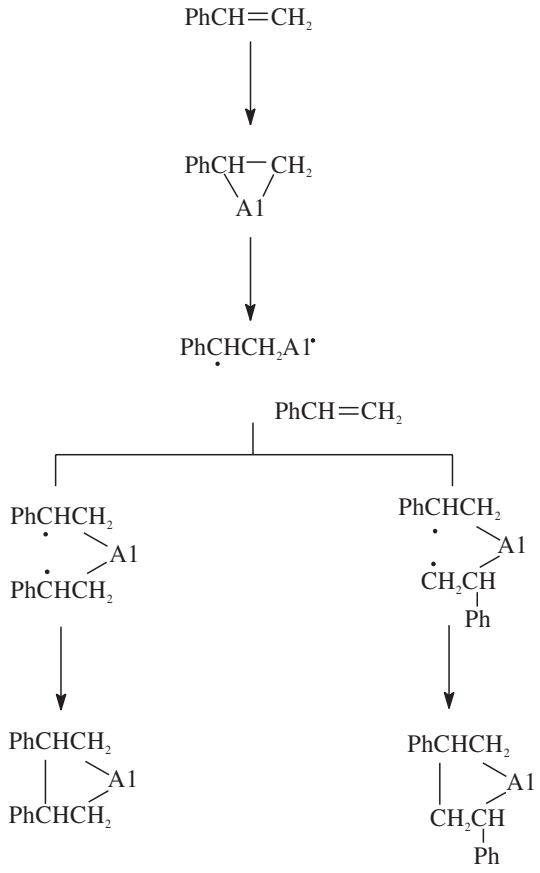

A possible mechanism for the formation of the aluminacyclopentane adducts involves the three-step process shown in Scheme 2. In the first step, Al atoms add in a concerted fashion to styrene to give 2-phenylaluminacyclopropane. The C—Al bond dissociates in a second step to give the most stable alumina–carbon radical. Then, the addition of a second molecule of styrene results in the formation of a diradical. To explain the formation of both 2,3- and 1,3-diphenylbutane, two different diradical intermediates must form, i.e., attack of the β-carbon of styrene by the β-alumina carbon radical results in the diradical that is the precursor of 2,3-diphenylbutane, whereas attack of the α-carbon of styrene results in the diradical responsible for the formation of 1,3-diphenylbutane. In the third step, a bond forms between the two radical centres to form the aluminacyclopentane intermediates. The fact that the *dl* isomer is favoured over the *meso* isomer suggests that ring closure is stereoselective. One could argue that the transition state energy for ring closure is lower when the *gauche* interactions between the phenyl groups and the CH_2 groups are minimized, as is the case for structure **Ia**, Fig. 1. As a result, it is reasonable to expect that the formation of **Ia** will be favoured kinetically and that the *dl* isomer will form more readily than the *meso* isomer.

However, there is some concern about the fact that the diradical, which is proposed to be responsible for the formation

© 1998 NRC Canada

Fig. 1. Newman projections representing conformations of the *trans* (**Ia**, **Ib**) and *cis* (**IIa**, **IIb**) 3,4-diphenylaluminacyclopentane.

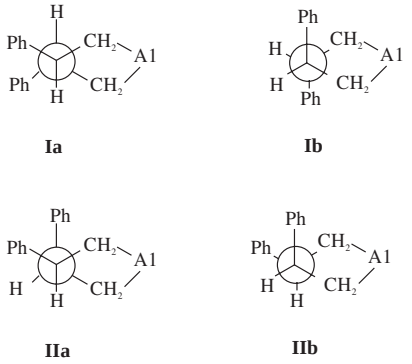

of 1,3-diphenylbutane, has a primary radical centre. The relative stabilities of the primary versus the benzyl radical centre can be estimated by comparing bond dissociation energies. For instance, the bond dissociation energy of the secondary C—H bond of phenylethane (18) is 357.3 kJ/mol whereas the bond dissociation energy of the primary C—H bond of ethane (18) is 422.8 kJ/mol. The benzyl radical is therefore significantly more stable than the primary radical centre. Considering that the 1,3 isomer represents anywhere from 3.4 to 9.4% of the reaction mixture, one would expect that the difference in energies of the intermediates leading to formation of the 1,3 and 2,3 isomers would only be of the order of 4.184 kJ/mol and not of the order of 422.8 – 357.3 or 65.5 kJ/mol. Therefore, it is unlikely that the Al atom reaction of styrene proceeds via the stepwise mechanism proposed above.

Shusterman et al. (19) have suggested that dimethylgermylene produced by the thermal decomposition of 7,7-dimethyl-1,4,5,6-tetraphenyl-7-germabenzonorbornadiene adds to (*E*)-2-deuteriostyrene by a mechanism comparable to that shown in Scheme 2. These workers found that only the *cis* and *trans* isomers of 2,5-dideuterio-1,1-dimethyl-3,4-diphenylgermacyclopentane were formed. There was no evidence for the formation of 1,1-dimethyl-2,4-diphenylgermacyclopentane. In addition, unlike the Al atom reaction, the *cis* and *trans* isomers were formed in a 1:1 ratio.

Alternatively, the Al–styrene reaction could proceed by a two-atom insertion into the 2-phenylaluminacyclopropane, Scheme 3. In this process, the β-alumina radical, PhĊH-CH_2Al, is trapped by styrene in a concerted manner. The fact that three isomers of diphenylbutane were observed suggests that the radical character of the α and β carbons in the transition state is not very advanced, i.e., the transition state is early. The observation that the reaction mixtures always contain greater amounts of the *dl* isomer can be explained in terms of a steric effect. The transition state energy is lowest for the structure where the phenyl rings are *trans*. The phenylethane forms from the hydrolysis of 2-phenylaluminacyclopropane. The incorporation of two deuterium atoms into the phenylethane, at the α and β carbons, is consistent with this interpretation.

Seyferth and co-workers (20, 21) suggested that hexamethylsilirane transfers Me_2Si to styrene, giving 1,1,2,2,3,3-hexamethyl-5-phenylsilacyclopentane by a two-atom insertion comparable to that proposed for the Al–styrene reaction.

Next, Al atoms were added to α-methylstyrene. The hydrolysis of the organoaluminium intermediates gave two main products. The compound that eluted first had a retention time and mass spectrum identical to those of an authentic sample of 2-phenylpropane. The *m*/*z* values of the main mass spectral fragments (and the percentage abundance relative to the base peak) observed for the second compound were 119 (100%), 103 (7.2%), 91 (57.5%), 77 (11.9%), 65 (3.3%), and 51 (6.2%). These data are consistent with 2,3-dimethyl-2,3-diphenylbutane. The base peak has an *m*/*z* of 119 and is assigned to $[C_6H_5C(CH_3)_2]^+$. The peak at an *m*/*z* of 91 is due to $[C_7H_7]^+$ and forms as a result of the elimination of C_2H_4 from $[C_6H_5C(CH_3)_2]^+$. A molecular ion was not observed, as was the case for the symmetric compound, 2,3-diphenylbutane. The 2-phenylpropane can be explained by the hydrolysis of 2-methyl-2-phenylaluminacyclopropane, formed by the concerted addition of Al atoms to α-methylstyrene. The 2,3-dimethyl-2,3-diphenylbutane is formed upon hydrolysis of 3,4-dimethyl-3,4-diphenylaluminacyclopentane. Support for this structure comes from the deuterolysis experiments, which indicate that deuterium is incorporated in the methyl groups (at C1 and C4), Table 3. The aluminacyclopentane intermediate could form in one of at least two ways. The first reaction pathway involves the addition of the β-alumina-α-methylstyrl radical, PhĊ$(CH_3)CH_2$Al, to α-methylstyrene yielding the diradical, PhĊ$(CH_3)CH_2AlCH_2(CH_3)$Ċ Ph. The diradical ring closes in a subsequent step to give Ph$\overline{C(CH_3)CH_2AlCH_2(CH_3)C}$Ph. The

Scheme 3.

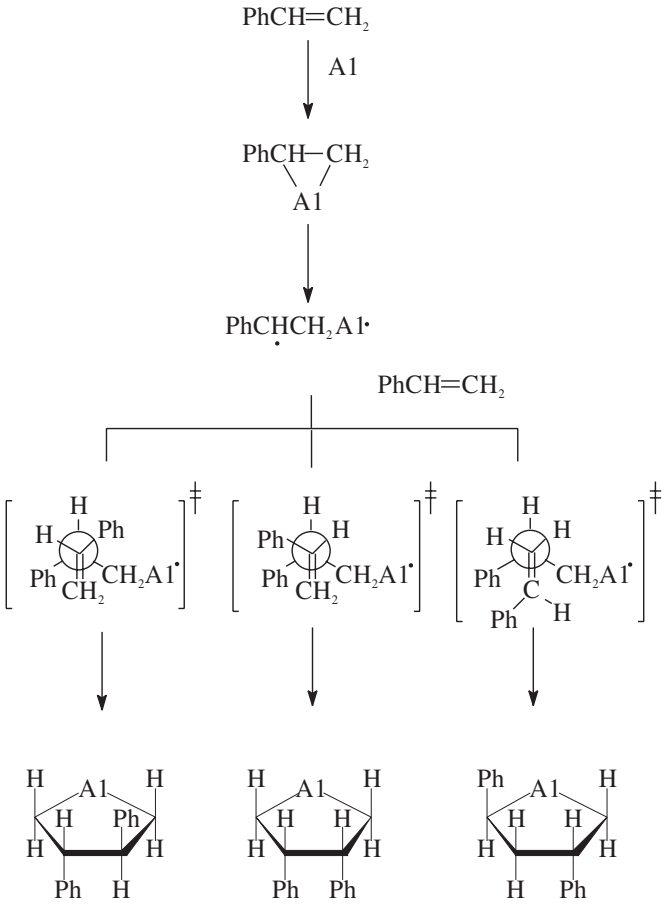

© 1998 NRC Canada

Table 3. Mass spectral data for the hydrolysis and deuterolysis products of the Al–α-methylstyrene reaction mixture.

Compound	*m/z* for the main mass spectral fragments[a]
2-Phenylpropane	119 (16.3, $[M - 1]^+$), 105 (100, $[M - CH_3]^+$), 91 (8.1, $[C_7H_7]^+$), 77 (20.5), 63 (4.7), 51 (16.9)
2-Phenylpropane-1,2-d_2	121 (12.2, $[M - 1]^+$), 107 (99, $[M - CH_3]^+$), 106 (100, $[M - CH_2D]^+$), 92 (7.6, $[C_7H_6D]^+$), 77 (13.8), 63 (5.6), 51 (18.4)
2,3-Dimethyl-2,3-DPB	119 (100, $[C_6H_5C(CH_3)_2]^+$), 103 (7.2), 91 (57.5), 77 (11.9), 65 (3.3), 51 (6.2)
2,3-Dimethyl-2,3-DPB-1,4-d_2	120 (100, $[C_6H_5C(CH_3)(CH_2D)]^+$), 104 (5.2), 92 (32.7), 91 (64.8), 77 (15.0), 65 (4.5), 51 (9.3)

[a] The numbers in parentheses represent the relative abundance of the fragment.

β-alumina-α-methylstyrl radical could form by the ring opening of 2-methyl-2-phenylaluminacyclopropane.

Alternatively, the β-alumina-α-methylstyrl radical could insert into an α-methylstyrene molecule by a concerted two-atom insertion, as was suggested for styrene, yielding 3,4-dimethyl-3,4-diphenylaluminacyclopentane. We are not able to tell by which mechanism the reaction proceeds. However, it is interesting to note that there is no evidence for the formation of $PhC(CH_3)CH_2AlC(CH_3)PhCH_2$, suggesting that if the process were concerted the radical character of the transition state is advanced.

Reaction of other Group 13 metal atoms with styrene

The study was extended to include the reactions of several other Group 13 metal atoms, namely, Ga, In, and Tl, with styrene. In addition to phenylethane, *dl*-2,3-, *meso*-2,3-, and 1,3-DPB, hydrolysis of the Ga–styrene reaction intermediates resulted in the formation of compounds with retention times and mass spectral data identical to those of authentic samples of 1-phenylethanone and styrene oxide. A compound with mass spectral data consistent with 1-phenylethanol was also detected. (The formation of 1-phenylethanone, styrene oxide, and 1-phenylethanol will be the subject of a separate publication.) The ratio of the diphenylbutane isomers in the mixture is similar to that observed for the Al atom reaction in that the [*dl*] > [*meso*] > [1,3], Table 4. Also, the relative amounts of the *dl* and *meso* compounds are similar. However, there appears to be more of the 1,3-DPB formed in the Ga–styrene hydrolysis reaction. The deuterolysis of the Ga–styrene reaction mixture yielded phenylethane-1,2-d_2 (78%), *meso*-2,3-DPB-1,4-d_2 (13%), *dl*-2,3-DPB-1,4-d_2 (5.8%), and 1,3-DPB-1,4-d_2 (3.2%).

Phenylethane and the isomeric diphenylbutanes are the hydrolysis products of 2-phenylgallacyclopropane, *cis*- and *trans*-3,4-diphenylgallacyclopentane, and *cis*- and *trans*-2,4-diphenylgallacyclopentane. It would seem likely that the mechanism for the formation of the organogallium intermediates is comparable to that suggested for the reaction of Al atoms with styrene as the same product ratios and deuterium incorporation were observed for both cases. It is also worth noting that there is tentative EPR evidence for the formation of gallacyclopentane when Ga atoms are reacted with ethene (13).

Table 4. Relative amounts[a] of the isomeric diphenylbutanes found for the organoaluminium adducts formed in the reaction of Ga atoms with styrene at 77 K.

Entry	Relative amounts of the hydrolysis products[a]		
	2,3-DPB *dl*	2,3-DPB *meso*	1,3-DPB
1	60.8	23.1	16.1
2	67.3	21.7	11.0
3	65.8	22.1	12.1
4	67.7	21.5	10.8
5[b]	58.5	26.6	14.9
6[c]	52.5	28.5	19.9

[a] Based on $AC_i/\Sigma AC_i \times 100$ where AC_i is the area counts for product *i*, obtained from the electronic integration of the peaks in the total ion current chromatogram.

[b] D_2O was substituted for H_2O in the hydrolysis reaction.

[c] Cyclohexane was deposited as an inert matrix (vapour pressure 1 Torr) along with Ga and styrene (vapour pressure 0.1 Torr). No water was added to the reaction mixture until after the sample had been annealed to room temperature.

Indium and thallium atoms are not very reactive towards styrene. We were only able to detect traces of phenylethane in the hydrolyzed reaction mixtures. Klabunde and co-workers (22) found the reactivity order of Group 13 metal atoms/clusters for the reaction with methyl bromide to be Al > Ga > In > Tl. They argued that the reactivity displayed by the atoms would be influenced by the heats of vaporization (which are also in the order Al > Ga > In > Tl) in that the reactivity would depend on the energy put into the system during vaporization. Hauge et al. (23) have reported a similar reactivity dependency in Group 13 atom – water reactions. Whereas aluminium atoms were found to react spontaneously with water to form HAlOH, the corresponding Ga and In products were only formed after photolysis of the reaction matrix and no insertion product could be detected for the case of Tl and water.

Acknowledgements

The authors wish to express thanks to Drs. K.C. Westaway, W. Rank, and J.A. Howard for useful discussions. The comments made by the referees are also greatly appreciated. The authors gratefully acknowledge the financial support provided by the Natural Sciences and Engineering Research Council of Canada in the form of an operating grant (H.A.J.), an equipment grant (H.A.J.), and a student summer fellowship (N.R.). Financial support from the Laurentian University research fund is also acknowledged.

References

1. P.H. Kasai and D. McLeod, Jr. J. Am. Chem. Soc. **97**, 5609 (1975).
2. P.H. Kasai. J. Am. Chem. Soc. **104**, 1165 (1982).
3. J.H.B. Chenier, J.A. Howard, and B. Mile. J. Am. Chem. Soc. **109**, 4109 (1987).

© 1998 NRC Canada

4. J.A. Howard, B. Mile, J.S. Tse, and H. Morris. J. Chem. Soc. Faraday Trans. 1, **83**, 3701 (1987).
5. P.S. Skell and L.R. Wolf. J. Am. Chem. Soc. **94**, 7919 (1972).
6. M.J. McGlinchey and P.S. Skell. Angew. Chem. Int. Ed. Engl. **14**, 1975 (1975).
7. M. Histed, J.A. Howard, H. Morris, and B. Mile. J. Am. Chem. Soc. **110**, 5290 (1988).
8. J.A. Howard, H.A. Joly, B. Mile, M. Histed, and H. Morris. J. Chem. Soc. Faraday Trans. 1, **84**, 3307 (1988).
9. J.H.B. Chenier, J.A. Howard, J.S. Tse, and B. Mile. J. Am. Chem. Soc. **107**, 7290 (1985).
10. P.H. Kasai and D. McLeod, Jr. J. Am. Chem. Soc. **101**, 5860 (1979).
11. J.A. Howard, H.A. Joly, and B. Mile. J. Am. Chem. Soc. **111**, 8094 (1989).
12. P.M. Jones and P.H. Kasai. J. Phys. Chem. **92**, 1060 (1988).
13. J.A. Howard, H.A. Joly, and B. Mile. J. Phys. Chem. **96**, 1233 (1992).
14. J.A. Howard, H.A. Joly, B. Mile and R. Sutcliffe. J. Phys. Chem. **95**, 6820 (1991).
15. A.J. Buck, B. Mile, and J.A. Howard. J. Am. Chem. Soc. **105**, 3381 (1983).
16. J.K. Kochi. J. Org. Chem. **28**, 1960 (1963).
17. M. Casey, J. Leonard, B. Lygo, and G. Procter. Advanced practical organic chemistry. Blackie Academic and Professional, New York, 1993. pp. 236–237.
18. Handbook of chemistry and physics. 76th ed. CRC Press, New York. 1995–1996. pp. 9–51.
19. A.J. Shusterman, B.E. Landrum, and R.L. Miller. Organometallics, **8**, 1851 (1989).
20. D. Seyferth and D.C. Annarelli. J. Organomet. Chem. **117**, C51 (1976).
21. D. Seyferth, D.P. Duncan, and S.C. Vick. J. Organomet. Chem. **125**, C5 (1977).
22. Y. Tanaka, S.C. Davis, and K.J. Klabunde. J. Am. Chem. Soc. **104**, 1013 (1982).
23. R.H. Hauge, J.W. Kauffman, and J.L. Margrave. J. Am. Chem. Soc. **102**, 6005 (1980).

© 1998 NRC Canada

Solvent effects on electrical conductivities of sodium tetraphenylboride in water methanol, ethanol, and 2-propanol mixed solvents

Yixing Zhao and Gordon R. Freeman

Abstract: As a foundation for a future measurement of solvated electron mobilities in alcohol–water mixed solvents, the electrical conductances of sodium tetraphenylboride (STPB) in methanol–water, ethanol–water, and 2-propanol–water were measured at different temperatures. The molar conductivity Λ_0 (10^{-4} S m^2 mol^{-1}) of STPB at 298 K is 70 in pure water and 82 in pure methanol; in methanol–water mixed solvents it passes through a minimum, the value being 45 at 70 mol% water. In 2-propanol–water Λ_0 (10^{-4} S m^2 mol^{-1}) at 298 K decreases rapidly from 70 in pure water to 22.6 in 80 mol% water, then gradually to 16.5 in pure 2-propanol. Behavior in ethanol–water is intermediate, with a minimum of 29.5 in 70 mol% water, gradually increasing to 35.5 in pure ethanol. The product of Λ_0 and the solvent viscosity η has a maximum at about 75 mol% water in methanol, 90 mol% water in ethanol, and 95 mol% water in 2-propanol. The effects are attributed to changes of solvent structure and of solvated ion radius as alcohol is added to water.

Key words: alcohol–water mixed solvents, electrical conductivity, large ions, solvent effects, activation energy.

Résumé : Dans le but de préparer le terrain pour de futures mesures des mobilités d'électrons solvatés dans des mélanges de solvants formés d'alcool et d'eau, on a mesuré les conductances du tétraphénylborure de sodium (TPBS) dans des mélanges de méthanol–eau, éthanol–eau et propan-2-ol–eau, à diverses températures. La conductivité molaire, Λ_0 (10^{-4} S m^2 mol^{-1}), du TPBS à 298 K est égale à 70 dans l'eau pure et de 82 dans le méthanol pur; dans des solvants mixtes méthanol–eau, elle passe par une valeur minimum de 45 à 70 mol% d'eau. Dans le mélange propan-2-ol–eau, la valeur de Λ_0 (10^{-4} S m^2 mol^{-1}) à 298 K diminue rapidement de 70 dans l'eau pure à 22,6 dans un mélange à 80 mol% d'eau; elle diminue ensuite graduellement jusqu'à une valeur de 16,5 dans le propan-2-ol pur. Le comportement dans des mélanges éthanol–eau est intermédiaire avec un minimum de 29,5 dans un mélange contenant 70 mol% d'eau, qui augmente graduellement jusqu'à 33,5 dans l'éthanol pur. Le produit de Λ_0 par la viscosité du solvant, η, passe par un maximum dans des mélanges à 75 mol% d'eau dans le méthanol, de 90 mol% d'eau dans l'éthanol et de 95 mol% d'eau dans le propan-2-ol. Les effets sont attribués à des changements dans la structure du solvant et dans les rayons des ions solvatés lorsqu'on ajoute de l'alcool à l'eau.

Mots clés : solvants mixtes alcool–eau, conductivité électrique, gros ions, effets de solvant, énergie d'activation.

[Traduit par la rédaction]

Introduction

The study of electrical conductances of electrolytes in different solvents elucidates properties of ions and solvents (1–4), and provides reference data for solvent effects on the mobilities of solvated electrons (5–8). The electrical conductances of large-ion tetraphenylphosphonium and tetraphenylboride salts in C_1–C_4 alcohols were recently reported (2). The present paper extends the study to mixed alcohol–water solvents, as a foundation for a future measurement of solvated electron mobilities in these solvents. We have chosen sodium tetraphenylboride because its photoionization in solution would produce solvated electrons. In the solvent sequence methanol, ethanol, and 2-propanol, the molecular size increases and the molecule becomes more spherelike.

Received October 20, 1997.

Y. Zhao and G.R. Freeman.[1] Department of Chemistry, University of Alberta, Edmonton, AB T6G 2G2, Canada.

[1] Author to whom correspondence may be addressed. Telephone: (403) 492-3468. Fax: (403) 492-8231. E-mail: k.np@ualberta.ca

Experimental

The solute, solvents, purification method, and techniques of the conductance measurements have been reported in ref. 2.

Results and discussion

Low concentrations (0.025–0.125 mol m^{-3}) were used in the measurement of the electrical conductances of sodium tetraphenylboride (STPB) in all the solvents, and straight lines were obtained in the plots of specific conductance against solute concentration. This indicates that the ionic atmosphere effect (9) and ion association (10) were negligible.

Arrhenius plots of molar conductivities of STPB in water–methanol (Fig. 1), water–ethanol (Fig. 2), and water–2-propanol (Fig. 3) mixed solvents display considerable variation with solvent composition. Symbols used in Figs. 1–3 are listed in Table 1.

Molar conductivities of STPB

The molar conductivities Λ_0 of STPB in the three mixed solvent systems at 298 K are listed in Table 2 and plotted in Fig. 4*a* along with the viscosities η of the solvents (11, 12)

© 1998 NRC Canada

Fig. 1. Arrhenius plots of molar conductivities of sodium tetraphenylboride (STPB) in water–methanol mixed solvents. Refer to Table 1 for symbols.

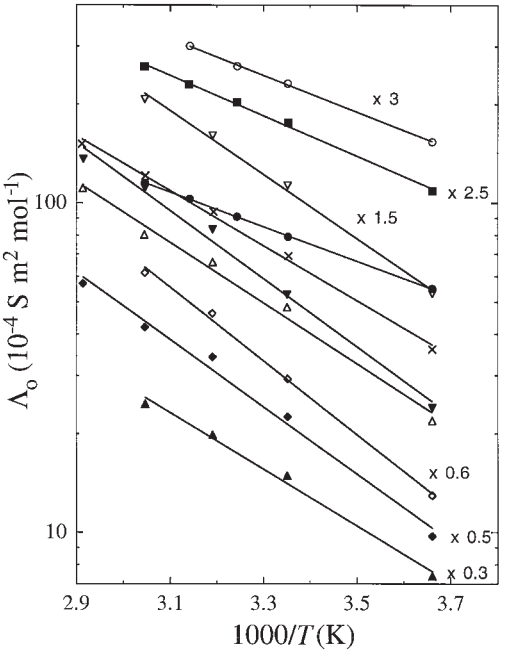

Fig. 2. Arrhenius plots of molar conductivities of STPB in water–ethanol mixed solvents. Refer to Table 1 for symbols.

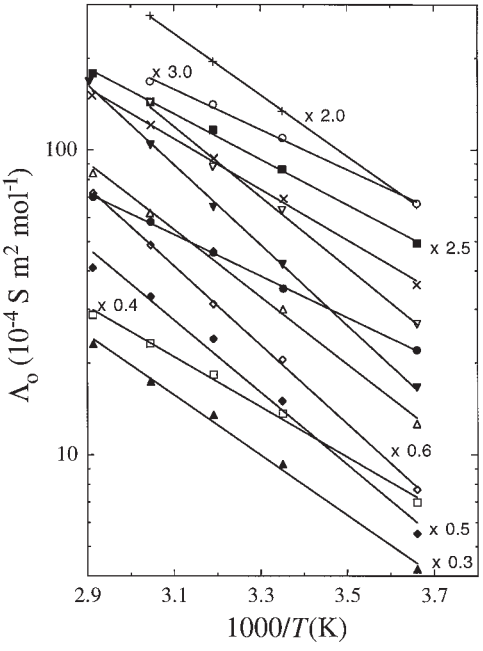

(Fig. 4*b*). The value of Λ_0 does not vary simply inversely as η in these three mixed solvent systems.

In pure ethanol at 298 K, $\Lambda_0 = 35.5$ (10^{-4} S m^2 mol^{-1}, Table 2) is preferred to the previously reported value of 35.0 (2).

Plots of $\eta\Lambda_0$ against solvent composition display a maximum at about 75 mol% water in methanol, 90 mol% water in ethanol, and 95 mol% water in 2-propanol (Fig. 5). The presence of a small amount of alcohol in water alters the solvent

Fig. 3. Arrhenius plots of molar conductivities of STPB in water–2-propanol mixed solvents. Refer to Table 1 for symbols.

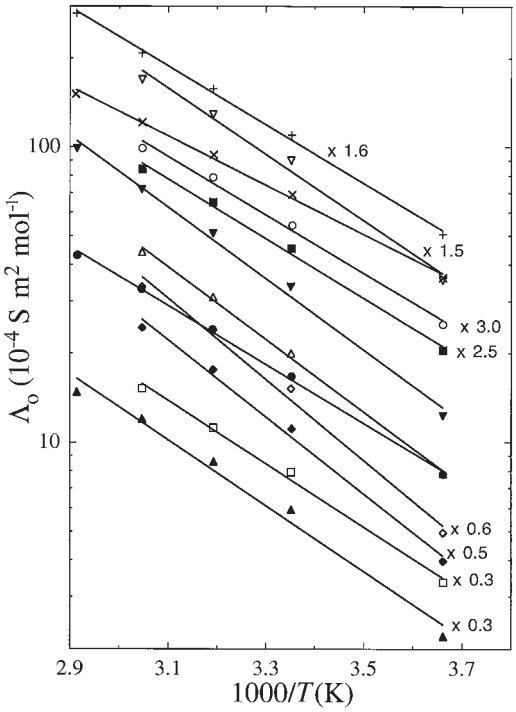

Table 1. Symbols for Figs. 1–3.

	Mol% water		Mol% water
×	100	△	60
+	99	▲	45
▽	97	□	30
▼	90	■	15
◇	80	○	5
◆	70	●	0 (Alcohol) [a]

[a] Methanol (Fig. 1), ethanol (Fig. 2), and 2-propanol (Fig. 3).

structure, probably by changing the hydrogen-bond configurations toward an ice-like structure, and thereby increasing the viscosity (11). However, the shear viscosity increases more rapidly than the ion mobilities decrease, possibly because the ions disrupt the solvent structure in their vicinity.

Addition of further alcohol to the water decreases $\eta\Lambda_0$, because some of the water molecules that solvate the ions are replaced by alcohol molecules, thereby increasing the solvated ion radius. In the pure alcohols or water the radii of the solvated ions are roughly proportional to $(N + 1)^{1/2}$, where N is the number of carbon atoms in the molecule, the 1 represents the oxygen atom, and the square root represents a randomly folded chain. The values of $\eta\Lambda_0(N + 1)^{1/2}$ at 298 K are 62 in water, 65 in methanol, 68 in ethanol, 69 in 2-propanol, in satisfactory agreement with Walden's rule.

Activation energy $E_{\Lambda 0}$ and E_η

The values of $E_{\Lambda 0}$ and E_η have the same pattern (Fig. 6), and the values of $E_{\Lambda 0}$ are close to those of E_η (Table 2). In the alcohol-rich regions the values of $E_{\Lambda 0}$ are slightly lower than those of E_η, whereas in the water-rich regions $E_{\Lambda 0}$ is equal to or slightly larger than E_η. This might indicate that the ions are

© 1998 NRC Canada

Fig. 4. Composition dependences of molar conductivity of STPB (*a*) and viscosity (*b*) in water–methanol (●), water–ethanol (○), and water–2-propanol (■) mixed solvents at 298 K.

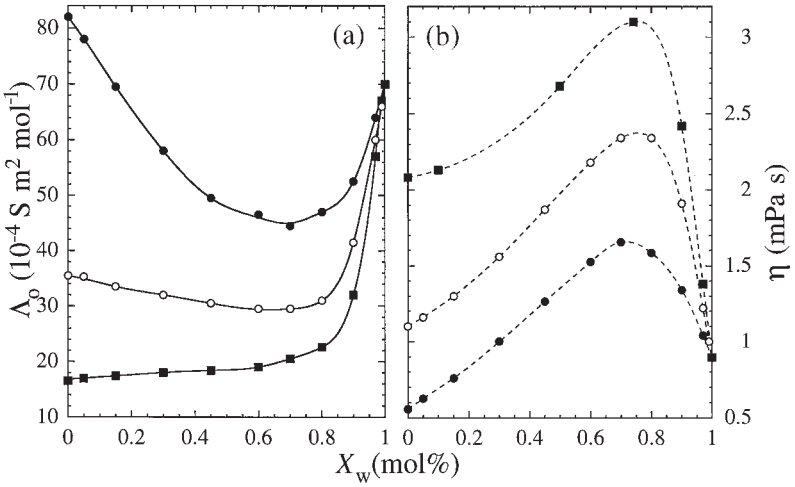

Table 2. Molar conductivities at 298 K and temperature coefficients of sodium tetraphenylboride in water–alcohol mixed solvents.

Mol% water	η (mPa s)[a]	Λ_0 (10^{-4} S m^2 mol^{-1})	E_η (kJ mol^{-1})[a]	$E_{\Lambda 0}$ (kJ mol^{-1})
Water–methanol mixed solvents				
100	0.89	70	16.0	16.0
97	1.04	64	17.0	20.4
90	1.34	53	19.0	22.3
80	1.59	47.0	19.9	22.2
70	1.66	44.5	20.9	21.0
60	1.53	46.5	20.8	18.0
45	1.27	49.5	18.6	16.0
30	1.00	58	16.2	14.0
15	0.76	70	13.6	12.0
5	0.63	78	11.5	10.3
0	0.56	82	10.7	9.6
Water–ethanol mixed solvents				
100	0.89	70	16.0	16.0
99	1.00	66		19.2
97	1.22	60	21.0	22.8
90	1.91	41.5	26.3	24.6
80	2.34	31.0	27.3	25.3
70	2.34	29.5	25.5	24.3
60	2.18	29.5	23.0	22.6
45	1.87	30.5	20.4	19.0
30	1.56	32.0	18.2	17.0
15	1.30	33.5	16.0	15.2
5	1.16	35.3	14.8	13.4
0	1.10	35.5	14.1	13.2
Water–2-propanol mixed solvents				
100	0.89	70	16.0	16.0
99	1.00	67		19.0
97	1.38	55	20.0	20.5
90	2.42	32.0	23.0	23.2
80	3.06	22.6	24.5	24.7
70	3.07	20.5	25.1	24.8
60	2.90	19.0	24.7	24.4

Table 2 (*concluded*).

Mol% water	η (mPa s)[a]	Λ_0 (10^{-4} S m^2 mol^{-1})	E_η (kJ mol^{-1})[a]	$E_{\Lambda 0}$ (kJ mol^{-1})
45	2.57	18.4	23.6	22.3
30	2.33	18.0	23.0	21.0
15	2.17	17.4	22.5	20.7
5	2.13	17.0	22.4	20.3
0	2.08	16.5	22.2	20.1

[a] Viscosity (η) and activation energy (E_η): water–methanol and water–ethanol mixed solvents, ref. 11, and water–2-propanol mixed solvents, ref. 12.

Fig. 5. Composition dependences of $\eta\Lambda_0$ of STPB in water–methanol (●), water–ethanol (○), and water–2-propanol (■) mixed solvents at 298 K.

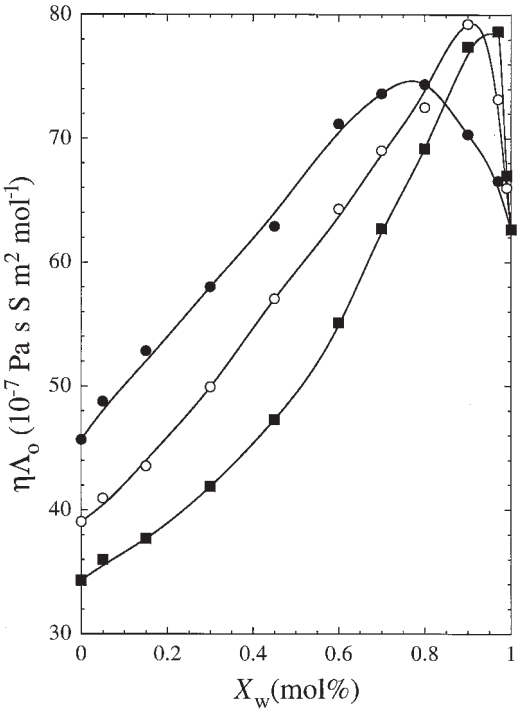

© 1998 NRC Canada

Fig. 6. Comparison of E_Λ of STPB and E_η of water–methanol (●), water–ethanol (○), and water–2-propanol (■) mixed solvents.

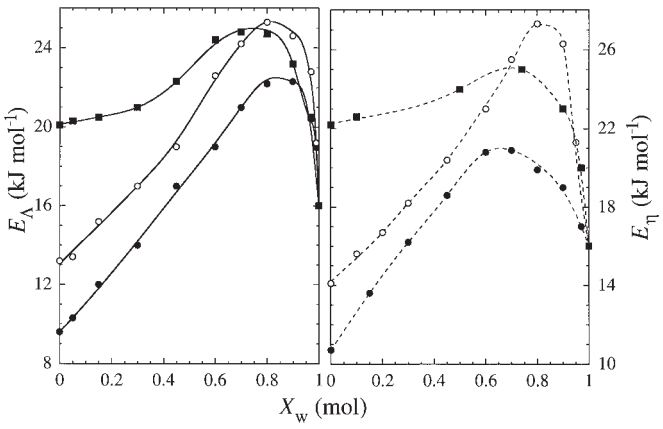

less tightly solvated by alcohol molecules than by water molecules.

Conclusions

The present work provides a foundation for the measurement of solvated electron mobilities in alcohol–water mixed solvents. Values of the mobilities are needed to better understand the solvent composition dependence of reaction rate constants of solvated electrons with diverse solutes in alcohol–water mixtures (5, 6, 8, 11–14). Knowledge of the transport behavior of electrons in these molecular-scale structures (hydrogen-bonded liquids) would also provide insight into the behavior of electrons in sub-nanometer-component systems.

Mixtures of water with the sequence of alcohols CH_3OH, CH_3CH_2OH, and $(CH_3)_2CHOH$ should be extended to $(CH_3)_3COH$, to include the most globular alcohol that is completely miscible with water. Unfortunately, G.R.F. passed retirement age, the Radiation Research Centre was closed, research always opens new questions, so this last experimental article from our group is left with open circuits.

It would also be valuable to measure the change of transference numbers of $Na^+$and $(C_6H_5)_4B^-$ ions with solvent composition, to give information about selective solvation of small inorganic and large organic ions in the alcohol–water mixtures.

We hand a torch, not a baton, to the next generation.

Acknowledgement

We thank the Natural Sciences and Engineering Research Council of Canada for financial assistance and Mr. Ronald Gardner for maintaining the electric equipment.

References

1. Y. Zhao and G.R. Freeman. Can. J. Chem. **75**, 559 (1997).
2. Y. Zhao and G.R. Freeman. J. Phys. Chem. **100**, 17568 (1996).
3. M.C. Blanco and D.C. Champeny. Phys. Chem. Liq. **23**, 93 (1991).
4. Y. Zhao and G.R. Freeman. Can. J. Chem. **73**, 2131 (1995).
5. Y. Zhao and G.R. Freeman. Can. J. Chem. **73**, 392 (1995).
6. R. Chen and G.R. Freeman. J. Phys. Chem. **99**, 4970 (1995).
7. K.H. Schmidt, P. Han, and D.M. Bartels. J. Phys. Chem. **96**, 199 (1992).
8. R. Chen and G.R. Freeman. Can. J. Chem. **71**, 1303 (1993).
9. P.W. Atkins. Physical chemistry. 4th ed. W.H. Freeman and Company, New York. 1990. pp. 251, 752, 765–766.
10. J.O'M. Bockris and A.K.N. Reddy. Modern electrochemistry. Vol. 1. Plenum Press, New York. 1975. p. 450.
11. C.C. Lai and G.R. Freeman. J. Phys. Chem. **94**, 302 (1990).
12. A.P. Sedigallage and G.R. Freeman. Can. J. Phys. **68**, 940 (1990).
13. P.C. Senanayake and G.R. Freeman. J. Chem. Phys. **87**, 7007 (1987).
14. J. Cygler and G.R. Freeman. Can. J. Chem. **62**, 1265 (1984); many subsequent articles by GRF and co-workers, in Can. J. Chem. and J. Phys. Chem.

© 1998 NRC Canada

Optical absorption spectrum of solvated electrons in pure *tert*-butanol: effect of temperature

Yixing Zhao and Gordon R. Freeman

Abstract: The energy and asymmetry of the optical absorption spectrum of solvated electrons, e_s^-, change in a nonlinear fashion on changing the solvent through the series HOH, CH_3OH, CH_3CH_3OH, $(CH_3)_2CHOH$, $(CH_3)_3COH$. The ultimate, quantum-statistical mechanical, interpretation of solvated electron spectra is needed to describe the solvent dependence. The previously reported optical spectrum of e_s^- in *tert*-butanol was somewhat inaccurate, due to a small amount of water in the alcohol and to limitations of the infrared light detector. The present note records the remeasured spectrum and its temperature dependence. The value of the energy at the absorption maximum (E_{Amax}) is 155 zJ (0.97 eV) at 299 K and 112 zJ (0.70 eV) at 338 K; the corresponding values of $G\varepsilon_{max}$ (10^{-22} m^2 aJ^{-1}) are 1.06 and 0.74. These unusually large changes are attributed to the abnormally rapid decrease of dielectric permittivity of *tert*-butanol with increasing temperature. The band asymmetry at 299 K is $W_b/W_r = 1.8$.

Key words: optical absorption spectrum, solvated electron, solvent effects, *tert*-butanol, temperature dependence.

Résumé : L'énergie et l'asymétrie des spectres d'absorption optique des électrons solvatés, e_s^-, changent d'une façon non linéaire lorsqu'on passe de l'un à l'autre des solvants suivants : HOH, CH_3OH, CH_3CH_2OH, $(CH_3)_2CHOH$, $(CH_3)_3COH$. Pour décrire l'influence du solvant, il sera nécessaire de faire appel à l'interprétation ultime des spectres des électrons solvatés, basée sur la mécanique quantique statistique. Le spectre optique de e_s^- dans le *tert*-butanol qui a été rapporté antérieurement n'était pas complètement exact à cause d'une faible quantité d'eau dans l'alcool et des limitations du détecteur de la lumière infrarouge. La présente note corrige les données relatives au spectre et à sa dépendance sur la température. La valeur de l'énergie au niveau de l'absorption maximale (E_{Amax}) est égale à 155 zJ (0,97 eV) à 299 K et de 112 zJ (0,70 eV) à 338 K; les valeurs correspondantes de $G\varepsilon_{max}$ (10^{-22} m^2 aJ^{-1}) sont égales à 1,06 et 0,74. On attribue ces changements particulièrement importants à la diminution anormalement rapide de la permittivité diélectrique du *tert*-butanol avec une augmentation de la température. L'asymétrie de la bande à 299 K est $W_b/W_r = 1,8$.

Mots clés : spectre d'absorption optique, électron solvaté, effets de solvant, *tert*-butanol, dépendance sur la température.

[Traduit par la rédaction]

Introduction

The optical absorption spectrum of solvated electrons (e_s^-) in an alcohol solvent shifts to lower energy on going from a primary to a secondary to a tertiary alcohol (1). In the isomeric butanols at 298 K the energies at the absorption maximum (E_{Amax}) were reported to be 317 zJ (1.98 eV) in 1-butanol, 254 zJ (1.59 eV) in 2-butanol, and 179 zJ (1.12 eV) in *tert*-butanol (2-methyl-2-propanol). The absorption energy in *tert*-butanol is especially sensitive to the presence of a small amount of water, so we have measured the spectrum in more thoroughly dried *tert*-butanol, and determined the temperature dependence. The solvent density and dipole correlation decrease with increasing temperature, which decreases the e_s^- optical absorption energy (ref. 2, Fig. 6 and associated discussion; each ref. no. in Fig. 6 legend should be increased by 2).

Received November 13, 1997.

Y. Zhao and G.R. Freeman.[1] Department of Chemistry, University of Alberta, Edmonton, AB T6G 2G2, Canada.

[1] Author to whom correspondence may be addressed. Telephone: (403) 492-3468. Fax:(403) 492-8231. E-mail: k.np@ualberta.ca

When an adequate quantum-statistical mechanical model of solvated electrons is ultimately formulated, it will accommodate the nonlinear shifts in optical absorption energy and band asymmetry on changing the solvent through the series HOH, CH_3OH, C_2H_5OH, $(CH_3)_2CHOH$, and $(CH_3)_3COH$. The present note reports e_s^- spectrum data for the last solvent in that series, *tert*-butanol; data for the spectra in the other solvents are recorded elsewhere (refs. 1, 2, and refs. therein).

In the report of solvent effects on the reactivity of e_s^- with $NO_{3,s}^-$ in C_1–C_4 alcohols (3) and in *tert*-butanol–water mixed solvents (4), an optical absorption energy E_r (halfway up the low-energy side of the band) in *tert*-butanol at 299 K was listed from unpublished work. The present note reports that work.

Experimental

The *tert*-butanol was obtained from Fluka (> 99.7%). Reference 4 reports the purification method. The water content, measured by Karl-Fisher titration, was <0.05 mol%. The freezing point of pure *tert*-butanol is 298.6 K.

The optical absorption spectrum of e_s^- was measured at 299 K, 319 K, and 338 K over the energy range 99–397 zJ (λ = 2000–500 nm). A fresh sample of purified *tert*-butanol was

© 1998 NRC Canada

Table 1. Comparison of parameters of solvated electron spectra.

Solvent	T (K)	D [a]	d [b] (kg/m^3)	$G\varepsilon_{max}$ (10^{-22} m^2/aJ)[c]	E_{Amax} (zJ)	E_b (zJ)	E_r (zJ)	$W_{1/2}$ (zJ)	W_b/W_r.[d]	d(ln E_{amax})/dT (K^{-1})
tert-Butanol	299	12.4	779	1.06	155	246	104	142	1.8	
	319	8.7	757	0.83	131	208				0.0084
	338	6.9	735	0.74	112	177				
Water [e]	298	78.4	997	5.19	278	362	223	139	1.5	0.0014
1-Butylamine [e]	298	4.7	737	0.89	115	215				
	225		803	1.35	147	251	102[f]	149[f]	2.3	0.0033

[a] Dielectric permittivity: water and *tert*-butanol, ref. 13*a*; 1-butylamine, ref. 13*b*.

[b] Density: water and 1-butylamine, ref. 14; *tert*-butanol, ref. 12.

[c] SI units for $G\varepsilon_{max}$, where G is the number of free ions e_s^- formed per 16 aJ absorbed and ε is the molar extinction coefficient; 1.00 m^2/aJ = 9.63 × 10^{25} e_s^-·L/100 eV mol cm (old units). For e_s^- in water (ref. 5), $G\varepsilon_{max}$ = 5.0 × 10^4 e_s^-·L/100 eV mol cm = 8.3 × 10^{-21} m^2/16 aJ = 5.2 × 10^{-22} m^2/aJ.

[d] Asymmetry of the absorption band. $W_b = E_b - E_{Amax}$; $W_r = E_{Amax} - E_r$.

[e] Reference 5.

[f] Near the freezing point, 224 K (ref. 5).

Fig. 1. Optical absorption spectra of solvated electrons in pure *tert*-butanol at 299 K (●), 319 K (○), and 338 K (▲). $G\varepsilon$ is the product of the yield of free ions, $G_{fi}(e_s^-)$, and the optical extinction coefficient ε. Photon wavelength λ (μm) = 198.6/E (zJ).

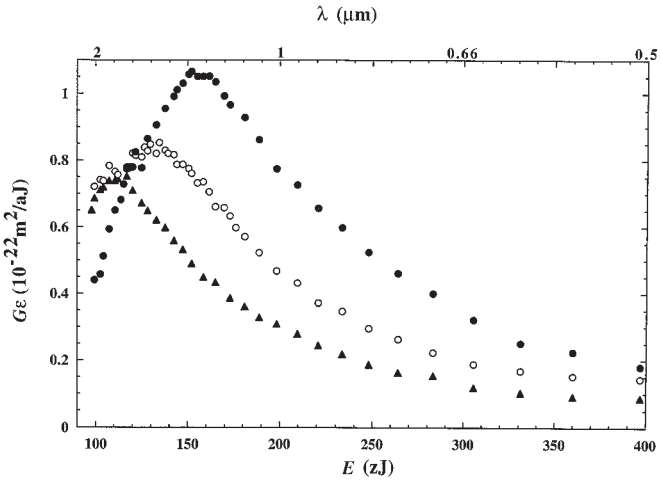

used for the measurement at each temperature. The technique of the optical measurement has been reported in ref. 5.

Results and discussion

The optical absorption spectra of e_s^- in pure *tert*-butanol at 299 K, 319 K, and 338 K are shown in Fig. 1. The spectra are broad and asymmetric, skewed toward higher energies. The nonhomogeneously broadened spectrum has no fine structure (6, 7).

As the temperature was increased the magnitude of absorption decreased and the energy at the absorption maximum (E_{Amax}) shifted to a lower energy (Fig. 1). The decrease in magnitude of absorption is attributed to a decrease of free ion yield, because the value of the product of the dielectric permittivity D and the temperature T decreases with increasing temperature in *tert*-butanol (8, 9). The value of E_{Amax} decreases with increasing temperature because thermal agitation of the solvent molecular dipoles makes the electron traps more shallow (1).

The relative rate of decrease of E_{Amax} with increasing temperature, expressed as $(E_{Amax})^{-1}(-dE_{Amax}/dT) = -d(\ln E_{Amax})/dT$, is much larger in *tert*-butanol (0.0084 K^{-1}) than in water (0.0014 K^{-1}), methanol (0.0013 K^{-1}), ethanol (0.0018 K^{-1}), or 2-propanol (0.0030 K^{-1}); the values other than that for *tert*-butanol were calculated from data in ref. 1*a*, pp. 169 and 211, ref. 1*b*, Table 1, and ref. 2, Fig. 6. The relative temperature coefficient in an alcohol is larger when the alkyl group is more globular. The globular *tert*-butanol molecules are sterically hindered from strongly aligning four -O–H dipoles in the field of the electron, and the alignment is more easily disturbed by thermal agitation than appears to be the case in the other liquids. The relatively easy thermal disturbance of dipole alignment in *tert*-butanol is reflected in the relatively rapid decrease of DT with increasing T (ref. 8, Fig. 4).

Optical excitation energies of e_s^- in 1-butylamine (5) are even lower than those in *tert*-butanol, which made the amine an interesting solvent in which to study e_s^- reaction rate constants (10). Reaction rate constants of e_s^- with certain solutes are larger when the e_s^- optical absorption energies are smaller. Parameter values of the optical absorption spectrum of e_s^- in *tert*-butanol are compared with those in 1-butylamine and in water (the usual standard for comparison) in Table 1: E_{Amax}, the maximum absorption $G\varepsilon_{max}$, the energies E_r and E_b halfway up the low- (red) and high- (blue) energy sides of the band, the width of the band at half-height ($W_{1/2}$), the band asymmetry W_b/W_r, and the relative temperature dependence of the optical absorption energy $-d(\ln E_{Amax})/dT$. From the data in Table 1 one may interpolate that, at a given temperature, on going from water to *tert*-butanol to 1-butylamine the values of $G\varepsilon_{max}$ and E_{Amax} decrease, while the band asymmetry increases. The relative temperature dependence of the optical absorption is anomalously high in *tert*-butanol, due to the unusually rapid decrease of D with increasing T of that liquid (Table 1; ref. 8, Fig. 4).

The values of E_{Amax} correlate roughly with the product of D and the density d of these solvents (11).

The values of $G\varepsilon_{max}$ in these solvents correlate roughly with the product DT, due mainly to the variation of G, the free ion yield of e_s^- (9). The values of G (free ion e_s^-/16 aJ) at 298 K are 2.7 in water (2), 0.67 in *tert*-butanol (15), and about 0.27

© 1998 NRC Canada

in 1-butylamine (5), which give respective values of ε_{max} (10^{-21} m^2/e_s^-) = 3.1, 2.5, and about 5.3.

The values of the band width $W_{1/2}$ are similar in these three solvents (Table 1). We suggest that as E_{Amax} decreases, excitation to the continuum contributes an increasing portion of the total band (ref. 16, and references therein).

We await a quantum-statistical mechanical model that is consistent with these behaviors of e_s^-. The all-atom force field model (17), applied through Monte Carlo techniques to molecular reactions (18), holds promise for e_s^- properties and reactions. Polarization effects are important in low-dielectric media (19), but must also be very important in all organic liquids, including alcohols.

Acknowledgments

We thank the Natural Sciences and Engineering Research Council of Canada for financial assistance, and the staff of the Radiation Research Center for maintaining the electronic equipment. G.R.F. is grateful to the University of Alberta for generous support of the Radiation Research Center and its personnel during three decades. The R.R.C. is now closed, and the personnel are members of the Chemistry Department.

References

1. (*a*) A.-D. Leu. Ph.D. Thesis, University of Alberta, 1980; (*b*) A.-D. Leu, K.N. Jha, and G.R. Freeman. Can. J. Chem. **60**, 2342 (1982).
2. F.-Y. Jou and G.R. Freeman. J. Phys. Chem. **83**, 2383 (1979).
3. Y. Zhao and G.R. Freeman. Can. J. Chem. **73**, 284 (1995).
4. Y. Zhao and G.R. Freeman. Can. J. Chem. **73**, 392 (1995).
5. Y. Zhao and G. R. Freeman. Can. J. Chem. **73**, 2126 (1995).
6. T.R.J. Tuttle, S. Golden, S. Lwenje, and C.M. Stupak. J. Phys. Chem. **88**, 3811 (1984).
7. N. Okabe, T. Kimura, and K. Fueki. Can J. Chem. **61**, 2199 (1983).
8. Y. Zhao and G.R. Freeman. Can. J. Chem. **75**, 559 (1997).
9. G.R. Freeman. Kinetics of nonhomogeneous processes: a practical introduction for chemists, biologists, physicists, and materials scientists. Wiley–Interscience, New York. 1980. Chap. 2.
10. Y. Zhao and G.R. Freeman. Can. J. Chem. **74**, 300 (1996).
11. G.R. Freeman. J. Phys. Chem. **77**, 7 (1973).
12. P.C. Senanayake, N. Gee, and G.R. Freeman. Can. J. Chem. **65**, 2441 (1987).
13. Y.Y. Akhadov. Dielectric properties of binary solutions. Pergamon Press, New York. 1980. (*a*) p. 456; (*b*) p. 144.
14. R.W. Gallant. Physical properties of hydrocarbons. Vol. 2. Gulf Publishing Co., Houston, Tex. 1970. pp. 109, 186.
15. C. Capellos and A.O. Allen. J. Phys. Chem. **74**, 840 (1970).
16. F.-Y. Jou and G.R. Freeman. Can. J. Chem. **57**, 591 (1979).
17. W.L. Jorgensen, D.S. Maxwell, and J. Tirado-Rives. J. Am. Chem. Soc. **118**, 11225 (1996).
18. D. Lim and W.L. Jorgensen. J. Phys. Chem. **100**, 17490 (1996).
19. W.L. Jorgensen, N.A. McDonald, M. Selmi, and P.R. Rablen. J. Am. Chem. Soc. **117**, 11809 (1995).

© 1998 NRC Canada

Tripodal trisamides based on nicotinic and picolinic acid derivatives

H.R. Hoveyda, Veranja Karunaratne, Christopher J. Nichols, Steven J. Rettig, Ashley K.W. Stephens, and Chris Orvig

Abstract: A number of polydentate arylamide ligands have been prepared by coupling various acyclic tripodal or linear polyamines with derivatives of nicotinic and picolinic acids. Two synthetic procedures were utilized; tris{[(2-hydroxynicotinyl)carbonyl]-2-aminoethyl}amine (H_3NICTREN) was prepared by Method A, the HOSu/DCC method, and the other arylamides in this study were prepared by Method B, the CDI method. Method A involved the reaction of *N*-hydroxysuccinimide with 2-hydroxynicotinic acid (in the presence of dicyclohexylcarbodiimide (DCC) as a dehydrative coupling reagent) to form the succinimide ester, followed by reaction with TREN to yield H_3NICTREN. Method B involved reaction of a carboxylic acid (2-hydroxynicotinic, 3-hydroxypicolinic, nicotinic, or picolinic acids) with carbonyldiimidazole (CDI) to form the *N*-acylimidazolide, followed by reaction with the amine (TREN, TAME, spermidine, or TRPN) to yield the desired arylamide. The X-ray structure of 1,1,1-tris{[(3-hydroxypicolinyl)carbonyl]-2-aminomethyl}ethane (H_3PICTAME) was determined; crystals of H_3PICTAME are monoclinic, $a = 10.257(2)$, $b = 15.572(3)$, $c = 15.208(2)$ Å, $\beta = 96.124(15)°$, $Z = 4$, space group $P2_1/a$. The structure was solved by direct methods and refined by full-matrix least-squares procedures to $R = 0.041$ and $R_w = 0.038$ for 2506 reflections with $I \geq 3\sigma(I)$. In the solid state, H_3PICTAME contains an extensive hydrogen-bonding network, with eight intra- and one intermolecular H-bonds per molecule; the ligand is partially preorganized for metal ion chelation. The acid dissociation constants of H_3NICTREN and those of 1,1,1-tris{[(2-hydroxynicotinyl)carbonyl]-2-aminomethyl}ethane (H_3NICTAME) have been determined; $pK_{a1} = 11.2$ (10.68), $pK_{a2} = 10.7$ (10.58), $pK_{a3} = 10.0$ (9.71), and $pK_{a4} = 6.25$ for H_3NICTREN (H_3NICTAME); the high phenolic pK_a'*s* are consistent with the hydrogen bonding observed in the solid state.

Key words: arylamide, hydrogen bonding, preorganization.

Résumé : On a préparé une série de ligands arylamides polydentates en procédant au couplage de diverses polyamines linéaires ou acycliques tripodaux avec des dérivés des acides nicotinique et picolinique. On a fait appel à deux voies de synthèse : on a préparé la tris{[(2-hydroxynicotinyl)carbonyl]-2-aminoéthyl}amine (H_3NICTREN) par la méthode A, la méthode au HOSu/DCC, alors que les autres arylamides examinés dans cette étude ont été préparés par la méthode B, la méthode CDI. La méthode A implique la réaction du *N*-hydroxysuccinimide avec l'acide 2-hydroxynicotinique (en présence de dicyclohexylcarbodiimide (DCC) comme agent de couplage déshydratant) qui conduit à l'ester succinimide, suivie d'une réaction avec du « TREN » pour obtenir le H_3NICTREN. La méthode B implique la réaction d'un acide carboxylique (acides 2-hydroxynicotinique, 3-hydroxypicolinique, nicotinique ou picolinique) avec le carbonyldiimidazole (CDI) pour former le *N*-acylimidazolide, suivie d'une réaction avec l'amine (« TREN », « TAME », spermidine ou « TRPN ») conduisant à l'arylamide désiré. On a déterminé la structure cristalline du 1,1,1-tris{[(3-hydroxypicolinyl)carbonyl]-2-aminométhyl}éthane (H_3PICTAME). Les cristaux sont monocliniques, groupe d'espace $P2_1/a$, avec $a = 10{,}257(2)$, $b = 15{,}572(3)$ et $c = 15{,}208(2)$ Å, $\beta = 96{,}124(15)°$ et $Z = 4$. On a résolu la structure par des méthodes directes et on l'a affinée par la méthode des moindres carrés (matrice entière) jusqu'à des valeurs de $R = 0{,}041$ et $R_w = 0{,}038$ pour 2506 réflexions avec $I \geq 3\sigma(I)$. À l'état solide, le H_3PICTAME comporte un important réseau de liaisons hydrogènes, avec huit liaisons intra- et une liaison intermoléculaire par molécule; le ligand est partiellement préorganisé pour donner une chélation avec le métal. On a déterminé les constantes de dissociation acide du H_3NICTREN et du 1,1,1-tris{[(3-hydroxypicolinyl)carbonyl]-2-aminométhyl}éthane (H_3PICTAME) qui sont respectivement : $pK_{a1} = 11{,}2$ (10,68), $pK_{a2} = 10{,}7$ (10,58), $pK_{a3} = 10{,}0$ (9,71) et $pK_{a4} = 6{,}25$; les valeurs élevées du pK_a des phénols sont en accord avec les liaisons hydrogènes observées à l'état solide.

Mots clés : arylamide, liaison hydrogène, préorganisation.

[Traduit par la rédaction]

Received August 25, 1997.

H.R. Hoveyda, V. Karunaratne, C.J. Nichols, S.J. Rettig, A.K.W. Stephens, and C. Orvig.[1] Medicinal Inorganic Chemistry Group, Department of Chemistry, University of British Columbia, 2036 Main Mall, Vancouver, BC V6T 1Z1, Canada.

[1] Author to whom correspondence may be addressed. Telephone: (604) 822-4449. Fax: (604) 822-2847. E-mail: orvig@chem.ubc.ca

© 1998 NRC Canada

Introduction

In searching for new ligands to be used in the sequestration of trivalent metal ions (e.g., group 13 and lanthanides), much insight can be gained from an examination of naturally occurring chelating agents for trivalent iron. The physical and chemical similarities between Fe(III) and group 13 metals, especially Ga(III), are rather pronounced; they share the same charge and similar ionic radii, e.g., 0.645 Å for Fe(III) compared to 0.620 Å for Ga(III) (1). In addition, the electronic configuration of (aqueous) ferric ion is high-spin d^5, while the group 13 metal ions are diamagnetic (Al(III), d^0; Ga(III) and In(III), d^{10}), and, accordingly, none of these metal ions or the lanthanides are perturbed by crystal field effects (2). The kinship between Ga(III) and Fe(III) is nicely reflected in the kinetics of ligand exchange, for instance, the first-order water exchange rates for Ga(III) and Fe(III) (at 298 K) are 4.0×10^2 and 1.6×10^2 s^{-1}, respectively (3). Also, microorganisms and plants have evolved a host of low-molecular-weight ligands; the *siderophores* (for a general overview, see ref. 4), which show both a high affinity and a high specificity for Fe(III) (formation constants ranging from 10^{25} to 10^{49}) (5). Therefore, in a biomimetic approach, the knowledge gained from ferric ion transport can be applied, for example, to the development of ^{67}Ga radiopharmaceuticals (6, 7). Our approach in designing the ligands prepared in this paper has been biomimetic, as is outlined below.

Enterobactin forms one of the most stable Fe(III) complexes known (8), with an overall stability constant of 10^{49} (9). The backbone of this macrocyclic ligand is derived from three L-serine units, and it utilizes three catechol moieties to sequester Fe(III) in a hexadentate coordination sphere as in Fig. 1a (10–12). However, since the effective ligand is the conjugate base form (the catecholate), the coordination environment of the metal ion is a function of pH. In a series of studies (13–15), Raymond and co-workers have unequivocally established that sequential protonation of the ferric enterobactin complex (three one-proton steps) results in a concomitant shift from a "catechol binding mode" to a "salicylate binding mode" (see Fig. 1). The "arylamides" that possess the structural features depicted in Fig. 1c may thus be considered as "salicylate type"

Fig. 1. Catecholate (**a**) and salicylate (**b**) modes of bonding for the pH-dependent coordination environments of Fe(III) bound to catechoylamide ligands. Prototypical "arylamide" ligand in protonated form (**c**).

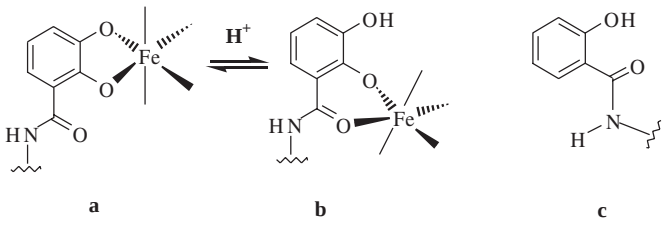

a **b** **c**

ligands, potentially capable of metal ligation via the phenolate oxygen and the amide carbonyl oxygen.

It was our interest in maltol as an effective bidentate chelating ligand for group 13 metal ions (16, 17) that instigated the investigation of its structural isomer, isomaltol, as yet another naturally occurring bidentate chelator (18). However, once it was established that isomaltol was not a good ligand for the formation of other hexadentate ligands (i.e., its denticity cannot be increased via an imine linkage), due to nucleophilic attack being favored at the C-5 carbon (19), attention was turned to using the amide linkage both as a metal binding group, as well as the "arm" to increase the denticity of the ligand. As a consequence, a bidentate analog Hahm was synthesized starting from the appropriate ethyl ester Hehm (19). In spite of the fact that Al and Ga tris(ligand) complexes could be isolated with Hahm, it was discovered that in H_2O, Hahm undergoes decomposition that is time, concentration, and pH dependent (19).

Given the fact that, in general, the half-life for hydrolysis of an amide bond (in neutral aqueous solution) is ca. 7 years (20), it is clear that replacement of the furan with another aromatic ring system would do much to alleviate the instability of these ligands, not to mention the reduction in the number of steps required for the ligand synthesis. Therefore, we have used derivatives of nicotinic and picolinic acid as (commercially available) starting materials for the formation of new arylamide ligands.

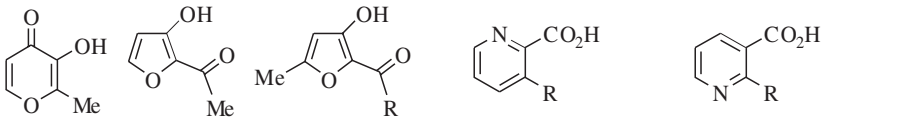

Maltol Isomaltol R = OEt (Hehm) R = N(H)Me (Hahm) R = H OH nicotinic acid 2-hydroxy-nicotinic acid (H_2nic) R = H OH picolinic acid 3-hydroxy-picolinic acid (H_2pic)

Experimental

Materials and methods

All chemicals were reagent grade and were used as received from commercial vendors (Aldrich and Sigma) unless otherwise stated. 1,1,1-Tris(azidomethyl)ethane was prepared according to a literature procedure (21). THF was distilled from Na benzophenone ketyl under Ar prior to use; 1,4-dioxane was predried over activated 4Å molecular sieves before use. Water was deionized (Barnstead D8902 and D8904 cartridges) and distilled (Corning MP-1 Megapure still). Plates used for thin-layer chromatography (TLC) were aluminum-supported 0.2 mm silica gel 60 F_{254} (EM Science). Column chromatography was carried out using 230–400 mesh size silica gel

© 1998 NRC Canada

(E. Merck, Silica Gel 60) and the "flash" technique (22), or by using lipophilic Sephadex LH-20™. All reactions were carried out under N_2 unless otherwise noted. The yields reported refer to isolated yields.

Instrumentation

NMR spectra were recorded on Bruker WH-400 (^{1}H NMR, 400 MHz), or Bruker AC-200E (^{1}H NMR, 200 MHz; ^{13}C NMR, 50 MHz) instruments. ^{1}H NMR data are reported as δ downfield from TMS (external reference) at 400 MHz in DMSO-d_6 unless otherwise noted. ^{13}C NMR data are reported as δ downfield from TMS (external reference) at 50 MHz in DMSO-d_6 unless otherwise noted. Infrared (IR) spectra were recorded as KBr disks in the range 4000–400 cm^{-1} on a Perkin Elmer PE 783 spectrophotometer and were referenced to polystyrene unless stated otherwise. Mass spectra (MS) were obtained with a Kratos MS 50 (electron-impact ionization, EI), an AEI MS 9, or a Kratos Concept IIH (fast-atom-bombardment ionization, FAB). Melting points were measured on a Mel-Temp apparatus and are uncorrected. Analyses were performed on a Carlo Erba elemental analyzer by Mr Peter Borda of this department.

Syntheses

Caution! *The handling of polyazides in large quantities may be hazardous. DCC is a severe skin irritant!*

1,1,1-Tris(aminomethyl)ethane (TAME)

TAME was prepared with some modifications to the reported method (21). To a solution of 1,1,1-tris(azidomethyl)ethane (16.8 g, 0.086 mol) in THF (200 mL) at 0°C, lithium aluminium hydride (LAH) (14.0 g, 0.364 mol) was added in small portions over 30 min. The resulting white-grey slurry was stirred at 0°C for 10 min, allowed to warm up to 20°C, and then refluxed for 24 h. The mixture was cooled to 0°C and NaOH (50 mL, 8 M) was added slowly to quench the excess LAH. To the resulting off-white slurry was added Et_2O (500 mL) and the reaction mixture was stirred for 30 min. The off-white precipitate was filtered off and washed with Et_2O. The combined filtrate and washings were dried ($MgSO_4$), and the solvent was removed on a rotary evaporator to afford TAME (8.6 g, 86%) as a pale yellow oil. ^{1}H NMR and IR spectra of the product thus obtained were identical with those previously reported (21). This product was used without any further purification.

Tris(aminopropyl)amine (TRPN)

TRPN was made by reduction of nitrilotrispropionamide with LAH in THF with some modifications to the reported method (23). The intermediate trisamide was synthesized as follows. To a suspension of acrylamide (43.0 g, 0.60 mol) in H_2O (20 mL) was added 26 g of 30% NH_4OH (0.22 mol). The solution became clear in ca. 10 min, and the mixture was left stirring at 20°C for 24 h. The precipitate thus formed was filtered, washed with H_2O (3 × 10 mL), and dried in vacuo, yielding nitrilotrispropionamide (25 g, 57%). ^{1}H NMR and IR spectra of the product were identical with those previously reported.

To a suspension of the dry trisamide thus obtained (10.0 g, 0.04 mol) in 1000 mL of THF at 0°C, LAH (10.0 g, 0.26 mol) was added in small portions over 30 min. The resulting white-grey slurry was stirred at 0°C for 10 min, allowed to warm up to 20°C, and then stirred for 18 h. The mixture was then cooled to 0°C and NaOH (50 mL, 8 M) was added slowly to quench the excess LAH. To the resulting off-white slurry was added Et_2O (500 mL) and the reaction mixture was stirred for 30 min. The off-white precipitate was filtered and washed with Et_2O. The organic layer was separated, dried ($MgSO_4$), and evaporated to afford a yellow oil. The crude product was vacuum distilled (0.2 Torr; 1 Torr = 133.3 Pa) to remove the bisamine impurity (ca. 10% by ^{1}H NMR; 65°C) from the product (97–100°C), yielding 2.6 g (35%) of TRPN. ^{1}H and ^{13}C NMR spectra of TRPN thus synthesized were identical with those reported in the literature (23).

Method A: Succinimido 2-hydroxynicotinate (HOSuNic)

To a mixture of 2-hydroxynicotinic acid (1.370 g, 9.85 mmol) in THF (100 mL) was added *N*-hydroxysuccinimide (1.148 g, 9.98 mmol) and DCC (2.275 g, 11.03 mmol). The mixture was then refluxed for 20 h, whereupon it was allowed to cool to 20°C. The white precipitate was filtered, washed with CH_2Cl_2 (3 × 50 mL), and dried in vacuo. The crude product thus obtained was still contaminated with dicyclohexylurea (DCU). The product was purified via Soxhlet extraction (48 h) using CH_2Cl_2 to yield 1.02 g (42%) of HOSuNic. ^{1}H NMR: 2.98 (s, 4H^{1,2}), 6.49 (t, 1H$^{\beta}$, J = 7 Hz), 7.99 (dd, 1H$^{\gamma}$, J = 7, 2 Hz), 8.44 (dd, 1H$^{\alpha}$, J = 7, 2 Hz), 12.56 (br s, O*H*). MS (EI), *m/z*: 236 (M^+).

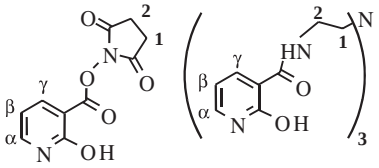

HOSuNic

H_3NICTREN

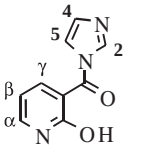

HImNic

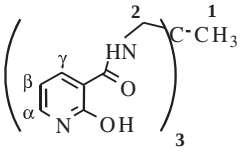

H_3NICTAME

Tris{[((2-hydroxynicotinyl)carbonyl]-2-aminoethyl}amine (H_3NICTREN)

To a mixture of HOSuNic (1.17 g, 4.95 mmol) in THF (200 mL) was added TREN (0.240 g, 1.64 mmol) in one portion. The resultant mixture was refluxed for 18 h, whereupon it was left to cool to 20°C. The white precipitate was filtered, washed with CH_2Cl_2 and Et_2O, and dried in vacuo to afford H_3NICTREN (0.73 g, 87%), mp 242°C (dec.). IR: 3640–2600 (br, ν_{OH}), 3280 (m, ν_{NH}), 1680 (s, $\nu_{C=O}$), 1610 (m, $\nu_{C=C}$), 1560 (s, amide II (24)), 1473 (m, $\nu_{C=C}$), 1328, 1255, 1060, 980. ^{1}H NMR: 2.68 (t, 6H^1, J = 6 Hz), 3.10–3.60 (partially obscured m, 6H^2), 6.43 (t, 3H$^{\beta}$, J = 6 Hz), 7.64 (dd, 3H$^{\gamma}$, J = 6, 4 Hz), 8.28

© 1998 NRC Canada

(dd, 3H$^{\alpha}$, J = 6, 4 Hz), 9.79 (t, 3H, C(O)N*H*, J = 6 Hz), 12.20 (br s, 3H, O*H*). ^{13}C NMR (DMSO-d_6): 37.42 (C*1*), 53.46 (C*2*), 106.14 (Cb), 120.63 (Cγ), 139.30 (Cα), 143.77 (Cδ), 162.32 (*C*-OH), 163.36 (*C*═O). Anal. calcd. (found) for $C_{24}H_{27}N_7O_6 \cdot 0.5H_2O$: C 55.60 (55.42), H 5.21 (5.33), N 18.90 (18.83).

Method B: N-*(2-Hydroxynicotinyl)-imidazole (HImNic)*
To a mixture of 2-hydroxynicotinic acid (5.34 g, 38.4 mmol) in THF (200 mL) was added CDI (6.43 g, 39.4 mmol) in one portion. The mixture was refluxed for 19 h. After cooling the reaction mixture to 20°C, the white precipitate was filtered, washed with Et_2O, and dried in vacuo to afford HImNic (6.65 g, 98%). ^{1}H NMR: 6.38 (t, 1H$^{\beta}$, J = 6.6 Hz), 7.05 (dd, 1H^{4}, J = 1.6, 0.8 Hz), 7.61 (t, 1H^{5}, J = 1.6 Hz), 7.74 (dd, 1H$^{\gamma}$, J = 6.3, 2.2 Hz), 7.93 (dd, 1H$^{\alpha}$, J = 6.3, 2.2 Hz), 8.16 (t, 1H^{2}, J = 0.8 Hz), 12.32 (br s, O*H*). MS (EI), *m/z*: 189 (M$^+$). Anal. calcd. (found) for $C_9H_7N_3O_2$: C 57.14 (56.95), H 3.73 (3.81), N 22.21 (22.15).

Tris{[(2-hydroxynicotinyl)carbonyl]-2-aminoethyl}amine (H$_3$NICTREN)
To a mixture of HImNic (6.30 g, 33.3 mmol) in 1,4-dioxan (400 mL) was added TREN (1.56 g, 10.67 mmol) in one portion. The resulting mixture was refluxed for 18 h. After cooling the reaction mixture to 20°C, the precipitate was filtered, washed with THF and Et_2O, and dried in vacuo to afford H_3NICTREN as a white solid (5.20 g, 95%). ^{1}H NMR, ^{13}C NMR, IR, and MS spectra were identical to those reported for the sample obtained by Method A. Anal. calcd. (found) for $C_{24}H_{27}N_7O_6 \cdot 0.25H_2O$: C 56.08 (56.15), H 5.39 (5.57), N 19.07 (19.07).

1,1,1-Tris{[(2-hydroxynicotinyl)carbonyl]-2-aminomethyl}ethane (H$_3$NICTAME)
To a mixture of HImNic (6.05 g, 32.0 mmol) in 1,4-dioxan (400 mL) was added TAME (1.10 g, 9.39 mmol) in one portion. The resulting mixture was refluxed for 19 h. After cooling the reaction mixture to 20°C, the precipitate was filtered, washed with THF and Et_2O, and dried in vacuo to afford H_3NICTAME as an off-white solid (4.22 g, 89 %), mp 270°C (dec.). IR: 3600–2600 (br, ν_{OH}), 3280 (m, ν_{NH}), 1665 (s, $\nu_{C=O}$), 1600 (m, $\nu_{C=C}$), 1562 (s, amide II), 1480 (m, $\nu_{C=C}$), 1430, 1320, 1235, 1150, 790, 770. ^{1}H NMR: 0.91 (s, 3H^{1}), 3.14–3.47 (partially obscured d, 6H^{2}, J = 6 Hz), 6.46 (t, 3H$^{\beta}$ J = 6 Hz), 7.69 (dd, 3H$^{\gamma}$, J = 8, 1.2 Hz), 8.30 (dd, 3H$^{\alpha}$, J = 8, 1.2 Hz), 10.01 (t, 3H, C(O)N*H*, J = 6 Hz), 12.38 (br s, 3H, O*H*). MS (FAB), *m/z*: 481 (M+H)$^+$. Anal. calcd. (found) for $C_{23}H_{24}N_6O_6 \cdot H_2O$: C 55.42 (55.68), H 5.22 (5.28), N 16.87 (16.55).

N^1,N^5,N^{10}-*Tris(2-hydroxynicotinyl)spermidine (H$_3$NICSPERM)*
To a suspension of HImNic (2.639 g, 13.96 mmol) in 1,4-dioxane (200 mL) was added spermidine (0.658 g, 4.53 mmol) in one portion. The resulting mixture was refluxed for 19 h. After cooling the reaction mixture to 20°C, the brown-orange precipitate was filtered, washed with Et_2O, and dried in vacuo to yield 1.611 g of the crude product; 205 mg of this was column chromatographed on lipophilic Sephadex LH-20™ (3 × 120 cm column; eluant: 50% MeOH in EtOAc) to afford pure product (150 mg, 73% recovery), equivalent to a 51% overall yield; mp 115–117°C. TLC (eluant: 50% MeOH in EtOAc) R_f = 0.3. IR: 3600–2600 (br,ν_{OH}), 3260 (m, ν_{NH}), 1675 (s, $\nu_{C=O}$), 1605 (m, $\nu_{C=C}$), 1560 (s, amide II), 1230, 775. ^{1}H NMR (δ at 200 MHz in DMSO-d_6): 1.3–1.9 (three overlapping m, 6 H^{3,7,8}), 2.9–3.6 (partially obscured overlapping m, 8H^{2,4,6,9}), 6.03–6.22 (m, 1H$^{\beta}$), 6.40–6.51 (m, 2H$^{\beta',\beta''}$), 7.24–7.45 (two overlapping m, 2H$^{\alpha,\gamma}$), 7.60–7.75 (m, 2H$^{\gamma,\gamma'}$), 8.22–8.38 (m, 2H$^{\alpha',\alpha''}$), 9.60–9.90 (m, 2H, C(O)N*H*), 11.85 (br s, 1H, O*H*), 12.45 (br s, 2H, O*H*). MS (FAB), *m/z*: 510 ± 1 (M+H)$^+$. Anal. calcd. (found) for $C_{25}H_{28}N_6O_6 \cdot H_2O$: C 57.03 (57.13), H 5.74 (5.80), N 15.96 (15.82).

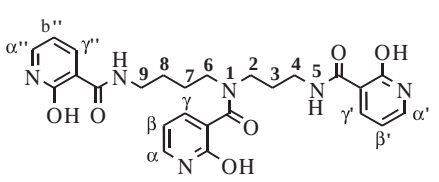

H$_3$NICSPERM

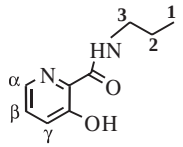

HpropylPic

[(3-Hydroxypicolinyl)carbonyl]propylamine (HpropylPic)
To a mixture of 3-hydroxypicolinic acid (1.48 g, 10.6 mmol) in THF (200 mL) was added CDI (1.92 g, 11.8 mmol) in one portion. The mixture was refluxed for 2 h whereupon *n*-propylamine (10.1 g, 0.12 mol) was added and the resultant mixture was refluxed for a further 19 h. After cooling the reaction mixture to 20°C, the volatiles were removed under reduced pressure and the resultant oil was column chromatographed on silica gel (eluant: 50% pentane in Et_2O, R_f = 0.84) to afford Hpropylpic (1.40 g, 74%) as a yellow-brown liquid. IR (neat on KBr plates): 3600–2600 (br, ν_{OH}), 3380 (m, ν_{N-H}), 1650 (s, $\nu_{C=O}$), 1580 (m, $\nu_{C=C}$), 1535 (s, amide II), 1450 (m, $\nu_{C=C}$), 1340, 1295, 1255, 1195, 810, 795. ^{1}H NMR: 0.85 (t, 3H^{1}, J = 7 Hz), 1.54 (m, 2H^{2}), 3.25 (dt, 2H^{3}, J = 8, 7 Hz), 7.36 (dd, 1H$^{\gamma}$, J = 8, 0.8 Hz), 7.48 (dd, 1H$^{\beta}$, J = 8, 4 Hz), 8.12 (dd, 1H$^{\alpha}$, J = 4, 0.8 Hz), 9.14 (t, 1H, C(O)N*H*, J = 6 Hz), 12.70 (br s, O*H*). ^{13}C NMR: 11.32 (C*1*), 22.27 (C*2*), 40.05 (C*3*), 125.84 (Cγ), 128.95 (Cβ), 131.49 (Cα), 139.66 (*C*C(O)NH), 157.37 (*C*-OH), 168.70 (*C*═O). Exact Mass calcd. (found) for $C_9H_{12}N_2O_2$: 180.0904 (180.0898). Anal. calcd. (found) for $C_9H_{12}N_2O_2$: C 59.99 (59.77), H 6.71 (6.78), N 15.55 (15.50).

1,1,1-Tris{[(3-hydroxypicolinyl)carbonyl]-2-aminomethyl}-ethane (H$_3$PICTAME)
To a mixture of 3-hydroxypicolinic acid (5.34 g, 38.39 mmol) in THF (150 mL) was added CDI (6.43 g, 39.65 mmol) in one portion. The mixture was refluxed for 5 h whereupon TAME (1.50 g, 12.80 mmol) was added and the solution was refluxed for a further 26 h. After cooling the reaction mixture to 20°C, the precipitate was filtered and the filtrate was concentrated in vacuo to yield a dark reddish-brown residue. This residue was redissolved in a minimum amount of hot MeOH (ca. 40 mL), which, after cooling to room temperature, was triturated with Et_2O to yield the product as a brown solid (1.25 g, 20%), mp 165–167°C. X-ray quality crystals were obtained by slow evaporation of a MeOH:Et_2O (1:20) solution at room temperature (rt). IR: 3600–2600 (br, ν_{OH}), 3355 (m, ν_{NH}), 1650 (s, $\nu_{C=O}$), 1580 (m, $\nu_{C=C}$), 1530 (s, amide II), 1448 (m, $\nu_{C=C}$), 1355, 1315, 1295, 1245, 1200, 1160, 810, 695, 660. ^{1}H NMR:

© 1998 NRC Canada

0.88 (s, 3H^{1}), 3.20–3.41 (partially obscured d, 6H^{2}, J = 6 Hz), 7.43 (dd, 3H$^{\gamma}$, J = 8, 0.8 Hz), 7.55 (dd, 3H$^{\beta}$, J = 8, 4 Hz), 8.19 (dd, 3H$^{\alpha}$, J = 4, 0.8 Hz), 9.62 (t, 3H, C(O)N*H*, J = 6 Hz), 12.46 (br s, 3H, O*H*). MS (FAB), *m/z*: 481 $(M+H)^+$. Anal. calcd. (found) for $C_{23}H_{24}N_6O_6$: C 57.50 (57.39), H 5.03 (4.90), N 17.49 (17.55).

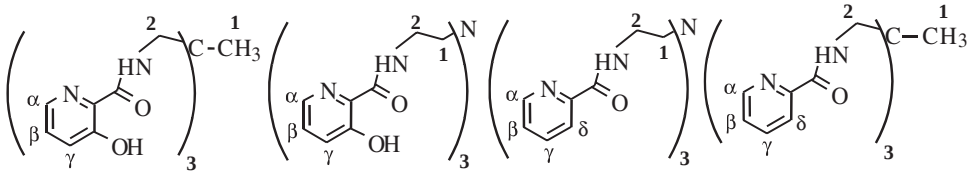

H_3PICTAME H_3PICTREN PICTREN PICTAME

Tris{[(3-hydroxypicolinyl)carbonyl]-2-aminoethyl}amine (H_3PICTREN)

To a mixture of 3-hydroxypicolinic acid (2.52 g, 18.12 mmol) in THF (150 mL) was added CDI (3.50 g, 21.6 mmol) in one portion. The mixture was refluxed for 5 h whereupon TREN (0.883 g, 6.04 mmol) was added and the solution was refluxed for a further 18 h. After cooling the reaction mixture to 20°C, the precipitate was filtered and the filtrate was concentrated in vacuo to yield a dark reddish-brown residue. This residue was redissolved in a minimum amount of hot MeOH (ca. 20 mL), which, after cooling to rt, was triturated with Et_2O to yield the product as a light-brown solid (2.15 g, 70%), mp 156–158°C. IR: 3600–2700 (br, ν_{OH}), 3350 (m, ν_{NH}), 1640 (s, $\nu_{C=O}$), 1590 (m, $\nu_{C=C}$), 1540 (s, amide II), 1450 (m, $\nu_{C=C}$), 1300, 1240, 1200, 1180, 1150, 860, 820, 685, 665. ^{1}H NMR: 2.78 (t, 6H^{1}, J = 6 Hz), 3.36–3.47 (partially obscured m, 6H^{2}), 7.33 (dd, 3H$^{\gamma}$, J = 8, 0.8 Hz), 7.42 (dd, 3H$^{\beta}$, J = 8, 4 Hz), 7.97 (dd, 3H$^{\alpha}$, J = 4, 0.8 Hz), 8.96 (t, 3H, C(O)N*H*, J = 6 Hz), 12.52 (br s, 3H, O*H*). MS (FAB), *m/z*: 510 $(M+H)^+$. Anal. calcd. (found) for $C_{24}H_{27}N_7O_6$: C 56.58 (56.46), H 5.34 (5.41), N 19.24 (19.21).

Tris{[(picolinyl)carbonyl]-2-aminoethyl}amine (PICTREN)

To a mixture of picolinic acid (3.0 g, 24.4 mmol) in THF (200 mL) was added CDI (4.35 g, 26.8 mmol) in one portion. The resultant mixture was refluxed for 1 h whereupon TREN (1.17 g, 8.02 mmol) was added and the mixture was refluxed for a further 19 h. After cooling the reaction mixture to 20°C and removal of the solvent under reduced pressure, the dark-brown residue thus obtained was column chromatographed on lipophilic Sephadex LH-20™ (3 × 120 cm column; eluant: MeOH) to afford PICTREN (3.43 g, 93%) as a deep red-brown viscous liquid. IR (in $CHCl_3$): 3390 (m, ν_{NH}), 1665 (s, $\nu_{C=O}$). ^{1}H NMR: 2.76 (t, 6H^{1}, J = 6 Hz), 3.34–3.50 (partially obscured m, 6H^{2}), 7.49-7.56 (m, 3Hβ), 7.90–8.00 (m, 6H$^{\gamma,\delta}$), 8.43-8.47 (m, 3H$^{\alpha}$), 8.70 (t, 3H, C(O)N*H*, J = 6 Hz). MS (FAB), *m/z:* 462 $(M+H)^+$. Anal. calcd. (found) for $C_{24}H_{27}N_7O_3\cdot 0.5H_2O$: C 61.26 (60.99), H 6.00 (5.94), N 20.84 (20.92).

1,1,1-Tris{[(picolinyl)carbonyl]-2-aminomethyl}ethane (PICTAME)

To a mixture of picolinic acid (1.576 g, 12.80 mmol) in THF (150 mL) was added CDI (2.283 g, 14.08 mmol) in one portion. The resultant mixture was refluxed for 2 h whereupon TAME (0.5 g, 4.30 mmol) was added and the mixture was refluxed for a further 19 h. After cooling the reaction mixture to 20°C, and removal of the solvent under reduced pressure, the residue so obtained was column chromatographed on silica gel (eluant: 5% MeOH:45% Et_2O:50% EtOAc; R_f = 0.58) to afford PICTAME (1.30 g, 70%) as a white solid, mp 207–208°C. IR: 1670 (s, $\nu_{C=O}$), 1590 (m, $\nu_{C=C}$), 1535 (s, amide II), 1465 (m, $\nu_{C=C}$), 1435, 1335, 1000, 760, 690. ^{1}H NMR: 0.53 (s, 3H^{1}), 3.22 (d, 6H^{2}, J = 6 Hz), 7.62 (ddd, 3H$^{\beta}$, J = 8, 4, 1.2 Hz), 8.01 (dt, 3H$^{\gamma}$, J = 8, 8, 1.6 Hz), 8.06-8.16 (m, 3H$^{\delta}$), 8.66-8.74 (m, 3H$^{\alpha}$), 9.37 (t, 3H, C(O)N*H*, J = 6 Hz). MS (FAB), *m/z*: 433 $(M+H)^+$. Anal. calcd. (found) for $C_{23}H_{24}N_6O_3$: C 63.88 (63.63), H 5.59 (5.53), N 19.43 (19.20).

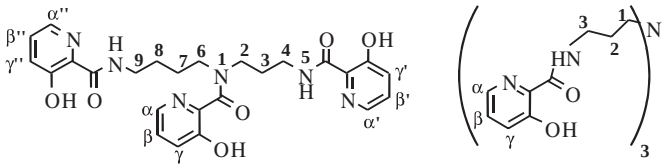

H_3PICSPERM H_3PICTRPN

N^1,N^5,N^{10}-*Tris(3-hydroxypicolinyl)spermidine (H_3PICSPERM)*

To a mixture of 3-hydroxypicolinic acid (2.657 g, 19.1 mmol) in THF (275 mL), CDI (3.103 g, 19.1 mmol) was added and the solution refluxed for 3 h. Spermidine (0.87 g, 5.97 mmol) was added to the mixture, which was refluxed for an additional 15 h. After cooling the reaction mixture to 20°C, the solution was filtered and the filtrate was concentrated in vacuo to a yellowish oil. The slow-moving contaminants (R_f 0.05) in the mixture were removed by column chromatography on silica gel (eluant: 5% MeOH in EtOAc). Combining the appropriate fractions and evaporating the solvent yielded a yellow oil. This material was then triturated with MeOH (ca. 50 mL) to afford H_3PICSPERM (1.31 g, 42%) as a white solid, mp 99–100°C. TLC (eluant: 5% MeOH in EtOAc) R_f = 0.48. IR: 3600–2600 (br, ν_{OH}), 3360 (m, ν_{NH}), 1650 (s, $\nu_{C=O}$), 1610 (m, $\nu_{C=C}$), 1535 (s, amide II), 1445 (m, $\nu_{C=C}$), 1610, 1390, 1190, 990, 810, 795. ^{1}H NMR (δ at 400 MHz in $CDCl_3$): 1.62–2.13 (series of overlapping m, 6H^{3,7,8}), 3.43–3.60 (m, 5H$^{4,6',9}$), 3.64, 4.04, 4.12 (three t each, 3H$^{2,6''}$, J = 6 Hz), 7.20–7.37 (m, 6H$^{\beta,\beta',\beta'',\gamma,\gamma,\gamma''}$), 7.98–8.24 (m, 3H$^{\alpha,\alpha',\alpha''}$), 8.33, 8.56 (two br s, 2H, C(O)N*H*, $W_{1/2}$ = 14 Hz), 12.2 (br s, 2H, O*H*), 12.3 (br s, 1H, O*H*). ^{13}C NMR (δ at 50 MHz in $CDCl_3$): 169.4, 169.1, 168.9, 158.8, 158.7, 157.8, 139.4, 138.8, 134.3, 131.4, 128.6,

© 1998 NRC Canada

127.4, 126.1, 102.9, 49.7, 47.8, 38.8, 36.3, 28.8, 27.6, 26.7, 24.6. MS (FAB), *m/z*: 509 $(M+H)^+$. Anal. calcd. (found) for $C_{25}H_{28}N_6O_6$: C 59.05 (59.06), H 5.55 (5.63), N 16.53 (16.60).

Tris{[(3-hydroxypicolinyl)carbonyl]-2-aminopropyl}amine (H_3PICTRPN)

To a mixture of 3-hydroxypicolinic acid (1.145 g, 8.23 mmol) in THF (120 mL) was added CDI (1.335 g, 8.23 mmol) in one portion. The mixture was refluxed for 2 h whereupon TRPN (0.5 g, 2.66 mmol) was added and the resultant mixture was refluxed for a further 19 h. After cooling the reddish-brown reaction mixture to 20°C, the solvent was removed under reduced pressure and the viscous dark-brown liquid was redissolved in a minimum amount of hot MeOH (ca.40 mL) and triturated with Et_2O to remove any unreacted starting acid (0.45 g, 39%) that precipitated. The filtrate was concentrated under reduced pressure and the brownish oil thus obtained was column chromatographed twice on lipophilic Sephadex LH-20™ (3 × 120 cm column; eluant: MeOH) and on silica gel (eluant: 10% MeOH in EtOAc, R_f = 0.13) to afford H_3PICTRPN (0.13 g, 9%) as a glassy (sticky) brown solid. IR: 3600–2600 (br, ν_{OH}), 3350 (m, ν_{NH}), 1655 (s, $\nu_{C=O}$), 1595 (m, $\nu_{C=C}$), 1540 (s, amide II), 1445 (m, $\nu_{C=C}$), 1350, 1289, 1248, 1198, 1150, 807, 695. ^{1}H NMR: 1.75 (t, 6H^1, J = 6 Hz), 2.35–2.70 (partially obscured m, 6H^2), 3.35 (dt, 6H^3, J = 8, 7 Hz), 7.38 (d, 3H$^\gamma$, J = 8 Hz), 7.48 (dd, 3H$^\beta$, J = 8, 3 Hz), 8.10 (d, 3H$^\alpha$, J = 3 Hz), 9.22 (br s, 3H, C(O)N*H*, $W_{1/2}$ = 20 Hz), 12.62 (br s, 3H, O*H*). MS (FAB), *m/z*: 552 $(M+H)^+$. Anal. calcd. (found) for $C_{27}H_{33}N_7O_6 \cdot 0.25H_2O$: C 58.32 (58.43), H 6.07 (5.90), N 17.63 (17.55).

Potentiometric equilibrium measurements

All potentiometric measurements on H_3NICTREN and H_3NICTAME were made with an automatic titrator system consisting of a Fisher model 950 digital pH meter equipped with Orion–Ross glass and calomel reference electrodes, a Metrohm Dosimat model 665 autoburet, and water-jacketed titration vessels maintained at 25.0 ± 0.1°C with a Julabo UC circulating bath (25). Both autoburet and pH meter were interfaced to an IBM-compatible PC so that the titrations were automated. During the titrations, the solutions were kept under an argon atmosphere that was first passed through 2 M NaOH solution.

The electrodes were calibrated before each titration, and often afterwards, by titrating a known amount of aqueous HCl with a known concentration of NaOH. A plot of mV (calculated) vs. pH gave a working slope and intercept so that the pH could be read directly as $-\log[H^+]$. The value of pK_w used was 13.76.

All solutions were prepared at an ionic strength of 0.16 M NaCl. Carbonate-free NaOH (~0.16 M) was prepared with deionized, distilled water that was boiled and purged with argon while cooling to ensure removal of CO_2. This solution was standardized potentiometrically with potassium hydrogen phthalate. Standard HCl solutions were prepared similarly and were standardized with the NaOH prepared above. Stock ligand solutions (~ 0.5 mM) were prepared using deionized, distilled water and were used within 3–4 days. The compounds were titrated in the pH range 2–11.5; a minimum of five titrations was performed for each compound.

Potentiometric calculations

The deprotonation constants of the ligands were calculated using the program BEST (26). The program sets up simultaneous mass-balance equations for all the components present at each addition of base and calculates the pH at each data point according to the current set of stability constants and total concentrations of each component. The stability constants are iteratively varied to minimize the sum of the square of the difference between observed (pH_{obs}) and calculated (pH_{calc}) pH values. An indication of the fit is given by σ_{fit}, where σ_{fit} is

$$\sigma_{fit} = \Sigma\,(pH_{calc} - pH_{obs})^2/(N-1)$$

and N is the total number of data points (typically ~100). In all the titrations considered, $\sigma_{fit} < 0.01$. The final calculated deprotonation constants are the average of the deprotonation constants determined from individual titrations; an estimate of the error in these values is given by one standard deviation (1σ) for these results.

X-ray crystallographic analysis of H_3PICTAME

Crystallographic data for H_3PICTAME appear in Table 1. The final unit-cell parameters were obtained by least squares on the setting angles for 25 reflections with 2θ = 55.1°–82.4°. The intensities of three standard reflections, measured every 200 reflections throughout the data collection, showed only small random fluctuations. The data were processed,[2] corrected for Lorentz and polarization effects, and for absorption (empirical, based on azimuthal scans).

The structure was solved by direct methods. Non-hydrogen atoms were refined with anisotropic thermal parameters, the O-bound hydrogen atoms were refined with isotropic thermal parameters, and the remaining hydrogen atoms were fixed in calculated positions with N—H = 0.91 Å, C—H = 0.98 Å, and $B_H = 1.2\,B_{\text{bonded atom}}$. A correction for secondary extinction was applied (Zachariasen type, isotropic), the final value of the extinction coefficient being $5.7(3) \times 10^{-7}$. Neutral atom scattering factors for all atoms and anomalous dispersion corrections for the non-hydrogen atoms were taken from the *International tables for X-ray crystallography* (27). Final atomic coordinates and equivalent isotropic thermal parameters, bond lengths, bond angles, and hydrogen bond geometry appear in Tables 2–5, respectively. Hydrogen atom parameters, anisotropic thermal parameters, torsion angles, intermolecular contacts, and least-squares planes are available as supplementary material.[3]

Results and discussion

Synthetic procedures

HOSu/DCC method (Method A) (28)

Depending on the nature of the starting materials, *N,N′*-dicyclohexylcarbodiimide (DCC) by itself can act in situ as a

[2] *teXan*: Crystal Structure Analysis Package. Molecular Structure Corp., The Woodlands, Texas. 1985 and 1992.

[3] Supplementary material mentioned in the text can be purchased from: The Depository of Unpublished Data, Document Delivery, CISTI, National Research Council Canada, Ottawa, Canada K1A 0S2. Tables of hydrogen atom coordinates and bond distances have also been deposited with the Cambridge Crystallographic Data Centre, and can be obtained on request from The Director, Cambridge Crystallographic Centre, 12 Union Road, Cambridge, CB1 1EZ. U.K.

© 1998 NRC Canada

Table 1. Crystallographic data for H_3PICTAME.[a]

Formula	$C_{23}H_{24}N_6O_6$
fw	480.48
Crystal system	Monoclinic
Space group	$P2_1/a$
a, Å	10.257(2)
b, Å	15.572(3)
c, Å	15.208(2)
β,°	96.124(15)
V, Å^3	2415.2(8)
Z	4
ρ_{calc}, g/cm^3	1.321
F(000)	1008
Radiation (λ, Å)	Cu (1.54178)
μ, cm^{-1}	8.21
Crystal size, mm	0.12 × 0.25 × 0.30
Transmission factors	0.97–1.00
Scan type	ω–2θ
Scan range, deg in ω	0.89 + 0.20 tan θ
Scan speed, deg/min	32 (up to 8 rescans)
Data collected	$+h$, $+k$, $\pm l$
$2\theta_{max}$, deg	155
Crystal decay, %	Negligible
Total reflections	5368
Total unique reflections	5099
R_{merge}	0.022
Reflections with $I \geq 3\sigma(I)$	2506
No. of variables	329
R	0.041
R_w	0.038
gof	2.27
Max Δ/σ (final cycle)	0.0003
Residual density e/Å^3	–0.12 to 0.25

[a] Temperature 294 K, Rigaku AFC6S diffractometer, graphite monochromator, takeoff angle 6.0°, aperture 6.0 × 6.0 mm at a distance of 285 mm from the crystal, stationary background counts at each end of the scan (scan/background time ratio 2:1), $\sigma^2(F^2) = [S^2(C + 4B)]/Lp^2$ (S = scan rate, C = scan count, B = normalized background count), function minimized $\Sigma w(|F_o| - |F_c|)^2$ where $w = 4F_o/\sigma^2(F_o^2)$, $R = \Sigma ||F_o| - |F_c||/\Sigma |F_o|$, $Rw = (\Sigma w(|F_o| - |F_c|)^2/\Sigma w|F_o|^2)^{1/2}$, and gof $= [\Sigma w(|F_o| - |F_c|)^2/(m - n)]^{1/2}$. Values given for R, R_w, and gof are based on those reflections with $I \geq 3\sigma(I)$.

Table 2. Final atomic coordinates (fractional) and B_{eq} (Å^2) for H_3PICTAME.[a]

Atom	x	y	z	B_{eq}
O(1)	0.5379(2)	0.19534(12)	0.22904(12)	5.56(5)
O(2)	0.5327(3)	0.0389(2)	0.1759(2)	7.88(8)
O(3)	0.3223(2)	0.57156(12)	0.45428(12)	5.52(5)
O(4)	0.1540(2)	0.69186(15)	0.46730(15)	6.83(7)
O(5)	0.4835(2)	0.51490(15)	0.14869(13)	6.53(6)
O(6)	0.6443(4)	0.5781(2)	0.0469(2)	9.72(9)
N(1)	0.4708(2)	0.22750(13)	0.36175(14)	4.62(6)
N(2)	0.3842(3)	0.0661(2)	0.3798(2)	6.38(8)
N(3)	0.3942(2)	0.54131(13)	0.32155(14)	4.60(6)
N(4)	0.2565(3)	0.67422(15)	0.24658(15)	5.64(7)
N(5)	0.4902(2)	0.37287(15)	0.18000(14)	5.10(6)
N(6)	0.6955(3)	0.3500(2)	0.0871(2)	8.09(10)
C(1)	0.4177(3)	0.3826(2)	0.3313(2)	3.88(6)
C(2)	0.2945(3)	0.3734(2)	0.3794(2)	5.10(7)
C(3)	0.5197(3)	0.3153(2)	0.3664(2)	4.18(6)
C(4)	0.4863(3)	0.1737(2)	0.2961(2)	4.52(7)
C(5)	0.4439(3)	0.0838(2)	0.3080(2)	4.87(8)
C(6)	0.4710(3)	0.0208(2)	0.2472(2)	5.76(9)
C(7)	0.4358(4)	–0.0632(2)	0.2641(3)	7.41(11)
C(8)	0.3773(4)	–0.0809(2)	0.3373(3)	8.10(12)
C(9)	0.3524(4)	–0.0152(2)	0.3938(3)	8.06(12)
C(10)	0.4804(3)	0.4707(2)	0.3516(2)	4.30(6)
C(11)	0.3232(3)	0.5867(2)	0.3741(2)	4.49(7)
C(12)	0.2444(3)	0.6585(2)	0.3317(2)	4.49(7)
C(13)	0.1655(3)	0.7071(2)	0.3813(2)	5.04(8)
C(14)	0.0950(3)	0.7739(2)	0.3397(2)	6.52(10)
C(15)	0.1050(4)	0.7895(2)	0.2529(3)	7.03(10)
C(16)	0.1874(4)	0.7392(2)	0.2085(2)	6.81(10)
C(17)	0.3797(3)	0.3717(2)	0.2318(2)	4.63(7)
C(18)	0.5335(3)	0.4421(2)	0.1416(2)	5.60(9)
C(19)	0.6459(4)	0.4294(3)	0.0898(2)	6.42(10)
C(20)	0.6950(4)	0.4972(3)	0.0444(2)	8.12(13)
C(21)	0.7968(5)	0.4827(4)	–0.0053(3)	10.5(2)
C(22)	0.8473(5)	0.4034(5)	–0.0085(3)	11.9(2)
C(23)	0.7953(5)	0.3367(4)	0.0397(3)	10.36(15)

[a] $B_{eq} = (8/3)\pi^2\Sigma\Sigma(U_{ij}\, a_i^* a_j^* (\boldsymbol{a_i}\cdot\boldsymbol{a_j}))$.

dehydrative coupling reagent, leading to the formation of the amide bond. In the present work, however, it was important that an activated ester be isolated, as the reaction between the amines (e.g., TREN or TAME) and the pyridine carboxylic acids used was fast enough to result in the quantitative precipitation of the corresponding ammonium salt. The main drawback in using this method was the practical difficulty of purifying the activated ester from the dicyclohexylurea that formed as a side product. This problem was circumvented by adopting the more efficient CDI method.

CDI method (Method B) (31)

The advantage of method B is that it obviates the intermediacy of DCC (and hence the DCU side product). The side products formed in method B (imidazole and CO_2) are easier to remove. This method, although it involves two steps, allows for a single-step synthesis of the amide unless practical reasons call for the isolation of the intermediate imidazolide. Due to the lack of sufficient solubility in THF (bp 67°C), the *N*-acylimidazolide of 2-hydroxynicotinic acid was isolated, and the next step performed in a more suitable, i.e., more polar, solvent, dioxane. Conveniently enough, these crystalline intermediates, although highly reactive in solution towards nucleophiles such as amine nitrogen, are stable in air at room temperature for at least a week.

X-ray crystal structure of H_3PICTAME

In X-ray crystallography, the main criterion for identification of an H-bond is the distance between the hydrogen and the acceptor atom (that is, the distance H···A in B—H···A where A and B are frequently nitrogen or oxygen atoms). However, in using X-ray diffraction data to extract bond distances involving a hydrogen atom, one must be aware of the fact that such bond lengths are systematically shortened (relative to the "true" internuclear separation) since these distances are, strictly speaking, a measure of the distance between the

© 1998 NRC Canada

Table 3. Bond lengths (Å) in H_3PICTAME with estimated standard deviations in parentheses.

Bond	Length	Bond	Length
O(1)—C(4)	1.245(3)	O(2)—C(6)	1.343(4)
O(3)—C(11)	1.243(3)	O(4)—C(13)	1.347(3)
O(5)—C(18)	1.254(3)	O(6)—C(20)	1.365(5)
N(1)—C(3)	1.456(3)	N(1)—C(4)	1.326(3)
N(2)—C(5)	1.336(3)	N(2)—C(9)	1.331(4)
N(3)—C(10)	1.454(3)	N(3)—C(11)	1.339(3)
N(4)—C(12)	1.336(3)	N(4)—C(16)	1.332(4)
N(5)—C(17)	1.447(3)	N(5)—C(18)	1.325(4)
N(6)—C(19)	1.339(4)	N(6)—C(23)	1.330(5)
C(1)—C(2)	1.532(3)	C(1)—C(3)	1.535(3)
C(1)—C(10)	1.533(3)	C(1)—C(17)	1.531(3)
C(4)—C(5)	1.482(4)	C(5)—C(6)	1.396(4)
C(6)—C(7)	1.388(4)	C(7)—C(8)	1.349(5)
C(8)—C(9)	1.377(5)	C(11)—C(12)	1.486(4)
C(12)—C(13)	1.388(4)	C(13)—C(14)	1.381(4)
C(14)—C(15)	1.357(4)	C(15)—C(16)	1.381(4)
C(18)—C(19)	1.478(4)	C(19)—C(20)	1.385(5)
C(20)—C(21)	1.370(6)	C(21)—C(22)	1.342(7)
C(22)—C(23)	1.409(7)		

centroids of electron density of the two atoms concerned. In the case of hydrogen, this does not coincide with its nuclear position, but is displaced significantly in the direction of the covalent bond (i.e., B—H). For example, O—H and N—H covalent bond lengths, which are observed to be 0.97 and 1.03 Å by neutron diffraction, can be determined to be as short as 0.6 and 0.7 Å, respectively, by X-ray diffraction (33). Hence, in order to identify an H-bond based on X-ray diffraction data, the H···A bond length should be at least 0.09 Å (34) shorter than the sum of the van der Waals radii (35) of H and A (36). Angular orientations are also of importance, viz. the extent of deviation from linearity of the A—H···B bond. Statistical surveys of H-bond geometry in small molecules have revealed a mean value close to 180° (37), although exceptions to this finding are plentiful and are often due to the geometric constraints imposed elsewhere in the structure.

In the solid state structure, an H-bond will form whenever it can because its formation will raise the stability of a molecular crystal by a few kilocalories per mole (38). The H_3PICTAME solid state structure nicely demonstrates this observation, with eight *intra*- and one *inter*molecular H-bonds per molecule. Following the nomenclature of H-bonding geometry, two types of such interactions are present in H_3PICTAME: two-center (chelate) and three-center (bifurcated) H-bonds (Fig. 2).

The atom labelling and numbering scheme used is shown in the ORTEP diagram of the X-ray crystal structure of H_3PICTAME (Fig. 3*a*). In each arm of the molecule, the arylamide moiety is held strictly planar (Fig. 3*c*) due to the extended π network of the aromatic amide linkage. The H-bond distances and some of the relevant bond angles are listed in Table 5, a perusal of which clearly indicates that all the H-bonds identified are well within the H···A distance criterion (H···O = 2.5 Å; H···N = 2.6 Å) and, as expected, the three-center H-bonds (H(5) H-bonded to N(3), N(4), and O(5) and H(6) H-bonded to N(5), N(6), and O(1), respectively) display a greater deviation from linearity.

Table 4. Bond angles (deg) in H_3PICTAME with estimated standard deviations in parentheses.

Bonds	Angle (deg)	Bonds	Angle (deg)
C(3)-N(1)-C(4)	124.2(2)	C(5)-N(2)-C(9)	117.9(3)
C(10)-N(3)-C(11)	124.2(2)	C(12)-N(4)-C(16)	117.4(3)
C(17)-N(5)-C(18)	124.7(3)	C(19)-N(6)-C(23)	118.5(4)
C(2)-C(1)-C(3)	109.7(2)	C(2)-C(1)-C(10)	109.7(2)
C(2)-C(1)-C(17)	109.0(2)	C(3)-C(1)-C(10)	106.5(2)
C(3)-C(1)-C(17)	111.1(2)	C(10)-C(1)-C(17)	110.8(2)
N(1)-C(3)-C(1)	113.9(2)	O(1)-C(4)-N(1)	122.7(3)
O(1)-C(4)-C(5)	120.8(3)	N(1)-C(4)-C(5)	116.4(3)
N(2)-C(5)-C(4)	117.4(3)	N(2)-C(5)-C(6)	122.5(3)
C(4)-C(5)-C(6)	120.1(3)	O(2)-C(6)-C(5)	122.1(3)
O(2)-C(6)-C(7)	120.1(3)	C(5)-C(6)-C(7)	117.8(3)
C(6)-C(7)-C(8)	119.5(3)	C(7)-C(8)-C(9)	119.5(3)
N(2)-C(9)-C(8)	122.8(3)	N(3)-C(10)-C(1)	112.7(2)
O(3)-C(11)-N(3)	123.2(3)	O(3)-C(11)-C(12)	120.5(3)
N(3)—C(11)-C(12)	116.3(3)	N(4)-C(12)-C(11)	117.1(3)
N(4)-C(12)-C(13)	123.1(3)	C(11)-C(12)-C(13)	119.7(3)
O(4)-C(13)-C(12)	123.2(3)	O(4)-C(13)-C(14)	118.8(3)
C(12)-C(13)-C(14)	117.9(3)	C(13)-C(14)-C(15)	119.4(3)
C(14)-C(15)-C(16)	119.2(3)	N(4)-C(16)-C(15)	122.9(3)
N(5)-C(17)-C(1)	113.9(2)	O(5)-C(18)-N(5)	122.6(3)
O(5)-C(18)-C(19)	121.1(3)	N(5)-C(18)-C(19)	116.4(3)
N(6)-C(19)-C(18)	117.4(3)	N(6)-C(19)-C(20)	121.9(4)
C(18)-C(19)-C(20)	120.7(4)	O(6)-C(20)-C(19)	121.9(4)
O(6)-C(20)-C(21)	118.8(5)	C(19)-C(20)-C(21)	119.3(5)
C(20)-C(21)-C(22)	119.4(6)	C(21)-C(22)-C(23)	119.3(5)
N(6)-C(23)-C(22)	121.5(5)		

Table 5. Hydrogen bonds (Å) and C—H···O interaction geometries (deg) in H_3PICTAME with estimated standard deviations in parentheses.

Interaction	D—H	H···A	D···A	D—H···A
O(2)—H(1)···O(1)[b]	0.96(3)	1.68(4)	2.565(3)	152(3)
O(4)—H(2)O(3)[b]	1.01(4)	1.65(4)	2.569(3)	148(3)
O(6)—H(3)O(5)[b]	1.29(5)	1.28(5)	2.575(3)	178(4)
N(1)—H(4)O(1)[a,b]	0.91	2.18	3.069(3)	164
N(1)—H(4)···N(2)[b]	0.91	2.29	2.689(3)	106
N(3)—H(5)···O(5)[c]	0.91	2.18	2.904(3)	136
N(3)—H(5)···N(4)[c]	0.91	2.29	2.690(3)	107
N(5)—H(6)···O(1)[c]	0.91	2.15	2.891(3)	138
N(5)—H(6)···N(6)[c]	0.91	2.27	2.682(3)	107
C(3)—H(11)···O(1)	0.98	2.51	2.824(3)	99
C(10)—H(16)···O(3)	0.98	2.49	2.842(3)	101
C(17)—H(20)···O(5)	0.98	2.51	2.827(3)	98

[a] Symmetry operation: ½ + *x*, –1/2 + *y*, 1 – *z*.
[b] Two centred H-bond.
[c] Three centred H-bond.

Fig. 2. The two types of H-bond present in the H_3PICTAME X-ray crystal structure.

two-center (chelate) three-center (bifurcated)

© 1998 NRC Canada

Fig. 3. (*a*) ORTEP representation of the X-ray crystal structure of H_3PICTAME; (*b*) torsion angles between amide nitrogens and apical C(2); (*c*) wire frame diagram showing only the three arylamide moieties with arrows representing the dihedral angles between the least-squares planes. In the wire framework representation, the arrangement and orientation of atoms are identical to that in (*a*). All values shown are based on the X-ray diffraction data; the planes include refined hydrogen atoms as well as all other non-hydrogen atoms of the arylamide moiety, but the backbone carbons are omitted for clarity.

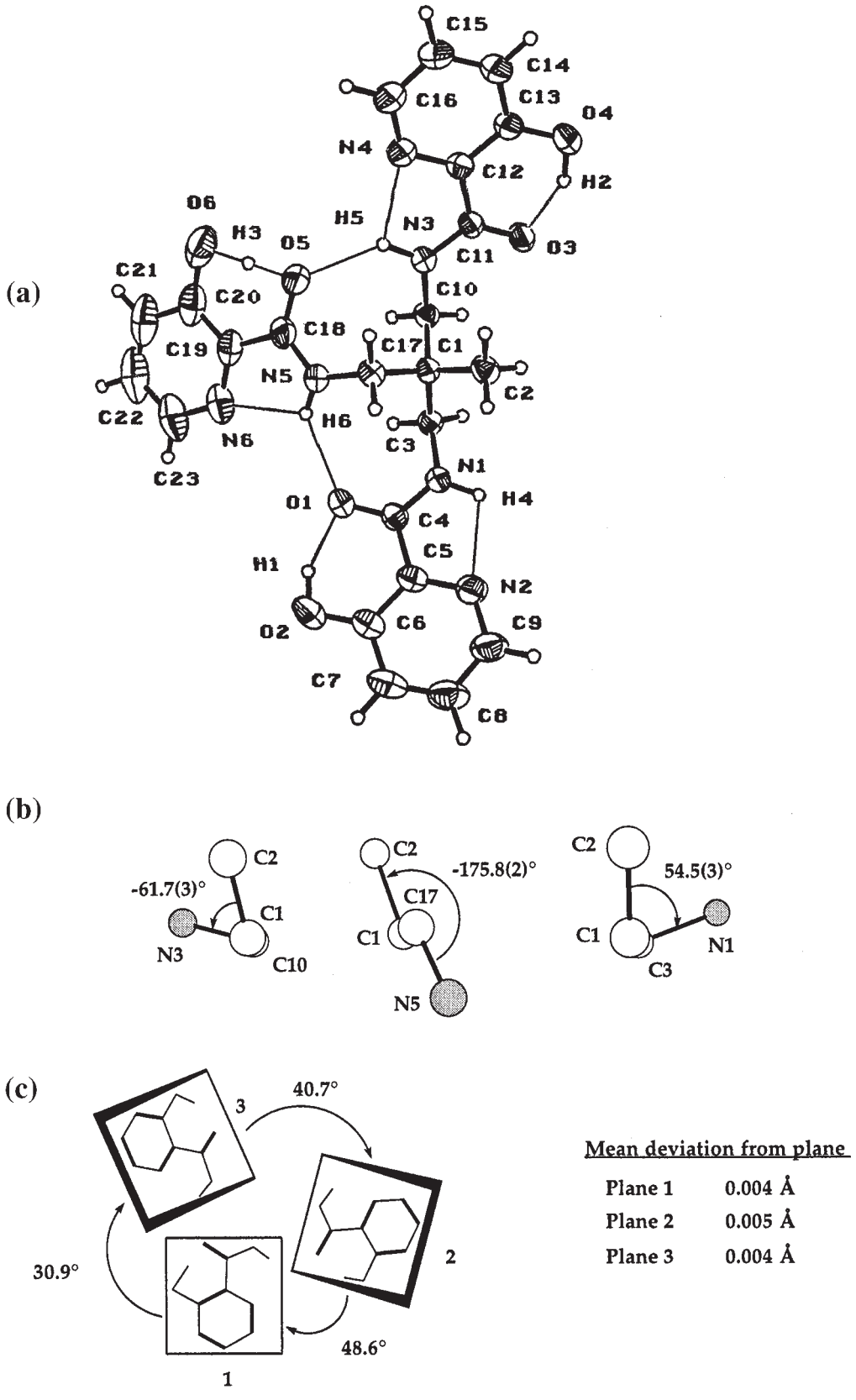

© 1998 NRC Canada

Table 6. pK_a values[a] of H_3NICTAME, H_3NICTREN, and related ligands (0.16 M NaCl, 25°C).

pK_a	H_3NICTAME	H_3NICTREN	H_2nic[e]	H_2pic[e]	H_6TRNS[f]	H_6TAMS[f]
1	10.68 (2)[b]	11.2 (2)[b]	11.99[b]	11.06[b]	11.2 (1)[c]	11.19 (4)[c]
2	10.58 (4)[b]	10.7 (2)[b]	4.98[d]	5.03[d]	10.6 (1)[c]	9.81 (4)[c]
3	9.71 (3)[b]	10.0 (1)[b]	< 0	< 0	9.59 (3)[c]	8.91 (2)[b]
4		6.25 (4)[c]			8.07 (3)[b]	7.95 (3)[b]
5					7.29 (3)[b]	6.56 (2)[b]
6					6.17 (3)[b]	2.92 (2)[c]

[a] The numbers in parentheses refer to 1σ.
[b] Phenol deprotonation.
[c] Ammonium deprotonation.
[d] Pyridinium deprotonation.
[e] Reference 44.
[f] Reference 45.

The molecule in the solid state lacks a C_3 axis of symmetry; the torsion angles about the apical C(2), the intervening methylene carbon, and the amidic nitrogen succinctly depict this fact (Fig. 3*b*). The apical carbon (C2) is in a staggered conformation with respect to N5; whereas the analogous torsion angles in the other two arms are roughly 60°, corresponding to a *gauche* conformation with one in a positive (clockwise) and the other in a negative (counterclockwise) sense. Since nearly all H-bond donors and acceptors are "buried" intramolecularly, preorganizing the molecule for chelation, only one *inter*molecular H-bond forms in each molecule as shown in Fig. 3. It is reasonable to conjecture, in the absence of an X-ray structure, that the structural isomer, H_3NICTAME, should show a greater propensity toward aggregation (as opposed to intramolecular H-bond formation) based merely on geometric considerations.

A noteworthy detail in the solid state H-bonding network present in H_3PICTAME is the variation in the H-bond distances (and angles) of the two-center O—H···O (Table 5). Thus, whereas O(6)—H(3)···O(5) constitutes a symmetrical H-bonding site, the other two analogous H-bonds are asymmetric and, accordingly, the corresponding H···O distances are significantly longer. The most interesting aspect about the geometry of the symmetrical site is that, as a result of its perfect linearity (within experimental error), an unseemly angle of 87(2)° is imposed upon the C(20)-O(6)-H(3) bond — in contrast to 105(2)° for the other two analogous angles (Fig. 3). In spite of this anomalous bond angle, however, the symmetrical disposition of the H3, with respect to the two adjacent oxygens (O6 and O5), is corroborated by the significant lengthening of the respective C(18)—O(5) bond to 1.254 Å, (C(4)—O(1) = 1.245 Å, C(11)—O(3) = 1.243 Å) and a decrease in the C(18)—N(5) bond to 1.324 Å (C(4)—N(1) = 1.327 Å, C(11)—N(3) = 1.333 Å). This observation would be expected if the amide resonance structure **ii** (Fig. 4) were more predominant; the more the type **ii** resonance contributes to the overall resonance hybrid structure, the better the H-bonding acceptor ability of that amidic oxygen. The structural data summarized above clearly reflect this fact: the concomitant increase in C═O and decrease in C—N bond lengths is paralleled by a shortening of the H-bond distance. Thus, not too surprisingly, the longest C═O bond length, C(18)—O(5), corresponds to the shortest H-bond (1.28(5) Å, O(5)···H(3)).

Fig. 4. The amide resonance and H-bonding (see text).

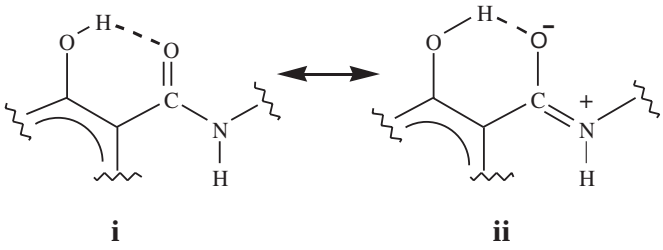

General characterization

The preorganization of a multidentate ligand is governed by two factors, each capable of diminishing the entropic penalty attendant upon metal ion complexation: (*i*) the conformation of each metal binding moiety in the molecule; (*ii*) the conformation of the "arms" (containing the binding moiety) with respect to each other. The first factor determines, for instance, the ease with which a chelate ring will form, while the second factor contributes to the complete encapsulation of the metal ion. Based on the solid state structure of H_3PICTAME, it is evident that although the structure is preorganized in the first sense, the three arms are not favorably disposed to define the cavity necessary for the coordination of a group 13 metal ion in a hexacoordinate octahedral polyhedron. In fact, in solution, as evinced by ^{1}H NMR spectroscopy, one set of signals is observed for the tripodal arylamides prepared, indicating that each arm rotates freely. The exceptions to this finding are, of course, H_3PICSPERM and H_3NICSPERM, which are asymmetric by virtue of their spermidine backbones. Therefore, for the purposes of solution coordination chemistry, the latter facet of preorganization is of no relevance in the case of the arylamides.

In considering the local conformation of each individual metal binding moiety, it is possible to predict which conformer is preferred (Fig. 5) by comparing the strengths of the hydrogen bonds available to the two forms. The strength of an H-bond (A—H···B) is known to depend on the relative acidity of A and the basicity of B; the strength of the H-bond should increase as the acid becomes more acidic and the base more basic (39). Since the phenolic hydrogens (pK_a ca. 10) (40) are more acidic than the amide (pK_a ca. 15) (41), the strongest H-bonds ought to occur in conformations **1a** and **2a** (Fig. 5). The ^{1}H NMR and IR spectroscopic results, although not unequivocally conclusive, appear to be in accord with the qualitative prediction that conformers **1a** and **2a** are prevalent in solution.

The ^{1}H NMR chemical shifts of the phenolic hydrogens of the arylamides show extensive downfield shifts (ca. 12 ppm in DMSO-d_6) indicative of H-bonding. The same observation was found to hold true in the less polar solvent $CDCl_3$, in the case of the picolinic amides; the nicotinic derivatives were not soluble enough in chloroform to allow for ^{1}H NMR spectroscopy (vide infra). On the other hand, the IR spectrum of H_3PICTAME in CCl_4 shows a broad band ranging from ca. 3200 to 2700 cm^{-1} characteristic of an intramolecular chelated phenolic OH stretching frequency (42). In the solid state IR spectrum of H_3PICTAME (KBr pellet), however, the phenolic stretching frequency ranges over a greater span from ca. 3600

© 1998 NRC Canada

Fig. 5. The two conformers of 3-hydroxypicolinyl (**1a**, **1b**) and 2-hydroxynicotinyl amide derivatives (**2a**, **2b**). (The dipole moments are depicted merely in a qualitative sense; they are not drawn to scale).

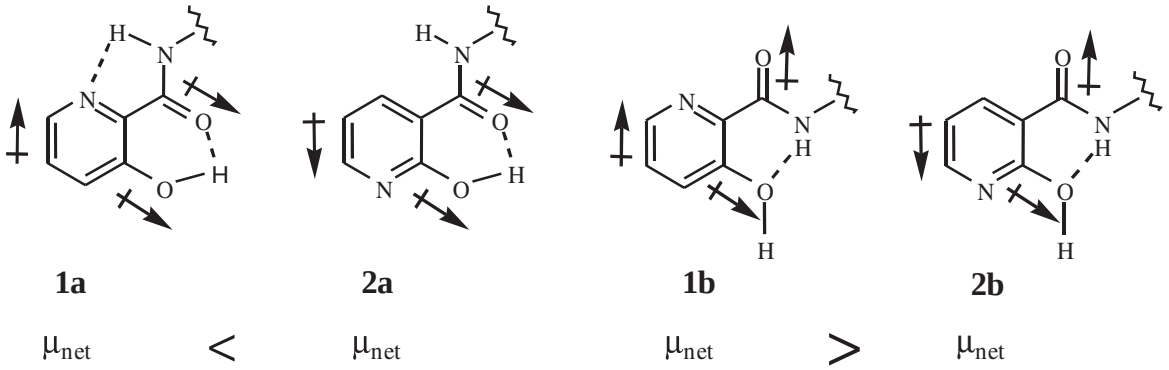

to 2700 cm^{-1}, in agreement with the solid state structure provided by X-ray crystallography wherein both intra- and intermolecular H-bonds are found to exist (the intermolecularly H-bonded OH stretching frequencies are found in the 3550–3450 cm^{-1} range) (42).

It is worthwhile to reflect on the significant solubility difference between the 2-hydroxynicotinyl and the 3-hydroxypicolinyl amide derivatives. The water solubility (at neutral pH) of the 3-hydroxypicolinyl amide derivatives is typically on the order of tens of μM as opposed to the 2-hydroxynictonyl counterparts that are soluble to the extent of ca. 0.5 mM, which is in accord with the polarity differences expected based on a qualitative consideration of dipole moments. In calculating the dipole moments of the molecule (μ_{net}) it is convenient to employ the moments of groups of atoms (amide, pyridine, OH) as an approximation (43) as shown in Fig. 5, where the magnitude of the three group moments are taken to be the same. It is clear that *only* type **a** conformers (Fig. 5) corroborate the observed water solubility trend.

The fact that 2-hydroxynicotinic amides adopt the type **2a** conformation is unexpected from the point of view of the electroneutrality principle (ref. 35, pp. 172 and 273), which would favor a conformation with a smaller electric dipole moment, i.e., the **2b** conformer. The reason for this conformational preference lies in H-bonding (cf. Fig. 5): the H-bonding in **2a** is more fortified, as discussed previously. Thus, the O—H···O hydrogen bond should still be stronger than N—H···O in water, even though this effect is mitigated in the presence of such a polar solvent; the H-bond energy decreases in more polar environments, since the H-bond has a substantial electrostatic component. Based on the evidence discussed here, the 2-hydroxynicotinic and the 3-hydroxypicolinic arylamides display an intramolecular H-bonding network that is sustained in water. Therefore, it can be concluded that these arylamide ligands are significantly partially preorganized for metal ion chelation.

Ligand deprotonation constants

The deprotonation constants[4] were obtained on the basis of a three- or four-proton model for H_3NICTAME and H_3NICTREN, respectively, in the pH 2.2–11.5 region at 25°C and in 0.16 M NaCl. The deprotonation constants thus obtained appear in Table 6, and correspond to the successive deprotonation equilibria of the three phenols (pK_{a1}, pK_{a2}, pK_{a3}) and, in the case of H_3NICTREN, the deprotonation of the protonated apical nitrogen. The pK_a values of the pyridine ring nitrogens are too low to be measured in the pH range examined, while those of the amides fall outside the upper pH limit of the measurements. The water solubility of H_3PICTAME and H_3PICTREN was too low for potentiometric measurements.

It is appropriate to compare the pK_a's of H_3NICTAME and H_3NICTREN with those of the parent acids and some related aminephenol ligands (Table 6). The phenolic pK_a's of H_3NICTAME, H_3NICTREN, H_2nic, and H_2pic are particularly high. This would be anticipated for H_3NICTAME on the basis of its crystal structure, where all three phenol groups are involved in hydrogen bonding with the adjacent amide carbonyl oxygen. A similar explanation would account for the phenolic pK_a's of H_3NICTREN, and the high pK_{a1} of H_2nic and H_2pic is consistent with the presence of a six-membered H-bond ring involving the phenolic group and the deprotonated carboxylate oxygen of these ligands. These arguments are reinforced with the observation that for the aminephenols H_6TRNS and H_6TAMS, the phenolic pK_a's are much lower as there is no possibility of hydrogen bonding for the protonated phenol. In fact, the deprotonated phenolate oxygen may H-bond with an adjacent ammonium group, which would tend to favour deprotonation of the phenol and a low pK_a.

Concluding remarks

A series of potentially polydentate arylamide ligands have been synthesized from the coupling of several tripodal amines with nicotinic and picolinic acids and their derivatives. Two synthetic procedures were utilized in this study but the HOSuNic method was not favoured due to the difficulty of separating the DCU side product from the activated ester. Hence, the CDI method was used in the synthesis of the compounds in this work.

The X-ray crystal structure of H_3PICTAME revealed extensive hydrogen bonding, with eight intra- and one

[4] The acid dissociation constant, K_a, is defined as:
$H_nL^{m+} \rightleftharpoons H_{n-1}L^{(m-1)+} + H^+$
$K_{an} = ([H_{n-1}L^{(m-1)+}]\,[H^+]) / [H_nL^{m+}]$
$pK_a = -\log K_a$

© 1998 NRC Canada

intermolecular H-bonds per molecule. In solution each arm of the tripodal arylamides rotates freely. Nevertheless, the NMR, IR, and solubility results indicate that the intramolecular H-bonding network of these arylamides is sustained in solution and, thus, these ligands are partially preorganized for the complexation of metal ions.

Acknowledgments

Acknowledgement is made to the Natural Sciences and Engineering Research Council of Canada (NSERC), to the U.S. National Institutes of Health (CA48964), and to the B.C. Health Research Foundation for operating funds as well as to the University of British Columbia for fellowships to H.R.H. (University Graduate Fellowship) and A.K.W.S. (Killam Trust).

References

1. R.D. Shannon. Acta Crystallogr. Sect. A: Cryst. Phys. Diffr. Theor. Gen. Crystallogr. **A32**, 751 (1976).
2. F.A. Cotton and G. Wilkinson. Advanced inorganic chemistry. 4th ed. Wiley, Toronto. 1980. p. 682.
3. H. Kido and K. Saito. J. Am. Chem. Soc. **110**, 3187 (1980).
4. Struct. Bonding. **58**, (1984).
5. K.N. Raymond. Coord. Chem. Rev. **105**, 135 (1990).
6. S.M. Moerlien, M.J. Welch, K.N. Raymond, and F.L. Weitl. J. Nucl. Med. **22**, 720 (1982).
7. M.A. Green and M.J. Welch. J. Nucl. Med. Biol. **16**, 435 (1989).
8. T.B. Karpishin, T.M. Dewey, and K.N. Raymond. J. Am. Chem. Soc. **115**, 1842 (1993).
9. L.D. Loomis and K.N. Raymond. Inorg. Chem. **30**, 906 (1991).
10. K. Spartalian, W.R. Oosterhuis, and J.B. Neilands. J. Chem. Phys. **62**, 3538 (1975).
11. W.R. Harris, C.J. Carrano, S.R. Cooper, S.R. Sofen, A. Avdeef, J.V. McArdle, and K.N. Raymond. J. Am. Chem. Soc. **101**, 6097 (1979).
12. K.N. Raymond and C.J. Carrano. Acc. Chem. Res. **12**, 183 (1979).
13. W.R. Harris and K.N. Raymond. J. Am. Chem. Soc. **101**, 6534 (1979).
14. V.L. Pecoraro, W.R. Harris, G.B. Wong, C.J. Carrano, and K.N. Raymond. J. Am. Chem. Soc. **105**, 4623 (1983).
15. M.E. Cass, M. Garrett, and K.N. Raymond. J. Am. Chem. Soc. **111**, 1677 (1989).
16. M.M. Finnegan, S.J. Rettig, and C. Orvig. J. Am. Chem. Soc. **108**, 5033 (1986).
17. M. Finnegan, T.G. Lutz, W.O. Nelson, A. Smith, and C. Orvig. Inorg. Chem. **26**, 2171 (1987).
18. T.G. Lutz, D.J. Clevette, S.J. Rettig, and C. Orvig. Inorg. Chem. **28**, 715 (1989).
19. T.G. Lutz, D.J. Clevette, H.R. Hoveyda, V. Karunaratne, A. Nordin, S. Sjöberg, M.Winter, and C. Orvig. Can. J. Chem. **72**, 1362 (1994).
20. D. Kahne and W.C. Still. J. Am. Chem. Soc. **110**, 7529 (1988).
21. E.B. Fleischer, A.E. Gebala, A. Levey, and P.A. Tasker. J. Org. Chem. **36**, 3042 (1971).
22. W.C. Still, M. Kahn, and A. Mitra. J. Org. Chem. **43**, 2923 (1978).
23. F.E. Hahn and M. Tamm. Angew. Chem. Int. Ed. Engl. **30**, 203 (1991).
24. T. Miyazawa, T. Shimanouchi, and S.-I. Mizuchima. J. Chem. Phys. **24**, 408 (1956).
25. P. Caravan, T. Hedlund, S. Liu, S. Sjoberg, and C. Orvig. J. Am. Chem. Soc. **117**, 11230 (1995).
26. A.E. Martell and R.J. Motekaitis. Determination and use of stability constants. VCH, New York. 1988. p. 4.
27. *(a)* International tables for X-ray crystallography. Vol. IV. Kynoch Press, Birmingham, U.K. (present distributor Kluwer Academic Publishers: Boston, Mass., U.S.A.). 1974. pp. 99–102; *(b)* International tables for crystallography. Vol. C. Kluwer Academic Publishers, Boston, Mass., U.S.A. 1992. pp. 200–206.
28. G.W. Anderson, J.,E. Zimmerman and F.M. Callahan. J. Am. Chem. Soc. **86**, 1839 (1964).
29. J.C. Sheehan and G.P. Hess. J. Am. Chem. Soc. **77**, 1067 (1955).
30. A. Williams and I.T. Ibrahim. Chem. Rev. **81**, 589 (1981).
31. R. Paul and G.W. Anderson. J. Am. Chem. Soc. **82**, 4596 (1960).
32. H.A. Staab and W. Rohr. *In* Newer methods of preparative organic chemistry. *Edited by* W. Foerst. Academic, New York. 1968. pp. 72–74.
33. G.A. Jeffrey and W. Saenger. Hydrogen bonding in biological structures. Springer, Berlin. 1991. p. 108.
34. M.R. Churchill. Inorg. Chem. **12**, 1213 (1973).
35. L. Pauling. The nature of the chemical bond. 3rd ed. Cornell University Press, Ithaca, N.Y. 1960. p. 449.
36. W.C. Hamilton and J.A. Ibers. Hydrogen bonding in solids. Benjamin, New York. 1968. p. 14.
37. E.N. Baker and R.E. Hubbard. Prog. Biophys. Mol. Biol. **44**, 98 (1984), and references cited therein.
38. J. Donohue. J. Phys. Chem. **56**, 502 (1952).
39. T.M. Garrett, M.E. Cass, and K.N. Raymond. J. Coord. Chem. **25**, 241 (1992).
40. H.O. House. Modern synthetic reactions. 2nd ed. Benjamin, Menlo Park, N.J. 1972. p. 494.
41. H. Sigel and R.B. Martin. Chem. Rev. **82**, 385 (1982).
42. L.J. Bellamy. Infrared spectra of complex molecules. Vol. 1. 3rd ed. Chapman and Hall, New York. 1980. p. 108.
43. O. Exner. Dipole moments in organic chemistry. Georg Thieme, Stuttgart. 1975. pp. 30–34.
44. A.K. W. Stephens and C. Orvig. Inorg. Chim. Acta, **273**, 47 (1998).
45. P. Caravan and C. Orvig. Inorg. Chem. **36**, 236 (1997).

© 1998 NRC Canada

Structure and dynamics of azapropazone derivatives studied by crystallography and nuclear magnetic resonance

Theresa Fauconnier, Alex D. Bain, Paul Hazendonk, R.A. Bell, and Colin J.L. Lock

Abstract: The X-ray crystal structure of a derivative of the nonsteroidal anti-inflammatory drug, azapropazone, has been determined using a data set obtained from a charge-coupled device (CCD) area detector. Azapropazone itself, 5-(dimethylamino)-9-methyl-2-propyl-1*H*-pyrazolo[1,2-*a*][1,2,4]benzotriazine-1,3(2*H*)-dione, has previously been shown to be nonplanar, probably due to steric interactions between the pyrazolidine ring and the exocyclic dimethylamino group. The derivative studied in this work, 3-dimethylamino-7-methyl-1,2,4-benzotriazine, does not have the pyrazolidine ring and is shown here to be strictly planar. There is also a significant difference in the kinetics of restricted rotation around the bond joining the dimethylamino group to the triazine ring, as measured by NMR. Both the enthalpy and entropy of activation are quite different. For the chemical exchange of the two methyl groups in azapropazone, $\Delta H^{\ddagger} = 36 \pm 0.5$ kJ mol^{-1}, and $\Delta S^{\ddagger} = -34 \pm 2$ J K^{-1}. For the derivative, $\Delta H^{\ddagger} = 48 \pm 0.4$ kJ mol^{-1}, and $\Delta S^{\ddagger} = -12 \pm 2$ J K^{-1}. This is rationalized by assuming the equilibrium state of the derivative is planar, and this defines the potential energy curve. The ground state of azapropazone is relatively destabilized, and somewhat disordered, by the steric interaction. Therefore, azapropazone has a small barrier to surmount, and the entropy of activation should be negative.

Key words: NMR, chemical exchange, entropy, barriers to rotation, crystal structure.

Résumé : Utilisant un ensemble de données obtenues à l'aide d'un dispositif à couplage de charge (DCC) comme détecteur de surface, on a déterminé la structure cristalline aux rayons X d'un dérivé d'un médicament anti-inflammatoire non stéroïdal. Il a été démontré antérieurement que l'azapropazone de base, 5-(diméthylamino)-9-méthyl-2-propyl-1*H*-pyrazolo[1,2-*a*][1,2,4]benzotriazine-1,3(2*H*)-dione, n'est pas planaire, probablement à cause d'interactions stériques entre le noyau pyrazolidine et le groupe diméthylamino exocyclique. Le dérivé examiné dans ce travail, la 3-diméthylamino-7-méthyl-1,2,4-benzotriazine, ne comporte pas de noyau pyrazolidine et on démontre qu'il est strictement planaire. Sur la base de mesures RMN, il existe aussi des différences importantes dans la cinétique de la rotation empêchée autour de la liaison reliant le groupe diméthylamino et le noyau triazine. Tant l'enthalpie que l'entropie d'activation sont très différentes. Pour l'échange chimique des deux groupes méthyles de l'azapropazone, $\Delta H^{\ddagger} = 36 \pm 0{,}5$ kJ mol^{-1} et $\Delta S^{\ddagger} = -34 \pm 2$ J K^{-1}. Pour le dérivé, $\Delta H^{\ddagger} = 48 \pm 0{,}4$ kJ mol^{-1} et $\Delta S^{\ddagger} = -12 \pm 2$ J K^{-1}. On rationalise ces résultats en suggérant, pour le dérivé, un état d'équilibre plan qui définit la courbe de l'énergie potentielle. L'état fondamental de l'azapropazone est relativement déstabilisé et assez désordonné à cause de l'interaction stérique. Il en découle que l'azapropazone comporte une faible barrière qu'il lui faut surmonter et il en découle que l'entropie d'activation devrait être négative.

Mots clés : RMN, échange chimique, entropie, barrières à la rotation, structure cristalline.

[Traduit par la rédaction]

Introduction

Azapropazone, or 5-(dimethylamino)-9-methyl-2-propyl-1*H*-pyrazolo[1,2-*a*][1,2,4]benzotriazine-1,3(2*H*)-dione (**1**), is one of a class of nonsteroidal anti-inflammatory drugs (1, 2) and is used to treat various forms of arthritis. The determination of the structure of a drug is invaluable for its characterization, but it can also be used to investigate the action of the drug at the molecular level. Rapid developments in structural biology and computational chemistry have helped determine what a molecule recognizes as a receptor in the body. For azapropazone, there has been some controversy in the literature over its structure (3): in particular, over the planarity of the ring and the positions of the hydrogens. Recent crystal structures (3) of azapropazone (Fig. 1) and one of its derivatives resolved these questions. For instance, the structure in the Merck Index (4) (called apazone there) is incorrect in that a proton is in the wrong position. The drug exists as a zwitterion, and the tricyclic part of the molecule is distinctly nonplanar.

A related observation was that at low temperature, the two methyls in the dimethylamino group in azapropazone were nonequivalent in the NMR spectrum below 220 K (3). There

Received August 26, 1998.

T. Fauconnier, A.D. Bain,[1] P. Hazendonk, R.A. Bell, and C.J.L. Lock.[2] Department of Chemistry, McMaster University, Hamilton, ON L8S 4M1, Canada.

[1] Author to whom correspondence may be addressed. E-mail: bain@mcmaster.ca

[2] Deceased.

© 1998 NRC Canada

Fig. 1. Structure of azapropazone (**1**) (*a*) and view of azapropazone along the C(5)—N(5) bond (*b*), showing how the dimethylamino group is not in the plane of the triazine ring. Structure taken from (3).

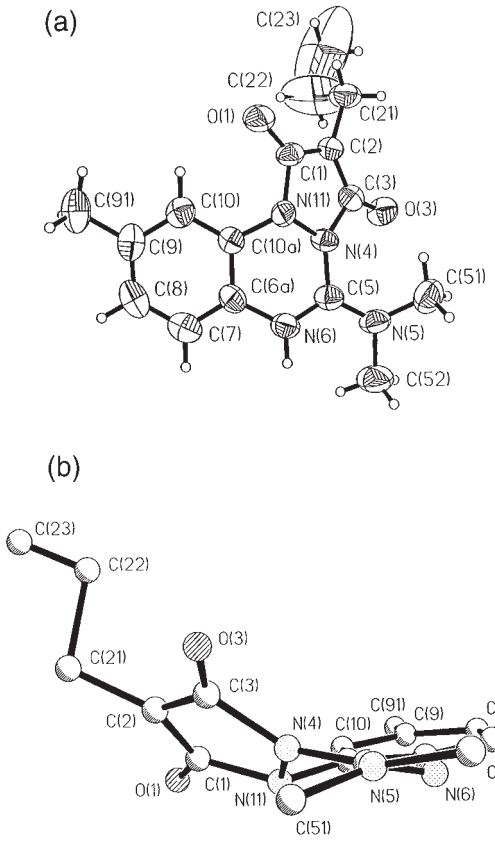

is sufficient steric crowding between the pyrazolidine ring and the dimethylamino group so that they cannot be coplanar. The rotation about the bond joining the dimethlyamino group to the triazine ring is restricted in some way.

The molecule in Fig. 2, 3-dimethylamino-7-methyl-1,2,4-benzotriazine (**2**), could help to understand these observations, since the pyrazolidine ring in azapropazone is absent and there are no steric interactions. This molecule is also an azapropazone derivative and has been identified as a photodegradation product of azapropazone, responsible for the photodermatitis that sometimes occurs to patients taking the drug (5). In this paper we present a crystal structure of **2**, derived from a data set obtained on a CCD detector. We also present a more detailed analysis of the dynamic NMR spectra of the dimethylamino group in the two molecules, using a powerful combination of NMR experiments (6). From these data, reliable values of both the enthalpy and entropy of activation for each molecule are derived.

Experimental

Azapropazone (**1**) was kindly provided as a yellow powder by Siegfried Pharma AG, Zotingen, Switzerland. To prepare 3-dimethylamino-7-methyl-1,2,4-benzotriazine (**2**), crude azapropazone (2 g) was dissolved in 1 M NaOH (20 mL). The reaction mixture was cooled in an ice bath while 30% H_2O_2 was added dropwise. The dark orange solution was allowed to

Fig. 2. Structure of 3-dimethylamino-7-methyl-1,2,4-benzotriazine (**2**), with the atoms numbered by analogy to **1**. Note the absence of the pyrazolidine ring (compare Fig. 1) at N(4)–N(11). The molecule is essentially planar.

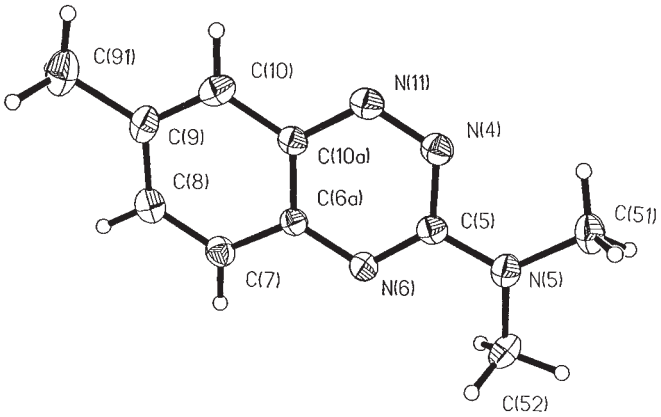

cool. The solution sat open to the air for three days, whereupon bright orange parallelepiped crystals appeared (mp 58–61°C, lit. (1) 61–63°C). ^{1}H NMR (200 MHz in $CDCl_3$ at 300 K) δ: 2.48 (3H, s, aromatic CH_3), 3.39 (6H, s, collapsed N-$(CH_3)_2$), 7.24 (1H, d, aromatic H(7)), 7.50 (1H, d, aromatic H(8)), 7.96 (1H, s, aromatic H(10)). ^{13}C NMR (125 MHz, 500 MHz for ^{1}H, in DMSO-d_6 at 300 K) δ: 20.68 (aromatic CH_3), 36.74 (N-$(CH_3)_2$), 125.8 (aromatic C(7)), 127.41 (aromatic C(8)), 134.66 (aromatic C(9)), 138.26 (aromatic C(10)), 140.23 (aromatic C(6-*a*)), 141.47 (aromatic C(10-*a*)), 158.83 (C-5). EI-MS *m*/*z*(%): 188 (20, M^+), 160 (70), 145 (100, $M - NC_2H_6$).

For the structure determination, a crystal was selected after examination for clarity and sharp extinction in a polarizing microscope. The crystal was soluble in all solvents and adhesives used to try to mount the crystal. Instead a glass capillary was drawn out over a Bunsen burner and broken off at the top, so the crystal could sit in the top. The bottom of the capillary was glued to a brass pin. Unit cell determination and intensity data collection were performed on a Siemans SMART Platform CCD 3-circle diffractometer with monochromatized MoK_α (λ = 0.71073 Å). An initial set of cell constants was calculated from reflections harvested from three sets of 30 frames. This produced orientation matrices determined from 46 reflections. Final cell constants were calculated from a set of 2079 strong reflections from the actual data collection. A semiempirical ψ-scan absorption correction was applied. The structure was solved by direct methods and refined on F^2 by full-matrix least squares. The details of data acquisition and treatment are given in Table 1. The atomic coordinates and isotropic temperature factors are in Table 2, and the interatomic distances and angles are given in Table 3. The molecule is shown in Fig. 2, and the packing diagrams in Fig. 3.

For the exchange measurements, an approximately 2% solution of **2** in acetone-d_6 was made up. Proton NMR spectra were obtained at 300 MHz on a Bruker AC300 spectrometer equipped with a 5 mm 4-nucleus probe and a BVT 2000 variable temperature unit. The 90° pulse width was 9.0 μs. The number of points in the FID was 64 k words, and the sweep width used was 5208 Hz. After acquisition, data were transferred to Silicon Graphics Indy workstation and processed

© 1998 NRC Canada

Table 1. Crystallographic data for 3-dimethylamino-7-methyl-1,2,4-benzotriazine (**2**).

Formula	$C_{10}H_{12}N_4$
Formula weight	188.24
Crystal colour, shape, size (mm)	Orange plate, $0.50 \times 0.28 \times 0.12$
Space group	$P2_12_12_1$
λ (Å)	0.71073
Unit cell parameters (Å)	$a = 4.9123(4)$
	$b = 12.392(1)$
	$c = 16.218(1)$
Volume (Å^3)	987.3(1)
Z	4
D_{calc} (g cm^{-3})	1.266
Index ranges	$-4 \le h \le 5, -14 \le k \le 13, -16 \le l \le 19$
Max 2θ (°)	50.4
Temperature (°C)	–100
Absorption coefficient (mm^{-1})	0.081
$F(000)$	400
Transmission factor (range)	0.679, 0.801
Reflections collected	4862
Independent reflections	1720 ($R_{int} = 0.0547$)
Reflections used	1720
Number of parameters refined	142
Final R indices ($I > 2\sigma(I)$)	$R1 = 0.0585$, $wR2 = 0.1154$
Final R indices (all data)	$R1 = 0.0862$, $wR2 = 0.1281$
Goodness of fit on F^2, S	1.168
Data:parameter ratio	12.11:1
Largest difference peak (e Å^{-3})	0.148
Largest difference hole (e Å^{-3})	–0.136

Table 2. Atomic coordinates (Å $\times 10^4$) and equivalent isotropic displacement parameters (Å$^2 \times 10^3$) for **2**.

	x	y	z	U_{eq}[a]
N(6)	1294(5)	6712(2)	3747(2)	37(1)
N(4)	2336(6)	5308(2)	2760(2)	43(1)
N(11)	597(6)	4649(2)	3088(2)	44(1)
N(5)	4515(6)	6962(2)	2729(2)	48(1)
C(5)	2646(6)	6319(2)	3096(2)	37(1)
C(6A)	–513(6)	6014(2)	4087(2)	33(1)
C(7)	–2041(7)	6313(3)	4788(2)	42(1)
C(8)	–3812(7)	5594(3)	5128(2)	48(1)
C(9)	–4210(7)	4544(3)	4809(2)	45(1)
C(10)	–2723(7)	4250(2)	4123(2)	45(1)
C(10A)	–880(6)	4979(2)	3763(2)	34(1)
C(91)	–6189(8)	3781(3)	5218(2)	65(1)
C(52)	4968(8)	8045(3)	3040(2)	55(1)
C(51)	6180(7)	6588(3)	2043(2)	53(1)

[a] Defined as one third of the trace of the orthogonalized U_{ij} tensor.

using Bruker's XWINNMR program. Lineshapes in the intermediate exchange regime were calculated using the program MEX (available from ADB) (7) and compared with experimental data using the dual display routine of XWINNMR. Figure 4 shows the match between simulated and experimental lineshapes, and the decomposition of the lineshape into individual transitions. For fast exchange, T_2 measurements using the offset saturation experiment provided the rate information (8). For slow exchange, selective inversion experiments were used (9).

Table 3. Bond lengths (Å) and angles (°) for **2**.

Bond	Length	Bond	Length
N(6)—C(5)	1.339(4)	N(6)—C(6A)	1.356(4)
N(4)—N(11)	1.296(3)	N(4)—C(5)	1.375(4)
N(11)—C(10A)	1.377(4)	N(5)—C(5)	1.353(4)
N(5)—C(52)	1.452(4)	N(5)—C(51)	1.456(4)
C(6A)—C(10A)	1.397(4)	C(6A)—C(7)	1.412(4)
C(7)—C(8)	1.362(4)	C(8)—C(9)	1.413(5)
C(9)—C(10)	1.381(4)	C(9)—C(91)	1.510(4)
C(10)—C(10A)	1.406(4)		
Bond	**Angle**	**Bond**	**Angle**
C(5)-N(6)-C(6A)	114.4(2)	N(11)-N(4)-C(5)	119.0(3)
N(4)-N(11)-C(10A)	119.1(3)	C(5)-N(5)-C(52)	119.7(3)
C(5)-N(5)-C(51)	122.0(3)	C(52)-N(5)-C(51)	118.3(3)
N(6)-C(5)-N(5)	118.0(3)	N(6)-C(5)-N(4)	126.1(3)
N(5)-C(5)-N(4)	115.9(3)	N(6)-C(6A)-C(10A)	121.2(3)
N(6)-C(6A)-C(7)	120.5(2)	C(10A)-C(6A)-C(7)	118.3(3)
C(8)-C(7)-C(6A)	119.6(3)	C(7)-C(8)-C(9)	122.9(3)
C(10)-C(9)-C(8)	117.7(3)	C(10)-C(9)-C(91)	122.0(3)
C(8)-C(9)-C(91)	120.3(3)	C(9)-C(10)-C(10A)	120.3(3)
N(11)-C(10A)-C(6A)	120.2(3)	N(11)-C(10A)-C(10)	118.6(3)
C(6A)-C(10A)-C(10)	121.2(3)		

Fig. 3. Crystal packing diagram of **2**.

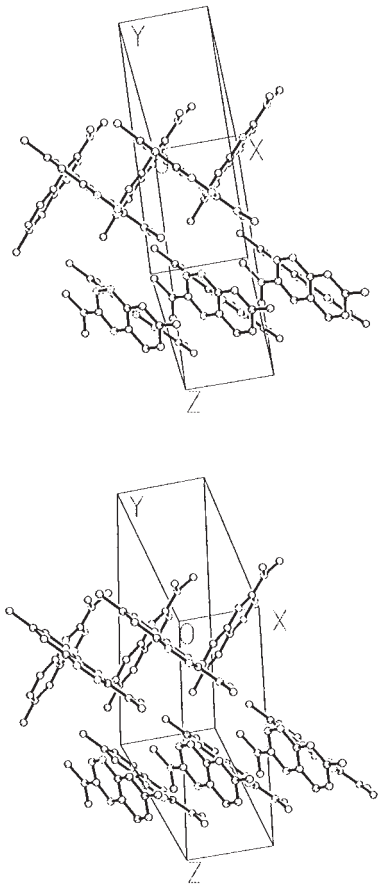

© 1998 NRC Canada

Fig. 4. Experimental (top) and simulated lineshapes for the two methyl signals of the dimethylamino group in **2** at 253 K. The bottom trace shows the decomposition of the lineshape into individual transitions.

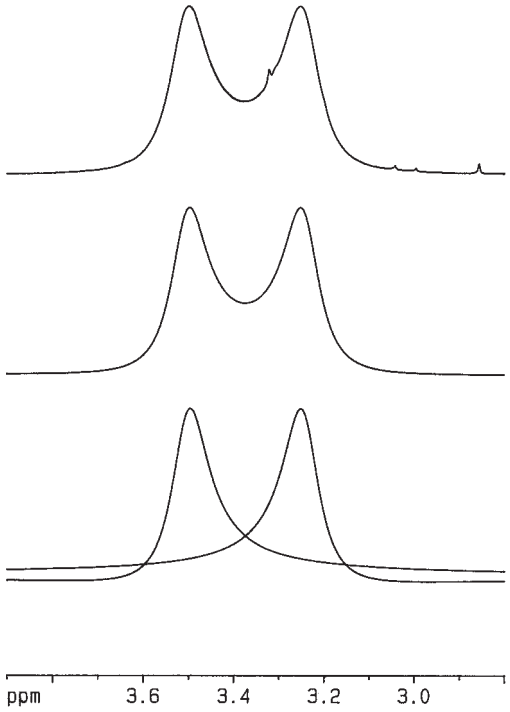

Fig. 5. Eyring plot of log(rate/*T*) versus 1/*T* for the exchange rates of the dimethylamino group in azapropazone (**1**) and its derivative (**2**). The intercept with the axis at $1/T = 0$ is shown to indicate the entropy of activation for the reaction.

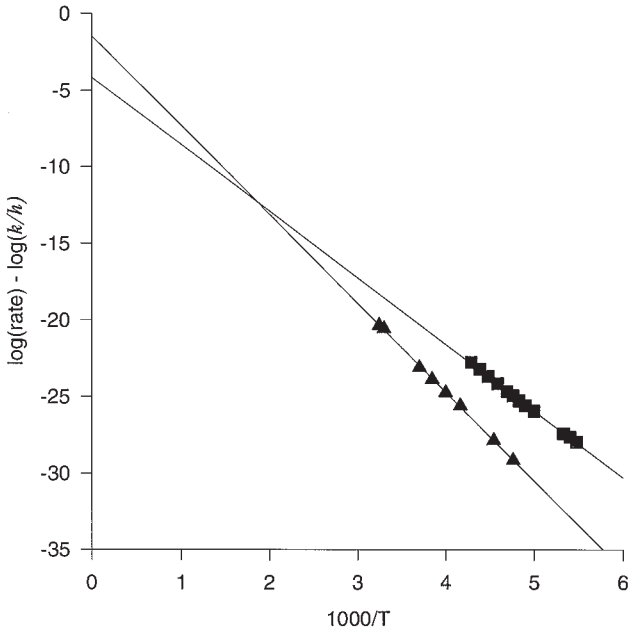

The activation parameters were estimated from a linear regression on an Eyring plot of log(rate/*T*) versus 1/T. The error in $\Delta H^{\ddagger}$ was taken directly from the error in the slope, and the error in $\Delta S^{\ddagger}$ was calculated from the combined effect of the error in the intercept and the extrapolation error due to the error in the slope.

Fig. 6. Schematic potential energy diagram for the rotation about the C—N bond joining the dimethylamino group to the triazine ring.

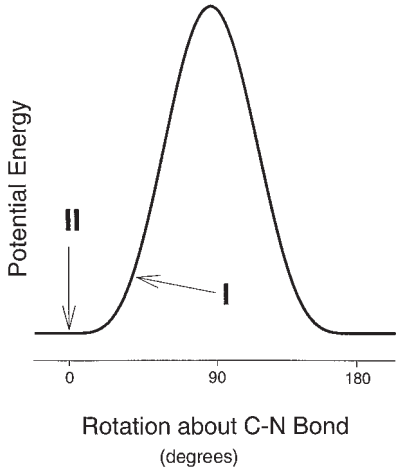

Discussion

The molecule is planar (maximum deviation, C(51), 0.077 Å). There appears to be considerable delocalization through the N(5)–C(5)–N(6)–C(6*a*) system (N(5)—C(5), 1.353(4) Å; C(5)—N(6), 1.339(4) Å; N(6)—C(6*a*), 1.356(4) Å) and less delocalization around the N(4)—N(11) double bond (N(4)—N(11), 1.296(4) Å; N(4)—C(10*a*), 1.377(4) Å; N(11)—C(5), 1.375(4) Å). The dihedral angle between the best planes of the benzene and triazine ring is 1.2°, and the dihedral angle between the dimethylamino group, C(51)-N(5)-C(52) and the plane of N(4)-C(5)-N(6) is 2.8°. For azapropazone itself, the corresponding angle that the dimethylamino groups make with the ring is 24.1(8)°.

The crystal packing of **2**, shown in Fig. 3, consists of spiral chains along the *b* and *c* direction. In the *a* direction, translationally equivalent molecules are stacked 3.5 Å apart, indicating some π–π interaction. The interactions between the chains appear to be van der Waals type.

For **2**, exchange of the two methyl groups simply involves a rotation about the bond joining the dimethylamino group to the triazine ring. However, azapropazone (**1**) is chiral, since it is not planar (Fig. 1). Exchange of the two methyl groups involves not only bond rotation, but also inversion at N(11), the junction of the triazine and pyrazolidine rings. Figure 5 shows an Eyring plot of log(*k*/*T*) vs. 1/*T* for the exchange rates, *k*, for both azapropazone and its derivative, II. It is clear from this plot that both the enthalpy and entropy of activation for the exchange process are significantly different in the two molecules. For the drug itself, $\Delta H = 36 \pm 0.5$ kJ mol^{-1}, and $\Delta S = -34 \pm 2$ J K^{-1}, and for the derivative $\Delta H = 48 \pm 0.4$ kJ mol^{-1}, and $\Delta S = -12 \pm 2$ J K^{-1}. We interpret these parameters as follows.

Figure 6 shows schematically the potential energy of the molecule as a function of the angle between the plane of the dimethylamino group and the triazine ring in the derivative (**2**). The molecule is planar, so the energy is a minimum when the angle is zero, and the transition state is at 90°. For **2**, the

© 1998 NRC Canada

behaviour is as might be expected: there is a barrier of about 48 kJ mol^{-1}, and the entropy of activation is close to zero, since the ground and transition states are both quite symmetrical. There are few reports of barriers to rotation in closely related compounds (10, 11), but the value is well within the normal range for dimethylamino groups attached to aromatic rings (12).

However, azapropazone (**1**) is nonplanar, so the dimethylamino group cannot correspond to the bottom of the curve in Fig. 6. The ground state for azapropazone is part way up the curve, so the barrier to exchange is lower. Also, the ground state is considerably less symmetrical than the postulated transition state with the dimethylamino group perpendicular to the ring. This would lead to a decrease in entropy on going to the transition state. The observed entropy of activation in azapropazone is significantly more negative than in its planar derivative, **2**.

The lower barrier in azapropazone is perhaps surprising in other contexts. The C(5)—N(5) bond, about which rotation occurs, is significantly shorter in azapropazone (1.313(7) Å) than in **2** (1.353(4) Å). Also, the exchange of the two methyl groups in azapropazone involves inversion at N(11) as well as bond rotation. An alternative explanation for the different barriers is that perhaps the transition states are different. The transition state for **2** presumably has the dimethylamino group perpendicular to the plane of the molecule. Another possible transition state for azapropazone is that the whole molecule is planar, including the dimethylamino group. That would mean that the exchange occurs by inversion at N(11), and the methyl group slides by the pyrazolidine ring, rather than rotating through a large angle and a perpendicular orientation. However, since the ground state of azapropazone is significantly distorted from planarity, we feel that the steric interactions in a completely planar transition state would preclude this mechanism.

Conclusions

The crystal structure of 3-dimethylamino-7-methyl-1,2,4-benzotriazine (**2**) is quite different from the parent compound, azapropazone (**1**). Removal of the pyrazolidine ring from **1** allows the molecule to become planar, since it removes the steric interaction with the exocyclic dimethylamino group. This change also has a dramatic effect on the rate of chemical exchange between the nonequivalent methyl groups in the dimethylamino moiety. In azapropazone, the enthalpy of activation is 36 kJ mol^{-1}, and the entropy of activation is significantly negative. In **2**, the enthalpy of activation is 48 kJ mol^{-1}, and the entropy is close to zero. We interpret these results to indicate that since the dimethylamino group in **1** cannot lie flat, it is trapped partway up a potential energy barrier. This means that it will take less energy to surmount the barrier. The entropy of activation for a unimolecular chemical exchange process is normally expected to be small. However, the ground state in azapropazone is nonplanar, and relatively disordered compared to a postulated transition state in which the tricyclic ring structure is planar and the dimethylamino group is perpendicular to the plane.

Acknowledgments

We would like to thank Victor Young of the X-ray Crystallographic Laboratory at the University of Minnesota, Twin Cities Campus, for obtaining the data and Dr. K.D. Rainsford of the University of Sheffield for samples of azapropazone. We would also like to thank the Natural Sciences and Engineering Research Council of Canada for financial support.

References

1. G. Mixich. Helv. Chim. Acta, **51**, 532 (1968).
2. F.M. Dean. *In* Azapropazone: over two decades of clinical use. *Edited by* K.D. Rainsford. Kluwer Academic Publishers, Dordrecht. 1991.
3. T. Fauconnier, C.J.L. Lock, R.A. Bell, J.F. Britten, and K. Rainsford. Can. J. Chem. **72**, 382 (1994).
4. The Merck Index. 11th ed. Merck and Company, Rahway, N.J. 1989.
5. K. Yamasaki, T. Maruyama, U. Kragh-Hansen, and M. Otagiri. Biochim. Biophys. Acta, **1295**, 147 (1996).
6. A.D. Bain, G.J. Duns, S. Ternieden, J. Ma, and N.H. Werstiuk. J. Phys. Chem. **98**, 7458 (1994).
7. A.D. Bain and G.J. Duns. Can. J. Chem. **74**, 819 (1996).
8. A.D. Bain and G.J. Duns. J. Magn. Reson. **109A**, 56 (1994).
9. A.D. Bain and J.A. Cramer. J. Magn. Reson. **118A**, 21 (1996).
10. N.W. Jacobsen and I. de Jonge. Aust. J. Chem. **40**, 1979 (1987).
11. E. Kleinpeter. J. Mol. Struct. **380**, 139 (1996).
12. L.M. Jackman and F.A. Cotton. Dynamic nuclear magnetic resonance spectroscopy. Academic Press, New York. 1975.

© 1998 NRC Canada

Synthesis and evaluation of a bicyclic deoxymannojirimycin derivative as a potential glycosidase inhibitor

Kelly S.E. Tanaka and Andrew J. Bennet

Abstract: A bicyclo[2.2.2] analogue of the glycosidase inhibitor 1-deoxynojirimycin, 2,6-anhydro-1-deoxymannojirimycin (**6**), has been synthesized in nine steps from 1,5-anhydro-D-glucitol. This conformationally restricted aza-sugar has been shown to inhibit, albeit weakly, several glycosidase enzymes.

Key words: glycosidase, inhibitor, bicyclic, deoxymannojirimycin, deoxynojirimycin.

Résumé : Utilisant le 1,5-anhydro-D-glucitol comme produit de départ, on a réalisé une synthèse en neuf étapes de la 2,6-anhydro-1-désoxymannojirimycine (**6**), un analogue bicyclo[2.2.2] de la 1-désoxynojirimyrine, un inhibiteur de glycosidase. Il a été démontré que cet aza-sucre conformationnellement restreint inhibe plusieurs enzymes glycosidase, même si ce n'est que faiblement.

Mots clés : glycosidase, inhibiteur, bicyclique, désoxymannojirimycine, désoxynojirimycine.

Introduction

Recent advances in the understanding of the diverse biological function of carbohydrates have led to a renewed interest in carbohydrate-processing enzymes (for recent examples of the use of carbohydrate-processing enzymes for synthesis, see ref. 1). These enzymes can be classified as either (*a*) glycosyl transferases, enzymes that are involved in the construction of oligosaccharides, or (*b*) glycosidases, enzymes that hydrolyze glycosidic linkages. Of particular interest in recent years is the design and synthesis of glycosidase inhibitors. In addition to providing insight into the hydrolytic mechanism of glycosidases (2), these inhibitors have potential therapeutic value in the treatment of metabolic disorders (3), tumor metastasis (4), and viral infections (5). A large class of glycosidase inhibitors are aza-sugars, compounds where a nitrogen atom has replaced the endocyclic oxygen atom of the corresponding carbohydrate. The most noted example is 1-deoxynojirimycin (**1**), an aza-sugar with the same hydroxyl configuration as 1-deoxyglucose (6). These aza-sugars are good inhibitors of glycosidases since the basic nitrogen atom is protonated at physiological pH, and the resultant positive charge is believed to mimic an enzyme-catalyzed transition state (TS). For retaining glycosidase enzymes, the reaction occurs through a double displacement mechanism that was first proposed by Koshland in 1953 (2, 7). In this mechanism, both the glycosylation and deglycosylation steps are believed to occur through TSs containing a distorted glycone ring that has significant oxocarbenium ion character (Fig. 1) (2*a*, 2*c*). Thus, the N-protonated forms of **1** (6) and its C-2 epimer **2** (8) inhibit glucosidases and mannosidases, respectively. Similarly, the glucosidase inhibitor castanospermine (**3**), is a bicyclic molecule that is locked in a $^4C_1$ conformation, and possesses a basic endocyclic nitrogen atom that is protonated at physiological pH (9). Another class of bicyclic glycosidase inhibitors is the calystegines (10), for example, calystegine B_2 (**4**), a molecule that possessess a basic nitrogen atom and is locked in a $^4C_1$ conformation (11). On the other hand, it is believed that the neutral compound nojiritetrazole **5** is a glucosidase inhibitor because the tetrazole ring distorts the glycosyl ring from the $^4C_1$ to the $^4H_3$ conformation (12).

From these studies it is evident that, in addition to the relative configuration of the hydroxyl groups, conformation and charge are two important factors in the design and synthesis of potential glycosidase inhibitors. The relative importance of these two factors in determining the potency of glycosidase inhibitors remains an active area of research (for example, see two recent sialidase inhibitor studies, ref. 13).

With regard to structure, there are four possible ring conformations a glycopyranosyl oxocarbenium ion intermediate can adopt (Fig. 2) and the thermodynamically most favourable $^4H_3$ has been the structural motif used in the design of many glycosidase inhibitors (2*b*, 12, 14). Variability in the inhibitory potency of these compounds suggests that this may not be the TS conformation of the substrate during the hydrolysis reaction catalyzed by all glycosidase enzymes. In 1985 Hosie and Sinnott proposed that yeast α-glucosidase-catalyzed hydrolysis of α-D-glucopyranosyl 4-bromoisoquinolinium bromide proceeded via a $^{2,5}B$ TS conformation (15). The two key results in this study that led to this hypothesis were (*a*) the measured β-secondary kinetic isotope effect for hydrolysis of α-D-glucopyranosyl 4-bromoisoquinolinium bromide (15) and (*b*) the inability of the conformationally rigid castanospermine to inhibit this α-glucosidase enzyme (9).

To further probe possible inhibitor conformations it was decided to synthesize nojirimycin analogues that are forced to adopt a boat-like conformation. Specifically, the target

Received October 27, 1997.

K.S.E. Tanaka and A.J. Bennet.[1] Department of Chemistry, Simon Fraser University, Burnaby, BC V5A 1S6, Canada.

[1] Author to whom correspondence may be addressed. Telephone: (604) 291-3532. Fax: (604) 291-3765. E-mail: bennet@sfu.ca

© 1998 NRC Canada

Fig. 1. The generally accepted transition states for glucoside hydrolysis catalyzed by a retaining α-glucosidase.

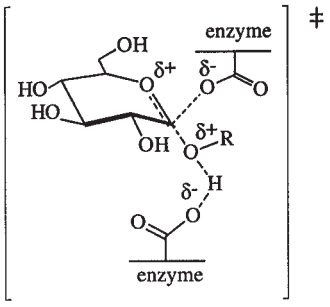

Glycosylation R = sugar
Deglycosylation R = H

compound chosen was 2,6-anhydro-1-deoxymannojirimycin (**6**), a dihydroxylated bicyclic amine that is locked in a $^{2,5}B$ conformation.

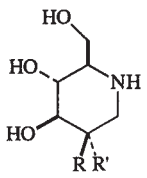

1 R = H, R' = OH
2 R = OH, R' = H

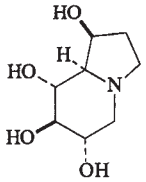

3

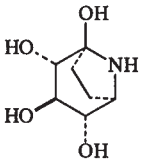

4

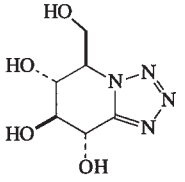

5

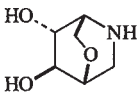

6

Results and discussion

The symmetry of the bicyclic target **6** allows four possible synthetic pathways (**a**–**d**) for the cyclization reaction using carbohydrate-based precursors (Scheme 1). It was anticipated that an efficient cyclization would occur via route **a** using a 2-amino-1,2-dideoxymannose precursor. Synthesis of the 2-*O*-methanesulfonate ester **8**, in five steps from D-glucose, was completed using a combination of literature procedures (16). Using a slightly modified procedure, the yield for the selective mesylation of the 2-OH group of 1,5-anhydro-4,6-*O*-benzylidene-D-glucitol **7** was modestly improved from 53% (16*d*) to 60% by increasing the reaction time at –40°C from 1 h to 10 h (Scheme 2). Nucleophilic displacement of the 2-*O*-methanesulfonate group in **8** with azide introduced the required nitrogen atom at the C-2 position, with the appropriate stereochemistry for the subsequent cyclization reaction (Scheme 2). Protection of the 3-*O* hydroxyl group, by benzylation, was necessary at this stage because cyclization of **13.2** led to formation of a [3.2.1] bicyclic product. The benzylation reaction was carried out to afford the 3-*O*-benzyl ether **10**, in good yield (89%) (Scheme 2).

Removal of the 4,6-*O*-benzylidene group followed by controlled hydrogenation resulted in the formation of the 2-amino-3-*O*-benzyl-2-deoxy compound **12** in a combined crude yield of 78% (Scheme 3). In a single step, ditosylation of the 6-OH and the 2-NH_2 groups efficiently introduced a leaving group and acidified the remaining nitrogen-bound hydrogen (TsCl, pyridine 77%; Scheme 3). Ditosylate **13** was efficiently cyclized using a hydroxide-promoted reaction to give **14** in 94% yield (Scheme 4). Simultaneous deprotection of the 4-*O*-benzyl ether and the *N*-toluenesulfonamido groups[2] was readily accomplished to give **6** in an unoptimized yield after recrystallization of 35% (Na, NH_3; Scheme 4). Confirmation that the final product **6** had the required [2.2.2]-bicyclic ring structure was accomplished by ^1H NMR spectroscopy using the measured ^1H coupling constants and the observed nOe contacts (Fig. 3).

Inhibition of four commercial glycosidases by **6** was measured using standard kinetic techniques (see experimental section for details). The kinetic data were fit, using a nonlinear least-squares routine, to a standard competitive-inhibitor rate equation because the corresponding Lineweaver–Burke plots (not shown) displayed the expected behaviour for a competitive inhibitor. Listed in Table 1 are the calculated inhibition constants (K_i) for **6** with these glycosidases. Although these measured K_i values are relatively high, this is the first demonstration that a [2.2.2]-bicyclic aza-sugar analogue can bind to the active site of glycosidases. This observation is particularly noteworthy since this inhibitor (**6**) lacks both the 2- and the 6-hydroxyl groups found in deoxynojirimycin. These hydroxyl groups can form H-bonds, and these interactions are known to be important in glycosidase-catalyzed hydrolysis reactions (17).

In conclusion, a novel, conformationally restricted, aza-sugar **6** has been synthesized (20% yield from **8**) and has been shown to inhibit, albeit weakly, several glycosidase enzymes.

Experimental

Thin-layer chromatography (TLC) was performed on analytical plates of aluminum precoated with Merck Silica Gel 60 F_{254}. Compounds were visualized on developed plates by UV light and (or) charring with 10% H_2SO_4 in methanol. Flash column chromatography was performed using Merck Silica Gel 60 (230–400 mesh). Melting point values are uncorrected. THF was distilled from the sodium ketyl of benzophenone, pyridine was distilled from CaH_2, and DMSO and DMF were distilled from CaH_2 at reduced pressure. All other reagents were used as purchased. Reactions using moisture-sensitive reagents were carried out under a nitrogen atmosphere using oven-dried glassware. Solutions of methanolic HCl (1% w/v) were prepared by the in situ reaction of acetyl chloride with methanol. NMR spectra were recorded on a Bruker AMX-400 NMR spectrometer operating at 400.13 MHz and 100.61 MHz for ^1H and ^{13}C, respectively. Chemical shifts (δ) for all compounds are listed in ppm downfield from TMS using residual $CHCl_3$ (δ 7.24 ppm) or HDO (δ 4.63 ppm) as the internal reference for ^1H spectra and $CDCl_3$ (δ 77.0 ppm) as the internal reference for ^{13}C spectra. Characterization of all new compounds included ^1H and $^{13}C\{^1H\}$ NMR spectra. The observed resonances in the NMR spectra were fully assigned using

[2] The numbering system of compound **5** is derived on the basis that the molecule is a derivative of 1-deoxymannojirimycin.

© 1998 NRC Canada

Fig. 2. The four possible conformations of a glycopyranose oxocarbenium ion. The coplanar atoms are indicated by the asterisk symbol; all hydroxyl groups are omitted for simplicity.

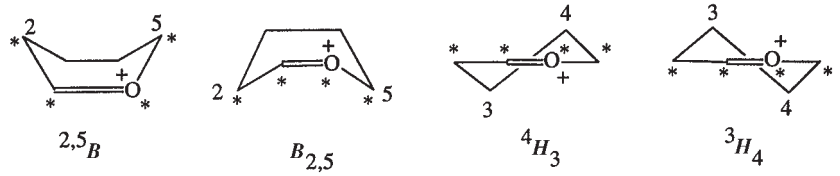

Scheme 1.

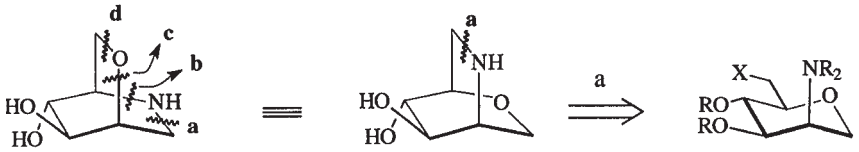

Scheme 2. (i) MsCl (1.1 equiv.), py –40°C, 10 h; (ii) NaN_3 (4 equiv.), DMSO, 85°C, 2 d; (iii) NaH (1.1 equiv.), BnBr (1.1 equiv.), THF, 30 min; (iv) 1% HCl (w/v) in methanol.

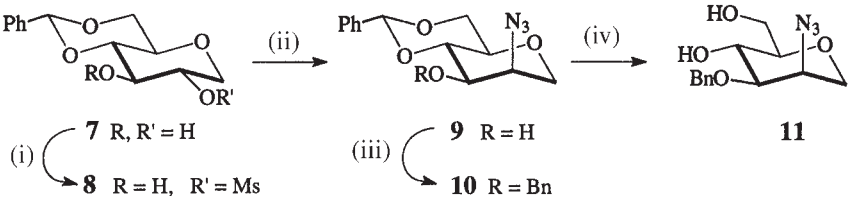

Scheme 3. (i) H_2, 10% Pd–C, EtOH, RT; (ii) TsCl (2.8 equiv.), pyridine, RT, 12 h.

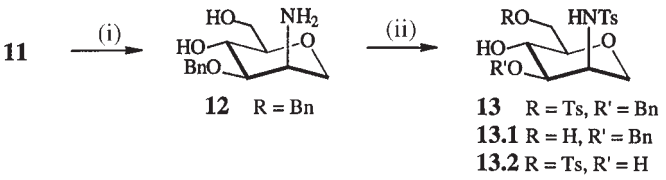

^{1}H–homonuclear (18) and ^{1}H–^{13}C-heteronuclear (19) chemical-shift correlated NMR spectroscopy techniques. Optical rotation values were measured using a Rudolph Research Autopol II polarimeter.

1,5-Anhydro-4,6-*O*-benzylidene-2-*O*-methanesulfonyl-D-glucitol (8)

A solution of 1,5-anhydro-4,6-*O*-benzylidene-D-glucitol **(7)** (16*a*–*c*) (3.00 g, 11.9 mmol) in dry pyridine (10 mL) was cooled to –40°C (Dry Ice – acetone) after which methanesulfonyl chloride (1.5 mL, 1.1 equiv.) was added dropwise over a period of 60 min. The resulting yellow solution was stirred at –40°C for a further 10 h and allowed to warm to –20°C overnight. After the reaction was quenched by the addition of cold H_2O–ice (100 mL), stirring was continued for 1 h and the product was extracted with EtOAc (3 × 75 mL). The organic extracts were combined, washed with cold 10% (v/v) H_2SO_4 (3 × 100 mL), saturated aqueous $NaHCO_3$ (100 mL), brine (100 mL), and dried (Na_2SO_4). After filtration the solvent was removed at reduced pressure to give a pale-yellow solid. The crude product was purified by flash column chromatography (toluene/EtOAc 9:1) to yield **8** (2.36 g, 60%) as a colourless solid: mp 149–150°C; $[\alpha]_D^{22}$ –12 (*c* 1.0, $CHCl_3$) (lit. (16*d*) mp 155–157°C; $[\alpha]_D^{22}$ –10.6 (*c* 1.1, $CHCl_3$)); R_f 0.48 (EtOAc/toluene 1:3); IR (cm^{-1}): 1182 S(═O)$_2$, 1348 S(═O)$_2$, 3434 (OH); ^{1}H NMR ($CDCl_3$) δ: 3.16 (s, 3 H, SO_2CH_3), 3.39 (dt, 1 H, $J_{4,5} + J_{5,6a}$ = 19.4 Hz, $J_{5,6e}$ = 5.0 Hz, H-5), 3.45–3.52 (m, 2 H, H-1a, H-4), 3.69 (t, 1 H, $J_{5,6a} + J_{6a,6e}$ = 20.5 Hz, H-6a), 3.94 (t, 1 H, $J_{2,3} + J_{3,4}$ = 18.2 Hz, H-3), 4.21 (dd, 1 H, $J_{1e,2}$ = 6.0 Hz, $J_{1e,1a}$ = 11.5 Hz, H-1e), 4.34 (dd, 1 H, $J_{6e,6a}$ = 10.5 Hz, H-6e), 4.59 (ddd, 1 H, $J_{2,3}$ = 8.7 Hz, $J_{1a,2}$ = 10.6 Hz, H-2), 5.52 (s, 1 H, CHC_6H_5), 7.35–7.41 (m, 3 H, CHC_6H_5), 7.45–7.50 (m, 2 H, CHC_6H_5); ^{13}C NMR (CDCl) δ: 38.3 (SO_2CH_3), 68.2 (C-6), 68.6 (C-1), 70.9 (C-5), 72.9 (C-3), 78.1 (C-4), 81.1 (C-2), 102.1 (Ar), 126.3 (Ar), 128.4 (Ar), 129.5 (Ar), 136.8 (Ar). Anal. calcd. for $C_{14}H_{18}O_7S$: C 50.91, H 5.49; found: C 51.21, H 5.57.

1,5-Anhydro-2-azido-2-deoxy-4,6-*O*-benzylidene-D-mannitol (9)

A stirred solution of **8** (1.16 g, 3.52 mmol) and sodium azide (0.915 g, 4.0 equiv.) in dry DMSO (5 mL) was heated to 85°C (oil bath) for 2 days. After the addition of H_2O–ice (50 mL) the product was extracted with EtOAc (3 × 50 mL). The organic extracts were combined and washed with cold H_2O (100 mL) and brine (100 mL), then dried (Na_2SO_4) and filtered. After removing the solvent at reduced pressure, the crude yellow solid was purified by flash column chromatography (EtOAc/hexane 1:3) to give **9** (0.864 g, 89%) as a colourless solid; R_f 0.49 (EtOAc/hexane 1:2); mp 80–81°C; $[\alpha]_D^{22}$ –66 (*c* 0.89, $CHCl_3$); IR (cm^{-1}): 2102 (N_3), 3445 (OH); ^{1}H NMR ($CDCl_3$) δ: 2.82 (d, 1 H, *J* = 4.0 Hz, 3-OH), 3.35 (ddd, 1 H, $J_{5,6e}$ = 5.0 Hz, $J_{5,6a}$ = 9.5 Hz, $J_{4,5}$ = 14.4 Hz, H-5), 3.68 (dd, 1 H, $J_{1e,2}$ = 1.7 Hz, $J_{1e,1a}$ = 12.7 Hz, H-1e), 3.77 (t, 1 H, H-6a), 3.90 (t, 1 H, $J_{3,4} + J_{4,5}$ = 18.8 Hz, H-4), 4.00 (m, 1 H, H-1a), 4.03–4.08 (m, 2 H, H-2, H-3), 4.29 (dd, 1 H, $J_{6a,6e}$ = 10.4 Hz, H-6e), 5.52

© 1998 NRC Canada

Scheme 4. (i) DMF–H_2O, 1 equiv. NaOH; (ii) Na–NH_3, THF, –78°C.

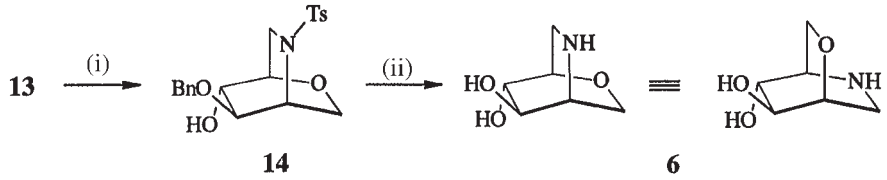

Fig. 3. Observed nOe contacts in the 2D ^{1}H NMR NOESY spectrum of compound **6**.

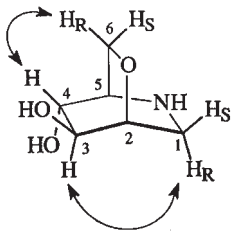

(s, 1 H, C*H*C$_6$H$_5$), 7.35–7.41 (m, 3 H, CHC$_6$*H*$_5$), 7.45–7.50 (m, 2 H, CHC$_6$*H*$_5$); ^{13}C NMR ($CDCl_3$) δ: 61.8 (C-2), 68.5 (C-6), 68.9 (C-1), 71.9 (C-5), 72.1 (C-3), 79.2 (C-4), 102.3 (*C*HC$_6$H$_5$), 126.3 (Ar), 128.4 (Ar), 129.3 (Ar), 137.2 (Ar). Anal. calcd. for $C_{13}H_{15}O_4N_3$: C 56.30, H 5.46, N 15.16; found: C 56.37, H 5.50, N 15.01.

1,5-Anhydro-2-azido-3-*O*-benzyl-4,6-*O*-benzylidene-2-deoxy-D-mannitol (10)

A suspension of sodium hydride (0.54 g, 13.4 mmol) and **9** (3.11 g, 11.2 mmol) in dry THF (50 mL) was stirred at room temperature (RT) for 30 min. Benzyl bromide (1.1 equiv., 1.47 mL) and tetrabutylammonium iodide (0.1 equiv., 42 mg) were added to this suspension and the resulting mixture was stirred at RT for 12 h. After the solvent was removed at reduced pressure the residue was suspended in brine (20 mL), and the product was extracted with ether (3 × 50 mL). The combined organic extracts were concentrated at reduced pressure to give a pale-yellow oil that, after purification by flash column chromatography (EtOAc/hexane 2:1), yielded **10** (3.75 g, 91%) as a colourless oil: $[\alpha]_D^{22}$ –50 (*c* 0.98, $CHCl_3$); R_f 0.45 (EtOAc/hexane 1:2); IR (cm^{-1}): 1124, 2105 (N_3); ^{1}H NMR ($CDCl_3$) δ: 3.33 (ddd, 1 H, $J_{5,6e}$ = 5.0 Hz, $J_{4,5}$ = 9.4 Hz, $J_{5,6a}$ = 10.1 Hz, H-5), 3.59 (dd, 1 H, $J_{1e,2}$ = 1.5 Hz, $J_{1e,1a}$ = 12.5 Hz, H-1e), 3.80 (t, 1 H, H-6a), 3.85 (dd, 1 H, $J_{2,3}$ = 3.9 Hz, $J_{3,4}$ = 9.4 Hz, H-3), 3.93 (m, 1 H, H-2), 3.98 (dd, 1 H, $J_{1a,2}$ = 1.9 Hz, H-1a), 4.11 (t, 1 H, $J_{3,4}+J_{4,5}$ = 18.6 Hz, H-4), 4.28 (dd, 1 H, $J_{6e,6a}$ = 10.1 Hz, H-6e), 4.77 (d, 1 H, $J_{A,B}$ = 12.5 Hz, CH_AH$_B$C$_6$H$_5$), 4.91 (d, 1 H, CH$_A$*H*$_B$C$_6$H$_5$), 5.64 (s, 1 H, C*H*C$_6$H$_5$), 7.30–7.40 (m, 8 H, Ar), 7.45–7.50 (m, 2 H, Ar); ^{13}C NMR ($CDCl_3$) δ: 61.0 (C-2), 68.5 (C-6), 69.3 (C-1), 72.5 (C-5), 73.1 (*C*H$_2$C$_6$H$_5$), 78.1 (C-3), 79.4 (C-4), 101.6 (*C*HC$_6$H$_5$), 126.1 (Ar), 127.7 (Ar), 127.8 (Ar), 128.2 (Ar), 128.5 (Ar), 128.9 (Ar), 137.5 (Ar), 138.1 (Ar). Anal. calcd. for $C_{20}H_{21}O_4N_3$: C 65.38, H 5.76, N 11.44; found: C 65.21, H 5.71, N 11.46.

1,5-Anhydro-2-azido-3-*O*-benzyl-2-deoxy-D-mannitol (11)

A solution of **10** (1.14 g, 3.11 mmol) in MeOH (25 mL) containing 1% HCl (w/v) was stirred at RT for 1.5 h, after which analysis by TLC (R_f 0.21, EtOAc/hexane 2:1 for **10**) indicated that the deprotection was complete. The solution was neutralized by stirring with Amberlite resin (IRA-400L, $^-$OH form). The resin was removed and the solution was concentrated at reduced pressure to give **11** (0.84 g, 97%) as a colourless solid. An analytically pure sample of **11** was obtained by recrystallization from EtOAc/ether/hexane (5:1:1): mp 98–99°C; $[\alpha]_D^{22}$ –86 (*c* 0.94, $CHCl_3$); IR (cm^{-1}): 1120, 2100 (N_3), 3450 (OH); ^{1}H NMR ($CDCl_3$) δ: 2.03 (brd, 1 H, *J* = 5.8 Hz, 6-O*H*), 2.44 (d, 1 H, *J* = 2.6 Hz, 4-O*H*), 3.26 (ddd, 1 H, $J_{5,6A}$ = 3.3 Hz, $J_{5,6B}$ = 5.3 Hz, $J_{4,5}$ = 9.4 Hz, H-5), 3.55 (dd, 1 H, $J_{1e,2}$ = 1.5 Hz, $J_{1e,1a}$ = 12.6 Hz, H-1e), 3.59 (dd, 1 H, $J_{3,2}$ = 3.7 Hz, $J_{3,4}$ = 9.2 Hz, H-3), 3.70 (dd, 1 H, $J_{6A,6B}$ = 11.9 Hz, H-6$_A$), 3.75 (dd, 1 H, H-6$_B$), 3.86–3.92 (m, 2 H, H-2, H-4), 4.01 (dd, 1 H, $J_{1a,2}$ = 2.0 Hz, H-1a), 4.60 (d, 1 H, $J_{A,B}$ = 11.6 Hz, C*H*$_A$H$_B$C6H5), 4.80 (d, 1 H, CH$_A$*H*$_B$C$_6$H$_5$), 7.32–7.40 (m, 5 H, Ar); ^{13}C NMR ($CDCl_3$) δ: 58.5 (C-2), 62.9 (C-6), 67.7 (C-4), 68.2 (C-1), 72.1 (*C*H$_2$C$_6$H$_5$), 80.3 (C-5), 82.4 (C-3), 128.0 (Ar), 128.3 (Ar), 128.7 (Ar), 137.3 (Ar). Anal. calcd. for $C_{13}H_{17}O_4N_3$: C 55.91, H 6.14, N 15.05; found: C 55.80, H 6.17, N 15.11.

1,5-Anhydro-3-*O*-benzyl-2-deoxy-2-*N*-toluenesulfonamido-6-*O*-toluenesulfonyl-D-mannitol (13)

A suspension of **11** (0.296 g, 1.06 mmol) and 10% Pd–C (0.15 g) in MeOH (15 mL) was stirred under a H_2 atmosphere (6 psi; 1 psi = 6.9 kPa) at RT for 45 min. After the suspension was filtered through a Celite pad and the pad was washed thoroughly with MeOH, the filtrate and washings were concentrated at reduced pressure and dried under high vacuum (0.01 Torr; 1 Torr = 133.3 Pa) to give crude 2-amino-1,5-anhydro-3-*O*-benzyl-2-deoxy-D-mannitol (**12**) (0.268 g, 100%) as a colourless oil: IR (cm^{-1}): 3364 (OH). Crude **12** (1.48 g, 5.84 mmol) was added to a solution containing *p*-toluenesulfonyl chloride (1.5 equiv., 1.6 g) in dry pyridine (30 mL) and the resulting mixture was stirred at RT. After 20 min a second aliquot of *p*-toluenesulfonyl chloride (1.3 equiv., 1.4 g) was added and the resulting mixture was stirred at RT for a further 12 h. The reaction mixture was diluted by the addition of H_2O–ice (50 mL) and the product was extracted with EtOAc (3 × 50 mL). The combined organic extracts were washed with cold 20% H_2SO_4 (50 mL), saturated aqueous $NaHCO_3$ (50 mL), H_2O (50 mL), brine (40 mL), and dried (Na_2SO_4). The resulting solution was filtered and concentrated at reduced pressure to give a pale-yellow solid. Purification of the solid by flash column chromatography (EtOAc/hexane 1:1) gave **13** (2.52 g, 77%) as a colourless solid. In addition the 2-*N*-monotosylated compound **13.1**, was obtained as a colourless solid (0.26 g, 8%; R_f 0.41, EtOAc/hexane 3:1). For compound **13**; mp 68–70°C; $[\alpha]_D^{22}$ –59 (*c* 0.97, $CHCl_3$); IR (cm^{-1}): 1160, 1174 S(═ O)$_2$, 1191 S(═ O)$_2$, 1349 S(═ O)$_2$, 3450 (OH); ^{1}H NMR ($CDCl_3$) δ: 2.35 (d, 1 H, *J* = 2.6, 4-O*H*), 2.39 (s, 3 H, Me), 2.45 (s, 3 H, Me), 3.25–3.32 (m, 2 H, H-1a, H-5), 3.36

© 1998 NRC Canada

Table 1. Binding constants for compounds **1**, **2**, and **6**, and the corresponding 4-nitrophenyl glycosides.

			K_i [a] (mM) for competitve inhibition		
Enzyme	K_m (mM)	pH	1	2	6
α-Glucosidase (yeast)	0.210 ±.008	6.8	0.015 ± 0.001[b]	ND	7.0 ± 1.0
α-Glucosidase (rice)[c]	0.73 ± 0.07[d]	5.0	$(2.4 \pm 0.4) \times 10^{-6}$ [e]	ND	0.8 ± 0.2
β-Glucosidase (almonds)	2.39 ± 0.07	6.8	0.018 ± 0.001[f]	ND	1.01 ± 0.06
α-Mannosidase (almonds)	2.6 ± 0.2	5.0	ND[g]	0.24 ± 0.05[h]	15 ± 2[i]

[a] Data were analysed using nonlinear least-squares regression; estimate of standard error in brackets
[b] Reference 8 lists $K_i = 0.013$ mM at a pH of 6.8.
[c] Slow onset to inhibition was observed for this enzyme.
[d] Substrate used was α-D-glucopyranosyl 4-bromoisoquinolinium bromide.
[e] Reference 17*a* lists $K_i = 1.0 \times 10^{-5}$ mM at a pH of 6.0.
[f] Reference 17*d* lists $K_i = 0.029$ mM at a pH of 6.2.
[g] ND (not determined).
[h] Reference 8 lists $K_i = 0.11$ mM at a pH of 4.5.
[i] Value estimated using data acquired at two inhibitor concentrations (1.65 and 3.30 mM).

(dd, 1 H, $J_{2,3}$ = 6.4 Hz, $J_{3,4}$ = 9.5 Hz, H-3), 3.58 (dt, 1 H, $J_{4,5}$ = 9.5 Hz, H-4), 3.77 (m, 1 H, H-2), 3.82 (dd, 1 H, $J_{1e,2}$ = 1.9 Hz, $J_{1e,1a}$ = 12.4 Hz, H-1e), 4.18 (dd, 1 H, $J_{5,6A}$ = 5.5 Hz, $J_{6A,6B}$ = 11.1 Hz, H-6_A), 4.19 (d, 1 H, $J_{A,B}$ = 11.4 Hz, CH_AH$_B$C$_6$H$_5$), 4.31 (dd, 1 H, $J_{5,6B}$ = 2.0 Hz, H-6_B), 4.47 (d, 1 H, CH$_A$$H_BC_6H_5$), 4.93 (d, 1 H, $J_{NH,2}$ = 7.1 Hz, TsN*H*), 7.19–7.28 (m, 5 H, CH$_2$C$_6$$H_5$), 7.30–7.36 (m, 4 H, *Ar*), 7.77 (d, 2 H, *J* = 8.5 Hz, *Ar*), 7.79 (d, 2 H, *Ar*); ^{13}C NMR (CDCl$_3$) δ: 21.5 (*C*H$_3$Ar), 21.6 (*C*H$_3$Ar), 50.7 (C-2), 66.4 (C-4), 68.6 (C-1), 68.8 (C-6), 70.9 (*C*H$_2$C$_6$H$_5$), 78.0 (C-5), 79.5 (C-3), 127.1 (Ar), 127.9 (Ar), 128.0 (Ar), 128.2 (Ar), 128.6 (Ar), 129.7 (Ar), 129.8 (Ar), 133.2 (Ar), 137.0 (Ar), 137.9 (Ar), 143.6 (Ar), 144.9 (Ar). Anal. calcd. for $C_{27}H_{31}NO_8S_2$: C 57.74, H 5.56, N 2.49; found: C 57.71, H 5.63, N 2.30.

1,5:2,6-Dianhydro-3-*O*-benzyl-2-deoxy-2-*N*-toluenesulfonamido-D-mannitol (14)

A solution of **13** (2.52 g, 4.49 mmol) in DMSO (70 mL) and H$_2$O (50 mL) containing NaOH (1 equiv.) was stirred at RT for 24 h. After the removal of the solvent at reduced pressure the residue was purified by flash column chromatography (EtOAc/hexane 1:1) to give **14** (1.64 g, 94%) as a colourless solid: mp 113–115°C; $[\alpha]_D^{22}$ –79 (*c* 1.2, CHCl$_3$); R_f 0.43 (EtOAc/hexane 2:1); IR (cm^{-1}): 1163, 1192 S(═ O)$_2$, 1345 S(═ O)$_2$, 3446 (OH); ^{1}H NMR (CDCl$_3$) δ: 2.24 (d, 1 H, *J* = 8.1, 4-O*H*), 2.40 (s, 3 H, Me), 3.40 (dd, 1 H, $J_{5,6A}$ = 1.7 Hz, $J_{6A,6B}$ = 10.7 Hz, H-6_A), 3.59 (m, 1 H, H-3), 3.69 (dd, 1 H, $J_{5,6B}$ = 3.3 Hz, H-6_B), 3.77 (dd, 1 H, $J_{1A,2}$ = 1.58 Hz, $J_{1A,1B}$ = 10.0 Hz, H-1_A), 3.81 (brd, 1 H, H-4), 3.89 (m, 1 H, H-5), 3.90 (dd, 1 H, $J_{1B,2}$ = 2.4 Hz, H-1_B), 4.21 (m, 1 H, H-2), 4.51 (d, 1 H, $J_{A,B}$ = 11.6 Hz, CH_AH$_B$C6H5), 4.75 (d, 1 H, CH$_A$$H_BC_6H_5$), 7.21 (d, 2 H, *J* = 8.52 Hz, Ar), 7.36–7.40 (m, 5 H, Ar), 7.73 (d, 2 H, Ar); ^{13}C NMR (CDCl$_3$) δ: 21.5 (*C*H$_3$Ar), 47.2 (C-6), 50.0 (C-2), 67.4 (C-1), 70.4 (C-5), 70.8 (*C*H$_2$C$_6$H$_5$), 75.6 (C-4), 83.1 (C-3), 127.4 (Ar), 127.8 (Ar), 128.0 (Ar), 128.4 (Ar), 129.6 (Ar), 136.4 (Ar), 137.6 (Ar), 143.5 (Ar). Anal. calcd. for $C_{20}H_{23}NO_5S$: C 61.68, H 5.95, N 3.60; found: C 61.53, H 5.85, N 3.46.

2,6-Anhydro-1-deoxymannojirimycin (6)

A solution of **14** (0.380 g, 0.976 mmol) in dry THF (5 mL) was cooled to –78°C (Dry Ice – acetone) in a three-neck flask fitted with a cold finger. After approximately 15 mL of ammonia was condensed in the flask, Na (0.11 g, 5 equiv.) was added to the suspension and the resulting mixture was stirred at –78°C for 30 min after a persistent blue colour was observed. The reaction was quenched by the addition of MeOH (30 mL) followed by evaporation to dryness. The crude product was dissolved in MeOH and again evaporated to dryness. The crude product was recrystallized from EtOH–ether–HCl to give the HCl salt of **6** as a colourless solid (62 mg, 35%): mp 227–230°C: $[\alpha]_D^{22}$ –44 (*c* 1.2, H$_2$O); ^{1}H NMR (D$_2$O) δ: 3.13 (dd, 1 H, $J_{1R,2}$ = 1.2 Hz, $J_{1R,1S}$ = 13.2 Hz, H-1_R), 3.66 (dd, 1 H, $J_{1S,2}$ = 3.6 Hz, H-1_S), 3.71 (m, 1 H, H-5), 3.82 (m, 1 H, H-3), 3.95 (dd, 1 H, $J_{6R,5}$ = 1.6 Hz, $J_{6R,6S}$ = 11.6 Hz, H-6_R), 4.02–4.06 (m, 2 H, H-2, H-4), 4.20 (dd, 1 H, $J_{6S,5}$ = 2.4 Hz, H-6_S); ^{13}C NMR (D$_2$O) δ: 46.0 (C-1), 53.2 (C-5), 64.5 (C-6), 69.9 (C-2), 74.0 (C-4), 76.7 (C-3). Anal. calcd. for $C_6H_{12}NO_3Cl$: C 39.68, H 6.66, N 7.71; found: C 39.46, H 6.76, N 7.52.

Enzyme kinetics

Yeast α-glucosidase (G-7256), rice α-glucosidase (G-9259), almond β-glucosidase (G-0395), and almond α-mannosidase (M-1266) were purchased from Sigma. Ammonium sulfate was removed from the stock yeast enzyme solution by washing through a Centricon-30 filter with 50 mM phosphate buffer (3 × 100 μL, pH 6.8), and diluting the final suspension 10-fold with 50 mM phosphate buffer (pH 6.8, 0.1% w/v BSA). All other enzymes were used as purchased. Inhibitor **1** was synthesized using a combination of literature procedures (20) and **2** was purchased from Sigma. Inhibition constants (K_i) of glycosidase-catalyzed hydrolyses were measured using a range of inhibitor concentrations (typically five concentrations) encompassing the K_i value, and a range of six substrate concentrations surrounding the Michaelis–Menton constant (K_m). The total volume for all assays was 350 μL. All assays were carried out using reaction times where less than 10% of the total amount of substrate was hydrolyzed. The K_m and the K_i values were calculated using nonlinear least-squares regression analysis of the data to a standard competitive-inhibition equation. The hydrolysis kinetics were followed using a CARY-3E UV–Vis spectrophotometer equipped with a Cary six-cell Peltier constant-temperature controller.

Yeast α-glucosidase and almond β-glucosidase kinetics

© 1998 NRC Canada

were carried out at 25°C in 50 mM phosphate buffer (0.1% w/v BSA) at pH 6.8 using 4-nitrophenyl α-(or β-)D-glucopyranoside as the substrate. The increase in absorbance due to the liberation of 4-nitrophenol was monitored at 400 nm and was linear with respect to time over the course of the measurements (1–3 min). The slope of the line was taken as the velocity for the hydrolysis of the substrate. A typical assay involved the incubation of the substrate (S) and inhibitor (I) for 10 min prior to the addition of enzyme (E).

The rice α-glucosidase kinetics were carried out at 37°C in 50 mM acetate buffer (0.1% w/v BSA) at pH 5.0 using α-D-glucopyranosyl 4-bromoisoquinolinium bromide as the substrate. The increase in absorbance due to the liberation of 4-bromoisoquinoline was monitored at 345 nm and was linear with respect to time over the course of the measurements (1–3 min). Due to the slow onset of inhibitor binding with this enzyme, assays were carried out where the inhibitor and glycosidase were preincubated together for 15 min before the addition of the substrate. Due to substrate inhibition, the substrate concentrations used did not exceed more than two times K_m.

Almond α-mannosidase kinetics were carried out at 25°C in 50 mM acetate buffer at pH 5.0 using 4-nitrophenyl α-D-mannopyranoside as the substrate. The increase in absorbance due to the liberation of 4-nitrophenol was monitored at 343 nm and was linear with respect to time for the duration of the measurements (10 min). The 4-nitrophenyl α-D-mannopyranoside and inhibitor were incubated together for 10 min prior to the addition of enzyme.

Acknowledgments

The authors are grateful to the Natural Sciences and Engineering Research Council of Canada, the British Columbia Health Research Foundation, and Simon Fraser University for financial support. In addition, the authors would like to thank M.K. Yang for carrying out the elemental analyses and M.M. Tracey for the acquisition of numerous NMR spectra.

References

1. (*a*) C.-H. Wong, R.L. Halcomb, Y. Ichikawa, and T. Kajimoto. Angew. Chem. Int. Ed. Engl. **34**, 412 (1995); (*b*) Angew. Chem. Int. Ed. Engl. **34**, 521 (1995); (*c*) S.H. Khan and R.A. O'Neill (*Editors*). Modern methods in carbohydrate synthesis. Vol. 1. Harwood Academic Publishers, The Netherlands. 1996.
2. (*a*) M.L. Sinnott. Chem. Rev. **90**, 1171 (1990); (*b*) G. Legler. Adv. Carbohydr. Chem. **48**, 319 (1990); (*c*) J.D. McCarter and S.G. Withers. Curr. Opin. Struct. Biol. **4**, 885 (1994).
3. K.M. Robinson, M.E. Begovic, B.L. Rhinehart, E.W. Heineke, J.-B. Ducep, P.R. Kastner, F.N. Marshall, and C. Danzin. Diabetes, **40**, 825 (1991).
4. M.J. Humphries, K. Matsumoto, S.L. White, and K. Olden. Cancer Res. **46**, 5215 (1986).
5. A. Karpas, G.W.J. Fleet, R.A. Dwek, S. Petursson, S.K. Namgoong, H.G. Ramsden, G.S. Jacob, and T.W. Rademacher. Proc. Natl. Acad. Sci. USA, **85**, 9229 (1988).
6. (*a*) S. Inouye, T. Tsuruoka, and T. Niida. J. Antibiot. **19**, 288 (1966); (*b*) A.B. Hughes and A.J. Rudge. Nat. Prod. Rep. 135 (1994).
7. D.E. Koshland. Biol. Rev. **28**, 416 (1953).
8. G. Legler and E. Julich. Carbohydr. Res. **128**, 61 (1984).
9. R. Saul, J.P. Chambers, R.J. Molyneux, and A.D. Elbein. Arch. Biochem. Biophys. **221**, 593 (1983).
10. N. Asano, A. Kato, M. Miyauchi, H. Kizu, T. Tomimori, K. Matsui, R.J. Nash, and R.J. Molyneux. Eur. J. Biochem. **248**, 296 (1997).
11. N. Asano, K. Oseki, E. Tomioka, H. Kizu, and K. Matsui. Carbohydr. Res. **259**, 243 (1994).
12. (*a*) P. Ermert and A. Vasella. Helv. Chim. Acta, **74**, 2043 (1991); (*b*) P. Ermert, A. Vasella, M. Weber, K. Rupitz, and S.G. Withers. Carbohydr. Res. **250,** 113 (1993).
13 (*a*) C.U Kim, W. Lew, M.A. Williams, H. Liu, L. Zhang, S. Swaminathan, N. Bischofberger, M.S. Chen, D.B. Mendel, C.Y. Tai, W.G. Laver, and R.C. Stevens. J. Am. Chem. Soc. **119**, 681 (1997); (*b*) I.B. Parr and B.A. Horenstein. J. Org. Chem. **62**, 7489 (1997).
14. T. Kajimoto, K.K.-C. Liu, R.L. Pederson, Z. Zhong, Y. Ichikawa, J.A. Porco, Jr., and C.-H. Wong. J. Am. Chem. Soc. **113**, 6187 (1991).
15. L. Hosie and M.L. Sinnott. Biochem. J. **226**, 437 (1985).
16. (*a*) A.I. Vogel. *In* Vogel's textbook of practical organic chemistry. 5th ed. *Edited by* B.S. Furniss, A.J. Hannaford, P.W.G. Smith, and A.R. Tatchell. The Bath Press, U.K. 1989. p. 647; (*b*) P. Kocienski and C. Pant. Carbohydr. Res. **110**, 330 (1982); (*c*) C. Brockway, P. Kocienski, and C. Pant. J. Chem. Soc. Perkin Trans. 1, 875 (1984); (*d*) Y. Kondo, K. Yabuuchi, H. Ono, and S. Hirano. Agric. Biol. Chem. **42**, 673 (1978).
17. (*a*) S.M. Anderson, M. Ebner, C.W. Ekhart, G. Gradnig, G. Legler, I. Lundt, A.E. Stutz, S.G. Withers, and T. Wrodnigg. Carbohydr. Res. **301**, 155 (1997); (*b*) M.N. Namchuck and S.G. Withers. Biochemistry, **34**, 16194 (1995); (*c*) K.-R. Roeser and G. Legler. Biochem. Biophys. Acta, **657**, 321 (1981); (*d*) M.P. Dale, H.E. Ensley, K. Kern, K.A.R. Sastry, and L.D. Byers. Biochemistry, **24**, 3530 (1985).
18. A.E. Derome and M.P. Williamson. J. Magn. Reson. **8**, 177 (1990).
19. A. Bax and S. Subramanian. J. Magn. Reson. **67**, 565 (1986).
20. (*a*) T. Kitahara, T. Ogawa, T. Naganuma, and M. Matsui. Agric. Biol. Chem. **38**, 2189 (1974); (*b*) B.P. Bashyal, H.-F. Chow, L.E. Fellows, and G.W.J. Fleet. Tetrahedron, **43**, 415 (1987); (*c*) S. Saito, H. Nakajima, M. Inaba, and T. Moriwake. Tetrahedron Lett. **30**, 837 (1989); (*d*) P.B. Anzeveno and L.J. Creemer. Tetrahedron Lett. **31**, 2085 (1990).

© 1998 NRC Canada

Thermodynamics of dissolving gaseous argon in different solvents

Giuseppe Graziano

Abstract: The solvation of argon in 10 different solvents at room temperature is analysed in terms of the theoretical framework developed by Lee. In order to perform calculations, we used the approach devised by Pierotti and firmly validated by Lee's theory. The fair agreement between the experimental and the calculated values of $\Delta G^{\bullet}$, $\Delta H^{\bullet}$, and $\Delta S^{\bullet}$ is carefully analysed. It proves that the excluded volume effect, due to cavity creation in the solvent, opposes the solubility process. This effect in water is exaggerated by the small size of the water molecules and is the cause of hydrophobicity. The qualitative difference between water and hydrazine with regard to the solvation enthalpy and entropy changes is rationalized on the basis of the contributions arising from the structural reorganization in the two solvents on solute insertion.

Key words: hydrophobic hydration, cavity creation, structural solvent reorganization.

Résumé : On utilise une approche théorique développée par Lee pour faire l'analyse de la solvatation de l'argon dans 10 solvants différents, à la température ambiante. Afin d'effectuer ces calculs, on a utilisé l'approche développée par Pierotti pour bien valider la théorie de Lee. On a fait une analyse approfondie du bon accord entre les valeurs expérimentales des $\Delta G^{\bullet}$, $\Delta H^{\bullet}$, et $\Delta S^{\bullet}$ et les valeurs calculées correspondantes. Il démontre que l'effet de volume exclu, provoqué par la création d'une cavité dans le solvant, s'oppose au processus de solubilité. Dans l'eau, cet effet est exagéré par la faible taille des molécules d'eau et elle est la cause du caractère hydrophobe. La différence qualitative entre l'eau et l'hydrazine concernant l'enthalpie et l'entropie de solvatation peut s'expliquer sur la base des contributions provenant de la réorganisation structurale dans les deux solvants lors de l'insertion du soluté.

Mots clés : hydratation hydrophobe, création de cavité, réorganisation structurale du solvant.

[Traduit par la rédaction]

Introduction

Hydrophobicity is a well-known natural phenomenon, but the actual cause of the low solubility of hydrocarbons in water is not yet completely understood (1). The importance of the topic is readily recognized, being mindful of its correlation with the formation and stability of micelles, double-layer membranes, and globular proteins (2). The most intriguing feature of hydrophobicity is the fact that, at room temperature, it arises from a negative entropy change. This experimental evidence has been difficult to reconcile with basic mixing thermodynamic theories, but in 1945 Frank and Evans suggested that the entropy decrease was due to "iceberg" formation around the nonpolar molecules (3). Water molecules, in order to avoid the waste of hydrogen bonds and to minimize the perturbation caused by the hydrocarbon moiety, reorganize themselves to give rise to an ordered structure, similar to the arrangement found in ice. The original idea of an enhancement of water structure around a nonpolar solute was largely accepted by the scientific community and reformulated in more sophisticated approaches by various authors (4, 5). It was also the basis for the introduction by Kauzmann of the concept of hydrophobic interaction, which should play a major role in determining the stability of globular proteins (6). However, thermodynamic investigations over large temperature ranges have shown that this simple picture is unable to explain satisfactorily all the details of the phenomenon (7, 8). The enthalpy and entropy changes associated with the transfer of nonpolar solutes from gas phase or organic liquid into water are strongly temperature dependent: at 25°C they are negative, pass through zero at a certain temperature, and then become positive. Around room temperature hydrophobicity would be caused by entropy, whereas at higher temperatures it would be governed by enthalpy (9). This finding is difficult to rationalize in terms of iceberg formation. The temperature dependence originates from the large positive heat capacity change (10) that is generally ascribed to the gradual melting of the structure formed. The heat capacity change, however, is large positive even beyond 100°C, where the iceberg would be melted (11–14). Finally, the Gibbs transfer energy change is little affected by temperature, being always positive and showing a very broad maximum around 100°C (7). This means that the temperature-dependent changes in enthalpy and entropy are large in magnitude, but largely compensate one another (15). These experimental results point out the inherent limitations of the structure-formation hypothesis to explain hydrophobicity. Moreover, many computer simulation studies have made clear that there is no iceberg formation around nonpolar moieties in water at room temperature (16). In addition, recent neutron-scattering measurements have shown that the structure of water in the hydration shell of a

Received September 30, 1997.

G. Graziano.[1] Dipartimento di Chimica, Università di Napoli "Federico II," Via Mezzocannone, 4–80134 Naples, Italy, and Dipartimento di Chimica, Università di Salerno, Via Salvador Allende – 84081 Baronissi (SA), Italy.

[1] Telephone: +39-81-547-6508. Fax: +39-81-552-7771. E-mail: barone@chemna.dichi.unina.it

© 1998 NRC Canada

nonpolar group is by no means more ordered than that of bulk water (17). This indicates that there is one molecular mechanism that determines hydrophobicity and is little dependent on temperature.

To study the solvation process it is necessary to consider the transfer of a molecule from a fixed position in the ideal gas phase to a fixed position in a liquid phase. The thermodynamic quantities of this process do not contain the effects associated with the difference in volume of the two phases. The thermodynamics of solvation processes were analysed in detail by Ben-Naim (18), who showed that the effects of volume and translational motion can be excluded by using the molar concentration scale. The thermodynamic quantities reported in the literature are usually defined using a mole-fraction-based standard state. Therefore they have to be corrected for the Ben-Naim standard state. The relationships required to pass from the conventional standard to the Ben-Naim standard are the following:

$$[1] \quad \Delta G^{\bullet} = \Delta G^{\circ} - RT \ln (RT/p^{\circ}v^{\circ}_1)$$

$$[2] \quad \Delta H^{\bullet} = \Delta H^{\circ} + RT(1 - \alpha^{\circ}_1 T)$$

$$[3] \quad \Delta S^{\bullet} = (\Delta H^{\bullet} - \Delta G^{\bullet})/T$$

$$[4] \quad \Delta C_p^{\bullet} = \Delta C_p^{\circ} + R\,[1 - 2\alpha^{\circ}_1 T - (\alpha^{\circ}_1)' T^2]$$

where $p^{\circ} = 1$ atm, v°_1 is the molar volume of the solvent, α°_1 is the thermal expansion coefficient of the solvent, $(\alpha^{\circ}_1)'$ is the corresponding temperature derivative, and the filled circle denotes the Ben-Naim standard.

In this paper, first the theory developed by Lee (19–22), to analyse and interpret the solvation process of nonpolar gases, is reexamined because, in our opinion, it seems the most reliable, proposed so far, from a physico-chemical point of view. Then, the solvation process of argon at room temperature in 10 different solvents is analysed, using the simple approach devised by Pierotti (23, 24), grounded on Scaled Particle Theory, SPT (25), and strongly validated by Lee's theory. The calculated values of $\Delta G^{\bullet}$, $\Delta H^{\bullet}$, and $\Delta S^{\bullet}$ are in satisfactory agreement with the experimental values. On this basis, the physical origin of hydrophobicity, or better, of solvophobicity, and the contribution arising from structural solvent reorganization upon solute insertion are rediscussed. Finally, an in-depth comparison between the transfer thermodynamics of He, Ar, and N_2 in water and hydrazine is carried out. Hydrazine shows slightly larger values of $\Delta G^{\bullet}$ than does water, but qualitatively different values of $\Delta H^{\bullet}$. Lumry and co-workers (26) used these experimental findings to propose a drastic reexamination of the origin of hydrophobicity. Actually, SPT calculations are also able to reproduce the values of thermodynamic quantities for hydrazine, and allow us to clarify the physical origin of the different behaviour of N_2H_4 and H_2O for the enthalpy changes. This fact lends further support to the physical interpretation of the low solubility of nonpolar gases in liquids arising from Lee's theory.

Lee s theory

From a microscopic point of view, according to the liquid perturbation theory (27), the process of inserting a solute molecule at a fixed point in a solvent can be dissected into two steps: (*a*) creation, in the solvent, of a cavity of suitable size to accommodate the solute molecule; (*b*) introduction, into the cavity, of the solute molecule, which then interacts with the solvent according to some potential law. Thus, the Gibbs energy change upon transferring the solute from the gas phase to a liquid phase is given by

$$[5] \quad \Delta G^{\bullet} = \Delta G_c + \Delta G_a$$

where ΔG_c is the reversible work to create a mole of cavities in the solvent, and ΔG_a is the Gibbs energy change associated with the turning on of solute–solvent interactions.

Lee pointed out that ΔG_c can be calculated from the following exact relationship of statistical mechanics (20, 28):

$$[6] \quad \Delta G_c = -RT \ln P_0 = RT\nu$$

where P_0 is the fraction of pure solvent molecular configurations that have a cavity of desired dimension at the point considered, and ν is a dimensionless number that has to be considered an effective solvation number of the solute. Unfortunately, this exact formula is not directly applicable, because it would require knowledge of the molecular distribution function of pure solvent, a system with a very large number of interacting particles. Actually, in recent years, eq. [6] has been used by performing computer simulations of the liquid phase and counting those instances possessing the desired cavity (29, 30). Additionally, eq. [6] demonstrates that ΔG_c arises from a purely entropic contribution, since it measures the fraction of molecular configurations of the pure solvent that become inaccessible to solvent molecules upon creation of the cavity (19, 20). Lee, by using fundamental relations of equilibrium thermodynamics, showed that the purely structural solvent reorganization associated with cavity creation is a compensating process, i.e., it does not affect the net Gibbs energy change because the enthalpic contribution exactly cancels the entropic one. In fact, it is

$$[7] \quad \Delta H_c = -RT^2 (\partial\nu/\partial T)_p$$

$$[8] \quad T{\cdot}\Delta S_c = -RT\nu - RT^2 (\partial\nu/\partial T)_p$$

The purely structural solvent reorganization is proportional to the temperature derivative of the effective solvation number. From a microscopic point of view, it can be stated that the enthalpy change due to the rupture of non-covalent interactions among solvent molecules exactly matches the entropy change associated with the gain of degrees of freedom upon breakage of the solvent–solvent interactions.

For the Gibbs energy change upon turning on the solute–solvent interactions, Lee (21, 22) pointed out that, on the basis of the potential distribution theorem of Widom (31), it can be expressed as

$$[9] \quad \Delta G_a = -RT \ln \langle \exp(-\psi_a/RT) \rangle$$

where ψ_a is the potential energy describing the solute–solvent interactions, and the brackets represent the ensemble average over the solvent molecular configurations containing the cavity. The enthalpy change is

$$[10] \quad \Delta H_a = \langle \psi_a \rangle + \Delta H_{ra}$$

where $\langle \psi_a \rangle$ is the ensemble average of the interaction energy and ΔH_{ra} represents the contribution of the structural solvent reorganization upon turning on the solute–solvent interactions. Lee (21, 22), exploiting an inversion relationship demonstrated

© 1998 NRC Canada

by Widom (31), showed that, when the fluctuations in the value of $< \psi_a >$ are small, the entropy change is

[11] $T \cdot \Delta S_a \approx \Delta H_{ra}$

On the basis of calculations by several authors (32), the condition of small fluctuations in the value of $< \psi_a >$ is valid for the interaction of nonpolar molecules with water. Therefore, the structural solvent reorganization associated with the process of turning on the attractive potential ψ_a around the cavity is a compensating process, because the entropy change cancels the enthalpy change. The net Gibbs energy change is due to a purely enthalpic contribution arising from the establishment of attractive interactions between the solute molecule in the cavity and all the surrounding solvent molecules, i.e., $\Delta G_a \approx < \psi_a >$.

In conclusion, the overall Gibbs energy change upon transferring the solute from gas phase to liquid phase is given by

[12] $\Delta G^\bullet = \Delta G_c + \Delta G_a = RT\nu + < \psi_a >$

This formula exactly matches that first proposed and used by Pierotti in the middle sixties (23). On the basis of this theoretical validation, we used Pierotti's approach, which is briefly outlined in the following section, to perform a series of calculations.

Pierotti s approach

Pierotti (23, 24) evaluated the Gibbs energy change to create a cavity in a solvent using the following theoretical equation derived from Scaled Particle Theory, SPT (25):

[13] $\Delta G_c = RT[K_0 + K_1(\sigma_2/\sigma_1) + K_2(\sigma_2/\sigma_1)^2 + K_3(\sigma_2/\sigma_1)^3]$

where $K_0 = -\ln(1-\xi)$; $K_1 = u = 3\xi/(1-\xi)$; $K_2 = u(u+2)/2$; $K_3 = \xi \cdot p v^\circ_1/RT$.

In these relations R is the gas constant; ξ is the volume packing density of pure solvent, which is defined as the ratio of the physical volume of a mole of solvent molecules over the molar volume of the solvent, v°_1 (i.e., $\xi = \pi \cdot \sigma_1^3 \cdot N_{Av}/6 \cdot v^\circ$); p is the hydrostatic pressure over the liquid; σ_1 and σ_2 are the hard-sphere diameters of the solvent and solute molecules, respectively. The temperature dependence of ΔG_c is due to the solvent packing density, which is a function of volume, which in turn depends on the temperature. The slight temperature dependence of molecular diameters is not considered in this work. The enthalpy change is calculated from the appropriate temperature derivative:

[14] $\Delta H_c = [\xi \alpha^\circ_1 \cdot RT^2/(1-\xi)^3]\,[(1-\xi)^2 + 3(1-\xi)(\sigma_2/\sigma_1) + 3(1+2\xi)(\sigma_2/\sigma_1)^2] + \xi p v^\circ_1 (\sigma_2/\sigma_1)^3$

where α°_1 is the thermal expansion coefficient of the solvent. The entropy change is

[15] $\Delta S_c = (\Delta H_c - \Delta G_c)/T$

Pierotti calculated the Gibbs energy change needed to turn on the attractive interactions between solute and solvent molecules, using the Lennard-Jones 6-12 potential, and a permanent dipole-inductive dipole term, integrated over the solvent molecules. In addition, he assumed that the solvent structure around the solute is uniform with the density equal to that of pure solvent. The resulting expression is

[16] $\Delta G_a = -(64/3) \cdot \xi \cdot \varepsilon_{12} \cdot (\sigma_{12}/\sigma_1)^3 - (8 \cdot \xi \cdot \mu_1^2 \cdot \alpha_2)/(\sigma_1 \cdot \sigma_{12})^3$

Table 1. Gibbs energy, enthalpy, and entropy changes associated with the dissolution of argon in several solvents at 298.15 K, according to the Ben-Naim standard state. For each solvent the experimental values are given in the first line, while the values calculated using Pierotti's procedure are given in the second line.

	$\Delta G^\bullet$	$\Delta H^\bullet$	$\Delta G^\bullet$
	J mol^{-1}	J mol^{-1}	J K^{-1} mol^{-1}
H_2O [a]	8367	–9629	–60.36
	7531	–8086	–52.38
D_2O [b]	8192	–11371	–65.61
	7390	–8444	–53.11
n-Hexane [c]	1890	–1182	–10.30
	986	591	–1.32
c-Hexane [c]	2726	661	–6.93
	1537	1088	–1.51
CCl_4 [c]	2654	1154	–5.03
	1539	823	–2.40
Benzene [c]	3538	2817	–2.42
	2235	2097	–0.46
MeOH [c]	3249	738	–8.42
	2599	–978	–12.00
EtOH [c]	3343	1289	–6.89
	2454	–1126	–12.01
N_2H_4 [d]	11546	10367	–3.95
	10666	3711	–23.33
EG [e]	8150	–830	–30.12
	7686	–815	–28.51

[a] Reference 8.
[b] Reference 33.
[c] Reference 34.
[d] Reference 35.
[e] EG stands for ethylene glycol; ref. 36.

where μ_1 is the dipole moment of the solvent molecule, α_2 is the polarizability of the solute molecule, $\sigma_{12} = (\sigma_1 + \sigma_2)/2$, and $\varepsilon_{12} = (\varepsilon_1 \varepsilon_2)^{1/2}$, where ε_1 and ε_2 are the Lennard-Jones potential parameters for the solvent and solute, respectively, measuring the magnitude of the maximum attractive potential energy. Pierotti considered ΔG_a purely enthalpic, $\Delta G_a = \Delta H_a$ (i.e., the interaction term has no entropic contribution), and independent of temperature. Therefore, in Pierotti's approach, the overall enthalpy and entropy changes are given by

[17] $\Delta H^\bullet = \Delta H_c + \Delta G_a$ and $\Delta S^\bullet = \Delta S_c$

The solvation of argon

The experimental values of the change in Gibbs energy, enthalpy, and entropy, corrected for the Ben-Naim standard state, associated with the dissolution of argon in several solvents at 25°C, are collected in Table 1 (8, 33–36). It is readily recognized that the values of $\Delta G^\bullet$ are always positive, also for nonpolar solvents such as *n*-hexane and CCl_4. The solvation process for argon at 25°C is not thermodynamically favoured under Ben-Naim standard state conditions, regardless of the physico-chemical properties of the solvent. Furthermore, this solvation process is strongly exothermic only in H_2O and D_2O, is slightly exothermic in *n*-hexane and ethylene glycol, slightly endothermic in all other solvents except hydrazine, where it is

© 1998 NRC Canada

Table 2. Molecular parameters and physical properties at 298.15 K: σ is the hard-sphere diameter, v°_1 is the molar volume, ε/*k* is the Lennard-Jones potential parameter, α°_1 is the thermal expansion coefficient, ξ is the volume packing density, and μ is the dipole moment.

	σ Å	v°_1 cm^3 mol^{-1}	ε/*k* K	$\alpha^\circ_1 \times 10^{-3}$ K^{-1}	ξ	μ debye
Helium	2.63[a]	—	6.03[a]	—	—	—
Argon	3.41[b]	—	125[b]	—	—	—
Nitrogen	3.70[a]	—	95[a]	—	—	—
H_2O	2.75[c]	18.08[c]	85.3[c]	0.255[c]	0.363[c]	1.84[c]
D_2O	2.75[d]	18.13[e]	85.3[d]	0.221[e]	0.361[d]	1.84[d]
n-Hexane	5.92[a]	131.62[a]	517[a]	1.296[f]	0.496[a]	—
c-Hexane	5.63[a]	108.75[a]	573[a]	1.214[c]	0.517[a]	—
CCl_4	5.37[a]	97.09[a]	536[a]	1.226[c]	0.503[a]	—
Benzene	5.26[a]	89.41[a]	531[a]	1.240[c]	0.513[a]	—
MeOH	3.69[a]	40.73[a]	234[a]	1.189[g]	0.389[a]	1.71[h]
EtOH	4.34[a]	58.68[a]	324[a]	1.089[g]	0.439[a]	1.69[h]
N_2H_4	3.62[a]	31.94[a]	138[a]	0.893[c]	0.468[a]	1.75[c]
EG	4.40[i]	55.36[h]	185[i]	0.663[g]	0.485[i]	2.28[h]

[a] Reference 37.
[b] Reference 24.
[c] Reference 19.
[d] We assumed that σ, ε/*k*, and μ are the same for H_2O and D_2O.
[e] Reference 38.
[f] Reference 23.
[g] Reference 39.
[h] Reference 40.
[i] We assumed these values for σ and ε/*k* on the basis of a comparison with ethanol and water. Additional data used: polarizability of helium, 0.204 Å^3; polarizability of argon, 1.63 Å^3; polarizability of nitrogen, 1.73 Å^3.

strongly endothermic. Therefore, there are large differences among the solvents for the values of $\Delta H^\bullet$. The entropy change is negative for all the solvents, but is very large only in H_2O and D_2O. It is useful to test whether Pierotti's approach is able to reproduce these experimental findings. The molecular parameters and physical properties, at 25°C, of the compounds considered in this work are collected in Table 2 (19, 23, 24, 37–40). The calculated values of ΔG_c, ΔG_a, and ΔH_c for all the solvents are reported in Table 3. The comparison between the experimental and calculated values of $\Delta G^\bullet$, $\Delta H^\bullet$, and $\Delta S^\bullet$ is made in Table 1. It is readily recognized that the agreement is satisfactory, in view of the physical features of the considered solvents, most of them being extensively hydrogen bonded.

The $\Delta G^\bullet$ values are reproduced quite well, as expected from Lee's theoretical analysis. The calculated values of $\Delta H^\bullet$ and $\Delta S^\bullet$ do not agree so well with the experimental values, as expected in view of the assumptions made by Pierotti. In any case the overall agreement is satisfactory, considering that no explicit information about the solvent structure has been introduced into the calculations. The success of SPT in reproducing the experimental data of the solvation process for nonpolar gases, first pointed out by Pierotti (22) and confirmed by several authors (1, 41), is striking and cannot be disregarded. Therefore, let us analyse the calculated values in detail.

The term ΔG_a is negative and little affected by the solvent considered, as can be seen from the values reported in Table 3. This finding is strongly validated by the theoretical calculations of dispersive interactions carried out by various authors

Table 3. Cavity and attractive terms contributing to the thermodynamics of dissolution of argon in several solvents. All values are calculated at 298.15 K, using Pierotti's procedure.

	ΔG_c J mol^{-1}	ΔG_a J mol^{-1}	ΔH_c J mol^{-1}
H_2O	18 460	–10 929	2 843
D_2O	18 260	–10 870	2 426
n-Hexane	11 929	–10 943	11 534
c-Hexane	14 236	–12 699	13 787
CCl_4	14 156	–12 617	13 440
Benzene	15 358	–13 123	15 220
MeOH	13 502	–10 903	9 925
EtOH	13 815	–11 361	10 235
N_2H_4	21 193	–10 527	14 238
EG	17 222	–9 536	8 721

(32). In addition, measurements of surface tension suggest that dispersive interactions between alkanes, and between alkanes and water, are very similar (42). Therefore, the term ΔG_a cannot be the cause of the low solubility of nonpolar gases in water. On the contrary, the term ΔG_c is large positive and strongly affected by the solvent considered: $\Delta G_c = 11\,929$ J mol^{-1} in *n*-hexane, 15 358 J mol^{-1} in benzene, 18 460 J mol^{-1} in water, and 21 193 J mol^{-1} in hydrazine. Equation [13] indicates that ΔG_c, for a fixed cavity size, is strongly dependent on the size of solvent molecules and on the solvent packing density. The Gibbs energy cost to create a cavity of a given radius is larger when the solvent molecules are smaller and the solvent packing density is higher. In other words, it is more difficult to create a cavity in a liquid of high packing density and constituted by small molecules, because the cavity does affect a larger number of solvent configurations. Water has the smallest molecular size among all other solvents (i.e., it corresponds roughly to the size of an oxygen atom), and this raises the value of ΔG_c. On the other hand, water also has a very low value of packing density because there are three-dimensional networks of H-bonds and this lowers the value of ΔG_c. Actually, the size effect in the case of water prevails, rendering ΔG_c very large. For the organic solvents the size effect prevails again but, in view of their large molecular diameters, the ΔG_c term is substantially lower than in water (see Table 3). Therefore, as stressed by Lucas (43) and mainly by Lee (19, 21), the origin of hydrophobicity is in the small size of the water molecules through an amplification of the excluded volume effect associated with the cavity creation (i.e., restriction of the translational degrees of freedom of the solvent molecules due to the cavity creation).

It is worth noting that SPT calculations also reproduce the experimental finding that argon is slightly more soluble in D_2O than in H_2O. The increase in solubility arises from the lower packing density of heavy water with respect to water ($\xi = 0.361$ for D_2O against 0.363 for H_2O), which renders the Gibbs energy cost to create the cavity smaller, as already pointed out by Jolicoeur and co-workers (44).

The overall enthalpy change represents the sum of two terms: (*i*) ΔG_a, which is negative and more or less similar for all the solvents (see above); (*ii*) ΔH_c, which is positive and strongly dependent on the solvent considered. Indeed, ΔH_c is a function of σ_1, ξ, and α°_1. Actually, it is directly proportional to α°_1, the thermal expansion coefficient of the solvent. It is

© 1998 NRC Canada

well known that the value of α°_1 for water and heavy water is abnormally small with respect to all other solvents at room temperature. As a consequence, the values of ΔH_c in H_2O and D_2O are the lowest among all other solvents, and the total enthalpy change, dominated by the ΔG_a term, proves to be large negative. In addition, the process is slightly more exothermic in D_2O than in H_2O, because α°_1 is lower for heavy water than for water. For the other solvents, except for hydrazine (see next section), the ΔH_c term is almost equal to ΔG_a but of opposite sign, and the solvation process proves to be very slightly endothermic or exothermic.

In Pierotti's approach, the overall entropy change takes into account only the entropy change associated with cavity creation, since ΔG_a is considered purely enthalpic. The entropy of cavity creation, according to eq. [8], is given by the sum of two terms: the first represents the contribution from the excluded volume effect (i.e., the exclusion of solvent molecules from the space occupied by the solute molecule) and has a negative sign; the second term represents the structural solvent reorganization as a response to volume exclusion (i.e., the breakage of some non-covalent interactions among solvent molecules) and has a positive sign. The contribution from the excluded volume effect is the prevailing one, and the calculated values of $\Delta S^\bullet$ are negative for all solvents, as can be seen in Table 1.

It is worth noting that, although the calculated values of $\Delta G^\bullet$ in some cases are very close to the experimental ones, Pierotti's approach does not really constitute a method for the prediction of $\Delta G^\bullet$ values. It strongly depends on the value of σ_1, which is determined from experimental solubility data (37), as already stressed by several authors (45). In this respect, it is not obvious that molecules such as water, *n*-hexane, and benzene can be described accurately as impenetrable spheres with a defined hard-sphere diameter. Indeed, Madan and Lee (30) emphasized that there are two sizes associated with water: the commonly used hard-sphere diameter, 2.75 Å, close to the first peak of the radial oxygen–oxygen distribution function, and the Lennard-Jones size parameter, which ranges from 2.96 to 3.24 Å for the different water models (46). Furthermore, experimentally known properties of the solvent, such as v°_1 and α°_1, are used in the application of SPT. These quantities serve to preserve as much information as possible about the real attractive interactions among the solvent molecules (i.e., H-bonds play important roles in determining the unusually small values for the molar volume and thermal expansion coefficient of water).

In any case, the success of Pierotti's approach in the case of water is a strong validation of Lee's theory, since in SPT the water molecules do not have orientational degrees of freedom. The work of cavity formation depends on the ability of the solvent to spontaneously generate atomic-sized cavities (20, 25, 29, 47). SPT indicates that the frequency of occurrence of atomic-sized cavities is low in water compared to that in common organic solvents, because the size of a water molecule is small and, consequently, the free volume in water is distributed in smaller packets. Computer simulations on water models with and without H-bonding potential (29, 30, 48) have confirmed that the Gibbs energy cost to create a cavity in water does not depend on the presence of H-bonds. This means that the purely structural reorganization of H-bonds is a compensating process that does not affect the Gibbs energy change. Recently, various authors (49–51), by using different theoretical approaches, concluded that the solvent reorganization contributions to the enthalpy and the entropy exactly cancel one another. The possibility of neglecting the solvent reorganization in calculating the hydration Gibbs energies also explains the success of the integral equation theory of Pratt and Chandler (52), because an essential ingredient of the theory is the assumption that water does not reorganize itself around nonpolar solutes. Finally, de Souza and Ben-Amotz (53) showed that large positive solvation Gibbs energies in water can be accounted for by a hard-sphere model, which has no orientational order, as a consequence of entropy changes associated with the repulsive translational constraints imposed on water molecules by a solute. Therefore, the analysis performed leads to the conclusion, with Lucas, Lee, and Ben-Amotz, that the low solubility of nonpolar gases in water is determined by the small size of water molecules, which amplifies the excluded volume effect due to cavity creation.

Hydrazine versus water behaviour

The dissolution of helium, argon, and nitrogen in water and hydrazine at room temperature has the following thermodynamic features (see Table 4): (*i*) $\Delta G^\bullet$ is large positive in both H_2O and N_2H_4; (*ii*) $\Delta H^\bullet$ is large negative in H_2O, but large positive in N_2H_4 (this is not true for He because it has very small values of both the polarizability and the Lennard-Jones parameter); (*iii*) $\Delta S^\bullet$ is large negative in H_2O and small negative in N_2H_4; (*iv*) $\Delta C_p{}^\bullet$ is large positive in H_2O and equal to zero in N_2H_4. On the basis of the experimental values collected in Table 4, the solvation process in water at 25°C seems to be dominated by entropy, whereas the solvation process in hydrazine at 25°C seems to be dominated by enthalpy. However, as well emphasized by the calculated values of ΔG_c and ΔG_a (see Table 5), it is always the excluded volume effect associated with cavity creation that plays the fundamental role in the transfer process. For the sake of clarity, in the following, we restrict our attention to the solvation of argon, but the conclusions are valid also for helium and nitrogen.

The values of ΔG_a are practically identical in the two solvents: $\Delta G_a = -10\,929$ J mol^{-1} in H_2O and $-10\,527$ J mol^{-1} in N_2H_4. On the contrary, $\Delta G_c = 18\,460$ J mol^{-1} in H_2O and 21 193 J mol^{-1} in N_2H_4. The reversible work necessary to create a suitable cavity for accommodating argon is larger in hydrazine than in water because, even though the water molecule is smaller ($\sigma_1 = 2.75$ Å for H_2O against 3.62 Å for N_2H_4), liquid hydrazine has a packing density greater than that of water ($\xi = 0.468$ for N_2H_4 against 0.363 for H_2O). For the pair H_2O–N_2H_4 the effect of the solvent packing density on ΔG_c prevails over the effect of the molecular dimension and argon is less soluble in hydrazine than in water. It has to be stressed that this experimental finding emerges directly from SPT calculations, which reproduce well the measured values of $\Delta G^\bullet$. According to Lee's theory, the substantial difference between N_2H_4 and H_2O for the value and sign of $\Delta H^\bullet$ and the value of $\Delta S^\bullet$ must be due to the purely structural reorganization process of solvent molecules upon cavity creation and turning on of solute–solvent interactions. Pierotti's approach allows us to estimate only the structural reorganization upon cavity creation and so the agreement between the calculated and the experimental values of $\Delta H^\bullet$ and $\Delta S^\bullet$ is expected to be less

© 1998 NRC Canada

Table 4. Gibbs energy, enthalpy, entropy, and heat capacity changes associated with the dissolution of helium, argon, and nitrogen in water and hydrazine at 298.15 K, according to the Ben-Naim standard state. For each solvent the experimental values are given in the first line, while the values calculated using Pierotti's procedure are given in the second line.

	$\Delta G^\bullet$	$\Delta H^\bullet$	$\Delta S^\bullet$	$\Delta C_p^\bullet$	
	J mol^{-1}	J mol^{-1}	J K^{-1} mol^{-1}	J K^{-1} mol^{-1}	
	11 525	1 753	–32.78	121.8	Water[a]
	10 695	179	–35.27	—	
He					
	13 686	7 108	–22.06	0	Hydrazine[b]
	12 688	7 608	–17.04	—	
	8 367	–9 629	–60.36	194.5	Water[a]
	7 531	–8 086	–52.38	—	
Ar					
	11 546	10 367	–3.95	0	Hydrazine[b]
	10 666	3 711	–23.33	—	
	10 725	–8 149	–61.79	221.1	Water[c]
	10 232	–7 549	–59.64	—	
N_2					
	12 873	11 697	–3.95	0	Hydrazine[b]
	13 767	6 037	–25.93	—	

[a] Reference 8.
[b] Reference 35.
[c] Reference 33.

Table 5. Cavity and attractive terms contributing to the thermodynamics of dissolution of helium, argon, and nitrogen in water (first line) and hydrazine (second line). All values are calculated at 298.15 K, using Pierotti's procedure.

	ΔG_c	ΔG_a	ΔH_c
	J mol^{-1}	J mol^{-1}	J mol^{-1}
Helium	12 361	–1 666	1 845
	14 327	–1 639	9 247
Argon	18 460	–10 929	2 843
	21 193	–10 527	14 238
Nitrogen	21 051	–10 819	3 270
	24 105	–10 338	16 375

satisfactory. In any case, ΔH_c = 2843 J mol^{-1}, $\Delta H^\bullet$ = –8086 J mol^{-1}, and $\Delta S^\bullet$ = –52.38 J K^{-1} mol^{-1} in H_2O, whereas ΔH_c = 14 238 J mol^{-1}, $\Delta H^\bullet$ = 3711 J mol^{-1}, and $\Delta S^\bullet$ = –23.33 J K^{-1} mol^{-1} in N_2H_4. It is worth noting that the calculations indicate, without any special assumptions, that the solvation of argon is strongly exothermic in water and endothermic in hydrazine. This striking difference requires an explanation.

The importance of the comparison between the two liquids was first recognized by Bernal and Fowler in their pioneering work of 1933 (54). Many of the physical properties of water and hydrazine are almost identical. Melting points, boiling points, heats and entropies of vaporization, densities, surface tensions, dipole moments, and viscosities are very similar. In all probability, the existence in both liquids of a three-dimensional network of H-bonds is the origin of the similarities (26). The two liquids, however, differ in those properties that are attributed to the unique structural features of water. Hydrazine does not expand upon freezing, exhibits no liquid density maximum, has a remarkably lower dielectric constant, and a heat capacity per atom lower than that of water (26). Indeed, one essential difference between H_2O and N_2H_4 that is readily recognized is their difference in functionality. Water is almost unique in being 2–2 functional, so that there is an exact matching. In addition, these functions exert their maximum action along the tetrahedral directions that are equivalent in each function. Thus a variety of three-dimensional structures possessing similar connectivity are favoured, and external perturbations do not cause drastic alterations (i.e., the number of H-bonds is very little affected). Hydrazine is 2–4 functional, with an excess of hydrogens over lone-pairs, and is involved in a conformational equilibrium between the *gauche* and *cis* rotamers, which are separated by an energy barrier. Therefore, hydrazine would be a model of inhibited water, a liquid with a connectivity system similar to that of water, but free of the fluctuational processes responsible for the anomalous behaviour of water (26). These features of N_2H_4 significantly affect the purely structural reorganization of solvent molecules upon solute insertion. In all probability, ΔH_c is large positive in N_2H_4 because hydrazine is forced to sacrifice some H-bonds in the reorganization upon cavity creation, due to its molecular structure. The loss of H-bonds, in view of their strength, gives a large positive contribution to the enthalpy change, overwhelming the negative contribution arising from the solute–solvent interactions. From this analysis, the large positive value of $\Delta H^\bullet$ found for solvation in N_2H_4 is understandable. At the same time, the breakage of H-bonds gives a large positive contribution to the entropy change, partially compensating for the large negative contribution arising from the excluded volume effect associated with cavity creation. Therefore, $\Delta S^\bullet$ in N_2H_4 is negative, but lower than in H_2O. In addition, the experimental evidence that the transfer heat capacity change is zero demonstrates the absence of significant enthalpy fluctuations in liquid hydrazine.

In water the molecules are capable of assuming a variety of three-dimensional structures without sacrificing H-bonds, in view of the 2–2 tetrahedral functionality. Therefore, the structural reorganization process associated with solute insertion does not significantly affect the number of H-bonds and $\Delta H^\bullet$ is dominated by the negative contribution of solute–solvent interactions, while $\Delta G^\bullet$ is dominated by the excluded volume effect. Indeed, for H_2O, $\Delta H^\bullet$ and $\Delta S^\bullet$ are both large negative. It has to be stressed that the purely structural reorganization process of water molecules can be described, in thermodynamic terms, with the simple two-state model developed by Muller (55), and later modified by Lee and Graziano (56) to render it compensating, as required by the theory. This model reproduces well the large positive heat capacity change associated with the transfer into water of nonpolar solutes and its temperature dependence.

The analysis performed shows that the striking difference between H_2O and N_2H_4 for the values of $\Delta H^\bullet$ and $\Delta S^\bullet$ is perfectly understandable within Lee's theory. Indeed, the calculations performed following Pierotti's procedure are in qualitative agreement with experimental values. The existence of a very poor (unfavourable) reaction field between water and nonpolar solutes, giving rise to a positive contribution to the

© 1998 NRC Canada

enthalpy change, and masked by the negative contribution arising from the relaxation process of water clusters as inferred by Lumry and co-workers (26) on the basis of the experimental values of $\Delta H^{\bullet}$ in hydrazine, is not justified. All theoretical calculations, both ab initio and semi-empirical, performed so far to characterize the interaction of water with nonpolar molecules, have shown the existence of a net attractive reaction field (32). Therefore, the reexamination of the origin of hydrophobicity carried out by Lumry and co-workers, being grounded in a physically incorrect idea, is simply wrong.

Acknowledgments

This work was supported by grants from the Italian National Research Council (C.N.R., Rome) and the Italian Ministry for University and Scientific and Technological Research (M.U.R.S.T., Rome).

References

1. W. Blokzijl and J.B.F.N. Engberts. Angew. Chem. Int. Ed. Engl. **32**, 1545 (1993).
2. C. Tanford. The hydrophobic effect. Wiley, New York. 1980.
3. H.S. Franks and M.W. Evans. J. Chem. Phys. **13**, 507 (1945).
4. G. Nemethy and H.A. Scheraga. J. Chem. Phys. **36**, 3382 (1962); J. Chem. Phys. **36**, 3401 (1962); J. Phys. Chem. **66**, 1773 (1962).
5. F. Franks (*Editor*). Water, a comprehensive treatise. Vol. 2. Plenum Press, New York. 1973.
6. W. Kauzmann. Adv. Protein Chem. **14**, 1 (1959).
7. P.L. Privalov and S.J. Gill. Adv. Protein Chem. **39**, 191 (1988).
8. D. Krause and B.B. Benson. J. Solution Chem. **18**, 823 (1989).
9. K.A. Dill. Biochemistry, **29**, 7133 (1990).
10. G. Graziano and G. Barone. J. Am. Chem. Soc. **118**, 1831 (1996).
11. M. Costas, B. Kronberg, and R. Silveston. J. Chem. Soc. Faraday Trans. **90**, 1513 (1994).
12. S.J. Gill, S.F. Dec, G. Olofsson, and I. Wadso. J. Phys. Chem. **89**, 3758 (1985).
13. G.I. Makhatadze and P.L. Privalov. J. Chem. Thermodyn. **19**, 467 (1988); J. Solution Chem. **18**, 927 (1989).
14. R. Crovetto, R. Fernandez-Prini, and M.L. Japas. J. Chem. Phys. **76**, 1077 (1982).
15. A. Ben-Naim. Biopolymers, **14**, 1337 (1975); R. Lumry, E. Battistel, and C. Jolicoeur. Faraday Symp. Chem. Soc. **17**, 93 (1982); E. Grunwald. J. Am. Chem. Soc. **108**, 5726 (1986).
16. P.J. Rossky and M.J. Karplus. J. Am. Chem. Soc. **101**, 1913 (1979); M. Mezei and D.L. Beveridge. J. Chem. Phys. **74**, 622 (1981); D.C. Rapaport and H.A. Scheraga. J. Phys. Chem. **86**, 873 (1982); D. van Belle and S.J. Wodak. J. Am. Chem. Soc. **115**, 647 (1993).
17. J.L. Finney and A.K. Soper. Chem. Soc. Rev. **23**, 1 (1994); J.L. Finney. Faraday Discuss. Chem. Soc. **103**, 1 (1996).
18. A. Ben-Naim. Hydrophobic interactions. Plenum Press, New York. 1980; Solvation thermodynamics. Plenum Press, New York. 1987.
19. B.K. Lee. Biopolymers, **24**, 813 (1985); *In* Mathematics and computers in biomedical applications. *Edited by* J. Eisenfeld and C. De Lisi. Elsevier, North-Holland. 1985. pp. 3–11.
20. B.K. Lee. J. Chem. Phys. **83**, 2421 (1985).
21. B.K. Lee. Biopolymers, **31**, 993 (1991); Methods Enzymol. **259**, 555 (1995).
22. B.K. Lee. Biophys. Chem. **51**, 271 (1994).
23. R.A. Pierotti. J. Phys. Chem. **67**, 1840 (1963); J. Phys. Chem. **69**, 281 (1965).
24. R.A. Pierotti. Chem. Rev. **76**, 717 (1976).
25. H. Reiss. Adv. Chem. Phys. **9**, 1 (1966).
26. M.S. Ramadan, D.F. Evans, and R. Lumry. J. Phys. Chem. **87**, 4538 (1983); M.S. Ramadan, D.F. Evans, R. Lumry, and S. Philson. J. Phys. Chem. **89**, 3405 (1985); R. Lumry. Methods Enzymol. **259**, 628 (1995).
27. D. Chandler, J.D. Weeks, and H.C. Andersen. Science, **220**, 787 (1983).
28. R.C. Tolman. The principles of statistical mechanics. Oxford University, London. 1938.
29. A. Pohorille and L.R. Pratt. J. Am. Chem. Soc. **112**, 5066 (1990); L.R. Pratt and A. Pohorille. Proc. Natl. Acad. Sci. U.S.A. **89**, 2995 (1992).
30. B. Madan and B.K. Lee. Biophys. Chem. **51**, 279 (1994).
31. B. Widom. J. Phys. Chem. **86**, 869 (1982).
32. W.L. Jorgensen, J. Gao, and C. Ravimohan. J. Phys. Chem. **89**, 3470 (1985); F. Floris and J. Tomasi. J. Comput. Chem. **10**, 616 (1989); P. Linse. J. Am. Chem. Soc. **112**, 1744 (1990).
33. E. Wilhelm, R. Battino, and R.J. Wilcock. Chem. Rev. **77**, 219 (1977).
34. E. Wilhelm and R. Battino. Chem. Rev. **73**, 1 (1973).
35. E.T. Chang, N.A. Gokcen, and T.M. Poston. J. Phys. Chem. **72**, 638 (1968).
36. A. Ben-Naim. J. Phys. Chem. **72**, 2998 (1968).
37. E. Wilhelm and R. Battino. J. Chem. Phys. **55**, 4012 (1971).
38. G.S. Kell. J. Chem. Eng. Data, **12**, 66 (1967).
39. J.F. Alary, M.A. Simard, J. Dumont, and C. Jolicoeur. J. Solution Chem. **11**, 755 (1982).
40. R.C. Weast (*Editor*). Handbook of chemistry and physics. Chemical Rubber Co., Cleveland, Ohio. 1970.
41. J. Tomasi and M. Persico. Chem. Rev. **94**, 2027 (1994).
42. A. Nicholls, K.A. Sharp, and B. Honig. Proteins, **11**, 281 (1991); R.M. Jackson and M.J.E. Sternberg. Protein Eng. **7**, 371 (1994).
43. M. Lucas. J. Phys. Chem. **80**, 359 (1976).
44. C. Jolicoeur and G. Lacroix. Can. J. Chem. **51**, 3051 (1973); P.R. Philip and C. Jolicoeur. J. Solution Chem. **4**, 105 (1975).
45. M.H. Abraham and A. Nasehzadeh. J. Chem. Soc. Faraday Trans. **77**, 321 (1981); N. Morel-Desrosiers and J.P. Morel. Can. J. Chem. **59**, 1 (1981); J.P.M. Postma, H.J.C. Berendsen, and J.R. Haak. Faraday Symp. Chem. Soc. **17**, 55 (1982).
46. W.L. Jorgensen, J. Chandrasekhar, J.D. Madura, R.W. Impey, and M.L. Klein. J. Chem. Phys. **79**, 926 (1983).
47. B.J. Berne. Proc. Natl. Acad. Sci. U.S.A. **93**, 8800 (1996); G. Hummer, S. Garde, A.E. Garcia, A. Pohorille, and L.R. Pratt. Proc. Natl. Acad. Sci. U.S.A. **93**, 8951 (1996).
48. A. Wallquist and D.G. Covell. Biophys. J. **71**, 600 (1996); S.R. Durell and A. Wallquist. Biophys. J. **71**, 1695 (1996).
49. H.A. Yu and M.J. Karplus. J. Chem. Phys. **89**, 2366 (1988).
50. B. Guillot, Y. Guissani, and S. Bratos. J. Chem. Phys. **95**, 3643 (1991); B. Guillot and Y. Guissani. J. Chem. Phys. **99**, 8075 (1993).
51. T. Lazaridis and M.E. Paulaitis. J. Phys. Chem. **98**, 635 (1994); H.S. Ashbaugh and M.E. Paulaitis. J. Phys. Chem. **100**, 1900 (1996).
52. L.R. Pratt and D.J. Chandler. J. Chem. Phys. **67**, 3683 (1977); J. Chem. Phys. **73**, 3434 (1980).
53. L.S.E. de Souza and D. Ben-Amotz. J. Chem. Phys. **101**, 9858 (1994).
54. J.D. Bernal and R.H. Fowler. J. Chem. Phys. **1**, 515 (1933).
55. N. Muller. Acc. Chem. Res. **23**, 23 (1990).
56. B.K. Lee and G. Graziano. J. Am. Chem. Soc. **118**, 5163 (1996).

Appendix

It may be useful to verify how small changes in the parameter values can affect the results of Pierotti's approach. By fixing σ_1 = 2.80 Å (ξ = 0.383) for water, ΔG_c = 20043 J mol^{-1} and ΔH_c

© 1998 NRC Canada

= 3226 J mol^{-1}: the cavity terms are sensitive to small variations in the value of the hard-sphere diameter. Furthermore, by using $\mu_1 = 2.45$ D, the dipole moment of a water molecule in liquid water, in connection with $\sigma_1 = 2.80$ Å, $\Delta G_a = -12\,313$ J mol^{-1}. The corresponding thermodynamic functions calculated for the hydration of argon at 25°C are $\Delta G^\bullet = 7730$ J mol^{-1}, $\Delta H^\bullet = -9087$ J mol^{-1}, and $\Delta S^\bullet = -56.40$ J K^{-1} mol^{-1}. Such figures are in slightly better agreement with the experimental values than those calculated with $\sigma_1 = 2.75$ Å and $\mu_1 = 1.84$ D (see Table 1). The aim of the work, however, is not the optimization of the values calculated by means of Pierotti's approach. The purpose is to show that the excluded volume effect, the fundamental ingredient of SPT, plays the dominant role in determining solvophobicity.

© 1998 NRC Canada

Syntheses and Fe(II)/Fe(III) equilibria of the new multidentate ligands pyridine-2-phosphonic-6-carboxylic acid and 2,6-pyridinediphosphonic acid for the use of their iron chelates as catalysts for the oxidation of H_2S to S_8 by air

Dian Chen, Arthur E. Martell, Ramunas J. Motekaitis, and Derek McManus

Abstract: The syntheses of two terdentate chelating agents, pyridine-2-phosphonic-6-carboxylic acid (2PP6C) and 2,6-pyridinediphosphonic acid (2,6PDPA), are described. The stepwise stability constants for the ferric complexes at 25.0°C and $\mu = 0.100$ M (KNO_3) are log $K_{ML} = 15.97$ and log $K_{ML_2} = 9.50$ for 2PP6C, and log $K_{ML} = 20.87$ and log $K_{ML_2} = 7.81$ for 2,6PDPA. Under the same conditions the stepwise formation constants for the ferrous chelates are log $K_{ML} = 8.70$ and log $K_{ML_2} = 5.10$ for 2PP6C, and log $K_{ML} = 10.12$ and log $K_{ML_2} = 5.33$ for 2,6PDPA. The stabilities of the Fe(III) and Fe(II) chelates are high enough to prevent precipitation of $Fe(OH)_3$ and FeS, respectively, from solutions having pH as high as 10.0. The rates of oxidative degradation of these ligands are very slow when the iron chelates are used as redox catalysts for the oxidation of H_2S to S_8 by air. The rates of oxidative degradation are immeasurably slow when the iron chelates are used with sodium thiosulfate as a radical scavenger.

Key words: 2,6-pyridinediphosphonic acid, pyridine-2-phosphonic-6-carboxylic acid, hydrogen sulfide oxidation, oxidative degradation, nitrilotriacetic acid.

Résumé : On décrit les synthèses de deux agents chélatants terdentates, l'acide pyridine-2-phosphonique-6-carboxylique (2PP6C) et l'acide pyridine-2,6-diphosphonique (2,6PDPA). Les constantes de stabilité progressives pour les complexes ferriques à 25°C et à $\mu = 0{,}100$ M (KNO_3) sont log $K_{ML} = 15{,}97$ et log $K_{ML_2} = 9{,}50$ pour le 2PP6C et log $K_{ML} = 20{,}87$ et log $K_{ML_2} = 7{,}81$ pour le 2,6PDPA. Dans les mêmes conditions, les constantes de formation progressives pour les chélates ferreux sont log $K_{ML} = 8{,}70$ et log $K_{ML_2} = 5{,}10$ pour le 2PP6C et log $K_{ML} = 10{,}12$ et log $K_{ML_2} = 5{,}33$ pour le 2,6PDPA. Les stabilités des chélates Fe(III) et Fe(II) sont suffisamment élevées pour empêcher la précipitation respectivement du $Fe(OH)_3$ et du FeS à partir de solutions ayant des pH allant jusqu'à 10,0. Les vitesses de dégradation oxydantes de ces ligands sont extrêmement lentes lorsqu'on utilise des chélates de fer comme catalyseurs redox pour l'oxydation du H_2S en S_8 par l'air. Les vitesses de dégradations oxydantes sont extrêmement lentes lorsqu'on utilise les chélates de fer avec du thiosulfate de sodium comme piège à radicaux.

Mots clés : acide pyridine-2,6-diphosphonique, acide pyridine-2-phosphonique-6-carboxylique, oxydation du sulfure d'hydrogène, dégradation oxydante, acide nitrilotriacétique.

[Traduit par la rédaction]

Introduction

In industrial, chelated iron sulfur recovery processes, which generally operate within a pH range of 7.0–8.5, NTA, EDTA, and HEDTA are typically used as the primary iron(III) chelators (1–4). In some cases the iron sequestering ability of the solution is increased by addition of compounds such as hexitols that form stable, soluble iron(III) complexes at high pH. High stability of the Fe(III) chelate is an important requirement for catalysts that are effective for the conversion of H_2S to S_8, since the acidic gas H_2S is best absorbed in a mildly alkaline solution in which HS^- is formed and is oxidized under these conditions to S_8. In this pH range the precipitation of $Fe(OH)_3$ must be prevented by using chelates of sufficiently high stability.

The Fe(III) chelates of dipicolinic acid (pyridine-2,6-dicarboxylic acid, PDCA) are less stable than those of NTA and EDTA (5, 6), and Fe(III) PDCA cannot be used as a catalyst above pH about 6.0 without the precipitation of $Fe(OH)_3$. This is highly unsatisfactory, since the low solubility of H_2S at this pH would require both a larger absorber vessel and a catalyst solution volume. One advantage of PDCA, however, is the

Received July 25, 1997.

D. Chen, A.E. Martell,[1] and R.J. Motekaitis. Department of Chemistry, Texas A&M University College Station, Texas 77842-3012, U.S.A.
D. McManus. U.S. Filter Corporation. Plainfield, Illinois 60544, U.S.A.

[1] Author to whom correspondence may be addressed. Telephone: (409) 845-2011. Fax: (409) 845-4719. E-mail: martell@chemvx.tamu.edu

© 1998 NRC Canada

very slow rate of oxidative degradation of the ligand, relative to aminocarboxylates, in the reoxidation by air of the ferrous chelate to the ferric form. With EDTA, NTA, and other aminocarboxylates, the rate of oxidative degradation of the ligand in the reoxidation step, even in the presence of free-radical scavengers such as thiosulfate, is appreciable (2, 3) and generally requires continuous replenishment of the chelating ligand in an amount equivalent to that lost by oxidative degradation. The replenishment of the chelating ligand increases the operating cost and is a significant factor in generally limiting the capacity of the plant.

In this paper two ligands are described, pyridine-2-phosphonic-6-carboxylic acid (2PP6C) and 2,6-pyridinediphosphonic acid (2,6PDPA) (7), which form stable Fe(III,II) chelates and are effective catalysts for the oxidation of H_2S to S_8. As shown by molecular mechanics the replacement of a carboxylate in PDCA by a phosphonate donor group produces a ligand with dimensions more suitable for coordinating iron(III) (8). Moreover these phosphonates resemble PDCA in that they undergo negligible degradation when the ferrous chelate is oxidized to the ferric form. The ligand 2PP6C was first described by Boduszek (9). The disphosphonic acid 2,6PDPA is apparently a new compound. Syntheses and iron(II,III) equilibria of 2PP6C and 2,6PDPA have been deposited as supplementary material.[2]

Experimental

Materials and reagents

The following are the sources of reagents and starting materials used in synthesis: butyllithium (10.0 M solution in hexane, Aldrich Co.); picolinic acid (99%, Aldrich Co.); HAc (GR, Glacial, EM Sciences, a Division of EM Industries, Inc.); H_2O_2 (30% aqueous solution EM Sciences); Me_2SO_4 (99%, Aldrich Co.); CH_2Cl_2 (Reagent ACS, Fisher Scientific Co.); pyridine-*N*-oxide (98%, Janssen Chimica); $Fe(NO)_3{\cdot}9H_2O$ (certified ACS, Fisher Scientific Co.); $Na_2S_2O_3$ (GR, EM Sciences); $CuCl_2{\cdot}2H_2O$ (Baker analyzed reagent); MeOH (HPLC grade, EM Sciences); H_2S (99.5%, Gas Analytical Service); hexadecyltrimethylammonium bromide (99%, Sigma); EDTA (ACS, Aldrich Co.); KNO_3 (ACS, Aldrich Co.). *Standard KOH*: a carbonate-free solution of the titrant, KOH, was prepared by dilution of analytical concentrate "Dilut-It" (J.T. Baker Chemical Co.) with double-distilled water under a stream of purified Ar gas. The solution was standardized by titration with primary standard potassium acid phthalate.

Synthesis of pyridine-2-phosphonic-6-carboxylic acid (2PP6C)

Pyridine-2-carboxylic acid N-*oxide*, **1**. Picolinic acid (20.0 g) was treated with 125 mL glacial acetic acid and 22 mL of 30% H_2O_2, and the reaction mixture was heated to 70–80°C for 3 h. Another 11 mL of 30% H_2O_2 was then added, and the temperature was maintained at 70°C for 18 h. The solvent was removed by vacuum evaporation. Compound **1** was obtained as a white solid and was used directly in the next step.

Ethyl pyridine-N-*oxide-2-carboxylate,* **2**. To compound **1** 130 mL of EtOH was added, and the mixture was treated with HCl gas for 30 min. Then the solution was heated to reflux for 30 min. The solvent was removed by evaporation under reduced pressure. To the residue, 130 mL of EtOH was then added, and the above procedure was repeated twice. Compound **2** was obtained as a white solid and was used directly in the next step.

Ethyl N-*methoxypyridinium-2-carboxylate methyl sulfate*, **3**. Dimethyl sulfate (19.5 mL) was slowly added to compound **2**, prepared in the previous step, over a 30 min period. The reaction mixture was then heated at 85°C for 3 h to ensure complete reaction. Compound **3** was obtained as a yellow oil and was used directly in the next step.

Triethyl pyridine-2-phosphate-6-carboxylate, **4**. *n*-Butyllithium (20.0 mL of 10.0 M solution in hexane) was added dropwise to 30.0 g of diethyl phosphite at –40 to –35°C over a 2 h period. (This procedure was first described by Redmore (10).) To the resulting solution of lithium diethyl phosphite, compound **3** (obtained above) in diethyl phosphite (40 mL) was added in 1 h at –25 to –30°C. The reaction mixture was stirred at room temperature for 16 h and heated at 70°C for 2 h. After the mixture was cooled to room temperature, 140 mL of water was added. The mixture was extracted three times with 75 mL CH_2Cl_2. The organic extracts were combined and were extracted with 4 M HCl (100 mL). The organic solvent was removed by evaporation under vacuum. The residue (yellow oil) was chromatographed on silica gel. Compound **4** was eluted with CH_2Cl_2. After the solvent was removed, a viscous oil was obtained (53 g, yield 88%).

Pyridine-2-phosphonic-6-carboxylic acid, **5**. This compound was synthesized by a modification of the method of Redmore (10). Compound **4** (53 g) was heated under reflux with 150 mL conc. HCl for 16 h. After the mixture was cooled to room temperature, the solution was extracted four times with 50 mL CH_2Cl_2, and the organic extracts were discarded. The aqueous acid solution was evaporated, treated with a small amount of mixed solvent (CH_2Cl_2:MeOH = 4:1), and the white solid formed was filtered off. The residue was washed with the same mixed solvent several times. The product, **5**, was dried under vacuum at 60°C for 4 h (10.3 g, yield 58.1%). The overall yield based on picolinic acid was 31.2%.

Proton NMR (in D_2O): 8.42 (m, 1H, pyridine), 8.26 (d, 1H, pyridine), 8.18 (t, 1H, pyridine). ^{13}C NMR: 165.4 (COOH), 156.8 (C-$PO(OH)_2$), 146.3 (C-COOH), 143.1, 128.6, 124.8 (pyridine). ^{31}P NMR: 0.46 (s, 1P, $PO(OH)_2$). λ_{max} = 273 nm, $\varepsilon = 8.49 \times 10^3$; MS gave the molecular ion 202 $(M - H)^-$. Anal. calcd. for $C_6H_6NPO_5$: C 35.48, H 2.98, N 6.90, P 15.26; found: C 35.31, H 3.33, N 7.01, P 15.66.

Synthesis of 2,6-pyridinediphosphonic acid (2,6PDPA, 10)

Diethylpyridine-2-phosphate, **6**. This compound was prepared by a modification of the method of Redmore (10). *n*-Butyllithium (10.0 M in hexane) 31.5 mL (0.315 mol) was added dropwise to 12.5 g (0.090 mol) of diethyl phosphite at –20.0 to –30.0°C over a 2 h period. To the resulting solution of lithium diethyl phosphite, a solution of *N*-methoxypyridiniummethylsulfate, (from 7.15 g (0.075 mol) pyridine *N*-oxide, **2**, and 9.5 g (0.075 mol) of dimethyl sulfate in diethyl phosphite (20 mL) was added at –15.0°C in 1 h. The reaction mixture was stirred at room temperature for 16 h, then 50 mL of water was added. The mixture was extracted with $CHCl_3$ (3/38 mL),

[2] Supplementary material may be purchased from: The Depository of Unpublished Data, Document Delivery, CISTI, National Research Council of Canada, Ottawa, Canada, K1A 0S2.

© 1998 NRC Canada

and the organic extracts were combined and extracted with 4 N HCl, neutralized with base, and re-extracted with $CHCl_3$. From this $CHCl_3$ solution after distillation 10.8 g of product, **6**, was obtained: yield 71%.

Diethylpyridine-N-*oxide-2-phosphate*, **7**. Compound **6** (10.8 g), 36 mL of glacial acetic acid, and 6 mL of 30% H_2O_2 were mixed, and the reaction mixture was heated to 70.0–80.0°C for 3 h. Another 3 mL of 30% H_2O_2 was added, and the temperature was maintained at 70.0°C for 16 h. The solvent was removed by rotovaporation. To the residue, 100 mL of $CHCl_3$ was added, the organic phase was washed with concentrated sodium carbonate solution and was then dried with magnesium sulfate for 16 h. After the solvent was removed, 7.9 g of the product, **7**, was obtained: yield 68%.

Diethyl-N-*methoxypyridinium-2-phosphonate methyl sulfate*, **8**. Dimethyl sulfate (4.3 g) was slowly added to 7.9 g of compound **7** within 30 min. This reaction mixture was heated with a steam bath for 2 h to ensure complete reaction. The compound was purified by silica gel, with a mixed solvent of CH_2Cl_2 and MeOH used as eluant. After the solvents were removed, 8.4 g of compound **8** was obtained: yield 69%.

Pyridine-bis(2,6-diethylphosphonate), **9**. The same procedure as in the preparation of compound **4** was used: yield 72%.

2,6-Pyridinediphosphonic acid, **10**. Compound **9** (3.0 g) was heated under reflux with 30 mL of 6 M HCl for 12 h. The solvent was removed by evaporation under reduced pressure, and a yellow oil was obtained. Addition of methanol yielded a yellow solid, which was then recrystallized three times from methanol. The sample of pure product 2,6-pyridinediphosphonic acid, **10**, amounted to 0.95 g: yield 40%. Proton NMR (in D_2O): 8.7 (m, 1H, pyridine-4); 8.4 (t, 2H, pyridine-3,5). ^{31}P NMR (in D_2O): –2.0 (s, 2P, $-PO(OH)_2$). ^{13}C NMR (D_2O): 153.6, 150.1 (C-$PO(OH)_2$), 146.8, 130.3 (pyridine) λ_{max} = 272 nm, $\varepsilon = 6.62 \times 10^3$. Anal. calcd. for $C_5H_7NP_2O_6$: C 25.10, H 2.95, N 5.86, P 25.94; found: C 24.98, H 3.06, N 5.69, P 26.56. MS gave the molecular ion 240 ($239 + H^+$).

Quantitative analysis of 2PP6C

Preparation of iron-free sample. To 4.0 mL of solution taken from the continuous reactor (1), 100 mg of NaOH in 20 mL water was added dropwise with stirring. The mixture was heated to 70–80°C for 30 min. The $Fe(OH)_3$ that precipitated was filtered off carefully and was washed several times with water. The filtrate was combined with the washings and was transferred to a 50 mL volumetric flask. The pH of the solution was adjusted with acid to 4.2 and then diluted with distilled water to 50 mL.

Operating conditions. Analytical column: IBM-SIL 5 C8, reverse phase 4.5 × 150 mm; column temperature: ambient; mobile phase flow rate: 1.5 mL/min; detector: UV at 275 nm, 0.20 AUFS; sample volume: 20 μL; recorder: 10 mV full-scale; chart speed: 0.5 cm/min. The mobile phase contained: 0.0010 M Cu(II), 60:40 H_2O:MeOH, 2% HAc, 0.2% $CH_3(CH_2)_{15}(CH_3)_3NBr$, adjusted to pH 4.2 with NaOH solution.

The calibration of the HPLC analysis of 2PP6C by this method results in a linear correlation between the peak height and concentration up to 5×10^{-4} M.

Quantitative determination of 2,6PDPA

The compound 2,6PDPA was measured quantitatively by its absorption spectrum. To 1.000 mL of solution taken from the continuous reactor, 150 mg of NaOH in 15 mL water was added with stirring. The mixture was heated with a steam bath for 2 h, then it was allowed to stand at room temperature for 2 h. The $Fe(OH)_3$ that precipitated was filtered off carefully and was washed several times with water. The filtrate, combined with the washings, was transferred to a 50 mL volumetric flask and then diluted with distilled water to 50 mL. A 5 mL sample of solution was taken from the volumetric flask and placed in a 10 mL volumetric flask and was diluted to 10 mL with 6 N HCl. This solution was ready for UV-vis spectrophotometric analysis. The calibration of the UV-vis analysis of 2,6PDPA by this method results in Beer's Law behavior up to 2×10^{-4} M.

Potentiometric titrations

Potentiometric measurements were conducted in a jacketed cell thermostated at 25 ± 0.1°C and under an inert atmosphere of purified Ar. A Corning Model 350 pH meter fitted with glass and calomel reference electrodes was used. The apparatus was calibrated in terms of $-\log[H^+]$, designated as pH, by titration of a small quantity of dilute HCl at 0.10 M ionic strength and 25.0°C, followed by adjustment of the meter so as to minimize the calculated pH versus observed values. Log K_w for the system, defined in terms of $\log[H^+][OH^-]$, was found to be –13.78 at the ionic strength employed (11) and was maintained fixed during refinements.

Potentiometric measurements of solutions containing ligand or equimolar amounts of ligand and metal ion were made at concentrations of approximately 2.0×10^{-3} M and ionic strength $m = 0.10$ M. Each titration produced at least 10 points per neutralization of a hydrogen ion, equivalent with titrations being repeated until satisfactory agreement was obtained. A minimum of three sets of data were used in each case to calculate the overall stability constants. The range of accurate pH measurement was considered to be 2–12. Equilibrium constants and species distribution diagrams were calculated using the programs BEST and SPE, respectively (11).

Degradation studies

Preparation of iron(III) chelate solution. The chelated metal catalyst solution is prepared by dissolving 0.018 mol $Fe(NO)_3 \cdot H_2O$ in about 200 mL water, separately dissolving 0.036 mol chelating agent (2,6PDPA or 2PP6C) in about 300 mL water and mixing the two solutions together. The pH is adjusted to 8.5 by NaOH solution, and the mixture is diluted to 1 L with water. This solution is ready for the following degradation study.

Oxidative degradation of chelating agents was carried out in the manner previously described (1) in a 1 L glass apparatus designed to simulate industrial conditions. The pH was continually monitored and kept close to 8.5. The H_2S was introduced into the absorber at the rate of 2.0 mL/min, and air was introduced into the oxidizer at the rate of 1.0 L/min. Both the absorber and oxidizer, as part of the glass apparatus, were operated at room temperature. The ligand 2PP6C was measured as a function of time by HPLC, as described above, while 2,6PDPA was measured quantitatively, as described above, from its UV-visible absorbance.

© 1998 NRC Canada

Scheme 1. Outline of the synthesis of 2PP6C.

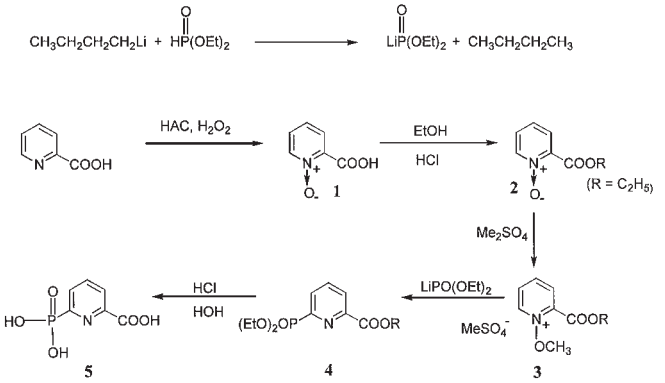

Scheme 2. Outline of the synthesis of 2,6PDPA.

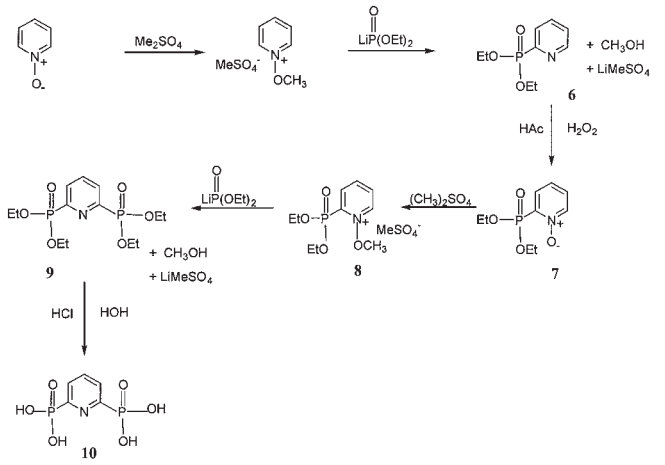

Results and discussion

Synthesis

The reaction sequences by which the phosphonate ligands 2PP6C and 2,6PDPA were synthesized are given in outline form in Schemes 1 and 2. In these syntheses the pyridine is activated toward nucleophilic substitution by formation of the *N*-oxide as an intermediate before the substitution reaction. The many steps required in these synthetic schemes drive down the overall yield. Thus, while the individual steps in the synthesis of 2,6PDPA are reasonable to good, the overall yield based on starting material was less than 10%. Caution should be exercised in the use of dimethyl sulfate, which is known to be very toxic. It is also probable that the mono methyl sulfate intermediates and by-products shown in Schemes 1 and 2 are also very toxic.

Thermodynamic stabilities

Protonation constants. The protonation constants of 2PP6C and of 2,6PDPA were determined by direct potentiometric titration and are listed in Table 2. The values of K_3^H for 2PP6C and K_4^H for 2,6PDPA are too low to be measured potentiometrically. Protonation sequences for 2PP6C and 2,6PDPA are illustrated by Schemes 3 and 4, respectively. The most basic group is the pyridine nitrogen (12). The higher basicity of the first phosphonate in 2,6PDPA over the phosphonate group in 2PP6C is due to the greater electronic withdrawing effect of a

Scheme 3. Protonation of 2PP6C.

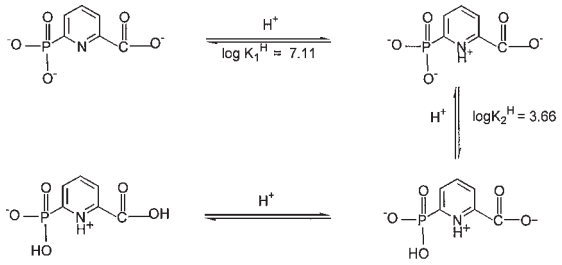

Scheme 4. Protonation of 2,6PDPA.

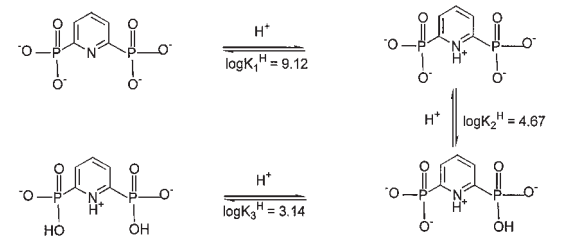

phosphonate relative to a carboxylate group transmitted through the pyridine ring. The phosphonate is probably the next lower in basicity, and it is therefore shown to become protonated after the pyridine nitrogen becomes protonated. The carboxylate group is considered to have the lowest basicity and is shown in Scheme 3 to be the last to be protonated. These assignments are in accordance with the p*K*s of several related compounds described by Redmore (12).

The equilibrium constants for the Fe(III)–2PP6C and the Fe(III)–PDPA chelate systems

It was found that the 1:1 complexes of Fe(III)–2PP6C and Fe(III)–2,6PDPA are completely formed at pH 2.0, and their stability constants could not be determined potentiometrically by direct titration. The formation constants of these complexes were therefore determined by competition with EDTA. In these systems at low pH, the Fe(III)–EDTA chelate is completely formed, but as the pH is raised this chelate is completely converted to the Fe(III)–2PP6C and Fe(III)–2,6PDPA chelates. The formation constants of these complexes were calculated from the degree of formation of the complex in competition with EDTA and all other known data (6), such as the protonation constants of EDTA and the phosphonates, and the stability constant of the Fe(III)–EDTA chelate.

In the competition solution with EDTA present, equilibrium took place rapidly enough to be investigated by direct potentiometric titration. Therefore the mixed ligand Fe(III) systems containing EDTA and 2PP6C or EDTA and 2,6PDPA were subjected to standard titration from pH 2 to 10 by the incremental addition of standard KOH solution.

The equilibrium constants involving metal chelate hydrolysis (hydroxo complex formation) and protonation were calculated from direct potentiometric titration of the phosphonic acids and Fe(III) without EDTA (11). Because of the very slow equilibrium for the direct titration, a batch method (13) was used. The pH of each point was read 8 and 10 days after preparation of the solution. Identical readings after this length of time confirmed that equilibrium had been reached.

The equilibrium constants for the Fe(III)–2PP6C and

© 1998 NRC Canada

Table 1. Comparison of the protonation constants of various ligands and the stability constants and their Fe(II) and Fe(III) chelates.

Quotient, *K*	log *K*							
	2,6-PDPA[a]		**2PP6C**[a]		**NTA**[b]		**PDCA**[c]	
[HL]/[H][L]	9.12 (3)		7.11 (3)		9.59		4.66	
$[H_2L]/[HL][H]$	4.67 (2)		3.66 (2)		2.52		2.09	
$[H_3L]/[H_2L][H]$	3.14 (3)				1.50			
	Fe(II)[a]	**Fe(III)**[a]	**Fe(II)**[a]	**Fe(III)**[a]	**Fe(II)**	**Fe(III)**	**Fe(II)**	**Fe(III)**
$[M(OH)_2L]/[M(OH)_3L][H]$						10.72		
$[M(OH)L]/[M(OH)_2L][H]$	11.38 (6)	8.36 (7)	10.77 (4)	8.53 (6)		7.58		
$[ML]/[M(OH)L][H]$	9.81 (6)	6.40 (6)	9.09 (1)	3.25 (5)	10.82	4.36		
[ML]/[M][L]	10.12 (6)	20.87 (5)	8.70 (1)	15.97 (5)	8.90	15.90	5.71	10.91
[MHL]/[ML][H]	4.50 (6)	4.06 (3)	3.46 (2)					
$[MH_2L]/[MHL][H]$	3.36 (6)							
$[ML_2]/[ML][L]$	5.33 (2)	7.81 (4)	5.10 (5)	9.50 (3)	3.08	8.07	4.65	6.22
$[MHL_2]/[ML_2][H]$	6.51 (1)	3.86 (3)	5.13 (8)	2.60 (2)				
$[MH_2L_2]/[MHL_2][H]$	4.78 (1)		3.83 (8)					
$[MH_3L_2]/[MH_2L_2][H]$	4.18 (5)							
$[MH_4L_2]/[MH_3L_2][H]$	3.57 (7)							

[a] This work; numbers in parentheses are standard deviations.
[b] Reference 4.
[c] Reference 6.

Fe(III)–2,6PDPA systems are shown in Table 1. The species distribution curves of the 1:2 Fe(III)–2PP6C and Fe(III)–2,6PDPA systems calculated from the data in Table 1 are shown in Figs. 1*a* and *b*. It is seen that the 1:2 chelates are the major species over the pH range from 3 to 9 for the 2PP6C system and from 4.5 to 9.5 for the 2,6PDPA system, reaching a maximum of about 95% in both cases.

Because complexes of 2:1 stoichiometry of 2PP6C and 2,6PDPA with Fe(III) are formed, the systems are concentration dependent. At higher concentration the relative concentration of the 2:1 chelate is increased. The 2:1 complexes of 2PP6C and 2,6PDPA with Fe(III) under these conditions predominate over a larger pH range.

The hydroxo complexes listed in Table 1 of the 1:1 ligand:metal complexes are expected, since combination of Fe(III) with a terdentate ligand results in three or more water molecules in the coordination sphere, giving rise to mono- and dihydroxo complexes at high pH. The protonated complexes are probably formed because of the presence of the uncoordinated phosphonate oxygens as protonation sites.

The equilibrium constants for the Fe(II)–2PP6C and the Fe(II)–PDPA chelate systems

Potentiometric determination of the stability constants of Fe(II)–2PP6C and Fe(II)–2,6PDPA system requires special precautions to prevent the oxidation of the ferrous chelate by oxygen of air. In this work the dry, weighed solid $FeSO_4 \cdot 7H_2O$ was kept separated for 1 h from the gently stirred 2PP6C solution by placing the weighed salt on a small ceramic boat kept afloat over the prepurified solution in the sealed titration cell (4). The Ar purging was continued during the 1 h period. At the end of 1 h the ferrous salt was tipped into the solution through agitation. The ferrous salt was considered dissolved (within a few minutes) after the pH meter reading stabilized (4).

The equilibrium constants for the Fe(II)–2PP6C and Fe(II)–2,6PDPA systems are shown in Table 1. From calculations based on these equilibrium data it is seen that the 1:1 complex is formed at low pH for both of the above systems and predominates between pH 3.5 and 9.0, reaching a maximum of 99.4% for the Fe(II)–2PP6C, and from pH 4.5 to 9.5, reaching a maximum and 99.5% for the Fe(II)–2,6PDPA system. At low pH the MHL species is formed and is the major species over the pH range 2–3.5, reaching a maximum of about 70% for the Fe(II)–2PP6C system. The MH_2L species is also formed in addition to the MHL species for the Fe(II)–2,6PDPA system. At high pH the hydroxo chelate M(OH)L is formed at pH about 7, and $M(OH)_2L$ is formed at about pH 9 for the Fe(II)–2PP6C system. Above pH 8 the hydroxo chelates M(OH)L and $M(OH)_2L$ begin to form and are the dominant species above pH 9.5 for the Fe(II)–2,6PDPA system. The solution of the Fe(II)–2,6PDPA system is yellow in color at pH about 2.0 and above. More than 50% ferrous chelates, initially in the protonated species, are formed at pH 2.0 and above. The protonated and nonprotonated ferrous chelates are probably responsible for the yellow color of the solution.

The species distribution curves of the 2:1 Fe(II)–2PP6C and Fe(II)–2,6PDPA systems are shown in Figs. 2 and 3. It is seen that the 2:1 chelate is formed about at pH 4 and is the major species over the pH range 4.4–10.5, reaching a maximum of about 93% at pH 8 for the Fe(II)–2PP6C system. In the Fe(II)–2,6PDPA system the 2:1 chelate is formed at about pH 5 and is the major species over the pH range 7.0–11.5, reaching a maximum of about 93.1% at pH 9.4. At low pH MHL_2 and MH_2L_2 form in addition to MHL for the Fe(II)–2PP6C system. In the Fe(II)–2,6PDPA system the species MHL_2, MH_2L_2, MH_3L_2, and MH_4L_2 form besides MHL and MH_2L. At 10 times the concentration of Fe(II) and ligand the concentration of the 2:1 chelates are increased relative to the concentration of species found in the more dilute solution. Thus the maximum concentration of MHL_2 is increased from 39.2% to 57.5%, that of MH_2L_2 is increased from 34.0% to

© 1998 NRC Canada

Fig. 1. (*a*) Species distribution curves of 1:2 Fe(III)–2PP6C; μ = 0.100 M (KNO_3), t = 25.0°C, [2PP6C] = 4.55×10^{-3} M, 1:2 [Fe(III)] = 2.27×10^{-3} M. H_{-n} represents $(OH)_n$; PP = 2PP6C. (*b*) Species distribution curves of Fe(III)–2,6PDPA; μ = 0.100 M (KNO_3), t = 25.0°C, [2,6PDPA] = 4.00×10^{-3} M, [Fe(III)] = 2.00×10^{-3} M. H_{-n} represents $(OH)_n$; PD = 2,6PDPA.

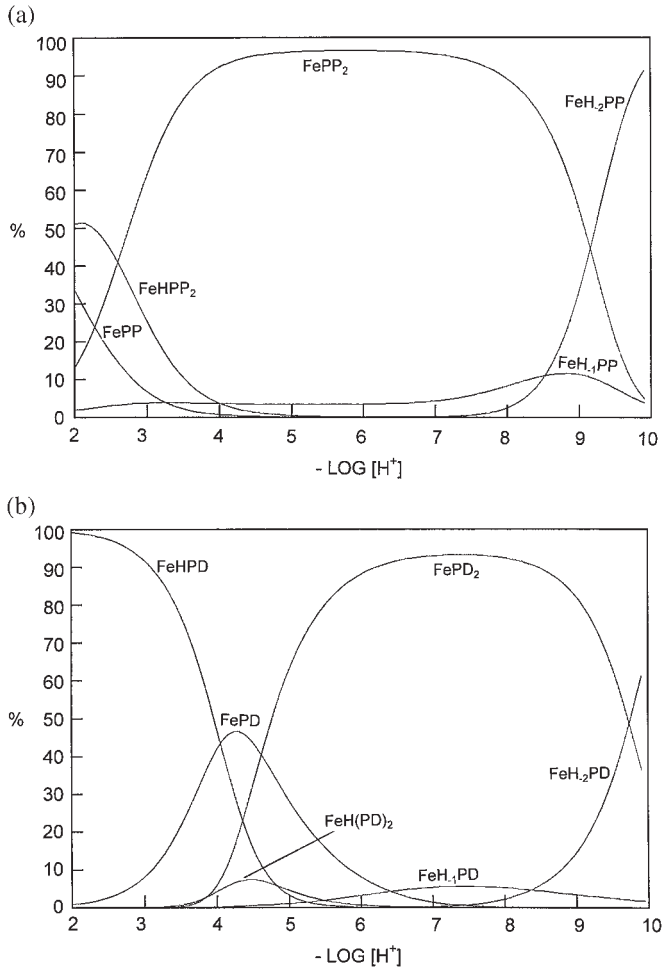

62.8% and that of ML_2 is increased from 93.1% to 97.7% for the Fe(II)–2PP6C system. In the Fe(II)–2,6PDPA system the maximum concentration of ML_2 is increased from 93.1% to 97.7%, that of MHL_2 is increased from 32.0% to 58.3%, that of MH_2L_2 is increased from 16.0% to 33.9%, and MH_3L_2 is increased from 14.9% to 32.8%, and MH_4L_2 is increased from 17.9% to 48.1%.

In the 2:1 system, because of formation of the more stable 2:1 chelate, the concentration of M(OH)L is decreased from 76.2% (in the 1:1 system) to 21.6% when the molar ratio of ligand to metal ion is 2:1. Its relative concentration is further decreased to 9.0% in the system in which the metal ion and ligand concentrations are 10 times higher for the Fe(II)–2PP6C system. Similar phenomena were also observed in the Fe(II)–2,6PDPA system.

A comparison of log stability constants of the ferric complexes of 2,6-pyridinedicarboxylic acid (PDCA), 2PP6C, 2,6PDPA, and NTA is indicated in Table 1, together with the corresponding protonation constants of each ligand. The data show that among the four ligands compared, the ferric complex of 2,6PDPA is the most stable. The stability constant of Fe(III)–2,6PDPA (1:1) is about 5 log units higher than that of Fe(III)–2PP6C and 10 log units higher than that of Fe(III)–PDCA. This difference indicates that $-PO(O^-)_2$ is a much more powerful coordinating group for Fe(III) ion than is COO^-. As expected, the stability constant of Fe(III)–2PP6C is between those of Fe(III)–PDCA and Fe(III)–PDPA, because the ligand 2PP6C contains one strong coordinating group, $PO(O^-)_2$, and a weaker donor, COO^-. The stability constant sequence for the above four ferric chelates (2:1) is as follows: 2,6PDPA > 2PP6C > NTA > PDCA. The same sequence applies to the ferrous chelates (2:1).

Fig. 2. Species distribution curves of the 1:2 Fe(II)–2PP6C; μ = 0.100 M (KNO_3), t = 25.0°C, [2PP6C] = 3.95×10^{-3} M, [Fe(II)] = 1.97×10^{-3} M. H_{-n} represents $(OH)_n$; PP = 2PP6C.

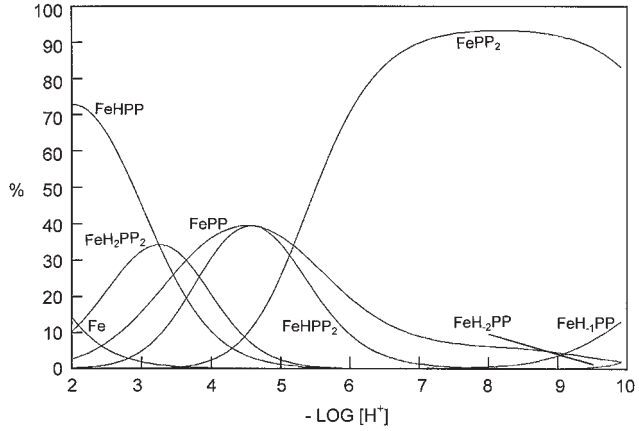

Fig. 3. Species distribution curves of the 1:2 Fe(II)–2,6PDPA, μ = 0.100 M (KNO_3), t = 25.0°C, [2,6PDPA] = 4.00×10^{-3} M, [Fe(II)] = 2.00×10^{-3} M. H_{-n} represents $(OH)_n$; PD = 2,6PDPA.

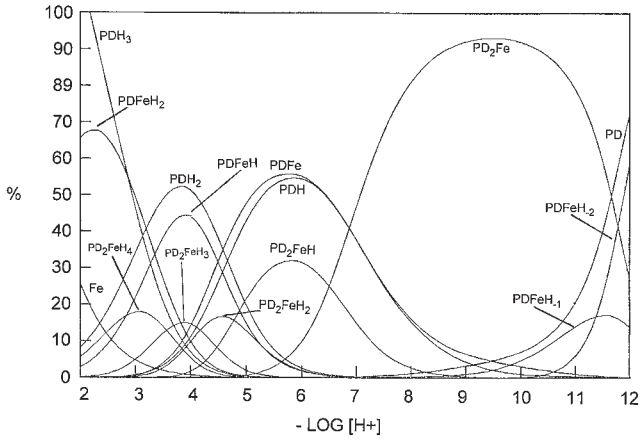

Calculation of reduction potential *E*(Fe(III) chelate→Fe(II) chelate) and K_c (conditional stability constants) for the oxidation of H_2S to S and pM values of Fe(II) and Fe(III) for the Fe(II)–2PP6C, Fe(III)–2PP6C, Fe(II)–2,6PDPA, and Fe(III)–2,6PDPA systems

The calculated pM of Fe(II) and Fe(III), E and log K_c (3) for the above two systems are shown in Table 2. The data show that the conditional constants (log K_c) of both Fe(III)–2PP6C

© 1998 NRC Canada

Table 2. The pM of Fe(II) and Fe(III), E, and log K_c.

	pM[a]				
	Fe(II)	Fe(III)	Δ pM	E[b]	log K_c[c]
NTA	8.0	20.8	12.8	0.013	7.98
2PP6C	12.3	24.0	11.7	0.080	10.26
2,6PDPA	12.6	25.9	13.3	–0.015	7.06

[a] The pM for Fe(II)–NTA and Fe(III)–NTA, taken from ref. 5, and for 100% excess ligand, 10^{-2} M metal chelate.

[b] E for reduction of ferric to ferrous ions, taken from pM values of the metal ions and the equation: $E = 0.770 - 0.059\log([Fe(II)]/[Fe(III)])$.

[c] K_c conditonal constants for the reaction: $2Fe(III)L + HS^- \rightarrow 2Fe(II)L + H^+ + S_{(s)}$ at pH 8.5 and $[HS^-]$ taken as 10^{-3} M.

and Fe(III)–2,6PDPA systems are sufficiently high for the oxidation of H_2S to S (3). The conditional constant sequence for the above three systems is as follows: 2PP6C > NTA > 2,6PDPA.

Oxidative degradation of Fe(III)–2PP6C at pH 8.5

The concentration of 2PP6C was analyzed by HPLC by the method described in Experimental. After the redox reaction was carried out for 100 h, about 20% of the 2PP6C was lost, presumably by hydroxylation of the pyridine ring (1, 2).

The experimental run on the degradation of the 2:1 chelate of 2-phosphonopyridine-6-carboxylate and Fe(III) was also carried out in the presence of 5% sodium thiosulfate. After the redox reaction was continued for 100 h, no significant degradation of 2PP6C was observed. The HPLC analysis of the degradation of 2PP6C shows that in the presence of 5% $Na_2S_2O_3$, the hydroxyl radical does not oxidize this ligand at a measurable rate, and this ligand can therefore be used over a long time period without significant degradation. The stabilizing effect of $Na_2S_2O_3$ (14) seems to be much more efficient in preventing free-radical oxidation of 2PP6C than for NTA. The action of thiosulfate has been explained as follows (15):

Radical scavenger:

$$S_2O_3^{2-} + \cdot OH \rightarrow \cdot S_2O_3^- + OH^-$$

Regeneration:

$$\cdot S_2O_3^- + Fe(II)NTA^- \rightarrow S_2O_3^{2-} + Fe(III)NTA$$

The use of 2PP6C as the redox catalyst has additional advantages in that no FeS or $Fe(OH)_3$ precipitate was formed in the process, and the sulfur was easily filtered off during the reaction.

Because the stabilities of the Fe(III)–2PP6C chelates are higher than those formed in the NTA system (4) (see Table 1), the redox reaction for the Fe(III)–2PP6C system can be carried out at pH 9.0 (no $Fe(OH)_3$ precipitate appears). The Fe(II)–2PP6C system is also more stable than the corresponding Fe(II)–NTA system (see Table 1) thus the FeS does not precipitate at pH as high as 9.0. The difference in the stabilities of the Fe(III) and Fe(II) chelates at higher pH is still large enough to oxidize H_2S to S_8. The use of higher pH has the advantage that absorption of H_2S is more rapid. Industrially this means that a smaller and less expensive absorber may be used. A further advantage is that the degradation of the ligand decreases as the pH is increased (1), so that the oxidation of H_2S to S may be carried out with even less degradation of the catalyst.

Degradation of Fe(III)–2,6PDPA at pH 8.5 (Fe(III) 0.0090 M, 2,6PDPA 0.018 M)

The concentration of 2,6PDPA was analyzed with its UV-vis spectrum by the method described in Experimental. The spectral analysis of the degradation of 2,6PDPA shows that the degradation of 2,6PDPA is less than 5% over a 100 h period. When the degradation run was repeated in the presence of 5% sodium thiosulfate, no degradation of 2,6PDPA was detected over a 100 h period. Thus 2,6PDPA forms a 2:1 iron(III) chelate that seems to survive as long as the iron(III) chelate of 2PP6C as a catalyst for the oxidation of H_2S to S_8 by air. Previously it was found that the iron chelate of pyridine-2-phosphonic acid undergoes facile oxidative degradation when used as a catalyst for the oxidation of H_2S to S_8 by air.[3] Apparently when a second phosphonic acid or a carboxylic acid function is substituted at the other alpha position of the pyridine ring, the new ligands, 2PP6C and 2,6PDPA, form iron(III) chelates that are much more resistant to oxidative degradation than are the iron(III) chelates of the parent ligand. This interesting phenomenon was also observed for pyridinedicarboxylic acid, PDCA, the iron chelate of which is much more resistant to oxidative degradation than is pyridine-2-carboxylic acid (picolinic acid).

References

1. D. Chen, R.J. Motekaitis, A.E. Martell, and D. McManus. Can. J. Chem. **71**, 1524 (1993).
2. D. Chen, A.E. Martell, and D. McManus. Can. J. Chem. **73**, 264 (1995).
3. A.E. Martell, R.J. Motekaitis, D. Chen, R.D. Hancock, and D. McManus. Can. J. Chem. **74**, 1872 (1996).
4. R.J. Motekaitis and A.E. Martell. J. Coord. Chem. **31**, 67 (1994).
5. R.M. Smith and A.E. Martell. Critical stability constants. Vol. 5. Plenum Press, New York. 1974. p.76; Critical stability constants. Vol. 6. Plenum Press, New York. 1989. p.163.
6. R.M. Smith, A.E. Martell, and R.J. Motekaitis. Critical stability constants database. NIST Standard Reference Data No. 46, Version 2, Gaithersburg, Md. 1995.
7. D. McManus, A.E. Martell, and D. Chen. U.S. Patent, 5,591,419, Jan. 7, 1997; U.S. Patent, 5,686,613, Nov. 11, 1997.
8. R.D. Hancock, A.E. Martell, D. Chen, R.J. Motekaitis, and D. McManus. Can. J. Chem. **75**, 591 (1997).
9. B. Boduszek. J. Prakt. Chem. **334**, 5 (1992); Chem.-Ztg. 444 (1992).
10. D. Redmore. J. Org. Chem. **35**, 4114 (1970).
11. A.E. Martell and R.J. Motekaitis. The determination and use of stability constants. 2nd ed. VCH Publishers, New York. 1992.
12. D. Redmore. J. Org. Chem. **38**, 1306 (1973).
13. R. Delgado, Y. Sun, R.J. Motekaitis, and A.E. Martell. Inorg. Chem. **32**, 3326 (1993).
14. D. McManus and F.R. Kin. U.S. Patent, 4,622,212, Nov. 11, 1986.
15. D.W.De Berry. 1996 AICHE Spring Natl. Meet. Paper 46*a*. New Orleans, La.

[3] D. Chen, A.E. Martell, and D. McManus. Unpublished results.

© 1998 NRC Canada

Étude d'ions négatifs préparés « in situ » dans un piège ionique quadripolaire

Sébastien Gregoire, Jean-Charles Mathurin, Raymond E. March et Jean-Claude Tabet

Résumé : Le piège ionique quadripolaire constitue un appareil d'analyse de grand intérêt en spectrométrie de masse. Pourtant, dans sa configuration à ionisation interne (les ions sont formés au sein du piège), l'étude des ions négatifs est difficile. L'objet de ce travail est de déterminer les problèmes rencontrés lors d'analyse en mode négatif sur un piège ionique quadripolaire à ionisation interne. La première difficulté, due à la détection simultanée des ions positifs et des ions négatifs, s'explique par la grande énergie cinétique des ions éjectés. De plus, la formation des ions négatifs, par capture électronique, est fortement limitée en raison de la forte accélération des électrons par le champ quadripolaire, limitant le nombre d'électrons d'énergie thermique nécessaire au processus de capture électronique. Enfin, le confinement simultané des ions positifs et des ions négatifs perturbe fortement les spectres de masse enregistrés. Les potentiels de charge d'espace qui règnent au sein du piège (due aux conditions d'ionisation nécessaires à la détection d'ions négatifs) déstabilisent les ions positifs de hauts rapports *m/z*, tandis que les ions négatifs stabilisés sont observés. De plus, des pertes de résolution et de décalibration peuvent survenir, dans certains cas, pour les ions négatifs, lorsque ces derniers sont éjectés en présence d'ions positifs de plus hauts rapports *m/z*. Enfin, les interactions ion–ion semblent limiter l'observation des ions négatifs au sein du piège. La compréhension de tous ces phénomènes, détection, formation et confinement simultané, permettra de proposer des solutions possibles aux problèmes rencontrés pour la production d'ions négatifs dans les pièges ioniques quadripolaires à ionisation interne.

Mots clés : spectrométrie de masse, piège ionique quadripolaire, ion négatif, perfluorotributylamine, charge d'espace.

Abstract: The quadrupole ion trap mass spectrometer is of great interest for chemical analysis. Nevertheless, negative ion studies using in situ ionization (negative ions created inside the ion trap) are difficult and limited. This paper describes the difficulties that occurred during negative ion analysis when using a commercial gas chromatography quadrupole ion trap mass spectrometer (GC/MS) system. Detection problems, due to simultaneous trapping of both positive and negative ions, are explained by the large kinetic energies of the ejected ions. Negative ion formation, produced by electron capture, is limited by the fundamental RF field, which imparts high kinetic energy to the electrons, precluding the possibility that the electrons will reach the thermal energies needed for electron capture processes. In addition, simultaneous confinement of negative and positive ions affects the recorded mass spectra. Space charge potentials that exist inside the ion trap (due to the ionization conditions necessary to detect negative ions) induce the destabilization of positive ions at higher *m/z* ratios, while negative ions in the same *m/z* range are stabilized. Moreover, loss of resolution and decalibration could occur for negative ions when they are ejected in the presence of positive ions with higher *m/z* ratios. At the very least, ion–ion reactions could limit the observation of negative ions. The understanding of these phenomena, viz. detection, formation, and simultaneous confinement, will permit the proposal of solutions for negative ion analysis with quadrupole ion trap mass spectrometers using in situ ionization.

Key words: mass spectrometry, quadrupole ion trap, negative ion, perfluorotributylamine, space charge.

Introduction

La « préhistoire » du piège ionique quadripolaire débute en 1953 avec les travaux de Paul et Steinwedel sur les champs électriques de nature alternative; ces derniers conduisirent à la réalisation du premier analyseur de masse de type quadripolaire (filtre de Paul) et au dispositif à piégeage d'ions appelé piège de Paul (1). Par la suite le développement de ce dernier s'effectua avec les travaux de Fisher en spectrométrie de masse (2) et par Dehmelt (3, 4) dans le domaine de spectroscopie d'ions confinés. Le prix Nobel de physique de 1989 fut d'ailleurs attribué à Paul pour l'invention du piège ionique qui porte son nom et à Dehmelt pour l'utilisation de ce dernier en spectroscopie atomique.

Les temps modernes de ces spectromètres de masse débutent dans les années 80 avec les travaux des ingénieurs de la société Finnigan (5), qui conduisent à la commercialisation d'un GC/MS (Gas Chromatograph/Mass Spectrometer) : l'ITD™ (Ion Trap Detector), suivi peu après par une version améliorée : l'ITMS™ (Ion Trap Mass Spectrometrer) en 1985. Le piège ionique quadripolaire entre alors dans le domaine de l'analyse, notamment avec la possibilité d'obtenir aisément

Reçu le 3 mars 1997.[1]

S. Gregoire, J.-C. Mathurin et J.-C. Tabet.[2] Laboratoire de chimie organique structurale et biologique, Centre national de la recherche scientifique EP 103, Université Pierre et Marie Curie, 4 Place Jussieu, 75270 Paris Cedex 05, France.
R.E. March. Department of Chemistry, Trent University, Peterborough, ON K9J 7B8, Canada.

1. Revision reçue le 26 janvier 1998.
2. Auteur à qui la correspondance doit être adrésée. Tél. : (33) 01 44 27 32 63. Téléc : (33) 01 44 27 38 43. Mél : tabet@ccr.jussieu.fr

© 1998 NRC Canada

des spectres de masse grâce à la technique de l'instabilité axiale (6), ainsi qu'à l'apport d'un bain d'hélium (6, 7) qui augmente la sensibilité et la résolution. Deux autres fonctions améliorent les performances de l'appareil : la modulation axiale (8) qui améliore la résolution, et l'AGC (Automatic Gain Control) (9) qui permet de calculer le temps d'ionisation optimal de façon à donner le signal d'intensité maximum sans conduire à une perte de résolution par effet de charge d'espace (dû à des densités de charge suffisamment importantes pour perturber le champ quadripolaire).

Il s'avère alors que le piège de Paul est un instrument de choix dans des champs d'investigation très variés, dont celui de l'environnement, pour la détection de traces (10), en raison de sa sensibilité (11) et des possibilités de $(MS)^n$ en routine (12). Les potentiels affichés par cet appareil, que constituent l'accès à des ions de masse relativement élevée (13) ou à la très haute résolution (14), laissent présager un avenir grandissant. Enfin la pluralité des couplages réalisables (15) (Matrix Assisted Laser Desorption and Ionization (MALDI) (16), Electrospray Ionization (ESI) (17),...) associée à une résolution moyenne de $\Delta m/z = 0{,}2$ Th[3] et à l'accès aux hautes masses (= 6000 Th) augmente l'attrait analytique pour cet instrument. Ce dernier type de couplage fait actuellement l'objet d'un effort considérable de la part des constructeurs avec la mise sur le marché d'appareils du type ESI-Trap (l'Esquire™ de Brüker ou le LCQ™ de Finnigan).

Il faut toutefois relativiser ces particularités. Actuellement, le parc mondial de pièges ioniques quadripolaires commerciaux est principalement constitué de GC/MS, où l'introduction des échantillons se fait par l'intermédiaire d'un chromatographe en phase gazeuse, et l'ionisation est dite « interne » (création des ions dans le piège). Cette approche permet de limiter les pertes de sensibilité qui se produiraient en utilisant une source externe, les ions étant créés au sein même du piège, où se feront les étapes ultérieures (manipulation et analyse en masse). Néanmoins, la gamme de rapport m/z est limitée à 650 Th avec un pouvoir de résolution unitaire. Ce type d'appareil a montré des capacités pour l'analyse en ionisation chimique positive (18, 19), sans pouvoir utiliser des hautes pressions en gaz réactif (utile à des fins de stabilisation d'ions adduits non covalents).

D'un autre côté, la formation d'ions négatifs par capture électronique (20) donne accès à une meilleure sensibilité, ceci étant en partie dû à la faible proportion de fragmentation et à la forte section efficace de capture électronique (21). En outre, ce même mode d'ionisation présente une bonne sélectivité. Il est ainsi possible de détecter des composés à forte affinité électronique à l'état de trace dans des mélanges complexes (21).

De ce point de vue, le potentiel analytique du piège ionique quadripolaire allié aux spécificités de la capture électronique laisse présager de bonnes perspectives. Malheureusement, il s'avère que le piège quadripolaire à ionisation interne ne permet pas de former efficacement des ions négatifs. La principale raison avancée concerne la difficulté d'avoir des électrons thermiques donc de faible énergie cinétique nécessaires à la création d'ions négatifs; mais il est également impossible d'avoir recours à des pressions partielles élevées en gaz tampon nécessaires à leur formation en forte abondance, sous peine d'une forte perte de signal. De telles conditions sont habituellement utilisées dans les sources haute pression des spectromètres de masse conventionnels pour produire des ions négatifs (22).

Ces points expliquent le faible engouement pour l'étude des ions négatifs sur ce type d'appareil. La première étude faite par Schermann et Major décrit le confinement d'ions iodure (I^-) formés par photodissociation de l'iodure de thallium (23). Plus tard, Hughes observe des ions négatifs dans des spectres d'impact électronique de petites molécules (24). En 1987, McLuckey et Glish (25) mirent en évidence la possibilité de confiner des ions négatifs formés par ionisation chimique, utilisant des ions négatifs réactifs OH^- et $O^{\bullet -}$ créés au sein du piège. En 1994, Berberich et Yost ont étudié les paramètres d'ionisation influençant l'efficacité de formation des ions négatifs (26). Plus récemment, quelques exemples d'applications analytiques pour des composés à forte affinité électronique (composés polychlorés) ont été reportés (27, 28).

Dans cette étude, les raisons pour lesquelles le piège quadripolaire se prête difficilement aux applications analytiques des ions négatifs, seront discutées. Après une description sommaire du principe de fonctionnement de cet instrument, la détection des ions négatifs, qui constitue une difficulté sérieuse, sera décrite. Il s'avère que le piège possède un comportement particulier nécessitant une bonne compréhension des processus de piègeage et de détection. Les moyens disponibles pour identifier la charge d'un ion seront décrits, d'autant plus que les ions négatifs et positifs créés dans le piège pendant l'ionisation sont détectés simultanément; d'où l'intérêt porté aux méthodes d'identification de la polarité des ions. Puis le rôle joué par l'énergie des électrons de capture sur la limitation de la formation des ions négatifs sera étudié. Enfin, la conséquence directe du confinement simultané des ions positifs et négatifs est la création d'importants potentiels de charge d'espace affectant la stabilité des ions positifs et des ions négatifs. Un autre aspect de ce confinement simultané concerne la résolution des ions positifs comme celle des ions négatifs éjectés en présence d'ions de polarité opposée. Enfin, des indices concernant les interactions possibles entre les ions positifs et les ions négatifs, second facteur limitant l'utilisation analytique des ions négatifs dans le piège, seront aussi présentés.

Partie expérimentale

Toutes les expériences ont été réalisées sur un piège ionique quadripolaire Varian Saturn III™ qui possède une géométrie « étirée ». Une jauge de pression Penning (CF2P, Alcatel) a été installée sur la partie inférieure de l'enceinte de l'appareil qui a été modifiée. La jauge n'ayant pas été calibrée, les valeurs de pression données ne sont donc pas corrigées.

L'hélium est introduit dans la cavité du spectromètre de masse par l'intermédiaire du chromatographe en phase gazeuse (Varian Star 3400 CX™). La pression en gaz tampon (hélium) est d'environ 10^{-3} Torr (pression réelle) (1 Torr = 133,3 Pa). La perfluorotributylamine (FC43) (purifiée par Aldrich) employée dans ces expériences pénètre en continu dans le piège par l'intermédiaire d'une vanne aiguille à une pression partielle lue de $(1–2) \times 10^{-5}$ mbar. L'enceinte de l'appareil est maintenue à une température de 170°C. L'acquisition des spectres de masse est réalisée à la vitesse de balayage de

3. Le Thomson (Th) est défini comme le rapport entre la masse exprimée en unité de masse atomique (u) et le nombre de charges.

© 1998 NRC Canada

Fig. 1. Diagramme de stabilité décrivant les différences entre les ions positifs (*a*) et négatifs (*b*). La zone de recouvrement dénote une stabilité simultanée des ions positifs et négatifs. Les axes choisis nécessitent une pondération des paramètres de stabilité par la polarité, a_u/p, q_u/p. La droite de fonctionnement représentée correspond à l'application d'une tension continue négative permettant l'isolement des ions négatifs (vide supra).

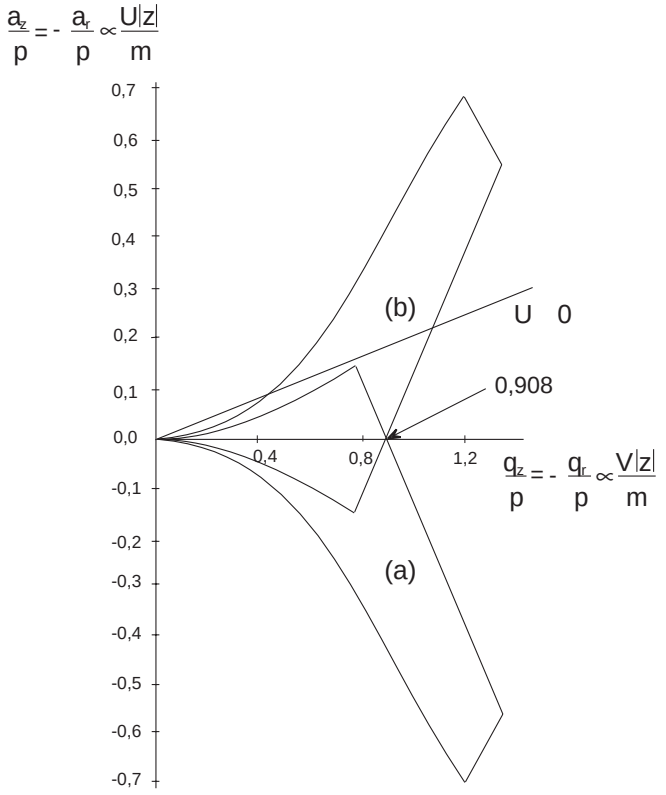

5555 Th/s, avec une segmentation standard entre 25 et 650 Th (29) et correspondant à la moyenne d'une centaine de balayages.

Les conditions d'ionisation en mode positif sont standards. Le niveau RF d'ionisation (LMCO) est de 50 Th (pendant l'ionisation, seule une tension RF d'amplitude constante, exprimée comme la limite de basse masse, est appliquée à l'électrode circulaire). Le courant d'émission du filament (FEC) est relativement faible (10 µA), tandis que le temps d'ionisation est ajusté de façon à conserver une résolution unitaire tout en optimisant l'intensité du signal (typiquement un temps d'ionisation de 300 µs pour la pression partielle en échantillon utilisée).

Il a été au préalable nécessaire d'équiper l'appareil d'un système de détection modifié afin de détecter les ions négatifs. Ce dernier est constitué d'un channeltron classique devant lequel est placée une dynode de conversion de géométrie du type « Venetian Blind » (Torn Emi, Fairfield, Conn., U.S.A.). L'alimentation de la dynode est comprise entre +5 kV et –5 kV.

La formation des ions négatifs étant défavorisée, il est nécessaire d'utiliser un temps d'ionisation de 25 ms (valeur maximale) et un FEC intense (typiquement compris entre 40 et 80 µA), de façon à augmenter la probabilité de formation des ions négatifs. Enfin, le LMCO est classiquement de 10 Th. Les expériences portant sur l'effet du niveau RF d'ionisation utilisent un FEC de 50 µA. L'étude des effets du FEC (cf. les figures 7 et 8) a été effectuée à un LMCO de 35 Th (pour pouvoir confiner simultanément des ions positifs et négatifs ayants des rapports *m*/*z* proches) avec une variation du FEC comprise entre 10 et 50 µA avec un incrément de 1 µA.

Enfin les simulations ont été effectuées avec le logiciel ITSIM™ (30). Celles-ci utilisent un piège avec une géométrie étirée, comme celle employée dans ce travail. Toutefois, aucune contribution des champs d'ordre élevé n'est considérée (ceux-ci n'introduisent qu'une faible dispersion des trajectoires et ne modifient pas l'énergie cinétique maximale des électrons) : le champ quadripolaire est donc pur. De plus, aucun ion n'est supposé présent au sein du piège; le potentiel de charge d'espace est négligé. Les collisions des électrons avec l'hélium ne sont pas prises en compte (en effet, le temps de résidence des électrons est au maximum de 20 ns, alors que le temps moyen entre deux collisions est au minimum de 1 µs, estimé à partir du modèle de Langevin (31) en supposant des électrons thermiques). Seule une tension RF de fréquence fixe 1,05 MHz et d'amplitude constante 114 $V_{0\text{-}p}$ (LMCO = 10 Th) est appliquée à l'électrode circulaire. Chaque simulation considère 100 électrons créés simultanément à un angle de phase RF donné. Les électrons pénètrent dans le piège par l'électrode chapeau supérieure, avec une distribution uniforme de 2 mm de large suivant les directions *x* et *y* et centrée sur l'axe *z*. La vitesse de chaque électron est axiale et sans composante radiale, et correspond à une valeur fixe d'énergie cinétique de 12,5 eV (tension du filament conseillée par défaut pour le Saturn™).

Partie théorique

Le mode de fonctionnement des pièges ioniques quadripolaires a été amplement décrit dans la littérature (32). Le diagramme de stabilité permet de déterminer si un ion est stable ou non au sein du piège. Il est typiquement représenté en coordonnée a_u et q_u connues sous le nom de paramètres de stabilité :

$$[1] \qquad a_z = -2a_r = -\frac{16zeU}{m(r_o^2 + 2z_o^2)\Omega^2}$$

$$[2] \qquad q_z = -2q_r = -\frac{8zeV}{m(r_o^2 + 2z_o^2)\Omega^2}$$

où *u* représente les coordonnées (*r* et *z*); *m* est la masse de l'ion et *z* son nombre de charges; *V* représente l'amplitude zéro à crête de la tension radiofréquence (RF) de pulsation Ω et *U* est l'amplitude de la tension continue (DC) appliquées toutes deux à l'électrode circulaire de rayon r_0 ; z_0 décrit la distance entre les électrodes chapeaux.

Dans le cas présent, les paramètres de stabilité a_u et q_u sont pondérés par la polarité *p* de l'ion considéré (avec $z = p|z|$ et $p = \pm 1$) de façon à différencier le diagramme de stabilité des ions négatifs de celui des ions positifs. Le diagramme de stabilité de ces derniers est le symétrique par rapport à l'axe q_u/p de celui des ions négatifs (figure 1). Toutefois, la pondération des paramètres de stabilité par la polarité n'est généralement pas prise en compte dans la représentation des diagrammes de stabilité des ions positifs et négatifs.

Cette figure présente une zone commune aux ions positifs et négatifs, notamment pour le mode de fonctionnement classique ($a_u/p = 0$). Ainsi, dans ces conditions il y a confinement

© 1998 NRC Canada

simultané. Il est toutefois possible d'isoler sélectivement des ions négatifs et positifs, en travaillant sur l'axe a_u/p ($U \neq 0$).

Il reste à déterminer la stabilité relative d'un ion par rapport à un autre, ou d'un ion en fonction des tensions U et V employées. Il faut savoir que la détermination de l'allure d'une trajectoire est une approche complexe. Différentes méthodes ont été mises au point pour étudier le mouvement des ions piégés dans un champ quadripolaire (33–35). Plus récemment, de nombreux auteurs ont étudié, à l'aide de simulations (ITSIM™ (30), SIS™ (31)), l'influence de différents paramètres sur les conditions de piégeage : effet de l'hélium (31), de l'instabilité axiale (30), de l'excitation résonnante (36) ou des phénomènes de charge d'espace (37, 38). Malgré les promesses engendrées par ces méthodes, les moyens mis en oeuvre sont difficiles (logiciel et traitement informatique complexes). Toutefois un traitement beaucoup plus accessible, mais moins rigoureux, a été développé par Major et Dehmelt (33). Il permet d'avoir une idée de la stabilité relative d'un ion donné dans des conditions opératoires données (paramètres a_u et q_u fixés). Ce traitement conçoit le mouvement d'un ion comme un simple mouvement oscillatoire à la fréquence séculaire selon une direction u, ω_u (cette dernière est liée au facteur m/z de la façon suivante, $\omega_u = \beta_u\Omega/2$) dans un puits de pseudo-potentiel de profondeur $\overline{D}_u$. Ce modèle n'est cependant quantitativement valable que pour des valeurs de q_u inférieures à 0,4 où $\beta_u = \sqrt{a_u + q_u^2/2}$. Si l'on considère que seule une tension RF est appliquée à l'électrode circulaire ($a_u = 0$), on a :

$$[3] \qquad \overline{D}_u = \frac{mq_u^2\Omega^2}{16ze}u_0^2$$

En considérant la relation $r_0^2 = 2z_0^2$, on a $\overline{D}_z = 2\overline{D}_r$. Un ion est donc d'autant plus stable que sa valeur de q_z est élevée et que son rapport m/z est faible.

Détection et identification des ions négatifs

La détection d'ions négatifs implique un détecteur approprié (39). La difficulté à les détecter est liée au principe même du fonctionnement des détecteurs conventionnels en mode analogique (channeltron, galettes de microcanaux ou multiplicateur d'électrons). Un ion incident entre en collision avec le haut du détecteur, ce qui induit la production d'électrons secondaires en cascades depuis le site d'impact porté à un potentiel négatif vers le collecteur porté à la masse.

Dans les générations précédentes de spectromètres à faisceau d'ions de hautes énergies, l'ion négatif incident possède une énergie cinétique suffisante pour passer la barrière de potentiel imposée par un détecteur conventionnel. Ainsi un ion négatif peut être détecté malgré le fait que le détecteur soit porté à un potentiel négatif (40). Dans un cadre plus général, pour détecter des ions négatifs, il faut les accélérer vers le détecteur au moyen d'un potentiel positif; il est alors nécessaire d'avoir un collecteur porté à un haut potentiel positif (41). Cependant, cela pose des difficultés technologiques importantes en détection analogique. La deuxième solution plus couramment utilisée depuis une vingtaine d'années sur les spectromètres de masse conventionnels utilise une dynode de conversion (42, 43). Les ions négatifs sont accélérés vers une surface métallique portée à un haut potentiel positif de plusieurs kV. De la collision sur surface, résultent des espèces

Fig. 2. Dépendance linéaire liant l'énergie cinétique (en eV) maximale estimée (obtenue au travers de la mesure du seuil de disparition du signal d'un ion donné par variation du potentiel positif appliqué à la dynode) au rapport m/z des ions du FC43 (les conditions opératoires étant des conditions d'impact électronique standard : FEC = 10 μA, LMCO = 35 Th, TI = 300 μs).

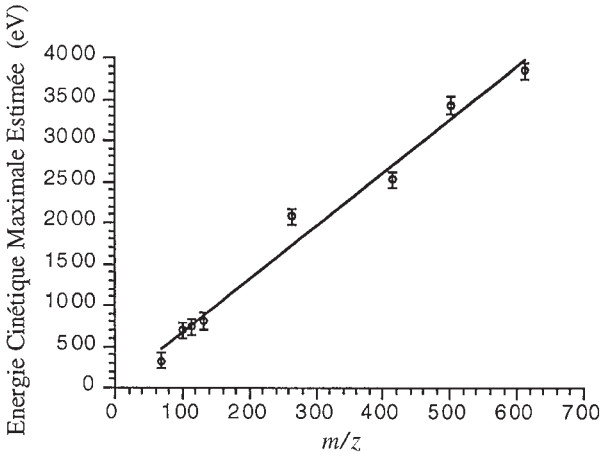

secondaires positives qui dans un second temps seront détectées par un channeltron classique. L'utilisation d'un « Venetian Blind » comme dynode de conversion permet une émission des espèces secondaires suivant le même axe que les ions incidents. Le gain de place ainsi occasionné permet d'utiliser ce système sur des pièges ioniques commerciaux avec peu de soucis technologiques.

En 1980, Mather et Todd (44) ont reporté la détection simultanée d'ions positifs et d'ions négatifs. Pour cela, il faut que les ions négatifs possèdent une énergie cinétique suffisante pour passer la barrière de potentiel imposée par le détecteur. Cooks et coll. (45) ont précédemment déterminé expérimentalement la distribution d'énergie cinétique des ions éjectés sous instabilité axiale. Il apparaît selon cette étude que les ions sont éjectés à vitesse constante; autrement dit, l'énergie cinétique des ions éjectés augmente linéairement avec le rapport m/z.

Les résultats présentés dans ce travail montrent que le signal des ions positifs décroît avec l'augmentation de la tension positive appliquée au Venetian Blind. Cette diminution résulte de deux facteurs : premièrement les ions positifs sont ralentis et l'efficacité de conversion diminue, celle-ci étant fonction de l'énergie des ions incidents (46); deuxièmement la décroissance reflète la distribution d'énergie cinétique (normalement accessible en effectuant la dérivée de la courbe du signal en fonction du potentiel retardateur). L'efficacité de conversion étant une inconnue, seule une estimation de l'énergie cinétique maximale peut être faite. Cette dernière correspond à la tension seuil appliquée à la dynode pour laquelle le signal des ions positifs détectés disparaît. L'utilisation du Venetian Blind permet de confirmer la détection simultanée au travers de la grande énergie cinétique caractérisant les ions positifs et négatifs. La figure 2 montre la corrélation liant l'énergie cinétique maximum estimée d'un ion donné en fonction de son rapport masse sur charge. Cette dépendance linéaire est proche de $E_{cin_{max}} = [27{,}15+6{,}44m/z]$ eV selon un coefficient de corrélation de 0,9913.

Cependant, la détection simultanée ne résulte pas uniquement de l'énergie cinétique des ions éjectés; il existe, comme

© 1998 NRC Canada

Fig. 3. Résultats de la simulation de la variation des énergies cinétiques (en eV) maximale et minimale des électrons en fonction de l'angle phase RF initial (E_{init} = 12,5 eV, V = 114 $V_{0\text{-}p}$ soit 10 Th et $\Omega/2\pi$ = 1,05 MHz).

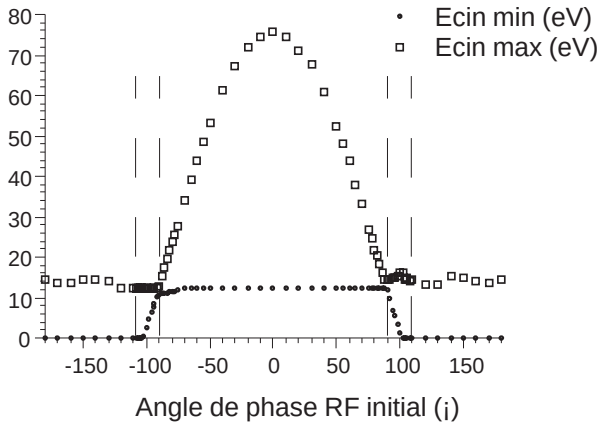

cela a été précédemment montré, la possibilité de conversion par collision sur l'électrode chapeau supérieure (47). En effet, les ions négatifs, ne possédant pas suffisamment d'énergie cinétique pour passer la barrière de potentiel imposé par le détecteur, sont repoussés vers l'électrode chapeau inférieure. La collision sur surface qui en résulte libère des espèces positives secondaires, qui peuvent être détectées.

La détection simultanée des ions positifs et des ions négatifs repose sur le principe de fonctionnement du piège quadripolaire. Cependant, à partir du moment où l'on peut détecter des ions de polarité différente sans aucun moyen d'identification, des confusions peuvent être faites. Différentes méthodes sont à notre disposition pour passer outre ce problème. La première solution utilise le fait même que les ions éjectés possèdent une grande énergie cinétique. Suivant la polarité de l'ion étudié, l'évolution de son signal en fonction de la tension appliquée à la dynode sera différente. Il est possible aussi de s'affranchir de ces difficultés causées, premièrement par l'énergie cinétique à l'éjection en utilisant une dynode de conversion située hors de l'axe z et portée à un très haut potentiel (jusqu'à ±15 kV), avec les difficultés technologiques que comportent l'utilisation de très hautes tensions ainsi que le volume occupé par le détecteur, deuxièmement en insérant un isolant derrière l'électrode chapeau et devant le système de détection (pour s'affranchir de la conversion par collision sur l'électrode chapeau, et éviter une perturbation éventuelle du champ quadripolaire par le potentiel élevé appliqué à la dynode). La société Finnigan sur le GCQ™ et le LCQ™ et la société Brüker sur l'Esquire™ proposent des systèmes, brevetés, de détection analogues.

Récemment, une étude a confirmé la polarité des ions négatifs à m/z 452, m/z 595 et m/z 633 étudiés dans le présent travail (27), en utilisant la solution la plus courante : l'application à l'électrode circulaire d'une tension continue U. Comme il l'a été montré précédemment, le diagramme de stabilité des ions négatifs présente certaines parties communes avec celui des ions positifs. Par contre, dans les parties indépendantes, il est possible de confiner sélectivement soit des ions positifs soit des ions négatifs. Ainsi en appliquant une combinaison d'une tension RF et d'une tension continue positive appropriée (a_u/p <0) à l'électrode circulaire, la droite de fonctionnement (sur laquelle se positionnent les points de fonctionnement (a_u/p, q_u/p) des ions négatifs et positifs) est hors des limites du diagramme de stabilité des ions négatifs. Les ions positifs sont alors piégés sélectivement. Inversement, avec une tension continue négative, les ions négatifs sont isolés. Sur la figure 1, décrivant les diagrammes de stabilité des ions négatifs et des ions positifs avec la représentation a_u/p, q_u/p, est reportée la droite de fonctionnement pour une tension continue négative. Pour avoir un isolement en l'absence de tout ion positif, la droite de fonctionnement doit passer au delà de l'extrémité supérieure du diagramme de stabilité des ions positifs. Dans ces conditions, la gamme de masse d'ions négatifs isolés se réduit, puisque certains ions négatifs de hauts rapports m/z ($m/z > M$) sont situés au-delà de la limite de stabilité $\beta_z = 0$. Afin d'isoler les ions négatifs de rapports m/z supérieurs à M, les tensions U et V sont modifiées (tout en les maintenant dans un rapport constant) de façon à ce que le point de fonctionnement de l'ion de masse M se retrouve à la place de celui de l'ion de masse m. Ceci permet d'isoler des ions négatifs de plus hauts rapports m/z, et déplace la limite de haute masse à une valeur plus élevée.[4] Ainsi, si l'on veut enregistrer un spectre de masse d'ions négatifs en l'absence de tout ion positif, il convient d'utiliser six séquences différentes correspondant à six combinaisons de tension U et V. Ceci présente alors un net désavantage d'un point de vue analytique, puisque dans un pic chromatographique il faut enregistrer cinq balayages différents pour avoir le spectre de masse des ions négatifs sur toute la gamme de masse.

Marquette et Wang (48) ont proposé une solution permettant de s'affranchir de la tension continue. L'utilisation d'une tension RF dipolaire, à la même fréquence que celle du champ de piégeage Ω, appliquée aux électrodes chapeaux permet l'éjection unidirectionnelle des ions confinés. Dans le cas d'ions négatifs et positifs confinés simultanément, chacun d'entre eux sera alors éjecté suivant des directions opposées, et donc pourra être analysé séparément.

La formation des ions négatifs

Trois types de réactions sont invoquées sous le terme générique de capture électronique (49). La première est la capture résonnante d'électron (réaction [4]), la seconde la capture d'électron dissociative (réaction [5]), la troisième enfin est la formation de paire d'ions (réaction [6]).

[4] $A + e^- \rightarrow A^{\bullet -}$

[5] $A + e^- \rightarrow [A^{\bullet -}]^* \rightarrow F^- + N$

[6] $AB + e^- \rightarrow A^- + B^+ + e^-$

Quelle que soit la réaction envisagée, l'énergie cinétique des électrons ionisants doit être faible. Or l'électron, compte tenu de son rapport m/z, est instable au sein du piège et est fortement accéléré par le champ quadripolaire, limitant ainsi les processus de capture.

4. En pratique, la gamme de masse est plus restreinte. La limite de basse masse m est située à l'aplomb de la limite de stabilité à q_z = 0,908, à cause de la séquence d'isolement utilisée : la tension RF est augmentée jusqu'à une valeur, correspondant à un seuil de basse masse de m, puis est appliquée la tension DC, déplaçant le point de fonctionnement de cet ion m à la verticale de la limite à q_z = 0,908.

© 1998 NRC Canada

Fig. 4. Variation expérimentale de l'intensité absolue du signal de l'ion négatif *m*/*z* 452 du FC43 en fonction du niveau RF d'ionisation, exprimé en *m*/*z* (TI = 25ms, FEC = 50 μA).

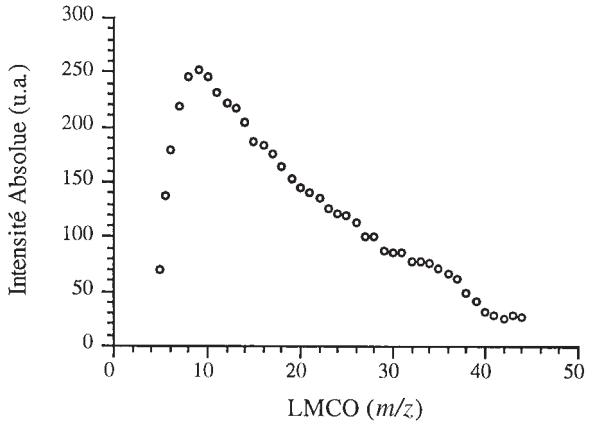

L'utilisation du programme de simulation ITSIM™ a permis de déterminer l'influence de l'angle de phase RF initial $2\xi_0$ de la tension RF (autrement dit la tension $V \cos 2\xi_0$), appliquée à l'électrode circulaire lors de la période d'ionisation, sur la trajectoire des électrons. La figure 3 reporte l'évolution de l'énergie cinétique maximale et minimale des électrons, au cours de la trajectoire, en fonction de l'angle de phase RF initial. Les électrons sont injectés par l'électrode chapeau supérieure avec une vitesse correspondant à une énergie cinétique de 12,5 eV (la vitesse est supposée sans composante radiale). Les résultats obtenus sont comparables à ceux de Pedder et al. (50).

Cette courbe peut être découpée en trois zones distinctes. La zone I correspond aux angles de phase RF initiaux pour lesquels le potentiel $V \cos 2\xi_0$ est supérieur à –25 eV (soit $2\xi_0$ = 102.7° et –102.7°). Dans ces conditions, les électrons traversent le piège de part en part et viennent frapper l'électrode chapeau inférieure. Lorsque le potentiel $V \cos 2\xi_0$ augmente, leurs énergies cinétiques maximales croient jusqu'à un maximum à $2\xi_0 = 0°$; parallèlement leurs temps de résidence diminuent. La variation de l'énergie cinétique maximale suit la relation suivante :

$$[7] \qquad E_{e^-}(\max) = 0{,}5V \cos 2\xi_0 + E_{\text{init}}$$

Cette relation est différente de celle donnée par Pedder et al. (50). Ceci est dû aux conditions de simulation utilisées, où la vitesse est supposée sans composante radiale. Les électrons passent donc au centre du piège, où le potentiel est de $0{,}5V \cos 2\xi_0$ (32). L'énergie cinétique maximale suit, dans ce cas particulier, la relation [7].

La zone II correspond à une période de transition. Elle est centrée sur une valeur d'angle de phase où $V \cos 2\xi_0 = -2E_{\text{init}}$. Cette zone caractérise le passage des trajectoires de type I (associées à la zone qui les caractérise) à des trajectoires de type III. Les électrons vont voir leur temps de confinement progressivement augmenter, et leur énergie cinétique minimale diminuer. Lorsque l'électron passe au centre du piège, son énergie cinétique atteint un minimum. À ce moment, le potentiel est légèrement supérieur à $-2E_{\text{init}}$. Le potentiel RF devient plus négatif et l'électron ne traverse plus le piège de part en part. Il pénètre alors celui-ci plus ou moins profondément, selon la valeur de $V \cos 2\xi_0$, puis est repoussé vers l'électrode chapeau supérieure. L'énergie cinétique minimale est nulle, lorsque l'électron a effectué son incursion maximale au sein du piège. Cette zone II correspond aux électrons ayant une faible énergie cinétique (proche de zéro) lorsqu'ils sont au centre du piège. Ceux-ci sont très probablement à l'origine des interactions électron–molécule nécessaires à la formation des ions négatifs, car ils possèdent une faible énergie cinétique nécessaire au processus de capture.

Durant la troisième période (zone III), les électrons sont repoussés vers l'électrode chapeau supérieure. L'incursion axiale décroît lorsque le potentiel $V \cos 2\xi_0$ devient plus négatif, et le temps de résidence décroît aussi. L'énergie cinétique maximale garde une valeur constante égale à l'énergie cinétique initiale.

Le même raisonnement peut être tenu avec les électrons secondaires issus de l'impact électronique (équation [8]). Ceux-ci créés au centre du piège avec une énergie thermique initiale ont des temps de confinement bien plus longs, et interviennent donc fort probablement dans les processus de capture (51). Toutefois, ces simulations montrent aussi le rôle joué par les électrons primaires issus du filament. Il est cependant très difficile de faire la part des choses entre ces deux origines.

$$[8] \qquad \mathrm{M} + e^-_{\text{prim}} \rightarrow M^{\bullet +} + \mathrm{e}^{\prime -}_{\text{prim}} + \mathrm{e}^-_{\text{sec}}$$

D'après l'équation [8], l'énergie cinétique maximale des électrons est affectée par la tension RF d'ionisation *V*. La figure 4 reporte le signal de l'ion négatif *m*/*z* 452 en fonction du niveau RF d'ionisation (noté LMCO). Les courbes pour les autres ions négatifs à *m*/*z* 595 et *m*/*z* 633 ont une évolution similaire.

Ce paramètre affecte le courant ionique selon deux facteurs : (*i*) le paramètre de stabilité q_u de chaque ion confiné selon son rapport *m*/*z*, ce qui affecte par la même la stabilité des ions piégés, estimée selon le modèle du puits de pseudo-potentiel de Dehmelt (équation [3]) et (*ii*) l'énergie cinétique et la trajectoire des électrons primaires issus du filament et des électrons secondaires. Ces deux points conduisent à une dépendance caractérisée par la présence d'un maximum du courant ionique, et illustrent deux effets antagonistes. Lorsque le LMCO augmente, l'efficacité d'ionisation diminue, car l'énergie cinétique des électrons croît; parallèlement le puits de pseudo-potentiel est plus profond et l'ion *m*/*z* 452 est d'autant plus stable. La figure 4 présente certaines particularités propres au fait qu'elle caractérise un ion négatif : l'optimum se situe autour du rapport 10 *m*/*z* suivi d'une diminution monotone pour atteindre une faible valeur vers *m*/*z* 45, alors que pour un ion positif ayant un rapport *m*/*z* équivalent (*m*/*z* 464) le maximum se situe autour de la valeur de 25 Th suivi d'une lente décroissance (50). La formation des ions négatifs nécessitant des électrons de faible énergie cinétique, le LMCO joue donc un rôle particulièrement néfaste sur le courant de ces ions.

La présence d'ions négatifs ayant des rapports *m*/*z* élevés (*m*/*z* 633, *m*/*z* 595,...) à de faibles LMCO est remarquable, or dans ces conditions la valeur du D_z est très faible (eq. [3]) : D_z = 0,225 V pour l'ion à *m*/*z* 633 avec une tension RF d'ionisation de 114 $V_{0\text{-}p}$ (LMCO = 10 Th). Par contre, l'ion positif à *m*/*z* 614 avec un seuil de basse masse analogue présente une intensité très faible, car cet ion n'est pas suffisamment stable au sein du piège. Cet aspect résulte des conditions d'ionisation particulières utilisées et sera discuté plus en détail.

Le recours à des pressions partielles élevées en gaz tampon

© 1998 NRC Canada

Fig. 5. Spectre de masse d'ions négatifs du FC43 (TI = 25 ms, FEC = 80 μA, LMCO = 10 Th). Il apparaît une forte abondance d'ions positifs de faible rapport *m*/*z* et corrélativement la disparition des ions de hauts rapports *m*/*z*, ainsi que l'apparition d'ions négatifs de hauts rapports *m*/*z* avec des signaux bien résolus.

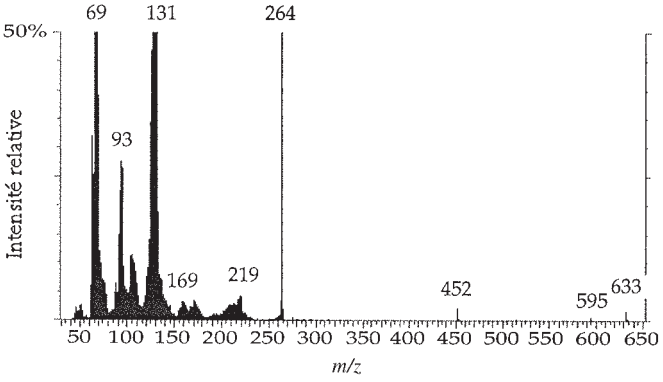

(22) est la solution couramment employée pour limiter les problèmes de reproductibilité qui se posent lorsqu'on étudie les ions négatifs (52). Ce gaz tampon permet de thermaliser les électrons et donc de favoriser les processus de capture, mais aussi il stabilise les ions négatifs et limite les pertes de signal qui surviennent par autodétachement (49). Sears et Grimsrud ont comparé les sensibilités relatives de détection d'ion négatif moléculaire du nitrobenzène avec différents gaz tampons à la même pression (53). Avec CO_2 et CH_4, des sensibilités similaires ont été obtenues, alors qu'avec l'azote ou l'argon les sensibilités sont plus faibles d'un facteur 30, tandis qu'avec l'hélium la sensibilité est plus faible d'un facteur 100. Malheureusement, dans les pièges ioniques quadripolaires, les gaz les plus performants (CO_2, CH_4) induisent des diminutions de l'intensité du signal (54), tandis que l'hélium, qui améliore la sensibilité dans le piège (7), donne des résultats plus modestes. Il n'est donc pas possible de bénéficier de l'avantage de ces gaz tampons dans les pièges ioniques quadripolaires, même si ces derniers sont présents en mélange avec l'hélium (55).

Influence des ions positifs sur les ions négatifs

Comme cela vient d'être décrit, la principale raison pour laquelle les ions négatifs sont peu étudiés est due à la faible probabilité de les créer. Il est alors nécessaire d'utiliser des conditions d'ionisation extrêmes de façon à favoriser l'observation de ces espèces. Le temps d'ionisation utilisé est donc maximal, ainsi que le courant d'émission du filament. Enfin, il est préférable d'avoir des quantités importantes d'échantillon. Étant donné que seule une tension RF est appliquée à l'électrode circulaire pendant l'ionisation, les ions positifs et les ions négatifs créés au cours de cette période sont confinés simultanément. De plus, la formation d'ions positifs est beaucoup plus probable (56). Aussi pendant l'ionisation, une quantité considérable d'ions positifs est produite, ce qui induit des potentiels de charge d'espace particulièrement intenses. Il faut préciser que lorsque le piège ionique est utilisé en condition normale d'étude des ions positifs (avec contrôle du nombre d'ions formés par l'AGC (9)) la quantité d'ions négatifs simultanément formée est trop faible pour perturber l'enregistrement des spectres de masse.

L'effet de l'environnement subi par les ions négatifs est dû à la présence d'un grand nombre d'ions positifs, et cet effet a été très peu étudié (32, 47). Pourtant, compte tenu de l'allure des spectres de masse enregistrés, l'influence des ions positifs est loin d'être négligeable. La figure 5 représente un spectre de masse du FC43 comportant des ions négatifs obtenus pour le FC43 (TI = 25 ms, FEC = 60 μA, LMCO = 35 Th).

Ce spectre de masse présente plusieurs particularités, dont la première est la détection simultanée, dont les raisons ont été déjà discutées, d'ions positifs et des trois ions négatifs de haute masse à *m*/*z* 633, *m*/*z* 595 et *m*/*z* 452 (détectés avec la dynode de conversion portée à un potentiel de –3 kV). Les autres points sont imputables au potentiel de charge d'espace. Ainsi, les profils des ions positifs de faibles rapports *m*/*z* sont fortement perturbés : décalibration accompagnée d'un élargissement des signaux.

Ces perturbations sont dues aux interactions coulombiennes répulsives entre espèces chargées de même polarité. À cet égard, la prédominance des ions positifs de faibles rapports *m*/*z* par rapport aux ions négatifs permet en première approximation de négliger les éventuelles perturbations induites par ces derniers. Lorsque la quantité d'ions positifs présents au sein du piège, lors de l'éjection d'ions positifs de rapport *m*/*z* donné par instabilité sélective en masse, est importante, le profil des ions éjectés est déplacé vers les hauts rapports *m*/*z* et sa largeur à mi-hauteur augmente (57). Étant donné que cette perte de résolution (élargissement et déplacement des pics vers les hautes valeurs de *m*/*z*) est fonction du nombre d'ions, ceux de plus faible rapport *m*/*z* seront les plus affectés. En effet, le capital d'ions formés et piégés pendant l'ionisation, dont les rapports *m*/*z* sont supérieurs au seuil de basse masse, diminue par éjection, lors du balayage de la tension RF, depuis les ions de bas rapports *m*/*z* vers ceux de hauts rapports *m*/*z*. La deuxième conséquence du potentiel de charge d'espace porte sur la déstabilisation des ions positifs de hauts rapports *m*/*z* (58). Ainsi, le spectre reporté figure 5 ne présente aucun ion positif ayant un rapport *m*/*z* supérieur à 270 Th, le signal à *m*/*z* 264 a donc une résolution unitaire. Il n'est pas possible d'éviter ces perturbations rencontrées au cours de l'étude des ions négatifs à l'aide d'algorithme permettant de contrôler le temps d'ionisation tel que l'AGC. En effet, les ions négatifs étant formés en beaucoup plus faible proportion que les ions positifs, une diminution trop importante de la période d'ionisation pour limiter le nombre d'ions positifs créés empêcherait l'observation d'ions négatifs.

Déstabilisation des ions positifs et stabilisation des ions négatifs

La déstabilisation des ions positifs survient pendant l'ionisation, au cours de laquelle la population d'ions positifs peut être modifiée. Les répulsions coulombiennes entre les ions positifs déstabilisent les ions positifs les moins stables au sein du piège, qui sont d'après le modèle du puits de pseudo-potentiel les ions de hauts rapports *m*/*z*. Ainsi, par augmentation progressive de la quantité d'ions et donc du potentiel de charge d'espace, les ions positifs sont éjectés selon les rapports *m*/*z* décroissants. Si le nuage d'ions est majoritairement constitué d'ions positifs de hauts rapports *m*/*z*, ceux-ci ne seront pas forcément éjectés,

© 1998 NRC Canada

Fig. 6. Spectre du FC43 montrant la présence simultanée d'ions positifs de hauts rapports *m*/*z* ▲ (*m*/*z* 414, *m*/*z* 464 et *m*/*z* 502) et d'ions négatifs ● (*m*/*z* 452, *m*/*z* 595 et *m*/*z* 633). Le profil des ions *m*/*z* 452, éjectés en présence d'ions positifs (*m*/*z* 464 et *m*/*z* 502), est déplacé vers les faibles rapports *m*/*z* (*m*/*z* 451) (TI = 25 ms, LMCO = 35 Th, FEC = 20 μA).

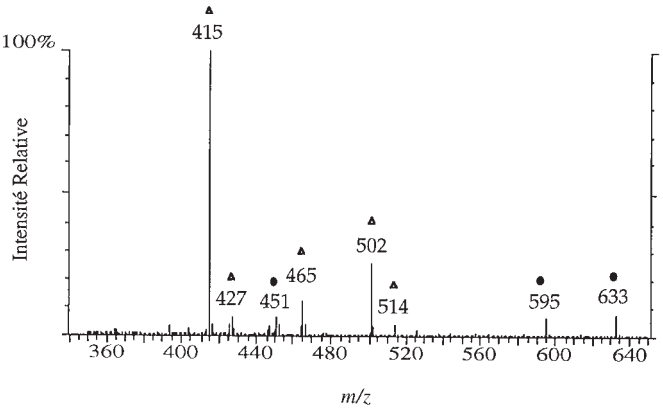

mais leurs abondances relatives pourront être modifiées. Ces résultats ont fait l'objet d'une publication (58), dont les résultats majeurs sont résumés ci-dessous.

Le modèle employé pour interpréter la déstabilisation des ions positifs est basé sur le modèle du puits de pseudo-potentiel. Le potentiel de charge d'espace induit par les ions de faibles rapports *m*/*z* va compenser le potentiel de piègeage des ions de hauts rapports *m*/*z* conduisant à une déstabilisation de ces derniers. Les ions de hauts rapports *m*/*z* étant d'autant moins stables que leur rapport *m*/*z* est élevé, ceux-ci seront déstabilisés suivant leur rapport *m*/*z* décroissant (c'est à dire, dans le cas de la figure 5, depuis *m*/*z* 614 jusqu'à *m*/*z* 300).

Cette déstabilisation des ions positifs s'accompagne d'une déformation du diagramme de stabilité. Des mesures expérimentales de déformation du diagramme de stabilité ont été précédemment reportées qui confirment ces résultats (59).

Intuitivement, il est probable qu'il en va différemment pour des ions de charge opposés. En effet, la figure 5 montre la présence indiscutable d'ions négatifs de hauts rapports *m*/*z*. Ceux-ci ne sont donc pas déstabilisés par le potentiel de charge d'espace dû aux ions positifs de faibles rapports *m*/*z* en quantité abondante; ils sont au contraire stabilisés (58). En fait, le diagramme de stabilité des ions négatifs en présence d'ions positifs subit une déformation inverse de celui des ions positifs (59), confirmant aussi l'effet de stabilisation des ions négatifs par le potentiel de charge d'espace dû aux ions positifs.

Décalibration des ions positifs par les ions négatifs et réciproquement

L'hypothèse faite au préalable sur l'influence négligeable des ions négatifs peut s'avérer dans certains cas hasardeuse. Sur le spectre de masse reporté figure 6, le signal des ions négatifs est bien résolu; en effet, il a été dit précédemment que la résolution du signal d'ions donnés est affectée par la quantité d'ions présents lors de l'éjection de ces derniers. Pour les conditions utilisées dans la figure 5, lors de leur éjection, les ions négatifs ne sont pas perturbés par d'éventuels ions positifs, car ceux de hauts rapports *m*/*z* ont déjà été déstabilisés par le potentiel de charge d'espace tandis que ceux de faibles rapports *m*/*z* ont été éjectés au préalable par balayage de la tension RF, ni par les ions négatifs eux-mêmes, car ils sont en quantité trop faible pour induire un potentiel de charge d'espace.

Toutefois, les ions négatifs peuvent être dans certains cas en quantité suffisamment abondante pour induire des pertes de résolution, déplaçant leurs profils vers de hauts rapports *m*/*z* (60), comme c'est le cas pour les ions positifs (57). À cet égard, il est difficile d'estimer la quantité d'ions négatifs présents au sein du piège, bien que celle-ci soit probablement plus faible que celle des ions positifs, mais tout de même suffisante pour induire un potentiel de charge d'espace. De plus, il est difficile de comparer les intensités relatives des ions positifs et des ions négatifs, les efficacités de détection n'étant pas identiques.

Parallèlement, il est possible d'observer, dans certaines conditions, la présence simultanée d'ions négatifs et d'ions positifs de plus haut rapport *m*/*z*. La figure 6 est obtenue dans des conditions similaires à celle de la figure 5, mais avec un FEC plus faible, de 20 μA, de façon à limiter l'éjection des ions positifs de hauts rapports *m*/*z* en réduisant le potentiel de charge d'espace. La résolution du signal d'ions de rapport *m*/*z* donné est affectée par la quantité d'ions ayant des rapports *m*/*z* plus élevés. Aucun ion positif ayant un rapport *m*/*z* supérieur à 526 n'est détecté. Le pic à *m*/*z* 502 est bien résolu, tandis que celui à *m*/*z* 464 est déplacé vers *m*/*z* 465, car les ions à *m*/*z* 464 subissent un potentiel de charge d'espace induit par leur propre densité ainsi que celle des ions à *m*/*z* 502. De même, les ions avec des rapports *m*/*z* plus faibles sont aussi décalibrés : *m*/*z* 426 à *m*/*z* 427, *m*/*z* 414 à *m*/*z* 415. Concernant les ions négatifs, ceux à *m*/*z* 633 et *m*/*z* 595 ne sont pas éjectés en présence d'ions positifs de plus haut rapport *m*/*z*, car ces derniers sont déstabilisés par le potentiel de charge d'espace, de plus ils ne sont pas en quantité suffisamment abondante pour affecter leurs résolutions. Par contre, les ions négatifs à *m*/*z* 452 sont éjectés en présence d'ions positifs à *m*/*z* 464 et *m*/*z* 502. Leur profil est alors déplacé vers de plus faibles rapports *m*/*z* (massif à *m*/*z* 451).

Inversement, il est fort probable que le signal d'ions positifs soit déplacé vers de plus faible rapport *m*/*z*, lorsque ces derniers sont éjectés en présence d'ions négatifs abondants. La figure 7*a* montre le profil des ions à *m*/*z* 414 en fonction de la valeur du FEC dans des conditions d'ions négatifs (TI = 25 ms, LMCO = 35 Th; ce profil a été enregistré dans des conditions de pression en FC43 légèrement différentes de celles utilisées pour les figures 5 et 6). À de faibles FEC (≤ 12 μA), le profil de ces ions est très large, dû à la présence d'ions positifs en très fortes abondances lors de l'éjection de ce dernier. À de telles valeurs de FEC, le signal semble plus faible car le courant ionique des ions à *m*/*z* 414 se répartit sur plusieurs masses. Par augmentation du FEC, le potentiel de charge d'espace est plus intense, conduisant à la déstabilisation d'ions positifs de hauts rapports *m*/*z*. Ainsi, la résolution s'améliore lorsque le FEC augmente; le profil est moins large. La figure 7*b* montre le profil de ces ions pour des valeurs de FEC comprises entre 14 et 20 μA. Quant la valeur du FEC est de 14 μA, le pic à *m*/*z* 414 est déplacé à *m*/*z* 415. À 15 μA, le nombre total d'ions à *m*/*z* 414 a légèrement diminué; le potentiel de charge d'espace subi par ces ions lors de leur éjection est plus faible et leur profil est alors redéplacé vers *m*/*z* 414 (bien que dans ces conditions, le signal ne soit pas parfaitement résolu). À 16 μA, le nombre d'ions à *m*/*z* 414 a considérablement diminué, le profil

© 1998 NRC Canada

Fig. 7. (*a*) Profil des ions positifs à *m*/*z* 414 en fonction de la valeur du FEC. La perte de signal est due au potentiel de charge d'espace. Lorsque le signal est suffisamment faible, et que la quantité d'ions négatifs est assez importante, le profil des ions positifs à *m*/*z* 414 est décalibré vers les bas rapports *m*/*z*, avant de disparaître. Le signal au rapport *m*/*z* 414 est indiqué par *. Agrandissement du profil de cet ion positif pour des valeurs de FEC comprise entre 14 et 20 μA (*b*).

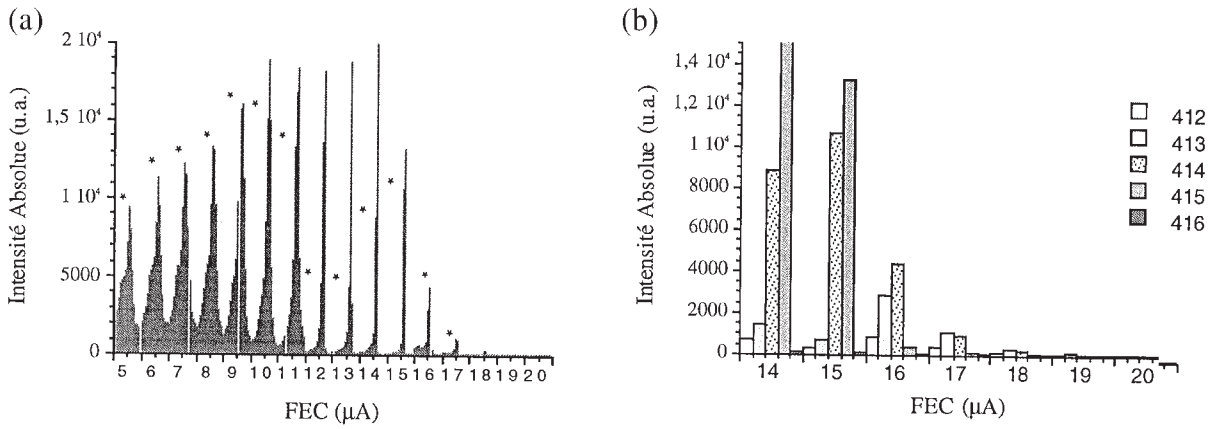

de ces ions se déplace à des rapports *m*/*z* inférieurs à *m*/*z* 414. À une telle valeur de FEC, des ions négatifs intenses à *m*/*z* 452, *m*/*z* 595 et *m*/*z* 633 sont présents, de telle façon que le potentiel de charge d'espace induit par ces ions déplace le profil des ions positifs à *m*/*z* 414 à de faibles rapports *m*/*z*. À des valeurs de FEC plus élevées, le déplacement se confirme, tandis que le signal de ces ions continue à décroître jusqu'à sa disparition totale à 20 μA.

Ainsi le suivi rigoureux du profil des ions positifs à *m*/*z* 414 en fonction du FEC montre l'effet des ions négatifs de hauts rapports *m*/*z* (*m*/*z* 452, *m*/*z* 595 et *m*/*z* 633) sur la résolution des pic des ions positifs.

Des réactions insolites : les interactions ion–ion

L'influence du confinement simultané des ions positifs et des ions négatifs ne se limite pas à des effets de charge d'espace. En effet, il a été envisagé la possibilité de réaction ion–ion pouvant limiter l'observation des ions négatifs (26) sans en spécifier la nature. Cependant, McLuckey et coll. (61) ont reporté récemment l'observation effective de transfert de proton entre des ions négatifs multichargés et une base forte protonnée, la pyridine. La réaction conduit à un ion négatif ayant perdu un état de charge. Ce type de réaction peut être utilisé pour améliorer les limites de détection en électrospray (62). Dans le cas d'interactions entre deux ions de même état de charge, mais de polarité opposée, il se produit une neutralisation (63). Deux types de réactions sont possibles (64).

[9] $A^+ + B^- \rightarrow A + B$

[10] $A^+ + B^- \rightarrow C + D$

La première possibilité consiste en une neutralisation par transfert d'électron, conduisant aux neutres de mêmes structures que les ions de départ (réaction [9]). Le deuxième cas concerne la formation de neutres de structures différentes (réaction [10]). La réaction chimique placée sous le label de « neutralisation » peut prendre différentes orientations : transfert d'électron, de proton, d'hydrure et autres, ou attachement,... Tout dépendra du comportement chimique des deux ions réactifs. La difficulté concernant l'étude de ces réactions réside dans l'identification des produits finaux (64). Cependant, quelle que soit la nature de la réaction, ces interactions ion–ion sont caractérisées par de fortes sections efficaces (10^{-7} cm^3 s^{-1}) (65), plus grandes que celles des réactions ion–molécule classiques (66). Ainsi la probabilité d'avoir ce type de réaction est grande. C'est pourquoi ces réactions ne peuvent être négligées au sein du nuage constitué des ions positifs et des ions négatifs piégés.

Dans le cas du FC43, des indices indirects ont montré la possibilité de rencontrer ce type de réaction. Ainsi l'évolution du signal des ions négatifs (figure 8*a*) et celle du signal des ions positifs de hauts rapports *m*/*z* (figure 8*b*) en fonction du FEC montrent une complémentarité frappante.

L'observation des ions négatifs (à *m*/*z* 452, *m*/*z* 595 et *m*/*z* 633) n'est possible qu'à partir du moment où la quantité d'ions positifs ayant des rapports *m*/*z* proches (614, 576, 502, 464, 414,...) diminue sous l'effet de déstabilisation dû au potentiel de charge d'espace (la contribution éventuelle apportée par les interactions ion–ion à la diminution du signal des ions positifs est supposée négligeable, compte tenu de la faible proportion des ions négatifs). En outre, l'évolution du courant des ions négatifs en fonction du FEC (figure 8*b*) montre deux droites de pentes différentes, ce qui semble caractériser deux types de processus. Dans un premier temps, le signal augmente grâce à une diminution des neutralisations; puis après déstabilisation des ions positifs de rapports *m*/*z* proches, l'augmentation du FEC assure seul la croissance du signal des ions négatifs. Un indice allant dans ce sens est l'extrapolation de cette deuxième droite qui passe près de l'origine, ce qui indiquerait que les interactions ion–ion empêcheraient la détection des ions négatifs entre 0 et 16 μA. Cet aspect mérite une étude plus approfondie. Notamment il faut déterminer l'impact des différents ions positifs sur les neutralisations (dans l'explication rapportée ici, les ions positifs de bas rapports *m*/*z* ne semblent avoir aucun effet).

S'il semble que les interactions ion–ion aient un effet non négligeable sur la faibles quantité d'ions négatifs présents au sein du piège, ce n'est pas la principale raison avancée. En effet, cette dernière est l'énergie des électrons nécessaire à la capture électronique.

© 1998 NRC Canada

Fig. 8. Évolution de l'intensité du signal des ions positifs à *m/z* 464, *m/z* 502 et *m/z* 614 en fonction de la valeur du FEC (*a*). Les ions positifs disparaissent suivant leur rapport *m/z* décroissant dû à l'augmentation du potentiel de charge d'espace avec le FEC. L'évolution de l'abondance des ions négatifs à *m/z* 595 et *m/z* 633

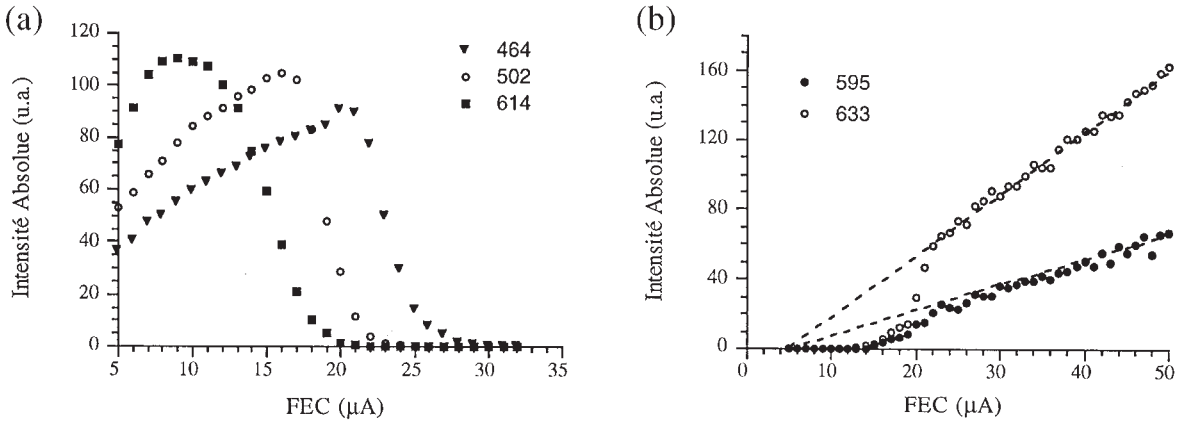

Conclusion

Ce travail a permis de dégager les difficultés relatives à l'étude des ions négatifs générés dans un piège ionique quadripolaire. Il a été montré que de tels ions peuvent être observés avec des GC/MS commerciaux, comme ceux du type Saturn™, sans aucune modification instrumentale, avec cependant quelques limitations. En effet, la détection simultanée des ions positifs et des ions négatifs, rendue possible par la forte énergie cinétique des ions lors de leur éjection analytique, peut conduire à des ambiguités d'attribution de la polarité des ions détectés, si l'on n'a pas recours à un isolement RF/DC ou à un détecteur modifié. En outre, la gamme de masse d'ions négatifs qui peut être détectée est alors restreinte, car seul les ions négatifs de plus hauts rapports *m/z* peuvent être détectés. L'utilisation d'un système de détection comportant une dynode de conversion peut être une alternative intéressante.

L'efficacité de formation des ions négatifs reste un problème plus épineux. Sa résolution doit permettre de favoriser l'abondance des électrons thermiques, nécessaires au processus de capture électronique, au sein du piège. Deux solutions sont envisageables. La première concerne l'utilisation d'une vanne pulsée, qui injecterait pendant la période d'ionisation une forte quantité de gaz, autre que l'hélium (ce dernier n'apportant pas de gain de sensibilité significatif pour la formation des ions négatifs), favorisant la thermalisation des électrons. Les vannes pulsées sont d'ores et déjà utilisées pour améliorer l'efficacité d'injection des ions à partir d'une source externe (67), ou pour améliorer l'efficacité des processus de CID (dissociations induites par collision) (68), ou encore pour limiter les réactions ion–molécule parasites (69). La deuxième solution serait de pulser la tension RF pendant l'ionisation. La formation des ions négatifs serait favorisée au cours de la période sans RF, où les électrons ne sont plus accélérés, le pulse RF assurant alors le confinement des ions négatifs créés. Des simulations de ce type de séquence sont en cours d'étude.

Il reste malgré tout une difficulté majeure : le confinement simultané des ions négatifs et des ions positifs. Celui-ci conduit à des potentiels de charge d'espace, qui se présentent comme un avantage. En effet, ces derniers déstabilisent les ions positifs de hauts rapports *m/z*, permettant ainsi l'observation des ions négatifs dans cette même gamme de rapports *m/z,* et stabilisent les ions négatifs permettant l'utilisation de faible niveaux RF d'ionisation plus favorable à la formation de ces derniers. Cependant, ce confinement simultané peut induire des pertes de résolution pour des ions négatifs, lorsque ceux-ci sont détectés en présence d'ions positifs de plus hauts rapports *m/z*. En outre, des réactions ion–ion semblent contribuer à la limitation de la quantité d'ions négatifs détectables. La solution à ce confinement simultané est l'emploi d'un isolement RF/DC qui fait suite à l'ionisation, mais en limitant la gamme de masse d'ions négatifs isolables.

L'étude des ions négatifs avec un piège ionique quadripolaire à ionisation interne devrait rester sporadique et n'être utile que pour des applications bien particulières. Par contre le développement de couplage permettant d'injecter des ions négatifs préparés dans une source externe (70) devrait favoriser l'étude et l'emploi des ions négatifs, si l'on parvient à maitriser les problèmes d'éfficacité d'injection et de discrimination en masse que l'on peut rencontrer avec ces appareils. Une solution alternative est d'utiliser une source externe qui se limite à produire des ions réactifs injectés par la suite dans le piège (71). Les échantillons arrivent par l'intermédiaire du chromatographe en phase gazeuse dans le piège, les réactions ion–molécule conduisant à la formation des ions négatifs se produisant alors au sein de celui-ci. Une telle solution permet de s'affranchir des pertes de signal des ions négatifs de l'échantillon à l'injection ainsi que des discriminations en masse. En outre, les ions produits par ionisation chimique sont bien contrôlés au moyen d'un isolement préalable des ions réactifs injectés.

Remerciements

Les auteurs remercient le Centre d'Études du Bouchet (DGA), l'Université Pierre et Marie Curie, le Centre National de la Recherche Scientifique ainsi que le Ministère de la Recherche et de l'Enseignement Supérieur pour leur support financier. La société Varian-France est remerciée pour son support technique et financier, ainsi que la société Varian Associates pour avoir fourni le logiciel QISMS™. Enfin, des remerciements

© 1998 NRC Canada

sont adressés au Professeur R.G. Cooks, et aux Docteurs C. Weil et M. Nappi pour nous avoir gracieusement fourni le logiciel de simulation ITSIM™.

Bibliographie

1. W. Paul et H. Steinwedel. US Patent **2**, 939 (1960).
2. E. Fisher. Z. Phys. **156**, 1 (1959).
3. H.G. Dehmelt. Adv. At. Mol. Phys. **3**, 53 (1967).
4. H.G. Dehmelt. Adv. At. Mol. Phys. **5**, 109 (1969).
5. J.E.P. Syka. *Dans* Practical aspects of ion trap mass spectrometry. Vol. 1. Fundamentals of ion trap mass spectrometry. *Edité par* R.E. March et J.F.J. Todd. CRC Press, Boca Raton, Fla. 1995. p. 169.
6. G.C. Stafford, P.E. Kelley, J.E.P. Syka, W.E. Reynolds et J.F.J. Todd. Int. J. Mass Spectrom. Ion Processes, **60**, 85 (1984).
7. H.F. Wu et J.S. Brodbelt. Int. J. Mass Spectrom. Ion Processes, **115**, 67 (1992).
8. M. Weber-Grabau, P.E. Kelley, S.C. Bradshaw et D.J. Hoekman. Proc. 36th ASMS Conference on Mass Spectrometry and Allied Topics. San Francisco, Calif. 1988. p. 1106.
9. G.C. Stafford, D.M. Taylor, S.C. Bradshaw, J.E.P. Syka et M. Uhrich. Proc. 35th ASMS Conference on Mass Spectrometry and Allied Topics. Denver, Colo. 1987. p. 775.
10. J.B. Plomley, C.J. Koester et R.E. March. Org. Mass Spectrom. **29**, 372 (1994).
11. B.A. Eckenrode, S.A. McLuckey et G.L. Glish. Int. J. Mass Spectrom. Ion Processes, **106**, 137 (1991).
12. J.N. Louris, J.S. Brodbelt-Lustig, R.G. Cooks, G.L. Glish, G.J. Van Berkel et S.A. McLuckey. Int. J. Mass Spectrom. Ion Processes, **96**, 117 (1990).
13. R.E. Kaiser, J.N. Louris, J.W. Amy et R.G. Cooks. Rapid Commun. Mass Spectrom. **3**, 225 (1989).
14. F.A. Londry, G.J. Wells et R.E. March. Rapid Commun. Mass Spectrom. **7**, 43 (1993).
15. S.A. McLuckey, G.J. Van Berkel, D.E. Goeringer et G.L. Glish. Anal. Chem. **66**, 689 (1994).
16. J. Qin, R.J.J.M. Steenvoorden et B.T. Chait. Proc. 42nd ASMS Conference on Mass Spectrometry and Allied Topics. Chicago, Ill. 1994. p. 696.
17. G.J. Van Berkel, G.L. Glish et S.A. McLuckey. Anal. Chem. **62**, 1284 (1990).
18. J.S. Brodbelt, J.N. Louris et R.G. Cooks. Anal. Chem. **59**, 1278 (1987).
19. D.W. Berberich, M.E. Hail, J.V. Johnson et R.A. Yost. Int. J. Mass Spectrom. Ion Processes**, 94**, 115 (1989).
20. J.H. Bowie. Mass Spectrom. Rev. **3**, 161 (1984).
21. V.S. Ong et R.A. Hites. Mass Spectrom. Rev. **13**, 259 (1994).
22. J.E. Szulejko, I. Howe, J.H. Beynon et U.P. Schlunegger. Org. Mass Spectrom. **15**, 263 (1980).
23. J.P. Schermann et F.G. Major. Appl. Phys. **16**, 225 (1978).
24. R.J. Hughes. M. Sc. Thesis, Trent University, Peterborough, Ont. 1980.
25. S.A. McLuckey et G.L. Glish. Anal. Chem. **59**, 1674 (1987).
26. D.W. Berberich et R.A. Yost. J. Am. Soc. Mass Spectrom. **5**, 757 (1994).
27. S. Catinella, P. Traldi, X.W. Jiang, F.A. Londry, R.J.S. Morrison, R.E. March, S. Gregoire, J.C. Mathurin et J.C. Tabet. Rapid Commun Mass Spectrom **9**, 1302 (1995).
28. M. Lausevic, M. Splendore, X. Jiang et R.E. March. Proc. 44th ASMS Conference on Mass Spectrometry and Allied Topics. Portland, Oreg. 1996. p. 143.
29. C.K. Huston. J. Chromatogr. **606**, 203 (1992).
30. H.P. Reiser, R.K. Julian et R.G. Cooks. Int. J. Mass Spectrom. Ion Processes **121**, 49 (1992).
31. F.A. Londry, R.A. Alfred et R.E. March. J. Am. Soc. Mass Spectrom. **4**, 687 (1993).
32. R.E. March. J. Mass. Spectrom. **32**, 351 (1997).
33. F.G. Major et H.G. Dehmelt. Phys. Rev. **170**, 91 (1968).
34. R.B. Turner, G. Lawson et J.F.J. Todd. *Dans* Dynamic mass spectrometry. Vol. 4. *Edité par* D. Price et J.F.J. Todd. Heyden, London. 1976. p. 79.
35. R.E. Pedder et R.A. Yost. Proc. 36th ASMS Conference on Mass Spectrometry and Allied Topics. San Francisco, Calif. 1988. p. 632.
36. R.K. Julian, M. Nappi, C. Weil et R.G. Cooks. J. Am. Soc. Mass Spectrom. **6,** 57 (1995).
37. S. Guan et A.G. Marshall. J. Am. Soc. Mass Spectrom. **5**, 64 (1994).
38. J.H. Parks et A. Szoke. J. Chem. Phys. **103**, 1422 (1995).
39. M. McKeown. Environ. Health Perspect. **30**, 97 (1980).
40. J. Rullkötter et H. Budzikiewicz. Int. J. Mass Spectrom. Ion Phys. **20**, 269 (1976).
41. M.A. Armitage. Ph. D. Thesis, Trent University, Peterborough, Ont. 1979.
42. G.C. Stafford, J. Reeher, R. Smith et M. Story. *Dans* Dynamic mass spectrometry. Vol. 5. *Edité par* D. Price et J.F.J. Todd. Heyden, London. 1978. p. 55.
43. G.C. Stafford. Environ. Health Perspect. **36**, 85 (1980).
44. R.E. Mather et J.F.J. Todd. Int. J. Mass Spectrom. Ion Phys. **33**, 159 (1980).
45. H.P. Reiser, R.E. Kaiser, P.J. Sacickas et R.G. Cooks. Int. J. Mass Spectrom. Ion Processes, **106**, 237 (1991).
46. R.J. Beuhler et L. Friedman. Int. J. Mass Spectrom. Ion Phys. **23**, 81 (1977).
47. J.D. Williams et R.G. Cooks. Rapid Commun. Mass Spectrom. **7**, 380 (1993).
48. E. Marquette et M. Wang. Proc. 41st ASMS Conference on Mass Spectrometry and Allied Topics. San Franscico, Calif. 1993. p. 698.
49. J.C.J. Thynne. *Dans* Dynamic mass spectrometry. Vol. 3. *Edité par* D. Price. Heyden, London. 1972. p. 67.
50. R.. Pedder, J.V. Johnson et R.A. Yost. Proc. 40th ASMS Conference on Mass Spectrometry and Allied Topics. Washington, D.C. 1992. p. 1761.
51. R.W. Vachet, S.D. Clark et G.L. Glish. Proc. 43rd ASMS Conference on Mass Spectrometry and Allied Topics. Atlanta, Ga. 1995. p. 1111.
52. V.S. Ong et R.A. Hites. J. Am. Soc. Mass Spectrom. **4**, 270 (1993).
53. L.J. Sears et E.P. Grimsrud. Anal. Chem. **61**, 2523 (1986).
54. J.N. Louris, J.W. Amy, T.Y. Ridley et R.G. Cooks. Int. J. Mass Spectrom. Ion Processes, **88**, 97 (1989).
55. S. Grégoire. Doctorat d'Université, Université Pierre et Marie Curie, Paris. 1997.
56. K.G. Asano, G.L. Glish et S.A. McLuckey. Proc. 36th ASMS Conference on Mass Spectrometry and Allied Topics. San Francisco, Calif. 1988. p. 636.
57. D.C. Cleven, K.A. Cox et R.G. Cooks. Rapid Commun. Mass Spectrom. **8**, 451 (1994).
58. J.C. Mathurin, S. Grégoire, A. Brunot, J.C. Tabet, R.E. March, S. Catinella et P. Traldi. J. Mass Spectrom. **32**, 829 (1997).
59. S. Grégoire, J.C. Mathurin, R.E. March et J.C. Tabet. ICR/Ion Trap News Lett. **43**, 12 (1996).
60. J.C. Mathurin, S. Grégoire, A. Brunot, J.C. Tabet et R.E. March. Proc. 44th ASMS Conference on Mass Spectrometry and Allied Topics. Portland, Oreg. 1996. p. 144.
61. W.J. Herron, D.E. Goeringer et S.A. McLuckey. J. Am. Soc. Mass Spectrom. **6**, 529 (1995).
62. R.S. Ramsey, D.E. Goeringer et S.A. McLuckey. Proc. 44th ASMS Conference on Mass Spectrometry and Allied Topics. Portland, Oreg. 1996. p. 1284.

© 1998 NRC Canada

63. S.V.K. Kumar, S. Mazumdar et S.K. Mitra. Chem. Phys. Lett. **237**, 448 (1995).
64. C.A. Valkenburg, L.A. Krieger et E.P. Grimsrud. J. Chem. Phys.**86**, 6782 (1987).
65. M.R. Flannery. Adv. At. Mol. Opt. Phys. **32**, 117 (1994).
66. W. Lindinger. *Dans* Gaseous ion chemistry and mass spectrometry. *Edité par* J.H. Futrell. John Wiley & Sons, New York. 1986. p. 237.
67. S.M. Boué, J.L. Stephenson et R.A. Yost. Proc. 44th ASMS Conference on Mass Spectrometry and Allied Topics. Portland, Oreg. 1996. p. 475.
68. V.M. Doroshenko et R.J. Cotter. Anal. Chem. **68**, 463 (1996).
69. B.I. Coopersmith et R.A. Yost. J. Am. Soc. Mass Spectrom. **6**, 976 (1995).
70. S.A. McLuckey, G.J. Van Berkel, D.E. Goeringer et G.L. Glish. Anal. Chem. **66**, 689 (1994).
71. B.A. Eckenrode, G.L. Glish et S.A. McLuckey. Int. J. Mass Spectrom. Ion Processes, **99**, 151 (1990).

© 1998 NRC Canada

Ultrasonic velocity and volumetric properties of isomeric butanediols plus water systems

Brent Hawrylak, Kim Gracie, and R. Palepu

Abstract: Ultrasonic velocities and densities of binary aqueous solutions of isomeric butanediols were measured in the temperature range 298–318 K at 10 degree intervals over the entire composition range, and 5 degree intervals in the water-rich region. The experimental data in the dilute region, with mole fraction of water less than 0.1, was analysed to determine the partial molar volumes and adiabatic compressibilities of water at infinite dilution. The standard thermodynamic transfer functions were calculated to evaluate the environment of water at infinite dilution in these systems. From the compressibility isotherms, as a function of temperature in the water-rich region, the formation and the composition of clathrate-like structures in the liquid solutions was determined, and the nature of these structures was discussed.

Key words: ultrasonic velocity, adiabatic compressibility, density, partial molar quantities, standard thermodynamic transfer functions.

Résumé : Opérant de 298 à 318 K, à des intervalles de 10 degrés sur l'ensemble des plages de compositions et de 5 degrés dans la région riche en eau, on a mesuré les vélocités ultrasoniques et les densités de solutions aqueuses binaires des butanediols isomères. Dans le but de déterminer les volumes molaires partiels et les compressibilités adiabatiques de l'eau à dilution infinie, on a analysé les données expérimentales dans la région diluée, à des fractions molaires d'eau inférieures à 0,1. Afin d'évaluer l'environnement de l'eau à dilution infinie dans ces systèmes, on a calculé les fonctions thermodynamiques standard de transfert. Sur la base des isothermes de compressibilité en fonction de la température dans la région riche en eau, on a déterminé la formation et la composition de structures ressemblant à des clathrates en solutions liquides et on discute de la nature de ces structures.

Mots clés : vitesse ultrasonique, compressibilité adiabatique, densité, quantités molaires partielles, fonctions thermodynamiques standard de transferts.

[Traduit par la rédaction]

Introduction

The strengthening of structure of water in dilute aqueous non-polar solutes containing hydrophobic functional groups is well known in the literature (1–5). The thermodynamic properties of aqueous polar organic compounds are determined predominantly by the hydrophobic interactions. The stabilization of water structure in dilute solutions of aqueous polar organic compounds was extensively studied using ultrasonic velocity measurements (6–13). The solute molecules are expected to be accommodated in short-lived water cages of a bulky water lattice with tetrahedrally coordinated water molecules. The water lattice is similar to that of the well known solid clathrate hydrates of many organic compounds (14–17). Wagner et al. (10) provided an evidence to this clathrate-like image of the structure of dilute organic compounds.

Received July 18, 1997.

B. Hawrylak. Graduate Student, Dept. of Chemistry, Memorial University, St. Johns, NF A1B 3X7, Canada.
K. Gracie. Graduate Student, Dept. Of Chemistry, McMaster University, Hamilton, ON L8S 4Ml, Canada.
R. Palepu.[1] Department of Chemistry, St. Francis Xavier University, Antigonish, NS B2G 2W5, Canada.

[1] Author to whom correspondence may be addressed. Telephone: (902) 867-3886. Fax: (902) 867-2414. E-mail: rpalepu@juliet.stfx.ca

Recently it has been concluded from the study of adiabatic compressibility isotherms, quasi clathrate-like structures exist in the dilute aqueous solutions of γ-Picoline (11, 13, 18). Studies on aqueous solutions of polyhydroxy compounds, especially those related to biological systems, have been conducted in the literature to obtain the information on the hydrophobic interactions present in these systems (19, 20).

We have undertaken a systematic investigation of isomeric butanediols (BTD) to obtain a deeper understanding of solute–solute and solute–solvent interactions in these systems and the influence of the position of the hydroxy groups on the acoustic and volumetric properties (21). In this paper we present the results dealing with standard transfer functions, to evaluate the environment of water at infinite dilution in these systems.

The standard function of transfer ($Y_s^{m\to n}$) is defined as follows:

$$[1] \qquad Y_s^{m\to n} = -Y_s^{n\to m} = Y_s^{\infty(n)} - Y_s^{\infty(m)}$$

where $Y_s^{\infty(m)}$ and $Y_s^{\infty(n)}$ are the partial molar quantities at infinite dilution of solute (s) in solvents m and n, respectively. The standard function of transfer provides valuable information on the difference in the interaction of a given solute in two different solvent systems.

Normal practice is to study the standard function of transfer of a solute molecule from an organic polar solvent to water. A study of standard function of transfer of water between two

© 1998 NRC Canada

Table 1. Experimental density and sound velocities of isomeric butanediols.

	Density		Sound
	This work	Literature	velocity
T (K)	ρ (g cm^3)	ρ (g cm^3)	U (m s^{-1})
	1,2-Butanediol		
298	0.99887	0.9987,[a]	
		0.9990[d]	1453.0
308	0.99143		1423.6
318	0.98392	0.9848[b]	1395.2
	1,3-Butanediol		
298	1.00089	1.0000,[c]	
		1.0002[d]	1524.1
308	0.99420		1495.6
318	0.98871		1469.0
	1,4-Butanediol		
298	1.01259	1.0150,[a]	
		1.0129,[c]	
		1.01258[d]	1601.3
308	1.00647		1578.5
318	1.00078	1.0002[c]	1423.6
	2,3-Butanediol		
298	0.99858	0.9871,[b]	
		0.9975[d]	1471.8
308	0.99074		1439.0
318	0.98233		

[a] Reference 22.
[b] Reference 23.
[c] Reference 24.
[d] Reference 25.

different polar organic solvents also provides useful information in terms of coupling of water with the pure solvents. A similar environment should result in a smaller value of the function of transfer, while increasing in differences in the interactions of a water molecule with both solvents should lead to a larger value of standard function of transfer.

In the present study isomeric butanediols plus water systems were investigated using ultrasonic velocity and density measurements to calculate the function of transfer of water between different isomeric butanediols. Transfer functions reflect the differences in the surroundings of the water molecule in the corresponding isomers. Ultrasonic velocity and volumetric properties of isomeric butanediols plus water systems have been deposited.[2]

Experimental

Isomeric butanediols were obtained from Aldrich Chemical Company (>99.5%) and used without further purification. The water was nanopure quality with specific conductivity less than 2 μS cm^{-1}.

Densities of butanediol solutions were measured at five different temperatures (298–318 K) using an Anton–Paar DMA 45 vibrating tube digital densimeter operating in a static mode. The measurements obtained are accurate to 5 × 10^{-5} g cm^{-3}. The ultrasonic velocity at three different temperatures were measured at 4 MHz using a Nusonics velocimeter (Mapco model 6080) employing the sing-around technique. Rapid and accurate measurements of sound velocity as a function of butanediol concentration were made by successive additions of a known mass of diol to the thermostated beaker containing a known amount of water. The velocity measurements are accurate to ±0.1 m s^{-1}. The temperature for the density and velocity measurements was controlled to within ±0.001 K by means of a thermostatically control SODEV bath.

[2] Supplementary material may be purchased from: The Depository of Unpublished Data, Document Delivery, CISTI, National Research Council of Canada, Ottawa, Canada, K1A 0S2.

Table 2. Partial molar quantities at infinite dilution as a function of temperature.

T (K)	V_{H_2O} (cm^3 mol^{-1})	K_{H_2O} (m^5 N^{-1} mol^{-1} × 10^{-16})
	1,2 BTD	
298	16.75	–1.57
308	16.85	–4.90
318	17.07	–9.13
	1,3 BTD	
298	16.28	–4.05
308	16.42	–7.11
318	16.64	–9.98
	1,4 BTD	
298	16.35	–5.47
308	16.49	–8.15
318	16.73	–10.2
	2,3 BTD	
298	16.36	–4.90
308	16.52	–7.24
318	16.67	—

Table 3. Standard function of transfer of water between butanediol isomers.

T (K)	1,2→1,3	1,2→1,4	1,2→2,3	1,3→1,4	1,3→2,3	1,4→2,3
	Volumes (cm^3 mol^{-1})					
298	–0.47	–0.40	–0.39	0.07	0.08	0.01
308	–0.43	–0.36	– 0.33	0.07	0.10	–0.03
318	–0.43	–0.34	–0.40	0.09	0.03	–0.06
	Molar compressibilities (m^5 N^{-1} m^{-1} × 10^{-16})					
298	–2.48	–3.90	–3.33	–1.42	–0.85	0.57
308	–2.11	–3.25	–2.34	–1.04	–0.13	0.91
318	–0.85	–1.07	—	–0.22	—	—

Results

The densities and ultrasonic velocities of pure isomers together with the literature values (21–24) are presented in Table 1. Molar volumes (V) of the solution were calculated as follows:

$$[2] \qquad V = \frac{X_1 M_1 + (1 - X_1) M_2}{\rho}$$

© 1998 NRC Canada

Fig. 1. Plot of densities of butanediols as a function of concentration at 298 K.

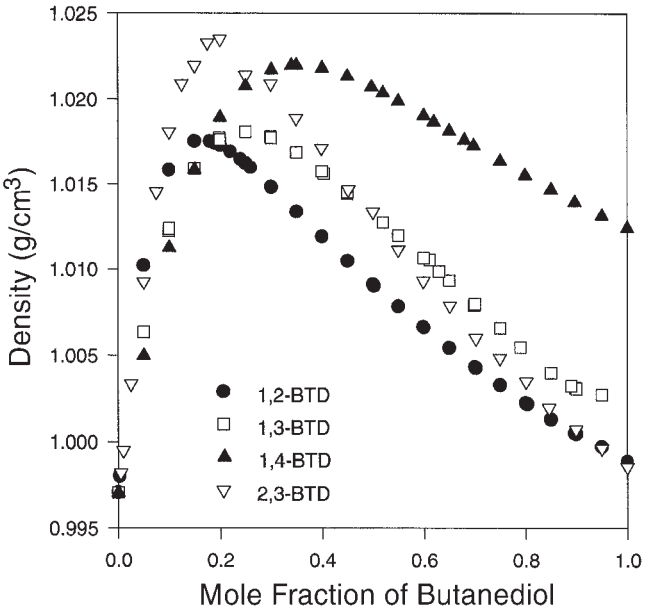

Fig. 2. Plot of adiabatic compressibilities of butanediols as a function of concentration at 298 K.

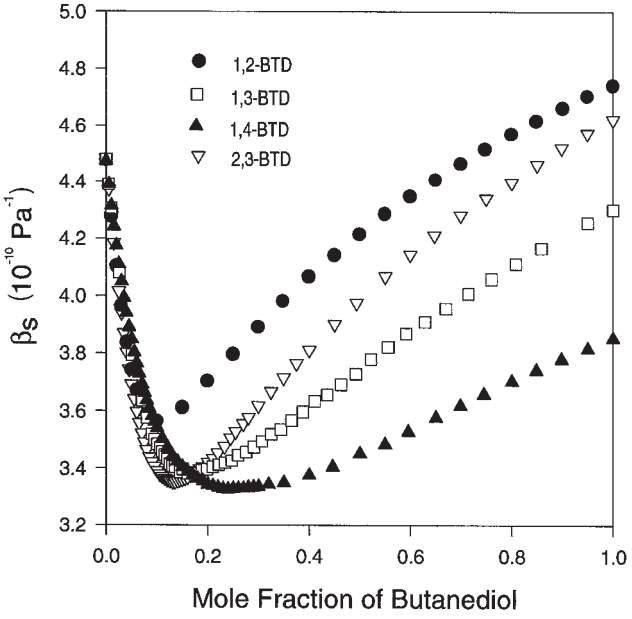

where X_1, M_1, and M_2 are mole fraction of water, molar masses of water and butanediols, respectively, and ρ is the density of the solution. Adiabatic compressibility (β_s) and molar adiabatic compressibility (K_s) were calculated using the following equations.

$$[3] \qquad \beta_s = \frac{1}{U^2\rho}, \qquad K_s = V\beta_s$$

The density and ultrasonic data in the entire composition range was reported in our previous publication (21).

The molar volumes and molar adiabatic compressibilities in the dilute region are fitted to the following equation.

$$[4] \qquad Y = a_o + a_1(1 - X)$$

The values of the coefficient a_o and a_1 were determined by least-squares method:

$$[5] \qquad Y_m = Y - (1 - X_m)\left[\frac{\partial Y}{\partial(1 - X_m)}\right]_{T,P}$$

The partial molar quantities Y_m of the mth component of a binary solution is given by the following, where $m = 1$ or 2, Y is the corresponding molar property, and X_m is the mole fraction of the mth component. From eqs. [4] and [5], one can deduce that the partial molar quantity of water at infinite dilution in the solution of butanediol is equal to the value of a_o. The partial molar quantities of water at 298, 308, and 318 K were determined at a concentration of water <0.1 and are presented in Table 2. The values of transfer functions of water $V^{m\rightarrow n}$ and $K_s^{m\rightarrow n}$ between binary isomeric butanediols were calculated from eq. [1] and presented in Table 3.

Densities and adiabatic compressibilities (β_s) at 298 K of binary aqueous mixtures of isomeric butanediols as function of composition are presented in Figs. 1 and 2, respectively. The adiabatic compressibility isotherms in the dilute aqueous solution are presented in Fig. 3. The intersection point in these isotherms was taken as the composition of quasi clathrate formation in these systems. The compositions along with the composition of density maxima and adiabatic minima are presented in Table 4.

Discussion

Transfer functions

The partial molar volumes of water at infinite dilution are smaller than the corresponding molar volume V^o values. The observation is consistent with the idea that the molar volume of pure water is a result of the sum of actual molecular volume plus empty volume that arises from the hydrogen-bonded open structure of liquid water.

Examination of Table 3 indicates that the standard transfer function of volume for water molecules from 1,2 BTD to 1,3, 1,4, and 2,3 BTD is accompanied by larger volume effects compared to the transfer of water from 1,3 to 1,4 and 2,3 or 1,4 to 2,3. The smaller values of volume for the transfer of water in 1,3, 1,4, and 2,3 indicate that the surroundings of water in these three systems are very similar at infinite dilution compared to 1,2 BTD.

The values of partial molar adiabatic compressibilities at infinite dilution are negative in all cases, indicative that water molecules are likely to fill in the intermolecular free spaces in liquid BTD or from hydrogen bonds with the neighbouring diol molecules. Both these effects will result in a decrease in the structural compressibility resulting in negative K_s. The transfer function of molar compressibilities also indicate that the nature of water in 1,3, 1,4, and 2,3 BTD is very similar and different in 1,2 BTD. Ultrasonic relaxation, calorimetric (26–28) surface tension (29), and also a complete analysis of acoustic and volumetric properties in the entire concentration range (21), indicate that 1,2 BTD molecules are more hydrophobic compared to the other isometric butanediols and differ in terms of interactions with water.

© 1998 NRC Canada

Fig. 3. Adiabatic isotherms of butanediols as a function of concentration.

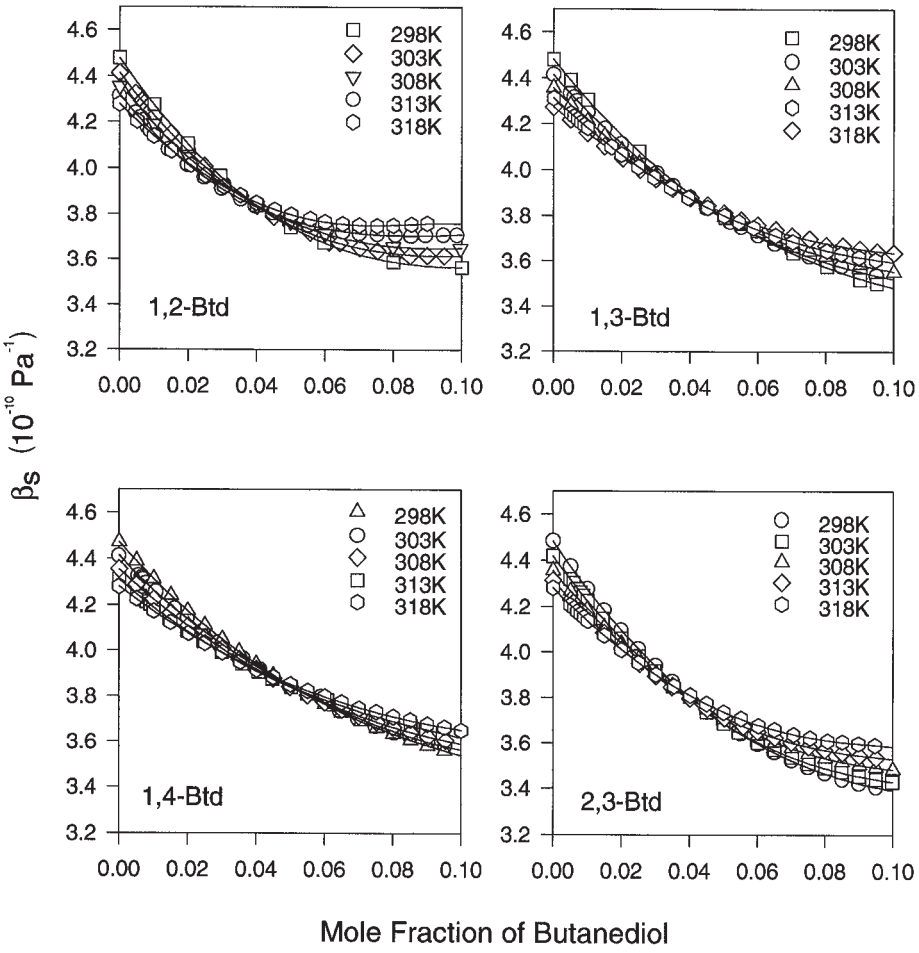

Clathrate formation

Many dilute aqueous solutions of nonelectrolyte exhibited a common intersection point in adiabatic isotherms, and this phenomenon is attributed to the formation of clathrate-like structures in liquid water–organic systems. Endo (11) attributed the concentration of the zero temperature coefficient of adiabatic compressibility ($\partial\beta/\partial T$) = 0 to the composition of liquid clathrate-like hydrate, since the instantaneous compressibilities (β_∞), due to compression of molecules, intermolecular distances, as well as the structural compressibilities (β_{ST}) due to breakdown of intermolecular bonds, become simultaneously temperature independent. According to Endo (11), the cross-point concentration of solution structure corresponds either to a solid clathrate structure (**1** or **11**) or consists of polyhedra occupied by a solute molecule, and the polyhedra freely floating in water is not involved in the clathrate formation. In the present study based on the hydration numbers calculated from cross-point compositions, one can conclude that these clathrate can be viewed as clathrate **11** structure, with the larger voids (14-hedra) occupied by 1,3 and 1,4 BTD and 12-hedra occupied by 1,2 and 2,3 BTD molecules. The smaller voids are occupied by nonbonded water molecules. The stoichiometry of the clathrate-like structure formed in the solution may not correspond to the concentration of the intersection point. This can be attributed to a shift in the concentration at which $\partial\beta/\partial T = 0$ to higher value than true clathrate composition, due to the incomplete occupancy of the available empty spaces. Also, the approximation $\partial\beta/\partial T \approx \partial\beta_{ST}/\partial T$ is only applicable if $\partial\beta_\infty/\partial T \approx 0$ in the temperature range investigated.

Table 4. Concentrations of intersection points of the compressibility isotherms (X_c), compressibility minima (X_{min}), density maxima (X_{max}), and composition of the corresponding hydrates.

		X_{min}			X_{max}		
System	X_c	298 K	308 K	318 K	298 K	308 K	318 K
1,2 BTD + water	0.040	0.10	0.10	0.08	0.15	0.15	0.15
BTD:H_2O	1:24	1:9	1:9	1:11.5	1:5.8	1:5.8	1:5.8
1,3 BTD + water	0.045	0.16	0.15	0.13	0.25	0.25	0.25
BTD:H_2O	1:21	1:5.3	1:5.8	1:6.7	1:3.0	1:3.0	1:3.0
1,4 BTD + water	0.0475	0.23	0.21	0.20	0.40	0.35	0.35
BTD:H_2O	1:20	1:3.5	1:3.8	1:4.0	1:1.5	1:1.9	1:1.9
2,3 BTD + water	0.040	0.13	0.12	—	0.20	0.20	0.18
BTD:H_2O	1:24	1:6.7	1:7.3		1:4.0	1:4.0	1:4.6

Conclusions

The model of aqueous solution of isomeric butanediols can be

© 1998 NRC Canada

represented as the formation of clathrate structure of type **11** arising due to hydrophobic hydration. At a higher concentration these structures gradually decay with increase in BTD content. The hydrophobic hydration is also accompanied by hydrophilic interactions through hydrogen bonding. The nature of water at infinite dilution is very similar in 1,3, 1,4, and 2,3 and different in 1,2 BTD and can be attributed to the more hydrophobic nature of 1,2 BTD compared to the other isomers of butanediols.

Acknowledgments

The authors are grateful to Natural Sciences and Engineering Research Council of Canada for an operating grant. B.H. is grateful to the undergraduate summer research award by NSERC, and K.G. to Economic Renewal Agency of the Government of Nova Scotia in the form of a salary supplement.

References

1. H.S. Frank and M.W. Evans. J. Chem. Phys. **13**, 507 (1945).
2. H.S. Frank and A.S. Quist. J. Chem. Phys. **34**, 604 (1961).
3. G. Nemethy and H.A. Scheraga. J. Chem. Phys. **35**, 3401 (1962).
4. H.S. Franks. *In* hydrogen-bonded solvent systems. *Edited by* A.K. Covington and P. Jones. Taylor and Frances Ltd. (London). 1968. p.31
5. M.D. Danford and H.A. Levy. J. Am. Chem. Soc. **84**, 3965 (1962).
6. M.J. Blandamer and D. Waddington. Adv. Mol. Relax. Processes, **2**, 1 (1970).
7. E.K. Baumgartner and G.J. Atkinson. J. Phys. Chem. **75**, 2336 (1975).
8. E.K. Baumgartner and G.J. Atkinson. Z. Phys. Chem (Leipzig), **252**, 392 (1973).
9. P. Bourton and A. Kaufmann. J. Chem. Phys. **68**, 5032 (1978).
10. E. Wagner, J.V. Weidner, and G.W. Zimmermann. Ber. Bunsenges. Phys. Chem. **81**, 1143 (1977).
11. H. Endo. Bull. Chem. Soc. Jpn. **46**, 1586 (1973).
12. M.V. Kaulgud and K.J. Patel. Indian J. Pure. Appl. Phys. **13**, 322 (1975).
13. S. Ernst and J. Glinki. J. Mater. Sci. **3**, 69 (1977).
14. S.F. Dey and S.J. Gill. J. Solution Chem. **14**, 417 (1985).
15. S.F. Dey and S.J. Gill. J. Solution Chem. **14**, 827 (1985).
16. G.A. Jeffery and R.K. McMullan. Prog. Inorg. Chem. **8**, 43 (1967).
17. M. Von Stackelberg and H. Muller. Z. Elektrochem. **58**, 25 (1954).
18. J. Glinski and S. Ernst. Pol. J. Chem. **56**, 339 (1982).
19. J.J. Savage and R.H. Wood. J. Solution Chem. **5**, 733 (1975).
20. G. Barone, B. Bove, G. Castranuovo, and V. Elia. J. Solution Chem. **10**, 803 (1981).
21. B. Hawrylak, K. Gracie, and R. Palepu. J. Solution Chem. **27**, 17 (1998).
22. T. Sun, R.M. DiGuilio, and A.S. Teja. J. Chem. Eng. Data, **37**, 246 (1992).
23. G. Czechowski, B. Zywucki, and J. Jadzyn. J. Chem. Eng. Data, **33**, 55 (1988).
24. A. Bald and A. Szejgis. J. Chem. Res. Synop. 923 (1992).
25. H. Piekarski, M. Jozwiak, J. Woznicka, A. Bald, and A. Szejgis. Phys. Chem. Liquids, **30,** 195 (1995).
26. S. Nishikawa and M. Mashima. J. Chem. Soc. Faraday Trans. **78**, 1249 (1982).
27. S. Adini, G. Castranuovo, V. Elia, and L. Fasano. J. Chem. Soc. Faraday Trans. **86**, 3567 (1990).
28. G. Borghesani, R. Pedriali, F. Pulidoro, and I. Scaroni. J. Solution Chem. **15**, 397 (1986).
29. B. Hawrylak, K. Gracie, and R. Palepu. J. Solution Chem. (1998). In press.

© 1998 NRC Canada

New heterocycles from thienopyridocinnolines

M.Z.A. Badr, A.A. Geies, M.S. Abbady, and A.A. Dahy

Abstract: 3-Cyano-4-(*p*-tolyl)pyrido[3,2-*c*]cinnolin-2(1*H*) thione **3** was reacted with α-halo ketones, esters, or amides to give the intermediates, S-alkylated products **5b**–**h**, respectively, which underwent intramolecular ring closure reactions with ethanolic sodium ethoxide to give thienopyridocinnolines **6a**–**h**. Pyrimidothienopyridocinnolines **9** and **11** were obtained by treatment of oxazino compound **8** with hydrazine hydrate and ammonium acetate. Treatment of hydrazino derivative **13** with acetylacetone, triethylorthoformate, carbon disulphide, ethyl chloroformate, and acetic anhydride afforded triazolopyrimidothienopyridocinnolines **14**–**16, 18,** and **21,** while with nitrous acid the corresponding tetrazolo compound **19** was produced.

Key words: thienopyridocinnolines; their pyrimido, triazolopyrimido, and heteroannelated systems.

Résumé : La 3-cyano-4-(*p*-tolyl)pyrido[3,2-*c*]cinnolin-2(1*H*) thione (**3**) réagit avec les α-halogéno cétones, esters ou amides pour conduire respectivement aux produits S-alkylés intermédiaires **5b**–**h** qui, sous l'influence de l'éthylate de sodium en solution dans l'éthanol, subissent des réactions de fermetures de cycle intramoléculaires fournissant les thiénopyridocinnolines **6a**–**h**. On a obtenu les pyrimidothiénopyridocinnolines **9** et **11** par traitement du composé oxazine **8** avec de l'hydrate d'hydrazine et de l'acétate d'ammonium. Le traitement du dérivé hydrazino **13** par de l'acétylacétone, de l'orthoformate d'éthyle, du disulfure de carbone, du chloroformate d'éthyle et de l'anhydride acétique conduit aux triazolopyrimidothiénopyridocinnolines **14**–**16, 18** et **21** alors que sa réaction avec l'acide nitreux conduit à la formation du composé tétrazolo correspondant **19**.

Mots clés : thiénopyridocinnolines; systèmes pyrimido, triazolopyrimido et hétérocycliques correspondants.

[Traduit par la rédaction]

Introduction

Cinnoline derivatives have been reported to constitute an important class of biologically active reagents (1). They have shown antibacterial (2), antifungal (3), and other microbicide (4) activities. Similarly, thienocinnolines and other derivatives have shown various pharmacological activities, such as acting as antihypertensive agents (5), bronchodilators (6), antioxylate drugs to improve brain functions (7), and immunostimulants (8), together with many other activities reported in the literature (9).

Results and discussion

As a continuation of our studies on the synthesis and chemistry of different new heteroannelated ring systems related to phthalazines, quinoxalines, pyrimidines, and other systems (10), we report in the present paper the synthesis and chemistry of a novel series of linear and angular tetra-, penta-, and hexaheterocyclic ring systems based on the cinnoline moiety. An approach to ring closure reactions leading to target compounds started from 4-amino-3-(*p*-methylbenzoylcinnoline **1** (11), which reacted with ethyl cyanoacetate and ammonium acetate to produce 3-cyano-4-(*p*-tolyl)pyrido[3,2-*c*]cinnolin-2(1*H*)-one **2**, which in turn, on refluxing with phosphorus pentasulphide in dry pyridine, gave the corresponding-2(1*H*)thione derivative **3**. Alkylation of **3** with alkyl (benzyl)halides or ethyl chloroformate in the presence of anhydrous sodium acetate gave the corresponding 2-alkylthio compounds **4a**–**d** (Scheme 1).

Similarly, treatment of **3** with α-halo ketones, esters, and (or) acylamides or acetanilides in basic medium gave the corresponding 2-substituted thio compounds **5b**–**h**, which in turn, as active starting materials, underwent nucleophilic ring closure reactions when treated with ethanolic sodium ethoxide solution to produce a new series of tetracyclic substituted thieno[3′,2′:5,6]pyrido[3,2-*c*]cinnolines **6b**–**h**. The corresponding **6**a isomer was produced directly from treatment of **3** with α-chloroacetone without separation of the acyclic alkylthio intermediate **5a**. 3-Amino-2-ethoxycarbonyl-4-(*p*-tolyl)thieno[3′,2′:5,6]pyrido[3,2-*c*]cinnoline **6c** was successfully used as a strategic starting material to synthesize the novel pentaheterocyclic target compound **11** together with other analogs **9** and **10** through the intermediate oxazine compound **8**.

Alkaline hydrolysis of 2-ethoxycarbonyl derivative **6c** gave the corresponding 2-carboxylic acid derivative **7**.

Ring closure reactions of the 3-amino-2-carboxylic acid compound **7** by heating with acetic anhydride gave the pentacyclic intermediate oxazino [4″,5″:4′,5′]thieno[3′,2′:5,6]-pyrido[3,2-*c*]cinnolin-11-one **8**. Refluxing of oxazino compound **8** with ammonium acetate in acetic acid produced pyrimido thienopyridocinnolin-11(10*H*)one **11**. Refluxing **8** with hydrazine hydrate in dry pyridine produced the corresponding 10-amino-11(10*H*)pyrimidone **9**, which condensed with aromatic aldehydes to give the corresponding arylideneamine derivatives **10a** and **10b.** Treatment of the 11-pyrimidone

Received April 18, 1997.[1]

M.Z.A. Badr,[2] A.A. Geies, M.S. Abbady, and A.A. Dahy. Chemistry Department, Faculty of Science, Assiut University, Assiut, Egypt.

[1] Revision received October 10, 1997.
[2] Author to whom correspondence may be addressed.

© 1998 NRC Canada

Scheme 1.

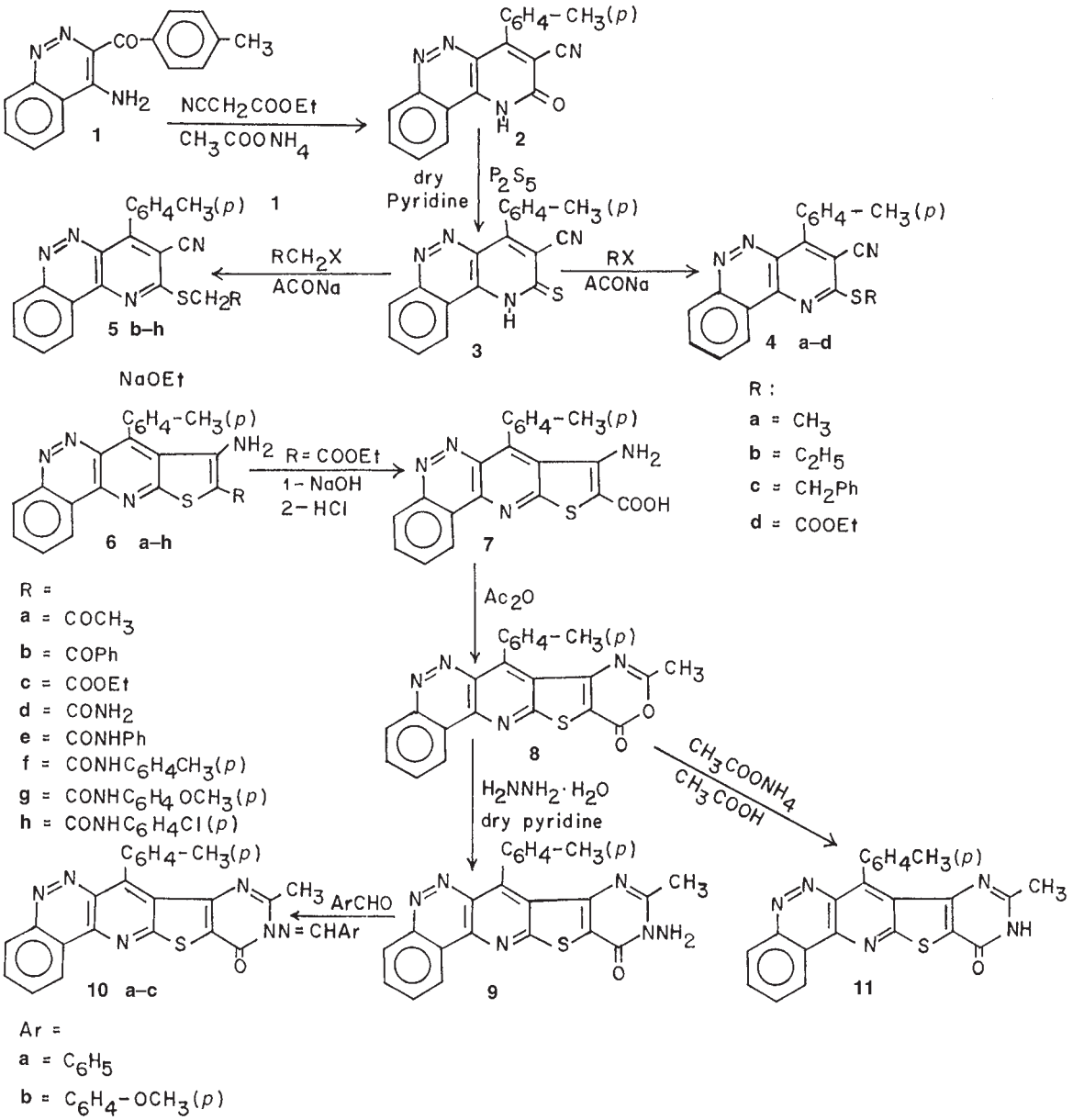

11 with phosphorus oxychloride gave the corresponding 11-chloropyrimidine derivative **12** (Scheme 2). The chlorine group of **12** underwent nucleophilic displacement by reflux with hydrazine hydrate in dioxane to produce 11-hydrazinopyrimidothienopyridocinnoline **13**, which condensed with aromatic aldehydes to give the corresponding 11-arylidinehydrazono derivatives **18a** and **18b**. Similarly, heating **13** with acetylacetone produced the corresponding 11-(3,5-dimethylpyrazolyl) derivative **14**.

The hydrazino compound **13** containing an active nitrogen nucleophile was used as strategy material and on treatment with carbonyl, thionyl, or other electrophilic reagents underwent ring closure reactions into a novel series of hexaheterocyclic target compounds. Such reactions favor the existence of the hydrazone tautomer **13** (12).

Treatment of **13** ⇌ **13′** with triethylorthoformate in acetic acid afforded 5-methyl-7-(*p*-tolyl)triazolo[3‴,4‴:1″,6″]-pyrimido[4″,5″:4′5′]thieno[3′,2′:5,6]pyrido[3,2-*c*]-cinnoline **15**. The reaction between **13** and acetic anhydride produced the corresponding 3-methyltriazolo derivative **21**.

The interaction of **13** with carbon disulphide in pyridine produced the triazolopyrimidothienopyridocinnolin-3-thione **16**. The latter interacted with ethyl chloroacetate to give the 3-ethoxycarbonylmethylthio derivative **17**. On the other hand, condensation of **13** with ethyl chloroformate led to the formation of the correspondingtriazolo-3-one compound **20**. The interaction of **13** with sodium nitrite in dilute hydrochloric acid, while cooling, afforded the corresponding tetrazolopyrimidothieno-pyridocinnoline **19**.

Experimental

All melting points are uncorrected and were determined on an electric melting point (Gallenkamp) apparatus. IR spectra were

© 1998 NRC Canada

Scheme 2.

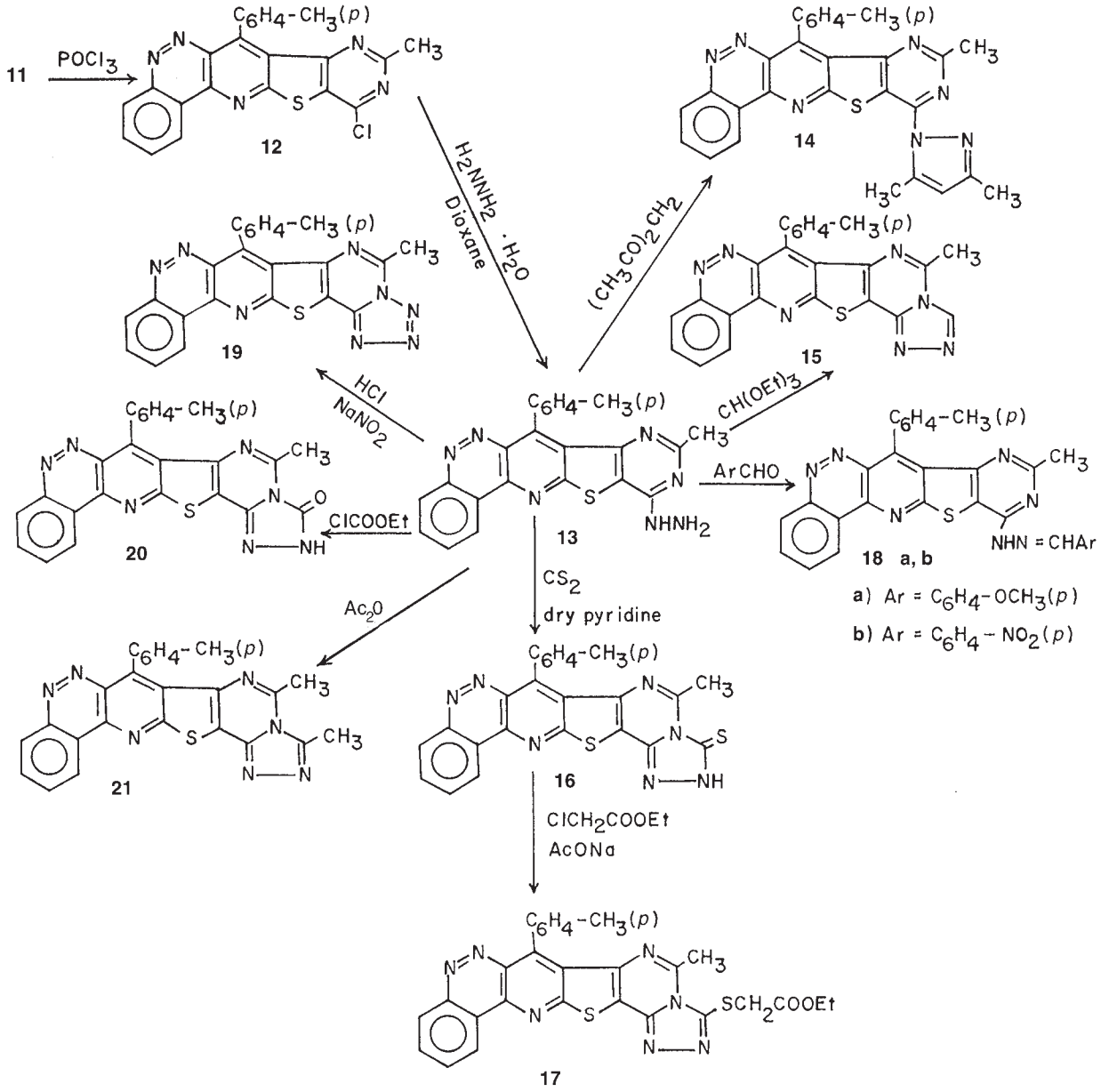

determined with a Shimadzu 470 IR spectrophotometer using KBr wafer technique. ^{1}H NMR spectra were recorded on a 90 MHz Varian EM-390 spectrometer in an appropriate solvent ($CDCl_3$, DMSO-d_6, or deuterated trifluoroacetic acid (TFA)) using TMS as internal standard. ^{1}H NMR signals for NH or NH_2 in TFA-*d* solvent were downfield. Chemical shifts are expressed in δ (ppm). Mass spectra were measured on a GC–MS QP 1000 EX spectrometer at an ionizing potential of 70 eV. Elemental analyses were carried out using a 240C Perkin Elmer analyser.

4-Amino-3-(*p*-methyl benzoyl)cinnoline (1)
A mixture of phenylhydrazonomalononitrile (0.1 mol), toluene (150 mL), and aluminium chloride (0.4 mol) was refluxed for 3 h. The separated product was crystallized from ethanol, mp 210°C (lit. (11) mp 210–212°C).

3-Cyano-4-(*p*-tolyl)pyrido[3,2-*c*]cinnolin-2(1*H*)-one (2)
A mixture of 1 (0.1 mol), ethyl cyanoacetate (0.03 mol), and ammonium acetate (0.05 mol) was heated under reflux for 3 h. After cooling, the precipitate was filtered off, washed with boiling ethanol, and recrystallized from dioxane as yellow crystals, mp >360°C, yield 56%. IR: 3100 (NH); 2200 (CN), 1650 (CO) cm^{-1}; ^{1}H NMR (DMSO) δ: 3.50 (s, 3H, CH_3) and 7.2–9.1 (m, 8H, ArH). Anal. calcd. for $C_{19}H_{12}N_4O$: C 73.07, H 3.87, N 17.94; found: C 72.92, H 3.76, N 17.62%.

3-Cyano-4-(*p*-tolyl)pyrido[3,2-*c*]cinnolin-2(1*H*)-thione (3)
A mixture of **2** (0.01 mol) and phosphorus pentasulphide (0.01 mol) in dry pyridine (20 mL) was refluxed for 4 h, then poured into ice-water. The precipitated solid was filtered, washed with water, and recrystallized from dioxane as orange crystals, mp 315–317°C, yield 86%. IR: 3280 (NH), 2200 (CN), 1250

© 1998 NRC Canada

Table 1. Analytical, spectral, and physical data of compounds, **4a**–**4d**.

Comp. no.	mp,°C	Color	Yield%	Mol. formula	Analysis calcd./found (%) C	H	N	S	Spectral data IR (KBr) cm^{-1}	^1H NMR δ (ppm)
4a[a]	306°C	Yellow	87	$C_{22}H_{14}N_4S$	70.15 69.89	4.12 4.07	16.36 16.08	9.36 9.18	(CN) 2200	^1H NMR (TFA-*d*) δ: 2.50 (s, 3H, *p*-CH_3), 3.20 (s, 3H, SCH_3), 7.5–9.5 (m, 8H, ArH)
4b	285°C	Yellow	80	$C_{21}H_{16}N_4S$	70.76 70.55	4.52 4.72	15.72 15.54	8.99 8.67	(CN) 2200	^1H NMR ($CDCl_3$) δ: 1.60 (t, 3H, CH_3 ester), 2.50 (s, 3H, *p*-CH_3), 3.60 (q, 2H, CH_2), 7.4–9.2 (m, 8H, ArH)
4c	265°C	Yellow	83	$C_{26}H_{18}N_4S$	74.60 74.50	4.30 4.18	13.39 13.56	7.66 7.38	(CN) 2200	^1H NMR ($CDCl_3$) δ: 2.50 (s, 3H, *p*-CH_3), 4.80 (s, 2H, CH_2), 7.2–9.2 (m, 13H, ArH)
4d	154°C	Yellow-orange	70	$C_{22}H_{16}N_4O_2S$	65.98 65.86	4.30 3.90	13.99 13.77	8.01 7.65	(CN) 2200, (CO) 1720	^1H NMR ($CDCl_3$) δ: 1.45 (t, 3H, CH_2CH_3), 2.55 (s, 3H, *p*-CH_3), 4.50 (q, 2H, CH_2), 7.25–9.3 (m, 8H, ArH)

[a] All products were recrystallized from ethanol except **4a** from acetic acid.

(C═S) cm^{-1}.^1H NMR (TFA-*d*) δ: 2.42 (s, 3H, *p*-CH_3) and 7.2–9.4 (m, 8H, ArH). Anal. calcd. for $C_{19}H_{12}N_4S$: C 69.5, H 3.68, N 17.06, S 8.76; found: C 69.65, H 3.80, N 17.12, S 8.68%.

2-Alkyl (aralkyl)thio-3-cyano-4-(*p*-tolyl)pyrido[3,2-*c*]-cinnoline (4a–d)

General procedure

A mixture of **3** (0.01 mol) and alkyl (or benzyl) halide or ethyl chloroformate (0.01mol) was refluxed in ethanol (30 mL) and anhydrous sodium acetate (2 g) for 1 h. The reaction mixture was concentrated to half volume and cooled. The precipitated solid was filtered and recrystallized from an appropriate solvent. The analytical, spectral, and physical data are summarized in Table 1.

3-Cyano-4-(*p*-tolyl)-2-substituted thiopyrido[3,2-*c*]cinnoline (5b–h)

The corresponding α-halo compound was treated with **3** following the same procedure as above. The separated solid was filtered, washed with water, and recrystallized from an appropriate solvent. The analytical, spectral, and physical data are summarized in Table 2.

3-Amino-2-substituted-4-(*p*-tolyl)thieno[3′,2′:5,6]pyrido-[3,2-*c*]cinnoline (6a–h)

General procedure

A mixture of each of the mercapto derivatives (**5b**–**h**) (0.01 mol) in ethanol (50 mL) and five drops of ethanolic sodium ethoxide was refluxed for 30 min. The solid product was filtered and recrystallized from a suitable solvent. **6a** was separated directly on treating α-chloracetone and **3** with anhydrous sodium acetate as above. The analytical, spectral, and physical data are summarized in Table 3.

2-(3-Amino-4-(*p*-tolyl)thieno[3′,2′:5,6]pyrido[3,2-*c*]-cinnolinyl)carboxylic acid (7)

A mixture of **6c** (0.01 mol) and alcoholic sodium ethoxide (30 mL, 25%) was refluxed for 3 h. Sodium salt precipitated and was filtered and acidified in water (200 mL) with dilute HCl. The solid free acid was filtered and recrystallized from acetic acid as yellow crystals, mp 330°C, yield 70%. IR: 3400, 3300 (NH_2) cm^{-1}. ^1H NMR (DMSO) δ: 2.48 (s, 3H, CH_3), 6.55 (s, 2H, NH_2), 10.20 (s, 1H, OH), both of them exchangeable with D_2O, and 7.1–9.2 (m, 8H, ArH). Anal. calcd. for $C_{21}H_{14}N_4O_2S$: C 65.27, H 3.65, N 14.50, S 8.30; found: C 65.31, H 3.87, N 14.06, S 7.97%.

9-Methyl-7-(*p*-tolyl)oxazino[4″,5″:4′,5′]thieno[3′,2′:5,6]-pyrido[3,2-*c*]cinnolin-11-one (8)

A mixture of **7** (0.01 mol) and acetic anhydride (20 mL) was refluxed for 2 h. The solid separated on cooling was filtered and recrystallized from dioxane as yellow crystals, mp 320°C, yield 74%. IR: 1750 (CO) cm^{-1}. ^1H NMR (TFA-*d*) δ: 2.58 (s, 3H, *p*-CH_3), 2.70 (s, 3H, CH_3), 7.4–9.85 (m, 8H, ArH). MS, *m*/*z* (%): 411 (M + 1, 29), 410 (M^+, 100). Anal. calcd. for $C_{23}H_{14}N_4O_2S$: C 67.3, H 3.44, N 13.65, S 7.81; found: C 66.96, H 3.89, N 13.60, S 8.00%.

10-Amino-9-methyl-7-(*p*-tolyl)pyrimido[4″,5″:4′,5′]thieno-[3′,2′:5,6]pyrido[3,2-*c*]-cinnolin-11(10*H*)-one (9)

A mixture of the oxazino compound **8** (0.01 mol) and hydrazine hydrate (0.01 mol) in dry pyridine (30 mL) was refluxed for 1 h. The solid separated on cooling was filtered and recrystallized from dioxane into yellow crystals, mp >360°C, yield 82%. IR: 3402, 3300 (NH_2), 1660 (CO) cm^{-1}. ^1H NMR (TFA-*d*) δ: 2.90 (s, 3H, *p*-CH_3), 3.18 (s, 3H, CH_3), 7.65–9.95 (m, 8H, ArH). Anal. calcd. for $C_{23}H_{16}N_6OS$: C 65.08, H 3.80, N 19.80, S 7.55; found: C 64.90, H 4.00, N 19.32, S 7.23%.

10-Arylidene amine derivatives of 9 (10a and 10b)

These were prepared by refluxing **9** (0.01 mol) with each of (*a*) benzaldehyde and (*b*) *p*-anisaldehyde (0.01 mol) in glacial acetic acid (20 mL) for 30 min. The solid product in each case

© 1998 NRC Canada

Table 2. Analytical, spectral, and physical data of compounds, **5b**–**5h**.

Comp. no.	mp, °C	Color	Yield%	Mol. formula	Analysis calcd./found (%) C	H	N	S	Spectral data IR (KBr) cm^{-1}	^1H NMR δ (ppm), and MS, *m/z* (%)
5b	230°C	Yellow	75	$C_{27}H_{18}N_4OS$	72.63 72.78	4.03 3.89	12.55 12.32	7.18 7.32	(CN) 2200, (CO) 1670	^1H NMR (DMSO) δ: 2.85 (s, 3H, *p*-CH_3), 5.00 (s, 2H, SCH_2), 7.3–8.9 (m, 13H,ArH)
5c	221°C	Yellow	79	$C_{23}H_{18}N_4O_2S$	66.65 66.85	4.38 4.36	13.52 13.29	7.74 7.48	(CN) 2200, (CO) 1720	^1H NMR ($CDCl_3$) δ: 1.20 (t, 3H, CH_2 CH_3), 2.40 (s, 3H, *p*-CH_3), 4.20 (q, 2H, CH_2), 7.2–9.2 (m, 8H, ArH)
5d	286–287°C	Yellow	76	$C_{21}H_{15}N_5OS$	65.43 65.21	3.90 3.88	18.17 18.34	8.37 8.16	(NH_2) 3800, 3600, (CN) 2200, (CO) 1670	^1H NMR (TFA-*d*) δ: 2.50 (s, 3H, *p*-CH_3), 4.55 (s, 2H, CH_2), 7.2–9.5 (m, 8H, ArH)
5e	289–290°C	Green-yellow	76	$C_{27}H_{19}N_5OS$	70.26 70.06	4.15 4.10	15.17 14.98	6.95 6.82	(NH) 3300, (CN) 2200, (CO) 1660	^1H NMR ($CDCl_3$ + drop TFA-*d*) δ: 2.50 (s, 3H, CH_3), 4.35 (s, 2H, CH_2), 6.9–9.4 (m, 13H, ArH) MS, *m/z* (%): 461 (M^+, 51%)
5f	300°C	Green-yellow	70	$C_{28}H_{21}N_5OS$	70.72 70.53	4.45 4.28	14.73 14.64	6.74 6.48	(NH) 3300, (CN) 2200, (CO) 1655	^1H NMR (DMSO) δ: 2.20 (s, 3H, *p*-CH_3), 2.50 (s, 3H, *p*-CH_3), 4.40 (s, 2H, CH_2), 6.95–9.2 (m, 12H, ArH), 10.55 (s, 1H, NH)
5g	300–302°C	Green-yellow	81	$C_{28}H_{21}N_5OS$	68.42 68.66	4.31 4.45	14.25 14.14	6.52 6.51	(NH) 3300, (CN) 2200, (CO) 1650	^1H NMR (DMSO) δ: 2.20 (s, 3H, *p*-CH_3), 3.20 (s, 3H, OCH_3), 4.20 (s, 2H, CH_2), 6.5–8.95 (m, 12H, ArH), 10.30 (1H, NH)
5h[a]	325°C	Green-yellow	84	$C_{27}H_{18}ClN_4OS$	65.38 65.28	3.66 3.76	14.12 14.00	6.47 6.35	(NH) 3300, (CN) 2200, (CO) 1660	^1H NMR (DMSO) δ: 2.50 (s, 3H, *p*-CH_3), 4.50 (s, 2H, CH_2), 7.2–9.2 (m, 12H, ArH), 7.85 (s, 1H, NH)

[a] Chlorine analysis for **5h**, calcd.: 7.15; found: 7.34%.

was filtered and recrystallized from ethanol. The analytical, spectral, and physical data are summarized in Table 4.

9-Methyl-7-(*p*-tolyl)pyrimido[4″,5″:4′,5′]thieno[3′,2′:5,6]-pyrido[3,2-*c*]cinnolin-11(10*H*)-one (11)

Refluxing the oxazino compound **8** (0.01 mol) and ammonium acetate in acetic acid (30 mL) for 30 min precipitated a solid that was filtered and recrystallized from acetic acid as yellow crystals, mp 320°C, yield 80%. IR: 3600 br (NH), 1650 (CO) cm^{-1}; ^1H NMR (TFA-*d*) δ: 2.70 (s, 3H, *p*-CH_3), 2.92 (s, 3H, CH_3), 7.7–9.9 (m, 8H, ArH). Anal. calcd. for $C_{23}H_{15}N_5OS$: C 67.47, H 3.69, N 17.10, S 7.83; found: C 65.7, H 4.00, N 16.95, S 7.69%.

11-Chloro-9-methyl-7-(*p*-tolyl)pyrimido[4″,5″:4′,5′]thieno-[3′,2′:5,6] pyrido[3,2-*c*]-cinnoline (12)

The pyrimidinone **11** (0.01 mol) in phosphorus oxychloide (40 mL) was refluxed for 4 h. The cooled mixture was stirred in ice-water for 30 min. The solid product was filtered, washed with water, and recrystallized from dioxane as yellow crystals, mp 283°C, yield 68%. IR: both NH and CO absorptions disappeared. ^1H NMR (TFA-*d*) δ: 2.60 (s, 3H, *p*-CH_3), 2.85 (s, 3H, CH_3), 7.55–9.8 (m, 8H, ArH). Anal. calcd. for $C_{23}H_{14}N_5SCl$: C 64.56, H 3.30, N 16.37, S 7.49, Cl 8.29; found: C 64.50, H 3.60, N 16.02, S 7.60, Cl 8.58%.

11-Hydrazino-9-methyl-7-(*p*-tolyl)pyrimido[4″,5″:4′,5′]-thieno[3′,2′:5.6]pyrido[3.2-*c*]-cinnoline (13)

The chloro compound **12** (0.01 mol) and hydrazine hydrate (0.01 mol) in dioxane (30 mL) were refluxed for 30 min. The separated solid was filtered and recrystallized from dioxane as yellow crystals, mp 300°C, yield 85%. IR: 3350 (NH_2), 3200 (NH) cm^{-1}; ^1H NMR (TFA-*d*) δ: 2.69 (s, 3H, *p*-CH_3), 2.73 (s, 3H, CH_3), 7.6–9.9 (m, 8H, ArH). Anal. calcd. for $C_{23}H_{17}N_7S$: C 65.23, H 4.05, N 23.15, S 7.57; found: C 64.92, H 4.25, N 23.25, S 7.87%.

9-Methyl-11-(3,5-dimethylpyrazolyl)-7-(*p*-tolyl)pyrimido-[4″,5″:4′,5′]thieno[3′,2′:5,6]pyrido[3,2-*c*]cinnoline (14)

The hydrazino compound **13** (0.001 mol) and acetylacetone (0.005 mol) in ethanol (40 mL) were refluxed for 6 h. The separated solid was filtered and recrystallized from ethanol as pale brown crystals, mp 320°C, yield 77%. IR: NH and NH_2 absorptions disappeared. ^1H NMR (TFA-*d*) δ: 2.45 (s, 3H, *p*-CH_3), 2.60 (s, 3H, CH_3), 2.80 (s, 3H, CH_3), 6.40 (s,,1H, ═CH), 7.6–9.8 (m, 8H, ArH). MS, *m/z* (%): 488 (M + 1, 35), 487(M^+, 100), 486(M – 1, 16). Anal. calcd. for $C_{28}H_{21}N_7S$: C 68.97, H 4.34, N 20.11, S 6.58; found: C 64.10, H 4.62, N 19.90, S 6.82%.

5-Methyl-7-(*p*-tolyl)-1,2,4-triazolo[4‴,3‴:1″,6″]pyrimido-[4″,5″:4′,5′]thieno-[3′,2′:5,6]pyrido[3,2-*c*]cinnoline(15).

The hydrazino compound **13** (0.001 mol), triethylorthoformate

© 1998 NRC Canada

Table 3. Analytical, spectral, and physical data of compounds, **6a**–**6h**.

Comp. no. [a]	mp, °C	Color	Yield %	Mol. formula	Analysis calcd./found (%) C	H	N	S	Spectral data IR (KBr) cm^{-1}	^1H NMR δ (ppm), and MS, *m/z* (%)
6a	310°C	Orange	69	$C_{22}H_{16}N_4OS$	68.73 68.46	4.19 4.35	14.57 14.55	8.34 8.11	(NH_2) 3500, 3300(CO), 1610	^1H NMR ($CDCl_3$) δ: 2.55 (s, 3H, *p*-CH_3), 2.90 (s, 3H, $COCH_3$), 6.20 (s, 2H, NH_2), 7.2–9.1 (m, 8H, ArH)
6b	265°C	Red	78	$C_{27}H_{18}N_4OS$	72.63 72.70	4.06 4.12	12.55 12.36	7.18 7.31	(NH_2) 3400, 3300, (CO) 1560	^1H NMR ($CDCl_3$)δ: 2.60 (s, 3H, *p*-CH_3), 7.12 (s, 2H, NH_2), 7.2–9.3 (m, 13H, ArH); MS, *m/z* (%): 446 (M^+, 100%)
6c	290°C	Orange	82	$C_{23}H_{18}N_4O_2C$	66.65 66.82	4.38 4.31	13.52 13.30	7.74 7.52	(NH_2) 3470, 3350, (CO) 1670	^1H NMR ($CDCl_3$) δ: 1.50 (t, 3H, CH_3 ester), 2.60 (s, 3H, *p*-CH_3), 4.10 (q, 2H, CH_2), 5.90 (s, 2H, NH_2), 7.2–9.3 (m, 8H, ArH); MS, *m/z* (%): 414(M^+, 100%)
6d	270°C	Red	75	$C_{21}H_{15}N_5OS$	65.43 65.60	3.90 3.98	18.17 17.94	8.32 8.16	(NH_2) 3450, 3300, (CO) 1630	^1H NMR (DMSO) δ: 3.30 (s, 3H, *p*-CH_3), 6.00 (s, 2H, NH_2), 7.35 (s, 2H, $CONH_2$), 7.35–9.1 (m, 8H, ArH); MS, *m/z* (%); 385 (M^+, 69%)
6e	297°C	Orange	69	$C_{28}H_{19}N_5OS$	70.26 70.36	4.15 4.28	15.17 15.32	6.95 6.80	(NH_2) 3450, 3400, (NH) 3300, (CO) 1640	^1H NMR ($CDCl_3$) δ: 3.00 (s, 3H, *p*-CH_3),6.05 (s, 2H, NH_2), 7.73 (s, 1H, NH), 7–9.2 (m, 13H, ArH)
6f	194°C	Red	70	$C_{28}H_{21}N_5OS$	70.72 70.53	4.45 4.25	14.73 14.50	6.74 6.81	(NH_2) 3460–3400, (NH) 3300, (CN) 2200, (CO) 1622	^1H NMR (DMSO) δ: 2.25 (s, 3H, *p*-CH_3), 2.52 (s, 3H, *p*-CH_3), 6.03 (s, 2H, NH_2), 7.52 (s, 1H, NH), 7–9.1 (m, 12H, ArH)
6g	257°C	Red	72	$C_{28}H_{21}N_5O_2S$	69.17 68.94	4.20 4.06	13.91 13.72	6.37 6.57	(NH_2) 3500, 3450, (NH) 3300, (CO) 1630	^1H NMR ($CDCl_3$) δ: 2.60 (s, 3H, *p*-CH_3), 2.80 (s, 3H, *p*-OCH_3), 6.15 (s, 2H, NH_2), 7.80 (s, 1H, NH), 6.8–9 (m, 12H, ArH)
6h[b]	285°C	Red	74	$C_{27}H_{18}ClN_5OS$	65.38 65.20	3.66 3.71	14.12 13.92	6.47 6.32	(NH_2) 3450, (NH) 3300, (CO) 1620	^1H NMR ($CDCl_3$) δ: 2.60 (s, 3H, CH_3), 6.20 (s, 2H, NH_2), 8.90 (s, 1H, NH), 7.15–9.3 (m, 12H, ArH)

[a] All products were recrystallized from ethanol except **6a** from acetic acid.
[b] Chlorine analysis for **6h**, calcd.: 7.15; found: 7.23%.

(5 mL) and five drops of acetic acid were refluxed for 6 h. The separated product was filtered and recrystallized from acetic acid as yellow crystals, mp >360 °C, yield 75%. IR: NH and NH_2 absorptions disappeared. ^1H NMR (TFA-*d*) δ: 2.40 (s, 3H, *p*-CH_3), 2.96 (s, 3H, CH_3), 7.35–9.9 (m, 8H, ArH), 9.65 (s, 1H, =CH). MS, *m/z* (%); 434 (M + 1, 48), 433 (M^+, 60), 432 (M – 1, 32). Anal. calcd. for $C_{24}H_{15}N_7S$: C 66.50, H 3.49, N 22.62, S 7.40; found: C 66.26, H 3.86, N 22.81, S 7.73%.

5-Methyl-7-(*p*-tolyl)1,2,4-triazolo[4‴,3‴:1″,6″]pyrimido-[4″,5″:4′,5′]thieno-[3′,2′:5,6]pyrido[3,2-*c*]cinnolin-3(2*H*)-thione (16)

The hydrazino compound **13** (0.001 mol) and carbon disulphide (2 mL) in dry pyridine (20 mL) were refluxed for 8 h. The separated solid was filtered and recrystallized from ethanol as brown crystals, mp >360°C. IR: 3450 (NH), 1280 (C=S) cm^{-1}. ^1H NMR (TFA-*d*) δ: 2.70 (s, 3H, *p*-CH_3), 3.30 (s, 3H, CH_3), 7.5–9.82 (m, 8H, ArH). Anal. calcd. for $C_{24}H_{15}N_7S_2$: C 61.92, H 3.25, N 21.06, S 13.78; found: C 62.06, H 3.57, N 20.89, S 13.56%.

5-Methyl-7-(*p*-tolyl)-3-(ethoxycarbonylmethylthio)1,2,4-triazolo-[4‴,3‴:1″,6″]pyrimido[4″,5″:4′,5′]thieno-[3′,2′:5,6]pyrido[3,2-*c*]cinnoline (17)

The triazolo compound **16** (0.001 mol) and ethyl chloroacetate (0.5 mL) in ethanol (30 mL) were refluxed for 30 min. The separated solid was filtered and recrystallized from ethanol as greenish yellow crystals, mp 275°C, yield 77%. IR: 1720 (CO) cm^{-1}. ^1H NMR ($CDCl_3$) δ: 1.17 (t, 3H, CH_3 ester), 2.50 (s, 3H, *p*-CH_3), 2.77 (s, 3H, CH_3), 4.08 (s, 2H, SCH_2), 4.17 (q, 2H, CH_2 ester), 7.2–9 (m, 8H, ArH). Anal. calcd. for $C_{28}H_{21}N_7O_2S_2$: C 60.96, H 3.84, N 17.77, S 11.63; found: C 59.51, H 3.89, N 17.56, S 11.80%.

© 1998 NRC Canada

Table 4. Analytical, spectral, and physical data of compounds **10a**, **10b** and **18a**, **18b**.

Comp. no.	mp, °C[a]	Color	Yield %	Mol. formula	Analysis calcd./found (%) C	H	N	S	Spectral data IR (K Br) cm^{-1}	^{1}H NMR δ (ppm) and MS, *m/z* (%)
10a	325°C	Pale yellow	74	$C_{30}H_{20}N_6OS$	70.30 70.04	3.93 4.20	16.40 13.21	6.26 6.40	(CO) 1650	^{1}H NMR (TFA-*d*) δ: 2.70 (s, 3H, *p*-CH_3), 2.90 (s, 3H, CH_3), 8.98 (s, 1H, =CH), 7.4–9.9 (m, 14H, ArH)
10b	315°C	Yellow	78	$C_{31}H_{22}N_6O_2S$	68.62 68.39	4.09 4.10	15.49 15.67	5.91 6.08	(CO) 1660	^{1}H NMR (TFA-*d*) δ: 2.70 (s, 3H, *p*-CH_3), 2.93 (s, 3H, CH_3), 4.20 (s, 3H, *p*-OCH_3), 7.1–9.8(m, 13H, ArH+ 1H, =CH)
18a	320°C	Yellow	81	$C_{31}H_{23}N_7OC$	68.74 68.48	4.28 4.40	18.10 17.89	5.92 5.78	(NH) 3250	^{1}H NMR (TFA-*d*) δ: 2.30 (s, 3H, *p*-CH_3), 2.63 (s, 3H,CH_3), 4.15 (s, 3H, *p*-OCH_3), 8.50 (s, 1H, =CH), 7.1–9.9 (m, 12H, ArH)
18b	330°C	Pale yellow	74	$C_{30}H_{20}N_8O_2S$	64.50 64.69	3.61 3.81	20.06 19.91	5.74 5.48	(NH) 3210	^{1}H NMR (TFA-*d*) δ: 2.20 (s, 3H, *p*-CH_3), 2.64 (s, 3H, CH_3), 7.7–9.8 (m, 13H, ArH + H, = CH)

[a] All products were recrystallized from ethanol.

11-(Arylidenehydrazono)-9-methyl-7-(*p*-tolyl)pyrimido-[4″,5″:4′,5′]thieno-[3′,2′:5,6]pyrido[3,2-*c*]cinnoline (18a and 18b)

The hydrazino compound **13** and each of (*a*) *p*-anisaldehyde and (*b*) *p*-nitrobenzalehyde (0.001 mol) in acetic acid (20 mL) were refluxed for 30 min. The solid product was filtered and recrystallized from ethanol. The analytical, spectral, and physical data are reported in Table 4.

5-Methyl-7-(*p*-tolyl)tetrazolo[4‴,3‴:1″,6″]pyrimido-[4″,5″:4′,5′]thieno- [3′,2′:5,6]pyrido[3,2-*c*]cinnoline (19)

Sodium nitrite (7 mL, 10%, 0.01 mol) was added dropwise to a solution of the hydrazino derivative **13** (0.002 mol) in dilute hydrochloric acid (10 mL, 50%) at 0°C and stirred for 10 min. The solid product separated and recrystallized from ethanol as pale yellow crystals, mp >360°C, yield 70%. IR: NH and NH_2 absorptions disappeared. ^{1}H NMR (TFA-*d*) δ: 2.65 (s, 3H, *p*-CH_3), 3.30 (s, 3H, CH_3), 7.4–9.95 (m, 8H, ArH). Anal. calcd. for $C_{23}H_{14}N_8S$: C 63.58, H 3,25, N 25.79, S 7.38; found: C 63.30, H 3.40, N 25.37, S 7.19%.

5-Methyl-7-(*p*-tolyl)-1,2,4-triazolo[4‴,3‴:1″,6″]pyrimido-[4″,5″:4′,5′]thieno-[3′,2′:5,6]pyrido[3,2-*c*]cinnolin-3(2*H*)-one (20)

The hydrazino compound **13** (0.001 mol) and ethyl chloroformate (0.002 mol) in acetic acid (20 mL) were refluxed for 30 min. The solid product was recrystallized from acetic acid as yellow crystals, mp 300°C, yield 66%. IR: 1725 (CO), 3400 (NH) cm^{-1}. ^{1}H NMR (TFA-*d*) δ: 2.60 (s, 3H, *p*-CH_3), 2.95 (s, 3H, CH_3), 7.45–9.8 (m, 8H, ArH). MS, *m/z* (%): 449 (M^+, 4). Anal. calcd. for $C_{24}H_{16}N_7OS$: C 24.0, H 3.28, N 21.76, S 7.12; found: C 64.20, H 3.76, N 21.58, S 6.96%.

3,5-Dimethyl-7-(*p*-tolyl)-1,2,4-triazolo[4‴,3‴:1″,6″]pyrimido-[4″,5″:4′,5′]- thieno[3′,2′:5,6]pyrido[3,2-*c*]cinnoline (21)

The hydrazino compound **13** (0.001 mol) and acetic anhydride (20 mL) were refluxed for 6 h. The solid product was recrystallized from acetic acid as greenish yellow crystals, mp >360°C, yield 71%. IR: NH and NH_2 absorptions disappeared. ^{1}H NMR (TFA-*d*) δ: 2.50 (s, 3H, *p*-CH_3), 2.95 (s, 3H, CH_3), 3.20 (s, 3H, CH_3 triazol), 7.2–9.7 (m, 8H, ArH). Anal. calcd. for $C_{25}H_{17}N_7S$: C 67.10, H 3.83, N 21.91, S 7.17; found: C 63.70, H 4.05, N 22.10, S 6.98%.

References

1. S. Kneubuehler, V. Carta, A. Vincengo, C. Altomare, A. Carotti, and B. Testa. Helv. Chim. Acta, **76**, 1956(1993); T. Nakao, M. Kawakami, M. Hisadome, and T. Tahara. PCT Int. Appl. WO 89 04,306, 18 May, 1989; JP Appl. 87/278,009, 2 Nov. 1987; Chem. Abstr. **111**, 214498 (1989).
2. S. Inoue, A. Yazaki, H. Mochizuki, H. Tsutsumi, M. Murata, and K. Sakane. Jpn. Kokai Tokkyo Koho, JP 06 228, 138[94, 228, 138]; Chem. Abstr. **123**, 9452 (1995); S. Inoe, J. Yoshida, M. Yokomoto, A. Yazaki, N. Hayashi, and H. Amano. Jpn. Kokai Tokkyo Koho, JP 06, 228, 138 [94, 228, 138], JP Appl. 92/22, 407; Chem. Abstr. **121**, 179602 (1994); M. Yokomoto, A. Yazaki, N. Hayashi, S. Hatono, S. Inoue, and Y. Kuramato. Eur. Pat. Appl. Ep 470, 578; JP Appl 90/211, 190; Chem. Abstr. **117**, 7943(1992); R. Fusco, L.F. Piselli, and P.M. Boschi. Eur. Pat. Appl. Ep 287, 853 IT Appl. 87/20,230; Chem. Abstr. **110**, 75540 (1989); T. Miyamoto and J. Matsumoto. Chem. Pharm. Bull. **37**, 93 (1989); **36**, 1321 (1988).
3. M. Mizutani, M. Shiroshita, M. Sasaki, H. Okuda, and N. Mito. Eur. Pat. Appl. EP 273, 325; JP Appl. 86/309, 981; Chem. Abstr. **110**, 75532 (1989).
4. G.A. Pinna, M.M. Curzu, G. Cignarella, D. Barlocco, M. D'Amico, A. Filippelli, V. DeNovellis, and F. Rossi. Eur. J. Med. Chem. **29**, 447 (1994); G. Cignarella, D. Barrlocco, S. Villa, M.M. Curzu, G.A. Pinna, A. Lavezzo, and A. Bestetti. **27**, 819 (1992); G. Cignarella, D. Barlocco, M.M. Curzu, G.A. Pinna, P. Cazzulani, M. Cassin, and B. Lumachi. Eur. J. Med. Chem. **25**, 749,(1990); G. Cignarella, D. Barlocco, G.A. Pinna, M. Loriga, M.M. Curzu, O. Toffametti, M. Germini, P. Cazzulani, and E. Cavelletti. J. Med. Chem. **32**, 2277 (1989).
5. N. Garcia-Dominguez, E. Ravina, L. Santana, C. Teran, G. Garcia-Mera, F. Orallo, M. Crespo, and J.A. Fontenla. Arch. Pharm. **321**, 735 (1988).
6. J.F. Patoiseau, J.M. Autin, J.L. Maurel, and D. Bigg. PCT Int. Appl. Wo 93/09, 098, FR Appl. 91/13,571; Chem. Abstr. **119**,

© 1998 NRC Canada

225963 (1993); E. Ravina, J. Fueyo, C. Teran, J. Cid, G. Garcia-Mera, F. Orallo, and B. Bardan. Pharmazie, **47**, 574(1992).
7. J.F. Resch. Ger. (East) DD 249, 011, Appl. 291, 515, 86; Chem. Abstr. **108**, 186758 (1988).
8. G. Doria, A.M. Isetta, M. Ferrari, and D. Trizio. Eur. Pat. Appl. Ep 277, 791, IB Appl. 87/2,288; Chem. Abstr. **109**, 231043 (1988); L.V.G. Nargund, V.V. Badiger, and S.M. Yarnal. J. Pharm. Sci. **81**, 365 (1992).
9. G. Dattolo, G. Cirrincione, A.M. Almerico, E. Aiello, and I. D'Asdia. J. Heterocycl. Chem. **23**, 1371 (1986); S. Radl, J. Moural, and R. Bendova. Collect. Czech. Chem. Commun. **55**, 1311 (1989); S.J. Bakewell, W.J. Coates, M.B. Comer, M.L. Reeves, and B.H. Warrington. Eur. J. Med. Chem. **25**, 765 (1990); G.A. Pinna, M.M. Curzu, G. Cignarella, D. Barlocco, M. Cassin, and B. Lumachi. Eur. J. Med. Chem. **25**,249 (1990); H. Sasaki, H. Tsutsumi, M. Murata, T. Terasawa, and K. Sakane. J. Org. Chem. **60**, 3928 (1995).
10. M.Z.A. Badr, G.M. El-Naggar, H.A. El-Sherief, and S.A. Mahgoub. Bull. Chem. Soc. Jpn. **57**, 1653 (1984); M.Z.A. Badr, S.A. Mahgoub, O.S. Moustafa, and F.F.A. Latif. J. Indian Chem. Soc. **67**, 216 (1990); M.Z.A.Badr, S.A. Mahgoub, F.M. Atta, and O.S. Moustafa. J. Indian Chem. Soc. **74**, 30 (1997); M.Z.A. Badr, S.A. Mahgoub, O.S. Moustafa, and A.A. Geies. Phosphorus, Sulfur Silicon Relat. Elem. **73**, 27, (1992); M.Z.A..Badr, S.A. Mahgoub, O.S. Moustafa, and A.A. Geies. Phosphorus, Sulfur Silicon Relat. Elem. **79**, 77 (1993); M.Z.A. Badr and O.S. Moustafa. Phosphorus, Sulfur Silicon Relat. Elem. **1**,127(1996).
11. K. Gewald, O. Calderon, H. Schafer, and U Hain. Liebigs Ann. Chem. 1390 (1983), and ref. 5 cited therein.
12. M.Z.A. Badr, H.A. El-Sherief, G.M. El-Naggar, and S.A. Mahgoub. J. Heterocycl. Chem. **21**, 471 (1984); K.T. Potts and C. Lovelette. J. Org. Chem. **34**, 3221 (1969); A. Amer, K. Weisz, and H. Zimmer. Heterocycles, **26**, 1853 (1987); H.Zimmer, J. McManus, T. Novinson, E.V. Hess, and A. Litwin. Arzneim.-Forsch. **20**, 1586 (1970).

© 1998 NRC Canada

Generalized valence bond study of rotational singlet structures and π bond energies for systems containing C═C, Si═Si, and C═Si double bonds

Youliang Wang and Raymond A. Poirier

Abstract: Ab initio GVB(6/12)/6-31G** calculations were performed on $A_2X{=}YB_2$ (A, B = H, F; X, Y = C, Si) to obtain the optimized geometries for planar and twisted singlet structures, and to also calculate π bond energies (rotational barriers). The nature of C—C, Si—Si, and C—Si π bonds has been investigated. The results show that the C–C π bond energy (E_π(ethene) = 65.4 kcal/mol) decreases with increasing fluorine substitution. The pyramidalization at the carbon or silicon center for the twisted structures decreases the π bond energies in the substituted ethenes and their silicon counterparts. The Si—Si (E_π(disilene) = 23.2 kcal/mol) and C—Si (E_π(silaethene) = 31.6 kcal/mol) π bonds become much weaker. Fluorine substitution stabilizes both the diradical and the dipolar twisted singlet structures.

Key words: π bond energy, ab initio calculations, generalized valence bond, fluorine substitution, disilene, and silaethene.

Résumé : On a effectué des calculs ab initio au niveau GVB(6/12)/6-31G** sur des molécules du type $A_2X{=}YB_2$ (A, B = H, F; X, Y = C, Si) dans le but d'obtenir des géométries optimisées pour les structures singulets planes et déformées ainsi que pour calculer les énergies de liaison π (barrières rotationnelles). On a étudié la nature des liaisons π dans C—C, Si—Si et C—Si. Les résultats montrent que l'énergie de liaison π dans C–C (E_π(éthène) = 65,4 kcal/mol) diminue lorsqu'on augmente le nombre d'atomes de fluor comme substituants. La pyramidalisation au niveau des atomes de carbone ou de silicium pour les structures déformées diminue les énergies des liaisons π dans les éthènes substitués ainsi que dans leurs équivalents contenant du silicium. Les liaisons π dans Si—Si (E_π(disilène) = 23,2 kcal/mol) et dans C—Si (E_π(silaéthène) = 31,6 kcal/mol) deviennent beaucoup plus faibles. Une substitution par le fluor stabilise les structures tant diradicalaire que singulet déformée dipolaire.

Mots clés : énergie de liaison π, calculs ab initio, liaison de valence généralisée, substitution par le fluor, disilène, silaéthène.

[Traduit par la rédaction]

1. Introduction

Double-bond energies are often divided into σ and π contributions, but these are not directly observable quantities. Ab initio molecular orbital theory affords an excellent way to assess these components. There are two ways to obtain the π bond energies. The first procedure is to compare the bond dissociation energies of double bonds, D_e(X═Y), and single bonds, D_e(X—Y). However, the energy difference between them, D_e(X═Y) – D_e(X—Y), does not correspond to the barrier to rotation about the X═Y bond. For example, the experimental data (1) for ethene are 173.3 and 86.1 kcal/mol for D_e(X═Y) and D_e(X—Y), respectively. The difference, 87.2 kcal/mol, is far greater than the rotational barrier (65 kcal/mol) (2). Obviously, the directly deduced quantity from D_e(X═Y) – D_e(X—Y) is not the π bond energy in ethene. Schleyer and Kost (3) used isogyric reactions,

$$H_2X{=}YH_n + XH_4 + YH_{n+2} \rightarrow 2H_3X{-}YH_{n+1}$$

to compare the energies of X═Y double bonds with those of X—Y single bonds. For ethene, a π bond energy (E_π) of 69.6 kcal/mol was obtained at MP4/6-31G*//6-31G*+ZPE. Meanwhile, Schmidt et al. (4) used hydrogenation thermochemical cycles to give similar results, e.g., E_π(ethene) = 62 kcal/mol. However, there are some discrepancies between their calculated π bond energies. For instance, the calculated C═N π bond energy by Schmidt et al. (4) is 65 kcal/mol, compared to 81 kcal/mol obtained by Schleyer and Kost (3). The discrepancies are due to the use of different sets of reference species in the thermochemical cycles.

Another commonly used procedure is to equate the π bond energy with the rotational barrier (2, 4, 5), provided that the transition state has no π bond character while retaining all σ bonds. The transition state, for singlet rotation around a double bond, is the 90° twisted singlet diradical. For this diradical structure, a single determinantal wave function cannot afford

Received September 29, 1997.

Y. Wang[1] and R.A. Poirier.[2] Department of Chemistry, Memorial University of Newfoundland, St. John's, NF A1B 3X7, Canada.

[1] Current address: Materials and Process Simulation Center, Beckman Institute(139-74), Division of Chemistry and Chemical Engineering, California Institute of Technology, Pasadena, CA 91125, U.S.A.

[2] Author to whom correspondence may be addressed. Telephone: (709) 737-8609. Fax: (709) 737-3702. E-mail: rpoirier@morgan.ucs.mun.ca

© 1998 NRC Canada

a proper description, and a multiconfiguration calculation must be used. Due to the difficulty in characterizing the twisted singlet transition state, which is very sensitive to the basis set and correlation energy, few efforts have been made to obtain the optimized geometries with extensive basis sets. Schmidt et al. (4) reported MCSCF/6-31G*//3-21G* results of the rotational barrier, or π bond energy, for ethene of 65.4 kcal/mol. Borden and co-workers (6) carried out GVB-PP(1/2)/6-31G* calculations of the rotational barrier in ethene (65.6 kcal/mol) and TCSCF (two configuration SCF) calculations of the rotational barrier in disilene (22.1 kcal/mol). Our preliminary GVB(2/4)/6-31G** calculations (7) gave a proper description of the rotation about the π bond in C_2H_4 and gave a π bond energy of 63.6 kcal/mol.

A number of ab initio (SCF (5, 8), CI (9), MCSCF (4, 6, 10), GVB (7, 11)) calculations have been performed to study the planar singlets and twisted structures triplets for ethene, silaethene, disilene, and their derivatives and isomers. However, the previous calculated geometries for the twisted singlets are far from agreement, due to the difficulty in characterizing the correct transition states, which are very sensitive to the basis set and correlation energy. For example, the MCSCF/3-21G* (4) geometry for the twisted singlet silaethene is very different from MP2/6-31G** (11*c*). As known, the twisted singlet structure is close to the twisted triplet. However, the MCSCF/3-21G* triplet (4) HSiC angle is different from Lischka's result (10*a*), i.e., 119° vs. 111.4°, while the flap angles of SiH_2 and the HCSi bond are very close to each other. The MCSCF/3-21G* and TCSCF/6-31G* (6) structures for twisted singlet disilene are also different in the flap angle of SiH_2, 17.3° vs. 47.6°. The calculated geometrical structure of disilene, especially the trans-bent angle formed by the SiH_2 plane and Si—Si bond, strongly depends on the basis sets and the electron correlation energy (11*b*). Although many studies have been done to investigate fluorine substitution effects on C═C bonding and electronic structures, no transition-state structures of fluorine substituents have been reported.

On the other hand, the early studies (11*c*–*e*) indicated that the nature of C═Si bond in silaethene is similar to that of C═C bond in ethene from their GVB orbital analysis. This may be true in the planar structure. However, the π bond energy is not only related to the planar structure, but more importantly to the transition-state structure. Most of the other experimental (12) and theoretical studies (3–5, 10*b*, 13) give a C═Si π bond energy of ~40 kcal/mol, which is only a fraction of the value in ethene.

Our objective of this study is to characterize the correct transition state for singlet rotation around the C═C, C═Si, and Si═Si double bonds. By employing GVB calculations, the π bond energies and the fluorine substitution effects are further studied.

2. Computational details

In this study, GVB(6/12)/6-31G** calculations were carried out for $A_2X{=}YB_2$ (A, B = H, F; X, Y = C, Si). The GVB(6/12) wave function includes two X—A bonds, two B—Y bonds, one X—Y σ, and one X—Y π bond, i.e.,

$$[1]\quad \Psi^{GVB}_{A_2X=YB_2} = A[\Psi_{core}\Psi_{X-Y(\sigma)}\Psi_{X-Y(\pi)}\Psi_{X-A1}\Psi_{X-A2}\Psi_{Y-B1}\Psi_{Y-B2}]$$

The planar or trans-bent structures of $A_2X{=}YB_2$ were optimized with the Davidon's optimally conditioned method (14). The singlet transition-state structures were optimized with a minimization of sum-of-squares method.[3] All equilibrium structures were characterized to have no imaginary frequency, while the transition states have only one imaginary frequency. In the transition state, the GVB CI-coefficients for π orbitals are 0.707 ± 0.005.

When a doubly bonded $A_2X{=}YB_2$ molecule is rotated by 90° to the diradical transition state, the X—Y π bond is broken while retaining all σ bonds. The barrier to X═Y double-bond rotation can be defined as the π bond energy, E_π. The π bond energies reported here are not corrected for zero-point energy (ZPE).[4]

All calculations are carried out with the GVB program in the MUNGAUSS ab initio package (15),[5] which is written using the OSIPE (open structured interfaceable programming environment) tools and automatically generates reliable initial GVB orbitals leading to the proper and fast energy convergence (7).The OSIPE is an "object-oriented" approach to programming in which objects are computed dynamically.

3. Results and discussion

The computed GVB total energies for ground states and transition states, and rotational barriers are summarized in Table 1. The optimized geometrical parameters are given in Tables 2 and 3 for reactants and transition states, respectively. The results of X–Y bond order and Mulliken charges on X and Y are also listed in Table 4. The transition-state structures for ethene, silaethene, and disilene are illustrated in Fig. 1.

3.1 The C═C bond

The C═C π bond in ethene is probably the best characterized π bond, both experimentally and theoretically. A number of theoretical papers (4, 11*a*, 16) have indicated that the triplet state and the rotated singlet state (which is usually referred to as the N state) represent a violation of Hund's rule. In accordance with Hund's rule, the two unpaired π electrons should give the triplet ground state. The GVB treatments (11*a*), along with MCSCF (4), CI (16), UHF (5), predict that the lowest energy rotation path on the singlet N state potential-energy surface is entirely below the triplet surface, for ethene. In the other $A_2X{=}YB_2$ (A, B = H, F; X, Y = C, Si), the 90° twisted triplet is about 1–3 kcal/mol lower than the rotated singlets, with geometries similar to their singlets. The rotated singlets are considered as the transition states for X═Y double bond rotation in this study.

(i) Optimized geometries

For planar $H_2C{=}CH_2$, $H_2C{=}CF_2$, and $F_2C{=}CF_2$, the GVB geometries are very close to the CISD (8*d*) and MCSCF (4)

[3] M.J.D. Powell. Subroutine VA05AD, AERE Subroutine Library Harwell, Didcot, Berkshire, U.K.

[4] The MCSCF/3-21G* (4) ZPE correction for the π bond energies in $CH_2{=}CH_2$, $CH_2{=}SiH_2$, and $SiH_2{=}SiH_2$ are 4.2, 1.4, and 0.6 kcal/mol, respectively.

[5] R.A. Poirier, Y. Wang, and C.C. Pye. MUNGAUSS V1.0, Department of Chemistry, Memorial University of Newfoundland, St. John's, Newfoundland, Canada; OSIPE Version, 1995. See ref. 15.

© 1998 NRC Canada

Table 1. The GVB(6/12)/6-31G** total energies and π bond energies.

	Total energy[a]		E_π[b]	E_π[b]
Molecule	Planar	Twisted	(This work)	(Reference)
$H_2C{=}CH_2$	–78.13651	–78.03224	65.4	65.4 (4), 67.9 (9*a*)
$H_2C{=}SiH_2$	–329.13391	–329.08352	31.6	35.6 (4), 34 (11*c*)
$H_2Si{=}SiH_2$	–580.16608	–580.12900	23.2	22.7 (4), 25.0 (6)
$H_2C{=}CF_2$	–275.85207	–275.75140	63.2	63.3 (18)
$F_2C{=}CF_2$	–473.54140	–473.45909	51.7	50.3 (18)
$F_2C{=}SiH_2$	–526.83074	–526.79163	24.6	—
$H_2C{=}SiF_2$	–526.96988	–526.93590	21.3	—

[a] In hartrees.
[b] In kcal/mol.

Table 2. The GVB(6/12)/6-31G** reactant geometries for $A_2X{=}YB_2$.[a]

Molecule	r_1	r_2	r_3	θ_1	θ_2	ϕ_1	ϕ_2	ϕ_3
$H_2C{=}CH_2$	1.346	1.093	1.093	121.7	121.7	180.0	0	180.0
$H_2C{=}SiH_2$	1.734	1.093	1.486	122.4	122.1	180.0	0	180.0
$H_2Si{=}SiH_2$	2.240	1.498	1.498	116.3	116.3	131.5	48.5	131.5
$H_2C{=}CF_2$	1.327	1.087	1.329	119.9	125.1	180.0	0	180.0
$F_2C{=}CF_2$	1.324	1.325	1.325	123.4	123.4	180.0	0	180.0
$F_2C{=}SiH_2$	1.749	1.339	1.477	125.3	118.7	180.0	0	180.0
$H_2C{=}SiF_2$	1.688	1.091	1.586	121.2	126.6	180.0	0	180.0

[a] Bond lengths in Å; bond angles in degree. r_1, X—Y bond length; r_2, A1—X bond length; r_3, B1—Y bond length; θ_1, bond angle A1-X-Y; θ_2, bond angle B1-Y-X; ϕ_1, torsion angle A2-X-Y-A1; ϕ_2, torsion angle B1-Y-X-A1; ϕ_3, torsion angle B2-Y-X-B1.

Table 3. The GVB(6/12)/6-31G** transition-state geometries for $A_2X{=}YB_2$.[a]

Molecule	r_1	r_2	r_3	θ_1	θ_2	ϕ_1	ϕ_2	ϕ_3
$H_2C{=}CH_2$	1.492	1.091	1.091	121.1	121.1	180.0	90.0	180.0
$H_2C{=}SiH_2$	1.884	1.093	1.496	122.7	112.1	180.0	118.1	123.8
$H_2Si{=}SiH_2$	2.358	1.496	1.497	112.5	114.7	126.7	161.4	126.8
$H_2C{=}CF_2$	1.490	1.087	1.341	119.9	115.2	180.0	115.7	128.6
$F_2C{=}CF_2$	1.501	1.330	1.330	113.9	113.9	129.0	155.4	129.0
$F_2C{=}SiH_2$	1.912	1.346	1.489	117.8	110.8	134.3	156.8	123.3
$H_2C{=}SiF_2$	1.858	1.093	1.603	122.5	109.7	180.0	121.8	116.4

[a] Bond lengths in Å; bond angles in degree. r_1, X—Y bond length; r_2, A1—X bond length; r_3, B1—Y bond length; θ_1, bond angle A1-X-Y; θ_2, bond angle B1-Y-X; ϕ_1, torsion angle A2-X-Y-A1; ϕ_2, torsion angle B1-Y-X-A1; ϕ_3, torsion angle B2-Y-X-B1. In transition state, A1—X and A2—X bond lengths, and the related bond angles, are not equal but very close. Only the above parameters are listed.

Table 4. The GVB(6/12)/6-31G** results of X=Y bond order and Mulliken charges at atoms X and Y for planar and twisted singlets.

	Planar			Twisted		
Molecule	Q_X	Q_Y	X=Y bond order	Q_X	Q_Y	X=Y bond order
$H_2C{=}CH_2$	–0.214	–0.214	1.778	–0.227	–0.227	0.966
$H_2C{=}SiH_2$	–0.446	0.431	1.709	0.017	0.337	0.899
$H_2Si{=}SiH_2$	0.241	0.241	1.380	0.250	0.250	0.863
$H_2C{=}CF_2$	–0.355	0.716	1.738	–0.292	0.679	0.950
$F_2C{=}CF_2$	0.622	0.622	1.670	0.637	0.637	0.903
$F_2C{=}SiH_2$	0.486	0.317	1.576	0.423	0.499	0.837
$H_2C{=}SiF_2$	–0.556	1.192	1.771	–0.494	1.165	0.881

results. The C=C and C—F bond lengths decrease with increasing fluorine substitution, as observed from early Hartree–Fock calculations (8*d*).

The twisted structure of ethene is illustrated in Fig. 1*a*. For twisted $H_2C{=}CH_2$, $H_2C{=}CF_2$, and $F_2C{=}CF_2$, the GVB C—C bond lengths are 1.492, 1.490, and 1.501 Å, respectively, which are very close to Schaefer's CI C—C bond length of 1.494 Å for $H_2C{=}CH_2$ (9*a*). The C—C bond length in the twisted structure is close to the single C—C bond length of 1.531 Å in C_2H_6, obtained at full valence GVB/6-31G** (17).

The F-C-C bond angle (θ_2 in Tables 2 and 3) clearly shows that the bond at which substitution occurs (CF_2) is changed from a planar (sp^2 hybridization, ~120°) conformation to a tetrahedral (sp^3 hybridization, ~113°) conformation, indicating the pyramidalization at CF_2 in the twisted structure.

(ii) C–C π bond energies

Our GVB/6-31G** results of C–C π bond energies (E_π) are in very good agreement with the previous ab initio calculations and the available experimental results. For instance, E_π(ethene) is 65.4 kcal/mol, compared to 67.9 (Schaefer's CI (9*a*)), 65.4 (MCSCF (4)), 65.6 (GVB(1/2) (18)), and 64 kcal/mol (experiment (2)). The E_π of fluoroethene contains a contribution from pyramidalization of the CF_2 radical center. The intrinsic π bond energy is the calculated result without the pyramidalization. Constraining the CF_2 radical center to planarity in the 1,1-difluoroethene diradical results in a E_π that is higher than E_π(ethene) by 11.5 kcal/mol. The actual E_π is, however, obtained from the transition state in which pyramidalization is allowed and is lower than E_π(ethene) by 2.2 kcal/mol. Therefore, the pyramidalization at the carbon or silicon center from sp^2(120°) to sp^3(109.5°) stabilizes the diradical transition state. The value of E_π is related to the B-Y-X bond angle in the transition state, i.e., θ_2 in Table 3. For example, the θ_2 values are 121.1°, 115.2°, 113.9° for $CH_2{=}CH_2$, $CH_2{=}CF_2$, and $CF_2{=}CF_2$, respectively. Their differences from 109.5° are 10.6°, 5.7°, and 4.4°, which correlates well with the calculated E_π values of 65.4, 63.2, and 51.7 kcal/mol, respectively. With two carbon centers pyramidalized, the rotational barrier in tetrafluoroethene is much lower. The C–C π bond energy decreases with increase fluorine substitution.

For the isodesmic reaction,

$$CH_2{=}CH_2 + CF_2{=}CF_2 \rightarrow 2CH_2{=}CF_2$$

the calculated GVB reaction energy (ΔE) of –16.5 kcal/mol is in excellent agreement with the experimental value of –14.6 kcal/mol (18) of which –9.3 kcal/mol can be attributed to differences in the π bond energies. The exothermicity of this reaction can be attributed to the replacement of the homopolar σ and π C—C bonds in ethene and tetrafluoroethene with the heteropolar σ and π C—C bonds in 1,1-difluoroethene.

The C–C bond orders clearly show that the π bond is totally broken in the twisted structures, with the C–C bond order of -0.9. The C–C bond orders are 1.778, 1.738, and 1.670 for planar $CH_2{=}CH_2$, $CH_2{=}CF_2$, $CF_2{=}CF_2$, respectively, decreasing with increasing fluorine substitution. The differences in the C–C bond order between planar and transition-state

© 1998 NRC Canada

Fig. 1. The structure of $A_2X{=}YB_2$ planar and perpendicular conformation. (*a*) twisted C_2H_4; (*b*) twisted $CH_2{=}SiH_4$; (*c*) trans-bent Si_2H_4; (*d*) twisted Si_2H_4.

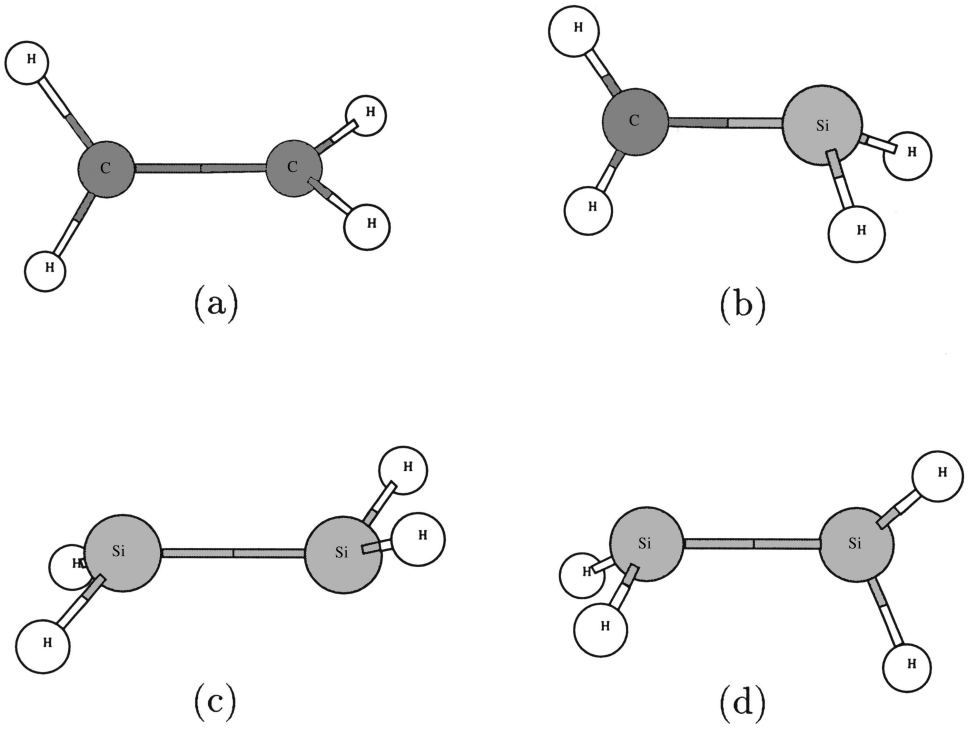

structures (0.812, 0.788, and 0.767, respectively), are the measure of π bond order and are related to the π bond energies. Overall, the C–C π bond energy decreases with increasing fluorine substitution, due to the strong pyramidalization of CF_2 in the twisted structures.

3.2 The C═Si bond

Silaethenes have long been implicated as reactive intermediates. 1,1-Dimethylsilaethene (DMSE) is the simplest silaethene that has been detected in the gas phase. Shin et al. (11*c*) experimentally found that silaethene is more stable than methylsilylene by 10 ± 3 kcal/mol, which is corroborated by GVB calculations. Their experimentally estimated π bond energy is 34 ± 4 kcal/mol for silaethene, which is less than the earlier estimate of 41 ± 5 kcal/mol for DMSE (12). However, their GVB calculations predicted a much higher value of 59.9 kcal/mol, since they did not allow for pyramidalization at the Si center in the twisted structure and the barrier was incorrectly calculated for a rotation from a planar singlet (two pairs GVB) to a twisted triplet (one pair GVB). The correct C–Si π bond energy can be equated to the barrier calculated by a consistent wave function for a rotation from a planar singlet to a twisted singlet with pyramidalization at the Si atom.

(i) Optimized geometries

For silaethene $H_2C{=}SiH_2$, the GVB C—Si distance is 1.734 Å, compared to 1.743 Å for MCSCF/3-21G* (4). These values are in reasonable agreement with experimental C—Si bond lengths of complex silaethenes 1.747 Å (19) and 1.702 Å (20). For planar (C_{2v}) $F_2C{=}SiH_2$ and $H_2C{=}SiF_2$, the GVB C—Si bond lengths are 1.749 and 1.688 Å, respectively. For twisted (C_s) structure, the GVB C—Si bond lengths are 1.884, 1.912, and 1.858 Å for $H_2C{=}SiH_2$, $F_2C{=}SiH_2$, and $H_2C{=}SiF_2$, respectively. From our GVB results, it can be found that a very short C—Si double bond in $H_2C{=}SiF_2$ is due to the strong dipolar (ionic) interaction between C and Si. The C—Si bond in the twisted structure is still a short single bond.

In the twisted singlet silaethene as shown in Fig. 1*b*, our GVB calculated H-Si-C bond angle (θ_2 in Table 3) is 112.1°, which is in good agreement with the H-Si-Si, H-Si-N, H-Si-P bond angle of ~110° reported by the previous MCSCF/3-21G* calculations (4). It is also in good agreement with the H-Si-C bond angle (111.4°) in the triplet structure reported by others (10*a*), supporting that the twisted singlet and triplet structures are similar. The flap angle for Si═Si transition state was incorrectly reported to be 17.6° in ref. 4. The correct value is 45.5°.

(ii) C–Si π bond energies

Our GVB calculations give a C═Si π bond energy (without pyramidalization at silicon) of 40.7 kcal/mol. Pyramidalization of the silicon center from sp^2 to sp^3 stabilizes the diradical transition state and decreases the π bond energy. Our GVB(6/12)/6-31G** E_π(silaethene) is 31.6 kcal/mol, which is close to the experimental result of 34 ± 4 kcal/mol (11*c*) and the MCSCF/6-31G*//3-21G* result of 35.6 kcal/mol (4). The E_π(silaethene) is less than the experimental estimate of 41 ± 5 kcal/mol for 1,1-dimethyl-silaethene (12). As mentioned before, the previous GVB result of 59.9 kcal/mol (11*c*) is too high, because the geometries were constrained in the twisted conformation.

The $H_2C{=}SiF_2$ bond is more stable than the $F_2C{=}SiH_2$ bond with a larger C–Si bond order in the planar structure. This large C–Si bond order is from the strong ionic interaction, so

© 1998 NRC Canada

that the bond order difference (0.89) between the transition state and the planar structure is larger than the actual C–Si π bond order. In general, the closer θ_2 is to 109.5° (sp^3) in the transition state, the smaller the π bond energy. Because of pyramidalization at silicon, the GVB H(F)-Si-C bond angles (θ_2 in Table 3) in the transition states are 112.1°, 110.8°, and 109.7° for silaethene, 2,2-difluorosilaethene, and 1,1-difluorosilaethene, respectively. Their deviations from 109.5° are 2.6°, 1.3°, and 0.2°, which correlate well with the π bond energies of 31.6, 24.6, and 21.3 kcal/mol.

In general, the pyramidalization at carbon or silicon will decrease the energy of the transition state more than that of the reactant, thus decreasing the rotational barrier. In contrast to the early suggestion (11*c–e*) that the nature of C═Si bond in silaethene is similar to that of the C═C bond in ethene, our GVB results clearly show that the C—Si π bond is very different from C—C π bond and much weaker.

3.3 The Si═Si bond

Because disilene Si_2H_4 is the simplest species with a Si—Si double bond, and its ground state shows an unusual preference for a trans-bent C_{2h} structure rather than a planar D_{2h} structure, it has been the subject of much interest experimentally and theoretically, since the isolation of tetramesityldisilene in 1981 (4, 6, 8*a,* b, 10*a*, 11*b*).

(i) Optimized geometries

The trans-bent singlet disilene, as shown in Fig. 1*c*, is more stable than the planar structure. Our GVB equilibrium geometry is very close to TCSCF/6-31G* result (6). For $H_2Si{=}SiH_2$ (C_{2h} for trans-bent structure), the Si—Si bond distance is 2.240 Å, compared to 2.160 Å (experimental observation for tetramesityldisilene (21)), 2.217 Å (MCSCF/3-21G* (4)), 2.242 Å (TCSCF/6-31G* (6)), 2.248 Å (GVB(2/4)/6-31G** (8*b*)), and 2.236 Å (CASSCF/6-31G** (8*b*)). Such a long bond length reflects the diradical character of the Si—Si bond, even though it is still shorter than that of the single bond. However, some double-bond character exists in disilene (C_{2h}) as illustrated by the Si–Si bond order of 1.380. For the twisted (C_{2h}) structure as shown in Fig. 1*d*, the Si—Si bond distance is 2.358 Å, compared to 2.351 Å (TCSCF/6-31G*), 2.355 Å (MCSCF/3-21G*), which is a single bond with a bond order of 0.863.

(ii) Si–Si π bond energies

The energetics of disilene are significantly affected by the incorporation of the electron correlation corrections. The calculated GVB barrier to rotation is 23.2 kcal/mol, which is close to 22.1 (TCSCF/6-31G* (6)), 22.7 (MCSCF/6-31G*//3-21G* (4)), and 25.0 kcal/mol (CISD/DZP (6)). The small Si–Si π bond energy is consistent with the Si–Si bond order of 1.380 in the trans-bent structure, and the difference of the Si–Si bond order between the trans-bent and twisted structures is 0.517, which is considered as the Si–Si π bond order. It is noticed that the rotation increases the positive charge at silicon in disilene, which increases the negative charge at carbon in ethene. The pyramidalization at silicon will decrease the energy of the transition state more than that of the reactant, thus decreasing the rotational barrier. The E_π(disilene) is much weaker than E_π(ethene).

For the following reaction:

$$H_2C{=}CH_2 + H_2Si{=}SiH_2 \rightarrow 2H_2C{=}SiH_2$$

the GVB reaction energy (ΔE) is 21.8 kcal/mol of which 25.4 kcal/mol can be attributed to differences in the π bond energies. For

$$H_2Si{=}SiH_2 + F_2C{=}CF_2 \rightarrow 2F_2C{=}SiH_2$$

the GVB reaction energy (ΔE) is 28.9 kcal/mol of which 25.7 kcal/mol can be attributed to differences in the π bond energies. The results show that the π bond change is the dominant contribution to the total enthalpy change in the above reactions. However, these two reactions are endothermic rather than exothermic. Because the C—C π bond is much stronger than the C—Si π bond, the breaking of C═C and Si═Si bonds to form C═Si bonds is not favoured energetically.

Conclusions

The GVB(6/12)/6-31G** study on the singlet state rotation around the double bond of $A_2X{=}YB_2$ (X, Y = C, Si and A, B = H, F), gives the twisted singlet structures and π bond energies. The X—Y π bond is essentially broken in the transition state while retaining all σ bonds. Our GVB results of C–C π bond energies (E_π(ethene) = 65.4 kcal/mol) are in very good agreement with the previous ab initio calculations and the available experimental results. The results indicate that the C–C bond energy decreases with increasing fluorine substitution. The pyramidalization at carbon or silicon decreases the energy of the transition state more than that of the reactant, thus decreasing the rotational barrier. In general, the pyramidalization at carbon or silicon center from sp^2 to sp^3 stabilizes both diradical and dipolar transition states. The closer θ_2 is to 109.5° in transition state, the smaller the π bond energy for the same type of X–Y bonding. Our GVB results show that the C—Si π bond (E_π(silaethene) = 31.6 kcal/mol) and Si—Si π bond (E_π(disilene) = 23.2 kcal/mol) are much weaker than the C═C bond.

Acknowledgements

The continuing financial support (to R.A.P.) of the Natural Sciences and Engineering Research Council of Canada (NSERC) is gratefully acknowledged. The authors would like to thank Mr. James Xidos for reading the manuscript.

References

1. H.M. Rosenstock, K. Praxl, B.W. Steiner, and J.T. Heron. J. Phys. Chem. Ref. Data Suppl. **6** (1977).
2. J.E. Douglas, B.S. Rabinovitch, and F.S. Looney. J. Chem. Phys. **23**, 315 (1955).
3. P.v.R. Schleyer and D. Kost. J. Am. Chem. Soc. **110**, 2105 (1988).
4. M.N. Schmidt, P.N. Truong, and M.S. Gordon. J. Am. Chem. Soc. **109**, 5217 (1987).
5. K.D. Dobbs and W.J. Hehre. Organometallics, **5**, 2057 (1986).
6. D.A. Hrovat, H. Sun, and W.T. Bordon. J. Mol. Struct. (Theochem), **163**, 51 (1988).
7. Y. Wang and R.A. Poirier. J. Comput. Chem. **13**, 313 (1996).
8. (*a*) R.A. Poirier and J.D. Goddard. Chem. Phys. Lett. **80**, 37 (1981); (*b*) H. Lischka and H.J. Kohler. Chem. Phys. Lett. **85**, 467 (1982); (*c*) Y. Yoshioka, J.D. Goddard, and H.F. Schaefer III. J. Am. Chem. Soc. **103**, 2452 (1981); (*d*) D.A. Dixon,

© 1998 NRC Canada

T. Fukunaga, and B.E. Smart. J. Am. Chem. Soc. **108**, 1585 (1986).
9. (*a*) B.R. Brook, and H.F. Schaefer III. J. Am. Chem. Soc. **101**, 307 (1979); (*b*) J.D. Goddard, Y. Yoshioka, and H.F. Schaefer III. J. Am. Chem. Soc. **102**, 7644 (1980).
10. (*a*) H.J. Kohler and H. Lischka. J. Am. Chem. Soc. **104**, 5884 (1982); (*b*) M.W. Schmidt, M.S. Gordon, and M. Dupuis. J. Am. Chem. Soc. **107**, 2585 (1985).
11. (*a*) A.F. Voter, M.M. Goodgame, and W.A. Goddard III. Chem. Phys. **98**, 7 (1985); (*b*) H. Teramae. J. Am. Chem. Soc. **109**, 4140 (1987); (*c*) S.K. Shin, K.K. Irikura, J.L. Beauchamp, and W.A. Goddard III. J. Am. Chem. Soc. **110**, 24 (1988); (*d*) E.A. Carter and W.A. Goddard III. J. Am. Chem. Soc. **108**, 2180 (1986); (*e*) E.A. Carter and W.A. Goddard III. J. Phys. Chem. **88**, 1485 (1984).
12. (*a*) R. Walsh. Acc. Chem. Res. **14**, 246 (1981); (*b*) W.J. Pietro and W.J. Hehre. J. Am. Chem. Soc. **104**, 4329 (1982).
13. (*a*) M. Hanamura, S. Nagase, and K. Morokuma. Tetrahedron Lett. **22**, 1813 (1981); (*b*) M.J.S. Dewar, D.H. Lo, and C.A. Ramsden. J. Am. Chem. Soc. **97**, 1311 (1975).
14. W.C. Davidon. Math. Prog. **9**, 1 (1975).
15. F. Colonna, L.-H. Tolly, R.A. Poirier, J.G. Angyan, and G. Jansen. Comput. Phys. Commun. **81**, 293 (1994).
16. (*a*) Y. Yamaguchi, Y. Osamura, and H.F. Schaefer III. J. Am. Chem. Soc. **105**, 7506 (1983); (*b*) R.J. Buenker and S.D. Peyerimhoff. Chem. Phys. **9**, 75 (1976).
17. Y. Wang and R. Poirier. J. Mol. Struct. (Theochem), **340**, 1 (1995).
18. A. Nicolaidas and W.T. Borden. J. Am. Chem. Soc. **114**, 8682 (1992).
19. N. Wiberg, G. Wagner, G. Muller, and J. Riede. J. Organomet. Chem. **271**, 381 (1984).
20. N. Wiberg, G. Wagner, and G. Muller. Angew. Chem. Int. Ed. Engl. **24**, 229 (1985).
21. M.J. Fink, M.J. Michalczyk, K.J. Haller, R. West, and J. Michl. J. Chem. Soc. Chem. Commun. 1010 (1983).

© 1998 NRC Canada

Average energy approximations for anisotropic triple-dipole dispersion energy coefficients using three-body interactions involving O_2, NO, CO, N_2, H_2, and the rare gases as tests

Sean A.C. McDowell and W.J. Meath

Abstract: Average energy approximations for the anisotropic triple-dipole dispersion energy coefficients are tested using reliable results for these coefficients, which are available for all interactions involving the rare gases, H_2, N_2, CO, O_2, and NO. The original average energy approximation does not reproduce any of the anisotropic coefficients to within their estimated uncertainties. More recently derived average energy approximation formulae, requiring the isotropic and anisotropic polarizabilities and average energies for the interacting species as input, reproduce all but 69 of the 680 isotropic and anisotropic coefficients considered to within their estimated uncertainties.

Key words: nonadditive, three-body interactions, dispersion energies.

Résumé : On a vérifié des approximations de l'énergie moyenne pour les coefficients d'énergie de dispersion anisotrope de triples dipôles en faisant appel à des résultats fiables pour tous les coefficients disponibles pour toutes les interactions impliquant les gaz rares ainsi que H_2, N_2, CO, O_2 et NO. L'approximation originale de l'énergie moyenne ne permet pas de reproduire les coefficients anisotropes à des valeurs situées dans les limites des évaluations des incertitudes. Des formules d'approximation de l'énergie moyenne développées plus récemment, dans lesquelles il est nécessaire d'introduire des polarisabilités isotropes et anisotropes ainsi que les énergies moyennes des espèces interagissantes, permettent de reproduire l'ensemble des 680, à l'exception de 69 d'entre eux, coefficients isotropes et anisotropes à des valeurs considérées dans les limites des évaluations des incertitudes.

Mots clés : non additif, interactions entre trois corps, énergies de dispersion.

[Traduit par la rédaction]

1. Introduction

Nonadditive interaction energies are important for the understanding and the evaluation of many bulk properties of matter, ranging from third virial coefficients and absorption spectra of fluids, surface tension, binding energies of solids, molecular adsorption and interactions on surfaces, pressure–volume relations, internal energies, and structures of solids and fluids (refs. 1–9 and many refs. therein). The importance of these effects has also been stressed recently for microscopic molecular properties, namely the spectroscopy of van der Waals complexes (10–13).

Nonadditive interactions arising from dispersion forces, and for rare gas systems, are perhaps the best understood of the nonadditive interactions (however, see refs. 7, 8, 14–19), and of these the lead triple-dipole dispersion energy (20, 21), DDD, is most important. It is now well known that there are many types of nonadditive effects, which are of the same order of magnitude as DDD for interatomic or intermolecular distances of interest in rare gas or molecular systems (7, 8, 10–19). Nevertheless, the triple-dipole dispersion energy continues to play a significant role in representing nonadditive effects in both bulk and microscopic systems (1–19, 22).

Accurate results have been available, for some time, for the isotropic DDD energy for many interactions involving three rare gas atoms and (or) molecules (23–28). To date, however, the only reliable results for the anisotropic triple-dipole coefficients for interactions involving molecules are for three-body systems made up of He, Ne, Ar, Kr, Xe, H_2, N_2, CO, O_2, and NO (29). In applications these anisotropic coefficients have usually been evaluated using an average energy approximation developed by Stogryn (30), and it has recently been shown, using prototype interactions as examples, that the results so obtained can lead to poor representations of the anisotropy of

Received January 26, 1998.

S.A.C. McDowell[1,2] **and W.J. Meath.**[1,3] Department of Chemistry, University of Western Ontario, London, ON N6A 5B7, Canada.

[1] Present address: Department of Biological and Chemical Sciences, University of West Indies, Cave Hill Campus, Bridgetown, Barbados.
[2] Associated with the Centre for Chemical Physics, University of Western Ontario, London, ON N6A 3K7.
[3] Author to whom correspondence may be addressed. Telephone: (519) 679-2111 (ext. 6334). Fax: (519) 661-3022. E-mail: wmeath@julian.uwo.ca

© 1998 NRC Canada

the DDD for interactions involving molecules (22, 31). Part of the purpose of this paper is to use the available reliable anisotropic DDD coefficients to explicitly test the validity of the original average energy approximation (30) for the anisotropic DDD, on a coefficient by coefficient basis, and to further test a recently derived (32) anisotropic average energy approximation for these coefficients.

The recent average energy approximations for the isotropic and anisotropic DDD coefficients are reviewed in Sect. 2.2; the corresponding average energy approximations for the isotropic and anisotropic two-body dipole–dipole dispersion energy coefficients are reviewed in Sect. 2.1. The approach is tested in Sect. 3.1 and Sect. 3.2, for all two-body and three-body interactions, respectively, involving O_2 and NO, both with each other and with the rare gases, H_2, N_2, and CO. This augments the analogous tests for all two- and three-body interactions arising from the rare gases and H_2, N_2, and CO discussed previously in this journal (32). The new tests involve 54 unique two-body dispersion energy coefficients and 394 unique three-body dispersion energy coefficients of which all but 11 and 51, respectively, are reproduced to within the recently established (29) error estimates in the reliable results for the coefficients. Requiring a 1% reproducability for all the coefficients, the criteria used in earlier tests (32), increases the number of species failing the test to 17 and 94, respectively. The earlier tests involved 66 unique two-body and 286 unique three-body coefficients of which 13 and 26, respectively, cannot be reproduced to within 1% by the new average energy approximation. Section 3.2 also contains a test of the Stogryn average energy approximation (30) for all three-body interactions arising from the rare gases, H_2, N_2, CO, O_2, and NO, where at least one species is a molecule; none of the 460 unique anisotropic DDD coefficients are reproduced within their estimated uncertainties by this original anisotropic DDD average energy approximation. Finally, Sect. 4 contains a brief discussion of some of our results, and their relevance, in the context of nonadditive interactions.

2. Average energy approximations for the anisotropic dipolar dispersion energy coefficients

Here we summarize the average energy approximations for the anisotropic dipole–dipole and triple-dipole dispersion energy coefficients to be considered later in this paper.

2.1 The dipole–dipole dispersion energy

The long range dipole–dipole dispersion energy, which depends on the relative orientations of the two linear molecules, is given by (33, 34)

$$[1]\qquad E^{ab}_{dis,R^{-1}} = -\frac{C_6(a,b)}{R^6}\left[1 + \Gamma_{ab}P_2(\cos\theta_a) + \Gamma_{ba}P_2(\cos\theta_b) + \Delta_{ab}\left(\frac{4\pi}{5}\right)\sum_{m=-2}^{m=2}(3-|m|)Y_2^m(\theta_a,\phi_a)Y_2^{-m}(\theta_b,\phi_b)\right]$$

where R is the distance between the interacting molecules, and P_2 and Y_2^m are Legendre and spherical harmonic functions of the spherical polar angles (θ_a, ϕ_a) and (θ_b, ϕ_b) specifying the relative orientations of the interactioning molecules a and b (as specified in refs. 33 and 34). The isotropic dispersion energy coeffient, $C_6(a, b)$, and the anisotropy parameters Γ_{ab}, Γ_{ba}, and Δ_{ab}, can be expressed (33–36) in terms of anisotropic dispersion energy coefficients $C^{\zeta,\zeta'}_{ab}$, ζ, $\zeta' = \parallel$ or $\perp$ (see ref. 32 for explicit expressions). Without loss of accuracy (26, 35–37), these coefficients are most easily evaluated using pseudo dipole oscillator strength distributions (DOSDs), which provide a discrete representation of the recommended original DOSDs for the molecule. Thus,

$$[2]\qquad C^{\zeta,\zeta'}_{ab} = \frac{1}{4}\sum_{k_a=1}^{N_a}\sum_{k_b=1}^{N_b}\frac{f^{\zeta}_{k_a}f^{\zeta'}_{k_b}}{E^{\zeta}_{k_a}E^{\zeta'}_{k_b}[E^{\zeta}_{k_a}+E^{\zeta'}_{k_b}]}$$

where the ζ-component of the pseudo-DOSD for molecule a, say, is given by $\{E^{\zeta}_{k_a}, f^{\zeta}_{k_a}\}$ where the $E^{\zeta}_{k_a}$ and $f^{\zeta}_{k_a}$ are the excitation energy – oscillator strength pairs defining the pseudo-DOSD for the molecule a. If one of the species is isotropic, a say, then eq. [2] is written as $C^{0,\zeta'}_{ab}$ and is given by eq. [2] with the ζ-pseudo-DOSD for molecule a replaced by the isotropic atomic DOSD (35, 36).

The Unsöld average energy approximation (38) can be applied to eq. [2] to obtain (32)

$$[3]\qquad C^{\zeta,\zeta'}_{ab} = \frac{1}{4}\alpha_a^{\zeta}\alpha_b^{\zeta'}\frac{U_a^{\zeta}U_b^{\zeta'}}{(U_a^{\zeta}+U_b^{\zeta'})}$$

where U_a^{ζ} is a molecular ($\zeta = \parallel$ or $\perp$) or an atomic ($\zeta = 0$, $U_a^0 = U_a$) average energy, which is independent of k_a, and α_a^{ζ} is either the ζ-component of the anisotropic dipole polarizability for a molecule ($\zeta = \parallel$ or $\perp$) or the isotropic dipole polarizability α_a for an atom. Using eq. [3] it can be shown that the average energies U_a and U_b for atoms a and b can be related to the isotropic $C_6(a,b)$ dispersion energy coefficient by (30, 39)

$$[4]\qquad C_6(a,b) = \frac{3}{2}\frac{U_aU_b}{(U_a+U_b)}\alpha_a\alpha_b$$

and for two like atoms this yields

$$[5]\qquad U_a = \frac{4C_6(a,a)}{3\alpha_a^2}$$

For linear molecules average energies $U_a^{\parallel}$ and $U_a^{\perp}$ can be determined from $C^{\parallel,\parallel}_{aa}$ and $C^{\perp,\perp}_{aa}$ via eq. [3],

$$[6]\qquad U_a^{\zeta} = \frac{8C^{\zeta,\zeta}_{aa}}{(\alpha_a^{\zeta})^2},\qquad \zeta = \parallel \text{ or } \perp$$

Thus average energies for each of the rare gas atoms can be evaluated from eq. [5] from reliable values (23–25) of the isotropic C_6 coefficients and isotropic dipole polarizabilities, while the parallel and perpendicular average energies $U_a^{\parallel}$ and $U_b^{\perp}$ for H_2, N_2, CO, O_2, and NO can be obtained from eq. [6] using reliable values of the anisotropic polarizabilities and the $C^{\zeta,\zeta}_{aa}$, which have been computed from molecular pseudo-DOSDs (35, 36, 40, 41). The rare gas and H_2, N_2, and CO polarizabilities, α_a^{ζ}, and average energies, U_a^{ζ}, are given in ref. 32; those for O_2 and NO are in Table 1.

2.2 The triple-dipole dispersion energy

The triple-dipole dispersion energy (DDD) for the interaction of three linear molecules can be written in the form (22, 31)

© 1998 NRC Canada

$$[7]\quad \mathrm{DDD} = \frac{(1 + 3\cos\theta_A\cos\theta_B\cos\theta_C)C_9(a,b,c)}{R_{ab}^3 R_{bc}^3 R_{ac}^3}\,\mathrm{Re}[1 - \Gamma(a)W(\theta_a, \phi_a, \theta_A, \theta_B) - \Gamma(b)W(\theta_b, \phi_b, \theta_A, \theta_B) - \Gamma(c)W(\theta_c, \phi_c, \theta_A, \theta_B) + \Gamma(a,b)W(\theta_a, \phi_a, \theta_b, \phi_b, \theta_A, \theta_B) + \Gamma(a,c)W(\theta_a, \phi_a, \theta_c, \phi_c, \theta_A, \theta_B) + \Gamma(b,c)W(\theta_b, \phi_b, \theta_c, \phi_c, \theta_A, \theta_B) - \Gamma(a,b,c)W(\theta_a, \phi_a, \theta_b, \phi_b, \theta_c, \phi_c, \theta_A, \theta_B)]$$

where Re[···] indicates the real part of [···], θ_A, θ_B, and θ_C are the internal angles of the triangle formed by the centres of mass of molecules a, b, and c, and R_{ab} represents the distance between molecules a and b. The coefficients, W, are complicated functions of the spherical polar angles, (θ_i, ϕ_i) for i = a, b, c, specifying the relative orientations of the interacting molecules; expressions for the W's and details of the coordinate system used to define eq. [7] can be found in ref. 31.

The C_9 and the Γ's occurring in eq. [7] are the isotropic and anisotropic triple-dipole dispersion energy coefficients for the a–b–c interaction and are defined in terms of individual anisotropic triple-dipole dispersion energy coefficients defined by (31)

$$[8]\quad C_{abc}^{\zeta,\zeta',\zeta''} = \frac{1}{2}\sum_{k_a=1}^{N_a}\sum_{k_b=1}^{N_b}\sum_{k_c=1}^{N_c}\frac{f_{k_a}^{\zeta} f_{k_b}^{\zeta'} f_{k_c}^{\zeta''}\,[E_{k_a}^{\zeta} + E_{k_b}^{\zeta'} + E_{k_c}^{\zeta''}]}{E_{k_a}^{\zeta} E_{k_b}^{\zeta'} E_{k_c}^{\zeta''}[E_{k_a}^{\zeta} + E_{k_b}^{\zeta'}][[E_{k_a}^{\zeta} + E_{k_c}^{\zeta''}][[E_{k_b}^{\zeta'} + E_{k_c}^{\zeta''}]}$$

where $\zeta, \zeta', \zeta'' = \parallel, \perp$. Explicit expressions for C_9 and the various Γ's occurring in eq. [7], in terms of these coefficients, are given in refs. 31 and 32.

The extension of the average energy approximation for the dipole–dipole dispersion energy, Sect. 2.1, to DDD has been discussed previously (32). Applying this approximation to eq. [8] leads to

$$[9]\quad C_{\bar{a}bc}^{\zeta,\zeta',\zeta''} = \frac{1}{2}\frac{[U_a^{\zeta} + U_b^{\zeta'} + U_c^{\zeta''}]U_a^{\zeta} U_b^{\zeta'} U_c^{\zeta''}}{[U_a^{\zeta} + U_b^{\zeta'}][U_a^{\zeta} + U_c^{\zeta''}]\,[U_b^{\zeta'} + U_c^{\zeta''}]}\alpha_a^{\zeta}\alpha_b^{\zeta'}\alpha_c^{\zeta''} = \frac{1}{2}U_{\bar{a}bc}^{\zeta,\zeta',\zeta''}\alpha_a^{\zeta}\alpha_b^{\zeta'}\alpha_c^{\zeta''}$$

For isotropic interactions the parameter $U_{\bar{a}bc}^{\zeta,\zeta',\zeta''} = U_{abc}$ is independent of ζ, ζ', ζ''. Following Stogryn (30), U_{abc} can expressed in terms of the isotropic C_9(a, b, c) and polarizabilities,

$$[10]\quad U_{abc} = \frac{2C_9(a,b,c)}{3\alpha_a\alpha_b\alpha_c}$$

which leads to an average energy, for each rare gas atom a, given by (32)

$$[11]\quad U_a = \frac{16C_9(a,a,a)}{3(\alpha_a)^3}$$

Similarly to the two-body interactions involving linear molecules discussed in Sect. 2.1, average energies $(U_a^{\parallel}, U_a^{\perp})$ for each molecule can be obtained from the anisotropic DDD coefficients defined by eq. [9] with $\zeta = \zeta' = \zeta'' = \parallel$ or $\perp$ (32);

$$[12]\quad U_a^{\zeta} = \frac{16C_{\bar{a}\bar{a}\bar{a}}^{\zeta,\zeta,\zeta}}{3(\alpha_a^{\zeta})^3}, \qquad \zeta = \parallel \text{or} \perp$$

Average energies for the rare gases can therefore be evaluated using eq. [11] and reliable values (23–25) for the like rare gas C_9 triple-dipole coefficients and rare gas polarizabilities. The molecular parallel and perpendicular average energies are obtained from eq. [12] using reliable results for the molecular anisotropic polarizabilities and the like molecule anisotropic triple-dipole coefficients $C_{\bar{a}\bar{a}\bar{a}}^{\zeta,\zeta,\zeta}$, $\zeta = \parallel$ or $\perp$, that have been computed from the pseudo-DOSDs for the molecules (35, 36, 40, 41). The rare gas and H_2, N_2, and CO results are listed in ref. 32; the average energies and polarizabilities for O_2 and NO are included in Table 1.

3. Further tests of the average energy approximations

The average energy approximations, reviewed in Sect. 2, have been tested for all pair and three-body interactions involving the rare gases, H_2, N_2, and CO previously. Here the earlier analysis is extended to include O_2 and NO. Also, an analysis of the validity of results for the DDD coefficients obtained using Stogyn's original average energy approximation (30) for all three-body interactions arising from the rare gases and H_2, N_2, CO, O_2, and NO, which include at least one molecule, is included in Sect. 3.2. It should be noted that the expressions for the anisotropic dipole–dipole and triple-dipole dispersion energies, given by eqs. [1] and [7], do not contain additional terms arising from degeneracy of the $^2\Pi$ ground state of NO (29, 41, 42). Their computation requires the separate $\Pi\rightarrow\Sigma$ and $\Pi\rightarrow\Delta$ components of the $\perp$-DOSD, which are not available (41). Indeed the extra terms have been developed only for the interaction of a Π state molecule with an S state atom, for the two-body dispersion energy, where they have been shown to be small (42).

3.1 Results for the dipole–dipole dispersion energy

To test the validity of the average energy approximation, all the two-body dispersion energy coefficients C_6(a, b), $\Gamma_{a,b}$, Γ_{ba}, and Δ_{ab} are computed, in the average energy approximation discussed in Sect. 2.1, for all two-body interactions involving O_2 and NO, both with each other and with the rare gases, H_2, N_2, and CO. The expressions for the various coefficients, in terms of the $C_{ab}^{\zeta,\zeta'}$, are given explicitly by eqs. [2]–[5] of ref. 32, and the results for the $C_{ab}^{\zeta,\zeta'}$, in the average energy approximation, are obtained from eq. [3]; the polarizabilities and dipole–dipole average energies for O_2 and NO given in Table 1, and the analogous results for the other species given in ref. 32. In all cases the average energies are obtained using the like-species interaction coefficients $C_{\bar{a}b}^{\zeta,\zeta}$, $\zeta = \parallel$ or $\perp$, and C_6(a, a). The average energy results are compared against the reliable DOSD results for the two-body dispersion energy coefficients, which are available in the literature (25, 35, 36, 40, 41).

© 1998 NRC Canada

For the interactions considered explicitly here, there are 54 unique two-body dispersion energy coefficients C_6, Γ's, and Δ's. Of these, all but 17 can be generated, within the 1% uncertainty claimed (25, 35, 36, 40, 41) for C_6(a, a), Γ_{ab}, and Γ_{ba}, by the average energy approximation discussed in Sect. 2.1. The reliable DOSD values for the 17 coeffients, together with the percent difference between them and the average energy results, are listed in Table 2. As discussed in refs. 25, 35, 36, 40, 41, the estimated uncertainties in the reliable DOSD results for the small coefficient Δ_{ab} is often ≤2%, not ≤1%, and using a greater than 2% criteria for Δ_{ab} would eliminate six entries from Table 2.

Generally the percent differences are reasonably small with, as expected, those for Δ_{ab} being largest. Relatively high discrepancies are generally due to cumulative errors arising from "summing" the individual $C_{ab}^{\zeta,\zeta'}$ to obtain the overall dispersion energy coefficients (29, 32). In general the DOSD results for the individual $C_{ab}^{\zeta,\zeta'}$ coefficients are reproduced to within ~1%. For example for O_2–O_2 the discrepancy between the average energy and DOSD results for $\Delta = 2(C^{\|,\|} + C^{\perp,\perp} - 2C^{\|,\perp})/(3C_6)$ is –12%. The errors in using the average energy approximation to evaluate the (large) individual $C^{\zeta,\zeta'}$ is ≤1%, but since $(C^{\|,\|} + C^{\perp\perp}) \sim 2C^{\|,\perp}$, the cumulative effect of these small errors is large for this small interaction coefficient.

3.2 Results for the triple-dipole dispersion energy

All the triple-dipole dispersion energy coefficients (C_9 and Γ's) for all three-body interactions involving O_2 and NO, both with each other and with the rare gases and H_2, N_2, CO, have been evaluated using the average energy approximation detailed in Sect. 2.2. The expressions for the various coefficients, in terms of the $C_{abc}^{\zeta,\zeta',\zeta''}$, are given by eqs. [14]–[18] of ref. 32, and related symmetry conditions, and the results for the $C_{abc}^{\zeta,\zeta',\zeta''}$ are obtained from eq. [9]; the polarizabilities and the triple-dipole average energies for O_2 and NO given in Table 1, and the analogous results for the other species given in ref. 32. As for the two-body case, the average energies are determined using input concerning like-species interactions only. A comparison of the average energy results, with reliable values (29) obtained by directly evaluating the C_9's and Γ's using the relevant atomic and molecular DOSDs (25, 35, 36, 40, 41), is made below.

There are 394 unique three-body triple-dipole dispersion energy coefficients for the interactions considered explicitly here. Of these there are 60 atom–atom–molecule, 170 atom–molecule–molecule, and 164 molecule–molecule–molecule coefficients, and of these, respectively, all but 10, 43, and 41 can be reproduced to within 1% by the average energy approximation outlined in Sect. 2.2. A realistic assessment of the errors in the reliable DOSD results for the triple-dipole dispersion energy coefficients for the interactions of interest has been made (29) and yields error estimates of ≤1–2% for C_9 and Γ(i), ≤2–3% for Γ(i, j), and ≤5–10% for Γ(i, j, k) with the latter probably being excessive; these estimates were not available in the context of ref. 32. Therefore to reduce the tabular data to be presented, we report, in Tables 3–5, the reliable DOSD results for the relevant coefficients, together with the percent deviation of the average energy results from the reliable values, only if the average energy values disagree by more than 1%, 1.5%, and 2% for C_9 and Γ(i), Γ(i, j), and Γ(i, j, k), respectively. This reduces the tabular entries to 29 and 25 for the atom–molecule–molecule and the molecule–molecule–molecule results, relative to the 43 and 41 entries that would have been obtained if the 1% criteria for all coefficients, used in our previous analysis (32) of the three-body interactions arising from the rare gases, H_2, N_2, and CO, had been used. Using the error estimates themselves as criteria regarding Tables 4 and 5, namely 2% and 5%, would reduce the entries in these tables only by 1, to 28, and by 12, to 13, respectively. With respect to Table 5, only one Γ(i, j, k) value is not reproduced within the estimated error of 5%, while five Γ(i, j) values are not reproduced within 2%.

Table 1. Polarizabilities (40, 41) and average energies for O_2 and NO. Two sets of average energies are provided. One, labelled U_{DD}^{ζ}, is obtained from like molecule–molecule dipole–dipole dispersion energy interaction coefficients and the other, labelled U_{DDD}^{ζ}, from like molecule–molecule–molecule triple-dipole dispersion energy interaction coefficients (see main text for definitions). All quantities are in atomic units. The analogous results for the rare gases and H_2, N_2, and CO can be found in ref. 32.

	α	$\alpha^{\|}$	$\alpha^{\perp}$	$U_{DD}^{\|}$	$U_{DD}^{\perp}$	$U_{DDD}^{\|}$	$U_{DDD}^{\perp}$
O_2	10.59	15.29	8.238	0.5605	0.9275	0.5218	0.8825
NO	11.53	15.24	9.669	0.6375	0.7544	0.6078	0.7006

Until recently (22, 31), the only available computationally viable expression for the anisotropic triple-dipole dispersion energy was that due to Stogryn (30) in an average energy approximation. Relative to the average energy approximation discussed in Sect. 2.2, Stogryn's average energy approximation for DDD assumes all average energies $U_{abc}^{\zeta,\zeta',\zeta''}$ occurring in eq. [9] are the same and given by eq. [10]. Thus in this original average energy approximation, the molecular anisotropy of the DDD coefficients $C_{abc}^{\zeta,\zeta',\zeta''}$, defined by eq. [9], are given by those of the molecular polarizabilities only. The input for the Stogryn average energy eq. [10] are the isotropic DDD coefficient and polarizabilities only.

We have evaluated the anisotropic DDD coefficients Γ for all three-body interactions involving all the rare gases and H_2, N_2, CO, O_2, and NO and at least one molecule. There are 460 such unique coefficients and none of these are reproduced, by Stogryn's average energy approximation, within the error estimates of ≤1–2% for C_9 and Γ(i), ≤2–3% for Γ(i, j), and ≤5–10% for Γ(i, j, k), for the reliable results (29) for these coefficients. The discrepancies vary from ~5.0% to –58.7% for the Γ(i), from ~10.5% to ~ –91.3% for the Γ(i, j), and from ~16.0% to ~ –105.5% for the Γ(i, j, k). With a few exceptions, namely –4.9%, –4.4%, –3.7%, –4.6%, –3.8%, -4.7%, –4.9%, –4.6%, 1.3%, and 1.0% for Γ(N_2, CO), for the Ar–N_2–CO, Kr–N_2–CO, and Xe–N_2–CO interactions, Γ(CO–NO) for the Kr–CO–NO and Xe–CO–NO interactions, Γ(CO–N_2) for the CO–CO–N_2 interaction, Γ(CO–NO) for the CO–CO–NO interaction, Γ(CO–CO–H_2), Γ(CO–CO–N_2), and Γ(CO–CO–NO), respectively, the magnitude of the discrepancies exceed 5% and are generally large, and negative, especially for interactions involving the O_2 molecule. As discussed previously for some prototype interactions (22, 31), errors of this magnitude for the individual Γ's can lead to very poor representations for

© 1998 NRC Canada

Table 2. Reliable anisotropic dipole–dipole dispersion energy coefficients, refs. 40, 41 or evaluated using the pseudo-DOSDs of refs. 25, 35, 36, 40, 41, for all two-body interactions involving O_2 and NO, both with each other and with the rare gases, H_2, N_2, and CO, which are not reproduced to within 1% by the average energy approximation discussed in Sect. 2.1. The percentage difference, [(reliable – approximate)/reliable] × 100%, is shown in parentheses.

a–b		a–b	
NO–He	$\Gamma_{ab} = 0.1249$ (1.2%)	CO–O_2	$\Delta_{ab} = 0.0128$ (3.6%)
CO–NO	$\Delta_{ab} = 0.0126$ (2.6%)	H_2–O_2	$\Gamma_{ab} = 0.0956$ (–1.8%)
H_2–NO	$\Gamma_{ab} = 0.0963$ (–2.0%)		$\Delta_{ab} = 0.0156$ (–2.3%)
	$\Delta_{ab} = 0.0140$ (1.1%)	O_2–N_2	$\Gamma_{ab} = 0.1305$ (1.0%)
N_2–NO	$\Delta_{ab} = 0.0149$ (1.8%)	NO–O_2	$\Delta_{ab} = 0.0193$ (–1.2%)
NO–NO	$\Delta_{ab} = 0.0182$ (2.0%)	O_2–O_2	$\Gamma_{ab} = 0.1276$ (1.01%)
O_2–He	$\Delta_{ab} = 0.1192$ (5.9%)		$\Delta_{ab} = 0.0218$ (–12%)
O_2–Ne	$\Delta_{ab} = 0.1130$ (6.6%)		
O_2–Ar	$\Delta_{ab} = 0.1318$ (1.3%)		
O_2–Xe	$\Delta_{ab} = 0.1410$ (–1.7%)		

the anisotropy of the total triple-dipole dispersion energy for interactions involving molecules.

4. Discussion

Combining the results of this paper, with those of our earlier tests of the average energy approximation reviewed in Sect. 2, for all the two- and three-body interactions arising from He, Ne, Ar, Kr, Xe, H_2, N_2, CO, O_2, and NO, 120 unique two-body C_6's, Γ's, and Δ's corresponding to 55 unique two-body interactions, and 680 unique three-body C_9's and Γ's for 220 unique three-body interactions, are involved in the testing of the average energy approximation. In global summary, the average energy approximation expressions, with the provided input (Table 1 and Tables 1 and 2 of ref. 32), reproduce all but 19 of the two-body dispersion energy coefficients and all but 69 of the three-body dispersion energy coefficients to within the estimated uncertainties in the reliable results for these coefficients (25, 29, 35, 36, 40, 41). Thus a relatively small body of input data, and an average energy approximation, can be used to represent are large number of dipolar dispersion energy coefficients, especially for the triple-dipole dispersion energy interaction coefficients. Section 3.2 also contains a test of Stogryn's (30) average energy approximation for the anisotropic triple-dipole coefficients Γ. In summary, none of these 460 unique Γ's are reproduced to within their estimated uncertainties by this original DDD average energy approximation.

In general the anisotropic DDD energy will not be well represented by Stogryn's average energy approximation. However, until recently, this average energy approximation result for the anisotropic DDD energy was the only computationally viable result for this important nonadditive energy, and it has therefore been used in a variety of applications in the literature. It is also relevant to note that this average energy expression requires much less molecular input than does the exact expression for DDD or our average energy approximations. Indeed the reliable input required to evaluate the exact expression (31), of the form of eq. [7], is still only available for relatively few molecules at the present time. Thus, for example, in investigations of the effects of nonadditivity in the spectroscopy of van der Waals complexes, such as Ar_2–HF, Ar_2–HCl, and Ar_2–DCl, the anisotropic DDD energy has been evaluated in the Stogryn average energy approximation (10–13) (see also relevant discussion in ref. 22). Reliable results apparently are only available for the isotropic triple-dipole dispersion energy for interactions involving hydrogen halides (HX, X = Br, Cl, F) and one or two rare gases (25).

Table 3. Reliable anisotropic triple-dipole dispersion energy coefficients (29) for rare gas – rare gas – molecule interactions involving the rare gases, NO and O_2, evaluated using DOSDs (25, 35, 36, 40, 41), which are not reproduced to within 1% by the average energy approximation discussed in Sect. 2.2. The percentage difference, [(reliable – approximate)/reliable] × 100%, is shown in parentheses. The isotropic C_9 coefficient for He–Xe–O_2 is 148.6 (1.04%). All quantities are in atomic units.

a–b–c	
He–He–O_2	Γ(c) = 0.1428 (5.2%)
He–Ne–O_2	Γ(c) = 0.1399 (5.4%)
He–Ar–O_2	Γ(c) = 0.1514 (2.8%)
He–Kr–O_2	Γ(c) = 0.1545 (1.9%)
Ne–Ne–O_2	Γ(c) = 0.1367 (5.5%)
Ne–Ar–O_2	Γ(c) = 0.1491 (3.0%)
Ne–Kr–O_2	Γ(c) = 0.1524 (2.0%)
Ar–Ar–O_2	Γ(c) = 0.1588 (1.3%)
Xe–Xe–O_2	Γ(c) = 0.1710 (–1.04%)

As discussed in the introduction, it is clear that nonadditive energies are important for the understanding and evaluation of many properties of matter and that the triple-dipole dispersion energy is only one of several competing nonadditive interaction energies occurring in many (greater than two) body systems. It is important to quantify as many of these competing interactions as possible so that experiments can be used to study other, more difficult to compute, nonadditive energies (7, 8). Hopefully the results of this paper are a contribution to this end and will also help lead to improved average energy approximations, analogous to Stogryn's work, for the anisotropic triple-dipole energy that will be both tractable, and reliable, for a wide variety of three-body molecular interactions.

© 1998 NRC Canada

Table 4. Reliable anisotropic triple-dipole dispersion energy coefficients (29) for rare gas–molecule–molecule interactions involving the rare gases, H_2, N_2, CO, NO, and O_2, where at least one of the molecules is NO or O_2, evaluated using DOSDs (25, 35, 36, 40, 41), which are not reproduced to within 1% for C_9 and $\Gamma(i)$, and to within 1.5% for $\Gamma(i, j)$, by the average energy approximation discussed in Sect. 2.2. The percentage difference, [(reliable – approximate)/reliable] × 100%, is shown in parentheses. The isotropic C_9 coefficients for He–CO–O_2, He–O_2–O_2, and Ne–O_2–O_2 are 78.00 (1.1%), 66.47 (1.2%), and 131.9 (1.06%), respectively. All quantities are in atomic units.

a–b–c		a–b–c	
He–CO–NO	Γ(b) = 0.0960 (–1.2%)	Ne–N_2–O_2	Γ(c) = 0.1484 (2.7%)
He–CO–O_2	Γ(b) = 0.0960 (–1.4%)	Ne–NO–O_2	Γ(c) = 0.1482 (1.8%)
	Γ(c) = 0.1531 (1.2%)	Ne–O_2–O_2	Γ(c) = 0.1469 (2.2%)
	Γ(b, c) = 0.0147 (3.3%)		Γ(b, c) = 0.0258 (–4.9%)
He–H_2–NO	Γ(b) = 0.1035 (–1.2%)	Ar–CO–O_2	Γ(b, c) = 0.0154 (2.1%)
He–N_2–O_2	Γ(c) = 0.1508 (2.6%)	Ar–N_2–O_2	Γ(c) = 0.1584 (1.2%)
He–NO–O_2	Γ(c) = 0.1506 (1.8%)	Ar–O_2–O_2	Γ(b, c) = 0.0283 (–4.3%)
He–O_2–O_2	Γ(c) = 0.1495 (2.2%)	Kr–CO–O_2	Γ(b, c) = 0.0156 (1.6%)
	Γ(b, c) = 0.0263 (–4.5%)	Kr–O_2–O_2	Γ(a, b) = 0.0291 (–4.5%)
Ne–CO–NO	Γ(b) = 0.0958 (–1.7%)	Xe–O_2–O_2	Γ(b, c) = 0.0301 (–4.8%)
Ne–CO–O_2	Γ(b) = 0.0957 (–1.9%)		
	Γ(c) = 0.1508 (1.2%)		
	Γ(b, c) = 0.0145 (3.3%)		
Ne–H_2–NO	Γ(b) = 0.1027 (–1.4%)		
Ne–H_2–O_2	Γ(b) = 0.1022 (–1.4%)		
	Γ(c) = 0.1560 (2.3%)		

Table 5. Reliable anisotropic triple-dipole dispersion energy coefficients (29) for molecule–molecule–molecule interactions involving H_2, N_2, CO, NO, and O_2, where at least one of the molecules is NO or O_2, evaluated using DOSDs (25, 35, 36, 40, 41), which are not reproduced to within 1% for C_9 and $\Gamma(i)$, 1.5% for $\Gamma(i, j)$, and 2% for $\Gamma(i, j, k)$, by the average energy approximation discussed in Sect. 2.2. The percentage difference, [(reliable – approximate)/reliable] × 100%, is shown in parentheses. All quantities are in atomic units.

a–b–c		a–b–c	
CO–CO–O_2	Γ(a, b, c) = 0.0015 (3.1%)	H_2–NO–NO	Γ(a) = 0.1060 (–1.2%)
CO–H_2–NO	Γ(b) = 0.1064 (–1.1%)		Γ(b, c) = 0.0218 (2.0%)
	Γ(a, c) = 0.0159 (1.9%)	H_2–NO–O_2	Γ(a) = 0.1056 (–1.2%)
CO–H_2–NO	Γ(b) = 0.1067 (–1.1%)	H_2–O_2–O_2	Γ(a) = 0.1053 (–1.2%)
	Γ(a, c) = 0.0141 (1.6%)		Γ(b, c) = 0.0298 (–3.8%)
CO–N_2–O_2	Γ(a, c) = 0.0153 (2.0%)		Γ(a, b, c) = 0.0035 (–3.8%)
CO–NO–NO	Γ(a, b, c) = 0.0020 (2.1%)	N_2–N_2–O_2	Γ(c) = 0.1580 (1.02%)
CO–O_2–O_2	Γ(a, b) = 0.0152 (1.6%)	N_2–O_2–O_2	Γ(b, c) = 0.0282 (–4.5%)
	Γ(b, c) = 0.0288 (–5.2%)		Γ(a, b, c) = 0.0035 (–4.1%)
	Γ(a, b, c) = 0.0027 (–3.4%)	NO–NO–NO	Γ(a, b, c) = 0.0032 (2.1%)
H_2–H_2–NO	Γ(c) = 0.1481 (1.2%)	O_2–O_2–NO	Γ(a, b) = 0.0282 (–5.2%)
			Γ(a, b, c) = 0.0044 (–4.1%)
		O_2–O_2–O_2	Γ(a, b) = 0.0280 (–5.2%)
			Γ(a, b, c) = 0.0053 (–7.3%)

Acknowledgement

This research was supported by a grant from the Natural Sciences and Engineering Research Council of Canada.

References

1. J.A. Barker. *In* Rare gas solids. Vol. 1. *Edited by* M.L. Klein and J.A. Venables. Academic Press, New York. 1976. Chap. 4.
2. B. Guillot. J. Chem. Phys. **91**, 3456 (1989); B. Guillot, R.D. Mountain, and G. Birnbaum. J. Chem. Phys. **90**, 650 (1989); Mol. Phys. **64**, 747 (1988).
3. J.K. Lee, J.A. Barker, and G.M. Pound. J. Chem. Phys. **60**, 1976 (1974).
4. R.J. Bell and I.J. Zucker. *In* Rare gas solids. Vol. 1. *Edited by* M.L. Klein and J.A. Venables. Academic Press, New York. 1976. Chap.1.
5. W.-K. Liu. Phys. Rev. B: Condens. Matter, **32**, 868 (1985); J. Mahanty. Phys. Rev. B: Condens. Matter, **35**, 4113 (1987).
6. J.J. Salcuse and P.A. Egelstaff. Phys. Rev. A: Gen. Phys. **38**, 4313 (1988).

© 1998 NRC Canada

7. W.J. Meath and R.A. Aziz. Mol. Phys. **52**, 225 (1984); Faraday Discuss. Chem. Soc. **80**, 225 (1985).
8. W.J. Meath and M. Koulis. J. Mol. Struct. Spectrosc. (Theochem), **226**, 1 (1991).
9. D.E. Stogryn. J. Chem. Phys. **50**, 4967 (1969); J. Chem. Phys. **50**, 3671 (1970).
10. A. Ernesti and J.M. Hutson. Faraday Discuss. **97**, 1 (1994); M.J. Elrod, R.J. Saykally, A.R. Cooper, and J.M. Hutson. Mol. Phys. **81**, 579 (1994); A.R. Cooper and J.M. Hutson. J. Chem. Phys. **98**, 5337 (1993); M.J. Elrod, D.W. Steyert, and R.J. Saykally. J. Chem. Phys. **94**, 58 (1991); M.J. Elrod, D.W. Steyert, and R.J. Saykally. J. Chem. Phys. **95**, 3182 (1991); M.J. Elrod, J.G. Loeser, and R.J. Saykally. J. Chem. Phys. **98**, 5352 (1993).
11. A. Ernesti and J.M. Hutson. J. Chem. Phys. **103**, 3386 (1995).
12. A. Ernesti and J.M. Hutson. Phys. Rev. **A51**, 239 (1995).
13. A. Ernesti and J.M. Hutson. J. Chem. Phys. **106**, 6288 (1997).
14. Z.C. Zhang, A.R. Allnatt, J.D. Talman, and W.J. Meath. Mol. Phys. **81**, 1425 (1994).
15. A.D. McLean, B. Liu, and J.A. Barker. J. Chem. Phys. **89**, 6339 (1988); J.A. Barker. J. Stat. Phys. **52**, 1359 (1988).
16. R. LeSar. Phys. Rev. B.: Condens. Matter, **28**, 6812 (1983); Phys. Rev. Lett. **61**, 2121 (1988).
17. G. Chalasinski, S.M. Cybulski, M.M. Szczesniak, and S. Scheiner. J. Chem. Phys. **91**, 7048 (1989); G. Chalasinski, M.M. Szczesniak, P. Cieplak, and S. Scheiner. J. Chem. Phys. **94**, 2873 (1991), and refs. therein.
18. S.F. O'Shea and W.J. Meath. Mol. Phys. **28**, 1431 (1974); Mol. Phys. **31**, 515 (1976).
19. V.F. Lotrich and K. Szalewicz. J. Chem. Phys. **106**, 9688 (1997).
20. B.M. Axilrod and E. Teller. J. Chem. Phys. **11**, 299 (1943).
21. Y. Muto. Proc. Phys.– Math. Soc. Jpn. (Nippon Sugaku-Butsurigakki Kiji), **17**, 629 (1943).
22. S.A.C. McDowell and W.J. Meath. Chem. Phys. **223**, 23 (1997).
23. P.J. Leonard and J.A. Barker. Theor. Chem. Adv. Perspect. **1**, 117 (1975).
24. J.A. Barker and P.J. Leonard. Phys. Lett. **13**, 127 (1964).
25. A. Kumar and W.J. Meath. Mol. Phys. **54**, 823 (1985).
26. D.J. Margoliash, T.R. Proctor, G.D. Zeiss, and W.J. Meath. Mol. Phys. **35**, 747 (1978).
27. A. Kumar, G.R.G. Fairley, and W.J. Meath. J. Chem. Phys. **83**, 70 (1985).
28. R.J. Pazur, A. Kumar, R.A. Thuraisingham, and W.J. Meath. Can. J. Chem. **66**, 615 (1988).
29. S.A.C. McDowell and W.J. Meath. Mol. Phys. **90**, 713 (1997).
30. D.E. Stogryn. Phys. Rev. Lett. **24**, 971 (1970).
31. S.A.C. McDowell, A. Kumar, and W.J. Meath. Mol. Phys. **87**, 845 (1996).
32. S.A.C. McDowell, A. Kumar, and W.J. Meath. Can. J. Chem. **74**, 1180 (1996).
33. G.A. Victor and A. Dalgarno. J. Chem. Phys. **50**, 2535 (1969); **53**, 1316 (1970).
34. P.W. Langhoff, R.G. Gordon, and M. Karplus. J. Chem. Phys. **55**, 2126 (1971).
35. W.J. Meath and A. Kumar. Int. J. Quantum Chem. **24**, 501 (1990).
36. A. Kumar and W.J. Meath. Chem. Phys. **189**, 467 (1994).
37. D.J. Margoliash and W.J. Meath. J. Chem. Phys. **68**, 1426 (1978).
38. A. Unsöold. Z. Phys. **43**, 563 (1927).
39. A.D. Buckingham. Adv. Chem. Phys. **12**, 107 (1967).
40. A. Kumar, W.J. Meath, P. Bundgen, and A.J. Thakkar. J. Chem. Phys. **105**, 4927 (1997).
41. P. Bundgen, A.J. Thakkar, A. Kumar, and W.J. Meath. Mol. Phys. **90**, 721 (1997).
42. G.C. Nielson, G.A. Parker, and R.T. Pack. J. Chem. Phys. **64**, 2055 (1976).

© 1998 NRC Canada

Complexes of ketodiesters and related compounds with $TiCl_4$. Attempts to use chelation to promote the simultaneous coordination of ketones by two Lewis acids

Okba Saied, Benoit Bachand, and James D. Wuest

Abstract: Carbonyl oxygen atoms have two formal lone pairs of electrons. In principle, both can be used simultaneously to form complexes with two or more Lewis acids. This multiple coordination promises to have a variety of interesting consequences; unfortunately, however, complexes of carbonyl compounds with multiple Lewis acids are extremely rare. To promote multiple coordination, we have made a series of symmetric ketodiesters and related compounds in which the carbonyl group of a ketone is flanked by two additional sites of Lewis basicity. In such compounds, the flanking bases and both lone pairs of the central ketone are available for binding two equivalents of suitable Lewis acids, thereby producing symmetric double chelates in which the central ketone interacts with two Lewis acids at the same time. As expected, treatment of 3-oxoglutarates and 4-oxopimelates with $TiCl_4$ in a 1:1 ratio yielded unsymmetric single chelates in which the carbonyl groups of the ketone and one ester bind $TiCl_4$, while the other ester remains free. Unfortunately, treatment of the same ketodiesters with $TiCl_4$ in a 1:2 ratio did not produce the desired symmetric double chelates. Instead, 2:4 complexes were formed in which the free esters of the unsymmetric single chelates bind $TiCl_4$ in the normal way, without assistance from the keto group. We attribute this observation to the inherent reluctance of ketones to bind multiple Lewis acids, as well as to unfavorable Cl···Cl interactions created in the hypothetical double chelates by the simultaneous attachment of two octahedrally coordinated atoms of titanium to a single carbonyl oxygen atom.

Key words: Lewis acids, chelation, ketodiesters, $TiCl_4$.

Résumé : Les atomes d'oxygène des groupes carbonyles possèdent formellement deux paires d'électrons non partagés. En principe, chacune peut être utilisée simultanément pour former des complexes avec deux ou plusieurs acides de Lewis. Cette coordination multiple suggère la possibilité de plusieurs conséquences intéressantes; toutefois, malheureusement, les complexes des composés carbonylés avec divers acides de Lewis sont extrêmement rares. Dans le but de promouvoir des coordinations multiples, on a préparé une série de cétoesters et de composés apparentés symétriques dans lesquels le groupe carbonyle de la cétone est entouré de deux sites additionnels de basicité de Lewis. Dans de tels composés, les bases périphériques ainsi que les deux paires d'électrons non partagés de la cétone centrale sont toutes disponibles pour se lier à deux équivalents d'acides de Lewis appropriés conduisant à la formation de chélates doubles symétriques dans lesquels la cétone centrale interagit avec deux acides de Lewis en même temps. Tel que prévu, le traitement des 3-oxoglutarate et 4-oxopimélate avec du $TiCl_4$ dans un rapport 1 : 1 conduit à des chélates simples non symétriques dans lesquels les groupes carbonyles de la cétone et d'un ester sont liés au $TiCl_4$ alors que l'autre ester reste libre. Malheureusement, le traitement des mêmes cétodiesters avec le $TiCl_4$ dans un rapport de 1 : 2 ne conduit pas aux doubles chélates symétriques désirés. Il se forme plutôt des complexes 2 : 4 dans lesquels les esters libres des chélates simples non symétriques se lient au $TiCl_4$ de façon normale, sans l'aide du groupe cétonique. On attribue cette observation à la faible disposition des groupes cétoniques à se lier à plusieurs acides de Lewis ainsi qu'aux interactions Cl···Cl non favorables qui se créeraient dans les chélates doubles hypothétiques lors de la fixation simultanée de deux atomes de titane à coordination octaédrique sur un seul atome d'oxygène d'un carbonyle.

Mots clés : acides de Lewis, chélation, cétodiesters, $TiCl_4$.

[Traduit par la rédaction]

Received February 24, 1998.

O. Saied, B. Bachand,[1] and J.D. Wuest.[2] Département de chimie, Université de Montréal, Montréal, QC H3C 3J7, Canada.

[1] Fellow of the Natural Sciences and Engineering Research Council of Canada, 1986–1990. Fellow of the Ministère de l'Éducation du Québec, 1990–1991.

[2] Author to whom correspondence may be addressed. Telephone: (514) 343-6266. Fax: (514) 343-6281. E-mail: wuest@ere.umontreal.ca

Introduction

Carbonyl oxygen atoms have two formal lone pairs of electrons in sp^2 orbitals (1), and both are potentially available for interaction with Lewis acids. Simultaneous coordination of ketones by two or more Lewis acids is therefore plausible, although ketones are among the least basic carbonyl compounds (2). Such multiple coordination can be expected to have a variety of interesting consequences (3, 4). Of particular

© 1998 NRC Canada

importance to organic chemists is the possibility that ketones interacting with multiple Lewis acids may experience an unusually high degree of electrophilic activation (3, 4). Unfortunately, complexes of this type are extremely uncommon. No complexes in which simple ketones interact *inter*molecularly with multiple Lewis acids are known, although related structures involving carbonyl compounds more basic than ketones have been characterized (3). In addition, we have established that the carbonyl oxygen atom of relatively simple ketones can form complexes **1** by interacting *intra*molecularly with two nearby sites of Lewis acidity when they are held by covalent

1 **2**

(LA = Lewis acid, LB = Lewis base)

bonds in a suitable orientation (5). As expected, this double coordination has marked effects on the geometry, spectroscopic properties, and reactivity of the bound carbonyl group (3–5). An even more ambitious objective is to construct related doubly coordinated complexes **2** in which the carbonyl group is flanked by two nearby sites of Lewis acidity that are held in place only by relatively weak dative bonds involving adjacent sites of Lewis basicity (6). In such complexes, the carbonyl oxygen atom of the central ketone uses both of its lone pairs in order to participate in the simultaneous formation of two chelates. Chelation is thereby used to promote the simultaneous coordination of the ketone by two Lewis acids. In this paper, we describe our efforts to prepare novel complexes of this type by treating selected ketodiesters and related compounds with $TiCl_4$.

Results and discussion

Transesterification of diethyl 4-ketopimelate provided the corresponding diphenethyl ester **3**, which forms complexes with $TiCl_4$ that proved to be soluble enough in CH_2Cl_2 to permit their ^1H and ^{13}C NMR spectra to be recorded at low temperatures. The carbonyl region of the ^{13}C NMR spectrum of ketodiester **3** ($CDCl_3$, 25°C) showed two peaks at δ 172.4 and

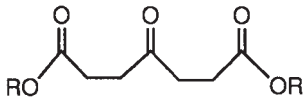

3 (R = CH_2CH_2Ph)

206.7, which can be assigned to the carbonyl carbon atoms of the ester and the ketone, respectively. In the ^{13}C NMR spectrum of a solution prepared by mixing ketodiester **3** and $TiCl_4$ in a 1:1 ratio (0.50 M in CD_2Cl_2, 25°C), the corresponding peaks appeared at δ 177.7 and 222.2. The pronounced downfield shifts indicate that complexation occurs, as expected, and that the ester and ketone groups must both participate. A similar spectrum recorded at –85°C revealed a total of 19 peaks, including 3 in the carbonyl region at δ 171.6, 180.9, and 225.2.

Fig. 1. The carbonyl region of the low-temperature ^{13}C NMR spectrum of a solution prepared by mixing ketodiester **3** and $TiCl_4$ in a 1:2 ratio (0.060 M in CD_2Cl_2, –65°C).

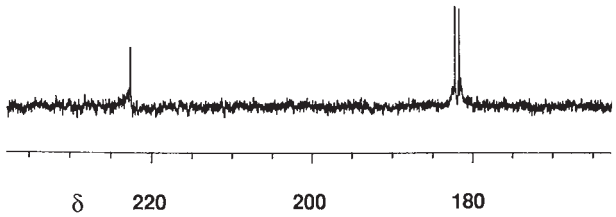

Together, these observations demonstrate that solutions prepared from equimolar amounts of ketodiester **3** and $TiCl_4$ must contain primarily a single 1:1 complex; moreover, the complex must be the unsymmetric chelate **4**, in which the carbonyl groups of the ketone and one ester are bound to $TiCl_4$ and their carbonyl carbon atoms are shifted downfield, while the other ester remains free and essentially unshifted. Analogous chelates of simple dicarbonyl compounds are well known (7).

[1]

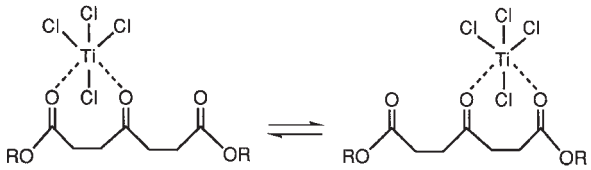

4 (R = CH_2CH_2Ph)

Symmetrization of the complex (eq. [1]) is sufficiently rapid at 25°C that the two esters can no longer be distinguished by ^{13}C NMR spectroscopy.

We hoped that the ^1H and ^{13}C NMR spectra of solutions prepared by mixing ketodiester **3** and $TiCl_4$ in a 1:2 ratio would provide evidence for the formation of the symmetric double chelate **5**. In fact, the carbonyl region of the ^{13}C NMR spectrum (0.33 M in CD_2Cl_2, 25°C) showed two peaks at δ 180.4 and 223.2, which are both farther downfield than those observed in the spectrum of the 1:1 mixture under similar conditions (δ 177.7 and 222.2). The relatively large downfield shift of the upfield carbonyl carbon atom (Δδ 2.7) indicates that both ester groups must now be bound to $TiCl_4$; however, the

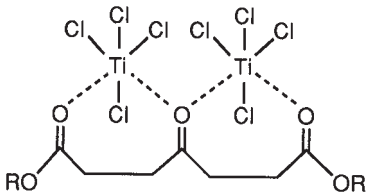

5 (R = CH_2CH_2Ph)

downfield shift of the ketonic carbonyl carbon atom (Δδ 1.0) appears to be too small to be consistent with the formation of the desired symmetric double chelate **5**. Furthermore, a similar spectrum recorded at –65°C revealed three peaks in the carbonyl region at δ 181.5, 182.0, and 222.4 (Fig. 1). This confirms that addition of an equimolar amount of $TiCl_4$ to the unsymmetric single chelate **4** under these conditions does not produce the symmetric double chelate **5**. Instead, we propose that the free ester group of unsymmetric chelate **4** behaves in

© 1998 NRC Canada

Fig. 2. ORTEP view of the structure of complex **6a**, which is obtained when ketodiester **3** and $TiCl_4$ are mixed in CH_2Cl_2 in a 1:2 ratio. Non-hydrogen atoms are represented by ellipsoids corresponding to 40% probability, and hydrogen atoms are shown as spheres of arbitrary size. All bonds to titanium are drawn using solid lines. Included CH_2Cl_2 is not shown.

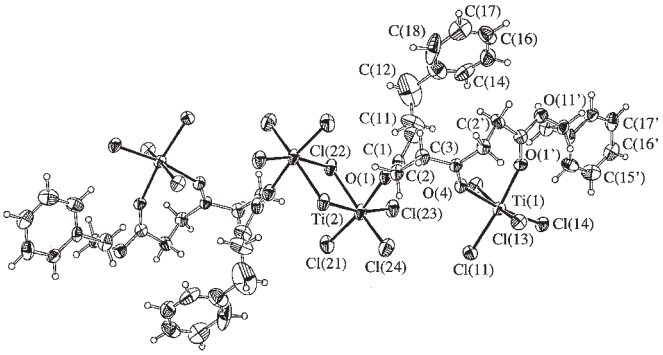

Table 1. Crystallographic data for the CH_2Cl_2 solvate of the 2:4 adduct **6a** of bis(2-phenylethyl) 4-oxoheptanedioate (**3**) and $TiCl_4$.

Formula	$C_{46}H_{52}Cl_{16}O_{10}Ti_4 \cdot CH_2Cl_2$
fw	1608.60
System	Triclinic
Space group	$P\bar{1}$
Cell constants	
a, Å	7.982(2)
b, Å	9.264(4)
c, Å	22.362(11)
α, deg	86.26(4)
β, deg	86.13(3)
γ, deg	80.73(3)
Cell volume, Å^3	1625.8(11)
Z	1
T, K	205
D_{calcd}, g cm^{-3}	1.643
μ_{calcd}, mm^{-1}	11.50
Radiation (λ, Å)	Graphite-monochromated, Cu Kα (1.54056)
Cryst. dimens., mm	0.78 × 0.33 × 0.21
Data collect. range	±*h*, ±*k*, +*l*
No. of reflcns. collectd.	12 119
No. of reflcns. refined	6164
Goodness-of-fit	0.965
*R*1	0.1136
w*R*2	0.2804
$\Delta\rho_{max}$, e Å^{-3}	1.571
$\Delta\rho_{min}$, e Å^{-3}	–1.185

the conventional way and binds $TiCl_4$ without assistance from the keto group, thereby forming a chloride-bridged complex

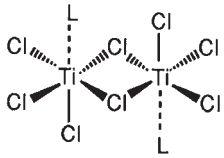

6a (L = **4**, bound by free ester)

6b (L = **16**, bound by free ester)

Table 2. Selected bond lengths and angles for the CH_2Cl_2 solvate of the 2:4 adduct **6a** of bis(2-phenylethyl) 4-oxoheptanedioate (**3**) and $TiCl_4$.

Bond lengths (Å)	
Ti(1)—O(1′)	2.076(6)
Ti(1)—O(4)	2.141(6)
Ti(2)—O(1)	2.050(7)
Ti(1)—Cl(11)	2.226(3)
Ti(1)—Cl(12)	2.289(3)
Ti(1)—Cl(13)	2.285(3)
Ti(1)—Cl(14)	2.225(3)
Ti(2)—Cl(21)	2.205(3)
Ti(2)—Cl(22)[a]	2.450(3)
Ti(2)[a]—Cl(22)	2.450(3)
Ti(2)—Cl(23)	2.217(3)
Ti(2)—Cl(24)	2.203(4)
O(1)—C(1)	1.231(11)
O(1′)—C(1′)	1.206(11)
O(4)—C(4)	1.242(10)
Bond angles (deg)	
O(1′)-Ti(1)-O(4)	82.4(2)
O(1′)-Ti(1)-Cl(11)	172.0(2)
O(1′)-Ti(1)-Cl(12)	84.8(2)
O(1′)-Ti(1)-Cl(13)	86.9(2)
O(1′)-Ti(1)-Cl(14)	88.9(2)
O(4)-Ti(1)-Cl(11)	89.6(2)
O(4)-Ti(1)-Cl(12)	82.6(2)
O(4)-Ti(1)-Cl(13)	85.5(2)
O(4)-Ti(1)-Cl(14)	171.2(2)
Cl(11)-Ti(1)-Cl(12)	93.7(1)
Cl(11)-Ti(1)-Cl(13)	93.0(1)
Cl(11)-Ti(1)-Cl(14)	99.1(1)
Cl(12)-Ti(1)-Cl(13)	166.4(1)
Cl(12)-Ti(1)-Cl(14)	95.4(1)
Cl(13)-Ti(1)-Cl(14)	95.3(1)
O(1)-Ti(2)-Cl(21)	169.9(2)
O(1)-Ti(2)-Cl(22)[a]	83.5(2)
O(1)-Ti(2)-Cl(23)	87.4(2)
O(1)-Ti(2)-Cl(24)	91.1(2)
Cl(21)-Ti(2)-Cl(22)[a]	90.0(1)
Cl(21)-Ti(2)-Cl(23)	97.5(1)
Cl(21)-Ti(2)-Cl(24)	96.7(2)
Cl(22)[a]-Ti(2)-Cl(23)	165.9(2)
Cl(22)[a]-Ti(2)-Cl(24)	91.4(1)
Cl(23)-Ti(2)-Cl(24)	99.4(1)
Ti(1)-O(1′)-C(1′)	152.4(6)
Ti(1)-O(4)-C(4)	140.3(6)
Ti(2)-O(1)-C(1)	153.2(8)
Dihedral angles (deg)	
Ti(1)-O(1′)-C(1′)-C(2′)	23.0(20)
Ti(1)-O(4)-C(4)-C(3′)	2.0(20)
Ti(2)-O(1)-C(1)-C(2)	–6.0(20)

[a] –*x*, –*y*, –*z* + 1.

6a of stoichiometry 2 **3**·4 $TiCl_4$. This hypothesis is reasonable because a wide range of simple esters are known to form structurally analogous chloride-bridged 2:2 complexes with $TiCl_4$ (8).

Direct confirmation was provided by an X-ray crystallographic study of crystals of a CH_2Cl_2 solvate of complex **6a**,

© 1998 NRC Canada

Scheme 1.

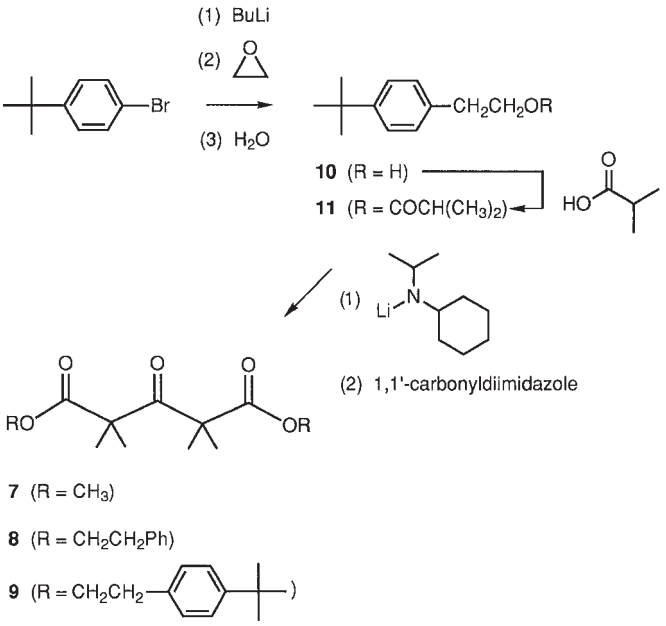

which were obtained by allowing pentane to diffuse into a solution prepared by mixing ketodiester **3** and $TiCl_4$ in CH_2Cl_2 in a 1:2 ratio. The results of this study are summarized in Fig. 2 and in Tables 1 and 2. Most of the observed bond lengths and angles are similar to those found in related structures (7, 8). For example, normal values are observed for the average lengths of Ti(1)—Cl bonds *trans* to the chelating oxygen atoms (2.226(3) Å), Ti(1)—Cl bonds *cis* to the chelating oxygen atoms (2.287(3) Å), terminal Ti(2)—Cl bonds (2.208(3) Å), bridging Ti(2)—Cl bonds (2.450(3) Å), Ti(1)···O bonds to the carbonyl groups of the chelating ester (2.076(6) Å) and ketone (2.141(6) Å), Ti(2)···O bond to the carbonyl group of the non-chelating ester (2.050(7) Å), and C = O bonds of the chelating ester (1.206(11) Å), ketone (1.242(10) Å), and non-chelating ester (1.231(11) Å). Typically large values are observed for the carbonyl C=O···Ti(1) angles involving the chelating ester (152.4(6)°) and the ketone (140.3(6)°), as well as for the carbonyl C=O···Ti(2) angles involving the non-chelating ester (153.2(8)°). In addition, both atoms of titanium have approximate octahedral coordination. As expected, the dihedral angles Ti(1)···O(4)-C(4)-C(3′) (2.0(20)°) and Ti(2)···O(1)-C(1)-C(2) (–6.0(20)°) are small, indicating that normal $\eta^1(\sigma)$ complexation is favored by the ketone and the non-chelating ester, with Ti lying close to the carbonyl plane. However, an unusual value is observed for the dihedral angle Ti(1)···O(1′)-C(1′)-C(2′) involving the chelating ester (23.0(20)°), which reveals that Ti(1) lies far from the carbonyl plane and that the interaction must therefore have important π character (9).

In principle, the conversion of 2:4 complex **6a** into two equivalents of symmetric double chelate **5** is entropically favorable and should be favored by dilution. Even at the lowest concentrations that could be studied, however, low-temperature ^{13}C NMR spectra of solutions prepared by mixing ketodiester **3** and $TiCl_4$ in a 1:2 ratio provided no evidence for the formation of symmetric double chelate **5**.

We reasoned that hypothetical structure **5** and other double chelates derived from 4-ketopimelates might be disfavored because they contain two seven-membered rings, so we also examined the interaction of representative 3-ketoglutarates with $TiCl_4$. Neither dimethyl 2,2,4,4-tetramethyl-3-oxopentanedioate (**7**) (10) nor the corresponding diphenethyl ester **8** formed complexes with $TiCl_4$ that were sufficiently soluble in CH_2Cl_2 at low temperatures, so we prepared derivative **9** by the route summarized in Scheme 1.[3] Lithiation of 1-bromo-4-(1,1-dimethylethyl)benzene, followed by the addition of excess ethylene oxide and then water, provided 4-(1,1-dimethylethyl)benzeneethanol (**10**) in 77% yield. Subsequent esterification then gave the corresponding 2-methylpropanoate **11** in 88% yield. Deprotonation of ester **11**, followed by treatment of the resulting enolate with 1,1′-carbonyldiimidazole, finally provided the required 3-ketoglutarate **9** in 43% yield.

Fig. 3. The carbonyl region of the low-temperature ^{13}C NMR spectrum of a solution prepared by mixing ketodiester **9** and $TiCl_4$ in a 1:1 ratio (0.064 M in CD_2Cl_2, –85°C).

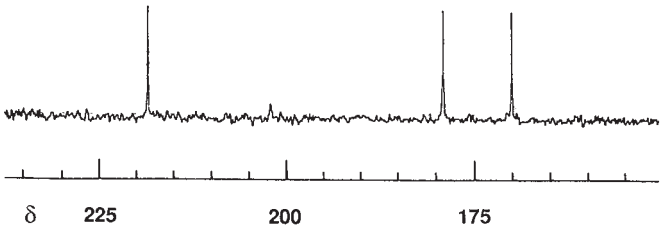

The carbonyl region of the ^{13}C NMR spectrum of compound **9** (CD_2Cl_2, 25°C) showed two peaks at δ 173.6 and 205.4, which correspond to the carbonyl carbon atoms of the ester and the ketone, respectively. As expected, the low-temperature ^{13}C NMR spectrum of a solution prepared by mixing ketodiester **9** and $TiCl_4$ in a 1:1 ratio (0.064 M in CD_2Cl_2, –85°C) contained three peaks in the carbonyl region at δ 170.2, 179.1, and 218.6 (Fig. 3). This provides strong evidence for the formation of the unsymmetric single chelate **12**. Low-temperature spectra of solutions prepared by mixing ketodiester **9** and $TiCl_4$ in a 1:2 ratio were also recorded, but peaks in the carbonyl region remained too broad to permit detailed analysis; however, no conspicuous downfield shift of the carbonyl

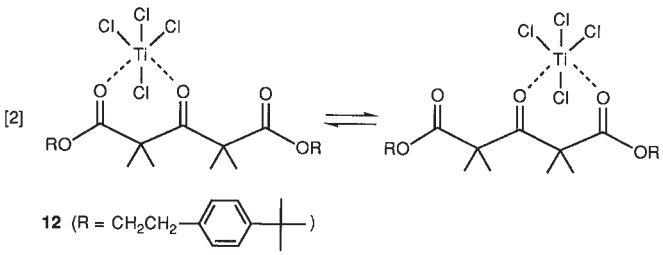

carbon atom of the ketone was observed, so we doubt that symmetric double chelate **13** is the principal product.

Although the two ester groups of unsymmetric single chelate **12** can be distinguished by ^{13}C NMR spectroscopy at –85°C, symmetrization is nevertheless rapid (eq. [2]). Variable-temperature ^{13}C NMR spectroscopy established that coalescence of the ester peaks occurred at T_c = –35°C, enabling

[3] This synthesis resembles the one previously used to make dimethyl 2,2,4,4-tetramethyl-3-oxopentanedioate (**7**) (10).

© 1998 NRC Canada

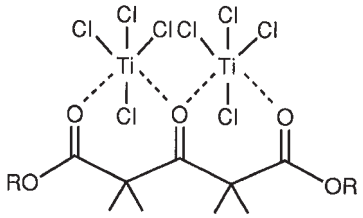

13 (R = CH_2CH_2–C$_6$H$_4$–C(CH$_3$)$_3$)

us to estimate that $\Delta G^{\ddagger} = 10.2 \pm 0.2$ kcal mol^{-1} for the symmetrization of single chelate **12** (11). In principle, this process can occur by three distinct mechanisms: (*i*) intermolecular or intramolecular attack of the free ester on chelated $TiCl_4$, with displacement of the other ester; (*ii*) complete dissociation of $TiCl_4$, followed by reassociation; or (*iii*) partial dissociation to form the ketone complex **14**, followed by rapid *syn–anti* isomerization (12) and reassociation. Because exchange in complexes of $TiCl_4$ normally occurs by dissociation (12), mechanisms (*ii*) and (*iii*) are more probable. Furthermore, the

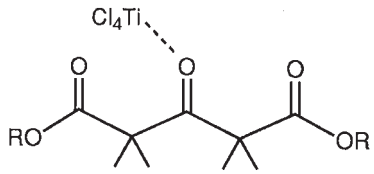

14 (R = CH_2CH_2–C$_6$H$_4$–C(CH$_3$)$_3$)

observed $\Delta G^{\ddagger}$ is closely similar to those measured for loss of a single ligand from 1:2 complexes of simple carbonyl compounds with $TiCl_4$ (12). As a result, we propose that the symmetrizations of unsymmetric single chelates **4** and **12** both occur by dissociation of the bound ester and reassociation of the free ester.

The absence of the desired double chelates **5** and **13** is noteworthy, because previous experimental and theoretical studies have suggested that the simultaneous coordination of simple ketones by two Lewis acids is enthalpically feasible (3, 5, 13, and footnote 4). Two factors may account for our failure to observe double chelates derived from 4-ketopimelates and 3-ketoglutarates:

1. Simple ketones are inherently reluctant to form complexes with multiple Lewis acids, so the formation of double chelates by the addition of $TiCl_4$ to unsymmetric single chelates **4** and **12** may not be sufficiently exothermic to compete with the formation of 2:4 complexes such as structure **6a**, even at low concentrations; moreover, ΔS for the formation of double chelates **5** and **13** is made particularly unfavorable by the conformational mobility of ketodiesters **3** and **9**.

2. Careful examination of the octahedral coordination geometry of Ti in complex **6a** and other simple chelates of $TiCl_4$ (7) reveals that hypothetical double chelates **5** and **13** are likely to be destabilized by nonbonded Cl···Cl interactions created when a single carbonyl oxygen atom binds two molecules of $TiCl_4$ at the same time.

[4] P. Deschatelets and J.D. Wuest. Unpublished results.

Fig. 4. The carbonyl region of the ^{13}C NMR spectrum of (*a*) a solution of pure bicyclic ketodiester **15** (CD_2Cl_2, 25°C); (*b*) a solution prepared by mixing ketodiester **15** with $TiCl_4$ in a 1:1 ratio (0.050 M in CD_2Cl_2, –85°C); and (*c*) a solution prepared by mixing ketodiester **15** with $TiCl_4$ in a 1:2 ratio (0.050 M in CD_2Cl_2, –85°C).

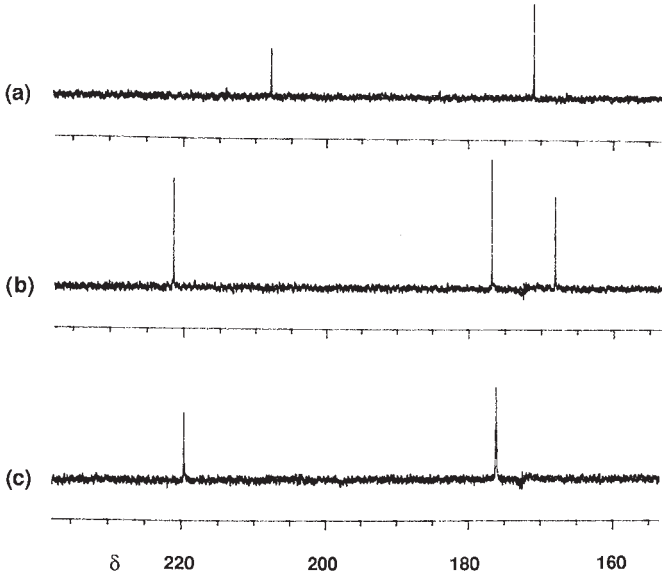

To evaluate the importance of conformational mobility, we decided to study the interaction of $TiCl_4$ with bicyclic 3-ketoglutarate **15**, which is a more rigid analogue of ketodiesters **7**–**9**. Compound **15** could be made in a single step in 34% yield by treating diethyl 3-ketoglutarate with two equivalents of 3-chloro-2-(chloromethyl)-1-propene in refluxing toluene in the presence of K_2CO_3 and catalytic amounts of $(PPh_3)_2PdCl_2$ (14). The carbonyl region of the ^{13}C NMR spectrum of bicyclic

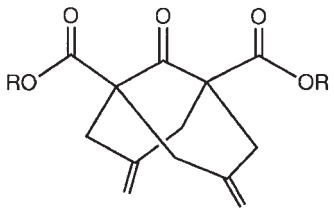

15 (R = CH_2CH_3)

ketodiester **15** (CD_2Cl_2, 25°C) showed two peaks at δ 170.7 and 207.6, which correspond to the carbonyl carbon atoms of the ester and the ketone, respectively (Fig. 4*a*). In the low-temperature ^{13}C NMR spectrum of a solution prepared by mixing bicyclic ketodiester **15** and $TiCl_4$ in a 1:1 ratio (0.050 M in CD_2Cl_2, –85°C), a total of 13 peaks appeared as anticipated, including 3 in the carbonyl region at δ 167.9, 176.6, and 221.2 (Fig. 4*b*). This provides strong evidence for the formation of the expected unsymmetric single chelate **16**. A similar low-temperature spectrum of a solution prepared by mixing bicyclic ketodiester **15** and $TiCl_4$ in a 1:2 ratio (0.050 M in CD_2Cl_2, –85°C) also consisted of 13 peaks, including 3 at δ 175.8, 175.9, and 219.3 (Fig. 4*c*). We conclude that the behavior of bicyclic ketodiester **15** resembles that of its more flexible analogues **3** and **9**, and that detectible amounts of symmetric

© 1998 NRC Canada

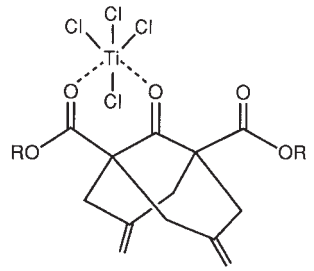

16 (R = CH_2CH_3)

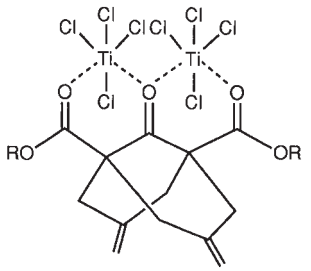

17 (R = CH_2CH_3)

double chelate **17** are not formed when compound **15** and $TiCl_4$ are mixed in a 1:2 ratio, even at the lowest accessible concentrations. Instead, the principal product must again be a 2:4 complex, presumably structure **6b**.

In a final effort to exploit the double chelation of $TiCl_4$ to promote the simultaneous coordination of a ketone by two Lewis acids, we decided to replace ketodiesters by analogues in which the ketone is flanked by stronger Lewis bases (2). In bicyclic ketone **18**, for example, the carbonyl group is flanked by two pyridines, and we hoped that strong binding of $TiCl_4$ by the pyridines would favor formation of the double chelate **19** by helping compensate for the weakly exothermic double coordination of the central carbonyl group. Compound **18** could be prepared conveniently in one step in 21% yield by treating 1,3-bis(2-pyridyl)-2-propanone (15) with 2-methylene-1,3-propanediol diacetate (16) in refluxing toluene in the presence of K_2CO_3 and catalytic amounts of $Pd(OOCCH_3)_2$ and PPh_3. The carbonyl region of the ^{13}C NMR spectrum of bicyclic dipyridylketone **18** ($CDCl_3$, 25°C) showed a single peak at δ 213.0. Unfortunately, complexes of compound **18** with $TiCl_4$ were not soluble enough in CD_2Cl_2 to allow their ^1H and ^{13}C NMR spectra to be recorded conveniently at low temperatures. However, in the ^{13}C NMR spectrum of a solution prepared by mixing bicyclic dipyridylketone **18** and $TiCl_4$ in a 1:2 ratio (0.17 M in $CDCl_3$, 25°C), the carbonyl peak appeared at δ 225.9, which corresponds to a downfield shift of Δδ 12.9. Because our previous experiments show

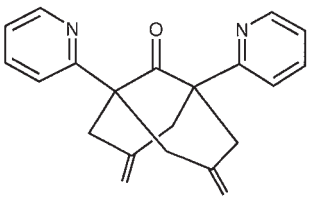

18

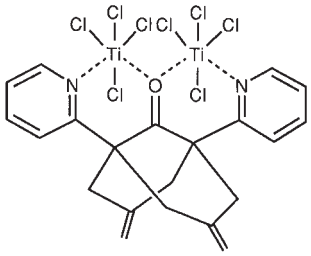

19

that similar shifts are characteristic of single chelates, we conclude that bicyclic dipyridylketone **18** resembles ketodiesters **3**, **9**, and **15** and does not yield significant amounts of a symmetric double chelate with $TiCl_4$.

Conclusions

In principle, compounds in which the carbonyl group of a simple ketone is flanked by two nearby sites of Lewis basicity are well designed to form symmetric double chelates **2**. In these hypothetical chelates, the oxygen atom of the central carbonyl group uses both of its lone pairs to bind two Lewis acids simultaneously. Unfortunately, persistent efforts to prepare such double chelates by treating ketodiesters and related compounds with two equivalents of $TiCl_4$ were unsuccessful. These instructive failures presumably result from the inherent reluctance of simple ketones to form complexes with multiple Lewis acids and from unfavorable Cl···Cl interactions that are created in the hypothetical double chelates by the simultaneous attachment of two octahedrally coordinated atoms of titanium to a single carbonyl oxygen atom. We are optimistic that double chelates can be formed when these destabilizing interactions are not present, and we are now studying the complexation of ketodiesters and related compounds with strong Lewis acids that favor non-octahedral coordination.

Experimental section

Ether and tetrahydrofuran (THF) were dried by distillation from the sodium ketyl of benzophenone, CH_2Cl_2 was dried by distillation from P_2O_5, *N*-isopropylcyclohexylamine was dried by distillation from CaH_2, ethylene oxide was dried by passage over anhydrous $CaSO_4$, and toluene was dried by distillation from sodium. $TiCl_4$ was purified by distillation, and 1,3-bis(2-pyridyl)-2-propanone (15), 2-methylene-1,3-propanediol diacetate (16), and $PdCl_2(PPh_3)_2$ (17) were made by published procedures. Other reagents were commercial products that were used without further purification. Flash chromatography was performed in the normal way (18).

Bis(2-phenylethyl) 4-oxoheptanedioate (3)

A solution of diethyl 4-oxo-heptanedioate (2.00 g, 8.69 mmol) and excess 2-phenylethanol (6.34 g, 51.9 mmol) in toluene (15 mL) was treated with a catalytic amount of concentrated H_2SO_4 (85 mg, 0.87 mmol), and the mixture was heated at reflux for 5 h in an apparatus equipped with a Dean–Stark trap. Saturated aqueous $NaHCO_3$ (100 mL) was then added, and the mixture was extracted with ether. Volatiles were removed from the combined extracts by evaporation under reduced pressure, and the residue was purified by flash chromatography (silica, toluene (80%) – ether (20%)). This yielded colorless crystals of bis(2-phenylethyl) 4-oxoheptanedioate (**3**; 3.25 g, 8.50 mmol, 98%): mp 37–38°C; IR (melt): 1735, 1714 cm^{-1}; ^1H NMR (300 MHz, $CDCl_3$) δ: 2.59 (t, 4H, ^3J = 6.7 Hz), 2.73 (t, 4H, ^3J = 6.7 Hz), 2.95 (t, 4H, ^3J = 7.1 Hz), 4.30 (t, 4H, ^3J = 7.1 Hz), 7.21–7.32 (m, 10H); ^{13}C NMR (75.4 MHz, $CDCl_3$) δ: 27.9, 35.0, 36.9, 65.0, 126.5, 128.4, 128.8, 137.7, 172.4, 206.7; HRMS (FAB) calcd. for $C_{23}H_{26}O_5$ + H, *m/e:* 383.1859; found, *m/e*: 383.1840. Anal. calcd. for $C_{23}H_{26}O_5$: C 72.23, H 6.85; found: C 72.52, H 6.88.

2:4 Adduct 6a of bis(2-phenylethyl) 4-oxoheptanedioate (3) and $TiCl_4$

A solution of ketodiester **3** (37.5 mg, 0.0981 mmol) in CH_2Cl_2 was stirred at 25°C under dry N_2 and treated dropwise with $TiCl_4$ (37.2 mg, 0.196 mmol). A supernatant layer of pentane (0.5 mL) was carefully added and allowed to diffuse slowly into the lower phase. This yielded yellow-orange crystals of adduct **6a** as a 1:1 CH_2Cl_2 solvate (67.2 mg, 0.0418 mmol, 85%).

© 1998 NRC Canada

X-ray crystallographic study of the CH_2Cl_2 solvate of the 2:4 adduct 6a of bis(2-phenylethyl) 4-oxoheptanedioate (3) and $TiCl_4$

Data were collected on an Enraf–Nonius CAD-4 diffractometer. Cell constants were obtained using 25 well-centered reflections ($20° \leq \theta \leq 25°$). Five standard reflections were measured every 1 h of exposure time and showed only small fluctuations. The data were corrected for absorption by Gaussian integration. The structure was solved by direct methods using SHELXS-85 (19). Full-matrix least-squares refinement on F^2 was carried out with SHELXL-93 (20). All non-hydrogen atoms were refined anisotropically. Hydrogen atoms were placed in ideal positions and refined using a riding model with isotropic thermal parameters 1.2 times those of their carrier atoms. A detailed description of the structure determination and tables of atomic coordinates and isotropic thermal parameters, complete bond lengths and angles, anisotropic thermal parameters, hydrogen atom coordinates and thermal parameters, and distances to weighted least-squares planes are available as supplementary material.[5]

4-(1,1-Dimethylethyl)benzeneethanol (10)

A solution of 1-bromo-4-(1,1-dimethylethyl)benzene (2.46 g, 11.5 mmol) in ether (40 mL) was stirred at 0°C under dry N_2 and treated dropwise with a solution of BuLi (7.40 mL, 1.55 M in hexane, 11.5 mmol). The solution was kept at 0°C for 1 h, and then a solution of ethylene oxide (3.6 g, 82 mmol) in ether (10 mL) was added dropwise. The resulting mixture was stirred at 0°C for 2 h, treated with water, and extracted with ether. Volatiles were removed from the combined extracts by evaporation under reduced pressure, and the residue was purified by flash chromatography (silica, hexane (85%) – ethyl acetate (15%)). This yielded 4-(1,1-dimethylethyl)benzeneethanol (**10**; 1.57 g, 8.81 mmol, 77%) as a colorless oil: IR (liquid film): 3330 (br) cm^{-1}; ^1H NMR (300 MHz, $CDCl_3$) δ: 1.32 (s, 9H), 1.43 (s, 1H), 2.85 (t, 2H, ^3J = 6.6 Hz), 3.87 (t, 2H, ^3J = 6.6 Hz), 7.18 (d, 2H, ^3J = 8.2 Hz), 7.35 (d, 2H, ^3J = 8.2 Hz); ^{13}C NMR (75.4 MHz, $CDCl_3$) δ: 31.3, 34.4, 38.6, 63.6, 125.5, 128.7, 135.3, 149.3; HRMS (EI) calcd. for $C_{12}H_{18}O$, *m/e:* 173.1358; found, *m/e:* 173.1355.

2-[4-(1,1-Dimethylethyl)phenyl]ethyl 2-methylpropanoate (11)

A solution of 4-(1,1-dimethylethyl)benzeneethanol (**10**; 1.03 g, 5.78 mmol) and 2-methylpropanoic acid (0.52 g, 5.9 mmol) in benzene (10 mL) was treated with a catalytic amount of (1*S*)-10-camphorsulfonic acid (30 mg, 0.13 mmol), and the mixture was heated at reflux for 12 h in an apparatus equipped with a Dean–Stark trap. Saturated aqueous $NaHCO_3$ (10 mL) was then added, and the mixture was extracted with ether. Volatiles were removed from the combined extracts by evaporation under reduced pressure, and the residue was purified by distillation (100°C/0.3 Torr; 1 Torr = 133.3 Pa) to give 2-[4-(1,1-dimethylethyl)phenyl]ethyl 2-methylpropanoate (**11**; 1.27 g, 5.11 mmol, 88%) as a colorless liquid: IR (film): 1731 cm^{-1}; ^1H NMR (300 MHz, $CDCl_3$) δ: 1.14 (d, 6H, ^3J = 7.0 Hz), 1.31 (s, 9H), 2.53 (septuplet, 1H, ^3J = 7.0 Hz), 2.91 (t, 2H, ^3J = 7.1 Hz), 4.27 (t, 2H, ^3J = 7.1 Hz), 7.16 (d, 2H, ^3J = 8.2 Hz), 7.33 (d, 2H, ^3J = 8.2 Hz); ^{13}C NMR (75.4 MHz, $CDCl_3$) δ: 18.9, 31.3, 34.0, 34.4, 34.6, 64.7, 125.3, 128.6, 134.8, 149.3, 177.0; HRMS (EI) calcd. for $C_{16}H_{24}O_2$, *m/e:* 248.1776; found, *m/e:* 248.1756.

Bis{2-[4-(1,1-Dimethylethyl)phenyl]ethyl} 2,2,4,4-tetramethyl-3-oxopentanedioate (9)

A solution of *N*-isopropylcyclohexylamine (1.13 g, 8.00 mmol) in THF (10 mL) was stirred at –78°C under dry N_2 and treated dropwise with a solution of BuLi (5.3 mL, 1.5 M in hexane, 8.0 mmol). The solution was kept at –78°C for 40 min, and then a solution of 2-[4-(1,1-dimethylethyl)phenyl]ethyl 2-methylpropanoate (**11**; 1.98 g, 7.97 mmol) in THF (10 mL) was added dropwise. The resulting solution was kept at –78°C for 30 min and was then added dropwise to a stirred solution of 1,1′-carbonyldiimidazole (0.630 g, 3.89 mmol) in THF (10 mL) at 25°C. The mixture was kept at 25°C for 12 h, treated with water, and extracted with ether. Volatiles were removed from the combined extracts by evaporation under reduced pressure, and the residue was purified by flash chromatography (silica, hexane (95%) – ethyl acetate (5%)) to give bis{2-[4-(1,1-dimethylethyl)-phenyl]ethyl} 2,2,4,4-tetramethyl-3-oxopentanedioate (**9**; 0.882 g, 1.69 mmol, 43%) as a colorless solid. An analytically pure sample was prepared by recrystallization from hexane: mp 95–97°C; IR (melt): 1740, 1730, 1710 cm^{-1}; ^1H NMR (300 MHz, $CDCl_3$) δ: 1.24 (s, 12H), 1.29 (s, 18H), 2.87 (t, 4H, ^3J = 6.9 Hz), 4.25 (t, 4H, ^3J = 6.9 Hz), 7.11 (d, 4H, ^3J = 8.2 Hz), 7.31 (d, 4H, ^3J = 8.2 Hz); ^{13}C NMR (75.4 MHz, $CDCl_3$) δ: 23.4, 31.3, 34.2, 34.3, 55.1, 65.8, 125.4, 128.5, 134.3, 149.4, 173.3, 205.1; HRMS (FAB) calcd. for $C_{33}H_{46}O_5$ + H, *m/e:* 523.3423; found, *m/e:* 523.3465.

Diethyl 3,7-dimethylene-9-oxobicyclo[3.3.1]nonane-1,5-dicarboxylate (15)

A mixture of diethyl 3-ketoglutarate (5.04 g, 24.9 mmol), 3-chloro-2-(chloromethyl)-1-propene (6.91 g, 55.3 mmol), K_2CO_3 (15.2 g, 110 mmol), and $PdCl_2(PPh_3)_2$ (1.75 g, 2.49 mmol) in toluene (18 mL) was stirred at reflux for 36 h. The mixture was then cooled to 25°C and filtered, and volatiles were removed from the filtrate by evaporation under reduced pressure. The residue was purified by flash chromatography (silica, hexane (85%) – ethyl acetate (15%)) to give colorless crystals of diethyl 3,7-dimethylene-9-oxobicyclo-[3.3.1]nonane-1,5-dicarboxylate (**15**; 2.60 g, 8.49 mmol, 34%): mp 48–49°C; IR (melt): 1735, 1713, 1652 cm^{-1}; ^1H NMR (300 MHz, $CDCl_3$) δ: 1.29 (t, 6H, ^3J = 7.1 Hz), 2.76 (d, 4H, ^2J = 15.4 Hz), 3.33 (d, 4H, ^2J = 15.4 Hz), 4.26 (q, 4H, ^3J = 7.1 Hz), 4.87 (t, 4H, ^4J = 2.2 Hz); ^{13}C NMR (75.4 MHz, $CDCl_3$) δ: 14.1, 44.0, 56.9, 61.6, 115.0, 138.7, 170.5, 206.9; HRMS (FAB) calcd. for $C_{17}H_{22}O_5$ + H, *m/e:* 307.1545; found, *m/e:* 307.1546. Anal. calcd. for $C_{17}H_{22}O_5$: C 66.65, H 7.24; found: C 66.35, H 7.28.

[5] Copies of material on deposit may be purchased from: The Depository of Unpublished Data, Document Delivery, CISTI, National Research Council Canada, Ottawa, Canada K1A 0S2. In addition, the authors have deposited X-ray crystallographic data, a description of the structure determination, and tables of atomic coordinates and isotropic thermal parameters, bond lengths and angles, anisotropic thermal parameters, and refined and calculated hydrogen atom coordinates with the Cambridge Crystallographic Data Centre. These data can be obtained, on request, from the Director, Cambridge Crystallographic Data Centre, 12 Union Road, Cambridge CB2 1EZ, U.K.

© 1998 NRC Canada

3,7-Dimethylene-1,5-bis(2-pyridyl)bicyclo[3.3.1]nonan-9-one (18)

A suspension of $Pd(OOCCH_3)_2$ (0.106 g, 0.472 mmol) and PPh_3 (0.493 g, 1.88 mmol) in toluene (25 mL) was stirred at 25°C for 30 min, and then a solution of 2-methylene-1,3-propanediol diacetate (3.57 g, 20.7 mmol) in toluene (20 mL) was added, followed by a suspension of 1,3-bis(2-pyridyl)-2-propanone (2.00 g, 9.42 mmol) and K_2CO_3 (7.82 g, 56.6 mmol) in toluene (10 mL). The resulting mixture was stirred at reflux for 45 h, cooled to 25°C, and filtered. Volatiles were removed from the filtrate by evaporation under reduced pressure, and the residue was purified by flash chromatography (silica, hexane (70%) – ethyl acetate (30%)) to give a mixture of 3,7-dimethylene-1,5-bis(2-pyridyl)bicyclo[3.3.1]-nonan-9-one (**18**) and the corresponding hydrate. Dehydration was achieved by dissolving the crude product in chlorobenzene (60 mL) and removing water by azeotropic distillation (21). This provided bicyclic dipyridylketone **18** (0.621 g, 1.96 mmol, 21%) as a tan solid. Recrystallization from hexane provided an analytically pure sample: mp 115–116°C; IR (melt): 1712, 1646 cm^{-1}; ^1H NMR (300 MHz, $CDCl_3$) δ: 3.11 (d, 4H, ^2J = 15.3 Hz), 3.46 (d, 4H, ^2J = 15.3 Hz), 4.96 (t, 4H, ^4J = 2.1 Hz), 7.16 (m, 2H), 7.37 (m, 2H), 7.65 (m, 2H), 8.60 (m, 2H); ^{13}C NMR (75.4 MHz, $CDCl_3$) δ: 47.6, 55.4, 114.2, 121.7, 123.0, 135.6, 141.2, 148.3, 160.5, 213.0; HRMS (FAB) calcd. for $C_{21}H_{20}N_2O$ + H, *m/e:* 317.1654; found, *m/e:* 317.1665. Anal. calcd. for $C_{21}H_{20}N_2O$: C 79.72, H 6.37; found: C 76.89, H 6.38.

Acknowledgments

We are grateful to the Natural Sciences and Engineering Research Council of Canada, the Ministère de l'Éducation du Québec, and Merck Frosst for financial support. In addition, acknowledgment is made to the donors of the Petroleum Research Fund, administered by the American Chemical Society, for support of this research. We also thank Dr. Michel Simard of the Laboratoire de Diffraction des Rayons-X, Département de Chimie, Université de Montréal, for having determined the structure of complex **6a**.

References

1. K. Wiberg, M. Marquez, and H. Castejon. J. Org. Chem. **59**, 6817 (1994); P. Murray-Rust and J.P. Glusker. J. Am. Chem. Soc. **106**, 1018 (1984).
2. J.-F. Gal and P.-C. Maria. Prog. Phys. Org. Chem. **17**, 159 (1990); P.-C. Maria and J.-F. Gal. J. Phys. Chem. **89**, 1296 (1985); M. Berthelot, J.-F. Gal, M. Helbert, C. Laurence, and P.-C. Maria. J. Chim. Phys. **82**, 427 (1985); J.-F. Gal, C. Calleri, L. Elegant, and M. Azzaro. Bull. Soc. Chim. Fr. 311 (1979); L. Elegant, A. Pagliardini, G. Torri, and M. Azzaro. Bull. Soc. Chim. Fr. 4422 (1972).
3. J. Vaugeois, M. Simard, and J.D. Wuest. Coord. Chem. Rev. **145**, 55 (1995).
4. T. Ooi, M. Takahashi, and K. Maruoka. J. Am. Chem. Soc. **118**, 11307 (1996); M. Reilly and T. Oh. Tetrahedron Lett. **36**, 221 (1995); Tetrahedron Lett. **36**, 217 (1995).
5. V. Sharma, M. Simard, and J.D. Wuest. J. Am. Chem. Soc. **114**, 7931 (1992).
6. A. Haaland. Angew. Chem. Int. Ed. Engl. **28**, 992 (1989).
7. P. Sobota, S. Szafert, and T. Głowiak. J. Organomet. Chem. **526**, 329 (1996); H.J. Kakkonen, J. Pursiainen, T.A. Pakkanen, M. Ahlgrén, and E. Iiskola. J. Organomet. Chem. **453**, 175 (1993); G. Quinkert, H. Becker, M. Del Grosso, G. Dambacher, J.W. Bats, and G. Dürner. Tetrahedron Lett. **34**, 6885 (1993); P. Sobota, S. Szafert, and T. Lis. J. Organomet. Chem. **443**, 85 (1993); T. Carofiglio, P.G. Cozzi, C. Floriani, A. Chiesi-Villa, and C. Rizzoli. Organometallics, **12**, 2726 (1993); V. Jonas, G. Frenking, and M.T. Reetz. Organometallics, **12**, 2111 (1993); P. Sobota, S. Szafert, J. Utko, and T. Lis. J. Organomet. Chem. **423**, 195 (1992); P. Sobota, J. Utko, and T. Lis. J. Organomet. Chem. **393**, 349 (1990); J. Utko, P. Sobota, and T. Lis. J. Organomet. Chem. **334**, 341 (1987); G. Maier, U. Seipp, and R. Boese. Tetrahedron Lett. **28**, 4515 (1987); T. Poll, J.O. Metter, and G. Helmchen. Angew. Chem. Int. Ed. Engl. **24**, 112 (1985); B. Viard, M. Poulain, D. Grandjean, and J. Amaudrut. J. Chem. Res. (S), 84 (1983).
8. P. Sobota, J. Utko, and T. Lis. J. Organomet. Chem. **447**, 213 (1993); I.W. Bassi, M. Calcaterra, and R. Intrito. J. Organomet. Chem. **127**, 305 (1977); L. Brun. Acta Crystallogr. **20**, 739 (1966).
9. D.K. Singh, J.B. Springer, P.A. Goodson, and R.C. Corcoran. J. Org. Chem. **61**, 1436 (1996).
10. M.J. Bourgeois, E. Montaudon, M. Campagnole, and B. Maillard. Bull. Soc. Chim. Belg. **91**, 871 (1982).
11. J. Sandström. Dynamic NMR spectroscopy. Academic Press, London. 1982. p. 96.
12. B. Bachand and J.D. Wuest. Organometallics, **10**, 2015 (1991).
13. T.J. LePage and K.B. Wiberg. J. Am. Chem. Soc. **110**, 6642 (1988).
14. D. Gravel, S. Benoit, S. Kumanovic, and H. Sivaramakrishnan. Tetrahedron Lett. **33**, 1407 (1992). Y. Huang and X. Lu. Tetrahedron Lett. **29**, 5663 (1988).
15. R. Bodalski, J. Michalski, and B. Mlotkowska. Rocz. Chem. **43**, 677 (1969).
16. Y. Ducharme, S. Latour, and J.D. Wuest. Organometallics, **3**, 208 (1984).
17. F.R. Hartley. Organomet. Chem. Rev. Sect. A **6**, 119 (1970).
18. W.C. Still, M. Kahn, and A. Mitra. J. Org. Chem. **43**, 2923 (1978).
19. G.M. Sheldrick. Acta Crystallogr. Sect. A: Found. Crystallogr. **A46**, 467 (1990).
20. G.M. Sheldrick. SHELXL-93. University of Göttingen, Göttingen, Germany. 1993.
21. G.B. Gill, M.S.H. Idris, and K.S. Kirollos. J. Chem. Soc. Perkin Trans. 1, 2355 (1992).

© 1998 NRC Canada

ADDITIONS AND CORRECTIONS/AJOUTS ET CORRECTIONS

Additions and corrections: Folding strain stereocontrol in cyclohexane ring formation by means of an intramolecular ester enolate alkylation reaction

Takashi Tokoroyama and Hisashi Kusaka

Ref.: Can. J. Chem. **74**, 2487 (1996).
On page 2491, the Diastereomeric ratio (yield) in Entry 2 of Table 1 should be **42** : **43** 99 : 1.

© 1998 NRC Canada

1997 McBryde Medal Award Lecture Radio frequency quadrupole ion guides in modern mass spectrometry[1]

Bruce A. Thomson

Abstract: The role of RF quadrupoles in modern mass spectrometer and tandem mass spectrometer systems is described. A good deal of the success in the application of tandem quadrupole mass spectrometers and atmospheric pressure ionization mass spectrometers is due to new applications of the RF quadrupole ion guide. Developments that led from the use of very open, "transparent" electrodes in a cryopumped system to the opposite extreme of well-confined RF quadrupoles that operate advantageously at pressures of several mTorr are described. The ion containment properties of RF quadrupoles are remarkably insensitive to the accuracy of the electrode positions. This has allowed the use of novel quadrupole designs in order to provide unique solutions to instrumentational and physical-chemical problems.

Key words: quadrupole, focusing, mass spectrometer.

Résumé : On décrit le rôle des quadripôles de radiofréquence (RF) dans les spectromètres de masse modernes ainsi que ceux en tandem. Une grande partie des succès obtenus dans l'application des spectromètres de masse quadripolaires en tandem et dans les spectromètres de masse à ionisation à pression atmosphérique est due à de nouvelles applications du guide d'ion quadripolaire de RF. On décrit les développements qui ont conduit à l'utilisation d'électrodes « transparentes » très ouvertes dans un système à pompe cryogénique, à l'extrême opposé des quadripôles de RF bien confinés qui opèrent avantageusement à des pressions de plusieurs mTorr. Les propriétés de confinement des ions des quadripôles de RF sont remarquables par leur insensibilité à la précision des positions de l'électrode. Cette caractéristique a permis d'utiliser de nouveaux arrangements dans le but d'offrir des solutions uniques à des problèmes d'instrumentation et nature physicochimique.

Mots clés : quadripôle, focalisation, spectromètre de masse.

[Traduit par la rédaction]

Introduction

Quadrupole mass spectrometers have assumed a commanding place in the field of analytical mass spectrometry, due to their relatively high sensitivity, reliability, and ruggedness. As a measure of how routine they have become, the quadrupole mass spectrometer is often employed as simply another detector for a gas chromatograph. Recent developments in techniques of coupling liquid chromatography to mass spectrometry are rapidly moving the quadrupole mass spectrometer to the same level as a routine detector for a liquid chromatograph. For example, liquid chromatography, combined with tandem mass spectrometry in the form of a triple quadrupole (a technique designated as LC/MS/MS) has become the method of choice for the high-sensitivity quantitative analysis of drugs and metabolites in biological fluids. To the manufacturer, the ongoing challenge is to make the instrument ever more sensitive, selective, and cost effective (the latter factor includes price, ease of use, automation, and the ability to process more samples per unit time). This competitive challenge has resulted over the last decade in an explosion of interest directed at the quadrupole mass spectrometer, aimed at finding new ways to improve the performance or to find alternate modes of operation that improve analytical and instrumentational characteristics. As a result, new methods of using the two-dimensional and three-dimensional (i.e., ion trap) quadrupole are being discovered (1, 2) or revived (3).

However, the interesting and useful characteristics of the quadrupole are not limited to its use as a mass filter or spectrometer. The quadrupole also has the very useful property of acting as an ion guide, capable of either focusing ions or simply confining them in a beam by counteracting dispersive effects. In this mode, the strong ion containment properties of the radio-frequency (RF) quadrupole have resulted in its development as an ion storage device (a "trap") to suspend ions in space for spectroscopic measurement (4, 5), to accumulate ions from a weak beam prior to time-of-flight mass spectrometry (2) or Penning trap mass analysis (6), or to trap ions for nondestructive mass analysis using properties of ion motion in the RF field itself (7, 8). The two-dimensional RF quadrupole is used as the collision cell in triple quadrupoles (although some manufacturers prefer to use a hexapole or octapole, rather than a quadrupole), as a guide to transfer ions from the atmosphere-to-vacuum orifice of an atmospheric pressure

Received January 6, 1998.

B.A. Thomson.[2] PE SCIEX, 71 Four Valley Drive, Concord, ON L4K 4V8, Canada.

[1] This is an invited review article based on the 1997 McBryde Medal award lecture presented by Dr. Thomson at the 80th Annual Conference of the Canadian Society for Chemistry, held in Windsor, Ontario, in June 1997.

[2] Telephone: (905) 660-9005. Fax: (906) 660-2600. E-mail: brucet@sciex.com

© 1998 NRC Canada

Fig. 1. Cross-sectional view of a conventional quadrupole with cylindrical electrodes. Opposite electrodes are connected together, with opposite phases applied to the two pairs of electrodes. The resulting equipotentials at any point in time are shown between the electrodes.

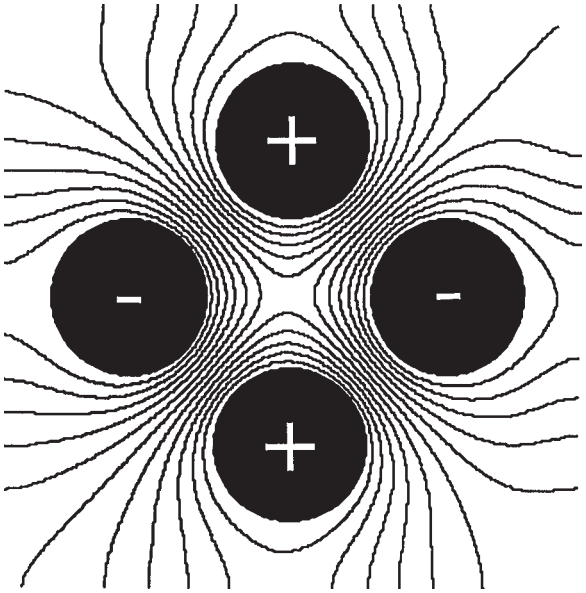

Fig. 2. The *x* and *y* components of motion of an ion inside the quadrupole at a *q* value of 0.15, with distance expressed in units of r_0, the radius of the inscribed circle between the rods. The motion consists mainly of a small "wiggle" at the RF frequency, superimposed on the higher amplitude secular motion, whose frequency is a unique function of the *q* value.

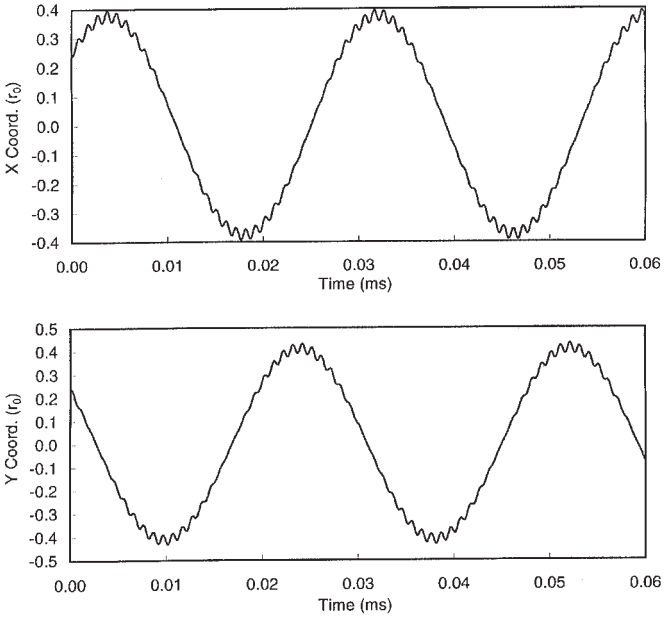

ionization (API) source (9), as the entrance optics into a mass-resolving quadrupole (a so-called Brubaker lens (10)), and as a guide from an external ion source through the strong fringing magnetic field of a Fourier-transform mass spectrometer (11).

One of the interesting things about the RF quadrupole ion guide is that, in contrast to the quadrupole mass spectrometer, the confinement characteristics are particularly insensitive to the accuracy and precision of the surrounding electrodes. While a mass filter must have electrodes that are accurately shaped and positioned to a tolerance of several parts per million (i.e., less than 1 μm), in many cases the RF-only beam guide can in principle be constructed of copper plumbing pipe without significant loss of efficiency (ignoring for the sake of this argument the fact that copper is not a suitable conductive surface for ion optical elements). Aside from the obvious benefits of cost, this factor, along with the strong containment properties, has resulted in the development of novel RF quadrupole guides that provide unique solutions or benefits in the design and performance of the triple quadrupole. The developments to be described here are the outcome of the last 15 years of research at SCIEX, and are the product of many contributing scientists in the research department. Acknowledgments for specific developments will be made at each point.

The physics of the quadrupole

The properties of quadrupole fields, along with recognition of almost all of the practical applications for operation as a mass spectrometer or ion-containment device, are found in the early papers and patents of Wolfgang Paul in Germany (12, 13), and Weurker and Langmuir in California (14, 15). For the purposes of this article, however, a thorough and comprehensive description of the development and use of multipoles (including, but not emphasizing, quadrupoles) is found in an article by Gerlich (16), following from the earlier work of Teloy and Gerlich (17) in developing the octapole beam guide for spectroscopic measurements.

The conventional RF quadrupole consists of four electrodes (usually cylindrical in shape) symmetrically disposed about a central axis, to which RF voltages are applied. The quadrupolar field results from opposite electrodes being at the same phase, and adjacent electrodes at opposite phases. Figure 1 shows the electrode arrangement, as well as the equipotentials in the *x*–*y* plane (forming rectilinear hyperbola). The equations of motion for an ion in this potential field are well known (the Mathieu equations (18)). The solution, which is a function of the ion mass (*m*), the radius of the inscribed circle between the rods (r_0), and the angular frequency and amplitude of the RF voltage applied to the electrodes (ω and *V*, respectively), is characterized by regions of stability and instability according to whether the amplitude of ion motion grows exponentially or remains bounded in space. Stability criteria can be expressed in terms of the non-dimensional parameter $q = 4eV/m\omega^2 r_0^2$; for values of $q > 0.907$, the ion motion is unstable (other, smaller regions of stability in *q*-space are ignored here).

At low values of *q* (less than approximately 0.4), the motion of an ion in the field is largely composed of a small high-frequency component (at the RF frequency), superimposed on a larger amplitude, lower frequency motion, the frequency of which is a unique function of *q*. Figure 2 shows a typical trajectory at a *q* of 0.15 (shown as the *x* and *y* components of motion, which, in a perfect quadrupolar field, are uncoupled).

An explanation of the low-frequency (so called "secular") motion is found in the mathematical derivations of the pseudopotential well model by Dehmelt (19), and the "adiabicity" model by Gerlich (16). Even though the ion motion

© 1998 NRC Canada

contains an infinite series of frequencies, to a very good approximation it can be treated as the secular motion with a small RF oscillation superimposed. The secular frequency can be viewed as simple harmonic motion in a pseudopotential well of depth $qV/8$. The physical justification for the concept of a potential well formed by the RF field is expressed by Gerlich (16): inhomogeneous oscillatory fields result in an average force toward the region of weakest field. In the case of a quadrupole, the region of weakest field is at the center of the rods. Thus, the RF field produces a net inward (restoring) force on every ion that is stable, resulting in oscillation about the center with an amplitude that depends on the initial position and velocity in the field. In the absence of any dissipation, the system is on average conservative, so that (on average) there is no gain or loss of kinetic energy by the ion. An ion that enters the quadrupole with a radial energy that is less than the depth of the pseudopotential well is radially confined by the field, and thus transmitted unless its amplitude of oscillation is large enough to cause it to strike a rod surface.

Applications in a triple quadrupole mass spectrometer system

The first commercial use of the RF quadrupole as an ion-containment and transport device was as a gas cell for collisionally induced dissociation in a triple quadrupole mass spectrometer (20). In a triple quadrupole (Fig. 3), ions from the source are selected by the first quadrupole, and accelerated at several tens of electron volts energy into a low-pressure gas in the center quadrupole. Fragment ions formed by collisions with the gas are mass analyzed by the third quadrupole (operated in a resolving mode). The strong containment field in the center RF quadrupole minimizes the scattering losses as ions collide with the gas molecules, allowing high sensitivity to be achieved. While the conventional RF quadrupole collision cell was a pressurized cell (a chamber with entrance and exit apertures that maintained a uniform gas density in the cell), one of the first innovations at SCIEX (by Barry French (9)) was to use a supersonic gas jet crossing the axis of the quadrupole as the collision region. This allowed the quadrupole to be closely coupled to the following mass-resolving quadrupole without an intervening aperture, and produced a well-defined collision region defined by the boundaries of the free jet. However, it required development of an RF quadrupole with electrodes that were "transparent" in order to avoid blocking or interfering with the transverse gas flow. The quadrupole was constructed of fine stainless steel wire strung between cylindrical end pieces, with the wires forming the contour of each of the four electrode surfaces (Fig. 4). Critical to the design was the use of cryopumping to condense the nitrogen or argon gas jet on a cold surface just outside of the wire quadrupole. This provided a one-pass system for the gas molecules, ensuring that no gas was scattered outside of the collision region. This wire quadrupole design was used on the SCIEX TAGA 6000 system (a triple quadrupole mass spectrometer system equipped with high-pressure ion sources), the first commercial triple quadrupole mass spectrometer to be introduced.

The concept of a "transparent" quadrupole to guide ions through a region of directed gas flow was also employed in the vacuum interface region for the TAGA 6000, which used an atmospheric pressure chemical ionization (APCI) source. Ions

Fig. 3. Schematic view of a triple quadrupole mass spectrometer system. Q1 and Q3 are mass resolving quadrupoles, while Q2 is an RF quadrupole collision cell. The Q1/Q2/Q3 configuration is generic; the use of Q0 as an ion guide in front of Q1 is usually limited to those triple quadrupole systems which use atmospheric pressure ion sources, such as electrospray.

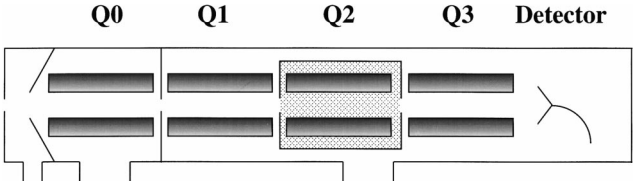

and gas entered the chamber through a small orifice in an expanding supersonic jet. An RF quadrupole constructed of small wires outlining the electrode surfaces produced the same effect of confining the ions along the axis while allowing the gas to escape to surrounding cryosurfaces. Both of these developments demonstrated that highly efficient ion containment and transmission could be achieved with electrodes that were far from accurately defined and positioned. The same configurations were employed in the API III LC/MS/MS system several years later. The API III, based on the earlier TAGA platform, became the gold standard in the field of quantitative LC/MS/MS.

Collisional focusing in an RF quadrupole

One of the most significant breakthroughs to follow was the development of "collisional focusing" by Don Douglas and Barry French (21). The term refers to the combined effect of gas drag (due to multiple collisions between the ions and the gas) and radial containment by the RF field. The dissipative action of the collisions (damping ion motion in both the radial and axial directions) allows the ions to fall toward the centre of the potential well, thus effectively focusing the ions toward the axis. This effect can be seen in Fig. 5, which shows the results of a numerical simulation of ion motion in an RF field, including the effect of collisions with nitrogen gas at a pressure of 7×10^{-3} Torr (using a hard-sphere model) (1 Torr = 133.3 Pa). The effects are beneficial in two important regards: (*i*) gas drag in the axial direction reduces the energy spread of the ions, improving the mass resolution in the following quadrupole; (*ii*) the radial focusing improves ion transmission efficiency through a following aperture, and provides a narrower ion beam that better matches the acceptance of the following quadrupole mass filter. The use of collisional focusing was key to the design of the API 300, the triple quadrupole product that succeeded the API III and used differential pumping (with turbo pumps) rather than cryopumping. By staging the pumping so that the first ion guide (Q0) is at a pressure of about 7×10^{-3} Torr, ions that enter Q0 at an energy of several electron volts are slowed to 1–2 eV (with a spread of less than 1 eV), and are collisionally focused through an aperture of less than 2 mm diameter at the end of Q0. This provides highly efficient (greater than 50%) capture and transfer of ions from a region at moderate pressure (7×10^{-3} Torr) into a vacuum regime (10^{-5} Torr), with an ion energy spread that allows good mass resolution in the following mass-resolving quadrupole (Q1).

Recently, the same principal has been employed to

© 1998 NRC Canada

Fig. 4. The "transparent" RF quadrupole with transverse free jet (used on the TAGA 6000 and the API III triple quadrupoles). (*a*) Side view. (*b*) End view.

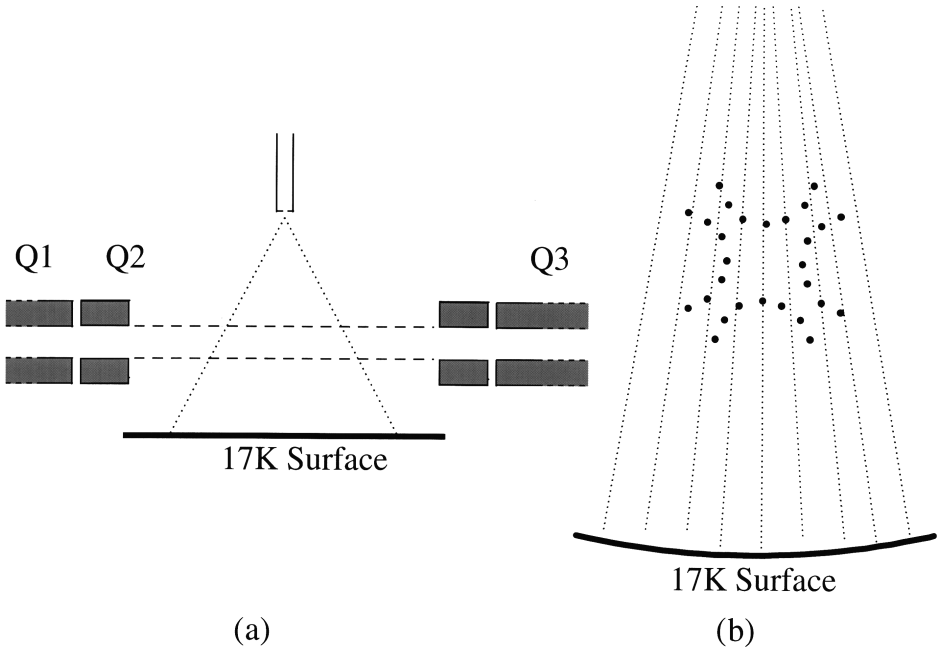

introduce ions into a time-of-flight mass spectrometer system (22). Even at a pressure of 7×10^{-2} Torr, ions are effectively cooled and focused into the orthogonal extraction region of the time-of-flight mass spectrometer, thereby providing the reduced spatial and energy spread required to achieve good mass resolution.

Precisely the same principles were applied to the development of a high-pressure collision cell (23). The transparent quadrupole with the transverse gas jet was replaced with an RF quadrupole in a chamber pressurized to 7×10^{-3} Torr, a pressure significantly higher than that used in earlier versions of the enclosed collision cell. The application of collisional focusing in the collision cell provided the unusual (but very desirable) benefit of simultaneously increasing both the sensitivity and the mass resolution for fragment ions. The sensitivity in an MS/MS mode was increased by a factor of 5–10 over that previously achieved with the open collision cell, while the mass resolution increased to the point of being able to distinguish the separate isotopic peaks from multiply charged ions with up to four charges. Figure 6 (reproduced, with permission, from ref. 23) shows the fragment ion spectrum from the *m*/*z* 440 quadruply charged ion of renin substrate, a peptide of MW 1758. The expanded views of several regions of the spectrum show the ability to resolve individual peaks that are separated by as little as 0.25 mass-to-charge units.

Axial electric fields in RF quadrupoles

An unwanted effect of employing collisional focusing in Q0 and in Q2 is that some ions undergo so many collisions that they are effectively brought to rest (with no average forward motion) before reaching the exit from the high-pressure region. Since in a conventional quadrupole there is no electric field in the axial direction (all of the fields being radially directed), there is nothing to force the ions toward the exit end. While all of the ions do eventually reach the exit (presumably due to diffusion and space charge forces), the significant time delay causes problems in certain modes of operation. For example, selected-reaction monitoring (SRM) is an MS/MS scan mode in which Q1 and Q3 are used to monitor several fragmentation reactions of interest by stepping several times per second between mass values corresponding to the ions of interest. If two different precursor ions happen to form the same product (fragment) ion, then ions that take longer to reach the exit of the collision cell than the measurement time being used (typically 50–200 ms) can be recorded in the wrong channel. This leads to an effect known as "cross-talk," in which some ions from one transition (*m*/*z* 500 fragmenting to *m*/*z* 230, for example) are recorded during the measurement time for the transition monitored immediately after (*m*/*z* 517 fragmenting to *m*/*z* 230). As a result, false readings can be recorded in the second channel. In another type of scan mode (the precursor ion scan mode, in which Q3 is fixed at a fragment ion of interest, and Q1 is scanned in order to reveal all of the precursors that form that fragment), the effect of time dispersion in Q2 due to the highly damped axial motion leads to a loss in mass resolution and sensitivity.

Observation of these effects stimulated the development of several methods of generating an axial field directed along the axis of the quadrupole, in order to move the ions quickly toward the exit (24). In all cases, the goal was to provide enough force on the ions to cause them to drift through the high-pressure quadrupole within much less than the typical measurement time, without inducing effects that would couple to their radial motion and reduce the collisional focusing effects.

One method involved simply dividing the RF quadrupole into several segments, and applying a different rod-offset voltage to each segment. This establishes a different dc potential within each segment, and, by arranging the voltages to decrease monotonically toward the exit, an approximately

© 1998 NRC Canada

Fig. 5. Numerical simulation of an ion trajectory in a quadrupole at a pressures of (*a*) 0, (*b*) 5, and (*c*) 7 mTorr of nitrogen, showing how collisions damp the ion motion toward the centre of the quadrupole. Conditions for this simulation: *m*/*z* 1000, hard-sphere collisions with a collision cross section of 200×10^{-16} cm^2, *q*-value = 0.35. At the higher pressure, the ion does not reach the end of the quadrupole during the simulation time (0.8 ms), because neither space charge nor axial field effects have been included.

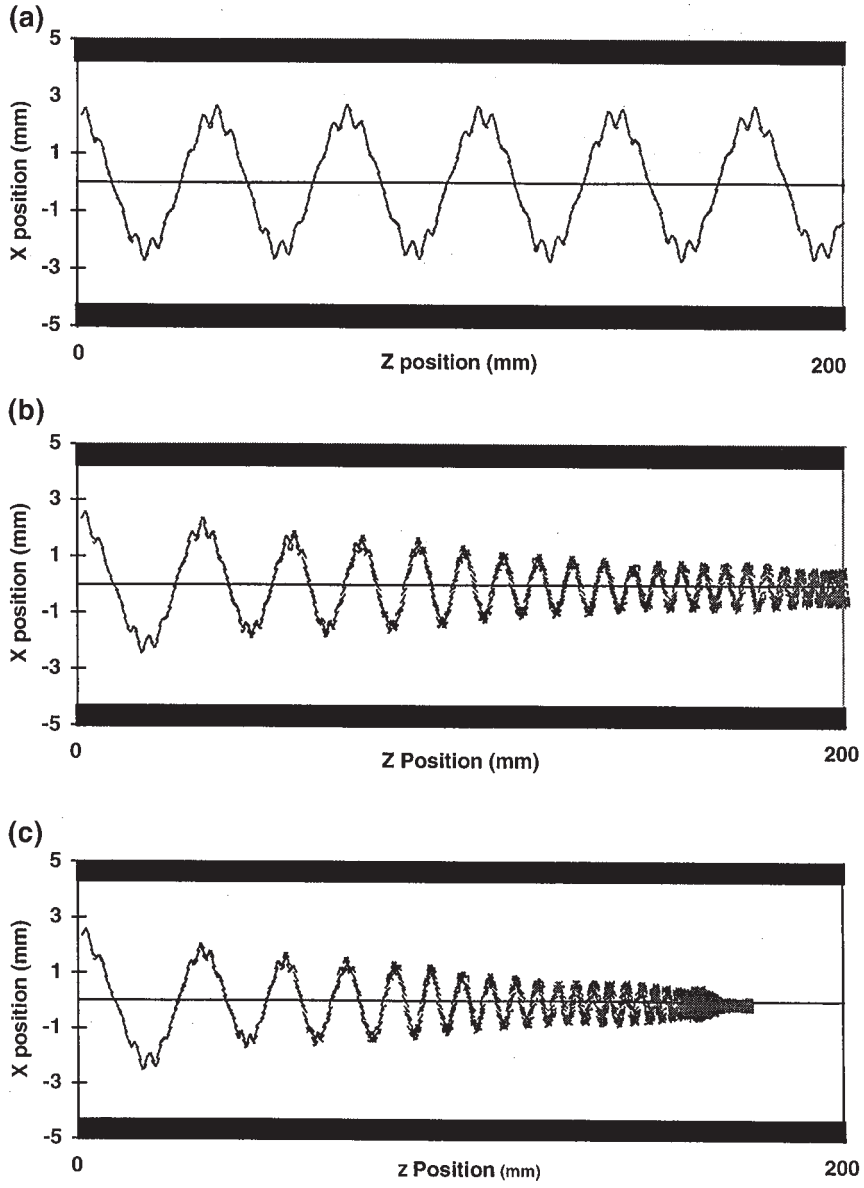

uniform dc field can be generated inside the device, parallel to the axis. This method is analogous to the use of guard rings in an ion mobility drift tube to establish a potential gradient along the axis. An RF quadrupole consisting of six separate segments, with a total potential drop of 2–3 V over the 20 cm length, was sufficient to eliminate effects produced by the loss of axial ion energy. A 20-segment RF quadrupole collision cell has also been constructed, and was used to measure the cross sections of various mass-selected ions in a triple quadrupole mass spectrometer (25). This device is described more fully in the following section.

Although the segmented quadrupole provided the desired characteristics of eliminating the problems described above, this method is mechanically complex, requiring separate connections to all 24 small rods (for 6 segments). A simpler method of generating an axial field was developed by using an asymmetric electrode geometry combined with a differential dc voltage on the two pairs of rods. Referred to as the Linac®, it has one pair of cylindrical rods tilted toward the entrance, the other pair toward the exit (Fig. 7). This configuration results in one pair of opposing rods being closer to the axis at the entrance end, and the other pair of rods being closer to the axis at the exit end. With slightly different dc voltages applied to each rod pair, an axial potential gradient (electric field) is established. This follows from the fact that the electric potential on the axis is dominated by the voltage applied to one pair of rods at the entrance, and by the voltage applied to the other pair of rods at the exit. In practice, a potential difference of

© 1998 NRC Canada

Fig. 6. Fragmentation spectrum (MS/MS) of $(M + 4H)^{4+}$ (m/z 440) from renin substrate at high fragment ion resolution, showing separation of the isotopic peaks for fragment ions with 1, 2, 3, and 4 charges (attached protons). Collision energy, 112 eV; collision gas thickness (CGT), $4 \times 10^{15}/cm^2$. Reprinted with permission from ref. 23. © 1995 American Chemical Society.

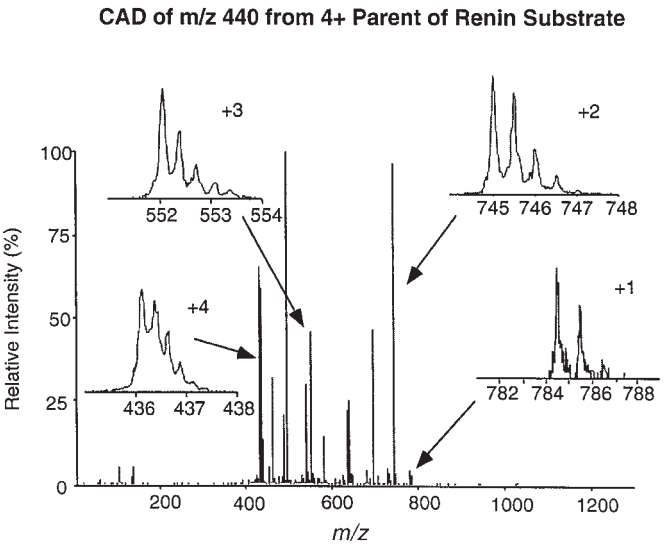

approximately 2 V between the rod pairs is sufficient to reduce or eliminate the cross-talk problem and the parent scan problems described above. Numerical modeling of the Linac electrode geometry reveals that the field gradient along the center axis due to a potential difference of 2 V is only 0.075 V cm^{-1} over the 20 cm length. This weak field is nevertheless enough to cause the ions to rapidly drift toward the exit end of the quadrupole. For example, an ion with a reduced ion mobility of 1 cm^2 V^{-1} s^{-1} would require only 2.4 ms to traverse the 20 cm length of the quadrupole at a pressure of 7 mTorr.

Other configurations that were designed to generate an axial field were also effective. These included using a segmented case surrounding the quadrupole, with different dc voltages applied to each segment, as well as using a high-resistance surface on auxiliary electrodes located between the main electrodes, with different dc potentials applied to each end of the rods to generate a continuous potential gradient. One aspect common to all geometries, however, is that in spite of using non-ideal electrode shapes and positions (far from ideal, in the case of the Linac®), in configurations that inevitably produced some non-quadrupolar radial field components in addition to the desired axial fields, the performance as an ion guide was not significantly affected. Recently, the original Linac® prototype, which used truncated conical rods rather than cylindrical rods to produce the axial field, was thoroughly investigated, both for its operational characteristics and for its function as the collision cell in a triple quadrupole. This study, conducted by B.A. Mansoori, E.W. Dyer, C.M. Lock, and R.K. Boyd of the National Research Council in Halifax, confirmed that the Linac® configuration is effective at eliminating the undesirable trapping associated with the high-pressure RF quadrupole, without affecting the transmission and focusing characteristics. (The full results of this study will soon be submitted for publication.) The conclusion supports the original contention that the confinement properties of RF quadupole

Fig. 7. The Linac® collision cell, with one set of cylindrical rods tilted toward the axis, the other set tilted away from the axis. Combined with slightly different dc voltages applied to the two sets of rods (V_1 and V_2), this produces a small axial field.

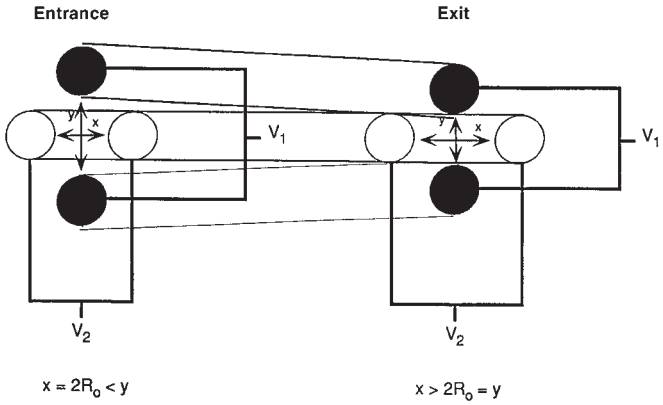

devices are very insensitive to the purity of the quadrupole field.

Cross sections of protein ions

The development of electrospray mass spectrometry has greatly expanded the range of applications to which mass spectrometry can be applied. This ionization method allows ionic and labile compounds to be easily and sensitively detected without unwanted fragmentation. Combined with MS/MS, it offers unmatched specificity and sensitivity for the analysis of biological compounds, including biopolymers such as proteins, peptides, and nucleotides. The introduction of electrospray mass spectrometry into the field of biochemistry has also led to its application for the study of the structure of proteins and biopolymers. For example, Covey and Douglas (26) used the collision cell of a triple quadrupole mass spectrometer to measure the cross section of protein ions, by measuring the rate of energy loss of ions as they experienced gas drag in traversing the cell. Herron et al. (27) have used an ion trap mass spectrometer to study ion–ion reactions of electrospray negative ions, in order to learn more about their structure and reactivity. Jarrold and co-workers (28) have combined a low-pressure drift cell with a mass spectrometer to investigate the cross section of protein ions.

The development of the axial field quadrupole described in the previous section led us to apply this device to measure the ion mobility of mass-selected ions in a segmented quadrupole collision cell (25). We replaced the conventional quadrupole collision cell in the API 300 triple quadrupole mass spectrometer with the 20-segment quadrupole described above. We were able to establish a low, uniform, electric field along the axis by applying decreasing potentials to each quadrupole segment, using a potential divider network. Using the electrospray ion source to generate multiply charged ions from proteins such as myoglobin and ubiquitin, ions were selected by Q1, allowing only one m/z value into the collision cell at one time. By gating the ions into Q2, and using a multichannel scalar to detect the ion pulse at the detector, we were able to measure the drift time of the ions. Ion mobilities were measured by varying the electric field and, from these, the ion-neutral

© 1998 NRC Canada

ollision cross sections were calculated. Results obtained with this method were in good agreement with the cross sections measured by Collings and Douglas using their energy loss method (29).

Determination of cross sections allows insight into the shape and size of large biopolymers. For example, the cross section of different charge states of apomyoglobin was observed to increase with charge state, indicating that ions with more attached charges (protons) probably exist in a more extended form (at least in the gas phase) than those with fewer charges. Holomyoglobin (myoglobin with the heme group attached) was observed to have a smaller cross section than myoglobin without the heme, supporting the view that holomyoglobin is a more compact structure than apomyoglobin (myoglobin without the heme). Douglas and others continue to use electrospray mass spectrometry to probe the structure, binding energies, and reaction kinetics of proteins.

Conclusions

Radio-frequency quadrupoles have found diverse applications in analytical mass spectrometer and tandem mass spectrometer systems where mass analysis and quantitation are the primary goals, as well as in physical chemistry applications where other properties of ions are measured while confined by an RF field. The high tolerance toward "imperfect" quadrupolar fields allows RF multipoles to be applied in unique and creative ways in order to solve problems. This tolerance has the added benefit of loosening conventional design constraints on quadrupole design, thus contributing to reduced cost and higher performance in commercial mass spectrometer systems.

References

1. A.E. Schoen and J.E.P. Syka. U.S. Patent 5,089,703 (1991).
2. M.K. Qian and D.M. Lubman. Anal. Chem. **67**, 243A (1995).
3. R.E. Pedder and R.A. Schaeffer. Proc. Conf. Mass Spectrometry and Allied Topics, 43rd. Atlanta, Ga. May 1995. p. 1070.
4. M. Tachikawa, M. Kajita, and T. Shimizu. IEEE Trans. Instrum. Meas. **42**, 281 (1993).
5. R.C. Thompson. Adv. At. Mol. Opt. Phys. **31**, 63 (1993).
6. R.B. Moore and G. Rouleau. J. Mod. Opt. **39**, 361 (1992).
7. D.E. Goeringer, R.I. Crutcher, and S.A. McLuckey. Anal. Chem. **67**, 4164 (1995).
8. M. Soni, V. Frankevich, M. Nappi, R.E. Santini, J.W. Amy, and R.G. Cooks. Anal. Chem. **68**, 3314 (1996).
9. J.B. French. U. S. Patent No. 4,328,420 (1982).
10. W.M. Brubaker. Adv. Mass Spectrom. **4**, 293 (1968).
11. R.T. McIver, Jr., R.L. Hunter, and W.D. Bowers. Int. J. Mass Spectrom. Ion Processes, **64**, 67 (1995).
12. W. Paul and H.Z. Steinwedel. Z. Naturforsch. A: Astrophys. Phys. Phys. Chem. **8A**, 448 (1953).
13. W. Paul and H.Z. Steinwedel. U.S. Patent No. 2,939,952 (1960).
14. R.F. Wuerker, H. Shelton, and R.V. Langmuir. J. Appl. Phys. **30**, 342 (1959).
15. D.B. Langmuir, R.V. Langmuir, and R.F. Wuerker. U. S. Patent No. 3,065,640 (1962).
16. D. Gerlich. *In* State-selected and state-to-state ion–molecule reaction dynamics, Part 1: experiment. *Edited by* C.-Y. Ng and M. Baer. Adv. Chem. Phys. Vol. **82**. John Wiley and Sons, Inc., New York. 1992.
17. E. Teloy and D. Gerlich. Chem. Phys. **4**, 417 (1974).
18. P.H. Dawson. Quadrupole mass spectrometry and its applications. Elsevier, Amsterdam. 1976.
19. H.G. Dehmelt. Adv. At. Mol. Phys. **3**, 53 (1967).
20. R.A. Yost and C.G. Enke. J. Am. Chem. Soc. **100**, 2274 (1978).
21. D.J. Douglas and J.B. French. J. Am. Soc. Mass Spectrom. **3**, 398 (1982).
22. A.N. Krutchinsky, I.V. Chernushevich, V. Spicer, V. Ens, and K.G. Standing. Proc. Conf. Mass Spectrometry and Allied Topics, 43rd. Atlanta, Ga. May 1995. p. 126.
23. B.A. Thomson, D.J. Douglas, J.J. Corr, J.W. Hager, and C.L. Jolliffe. Anal. Chem. **67**, 1696 (1995).
24. B.A. Thomson, C. Jolliffe, and R. Javahery. Proc. Conf. Mass Spectrometry and Allied Topics, 44th. Portland, Oreg. May 1995. p. 1155.
25. G. Javahery and B.A. Thomson. J. Am. Soc. Mass Spectrom. **8**, 697 (1997).
26. T. Covey and D.J. Douglas. J. Am. Soc. Mass Spectrom. **4**, 616 (1993).
27. W.J. Herron, D.E. Goeringer, and S.A. McLuckey. J. Am. Soc. Mass Spectrom. **6**, 529 (1995).
28. D.E. Clemmer, R.R. Hudgins, and M.F. Jarrold. J. Am. Chem. Soc. **117**, 10141 (1995).
29. B.A. Collings and D.J. Douglas. J. Am. Chem. Soc. **118**, 4488 (1996).

© 1998 NRC Canada

On the formation of diphenylmethane structures in lignin under kraft, EMCC®, and soda pulping conditions

Behzad C. Ahvazi, Gerry Pageau, and Dimitris S. Argyropoulos

Abstract: This paper describes our efforts focused at defining the formation of diphenylmethane moieties in lignin during conventional kraft and soda pulping conditions. This objective was realized by confirming, initially, the assignment of a ^{31}P NMR signal as being due exclusively to the presence of phosphitylated diphenylmethane (DPM) phenolic hydroxyl groups. More specifically, softwood milled wood lignin (*Picea mariana*) was subjected to kraft pulping conditions in the presence and absence of varying amounts of formaldehyde. After quantitative recovery of the lignin, the ^{31}P NMR spectra were recorded and the spectra revealed selective signal growth in the region confined between 142.8 and 144.3 ppm, in accordance with previous model compound work and detailed calculations based on the Hammett principles. To further substantiate our conclusions we also carried out two series of isothermal (120°C) kraft and soda pulping experiments followed by quantitative determinations of the DPM moieties, and correlated our findings with the differences in chemistry known to occur between the two processes. Finally, diphenylmethane phenolic moieties were determined in isolated residual lignins from two western hemlock kraft pulp samples produced via an EMCC® mill protocol and a laboratory batch digester, respectively. These structures prevailed amongst the condensed phenolic units of the conventional pulp, providing additional evidence to support the fact that modern modified pulping technologies beneficially alter the structure of residual kraft lignin.

Key words: phenyl groups, kraft pulping, modified kraft process, nuclear magnetic resonance (NMR), phosphorus spectroscopy.

Résumé : Dans ce travail, on décrit nos travaux orientés vers la démonstration de conditions de formation d'entités diphénylméthane dans les conditions de fabrication de pâtes kraft et à la soude. L'objectif de ces travaux a été réalisé en confirmant initialement l'attribution d'un signal RMN du ^{31}P uniquement à la présence de groupes hydroxyles phénoliques phosphylatés du diphénylméthane. D'une façon plus précise, on a soumis de la lignine de bois mou broyé (*Picea mariana*) à des conditions de fabrication de pâte kraft, en l'absence et en présence de quantités variables de formaldéhyde. Après avoir récupéré la lignine d'une façon quantitative, on a enregistré les spectres RMN du ^{31}P qui révèlent la croissance sélective de signaux dans la région comprise entre 142,8 et 144,3 ppm, en accord avec le travail antérieur sur un composé modèle et avec des calculs détaillés basés sur les principes de Hammett. Afin de confirmer nos conclusions, on a aussi effectué deux séries d'expériences isothermes (120°C) de formation de pâte kraft et de pâte à la soude, suivies de déterminations quantitatives des portions de DPM, et on a établi une corrélation entre nos résultats et les différences bien connues dans les chimies de ces deux procédés. Enfin, on a déterminé les portions phénoliques de diphénylméthane présentes dans des lignines résiduelles isolées à partir de deux échantillons de pâte kraft de la pruche de l'ouest obtenues respectivement par le biais d'un protocole EMCC® en usine et d'un lessiveur discontinu de laboratoire. Ces structures sont prévalentes dans les unités phénoliques condensées de la pâte conventionnelle; ces résultats fournissent des preuves supplémentaires relatives au fait que les technologies modernes de fabrication de pâte altèrent de façon avantageuse la structure de la lignine kraft résiduelle.

Mots clés : groupes phényles, fabrication de pâte kraft, procédé de fabrication kraft modifié, résonance magnétique nucléaire (RMN), spectroscopie du phosphore.

[Traduit par la rédaction]

Received December 8, 1997.

B.C. Ahvazi. Department of Chemistry, McGill University, Pulp and Paper Research Centre, 3420 University St., Montréal, QC H3A 2A7, Canada.
G. Pageau. Howe Sound Pulp and Paper, Port Melon, BC V0N 2S0, Canada.
D.S. Argyropoulos.[1] PAPRICAN, and Department of Chemistry, McGill University, Pulp and Paper Research Centre, 3420 University St., Montréal, QC H3A 2A7, Canada.

[1] Author to whom correspondence may be addressed. Telephone: (514) 398-6187. Fax: (514) 398-8254. E-mail: DIMITRIA@SHARED 1.LAN.McGILL. CA

Introduction

While the ether bonds of lignin cleave efficiently under alkaline pulping conditions, the formation of condensed structures decreases its reactivity and diminishes the solubility of the residual lignin (1). This phenomenon seriously interferes with the complete removal of lignin and the rate of delignification, especially during the final stages of most pulping processes.

During the past several years a number of modifications aimed at enhancing delignification have been proposed for the conventional kraft pulping process (2–5). Rapid displacement heating (RDH) (6–9) and modified continuous cooking (MCC) (10–13) are two examples of these processes. In addition, the

© 1998 NRC Canada

Scheme 1.

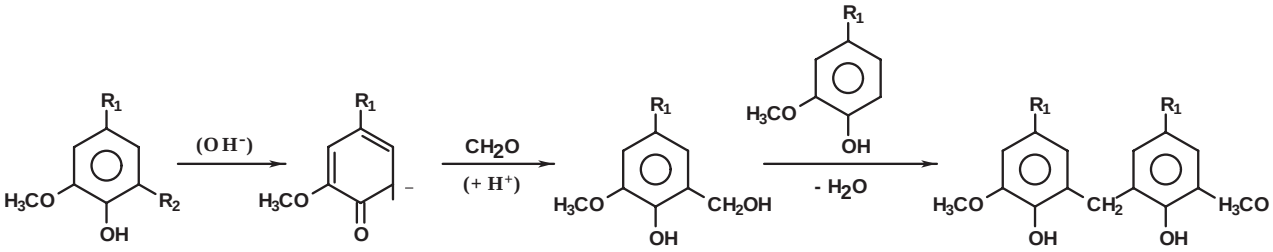

use of pulping additives such as polysulphide (14–16) and anthraquinone (16–18) have also been advocated.

Amongst the reactions that are known to interfere with the process of alkaline delignification are those involving the formation of carbon–carbon bonds. Formaldehyde is known to be liberated (19) as early as 100°C, as a result of C_γ elimination from phenylcoumaran (20, 21) and from guaiacylglycerol-β-aryl ether structures, both abundant in native lignin (22–24). The released formaldehyde is known to cause the substitution of hydroxymethyl groups at positions *ortho* to the phenolate moieties (22). This potentially represents a very important reaction since one third of the phenolic nuclei in softwood kraft lignin (25) and about one half of the phenolic and non-phenolic units in softwood milled wood lignin contain free C5 positions (23). The methylolated phenols may undergo further reaction to yield diphenylmethane moieties (1, 26, 27) (Scheme 1).

A number of these structures (**1**–**4**) have been suggested (28–31). Another condensation reaction caused by the liberation of formaldehyde during alkaline hydrolysis is Tollen's reaction (1). This reaction involves the substitution of hydroxymethyl groups at side-chain positions provided activating carbonyl groups are present (1, 25).

Although several studies by Chiang and Funaoka (32–34) have claimed to show convincing qualitative and quantitative evidence for the presence of diphenylmethanes in residual kraft lignin, a number of questions in relation to the method of detection have recently surfaced (35). Since the development of ^{31}P NMR spectroscopy for probing lignin structure (36–40), the technique has been successfully implemented for the absolute determination of the various phenolic and non-phenolic structures in several native and technical lignins (41–44). The availability of a phosphitylating reagent (40) that permits excellent resolution and the quantitative spectroscopic detection of several phenolic moieties with varying substitution patterns (44–46) provides an excellent opportunity for systematically exploring the complex reactions that occur in lignin during alkaline pulping. For example, such an effort has already led to the definition of the fundamental thermodynamic parameters that govern the stereoselective degradation of the arylglycerol-β-aryl ether bonds in milled wood lignin under kraft pulping conditions (47).

As mills move toward elemental chlorine free bleaching (ECF), the negative impact of condensed lignin structures on the final pulp brightness ceiling provides additional incentives to minimize the possibility that condensation reactions may occur in the digester and during oxygen delignification. The precise identification of such structures and their formation kinetics could be a major step forward toward understanding and minimizing their detrimental effects.

In this paper we describe our efforts focused on defining the formation of diphenylmethane moieties in lignin during conventional kraft and soda pulping conditions. This objective was realized by initially confirming the assignment of a ^{31}P NMR signal as being due exclusively to the presence of phosphitylated diphenylmethane phenolic hydroxyl groups. The overall phosphitylation reaction of labile protons is depicted in Scheme 2. We then accumulated kinetic data for the formation of these species under soda and kraft pulping conditions and correlated this information to known chemistry.

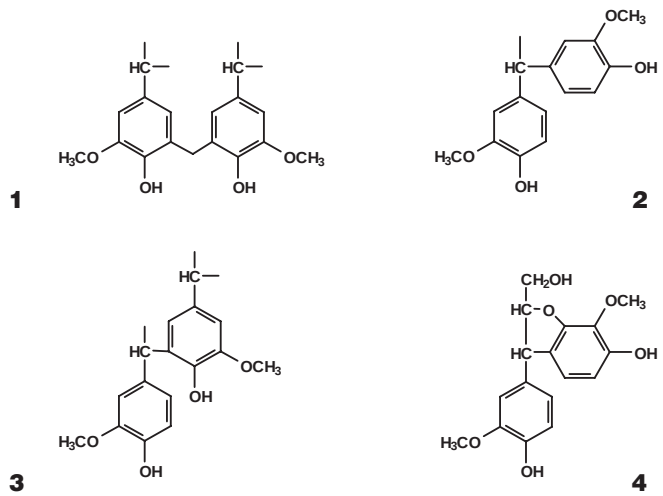

Experimental

Treatment of milled wood lignin under homogeneous kraft or soda pulping conditions

Initially, a white liquor solution containing 7.0 g of sodium hydroxide (0.175 mol NaOH) and 6.2 g of sodium sulphide (0.026 mol $Na_2S{\cdot}9H_2O$) per 100 mL deionized water was prepared. For the case of the soda "cooks" the molar amount of sodium sulphide ($Na_2S{\cdot}9H_2O$) used for the kraft pulping experiments was substituted with sodium hydroxide dissolved in 200 mL of deionized water and dioxane (1:1 v/v). This solution was then mixed with an equal volume of dioxane. During a typical experiment, 0.1 g of softwood milled wood lignin, prepared according to the Björkman procedure (47, 48) and having the following elemental composition: 60.86% carbon, 5.71% hydrogen, and 15.45% methoxy, was used. This lignin was dissolved in 1.33 g of the previously described white

© 1998 NRC Canada

Scheme 2.

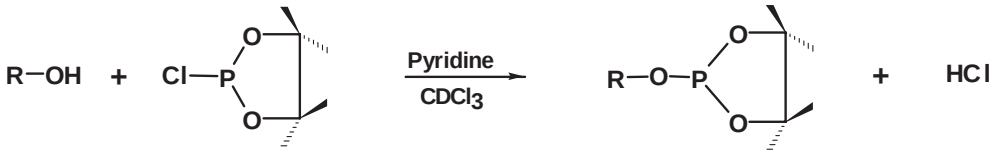

liquor (the ratio of liquor to lignin was 4:1). The reaction was carried out in a 10 mL stainless steel bomb whose air was displaced by nitrogen. The kraft cooking was simulated by heating and occasionally shaking the bomb in an oil bath preheated to the desired temperature and for specific time intervals. At the end of the reaction period, the bomb was cooled with cold water and its contents were acidified to pH 2 using dilute hydrochloric acid (0.2 M HCl). The precipitate was allowed to settle overnight. It was then collected by centrifugation and washed with acidic water to remove the inorganic salts. The precipitated degraded lignin was then freeze-dried and brought to constant weight at room temperature under reduced pressure. This material accounted for approximately 80% of the initial weight of lignin used. In an effort to isolate the remaining 20%, the solution containing the water-soluble low molecular weight lignin resulting from the first aqueous acidic precipitation was allowed to dry at room temperature. The remaining low molecular weight lignin was extracted by addition of 10–15 mL high-grade tetrahydrofuran. This was followed by evaporation of the solvent to a fine viscous residue, and dropwise addition to 20 mL of diethyl ether. This step was repeated 2–3 times, allowing the collection of more lignin, free from inorganic salts. Finally, the diethyl ether was evaporated and the remaining lignin was freeze-dried. The samples, after being brought to constant weight under reduced pressure, accounted for almost 16% of the starting lignin. The two sets of degraded lignin samples collected were then mixed thoroughly prior to subsequent analyses.

Addition of formaldehyde to milled wood lignin followed by homogeneous kraft pulping

Milled wood lignin (100 mg) was placed in a 10 mL stainless steel bomb. The lignin was then dissolved by the addition of 1.33 g of white liquor solution, prepared by dissolving 7.0 g of sodium hydroxide (NaOH) and 6.2 g of sodium sulphide ($Na_2S{\cdot}9H_2O$) in a solution (200 mL) of deionized water and absolute dioxane (1:1 v/v). Two separate sets of experiments, in which the amount of formaldehyde added was varied, were carried out at 120°C. For the first series of experiments, 11.1 μL of a 30% formaldehyde solution, accounting for 50% of the total β-aryl ether bonds, was added to each sample, while for the second series, 22.2 μL (representing 100% of the total β-aryl ether bonds) was added. After replacing the air with nitrogen, each bomb was sealed. Four reaction bombs (each containing the above mixture) were then placed in a preheated oil bath and after occasional shaking they were removed after 1, 2, 3, and 4 h of treatment. The isolation and purification procedures were conducted in a manner identical to those discussed in the previous section.

Preparation of kraft pulps and residual lignin isolation

A conventional western hemlock kraft pulp was prepared at Paprican in a laboratory batch digester using conditions described previously (46). The western hemlock EMCC® (extended modified continuous cooking) pulp was supplied by a Canadian mill. The isolation of residual lignin was carried out from pre-extracted pulp meal following a procedure described previously (46).

Quantitative ^{31}P NMR spectroscopy

The derivatizing reagent 2-chloro-4,4,5,5-tetramethyl-1,3,2-dioxaphospholane was synthesized (40) and used as the phosphitylation reagent. Approximately 30 mg of dry lignin was added to 800 μL of a solvent mixture containing pyridine and $CDCl_3$ at a volume ratio of 1.6:1. The mixture was stirred with a magnetic bar until the lignin was fully dissolved. This was followed by the addition of 100 μL of a solution containing both cyclohexanol (11 mg/mL) as an internal standard and chromium acetylacetonate (5 mg/mL) as a relaxation reagent. Finally, 100 μL of 2-chloro-4,4,5,5-tetramethyl-1,3,2-dioxaphospholane was added and the flask was sealed and shaken to ensure thorough mixing. The ^{31}P NMR spectra were obtained by using inverse gated decoupling on a Varian XL-300 FT-NMR spectrometer at 121.5 MHz. The obtained spectra were integrated 3 times on separate occasions and the resulting data were averaged out as reported here. Further details dealing with acquisition and spectral processing have been described elsewhere (40, 49).

Results and discussion

In our earlier work the phosphorus NMR spectra of solubilized kraft lignin contained, among others, a signal centred around 143.5 ppm (40). On the basis of model compound work and calculations based on the Hammett principles (50), this signal was tentatively assigned to diarylmethane structures possessing free phenolic hydroxyl groups (40). In an effort to confirm the validity of our earlier work, the interaction of milled wood lignin with formaldehyde under kraft pulping conditions was clarified by conducting experiments in which different amounts of formaldehyde were introduced into the reaction mixture prior to the cook. More specifically, two different sets of experiments were carried out with four samples of milled wood lignins being subjected to kraft pulping at 120°C with the addition of formaldehyde accounting for 50 and 100% of the total aryl ether units of lignin, respectively (51). After quantitative recovery of the lignin, the ^{31}P NMR spectra were recorded and the spectra critically examined. Figure 1 shows a representative series of such spectra.

A comparison of the ^{31}P NMR spectra of milled wood lignin (*A*) to those treated under kraft pulping conditions without (*B*) and with (*C* and *D*) addition of formaldehyde reveals substantial signal growth (Table 1) at around 143.5 ppm. Indeed, the area under the broad signal (142.8–144.3 ppm), labelled DPM, was increased in spectra *C* and *D* where significant amounts of formaldehyde had been added (Table 1). In addition, the spectra of the samples to which formaldehyde was

© 1998 NRC Canada

Fig. 1. Quantitative ^{31}P NMR spectra of milled wood lignin before and after being subjected to isothermal (120°C, 3 h) homogeneous kraft pulping conditions; (*A*) blank, (*B*) control kraft pulping, (*C*) with the addition of 11 μL, and (*D*) 22 μL formaldehyde corresponding to 50% and 100% of the aryl ether structures in lignin.

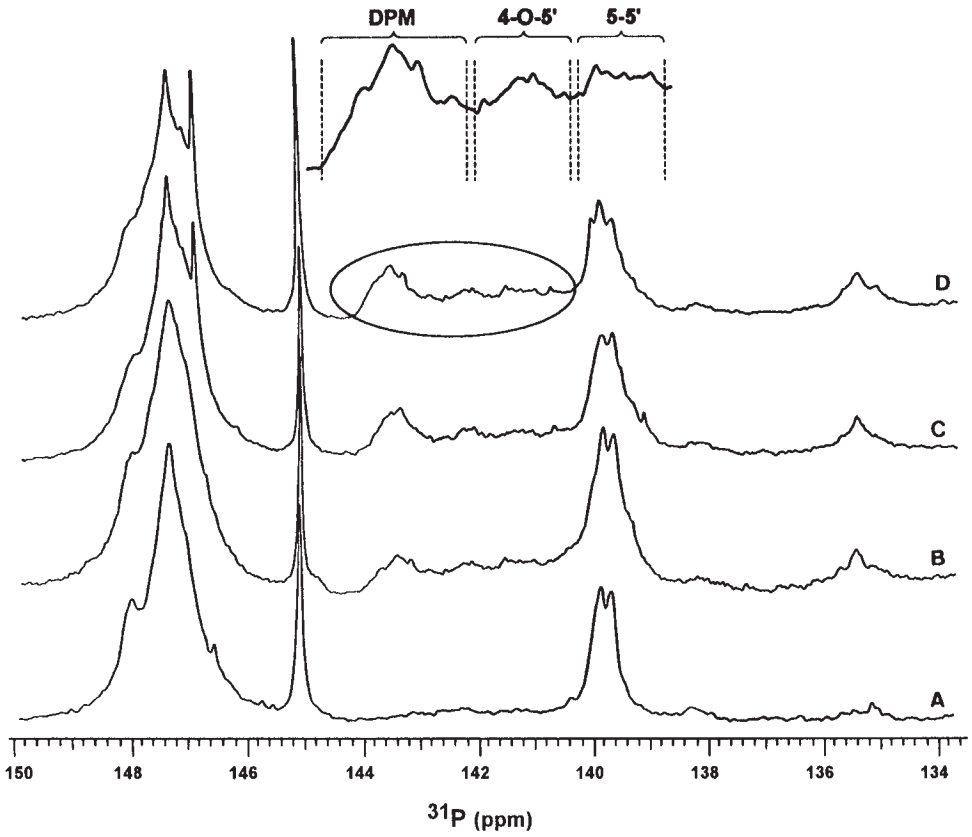

added display a new signal at 147.01 ppm that appears in the aliphatic OH region. In accordance with the chemistry of the formaldehyde–phenol interaction, which is known to occur under alkaline conditions (19, 20), it is very likely that this signal is due to the aliphatic primary hydroxyl group of methylolated aromatic rings.

When the ^{31}P NMR signal in the region 142.8–144.3 ppm was integrated, the determination of the actual concentrations of diphenylmethane structures in milled wood lignin, in the presence and absence of formaldehyde under kraft pulping conditions, was made possible as a function of reaction time at 120°C (Table 1).

The quantitative data thus collected revealed that under isothermal conditions (120°C) the addition of formaldehyde to the kraft reaction medium causes the buildup of DPM structures within lignin, while in the absence of externally added formaldehyde, these structures predominate after 3–4 h of reaction. It is also interesting to note that when a large excess of formaldehyde was added (amounting to 100% of the total aryl ethers) the amount of DPM structures reached a value of 0.4 mmol/g within 60 min at 120°C, remaining approximately constant beyond this point.

In an effort to further substantiate our conclusions we then carried out two series of isothermal (120°C) kraft and soda pulping experiments followed by quantitative determinations of the DPM moieties, and correlated our findings with the differences in chemistry known to occur between the two processes.

Table 1. Showing the actual amounts of DPM[a] structures present in MWL[b] before and after the addition of formaldehyde[c] under homogeneous kraft pulping conditions.[d]

	DPM × 10^4 (mol/g)		
Reaction time (min)	Control kraft	50%[c]	100%[c]
60	0.83	1.60	4.0
120	1.41	2.20	4.2
180	2.41	3.00	4.4
240	4.10	4.10	4.6

[a] Diphenylmethane structures.
[b] Milled wood lignin (softwood, *Picea mariana*).
[c] Amount of formaldehyde added, expressed as percentage of the total amount of aryl ethers present in MWL.
[d] The temperature of the kraft pulping experiment was set at 120°C.

The data of Table 2 clearly demonstrate that the formation of diphenylmethane moieties is a considerably more facile reaction under soda pulping conditions than under kraft pulping conditions. Sulphide ions present in kraft liquors are responsible for promoting and accelerating lignin fragmentation reactions as well as suppressing undesirable condensation reactions (1, 52, 53).

The presence of sulphide ions within sulfate liquors has been suggested to preclude the liberation of formaldehyde from the lignin biopolymer (19). Alternatively, the absence of sulphide, i.e., soda pulping, allows the intermediate quinone-

© 1998 NRC Canada

Scheme 3.

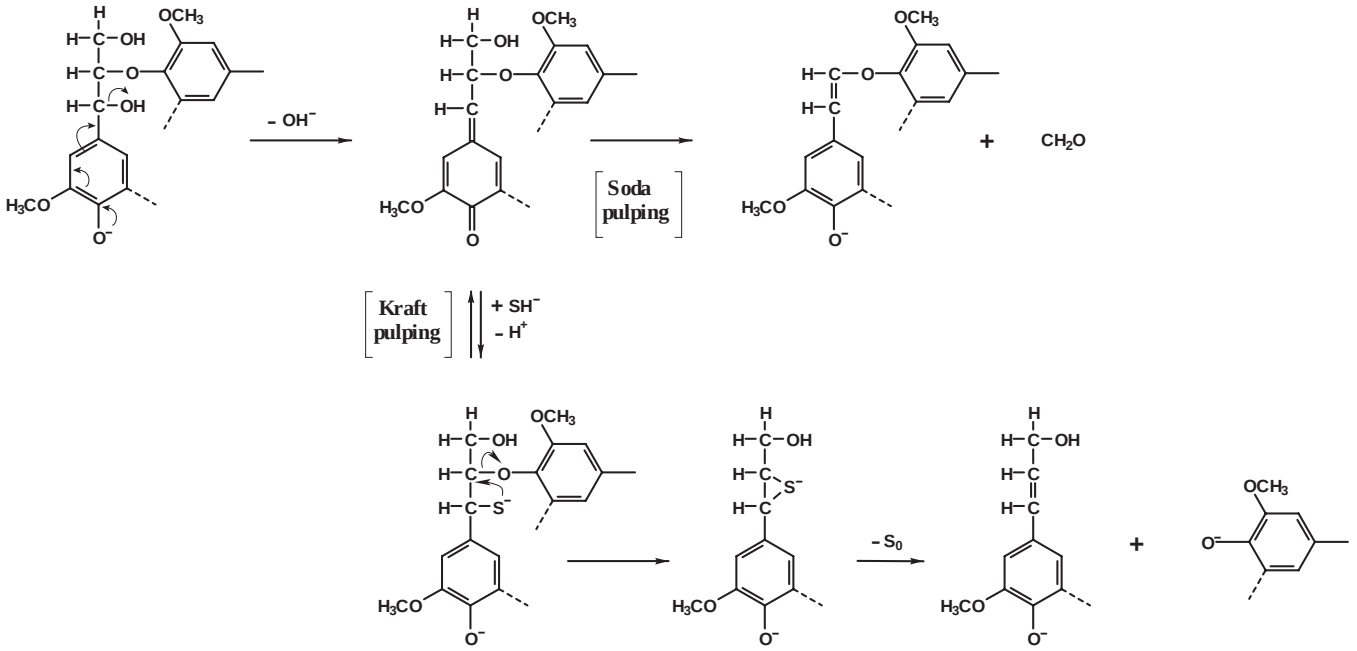

Table 2. Showing the actual amounts of DPM[a] structures present in MWL[b] under homogeneous kraft and soda[c] pulping conditions.[d]

	DPM × 10^4 (mol/g)	
Reaction time (min)	Kraft pulping	Soda pulping
60	0.83	1.60
120	1.41	2.20
180	2.41	3.10
240	4.10	4.30

[a] Diphenylmethane structures.
[b] Milled wood lignin (softwood, *Picea mariana*).
[c] Amount of sodium sulphide was replaced with sodium hydroxide.
[d] The temperature of the pulping experiments was set at 120°C.

Table 3. Showing the actual distribution of condensed and diphenylmethane structures present in conventional and EMCC® kraft pulps of similar κ number.

	Total concentration × 10^4(mol/g)	
Pulp sample identity	Condensed units[a]	DPM units[b]
Conventional kraft (κ = 26.8)[c]	17.0	3.0
EMCC® kraft (κ = 26.0)[c]	15.0	2.0

[a] Total condensed phenolic structures.
[b] Diphenylmethane phenolic OH structures.
[c] κ number.

methides to lose formaldehyde, causing the formation of undesirable alkaline stable enol ethers (1, 54). The rate data of Table 2 clearly demonstrate the efficiency of formation of diphenylmethanes under soda pulping conditions, especially early in the process. Therefore, it is not surprising that bleaching a soda–AQ pulp is more difficult than bleaching a kraft pulp of a similar κ (kappa) number (55) (Scheme 3).

Among the various principles that operate during modified pulping, the control of alkalinity is of prime importance. Maintaining hydroxide concentration at a uniformly low level offers distinct advantages as far as carbohydrate degradation is concerned. In this context, maintaining a uniformly low alkalinity may also have an impact on the actual amount of diphenylmethane structures that form within the residual kraft lignin. For this reason residual lignin was isolated from two hemlock kraft pulp samples (κ number 26.0) produced via an EMCC® mill protocol and a laboratory batch digester, respectively. The data of Table 3 are in accord with the previous observations. While in the conventional kraft pulp the overall amount of C-5 substituted phenolic environments is higher by 11%, the diarylmethane structures prevail amongst them by 37%. These data, coupled with the earlier account of Froass et al. (43), provide convincing evidence supporting the fact that modern modified cooking technologies alter the structure of lignin beneficially.

The region of the ^{31}P NMR spectra assigned to the overall condensed phenolic units (140.2–144.3 ppm), in addition to the diphenylmethane moieties, also includes phenolic hydroxyl groups belonging to 4-O-5′ and 5,5′ structures. More specifically, on the basis of model compound work and detailed calculations these structures have been assigned to the signals ranging between 142.8 and 141.7 ppm and 141.7 and 140.2 ppm, respectively (40, 50) (Fig. 1). This assignment was also confirmed by the efforts of Smit et al. (44). In 1995, Brunow's group announced the discovery of the dienzodioxocin bonding patterns as being prevalent in softwoods lignins (56, 57). This involves the formation of α,β ethers on the same 5–5′ biphenyl structure. The new moiety, when subjected to soda pulping conditions, was shown to release significant amounts of structures bearing 5,5′ biphenolic hydroxyl groups (58). Therefore under kraft pulping conditions it is likely that similar reactions, releasing 5,5′ biphenolic hydroxyl groups,

© 1998 NRC Canada

Fig. 2. Kinetic data showing the development of the actual amounts of 4-*O*-5′,5,5′ biphenolic and diphenylmethane phenolic hydroxyl structures on softwood milled wood lignin under homogeneous kraft pulping conditions at 120°C in the presence and absence of formaldehyde. The amount of formaldehyde added is expressed as percentage of the total amount of aryl ethers present in MWL.

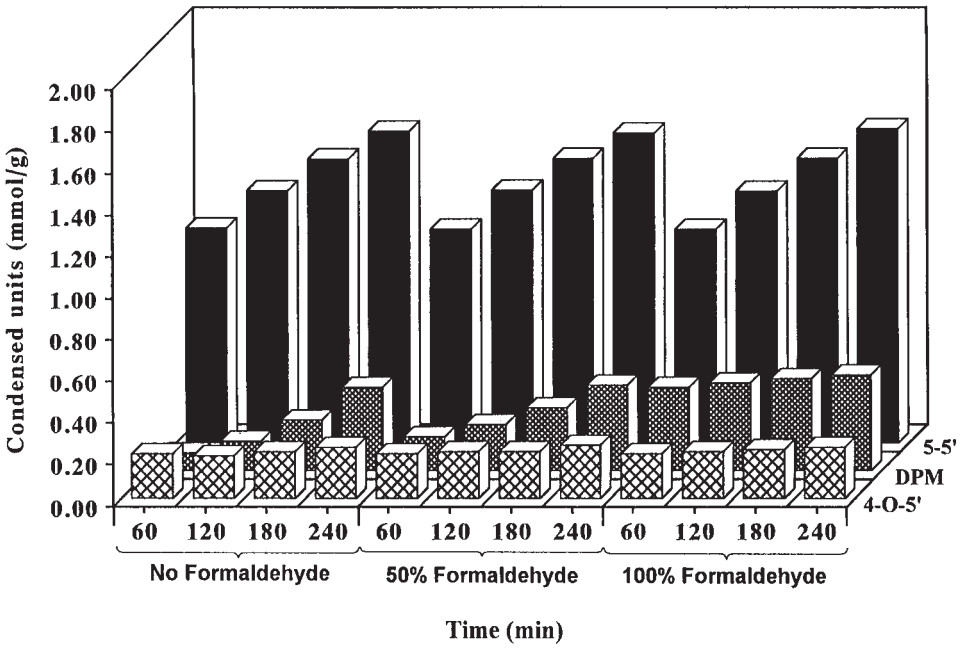

will occur. The data of Fig. 2 show that indeed such structures are released in very significant amounts after 4 h at 120°C (about 1.5 mmol/g are formed within milled wood lignin). As anticipated, the presence of formaldehyde does not seem to affect the rate of formation of 5,5′ biphenolic hydroxyl groups or the concentration of dibenzyl ether (4-O-5′) structures (Fig. 2).

Finally, the formation of diphenylmethane structures under kraft and soda pulping conditions was found to follow pseudo-first-order kinetics with rate constants $14.8 \times 10^{-5} \pm 2.2 \times 10^{-7}$ s^{-1} and $9.2 \times 10^{-5} \pm 8.8 \times 10^{-7}$ s^{-1}, respectively.

Conclusions

By using quantitative ^{31}P NMR spectroscopy it is possible to identify, quantify, and follow the formation of phenolic hydroxyl groups that belong to diphenylmethane units under kraft and soda pulping conditions. These units exhibit a ^{31}P chemical shift signal that is confined between 142.8 and 144.3 ppm. Data derived during the course of this work implied that diphenylmethanes are formed in higher quantities during a conventional pulping than are their EMCC® counterparts, at the same κ number.

Acknowledgements

This investigation was made possible by the support of the Canadian Pulp and Paper Industry and a strategic grant provided by the Government of Canada.

References

1. J. Marton. *In* Lignins: occurrence, formation, structure, and reactions. *Edited by* K.V. Sarkanen and C.H. Ludwig. Wiley–Interscience, New York. 1971. pp. 639–694.
2. B. Johansson, J. Mjoberg, P. Sandstrom, and A. Teder. Sven. Papperstidn. **10**, 30 (1984).
3. A. Backlund. Tappi, **67**, 62 (1984).
4. A. Teder and P. Sandstrom. Tappi, **68**, 94 (1985).
5. F.E. Mera and J.L. Chamberlin. TAPPI Proc. Pulping Conference. Book 3. TAPPI Press, Washington, D.C. November 1987. pp. 459–465.
6. L.K. Swift and J.S. Dayton. CPPA Energy Management Conference, Toronto, Ont. April 1987. pp. 31–37.
7. P.O. Tikka, N.E. Virkola, S.A. Pursiainen, and I.T. Hamala. TAPPI Proc. Pulping Conference. Book 3. TAPPI Press, Washington, D.C. November 1987. pp. 635–645.
8. K.B. Barratt. Proc. TAPPI Annual Meeting. TAPPI Press, Atlanta, Ga. March 1990, pp. 95–102.
9. N.H. Shin, V.S.M. Sundaram, H. Jameel, and H. Chang. Proc. TAPPI Annual Meeting. Pulping Conference. Book 2. TAPPI Press, Toronto, Ont. October 1990. pp. 817–828.
10. B. Dillner, L.O. Larsson, and P. Tibbling. Tappi, **73**, 167 (1990).
11. D.L. Whitley, J.R. Zierdt, and D.J. Lebel. Tappi, **73**, 103 (1990).
12. B. Stromberg. TAPPI Proc. Pulping Conference. Book 3. TAPPI Press, Washington, D.C. November 1987. pp. 453–458.
13. D.Y. Prasad, A. Gnanasekaran, and N.R. Mohan Rao. Tappi, **77**, 141 (1994).
14. J.E. Jiang. Tappi, **77**, 120 (1994).
15. B. Mao and N. Hartler. Tappi, **77**, 149 (1994).
16. H. Jmeel, J. Gratzl, D.Y. Prasad, and S. Chivukula. Tappi, **78**, 151 (1995).
17. T.J. Blain. Tappi, **76**, 137 (1993).
18. L.G. Sturgeoff and Y. Pitl. Tappi, **77**, 95 (1994).
19. K.H. Ekman. Tappi, **84**, 398 (1965).
20. E. Adler, J. Marton, and S.I. Falkehag. Acta Chem. Scand. **18**, 1311 (1964).
21. J. Gierer and S. Söderberg. Acta Chem. Scand. **13**, 127 (1959).
22. E. Adler, S.I. Falkehag, J. Marton, and H. Halvarson. Acta Chem. Scand. **18**, 1313 (1964).
23. E. Adler and K. Lundquist. Acta Chem. Scand. **15**, 223 (1961).
24. J. Gierer, B. Lenz, and N.H. Wallin. Tappi, **48**, 402 (1965).

© 1998 NRC Canada

25. J. Marton, T. Marton, and S.I. Falkehag. Adv. Chem. Ser., **59**, 125 (1966).
26. G. Chirkin, and D. Tishschenko. Zh. Prikl. Khim. **35**, 153 (1962).
27. J. M. Harkin. Adv. Chem. Ser. **59**, 65 (1966).
28. J. Gierer. J. Wood Sci. Technol. **19**, 289 (1985).
29. G. Brunow and G.E. Miksche. Appl. Polymer Symp. **28**, 1155 (1976).
30. J. Gierer, F. Imsgard, and I. Pettersson. Appl. Polymer Symp. **28**, 1195 (1976).
31. B.Johansson and G.E. Miksche. Acta Chem. Scand. **23**, 824 (1969).
32. V.L. Chiang and M. Funaoka. Holzforschung, **42**, 385 (1988).
33. V.L. Chiang and M. Funaoka. Holzforschung, **44**, 147 (1990).
34. V.L. Chiang and M. Funaoka. Holzforschung, **44**, 309 (1990).
35. F.D. Chan, K.L. Nguyen, and A.F.A. Wallis. J. Wood Chem. Technol. **15**, 473 (1995).
36. Y. Archipov, D.S. Argyropoulos, H.I. Bolker, and C. Heitner. J. Wood Chem. Technol. **11**, 137 (1991).
37. Y. Archipov, D.S. Argyropoulos, H.I. Bolker, and C. Heitner. Carbohydr. Res. **220**, 49 (1991).
38. D.S. Argyropoulos, Y. Archipov, H.I. Bolker, and C. Heitner. Holzforschung, **47**, 50 (1992).
39. D.S. Argyropoulos, H.I. Bolker, C. Heitner, C. Archipov, and Y. Archipov. J. Wood Chem.Technol. **13**, 187 (1993).
40. A. Granata and D.S. Argyropoulos. J. Agric. Food Chem. **43**, 1538 (1995).
41. D.S. Argyropoulos, Y. Sun, and M. Mazur. Nord. Pulp Pap. Res. J. **10**, 68 (1995).
42. Y. Sun and D.S. Argyropoulos. J. Pulp Pap. Sci. **21**, 185 (1995).
43. P.M. Froass, A.J. Ragauskas, and J. Jiang. J. Wood Chem. Technol. **16**, 347 (1996).
44. R. Smit, I.D. Suckling, and R.M. Ede. Int. Symp. Wood and Pulping Chemistry, 9th. Montréal, Que. June 1997. L4-1–L4-6.
45. Z.H. Jiang and D.S. Argyropoulos. Int. Symp. Wood and Pulping Chemistry, 8th. Helsinki, Finland. June 1995. Vol. I. pp. 511–525.
46. Z.H. Jiang and D.S. Argyropoulos. Int. Symp. Wood and Pulping Chemistry, 9th. Montréal, Que. June 1997. pp. J2-1–J2-6.
47. B.C. Ahvazi and D.S. Argropoulos. Nord. Pulp Pap. Res. J. **12**, 282 (1997).
48. A. Björkman. Sven. Papperstidn. **59**, 477 (1956).
49. D.S. Argyropoulos. J. Wood Chem. Technol. **14**, 45 (1994).
50. Z.H. Jiang, D.S. Argyropoulos, and A. Granata. Magn. Reson. Chem. **33**, 375 (1995).
51. E. Adler. J. Wood Sci. Technol. **11**, 169 (1977).
52. E. Hägglund. Tappi, **32**, 241 (1949).
53. T. Enkvist and E. Hägglund. Sven. Papperstidn. **53**, 85 (1950).
54. J. Gierer. J. Wood Sci. Technol. **14**, 267 (1980).
55. V.R. Parthasarathy, R.C. Grygotis, K.W. Wahoske, and D.M. Bryer. Tappi, **79**, 189 (1996).
56. P. Karhunen, P. Rummakko, J. Sipilä, G. Brunow, and I. Kilpeläinen. Tetrahedron Lett. **36**, 169 (1995).
57. P. Karhunen, P. Rummakko, J. Sipilä, G. Brunow, and I. Kilpeläinen. Tetrahedron Lett. **36**, 4501 (1995).
58. P. Karhunen, J. Mikkola, and G. Brunow. Int. Symp. Wood and Pulping Chemistry, 9th. Montréal, Que. June 1997. pp. R1-1–R1-3.

© 1998 NRC Canada

The solid-state structure of bis(pentafluorophenyl)zinc

Yimin Sun, Warren E. Piers, and Masood Parvez

Abstract: Using the published method of Wiedenbruch, bis(pentafluorophenyl)zinc, **1**, was prepared from anhydrous $ZnCl_2$ and 2 equiv. of LiC_6F_5 in diethyl ether. Base-free **1** was obtained in 60–65% yield by repeated distillation of the initially formed bis(diethyl) ether adduct of **1**. The X-ray quality crystals of **1** were obtained from benzene solution. The molecular structure of **1** revealed a near linear geometry for the two-coordinate zinc center (C(1)-Zn-C(7) = 172.6(2)°), typical of monomeric ZnR_2 derivatives. In the crystal structure, stacking interactions between C_6F_5 rings on adjacent molecules is a dominant motif, with ring centroid to ring centroid distances of 3.503 and 3.563 Å observed. A weak intermolecular C-F···Zn interaction between F(2) and an adjacent zinc center, as judged by the close contact of 2.849(2) Å, also appears to be an important aspect of the crystal structure. Compound **1** is an effective but nonselective C_6F_5 transfer agent to BCl_3; **1**: monoclinic, space group $P2_1/n$, a = 11.902(2) Å, b = 7.732(2) Å, c = 13.735(2) Å, β = 110.58(1)°, V = 1183.4(4) Å^3, Z = 4, R = 0.048, R_w = 0.069.

Key words: organozinc complex, pentafluorophenyl transfer agent.

Résumé : En faisant appel à la méthode non publiée de Wiedenbruch, on a préparé le bis(pentafluorophényl)zinc, **1**, à partir du $ZnCl_2$ et de deux équivalents de LiC_6F_5 dans l'éther. On a obtenu le composé **1** sous la forme de base libre avec un rendement de 60 à 65% en procédant à la distillation répétée de l'adduit formé initialement du composé **1** avec deux molécules d'éther. À partir d'une solution de benzène, on a obtenu des cristaux de **1** pouvant être utilisés pour études par diffraction des rayons X. La structure moléculaire du composé **1** révèle que ce composée présente une géométrie pratiquement linéaire pour le zinc central bicoordiné (C(1)-Zn-C(7) = 172,62(2)°) typique de dérivés ZnR_2 monomères. Dans la structure cristalline, les interactions d'empilement entre les noyaux C_6F_5 de molécules adjacentes correspondent au motif dominant et on observe des distances 3,503 et de 3,563 Å entre les centroïdes de noyaux. Il semble qu'une faible interaction intermoléculaire C-F···Zn entre F(2) et le zinc central adjacent, détectée par un contact de 2,849(2) Å, corresponde à un aspect important de la structure. Le composé **1** est un agent de transfert efficace, mais non sélectif, de C_6F_5 vers le BCl_3. Le composé est monoclinique, groupe d'espace $P2_1/n$, avec a = 11,902(2) Å, b = 7,732(2) Å et c = 13,735(2) Å, β = 110,58(1)°, V = 1183,4(4) Å^3, Z = 4, R = 0,048 et R_w = 0,069.

Mots clés : complexe organozincique, agent de transfert de pentafluorophényle.

[Traduit par la rédaction]

Introduction

The increasing commercial importance of $B(C_6F_5)_3$ (1) has stimulated interest in other perfluorinated boranes (2). The robust nature of the B—C_6F_5 bond and the heightened Lewis acidity, which the C_6F_5 group confers upon the boron center, contributes to the utility of these compounds. Increasingly, bis(pentafluorophenyl) boranes of general formula $X[B(C_6F_5)_2]_n$ are finding utility as catalysts or reagents in organic synthesis (X = OH, n = 1 (3); X = H, n = 1 (4)) and as alternative co-catalysts in homogeneous olefin polymerization (X = t-$C_4H_9CH_2CH$, n = 2 (5)).

The syntheses of such compounds is not, however, straightforward at this point. For example, the borane $HB(C_6F_5)_2$ and the boronic acid $HOB(C_6F_5)_2$ both rely on the chloroborane $ClB(C_6F_5)_2$ as a starting material. While a reliable published procedure for the preparation of this compound exists (6), it is not ideal in that it depends on the organotin compound $Me_2Sn(C_6F_5)_2$ as a reagent capable of selectively delivering two C_6F_5 groups to BCl_3. The tedious procedures necessary for separating Me_2SnCl_2 completely from the chloroborane product and concerns around the handling of this volatile organotin by-product have led us to explore other reagents for C_6F_5 transfer to boron. While testing the known compound bis(pentafluorophenyl)zinc, **1**, as a possible reagent for preparing $ClB(C_6F_5)_2$, we obtained its molecular structure, which had not previously been determined.

Received January 28, 1998.

Y. Sun, W.E. Piers,[1] and M. Parvez. Department of Chemistry, University of Calgary, 2500 University Drive N.W., Calgary, AB T2N 1N4, Canada.

[1] Fellow of the Alfred P. Sloan Foundation, 1996–1998. Author to whom correspondence may be addressed. Telephone: (403) 220–5746. Fax: (403) 289–9488. E-mail: wpiers@chem.ucalgary.ca.

Results and discussion

To our knowledge, four routes to $Zn(C_6F_5)_2$, **1**, have been published (eqs. [1]–[4]). The original preparation of **1** utilized the Grignard reagent $BrMgC_6F_5$ for introducing the pentafluorophenyl groups to $ZnCl_2$, by refluxing in toluene for 2 h after an initial contact of the reagents in diethyl ether solution

© 1998 NRC Canada

[1] $$2\ BrMgC_6F_5 + ZnCl_2 \xrightarrow[2.\ \text{toluene, } 110^\circ C]{1.\ Et_2O} Zn(C_6F_5)_2\bullet(Et_2O)_2 \xrightarrow[10^{-2}\ \text{torr}]{140^\circ C} \mathbf{1}$$

[2] $$Zn(O_2C\text{-}C_6F_5)_2 \xrightarrow[-\ 2\ CO_2]{220^\circ C} Zn(C_6F_5)_2 \quad \mathbf{1}$$

[3] $$2\ IC_6F_5 + ZnEt_2 \xrightarrow[2\ L = \text{diglyme or pyridine}]{2\ L} Zn(C_6F_5)_2\bullet L_2 \not\rightarrow \mathbf{1}$$

[4] $$2\ LiC_6F_5 + ZnCl_2 \xrightarrow{-78^\circ C,\ Et_2O} Zn(C_6F_5)_2\bullet(Et_2O)_2 \xrightarrow[10^{-2}\ \text{torr}]{140^\circ C} \mathbf{1}$$

(7). The crude product mixture contained the ether adduct of **1**, which was isolated base-free by distillation of $Zn(C_6F_5)_2\cdot(Et_2O)_2$ under high vacuum at 140°C, resulting in a 15% yield of $Zn(C_6F_5)_2$. However, significant amounts of an unidentified colorless liquid by-product was also produced in this reaction.

In our hands, this procedure produced very little $Zn(C_6F_5)_2$ but large amounts of the liquid by-product, which we identified as an isomeric mixture of the Diels–Alder products formed upon reaction with tetrafluorobenzyne and toluene.[2] It is not clear which species in the reaction mixture is the source of tetrafluorobenzyne but, given the thermal stability of **1** itself, it is likely to be an intermediate in this process or perhaps $BrMgC_6F_5$. In a second route to **1**, loss of CO_2 from the dicarboxylate compound $Zn(O_2CC_6F_5)_2$ (eq. [2]) provides the driving force for relatively clean formation of **1** directly (8). Third, eq. [3] represents a relatively safe route to pentafluorophenyl zinc derivatives, but the bases employed in the published procedure (9) are not easy to remove; for our purposes, we must have base free **1**.

Despite the potential hazards associated with the more reactive reagent pentafluorophenyllithium, we turned to the fourth procedure, also developed by Weidenbruch (8), which produces **1** much more cleanly (eq. [4]). A diethyl ether solution of $ZnCl_2$ was added to in situ generated C_6F_5Li, and the resulting mixture was allowed to warm slowly to room temperature. Work-up led to base-free **1**, which gave a ^{19}F NMR spectrum essentially identical to that reported, with no trace of the Diels–Alder by-product in evidence. For larger scale preparations (>2 g), multiple distillations were required to fully remove the diethyl ether, which was judged complete when the distillate was a free-flowing powder as opposed to the oily white solid characteristic of **1** contaminated with its ether adduct.

While a few Lewis base adducts $\mathbf{1}\cdot L_2$ have been structurally characterized (L = THF (10); tetramethyltetrazene (11)), that of base free **1** has not. We therefore obtained X-ray quality crystals of **1** and evaluated its solid-state structure; an ORTEP diagram is shown in Fig. 1, while metrical parameters are given in Table 1, and atomic coordinates are given in Table 2. Two coordinate organozinc compounds are typically monomeric with linear geometries (12), and most of those whose structures have been determined bear this out (13). The exception is diphenylzinc (13*a*), which is dimeric in the solid state by virtue of an interaction between an ipso carbon of one σ-bound phenyl group and the zinc center of another $Zn(C_6H_5)_2$ unit. This interaction was rationalized as being akin to an electrophilic attack on the zinc phenyl group by an adjacent Lewis acidic zinc center. This feature is not replicated in the structure of perflouro diphenylzinc, **1**, presumably because the C_6F_5 groups are much less susceptible to electrophilic attack even though the zinc centers must also be more powerful electrophiles.

Thus, in contrast to its perproteo cousin, **1** behaves like most other ZnR_2 derivatives and is monomeric in the solid state with with C(1)-Zn-C(7) approaching ideal linearity at 172.6(2)°. The Zn—C bonds in **1** are typical of ZnR_2 compounds, which range from 1.93–1.95 Å in compounds where R is not sterically bulky. These lengths are slightly shorter than those found in four coordinate $Zn(C_6F_5)_2\cdot L_2$ compounds (cf. Zn—C lengths of 1.999(4) and 2.102(3) Å in $Zn(C_6F_5)_2(THF)_2$) (10). The two C_6F_5 rings in **1** are almost orthogonal to one another, with an angle between the planes of the aromatic rings of 76.7(2)°. This compares to 67.1° for the same parameter in $Zn[2,4,6\text{-}(CF_3)_3C_6H_3]_2$ (13*c*).

In addition to alleviating intramolecular steric interactions between the C_6F_5 rings, the orthogonality of the C_6F_5 rings in **1** allows for intramolecular stacking interactions between rings on adjacent molecules in the crystal structure of the compound. These stacking interactions engender a layered structure in the crystal; Fig. 2 shows a chemical 3-D representation of the molecular arrangement in the crystal looking down on a portion of one layer (*A*) and from the side (*B*). The distances between the centroids of each C_6F_5 ring and its stacking partner are 3.503 and 3.563 Å, similar to the ring separations observed in stacking interactions between phenyl and pentafluorophenyl rings (14). Between the layers, a weak interaction between one of the meta fluorines, F(2), and a Zn center of an adjacent molecule may be present, as judged by the intermolecular separation of 2.849(2) Å. Although this is at the long end of the range (2.532(6)–2.733(6) Å) of previously observed intramolecular C-F···Zn interactions (15), the intermolecular nature of the contact here might be expected to be slightly longer. Furthermore, the distance is within the sum of the van der

[2] D.J. Parks and W.E. Piers. Unpublished results.

© 1998 NRC Canada

Fig. 1. An ORTEP drawing of $Zn(C_6F_5)_2$, **1** (thermal ellipsoid probability = 50%).

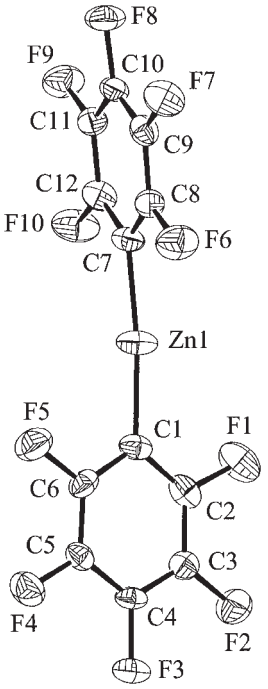

Fig. 2. Two views of the molecular arrangment of $Zn(C_6F_5)_2$ molecules in the crystal structure of **1**. (*A*) View looking down on one of the layers of stacked $Zn(C_6F_5)_2$ molecules. (*B*) Side view of layer shown in *A*.

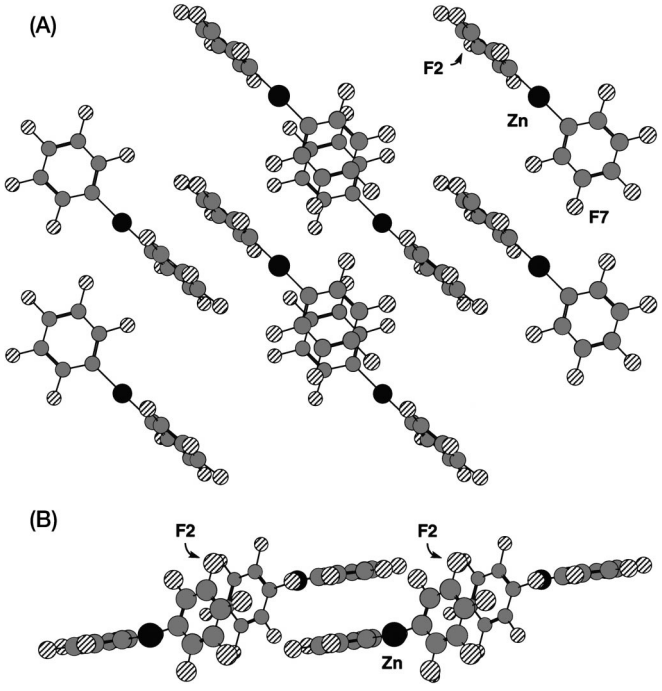

Waals radii(16) for fluorine (1.50–1.60 Å) and zinc (1.40 Å). The fact that the slight bend in the C(1)-Zn-C(7) angle is oriented away from the C(3)-F(2) vector is further evidence in favor of this interaction. The tendency of ZnR_2 complexes to coordinate Lewis bases is thus partially satisfied in the crystal structure of "base free" **1** through this intermolecular contact.[3]

Table 1. Bond distances and angles for $Zn(C_6F_5)_2$, **1**.

Bond lengths (Å)			
Zn(1)—C(1)	1.930(4)	C(1)—C(2)	1.382(5)
Zn(1)—C(7)	1.926(4)	C(1)—C(6)	1.379(5)
F(1)—C(2)	1.358(4)	C(2)—C(3)	1.370(5)
F(2)—C(3)	1.343(4)	C(3)—C(4)	1.384(5)
F(3)—C(4)	1.340(4)	C(4)—C(5)	1.371(5)
F(4)—C(5)	1.347(4)	C(5)—C(6)	1.364(5)
F(5)—C(6)	1.360(4)	C(7)—C(8)	1.385(5)
F(6)—C(8)	1.361(4)	C(7)—C(12)	1.370(5)
F(7)—C(9)	1.344(4)	C(8)—C(9)	1.367(5)
F(8)—C(10)	1.339(4)	C(9)—C(10)	1.378(5)
F(9)—C(11)	1.344(4)	C(10)—C(11)	1.371(5)
F(10)—C(12)	1.354(4)	C(11)—C(12)	1.378(5)
Bond angles (°)			
C(1)-Zn(1)-C(7)	172.6(2)	Zn(1)-C(7)-C(8)	121.5(3)
Zn(1)-C(1)-C(2)	126.2(3)	Zn(1)-C(7)-C(12)	123.8(3)
Zn(1)-C(1)-C(6)	119.2(3)	C(8)-C(7)-C(12)	114.7(3)
C(2)-C(1)-C(6)	114.6(3)	F(6)-C(8)-C(7)	119.1(3)
F(1)-C(2)-C(1)	120.0(3)	F(6)-C(8)-C(9)	116.9(4)
F(1)-C(2)-C(3)	116.4(3)	C(7)-C(8)-C(9)	123.9(4)
C(1)-C(2)-C(3)	123.6(3)	F(7)-C(9)-C(8)	121.4(3)
F(2)-C(3)-C(2)	122.1(3)	F(7)-C(9)-C(10)	119.8(3)
F(2)-C(3)-C(4)	118.9(3)	C(8)-C(9)-C(10)	118.8(4)
C(2)-C(3)-C(4)	119.0(3)	F(8)-C(10)-C(9)	120.0(3)
F(3)-C(4)-C(3)	120.1(3)	F(8)-C(10)-C(11)	120.1(3)
F(3)-C(4)-C(5)	120.3(3)	C(9)-C(10)-C(11)	119.8(3)
C(3)-C(4)-C(5)	119.6(3)	F(9)-C(11)-C(10)	119.5(3)
F(4)-C(5)-C(4)	119.6(3)	F(9)-C(11)-C(12)	121.6(4)
F(4)-C(5)-C(6)	121.4(3)	C(10)-C(11)-C(12)	118.9(3)
C(4)-C(5)-C(6)	119.0(3)	F(10)-C(12)-C(7)	119.1(3)
F(5)-C(6)-C(1)	118.7(3)	F(10)-C(12)-C(11)	117.1(3)
F(5)-C(6)-C(5)	117.0(3)	C(7)-C(12)-C(11)	123.8(4)
C(1)-C(6)-C(5)	124.3(3)		

As expected, **1** rapidly reacts with Lewis bases to form $\mathbf{1}\cdot L_2$ adducts in toluene solution. For example, the known adducts of diethyl ether (8, 10) and THF (10) can be generated quantitatively upon treatment with these solvents. Base free, **1** is an efficient C_6F_5 transfer agent, although it does not react selectively with BCl_3 (eq. [5]). Unfortunately, inseparable mixtures of $Cl_2B(C_6F_5)$, $ClB(C_6F_5)_2$, and $B(C_6F_5)_3$ were formed when **1** was reacted with 1 equiv. of BCl_3 under various conditions, a similar situation to that observed in the reaction of C_6F_5Li with BCl_3. Thus, **1** is too reactive to be a suitable reagent for selective formation of $ClB(C_6F_5)_2$; however, it has promise as a C_6F_5 transfer agent to compounds of general formula $RBCl_2$. We will report on its utility in this capacity in due course.

[5] $$\underset{\mathbf{1}}{Zn(C_6F_5)_2} \xrightarrow[-\ ZnCl_2]{BCl_3} \underset{\text{major (≈80\%)}}{Cl_2B(C_6F_5)} + ClB(C_6F_5)_2 + B(C_6F_5)_3$$

[3] The second closest contact between the zinc centers and a fluorine atom is that of meta fluorine F(7) at 3.200(3) Å. This interaction occurs within the layers mentioned in the text; however, due to the rather large separation, caution must be employed in interpreting this interaction as the second incipient zinc/base interaction.

© 1998 NRC Canada

Table 2. Atomic coordinates x, y, z and B_{eq} for $Zn(C_6F_5)_2$, **1**.

Atom	x	y	z	B_{eq}[a]
Zn(1)	0.15686(4)	0.12335(6)	0.89789(4)	3.33(1)
F(1)	0.2482(2)	–0.1429(3)	0.7609(2)	4.30(6)
F(2)	0.4394(2)	–0.3549(3)	0.8233(2)	3.77(6)
F(3)	0.5844(2)	–0.3629(3)	1.0255(2)	3.16(5)
F(4)	0.5285(2)	–0.1749(3)	1.1691(2)	3.62(5)
F(5)	0.3401(2)	0.0414(3)	1.1082(2)	3.81(6)
F(6)	0.1779(2)	0.5214(3)	0.9004(2)	4.08(6)
F(7)	0.0128(2)	0.7687(3)	0.8797(2)	3.89(6)
F(8)	–0.2165(2)	0.6805(3)	0.8550(2)	3.71(6)
F(9)	–0.2816(2)	0.3437(3)	0.8438(2)	3.97(6)
F(10)	–0.1162(2)	0.0942(3)	0.8647(2)	4.21(6)
C(1)	0.2857(3)	–0.0434(5)	0.9330(3)	2.54(8)
C(2)	0.3156(3)	–0.1471(5)	0.8638(3)	2.63(8)
C(3)	0.4127(3)	–0.2559(5)	0.8925(3)	2.48(8)
C(4)	0.4857(3)	–0.2637(4)	0.9962(3)	2.26(8)
C(5)	0.4581(3)	–0.1662(5)	1.0681(3)	2.29(8)
C(6)	0.3612(3)	–0.0585(5)	1.0350(3)	2.45(8)
C(7)	0.0360(3)	0.2976(5)	0.8817(3)	2.54(8)
C(8)	0.0628(3)	0.4722(5)	0.8836(3)	2.66(9)
C(9)	–0.0189(3)	0.6011(5)	0.8744(3)	2.40(8)
C(10)	–0.1357(3)	0.5569(5)	0.8606(3)	2.43(8)
C(11)	–0.1676(3)	0.3860(5)	0.8568(3)	2.60(8)
C(12)	–0.0815(3)	0.2613(5)	0.8667(3)	2.73(9)

[a] $B_{eq} = (8/3)\pi^2[U_{11}(aa^*)^2 + U_{22}(bb^*)^2 + U_{33}(cc^*)^2 + 2U_{12}aa^*bb^* \cos\gamma + 2U_{13}aa^*cc^* \cos\beta + 2U_{23}bb^*cc^* \cos\alpha]$.

Experimental

General procedures have been presented in detail elsewhere (17). Pentafluorobromobenzene and zinc dichloride were purchased from Aldrich Chemicals. The former was used without further purification, while the latter was rendered completely anhydrous by refluxing in dry dioxane along with zinc dust. The suspension was filtered hot and cooled; the resulting crystalline $ZnCl_2$·dioxane adduct was isolated by filtration and exposed to high vacuum at 110°C for several hours to liberate the coordinated dioxane.

Preparation of 1

A procedure similar to that reported earlier by Sartori and Weidenbruch (8) was employed to generate **1**·$(OEt_2)_2$. (CAUTION! Do not allow solutions of C_6F_5Li to warm above –40°C; spontaneous elimination of LiF is possible above this temperature.) The only modification involved quenching the reaction with a small amount of methanol (≈1–2%) to ensure that no C_6F_5Li remained for the workup procedure. For smaller scale reactions (≈0.5–1.0 g), distillation of **1**·$(OEt_2)_2$ at 140°C and high vacuum was sufficient to completely remove the ether. For larger scale preparations (>2 g), multiple distillations were required to generate pure **1**. This was most conveniently accomplished by repeatedly subliming the material in a long glass tube. Loss of the oily appearance of the sublimate signalled the complete removal of ether. The material thus obtained had essentially identical ^{19}F NMR data as that reported previously for **1** by Weidenbruch et al. (10).

X-ray determination of 1

A suitable crystal was affixed to a glass fiber with epoxy resin and mounted onto a Rigaku AFC6S diffractometer. A summary of data collection, reduction, and refinement parameters are given in Table 3. Measurements were made at 103°C using graphite monochromated Mo-Kα radiation (λ = 0.71069 Å). Omega scans of several intense reflections, made prior to data collection, had an average width at half-height of 0.39° with a take-off angle of 6.0° For data collection, the weak reflections ($I < 10\sigma(I)$) were rescanned, and the counts were accumulated to ensure good counting statistics. No decay correction was required. The data were corrected for Lorentz, polarization, and for absorption correction by ψ scans of a few reflections (18). A correction for secondary extinction was also applied (coefficient = 5.11673×10^{-6}) (19). The structure was solved by direct methods and expanded using Fourier techniques. The non-hydrogen atoms were refined anisotropically. The function minimized was $\Sigma\, w(|F_o| - |F_c|)^2$ where $w = 1/\sigma^2(F_o) = [\sigma^2_c(F_o) + p^2/4(F_o)^2]^{-1}$ and the p-factor was 0.0200. The final cycle of full-matrix least-squares refinement converged with unweighted ($R = \Sigma\, ||F_o|| - |F_c||/\, \Sigma\, |F_o|$) and weighted ($R_w = [\Sigma\, w(|F_o| - |F_c|)^2/\, \Sigma\, w|F_o|^2)]^{1/2}$] agreement factors of 0.048 and 0.069, respectively. All calculations were performed using the TEXAN[4] crystallographic software package of Molecular Structure Corporation. Anisotropic thermal parameters along with a full listing of torsion angles and nonbonded contacts to 3.60 Å are available as supplementary material.[5]

Table 3. Summary of data collection and structure refinement details for $Zn(C_6F_5)_2$, **1**.

Formula	$ZnC_{12}F_{10}$
fw	399.50
Crystal system	Monoclinic
Space group	$P2_1/n$ (no. 14)
a, Å	11.902(2)
b, Å	7.732(2)
c, Å	13.735(2)
β,°	110.58(1)
V, Å^3	1183.4(4)
Z	4
d_{calc}, mg m^{-3}	2.242
$F(000)$	768
μ, cm^{-1}	22.02
T, °C	–103
Crystal dimensions, mm^3	0.45 × 0.40 × 0.13
Rel. transmission factors	0.71–1.0000
Scan type	ω – 2θ
Scan range, deg	1.68 + 0.34 tan θ
Scan speed, deg/min	16.0
2θ (max), deg	55.1
Unique reflections	2940
Reflections with $I > 3\sigma I$	1655
No. of variables	209
R	0.048
R_w	0.069
gof	1.72
Max. Δ/σ (final cycle)	0.00
Residual density, e/Å^3	–0.46–0.52

[4] Crystal structure analysis package, Molecular Structure Corporation, 1985 and 1992.

[5] Supplementary material may be purchased from: The Depository of Unpublished Data, Document Delivery, CISTI, National Research Council of Canada, Ottawa, Canada, K1A 0S2.

© 1998 NRC Canada

Acknowledgments

Financial support for this work was provided by the NOVA Research & Technology Corporation of Calgary, Alberta, and NSERC of Canada's Research Partnerships office (CRD program).

References

1. (*a*) A.G. Massey and A.J. Park. J. Organomet. Chem. **2**, 245 (1964); (*b*) W.E. Piers and T. Chivers. Chem. Soc. Rev. 345 (1997).
2. Y.-X. Chen, C.L. Stern, S. Yang, and T.J. Marks. J. Am. Chem. Soc. **118**, 12 451 (1996).
3. K. Ishihara, H. Kurihara, and H. Yamamoto. J. Org. Chem. **62**, 5664 (1997).
4. D.J. Parks, R.E.v.H. Spence, and W.E. Piers. Angew. Chem. Int. Ed. Engl. **34**, 809 (1995).
5. L. Jia, X. Yang, C. Stern, and T. J. Marks. Organometallics, **13**, 3755 (1994).
6. R.D. Chambers and T. Chivers. J. Chem. Soc. 3933 (1965).
7. J.G. Noltes and J.W.G. Vanden Hurk. J. Organomet. Chem. **1**, 377 (1964).
8. P. Sartori and M. Weidenbruch. Chem. Ber. **100**, 3016 (1967).
9. H. Lange and D. Naumann. J. Fluorine Chem. **26**, 435 (1984).
10. M. Weidenbruch, M. Herrndorf, A. Schäfer, S. Pohl, and W. Saak. J. Organomet. Chem. **361**, 139 (1989).
11. V.W. Day, D.H. Campbell, and C.J. Michejda. J. Chem. Soc. Chem. Commun. 118 (1975).
12. J. Boersma. *In* Comprehensive organometallic chemistry. Vol. 2. *Edited by* G. Wilkinson. Pergammon, Oxford, U.K. 1982. p. 823.
13. (*a*) P.R. Markies, G. Schat, O.S. Akkerman, F. Bickelhaupt, W.J.J. Smeets, and A.L. Spek. Organometallics, **9**, 2243 (1990), and refs. therein; (*b*) M. Westerhausen, B. Rademacher, and W. Pohl. J. Organomet. Chem. **421**, 175 (1991); (*c*) S. Brooker, N. Bertel, D. Stalke, M. Noltemeyer, H.W. Roesky, G.M. Sheldrick, and F.T. Edelmann. Organometallics, **11**, 192 (1992).
14. G.W. Coates, A.R. Dunn, L.M. Henling, D.A. Dougherty, and R.H. Grubbs. Angew. Chem. Int. Ed. Engl. **36**, 248 (1997), and refs. therein; J.H. Williams. Acc. Chem. Res. **26**, 593 (1993).
15. H. Plenio. Chem. Rev. **97**, 3363 (1997).
16. A. Bondi. J. Phys. Chem. **68**, 441 (1964).
17. Y. Sun, R.E.v.H. Spence, W.E. Piers, M. Parvez, and G.P.A. Yap. J. Am. Chem. Soc. **119**, 5132 (1997).
18. A.C.T. North, D.C. Phillips, and F.S. Matthews. Acta Cryst. **A24**, 351 (1968).
19. W. H. Zachariasen. Acta Crystallogr. Sect. A: Cryst. Phys. Diffr. Theor. Gen. Crystallogr. **A24**, 212 (1968).

© 1998 NRC Canada

Cyclic–acyclic equilibrium and selective P—O bond cleavage in 2-hydroxyphenyldiphenylphosphinate, $Ph_2P(O)OC_6H_4OH$

Edward Paul Segstro, Kerry Davie, Xiaoling Huang, and Alexander Frank Janzen

Abstract: The equilibrium in the $Ph_2P(O)OC_6H_4OH$–base system may be shifted by varying the base concentration, where base = imidazole, triethylamine, dimethyl sulfoxide, pyridine, and 1,4-dioxane. This equilibrium was studied by ^{31}P and ^{1}H NMR, and information about the symmetry of phosphorus-containing intermediates is provided by the ^{1}H NMR spectrum of the catecholyl ring, with its *ABCD* spin system. The equilibrium is also affected by trifluoroacetic acid. A mechanism is proposed that involves protonation–deprotonation, cyclic–acyclic equilibria, and selective P—O bond cleavage, with all steps occurring rapidly on the NMR time scale.

Key words: $Ph_2P(O)OC_6H_4OH$–base system, cyclic–acyclic equilibrium, and selective P—O bond cleavage.

Résumé : On peut déplacer la position de l'équilibre du système $Ph_2P(O)OC_6H_4OH$–base en faisant varier la concentration de base (base = imidazole, triéthylamine, diméthylsulfoxyde, pyridine, 1,4-dioxane). On a étudié cet équilibre par RMN du ^{31}P et du ^{1}H et l'information relative à la symétrie des intermédiaires contenant du phosphore découle du spectre RMN du ^{1}H du noyau catécholyle comportant un système de spin *ABCD*. L'équilibre est aussi affecté par l'acide trifluoroacétique. On propose un mécanisme pour cet équilibre qui implique une protonation–déprotonation, un équilibre cyclique–acyclique et la rupture sélective de la liaison P—O; toutes les étapes se produiraient rapidement à l'échelle de temps de la RMN.

Mots clés : système $Ph_2P(O)OC_6H_4OH$–base, équilibre cyclique–acyclique, rupture sélective de la liaison P—O.

[Traduit par la rédaction]

Introduction

Five-membered rings, cyclic–acyclic equilibria, and protonation–deprotonation are common features of the hydrolysis, and enzymatic hydrolysis, of phosphorus esters (see examples in ref. 1). Previously, we studied the base-initiated cyclic–acyclic equilibrium of a perfluoropinacolyl phosphorus compound (2). The perfluoropinacolyl septets in the ^{19}F NMR spectrum collapsed to a broad peak with increasing base concentration or temperature, which is consistent with the cyclic–acyclic equilibrium of Scheme 1, but line broadening made it impossible to distinguish between trigonal bipyramidal or square pyramidal intermediates; both structural types have been established by X-ray crystallography for phosphorus compounds that contain five-membered rings (3).

In this study, perfluoropinacol was replaced by catechol, and the equilibrium of 2-hydroxyphenyldiphenylphosphinate, $Ph_2P(O)OC_6H_4OH$ **1**, in the presence of base was monitored by ^{31}P and ^{1}H NMR. Analysis of the ^{1}H NMR spectrum of the planar catecholyl ring, with its *ABCD* spin system, was carried out in an attempt to obtain information about the symmetry of phosphorus-containing intermediates.

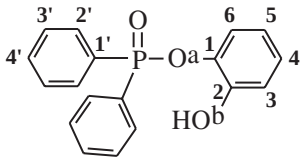

1

Results and discussion

In a series of experiments, the ^{31}P chemical shift of **1** was measured in CH_2Cl_2 solution as a function of base concentration. As seen in Fig. 1, there is an upfield shift with increasing base concentration, i.e., towards five-coordinate phosphorus (4), and the relative shift is in the order: imidazole ~ Et_3N > DMSO > pyridine > 1,4-dioxane. Only limited data are available for imidazole and triethylamine because these bases bring about decomposition of **1**, but solutions of **1** in excess DMSO, pyridine, or 1,4-dioxane are stable in CH_2Cl_2, as judged by ^{31}P and ^{1}H NMR.

To eliminate the possibility that changes in $\delta^{31}P$ are due to solvent or concentration effects, two compounds were chosen that lack a hydroxyl substituent, namely, $(MeO)_3PO$ and $Ph_2P(O)OC_6H_4OSiMe_3$. Addition of pyridine to these compounds produced only minor changes in $\delta^{31}P$. For example, $\delta^{31}P$ of $(MeO)_3PO$ (0.071 M in CH_2Cl_2 at 27°C) shifts from 1.39 to 1.10 ppm as the pyridine concentration increases from

Received November 3, 1997.

E.P. Segstro. Department of Chemistry, University of Winnipeg, Winnipeg, MB R3B 2E9, Canada.
X. Huang. Department of Chemistry, Wuhan University, Wuhan 430072, China.
K. Davie and A.F. Janzen.[1] Department of Chemistry, University of Manitoba, Winnipeg, MB R3T 2N2, Canada.

[1] Author to whom correspondence may be addressed. Telephone: (204) 474-9731. Fax: (204) 474-7608. E-mail: ajanzen@cc.umanitoba.ca

© 1998 NRC Canada

Scheme 1. Cyclic–acyclic equilibrium in a perfluoropinacolyl phosphorus compound.

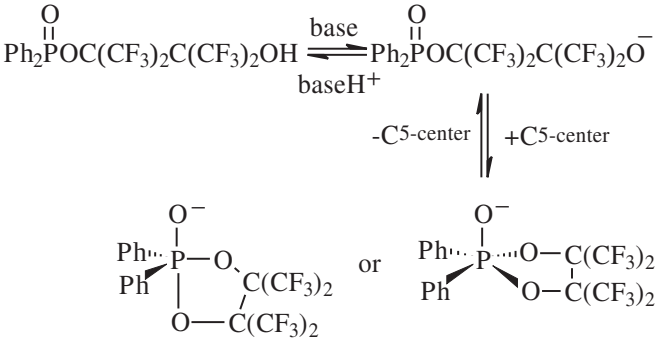

Fig. 1. Plot of $\delta^{31}P$ of $Ph_2P(O)OC_6H_4OH$ **1** as a function of base concentration, and of CF_3COOH concentration. Temperature is 27°C, solvent is CH_2Cl_2, and [**1**] = 0.032 M in all experiments.

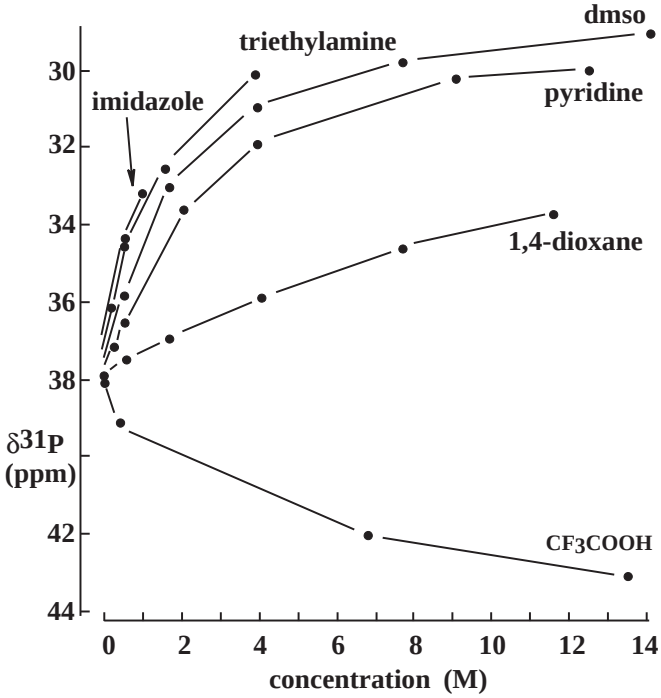

0 to 12.4 M. Similarly, $\delta^{31}P$ of $Ph_2P(O)OC_6H_4OSiMe_3$ in CH_2Cl_2 at 27°C changes from 29.83 to 29.04 ppm as the pyridine concentration increases from 0 to 9.3 M.

A mechanism is proposed in Scheme 2 to account for the behaviour of the **1**-base system. This mechanism is written in sufficient detail so that the connectivity of atoms along the reaction pathway is evident, and ring-opening and rapid ring-closing of five-membered rings is denoted as $-C^{5\text{-center}}$ and $+C^{5\text{-center}}$, respectively (5). The overall shift towards five-coordinate phosphorane is rather modest, for example, $\delta^{31}P$ of **1** (37.80 ppm in CH_2Cl_2) shifts to 29.85 ppm in excess pyridine (Fig. 1). Much greater changes of 63–79 ppm have been found in related compounds as they are converted to authentic five-coordinate phosphoranes (4). If a chemical shift of about –32 ppm is assumed for **6**, i.e., 70 ppm upfield from that of **1**, then an equilibrium constant can be crudely estimated for Scheme 2 by assuming an equilibrium between two species only,

Scheme 2. Proposed protonation–deprotonation and cyclic–acyclic equilibrium in the $Ph_2P(O)OC_6H_4OH$–base system.

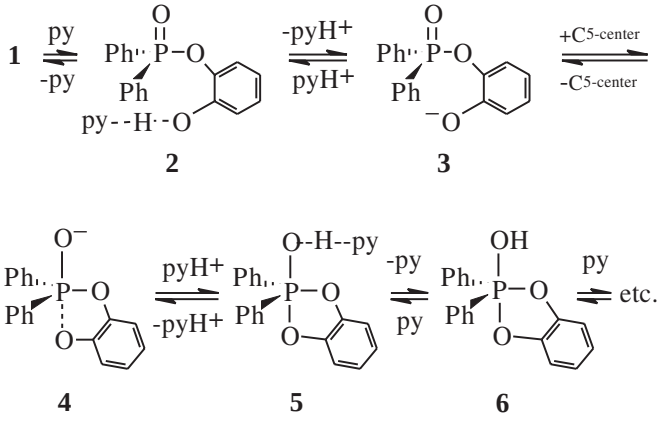

Scheme 3. Proposed protonation–deprotonation and cyclic–acyclic equilibrium in the $Ph_2P(O)OC_6H_4OH$–acid system.

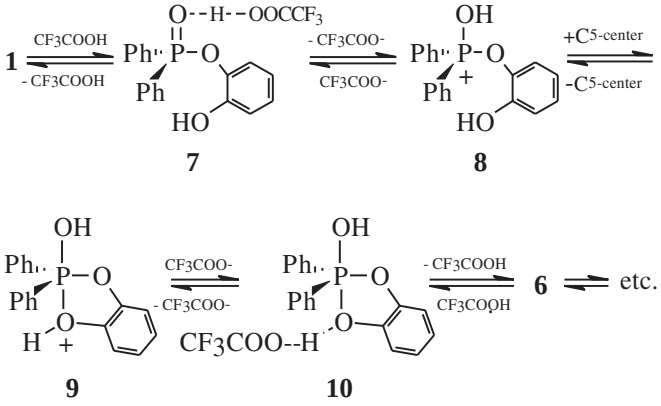

namely, **1** and **6**. In that case, from the weighted average of $\delta^{13}P$, and standard equations (6), equilibrium constants are estimated as ~0.09 for imidazole and triethylamine, ~0.04 for DMSO and pyridine, and ~0.01 for 1,4-dioxane. Thus the concentration of five-coordinate phosphorane depends on the nature and concentration of base, but the equilibrium in Scheme 2 favours phosphinate **1** in all experiments.

All samples of **1** and base (Fig. 1) give only single ^{31}P peaks at 27°C, and individual species cannot be observed by NMR at ambient temperature. On lowering the temperature of a sample of **1** (0.031 M) and pyridine (9.31 M) in CH_2Cl_2, $\delta^{31}P$**1** shifts from 31.07 ppm at 27°C to 29.62 ppm at –63°C, in the direction of five-coordinate phosphorane. However, no appreciable line-broadening was evident, confirming that all steps of Scheme 2 are rapid on the NMR time scale, even at –63°C. It follows from this result that only very weak bonds are cleaved, and these are identified in Scheme 2 as bridging

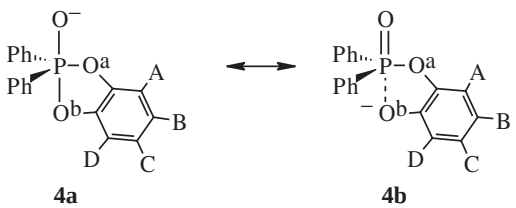

© 1998 NRC Canada

Table 1. Effect of pyridine on *J*(P,H) and *J*(H,H) of the catecholyl ring of **1**.[a,b,c]

[Py]/[**1**]	^5J(P,3)	^6J(P,4)	^5J(P,5)	^4J(P,6)	^3J(3,4)	^4J(3,5)	^5J(3,6)	^3J(4,5)	^4J(4,6)	^3J(5,6)
0	–0.25	1.00	–0.84	1.36	8.13	1.63	0.32	7.37	1.59	8.08
8.1	–0.29	0.97	–0.80	1.37	8.13	1.62	0.32	7.37	1.59	8.09
9.8	–0.32	0.97	–0.77	1.37	8.12	1.60	0.31	7.41	1.59	8.09
17.1	–0.43	0.97	–0.72	1.38	8.12	1.62	0.31	7.38	1.60	8.10
34.7	–0.51	0.93	–0.64	1.38	8.11	1.59	0.30	7.42	1.60	8.09
67.7	–0.64	0.91	–0.55	1.42	8.08	1.62	0.26	7.41	1.58	8.10

[a] Temperature 27°C; [**1**] = 0.032 M. Internal reference with respect to $CHDCl_2$, δ H 5.32 ppm.
[b] ^{1}H in CD_2Cl_2 (without pyridine): δ H3 6.89, δ H4 6.99, δ H5 6.69, δ H6 6.95 ppm.
[c] Coupling constant, Hz.

Fig. 2. Plot of δH of catecholyl and phenyl protons of **1** as a function of pyridine concentration, showing retention of an *ABCD* spin system in the catecholyl ring. H3-H6 are catecholyl hydrogens, and H2′-H4′ are phenyl hydrogens.

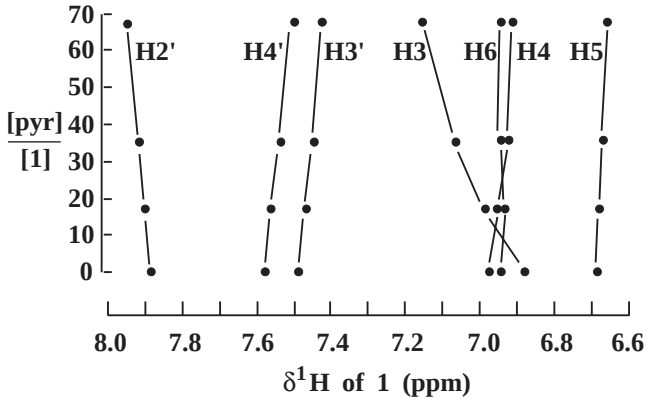

N--H--O bonds in **2** and **5**, and a P—O^b bond in **4**. The latter bond is *trans* to an oxo substituent, and contributing structures **4a** and **4b** may account for the weakness of the *trans* P—O^b bond.

Trifluoroacetic acid was also added to **1**, and the chemical shift of **1** moves downfield, as seen in Fig. 1, presumably as a result of protonation at the phosphoryl bond. Authentic phosphonium ions have downfield ^{31}P chemical shifts (7), and a mechanism that accounts for the behaviour of **1** in the presence of acid is shown in Scheme 3.

According to the mechanism of Scheme 2, the axial P—O^b bond in **4** is cleaved, but not the equatorial P—O^a bond. Evidence that the P—O^a bond remains intact is based on the ^{1}H NMR spectrum of the catecholyl ring. Its *ABCD* spectrum contains information about the symmetry of the intermediates and the stereospecificity of the overall reaction, and the question is whether this *ABCD* spin system is maintained at all stages of the equilibrium, as required by Scheme 2, or whether it is converted into an A_2B_2 (or *AA′BB′*) spin system.

The ^{1}H NMR spectra of **1** were recorded at 300 MHz, and a complete assignment was carried out for the catecholyl and phenyl regions at various pyridine concentrations. Hydrogens are assigned by comparison with 2-methoxyphenol (8) and related compounds (9). The downfield shift of H3 with increasing pyridine concentration is in agreement with the effect of base on the chemical shift of *ortho* hydrogens in phenol (10), but no argument that depends on the *ABCD* spin pattern is changed if the assignment of hydrogens is interchanged.

The variation in δH as a function of pyridine concentration is shown in Fig. 2, and the corresponding changes in *J*(H,P) and *J*(H,H) are given in Table 1. As seen in Fig. 2 and Table 1, the NMR parameters depend on pyridine concentration, but H3 and H6 never become equivalent, nor H4 and H5, and therefore the *ABCD* spin system is preserved. Selective P—O^b bond cleavage in **4**, and trigonal bipyramidal geometry of **4**–**6**, as postulated in Scheme 2, is entirely compatible with this "*ABCD* criterion."

Our results do not allow us to eliminate square pyramidal intermediate **11** from consideration, however, square pyramidal **12** is incompatible with an *ABCD* spin system, moreover, any polytopal rearrangement such as Berry pseudorotation or turnstile rotation that generates **12** is eliminated. Bond breaking of the P—O^a bond is not allowed by the *ABCD* criterion, nor complete loss of catechol, and there cannot be any pathways that interchange O^a and O^b substituents.

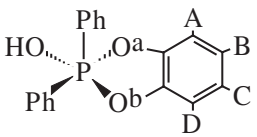

11

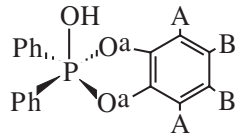

12

Experimental

All solvents were dried and stored over molecular sieve under N_2 in a dry box. Diphenylchlorophosphane, Ph_2PCl, and bis(pentafluorophenyl)chlorophosphane, $(C_6F_5)_2PCl$, were oxidized to $Ph_2P(O)Cl$ and $(C_6F_5)_2P(O)Cl$ by bubbling O_2 through a benzene solution. Elemental analyses were carried out by Galbraith Laboratories, Knoxville, Tenn.

The ^{31}P and phosphorus-decoupled ^{1}H NMR spectra were recorded on a Bruker WH90 spectrometer, and the ^{13}C and ^{1}H NMR spectra were recorded on a Bruker AM300 spectrometer. A complete assignment of ^{1}H NMR spectra was carried out of the catecholyl and phenyl regions of **1** at various pyridine concentrations, with the aid of computer program LAME (11).

2-Hydroxyphenyldiphenylphosphinate 1

The $Ph_2P(O)Cl$ (9.5 g, 40 mmol) in benzene (25 mL) was added dropwise over 30–40 min to a stirred solution of 1,2-benzenediol (catechol) (4.4 g, 40 mmol) and pyridine (3.2 g, 40 mmol) in benzene (30 mL). At the completion of the reaction, solid was filtered off, washed several times with water, dried under vacuum and recrystallized from 1:1 benzene:methanol, and identified as 2-hydroxyphenyldiphenylphosphinate **1**. Anal. calcd. for $C_{18}H_{15}O_3P$: C 69.68, H 4.87; found: C 69.51, H 4.87. The filtrate was concentrated on a

© 1998 NRC Canada

rotary evaporator and solids filtered off and purified as above to give a total yield of **1** of 40%; mp 185°C; MS, *m/z*: 310 $(M)^+$, 233 $(M - C_6H_5)^+$, 232 $(M - C_6H_6)^+$, 201 $(Ph_2PO)^+$.

^1H NMR of **1** is given in Table 1 and Fig. 2. Variable-temperature ^1H NMR of OH in CD_2Cl_2, δ: 9.02 ppm (+40°C), 9.19 ppm (–25°C), 9.35 ppm (–56°C); in DMSO: 8.96 ppm (+39°C), 9.29 ppm (–23°C), 9.57 ppm (–60°C). ^1H NMR of OH as a function of molar ratio of pyridine/**1** in CD_2Cl_2, δ: 9.01 ppm (py/**1** = 0), 9.10 ppm (py/**1** = 1.83), 9.57 ppm (py/**1** = 14.9), 10.52 ppm (py/**1** = 125.4). $\delta^{31}P$ of **1** (0.032 M) in various solvents: (CH_2Cl_2) δ 37.80, ($CDCl_3$) δ 38.04, (1,4-dioxane) δ 33.75, (pyridine) δ 29.85, (DMSO) δ 29.07, (CF_3COOH) δ 43.16.

^{13}C NMR of **1** (CD_2Cl_2): C1 δ 139.6, ^2J(PC) = 9.50 Hz; C2 δ 148.6, ^3J(PC) = 3.15 Hz; C3 δ 119.9, ^4J(PC) = 1.23 Hz; C4 δ 126.8, ^5J(PC) = 1.27 Hz; C5 δ 120.8, ^4J(PC) = 0.68 Hz; C6 δ 122.9, ^3J(PC) = 4.56 Hz; C1′ δ 129.2, ^1J(PC) = 137.1 Hz; C2′ δ 132.2, ^2J(PC) = 10.62 Hz; C3′ δ 129.2, ^3J(PC) = 13.58 Hz; C4′ δ 133.6, ^4J(PC) = 2.89 Hz.

A similar reaction of 1,2-benzenediol and $(C_6F_5)_2P(O)Cl$ gave 2-$HOC_6H_4OP(O)(C_6F_5)_2$; MS, *m/z*: 490$(M)^+$.

2-$Me_3SiOC_6H_4OP(O)Ph_2$ and 2-$MeOC_6H_4OP(O)Ph_2$

$Ph_2P(O)OC_6H_4OH$ **1** (0.11 g, 0.35 mmol) and Me_3SiCl (0.038 g, 0.35 mmol) and 2 drops of Et_3N in CH_2Cl_2 (2 mL) were refluxed for 2 h. The solvent was removed by rotary evaporator and a white solid remained, which was washed with 1:1 benzene:methanol and identified by mass spectrometry as $Ph_2P(O)OC_6H_4OSiMe_3$; MS, *m/z*: 382 $(M)^+$, 367 $(M - CH_3)^+$. This product was also formed if **1** was treated with $(Me_3Si)_2NH$ or with a mixture of $(Me_3Si)_2NH$, Me_3SiCl, and pyridine, but a red solid was formed in the reaction of **1** with Et_2NSiMe_3.

Reaction of 2-$MeOC_6H_4OH$ (1.4 g, 11 mmol) and $Ph_2P(O)Cl$ (2.37 g, 10 mmol) in pyridine (13 mL) gave 2-$MeOC_6H_4OP(O)Ph_2$; MS, *m/z*: 324 $(M)^+$, 306 $(M - 18)^+$, 293 $(M - OMe)^+$. The NMR spectra of these compounds, as well as of 2-methoxyphenol (8), and others (9), were helpful in assigning the ^1H NMR spectrum of **1**.

***cis*-3-Diphenylphosphinatotetrahydro-3,4-furandiol**

$Ph_2P(O)Cl$ (8.5 g, 36 mmol) in benzene was added dropwise to a stirred solution of *cis*-tetrahydro-3,4-furandiol (3.70 g, 36 mmol) and pyridine (2.82 g, 36 mmol) in CH_2Cl_2 (30 mL) over 30 min. The mixture was stirred for 24 h, then *n*-hexane added and the precipitate washed with water, dried under vacuum, and recrystallized from 1:1 benzene:methanol to give *cis*-3-diphenylphosphinatotetrahydro-3,4-furandiol (37%). Anal. calcd. for $C_{16}H_{17}O_4P$: C 63.16, H 5.63; found: C 63.35, H 5.47. MS, *m/z*: 304 $(M)^+$, 286 $(M - H_2O)^+$. ^{31}P NMR ($CDCl_3$), δ: 32.3 ppm. ^1H NMR ($CDCl_3$), δ: 3.72–4.78 (aliphatic), 7.33–7.96 (phenyl), 5.80 (OH). Its complex ^1H NMR spectrum made this compound less suitable for NMR study than **1**.

Acknowledgements

This work was supported financially by the Natural Sciences and Engineering Research Council of Canada. We thank Mr. R. Sebastian for assistance with the calculation of NMR spectra.

References

1. (*a*) F.H. Westheimer. Acc. Chem. Res. **1**, 70 (1968); (*b*) F. Ramirez and J.F. Marecek. Pure. Appl. Chem. **52**, 1021 (1980); (*c*) D.A. Usher, D.I. Richardson, Jr., and D.G. Oakenfull. J. Am. Chem. Soc. **92**, 4699 (1970); (*d*) A. Queen, A.E. Lemire, and A.F. Janzen. Int. J. Chem. Kinet. **13**, 411 (1981); (*e*) D.B. Denney, D.Z. Denney, P.J. Hammond, and K.-S. Tseng. J. Am. Chem. Soc. **103**, 2054 (1981); (*f*) G.H. McGall and R.A. McClelland. Can J. Chem. **69**, 2064 (1991); (*g*) C.N. Pace, U. Heinemann, U. Hahn, and W. Saenger. Angew. Chem. Int. Ed. Engl. **30**, 343 (1991).
2. A.F. Janzen, A.E. Lemire, R.K. Marat, and A. Queen. Can. J. Chem. **61**, 2264 (1983).
3. (*a*) R.R. Holmes. Acc. Chem. Res. **12**, 257 (1979); (*b*) R.R. Holmes. Chem. Rev. **96**, 927 (1996).
4. (*a*) I. Granoth and J.C. Martin. J. Am. Chem. Soc. **100**, 5229 (1978); (*b*) I. Granoth and J.C. Martin. J. Am. Chem. Soc. **101**, 4618 (1979); (*c*) Y. Segall and I. Granoth. J. Am. Chem. Soc. **100**, 5130 (1978).
5. (*a*) A.F. Janzen. Coord. Chem. Rev. **130**, 355 (1994); (*b*) X. Ou and A.F. Janzen. Inorg. Chem. **36**, 392 (1997); (*c*) A.F. Janzen and M. Jang. Can. J. Chem. **67**, 71 (1989).
6. R.S. Drago. Physical methods in chemistry. W.B. Saunders, Philadelphia. 1977. pp. 252–253.
7. (*a*) V. Mark, C.H. Dungan, M.M. Crutchfield, and J.R. van Wazer. Top. Phosphorus Chem. **5**, 227 (1967); (*b*) K.B. Dillon and R.N. Reeve. Polyhedron, **4**, 1533 (1985).
8. T. Schaefer and T.A. Wildman. Can. J. Chem. **57**, 450 (1979).
9. (*a*) W.J.E. Parr. J. Chem. Soc. Faraday Trans. 2, **74**, 933 (1978); (*b*) W.B. Smith and T.W. Proulx. Org. Magn. Reson. **8**, 205 (1976); (*c*) K.W. Scott. J. Am. Chem. Soc. **94**, 8564 (1972); (*d*) T.A. Modro. Can. J. Chem. **55**, 3681 (1977); (*e*) F. Lambert, M. Ellenberger, L. Merlin, and Y. Cohen. Org. Magn. Reson. **7**, 266 (1975). (*f*) S. Castellano and R. Kostelnik. Tetrahedron Lett. 5211 (1967).
10. I. Gränacher. Helv. Phys. Acta, **34**, 272 (1961).
11. (*a*) S. Castellano and A.A. Bothner-By. J. Chem. Phys. **41**, 3863 (1964); (*b*) C.W. Haigh and J.M. Williams. J. Mol. Spectrosc. **32**, 398 (1969).

© 1998 NRC Canada

Bisthiosemicarbazones of 2,4-pentanedione are pyrazolines

Duncan H. Hunter, Chantelle McRoberts, and Jagadese J. Vittal

Abstract: Attempts to prepare 2,4-bisthiosemicarbamoylpentanediones **1** via literature precedent from 2,4-pentanedione and three different thiosemicarbazides resulted instead in the formation of cyclic pyrazolines **5**. The preparation was attempted with thiosemicarbazide, 4-methylthiosemicarbazide, and 4-ethylthiosemicarbazide, respectively. A single-crystal X-ray structure study of the product from 4-methylthiosemicarbazide confirmed the pyrazoline structure. This observation serves to correct earlier misassignments of structure.

Key words: pentanedione, bisthiosemicarbazone, pyrazoline, ethylenediamine.

Résumé : Les efforts déployés en vue de préparer les 2,4-bisthiosemicarbamoylpentanediones, **1**, par le biais de méthodes décrites dans la littérature à partir de la pentane-2,4-dione et de trois thiosemicarbazides différentes ont tous conduit plutôt à la formation de pyrazolines cycliques, **5**. On a tenté les préparations à l'aide de la thiosemicarbazide, de la 4-méthylthiosemicarbazide et de la 4-éthylthiosemicarbazide respectivement. Une étude de structure par diffraction des rayons X sur un cristal unique du produit obtenu à partir de la 4-méthylthiosemicarbazide a permis de confirmer la structure pyrazoline. Cette observation permet de corriger de mauvaises attributions de structures proposées antérieurement.

Mots clés : pentanedione, bisthiosemicarbazone, pyrazoline, éthylènediamine.

[Traduit par la rédaction]

Metal complexes of bisthiosemicarbazones have long been known for anticarcinogenic, antibacterial, and antifungal properties (1). The N_2S_2 chelation system of bisthiosemicarbazones has been used with a variety of metals, including Ni(II), Cu(II), Zn(II), Hg(II) (2), as well as ^{99m}Tc (3). Technetium chelates present many interesting possibilities for nuclear medicine applications. As part of a project on the preparation of N_2S_2 ^{99m}Tc chelates for diagnostic imaging, bisthiosemicarbazones of 2,4-pentanedione **1** were targeted. This molecule, after substitution at the 3-position of the dione, would provide a simple and versatile chelation system for ^{99m}Tc nuclear imaging agents **2** (Fig. 1).

Typically, bisthiosemicarbazones have been synthesized directly from a 2:1 ratio of thiosemicarbazide and dicarbonyl compound (4). However, there is confusion in the literature regarding the specific case of 2,4-pentanedione. In 1967, it was reported that the bisthiosemicarbazones of 2,4-pentanedione could not be prepared by the direct reaction of 2,4-pentanedione and various thiosemicarbazides (5). Instead, a method involving the use of ethylenediamine was devised, resulting in the reported preparation of bisthiosemicarbazones of 2,4-pentanedione **1** with R = H, methyl, ethyl, cyclohexyl, and phenyl (Fig. 1). However, in 1986, the direct reaction was reported to be successful with 4-phenylthiosemicarbazide and 2,4-pentanedione (6). Independent of this paper, the structure assigned to the bisthiosemicarbazones of 2,4-pentanedione **1** in the original 1967 report was questioned on the basis of the ^{1}H NMR spectra of two adducts, prepared from thiosemicarbazide and 4-methylthiosemicarbazide. A pyrazoline structure **5** (Fig. 3) was suggested instead (7).

In 1990, a modified ethylenediamine route was employed to synthesize the bis(4-methylthiosemicarbazone) of 2,4-pentanedione (8), which was assigned structure **1** based on the ^{1}H NMR spectrum. This material was then used to prepare a technetium-99m chelate and biodistribution studies were carried out. Surprisingly, labelling with technetium-99m resulted in two radioactive species as observed by HPLC analysis of a hexane extract. This observation led the authors to a further study in which 3,3-dimethyl-2,4-pentanedione was prepared and reacted with 4-methylthiosemicarbazone by the same procedure (9). Again, the product was characterized by the ^{1}H NMR spectrum and assigned a structure similar to **1**. Radiolabelling of this material with technetium-99m resulted in just one radioactive species being observed by HPLC analysis of a chloroform extract.

Results

Because we were interested in preparing similar bisthiosemicarbazones as technetium-99m bioconjugates, the reaction of three thiosemicarbazides with 2,4-pentanedione was repeated. In our hands, the direct reaction of thiosemicarbazides with 2,4-pentanedione failed. Specifically, reaction of 2,4-pentanedione with thiosemicarbazide, 4-methylthiosemicarbazide, and 4-ethylthiosemicarbazide in 20% acetic acid solution resulted in recovery of starting materials. This finding is consistent with the report of 1967 (5) but not the 1986 report (6).

Received November 4, 1997.

D.H. Hunter[1] and C. McRoberts. Department of Chemistry, University of Western Ontario, London, ON N6A 5B7, Canada. **J.J. Vittal.** Department of Chemistry, National University of Singapore, Singapore 119 260.

[1] Author to whom correspondence may be addressed. Telephone: (519) 679-2111. Fax: (519) 661-3022. E-mail: dhunter@julian.uwo.ca

© 1998 NRC Canada

Fig. 1. 2,4-Bisthiosemicarbamoylpentanedione and 99m-Tc 2,4-bisthiosemicarbamoylpentanedione (R = H, CH_3, CH_2CH_3 and X = H, or linker).

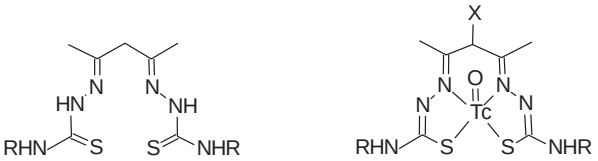

1 **2**

Fig. 2. Ethylenediamine intermediates of 2,4-pentanedione.

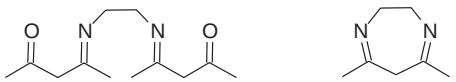

3 **4**

In contrast, the modified ethylenediamine preparation of 1990 led to products with the same melting point and mass spectra as those originally published (5).

The 1967 route (5) through compounds **3** and **4** (Fig 2.), adducts of dione and diamine, was repeated. A 2:1 adduct of dione to diamine, 1,2-bis(1-methyl-3-oxobutylideneamino)ethane **3**, was prepared in 70% yield. The proton NMR spectrum indicated the product to be an enol (10), mp 110–113°C; ^{1}H NMR ($CDCl_3$), ppm: 1.85 (3H, s, CH_3), 1.88 (3H, s, CH_3), 3.38 (1H,m, CH_2), 4.9 (1H,s, CH), 10.9 (1H,s, OH); MS, *m*/*z* calcd. for $C_{12}H_{20}N_2O_2$: 224.1524; found: 224.1516.

This 2:1 dione:diamine adduct was converted to 1:1 adduct **4** in 20% acetic acid over 24 h at room temperature. An ^{1}H NMR spectrum indicated only the 1:1 adduct as judged by the dione methyl equivalency at 1.9 ppm in the crude spectrum ($CDCl_3$). Adduct **4** was reacted with thiosemicarbazide, 4-methylthiosemicarbazide, and 4-ethylthiosemicarbazide in a 50% methanolic solution at reflux, yielding crystalline material in each case. Specifically for the 4-methylthiosemicarbazide example, colourless, block-like crystals were isolated in 40% purified yield. MS, *m*/*z* calcd. for $C_9H_{18}N_6S_2$: 274.1034; found: 274.1032. On the basis of the melting point (mp 174–176°C), this product and that previously reported in 1967 (5) are the same compound.

The 1990 modification of the dione–ethylenediamine route (7) was repeated successfully for 2,4-pentanedione and 4-methylthiosemicarbazide with addition of ethylenediamine. This modified route was not repeated for the thiosemicarbazide and 4-ethylthiosemicarbazide examples. Small, colourless needles precipitated in 24% crude yield and were found to be identical to the material produced above (melting point and mixture melting point). The melting point of this product was also in agreement with the 1990 report.

However, ^{1}H and ^{13}C NMR spectra were more complicated than anticipated symmetrical product **1** would suggest and are consistent with pyrazoline **5** (R = CH_3). In particular, the ^{1}H NMR spectrum in $CDCl_3$ showed 10 sets of signals rather than the anticipated 5. ^{1}H NMR ($CDCl_3$), ppm: 1.8 (3H, s, CH_3), 1.98 (3H, s, CH_3), 2.59 and 2.97 (2H, CH_AH_B, J_{AB} = 18 Hz), 3.07 (3H, d, CH_3), 3.15(3H, d, CH_3), 6.63 (1H, s, NH), 6.85 (1H, s, NH), 7.25(1H, brq, $NHCH_3$), and 7.38 (1H, brq, $NHCH_3$). Similarly, the ^{13}C NMR spectrum showed nine separate signals instead of the anticipated five: ^{13}C NMR ($CDCl_3$), ppm: 183.7, 175.5 (C═S); 153.5 (C═N); 85.0 (C6); 47.2 (C5); 30.9, 30.2 ($NHCH_3$); 23.5, 16.2 (CH_3). The products of the thiosemicarbazide and 4-ethylthiosemicarbazide reactions with adduct **4** showed analogous NMR patterns. Because of the confusion already present in the literature, we obtained a single-crystal X-ray structural determination of the product of the 4-methylthiosemicarbazide reaction. The results of the crystallographic analysis shown in Fig. 4 confirm the 1986 proposal of a pyrazoline **5**.

Fig. 3. Thiosemicarbazido-pyrazoline (R = H, CH_3, CH_2CH_3).

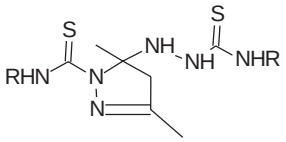

5

Fig. 4. Structure of **5** in the crystal.

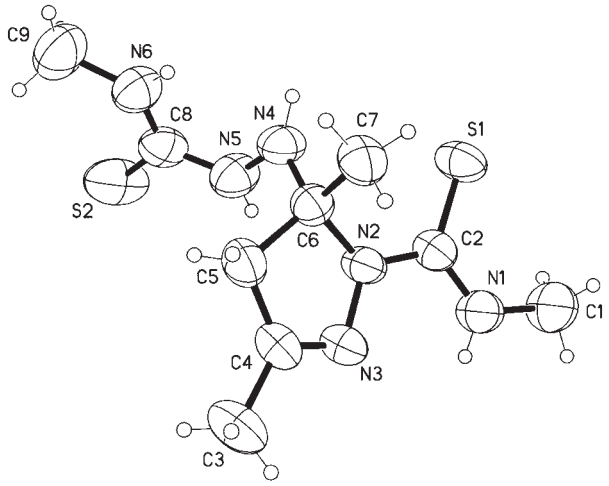

Crystallographic data for 5

$C_9H_{18}N_6S_2$, fw = 274.14, monoclinic space group: *P*2(1)/*c*, *a* = 8.678(1), *b* = 10.031(1), *c* = 17.415(3) Å, β = 100.13(1)°, *V* = 1492.3(3) Å^3, *Z* = 4, ρ_{calcd} = 1.221 g cm^{-3}, μ = 0.347 mm^{-1}. Data were collected at 20°C on a Siemens P4 diffractometer equipped with a sealed tube containing graphite-monochromated Mo Kα radiation. All the H atoms were located successfully. In the final least-squares refinement cycles on F^2, the model converged at $R1 = 0.0532$, $wR2 = 0.1275$, and goodness-of-fit = 1.066 for 1803 reflections with $F_o > 4\sigma F_o$ and 160 parameters. Further details of the crystallographic measurements are available as supplementary data.[2]

[2] Experimental details of the X-ray structure determination and tables of positional and thermal parameters, bond distances and angles, anisotropic thermal parameters, calculated hydrogen atom coordinates, and selected torsion angles, as well as the .cif file, can be purchased from: The Depository of Unpublished Data, Document Delivery, CISTI, National Research Council Canada, Ottawa, Canada K1A 0S2. The tables of bond distances and angles, positional parameters, and hydrogen atom coordinates have also been deposited with the Cambridge Crystallographic Data Centre, and can be obtained on request from The Director, Cambridge Crystallographic Centre, 12 Union Road, Cambridge, CB1 1EZ. U.K.

© 1998 NRC Canada

Conclusions

In conclusion, in our hands, reaction of 2,4-pentanedione with thiosemicarbazide, 4-methylthiosemicarbazide, and 4-ethylthiosemicarbazide proceeded only with the involvement of ethylenediamine as initially reported in 1967 and as modified in 1990. The products obtained are not the desired **1** but instead pyrazoline **5**, as confirmed by X-ray crystallographic analysis for the 4-methylthiosemicarbazide reaction. It should be noted that the material prepared in 1990 and used to form technetium-99m chelates was actually a pyrazoline that had been misidentified on the basis of its ^{1}H NMR spectrum. This might be a consequence of the dramatic solvent dependence of the ^{1}H NMR spectrum of the pyrazoline in $CDCl_3$ versus DMSO-d_6. The bisthiosemicarbazone **1** reported in the literature was misidentified, possibly due to the lack of an obvious AB pattern for the dione methylene protons and the coincidental methyl amine protons of the thiosemicarbazide in the ^{1}H NMR when analysed in DMSO-d_6 versus $CDCl_3$. Thus, the report of technetium-99m chelates of bisthiosemicarbazones of pentanedione (8) should be regarded with suspicion.

A subsequent article (9) by the same researchers in 1991 attempts to explain why a supposed symmetrical molecule would lead to two isomers upon radiolabelling. On the basis of the misidentification of the bis(4-methylthiosemicarbazone) of pentanedione, this 1991 report should be viewed with some suspicion as well. Although we did not repeat the 1991 preparation with 3,3-dimethyl-2,4-pentanedione and 4-methylthiosemicarbazide, the reported ^{1}H NMR spectrum seems more consistent with a pyrazoline, similar to structure **5**, than the proposed bisthiosemicarbazone.

References

1. (*a*) E.A. Coats, S.R. Milstein, G. Holbein, J. McDonald, R. Reed, and H.G. Petering. J. Med. Chem. **19**, 131 (1976); (*b*) H.G. Petering, H.H. Buskirk, and G.E. Underwood. Cancer Res. **24**, 367 (1964); (*c*) D.T. Minkel, C. Chan-Stier, and D.H. Petering. Mol. Pharmacol. **12**, 1036 (1976).
2. M.J.M. Campbell. Coord. Chem. Rev. **15**, 279 (1975).
3. A. Yokoyama and T. Hosotani. Int. J. Nucl. Med. Biol. **12**, 431 (1986).
4. B.A. Gingras, T. Suprunchuk, and C.H. Bayley. Can. J. Chem. **40**, 1053 (1962).
5. C.N. O'Callaghan and D. Twomey. J. Chem. Soc. (C), 2400 (1967).
6. A.A. El-Asmy, M.A. Morsi, and A.A. El-Shafei. Transition Met. Chem. **11**, 494 (1986).
7. K.N. Zelenin, A.B. Tomchin, O.V. Solod, and M.Y. Malov. Khim. Geterot. Soed. **1**, 128 (1986).
8. Y. Arano, M. Yabuki, T. Yahata, K. Horiuchi, and A. Yokoyama. Chem. Pharm. Bull. (Tokyo), **38**, 3099 (1990).
9. Y. Arano, M. Yabuki, A.G. Jones, and A. Yokoyama. Chem. Pharm. Bull. (Tokyo), **39**, 104 (1991).
10. G.O. Dudek and R.H. Holm. J. Am. Chem. Soc. **83**, 2099 (1961).

© 1998 NRC Canada

Rate enhancement of organic reactions by microwaves at atmospheric pressure

R.N. Gedye and J.B. Wei

Abstract: Several different reactions have been studied to determine whether they occur more rapidly than conventionally heated reactions at atmospheric pressure. Small rate enhancements have been observed for some reactions carried out under microwave reflux in a modified domestic microwave oven. The Knoevenagel reaction of acetophenone with ethyl cyanoacetate was shown to have a rate enhancement of 2.5 times. However this reaction showed no rate increase over conventional heating, at the same temperature, in a variable-frequency microwave oven. It is therefore probable that the small rate enhancements observed in these experiments, using microwave heating, were due to hot spots or superheating of the solvent rather than to nonthermal effects.

Key words: microwave, nonthermal effects, superheating, hot spots.

Résumé : On a étudié plusieurs réactions différentes pour déterminer si elles se produisent plus rapidement que les réactions chauffées normalement, à la pression ambiante. On a observé de légères augmentations de vitesse pour quelques réactions effectuées sous reflux à microondes, dans un four à microondes domestique modifié. Il a été démontré que la vitesse de la réaction de Knoevenagel de l'acétophénone avec le cyanoacétate d'éthyle est multipliée par 2,5. Toutefois, lorsqu'on utilise un four à microonde à fréquence variable, cette réaction ne présente aucune augmentation de vitesse par rapport à un chauffage conventionnel, à la même température. Il donc probable que les faibles augmentations de vitesse observées au cours de ces expériences, par chauffage à microondes, seraient le résultat de points chauds ou de surchauffe du solvant plutôt que d'effets non thermiques.

Mots clés : microonde, effets non thermiques, surchauffe, points chauds.

[Traduit par la rédaction]

Introduction

Substantial rate enhancements are frequently observed when chemical reactions are carried out under microwave irradiation in sealed vessels (1–4). These rate enhancements are generally attributed to superheating of the solvent due to the increased pressures generated when reactions are carried out in this manner (3, 5). However, there have been a number of reports that claim that significant rate increases occur in some reactions under microwave irradiation in open vessels (6–14), suggesting a specific or nonthermal microwave effect. Some of these reactions have been reexamined, however, and shown to occur at similar rates under microwave and conventional heating at the same temperature (15–17).

Berlan et al. (6) reported that certain Diels–Alder reactions occur more rapidly under microwave heating than under conventional heating at the same temperature. In a subsequent paper (18), however, he cast doubt on the existence of nonthermal effects, attributing the rate increases to localized "hot spots" in the reaction mixture or to superheating of the solvent above its boiling point. He emphasized the difficulty in measuring the temperature accurately in microwave cavities. In fact, kinetic studies by Raner et al. (15) on the Diels–Alder reaction of anthracene with diethyl maleate, previously reported by Berlan et al. (6) to show a microwave effect, showed no microwave enhancement compared with conventional heating at the same temperature.

Jahngen and co-workers (7) reported that the rate of hydrolysis of the biomolecule ATP was 25 times greater during microwave heating than conventional heating at comparable temperatures. However Jahngen et al. (16) later showed that, with more accurate temperature control, no such effect could be observed.

Bose et al. (8) suggested that the rapid reaction rates achieved in the synthesis of a variety of heterocycles in microwave ovens, at low power levels in open vessels, were not only due to thermolysis. This implied specific activation by microwaves. However, Westaway and Gedye (17) have shown that the rates of two of these syntheses were not accelerated appreciably by microwave heating compared with conventional heating at similar temperatures.

There have also been reports (9, 10) that racemization of amino acids occurs more rapidly on microwave heating than conventional heating at similar temperatures. This could have important negative consequences in nutrition, since proteins and peptides in food are hydrolyzed to amino acids (10). Again no real evidence for a nonthermal effect was found in a study of the racemization of L-proline under microwave and conventional reflux in aqueous solution (17). The increase in

Received October 28, 1997.

R.N. Gedye.[1] Department of Chemistry & Biochemistry, Laurentian University, Sudbury, ON P3E 2C6, Canada.
J.B. Wei. Lambda Technologies Inc., 960 Aviation Parkway, Morrisville, NC 27560, U.S.A.

[1] Author to whom correspondence may be addressed. Telephone: (705) 675-1151 (ext. 2104). Fax: (705) 675-4844. E-mail: RGEDYE@NICKEL.LAURENTIAN.CA

© 1998 NRC Canada

racemization rate was found to be very small, and could be attributed to localized hot spots or superheating of the solvent.

It should be noted that Baghurst and Mingos (19) have reported recently that some solvents superheat under microwave heating at atmospheric pressure and that this could account for any small rate enhancements observed. Furthermore, Mingos (20) suggests that rate enhancements should only be attributed to nonthermal effects if they are substantial (100 times or more).

A number of other reactions have been shown to occur at the same rate under microwave and conventional heating at the same temperature These include the esterification of carboxylic acids with alcohols (3, 5), the acid-catalyzed isomerization of carvone (15), and ene reactions involving carbonyl enophiles (18).

On the other hand kinetic studies by Lewis et al. (21) showed that microwave irradiation enhanced the rate of imidization of a polymer (BTDA–DDS polyamic acid) and that the apparent activation energy was reduced from 105 kJ/mol (conventional heating) to 55 kJ/mol. It was suggested, however, that this enhancement was due to nonuniform temperature on a molecular scale rather than a nonthermal effect. Wei et al. (22) have reported that the cross-linking of epoxies using the curing agents diaminodiphenyl sulfone (DDS) and *m*-phenylenediamine (*m*-PDA) occurred more rapidly using microwave heating than conventional heating at similar temperatures and resulted in higher Tg (glass transition temperature) values. Higher rate enhancements and Tg values were observed for the higher lossy curing agent, DDS, than the lower lossy *m*-PDA. The higher Tg values for the microwave-cured samples was regarded as evidence for a nonthermal effect.

Recently Shibata et al. (23) reported a reduction in activation energy in the microwave assisted decomposition of sodium bicarbonate in water, attributing their results to a nonthermal effect. It should be noted, however, that the reaction was carried out using a 20% suspension of sodium bicarbonate, i.e., under heterogeneous conditions. Thus it is possible that selective superheating of the solid $NaHCO_3$ might have caused the rate increase.

This paper describes the study of a number of reactions, including reactions previously claimed to show a microwave effect at atmospheric pressure, in order to determine whether they occur more rapidly under microwave irradiation than under conventional heating at the same temperature.

Results & discussion

Srikrishna and Nagaraju (11) reported that microwave irradiation accelerated the *ortho* ester Claisen rearrangement of allylic alcohols in DMF in open vessels. For example, alcohol **1** gave an 83% yield of product **2** in 10 min, using a commercial microwave oven (eq. [1]).

[1] 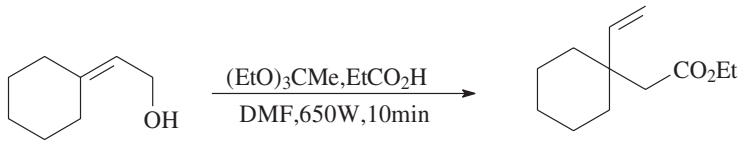

1 **2**

A similar reaction, heated conventionally in a sealed tube at 180°C took 48 h. It is not clear, however, whether DMF was used in this experiment. In the present study the rearrangement of geraniol (**3**) to compound **4** was investigated (eq. [2]).

[2] 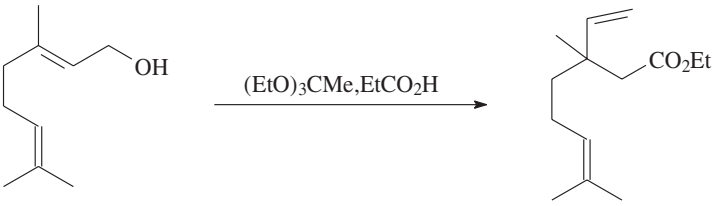

3 **4**

This reaction had been reported (11) to give an 87% yield of **4** in 12 min in a microwave oven. Identical reaction mixtures (i.e., geraniol, TEOA, propanoic acid in DMF) were heated at the boiling point (153°C) of DMF conventionally (heating mantle) and in a microwave oven for 10 min in an open vessel. The yield of **4** (52%) in the microwave reaction was not significantly higher, however, than that of **4** (47%) obtained by conventional heating.

Recently, Gupta et al. (12) have reported considerable rate enhancements in the synthesis of chalcones by Crossed–Aldol condensations in a microwave oven at atmospheric pressure. The reaction times and yields were compared with those reported earlier using conventional conditions, and it was claimed that reaction times were reduced from hours to minutes using microwave heating. For example, the chalcone **5** was synthesized from cyclohexanone and benzaldehyde in ethanol in the presence of one or two pellets of NaOH (catalyst) in 1 min in a 90% yield, compared with a "standard time" of 2 h, giving a 72% yield (eq. [3]).

[3] 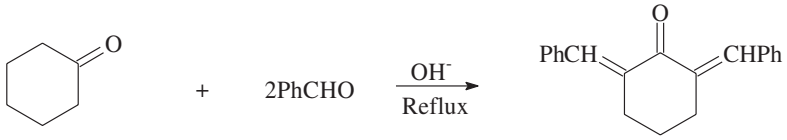

5

© 1998 NRC Canada

Table 1. Reaction of cyclohexanone with benzaldehyde in the presence of a basic catalyst.

Method	Catalyst[a]	Time (min)	% yield[b]
Microwave	NaOH (s)	2	38
Conventional	NaOH (s)	2	32
Microwave	KOH (alc)	2	35
Conventional	KOH (alc)	2	30
Microwave	NaOH (s)	3	45
Conventional	NaOH(s)	3	38

[a] s, solid; alc, alcoholic.
[b] Average of three runs. Product was isolated.

Table 2. Reaction of styrene with CCl_4 in the presence of a Cu(I)-amine catalyst in CH_3CN under reflux.

Method[a]	Time (min)	% product
MW	15	8.5
CONV	15	7.9
MW	35	16.0
CONV	35	18.1
MW	70	18.7
CONV	77	20.3
CONV	80	23.0
MW (hetero)	15	19.4

[a] MW, microwave; CONV, conventional. Microwave reaction carried out under homogeneous conditions unless otherwise indicated.

Table 3. Reaction of styrene with CCl_3CO_2Et in the presence of a Cu(I)-amine catalyst in CH_3CN under reflux.

Method[a]	Time (min)	% product
MW	15	21.8
CONV	15	15.1
MW	35	27.2
CONV	35	22.6
MW	70	38.3
CONV	70	33.2
MW	170	48.7
CONV	250	51.8
MW (hetero)	16	49.1

[a] MW, microwave; CONV, conventional. Microwave reaction carried out under homogeneous conditions unless otherwise indicated.

The same reaction was carried out under microwave and conventional heating in an open vessel, with the same proportions of reactants, catalyst, and solvent used by Gupta. Initial experiments showed a two- to five-fold rate increase in the microwave heated reactions. A more careful investigation showed, however, that substantial evaporation of ethanol occurred in the microwave-heated reactions, whereas the conventionally heated reactions lost less solvent. Thus the microwave-heated reactions would have been expected to give higher yields in the same time period because of a more concentrated solution and a higher reaction temperature. It was also considered possible that, since the NaOH pellets did not dissolve appreciably under the reaction conditions, the rate enhancement could be caused by selective heating of the solid catalyst. To test this hypothesis, the reactions were also carried out using a solution of KOH in ethanol, but the rate enhancements were comparable to those observed in the reactions carried out with pellets of solid NaOH.

To prevent evaporation of the solvent, the reaction was carried out in a microwave oven modified to enable the reaction vessel to be connected to a reflux condenser outside the microwave oven (24). The reaction was carried out under reflux in the microwave oven and compared with a similar reaction carried out under conventional reflux. The results are shown in Table 1.

However, it can be seen (Table 1) that only slightly higher yields were obtained in the microwave reactions than in the conventionally heated reactions, in the same time period, when either solid NaOH (heterogeneous catalyst) or alcoholic KOH (homogeneous catalyst) were used. The rate enhancement using solid NaOH was only 1.5 times, and this could be attributed to superheating of the solvent or to hot spots in the reaction mixture in the microwave reactions rather than to a nonthermal effect (18, 19).

Adamek and Hajek (13) have reported that the addition of CCl_4 and CCl_3CO_2Et to styrene in the presence of a homogeneous Cu(I)-amine catalyst in CH_3CN occurs more rapidly under microwave heating than conventional heating at the same temperature (eq. [4]). Rate enhancements of 21 times were observed for the CCl_3CO_2Et addition and 7 times for the CCl_4 addition to styrene. The present investigation, in which the rates of the reaction using microwave reflux and conventional reflux were compared, showed a rate enhancement of only 1.5 times for the addition of CCl_3CO_2Et and no rate increase for the addition of CCl_4.

[4] 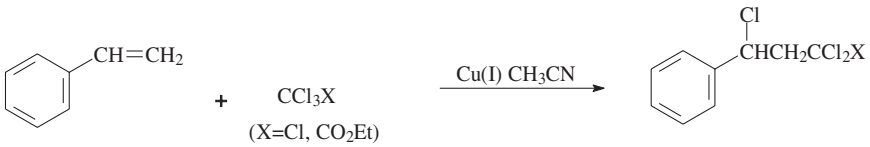

Higher rate enhancements were observed, however, when the reactions were done in the presence of a small amount of solid CuCl (heterogeneous conditions). The rate enhancements for the additions of CCl_3CO_2Et and CCl_4 to styrene were 11 and 3 times, respectively. The results of these experiments are summarized in Tables 2 and 3 and Fig. 1.

The larger rate enhancements observed under heterogeneous conditions can be accounted for by the increased temperature

© 1998 NRC Canada

Fig. 1. The effect of microwave heating on the rate of the reaction of styrene with carbon tetrachloride and ethyl trichloroacetate in the presence of a Cu(I) catalyst in refluxing acetonitrile.

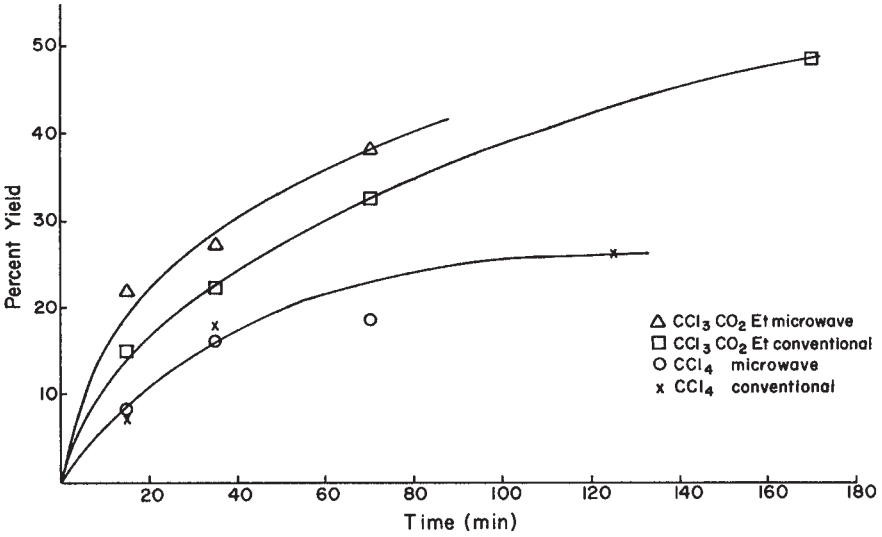

of the solid CuCl in the microwave reaction. It has been reported that CuCl is a strong absorber of microwaves and heats very rapidly (20°C/s) in a 2.45 GHz microwave cavity (25).

Soufaioui and co-workers (14) synthesized a series of 1,5-aryldiazepin-2-ones in high yield by the condensation of *o*-β-arylenediamines with β-ketoesters in xylene under microwave heating in open vessels. The reaction time was only 10 min with a final reaction temperature of 136–139°C. They reported, however, that no reaction occurred when similar reactions were heated classically under the same conditions of time and temperature. This would suggest a very dramatic rate increase under microwave heating at atmospheric pressure, and these results were taken as evidence for a specific microwave effect (14).

The reaction of *o*-phenylenediamine with ethyl acetoacetate was repeated using the same quantities of reagents and solvent used by Soufaioui. Care was taken to carry out the microwave- and conventionally heated reactions in the same vessels and at, as close as possible, the same temperature. Initially an attempt was made to carry out the reactions under microwave and classical reflux, respectively. Unfortunately it was found that insufficient microwave energy was absorbed in the low-polarity solvent *o*-xylene for the reaction to reach reflux temperature in 10 min. Even when a solution of *o*-phenylendiamine in *o*-xylene was preheated to reflux temperature (143°C) and the ethyl acetoacetate then added followed immediately by heating at 720 W in the microwave oven, the temperature slowly dropped and was only 105°C at the end of 10 min of microwave heating. In this experiment, the product failed to crystallize on cooling overnight although GC analysis indicated about 50% conversion to the expected product. Under classical reflux (oil bath heating), refluxing was maintained throughout the 10 min heating period, but the temperature dropped from 143 to 122°C due to containment of the ethanol liberated in the reaction. The product crystallized on cooling, giving a 37% yield.

Since the reflux conditions were unsatisfactory the reactions were then carried out in open Erlenmeyer flasks. The results obtained in the conventionally heated experiments were very different from these reported by Soufiaoui, and showed that there was virtually no difference in the rate of the microwave and conventionally heated reactions (Table 4). The temperature of the microwave-heated reaction, carried out at 720 W, was initially 143°C (after preheating), and fell to 105–115°C in different runs. The temperature profiles were simulated as far as possible in the conventionally heated (oil bath) experiments, giving comparable yields of the crystalline product (Table 4). In each case the product was shown, by GC – mass spectrometry and NMR to be the expected 2-methyl-1,5-phenyldiazepin-2-one **6** (eq. [5]).

[5] 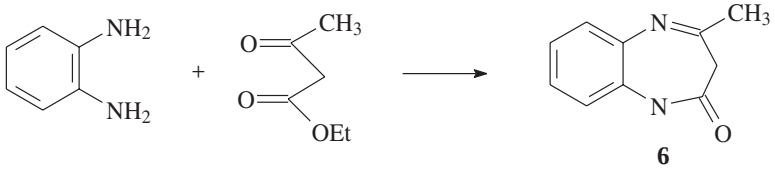

6

It can also be seen from Table 4 that the yields were affected by reaction temperature but not by the heating method (microwave or classical). For example, the microwave-heated reaction, with a temperature range 143–115°C gave a yield of 53%, and a comparable yield of 46% was obtained in the conventionally heated reaction with a similar temperature range

© 1998 NRC Canada

Table 4. Reaction of *o*-phenylenediamine with ethylacetoacetate (heating time 10 min).

Method[a]	Temp. (°C)	% yield[c]
MW (reflux)[b]	143–105	0[d]
CONV (reflux)	143–122	37
MW (open)	143–105	33
MW (open)	143–115	53
CONV (open)	143–108	41
CONV (open)	143–110	46
CONV (open)	143–140	75

[a] MW, microwave; CONV, conventional.
[b] Reaction mixture observed to have ceased boiling after about 2 min.
[c] Yields of isolated crystalline product. Yields estimated by GC were considerably higher, but showed the same trends.
[d] The GC analysis indicated approx. 50% conversion to product.

(143–110°C). A higher yield (75%) was obtained by conventional heating for 10 min at the boiling point of xylene (143–140°C). Hence, there was no evidence for specific microwave effects.

Table 5. Reaction of acetophenone with ethyl cyanoacetate in the presence of piperidine in ethanol under reflux.

		% yield			
Method[a]	Time (min)	*Z*-Isomer	*E*-Isomer	Total	Ratio *E*/*Z*
MW	30	2.2	3.0	5.2	1.4
CONV	30	0.8	1.3	2.1	1.6
MW	60	4.2	5.5	9.7	1.3
CONV	60	1.5	2.3	3.5	1.5
MW	120	7.6	9.4	17.0	1.2
CONV	120	3.4	4.7	8.1	1.4
CONV	240	7.1	9.3	16.4	1.3
CONV	465	9.7	12.6	22.3	1.3
CONV	990	15.4	18.4	33.8	1.2

[a] MW, microwave; CONV, conventional. Microwave reaction carried out in a modified microwave oven with a reflux condenser.

Bose et al. (8) reported the rapid synthesis of a variety of heterocyclic compounds in microwave ovens using open vessels. Among these reactions, the Knoevenagel reaction between sacilylaldehyde and ethyl malonate in the presence of piperidine (eq. [6]) was reported to give an 82% yield of 3-carbethoxycoumarin **7** in 3 min in a microwave oven.

[6] 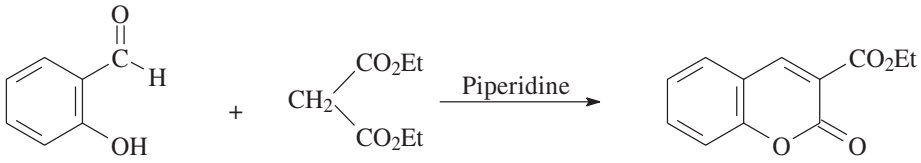

7

Initial studies on this reaction by Westaway and Gedye (17) showed slightly increased rates both in the presence of ethanol and in the absence of a solvent, when microwave heating was used at approximately the same temperature as the conventionally heated reactions. However, it was difficult to measure the temperature accurately in the microwave reaction without solvent, and in the presence of ethanol, evaporation of the solvent proved to be a problem. In the present study, the reaction in ethanol was carried out using a reflux condenser as described earlier, and it was found that the rate enhancement of the microwave reaction was approximately 2.5 times, since the yield of the product **7** was found to be 73% in 8 min using microwave heating compared with a yield of 71% in 20 min using conventional heating under reflux.

A similar rate enhancement (2.5 times) was observed in the much slower Knoevenagel reaction of acetophenone with ethyl cyanoacetate in ethanol in the presence of piperidine (eq. [7]).

[7] 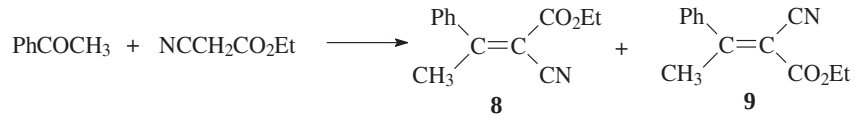

8 **9**

The results are shown in Table 5 and Fig. 2. It can been seen that the same yield (17%) of the isomer mixture **8** and **9** was obtained after refluxing for 120 min in the microwave oven and 320 min of conventional reflux. The isomer ratio *E*:*Z* was not affected by the heating method, and it was concluded that microwave irradiation did not effect the stereochemical outcome of this reaction.

The question that remained was whether these rate increases were due to a nonthermal microwave effect. To investigate this, the reaction was carried out using a variable-frequency (Variwave) microwave system. This instrument includes temperature measurement and provides very uniform heating, minimizing the possibility of hot spots. Ethanol was not suitable as a solvent because it would evaporate in the Variwave system. For this reason both microwave and conventional reactions were carried out at 80°C in the absence of solvent. The results are shown in Table 6 and Fig. 3. It can be seen that there is no significant difference in the rate of the microwave and conventional reactions. The microwave (Variwave) and conventional reactions were also carried out in anisole as a solvent at 100°C. Again the microwave and conventional reactions occurred at virtually the same rate (Table 7, Fig. 4).

These results suggest that the rate enhancement (2.5 times)

© 1998 NRC Canada

Table 6. Reaction of acetophenone with ethyl cyanoacetate in the presence of piperidine at 80°C (no solvent).

		% yield			
Method[a]	Time (min)	*Z*-Isomer	*E*-Isomer	Total	Ratio *E*/*Z*
MW	10	—	—	4.7	—
MW	30	3.4	10.1	13.5	3.0
CONV	31	4.1	10.1	14.2	2.5
MW	60	6.7	13.8	20.5	2.1
CONV	64	7.3	14.5	21.8	2.0
MW	120	8.8	15.8	24.6	1.8
CONV	124	10.2	15.7	25.9	1.5
CONV	201	11.9	17.1	29.0	1.4

[a] MW, microwave; CONV, conventional. Microwave reaction carried out in Variwave frequency (Variwave) microwave oven.

Fig. 2. The effect of microwave heating on the rate of the reaction of acetophenone with ethyl cyanoacetate in the presence of piperidine in refluxing ethanol.

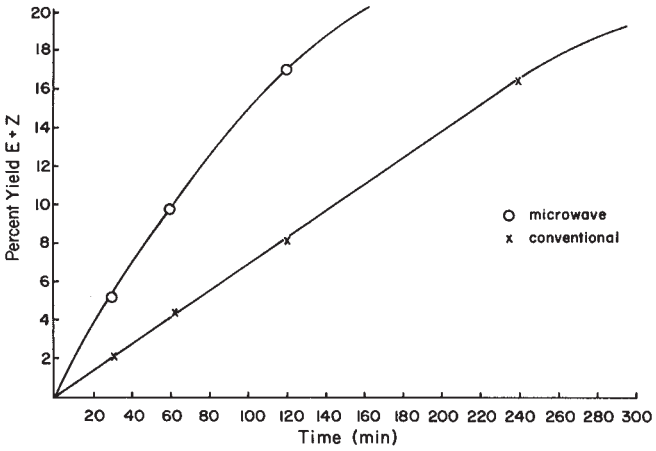

of the same reaction carried out under reflux in the microwave oven was due to hot spots or to general superheating of the solvent (ethanol) rather than to a nonthermal effect.

Conclusions

Several reactions, previously reported to show substantial rate enhancements using microwave heating at atmospheric pressure, were shown to occur at the same rate or only slightly faster than under conventional heating at the same temperature. The largest rate enhancement found in this study under homogeneous conditions, was 2.5 times in the Knoevenagel reaction of acetophenone with ethyl cyanoacetate. However, when this reaction was carried out in a variable-frequency microwave oven, it showed no rate enhancement compared with a conventionally heated reaction at the same temperature. It is therefore probable that the small rate enhancements observed in some reactions at atmospheric pressure are due to hot spots or to general superheating of the solvent under microwave heating.

Higher rate enhancements may be observed for reactions carried out under heterogeneous conditions, for example, in the presence of a solid catalyst that absorbs microwave energy.

Fig. 3. The effect of microwave heating on the rate of the reaction of acetophenone with ethyl cyanoacetate in the presence of piperidine at 80% (no solvent).

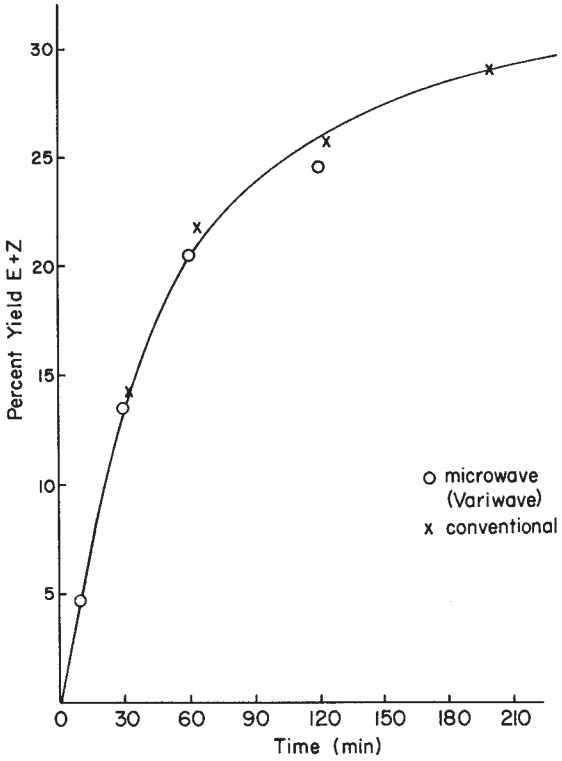

This can be attributed to localized heating of the catalyst to a temperature higher than that of the reaction mixture.

Experimental

Apparatus

The microwave ovens used in this study were the following:

(*i*) A Kenmore model 88560 microwave oven with 10 power settings, maximum output 900 W, modified to allow reactions to be carried out under reflux. A 7/8 in. (1 in. = 25.4 mm) hole was punched in the centre of the top of the oven to permit insertion of a B-14 air condenser surrounded by a 3/4 in. internal diameter copper tube, 4 in. long. A B-14 water-cooled condenser was inserted in the air condenser above the microwave oven.

(*ii*) A Toshiba model ER-8000 BTC microwave oven with a maximum output of 720 W.

(*iii*) A variable-frequency (Variwave) microwave furnace, Model 1500 manufactured by Lambda Technologies, Raleigh, North Carolina, U.S.A.

Product analysis

Reaction products were identified by their melting and boiling points (uncorrected), by GC – mass spectrometry and by NMR spectroscopy. GC–MS analysis was carried out using a Varian 3400 gas chromatograph, fitted with a 30 m × 0.25 nm PTE-5 silica column coupled to a Saturn II mass spectrometer operated in the electron impact mode. Proton NMR spectra were recorded with a Varian Gemini 200 MHz FT–NMR spectrometer. Reactions were monitored by GC using a Varian

© 1998 NRC Canada

Table 7. Reaction of acetophenone with ethyl cyanoacetate in the presence of piperidine in anisole at 100°C.

		% yield			
Method[a]	Time (min)	*Z*-Isomer	*E*-Isomer	Total	Ratio *E*/*Z*
MW	30	3.7	11.9	15.6	3.2
CONV	30	4.9	12.8	17.7	2.0
MW	60	6.7	13.4	20.1	2.0
CONV	70	7.7	16.2	23.9	2.1
MW	120	11.1	17.6	28.7	1.6
CONV	120	10.7	17.5	28.2	1.6
MW	150	12.5	19.7	32.2	1.6
CONV	210	13.0	20.4	33.4	1.6

[a] MW, microwave; CONV, conventional. Microwave reaction carried out in Variwave microwave oven.

3700 gas chromatograph fitted with a 5 ft × 0.25 in. (1 in. = 25.4 mm) 3% silicone SE-30 column.

Temperature measurement

In the microwave experiments carried out in the Variwave microwave oven, temperatures were measured using a fibre-optic probe manufactured by Luxtron.

Temperatures quoted in other microwave experiments were estimated either pointing a Williamson 600 infrared sensor at the reaction mixture or by inserting a standard thermometer into the reaction mixture immediately after heating was completed. It was recognized that the temperatures observed using the former method were not very accurate (± 5°C) and using the latter method were a few degrees lower than the actual final temperature.

General procedure

Each experiment was carried out both by conventional heating and by microwave heating using the same quantities of reagents and solvent. Most of the experiments were carried out under reflux (conventional and microwave) and the reactions monitored by withdrawing samples at regular time intervals and analyzing them by GC. In reactions that required catalysts, the mixture of reactants and solvent was heated until refluxing commenced, and the catalyst was then added. The reaction time was the reflux time after the addition of the catalyst. This procedure eliminated the problem caused by the fact that the conventionally heated reactions took longer to reach the boiling point than the microwave heated reactions.

Reaction rates of the Knoevenagel reaction of acetophenone with ethyl cyanoacetate using the variable-frequency (Variwave) microwave oven were compared with the conventional reactions at the same temperature. The temperature of the Variwave reactions was monitored and held constant, and the conventional reactions were heated at the same temperature in a constant-temperature oil bath. Again the catalyst was added after the temperature had equilibrated to the required value, and the reaction time measured from this point.

The individual microwave heated reactions are described in the following section.

Ortho ester Claisen rearrangement

A mixture of geraniol (230 mg, 1.5 mmol), triethyl orthoacetate (1.3 g, 8.2 mmol), and propanoic acid (5 drops) in dry

Fig. 4. The effect of microwave heating on the rate of the reaction of acetophenone with ethyl cyanoacetate in the presence of piperidine in anisole at 100°C.

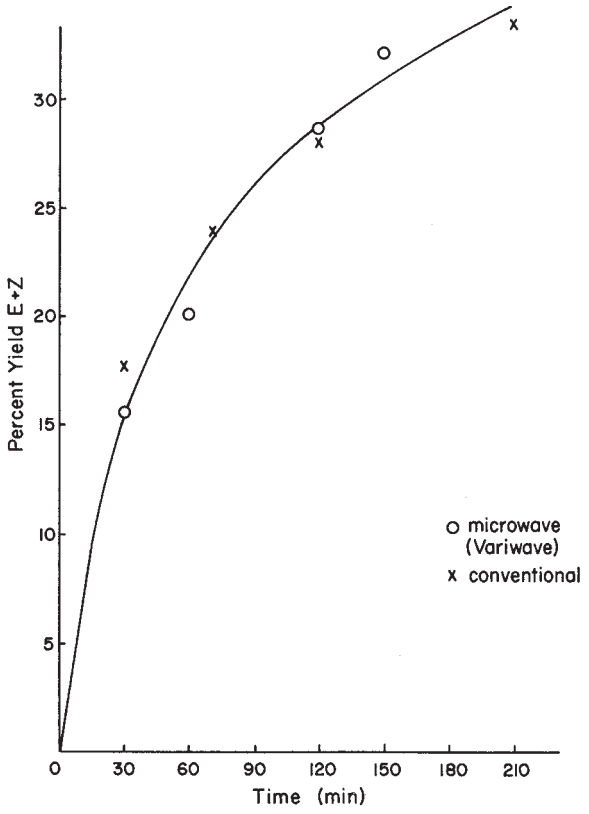

DMF (5 mL) was placed in an open Erlenmeyer flask and heated in the Toshiba microwave oven for 10 min at 640 W.

Crossed–Aldol condensation

A mixture of cyclohexanone (0.98 g, 10 mmol), benzaldehyde (2.12 g, 20 mmol), and anhydrous ethanol (20 mL) was heated to reflux in the Kenmore microwave oven. Two pellets of solid NaOH were then added, and the mixture refluxed in the microwave oven at 180 W for the specified time. The yield was estimated by GC and also by isolating the product. The product was cooled for 15 min in an ice bath, the pale yellow crystalline solid filtered, washed repeatedly with water, and dried in a dessicator.

Addition of CCl_3X to styrene

A mixture of styrene (2.1 g, 20 mmol), carbon tetrachloride (6.2 g, 40 mmol), copper(I) chloride (0.020 g, 0.2 mmol), *n*-butylamine (0.030 g, 0.4 mmol), and acetonitrile (5 mL) was refluxed in the Kenmore microwave oven at 180 W for the specified time.

The reaction was repeated using ethyl trichloroacetate (7.7 g, 40 mmol) and the above amounts of the other reagents.

Reaction of *o*-phenylenediamine with ethyl acetoacetate

(*i*) A mixture of *o*-phenylenediamine (1.08 g, 10 mmol) and *o*-xylene (20 mL) was heated to reflux (143°C) on a hot plate, forming a homogeneous solution. Ethyl acetoacetate (1.95 g, 15 mmol) was added and the mixture heated briefly (about 30 s) to reflux. The resulting mixture was immediately placed

© 1998 NRC Canada

in the Kenmore microwave oven (boileezers added) and heated with a reflux condenser attached for 10 min at 720 W. It was observed that the mixture ceased boiling after about 2 min. At the end of the heating period the temperature was measured and found to be approximately 105°C. An aliquot was analyzed by GC. The mixture was left to stand overnight in the refrigerator but failed to crystallize.

(*ii*) The above experiment was repeated except that the preheated mixture, in an open 125 mL Erlenmeyer flask, was heated in the Toshiba microwave oven at 720 W for 10 min. The temperature of the mixture fell to 105–115°C (in different experiments) by the end of the heating period. The crystalline product (yellow needles) was filtered off and washed with two 5 mL portions of ether.

Knoevenagel reaction of salicylaldehyde and diethyl malonate

A mixture of salicylaldehyde (3.0 g, 25 mmol), diethyl malonate (4.4 g, 27.5 mmol), acetic acid (40 μL), and anhydrous ethanol (10 mL) was heated to reflux in the Kenmore microwave oven. Piperidine (0.25 mL) was then added and the mixture refluxed for the specified time. The yield of the product was estimated by GC and by isolation after cooling and recrystallization from aqueous ethanol.

Knoevenagel reaction of acetophenone with ethyl cyanoacetate in the presence of piperidine

(i) In refluxing ethanol

A mixture of acetophenone (3.0 g, 25 mmol), ethyl cyanoacetate (2.9 g, 25 mmol), acetic acid (40 μL), and ethanol (10 mL) was heated to reflux in the Kenmore microwave oven. Piperidine (250 mL) was then added, and the mixture refluxed in the microwave oven at 180 W. Heating was interrupted at regular time intervals and samples withdrawn for GC analysis.

(ii) In the absence of solvent in the Variwave microwave oven at 80°C

The same amounts of reagents were used as in (*i*) except that no ethanol was used. The temperature of the Variwave was set at 80°C with a microwave central frequency of 8.1 GHz, a bandwidth of 0.30 GHz and a scan rate of 0.10 s. Initially a power of 80 W was used to preheat the mixture to 80°C. Piperidine was then added and the mixture maintained at 80°C using a power of 15 W. The heating was interrupted at regular time intervals and aliquots taken for GC analysis.

(iii) Using anisole as a solvent in the Variwave microwave oven at 100°C

The above reaction was repeated except that 5 mL of anisole was used as the solvent. The temperature was set at 100°C and maintained at that temperature with a power of 22 W. The central frequency was 12.2 GHz, bandwidth 0.40 GHz, and scan rate 0.5 s.

Acknowledgements

The authors wish to thank D. Morris for carrying out some of the experimental work and Drs. K. Westaway, F. Smith, H. Joly, and W. Rank of Laurentian University, and Drs. J. Methven and S. Bush of UMIST for helpful discussions. The authors also wish to thank Todd Ellis and Lambda Technologies for the use of the Variwave microwave furnace.

References

1. R. Gedye, F. Smith, K. Westaway, H. Ali, L. Baldisera, L. Laberge, and J. Rousell. Tetrahedron Lett. **27**, 279 (1986).
2. R.J. Giguere, T.L. Bray, S.M. Duncan, and G. Majetich. Tetrahedron Lett. **27**, 4945 (1986).
3. R. Gedye, F. Smith and K. Westaway. Can. J. Chem. **66**, 17 (1988).
4. D.M.P. Mingos and D.R. Baghurst. Chem. Soc. Rev. **20**, 1 (1991).
5. S. Pollington, G. Bond, R. Moyes, D. Whan, J. Candlin, and J. Jennings. J. Org. Chem. **56**, 1313 (1991).
6. J. Berlan, P. Giboreau, S. Lefeuvre, and C. Marchand. Tetrahedron Lett. **32**, 2363 (1991).
7. W.-C. Sun, P.M. Guy, J.H. Jahngen, E.F. Rossomando, and E.G.E. Jahngen. J. Org. Chem. **53**, 4414 (1988).
8. A.K. Bose, M.S. Manhas, M. Ghosh, V.S. Raju, K. Tabei, and Z. Urbanczyk-Lipkowska. Heterocycles, **30**, 741 (1990).
9. S.T. Chen, S.H. Wu, and K.T. Wang. Int. J. Pept. Protein Res. **33**, 73 (1989).
10. G. Lubec, C. Wolf, and B. Bartosch. The Lancet, 1392 (1989).
11. S. Srikrishna and S. Nagaraju. J. Chem. Soc. Perkin Trans. 1, 311 (1992).
12. R. Gupta, A.K. Gupta, S. Paul, and P.L. Kachroo. Ind. J. Chem. **34B**, 61 (1995).
13. F. Adámek and M. Hájek. Tetrahedron Lett. **33**, 2039 (1992).
14. K. Bougrin, A.K. Bennani, S.F. Tétouani, and M. Soufiaoui. Tetrahedron Lett. **35**, 8373 (1994).
15. K.D. Raner, C.R. Strauss, F. Vyskoc, and L. Mokbel. J. Org. Chem. **58**, 950 (1993).
16. E.G.E. Jahngen, R.R. Lentz, P.S. Pesheck, and P.H. Sackett. J. Org. Chem. **55**, 3406 (1990).
17. K.C. Westaway and R.N. Gedye. J. Microwave Power and Electromagnetic Energy, **30**, 219 (1995).
18. R. Laurent, A. Laporterie, J. Dubac, J. Berlan, S. Lefeuvre, and M. Audhuy. J. Org. Chem. **57**, 7099 (1992).
19. D.R. Baghurst and D.M.P. Mingos. J. Chem. Soc. Chem. Commun. 674 (1992).
20. D.M.P. Mingos. Res. Chem. Intermed. **20**, 85 (1994).
21. D.A. Lewis, J.D. Summers, T.C. Ward, and J.E. McGrath. J. Polym. Sci. Part A: Polymer Chem. **30**, 1647 (1992).
22. J.B. Wei, Z. Fathi, and M.C. Hawley. Proc. 30th Microwave Power Symp. Denver, Colorado. 1995. p. 11.
23. C. Shibata, T. Kashima, and K. Ohuchi. Jpn. J. Appl. Phys. **35**, 316 (1996).
24. D.R. Baghurst and D.M.P. Mingos. J. Organomet. Chem. **384**, C57 (1990).
25. Atomic Energy Canada Ltd. and Voss Engineering Ltd. Microwaves and Minerals, Industrial Mineral Background Paper No. 14, Part 1. 1990. p. 21.

© 1998 NRC Canada

Structure bifurcation in containerless low-temperature syntheses of solid state niobium chloride compounds from lanthanoid atoms: an X-ray absorption and ab initio EXAFS analysis

C. Den Auwer, M.P. Andrews, V. Briois, C. Cartier dit Moulin, and H. Dexpert

Abstract : A new method of preparing solid state chlorometallates by reductive dechlorination of solvated niobium pentachloride with the vapour of nominally free atoms of erbium and samarium is described. Products were prepared in a model of a rotatable Pyrex cryostat by evaporating Sm or Er into a turbulently mixed solution of $NbCl_5$ in toluene at 130 K. Since no single crystal had been isolated, local order around the Nb atom was probed by far-IR, XPS, and EXAFS spectroscopy. Depending on the vaporized rare earth, two structurally distinct products were found. Combining information gathered by EXAFS results and ab initio EXAFS calculations on clusters to model the growing solid state compound using the FEFF6 code, two different condensation patterns were proposed: chlorine edge-shared aggregation was preferred for Er vaporization, face-shared condensation patterns emerged from Sm vaporization.

Key words: X-ray absorption spectroscopy, niobium, metal vapour synthesis, XPS.

Résumé : Ce travail décrit une nouvelle méthode de synthèse de composés chlorométalliques par abstraction réductrice des atomes de chlore à partir de pentachlorure de niobium solvaté et de vapeur d'atomes libres d'erbium et de samarium. Les produits ont été préparés dans un cryostat rotatif par évaporation de Sm et Er sur la solution de $NbCl_5$ dans le toluène, agitée et refroidie à 130 K. Aucun monocristal n'ayant pu être isolé, l'ordre local autour du Nb a été sondé par spectroscopie IR, XPS et EXAFS. Deux structures différentes dépendantes de la terre rare vaporisée ont été identifiées. Additionnant les informations EXAFS aux calculs ab initio d'EXAFS par FEFF6 et simulant la croissance des clusters formés, deux modes de condensation ont été proposés : condensation via les chlores des arêtes de l'octaèdre pour la vaporisation d'Er et condensation via les chlores des faces de l'octaèdre pour la vaporisation de Sm.

Mots clés : spectroscopie d'absorption des rayons X, niobium, synthèse à l'aide de métaux à l'état vapeur, spectroscopie photoélectronique des rayons X, « XPS ».

Introduction

It is surprising how little is known about reactions that take molecular compounds to infinite solids. This is due in part to a traditional reliance on high-temperature reactions in sealed containers to carry out syntheses that involve complex equilibria and heterogeneous reactions among components at solid, liquid, and gas interfaces. Among the low-temperature methods for making solid state materials from molecular precursors, those based on the so-called "chimie douce" approaches offer the potential of access to mechanistic details of growth by chemical or spectroscopic interception and interrogation. More generally, molecular building block approaches to solid state materials at reduced temperatures may provide control over molecular assembly, and thus allow systematic amplification of physical properties by chemical tuning at the molecular level. This kind of approach converges to the limit of the so-called "top down" methods of microfabrication technologies, while carrying with it all the advantages of "bottom up" molecular-scale chemistry. Synthetic tactics have included decomposition of precursor transition metal mononuclear and cluster chalcogenides (1–3), reactions of molecules in low-temperature molten salts (3), combinations of transition metal halides and carbonyls with soluble polychalcogenide anions, excision of cluster fragments from solid state lattices (4), and Rieke-type reductive condensations (5–7). These methods offer the advantage of access to significant quantities of metastable products, therefore giving considerable impetus to the study of new compounds not accessible under more forcing conditions. Our interest in this subject is twofold: (*i*) to develop so called "containerless," low-temperature syntheses of new solid state compounds using atoms and molecules as starting

Received August 25, 1997.

C. Den Auwer.[1] Department of Chemistry, McGill University, Montreal QC H3A 2K6, Canada; LURE, Université Paris Sud, 91405 Orsay Cedex, France; present address: CEA ValRhô, DCC/DRRV/SEMP Laboratoire de chimie théorique et structurale, 30207 Bagnols sur Cèze, France.
M.P. Andrews. Department of Chemistry, McGill University, Montreal QC H3A 2K6, Canada.
V. Briois, C. Cartier dit Moulin, and H. Dexpert. LURE, Université Paris Sud, 91405 Orsay Cedex, France.

[1] Author to whom correspondence may be addressed. Telephone: +(0)4 66 79 65 89. Fax: +(0)4 66 79 65 31. E-mail: Denauwer@concerto.valrho.cea.fr

© 1998 NRC Canada

materials and building blocks; and (*ii*) to identify structural intermediates, or proto-forms, of bulk solids in order to understand more about how structure–property relationships develop as molecules are elaborated into extended solids. This is undertaken in the present study by introducing a method to elaborate $NbCl_5$ into chains by reaction with vaporized atoms of samarium and erbium.

$NbCl_5$ was selected for our study in part because of the prominent role it has played as an entry into a large number of early transition metal halide solids in groundbreaking studies that have linked electronic properties with the extraordinary structures and patterns of their ramifying substructural motifs (8–10). More recently, $NbCl_5$ has served as a material source for a new series of mixed ternary rare earth $RENb_6Cl_{18}$ and quaternary $MRENb_6Cl_{18}$ (RE = rare earth, M = group 1 element) compounds showing the trademark Nb_6 octahedral cluster motif (10). Erbium and samarium were selected as reducing agents based on their ease of vaporization and their well-known trivalent (Er, Sm) and bivalent (Sm) oxidation-state chemistry. The lanthanoids are attractive because they offer a range of ionic radii (0.86–1.03 Å) depending on the choice of element, tunable redox properties, and a host of magnetic properties related to *f*-orbital occupancy. Sm^{3+} and Er^{3+}, respectively, are valence state $4f^6$ and $4f^{12}$ ions. Differences in the radii of these ions show up in solid state quaternary niobium halides where unit cell volumes are observed to increase on changing from Er^{3+} to Sm^{3+} (11). In their own right, lanthanoid halides show interesting structural variations (12). Additional points of contact of our work can be found in the literature on synthesis of chloroniobates or chlorotantalates (13). The preparation of colloids of samarium by freezing Sm vapor with alkane at liquid nitrogen temperature was described. Colloid slurries were active in Rieke-like reductions of large excesses of Nb_2Cl_{10} and Ta_2Cl_{10}.

Synthesis with atoms and molecules has much in common with so called *chimie douce*. Our method is "containerless" in the following sense: we replace the high-temperature container and the metal powder reducing agent with a vapour of erbium or samarium. The target molecule is dissolved in an organic solvent whose purpose is to maximize the "surface area" of the $NbCl_5$, and to provide a kind of dilution factor so that atom–atom encounters that would favor lanthanoid atom repolymerization are diminished. Timms and Turney (14) have described a high-temperature variation of the approach, in which atoms have been deposited into molten eutectic salt mixtures, with product work-up in the laboratory. Our method differs in that atoms are deposited into low-temperature solutions of dissolved inorganic molecules: atoms of erbium and samarium are used in the reductive condensation of $NbCl_5$ and its elaboration into the extended solid state compound.

A drawback to the *chimie douce* approaches is that products are not usually obtained in single-crystal form, so that elaborate techniques of structure refinement must be brought to bear on the materials. X-ray Absorption Spectroscopy (XAS) figures prominently among the characterization tools. A major challenge to using Extended X-ray Absorption Fine Structure spectroscopy (EXAFS) in this manner to extract quantitative structural information is that accurately known experimental reference standards must be applied against each intermediate composition. Since each EXAFS wave implies two sets of highly correlated variables: ($F(\theta,k)$, σ, N) and ($\Phi(k)$, r), (*i*) the amplitude function $F(\theta,k)$ must be well known to obtain reliable coordination numbers (N) and Debye–Waller factors (σ); (*ii*) bond distances (r) must be determined from accurate phase functions ($\Phi(k)$) (15). This is clearly a formidable problem when studying sequences of reactions like those described in the present work. Our atom reactions generate samples of unknown structure or samples that exhibit subtle variations in structural parameters. The problem is certainly exacerbated in the kind of problem undertaken in our studies because suitable standards are simply lacking. This makes ab initio theoretical standards essential. But until recently, ab initio methods have been less successful than experimental standards because of the approximations and ad hoc parameters required by the models.

Most widely used among the theoretical phase and amplitude functions are the tabulations of Teo and Lee (16) or of McKale et al. (17). Their approaches either ignore curved-wave effects (Teo) (16) known to be important, or neglect inelastic losses (McKale) (17). To overcome these limitations and provide a flexible framework for XAS analysis, we use the recently developed ab initio multiple-scattering curved-wave XAFS method, FEFF6, introduced by Rehr and co-workers (18). The method offers theoretical standards that can be tailored to a particular chemical environment. The theory has the added advantage that multiple-scattering effects are taken into account.

The first part of this paper is devoted to spectroscopic results. Far-IR, XPS, and EXAFS spectroscopy are used to follow an unusual low-temperature assembly process. We identify a surprising dependence of the final cluster structure on the choice of rare earth atom. We then discuss, in the second part, two possible condensation routes. Ab initio calculations are compared with experimental EXAFS spectra and conclusions are drawn regarding dependence of the condensation route on the identity of rare earth atom.

Experimental section

Materials and atom syntheses

Manipulations of all air-sensitive compounds and starting materials were carried out under argon in a dry box. All solvents were dried and distilled under argon prior to use. $NbCl_5$ (Alfa) was purified by sublimation. Lanthanides (Alfa) were evaporated from fragments of the bulk solid elements after removal of the oxide layer on the surface by mechanical abrasion. Boron nitride crucibles suspended from dual-strand tungsten wire baskets were used as containers (19, 20).

Reactions were conducted at low temperature (~170 K) by resistive vaporization of Sm or Er under vacuum into deoxygenated red-orange liquid toluene solutions saturated with $NbCl_5$. Atom reactions were carried out in a 5 L rotatable cyostat. The rotatable cryostat – atom reactor has been described elsewhere (20, 21). The solution was metered into the Pyrex reaction vessel through connecting valves and cannulae, and then spun into a thin liquid film on the inner surface of the rotating vessel. Current to the crucible was set to obtain a constant atom vaporization flux of about 4 mg Er/min and 6 mg Sm/min. The difference between these two rates is due to the difference between the vaporization enthalpy of Er and Sm (65 kcal/mol and 46 kcal/mol, respectively). Metal atoms

© 1998 NRC Canada

impinging on the film reacted with dissolved $NbCl_5$ and deposited a fine brown-black solid in liquid. When erbium was vaporized initially at a constant rate of 3.6 mg/min, the deep red-orange solution characteristic of $NbCl_5$ in toluene rapidly turned red-brown. After approximately 15 min the solution was distinctly brown, consisting of a suspension of fine, brown particles. Electronic absorption spectroscopy was carried out on anaerobic samples of the supernatant liquid acquired after increasing amounts of Er were deposited. The absorption band intensity located at 370 nm and characteristic of $NbCl_5$ in toluene systematically decreased as the starting material was consumed. Similarly, samples of precipitate were extracted at intervals from the reaction vessel so that changes in spectral features of the products could be evaluated. Color change from deep red-orange solution for $NbCl_5$ in toluene to brown-black powder was observed upon samarium vaporization.

Typically, 2 g of $NbCl_5$ was dissolved in 150 mL of degassed toluene. Er vaporizations were sampled at intervals of time during the reaction. The products are identified in the text under the name ErNb5, ErNb30, and ErNb45, indicating 5-, 30-, and 45-min vaporizations during one reaction. These correspond to about 20, 120, and 180 mg of Er vaporized, respectively. Elemental analysis gave the following stoechiometry: $NbCl_{4.30}Er_{0.10}$, $NbCl_{4.98}Er_{0.15}$, and $NbCl_{3.28}Er_{0.20}$ for ErNb5, ErNb30, and ErNb45, respectively. The non-proportionality between the vaporization time and the Er stoechiometry is believed to be mainly related to vaporization rate fluctuations. Because small changes in current to the electrodes led to dramatic changes in the Sm vaporization rate, we chose to fix the current to complete sets of experiments for Sm atom reactions. Samarium atom evaporations were conducted for 15, 30, and 50 min (SmNb15, SmNb30, SmNb50), corresponding to about 90, 180, and 300 mg of Sm in sequence. After vaporization, insoluble reaction products were filtered from unreacted solution and washed three times with dry, oxygen-free toluene to remove unreacted $NbCl_5$. Other side products of the reactions (as oxides) are minor since both reaction medium and all starting materials were carefully manipulated under argon. The filtrate was then dried under vacuum to give red-brown (Er) or brown-black (Sm) powders.

Infrared spectroscopy

Far-IR spectra were recorded on a Bruker IFS 88 FT spectrometer. Samples were prepared under argon in a dry box as Nujol mulls between two sealed CsI windows.

X-ray photoelectron spectroscopy (XPS)

XPS spectra of solid products were recorded on a VG Instrument ESCALAB MKII unit, using a Mg twin anode source (1253.6 eV). Samples were transported to UHV via an anaerobic transfer device adapted to the preparation chamber of the ESCALAB unit. Rigorous exclusion of air during sample transport and manipulation was achieved in this way. Spectra were energy calibrated versus the carbon binding energy peak at –285 eV. Cl 2*p* XPS spectra for the products have been adjusted with the same parameters as those used to fit the $NbCl_5$ XPS spectrum. Considering a spin-orbit coupling ζ_{2p} = 1.6 eV, we performed a deconvolution of each spin orbit component with two Gaussian functions representative of two types of chlorine bridging and terminal ligands (Full Width at Half Maximum FWHM = 1.45 eV).

Fig. 1. Schematic representation of the solid state structure of $NbCl_5$ dimer and $NbCl_4$ infinite chain.

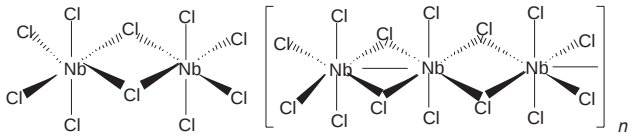

$NbCl_5$ $NbCl_4$

X-ray absorption spectroscopy

Data measurement

All samples were prepared in an argon-filled dry box. Quantities of materials were chosen to ensure an absorption jump $\Delta\mu$ close to 1. Ground powders were placed between two sheets of parafilm in a copper sample holder, which was then attached to a liquid nitrogen cryostat tip and enclosed in an evacuable cryostat shroud before data acquisition at 77 K.

Data were collected on beam-line D42 of the DCI 1.800 GeV synchrotron light source (LURE, Orsay, France) at the Nb K edge (18 986 eV). A channel cut Si 331 monochromator was used. Calibration of the monochromator was achieved by measuring the absorption K edge of a Zr metal foil at 17 998 eV. Spectra were taken in transmission mode using argon ionization chamber detectors coupled with Keithley pico-ampermeters (energy range from 18 850 to 19 850 eV with energy steps of 2 eV and 2 s acquisition time per point). Energy resolution at 19 000 eV was 9.7 eV.

Data treatment

EXAFS analysis was performed with a set of locally written programs called "EXAFS pour le Mac" that have been fully described elsewhere (22, 23). A straight-line approximation was used to remove background absorption. Heitler–Eisenberger normalization after 4th degree polynomial removal of the atomic absorption gave EXAFS oscillations in *k*-space. Fourier transformation of the EXAFS signal was achieved between 3.0 and 13.5 $Å^{-1}$ using a Kaiser window with τ = 1.5. Filtering of the main peak (Nb-Cl contribution) of the FT was done by back-Fourier transformation between 1.5 and 2.4 Å. Theoretical phase and amplitude functions used in adjustments of the Nb–Cl contributions were obtained by using the code FEFF6 (24). An effective curved-wave scattering amplitude plays a central role in this computation. The code is equipped with efficient filtering algorithms to enumerate scattering paths that contribute meaningfully to the EXAFS signal. It was first calibrated by comparison of the simulations with experimental spectra of reference compounds $NbCl_5$ and $NbCl_4$, which are schematically represented in Fig. 1 (25, 26). In the repeating dimer motif of $NbCl_5$ there is no Nb—Nb chemical bond, given the large 3.97 Å Nb–Nb separation. In $NbCl_4$, one recognizes alternating short (3.03 Å) and long (3.79 Å) Nb–Nb distances due to the presence of one bonding electron on each niobium atom.

The main lines of the FEFF6 used to reproduce the references are summarized below. Solid state $NbCl_5$ was simulated by a cluster of 12 atoms, namely Nb_2Cl_{10}. Plane waves were first used to accelerate the computation by determining normalized contributions to each path (18). In subsequent steps

© 1998 NRC Canada

Fig. 2. Experimental (—) and calculated (FEFF6) (– – –) EXAFS spectra of reference compounds $NbCl_5$ and $NbCl_4$. Both EXAFS oscillations in *k*-space and Fourier transform in *R*-space (not phase-shift corrected) are shown.

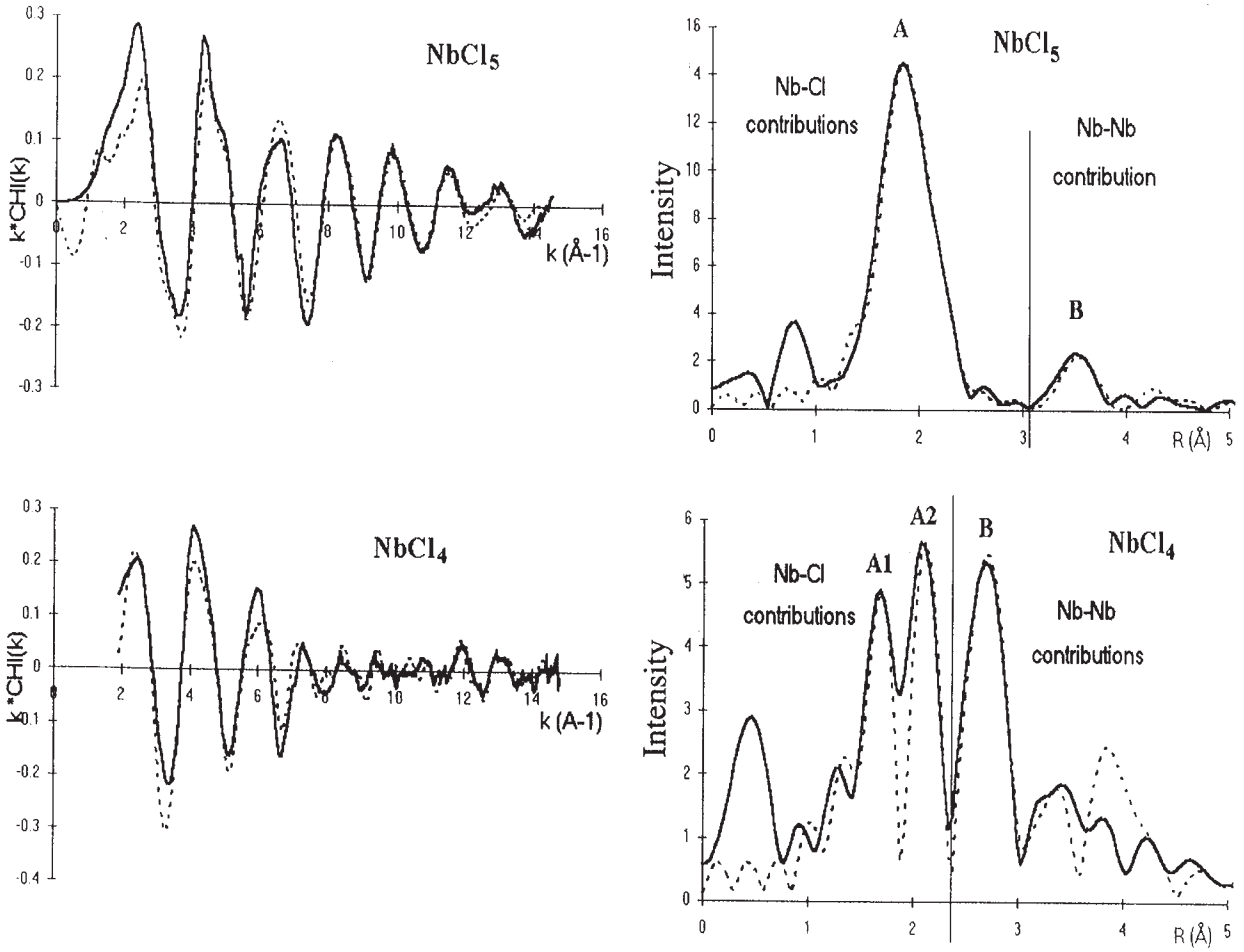

the curved-wave formalism was invoked to eliminate those paths that contributed intensity less than the threshold value of 2.5%. A second round of calculations, again within the curved-wave approximation, enabled us to delete those paths with relative intensity less than 4%. The EXAFS signal was then computed as the sum of contributions of all surviving paths. For $NbCl_5$ the maximum effective paths were determined to be no longer than 6 Å. Paths corresponding to scattering between Nb–Cl centers were the most intense. The contribution of the neighboring Nb atom itself was shown to be rather weak (13%). This is as expected because of the long metal–metal distance. The agreement between experimental results and ab initio calculations is shown in Fig. 2 in *k* space and in *R* space. Peak A is due to chlorine contribution whereas peak B is related mainly to niobium–niobium single scattering contribution. In fact, we found that multiple scattering paths less than fifth order also contribute to peak B and, in particular, paths including bonds that make an angle close to 180° with respect to each other. Overall, multiple scattering effects were found to reinforce the major single scattering contribution beyond 3 Å, so that multiple scattering needs to be included to fully rationalize this region of the FT.

In a similar manner, $NbCl_4$ was simulated for an aggregate of 27 atoms, where 3 chemically distinct chlorine centers can be identified. The comparison between experimental and ab initio calculations is presented in Fig. 2. As for $NbCl_5$, peak A, which is now split into two components A1 and A2, is due to chlorine contributions whereas peak B is related to Nb–Nb contribution. Contributions A1,2 and B were well reproduced by the calculation in the single scattering approximation. Amplitude enhancement due to the so-called focusing effect was clearly evident for the short Nb—Nb bond in $NbCl_4$. This effect accounts for the large intensity of peak B in the FT of $NbCl_4$. Multiple scattering corrections to the spectrum gave only minor cosmetic improvements, not because there were no such events of significant amplitude, but because the imaginary parts of the scattering contributions of order 3 and 4 were shown to be completely out of phase from 2 to 5 Å.

According to the structure of $NbCl_5$, three phases and amplitudes obtained in the curved-wave formalism can be extracted from the FEFF6 calculation: one for equatorial Cl_{eq} at 2.25 Å, one for apical Cl_{ap} at 2.29 Å, and one for bridging Cl_{br} at 2.57 Å. These theoretical functions, introduced in the "EXAFS pour le Mac" codes, were checked in the simulation of the Nb–Cl contributions of $NbCl_5$ in order to determine unknown electronic parameters like G, related to the mean free path λ of the photoelectron ($\lambda = k/\Gamma$) and the ionization threshold, $E_0 + \Delta E_0$, used to convert from energy to wave vector. The electronic parameters used in the fit of the Nb–Cl contribution of the reaction products were: $\Gamma = 1.2$ Å^{-2} for the three chlorine

© 1998 NRC Canada

layers and $E_0 + \Delta E_0 = 19\,000 - 0.2$ eV for equatorial chlorine, 19 000 – 1.0 eV for apical chlorine, and 19 000 + 6.2 eV for bridging chlorine. Accurate structural parameters are then determined on the Er and Sm reaction products by keeping the Γ and ΔE_0 parameters to these values and by using phases and amplitude functions extracted from the above ab initio simulation of $NbCl_5$.

The residual of the fit of the experimental spectra is given by the function (22):

$$[1] \qquad \rho = \frac{\sum_k [\chi^{exp}(k) - \chi^{fit}(k,\pi)]^2}{\sum_k [\chi^{exp}(k)]^2}$$

where $\chi^{exp}(k)$ is the extracted experimental EXAFS signal and $\chi^{fit}(k,\pi)$ is the fitted signal with π parameters.

Results and discussion

Part I: Chlorine environment probed by IR, XPS, and EXAFS spectroscopies

The X-ray diffraction patterns of the solid products show, exclusively, the broadened diffraction peaks that account for the presence of microcrystalline materials and which made further quantitative analysis impossible. Attempts to produce single crystals for X-ray diffraction structure determination, by either heat treatment or reaction-blocking units (such as phosphine groups), have failed. We then investigated the chlorine environment of the solid products with infrared and X-ray photoelectron spectroscopies. Both probes suggest that new products are formed when Er or Sm react with $NbCl_5$.

It is convenient to view the starting $NbCl_5$ dimer (Nb_2Cl_{10} in the solid state) and the $NbCl_4$ infinite chain (representing an infinite condensation of the $NbCl_5$ units) as material boundary conditions for the chlorometallate reductive condensation process and consequently compare systematically the products of reactions with these references. Higher condensation processes leading to Nb oxidation states lower than (III) were a priori considered as very unlikely (and confirmed by further EXAFS measurements, *see after*). In fact, infinite chain Nb_3Cl_8 or well-known Nb_6 clusters such as $RENb_6Cl_{18}$ (RE = rare earth metal) are obtained under different reductive conditions with a large excess of Nb metal (10, 27).

Infrared analysis

Figure 3 shows far-IR spectra of $NbCl_5$ and $NbCl_4$ compared with two reaction products (ErNb45 and SmNb50, respectively). We recall here the nomenclature used: the number after the product's name represents the vaporization time, here 45 and 50 min vaporization, respectively). Bond vibrations corresponding to Nb–Cl stretches in the solid are located in the region between 100 and 500 cm^{-1}. Despite the apparent simplicity of the $NbCl_5$ dimer, a definitive asignment of the vibrational spectrum is still unavailable (28). The most complete treatment belongs to Beattie et al., and so we have chosen to follow their assignments (29, 30). One can distinguish two regions in the vibrational spectra of $NbCl_5$. The first is located between 200 and 300 cm^{-1} and is due to Nb–Cl_{br} vibrational modes. These are not pure modes, but the vibrations are sufficiently characteristic that this region can be distinguished

Fig. 3. Far-infrared spectra of solid state (*a*) $NbCl_5$ and (*d*) $NbCl_4$ compared with those of (*b*) ErNb45 and (*c*) SmNb50.

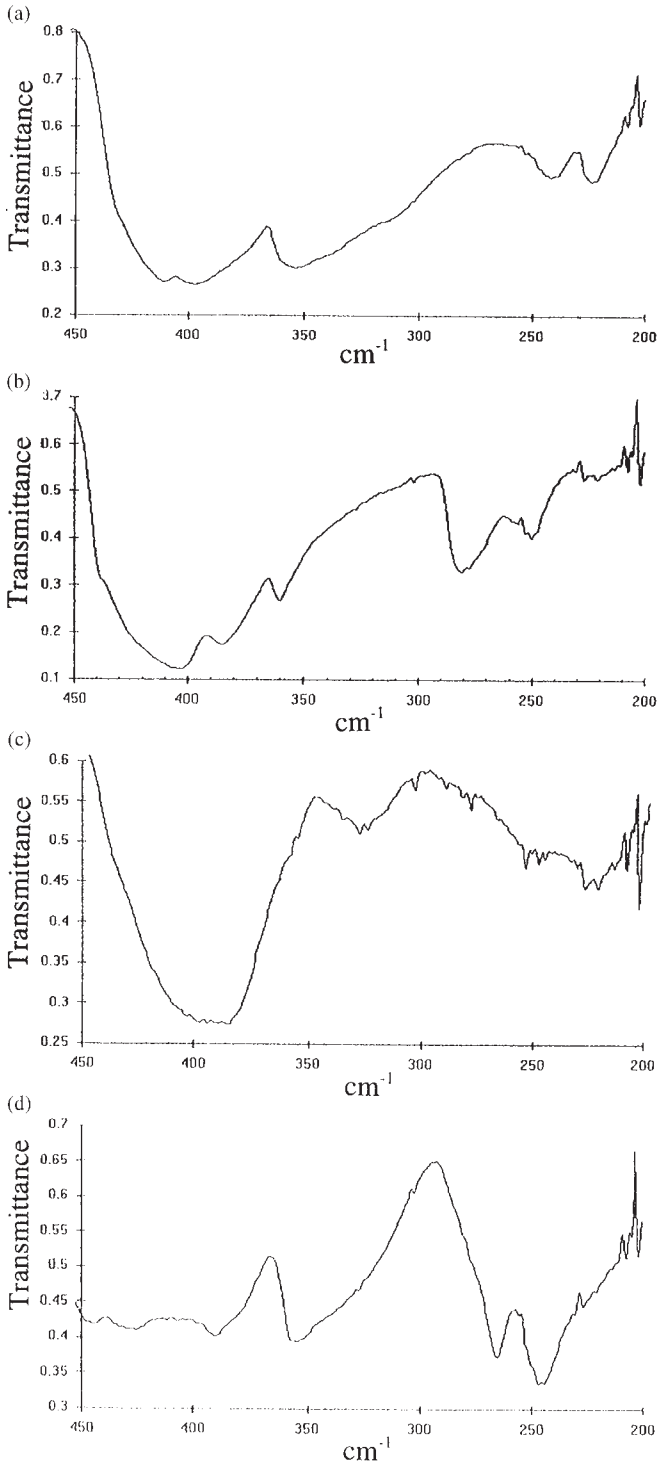

neatly from the second one falling between 300 and 450 cm^{-1}. The latter arises from modes that are terminal Nb–Cl_{term} stretches. It is interesting to contrast these data with data obtained in a study of Nb–Cl vibrations derived from Cl associated with the octahedral core of Nb_6 in the compound $MRENb_6Cl_{18}$ (M is a group 1 element and RE is a rare earth atom) (31). In this study, the higher frequency vibration at

© 1998 NRC Canada

340 cm^{-1} has been assigned to bridging Cl, whereas the lower frequency modes at 280 and 230 cm^{-1} have been attributed to terminal Cl ligands. To our knowledge, only Pisarev and coworkers (32) have reported the IR spectrum of $NbCl_4$, and with only a qualitative interpretation. Bands that we detect at 425, 390, 354, 265, and 244 cm^{-1} correspond to those given by Pisarev (32). Below 550 cm^{-1} we have also located bands maximizing at 530, 490, and 440 cm^{-1}. For comparison, we assign the doublet at 265 and 244 cm^{-1} in $NbCl_4$ to vibrations of the bridging chlorine atoms. The shift to higher frequency compared with the corresponding doublet exhibited by $NbCl_5$ is a consequence of stronger in-plane bonding associated with the decrease in oxidation state of Nb in the tetrachloride. Given that $NbCl_4$ corresponds roughly to a one-electron reduction and infinite condensation of $NbCl_5$ units, one might anticipate that reductive polycondensation of $NbCl_5$ by rare earth atoms might be accompanied by a similar shift to higher energy of the modes related to bridging chlorine, were the product to bear some structural congruity with $NbCl_4$.

The infrared spectra of the products of reaction of $NbCl_5$ with samarium or erbium vapors were found to be rather insensitive to the quantity of deposited atoms, for a reason that is still not clear. However, we are not sure that IR bands are very sensitive to whether or not trimers, tetramers,... are involved. Vaporizing the rare earth atoms modifies the electronic configuration of the cluster and this accounts for the evolutions between $NbCl_5$ and our products. We therefore present only two spectra for Er and Sm vaporizations in Fig. 3. The first important result of the IR study is the shift to higher energy of the Nb–Cl_{br} bands (ErNb45, the doublet 250, 280 cm^{-1} in Fig. 3*b*) observed for compounds derived from Er atom reactions, relative to both $NbCl_4$ and $NbCl_5$. Moreover, we detect relative intensity changes, the higher energy component of the doublet being the more intense of the two bands. Interestingly, the 350–500 cm^{-1} region of the spectrum of sample ErNb45 shows a band profile similar to that of $NbCl_5$. The second important point of this study lies in the significant differences between the spectra for SmNb50 (Fig. 3*c*) and ErNb45 over the 200–500 cm^{-1} region. This is evidence that reactions with Er atoms yield products that differ from those of Sm. The doublet feature at lower energy (225 and 250 cm^{-1}) is still retained in SmNb50, but is clearly shifted to lower wave number. An intense broad band centered near 380 cm^{-1} now replaces the articulated band located near this position for ErNb45. SmNb50 also manifests a new absorption at 330 cm^{-1} that has no correspondence in either $NbCl_5$ or $NbCl_4$.

X-ray photolectron spectroscopy

The binding energy of 210.7 eV for the Nb $3d_{3/2}$ level in $NbCl_5$ agrees well with the literature value (33). Shifts in the binding energy of Nb for products of Er or Sm atom reactions differed little from those of the parent $NbCl_5$ compound: binding energies for Er-containg products were consistently 0.1–0.3 eV lower than in $NbCl_5$, whereas those of the Sm products were 0.1–0.2 eV higher. In fact, data relative to the Nb $3d_{3/2}$ binding energy are not very informative about the condensation process involved during the vaporization, and interesting results come from the chlorine 2*p* XPS spectra since the presence of bridging and terminal chlorine atoms has been again evidenced. Table 1 gives the binding energy of the Cl $2p_{1/2}$ contribution for terminal and bridging chlorines of $NbCl_5$, and of the products of the atom reactions. Figure 4 represents the analysis of the Cl 2*p* binding energy peak for $NbCl_5$, ErNb45, and SmNb50. The fit with two types of chlorine ligands for $NbCl_5$ gave an area ratio R^{XPS} = (terminal chlorine peak area / bridging chlorine peak area) of 3.8. This corresponds satisfactorily to the ratio of the number of terminal to the number of bridging Cl atoms in this compound. The value carries an error of 5% compared with the expected value of 4.0 for the D_{2h} dimer. R^{XPS} extracted from the fits are on the order of 1.5 for Er products and 0.5 for Sm products. These values are strikingly smaller than those of $NbCl_5$ and support the idea of some kind of condensation of the target molecule (i.e., a decrease in the number of terminal chlorine atoms compared with the number of bridging atoms). The different R^{XPS} ratios for Er and Sm products also point to structural differences between them, as suggested by the IR studies.

Table 1. Cl 2*p* binding energy (eV) of the solid products. R^{XPS} is defined as the ratio of terminal Cl peak area to the bridging Cl peak area, as explained in the text.

Compound	Cl $2p_{1/2}$ term.	Cl $2p_{1/2}$ br.	R^{XPS}
$NbCl_5$	–200.8	–200.1	3.8
ErNb5	–200.7	–200	1.5
ErNb30	–200.8	–200.1	1.45
ErNb45	–200.8	–200.7	0.42
SmNb30	–201.5	–200.7	0.54
SmNb50	–201.6	–200.7	0.54

EXAFS

The local niobium environment was probed by EXAFS measurements at the Nb K edge for both Er and Sm atom reaction products.

These experiments confirmed the structural differences anticipated from the IR and XPS spectra. The moduli of the Fourier transformed EXAFS spectra of the atom reaction products are compared to the $NbCl_5$ and $NbCl_4$ reference compounds in Figs. 5*a* and 5*b*. As for the references, peaks in *R* ranging between 1.3 and 2.4 Å are related to chlorine contributions. This contribution, labeled A, is structured in the vaporization products into two components. Regarding the Er products, contribution A splits into peak A1 and a shoulder A2 on the right side of A1. The main peak A1 is shifted towards shorter distances on going from sample ErNb5 to sample ErNb45 in Fig. 5*a*, i.e., for increasing erbium content. Simultaneously, the shoulder identified as A2 becomes better resolved as the amount of lanthanoid in the reaction medium increases. This compares well with the features of contribution A in infinite chain $NbCl_4$. The Sm atom reaction products show different trends in Fig. 5*b*. Contribution A splits into a peak A2′ and shoulder A1′ on the left side of A2′. Main peak A2′ is shifted towards larger distances on going from SmNb15 to SmNb50. These differences between the main contribution of the Fourier transform reflect structural differences as suggested by XPS and IR. This is also confirmed in Figs. 5*c* and 5*d* by comparing the filtered EXAFS oscillations of Er and Sm compounds for the chlorine contribution. On one hand, the filtered EXAFS oscillations of Er reaction products present a "beating" between 6 and 10 $Å^{-1}$ (weak around 7 $Å^{-1}$ for ErNb5)

© 1998 NRC Canada

Fig. 4. Deconvolution of the Cl 2*p* binding energy contributions of (*a*) $NbCl_5$; (*b*) ErNb45; and (*c*) SmNb50.

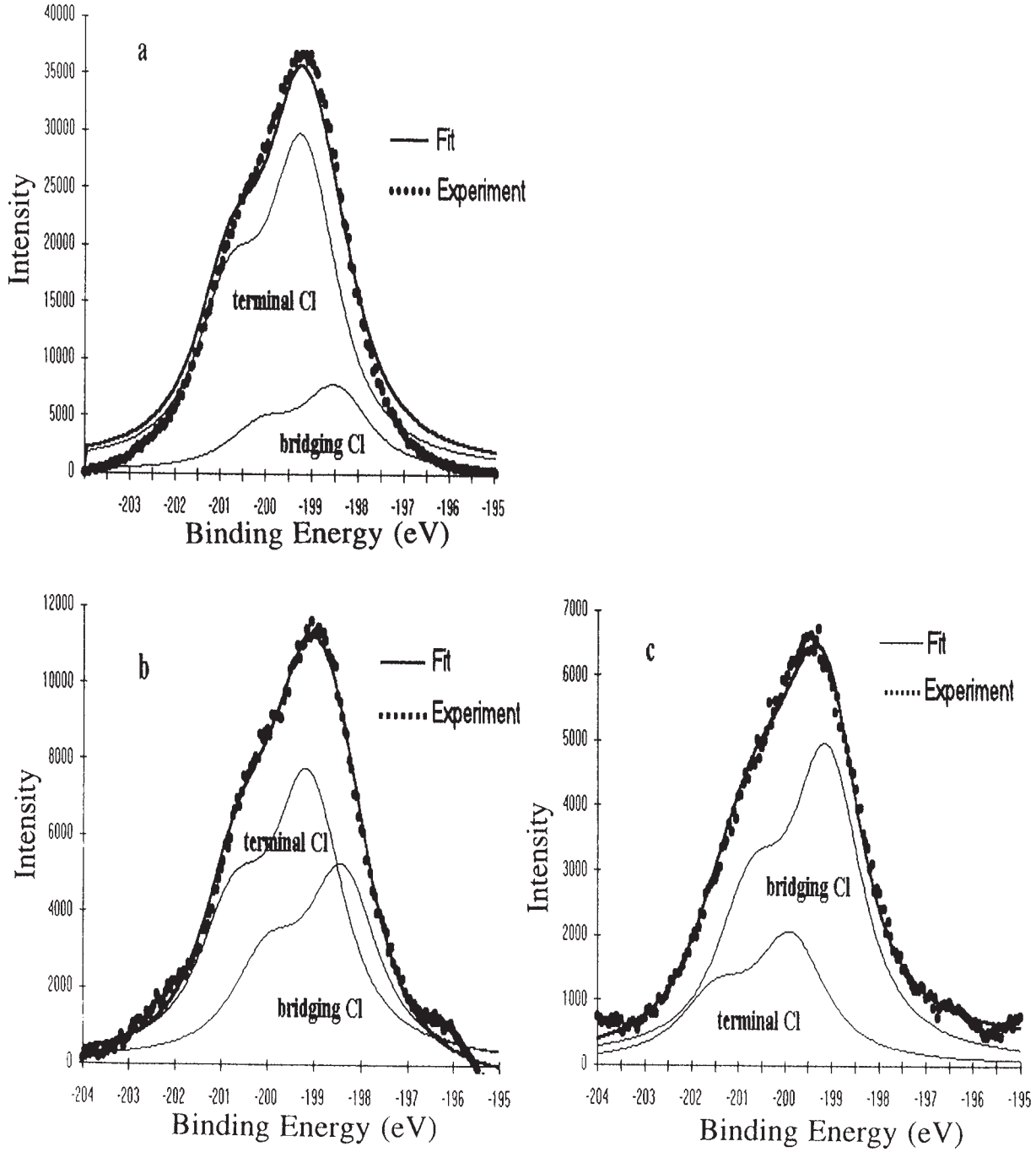

(Fig. 5*c*). Beating is caused by interference between scattered waves emerging from two or more chlorine shells around the niobium atom. The effect becomes correspondingly pronounced as the amount of deposited Er increases. On the other hand, Fig. 5*d* shows that there is no beating in any of the spectra of the Sm atom products. This is evidence again that the chlorine contributions for both Er and Sm atom reaction products are not the same.

The Nb contribution (contribution B in $NbCl_5$) is too weak to be analyzed. However, the weak intensity of this contribution and its position confirm that the condensation involved during the vaporization does not lead to the formation of more reduced Nb species as, for instance, Nb_6Cl_{14} units or even $Nb^{(0)}$: the FT of the EXAFS spectrum that we recorded on $LuNb_6Cl_{18}$ compound exhibits a very strong Nb–Nb contribution because each Nb atom has four Nb neigbhours at 2.91 Å (34), which is not the case for the samples.

Part II: Ab initio EXAFS simulations to distinguish condensation patterns

According to IR, XPS, and EXAFS analyses, Er and Sm atom reactions with $NbCl_5$ give different reaction products that are evolving as a function of the rare earth content. It is very likely that a mixture of phases is present during the reaction.

© 1998 NRC Canada

Fig. 5. Moduli of the FT of the EXAFS spectra (at the same scale, shifted in ordinates for clarity not phase-shift corrected) of (*a*) Er atom reaction products and (*b*) Sm atom reaction products, compared to the model compounds $NbCl_5$ and $NbCl_4$. EXAFS spectra of (*c*) Er reaction products and (*d*) Sm atom reaction products are also presented.

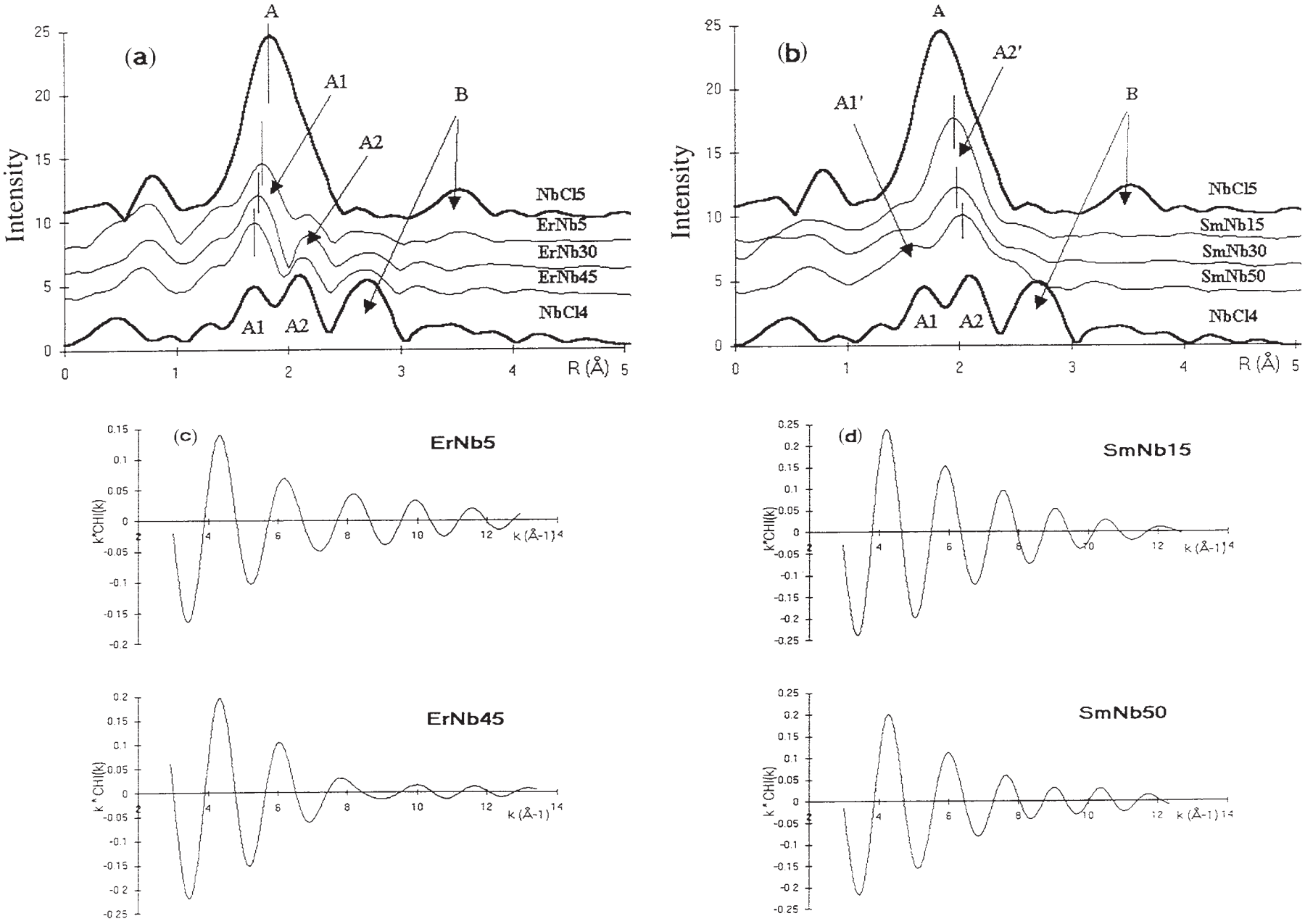

© 1998 NRC Canada

Fig. 6. Proposed condensation patterns to account for the assembly of dimer $NbCl_5$.

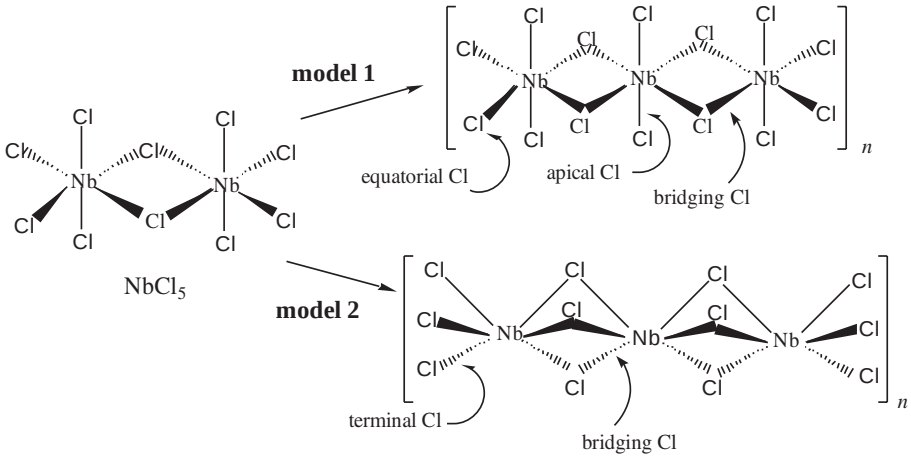

However, here, we first intend to fit the observed evolutions, using simple models of ideal reaction products. IR and XPS data together suggest that the product phases may contain bridging and terminal chlorine atoms. After considering a number of possible models for the products, we converged on two pathways that involve linear condensation. These condensations incorporate the starting $NbCl_5$ units in a manner that preserves the sixfold coordination of chlorine substituents about niobium. Accordingly, we offer two assembly routes as shown in Fig. 6. One route involves an edge-sharing condensation process, whereas the other is based on a face-sharing condensation mechanism. Both Nb environnements will be referred to in the text as edge-sharing octaedra and face-sharing octaedra for purposes of clarity. However, distortion of the Nb coordination sphere toward a trigonal prism geometry cannot be precluded.

The models are closely related since both contain bridging chlorine substituents. This is why the use of an ab initio code such as FEFF (with which absorption spectra are directly calculated from atomic coordinates of the cluster) is of particular interest in this case.

Confident that the ab initio method based on the use of the FEFF code functioned well to reproduce all features of the EXAFS of the model compounds $NbCl_5$ and $NbCl_4$, we chose to explore the proposed condensation patterns of models 1 and 2. Calculations were carried out on trimer, tetramer, and pentamer molecular fragments. Reduction of the Nb oxidation state due to polycondensation was simulated by contracting Nb–Nb and Nb–Cl_{br} (br = bridging) intracluster distances in the following way: bond angles and distances were estimated from the Nb–Nb distance *D* and the Nb-Nb-Cl_{br} bond angle α correlations from structures of known Nb_xCl_y compounds (25–27), as shown in Fig. 7. In general, polycondensation of niobium chloride fragments to give clusters of increasing size is accompanied by shortening of the Nb–Cl_{br} distances. Decreasing the Nb–Nb distance *D* implies an increase in the Nb-Nb-Cl_{br} bond angle. Simulations were required to account then for both the effect of increasing degree of polymerization of molecular subunits and the effect of shortening of the Nb–Cl_{br} distance. These two features of the process are closely related, but in a way that is not known in detail. We simplify the problem by separating it into two distinct studies: (*i*) the influence of bond contraction (i.e., decrease of distance *D*) on trimer units (Fig. 8*a*), and (*ii*) the influence of increasing cluster nuclearity, *n*, on trimers, tetramers, and pentamers, with fixed *D* (Fig. 8*b*). Finally, coordinates of the terminal Cl atoms were deduced from those of the $NbCl_5$ fragment.

Fig. 7. Bond angle α as a function of the Nb–Nb distance *D* for several niobium halide clusters.

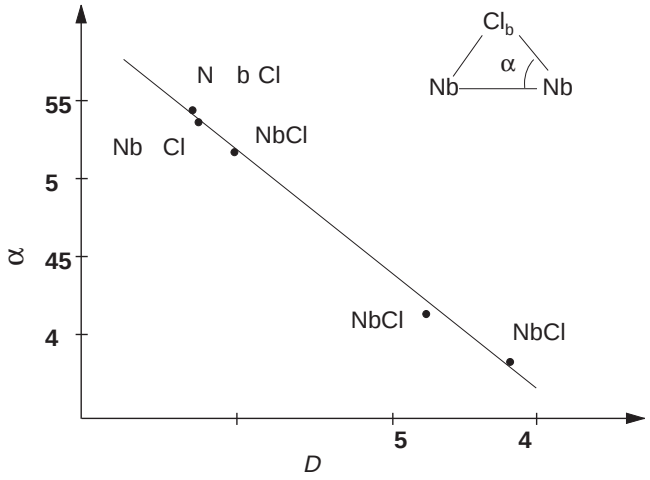

In Fig. 8, the intense peak around 3 Å is due to the overestimation of the Nb–Nb contribution by FEFF. This is not significant for the following discussion, which is based on the Nb–Cl contributions. In the case of constant nuclearity (trimers), the moduli of the EXAFS (Fig. 8*a*) exhibit the same gross features as those derived from experiment. Regarding more precisely model 1, our ab initio simulations indeed show that contribution A splits into a peak A1 at 1.7 Å, and peak A2 at 2.1 Å, which dominates A1. This formation of a shoulder A2 is what is observed in the FT derived from atom experiments with Er and also expressed by $NbCl_4$ (Fig. 5*a*). The similarity of our simulations to the FT of $NbCl_4$ is perhaps not surprising since $NbCl_4$ is an infinite chain model that rather closely resembles the structure postulated for the product derived from Er. For model 2, a shoulder A1′ is formed on the left of peak A2′, as observed experimentally in the case of Sm vaporization. Again, this shoulder becomes more resolved as the polycondensation is simulated to increase. In the case of

© 1998 NRC Canada

Fig. 8. Moduli of the simulated (FEFF6) EXAFS spectra pf clusters derived from models 1 and 2.

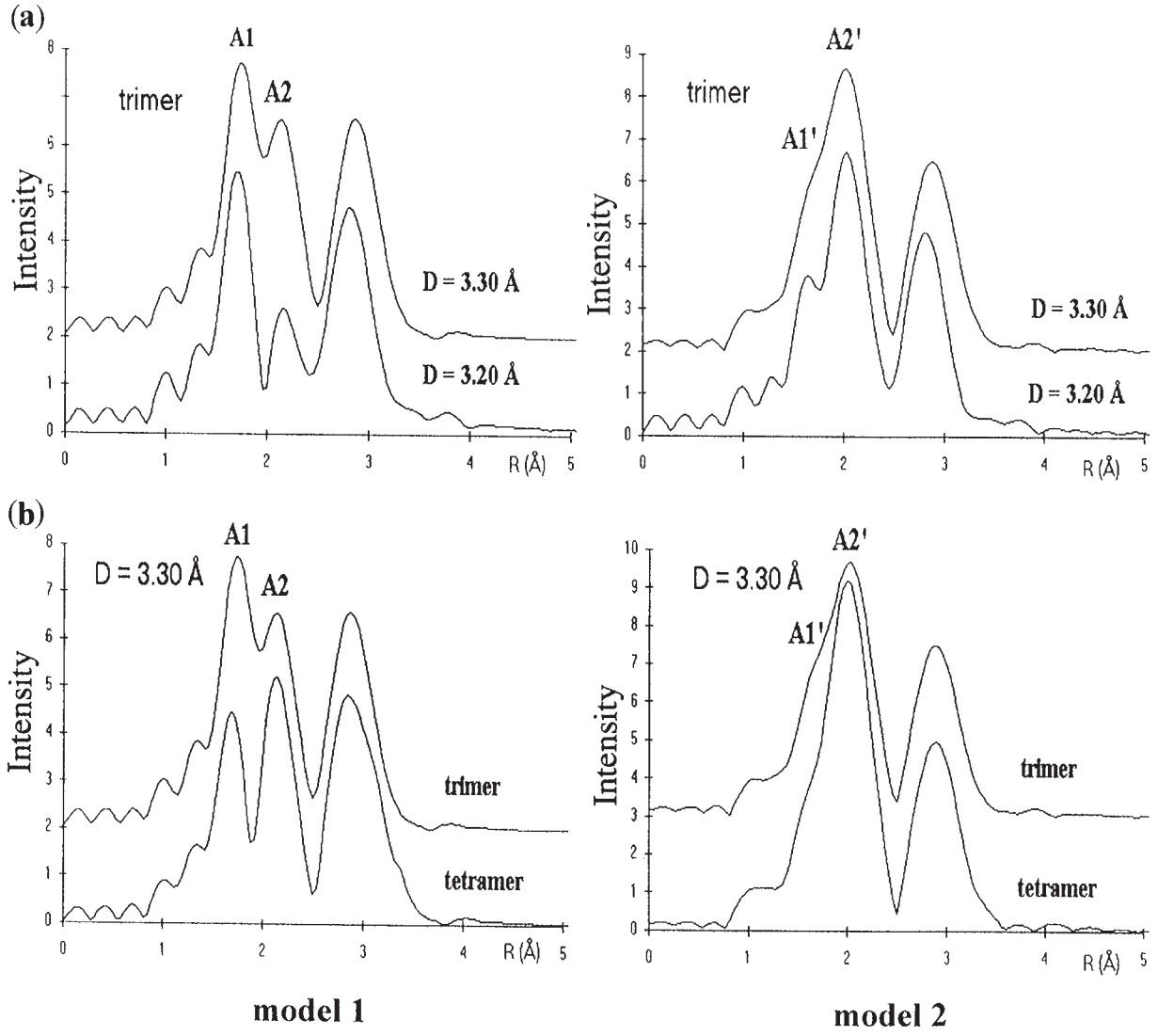

constant Nb–Nb distance and increasing nuclearity from trimer to tetramer (Fig. 8*b*), the features observed for trimers (formation of a shoulder A2 for model 1 and a shoulder A1′ for model 2) are not significantly evolving. In fact, a more realistic simulation of the polycondensation would involve both variations in the same time (*n* and *D*). Figure 9 shows the simulated EXAFS oscillations of the Nb–Cl contribution of trimers for Nb—Nb bond distances of 3.30 Å and 3.20 Å. It is striking that simulations of model 1 show a beating between 6 and 10 $Å^{-1}$ in the filtered EXAFS oscillations, whereas simulations of model 2 show no beating under any circumstances. Furthermore, beating is displaced towards higher *k*-values as the inter-niobium bond distance *D* diminishes for model 1, reflecting the trend in the experimental spectra for the erbium atom reaction products.

In light of these results and comparing findings of the previous section (Fig. 5), we propose that model 1 corresponds to the outcome of Er vaporization and model 2 to Sm vaporization. This also suggests an evolution of the cluster structures according to the amount of metal deposited, as demonstrated by comparison of the experimental EXAFS spectra with FEFF6 simulation of tetramer and pentamer clusters. Quantitative EXAFS analysis and XPS as discussed here would seem to support these assignments. Accordingly, the filtered EXAFS oscillations of chlorine contribution of Er atom/$NbCl_5$ reaction products were fitted using model 1 (i.e., three Nb–Cl layers: equatorial, apical, and bridging). The filtered EXAFS oscillations of Sm atom reaction products were fitted to model 2 (i.e., two Nb–Cl layers: terminal and bridging). Fits of ErNb45 and SmNb50 in real space are given as examples in Fig. 10. The fitting parameters in Table 2 illustrate, in the case of Er vaporization, a reduction of $Nb–Cl_{br}$ distances from 2.55 Å after 5 min Er vaporization, to 2.50 Å after 45 min of vaporization. A ratio, R^{EXAFS}, corresponding to the number of terminal to bridging chlorine atoms, was extracted from these fits. We have calculated R^{EXAFS} for each model as a function of the cluster nuclearity, *n*. For model 1, $R_1^{EXAFS} = (n + 2)/2(n - 1)$. For model 2, $R_2^{EXAFS} = 1/(n - 1)$. These ratios are bounded for minimum condensation ($n = 3$) and infinite condensation ($n = \infty$): model 1 gives $0.5 < R_1^{EXAFS} < 1.25$, whereas model 2 gives $0.0 < R_2^{EXAFS} < 0.5$. The value of 1.1 for R^{EXAFS} extracted from fits of ErNb5, ErNb30, and ErNb45 displayed in

© 1998 NRC Canada

Fig. 9. FEFF6 filtered EXAFS spectra simulated for trimers according to models 1 and 2 for two different Nb–Nb distances.

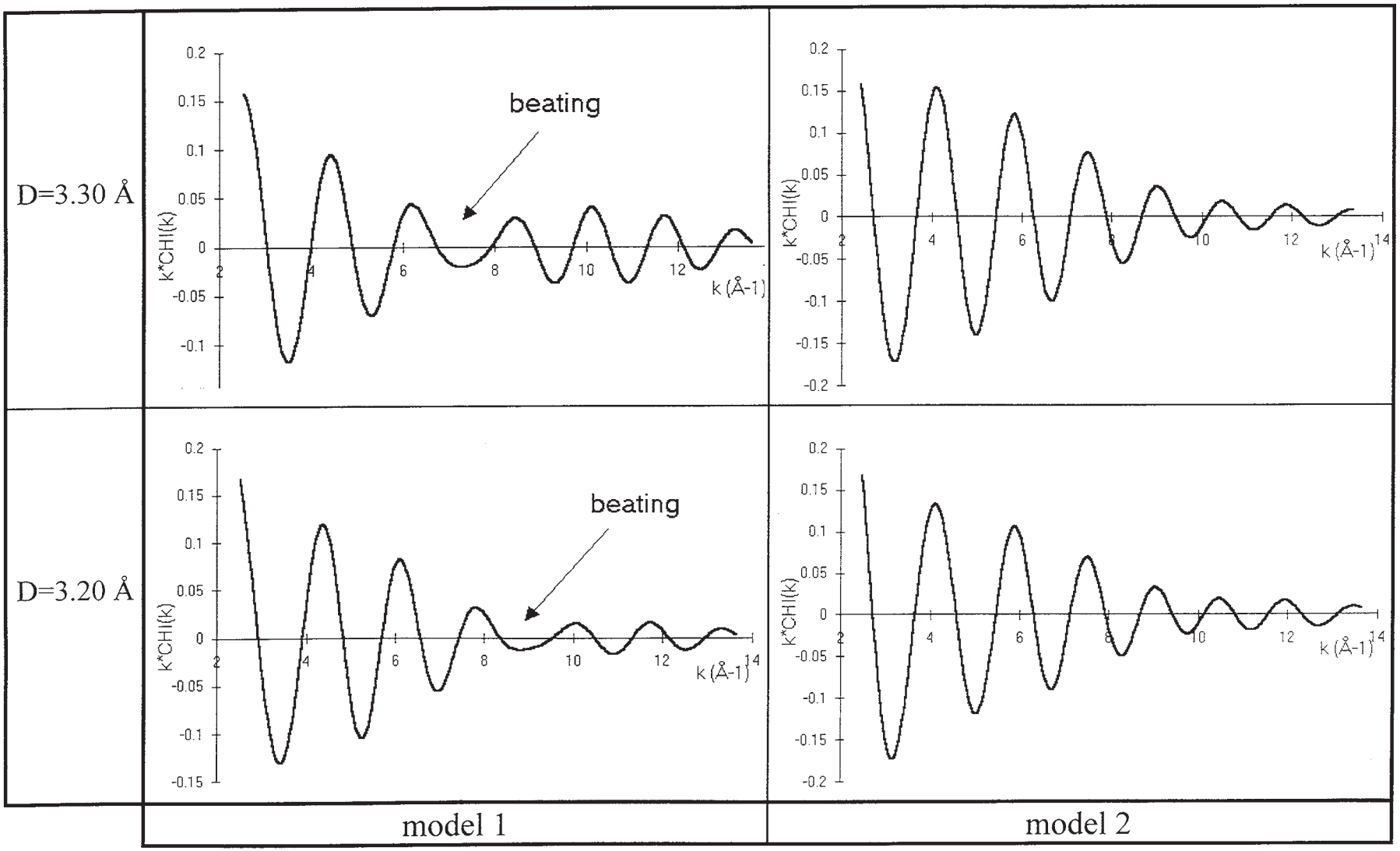

© 1998 NRC Canada

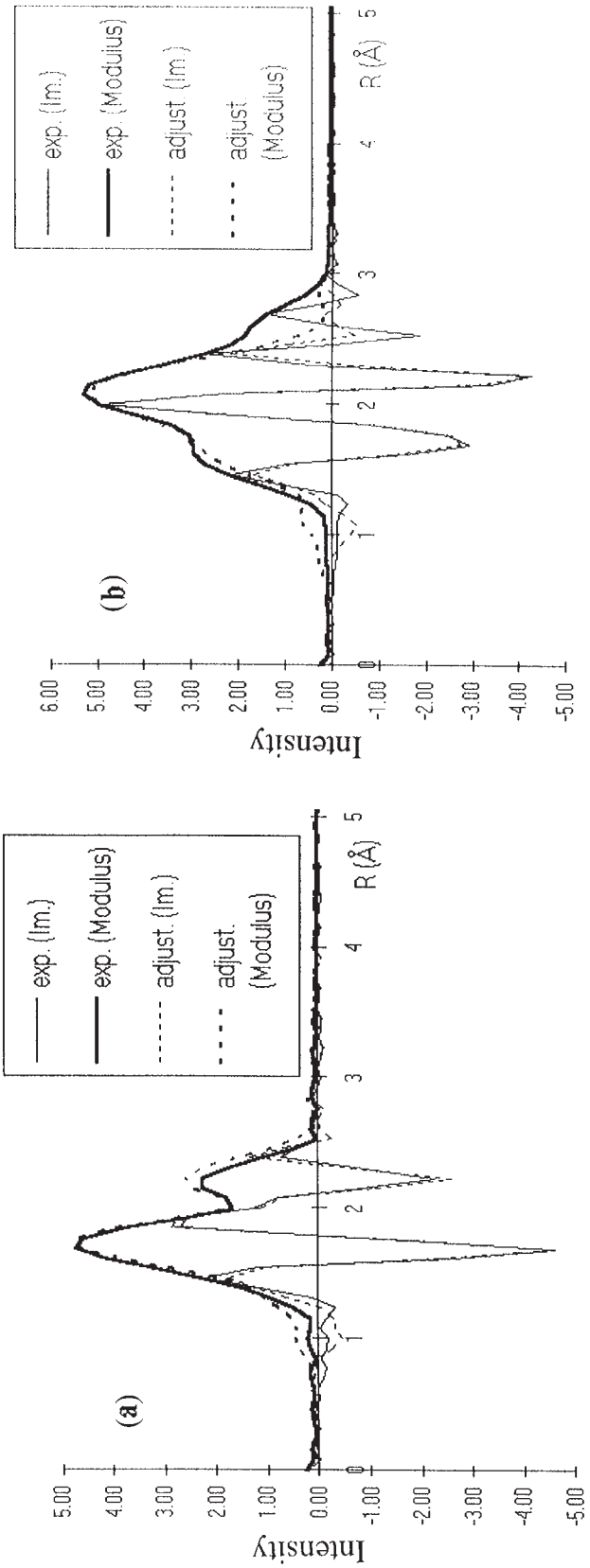

Fig. 10. Fits in *R*-space (not phase-shift corrected) of (*a*) ErNb45 and (*b*) SmNb50.

Table 2. EXAFS best-fit parameters of the Nb–Cl contributions.

Compound	*N*	σ (Å)	*r* (Å)	Cl type	R^{EXAFS}	Residual
	2.0[a]	0.04	2.25[a]	Equatorial		
$NbCl_5$	2.0[a]	0.04	2.29[a]	Apical	2	1.9%
	2.0[a]	0.09	2.57[a]	Bridging		
	1.2	0.1	2.28	Equatorial		
ErNb5	2	0.06	2.3	Apical	1.14	2.1%
	2.8	0.1	2.55	Bridging		
	1.2	0.05	2.28	Equatorial		
			2.35			
ErNb30	2	0.08		Apical	1.14	2.5%
	2.8	0.09	2.52	Bridging		
	1.1	0.04	2.26	Equatorial		
ErNb45	2	0.07	2.35	Apical	1.07	3.1%
	2.9	0.08	2.5	Bridging		
SmNb15	2	0.06	2.37	Terminal	0.5	4.2%
	4	0.06	2.5	Bridging		
SmNb30	2	0.1	2.36	Terminal	0.5	2.7%
	4	0.1	2.49	Bridging		
SmNb50	2	0.08	2.3	Terminal	0.5	3.5%
	4	0.07	2.48	Bridging		

[a] These values are fixed to the crystallographic data (25, 26).

N: number of neighbours; s: Debye–Waller factor. R^{EXAFS} is defined by the number of terminal Cl over the number of bridging Cl, as defined in the text.

Table 2 falls within the range of R_1^{EXAFS}. The R^{EXAFS} value of 0.5 extracted from fits of SmNb15, SmNb30, and SmNb50 is within the range of R_2^{EXAFS} values. The fact that the value of R^{EXAFS} does not seem to depend on the quantity of lanthanoid vaporized is simply due to insensitivity of these ratios to small changes in nuclearity. This is also the reason why these ratios are not used for the cluster nuclearity determination.

Our assignments find further support from the XPS spectra. As shown in Table 1, R^{XPS} values extracted from fits of the Cl 2*p* electron binding energy differ for Er and Sm vaporizations. Theoretical limits to R^{XPS} can be also calculated according to models 1 and 2 as a function of *n*. For model 1, $R_1^{XPS} = (n + 2)/(n - 1)$, and for model 2, $R_2^{XPS} = 2/(n - 1)$. These ratios give the following bounds for *n* ranging from 3 to ∞ : $1.00 < R_1^{XPS} < 2.50$ and $0.0 < R_2^{XPS} < 1.0$. Experimental ratios are of the order of 1.5 for Er products and 0.5 for Sm products. This confirms unambiguously the condensation patterns attribution for each rare earth vaporization.

Our results should be compared with studies of Ginsberg and Wayda (13) who produced niobium halide trimers by reacting Rieke-type colloidal samarium with $NbCl_5$. Their analysis was consistent with the formulation $Sm^{3+}[Nb_3Cl_{14}]^{3-}$, but the authors were unable to distinguish between face- or edge-sharing structural models. In a qualitative manner, formation of a shoulder on the right of main contribution Nb–Cl for $Sm^{3+}[Nb_3Cl_{14}]^{3-}$ would suggest, according to our study, a model 1 condensation pattern. This differs from our conclusions with Sm vaporization. However, the use of colloidal samarium instead of vaporized samarium atoms accounts, to our mind, for the structural differences. Why the condensation patterns observed in our studies exhibit structural bifurcation is not yet completely understood. It is well known that rare earth trichlorides crystallize in different crystal systems: hexagonal UCl_3 type (*P*63/*m*) from La to Gd; monoclinic YCl_3 type (*C*2/*m*) from Dy to Yb (11, 35). The change in size of the radii

© 1998 NRC Canada

in the 3+ lanthanides may account for these structural differences in the solid state. A possible 2+ oxidation state for the Sm atom may also explain the differences. Further support is given by Templeton and Dauben (11), who calculated the rare earth radii, based primarily on the cubic oxides. With a radius (coordination number = 6) of 0.958 Å (1.19 Å for Sm^{2+}), Sm^{3+} differs significantly from Er^{3+} (R = 0.890 Å) (36).

To confirm the role of (*i*) the increasing quantity of metal atoms that are condensed and (*ii*) the role of the rare earth, we intended to first look at the early stages of the cluster formation and to study the rare earth local order. In the first case, small metal quantities are deposited into $NbCl_5$/toluene molecules on a cryogenic matrix isolation quartz window. Reaction is followed in situ by EXAFS spectroscopy. First results with Sm vaporization already confirm our interpretation of a condensation route based on model 2. In the second case, post-mortem compounds from both Er and Sm vaporization are studied by EXAFS at the rare earth L_{III} edge to examine RE–Cl interactions. We shall discuss the results in detail in upcoming papers.

Conclusions

We have demonstrated in this study the usefulness of metal atom vaporization techniques to achieve controlled new solid state structures. The obtention of non-crystallized materials led us to the use of EXAFS, XPS, and IR spectroscopy to study the structural evolutions of $NbCl_5$ upon Er and Sm vaporization. EXAFS Nb *K* edge spectra of the products suggested different condensation patterns depending on the metal atom deposited. XPS and IR measurements confirmed that Sm and Er vaporization do not yield the same condensation route: edge-sharing octahedra for Er vaporization and face-sharing octahedra for Sm vaporization. Furthermore, we observed the effect of vaporization time upon evolution of the cluster structures. An in situ matrix isolation study by EXAFS spectroscopy has been undertaken and has already confirmed these findings (37).

Acknowledgements

The authors are very grateful to F. Villain (LURE) and L. Deakin (McGill) for their help during this work. We are also very grateful to the technicians of both laboratories for their indispensable technical competencies.

References

1. J.-F. You, B.S. Snyder, G.C. Papaefthymiou, and R.H. Holm. J. Am. Chem. Soc. **112**, 1067 (1990).
2. J.-F. You, G.C. Papaefthymiou, and R.H. Holm. J. Am. Chem. Soc. **114**, 2697 (1992).
3. M.G. Kanatzidis. Chem. Mater. **2**, 353 (1990).
4. J.R. Long, A.S. Williamson, and R.H. Holm. Angew. Chem. Int. Ed. Engl. **34**, 226 (1995).
5. R.D. Rieke. Science, **246**, 1260 (1989).
6. R.D. Rieke and P.M. Hudnall. J. Am. Chem. Soc. **94**, 7178 (1972).
7. R.D. Rieke, S.J. Uhm, and P.M. Hudnall. J. Chem. Soc. Chem. Commun. **269** (1973).
8. J.E. Fergusson. Prep. Inorg. React. **7**, 93 (1971).
9. M. Sergent, C. Perrin, S. Ihmaïne, A. Perrin, H. Ben Yaich, O. Peña, R. Chevrel, P. Gougeon, and M. Potel. J. Chim. Phys. **88**, 2123 (1991).
10. C. Perrin, S. Ihmaïne, and M. Sergent. New J. Chem. **12**, 321 (1988).
11. D.H. Templeton and C.H. Dauben. J. Am. Chem. Soc. **76**, 5237 (1954).
12. G. Meyer. Inorg. Synth. **22**, 1 (1983).
13. A.P. Ginsberg and A.L. Wayda. Inorg. Chem. **24**, 4749 (1985).
14. P.L. Timms and T.W. Turney. *In* Advances in organometallic chemistry. Vol. 15. Academic Press, New York. 1977.
15. P.A. O'Day, J.J. Rehr, S.I. Zabinsky, and G.E. Brown. J. Am. Chem. Soc. **116**, 2938 (1994).
16. B. Teo and P.A. Lee. J. Am. Chem. Soc. **101**, 2815 (1979).
17. A.G. McKale, B.W. Veal, A.P. Paulikas, S.-K. Chan, and G.S. Knapp. J Am Chem. Soc. **110**, 3763 (1988).
18. S.I. Zabinsky, J.J. Rehr, A. Ankudinov, R.C. Albers, and M. Eller. Phys. Rev. B: Condens. Matter, **52**, 2995 (1995).
19. K.J. Klabunde. *In* Reactive intermediates. Vol 1. *Edited by* Abramovitch. Plenum Press, New York. 1980.
20. J. R. Blackborow and D. Young. *In* Metal vapour synthesis in organometallic chemistry. Springer Verlag, Berlin. 1979.
21. M. P. Andrews. Encycl. Polym. Sci. Eng. [2nd Revis. Ed.], **9**,. 623 (1987).
22. A. Michalowicz. Thesis. Université Paris Val de Marne, Marne la Vallée, France. 1990.
23. A. Michalowicz. *In* Logiciels pour la chimie : EXAFS pour le Mac. Société Française de Chimie, Paris. 1991.
24. S.I. Zabinsky. Thesis. University of Washington, Seatle, Wash., U.S.A. 1993.
25. F.A. Cotton, P.A. Kibala, M. Matusy, and R.B. Sandor. Acta Crystallogr. Sect C: Cryst. Struct. Commun. **C47**, 2435 (1991).
26. D.R. Taylor, J.C. Calabrese, and E.M. Larsen. Inorg. Chem. **16**, 721 (1977).
27. S. Ihmaïne, C. Perrin, O. Peña, and M. Sergent. J. Less-Common Met. **137**, 323 (1988).
28. R.A. Walton and B.J. Brisdon. Spectrochim. Acta, Part A: **23A**, 2489 (1967).
29. I.R. Beattie, T.R. Gilson, and G.A. Ozin. J. Chem. Soc. A, 2765 (1968).
30. D.M. Adam and P.J. Chandler. J. Chem. Soc. Chem. Commun. 69 (1966).
31. P. Caillet, S. Ihmaïne, and C. Perrin. J. Mol. Struct. **216**, 27 (1990).
32. E.A. Pisarev, D.V. Drobat, and I.V. Makarchuk. Russ. J. Inorg. Chem. **27**, 19 (1982).
33. G.E. McGuire, G.K. Schweitzer, and T.A. Carlson. Inorg. Chem. **12**, 2450 (1973).
34. S. Ihmaïne, C. Perrin, and M. Sergent. Acta Crystallogr. Sect. C: Cryst. Struct. Commun. **C45**, 705 (1989).
35. D.H. Templeton and G.F. Carter. J. Phys. Chem. **58**, 940 (1954).
36. D.R. Lide (*Editor*). Handbook of chemistry and physics. 76th ed. CRC Press, Boca Raton, Fla. 1995.
37. C. Den Auwer, M.P. Andrews, V. Briois, C. Cartier dit Moulin, and H. Dexpert. J. Phys. IV (Colloque C2), **7**, 1051 (1997).

© 1998 NRC Canada

Synthesis of the first [*n*]paracyclophane with an annulene as the aromatic, a necklace-like molecule; NMR, X-ray, and MMX structural comparisons

Reginald H. Mitchell, Danny Y.K. Lau, Thomas C.W. Mak, Bo-mu Wu, and Clemens Anklin

Abstract: The [18]paracyclo[14]annulene, **6**, a *trans*-10b,10c-dimethyldihydropyrene bridged by an 18 atom chain at the 2,7-positions, was prepared in 33% yield from 1,14-tetradecanedioyl dichloride and 2,7-bis(hydroxymethyl)-10b,10c-dimethyldihydropyrene (**7**). Molecular mechanics calculations were carried out to correlate the lowest energy conformers of **6** with the experimental X-ray structure. High field NMR spectra of **6** were fully assigned and correlated with the lower energy conformers, which in solution equilibrate such that the annulene ring can freely spin. The molecule, which is necklace shaped, has the protons H(9/6), and not those at the centre of the chain of the necklace [H(8/7)], closest to the centre of the annulene ring, and most shielded by the ring current. Shielding of various protons of the chain approximately correlates with the distances of their appropriate carbons, averaged over the 10 lowest energy conformers, from the centre of the ring current.

Key words: paracyclophane, bridged annulene, molecular mechanics, ring current.

Résumé : Utilisant le dichlorure de 1,14-tétradécanedioyle et le 2,7-bis(hydroxyméthyl)-10b,10c-diméthyldihydropyrène (**7**) comme produits de départ, on a préparé (rendement de 33%) le [18]paracyclo[14]annulène (**6**), un *trans*-10b,10c- diméthyl-dihydropyrène portant une chaîne de 18 atomes qui relient les positions 2 et 7. On a effectué des calculs de mécanique moléculaire pour établir une corrélation entre les conformères de basse énergie du composé **6** et la structure déterminée par diffraction des rayons X. Les spectres RMN de haut champ du composé **6** ont permis de faire une attribution complète et d'établir une corrélation avec les conformères de basse énergie qui, en solution, s'équilibrent d'une façon telle que le noyau annulène peut tourner librement. Dans la molécule en forme de collier, ce sont les protons H(9/6) et non pas ceux au centre de la chaîne du collier [H(8/7)] qui sont le plus près du centre du noyau annulène et, par conséquent, les plus blindés par le courant du cycle. Il existe une corrélation approximative entre le blindage des divers protons de la chaîne et les distances de leurs carbones, établies comme moyenne des 10 conformères de plus basse énergie, du centre du courant de cycle.

Mots clés : paracyclophane, annulène ponté, mécanique moléculaire, courant de cycle.

[Traduit par la rédaction]

Introduction

Despite the huge interest in cyclophanes (1), examples in which the aromatic residues are the more highly condensed aromatics rather than benzene, naphthalene, anthracene, or phenanthrene derivatives are sparse. For example, even though three groups (2) reported the pyrenophane **1** in the mid 1970s, only recently has Bodwell et al. (3) reported the [8]paracyclopyrenophane **2**, and Siegel and co-workers (4) a paracyclocorrannulene. Examples in which the aromatic is a higher annulene are even rarer, despite the fact that Ito (5) has pointed out that non-benzenoid phanes should have interesting properties, because they can be distorted more easily. To our knowledge, only three cyclophanes, **3**–**5**, containing 10π or larger annulenes have been reported (6, 7).

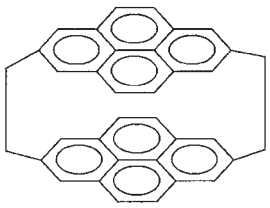

1

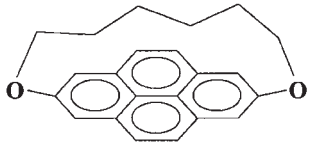

2

We now report the first singly bridged higher annulene, **6**, an [18]paracyclo[14]annulene.

Received December 21, 1997.

R.H. Mitchell[1] **and D.Y.K. Lau.** Department of Chemistry, University of Victoria, P.O. Box 3065, Victoria, BC V8W 3V6, Canada.
T.C.W. Mak and B-M. Wu.[2] Department of Chemistry, The Chinese University of Hong Kong, Shatin, New Territories, Hong Kong.
C. Anklin. Bruker Instruments, Inc., Fortune Drive, Manning Park, Billerica, MA 01821, U.S.A.

[1] Author to whom correspondence may be addressed. Telephone: (250) 721–7159. Fax: (250) 721–7147. E-mail: regmitch@uvvm.uvic.ca
[2] On leave from The Institute of Biophysics, The Chinese Academy of Sciences, Beijing, PRC.

© 1998 NRC Canada

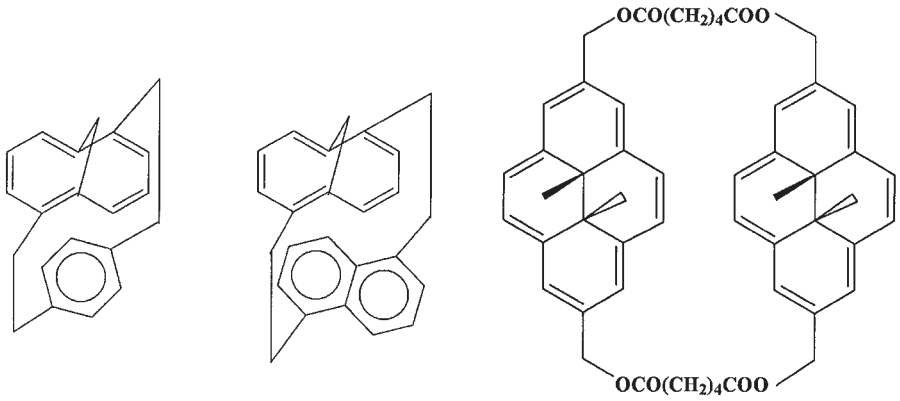

3 4 5

Results and discussion

Synthesis of cyclophane 6

The lack of cyclophanes containing higher annulenes is probably partly due to the problems encountered in synthesis, either difficulty in obtaining the annulene or difficulty because of its reactivity. Annulenes are generally highly electron-rich species and so often decompose on attempted alkylation. In the synthesis of **5** (7), we avoided this problem by proceeding through the dialcohol **7**, which was obtained not by direct alkylation, but rather by reacting the quinone **8** with the Corey reagent $(CH_3)_2S{=}CH_2$, and then reduction of the products to **7** (7). Not surprisingly reaction of **7** with 1,6-hexanedioyl chloride yielded only cyclic dimer **5** and none of the monomer **9**, a [10]paracylo[14]annulene. However, reaction of **7** with the longer 1,14-tetradecanedioyl dichloride in the presence of enough pyridine to complex any HCl formed, did yield 33% of the singly bridged cyclophane **6**, and to our surprise only minute amounts (that we could detect by mass spectrometry) of the cyclic dimer. The dark green crystals of **6** obtained, showed mp 124–126°C. Both a high-resolution mass spectrum, (MH^+ calcd. for $C_{34}H_{43}O_4$: 515.3161; found: 515.3135) and a single-crystal X-ray structure proved the identity of 6 as the monomer.

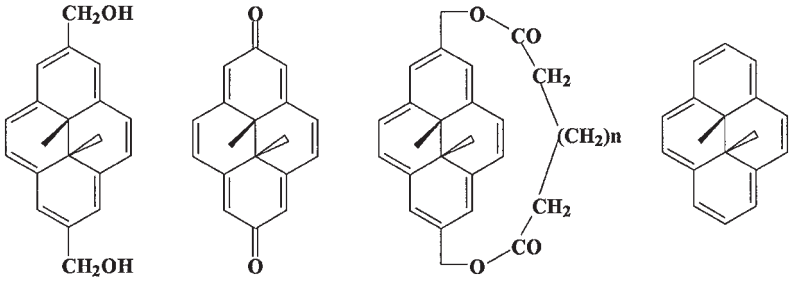

7 8 6: n = 10 9: n = 2 10

X-ray structure of 6

Suitable crystals of **6** could be obtained by crystallization from acetonitrile; small crystals appear yellow–green, while bulk quantities appear darker green. A yellow–green crystal, 0.15 × 0.25 × 0.60 mm, was mounted on a glass fibre to obtain the data summarized in Table 1. Full data containing molecular structures, crystal data, data collection, solution and refinement, sample experimental information, atomic coordinates, isotropic displacement coefficients, bond lengths and angles, anisotropic displacement coefficients, and H-atom coordinates have been deposited.[3]

An ORTEP drawing of cyclophane **6** is shown in Fig. 1. The molecule exhibits two-fold disorder associated with two alternate arrangements of its internal bridge system (see Fig. 1). Some important bond lengths are given in Table 2.

The C—C bond lengths around the periphery of the annulene are 1.37–1.41 Å, consistent with those (8) in the parent dimethyldihydropyrene **10**, and indicate that the annulene is fully delocalized. The C—C bond lengths of the long chain are mostly normal at 1.51–1.52 Å, but the C(6)—C(7) bond seems shorter, 1.41 Å, and the C(6)—C(5) bond longer, 1.59 Å, than would be expected. Interestingly, in the calculations described

[3] Supplementary material may be purchased from: The Depository of Unpublished Data, Document Delivery, CISTI, National Research Council of Canada, Ottawa, Canada, K1A 0S2. With the exception of the anisotropic displacement coefficients, these data have also been deposited with the Cambridge Crystallographic Data Centre and can be obtained on request from: The Director, Cambridge Crystallographic Data Centre, University Chemical Laboratory, 12 Union Road, Cambridge, CB2 1EZ, U.K.

© 1998 NRC Canada

Table 1. X-ray crystal data and parameters for **6**.

Formula	$C_{34}H_{42}O_4$
Formula weight	514.7
Temperature (°C)	21
System	Triclinic
Space group	p^{-1}
a	10.612(2)
b	11.400(2)
c	12.899(2)
α	102.09(1)°
β	97.00(1)°
γ	103.58(1)°
V	1471.9(7) Å^3
Z	2
D_c	1.161 g cm^{-3}
Crystal dimensions (mm)	0.15 × 0.25 × 0.60
μ	0.074 mm^{-1} (no abs corr.)
No. of independent reflections	4960
No. of observed reflections $\|F\| \geq \sigma(\|F\|)$	2850
Radiation	Mo Kα, 0.71073 Å
R_F	0.0798
$R_{wF}{}^2$	0.0952

below, one of the hydrogen atoms on C(6) is calculated to have the closest interaction with the C(32) methyl group, at 2.60 Å.

The ORTEP view shown in Fig. 1 is a little deceptive. Better perceptiveness of the molecule can be obtained by examination of Fig. 2.

From Fig. 2, it can be seen that the chain does not form vertically above the plane of the dihydropyrene, as in a basket, but goes off to one side, at least in the crystalline state. From the distances involved, one would expect in solution there to be many contributing conformations, with even the dihydropyrene ring being able to freely rotate. This aspect is discussed below.

Molecular mechanics calculations

The program[4] GMMX was used to search conformational space to determine the lowest energy conformers of **6**. This program uses an MM2 + PI calculation to search out unique conformers. It found 423 conformers within 3.5 kcal/mol energy of the most stable conformer. In fact the lowest energy calculated structure was not the X-ray structure, but the one almost identical, with the two carbonyl groups pointed to the same side of the molecule and not to opposite sides as in the X-ray structure, which it calculated had higher energy by about 0.3 kcal/mol. The fifth lowest energy conformer in fact corresponds most closely to the X-ray structure. Views of conformers **1** and **5** and the X-ray structure are compared in Fig. 3.

Clearly the molecular mechanics calculations do a reasonably good job in predicting the structure of **6**, especially since this is an annulene for which calculations can be a problem (9). To meaningfully discuss the NMR spectra of **6** (below), we need to have reasonable estimates of the distances between the chain atoms and those of the annulene ring. In the NMR spectrum, because the annulene ring can spin, the chain carbons and hydrogens average, thus C(13) and C(2) are equivalent,

[4] GMMX, V1.0, Serena Software, Box 3076, Bloomington, Ind. 47402-3076, U.S.A.

Fig. 1. Perspective view (35% thermal ellipsoids) of the molecular structure of cyclophane **6**, which has two equally populated sets of "half-carbon" atoms, namely C(30)-C(33) and C(30′)-C(33′), that represent alternate arrangements of the internal bridge unit. For clarity only one alternate arrangement is illustrated.

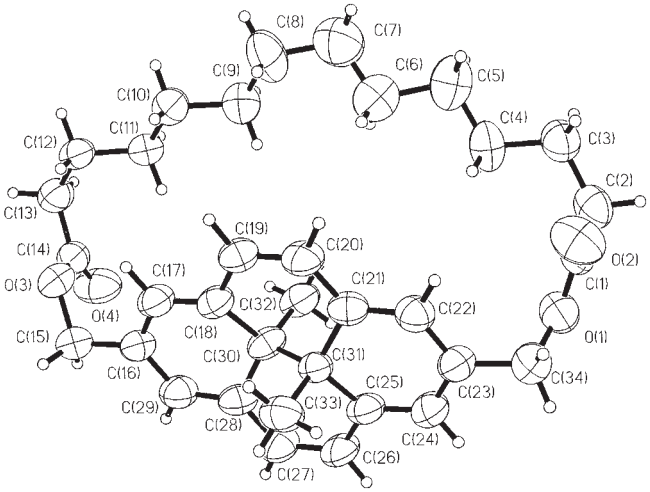

Table 2. Selected bond lengths (Å) of **6**.

C(16)—C(17)	1.409(6)	C(16)—C(15)	1.511(6)
C(17)—C(18)	1.371(6)	C(23)—C(34)	1.504(6)
C(18)—C(19)	1.401(6)	C(15)—O(3)	1.448(6)
C(19)—C(20)	1.374(6)	C(34)—O(1)	1.462(6)
C(20)—C(21)	1.398(6)	O(3)—C(14)	1.345(6)
C(21)—C(22)	1.381(6)	O(1)—C(1)	1.336(6)
C(22)—C(23)	1.398(6)	C(14)—C(13)	1.481(7)
C(23)—C(24)	1.381(6)	C(1)—C(2)	1.503(7)
C(24)—C(25)	1.390(6)	C(13)—C(12)	1.527(7)
C(25)—C(26)	1.381(6)	C(2)—C(3)	1.519(7)
C(26)—C(27)	1.382(6)	C(12)—C(11)	1.517(5)
C(27)—C(28)	1.382(6)	C(3)—C(4)	1.513(6)
C(28)—C(29)	1.393(6)	C(11)—C(10)	1.524(7)
C(29)—C(16)	1.382(6)	C(4)—C(5)	1.503(8)
C(18)—C(30)	1.523(11)	C(10)—C(9)	1.522(6)
C(21)—C(31)	1.509(12)	C(5)—C(6)	1.593(8)
C(25)—C(31)	1.564(9)	C(9)—C(8)	1.512(8)
C(28)—C(30)	1.531(16)	C(6)—C(7)	1.405(9)
C(30)—C(31)	1.519(16)	C(7)—C(8)	1.517(8)
C(30)—C(32)	1.572(18)	C(14)—O(4)	1.181(5)
C(31)—C(33)	1.576(16)	C(1)—O(2)	1.193(5)

C(12) and C(3) are equivalent, and so on. We therefore calculated average distances of each type of chain carbon from the closest methyl group, C(32), for comparison between the various structures. This data is presented in Table 3.

It can be seen that except for C(13/2), in terms of distances from the chain carbons to C(32), the X-ray structure is in fact closest to the lowest energy conformer **1** rather than conformer **5**. However in both conformers **1** and **5**, and in the X-ray structure the order of distance from C(32) is

9/6 < 11/4 < 10/5 < 8/7 < 12/3 < 13/2

Only when conformers **6**–**10** are included in the average does the order significantly change:

9/6 < 8/7 < 11/4 < 10/5 < 12/3 < 13/2

and the pair 8/7 moves closer to C(32), however pair 9/6 still

© 1998 NRC Canada

Fig. 2. Alternative views of the cyclophane **6**. View *A*: from above the dihydropyrene, which is in the plane of the paper. View *B*: from the edge of the plane containing the dihydropyrene. View *C*: from the end of the plane containing the dihydropyrene.

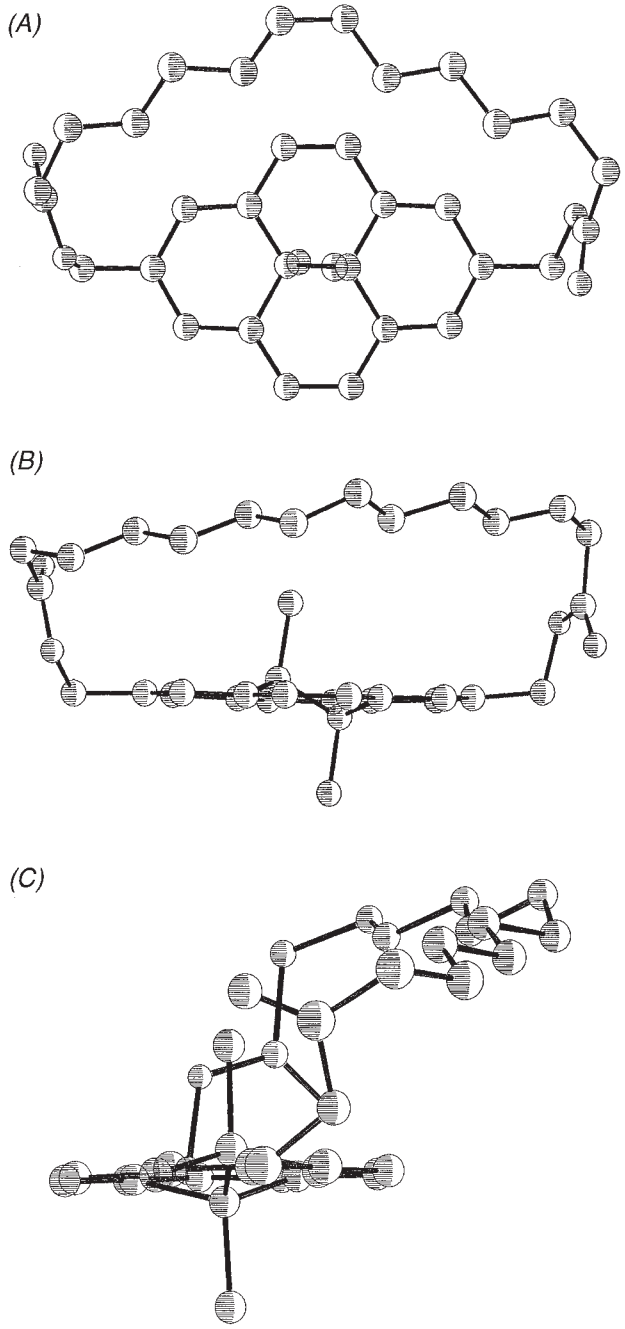

remains closest to the internal methyl carbon. This will have ramifications for the proton spectra (below).

NMR spectra of 6

The ^{1}H and ^{13}C NMR spectra of **6** were run at 600.13 and 150.91 MHz, respectively. The chemical shifts are given in Table 4.

The fact that the singlets at δ –4.07, 5.85, and 8.62 remained so even at –100°C suggests that in solution, the molecule has the annulene ring freely rotating.

Fig. 3. Comparison *A* of the GMMX lowest energy structure with the X-ray structure of **6**, and *B* of the fifth lowest energy conformer with the X-ray structure of **6**.

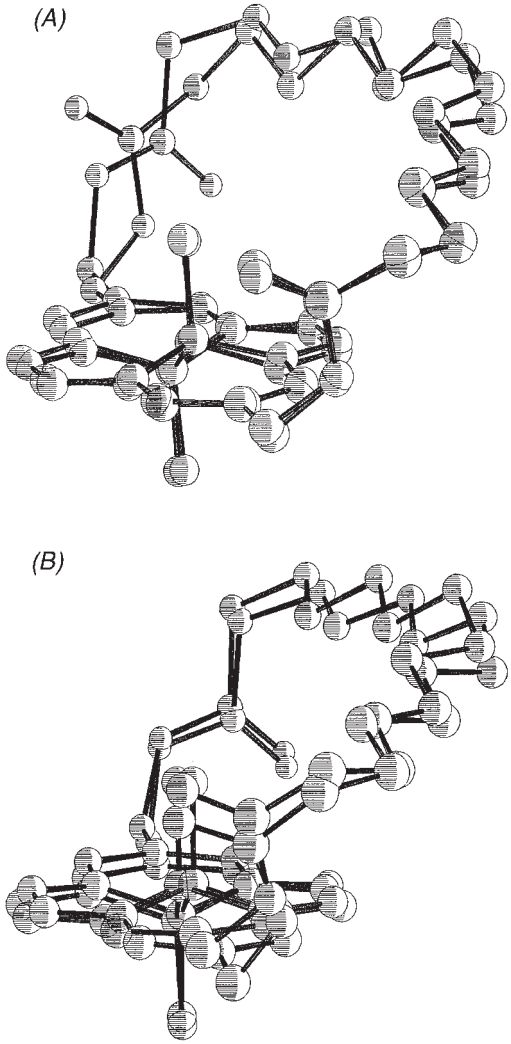

Table 3. Average distances (Å) from C(32) to each pair of chain carbon atoms in **6** for various conformers.

Carbon pairs	13/2	12/3	11/4	10/5	9/6	8/7
Conf. **1**–**10**[a]	6.42	6.34	5.18	5.49	4.73	4.94
Conf. **1**	6.62	6.26	5.10	5.34	4.63	5.55
X-ray	6.44	6.25	5.10	5.38	4.58	5.48
Conf. **5**	6.45	6.14	4.81	5.06	4.23	5.16
X-ray (min)[b]	6.44	6.17	4.88	5.19	4.39	5.33

[a] Average of 10 lowest energy conformers, ~25% of populated conformers.

[b] X-ray structure minimized using PCMODEL.[5]

The assignments were made as follows: the protons on C(13/2) are known unambiguously because of their chemical shift at δ 2.39. A 2-D phase-sensitive, double quantum filtered COSY spectrum, Fig. 4, indicated that these were coupled to the protons at δ 1.53, which must therefore be H(12/3); likewise these were coupled to those at δ 0.75, H(11/4), which

[5] PCMODEL, V5.0, Serena Software, Box 3076, Bloomington, Ind. 47402-3076, U.S.A.

© 1998 NRC Canada

Table 4. Proton and carbon NMR chemical shifts (δ) for **6** in $CDCl_3$.

Atom nos.[a]	34/15	14/1	13/2	12/3	11/4	10/5	9/6	8/7	
^{1}H (δ)	5.85	—	2.39[b]	1.53[b]	0.75[b]	0.88[b]	0.46[b]	0.68[b]	
^{13}C (δ)	67.79	173.99	35.03	26.38	29.12	30.62	29.85	30.07	
Atom nos.	16/23	17,29/22,24		18,28/21,25		19,27/20,26		30/31	32/33
^{1}H (δ)	—	8.619		—		8.616		—	–4.07
^{13}C (δ)	131.92	124.57		137.20		124.65		30.26	14.73

[a] X-ray nos., see Fig. 1.
[b] Centre of multiplet.

Fig. 4. A 2-D phase-sensitive, double quantum filtered COSY spectrum of **6** between 2.5 and 0.0 ppm.

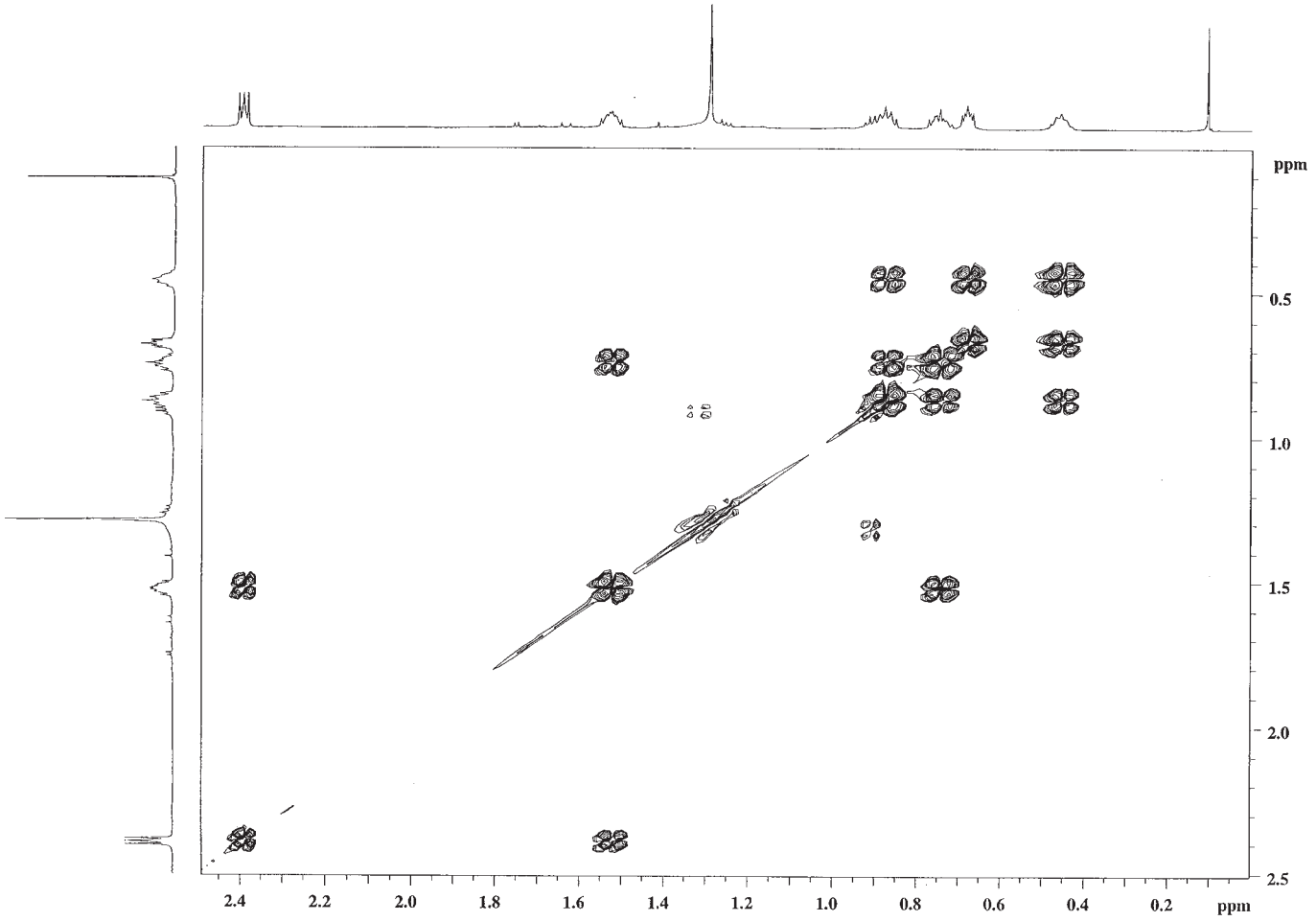

were coupled to those at δ 0.88, H(10/5), which were coupled to those at δ 0.46, H(9/6), which finally were coupled to those at δ 0.68, H(8/7). Additionally, H(17) could be distinguished from H(19) by the very weak cross peak from the former to the benzyl protons, H(15). With the protons fully assigned, their corresponding carbons were assigned using 2-D HMQC and HSQC 1H/13C correlation spectra. The quaternary carbons were assigned using 2-D HMBC 1H/13C long-range correlation spectra: specifically the methyl protons at δ –4.07 correlated to C(30) at δ 30.26 and C(18) at δ 137.2, while the benzylic protons at δ 5.83 correlated to C(16) at δ 131.9.

A series of 1-D GOESY gradient Overhauser spectra were run: irradiation of the internal methyl protons indicated interactions decreasing in intensity in the order H(9/6), H(8/7), H(11/4), and H(10/5) (see Fig. 5), which is exactly the order obtained above in the calculation of the chain carbon distances to the methyl carbons, averaged over the 10 lowest energy conformers. For the X-ray structure, the minimum and average H—H distances were calculated for the C(32) methyl and the hydrogens on the chain. These are given in Table 5.

The Me–H interactions nicely follow the calculated H—H distances, except that the interaction with H(8/7) is stronger than would be expected on the basis of the X-ray conformer, but as explained above, when the other conformers are mixed in, these hydrogens average closer to the methyl groups.

Table 5 also shows the minimum ring—H distances.

© 1998 NRC Canada

Table 5. Minimum and average H—H distances (Å) between the hydrogens of methyl C(32) [Me] or the hydrogens on the ring, H(17) or H(19) [Ring], and the hydrogens on the chain [H] in the X-ray conformer.

H no.	9/6	11/4	8/7	10/5	12/3	13/2
$[Me - H]_{min}$	2.60	2.90	4.53	4.65	5.28	5.45
$[Me - H]_{ave}$	3.94	4.49	5.93	5.82	6.74	6.93
$[Ring - H]_{min}$	2.41	2.58	3.46	3.08	2.88	4.71

Table 6. Chemical-shift shielding (Δδ, ppm) of the chain hydrogens in **6** compared to those in 1,14-tetradecanedioic acid (**11**).

H no.	13/2	12/3	11/4	10/5	9/6	8/7
δ (**6**)	2.39	1.53	0.75	0.88	0.46	0.68
δ (**11**)	2.15	1.48	1.14	1.14	1.14	1.14
Δδ	–0.24	–0.05	0.39	0.26	0.68	0.48
C—C[a]	6.42	6.34	5.18	5.49	4.73	4.94

[a] Å, from Table 3.

Irradiation of the ring hydrogens at δ 8.62 indicates interaction with H(9/6) and H(11/4) most strongly, consistent with the closest approach distances in Table 5, and then weaker interactions with the other chain hydrogens.

Thus overall, the annulene ring can spin freely about the chain, and although the chain is obviously averaging many conformations, the Overhauser experiments indicate that on average the internal methyl protons come closest to H(9/6) and H(8/7) in the centre of the chain of the necklace, while the ring hydrogens approach closest on average H(9/6) and H(11/4) during the rotation.

The chemical-shift shielding of the chain hydrogens depends upon the distance from the centre of the dihydropyrene ring, where the ring-current effect is strongest. The observed order of chemical-shift shielding, which can be obtained by subtracting the chemical shift of the appropriate hydrogens in the free acid (Table 6) is H(9/6) > H(8/7) > H(11/4) > H(10/5) > H(12/3).

This is exactly the order observed above for the increasing chain C — methyl C distances averaged for the 10 lowest energy conformers. We have carried out the comparison between both the minimum and average "chain H to centre of ring" distance and the "C—C" distances given in Table 3 for the X-ray conformer and found an exact correspondence of order. Thus using the C—C distances averaged over the 10 lowest energy conformers to correlate with the ring-current shielding is a reasonable approximation. Both DuVernet and Boekelheide (10) and Lai and Zhou (11) have attempted to correlate ring-current shielding of the internal substituents in dihydropyrenes to distance from the plane of the ring. Unless a frozen conformer is available, this has some difficulty. In the case of our necklace **6**, correlation would need to include both the out-of-plane and in-plane distances from the centre of the ring and then would best be done in a fixed conformer. Our approximation, which uses the C—C distances averaged over the 10 lowest energy conformers, gives surprisingly good results, but correlation with a more precise Johnson–Bovey model (12) will have to wait until we are able to synthesize a necklace with a shorter chain that is unable to move very much. This we will attempt.

Fig. 5. (*Top*) A portion of the 600 MHz ^{1}H NMR spectrum of **6** between δ 4 and δ –2 showing protons 13/2 (*a*), 12/3 (*b*), 10/5 (*c*), 11/4 (*d*), 8/7 (*e*), and 9/6 (*f*). (*Bottom*) The 1-D GOESY (gradient Overhauser) spectrum of the same portion with irradiation of the internal methyl protons.

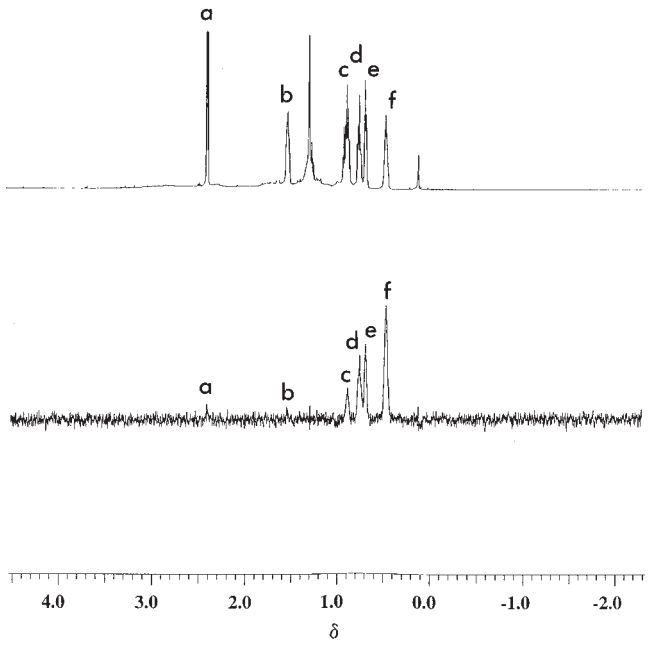

Conclusions

We have synthesised the first "paracyclo" dihydropyrene, **6**, a molecule shaped like a necklace. The pendant, the dihydropyrene ring, can freely spin in solution at room temperature. The dihydropyrene ring appears unstrained on the basis of the X-ray structure and by comparison of the proton spectrum and UV spectrum to those of the parent **10** and its 2,7-dimethyl derivative (13). Molecular mechanics calculations were carried out to obtain the lowest energy conformers of **6**, and these were compared to the X-ray conformer, and calculations based on these gave good correlation with NMR chemical-shift data.

Experimental

Melting points were determined on a Reichert 7905 melting point apparatus integrated to a chrome–alumel thermocouple. Infrared spectra, major peaks only, calibrated with polystyrene, were recorded on a Bruker IFS25 FT–IR spectrometer as KBr disks. Ultraviolet-visible spectra were recorded on a Cary 5 or a Perkin–Elmer Lambda-4B spectrometer in chloroform. Proton NMR spectra were recorded at 360 MHz on a Bruker AMX 360 or at 600MHz on a Bruker DRX600 using $CDCl_3$ as solvent. Carbon NMR spectra were recorded at 90.6 MHz or 151 MHz in $CDCl_3$, using the solvent peak at 77.0 ppm for calibration. Exact mass measurements used a Kratos Concept-H instrument with perfluorokerosene as calibrant. Elemental analyses were carried out by Canadian Microanalytical Services Ltd, Vancouver, B.C. All evaporations were carried out under reduced pressure on a rotary evaporator, and all organic

© 1998 NRC Canada

extracts were washed with water and dried over anhydrous $MgSO_4$. SiGel refers to Merck Silica Gel, 70–230 mesh.

2,7-Bis(hydroxymethyl)-*trans*-10b,10c-dimethyl-10b,10c-dihydropyrene (7)

NaH (1.0 g, 20 mmol, 52% dispersion in mineral oil) was washed thrice with dry hexane (5 mL), and then heated at 60°C for 45 min with dry DMSO (20 mL) under N_2. The resulting grey solution was diluted with dry THF (50 mL) and cooled to –20°C, and then a solution of trimethylsulfonium iodide (4.08 g, 20 mmol) in dry DMF (40 mL) was added and the mixture stirred for 15 min. It was then cooled to –78°C, and with good stirring a solution of the quinone **8** (7) (0.524 g, 2.0 mmol) in dry THF (20 mL) was added dropwise. After further stirring at –78°C for 30 min, the reaction was warmed to room temperature over 2 h, and then the reaction mixture was poured into water and dichloromethane. The aqueous layers were further extracted with dichloromethane, and the extracts were washed, dried, and evaporated. The resulting purple coloured residue was dissolved in THF (50 mL) and $NaBH_4$ (80 mg, 2 mmol) was added, and then the reaction mixture stirred for 14 h at 20°C. The resulting green solution was treated with dichloromethane (at least 100 mL) and water. Any remaining green dialcohol **7** was extracted from the aqueous layer with dichloromethane, and then the combined extracts were washed, dried, and evaporated. The residue was dissolved in dichloromethane and chromatographed on 10% water deactivated SiGel using N_2 degassed dichloromethane–diethyl ether (8:2) as eluant to give 430 mg (73%) of dialcohol **7**, as green needles from methanol–hexane, mp 192–193°C. ^{1}H NMR (360 MHz, d_6-acetone) δ: 8.58 (s, 4H), 8.56 (s, 4H), 5.31 (d, J = 5.8 Hz, 4H), 4.68 (t, 2H, -OH), –4.11 (s, 6H); ^{13}C NMR δ: 138.1, 137.4, 123.9, 122.7, 66.2, 31.0, 14.6; IR 3280 (vb) cm^{-1}; UV (CH_2Cl_2) λ_{max} nm (ϵ_{max}): 343 (79 000), 361 sh (37 000), 381 (31 000), 457 (6400), 480 (8600), 650 (~400); MS (CI) *m*/*z*: 293 MH$^+$. Anal. calcd. for $C_{20}H_{20}O_2$: C 82.15, H 6.90; found: C 81.97; H, 6.80.

Cyclophane 6

Dry pyridine (0.35 mL, 4.4 mmol) was added to a solution of dialcohol **7** (511 mg, 1.75 mmol) in dry dichloromethane (500 mL) and was stirred for 15 min. Then a solution of 1,14-tetradecanedioyl dichloride (516 mg, 1.75 mmol) in dry dichloromethane (120 mL) was added fast in one portion with vigorous stirring under argon protection. The reaction mixture was further stirred for 4 h, and then was concentrated to about 5 mL and was loaded onto a neutral alumina column (deactivated with 5% water). The green band eluted with dichloromethane was collected and evaporated to yield 300 mg (33%) of the cyclophane **7**. Recrystallization from benzene yielded dark green crystals, mp 124–126°C. NMR: see text, Table 4. The multiplets referred to in Table 4 appeared at the following chemical-shift ranges: 2.41–2.37, 1.57–1.49, 0.94–0.84, 0.78–0.71, 0.71–0.65, 0.49–0.42 ppm. IR 1732, 1446, 1377, 1341, 1263, 1216, 1158, 1101, 882, 756, 664 cm^{-1}; UV λ_{max} nm (ϵ_{max}): 344 (78 400), 359 (17 400), 384 (31 100), 446 (7600), 483 (13 200), 590 (380), 637 (440), 646 (430). MS (CI) *m*/*z*: 515 MH$^+$; HRMS (LSIMS) calcd. for $C_{34}H_{43}O_4$: 515.3161; found: 515.3135.

Acknowledgements

We thank the Natural Sciences and Engineering Research Council of Canada, The University of Victoria, and the Hong Kong Research Grants Council (ref. no. CUHK 456/95P) for financial support.

References

1. F. Diederich. Cyclophanes. Royal Society of Chemistry, Cambridge, U.K. 1991; P.M. Keehn and S.M. Rosenfeld. Org. Chem. **45**, 1 (1983); F. Vogtle. Top. Curr. Chem. **115**, 1 (1983); Top. Curr. Chem. **113**, 1 (1983).
2. T. Umemoto, S. Satani, Y. Sakata, and S. Misumi. Tetrahedron Lett. **16**, 3159 (1975); R.H. Mitchell, R.J. Carruthers, and J.C. Zwinkels. Tetrahedron Lett. **17**, 2585 (1976); H. Irngartin, R.G. Kirrstetter, C. Krieger, H. Rodewald, and H.A. Staab. Tetrahedron Lett. **18**, 1425 (1977).
3. G.J. Bodwell, J.N. Bridson, T.J. Houghton, J.W. Kennedy, and M.R. Mannion. Angew. Chem. Int. Ed. Engl. **35**, 1320 (1996).
4. T.J. Seiders, K.K. Baldridge, and J.S. Siegel. J. Am. Chem. Soc. **118**, 2754 (1996).
5. S. Ito. Pure. Appl. Chem. **54**, 957 (1982).
6. M. Matsumoto, T. Otsubo, Y. Sakata, and S. Misumi. Tetrahedron Lett. **18**, 4425 (1977).
7. R.H. Mitchell and X. Jin. Tetrahedron Lett. **36**, 4357 (1995).
8. R.H. Mitchell, V.S. Iyer, N. Khalifa, R. Mahadevan, S. Venugopalan, S.A. Weerawarna, and P. Zhou. J. Am. Chem. Soc. **117**, 1514 (1995); R.V. Williams, W.D. Edwards, A. Vij, R.W. Tolbert, and R.H. Mitchell. J. Org. Chem. **63**, 3125 (1998).
9. R.H. Mitchell, Y. Chen, V.S. Iyer, D.Y. Lau, K.K. Baldridge, and J.S. Siegel. J. Am. Chem. Soc. **118**, 2907 (1996); R.H. Mitchell, V.S. Iyer, R. Mahadevan, S. Venugopalan, and P. Zhou, J. Org. Chem. **61**, 5116 (1996).
10. R. DuVernet and V. Boekelheide. Proc. Natl. Acad. Sci. U.S.A. **71**, 2961 (1974).
11. Y.H. Lai and Z.L. Zhou. J. Org. Chem. **62**, 925 (1997).
12. C.E. Johnson and F.A. Bovey. J. Chem. Phys. **29**, 1012 (1958).
13. R.H. Mitchell, I. Calder, H. Huisman, and V. Boekelheide. Tetrahedron, **31**, 1109 (1975).

© 1998 NRC Canada

Solubility prediction of *n*-fatty alcohols and sterols in complexing and non-complexing solvents according to the mobile order theory

Paul Ruelle and Ulrich W. Kesselring

Abstract: The volume fraction solubilities of a number of solid *n*-fatty alcohols and sterols are predicted in neat organic nonpolar, polar, and hydrogen-bonded solvents including water. In the frame of the mobile order thermodynamics, the predictions are based on the knowledge (*a*) of the melting properties of the alcohols, which affect the fluidization process, (*b*) of their molar size, which mainly rules the exchange entropy and the hydrophobic effect, and (*c*) of the group interaction stability constants, which are responsible for the balance between the competing self-association and strong intermolecular interactions of the alcohols in solution. Owing to its ability to deal properly with these various elementary processes, the proposed thermodynamic solubility model derived from the mobile order theory in H-bonded liquids represents an advance towards reliable and comprehensive estimates of the solubilizing capacity of common solvents for nonideal complexing systems, i.e., the solid alcohols.

Key words: solubility prediction, solution thermodynamics, mobile order theory, *n*-fatty alcohols, sterols.

Résumé : On prédit les fractions volumiques de solubilité d'un certain nombre d'alcools gras et de stérols dans des solvants organiques non polaires, polaires et à liaisons hydrogènes, y compris dans l'eau. Dans le cadre de la thermodynamique de l'ordre mobile, on base les prédictions sur la connaissance (*a*) des propriétés de fusion des alcools affectés au cours du processus de fluidisation, (*b*) de la taille molaire qui détermine principalement l'entropie d'échange et l'effet hydrophobe (*c*) ainsi que des constantes de stabilité des interactions entre groupes qui sont responsables de la balance entre les interactions d'autoassociation et les fortes interactions intermoléculaires des alcools en solution. À cause de sa capacité à traiter ces divers processus élémentaires, le modèle thermodynamique de solubilité proposé — qui dérive de la théorie de l'ordre mobile dans des liquides à liaisons hydrogènes — représente une amélioration vers des évaluations plus fiables et plus complètes de la capacité des solvants ordinaires à solubiliser des substances formant des complexes non idéaux, comme les alcools solides.

Mots clés : prédiction de la solubilité, thermodynamique des solutions, théorie de l'ordre mobile, alcools gras, stérols.

[Traduit par la rédaction]

1. Introduction

Over the years, a large number of studies have been carried out to find a general solubility model enabling a priori predictions. An important step towards solubility predictions was achieved around 1930 with the development by Hildebrand and Scott of the *regular* solution theory (1, 2). Expressions such as "*polar solutes dissolve in polar solvents*," "*like dissolves like,*" or "*similia similibus solvuntur*" are based on this theory. Although this treatment originally was strictly intended for systems involving dispersion forces, its use has largely been extended to include highly polar solvents and solutes, and still constitutes the background of practically all theoretical approaches of solubility prediction found in the literature (3–9). These predictive models rely on the premise that the solubility of a solute in a particular solvent is simply related to the bulk properties of the pure components. However, whenever hydrogen bonds are involved in the solution process, solubilities may no longer be described in terms of bulk properties of the components such as their solubility parameters, and may not be obtained either by the regular solution theory or by any of its further expanded developments. The regular solution theory and the Scatchard–Hildebrand expression are mainly based on two fundamental assumptions: (*a*) the rule of the geometric mean, i.e., the adhesive energy of a pair of unlike molecules is the geometric mean of the cohesive energies of the two equivalent like pairs; and (*b*) the interactions between molecules in solution occur "at random," i.e., there are no preferential contacts in solution and the randomness of ideal mixtures is preserved. A direct consequence of the geometric mean rule is that regular solutions always give positive deviations from Raoult's law and positive enthalpies of mixing. This implies that adhesive forces are always inferior to cohesive forces. Consequently, the regular solution theory is a reasonable approximation for relatively nonpolar systems, in which attraction forces essentially result from dispersion, but it no longer holds for solutions in which specific interaction forces or hydrogen bonds occur, because hydrogen bonds do not obey the

Received September 8, 1997.[1]

P. Ruelle[2] and U.W. Kesselring. Institut d'analyse pharmaceutique, Section de pharmacie, Université de Lausanne, BEP, CH-1015 Lausanne, Switzerland.

[1] Revision received March 20, 1998.

[2] Author to whom correspondence may be addressed. Fax: +41 21/ 692 45 05. E-mail: Paul.Ruelle@iap.unil.ch

© 1998 NRC Canada

rule of the geometric mean and do not lead to random contacts. In contrast, one of the most important characteristics of H-bonding in the liquid phase is the establishment of "*highly preferential contacts*" between the proton-donor and proton-acceptor sites of the various molecules. These contacts in turn confer to H-bonded liquids a higher degree of "order" and a kind of structure. The structuration produced by H-bonding is, however, intermittent and labile. The fundamental difference with the crystalline state lies in the "mobility" of the H-bonds in the liquid phase: the disorder or the order in an associated liquid is dynamic. Both the temporary order introduced in the liquid by the formation of hydrogen bonds (preferential contacts) as well as the labile nature and the perpetually moving character of these bonds (their mobility) constitute the basic foundations of the "mobile order" theory developed by Huyskens et al. (10–12). The mobile order theory is at the origin of the nonergodic thermodynamic treatment of the H-bonded liquids, which is based not on static configurations but on movements and time fractions. In effect, the thermodynamics of the mobile order (13–16) consider equilibrium between the fractions of the time during which an amphiphilic proton follows the electron-donor site of one or another molecule in its walk through the liquid, rather than equilibria between concentrations of the various H-bonded (dimers, trimers, tetramers,...) or non-H-bonded (monomers) entities present in solution. The quantitative development of the mobile order theory then led to a universal predictive equation for solubility (17, 18) accounting for all the contributions to the free energy change implied when a solute is dissolved in a solvent.

Up to now, the mobile-order-derived solubility model has been sucessfully applied to predict the solubilities of low-polarity substances in one- and two-components solvent systems (19–33), the mutual solubilities of water and hydrocarbons (34, 35), the solubilities of proton-acceptor mono- and polyfunctional substances in aprotic and protic solvents (36–41), and the aqueous solubility of aliphatic alcohols (42). The mobile order theory has furthermore been used to make reliable estimates of the *n*-octanol–water partition coefficient of various hydrophobic compounds (43), and to explain the peculiarities of the conductance of LiCl solutions as well as the paradoxical effects of the addition of LiCl on both the conductivity of Polystyryl$^-$Li$^+$ solutions and the kinetics of the anionic polymerization (44). The apparent success obtained in these different studies already tends to demonstrate the high potential of the mobile order thermodynamics for predicting solubility in real systems, and confirms that this model may also be of great help in providing explanations of various solution phenomena (45–49). The mobile order theory undoubtedly constitutes an advancement in particular over the regular solution thermodynamic approaches against which the present model has been tested in the past (50). Contrary to the "solubility parameters"-based models (issued from the regular solution theory), which do not explicitly consider preferential contacts and entropy effects, the present approach is based, for H-bonds, on stability constants and on concentrations of the interacting sites that permit taking into account the important entropy effects accompanying the formation of the specific interactions.

The aim of the present paper then is twofold: (*i*) to further apply the mobile order thermodynamic model to predict the solubility of amphiprotic substances capable not only of self-association in solution — no matter the nature of the solvent — but also of interacting by hydrogen bond with proton-donor and proton-acceptor solvents; (*ii*) to determine the stability constants characterizing the various solute–solvent hydrogen bonds. For that purpose, five primary *n*-fatty alcohols, i.e., 1-dodecanol, 1-tetradecanol, 1-hexadecanol, 1-octadecanol, and 1-eicosanol, and two sterols, i.e., cholesterol and β-sitosterol, have been considered. Their solubilities are predicted in a wide range of both complexing and noncomplexing organic solvents. In the case of solid *n*-fatty alcohols, the knowledge of their solubility characteristics is of relevance to fat, cosmetic, and oil technology, whereas the knowledge of the solubility behavior of the sterols is of importance for understanding their pathophysiological role, as in gallstone disease and atherosclerosis. From the comparison of the relative importance of the different contributions involved in the solubility calculation, the origin of the solubility of the alcohols is analyzed, leading to a thorough understanding of the solution process of these substances.

2. Theoretical section

The ability to estimate solubility in real solutions certainly depends on the proper knowledge of the physical phenomena implied in the solubility process as well as of the forces that operate between molecules in solution, but also on the possibility of describing these phenomena correctly by thermodynamic expressions. Considering both the enthalpy and entropy changes accompanying the fusion and solvation processes, different thermodynamic expressions (17, 18) were previously derived in the frame of the mobile order theory to account for the influence of the solvent–solvent, solute–solute, and solute–solvent interactions on the chemical potential of the solute. According to these developments, the volume fraction solubility, Φ_B, of the solid alcohols in pure organic solvents may be considered to arise from the sum of maximum five contributions.

$$[1] \qquad \ln \Phi_B = A + B + D + F + \mathrm{OH}$$

Representing a particular physical phenomenon of the whole solubility process, each contribution reported hereafter has a thermodynamically well-defined expression, and plays either in favor or against solubility. (The interested reader will find, for each appropriate solubility contribution given hereafter, the appropriate references concerning the origin and derivation of its thermodynamic expression.)

"*A*" represents the fluidization (the ideal solubility) of the crystalline substance. This contribution corresponds to the suppression of the collective forces that bind the alcohol molecules within their crystalline state. Being in general an endothermic process, the fluidization is independent of the solvent and affects solubility unfavorably. At first approximation, the ideal solubility (51) is calculated from the knowledge of the enthalpy of melting, $\Delta_m H$, of the pure crystalline substance and from the difference between the melting point, T_m, and the absolute temperature, T, of interest.

$$[2] \qquad A = -\frac{\Delta_m H}{R}\left(\frac{1}{T} - \frac{1}{T_m}\right)$$

The fluidization is, however, not always a simple mathematical transformation of the Gibbs energy of melting, because it

© 1998 NRC Canada

may contain additional terms if some solid–solid or solid–liquid crystal transitions occur between the temperature of interest and the melting point temperature (52–54). This is especially the case for the long-chain 1-alkanols and for cholesterol, for which polymorphism is now well established as a characteristic feature.

"*B*" represents the correction factor for the entropy of mixing and is related to the difference between the sizes of the solvent (S) and alcohol (B) molecules in solution. This term essentially depends on the ratio, V_B/V_S, between the molar volumes, and contributes positively to the solubility as long as V_B is greater than V_S. Remember that, in the mobile order theory, the entropy of mixing in liquids is calculated by a hybrid expression (10, 18) taking into account both the nominal exchanges of place between unlike molecules, and the expansion of the individual domains available for the motions within the solution.

$$[3] \qquad B = 0.5\Phi_S\left(\frac{V_B}{V_S} - 1\right) + 0.5\ln\left(\Phi_B + \Phi_S\frac{V_B}{V_S}\right)$$

"*D*" accounts for the effect of the difference in the solute–solute, solvent–solvent, and solvent–solute nonspecific cohesion forces in the liquid phase. This effect brings about a reduction of the solubility that may, as a first approximation, be estimated from an expression of the usual Scatchard–Hildebrand type (55) using nonspecific solubility parameters δ' instead of the Hildebrand solubility parameters, δ. This equation, which is essentially based on the assumption of random contacts in solution, is, however, no longer valid when H-bonds are formed between the solute and solvent molecules, because these interactions modify the random distribution of the molecules. The effect of the new mode of distribution on the solubility is then accounted for by multiplying the Scatchard–Hildebrand expression by the fraction of the time during which the solute is not bound to the solvent, i.e., during which the distribution between the solvent and unbound solute molecules can still be considered to occur at random. As previously demonstrated (56), the new expression for *D* is then given by eq. [4]:

$$[4] \qquad D = -\frac{1}{(1.0 + K_{OH}\frac{\Phi_S}{V_S})}\frac{\Phi_S^2 V_B}{RT}\left(\delta'_B - \delta'_S\right)^2$$

where K_{OH} denotes the stability constant governing the solute–solvent H-bonds. Note that this equation assumes that the nonspecific interactions involving the bound solute are negligible.

"*F*" accounts for the reduction in the solubility of the alcohol in amphiphilic solvents that results from the solvent–solvent self-association, i.e., the hydrophobic effect. The hydrophobic effect has been properly defined and quantified in the frame of the mobile order theory (17, 18, 42). This contribution is composed of three parts (eq. [5]): the first term describes the loss of the mobile order entropy of the self-associated solvent molecules related to the hindrance of these molecules to dispose of a larger domain consecutive to the addition of the solute. For solutes involving amphiprotic groups (42), such as alcohols, this loss of entropy is, however, partially reduced by the insertion of these proton-donor groups in the solvent H-bond chains, which reduces the fraction of the time during which the solvent molecules are free from H-bonding. This reduction of the loss of entropy is expressed by the second part of eq. [5]. In the particular case of water, the effect on solubility of the strengthening of the water hydrogen bonding network by the formation of stronger mixed water–alcohol H-bonds from homogeneous chains is accounted for by the last term of eq. [5]

$$[5] \qquad F = -r_S\,\Phi_S\frac{V_B}{V_S} + \Phi_S r_S + \Phi_S b$$

In this equation, r_S represents the "structuration factor" of the solvent, and *b* is a constant accounting for the degree of branching of the alcohol, amounting to 1.2, 2.0, and 2.9 for primary, secondary, and tertiary alcohols, respectively (42). At room temperature, the value of r_S is equal to zero for non-associated solvents (aliphatic and aromatic hydrocarbons, esters, ethers, ketones, nitriles); r_S is approximately 1 for strongly associated solvents forming single H-bonded chains (alcohols), and amounts to 2 for water and diols whose molecules are involved in double hydrogen-bonded chains.

"OH" describes the effect of the amphiphilic OH group of the alcohol on its solubility (with the exception of the reduction of the hydrophobic effect considered in eq. [5]). The way that these groups affect the solubility is twofold: (*a*) the insertion of the alcohol molecules in their own hydrogen-bonded chains in solution (self-association) tends to decrease the solubility; (*b*) with proton-acceptor and amphiphilic solvents, either the formation of single solute–solvent H-bonds or the solute insertion in mixed solute–solvent hydrogen-bonded chains promotes the solubility. The OH chemical contribution depends upon the relative strengths of these various molecular interactions, and is expressed by eq. [6] (18, 42).

$$[6] \qquad OH = \ln\left(1 + K_{OH}\frac{\Phi_S}{V_S} + K_{BB}\frac{\Phi_B}{V_B}\right) - \ln\left(1 + \frac{K_{BB}}{V_B}\right)$$

In this expresion, the constants K_{BB} and K_{OH} represent the stability constants that govern, respectively, the alcohol self-association and the alcohol–solvent complexation in solution.

The complete universal solubility equation (18) derived from the mobile order theory would still contain an additional term called the "O term" to account for the positive effect of the H-bond formation between proton-acceptor sites on the solute and proton-donor solvents. In the present study, this contribution vanishes since the fatty alcohols and sterols of interest do not display such proton-acceptor groups.

3. Results and discussion

From the foregoing, the solubility of the *n*-fatty alcohols and sterols can be estimated on the basis of a limited number of properties characterizing both the alcohol and solvent molecules and their interactions in solution. Considering the fatty alcohols and sterols, all the physico-chemical parameters needed to estimate their solubility are collected in Table 1. Remember that for the compounds of interest, which are solid at room temperature, the molar volume, V_B, to be considered is not that of the crystalline compound, but the volume of the dissolved substance, which is, in general, larger by a few percentage points. Practically, these molar volumes are estimated from the addition of the volume contributions for the various

© 1998 NRC Canada

groups constituting the molecule (18, 39). The modified nonspecific cohesion parameter, δ_B', of all 1-alcohols and sterols has been set to 16.30 $MPa^{1/2}$, as the lowest limit of the decreasing cohesion parameter values with respect to the number of carbon atoms in the homologous 1-alcohol series. As for the fluidization constants, *A*, of the fatty alcohols and sterols, their values were not calculated from their melting and transition properties, but were directly estimated to fit the experimental solubilities in hydrocarbons. This procedure allows us to avoid the discrepancies observed between the existing data concerning the phase transformation enthalpies and temperatures. It is well known (59–69) that solid–solid transitions of the long-chain 1-alcohols and cholesterol are affected by the presence of minute amounts of impurities, as well as by variations in the measurement technique and by variations in the thermal histories of the materials. It is also noted that the solid–solid transition points of these materials, as well as the types and sequences of the solid phases, vary with the solvent, as a result of solute–solvent intermolecular interactions (70–80).

Concerning the solvents, their molar volumes and their modified nonspecific cohesion parameters are reported in Table 2. Numerical values were obtained from our previous published compilations (21, 36), or were calculated either according to the correlations reported by Huyskens et al. (40), or from the Hansen's dispersive, d_d, and polar, d_p, partial cohesion parameter values (81), or were simply estimated on the analogy of similar organic solvents with known modified nonspecific cohesion parameters.

Finally, predictions of solubility in complexing solvents still require the knowledge of the stability constants, K_{OH}, characteristic of the interactions between the OH group of the solute and the functional group of the solvent. Assuming that a given type of interaction, such as alcohol–ketone, has always the same strength regardless of its chemical environment, one therefore uses for each type of intermolecular interaction a "standard" stability constant whose values were deduced to fit the experimental solubilities (Table 3). Notice that the insertion constant of alcohol molecules in the hydrogen-bonded chains of such amphiphilic solvents as alcohols and water is considered to be identical to the alcohol–alcohol self-association constant in solution, i.e., $K_{BB} \cong 5000$ cm^3 mol^{-1}.

On the basis of the aforementioned physico-chemical data, the solubilities of five *n*-fatty alcohol (1-dodecanol, 1-tetradecanol, 1-hexadecanol, 1-octadecanol, 1-eicosanol) and of two sterols (cholesterol, β-sitosterol) have been calculated in a wide range of complexing and non-complexing solvents at 25°C and (or) 37°C according to eq. [1]. The results as well as the corresponding experimental data are given in Table 4 together with the contributions of the different terms involved in the solubility calculations. The agreement between observed and predicted solubilities is illustrated in Fig. 1, whereas the predictive ability of the model is furthermore characterized by the calculated vs. experimental volume fraction solubility ratios, $\Phi_B^{calc}/\Phi_B^{exp}$, given in the fifth column of Table 4. Apart from a few exceptions, most predictions, i.e., 98% of the 210 solubilities, show a solubility ratio between 0.1 and 10.0, whereas 70% of the predicted values are even less than twice higher or lower than the experimental values. Several reasons may be invoked to explain the small disagreement observed between calculated and experimental results. From the theoretical point of view, different errors could stem (*a*) from the uncertainties concerning both the molar volumes and the modified nonspecific cohesion parameters of the sterols and *n*-fatty alcohols in solution, (*b*) from the assignment of a common value, K_{BB}, to characterize the self-association of all the hydroxy compounds, and (*c*) from the use of standard solute–solvent stability constants instead of using particular values depending on the chemical environment of the interacting functional groups. Moreover, the values of all these parameters have not been modified for the predictions at 37°C. From the experimental point of view, variations in solid state factors such as hydration state, polymorphism, crystallinity, crystal inhomogeneity, and impurities may affect the solubility determination. The largest deviation between calculated and experimental solubilities is observed for cholesterol in water. Although we actually are unable to explain so large a discrepancy, it is important to mention that, for sparingly soluble compounds, like cholesterol, in water, accurate measurements of solubility are particularly difficult, and solubility values may vary considerably. Notwithstanding, the results on the whole clearly confirm the ability of the mobile-order-derived solubility model to provide reliable estimates of solubility of the solid long-chain *n*-alcohols and sterols in a wide range of organic solvents.

Table 1. Physico-chemical properties of the solutes.

Solute [a]	*A*	V_B (cm^3/mol)	δ'_B $MPa^{1/2}$	*b*
1-Dodecanol	–0.110	219.8	16.3	1.2
1-Tetradecanol	–0.174	252.3	16.3	1.2
1-Hexadecanol	–1.172	284.8	16.3	1.2
1-Octadecanol	–2.389	317.3	16.3	1.2
1-Eicosanol	–2.606	349.8	16.3	1.2
Cholesterol [b]	–2.707	390.5	16.3	2.0
Cholesterol (37°C) [b]	–1.957	390.5	16.3	2.0
β-Sitosterol (37°C) [c]	–2.620	428.5	16.3	2.0

[a] The self-association constant K_{BB} for all *n*-alcohols and sterols is equal to 5000 cm^3 mol^{-1}.

[b] The molar volume of cholesterol corresponds to the infinite partial molar volume determined in toluene, carbon tetrachloride, chlorobenzene, and nitrobenzene (ref. 57).

[c] In the absence of available solubilities in hydrocarbons, the solute crystallinity contribution, *A*, is calculated according to Yalkowsky's equation (58): $A = -0.023\ (T_m - 298.15)$.

The solubility behavior of the hydroxy compounds appears as a complex phenomenon subject to the balance of enthalpic and entropic contributions, depending in particular on the relative importance of the competing self-association and strong intermolecular interactions. Such information can be learned from the present thermodynamic solubility model, which, beyond its satisfactory predictive ability, also enables us to assess the factors that affect solubility differences between the hydroxy compounds, and the parameters that are responsible for the solubility changes from one solvent to another. A comprehensive understanding can be obtained either by comparing the relative importance of the terms involved in the solubility calculation or by considering their evolution with respect to the solvent or solute properties.

Irrespective of the nature of the solvent, the fluidization constant (term *A*), i.e, the removal of the alcohol molecule from its crystal lattice, always represents a barrier, the height of which is inversely related to the solubility. Practically, in a

© 1998 NRC Canada

Table 2. Molar volume and modified nonspecific cohesion parameter of solvents.

Solvent	V_S cm^3 mol^{-1}	δ'_S MPa$^{1/2}$	Solvent	V_S cm^3 mol^{-1}	δ'_S MPa$^{1/2}$
n-Hexane	131.6	14.56	Ethyl decanoate	231.6	18.30
n-Heptane	147.5	14.66	Ethyl undecanoate	244.1	18.21
n-Octane	163.5	15.85	Ethyl dodecanoate	260.3	18.11
n-Nonane	179.7	15.07	Ethyl tetradecanoate	292.8	17.94
n-Decane	195.9	15.14	Ethyl hexadecanoate	325.3	17.80
n-Undecane	213.3	15.25	Isoamyl acetate	148.8	19.27
n-Dodecane	228.6	15.34	Isopropyl myristate	317.0	17.83
n-Tridecane	245.0	15.42	Methyl benzoate	125.0	19.62
n-Tetradecane	260.3	15.49	Methanol	40.7	19.25
n-Pentadecane	277.7	15.56	Ethanol	58.7	17.81
n-Hexadecane	294.1	15.61	1-Propanol	75.1	17.29
Cyclohexane	108.8	14.82	Isopropanol	76.9	16.80
Benzene	89.4	18.95	1-Butanol	92.0	17.16
Toluene	106.9	18.10	2-Butanol	92.4	16.60
CCl_4	97.1	17.04	Isobutanol	92.8	16.14
$CHCl_3$	80.7	18.77	*tert*-Butanol	94.3	15.78
1,2-Diclhoroethane	78.8	20.99	1-Pentanol	108.6	16.85
Nitroethane	71.8	22.44	1-Hexanol	125.2	16.40
Acetonitrile	52.9	23.62	1-Heptanol	141.9	16.39
N,N-Dimethylformamide	77.0	22.15	1-Octanol	158.3	16.38
Pyridine	80.9	20.94	1-Nonanol	174.3	16.37
Acetone	74.0	21.91	1-Decanol	191.6	16.35
Methyl ethyl ketone	90.2	20.90	1-Undecanol	203.5	16.34
Diethyl ether	104.8	18.78	1-Dodecanol	219.8	16.33
Dipropyl ether	141.8	17.96	Ethylene glycol	55.8	19.90
Dibutyl ether	170.3	17.45	Propylene glycol	73.7	19.23
Dipentyl ether	204.0	16.16	1,4-Butanediol	88.9	20.24
Ethyl acetate	98.5	20.79	2,3-Butanediol	91.3	19.40
Butyl acetate	132.5	19.66	1,3-Butanediol	89.4	19.40
Ethyl propionate	115.5	20.05	Methyl cellosolve	79.1	18.63
Ethyl butyrate	132.2	19.61	Cellosolve	97.4	18.63
Ethyl pentanoate	148.5	19.27	Carbitol	136.1	18.60
Ethyl hexanoate	165.6	18.99	Butyl carbitol	170.1	17.40
Ethyl octanoate	198.2	18.59	Water	18.1	20.50
Ethyl nonanoate	215.2	18.43			

given solvent, both experimental and predicted solubilities decrease as one moves forward through the series of the higher 1-alcohols. There is even an almost direct linear relationship between the lowering of the logarithm of the volume fraction solubility and the increase of the fluidization constant (*A* term) as a result of the addition of a methylene group in the hydrocarbon chain on going to higher homologues. Given a particular solvent, more than 90% of the solubility dependence on the length of the paraffin chain is dictated by the melting and transition properties of the pure solid alcohols. Such an evolution means that all parameters other than the crystal properties of the fatty alcohols of interest exert nearly the same influence, or cancel each other to produce the same influence, in determining the solubility in a fixed solvent. In contrast, the solubility of a particular *n*-alcohol or sterol is favorably or unfavorably affected according to whether the solvent is of complexing or non-complexing, polar or nonpolar, nature. Once the melting has occurred, the solute forms a homogeneous solution with the solvent following the solvation process whose enthalpic and entropic contributions determine the overall noncrystalline solubility. At this stage, it is interesting to observe that solvents can be sorted roughly into four groups with respect to their solubilizing capacity for the hydroxy compounds (Fig. 2): the *n*-fatty alcohols and sterols are very insoluble in very polar associated solvents with strong hydrophobic

Table 3. Standard stability constants of hydrogen bond association, K_{OH}, between the alcohol OH group and proton-acceptor sites on the solvent.

Solute donor	Solvent acceptor	K_{OH} cm^3 mol^{-1}
-OH	-C≡N	40.0
-OH	$-NO_2$	40.0
-OH	Arom. ring	200.0
-OH	CH_2Cl_2	200.0
-OH	$CHCl_3$	300.0
-OH	Ketone	2000.0
-OH	Ester	2500.0
-OH	Ether	2500.0
-OH	OH (alcohol)	5000.0
-OH	OH (water)	5000.0

© 1998 NRC Canada

Table 4. Experimental and calculated solubilities of the alkanols and sterols, and the contributions to the solubility (crystalline solubility contributions, *A*, are given in Table 1).

Solute	Solvent	Φ_B^{calc}	Φ_B^{exp}	$\frac{\Phi_B^{calc}}{\Phi_B^{exp}}$	*B*	*D*	*F*	OH	Ref.
1-Dodecanol	*n*-Hexane	0.833	0.848	1.0	0.109	–0.008		–0.175	82
	Cyclohexane	0.892	0.882	1.0	0.107	–0.002		–0.109	78
	Benzene	0.928	0.900	1.0	0.102	–0.003		–0.064	77
	Toluene	0.903	0.890	1.0	0.100	–0.002		–0.089	77
	CCl_4	0.914	0.895	1.0	0.106	–0.000		–0.086	78
	$CHCl_3$	0.941	0.935	1.0	0.099	–0.002		–0.048	83
	Diethyl ether	0.949	0.889	1.1	0.056	–0.001		0.002	83
	Dipropyl ether	0.919	0.856	1.1	0.044	–0.001		–0.018	80
	Dibutyl ether	0.890	0.816	1.1	0.032	–0.001		–0.038	80
	Ethyl acetate	0.925	0.912	1.0	0.058	–0.002		0.005	83
	Butyl acetate	0.926	0.910	1.0	0.048	–0.002		–0.012	83
	Acetone	0.964	0.914	1.1	0.069	–0.002		0.006	83
	2-Butanone	0.954	0.916	1.0	0.066	–0.002		–0.001	83
	Acetonitrile	0.206	0.133	1.6	1.880	–2.008		–1.343	83
	Nitroethane	0.887 E-01	0.199	0.5	1.468	–1.873		–1.907	83
	Methanol	0.978	0.956	1.0	0.096	–0.000	–0.098	0.090	83
	Ethanol (95%)	0.968	0.952	1.0	0.085	–0.000	–0.087	0.080	83
	Isopropanol	0.959	0.925	1.0	0.074	–0.000	–0.076	0.070	83
	1-Butanol	0.952	0.900	1.1	0.066	–0.000	–0.067	0.062	83
	Water	0.662 E-05	0.348 E-05	1.9	6.820	–0.006	–21.087	2.457	84
1-Tetradecanol	*n*-Hexane	0.806	0.574	1.4	0.171	–0.008		–0.204	82
	n-Heptane	0.751	0.453	1.7	0.170	–0.011		–0.270	85
	n-Octane	0.683	0.455	1.5	0.166	–0.014		–0.360	74
	n-Nonane	0.598	0.414	1.4	0.157	–0.014		–0.483	74
	n-Decane	0.482	0.374	1.3	0.144	–0.020		–0.679	74
	n-Undecane	0.356	0.358	1.0	0.115	–0.024		–0.950	74
	n-Dodecane	0.268	0.305	0.9	0.075	–0.024		–1.194	74
	n-Tridecane	0.203	0.284	0.7	0.024	–0.022		–1.420	74
	n-Tetradecane	0.162	0.258	0.6	–0.029	–0.019		–1.598	74
	n-Pentadecane	0.134	0.209	0.6	–0.081	–0.015		–1.737	74
	n-Hexadecane	0.114	0.187	0.6	–0.130	–0.012		–1.853	85
	Cyclohexane	0.866	0.399	2.2	0.169	–0.003		–0.136	78
	Benzene	0.906	0.644	1.4	0.165	–0.006		–0.083	77
	Toluene	0.877	0.606	1.4	0.161	–0.005		–0.112	77
	CCl_4	0.890	0.656	1.4	0.170	–0.001		–0.111	78
	$CHCl_3$	0.922	0.774	1.2	0.159	–0.004		–0.062	83
	Diethyl ether	0.933	0.668	1.4	0.093	–0.001		0.013	83
	Dipropyl ether	0.898	0.521	1.7	0.078	–0.001		–0.011	80
	Dibutyl ether	0.865	0.448	1.9	0.064	–0.001		–0.034	80
	Ethyl acetate	0.937	0.625	1.5	0.096	–0.004		0.017	83
	Butyl acetate	0.906	0.635	1.4	0.084	–0.004		–0.004	83
	Acetone	0.952	0.639	1.5	0.112	–0.004		0.016	83
	2-Butanone	0.938	0.656	1.4	0.108	–0.004		0.007	83
	Acetonitrile	0.575 E-01	0.399 E-01	1.4	2.534	–3.228		–1.988	83
	Nitroethane	0.525 E-01	0.927 E-01	0.6	1.800	–2.480		–2.093	83
	Methanol	0.968	0.828	1.2	0.161	–0.000	–0.168	0.148	83
	Ethanol (95%)	0.955	0.774	1.2	0.144	–0.000	–0.149	0.133	83
	Isopropanol	0.942	0.756	1.2	0.128	–0.000	–0.132	0.119	83
	1-Butanol	0.932	0.658	1.4	0.115	–0.000	–0.119	0.107	79
	1-Hexanol	0.911	0.595	1.5	0.089	–0.000	–0.091	0.083	79
	1-Octanol	0.891	0.547	1.6	0.064	–0.000	–0.065	0.060	79
	1-Decanol	0.872	0.510	1.7	0.040	–0.000	–0.041	0.038	79
	Water	0.512 E-06	0.365 E-06	1.4	7.787	–0.007	–24.678	2.589	84
1-Hexadecanol	*n*-Hexane	0.814 E-01	0.149	0.5	0.898	–0.201		–2.033	82
	n-Heptane	0.611 E-01	0.872 E-01	0.7	0.751	–0.182		–2.192	71

© 1998 NRC Canada

Table 4 (*continued*).

Solute	Solvent	Φ_B^{calc}	Φ_B^{exp}	$\frac{\Phi_B^{calc}}{\Phi_B^{exp}}$	*B*	*D*	*F*	OH	Ref.
	n-Octane	0.514 E-01	0.528 E-01	1.0	0.618	–0.137		–2.278	75
	n-Nonane	0.450 E-01	0.408 E-01	1.1	0.501	–0.091		–2.338	75
	n-Decane	0.386 E-01	0.323 E-01	1.2	0.399	–0.079		–2.404	75
	n-Undecane	0.339 E-01	0.289 E-01	1.2	0.302	–0.060		–2.454	75
	n-Dodecane	0.307 E-01	0.241 E-01	1.3	0.226	–0.047		–2.490	75
	n-Tridecane	0.279 E-01	0.219 E-01	1.3	0.152	–0.037		–2.522	75
	n-Tetradecane	0.256 E-01	0.262 E-01	1.0	0.086	–0.028		–2.549	75
	n-Pentadecane	0.237 E-01	0.169 E-01	1.4	0.024	–0.021		–2.573	75
	n-Hexadecane	0.221 E-01	0.162 E-01	1.3	–0.031	–0.017		–2.593	85
	Cyclohexane	0.192	0.291	0.7	1.072	–0.105		–1.448	71
	Benzene	0.391	0.243	1.6	1.089	–0.157		–0.699	77
	Toluene	0.299	0.231	1.3	0.970	–0.108		–0.899	77
	CCl_4	0.294	0.332	0.9	1.113	–0.062		–1.102	78
	$CHCl_3$	0.507	0.467	1.1	1.027	–0.076		–0.458	83
	Nitroethane	0.477 E-01	0.741 E-02	6.4	2.083	–2.096		–1.856	83
	Diethyl ether	0.617	0.300	2.1	0.581	–0.013		0.122	83
	Dipropyl ether	0.489	0.191	2.5	0.466	–0.012		0.002	80
	Dibutyl ether	0.403	0.142	2.8	0.369	–0.009		–0.097	80
	Ethyl acetate	0.634	0.187	3.4	0.608	–0.034		0.143	83
	Butyl acetate	0.511	0.237	2.2	0.504	–0.036		0.034	83
	Acetone	0.706	0.149	4.7	0.723	–0.039		0.140	83
	2-Butanone	0.639	0.233	2.7	0.678	–0.040		0.086	83
	Methanol	0.545	0.350	1.6	2.024	–0.004	–2.731	1.276	83
	Ethanol (95%)	0.565	0.329	1.7	1.329	–0.002	–1.674	0.949	83
	Isopropanol	0.541	0.379	1.4	1.023	–0.001	–1.240	0.776	71
	1-Butanol	0.517	0.322	1.6	0.855	–0.001	–1.011	0.671	79
	1-Hexanol	0.469	0.290	1.6	0.597	–0.000	–0.677	0.495	79
	1-Octanol	0.426	0.266	1.6	0.418	–0.000	–0.459	0.360	79
	1-Decanol	0.389	0.243	1.6	0.279	–0.000	–0.297	0.248	79
	Water	0.152 E-07	0.284 E-07	0.5	8.745	–0.008	–28.270	2.704	84
1-Octadecanol	*n*-Hexane	0.165 E-01	0.121 E-01	1.4	1.129	–0.257		–2.588	82
	n-Heptane	0.137 E-01	0.140 E-01	1.0	0.947	–0.224		–2.623	72
	n-Octane	0.122 E-01	0.112 E-01	1.1	0.793	–0.165		–2.643	72
	n-Nonane	0.112 E-01	0.111 E-01	1.0	0.660	–0.108		–2.657	72
	n-Decane	0.997 E-02	0.906 E-02	1.1	0.546	–0.093		–2.673	72
	n-Undecane	0.904 E-02	0.818 E-02	1.1	0.439	–0.071		–2.686	72
	n-Dodecane	0.837 E-02	0.803 E-02	1.0	0.355	–0.055		–2.695	72
	n-Tridecane	0.775 E-02	0.669 E-02	1.2	0.275	–0.042		–2.704	72
	n-Tetradecane	0.723 E-02	0.756 E-02	0.9	0.203	–0.033		–2.711	72
	n-Pentadecane	0.678 E-02	0.614 E-02	1.1	0.137	–0.024		–2.717	72
	n-Hexadecane	0.638 E-02	0.577 E-02	1.1	0.077	–0.019		–2.723	76
	Cyclohexane	0.289 E-01	0.449 E-01	0.6	1.456	–0.168		–2.444	71
	Benzene	0.108	0.651 E-01	1.7	1.730	–0.296		–1.272	77
	Toluene	0.749 E-01	0.685 E-01	1.1	1.429	–0.177		–1.455	77
	CCl_4	0.424 E-01	0.977 E-01	0.4	1.663	–0.127		–2.307	78
	$CHCl_3$	0.197	0.235	0.8	1.783	–0.159		–0.861	83
	Diethyl ether	0.347	0.125	2.8	1.083	–0.025		0.274	83
	Dipropyl ether	0.222	0.636 E-01	3.5	0.819	–0.020		0.083	80
	Dibutyl ether	0.161	0.552 E-01	2.9	0.634	–0.014		–0.055	80
	Ethyl acetate	0.366	0.653 E-01	5.6	1.143	–0.069		0.310	83
	Butyl acetate	0.239	0.104	2.3	0.892	–0.065		0.132	83
	Acetone	0.463	0.364 E-01	12.7	1.392	–0.083		0.309	83
	2-Butanone	0.372	0.724 E-01	5.1	1.265	–0.081		0.216	83
	Methanol	0.728 E-01	0.318 E-01	2.3	4.145	–0.010	–6.301	1.935	83
	Ethanol (95%)	0.137	0.112	1.2	2.686	–0.004	–3.803	1.521	83

© 1998 NRC Canada

Table 4 (*continued*).

Solute	Solvent	Φ_B^{calc}	Φ_B^{exp}	$\frac{\Phi_B^{calc}}{\Phi_B^{exp}}$	*B*	*D*	*F*	OH	Ref.
	Isopropanol	0.163	0.105	1.6	1.951	–0.001	–2.617	1.241	71
	1-Butanol	0.168	0.110	1.5	1.574	–0.003	–2.038	1.070	79
	1-Hexanol	0.161	0.116	1.4	1.057	–0.000	–1.287	0.793	79
	1-Octanol	0.147	0.113	1.3	0.738	–0.000	–0.857	0.591	79
	1-Decanol	0.133	0.104	1.3	0.510	–0.000	–0.569	0.429	79
	Water	0.356 E-09	0.120 E-08	0.3	9.697	–0.009	–31.861	2.806	84
1-Eicosanol	*n*-Heptane	0.136 E-01	0.984 E-02	1.4	1.104	–0.247		–2.550	71
	n-Octane	0.121 E-01	0.110 E-01	1.1	0.940	–0.182		–2.568	73
	n-Nonane	0.110 E-01	0.856 E-02	1.3	0.798	–0.119		–2.581	73
	n-Decane	0.977 E-02	0.690 E-02	1.4	0.677	–0.102		–2.597	73
	n-Undecane	0.883 E-02	0.801 E-02	1.1	0.563	–0.078		–2.609	73
	n-Dodecane	0.815 E-02	0.688 E-02	1.2	0.474	–0.060		–2.617	73
	n-Tridecane	0.753 E-02	0.142 E-01	0.5	0.389	–0.047		–2.625	73
	n-Tetradecane	0.701 E-02	0.837 E-02	0.8	0.313	–0.036		–2.632	73
	n-Pentadecane	0.656 E-02	0.579 E-02	1.1	0.243	–0.027		–2.638	73
	n-Hexadecane	0.616 E-02	0.488 E-02	1.3	0.180	–0.021		–2.643	76
	Cyclohexane	0.279 E-01	0.421 E-01	0.7	1.648	–0.185		–2.373	71
	Isopropanol	0.123	0.465 E-01	2.7	2.262	–0.001	–3.111	1.363	71
	1-Butanol	0.132	0.604 E-01	2.2	1.832	–0.003	–2.431	1.186	79
	1-Hexanol	0.133	0.707 E-01	1.9	1.247	–0.000	–1.555	0.898	79
	1-Octanol	0.124	0.676 E-01	1.8	0.891	–0.001	–1.060	0.688	79
	1-Decanol	0.113	0.608 E-01	1.9	0.641	–0.001	–0.732	0.521	79
Cholesterol	Cyclohexane	0.325 E-01	0.326 E-01	1.0	1.880	–0.323		–2.277	70
	Benzene	0.145	0.123	1.2	2.117	–0.278		–1.062	70
	Toluene	0.998 E-01	0.176	0.6	1.804	–0.154		–1.248	70
	1,2-Dichloroethane	0.254 E-02	0.124 E-01	0.2	2.772	–3.447		–2.593	70
	CCl_4	0.665 E-01	0.267	0.3	2.081	–0.075		–2.009	70
	$CHCl_3$	0.245	0.979 E-01	2.5	2.130	–0.144		–0.688	70
	Methanol	0.270 E-01	0.521 E-02	5.2	5.299	–0.011	–8.362	2.170	86
	Ethanol (95%)	0.706 E-01	0.210 E-01	3.4	3.543	–0.004	–5.253	1.770	86
	1-Propanol	0.991 E-01	0.501 E-01	2.0	2.674	–0.002	–3.784	1.506	86
	1-Butanol	0.114	0.546 E-01	2.1	2.114	–0.002	–2.874	1.299	86
	1-Pentanol	0.120	0.889 E-01	1.4	1.736	–0.001	–2.283	1.137	86
	1-Hexanol	0.121	0.100	1.2	1.457	–0.000	–1.862	1.003	86
	1-Heptanol	0.120	0.127	0.9	1.238	–0.000	–1.542	0.888	86
	1-Octanol	0.117	0.106	1.1	1.064	–0.000	–1.296	0.787	86
	1-Nonanol	0.113	0.993 E-01	1.1	0.921	–0.000	–1.101	0.703	86
	1-Decanol	0.108	0.136	0.8	0.790	–0.000	–0.926	0.620	86
	Water	0.180 E-11	0.273 E-07		11.823	–0.010	–39.149	3.000	87
Cholesterol (37°C)	Cyclohexane	0.108	0.108	1.0	1.753	–0.264		–1.755	70
	Tetradecane (38°C)	0.178 E-01	0.256 E-01	0.7	0.445	–0.096		–2.419	88
	1,2-Dichloroethane	0.656 E-02	0.482 E-01	0.1	2.762	–3.287		–2.544	70
	$CHCl_3$	0.428	0.159	2.7	1.678	–0.097		–0.472	70
	CCl_4	0.222	0.341	0.7	1.781	–0.050		–1.280	70
	Benzene	0.318	0.258	1.2	1.745	–0.196		–0.738	70
	Toluene	0.238	0.293	0.8	1.564	–0.117		–0.925	70
	Acetone	0.637	0.394 E-01	16.2	1.246	–0.058		0.318	89
	Acetonitrile	0.134 E-01	0.211 E-02	6.4	4.142	–4.524		–1.974	89
	N,N-Dimeformamide	0.101 E-02	0.473 E-02	0.2	2.845	–5.172		–2.612	86
	Methyl benzoate	0.456	0.943 E-01	4.8	0.962	–0.042		0.250	86
	Isoamyl acetate	0.376	0.956 E-01	3.9	0.857	–0.045		0.166	86
	Isopropyl myristate	0.114	0.611 E-01	1.9	0.196	–0.035		–0.379	86
	Ethyl acetate	0.556	0.687 E-01	8.1	1.079	–0.049		0.340	86
	Ethyl propionate	0.489	0.891 E-01	5.5	1.006	–0.046		0.283	86
	Ethyl butyrate	0.429	0.904 E-01	4.7	0.932	–0.046		0.225	86

© 1998 NRC Canada

Table 4 (*concluded*).

Solute	Solvent	Φ_B^{calc}	Φ_B^{exp}	$\frac{\Phi_B^{calc}}{\Phi_B^{exp}}$	*B*	*D*	*F*	OH	Ref.
	Ethyl pentanoate	0.377	0.978 E-01	3.9	0.858	–0.045		0.167	86
	Ethyl hexanoate	0.328	0.895 E-01	3.7	0.781	–0.044		0.106	86
	Ethyl octanoate	0.253	0.874 E-01	2.9	0.635	–0.043		–0.010	86
	Ethyl nonanoate	0.222	0.845 E-01	2.6	0.562	–0.041		–0.069	86
	Ethyl decanoate	0.197	0.787 E-01	2.5	0.495	–0.040		–0.124	86
	Ethyl undecanoate	0.180	0.903 E-01	2.0	0.445	–0.040		–0.165	86
	Ethyl dodecanoate	0.161	0.760 E-01	2.1	0.385	–0.039		–0.216	86
	Ethyl teradecanoate	0.131	0.704 E-01	1.9	0.272	–0.037		–0.313	86
	Ethyl hexadedanoate	0.108	0.689 E-01	1.6	0.172	–0.034		–0.401	86
	Methanol	0.637 E-01	0.105 E-01	6.1	5.125	–0.010	–8.047	2.136	89
	Ethanol	0.173	0.385 E-01	4.5	3.206	–0.003	–4.675	1.675	89
	1-Propanol	0.230	0.821 E-01	2.8	2.337	–0.002	–3.232	1.386	86
	Isopropanol	0.234	0.451 E-01	5.2	2.271	–0.003	–3.125	1.361	86
	1-Butanol	0.252	0.841 E-01	3.0	1.829	–0.002	–2.426	1.179	86
	Isobutanol	0.253	0.850 E-01	3.0	1.809	–0.000	–2.396	1.170	86
	sec-Butanol	0.253	0.106	2.4	1.819	–0.000	–2.410	1.174	86
	tert-Butanol	0.254	0.185 E-01	13.7	1.775	–0.001	–2.344	1.155	86
	1-Pentanol	0.257	0.132	2.0	1.502	–0.001	–1.929	1.026	86
	1-Hexanol	0.254	0.138	1.8	1.265	–0.000	–1.581	0.903	86
	1-Heptanol	0.247	0.169	1.5	1.080	–0.000	–1.319	0.799	86
	1-Octanol	0.239	0.143	1.7	0.933	–0.000	–1.116	0.710	86
	1-Nonanol	0.231	0.137	1.7	0.808	–0.000	–0.948	0.631	86
	1-Decanol	0.222	0.170	1.3	0.700	–0.000	–0.808	0.559	86
	1-Undecanol	0.216	0.184	1.2	0.632	–0.000	–0.721	0.512	86
	1-Dodecanol	0.207	0.964 E-01	2.1	0.548	–0.000	–0.616	0.452	86
	Methyl cellosolve	0.236	0.255 E-01	9.2	2.198	–0.010	–3.008	1.332	86
	Cellosolve	0.252	0.775 E-01	3.2	1.714	–0.012	–2.250	1.127	86
	Carbitol	0.246	0.489 E-01	5.0	1.144	–0.016	–1.409	0.836	86
	Butyl carbitol	0.232	0.935 E-01	2.5	0.843	–0.005	–0.995	0.654	86
	Ethylene glycol	0.307 E-03	0.289 E-03	1.1	3.957	–0.022	–11.943	1.878	86
	Propylene glycol	0.256 E-02	0.172 E-02	1.5	2.976	–0.017	–8.575	1.605	86
	1,3-Butanediol	0.783 E-02	0.151 E-02	5.2	2.405	–0.025	–6.683	1.411	86
	2,3-Butanediol	0.871 E-02	0.607 E-02	1.4	2.348	–0.026	–6.497	1.390	86
	1,4-Butanediol	0.749 E-02	0.207 E-02	3.6	2.421	–0.041	–6.734	1.417	86
β-Sitosterol (37°C)	Acetone	0.547	0.400 E-01	13.7	1.661	–0.081		0.437	89
	Methanol	0.209 E-01	0.527 E-02	4.0	5.832	–0.011	–9.329	2.261	89
	Ethanol	0.642 E-01	0.299 E-01	2.1	3.913	–0.004	–5.895	1.861	89
	1-Propanol	0.978 E-01	0.175	0.6	2.951	–0.002	–4.245	1.591	86
	1-Butanol	0.118	0.224	0.5	2.333	–0.002	–3.225	1.379	86
	1-Pentanol	0.128	0.248	0.5	1.920	–0.001	–2.568	1.214	86
	1-Hexanol	0.132	0.256	0.5	1.618	–0.000	–2.104	1.078	86
	1-Heptanol	0.132	0.244	0.5	1.384	–0.000	–1.754	0.962	86
	1-Octanol	0.129	0.246	0.5	1.198	–0.000	–1.486	0.862	86
	1-Nonanol	0.126	0.245	0.5	1.043	–0.000	–1.267	0.773	86
	1-Decanol	0.122	0.248	0.5	0.910	–0.000	–1.085	0.693	86

propensity, such as water or diols, but have appreciable solubility either in associated solvents with moderate hydrophic propensity, like alcohols, or in nonpolar solvents like the aliphatic hydrocarbons. The highest solubilities are observed in proton-acceptor aprotic solvents with partial polarity, such as aromatics, ethers, esters, and ketones. A more in-depth analysis of the various contributions encoded in the overall solubility value can then reveal, for each class of solvents, which physical elementary processes are responsible for the alcohol noncrystalline solubility.

1. In aprotic noncomplexing solvents, the sum of the *B*, *D*, and OH terms is negative or close to zero. Because of the closeness of the modified nonspecific cohesion parameters between these solvents and the hydroxy compounds, the *D* component generally remains very low, and the noncrystalline solubility of the higher 1-alcohols and sterols thus results essentially from the balance between the *B* and OH terms. In such solvents, the solute–solute self-association in solution, not being counterbalanced by the formation of strong intermolecular interactions, disfavors the solubility process (OH term

© 1998 NRC Canada

Fig. 1. Predicted vs. experimental volume fraction solubility of the *n*-fatty alcohols and sterols.

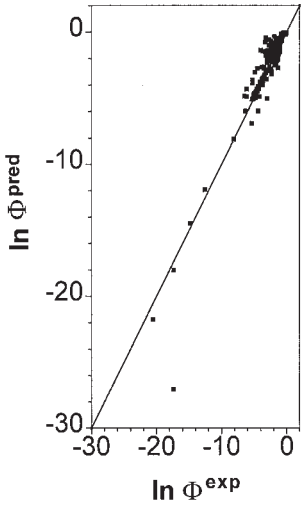

Fig. 2. Neperian logarithm of the experimental volume fraction solubility of the *n*-fatty alcohols and sterols versus the *B*+*D*+OH noncrystalline solubility contribution.

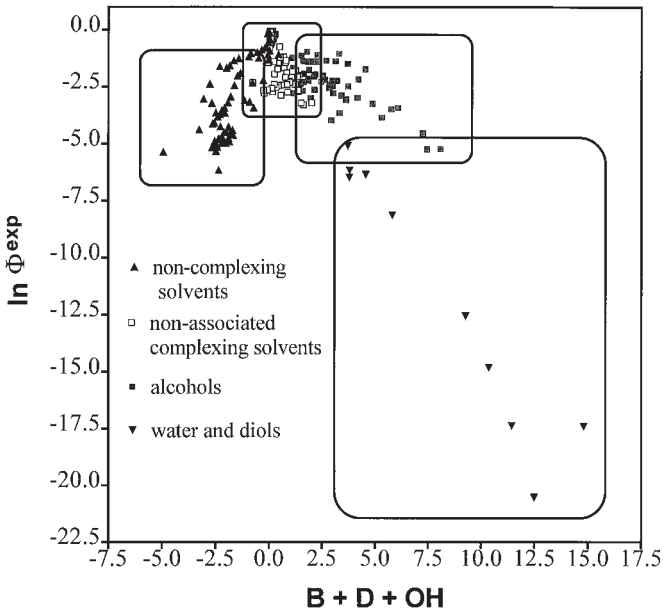

is negative). This explains why the hydroxy compounds are generally less soluble in aprotic noncomplexing solvents than in aprotic but complexing solvents of similar volume. For instance, the volume fraction solubilities of all *n*-fatty alcohols are always lower in *n*-hexane than in *n*-butyl acetate. Furthermore, the continuous lowering of the alcohol solubility with increasing alkyl chain length of the hydrocarbons used as solvents (Fig. 3) can also be explained from a consideration of the *B* and OH terms. Given a solute, any increase of the solvent size by addition of a methylene group in the homologous alkane series acts against solubility by simultaneously reducing the positive *B* term and increasing the unfavorable OH term.

2. In aprotic complexing solvents (aromatic hydrocarbons, halogenated hydrocarbons, ethers, esters, ketones), the addition of the *B*, *D,* and OH contributions is in most cases positive. As the *D* values remain generally low, the noncrystalline solubility of the 1-alcohols and sterols in these solvents is still governed by the balance between the *B* and OH terms. However, if the hydroxy compounds appear to be more soluble in the present class of solvents than in the previous one, this does not result from an increase of the positive *B* term, but rather stems from the less negative OH contribution. The solubility in polar non-associated complexing solvents is in fact enhanced by the formation of specific molecular interactions between the proton-donor hydroxyl group of the solute and the various proton-acceptor sites of the solvents. These intermolecular H-bonds sometimes counterbalance, but overcome in most cases the alcohol–alcohol self-association as demonstrated by the existence of slightly negative and positive values of the OH term, which expresses the net result of the two opposite effects. In the present class of solvents, as in the previous one, any increase in the molar volume of the solvent in a chemical homologous series leads to both the decrease in the *B* term and the increase in the OH term, resulting in a lowering of the solubility. Indeed, although more irregular, the solubility profile of cholesterol versus the carbon chain length of the ethyl carboxylate derivatives at 37°C (Fig. 4) presents the same trend as that given by the sum of the *B* and OH solubility components.

3. In the third group of solvents, namely, the alkanols, the sum of the *B* and *D* terms favors the solubility, and the OH term is even more positive than in the previous classes. Although, in these solvents, the insertion of the fatty alcohol molecules into the molecular hydrogen bond chains of the solvent contributes more efficiently to promoting the solubility process, the solubility values remain generally lower than those observed in ketones, ethers, or esters, but are rather comparable to those observed in the aliphatic hydrocarbons of similar volume. The reason for such behavior is that, in amphiphilic solvents and in alkanols in particular, the noncrystalline part of the solubility is not only determined by the sum of the *B* and OH components (*D* term ≈ 0), but is also ruled by an additional component, i.e., the hydrophobic effect (*F* term), which acts against solubility. Practically, this effect related to the solvent–solvent self-association reduces the solubility by a factor depending on the solute/solvent molar volume ratio. According to whether or not the *F* term predominates over the other solubility components, one can expect that the solubility will either increase (19), decrease, or pass through a maximum with increasing alkyl chain length of the alkanol solvent molecules. Actually, the hydrophobic propensity of the alkanols towards the *n*-fatty alcohols and sterols remains relatively small because of the possible insertion of the solute molecules into the solvent H-bond chains, and two types of solubility pattern are experimentally observed (Fig. 5). On the one hand, for the lower solid *n*-fatty alcohols, i.e., 1-dodecanol and 1-tetradecanol, the plots of the experimental solubility versus the carbon chain length of the alkanol are similar to those previously observed for *n*-fatty alcohol solubility in the alkane or

© 1998 NRC Canada

Fig. 3. Comparison between the experimental solubility profile and the variation of the non-crystalline solubility components (*B*+OH) of 1-tetradecanol and 1-octadecanol in the *n*-alkane series (C_6–C_{16}).

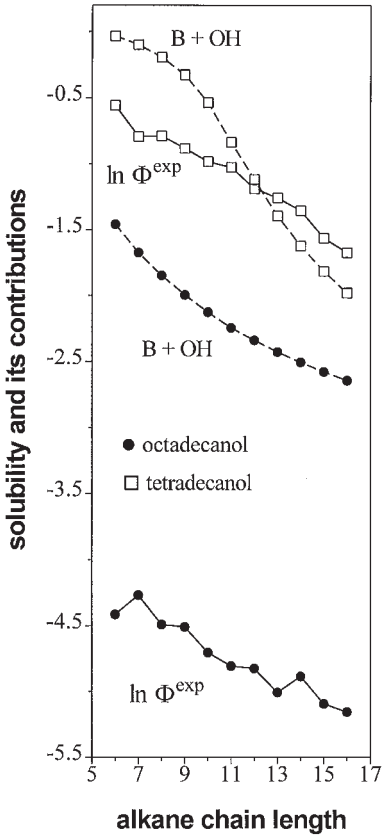

Fig. 4. Comparison between the experimental solubility profile and the variation of the non-crystalline solubility components (*B*+OH) of cholesterol in the homologous ethyl carboxylate series at 37°C.

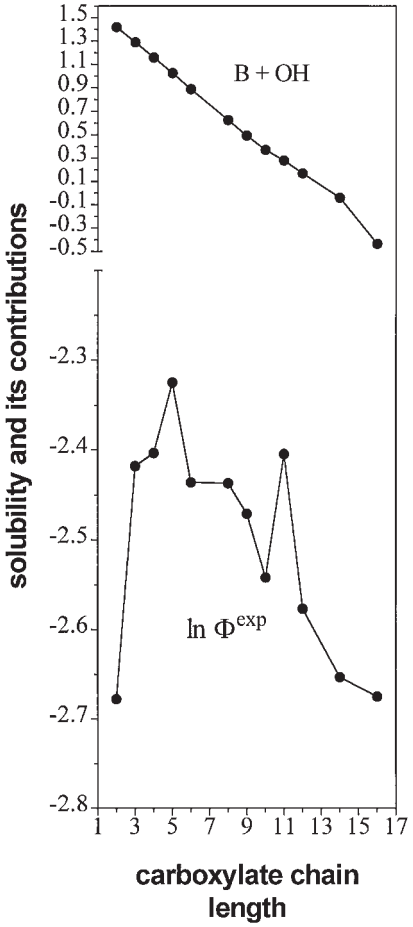

ethyl carboxylate series: the solubility decreases with the increasing length of the alkyl chain of the alkanol. On the other hand, for the upper *n*-fatty alcohols and for the sterols, a maximum of the solubility is observed in the curves presenting the experimental solubility versus the alkanol carbon chain length: the solubility first sharply increases up to a maximum (the position of which varies from one solute to another between a length of six and seven carbon atoms), and then slowly decreases with further lengthening in the alkanol chain length. It is remarkable that both types of behavior are correctly accounted for by the sum of the *B*, *F*, and OH components involved in the solubility estimation. The present thermodynamic solubility model is thus also able to account for subtle changes concerning the dependence of the solubility on the molar size of the solvent.

4. The fourth category of solvents is represented by water and diols. In these solvents, the solubilities of the *n*-fatty alcohols and sterols are the lowest observed, notwithstanding the fact that the positive *B* and OH contributions are larger than in the other groups of solvents, and that the negative *D* contributions remain close to zero. In fact, in water and diols, the solubilities are predominantly governed by the hydrophobic effect (*F* term). The very large hydrophobic propensity of these solvents towards the alcohol substances is due either to the exceptional smallness of the water molar volume with respect to that of the fatty alcohol and sterol molecules ($V_B >> V_S$), or to the fact that the water and diol molecules are involved in double hydrogen bond chains ($r_s = 2$). Practically, the solubility is reduced by a factor of $2V_B/V_S$. In these solvents, the extremely important loss of the mobile order entropy of the H-bonded solvent molecules following the addition of the solute cannot be counterbalanced by the exothermic energy gained by the various solute–solvent specific interactions. A direct consequence of the hydrophobic effect is that any increase of the molar volume of the solute, which normally promotes its noncrystalline solubility in non-associated solvents via the *B* term of the solubility equation, will lessen it in water and diols because of the *F* contribution.

The foregoing analysis thus provides better understanding of the factors that govern the solubility of the *n*-fatty alcohols as well as some practical rules that might help in choosing a suitable solvent system for a substance involving a hydroxyl amphiphilic group.

4. Conclusion

Based on the knowledge of a limited number of physicochemical parameters characterizing both the high molecular weight alcohols and solvent molecules and their specific interactions in solution, the mobile-order-derived solubility equation permits reliable predictions of the solubilities of solid *n*-fatty alcohols and sterols in common organic solvents including

© 1998 NRC Canada

Fig. 5. Comparison between the experimental solubility profile and the variation of the non-crystalline solubility components (*B*+*F*+OH) of 1-tetradecanol and 1-octadecanol in the 1-alkanol series (C_1–C_{10}).

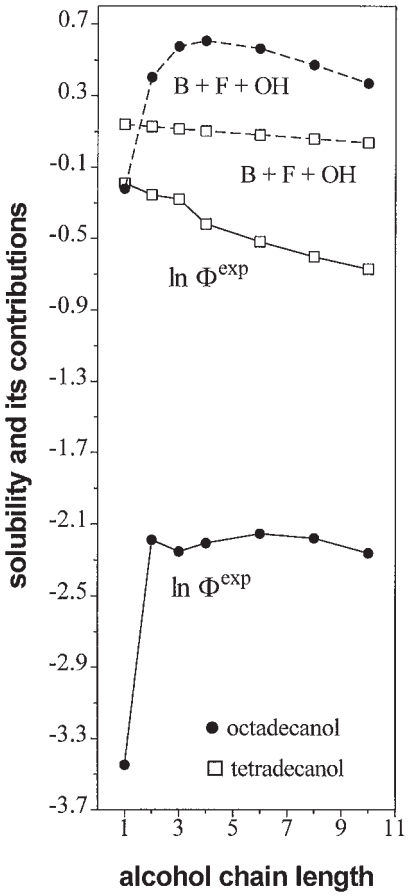

water. The model provides better understanding of their solution process by assessing the factors that determine their solubility behavior. By considering the relative importance of the noncrystalline solubility components involved in the solubility calculation, four groups of solvents can be differentiated with respect to their solubilizing capacity: the aliphatic hydrocarbons, the non-associated polar solvents, the alkanols, and water and diols. Furthermore, the detailed analysis of the solubility components provides both the grounds for the *n*-fatty alcohol and sterol solubility dependence on the solvent carbon chain length for different homologous chemical series of solvents, and the interpretation of the solubility differences between the *n*-fatty alcohols in a particular solvent. At the present time, the solubility theory has a sound theoretical basis, and a priori prediction of solubility in a number of systems has become a reality.

Acknowledgment

The authors thank Professor P.L. Huyskens for stimulating discussions.

References

1. J.H. Hildebrand and R.L. Scott. Regular solutions. Prentice-Hall, New York. 1962.
2. J.H. Hildebrand, J.M. Prausnitz, and R.L. Scott. Regular and related solutions. Van Nostrand Reinhold, New York. 1970.
3. A. Martin, A.N. Paruta, and A. Adjei. J. Pharm. Sci. **70**, 1115 (1981).
4. A. Beerbower, P.L. Wu, and A. Martin. J. Pharm. Sci. **73**, 179 (1984).
5. A. Martin, P.L. Wu, and A. Beerbower. J. Pharm. Sci. **73**. 188 (1984).
6. J. Barra, F. Lescure, E. Doelker, and P. Bustamante. J. Pharm. Pharmacol. **49**, 644 (1997).
7. S. Romero, A. Reillo, B. Escalera, and P. Bustamante. Chem. Pharm. Bull. **44**, 1061 (1996).
8. A. Regosz, A. Chmielewska, T. Pelplinska, and P. Kowalski. Pharmazie, **49**, 371 (1994).
9. C. Sunwoo and H. Eisen. J. Pharm. Sci. **60**, 238 (1971).
10. P.L. Huyskens and M.C. Haulait-Pirson. J. Mol. Liq. **31**, 135 (1985).
11. P.L. Huyskens and G.G. Siegel. Bull. Soc. Chim. Belg. **97**, 809 (1988).
12. P.L. Huyskens. J. Mol. Struct. **274**, 223 (1992).
13. P.L. Huyskens and F. Kapuku, and C. Colemonts-Vandevyvere. J. Mol. Struct. **237**, 207 (1990).
14. P.L. Huyskens. J. Mol. Struct. **297**, 141 (1993).
15. P.L. Huyskens, D.P. Huyskens, and G.G. Siegel. J. Mol. Liq. **64**, 283 (1995).
16. W.E. Acree, Jr., J.R. Powell, M.E.R. McHale, S. Pandey, T.L. Borders, and S.W. Campbell. Trends Phys. Chem. **6**, 197 (1997).
17. P.L. Huyskens, M.C. Haulait-Pirson, G.G. Siegel, and F. Kapuku. J. Phys. Chem. **92**, 6841 (1988).
18. P. Ruelle, C. Rey-Mermet, M. Buchmann, N.-T. Hô, U.W. Kesselring, and P.L. Huyskens. Pharm. Res. **8**, 840 (1991).
19. P. Ruelle, M. Buchmann, H.-T. Hô, and U.W. Kesselring. Int. J. Pharm. **87**, 47 (1992).
20. P.Ruelle, M. Buchmann, H.-T. Hô, and U.W. Kesslering. Environ. Sci. Technol. **27**, 266 (1993).
21. P. Ruelle, M. Buchmann, and U.W. Kesselring. J. Pharm. Sci. **83**, 396 (1994).
22. P. Ruelle and U.W. Kesselring. Chemosphere, **34**, 275 (1997).
23. J.R. Powell, D. Voisinet, A. Salazar, and W.E. Acree, Jr. Phys. Chem.Liq. **28**, 269 (1994).
24. K.A.Fletcher, S. Pandey, M.E.R McHale, and W.E Acree, Jr. Phys. Chem. Liq. **33**, 181 (1996).
25. K.A. Fletcher, M.E.R. McHale, K.S. Coym, and W.E. Acree, Jr. Can. J. Chem. **75**, 258 (1997).
26. K.A. Fletcher, M.E.R. McHale, J.R. Powell, K.S. Coym, and W.E. Acree, Jr. Phys. Chem. Liq. **34**, 41 (1997).
27. K.A. Fletcher, K.S. Coym, L.S. Roy, C.E. Hernández, M.E.R. McHale, and W.E. Acree, Jr. Phys. Chem. Liq. **35**, 243 (1998).
28. P. Ruelle and U.W. Kesselring. J. Mol. Liq. **67**, 81 (1995).
29. W.E. Acree, Jr. and S.A. Tucker. Int. J. Pharm. **101**, 199 (1994).
30. A.I. Zvaigzne, J.R. Powell, W.E. Acree, Jr., and S.W. Campbell. Fluid Phase Equilib. **121**, 1 (1996).
31. M.E.R. McHale, J.R. Powell, A.-S.M. Kauppila, W.E. Acree, Jr., and P.L. Huyskens. J. Solution Chem. **25**, 1089 (1996).
32. M.E.R. McHale, A.I. Zvaigzne, J.R. Powell, A.-S.M. Kauppila, W.E Acree, Jr., and S.W. Campbell. Phys. Chem. Liq. **32**, 67 (1996).
33. M.E.R. McHale, K.A. Fletcher, K.S. Coym, W.E. Acree, Jr., V.G.Varanasi, and S.W. Campbell. Phys. Chem. Liq., **34**, 103 (1997).
34. P. Ruelle, N.-T. Hô, M. Buchmann, and U.W. Kesselring. J. Comput.-Aided Mol. Des. **6**, 431 (1992).
35. P. Ruelle and U.W.Kesselring. J. Solution Chem. **25**, 657 (1996).
36. P. Ruelle, E. Sarraf, L. Van Den Verge, K. Seghers, M. Buchmann, and U.W. Kesselring. Pharm. Acta Helv. **68**, 49 (1993).
37. P. Ruelle and U.W. Kesselring. Pharm. Res. **11**, 201 (1994).

© 1998 NRC Canada

38. P. Ruelle and U.W. Kesselring. J. Chem. Soc. Faraday Trans. **93**, 2049 (1997).
39. P. Ruelle, A. Fãrina-Cuendet, and U.W. Kesselring. Int. J. Pharm. **157**, 219 (1997).
40. P.L. Huyskens, K. Seghers, and H. Morissen. Fluid Phase Equilib. **96**, 1 (1994).
41. P.L. Huyskens and K. Seghers. J. Mol. Struct. **322**, 75 (1994).
42. P. Ruelle and U.W. Kesselring. J. Pharm. Sci. **86**, 179 (1997).
43. P. Ruelle and U.W. Kesselring. Pharm. Res. **12**, S-203 (1995).
44. P. Huyskens, M. Van Beylen, and H. Verheyden. Pure Appl. Chem. **68**, 1535 (1996).
45. P.L. Huyskens, F. Huyskens, and K. Nelis. Bull. Pol. Acad. Sci. Chem. **42**, 389 (1994).
46. M. Van Beylen, P. Jappens-Loosen, and D. Huyskens. J. Mol. Liq. **67**, 1 (1995).
47. P. Huyskens, K. Platteborze, and T. Zeegers-Huyskens. J. Mol. Struct. **437**, 91 (1997).
48. P.L. Huyskens, F. Vandenbroeck, and T. Zeegers-Huyskens. J. Mol. Struct. **416**, 91 (1997).
49. P. Huyskens, H. Verheyden, P. Van Lierde, J. Bastiaens, and B. Kapuku. J. Mol. Liq. **73–74**, 41 (1997).
50. P. Ruelle, M. Buchmann, N.-T. Hô, and U.W. Kesselring. Pharm. Res. **9**, 788 (1992).
51. K.C. James. *In* Drugs and the pharmaceutical sciences. Vol. 28. *Edited by* J. Swarbrick. Marcel Dekker, New York. 1986. p. 130.
52. R.F. Weimer and J.M. Prausnitz. J. Chem. Phys. **42**, 3643 (1965).
53. P.B. Choi and E. McLaughlin. AIChE J. **29**, 150 (1983).
54. J.E. Coon, J.E. Auwaerter, and E. McLaughlin. Fluid Phase Equilib. **44**, 305 (1989).
55. K.C. James. *In* Drugs and the pharmaceutical sciences. Vol. 28. *Edited by* J. Swarbrick. Marcel Dekker, New York. 1986. p. 161.
56. P. Ruelle, E. Sarraf, and U.W. Kesselring. Int. J. Pharm. **104**, 125 (1994).
57. Z. Liron and S. Cohen. J. Pharm. Sci. **72**, 499 (1983).
58. S.H. Yalkowsky. Ind. Eng. Chem. Fundam. **18**, 108 (1979)
59. A. Watanabe. Bull. Chem. Soc. Jpn. **34**, 1728 (1964).
60. Y.K. Kuchhal, R.N.Shukla, and A.B. Biswas. Thermochim. Acta, **31**, 61 (1979).
61. Y.K. Kuchhal, R.N. Shukla, and A.B. Biswas. Indian J. Chem. **20A**, 837 (1981).
62. J.D. Meyer and E.E. Reid. J. Am. Chem. Soc. **55**, 1574 (1933).
63. J.D. Hoffman and C.P. Smyth. J. Am. Chem. Soc. **71**, 431 (1949).
64. C. Mosselman, J. Mourik, and H. Dekker. J. Chem. Thermodyn. **6**, 477 (1974).
65. T. Eckert and J. Müller. Arch. Pharm. **311**, 31 (1978).
66. M. Davies and B. Kybett. Trans. Faraday Soc. **61**, 1608, 2646 (1965).
67. N. Garti, L. Karpuj, and S. Sarig. Thermochim. Acta, **35**, 343 (1980).
68. N. Garti, L. Karpuj, and S. Sarig. Cryst. Res. Technol. **16**, 1111 (1981).
69. T. Hofman, B. Barbés, and C. Casanova. Ber. Bunsen-Ges. Phys. Chem. **102**, 25 (1998).
70. U. Domanska, C. Klofutar, and S. Paljk. Fluid Phase Equilib. **97**, 191 (1994).
71. U. Domanska and A.M. Szafranski. Int. DATA Ser. Sel. Data Mixtures, Ser. A: **4**, 277 (1987).
72. U. Domanska and J. Rolinska. Int. DATA Ser. Sel. Data Mixtures, Ser. A: **1**, 1 (1991).
73. U. Domanska and J. Rolinska. Int. DATA Ser. Sel. Data Mixtures, Ser. A: **2**, 90 (1991).
74. U. Domanska and J. Rolinska. Int. DATA Ser. Sel. Data Mixtures, Ser. A: **2**, 76 (1992).
75. U. Domanska and J. Rolinska. Int. DATA Ser. Sel. Data Mixtures, Ser. A: **2**, 84 (1992).
76. U. Domanska and J. Rolinska. Fluid Phase Equilib. **86**, 233 (1993).
77. U. Domanska and J.A. Gonzalez. Fluid Phase Equilib. **119**, 131 (1996).
78. U. Domanska and J.A. Gonzalez. Fluid Phase Equilib. **123**, 167 (1996).
79. U. Domanska and J.A. Gonzalez. Fluid Phase Equilib. **129**, 139 (1997).
80. J. Rolinska, E. Krumplewska, and T. Hofman. Fluid Phase Equilib. **119**, 131 (1996).
81. A.F.M. Barton (*Editor*). CRC handbook of solubility parameters and other cohesion parameters. CRC Press, Boca Raton, Fla. 1983.
82. C.W. Hoerr and H.J. Harwood. J. Org. Chem. **16**, 779 (1951).
83. C.W. Hoerr, H.J. Harwood, and A.W. Ralston. J. Org. Chem. **9**, 267 (1944).
84. T. Suzuki. J. Comput.-Aided Mol. Des. **5**, 149 (1991).
85. U. Domanska. Fluid Phase Equilib. **114**, 175 (1996).
86. G.L. Flynn, Y. Shah, S. Prakongpan, K.H. Kwan, W.I. Higuchi, and A.F. Hofmann. J. Pharm. Sci. **68**, 1090 (1979).
87. S. Budavari (*Editor*). The Merck Index. An encyclopedia of chemicals, drugs, and biologicals. 11th ed. Rahway, N. J., U.S.A. 1989.
88. S. Pal and S.P. Moulik. Indian J. Biochem. Biophys. **24**, 24 (1987).
89. L.-K. Bar, N. Garti, S. Sarig, and R. Bar. J. Chem. Eng. Data, **29**, 440 (1984).

© 1998 NRC Canada

Ab initio conformational analysis of the model tripeptide *N*-formyl-L-alanyl-L-alanine amide

Michael Ramek, Ching-Hsing Yu, and Lothar Schäfer

Abstract: The ab initio conformational energy minima of the model tripeptide *N*-formyl-L-alanyl-L-alanine amide (ALA-ALA) were determined by ab initio RHF/4-21G and RHF/6-31G* gradient geometry refinement. For the current investigation, 11 664 RHF/4-21G structures were optimized, representing grid points in the four-dimensional (ϕ_1, ψ_1, ϕ_2, ψ_2) conformational space, which were constructed in 40° increments along the outer torsions ϕ_1 and ψ_2 and in 30° increments along the inner torsions ψ_1 and ϕ_2 of ALA-ALA. Two new energy minima, previously not reported, are described. The positions of the RHF/6-31G* energy minima in ϕ,ψ-space can differ significantly from the corresponding RHF/4-21G locations, and both sets are not clustered in the centers but on the fringes of the most populated regions of ϕ,ψ-space in protein crystal structures. Thus, the torsion angles of the ab initio energy minima are not those of the typical substructures of proteins: the most stable helices are not α_R, and the torsion angles of the most stable bend forms are not those most frequently encountered in protein bends. Limitations of the dipeptide approximation are explored, illustrating how the conformational energies of an amino acid residue depend on the state of its neighbor.

Key words: alanyl alanine amide, dipeptide approximation, model tripeptide, peptide models, structure of peptides.

Résumé : On a effectué des calculs ab initio, RHF/4-21G et RHF/6-31G* avec affinement de gradient de la géométrie, de minimums d'énergie conformationnelle du tripeptide modèle *N*-formyl-L-alanyl-L-alanine amide (ALA-ALA). Pour la présente étude, on a optimisé 11 664 structures RHF/4-21G qui représentent des points de la grille de l'espace conformationnel en quatre dimensions (ϕ_1, ψ_1, ϕ_2, ψ_2) construits avec des augmentations de 40° autour des torsions externes, ψ_1 et ϕ_2, et des augmentations de 30° le long des torsions internes, ψ_1 et ϕ_2, de ALA-ALA. On décrit deux nouveaux minimums qui n'avaient pas été rapportés antérieurement. Les positions des minimums d'énergie RHF/6-31G* dans l'espace ϕ,ψ peuvent être assez différents des locations correspondantes de RHF/4-21G; les deux ensembles ne sont toutefois pas groupés dans les centres, mais plutôt sur les bordures des régions les plus populeuses de l'espace ϕ,ψ des structures cristallines de la protéine. Ainsi, les angles de torsion des minimums d'énergie ab initio ne correspondent pas à ceux des sous-structures types des protéines: les hélices les plus stables ne sont pas α_R et les angles de torsion des formes courbées les plus stables ne sont pas celles que l'on rencontre le plus fréquemment dans les courbures des protéines. On a exploré les limitations de l'approximation du dipeptide qui montrent comment les énergies conformationnelles d'un résidu d'acide aminé dépend de l'état de son voisin.

Mots clés : alanyl alanine amide, approximation du dipeptide, tripeptide modèle, modèles de peptide, structure de peptides.

[Traduit par la rédaction]

Introduction

Model tripeptides, such as the *N*-formyl or *N*-acetyl derivatives of diamino acid amides, are of great interest in computational chemistry because they allow for the computer modeling of structural aspects of relevance for larger systems, such as oligopeptides and proteins (1–21), which are not readily amenable to study by advanced computational techniques. In the recent past there has been considerable interest in ab initio conformational analyses of such model compounds (22–30) and, specifically, in *N*-acetyl-L-alanyl-L-alanine-*N*′-methyl amide (31–33) and the title compound *N*-formyl-L-alanyl-L-alanine amide (ALA-ALA, henceforth; Fig. 1) (33–39).

In attempts to find a working basis for dealing with the considerable complexity of the conformational properties of proteins, the *dipeptide approximation* has frequently been applied (40–48). In this approximation it is assumed that the conformational properties of the *i*th residue of a peptide chain, particularly the values of the torsional angles ϕ_i and ψ_i (Fig. 1), depend mainly on the nature of the residue R_i and are largely independent of the neighboring pairs, ϕ_{i-1},ψ_{i-1} and ϕ_{i+1},ψ_{i+1}. More specifically (48), "the interactions associated with rotations of a ϕ_i,ψ_i pair are largely independent of the angles assumed by the neighbouring pairs ϕ_{i-1},ψ_{i-1} and ϕ_{i+1},ψ_{i+1}." Since short-range interactions are highly important in the folding of polypeptide chains, the dipeptide model has been rather effective, in spite of the fact that it neglects cooperative phenomena and long-range interactions in polymer chains.

Investigations of systems like ALA-ALA allow one to step beyond the limits of the dipeptide approximation. For this

Received November 24, 1997.

M. Ramek.[1] Institut für Physikalische und Theoretische Chemie, Technische Universität Graz, A-8010 Graz, Austria.
C.-H. Yu and L. Schäfer. Department of Chemistry and Biochemistry, University of Arkansas, Fayetteville, AR 72701, U.S.A.

[1] Author to whom correspondence may be addressed. Telephone: +43-316-873-8227. Fax: +43-316-873-8720. E-mail: ramek@ptc.tu-graz.ac.at

© 1998 NRC Canada

Fig. 1. *N*-Formyl alanyl alanine amide. Notation for backbone torsional angles.

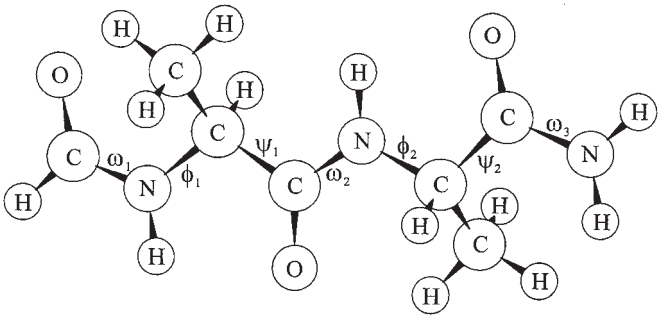

reason we have optimized the geometries of this compound at grid points in its four-dimensional (ϕ_1, ψ_1, ϕ_2, ψ_2) conformational space (Fig. 1) defined by 40° increments along the outer torsions ϕ_1 and ψ_2, and by 30° increments along the inner torsions ψ_1 and ϕ_2. The smaller stepsize for the latter was chosen because the properties of the central peptide bond are of particular interest to us. At each of the $9 \times 12 \times 12 \times 9 = 11\,664$ grid points geometry optimizations were performed via RHF/4-21G (49) calculations, in which the torsions ϕ_1, ψ_1, ϕ_2, and ψ_2 were kept constant while all other structural parameters were relaxed without any constraints. The orientation of the torsions ω_1 (i.e., H-C-N-C) and ω_2 was *trans* in all cases.

Previous ab initio geometry optimizations of ALA-ALA involved the all-extended and $C_7^{eq} - C_7^{eq}$ conformations (36), followed by studies of bend and helical forms (37–39). On the basis of these studies it was concluded that the latter are stable in ALA-ALA, in contrast to model dipeptides, such as the *N*-acetyl-*N*′-methyl derivatives of amino acids, where bends and helices are not energy minima (50–54). It was a further characteristic (38) of ALA-ALA that its stable helical form is displaced from the standard right-handed α_R-helical region to that of the 3/10 helix. This result is important in view of the experimental finding (55) that 3/10 helices, rather than α_R, are preferred by short alanine-based peptides in aqueous solution.

Perczel et al. (37, 39) have reported a particularly extensive study of ALA-ALA in an ambitious attempt to present a complete set of minimum energy conformations. The current investigation will add two more energy minima not found previously.

The current paper is focused on the conformational energies of ALA-ALA. The structures of all RHF/4-21G energy minima found by our analysis were also optimized at the RHF/6-31G* level of theory because the latter will yield better estimates of the locations of minima in ϕ,ψ-space. Apart from the concerns of the current paper, this data base is intended for use in developing improved parameters for computer simulations of organic compounds adsorbing to clay mineral surfaces (56).

Computational procedures

The RHF optimizations were carried out with Pulay's original 4-21G basis set (49) using the program GAMESS (57) on a variety of different machines until the maximum gradient was less than 10^{-4} H/Bohr, and the root mean square gradient was below 3.33×10^{-5} H/Bohr. The nature of all local minima reported here was confirmed by calculating the eigenvalues of the Hessian matrix.

Cubic spline functions were used to generate an analytical approximation of the potential-energy surface (PES) from the 11 664 grid points. Subsequently the local minima of this analytical approximation were determined and their positions in the four-dimensional space (ϕ_1, ψ_1, ϕ_2, ψ_2) were used as starting points for unrestricted geometry optimizations with the 4-21G basis set. The 4-21G energy minima were then reoptimized with the 6-31G* (58, 59) basis set.

On the basis of some recent analyses (60–62), the following error estimates can be given for the 4-21G results of this study: in calculations of glycine and *N*-formyl alanine amide (60, 61), HF/4-21G energies were found closer to MP2 energies or experimental values than results obtained with larger basis sets, with maximum inaccuracies of 1.5 kcal/mol for HF/4-21G (60, 61). This result shows that the 4-21G basis set is well balanced for compounds like ALA-ALA. Similarly, essential geometry trends, differences between comparable bond distances and angles in different conformations, are well determined at the 4-21G level (60–62), but the exact minima of torsional angles were found (60) inaccurate by up to 15°. On the basis of the previous comparisons (60, 61) we expect that the ϕ,ψ-torsions of the RHF/6-31G* optimized energy minima are within ~5° of comparable MP2-optimized geometries.

Results and discussion

The results of our analysis are given in Tables 1–4. The ϕ,ψ-torsional angles, conformational energies, and notation used to characterize the RHF/4-21G and RHF/6-31G* optimized minimum energy structures of ALA-ALA are given in Table 1. Some selected conformational energies and their transitions are presented in Tables 2 and 3. The RHF/3-21G data of two previously not reported energy minima are listed in Table 4.

The notation adopted for this study makes use of a convention generally accepted for characteristic regions of peptide ϕ,ψ-space in protein crystallography (63) (Fig. 2). The nomenclature introduced by Perczel et al. (64) is also included in Table 1, but merely for the sake of comparing the current and previous (39) data sets. We do not wish otherwise to adhere to it because it uses the same symbol, $\alpha_L\alpha_L$, for both type I and type III bends, which are usually (65, 66) considered as different types; furthermore, the same symbol, $(\alpha_L)_n$, is used to denote both standard α-helices and helices in model tripeptides (39), omitting the important detail that the latter are 3/10 helices and not α_R (36, 38, 55). Moreover, characterizing regions of ϕ,ψ-space in accordance with frequently populated regions in protein crystal structures, rather than with the energy minima of model dipeptides, helps to clarify an important result of the current study. That is (see below) that the torsional angles of the ab initio energy minima of ALA-ALA are not typical of the most populated regions of ϕ,ψ-space in protein crystal structures and, furthermore, cannot be extrapolated from the corresponding model dipeptide in all cases.

In addition to the crystallographic regions specified in Fig. 2, the results of the geometry optimizations of ALA-ALA require the definition of a provisional region, denoted as "p" in Table 1, whose approximate boundaries are given by $\phi > 150°$ or $\phi < -150°$ and $-90° < \psi < 0°$. Some of the calculated

© 1998 NRC Canada

Table 1. Torsions angles ϕ_1, ψ_1, ϕ_2, ψ_2 and relative energies (kcal/mol) for all local minima in the RHF/4-21G (top lines) and RHF/6-31G* (bottom lines) potential-energy surfaces. The absolute energies (Hartree) of the global minima are –659.1328881522 (4-21G) and –660.6397182345 (6-31G*).

Conformer	ϕ_1	ψ_1	ϕ_2	ψ_2	E_{rel}	Alternate symbol (39)
$\gamma'\gamma'$	–84.28	66.43	–84.84	65.76	0.000	$\gamma_L\gamma_L$
$\gamma'\gamma'$	–86.16	73.99	–87.49	75.22	0.000	
$\beta_S\gamma'$	–165.85	168.67	–85.24	67.66	1.736	$\beta_L\gamma_L$
$\beta_S\gamma'$	–157.06	156.33	–85.38	79.57	0.329	
$\gamma\gamma'$	74.13	–57.98	–83.56	66.68	2.073	$\gamma_D\gamma_L$
$\gamma\gamma'$	75.79	–55.51	–84.87	77.51	2.273	
$\gamma'\gamma$	–84.73	67.76	73.05	–56.81	2.234	$\gamma_L\gamma_D$
$\gamma'\delta_L$	–86.28	73.25	73.36	–46.98	2.468	
$\beta_S\beta_S$	–166.76	170.60	–165.73	169.84	2.339	$\beta_L\beta_L$
$\beta_S\beta_S$	–158.10	160.42	–156.53	162.40	0.082	
$\gamma'\zeta$	–84.74	70.86	–127.43	22.34	3.262	$\gamma_L\delta_L$
$\gamma'\delta_R$	–85.96	78.61	–134.03	17.29	1.829	
$\zeta\gamma'$	–123.75	19.74	–84.75	66.44	3.553	$\delta_L\gamma_L$
$\zeta\gamma'$	–124.81	13.65	–85.31	76.91	2.071	
$\delta_R\delta_R$	–73.25	–10.71	–113.69	18.97	3.648	$\alpha_L\delta_L$
$\delta_R\delta_R$	–71.92	–18.75	–104.32	8.64	1.599	
$\beta_S\gamma$	–165.59	167.72	75.57	–56.88	4.390	$\beta_L\gamma_D$
$\beta_S\gamma$	–157.28	156.76	76.69	–50.37	3.086	
$\gamma'\beta_S$	–87.16	71.70	–162.00	167.56	4.499	$\gamma_L\beta_L$
$\gamma'\beta_S$	–86.98	92.85	–156.39	155.71	2.100	
$\gamma\gamma$	74.14	–55.64	74.39	–56.04	4.552	$\gamma_D\gamma_D$
$\gamma\delta_L$	75.74	–55.40	75.37	–46.42	4.808	
$\delta_R\beta_S$	–120.40	16.55	–167.67	168.86	4.746	$\delta_L\beta_L$
$\delta_R\beta_S$	–105.72	1.51	–157.68	161.56	2.215	
$\gamma'p$	–79.73	74.07	178.63	–34.46	4.989	$\gamma_L\delta_D$
$\gamma'p$	–81.63	76.83	–171.02	–37.75	4.372	
$\beta_P\alpha_L$	–72.28	98.22	69.22	31.89	5.037	
$\beta_P\delta_L$	–61.38	132.07	64.91	25.76	2.835	
$\beta_S\zeta$	–166.37	170.89	–126.80	27.95	5.171	$\beta_L\delta_L$
$\beta_S\zeta$	–157.74	162.92	–131.91	22.32	2.588	
$\delta_L\gamma'$	66.24	26.66	–87.08	66.76	5.210	$\alpha_D\gamma_L$
$\delta_L\gamma'$	66.69	27.78	–89.65	76.85	3.651	
$\gamma\delta_R$ $\rightarrow\varepsilon\delta_R$	70.09	–75.60	–128.64	3.13	5.289	
$\varepsilon\zeta$	57.37	–128.33	–112.14	24.93	5.359	$\varepsilon_D\delta_L$
$\varepsilon\delta_R$	55.37	–130.39	–98.72	7.86	3.276	
$\gamma'\alpha_L$	–86.04	63.98	65.09	30.04	5.573	$\gamma_L\alpha_D$
$\gamma'\alpha_L$	–88.42	64.99	64.16	32.91	4.105	
$\zeta\gamma$	–120.33	21.63	75.95	–57.80	5.691	$\delta_L\gamma_D$
$\delta_R\gamma$	–114.26	14.08	76.49	–51.40	4.507	
$\gamma'\beta_P$ $\rightarrow\gamma'\gamma'$	–84.19	64.82	–75.10	160.92	5.892	$\gamma_L\varepsilon_L$
$\gamma'\varepsilon$	–81.77	74.38	64.19	–173.91	5.983	$\gamma_L\varepsilon_D$
$\gamma'\varepsilon$	–83.11	77.92	54.71	–151.44	3.243	
$\alpha_L\delta_L$	61.26	28.05	64.85	22.34	6.045	$\alpha_D\alpha_D$
$\alpha_L\delta_L$	61.39	32.46	63.34	28.17	5.037	
$\gamma\zeta$	75.66	–52.32	–120.00	21.49	6.085	$\gamma_D\delta_L$
$\delta_L\delta_R$	77.53	–49.49	–111.61	8.53	4.693	
$\alpha_L\beta_S$	63.51	30.05	–169.88	169.41	6.434	$\alpha_D\beta_L$
$\alpha_L\beta_S$	64.80	30.84	–162.62	158.40	3.996	
$p\beta_P$	–171.82	–55.29	–81.92	171.86	6.651	$\delta_D\varepsilon_L$
$p\beta_P$	–164.44	–59.06	–68.08	159.93	4.226	
$\zeta\varepsilon$	–160.48	54.18	62.84	–172.10	6.743	$\delta_L\varepsilon_D$
$\zeta\varepsilon$	–153.35	53.21	56.55	–159.43	4.834	
$\gamma\beta_P$	73.58	–64.70	–76.86	167.57	6.924	$\gamma_D\varepsilon_L$
$\gamma\beta_P$	74.09	–67.21	–63.04	146.38	3.481	
$\delta_L\beta_S$	76.28	–48.07	–158.14	168.71	7.083	$\gamma_D\beta_L$
$\delta_L\beta_S$	77.80	–38.06	–151.02	157.23	4.927	
$p\gamma'$	–179.00	–44.48	–85.52	68.25	7.316	$\delta_D\gamma_L$
$p\gamma'$	–170.62	–41.67	–87.26	79.73	5.364	
$\beta_S\alpha_L$	–165.69	167.39	64.56	32.53	7.534	$\beta_L\alpha_L$
$\beta_S\alpha_L$	–157.42	156.45	65.81	33.15	4.395	
$\varepsilon\gamma'$	62.82	–166.01	–86.32	65.10	7.537	$\varepsilon_D\gamma_L$
$\varepsilon\gamma'$	57.66	–148.30	–86.82	76.90	4.593	
$\gamma\alpha_L$	74.04	–60.19	65.20	32.70	7.540	$\gamma_D\alpha_D$
$\gamma\alpha_L$	75.42	–63.53	65.20	34.70	6.111	
$p\beta_S$	–173.46	–44.02	–165.32	169.73	7.949	$\delta_D\beta_L$
$p\beta_S$	–166.89	–40.22	–159.19	159.89	5.134	
$\alpha_L\gamma$	64.55	34.82	74.19	–57.44	8.430	$\alpha_D\gamma_D$
$\alpha_L\gamma$	64.18	36.78	74.54	–63.81	6.792	
β_Sp	–165.54	168.67	–171.34	–46.99	8.885	$\beta_L\delta_D$
β_Sp	–157.11	157.42	–163.42	–42.14	5.471	
γp $\rightarrow\varepsilon\delta_R$	73.75	–52.71	–166.53	–42.97	8.910	$\gamma_D\delta_D$
$\varepsilon\beta_S$	65.37	–168.83	–164.79	169.23	8.914	$\varepsilon_D\beta_L$
$\varepsilon\beta_S$	60.17	–147.35	–154.83	162.80	5.070	
$\alpha_L\zeta$	59.06	37.39	–130.30	28.50	8.984	$\alpha_D\delta_L$
$\alpha_L\ \delta_R$	64.00	34.71	–130.23	18.82	6.136	
$\beta_S\varepsilon$	–167.28	171.77	64.71	–168.22	9.321	$\beta_L\varepsilon_D$
$\beta_S\varepsilon$	–158.41	163.21	58.62	–141.50	4.938	
δ_Lp	65.74	14.63	151.25	–38.17	9.407	$\alpha_D\delta_D$
δ_Lp	69.10	10.24	165.77	–34.97	8.257	
$\gamma\varepsilon$	73.42	–58.92	63.43	–177.02	9.743	$\gamma_D\varepsilon_D$
$\gamma\varepsilon$	74.97	–50.54	55.29	–135.47	7.140	
$p\gamma$	–177.83	–41.77	74.47	–57.52	10.036	$\delta_D\gamma_D$
$p\gamma$	–169.75	–39.76	74.04	–52.26	8.201	
$\zeta\alpha_L$	–120.75	24.38	65.91	31.81	10.206	$\delta_L\alpha_D$
$\delta_R\alpha_L$	–113.61	17.69	66.36	31.81	6.703	
$\varepsilon\gamma$	60.56	–146.30	76.35	–57.58	10.387	$\varepsilon_D\gamma_D$
$\varepsilon\delta_L$	59.47	–128.56	78.49	–49.58	7.445	
ζp	–125.21	23.59	–171.44	–45.48	11.557	$\delta_L\delta_D$
δ_Rp	–128.23	17.35	–163.74	–39.29	7.848	
$p\alpha_L$	–179.35	–46.55	64.45	30.42	13.833	$\delta_D\alpha_D$
$p\alpha_L$	–171.45	–45.62	64.34	31.33	10.332	
$p\varepsilon$	–176.03	–39.63	63.89	–164.98	14.668	$\delta_D\varepsilon_D$
$p\varepsilon$	–165.93	–36.89	58.15	–142.93	9.441	
pp	–179.38	–45.43	–169.54	–51.08	14.915	$\delta_D\delta_D$
pp	–170.79	–42.27	–159.28	–54.76	11.052	
$\varepsilon\varepsilon$	67.27	–174.04	62.98	–163.67	15.128	$\varepsilon_D\varepsilon_D$
$\varepsilon\varepsilon$	63.22	–157.52	56.84	–139.62	9.542	

Table 1 (*concluded*).

© 1998 NRC Canada

Fig. 2. Notation for characteristic regions of peptide ϕ,ψ-space taken from Karplus (63). The frequencies of observed peptide conformations in protein crystal structures are also indicated. They decrease from areas enclosed by heavy solid lines to regions enclosed by plain solid lines and broken lines. The outlines are an approximate rendering of the exact contours given by Karplus (63).

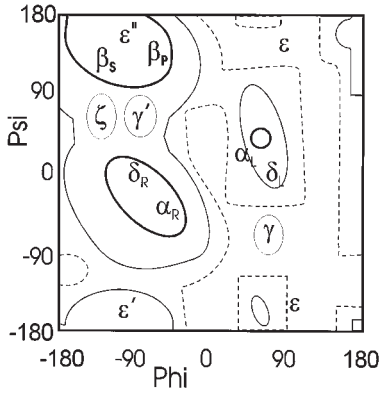

energy minima (Table 1) are situated in this part of ϕ,ψ-space, even though it is seldom populated in protein crystal structures.

Comparisons with previous ab initio studies

Even though a search for stationary points on the potential-energy surface (PES) of ALA-ALA was not the purpose of our geometry optimizations, it is a relatively easy by-product: once the energies at all grid points are determined, effective functions can be fitted to give a mathematical representation of the PES, which can then be used to search for minima and saddle points. The set by Perczel et al. (39) seemed to be a good test for the quality of the PES engendered by our approach. Indeed, most of the local minima encountered on the 4-21G PES are a good match with the RHF/3-21G optimized structures reported by Perczel et al., with deviations in backbone torsions of less than 1°. Several of the local minima reported in ref. 39, however, did not match and were therefore reoptimized with the 3-21G basis set. The resulting structures indicate that the data of ref. 39 contain a number of typographical errors[2] that are relevant to point out for this important molecule.

We cannot be sure that the 4-21G grid search of ALA-ALA has led to the discovery of all the local energy minima of ALA-ALA, but it has revealed two additional minima not listed in ref. 39. Reoptimization of these structures with the 3-21G basis set followed by calculations of the vibrational frequencies showed that these conformers are true minima in the RHF/3-21G space. Their 3-21G optimized energies and backbone torsional angles are given in Table 4. The two new conformers, $\beta_P\alpha_L$ and $\gamma\delta_R$, are relatively close to other energy minima reported by Perczel et al. (39), namely to $\gamma'\alpha_L$ and $\gamma\zeta$ ($\gamma_L\alpha_D$ and $\gamma_D\delta_L$ in the notation of ref. 39), but they are separated from them by distinct saddle points. Both of the conformers identified in Table 4 are characterized by two intramolecular C═O···H—N hydrogen bonds, one between the formyl group and the central peptide bond (1←3) and the other between the two terminal groups (1←4). The bond orders (67), which are also listed in Table 4, indicate that the latter is stronger than the former.

In further deviation from the results reported in ref. 39, we note that the RHF/3-21G $\varepsilon_D\delta_D$ conformer is not a local minimum in either the RHF/4-21G or the RHF/6-31G* calculations. Geometry optimizations starting with that conformation yield γp (labeled $\gamma_D\delta_D$ in ref. 39) in the former and $\varepsilon\delta_R$ ($\varepsilon_D\delta_L$) in the latter.

The previously noted (38) type of the helical form of ALA-ALA, i.e., 3/10 rather than α_R, was confirmed by the present investigation and, most importantly (see conformation $\delta_R\delta_R$ in Table 1), this finding was not changed by optimizing the structure of $\delta_R\delta_R$ at the RHF/6-31G* level of theory. When α_R-helical forms of *N*-formyl-pentaglycine amide and pentaalanine

Table 2. The RHF/4-21G conformational energies of *N*-formyl alanyl alanine amide calculated at specific points in ϕ,ψ-space.[a]

CONF	ϕ_1	ψ_1	ϕ_2	ψ_2	ENG
β,β	–165	165	–165	165	0.0
β,α_R	–165	165	–75	–45	6.1
β,α_L	–165	165	55	55	6.9
β,δ_R	–165	165	–90	0	3.8
β,γ	–165	165	–85	65	–0.2
α_R,β	–75	–45	–165	165	5.2
α_R,α_R	–75	–45	–75	–45	11.9
α_R,α_L	–75	–45	55	55	13.1
α_R,δ_R	–75	–45	–90	0	6.6
α_R,γ	–75	–45	–85	65	4.4
α_L,β	55	55	–165	165	5.3
α_L,α_R	55	55	–75	–45	12.5
α_L,α_L	55	55	55	55	10.5
α_L,δ_R	55	55	–90	0	9.9
α_L,γ	55	55	–85	65	4.8
δ_R,β	–90	0	–165	165	2.9
δ_R,α_R	–90	0	–75	–45	6.4
δ_R,α_L	–90	0	55	55	10.5
δ_R,δ_R	–90	0	–90	0	2.0
δ_R,γ	–90	0	–85	65	2.7
γ,β	–85	65	–165	165	2.1
γ,α_R	–85	65	–75	–45	3.7
γ,α_L	–85	65	55	55	5.2
γ,δ_R	–85	65	–90	0	2.2
γ,γ	–85	65	–85	65	–2.1

[a] Symbols for conformational regions (CONF) were taken from Fig. 2. The ϕ,ψ-torsional angles are in degrees and identified in Fig. 1. Energies (ENG) are in kcal/mol relative to the β,β conformation.

[2] In Table 6 of ref. 39 the values of the ϕ_1 torsions of $\delta_L\delta_D$, $\delta_L\varepsilon_D$, $\delta_L\gamma_D$, and $\delta_L\gamma_L$, in Table 9 the value of ϕ_1 for $\gamma_D\beta_L$, and in Table 5 the value of ψ_1 for $\varepsilon_D\beta_L$ should have the opposite sign. Also in Table 5, the correct value of ψ_2 for $\varepsilon_D\gamma_D$ should be –58.1°. The last two misprints also appear in Figs. 2 and 3 (39). Also in Table 5 (39), the optimized value of ψ_1 should be –60.9° for conformer $\varepsilon_D\alpha_D$; in the nomenclature used by Perczel et al. this will require to change the label of $\varepsilon_D\alpha_D$ to $\gamma_D\alpha_D$. As it is, the paper (39) contains an inconsistency, because on p. 2055 $\varepsilon_D\alpha_D$ is listed as an unstable conformation, but in Table 5 it is an energy minimum. The correction suggested here, changing $\varepsilon_D\alpha_D$ to $\gamma_D\alpha_D$, will remove this inconsistency. The same change should also be considered in Scheme 7 (39) and in the footnote to Table 5 (39) regarding conformational shifts. It also vitiates the first part of footnote (a) in Table 9 (39). Finally, in Table 4, the notation of $\beta_L\alpha_L$ is not in agreement with scheme 2 (39). Similarly, Table VI of ref. 37 should be corrected for the ψ_2 value (–58.1°) of conformer $\varepsilon_D\gamma_D$.

© 1998 NRC Canada

Table 3. The RHF/4-21G transition energies (kcal/mol) between various conformations of *N*-formyl alanyl alanine amide.[a]

CONF	β	α_R	α_L	δ_R	γ′
β,β	0	6.1	6.9	3.8	–0.2
α_R,β	0	6.6	7.8	1.3	–0.9
α_L,β	0	7.2	5.2	4.6	–0.5
δ_R,β	0	3.5	7.6	–0.9	–0.2
γ′,β	0	1.7	3.1	0.1	–4.2
β[b]	0	5.6	6.5	3.3	–1.1

[a] The energies listed are transition energies (final minus initial state) when the second residue in the conformations listed in column CONF changes to the conformation listed as column heading in columns 2–6. The values of Table 2 were used to calculate the energy differences.

[b] The last row presents RHF/4-21G energy differences (100) for the model dipeptide, *N*-formyl alanine amide.

amide were optimized at the HF/4-21G level (36), the same result was obtained.

Comparison of RHF/6-31G* and RHF/4-21G energy minima

Previous investigations of basis-set effects on the structures of amino acids and peptides (60, 61) have shown that backbone torsional angles in glycine and *N*-formyl alanine amide can vary by up to ~15° when the same structures are optimized at the RHF/4-21G, RHF/6-311G**, and MP2/6-311G** levels of theory. The largest parts of these changes were encountered (60, 61) in going from RHF/4-21G to RHF/6-311G*, with the latter yielding backbone torsional angles in close proximity, within 4°, of the MP2/6-311G** optimized geometries. Similar variations can be noted in the case of ALA-ALA, which cause a change in the conformer symbol in several cases. The most significant variations are found for $\gamma'\beta_S$ (4-21G) for which ψ_1 shifts more than 20° (Table 1), and the conformers $\beta_P\alpha_L/\beta_P\delta_L$ ($\Delta\psi_1 > 30°$), γε ($\Delta\psi_2 > 40°$),γβ_P, β_Sε, pε, and εε ($\Delta\psi_2 > 20°$). Similar differences were found by Möhle et al. (32) in the case of Ac-Ala-Ala-NHMe. Uncertainties of that order in backbone torsional angles are highly significant when they are propagated along a polypeptide chain. We expect the 6-31G* structures to yield more realistic estimates of the positions of minima on the φ,ψ-PES than their 4-21G counterparts. Several RHF/4-21G energy minima are no local minima in the RHF/6-31G* PES, as indicated in Table 1.

In Fig. 2 a φ,ψ-map is presented that illustrates the frequencies of observed peptide conformations in protein crystal structures as found by Karplus (63) on the basis of a critical analysis of protein crystal data. Figure 3 summarizes the positions of the ab initio energy minima of ALA-ALA in φ,ψ-space. Comparison of Figs. 2 and 3 reveals that the energy minima of the model tripeptide are not clustered in the centers but on the fringes of the most populated regions of φ,ψ-space in proteins. Möhle et al. (32) noted the same deviation for the special case of β-turns; the present comparison seems to show that this is a general feature. Thus it is true that examples for the substructures of the ab initio energy minima of ALA-ALA can be found in the X-ray data of proteins (39) but, at the same time, these substructures are not typical for proteins. It is seen from Fig. 4 that the same result is obtained when only ala-ala sequences

Table 4. Backbone torsions (degree), hydrogen bond distances (Å), bond orders (67), and RHF/3-21G energies (Hartree and kcal/mol) of the two conformers of ALA-ALA not listed in ref. 39.

		$\beta_P\alpha_L$	$\gamma\delta_R$
Torsions	ω_1	–179.1	178.5
	ϕ_1	–70.0	69.4
	ψ_1	101.7	–77.6
	ω_2	–175.9	179.3
	ϕ_2	66.2	–134.1
	ψ_2	32.4	8.6
	ω_3	–179.8	177.1
H-bond distances	O1···H3	2.4377	2.1265
	O1···H4	2.1278	2.1090
H-bond orders	O1···H3	0.024	0.044
	O1···H4	0.064	0.064
Energies	*E*	–656.956613	–656.955314
	E_{rel}	4.44	5.25

Fig. 3. Location of the RHF/6-31G* energy minima of *N*-formyl alanyl alanine amide in φ,ψ-space.

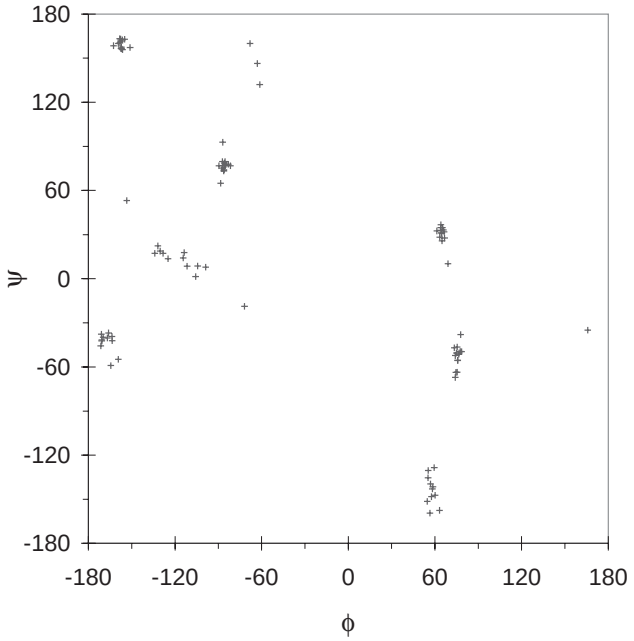

in protein structures are included in this comparison. It follows that, like dipeptides (50–54, 64, 68–100) whose global energy minimum (C_7^{eq}) is rarely populated in proteins and whose PES does not contain a minimum for one of the most frequently populated conformations (α_R) of proteins, tripeptides, too, are not sufficient to model the exact positions of energy minima of polypeptide chains in the solid state.

Limitations of the dipeptide approximation

In the dipeptide approximation the conformations A and B of two amino acid residues linked in a chain are considered independent of one another. In contrast, the peptide sequence AB, as a rule, is noncommutative and AB ≠ BA. The current study provides some quantitative estimates as to what extent the conformational energy of an amino acid residue in a peptide sequence depends on the state of its neighbor.

© 1998 NRC Canada

Fig. 4. Values of the ϕ,ψ-torsional angles of alanine residues in ala-ala sequences in protein crystal structures, according to the protein data file by Karplus (63).

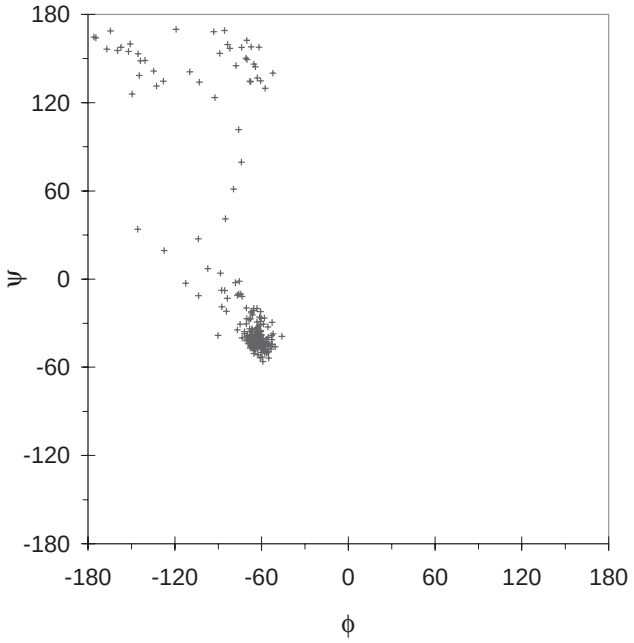

Fig. 5. The conformational energy surface (kcal/mol) PES_2 of residue 2 of *N*-formyl alanyl alanine amide as a function of ϕ_2 and ψ_2 calculated with residue 1 being held fixed at $f = -165°$ and $y = +165°$. The upper graph shows a projection of the three-dimensional rendering of PES_2. The lower graph shows a linearized version, plotting average energies on PES_2 as a function of region numbers in ϕ,ψ-space. Each region is a segment of a 15° grid in ϕ,ψ-space. Region numbering was started with segment $-180° \le \phi < -165°$ and $-180° \le \psi < -165°$ and proceeded from –180° to 180°, moving along the ψ-axis first. In each segment energy values were calculated at 5° intervals and averaged.

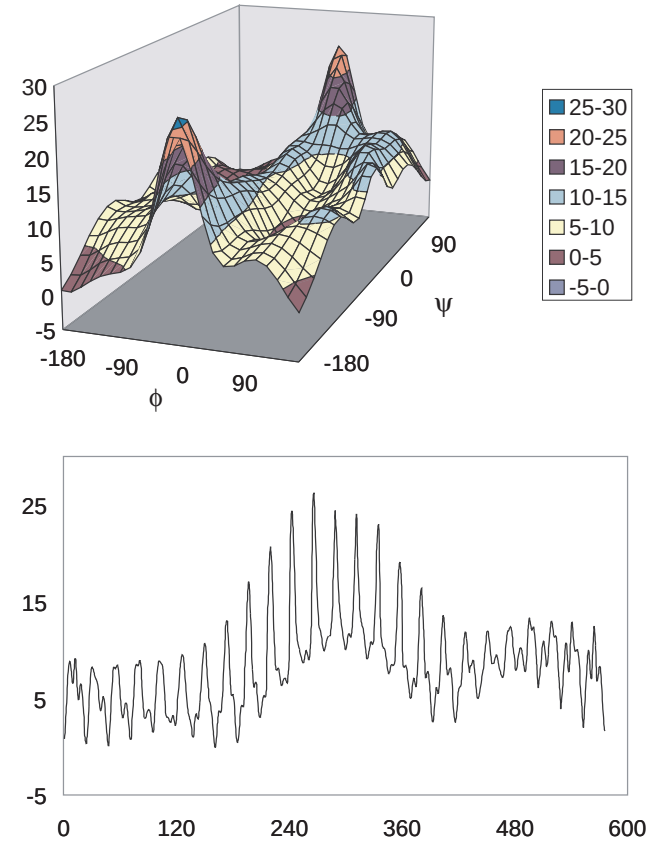

Figure 5 presents the conformational energy surface, PES_2, of residue 2 of ALA-ALA as a function of ϕ_2 and ψ_2, which was calculated with residue 1 being held constant on its own PES (i.e., PES_1) in the β-region at $\phi_1 = -165°$ and $\psi_1 = +165°$. In a qualitative way PES_2 is similar to the RHF/4-21G ϕ,ψ-PES of the model dipeptide *N*-formyl alanine amide (ALA) (100) shown in Fig. 6. Both surfaces have regions of high and low energy at approximately the same locations in ϕ,ψ-space, and in general they display similar topologies. However, quantitatively the energy surfaces of ALA-ALA are not identical with those of ALA, because PES_i in the former varies with PES_j (Fig. 6).

To simplify the comparisons described below, we shall concentrate on four characteristic and frequently populated regions in protein ϕ,ψ-space, that is α_L, α_R, β, and the bridge region, δ_R (Fig. 2). Due to limitations of the graphics software, the latinicized symbols "al," "ar," "bt," and "br," respectively, were used in our graphs to denote these regions, associating with them fixed points at the ϕ,ψ-values of –75°, –45° for ar; +55°, +55° for al; –90°, 0° for br; and –165°, +165° for bt. As a further shorthand convention we mean by xx.1 the PES_1 calculated when residue 2 is being held constant on PES_2 in conformation xx, where xx is either ar, al, bt, or br, as defined above. Similarly, xx.2 is PES_2 calculated when residue 1 is being held fixed at xx equal to either ar, al, bt, or br. To display differences between comparable PES, it is advantageous to transform the three-dimensional surface to two-dimensional line drawings. This was done in Figs. 5–7 by forming a 15° grid in ϕ,ψ-space, numbering the grid regions as described in Fig. 5 and presenting energies as functions of region numbers. Figure 5 shows both the three-dimensional surface and the corresponding line drawing that results when bt.2 (i.e., PES_2 calculated with residue 1 fixed at bt) is transformed in this way.

The asymmetry AB ≠ BA is apparent when the conformational properties of commutated pairs, AB and BA, are compared. It can be seen from Table 1 that ϕ,ψ-torsions and energies can differ significantly for pairs of energy minima such as $\beta_S\gamma'$ and $\gamma'\beta_S$; γ'p and pγ'; $\gamma'\varepsilon$ and $\varepsilon\gamma'$; and others. In some of these cases, the ϕ,ψ-torsions in same-name conformations of a given pair differ by only a few degrees. In others, for example $\gamma'\varepsilon$, they differ almost 10°. Similarly, the conformational energies of the members of a pair may differ by less than 0.5 kcal/mol, or by more than 2.5 kcal/mol, as in the case of $\beta_S\gamma'$.

Further illustrations of inter-residue conformation transmission effects are provided by Fig. 7, which shows differences of type xx.*i* minus yy.*i*; that is, between different PES_i, which were calculated with residue *j* being held constant in different regions, xx or yy, of PES_j, where $i \neq j = 1$ or 2. Furthermore, differences xx.1 minus xx.2 are shown in Fig. 7; that is, differences $PES_1 - PES_2$, which were calculated with residue 2 or 1, respectively, being held fixed at identical points in ϕ,ψ-space. From all these data it is seen that the conformational energy of a residue in ALA-ALA can be significantly affected by the state of its neighbor. These results further

© 1998 NRC Canada

Fig. 6. The conformational energy surface (kcal/mol) of *N*-formyl alanine amide (100) (top) plotted relative to the energy at $\phi = -165°$ and $\psi = +165°$. The lower graph is the difference curve (energy differences as a function of the region numbers defined in Fig. 5) between PES_2 of *N*-formyl-alanyl alanine amide (Fig. 5) and the PES of *N*-formyl alanine amide (top).

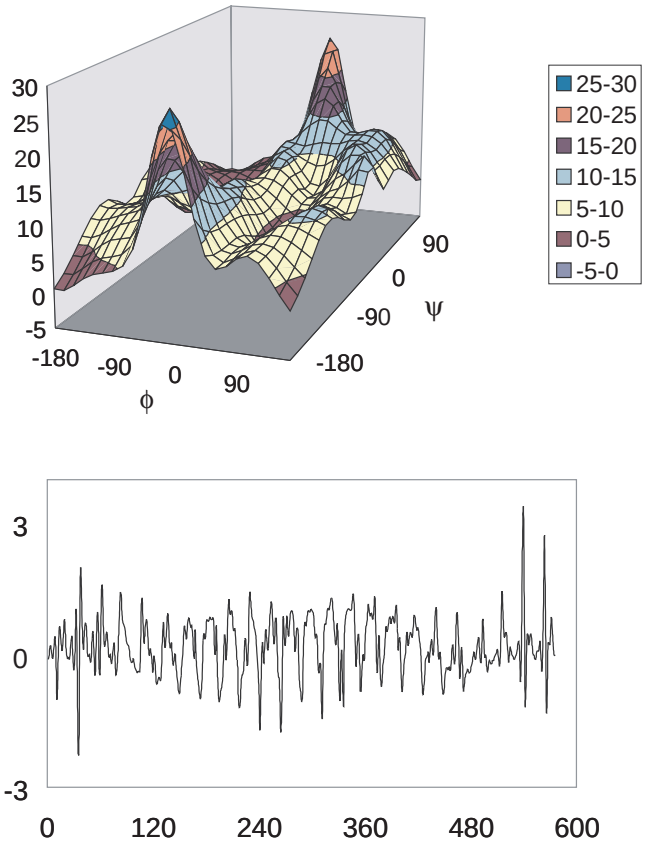

Fig. 7. Energy differences (kcal/mol) for *N*-formyl alanyl alanine amide. The sequence of curves from top to bottom is the same as that of the curve identifiers in the legends. Notation used for the identifiers is "al" for α_L; "ar" for α_R; "bt" for β; and "br" (bridge region) for δ_R. The symbol xx.*i* denotes PES_i (that is, the PES for residue *i* of *N*-formyl alanyl alanine amide as a function of ϕ_i and ψ_i) calculated when residue *j* is being held fixed at α_L, α_R, β, or δ_R on PES_j, where $i \neq j = 1$ or 2. To avoid overlap, some curves have been offset by constant energy amounts (kcal/mol) as indicated at the end of each identifier.

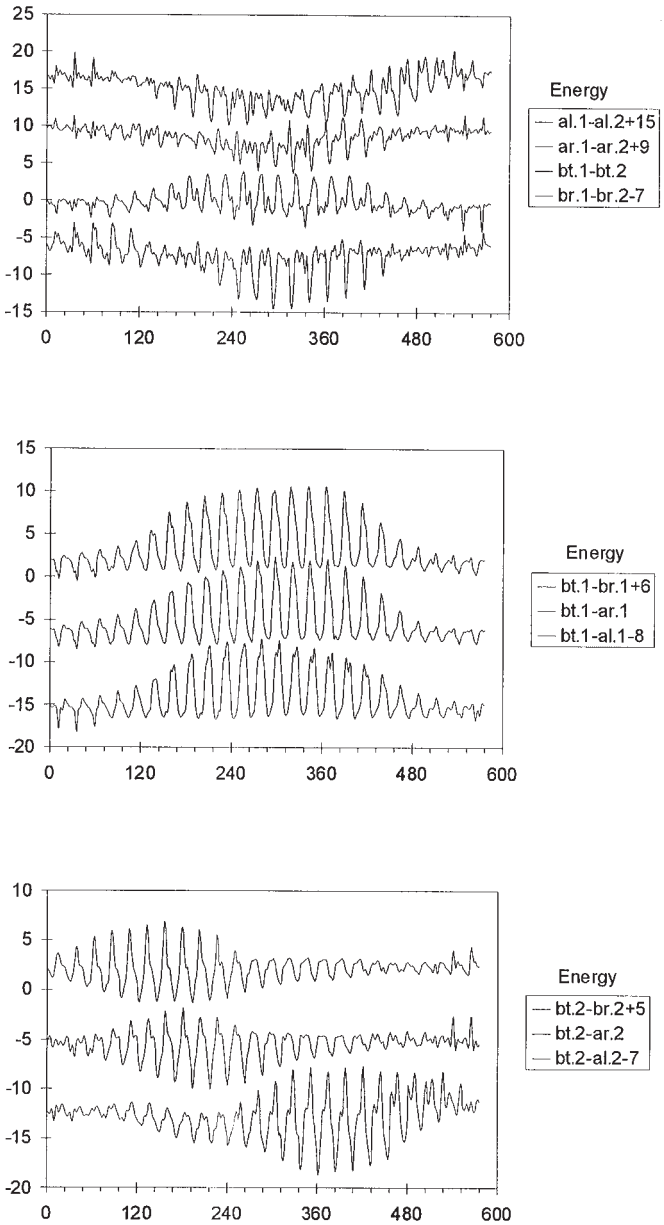

illustrate the asymmetry of the case. For example (Fig. 7), differences of type xx.1 – yy.1 are entirely different from xx.2 – yy.2.

In Tables 2 and 3 relative energies of specific points in the ϕ,ψ-space of ALA-ALA are listed, including the region γ', which is rarely populated in protein crystal structures but of low energy in ALA-ALA. Tables 2 and 3 show that, regardless of what the nature of the first residue is, preference is always for the second residue to be added in the γ'- or β-conformations. Table 3 also shows the importance of cooperative phenomena in the structures of ALA-ALA. That is, energy differences between the same conformational regions in the dipeptide and tripeptide are not the same. In addition it can be seen that transitions between the same conformations of residue 2 depend on the state of residue 1.

These results also show that the conformational energies of small model peptides such as ALA-ALA cannot be used to predict the conformational frequencies of peptide units in proteins. If the population frequencies of residues R_i in protein crystal structures (63) are investigated as a function of the conformational state of the preceding residue R_{i-1}, then the results of Fig. 8 are obtained. Restricting the analysis to the most common cases, i.e., to residues following a preceding neighbor in either the α_R, α_L, β, or δ_R state, Fig. 8 is in agreement with the general expectation of finding β-sheets, α-helices, turns of type (α_L,α_L), (α_L,β), (β,δ_R), (β,α_L), etc., in peptide chains, but the relative frequencies are not in accordance with the energy pattern of ALA-ALA shown in Table 3. The comparison is, of course, not perfect because residues of any kind, not only alanine, were included in Fig. 8, and much of the driving force of conformational selection is by the nature of the side chain. If the analysis underlying Fig. 8 is restricted

© 1998 NRC Canada

Fig. 8. Values of the ϕ,ψ-torsional angles of amino acid residues, R_i, in protein crystal structures, which are found when the preceding residue, R_{i-1}, is in the α_L (top left), α_R (top right), β (lower left), or δ_R-conformation (lower right). The protein data file by Karplus (63) was used. The following simplified boundaries were used (in degrees): $-165 \le \phi \le -60$ and $105 \le \psi \le 180$ for β; $-75 \le \phi \le -30$ and $-75 \le \psi \le -30$ for α_R; $45 \le \phi \le 70$ and $30 \le \psi \le 60$ for α_L; $-120 \le \phi \le -75$ and $-30 \le \psi \le 20$ for δ_R.

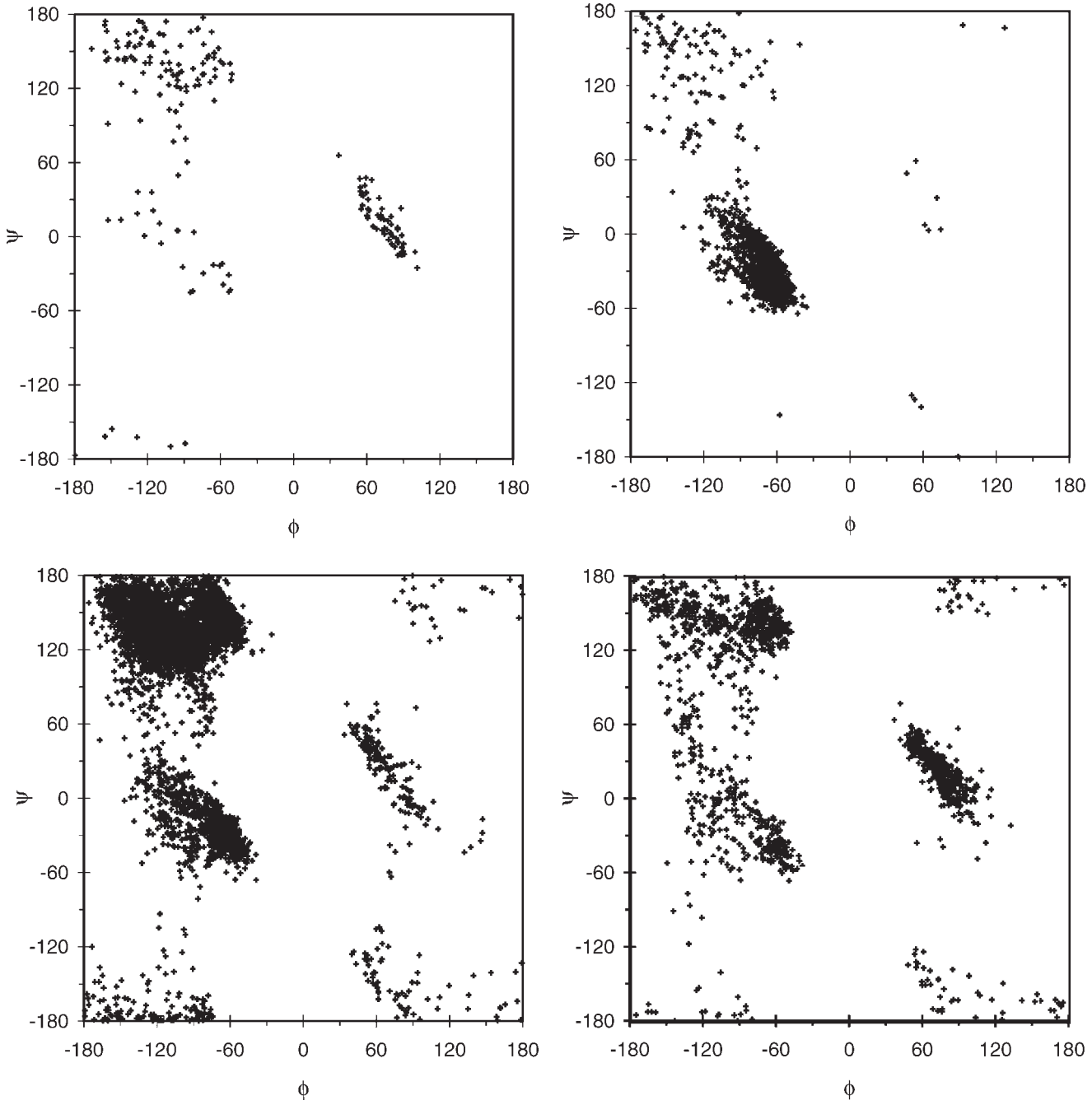

to two alanine residues in sequence, only a small number of cases is found. They indicate preference mainly for α_R to follow α_R and β to follow β, again not in accordance with the conformational energy pattern of Table 3.

Conclusions

In the current study we present, in the 6-31G* geometries of the energy minima of *N*-formyl alanyl alanine amide summarized in Table 1, a data base from which improved parameters can be refined for empirical molecular modeling procedures of organic compounds with functional groups of the kind exhibited by ALA-ALA.

From the ab initio conformational energies of ALA-ALA quantitative estimates can be made of the extent to which the conformational energies of individual residues in peptide chains are affected by the states of neighboring peptide units. The concomitant limitations of the dipeptide approximation (40–48) are more extensive in the ab initio results than previously estimated (101) on the basis of empirical modeling

© 1998 NRC Canada

calculations. Nishikawa et al. (101) found significant departure from additivity of single-residue energies mainly for minimum-energy bends. Figure 7 indicates that significant departures from additivity are found in many regions of ϕ,ψ-space.

Small peptides contain a great deal of information that is relevant for understanding structural trends, specifically those involving bond angles of larger systems such as oligopeptides and proteins (100, 102). However, as far as the exact positions of conformations in ϕ,ψ-space are concerned, small peptides seem to be much less informative. In the case of ALA-ALA, specifically, the torsion angles of the ab initio energy minima are not those of the typical substructures of proteins: the most stable helices are not α_R, and the torsion angles of the most stable bend forms deviate from those most frequently encountered in protein bends.

Acknowledgements

The authors gratefully acknowledge partial support of this work by U.S. Department of Agriculture National Research incentive grant 97-35107-4362.

References

1. L.L. Shipman and R.E. Christoffersen. J. Am. Chem. Soc. **95**, 4733 (1973).
2. D.A. Kleier and W.N. Lipscomb. Int. J. Quantum Chem. Quantum Biol. Symp. **4**, 73 (1977).
3. D. Peters and J. Peters. J. Mol. Struct. **68**, 255 (1980).
4. D. Peters and J. Peters. J. Mol. Struct. **69**, 249 (1980).
5. M. Kertész, J. Koller, and A. Azman. Int. J. Quantum Chem. Quantum Biol. Symp. **7**, 177 (1980).
6. R.S. Day, S. Suhai, and J. Ladik. Chem. Phys. **62**, 165 (1981).
7. P.T. van Duijnen and B.T. Thole. Biopolymers, **21**, 1749 (1982).
8. S. Suhai. J. Mol. Struct. (Theochem), **123**, 97 (1985).
9. L. Skála and P. Pancoska. Chem. Phys. **125**, 21 (1988).
10. A.K. Bakhshi, P. Otto, and J. Ladik. J. Mol. Struct. (Theochem), **180**, 113 (1988).
11. C.-M. Liegener, A.K. Bakhshi, P. Otto, and J. Ladik. J. Mol. Struct. (Theochem), **188**, 205 (1989).
12. A.K. Bakhshi, P. Otto, C.-M. Liegener, E. Rehm, and J. Ladik. Int. J. Quantum Chem. **38**, 573 (1990).
13. V. Barone, F. Fraternali, and P.L. Cristinziano. Macromolecules, **23**, 2038 (1990).
14. C.-M. Liegener, A. Sutjianto, and J. Ladik. Chem. Phys. **145**, 385 (1990).
15. P. Otto and A. Sutjianto. J. Mol. Struct. (Theochem), **231**, 277 (1991).
16. C. Chang and R.F.W. Bader. J. Phys. Chem. **96**, 1654 (1992).
17. H. Torii and M. Tasumi. J. Mol. Struct. **300**, 171 (1993).
18. K. Zhang, D.M. Zimmerman, A. Chung-Phillips, and C. J. Cassady. J. Am. Chem. Soc. **115**, 10 812 (1993).
19. P.D. Walker and P. G. Mezey. J. Am. Chem. Soc. **115**, 12 423 (1993).
20. P.D. Walker and P. G. Mezey. J. Am. Chem. Soc. **116**, 12 022 (1994).
21. G. Endredi, C.-M. Liegener, M.A. McAllister, A. Perczel, J. Ladik, and I.G. Csizmadia. J. Mol. Struct. (Theochem), **306**, 1 (1994).
22. J.A. Ryan and J.L. Whitten. J. Am. Chem. Soc. **94**, 2396 (1972).
23. D. Peters and J. Peters. J. Mol. Struct. **68**, 243 (1980).
24. R. Ramani and R.J. Boyd. Int. J. Quantum Chem. Quantum Biol. Symp. **8**, 117 (1981).
25. L.R. Wright and R.F. Borkman. J. Phys. Chem. **86**, 3956 (1982).
26. A.-M. Sapse, S.B. Daniels, and B.W. Erickson. Tetrahedron, **44**, 999 (1988).
27. J. Mavri, F. Avbelj, and D. Hadži. J. Mol. Struct. (Theochem), **187**, 307 (1989).
28. A.-M. Sapse, D.C. Jain, D. de Gale, and T.C. Wu. J. Comput. Chem. **11**, 573 (1990).
29. H.-J. Böhm. J. Am. Chem. Soc. **115**, 6152 (1993).
30. O. Antohi, F. Naider, and A.-M. Sapse. J. Mol. Struct. (Theochem), **360**, 99 (1996).
31. A. Perczel, M. Kajtár, J.-F. Marcoccia, and I.G. Csizmadia. J. Mol. Struct. (Theochem), **232**, 291 (1991).
32. K. Möhle, M. Guβmann, and H.-J. Hofmann. J. Comput. Chem. **18**, 1415 (1997)
33. M.A. McAllister, A. Perczel, P. Császár, and I.G. Csizmadia. J. Mol. Struct. (Theochem), **288**, 181 (1993).
34. D. Peters and J. Peters. J. Mol. Struct. (Theochem), **85**, 267 (1981).
35. A. Perczel, G. Endredi, M.A. McAllister, O. Farkas, P. Császár, J. Ladik, and I.G. Csizmadia. J. Mol. Struct. (Theochem), **331**, 5 (1995).
36. L. Schäfer, S.Q. Newton, M. Cao, A. Peeters, C. Van Alsenoy, K. Wolinski, and F.A. Momany. J. Am. Chem. Soc. **115**, 272 (1993).
37. A. Perczel, M.A. McAllister, P. Császár, and I.G. Csizmadia. J. Am. Chem. Soc. **115**, 4849 (1993).
38. C. Van Alsenoy, M. Cao, S.Q. Newton, B. Teppen, A. Perczel, I. G. Csizmadia, F.A. Momany, and L. Schäfer. J. Mol. Struct. **286**, 149 (1993).
39. A. Perczel, M.A. McAllister, P. Császár, and I.G. Csizmadia. Can. J. Chem. **72**, 2050 (1994).
40. V. Sasisekharan. *In* Collagen. *Edited by* N. Ramanathan. John Wiley and Sons, Interscience Publishers, New York. 1962. p. 39.
41. G.N. Ramachandran, C. Ramakrishnan, V. Sasisekharan. J. Mol. Biol. **7**, 95 (1963).
42. C. Ramakrishnan and G.N. Ramachandran. Biophys. J. **5**, 909 (1965).
43. S.J. Leach, G. Nemethy, and H.A. Scheraga. Biopolymers, **4**, 369 (1966).
44. K.D. Gibson and H.A. Scheraga. Biopolymers, **4**, 709 (1966).
45. P.K. Ponnuswamy and V. Sasisekharan. Biopolymers, **10**, 565 (1971).
46. G.N. Ramachandran, C.M. Venkatachalam, and S. Krimm. Biophys. J. **6**, 849 (1966).
47. P.N. Lewis, F.A. Momany, and H.A. Scheraga. Isr. J. Chem. **11**, 121 (1973).
48. B. Pullman and A. Pullman. Adv. Prot. Chem. **28**, 347 (1974).
49. P. Pulay, G. Fogarasi, F. Pang, and J.E. Boggs. J. Am. Chem. Soc. **101**, 2550 (1979)
50. L. Schäfer, C. van Alsenoy, and J.N. Scarsdale. J. Chem. Phys. **76**, 1439 (1982).
51. J.N. Scarsdale, C. van Alsenoy, V.J. Klimkowski, L. Schäfer, and F.A. Momany. J. Am. Chem. Soc. **105**, 3438 (1983).
52. L. Schäfer, V.J. Klimkowski, F.A. Momany, H. Chuman, and C. van Alsenoy. Biopolymers, **23**, 2335 (1984).
53. V.J. Klimkowski, L. Schäfer, F.A. Momany, and C. van Alsenoy. J. Mol. Struct. **124**, 143 (1985).
54. K. Siam, V.J. Klimkowski, C. van Alsenoy, J.D. Ewbank, and L. Schäfer. J. Mol. Struct. **152**, 261 (1987).
55. S.M. Miick, G.V. Martinez, W.R. Fiory, A.P. Todd, and G.L. Millhauser. Nature (London), **359**, 653 (1992).
56. B.J. Teppen, C-H. Yu, D.M. Miller, and L. Schäfer. J. Comput. Chem. **19**,144 (1998).
57. M.W. Schmidt, K.K. Baldridge, J.A. Boatz, S.T. Elbert, M.S. Gordon, J.H. Jensen, S. Koseki, N. Matsunaga, K.A. Nguyen, S. Su, T. L. Windus, M. Dupuis, and J.A. Montgomery, Jr. J. Comput. Chem. **14**, 1347 (1993).

© 1998 NRC Canada

58. W.J. Hehre, R. Ditchfield, and J.A. Pople. J. Chem. Phys. **56**, 2257 (1972).
59. P.C. Hariharan and J.A. Pople. Theor. Chim. Acta, **28**, 213 (1973).
60. R.F. Frey, J. Coffin, S.Q. Newton, M. Ramek, V.K.W. Cheng, F.A. Momany, and L. Schäfer. J. Am. Chem. Soc. **114**, 5369 (1992).
61. M. Ramek, V.K.W. Cheng, R.F. Frey, S.Q. Newton, and L. Schäfer. J. Mol. Struct. **235**, 1 (1991).
62. J. de Smedt, F. Vanhouteghem, C. van Alsenoy, H.J. Geise, and L. Schäfer. J. Mol. Struct. **259**, 289 (1992).
63. P.A. Karplus. Protein Sci. **5**, 1406 (1996).
64. A. Perczel, J.G. Ángyán, M. Kajtár, W. Viviani, J.-L. Rivail, J.-F. Marcoccia, and I.G. Csizmadia. J. Am. Chem. Soc. **113**, 6256 (1991).
65. C.M. Venkatachalam. Biopolymers, **6**, 1425 (1968).
66. P.N. Lewis, F.A. Momany, and H.A. Scheraga. Biochim. Biophys. Acta, **303**, 211 (1973).
67. I. Mayer. Chem. Phys. Lett. **97**, 270 (1983).
68. L. Schäfer, I.S. Bin Drees, R.F. Frey, C. Van Alsenoy, and J.D. Ewbank. J. Mol. Struct. **338**, 71 (1995).
69. D. Peters and J. Peters. J. Mol. Struct. **53**, 103 (1979).
70. D. Peters and J. Peters. J. Mol. Struct. (Theochem), **85**, 107 (1981).
71. D. Peters and J. Peters. J. Mol. Struct. (Theochem), **85**, 257 (1981).
72. D. Peters and J. Peters. J. Mol. Struct. (Theochem), **90**, 305 (1982).
73. D. Peters and J. Peters. J. Mol. Struct. (Theochem), **90**, 321 (1982).
74. P.S. Stern, M. Chorev, M. Goodman, and A.T. Hagler. Biopolymers, **22**, 1901 (1983).
75. D. Peters and J. Peters. J. Mol. Struct. (Theochem), **109**, 137 (1984).
76. D. Peters and J. Peters. J. Mol. Struct. (Theochem), **109**, 149 (1984).
77. S.J. Weiner, U.C. Singh, T.J. O'Donnell, and P.A. Kollman. J. Am. Chem. Soc. **106**, 6243 (1984).
78. P.K. Mehrotra, M. Mezei, and D.L. Beveridge. Int. J. Quantum Chem. Quantum Biol. Symp. **11**, 301 (1984).
79. M. Mezei, P.. Mehrotra, and D.L. Beveridge. J. Am. Chem. Soc. **107**, 2239 (1985).
80. K. Siam, S. Q. Kulp, J.D. Ewbank, and L. Schäfer. J. Mol. Struct. (Theochem), **184**, 143 (1989).
81. T.C. Cheam and S. Krimm. J. Mol. Struct. **193**, 1 (1989).
82. T.C. Cheam and S. Krimm. J. Mol. Struct. (Theochem), **188**, 15 (1989).
83. T. Head-Gordon, M. Head-Gordon, M.J. Frisch, C. Brooks III, and J.A. Pople. Int. J. Quantum Chem. Quantum Biol. Symp. **16**, 311 (1989).
84. D.E. Williams. Biopolymers, **29**, 1367 (1990).
85. H.-J. Böhm and S. Brode. J. Am. Chem. Soc. **113**, 7129 (1991).
86. T. Head-Gordon, M. Head-Gordon, M.J. Frisch, C.L. Brooks III, and J.A. Pople. J. Am. Chem. Soc. **113**, 5989 (1991).
87. A. Perczel, W. Viviani, and I.G. Csizmadia. *In* Molecular aspects of biotechnology: computational models and theories. *Edited by* J. Bertran. Kluwer Academic Publishers, Norwell, Mass. 1992. pp. 39–82.
88. I.R. Gould and P.A. Kollman. J. Phys. Chem. **96**, 9255 (1992).
89. I.R. Gould and I.H. Hillier. J. Chem. Soc. Chem. Commun. 951 (1993).
90. D. Jiao, M. Barfield, and V.J. Hruby. J. Am. Chem. Soc. **115**, 10 883 (1993).
91. W. Viviani, J.-L. Rivail, A. Perczel, and I.G. Csizmadia. J. Am. Chem. Soc. **115**, 8321 (1993).
92. W. Viviani, J.-L. Rivail, and I.G. Csizmadia. Theor. Chim. Acta, **85**, 189 (1993).
93. M.A. McAllister, A. Perczel, P. Császár, W. Viviani, J.-L. Rivail, and I. G. Csizmadia. J. Mol. Struct. (Theochem), **288**, 161 (1993).
94. I.R. Gould, W.D. Cornell, and I.H. Hillier. J. Am. Chem. Soc. **116**, 9250 (1994).
95. M. Ramek, A.-M. Kelterer, B.J. Teppen, and L. Schäfer. J. Mol. Struct. **352/353**, 59 (1995).
96. A. Perczel, O. Farkas, and I.G. Csizmadia. J. Comput. Chem. **17**, 821 (1996).
97. O. Farkas, M.A. McAllister, J.M. Ha, A. Perczel, M. Hollosi, and I.G. Csizmadia. J. Mol. Struct. (Theochem), **369**, 105 (1996).
98. G. Endredi, A. Perczel, O. Farkas, M.A. McAllister, G.I. Csonka, J. Ladik, and I.G. Csizmadia. J. Mol. Struct. (Theochem), **391**, 15 (1997).
99. W.D. Cornell, I.R. Gould, and P.A. Kollman. J. Mol. Struct. (Theochem), **392**, 101 (1997).
100. L. Schäfer, M. Cao, and M.J. Meadows. Biopolymers, **35**, 603 (1994).
101. K. Nishikawa, F.A. Momany, H.A. Scheraga. Macromolecules, **7**, 797 (1974).
102. X. Jiang, M. Cao, B. Teppen, S.Q. Newton, and L. Schäfer. J. Phys. Chem. **99**, 10 521 (1995).

© 1998 NRC Canada

Determination of the acid dissociation constants for some mycotoxins of the *Alternaria alternata* genus

Patricia Gabriela Molina, María Alicia Zón, and Héctor Fernández

Abstract: The acid dissociation constants for alternariol monomethyl ether (AME), altertoxin-I (ATX-I), and alternariol (AOH), three of the *Alternaria alternata* genus mycotoxins, are estimated through conventional UV–VIS spectroscopic studies at different pH values. Experimental variations of absorbance as a function of pH at a given wavelength were fitted by using the exact equations that describe the systems studied. Good agreement between the experimental absorbance vs. pH plots and the curves generated by the fitting process was found. A comparison between the acidic constants for the first step of dissociation of these mycotoxins and the value for the acidic constant of phenol is discussed by assuming that phenolic structures are responsible for the acidity of these mycotoxins.

Key words: mycotoxins, alternariol monomethyl ether, altertoxin-I, alternariol, acidic constants.

Résumé : En se basant sur des études spectroscopiques UV–VIS conventionnelles réalisées à diverses valeurs de pH, on a évalué les constantes de dissociation acide de l'éther monométhylique de l'alternariol (EMA), de l'altertoxine-1 (ATX-1) et de l'alternariol (AOH), trois mycotoxines du genre *Alternaria alternata*. On a ajusté les variations expérimentales d'absorption en fonction du pH à une longueur d'onde donnée à l'aide d'équations exactes qui décrivent les systèmes étudiés. On a observé de bons accords entre l'absorption expérimentale en fonction des courbes de pH et celles générées par le procédé d'ajustement. Pour discuter de la comparaison entre les constantes d'acidité de la première étape de dissociation de ces mycotoxines et la valeur de la constante d'acidité du phénol, on fait l'hypothèse que les structures phénoliques sont responsables de l'acidité de ces mycotoxines.

Mots clés : mycotoxines, éther monométhylique de l'alternariol, altertoxine-1, alternariol.

[Traduit par la rédaction]

Introduction

Alternaria species are common in many foods and feed crops. In grain or seeds, *Alternaria* infection usually occurs before harvest when the seed moisture content is still high. The infection becomes extensive enough to produce secondary metabolites only when drying in the field is delayed by rainfall and high humidity. Post-harvest infection by *Alternaria* is more likely to occur in fruits and vegetables that remain high in moisture content after harvest, resulting in economic loss to growers and commercial marketers (1–7).

Alternariol monomethyl ether (AME), alternariol (AOH), and alternuene (ALT), which are benzopyrone derivatives; altertoxin-I (ATX-I) and altertoxin-II (ATX-II), which are perylene derivatives; and tenuazonic acid (TA), a tetramic acid derivative, are considered to be the most important *Alternaria* mycotoxins (see Fig. 1) (1). They are toxic in many biological systems, including animal and mammalian cells (8–13).

Given the fact that these secondary metabolites have multibasic sites, it is expected that more than one acid–base pair will be under equilibrium conditions depending on the pH of the medium. The knowledge of the acid dissociation constants is of utmost importance both for understanding their reaction mechanisms and for firmly grounding their toxicological properties.

In this paper, we estimate the acidity constants for AME, ATX-I, and AOH through conventional UV–VIS spectrophotometric studies at different pH values as part of a general program for the study of the properties of mycotoxins recently started by our group.

Received November 19, 1997.

P.G. Molina, M.A. Zón, and H. Fernández.[1] Departamento de Química y Física, Universidad Nacional de Río Cuarto, Agencia Postal Nº 3, (5800) - Río Cuarto, Córdoba, Argentina.

[1] Author to whom correspondence may be addressed. Telephone: 54-58-676221 / 33. Fax: 54-58-676224. E-mail: HFERNANDEZ@EXA.UNRC.EDU.AR

Experimental

Reagents

AME, ATX-I, and AOH were obtained from Sigma Chemical Company and were used as received. Acetonitrile (ACN), methanol (MeOH), and acetone (Ac) were Sintorgan, HPLC grade. They were dried over 3 Å molecular sieves for 48 h prior to use and were then employed without further purification. Water was obtained from the Labconco WaterPro Mobile system model 90901–01 (HPLC grade water).

Working solutions of mycotoxin were prepared daily at concentrations in the $(0.3–3) \times 10^{-5}$ M range from stock solutions of AME, ATX-I, and AOH (prepared in ACN, Ac, and MeOH, respectively). The pH region 0–1 was covered using 1 and 0.1 mol dm^{-3} HCl and pH 12–13 by 0.01 and 0.1

© 1998 NRC Canada

Fig. 1. Chemical structures of some *Alternaria alternata* genus mycotoxins.

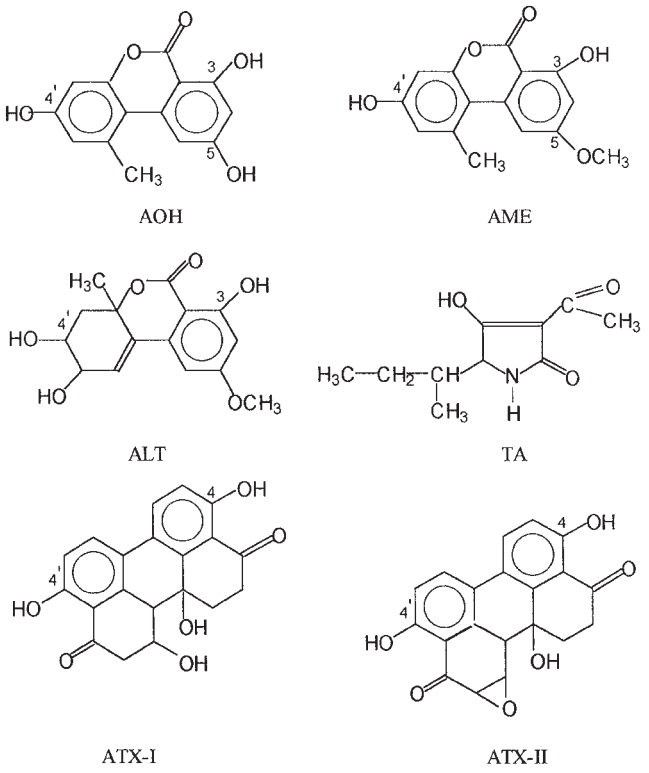

mol dm^{-3} NaOH. The pH range 2–12 was covered by the appropriate buffer with the pH adjusted by the addition of various volumes of 1 mol dm^{-3} HCl or NaOH. Twenty percent of ACN in the medium studied was necessary to allow the complete solubilization of mycotoxins.

Apparatus and methods

UV-VIS spectra were recorded immediately after the preparation of solutions by using a Hewlett–Packard model 8452A spectrophotometer equipped with a temperature controller. Absorbances at three selected wavelengths for each toxin were obtained from the spectra recorded against the corresponding blanks. Silica cells were of 1 cm pathlength.

pH Measurements were performed by using an Orion model 720A pH meter that was calibrated daily with three commercial buffers (manufactured according to the National Institute for Standards and Technology recommendations). The pH meter was used with an Orion 8104 Ross (pH 0–14) combination electrode. All measurements were performed at 25 ± 0.5°C.

Manipulation of all the experimental laboratory material was done by using thin plastic gloves for security.

In our calculations, the unknown parameters were the acid dissociation constants (K_i) and extinction coefficients (ε); nevertheless, the ε value for some species in solution at a given pH could always be experimentally determined for each one of the toxins. This provides a way of checking the accuracy of our data and calculations by comparing the experimental and calculated values. Treatment of experimental data was by the nonlinear least-squares fitting procedure (14, 15). The nonlinear regression method is based on the Levenberg–Marquardt algorithm. The two necessary building blocks of any fitting procedure are: (*i*) data that represent the results of certain measurements in which one or several independent variables ($X_1, X_2, X_3,....$) was varied over a certain range in a controllable manner to produce the measured dependent variable(s) Y_1, Y_2, Y_3, and (*ii*) mathematical expressions in the form:

$$[1] \quad Y_1 = f_1\,(X_1, X_2, X_3,....; p_1, p_2, p_3,....)$$

$$[2] \quad Y_2 = f_2\,(X_1, X_2, X_3,....; p_1, p_2, p_3,....)$$

$$[3] \quad Y_3 = f_3\,(X_1, X_2, X_3,....; p_1, p_2, p_3,....)$$

which represent the theoretical model believed to explain the process that produced the experimental data. The model usually depends on one or more parameters. The search for the values of the parameters that best describe the experimental data was performed by minimization of the Chi-square function (χ^2), being the sum of the squares of the differences between the absorbances calculated according to the model and the corresponding experimental absorbances for a range of independent variables. For the case where there is only one independent and one dependent variable the function simplifies to

$$[4] \quad \chi^2\,(p_1, p_2, p_3,....) = (1/d) \sum w_i\,[Y_i - f\,(x_i; p_1, p_2,...)]^2$$

where Y_i are the measured values of the dependent variable for the values of the independent variable x_i; d is the number of degrees of freedom defined as $d = n^{\text{eff}} - p$, where n^{eff} is the total number of experimental points and p the total number of adjustable parameters used in the fitting. The quantities w_i represent the weight of each experimental point. In this work w_i was taken as equal to 1.

The presence of intramolecular hydrogen bonds in mycotoxin structures was inferred from calculations performed by using the HyperChem software package (Autodesk, Inc.). Mycotoxin molecular geometries were optimized by using the MM+ molecular mechanics force field and hydrogen bonds were recomputed. HyperChem creates a hydrogen bond if the distance between the donor hydrogen and acceptor atom is less than 3.2 Å and the angle made by covalent bonds to the donor and acceptor atoms is greater than 150°.

Results and discussion

The equilibria involved in aqueous solutions containing AME or ATX-I (diprotic acids) can be represented in the usual way by the following equations (16):

$$[5] \quad AH_2 \Leftrightarrow AH^- + H^+ \qquad K_1 = [AH^-]\,[H^+] / [AH_2]$$

$$[6] \quad AH^- \Leftrightarrow A^{2-} + H^+ \qquad K_2 = [A^{2-}]\,[H^+] / [AH^-]$$

while those corresponding to AOH (triprotic acid) aqueous solutions must be represented by the following sequence:

$$[7] \quad AH_3 \Leftrightarrow AH_2^- + H^+ \qquad K_1 = [AH_2^-]\,[H^+] / [AH_3]$$

$$[8] \quad AH_2^- \Leftrightarrow AH^{2-} + H^+ \qquad K_2 = [AH^{2-}]\,[H^+] / [AH_2^-]$$

$$[9] \quad AH^{2-} \Leftrightarrow A^{3-} + H^+ \qquad K_3 = [A^{3-}]\,[H^+] / [AH^{2-}]$$

where K_1, K_2, and K_3 are, by definition, the acid dissociation constants for the first, the second, and the third ionization steps, respectively. The brackets represent the equilibrium molar concentrations of the corresponding species. They are

© 1998 NRC Canada

related to the analytical concentration, C_A, through either of the following mass balance equations:

[10] $C_A = [AH_2] + [AH^-] + [A^{2-}]$

or

[11] $C_A = [AH_3] + [AH_2^-] + [AH^{2-}] + [A^{3-}]$

depending upon whether the different equilibria are represented by eqs. [5] and [6] or [7]–[9], respectively.

On the other hand, by assuming that Beer's law holds under the experimental conditions used, the absorbance at a given wavelength, A^λ, can be expressed either as (17)

[12] $A^\lambda = \varepsilon^\lambda_{AH_2}\, b\, [AH_2] + \varepsilon^\lambda_{AH^-}\, b\, [AH^-] + \varepsilon^\lambda_{A^{2-}}\, b\, [A^{2-}]$

or

[13] $A^\lambda = \varepsilon^\lambda_{AH_3}\, b\, [AH_3] + \varepsilon^\lambda_{AH_2^-}\, b\, [AH_2^-] + \varepsilon^\lambda_{AH^{2-}}\, b\, [AH^{2-}] + \varepsilon^\lambda_{A^{3-}}\, b\, [A^{3-}]$

for the di- and triprotic acids, respectively; b represents the pathlength of light and ε^λ are the extinction coefficients of the corresponding species for a given wavelength.

The exact analytical solutions for eqs. [12] and [13] are obtained by expressing the concentration of each species in equilibrium as a function of the acid dissociation constants and of the analytical concentration of the corresponding species. Then, the rearranged forms for eqs. [12] and [13] are

[14] $A^\lambda = C_A\, b\, \{[A(10^{-x})^2 + B\, 10^{-x} + C] / [(10^{-x})^2 + D\, 10^{-x} + E]\}$

and

[15] $A^\lambda = C_A\, b\, \{[F(10^{-x})^3 + G(10^{-x})^2 + H\, 10^{-x} + I] / [(10^{-x})^3 + J(10^{-x})^2 + L\, 10^{-x} + M]\}$

respectively, with x = pH; $A = \varepsilon^\lambda_{AH_2}$; $B = \varepsilon^\lambda_{AH^-} K_1$; $C = \varepsilon^\lambda_{A^{2-}} K_1K_2$; $D = K_1$; $E = K_1K_2$; $F = \varepsilon^\lambda_{AH_3}$; $G = \varepsilon^\lambda_{AH_2^-} K_1$; $H = \varepsilon^\lambda_{AH^{2-}} K_1K_2$; $I = \varepsilon^\lambda_{A^{3-}} K_1K_2K_3$; $J = K_1$; $L = K_1K_2$; and $M = K_1K_2K_3$.

UV–VIS spectra recorded at different pH values for AME, ATX-I, and AOH are shown in Figs. 2(*a*)–(*c*), respectively. They show changes with pH, mainly above pH 8. The absence of an isosbestic point in the pH range was, at first sight, an argument in favor of the occurrence of more than one equilibrium.

The unknown parameters for each system were estimated by fitting the variation of experimental absorbance with the pH at selected wavelengths (see experimental section).

The theoretical functions chosen to start the fitting were selected as those given by eqs. [14] and [15] for di- and triprotic compounds, respectively. Before starting the fitting procedure the experimental data of A^λ vs. pH were interpolated by a polynomial regression or a sigmoidal curve in order to generate a greater number of points on the select dataset for fitting (experimental curve). At the end of the procedure the fitted parameter values were listed with the corresponding estimated standard errors (σ_i).

A detailed discussion about the choice of the best parameters for each system studied is described as follows.

For AME and ATX-I, values reported for the D and E parameters corresponded to the best fit (the lowest χ^2) for the three wavelengths chosen by considering that those parameters must be independent of the wavelength ($D = K_1$ and $E = K_1K_2$).

Fig. 2. Absorption spectra at different pH for: (*a*) AME (pH = 1.463, 4.616, 8.900, and 12.050 from 1 to 4, respectively), [AME] = 2.35×10^{-5} M; (*b*) ATX-I (pH = 1.066, 4.492, 8.664, and 12.595 from 1 to 4, respectively), [ATX-I] = 2.83×10^{-6} M; and (*c*) AOH (pH = 1.060, 4.360, 8.620, and 13.380 from 1 to 4, respectively), [AOH] = 7.74×10^{-6} M.

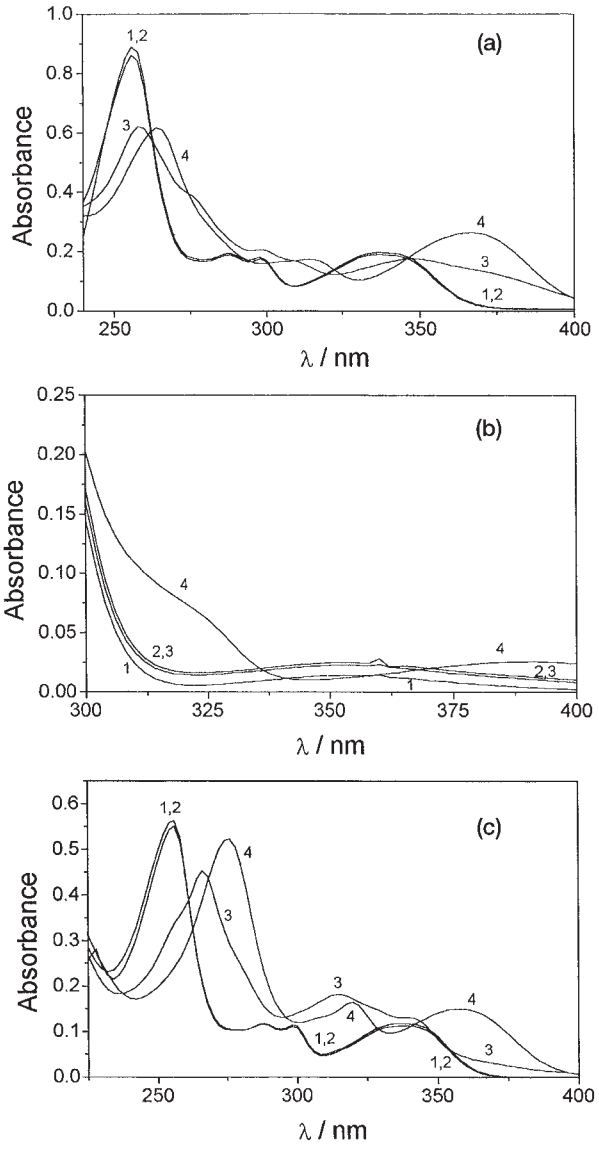

Then, they were used as constants for the determination of A, B, and C at the three wavelengths. In the same way, for AOH, the J, L, and M parameters were chosen from the best fit (the lowest χ^2) following the same criteria as explained above. They were then kept constant for the determination of the F, G, H, and I parameters at the three wavelengths chosen ($J = K_1$, $L = K_1K_2$, and $M = K_1K_2K_3$).

AME

Fitting results as well as the extinction coefficients calculated for the different species from the fitting parameters obtained at three wavelengths (λ = 256, 330, and 374 nm) are gathered in Table 1. In Table 1 is also included an estimate of the $\varepsilon^{exp}_{AH_2}$ value at a given wavelength, reached from the experimental

© 1998 NRC Canada

Table 1. Final results of the fitting process, extinction coefficients of different species at the wavelengths indicated, as well as dissociation constants for AME and ATX-I.

	AME			ATX-I		
Parameters	$\lambda = 256$ nm	$\lambda = 330$ nm	$\lambda = 374$ nm	$\lambda = 306$ nm	$\lambda = 324$ nm	$\lambda = 390$ nm
A	$(3.644 \pm 0.002) \times 10^4$	$(7.540 \pm 0.006) \times 10^3$	329 ± 15	$(2.178 \pm 0.002) \times 10^4$	$(3.04 \pm 0.02) \times 10^3$	$(3.67 \pm 0.04) \times 10^3$
B	$(6.53 \pm 0.12) \times 10^{-5}$	$(1.513 \pm 0.003) \times 10^{-5}$	$(2.967 \pm 0.008) \times 10^{-5}$	$(7.56 \pm 0.01) \times 10^{-7}$	$(2.4 \pm 0.1) \times 10^{-7}$	$(1.13 \pm 0.03) \times 10^{-7}$
C	$(3.3 \pm 0.7) \times 10^{-17}$	$(6.47 \pm 0.02) \times 10^{-18}$	$(2.17 \pm 0.01) \times 10^{-17}$	$(5.449 \pm 0.006) \times 10^{-19}$	$(3.3 \pm 0.3) \times 10$–19	$(1.52 \pm 0.01) \times 10^{-19}$
D		$(3.34 \pm 0.06) \times 10^{-9}$			$(1.8 \pm 0.1) \times 10^{-11}$	
E		$(1.45 \pm 0.31) \times 10^{-21}$			$(1.1 \pm 0.1) \times 10^{-23}$	
χ^2	2.3×10^{-5}	1.7×10^{-5}	8.4×10^{-5}	3.0×10^{-6}	3.5×10^{-7}	1.3×10^{-6}
$\varepsilon^{\lambda}_{AH_2}$ / M^{-1} cm^{-1}	$(3.644 \pm 0.002) \times 10^4$	$(7.540 \pm 0.006) \times 10^3$	$(3.3 \pm 0.1) \times 10^2$	$(2.178 \pm 0.002) \times 10^4$	$(3.04 \pm 0.02) \times 10^3$	$(3.67 \pm 0.04) \times 10^3$
$\varepsilon^{\lambda}_{AH^-}$ / M^{-1} cm^{-1}	$(1.96 \pm 0.07) \times 10^4$	$(4.53 \pm 0.09) \times 10^3$	$(8.8 \pm 0.2) \times 10^3$	$(4.2 \pm 0.3) \times 10^4$	$(1.3 \pm 0.1) \times 10^4$	$(6.3 \pm 0.6) \times 10^3$
$\varepsilon^{\lambda}_{A^{2-}}$ / M^{-1} cm^{-1}	$(2.3 \pm 0.9) \times 10^4$	$(4.4 \pm 0.9) \times 10^3$	$(1.4 \pm 0.3) \times 10^4$	$(5.0 \pm 0.5) \times 10^4$	$(3.1 \pm 0.6) \times 10^4$	$(1.4 \pm 0.2) \times 10^4$
$\varepsilon^{exp}_{AH_2}$ / M^{-1} cm^{-1}	3.7×10^4 [a]	7.6×10^3 [a]	3.2×10^2 [a]	2×10^4 [b]	2.7×10^3 [b]	3.7×10^3 [b]
$\Delta\varepsilon_{AH_2}\%$ [c]	1.5	0.8	3	9	12	0.8
Dissociation constants	$K_1 = (3.34 \pm 0.05) \times 10^{-9}$	$K_2 = (4.4 \pm 0.9) \times 10^{-13}$		$K_1 = (1.8 \pm 0.1) \times 10^{-11}$	$K_2 = (6 \pm 1) \times 10^{-13}$	

[a, b] Determined at pH = 1.97 and 1.513, respectively.

[c] $\Delta\varepsilon_{AH_2}\% = (\varepsilon^{exp}_{AH_2} - \varepsilon^{\lambda}_{AH_2}) \times 100 / \varepsilon^{exp}_{AH_2}$.

absorbance in the pH range of 1–2 by considering that the species should be the only one in solution in an acidic pH range (see below). A reasonably good agreement between the experimental data and the curve generated with the fitting results was found, as can be seen in Fig. 3(I). On the other hand, the low relative percent error, $\Delta\varepsilon_{AH_2}\%$ (Table 1) shows good agreement between experimental and calculated extinction coefficients.

A distribution of AME acid species as a function of pH was calculated with the parameters determined from the fitting procedure. The results are shown in Fig. 4(*a*). It can be seen that below pH ≈ 7 the only species present is AH_2. This is in agreement with the fact that no change in absorption spectra is observed up to a pH of ≈7. Above this pH, two species are present in an appreciable amount up to about pH ≈10.5 where AH^{-} should be the only predominant species. This can be taken as an additional proof of the quality of the fitting. The experimental ε values at a given wavelength calculated at pH = 10.31 ($\varepsilon^{256}_{exp} = 1.9 \times 10^4$ M^{-1} cm^{-1}; $\varepsilon^{330}_{exp} = 4.4 \times 10^3$ M^{-1} cm^{-1}; and $\varepsilon^{374}_{exp} = 9.0 \times 10^4$ M^{-1} cm^{-1}) are in good agreement with those obtained from the ratio between the *B* and *D* fitting parameters ($\varepsilon_{AH^-} = B/D$) shown in Table 1.

The estimated values of K_1 and K_2 for AME are also gathered in Table 1. A value of $K_1 = 3.34 \times 10^{-9}$ is reasonable when comparing it with the acidity constant value of phenol ($K_a = 1.3 \times 10^{-10}$ (17)) by assuming that two phenolic structures can be found in the AME structure (see Fig. 1). On the other hand, it may be argued that the hydroxyl group in C(3) for AME (see Fig. 1) should be responsible for the first stage of dissociation for this mycotoxin by considering that a K_1 value rather higher than the K_a of phenol was found. This might be explained by assuming that the phenoxide ion generated should be stabilized by resonance in an extension greater than that of the corresponding ion in phenol as a consequence of AME having an electron-withdrawing group (C═O) close to the hydroxyl group in C(3) (see Fig. 1), leading AME to be more acidic than phenol itself. In this way, the second ionization step should correspond to the loss of hydrogen atom bonded to the hydroxyl group in C(4′) (see Fig. 1). Besides, the absence of an intramolecular hydrogen bond between the hydroxyl group in C(3) and the δ-lactone carbonyl group could be verified by theoretical MM+ calculations as indicated in the Experimental.

On the other hand, no change in the absorption spectra recorded at different times during a period of 40 min was observed either at pH = 1.224 (acidic medium) or pH = 10.825 and 12.865 (basic media). This indicates that if a basic hydrolysis of the six-membered ring of the δ-lactone occurs in the AME structure, its kinetics should be very slow, at least up to pH 12.865. This behavior might be understood by assuming that the reaction hydrolysis would take place through a typical nucleophilic acyl substitution pathway in which the hydroxide ion is added to the lactone carbonyl group, giving a tetrahedral intermediate. This could be sterically hindered in AME as a consequence of the bulky substituents involved in that structure. As well, when the solution composed of AME – basic medium was acidified it spontaneously recovered the characteristic form of the absorption spectra for this mycotoxin in an acidic medium. This appears as powerful evidence that true acid–base equilibria exist in solution.

ATX-I

Absorption spectra at different bulk concentrations of ATX-I

© 1998 NRC Canada

Fig. 3. Comparison between the experimental and theoretical variation of absorbance as a function of pH for: (I) AME: (*a*) = 256 nm, (*b*) = 330 nm, and (*c*) = 374 nm, [AME] = 2.35×10^{-5} M; (II) ATX-I: (*a*) = 306 nm, (*b*) = 324 nm, and (*c*) = 390 nm, [ATX-I] = 2.83×10^{-6} M; and (III) AOH: (*a*) = 256 nm, (*b*) = 280 nm, and (*c*) = 374 nm, [AOH] = 7.74×10^{-6} M. The open and closed circles are the experimental points; the solid lines represent the theoretical curves obtained by the fitting process.

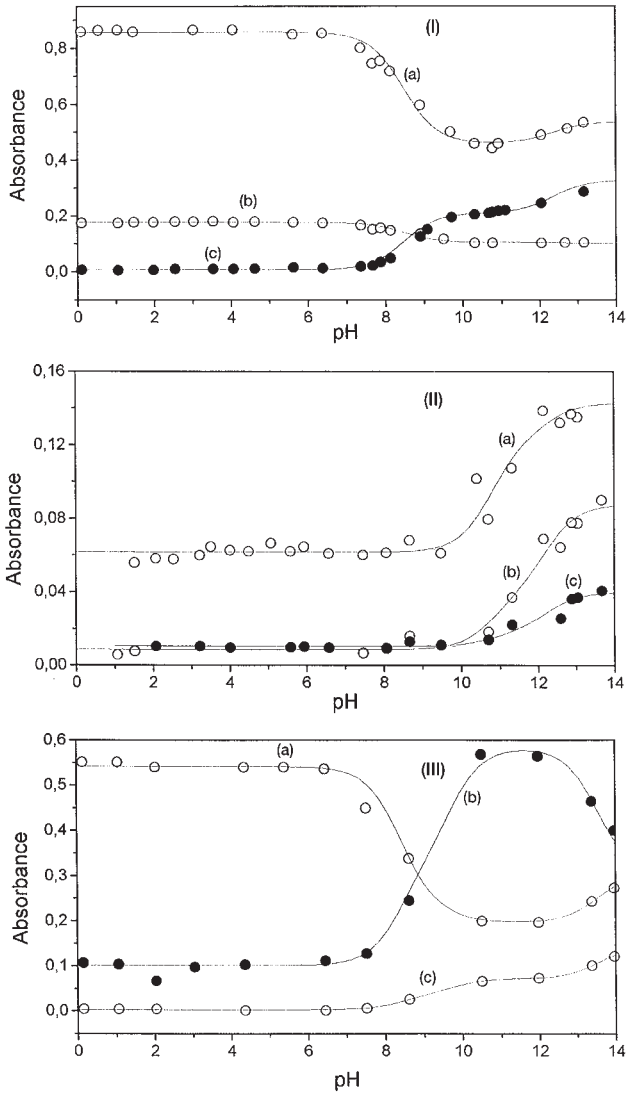

were recorded in the ACN – 1 M $HClO_4$ medium. An absorption maximum was observed at $\lambda = 264$ nm. A plot of A^{264} vs. [ATX-I] was linear, with a correlation coefficient $r = 0.9905$ and a standard deviation sd = 0.05. From the slope of this plot the ε value ($\varepsilon^{264}_{ATX-I} = 3.4 \times 10^4$ M^{-1} cm^{-1}) was calculated.

On the other hand, absorption spectra did not show any change when they were recorded at different times in an acidic medium (pH = 1.224). However, spectral changes with time were observed in basic media (pH = 9.502 and 12.865), showing a solution decomposition. The origin of these spectral changes was not analyzed. However, they were insignificant for time periods below 1 min from the beginning of the solution preparation. Therefore, when absorption spectra for ATX-I solutions as a function of pH were measured, the whole

Fig. 4. Diagram of distribution of species as a function of pH for: (*a*) AME (▲ [AH_2], ○ [AH^-], ● [A^{2-}]); (*b*) ATX-I (▲[AH_2], ○[AH^-], ●[A^{2-}]); and (*c*) AOH (▲[AH_3], ○[AH_2^-], ●[AH^{2-}], △[A^{3-}]).

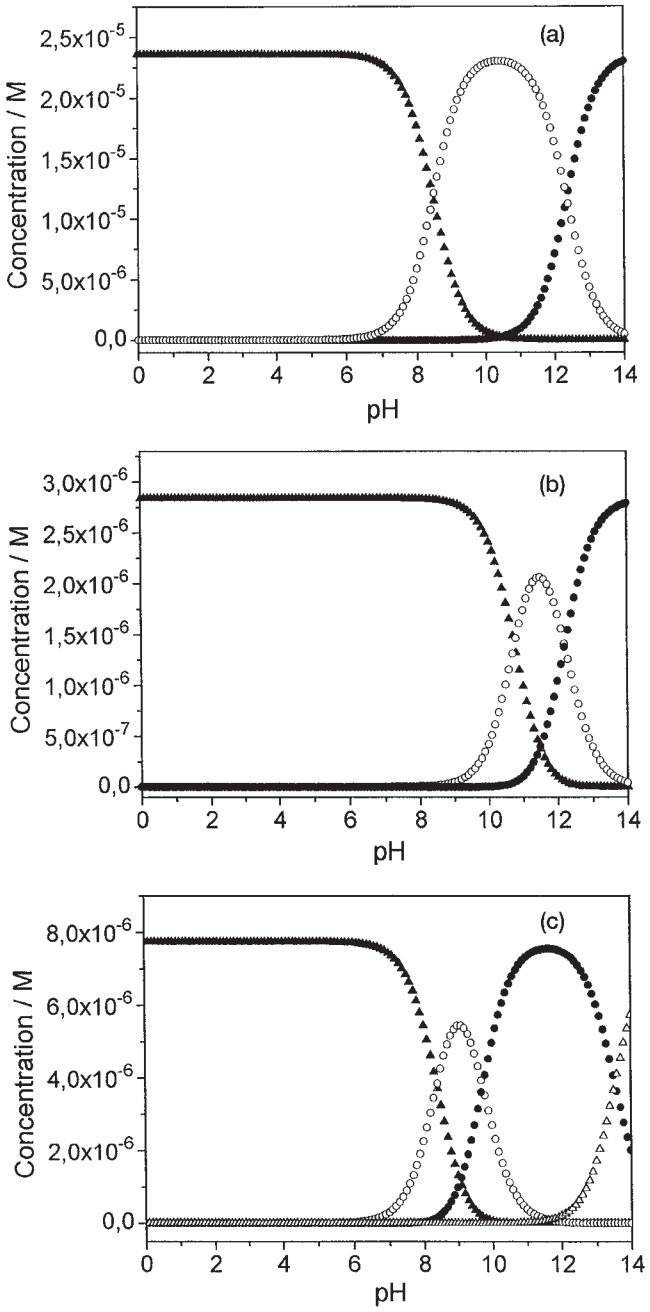

process (mixing of solutions and recording) did not exceed 1 min (these spectra at different pH values are shown in Fig. 2*b*).

The experimental curves of A^{λ} vs. pH were fitted by the procedure previously described. Results of the fitting process at three wavelengths (λ = 306, 324, and 390 nm) are gathered in Table 1.

A previous estimate of the quality of *A* values can be drawn from the comparison with the $\varepsilon^{exp}_{AH_2}$ by assuming that AH_2 is the only species in solution in an acidic pH range. Thus, the relative percent errors, $\Delta\varepsilon_{AH_2}\%$, are about 10% or lower for the

© 1998 NRC Canada

Table 2. Final results of the fitting process, extinction coefficients of different species at the wavelengths indicated, as well as dissociation constants for AOH.

Parameters	λ = 256 nm	λ = 280 nm	λ = 374 nm
F	$(6.992 \pm 0.008) \times 10^4$	$(1.29 \pm 0.04) \times 10^4$	$(3.79 \pm 0.06) \times 10^2$
G	$(1.26 \pm 0.01) \times 10^{-4}$	$(1.76 \pm 0.06) \times 10^{-4}$	$(1.91 \pm 0.04) \times 10^{-5}$
H	$(1.93 \pm 0.01) \times 10^{-14}$	$(5.74 \pm 0.05) \times 10^{-14}$	$(7.1 \pm 0.4) \times 10^{-15}$
I	$(8.6 \pm 0.1) \times 10^{-28}$	$(8.5 \pm 0.5) \times 10^{-28}$	$(4.0 \pm 0.2) \times 10^{-28}$
J		$(4.1 \pm 0.1) \times 10^{-9}$	
L		$(7.6 \pm 0.5) \times 10^{-19}$	
M		$(2.2 \pm 0.1) \times 10^{-32}$	
χ^2	3.2×10^{-4}	3.1×10^{-4}	1.3×10^{-6}
$\varepsilon^{\lambda}_{AH_3}$ / M^{-1} cm^{-1}	$(6.992 \pm 0.008) \times 10^4$	$(1.29 \pm 0.04) \times 10^4$	$(3.79 \pm 0.06) \times 10^2$
$\varepsilon^{\lambda}_{AH_2^-}$ / M^{-1} cm^{-1}	$(3.1 \pm 0.1) \times 10^4$	$(4.3 \pm 0.2) \times 10^4$	$(4.6 \pm 0.2) \times 10^3$
$\varepsilon^{\lambda}_{AH^{2-}}$ / M^{-1} cm^{-1}	$(2.5 \pm 0.2) \times 10^4$	$(7.5 \pm 0.5) \times 10^4$	$(9.3 \pm 0.1) \times 10^3$
$\varepsilon^{\lambda}_{A^{3-}}$ / M^{-1} cm^{-1}	$(4.1 \pm 0.3) \times 10^4$	$(4.1 \pm 0.3) \times 10^4$	$(1.9 \pm 0.2) \times 10^4$
$\varepsilon^{exp}_{AH^{2-}}$ / M^{-1} cm^{-1} [a]	2.55×10^4	7.3×10^4	9.5×10^3
$\Delta\varepsilon_{AH^{2-}}$ % [b]	2	3	2
Dissociation constants	$K_1 = (4.1 \pm 0.1) \times 10^{-9}$	$K_2 = (1.8 \pm 0.2) \times 10^{-10}$	$K_3 = (2.8 \pm 0.4) \times 10^{-14}$

[a] Determined at pH = 11.98.
[b] $\Delta\varepsilon_{AH^{2-}}\% = (\varepsilon^{exp}_{AH^{2-}} - \varepsilon^{\lambda}_{AH^{2-}}) \times 100 / \varepsilon^{exp}_{AH^{2-}}$.

three wavelengths chosen (Table 1). However, a reasonably good agreement was found between the experimental A^{λ} vs. pH plots and the calculated curves by using the fitting results at the three wavelengths studied (see Fig. 3(II)).

Values of K_1 and K_2 for ATX-I determined from the fitting process are also collected in Table 1. A K_1 value rather lower than the value of the acidity constant of phenol was estimated. A tentative explanation for this behavior might be given by considering that carbonyl groups near the hydroxyl groups in C(4) or C(4′) in the ATX-I structure (see Fig. 1) can be in solution in a keto–enol tautomeric equilibrium. The probable formation of an intramolecular hydrogen bond between the hydroxyl groups in C(4) or C(4′) and those of the corresponding enol tautomers could be responsible for an ATX-I acidity weaker than that of phenol. Theoretical calculations were used to confirm the probable existence of the intramolecular hydrogen bonds between the above-mentioned hydroxyl groups. Furthermore, it should be noticed that a marked structural difference can be found between the ATX-I structure and those corresponding to AME and AOH. When comparing the structures of ATX-I, AME, and AOH, a greater flexibility for ATX-I could be suspected by considering that three aliphatic six-membered rings are found in ATX-I. Besides, it is more difficult to decide which of the two phenolic hydroxyl groups in ATX-I is involved in the first ionization step. A distribution of species as a function of pH for this mycotoxin is shown in Fig. 4(*b*). As can be seen, AH_2 is the only species present in solution below a pH of ≈9. The contribution of AH^- and A^{2-} begins to be appreciable above that pH value.

AOH

AOH absorption spectra in ACN – 1 M $HClO_4$ were very similar to those recorded for AME in the same reaction medium. This can be explained by assuming that there is a similarity between the molecular structures of both compounds (see Fig. 1). These spectra showed an absorption maximum at λ = 256 nm. A plot of A^{256} as a function of the bulk concentration of AOH was linear in the concentration range from 7×10^{-6} to 2×10^{-5} M. From the slope of this plot, ε for AOH ($\varepsilon^{256}_{AOH} = 7.5 \times 10^4$ M^{-1} cm^{-1}) was calculated.

Absorption spectra of AOH did not show any change with time when recorded either at pH = 1.224 (acidic medium) or at pH = 10.825 and 12.825 (basic media) as was previously observed for AME. Also, the acidification of AOH – basic medium solutions allowed recovery of the characteristic form of the AOH absorption spectra obtained in acidic medium. This is evidence that the opening of the δ-lactone ring in the AOH structure in a basic medium should be sufficiently slow to be detected in the time period analyzed (40 min), at least up to pH 13.

The fitting was performed at three wavelengths (256, 280, and 374 nm) in a manner similar to that previously explained for other mycotoxins. Characteristic fitting parameters as well as calculated and experimental ($\varepsilon_{AH^{2-}}$) extinction coefficients with their relative percent errors are collected in Table 2. Good agreement was found between the experimental variation of A^{λ} as a function of pH and the curves calculated for a given wavelength by using the fitting results (see Fig. 3(III)).

Values of K_1, K_2, and K_3 determined from the fitting process are also collected in Table 2. The K_1 value ($K_1 = 4.1 \times 10^{-9}$) is very similar to that previously obtained for AME ($K_1 = 3.34 \times 10^{-9}$). This can be explained by assuming that the molecules are structurally related to one another (see Fig. 1). On the other hand, the fact that K_1 values calculated for AME and AOH are greater than the K_a value of phenol should allow us to infer that the formation of an intramolecular hydrogen bond between the hydroxyl group in C(3) of both AME and AOH and the carbonyl group of the corresponding δ-lactone rings should be absent. This hypothesis was later verified through the MM+ theoretical calculation. A similar conclusion was also reached by other authors (18) who performed a study about solvent effects on these mycotoxins by using both UV–VIS spectroscopic measurements as well as the retention times in normal-phase HPLC. They found that the changes in both spectroscopic and chromatographic properties could be explained by applying Taft's solvatochromic comparison

© 1998 NRC Canada

method (19). Only the Taft β-parameter, which measures the hydrogen-bond acceptor capacity of the solvent, had statistical significance in the correlation. It was also observed that the sensitivity of AOH to that parameter was greater than that of AME. They explained this behavior by assuming that AOH has one more free hydroxyl group than AME (18) (see Fig. 1).

A distribution of AOH species is shown in Fig. 4(*c*). AH_3 is the only species present in solution below pH 7. An appreciable contribution of AH_3, AH_2^-, and AH^{2-} is found from pH 7 to pH 12. $AH^{2-}$and A^{3-} are practically the only species present in solution above pH 12.

By assuming that AH^{2-} should be the only species present in solution close to pH = 12 (see Fig. 4(*c*)), additional proof concerning the quality of the fitting process for this mycotoxin can be reached by comparing the $\varepsilon_{AH^{2-}}$ value determined at pH = 11.98 and the $\varepsilon^{\lambda}_{AH^{2-}}$ value calculated from the fitting results ($\varepsilon^{\lambda}_{AH^{2-}} = H / L$). As can be observed in Table 2, good agreement was found between the $\varepsilon_{AH^{2-}}$ values obtained at that pH value and the $\varepsilon^{\lambda}_{AH^{2-}}$ values obtained from the ratio between the *H* and *L* parameters.

Acknowledgments

Financial support from the Consejo de Investigaciones Científicas y Tecnológicas de la Provincia de Córdoba (CONICOR) and the Secretaría de Ciencia y Técnica of the Universidad Nacional de Río Cuarto is gratefully acknowledged. P.G. Molina thanks CONICOR for a research fellowship. We are indebted to Lilia Fernández for language assistance.

References

1. (*a*) J. Chelkowsky and A. Visconti (*Editors*). *Alternaria*: biology, plant diseases and metabolites. Elsevier, New York. 1992; (*b*) A. Visconti and A. Sibilia. *In* Mycotoxins in grain. Compound other than aflatoxins. *Edited by* J.D. Miller and H.L. Trenholm. Eagan Press, Minnesota, U.S.A. 1994. Chap. 7.
2. L.M. Seitz. *In* Mycotoxins — production, isolation, separation and purification. *Edited by* V. Bettina. Elsevier, Amsterdam. 1984. Chap. 20.
3. E.E. Stinson, D.D. Bills, S.F. Osman, J. Siciliano, M.J. Ceponis, and E.G. Heisler. J. Agric. Food Chem. **28**, 960 (1980).
4. A. Visconti, A. Logrieco, and A. Bottalico. Food Addit. Contam. **3**, 323 (1986).
5. A.A. Ansari and A.K. Shrivastava. Food Addit. Contam. **7**, 815 (1990).
6. D. Prusky, Z. Gat, and P. Burd. Plant Dis. **77**, 249 (1993).
7. M.M. Wall and C.L. Biles. Phytopathology, **83**, 324 (1993).
8. R.W. Pero, H. Posner, M. Blois, D. Harvan, and J.W. Spalding. Environ. Health Perspect. June 87 (1973).
9. P.S. Steyn and C.J. Rabie. Phytochemistry, **15**, 1977 (1976).
10. D.B. Sauer, L.M. Seitz, R. Burroughs, H.E. Mohr, J.L. West, R.J. Milleret, and H.D. Anthony. J. Agric. Food Chem. **26**, 1380 (1978).
11. J.F. Griffin and F.S. Chu. Appl. Environ. Microbiol. **46**, 1420 (1983).
12. M.E. Stack and M.J. Prival. Appl. Environ. Microbiol. **52**, 718 (1986).
13. Y.-H. An, T.-Z. Zhao, J. Miao, G.-T. Liu, Y.-Z. Zheng, Y.-M. Xu, and R.L. van Etten. J.Agric. Food Chem. **37**, 1341 (1989).
14. B. Legovin and J.L. Burgot. Analyst, **121**, 43 (1996).
15. L. Davies. *In* Efficiency in research, development and production: the statistical design and analysis of chemical experiments. Royal Society of Chemistry, Cambridge, U.K. 1993.
16. J.N. Butler. *In* Ionic equilibrium. A mathematical approach. Addison–Wesley, Reading, Mass. 1964.
17. (*a*) T.W.G. Solomons. *In* Fundamentals of organic chemistry. John Wiley & Sons, Inc., New York. 1982; (*b*) S.H. Pine, J.B. Hendrikson, D.J. Cram, and G.S. Hammond. *In* Química Orgánica. 4th ed. McGraw–Hill, México. 1993.
18. L. Giacomelli, H. Bogetti, H. Agnelli, J. Anunziata, J.J. Silber, and R. Cattana. Anal. Chem. Acta. In press..
19. M.J. Kamlet, J.L. Abboud, M.H. Abraham, and R.W. Taft. J. Org. Chem. **48**, 2877 (1983).

© 1998 NRC Canada

Crystal chemistry of tetraradial species. Part 9. The versatile BPh_4^- anion, or how organoammonium H(N) atoms compete for hydrogen bonding[1]

Katherine N. Robertson, Pradip K. Bakshi, Susanne D. Lantos, T. Stanley Cameron, and Osvald Knop

Abstract: In organoammonium cations containing two or more N atoms, the H(N) atom introduced by the protonation may engage in an N—H(N)···Y bond to an external acceptor (anion or solvent molecule); in an *intra*-cation (intra-annular) N—H(N)···N′ bond; or in a branched N—H(N)···N′,Y bond(s), simultaneously intra-cation and to one or more external acceptors. The outcome of the competition for these bond types is determined by various factors, e.g., the size of the ring to be closed by insertion of the H(N) atom, steric accessibility of H(N), and the H-bond-forming strength of Y. Some of these are discussed in considerable detail and are exemplified by the hitherto unreported crystal structures of the tetraphenylborates (solvated or unsolvated) of the 2,2′:6′,2″-terpyridinium (**1**), 2,3-bis(2-pyridyl)pyrazinium (**2**), 2,2′-dipyridylammonium (**3**), 6,7-dihydro[*b*,*j*][1,10]phenanthrolinium (**9**), 2,4,7-triamino-6-pteridinium (triamterenium, **10**), proton-sponge (1-Me_2N-8-Me_2NH-naphthalene, **11**, **12**), and 9-amino-1,2,3,4-tetrahydroacridinium (tacrinium, **13**) cations. The crystal structures of the comparison compounds 2,3-bis(2-pyridyl)pyrazine (**4**) and its mono- (**2A**) and diprotonated (**3**) chlorides, and of 2-phenylpyridinium (**6**) and 7,8-benzoquinolinium (**7**, **8**) tetraphenylborates, have also been determined. The many interesting features of these crystal structures, such as the X—H(X)...phenyl bonding (X = N, O, C), are commented upon and crystallographic comparisons with numerous literature compounds are offered. Included in the discussion are the monoprotonated intrabridgehead cations of the bicyclic diamines of Alder et al., the N-H(N)-N′ angle of which has been shown, analytically, to be dominated by the size of the smallest of the rings in these tricyclic systems.

Key words: crystal structures, hydrogen bonding, intrabridgehead cations, proton sponges, tetraphenylborates.

Résumé : Dans les cations organoammonium contenant deux ou plusieurs atomes d'azote, l'atome H(N) introduit par la protonation peut donner lieu à une liaison N—H(N)···Y avec un accepteur externe (anion ou molécule de solvant); à une liaison N—H(N)···N′ intra-annulaire à l'intérieur du cation; ou à une (ou plusieurs) liaison(s) ramifiée(s), N—H(N)···N′,Y qui sont simultanément intra-cation et à l'un ou plusieurs accepteurs externes. Le résultat de la compétition pour ces types de liaisons est déterminé par divers facteurs, comme la grandeur du cycle à fermer par l'insertion de l'atome H(N), l'accessibilité stérique du H(N) et par la force de la liaison hydrogène qui se forme avec Y. On discute en détail de quelques-uns de ces facteurs et on en donne des exemples à l'aide de structures cristallines de tétraphénylborates (solvatés et non solvatés) des ions 2,2′:6′,2″-terpyridinium (**1**), 2,3-bis(2-pyridyl)pyridinium (**2**), 2,2′-dipyridylammonium (**3**), 6,7-dihydro[*b*,*j*][1,10]phénanthrolinium (**9**), 2,4,7-triamino-6-ptéridinium (triamtérénium, **10**), de l'éponge à proton (1-Me_2N-8-Me_2NH-naphtalène, **11**, **12**) et 9-amino-1,2,3,4-tétrahydroacridinium (tacrinium, **13**) qui n'avaient pas été rapportées jusqu'à maintenant. On a aussi déterminé les structures cristallines des composés de référence suivants : 2,3-bis(2-pyridyl)-pyrazine (**4**) et de ses chlorures mono- (**2A**) et diprotonés (**3**) et tétraphénylborates de 2-phénylpyridinium (**6**) et 7,8-benzoquinolinium (**7**, **8**). On commente plusieurs caractéristiques intéressantes de ces structures cristallines, telles les liaisons X—H(X)···phényle (X = N, O, C) et on présente des comparaisons cristallographiques avec de nombreux composés de la littérature. La discussion comporte les cations monoprotonés entre les têtes de pont de diamines bicycliques d'Alder et al., l'angle N-H(N)-N′ pour lequel il a été démontré d'une façon analytique qu'il est déterminé en grande partie par la grandeur du plus petit des cycles de ces systèmes tricycliques.

Mots clés : structures cristallines, liaison hydrogène, cations entre les têtes de pont, éponges de protons, tétraphénylborate.

[Traduit par la rédaction]

Received September 12, 1997.[2]

K.N. Robertson, P.K. Bakshi,[3] S.D. Lantos, T.S. Cameron, and O. Knop.[4] Department of Chemistry, Dalhousie University, Halifax, NS B3H 4J3, Canada.

[1] For Part 8 see ref. 1.

[2] Revision received April 15, 1998.
[3] Holder of a graduate scholarship, Canadian Commonwealth Scholarship and Fellowship Plan, and a Killam Graduate Scholarship.

[4] Author to whom correspondence may be addressed. Telephone: (902) 494-3317 or (902) 494-3305. Fax: (902) 494-1310.

© 1998 NRC Canada

The existence of N—H···phenyl hydrogen bonds in tetraphenylborates (TB) of organoammonium cations is by now well documented (1–3). As might be expected, these H-bonds are ordinarily of the *inter*-ion type. The H(N)···phenyl bond has only moderate or weak strength, and the size and shape of the TB anion are such that under favourable circumstances the H(N) may participate in bonds to other acceptors, viz. in an *intra*-cation N—H···N′ bond, in a normal N—H···Y bond to an external (neutral) acceptor Y, or in a branched N—H···phenyl,N′ or N—H···phenyl,Y bond. Such competition for bonding to the H(N) atom(s) will occur when the free-base molecule contains two or more N atoms, some or all protonable, or when the TB crystal contains solvent molecules with good H-bonding properties (H_2O, MeCN, Me_2CO, etc.), or when both conditions exist. Examples of various combinations of these bonds have been reported previously (1–3). In this paper we focus on providing conditions that are conducive to the formation of *intra*-cation N—H···N′ bonds in tetraphenylborates, sometimes to the exclusion of N—H···phenyl or even any other kind of H(N)-bonding in the crystal.

The cations selected for this investigation (Table 1) contain two or more rings that either form a planar system to begin with (fused-ring systems, **9**–**13**) or are converted to a planar ring system on protonation (*syn* rotamers; **1**, **2**, **5**). The two single-nitrogen cations, in **6** and **7**, have been included for comparison with their two-nitrogen counterparts, the previously (1) investigated cations in **15** and **17** that were found to be singly protonated. In the case of 7,8-benzoquinolinium TB, the crystal structures of both the unsolvated (**7**) and the solvated (**8**) forms have been determined. Also investigated were two solvates of the classical proton-sponge TB, the Me_2CO (**11**) and the $MeCN{\cdot}H_2O$ (**12**) forms. Included for comparison are 2,3-bis(2-pyridyl)pyrazine (**4**) and its mono- and dihydrochlorides (**2A**, **3**).

The two more exotic-sounding cations of **10** and **13**, triamterenium(1+) and tacrinium(1+), were chosen for investigation primarily because of the expected engagement of their several ring and exocyclic nitrogens in N—H···phenyl bonds. However, both are important also for their therapeutically noteworthy activity (18, 29). Triamterene, which contains a rigid pteridine ring system, is a "valuable potassium-sparing diuretic and also a modest inhibitor of dihydrofolate reductase" (17). Tacrine contains a 1,2,3,4-tetrahydroacridine ring system and has found application as an apparently effective acetylcholinesterase inhibitor in the treatment of Alzheimer disease (29).

We also report on our examination of the N—H···N′ bond geometry in the inside-protonated, intrabridgehead bicyclic diamines **44**–**50** investigated by Alder and co-workers (Table 1). These cations afford interesting comparisons with the above aromatic planar-ring cations.

Housekeeping

Crystal data of compounds **1**–**13** are listed in Table 2. The atom numbering adopted for **1**–**13** is a compromise between the IUPAC system and the desire for consistency when comparing corresponding structural features of the ring skeleton systems. The conformations shown in Fig. 1 anticipate those actually found in the crystal structures determined.

Phenyl rings in a TB anion are numbered R1–R4. Aromatic and other rings in a cation are numbered c1, c2, etc.; cat designates the skeleton of the whole cation, and c2/c1, etc. represents the angle between the best planes through the ring skeletons cl and c2, etc. In discussions involving H-bonding to phenyl rings, $\bar{d}$(X···R3), etc. is the mean of the X···C distances to the carbon atoms in ring R3, etc.; Δ(X···C) = $d(X{\cdots}C)_{max} - d(X{\cdots}C)_{min}$ for the same phenyl ring; π_c(R3), etc. refers to the centre of the phenyl ring R3, etc. skeleton.

Unless stated otherwise, the bond lengths and angles have not been corrected for the effects of thermal motion. Corrections, where made, are based on the rigid-body-motion (RBM) model. Crystallographic esd's are quoted in parentheses. No esd's are quoted for bond lengths and angles involving placed and not refined hydrogen atoms. Standard deviations of means of bond lengths and angles are quoted in square brackets. The means were computed with unit weights and their standard deviations do not take account of the esd's of the individual component values.

In discussing N—H bond lengths in N—H···N* bonds, use will be made of the expression

$$[1] \qquad d^* = d_o - b\ \ln\{1 - \exp[(d_0 - d)/b]\}$$

proposed by Steiner (30) for correlating d = N—proton and d = proton···N* distances. For moderately strong, essentially straight N—H···N* bonds (cf. also ref. 31), on introducing $D = d(N{\cdots}N^*) - d + d^*$ and setting $d_0 = 0.996$ Å and $b = 0.381$ Å from ref. 30, eq. [1] can be recast as

$$[2] \qquad d^* = D - 0.996 + 0.381\ \ln\{1 - \exp[(0.996 - d^*)/0.381]\}$$

Since in X-ray diffraction D is always determined with greater accuracy than d or d^*, eq. [2] makes it possible to estimate d and d^* from the N···N* separation alone, thus circumventing the uncertainty in the location of the H(N) atom.

The following tables and figures have been deposited:[5]

A. Positional parameters of the nonhydrogen atoms.
B. Positional parameters and isotropic temperature factors of the H atoms.
C. Anisotropic thermal parameters of the nonhydrogen atoms.
D. Geometry of the tetraphenylborate anions.
E. Planarity of the phenyl rings in the tetraphenylborate anions.
F. X···C and H(X)···C distances in the X—H(X)···phenyl bonds.
G. XOH_2 distances in TPTBw.
Fig. A. 2PyPzTB: difference map in the N(2)-N(2′)-C(2) plane.
Fig. B. 2PyPzCl: difference map in the N(2′)-C(2′2)-C(2′6) plane.

Results and discussion

Intra-cation N—B···N′ ring closure: general considerations

The skeleton topology, the suitability of the local cation

[5] This material may be purchased from: The Depository of Unpublished Data, Document Delivery, CISTI, National Research Council Canada, Ottawa, Canada K1A 0S2. Tables A, B, and D have also been deposited with the Cambridge Crystallographic Data Centre and can be obtained on request from The Director, CCDC, University Chemical Laboratory, 12 Union Road, Cambridge CB2 lEX, U.K.

© 1998 NRC Canada

Table 1. Crystal structures discussed in this paper.

No.	Compound	Code
This work		
1	$[2,2'{:}6',2''$-Terpyridine $H_2]^{2+}$ $(BPh_4)_2{\cdot}H_2O$	TPTBw
2	2,3-Bis (2-pyridyl) pyrazinium (1+) BPh_4[a]	2PyPzTB
2A	2,3-Bis (2-pyridyl) pyrazinium (1+) Cl[a]	2PyPzCl
3	2,3-Bis (2-pyridyl) pyrazinium (2+) Cl_2[a]	2PyPz2Cl
4	2,3-Bis (2-pyridyl) pyrazine[a]	2PyPz
5	2,2′-Dipyridylammonium (1+) $BPh_4{\cdot}H_2O$	DPATBw
6	2-Phenylpyridinium BPh_4	PPTB
7	7,8-Benzoquinolinium BPh_4	BQTB
8	7,8-Benzoquinolinium BPh_4·MeCN	BQTBs
9	6,7-Dihydro-5,6-dibenzo[*b*,*j*][1,10]phenanthrolinium (1+) BPh_4	DDPTB
10	Triamterenium (1+) $BPh_4{\cdot}$MeCN[b]	TTTBs
11	1-Me_2N-8-Me_2NH-Naphthalene (1+) $BPh_4{\cdot}Me_2CO$[c]	PSTBs
12	1-Me_2N-8-Me_2NH-Naphthalene (1+) $BPh_4{\cdot}$MeCN$\cdot H_2O$[c] (1)	PSTBw
13	Tacrinium (1+) BPh_4 ·MeCN[d]	TcTBs
Literature[e]		
14	18[(2,6)pyridino$_6$coronand-6], "sexipyridine" (4)	
15	2,2′-Bipyridinium (1+) BPh_4 (1) (ZUTDAT)	BPTB
16	TCNQ-BQ[f] (5) (BZQTCQ)	
17	1,10-Phenanthrolinium (1+) BPh_4 (1) (ZUTDEX)	PTB
18	1,10-Phenanthrolinium (2+) $(ClO_4)_2{\cdot}H_2O$ (6) (PENPCM)	
4	2,3-Bis (2-pyridyl) pyrazine[a] (7) (JITPIL)	2PyPz
19	2,3,5,6-Tetra (2-pyridyl) pyrazine, monoclinic (8) (VUKGAJ01)	
20	2,3,5,6-Tetra (2-pyridyl) pyrazine, tetragonal (9) (VUKGAJ)	
21	2,3,5,6-Tetra (2-pyridyl) pyrazinium (2+) Cl_2, 100 K (8) (VOWDOA)	4PyPz2Cl
22	2,3,5,6-Tetra (2-pyridyl) pyrazinium (2+) $(BPh_4)_2$, 100 K (8) (VOWDUG)	4PyPzTB
23	2,3-Bis (2-pyridyl) quinoxaline (10) (]EWLIG)	
24	2,3-Bis (2-pyridyl) quinoxaline[g] (11) (SENDEU)	
25	1,4-$(Me_2N)_2$-2,5-$(Me_2NH)_2$-benzene (2+) $Br_2{\cdot}2H_2O$ (12) (FANDIH)	
26	2,6-$(Me_2N)_2$-3,7-$(Me_2NH)_2$-naphthalene (2+) $Br_2{\cdot}4H_2O$ (13) (SETZIA)	
27	4-Me_2N-5-Me_2NH-phenanthrene (1+) $ClO_4{\cdot}0.3H_2O$ (14, 15) (DUBFAH)	
28	1,4-$(Me_2N)_2$-5,8-$(Me_2NH)_2$-naphthalene (2+) $Br_2{\cdot}5H_2O$ (16) (VIZNUN)	
29	Triamterene[b] (17) (FITZAJ)	TT
30	Triamterene·DMF$\cdot H_2O$[b] (18) (SEWZOJ)	TTsw
31	Pteridine (19) (PTERID11)	
32	2,4-Diaminopteridine$\cdot H_2O$ (20) (AMPTRA10)	
33	2,4-Diamino-6,7-Me_2-pteridine$\cdot$HCl$\cdot H_2O$ (21) (AMPTRB10)	
34	Tacrine$\cdot$HCl$\cdot H_2O$[d] (22) (GICMEK)	TcClw
34	Tacrine$\cdot$HCl$\cdot H_2O$[d] (23) (GICMEK01)	TcClw
35	7-Methoxytacrine$\cdot$HCl$\cdot H_2O$[d] (23) (WIDDAO)	MTcClw
36	9-Aminoacridine HCl$\cdot H_2O$ (24) (AMACRD)	AcClw
37	9-Aminoacridine$\cdot$HCl$\cdot 2H_2O$ (25) (AMACCL)	AcCl2w
38	4-Aminopyridine (26) (AMPYRE)	

Table 1 (*concluded*).

No.	Compound	Code
39	(4-Aminopyridine) $_2HClO_4$ (α), neutron diffraction (27) (APYRDN)	
40	(4-Aminopyridine) $_2HClO_4$ (β), 193 K (28) (CUTBUO)	
41	2,3-Bis (2-pyridyl)-6,7-Me_2-quinoxaline (32) (KIXKUX10)	
42	2,3-Bis (2-pyridyl)-6,7-Me_2-quinoxalinium (1+) BF_4 (32) (HAPKUE)	
43	2,3-Bis (2-pyridyl) benzoquinoxaline (33) (SOSREX)	
44	1,6-Diazabicyclo[4.4.4]tetradecanium (1+) Cl (35-37) (CABMOH)	
45	1,7-Diazabicyclo[5.4.2]tetradecanium (1+) picrate (43) (VUY CAT)	
46	1,7-Diazabicyclo[5.4.3]tetradecanium (1+) CF_3SO_3 (39) (GERZUY)	
47	1,7-Diazabicyclo[5.5.2]tetradecanium (1+) picrate (40) (GESBAH)	
48	1,7-Diazabicyclo[5.5.4]hexedecanium (1+) $(p\text{-}C_7H_4NO_4^-)(p\text{-}C_7H_5NO_4)$[h] (42) (VUXTUD)	
49	1,8-Diazabicyclo[6.4.3]pentadecanium (1+) picrate (38) (GASWOM)	
50	1,8-Diazabicyclo[6.5.3]hexadecanium (1+) picrate (41) (VUWXIU)	
51	{1,4,7,10-Tetraazabicyclo[5.5.3]pentadecane H_3}$(ClO_4)Br_2$, 120 K (47) (HIDSAO)	
52	{4,10-Me_2-1,4,7,10-Tetraazabicyclo[5.5.4]hexadecane H}ClO_4 (48) (JURGAE)	
53	{1,4,8,11-Tetraazatricyclo[6.6.2.$2^{4,11}$]octadecane H}$[Zn(H_2O)Cl_3]{\cdot}H_2O$, 120 K (49) (HIDRUH)	
54	2,2′-Dipyridylamine, *Pccn* (low mp) (50) (DPYRAM)	
55	2,2′-Dipyridylamine, $P\bar{1}$ (high mp) (51) (DPYRAM01)	
56	1-Me-2-(2′-pyridyl) aminopyridinium chloride (52) (VEKSAF)	
57	1,2-*trans*-Diaminocyclohexane HBr (53) (DACHXB)	

[a] 2,3-Di-2-pyridylpyrazinium(1+).
[b] Triamterene = 2,4,7-triamino-6-phenylpteridine.
[c] 1,8-$(Me_2N)_2$-naphthalene, proton sponge.
[d] Tacrine = 9-amino-1,2,3,4-tetrahydroacridine.
[e] In parentheses, reference code in the Cambridge Strutural Database.
[f] 7,7,8,8-Tetracyanoquinodimethane–7,8-benzoquinoline (1:1).
[g] Nonbonded dpq molecule in bromobis[2,3-di(2-pyridyl)quinoxaline]copper(II)–hydrogensulfate-2,3-di(2-pyridyl)quinoxaline (1:1).
[h] *p*-Nitrobenzoate *p*-nitrobenzoic acid solvate.

geometry for intra-cation H-bonding, and the anticipated type of bond in the compounds of Table 1 can be conveniently assessed with the aid of an appropriate planar template. In their idealized, flattened conformations *all* the cations of Table 1 except **43**–**53** can be embedded, schematically, in the 13-cell honeycomb template of Fig. 1 and most in the heavily outlined 7-cell subtemplate. The embedding classifies possible intra-cation N—H···N′ interactions according to the idealized N···N′

© 1998 NRC Canada

Table 2. Crystal data of the compounds investigated in this work.[a]

Parameter	TPTBw	2PyPzTB[b]	2PyPzCl[b]	2PyPz2Cl[b]	2PyPz[b]	DPATBw[b]
Formula	$B_2C_{63}H_{55}N_3O$	$BC_{38}H_{31}N_4$	$C_{14}H_{11}ClN_4$	$C_{14}H_{12}Cl_2N_4$	$C_{14}H_{10}N_4$	$BC_{34}H_{32}N_3O$
fw	891.8	554.5	270.7	307.2	234.3	509.5
Crystal size, mm^3	$0.5 \times 0.3 \times 0.25$	$0.25 \times 0.35 \times 0.60$	$0.2 \times 0.2 \times 0.25$	$0.2 \times 0.2 \times 0.35$	0.3×0.25[d]	$0.21 \times 0.09 \times 0.08$
μ, cm^{-1}	0.7	5.2	25.2	40.4	6.7	5.5
Max/min[e]	—	1.00–0.93	1.00–0.86	1.00–0.63	1.00–0.80	1.00–0.66
θ-range[f]	2–23/20	2–60/25	2–60/25	2–60/25	2–60/25	2–60/25
a, Å	27.148(8)	18.336(3)	8.017(2)	8.630(1)	16.472(2)	14.626(2)
b, Å	11.965(9)	18.336(3)	16.906(1)	11.428(2)	9.469(2)	8.886(2)
c, Å	15.751(3)	35.670(6)	9.735(1)	8.051(1)	7.505(1)	22.338(2)
α, deg	90	90	90	95.91(1)	90	90
β, deg	109.58 (4)	90	99.84(1)	107.90(1)	90	95.79(1)
γ, deg	90	90	90	70.96(1)	90	90
V, $Å^3$	4820(6)	11992(3)	1300.1(3)	714.3(2)	1170.5(6)	2889(1)
Z	4	16	4	2	4	4
ρ_c, g/cm^3	1.229(2)	1.228(1)	1.383(1)	1.428(1)	1.329(1)	1.171(1)
F(000), e	1888	4672	560	316	488	1080
Space group	*C*2/*c* (no. 15)	$I4_1/a$ (no. 88)	$P2_1/n$ (no. 14)	*P*$\bar{1}$ (no. 2)	*Pbcn* (no. 60)	$P2_1/c$ (no. 14)
h, *k*, *l* ranges	0/29,0/13,–16/16	0/20,0/20,0/40	0/8,0/19,–10/10	0/9,–12/12,–8/8	0/18,0/10,–8/0	0/16,0/9,–24/24
Reflections:						
total measured	3639	4872	2157	2274	1051	4805
unique total	3551	4553	2002	2110	1051	4608
unique used[g]	1326	2529	1074	1495	501	1745
$100R_{merg}$	3.7	3.0	3.5	2.3	3.2	2.9
data/parameters	4.1	6.4	6.2	8.2	6.0	4.9
$100R$; $100R_w$	3.8; 3.9	3.8; 3.6	3.7; 3.7	3.1; 3.2	3.7; 3.5	4.7; 5.3
G.O.F.	1.89	1.95	1.57	1.88	2.00	2.59
Weighting scheme[i]	Sigma	Unit	Sigma	Sigma	Sigma	Sigma
Residual e.d.[j]	–0.13/0.14	–0.14/0.11	–0.17/0.23	–0.16/0.13	–0.14/0.10	–0.18/0.18

[a] Rigaku AFC5 single-crystal diffractometer, sealed 2.4 kW tube, λ(Mo Kα) = 0.710 69 Å (graphite monochromator); $T = 20$ (2)°C. For code words see Table 1; for additional details see Experimental.

[b] 12 kW rotating-anode tube, λ(Cu Kα) = 1.54178 Å (graphite monochromator).

[c] 12 kW rotating-anode tube, λ(Mo Kα) = 0.71069 Å (graphite monochromator).

[d] Approximate trigonal pyramid, 0.30 mm base, 0.25 mm height.

[e] Maximum and minimum transmission factors applied (ψ-scans).

[f] $\theta_{min} \leq \theta \leq \theta_{max}/n$. The lattice paramaters and orientation matrices were obtained by least squares from the setting angles θ of *n* suitable reflections.

[g] $I > 3\sigma(I)$.

[h] $I > 2\sigma(I)$.

[i] See Experimental.

[j] Minimum and maximum residual peaks ($e/Å^3$) in the final difference map.

distances in the pertinent (completed) hexagonal cell: *ortho* (*o*) for the two N atoms in a cell edge, at a nominal distance in the template plane of ~1.4 Å (but see below), *meta* (*m*) and *para* (*p*) across the hexagon, at ~2.4 and ~2.8 Å, respectively.[6]

The planar template cell containing the two N atoms cannot be completed, i.e., the ring cannot be closed by an intra-annular N—H(N)···N′ bond, without distortion of the cation geometry. Insertion of a H(N) atom into the free-base molecule will result, on closure, in a 7-membered ring for the *o* type, a 6-membered ring for the *m* type, and a 5-membered ring for the *p* type; the template geometry for a 4-membered ring is unfavourable for closure (Fig. 2). Because the N—H(N) bond (nominally 1 Å) is shorter than the mean cell edge, the H(N) atom will not fall on any cell apex in the template.

It is immediately obvious that in the *o* case the H(N) atom introduced by the protonation cannot be accommodated between the two N atoms ~1.4 Å apart without a significant departure from planarity if reasonable skeleton bond angles are to be maintained. There will also be some "hydrophobic" shielding of the H(N) proton from involvement in *external* H-bonding by the H(C) atoms on the neighbouring exposed ring carbons.[8] In the *m* and *p* cases an appreciable departure from planarity on ring closure would not be expected, but some in-plane distortion should result, partly because of the H(N)···N′ interaction and partly because of the expansion of the endocyclic *ipso* angle at the N atom on protonation. The

[6] Genuinely three-dimensional situations (e.g., **57**) would require a three-dimensional template, less likely to be useful than the planar template of Fig. 1. For the special case of the inside-protonated, intrabridgehead cations of bicyclic diamines (34–46; see also footnote 7), see a later section.

[7] R.W. Alder, J.M. White, A.G. Orpen, and T.F. Koetzle. Unpublished data (communicated to the authors by R.W. Alder).

[8] For a discussion of this point see ref. 14.

© 1998 NRC Canada

Table 2.

PPTB	BQTB[b]	BQTBs[c]	DDPTB[b]	TTTBs	PSTBs[b]	PSTBw[b]	TcTBs[b]
$BC_{35}H_{30}N$	$BC_{37}H_{30}N$	$BC_{39}H_{33}N_2$	$BC_{46}H_{39}N_2$	$BC_{38}H_{35}N_8$	$BC_{41}H_{45}N_20$	$BC_{40}H_{46}N_30$	$BC_{39}H_{38}N_3$
475.4	499.5	540.5	630.6	614.6	592.6	595.6	559.5
0.23 × 0.25 × 0.41	0.12 × 0.27 × 0.45	0.2 × 0.015 × 0.25	0.1 × 0.25 × 0.3	0.1 × 0.15 × 0.55	0.2 × 0.25 × 0.25	0.15 × 0.2 × 0.25	0.12 × 0.04 × 0.02
0.6	5.3	0.6	4.9	0.7	5.1	5.2	5.2
—	1.00–0.42	—	1.00-0.49	—	1.00–0.57	1.00–0.61	1.00–0.64
2-23/22	2-58/22	2–20/22	3–60/22	2–23/20	3–60/24	3–60/25	4–60/25
12.208 (2)	12.499(2)	11.502(5)	10.168(8)	14.329(4)	8.258(2)	11.215(1)	12.737(7)
13.182 (5)	12.984(2)	14.949(4)	21.239(10)	10.544(4)	21.950(2)	18.806(2)	12.995(5)
17.015 (1)	17.581(2)	9.810(2)	16.066(8)	22.133(4)	19.218(2)	8.336(1)	12.284(3)
90	90	104.11(2)	90	90	90	92.86(1)	90.19(3)
107.28 (1)	107.86(1)	101.92(3)	91.03(6)	98.75(2)	91.83 1)	97.94(1)	113.83 (2)
90	90	70.26(3)	90	90	90	97.72(1)	61.09 (2)
2614 (2)	2716(1)	1525(2)	3469(3)	3305(3)	3482(1)	1721(1)	1581 (1)
4	4	2	4	4	4	2	2
1.208 (1)	1.222(1)	1.177(2)	1.207(1)	1.235(1)	1.130(1)	1.149(1)	1.176 (1)
1008	1056	$\bar{1}$572	1336	1296	1272	$\bar{1}$640	$\bar{1}$596
$P2_1/c$ (no. 14)	$P2_1/c$ (no. 14)	$P\bar{1}$ (no. 2)	$P2_1/n$ (no. 14)	$P2_1/n$ (no. 14)	$P2_1/n$ (no. 14)	$P\bar{1}$ (no. 2)	$P\bar{1}$ (no. 2)
0/13,0/14,–18/17	0/13,0/14,–19/18	0/9,–13/14,–9/9	0/10,0/23,–18/18	0/16,0/9,–24/25	0/8,0/24,–21/21	0/12,–21/20,-9/9	0/12,–12/14,–13/12
4032	4213	3766	4258	5124	5413	5591	4483
3831	4002	2699	3924	4898	4998	5127	4238
2025	1726	1758[h]	794	1901	1672	1625	1304[h]
4.1	2.7	5.0	11.8	3.0	5.1	7.9	6.6
6.1	4.9	5.0	4.0	4.5	4.1	4.1	3.9
4.1; 4.0	3.6; 3.4	5.6; 8.5	7.0; 7.1	4.1; 4.5	3.9; 4.0	5.4; 5.6	6.9[h]; $wR2 = 0.191$[h]
2.03	1.54	1.90	2.19	0.74	1.40	2.41	1.00 (on F^2)
Sigma	Unit	Sigma	Unit	Unit	Sigma	Sigma	SHELX
–0.19/0.15	–0.13/0.10	–0.19/0.17	–0.18/0.23	–0.26/0.20	–0.13/0.12	–0.19/0.15	–0.23/0.23

situations obtained are illustrated, in terms of the template geometry, in Fig. 2. The N-H(N)-N′ angle, which decreases with the decreasing ring size, is favourable for the formation of a bifurcated H(N)···N′,Y bond to an external acceptor Y in both the *m* and *p* systems, until exclusive formation of unbranched H-bonds to external acceptors is-expected for 3-membered N-C-N′ groups.

Intra-cation ring closure: present results

Tables 3 and 4 provide synoptic presentations of the N—H···N′ ring-closure situations in our structures as well as in the comparison structures of Table 1.[9] The results, without exception, agree with the expectations outlined in the preceding section.

[9] For details and for other aspects of the structures the reader is referred to the descriptions of the individual crystal structures below.

In the ortho case, analysis of our example, 2PyPzTB (**2**), substantiates two points: (*i*) protonation, of only one of the pyridine nitrogens, does result in ring closure, and (*ii*) the expected nonplanarity of the pyridine rings is confirmed, c2′/c2 = 14.3°. The first point is not trivial. Ring closure very similar to that in **2** is observed in the counterparts of **2**, the analogous TBs of the 2,3,5,6-tetra(2-pyridyl)pyrazinium(2+) (**22**) and 2,3-bis(2-pyridyl)quinoxalinium(1+) cations (S.D. Lantos, T.S. Cameron, and O. Knop, to be published). In **22** the centrosymmetric diprotonated (two protons per four pyridine nitrogens) cation has ring closure on both sides of the pyrazine ring, with a c2′/c2 angle between the two ipsolateral pyridine rings of ~37°. The relevant geometry of the 2,3-bis(2-pyridyl)-quinoxalinium(1+) cation is practically the same as that of the cation in **2**. The free bases of the cations in these last two TBs are known to occur with both the *syn* and the *anti* conformations (**19** and **20**, **23** and **24**). If the ground-state conformation

© 1998 NRC Canada

Fig. 1. Idealized (flattened) ring systems of cations in Table 1; all can be embedded in the heavily outlined portion (**a**–**g**) of the honeycomb template. Large black circles, N atoms; small black circles, H(N) atoms introduced by protonation; small open circles, H(N) atoms present before protonation. The conformations shown correspond to those actually found. The atom and ring numbering in **6** and **7** matches that in **15** and **17**, respectively (1). The Me groups on N(1) and N(8) of **11** and **12** are not shown.

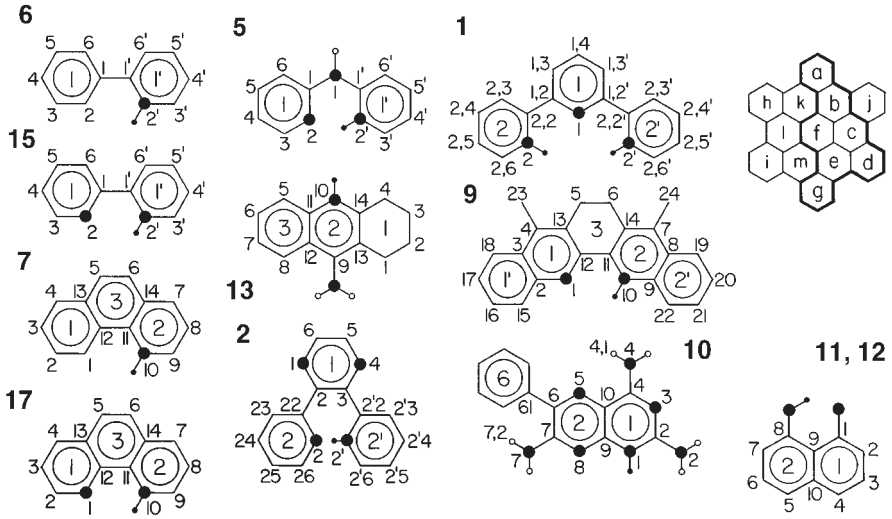

Fig. 2. Possible formation of intra-cation H-bonds through intra-annular N—H···N′ ring c1osure resulting in 6-, 5-, and 4-membered rings. The approximate distances and angles shown are for undistorted planar ring systems of Fig. 1 and for N—H bond lengths of nominally 1 Å. H(N) atoms in the 6- and 5-membered rings are likely to form bifurcated H(N)···N′,Y bonds to external Y acceptors, while those in the putative 4-membered ring are likely to form normal, possibly somewhat bent H(N)···Y bonds (see text).

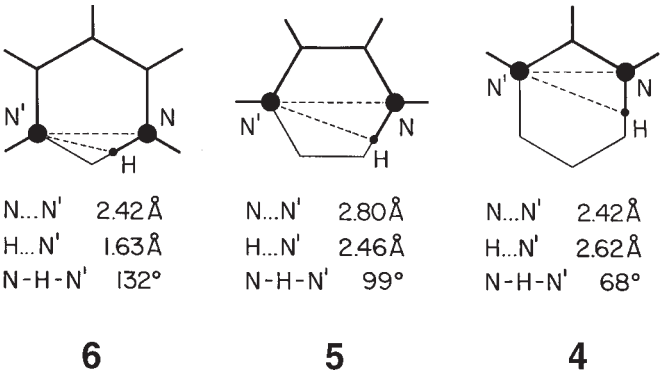

of the free base is *syn* and is maintained in the crystal, the ring closure on formation of the TB will merely correspond to a natural, minimum-energy conformational adjustment. If, however, the ground-state conformation is *anti*, the existence of a crystalline *syn* form of the free base must be due to crystal forces. The existence, then, of a protonated *syn* conformation in the TB crystal means that the energy of the ring closure must be sufficient to overcome the *anti–syn* conversion barrier, with or without assistance from crystal forces. If the ground-state conformation of the free base is *anti*, the *syn* conformation in the TB is then the result of a positive tendency of the proton to effect ring closure. Adequate conformation-energy calculations or, better still, experimental evidence of the conformational preference in the free base would be required to resolve this problem. For the free base of **2** only the *syn* form (**4**) has been reported, but it seems possible that the situation here parallels that of the two preceding cations and that an *anti* form may eventually be found.[10]

The ring closures in the TBs **2** and **22** correspond to short normal (i.e., unbranched) N—H(N)···N′ bonds (Table 4). There is no effective H-bonding interaction between H(N) and the anion. In **2** the three shortest H(N)···C(phenyl) distances are H(2′)···C(132) = 3.66(4) Å (N(2′)···C(132) = 3.656(4) Å, N(2′)-H(2′)-C(132) = 80(2)°); H(2′)···C(142) = 3.87(4) Å (N(2′)···C(142) = 4.225(4) Å, N(2′)-H(2′)-C(142) = 100(4)°); and H(2′)···C(133) = 3.90(4) Å (N(2′)···C(133) = 3.493(4) Å, N(2′)-H(2′)-C(133) = 61(2)°); all the other H(N)···C(phenyl) distances are longer than 4.0 Å (Tables 5 and F). In **22** the two shortest H(N)···C(phenyl) distances are ~3.15 Å (N···C = 3.54 Å, N-H(N)-C ~ 98°) and ~3.43 Å (N···C = 3.65 Å, N-H(N)-C ~ 90°), both to the same phenyl ring; all the other H(N)···C(phenyl) distances are ≥ 3.6 Å, with the corresponding N-H(N)-C angles between 61° and 99°.

In the corresponding *chlorides* **2A** and **21**, both with the pyridine nitrogens *syn* to each other, closure of the 6-membered ring through proton insertion is precluded by the large c2′/c2 angle, 55.5° and 60.0°, respectively, the consequence of a competing strong inter-ion N—H(N)···Cl bond (Fig. 3). In **3**, in which *both* pyridine nitrogens are protonated, closure of the

[10] The pyridinium nitrogens are *syn* also in **41** and **43**. In **41** the angles between the pyridine and pyrazine rings are ~43° and ~24°, respectively. Protonation of **41** is reported to result, in the tetrafluoroborate **42**, in ring c1osure but with the proton in two locations with, respectively, 0.8 and 0.2 occupancy factors and N—H and H···N′ distances of 0.79(4) and 1.80(4) Å, and 1.08(11) and 1.49(10) Å. The occurrence of alternative locations may be associated with the disorder of the BF_4^- anion, although in the analogous case of the perchlorate **27** (Table 4) only one proton location is mentioned. For the stated N···N′ distance of 2.574(4) Å in **42**, eq. [2] yields *d*(N···H) of ~1.14 Å and ~1.43 Å if the stated N-H-N′ angles of 169(4)° and 172(4)°, respectively, are taken as sufficiently c1ose to 180°.

© 1998 NRC Canada

Table 3. Hydrogen bonding in compounds of Table 1 with cations or molecules containing two or more (protonable) N atoms.[a]

				H(N) bonds[b]						H(N) bonds[b]	
Type	No.	Anion	Solvation	Intra	Inter	Type	No.	Anion	Solvation	Intra	Inter
o	**2**	TB^-	No	Yes	No[c]	*p*	**18**	ClO_4^-	H_2O	Yes[e,i]	H_2O
o	**27**	ClO_4^-	$0.3H_2O$	Yes	No	*p*	**29**	—	No	Yes[j]	N[k]
o	**42**	BF_4^-	No	Yes	No	*p*	**30**	—	DMF, H_2O	Yes[j]	N[k]
o	**2A**	Cl^-	No	No	Cl^-	*p*	**10**	TB^-	MeCN	Yes[e,j]	Phenyl
o, *o*	**22**[d]	TB^-	No	Yes	No	*p*	**32**	—	H_2O	Yes[j]	Phenyl
o, *o*	**21**[d]	Cl^-	No	No	Cl^-	*p*	**33**	Cl^-	H_2O	Yes[j]	Cl^-
o, *p*	**3**	Cl^-	No	Yes	Cl^-[e]	*p*, *p*	**1**	TB^-	H_2O	Yes	H_2O[m]
m	**5**	TB^-	H_2O	Yes	Phenyl[f]	*p*, *p*	**25**	Br^-	$2H_2O$	Yes	H_2O
m	**11**	TB^-	Me_2CO	Yes	No[e,g]	*p*, *p*	**26**	Br^-	$4H_2O$	Yes	H_2O
m	**12**	TB^-	MeCN, H_2O	Yes	No[e,g]	—	**13**	TB^-	MeCN	No	MeCN; phenyl[n]
m, *m*	**28**	Br^-	$5H_2O$	Yes	No (?)[h]	—	**34**	Cl^-	H_2O	No	H_2O; Cl^-[p]
p	**9**	TB^-	No	Yes	Phenyl	—	**35**	Cl^-	H_2O	No	H_2O; Cl^-[p]
p	**15**	TB^-	No	Yes	Phenyl	—	**36**	Cl^-	H_2O	No	H_2O; Cl^-[p]
p	**17**	TB^-	No	Yes	Phenyls	—	**37**	Cl^-	$2H_2O$	No	H_2O; Cl^-[p]

[a] Other examples will be found in Tables 3 and 4 of ref. 1. *o*,*o*, *m*,*m*, *p*,*p*: *two* pairs of eligible N atoms.

[b] Intra, N—H(N)···N′ intra-cation bond; inter, external N—H(N)···Y bond to an anion, to an adjacent molecule, or to a solvent molecule, involving the H(N) atom of the N—H(N)···N' intra-cation bond. H(N)···N',Y bonds are bifurcated.

[c] H(N) partially shielded from possible external acceptors by vicinal H(C) atoms.

[d] Free base (**19**, **20**) and dihydrochloride (**21**) colourless; **22** yellow both in crystal and in solution (MeCN + MeOH).

[e] See text.

[f] Also N(1)—H(1)···O and O—H(O)···phenyl interactions.

[g] Also H(C)···phenyl interactions.

[h] H_2O molecules disordered.

[i] Both N atoms protonated. The H(1)-N(1)-C(12)-C(11)-N(10)-H(10) group is closed by the O atom of a H_2O molecule to yield a 7-membered ring.

[j] The pertinent H(N) atom(s) is present before protonation.

[k] N atom of a neighbouring molecule.

[m] Also O—H(O)···phenyl interactions.

[n] N(10)—H(10)···MeCN, N(9)—H(9A/B)···phenyl.

[p] N(10)···H(10)···H_2O, N(9)—H(9A/B)···Cl.

6-membered ring is prevented by the change in the orientation of ring c2 from *syn* to *anti* relative to c2′. This change is associated with the formation of a *second* H(N)C1 bond and results in the closure of the *4-membered* ring between c2 and cl, i.e., between N(2) and the pyrazine nitrogen N(1). This closure, with a strong inter-ion component, belongs to the *p* class (Table 4).

In the meta case, conversion of the free base into the cation of **5** brings the two pyridine rings into a *syn* conformation and results in the closure of the N(2)-C(l)-N(l)-C(l′)-N(l′) group and thus in the formation of a relatively unstrained 6-membered ring (Fig. 1). An analogous N(l)-C(l)-C(9)-C(8)-N(8)-H(8) ring is formed when the classical, rigid-skeleton proton sponge 1,8-$(Me_2N)_2$-naphthalene is protonated to the cation of **11** and **12** (Fig. 1); an example of the corresponding *two-sided* proton-sponge cation is provided in **28**. The N-H(N)-N′ angles in these cations are more or less in the expected range of 130°–140°.[11] The eligible acceptors of H(N) are a phenyl group in **5**, the acetone oxygen in **11**, the MeCN nitrogen in **12**, and a Br^- anion in **28**. The H(N)···Y distances to these acceptors (Tables 4 and 5) are considerably longer than would be expected for unbranched H-bonds, but the orientations of the acceptors with respect to the cation are such as to support the existence of weak H-bonding interactions, cf. the N-H(N)-Y angles, all in the same general range of 100°–120°. The question of whether such H(N)···Y distances represent H-bonds will have to await detailed deformation electron density studies.

In the para case, the N-H(N)-N′ angles (Table 4) are, as expected, significantly smaller, in the range of 85°–110°. The estimated shortest H(N)···C(phenyl) distances range from ~2.35 to ~2.9 Å. The distances from H(N) to other acceptors appear to qualify for weak or very weak H-bonds, but in several cases the geometries are not clear-cut, since the acceptor atom is involved in positional disorder. The N-H(N)-Y angles form a reasonably homogeneous set, with an approximate mean value of 135[15]°. On the whole, ring closure in the *p* groupings can be said to result in the formation of bifurcated N—H(N)···N′,Y bonds to phenyl as well as other acceptors.

An interesting *p* case is **18**, which contains a *doubly*-protonated 1,10-phenanthrolinium(2+) cation. Since both N atoms of the rigid ring system are protonated, closure of the six-atom H(1)-N(1)-C(12)-C(11)-N(10)-H(10) group can only take place by co-option of an external acceptor capable of simultaneous bonding to both H(1) and H(10). This atom is the oxygen of an H_2O molecule. The structure of **18** contains two nonequivalent cations and two nonequivalent water molecules; the bond lengths and angles averaged over the two cations can be compared with the corresponding mean values in the monoprotonated 1,10-phenanthrolinium(l+) cation (Tables 3 and G of ref. 1):

[11] The mean of the N-H(N)-N′ angles in the c1assical proton-sponge cations in Table 4 of ref. 1 is 155[5]°.

© 1998 NRC Canada

Table 4. N—H(N)···N′ ring closure geometries and hydrogen bonding to external acceptors Y in crystal structures of Table 1.[a]

		Intra-cation bond			External bond			
Type	No.	N···N′	H(N)···N′	N-H(N)-N′	Y	N···Y	H(N)···Y	N-H(N)-Y
o	**2**	2.52	1.37	168°	None[b]			
	27	2.54	1.36	168°	[ClO_4[c]	4.22	3.69	108°]
	42	2.57			[BF_4[d]			]
	2A	[2.90	2.96	75°][b]	Cl	2.92	1.77	171°
o,*o*	**22**	2.53	1.33	160°	None[b]			
	21	[2.88	2.90	81°][b]	Cl	2.95	2.05	171°
o,*p*	**3**	[4.46	3.90	112°][b,e]	Cl(1)	2.98	1.83	179°
		2.65	2.25	99°[f]	Cl(2)	3.00	2.07	142°
m	**5**	2.63	1.87	129°	Phenyl[g]	3.51	2.81	125°
	11	2.68	1.54	158°	[O	3.35	-3.00	-97°]
	12	2.62	1.63	138°	[N(5)	3.54	-2.84	-117°]
m,*m*	**28**	2.57	1.39	158°	[Br	3.91	3.42	104°]
p	**9**	2.61	2.18	106°	Phenyl[h]	3.34	2.88	126°
	15	2.61	2.11	105°	Phenyl[i]	3.28	2.52	123°
						3.31	2.37	142°
	17	2.71	2.33	98°	Phenyls[j]			
	18[b]	2.87	2.56[4]	97[5]°	O_w	2.76[3]	1.76[2]	169°
	29	2.77	2.48	105°	N[m,n]			
		2.76	2.74	83°	N[m,n]			
	30	2.80	2.43	97°	O_w	3.33		112°
	10	2.80	2.73	84°	C(13A)	3.49	2.61	155°
	32	2.79	2.48	97°	N[m]	3.07	2.20	144°
	33	2.74	2.27	111°	Cl	3.20	2.48	135°
		2.74	2.37	102°	Cl	3.15	2.34	142°
p,*p*	**1**	2.64	2.20	104°	O_w	2.82	1.93	144°
	25	2.72			O_w	2.94		119°
	26	2.69			O_w	2.92		

[a] Distances (Å) involving H(N) atoms are estimated to be accurate to within ±0.05 Å, angle to within ±5°. For N···Y distances see Table 8. O_w, oxygen atom of an H_2O molecule. Entries in square brackets refer to H(N)···Y bonds that are at best marginal.

[b] See text.

[c] No external bond. Oxygens of the ClO_4^- anion are disordered; the values quoted here refer to one O set only.

[d] Disordered BF_4^- anion (see footnote 10 in text).

[e] N(2')—H(N2′)···Cl(1); potentially *o* type but no intra-cation ring closure.

[f] N(2)—H(N2)···N(1),Cl(2); intra-cation ring closure to pyrazine N(1) atom.

[g] The shortest N···C(R2) and H(N)···C(R2) distances in **5**.

[h] The shortest N···C(R1) and H(N)···C(R1) distances in **9**.

[i] The shortest N···C(R2A) and H(N)···C(R2A) distances in **15**.

[j] Trifurcated H(N)···N',R3,R1 bond, see ref. 1.

[k] These are the averages of the distances in the two nonequivalent *diprotonated* cations in **18**, in which an O_w atom closes the H(1)-N(1)-C(12)-C(11)-N(10)-H(10) group to form a 7-membered ring. Each H(N) atom may be regarded as involved in a weakly bifurcated N—H(N)···N',O_w bond with H(N)···O_w as the principal component (see text).

[m] N atom of an adjacent molecule.

[n] H(N) disordered.

	Dication	Monocation
C(11)—C(12)	1.421[7] Å	1.431[3] Å
N(1)···N(10)	2.873[4] Å	2.722[9] Å
H(1)···H(10)	1.94 Å	—
N(1)—C(12) } N(10)—C(11) }	1.366[6] Å	{ 1.356[1] Å, 1.358[6] Å }
H(N)···N′	2.56[4] Å	2.38[3] Å
N-H(N)-N′	97[3]°	102[3]°
N···O	2.757[24] Å	—
H(N)···O	1.76[2] Å	—
N-H(N)-O	169[12]°	—

The differences for N(1)···N(10) and H(N)···N′ are statistically highly significant, whereas the difference for N-H(N)-N′ is not significant (*t* test for two means). Thus while the protonation at N(1) has little if any effect on the C(11)—C(12) bond length, the significant expansion of the N(1)···N(10) distance and the attendant changes in the bond angles (cf. Fig. 8 of ref. 1) are such as to separate H(1) and H(10) by ~1.94 Å. This separation apparently is sufficient, on closure by the O atom, to maintain planarity of the resulting 7-membered ring;[12] the N···O ~ 2.76 Å

[12] The skeleton of cation 1 is planar to 0.01[1] Å and that of cation 2 to 0.02[1] Å; the deviation of the pertinent O atom from the cation plane is 0.07 Å for cation 1 and 0.00 Å for cation 2.

© 1998 NRC Canada

Fig. 3. Conformations in the crystal structures of 2-pyridyl-substituted pyrazines (**4**, **19**, **20**) and quinoxalines (**23**, **24**), and H-bonding in their chlorides (**2A**, **3**, **21**) and tetraphenylborates (**2**, **22**). The angle between the pyrazine (or quinoxaline) and the pyridine planes is indicated next to the pyridine ring, and that between the planes of the two ipsolateral pyridine rings (the acute angle) at the bottom of each figure. Large black circles, N atoms; small black circles, H(N) atoms; large open circles, Cl atoms; broken-line hexagons, anion phenyl rings potentially eligible for N—H(N)···phenyl bonding. The orientations of the ring systems match those of Fig. 1. Note the similarity of the pyridine/pyridine angles in the free bases.

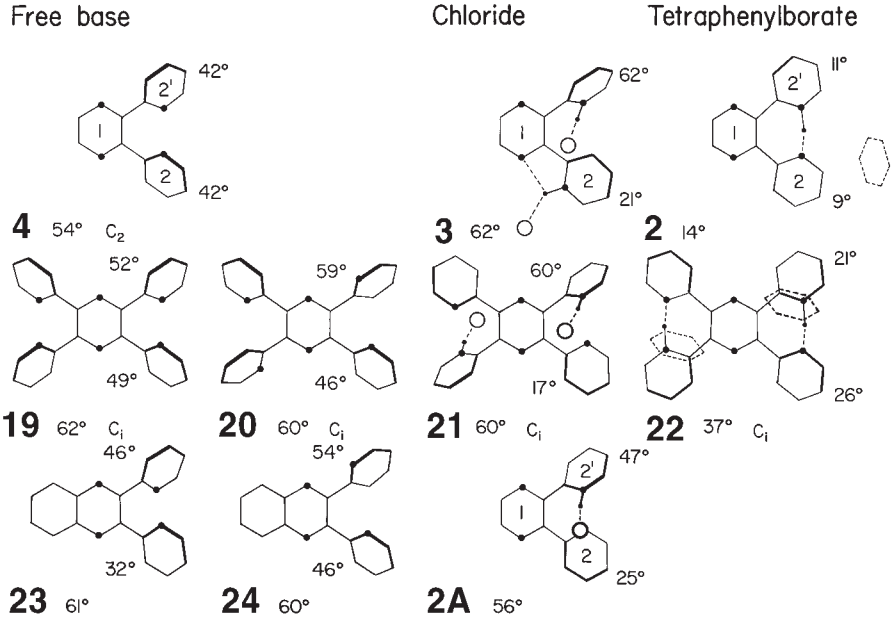

Fig. 4. N-H-N′ angle vs. *d*(N···N′) in the inside-protonated cations **44**–**50**. Large circles, experimental values (with N-H-N′ esd bars); small circles, values obtained from eq. [3]. The results of a regression of N-H-N′ on *w* and *d*(N···N′) alone are indicated by broken lines.

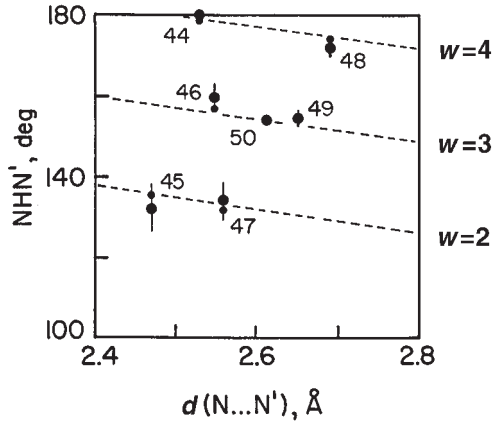

distance and the N-H(N)-O ~ 169° angle are in the normal range for weak to moderately strong N—H···O bonds.

It is interesting to note that the N-H(N)-N′ angles in **18** are much the same as the corresponding angles in the monocation, i.e., the intra-cation N-H(N)-N′ closure angle appears to be unaffected by the presence of the second H(N) atom.

Intra-cation N—H···N′ ring closure: intrabridgehead cations

In saturated, nonplanar ring systems, ring closure on protonation leads to less predictable results. Nevertheless, circumstances exist in which the cation system may possess sufficient rigidity to permit the N—H···N′ geometry to be rationalized. A case in point that merits examination in this context are the bicyclic diamines extensively investigated by Alder and coworkers (34–46, and footnote 7). Protonation of these molecules may result in the formation of inside-protonated intrabridgehead cations. When it does, insertion of the proton effects simultaneous closure of *three* saturated rings (**44**–**50**) with little or no opportunity for bifurcation to external acceptors:

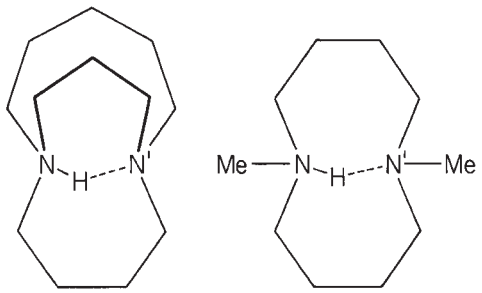

46 [5.4.3] [4.4.Me_2]

Of particular interest here is the wide variation of the N-H-N′ angle, which is reported to range from ~132° to ~180°.

Inspection of the pertinent geometric parameters of **44**–**50** (Table 6) suggests that these parameters are interrelated and that the dominant correlation occurs between the N-H-N′ angle ϕ and the size of the smallest, (*w*+3)-membered cation ring, with possible secondary association with *d*(N···N′). The sample is too small for a more elaborate statistical treatment, but even the simplest model, a linear regression of ϕ on *d*(N···N′)

© 1998 NRC Canada

Table 5. Conspectus of the geometric X—H(X)···phenyl bond parameters.[a]

X[b]	H(X)[b]	Ring	d_{min}	$\overline{d}$	$d(\pi_c)$	Δ	X-H-π_c	X-H-C_{min}	X-H/R
TPTBw[c]									
C(2,6)		2	3.518(8)	3.81[23]	3.55	0.54			
	2,6	2	2.57	2.90[27]	2.56	0.69	164°	161[19]°	67°
2PyPzTB									
2′		13	3.493(4)	4.06[44]	3.84	1.08			
	2′	13	3.66	4.36[53]	4.16	1.34	66°	71[10]°	5°
DPATBw[d]									
2′		2	3.508(8)	3.98[34]	3.74	0.89			
	2′	2	2.81	3.51[54]	3.26	1.33	112°	129[4]°	55°
2′		3	3.46(1)	4.04[44]	3.82	1.12			
	2′	3	3.27	4.10[57]	3.40	1.57	78°	87[9]°	18°
O		1A	3.331(7)	3.55[14]	3.27	0.40			
	H(O1)	1A	2.51	2.99[33]	2.67	0.90	122°	146°	54°
O		4A	3.361(7)	3.49[9]	3.21	0.25			
	H(O2)	4A	2.47	2.79[22]	2.43	0.61	139°	154[15]°	62°
PPTB									
2′		3	3.320(5)	4.15[61]	3.86	1.59			
	2′	3	2.29	3.08[57]	2.84	1.48	144°	144°	51°
BQTB									
10		1	3.304(5)	4.11[59]	3.78	1.53			
	10	1	2.42	3.21[57]	2.90	1.49	149°	148°	51°
DDPTB									
10		1	3.34(3)	4.39[76]	4.24	1.99			
	10	1	2.88	3.99[81]	3.82	2.08	110°	114[13]°	35°
TTTBs[e]									
1		2	3.195(7)	3.80[42]	3.57	1.15			
	1	2	3.01	3.74[50]	3.51	1.39	85°	92°	13°
1		3	3.421(7)	3.54[8]	3.25	0.21			
	1	3	2.51	2.71[13]	2.34	0.37	160°	161°	80°
2		N(9A)[f]	3.041(8)	—	—	—			
	2,2	N(9A)	2.53	—	—	—	—	114°	—
2		2	3.722(7)	3.94[16]	3.69	0.42			
	2,1	2	3.05	3.53[33]	3.27	0.92	110°	129°	39°
2		3	3.344(7)	3.97[49]	3.75	1.21			
	2,1	3	2.55	3.43[59]	3.20	1.65	119°	141°	53°
4		N(5)[g]	2.802(7)	—	—	—			
	3,1	N(5)	2.73	—	—	—	—	84°	—
4		1A	3.494(8)	3.53[3]	3.24	0.08			
	4,1	1A	2.61	2.93[23]	2.57	0.59	128°	155°	51°
	4,2	1A	3.21	3.53[25]	3.25	0.65	81°	84[21]°	7°
4		4A	3.391(7)	4.02[43]	3.80	1.21			
	4,2	4A	2.48	3.32[55]	3.07	1.57	135°	161°	83°
7		2B	3.365(7)	3.49[9]	3.21	0.25			
	7,1	2B	2.61	2.72[9]	2.34	0.23	154°	138[10]°	65°
	7,2	2B	3.31	3.73[31]	3.47	0.81	66°	85[4]°	4°
7		c6	2.960(8)	4.10[86]	3.96	2.17			
	7,2	c6	2.44	3.67[85]	3.51	2.30	112°	108[15]°	13°
PSTBs[h]									
C(4)		2	3.643(9)	3.94[20]	3.48	0.56			
	4	2	3.02	3.31[20]	2.76	0.57	133°	126[12]°	45°
C(4)		3	3.551(9)	3.76[16]	3.51	0.45			
	4	3	3.09	3.15[5]	2.83	0.13	129°	120[17]°	42°
C(O22A)		1	3.802(9)	3.97[12]	3.72	0.36			
	H(O221A)	1	3.17	3.26[6]	2.95	0.18	139°	133[18]°	52°

© 1998 NRC Canada

Table 5 (*concluded*).

X[b]	H(X)[b]	Ring	d_{min}	$\overline{d}$	$d(\pi_c)$	Δ	X-H-π_c	X-H-C_{min}	X-H/R
C(O22A)		4	3.989(9)	4.13[9]	3.90	0.26			
	H(O221A)	4	3.41	3.59[14]	3.31	0.38	122°	126[20]°	39°
PSTBw[i]									
C(4)		2	3.55(1)	4.07[36]	3.84	0.99			
	4	2	2.91	3.44[38]	3.17	1.00	129°	126°	46°
C(5)		1	3.54(1)	3.78[19]	3.52	0.49			
	5	1	3.01	3.14[10]	2.82	0.25	131°	129[13]°	43°
C(5)		2	3.68(1)	4.08[28]	3.85	0.75			
	5	2	3.02	3.46[30]	3.19	0.86	128°	127[13]°	44°
C(52A)		3	3.71(1)	3.76[5]	3.50	0.13			
	521A	3	2.95	3.18[17]	2.87	0.45	125°	124[18]°	45°
C(52A)		4	3.71(1)	3.82[9]	3.57	0.21			
	521A	4	2.97	3.33[25]	3.04	0.68	117°	124[13]°	42°
TcTBs[j]									
9		2A	3.281(8)	3.66[27]	3.40	0.74			
	9a	2A	2.76	2.95[15]	2.60	0.41	135°	122[11]°	42°
9		4	4.263(8)	5.02[55]	4.85	1.50			
	9b	4	3.27	4.05[55]	3.84	1.52	171°	164°	58°
10		N(3)[f]	3.018(7)	—	—	—			
	10	N(3)	2.01	—	—	—	—	170°	

[a] Distances in Å; for d(X—H) see Experimental. $d_{min} = d[X\cdots C(R)]_{min}$ or $d[H(X)\cdots C(R)]_{min}$, i.e., the shortest X···C(R) or H(X)···C(R) distance, respectively; $d(\pi_c) = d[X\cdots\pi_c(R)]$ or $d[H(X)\cdots\pi_c(R)]$. X-H-C_{min} is the X-H(X)-C angle corresponding to $d[H(X)\cdots C(R)]_{min}$; when the shortest X···C distance is to a different carbon of R than the shortest H(X) distance, the mean of the X-H-C′ and the X-H-C″ angles is given. X-H/R = angle formed by the X–H(X) vector with the R plane. For distances to individual C atoms see Table F.

[b] In the absence of another indication, X = N, H(X) = H(N).

[c] $\pi_c(c2)...\pi_c(R2) = 4.87$ Å.

[d] A: x, ½ – y, ½ + z.

[e] A: ½ + x, ½ – y, ½ + z; B: (3/2) – x, y – ½, (3/2) – z.

[f] N atom of MeCN.

[g] Bifurcated intra-cation N(4)—H(4,1)···N(5), R(1A) bond; N(4)-H(4,1)-N(5) - 84°.

[h] A: x, y, z + 1.

[i] A: x, y – 1, z.

[j] A: 1 – x, 1 – y, 1 – z.

(which is better determined than d(N—H)) and the numbers u, v, and w of the carbon atoms in the three rings ($u \geq v \geq w$),

[3] $\phi = 145.3 + 0.19u - 1.72v + 22.39w - 19.72d(N\cdots N')$

confirms that ϕ is indeed strongly correlated with w but only weakly with d(N···N′) and shows that changes in w and d(N···N′) work in opposite directions: $r^2 = 0.986$, with the residual standard error of the regression $\sigma = 3.6° \sim 7.5\%$ of range and with the pairwise correlation coefficients

	u	v	w	d(N...N′)
ϕ	–0.36	–0.09	0.99	0.41
d(N···N′)	0.52	0.45	0.50	1

The other correlations, while not negligible, have an even smaller effect on ϕ than d(N···N′); in fact, regressing ϕ on w and d(N···N′) alone gives a fit not significantly different from that of eq. [3]. The distance d(N···N′) correlates very weakly but about equally with the other four variables.[13]

While approximating ϕ by a *linear* function is not unassailable, it is clear that w will dominate ϕ far more strongly than any of the other parameters no matter what the representation (Fig. 4). This undoubtedly reflects the limits on conformational adjustment that are narrowest for the smallest ring and thus determine the relative orientations of the N–H vector and of the axis of the lone pair at N′.[14] This finding may not come as a surprise, but eq. [3] puts it in proper perspective.

Since no structures of *simple* cations of this type other than **44**–**50** appear to have been reported, the extent of the usefulness of eq. [3] remains to be seen. However, the applicability of the correlation may well extend to more varied systems. Thus the ϕ angle calculated from eq. [3] for the inside-monoprotonated [5.5.3] cation in **51** is 154° compared to the ~158° estimated from the crystal-structure determination. For the [5.5.4] cation in **52** the agreement between the calculated ϕ of 173° and the experimental value of ~167° is less satisfactory. In the inside-monoprotonated cation of the macrocyclic amine in **53** the acidic H(N) atom is inside a pseudo-C_2 tetrahedron

[13] When d(N···N′) is regressed on the ring-size parameters only (thus exc1uding the uncertainties in the H(N) location), the result is $d(N\cdots N') = 1.838 + 0.073u + 0.040v + 0.065w$ ($r^2 = 0.81$, σ = 0.048 Å ~ 22% of range), i.e., the increase in d(N···N′) with each of u, v, and w is of the same order but the correlation is weak.

[14] The problem of which N—H···N′ geometry in these cations corresponds to a single-well, a symmetric double-well, or an asymmetric double-well potential does not appear to have been completely solved as yet (44). For ir and nmr spectra of the intrabridgehead cations in solution, see ref. 36.

© 1998 NRC Canada

Table 6. Geometric parameters of the N—H···N′ bonds in the inside-protonated cations **44**–**50**.[a]

No.	[*u*.*v*.*w*]	*d*(N···N′)	*d*(N—H)	NHN'_{obsd}	NHN'_{calcd}	Difference
45	5.4.2	2.474 (7)	1.37 (7)	132 (6)°	135.4°	3.4°
47	5.5.2	2.555 (7)	1.09 (5)	134 (5)°	132.0°	–2.0°
46	5.4.3[b]	2.555 (3)	1.268 (3)	157.8 (2)°	156.2°	–1.0°
49	6.4.3	2.663 (4)	0.950 (19)	154.8 (13)°	154.2°	–0.6°
50	6.5.3	2.610 (5)	1.19 (3)	154 (3)°	153.5°	–0.5°
44	4.4.4[c]	2.526 (3)	1.278 (2)	180°	178.9°	–1.1°
48	5.5.4	2.690 (4)	1.096 (33)	171.7 (17)°	174.2°	2.5°

[a] Parameter values from refs. 35 and 38–43; distances in Å; $u \geq v \geq w$, numbers of C atoms in the respective (—$(CH_2)_n$N—H···N′-) rings of the cation. NHN'_{calcd} from eq. [3].
[b] Neutron diffraction at 130 K.[7]
[c] Neutron diffraction at 20 K[7].

of the *endo* atoms N(1)–N(4), with the in-plane bridgehead atoms N(2) and N(4) at 2.636(7) Å and the off-plane atoms N(1) and N(3) at 3.081 Å; the N···H(N) distances are 1.35(9) Å to N(4), 1.38(9) Å to N(2), 2.13(9) Å to N(3), and 2.29(9) Å to N(1). The intrabridgehead bond is thus essentially N(2)—H(N)···N(4), with an N(2)-H(N)-N(4) angle of ~150°. The cation may therefore be regarded as an inside-protonated three-ring [5.5.3] system, with N(2) and N(4) as the bridgehead atoms, one 3C ring, two 2C + N + 2C rings, and a 3C bridge between N(1) and N(3). Setting $u = v = 5$, $w = 3$, *d*(N···N′) = 2.636 Å, the ϕ angle obtained from eq. [3] is 153°, in agreement with the experimental value if the uncertainty in the location of H(N) is taken into account. The distance between a bridgehead and a nonbridgehead N atom ranges from ~2.75 to ~2.85 Å and is thus not appreciably longer than N(2)···N(4), but the ϕ angle spanning it is only about 100° and must correspond to a substantially weaker H-bonding interaction.[15]

Equation [3] also accommodates the unbridged two-ring *cis*-1,6-Me_2-1,6-diazacyclodecanium(1+) cation (= [4.4.Me_2] (44, 45); see line drawing). Substitution of the experimental values ϕ = 169(2)° and *d*(N···N′) = 2.60 Å into eq. [3] yields $w = 3.6$. This cation thus fits between the [4.4.3] and [4.4.4] systems, which seems reasonable since the two *N*-Me carbons, although not in a ring and thus not constrained, may be regarded as parts of a virtual, uncompleted low-strain 5- or 6-membered third ring.

The ϕ angle in **44**–**50** for a given *w* is larger than the ϕ angle in a ring of corresponding size in the quasi-planar cations discussed in the preceding section (Fig. 2): $\phi(w)_{intrabr.} = 76.5 + 0.58\ \phi(w)_{planar}$. The conditions for the formation of an N—H···N′ bond are thus more favourable in the former, in spite of the conformational constraints imposed by the three-dimensional aliphatic three-ring system on protonation.

Geometry of the H(X)···phenyl interactions

The relevant numerical parameters are assembled in Table 5; the corresponding structural details will be found under the individual crystal structures below. As shown in ref. 3, such a body of information can be examined in various ways and treated statistically depending on the specific purpose. Here we limit ourselves to consideration of the two perhaps most important parameters, $d[X\cdots C(phenyl)]_{min}$ and $d[H(X)\cdots C(phenyl)]_{min}$. For X = N and N-H(N)-$C_{min} \geq 90°$, the means of the 14 values are 3.37[17] Å ($\gamma_1 = -0.34$, $\gamma_2 = 4.03$) for $d[N\cdots C(phenyl)]_{min}$ and 2.64[22] Å ($\gamma_1 = 0.45$, $\gamma_2 = 2.18$) for $d[H(N)\cdots C(phenyl)]_{min}$.[16] This compares with the means 3.37[12] Å ($\gamma_1 = 0.76$, $\gamma_2 = 3.23$) and 2.60[20] Å ($\gamma_1 = 0.67$, $\gamma_2 = 3.07$) for the 47 TB structures in Table 7 of ref. 3.[17] The corresponding means for the two X = O cases in **5** are 3.34[2] Å and 2.49[2] Å, respectively,[18] and for the nine X = C bonds in the two proton-sponge TBs **11** and **12**, 3.69[14] Å ($\gamma_1 = 0.95$, $\gamma_2 = 3.19$) and 3.06[14] Å ($\gamma_1 = 1.44$, $\gamma_2 = 4.18$).

Based on these statistics, the expectation values of the minimum X···C(phenyl) and H(X)···C(phenyl) distances to the associated-ring carbons in TB structures would appear to be 3.4[2] Å and 2.6[3] Å for X = N, O, and 3.7[2] Å and 3.1[2] Å for X = C. Thus with some exceptions (e.g., BQTBs, PSTBs, PSTBw), in organoammonium TBs the anion always provides an opportunity for an H(N)···phenyl separation in a range acceptable for an effective H-bonding interaction. In BQTBs, the introduction of MeCN results in a winning competition for H-bonding in favour of the strongly polar solvent molecule; in **11** and **12** the combination of overall packing requirements, closure of the 6-membered ring, and the presence of polar solvent molecules supervenes, with the result that a priori conceivable H(N)···phenyl interactions are replaced by H(C)···phenyl interactions (cf. below).

Noteworthy also is the variability of the angle of inclination X-H(X)/R of the X-H(X) vector to the phenyl plane, and of the related quantity Δ, which indicates the displacement of X or H(X) from the perpendicular through the centre π_c of the phenyl ring (cf. Housekeeping and ref. 3). For the 30 H(X)···phenyl bonds of Table 5 the means of Δ(X···C) and Δ[H(X)···C] are 0.76[57] Å ($\gamma_1 = 0.79$, $\gamma_2 = 2.67$) and 0.95[57] Å ($\gamma_1 = 0.51$, $\gamma_2 = 2.35$), respectively, with both distributions skewed toward zero. This means that only rarely would X or H(X) be above π_c. Information concerning X-H(X)/R and Δ acquires special relevance when deformation electron density and bond-path topology in X—H(X)···phenyl

[15] If the H(N) atom is regarded as located between a bridgehead and a nonbridgehead N atom, and the cation as a [6.6.2] three-ring system with an extra bridge between two N atoms, the ϕ angle from eq. [3], for *d*(N···N′) = 2.80 Å, is 125°.

[16] $\gamma_1 = m_3/m_2^{3/2}$, moment coefficient of skewness; $\gamma_2 = m_4/m_2^2$, moment coefficient of kurtosis. For a normal distribution, $\gamma_1 = 0$, $\gamma_2 = 3$.

[17] Bond lengths in ref. 3 calculated assuming N—H = 1.02 Å, O—H = 1.00 Å.

[18] 3.41[5] Å ($\gamma_1 = -0.05$, $\gamma_2 = 2.15$) and 2.62[17] Å ($\gamma_1 = 1.28$, $\gamma_2 = 2.94$) for the ten X = O cases in Table 7 of ref. 3.

© 1998 NRC Canada

Table 7. Comparison of the unit-cell dimensions and cation conformations in the PPTB/BPTB and BQTB/PTB pairs and in BQTBs.[a]

	PPTB	BPTB[b]		BQTB	PTB[b]	BQTBs[c]
S.G.	$P2_1/c$	$P2_1/n$	S.G.	$P2_1/c$	$P2_1/c$	$P\bar{1}$
a'	0.886	0.669	a'	0.896	0.804	0.793
b'	0.957	1.020	b'	0.931	0.994	1.031
c'	1.235	1.468	c'	1.260	1.315	1.353
$\bar{\delta}$(c1)	0.002[2]	0.003[1]	$\bar{\delta}$(c1)	0.009[5]	0.010[4]	0.002[1]
$\bar{\delta}$(c1′)	0.010[6]	0.002[1]	$\bar{\delta}$(c2)	0.013[6]	0.011[5]	0.013[6]
			$\bar{\delta}$(c3)	0.008[5]	0.007[4]	0.008[4]
$\bar{\delta}$(cat)	0.111[68]	0.041[16]	$\bar{\delta}$(cat)	0.025[19]	0.029[17]	0.045[28]
c1′/c1	15.3°	5.2°	c2/c1	3.4°	3.7°	6.2°
			c3/c1	1.1°	1.2°	2.8°
			c3/c2	2.3°	2.6°	3.4°
cat/c1′	7.0°	2.6°	cat/c1	1.2°	2.0°	2.5°
cat/c1	8.4°	2.6°	cat/c2	2.2°	2.6°	3.7°
			cat/c3	0.3°	0.8°	0.5°

[a] S.G., space group; a', b', c' = unit-cell dimensions normalized to $V^{1/3}$; $\bar{\beta}$ = 107.65[26]° for the three $P2_1/c$ structures; $\bar{\delta}$, mean deviation of the ring C and N atoms from the respective best plane through the ring skeleton.

[b] At –20°C.

[c] $a' = a(2V)^{-1/3}$, $b' = b(2V)^{-1/3}$, $c' = 2c(2V)^{-1/3}$.

Fig. 5. Matching projections of the unit cells and of the B atom and cation centroid $\bar{c}$ positions designed to display similarity of ion packing in PPTB, BQTB, and PTB ($P2_1/c$), BQTBs ($P\bar{1}$, see text), and BPTB ($P2_1/n$). *Bottom*: Large circles, B atoms at $x \sim$ ¼ (open) and $x \sim$ ¾ (stippled). The symmetry centres, at x = ½, relating the $\bar{c}$ in closest cation pairs define the corners of CdI_2-type cells (broken lines). *Top*: Large circles, B atoms at $y \sim 0$ (open) and $y \sim$ ½ (stippled). Small circles, cations centroids $\bar{c}$ at $y \sim 0$ (open) and $y \sim$ ½ (stippled). Note that for BPTB x and y are reversed.

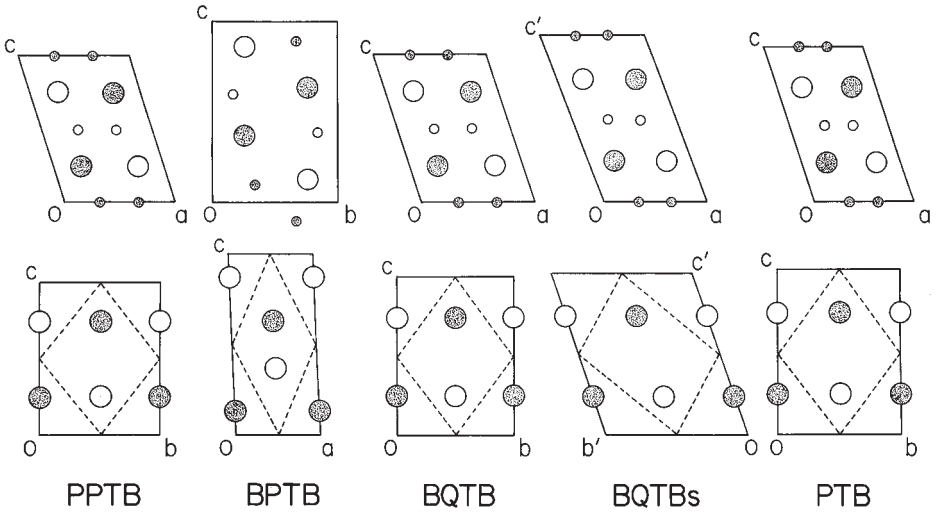

bonds are investigated (W. Kwiatkowski, K.N. Robertson, T.S. Cameron, and O. Knop, work in progress).

PPTB, BQTB, and BQTBs: comparison with BPTB and PTB

The unsolvated PPTB (**6**) and BQTB (**7**) investigated in this work form chemically matched pairs with the TBs BPTB (**15**) and PTB (17) reported previously (1). The introduction of a second ring nitrogen into the cation skeletons of PPTB and BQTB opens up the possibility of formation of an intra-cation N—H···N′ bond that is absent in the single-nitrogen cations. This provides an opportunity for examining the effect of the intra-cation bond on the geometry of the cation and on the ion packing.

PPTB, BQTB, and PTB crystallize in the same space group, $P2_1/c$, and their cell dimensions and axial ratios are similar; the monoclinic angle β is almost constant, $\bar{\beta}$ = 107.65[26]° (Table 7). The packing of the *ions* cannot be related directly in a natural manner to any of the simple 1:1 packing types. However, the cations in each of the three structures occur in centrosymmetric pairs in which the minimum separation $\bar{c}\cdots\bar{c}$ of the cation centroids is of the order of 4 Å.[19] When the three structures are juxtaposed, after appropriate shifts of origin to match up the atom positions with those tabulated for

[19] The smallest $\bar{c}\cdots\bar{c}$ separations in PPTB, BQTB, and PTB are 4.30, 4.13, and 4.61 Å, respectively; in BPTB, 6.29 Å.

© 1998 NRC Canada

PTB in ref. 1 (Fig. 5),[20] the symmetry centres relating the cations in each pair are seen to be located at equipoints 2(*d*) of $P2_1/c$, i.e., at points of a lattice complex *A*2/*m*. The B atoms of the anions, which are close to the anion centroids, occupy, in the standardized $P2_1/c$ cells, positions that differ only slightly from (¼, 0, ¾) etc. The packing of the cation-pair centres and the anion centroids can thus be regarded as a monoclinically distorted packing of the CdI_2 type. This is illustrated in the projections of the three structures on (100) in Fig. 5. However, the inclination to (100) of the cation planes in the pairs varies considerably, as does the shortest $\bar{c}\cdots\bar{c}$ distance, so that the actual ion packing has a different appearance in each of the projections. The characteristic orientation of the phenyl rings of the anion (in a conformation of approximate C_s symmetry) is one in which one of the rings is in the quasi *m* plane approximately ||*a*, another approximately perpendicular to that plane, and the remaining two more or less symmetrically disposed about the quasi *m* plane.

The similarity of ion packing is seen to extend even to the solvated BQTBs if the triclinic $P\bar{1}$ cell is transformed into an *A*-centred double cell by $(a'/b'/c') = (1,0,0/0,1,1/0,1,-1)(a/b/c)$ and the atom coordinates by $(x'/y'/z') = (1,0,0/0,½,½/0,½,-½)(x/y/z)$ (Fig. 5).[21] The minimum $\bar{c}\cdots\bar{c}$ distance in BQTBs is 3.88 Å.

The effect of the second ring nitrogen on the cation bond lengths and angles in the BPTB/PPTB and PTB/BQTB pairs is discussed under the structures of **6** and **7** below.

Conclusions

In heterocyclic amines that contain N—$C_1\cdots C_{n-2}$—N′ atom groups G_n in pro-closure configurations, intra-cation ring closure can be accomplished through insertion of the H atom introduced by the protonation of one of the nitrogens, i.e., through formation of an intra-annular N—H···N′ bond contained in an (*n*+1)-membered ring. In the present work, the skeleton of the aromatic free-base molecule either is planar or becomes so on protonation, i.e., the tendency to form an intra-cation H-bond is at the very least a cofactor in bringing about a *syn* conformation of N and N′. On geometric evidence, intra-cation ring closure is present in the TBs **1**, **2**, **5**, **9**, **11**, **12**, **15**, **17**, **22**; in **3**, **28**, and **33**; and almost certainly also in **25** and **26**. In **10** it is present independently of protonation, between an H atom of an exocyclic amino group and a ring nitrogen.

The magnitude of the N-H-N′ angle depends primarily on *n* (Fig. 2, Table 4). For G_6, where there is steric crowding and where ring closure requires departure from planarity, the angle tends to be large, >160°. For G_5 the closed 6-membered ring is relatively strain-free, with N-H-N′ > 120°; values as high as ~158° are seen. For G_4 the mean N-H-N′ angle expected from molecular geometry is ~100°, and this is observed.

Whether or not the H(N) atom is involved in a secondary H-bonding interaction with an external acceptor Y will depend on *n* and on the nature of the counter anion and the extent of solvation. Conversely, the two last-named factors may codetermine the occurrence of a ring closure and influence the N-H-N′ angle. In the unsolvated G_4 TBs **9**, **15**, and **17**, Y = phenyl, and H(N) forms a bifurcated H(N)···phenyl bond, whereas in the G_6 TBs **2** and **22** the bifurcation is tenuous at best and in **2** probably absent owing to unfavourable packing geometry.

In the *solvated* G_5 TBs **5** and **10**–**12** the acceptor Y is either a phenyl (**5**, **10**) or a solvent molecule (**11**, **12**), but while the *orientation* of Y with respect to the N–H(N) vector is favourable, the H(N)···Y distances are longer and the N-H-Y angles smaller than would be thought acceptable for H-bonds of conventional types. In the G_4 TB **1** there is an unmistakable H(N)···N′,H_2O bifurcation, but the oxygen atom of the H_2O molecule is positionally disordered (probably dynamically), the result of a compromise involving several simultaneous H-bonding interactions (Figs. 6 and 7).

In none of the TBs does the H-bond to the anion or the solvent molecule prevent ring closure. However, this is not necessarily so when the anion is Cl or Br. In the unsolvated G_6 chlorides **2A** and **21** the H-bonding is dominated by the N—H(N)···Cl interaction, which directs the N-H(N) vector away from the potential N′ acceptor and which is associated with a large inclination of the protonated pyridine ring to the pyrazine ring (Fig. 3). A similar absence of ring closure is observed for one of the pyridine H(N) atoms in the doubly protonated chloride **3**; the second pyridine H(N) atom is involved in a bond to the second Cl atom, but in this case it also closes a G_4 ring containing a pyrazine nitrogen and forms a bifurcated N—H(N)···Cl,N(pyrazine) bond. By contrast, in **25**, **26**, **28**, and **33** the G_4 group is closed in spite of the presence of a halide anion, and there appears to be bifurcation from H(N) to N′ and Br^- (**28**) or to H_2O.[22]

In sum, for the amines under discussion, intra-cation ring closure will result on protonation except where there is disruptive competition from a strongly H-bonding anion (Cl^-, Br^-). Where ring closure does occur, the H(N) atom may be involved in a branched H(N)···N′,Y bond to an external acceptor. This appears to be always the case for G_4 cations but less so for G_5 cations (weaker H(N)···Y interaction) and even less so for G_6 cations.

The cations in BPTB (**15**) and PTB (**17**) each contain two ring nitrogens in pro-closure configurations, whereas the corresponding, matching cations in PPTB (**6**) and BQTB (**7**) each contain one ring nitrogen only. Intra-annular N—H···N′ bonding therefore occurs in the former two but not in the latter two, the cation geometry otherwise being similar. The effect of the ring closure on ion packing and on H(N) bonding in the PPTB/BPTB and BQTB/PTB pairs can thus be examined. While the effect in the rigid-cation BQTB/PTB pair is minor and BQTB and PTB are practically isostructural and not dramatically different from PPTB, the packing in BPTB is significantly different and not for reasons that are immediately apparent.

While in the above aromatic ammonium cations the N-H-N′ angle is largely determined by the size of the pro-closure grouping G_n, in the analogous inside-protonated intrabridge-

[20] For PPTB this requires a transformation $(x, y, z) \rightarrow (x - ½, y, z + ½)$ and for BQTB, $(x, y, z) \rightarrow (x, y, z + ½)$, where (x, y, z) are the tabulated coordinates (Table A). The transformed coordinates match the tabulated PTB(x, y, z) coordinates (1).

[21] To match the tabulated positions of the B atom and of the cation centroid $\bar{c}$ in PTB, approximately (¼, 0, ¾) and $(x, \sim0, \sim½)$, respectively, the atom coordinates in BQTBs (Table A) are transformed by $(x, y, z) \rightarrow [x - ½, ½(1 - y - z), ½(1 - y + z)]$.

[22] Location of some of the acceptors may not be adequately characterized because of disorder.

© 1998 NRC Canada

Fig. 6. (*a*) Atom numbering and bond angles (deg) in TPTBw. (*b*) H-bond system, cation and H_2O oxygen in the page. Large filled circles, N atoms; small filled circles, H(N) atoms; stippled circles, O atoms (resolved disorder, partial occupancy; see text). Ring R4 and H(C) atoms omitted for c1arity. H-bonds shown in broken lines.

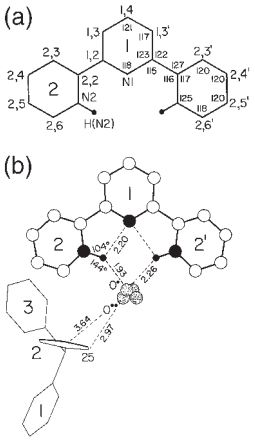

head cations reported to date (**44**–**50**) the N—H···N′ group is intra-annular simultaneously to *three* (aliphatic) rings. The N-H-N′ angle, which ranges from ~132° to ~180°, would then be expected to be codetermined by the sizes of all three rings. Our analysis shows that the angle is in fact determined almost entirely by the size of the *smallest* of the three rings and that the N···N′ separation plays a relatively minor role.

N—H···phenyl interaction is a common (though not universal, as already noted) feature of the present as well as of previously reported (1–3) TB structures. The geometry of this interaction is noteworthy for its variability (Table 5). Particularly striking is the range of positions and orientations the N–H(N) vector can assume with respect to the associated phenyl ring, and the angle between this vector and the ring plane. The fundamental questions of (*i*) how to account for the observed variability, and (*ii*) whether the H···phenyl interaction is in fact a *bond* in the chemical sense (with nonvanishing electron density at the bond critical point and a demonstrable bond path), are currently being investigated on selected TB structures.

In addition to the H(N)···phenyl interactions, some of the structures of Table 1 contain evidence of H(O)···phenyl and H(C)···phenyl interactions. The former involve solvent molecules, the latter come to prominence in the two solvated proton-sponge TBs **11** and **12**, where they appear to compensate for the absence of H(N)···phenyl bonds.

Individual crystal structures

Crystallographic information for **1**–**13** and details of the structure determinations are presented in Table 2 (cf. also Experimental). Information concerning cation geometry will be found in Tables 8 and 9, and that for H-bonding in Table 5. Relevant X···C and H(X)···C distances in the X—H(X)···phenyl bonds are listed in Table F.

The average geometry of the TB anion in **1**, **2**, and **5**–**13** (Tables D and E) is virtually the same as that reported previously (3): $\bar{d}$(B—C) for the 28 more accurate bond lengths (not corrected for thermal motion) is 1.646[10] Å (γ_1 = –0.82, γ_2 = 3.69) compared to 1.646[18] Å (n = 88, γ_1 = 0.81, γ_2 = 4.49) in ref. 3; the mean deviation δ(C) of the C atoms from their respective best planes is 0.006[4] Å (44 phenyl rings, γ_1 = 1.68, γ_2 = 5.79) for the present structures compared to 0.007[4] Å for the 60 rings in ref. 3.

Fig. 7. TPTBw: H-bonding and T-shape π–π interaction. (*a*) View down the cation C_2 axis. (*b*) View with the cation C_2 axis in the page. For legend see caption of Fig. 6.

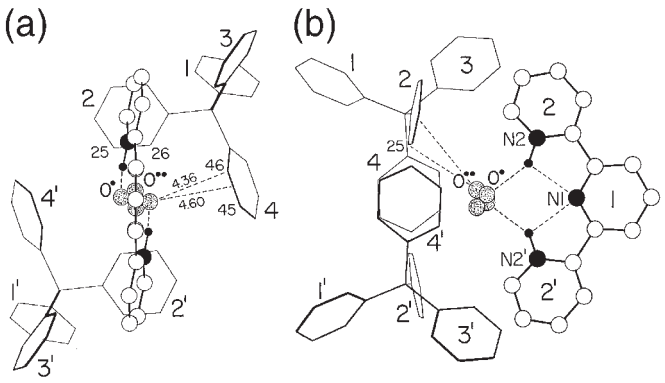

TPTBw (1)

The geometry of the TP^{2+} cation (Figs. 6 and 7) is related to that of the 2,2′-bipyridinium(1+) and 1,10-phenanthrolinium(1+) cations (1).[23] The cation, of symmetry C_2, is not completely planar: c2/c1 = 13.5°, c2′/c2 = 21.5° (Table 9). Noteworthy are the small exocyclic angles at carbons C(1,2) and C(1,2′), 115.1°, and at C(2,2) and C(2,2′), 115.7°, and the corresponding large exocyclic angles at C(2,2) and C(2,2′), 127.4°. The departures of all three angles from 120° are in directions that make the cation bend in its approximate molecular plane, i.e., so as to decrease the N(2)···N(1) and N(2′)···N(1′) separations, consistent with the presence of N(2)—H(N2)···N(1) and N(2′)—H(N2′)···N(1) intra-cation H-bonds (Fig. 6*b*). In this, $TP2^+$ strongly resembles the 2,2′-bipyridinium(1+) cation: the mean N(2)···N(2′), C(1)···C(1′), and C(6)···C(6′) distances in the latter (Table F of ref. 1; cf. also **15**) are statistically indistinguishable from the corresponding distances in **1**.

The cation is approximately perpendicular to R2 of the associated anions, c2/R2 = 92.6° (Figs. 6*b*, 7). The ring centres π_c(c2) and π_c(R2) are 4.87 Å apart. The mean distances to R2 carbons of the cation atoms nearest to R2, C(2,6) and H(2,6), are 3.81[2] and 2.90[3] Å, respectively, the minimum distances being C(2,6)···C(23) = 3.52 Å and H(2,6)···C(24) ~ 2.57 Å; the C(2,6)···π_c(R2) and H(2,6)···π_c(R2) distances are 3.55 and 2.56 Å, respectively. The spatial relationship of c2 and R2 thus qualifies for a T-shape π–π interaction.[24] However, unlike the 1,10-phenanthrolinium(1+) (**17**) and paraquat(1+) (PQTB) TBs (discussed in ref. 1), in which *both* cofacial and T-shape geometries are present, the aromatic-ring relationship found in TPTBw represents a clear-cut case of a

[23] The unprotonated TP^0 molecule may be regarded as one half of the sexipyridine **14** molecule.

[24] These interactions may manifest themselves also in the pale lemon-yellow colour of freshly prepared TPTBw; on dissolution of the solid in acetone the colour disappears.

© 1998 NRC Canada

Table 8. Interatomic distances (Å) and bond angles (deg) in the cations.

Atoms	Distance	Atoms	Angle
TPTBw			
N(1)—C(1,2)	1.336(6)	C(1,2)-N(1)-C(1,2′)	118.2(7)
C(1,2)—C(1,3)	1.394(7)	N(1)-C(1,2)-C(1,3)	123.2(6)
C(1,3)—C(1,4)	1.383(6)	N(1)-C(1,2)-C(2,2)	115.1(5)
C(1,2)—C(2,2)	1.473(7)	C(1,3)-C(1,2)-C(2,2)	121.6(5)
N(2)—C(2,2)	1.351(7)	C(1,2)-C(1,3)-C(1,4)	117.1(6)
C(2,2)—C(2,3)	1.377(7)	C(1,3)-C(1,4)-C(1,3′)	121.1(7)
C(2,3)—C(2,4)	1.391(7)	C(2,2)-N(2)-C(2,6)	125.1(5)
C(2,4)—C(2,5)	1.375(8)	N(2)-C(2,2)-C(1,2)	115.7(6)
C(2,5)—C(2,6)	1.355(7)	N(2)-C(2,2)-C(2,3)	116.8(5)
C (2,6)—N (2)	1.351(8)	C(1,2)-C (2,2)-C(2,3)	127.4(5)
N(1)···N(2)	2.637(5)	C(2,2)-C(2,3)-C(2,4)	119.9(5)
H(N2)···N(l)	2.20	C(2,3)-C(2,4)-C(2,5)	120.1(6)
		C(2,4)-C(2,5)-C(2,6)	120.0(6)
X′ –x y	(3/2) – *z*	C(2,5)-C(2,6)-N(2)	118.1(6)
		N(2)-H(N2)-N(1)	104
2 PyPzTB			
N(1)—C(2)	1.350(4)	C(2)-N(1)-C(6)	119.9(3)
C(2)—C(3)	1.413(4)	N(1)-C(2)-C(3)	118.9(3)
C(3)—N(4)	1.349(4)	N(1)-C(2)-C(22)	110.5(3)
N(4)—C(5)	1.320(4)	C(3)-C(2)-C(22)	130.6(3)
C(5)—C(6)	1.375(5)	C(2)-C(3)-N(4)	119.5(3)
C(6)—N(1)	1.319(4)	C(2)-C(3)-C(2′2)	130.6(3)
C(2)—C(22)	1.493(4)	N(4)-C(3)-C(2′2)	109.9(3)
C(22)—C(23)	1.389(4)	C(3)-N(4)-C(5)	119.8(3)
C(23)—C(24)	1.381(5)	N(4)-C(5)-C(6)	120.7(4)
C(24)—C(25)	1.367(5)	C(5)-C(6)-N(1)	121.4(4)
C(25)—C(26)	1.375(5)	C(22)-N(2)-C(26)	121.8(3)
C(26)—N(2)	1.350(4)	C(2)-C(22)-N(2)	119.7(3)
N(2)—C(22)	1.340(4)	C(2)-C(22)-C(23)	120.9(3)
C(3)—C(2′2)	1.498(4)	N(2)-C(22)-C(23)	119.3(3)
C(2′2)—C(2′3)	1.379(4)	C(22)-C(23)-C(24)	119.1(4)
C(2′3)—C(2′4)	1.382(5)	C(23)-C(24)-C(25)	120.5(3)
C(2′4)—C(2′5)	1.364(5)	C(24)-C(25)-C(26)	119.0(4)
C (2′5)—C (2′6)	1.373 (4)	C(25)-C(26)-N(2)	120.3 (4)
C(2′6)—N(2′)	1.337(4)	C(2′2)-N(2′)-C(2′6)	121.8(3)
N(2′)—C(2′2)	1.338(4)	C(3)-C(2′2)-N(2′)	121.2(3)
N(2)···N(2′)	2.524(4)	C(3)-C(2′2)-C(2′3)	120.3(2)
C(22)···C(2′2)	3.362(4)	N(2′)-C(2′2)-C(2′3)	118.5(3)
C(26)···C(2′6)	4.241(5)	C(2′2)-C(2′3)-C(2′4)	120.0(3)
N(2′)—H(2′)	1.17(4)	C(2′3)-C(2′4)-C(2′5)	120.3(3)
H(2′)···N(2)	1.37(4)	C(2′4)-C(2′5)-C(2′6)	117.8(3)
		C(2′5)-C(2′6)-N(2′)	121.6(3)
		N(2′)-H(2′)-N(2)	168(3)
2PyPzCl			
N(1)—C(2)	1.343(4)	C(2)-N(1)-C(6)	117.3(3)
C(2)—C(3)	1.400(5)	N(1)-C(2)-C(3)	119.8(3)
C(3)—N(4)	1.341(4)	N(1)-C(2)-C(22)	115.7(3)
N(4)—C(5)	1.330 (5)	C(3)-C(2)-C(22)	124.5(3)
C(5)—C(6)	1.366(5)	C(2)-C(3)-N(4)	121.4(3)
C(6)—N(1)	1.328(5)	C(2)-C(3)-C(2′2)	126.0(3)
C(2)—C(22)	1.482(5)	N(4)-C(3)-C(2′2)	112.6(3)
C(22)—C(23)	1.383(5)	C(3)-N(4)-C(5)	117.2 (3)
C(23)—C(24)	1.377(5)	N(4)-C(5)-C(6)	121.2(4)
C(24)—C(25)	1.369(5)	C(5)-C(6)-N(1)	122.5(4)
C(25)—C(26)	1.369(5)	C(22)-N(2)-C(26)	117.1 (3)
C(26)—N(2)	1.330(5)	C(2)-C(22)-N(2)	116.9(3)
N(2)—C(22)	1.338(4)	C(2)-C(22)-C(23)	120.7(3)
C(3)—C(2′2)	1.485(5)	N(2)-C(22)-C(23)	122.3(3)
C(2′2)—C(2′3)	1.375(5)	C(22)-C(23)-C(24)	119.5(4)
C(2′3)—C(2′4)	1.368(6)	C(23)-C(24)-C(25)	118.2(4)
C(2′4)—C(2′5)	1.365(7)	C(24)-C(25)-C(26)	119.0(4)
C(2′5)—C(2′6)	1.372(6)	C(25)-C(26)-N(2)	123.9(4)
C(2′6)—N(2′)	1.342(5)	C(2′2)-N(2′)-C(2′6)	121.7(3)
N(2′)—C(2′2)	1.342(4)	C(3)-C(2′2)-N(2′)	119.1(3)
N(2)···N(2′)	2.897(4)	C(3)-C(2′2)-C(2′3)	122.0(3)
C(22)···C(2′2)	3.121(5)	N(2′)-C(2′2)-C(2′3)	118.8(3)
C(26)···C(2′6)	4.359(6)	C(2′2)-C(2′3)-C(2′4)	120.2(4)
N(2′)—H(N2′)	1.16	C(2′3)-C(2′4)-C(2′5)	120.0(4)
H(N2′)···N(2)	2.96	C(2′4)-C(2′5)-C(2′6)	118.9(4)
N(2′)···C1	2.924(3)	C(2′5)-C(2′6)-N(2′)	120.4(4)
H(N2′)···C1	1.77	N(2′)-H(N2′)-C1	171
N(2)···C1	3.927(4)	N(2′)-H(N2′)-N(2)	75
2PyPz2CI			
N(1)—C(2)	1.340(4)	C(2)-N(1)-C(6)	117.4(3)
C(2)—C(3)	1.396(4)	N(l)-C(2)-C(3)	121.1(3)
C(3)—N(4)	1.351(4)	N(1)-C(2)-C(22)	113.8(3)
N(4)—C(5)	1.332 (4)	C(3)-C(2)-C(22)	125.0 (3)
C(5)—C(6)	1.377(5)	C(2)-C(3)-N(4)	121.1(3)
C(6)—N(1)	1.337(4)	C(2)-C(3)-C(2′2)	125.5(3)
C(2)—C(22)	1.489(4)	N(4)-C(3)-C(2′2)	113.4(3)
C(22)—C(23)	1.382(4)	C(3)-N(4)-C(5)	116.4(3)
C(23)—C(24)	1.380(4)	N(4)-C(5)-C(6)	122.7 (3)
C(24)—C(25)	1.375(4)	C(5)-C(6)-N(1)	121.1(3)
C(25)—C(26)	1.368(4)	C(22)-N(2)-C(26)	122.6(3)
C(26)—N(2)	1.337(4)	C(2)-C(22)-N(2)	115.4(3)
N(2)—C(22)	1.353(4)	C(2)-C(22)-C(23)	126.2(3)
C(3)—C(2′2)	1.481(4)	N(2)-C(22)-C(23)	118.3(3)
C(2′2)—C(2′3)	1.376(4)	C(22)-C(23)-C(24)	119.5(3)
C(2′3)—C(2′4)	1.392 (5)	C(23)-C(24)-C(25)	120.5 (3)
C(2′4)—C(2′5)	1.364(5)	C(24)-C(25)-C(26)	118.5(3)
C(2′5)—C(2′6)	1.367(5)	C(25)-C(26)-N(2)	120.4(3)
C(2′6)—N(2′)	1.342(4)	C(2′2)-N(2′)-C(2′6)	121.7(3)
N(2′)—C(2′2)	1.351(4)	C(3)-C(2′2)-N(2′)	117.0(3)
N(2)···N(2′)	4.462(3)	C(3)-C(2′2)-C(2′3)	123.1(3)
C(22)···C(2′2)	3.111(4)	N(2′)-C(2′2)-C(2′3)	120.0(3)
N(2)···H(N2)	1.09	C(2′2)-C(2′3)-C(2′4)	118.1(3)
N(2)···C1(2)	3.006(3)	C(2′3)-C(2′4)-C(2′5)	120.7(3)
H(N2)···C1(2)	2.07	C(2′4)-C(2′5)-C(2′6)	119.3(3)
N(2)···N(1)	2.648(3)	C(2′5)-C(2′6)-N(2′)	120.1(3)
H(N2)···N(l)	2.25	N(2)-H(N2)-C1(2)	142
N(2′)—H(N2′)	1.15	N(2)-H(N2)-N(1)	99
N(2′)...C1(1)	2.988(3)	N(2′)-H(N2′)-C1(1)	176
H(N2′)...Cl(l)	1.83		
N(2′)...N(4)	3.361(3)		
H(N2′)...N(4)	3.60		
N(2′)...C(23)	3.172(4)		
N(l)...Cl(l)	4.093(3)		
2PyPz			
N(1)—C(2)	1.347(4)	C(2)-N(1)-C(6)	116.6(3)
C(2)—C(2*)	1.387(6)	N(1)-C(2)-C(2*)	121.2(2)
C(6)—C(6*)	1.370(7)	N(1)-C(2)-C(22)	113.8(3)

© 1998 NRC Canada

Table 8 (*continued*).

Atoms	Distance	Atoms	Angle
C(6)—N(1)	1.327(4)	C(2*)-C(2)-C(22)	125.0(2)
C(2)—C(22)	1.493(4)	N(1)-C(6)-C(6*)	122.2(2)
C(22)—C(23)	1.388(4)	C(22)-N(2)-C(26)	116.4(3)
C(23)—C(24)	1.382(5)	N(2)-C(22)-C(23)	123.5(3)
C(24)—C(25)	1.363(5)	N(2)-C(22)-C(2)	116.8(3)
C(25)—C(26)	1.372(5)	C(2)-C(22)-C(23)	119.6(3)
C(26)—N(2)	1.352(4)	C(22)-C(23)-C(24)	117.8(4)
N(2)—C(22)	1.345(4)	C(23)-C(24)-C(25)	119.9(3)
N(2)···N(2*)	2.963(6)	C(24)-C(25)-C(26)	118.9(4)
C(26)···C(26*)	4.446(8)	C(25)-C(26)-N(2)	123.5(4)
N(1)···C(23)	2.853(5)	C(23)-H(23)-N(1)	91
N(1)···H(23)	2.66		
C(22)···C(22*)	3.102(6)	*X** 1 – *x* *y* ½ – *z*	
DPATBw			
N(1)—C(1)	1.409(6)	C(l)-N(l)-C(1′)	127.7(5)
C(1)—N(2)	1.325(7)	N(l)-C(l)-N(2)	117.9(6)
N(2)—C(3)	1.352(7)	N(l)-C(l)-C(6)	118.1(6)
C(3)—C(4)	1.355(8)	N(2)-C(1)-C(6)	124.0(6)
C(4)—C(5)	1.375(9)	C(1)-N(2)-C(3)	116.7(5)
C(5)—C(6)	1.378(7)	N(2)-C(3)-C(4)	123.3(6)
C(6)—C(1)	1.369(8)	C(3)-C(4)-C(5)	118.8(6)
N(1)—C(1′)	1.339(7)	C(4)-C(5)-C(6)	119.1(6)
C(1′)—N(2′)	1.342(7)	C(5)-C(6)-C(1)	118.1(6)
N(2′)—C(3′)	1.360(7)	N(l)-C(l′)-N(2′)	121.3(6)
C(3′)—C(4′)	1.354(8)	N(l)-C(l′)-C(6′)	121.9(6)
C(4′)—C(5′)	1.383(9)	N(2′)-C(1′)-C(6′)	116.7(6)
C(5′)—C(6′)	1.360(8)	C(1′)-N(2′)-C(3′)	123.7(5)
C(6′)—C(1′)	1.411(7)	N(2′)-C(3′)-C(4′)	119.9(6)
N(2)···N(2′)	2.633(6)	C(3′)-C(4′)-C(5′)	118.6(7)
N(2′)—H(N2′)	1.03	C(4′)-C(5′)-C(6′)	121.1(6)
H(N2′)···N(2)	1.87	C(5′)-C(6′)-C(1′)	120.0(6)
N(1)···O	2.806(7)	N(2′)-H(N2′)-N(2)	128
H(N1)···O	1.80	N(l)-H(Nl)-O	173
PPTB			
C(1)—C(2)	1.388(5)	C(2)-C(1)-C(6)	119.0(3)
C(2)—C(3)	1.375(5)	C(2)-C(l)-C(1′)	122.0(3)
C(3)—C(4)	1.390(6)	C(l′)-C(l)-C(6)	119.0(4)
C(4)—C(5)	1.372(6)	C(1)-C(2)-C(3)	120.7(4)
C(5)—C(6)	1.370(6)	C(2)-C(3)-C(4)	119.2(4)
C(6)—C(1)	1.384(5)	C(3)-C(4)-C(5)	120.4(4)
C(1)—C(1′)	1.471(5)	C(4)-C(5)-C(6)	120.1(4)
C(1′)—N(2′)	1.357(4)	C(5)-C(6)-C(1)	120.5(4)
N(2′)—C(3′)	1.353(5)	C(l)-C(l′)-N(2′)	118.5(3)
C(3′)—C(4′)	1.371(6)	C(l)-C(l′)-C(6′)	125.1(4)
C(4′)—C(5′)	1.365(6)	N(2′)-C(1′)-C(6′)	116.4(3)
C(5′)—C(6′)	1.380(5)	C(1′)-N(2′)-C(3′)	123.5(3)
C(6′)—C(1′)	1.390(5)	N(2′)-C(3′)-C(4′)	120.2(4)
C(2)—N(2′)	2.870(5)	C(3′)-C(4′)-C(5′)	118.0(4)
C(6)···C(6′)	2.960(6)	C(4′)-C(5′)-C(6′)	121.2(4)
		C(5′)-C(6′)-C(1′)	120.5(4)
BQTB			
C(1)—C(2)	1.362(6)	C(2)-C(1)-C(12)	121.1(4)
C(2)—C(3)	1.368(8)	C(1)-C(2)-C(3)	119.7(5)
C(3)—C(4)	1.347(8)	C(2)-C(3)-C(4)	122.0(6)
C(4)—C(13)	1.420(7)	C(3)-C(4)-C(13)	120.0(6)
C(13)—C(5)	1.409(7)	C(6)-C(5)-C(13)	122.4(5)
C(5)—C(6)	1.347(7)	C(5)-C(6)-C(14)	120.5(5)
C(6)—C(14)	1.431(7)	C(8)-C(7)-C(14)	121.3(5)
C(14)—C(7)	1.383(7)	C(7)-C(8)-C(9)	119.8(5)
C(7)—C(8)	1.351(7)	C(8)-C(9)-N(10)	119.2(5)
C(8)—C(9)	1.366(7)	C(9)-N(10)-C(11)	123.6(4)
C(9)—N(10)	1.348(5)	N(10)-C(11)-C(12)	121.3(4)
N(10)—C(11)	1.354(5)	C(12)-C(11)-C(14)	121.5(4)
C(11)—C(12)	1.427(5)	N(10)-C(11)-C(14)	117.2(4)
C(12)—C(1)	1.398(5)	C(l)-C(12)-C(11)	123.1(4)
C(12)—C(13)	1.410(5)	C(1)-C(12)-C(13)	119.0(4)
C(11)—C(14)	1.414(5)	C(11)-C(12)-C(13)	118.0(4)
C(l)···N(10)	2.895(6)	C(4)-C(13)-C(5)	122.1(6)
C(13)···C(14)	2.828(6)	C(4)-C(13)-C(12)	118.2(5)
		C(5)-C(13)-C(12)	119.7(5)
		C(6)-C(14)-C(7)	123.4(5)
		C(6)-C(14)-C(11)	117.9(5)
		C(7)-C(14)-C(11)	118.7 (5)
DDPTB			
C(12)—N(1)	1.30(2)	C(2)-N(1)-C(12)	111(2)
N(1)—C(2)	1.38(2)	N(1)-C(2)-C(3)	127(2)
C(2)—C(3)	1.40(2)	N(1)-C(2)-C(15)	110(2)
C(3)—C(4)	1.37(2)	C(3)-C(2)-C(15)	121(2)
C(4)—C(13)	1.39(3)	C(2)-C(3)-C(4)	116(2)
C(13)—C(5)	1.50(3)	C(2)-C(3)-C(18)	115(2)
C (5)—C(6)	1.45(3)	C(4)-C(3)-C(18)	127(2)
C(6)—C(14)	1.51 (2)	C(3)-C(4)-C(13)	118(2)
C(14)—C(7)	1.38(2)	C(3)-C(4)-C(23)	118(2)
C(7)—C(8)	1.43(2)	C(13)-C(4)-C(23)	122(2)
C(8)—C(9)	1.35(2)	C(6)-C(5)-C(13)	119(2)
C(9)—N(10)	1.40(2)	C(5)-C(6)-C(14)	117(2)
N(10)—C(11)	1.35(2)	C(8)-C(7)-C(14)	119(2)
C(11)—C(12)	1.49(2)	C(8)-C(7)-C(24)	121(1)
C(12)—C(13)	1.39(2)	C(14)-C(7)-C(24)	118(1)
C(11)—C(14)	1.37(2)	C(7)-C(8)-C(9)	120(2)
C(2)—C(15)	1.45(3)	C(7)-C(8)-C(19)	121(2)
C(15)—C(16)	1.44(3)	C(9)-C(8)-C(19)	118(2)
C(16)—C(17)	1.38(3)	C(8)-C(9)-N(10)	117(2)
C(17)—C(18)	1.35(3)	C(8)-C(9)-C(22)	123(2)
C(18)—C(3)	1.44(3)	N(10)-C(9)-C(22)	118(2)
C(8)—C(19)	1.43(2)	C(9)-N(10)-C(11)	122(1)
C(l9)—C(20)	1.33(3)	N(10)-C(11)-C(12)	112(2)
C(20)—C(21)	1.40(3)	N(10)-C(11)-C(14)	120(2)
C(21)—C(22)	1.38(3)	C(12)-C(11)-C(14)	127(2)
C(9)—C(22)	1.39(3)	N(l)-C(12)-C(11)	117(2)
C(4)—C(23)	1.52(3)	N(1)-C(12)-C(13)	126(2)
C(7)—C(24)	1.50(2)	C(11)-C(12)-C(13)	115(2)
N(l)...N(10)	2.61(2)	C(4)-C(13)-C(5)	119(2)
N(10)—H(10)	0.95	C(4)-C(13)-C(12)	119(2)
H(10)···N(1)	2.18	C(5)-C(13)-C(12)	120(2)
C(13)···C(14)	2.93(2)	C(6)-C(14)-C(7)	124(2)
		C(6)-C(14)-C(11)	115(2)
		C(7)-C(14)-C(11)	119(1)
		C(2)-C(15)-C(16)	119 (2)
		C(15)-C(16)-C(17)	115(2)
		C(16)-C(17)-C(18)	125(2)

© 1998 NRC Canada

Table 8 (*continued*).

Atoms	Distance	Atoms	Angle
		C(3)-C(18)-C(17)	121(2)
		C(8)-C(19)-C(20)	118 (2)
		C(l9)-C(20)-C(21)	121(2)
		C(20)-C(21)-C(22)	120(2)
		C(9)-C(22)-C(21)	116(2)
		N(10)-H(10)-N(1)	106
TTT Bs			
N(1)—C(2)	1.367(7)	C(2)-N(l)-C(9)	119.2(5)
C(2)—N(2)	1.334(7)	N(1)-C(2)-N(3)	123.9(6)
C(2)—N(3)	1.328(7)	N(l)-C(2)-N(2)	117.3(6)
N(3)—C(4)	1.337(7)	N(2)-C(2)-N(3)	118.8(6)
C(4)—N(4)	1.319(7)	C(2)-N(3)-C(4)	117.9(5)
C(4)—C(10)	1.444(7)	N(3)-C(4)-C(l0)	121.7(5)
C(10)—N(5)	1.356(6)	N(3)-C(4)-N(4)	118.6(6)
N(5)—C(6)	1.321(6)	N(4)-C(4)-C(l0)	119.7(6)
C(6)—C(7)	1.443(7)	C(6)-N(5)-C(10)	117.6(5)
C(7)—N(7)	1.344(7)	N(5)-C(6)-C(7)	120.0(5)
C(7)—N(8)	1.341(7)	N(5)-C(6)-C(61)	116.6(5)
N(8)—C(9)	1.336(6)	C(7)-C(6)-C(61)	123.4(5)
C(9)—C(10)	1.373(7)	C(6)-C(7)-N(7)	121.2(6)
C(9)—N(1)	1.380(7)	C(6)-C(7)-N(8)	122.6(5)
C(6)—C(61)	1.491(7)	N(7)-C(7)-N(8)	116.2(5)
N(9)—C(91)	1.135(8)	C(7)-N(8)-C(9)	114.4(5)
C(91)—C(92)	1.442(10)	N(l)-C(9)-C(l0)	119.1(5)
N(4)···N(5)	2.803(2)	N(l)-C(9)-N(8)	116.4(5)
		N(8)-C(9)-C(10)	124.5(6)
		C(4)-C(10)-N(5)	121.3(5)
		C(4)-C(10)-C(9)	117.8(5)
		N(5)-C(10)-C(9)	120.8(5)
		N(9)-C(91)-C(92)	179.5(8)
PSSTBs			
C(1)—N(1)	1.465(7)	N(l)-C(l)-C(2)	121.7(6)
C(1)—C(2)	1.359(8)	N(l)-C(l)-C(9)	117.1(5)
C(2)—C(3)	1.407(9)	C(2)-C(l)-C(9)	121.1(6)
C(3)—C(4)	1.346(10)	C(1)-C(2)-C(3)	119.8(7)
C(4)—C(10)	1.395(9)	C(2)-C(3)-C(4)	120.3(7)
C(10)—C(5)	1.404(9)	C(3)-C(4)-C(10)	122.0(7)
C(10)—C(9)	1.426(7)	C(6)-C(5)-C(10)	120.8(7)
C(5)—C(6)	1.323(9)	C(5)-C(6)-C(7)	121.4(7)
C(6)—C(7)	1.412(9)	C(6)-C(7)-C(8)	119.2(7)
C(7)—C(8)	1.345(8)	C(7)-C(8)-N(8)	119.2(6)
C(8)—N(8)	1.456(7)	C(7)-C(8)-C(9)	122.1(6)
C(8)—C(9)	1.413(7)	N(8)-C(8)-C(9)	118.6(5)
C(1)—C(9)	1.421(7)	C(l)-C(9)-C(8)	125.1(6)
N(1)—C(N11)	1.493(7)	C(l)-C(9)-C(10)	118.0(6)
N(1)—C(N12)	1.475(7)	C(8)-C(9)-C(10)	116.9(6)
N(8)—C(N81)	1.487(7)	C(4)-C(10)-C(5)	121.9(7)
N(8)—C(N82)	1.494(7)	C(4)-C(10)-C(9)	118.6(6)
N(8)—H(N8)	1.18	C(5)-C(10)-C(9)	119.5(6)
H(N8)···N(1)	1.40	C(1)-N(l)-H(N8)	95
O—C(O1)	1.200(8)	C(1)-N(1)-C(N11)	113.3(5)
C(1)···C(8)	2.516(9)	C(1)-N(1)-C(N12)	111.3(5)
N(1)···N(8)	2.552(9)	C(N11)-N(1)-C(N12)	111.8(5)
N(1)···O	3.424(9)	C(8)-N(8)-H(N8)	96
N(8)···O	3.350(9)	C(8)-N(8)-C(N81)	112.4(5)
H(N8)···O	3.00	C(8)-N(8)-C(N82)	114.1(5)
		C(N81)-N(8)-C(N82)	111.4(5)
		N(1)-H(N8)-N(8)	163
		N(1)-H(N8)-O	95
		N(8)-H(N8)-O	97
PSTBw			
C(1)—N(1)	1.464(9)	N(l)-C(l)-C(2)	121.7(8)
C(1)—C(2)	1.36(1)	N(l)-C(l)-C(9)	117.1(7)
C(2)—C(3)	1.39(1)	C(2)-C(l)-C(9)	121.1(8)
C(3)—C(4)	1.33(1)	C(1)-C(2)-C(3)	120.7(10)
C(4)—C(10)	1.42(1)	C(2)-C(3)-C(4)	121(1)
C(10)—C(5)	1.40(1)	C(3)-C(4)-C(10)	119(1)
C(10)—C(9)	1.43(1)	C(6)-C(5)-C(10)	120(1)
C(5)—C(6)	1.33(1)	C(5)-C(6)-C(7)	121(1)
C(6)—C(7)	1.42(1)	C(6)-C(7)-C(8)	119.5(10)
C(7)—C(8)	1.37(1)	C(7)-C(8)-N(8)	121.3(9)
C(8)—N(8)	1.455(9)	C(7)-C(8)-C(9)	120.6(9)
C(8)—C(9)	1.41(1)	N(8)-C(8)-C(9)	118.1(8)
C(1)—C(9)	1.42(1)	C(l)-C(9)-C(8)	125.5(7)
N(1)—C(N11)	1.464(10)	C(l)-C(9)-C(10)	116.3(9)
N(1)—C(N12)	1.48(1)	C(8)-C(9)-C(10)	118.1(8)
N(8)—C(N81)	1.505(10)	C(4)-C(10)-C(5)	120(1)
N(8)—C(N82)	1.46(1)	C(4)-C(10)-C(9)	120.3(9)
N(8)—H(N8)	1.17	C(5)-C(10)-C(9)	119(1)
H(N8)...N(1)	1.56	C(1)-N(1)-H(N8)	106
N(5)—C(51)	1.12(1)	C(1)-N(1)-C(N11)	110.5(6)
C(51)—C(52)	1.43(1)	C(1)-N(1)-C(N12)	112.2(7)
C(1)···C(8)	2.52(1)	C(N11)-N(1)-C(N12)	111.9(7)
N(1)···N(8)	2.55(1)	C(8)-N(8)-H(N8)	110
		C(8)-N(8)-C(N81)	110.6(7)
		C(8)-N(8)-C(N82)	113.8(7)
		C(N81)-N(8)-C(N82)	111.7(7)
		N(1)-H(N8)-N(8)	137
		N(5)-C(51)-C(52)	179(2)
TcTBs			
C(5)—C(6)	1.347(10)	C(6)-C(5)-C(11)	119.4(9)
C(5)—C(11)	1.412(10)	C(5)-C(6)-C(7)	119.8(9)
C(6)—C(7)	1.412(11)	C(6)-C(7)-C(8)	120.9(9)
C(7)—C(8)	1.352(11)	C(7)-C(8)-C(12)	120.9(9)
C(8)—C(12)	1.401(11)	N(9)-C(9)-C(12)	118.7(9)
C(9)—N(9)	1.365(9)	N(9)-C(9)-C(l3)	119.6(8)
C(9)—C(12)	1.439(10)	C(12)-C(9)-C(13)	121.7(7)
C(9)—C(13)	1.406(10)	C(11)-N(10)-C(14)	122.5(6)
N(10)—C(11)	1.379(9)	C(5)-C(11)-N(10)	118.5(8)
N(10)—C(14)	1.361(8)	C(5)-C(11)-C(12)	121.4(8)
C(11)—C(12)	1.387(10)	N(10)-C(11)-C(12)	120.2(8)
C(13)—C(14)	1.381(7)	C(8)-C(12)-C(9)	125.3(9)
C(1A)—C(2A)	1.520(10)	C(8)-C(12)-C(11)	117.7(9)
C(1A)—C(13)	1.515(10)	C(9)-C(12)-C(11)	116.9(8)
C(2A)—C(3A)	1.519(10)	C(9)-C(13)-C(14)	117.9(7)
C(3A)—C(4A)	1.534(9)	N(10)-C(14)-C(13)	120.6(7)
C(4A)—C(14)	1.517(10)	C(2A)-C(1A)-C(13)	113.1(10)
C(1B)—C(2B)	1.537(9)	C(1A)-C(2A)-C(3A)	109.4(11)
C(1B)—C(13)	1.525(10)	C(2A)-C(3A)-C(4A)	107.4(12)
C(2B)—C(3B)	1.519(10)	C(3A)-C(4A)-C(14)	109.0(9)
C(3B)—C(4B)	1.522(10)	C(1A)-C(13)-C(9)	129.1(9)
C(4B)—C(14)	1.510(9)	C(1A)-C(13)-C(14)	112.9(8)

© 1998 NRC Canada

Table 8 (*concluded*).

Atoms	Distance	Atoms	Angle
N(3)—C(31)	1.132(8)	C(4A)-C(14)-N(10)	108.9(9)
C(31)—C(32)	1.434(10)	C(4A)-C(14)-C(13)	130.5(9)
		C(2B)-C(1B)-C(13)	109.5(9)
		C(1B)-C(2B)-C(3B)	107.5(12)
		C(2B)-C(3B)-C(4B)	107.3(11)
		C(3B)-C(4B)-C(14)	112.4(11)
		C(1B)-C(13)-C(9)	115.8(9)
		C(1B)-C(13)-C(14)	126.2(9)
		C(4B)-C(14)-N(10)	122.6(8)
		C(4B)-C(14)-C(13)	116.7(7)
		N(3)-C(31)-C(32)	177.9(9)

T-shape only π–π interaction (alternatively, a perpendicular C(2,6)—H(2,6)···R2 H-bonding interaction).

In the intra-cation N(2)—H(N2)···N(1) and N(2′)—H(N2′)···N(1) bonds, N(2)···N(1) = 2.637(5) Å, H(N2)···N(1) ~ 2.20 Å, and N(2)-H(N2)-N(1) ~ 104° (assuming N(2)—H(N2) = 1.02 Å). This geometry again is very similar to the corresponding intra-cation H-bond geometry in the 2,2′-bipyridinium(1+) cation, in which the mean distance analogous to H(N2)···N(1) is 2.23[8] Å and the mean angle analogous to N(2)-H(N2)-N(1) is 106[5]° (Table 3 of ref. 1). The H(N2)···H(N2′) ~ 2.65 Å separation in TPTBw may be co-responsible for the nonplanarity of the cation, although the H(1,3)···H(2,3) repulsion, at ~2.23 Å, is probably the principal factor.

The location of the H_2O molecule suggests H-bonding interactions with N(2) and possibly with R2 or R4 or both (Figs. 6*b*, 7). The refined coordinates of the O atom, on the cation C_2 axis, were (0, 0.5040(5), ¾), with U_{11} = 0.121(6), U_{22} = 0.058(4), U_{33} = 0.45(1), U_{12} = U_{23} = 0, and U_{13} = 0.118(7) Å^2. The very large U_{33} (perpendicular to the cation plane) and the interatomic distances from the oxygen (which were compatible with the suspected interactions) pointed to disorder of the H_2O molecule. An attempt was therefore made to resolve the disorder by placing the O atom at partial occupancy between two pairs of C_2-related but otherwise unconstrained sites O* and O**. The oxygen positions that resulted from the ensuing refinement are shown in Fig. 7, with 74% of the oxygen occupying positions O* and 26% positions O**. Although the refinement was unconstrained (i.e., unbiased), the resulting location at O* is such that it improves the geometry of the N(2)—H(N2)···O bond (Table G), and the location at O** is in the natural direction for the formation of an O**···R2 hydrogen bond given a favourable (dynamic?) orientation of the H_2O hydrogens, as also shown by the reasonable O**···R2 interatomic distances. The O*···R4 and O**···R4 separations are too long for effective O—H···π bonding, but it should be noted that the U_{22} of the R4 carbons C(43), C(44), and C(45) are large, 0.13–0.17 Å^2 (Table C), so that a dynamic O···R4 interaction cannot be entirely excluded. The U_{ij} of the cation-skeleton atoms could not be satisfactorily accounted for on an RBM model.

The H-bonding at N(2) can then be described as a bifurcated N(2)—H(N2)···N(1),O* bond with H(N2)···N(1) ~ 2.20 Å, H(N2)···O* ~ 1.93 Å, N(2)-H(N2)-N(1) ~ 104°, N(2)-H(N2)-O* ~ 144°, and N(1)-H(N2)-O* ~ 108° (Fig. 6*b*). The H_2O molecule is loosely H-bonded to N(2) and N(2′) as well as to R2 and R2′. The H-bonding at room temperature has a strong dynamic component, not easily described in detail.

2PyPzTB (2)

The anions in the large tetragonal cell (origin at $\bar{1}$) of **2** are arranged in tightly wound helices with 4_1 as axes. The B atoms, at z ~ 0, ± ¼, ½, tesselate the structure into a stack ⊥(001) of four successive layers of cuboids. In each layer, cuboids containing a cation pair alternate with "empty" cuboids, and the orientations of the cation pairs in this square tiling again alternate in an *antiferro* manner. The near-planar (see below) cations in a pair are related by a $C_2 \subset S_4$ rotation; the cation planes are perpendicular to (001) and their perpendicular separation in a pair is ~3.7 Å. The 2PyPzTB structure may then be regarded as a three-dimensional *antiferro* mosaic of alternating $[cat_2an]^+$ and $[0,an]^-$ CsCl-like cells.

The pyrazine ring c1 is less planar than the two pyridine rings (Table 9). The c1 plane forms angles ~10° with the pyridine rings, while the c2′/c2 angle between the two pyridine planes is ~14°; the mean deviation of the nonhydrogen atoms from the best plane through the cation is ~0.1 Å.

The H(2′) atom effecting the intra-cation ring closure was clearly seen in an otherwise flat difference map (Fig. A) and was refined isotropically. The cation geometry and that of the N(2′)—H(2′)···N(2) bond are described in Tables 5, 8, 9, and Fig. 3. The shortest H(2′)···C(phenyl) distance is to C(132), 3.66(4) Å (N(2′)···C(132) = 3.656(4) Å, N(2′)-H(2′)-C(132) = 80(2)°), followed by H(2′)···C(142) = 3.87(4) Å (N(2′)···C(142) = 4.225(4) Å, N(2′)-H(2′)-C(142) = 100(2)°) and H(2′)···C(133) = 3.90(4) Å (N(2′)···C(133) = 3.493(4) Å, N(2′)-H(2′)-C(133) = 61(2)°). All the other H(2′)···C(phenyl) distances are longer than 4 Å. The intra-cation N(2′)—H(2′)···N(2) bond, N(2′)-H(2′)-N(2) = 168(3)°, cannot thus be said to be bifurcated, i.e., there is no significant H-bonding interaction with the anion.

Comparison of **2** with the analogous **22** (Fig. 3) shows that with respect to H-bonding the situations in these two structures are not completely similar. Although the N—H(N)···N′ geometry in the double-sided, centrosymmetric cation of **22** closely resembles that in the cation of **2** (Table 4), in the latter the two pyridine rings are significantly more coplanar than the corresponding ipsolateral rings in **22**. Furthermore, the opportunity for H(N)···phenyl bonding is somewhat more favourable in **22**, even though effective interaction would be difficult to claim. The shortest N···C(phenyl) and H(N)···C(phenyl) distances in **22** are 3.54 and 3.15 Å, N-H(N)-C ~ 98°. All the other H(N)···C(phenyl) distances are ≥ 3.4 Å, with N-H(N)-C angles of 61°–99°.

2PyPzCl (2A)

The H-bonding in **2A** is completely dominated by the Cl^- anion: N(2′)···Cl = 2.92 Å, H(N2′)···Cl ~ 1.77 Å, N(2′)-H(N2′)-Cl ~ 171°. The essentially straight, strong N—H···Cl bond minimizes the opportunity for intra-cation ring closure to an extent that renders the N—H···N′ interaction structurally ineffective even though the pyridine nitrogens are *syn* to each other: H(N2′)···N(2) ~ 2.96 Å, N(2′)-H(N2′)-N(2) ~ 75°.[25] The

[25] The location of H(N2′) in a difference map was very well defined (Fig. B).

© 1998 NRC Canada

Table 9. Planarity of the cation rings.[a]

Ring	$\bar{\delta}$(C,N), Å	X	δ(X), Å	Interplanar angles
TPTBw				
c1	0.002[2]			
c2	0.003[1]			c2/c1, 13.5°; c2/R2, 92.6°
c2′	0.003[1]			c2′/c2, 21.5°
2PyPzTB				
c1	0.012[7]			
c2	0.002[1]	H(2′)	–0.036	c2/c1, 8.5°
c2′	0.008[4]	H(2′)	0.173	c2′/c1, 10.6°; c2′/c2, 14.3°
cat	0.103[82]	H(2′)	–0.176	cat/c1, 4.6°; cat/c2, 4.0°; cat/c2′, 11.4°
2PyPzCI				
c1	0.027[13]			
c2	0.004[3]			c2/c1, 24.3°
c2′	0.006[3]			c2′/c1, 46.9°; c2′/c2, 55.4°
2PyPz2CI				
c1	0.014[7]	H(N2)	0.544	
c2	0.011[6]	H(N2′)	0.123	c2/c1, 159°
c2′	0.006[3]	H(N2′)	0.091	c2′/c1, 118°; c2′/c2, 62°
2PyPz				
c1	0.008[5]			
c2	0.003[3]			c2/c1, 138°
c2*	0.003[3]			c2*/c1, 138°; c2*/c2, 54°
DPATBw				
c1	0.005[3]	N(1)	0.025	
		H(N1)	–0.050	
c1′	0.006[2]	N(1)	–0.029	c1′/c1, 3.9°
		H(N1)	–0.092	
		H(N2′)	0.049	
PPTB				
c1	0.002[2]			
c1′	0.010[6]			c1′/c1, 15.3°
c1+c1′	0.111[68]			(c1+c1′)/c1, 8.4°; (c1+c1′)/c1′, 7.0°
BQTB				
c1	0.009[5]			
c2	0.013[6]			c2/c1, 3.4°
c3	0.008[5]			c3/c1, 1.1°; c3/c2, 2.3°
cat	0.025[19]			cat/c1, 1.2°; cat/c2, 2.3°; cat/c3, 0.3°
BQTBs				
c1	0.003[2]			
c2	0.011[8]			c2/c1, 6.1°
c3	0.009[7]			c3/c1, 2.5°; c3/c2, 3.6°
cat	0.046[28]			cat/c1, 2.4°; cat/c2, 3.7°; cat/c3, 0.4°
DDPTB				
c1	0.008[6]	N(10)	0.107	c1/c1′, 2.6°; c1/c2′, 8.3°
c2	0.017[10]	N(1)	–0.206	c2/c1, 4.9°; c2/c1′, 6.9°; c2/c2′, 3.4°
c3	0.056[45]	N(1)	–0.128	c3/c1, 3.4°; c3/c2, 2.1°; c3/c1′, 5.8°; c3/c2′, 5.3°
c1′	0.011[7]	N(1)	–0.075	
c2′	0.016[10]	N(1)	–0.317	c2′/c1′, 10.1°
c1+c1′	0.018[12]			
c2+c2′	0.034[17]			(c2+c2′)/(c1+c1′), 7.1°
cat	0.081[48]	C(23)	0.091	cat/c1, 2.1°; cat/c2, 3.4°; cat/c3, 2.8°;
		C(24)	–0.116	cat/c1′, 3.5°; cat/c2′, 6.6°

© 1998 NRC Canada

Table 9 (*concluded*).

Ring	$\bar{\delta}$(C,N), Å	X	δ(X), Å	Interplanar angles
TTTBs				
c6	0.003[2][b]			c6/c1, 50.1°; c6/c2, 46.7°
c1	0.021[11]	N(2)	–0.083	
		N(4)	0.079	
c2	0.007[5]	N(7)	–0.019	c2/c1, 4.2°
		C(61)	0.067	
c1+c2	0.037[16][c]	N(2)	–0.134	(c1+c2)/c1, 2.0°; (c1+c2)/c2, 2.1°;
		N(4)	0.053	(c1+c2)/c6, 48.4°
		N(7)	–0.115	
PSTBs				
c1	0.010[6]	N(1)	–0.076	
		N(8)	0.230	
c2	0.008[5]	N(1)	–0.193	c2/c1, 2.4°
		N(8)	0.101	
c1+c2	0.023[14]	N(1)	–0.139	(c1+c2)/c1, 1.3°; (c1+c2)/c2, 1.1°
		N(8)	0.155	
PSTBw				
c1	0.014[7]	N(1)	–0.077	
		N(8)	0.138	
c2	0.008[6]	N(1)	–0.174	c2/c1, 2.1°
		N(8)	0.028	
c1+c2	0.020[15]	N(1)	–0.128	(c1+c2)/c1, 1.1°; (c1+c2)/c2, 1.1°
		N(8)	0.081	
TcTBs				
c2	0.020[8]	N(9)	0.083	
		[N(10)	0.033]	
c3	0.004[3]	N(9)	0.028	c3/c2, 3.2°
		N(10)	–0.021	
c2+c3	0.029[14]	N(9)	0.090	(c2+c3)/c2, 1.8°; (c2+c3)/c3, 1.4°
		[N(10)	0.042]	

[a] $\bar{\delta}$(C,N), mean deviation of the C atoms in carbocyclic or of the C and N atoms in heterocyclic cation rings from the fitted ring plane; δ(X), deviation of the exocyclic atom X (in brackets, of the endocyclic atom X) from the fitted ring plane; cat, the complete cation ring system.

[b] 0.006 and 0.008 Å in TT, 0.007 Å in TTsw.

[c] 0.040 and 0.027 Å in TT, 0.022 Å in TTsw.

H-bonding in **2A** resembles that in **21** except for the somewhat smaller deviations of the cation rings from coplanarity (Fig. 3, Table 4). The shortness of the N(2′)—H(N2′)···Cl bond and the lack of interactive neighbours of the Cl atom other than H(N2′) permit the structure of **2A** to be viewed as composed of neutral [cat$^+$Cl$^-$] units.

2PyPz2Cl (3)

In the divalent (one Cl per pyridine) cation of **3** the protonation is on both pyridine nitrogens and both *N*-hydrogens are involved in N—H···Cl bonds (Fig. 3). While the N(2′)—H(N2′)···Cl(1) bond (N(2′)···Cl(1) = 2.988(3) Å, H(N2′)···Cl(1) ~ 1.83 Å, N(2′)-H(N2′)-Cl(1) ~ 176°) is analogous to the N(2′)—H(N2′)···Cl bond in **2A** and to the corresponding bond in **21**, formation of the second N—H···Cl bond changes the conformation of the two pyridine rings from *syn* to *anti* and results in an intra-cation ring closure between N(2) and the *pyrazine* nitrogen N(1). The H(N2) atom (N(2)—H(N2) ~ 1.09 Å) engages Cl(2) at ~2.07 Å, N(2)-H(N2)-Cl(2) ~ 142°, and N(1) at ~2.25 Å, N(2)-H(N2)-N(1) ~ 99°, to form a bifurcated N(2)—H(N2)···Cl(2),N(l) bond.[26] The distances from H(N2′) to N(4) and N(2), ~3.60 and ~3.90 Å, respectively, are too long and the corresponding N(2′)-H(N2′)-N angles too small, ~69° and ~112°, respectively, to qualify even for a bifurcated H-bonding interaction.

The cations are arranged in layers approximately ∥(001). The pyrazine rings are stacked face-to-face along *c*; neighbouring rings form centrosymmetric pairs with minimum vertical C—C and C—H separations of ~3.7 Å, too long for an effective facial π–π overlap. Similar to **2A**, the structure of **3** may be viewed as composed of neutral [cat^{2+}·2Cl$^-$] units.

2PyPz (4)

The crystal structure of **4** determined here from Cu *K*α data agrees very well with a previous determination (7) based on

[26] The N(1)-C(22)-C(2)-N(2) group is planar to 0.070[27] Å and N(1)-C(22)-C(2)-N(2)-H(N2) to 0.081[33] Å. The H(N2) atom is 0.20 Å out of the first plane; the Cl(2) atom is 0.43 Å out of the first and 0.16 Å out of the second plane.

© 1998 NRC Canada

Fig. 8. Hydrogen bonding in **5** and **9**. Projection on the plane of the cation ring 1′ or 2. Stippled circles, N atoms; black circles, H(N) atoms; large open circle, O atom; small open circles, H(O) atoms. Atom numbering as in Tables 8 and A.

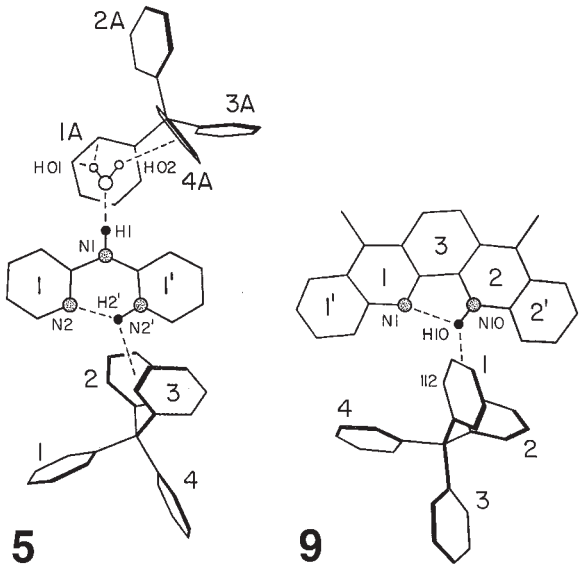

Mo *K*α data. The differences between corresponding bond lengths (11 pairs, Table 8) and bond angles (13 pairs) in the two determinations are all within three times the pooled esd's (9 of the bond lengths and 11 of the bond angles are within twice the pooled esd's).[27] The c2′/c2 angles are the same, 54°, and c2/cl differs by only 0.3° (41.9° against 42.2° in ref. 7).

The molecules, of C_2 symmetry (Fig. 3), are arranged in slightly puckered sheets ||(001).

DPATBw (5)

The cation in **5** is almost planar, cl′/cl = 3.9°, with the pyridine nitrogens *syn* to each other and C(1)-N(1)-C(1′) = 127.7(5)°. Direct comparison with the three related structures from the literature cannot be made, as the conformations in both the chloride **56** and the two forms of the free base (**54**, **55**) are *anti*. However, in none of these three structures are the two pyridine rings anywhere near coplanar: in **56** the interplanar angle is 50°, in **54** it is 23°, and in the two nonequivalent molecules in **55** the angles are 8° and 30°; the corresponding C-N-C angles at the amino nitrogen are 124.2(2)° (**56**), 131.4(4)° (**54**), and 129.9(2)° and 132.1(2)° (**55**), respectively. It is thus clear that, in the absence of a strong competition for an external H-bond, the ring closure in **5** on protonation is effective in producing a nearly planar *syn* conformation of the pyridine rings.

The ring closure results in the formation of a bifurcated N(2′)—H(N2′)···N(2),R2 bond (Fig. 8, Tables 4, 5, 8). The amino hydrogen H(N1) is involved in an almost straight bond to the oxygen of the H_2O molecule: N(1)-H(N1)-O ~ 173°. The H_2O molecule in turn is H-bonded to rings 1 and 4 of an adjacent anion (Fig. 8).

[27] Paired *t* statistic testing for equality of sample means gave t_{10} = 2.71 ($t_{0.01,\,10}$ = 3.17) for the bond lengths and t_{12} = 0.46 ($t_{0.01,\,12}$ = 3.06) for the bond angles.

Fig. 9. Effect of the second ring nitrogen on the cation bond lengths *d* (×10³, Å) and angles ε in the pairs BPTB/PPTB and PTB/BQTB. *Top left*: *d*(BPTB) – *d*(PPTB); *top right*: *d*(PTB) – *d*(BQTB); *bottom left*: ε(BPTB) – ε(PPTB); *bottom right*: ε(PTB) – ε(BQTB). The differences shown are equal to or exceed three pooled esd's of the respective *d* or ε values. c1′/c1(BPTB) – c1′/c1(PPTB) = –10.1°.

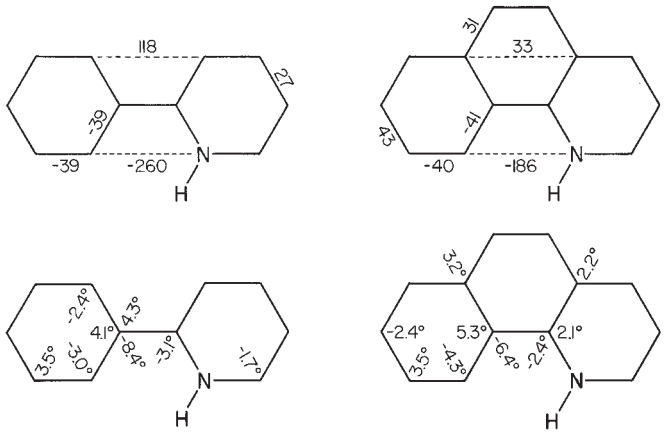

PPTB (6), BQTB (7), and BQTBs (8)

The bond lengths and angles in the cations of PPTB and BPTB (**15**), and in the cations of BQTB and PTB(**17**), are compared in Fig. 9, which displays differences exceeding three times the pooled esd's in respective pairs of corresponding bond lengths and angles. In the PPTB/BPTB pair, apart from the expected changes in ring c1, the effect of converting the phenyl ring into a pyridine ring on the geometry of ring c1′ is minor. However, the contraction of the X(2)···N(2′) (X = C, N) distance and the expansion of the C(6)···C(6′) distance on going from PPTB to BPTB are significant They and the simultaneous decrease in the dihedral c1′/c1 angle from 15.3° in PPTB to 5.2° in BPTB are associated with the appearance of the intra-cation N(2′)—H(N2′)···N(2) bond, which cannot exist in PPTB. Similarly, in the BQTB/PTB pair the effect of the introduction of N(1) on the geometry of ring 2 is minor. However, since the planarity of the cation skeleton remains practically the same

	$\bar{\delta}$(C,N)	c2/c1	c3/c1	c3/c2
BQTB	0.025[19] Å	3.4°	1.1°	2.3°
PTB	0.029[17] Å	3.7°	1.2°	2.6°

(Table 9; $\bar{\delta}$(C,N) = mean deviation of the C and N atoms from the fitted cation plane), comparisons of the compensatory changes in the bond lengths and angles in the BQTB/PTB and PPTB/BPTB pairs are not completely straightforward. Nevertheless, the change in the endocyclic angle at the X atom of ring 1 appears, on substituting N for C, to be larger in the BQTB/PTB pair, –4.3° as against –3.0° in the PPTB/BPTB pair. (For unprotonated 7,8-benzoquinoline and 1,10-phenanthroline see **16** and ref. 58, respectively.)

The similarities of the ion packing in the three $P2_1/c$ structures PPTB, BQTB, and PTB discussed above are reflected in the similarities of the H(N)···phenyl bond geometry, which are particularly conspicuous in the PPTB/BQTB pair (Fig. 5). The N···B and H(N)···B distances are much the same, as is the

© 1998 NRC Canada

Fig. 10. The ν(NH) and ν(ND) region of the FT-ir spectra of undeuterated PPTB and BQTB at 298 and 10 K, and of deuterated PPTB and BQTB at 298 K (Fluorolube mulls, CaF_2 plates). The principal ν(NH) and ν(ND) absorptions are marked with a dot.

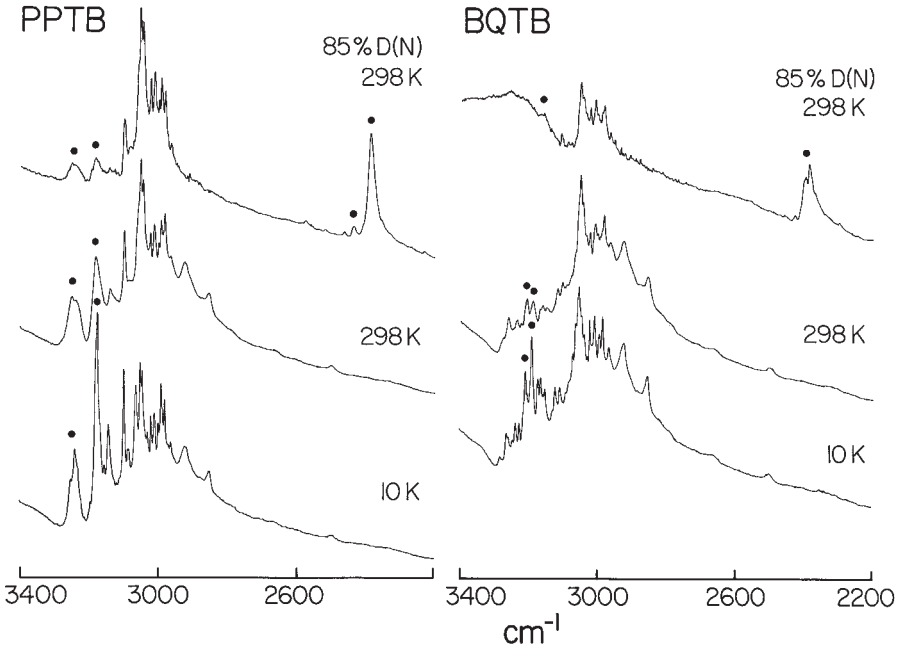

attitude of the associated anion with respect to the cation. In contrast,

	PPTB	BQTB	PTB
N···B, Å	4.21	4.20	4.28
H(N)···B, Å	3.37	3.75	3.69

the N···B and H(N)···B distances in BPTB and BQTBs differ considerably from the above (6.60 and 7.47 Å, respectively, in the former, and 4.72 and 4.60 Å, respectively, in the latter), and the H-bonded phenyl ring in BPTB is oriented differently. In BQTBs the H-bond is exclusively to MeCN (cf. below), so the phenyl involvement is irrelevant.

The main difference between the solvated BQTBs and the unsolvated BQTB arises from the manner in which the H(N) atom is engaged in H-bonding. In BQTB it forms an unbranched N—H(N)···phenyl bond, whereas in BQTBs the H-bond is exclusively to the N atom of the MeCN molecule: N(10)···N(50A) = 2.85(1) Å, H(10)···N(50A) ~ 1.99 Å, N(10)-H(10)-N(50A) ~ 147°, C(51A)-N(50A)-H(10) ~ 163° (A: $x + 1, y, z$). The shortest distance of H(10) to a phenyl carbon is to C(2,6), 3.55 Å; the distance of H(10) from the cation hydrogen H(1) is ~2.00 Å.

Within the accuracy of the structure determination the bond lengths and angles in BQTBs are the same as those in BQTB and are thus not included in Table 8. The cation rings in BQTBs appear to be slightly less coplanar than those in BQTB and PTB: in this order, c2/c1 = 6.1°, 3.4°, 3.7°; c3/c1 = 2.5°, 1.1°, 1.2°; c3/c2 3.6°, 2.2°, 2.6° (Table 9).

The external H(N)···phenyl bonding and the intra-cation ring closure would be expected to manifest themselves in the ir spectra of the four unsolvated compounds, primarily in the value of the ν(NH) stretching frequency and in the temperature coefficient $\delta\nu(NH)/\delta T$. Tracing the effect of the two bonding factors on ν(NH) is, however, difficult. The spectra are complex (Fig. 10; cf. also Fig. 12 of ref. 1) and contain a variety of features that seem to arise from coupling, Fermi resonance, or both, of vibrations involving the H(N) atom.[28] The principal ν(NH) adsorptions were identified by deuteration at N(2′) or N(10): over the observed ν(NH) range, ~3300 to ~3100 cm^{-1}, the corresponding ν(NH) and ν(ND) values show a linear correlation (Table 10, Fig. 11), with ν(NH)/ν(ND) ratios between 1.337 and 1.333. The ν(NH) shift with temperature is practically zero for BPTB and BQTB; in PPTB, ν(NH) decreases on cooling by a few wave numbers, while in PTB (1) it increases somewhat. This lack of pronounced temperature dependence over almost 300 K is consistent with weak or diffuse H-bonding. In addition, in PPTB $\delta\nu/\delta T > 0$ is indicative of an unbranched H-bond, whereas in PTB $\delta\nu/\delta T < 0$ points to branched H-bonds (cf. ref. 54), which indeed is what is observed (Fig. 12), even though the type of H-bond may not be the only factor responsible for this temperature dependence, given the smallness of the change in ν(NH) over such a substantial temperature range.

The relative lowering of ν(NH) in the sequence PTB, PPTB~BQTB (no ring closure), BPTB (Fig. 11) indicates that the decrease is the consequence of H-bonding both to a phenyl and to the unprotonated N atom. The present set of four compounds is too small for a meaningful statistical analysis. Nevertheless, exploratory regressions of averaged ν(NH) and ν(ND) frequencies on $d(\pi_c)$ (or $d[H(N)\cdots C(phenyl)]_{min}$) and $d[H(N)\cdots N']$, taking the latter in PPTB and BQTB arbitrarily as 10–50 Å, seem to show that the effect of the bonding to the phenyl on the stretching frequency by far exceeds that of the ring closure.

DDPTB (9)

The aromatic rings c1, c2, c1′, and c2′ are reasonably planar (Table 9), but the large B_{eq} of C(5) and C(6) and the significantly

[28] For further details of the BPTB and PTB spectra see ref. 1.

© 1998 NRC Canada

Table 10. ν(NH) and ν(ND) frequencies (cm^{-1}) in the room-temperature and 10 K spectra of PPTB, BPTB, BQTB, and PTB.[a]

	ν(NH)		ν(ND)[b]
Compound	RT	10 K	RT
PPTB	3248	3247 sh	2433
	3241	3237	
	3179	3175	2386
BPTB	3147	3147	2358
	3125	3125	2344
BQTB	3204	3204	2398
	3185	3186	2387
PTB	3279	3272	2451

[a] Principal components only. BPTB and PTB from ref. 1.
[b] Circa 85% D(N).

lower nominal planarity of c3 compared to cl and c2 indicate that these two atoms are positionally disordered. Since the volume of data was barely sufficient for an isotropic refinement of the structure, resolution of the disorder was not attempted (cf. Experimental).

The H-bond resulting from the intra-cation ring closure has the expected geometry. but the N(10)–H(l0)···phenyl distances, to the nearest phenyl R1, are long (Fig. 9, Tables 4, 5). Although some of the features of the structure appear to suggest the existence of π–π interactions, the pertinent distances and angles seem unfavourable for such interactions to be effective: the angle c2′/R2 is only 76°, at π_c(c2′)···π_c(R2) ~ 4.9 Å, and the shortest (perpendicular) separations in the centrosymmetric cation pairs are N(1)···C(14)* = N(1)*···C(14) ~ 3.63 Å.

The pattern generated by the projections of the cations and anions along *a* on (011) is essentially that found for a projection of a hexagonal NiAs-type structure on (0001):[29] the cation projections form almost equilateral triangles inside which are located the anion projections.

TTTBs (10)

The pteridine skeleton is essentially planar (Table 9). The phenyl ring c6 forms an angle of 48.4° with the best plane through the cation skeleton. This angle is almost the same as that in the neutral solvated TTsw (**30**), 47.1°, but larger than in the neutral unsolvated TT (**29**), 31.6° and 34.7°.

The cation is protonated at the N(1) ring atom, as in **33**. Corresponding bond lengths and angles in the skeleton ring system in the two structures are statistically indistinguishable within three, and in most cases two or fewer, stated esd's. To estimate the effect of the protonation on the geometry of the pteridine skeleton, corresponding mean bond lengths and angles in the two cations were compared with those in the unprotonated pteridine skeletons in **29**–**32**. Comparison of the means for the two groups (*t* test for two means and analysis of variance, both at the 0.01 significance level) shows that the only angles significantly affected are the angle C(9)-N(1)-C(2), which as expected is increased (119.7[3]° against 115.0[5]°), and the two flanking endocyclic angles N(l)-C(9)-C(10) and N(1)-C(2)-N(3) (119.1[2]° against 122.1[8]°, and 123.3[6]° against 127.8[8]°, respectively); the decrease in the latter two is a compensatory response to the increase in the angle at N(1). Also increased on protonation is the exocyclic angle N(3)-C(2)-N(2), 118.4[1]° against 115.7[5]°, whereas the exocyclic N(1)-C(2)-N(2) angle apparently remains unchanged, 118.1[8]° against 116.9[9]°. The sum of these five mean angles before protonation is 598.6°, and after protonation is 597.5°, i.e., the changes are compensatory and localized around N(1).

[29] *b*/*c* = 1.32 compared with the ideal $\sqrt{3}$ ~ 1.73 for the true orthohexagonal geometry.

Fig. 11. Correlation of the principal ν(NH) and ν(ND) absorption frequencies in PPTB, BQTB, BPTB, and PTB (FT-ir spectra at 298 K, see text). In the structural formulae the large dots represent N and the small dots H(N) atoms.

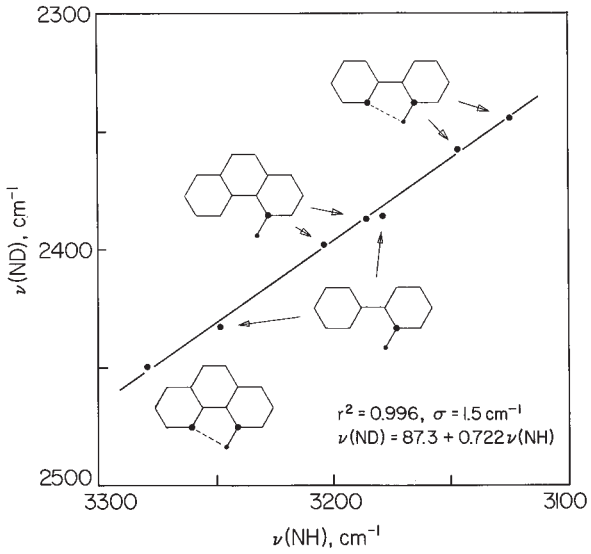

The H-bonding in TTTBs is illustrated in Fig. 13, with details of the relevant bond lengths and angles in Tables 3, 8, and F. All the H(N) atoms are engaged in H-bonds to phenyl groups of the neighbouring anions except H(2,2), which is bonded to the N atom of the MeCN molecule, and H(7,2), which interacts with phenyl c6 of its own cation. The three anions and the MeCN molecule coordinate the cation in such a way that there is no H-bonding between adjacent cations. Specifically, there is no pairing of cations across a centre (or pseudo centre) of symmetry to form cyclic

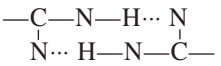

dimers. Such pairing of molecules (N···N ~ 3.00–3.09 Å)[30] occurs not only in anhydrous TT, but also in the solvated TTsw crystal and in **32**, and even between *cations* in the hydrated salt **33**, in all of which there is competition for H-bonds from the solvent molecules, and in the chloride **33** also from the Cl^- anion.[31] The disruption of the pairing and the absence of other cation–cation H-bonding interactions in TTTBs are attributable to the shape and size of the coordinating TB anions, which isolate the cations from one another; to the ample opportunity to form N—H···phenyl bonds provided by the acceptor-rich

[30] The N–proton distance estimated for N···N = 3.00 from eq. [3] is 1.027 Å, that for N···N = 3.09 Å is 1.020 Å.

[31] As pointed out in ref. 21, such paired N—H···N* bonds have been observed in almost every crystalline dihydrofolate reductase inhibitor investigated to that date.

© 1998 NRC Canada

Fig. 12. Competition of the H(N) atom in **6** and **15**, and in **7** and **17**, for hydrogen bonding. Projection on the c1′ or c2 plane. Large circles, N atoms; small circles, H(N) atoms; broken lines, H(N)···phenyl or H(N)···N′ bonds. Anion rings numbered as in Tables A, D, and E. Note the similarity of the anion orientations in the isostructural TBs **6** and **7**.

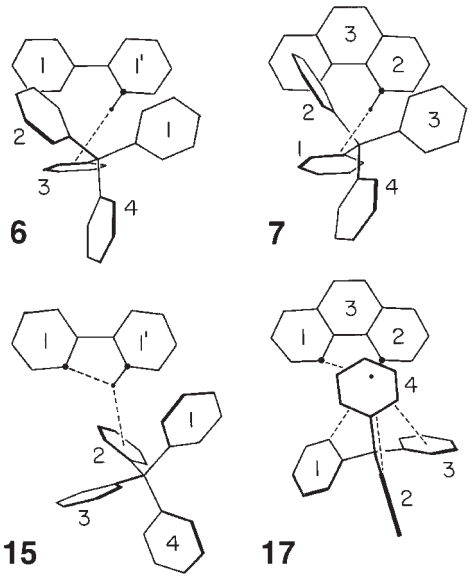

counter anion; and to the non-negligible strength of the H···phenyl interaction.

The H(1), H(4,2), and H(7,1) atoms are involved in unbranched N—H(N)···phenyl bonds to anion rings R3. R4A, and R2B, respectively; H(4,1) forms a bifurcated N(4)—H(4,1)···R1A,N(5) bond that effects a *p*-type intra-cation ring closure (Fig. 13, Tables 4, 5). The H(2,1) hydrogen forms an asymmetrically bifurcated bond to R2 and R3, while H(2,2) is bonded, at the unfavourable angle of only 114°, to the N(9) atom of the MeCN molecule: N(2)···N(9A) = 3.041(8) Å, H(2,2)···N(9A) ~ 2.53 Å. Oddly, this unexpectedly small angle is associated with an equally small H(2,2)-N(9A)-C(9A) angle, 107°, at the MeCN nitrogen. Examination of the immediate environment of H(2,2) and N(9A) reveals that the only other neighbour within a distance possibly eligible for H-bonding is R3C (C, 1 – *x*, –*y*, 2 – *z*): N(9A)···H(33C) ~ 3.06 Å, N(9A)-H(33C)-C(33C) ~ 120°, C(9A)-N(9A)-H(33C) ~ 144°. It is uncertain whether or not this geometry qualifies as corresponding to marginal —C≡N···N—C(phenyl) bonding (cf. ref. 55).

The minimum N···C distances in the bonds to the phenyl rings range from 2.96 to 3.72 Å and the minimum H(N)···C distances from ~2.48 to ~3.05 Å. The approach of an N–H(N) vector to the associated ring plane can be very oblique, cf. the (N-H)/R angle, which varies considerably (Table 5). With the exception of R2, which is the acceptor of H(2,1) and H(7,1) from two different cations, a phenyl ring is H-bonded from one side only.

An interesting feature of the cation geometry is the proximity of the NH_2 group on C(7) to the phenyl ring c6 of its own cation. As noted above, this ring forms a substantial angle with the pteridine skeleton not only in TTTBs but also in the neutral unsolvated as well as solvated triamterene, and the corresponding relevant N(7)···c6 distances are similar (Table 5):

Fig. 13. Hydrogen bonding in TTTBs. Open circles, N atoms; stippled circles, C atoms; filled circles, H(N) atoms. H(C) atoms omitted for clarity. H-bonds are indicated by broken lines. For atom numbering see Table A and Fig. 1.

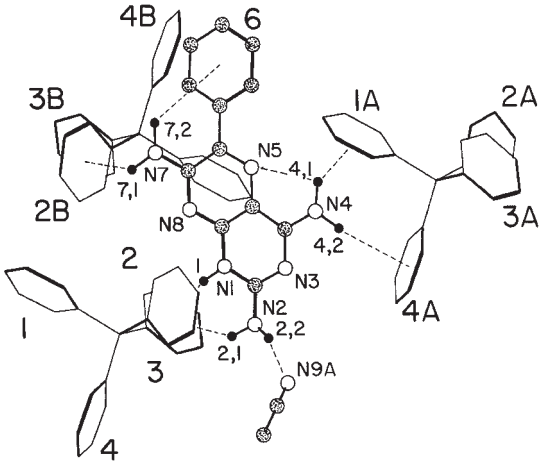

	TTTBs	TT (mean)	Ttsw
d(N···C)$_{min}$, Å	2.960(8)	2.998[10]	2.946
d(N···C), Å	4.10[86]	4.15[89]	4.05
$d(\pi_c)$, Å	3.96	4.13	3.92
Δ, Å	2.17	2.20	2.15

The shortest N···c6 distance, between N(7) and C(61), is shorter than any of the other N···C(phenyl) separations in TTTBs (Table 5). This distance and the corresponding N(7,2)···C(62) distance of 2.44 Å clearly point to the existence of an *intra*-cation N(7)—H(7,2)···c6 hydrogen bond. However, the very large Δ values, 2.17 Å for N(7)···C(c6) and 2.30 Å for H(7,2)···C(c6), indicate that the attitude of the N(7)-H(7,2) vector to the ring plane is very oblique, the [N(7)-H(7,2)]/c6 angle being only 13°. The H-bonding situations at the corresponding phenyl ring in TT and TTsw are similar.[32] Thus while the steric interaction with the NH_2 group at C(7) causes c6 to twist out of the pteridine plane, it simultaneously results in the observed distorted H-bonding geometry (cf. also refs. 56 and 57).

TLS analysis accounted only moderately well for the U_{ij} of the skeleton atoms: $R(U_{ij})$ = 10.1%, $R_w(U_{ij})$ = 9.7%, rms(U_{ij}) = 0.0035 Å, rms[esd(U_{ij})] = 0.0040[8] Å^2; the mean bond-length correction based on this model amounted to ≤ 0.003 Å, and that to the bond angles to ≤ | 0.04 |°. Comparison of the $\bar{U}_{ii}$ for the skeleton ring atoms with the $\bar{U}_{ii}$ for the exocyclic nonhydrogen atoms in TTTBs and **29**, **30**, **32**, and **33** resulted in $\bar{U}_{ii}$(exocyclic) = 1.43$\bar{U}_{ii}$(skeleton) (r^2 = 0.98), i.e., in these structures at room temperature there is substantial thermal activity of the substituent atoms.

PsTBs (11) and PsTBw (12)

The main difference between the structures of these two proton-sponge TBs is in the nature of their solvation: in the monoclinic **11** the solvent molecule is Me_2CO, whereas in the triclinic **12** it is MeCN and H_2O. This would suggest that the two structures are organized in a similar manner. Indeed,

[32] The shortness of this distance in TT is noted in ref. 17, but it is not interpreted there as arising from the intra-molecular N(7)—H(7)···c6 H-bond.

© 1998 NRC Canada

Fig. 14. Packing relationship between the monoc1inic **11** and the tric1inic **12**. The heavily-outlined subcell *S* of **11** corresponds to the unit cell of **12**. The *S* bands ||*c* alternate with bands of similar subcells roughly antiparallel to the *S* bands, with pseudo anticentres of inversion $\bar{1}'$ (at the corners of *S*) relating cations to the Me_2CO molecules. Black circles, O or N atoms of the solvent molecules.

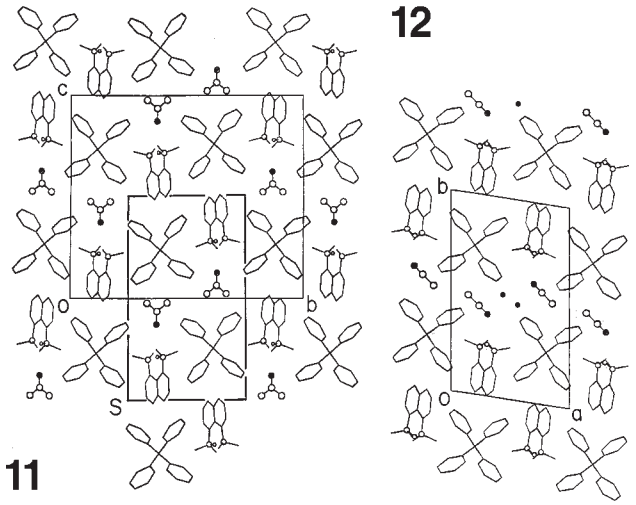

V_1(**11**) – V_1(**12**) = 871 – 861 ~ 10 Å, which is in the right direction of the difference for nominal space filling by C + H and N. Furthermore, the unit cells of **11** and **12** can be transformed with reasonable fidelity into each other: $(a, b, c)_{\mathbf{11}}$ = (0,0,1/2,0,0/0,1,0)$(a, b, c)_{\mathbf{12}}$ or $(a, b, c)_{\mathbf{12}}$ = (0,½,0/0,0,l/l,0,0) $(a, b, c)_{\mathbf{11}}$; a(**11**)/c(**12**) = 0.991, b(**11**)/2a(**12**) = 0.979, c(**11**)/b(**12**) = 1.022. The relationship of the two structures is represented in Fig. 14.

In **11**, the components of the structure are arranged in $[\cdots Me_2CO\cdots an\cdots cat\cdots]_\infty$ columns ||*c*, with the cation planes ⊥(001). Projections of these columns on (001) define the lattice points of a distorted rhombic tiling with rhombs of ~7.2 Å on the side.[33] The space in the channels between the columns is occupied by H(C) atoms of both the anions and the cations. The N(1)-C(1)-C(9)-C(8)-N(8) group of the cation is closed by H(N8) to form a 6-membered ring in which the nonhydrogen atoms are coplanar to 0.044[22] Å, with H(N8) 0.16 Å off their plane; the N(1)···N(8) distance, 2.552(9) Å, is ~1.4% longer than d[C(l)···C(8)] = 2.516(9) Å. The N(8)-H(N8)-N(1) angle of ~163° (N(8)—H(N8) ~ 1.18 Å, H(N8)···N(1) ~ 1.40 Å; H(N8) seen in the difference map) offers a poor opportunity for H-bond bifurcation at H(N8): the unique external acceptor atom is the acetone oxygen at ~3.00 Å from H(N8), which is too far for an effective H-bonding, and the relative orientations of the cation and the anion exclude any possibility of H(N8)···phenyl interaction. Nonetheless, the Me_2CO molecule is oriented in the right direction for an H(N8)···O bond (Fig. 15), and the two angles N(8)-H(N8)-O and N(1)-H(N8)-O, though small, are practically the same, ~97° and ~95°, respectively, and not inconsistent with the existence of a branched H-bond, however weak.[34] In this context it is of interest to recall the above observation that all three components of the structure are located on parallel strings in the sequence

[33] The tiling may also be regarded as corresponding to a distorted hexagonal honeycomb packing of the infinite columns.

[34] The O atom is 0.26 Å out of the N(1)-C(1)-C(9)-C(8)-N(8) plane.

Fig. 15. PSTBs: intra-cation and putative H(C)···phenyl hydrogen bonds (see text). Only those H atoms that participate in H-bonding are shown (small black circles). Large black circles, O atoms; large open circles, C atoms; small open circles, N atoms (A: x, y, 1 + z, cf. Table A). H-bonds in broken lines.

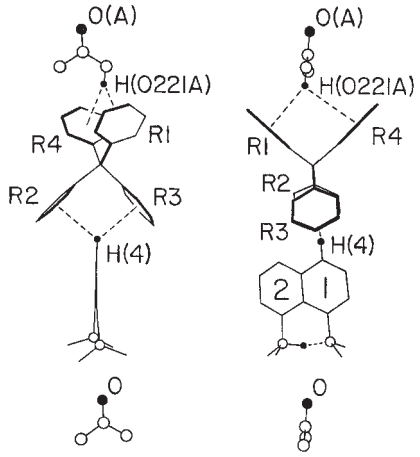

···[Me_2CO···an···cat]···. This arrangement permits a close approach of the neighbours on the string; notably, the cation plane, which is parallel to the string axis, fits almost symmetrically in the wedge-shaped space formed by the pair of anion phenyl rings closest to the cation, thus providing an opportunity for an H(C) atom(s) of the cation to interact with these phenyl groups (Fig. 15). Similarly, the Me groups of the solvent molecule fit between the other pair of phenyl rings of the flanking anion. Examination of the shortest H(C)···phenyl distances shows that H(4) of the cation is ~3.02 Å from C(26) and ~3.09 Å from C(32), the corresponding H(4)···π_c (R2) and H(4)···π_c (R3) distances being ~2.76 and ~2.83 Å, respectively. Similarly, the distance of the acetone hydrogen H(O221A) (A: x, y, 1 + z) from C(16) is ~3.17 Å, with H(O221A)···π_c (R1) ~ 2.95 Å, and from C(41), ~3.41 Å, with H(O221A)···π_c (R4) ~ 3.31 Å. The H(4) atom is thus engaged in a putative bifurcated C(4)—H(4)···R2,R3 bond (C(4)-H(4)-π_c (R2) ~ 133°, C(4)-H(4)-π_c (R3) ~ 129°) to one side of the anion, while the other side of the anion is involved in an asymmetric bifurcated C(O22A)—H(O221A)···R1,R4 bond, C(022A)-H(0221A)-π_c(R1) ~ 139°, C(022A)-H(O221A)-π_c(R4) ~ 122°; the cation and acetone planes are approximately mutually perpendicular. This arrangement is reminiscent of the ···cat···an··· strings ||*c* in the tetragonal alkali and ammonium TBs, in which the wedge-shaped spaces between the phenyl rings on each side of the S_4 anion are occupied by like cations (cf. ref. 3).

The C—H bond lengths used to place the H(C) atoms in the refinement of **11** were 0.95 Å. If allowance is made for this assumed thermal foreshortening, the H(C)···C and H(C)···π_c distances quoted here compare with those found in the terminal alkynes of ref. 55 and considered to correspond to weak —C≡C—H···phenyl bonds. A case can thus be made for the existence of similar, *bifurcated* weak H(C)···phenyl hydrogen bonds in **11**.

The overall features of the structure of **12** are quite similar to those of **11**. However, the solvent content of the reported structure is rendered somewhat ambiguous because of the ~30% decrease in the intensities of the standard reflections

© 1998 NRC Canada

Fig. 16. Hydrogen bonding in the 9-aminoacridine derivatives **13** and **34**–**37**. Only one conformation of ring c1 is shown for **34** and **35**. Black circles (decreasing size), C, N. and H atoms. Large open circles, Cl atoms; small open circles, O atoms. H-bonds are shown as broken lines. Projections of symmetry elements ($\bar{1}$, 2, 2_1) on the cation planes are indicated by dots or arrows.

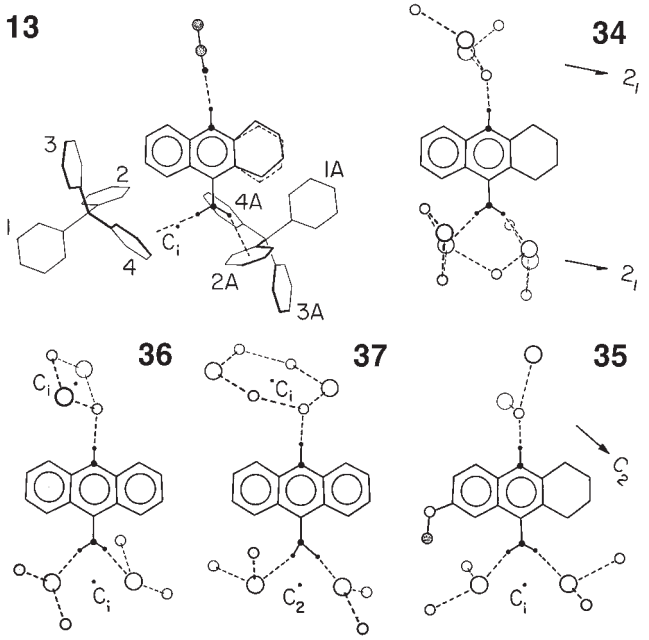

over the course of data collection. This decrease is taken to be the effect of a partial loss of solvent. Although an empirical correction was applied to the intensities (cf. Experimental), the degree of solvation remains uncertain, more so for H_2O than for MeCN on the evidence from the refined structure.

The components of the structure form [···MeCN···cat···an···]$_\infty$ strings ||*b* (Fig. 14). The distance of the MeCN nitrogen atom N(5) from H(N8) is ~2.84 Å, at an N(8)-H(N8)-N(5) angle of ~117°, both unfavourable for H-bonding. However, the C(51)-N(5)-H(N8) angle of ~135° indicates that N(5) may be involved in a weak bifurcated bond to the H_2O molecule. The O atom of the latter appears to be positionally disordered across a centre of symmetry, the O···O* distance being ~1.85 Å; the N(5)···O distance to the O position more likely to be engaged is ~3.44 Å. Thus here again the solvent molecule (MeCN) has a reasonable orientation for H-bonding to H(N8), but the interatomic distances are much longer than conventionally accepted for effective H-bonding. The H_2O molecule is almost certainly bonded to MeCN, but details of the bonding could not be ascertained.

Putative interaction can be claimed between the cation H(C) hydrogen H(5) and the phenyls R1 and R2 (H(5)···π_c(R1) ~ 2.82 Å, C(5)-H(5)-π_c(R1) ~ 131°, $\bar{d}$[H(5)···C(R1)] = 3.14(10) Å, mean C(5)-H(5)-C(R1) angle = 129[13]°; H(5)···π_c(R2) ~ 3.19 Å, C(5)-H(5)-π_c(R2) ~ 128°, $\bar{d}$[H(5)···C(R2)] = 3.46[30] Å), and between H(4) and R2 (H(4)···π_c(R2) ~ 3.17 Å, C(4)-H(4)-π_c(R2) ~ 129°, $\bar{d}$[H(4)···C(R2)] = 3.44[38] Å).[35] Furthermore, the H(521) atom of the MeCN molecule is situated appropriately for a bifurcated H(521)···R3,R4 bond (H(521)···π_c(R3) ~ 2.87 Å, C(52)-H(521)-π_cC(R3) ~ 125°; H(521)···π_c(R4) ~ 3.04 Å, C(52)-H(52)-π_c(R4) ~ 117°), so that the anion appears to be H-bonded from opposite sides. The nearly symmetric bifurcation at H(521) may well account for the seemingly unfavourable orientation of the MeCN molecule with respect to the H(N8) atom of the cation and probably represents a compromise between simultaneous weak interactions involving MeCN, the cation, two of the phenyl rings, and the H_2O molecule (Fig. 15).

It should be noted that in both **11** and **12** the solvent molecule engaged in the putative H(C)···phenyl interaction has an appreciable dipole moment (2.83 D for Me_2CO, 3.44 D for MeCN, both in benzene), and that the polar axis of the Me_2CO molecule in **11** is aligned with the column axis (Fig. 15), thus ensuring maximum dipolar interaction of Me_2CO with its neighbours in the column.

TcTBs (13)

The cation geometry is practically the same as that found for the monohydrated hydrochlorides **34** and **35**. The skeletons of the aromatic rings c2 and c3 are planar to 0.020[8] and 0.004[3] Å, respectively, and c3/c2 = 3.2° (Table 9). As in the hydrochlorides, atoms in the saturated portion of c1 are positionally disordered. The coordinates of atoms C(1)–C(4) listed in Table A are the result of modelling the disorder as a 1:1 superposition of two c1 conformations, A and B, with C(13) and C(14) stationary (cf. Experimental). The protonated atom is, as in **34** and **35**, the ring nitrogen N(10), C(11)-N(10)-C(14) = 122.5(6)°. It is weakly bonded to the N(3) atom of the MeCN molecule, N(10)···N(3) = 3.018(7) Å, H(10)···N(3) ~ 2.01 Å, N(10)-H(10)-N(3) ~ 172°. These distances agree well with the estimated obtained for N···N = 3.018 Å from eq. [2], N—H = 1.03 Å, H···N′ ~ 1.99 Å.

The interaction of the amino group with its anion neighbours is very asymmetric (Tables 5, F): the shortest H(9a)···C(phenyl) distance is to R2A, ~2.76 Å (H(9a)···π_c(R2A) ~ 2.60 Å), and the shortest H(9b)···C(phenyl) distance is to R4, ~3.27 Å (H(9b)···π_c(R4) ~ 3.84 Å). The former corresponds to only a weak H(N)···phenyl interaction, while the latter is much too long to qualify for any such significant interaction.[36] Moreover, the geometric H···phenyl parameters involving either amino hydrogen fit only poorly in the correlation plots of ref. 3 for H···phenyl bonds, indicating the absence of an ion-charge reinforcement at the amino group. Nevertheless, the *orientation* of the N(9)–H(9b) vector is favourable for potential H(N)···phenyl bonding.

The gross structure of TcTBs may be regarded as consisting of centrosymmetric [···(cat + MeCN)···an···]$_2$ ring dimers in which H(9a) is bonded to R2 (from one side only), N(9)—H(9b) points in the direction of R4, and rings R1 and R3 remain unengaged (Fig. 16). The dimer groups are thus discrete, i.e., there is no H-bonding interaction between them. In this, TcTBs differs from the structures of **34** and **35** as well as from the mutagenic hydrochloride hydrates **36** and **37**, in all of which the Cl^- anion is 4-coordinated by two amino and

[35] For further details see Table F.

[36] This H-bond engagement is reminiscent of 4-aminopyridine (38), in which only one of the amino hydrogens is involved in an H-bond: N···N′ = 3.01 Å, H···N′ ~ 2.13 Å, N-H-N′ ~ 169° (N, amino nitrogen; N′, ring nitrogen of a neighbouring molecule).

© 1998 NRC Canada

two water hydrogens, so that the anion and the water molecule are able to propagate the H-bonding three-dimensionally throughout the crystal (Fig. 16). Viewed along *b*, the centroids of the cations and anions project into a honeycomb array of irregular centrosymmetric hexagons with *b* as the column axis and with the MeCN molecules forming 2_1-helices about this axis.

In contrast to protonated 4-aminopyridine (**39**, **40**), the py_2H^+-type cation with mutually perpendicular pyridine rings and a short N···N′ separation (N···N′ ~ 2.70 Å, N—H ~ 1.17 Å, H···N′ ~ 1.52 Å. N-H-N′ ~ 177°) is not present in the structures of the 9-aminoacridine derivatives of Fig. 16. The reason for this might be the inefficient space filling that would result if the two three-ring acridine systems were mutually perpendicular. In fact, even the formation of an essentially coplanar biacridine cation appears to be stereochemically unfavourable (H(C) repulsions!).

It is noteworthy that the compounds discussed in this section, all of which contain a 4-aminopyridine core, have properties injurious to human biology (high toxicity, strong mutagenic activity, undesirable enzyme inhibitions.

Experimental

The TBs were prepared by precipitation from aqueous solutions of $NaBPh_4$ and the appropriate organoammonium halide, usually the chloride. After washing with water the precipitate was recrystallized from MeCN, or it was dissolved in acetone and water was added until a precipitate reappeared. Sufficient acetone was then added to restore the clear solution, and the resulting solution was allowed to crystallize by slow evaporation at room temperature. For X-ray work the crystals were sealed in glass capillaries.

The crystallographic information is summarized in Table 2. All intensities were corrected for Lorentz, polarization, absorption (ψ-scans), secondary extinction, and, where appropriate, for time-decay effects. We wish to reiterate that, in general, organoammonium TB crystals are weak and fickle scatterers. As pointed out previously (1–3), significant reflections are seldom observed above a (sin θ)/λ limit of 0.48 $Å^{-1}$ (θ_{Mo} ~ 20°, θ_{Cu} ~ 48°). Since in this laboratory X-ray data collection routinely extends to (sin θ)/λ ~ 0.55 $Å^{-1}$ (θ_{Mo} ~ 25°, θ_{Cu} ~ 60°), the ratio of observed reflections to total measured unique reflections never exceeds 50%. In several cases there was an observable decline in the intensities of the standard reflections over the course of data collection (see below). A linear correction was applied to take account of the decline unless stated otherwise.

The structures were solved by direct methods (59) and refined using the TEXSAN-TEXRAY software package (60) or SHELXL-93 (61) or both. The function minimized was $\Sigma w(|F_o| - |F_c|)^2$. The anisotropic temperature factor is defined as $\exp[-2\pi^2(U_{11}h^2a^{*2} + ... + 2\ U_{12}\ hka^*b^* + ...)]$; U_{iso} (H) = $1.2U_{eq}$(X) of the attached X atom. The H(C) atoms, though seen in the difference maps, were in the final refinement placed geometrically and not refined. The positions of the H(N) atoms were obtained from the difference maps; in favourable cases they were well defined (e.g., in Figs. A and B) and were kept fixed at the observed values during the final refinement, as noted. Otherwise the H(N) atoms were placed geometrically and not refined.[37] In addition to Table 2 the following experimental details are noted:

1: pale lemon yellow.[24] **2**: yellow crystals; H(N) refined isotropically, N—H, 1.17(4) Å. **2A**: crystal cut from a light-yellow needle; ~5% intensity decline. **3**: colourless needle; <1% decline. **4**: yellow needle, ~1% decline. **5**: colourless needle; ~6% decline. **6**: N—H. 1.18 Å. **7**: crystal cut from a faint yellow plate. **8**: in contrast to the unsolvated **7** obtained from aqueous acetone, the crystals obtained from MeCN were solvated. Although the colourless block crystal was in a sealed glass capillary, it appeared to lose solvent. To compensate for the ~70% intensity decline, a fourth-order polynomial correction was applied. ORTEP drawings before the last refinement showed that the thermal ellipsoids on the B and cation C(11)–C(14) atoms were essentially spherical; these atoms were therefore refined only isotropically. **9**: orange needle. **10**: colourless needle. **11**: colourless block; N—H. 1.18 Å, C—H = O—H = 0.95 Å. **12**: colourless prism; ~30% decline; N—H. 1.17 Å, C—H = O—H = 0.95 Å. In the final refinement the N(1) and N(8) atoms were treated isotropically, as their thermal ellipsoids in the preceding refinement were nearly spherical and the d/p ratio was not high. **13**: the quality of the yellow needles obtained from MeCN was rather poor; ~6% decline. To model the disorder in ring c1 the structure was refined by full-matrix least squares on F^2 using SHELXL-93, with the C—C bond lengths and angles involving carbons C(1)–C(4) loosely constrained. This treatment differs from that of **20** and **34** (22, 23), where only carbons C(2) and C(3) were assumed disordered. The anion was refined as a rigid body, and the nonhydrogen atoms of the MeCN molecule were refined isotropically. The H(N) atoms, though seen in the difference map, were placed geometrically (N—H. 1.02 Å) and not refined. The exocyclic NH_2 group was treated as an extension of the planar system of rings c2 + c3.

Acknowledgments

We thank Dr M. Falk and Mr Ping Seto for obtaining the FT-ir spectra, and Dr R.W. Alder for providing us with unpublished experimental data on the inside-protonated cations. This investigation was supported by grants from the Natural Sciences and Engineering Research Council of Canada to O.K. and T.S.C.

References

1. P.K. Bakshi, T.S. Cameron, and O. Knop. Can. J. Chem. **74**, 201 (1996).
2. O. Knop, T.S. Cameron, P.K. Bakshi, W. Kwiatkowski, S.C. Choi, and D. Adhikesavalu. Can. J. Chem. **71**, 1495 (1993).
3. P.K. Bakshi, A. Linden, B.R. Vincent, S.P. Roe, D. Adhikesavalu, T.S. Cameron, and O. Knop. Can. J. Chem. **72**, 1273 (1994).
4. G.R. Newkome and H.-W. Lee. J. Am. Chem. Soc. **105**, 5956 (1983).

[37] The structures of the 14 compounds were determined over a period of time and by different hands. This and the varying quality of the primary data accounts for a certain nonuniformity in the treatment of the H-atoms. The earlier refinements were based on assumed C—H, N—H, and O—H bond lengths of 1.08, 1.02, and 1.00 Å, respectively. In the more recent determinations the H-atoms were placed at C—H = 0.96 Å, N—H = O—H = 0.95 Å, or as mentioned under the individual structures.

© 1998 NRC Canada

5. B. Shaanan and U. Shmueli. Acta Crystallogr. Sect. B: Struct. Crystallogr. Cryst. Chem. **B36**, 2076 (1980).
6. G. Thevenet, N. Rodier, and P. Khodadad. Acta Crystallogr. Sect B: Struct. Crystallogr. Cryst. Chem. **B34**, 2594 (1978).
7. N.-T. Huang, W.T. Pennington, and J.D. Petersen. Acta Crystallogr. Sect. C: Cryst. Struct. Commun. **C47**, 2011 (1991).
8. H. Bock, T. Vaupel, C. Näther, K. Ruppert, and Z. Havlas. Angew. Chem. Int. Ed. Engl. **31**, 299 (1992).
9. B. Greaves and H. Stoeckli-Evans. Acta Crystallogr. Sect. C: Cryst. Struct. Commun. **C48**, 2269 (1992).
10. S.C. Rasmussen, M.M. Richter, E. Yi, H. Place, and K.J. Brewer. Inorg. Chem. **29**, 3926 (1990).
11. K.V. Goodwin, W.T. Pennington, and J.D. Petersen. Acta Crystallogr. Sect. C: Cryst. Struct. Commun. **C46**, 898 (1990).
12. H.A. Staab, K. Elbl, and C. Krieger. Tetrahedron Lett. **27**, 5719 (1986).
13. K. Elbl-Weiser, C. Krieger, and H.A. Staab. Angew. Chem. Int. Ed. Engl. **29**, 211 (1990).
14. H.A. Staab and T. Saupe. Angew. Chem. Int. Ed. Engl. **27**, 865 (1988).
15. T. Saupe, C. Krieger, and H.A. Staab. Angew. Chem. Int. Ed. Engl. **25**, 451 (1986).
16. T. Barth, C. Krieger, F.A. Neugebauer, and H.A. Staab. Angew. Chem. Int. Ed. Engl. **30**, 1028 (1991).
17. C.H. Schwalbe and G.J.B. Williams. Acta Crystallogr. Sect. C: Cryst. Struct. Commun. **C43**, 1097 (1987).
18. O. Dahl, K.H. Ziedrich, G.J. Marek, and H.H. Paradies. J. Pharm. Sci. **78**, 598 (1989).
19. C.D. Shirrell and D.E. Williams. J. Chem. Soc. Perkin Trans. 2, 40 (1975).
20. C.H. Schwalbe and G.J.B. Williams. Acta Crystallogr. Sect. C: Cryst. Struct. Commun. **C42**, 1252 (1986).
21. C.H. Schwalbe and G.J.B. Williams. Acta Crystallogr. Sect. C: Cryst. Struct. Commun. **C42**, 1254 (1986).
22. D.E. Zacharias and J.P. Glusker. Acta Crystallogr. Sect. C: Cryst. Struct. Commun. **C44**, 1656 (1988).
23. G. Bandoli, A. Dolmella, S. Gatto, and M. Nicolini. J. Chem. Crystallogr. **24**, 301 (1994).
24. R. Talacki, H.L. Carrell, and J.P. Glusker. Acta Crystallogr. Sect. B: Struct. Crystallogr. Cryst. Chem. **B30**, 1044 (1974).
25. C. Courseille, S. Geoffre, and B. Busetta. Cryst. Struct. Commun. **9**, 287 (1980).
26. M. Chao and E. Schempp. Acta Crystallogr. Sect. B: Struct. Crystallogr. Cryst. Chem. **B33**, 1557 (1977).
27. J. Rozière, J.M. Williams, E. Grech, Z. Malarski, and L. Sobczyk. J. Chem. Phys. **72**, 6117 (1980).
28. P. Teulon, R.G. Delaplane, I. Olovsson, and J. Rozière. Acta Crystallogr. Sect. C: Cryst. Struct. Commun. **C41**, 479 (1985).
29. R. Stevenson. Chem. Br. 165 (March) (1994).
30. T. Steiner. J. Chem. Soc. Chem. Commun. 1331 (1995).
31. O. Knop, S.C. Choi, and D.C. Hamilton. Can. J. Chem. **70**, 2574 (1992).
32. K. Woźniak, T.M. Krygowski, E. Grech, W. Kolodziejski, and J. Klinowski. J. Phys. Chem. **97**, 1862 (1993).
33. A. Escuer, R. Vicente, T. Comas, J. Ribas, M. Gomez, and X. Solans. Inorg. Chim. Acta, **177**, 161 (1990).
34. R.W. Alder, R.E. Moss, and R.B. Sessions. J. Chem. Soc. Chem. Commun. 997 (1983).
35. R.W. Alder, A.G. Orpen, and R.B. Sessions. J. Chem. Soc. Chem. Commun. 999 (1983).
36. R.W. Alder, R.E. Moss, and R.B. Sessions. J. Chem. Soc. Chem. Commun. 1000 (1983).
37. W.P. Schaefer and R.E. Marsh. J. Chem. Soc. Chem. Commun. 1555 (1984).
38. R.W. Alder, A.G. Orpen, and J.M. White. Acta Crystallogr. Sect. C: Cryst. Chem. Commun. **C44**, 287 (1988).
39. J.M. White, R.W. Alder, and A.G. Orpen. Acta Crystallogr. Sect. C: Cryst. Chem. Commun. **C44**, 662 (1988).
40. J.M. White, R.W. Alder, and A.G. Orpen. Acta Crystallogr. Sect. C: Cryst. Chem. Commun. **C44**, 664 (1988).
41. J.M. White, R.W. Alder, and A.G. Orpen. Acta Crystallogr. Sect. C: Cryst. Chem. Commun. **C44**, 872 (1988).
42. J.M. White, R.W. Alder, and A.G. Orpen. Acta Crystallogr. Sect. C: Cryst. Chem. Commun. **C44**, 1465 (1988).
43. J.M. White, R.W. Alder, and A.G. Orpen. Acta Crystallogr. Sect. C: Cryst. Chem. Commun. **C44**, 1467 (1988).
44. R.W. Alder. Tetrahedron, **46**, 683 (1990).
45. R.W. Alder, P. Eastment, N.M. Hext, R.E. Moss, A.G. Orpen, and J.M. White. J. Chem. Soc. Chem. Commun. 1528 (1988).
46. R.W. Alder and S.P. East. Chem. Rev. **96**, 2097 (1996).
47. J. Springborg, P. Kofod, C.E. Olsen, H. Toftlund, and I. Søtofte. Acta Chem. Scand. **49**, 547 (1995).
48. A. Bencini, A. Bianchi, C. Bazzicalupi, M. Ciampolini, P. Dapporto, V. Fusi, M. Micheloni, N. Nardi, P. Paoli, and B. Valtancoli. J. Chem. Soc. Perkin Trans. 2, 115 (1993).
49. J. Springborg, C.E. Olsen, and I. Søtofte. Acta Chem. Scand. **49**, 555 (1995).
50. J.E. Johnson and R.A. Jacobson. Acta Crystallogr. Sect. B: Struct. Crystallogr. Cryst. Chem. **B29**, 1669 (1973).
51. G.J. Pyrka and A.A. Pinkerton. Acta Crystallogr. Sect. C: Cryst. Chem. Commun **C48**, 91 (1992).
52. D. Kummer, S.C. Chaudhry, J. Seifert, B. Deppisch, and G. Mattern. J. Organomet. Chem. **382**, 345 (1990).
53. M.D. Morse and J.P. Chesick. Acta Crystallogr. Sect. B: Struct. Crystallogr. Cryst. Chem. **B32**, 954 (1976).
54. O. Knop, W.J. Westerhaus, and M. Falk. Can. J. Chem. **58**, 867 (1980).
55. T. Steiner, E.B. Starikov, A.M. Amado, and J.J.C. Teixeira-Dias. J. Chem. Soc. Perkin Trans. 2, 1321 (1995).
56. T.S. Osdene, P.B. Russell, and L. Rane. J. Med. Chem. **10**, 431 (1967).
57. T. Phillips and R.F. Bryan. Acta Crystallogr. Sect. A: Cryst. Phys. Diffr. Theor. Gen. Crystallogr. **A25**, S200 (1969).
58. S. Nishigaki, H. Yoshioka, and K. Nakatsu. Acta Crystallogr. Sect. B: Struct. Crystallogr. Cryst. Chem. **B34**, 875 (1978).
59. G.M. Sheldrick. SHELXS-86. *In* Crystallographic computing. *Edited by* G.M. Sheldrick, C. Kruger, and R. Goddard. Oxford University Press, Oxford, U.K. 1985.
60. TEXSAN-TEXRAY. Single-crystal structure analysis package. Molecular Structure Corporation, The Woodlands, Tex. 1993.
61. G.M. Sheldrick. SHELXL-93 crystal structure refinement program. Institute of Inorganic Chemistry, University of Göttingen, Göttingen. 1993.

© 1998 NRC Canada

Coupling P-31 NMR with the Mannich reaction for the quantitative analysis of lignin

Zhi-Hua Jiang and Dimitris S. Argyropoulos

Abstract: The reactivity of lignin model compounds under Mannich conditions with piperidine and formaldehyde was studied. The piperidinomethyl group was confirmed to be introduced quantitatively at sterically unhindered positions *ortho* to a phenolic hydroxyl when the substrate was allowed to react under ambient conditions. The sequential application of the Mannich reaction followed by quantitative ^{31}P NMR on a variety of lignin samples allowed the amounts of various aromatic groups bearing free phenolic hydroxyls to be determined. More specifically, the technique allowed the quantification of *para*-hydroxyl phenols, catechols, guaiacols, and phenols bearing C_5 or C_6 substituents. The quantitative reliability of the technique was also examined with a series of dissolved kraft lignins, isolated at various degrees of delignification. The data were found to favourably compare to those obtained by permanganate oxidation.

Key words: lignin, lignin model compounds, Mannich reaction, nuclear magnetic resonance (NMR), phenols, phosphorus, piperidine, quantitative analysis.

Résumé : On a étudié la réactivité de composés modèles de la lignine dans la réaction de Mannich avec de la pipéridine et du formaldéhyde. Il a été confirmé que, lorsque le substrat réagit dans des conditions ambiantes, le groupe pipéridinométhyle s'introduit quantitativement dans les positions stériquement non empêchées en *ortho* de l'hydroxyle phénolique. L'application séquentielle de la réaction de Mannich sur divers échantillons de lignine, suivie d'une étude quantitative RMN du ^{31}P, permet de déterminer les quantités de divers groupes aromatiques portant des hydroxyles phénoliques. D'une façon plus spécifique, la technique permet de quantifier les *para*-hydroxyphénols, les catéchols, les guaïacols et les phénols portant des substituants en C_5 et en C_6. On a aussi évalué la fiabilité quantitative de la technique avec une série de lignines kraft dissoutes, isolées à divers degrés de délignification. On a trouvé que les données se comparent favorablement à celles obtenues par oxydation avec le permanganate.

Mots clés : lignine, composés modèles de la lignine, réaction de Mannich, résonance magnétique nucléaire (RMN), phénols, phosphore, pipéridine, analyse quantitative.

[Traduit par la rédaction]

1. Introduction

Softwood lignin contains, amongst others, a variety of phenolic units that may be classified (1, 2), based on their substitution patterns, as shown in Fig. 1. The relative frequencies of these moieties have been determined by a variety of degradative techniques, i.e., oxidative degradation (3–5) and thioacidolysis–desulfuration (6). Amongst the nondegradative methods of analysis, advanced ^{13}C NMR spectroscopy may offer a quantitative estimate for some of these units (7). Its execution, however, requires acetylation, independent methoxyl analyses, and lengthy acquisition protocols. Therefore, at present, there is no facile, nondegradative means to determine these units.

The potential and unique features of 2-chloro-4,4,5,5-tetramethyl-1,3,2-dioxaphospholane as an additional phosphitylation reagent used in quantitative ^{31}P NMR analysis of lignin have been demonstrated by Jiang et al. (8) and Granata and Argyropoulos (9). This reagent offers some distinct advantages compared to 2-chloro-1,3,2-dioxaphospholane, i.e., better resolution of the various phenolic moieties (8, 9), permitting the accurate calculation of ^{31}P chemical shifts for various phenolic compounds (8), and better stability of the phosphitylated moieties (9).

However, the spectral resolution obtained using 2-chloro-4,4,5,5-tetramethyl-1,3,2-dioxaphospholane as the phosphitylation reagent is still not adequate for quantifying all types of phenolic structures. The ^{31}P NMR signals belonging to types (B), (C), and (D) phenolic units overlap in the region of 138.3–140.2 ppm as observed by Granata and Argyropoulos (9). The information about the amount of each type of phenolic units (B), (C), and (D) cannot therefore be determined using quantitative ^{31}P NMR alone. Data reported elsewhere by Jiang et al. (8) demonstrated that *ortho* substitution onto the aromatic ring of phenols has a considerably higher effect on the magnitude of the ^{31}P NMR chemical shifts than that of *para* and *meta* substitution patterns. As such it became of interest to investigate the potential of coupling quantitative ^{31}P NMR with the Mannich reaction, aimed at obtaining further structural information for lignin.

The Mannich reaction on phenols is a classic organic reaction. The essential feature of the reaction is the replacement of

Received December 4, 1997.

Z.-H. Jiang and D.S. Argyropoulos.[1] PAPRICAN and Department of Chemistry, McGill University, Pulp and Paper Research Centre, 3420 University St., Montreal, QC H3A 2A7, Canada.

[1] Author to whom correspondence may be addressed. Telephone: (514) 398-6178. Fax: (514) 398-8254.

© 1998 NRC Canada

Fig. 1. The major types of phenolic units in softwood lignin, where R represents a lignin interunit [1,2].

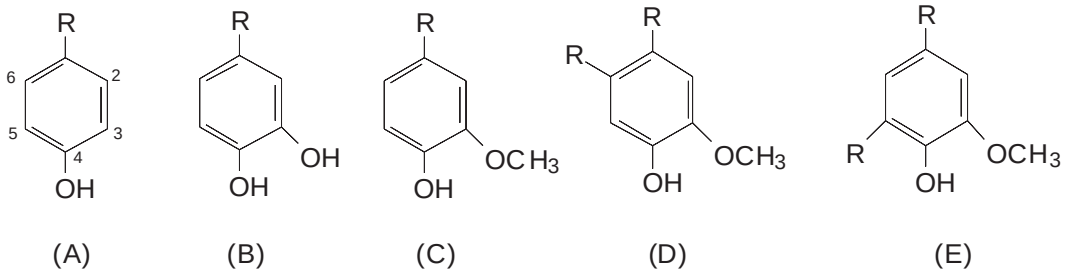

the active hydrogen atoms in phenols, especially active hydrogen atoms in positions *ortho* and *para* to phenolic hydroxyl groups, by aminomethyl or substituted aminomethyl groups (10–15).

The reactivity of various lignin model phenols toward the Mannich reaction with dimethylamine and (or) piperidine was first investigated by Mikawa et al. (17). They demonstrated that a dimethylaminomethyl or piperidinomethyl group was introduced quantitatively to free C_5 positions of lignin-related phenolic units (17). The application of the Mannich reaction to lignin, followed by nitrogen analysis, allowed Mikawa et al. (17) to quantify the phenolic units with free C_5 positions in lignin. Their data showed that about 25–40% of the phenolic hydroxyl groups in a dissolved softwood kraft lignin belong to this type of phenolic unit. The Mannich reaction has also been applied in the preparation of lignin derivatives with ion-exchange properties by Brezny et al. (18) and Rusina et al. (19).

This study examines the potential of coupling the Mannich reaction with quantitative ^{31}P NMR, to provide further fine structural information of lignin. Initially, the course and conditions of the Mannich reaction with piperidine were examined on 4-hydroxy-3-methoxybenzoic acid, and then the Mannich reaction with piperidine was carried on a variety of lignin model compounds. Finally the Mannich reaction was coupled with quantitative ^{31}P NMR for quantifying various types of phenolic units in lignin. The determined values were compared to those reported in the literature for similar samples.

2. Results and discussion

2.1 Studies on lignin model compounds

Although dimethylamine is the most frequently reported secondary amine for use in the Mannich reaction of phenols, piperidine was chosen in this study since the former also causes substitution at available methylol groups (17). Piperidine is more selective in this respect (unreactive with methylol groups) (17), yet of comparable reactivity to dimethylamine (15).

The work of Mikawa et al. (17), using either dimethylamine or piperidine as bases, has shown that type (C) lignin model compounds (see Fig. 1) give, without exception, C_5 substituted Mannich bases at very high yields. When the C_1 position of type (C) is a carboxyl group, it forms the Mannich base with simultaneous decarboxylation and substitution at the C_5 and C_1 positions. Other C_1 groups remain intact when piperidine is used. Mikawa et al. (17) also confirmed that type (E) moieties do not react, and also the Mannich reaction does not occur in all cases, when the phenolic hydroxyl group is etherified. These conclusions offered the basis for interpreting the ^{31}P NMR spectra obtained with the following lignin model compounds, using 2-chloro-4,4,5,5-tetramethyl-1,3,2-dioxaphospholane as a phosphitylation reagent. Since the ^{31}P chemical shifts of phenolic hydroxyls with various substitution patterns strongly depend on the nature of the substituents, they can be calculated using the parameters developed by Jiang et al. (8). All lignin-related phenols with *ortho*-mono substituents have ^{31}P chemical shifts within the range 138.3–140.5 ppm. These signals are completely separated from those of *ortho*-disubstituted phenols, including phenols with a substitution of a piperidinomethyl group at C_5 positions, which are located in the range 141.1–144.5 ppm (8).

Fig. 2. The ^{31}P NMR spectrum, phosphitylated with 2-chloro-4,4,5,5-tetramethyl-1,3,2-dioxaphospholane, of blank Mannich reaction medium, a mixture of equivalent amounts of piperidine and formaldehyde with 3.3 equiv. of ethanol.

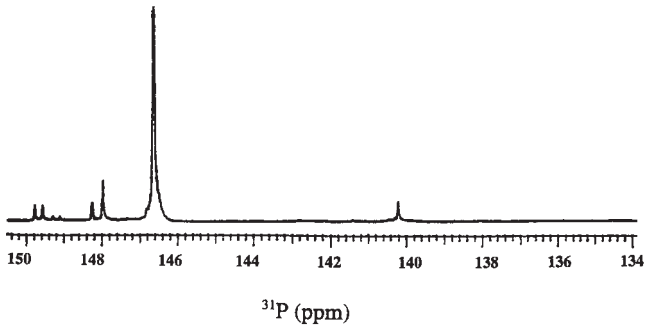

Furthermore, in the early phases of this study, it was found that the ^{31}P NMR technique could be applied to identify the Mannich reaction products even if the reaction products are not completely pure. A ^{31}P NMR spectrum of the Mannich reaction medium used in this work (a mixture of equivalent amounts of piperidine and formaldehyde with 3.3 equiv. of ethanol) is shown in Fig. 2. The major signals of the reaction medium are located in the downfield (146–150 ppm) and are well separated from those signals of phenols and carboxylic acids (8, 9).

The course and conditions of the Mannich reaction with piperidine were first reexamined on 4-hydroxy-3-methoxybenzoic acid **1** (see Fig. 3) as a lignin model compound. Figure 4 shows the ^{31}P NMR spectra of 4-hydroxy-3-methoxybenzoic acid under Mannich conditions as a function of time. The following progressive changes can be visualized from these spectra: (*i*) reduction of signal intensity at 139.1 and 135.1 due to the ^{31}P derivatives of the phenolic hydroxyl and the carboxylic acid of 4-hydroxy-3-methoxybenzoic acid respectively; (*ii*) increase of signal intensity at 143.7, which is assigned to the ^{31}P derivative of the phenolic hydroxyl of the Mannich

© 1998 NRC Canada

Fig. 3. The structure of model compounds examined in this work and their Mannich reaction products with piperidine and formaldehyde.

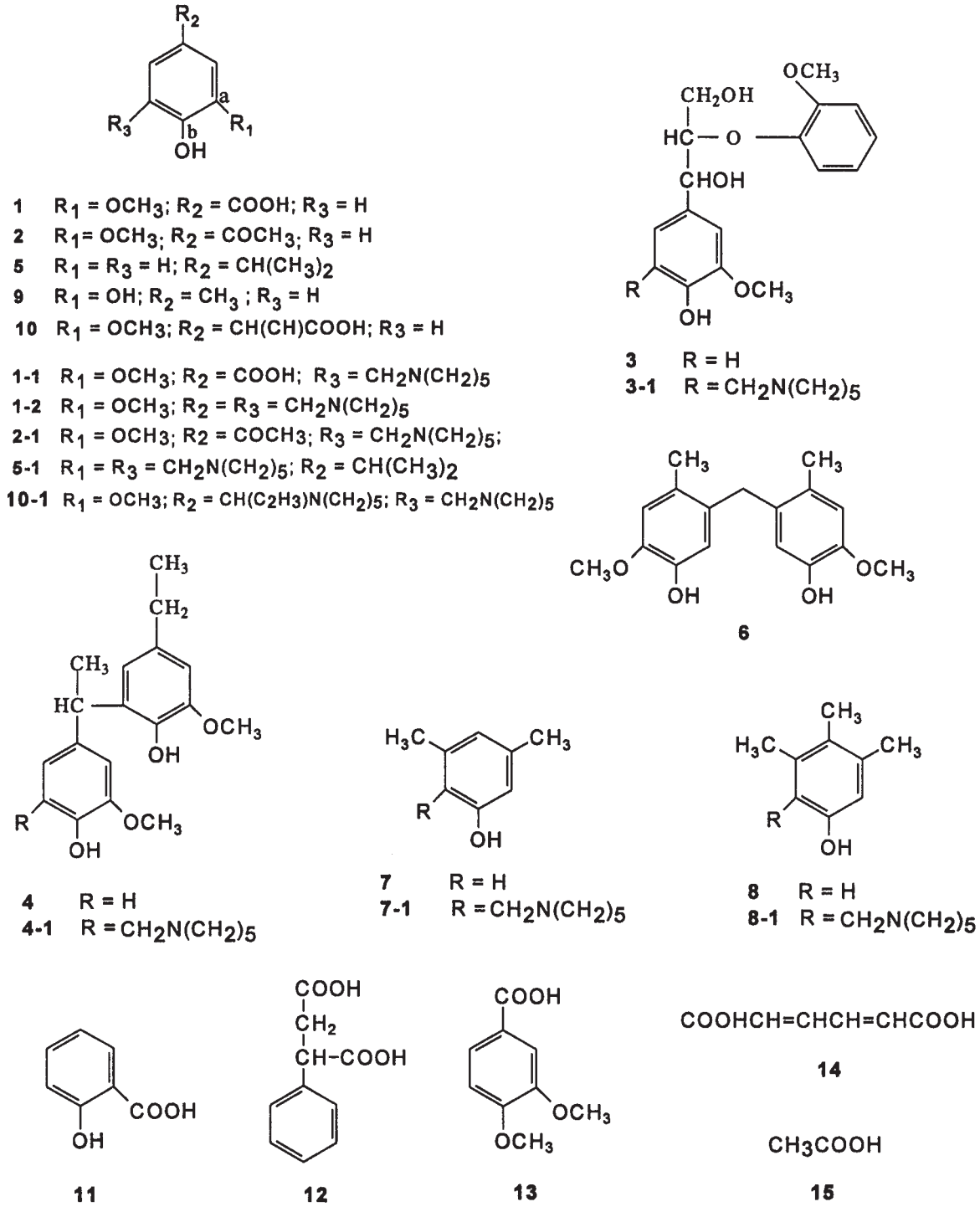

base, 2,4-dipiperidinomethyl-6-methoxyphenol **1-2** (see Fig. 3); (*iii*) increase over the first day and reduction thereafter of signal intensity at 143.4, which is assigned to the ^{31}P derivative of the phenolic hydroxyl of the Mannich base, 5-piperidinomethyl-4-hydroxy-3-methoxybenzoic acid **1-1** (see Fig. 3). Figure 5 shows further the results of this kinetic investigation.

As anticipated, the active hydrogen position *ortho* to the phenolic hydroxyl in 4-hydroxy-3-methoxybenzoic acid **1** was completely substituted to form the Mannich base **1-1** within 24 h. However, the displacement of the carboxyl group, which results in product **1-2**, was considerably slower as evidenced from quantitative ^{31}P NMR studies, which showed that the carboxyl groups reacted completely only after a 5-day reaction period. When the temperature was increased to 45°C, more than 50% of the carboxyl groups in model **1** were substituted within 2 h and about 85% of them were reacted after 6 h. Besides, the reaction of model **1** was found to be considerably

© 1998 NRC Canada

Fig. 4. The ^{31}P NMR spectra, phosphitylated with 2-chloro-4,4,5,5-tetramethyl-1,3,2-dioxaphospholane (shown as P), of 4-hydroxy-3-methoxybenzoic acid under the Mannich reaction conditions as a function of time: (*a*) before reaction; (*b*), (*c*), and (*d*) after reaction for 1, 3, and 5 day(s), respectively; (*e*) after reaction for 5 days followed by purification. The unassigned signals belong to the Mannich reaction medium (see Fig. 2).

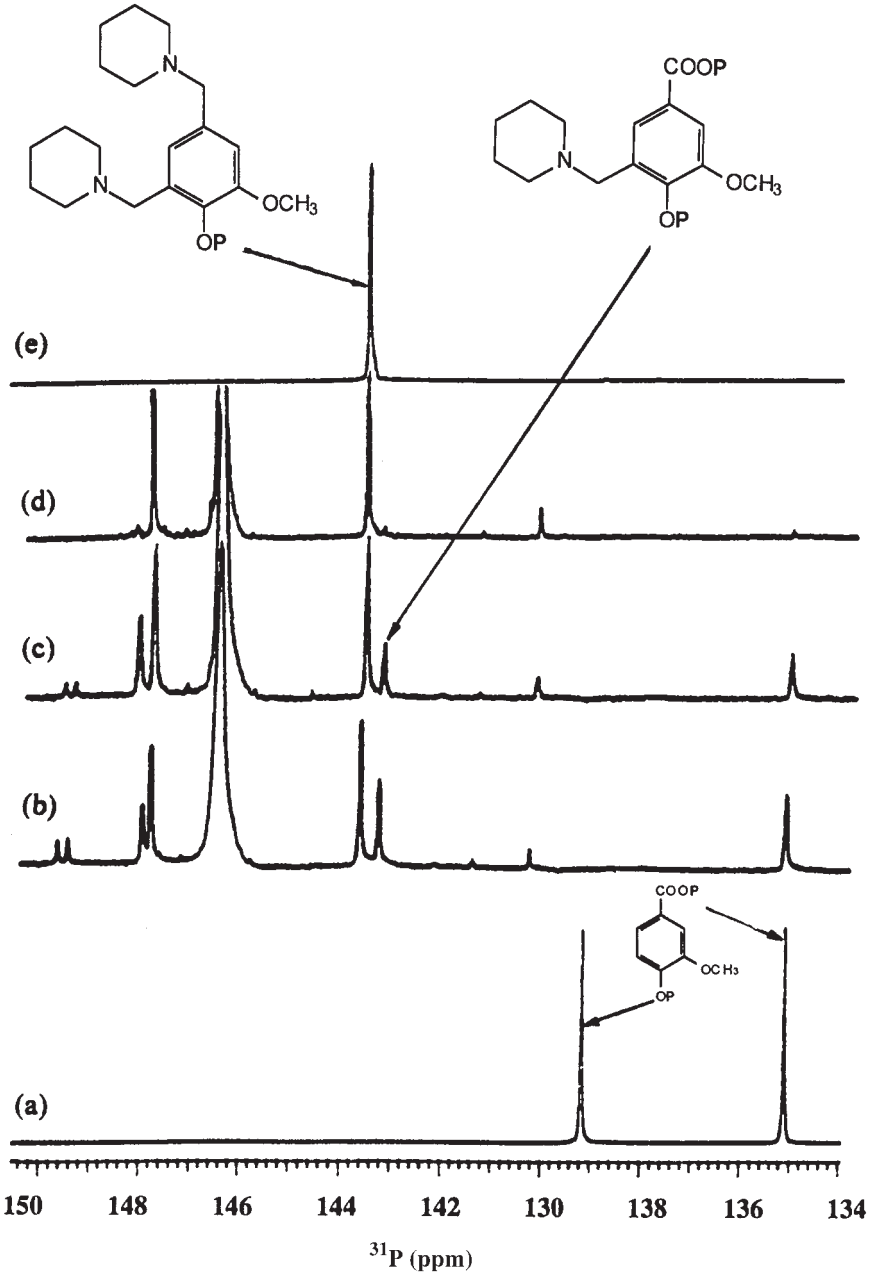

slower under acidic conditions. At pH 4–5 and after 3 days of reaction, only about 38% of the carboxylic groups and 92% of the active hydrogen position *ortho* to the phenolic hydroxyl were replaced. At the same pH and at 45°C, 11.5% of the carboxylic groups and 23.5% of the active hydrogen position *ortho* to the phenolic hydroxyl were replaced after 3 h.

The Mannich reaction was then carried out at room temperature on a variety of lignin-related model phenols. These model compounds were such chosen so as to represent all types of phenolic units in softwood lignin as shown in Fig. 1. The structure of these model compounds and their Mannich reaction products are shown in Fig. 3.

Acetovanillone **2** and lignin model dimer **3** over a period of 5 days gave the Mannich bases **2**-**1** and **3**-**1**, respectively. The active hydrogen positions *ortho* to the phenolic hydroxyl were substituted, however, the side chains of models **2** and **3** remained intact, in agreement with Mikawa et al. (17). Lignin model dimers **4**, over a period of 24 h, gave the Mannich base **4**-**1** with a 5-piperdinomethyl substituent at the C_5 position as expected.

p-Isopropylphenol **5**, which represents type (A) phenolic units, containing two active hydrogen positions *ortho* to the phenolic hydroxyl, was found to yield the Mannich base **5**-**1** within 5 days. Similar observations have also been reported

© 1998 NRC Canada

Fig. 5. The course of the Mannich reaction with piperidine on 4-hydroxy-3-methoxybenzoic acid under various conditions.

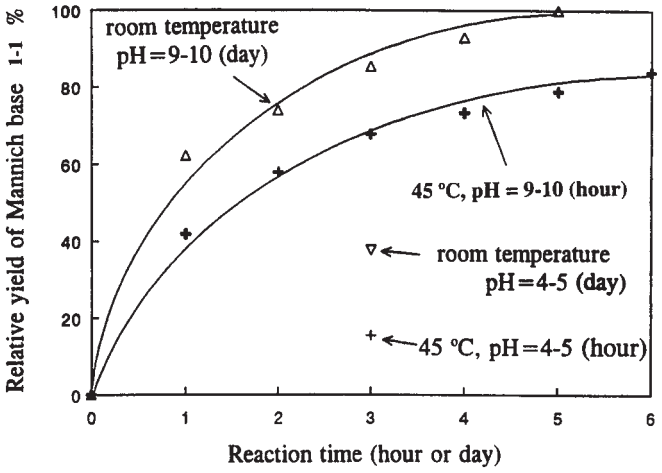

when unhindered phenols were allowed to react with dimethylamine and morpholine (15). No changes in terms of ^{31}P NMR chemical shifts were observed for model **6**, after the Mannich reaction was carried out for 5 days at room temperature. This seems to indicate that both unsubstituted positions *ortho* to the phenolic hydroxyls were unreactive because the substitution of the piperidinomethyl group at one of these positions is expected (8, 20) to result in a very significant change in the ^{31}P NMR chemical shift (downfield shift of about 4 ppm).

After the Mannich reaction, the ^{31}P NMR chemical shifts of both models **7** and **8** were found to shift downfield by about 0.7 ppm. For a similar reason as described above, these data seem to indicate that the reaction products were Mannich bases bearing a substituent *ortho* to the phenolic hydroxyl.

Although this information seems to be adequate as far as the main objective of this study is concerned, these products were further purified and identified. It was found that only one unsubstituted position *ortho* to the phenolic hydroxyl reacted. This is very likely due to steric effects exerted by the peri positions, inhibiting Mannich disubstitution. Steric factors are known to significantly affect the course of the Mannich reaction (15). For example, hydroquinone treated with 3 equiv. each of dimethylamine and formaldehyde gave 2,5-dimethylhydroquinone not tri-(dimethylaminomethyl)-hydroquinone (21). Also, 5,7-bis(piperidinomethyl)-8-quinolinol could not be prepared by means of the Mannich reaction with 8-quinolinol under usual conditions, since only monosubstituted Mannich base (7-piperidinomethyl-8-quinolinol) was formed (16).

When the Mannich reaction was carried out on model **9** (*m*-methylcatechol), using 3 equiv. of piperidine, a mixture of several Mannich bases was obtained. No attempts were made to identify these products. However ^{31}P NMR analyses of the products seem to indicate that the positions *ortho* to the phenolic hydroxyl (C_2 and C_5) were not simultaneously substituted, and one of them was substitued by the piperidinomethyl group, as evidenced by quantitative ^{31}P NMR analysis of the mixtures of the Mannich base products, which showed that the signal intensity in the range of 138.4–139.0 ppm is the same compared to those in the range of 143.0–144.4 ppm. The signals at around 138.4–139.0 and 143.0–144.4 ppm are known to be due to the phenolic hydroxyl groups with *ortho*-mono and *ortho*-disubstitutents, respectively (8).

Fig. 6. A possible six-membered ring in salicylic acid formed through hydrogen bonding.

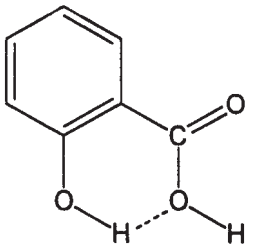

Similar to model **3**, 4-hydroxy-3-methoxycinnamic acid **10** gave Mannich base **10-1** with simultaneous decarboxylation. However, such decarboxylation reactions were not observed when the Mannich reaction was carried out, under similar conditions, on model acid compounds salicylic acid **11**, phenylsuccinic acid **12**, 3,4-dimethoxybenzoic acid **13**, muconic acid **14**, and acetic acid **15**, as evidenced by ^{31}P NMR analyses, which showed that the ^{31}P NMR signals of acid groups in these models did not change in terms of position and intensity. These observations seem to indicate that the decarboxylation reaction, during the Mannich reaction, may occur only to the carboxyl groups that link (i.e., model **1**) or are conjugated with (i.e., model **10**) aromatic units bearing a *para* hydroxyl substituent.

The Mannich reaction did not seem to occur on the positions *ortho* and *para* to the phenolic hydroxy of salicylic acid **11** because the ^{31}P NMR signal position due to the phenolic hydroxy group did not change after the Mannich reaction. Similar results were reported previously by Regnier et al. (22). A possible explanation for this phenomenon is that intramolecular interactions cause the formation of a six-membered ring and may consequently reduce the acidity of the phenol and prevent Mannich substitution as shown in Fig. 6.

2.2 Summary of studies on lignin model compounds

The results of the model compound studies described above confirmed and complemented the results reported by Mikawa et al. (17). These results showed that: (*i*) model compounds of type (A) gave Mannich bases with the substituents at both the C_3 and C_5 positions; (*ii*) a type (B) model compound gave a mixture of the Mannich bases with the substituent at the C_2 or C_5 position; (*iii*) model compounds of type (C) gave Mannich bases with the substituent at the C_5 position; (*iv*) those of type (D) and (E) do not react; (*v*) carboxyl groups that link or are conjugated with aromatic units bearing a phenolic hydroxyl group in the *para*-position gave Mannich bases with simultaneous decarboxylation; however, all other carboxyl groups do not react; (*vi*) all other groups attached to phenolic aromatic units at C_1 positions including methylol and methyl groups remain intact.

2.3 Summary of ^{31}P NMR chemical shifts of Mannich base products

A methodology for accurate prediction of the ^{31}P chemical shifts of lignin-related phenolic compounds was developed in our previous effort as a result of correlation analysis using the Hammett principles (8). This methodology has recently been

© 1998 NRC Canada

Table 1. The ^{31}P NMR chemical shifts of phenolic hydroxyls in various lignin model compounds and their Mannich reaction products. The calculations were carried out using the method and parameters previously described (8).

Lignin model compounds			Mannich reaction products		
	^{31}P chemical shift, ppm			^{31}P chemical shift, ppm	
No.[a]	Observed	Calculated	No.	Observed	Calculated
1	139.1	139.1	**1-1**	143.4	143.6
			1-2	143.7	—[b]
2	139.3	139.4	**2-1**	143.5	143.9
3	139.5	139.6	**3-1**	144.2	144.1
4	OH[a] 143.9	143.9	**4-1**	143.9	143.9
	OH[b] 139.8	139.8		144.4	144.3
5	138.1	138.1	**5-1**	144.3	—[b]
6	139.8	139.8	**6-1**	139.8	139.8
7	137.8	137.8	**7-1**	138.5	—[b]
8	138.1	138.1	**8-1**	138.8	—[b]
9	OH[a] 139.2 (d)	139.2	M[c]	138.4(d);138.7(d);	—[b]
	OH[b] 138.9 (d)	139.0		139.0 (d); 143.7(d)	
				144.4(d)	
10	139.4	139.4	**10-1**	143.8	—[b]
11[d]	OH[a] 137.4 (d)	137.2			
	OH[b] 139.2 (d)	—[b]			
12-15[d]	137.7	137.7			

[a] Roman number designations refer to Fig. 3.
[b] Parameters not available for calculation.
[c] A mixture of several Mannich products.
[d] For all these compounds, no changes in terms of signal positions were observed after the Mannich reaction.

successfully applied for calculating or assigning the ^{31}P chemical shifts of phenolic units in lignin (9, 20, 23). In the present study the methodology was also applied to calculate the changes of the ^{31}P chemical shifts occurring on model phenols before and after the Mannich reaction (Table 1). These changes were further generalized as shown in Table 2, using the parameters previously developed (8, 20) and taking the changes of the lignin structure after the Mannich reaction into account.

2.4 The Mannich reaction on lignin

2.4.1 Kinetics of the Mannich reaction with piperidine on lignin

Prior to embarking at an extensive investigation of the Mannich reaction on lignin, a kinetic study was carried out on a dissolved softwood kraft lignin isolated at a degree of delignification of 92.9%. When this lignin sample was treated with formaldehyde and piperidine, the nitrogen content of the lignin sample was found to increase as the reaction time was prolonged (Table 3). The increase was most pronounced during the first 2 days, which seems to reflect the rapid replacement of the active hydrogens in phenolic units by the piperidinomethyl group. This increase is unlikely to be attributed to piperidine contamination because the excess piperidine seems to be effectively removed by the work-up procedure applied (see relevant experimental section for more details). The nitrogen content was found to remain constant after 3 days. Very similar results were also reported by Mikawa et al. (17) with dimethylamine. The Mannich reaction on lignin was therefore carried out at room temperature for 5 days.

2.4.2 The determination of the various phenolic moieties in kraft lignin

A series of dissolved and well characterized (24) softwood kraft lignins, isolated at various degrees of delignification, were subjected to the Mannich reaction with piperidine at room temperature for 5 days. Quantitative ^{31}P NMR analyses prior to and after the Mannich reaction quantified the various phenolic units in the lignin samples. Figure 7 shows typical quantitative ^{31}P NMR spectra of such a lignin sample and its Mannich reaction product.

By integrating the region between 144.4–140.3 ppm and 138.2–137.3 ppm in the spectrum before the Mannich reaction (Fig. 7*a*), the amounts of type (E) and type (A) phenolic nuclei can be quantified. Integration of the region 140.2–138.3 ppm in the same spectrum allows the determination of the sum of phenolic types (B), (C), and (D) to be made. Furthermore, integration over from 144.4 to 137.3 ppm allows the determination of the amount of all phenolic moieties. These integration ranges applied are based on previous model compound (see Table 2 for details) and lignin studies by Granata and Argyropoulos (9). Such integration ranges have recently been adopted by Sun and Argyropoulos (25, 26), Froass et al. (27), and Senior et al. (28).

On the other hand, the ^{31}P NMR signals at 139.1–138.0, 140.4–139.1, and 144.8–138.0 ppm, in the spectrum after the Mannich reaction (Fig. 7*b*), could be assigned to the corresponding Mannich base products of phenolic (B), (D), and the sum of all types of phenolic units, respectively. These integration ranges are based on the results of early calculations (Table 2). Integrating the ranges between 139.1–138.0 and 140.0–139.1 ppm and dividing these integrals to the integral obtained by integrating the region 144.8–138.0, respectively, gives rise to the relative frequencies of type (B) and (D) phenolic units, expressed in terms of their percentages in the total phenolic hydroxyls. These relative frequencies should remain unchanged prior to and after the Mannich reaction. The absolute amounts of type (B) and (D) phenolic units in a given sample can therefore be obtained by multiplying their relative frequencies with the absolute amount of all phenolic hydroxyls obtained by integrating the region 144.4–137.3 ppm in the spectrum (*a*) of Fig. 7. By subtracting the absolute amounts of type (B) and (D) phenolic units from the sum of (B), (D), and (C), obtained by integrating the region 140.2–138.3 ppm in the spectrum (*a*) of Fig. 7, the amount of type (C) phenolic units in a given sample was calculated.

Using the method described above, the absolute amounts of all types of phenolic units shown in Fig. 1 could be quantified. This method when applied to a series of softwood dissolved kraft lignin samples revealed the data of Table 4. These data can now be compared to those reported in the literature with similar samples. The relative frequencies of individual phenolic units (A)–(E) were calculated and expressed as a percentage of the total phenolic hydroxyl content. The major phenolic units were then compared to those obtained by Gellerstedt and Gustafsson (29) using permanganate degradation analysis (Fig. 8). The agreement shown between the two sets of data is apparent, bearing in mind that different wood species and techniques were used to detect these moieties. In addition, a

© 1998 NRC Canada

Table 2. The ^{31}P chemical-shift ranges for various Mannich base products phosphitylated with 2-chloro-4,4,5,5-tetramethyl-1,3,2-dioxaphospholane. (For details see ref. 8.)

Type of phenolic unit[a]	Ranges of calculated ^{31}P chemical shift (ppm)		Detailed calculations for the ranges after the Mannich reaction
	Before[b]	After[c]	
(A)	137.3–138.2	143.8–144.4	Up-field: 138.02[d] – 0.37[e] + 6.2[f]; downfield: 138.02[d] + 0.13[g] + 6.2[f]
(B)	OH[a] 138.9–139.5 OH[b] 138.3–139.2	138.0–139.0;[h] 143.3–144.4	Up-field: 138.4[i] – 0.37;[e] downfield: 139.0[j]; up-field: 143.7[k]– 0.37;[e] downfield:144.4[l]
(C)	139.1–140.0	143.8–144.4	Up-field: 138.02[d] + 1.76[m] – 0.37[e] + 4.45[n]; downfield: 138.02[d] + 1.76[m] + 0.13[g] + 4.45[n]
(D)	139.0–140.5	139.3–140.5	Up-field: 138.02[d] + 1.76[m] – 0.37[e] – 0.11[o]; downfield: 138.02[d] + 1.76[m] + 0.13[g] + 0.50[p]
(E)	141.1–144.0	141.3–144.0	Up-field: 138.02[d] + 1.76[o] – 0.37[e] + 1.96[q]; downfield : 138.02[d] + 1.76[o] + 0.13[g] + 4.03[r]

[a] For structures see Fig. 1.
[b] Before the Mannich reaction.
[c] After the Mannich reaction.
[d] Value for phenol.
[e] Value for *p*-$COCH_3$.
[f] Value for *ortho* disubstitution of piperidinomethyl groups (from the chemical-shift difference between model **5** and its Mannich base **5-1**, Table 1).
[g] Value for *p*-CH_3.
[h] Range for one of the two phenolic hydroxyls.
[i] Up-field limit value of model **9** after the Mannich reaction (for signals in the range of 138.4–139.0 ppm, Table 1).
[j] Downfield limit value of model **9** after the Mannich reaction (for signals in the range of 138.4–139.0 ppm, Table 1).
[k] Up-field limit value of model **9** after the Mannich reaction (for signals in the range of 143.7–144.4 ppm, Table 1).
[l] Downfield limit value of model **9** after the Mannich reaction (for signals in the range of 143.7–144.4 ppm, Table 1).
[m] Value for *o*-OCH_3.
[n] Value for second *ortho* substitution by a piperidinomethyl group.
[o] Value for *m*-CH_2Ph.
[p] Value for *m*-$COCH_3$.
[q] Up-field limit value selected for second *ortho* disubstitution.
[r] Downfield limit value selected for second *ortho* disubstitution. Values from ref. 8 if unspecified.

comparison of the sum of types (A), (B), (C), and (D) phenolic units can also be made for a sample of softwood milled wood lignin. When these moieties are expressed per methoxyl group, Alder and Lundquist (30) obtained values of 0.15–0.18 using Fremy's salt oxidation, while the methodology of this work showed a value of 0.16.

2.4.3 The reproducibility of the Mannich – ^{31}P NMR analysis

Quantitative ^{31}P NMR analysis of lignin using 2-chloro-4,4,5,5-tetramethyl-1,3,2-dioxaphospholane as the phosphitylation reagent was found to have a high reproducibility by Sun and Argyropoulos (25). For all functional groups, the maximum error obtained between duplicate acquisitions was found to be below 1% (25). This is probably due to the better stability of the moieties phosphitylated with 2-chloro-4,4,5,5-tetramethyl-1,3,2-dioxaphospholane than with 2-chloro-1,3,2-dioxaphospholane moieties (9).

In an effort to examine the reproducibility of the Mannich – ^{31}P NMR technique, the dissolved softwood lignin with a degree of delignification of 92.9% was subjected to three Mannich – ^{31}P NMR analyses (Table 5). The relative standard derivation obtained for the major types of phenolic units (types (C) and (E)) was found to be less than 6.0%.

Table 3. Nitrogen contents of a dissolved softwood kraft lignin after the Mannich reaction with piperidine as a function of time.

Reaction time (days)	Nitrogen content (%)
Control	<0.01
1	1.64
2	1.87
3	2.02
4	2.18
5	2.15

3. Experimental

3.1 ^{31}P NMR spectroscopy

The lignin sample (about 40 mg), predried overnight in a vacuum oven set at 40°C, was dissolved with 800 μL of solvent (pyridine – deuterated chloroform 1.6:1 v/v) at room temperature in a 5 mL flask with magnetic stirring. Internal standard cyclohexanol (about 1.3 mg) and relaxation reagent chromium acetylacetonate (about 0.4 mg) were added as 200 μL in the same solvent mixture, and the solution was stirred until the lignin was fully dissolved. The phosphitylation reagent

© 1998 NRC Canada

Fig. 7. Quantitative ^{31}P NMR spectra, phosphitylated with 2-chloro-4,4,5,5-tetramethyl-1,3,2-dioxaphospholane, and signal assignment of (*a*) a softwood kraft dissolved lignin sample and (*b*) its Mannich reaction product with piperidine. The chemical shifts of type (E) phenolic units do not change after the Mannich reaction.

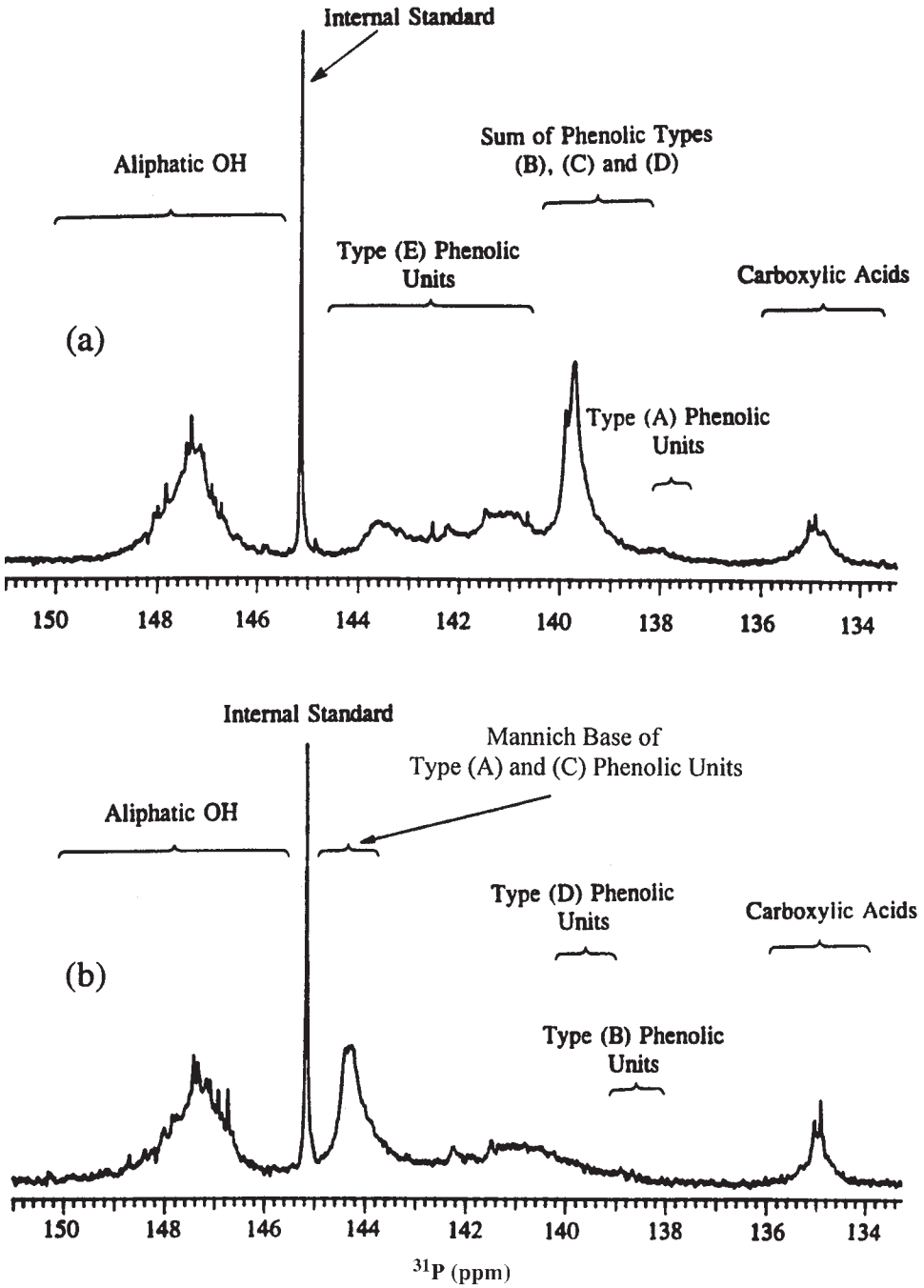

2-chloro-4,4,-5,5-tetramethyl-1,3,2-dioxaphosphalane (about 100 μL), was then added and the flask was sealed, stirred to ensure thorough mixing, and this slightly exothermic reaction was complete in about 20 min.

Quantitative ^{31}P NMR analysis was obtained in 5 mm sample tubes on a Varian XL-300 spectrometer at 125.5 MHz following the procedures described by Granata and Argyropoulos (9).

3.2 ^{1}H NMR spectroscopy

The ^{1}H NMR spectra were obtained in 5 mm sample tubes on a Varian XL-200 or Varian XL-300 NMR spectrometers, operating at 200.1 and 299.9 MHz, respectively. Deuterated chloroform was used as solvent and tetramethylsilane was used as internal reference. No relaxation delay was used during acquisition.

3.3 Gas chromatography – mass spectroscopy

The GC–MS analyses were carried out on a Hewlett–Packard 5792 mass spectrometer interfaced to a Hewlett–Packard 5890A gas chromatography with a 30 m × 0.25 mm packed silica capillary column DB-5. The injection port temperature was 280°C, and the oven temperature was varied from 100 to

© 1998 NRC Canada

Table 4. Phenolic hydroxyl contents of types (A)–(E) phenolic units present in softwood kraft solubilized lignin isolated at various degrees of delignification, determined by the Mannich – ^{31}P NMR technique.

Lignin sample[a]	Degree of delignification (%)	Various types of phenolic OH (mmol/g)					
		(A)	(B)	(C)	(D)	(E)	Total
MWL[b]	—	0.02	0.05	0.62	0.06	0.35	1.15
KSL[c] 1	18.1	0.07	0.04	1.35	0.08	0.86	2.44
KSL 2	22.1	0.06	n.d.[d]	n.d.	n.d.	0.96	2.49
KSL 3	26.7	0.05	n.d.	n.d.	n.d.	1.02	2.4
KSL 4	39.1	0.05	0.01	1.56	0.12	1.31	3.06
KSL 5	59.9	0.05	0.01	1.57	0.12	1.46	3.22
KSL 6	84.6	0.05	0.01	1.62	0.13	1.54	3.36
KSL 7[e]	92.9	0.04	0.04	1.49	0.19	1.80	3.6

[a] Lignin sample from black spruce (*Picea mariana*), see ref. 24 for their elemental composition, methoxyl, and total lignin contents.
[b] Milled wood lignin.
[c] Kraft solubilized lignin.
[d] Not determined.
[e] Average of triplicate results.

Table 5. The reproducibility of the Mannich – ^{31}P NMR analysis carried out on a softwood kraft dissolved lignin sample isolated at a degree of delignification of 92.9%.

Type of phenolic units	Mean value (mmol/g)	Standard error	Standard deviation	90% confidence limit
(A)	0.04	3.3×10^{-3}	5.8×10^{-3}	9.7×10^{-3}
(B)	0.04	5.8×10^{-3}	1.0×10^{-2}	1.7×10^{-2}
(C)	1.49	4.7×10^{-2}	8.1×10^{-2}	1.4×10^{-1}
(D)	0.2	1.5×10^{-2}	2.5×10^{-2}	4.2×10^{-2}
(E)	1.8	3.0×10^{-2}	5.1×10^{-2}	8.7×10^{-2}

250°C, with a gradient of 10°C/min. Samples were analyzed after silylation with chlorotrimethylsilane.

3.4 Elemental analyses

Elemental analyses were carried out by the Schwarzkopf microanalytical laboratories, Woodside, N.Y., in a Perkin–Elmer 2400 carbon, hydrogen, and nitrogen analyzer.

3.5 Mannich reaction with piperidine on 4-hydroxy-3-methoxybenzoic acid

4-Hydroxy-3-methoxybenzoic acid **1** (20 mmol) was dissolved in a mixture of 99% piperidine (60 mmol), aqueous formaldehyde (37%) (60 mmol), and absolute ethanol (20 mL). The reaction mixture was kept at a preset temperature for the required time with occasional shaking. When necessary, the solution was acidified to pH 4–5 with acetic acid prior to the onset of the reaction. After the reaction, a few drops of the solution were used for the ^{31}P NMR analyses without purification. The work-up prior to obtaining the spectrum of Fig. 1(*d*) was as follows: the solution was concentrated repeatedly in order to expel residual Mannich reagents by adding distilled water and freeze-dried. The solid product obtained was subjected to ^{31}P NMR and GC–MS. ^{31}P NMR δ (ppm): 143.7; MS *m/z*: 390 (M^+, 6), 375 (11), 307 (48), 232 (9), 222 (100), 207 (32), 191 (64), 149 (9), 98 (23), 73 (65), 55 (8). ^{1}H NMR (200 MHz, TMS, $CDCl_3$) δ (ppm): 1.30–1.80 (m, 12H), 2.25–2.90 (m, 8H), 3.75 (s, 4H), 3.86 (s, 3H), 6.68 (s, 1H), 6.94 (s, 1H).

Fig. 8. A comparison of the relative frequencies of type (C), circles, and type (E) phenolic units, squares, as obtained by this work, closed symbols, and those reported by Gellerstedt and Gustafsson (29), open symbols.

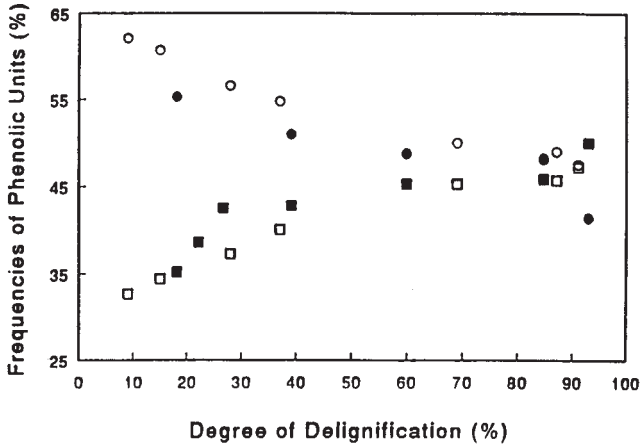

3.6 Mannich reaction with piperidine on other model compounds

*Acetonevanillone **2***

Acetonevanillone **2** (10 mmol), 99% piperidine (20 mmol), aqueous formaldehyde (37%) (20 mmol), and absolute ethanol (10 mL) were mixed and allowed to stand at room temperature for 5 days. After the reaction, the reaction mixture was concentrated repeatedly by adding distilled water and freeze-dried to give the Mannich base product 5-piperidinomethyl-acetonevanillone **2-1** in a quantitative yield based on ^{31}P NMR analysis. ^{31}P NMR δ (ppm): 143.5; ^{1}H NMR (200 MHZ, TMS, $CDCl_3$) δ (ppm): 1.50–1.75 (m, 6H), 2.40–2.80 (m, 7H), 3.76 (s, 2H), 3.92 (s, 3H), 7.28 (s, 1H), 7.43 (s, 1H). MS *m/z*: 335 (M^+, 22), 320 (15), 292 (11), 252 (42), 221 (57), 194 (19), 179 (8), 144 (11), 98 (39), 84 (100), 73 (66), 55 (8). For crystallization, 5-piperidinomethyl-acetonevanillone (6 mmol) was dissolved in absolute ethanol (5 mL), and concentrated hydrochloric acid (6.2 mmol) was added. The product precipitated as crystals when the mixture was cooled in a fridge. It was finally recrystallized from absolute ethanol, yield 59%. No correct elemental analysis results were obtained.

*1-(4-Hydroxy-3-methoxyphenyl)-2-(2-hydroxy-3-methoxyphenol)-1,3-propanediol **3***

To 1-(4-hydroxy-3-methoxyphenyl)-2-(2-hydroxy-3-methoxyphenol)-1,3-propanediol **3** (5 mmol) was added 99% piperidine (10 mmol), aqueous formaldehyde (37%) (10 mmol), absolute ethanol (5 mL). The reaction mixture was stirred and allowed to stand at room temperature for 5 days. After the reaction, the reaction mixture was concentrated repeatedly by adding distilled water and freeze-dried to give the Mannich base 1-(5-piperidinomethyl-4-hydroxy-3-methoxyphenyl)-2-(2-hydroxy-3-methoxyphenol)-1,3-propanediol **3-1** in a quantitative yield based on ^{31}P NMR analysis. ^{31}P NMR δ (ppm): 148.2 (1OH, OH_γ), 147.4 (1OH, OH_α), 144.2 (1OH, phenolic OH). MS *m/z*:

© 1998 NRC Canada

633 (M^+, 5), 618 (5), 460 (34), 394 (83), 311 (100), 281 (10), 247 (9), 149 (31), 123 (16), 73 (76).

*1-(4-Hydroxy-3-methoxybenzyl)-1′-(4-ethyl-3-methoxy-2-phenyl)-ethane **4***

To 1-(4-hydroxy-3-methoxybenzyl)-1′-(4-ethyl-3-methoxy-2-phenyl)-ethane **4** was added 99% piperidine (10 mmol), aqueous formaldehyde (37%) (10 mmol), absolute ethanol (5 mL). The reaction mixture was stirred and allowed to stand at room temperature for 1 day. After the reaction, the reaction mixture was concentrated repeatedly by adding distilled water and freeze-dried to give the Mannich base 1-(5-piperidinomethyl-4-hydroxy-3-methoxybenzyl)-1′-(4-ethyl-3-methoxy-2-phenyl)-ethane **4**-**1** in a quantitative yield based on ^{31}P NMR analysis. ^{31}P NMR δ (ppm): 143.9 (1OH^a), 144.4 (1OH^b). MS *m*/*z*: 543 (M^+, 5), 528 (7), 460 (34), 429 (11), 399 (7), 251 (100), 220 (31), 205 (11), 84 (13), 73 (94).

p-*Isopropylphenol **5***

To *p*-isopropylphenol **5** (10 mmol) was added 99% piperidine (30 mmol), aqueous formaldehyde (37%) (30 mmol), and absolute ethanol (10 mL). The reaction mixture was stirred and kept at room temperature for 5 days. After the reaction, the reaction mixture was concentrated repeatedly by adding distilled water and freeze-dried to give the Mannich base 2,6-dipiperidinomethyl-4-isopropylphenol **5**-**1** in a quantitative yield based on ^{31}P NMR analysis. ^{31}P NMR δ (ppm): 144.3. ^{1}H NMR (200 MHz, TMS, $CDCl_3$) δ (ppm): 1.00–1.24 (m, 6H), 1.30–1.80 (m, 12H), 2.20–2.90 (m, 9H), 3.61 (s, 4H), 6.60–6.84 (m, 1H), 6.90–7.00 (m, 1H). MS *m*/*z*: 402 (M^+, 5), 387 (11), 319 (83), 276 (34), 235 (55), 219 (53), 161 (24), 98 (42), 73 (100), 55 (15).

*3.3′-(6,6′-Dimethoxy-4,4′-dimethyl)-diphenylmethane **6***

To 3.3′-(6,6′-dimethoxy-4,4′-dimethyl)-diphenylmethane **6** (5 mmol) was added 99% piperidine (15 mmol), aqueous formaldehyde (37%) (15 mmol), and absolute ethanol (5 mL). The reaction mixture was stirred and kept at room temperature for 1 day. After the reaction, the reaction mixture was concentrated repeatedly by adding distilled water and freeze-dried. The product, obtained in a quantitative yield based on ^{31}P NMR analysis, has an identical structure as starting material 3.3′-(6,6′-dimethoxy-4,4′-dimethyl)-diphenylmethane **6**. ^{31}P NMR δ (ppm): 139.8; MS *m*/*z*: 432 (M^+, 84), 402 (47), 372 (12), 329 (12), 193 (13), 73 (100), 45 (17); ^{1}H NMR (200 MHz, TMS, $CDCl_3$) δ (ppm): 2.20 (s, 6H), 3.90 (s, 6H), 6.50 (s, 2H), 6.53 (s, 2H). The crystallization of the product was carried out from absolute ethanol, yield 48%. Anal. calc. for $C_{17}H_{20}O_4$: C 70.8, H 6.99; found: C 71.0, H 6.77.

*3.5-Dimethylphenol **7***

To 3,5-dimethylphenol **7** (10 mmol) was added 99% piperidine (20 mmol), aqueous formaldehyde (37%) (20 mmol), and absolute ethanol (10 mL). The reaction mixture was stirred and kept at room temperature for 1 day. After the reaction, the reaction mixture was concentrated repeatedly by adding distilled water and freeze-dried to give the Mannich base 2-piperidinomethyl-3,5-dimethylphenol **7**-**1** in a quantitative yield based on ^{31}P NMR analysis. ^{31}P NMR δ (ppm): 138.5; ^{1}H NMR (200 MHz, TMS, $CDCl_3$) δ (ppm): 1.40–1.75 (m, 6H), 2.19 (s, 3H), 2.23 (s, 3H), 2.40–2.70 (m, 4H), 3.65 (s, 2H), 6.46 (s, 1H), 6.51 (s, 1H). MS *m*/*z*: 291 (M^+, 11), 217 (21), 206 (79), 191 (20), 135 (27), 84 (100), 73 (27). The crystallization of 2-piperidinomethyl-3,5-dimethylphenol was carried out from absolute ethanol, yield 48%. Anal. calcd. for $C_{14}H_{20}ON$: C 77.1, H 9.24, N 6.42; found: C 76.6, H 9.40, N 6.58.

*3.4,5-Trimethylphenol **8***

To 3,4,5-dimethylphenol **8** (10 mmol) was added 99% piperidine (20 mmol), aqueous formaldehyde (37%) (20 mmol), and absolute ethanol (10 mL). The reaction mixture was stirred and kept at room temperature for 1 day. After the reaction, the reaction mixture was concentrated repeatedly by adding distilled water, diluted with distilled water, and freeze-dried to give the Mannich base 2-piperidinomethyl-3,4,5-trimethylphenol **8**-**1** in a quantitative yield based on ^{31}P NMR analysis. ^{31}P NMR δ (ppm): 138.8 (s); ^{1}H NMR (200 MHz, TMS, $CDCl_3$) δ (ppm): 1.40–1.70 (m, 6H), 2.12(s, 3H), 2.17 (s, 3H), 2.24 (s, 3H), 2.40–2.70 (m, 4H), 3.72 (s, 2H), 6.55 (s, 1H). MS *m*/*z*: 305 (M^+, 18), 290 (6), 220 (100), 205 (27), 191 (6), 149 (6), 105 (6), 73 (22).

m-*Methylcatechol **9***

To 3-methylcatechol **9** (10 mmol) was added 99% piperidine (30 mmol), aqueous formaldehyde (37%) (30 mmol), and absolute ethanol (10 mL). The reaction mixture was stirred and kept at room temperature for 5 days. After the reaction, the reaction mixture was concentrated repeatedly by adding distilled water and freeze-dried to give a mixture of Mannich bases. ^{31}P NMR δ (ppm): 138.4–139.0 (d, 1OH), 143.0–144.4 (d, 1OH).

*4-Hydroxy-3-methoxylcinnamic acid **10***

4-Hydroxy-3-methoxycinnamic acid **10** (10 mmol) 99% piperidine (20 mmol), aqueous formaldehyde (37%) (20 mmol), and absolute ethanol (10 mL) were mixed and allowed to stand at room temperature for 1 day. After the reaction, the reaction mixture was concentrated repeatedly by adding distilled water and freeze-dried to give the Mannich bases 3,5-dimethoxyl-4-hydroxycinnamic acid and 5-piperidinomethyl-4-hydroxy-3-methoxycinnamic acid **10**-**1** in a quantitative yield based on ^{31}P NMR analysis. ^{31}P NMR δ (ppm): 143.8 (1OH). MS *m*/*z*: 416 (M^+, 5), 401 (8), 333 (94), 248 (92), 233 (26), 217 (63), 110 (63), 98 (47), 73 (100).

*Mannich reaction on model carboxylic acids **11**–**15***

Individual model carboxylic acids (5 mmol) 99% piperidine (10 mol), aqueous formaldehyde (37%) (10 mol), and absolute ethanol (5 mL) were mixed and kept for 5 days at room temperature with stirring. After the reaction, the solution was concentrated under reduced pressure at room temperature and freeze-dried. The solid products were subjected to ^{31}P NMR analysis with 2-chloro-4,4,5,5-tetramethyl-1,3,2-dioxaphospholane as the phosphitylation reagent. In all cases, the spectra obtained for the products were identical with corresponding starting materials.

3.7 Mannich reaction with piperidine on lignin

The procedures used by Mikawa et al. (17) were essentially followed. Approximately 200 mg of lignin was dissolved in 2 mL of a mixture solution composed of 99% piperidine, aqueous formaldehyde (37%), and absolute ethanol in the following

© 1998 NRC Canada

molar proportions of 1.00:1.05:3.30. It was then kept at room temperature for 5 days with stirring or occasional shaking. After the reaction, the reaction mixture was concentrated repeatedly by adding distilled water and freeze-dried. The solid lignin was washed with diethyl ether three times, centrifuged, and dried in a vacuum oven at room temperature.

4. Conclusions

The absolute amounts of various phenolic nuclei such as, *para*-hydroxylphenyls, catechols, guaiacols, and phenols bearing C_5 or C_6 substituents in lignin, can be determined by using the combination of the Mannich reaction and quantitative ^{31}P NMR. The Mannich – ^{31}P NMR analysis is a facile and nondestructive technique that may provide detailed structural information of lignin samples, with minimum experimental complexity.

5. Acknowledgements

This research was supported by the Canadian Pulp and Paper Industry and the Natural Sciences and Engineering Research Council of Canada.

References

1. E. Alder. Wood Sci. Technol. **11**, 169 (1977).
2. A. Sakakibara. Wood Sci. Technol. **14**, 89 (1980).
3. S. Larson and G.E. Miksche. Acta Chem. Scand. **23**, 3337 (1969).
4. M. Erickon, S. Larson, and G.E. Miksche. Acta Chem. Scand. **27**, 127 (1973).
5. G. Gellerstedt and E.-L. Lindfors. Holzforschung, **38**, 151 (1991).
6. C. Lapierre, P. Brigitte, and B. Monties. Holzforschung, **45**, 61 (1991).
7. R.R. Danielle, M. Bardet, G. Gellerstedt, and E.L. Lindfors. J. Wood Chem. Technol. **4**, 239 (1984).
8. Z.-H. Jiang, D.S. Argyropoulos, and A. Granata. Mag. Reson. Chem. **33**, 375 (1995).
9. A. Granata and D.S. Argyropoulos. J. Agric. Food Chem. **43**, 1538 (1995).
10. F.F. Blicke. *In* Organic reactions. Vol. 1. *Edited by* A. Roger. John Wiley & Sons, Inc., New York. 1942. p. 303.
11. S.V. Lieberman and E.C. Wagner. J. Org. Chem. **14**, 1001 (1949).
12. K.W. Merz. Pharmazie, **11**, 505 (1956).
13. B. Reichert. Die Mannich-reaktion. Springer-Verlag, Berlin. 1959.
14. T.F. Cummings and J.R. Shelton. J. Org. Chem. **25**, 419 (1960).
15. D.Z. Wan. Mannich reaction and the chemistry of Mannich base. Science Press, Inc., Beijing. 1986.
16. J.H. Burckhalter and R.I. Leib. J. Org. Chem. **26**, 4078 (1961).
17. H. Mikawa, K. Sato, C. Takasaki, and K. Ebisawa. Bull. Chem. Soc. Jpn. **29**, 259 (1956).
18. R. Brezny, L. Paszner, M.M. Micko, and D. Uhrin. Holzforschung, **42**, 369 (1988).
19. M.N. Rusina, L.M. Timakova, G.F. Yaroshenko, M.Z. Branzburg, and V.Ya. Temkina. Zh. Obshch. Khim. **47**, 2112 (1977).
20. Z.-H. Jiang. Advances and applications of quantitative ^{31}P NMR for the structural elucidation of lignin. Ph.D. thesis, McGill University, August 1997.
21. W.T. Caldwell and T.R. Thompson. J. Am. Chem. Soc. **61**, 765 (1939).
22. G. Regnier, R. Canevari, and J.-C. Le Douarec. Bull. Soc. Chim. Fr. **9**, 2827 (1966).
23. R. Smit, I.D. Suckling, and R.M. Ede. Proc. 9th Int. Symp. Wood Pulping Chem. Oral presentations vol. L4-1. Montreal, Canada. 1997.
24. Z-H. Jiang and D.S. Argyropoulos. J. Pulp Paper Sci. **20**, J183 (1995).
25. Y. Sun and D.S. Argyropoulos. J. Pulp Paper Sci. **21**, J185 (1995).
26. Y. Sun and D.S. Argyropoulos. Holzforschung, **50**, 175 (1996).
27. P.M. Froass, A.J. Ragauskas, T.J. McDonough, and J. Jiang. Proc. Int. Pulp Bleaching Conf. Washington, D.C. **1**, 73 (1996).
28. D.J. Senior, J. Hamilton, A.J. Ragauskas, and P. Froass. Proc. Int. Pulp Bleaching Conf. Washington, D.C. **2**, 261 (1996).
29. G. Gellerstedt and K. Gustafsson. J. Wood Chem. Technol. **7**, 65 (1987).
30. E. Adler and K. Lundquist. Acta Chem. Scand. **15**, 223 (1961).

© 1998 NRC Canada

Escherichia coli β-galactosidase is heterogeneous with respect to the activity of individual molecules

Douglas B. Craig and Norman J. Dovichi

Abstract: *Escherichia coli* β-galactosidase molecules were incubated with fluorogenic substrate in a capillary. Upon flushing the reactor contents past the detector, individual randomly distributed peaks of product were observed, each representing the activity of an individual enzyme molecule. Individual molecules were found to differ with respect to their activities. Molecules showed a 23-fold distribution of activities with the majority of molecules within a 4-fold distribution.

Key words: single-molecule chemistry, β-galactosidase, capillary electrophoresis, laser-induced fluorescence, enzyme assay.

Résumé : On a incubé des molécules de β-galactosidase de l'*E. coli* avec un substrat fluorogénique dans un capillaire. Après avoir fait passé le contenu du réacteur hors du champ du détecteur, on a observé des pics individuels de produits distribués d'une façon aléatoire; chacun correspond à l'activité d'une molécule individuelle d'enzyme. On a trouvé que les activités des molécules individuelles diffèrent. Les molécules présentent une distribution d'activité de 23 alors que la majorité des molécules se trouve dans une distribution de 4.

Mots clés : chimie des molécules individuelles, β-galactosidase, électrophorèse capillaire, fluorescence induite par un laser, essai enzymatique.

[Traduit par la rédaction]

Introduction

Until recently, enzymology, and chemistry in general, has relied on measurements taken on large ensembles of molecules, with data representing average values for many individual molecules. Any differences between individual molecules is obscured by this averaging. To determine whether individual enzyme molecules are homogeneous or heterogeneous with respect to a particular characteristic, it is necessary to assay molecules one at a time.

Activities of individual molecules using a capillary reactor and laser-induced fluorescence detection have been determined on the enzymes lactate dehydrogenase (1) and bovine (2) and *E. coli*[3] alkaline phosphatase. These enzymes have been found to be heterogeneous with respect to individual molecule activities.

High-sensitivity assays of ensembles of β-galactosidase enzyme molecules have shown mass limits of detection close to single molecule (3). This study was undertaken to modify such methods to allow for the detection of the activities of individual molecules of β-galactosidase.

Received August 8, 1997.

D.B. Craig[1] and N.J. Dovichi.[2] Department of Chemistry, University of Alberta, Edmonton, AB T6G 2G2, Canada.

[1] Present address: Department of Chemistry, University of Winnipeg, Winnipeg, MB R3B 2E9, Canada.

[2] Author to whom correspondence may be addressed. Telephone: (403) 492-2825. Fax: (403) 492-8231. E-mail: norm.dovichi@ualberta.ca

[3] D.B. Craig and N.J. Dovichi. Unpublished results. 1997.

Experimental

Reagents

Sodium resorufin and resorufin β-D-galactopyranoside were obtained from Molecular Probes (Eugene, Oreg.). *Escherichia coli* β-galactosidase (E.C. 3.2.1.23) and *o*-nitrophenyl β-D-galactoside were purchased from Sigma (St. Louis, Mo.). Polymer 6 was from Applied Biosystems (Mississauga, Ont.).

Instrumentation

The injection end of a fused silica capillary (10 μm i.d., 145 μm o.d., 72.5 cm long, Polymicro Technologies, Phoenix, Ariz.) was immersed into sample or running buffer along with a platinum wire connected to a high-voltage power supply (CZE1000R, Spellman, Plainview, N.Y.). The polyimide coating from the detection end of the capillary was removed with a gentle flame and the capillary end was placed inside a 250 × 250 μm inner bore sheath flow cuvette. Molecules exiting the capillary were hydrodynamically focused post-capillary into a cone by sheath buffer flowing within the cuvette. Eluting species were excited by a 543.5 nm line from a 1 mW helium neon laser (Melles Griot, Nepean, Ont.) focused 20 μm below the capillary end by a 6.3×, 0.20 NA microscope objective (Melles Griot). Fluorescence was collected at right angle from the direction of excitation by a 60×, 0.70 NA microscope objective (model 60x-LWD, Universe Kogaku, Japan) and selectively passed through a slit and a 580DF40 bandpass filter (Omega Optical, Brattleboro, Vt.) to an R1477 photomultiplier tube (PMT) (Hamamatsu, Middlesex, N.J.). The analog PMT output was dropped across a 1 MΩ resistor and conditioned with a simple RC filter ($t_c = 0.022$ s). The resulting voltage was digitized at 10 Hz by a MacIntosh IIsi via an NB-MIO-16XH-

© 1998 NRC Canada

18 I/O board (National Instruments, Austin, Tex.). The same board controls the CE power supply. Sheath and running buffers were 50 mM HEPES (pH 7.3) containing a 1/100 dilution of the proprietary sieving matrix Polymer 6 marketed by Applied Biosystems.

Standards

Resorufin standards were used to determine the sensitivity of the detector. Dye at a concentration of 1 nM was injected for 5 s at 209 V/cm and swept past the detector at 400 V/cm.

Standard assay

The concentration of active enzyme was determined by monitoring the change in absorbance at 410 nm of a solution of 93 mM phosphate (pH 7.3) containing 2.3 mM *o*-nitrophenyl β-D-galactoside, 1 mM $MgCl_2$, 112 mM 2-mercaptoethanol, and 0.02–0.1 unit β-galactosidase at 37°C. One unit is defined as the amount of enzyme that will hydrolyze 1.0 μmol *o*-nitrophenyl β-D-galactoside under these conditions in 1 min. The millimolar extinction coefficient for *o*-nitrophenol is 3.5 at 410 nm. To convert activity to concentration, a specific activity of 1200 units/mg and a mass of 540 kDa was used.

Capillary coating

The capillary was flushed using a syringe with 100 mM NaOH for 30 min followed by a 1/10 dilution of Polymer 6 in 50 mM HEPES (pH 7.3) for 3 h. The capillary was then flushed with a 1/100 dilution of Polymer 6 in 50 mM HEPES (pH 7.3). This treatment resulted in the dynamic coating of the inner capillary wall with a layer of polymer. To maintain this coating buffers contained a 1/100 dilution of Polymer 6.

Single-molecule assay

The commercial suspension of enzyme was diluted by 10 orders of magnitude into a solution of final concentration of 50 mM HEPES (pH 7.3) containing 200 μM resorufin galactoside and a 1/100 dilution of Polymer 6. The sample was continuously injected with a syringe into the capillary for 10 min, filling the capillary, and was allowed to sit in the capillary for a 30 min incubation period. After incubation, the capillary contents were swept past the detector at an electric field of 400 V/cm, injection end negative, using 50 mM HEPES (pH 7.3) containing a 1/100 dilution of Polymer 6 as running buffer. Data were collected with a MacIntosh IIsi and converted to PC format to analyze peak areas using PeakFit (Jandel Scientific Software, San Rafael, Calif.) on a Pentium computer. Blanks contained no enzyme.

Results and discussion

In this assay, substrate concentration is approximately 12 orders of magnitude greater than that of the enzyme. Substrate concentration does not significantly drop over the course of the 30 min incubation period. A minute fraction of the resorufin galactoside is converted to the highly fluorescent product resorufin by the action of β-galactosidase. Resorufin galactosidase is itself mildly fluorescent. The sensitivity of the detector is such that the 200 μM residual substrate will saturate the detector, making it impossible to detect product. Fortunately, the relative electrophoretic mobilities of the substrate and product allow us to detect only the product, even in the presence of a huge excess of substrate. We coat the capillary with Polymer 6, which has the effect of reducing electroosmotic flow such that it is less than the electrophoretic mobility of the product resorufin. At pH 7.3, resorufin is negatively charged while resorufin galactosidase is neutral. When the injection end of the capillary is negative relative to the detection end, the residual electroosmotic flow is towards the injector.

Fig. 1. Assay protocol. A capillary was filled with a solution of substrate (shaded) containing a few enzyme molecules (black dots). The sample was incubated for 30 min, resulting in the accumulation of product in the vicinity of the enzyme molecules. An electric field was placed across the length of the capillary. The product migrated towards the detector, producing peaks observed on the electropherogram. The substrate migrated towards the injection end of the capillary and was not detected.

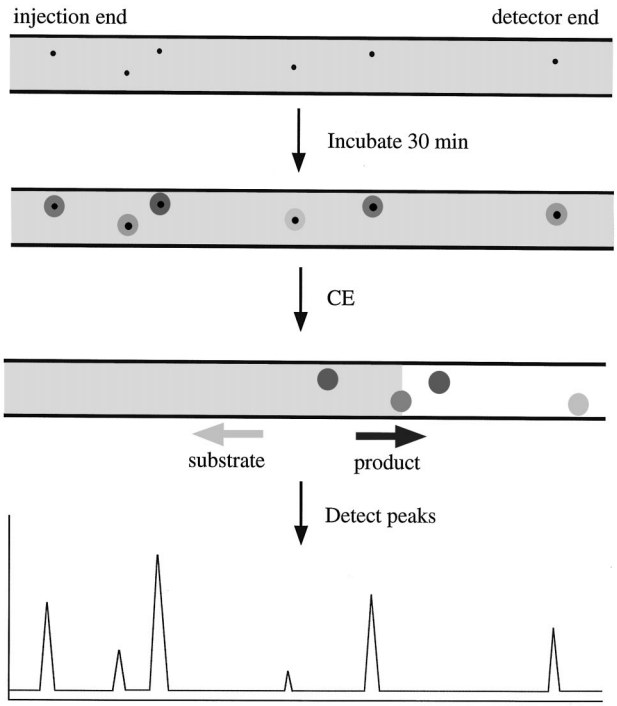

The capillary is filled with substrate and very dilute enzyme and incubated (Fig. 1). The concentration of enzyme is such that only a few of the molecules will be present and randomly spread along the 72.5 cm capillary. During the incubation period, the enzyme converts the substrate into product. Product molecules diffuse only a small distance from the enzyme molecule that produced them. After the incubation period, an electric field of 400 V/cm is placed across the capillary length. Residual electroosmotic flow directs the unreacted substrate towards the injection end of the capillary and away from the detector. The product has an electrophoretic mobility directed towards the detector. The product exits the capillary at the detector end and results in a set of peaks, each peak produced by the localized pool of product formed by a single enzyme molecule. If the reaction product from individual enzyme molecules is indeed being detected, the number of peaks detected should be similar to that expected by the product of the putative enzyme concentration and the capillary volume, the

© 1998 NRC Canada

Fig. 2. Single-molecule β-galactosidase assay. The capillary was filled with 200 μM resorufin galactoside in 50 mM HEPES (pH 7.3) containing 1/100 dilution of Polymer 6. The sample was incubated 30 min and electrophoretically flushed past the detector. A plateau was detected due to non-enzymatic hydrolysis of the substrate (bottom). Addition of putative 87 aM β-galactosidase to the reaction mixture resulted in the detection of five peaks atop this plateau, indicating the capture of five enzyme molecules within the capillary.

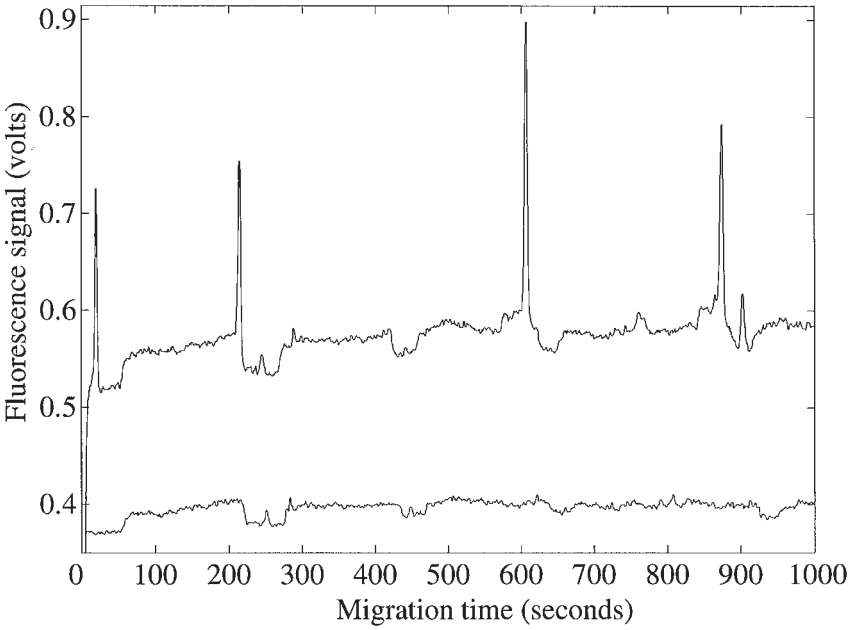

Fig. 3. Distribution of activities. The number of molecules with an activity within the given range is shown.

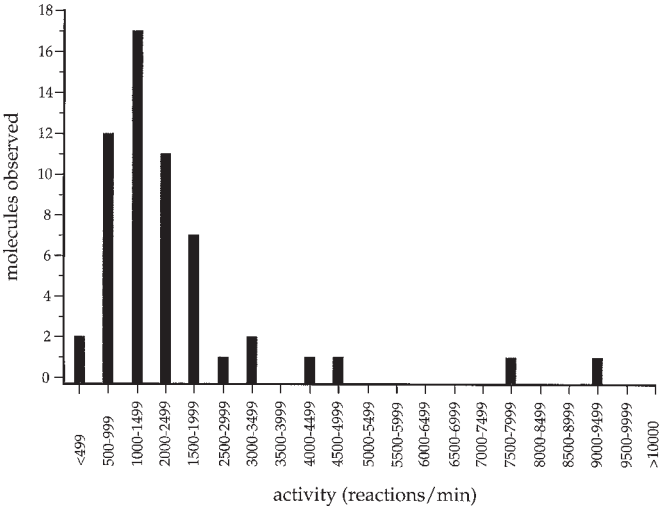

enzyme molecules should be randomly distributed along the capillary length, and the number of molecules observed per run should be dominated by Poisson statistics.

Resorufin galactoside contains a small amount of resorufin as an impurity. At the pH used for electrophoresis, resorufin is charged. However, near pH 5, the weak acid is protonated and neutral. To remove trace amounts of resorufin, the substrate, resorufin galactoside, was dissolved in 5 mM HEPES (pH 5) and extracted 3 times with an equal volume of $CHCl_3$ at the beginning of the day and once more immediately prior to use, and was diluted to give a final concentration of 200 μM in 50 mM HEPES (pH 7.3) containing 1/100 dilution Polymer 6 and enzyme. The neutral resorufin was extracted into the organic layer and removed from the substrate.

In the absence of enzyme, resorufin galactosidase hydrolyzes slowly to produce resorufin. This hydrolysis results in an increased background signal present in all runs. Enzyme product peaks will be present atop this background signal.

Figure 2 shows an electropherogram resulting from the 30 min incubation of $1/10^{10}$ dilution of enzyme in 200 μM resorufin galactosidase and a blank containing substrate but no enzyme. A plateau due to the non-enzymatic hydrolysis of substrate is observed in the blank. In the presence of enzyme, individual peaks are seen sitting atop this plateau. From the stock solution enzyme concentration determined by standard assay and the dilution factor, the enzyme concentration is estimated as 87 aM (1 aM = 10^{-18} M). With a capillary volume of 59 nL, we expect 5.1 ymol (1 ymol = 10^{-24} mol) or approximately three molecules. Experimentally, 5.1 ± 3.3 peaks were observed per run (N = 11) with no peaks observed in any of the blanks (N = 5). Exact enzyme concentrations are difficult to calculate due to the poor accuracy for the specific activity. Peak numbers were dominated by Poisson statistics and the peaks were randomly distributed along the length of the capillary.

A total of 56 molecules were detected. Converting the peak areas into product molecules was done by comparison to resorufin standards. Turnover numbers were calculated by dividing the number of product molecules formed by the incubation time. The average turnover was 1800 ± 1500 reactions/min. Figure 3 shows the distribution of activities of individual molecules. The majority of molecules (47/56) showed activities of between 500 and 2000 reactions/min. The total spread of activity detected was 23-fold, from 400 to 9200 reactions/min.

The range in activity appears to reflect differences in the

© 1998 NRC Canada

molecules. Experimental sources of noise would include shot noise in the number of product molecules generated during the incubation; this noise source would produce about 0.4% relative standard deviation in turnover numbers. Similarly, the shot noise in the photon flux can be calculated from the known charge generated per photon from this photomultiplier tube (4); this noise source contributes less than 2% relative standard deviation to the distribution in activity. Instead, we believe that the distribution in turnover number reflects differences in the structure of these enzyme molecules.

Conclusions

Single-enzyme molecule assays have previously been performed on lactate dehydrogenase (1) and bovine (2) and *E. coli*[3] alkaline phosphatases. All these enzymes were shown to be heterogeneous with respect to activity. Here we report on the activities of individual molecules of *E. coli* β-galactosidase. We find individual molecules to range 23-fold in turnover numbers with the majority of individuals varying by 4-fold. It is noteworthy that all the enzymes studied to date at the single-molecule level have shown microheterogeneity, leading one to speculate that such heterogeneity may be a common phenomenon amongst enzymes in general.

The central paradigm of chemistry states that structure affects function. Differences in function must arise from some differences in structure. There are two possible causes of structural differences. In the simplest case, all enzyme molecules would consist of the same atoms arranged in the same order. Differences in chemical behavior would arise from differences in the higher order structures into which the molecule has folded. This argument is a particularly attractive explanation for the behavior of enzymes such as lactate dehydrogenase that generate a single band in gel electrophoresis but individual molecules generate a broad distribution of activities (1).

As a second case, there is a vast menagerie of post-translational modifications found in nature. In this case, molecules have differences in activity because they have differences in primary structure. Proteins are usually decorated with sugars, lipids, phosphates, and other functional groups. A protease often forms the protein from a larger apoprotein, which is the original translation product from mRNA; different cutting sites lead to different product molecules. All of these post-translational modifications are generated in a somewhat haphazard fashion, leading to a population of product molecules that contain a range of different modifications. Further complication occurs for enzymes that are formed from two or more monomer peptides. Differences in each monomer could combine to form a huge number of different assembled products.

Acknowledgments

This work was supported by a research grant from the Natural Sciences and Engineering Research Council of Canada. D.B.C. acknowledges a post-doctoral fellowship from the Alberta Heritage Foundation for Medical Research.

References

1. Q. Xue and E.S. Yeung. Nature, **373**, 681 (1995).
2. D.B. Craig, E.A. Arriaga, J.C.Y. Wong, H. Lu, and N.J. Dovichi. J. Am. Chem. Soc. **118**, 5245 (1996).
3. D.B. Craig, E.A. Arriaga, P. Banks, Y. Zhang, A. Renborg, M.M. Palcic, and N.J. Dovichi. Anal. Biochem. **226**, 147 (1995).
4. S. Wu and N.J. Dovichi. J. Chromatogr. **480**, 141 (1989).

© 1998 NRC Canada

Kinetic studies of σ-adduct formation and nucleophilic substitution in the reactions of ethyl 2,4,6-trinitrophenyl ether, some phenyl 2,4,6-trinitrophenyl ethers, and phenyl 2,4-dinitronaphthyl ether with aniline in dimethyl sulfoxide

Michael R. Crampton and Ian A. Robotham

Abstract: The reaction of ethyl 2,4,6-trinitrophenyl ether with aniline in dimethyl sulfoxide containing Dabco occurs in two stages. The first gives **5**, the σ-adduct intermediate on the substitution pathway, which has been identified spectroscopically. The second yields 2,4,6-trinitrodiphenylamine, the substitution product. Kinetic studies show that proton transfer is rate limiting both in the formation of the intermediate and in its subsequent acid-catalysed decomposition. Phenoxide is a considerably better leaving group than ethoxide and the substitution reactions of phenyl 2,4,6-trinitrophenyl ethers and phenyl 2,4-dinitronaphthyl ether with aniline in DMSO occur without the accumulation of intermediates. The kinetics indicate both uncatalysed and base-catalysed pathways. The kinetic and equilibrium data for reaction of the ethyl and phenyl ethers are compared with data for σ-adduct formation from 1,3,5-trinitrobenzene and aniline.

Key words: nucleophilic substitution, proton transfer, base catalysis, σ-adducts.

Résumé : La réaction de l'oxyde d'éthyle et de 2,4,6-trinitrophényle avec l'aniline, dans le diméthylsulfoxyde contenant du DABCO, se produit en deux étapes. La première fournit le produit **5**, l'adduit-σ intermédiaire sur la voie de la substitution, que l'on a identifié par spectroscopie. La deuxième conduit à la 2,4,6-trinitrodiphénylamine, le produit de substitution. Des études cinétiques ont permis de montrer que le transfert de proton est l'étape cinétiquement limitante tant pour la formation de l'intermédiaire que pour sa décomposition acidocatalysée subséquente. L'ion phénolate est un bien meilleur groupe partant que l'éthanolate; les réactions de substitutions des oxydes de phényle et de 2,4,6-trinitrophényle, et de l'oxyde de phényle et de 2,4-dinitronaphtyle, avec l'aniline dans le DMSO se produisent sans accumulation d'intermédiaires. Les données cinétiques indiquent la présence de voies réactionnelles non catalysées et d'autres catalysées par les bases. On a comparé les données cinétiques et d'équilibre pour les réactions des oxydes d'éthyle et de phényle avec celles relatives à la formation de l'adduit-σ à partir du 1,3,5-trinitrobenzène et de l'aniline.

Mots clés : substitution nucléophile, transfert de proton, catalyse par les bases, adduits-σ.

[Traduit par la rédaction]

Introduction

Whereas the reaction of 1,3,5-trinitrobenzene, TNB, with primary and secondary aliphatic amines in dimethyl sulfoxide, DMSO, spontaneously produces σ-adducts (1–3), reaction with aromatic amines requires the presence of a strong base. Buncel and co-workers showed, by use of ^{1}H NMR spectroscopy, that reaction of the TNB–methoxide σ-adduct with aniline (4), or with ring-substituted anilines (5), resulted in the formation of TNB–anilide adducts, such as **1**.

Interestingly, kinetic studies (6, 7) showed that this conversion involved a dissociative mechanism rather than an S_N2

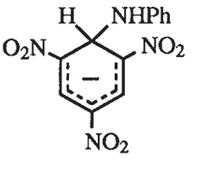

1

displacement on the σ-adduct. It was later found that **1** may be formed directly from TNB and aniline in DMSO (8), or in acetonitrile (9), in the presence of a tertiary amine, B, such as Dabco or triethylamine, to act as a proton acceptor. The

Received July 30, 1997.

This paper is dedicated to Professor Erwin Buncel in recognition of his outstanding contributions to the study of physical-organic chemistry.

M.R. Crampton[1] and I.A. Robotham. Chemistry Department, Durham University, Durham, U.K., DH1 3LE.

[1] Author to whom correspondence may be addressed. Telephone: +44 191 374 3130. Fax: +44 191 384 4737. E-mail: M.R.Crampton@durham.ac.uk

© 1998 NRC Canada

Scheme 1.

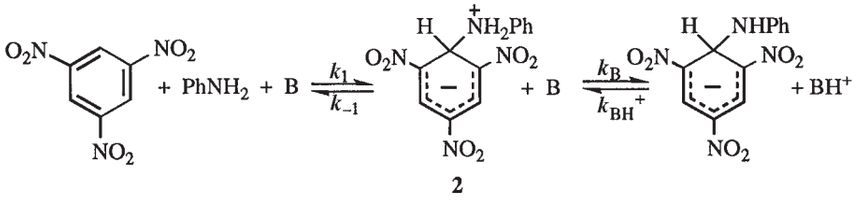

Fig. 1. Visible spectra of **3** (4×10^{-5} mol dm^{-3}) in DMSO containing aniline (0.1 mol dm^{-3}), Dabco (0.05 mol dm^{-3}), and Dabco hydrochloride (0.01 mol dm^{-3}) taken after (*a*) 1 min, (*b*) 5 min, and (*c*) 3 h. The spectra show the rapid formation of **5** followed by the slower conversion to **6**.

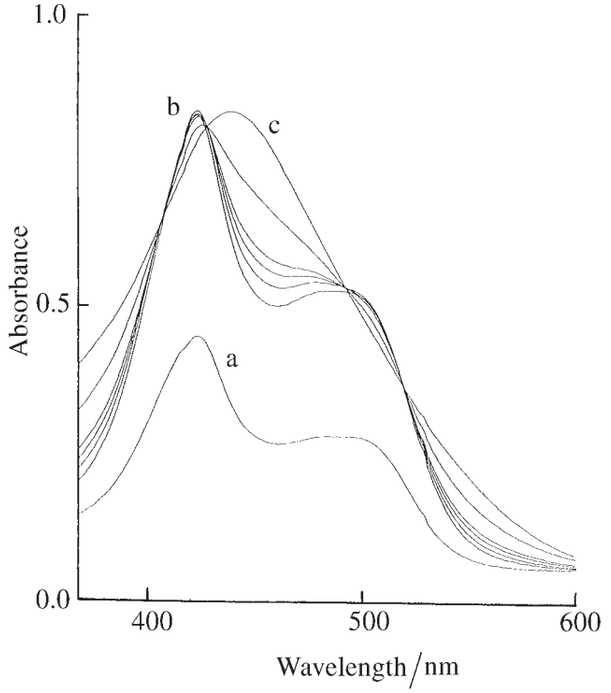

reaction involves two steps, as shown in Scheme 1. The first step is thermodynamically unfavourable due to the weak basicity of aniline. However, the presence of a strong base renders the proton transfer step sufficiently favourable to allow formation of the anionic adduct. Nevertheless, kinetic studies (10, 11) showed that the proton transfer from the zwitterion, **2**, is rate limiting, corresponding to the condition $k_{-1} > k_B[B]$. When Dabco was used as the added base, a specific salt effect involving association of protonated Dabco with chloride ions was observed (12). There is also clear kinetic evidence for rate-limiting proton transfer in the reactions of TNB with aliphatic amines (13–15).

We have previously examined the kinetics of the reaction of ethyl 2,4,6-trinitrophenyl ether (16), **3**, and some ring-activated phenyl aryl ethers (17) with aliphatic amines in DMSO. In agreement with the classic work of Orvik and Bunnett (18), the results for **3** indicated that substitution involves the specific base – general acid catalysis mechanism, SB–GA, in which leaving-group expulsion is the overall rate-limiting step. However, the observation of base catalysis in reactions of the phenyl aryl ethers was best explained in terms of rate-limiting proton transfer from a zwitterionic intermediate to base (17). Previous studies of nucleophilic substitution using aniline as the nucleophile have shown that in reaction with methyl 2,4,6-trinitrophenyl ether there is competition between attack at the ring carbon atom to give a diphenylamine derivative, and at the side-chain carbon to give picric acid (19). Reactions of aniline with phenyl 2,4,6-trinitrophenyl ether yield the diphenylamine derivative and are subject to base catalysis in methanol, acetonitrile, tetrahydrofuran, ethyl acetate, and benzene (20). However, there was little evidence for catalysis in DMSO (19, 21).

Here we examine the kinetics of the reactions of **3**, and of some ring-activated phenyl aryl ethers with aniline in DMSO. Our results show that in these substitution reactions, as in the reaction of aniline with TNB, proton transfer may be the rate-limiting step.

Results and discussion

Kinetic and equilibrium measurements of the reactions with aniline were generally made in the presence of Dabco and Dabco hydrochloride. The pK_a values (22) in DMSO of the protonated forms of the bases are, for aniline, 3.82, and for Dabco, 9.06. Hence the value of the equilibrium constant, K_a', for eq. [1] is 5.8×10^{-6}.

[1] aniline + DabcoH$^+$ ⇌ aniline H$^+$ + Dabco

$$K_a' = \frac{K_a(\text{DabcoH}^+)}{K_a(\text{AnilineH}^+)} = 5.8 \times 10^{-6}$$

Thus the concentrations of the reagents in the reaction mixture will be very similar to the stoichiometric concentrations; relatively little protonation of aniline will occur.

Reactions of ethyl 2,4,6-trinitrophenyl ether, 3

Ultraviolet–visible spectra of **3** in DMSO containing aniline (0.1 mol dm^{-3}) indicated no reaction during 90 min. When the reaction was repeated with the addition of Dabco and DabcoH$^+$ a biphasic reaction was observed. The spectra in Fig. 1 show that, in the first stage, a species with λ_{max} 430 nm and 500 nm is produced. The spectrum is typical of that for σ-adducts (2, 3) and ^{1}H NMR experiments confirm the formation of **5**, the intermediate on the substitution pathway. A second, much slower, reaction gave a species with λ_{max} 445 whose spectrum is identical to that of 2,4,6-trinitrodiphenylamine, **6**, in the reaction medium. Since the pK_a value (22) of **6** is 8.01, this species will be present largely in its deprotonated form, **7**.

The ^{1}H NMR spectrum of **3** in [$^2H_6$]DMSO shows bands at

© 1998 NRC Canada

Scheme 2.

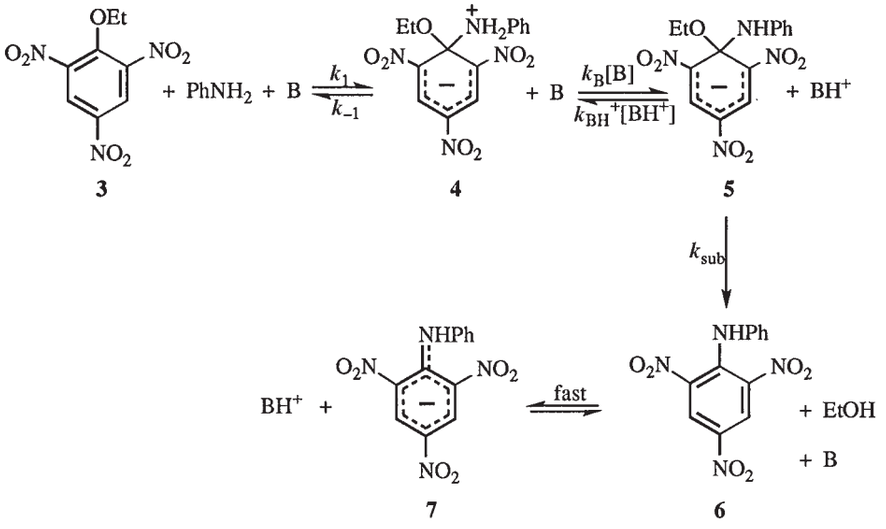

Table 1. Kinetic and equilibrium data for the equilibration of **3** and **5** in DMSO at 25°C.

[Aniline]/mol dm^{-3}	[Dabco]/mol dm^{-3}	[Dabco H$^+$]/mol dm^{-3}	Abs [a] (430 nm)	K_1K_{Dabco} [b]/dm^3 mol^{-1}	k_{fast}/10^{-3} s^{-1}	k_{calc} [c]/10^{-3} s^{-1}
0.10	0.02	0.01	0.63	7.5	14	14
0.10	0.04	0.01	0.79	7.6	14	14
0.10	0.06	0.01	0.81	5.6	16	16
0.10	0.10	0.01	0.88	5.2	20	20
0.10	0.15	0.01	—	—	24	25
0.01	0.10	0.01	0.43	6.9	3.5	3.3
0.02	0.10	0.01	0.58	6.2	4.9	4.7
0.04	0.10	0.01	0.80	8.0	8.5	7.9
0.06	0.10	0.01	0.88	8.6	12	12
0.08	0.10	0.01	—	—	16	16

[a] Absorbance at completion of fast reaction forming **5**.

[b] Calculated as $\frac{\text{Abs.[DabcoH}^+]}{(1.05 - \text{Abs})[\text{An}][\text{Dabco}]}$.

[c] Calculated from eq. [6] with $K_1k_{Dabco} = 1.17$ dm^6 mol^{-2} s^{-1}, $k_{DabcoH^+} = 0.2$ dm^3 mol^{-1} s^{-1}, and $k_{An}/k_{Dabco} = 0.46$.

δ 9.09 (ring hydrogens), 4.26 (q, J = 7 Hz, OCH_2), and 1.35 (t, CH_3). In the presence of aniline (1 equiv.) and Dabco (1 equiv.), bands due to **5** are observed at δ 8.62 (ring), 3.14 (q, J = 7 Hz, OCH_2), and 1.08 (t, CH_3). It is interesting (4, 5) that the anilide group of **5** shows a singlet at δ 5.98 attributed to the amino hydrogen together with spin-coupled, J = 8 Hz, bands due to ring hydrogens at δ 6.93(t), 6.52(t), and 6.35(d). Over a period of 1 h the bands due to **5** decrease in intensity while bands attributable to the substitution products, **7** and ethanol, increase in intensity. A small band at δ 8.58 is also observed, indicating the formation of some picric acid.

UV–visible measurements show that, in solutions containing Dabco but without aniline, **3** is very slowly converted to picric acid, λ_{max} = 380 nm. This reaction could be inhibited by the presence of Dabco hydrochloride. The latter observation indicates that picric acid formation is likely to be due to attack of hydroxide, formed from adventitious water in the solvent, at the 1-position rather than attack by Dabco at the side-chain ethyl group. All quantitative measurements involving aniline were made in buffered solutions, Dabco with Dabco hydrochloride, to suppress picric acid formation.

Our kinetic and equilibrium results are interpreted in terms of Scheme 2, in which the zwitterion, **4**, is expected to be an intermediate present in low concentrations. The first stage of the reaction, representing the equilibration of **3** and **5**, was monitored at 430 nm. With concentrations of aniline (An), Dabco, and Dabco hydrochloride in large excess of the concentration of **3**, first-order kinetics were observed. Rate constants, k_{fast}, and absorbances at completion of the equilibration are given in Table 1. All measurements were made in the presence of DabcoH$^+$, 0.01 mol dm^{-3}, to maintain constant ionic strength.

An equilibrium constant for formation of **5** may be defined in terms of the Dabco concentration by eq. [2]. The absorbance values in Table 1 lead to a value for K_1K_{Dabco} of 7 ± 1 dm^3 mol^{-1}.

$$[2] \qquad K_1K_{Dabco} = \frac{k_1\,k_{Dabco}}{k_{-1}\,k_{DabcoH^+}} = \frac{[\mathbf{5}]}{[\mathbf{3}]} \times \frac{[\text{DabcoH}^+]}{[\text{An}]\,[\text{Dabco}]}$$

© 1998 NRC Canada

Alternatively, the equilibrium constant may be defined in terms of the aniline concentration in eq. [3]:

$$[3] \quad K_1K_{An} = \frac{k_1}{k_{-1}} \times \frac{k_{An}}{k_{AnH^+}} = \frac{[\mathbf{5}]}{[\mathbf{3}]} \times \frac{[AnH^+]}{[An]^2}$$

Use of eq. [1] leads to eq. [4], showing that the value of K_1K_{An} will be many orders of magnitude lower than the value of K_1K_{Dabco}, and explaining why adduct formation is not observed in the absence of Dabco.

$$[4] \quad K_1K_{An} = K_1K_{Dabco}\, K_a'$$

The variation of k_{fast} with values of the Dabco and aniline concentrations is compatible only with proton transfer being rate determining in the formation of **5**. Using the condition $k_{-1} > k_B[B]$ and treating **4** as a steady-state intermediate leads to the rate expression given in eq. [5]:

$$[5] \quad k_{fast} = \frac{k_1}{k_{-1}}[An](k_{An}[An] + k_{Dabco}[Dabco]) + k_{DabcoH^+}[DabcoH^+] + k_{AnH^+}[AnH^+]$$

Here k_{Dabco} and k_{An} represent k_B when reaction involves Dabco and aniline, respectively, while k_{DabcoH^+} and k_{AnH^+} represent k_{BH^+} for reactions with the appropriate conjugate acids.

Since K_{An}/K_{Dabco} has a constant value (eq. [4]) it is possible to reduce the number of variables in eq. [5] to give eq. [6]:

$$[6] \quad k_{fast} = K_1k_{Dabco}[An]\left([Dabco] + \frac{k_{An}}{k_{Dabco}}[An]\right) + k_{DabcoH^+}[DabcoH^+]\left(1 + \frac{k_{An}}{k_{Dabco}}\frac{[An]}{[Dabco]}\right)$$

Excellent agreement between the calculated and observed values of k_{fast} was obtained with K_1k_{Dabco} 1.17 ± 0.10 dm^6 mol^{-2} s^{-1}, k_{DabcoH^+} 0.20 ± 0.05 dm^3 mol^{-1} s^{-1}, and k_{An}/k_{Dabco} 0.46 ± 0.10. The latter value indicates that aniline competes effectively with the much stronger base Dabco in the proton transfer step, **4** ⇌ **5**. This point is discussed later. It was not possible to obtain an acceptable fit between calculated and observed values of k_{fast} with lower values of the ratio k_{An}/k_{Dabco}. Combination of the values of K_1k_{Dabco} and k_{DabcoH}+ leads to a value of K_1K_{Dabco} of 5.9 dm^3 mol^{-1}, in acceptable agreement with that obtained independently from absorbance measurements at equilibrium.

The slow product-forming reaction was measured at 445 nm. Values of the first-order rate constants, k_{slow}, are reported in Table 2. Making the assumption that **3** and **5** are in rapid equilibrium during this stage of the reaction leads to the rate expression of eq. [7].

$$[7] \quad k_{slow} = \left(k_{sub,DabcoH^+}[DabcoH]^+ + k_{sub,AnH^+}[AnH^+]\right)\left(\frac{K_1K_{Dabco}[Dabco][An]}{K_1K_{Dabco}[Dabco][An] + [DabcoH^+]}\right)$$

Here $k_{sub,DabcoH^+}$ and k_{sub,AnH^+} are, respectively, the rate constants for the substitution reactions involving protonated Dabco and aniline. Use of eq. [1] results in eq. [8]:

$$[8] \quad k_{slow} = \left(k_{sub,DabcoH^+} + k_{sub,AnH^+}.\frac{[Dabco]}{[An]}\right)\left(\frac{K_1K_{Dabco}[Dabco][An][DabcoH^+]}{K_1K_{Dabco}[Dabco][An] + [DabcoH^+]}\right)$$

Analysis of the results using the known value for K_1K_{Dabco} of 7 dm^3 mol^{-1} showed that most of the reaction flux involved the protonated Dabco. Agreement between observed and calculated values of k_{slow} was optimized with values of 0.06 ± 0.01 dm^3 mol^{-1} s^{-1} for $k_{sub,DabcoH^+}$ and 0.005 ± 0.002 dm^3 mol^{-1} s^{-1} for $k_{sub,AnH^+}.K_a'$. Using the known value of K_a' leads to a value for k_{sub,AnH^+} of 860 dm^3 mol^{-1} s^{-1}.

Reactions of phenyl 2,4,6-trinitrophenyl ethers, 8

Reactions of **8a–c** with aniline in DMSO proceeded in a single stage. UV–visible spectra, and NMR spectra (in more concentrated solutions), at completion of reaction were identical to those of **6**, the expected substitution product, in the reaction medium.

Kinetic measurements were made with aniline and with solutions containing aniline, Dabco, and Dabco hydrochloride. With these concentrations in large excess of the substrate concentration, first-order kinetics were observed. Data obtained with aniline alone are shown in Fig. 2. Plots of the second-order rate constant, k_{obs}/[aniline], versus aniline concentration were linear with positive intercepts. At a constant aniline concentration, values of the first-order rate constant, k_{obs}, increased linearly with Dabco concentration, as shown in Fig. 3. These results are interpreted in terms of the process shown in Scheme 3. It is known (17, 23) that phenoxide is a considerably better leaving group than ethoxide, by a factor of ca. 10^6. Our failure to observe **10**, the intermediate on the substitution pathway, may be attributed to its rapid decomposition by loss of phenoxide. The assumption that **9** may be treated as a steady-state intermediate leads to the rate expression of eq. [9], where k_{An} and k_{Dabco} represent k_B for the respective bases.

$$[9] \quad k_{obs} = \frac{k_1[An]\,(k_2 + k_{An}[An] + k_{Dabco}[Dabco])}{k_{-1} + k_2 + k_{An}[An] + k_{Dabco}[Dabco]}$$

Our results, which provide evidence for base catalysis, indicate that the condition $k_{-1} >> k_2 + k_{An}[An] + k_{Dabco}[Dabco]$ applies so that eq. [9] reduces to eq. [10].

$$[10] \quad k_{obs} = K_1[An](k_2 + k_{An}[An] + k_{Dabco}[Dabco])$$

Values obtained for K_1k_2, K_1k_{An}, and K_1k_{Dabco} can be found in Table 3.

© 1998 NRC Canada

Table 2. Kinetic data for the formation of the product, **6**, in DMSO at 25°C.

[Aniline]/ mol dm^{-3}	[Dabco]/ mol dm^{-3}	[DabcoH$^+$]/ mol dm^{-3}	k_{slow}/10^{-4} s^{-1}	k_{calc} [a]/10^{-4} s^{-1}
0.10	0.02	0.01	3.4	3.5
0.10	0.04	0.01	4.3	4.5
0.10	0.06	0.01	5.1	5.1
0.10	0.10	0.01	5.5	5.7
0.10	0.15	0.01	5.9	6.1
0.01	0.10	0.01	4.7	4.5
0.02	0.10	0.01	5.1	5.0
0.04	0.10	0.01	5.5	5.3
0.06	0.10	0.01	5.6	5.5
0.08	0.10	0.01	5.7	5.6
0.05	0.05	0.003[b]	1.8	1.7
0.05	0.05	0.005[b]	2.6	2.5
0.05	0.05	0.007[b]	3.4	3.3
0.05	0.05	0.010	4.3	4.1

[a] Calculated from eq. [8] with $k_{sub,DabcoH^+}$ 0.060 dm^3 mol^{-1} s^{-1}, $k_{sub,AnH^+} \cdot K_a'$ 0.005 dm^3 mol^{-1} s^{-1}, and K_1K_{Dabco} 7.0 dm^3 mol^{-1}.
[b] Ionic strength was maintained at 0.01 mol dm^{-3} using tetrabutylammonium chloride.

Reactions of phenyl 2,4-dinitronaphthyl ether, 11

UV–visible and ^{1}H NMR studies showed that in the presence of aniline, or aniline with Dabco, **11** was smoothly converted into *N*-phenyl-2,4-dinitronaphthylamine. Kinetic measurements at 440 nm showed a single first-order process. Values of the rate constant, k_{obs}, are given in Table 4. Data are interpreted in a manner similar to that given for **8** so that Scheme 3 is applicable and eq. [10] will apply. Values calculated with K_1k_2 2.0×10^{-4} dm^3 mol^{-1} s^{-1}, K_1k_{An} 1.1×10^{-2} dm^6 mol^{-2} s^{-1}, and K_1k_{Dabco} 0.24 dm^6 mol^{-2} s^{-1} give excellent agreement with values of k_{obs}.

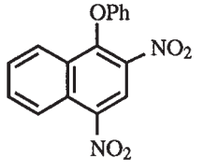

11

Comparisons

Data for reactions of **3**, **8,** and **11** are collected in Table 3, where they are compared with values for the formation of **1** from TNB. The value of K_1K_{Dabco}, the overall equilibrium constant for formation of the adduct **5** from **3**, is ca. 20 times larger than that for formation of **1** by reaction at an unsubstituted ring position of TNB. The major effect is likely to be an increase in K_1 due to relief of steric strain present in the parent (16, 24) when the ethoxy group is twisted from the ring plane. Stereoelectronic stabilization of **5** relative to **1** may also contribute, as described in related systems by Buncel et al. (25). The polar effect of the ethoxy group will be expected to result in an increase in the value of K_1 and may also give rise to a small increase in K_{Dabco}. For comparison (16), the equilibrium constant for formation of **12** from **3** and *n*-butylamine has a value 50 times larger than that for the corresponding formation of **13**. We have not observed an adduct formed by attack of

Fig. 2. Plots of the second-order rate constant, k_{obs}/[aniline], versus aniline concentration for reactions of **8a**, **8b,** and **8c** with aniline in DMSO.

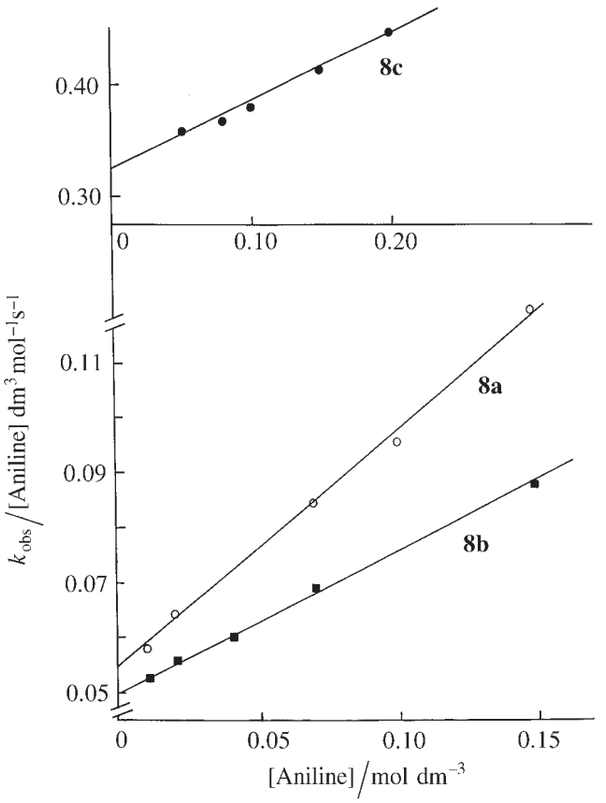

Fig. 3. Plots of k_{obs} versus [Dabco] for reactions of **8a**, **8b**, and **8c** with aniline (0.02 mol dm^{-3}) in DMSO containing Dabco hydrochloride (0.05 mol dm^{-3}).

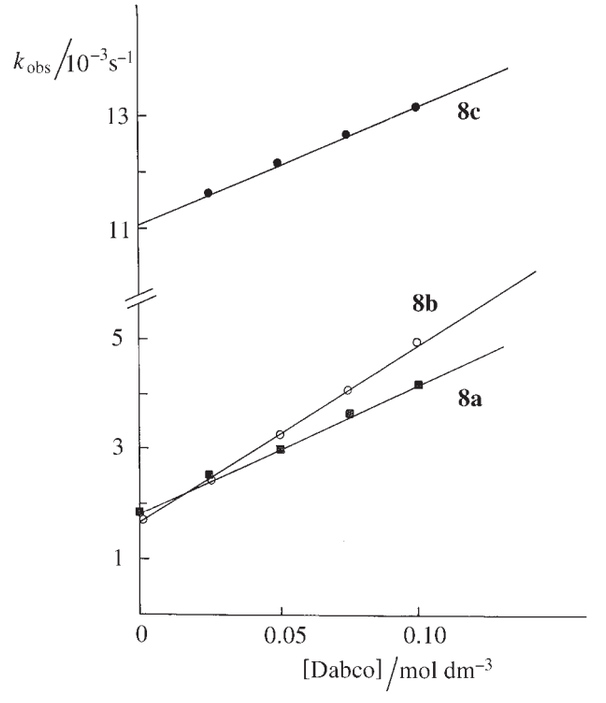

© 1998 NRC Canada

Scheme 3.

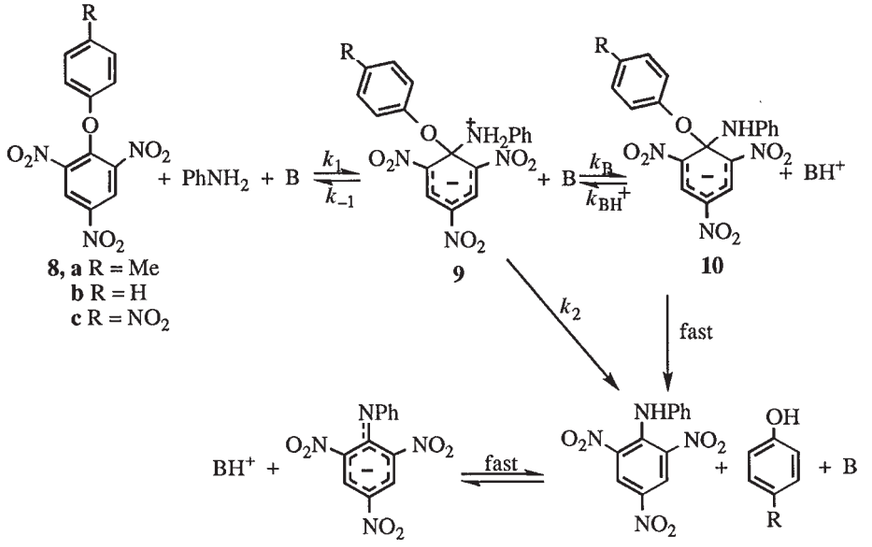

Table 3. Comparison of data in DMSO at 25°C.

Reactant	K_1k_{An}/ dm^6 mol^{-2} s^{-1}	K_1k_{Dabco}/ dm^6 mol^{-2} s^{-1}	K_1k_2/ dm^3 mol^{-1} s^{-1}	k_{DabcoH^+}/ dm^3 mol^{-1} s^{-1}	K_1K_{Dabco}/ dm^3 mol^{-1}	k_{An}/k_{Dabco}	k_{An}/ k_2 dm^3 mol^{-1}
3	0.54	1.17	—	0.2	7	0.46	—
TNB[a]	—	26	—	74	0.35	—	—
8a	0.42	1.2	0.055	—	—	0.35	8
8b	0.27	1.6	0.050	—	—	0.17	5.4
8c	0.65	0.9	0.32	—	—	0.72	2
11	0.011	0.24	0.0002	—	—	0.045	55

[a] From ref. 12. Values quoted are in presence of tetraethylammonium chloride 0.01 mol dm^{-3}, to correspond with data for reactant **3**.

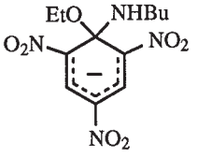

12

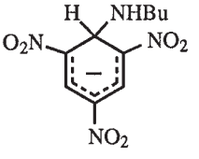

13

aniline at the unsubstituted 3-position of **3**. This may be explained by the much lower thermodynamic stability expected for this adduct compared with its isomer **5** or with the adduct **1** formed from TNB. Attack at the 3-position of **3** will not relieve the steric strain present in the parent, and work with aliphatic amines (16) suggests that the adduct so formed would have a stability ca. 100 times lower than that of the adduct **1** from TNB.

Buncel et al. (10, 11) showed that, in the formation of **1** from TNB and aniline, the proton transfer step is rate limiting. Similarly in the formation of **5** our results indicate rate-limiting proton transfer. From eqs. [1] and [4], K_{An}/K_{Dabco} has the value 5.8×10^{-6}, showing that the equilibrium constant for the proton-transfer step is very much smaller when the reaction involves aniline than when it involves Dabco. Nevertheless the ratio of 0.46 obtained for k_{An}/k_{Dabco} shows that *kinetically* aniline may compete effectively with Dabco, a much stronger base, in the proton-transfer step. This may seem surprising; however, it should be remembered that the proton-transfer step, **4** ⇌ **5**, in Scheme 2 will be thermodynamically favourable even when the reaction involves aniline as B and the anilinium ion as BH^+. Thus it is known (5, 26) that the trinitrocyclohexadienate group, even though negatively charged, is electron withdrawing relative to hydrogen. Hence **4** will be more acidic than the anilinium ion. Values of k_{An} and k_{Dabco} will be

Table 4. Kinetic results for reaction of phenyl 2,4-dinitronaphthyl ether with aniline in DMSO at 25°C.

[Aniline]/ mol dm^{-3}	[Dabco]/ mol dm^{-3}	k_{obs}/ 10^{-5} s^{-1}	k_{calc} [a]/ 10^{-5} s^{-1}
0.02	—	0.84	0.84
0.04	—	2.5	2.6
0.07	—	6.7	6.8
0.10	—	14	13
0.15	—	29	28
0.20	—	50	48
0.11	0.01	44	42
0.11	0.02	71	68
0.11	0.03	92	95
0.11	0.05	150	150
0.11	0.10	280	280

[a] Calculated from eq. [10] with K_1k_2 2.0×10^{-4} dm^3 mol^{-1} s^{-1}, K_1k_{An} 1.1×10^{-2} dm^6 mol^{-2} s^{-1}, and K_1k_{Dabco} 0.24 dm^6 mol^{-2} s^{-1}.

© 1998 NRC Canada

affected by steric factors rather than the relative basicities of the amines. It is likely that the proton to be transferred from **4** will be hydrogen bonded to a DMSO molecule in the solvent (13, 27, 28) and this, together with steric hindrance to the approach of the reagents, will reduce values of rate constants below the diffusion limit.

It is interesting to speculate on values of rate constants for the proton-transfer step. It has previously been estimated (15, 16) that the presence of the trinitrocyclohexadienate ring in zwitterions such as **4** will acidify the adjacent ammonium protons by a factor of ca. 500, as indicated in eq. [11]:

[11] $K_a(\mathbf{4})/K_a(AnH^+) = 500$

Use of eq. [1] allows the comparison of the relative acidities of **4** and protonated Dabco as shown in eq. [12]:

[12] $$K_a(\mathbf{4})/K_a(DabcoH^+) = \frac{500}{5.8 \times 10^{-6}} = 8.6 \times 10^7$$

The ratio obtained corresponds to k_{Dabco} / k_{DabcoH^+} and since k_{DabcoH^+} has been found experimentally to be 0.2 $dm^3\ mol^{-1}\ s^{-1}$ we obtain a value for k_{Dabco} of 1.7×10^7 $dm^3\ mol^{-1}\ s^{-1}$. This allows the calculation of values for k_{An} of 8×10^6 $dm^3\ mol^{-1}\ s^{-1}$ and for K_1 of 7×10^{-8} $dm^3\ mol^{-1}$. Since the ratio given in eq. [11] is not known precisely, the values calculated using it should be regarded only as estimates.

The data in Table 3 indicate that values of rate constants for proton transfer are larger in the formation of **1** from TNB, than in the formation of **5**. Here reaction occurs at an unsubstituted ring position so that there is less steric congestion at the reaction centre. A calculation analogous to that given above leads here to a value for k_{Dabco} in excess of 10^9 $dm^3\ mol^{-1}\ s^{-1}$.

The formation of **6** from **5** involves general acid-catalysed expulsion of the ethoxy group. Values of the rate constants for reaction with the anilinium ion, 860 $dm^3\ mol^{-1}\ s^{-1}$, and DabcoH$^+$, 0.06 $dm^3\ mol^{-1}\ s^{-1}$, may be used in conjunction with eq. [1] to calculate a Brønsted α value of 0.80.

Phenoxide is known to be a considerably better leaving group than ethoxide (17, 23), and we did not observe intermediates in the substitution reactions of the phenyl ethers **8a**–**c**. We interpret the increases in the rate constant shown in Figs. 2 and 3 as base catalysis. Previous work (19, 21), at lower base concentrations, did not find evidence for base catalysis. The effects we have observed are not particularly large. However, values calculated for K_1k_{An} and K_1k_{Dabco} for reactions of **8a**–**c** are similar to those found for reaction of **3**, where there is genuine base catalysis. These similarities are to be expected if proton transfer from zwitterion, **9** or **4**, to base is rate limiting. The presence of a phenoxy group rather than an ethoxy group at the 1-position is not expected to drastically affect the value of K_1 for formation of the zwitterion (29). Nor will this change be expected to greatly alter the values of k_{An} or k_{Dabco} for the proton-transfer step. A major difference between the phenyl ethers, **8**, and the ethyl ether, **4**, is that in the former case much of the reaction flux involves the direct uncatalysed decomposition of the zwitterions, **9**, by the k_2 step. This step is likely to involve intramolecular proton transfer from nitrogen to oxygen coupled with carbon–oxygen bond cleavage. Leaving-group expulsion is part of the rate-limiting step here, so that reaction of the 4-nitrophenoxy derivative, **8c**, is six times faster than that of the phenoxy derivative, **8b** (Table 3).

Comparison of data for reaction of phenyl 2,4-dinitronaphthyl ether, **11**, with that for phenyl 2,4,6-trinitrophenyl ether, **8b**, shows decreases in K_1k_2, K_1k_{An}, and K_1k_{Dabco} by factors of 250, 24, and 7, respectively. These changes may be attributed (2, 3) to two main factors: the decrease in ring activation in **11** compared to **8b**, and the reduction in steric crowding at the reaction centre in the zwitterionic

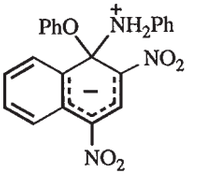

14

intermediate **14** compared to that in the corresponding intermediate, **9b**. The first factor will result in a decrease in the value of K_1 and hence in the value of K_1k_2. That the decreases observed for K_1k_{An} and K_1k_{Dabco} are smaller than that observed for K_1k_2 may be attributed to the second factor. A reduction in steric crowding in **14** compared to **9b** may allow the easier approach of a base molecule to accept a proton from the zwitterionic intermediate. Hence values of k_{An} and k_{Dabco} may be larger in the 2,4-dinitronaphthyl system. The k_{An}/k_{Dabco} ratio is somewhat decreased in the dinitronaphthyl system and this may indicate that the situation is being approached in which the reduction in the electron-withdrawing ability of the ring system renders the proton transfer from **14** to aniline thermodynamically unfavourable.

Experimental

Ethyl 2,4,6-trinitrophenyl ether (16), **3**, phenyl 2,4,6-trinitrophenyl ether (17), **8b**, and phenyl 2,4-dinitronaphthyl ether (17), **11**, were available from previous work. The 4-substituted phenyl 2,4,6-trinitrophenyl ethers **8a** and **8c** were prepared by reaction at 45°C for 3 h of picryl chloride (1 equiv.) with sodium hydroxide (1 equiv.) in an excess of the appropriate 4-substituted phenol containing a little water. On completion, water was added to remove any picric acid produced and recrystallization from ethanol yielded **8a**, mp 100°C (lit. (30) mp 103°C) and **8c**, mp 163°C (lit. (30) mp 157°C). 2,4,6-Trinitrodiphenylamine, **6**, and *N*-phenyl-2,4-dinitronaphthylamine were available from previous work (22). Solvent, amines, and amine salts were prepared and (or) purified as described previously (22).

^{1}H NMR spectra were recorded using Varian-200 XL or VXR-400 spectrometers. UV–visible spectra and kinetic measurements were made with Beckman Lambda 2 or Applied Photophysics SX.17 MV stopped-flow spectrophotometers at 25°C. Reported rate constants are the means of several determinations and are precise to ±5%.

Acknowledgements

We thank the Engineering and Physical Sciences Research Council (EPSRC) for a studentship and for a research grant to purchase the stopped-flow spectrophotometers. Mrs. J. Say is thanked for assistance with the NMR measurements.

© 1998 NRC Canada

References

1. M.R. Crampton and V. Gold. J. Chem. Soc. B, 23 (1967).
2. E. Buncel, M.R. Crampton, M.J. Strauss, and F. Terrier. Electron deficient aromatic- and heteroaromatic-base interactions. Elsevier, Amsterdam. 1984.
3. F. Terrier. Nucleophilic aromatic displacement. VCH, New York. 1991.
4. E. Buncel and J.G.K. Webb. Can. J. Chem. **50**, 129 (1972).
5. E. Buncel and J.G.K. Webb. Can. J. Chem. **52**, 630 (1974).
6. E. Buncel and J.G.K. Webb. Tetrahedron Lett. 4417 (1976).
7. E. Buncel, J.G.K. Webb, and J.F. Wiltshire. J. Am. Chem. Soc. **99**, 4429 (1977).
8. E. Buncel and H.W. Leung. J. Chem. Soc. Chem. Commun. 19 (1975).
9. T.O. Bamkole, J. Hirst, and I. Onyido. J. Chem. Soc. Perkin Trans. 2, 1201 (1981).
10. E. Buncel and W. Eggimann. J. Am. Chem. Soc. **99**, 5958 (1977).
11. E. Buncel, W. Eggimann, and H.W. Leung. J. Chem. Soc. Chem. Commun. 55 (1977).
12. E. Buncel and W. Eggimann. J. Chem. Soc. Perkin Trans. 2, 673 (1978).
13. C.F. Bernasconi, M.C Muller, and P. Schmid. J. Org. Chem. **44**, 3189 (1979).
14. C.F. Bernasconi. Acc. Chem. Res. **11**, 147 (1978).
15. M.R. Crampton and B. Gibson. J. Chem. Soc. Perkin Trans. 2, 533 (1981).
16. M.R. Crampton and P.J. Routledge. J. Chem. Soc. Perkin Trans. 2, 573 (1984).
17. R. Chamberlin and M.R. Crampton. J. Chem. Soc. Perkin Trans. 2, 1831 (1995).
18. J.A. Orvik and J.F. Bunnett. J. Am. Chem. Soc. **92**, 2417 (1970).
19. J. Hirst, G. Hussain, and I. Onyido. J. Chem. Soc. Perkin Trans. 2, 397 (1986).
20. O. Banjoko and P. Otiono. J. Chem. Soc. Perkin Trans. 2, 399 (1981).
21. T.A. Emokpae, P.U. Uwakwe, and J. Hirst. J. Chem. Soc. Perkin Trans. 2, 125 (1993).
22. M.R. Crampton and I.A. Robotham. J. Chem. Res. (S), 22 (1997).
23. C.F. Bernasconi and M.C. Muller. J. Am. Chem. Soc. **100**, 5530 (1978).
24. C.M. Gramaccioli, R. Destro, and M. Simonetta. Acta Crystallogr. Sect. B: Struct. Crystallogr. Cryst. Chem. **B24**, 129 (1968).
25. E. Buncel, J.M. Dust, and F. Terrier. Chem. Rev. **95**, 2261 (1995).
26. M.R. Crampton. J. Chem. Soc. B, 2112 (1971).
27. M.R. Crampton and S.D. Lord. J. Chem. Soc. Perkin Trans. 2, 369 (1997).
28. C.F. Bernasconi and F. Terrier. J. Am. Chem. Soc. **97**, 7458 (1975).
29. R. Chamberlin, M.R. Crampton, and R.L. Knight. J. Chem. Res. (S), 444 (1993).
30. K. Okon. Rocz. Chem. **32**, 213 (1958); **32**, 218 (1958).

© 1998 NRC Canada

Novel syntheses of 4-alkyl-2(*5H*)-thiophenones and 8-phenylimino-1,2,4-triazolo[5,1-*c*]-1,4-thiazines

Alan R. Katritzky, Daming Feng, Hengyuan Lang, Ming Qi, and Peter J. Steel

Abstract: 1,2,4-Triazole stabilized allene anions are intermediates for the synthesis of 4-alkyl-2(5*H*)-thiophenones and 8-phenylimino-1,2,4-triazolo[5,1-*c*]-1,4-thiazines. Structures are confirmed by X-ray crystallography.

Key words: allene anion, 4-alkyl-2(5*H*)-thiophenones, 8-phenylimino-1,2,4-triazolo[5,1-*c*]-1,4-thiazines, X-ray crystallography.

Résumé : Les anions alléniques stabilisés par un 1,2,4-triazole sont des intermédiaires dans la synthèse de 4-alkyl-(5*H*)-thiophén-2-ones et de 8-phénylimino-1,2,4-triazolo[5,1-*c*]-1,4-thiazines. Les structures ont été confirmées par diffraction des rayons-X.

Mots clés : anion allénique, 4-alkyl-(5*H*)-thiophén-2-ones, 8-phénylimino-1,2,4-triazolo[5,1-*c*]-1,4-thiazines, diffraction des rayons-X.

[Traduit par la rédaction]

Can. J. Chem. Downloaded from www.nrcresearchpress.com by China University of Science and Technology on 09/05/12
For personal use only.

Introduction

We recently reported convenient syntheses of α,β-unsaturated esters, α,β-unsaturated γ-lactones, and alkoxypyrroles (1) by reactions of triazole-stabilized allene–triazole dianions (formed from 1-(1,2,4-triazol-1-yl)-3-phenylpropargyl ethyl ether) with alkyl halide, aldehyde, ketone, and imine electrophiles. In these syntheses, treatment of **1** with two equivalents of BuLi at –78°C for a few minutes, followed by reactions with electrophiles, led to exclusive attack at the γ-carbon of **2** ⇌ **3** to form allene intermediate **4** (Scheme 1), which then underwent acidic hydrolysis. We now report further novel reactions of dianions **3** with carbon disulfide and phenyl isothiocyanate, which lead to synthetically useful preparations of a variety of compounds.

Results and discussion

Reactions of 1-(1,2,4-triazol-1-yl)propargyl ethyl ethers 1 and 5 with carbon disulfide

Treatment of **1** with two equivalents of BuLi at –90°C for a few minutes, followed by reaction with CS_2 (2 equiv.), unexpectedly formed the disulfide **8a** (Scheme 2). Acidic hydrolysis of **8a** and corresponding treatment of **5**, without isolation of the disulfide, produced the 4-alkyl-2-thiophenones **9a**,**b**. These reactions may proceed through intermediates **6**, which cyclize to the substituted thiophene derivatives **7**. Compounds **7** then oxidatively dimerize. The structures of bis(5-ethoxy-3-phenyl-2-thienyl) disulfide **8a** and the substituted thiophenones **9a**,**b** were supported by ^{1}H and ^{13}C NMR spectra and microanalysis and were confirmed by X-ray crystallography, as shown in Figs. 1 and 2.

The disulfide **8a** crystallizes in the monoclinic space group $P2_1/n$, with a complete molecule in the asymmetric unit. One of the two ethoxy substituents has the methyl group disordered over two sites (Fig. 1). Although the two halves of the molecule have similar bond lengths and angles (see Experimental), they differ in the relative orientations of the phenyl rings, which are inclined to the planes of their attached thiophene rings at angles of 39.9(9)° and 48.5(9)°. There are no unusually short intermolecular interactions in the solid state. The 2-thiophenone **9a** also crystallizes in the monoclinic space group $P2_1/n$, with a full molecule in the asymmetric unit (Fig. 2). As well as confirming the structure, the X-ray analysis unambiguously showed that this compound exists as the conjugated 5*H* tautomer, in accord with well-established rules for the tautomerism of thiophenones (2). The geometry of the thiophenone ring in **9a** differs somewhat from that reported in the only other X-ray structure determination of a monosubstituted 2-thiophenone (3), which, as a 4-alkylamino-substituted 2-thiophenone, exhibited the greater polarization, expected for a vinylogous amide. Surprisingly, the two rings in **9a** are almost coplanar (angle between mean planes = 5.5(2)°), which is undoubtedly associated with the molecular packing. The molecules pack in sheets approximately perpendicular to the *a* axis, with adjacent molecules exhibiting π–π stacking between phenyl and thiophene rings separated by approximately 3.6 Å.

Received June 26, 1997.

This paper is dedicated with affection to Professor Erwin Buncel (A.R.K.).

A.R. Katritzky,[1] **D. Feng, H. Lang, and M. Qi.** Center for Heterocyclic Compounds, Department of Chemistry, University of Florida, Gainesville, FL 32611-7200, U.S.A.

P. J. Steel. Department of Chemistry, University of Canterbury, Christchurch, New Zealand.

[1] Author to whom correspondence may be directed. Telephone: (352) 392-0554. Fax: (352) 392-9199. E-mail: katritzky@chem.ufl.edu

© 1998 NRC Canada

Can. J. Chem. Downloaded from www.nrcresearchpress.com by China University of Science and Technology on 09/05/12
For personal use only.

Scheme 1.

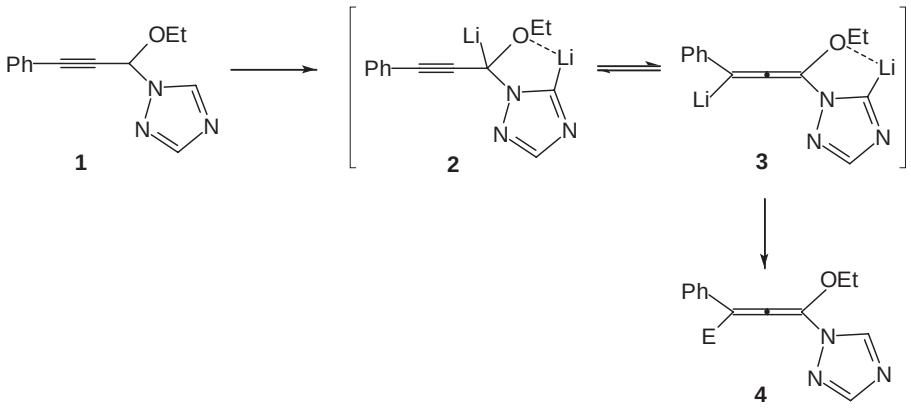

Scheme 2.

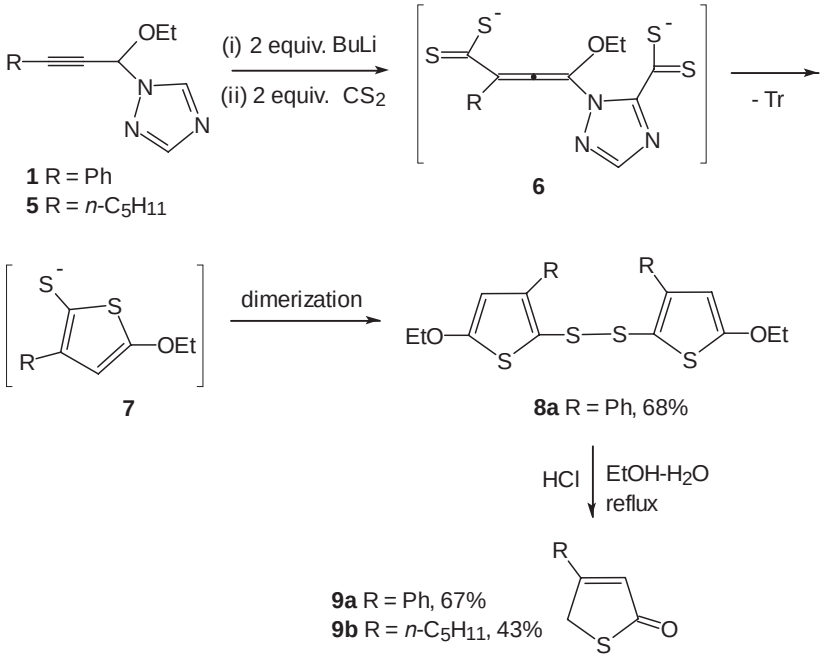

Fig. 1. Perspective view and atom labelling of the X-ray crystal structure of **8a**.

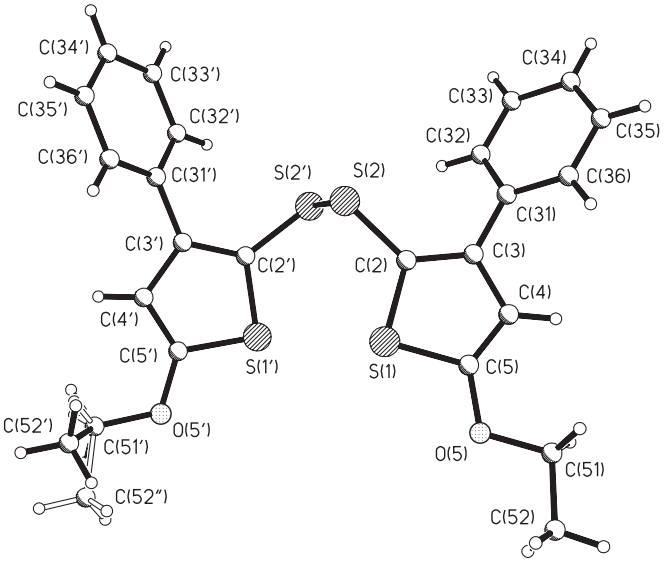

Fig. 2. Perspective view and atom labelling of the X-ray crystal structure of **9a**.

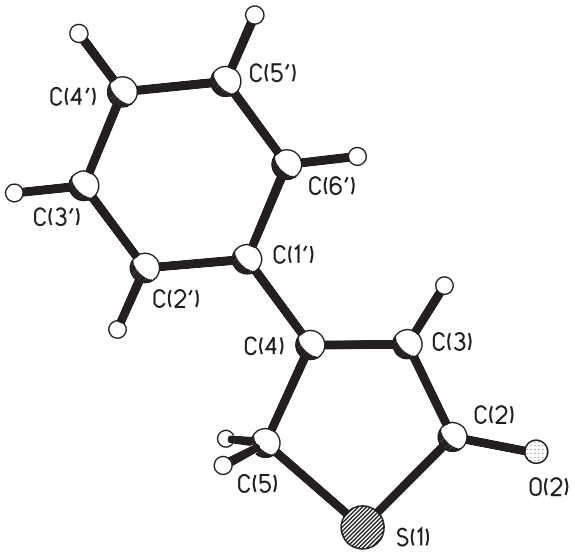

© 1998 NRC Canada

Scheme 3.

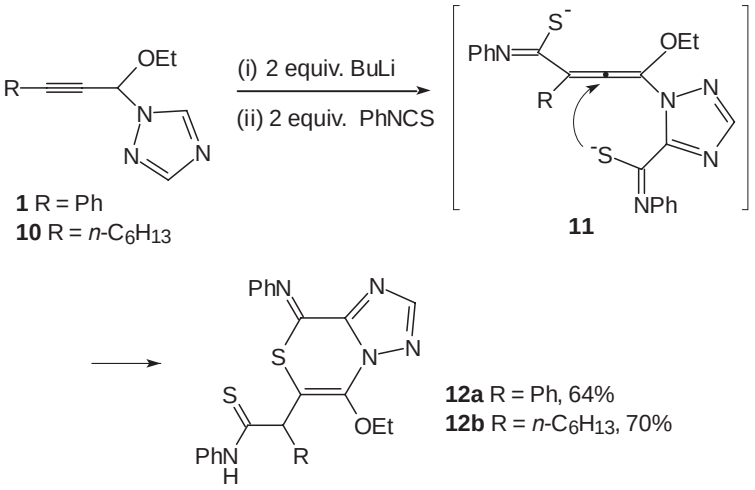

1 R = Ph
10 R = *n*-C_6H_{13}

11

12a R = Ph, 64%
12b R = *n*-C_6H_{13}, 70%

Table 1. Crystal data, data collection, and refinement parameters.

	8	**9a**	**12a**
Formula	$C_{24}H_{22}O_2S_4$	$C_{10}H_8OS$	$C_{28.5}H_{26}N_5O_{1.5}S_2$
M	235.33	176.22	526.66
Crystal system	Monoclinic	Monoclinic	Monoclinic
a, Å	15.722(3)	7.961(1)	17.563(3)
b, Å	10.401(3)	6.408(1)	15.425(3)
c, Å	15.839(4)	16.413(3)	19.902(3)
β,°	116.70(1)	96.61(1)	94.11(1)
V, Å^3	2314(1)	831.7(2)	5378(2)
Space group	$P2_1/n$	$P2_1/n$	$P2_1/c$
Z	4	4	8
F(000)	984	368	2208
D_x, g cm^{-3}	1.351	1.407	1.301
Crystal description	Yellow plate	Brown plate	Yellow block
Dimensions, mm	0.46 × 0.42 × 0.07	0.72 × 0.60 × 0.04	0.83 × 0.37 × 0.17
μ, mm^{-1}	4.29	3.29	2.31
Temperature, K	163	163	163
2θ range,°	4–48	4–52	4–48
Data collected	+*h*, +*k*, ±*l*	+*h*, +*k*, ±*l*	+*h*, +*k*, ±*l*
No. measured	3623	1623	8435
No. with $I > 2\sigma(I)$	1109	1060	4258
a	0	0.0573	0.0356
Parameters	278	109	669
wR (all data)	0.0496	0.1012	0.0903
*R*1 [$I > 2\sigma(I)$]	0.0448	0.0431	0.0451

Several previous methods exist for the synthesis of 4-alkyl-2-thiophenones of type **9**: (*i*) reaction of bismetallated thioacids with α-chloroacetophenone followed by dehydration (4); (*ii*) basic hydrolysis of 2-amino-4-phenyl-3-thenoic esters (5); (*iii*) two-step conversion of 4-(chloromethyl)-4-methyl-azetidin-2-one with sodium hydrosulfide (6). Kagabu and Kaku recently reported a novel route for the synthesis of 4-aryl-2-thiolenones via treatment of 2-substituted 3-ethoxycarbonyl-2-propenylisothiuronium salts with alkali in a two-phase system (7).

Reactions of 1-(1,2,4-triazol-1-yl)propargyl ethyl ethers 1 and 10 with phenyl isothiocyanate

When the allenic dianion **3** was treated with two equivalents of phenyl isothiocyanate, compound **12a** was isolated in 64% yield (Scheme 3). The structure of novel compound **12a** was determined by X-ray crystallography (Fig. 3), and its NMR spectra and microanalysis match this structure.

Crystals of **12a** suitable for X-ray structure determination were obtained only by recrystallization from acetone. At room temperature these underwent spontaneous decomposition, through loss of solvate upon removal from the mother liquor, but were stable at –110°C. This compound crystallizes in the monoclinic space group $P2_1/c$, with two molecules of **12a** and one acetone solvate molecule in the asymmetric unit. The two independent molecules of **12a**, one of which is shown (Fig. 3), have very similar bond lengths and angles (see Experimental) but differ in the relative orientations of the conformationally

© 1998 NRC Canada

Can. J. Chem. Downloaded from www.nrcresearchpress.com by China University of Science and Technology on 09/05/12
For personal use only.

Can. J. Chem. Downloaded from www.nrcresearchpress.com by China University of Science and Technology on 09/05/12
For personal use only.

Table 2. Atomic coordinates and equivalent isotropic displacement parameters (Å^2) for **8**.

Atom	$10^4\,x$	$10^4\,y$	$10^4\,z$	$10^3\,U_{eq}$
S1	8419(2)	562(3)	731(2)	36(1)
S2	6961(2)	2641(3)	208(2)	41(1)
C2	8102(6)	2186(9)	433(5)	28(3)
C3	8883(6)	2918(9)	567(6)	27(3)
C4	9735(6)	2168(9)	918(6)	30(3)
C5	9593(7)	918(10)	1020(6)	36(3)
C31	8877(7)	4305(10)	444(7)	32(3)
C32	8149(6)	4948(10)	–323(6)	40(3)
C33	8156(7)	6262(11)	–418(7)	46(3)
C34	8893(8)	6992(10)	248(7)	50(3)
C35	9628(8)	6400(10)	987(7)	50(3)
C36	9613(7)	5063(10)	1076(7)	40(3)
O5	10187(4)	–130(6)	1285(4)	40(2)
C51	11184(6)	157(9)	1600(6)	45(3)
C52	11709(5)	–1101(9)	1883(6)	54(3)
S1’	6331(2)	–399(3)	–1418(2)	48(1)
S2’	6158(2)	2468(3)	–1256(2)	51(1)
C2’	5660(6)	944(10)	–1420(6)	40(3)
C3’	4790(6)	569(12)	–1497(6)	42(3)
C4’	4664(7)	–793(11)	–1560(6)	39(3)
C5’	5430(7)	–1425(12)	–1542(7)	46(3)
C31’	4041(6)	1482(11)	–1533(6)	35(3)
C32’	3784(6)	2572(12)	–2105(6)	50(3)
C33’	3093(6)	3413(11)	–2117(6)	52(4)
C34’	2681(6)	3189(10)	–1519(6)	44(3)
C35’	2936(6)	2110(11)	–949(7)	47(3)
C36’	3613(6)	1260(10)	–957(6)	39(3)
O5’	5593(5)	–2690(8)	–1601(5)	57(2)
C51’	4898(6)	–3566(9)	–1618(8)	87(5)
C52’ [a]	5010(6)	–4025(9)	–727(8)	72(7)
C52" [b]	5339(16)	–4884(12)	–1350(16)	48(11)

[a] Disordered; occupancy 63%.
[b] Disordered; occupancy 37%.

Fig. 3. Perspective view and atom labelling of one of the two independent molecules of **12a**.

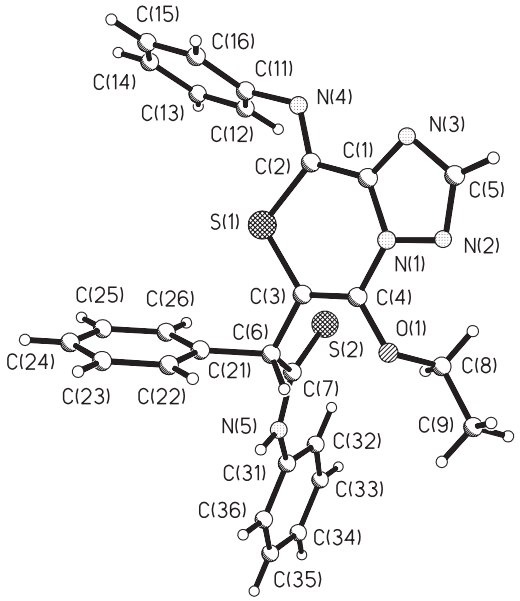

free phenyl and ethoxy substituents. The molecular packing is controlled by intermolecular hydrogen bonds between the thioamide NH and a nitrogen (N3 or N4) of an adjacent symmetry-related molecule. This represents the first X-ray structure of this heterocyclic ring system.

As indicated in Scheme 3, we believe that the thioamide anion at the 5-position of the triazole ring in **11** cyclizes to form the second ring. After hydrolysis, intermediate **11** is converted into 8-phenylimino-1,2,4-triazolo[5,1-*c*]-1,4-thiazine **12a**. This is different from the reaction between **3** and carbon disulfide, in which the triazole group was displaced by the dithiocarboxylate anion attached to the side chain (Scheme 2). Alkyl-substituted heterocycle **12b** was prepared in 70% yield in a manner similar to that for **12a**.

Table 3. Atomic coordinates and equivalent isotropic displacement parameters (Å^2) for **9a**.

Atom	10^4x	10^4y	10^4z	10^3U_{eq}
S1	6438(1)	2090(1)	3006(1)	36(1)
O2	5188(3)	5461(3)	3654(1)	42(1)
C2	5846(3)	3750(4)	3792(2)	32(1)
C3	6296(3)	2781(4)	4583(1)	31(1)
C4	7056(3)	923(4)	4574(1)	26(1)
C5	7266(3)	125(4)	3733(1)	33(1)
C1’	7686(3)	–324(4)	5298(1)	27(1)
C2’	8342(3)	–2321(4)	5210(2)	36(1)
C3’	8946(3)	–3473(4)	5895(2)	43(1)
C4’	8902(3)	–2691(5)	6672(2)	42(1)
C5’	8234(3)	–723(4)	6767(2)	39(1)
C6’	7638(3)	442(4)	6094(2)	34(1)

Only a few examples of 8*H*-1,2,4-triazolo[5,1-*c*]-1,4-thiazines have previously been recorded in the literature (8–11). They were prepared by the formation of the thiazine ring (8, 9) or the triazole ring (10, 11). No 8-phenylimino-1,2,4-triazolo[5,1-*c*]-1,4-thiazines have previously been known.

In conclusion, we have demonstrated that 1,2,4-triazole stabilized allenic anions, which can be easily prepared from available starting materials, have significant synthetic utility for the synthesis of a variety of polyfunctionalized heterocycles, as shown in the previous (1) and present papers. Many of these syntheses show advantages over previous literature methods.

Experimental

Melting points were measured on a hot-stage microscope and are uncorrected. ^{1}H and ^{13}C NMR data were collected on a 300 NMR spectrometer (300 MHz and 75 MHz, respectively) in $CDCl_3$, except where stated, with TMS or $CDCl_3$, respectively, as internal reference. Column chromatography was carried out using 230-400 mesh silica.

© 1998 NRC Canada

Table 4. Atomic coordinates and equivalent isotropic displacement parameters (Å^2) for **12a**.

Atom	10^4x	10^4y	10^4z	10^3U_{eq}	Atom	10^4x	10^4y	10^4z	10^3U_{eq}
S1	4581(1)	4080(1)	2024(1)	30(1)	O1'	9208(1)	5498(1)	3001(1)	31(1)
S2	6635(1)	3985(1)	2063(1)	42(1)	N1'	10007(2)	4293(2)	3105(1)	28(1)
O1	5593(1)	3174(1)	3750(1)	27(1)	N2'	9798(2)	4131(2)	3742(2)	37(1)
N1	4755(1)	4334(2)	3548(1)	22(1)	N3'	10635(2)	3108(2)	3420(2)	36(1)
N2	4733(2)	4469(2)	4225(1)	31(1)	N4'	11309(2)	3043(2)	2172(2)	37(1)
N3	3955(1)	5421(2)	3631(1)	27(1)	N5'	8422(1)	6502(2)	1530(1)	28(1)
N4	3780(1)	5545(2)	2191(1)	24(1)	C1'	10506(2)	3672(2)	2925(2)	28(1)
N5	6821(1)	2256(2)	2127(1)	28(1)	C2'	10862(2)	3666(2)	2290(2)	29(1)
C1	4290(2)	4910(2)	3207(2)	23(1)	C3'	9993(2)	5179(2)	2124(2)	25(1)
C2	4181(2)	4929(2)	2473(2)	23(1)	C4'	9730(2)	4993(2)	2718(2)	27(1)
C3	5139(2)	3485(2)	2629(2)	20(1)	C5'	10185(2)	3414(2)	3892(2)	38(1)
C4	5184(2)	3654(2)	3283(2)	21(1)	C6'	9687(2)	5969(2)	1734(2)	26(1)
C5	4247(2)	5130(2)	4237(2)	32(1)	C7'	8855(2)	5799(2)	1455(2)	26(1)
C6	5574(2)	2725(2)	2358(2)	23(1)	C8'	8446(2)	5096(2)	3019(2)	39(1)
C7	6388(2)	2971(2)	2177(2)	24(1)	C9'	7898(2)	5788(3)	3186(2)	62(1)
C8	6315(2)	3566(2)	4004(2)	36(1)	C11'	11690(2)	3032(2)	1560(2)	39(1)
C9	6670(2)	2987(3)	4534(2)	56(1)	C12'	11304(2)	2867(3)	942(2)	66(1)
C11	3669(2)	5555(2)	1474(2)	26(1)	C13'	11704(3)	2809(3)	375(2)	79(2)
C12	4273(2)	5743(2)	1086(2)	36(1)	C14'	12477(3)	2907(3)	410(2)	60(1)
C13	4153(2)	5780(2)	396(2)	46(1)	C15'	12857(2)	3070(3)	1019(2)	50(1)
C14	3440(3)	5656(2)	85(2)	49(1)	C16'	12474(2)	3132(2)	1595(2)	42(1)
C15	2836(2)	5480(2)	469(2)	50(1)	C21'	10216(2)	6286(2)	1206(2)	28(1)
C16	2950(2)	5443(2)	1165(2)	38(1)	C22'	10877(2)	6717(2)	1418(2)	37(1)
C21	5119(2)	2278(2)	1779(2)	24(1)	C23'	11364(2)	7038(3)	966(2)	51(1)
C22	4579(2)	1660(2)	1929(2)	41(1)	C24'	11197(2)	6935(3)	286(2)	50(1)
C23	4152(2)	1251(3)	1410(3)	60(1)	C25'	10543(2)	6496(3)	61(2)	46(1)
C24	4252(2)	1443(3)	748(3)	67(2)	C26'	10047(2)	6165(2)	516(2)	36(1)
C25	4786(2)	2051(3)	596(2)	52(1)	C31'	7626(2)	6638(2)	1388(2)	26(1)
C26	5218(2)	2471(2)	1111(2)	37(1)	C32'	7110(2)	6027(3)	1167(2)	61(1)
C31	7586(2)	2138(2)	1962(2)	26(1)	C33'	6350(2)	6244(3)	1047(2)	63(1)
C32	8100(2)	2799(2)	1854(2)	38(1)	C34'	6094(2)	7052(3)	1165(2)	39(1)
C33	8835(2)	2597(3)	1701(2)	42(1)	C35'	6609(2)	7657(3)	1394(2)	59(1)
C34	9074(2)	1754(3)	1657(2)	41(1)	C36'	7372(2)	7459(2)	1515(2)	47(1)
C35	8562(2)	1098(2)	1768(2)	40(1)	O41	7380(2)	4937(3)	4640(2)	114(1)
C36	7823(2)	1284(2)	1921(2)	33(1)	C41	7781(3)	5711(3)	5602(3)	103(2)
S1'	10683(1)	4561(1)	1740(1)	35(1)	C42	7895(3)	5115(4)	5046(3)	77(2)
S2'	8607(1)	4859(1)	1121(1)	40(1)	C43	8680(3)	4740(5)	5007(3)	150(3)

Can. J. Chem. Downloaded from www.nrcresearchpress.com by China University of Science and Technology on 09/05/12
For personal use only.

Crystallographic analyses

The crystal data, data collection, and refinement parameters for the three structures are listed in Table 1. All measurements were made with a Nicolet P4s diffractometer using graphite monochromatized Mo Kα (λ = 0.710 73 Å) radiation. Cell parameters were determined by least-squares refinement on diffractometer angles for at least 25 accurately centered reflections with 2 θ > 20°. Throughout data collection (ω scan mode) the intensities of three standard reflections were monitored at regular intervals and in no case showed variations of >5%. Intensities were corrected for Lorentz and polarization effects and for absorption using a technique based on azimuthal ψ scans.

The structures were solved by direct methods using SHELXS (12), and refined on F^2, using all data, by full-matrix least-squares procedures with SHELXL-96 (13). All non-hydrogen atoms were refined with anisotropic displacement parameters. Hydrogen atoms were included in calculated positions with isotropic displacement parameters 1.3 times the isotropic equivalent of their carrier atoms. The functions minimized were $w(F_o^2 - F_c^2)$, with $w = [\sigma^2(F_o^2) + aP^2]^{-1}$, where $P = [\max(F_o)^2 + 2F_c^2]/3$. Final non-hydrogen atom coordinates are listed in Tables 2–4. Tables 5–7 list bond lengths and angles for **8**, **9a**, and **12a**, respectively. Tables of hydrogen atom coordinates and anisotropic displacement parameters are available as supplementary data.[2]

1-(1,2,4-Triazol-1-yl)-3-phenylpropargyl ethyl ether (**1**)

[2] Copies of the supplementary data (Tables S1–S6) can be purchased from: The Depository of Unpublished Data, Document Delivery, CISTI, National Research Council Canada, Ottawa, Canada K1A 0S2. The tables of hydrogen atom coordinates have also been deposited with the Cambridge Crystallographic Data Centre, and can be obtained on request from The Director, Cambridge Crystallographic Data Centre, University Chemical Laboratory, 12 Union Road, Cambridge, CB2 1EZ, U.K.

© 1998 NRC Canada

Can. J. Chem. Downloaded from www.nrcresearchpress.com by China University of Science and Technology on 09/05/12
For personal use only.

Table 5. Bond lengths (Å) and bond angles (°) for **8**.

S1—C5	1.731(9)	S1—C2	1.765(9)	S2—C2	1.731(8)
S2—S2'	2.090(3)	C2—C3	1.377(10)	C3—C4	1.430(11)
C3—C31	1.455(12)	C4—C5	1.342(12)	C5—O5	1.372(10)
C31—C36	1.386(12)	C31—C32	1.409(11)	C32—C33	1.375(12)
C33—C34	1.390(12)	C34—C35	1.367(12)	C35—C36	1.399(12)
O5—C51	1.446(8)	C51—C52	1.504(11)	S1'—C5'	1.714(10)
S1'—C2'	1.750(10)	S2'—C2'	1.735(10)	C2'—C3'	1.374(11)
C3'—C4'	1.428(13)	C3'—C31'	1.494(13)	C4'—C5'	1.361(13)
C5'—O5'	1.352(13)	C31'—C36'	1.374(11)	C31'—C32'	1.393(13)
C32'—C33'	1.388(13)	C33'—C34'	1.386(10)	C34'—C35'	1.382(12)
C35'—C36'	1.389(12)	O5'—C51'	1.413(10)	C51'—C52'	1.425(20)
C51'—C52"	1.509(29)				
C5-S1-C2	90.3(5)	C2-S2-S2'	105.0(3)		
C3-C2-S2	130.5(7)	C3-C2-S1	111.3(6)		
S2-C2-S1	117.3(5)	C2-C3-C4	111.9(8)		
C2-C3-C31	125.2(9)	C4-C3-C31	122.7(9)		
C5-C4-C3	113.5(9)	C4-C5-O5	132.8(9)		
C4-C5-S1	113.0(8)	O5-C5-S1	114.2(7)		
C36-C31-C32	116.4(10)	C36-C31-C3	120.9(10)		
C32-C31-C3	122.7(10)	C33-C32-C31	121.5(10)		
C32-C33-C34	120.3(10)	C35-C34-C33	119.9(11)		
C34-C35-C36	119.3(11)	C31-C36-C35	122.6(11)		
C5-O5-C51	115.1(7)	O5-C51-C52	106.7(8)		
C5'-S1'-C2'	91.7(5)	C2'-S2'-S2	104.6(3)		
C3'-C2'-S2'	129.6(9)	C3'-C2'-S1'	110.5(9)		
S2'-C2'-S1'	119.8(5)	C2'-C3'-C4'	112.9(10)		
C2'-C3'-C31'	124.0(11)	C4'-C3'-C31'	123.1(9)		
C5'-C4'-C3'	112.6(10)	O5'-C5'-C4'	131.5(11)		
O5'-C5'-S1'	116.1(9)	C4'-C5'-S1'	112.4(9)		
C36'-C31'-C32'	118.8(10)	C36'-C31'-C3'	118.7(10)		
C32'-C31'-C3'	122.4(10)	C33'-C32'-C31'	121.2(9)		
C34'-C33'-C32'	119.2(10)	C35'-C34'-C33'	119.7(10)		
C34'-C35'-C36'	120.6(10)	C31'-C36'-C35'	120.4(11)		
C5'-O5'-C51'	117.3(9)	O5'-C51'-C52'	116.6(16)		
O5'-C51'-C52"	109.1(21)				

Table 6. Bond lengths (Å) and bond angles (°) for **9a**.

S1—C2	1.776(3)	S1—C5	1.806(3)	O2—C2	1.225(3)
C2—C3	1.447(3)	C3—C4	1.336(3)	C4—C1'	1.472(3)
C4—C5	1.499(3)	C1'—C2'	1.396(3)	C1'—C6'	1.399(3)
C2'—C3'	1.384(4)	C3'—C4'	1.375(4)	C4'—C5'	1.385(4)
C5'—C6'	1.372(3)				
C2-S1-C5	92.63(12)	O2-C2-C3	127.4(2)		
O2-C2-S1	123.1(2)	C3-C2-S1	109.6(2)		
C4-C3-C2	116.0(2)	C3-C4-C1'	126.0(2)		
C3-C4-C5	114.4(2)	C1'-C4-C5	119.7(2)		
C4-C5-S1	107.4(2)	C2'-C1'-C6'	117.9(2)		
C2'-C1'-C4	120.7(2)	C6'-C1'-C4	121.3(2)		
C3'-C2'-C1'	120.3(3)	C4'-C3'-C2'	121.0(3)		
C3'-C4'-C5'	119.2(3)	C6'-C5'-C4'	120.4(3)		
C5'-C6'-C1'	121.1(2)				

and 1-(1,2,4-triazol-1-yl)-2-nonynyl ethyl ether (**10**) were prepared by literature methods (1).

1-(1,2,4-Triazol-1-yl)-2-octynyl ethyl ether (5)

This compound was prepared in 97% yield using a previously reported method (1) and was purified by column chromatography on silica gel (eluent: hexane–EtOAc (5:1)); a colorless oil; ^{1}H NMR: 0.91 (3H, t, J = 7.1 Hz), 1.20 (3H, t, J = 7.1 Hz), 1.27–1.47 (4H, m), 1.52–1.67 (2H, m), 2.33 (2H, t, J = 7.1 Hz), 3.50–3.76 (2H, m), 6.27 (1H, s), 7.98 (1H, s), 8.53 (1H, s); ^{13}C

© 1998 NRC Canada

Can. J. Chem. Downloaded from www.nrcresearchpress.com by China University of Science and Technology on 09/05/12
For personal use only.

Table 7. Bond lengths (Å) and bond angles (°) for **12a**.

	Molecule 1	Molecule 2		Molecule 1	Molecule 2
S1—C3	1.755(3)	1.759(3)	S1—C2	1.760(3)	1.775(4)
S2—C7	1.644(3)	1.642(3)	O1—C4	1.354(3)	1.356(4)
O1—C8	1.463(4)	1.477(4)	N1—1	1.356(4)	1.364(4)
N1—N2	1.366(3)	1.366(4)	N1—C4	1.415(4)	1.394(4)
N2—C5	1.332(4)	1.322(4)	N3—C1	1.322(4)	1.322(4)
N3—C5	1.353(4)	1.354(4)	N4—C2	1.288(4)	1.273(4)
N4—C11	1.426(4)	1.430(4)	N5—C7	1.346(4)	1.339(4)
N5—C31	1.418(4)	1.422(4)	C1—C2	1.459(4)	1.450(4)
C3—C4	1.324(4)	1.331(4)	C3—C6	1.520(4)	1.523(4)
C6—C21	1.519(4)	1.532(4)	C6—C7	1.547(4)	1.547(4)
C8—C9	1.486(4)	1.491(4)	C11—C16	1.376(4)	1.382(5)
C11—C12	1.388(4)	1.386(5)	C12—C13	1.374(5)	1.375(5)
C13—C14	1.369(5)	1.362(5)	C14—C15	1.378(5)	1.365(5)
C15—C16	1.386(5)	1.373(5)	C21—C26	1.386(4)	1.396(4)
C21—C22	1.392(4)	1.378(4)	C22—C23	1.385(5)	1.377(4)
C23—C24	1.373(6)	1.372(5)	C24—C25	1.376(6)	1.381(5)
C25—C26	1.391(5)	1.397(5)	C31—C36	1.385(4)	1.371(5)
C31—C32	1.389(4)	1.359(4)	C32—C33	1.383(4)	1.379(5)
C33—C34	1.372(5)	1.351(5)	C34—C35	1.382(5)	1.356(5)
C35—C36	1.384(4)	1.379(5)			
O41—C42	1.201(5)		C41—C42	1.463(6)	
C42—C43	1.502(7)				
C3-S1-C2	105.3(2)	104.5(2)	C4-O1-C8	114.5(2)	114.1(2)
C1-N1-N2	109.6(3)	109.6(3)	C1-N1-C4	128.0(3)	127.2(3)
N2-N1-C4	122.3(3)	123.2(3)	C5-N2-N1	101.4(3)	101.2(3)
C1-N3-C5	102.3(3)	102.1(3)	C2-N4-C11	118.4(3)	119.9(3)
C7-N5-C31	132.1(3)	131.0(3)	N3-C1-N1	110.5(3)	110.2(3)
N3-C1-C2	126.4(3)	125.7(3)	N1-C1-C2	123.1(3)	124.0(3)
N4-C2-C1	118.7(3)	118.4(3)	N4-C2-S1	123.6(2)	123.9(3)
C1-C2-S1	117.7(2)	117.6(3)	C4-C3-C6	120.3(3)	119.5(3)
C4-C3-S1	124.2(3)	124.3(3)	C6-C3-S1	115.5(2)	116.2(2)
C3-C4-O1	124.0(3)	122.2(3)	C3-C4-N1	121.1(3)	121.9(3)
O1-C4-N1	114.8(3)	115.8(3)	N2-C5-N3	116.1(3)	116.8(3)
C21-C6-C3	111.7(3)	113.3(3)	C21-C6-C7	112.3(3)	114.3(3)
C3-C6-C7	113.0(3)	109.7(3)	N5-C7-C6	110.6(3)	110.6(3)
N5-C7-S2	127.9(2)	128.6(3)	C6-C7-S2	121.5(2)	120.7(2)
O1-C8-C9	107.8(3)	107.8(3)	C16-C11-C12	119.4(3)	119.1(4)
C16-C11-N4	120.1(3)	118.7(4)	C12-C11-N4	120.3(3)	122.0(4)
C13-C12-C11	119.7(3)	119.7(4)	C14-C13-C12	121.0(4)	121.1(4)
C13-C14-C15	119.6(4)	119.3(4)	C14-C15-C16	119.9(4)	121.1(4)
C11-C16-C15	120.3(4)	119.8(4)	C26-C21-C22	119.1(3)	118.7(3)
C26-C21-C6	122.3(3)	122.4(3)	C22-C21-C6	118.6(3)	118.9(3)
C23-C22-C21	119.5(4)	121.5(4)	C24-C23-C22	121.1(4)	120.2(4)
C23-C24-C25	119.7(4)	119.4(4)	C24-C25-C26	119.9(4)	120.8(4)
C21-C26-C25	120.5(4)	119.3(3)	C36-C31-C32	119.1(3)	118.8(3)
C36-C31-N5	115.4(3)	115.4(3)	C32-C31-N5	125.4(3)	125.8(3)
C33-C32-C31	119.8(3)	120.1(4)	C34-C33-C32	121.4(4)	121.6(4)
C33-C34-C35	118.6(3)	118.0(3)	C34-C35-C36	121.0(3)	121.5(4)
C35-C36-C31	120.1(3)	119.9(4)			
O41-C42-C41	121.1(6)		O41-C42-C43	121.8(6)	
C41-C42-C43	117.1(5)				

NMR: 13.4, 14.3, 18.1, 21.6, 27.3, 30.6, 63.0, 72.5, 77.8, 89.7, 142.2, 151.5. Anal. calcd. for $C_{12}H_{19}N_3O$: C 65.13, H 8.65, N 18.99; found: C 64.89, H 8.89, N 18.76.

General procedure for the preparation of disulfide 8 and 8-phenylimino-1,2,4-triazolo[5,1-*c*]-1,4-thiazines 12

To a solution of 1-(1,2,4-triazol-1-yl)propargyl ethyl ether **1**,

© 1998 NRC Canada

Can. J. Chem. Downloaded from www.nrcresearchpress.com by China University of Science and Technology on 09/05/12
For personal use only.

5, or **10** (5 mmol) in THF (70 mL) at –90°C was added *n*-butyllithium (2.5 M in cyclohexane, 4 mL, 10 mmol). The solution was stirred at this temperature for 5 min and the appropriate electrophile (carbon disulfide or phenyl isocyanate, 10 mmol) was then added. After the reaction mixture was stirred for an additional 10 min, it was quenched at this temperature with water (50 mL). HCl (5 N, 5 mL) was added to the above solution, which was then stirred at room temperature for 2 h. The resulting solution was extracted with ether (3 × 100 mL), and the organic extractant was dried over anhydrous $MgSO_4$. Evaporation of the solvent gave a residue that was purified by column chromatography on silica gel (eluent: hexane–EtOAc).

*Bis(5-ethoxy-3-phenyl-2-thienyl) disulfide (***8a***)*: yellow microcrystals, mp 93–94°C; ^{1}H NMR: 1.45 (6H, t, J = 7.1 Hz), 4.08 (4H, q, J = 7.1 Hz), 6.20 (2H, s), 7.22–7.32 (10H, m); ^{13}C NMR: 14.7, 69.0, 107.9, 127.3, 127.9, 129.1, 135.4, 148.5, 168.5. Anal. calcd. for $C_{24}H_{22}O_2S_4$: C 61.24, H 4.71; found: C 61.46, H 4.61.

*5-Ethoxy-6-[1-phenyl-1-(phenylaminothiocarbamoyl)methyl]-8-phenylimino-1,2,4-triazolo[5,1-c]-1,4-thiazine (***12a***)*: yellow microcrystals, mp 212–214°C; ^{1}H NMR (DMSO-d_6): 1.44 (3H, t, J = 7.1 Hz), 4.22–4.42 (2H, m), 6.03 (1H, s), 6.91 (2H, d, J = 7.7 Hz), 7.15 (1H, t, J = 7.4 Hz), 7.24–7.54 (10H, m), 7.71 (2H, d, J = 7.7 Hz), 8.57 (1H, s), 11.98 (1H, s); ^{13}C NMR (DMSO-d_6): 14.9, 57.2, 70.9, 110.0, 118.9, 123.7, 125.0, 126.5, 127.8, 128.4, 128.6, 128.7, 129.6, 137.2, 138.9, 139.1, 145.3, 146.7, 148.6, 152.8, 199.6. Anal. calcd. for $C_{27}H_{23}N_5OS_2$: C 65.17, H 4.66, N 14.07; found: C 65.57, H 4.78, N 13.92.

*5-Ethoxy-6-[1-(phenylaminothiocarbamoyl)heptanyl]-8-phenylimino-1,2,4-triazolo[5,1-c]-1,4-thiazine (***12b***)*: yellow microcrystals, mp 82–85°C; ^{1}H NMR: 0.86 (3H, t, J = 6.6 Hz), 1.10–1.45 (8H, m), 1.55 (3H, t, J = 7.2 Hz), 1.74–1.94 (1H, m), 2.04–2.23 (1H, m), 4.24–4.38 (2H, m), 4.46–4.59 (1H, m), 7.02 (2H, d, J = 7.2 Hz), 7.09–7.29 (2H, m), 7.30–7.40 (4H, m), 7.60 (2H, d, J = 7.8 Hz), 8.20 (1H, s), 9.40 (1H, s); ^{13}C NMR: 13.9, 15.2, 22.4, 27.3, 28.8, 31.4, 32.7, 54.2, 72.1, 110.2, 119.4, 123.5, 125.5, 126.9, 128.8, 129.5, 138.4, 138.6, 144.1, 147.3, 148.5, 152.5, 200.9. Anal. calcd. for $C_{27}H_{31}N_5OS_2$: C 64.13, H 6.18, N 13.85; found: C 64.09, H 5.82, N 13.58.

General procedure for the preparation of 2-thiophenones 9 by acidic hydrolysis

Disulfide **8** (3 mmol) was hydrolyzed in a mixture of ethanol (25 mL), water (25 mL), and concentrated HCl (2 mL) under reflux for 2 days. After the usual extraction work-up, the crude product was purified by column chromatography on silica gel (eluent: hexane–EtOAc).

*4-Phenyl-2-thiophenone (***9a***)*: yellow solid, mp 133–135°C (lit. (4) mp 134–136°C); ^{1}H NMR: 4.44 (2H, s), 6.69 (1H, t, J = 1.6 Hz), 7.46–7.62 (5H, m); ^{13}C NMR: 37.5, 111.1, 126.3, 126.8, 129.1, 131.1, 133.3, 165.2. Anal. calcd. for $C_{10}H_8OS$: C 68.15,H 4.58; found: C 68.32, H 4.46.

*4-Pentyl-2-thiophenone (***9b***)*: This compound was obtained directly from **5**, without isolation of the intermediate disulfide, as a brown oil; ^{1}H NMR: 0.91 (3H, t, J = 6.6 Hz), 1.25–1.35 (4H, m), 1.61 (2H, t, J = 7.3 Hz), 2.47 (2H, t, J = 7.7 Hz), 3.97 (2H, s), 6.09 (1H, s); ^{13}C NMR: 13.8, 22.2, 27.5, 31.2, 33.1, 39.7, 116.2, 128.1, 172.2; HRMS (EI) calcd. for $C_9H_{14}OS$: 170.0765; found: 170.0782.

References

1. A.R. Katritzky, D. Feng, and H. Lang. J. Org. Chem. **62**, 715 (1997).
2. J. Elguero, C. Marzin, A.R. Katritzky, and P. Linda. *In* Adv. Heterocycl. Chem., Suppl. 1. *Edited by* A.R. Katritzky and A.J. Boulton. Academic Press, New York. 1976. p. 229.
3. K.S. McCully and G.B. Carpenter. Acta Crystallogr. Sect. C: Cryst. Struct. Commun. **C43**, 2345 (1987).
4. A.M. Sarpeshkar, G.J. Gossick, and J. Wemple. Tetrahedron Lett. 703 (1979).
5. W. Offermann, K. Eger, and H.J. Roth. Arch. Pharm. (Weinheim), **314**, 168 (1981).
6. K. Clauss. Tetrahedron Lett. 1271 (1974).
7. S. Kagabu and I. Kaku. Biosci. Biotech. Biochem. **57**, 1899 (1993).
8. R.B. Mitra, Z. Muljiani, and S.R. Deshpande. Heterocycles, **27**, 2297 (1988).
9. R. Heckendorn. Helv. Chim. Acta, **70**, 2118 (1987).
10. G. Grandolini, C. Rossi, M.C. Tiralti, G. Orzalesi, and M. De Regis. Farmaco, Ed. Sci. **40**, 221 (1985); Chem. Abstr. **103**, 215244p (1985).
11. L. Bruche, L. Garanti, and G. Zecchi. Gazz. Chim. Ital. **111**, 337 (1981); Chem. Abstr. **96**, 52251j (1982).
12. G.M. Sheldrick. Acta Crystallogr. Sect. A: Found. Crystallogr. **A46**, 467 (1990).
13. G.M. Sheldrick. SHELXL-96. University of Göttingen, Göttingen, Germany. 1996.

© 1998 NRC Canada

On the relationship between the rate constants for racemization and isotopic exchange

John M.W. Scott and Danny Summers

Abstract: The relationship between the rate constants that describe the halide ion catalysis of the racemization (k_r) of optically alkyl halides and the related isotopic halide exchange reaction (k_e) is shown to be valid in two distinct cases. The first is when the racemization and exchange mechanisms follow the classical and conventional S_N2 path characterized by a symmetrical trigonal (sp^2) transition state. The second envisages the trigonal species characteristic of the S_N2 reaction as an intermediate instead of a transition state. The latter mechanism is also shown to be characterized by the relationship $k_r = 2k_e$, and hence this diagnostic test is seen to be a necessary but not a sufficient condition for invoking the S_N2 mechanism.

Key words: racemization, isotopic exchange, kinetics, bimolecular substitution, inversion.

Résumé : On montre que la relation entre les constantes de vitesse, qui décrit la racémisation (k_r) des halogénures d'alkyle optiquement actifs catalysée par un ion halogénure et la réaction apparentée d'échange isotopique d'halogénure (k_e), est valide dans deux cas distincts. Le premier cas est celui où la racémisation et le mécanisme d'échange suivent le chemin classique et conventionnel d'une réaction S_N2 caractérisée par un état de transition trigonal (sp^2). Le second cas met en jeu une espèce trigonale caractéristique d'une réaction S_N2 comme intermédiaire plutôt que comme état de transition. On montre également que le mécanisme, dans le deuxième cas, est caractérisé par la relation $k_r = 2k_e$, et par conséquent ce test caractéristique semble être une condition nécessaire mais pas suffisante pour invoquer le mécanisme S_N2.

Mots clés : racémisation, échange isotopique, cinétique, substitution bimoléculaire, inversion.

[Traduit par la rédaction]

Introduction

The racemizations of optically active alkyl halides catalysed by halide ions

$$[1] \qquad (\pm)\mathrm{RX} + \mathrm{X} \underset{k_\alpha}{\overset{k_\alpha}{\leftrightarrows}} (\mp)\mathrm{RX} + \mathrm{X}$$

and the related isotopic exchange reactions summarized

$$[2] \qquad \mathrm{RX} + \mathrm{X}^* \underset{k_\gamma}{\overset{k_\alpha}{\leftrightarrows}} \mathrm{RX}^* + \mathrm{X}$$

form an important part of the substance and theory of nucleophilic displacement reactions (1, 2). Some specific examples generally described by eqs. [1] and [2] are the following:
(*a*) RX = 2-octyl iodide with X = iodide ion (NaI in acetone);
(*b*) RX = 1-phenylethyl bromide with X = bromide ion (LiBr in acetone);
(*c*) RX = 1-bromopropionic acid with X = bromide ion (LiBr in acetone).

The kinetics of the process represented by eq. [1] are described by a pseudo-first-order rate constant k_α, which is related to a second-order rate constant k_1 and the concentration of the halide ion:

$$[3] \qquad k_\alpha = k_1[\mathrm{X}]$$

Similar rate constants k_β and k_γ, related respectively to the concentration of the alkyl halide and the halide ion, characterize the exchange process:

$$[4] \qquad k_\beta = k_1[\mathrm{RX}]$$

$$[5] \qquad k_\gamma = k_1[\mathrm{X}]$$

The rates of the processes described by eqs. [1] and [2] differ because the same potential energy surface is being probed in two distinct ways. The assumption that the two kinetic processes are underpinned by a single potential energy surface is limited only by departures from the Born–Oppenheimer Principle (BOP). For heavy atoms such as bromine and iodine, departures from the BOP are negligible.

Clearly, both the racemization and exchange processes for a given substrate at a fixed temperature relate to a common second-order rate constant k_1, which becomes a component of the pseudo-first-order rate constants k_α, k_β, and k_γ when the kinetics of any given experimental system are treated formally. Thus, eqs. [3], [4], and [5] merely emphasize the second-order character of the basic processes without, for instance, determining the condition of the ionic substances dissolved in acetone. The calculation of the true second-order rate constants

Received February 26, 1997.[1]

This paper is dedicated to Professor Erwin Buncel in recognition of his contributions to Canadian chemistry.

J.M.W. Scott.[2] 34 Poplar Ave., St. John's, NF A1B 1C8, Canada. Fax (Chem. Dept.): (709) 737-3702; (Math. Dept.): (709) 737-3010. E-mail: jmscott@morgan.ucs.mun.ca

D. Summers. Department of Mathematics and Statistics, Memorial University of Newfoundland, St. John's, NF A1C 5S7, Canada. E-mail: dsummers@math.mun.ca

[1] Revision received September 18, 1997.
[2] Author to whom correspondence may be addressed.

© 1998 NRC Canada

Table 1. Synthetic data related to eq. [23D].

[RX]	[X]	[X*]	k_1	k_2	k(calc.)	Ratio[a]
0.1000	0.1000	1.000^{-4}	1.00^{-4}	10.00	5.000^{-5}	2.00
0.1000	0.1000	1.000^{-4}	1.26^{-4}	10.00	6.295^{-5}	2.00
0.1000	0.1000	1.000^{-4}	1.58^{-4}	10.00	7.924^{-5}	2.00
0.1000	0.1000	1.000^{-4}	2.00^{-4}	10.00	9.976^{-5}	2.00
0.1000	0.1000	1.000^{-4}	3.16^{-4}	10.00	1.581^{-4}	2.00
0.1000	0.1000	1.000^{-4}	3.98^{-4}	10.00	1.991^{-4}	2.00
0.1000	0.1000	1.000^{-4}	5.01^{-4}	10.00	2.506^{-4}	2.00
0.1000	0.1000	1.000^{-4}	6.31^{-4}	10.00	3.155^{-4}	2.00
0.1000	0.1000	1.000^{-4}	1.00^{-3}	10.00	5.000^{-4}	2.00
0.1000	0.1000	1.000^{-4}	1.26^{-3}	10.00	6.295^{-4}	2.00
0.1000	0.1000	1.000^{-4}	1.58^{-3}	10.00	7.924^{-4}	2.00
0.1000	0.1000	1.000^{-4}	2.00^{-3}	10.00	9.976^{-4}	2.00
0.1000	0.1000	1.000^{-4}	3.16^{-3}	10.00	1.581^{-4}	2.00
0.1000	0.1000	1.000^{-4}	3.98^{-3}	10.00	1.991^{-4}	2.00
0.1000	0.1000	1.000^{-4}	5.01^{-3}	10.00	2.506^{-4}	2.00
0.1000	0.1000	1.000^{-4}	6.31^{-3}	10.00	3.155^{-4}	2.00
0.1000	0.1000	1.000^{-4}	1.00^{-2}	10.00	5.000^{-3}	2.00
0.1000	0.1000	1.000^{-4}	1.26^{-2}	10.00	6.295^{-3}	2.00
0.1000	0.1000	1.000^{-4}	1.58^{-2}	10.00	7.924^{-3}	2.00
0.1000	0.1000	1.000^{-4}	2.00^{-2}	10.00	9.976^{-3}	2.00
0.1000	0.1000	1.000^{-4}	3.16^{-2}	10.00	1.581^{-2}	2.00
0.1000	0.1000	1.000^{-4}	3.98^{-2}	10.00	1.991^{-2}	2.00
0.1000	0.1000	1.000^{-4}	5.01^{-2}	10.00	2.506^{-2}	2.00
0.1000	0.1000	1.000^{-4}	6.31^{-2}	10.00	3.155^{-2}	2.00
0.1000	0.1000	1.000^{-4}	1.00^{-1}	10.00	5.000^{-2}	2.00

[a] k_1C/k(calc.)

Table 2. Synthetic data related to eq. [23D].

[RX]	[X]	[X*]	k_1	k_2	k(calc.)	Ratio[a]
0.1000	0.1000	1.000^{-4}	1.00^{-4}	1.000^{-3}	5.000^{-5}	2.00
0.1000	0.1000	1.000^{-4}	1.00^{-4}	1.585^{-3}	5.000^{-5}	2.00
0.1000	0.1000	1.000^{-4}	1.00^{-4}	3.981^{-3}	5.000^{-5}	2.00
0.1000	0.1000	1.000^{-4}	1.00^{-4}	6.310^{-3}	5.000^{-5}	2.00
0.1000	0.1000	1.000^{-4}	1.00^{-4}	1.259^{-2}	5.000^{-5}	2.00
0.1000	0.1000	1.000^{-4}	1.00^{-4}	3.162^{-2}	5.000^{-5}	2.00
0.1000	0.1000	1.000^{-4}	1.00^{-4}	6.310^{-2}	5.000^{-5}	2.00
0.1000	0.1000	1.000^{-4}	1.00^{-4}	1.000^{-1}	5.000^{-5}	2.00
0.1000	0.1000	1.000^{-4}	1.00^{-4}	2.512^{-1}	5.000^{-5}	2.00
0.1000	0.1000	1.000^{-4}	1.00^{-4}	5.012^{-1}	5.000^{-5}	2.00
0.1000	0.1000	1.000^{-4}	1.00^{-4}	1.000	5.000^{-5}	2.00
0.1000	0.1000	1.000^{-4}	1.00^{-4}	1.585	5.000^{-5}	2.00
0.1000	0.1000	1.000^{-4}	1.00^{-4}	3.162	5.000^{-5}	2.00
0.1000	0.1000	1.000^{-4}	1.00^{-4}	7.943	5.000^{-5}	2.00
0.1000	0.1000	1.000^{-4}	1.00^{-4}	1.259^{+1}	5.000^{-5}	2.00
0.1000	0.1000	1.000^{-4}	1.00^{-4}	3.162^{+1}	5.000^{-5}	2.00
0.1000	0.1000	1.000^{-4}	1.00^{-4}	6.310^{+1}	5.000^{-5}	2.00
0.1000	0.1000	1.000^{-4}	1.00^{-4}	1.259^{+2}	5.000^{-5}	2.00
0.1000	0.1000	1.000^{-4}	1.00^{-4}	1.995^{+2}	5.000^{-5}	2.00
0.1000	0.1000	1.000^{-4}	1.00^{-4}	5.012^{+2}	5.000^{-5}	2.00
0.1000	0.1000	1.000^{-4}	1.00^{-4}	1.000^{+3}	5.000^{-5}	2.00

[a] k_1C/k(calc.)

from experimental data that may relate to either kinetically free ions or saline ion pairs is not a trivial matter. Nevertheless, such problems are of marginal concern here; rather the first-order character of eqs. [3], [4], and [5] with respect to the saline nucleophiles serves to highlight the bimolecular nature of the transition state, which is conventionally regarded as a symmetrical bipyramidal sp^2 structure. The overall mechanism represents a classical example of the S_N2 displacement reaction; indeed, the distinct relationships between racemization ($k_r = 2k_1$) and exchange ($k_e = k_1$) are central to the hypothesis that the activated complex is symmetric. For instance, Ingold (1) states categorically that this particular observation "requires that ***every*** (C.K.I's emphasis) individual act of bimolecular substitution inverts configuration" and thus "passes through" a trigonal bipyramidal transition state. Hammett (2) is characteristically more circumspect and suggests that "the data do not exclude the possibility of a detailed mechanism involving further intermediates," but concludes that "there seems to be no reason to take the uncertainty very seriously."

Notwithstanding the comments of Ingold and Hammett, the question arises as to the relative rates of racemization and exchange for more complex barriers. The purpose of the present paper is to examine this question for a reaction described by a symmetrical barrier with a single symmetrical intermediate, i.e., in the more complicated regime the structure of the intermediate is identical to that of the S_N2 transition state. The racemizations are now described by the reaction

$$[6] \qquad (+)\mathrm{A} + \mathrm{X} \underset{k_2}{\overset{k_\alpha}{\rightleftarrows}} \mathrm{I} \underset{k_\alpha}{\overset{k_2}{\rightleftarrows}} (-)\mathrm{A} + \mathrm{X}$$

where k_α is defined again by eq. [3] and I is the symmetrical intermediate. The related exchange reaction is analogously represented by

$$[7] \qquad \mathrm{RX} + \mathrm{X}^* \underset{k_2}{\overset{k_\beta}{\rightleftarrows}} \mathrm{I} \underset{k_\gamma}{\overset{k_2}{\rightleftarrows}} \mathrm{RX}^* + \mathrm{X}$$

where k_β and k_γ are as previously defined by eqs. [4] and [5].

It is useful to repeat the derivations of the kinetic equations for the S_N2 racemization and exchange reactions described by eqs. [1] and [2] using mathematical techniques that can be readily extended to more complex barriers. The methodology adopted here is similar to that described briefly by Ritchie (3), and some aspects are also covered in a translated Russian monograph (4). In summary, the mathematical solutions of the appropriate differential equations are derived via an auxiliary polynomial equation, the roots of which are always negative. These negative roots, *with their sign changed*, define the dynamic constants (necessarily positive), that describe the time evolution of the chemical systems of interest. For complex systems the dynamic constants are functions of the primitive component rate constants (for extensive details see ref. 4). In general, the symbols of chemical species *without square brackets* (but italicized to indicate that they possess numerical value) will be used to denote concentrations since the inclusion of such brackets would render the more involved expressions too cumbersome.

The kinetic expressions that relate to the simple S_N2 racemizations and isotopic exchanges are derived in Appendices A and B, respectively. The related kinetic formulae for the cases when an intermediate is present (eqs. [6] and [7]) are derived in Appendices C and D. Several calculations using synthetic composition–time data are examined in the

© 1998 NRC Canada

Fig. 1. Schematic energy (or free energy) versus reaction coordinate diagram for (*a*) a simple symmetrical S_N2 displacement (LHS) and (*b*) a symmetrical displacement involving an intermediate (RHS).

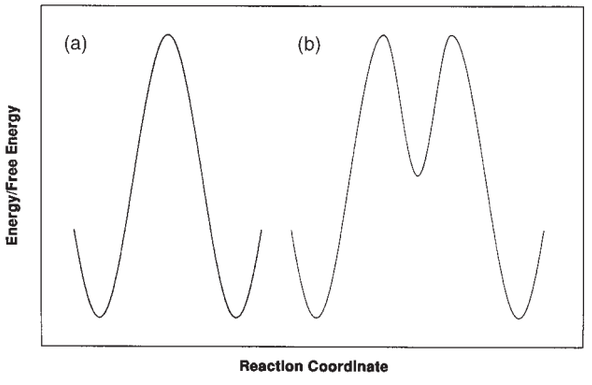

following section to verify numerically the formal conclusions established in Appendix D.

Calculations

The numerical tests were carried out using the analysis presented in Appendix D. Thus a range of synthetic data was calculated using eq. [23D] after solving the quadratic part of eq. [6D] to generate the dynamic constants γ_1 and γ_2. The concentrations of RX and X were arbitrarily fixed at 1.00×10^{-1} M L^{-1} and the tagged atom X^* concentration was set at 1.00×10^{-4} M L^{-1}, i.e., $0.001 \times$ [X]. The rate constant k_1 was set at 1×10^{-4} L M^{-1} s^{-1}, with 21 values of k_2 in the range $1.00 \times 10^{-3} < k_2 < 1.00 \times 10^3$. For each of the 21 pairs of k_1 and k_2, 100 values of X^*_n (n = 1–100) were calculated at equal intervals over a period estimated to be four half-lives ($4t_{1/2}$). Thus the time interval between each calculated value of X^*_n is approximately $t_{1/2}/25$. The half-life was estimated from the smaller dynamic constant of the pair γ_1 and γ_2. The values of X^*_n so calculated were then processed using the Guggenheim algorithm (5) and in the present context this approach is best considered in terms of eq. [7D].

Consider two sets of the quantities X^*_n; the first set is defined for n = 1–30 and the second set for n = 60–90. For the first set eq. [7D] gives

$$[8] \quad X^*_n\,(n = 1\text{–}30) = a_{11} + a_{12}\exp(-\gamma_1 t) + a_{13}\exp(-\gamma_2 t)$$

and, for the second set,

$$[9] \quad X^*_{n\tau}\,(n = 60\text{–}90) = a_{11} + a_{12}\exp\{-\gamma_1\,(t+\tau)\} + a_{13}\exp\{-\gamma_2(t+\tau)\}$$

where $\tau \approx 60t_{1/2}/25$. Subtracting eq. [9] from eq. [8], on the assumption that $\gamma_1 < \gamma_2$ and that $a_{12} > a_{13}$, gives

$$[10] \quad X^*_n - X^*_{n\tau} \approx a_{12}\{1 - \exp(-\gamma_1\,\tau)\}exp(-\gamma_1 t)$$

which in logarithmic form becomes an equation suitable for linear regression

$$[11] \quad \ln\{X^*_n - X^*_{n\tau}\} \approx \ln[a_{12}\{1 - \exp(-\gamma_1\,\tau)\}] - \gamma_1 t$$

A correlation with t as the "x" variable and $\ln\{X^*_n - X^*_{n\,\tau}\}$ as the "y" variable gives $-\gamma_1$ as the slope, which is equal to $-k$(calc.) and should, if the previous analysis is correct, be equal to $k_1C/2$. This requirement is amply confirmed by the data shown in Tables 1 and 2. In Table 2 the values of X, X*, and RX are the same as in Table 1, but k_2 is fixed at 10 s^{-1} and k_1 varies from 1×10^{-4} to 1×10^{-1} L M^{-1} s^{-1}. In all the cases numerically examined the ratio k_1C/k(calc.) = 2.

Conclusions

The diagnostic test for the S_N2 mechanism, which requires $k_r = 2k_e$, is necessary but not sufficient evidence for the operation of the S_N2 mechanism.

Acknowledgements

J.M.W.S. expresses gratitude to Memorial University of Newfoundland for a sabbatical year of leave starting May 1993. D.S. acknowledges support from the Natural Sciences and Engineering Research Council of Canada under grant A-0621.

References

1. C.K. Ingold. *In* Structure and mechanism in organic chemistry. 2nd ed. Bell, London. 1969.Chap.VII, p. 517.
2. L.P. Hammett. *In* Physical organic chemistry. 2nd ed. McGraw–Hill, New York. 1970. Chap.VI, p. 151
3. C.D. Ritchie. *In* Physical organic chemistry — the fundamental concepts. Marcel Dekker, New York. 1975.
4. N.M. Rodiguin and E.N. Rodiguina. *In* Consecutive chemical reactions. *Translated by* R.F. Schneider. Van Nostrand, New York. 1964.
5. E.A. Guggenheim. Philos. Mag. **2**, 538 (1926).
6. A. Stein. J.Org.Chem. **41**, 519 (1976).
7. J.H. Espenson. *In* Chemical kinetics and reaction mechanisms. McGraw–Hill, New York. 1981.

Appendix A

Racemization for the simple S_N2 case

The standard derivations for the racemization and exchange reactions are reported by Stein (6) and Espenson (7). For the racemization reaction, the experimental observables are the optical rotation (α) and time (t). For a given initial concentration of (+)RX represented by the symbol $(+)A_o$ the observed optical rotation at any time depends on the concentration of the two optical isomers present at that time, represented by the symbols (+)A and (–)A, hence

$$[1A] \quad \alpha = (+)\,\alpha_M\{(+)A + (-)\alpha_M\{(-)A\}$$

By definition

$$[2A] \quad (+)\alpha_M = -(-)\alpha_M = |\alpha_M|$$

Hence

$$[3A] \quad \alpha = \alpha_M\{(+)A - (-)A\}$$

At $t = 0$, if only one optical isomer is present the optical rotation (α_o) is given by

$$[4A] \quad \alpha_o = \alpha_M(+)A_o$$

The differential equations that describe reaction [1] are

$$[5A] \quad -\frac{d(+)A}{dt} = k_\alpha(+)A - k_\alpha(-)A$$

© 1998 NRC Canada

$$[6A] \quad -\frac{d(-)A}{dt} = -k_\alpha(+)A + k_\alpha(-)A$$

The auxiliary equation related to eqs. [5A] and [6A] is readily obtained from the determinant related to the matrix formulation of these equations:

$$[7A] \quad \begin{bmatrix} D + k_\alpha & -k_\alpha \\ -k_\alpha & D + k_\alpha \end{bmatrix} \begin{bmatrix} (+)A \\ (-)A \end{bmatrix} = 0$$

where D is the differential operator d/dt. The determinant is

$$[8A] \quad \begin{vmatrix} \lambda + k_\alpha & -k_\alpha \\ -k_\alpha & \lambda + k_\alpha \end{vmatrix} = 0$$

and the related auxiliary equation is

$$[9A] \quad \lambda(\lambda + 2k_\alpha) = 0$$

Equation [9A] has roots $\lambda = 0$ and $\lambda = -2k_\alpha$ and hence solutions of $(+)A$ and $(-)A$ as functions of time are of the form

$$[10A] \quad (+)A = a_{11} + a_{12}\exp(-2k_\alpha t)$$

and

$$[11A] \quad (-)A = a_{22} + a_{21}\exp(-2k_\alpha t)$$

where the quantities a_{nr} are constants evaluated from the boundary conditions, namely, $(+)A = (+)A_o$ at $t = 0$; $(+)A = (+)A/2$ at $t = \infty$; $(-)A = 0$ at $t = 0$; $(-)A = (+)A/2$ at $t = \infty$. These conditions yield the solutions

$$[12A] (+)A = \{(+)A_o/2\}\{1 + \exp(-2k_\alpha t)\}$$

$$[13A] (-)A = \{(+)A_o/2\}\{1 - \exp(-2k_\alpha t)\}$$

The observed optical rotation at any time (α) for the reacting system is related to the quantity $\{(+)A - (-)A\}$, which can be generated by subtracting eq. [13A] from eq. [12A]. Multiplication of both sides of the resulting equation by α_M gives

$$\alpha_M\{(+)A - (-)A\} = \alpha_M(+)A_o\exp(-2k_\alpha t)$$

or

$$[14A] \quad \alpha = \alpha_o\exp(-2k_\alpha t)$$

Equation [14A] is the usual form given for the change of optical activity with time for a labile optically active system (6).

Appendix B

Isotopic exchange for the simple S_N2 case

The kinetic equations for the isotopic exchange process are based on eq. [2]

$$[1B] \quad RX + X^* \underset{k_\gamma}{\overset{k_\beta}{\leftrightarrows}} RX^* + X$$

with the assumptions that the concentration of X^* is much less than the concentrations of X and RX, which are assumed to be comparable. The pseudo-first-order rate constants are those defined in eqs. [4] and [5]. The differential equations that describe the exchange process are

$$[2B] \quad -\frac{dX^*}{dt} = k_\beta X^* - k_\gamma RX^*$$

$$[3B] \quad -\frac{dRX^*}{dt} = -k_\beta X^* + k_\gamma RX^*$$

and their equivalent matrix form is

$$[4B] \quad \begin{bmatrix} D + k_\beta & -k_\gamma \\ -k_\beta & D + k_\gamma \end{bmatrix} \begin{bmatrix} X^* \\ RX^* \end{bmatrix} = 0$$

The related determinant

$$[5B] \quad \begin{vmatrix} \lambda + k_\beta & -k_\gamma \\ -k_\beta & \lambda + k_\gamma \end{vmatrix} = 0$$

gives the auxiliary equation

$$[6B] \quad \lambda(\lambda + k_\beta + k_\gamma) = 0$$

The roots of eq. [6B] are $\lambda = 0$ and $\lambda = -(k_\beta + k_\gamma)$, and the equation for X^* as a function of time is of the form (cf. eqs. [12A] and [13A])

$$[7B] \quad X^* = a_{11} + a_{12}\exp(-(k\beta + k_\gamma)t)$$

At $t = 0$, $X^* = X^*_o$, and at $t = \infty$, $X^* = X^*_\infty$. These conditions produce the result

$$[8B] \quad X^* - X^*_\infty = (X^*_o - X^*_\infty)\exp(-(k_\beta + k_\gamma)t)$$

Mass balance at all times requires that

$$[9B] \quad X^*_o = X^* + RX^*$$

and at $t = \infty$,

$$[10B] \quad X^*_o = X^*_\infty + RX^*_\infty$$

Eliminating X^*_o between eqs. [9B] and [10B] gives

$$[11B] \quad X^* - X^*_\infty = RX^*_\infty - RX^*$$

From eq. [9B],

$$[12B] \quad X^*_o - X^*_\infty = RX^*_\infty$$

Combining eqs. [11B] and [12B] with eq. [8B] gives

$$[13B] \quad RX^*_\infty - RX^* = RX^*_\infty\exp(-(k_\beta + k_\gamma)t)$$

or, in the more conventional form (7):

$$[14B] \quad \ln\{1 - (RX^*/RX^*_\infty)\} = -(k_\beta + k_\gamma)t$$

Combining eq. [14B] with eqs. [4] and [5] gives

$$[15B] \quad \ln\{1 - (RX^*/RX^*_\infty)\} = -k_1(RX + X)t$$

Note that the racemization rate constant is $k_r = 2k_1$ whereas the isotopic exchange rate constant is $k_e = k_1$. We now demonstrate in Appendices C and D that the same ratio, $k_r/k_e = 2$, characterizes racemization and exchange when an intermediate structurally identical to the S_N2 transition state is present in the reacting system.

Appendix C

Racemization with an intermediate present

The chemical equation for the racemization with an intervening intermediate is given by

$$[1C] \quad (+)A + X \underset{k_2}{\overset{k_\alpha}{\leftrightarrows}} I \underset{k_\alpha}{\overset{k_2}{\leftrightarrows}} (-)A + X$$

© 1998 NRC Canada

where k_α is defined in eq. [3].
The differential equations that describe this reaction are

$$[2C] \quad -\frac{d(+)A}{dt} = k_\alpha(+)A - k_2 I$$

$$[3C] \quad -\frac{dI}{dt} = -k_\alpha(+)A + 2k_2 I - k_\alpha(-)A$$

$$[4C] \quad -\frac{d(-)A}{dt} = -k_2 I + k_\alpha(-)A$$

The equivalent matrix form is

$$[5C] \quad \begin{bmatrix} (D + k_\alpha) & -k_2 & \\ -k_\alpha & (D + 2k_2) & -k_\alpha \\ & -k_2 & (D + k_\alpha) \end{bmatrix} \begin{bmatrix} (+)A \\ I \\ (-)A \end{bmatrix} = 0$$

and the related determinant gives the auxiliary equation

$$[6C] \quad \lambda(\lambda + k_\alpha)(\lambda + k_\alpha + 2k_2) = 0$$

for which the roots are $\lambda = 0$, $\lambda = -k_\alpha$, and $\lambda = -(k_\alpha + 2k_2)$. Hence the solutions of eq. [5C] are

$$[7C] \quad X_n = a_{1n} + a_{2n} \exp(-k_\alpha t) + a_{3n} \exp(-(k_\alpha + 2k_2)t)$$

where for $n = 1$, $X_n = (+)A$; for $n = 2$, $X_n = I$; and for $n = 3$, $X_n = (-)A$.

Standard methods give the following expressions for $(+)A$, $(-)A$, and I as functions of time

$$[8C] \quad (+)A = (+)A_o \left\{ \frac{k_2}{(k_\alpha + 2k_2)} + \frac{\exp(-k_\alpha t)}{2} + \frac{k_\alpha \exp(-(k_\alpha + 2k_2)t)}{2(k_\alpha + 2k_2)} \right\}$$

$$[9C] \quad I = \frac{(+)A_o k_\alpha}{k_\alpha + 2k_2} \{1 - \exp(-(k_\alpha + 2k_2)t)\}$$

$$[10C] \quad (-)A = (-)A_o \left\{ \frac{k_2}{(k_\alpha + 2k_2)} - \frac{\exp(-k_\alpha t)}{2} + \frac{k_\alpha \exp(-(k_\alpha + 2k_2)t)}{2(k_\alpha + 2k_2)} \right\}$$

Because the intermediate I is symmetrical, it makes no contribution to the optical activity of the system, which, as before, is defined (cf. eqs. [12A]–[14A]) by the difference $\{(+)A - (-)A\}$. This quantity can be generated in the present case by subtracting eq. [10C] from eq. [8C], yielding the result,

$$[11C] \quad (+)A - (-)A = (+)A_o \exp(-k_\alpha t)$$

Equation [11C] is analogous to eq. [14A] with the important exception that k_r is now equal to k_1 rather than $2k_1$. We now consider the exchange reaction when an intermediate is present.

Appendix D

Isotopic exchange with an intermediate present

Section I(D)
The reaction for the isotopic exchange process is now described by the equation

$$[1D] \quad RX + X^* \underset{k_2}{\overset{k_\beta}{\rightleftarrows}} I \underset{k_\gamma}{\overset{k_2}{\rightleftarrows}} RX^* + X$$

where the quantities k_β and k_γ have the same meaning as in eqs. [4] and [5]. The differential equations that describe this version of the isotopic exchange are

$$[2D] \quad -\frac{dX^*}{dt} = k_\beta X^* - k_2 I$$

$$[3D] \quad -\frac{dI}{dt} = -k_\beta X^* + 2k_2 I - k_\gamma RX^*$$

$$[4D] \quad -\frac{dRX^*}{dt} = -k_2 I + k_\gamma RX^*$$

The matrix form corresponding to eqs. [2D], [3D], and [4D] is

$$[5D] \quad \begin{bmatrix} (D + k_\beta) & -k_2 & \\ -k_\beta & (D + 2k_2) & -k_\gamma \\ & -k_2 & (D + k_\gamma) \end{bmatrix} \begin{bmatrix} X^* \\ I \\ RX^* \end{bmatrix} = 0$$

which yields, via the related determinant, the auxiliary equation

$$[6D] \quad \lambda\{\lambda^2 + k_\beta + k_\gamma + 2k_2)\,\lambda + k_2(k_\beta + k_\gamma) + k_\beta k_\gamma\} = 0$$

At this point there are several ways of comparing the present system with that described in Appendix B. This comparative analysis is presented with varying degrees of approximation and rigour below.

Section II(D)
Equation [6D] has three roots, $\lambda = 0$, $\lambda = \lambda_1$, and $\lambda = \lambda_2$. The time evolution of the system represented by eq. [5D] is characterized by three amplitude factors, a_{11}, a_{12}, and a_{13}, and two dynamic constants, γ_1 and γ_2, that correspond to the two nonzero roots of the quadratic part of eq. [6D] with the signs of the roots reversed (cf. eq. [6C] where the roots are $-(k_\alpha + 2k_2)$ and $-k_\alpha$ but the dynamic constants are $(k_\alpha + 2k_2)$ and k_α). Thus, in particular, we have

$$[7D] \quad X^* = a_{11} + a_{12}\exp(-\gamma_1 t) + a_{13}\exp(-\gamma_2 t)$$

Generally, the smaller of the dynamic constants (say γ_1) will dominate the time evolution of the system because the amplitude factors are inversely correlated with γ_1 and γ_2. If the intermediate I is labile, then the rate constant k_2, which characterizes the paths of its destruction, must be such that $k_2 > k_\beta = k_1 RX$. With these approximations, the quadratic part of eq. [6D] becomes

$$[8D] \quad \lambda^2 + 2k_2\lambda + k_2(k_\beta + k_\gamma) = 0$$

If $\lambda << 1$ then $\lambda^2 << \lambda$, and hence eq. [8D] can be linearized to the form

$$2k_2\lambda = -k_2(k_\beta + k_\gamma)$$

or

$$[9D] \quad \lambda \approx -(k_\beta + k_\gamma)/2 = -k_1(RX + X)/2 = -k_1 C/2 \text{ or } \gamma_1 = k_1 C/2$$

where C represents the concentration term related to RX and X in eq. [9D]. Thus, the approximate root of eq. [6D] leads to the same relationship between k_r and k_e as is observed in the classical S_N2 reaction, namely, $k_r = 2k_e$. If λ is large, then the

© 1998 NRC Canada

constant term in eq. [8D] is negligible, and the larger approximate dynamic constant is given by

[10D] $\lambda^2 = -2k_2\lambda$ or $\gamma_2 = 2k_2$

These approximate roots can be improved by solving eq. [8D] in the usual way, and then using the binomial theorem to expand the square-root term, giving the following expressions for the dynamic constants γ_1 and γ_2:

[11D] $\gamma_1 = \{2k_2 - (4k_2^2 - 4k_1k_2C)^{1/2}\}/2 \approx k_1C$

[12D] $\gamma_2 = \{2k_2 + (4k_2^2 - 4k_1k_2C)^{1/2}\}/2 \approx 2k_2 - k_1C/2$

The values of γ_1 and γ_2 established in eqs. [11D] and [12D] confirm the previous estimates of these quantities.

Section III(D)

In the present section the amplitude factors are calculated for eq. [7D] so that synthetic data for X^* as a function of time can be established. The synthetic data are then processed in the same manner as experimental data to recover the input rate constant k_1. Setting $t = 0$ and $X^* = X^*_o$ in eq. [7D] gives

[13D] $X^*_o = a_{11} + a_{12} + a_{13}$

Similarly, setting $X^* = X^*_\infty$ at $t = \infty$ in eq. [7D] gives

[14D] $X^*_\infty = a_{11}$

Using the condition that $I = 0$ at $t = 0$ gives $\left.\frac{dX^*}{dt}\right|_{t=0} = k_\beta X^*_o$

Hence

[15D] $k_\beta X^*_o = \lambda_1 a_{12} + \lambda_2 a_{13}$

Combining eqs. [13D] and [14*D*] gives

[16D] $X^*_o - X^*_\infty = a_{12} + a_{13}$

Solving eqs. [15D] and [16D] simultaneously gives

[17D] $a_{12} = \dfrac{\lambda_2(X^*_o - X^*_\infty) - k_\beta X^*_o}{(\lambda_2 - \lambda_1)}$

[18D] $a_{13} = \dfrac{\lambda_1(X^*_o - X^*_\infty) - k_\beta X^*_o}{(\lambda_1 - \lambda_2)}$

At $t = \infty$, mass balance requires

[19D] $X^*_o = X^*_\infty + I_\infty + RX^*_\infty$

with the further equilibrium condition that

[20D] $k_\beta X^*_\infty = k_2 I_\infty = k_\gamma RX^*_\infty$

Using the relationships between I_∞, RX^*_∞, and X^*_∞ given in eq. [20D] to eliminate the quantities I_∞ and RX^*_∞ in eq. [19D] gives

[21D] $X^*_o = X^*_\infty + (k_\beta/k_2)X^*_\infty + (k_\beta/k_\gamma)X^*_\infty$

which, after further manipulations, gives

$$X^*_o = X^*_\infty + (k_1RX/k_2)X^*_\infty + (RX/X)X^*_\infty$$

or

[22D] $X^*_\infty = \dfrac{k_2XX^*_o}{k_2X + k_1XRX + k_2RX}$

Equation [13D] combined with eqs. [17D], [18D], and [22D] gives

[23D] $X^* = \dfrac{k_2XX^*_o}{k_2X + k_1XRX + k_2RX} + \dfrac{\lambda_2(X^*_o - X^*_\infty) - k_\beta X^*_o}{(\lambda_2 - \lambda_1)}\exp(-\lambda_1 t) + \dfrac{\lambda_1(X^*_o - X^*_\infty) - k_\beta X^*_o}{(\lambda_1 - \lambda_2)}\exp(-\lambda_2 t)$

© 1998 NRC Canada

Lactams in sulfuric acid. The mechanism of amide hydrolysis in weak to moderately strong aqueous mineral acid media

Robin A. Cox

Abstract: Reaction rate constants obtained in moderately concentrated sulfuric acid for the hydrolysis of simple lactams of ring sizes five, six, seven, and eight as a function of acidity and temperature have been analyzed using the excess acidity kinetic method. The basicity constants for these substrates have been recalculated; the ^{13}C NMR spectra used to obtain these values are very sensitive to medium effects. It was found that the basicities of the lactams at 0.003–0.1 M lactam concentration were over half a p*K* unit more basic than they were at 0.5 M lactam, presumably because of the medium effect. Apart from this, the rate constant results obtained at different times by different groups using different techniques for monitoring the kinetics are in adequate agreement. The excess acidity analysis showed that the kinetics could be fitted according to the "three-water-molecule followed by one-water-molecule" mechanistic scenario previously found, or could just as well be fitted by a "one-water-molecule followed by unknown mechanism" scenario, with the mechanistic change taking place at 50 wt.% sulfuric acid for all the substrates. Other evidence makes the latter seem the more likely possibility of the two, and activation parameters based upon the "one-water-molecule" process were determined. Sufficient data points to enable the unknown mechanism to be established were not present; possible mechanisms applicable in media more concentrated than 50 wt.% sulfuric acid are discussed. Previously obtained values of the parameter *r*, the number of water molecules involved with the substrate in A2 processes, are now questionable.

Key words: amides, lactams, excess acidity, hydrolysis, mechanism.

Résumé : Faisant appel à la méthode cinétique d'excès d'acidité, on a analysé les constantes de vitesse d'hydrolyse de lactames simples, de cycles à cinq, six, sept et huit chaînons, obtenues en solution dans de l'acide sulfurique modérément concentré, en fonction de l'acidité et de la température. Les constantes de basicité de ces substrats ont été recalculées; les spectres RMN du ^{13}C utilisés pour obtenir ces valeurs sont très sensibles aux effets du milieu. À des concentrations de lactames allant de 0,003 à 0,1 M, on a trouvé que les basicités des lactames sont 0,5 unité de p*K* plus basique qu'à 0,5 M, probablement à cause d'un effet de milieu. À part cette différence, il existe un bon accord entre les constantes de vitesse obtenues à différents moments, par différents groupes utilisant des techniques de mesures cinétiques différentes. L'analyse d'excès d'acidité a montré que la cinétique peut tout aussi bien être accommodée par le scénario mécanistique de "trois molécules d'eau suivies par une molécule d'eau" proposé antérieurement que par le scénario d'"une molécule d'eau suivie d'un mécanisme inconnu;" le changement de mécanisme se produit pour tous les substrats à 50% en poids d'acide sulfurique. D'autres données laissent croire que la deuxième possibilité est la plus plausible des deux; on a déterminé les paramètres d'activation basés sur le scénario d'"une molécule d'eau." On ne disposait pas d'assez de données pour déterminer le mécanisme inconnu; on discute de divers mécanismes qui pourraient être appliqués dans des milieux plus concentrés que 50% en poids d'acide sulfurique. Les valeurs obtenues antérieurement pour le paramètre *r*, le nombre de molécules d'eau impliquées avec le substrat dans un processus A2, sont remises en question.

Mots clés : amides, lactames, excès d'acidité, hydrolyse, mécanisme.

[Traduit par la rédaction]

Introduction

The mechanism of the hydrolysis of amides in acidic media is now thought to be reasonably well established. Although nitrogen protonation has been advocated (1), it is now generally agreed that the reaction begins with protonation on the amide oxygen, followed by rate-determining attack of water at the carbonyl carbon and subsequent processes, as shown in Scheme 1 (2).

However, in moderately concentrated mineral acid media, the Yates *r*-parameter treatment (3) (which is an update of Bunnett's original proposal (4) that log rate constant minus H_0 for reactions like this should be linear in the log water activity, slope *w*, which becomes slope *r* if the H_A amide acidity function is used instead of H_0) showed that three water molecules rather than one were involved in the rate-determining step (3, 5). In consequence it is very tempting to write the N-protonated tetrahedral intermediate as being formed in the rate-determining

Received 1 October 1997.

This paper is dedicated to Professor Erwin Buncel in recognition of his contributions to Canadian chemistry.

R.A. Cox.[1] Department of Chemistry, University of Toronto, 80 St. George St., Toronto, ON M5S 3H6, Canada.

[1] Telephone: (416) 978-4581. Fax: (416) 978-8775. E-mail: rcox@alchemy.chem.utoronto.ca

© 1998 NRC Canada

Scheme 1.

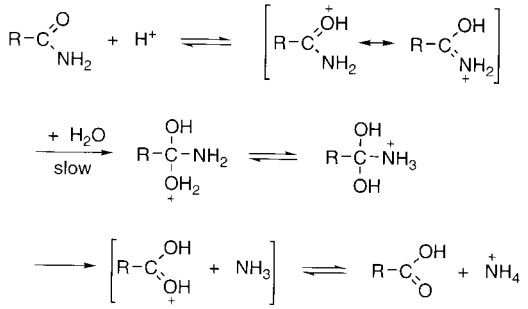

step directly, via a proton switch in a five-membered ring, as shown in eq. [1], since this involves no charge transfer (the positive charge merely becoming concentrated on the nitrogen) (6). This would also account quite well for the small amount of of ^{18}O exchange observed in amide hydrolysis (7), as compared to the considerable amounts found in ester hydrolysis (8), for instance, since the breakup of the N-protonated tetrahedral intermediate would be expected to be essentially irreversible.

[1] 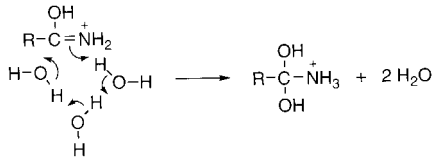

This proposal was made following an application of the excess acidity kinetic method (9) to rate data for the hydrolysis of a number of benzamides, benzimidates, and lactams (6). The analysis resulted in a two-mechanism scenario, with eq. [1] being followed at low acidities (high water activities), and the regular Scheme 1 process (one water molecule) taking over as the acidity increased and the water activity decreased, which seemed eminently reasonable (6). However, more recent work is not consistent with this. Small but measurable amounts of ^{18}O exchange accompanying hydrolysis have been reported for acetanilide (10), *N*-cyclohexylacetamide (10), and *N*,2,4-trimethylacetanilide (11) in reasonably concentrated aqueous HCl media. For *N*,2,4-trimethylacetanilide the solvent deuterium isotope effect was found to be close to one (11), which is a long way from what would be expected on the basis of eq. [1], which has three protons in flight at the transition state (11). For acetanilide and *N*-cyclohexylacetamide the amount of ^{18}O exchange was observed to decrease as the acidity increased (10), which is the reverse of what would be expected if only the high-acidity mechanism led to exchange, although later this was found not to be the case for acetanilide (11), the rate profiles for exchange and hydrolysis being parallel.

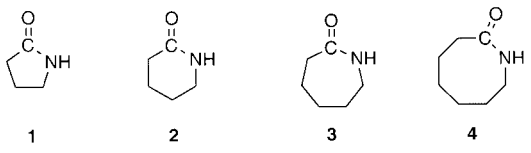

In view of this it was decided to reexamine the data for lactam hydrolysis in dilute to moderately concentrated sulfuric acid media. Subsequent to the publication of our previous paper (6), which included lactam hydrolysis data obtained by ^1H NMR spectroscopy for **1**, **2**, and **3** (12), an extensive new examination of lactam hydrolysis in aqueous sulfuric acid as a function of medium and temperature was published by Vinnik and Moiseev (13) for **1**–**4**, using UV-vis spectroscopy. Using both sets of data, together with that obtained by titration for **3** by Mhala and Jagdale (14) in the same medium, it should be possible to answer the nagging question as to whether amide hydrolysis data obtained by different kinetic methods are in fact comparable, as well as to shed some light on the mechanistic issues raised above. Again the excess acidity kinetic method was used (9); this has enabled mechanistic insights to be made into such diverse processes as ether cleavage (15), the benzidine rearrangement (16), aryl ring hydroxylation (17), acylimidazole hydrolysis (18), the reactions of *N*-nitro amides (19), *N*-nitroamine decomposition (20), alkene hydration (21), and imidazoline cyclization (22), to cite only the most recent examples.

Results

Since amides and lactams change their state of protonation over the acidity range covering most hydrolysis rate measurements, being unprotonated at low acid concentrations and protonated at high ones, it is necessary to know the pK_{BH^+} values of the substrates. These are determined from the variation of the spectrum of the substrate with acid concentration. Lactam (and amide) spectra, ^{13}C NMR, ^1H NMR, and UV-vis, are all very sensitive to medium effects. A method for accurately dealing with these has been devised (23), using the excess acidity method (24). This consists of determining slopes and intercepts of eq. [2]:

$$[2] \quad \log I - \log C_{H^+} = pK_{BH^+} + m^*X$$

where I is the ionization ratio, C_{BH^+}/C_B, obtained from the spectra, X is the excess acidity (essentially an activity coefficient ratio, $\log(f_{B^*}f_{H^+}/f_{B^*H^+})$ for a standard base B*), available for this medium along with log proton concentrations, $\log C_{H^+}$ (24), and m^* is a parameter characteristic of the substrate, having values of 1.0 for primary aromatic amines, 1.3 for tertiary amines, 0.6 for most carbonyl compounds, and so on (24). In simple cases where medium effects are negligible, the equation $I = (D_B - D)/(D - D_{BH^+})$ applies, where D is UV-vis optical density or NMR chemical shift, and D_B and D_{BH^+} refer to the pure unprotonated and protonated forms, respectively (23). This equation is then substituted into eq. [2] and the result curve-fitted in its entirety, giving D_B, D_{BH^+}, m^*, and pK_{BH^+} as coefficients (23).

With medium effects present, D_B or D_{BH^+} (or both) also become functions of the medium. For lactams the excess acidity treatment gives the medium dependence of D_{BH^+} as eq. [3]:

$$[3] \quad D_{BH^+} = D_{Aaq} + \delta D_A I'_A, \text{ where } I'_A = \Delta m^*_A X$$

Here D_{Aaq} is what the optical density (or chemical shift) of the acid form (A) (i.e., D_{BH^+}) would be in the standard state (water), δD_A is a constant, and I'_A is a medium variable controlled by the excess acidity X (24); Δm^*_A is another constant, with values typically around 0.1 (23). Substitution of eq. [3] into eq. [2] leads to two new coefficients that have to be calculated by the curve-fitting program, δD_A and Δm^*_A, giving six

© 1998 NRC Canada

Fig. 1. Plot of ^{13}C chemical shift differences for ε-caprolactam **3** against the substrate acidity function specifically applicable to it, $-H_S$. Open circles, $\delta_\varepsilon - \delta_\gamma$, plotted as differences from the value in water taken as being 1.0000; closed circles, $\delta_\alpha - \delta_\gamma$, plotted as differences from the value in water taken as being 0.0000. The points are experimental and the curves theoretical (see text). The numbers quoted are the fitted shift difference values for pure unprotonated **3** (values at center) and for pure protonated **3** (upper and lower values). The δD_A values were 2.350 ± 0.083 (upper curve) and 1.281 ± 0.062 (lower curve).

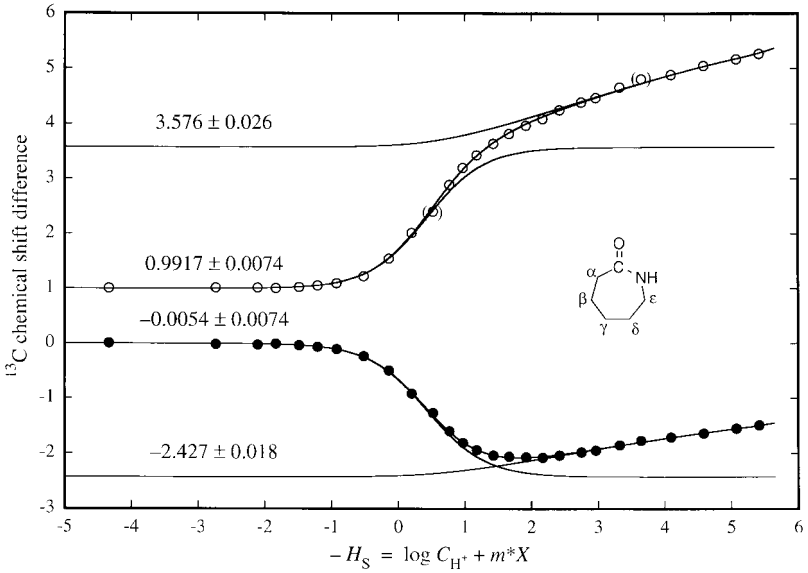

coefficients in all, which means that plenty of good data is required for the analysis to work.

Much good ^{13}C NMR chemical shift data is available for all of these lactams (25). As an example, a plot of two chemical shift differences for ε-caprolactam **3** as a function of the acidity function specifically applicable to it (24) is given as Fig. 1. As can be clearly seen, the chemical shift differences of the protonated form are strongly medium dependent, despite the fact that chemical shift differences are used rather than the chemical shifts themselves, which is supposed to minimize medium effects (26). The curve fitting to eqs. [2] and [3] is very good, as the excellent agreement with the theoretical curves in Fig. 1 and the very low errors on the parameters in Fig. 1 and Table 1 show; for **3** Δm^*_A was 0.1076 ± 0.0063. Precise ^{13}C NMR chemical shift measurements as a function of sulfuric acid concentration are available for all of the substrates, at a lactam concentration of 0.5 M (25). For this study I reworked these data, taking into account dilution of the acid solutions by the substrate and the NMR probe temperature of 33°C, but the resulting values were, within experimental error, identical with those already given (25). The reworked values are given here in Table 1; these values can be regarded as quite reliable, with the proviso that the lactam concentration is fairly high at 0.5 M. A standard curve-fitting program (27) was used throughout.

The pK_{BH^+} values are used to calculate protonation correction terms for the observed reaction rate constants as a function of acid concentration. These have the form $\log(C_{SH^+}/(C_S + C_{SH^+}))$ for amides and lactams (S for substrate) (6), and are easily calculated using eq. [2] and the data in Table 1. One complication is that they have to be calculated at the reaction temperature rather than at 25°C; we have found previously that this is best done by converting pK_{BH^+} to $\Delta G°$ and assuming that $\Delta S° = 0$ in the absence of any information regarding the variation of pK_{BH^+} with temperature (6, 28, 29).

Table 1. Basicities of the lactam substrates at 25°C.

Substrate	pK_{BH^+} (NMR)[a]	pK_{BH^+} (UV)[b]	m^*
1	–0.632 ± 0.014	–0.099	0.766 ± 0.047
2	–0.160 ± 0.016	0.373	0.934 ± 0.073
3	–0.439 ± 0.010	0.094	0.586 ± 0.028
4	–0.345 ± 0.011	0.188	0.715 ± 0.052

[a] Substrate concentration 0.5 M.
[b] Substrate concentration 0.003–0.1 M.

Values of log C_{H^+} and X were corrected to temperature as previously described; if this is done the m^* values are temperature-independent (28, 29).

Excess acidity kinetic expressions that apply to Scheme 1 and (or) eq. [1] are easily derived. Writing the number of water molecules involved in the mechanism as r and the substrate concentration as the sum of protonated and unprotonated forms, absolute rate theory requires that eq. [4] holds, where the observed rate constants are k_ψ.

$$[4] \qquad k_\psi(C_S + C_{SH^+}) = k_0 a_{SH^+} a_{H_2O}{}^r \frac{1}{f_\ddagger} = k_0 C_{SH^+} a_{H_2O}{}^r \frac{f_{SH^+}}{f_\ddagger}$$

Here k_0 is the standard-state rate constant and a_{H_2O} the water activity, and including the activity coefficient of the transition state $f_\ddagger$ enables equation of concentrations and activities. Rearranging and taking logs gives the relevant rate equation, eq. [5].

$$[5] \qquad \log k_\psi - \log \frac{C_{SH^+}}{C_S + C_{SH^+}} - r \log a_{H_2O} = \log k_0 + \log \frac{f_{SH^+}}{f_\ddagger} = \log k_0 + (m^\ddagger - 1) m^* X$$

In eq. [5] the activity coefficient ratio is linear in X as shown, with the value of $m^\ddagger$ being characteristic of the transition state,

© 1998 NRC Canada

Table 2. Standard-state rate constants, activation parameters, $m^{\ddagger}$ values, etc., for the lactam substrates at 25°C, assuming reaction with one water molecule.

Substrate	log k_0	$\Delta H^{\ddagger}_{25^\circ}$[a]	$\Delta S^{\ddagger}_{25^\circ}$[b]	$m^{\ddagger}$[c]	$\pm \sigma_y$[d]	N[e]
1	–6.309 ± 0.038	20.35 ± 0.30	–27.1 ± 1.0	0.838 ± 0.014	0.039	91(8)
2	–5.072 ± 0.028	16.34 ± 0.24	–34.92 ± 0.82	0.575 ± 0.035	0.044	90(3)
3	–5.703 ± 0.048	17.98 ± 0.39	–32.3 ± 1.3	0.441 ± 0.035	0.066	95(5)
4	–6.52 ± 0.13	20.7 ± 1.0	–27.9 ± 3.4	0.136 ± 0.074	0.054	26

[a]In kcal mol^{-1}.
[b]In cal mol^{-1} K^{-1}.
[c]Calculated from the observed $(m^{\ddagger} - 1)m^*$ slopes and the m^* values in Table 1.
[d]Root-mean-square deviation between the experimental points and the fitted lines in Figs. 2–5, in log k units.
[e]Number of points. Any rejected by the multiple linear regression program used as not being part of the same data set as the rest, to 95% confidence, are in parentheses here and in Figs. 2–5.

>1 for A1 reactions, <1 for A-S$_E$2 processes, and ~1 for A2 mechanisms (but see below) such as the ones under discussion here (9).

In calculating the protonation correction term (PCT) in eq. [5], it was found that the same pK_{BH^+} value could not be used for both the NMR kinetic data (12) and the UV-vis kinetic data (13). The PCT values calculated using the NMR entries in Table 1, obtained at a substrate concentration of 0.5 M, applied well to the rate data obtained by NMR spectroscopy, also at a substrate concentration of 0.5 M (12), and gave the same curve fits to the 3H$_2$O and 1H$_2$O mechanisms already described (6). However, using the same value with the UV-vis data, obtained at substrate concentrations of 0.003–0.1 M (13), did not lead to agreement with the NMR data. Consequently, the curve-fitting program was allowed to calculate a ΔG° value applicable to the UV-vis data, assuming that the same $\Delta H^{\ddagger}_{25^\circ}$, $\Delta S^{\ddagger}_{25^\circ}$, and m^* and $(m^*-1)m^*$ slope values applied to both data sets, and that the ΔG° value derived from the Table 1 NMR pK_{BH^+} values applied to the NMR data. For simplicity only rate data obtained in the more dilute acid media were used, where only one mechanism applies, but this still included a large majority of the data points. Within experimental error the difference between the NMR ΔG° and UV-vis ΔG° values obtained in this way was the same for all four substrates, +0.727 ± 0.072 kcal mol^{-1}, or +0.533 pK units at 25°C. Adding this to the NMR values gives the UV values in Table 1.

The availability of rate data at several different temperatures T was accommodated by replacing log k_0 in eq. [5] according to eq. [6] (6, 28), based upon the formulation given by Clarke and Glew (30), where the standard temperature θ is 25°C (298.15 K):

$$[6]\quad \log k_0 = 10.3188 + \log T - \frac{\Delta G^{\ddagger}_{25^\circ}}{R\theta \ln 10} - \left(\frac{\Delta H^{\ddagger}_{25^\circ}}{R\theta \ln 10}\right)\left(\frac{T-\theta}{T}\right)$$

Subsequently $\Delta S^{\ddagger}_{25^\circ}$ is calculated from $\Delta G^{\ddagger}_{25^\circ}$ and $\Delta H^{\ddagger}_{25^\circ}$.

Provided that the protonation correction terms were calculated using the correct pK_{BH^+} value, all of the rate constant data, NMR and UV-vis, could be fitted to the same "3H$_2$O mechanism followed by 1H$_2$O mechanism" scenario used before (6). The enthalpies and entropies of activation, etc., obtained according to this fit are not given here because they are not significantly different from the values already quoted (6). In view of the mechanistic situation noted in the introduction, however, other possible data fits were tested. It was soon found that all of the experimental data for all of the substrates obtained in sulfuric acid media more dilute than 50 wt.% acid were fitted by eq. [5] (including eq. [6]) with $r = 1$. A standard multiple linear regression program was used for this (31), curve fitting not being necessary. The resulting parameters are given in Table 2, and the fit for all four substrates is illustrated in Figs. 2–5.

These are difficult experimental data to obtain, and much scatter is evident in Figs. 2–5. Nevertheless the large amount of data available compensates for this to some extent, over 90 points in most cases, and the computer programs I use reject points which, to 95% confidence, do not form part of the same data set as the rest (32). As a result the experimental errors on the parameters obtained, quoted as standard deviations in Table 2, are acceptably low. The scatter on the points in Figs. 2–5 is mainly random; any remaining systematic deviations from linearity are probably due to the real variation of pK_{BH^+} with temperature being slightly different from the one assumed. The data for ε-caprolactam **3** includes that obtained by Mhala and Jagdale (14) at 97°C by titration; since the substrate concentration used was 0.1 M, the UV-vis pK_{BH^+} value was used to calculate the PCT. As is apparent from Fig. 4, most of these data are in agreement with the rest, but some are not and were rejected by the program.

Only data obtained at acidities below 50 wt.% H_2SO_4 were used to obtain the Table 2 parameters, so the fitted lines in Figs. 2–5 stop there; rate constants obtained in stronger acids all fall above the extrapolated lines, indicating that another mechanism is taking over at this point. However, all attempts to discover what this second mechanism is were inconclusive. The experimental scatter is too bad to enable a decision to be made between an A1 mechanism, a one-bisulfate-ion mechanism or another one-water-molecule mechanism, based upon a multiple linear regression using only the points obtained at acidities above 50 wt.% acid; there are too few points and the scatter is too bad. This is unrealistic anyway, since both mechanisms must contribute to the overall process at acidities well above and below 50 wt.%. All attempts to fit the entire data set as a sum of two mechanisms, by curve fitting, failed. This is probably because the multitude of data describing the first mechanism swamps the few data points describing the second, and the high random scatter on the points does not help. Undoubtedly many more data points at acidities greater than 50 wt.% acid would be needed for this approach to work.

© 1998 NRC Canada

Fig. 2. Excess acidity plot of log k_ψ – PCT – log a_{H_2O} against the excess acidity X, for the hydrolysis of γ-butyrolactam **1** in aqueous sulfuric acid at several temperatures. Closed symbols, data of Vinnik and Moiseev (13) at 69°C (circles), 78.5°C (side-up triangles), 88°C (squares), and 94°C (side-down triangles). Open symbols, data of Wan et al. (12) at 75.8°C (circles), 80.3°C (side-up triangles), 85.8°C (squares), 90.0°C (side-down triangles), 93.0°C (diamonds), and 97.0°C (circles). The points are experimental and the lines fitted (see text).

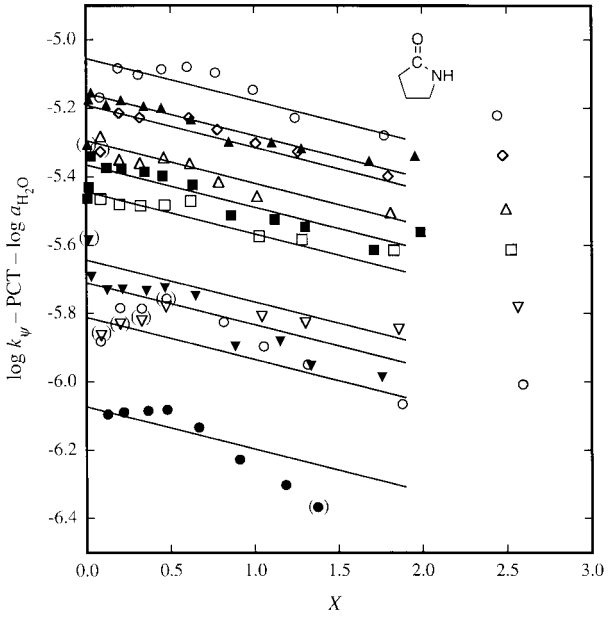

Fig. 3. Excess acidity plot of log k_ψ – PCT – log a_{H_2O} against the excess acidity X, for the hydrolysis of δ-valerolactam **2** in aqueous sulfuric acid at several temperatures. Closed symbols, data of Vinnik and Moiseev (13) at 59.5°C (circles), 69°C (side-up triangles), 78.5°C (squares), 88°C (side-down triangles), and 94°C (diamonds). Open symbols, data of Wan et al. (12) at 65.0°C (circles), 71.0°C (side-up triangles), 75.0°C (squares), 80.3°C (side-down triangles), and 85.0°C (diamonds). The points are experimental and the lines fitted (see text).

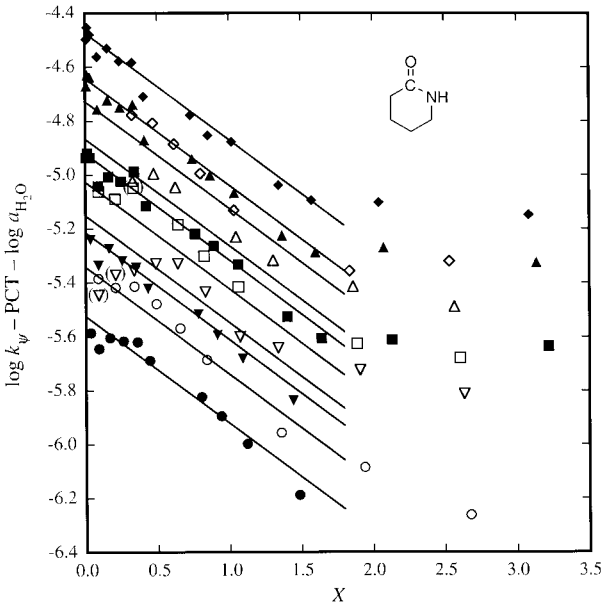

Fig. 4. Excess acidity plot of log k_ψ – PCT – log a_{H_2O} against the excess acidity X, for the hydrolysis of ε-caprolactam **3** in aqueous sulfuric acid at several temperatures. Closed symbols, data of Vinnik and Moiseev (13) at 69°C (circles), 78.5°C (side-up triangles), 88°C (squares), and 94°C (side-down triangles). Filled diamonds, data of Mhala and Jagdale (14) at 97°C. Open symbols, data of Wan et al. (12) at 65.8°C (circles), 70.8°C (side-up triangles), 75.6°C (squares), 80.3°C (side-down triangles), 90.0°C (circles), and 97.0°C (diamonds). The points are experimental and the lines fitted (see text).

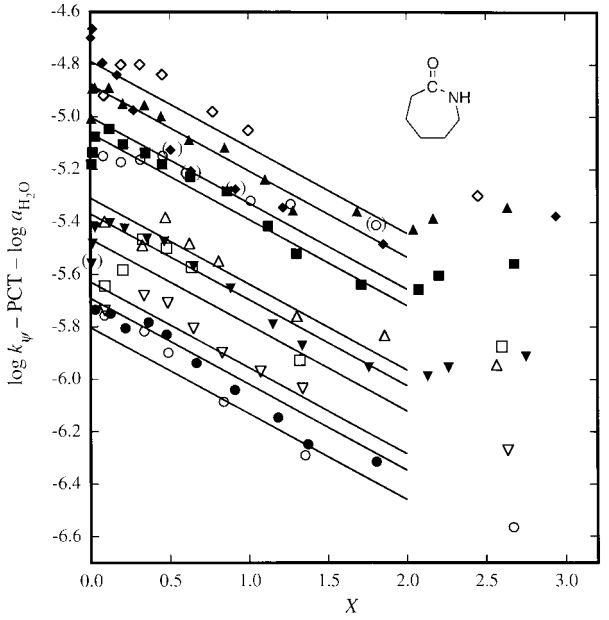

Fig. 5. Excess acidity plot of log log k_ψ – PCT – log a_{H_2O} against the excess acidity X, for the hydrolysis of enantholactam **4** in aqueous sulfuric acid at several temperatures. Data of Vinnik and Moiseev (13) at 78.5°C (circles), 88°C (side-up triangles), and 94°C (squares) The points are experimental and the lines fitted (see text).

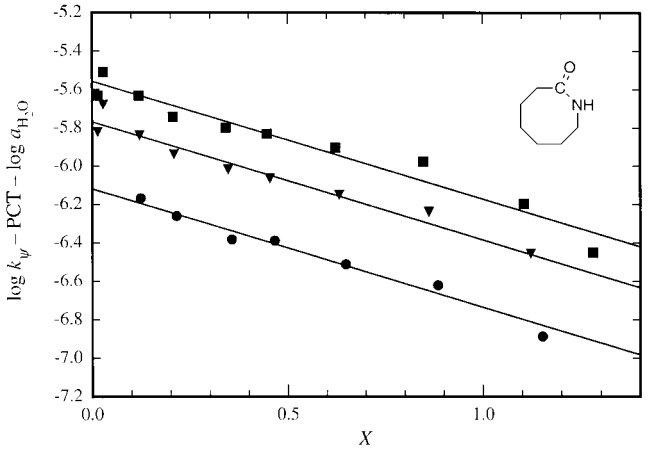

Discussion

With regard to the question raised in the introduction as to whether hydrolysis data obtained by different kinetic methods are in fact comparable, the best answer that this work can provide is "probably." Certainly the results obtained by three different sets of workers at different times by different

© 1998 NRC Canada

Scheme 2.

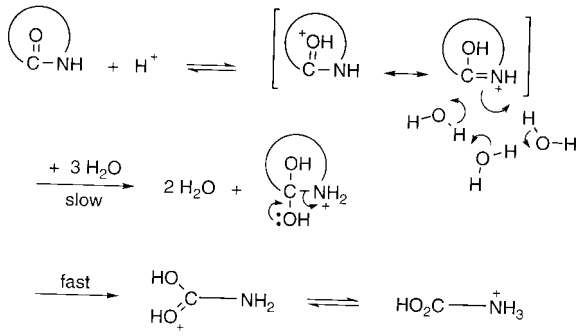

techniques, illustrated in Figs. 2–5, are highly comparable, considering the scatter present. However, to obtain the protonation correction terms used in these plots, different pK_{BH^+} values have to be used for the different data sets, NMR data obtained at a substrate concentration of 0.5 M (12) and UV-vis data obtained at a substrate concentration of 0.003–0.1 M (13). These are different media, with the organic content in one case being at least five times larger than that in the other case, and considering the high sensitivity of amide and lactam protonations to medium effects (25), illustrated in Fig. 1, it is perhaps not too surprising that this causes a difference of half a pK unit. In cases where comparison is possible amide pK_{BH^+} values obtained by NMR seem to be consistently more negative than those obtained by UV. For instance, for acetamide values between –0.48 and +0.37 are reported, using a variety of techniques including UV spectroscopy (33). An NMR value of –0.9 has been obtained (34), and our own value, obtained after accounting for the medium effect, was –0.73 (25). (The "best" value, obtained by conductance measurements, is probably –0.62 ± 0.07 (33).) For *N*-ethyl- and *N*,*N*-diethyl-acetamide our values of –0.49 and –0.33 (25) are both somewhat more negative than the conductance values of –0.42 ± 0.03 and –0.28 ± 0.03 reported for the *N*-methyl and *N*,*N*-dimethyl derivatives (33).

The three-water-molecule mechanism for the lactams is given in Scheme 2; this, in combination with a one-water-molecule process taking over in the stronger acids, is the mechanism given before for these substrates (6). Previously only the NMR data were available (12); adding in the UV-vis data (13) and the titration data for **3** (14) does not change anything, beyond having to use different substrate basicities as already noted. All of the data are fitted quite well according to this scheme. However, in this work it is found that a one-water-molecule mechanism, with another unidentified mechanism taking over above 50 wt.% H_2SO_4, fits the data equally well (the root-mean-square errors of the fit for the two mechanistic schemes being comparable, with no statistically significant differences between them evident for any of the substrates). A likely one-water-molecule mechanism is given in Scheme 3.

The difference between Schemes 2 and 3 boils down to: synchronous nucleophilic addition of a water molecule and a proton switch to the nitrogen (Scheme 2); and nucleophilic attack by a water molecule taking place *before* the proton switch to the nitrogen (Scheme 3). Guthrie's latest work (34) indicates that these processes are commonly stepwise rather than concerted, that charge separation can take place within

Scheme 3.

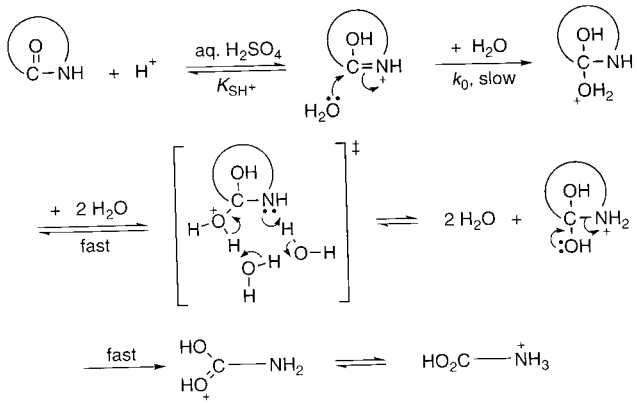

the ring of water molecules (typically two or three) involved in a proton switch, and that there is an intrinsic barrier for proton transfer reactions along a preformed hydrogen bond. Such theoretical calculational evidence as exists at present (36) does not enable an easy distinction between concerted and stepwise processes to be made, although better calculations are on the way.[2]

Since it is not possible from the kinetic evidence to statistically distinguish between the three-water-molecule followed by one-water-molecule mechanistic scheme given before (6) and the equally applicable one-water-molecule followed by unknown mechanism scenario under discussion here, additional information must be used. The only piece of compelling evidence in favour of the latter case is the lack of solvent isotope effect found in the case of *N*,2,4-trimethylacetanilide (11), since a large one would be expected if three protons were in flight at the transition state of Scheme 2. One could wish there were more evidence, but until this materializes I am forced to conclude that the one-water-molecule plus unknown mechanism scenario is in fact closer to the truth.

If this is the case, several questions present themselves. Because the one-water-molecule mechanism only applies up to 50 wt.% H_2SO_4, and all attempts to fit the lactam hydrolysis rate constants obtained at higher acidities failed, the first one to ask is "what is the nature of the second mechanism?" There is good evidence for a second A1 process in the stronger acid region for a number of acetanilides (37), for instance a rate increase at higher acidities being observed following on from the downside of the bell-shaped rate profile usually found for amide hydrolyses (38), and also for some benzamides (39) and ureas (40). This is shown for the lactams in Scheme 4; it is really only possible to visualize an A1 mechanism from the N-protonated lactam. This is not the most probable protonation site for a typical amide, but reaction from the N-protonated form is quite possible if this form is much more reactive than is the O-protonated form. In fact this mechanism is the one accepted for β-lactam hydrolysis (6, 12).

Another possibility is reaction with bisulfate ion as a nucleophile, as shown in Scheme 5. We have actually seen this before with benzamide (6); the problem is that 50 wt.% H_2SO_4 is rather dilute acid for bisulfate to take over from water, 80 wt.% being more typical (6, 20).

[2] S. Wolfe. Personal communication.

© 1998 NRC Canada

Scheme 4.

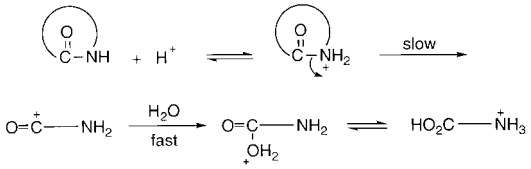

Scheme 5.

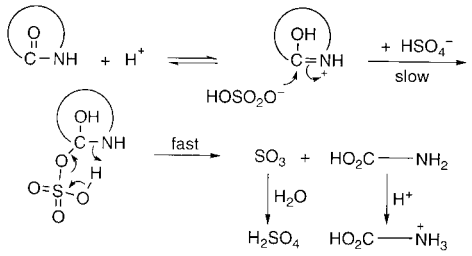

Scheme 6.

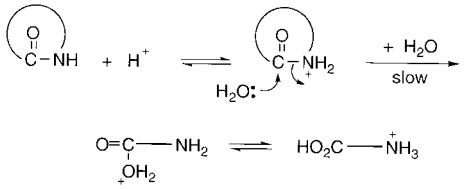

Scheme 7.

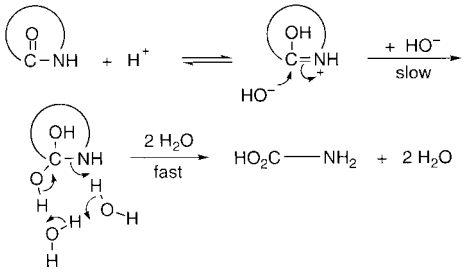

The only other one-water-molecule mechanism that seems possible is an A2 reaction with the N-protonated lactam, shown in Scheme 6. Although looking reasonable on the face of it, there is no evidence for a mechanism like this in the hydrolysis of simple amides. Also possible is bisulfate reacting with the N-protonated form, but this seems less likely still. At present there is not enough evidence to enable a decision to be made between Schemes 4, 5, and 6; this will have to await further experimental work at higher acid concentrations. This will be difficult as the reaction rates become quite slow in the stronger acids (12, 13).

While dealing with possible mechanistic schemes, it is interesting to note that there is no evidence for any reaction between protonated amide or lactam and hydroxide ion; this possibility is shown in Scheme 7. Evidence for Scheme 7 would be a zero slope in a plot of log rate constant against pH or log acid concentration, whereas it is found experimentally that plots of this type have good unit slopes for several amides in dilute HCl (10, 11). Recently several examples of the reaction of hydroxide ion with nitroamine and nitroamide substrates in acid media have been observed (18, 19); perhaps the clearest example of this is found in the hydrolysis of nitrourea in dilute H_2SO_4 (19). In 0.1 M HCl the hydroxide concentration would be 10^{-13} M, and if the lactam concentration was also 0.1 M then according to Table 1 the protonated lactam concentration should be about 10^{-2} M. If the two react with a diffusion-controlled rate constant of 10^{10}, we would obtain an observed rate constant of 10^{-5} s^{-1} at 25°C, and most amide hydrolyses, including those in this work, are carried out at higher temperatures. Stewart's proton activating factor analysis (41) indicates that protonated amide should react much faster with hydroxide than does unprotonated amide; however, the fact that no reaction is observed must mean that the reaction has a considerable activation energy.

If it is true that only one water molecule is involved in the reaction, then $m^{\ddagger}$ values other than one (9) will have to be accepted as normal for A2 reactions. The values for the lactams in Table 2 range from 0.8 to 0.1 and, interestingly, show a fairly steady decrease with increasing lactam ring size. What if anything this means is at yet unclear, since little attention has been paid to the magnitudes of these quantities for A2 processes, but it is suggestive of the possibility of their becoming valuable mechanistically. We have found systematic variation of $m^{\ddagger}m^{*}$ with substituent before, for instance in acylal and thioacylal hydrolyses (42), but in this and several other cases the m^{*} values were not known. However, variation due to changing substituent seems more likely than variation due to changing m^{*}, within a series of closely similar substrates.

The basicities and rate data in Tables 1 and 2 are interesting with respect to the effect of lactam ring size upon reactivity; see the discussion in ref. 12. The six-ring lactam **2** is unusually basic compared to the others, and has an unusually high m^{*} value for an amide, 0.6 being typical (24). It also has the fastest hydrolysis rate, the lowest activation energy, and the highest entropy of activation, followed by the seven-ring lactam **3**, the five-ring lactam **1**, and the eight-ring lactam **4**. It has been found that a six-ring lactam will rearrange to a five-ring lactam under suitable conditions (43), so it must be inherently less stable. The hydrolysis reaction is primarily enthalpy-controlled, with the enthalpy contributing about two-thirds of the overall free energy of activation; the entropies of activation for all four substrates are much the same as one another, quite negative at -32 ± 4 cal mol^{-1} K^{-1}. With the number of different bond angle changes, eclipsing interactions, and other ring strain effects possible in these systems, which will be different in the protonated and unprotonated forms, it is difficult to isolate any one factor as being the most important contributor to the relative basicities and reactivities, however.

If the r values of 3 associated with amide hydrolysis in fact turn out to be spurious, as the work in this paper would seem to indicate, then all reported r values other than 1 must be called into question too. For instance r values of 2 are commonly associated with the A2 ester hydrolysis mechanism (44). The excess acidity method has not been applied to many ester hydrolyses, but r values of 2 have been found for methyl benzoate and its *o*- and *p*-methyl derivatives (28), and to ethyl benzoate and various ethyl thiol- and thion-benzoates (45). (Values of $m^{\ddagger}$ for these substrates ranged from 0.74 to 1.30 (28, 45).) However, since the A2 ester hydrolysis mechanism

© 1998 NRC Canada

applies over a wide acidity range (typically 0–80 wt.% H_2SO_4), and the change in water activity with X is considerable over this range, allowing easy separation of variation due to one from variation due to the other, I think it likely that $r = 2$ for ester hydrolyses will hold up. Nevertheless, this will have to be checked.

What is needed to distinguish the mechanistic possibilities implied by Schemes 4–6 is an excess acidity analysis of much more amide hydrolysis data, preferably obtained at higher acidities. Fortunately there is quite a lot of this in the literature, and I hope to report further on this topic in future pages of this journal, probably starting with the benzamide and benzimidate results analyzed previously (6). More solvent isotope effect results would be useful too.

References

1. M. Liler. Reaction mechanisms in sulphuric acid. Academic Press, London. 1971. p. 189.
2. T.W.G. Solomons. Organic chemistry. 6th ed. Wiley, New York. 1996. p. 824; J. March. Advanced organic chemistry. 4th. ed. Wiley, New York. 1992. p. 385; T.H. Lowry and K.S. Richardson. Mechanism and theory in organic chemistry. 3rd. ed. Harper and Row, New York. 1987. p. 714; N.S. Isaacs. Physical organic chemistry. Longman Scientific and Technical, Harlow. 1987. p. 484.
3. K. Yates and J.B. Stevens. Can. J. Chem. **43**, 529 (1965).
4. J.F. Bunnett. J. Am. Chem. Soc. **83**, 4956 (1963); 4968 (1963); 4973 (1963); 4978 (1963).
5. K. Yates and J.C. Riordan. Can. J. Chem. **43**, 2328 (1965).
6. R.A. Cox and K. Yates. Can. J. Chem. **59**, 2853 (1981).
7. R.A. McClelland. J. Am. Chem. Soc. **97**, 5281 (1975).
8. M.L. Bender. J. Am. Chem. Soc. **75**, 5986 (1953); M.L. Bender, R.D. Ginger, and J.P. Uink. J. Am. Chem. Soc. **80**, 1044 (1958); C.A. Lane, M.F. Cheung, and G.F. Dorsey. J. Am. Chem. Soc. **90**, 6492 (1968).
9. R.A. Cox. Acc. Chem. Res. **20**, 27 (1987); R.A. Cox and K. Yates. Can. J. Chem. **57**, 2944 (1979).
10. H. Slebocka-Tilk, R.S. Brown, and J. Olekszyk. J. Am. Chem. Soc. **109**, 4620 (1987).
11. A.J. Bennet, H. Slebocka-Tilk, R.S. Brown, J.P. Guthrie, and A. Jodhan. J. Am. Chem. Soc. **112**, 8497 (1990).
12. P. Wan, T.A. Modro, and K. Yates. Can. J. Chem. **58**, 2423 (1980).
13. M.I. Vinnik and Y.V. Moiseev. Izv. Akad. Nauk SSSR Ser. Khim. 777 (708 in Engl. ed.) (1983).
14. M.M. Mhala and M.H. Jagdale. Indian J. Chem. **6**, 711 (1968).
15. M. Lajunen, M. Himottu, and K. Tanskanen-Lehti. Acta Chem. Scand. **51**, 515 (1997); M. Lajunen and J. Setälä. Acta Chem. Scand. **51**, 334 (1997).
16. R.A. Cox, K.-S. Cheon, and E. Buncel. Can. J. Chem. **76**, 896 (1998).
17. K.-S. Cheon, R.A. Cox, S.-R. Keum, and E. Buncel. J. Chem. Soc. Perkin Trans. 2, (1998). In press.
18. R.A. Cox. Can. J. Chem. **75**, 1093 (1997).
19. R.A. Cox. J. Chem. Soc. Perkin Trans. 2, 1743 (1997).
20. R.A. Cox. Can. J. Chem. **74**, 1774 (1996); 1779 (1996).
21. J.-P. Bégué, F. Benayoud, D. Bonnet-Delpon, A. D. Allen, R.A. Cox, and T. T. Tidwell. Gazz. Chim. Ital. **125**, 399 (1995); Y. Chiang, A.J. Kresge, P.A. Obraztsov, and J.B. Tobin. Croat. Chem. Acta, **65**, 615 (1992); M. Lajunen, M. Virta, and O. Kylläinen. Acta Chem. Scand. **48**, 122 (1994).
22. R.A. Cox, D.B. Moore, and R. S. McDonald. Can. J. Chem. **72**, 1910 (1994).
23. R.A. Cox and K. Yates. Can. J. Chem. **59**, 1560 (1981).
24. R.A. Cox and K. Yates. J. Am. Chem. Soc. **100**, 3861 (1978).
25. R.A. Cox, L.M. Druet, A.E. Klausner, T.A. Modro, P. Wan, and K. Yates. Can. J. Chem. **59**, 1568 (1981).
26. R.A. McClelland and W.F. Reynolds. Can. J. Chem. **54**, 718 (1976).
27. P.R. Bevington. Data reduction and error analysis for the physical sciences. McGraw–Hill, New York. 1969. pp. 232–245.
28. R.A. Cox, M.F. Goldman, and K. Yates. Can. J. Chem. **57**, 2960 (1979).
29. R.A. Cox and K. Yates. Can. J. Chem. **62**, 2155 (1984).
30. E.C.W. Clarke and D.N. Glew. Trans. Faraday Soc. **62**, 539 (1966).
31. P.R. Bevington. Data reduction and error analysis for the physical sciences. McGraw–Hill, New York. 1969. pp. 164–176.
32. R.A. Cox. J. Phys. Org. Chem. **4**, 233 (1991).
33. H.M. Grant, P. McTigue, and D.G. Ward. Aust. J. Chem. **36**, 2211 (1983).
34. M. Liler. J. Chem. Soc. B, 385 (1969).
35. J.P. Guthrie. J. Am. Chem. Soc. **118**, 12 886 (1996).
36. S. Antonczak, M.F. Ruiz-López, and J.L. Rivail. J. Am. Chem. Soc. **116**, 3912 (1994).
37. P. Denton, D. Horwell, C.D. Johnson, and D. Williamson. J. Chem. Res. Synop. 410 (1992); C.J. Giffney and C.J. O'Connor. J. Chem. Soc. Perkin Trans. 2, 1357 (1975); J.W. Barnett and C.J. O'Connor. J. Chem. Soc. Chem. Commun. 525 (1972); J. Chem. Soc. Perkin Trans. 2, 2378 (1972).
38. M.I. Vinnik and I.M. Medvetskaya. Zh. Fiz. Khim. **41**, 1775 (947 in Engl. ed.) (1967); M.I. Vinnik and L.R. Andreeva. Zh. Org. Khim. **9**, 2532 (2552 in Engl. ed.) (1973).
39. C.J. O'Connor and R.E. Ramage. Aust. J. Chem. **30**, 527 (1977).
40. C.J. Giffney and C.J. O'Connor. J. Chem. Soc. Perkin Trans. 2, 362 (1976).
41. R. Stewart and R. Srinivasan. Acc. Chem. Res. **11**, 271 (1978).
42. R.A. Cox and K. Yates. J. Org. Chem. **51**, 3619 (1986).
43. T. Fuji, S. Yoshifuji, and A. Tamai. Chem. Pharm. Bull. **19**, 369 (1971).
44. K. Yates. Acc. Chem. Res. **4**, 136 (1971).
45. R.A. Cox and K. Yates. Can. J. Chem. **60**, 3061 (1982).

© 1998 NRC Canada

The acid dissociation constant of triphenylethenethiol, a simple thioenol, and that of its oxygen-enol analog

Yvonne Chiang, A. Jerry Kresge, Norman P. Schepp, Vladimir V. Popik, Zvi Rappoport, and Tzvia Selzer

Abstract: The acidity constant, $pQ_a^E = 8.49$, for the stable thioenol, triphenylethenethiol, was determined by spectrophotometric titration, and that, $pQ_a^E = 11.37$, for its unstable oxygen analog, triphenylethenol, was determined by analysis of its ketonization rate using enol generated flash photolytically from triphenylvinyl bromide. (These acidity constants are *concentration* quotients applicable at 0.10 M ionic strength in 50 vol.% aqueous methanol.) This appears to be the first determination of the acid strength of a simple thioenol. Triphenylethenethiol was unreactive in dilute acid or base, but in concentrated perchloric acid solutions it was slowly transformed into diphenylacetophenone and 2,3-diphenylbenzo[*b*]thiophene; the mechanisms of these reactions are believed to involve rapid equilibrium protonation of the enol on the β-carbon followed by rate-determining capture of the cation so formed, either externally by solvent or internally by one of the β-phenyl groups of the ion.

Key words: enol ketonization, thioenol, flash photolysis, vinyl halide.

Résumé : Utilisant un titrage spectrophotométrique, on a déterminé la constante d'acidité, pQ_a^E, du thioénol stable, triphényléthènethiol, alors que l'on a déterminé celle, pQ_a^E, de son analogue oxygéné instable, le triphényléthénol, par analyse de sa vitesse de cétonisation en utilisant l'énol généré par photolyse éclair à partir du bromure de triphénylvinyle. (Ces constantes d'acidité sont les quotients de *concentration* applicables à une force ionique de 0,10 M, dans une solution aqueuse de méthanol à 50% en volume.) Il semble que ce travail corresponde à la première détermination de la force acide d'un thioénol simple. Le triphényléthènethiol ne réagit pas en milieux acide ou base faibles; toutefois, en solutions concentrées d'acide perchlorique, il se transforme lentement en diphénylacétophénone et en 2,3-diphénylbenzo[*b*]thiophène. On croit que les mécanismes de ces réactions impliquent une protonation à équilibre rapide de l'énol sur le carbone-β, suivie d'une capture cinétiquement limitante du cation ainsi formé, d'une façon externe par le solvant ou externe par l'un des groupes β-phényles de l'ion.

Mots clés : cétonisation des énols, thioénol, photolyse éclair, halogénure de vinyle.

[Traduit par la rédaction]

Introduction

Simple enols are generally much less stable than their aldehyde or ketone tautomers (1). The same, however, is not true of simple thioenols: in the sulfur systems, enol and keto isomers usually exist in comparable amounts, and the enol is sometimes even the dominant tautomer (2). A recently examined example of the latter situation is provided by triphenylethenethiol, **1**, which could not be converted to its keto isomer, diphenylthioacetophenone, **2**, eq. [1], under conditions much more drastic than usually required to equilibrate oxygen keto–enol systems (3). This predominance of the enol isomer in the system of eq. [1] is consistent with the estimate $pK_E = 2.7$ for the oxygen system[2] and the suggestion that the

[1] 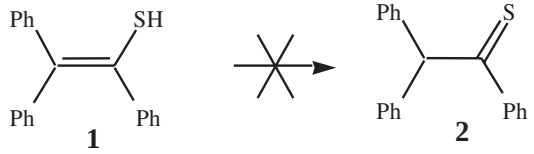

ratio of the keto–enol equilibrium constant of a sulfur system to that of its oxygen analog, $K_E(S)/K_E(O)$, will generally be equal to or greater than 10^6 (3).

We have taken advantage of this stability of triphenylethenethiol to measure the equilibrium constant for its ionization as an acid, eq. [2], using a conventional spectroscopic method based upon the difference in uv absorbance of

Received December 16, 1997.

This paper is dedicated to Professor Erwin Buncel in recognition of his contributions to Canadian chemistry.

Y. Chiang, A.J. Kresge,[1] N.P. Schepp, and V.V. Popik. Department of Chemistry, University of Toronto, Toronto, ON M5S 3H6, Canada.
Z. Rappoport and T. Selzer. Department of Organic Chemistry, The Hebrew University, Jerusalem 91904, Israel.

[1] Author to whom correspondence may be addressed. Telephone/Fax: (416) 978–7259. E-mail: akresge@alchemy.chem.utoronto.ca

[2] This estimate is based upon $pK_E = 0.98$ for diphenylacetaldehyde (4) and the effect of adding another phenyl group, obtained from $pK_E = 6.23$ for acetaldehyde (5) and $pK_E = 7.96$ for acetophenone (6).

© 1998 NRC Canada

[2] 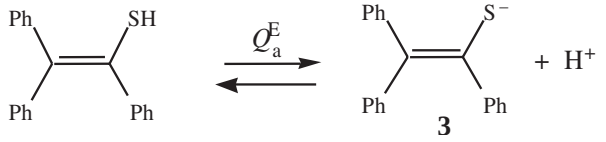

the enol (λ_{max} = 285 nm) and its enolate ion, **3** (λ_{max} = 315 nm). This, to the best of our knowledge, is the first determination of the acidity constant of a simple thioenol.

To assess the effect on enol acidity of replacing oxygen with sulfur, we also determined the equilibrium constant for the ionization of triphenylethenol, **4**, eq. [3]. This enol, however, is not stable with respect to its keto isomer, and it reverts to the latter too rapidly to allow measurements by the method we employed for the thio analog. We therefore used a flash

[3] 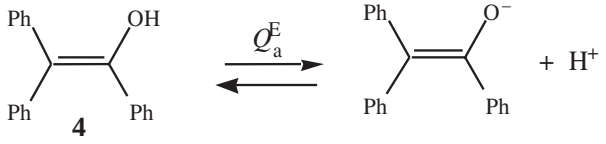

photolytic technique instead: we generated the enol by photoionization of triphenylvinyl bromide, **5**, and subsequent hydration of the ensuing vinyl cation, **6**, eq. [4], and then determined the acidity constant of the enol, **4**, from the dependence of its rate of ketonization to diphenylacetophenone, **7**, upon the acidity of the medium.

Because some of the substrates used were insufficiently soluble in a purely aqueous solvent, this work was done in 50 vol.% aqueous methanol.

[4] 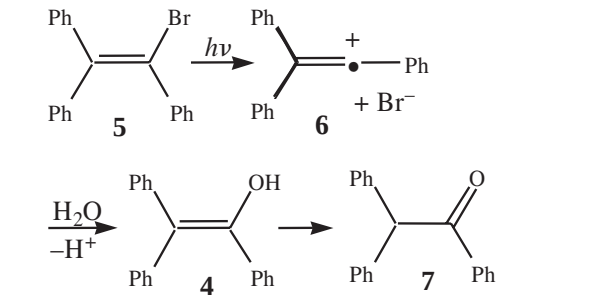

Experimental section

Materials

Triphenylethenethiol was a sample that had been prepared before (3), and 2,3-diphenylbenzo[*b*]thiophene was kindly provided by Dr. T. Kitamura (7). All other materials were best available commercial grades.

Spectrophotometric pK_a determination

The acid dissociation constant of triphenylethenethiol was determined by monitoring the absorbance of this substance in solutions of different acidity. The solvent was 50 vol.% aqueous methanol, and its acidity was controlled by using either perchloric acid or sodium hydroxide, or acetic acid, biphosphate ion, tris(hydroxymethyl)methylamine, or ammonia buffers; the ionic strength of these solutions was maintained at 0.10 M by adding sodium perchlorate as required.

Measurements were made at λ = 340 nm, the wavelength at which the difference in absorption between triphenylethenethiol and its thiolate anion is greatest. A Cary 2200 spectrometer, with cell compartment thermostatted at 25.0 ± 0.05°C, was used. The absorbance of the acid, base, or buffer solution without substrate was first recorded, a fixed amount of an acetonitrile stock solution of substrate (0.02 M) was then added (10.0 μL to 3.00 mL or 5.00 μL to 1.00 mL), and the absorbance was recorded again. The difference, Δ*A*, between such pairs of absorbance readings was then calculated, and the relationship between Δ*A* and the hydrogen ion concentration of the solutions was analyzed by least-squares fitting of eq. [5]; here A_B and A_A are the limiting absorbances of the basic and acidic forms of the substrate and *Q* is its acidity constant.[3]

$$[5] \qquad \Delta A = \frac{A_B Q_a^E + A_A[H^+]}{Q_a^E + [H^+]}$$

Hydrogen ion concentrations of the solutions in which the absorbances were recorded were determined by measuring their pH using a Beckman Research pH meter, in conjunction with a ROSS combination electrode model no. 81–02 (Orion Research Inc.), and then converting that reading into [H^+] with the aid of eq. [6] (8*a*).

$$[6] \qquad -\log[H^+] = pH_{meas} + \log \gamma_{H^+} - \delta = pH_{meas} - 0.205$$

In this equation, γ_{H^+} is the activity coefficient of H^+, which was calculated using the Debye–Hückel equation (8*b*) with parameters appropriate to the medium employed, and δ is an empirical parameter (8*a*). The validity of this method was checked by measuring the pH of five perchloric acid solutions of known concentration in the range 0.02–0.10 M. The results obtained gave an average value of ($-\log[H^+] - pH_{meas}$) = –0.2049 ± 0.0061, in excellent agreement with eq. [6].

Flash photolysis

Flash photolytic rate determinations were made using a conventional flash-lamp system with cell compartment thermostatted at 25.0 ± 0.05°C that has already been described (5). Measurements were carried out in perchloric acid and sodium hydroxide solutions whose ionic strength was maintained at 0.10 M; substrate (triphenylvinyl bromide) concentrations were (2–3) × 10^{-5} M. The lifetimes of the transient species observed in basic solution were short enough to be analyzed by the flash photolysis monitoring system, but those observed in acidic solution were too long-lived (*t* = 15–40 min). For rate measurements in acidic solutions, therefore, transients were generated by a single flash in the flash system, and the reacting solutions were then transferred to a Cary 118 spectrometer, with cell compartment thermostatted at 25.0 ± 0.05°C, for rate measurement there. Decay of the transients observed in both kinds of experiment obeyed the first-order rate law accurately, and observed first-order rate constants were calculated by least-squares fitting of an exponential function.

Results

Spectrophotometric pK_a determination

The equilibrium constant for ionization of triphenylethenethiol

[3] This is a *concentration* dissociation constant, applicable at ionic strength = 0.10 M.

© 1998 NRC Canada

Fig. 1. Spectrophotometric titration curve for the acid ionization of triphenylethenethiol in 50 vol.% aqueous methanol at 25°C.

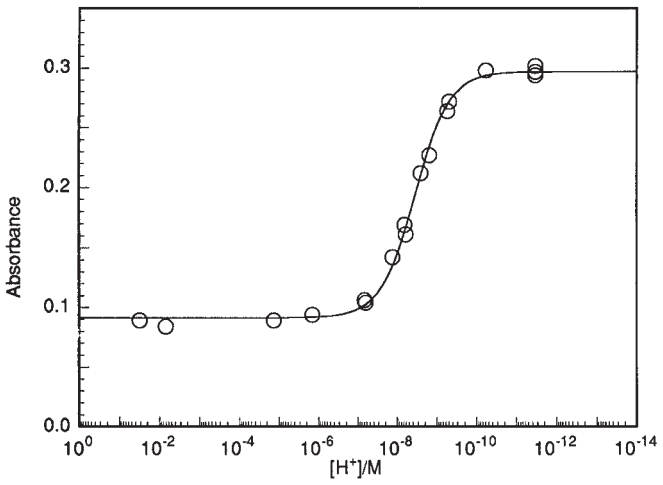

as an acid, eq. [2], was determined by measuring the absorbance of this substance dissolved in 50 vol.% aqueous methanol solutions of different acidity. Two series of experiments were carried out, one at a fixed total concentration of substrate of 7×10^{-5} M and another at 1×10^{-4} M. The data so obtained are summarized in Table S1.[4]

As Fig. 1 illustrates, these data describe the expected titration curve, eq. [5], well. Least-squares analysis gave the results $Q_a^E = (3.48 \pm 0.22) \times 10^{-9}$ M, $pQ_a^E = 8.46 \pm 0.03$, and $Q_a^E = (3.07 \pm 0.21) \times 10^{-9}$ M, $pQ_a^E = 8.51 \pm 0.03$. The weighted average of these gives $Q_a^E = (3.27 \pm 0.15) \times 10^{-9}$ M, $pQ_a^E = 8.49 \pm 0.02$, as the best value of this acidity constant.

Reaction of triphenylethenethiol in strong acid

Except for the acid ionization described above, triphenylethenethiol proved to be unreactive in dilute 50 vol.% aqueous methanol solutions of acid or base. In concentrated perchloric acid, however, its uv absorbance did decrease slowly in an acid-catalyzed process, and some rate measurements were made by monitoring this decay at $\lambda = 300$ nm. The rate constants so obtained are summarized in Table S2.[4] These data were extrapolated down to dilute solution by the Cox–Yates method (9) using the X_0 acidity function (10) on the assumption that values of X_0 in 50 vol.% aqueous methanol are the same as those in wholly aqueous solutions of the same acid concentration. This gave $k_{H^+} = (2.72 \pm 0.41) \times 10^{-8}$ M^{-1} s^{-1} as the dilute solution rate constant.

A product study was performed by allowing 0.0025 M triphenylethenethiol dissolved in 4 M perchloric acid in 2:1 methanol:water (vol/vol) to react for 36 h, and then subjecting the resulting solution to HPLC analysis. This showed that two products were formed in comparable amounts, and spiking with authentic samples showed them to be diphenylacetophenone, **7**, and 2,3-diphenylbenzo[*b*]thiophene, **8**.

[4] Tables S1–S4 may be purchased from: The Depository of Unpublished Data, Document Delivery, CISTI, National Research Council Canada, Ottawa, Canada K1A OS2.

Fig. 2. Relationship between sodium hydroxide concentration and rates of ketonization of triphenylethenol in 50 vol.% aqueous methanol solution at 25°C.

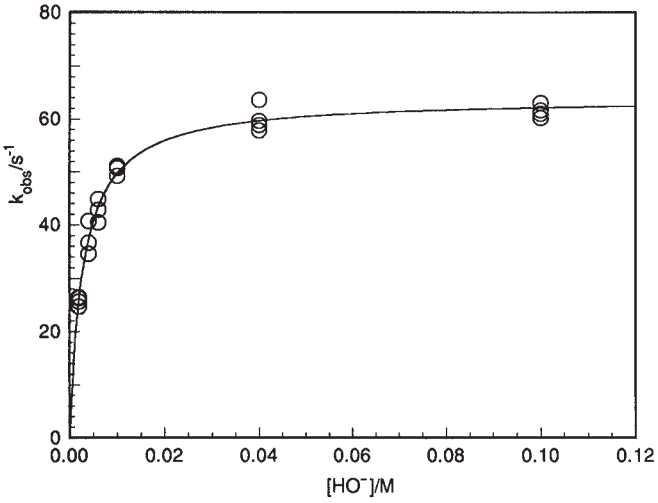

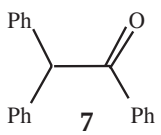

7

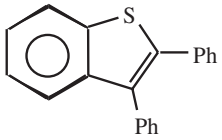

8

Flash photolysis

Flash photolysis of vinyl halides is known to produce vinyl cations (11), which, in the presence of water, are hydrated to enols; the enols then ketonize to their carbonyl isomers (11*b*,*c*). Evidence that this is the sequence of reactions that occurred in the present study upon flash photolysis of triphenylvinyl bromide, as depicted in eq. [4], is provided by the uv spectral changes that took place. The uv spectrum of triphenylvinyl bromide in 50 vol.% aqueous methanol consists of a strong absorption band with $\lambda_{max} = 290$ nm. Upon flashing, this band immediately increased in intensity in a process that was complete within the duration of the flash (50 ms). Such a change in intensity without the appearance of any new absorption bands is to be expected for the conversion of a vinyl halide to a vinyl alcohol with no change in the other double-bond substituents; the lifetime of vinyl cations in aqueous media, moreover, is known to be much shorter than 50 ms (11*c*), and formation of the enol would be expected to be immediate on the time scale of the present experiment. This increase in absorbance at $\lambda = 290$ nm was followed by a decrease whose velocity was catalyzed by both hydronium and hydroxide ions, with saturation of the hydroxide ion catalysis at high basicities. Such behavior is characteristic of the ketonization of simple enols, where saturation of hydroxide ion catalysis represents conversion of enol to enolate ion (12). The absorbance decrease at $\lambda = 290$ was also accompanied by an increase occurring at the same rate at $\lambda = 250$ nm, where diphenylacetophenone, the expected product of the present ketonization reaction, has an absorption maximum. It appears safe to conclude, therefore, that the process monitored here was ketonization of triphenylethenol to diphenylacetophenone.

Rates of this ketonization reaction were measured in

© 1998 NRC Canada

0.02–0.10 M perchloric acid solutions. The data are summarized in Table S3.[4] Observed rate constants proved to be accurately proportional to acid concentration, and the data were therefore analyzed by least-squares fitting of eq. [7]. This produced the result $k_{H^+} = (1.05 \pm 0.04) \times 10^{-2}$ M^{-1} s^{-1} for the acid-catalyzed reaction and $k_{uc} = (2.11 \pm 0.30) \times 10^{-4}$ s^{-1} for an "uncatalyzed" process.

[7] $$k_{obs} = k_{uc} + k_{H^+}[H^+]$$

Rates of ketonization of triphenylethenol were also measured in sodium hydroxide solutions over the concentration range 0.002–0.10 M. These data are summarized in Table S4.[4] As Fig. 2 shows, observed first-order rate constants increased with increasing basicity at low hydroxide ion concentrations, but at higher basicity the effect diminished, and rate constants finally reached a constant value independent of hydroxide ion concentration. Such behavior is commonly found in enol ketonization. It is known to be caused by a shift in the initial state of the reaction from enol to enolate ion, plus the facts that ketonization occurs by rate-determining protonation of the substrate on the β-carbon and that enolate ions are much more susceptible to such electrophilic attack than are enols (12). In weakly basic solutions, therefore, where the substrate exists mainly as un-ionized enol, ketonization will occur as shown in eq. [8]: rapid equilibrium ionization of the enol will be followed by rate-determining reaction of the more labile enolate ion by proton transfer from the only available proton donor, the hydroxylic solvent. Since hydrogen ions are produced in the pre-equilibrium step but are not used up in the rate-determining step, the overall reaction rate will show an inverse dependence on hydrogen ion concentration or a direct dependence on hydroxide ion concentration. This apparent hydroxide ion catalysis, however, will diminish as the hydroxide ion concentration increases and the position of the pre-equilibrium step

[8]

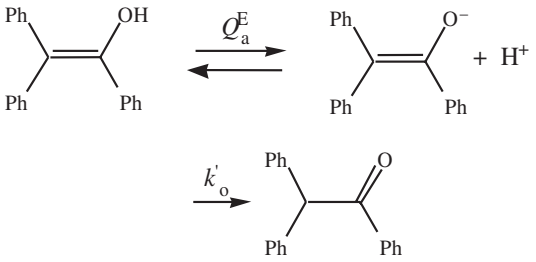

shifts toward enolate ion, and that will produce the saturation behavior shown in Fig. 2.

The rate law that applies to the reaction scheme of eq. [8] is shown in eq. [9]. Least-squares fitting of the data using this equation gave $k'_o = 63.1 \pm 0.07$ s^{-1} and $Q_a^E = (4.28 \pm 0.22) \times 10^{-12}$ M, $pQ_a^E = 11.37 \pm 0.02$.[3] Hydrogen ion concentrations needed for this purpose were obtained from pH meter readings with the aid of eq. [6].

[9] $$k_{obs} = \frac{k'_o Q_a^E}{[H^+] + Q_a^E}$$

Discussion

9 **10**

Comparison of the rate constants obtained here for the acid-catalyzed ketonization of triphenylethenol and the disappearance of triphenylethenethiol in concentrated perchloric acid solutions shows that the oxygen enol is 3.8×10^5 times as reactive as the thioenol. This is an unusually large oxygen-to-sulfur rate ratio for rate-determining protonation of a carbon–carbon double bond activated by these atoms; for example, the acid-catalyzed hydrolysis of ethyl vinyl ether, **9**, and ethyl vinyl sulfide, **10**, both of which occur by rate-determining protonation of the substrate on its β-carbon atom, give an oxygen-to-sulfur rate ratio of only 37 (13), some 10 000 times smaller than the present value.

This striking difference suggests that the disappearance of triphenylethenethiol in concentrated perchloric acid does not represent rate-determining protonation of this substance on its β-carbon atom, but rather that such protonation occurs rapidly and reversibly and is then followed by some other, much slower, reaction step. This hypothesis is consistent with the conclusion reached before (3) that the enol in this system is more stable than the thioketone, for the ketone, once formed, would then revert to the enol. It is also consistent with our observation that the oxygen ketone and a thiophene derivative, rather than the thioketone, are the products of the concentrated acid reaction. It is likely that the oxygen ketone is formed by occasional capture, by water or methanol, of the cation produced by reversible carbon protonation of the thioenol, followed by decomposition of that adduct, as shown in eq. [10], and that the thiophene product is formed by intramolecular capture of this cation by one of its β-phenyl groups, in an electrophilic aromatic substitution reaction, followed by aromatization of the thiophene ring, as shown in eq. [11]; a similar cyclization to a benzofuran has been observed in an analogous stable oxygen-enol system (14).

These observations reinforce the conclusion reached before (3) that the enol is the more stable tautomer in the diphenylthioacetophenone keto–enol system. Additional evidence that this is so is provided by the fact that we were able to determine the acidity constant of this thioenol by a conventional slow method. The limiting rate constant for ketonization of the corresponding oxygen enol, triphenylethenol, determined by our flash photolysis experiments, is 63 s^{-1}. Applying a sulfur-to-oxygen rate ratio of ca. 10^{-2} to this, as expected, for example, on the basis of the rates of reaction of ethyl vinyl

[10]

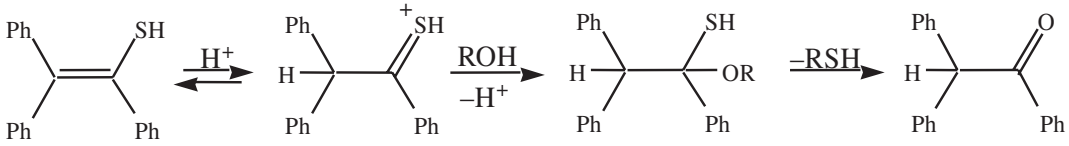

© 1998 NRC Canada

[11] 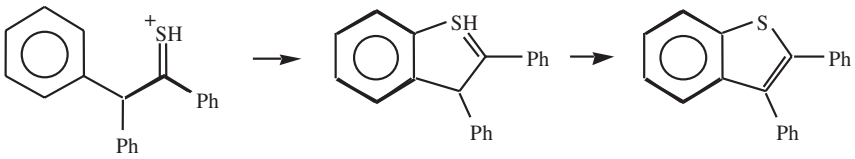

ether and ethyl vinyl sulfide discussed above, puts the lifetime of triphenylethenethiol at about 1 s; this short lifetime would have made our conventional measurements impossible if the enol were not the stable isomer.

We are aware of no previous determination of the acidity constant of a simple thioenol, and we consequently cannot compare the value we have obtained with other results. It is interesting, however, that our value makes triphenylethenethiol, with $pQ_a^E = 8.49$, a considerably stronger acid than its oxygen analog, triphenylethenol, with pQ_a^E = 11.37, for this is consistent with the fact that simple thiols are considerably stronger acids than simple oxygen alcohols (15). A quantitative comparison might be more appropriately based upon phenols rather than alcohols, for phenols, like enols, have their acidic groups attached to carbon–carbon double bonds, and enol pK_a's are in fact quite similar to phenol pK_a's (12). It is significant, therefore, that the difference in acid strength between the oxygen and sulfur enols examined here, ΔpQ_a^E = 2.88, is not unlike the difference in acidity between phenol (pK_a = 10.00 (16)) and thiophenol (pK_a = 6.49 (17)), ΔpK_a = 3.51.

Acknowledgements

We are grateful to Professor T. Kitamura for supplying 2,3-diphenylbenzo[*b*]thiophene and to the Natural Sciences and Engineering Research Council of Canada for financial support of this research.

References

1. J. Toullec. *In* The chemistry of enols. *Edited by* Z. Rappoport. Wiley–Interscience, New York. 1990. pp. 323–398.
2. F. Duus. *In* Comprehensive organic chemistry. Vol. 3. *Edited by* D. Barton and W.D. Ollis. Pergamon Press, Exeter, U K. 1979. pp. 385–388.
3. T. Selzer and Z. Rappoport. J. Org. Chem. **61**, 5462 (1996).
4. Y. Chiang, A.J. Kresge, and E.T. Krogh. J. Am. Chem. Soc. **110**, 2600 (1988).
5. Y. Chiang, M. Hojatti, J.R. Keeffe, A.J. Kresge, N.P. Schepp, and J. Wirz. J. Am. Chem. Soc. **109**, 4000 (1987).
6. J.R. Keeffe, A.J. Kresge, and J. Toullec. Can. J. Chem. **64**, 1224 (1986).
7. T. Kitamura, S. Soda, K. Morizane, Y. Fujiwara, and H. Taniguchi. J. Chem. Soc. Perkin Trans. 2, 473 (1996).
8. R.G. Bates. Determination of pH theory and practice. Wiley–Interscience, New York. 1973. (*a*) pp. 243–245; (*b*) p. 216.
9. R.A. Cox. Acc. Chem. Res. **20**, 27 (1987).
10. R.A.Cox and K. Yates. Can. J. Chem. **59**, 2116 (1981); A.J. Kresge, H.J. Chen, G.L. Capen, and M.F. Powell. Can. J. Chem. **61**, 249 (1983).
11. (*a*) W. Schnabel, I. Naito, T. Kitamura, S. Kobayashi, and H. Taniguchi. Tetrahedron, **36**, 3229 (1980); S. Kobayashi, T. Kitamura, H. Taniguchi, and W. Schnabel. Chem. Lett. 2101 (1983); S. Kobayashi, Q.Q. Zhu, and W. Schnabel. Z. Naturforsch. B: Chem. Sci. **43**, 825 (1988); F.I.M. van Ginkel, R.J. Wisser, C.A.G.O. Varma, and G. Lodder. J. Photochem. **30**, 453 (1985); R.A. McClelland, F. Cozens, and S. Steenken. Tetrahedron Lett. **31**, 2821 (1990); (*b*) A.J. Kresge and N.P. Schepp. J. Chem. Soc. Chem. Commun. 1548 (1989); (*c*) Y. Chiang, R. Eliason, J. Jones, A.J. Kresge, K.L. Evans, and R.D. Gandour. Can. J. Chem. **71**, 1964 (1993).
12. J.R. Keeffe and A.J. Kresge. *In* The chemistry of enols. *Edited by* Z. Rappoport. Wiley–Interscience, New York. 1990. pp. 399–480.
13. R.A.McClelland. Can. J. Chem. **55**, 548 (1977).
14. M. Schmittel and U Baumann. Angew. Chem. Int. Ed. Engl. **29**, 541 (1990).
15. R. Stewart. The proton: applications to organic chemistry. Academic Press, New York. 1985. pp. 45–46.
16. A.J. Biggs. Trans. Faraday Soc. **52**, 35 (1956).
17. C.L. Liotta, E.M. Perdue, and H.P. Hopkins, Jr. J. Am. Chem. Soc. **96**, 7981 (1974).

© 1998 NRC Canada

Carbon versus oxygen nucleophilic selectivity in the reaction of the aryloxide ions, 2,6- and 3,5-di-*tert*-butylphenoxide, with the 2-[(nitro)$_x$aryl]-4,6-dinitrobenzotriazole 1-oxide series of super-electrophiles. Stereoelectronic factors on C-7 Meisenheimer complex formation versus C-1′ S_NAr displacement

Julian M. Dust and Richard A. Manderville

Abstract: The 2-[(nitro)$_x$aryl]-4,6-dinitrobenzotriazole 1-oxides (**1**, Pi-DNBT ($x = 3$); **2**, DNP-DNBT ($x = 2$); **3**, NP-DNBT ($x = 1$)) are electron-deficient nitro-substituted heteroaromatic substrates that possess two sites for nucleophilic attachment: C-7 and C-1′. Generally, attack at the super-electrophilic C-7 site yields spectroscopically observable anionic σ-bonded adducts, whereas attack at C-1′ leads to displacement products in an overall process of nucleophilic aromatic substitution (S_NAr). To gain an understanding of the factors affecting C-1′ versus C-7 attack by potentially ambident aryloxide (C- and O-)nucleophiles, we have monitored the reactions of **1**–**3** with 2,6-di-*tert*-butylphenoxide (2,6-ArO$^-$) and 3,5-di-*tert*-butylphenoxide (3,5-ArO$^-$) using 400 MHz ^{1}H NMR spectroscopy (deuterated dimethyl sulfoxide solvent at ambient temperature). The results indicate that 2,6-ArO$^-$ acts only as a C-nucleophile with O-attack precluded, presumably by the sterically demanding *tert*-butyl groups flanking the O-nucleophilic centre. Although 2,6-ArO$^-$ reacts preferentially at C-7 of **1–3**, the biphenyl derivative that arises from C-1′ attack is also observed with **1**, the first time that C-nucleophilic attack has been seen at this electrophilic site. In contrast, 3,5-ArO$^-$ acts only as an O-nucleophile, also as a consequence of the steric hindrance to the C-4 position; this aryloxide reacts entirely at C-1′ of Pi-DNBT but also exclusively at C-7 of **3**. However, with DNP-DNBT, **2**, both the C-7 O-adduct and C-1′ displacement products are noted; attack at C-1′ is dominant. The selectivity (C-7 versus C-1′) found in these reactions is discussed with emphasis given to stereoelectronic factors that may stabilize the putative C-1′ O-adducts.

Key words: aryloxides, super-electrophiles, Meisenheimer complexes, 2-[(nitro)$_x$aryl]-4,6-dinitrobenzotriazole 1-oxides.

Résumé : Les 1-oxydes de 2-[(nitro)$_x$aryl]-4,6-dinitrobenzotriazole (**1**, Pi-DNBT ($x = 3$); **2**, DNP-DNBT ($x = 2$); **3**, NP-DNBT ($x = 1$)) sont des substrats hétéroaromatiques électrodéficients porteurs de groupes nitro qui possèdent deux sites, C-7 et C-1′, permettant d'effectuer des substitutions nucléophiles. En général, l'attaque du site superélectrophile C-7 conduit à la formation d'adduits anioniques à liaisons-σ qui peuvent être observés par spectroscopie alors que l'attaque en C-1′ conduit à des produits de déplacement résultant d'un processus global de substitution aromatique nucléophile (S_NAr). Afin de mieux comprendre les facteurs pouvant affecter les attaques en C-1′ et en C-7 par des nucléophiles aryloxydes ambidents (C- et O-), on a suivi les réactions des composés **1–3** avec le 2,6-di-*tert*-butylphénolate (2,6-ArO$^-$) et le 3,5-di-*tert*-butylphénolate (3,5-ArO$^-$) en faisant appel à la spectroscopie de résonance magnétique nucléaire du ^{1}H, à 400 MHz (diméthylsulfoxyde deutéré comme solvant, à la température ambiante). Les résultats indiquent que le 2,6-ArO$^-$ n'agit que comme nucléophile pour le C alors que l'attaque en O est empêchée, probablement à cause des contraintes stériques imposées par les groupes *tert*-butyles voisins du centre nucléophile O. Même si le 2,6-ArO$^-$ réagit préférentiellement en position C-7 des composés **1–3**, on a aussi observé, dans le cas du composé **1**, la formation du dérivé biphényle qui provient de l'attaque en C-1′; c'est la première fois que l'on observe une attaque nucléophilique C pour ce site électrophile. Par ailleurs, le 3,5-ArO$^-$ ne réagit que comme nucléophile O; ceci résultat de l'empêchement stérique en position C-4; cet aryloxyde ne réagit qu'en position C-1′ du

Received September 24, 1997.

This article is dedicated to Professor Erwin Buncel, who has been a mentor to us both and who first interested us in this area of research.

J.M. Dust.[1] Environmental Science Unit and Chemistry Department, Sir Wilfred Grenfell College, Corner Brook, NF A2H 6P9, Canada.
R.A. Manderville.[1] Department of Chemistry, Wake Forest University, P.O. Box 7486, Winston-Salem, NC 27109, U.S.A.

[1] Authors to whom correspondence may be addressed: JMD: Telephone (709) 637-6330. Fax: (709) 639-8125. E-mail: jdust@beothuk.swgc.mun.ca; RAM: Telephone (910) 759-5513. Fax: (910) 759-4656. E-mail: manderra@wfu.edu

© 1998 NRC Canada

Pi-DNBT, mais il réagit aussi en position C-7 avec le composé **3**. Toutefois, avec le DNP-DNBT, **2**, on observe la formation de l'adduit O en C-7 ainsi que des produits de substitution en C-1′; l'attaque en C-1′ est prédominante. On discute de la sélectivité (C-7 versus C-1′) observée dans ces réactions en insistant sur les facteurs stéréoélectroniques qui peuvent stabiliser les adduits O en C-1′.

Mots clés : aryloxydes, superélectrophiles, complexes de Meisenheimer, 1-oxydes de 2-[(nitro)$_x$aryl]-4,6-dinitrobenzotriazole.

[Traduit par la rédaction]

Introduction

The 2-[(nitro)$_x$aryl]-4,6-dinitrobenzotriazole 1-oxides (**1**–**3**, 2-Ar(NO$_2$)$_x$-DNBT) are novel electrophiles that yield anionic σ-bonded adducts, as well as displacement products, as a result of nucleophilic reaction (1). This series of compounds is related structurally to the super-electrophile, 4,6-dinitrobenzofuroxan (**4**, DNBF). As a neutral 10 π-electron heteroaromatic,

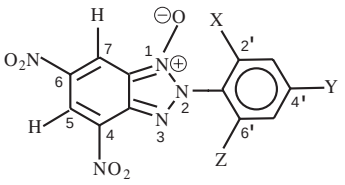

X = Y = Z = NO$_2$; **1**, Pi-DNBT

X = Y = NO$_2$, Z = H ; **2**, DNP-DNBT

X = Z = H, Y = NO$_2$; **3**, NP-DNBT

4, has been assessed to be a more powerful electron-pair or bond acceptor than such powerful electrophiles as the proton and the 4-nitrobenzenediazonium ion (2). Consequently, even weakly nucleophilic solvents such as water and methanol react with DNBF to yield the C-7 hydroxide and methoxide anionic σ-bonded (Meisenheimer) complexes, as shown (eq. [1]).

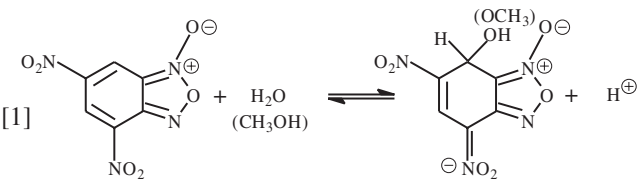

[1]

4

These adducts are more stable than the corresponding adducts formed by 1,3,5-trinitrobenzene (TNB), by a factor of 10^{10} (3–6). As implied by this comparison the TNB·OH$^-$ and TNB·OCH$_3^-$ Meisenheimer complexes are not formed unless the anionic nucleophiles, hydroxide and methoxide, are used. Further evidence for the super-electrophilicity of DNBF is provided by the observation that **4** reacts *quantitatively* with such weak carbon nucleophiles as aniline (7) and 1,3,5-trimethoxybenzene (8, 9), as well as pyrroles, indoles, thiophenes, and furans (10–12), to give Meisenheimer C-bonded adducts that are formally products of electrophilic aromatic substitution of the respective nucleophilic benzene rings (13). In general, DNBF is a very strong electrophile, notably towards weak oxygen or nitrogen bases and weakly nucleophilic double bonds (14, 15).

Two factors differentiate the 2-nitroaryl-4,6-dinitrobenzotriazole 1-oxide series, **1**–**3**, from its structural analog, **4**. First, each member of the series possesses two main electrophilic sites for nucleophilic attack: C-7 and C-1′. Second, the C-7 site appears to be less electrophilic than the corresponding position in DNBF.

With regard to the first factor, attack of alkoxide nucleophiles at C-7 generally leads to formation of relatively persistent C-7 σ-bonded anionic adducts. In contrast, attack at C-1′ results in formation of unobserved metastable Meisenheimer adducts that yield products of an overall S_NAr displacement (16). The C-7 site is super-electrophilic, whereas the C-1′ site is of normal electrophilicity, perhaps comparable to C-1 in picryl halides. In the strictest sense the two sites are not insulated from one another, but to a first approximation we may treat them as though they were, and consequently, we have an internal comparison of super-electrophilic and normal electrophilic centres built into the same molecule.

While prevailing evidence supports the view that the C-7 site is super-electrophilic, it also appears to be less electrophilic than the corresponding position in DNBF. Thus, the C-7 site in **1** (2-picryl-4,6-dinitrobenzotriazole 1-oxide, Pi-DNBT) has been assessed to be intermediate in electrophilicity: more electrophilic than the standard electrophile used in Meisenheimer complexation studies, TNB, but less electrophilic than DNBF, on the basis of the reactivity of the three electrophiles towards ethanethiol (7*b*). The C-7 sites of **2** and **3** also exhibit enhanced electrophilicity as compared to the C-1 site of TNB, on the basis of their reactivity with phenoxide ion, as a carbon-centred nucleophile (1*a*–*c*).

Recently we have examined the reactions of various aryloxide nucleophiles with DNBF (17) and with picryl halides (18). In the case of DNBF, the O-centred C-7 adduct of phenoxide could be observed at –40°C (400 MHz NMR) in the novel acetonitrile–dimethoxyethane (MeCN-d_6:DME-d_6 1:1 v/v) medium but *not at ambient temperature* in deuterated dimethyl sulfoxide (DMSO-d_6). Similar behaviour has been reported in the TNB–PhO$^-$ reaction system (19). Consequently, it is not surprising that the related O-adduct of phenoxide of Pi-DNBT was similarly not detected in the room temperature DMSO-d_6 system (1*e*); in accord with the intermediate C-7 electrophilicity assigned to Pi-DNBT as compared to TNB and DNBF. However, attack by PhO$^-$ as an O-nucleophile at C-1′ of **1** leads to facile displacement of the 4,6-dinitrobenzotriazole 1-oxyanion (DNBT$^-$) (1*e*, 20) similar to the reactivity observed with picryl chloride and picryl fluoride, where clean formation of the same phenoxy-2,4,6-trinitrobenzene product occurred (17). On the other hand, the phenoxide C-7 carbon-bonded adducts (*ortho* and *para*) of DNP-DNBT, **2**, and NP-DNBT, **3**, form promptly at room temperature; C-1′ displacement occurs via O-attack and is a relatively slow process (1*c*). Thus, reaction of aryloxides at C-7, whether as C- or O-nucleophiles, could only be observed on the time scale of these NMR experiments when the barrier to attack at C-1′ had

© 1998 NRC Canada

Table 1. The ^{1}H NMR spectroscopic characteristics of the O-bonded C-7 σ-adducts (**1a**, **2a**, **3a**, **4a**) formed by Pi-DNBT, **1**, DNP-DNBT, **2**, NP-DNBT, **3**, and DNBF, **4**, with 3,5-di-*tert*-butylphenoxide (3,5-ArO$^-$) and methoxide.[a,b]

	Chemical shifts, ppm (J = Hz)						
Adduct	H-7	H-5	H-2′	H-3′	H-5′	H-6′	Signals of C-7 attached group
4a·3,5-OAr$^-$	6.71, s	8.66, s					1.19, s, *meta*-di-*t*-Bu; 6.68, d, (1.5), H-*ortho*; 7.01, t, (1.5), H-*para*
1a·OCH_3^-	6.04, s	8.76, s		9.30, s	9.30, s		3.26, s, CH_3
2a·OCH_3^-	5.96, d (0.60)	8.76, d (0.60)		8.91, d (8.8)	8.78, d[c] (2.2)	8.19, d (2.2)	3.29, s, CH_3
2a·3,5-OAr$^-$	6.71, s	8.68, s		8.91, d (2.4)	8.78, dd (2.4, 8.8)	8.12, d (8.8)	1.18, s, *meta*-di-*t*-Bu; 6.74, s, H-*ortho*; 6.98, s, H-*para*
3a·OCH_3^-	5.98,d (0.50)	8.74, d (0.50)		8.35, 8.45, A_2X_2, (9.3)			3.41, s, CH_3
3a·3,5-OAr$^-$	6.84, s	8.72, s		8.34, 8.46, A_2X_2, (9.3)			1.16, s, *meta*-di-*t*-Bu; 6.72, d, (1.3), H-*ortho*; 6.95, br, s, H-*para*

[a] Spectra were recorded in DMSO-d_6 at ambient temperature (ca. 23°C) at 400.1 MHz.

[b] Data for the DNBF adduct and for the methoxide adducts of **1**, **2**, and **3** are taken from refs. 1*a* and 17, except for the characteristics of adduct **3a**·OCH_3^-, which are taken from ref. 20*b*. These data are included for purposes of comparison.

[c] Overlaps the H-5 doublet.

Table 2. The ^{1}H NMR spectroscopic characteristics of the C-bonded C-7 σ-adducts (**1a**, **2a**, **3a**) formed by reaction of Pi-DNBT, **1**, DNP-DNBT, **2**, and NP-DNBT, **3**, with 2,6-di-*tert*-butylphenoxide (2,6-ArO$^-$) ion.[a]

	Chemical shifts, ppm (J = Hz)						
Adduct	H-7	H-5	H-2′	H-3′	H-5′	H-6′	Signals of C-7 attached group
1a·2,6-ArOH$^-$	5.37, s	8.68, s		9.22, s	9.22, s		1.31, s, *meta*-di-*t*-Bu; 7.00, s, H-*ortho*; 6.87, s, O*H*
2a·2,6-ArOH$^-$	5.39, s	8.76, s		8.83, d (2.5)	8.71, dd (2.5, 8.8)	8.10, d (8.8)	1.31, s, *meta*-di-*t*-Bu; 7.03, s, H-*ortho*; 6.86, s, O*H*
3a·2,6-ArOH$^-$	5.38, s	8.79, s		8.39, 8.28, A_2X_2 (9.3)			1.31, *s, meta*-di-*t*-Bu; 7.07, s, H-*ortho*; 6.89, s, O*H*

[a] Spectra were recorded in DMSO-d_6 at ambient temperature (ca. 23°C) at 400.1 MHz.

been raised, in this case by the successive removal of groups from the 2-nitroaryl ring.

In the current study we have examined the reaction of two aryloxides with the 2-nitroaryl-4,6-dinitrobenzotriazole 1-oxide series, **1–3**. The aryloxides used are 2,6-di-*tert*-butylphenoxide (2,6-ArO$^-$) and 3,5-di-*tert*-butylphenoxide (3,5-ArO$^-$). Although, in principle, both may act as O- and (or) C-nucleophiles in attack at either position of the electrophiles **1–3**, previous work suggests that the latter will function only as an O-nucleophile while the former is effectively restricted from acting other than as a C-nucleophile (17, 18). The significance of using such hindered aryloxides derives from the sensitivity to steric factors that has been found for C-1′ displacement as compared to C-7 complexation with these substrates (1*a*, *b*). In essence, the choice of nucleophiles was made with a view to observing C-7 adducts, particularly oxygen-bonded ones, and consequently, assessing the selectivity of the two electrophilic sites to aryloxide O- versus C-attack.

We have had a long-term interest in the ambident reactivity of aryloxides (1, 19, 21, 22) and enolates (23) and in the regioselectivity found in nucleophilic attack on electron-deficient systems (17, 18, 22, 24). The current study is, therefore, a further foray into this field.

Results

1. Overview

The reactions of the aryloxide ions, 2,6- and 3,5-di-*tert*-butylphenoxides, with Pi-, DNP-, and NP-DNBT electrophiles, were studied by ^{1}H NMR (400 MHz) in deuterated dimethyl sulfoxide (DMSO-d_6) solvent at ambient (ca. 23°C) temperatures. Chemical shifts are reported in parts per million (ppm) relative to residual DMSO-d_5**H** in the solvent (δ 2.50 ppm), and coupling constants are given in Hertz (Hz). Initial spectra of the substrates **1–3** in the absence of added nucleophile demonstrated the purity of the starting materials; no signals for hydroxide adducts, formed by reaction of the substrates with traces of water in the solvent, were seen in these spectra. The ^{1}H NMR spectroscopic characteristics of the pertinent C-7 O-bonded adducts are given in Table 1, while the characteristics of the C-7 C-bonded adducts are listed in Table 2, along with NMR parameters for comparable C-7 methoxide O-adducts of **1–3** and aryloxide C-7 adducts of **4**. In these tables and throughout this report adducts are designated thus: for example, **1a**·3,5-OAr$^-$ denotes the C-7 O-adduct formed by substrate **1** and the aryloxide, 3,5-di-*tert*-butylphenoxide, while **3a**·2,6-ArO$^-$ indicates the C-7 C-adduct formed by **3** and 2,6-di-*tert*-butylphenoxide ion. Assignments partly rest on the chemical shift comparisons derived from Tables 1 and 2. The percentages of each adduct (or product derived from an adduct), determined from the earliest spectrum acquired (i.e., typically 3–4 min of mixing of the reagents), are listed in Table 3.

The salient features of the reactions, undertaken with equimolar aryloxide (i.e., under selective conditions) are as follows. First, neither O- nor C-adduct formation with 3,5-ArO$^-$ was observed at the C-7 site of Pi-DNBT, but **1** both forms a C-7 C-bonded adduct with 2,6-ArO$^-$ and shows significant C-1′ attack of 2,6-ArO$^-$ *as a C-nucleophile.* In contrast, DNP-DNBT, in reaction with 3,5-ArO$^-$ yields products of O-attack at both C-7 and C-1′, whereas reaction with the isomeric 2,6-ArO$^-$ gives only the C-7 C-bonded Meisenheimer complex of **2,** and C-1′ displacement is not observed over the period of

© 1998 NRC Canada

Table 3. The extent of formation of the O- and C-adducts with Pi-DNBT, DNP-DNBT, and NP-DNBT (**1**–**3**).

Substrate	Aryloxide	% C-7	% C-1′[a]	% Adducts[b]	Selectivity[c]
1	3,5-ArO⁻	0	100[d]	80	0
	2,6-ArO⁻	69[e]	31e	58	2.2
2	3,5-ArO⁻	9[d]	91[d]	88	0.1
	2,6-ArO⁻	100[e]	0	50	[f]
3	3,5-ArO⁻	100[d]	0	70	[f]
	2,6-ArO⁻	100[e]	0	90	[f]

[a] % C-1′ = % **1c**, **2c**, or **3c** = % DNBT⁻.

[b] The remainder (to 100%) consists of unchanged substrate and (or) C-7 hydroxide adduct and the corresponding C-1′ displacement product.

[c] Selectivity = $S = k_7/k_{1'} \approx$ % C-7/% C-1′ at earliest point of observation.

[d] Only O-attack is found in this system.

[e] Only C-attack is found in this system.

[f] Specific attack at C-7.

observation. Finally, NP-DNBT, **3**, reacts with 3,5-ArO⁻ *or with* 2,6-ArO⁻ to yield the products of addition at the C-7 position, **3a**·3,5-OAr⁻ and **3a**·2,6-ArO⁻, respectively; products of N-2:C-1′ bond scission are not observed. In the following sections details of these sequences will be given.

2. Reaction of the 2-[(nitro)$_x$aryl]-4,6-dinitrobenzotriazole 1-oxide series, 1–3, with 3,5-di-*tert*-butylphenoxide ion, 3,5-ArO⁻, in DMSO-d_6

The ^{1}H NMR spectrum recorded immediately after injection of 1 equiv. of 3,5-ArO⁻ (as the potassium salt in DMSO-d_6) into a DMSO-d_6 solution of Pi-DNBT, **1** (final concentrations of both reactants: 0.03 M), contains diminished signals for the substrate (refer to ref. 1*b* for substrate ^{1}H NMR data), accompanied by the appearance of signals that can be attributed to products of attack at C-1′. Therefore, the resonances of the 3,5-di-*tert*-butylphenyl picryl ether, **1c**-OAr (Scheme 1) are observed at 9.21 (s, H-3′,5′ picryl ring), 7.18 (t, J = 1.5, H-*para* aryl ether), 6.84 (d, J = 1.5, H-*ortho* aryl ether), and 1.25 (s, *meta*-di-*tert*-butyls). The spectrum of **1c** found in the reaction medium is in good agreement with the signals found for an authentic sample of the ether prepared by reaction of 3,5-ArO⁻ with picryl chloride (18). At the same time a pair of broad singlets can be seen at 8.77 and 8.73; these signals correspond to the 4,6-dinitrobenzotriazole 1-oxyanion, DNBT⁻, the other displacement product.

Even in this initial spectrum no signals could be noted that would correspond to a C-7 O-bonded adduct of 3,5-ArO⁻ with **1**. Comparison of the chemical shifts found for the diagnostic proton attached to the site of nucleophile attack (i.e., the proton bonded to the sp^3 hybridized carbon of the adduct) shows that aryloxide O-adducts have signals located in a very different place from that found for the structurally related alkoxide O-adducts (1, 17, 19*c*, 21). Thus, the C-7 proton (i.e., H-7) in aryloxide O-bonded complexes appears ca. 0.6–0.9 ppm downfield of H-7 in alkoxide O-adducts (cf. Table 1). (Conversely, in C-bonded aryloxide adducts H-7 appear ca. 0.6 ppm upfield of H-7 for the alkoxide O-adducts.) On this basis, the H-7 peak for a C-7 aryloxide O-adduct would be expected to be found in the 6.6–6.9 ppm region of the NMR spectrum. Close inspection of this region shows no such H-7 signal, nor are the peaks assigned to **1c**-OAr distorted (as would occur if the H-7 signal were hidden by an overlapping resonance of **1c**-OAr).

Scheme 1.

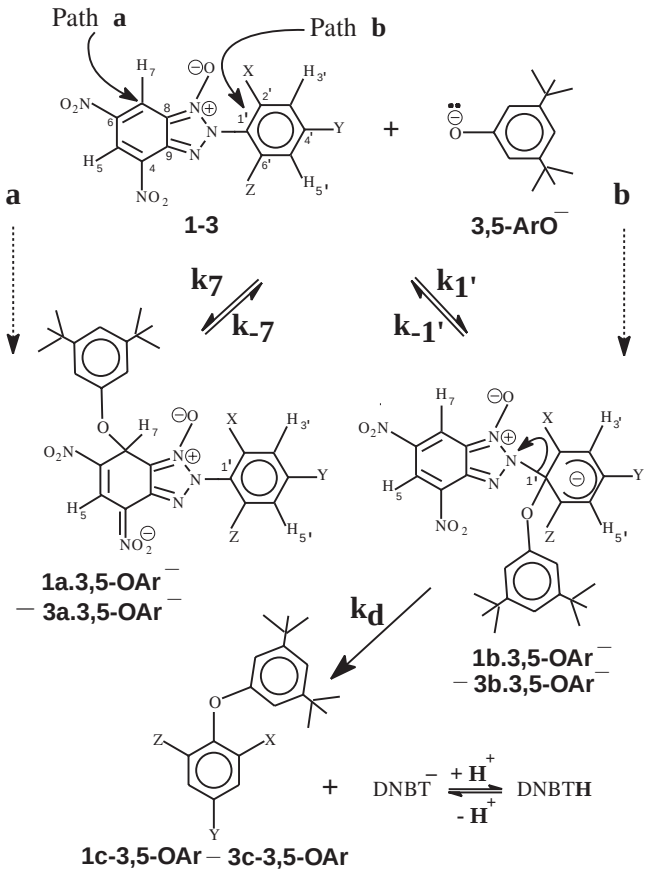

In short, *the reaction of* **1** *with the aryloxide at C-1′ is complete at the moment that the first spectrum could be recorded.*

In a separate control experiment, the reaction mixture was acidified with trifluoroacetic acid (TFA, 5 μL) immediately after the initial spectrum was recorded. Under these acidic conditions the peaks attributed to the 4,6-dinitrobenzotriazole 1-oxyanion leaving group are found to shift downfield to 9.12

© 1998 NRC Canada

and 8.89; these peaks now appear as well-resolved doublets for the ring protons ($J = 1.9$). These observations are consistent with protonation of DNBT$^-$to give DNBT**H**, the conjugate acid of the nucleofuge (1*a–c*). The peaks due to **1c**-OAr remain unchanged, as would be expected. However, small extraneous peaks are also apparent in the aromatic region (6.5–8.5 ppm). These peaks are as yet unidentified.[2]

Addition of one equiv. of the 3,5-ArO$^-$ nucleophile to the NMR tube containing DNP-DNBT, **2**, dissolved in DMSO-d_6 (final concentration: 0.06 M) results in an initial spectrum that includes small peaks ascribed to the C-7 O-bonded DNP-DNBT·3,5-OAr$^-$ adduct, **2a**·3,5-OAr$^-$. These peaks are located at 8.91 (d, $J = 2.4$, H-3′), 8.78 (d,d, $J = 8.8, 2.4$, H-5′), 8.68 (s, H-5), 8.12 (d, $J = 8.8$, H-6′), 6.98 (br s, H-*para* aryloxyl ring), 6.74 (br s, H-*ortho* aryloxyl ring), 6.71 (s, H-7), and 1.18 (s, *meta*-di-*tert*-butyls). Note the similarity in chemical shift of the sp^3-bound H-7 proton in this aryloxide O-adduct and that of H-7 of the C-7 DNBF·3,5-OAr$^-$ adduct (Table 1).

As expected for an O-bonded aryloxide adduct, the signals of **2a**·3,5-OAr$^-$ disappear from the spectrum upon acidification of the solution (5 μL TFA), and the original peaks of **2** are reinstated in the spectrum. Similar behaviour has been noted before with these types of O-bonded Meisenheimer complexes and, generally, serves to distinguish them from carbon-bonded aryloxide adducts that are not acid labile (1, 3, 17, 18, 22).

However, even in the initial (not acidified) spectrum the peaks due to **2a**·3,5-OAr$^-$ constitute a minority of the signals present. Broadened signals for starting material are present. The dominant peaks are ascribable to the products of N-2:C-1′ bond rupture and, importantly, these peaks indicate that such displacement proceeds exclusively through O-attack at C-1′. Peaks of 3,5-di-*tert*-butylphenyl 2′,4′-dinitrophenyl ether, **2c**-OAr (Scheme 1), appear at 8.87 (d, $J = 2.8$, H-3′), 8.44 (d,d, $J = 9.4, 2.8$, H-5′), 7.38 (t, $J = 1.6$, H-*para* aryl ether), 7.10 (d, $J = 1.6$, H-*ortho* aryl ether), and 1.29 (s, *meta*-di-*tert*-butyls). Under these conditions the signals of DNBT**H** (8.71, 8.69, d, $J = 1.9$) are also observed.

Thus, for the first time in these systems (**1**–**3** with aryloxide nucleophiles) *O-attack at both C-7 and C-1′ has been observed.* In the case of the reaction of **2** with phenoxide ion the C-7 adducts were formed via attack of the *ortho* and *para* carbons of phenoxide, while displacement at C-1′ occurred exclusively via the nucleophilic oxygen centre (1*c*).

When the reaction is not quenched by adding an excess of acid the C-7 O-bonded complex, **2a**·3,5-OAr$^-$, decomposes and is not present at the detection level of the method after 30 min. However, peaks that correspond to the C-7 DNP-DNBT·OH$^-$ adduct (cf. ref. 1*b*) can be noted. This adduct presumably arises from general base equilibration of adventitious water within the DMSO-d_6 solvent that generates low levels of OH$^-$, which attacks preferentially at the super-electrophilic site, C-7. The intervention of this adduct has been noted previously in the reactions of DNP-DNBT with various nucleophiles (1, 20), and comparable adducts are formed competitively in related electron-deficient aromatic–nucleophile systems (18, 22, 24) under conditions similar to those used in the present NMR study.

The reaction is complete within 1 h, at which time the only signals present are those of unchanged **2** and 3,5-di-*tert*-butylphenol, along with the anionic nucleofuge, DNBT$^-$, and **2c**-OAr, the ether formed as a result of C-1′ O-attack of the aryloxide.

A deep red solution is formed immediately upon reaction of equimolar 3,5-ArO$^-$ with NP-DNBT, **3**. The initial spectrum was acquired within 4 min of mixing; it includes the C-7 O-adduct, **3a**·3,5-OAr$^-$, with resonances recorded at 8.72 (d, $J = 0.8$, H-5), 8.46, and 8.34 (A_2X_2 d, $J = 9.3$), 6.95 (br s, H-*para* aryloxyl ring), 6.84 (d, $J = 0.8$, H-7), 6.72 (d, $J = 1.3$, H-*ortho* aryloxyl ring), and 1.16 (s, *meta*-di-*tert*-butyls). These are the dominant signals found in this first spectrum.

As observed in the other reaction systems, injection of TFA results in disappearance of the signals assigned to the C-**7** **3a**·3,5-OAr$^-$ adduct. Upon acidification the peaks of NP-DNBT are restored to close to their original intensity and 3,5-di-*tert*-butylphenol, also noted in the spectrum.

When the NP-DNBT–3,5-ArO$^-$ system is monitored without interruption, the signals of the **3a**·3,5-OAr$^-$ adduct decline below detection limits within 30 min. A number of unidentified signals are present in the spectrum, some of which may arise from reaction **3** with adventitious OH$^-$ or from NO_2 group displacement from the 2-nitroaryl ring.[2] However, resonances that could be attributed to the products of N-2:C-1′ bond cleavage (i.e., DNBT$^-$and the 3,5-di-*tert*-butylphenyl 4-nitrophenyl ether, **3c**-OAr) are not identified.

Therefore, only O-attack at the C-7 position can be unambiguously assigned in the NP-DNBT–3,5-ArO$^-$ reaction system.

3. Reaction of the 2-[(nitro)$_x$aryl]-4,6-dinitrobenzotriazole 1-oxide series, 1–3, with 2,6-di-*tert*-butylphenoxide ion, 2,6-ArO$^-$, in DMSO-d_6.

Equimolar 2,6-ArO$^-$ solution was injected into the NMR tube that contained Pi-DNBT, **1**, in DMSO-d_6 (final concentration: 0.03 M). The first spectrum was recorded within 4 min of mixing of the reagents. Among the signals found in the complex spectrum include those consistent with formation of the C-7 C-bonded **1a**·2,6-ArO$^-$ adduct (Table 2), the biphenyl product, **1c**-2,6-ArOH (Scheme 2), and DNBT$^-$/DNBT**H**, from C-1′ attack of the nucleophile. Hence, the peaks that represent the C-**7** **1a**·2,6-ArOH$^-$ adduct are found at 9.22 (s, H-3′,5′ picryl), 8.68 (s, H-5), 7.00 (s, H-*ortho* of C-7 aryl moiety), 6.86 (s, O**H** aryl), 5.37 (s, H-7), and 1.31 (s, *meta*-di-*tert*-butyls of aryl moiety).

The assignment is supported by the observation (vide supra) that the characteristic sp^3-bound proton (H-7) of aryl C-bonded adducts is found ca. 0.6 ppm upfield of the corresponding peak in alkoxide adducts, i.e., at about 5.4 ppm (cf. Tables 1 and 2). In separate experiments it was shown that the σ-adduct is stable to acid (5 μL TFA) and that the peak at δ 6.86 is exchangeable with D_2O. The former result supports the assignment of the signals to a C-7 C-adduct, since such aryloxide C-adducts have been found to be acid stable, while their O-bonded counterparts are acid labile. The latter result confirms the identity of the aryloxyl OH. Interestingly, this signal (6.86 ppm) is seen in the present system, whereas it could not be detected in the spectra of the *ortho* and *para* C-7 C-bonded adducts formed by phenoxide with **2** (1*a*).

[2] The current limited spectroscopic data supports assignment of the peaks to 3,5-di-*tert*-butylphenyl ethers arising from nitro group displacement from the substrate picryl ring or from similar displacement from **1c**, although full characterization awaits further work. Similar NO_2 displacement has been observed previously in these systems (1*b*).

© 1998 NRC Canada

Scheme 2.

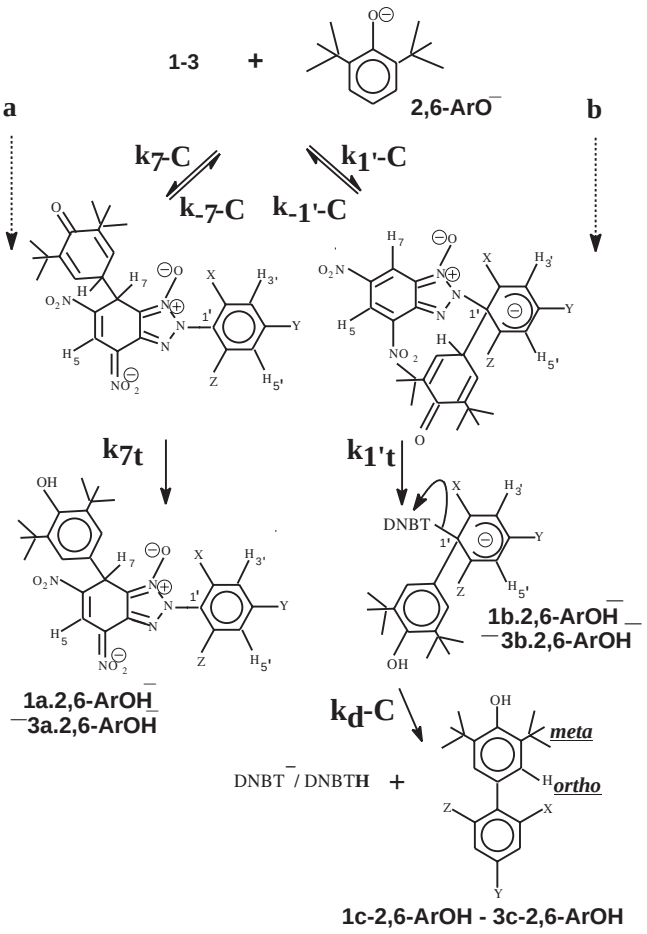

Attack at C-1′ via the *para* C-position of the 2,6-di-*tert*-butylphenoxide results in cleavage of the N-2:C-1′ bond and formation of the displacement products: 2,6-di-*tert*-butyl-4-(2′,4′,6′-trinitrophenyl)phenol, **1c**-2,6-ArOH (Scheme 2), and DNBT⁻/DNBTH. The signals for this biphenyl derivative are found at 9.12 (s, H- 3′,5′ picryl), 7.63 (br s, O**H**), 7.04 (s, H-3,5 phenolic moiety), and 1.35 (s, 2,6-di-*tert*-butyls). These peaks were previously observed in our study of the displacement reactions of 2,6-ArO⁻ with picryl chloride (17) and are in good agreement with the spectroscopic characteristics of authentic picryl 2,6-di-*tert*-butylphenol prepared separately (see Experimental). Interestingly, in our previous study the reaction medium was apparently basic enough to deprotonate the phenolic OH, whereas here this signal is observed and is seen to undergo exchange with D_2O.

Also apparent in the spectrum were resonances due to a small amount of PicO⁻, picrate anion, at 8.59 (s, H-3,5) and those assigned to 2,6-di-*tert*-butylphenol at 7.07 (d, J = 7.8, H-3,5), 6.89 (s, O**H**), 6.76 (t, J = 7.8, H-4), and 1.37 (s, 2,6-di-*tert*-butyl). These peaks also matched those recorded for the authentic materials. As would be expected, this initial spectrum remained unchanged over the period of observation (ca. 5 h).

Thus, for the first time in our examination of this series of electrophiles, **1**–**3***, C-attack at both the C-7 and C-1′ positions has been observed.*

The substrate DNP-DNBT, **2**, reacts with equimolar 2,6-ArO⁻ (as the potassium salt in DMSO-d_6; final concentration: 0.06 M) to yield a red-coloured mixture. In the spectrum acquired within 4 min of mixing, peaks attributable to the C-7 C-bonded adduct, **2a**·2,6-ArOH⁻, are seen at 8.83 (d, J = 2.5, H-3′), 8.76 (s, H-5), 8.71 (d,d, J = 8.8, 2,5, H-5′), 8.10 (d, J = 8.8, H-6′), 7.03 (s, H-*ortho* phenolic moiety), 6.86 (s, O**H**), 5.39 (s, H-7), and 1.31 (s, *meta*-di-*tert*-butyl). The σ-adduct meets the usual test for a C-bonded aryloxide adduct: the signals are stable to acid (5 μL TFA). The phenolic OH peak disappears when D_2O is added to the NMR tube, the tube is shaken, and then a new spectrum is recorded.

Unlike the Pi-DNBT–2,6-ArO⁻ reaction system, no signals are noted that could be assigned to the products of N-2:C-1′ bond scission; neither DNBT⁻/DNBT**H** nor 2,5-di-*tert*-butyl-4-(2′,4′-dinitrophenyl)phenol are formed. Again, the reaction is essentially complete at the time that the initial spectrum is recorded.

Here, only C-7 C-adduct formation is observed.

Consistent with its behaviour with the other aryloxide, NP-DNBT, **3**, reacts with 2,6-di-*tert*-butylphenoxide to give rise to the C-7 C-bonded adduct as the only product. Thus, when one equiv. of the 2,6-ArO⁻ solution (as the potassium salt in DMSO-d_6) is injected into the NMR tube that contains **3** (final concentration: 0.06 M), the first spectrum recorded consists of much diminished and broadened peaks for the starting material and dominant signals for the **3a**·2,6-ArOH⁻ σ-adduct. The characteristic resonances of this C-7 Meisenheimer complex are located at 8.79 (s, H-5), 8.39 (d), and 8.29 (d) (A_2X_2 system, J = 9.3), 7.07 (s, H-*meta* phenolic moiety), 6.89 (s, O**H**, D_2O-exchangeable), 5.38 (s, H-7), and 1.31 (s, *meta*-di-*tert*-butyl). The separate acidification experiment confirms the acid stability of this aryloxide C-adduct.

Attack at C-7 of **3** *by 2,6-ArO⁻ yields the C-7 C-bonded adduct and is complete within the time of mixing.*

Discussion

1. Reaction pathways: C-7 complexation versus C-1′ S_NAr displacement.

Although the aryloxides studied show a range of selectivity for the C-7 and C-1′ positions, a selectivity that is modulated for each substrate in turn, the basic pathways for reaction are shown by all the nucleophiles and all of the ambident electrophiles, **1**–**3.** However, the two nucleophiles show their own individual behaviours. Thus, 3,5-di-*tert*-butylphenoxide has been shown to act strictly as an O-nucleophile, and the pathways for its reaction with the substrates **1**–**3** are shown in Scheme 1. On the other hand, reactions with 2,6-di-*tert*-butylphenoxide proceed via attack of the *para*-carbon of the nucleophile; the *ortho* positions are blocked by the bulky *tert*-butyl groups, and this hindrance is also apparently large enough to effectively preclude attack of the aryloxide as an O-nucleophile. The pathways involving this aryloxide are detailed in Scheme 2.

As shown in Scheme 1, 3,5-ArO⁻ may attack at C-7 of any of the substrates to give rise to a σ-adduct via Path a. With Pi-DNBT, no C-7 adduct (e.g., **1a**·3,5-OAr⁻) was seen at the time of earliest observation. Instead, the only reaction noted was formation of the products of N-2:C-1′ bond scission via

© 1998 NRC Canada

Path b: the ether, **1c**·3,5-OAr, and the charge delocalized nucleofuge, DNBT⁻–DNBT**H**. Attack at C-1′ of 3,5-di-*tert*-butylphenoxide, as a "constrained phenoxide O-nucleophile," plausibly proceeds through a transient C-1′ adduct (or transition state modelled on such a C-1′ Meisenheimer complex), labelled **1b**·3,5-OAr⁻ in Scheme 1. The apparent preference for attack at this site is consistent with previous examinations of the Pi-DNBT–phenoxide and Pi-DNBT–mesitoxide reaction systems; in both cases reaction proceeded exclusively via C-1′ to give the corresponding ether products (or Meisenheimer adducts derived immediately from these ethers) (1, 20). (Stereoelectronic factors that may favour C-1′ attack have not previously been discussed for these types of systems (1) and will be discussed further in section 2). On the other hand, it should be recognized that the method of monitoring these reactions is a relatively slow one, and a rapidly formed C-7 O-adduct that also rapidly reverts to starting material may not be seen.

The rapid decomposition of adducts such as **1b**·3,5-OAr⁻ to the displacement products, **1c**·3,5-OAr and DNBT⁻, partly reflects the high nucleofugality of DNBT⁻, as a charge delocalized anion, and partly the relief of steric congestion that attends N-2:C-1′ bond rupture in **1b**·3,5-OAr⁻. As a result, C-1′ Meisenheimer adducts such as **1b** (or **2b** or **3b**) have not been observed in this or related studies (1, 7, 20).

Previous studies of the reactivity of DNP-DNBT, **2**, has shown that the removal of an *ortho* NO_2 group (in going from Pi-DNBT to DNP-DNBT) raises the barrier to attack at C-1′ more than it influences reaction at C-7. In the current study, then, reaction of 3,5-ArO⁻ as an O-nucleophile with **2** follows both Paths a and b, as outlined in Scheme 1. Here, a C-7 O-adduct, **2a**·3,5-OAr⁻, is observed along with the products of C-1′ displacement, via the putative **2b**·3,5-OAr⁻ adduct. This constitutes the first observation of an O-bonded C-7 aryloxide σ-adduct and illustrates the fine balance of C-7 stability (i.e., larger $K_7 = k_7/k_{-7}$, Scheme 1) and C-1′ barrier height (i.e., higher barrier = smaller $k_{1'}$) required to observe these adducts. Nonetheless, the C-7 adduct is present only as a minority product and within 30 min is no longer observed, presumably having decomposed back to **2** and the 3,5-ArO⁻; these rapidly recombine at C-1′ to yield the final S_NAr displacement products.

A further increase in the C-1′ kinetic barrier is associated with NP-DNBT, **3**, as substrate, as compared to **2**. In fact, the reduction in electrophilicity at the C-1′ position is now apparently significant enough to strongly bias the system towards C-7 adduct formation. Now the C-7 O-bonded adduct, **3a**·3,5-OAr⁻, is the only Meisenheimer complex formed in the system, and it persists over the period of observation. Note, however, that the overall percentage of O-adducts (C-7 plus C-1′) formed with **3** is lower than that found with **2** (Table 3 for 3,5-ArO⁻ as nucleophile, 70% vs. 88%), indicative of the reduction of overall electrophilicity that attends successive removal of electron-withdrawing groups from the 2-[(nitro)$_x$aryl] ring. (The comparison with 2,6-ArO⁻ as a nucleophile is not as straightforward and likely also reflects the generally higher barriers to attack via the C-centre.)

For 2,6-di-*tert*-butylphenoxide, reaction at the *ortho* carbon positions is prevented, and reaction via the oxygen centre is sterically demanding, to such an extent that no adducts (or products) have been observed to form in the present reaction systems or with either picryl chloride or fluoride (17). Rather, reaction proceeds via the *para*-carbon. With Pi-DNBT**, 1**, attack at C-7 according to Path a (Scheme 2) is the dominant process (Table 3). The comparison between the Pi-DNBT–2,6-ArO⁻ and Pi-DNBT–3,5-ArO⁻ reaction systems is striking. In the former, C-7 C-attack of the aryloxide is preferred over C-1′ C-attack and displacement, whereas in the latter system, only Path b attack can be observed via the oxygen-centre of the aryloxide. When the electrophilicity of the C-1′ site is reduced, as in **2** and even more so in **3**, reaction proceeds exclusively by Path a; the C-7 C-adducts, **2a**·2,6-ArOH⁻ and **3a**·2,6-ArOH⁻, are both persistent σ-complexes.

The selectivity towards C-7 complex formation found in these systems will now be considered in light of stereoelectronic factors.

2. Stereoelectronic factors: $n\rightarrow\sigma^*$ stabilization in C-1′ adducts.

In the course of our investigation of the regioselectivity shown in picryl ethers, and related electron-deficient aromatic–nucleophile systems (18, 22, 24, 25), we have found stereoelectronic stabilization of σ-adducts to be an important factor in determining the behaviour. In brief, C-1 dialkoxy adducts formed by alkoxides with 2,4,6-trinitroanisole (TNA), for example, can be viewed as acetals (26, 27). In such systems electron density from a lone pair of one OR group may be donated into the antibonding σ* orbital of the C(1)—OR bond, and vice versa, particularly when each OR group is aligned antiperiplanar to the relevant C—OR bond (22, 28–30). These $n\rightarrow\sigma^*$ interactions stabilize the C-1 methoxide adduct of TNA relative to the kinetically preferred C-3 Meisenheimer complex; the C-1 TNA·OCH_3^- adduct is the product of thermodynamic control (22, 31). In Buncel's nomenclature, this pattern of regioselectivity is termed K3T1 (kinetic preference for C-3 adduct formation, but the C-1 adduct is the thermodynamic product) (22). Where kinetic factors, such as F-strain to attack, are favourable an adduct that is stereoelectronically stabilized may be formed as the product of both kinetic and thermodynamic control. This is the case for the phenoxide O-adducts of TNA (22) and phenyl picryl ether (20); these systems are labelled K1T1. Note, however, that stereoelectronic stabilization is also generally considered to be less significant when it involves "unsymmetrical geminal disubstitution," that is, the stabilization is greatest when both acceptor fragment σ* orbitals are of equal energy, as would be expected for the methoxide C-1 adduct of TNA but as would not be expected for the O-centred phenoxide C-1 adduct of TNA (28). When stereoelectronic stabilization is diminished or precluded, for instance, because antiperiplanar rotameric forms of the geminally disubstituted adduct may not be populated as a result of steric congestion, an initially formed C-1 adduct may give way to its C-3 counterpart, as occurs in the case of 2,4,6-trimethylphenoxide (mesitoxide) reacting with TNA (32). In this case, the regioselectivity is denoted as K1T3. The preference of aryloxides, acting as O-nucleophiles, for C-1 of picryl chloride and fluoride was also partly attributed to $n\rightarrow\sigma^*$ stabilization of the C-1 adducts; no C-3 O-adducts were noted in these reaction systems (17).

In the context of the current study it should be recognized that Pi-DNBT, for example, can be viewed as "a 2-N substituted 4,6-dinitrobenzotriazole 1-oxide" or just as correctly be

© 1998 NRC Canada

Table 4. The ^{13}C NMR spectroscopic characteristics of the electrophiles, DNBF, PiCl, Pi-, DNP- and NP-DNBT (**4**, picryl chloride, **1**–**3**) in DMSO-d_6.[a]

	Chemical shift, ppm									
Substrate	C-4	C-5	C-6	C-7	C-8	C-9	C-1′		Other	
4[b]	136.6	126.5	144.8	120.8	116.7	145				
PiCl[c]							148.9	146.4	123.5	125.0
1	137.5	124.2	144.5	119.9	122.2	125.6	150.0	145.5	126.4	136.3
2	137.4	123.3	143.8	119.7	128.9	126.6	149.4	143.7	132	135.2
									130.2	122.6
3	137.0	122.8	143.1	119.6	128.2	138.3	148.2	134.2	125.0	125.1

[a] Spectra were recorded at 100.0 MHz using the J-mod pulse sequence (37). The numbering of the carbons follows that shown in Schemes 1 and 2 for the substrates **1**–**3**.

[b] Given in ref. 38.

[c] Given in ref. 17.

considered "a C-1 substituted 2,4,6-trinitrobenzene." The first description of the dinitrobenzotriazole 1-oxide series is the one that we have usually invoked in our comparison of the selectivity of nucleophilic attack on these substrates, **1**–**3**. In this case the C-7 site is super-electrophilic and should be expected to be the site of preferred attack. According to the second description, however, nucleophiles such as methoxide and phenoxide (as an O-nucleophile) could derive stabilization from $n\rightarrow\sigma^*$ interactions involving the oxygen lone pairs of the erstwhile nucleophiles and the N-2:C-1′ bond. While such an interaction is formally possible with the 2-nitrogen lone pair and the C-1′:OR (or :OAr) bond, donation of this pair of electrons would result in loss of aromaticity for the dinitrobenzotriazole 1-oxide fragment and is, therefore, likely unfavourable. Furthermore, stereoelectronic stabilization in these systems would be of the unsymmetrical kind and also energetically less rewarding, as a result.

However, when the possibility of $n\rightarrow\sigma^*$ stabilization is considered it should be conceded that the real comparison in selectivity lies between the C-7 site and the C-3′ site (at least in Pi-DNBT). Here, where the stereoelectronic stabilization is absent at both sites, an unbiased comparison should be possible. In this regard, note that in no system studied thus far has attack at C-3′ (or comparable unsubstituted centres on the 2-[(nitro)$_x$aryl] rings) been observed. Methoxide reacts with TNA to initially form the C-3 adduct that gives way to the more stable C-1 geminal dialkoxy adduct (K3T1 behaviour), but methoxide reacts preferentially at C-7 of **1** followed by C-1′ attack and displacement (K7T1′ pattern), without any apparent formation of a C-3′ adduct (1*c*, 22). This is an indirect confirmation of the super-electrophilicity of the C-7 position in **1**–**3**.

With this understanding we will now consider the selectivity data compiled in Table 3. The table gives the selectivity (*S*) as the ratio of the ratios of C-7 versus C-1′ adducts (i.e., displacement products) formed at the earliest point of observation. Properly, *S* should be defined only on the basis of the forward rate constants for formation of these adducts, that is, $S = k_7/k_{1'}$ or k_7-C/$k_{-1'}$-C (Schemes 1 and 2). In fact, the selectivities given in Table 3 reflect both the stability of the C-7 adduct (i.e., K_7) as well as the kinetic barrier to formation of it and its C-1′ analogue. In this sense, *S* here is a guide to the actual selectivity, though it has proved to be a useful construct for describing the behaviour in related systems (1). In considering the full series of substrates, we can see that the selectivity for C-7 attack increases from one end of the spectrum to the other as we proceed from **1** to **3**. Thus, 3,5-ArO$^-$ reacts entirely at C-1′ of **1**, as an O-nucleophile, shows a strong selectivity for C-1′ in **2** (i.e., the selectivity, $S = 0.1 = \%$ C-7/% C-1′, where % C-1′ = % DNBT$^-$ or % **1c**; Table 3, Scheme 1) but is specific in its reaction at C-7 for **3**. A somewhat similar situation is found for the reaction of 2,6-ArO$^-$ with the series, in that the preference for C-7 reaction increases in going from **1** to **3**. However, a preference for C-attack at C-7 over C-1′ exists even with **1** ($S = 2.2$), while with **2** and **3** C-7 regiospecificity of attack is found.

Further interesting comparisons arise from considering the aryloxide pairs with a given substrate. Therefore, in examining the reaction systems that involve Pi-DNBT, 2,6-di-*tert*-butylphenoxide ion shows significantly higher selectivity for C-7 than its isomer, the 3,5-di-*tert*-butylphenoxide ion; $S = 0$ for the former system and 2.2 for the latter. This is consistent with the reactivity–selectivity principle (33, 34[3]) in the sense that reaction via the *para*-C of 2,6-ArO$^-$ requires initial loss of aromaticity in formation of the quinoidal C-adduct ($k_{1'}$-C and k_7-C steps in Scheme 2). This adduct presumably tautomerizes rapidly ($k_{1't}$ and k_{7t}, Scheme 2) to give the observable C-7 adduct (**1c**·2,6-ArOH$^-$ in the case of Pi-DNBT) or the biphenyl product (**1c**-2,6-ArOH) of decomposition of the rearomatized C-1′ adduct (**1b**·2,6-ArOH$^-$). The loss of aromaticity that is required in C-attack as compared to O-attack would presumably raise the barrier for this step for 2,6-ArO$^-$ as a C-nucleophile as compared to 2,6-ArO$^-$ as a hypothetical O-nucleophile or 3,5-ArO$^-$ as an actual O-nucleophile. Thus, 2,6-ArO$^-$ is expected to be intrinsically less reactive than 3,5-ArO$^-$, and hence the 2,6-isomer is the most selective. That appears to be the case here, and the situation is confirmed in the DNP-DNBT systems where, again, the 2,6-ArO$^-$ ion favours C-7 attack more than the isomeric 3,5-ArO$^-$ ion does.

Reaction of either aryloxide with NP-DNBT gives the respective C-7 adducts, exclusively. This reflects the much lower electrophilicity of C-1′ as a site on an aryl ring that contains only a single electron-withdrawing NO_2 group.

These selectivity results support the notion that stereoelectronic stabilization plays a significant role in these systems. The 2,6-di-*tert*-butylphenoxide ion cannot act as an oxygen nucleophile, owing to the high steric congestion about the nucleophilic oxygen, and has been shown to react only via

[3] This is an issue devoted to articles about the RSP.

© 1998 NRC Canada

carbon, while the 3,5-di-*tert*-butyl isomeric ion is limited to reaction via oxygen. Neither the C-7 adduct nor the C-1′ adduct formed by 2,6-ArO^-, then, could derive stabilization via $n\rightarrow\sigma^*$ interactions, since the *para*-C fragment cannot be an *n* electron donor and, in the C-1′ adduct, it is unlikely that the N centre would be an *n* donor either. Conversely, the C-1′ adducts of 3,5-ArO^- could achieve a significant measure of such stereoelectronic stabilization.

The preferences for sites of attack parallel the possible stereoelectronic stabilization. Lacking any possibility of such stabilization, 2,6-ArO^- shows selectivity for C-7 of **1** whereas 3,5-ArO^- reacts entirely via the (presumably) stereoelectronically stabilized C-1′ O-adduct. From examination of models (Darling or Dreiding) it appears unlikely that any of the oxygen-centred C-1′ adducts would be able to take up the optimal orientations for full $n\rightarrow\sigma^*$ stabilization, as a result of steric hindrance. Nonetheless, the greater propensity for C-1′ attack shown by the 3,5-ArO^- nucleophile towards **2** also likely indicates some degree of stereoelectronic stabilization of the C-1′ adduct, a stabilization that the C-7 adduct does not share. That the **2a**·3,5-OAr^- adduct is observable under these conditions provides further support for our contention that C-7 is super-electrophilic. In the case of NP-DNBT the low electrophilicity of C-1′, linked largely to the diminished ability to conjugatively delocalize negative charge in the putative C-1′ adduct, is such that stereoelectronic stabilization cannot compete with C-7 electrophilicity: only C-7 adducts are formed by both nucleophiles.

It is interesting to compare the result of the reaction of 3,5-ArO^- with **3** and the reaction of phenoxide, as an O-nucleophile, with DNBF, **4**. Although phenoxide anionic σ-adducts of all common electron-deficient aromatic and heteroaromatic compounds have shown themselves to be elusive species (19, 35, 36) the DNBF.OPh^- adduct was recently observed at low temperature (17). In some senses, DNBF can be viewed as a truncated member of the current series of electrophiles. Unlike **1** and **2**, competition between complex formation and S_NAr displacement is not possible for **4**. This is similar to the situation with **3**, where the electrophilicity of C-1′ is no longer competitive with that of C-7, and the C-1′ adduct would clearly be less stable than its C-7 counterpart. In both cases, clean C-7 O-adduct formation can now be observed. With **3**, however, C-7 C-adduct formation with PhO^- is still preferred over O-adduct formation (1*c*), and only by barring C-adduct formation can the C-7 O-adduct be observed with 3,5-ArO^-, at room temperature in DMSO-d_6.

In conclusion, we have seen that selectivity for the C-7 complexation (defined as the ratio of the percentages of C-7 adduct to C-1′ adduct formed at the point of earliest observation) increases in going from **1** to **3** for either aryloxide. For the first time complexation via an aryloxide carbon has been observed along with attack of a ring carbon on C-1′. Thus, 2,6-di-*tert*-butylphenoxide ion, which cannot act as an O-nucleophile, reacts preferentially at C-7 ($S = 2.2$) of Pi-DNBT, but the biphenyl derivative that arises from C-1′ attack is also observed.

The preference for reaction at C-1′ of **1** that has been shown by phenoxide and mesitoxide (20) is also displayed by 3,5-di-*tert*-butylphenoxide. This is partly attributed to stereoelectronic stabilization of the C-1′ adduct.

Future work will focus on selectivity with less sterically demanding nucleophiles.

Experimental

Materials

Preparation of the 2-nitroaryl-4,6-dinitrobenzotriazole 1-oxide substrates, **1**–**3**, has been described previously (1). The ^{13}C NMR spectra of the substrates (**1**–**3**) have not previously been reported. These spectra were acquired using the J-modulated (JMOD) pulse sequence (37), which aided in assignment (38) of these spectra (Table 4). The DMSO-d_6 (CDN or Merck), used for the NMR studies, was dried by treatment with 4 or 3 Å molecular sieves prior to use, as advocated by Burfield and Smithers (39). The method of Kornblum and Laurie (40) was used for the preparation of the potassium aryloxide salts; the ^1H NMR spectroscopic characteristics of these salts have been reported previously (17, 18). For purposes of comparison the biphenyl derivatives (i.e., 2,6-di-*tert*-butyl-4-(2′,4′,6′-trinitrophenyl)phenol, **1c**·2,6-ArOH, and 2,6-di-*tert*-butyl-4-(2′,4′-dinitrophenyl)phenol, **2c**·2,6-ArOH) were prepared by reaction of potassium 2,6-di-*tert*-butylphenoxide with picryl chloride and fluoro-2,4-dinitrobenzene, respectively, as previously described (17, 41). Similarly, the ethers (namely, 3,5-di-*tert*-butylphenyl 2′,4′,6′-trinitrophenyl ether, **1c**·3,5-OAr, and 3,5-di-*tert*-butylphenyl 2′,4′-dinitrophenyl ether, **2c**·3,5-OAr), were prepared from potassium 3,5-di-*tert*-butylphenoxide with picryl chloride and fluoro-2,4-dinitrobenzene, respectively, again as reported previously (20*a*).

Methods

NMR experiments

The NMR spectra were recorded at Queen's University (Kingston) on a Bruker AM-400 spectrometer operating at 400.1 MHz (^1H) and 100.0 MHz (^{13}C). The spectrometer was typically tuned, as reported previously (22). Wilmad PP-507 NMR tubes were used in all experiments. Potassium aryloxide solutions were prepared in volumetric flasks (1 mL), from weighed quantities of the salts and dry DMSO-d_6 in a nitrogen dry-box; the flasks were capped with rubber septa before removal from the dry box.

Typically, an NMR tube that contained ca. 400 μL of dry DMSO-d_6 was septum-capped and swept out with nitrogen. Appropriate amounts of substrate, dissolved in DMSO-d_6, and 1,4-dibromobenzene (integration standard) in the same solvent were injected into the tube. An initial spectrum was acquired to demonstrate the purity of the starting material. Reaction was initiated by injection of the nucleophile solution, in an amount such that the final concentrations of substrate and nucleophile were equal (usually 0.03–0.06 M for each). The first spectrum was acquired as soon as possible (ca. 3 min), using 16 scans to obtain the FID. After the initial spectrum was obtained the system was monitored at varying intervals until the reaction was deemed complete.

Acknowledgments

Support of this research in the form of a grant from the Principal's Research Fund of Sir Wilfred Grenfell College (J.M.D.) and from the American Cancer Society (R.A.M.) is gratefully

© 1998 NRC Canada

acknowledged. We thank Queen's University for access to the NMR spectrometer and referees for helpful comments. For a fruitful and ongoing collaboration in the field of electron-deficient aromatic and heteroaromatic–nucleophile interactions, we especially thank Professor Erwin Buncel.

References

1. (*a*) J.M. Dust and E. Buncel. Can. J. Chem. **72**, 218 (1994); (*b*) Can. J. Chem. **69**, 978 (1991); (*c*) E. Buncel and J.M. Dust. Can. J. Chem. **66**, 1712 (1988); (*d*) E. Buncel, J.M. Dust, K.T. Park, R.A. Renfrow, and M.J. Strauss. *In* Nucleophilicity. *Edited by* J.M. Harris and S.P. McManus. Adv. Chem. Ser. 215. American Chemical Society, Washington, D.C. 1987. pp. 369–384; (*e*) R.A. Renfrow, M.J. Strauss, S. Cohen, and E. Buncel. Aust. J. Chem. **36**, 1843 (1983).
2. F. Terrier, E. Kizilian, J.C. Hallé, and E. Buncel. J. Am. Chem. Soc. **114**, 1740 (1992).
3. E. Buncel, M.R. Crampton, M.J. Strauss, and F. Terrier. Electron deficient aromatic- and heteroaromatic-base interactions. The chemistry of anionic sigma complexes. Elsevier, Amsterdam. 1984.
4. F. Terrier. Chem. Rev. **82**, 77 (1982).
5. F. Terrier, A.P. Chatrousse, Y. Soudais, and M. Hlaibi. J. Org. Chem. **49**, 4176 (1984).
6. C.F. Bernasconi. J. Am. Chem. Soc. **92**, 4682 (1970).
7. (*a*) M.J. Strauss, R.A. Renfrow, and E. Buncel. J. Am. Chem. Soc. **105**, 2473 (1983); (*b*) E. Buncel, R.A. Renfrow, and M.J. Strauss. J. Org. Chem. **52**, 488 (1987).
8. J.C. Hallé, M.P. Simonnin, M.J. Pouet, and F. Terrier. Tetrahedron Lett. **26**, 1307 (1985).
9. A.J. Kresge, H.J. Chen, L.E. Hakka, and J.E. Kouba. J. Am. Chem. Soc. **93**, 6174 (1971).
10. F. Terrier, M.J. Pouet, J.C. Hallé, S. Hunt, J.R. Jones, and E. Buncel. J. Chem. Soc. Perkin Trans. 2, 1665 (1993).
11. R.W. Read, R.J. Spear, and W.P. Norris. Aust. J. Chem. **77**, 985 (1984), and refs. therein.
12. (*a*) F. Terrier, M.J. Pouet, E. Kizilian, J.C. Hallé, F. Outurquin, and C. Paulmier. J. Org. Chem. **58**, 4696 (1983); (*b*) F. Terrier, J.C. Hallé, M.P. Simonnin, and M.J. Pouet. J. Org. Chem. **49**, 4363 (1984).
13. R. Taylor. Electrophilic aromatic substitution. Wiley, New York. 1990.
14. (*a*) H.J. Niclas and B. Göhrmann. Synth. Commun. **19**, 2141 (1989); (*b*) H.J. Niclas, B. Göhrmann, and E. Gründemann. Synth. Commun. **19**, 2789 (1989); (*c*) J. Kind and H.J. Niclas. Synth. Commun. **23**, 1569 (1993).
15. F. Terrier, M.P. Simonnin, M.J. Pouet, and M.J. Strauss. J. Org. Chem. **46**, 3537 (1981).
16. (*a*) F. Terrier. Nucleophilic aromatic displacement. The influence of the nitro group. Organic Nitro Chem. Ser. VCH, New York. 1991; (*b*) J. Miller. Nucleophilic aromatic substitution. Elsevier, Amsterdam. 1968.
17. E. Buncel, R.A. Manderville, and J.M. Dust. J. Chem. Soc. Perkin Trans. 2, 1019 (1997).
18. R.A. Manderville, J.M. Dust, and E. Buncel. J. Phys. Org. Chem. **9**, 515 (1996).
19. (*a*) E. Buncel and W. Eggimann. J. Am. Chem. Soc. **99**, 5958 (1977); (*b*) E. Buncel, A. Jończyk, and J.G.K. Webb. Can. J. Chem. **53**, 3761 (1975); (*c*) E. Buncel and R.A. Manderville. J. Phys. Org. Chem. **6**, 71 (1993), for leading refs.
20. (*a*) R.A. Manderville. Ph.D. thesis, Queen's University, Kingston, Ont. 1992; (*b*) J.M. Dust. Ph.D. thesis, Queen's University, Kingston, Ont. 1987.
21. E. Buncel, J.M. Dust, R.A. Manderville, K.T. Park, and I. Onyido. Bull. Soc. Chim. Fr. 371 (1988).
22. E. Buncel, J.M. Dust, A. Jończyk, R.A. Manderville, and I. Onyido. J. Am. Chem. Soc. **114**, 5610 (1992).
23. E. Buncel, J.M. Dust, and R.A. Manderville. J. Am. Chem. Soc. **118**, 2072 (1996).
24. E. Buncel, J.M. Dust, and F. Terrier. Chem. Rev. **95**, 2261 (1995).
25. (*a*) J.M. Dust and J.M. Harris. J. Polym. Sci. Part A: Polym. Chem. **28**, 1875 (1990); (*b*) J.M. Dust and M.D. Secord. J. Phys. Org. Chem. **8**, 810 (1995).
26. C.F. Bernasconi and K.A. Howard. J. Am. Chem. Soc. **104**, 7248 (1982).
27. (*a*) J.F. Bunnett and A.V. Cartano. J. Am. Chem. Soc. **103**, 4861 (1981); (*b*) J.F. Bunnett, S. Sekiguchi, and L.A. Smith. J. Am. Chem. Soc. **103**, 4865 (1981); (*c*) S. Sekiguchi, T. Suzuki, and M. Hosokawa. J. Chem. Soc. Perkin Trans. 2, 1783 (1989).
28. A.J. Kirby. The anomeric effect and related stereoelectronic effects at oxygen. Springer Verlag, Berlin. 1983. pp. 9–11, 82, 90.
29. E. Buncel, R.M. Tarkka, and J.M. Dust. Can. J. Chem. **72**, 1709 (1994).
30. P. Deslongchamps. Steroelectronic effects in organic chemistry. Pergamon, New York. 1983. pp. 5–20.
31. (*a*) K.L. Servis. J. Am. Chem. Soc. **89**, 1508 (1967); (*b*) J. Am. Chem. Soc. **87**, 5495 (1965).
32. R.A. Manderville and E. Buncel. J. Am. Chem. Soc. **115**, 8985 (1993).
33. E. Buncel and H. Wilson. J. Chem. Educ. **64**, 475 (1987).
34. Isr. J. Chem. **26** (1985).
35. (*a*) S.M. Shein and O.G. Byval'kevich. Zhur. Org. Khim. **8**, 323 (1972); (*b*) S.M. Shein, O.G. Byval'kevich, and AD. Khmelinskya. J. Org. Chem. U.S.S.R. **12**, 130 (1976).
36. V. Machacek, V. Sterba, A. Lycka, and D. Snobl. J. Chem. Soc. Perkin Trans. 2, 355 (1982).
37. J.K.M. Sanders and B.K. Hunter. Modern NMR spectroscopy. Oxford University Press, Oxford, U.K. 1987, pp. 93–207.
38. F. Terrier, J.C. Hallé, P. MacCormack, and M.J. Pouet. Can. J. Chem. **67**, 503 (1989).
39. D.R. Burfield and R.H. Smithers. J. Org. Chem. **43**, 3966 (1978).
40. N. Kornblum and A.P. Laurie. J. Am. Chem. Soc. **81**, 2705 (1959).
41. G.P. Stahley. J. Org. Chem. **50**, 3091 (1985).

© 1998 NRC Canada

A calculational and ultraviolet photoelectron spectroscopic study of distorted amides

N.H. Werstiuk, H.M. Muchall, C.D. Roy, J. Ma, and R.S. Brown

Abstract: Distorted amides 3,4-dihydro-2-oxo-1,4-ethanoquinoline (**1a**), 3,4-dihydro-2-oxo-1,4-propanoquinoline (**1b**), 3,3,4,5-tetrahydro-2-oxo-1,5-ethanobenzazepine (**1c**), and 3,3,4,5-tetrahydro-2-oxo-1,5-propanobenzazepine (**1d**) and the model compounds 2,*N*-dimethyl-acetanilide (**2a**), 2,*N*,*N*-trimethylaniline (**3**), and benzoquinuclidine (**4**) have been studied calculationally and with He(I) ultraviolet photoelectron spectroscopy. We find good agreement between experimentally obtained ionization energies for **1b**, **1c**, **1d**, **2a**, **3**, and **4** and values calculated with HAM/3 using the equilibrium geometries obtained at the HF/6-31G** level of theory. An excellent correlation between experimental ionization energies and orbital energies from Becke3LYP/6-31+G* calculations led to the characterization of the highest occupied molecular orbitals for these compounds and for **1a,** whose photoelectron spectrum could not be obtained due to its reactivity in the solid state.

Key words: distorted amides, He(I) photoelectron spectroscopy, Becke3LYP, molecular orbitals.

Résumé : Faisant appel à des calculs et à la spectroscopie photoélectronique ultraviolette He(I), on a étudié des amides déformés 3,4-dihydro-2-oxo-1,4-éthanoquinoléine (**1a**), 3,4-dihydro-2-oxo-1,4-propanoquinoléine (**1b**), 3,3,4,5-tétrahydro-2-oxo-1,5-éthanobenzazépine (**1c**) et 3,3,4,5-tétrahydro-2-oxo-1,5-propanobenzazépine (**1d**) ainsi que des composés modèles 2,*N*-diméthylacétanilide (**2a**), 2*N,N*-triméthylaniline (**3**) et benzoquinuclidine (**4**). On a observé un bon accord entre les énergies d'ionisation obtenues expérimentalement pour les composés **1b, 1c, 1d, 2a, 3a** et **4** et les valeurs calculées par la méthode HAM/3 en utilisant les géométries d'équilibre obtenues au niveau HF/6-31G** de la théorie. Une excellente corrélation entre les énergies d'ionisation expérimentales et les énergies d'orbitales obtenues à l'aide de calculs Becke3LYP/6-31+G* conduit à la caractérisation des orbitales moléculaires hautes occupées de ces composés et du produit **1a** dont on n'a pas pu obtenir le spectre photoélectronique à cause de sa réactivité à l'état solide.

Mots clés : amides déformés, spectroscopie photoélectronique He(I), Becke3LYP, orbitales moléculaires.

[Traduit par la rédaction]

Introduction

By studying a group of benzo-substituted bicyclic amides, Brown and co-workers showed that distorting the amide linkage away from planarity leads to a dramatic change in the basicity of the amides and their reactivities in H_2O (1, 2). The kinetics of hydrolysis of distorted amides 3,4-dihydro-2-oxo-1,4-ethanoquinoline (**1a**), 3,4-dihydro-2-oxo-1,4-propanoquinoline (**1b**), 3,3,4,5-tetrahydro-2-oxo-1,5-ethanobenzazepine (**1c**), and 3,3,4,5-tetrahydro-2-oxo-1,5-propanobenzazepine (**1d**) were studied as a function of pH and it was suggested that on going from **1d** to **1a** the site of protonation changes from oxygen to nitrogen, giving rise to N-protonated amides as reactive intermediates in the case of **1a**, **1b,** and **1c**. Because He(I) photoelectron spectroscopy provides a way of ordering the molecular orbitals (MOs) while quantum chemical calculations can be used to calculate orbital energies and MO coefficients, the availability of these distorted amides and the model compounds 2,*N*-dimethylacetanilide (**2a**), 2,*N*,*N*-trimethylaniline (**3**), and benzoquinuclidine (**4**) provided us with a unique opportunity to determine the impact of pyramidalizing the bridgehead nitrogen, twisting the amide linkage, and changing the ring size on the nature of the highest occupied molecular orbitals of the amides. This paper documents the results of our study.

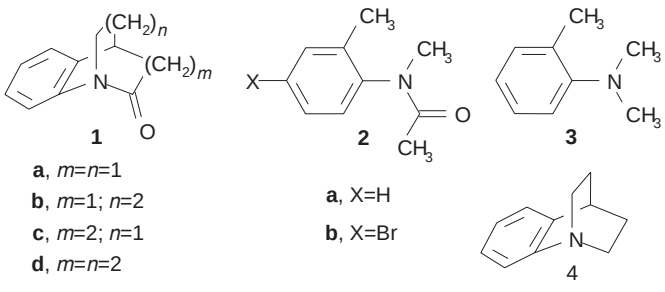

Received September 30, 1997.

This paper is dedicated to Professor Erwin Buncel in recognition of his contributions to Canadian chemistry.

N.H. Werstiuk,[1] H.M. Muchall,[1] C.D. Roy, and J. Ma. Department of Chemistry, McMaster University, Hamilton, ON L8S 4M1, Canada.
R.S. Brown.[2] Department of Chemistry, Queen's University, Kingston, ON K7L 3N6, Canada.

[1,2] Authors to whom correspondence may be addressed. N.H.W. and H.M.M.: Telephone: (905) 525-9140. Fax: (905) 522-2509. E-mail: werstiuk@mcmaster.ca, muchall@mcmaster.ca, R.S.B.: Telephone: (613) 545-2624. Fax: (613) 545-6669. E-mail: rsbrown@chem.queensu.ca

Experimental

Ultraviolet photoelectron spectroscopic studies

Photoelectron (PE) spectra were acquired with a versatile,

© 1998 NRC Canada

Fig. 1. He(I) ultraviolet photoelectron spectra:
(*a*) 2,*N*,*N*-trimethylaniline (**3**); (*b*) 3,4-dihydro-2,5-ethanoquinoline (benzoquinuclidine) (**4**); (*c*) 3,4-dihydro-2-oxo-1,4-propanoquinoline (**1b**); (*d*) 3,3,4,5-tetrahydro-2-oxo-1,5-ethanobenzazepine (**1c**); (*e*) 3,3,4,5-tetrahydro-2-oxo-1,5-propanobenzazepine (**1d**); (*f*) 2,*N*-dimethylacetanilide (**2a**). HAM/3 ionization energies are shown as vertical bars.

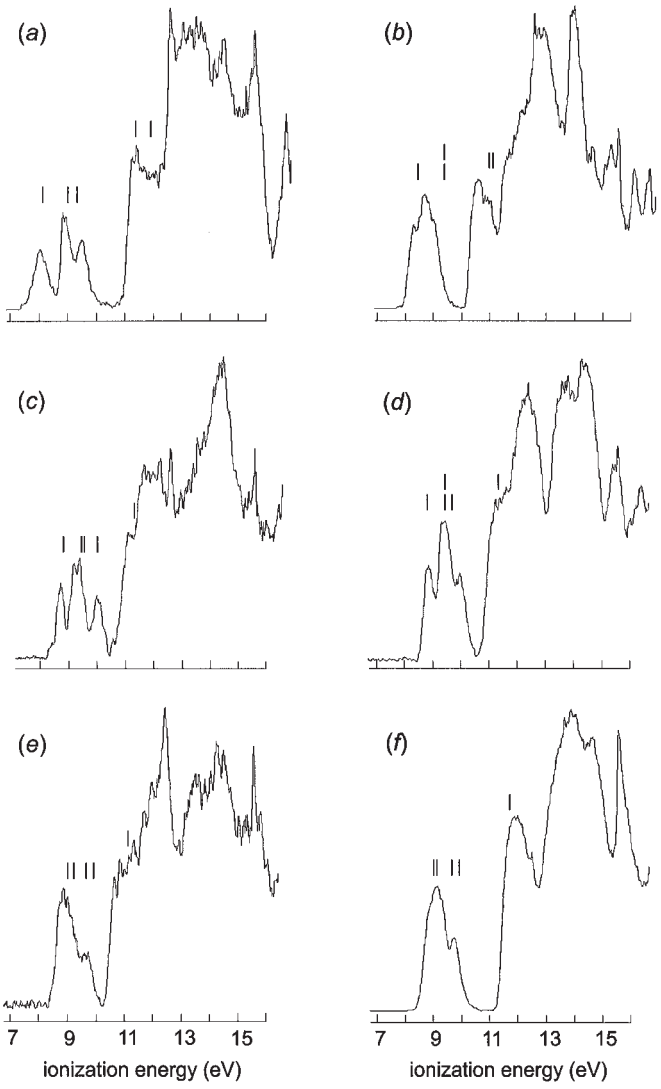

locally built spectrometer (3) designed to facilitate the handling of solids. Samples of the amides were placed in a 3 mm o.d. Pyrex tube — closed at one end — and inserted into the tip of a probe that could be electrically heated or cooled with circulating water. The tip of the sample tube was positioned 1 cm from the point of intersection with a He(I) photoionizing photon beam and the PE spectra were obtained by averaging 15–25 scans. During the acquisition of the spectra, the probe temperature was adjusted to maintain an acceptable signal level. The spectra were calibrated with N_2 (15.6 eV) and H_2O (12.6 eV), and linearity of the scale was ensured through calibrations with N_2 and acetone (9.7 eV) performed prior to the experiments. The spectra of **1b**, **1c**, **1d**, **2a**, **3,** and **4** are displayed in Fig. 1. Attempts to obtain the spectrum of **1a** failed because it rapidly polymerized when handled in the solid state. The vertical ionization energies (IEs) given in Table 1 were estimated from the maxima of the bands lying between 8 and 12 eV; shoulders are indicated (sh).

Calculational studies

Ab initio HF (4) and Becke3LYP (5) calculations were carried out on IBM RS/6000 model 39H, 350, and 530 computers with GAUSSIAN 92 (6) and GAUSSIAN 94 (7). The optimized equilibrium geometries of **1b**–**1d** and **2a** (geometrical structures not shown) correlated closely with the molecular structures of **1b**–**1d** and **2b** obtained with X-ray diffraction (1, 8, 9): the seven-membered ring of **1b** and **1c** adopts a chair conformation, the trimethylene bridge is oriented *syn* to the aromatic ring; the eight-membered ring of **1d** adopts a crown conformation; the planar amide group of acetanilide **2a** is nearly perpendicular to the plane of the phenyl ring. Table 2 lists calculated (HF/6-31G** and Becke3LYP/6-31+G*) and experimental N—C(O) and C═O bond lengths. HF/6-31G** optimized geometrical structures obtained with GAUSSIAN 92 were used in the semiempirical HAM/3 (10) calculations of the IEs (Table 1). PERGRA (11) was used to obtain displays of the Becke3LYP/6-31+G* MOs (which were found to compare well to HF/6-31G** eigenvectors).[3]

Results and discussion

The data in Table 2 show that calculations on **1b**–**1d** at both the HF/6-31G** and Becke3LYP/6-31+G* level of theory yield N—C(O) and C═O bond lengths that correlate well with the parameters obtained with X-ray diffraction. There is a progressive decrease in the calculated N—C(O) bond lengths on going from **1a** to **2a**, yet the C═O bonds lengthen only marginally, in keeping with the results of a calculational study on formamide reported by Wiberg and Breneman (13). The results are in accord with the expectation that the interaction of the nitrogen lone pair with the carbonyl group increases through the series **1a**–**1d** and **2b**. That the N—C(O) bond of **1d** is longer than the N—C(O) bond of **2b** (we expect that the experimental N—C(O) and C═O bond lengths of **2b** and **2a** are virtually identical) suggests that the interaction of the nitrogen lone pair with the carbonyl group of **1d** does not occur to the same extent in this case as in **2a** and **2b** even though **1d** has two 3-carbon bridges that allow the bridgehead nitrogen to become planar, a requirement for a maximal n_N–$\pi_{C=O}$ interaction in an amide. It is interesting to note that the calculated N—C(O) bond length of **1a** is substantially longer than the one calculated for **1b**. Because the N—C(O) and C═O bond lengths of **1b**, **1c**, and **1d** are reproduced with good accuracy by the calculations, we expect that the calculated N—C(O) and

[3] A rationale for the successful application of the Koopmans' Theory-like interpretation of the orbital energies obtained at the DFT level of theory in a PE spectroscopic study of a series of carbenes has recently been provided by Arduengo and co-workers (12). It is clear that applying a uniform shift, based on the difference in calculated HOMO energy and experimental first vertical IP, to orbital energies obtained with the hybrid HF/DFT Becke3LYP method nicely reproduces the PE spectra of compounds presented here (which are vastly different from the carbenes studied by Arduengo).

© 1998 NRC Canada

Table 1. HAM/3 calculated[a] and experimental vertical ionization energies (eV) of **1a**–**1d**, **2a**, **3**, and **4**.

1a		**1b**		**1c**		**1d**		**2a**		**3**		**4**	
Calcd.	Exp.[b]	Calcd.	Exp.	Calcd.	Exp.	Calcd.	Exp.	Calcd.	Exp.	Calcd.	Exp.	Calcd.	Exp.
8.76	–	8.79	8.7	8.76	8.9	8.97	9.0[c]	9.00	9.2[d]	8.14	8.0	8.42	8.3
9.46	–	9.36	9.2	9.43	9.4[c]	9.20	9.0[c]	9.13	9.2[d]	8.98	8.9	9.28	8.7
9.53	–	9.54	9.5(sh)	9.45	9.4[c]	9.61	9.4(sh)	9.61	9.2[d]	9.29	9.5	9.33	9.0
10.10	–	10.03	10.0	9.67	10.0	9.91	9.8	9.87	9.8	11.35	11.4	10.96	10.6
11.43	–	11.33	11.1	11.29	11.2	11.09	11.0	11.75	11.8	11.87	11.7	11.07	10.9

[a]HAM/3//HF/6-31G** level of theory.
[b]Because **1a** polymerized rapidly in the solid state, a spectrum could not be obtained.
[c]Value obtained at the maximum of the band resulting from two overlapping bands.
[d]Value obtained at the maximum of the broad band resulting from three overlapping bands.

Table 2. Selected experimental and calculated bond lengths *r* (Å) of amides **1a**–**1d**, **2a,** and **2b**.

	r (N—C(O))			*r* (C=O)		
	Exp.[a]	HF/ 6-31G**	B3LYP/ 6-31+G*	Exp.[a]	HF/ 6-31G**	B3LYP/ 6-31+G*
1a	—[b]	1.539	1.467	—[b]	1.252	1.206
1b	1.413[c]	1.414	1.422	1.225[c]	1.189	1.218
1c	1.401	1.411	1.421	1.216	1.191	1.219
1d	1.370[c]	1.382	1.394	1.233[c]	1.198	1.227
2a	—[d]	1.366	1.380	—[d]	1.201	1.230
2b	1.338	—[e]	—[e]	1.235	—[e]	—[e]

[a]Reference 2.
[b]The X-ray crystal structure was not determined due to the reactivity of **1a**.
[c]One of two molecules with slightly different structural parameters in the unit cell.
[d]The X-ray crystal structure was not determined.
[e]Not studied calculationally.

C═O bond lengths of **1a** are close to the experimental values, which have not yet been determined.

The computed four highest occupied MOs of amides **1b**–**1d** and **2a** comprise the electron lone pairs on nitrogen (n_N) and oxygen (n_O) as well as the two highest occupied MOs of the aromatic ring (π_3 and π_2). Ionizations from these four orbitals are expected in the low-energy region of the PE spectrum and, as seen in Figs. 1*c*–1*f*, bands arising from four ionizations are well separated from the main group of σ ionizations. On going from **1b** to **1d** and **2a**, the spectra exhibit increasing overlap of the respective bands: while for **1b** (Fig. 1*c*) all four ionizations can be assigned to individual peaks, for **2a** (Fig. 1*f*) only two maxima can be given (Table 1). This is due to a shift of the first band towards higher values, which eventually leads to a complete overlap with the former second band. PE spectra of amines **3** and **4** (Figs. 1*a* and 1*b*), which correspond well to those published earlier (14), possess one ionization less in this region due to the missing oxygen atom.

As seen from the data in Table 1 and the spectra displayed in Fig. 1, there is good agreement between the five lowest experimental vertical ionization energies of **1b**–**1d**, **2a**, **3,** and **4** and their IEs calculated with HAM/3 (shown as vertical bars in Fig. 1). Yet HAM/3 does not reproduce the gradual shift of the first ionization band towards higher energies in the amide series. As this seemed to be an important point, we performed ab initio calculations for amides **1a**–**1d** and **2a** and included amine **4** in the study. While orbital energies taken from HF/6-31G** calculations (not given) correspond only poorly to the experimental data, the correlation is excellent using Becke3LYP/6-31+G* orbital energies and applying Koopmans' Theorem (15).[3] For **1b**–**1d**, **2a**, and **4**, all relative orbital energy differences — for the single molecules as well as those between different molecules — are represented correctly (the rather large differences in absolute values are common with Becke3LYP and are not relevant to this analysis). Calculated Becke3LYP/6-31+G* orbital energies and assignments taken from the eigenvectors are given in Table 3.[3]

Table 3. Calculated Becke3LYP/6-31+G* orbital energies (eV) and assignments for amides **1a**–**1d** and **2a** as well as amine **4**.

1a	**1b**	**1c**	**1d**	**2a**	**4**
6.73 n_N[a]	6.52 n_N[b]	6.58 n_N[a]	6.61 n_O	6.75 n_O	6.12 n_N
6.92 π	6.96 n_O	7.06 n_O[a]	6.76 n_N[a]	6.85 n_N[a]	6.61 π
7.16 π	7.16 π	7.15 π	7.14 π	7.18 π	6.82 π
7.67 n_O	7.65 π[b]	7.49 π	7.51 π	7.49 π	

[a]n_N–n_O mixing.
[b]n_N–n_O–π mixing.

Graphical representations of the highest occupied molecular orbitals of amine **4** and amides **1a**–**1d** and **2a** determined with Becke3LYP/6-31+G* (these were checked against HAM/3//HF/6-31G** orbitals and found to compare well) are given in Figs. 2–7, respectively. The HOMO of **4** (Fig. 2) is of n_N character with σ electron density on the bridge C—C bonds. HOMO-1 and HOMO-2 are benzene-type π orbitals (π_3 and π_2). Introduction of the carbonyl group into the system leads to a loss of σ–π separation: n_N, which is in the plane of the aromatic ring in amine **4** and therefore does not interact with benzene π MOs, is twisted out of this plane in amides **1a**–**1d**. The HOMO of **1a** (Fig. 3) is essentially n_N with a small contribution from n_O (the torsional angle between these lone pairs estimated from the PERGRA plots is close to 0°)[4] and electron density on the C—C(O) bond; the nitrogen lone pair shows a pronounced tilt towards the benzene ring.

[4] In a detailed theoretical study of the topology of the charge densities of **1a**–**1d** and **2a** with the quantum theory of atoms in molecules (16) (the results will be documented in a following paper) we have characterized the outer and inner nonbonded charge concentrations (nbcc's) of the nitrogen atoms. The torsional angles between the outer (3, –3) critical points and the C—O linkages of **1a**, **1b**, **1c,** and **1d** are 4.2° ($\nabla^2\rho = -3.531$), 45.2° ($\nabla^2\rho = -3.225$), 50.3° ($\nabla^2\rho = -3.148$), and 72.8 ($\nabla^2\rho = -2.806$), respectively. In the case of **2a**, the nbcc's of the nitrogen atom exhibit two similar $\nabla^2\rho$ values of –2.553 (torsional angle 92.8°) and –2.168 (87.6°).

© 1998 NRC Canada

Fig. 2. HOMO to HOMO-2 of amine **4**.

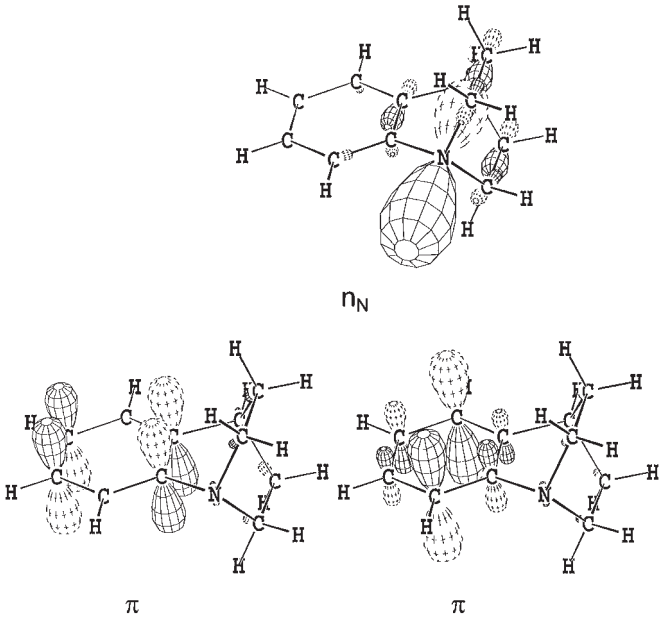

Fig. 3. HOMO to HOMO-3 of amide **1a**.

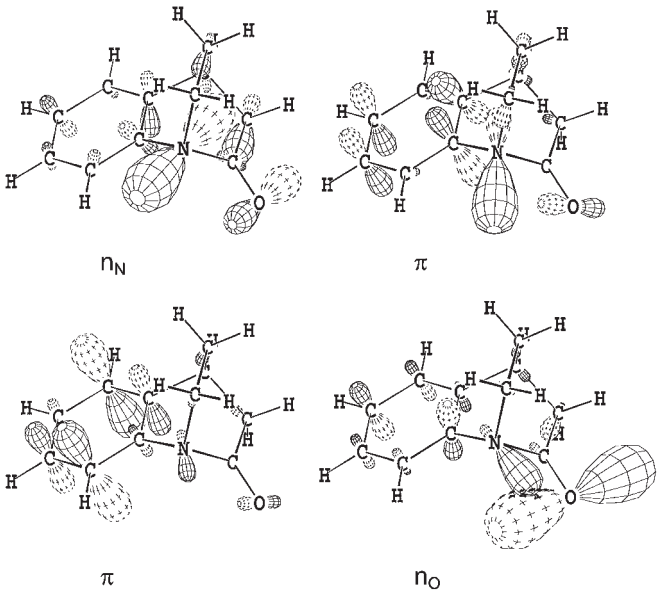

HOMO-1 and HOMO-2 have mainly π character on the benzene ring, with some n_N and n_O mixing. HOMO-3 is essentially n_O (with contributions on N—C(O) and C—C(O) bonds). As was found for **1a**, the HOMO of **1b** is n_N with n_O mixing, with a considerable additional amount of π mixing (Fig. 4). The torsional angle between the lone pairs is about 40°.[4] HOMO-1 is n_O, as described for **1a**. HOMO-2 is a benzene-type π MO while HOMO-3 shows π mixing with n_N and n_O, as was found for the HOMO: HOMO and HOMO-3 of **1b** seem to be two combinations of n_N and benzene π (n_O, which is always mixed with n_N, is found in different amounts according to individual interactions). For **1c**, HOMO and HOMO-1 are two combinations of nearly equal amounts of n_N and n_O

Fig. 4. HOMO to HOMO-3 of amide **1b**.

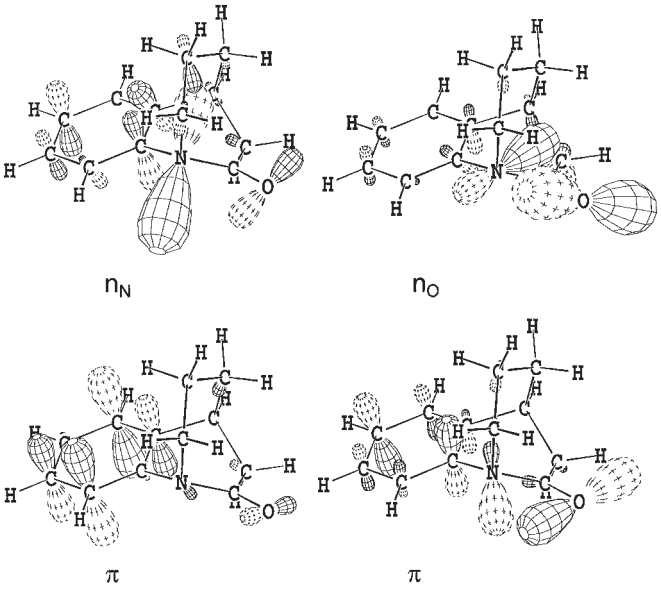

Fig. 5. HOMO to HOMO-3 of amide **1c**.

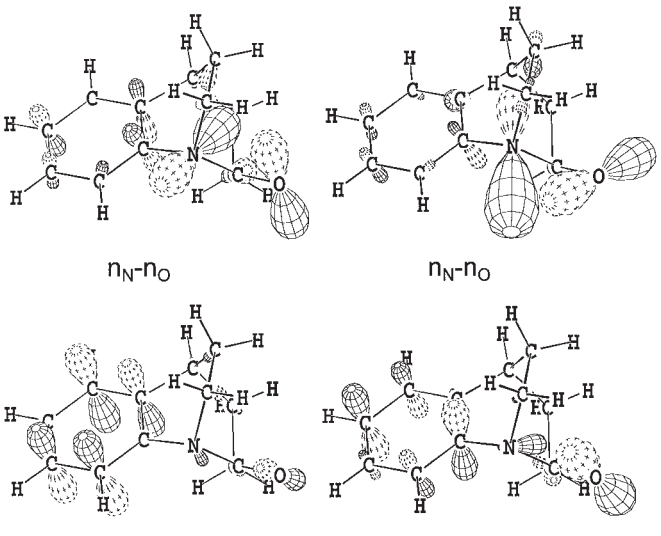

(Fig. 5). The torsional angle between n_N and n_O in the HOMO is comparable to that in the HOMO of **1b** (40°).[4] As in **1b**, HOMO-2 is of π character; HOMO-3 shows π–n_O mixing. For amides **1d** and **2a** (Figs. 6 and 7, respectively), the HOMO is n_O with pronounced coefficients along the N—C(O) and C—C(O) bonds. HOMO-1 is n_N with a large contribution from n_O (the torsional angle is greater than 60°);[4] HOMO-2 and HOMO-3 are benzene-type π orbitals. As for **1c**, HOMO-3 shows π–n_O mixing. It is apparent from inspection of the coefficients making up the various orbitals in Figs. 2–7 that the extensive mixing of the n_N, n_O, and π components does not fit with our simplistic notions of an isolated amide π system and C═O lone pair, even in the case of **2a** where such amidic resonance is allowed by the planarity of the amide unit.

The experimental (compare the spectra displayed in Fig. 1) and computational results, which are presented graphically in

© 1998 NRC Canada

Fig. 6. HOMO to HOMO-3 of amide **1d**.

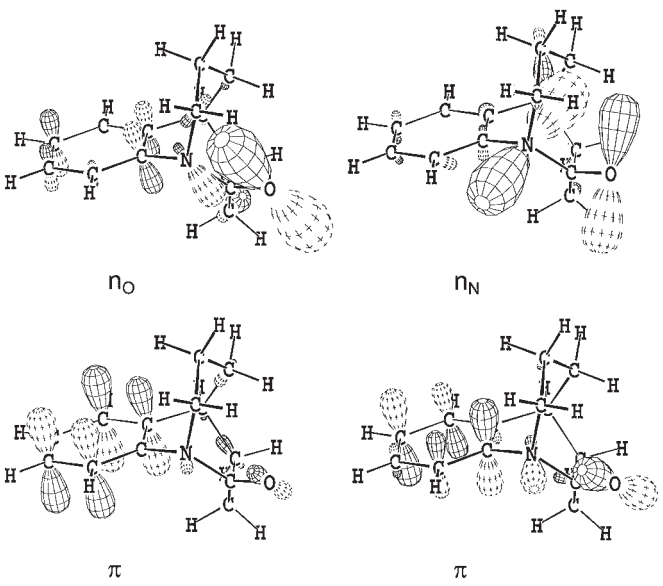

Fig. 7. HOMO to HOMO-3 of amide **2a**.

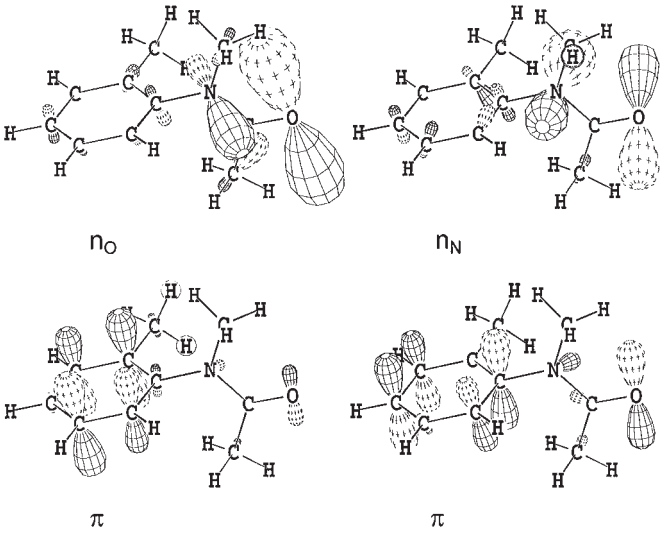

Fig. 8, show remarkable agreement. The high quality of the Becke3LYP calculations even allows for a prediction of the partial PE spectrum of **1a** (from orbital energies given in Fig. 8).[3] The first ionization should be close in energy to that of **2a** with the first three bands possibly overlapping.

Figure 8 shows that, in going from amine **4** to orthogonal amide **1a**, the n_N HOMO is stabilized by an inductive effect of the carbonyl group. The most striking feature obvious from Fig. 8 is the change of character of the HOMO: starting out as n_N in amine **4**, it is increasingly mixed with n_O in amides **1a**–**1c** and finally changes to n_O in **1d** and **2a**. This is nicely in accordance with findings on the site of protonation in these amides (2). While n_N is more or less energetically constant in the bicyclic amide series **1a**–**1d**, the energy of n_O changes dramatically. On going from **1a** to **1b**, n_O is destabilized by 0.71 eV. There is little change in n_O energy from **1b** to **1c** and, again, a destabilization from **1c** to **1d**. This can be correlated with the size of the amide ring in six-membered **1a**,

Fig. 8. Progression of orbital energies ε (Becke3LYP/6-31+G*) for amides **1a**–**1d** and **2a** as well as amine **4**. Unassigned orbitals are of aromatic π-character.

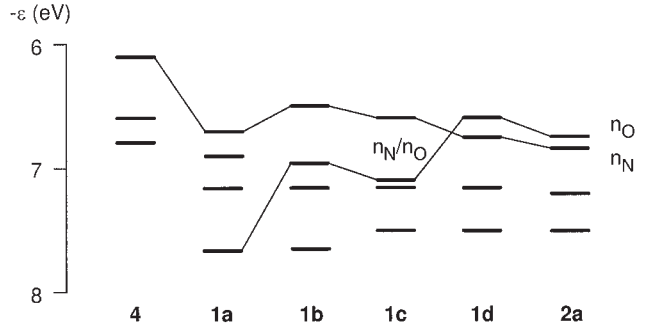

seven-membered **1b** and **1c,** and eight-membered **1d**. Such a correlation (shift of n_O due to ring expansion) in cyclic — undistorted — amides was shown before (17) and was explained by recognizing that n_O contains a significant coefficient at the carbon atom in the position α to the carbonyl group and is therefore strongly influenced by changes in ring size. There is no such contribution in the n_N of undistorted amides, which accordingly changes little in energy upon expansion or contraction of the ring. This explanation, modified, can also be applied to the ordering of n_N and n_O in distorted bicyclic amides **1a**–**1d**. It has to be modified for **1a** because of the coefficient at the carbon atom in the position α to the carbonyl group in the n_N HOMO, which explains why this orbital is destabilized on going from **1a** to **1c**. Thus a more or less constant energy n_N and a gradually destabilized n_O give rise to the computed and observed changes in orbital sequence. The conspicuously high HOMO energy of **1b** (which is confirmed by the low first IP of this amide, see Table 1) is due to an extraordinary amount of *n*–π mixing.

Conclusions

By combining PE spectroscopy with calculations at HAM/3 and Becke3LYP levels of theory, we gained detailed information about the highest occupied molecular orbitals of amides **1b**–**1d** and **2a**. This allowed the corresponding MOs of **1a** and its PE spectrum, which could not be obtained experimentally due to the extreme reactivity of **1a** in the solid state, to be predicted with certainty. Amide **1b** exhibits an unusually large degree of *n*–π mixing with the benzene ring. While the HOMO of **1a** is essentially n_N, destabilization of the n_O orbital as the ring size increases leads to a HOMO of n_O character in the case of **1d**.

Acknowledgments

We gratefully acknowledge the use of the IBM SP2 computer at Queen's University granted under the auspices of an IBM Canada – Queen's University collaborative project. We thank Ms. O. Donini for assistance with operational aspects of parallel GAUSSIAN 94, and the Natural Sciences and Engineering Research Council of Canada (NSERC) for financial support. We also gratefully acknowledge the use of the SGI computing installation in the Geochemistry Labs at McMaster funded by NSERC.

© 1998 NRC Canada

References

1. V. Somayaji and R.S. Brown. J. Org. Chem. **51**, 2676 (1986).
2. Q.-P. Wang, A.J. Bennet, R.S. Brown, and B.D. Santarsiero. J. Am. Chem. Soc. **113**, 5757 (1991).
3. N.H. Werstiuk, D.N. Butler, and E. Shahid. Can. J. Chem. **65**, 760 (1986).
4. W.J. Hehre, L. Radom, P.v.R. Schleyer, and J.A. Pople. Ab initio molecular orbital theory. John Wiley & Sons, New York. 1986.
5. A.D. Becke. J. Chem. Phys. **98**, 5648 (1993); C. Lee, W. Yang, and R.G. Parr. Phys. Rev. B: Condens. Matter, **37**, 785 (1988).
6. M.J. Frisch, G.W. Trucks, M. Head-Gordon, P.M.W. Gill, M.W. Wong, J.B. Foresman, B.G. Johnson, H.B. Schlegel, M.A. Robb, E.S. Replogle, R. Gomperts, J.L. Andres, K. Raghavachari, J.S. Binkley, C. Gonzalez, R.L. Martin, D.J. Fox, D.J. Defrees, J. Baker, J.J.P. Stewart, and J.A. Pople. Gaussian 92. Gaussian, Inc., Pittsburgh, Pa. 1992.
7. M.J. Frisch, G.W. Trucks, H.B. Schlegel, P.M.W. Gill, B.G. Johnson, M.A. Robb, J.R. Cheeseman, T. Keith, G.A. Petersson, J.A. Montgomery, K. Raghavachari, M.A. Al-Laham, V.G. Zakrzewski, J.V. Ortiz, J.B. Foresman, C.Y. Peng, P.Y. Ayala, W. Chen, M.W. Wong, J.L. Andres, E.S. Replogle, R. Gomperts, R.L. Martin, D.J. Fox, J.S. Binkley, D.J. Defrees, J. Baker, J.P. Stewart, M. Head-Gordon, C. Gonzalez, and J.A. Pople. Gaussian 94, Revision B.3. Gaussian, Inc., Pittsburgh, Pa. 1995.
8. V. Somayaji, K.I. Skorey, R.S. Brown, and R.G. Ball. J. Org. Chem. **51**, 4866 (1986).
9. Q. Wang, A.J. Bennet, R.S. Brown, and B.D. Santarsiero. Can. J. Chem. **68**, 1732 (1990).
10. L. Åsbrink, C. Fridh, and E. Lindholm. HAM/3. QCPE Bull. **13**, 393 (1981).
11. R. Sustmann and W. Sicking. Chem. Ber. **120**, 1323 (1987).
12. A.J. Arduengo III, H. Bock, H. Chen, M. Denk, D.A. Dixon, J.C. Green, W.A. Herrmann, N.L. Jones, M. Wagner, and R. West. J. Am. Chem. Soc. **116**, 6641 (1994).
13. K.B. Wiberg and C.M. Breneman. J. Am. Chem. Soc. **114**, 831 (1992).
14. J.P. Maier and D.W. Turner. J. Chem. Soc. Faraday Trans. 2, **69**, 521 (1973).
15. T. Koopmans. Physica, **1**, 104 (1933).
16. R.F.W. Bader. Atoms in molecules. A quantum theory. Clarendon Press, Oxford. 1990.
17. L. Treschanke and P. Rademacher. J. Mol. Struct. (Theochem), **122**, 35 (1985).

© 1998 NRC Canada

α-Effect nucleophiles and azide ion: effective charge studies of displacement reactions at esters

Matthew J. Colthurst, Angeline J.S.S. Kanagasooriam, Michael S.O. Wong, Christian Contini, and Andrew Williams

Abstract: The bimolecular reactions of azide, 2-iodosobenzoate, and acetohydroxamate ions and methoxyamine nucleophiles with substituted phenyl acetates possess Yukawa–Tsuno type correlations with substantial resonance interaction. The rate constants for hydroperoxide ion and the oxyanion of *N*,*N*-diethylhydroxylamine obey simple Hammett equations. The reactivities of azide, acetohydroxamate, hydroperoxide, and 2-iodosobenzoate ion nucleophiles exhibit modest α-effects when the reactivity in substitution at 4-nitrophenyl acetate is compared with that of phenoxide ions of similar pK_a values. The *N*,*N*-diethylhydroxylamine oxyanion is less reactive than its phenoxide ion analogue due to steric requirements, and the reactivities of the anionic nucleophiles exhibit changes in effective charge on the leaving oxygen similar to those for regular nucleophiles of similar pK_a. Methoxyamine possesses only a small enhancement compared with the reactivity of a normal primary amine of similar pK_a.

Values of the Leffler parameters for the bond fission process in the reactions of α-nucleophiles with phenyl acetates do not exhibit any special differences apart from those due to the pK_a of the nucleophile. The causes of the α-effect are considered to be due to steric and solvation requirements of the reactions.

Key words: α-effect, nucleophile, Yukawa–Tsuno, Leffler, Hammett, phenyl ester, effective charge, Brønsted.

Résumé : Les réactions bimoléculaires des acétates de phényles substitués avec les ions azoture, 2-iodosobenzoate et acétohydroxymate et la méthoxyamine, qui sont tous nucléophiles, présentent des corrélations du type Yukawa–Tsuno comportant une interaction de résonance importante. Les constantes de vitesse pour les réactions de l'ion hydroperoxyde et de l'oxyanion de la *N*,*N*-diéthylhydroxylamine obéissent à des équations de Hammett simples. Les réactions des ions nucléophiles iodure, acétohydroxamate, hydroperoxyde et 2-iodosobenzoate présentent de faibles effets σ lorsqu'on compare la réactivité de leurs réactions de substitution avec l'acétate 4-nitrophényle avec celle des ions phénolates de pK_a semblables. L'oxyanion *N*,*N*-diéthylhydroxylamine est moins réactif que l'ion phénolate correspondant à cause d'effets stériques et les réactivités des nucléophiles anioniques présentent des changements dans la charge effective présente sur l'oxygène partant qui sont semblables à ceux observés avec les nucléophiles réguliers de pK_a semblables. La méthoxyamine ne présente qu'une faible augmentation de réactivité par comparaison avec celle d'une amine primaire normale de pK_a semblable.

Les valeurs des paramètres de Leffler pour le processus de bris de liaison dans les réactions de nucléophiles α avec les acétates de phényle ne présentent pas de différences spéciales, à l'exception de celles dues au pK_a du nucléophile. On considère que l'effet α est causé par des effets stériques et des exigences imposées aux réactions par le solvant.

Mots clés : effet α, nucléophile, Yukawa–Tsuno, Leffler, Hammett, ester de phényle, charge effective, Brønsted.

[Traduit par la rédaction]

Introduction

A nucleophile with a lone pair of electrons on the atom adjacent to the nucleophilic atom often exhibits enhanced reactivity compared with that of a nucleophile of comparable Brønsted basicity (1, 2), which does not possess this structural feature. The phenomenon is called the α-effect, and it occurs to different degrees in reactions with many substrates. The α-effect phenomenon has been reviewed (3, 4), and several explanations have been advanced, none of which provides a universal explanation. Four major causes have been suggested for the α-effect and are ground-state destabilization of the nucleophile, transition-state stabilization, differences in solvation, and stabilization of the reaction products (3). Among other factors that may contribute to the above are hydrogen bonding in the transition state (5), intra-molecular general base catalysis (6), and cyclization in the transition state (7). The contribution of ground-state stabilization towards the α-effect via the repulsion of adjacent lone pairs (8) has been questioned

Received July 30, 1997.

M.J. Colthurst, A.J.S.S. Kanagasooriam, M.S.O. Wong, C. Contini, and A. Williams.[1] Chemical Laboratory, School of Physical Sciences, University of Kent, Canterbury, CT2 7NH, U.K.

[1] Author to whom correspondence may be addressed. Telephone: (44) (0)1227–82–3693. Fax: (44) (0)1227–475–475. E-mail: aw@ukc.ac.uk

© 1998 NRC Canada

Table 1. Kinetic data for the reaction of the azide ion and substituted phenyl acetates.[a]

Substituent	$k_2 \times 10^3/M^{-1}s^{-1}$[b]	pH[c]	$\Delta k_{obs} \times 10^3/s^{-1}$[d]	Δ[Nuc]/mM[e]	N[f]	λ/nm[g]
4-Cl	1.37 ± 0.085	10.00	0.43–0.77	0–240	6	295
H	0.361 ± 0.03	9.99	0.24–0.32	0–250	6	280
4-F	0.217 ± 0.034	9.98	0.36–0.41	0–240	6	300
4-MeO	0.0499 ± 0.006	10.11	0.27 – 0.28	0–240	6	290
4-CHO	13.6 ± 0.27	10.03	1.3–4.8	0–240	6	325
4-CN	13.6 ± 0.31	8.07	0.38–1.52	20–100	5	285
4-Cl,3-NO_2	22.9 ± 0.52	4.99	2.86–11.11	100–500	5	345
3-NO_2	7.60 ± 0.15	5.03	1.01–3.91	100–500	5	325
3-CHO	1.62 ± 0.091	5.01	0.46–0.91	200–500	4	315
4-NO_2	24.3 ± 0.61[h]	5.02	2.74–11.60	100–500	5	330
4-Ac	4.65 ± 0.11	8.89	0.577–0.853	40–100	4	330

[a] General conditions: 25°C; 10 mM $NaHCO_3$ buffer for pH values above 9.98; HEPES at 50 mM for pH values 8.07, 8.89; azide provided the buffer for pH ≈ 5; 0.5 M ionic strength maintained with KCl, solvent:water with 10% acetonitrile. HEPES, *N*-(2-hydroxyethyl)piperazine-*N*′-2-ethanesulphonic acid.

[b] Calculated using a fraction of base derived from the average pH using values of 4.0 (1) and 14 for pK_a azide and pK_w, respectively.

[c] Average measured pH for all runs.

[d] Range of observed first-order rate constants.

[e] Range of azide ion concentration employed.

[f] Number of data points not including duplicates.

[g] Wavelength used.

[h] Literature (1), 36.7×10^{-3} M^{-1} s^{-1}.

(3, 9) on the grounds that enhancement of nucleophilicity should also lead to an increase in the Brønsted basicity except where transition state stabilization is involved.

Recent literature suggests that stabilization of the transition state is a major factor (10–12) in the manifestation of the α-effect, and a contribution from solvation has been reported (12*b*). The reaction of 4-nitrophenyl acetate with various nucleophiles, such as oximate anions (12*b*, 13), has often been used in such experimental studies, although other reactions, such as that of phosphorylated pyridine monoanions with hydrogen peroxide, acetohydroxamate, and fluoride ions, have been investigated (10).

This work is to study the extent of fission in the C—OAr bond of reactions with substituted phenyl acetates as a function of the α-nucleophile structure and azide ion (**1**–**6**). Change in effective charge is a useful measure of bond formation or fission (14*a*), and there is a substantial body of data that can be used as a standard so that the charge distribution in reactions of nucleophiles with enhanced reactivity can be compared with

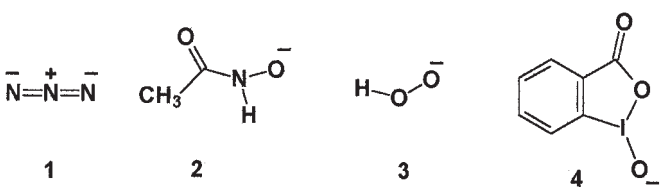

1 **2** **3** **4**

5 **6**

that of normal amines and oxyanions. The aim of this paper is to determine if there is a significant electronic difference between reactions of α-nucleophiles with substituted phenyl acetates compared with that of normal nucleophiles of similar pK_a.

Experimental

Materials

The nucleophiles (except hydrogen peroxide) were redistilled or recrystallized from bench-grade materials, and the substituted phenyl acetates were from a previous study or prepared by the method of Chattaway (14*b*). The 3-nitro-phenyl acetate, 4-formyl-phenyl, and 4-acetyl-phenyl acetates were donated by Dr. A.B. Maude. Hydrogen peroxide was of analytical reagent grade and was standardized by titration with $KMnO_4$.

Methods

All solutions were prepared with water double distilled from glass and degassed. Buffer materials were either of A.R. grade or purified before use. A series of buffered solutions for studies of rates at different nucleophile concentrations were prepared by dilution of a stock solution containing the nucleophile with a solution (identical in respect of buffer component concentration, pH, and ionic strength) but without nucleophile. Acetonitrile was added (to give 10% v/v) to counter solubility problems of the ester substrates; footnote *a* in Tables 1–6 gives the identities of the buffer components.

Reactions were initiated by the addition of an aliquot (0.01–0.05 mL) of a solution of the substrate (in acetonitrile) on the tip of a glass rod to 2.5 mL of buffered solution, contained in a 1 cm path-length silica cuvette in the thermostatted cell compartment of either a Pye Unicam SP 800 or a Perkin–Elmer Lambda 5 UV/visible spectrophotometer. A few vertical strokes of the glass rod effected mixing, and the

© 1998 NRC Canada

Table 2. Kinetic data for the reaction of the acetohydroxamate ion and substituted phenyl acetates.[a]

X	k_2/M^{-1} s^{-1}[b]	pH[c]	$\Delta k_{obs}/10^3$ s^{-1}[d]	Δ[Nuc]/mM[e]	N[f]	λ/nm[g]
4-NO_2	113 ± 0.89[h]	6.95	2.1–22	5.2–52	10	400
4-Cl,3-NO_2	119 ± 1.52	6.98	5.7–28	12–60	10	340
3-NO_2	55.8 ± 0.83	6.97	2.5–12	5.4–54	9	345
4-CO_2Me	29.1 ± 0.15	6.97	1.5–7.2	13–63	5	300
4-Cl	9.13 ± 0.83	8.02	4.7–25	13–64	5	290
4-F	4.85 ± 0.086	8.01	2.5–13	13–64	5	285
3-Cl	16.1 ± 0.23	7.99	8.4–42	13–64	5	280
4-MeO	1.60 ± 0.009	8.00	0.9–4.2	13–64	5	290
4-Ac	34.8 ± 0.11	7.99	7.2–87	12–58	6	325
4-CHO	49.4 ± 0.32	7.97	14–65	7.0–35	5	330
4-CN	58.9 ± 0.37	7.96	15–62	7.0–28	4	280

[a] General conditions: 25°C, 50 mM 2,6-lutidine (pH ≈ 7) or 50 mM HEPES (pH ≈ 8) buffers, 0.5 M ionic strength maintained with KCl, solvent:water with 10% acetonitrile.

[b] Calculated using a fraction of base derived from the average pH using values of 9.37 ± 0.04 and 14 for pK_a acetohydroxamic acid and pK_w, respectively.

[c,d] Footnotes as in Table 1.

[e] Range of acetohydroxamic acid concentration.

[f,g] Footnotes as in Table 1.

[h] Literature (8), 132 M^{-1} s^{-1}.

Table 3. Kinetic data for the reaction of hydrogen peroxide with substituted phenyl acetates.[a]

Substituent	$k_2 \times 10^{-3}$/M^{-1} s^{-1}[b]	pH[c]	$\Delta k_{obs} \times 10^2$/s^{-1}[d]	Δ[Nuc]/mM[e]	N[f]	λ/nm[g]
4-NO_2	3.48 ± 0.28[h]	9.00	0.31–4.00	0.25–1	5	400
4-CN	2.18 ± 0.35	9.00	0.26–2.06	0.5–3.7	5	280
4-Ac	1.37 ± 0.26	8.99	0.53–1.82	2–8	5	325
4-Cl	0.693 ± 0.031	9.00	0.68–2.80	4–16	5	290
3-NO_2	2.85 ± 0.14	8.99	0.61–5.00	0.5–7	5	345
3-Cl	0.71 ± 0.25	9.01	0.53–2.60	2–12	5	280
3-CHO	1.01 ± 0.25	9.00	1.1–3.91	4–16	5	315
H	0.335 ± 0.72	8.98	0.88–2.61	8–32	4	280
4-CHO	1.25 ± 0.30	8.98	0.48–1.48	1–4	4	330
4-F	0.55 ± 0.091	9.02	1.12–4.50	8–32	4	285

[a] General conditions: 25°, $NaHCO_3$ buffer at 50 mM; ionic strength maintained at 0.5 M with KCl; solvent was water with 10% acetonitrile.

[b] Calculated using a fraction of base derived from average pH using values of 11.62 ± 0.06 for pK_a for H_2O_2 and 14.00 for pK_w.

[c,d] Footnotes as in Table 1.

[e] Range of hydrogen peroxide concentrations employed.

[f,g] Footnotes as in Table 1.

[h] Literature (16), 3670 M^{-1} s^{-1}.

Table 4. Kinetic data for the reaction of 2-iodosobenzoate ion with substituted phenyl acetates.[a]

Substituent	k_2/M^{-1} s^{-1}[b]	pH[c]	$\Delta k_{obs} \times 10^2$/s^{-1}[d]	Δ[Nuc]/mM[e]	N[f]	λ/nm[g]
4-NO_2	1.47 ± 0.095	9.10	1–3.3	5–20	5	400
4-CN	1.13 ± 0.12	10.46	0.21–0.59	0.5–2	4	285
4-Ac	0.916 ± 0.084	10.46	0.33–0.88	2–8	4	325
4-Cl	0.376 ± 0.082	10.46	1.00–5.30	1.25–7.5	4	295
3-NO_2	1.2 ± 0.12	9.10	0.7–2.4	5–20	8	345
3-Cl	0.559 ± 0.063	9.10	1.49–2.4	0.5–2	8	280
3-CHO	0.53 ± 0.026	9.10	0.1–0.79	2.5–15	8	315
H	0.23 ± 0.011	10.46	0.067–0.15	1–2.5	4	280
4-F	0.317 ± 0.048	10.46	0.092–1.4	0.5–2.5	4	300
4-CHO	1.11 ± 0.09	9.6	0.7–16	5–12.5	4	330

[a] General conditions: 25°, Na tetraborate buffer at 30 mM; ionic strength maintained at 0.5 M with KCl; solvent was water with 10% acetonitrile.

[b] Calculated using a fraction of base derived from average pH using values of 7.52 ± 0.07 for the pK_a of 2-iodosobenzoic acid.

[c,d] Footnotes as in Table 1.

[e] Range of iodosobenzoic acid concentrations.

[f,g] Footnotes as in Table 1.

© 1998 NRC Canada

Table 5. Kinetic data for the reaction of *N*,*N*-diethylhydroxylamine with substituted phenyl acetates.[a]

Substituent	k_2/M^{-1} s^{-1}[b]	pH[c]	$\Delta k_{obs} \times 10^3$/s^{-1}[d]	Δ[Nuc]/mM[e]	λ/nm[f]
4-NO_2	64.1 ± 4	10.21	13.9–19.2	10–40	400
4-CN	47.2 ± 6	10.22	9.2–14.2	10–40	285
4-Ac	31.7 ± 3	10.22	7.98–9.60	10–40	325
4-Cl	17.9 ± 4	10.20	1.67–3.25	10–40	295
3-NO_2	63.1 ± 5	10.22	5.6–12.9	20–80	345
3-Cl	23.0 ± 5	10.20	4.81–7.02	10–40	280
3-CHO	21.0 ± 1	10.21	1.55–4.32	20–80	315
H	8.75 ± 1	10.22	0.42–1.2	40–80	280
4-CHO	28.9 ± 2	10.22	1.05–1.3	20–60	330
4-F	11.7 ± 2	10.21	1.84–3.0	40–80	300
4-COOMe	35.1 ± 4	10.22	7.1–9.0	20–40	300

[a] General conditions: 25°, $NaHCO_3$ buffer at 50 mM; ionic strength maintained at 0.5 M with KCl; solvent was water with 10% acetonitrile.
[b] Fraction of base was calculated employing the pK_a of the hydroxyl group (12.88 ± 0.04) determined by titration with KOH.
[c] Footnote as in Table 1.
[d] Range of observed first-order rate constants. Number of data points (not including duplicate runs) for each substituent is four.
[e] Range of *N*,*N*-diethylhydroxylamine concentrations.
[f] Wavelength used.

Table 6. Kinetic data for the reaction of methoxyamine with substituted phenyl acetates.[a]

Substituent	$k_2 \times 10^3$/M^{-1} s^{-1}[b]	pH[c]	$\Delta k_{obs} \times 10^4$/s^{-1}[d]	Δ[Nuc]/mM[e]	λ/nm[f]
4-NO_2	7.33 ± 0.053[g]	10.02	33–62.2	100–450	400
4-CN	4.33 ± 0.11	10.01	18.8–36.2	500–900	285
4-Ac	1.96 ± 0.052	10.01	11–20	500–900	325
4-Cl	0.833 ± 0.02	10.00	1.78–5.12	500–900	295
3-NO_2	4.16 ± 0.065	10.02	11.5–20.3	100–450	345
3-Cl	1.07 ± 0.049	10.01	4.67–12.8	200–450	280
3-CHO	1.35 ± 0.098	10.00	2.78–6.3	250–450	315
4-COOMe	1.92 ± 0.02	10.02	5.94–8	30–90	300

[a] General conditions: 25°, $NaHCO_3$ buffer at 50 mM; ionic strength maintained at 0.5 M with KCl; solvent was water with 10% acetonitrile.
[b] Fraction of neutral base taken as unity as measurements were carried out at pH values above that of the pK_a of the conjugate acid.
[c] Footnote as in Table 1.
[d] Range of observed first-order rate constants.Number of data points (not including duplicate runs) for each substituent is four.
[e] Range of methoxyamine concentrations.
[f] Wavelength used.
[g] Literature (2, 17), 3.33×10^{-3}, 2×10^{-3} M^{-1} s^{-1}.

reaction was followed by monitoring the change in absorbance with time at the optimal wavelength for analysis of the product. The pH values of the solutions were measured before and after each kinetic run using a Radiometer PHM62 meter with a Russell CMAWL combined electrode, calibrated with BDH buffers; data for experiments where the pH changed by more than 0.1 units were discarded.

Pseudo-first-order rate constants were obtained from linear plots of $\log(A_\infty - A_t)$ vs. time where A_t is the absorbance of the solution at the given wavelength at time t. Rate constants were also obtained by fitting the value of A_t (which increases with time in these cases) to the equation $A_t = A_\infty - (A_\infty - A_o)\exp(-kt)$. Ester concentrations employed in the kinetics were between 50 to 100 μM; some of the esters exhibited solubility problems, and for these esters concentrations near the lower limit were employed.

Values of pK_a for the nucleophilic species were determined by pH titration of solutions of the species with standard KOH solutions.

Data were fit to theoretical equations by use of programs operating on an Opus IV or V PC or by use of "grid-search" programs written in BASIC and employing a BBC Master 128 computer.

Results

The reactions of substituted phenyl acetates with the nucleophiles displayed good first-order kinetics for over 90% of the total reaction. The pseudo-first-order rate constants k_{obs} fitted eqn. [1] for all the nucleophiles studied here, and selected examples of the fit are illustrated in Fig. 1.

$$[1] \quad k_{obs} = k_{intercept} + k_2'[\text{total nucleophile}]$$

No buffer effect was observed, as deduced from the linearity of the rate–concentration plots. This was confirmed in the case of the reaction of acetohydroxamate ion with 4-chlorophenyl acetates by observing the effect on the pseudo-first-order rate constant (Fig. 2) of different concentrations of added buffer

© 1998 NRC Canada

Fig. 1. (*a*) Dependence of k_{obs} on the concentration of aceto-hydroxamic acid for reaction with substituted phenyl acetates. Conditions as in Table 2. (*b*) Dependence of k_{obs} on the concentration of azide ion for reaction with substituted phenyl acetates. Conditions as in Table 1.

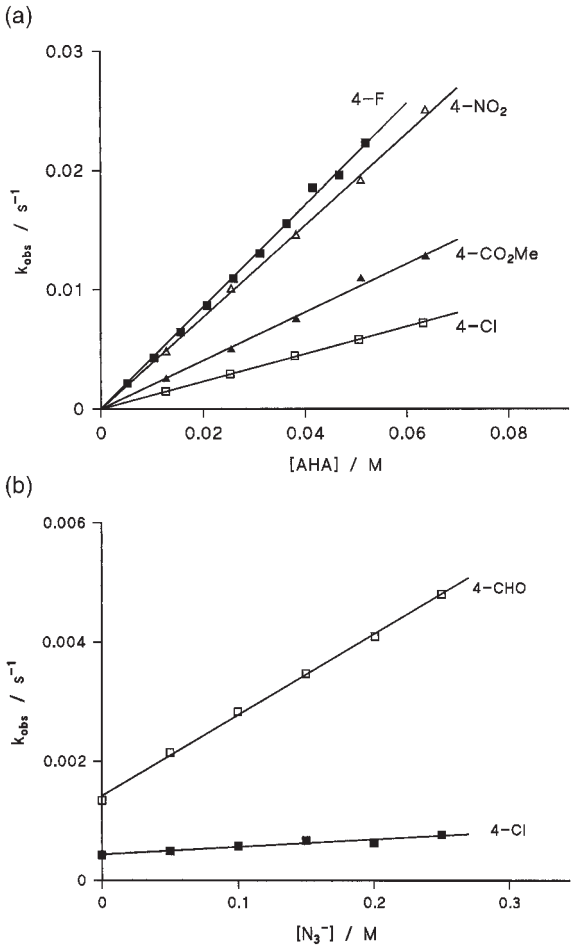

species. The second-order rate constants (k_2) were obtained by dividing the slope (k_2') of the rate-concentration plots by the fraction of base (FB) present at the pH of the reaction.

The values of k_2 are collected in Tables 1–6 together with experimental conditions, which include the ranges of nucleophile concentrations and the ranges of observed pseudo-first-order rate constants. The second-order rate constants for the nucleophiles with the 4-nitrophenyl ester agree with the literature values where these are known (1, 2, 8, 15–17).

The reactions of phenolate ions and amines with phenyl acetates involve nucleophilic attack (18). Since the nucleophiles studied here have reactivity close to or greater than that of the corresponding amine or phenolate ion of the same pK_a, it is reasonable that nucleophilic attack rather than general base catalysis of hydrolysis is occurring. Reaction of azide ion with phenyl cinnamates (19) has been demonstrated to be nucleophilic and acetohydroxamate ion has been shown to react as a nucleophile with 4-nitrophenyl acetate (20). The hydroxylamine species react via their oxyanions at the pH values studied here by analogy with the results for the parent hydroxylamine (21).

Fig. 2. The linear correlation of k_{obs} and acetohydroxamate ion-concentration at different HEPES buffer concentrations (○, 100 mM; ■, 50 mM; □, 25 mM) for the attack of the ion upon 4-chlorophenyl acetate. Conditions in Table 2.

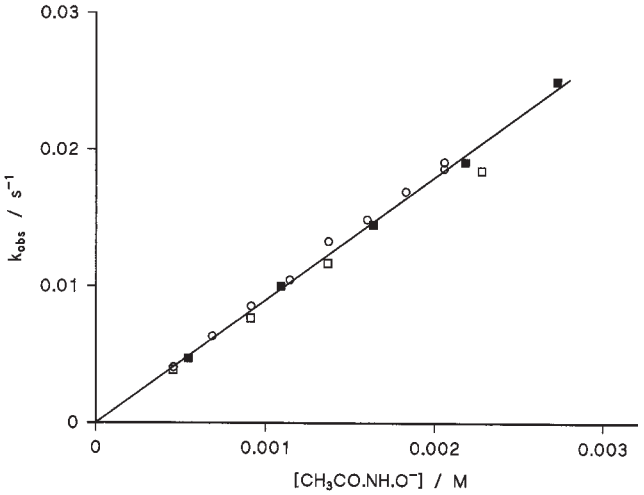

Fig. 3. The Hammett σ and σ⁻ correlations for the attack of the acetohydroxamate ion on substituted phenyl acetates. The conditions of measurement are listed in Table 2. The line is calculated from parameters in Table 7. ■, ▲, calculated from $\sigma + \rho r(\sigma^- - \sigma)$; ▲, resonating substituents; △, Hammett σ⁻ for resonating substituents; ○, Hammett σ value of resonating substituents.

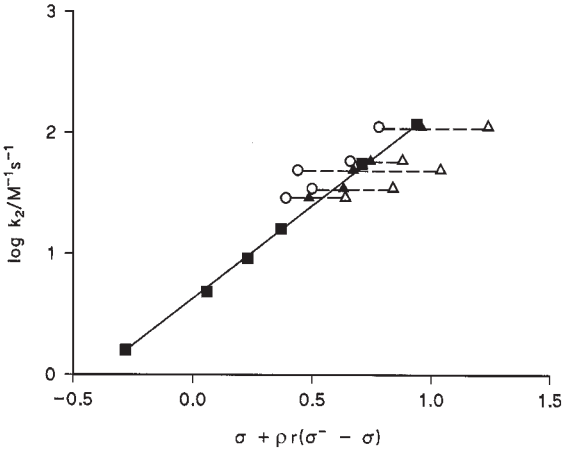

The second-order rate constants were fit to the Hammett eqn. [2], as modified by the Yukawa–Tsuno procedure for assessing resonance effects (22*a*).

[2] $$\log k_{nuc} = \rho\sigma + \rho r(\sigma^- - \sigma) + C$$

An example of the fit to the Yukawa–Tsuno type plot is illustrated in Fig. 3 for reaction of acetohydroxamate ion with phenyl acetates; the resonating substituents in the illustration (Fig. 3) are given sigma constants derived from the equation, sigma = $\sigma + r(\sigma^- - \sigma)$, which reduces to σ for all the non-resonating substituents. The parameters of the equations for each of the reactions in Tables 1–6 are recorded in Table 7.

The Leffler parameters, α_{lg} (Table 7), are obtained by division of the Hammett ρ_{lg} value for the reaction by the ρ_{eq} value

© 1998 NRC Canada

Table 7. Collection of parameters for the Yukawa–Tsuno relationship.[a]

Nucleophile	pK_a	ρ	r [b]	C	Leffler's α_{lg}	α-effect[c]
Azide ion	4.00	2.10 ± 0.152	0.50 ± 0.12	–3.584 ± 0.078	0.55	463 ± 44
Correlation coefficient (r)		0.9862				
Acetohydroxamate ion	9.37	1.53 ± 0.04	0.388 ± 0.045	0.630 ± 0.024	0.40	201 ± 18
Correlation coefficient (r)		0.9975				
Hydroperoxide ion	11.62	1.19 ± 0.129	0.032 ± 0.108	2.56 ± 0.046	0.31	128 ± 13
Correlation coefficient (r)		0.9785				
Iodosobenzoate ion	7.52	0.874 ± 0.07	0.372 ± 0.093	–0.590 ± 0.029	0.23	64 ± 3
Correlation coefficient (r)		0.9883				
N,*N*-diethylhydroxylamine	12.88	1.12 ± 0.05	–0.038 ± 0.045	–1.70 ± 0.02	0.30	0.27 ± 0.05
Correlation coefficient (r)		0.9945				
Methoxyamine	4.6	1.52 ± 0.15[d]	0.178 ± 0.099	–3.46 ± 0.07	0.40	48 ± 7
Correlation coefficient (r)		0.9853				

[a] Parameters calculated from data in Tables 1–6 for eq. [2].
[b] Resonance interaction parameter (see eq. [2]).
[c] Calculated from k_2/k_{normal}.
[d] A similar value was obtained (17) from a smaller number of data points.

for the equilibrium transfer of the acetyl group from the phenyl ester (3.79) obtained by multiplying the β_{eq} 1.7 (14*a*) by 2.23 (23), the r value for ionization of phenols. The values of the α-effect (see Table 7 for the definition) for the anionic nucleophiles are computed from the rate constants for the reaction of the nucleophiles with 4-nitrophenyl acetates (Tables 1–6), and the rate constants for reaction of 4-nitrophenyl acetate with phenolate ion of the same pK_a are calculated according to the equation: $\log k_{normal} = 0.75pK_a^{ArOH} - 7.28$ (18*a*). The α-effect of the methoxyamine is calculated using the rate constant for reaction of 4-nitrophenyl acetate with a primary amine of the same pK_a determined from the equation calculated from literature data (15):

$$\log k_{normal} = 0.82pK_a^{RNH3} - 7.59$$

Discussion

Reactions of substituted phenyl acetates with azide, acetohydroxamate, iodosobenzoate ions, and methoxyamine fit the Yukawa–Tsuno type equation (eqn. [2]), consistent with a substantial component of bond fission in the transition state (26). Although the general requirements for concerted displacement mechanisms at the acyl centre are known (25*b*) it is not possible to predict concerted or stepwise mechanisms with certainty, although reactions of phenyl esters with anionic nucleophiles are most likely to be concerted (25*b*). The more weakly basic anions (**1**, **2**, and **4**) would be expected to possess more bond fission in the transition state than more basic ones thus giving rise to resonance interaction. Hydrogen peroxide and diethylhydroxylamine oxyanions are more basic, and the transition state of the process would be expected to involve little bond fission and the absence of significant resonance interaction in these cases.

The reactions of **1**, **2**, **3**, **4**, and **6** with 4-nitrophenyl acetate exhibit enhanced reactivity compared with that of analogous "normal" nucleophiles (Table 7). The diminished reactivity of the *N*,*N*-diethylhydroxylamine ion (**5**) is simply ascribed to steric hindrance afforded by the ethyl groups even though the anion is an "α-nucleophile."

The Leffler parameter, α_{lg}, measures the change in effective charge on the leaving atom of the bond undergoing fission normalized by the change in effective charge for complete bond fission. The question of timing of bond fission and formation in the displacement reaction does not alter the conclusions to be obtained from knowledge of α_{lg} concerning bond fission. Molecular orbital theory predicts that the α-effect is dependent on the extent of bond formation between nucleophile and electrophilic centre (8). The theory was originally tested for amine (25*a*) and oxyanion nucleophiles (25*c*), but the data are equivocal. The observation in the case of aminolyses is based on a diverse series of reactions including ester aminolysis, aromatic substitution, alkyl substitution, phosphorolysis, and sulphation. In both amine and oxyanion nucleophiles the extent of bond formation was measured using β_{nuc} values and normalization by use of β_{eq} (14*a*) yields Leffler α_{nuc} values, which indicate a smaller value for bond formation than that expressed by the unnormalized β_{nuc} value.

The values of α_{lg} displayed in Table 7 may be compared with those from the literature for reaction of other nucleophiles with substituted phenyl esters. The α_{lg} values for amino nucleophiles show no correlation or trend and the α-effect of neutral nitrogen nucleophiles have α_{lg} values within the range observed for the regular amines (Fig. 4*a*). In the anion series there is an overall trend in α_{lg} to lower values as pK_a^{nuc} increases (Fig. 4*b*). Within the structurally related phenoxide ion series there is a good correlation between α_{lg} and pK_a (27). The azide ion is included in the oxyanion series simply because of its negative charge. The value of α_{lg} does not appear to be dependent on whether or not the nucleophile has a lone pair on its α-atom.

The role of solvation with regard to the α-effect remains a subject of controversy (3, 9). The range of α-effect enhancements, from 1 to 60 for amines (25*a*), is scarcely at levels to be regarded as energetically significant, and the deviations are within the range that might be expected for solvation effects. Similar arguments may be recruited for reactions of oxyanion α-nucleophiles, which exhibit enhancements corresponding to

© 1998 NRC Canada

Fig. 4. (*a*) Leffler's α_{lg} for attack of amines on substituted phenyl acetates. Identities of the neutral nitrogen nucleophiles are 1, imidazole; 2, ammonia; 3, trimethylamine; 4, tris(hydroxymethyl)aminomethane; 5, piperidine; 6, ethylenediamine; 7, morpholine; 8, ethylglycinate; 9, ethylamine; 10, propylamine; 11, 2-methoxyethylamine; 12, glycine; 13, glycylglycine; 14, ethylenediamine monocation; 15, 2,2,2-trifluoroethylamine; 16, aniline; 17, piperazine; 18, piperazine monocation; 19, quinuclidinol; 20, triethylenediamine; 21, triethylenediamine monocation; 22, hydrazine; 23, hydroxylamine; 24, semicarbazide; 25, methoxyamine; 26, 3-phenyl-3-hydroxyazetidine; 27, 3-phenylazetidine; 28, aziridine. Data is taken from Table 7 and calculated from data from refs. 15, 17, 30, and 33. ■, α-effect nitrogen; △, small ring nitrogen; □, primary, secondary, and tertiary amines. (*b*) Leffler's α_{lg} for attack of oxyanions on substituted phenyl acetates. Identities of the ions are as follows: 1, 2,3,5-trichlorophenolate; 2, 2,4,5-trichlorophenolate; 3, 4-formylphenolate; 4, 4-cyanophenolate; 5, 3-chlorophenolate; 6, phenolate; 7, azide; 8, 2-iodosobenzoate; 9, acetohydroxamate; 10, hydroperoxide; 11, *N*,*N*-diethylamino-oxy; 12, pentaerythritol (oxyanion); 13, tris(hydroxymethyl)aminomethane (oxyanion); 14, hydroxide. Data is taken from Table 7 and calculated from data from refs. 27 and 34. △, α-effect anions; □, phenolate ions; ■, alkoxide and hydroxide ions.

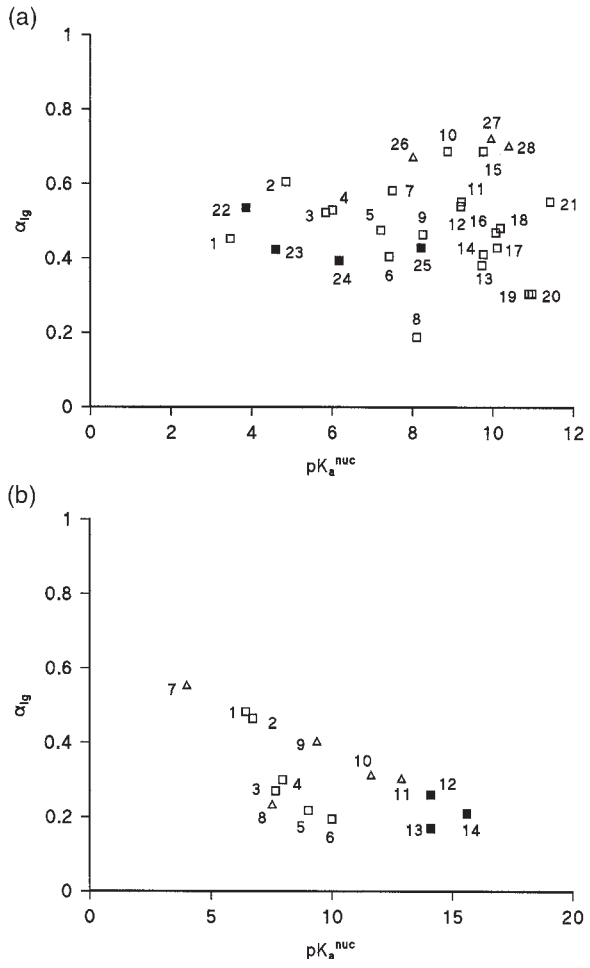

small energy differences. The α-effect is not manifest in a gas-phase reaction (22*b*) and is, therefore, caused by solvation, but it has also been suggested that the α-effect is less significant for low values of β_{nuc}; since a gas-phase reaction would be expected to have a low β_{nuc}, the absence of the α-effect is not surprising (3). Recent studies by Um and co-workers (22*c*) have shown that an α-effect is not apparent in the reaction of nitrophenyl acetates with α-nucleophiles in the presence of cetyltrimethylammonium bromide (CTAB), but is present in acetonitrile containing solutions (12*b*). It was concluded that solvation has a role in the manifestation of the α-effect. A desolvation effect was proposed by Terrier and co-workers (13) to account for the small Brønsted β_{nuc} obtained in the reaction of 4-nitrophenyl acetate and oximate anions of high pK_a. The reaction was considered to involve a rate-limiting desolvation of the nucleophile followed by a fast addition step. This explanation could, in part, explain the low α-effect of *N*,*N*-diethylhydroxylamine.

Deviations of nucleophiles from Brønsted and Hammett correlations have been discussed for many reactions, and these can have values of the same order as those ascribed to the α-effect (15, 28–31) while not possessing the structural requirements of the "α-nucleophile." When the rigorous test of hypernucleophilicity, discussed by Hoz and Buncel (3), is applied to many α-nucleophiles the enhancements are not substantial enough in our view to warrant a unique name, especially since nucleophiles without a lone pair on the α-atom can also exhibit similar enhancements of reactivity. The lower limit of rate enhancement commonly accepted as significant is about 50-fold (24), and this is larger than many α-effects in the amine series (25*a*). Prior to Hoz and Buncel's paper (3) the reactivity of the hydroxide ion nucleophile was employed as a standard, and it is now accepted that due to a solvation effect this nucleophile has a lower reactivity than its Brønsted basicity would predict. The enhanced reactivity of hydroperoxide ion over hydroxide ion is of significant practical importance, but a large component of the explanation must be due to the depressed activity of the latter ion due to solvation. It must be remembered that an α-effect (Table 7) remains for the hydroperoxide ion when a phenoxide ion is employed as the normal nucleophile in the α-effect calculation.

The acetate ion has two formal lone pairs of electrons on the oxygen atom β to the nucleophilic oxygen, and these could interact to cause an enhanced reactivity, as discussed for other similar nucleophiles (32). However, the nucleophilic reactivity of acetate ion towards 4-nitrophenyl acetate is only 0.016 of that of a phenolate of similar pK_a, even before it is statistically corrected for two possible centres. The most probable cause of the difference in reactivity is a solvation effect on the acetate ion, causing it to have substantial steric requirements compared with that of phenoxide ions.

We propose that the case for a special electronic explanation of the α-effect is not proven in view of the relatively small α-effects observed and the lack of any substantial difference between Leffler's α-parameter and those for normal nucleophiles of similar pK_a. Since the stability of the nucleophile component is independent of that of the electrophile in the ground state, it is clear that any effects on reactivity of hypernucleophiles relative to those of "regular" ones must be a result of differences in stability induced in the transition state where electrophile and nucleophile interact with each other.

© 1998 NRC Canada

References

1. W.P. Jencks and J. Carriuolo. J. Am. Chem. Soc. **82**, 1778 (1960).
2. W.P. Jencks and J. Carriuolo. J. Am. Chem. Soc. **82**, 675 (1960).
3. S. Hoz and E. Buncel. Isr. J. Chem. **26**, 313 (1985).
4. (*a*) J.O. Edwards and R.G. Pearson. J. Am. Chem. Soc. **84**, 16 (1962); (*b*) N.J. Fina and J.O. Edwards. Int. J. Chem. Kinet. **5**, 1 (1973); (*c*) A.P. Grekov and V.Ya. Veselov. Russ. Chem. Rev. (Engl. Transl.) **47**, 631 (1978).
5. (*a*) J. Epstein, M.M. Demek, and D.H. Rosenblatt. J. Org. Chem. **21**, 796 (1956); (*b*) W.P. Jencks. J. Am. Chem. Soc. **80**, 4585 (1958).
6. T.C. Bruice and R.G. Willis. J. Am. Chem. Soc. **87**, 531 (1965).
7. (*a*) E.G. Sander and W.P. Jencks. J. Am. Chem. Soc. **90**, 6154 (1968); (*b*) J.E. Dixon and T.C. Bruice. J. Am. Chem. Soc. **93**, 6592 (1971).
8. J.D. Aubort and R.F. Hudson. J. Chem. Soc. Chem. Commun. 938 (1970).
9. E. Buncel and S. Hoz. Tetrahedron Lett. **24**, 4777 (1983).
10. D. Herschlag and W.P. Jencks. J. Am. Chem. Soc. **112**, 1951 (1988).
11. (*a*) S. Hoz. J. Org. Chem. **47**, 3545 (1982); (*b*) M. Laloi-Diard, J.F. Vercherre, P. Gosselin, and F. Terrier. Tetrahedron Lett. **25**, 1267 (1984).
12. (*a*) I-H. Um, K-E. Choi, and D-S. Kwon. Bull. Korean Chem. Soc. **11**, 362 (1988); (*b*) I-H. Um, G-J. Hahn, G.J. Lee, and D-S. Kwon. Bull. Korean Chem. Soc. **13**, 642 (1992).
13. (*a*) F. Terrier, F. Degorre, D. Kiffer, and M. Laloi. Bull. Soc. Chim. Fr. 415 (1988); (*b*) F. Terrier, P. MacCormack, E. Kizilian, J-C. Hallé, P. Demerseman, F. Guir, and C. Lion. J. Chem. Soc. Perkin Trans. 2, 153 (1991); (*c*) G. Moutiers, E. Le Guével, L. Villien, and F. Terrier. J. Chem. Soc. Perkin Trans. 2, 7 (1977).
14. (*a*) A. Williams. Adv. Phys. Org. Chem. **27**, 1 (1991); (*b*) F.D. Chattaway. J. Chem. Soc. 2495 (1931).
15. W.P. Jencks and M. Gilchrist. J. Am. Chem. Soc. **90**, 2622 (1968).
16. R.A. Moss, K.W. Alwiss, and G.O. Bizzigotti. J. Am. Chem. Soc. **105**, 681 (1983).
17. L. do Amaral, K. Koehler, D. Bartenbach, T. Pletcher, and E. H. Cordes. J. Am. Chem. Soc. **89**, 3537 (1967).
18. (*a*) S. Ba-Saif, A.K. Luthra, and A. Williams. J. Am. Chem. Soc. **109**, 6362 (1987); (*b*) A.C. Satterthwaite and W.P. Jencks. J. Am. Chem. Soc. **96**, 7018 (1974).
19. J. Suh and B.H. Lee. J. Org. Chem. **45**, 3103 (1980).
20. T. Kunitake, Y. Okahata, and R. Ando. Bull. Chem. Soc. Jpn. **47**, 1509 (1974).
21. W.P. Jencks. J. Am. Chem. Soc. **80**, 4581 (1958).
22. (*a*) M.I. Page and A. Williams. Organic and bio-organic mechanisms. Longmans, Harlow, England. 1997. p. 59; (*b*) C.H. Depuy, E.W. Della, J. Filley, J.J. Grabowski, and V.M. Bierbaum. J. Am. Chem. Soc. **105**, 2481 (1983); (*c*) D-S. Kwon, S-E. Lee, J-K. Jung, J-Y. Park, and I-H. Um. Bull. Korean Chem. Soc. **13**, 486 (1992).
23. D.D. Perrin, B. Dempsey, and E.P. Serjeant. pK_a prediction for organic acids and bases. Chapman and Hall, London. 1981.
24. B. Capon. Q. Rev. Chem. Soc. **18**, 45 (1964).
25. (*a*) J.E. Dixon and T.C. Bruice. J. Am. Chem. Soc. **94**, 2052 (1972); (*b*) A. Williams. Acc. Chem. Res. **22**, 387 (1989); (*c*) R.F. Hudson. *In* Chemical reactivity and reaction paths. *Edited by* G. Klopman. J. Wiley and Sons, Inc., New York. 1974. p.167.
26. A. Williams and R.A. Naylor. J. Chem. Soc. B, 1967 (1971).
27. S.A. Basaif, A.K. Luthra, and A. Williams. J. Am. Chem. Soc. **111**, 2647 (1989).
28. R.P. Bell. The proton in chemistry. 2nd ed. Chapman and Hall, London. 1973. p. 217.
29. M.J Gregory and T.C. Bruice. J. Am. Chem. Soc. **89**, 4400 (1967).
30. T.C. Bruice, A. Donzel, R.W. Huffman, and A.R. Butler. J. Am. Chem. Soc. **89**, 2106 (1967).
31. D. Stefanidis, S. Cho, S. Dhe-Paganon, and W.P. Jencks. J. Am. Chem. Soc. **115**, 1650 (1993).
32. J.A. Zoltewicz and H.L. Jacobson. Tetrahedron Lett. 189 (1972).
33. T.C. Bruice and S.J. Benkovic. J. Am. Chem. Soc. **86**, 418 (1964).
34. T.C. Bruice and J.L. York. J. Am. Chem. Soc. **83**, 1382 (1961).

© 1998 NRC Canada

Pyridinium *N*-phenoxide betaines and their application to the determination of solvent polarities, XXIV.[1] Syntheses and UV-vis spectroscopic properties of new lipophilic *tert*-butyl- and 1-adamantyl substituted, negatively solvatochromic pyridinium *N*-phenolate betaine dyes

Christian Reichardt, Stefan Löbbecke, Abdol Mohammed Mehranpour, and Gerhard Schäfer

Abstract: Syntheses and negative solvatochromism of two new lipophilic pentaphenyl pyridinium *N*-phenolate betaine dyes, substituted with seven *tert*-butyl groups (**9**) or with three *tert*-butyl and two 1-adamantyl groups (**13**) in the peripheral phenyl rings, are described in order to get zwitterionic dyes that are more soluble in nonpolar solvents such as the standard betaine dye, **1**, which has been used for the construction of an empirical scale of solvent polarity, called the E_T(**30**) scale.

Key words: betaine dyes, E_T(**30**) values, lipophilic dyes, pyridinium *N*-phenolate betaine dyes, solvatochromism, solvent polarity.

Résumé : On décrit les synthèses et la solvatochromie négative de deux colorants bétaïnes lipophiles, le *N*-phénolate de pentaphényl pyridinium, dans lesquels les noyaux benzéniques périphériques sont respectivement substitués par sept groupes *t*-butyles (**9**) et trois groupes *t*-butyles ainsi que deux groupes 1-adamantyles (**13**). Ces produits ont été préparés dans le but d'obtenir des colorants zwitterioniques plus solubles dans les solvants non polaires que le colorant bétaïne standard, **1**, et ils ont été utilisés pour élaborer une échelle empirique de polarité de solvant appelée échelle E_T(**30**).

Mots clés : colorants bétaïnes, valeurs E_T(**30**), colorants lipophiles, colorants bétaïnes *N*-phénolate de pyridinium, solvatochromie, polarité de solvant.

[Traduit par la rédaction]

Introduction

Solutions of pyridinium *N*-phenolate betaine dyes such as **1** and **2** (Scheme 1) exhibit the phenomena of solvatochromism, thermochromism, piezochromism, and halochromism.[3] That means the longest wavelength, intramolecular charge-transfer (CT) absorption band of their UV-vis absorption spectra depends on solvent polarity, solution temperature, external pressure, and on the nature and concentration of added salts. The extraordinarily large negative solvatochromism of the standard pyridinium *N*-phenolate betaine dye **1** has been used to establish UV-vis spectroscopically derived empirical parameters of solvent polarity, called E_T(**30**) values (3).[4] The E_T(**30**) values are simply defined as the molar electronic transition energies (in kcal/mol) of the standard betaine dye **1**, measured in solvents of different polarity at room temperature (25°C) and normal pressure (1 bar) (1 bar = 100 kPa), according to eq. [1].

$$[1] \quad E_T(\mathbf{30})\ (\text{kcal/mol}) = hc\nu_{max}N_A = 2.8591(10^{-3})\nu_{max}\ (\text{cm}^{-1}) = 28\,591/\lambda_{max}\ (\text{nm})$$

where ν_{max} is the frequency and λ_{max} the wavelength of the maximum of the longest wavelength, intramolecular CT

Received November 22, 1997.

This paper is dedicated to Professor Dr. Erwin Buncel, honouring his valuable contributions to physical organic chemistry.

C. Reichardt,[2] A.M. Mehranpour, and G. Schäfer. Department of Chemistry and Scientific Center of Material Sciences, Philipps University, Hans-Meerwein-Strasse, D-35032 Marburg, Germany.
S. Löbbecke. Fraunhofer Institute for Chemical Technology, Joseph-von-Fraunhofer-Strasse 7, D-76327 Pfinztal, Germany.

[1] Part XXIII: see ref. 1.
[2] Author to whom correspondence may be addressed. Telephone (intl.): + 49(0)6421/285–544. Fax (intl.): + 49(0)/6421/288–917.
[3] For recent reviews on the various "-chromisms" of pyridinium *N*-phenolate betaine dyes see ref. 2.
[4] For recent reviews on empirical solvent polarity parameters see ref. 4.

© 1998 NRC Canada

Scheme 1.

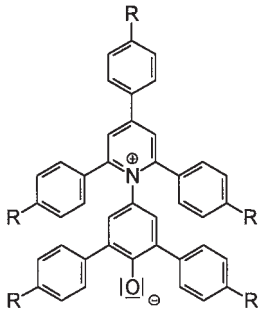

1: R = H
2: R = CMe_3

absorption band of betaine dye **1**. In the first publication (3*a*), the betaine dye **1** had, by chance, the formula number **30**. Therefore, the number (**30**) was later added in order to avoid confusion with E_T, which has been often used as an abbreviation for triplet energy in photochemistry. High E_T(**30**) values correspond to high solvent polarity (here defined as the overall solvation capability of a solvent[5]) and vice versa. The E_T(**30**) values are known for more than 360 solvents and for numerous binary solvent mixtures (4*d*, 6).[4] These and other empirical parameters of solvent polarity have been successfully used in the correlation analysis of solvent effects on chemical equilibria, reaction rates, and spectral absorptions (6).

The E_T(**30**) scale ranges from 63.1 kcal/mol for water, as the most polar solvent, to 30.7 kcal/mol for tetramethylsilane (TMS), as the least polar solvent. That means, a solvent change from water to TMS reduces the electronic excitation energy of the dissolved indicator dye **1** by 32.4 kcal/mol, caused by the differential solvation of the strongly dipolar ground state and the considerably less dipolar excited state of **1**. To avoid the non-SI unit kcal/mol, in 1983 the normalized E_T^N scale was introduced and defined according to eq. [2] (7).

$$[2] \quad E_T^N = \frac{E_T(\text{solvent}) - E_T(\text{TMS})}{E_T(\text{water}) - E_T(\text{TMS})} = \frac{E_T(\text{solvent}) - 30.7}{32.4}$$

The dimensionless E_T^N scale ranges now from 1.000 for water to 0.000 for TMS and is easier to handle, particularly in multiparameter equations (4*d*).[4]

The prerequisite to the measurement of E_T(**30**) and the resp. E_T^N values was the synthesis of the more lipophilic penta-*tert*-butyl-substituted betaine dye **2**, which is, in contrast to **1**, sufficiently soluble in nonpolar solvents such as aliphatic hydrocarbons and TMS. The excellent linear correlation between the E_T values of **1** and **2** for solvents in which both dyes are soluble allows the calculation of E_T(**30**) values, according to eq. [3] for nonpolar solvents in which the primary indicator dye **1** is not soluble enough. In eq. [3],

$$[3] \quad E_T(\mathbf{30}) \text{ (kcal/mol)} = (28\,591/\lambda'_{max}\text{ (nm)} - 1.808)/0.9424$$

λ'_{max} corresponds to the wavelength of the visible absorption maximum of the secondary indicator dye **2** (7).

[5] For a recent pragmatic definition of the term "solvent polarity" see ref. 5.

Nevertheless, the solubility of the penta-*tert*-butyl-substituted betaine dye **2** in nonpolar solvents is rather small, and the corresponding UV-vis spectroscopical measurements are sometimes cumbersome (see, for examples, ref. 1 and footnote 6). In perfluorohydrocarbons, **2** is completely unsoluble. Therefore, we have tried to obtain new, suitably substituted, solvatochromic betaine dyes, which are more lipophilic and hopefully more soluble in nonpolar solvents. In this paper, we describe the syntheses and UV-vis spectroscopic properties of two new negatively solvatochromic pyridinium *N*-phenolate betaine dyes, **9**, with seven *tert*-butyl groups, and **13**, with three *tert*-butyl and two 1-adamantyl groups in the peripheral phenyl groups of **1** (8). The increase in the number of lipophilic alkyl groups, corresponding to an increase in dispersion interactions with the solvent, and the introduction of bulky alkyl groups, distorting the crystal lattice of the betaine dyes, should lead to a better solubility of **9** and **13** in nonpolar solvents. The introduction of such lipophilic bulky substituents into the peripheral aryl groups of the already heavily twisted chromophore of **1** (9)[7] should not disturb its long-wavelength solvatochromic CT absorption.

Results and discussion

Syntheses of the substituted betaine dyes 9 and 13

The synthesis of betaine dye **9** is outlined in Scheme 2. The chalcone **5**, prepared from 3,5-di(*tert*-butyl)acetophenone **3** (10) and 4-(*tert*-butyl)benzaldehyde **4** (11)[8] by a base-catalyzed Aldol condensation reaction, undergoes in perchloric acid-containing solution an acid-catalyzed Michael addition with **3**, forming an intermediate nonisolated 1,5-diketone, which closes the ring to the new pyrylium salt **6** (12, 13). Condensation of **6** with 4-amino-2,6-bis[4-(*tert*-butyl)phenyl]phenol **7** (7) leads to the *N*-(4-hydroxyphenyl)pyridinium salt **8**, which, on deprotonation with sodium methanolate in methanol, gives the desired betaine dye **9** in good yield as black–green crystals, which contain some water of crystallization.

The preparation of the betaine dye **13** is shown in Scheme 3. 4-(Adamantane-1-yl)acetophenone **10** is synthesized from 1-phenyladamantane by Friedel–Crafts acylation with $CH_3COCl/AlCl_3$ (14). The latter is obtained by Friedel–Crafts alkylation of benzene with 1-bromoadamantane (14), which is prepared by bromination of adamantane (15). Synthesis of the pyrylium salt **11** analogous to **6** (cf. Scheme 2) from the corresponding chalcone (from **10** and **4**) and **10** leads to **11** with a yield of ca. 15% only (8). Therefore, another method first described by Dorofeenko and Krivun (16) was employed: condensation of two moles of **10** with one mole of **4** (11)[8] with aqueous perchloric acid (70% w/w) in Ac_2O/AcOH gives immediately the pyrylium salt **11** with a yield of 55% after recrystallization. Further condensation of **11** with the 4-aminophenol 7 (7) leads analogously to the *N*-(4-hydro-

[6] S. Löbbecke. Unpublished results.

[7] An X-ray analysis of a bromo-substituted derivative of **1** shows that the interplanar angle between the pyridinium and phenolate moiety is 65°; the interplanar angles between the five aryl groups and the corresponding two inner rings range from 18 to 70°.

[8] For a short time, aldehyde **4** is also commercially available (Aldrich, Fluka, Lancaster).

© 1998 NRC Canada

Scheme 2.

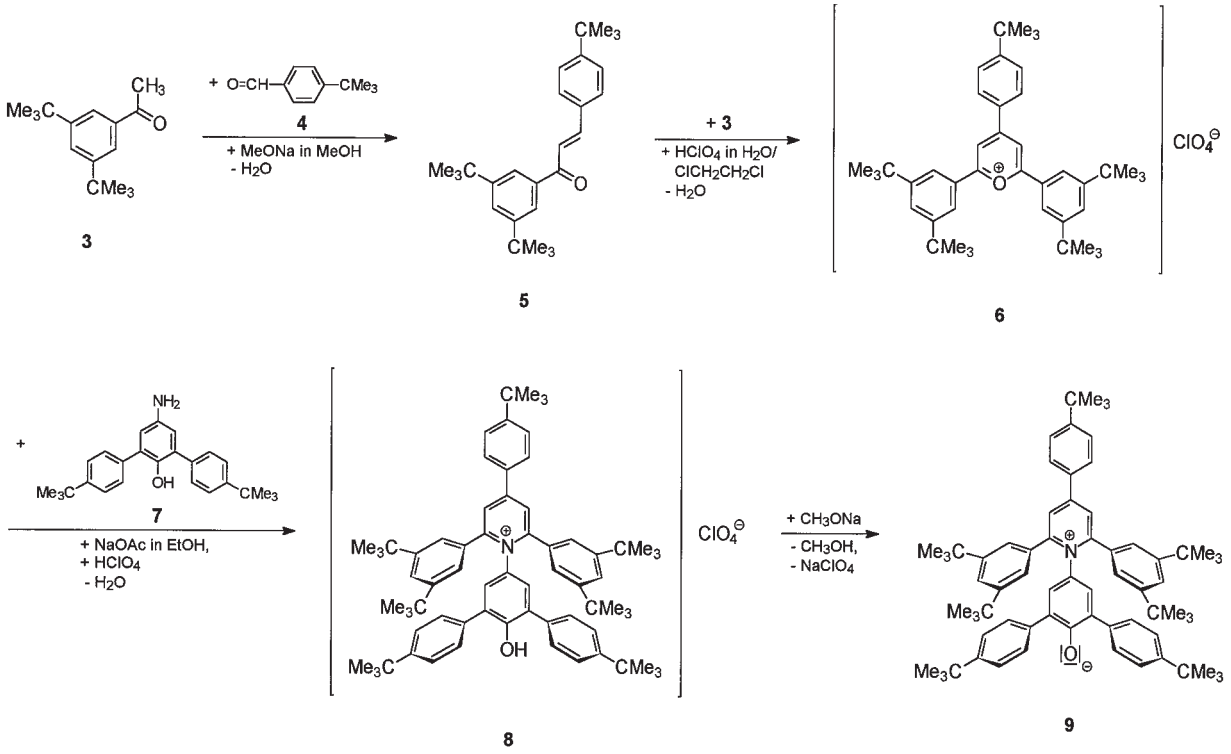

Scheme 3.

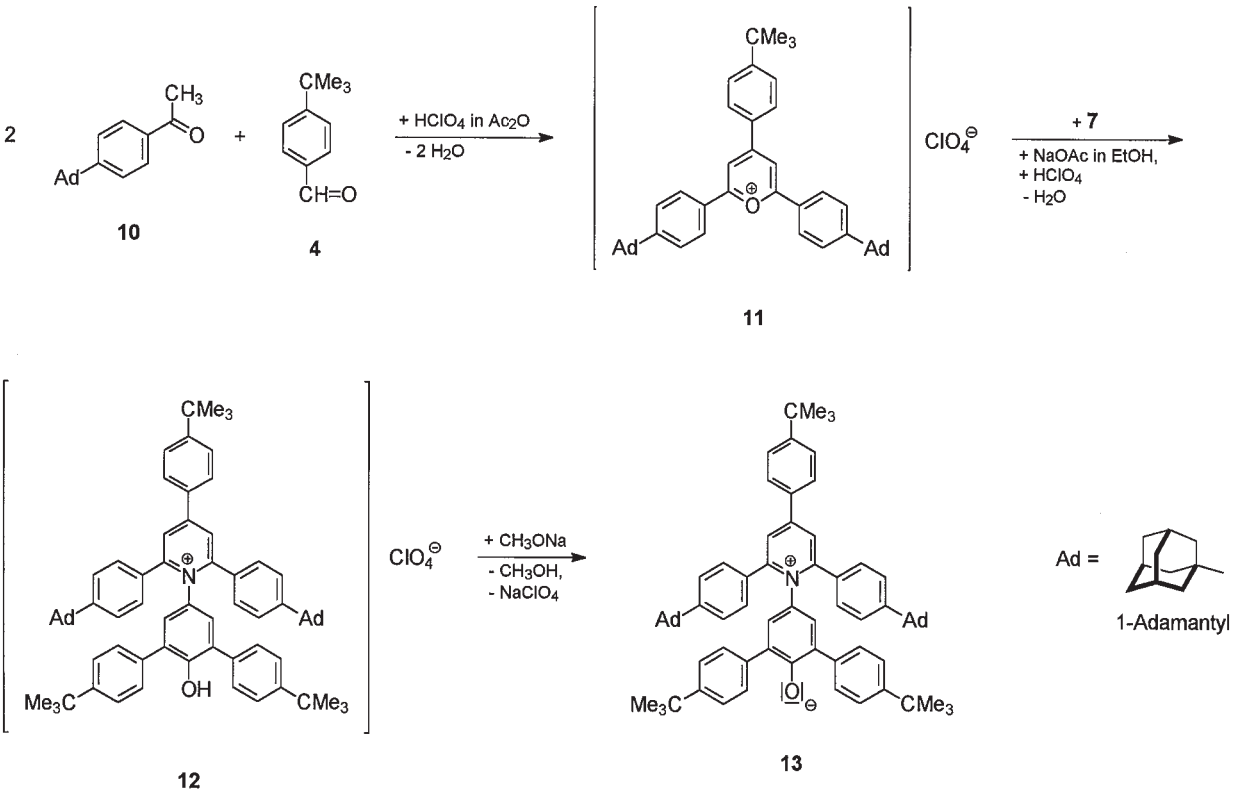

xyphenyl)pyridinium salt **12**, which on deprotonation gives the desired betaine dye **13** in good yield as black–green crystals, which again contain some water of crystallization.

The structure of all new compounds was ensured by elemental analyses, UV-vis, IR, ^{1}H and ^{13}C NMR as well as mass spectra (see experimental section).

© 1998 NRC Canada

Table 1. Vis–NIR absorption maxima of diluted solutions (ca. 10^{-3} M) of the betaine dyes **9** and **13**, measured in 29 solvents of different polarity at room temperature (ca. 25°C), the corresponding E_T(**9**) and E_T(**13**) values, as well as the E_T(**30**) values of **1**.

No.	Solvent	E_T(**30**)[a] (kcal/mol)	λ_{max}(**9**) (nm)	E_T(**9**)[b] (kcal/mol)	λ_{max}(**l3**) (nm)	E_T(**13**)[b] (kcal/mol)
1	2,2,2-trifluoroethanol	59.8	(not measurable)		482	59.3
2	1,2-ethanediol	56.3	528	54.1	520	55.0
3	methanol	55.4	533	53.6	528	54.1
4	*N*-methylformamide	54.1	550	52.0	537	53.2
5	2-methoxyethanol	52.0	562	50.9	558	51.2
6	ethanol	51.9	571.5	50.0	561	50.9
7	1-propanol	50.7	581	49.2	575	49.7
8	1-butanol	49.7	587	48.7	583	49.0
9	2-propanol	48.4	611	46.8	603	47.4
10	acetonitrile	45.6	667	42.9	641	44.6
11	dimethylsulfoxide	45.1	668.5	42.8	650	43.9
12	*N*,*N*-dimethylformamide	43.2	697	41.0	677	42.2
13	acetone	42.2	720	39.7	701	40.8
14	1,2-dichloroethane	41.3	725	39.4	700	40.8
15	dichloromethane	40.7	730	39.2	699	40.9
16	pyridine	40.5	738	38.7	715	40.0
17	trichloromethane	39.1	742	38.5	723	39.5
18	ethyl acetate	38.1	773	37.0	765	37.4
19	tetrahydrofuran	37.4	798	35.8	779	36.7
20	*tert*-butyl methyl ether	34.7	837	34.2	827	34.6
21	diethyl ether	34.5	845	33.8	830	34.4
22	benzene	34.3	857.5	33.3	839	34.1
23	toluene	33.9	846	33.8	837	34.2
24	tetrachloroethene	32.1	883	32.4	886	32.3
25	*n*-decane	31.0	902	31.7	904	31.6
26	*n*-heptane	31.1	906	31.6	898	31.8
27	*n*-hexane	31.0	904	31.6	896	31.9
28	*n*-pentane	31.0	918	31.1	910	31.4
29	cyclohexane	30.9	917	31.2	914	31.3
		ΔE_T(**30**) = 25.4 kcal/mol[c]	$\Delta\lambda$ = –389 nm[c]	ΔE_T(**9**) = 22.9 kcal/mol[c]	$\Delta\lambda$ = –394 nm[c]	ΔE_T(**13**) = 23.7 kcal/mol[c]

[a] Taken from ref. 4*d*.[4]
[b] Calculated according to eq. [1].
[c] Difference between the values measured in 1,2-ethanediol and cyclohexane.

Solvatochromic properties of the betaine dyes 9 and 13

The positions of the solvatochromic long-wavelength intramolecular CT absorption band of dyes **9** and **13** in various solvents of different polarity (as measured by the E_T(**30**) values (4*d*)[4]) are compiled in Table 1, together with the corresponding electronic transition energies E_T(**9**) and E_T(**13**) in kcal/mol. In analogy to the prior standard betaine dyes **1** and **2**, both new dyes **9** and **13** exhibit also an extraordinary negative solvatochromism: the intramolecular CT absorption band of **9** and **13** is hypsochromically shifted by $\Delta\lambda \approx 400$ nm (!) in changing the solvent from polar 1,2-ethanediol to nonpolar cyclohexane. This corresponds to an increase of their molar transition energies E_T of about 24 kcal/mol (or ca. 1 eV). With increasing solvent polarity, the highly dipolar ground state of these betaine dyes is increasingly stabilized by differential solvation, relative to the less dipolar CT excited state, with the observed hypsochromic band shift as consequence.

The completely analogous solvent-dependent behaviour of the new betaine dyes **9** and **13** with respect to standard dye **1**, necessary for their use as further standard betaines, is demonstrated by the good linear correlation between the E_T(**30**) values of **1** and the E_T values of **9** and **13** (Table 1), as exemplarily shown for the hepta-*tert*-butyl-substituted betaine dye **9** in Fig. 1. The correlation line of Fig. 1 follows eq. [4]:

[4] E_T(**9**) (kcal/mol) = 0.9084E_T(**30**) (kcal/mol) + 2.670

where pairs of values $n = 28$, correlation coefficient $r = 0.9961$, standard deviation of the estimate $s = 0.6886$. The analogous linear correlation between the E_T(**30**) and E_T(**13**) values is given by eq. [5]:

[5] E_T(**13**) (kcal/mol) = 0.9312E_T(**30**) (kcal/mol) + 2.438

where $n = 28$, $r = 0.9988$, $s = 0.3927$.

By means of these two equations, it is easily possible to calculate the empirical parameter of solvent polarity E_T(**30**) for those nonpolar solvents in which the standard betaines **1** and **2** are not sufficiently soluble. The excellent linear correlations between E_T(**30**) and the E_T values of both new betaine dyes **9** and **13** allow such calculations with great accuracy. The slope of the correlation lines as described by eqs. [4] and [5] is only a little smaller than unity, thus demonstrating that the

© 1998 NRC Canada

Fig. 1. Linear correlation between the E_T(**30**) values of standard betaine dye **1** and the E_T(**9**) values of the hepta-*tert*-butyl-substituted betaine dye **9** (cf. eq. [4]).

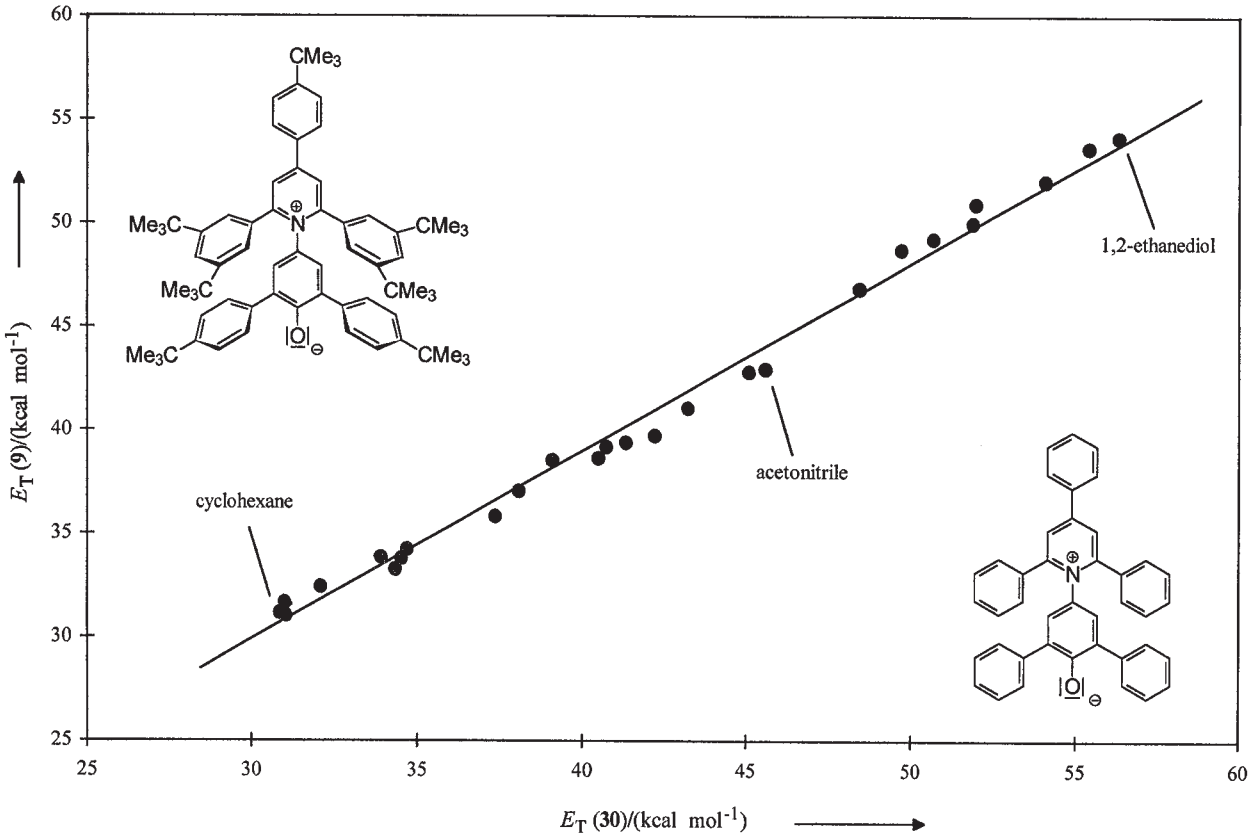

susceptibility of the light absorption of dyes **9** and **13** against a solvent change is nearly the same as for the standard dye **1**.

The introduction of more lipophilic and bulky alkyl substituents into the basic betaine chromophore **1** increases indeed the solubility of **9** and **13** in nonpolar solvents such as the hydrocarbons (e.g., *n*-hexane, *n*-pentane, cyclohexane, etc.), particularly for **9**. Therefore, the use of dyes **9** and **13** can be recommended for UV-vis spectroscopic studies of the polarity of such nonpolar solvents and their mixtures. More recently, dyes **2** and **9** have been used for the determination of the solvation capability of supercritical carbon dioxide (sc-CO_2) at various pressures and temperatures (1).[6] According to these measurements, the E_T(**30**) values of sc-CO_2 are comparable with the values for hydrocarbons such as *i*-octane (1).[6] However, to our disappointment, both new dyes are not soluble in perfluorohydrocarbons (also called perfluorocarbons, PFCs), the least polar solvents, which recently gain more and more interest as inert media for organic reactions and spectroscopic measurements (17). The introduction of a third 1-adamantyl group into the *para*-position of the 4-phenylpyridinium ring of dye **13** failed because we could not repeat the synthesis of the necessary 4-(adamantan-1-yl)benzaldehyde (18).

Conclusion and further considerations

Two new negatively solvatochromic betaine dyes **9** and **13** were prepared in good yield in four-step syntheses from easily available starting materials. Introduction of seven *tert*-butyl groups (**9**) or three *tert*-butyl and two 1-adamantyl groups (**13**) into the basic pentaphenyl pyridinium *N*-phenolate chromophore of **1** led to the desired increased solubility of these zwitterionic dyes in nonpolar solvents (except perfluorohydrocarbons). This and the excellent linear correlation between the molar electronic transition energies E_T of **9** and **13** with the E_T(**30**) values of the standard dye **1** make these new dyes potentially useful for the UV-vis spectroscopic determination of the empirical solvent polarity parameter E_T(**30**) for nonpolar solvents and solvent mixtures.

The particular structure of the betaine dyes **1**, **2**, **9**, and **13** (i.e., high permanent dipole moment, large polarizable π-electron system, strong electron-pair donor center Ar-O^s) enables them to interact with surrounding solvent molecules by means of nonspecific dipole–dipole, dipole – induced dipole, and dispersion interactions as well as specific hydrogen-bonding and electron-pair donor (EPD) – electron-pair acceptor (EPA) interactions. Therefore, the dissolved betaine dyes experience a rather complex combination of solute–solvent interactions, and the corresponding E_T values measure preferably the dipolarity and polarizability, the hydrogen-bond donating (HBD) capacity, and the Lewis acidity of solvents. An analysis of the E_T(**30**) values by means of the "master" eq. [6] for the empirical treatment of solute–solvent interactions, introduced by Kamlet and Taft (19*a*) in 1976, leads to eq. [7], as has been recently shown by Marcus (20).

$$[6] \quad XYZ = (XYZ)_0 + s\pi^* + a\alpha + b\beta + m\delta_H^2$$

$$[7] \quad E_T(\mathbf{30}) = 31.2 + 11.5\pi^* + 15.2\alpha$$

where n = 166 solvents, r = 0.979, $s[E_T(\mathbf{30})]$ = 2.1 kcal/mol

© 1998 NRC Canada

The XYZ value resp. $(XYZ)_0$ is the solvent-dependent physicochemical solute property under investigation in a given solvent and in the gas phase (or in an inert solvent). The π^*, α, and β values are UV-vis spectroscopically derived solvatochromic parameters measuring the dipolarity and polarizability of the solvent, its HBD capacity, and its hydrogen-bond accepting (HBA) capability, respectively. The value δ_H is Hildebrand's solubility parameter, accounting for the intermolecular solvent–solvent interactions, which must be overcome in producing a cavity in the solvent in order to accommodate the solute molecules. Since electronic transitions are not accompanied by a change in molar volume of the absorbing solute on excitation, the δ_H term drops out in application of eq. [6] to the correlation of solvent effects on spectra.

According to eq. [7] (20), the mutual interaction between the solvatochromic probe molecule **1** and solvent molecules is mainly determined by a blend of nonspecific dipolarity and polarizability interactions (as measured by π^*) as well as specific solute – HBD solvent interactions (as measured by α). The solute – HBA solvent interaction term, β, drops out in going from eq. [6] to [7]; that is, the HBA properties and the Lewis basicity of the solvents are not measured by the probe molecule **1**. The positive charge of the pyridinium moiety of **1** is delocalized and shielded by the peripheral phenyl groups, and a specific interaction with EPD solvent molecules is not possible. Hence, the betaine probe molecule **1** (as well as **2**, **9**, and **13**) measures in HBD solvents mainly the HBD acidity and Lewis acidity of the solvents: the ratio of regression coefficients of α and π^* in eq. [7] is $\alpha/\pi^* = 1.32$. In non-HBD solvents with $\alpha = 0$, the E_T(**30**) values are mainly determined by the nonspecific dipolarity and polarizability interactions. A recent thermodynamic analysis of the E_T(**30**) polarity scale comes to analogous conclusions (21). The unexpected success of the E_T(**30**) scale in correlating solvent effects of all kinds of organic solvent-dependent processes (cf. ref. 6)[3,4] stems from the fact that the composition of intermolecular solute–solvent interactions is for these processes often similar to that as described by eq. [7].

If in addition to the Lewis acidity the Lewis basicity of the solvents comes into the solvation play, then a two-parameter equation such as eq. [8], introduced by Krygowski and Fawcett (22) in 1975, should be used in the correlation of solvent effects.

$$[8] \quad XYZ = (XYZ)_0 + aE_T(\mathbf{30}) + b\mathrm{DN}$$

where DN is Gutmann's donor number, obtained by measuring the heat of reaction of the solvent with the strong Lewis acid $SbCl_5$ dissolved in 1,2-dichloroethane. Other Lewis basicity parameters can also be used; a critical compilation of solvent Lewis basicity parameters has been recently given by Gritzner (23). A linear correlation of solvent-dependent physicochemical solute properties with E_T(**30**) alone can only be expected if in eq. [8] $b = 0$. The E_T(**30**) values describe empirically the solvation capability (which is equal to solvent polarity)[5] of solvents as representatively experienced by the dissolved betaine dye **1** (as well as **2**, **9**, and **13**), representative for a large number of other solvent-dependent processes.

Experimental

General

The betaine dyes **1** and **2** were prepared according to the procedures described in refs. 3*a* and 24 (**1**) and 7 (**2**). Dye **1** is also commercially available (see advertisements in ref. 25).[9] For UV-vis and NIR measurements, the double-beam spectrophotometers U-3410 (Hitachi) and Omega 20 (Bruins Instruments) with 1 cm quartz cells SUPRASIL (Hellma) were used. Solvents were used as commercially supplied in the highest available quality (analytical or spectroscopic grade) and were additionally dried and purified by means of molecular sieves and, if necessary, by filtration through a column of basic alumina, activity grade I, in order to remove traces of acids. For the solvatochromic measurements, the solvents must be acid-free. Otherwise, the betaine dyes are (reversibly) protonated at the phenolate oxygen atom, and the long-wavelength solvatochromic CT absorption band disappears. Infrared spectra were obtained with the Interferometer IFS 88 (Bruker) with KBr discs. The ^1H and ^{13}C nuclear magnetic resonance spectra were performed on the spectrometer AC-300 (Bruker) in $CDCl_3$ or CD_3CN, with tetramethylsilane as an internal standard. Mass spectra were determined with the spectrometers MAT CH-7A (Varian) with electron impact (EI) and MAT 711 (Varian) with field desorption (FD) technique. Melting points were measured with a Kofler–Mikroheiztisch (Reichert) and are corrected. Elemental analyses were determined with the CHN-Rapid (Heraeus) by the Analytik-Servicelabor of the Department of Chemistry, Marburg.

Synthesis of the hepta-*tert*-butyl-substituted betaine dye 9

*3,5-Di(*tert*-butyl)acetophenone,* ***3***

In a three-necked, round-bottom 500 mL flask with dropping funnel, stirrer, and a reflux condenser with drying tube, magnesium ethanolate was prepared from magnesium turnings (4.62 g, 0.19 mol), dry ethanol (4.50 mL), and dry tetrachloromethane (0.45 mL). After addition of dry diethyl ether (70 mL) with stirring, a mixture of dry diethyl malonate (30.4 g, 29 mL, 0.19 mol), dry ethanol (18 mL), and dry diethyl ether (23 mL) was added, and the whole was heated under reflux for 3 h to give the ethoxymagnesium derivative of diethyl malonate. A solution of 3,5-di(*tert*-butyl)benzoyl chloride (50.6 g, 0.20 mol; prepared from 3,5-di(*tert*-butyl)benzoic acid and thionyl chloride) in diethyl ether (50 mL) was then added and heating under reflux was continued for 50 min. After cooling to room temperature, the mixture was made acidic by diluted sulfuric acid, and the two phases formed were separated. In the organic phase, some crystals of the intermediate acyl diethyl malonate were already formed; they were isolated by filtration and dissolved in diethyl ether. The aqueous phase was several times extracted with diethyl ether. The volume of the combined ethereal solutions of 3,5-di(*tert*-butyl)benzoyl diethyl malonate was reduced in a rotary evaporator until a suspension was obtained. This suspension was added to a mixture of acetic acid (54 mL), concentrated sulfuric acid (7 mL), and water (36 mL), and the whole was heated under reflux for 5 h until the hydrolysis and decarboxylation was finished. After cooling with an ice bath, the solution was made alkaline by addition of an aqueous NaOH solution (20% w/w), and the two phases formed were separated. The aqueous phase was

[9] Sigma–Aldrich Chemical Co., Milwaukee, Wisconsin, U.S.A. Order no. 27244–2; Fluka Chemie AG, Buchs/Switzerland. Order no. 43358.

© 1998 NRC Canada

extracted with diethyl ether. The combined ethereal phases were dried with Na_2SO_4 and filtered, the ether was distilled off in a rotary evaporator, and the oily residue was subjected to fractional distillation under reduced pressure (oil pump) to give **3** (10.10 g, 22%) as colorless crystals with mp 38°C (ref. 10*a,* 38.6–39.0°C).

*1-[3,5-Di(*tert-*butyl)phenyl]-3-[4-(*tert-*butyl)phenyl]-prop-2-en-1-one,* ***5***

A mixture of **3** (2.32 g, 10 mmol), 4-(*tert*-butyl)benzaldehyde **4** (11)[8] (1.62 g, 10 mmol), and sodium methanolate in methanol (10% w/w, 15 mL) was stirred at room temperature until stirring was impossible due to crystallization of the product. The reaction mixture was washed with water until the washing water was neutral. Recrystallization from methanol–water (3:1) gives **5** (3.19 g, 85%) as light yellow needles with mp 74°C. IR (KBr): 1651 cm^{-1} (C═O); ^1H NMR ($CDCl_3$) δ: 1.34 and 1.38 (27H, two close s, all CMe_3), 7.43–7.60 (6H, m, *p*-H of 1-phenyl, *o*- and *m*-H of 3-phenyl, β-CH), 7.66 (1H, d, ^3J = 15.7 Hz, α-CH), 7.81 (2H, d, ^4J = 6.9 Hz, *o*-H of 1-phenyl); ^{13}C NMR ($CDCl_3$) δ: 31.1 [*p*-C($\underline{C}H_3)_3$], 31.4 [*m*-C($\underline{C}H_3)_3$], 34.9 (*p*-$\underline{C}Me_3$), 35.0 (*m*-$\underline{C}Me_3$), 122.3 (*o*-C of 1-phenyl), 122.7 (α-CH), 125.9, 126.8, and 128.2 (aromatic C), 132.4 (ipso-C of 1-phenyl), 138.1 (ipso-C of 3-phenyl), 144.4 (β-CH), 151.2 (*m*-$\underline{C}$-CMe_3), 154.0 (*p*-$\underline{C}$-CMe_3), 191.8 (C═O); MS (EI, 70 eV) *m/z* (%): 376 (100) [M^+]; $C_{27}H_{36}O$ (376.6) calcd.: C 86.12, H 9.64; found: C 85.37, H 9.45.

*2,6-Bis[3,5-di(*tert-*butyl)phenyl]-4-[4-(*tert-*butyl)phenyl]-pyrylium perchlorate,* ***6***

A solution of ketone **3** (0.32 g, 1.36 mmol) and chalcone **5** (0.96 g, 2.55 mmol) in 1,2-dichloroethane (3.5 mL) in a three-necked, round-bottom 100 mL flask, equipped with stirrer, dropping funnel, and reflux condenser, was warmed to 70–75°C, and then aqueous perchloric acid (70% w/w; ca. 0.3 mL) was added dropwise during 30 min. First, the mixture became orange; subsequently the colour changed to brownish yellow. After the addition was completed, the mixture was heated under reflux for 1 h. Then, the solvent was distilled off in a rotary evaporator, and the solid residue was dissolved in diethyl ether (50 mL). This solution was added dropwise to *n*-pentane (400 mL), the yellow precipitate was filtered off, dried, recrystallized from ethanol–water (2:1), and dried with P_4O_{10} to give **6** (0.37 g, 39% related to **3**) as yellow microcrystalline powder with mp 312°C. ^1H NMR ($CDCl_3$) δ: 1.37 and 1.45 (45H, two close s, all CMe_3), 7.74–8.27 (10H, m, aromatic H), 8.49 (2H, s, 3/5-H of pyrylium ring); ^{13}C NMR ($CDCl_3$) δ: 30.9 [*p*-C($\underline{C}H_3)_3$], 31.3 [*m*-C($\underline{C}H_3)_3$], 35.3 (all $\underline{C}Me_3$), 114.5 (C-3/5 of pyrylium ring), 122.7 (*o*-CH of 2,6-phenyl), 126.6 (*m*-CH of 4-phenyl), 126.8 (*p*-CH of 2,6-phenyl), 128.5 (*o*-CH of 4-phenyl), 129.7 (ipso-C of 2,6-phenyl), 130.0 (ipso-C of 4-phenyl), 153.3 ($\underline{C}$-CMe_3 of 2,6-phenyl), 160.0 ($\underline{C}$-CMe_3 of 4-phenyl), 167.5 (C-4 of pyrylium ring), 171.1 (C-2/6 of pyrylium ring); MS (FD) *m/z* (%): 589 (100) [$M^+ - ClO_4$]; $C_{43}H_{57}C1O_5$ (689.3) calcd.: C 74.92, H 8.33; found: C 74.19, H 8.10.

*4-[4-(*tert-*Butyl)phenyl]-2,6-bis[3,5-di(*tert-*butyl)phenyl]-1-{4-hydroxy-3,5-bis[4-(*tert-*butyl)phenyl]phenyl}pyridinium perchlorate,* ***8***

A solution of pyrylium salt **6** (0.30 g, 0.43 mmol), 4-amino-2,6-bis[4-(*tert*-butyl)phenyl]phenol **7** (7) (0.19 g, 0.51 mmol), and water-free sodium acetate (0.29 g, 3.50 mmol) in dry ethanol (15 mL) was heated under reflux for 2.5 h in a three-necked, round-bottom 50 mL flask with stirrer, reflux condenser, and dropping funnel. To the still warm solution, aqueous perchloric acid (70% w/w, 0.70 mL, 8.2 mmol) was added with stirring. Then, the solvent was distilled off in a rotary evaporator, and the brown oily residue was dissolved in 1,2-dichloroethane (ca. 3 mL). This solution was added slowly to petroleum ether (bp 40–60°C, 300 mL). The yellow precipitate formed was filtered off. The crude product was recrystallized from methanol–water (2:1) and dried with P_4O_{10} at 80°C in vacuo (ca. 10^{-3} Torr) (1 Torr = 133.3 Pa) to give **8** (0.24 g, 54%) as light yellow microcrystalline powder with mp 345°C. IR (KBr): 3500 cm^{-1} (OH); UV-vis (CH_3CN) λ_{max} (log ε): 240 (4.092), 323 nm (4.024); ^1H NMR ($CDCl_3$) δ: 1.21, 1.31, and 1.42 (63 H, three close s, all CMe_3), 5.50 (1H, s, OH), 6.89–7.87 (16H, m, aromatic H and 3/5-H of phenol ring), 7.87–8.58 (4H, m, AA′BB′ system, aromatic H of 4-phenyl ring), 8.19 (2H, s, 3/5-H of pyridinium ring); ^{13}C NMR ($CDCl_3$) δ: 31.1 and 31.2 (all C($\underline{C}H_3)_3$), 35.0 and 35.2 (all $\underline{C}Me_3$), 123.8, 124.7, 125.5, 125.8, 126.7, and 128.3 (aromatic CH), 128.4 (C-3/5 of phenol ring), 128.9, 129.4, and 130.2 (quaternary aromatic C), 132.1 (C-3/5 of pyridinium ring), 132.3 (C-4 of pyridinium ring), 132.9 (C-2/6 of phenol ring), 149.5 (C-4 of phenol ring), 151.1, 151.5, and 155.7 (quaternary aromatic $\underline{C}$-CMe_3), 157.3 (C-2/6 of pyridinium ring), 157.4 (C-OH); MS (FD) *m/z* (%): 945 (100) [$M^+ - ClO_4$]; $C_{69}H_{86}ClNO_5$ (1044.9) calcd.: C 79.31, H 8.30, N 1.34; found: C 79.14, H 8.35, N 1.23.

*4-{4-[4-(*tert-*Butyl)phenyl]-2,6-bis[3,5-di(*tert-*butyl)phenyl]-1-pyridinio}-2,6-bis[4-(*tert-*butyl)phenyl]phenolate,* ***9***

To a stirred solution of perchlorate **8** (0.22 g, 0.21 mmol) in dry methanol (50 mL) a methanolic sodium methanolate solution (10% w/w, 1.3 mL) was added at room temperature, during which the solution changed from yellow to a dark colour. After heating under reflux for 3 min., cooling to room temperature, and filtration, the dark solution was poured into aqueous NaOH (10% w/w, 300 mL). After standing for ca. 12 h in a refrigerator, the precipitate formed was filtered off and dried with P_4O_{10} in vacuo. Purification by multiple hot extraction with 200 mL of boiling methanol–water (2:1) gave, after drying with P_4O_{10} at 70°C and 10^{-3} Torr in a drying pistol, betaine **9** (0.20 g, 95%) as black–green crystals with mp 239–240°C, which still contain ca. four moles water of crystallization. IR (KBr): 3550 cm^{-1} (OH from water); UV-vis (CH_3OH) λ_{max} (log ε): 321 (4.300), 327 (4.297), and 533 nm (3.106); UV-vis (CH_3CN): 317 (4.262), 379 (3.611), and 667 nm (3.251); ^1H NMR ($CDCl_3$) δ: 1.26, 1.29, and 1.39 (63H, three close s, all CMe_3), 2.96 (ca. 2H, broad s, H_2O), 6.67 (2H, s, 3/5-H of phenolate ring), 6.93–7.28 (14H, m, aromatic H), 7.52–7.91 (4H, m, AA′BB′ system, aromatic H of 4-phenyl ring), 8.17 (2H, s, 3/5-H of pyridinium ring), ^{13}C NMR ($CDCl_3$) δ: 31.1 and 31.2 (all C($\underline{C}H_3)_3$), 34.5 and 35.0 (all $\underline{C}Me_3$), 123.8, 124.7, 125.6, 125.7, 126.8, and 128.4 (aromatic CH), 128.5 (C-3/5 of phenolate ring), 128.8, 129.5, and 130.2 (quaternary aromatic C), 132.1 (C-3/5 of pyridinium ring), 132.2 (C-4 of pyridinium ring), 132.9 (C-2/6 of phenolate ring), 149.5 (C-4 of phenolate ring), 151.1, 151.6, and 155.7 (quaternary aromatic $\underline{C}$-CMe_3), 157.3 (C-2/6 of pyridinium ring), 157.4 (C-O^-); MS (FD) *m/z*

© 1998 NRC Canada

(%): 944 (100) [M^+]; $C_{69}H_{85}NO"4H_2O$ (944.4 + 72.1 = 1016.5) calcd.: C 81.53, H 9.22, N 1.38; found C 81.11, H 8.03, N 1.36.

Synthesis of the bis(adamantan-1-yl)-substituted betaine dye 13

4-(Adamantane-1-yl)acetophenone, ***10***

To a stirred solution of water-free aluminium trichloride (10.67 g, 0.08 mol) in dry trichloromethane (40 mL) acetylchloride (6.28 g, 0.08 mol) was added dropwise at 0–10°C. To this suspension was then dropwise added with stirring at –10°C a solution of 1-phenyladamantane (12.74 g, 0.06 mol) (prepared from 1-bromoadamantane (26)[10] and benzene, according to ref. 15) in dry trichloromethane (40 mL). After standing at room temperature for ca. 12 h, the mixture was carefully poured into ice water (200 mL). The precipitate of aluminium trihydroxide was dissolved by adding a small amount of concentrated HCl, and the two phases formed were separated. The aqueous phase was extracted twice with trichloromethane. The combined organic phases were washed with water, aqueous NaOH (2% w/w), again with water, and dried with K_2CO_3. The trichloromethane was distilled off and the residue was recrystallized from petroleum ether (bp 40–60°C) to give **10** (5.02 g, 33%) as colourless crystals with mp 106°C (ref. 14, 105–107°C).

*2,6-Bis[4-(adamantane-1-yl)phenyl]-4-[4-(*tert*-butyl)phenyl]-pyrylium perchlorate,* ***11***

To a solution of **10** (1.40 g, 5.50 mmol) and 4-(*tert*-butyl)benzaldehyde **4** (0.45 g, 2.75 mmol) (11)[8] in acetic acid (5.0 mL) and acetic anhydride (0.30 mL) was added aqueous perchloric acid (0.3 mL, 70% w/w), and the mixture was heated under reflux for 90 min. After cooling to room temperature, the dark brown solution was dropwise poured into diethyl ether (250 mL). The yellow precipitate was filtered off, recrystallized from methanol–water (3:1), and dried to give **11** (1.10 g, 55%) as yellow microcrystalline powder with mp 263°C. ^{1}H NMR ($CDCl_3$) δ: 1.40 (9H, s, CMe_3), 1.82–2.12 (30H, m, adamantyl-H), 7.70–7.78 (12H, m, aromatic H), 8.31 (2H, s, 3/5-H of pyrylium ring); ^{13}C NMR ($CDCl_3$) δ: 29.6 (CH_2 of adamantyl groups), 31.1 [$C(\underline{C}H_3)_3$], 37.0 ($\underline{C}Me_3$), 43.1 (CH of adamantyl groups), 115.1 (C-3/5 of pyrylium ring), 125.5, 127.4, 127.9, and 129.4 (aromatic CH), 130.5 (ipso-C of 2/6-phenyl rings), 130.8 (ipso-C of 4-phenyl ring and C-1 of adamantyl groups), 160.5 ($\underline{C}$-CMe_3), 160.6 (aromatic $\underline{C}$-adamantyl), 165.7 (C-4 of pyrylium ring), 170.8 (C-2/6 of pyrylium ring); MS (FD) *m/z* (%): 633 (100) [M^+ – $C1O_4$]; $C_{47}H_{53}C1O_5$ (733.4) calcd.: C 76.97, H 7.28; found: C 77.84, H 7.28.

*2,6-Bis[4-(adamantane-1-yl)phenyl]-4-[4-(*tert*-butyl)phenyl]-1-{4-hydroxy-3,5-bis[4-(*tert*-butyl)phenyl]phenyl}pyridinium perchlorate,* ***12***

A solution of pyrylium salt **11** (1.17 g, 1.60 mmol), 4-amino-2,6-bis[4-(*tert*-butyl)phenyl]phenol **7** (7) (0.70 g, 1.87 mmol), and water-free sodium acetate (0.29 g, 3.50 mmol) in dry ethanol (15 mL) was heated under reflux for 2.5 h in a three-necked, round-bottom 50 mL flask with stirrer, reflux condenser, and dropping funnel. To the still warm solution, aqueous perchloric acid (70% w/w, 0.70 mL, 8.2 mmol) was added with stirring. Then, the solvent was distilled off in a rotary evaporator, and the residue was dissolved in acetone (50 mL). This solution was added slowly to petroleum ether (bp 40–60°C, 300 mL). The yellow precipitate was filtered off. The crude product (1.50 g) was recrystallized from methanol–water (4:1) and dried with P_4O_{10} at 80°C in vacuo (ca. 10^{-3} Torr) to give **12** (1.40 g, 80%) as light yellow microcrystalline powder with mp 297–299°C. IR(KBr): 3526 cm^{-1} (OH); UV-vis (CH_3CN) λ_{max} (log ε): 237 (3.553), 324 nm (3.503); ^{1}H NMR ($CDCl_3$) δ: 1.35 and 1.42 (27 H, two s, all CMe_3), 1.53–2.10 (30H, m, adamantyl-H), 5.60 (1H, s, OH), 6.94 (2H, s, 3/5-H of phenol ring), 6.97–7.43 (16 H, m, aromatic H), 7.54–7.86 (4H, m, AA′BB′ system, aromatic H of 4-phenyl ring), 8.10 (2H, s, 3/5-H of pyridinium ring); ^{13}C NMR ($CDCl_3$) δ: 28.8 (CH_2 of adamantyl groups), 31.1 (all $C(\underline{C}H_3)_3$), 36.4 (all $\underline{C}Me_3$), 42.9 (CH of adamantyl groups), 121.3, 125.2, 125.9, and 126.0 (aromatic CH), 126.7 (CH_2 of adamantyl groups), 128.3 (ipso-C of 2/6-phenyl rings at the pyridinium ring), 128.7 (aromatic CH), 128.9 (C-3/5 of phenol ring), 129.4 (ipso-C of 4-phenyl ring at the pyridinium ring), 129.9 (C-1 of adamantyl groups), 130.8 (ipso-C of 2,6-phenyl rings at the phenol ring), 131.6 (C-3/5 of pyridinium ring), 131.9 (C-4 of pyridinium ring), 132.3 (C-2/6 of phenol ring), 149.8 (C-4 of phenol ring), 151.4 ($\underline{C}$-CMe_3 of 4-phenyl ring), 153.7 ($\underline{C}$-CMe_3 of 2/6-phenyl rings at the phenol ring), 155.8 (aromatic $\underline{C}$-adamantyl), 156.7 (C-2/6 of pyridinium ring), 157.2 (C-OH); MS (FD) *m/z* (%): 989 (100) [M^+ – ClO_4]; $C_{73}H_{82}ClNO_5$ (1088.9) calcd.: C 80.52, H 7.59, N 1.29; found: C 79.95, H 7.49, N 1.10.

*4-{2,6-Bis[4-(adamantane-1-yl)phenyl]-4[4-(*tert*-butyl)phenyl]-1-pyridinio}-2,6-bis[4-(*tert*-butyl)phenyl]phenolate,* ***13***

To a stirred solution of perchlorate **12** (1.09 g, 1.00 mmol) in dry methanol (100 mL) a methanolic sodium methanolate solution (10% w/w, 2.6 mL) was added at room temperature, during which the solution changed from yellow to a dark colour. After heating under reflux for 3 min., cooling to room temperature, and filtration, the dark solution was poured into aqueous NaOH (10% w/w, 300 mL). After standing for ca. 12 h in a refrigerator, the precipitate formed was filtered off and dried with P_4O_{10} in vacuo. Purification by multiple hot extraction with 200 mL of boiling methanol–water (2:1) gave, after drying with P_4O_{10} at 70°C and 10^{-3} Torr in a drying pistol, betaine **13** (0.97 g, 95%) as black–green crystals with mp 265–267°C, which still contain ca. 1.5 moles water of crystallization. IR (KBr): 3500 cm^{-1} (OH from water); UV-vis (methanol) λ_{max} (log ε): 326 (4.283) and 528 nm (3.211); UV-vis (CH_3CN): 379 (4.280) and 641 nm (3.977); ^{1}H NMR ($CDCl_3$) δ: 1.30 and 1.38 (27H, two s, all CMe_3), 1.72–2.10 (30H, m, adamantyl-H), 6.46 (2H, s, 3/5-H of phenolate ring), 7.12–7.47 (16H, aromatic H), 7.59–7.77 (4H, m, AA′BB′ system, aromatic H of 4-phenyl ring at the pyridinium ring), 8.02 (2H, s, 3/5-H of pyridinium ring); ^{13}C NMR ($CDCl_3$) δ: 28.8 (CH_2 of adamantyl groups), 31.4 (all $C(\underline{C}H_3)_3$), 36.6 (all $\underline{C}Me_3$), 42.9 (CH of adamantyl groups), 118.4, 124.0, 125.0, and 125.6 (aromatic CH), 126.9 (CH_2 of adamantyl groups), 127.3 (ipso-C of 2/6-phenyl rings at the pyridinium ring), 127.6 (aromatic CH), 128.9 (C-3/5 of phenolate ring), 129.1 (ipso-C of 4-phenyl ring at the pyridinium ring), 130.4 (C-3/5

[10] 1-Bromoadamantane is meanwhile also commercially available (Acros, Aldrich, Fluka, Lancaster).

© 1998 NRC Canada

of pyridinium ring), 131.3 (C-4 of pyridinium ring), 131.5 (C-2/6 of phenolate ring), 138.2 (C-4 of phenolate ring), 147.6 ($\underline{C}$-CMe_3 of 4-phenyl ring), 153.0 ($\underline{C}$-CMe_3 of 2/6-phenyl rings at the phenolate ring), 153.9 (aromatic $\underline{C}$-adamantyl), 156.0 (C-2/6 of pyridinium ring), 156.2 (C-O^-); MS (FD) *m/z* (%): 988 (100) [M^+]; $C_{73}H_{81}NO@1.5H_2O$ (988.4 + 27.1 = 1015.5) calcd.: C 86.34, H 8.34, N 1.38; found: C 86.00, H 8.32, N 1.17.

Acknowledgements

Financial support of this work by the Deutsche Forschungsgemeinschaft, Bonn, and the Fonds der Chemischen Industrie, Frankfurt (Main), is gratefully acknowledged. A.M.M. also thanks the Friedrich–Ebert–Stiftung, Bonn, for a grant.

References

1. R. Eberhardt, S. Löbbecke, B. Neidhart, and C. Reichardt. Liebigs Ann./Recueil (Part XXIII), 1195 (1997).
2. (*a*) C. Reichardt. Chem. Soc. Rev. **21**, 147 (1992); (*b*) C. Reichardt, S. Asharin-Fard, A. Blum, M. Eschner, A.M. Mehranpour, P. Milart, T. Niem, G. Schäfer, and M. Wilk. Pure Appl. Chem. **65**, 2593 (1993); (*c*) C. Reichardt, A. Blum, K. Harms, and G. Schäfer. Liebigs Ann./Recueil, 707 (1997).
3. (*a*) K. Dimroth, C. Reichardt, T. Siepmann, and F. Bohlmann. Liebigs Ann. Chem. **661**, 1 (1963); (*b*) C. Reichardt. The Chemical Intelligencer, **3**, 5 (1997).
4. (*a*) E. Buncel and S. Rajagopal. Acc. Chem. Res. **23**, 226 (1990); (*b*) C. Laurence. *In* Similarity models in organic chemistry, biochemistry and related fields. *Edited by* R.I. Zalewski, T.M. Krygowski, and J. Shorter. Elsevier, Amsterdam. 1991. Chap. 5, pp. 231–281; (*c*) W.R. Fawcett. J. Phys. Chem. **97**, 9540 (1993); (*d*) C. Reichardt. Chem. Rev. **94**, 2319 (1994).
5. (*a*) P. Müller. Glossary of terms used in physical organic chemistry — IUPAC Recommendations 1994. Pure Appl. Chem. **66**, 1077 (1994) (particularly p. 1151); (*b*) C. Reichardt. Nachr. Chem. Tech. Lab. **45**, 759 (1997).
6. (*a*) C. Reichardt. Solvents and solvent effects in organic chemistry. 2nd ed. VCH, Weinheim. 1988. Chap. 7. pp. 339–405; (*b*) J. Shorter. Correlation analysis of organic reactivity. Research Studies Press, Letchworth, and Wiley, Chichester. 1982.
7. C. Reichardt and E. Harbusch-Görnert. Liebigs Ann. Chem. 721 (1983).
8. A.M. Mehranpour. Ph.D. thesis, Philipps University. Marburg, Germany. 1992.
9. R. Allmann. Z. Kristallogr. **128**, 115 (1969)
10. (*a*) M.G.J. Beets, W. Meerburg, and H. van Essen. Recl. Trav. Chim. Pays-Bas, **78**, 570 (1959); (*b*) H.G. Walker and C.R. Hauser J. Am. Chem. Soc. **68**, 1386 (1946).
11. (*a*) J.W. Baker, W.S. Nathan, and C.W. Shoppee. J. Chem. Soc. 1847 (1935); (*b*) T.J. Broxton, L.W. Deady, A.R. Katritzky, A. Liu, and R.D. Topsom. J. Am. Chem. Soc. **92**, 6845 (1970); (*c*) W.E. Smith. J. Org. Chem. **37**, 3972 (1972); (*d*) B.S. Furniss, A.J. Hannaford, P.W.G. Smith, and A.R. Tatchell. Vogel's textbook of practical organic chemistry. 5th ed. Longman, Burnt Hill, England, and Wiley, New York. 1989. p. 997.
12. K. Dimroth, C. Reichardt, and K. Vogel. Org. Synth. **49**, 121 (1969); Org. Synth. (Collective Vol. V), 1135 (1973).
13. (*a*) A.T. Balaban, W. Schroth, and G. Fischer. Adv. Heterocycl. Chem. **10**, 241 (1969) (particularly p. 304 ff); (*b*) A.T. Balaban, A. Dinculescu, G.N. Dorofeenko, G.W. Fischer, A.V. Koblik, V.V. Mezheritskii, and W. Schroth. Adv. Heterocycl. Chem. Supplement 2. Academic Press, New York, London. 1982. p. 24.
14. T.J. Broxton, G. Capper, L.W. Deady, A. Lenko, and R.D. Topsom. J. Chem. Soc. Perkin Trans. 2, 1237 (1972).
15. (*a*) S. Landa and S. Hála. Chem. Listý, **51**, 2325 (1957); Chem. Abstr. **52**, 6213*a* (1958); (*b*) S. Landa and S. Hála. Collect. Czech. Chem. Commun. **24**, 93 (1959); Chem. Abstr. **53**, 7045*a* (1959).
16. G.N. Dorofeenko and S.V. Krivun. Zh. Obshch. Khim. **34**, 105 (1964); J. Gen. Chem. U.S.S.R. (Engl. Transl.) **34**, 104 (1964); Chem. Abstr. **60**, 10 641*b* (1964).
17. (*a*) A. Maciejewski. J. Photochem. Photobiol. A, **51**, 87 (1990); Chem. Abstr. **112**, 226 494*g* (1990); (*b*) D.-W. Zhu. Synthesis, 953 (1993); (*c*) I.T. Horváth and J. Rábai. Science, **226**, 72 (1994); (*d*) S.M. Pereira, G.P. Sauvage, and G.W. Simpson. Synth. Commun. **25**, 1023 (1995); (*e*) B. Cornils. Angew. Chem. **109**, 2147 (1997); Angew. Chem. Int. Ed. Engl. **36**, 2057 (1997).
18. L. Testaferri, M. Tiecco, M. Tingoli, M. Fiorentino, and L. Troisi. J. Chem. Soc. Chem. Commun. 93 (1978).
19. (*a*) M.J. Kamlet and R.W. Taft. J. Am. Chem. Soc. **98**, 377, 2886 (1976); (*b*) R.W. Taft, J.-L.M. Abboud, M.J. Kamlet, and M.H. Abraham. J. Solution Chem. **14**, 153 (1985); (*c*) C. Laurence, P. Nicolet, M.T. Dalati, J.-L.M. Abboud, and R. Notario. J. Phys. Chem. **98**, 5807 (1994).
20. Y. Marcus. Chem. Soc. Rev. **22**, 409 (1993).
21. D.V. Matyushov, R. Schmid, and B.M. Ladanyi. J. Phys. Chem. B **101**, 1035 (1997).
22. T.M. Krygowski and W.R. Fawcett. J. Am. Chem. Soc. **97**, 2143 (1975); Aust. J. Chem. **28**, 2115 (1975); Can. J. Chem. **54**, 3283 (1976).
23. G. Gritzner. J. Mol. Liq. **73/74**, 487 (1997).
24. (*a*) M.A. Kessler and O.S. Wolfbeis. Synthesis, 635 (1988); (*b*) M.C. Rezende and C.M. Radetski. Quim. Nova, **11**, 353 (1988); Chem. Abstr. **111**, 8876*w* (1989); (*c*) B.R. Osterby and R.D. McKelvey. J. Chem. Educ. **73**, 260 (1996); **73**, 737 (1996).
25. Aldrichimica Acta, **20** (No. 2), 59 (1987); **24** (No. 3), 81 (1991).
26. H. Stetter, M. Schwarz, and A. Hirschhorn. Chem. Ber. **92**, 1629 (1959).

© 1998 NRC Canada

Primary and secondary 5-(alkyloxy)thianthrenium perchlorates. Characterization with ^{1}H NMR spectroscopy, reactions with iodide and bromide ion, and thermal decomposition in solution

Wenyi Zhao and Henry J. Shine

Abstract: A series of 5-(alkyloxy)thianthrenium perchlorates has been made in which the alkyl group is primary (**1a**–**1p**) and secondary (**2a**–**2g**). Preparations were carried out by reaction of the corresponding alkanol with thianthrene cation radical perchlorate in CH_2Cl_2 solution followed by precipitation of the perchlorate salt with dry ether. ^{1}H NMR spectroscopy reveals that the presence of a stereogenic center in the alkyl group causes inequivalence in the ordinarily paired protons (e.g., H-4, H-6) of the thianthrenium ring. Reaction of iodide and bromide ion with primary alkyl-group compounds (e.g., methyl, ethyl, propyl, butyl) gave the alkyl halide in very good yield and by a second-order kinetic displacement. The second product was thianthrene 5-oxide (ThO). Rate constants for some of these reactions are reported. Reaction of secondary alkyl group compounds (e.g., 2-propyl, 2-pentyl, 2-hexyl, and 3-hexyl) with iodide ion gave good yields of alkyl iodide but also increasing evidence for a side reaction at the sulfonium sulfur, leading to I_2, thianthrene, and secondary alkanol. Decomposition of some compounds at 100°C in solution (acetonitrile or 1,2-dichloroethane) was studied and gave alkene(s) and ThO.

Key words: thianthrene cation radical, 5-(alkyloxy)thianthrenium perchlorates.

Résumé : On a préparé une série de perchlorates de 5-(alkyloxy)thianthrénium portant des groupes alkyles primaires (**1a–1p**) et secondaires (**2a–2g**). On a réalisé ces préparations en faisant réagir les alcanols correspondants avec le chlorate du cation radical thianthrène en solution dans du CH_2Cl_2 et en faisant ensuite précipiter le sel de perchlorate dans de l'éther anhydre. La spectroscopie RMN du ^{1}H révèle que la présence d'un centre stéréogène dans le groupe alkyle provoque une inéquivalence dans les protons généralement pairés (par exemple, H-4 et H-6) du noyau thianthrénium. Par un déplacement cinétique du premier ordre, la réaction des ions iodure et bromure avec les composés incorporant des groupes alkyles primaires (par exemple, méthyle, éthyle, propyle ou butyle) conduit à l'halogénure d'alkyle avec un très bon rendement alors que le deuxième produit est le 5-oxyde de thianthrène (ThO). On rapporte les constantes de vitesse d'un certain nombre de ces réactions. La réaction de l'ion iodure avec les composés comportant un groupe alkyle secondaire (par exemple, prop-2-yle, pent-2-yle, hex-2-yle et hex-3-yle) donne de bons rendements d'iodure d'alkyle; toutefois, on observe une augmentation d'une réaction secondaire au niveau de l'atome de sulfonium qui conduit à la formation de I_2, de thianthrène et d'alcanol secondaire. On a étudié la décomposition de certains de ces composés à 100°C, en solution (acétonitrile ou 1,2-dichloroéthane); elles conduisent à des alcènes et à du ThO.

Mots clés : cation radical du thianthrène, chlorhydrates de 5-(alkyloxy)thianthrénium.

[Traduit par la rédaction]

Introduction

The reactions of thianthrene cation radical ($Th^{\bullet+}$) with a diverse number of nucleophiles have been well documented during the last 20 or more years. Reaction occurs mainly at a sulfur atom and occasionally at a ring position (1–3). The reaction with water has been particularly well studied and it

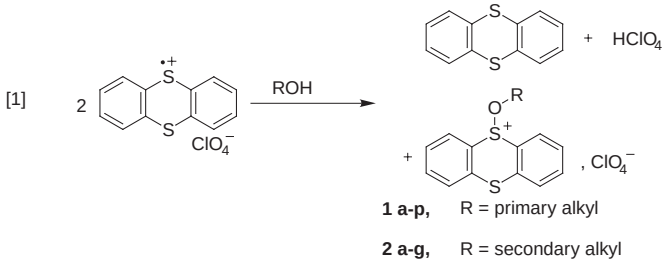

Received September 24, 1997.

This paper is dedicated to Professor Erwin Buncel in recognition of his contributions to Canadian chemistry.

W. Zhao and H.J. Shine.[1] Department of Chemistry and Biochemistry,Texas Tech University, Lubbock, TX 79409, U.S.A.

[1] Author to whom correspondence may be addressed. Telephone: (806) 742-3091. Fax: (806) 742-1289. E-mail: QVHJS@TTU.EDU

© 1998 NRC Canada

Scheme 1.

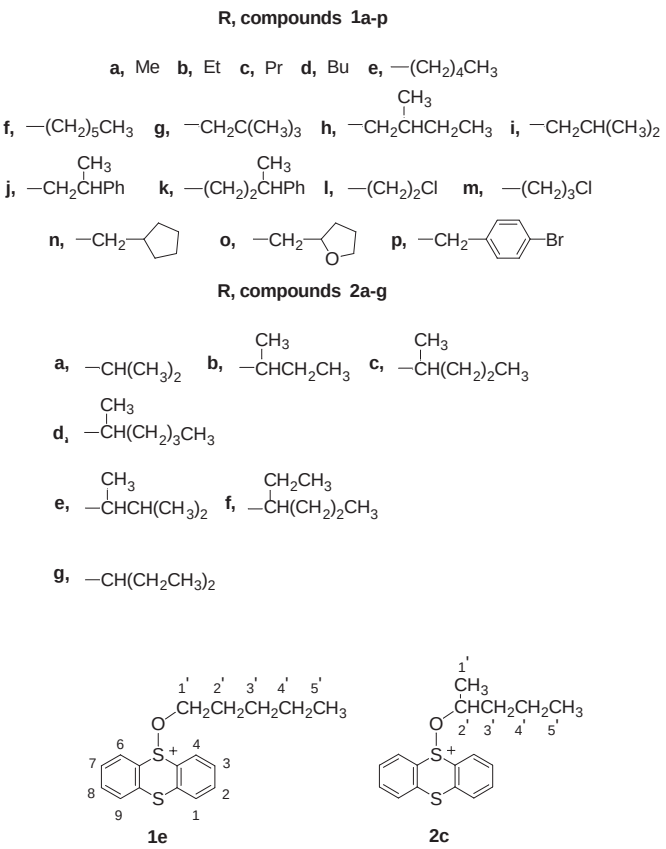

served as a model of the kinetics and mechanism of such reactions (1–4). In contrast, little was known until recently (5, 6) of the reaction of alcohols with $Th^{\bullet+}$. We have shown that thianthrene cation radical perchlorate ($Th^{\bullet+}ClO_4^-$) reacts readily with primary and secondary alcohols to form 5-(alkyloxy)thianthrenium perchlorates (eq. [1]).

When reaction was carried out in CH_2Cl_2 solution, the perchlorate salt could be precipitated easily by addition of ether. We have, in this way, reported the isolation, structure, and thermal decomposition of some 5-(cyclohexyloxy)thianthrenium perchlorates (5, 6). It was shown in these studies that when the cyclohexyl ring was stereogenic at its 1-position, inequivalence in ^1H and ^{13}C chemical shifts of the remote thianthrenium ring positions resulted.

We have now studied the reaction with alcohols in more depth and report here the isolation of a series of 5-(alkyloxy)thianthrenium perchlorates in which the alkyl group is primary (**1a**–**1p**) and a series in which it is secondary (**2a**–**2g**), Scheme 1. Inequivalence of aromatic ring protons where the alkyl group is stereogenic at its attachment to the oxygen atom is again recorded in the ^1H NMR spectra of **2a**–**2g**. In the spectra of some of compounds **1**, a similar effect is caused by stereogenicity at an even more remote position in the alkyl group. Reaction of compounds **1** having linear alkyl groups R with I^- and Br^- was essentially quantitative so that rates of formation of RI and RBr could be measured. Reaction of compounds **2a, 2c, 2d,** and **2f** with I^- also gave high yields of the alkyl iodides but small amounts of alkene were formed as well. Thermal decomposition of compounds **2** in solution was reasonably straightforward and is reported here. In contrast, we have been unable to quantify satisfactorily products of the thermal decomposition of several examples of **1** and further investigation of those reactions is in progress. Only decomposition of **1h** is reported.

^1H NMR spectra

Chemical shifts (δ) and coupling constants (*J*) are listed for convenience in Tables 1 and 2 (primary R) and Tables 3 and 4 (secondary R). Characteristics in δ for the thianthrenium protons are similar to some that have been noted recently (2). That is, where R is astereogenic, signals from four sets of equivalent protons are obtained, and the overall ^1H NMR spectrum is similar in most respects to that of thianthrene 5-oxide (ThO) but with shifts that are relatively further downfield (2). The presence of a stereogenic center in **2b–2f** can be seen in unequal shifts for H-4 and H-6 (**2b, 2e**), within each of sets H-4, -6 and H-2, -8 (**2c**), and H-4, -6, H-2, -8, and H-3, -7 (**2f**). Inequivalence in H-4 and H-6 resulted in two sets of doublet of doublets (dd) signals, while inequivalence in H-2 and H-8 and in H-3 and H-7 resulted in two groups of overlapping triplet of doublets (td) signals. The absence of inequivalence in the spectrum of **2a** with its small astereogenic isopropyl group, and of **2g** with its larger 3-pentyl group, is evident. Remarkably, the stereogenic center in **1j, 1k,** and **1o**, even more remote from the thianthrenium ring than in **2b**–**2f**, caused inequivalence in the H-4, -6 thianthrenium protons (**1j, 1k,**and **1o**) and H-3, -7 protons (**1o**) (Table 1). Inequivalence in more distant pairs H-2, -8, and H-1, -9 was, however, not found in **1j, 1k,** and **1o**. The effect of the stereogenic center in **1k** on nearby diastereotopic protons H-1′ and H-2′ was also seen. With **1h** only H-1′, and not H-4, -6, was affected by the stereogenic center.

In one respect, the NMR spectra of many of the compounds **1** differ from those of compounds **2** and the compounds of our earlier report (2). Coupling of H-3 with H-1, H-2, and H-4, i.e., H-3(2,4), 3(1), no longer led to a td, but to two sets of dd, namely, H-3(2), H-3(1) (equivalent to H-7(8), H-7(9)), and H-3(4), H-3(1) (equivalent to H-7(6), H-7(9)). This was the case with **1a, 1c**–**1f**, **1h, 1i**, and **1l**–**1o**. The expected td were observed in **1b** and **1g**.

As found earlier as well (2), δ for the -OC*H*$_2$ protons in compounds **1** and the –OC*H* proton in **2** were approximately 1 ppm downfield from the analogous proton in the corresponding alcohol. In the footnotes of Table 1 and Table 3 are listed the characteristics of signals from the alkyl-group protons.

Reactions with I^- and Br^-

Reactions with I^- were carried out in an acetonitrile solution of KI. Because KBr is itself not readily soluble in acetonitrile, it was used in conjunction with 18-crown-6. As a second source of Br^-, the more soluble Bu_4NBr was used.

Alkyl iodides (Table 5) and bromides (Table 6), along with

© 1998 NRC Canada

Table 1. ^{1}H chemical shifts (δ)[a] for **1a**–**1p**.

	δ							
H[b]	**1a**	**1b**[c]	**1c**[d]	**1d**[e]	**1e**[f]	**1f**[g]	**1g**	**1h**[h]
4	8.654	8.709	8.718	8.698	8.714	8.708	8.719	8.711
6								
1,9	7.979	7.947	7.945	7.952	7.943	7.945	7.954	7.951
2,8	7.930	7.881	7.878	7.885	7.877	7.879	7.882	7.883
3	7.788	7.770	7.768	7.766	7.764	7.764	7.767	7.765
7								
1′	3.854	4.298	4.198	4.218	4.222	4.221	3.885	4.079
								4.015
2′		1.271	1.622	1.562	1.574	1.566		1.612
								0.696
3′			0.737	1.148			0.708	1.155
					1.094			0.985
4′				0.752				0.713
5′					0.762			
6′						0.783		
	1i[i]	**1j**[j]	**1k**[k]	**1l**[l]	**1m**[m]	**1n**[n]	**1o**[o]	**1p**[p]
4		8.585	8.647				8.730	
	8.696			8.722	8.695	8.684		8.512
6		8.358	8.569				8.636	
1,9	7.958	[q]	7.931	7.978	7.984	7.958	7.936	[q]
2,8	7.891	[q]	7.860	7.911	7.919	7.891	7.858	[q]
3							7.757	[q]
	7.767	[q]	7.720	7.795	7.791	7.762		
7							7.736	
1′	3.989	4.356	4.176	4.572	4.357	4.076	4.283	5.297
			3.902					
2′	1.860	2.980	1.904	3.644	2.057			
			1.812					
3′	0.723	1.122	2.545		3.360			
4′			1.107					

[a]In $CDCl_3$ solution with TMS as reference.
[b]Listed in order of decreasing δ (*J* in Hz).
[c]H-1′, q, 2H, *J* = 7.01; H-2′, t, 3H, *J* = 7.01.
[d]H-1′, t, 2H, *J* = 6.45; H-2′, 2H, overlapping t, *J* = 6.54 and q, *J* = 7.33; H-3′, t, 3H, *J* = 7.40.
[e]H-1′, t, 2H, *J* = 6.35; H-2′, quintet, 2H, *J* = 6.94; H-3′, m, 2H, *J* = 7.98; H-4′, t, 3H, *J* = 7.25.
[f]H-1′, t, 2H, *J* = 6.46; H-2′, quintet, 2H, *J* = 6.90; H-3′, H-4′, m, 4H, δ = 1.094; H-5′, t, 3H, *J* = 6.78.
[g]H-1′, t, 2H, *J* = 6.43; H-2′, m, 2H; H-3′, -5′, m, 6H; H-6′, t, 3H, *J* = 6.52.
[h]H-1′, diastereotopic ABX coupling, 2H, *J* = 9.40 (AB), 6.69 (AX), 6.00 (BX); H-2′, m, 1H; H-2Me, d (overlapping H-4′), 6H, *J* = 7.02; H-3′, diastereotopic, two m, each 1H.
[i]H-1′, d, 2H, *J* = 6.60; H-2′, nonet, 1H, *J* = 6.70; H-3′, d, 6H, *J* = 6.72.
[j]H-1′, d, 2H, *J* = 7.06; H-2′, sextet, 1H, *J* = 7.01; H-3′, d, 3H, *J* = 7.06; phenyl, m, 3H, δ = 7.176; m, 2H, δ = 6.977.
[k]H-1′, diastereotopic, two m, each 1H; H-2′, diastereotopic, two m, each 1H; H-3′, m, 1H; H-4′, d, 3H, *J* = 6.97; phenyl, m, 3H, δ = 7.149; m, 2H, δ = 6.878.
[l]H-1′, t, 2H, *J* = 4.89; H-2′, t, 2H, *J* = 4.90.
[m]H-1′, t, 2H, *J* = 5.78; H-2′, quintet, 2H, *J* = 5.98; H-3′, t, 2H, *J* = 6.11.
[n]H-1′, d, 2H, *J* = 7.13; cyclopentyl ring, δ = 2.116, m, 1H; δ = 1.500, m, 6H; δ = 0.997, m, 2H.
[o]H-1′, overlapping peaks for two diastereotopic protons, m, 2H; tetrahydrofuranyl ring, four groups of overlapping peaks, δ = 3.943, m, 2H; δ = 3.785, m, 1H; δ = 1.769, m, 3H; δ = 1.504, m, 1H.
[p]H-1′, s, 2H; phenyl, δ = 7.393, d, 2H, *J* = 8.40; δ = 7.165, d, 2H, *J* = 8.42.
[q]Overlapping peaks, too complex for analysis.

thianthrene 5-oxide (ThO), were formed almost quantitatively from compounds **1**, shown schematically in eq. [2]. Assays were made by gas chromatography (GC) on reactions that were run to completion and also on aliquots taken at incomplete

© 1998 NRC Canada

Table 2. Coupling constants (J) for aromatic H in **1a**–**1p**.

	J^b							
Coupling[a]	**1a**	**1b**	**1c**	**1d**	**1e**	**1f**	**1g**	**1h**
4(3)								
	7.33	7.80	7.77	7.84	7.73	7.83	7..73	7.81
6(7)								
4(2)								
	1.13	1.45	1.60	1.56	1.50	1.37	1.01	1.16
6(8)								
4(1), 6(9)	[c]	[c]	[c]	[c]	[c]	[c]	[c]	[c]
1(2), 9(8)	8.00	8.09	7.83	8.10	7.89	8.08	8.00	7.88
1(3), 9(7)	1.67	1.91	1.85	1.99	1.78	1.86	1.63	1.78
1(4), 9(6)	[c]	[c]	[c]	[c]	[c]	[c]	[c]	[c]
2(1,3)								
	7.69	7.48	7.60	7.46	7.63	7.54	7.46	7.47
8(7,9)								
2(4), 8(6)	1.27	1.53	1.78	1.52	1.77	1.58	1.54	1.53
3(4), 7(6)[d]	7.70		7.77	7.78	7.78	7.75		8.07
		7.34					7.41	
3(2), 7(8)[d]	6.68		7.05	7.02	7.04	7.02		6.71
3(1)								
	2.25	1.99	1.93	1.92	1.93	1.87	1.76	1.72
7(9)								
	1i	**1j**	**1k**	**1l**	**1m**	**1n**	**1o**	**1p**
4(3)		7.41	7.22				7.88	
	7.58			7.31	7.90	8.03		7.81
6(7)		7.78	7.33				7.83	
4(2)			0.988				1.45	
	1.25			1.26	1.34	1.06		0.975
6(8)			1.07				1.33	
4(1), 6(9)	0.774				0.700		0.534	
1(2), 9(8)	7.98	[c]	[c]	7.94	7.94	8.00	7.87	[c]
1(3), 9(7)	1.82	[c]	[c]	1.77	1.84	1.83	1.84	[c]
1(4), 9(6)		[c]	[c]			0.602		[c]
2(1,3)								
	7.69	[c]	[c]	7.59	7.50	7.61	7.47	[c]
8(7,9)								
2(4), 8(6)	1.65	[c]	[c]	1.70	1.44	1.59	1.52	
3(4), 7(6)[d]	7.85	[c]	[c]	7.72	7.83	7.77	7.81[f]	
							7.41[e]	[c]
3(2), 7(8)[d]	6.93	[c]	[c]	7.05	6.96	7.04	7.19[f]	
3(1)							1.67	
	1.69	[c]	[c]	1.85	1.89	1.90		[c]
7(9)							1.80	

[a]Protons are listed in order of decreasing δ. For example, H-4 (before H-6) coupling with H-3, a doublet; and H-2 (before H-8) coupling with H-1 and H-3, a triplet.

[b]In Hz; coupling constants are averages when more than one value was measured. For example, the coupling pattern for H-4 in **1a** was a dd, so that coupling with H-2 gave two doublets with averaged J = 1.13 Hz.

[c]Overlapping peaks obscured coupling.

[d]In **1b**, for example, H-3 coupling equally with H-2 and H-4, and H-7 coupling equally with H-6 and H-8, leading to a triplet of doublets, δ = 7.770 ppm. In contrast, in **1c**, for example, coupling of H-3 with H-2 was not the same as coupling with H-4. Similarly, coupling of H-7 with H-6 was not the same as coupling with H-8, leading therefore to two sets of doublet of doublets, δ = 7.768 ppm.

[e]H-3 coupled equally with H-2 and H-4, leading to a triplet of doublets, δ = 7.757 ppm.

[f]Coupling of H-7 with H-6 was not the same as coupling with H-8, leading therefore to two sets of doublet of doublets, δ = 7.736ppm.

conversion in rate measurements. Some of the latter are reported in Tables 5 and 6 (e.g., runs 5 and 12 of Table 5), and in those cases we assayed also the alcohol (ROH) that was formed by reaction of the remaining **1** with the aqueous quench solution. Reaction of compounds **2** with I^- also gave good yields of alkyl iodide but not as close to quantitative as those

© 1998 NRC Canada

Table 3. ^{1}H chemical shifts (δ)[a] for 5-(alkyloxy)thianthreniumyl perchlorates (**2a**–**g**).

	δ						
H[b]	**2a**[c]	**2b**[d]	**2c**[e]	**2d**[f]	**2e**[g]	**2f**[h]	**2g**[i]
4		8.719	8.705	8.694	8.693	8.734	
	8.726						8.711
6		8.709	8.681	8.672	8.677	8.724	
1							
	7.924	7.928	7.932	7.938	7.944	7.923	7.932
9							
2			7.863	7.968		7.847	
	7.841	7.848			7.865		7.848
8			7.856	7.861		7.837	
3						7.742	
	7.746	7.744	7.738	7.738	7.742		7.739
7						7.739	
α	4.913	4.708	4.727	4.709	4.539	4.616	4.568

[a]In $CDCl_3$ solution with TMS as internal reference.

[b]The thianthrenium protons and the C*H* (α) attached to alkyloxy oxygen atom. Other alkyl-H assignments are given in footnotes; *J* in Hz.

[c]H-1′, -3′, d, 6H, *J* = 6.17, δ 1.316; H-2′(α), heptet, 1H, *J* = 6.18.

[d]H-1′, d, 3H, *J* = 6.22, δ = 1.337; H-2′(α), sextet, 1H, *J* = 6.18; H-3′, diastereotopic quintets, 1H, *J* = 7.31, δ 1.577, 1H, *J* = 6.80, δ 1.570; H-4′, t, *J* = 7.39, δ 0.663.

[e]H-1′, d, 3H, *J* = 6.20, δ 1.360; H-2′(α), sextet, 1H, *J* = 6.26; H-3′, m, diastereotopic 2H, δ 1.505; H-4′, m, diastereotopic 2H, δ 1.013; H-5′, t, 3H, *J* = 7.18, δ 0.728.

[f]H-1′, d, 3H, *J* = 6.22, δ 1.361; H-2′(α), sextet, *J* = 6.98; H-3′, m, diastereotopic 2H, δ 1.515 and δ 1.500; H-4′, 5′, m, 4H, δ 1.063; H-6′, t, 3H, *J* = 6.98, δ 0.729.

[g]H-1′, d, 3H, *J* = 6.14, δ 1.308; H-2′(α), quintet, 1H, *J* = 6.14; H-3′, septet of d, 1H, *J* (3′,4′) = 6.74, *J* (3′,2′) = 5.72, δ 1.757; H-4′, 2d, diastereotopic methyls, *J* = 6.710, δ 0.672, *J* = 6.84, δ 0.665.

[h]H-1′, t, 3H, *J* = 7.06, δ 0.764; H-2′, -4′, -5′ were not distinguishable; H-3′(α), quintet, 1H, *J* = 6.07; H-6′, t, 3H, *J* = 6.34, δ 0.698.

[i]H-1′, 5′, t, 6H, *J* = 7.35, δ 0.681; H-2′, -4′, diastereotopic quintets, 1H, *J* = 7.03, δ 1.627, 1H, *J* = 7.07, δ 1.620; H-3′(α), quintet, 1H, *J* = 6.04.

Table 4. Coupling constants *(J)* for aromatic H in **2a**–**g**.

	J[b]						
Coupling[a]	**2a**	**2b**	**2c**	**2d**	**2e**	**2f**	**2g**
4(3)		7.71	7.87	7.75	7.79	7.65	
	7.98						7.72
6(7)		7.68	7.37	7.85	7.91	7.71	
4(2)		1.94	1.28	1.44	1.52	1.86	
	1.46						1.44
6(8)		1.96	1.29	1.17[c]	1.40	1.80	
1(2)				[d]			
	7.09	7.89	8.05		7.84	7.78	7.71
9(8)				[d]			
1(3)				[d]			
	1.67	1.82	1.22		1.72	1.59	1.57
9(7)				[d]			
2(1,3)			7.53	7.51		8.01	
	7.84	7.53			7.35		7.52
8(7,9)			7.54	7.48		8.22	
2(4)			1.42	1.32		1.85	
	1.62	1.58			1.53		1.49
8(6)			1.30	1.40		1.35	
3(2,4)						7.71	
	7.42	7.44	7.41	7.48	7.46		7.47
7(6,8)						7.94	
3(1)						1.56	
	1.76	1.75	1.36	1.64	1.64		1.64
7(9)						1.59	

[a]Protons are in order of decreasing δ. For example, H-4 (before H-6) coupling with H-3; and H-2 (before H-8) coupling with H-1 and H-3, a triplet.

[b]In Hz; coupling constants are averages when more than one value was measured. For example (**2c**), the coupling pattern for H-4 was a dd so that coupling with H-2 gave two doublets with averaged *J* = 1.28 Hz.

[c]Average of *J* = 0.99 and 1.35.

[d]Resolution too poor to measure *J*.

of compounds **1**. Instead, small amounts of alkene were formed by a competitive bimolecular elimination, frequently designated as E_2C for eliminations by weakly basic nucleophiles (7, 8). Elimination, like substitution, gave ThO as the accompanying product, shown schematically in eq. [3], so that ThO is reported in the tables. Table 5 lists small amounts of I_2 and thianthrene (Th). These arose from reaction of I^- at sulfonium sulfur in compounds **1** and **2**, shown schematically in eq. [4]. Iodine was assayed by conventional iodometry after

[2]

[3] 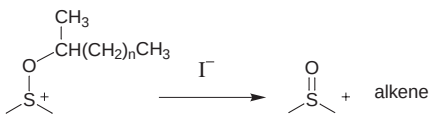

[4] 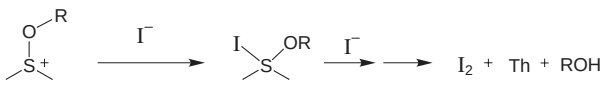

quenching the reaction solution with aqueous K_2CO_3. Table 6 lists, analogously, small amounts of Th and Br_2. We were unable, however, to assay Br_2 directly. Instead, it was converted into I_2 by addition of KI to the dry acetonitrile solution after reaction of **1** with Br^- was completed. I_2 was then assayed in the usual way, but is expressed as Br_2 in Table 6. In principle, the sum of amounts of alkyl halide and alkene (where formed) should be equal to the amount of ThO. Also, the amounts of Th and X_2 should be the same. For the most part these equalities are borne out by the data in the tables.

Rates of reaction (Table 7) were measured by quenching aliquots of the reaction solution with aqueous K_2CO_3 and assaying the amount of alkyl halide by GC. Good second-order rate plots were obtained, and led to the second-order rate constants listed in Table 7. These show the typical ordering expected of S_N2 displacements, namely Me > Et > Pr > Bu, pentyl, hexyl > isoPr (9). Rate constants of reactions with Br^- are somewhat larger than those of reactions with I^-. This can be attributed to our measuring rates in an aprotic solvent (10) or may have been caused by differences in counterion (11). The significance of the data of Tables 5–7 is in the demonstration of clean S_N2 displacements with **1** and **2**, the driving force being the departure of a good leaving group, ThO.

In accordance with S_N2 principles, displacement of the

© 1998 NRC Canada

Table 5. Formation of alkyl iodides from reaction of compounds **1** and **2** with KI in acetonitrile solution.

		Products, % yield				
Run	R	RI	ROH	Th	ThO	I_2
1	Me[a]	99		2.0	99	1.6
2	Me[b]	83		1.9	98	
3	Me[b]	92		1.8	99	
4	Et[b]	97	2.1	2.0	98	1.3
5	Et[b]	77	23	1.9	98	1.2
6	Pr[c]	100		1.3	100	2.5
7	Pr[b]	75		1.1	98	0.0
8	Bu[a]	100		4.2	96	3.9
9	Pentyl[b,c]	99		1.8	98	2.0
10	Hexyl[a]	98		2.2	98	2.3
11	iPr	92		3.7	95	3.3
12	iPr[b,c]	45	56	4.2	96	4.0
13	2-Pentyl[d]	88		7.0	93	7.0
14	2-Hexyl[e]	92		3.5	98	3.7
15	3-Hexyl[f]	87		8.1	92	

[a]Average of three runs.
[b]Assay of products from the last aliquot taken in rate measurement.
[c]Average of two runs.
[d]Small amounts of assumed 1- and 2- pentene (*cis* and *trans*) were seen but not measured.
[e]2.1% of *cis*-2-hexene and 4.6% of *trans*-2-hexene were formed.
[f]8.4% of a mixture of assumed *cis*- and *trans*-3-hexene was obtained.

Table 6. Formation of alkyl bromides from reaction of compounds **1** with KBr/18-crown-6 (A) and Bu_4NBr (B) in acetonitrile solution.

		Source	Products, % Yield				
Run	R	of Br^-	RBr	ROH	Th	ThO	Br_2
1[a]	Et	A	100	tr	1.7	98	3.7
2	Et[b,c]	A	83	19	4.7	98	
3[a]	Et	B	98	[e]	1.3	98	4.9
4	Et[b,c]	B	84		3.9	98	
5[a]	Pr	A	92	[f]	1.4	98	3.7
6	Pr[b,c]	A	71		1.6	98	
7[a]	Pr	B	95	[f]	1.6	101	3.5
8	Pr	B	75		3.2	97	
9[a]	Bu	A	98		5.6	97	3.1
10	Bu[b,c]	A	77		3.0	99	
11[a]	Pentyl	A	75		2.1	97	
12	Pentyl[d,c]	A	75		2.1	97	
13[a]	Pentyl	B	96		2.2	97	4.3

[a]GC analysis without prior addition of aqueous K_2CO_3.
[b]Average of two runs.
[c]These data were from the last aliquot taken in measuring rate of reaction.
[d]Average of three runs.
[e]GC peak overlapped that of an unknown from source B.
[f]GC peak broad, low intensity, and unintegrated.

neopentyl group from 5-(neopentyloxy)thianthrenium perchlorate (**1g**) by iodide ion did not occur. Instead, iodide ion reacted slowly at the sulfonium sulfur atom with the formation of Th, I_2, and neopentyl alcohol, eq. [4]. Details in the experimental section show that solutions containing **1g** and I^- decomposed to neopentyl iodide when injected onto the GC column, but that the only solution-reaction products were as shown in eq. [4].

Table 7. Rate constants[a,b] for formation of alkyl halides from **1a–f** and **2a**.

	Source of halide		
Compd.	KI	KBr/18-C-6	Bu_4NBr
1a	338 ± 6		
1b	7.30 ± 0.19	9.99 ± 0.13	10.7 ± 0.06
1c	4.30 ± 0.02	7.29 ± 0.19	7.32 ± 0.11
1d	2.41 ± 0.07	6.19 ± 0.08	
1e	3.12 ± 0.09	5.99 ± 0.19	5.12[c]
1f	2.49 ± 0.07		
2a	0.444 ± 0.008		

[a]10^2 k (M^{-1} s^{-1}). At room temperature, 23°C.
[b]Average of two runs.
[c]One run only.

Table 8. Yields (%) of products from thermal decompositions.[a]

	Yield, %		
Compd.	Alkene	Th	ThO
1h	91[b]	8.3	91
2d	98[c]	0.85	97
2e	88[d]	tr	100
2f	100[e]	4.7	93

[a]In DCE, except for **2e** in MeCN, at 100°C for 30 min, except for **1h**, 80 min.
[b]2-Methyl-1-butene, 40%; 2-methyl-2-butene, 51%.
[c]*trans*-2-Hexene, 70%; *cis*-2-hexene, 28%.
[d]3-Methyl-1-butene, 1.5%; 2-methyl-1-butene, 19%; 2-methyl-2-butene, 67%.
[e]A mixture of *cis*- and *trans*-3-hexene and *trans*-2-hexene, 82%; *cis*-2-hexene, 17%.

Thermal decompositions

Compounds **1** and **2** are stable to storage as solids and in dry solution. They decompose when heated in solution, forming alkenes and ThO. We report here (Table 8) the decomposition of **1h**, **2d,** and **2f** in 1,2-dichloroethane (DCE) and of **2e** in MeCN. Solvent MeCN was avoided for the most part because amides were formed in it along with the major alkene products, and the amides had broad, poorly shaped GC peaks that were not suited to reliable assay. The formation of amides was diagnostic of carbonium ion intermediates, and that diagnosis is also made from rearrangement alkenes in some of the examples reported here. The solutions were heated in sealed ampules at 100°C and, after cooling, aliquots were taken for GC analysis both before and after quenching with a small amount of aqueous K_2CO_3 solution. The data in Table 8 are from solutions that had been quenched. Heated solutions contained a small excess of 2,6-di-*tert*-butyl-4-methylpyridine (DTBMP) over the amount of substrate to prevent acid-catalyzed decompositions, and appropriate GC standards. In principle, only alkene and ThO in equal amounts should be formed in thermal decomposition. Thianthrene (Th) should not be formed, and the origin of the small amounts in Table 8 is unknown.

© 1998 NRC Canada

The only primary-alkyl-group compound in Table 8 is **1h**. From this, both 2-methyl-1- (40%) and 2-methyl-2-butene (51%) were obtained, the latter arising from rearrangement during decomposition. Rearrangement is also indicated in the formation of 2-methyl-1-butene (19%) from **2e**. From **2d** only *cis*- (28%) and *trans*-2-hexene (70%) were obtained, that is, unaccompanied by evidence of rearrangement. No 1-hexene was found. Isomeric **2f** gave both 2- and 3-hexenes. In that case, we could not distinguish by GC among *cis*- and *trans*-3-hexene and *trans*-2-hexene. We obtained 17% of *cis*-2-hexene and, if we assume that the same ratio of *cis*- and *trans*-2-hexenes was formed from **2f** as from **2d**, the mixture of inseparable hexenes from **2f** should have contained about 43% of *trans*-2-hexene. The addition of aqueous K_2CO_3 as a quench was to destroy any **1h** or **2d**–**2f** that was not decomposed in the heated solution. Undecomposed substrate would have decomposed to alkene in an uncontrolled way when injected onto the column. Reaction with aqueous K_2CO_3 converts **1** and **2** into ThO and the corresponding alcohol. Our assays (Table 8) did not show the presence of an alcohol in any quenched thermal reaction solution, attesting to the completeness of the thermal reaction.

Experimental section

Acetonitrile (MeCN, Eastman HPLC grade) was dried by distillation from CaH_2 and, again, from P_2O_5, each under N_2. 1,2-Dichloroethane (DCE) was from Baker Chemical Co, and was distilled from P_2O_5. Dichloromethane (CH_2Cl_2) was distilled from P_2O_5. All alcohols were from commercial sources, as were most of the authentic alkyl bromides and iodides. Neopentyl-, 2-pentyl-, and 2- and 3-hexyl iodides were prepared by reaction of the alcohols with iodotrimethylsilane, and had acceptable ^{1}H NMR spectra. All authentic alkenes, except 2-methyl-1-butene from Phillips Petroleum Co., were from Wiley Organics (now ChemSamp Co.), and were obtained as individual geometric isomers (where appropriate). Quantitative gas chromatographic (GC) assays were made with a Varian Associates model 3700 instrument attached to a Spectra Physics model 4290 recorder-integrator. Five columns were used, each of 1/8 in. (0.3175 cm) stainless steel: A, 10% OV-101 on 80–100 mesh Chrom-WHP, 4 ft (1.22 m); B, 10% Carbowax 20M on Chrom-WHP, 6 ft (1.83 m); C, 10% OV-17 on 80–100 mesh Chrom-Q11, 6 ft; D, 20% BEEA on 60–80 mesh Chrom PAW, 6 ft; E, 20% BEEA, on 60–80 mesh Chrom PAW, 8 ft (2.44 m). The conditions of usage of the columns were as follows: for A and C, injector at 250°C, detector at 300°C, oven at 50°C for 2 min and then ramped at 12°/min to 250°C; for B and D, initially similar settings but ramped only to 100°C; for E, ramping was omitted and the column was kept at 50°C. GC assays were made with the use of predetermined concentration factors for authentic compounds and internal standards: naphthalene for A and C; 2-butanone, acetone, or butyl methyl ether, as appropriate, for B; 2-butanone for D; and acetone for E.

Preparation of compounds 1 and 2

An example is given with **1a**.$Th^{\bullet+}ClO_4^-$ (253 mg, 0.80 mmol), *warning about explosiveness* (12), was weighed into a 50 mL flask containing a magnetic stirrer, and to this was added 15 mL of CH_2Cl_2. The flask was capped with a septum through which was added by syringe, after 5 min of stirring, an excess (2.1 mmol) of methanol in 5 mL of CH_2Cl_2. Stirring was continued at room temperature until the color of $Th^{\bullet+}$ had disappeared, about 15 h. The yellow solution was concentrated to about 5 mL on a rotary evaporator and was diluted with 25 mL of dry ether. The white precipitate of **1a** was filtered, washed three times with dry ether, and dried in air. Preparation of all other compounds was carried out in the same way except that higher concentrations of reactants were used and that, for **1p,** all procedures were conducted in an ice bath prior to concentration and dilution with ether. Compounds **1j**, **1k,** and **1m** were oils; they were reprecipitated from CH_2Cl_2 with ether and dried by pumping over P_2O_5. The times of stirring the reactants (h), % yield, and mp (dec.) °C of products were: **1a**, 15, 61, 93–96; **1b,** 2, 76, 91–107; **1c**, 2.5, 76, 70–90; **1d**, 1.5, 79, 87–90; **1e**, 1.5, 70, 85–86; **1f**, 1.0, 63, 64–65; **1g**, 7.5, 79, 105–123; **1h**, 1.0, 92, 88–90; **1i**, 1.5, 94, 91–94; **1j**, 3, 94, oil; **1k**, 1, 79, oil; **1i**, 72, 66, 69–71; **1m**, 26, 97, oil; **1n**, 1, 76, 89–91; **1o**, 5, 79, 82–84; **1p**, 7, 42, 71–74; **2a**, 2, 63, 82–84; **2b**, 2, 81, 76–82; **2c**, 3.5, 72, 72–73; **2d**, 2.5, 47, 68–70; **2e**, 2, 52, 75–77; **2f**, 2.5, 76, 84–86; **2g**, 4, 65, 75–80. Each of these compounds had a satisfactory ^{1}H NMR spectrum.

Reactions with iodide ion

An example is given with **1a**. Into a 5 mL volumetric flask containing a magnetic stirrer was weighed 36.4 mg (0.105 mmol) of **1a**. Measured amounts of internal GC standards naphthalene and acetone were added, followed by filling to the mark with a stock solution of KI in dry MeCN so as to provide 0.394 mmol of KI. The flask was capped with a septum and the solution was stirred at room temperature for 75 min, when 0.60 mL of 2 M aqueous K_2CO_3 was injected through the septum. Aliquots for GC assay were taken on column A for Th and ThO and on column B for MeI, giving 0.00192 mmol (1.8%) of Th, 0.104 mmol (99%) of ThO, and 0.104 (99%) of MeI. The solution was then titrated with aqueous sodium thiosulfate, giving 0.00152 mmol (1.5%) of I_2. This reaction was replicated three times. The averaged results are given in Table 5. Similar experiments were carried out with other 5-(alkyloxy)thianthrenium perchlorates (Table 5). All assays of Th and ThO were on column A. Assays of ethyl-, propyl-, and 2-propyl iodide, ethanol, 2-propanol, and propene were on column B, while assays of all other alkyl iodides were on column A.

Reaction of 5-(neopentyloxy)thianthrenium perchlorate (1g) with KI

A stirred solution of 47.9 mg (0.119 mmol) of **1g** and 166 mg (1.00 mmol) of KI in 5 mL of MeCN containing naphthalene and 2-butanone as GC standards was sampled for GC assay at 40, 160, and 350 min. 2-Methyl-1-butene (14.9, 12.2, 10.9%), 2-methyl-2-butene (19.9, 16.5, 15.5%), neopentyl iodide (35.3, 45.4, 31.5%), Th (31.1, 35.3, 37.0%), and ThO (68.1, 67.2, 58.0%) were obtained. After the solution had been stirred for 25 h, 0.30 mL of 2 M K_2CO_3 was added and stirring was continued for 7 h. GC assay gave 2-methyl-1-butene (0.21%), 2-methyl-2-butene (0.57%), Th (31.9%), and ThO (65.9%). No neopentyliodide was found. Neopentyl alcohol was formed but its GC peak overlapped that of the solvent, and assay was not possible. I_2 was titrated in the usual way, and gave 0.036 mmol (30.3%).

A second experiment gave, after 315 min of reaction and

© 1998 NRC Canada

stirring with K_2CO_3 for 30 min, 0.33% and 0.89% of the alkenes, 0.34% of neopentyliodide, 22% of Th, 72% of ThO, and 21% of I_2. The formation of the small amounts of alkenes and neopentyl iodide is assumed to stem from decomposition on the column of some residual **1g**.

Reactions with tetrabutylammonium bromide (TBAB)

An example is given with **1b** (run 3, Table 6). Into a 5 mL volumetric flask containing a magnetic stirrer were weighed measured amounts of naphthalene and **1b**. To this was added 5 mL of a 0.0716 M solution of TBAB in MeCN. The flask was capped with a septum and, after 10 min of stirring, a measured amount of GC standard acetone was injected. Aliquots were taken for GC assay. The solution was stirred for 2.5 h and 0.5 g of KI was added. The liberated I_2 was titrated as described.

Reactions with KBr/18-crown-6

A procedure similar to that with TBAB was followed with a solution of MeCN that was 0.0716 M in KBr and 0.132 M in 18-crown-6. Assays were conducted in the same way.

For GC assays of products of bromide ion reactions, column C rather than A was used for Th and ThO, because TBAB overlapped with Th on column A. Column B was used for assaying alkyl bromides except for bromopentane, which was assayed on column C. All results are listed in Table 6.

Measurement of rates of reaction

A, with KI

An example is given with **1a**. Into a 25 mL flask containing a magnetic stirrer were placed 358 mg (0.103 mmol) of **1a**, 27.8 mg (0.217 mmol) of naphthalene, and 0.02 mL (0.272 mmol) of acetone. The flask was made up to volume with a 5.18×10^{-3} M solution of KI in MeCN, and then was capped with a septum. The solutes dissolved rapidly. Aliquots of 4 mL were taken at 45, 75, 135, 195, and 315 s. Each aliquot was discharged into a screw-cap vial containing a magnetic stirrer and 0.1 mL of 2 M K_2CO_3, designed to hydrolyse any **1a** remaining in solution. GC assays for iodomethane were carried out after 35, 60, 90, 120, and 150 min of stirring the quenched aliquot, respectively. The amount of iodomethane (x_t) that was assayed at each time interval was assumed to be equated to the decrease in the initial amounts of **1a** (a_0) and KI (b_0). Consequently second-order rate plots $kt = \ln[b_0/a_0 \cdot a/b]/(a_0 - b_0)$ were made (by computer program) where $a = (a_0 - x_t)$ and $b = (b_0 - x_t)$.

After 18 min of stirring the reaction solution, it was quenched by adding 0.3 mL of 2 M K_2CO_3 solution and all products were assayed after 5 h of stirring. The results are given in run 3 of Table 5.

Rates of reaction of **1b**–**1f** and **2a** were measured similarly except that higher concentrations of reactants in a smaller volume (5 mL) were used for the slower reactions. The rate data are listed in Table 7.

B, with TBAB and KBr/18-crown-6

The procedure was analogous to that used in the KI reactions. The solution of TBAB was 0.0717 M, and the solution containing KBr /18-crown-6 was 0.0717 M in KBr and 0.132 M in 18-crown-6. Assays of alkyl bromides were made as described earlier. Second-order rate constants are listed in Table 7.

Thermal decompositions

An example is given with **2d**. A solution of 49.6 mg (0.119 mmol) of **2d** and 36.8 mg (0.179 mmol) of DTBMP in 5 mL of DCE, containing naphthalene and acetone as GC standards, was sealed in an ampule. The solution was heated at 100°C for 30 min and, after cooling and opening the ampule, was transferred to a 5 mL volumetric flask that was capped with a septum. The solution was then sampled for GC assay on columns A and E, giving 0.084 mmol (71%) of *trans*- and 0.033 mmol (28%) of *cis*-2-hexene (column E), 0.172 mmol (96%) of DTBMP, 0.00203 mmol (1.7%) of Th, and 0.118 mmol (99%) of ThO (column A). To verify that none of the **2d** had survived heating (and thus had decomposed to 2-hexene on the GC column), 0.30 mL of 2 M K_2CO_3 was injected through the septum after GC assays were complete, the solution was stirred for 120 min, and again sampled for GC assay, to give 70% of *trans*- and 28% of *cis*-2-hexene, 100% of DTBMP, 0.85% of Th, and 97% of ThO; these data are given in Table 8. Had **2d** survived heating to be hydrolysed by the K_2CO_3, the yields of 2-hexene would have been lower and 2-hexanol would have been found in the GC analysis.

Similar experiments were carried out with **1h**, **2e**, and **2f**. Results are listed in Table 8.

Acknowledgment

We thank the Robert A. Welch Foundation for financial support (Grant D-0028) and Professor J.N. Marx for discussions of NMR spectra.

References

1. A.J. Bard, A. Ledwith, and H.J. Shine. Adv. Phys. Org. Chem. **13**, 155 (1976).
2. H.J. Shine. *In* The chemistry of the sulphonuim group. *Edited by* C.J.M. Stirling and S.Patai. Wiley, New York. 1981. Chap. 14.
3. O. Hammerich and V.D. Parker. Adv. Phys. Org. Chem. **20**, 55 (1984).
4. E. Vieil, M. Maurey-Mey, and G. Cauquis. Electrochim. Acta, **29**, 1009 (1984).
5. W. Zhao and H.J. Shine. Tetrahedron Lett. **37**, 1749 (1996).
6. W. Zhao, H.J. Shine, and B.R. Whittlesey. J. Org. Chem. **62**, 8693 (1997).
7. W.T. Ford. Acc. Chem. Res. **6**, 410 (1973).
8. D.J. McLennan. Tetrahedron, **31**, 2999 (1975).
9. C.K. Ingold. Structure and mechanism in organic chemistry. Cornell University Press, Ithaca, N.Y. 1953. pp. 318, 319.
10. A.J. Parker. Chem. Rev. **69**, 1 (1969). See pp. 27, 28.
11. J. March. Advanced organic chemistry. 4th ed. John Wiley and Sons, New York. 1992. pp. 349, 350.
12. H.J. Shine and W. Yueh. J. Org. Chem. **59**, 3553 (1994).

© 1998 NRC Canada

The solubility of gases and vapours in ethanol — the connection between gaseous solubility and water–solvent partition

Michael H. Abraham, Gary S. Whiting, Wendel J. Shuely, and Ruth M. Doherty

Abstract: Ostwald solubility coefficients, as log L, for solutes in water and ethanol have been combined to give log P^{EtOH} for partition between the two pure solvents. Sixty-four such values have been correlated through our solvation equation, the coefficients of which lead to the conclusion that ethanol and water solvents are equally strong hydrogen-bond bases, but that ethanol is much weaker as a hydrogen-bond acid. A slightly different solvation equation has been used to correlate 68 values of log L^{EtOH}; the coefficients in this equation yield the same conclusions as to the hydrogen-bond acidity and basicity of bulk ethanol. In addition, an analysis of the various terms in the log L^{EtOH} correlation equation allows the elucidation of the various chemical factors that govern the solubility of gaseous solutes in ethanol solvent at 298 K.

Key words: solubility, partition, hydrogen-bonding, ethanol, water.

Résumé : On a combiné des coefficients de solubilité d'Ostwald (exprimés sous la forme de log L) de solutés dans l'eau et dans l'éthanol pour en tirer les valeurs de log P^{EtOH} exprimant le partage entre les deux solvants purs. On a établi une corrélation entre 64 de ces valeurs par le biais de notre équation de solvatation dont les coefficients conduisent à la conclusion que l'éthanol et l'eau sont deux solvants basiques avec de fortes liaisons hydrogènes; toutefois, l'éthanol est beaucoup plus faible comme acide de liaison hydrogène. On a utilisé une équation de solvatation légèrement différente pour établir une corrélation entre 68 valeurs de log L^{EtOH}; les coefficients de cette équation conduisent aux même conclusions relativement à l'acidité et à la basicité de l'éthanol dans les liaisons hydrogènes. De plus, une analyse des divers termes de l'équation de corrélation des log L^{EtOH} permet d'élucider les divers facteurs chimiques qui gouvernent la solubilité des solutés gazeux dans l'éthanol comme solvant, à 298 K.

Mots clés : solubilité, partage, liaison hydrogène, éthanol, eau.

[Traduit par la rédaction]

Introduction

The Gibbs energy of partition of a solute between two solvents, for example, water (W) and an organic solvent (S), is given by the difference between the Gibbs energies of solvation of the gaseous solute in the two solvents. In terms of equilibrium constants, the partition coefficient, as log P^S, is given by eq. [1]:

[1] $\log P^S = \log L^S - \log L^W$

L is the Ostwald solubility coefficient, or gas–liquid partition coefficient, defined as

[2] L = [conc. of solute in solution]/[conc. of solute in gas]

If the concentration units in eq. [2] are the same in each phase, for example mol dm^{-3}, then P^S, L^S, and L^W are all dimensionless. Equation [1] can be applied not only to two pure solvents, but also to solvents that are partially miscible, but then L^S and L^W must refer to the mutually saturated solvents.

Because there is such a clear connection between partitioning and gaseous solubility, it is evident that the solute properties that influence log L values must also influence log P values. However, this is not always the case as regards correlative and predictive methods. There are a number of empirical schemes that relate the solubility of gases in water (1, 2) and water–octanol partition coefficients (3, 4) to solute fragments, but without any connection between the two processes. Other methods for gaseous solubility are often characterized by individualistic approaches. Thus Jurs and co-workers (5) analyse gas chromatographic (GC) data of solutes on OV-101 and Carbowax 20M phases using solute descriptors such as the sum of the products of the partial negatively charged surface areas, a molecular connectivity parameter, the ratio of the first and second moments of inertia, etc., whilst Jalali-Heravi and Garkani-Nejad (6) discuss GC data on an Apiezon phase in terms of a zero-order valence term, the number of methyl groups, the solute volume, and dipole moment. One of the few investigations that considers the general problem of solvation is that of Cramer and co-workers (7–9) who set up a

Received December 9, 1997.

This paper is dedicated to Professor Erwin Buncel in recognition of his contributions to Canadian chemistry.

M.H. Abraham[1] **and G.S. Whiting.** The Department of Chemistry, University College London, 20 Gordon Street, London WC1H OAJ, U.K.
W.J. Shuely. SCBRD-RT, U.S. Army Edgewood Research, Development and Engineering Center, Aberdeen Proving Ground, MD 21010, U.S.A.
R.M. Doherty. NSWC Indian Head Division, Indian Head, MD 20640, U.S.A.

[1] Author to whom correspondence may be addressed. Telephone: + 44-171-387-7050. Fax: + 44-171-380-7463. E-mail: m.h.abraham@ucl.ac.uk

© 1998 NRC Canada

semiempirical quantum mechanical solvation model that can be used to correlate and predict log L values in water, hexadecane, and other solvents. Then, through eq. [1], they were able to calculate the corresponding log P^S values.

Our interest in the problem of partition and gaseous solubility arises through the use of the general solvation equation, eq. [3], for the characterization of water–solvent partitioning systems (10–13).

$$[3]\quad \log SP = c + rR_2 + s\pi_2^H + a\sum \alpha_2^H + b \sum \beta_2^H + vV_x$$

Here, log SP is a series of log P values for solutes in a given water–solvent system, and the independent variables are solute descriptors as set out before (10). These are, as follows: R_2, an excess molar refraction; π_2^H, the dipolarity/polarizability; $\sum\alpha_2^H$, the overall hydrogen-bond acidity; $\sum\beta_2^H$, the overall hydrogen-bond basicity; and V_X, the characteristic volume of McGowan (14). The coefficients in eq. [3] are found by the method of multiple linear regression analysis. They are not just fitting constants, but contain information on the properties of the system under investigation; in particular, they encode differences in chemical properties between the solvent phase and water. The r-coefficient reflects the differential interaction with solute π- and σ-lone pairs, the s-coefficient gives the difference in dipolarity/polarizability of the solvent and water, the a-coefficient the difference in hydrogen-bond basicity, and the b-coefficient the difference in hydrogen-bond acidity. The v-coefficient is a measure of the relative hydrophobicity of the solvent and water. Equation [3] has now been applied to numerous water–solvent partitions (11–13).

In the present work we extend the scope of eq. [3] to the water–ethanol system. There are two main reasons for the choice of ethanol as the solvent. Firstly, log P^{EtOH} values for the formal distribution between water and ethanol can only be obtained through eq. [1], and so the water–ethanol partition is a good example of the use of this equation. Secondly, there is considerable controversy over the hydrogen-bond basicity of water and alcohol (12): the solvatochromic comparison method of Kamlet, Taft, and co-workers (15) indicates that octanol and other alcohols are stronger hydrogen-bond bases than water (12), but studies (11) using eq. [3], as well as those using similar equations (16, 17) lead to the conclusion that water and (wet) octanol have the same hydrogen-bond basicity. Thus Abraham et al. (11) applied eq. [3] to 613 water–octanol partition coefficients, and obtained the regression:

$$[4]\quad \log P^{oct} = 0.09 + 0.56\,R_2 - 1.05\,\pi_2^H + 0.03 \sum \alpha_2^H - 3.46\,\Sigma\,\beta_2^H + 3.81\,V_x$$

The $s\pi_2^H$ and $b\sum\beta_2^H$ terms show that water is more polarizable/ dipolar and is a stronger hydrogen-bond acid than is wet octanol, but the negligible $a\sum\alpha_2^H$ term strongly suggests that water and wet octanol have the same hydrogen-bond basicity. Whether this similarity in basicity arises because wet octanol contains a considerable quantity of water, or whether octanol itself is as basic as water cannot be deduced from this particular data set. An analysis of log P^{EtOH} values will allow us to obtain the relative hydrogen-bond basicity of water and (dry) ethanol, and hence to address the problem of basicity of alcohols.

Values of log L^{EtOH} are required in order to calculate log P^{EtOH} through eq. [1]. Thus, it seems as though a straightforward application of eq. [3] to the log L^{EtOH} values would yield a direct measure of the hydrogen-bond basicity, and other properties of ethanol. However, we already know (18) that although eq. [3] correlates log P values very well, it is inferior to our second solvation equation, eq. [5], for the correlation of log L values in all nonaqueous solvents. The last descriptor in eq. [3], V_X, is replaced in eq. [5] by the descriptor log L^{16}, where L^{16} is the Ostwald solubility coefficient of solutes on hexadecane at 298 K (19).

$$[5]\quad \log L = c + rR_2 + s\,\pi_2^H + a \sum \alpha_2^H + b \sum \beta_2^H + l \log L^{16}$$

We can still explore solvent properties through eq. [5]. Indeed, the analysis is simpler than that through eq. [3], because the coefficients in eq. [5] are now directly related to the solvent phase properties. Although eqs. [3] and [5] are not identical, they have been constructed using the same chemical principles, and they include four out of five descriptors in common. Hence we can reasonably claim that the same general procedure is used to analyse both water–solvent partition and gas solubility. Another reason for analysis of log L^{EtOH} values is that a good correlative equation would be useful in the prediction of further values.

Our aims are thus to calculate log P^{EtOH} using eq. [1], to apply eq. [3] to these values, and to deduce properties of the solvent ethanol as compared to water; similarly, to apply eq. [5] to log L^{EtOH} values, and again to deduce properties of ethanol solvent.

Data collection

We have used various literature data to assemble log L^{EtOH} values from sources employing dry ethanol as the solvent. For the solution of permanent gases, directly determined log L^{EtOH} values have been recorded by Bo et al. (20), Pollack et al. (21), and Wilhelm and Battino (22). Other direct methods include that of Park et al. (23), who used a headspace analysis method. A useful indirect method involves combination of the infinite dilution activity coefficients of a solute in ethanol with the saturated vapour pressure of the solute, usually with the approximation that gas imperfections can be ignored. In addition, we have calculated log L^{EtOH} for some sparingly soluble aromatic hydrocarbons from their solubility in ethanol and their gaseous concentrations at 298 K (obtained from the saturated vapour pressures). This method can only be used, however, if the solute does not form any solvates with ethanol solvent; details are in Table 1. The gaseous concentrations, C^G, in mol dm^{-3}, are averages from various sources (24–26), and the solubilities of the solids in ethanol are also averages of the recorded values (27). Water solubilities, C^W, in mol dm^{-3} are included in Table 1 (25, 28–30) as they are needed for the calculation of log L^W values.

The final set of 68 values of log L^{EtOH} is in Table 2. There are four fewer log P^{EtOH} values, because the log L^W values for the long-chain alkanes are anomalous (31) and cannot be used to calculate log P^{EtOH}. The required descriptors in eqs. [3] and [5] have been listed before (10, 13, 26).

© 1998 NRC Canada

Table 1. Calculation of log L^{EtOH} and log P^{EtOH} for some aromatic hydrocarbons at 298 K.

Hydrocarbon	log C^{EtOH}	log C^{G}	log L^{EtOH}	log C^{W}	log L^{W}	log P^{EtOH}
Phenanthrene	–0.61	–7.97	7.36	–5.17	2.80	4.56
Anthracene	–1.84	–9.46	7.62	–6.43	3.03	4.59
Naphthalene	–0.13	–5.34	5.21	–3.61	1.73	3.48
Pyrene	–1.18	–9.65	8.47	–6.15	3.50	4.97

Table 2. Values of log L^{EtOH}, log L^{W}, and log P^{EtOH} obtained through eq. [1], at 298 K.

Solute	log L^{EtOH}	log L^{W} [a]	log P^{EtOH} [b]
Helium	–1.52 [c]	–2.02	0.51
Neon	–1.36 [c]	–1.96	0.59
Argon	–0.58 [c]	–1.47	0.89
Krypton	–0.16 [c]	–1.21	1.05
Xenon	0.37 [d]	–0.97	1.34
Radon	0.75 [e]	–0.65	1.39
Hydrogen	–1.07 [e]	–1.72	0.65
Oxygen	–0.62 [c]	–1.51	0.89
Nitrogen	–0.84 [c]	–1.80	0.96
Nitrous oxide	0.45 [e]	–0.23	0.68
Ammonia	2.01 [d]	3.15	–1.14
Carbon monoxide	–0.70 [f]	–1.63	0.94
Carbon dioxide	0.42 [f]	–0.08	0.50
Tetrafluoromethane	–0.72 [c]	–2.29	1.57
Sulfur hexafluoride	–0.12 [c]	–2.23	2.11
Methane	–0.29 [c]	–1.46	1.17
Ethane	0.44 [c]	–1.34	1.78
Propane	0.91 [g]	–1.44	2.35
Butane	1.40 [g]	–1.52	2.92
2-Methylpropane	1.20 [g]	–1.70	2.90
Pentane	1.78 [g]	–1.70	3.48
2,2-Dimethylpropane	1.61 [g]	–1.84	3.45
Hexane	2.24 [g]	–1.82	4.06
Heptane	2.71 [g]	–1.96	4.67
Octane	3.17 [h]	–2.11	5.28
Nonane	3.52 [g]	–2.30	5.82
Decane	3.92 [i]	–2.32	6.24
Hexadecane	6.57		
Octadecane	7.54 [j]		
Nonadecane	7.95 [j]		
Eicosane	8.34 [i]		
Cyclopentane	2.04 [g]	–0.88	2.92
Cyclohexane	2.55 [g]	–0.90	3.45
Ethene	0.41 [f]	–0.94	1.35
Trichloromethane	3.06 [k]	0.79	2.27
Tetrachloromethane	2.75 [l]	–0.06	2.81
Bromoethane	2.22 [m]	0.54	1.68
Iodomethane	2.19 [m]	0.65	1.54
Iodoethane	2.59 [m]	0.54	2.05
2-Iodopropane	2.92 [m]	0.34 [o]	2.58
$CFCl_2{\cdot}CFCl_2$	2.87 [n]	–0.64 [o]	3.51
1,1-Dichloroethene	2.38 [p]	–0.18	2.56
1,4-Dioxane	3.44 [h]	3.71	–0.27
Propanone	2.77 [m]	2.79	–0.02
Butanone	3.16 [h]	2.72	0.44
Methyl propanoate	3.04 [q]	2.15	0.89
Dimethylamine	2.40 [e]	3.15	–0.75
Trimethylamine	2.67 [r]	2.35	0.32

Table 2 (*concluded*).

Solute	log L^{EtOH}	log L^{W} [a]	log P^{EtOH} [b]
Triethylamine	3.57 [s]	2.36	1.21
Acetonitrile	2.90 [t,u]	2.85	0.05
Nitromethane	3.10 [h]	2.95	0.15
Water	3.72 [v]	4.64	–0.92
Methanol	3.40 [w]	3.74	–0.34
Ethanol	3.73 [x]	3.67	0.06
Propan–1-ol	4.20 [y]	3.56	0.64
Propan–2-ol	3.86 [y]	3.48	0.38
Carbon disulfide	2.27 [k]	–0.15 [z]	2.42
Benzene	2.78 [aa]	0.63	2.15
Toluene	3.28 [h]	0.65	2.63
p-Xylene	3.73 [ab]	0.59	3.14
Ethylbenzene	3.51 [ac]	0.58	2.93
Butylbenzene	4.20 [ac]	0.29	3.91
Chlorobenzene	3.68 [m]	0.82	2.86
Pyridine	4.18 [m,u]	3.44	0.74
Phenanthrene	7.36 [ad]	2.80 [ad]	4.56
Anthracene	7.62 [ad]	3.03 [ad]	4.59
Naphthalene	5.21 [ad]	1.73 [ad]	3.48
Pyrene	8.47 [ad]	3.50 [ad]	4.97

[a] From ref. 26 unless shown otherwise.
[b] From the previous two columns.
[c] Reference 20.
[d] Reference 21.
[e] Solubility Data Series.
[f] Reference 22.
[g] Reference 40.
[h] Reference 23.
[i] Reference 31.
[j] Reference 41.
[k] Reference 42.
[l] Reference 43.
[m] Reference 44.
[n] Reference 45.
[o] Reference 46.
[p] Reference 47.
[q] Reference 48.
[r] Reference 49.
[s] Reference 50.
[t] Reference 51.
[u] Reference 52.
[v] Reference 53.
[w] Reference 54.
[x] Taking the activity coefficient as unity.
[y] Reference 55.
[z] Estimated value from equations in ref. 29.
[aa] Reference 56.
[ab] Reference 57.
[ac] Reference 58.
[ad] From Table 1.

© 1998 NRC Canada

Table 3. Coefficients in eq. [3] for water–solvent partitions.

Solvent	*c*	*r*	*s*	*a*	*b*	*v*
Hexadecane[a]	0.09	0.67	–1.62	–3.59	–4.87	4.43
Cyclohexane[a]	0.13	0.82	–1.73	–3.78	–4.90	4.65
Benzene[b]	0.02	0.49	–0.60	–3.01	–4.63	4.59
Nitrobenzene[b]	–0.18	0.58	0.00	–2.36	–4.42	4.26
Chloroform[b]	0.12	0.12	–0.37	–3.39	–3.47	4.52
Decanol, wet[c]	0.01	0.48	–0.97	0.02	–3.80	3.95
Octanol, wet[a]	0.09	0.56	–1.05	0.03	–3.46	3.81
Isobutanol, wet[c]	0.23	0.51	–0.69	0.02	–2.26	2.78
Ethanol, dry[d]	0.21	0.41	–0.96	0.19	–3.64	3.93

[a] Reference 11.
[b] Reference 35.
[c] Reference 12.
[d] This work.

Table 4. Coefficients in eq. [5] for gas–solvent log *L* values at 298 K.

Solvent	*c*	*r*	*s*	*a*	*b*	*l*
Hexadecane[a]	0.00	0.00	0.00	0.00	0.00	1.000
$CH_2Cl.CH_2Cl$[b]	0.01	–0.15	1.44	0.65	0.74	0.936
Chloroform[c]	0.12	–0.47	1.20	0.14	1.43	0.994
Acetonitrile[b]	0.00	–0.22	2.19	2.38	0.41	0.733
DMSO[b]	–0.59	–0.20	2.89	5.46	0.00	0.732
3-Ethylphenol[d]	–1.08	–0.20	0.87	1.80	3.42	0.899
Water[e]	–1.27	0.82	2.74	3.90	4.81	–0.213
Ethanol[f]	0.01	–0.21	0.79	3.63	1.31	0.853

[a] By definition.
[b] M.H. Abraham, unpublished work.
[c] Reference 35.
[d] Reference 36.
[e] Reference 26.
[f] This work.

Analysis of the log P^{EtOH} data

Application of eq. [3] to the 64 log P^{EtOH} values yields the linear free energy relationship (LFER):

$$[6]\quad \log P^{EtOH} = 0.208 + 0.409\,R_2 - 0.959\,\pi_2^H + 0.186\sum \alpha_2^H - 3.645\sum \beta_2^H + 3.928\,V_x$$

where $n = 64$, sd = 0.17, $r^2 = 0.9904$, and $F = 1205$.

The number of solutes is *n*, the correlation standard deviation is sd, the correlation coefficient is *r*, and *F* is the *F*-statistic. Considering that log P^{EtOH} is the difference between two log *L* values, the statistics of eq. [6] are very good. The term in $\sum\alpha_2^H$ is significant at only the 70% level, and so could be omitted if required.

To interpret the coefficients in eq. [6] it is helpful to list the corresponding coefficients for regressions of log *P* values of solutes from water to other solvents; these are in Table 3. Note that decanol, octanol, and isobutanol are listed as "wet" because in equilibrium with water they contain appreciable quantities of water. The main coefficients are s, *a*, *b*, and *v*, which can be interpreted as follows.

The negative *s*-coefficients arise because water is much more dipolar than the organic solvents. The increased polarizability of organic solvents such as benzene or chloroform over that of water leads to rather less negative *s*-coefficients, and a combination of dipolarity and polarizability of nitrobenzene actually negates the dipolarity of water. Ethanol, itself, and the various wet alcohols appear to have rather low polarizability/ dipolarity.

The very negative *a*-coefficients are due to the pronounced hydrogen-bond basicity of water. Solvents such as hexadecane and cyclohexane have no hydrogen-bond basicity, and so the *a*-coefficient in any water–solvent equation cannot be more negative than around –3.8 units. Solvents with some basicity, such as nitrobenzene, give rise to less negative *a*-coefficients, as expected. An extraordinary feature of Table 3, however, is the almost-zero value of the *a*-coefficient for dry ethanol and the wet alcohols. This must indicate that the wet alcohols and dry ethanol have almost exactly the same hydrogen-bond basicity as water. Because dry ethanol has the same basicity as water, the basicity of the wet alcohols is unlikely to be due to just the presence of water; our findings suggest that dry alcohols are as hydrogen-bond basic as water. This is quite contrary to findings from the solvatochromic methods of Kamlet and Taft (32). Published lists of the Kamlet–Taft solvent hydrogen-bond basicity parameter, β, invariably show that dry alcohols, such as ethanol, have appreciably larger β-values than water (15, 33, 34).

In a similar vein, negative *b*-coefficients arise because water is so strong as a hydrogen-bond acid. The *b*-coefficients for the completely non-acidic solvents, hexadecane and cyclohexane, suggest that in eq. [3] for water-to-solvent partitions, this parameter cannot be more negative than around –4.9 units. The less negative the *b*-coefficient, the more acidic is the solvent, so that wet isobutanol is the most acidic solvent listed in Table 3. Dry ethanol, according to the coefficients in Table 3, is about as acidic as wet octanol or wet decanol and, perhaps surprisingly, no more acidic than bulk chloroform (35). Considering that a *b*-coefficient of –4.9 arises because the solvent has no acidity at all, a *b*-coefficient of –3.64 suggests that ethanol is markedly less hydrogen-bond acidic than is water. This is in line with solvatochromic measurements, because Marcus (33) lists the Kamlet–Taft hydrogen-bond solvent acidity, α, as 1.17 for water and 0.86 for dry ethanol. Goncalves et al. (34) give similar values, 1.16 for water and 0.88 for dry ethanol.

As mentioned above, the *v*-coefficient can be interpreted as a measure of the solvent hydrophobicity. Not surprisingly, alkanes and cycloalkanes have very large *v*-coefficients, and the wet alcohols somewhat lower coefficients. The value of 3.93 for dry ethanol seems unexceptional.

Analysis of the log L^{EtOH} data

The 68 values of log L^{EtOH} can be analysed through the LFER, eq. [5], to give the correlation:

$$[7]\quad \log L^{EtOH} = 0.012 - 0.206\,R_2 + 0.789\,\pi_2^H + 3.635\sum \alpha_2^H + 1.311\sum \beta_2^H + 0.853\log L^{16}$$

where $n = 68$, sd = 0.14, $r^2 = 0.9966$, $F = 3534$. The statistics of eq. [7] are a little better than those for eq. [6]. This is not surprising because the error in the log P^{EtOH} values will include the error in log L^W as well as the error in log L^{EtOH}. In any event, eq. [7] is good enough to predict further values of log L^{EtOH} to within around 0.2 log units. Once again, interpretation of eq. [7] is aided by comparison of coefficients for other like

© 1998 NRC Canada

Table 5. Some measures of the hydrogen-bond acidity and basicity of solvents.

Solvent	AN[a]	$\Delta_{acid}H^b$	α^c	α^d	α^e	b^f	b^g	$\delta\Delta H^h$	β^c	β^d	β^e	a^f	a^g
Cyclohexane	0.0	2.10	0.00	0.00	0.00	0.00	–4.90	1.46	0.00	0.00	0.00	0.00	–3.78
Chloroform	23.1	–5.60	0.20	0.44		1.43	–3.47	2.30	0.10	0.00	0.14	–3.39	
Ethanol	37.1	–9.14	0.86	0.83	0.88	1.25	–3.59	13.26	0.75	0.71/0.89	0.77	3.64	0.17
Water	54.8	–10.60	1.17	1.17	1.16	4.81	0.00	7.46	0.47	0.43/0.58	0.18	3.90	0.00

[a] Reference 39; the first datum is for hexane.
[b] Reference 37.
[c] Reference 33.
[d] Reference 15.
[e] Reference 34.
[f] The coefficient in eq. [5].
[g] The coefficient in eq. [3].
[h] Reference 38; the value for ethanol is an average of methanol (12.93) and butan-1-ol (13.60).

Table 6. The factors that influence the solubility of gaseous solutes in water and ethanol as log *L* values at 298 K.

						log *L*	
Solute	rR_2	$s\pi_2^H$	$a\sum\alpha_2^H$	$b\sum\beta_2^H$	$l \log L^{16}$	Calcd.[a]	Obsd.
Solvent ethanol							
Ethane	0.00	0.00	0.00	0.00	0.42	0.43	0.44
Octane	0.00	0.00	0.00	0.00	3.14	3.15	3.17
Toluene	–0.13	0.42	0.00	0.18	2.84	3.32	3.28
Butanone	–0.04	0.56	0.00	0.66	1.95	3.15	3.16
Propan-2-ol	–0.05	0.29	1.20	0.73	1.50	3.69	3.86
Ammonia	–0.03	0.31	0.58	0.73	0.27	1.88	2.01
Acetic acid	–0.06	0.52	2.22	0.55	1.49	4.74	—
Solvent water							
Ethane	0.00	0.00	0.00	0.00	–0.10	–1.37	–1.34
Octane	0.00	0.00	0.00	0.00	–0.78	–2.05	–2.11
Toluene	0.49	1.43	0.00	0.67	–0.71	0.61	0.65
Butanone	0.14	1.92	0.00	2.45	–0.49	2.75	2.29
Propan-2-ol	0.17	0.99	1.29	2.70	–0.38	3.50	3.48
Ammonia	0.11	1.07	0.62	2.70	–0.07	3.16	3.15
Acetic acid	0.22	1.78	2.38	2.11	–0.37	4.85	4.91

[a] Using eq. [5] with the coefficients in Table 4; note that $c = 0.01$ for ethanol and –1.27 for water.

regressions. Coefficients in eq. [5] are given in Table 4 for the solubility of gaseous solutes, as log *L* at 298 K, in a number of solvents.

Since the coefficients in Table 4 refer to transfers from the gas phase, where there are no solute–solvent interactions at all, to bulk solvents, they can be regarded as "absolute" measurements of the various solvent properties. By and large, they compare very well with the solvent properties, now referenced to water, obtained from log *P* values. Thus the rather low *s*-coefficient again indicates that dry ethanol has a low polarizability/dipolarity. Of considerable interest, in view of our comparison of the log *P* coefficients with solvatochromic parameters, are the *a*- and *b*-coefficients for ethanol. The *a*-coefficient shows clearly that ethanol is as strong a hydrogen-bond base as water, exactly as we found from the log *P* coefficients. But even ethanol and water are by no means as strong as dimethyl sulfoxide (DMSO). The *b*-coefficients in Table 4 confirm our above conclusion that ethanol is a much weaker hydrogen-bond acid than is water, and is only as strong as bulk chloroform. Again, this fits exactly with the *b*-coefficients in Table 3, viz: –3.47 for chloroform and –3.63 for ethanol.

Solvatochromic parameters are not the only measures of hydrogen-bond acidity and basicity of solvents. In Table 5 are collected the Kamlet–Taft α- and β-parameters, the $\Delta_{acid}H$ and the $\delta\Delta H$ (basicity) parameter of Catalan et al. (37, 38), and the AN acceptor parameter of Gutmann (39) for a number of solvents. We do not include the donor number, DN, because this is not a solvent property at all. In Table 5 are given the *a*- and *b*-coefficients in the relevant equations, eq. [3] and eq. [5]. The relative hydrogen-bond acidity of water and ethanol seems not in dispute, at least in a qualitative sense. All measures listed in Table 5 rank water as significantly more acidic than ethanol, although the coefficients obtained in this work suggest that water is much the better hydrogen-bond acid. From the *a*-coefficients obtained through eq. [3] or eq. [5], it is evident that water and ethanol behave as though they had almost the same hydrogen-bond basicity. However, the other four measures listed in Table 5 rank water as a much weaker hydrogen-bond base than ethanol. We have no explanation for this very large discrepancy, except to point out that, of the other four measures, three are spectroscopic in nature and one is enthalpy-related, whereas the *a*-coefficient is a Gibbs energy-related measure.

© 1998 NRC Canada

The *l*-coefficients in Table 4 are of some interest, in that for all nonaqueous solvents they are large and positive, but for water the *l*-coefficient is small and negative. As a result, large gaseous solutes will be much more soluble in ethanol than small solutes, but large solutes will be slightly less soluble in water than small solutes.

The factors that influence solubility in water and ethanol can be set out through a term-by-term analysis of eq. [5]. This is done in Table 6 for a few representative solutes. In the case of solubility in ethanol, the $l \log L^{16}$ term dominates, except for solutes that are strong hydrogen-bond acids. But for water, the three "polar" terms $s\pi_2^H$, $a \Sigma \alpha_2^H$, and $b \sum \beta_2^H$ are dominant, and the $l \log L^{16}$ term makes only a minor contribution. Hence solutes that are large will nearly always be more soluble in ethanol than in water; only if a large solute has substantial values of π_2^H and $\sum \beta_2^H$ will it be more soluble in water. Acetic acid is a case in point, where the large dipolarity and hydrogen-bond basicity together result in a very large solubility in water (note that the effect of hydrogen-bond acidity is very nearly the same in ethanol and water). For small solutes, where the $l \log L^{16}$ terms in ethanol and water do not differ so much, compounds that are strongly dipolar/polarizable and are hydrogen-bond bases will be more soluble in water; ammonia is such a case.

Conclusions

Values of log P^{EtOH} for the transfer of compounds from water to ethanol can be obtained from log *L* values in the two solvents, and the log P^{EtOH} values correlated very satisfactorily through eq. [3]. The coefficients in eq. [3] contain information on the relative chemical properties of water and ethanol, and lead to the conclusion that the two solvents have the same hydrogen-bond basicity, but that ethanol is a much weaker hydrogen-bond acid. The log L^{EtOH} values are well correlated through eq. [5], the coefficients of which now encode "absolute" chemical properties of ethanol, for example, properties relative to the gas phase. Once again, ethanol is seen to be a strong hydrogen-bond base, but only a moderate hydrogen-bond acid — no stronger than bulk chloroform. A term-by-term analysis of eq. [5] enables log L^{EtOH} values to be factored into contributions from particular solute–solvent interactions.

Acknowledgements

This paper is dedicated to Professor Erwin Buncel in recognition of his valuable work in the area of physical organic chemistry. We thank the US Army Research, Development and Standardization Group for support under Contract DAJA 45-87-C-0004.

References

1. J. Hine and P.K. Mookerjee. J. Org. Chem. **40**, 292 (1975).
2. S. Cabani, P. Gianni, V. Mollica, and L. Lepori. J. Solution Chem. **10**, 563 (1981).
3. A.J. Leo. Chem. Rev. **93**, 1281 (1993).
4. H. van de Waterbeemd and R. Mannhold. Quant. Struct.–Act. Relat. **15**, 410 (1996).
5. L.S. Anker, P.C. Jurs, and P.A. Edwards. Anal. Chem. **62**, 2676 (1990).
6. M. Jalali-Heravi and Z. Garkani-Nejad. J. Chromatogr. **648**, 389 (1993).
7. C.C. Chambers, G.D. Hawkins, C.J. Cramer, and D.G. Truhlar. J. Phys. Chem. **100**, 16385 (1996).
8. D.J. Giesson, C.C. Chambers, C.J. Cramer, and D.G. Truhlar. J. Phys. Chem. **101**, 2061 (1997).
9. D.J. Giesson, C.C. Chambers, C.J. Cramer, and D.G. Truhlar. J. Phys. Chem. **101**, 5084 (1997).
10. M.H. Abraham. Chem. Soc. Rev. **22**, 73 (1993).
11. M.H. Abraham, H.S. Chadha, G.S. Whiting, and R.C. Mitchell. J. Pharm. Sci. **83**, 1085 (1994).
12. M.H. Abraham, H.S. Chadha, J.P. Dixon, and A.J. Leo. J. Phys. Org. Chem. **7**, 712 (1994).
13. M.H. Abraham and H.S. Chadha. *In* Lipophilicity in drug action and toxicology. *Edited by* V. Pliska, B. Testa, and H. van de Waterbeemd. VCH, Weinheim. 1996.
14. M.H. Abraham and J.C. McGowan. Chromatographia, **23**, 243 (1987).
15. M.J. Kamlet, J.-L.M. Abboud, M.H. Abraham, and R.W. Taft. J. Org. Chem. **48**, 2877 (1983).
16. D.E. Leahy, J.J. Morris, P.J. Taylor, and A.R. Wait. J. Chem. Soc. Perkin Trans. 2, 705 (1992).
17. N. El Tayar, R.-S. Tsai, B. Testa, P.-A. Carrupt, and A. Leo. J. Pharm. Sci. **80**, 590 (1991).
18. M.H. Abraham, G.S. Whiting, R.M. Doherty, and W.J. Shuely. J. Chem. Soc. Perkin Trans. 2, 1451 (1990).
19. M.H. Abraham, P.L. Grellier, and R.A. McGill. J. Chem. Soc. Perkin Trans. 2, 797 (1987).
20. S. Bo, R. Battino, and E. Wilhelm. J. Chem. Eng. Data, **38**, 611 (1993).
21. G.L. Pollack, J.F. Himm, and J.J. Enyeart. J. Chem. Phys. **81**, 3239 (1984).
22. E. Wilhelm and R. Battino. Chem. Rev. **73**, 1 (1973).
23. J.H. Park, A. Hussam, P. Couasnon, D. Fritz, and P.W. Carr. Anal. Chem. **59**, 1970 (1987).
24. D. Mackay and W.Y. Shiu. J. Phys. Chem. Ref. Data, **10**, 1175 (1981).
25. R.M. Stephenson and S. Malinowski. Handbook of the thermodynamics of organic compounds. Elsevier, New York. 1987.
26. M.H. Abraham, J. Andonian-Haftvan, G.S. Whiting, A. Leo, and R.W. Taft. J. Chem. Soc. Perkin Trans. 2, 1777 (1994).
27. A. Seidell. Solubilities of organic compounds. 3rd ed. Van Nostrand, New York. 1941; A. Seidell and W.F. Linke. Solubilities of organic compounds. 3rd ed. supplement. Van Nostrand, New York. 1952.
28. G.L. Amidon and S.T. Anik. J. Chem. Eng. Data, **26**, 28 (1981).
29. R.S. Pearlman, S.H. Yalkowski, and S. Banerjee. J. Phys. Chem. Ref. Data, **13**, 555 (1984).
30. S.P. Wasik, M.M. Miller, Y.B. Tewari, W.E. May, W.J. Sonnefeld, H. DeVoe, and W.H. Zoller. Residue Rev. **85**, 29 (1983).
31. M.H. Abraham. J. Chem. Soc. Faraday Trans. 1, **80**, 153 (1984).
32. M.J. Kamlet and R.W. Taft. J. Am. Chem. Soc. **98**, 377 (1976); R.W. Taft and M.J. Kamlet. J. Am. Chem. Soc. **98**, 2886 (1976).
33. Y. Marcus. Chem. Soc. Rev. **22**, 409 (1993).
34. R.M.C. Goncalves, A.M.N. Simoes, L.M.P.C. Albuquerque, M. Roses, C. Rafols, and E. Bosch. J. Chem. Res. (M), 1380 (1993).
35. M.H. Abraham, J.A. Platts, A. Hersey, A.J. Leo, and R.W. Taft. Manuscript in preparation.
36. M.H. Abraham, I. Hamerton, J.B. Rose, and J.W. Grate. J. Chem. Soc. Perkin Trans. 2, 1417 (1991).
37. J. Catalan, J. Gomez, J.L. Saiz, A. Couto, M. Ferraris, and J. Laynez. J. Chem. Soc. Perkin Trans. 2, 2301 (1995).
38. J. Catalan, J. Gomez, A. Couto, and J. Laynez. J. Am. Chem. Soc. **112**, 1678 (1990).
39. U Mayer. Pure Appl. Chem. **51**, 1697 (1979).

© 1998 NRC Canada

40. M.H. Abraham, P.L. Grellier, and R.A. McGill. J. Chem. Soc. Perkin Trans. 2, 339 (1988).
41. U Domanska, T. Hofman, and J. Rolinska. Fluid Phase Equil. **32**, 273 (1987).
42. I.M. Barclay and J.A.V. Butler. Trans. Faraday. Soc. **34**, 1445 (1938).
43. E. Matteoli and L. Lepori. J. Chem. Thermodyn. **18**, 1085 (1986).
44. E.R. Thomas, B.A. Newman, T.C. Long, D.A. Wood, and C. Eckert. J. Chem. Eng. Data, **27**, 233 (1982); **27**, 399 (1982).
45. V. Dohnal and M. Novotna. Fluid Phase Equil. **23**, 303 (1985).
46. J. Hine and P.K. Mookerjee. J. Org. Chem. **40**, 292 (1975).
47. A. Kovac, J. Sroboda, and L. Ondrus. Chem. Zvesti, **39**, 729 (1985).
48. J. Polak and B.-C.Y. Lu. J. Chem. Eng. Data, **17**, 457 (1972).
49. M.H. Abraham. J. Chem. Soc. B, 299 (1971).
50. M.H. Abraham and P.L. Grellier. J. Chem. Soc. Perkin Trans. 2, 1735 (1976).
51. V. Dohnal, F. Vesely, R. Hobab, and J. Pick. Collect. Czech. Chem. Commun. **47**, 3177 (1982).
52. O. Mutha, P.J. Maher, and B.D. Smith. J. Chem. Eng. Data, **25**, 163 (1980).
53. J.A.V. Butler, D.W. Thomson, and W.H. Maclennan. J. Chem. Soc. 674 (1933).
54. A.C. Morris, L.T. Munn, and G. Anderson. Can. J. Res. **20B,** 207 (1942).
55. G.S. Parks and K.K. Kelly. J. Phys. Chem. **29**, 727 (1925).
56. S.-C. Hwang and R.L. Robinson. J. Chem. Eng. Data, **22**, 319 (1977).
57. R.H. Stokes and H.T. French. J. Chem. Soc. Faraday Trans. 1, **76**, 537 (1980).
58. C.J. Pierotti, C.H. Deal, and E.L. Durr. Ind. Eng. Chem. **51**, 95 (1959).

© 1998 NRC Canada

Kinetics and mechanism of the aminolysis of ethyl aryl carbonates in acetonitrile

Han Joong Koh, Ji-Won Lee, Hai Whang Lee, and Ikchoon Lee

Abstract: The aminolysis reactions of ethyl aryl carbonates with benzylamines in acetonitrile at 25.0°C are investigated. The base-catalyzed path, k_2, disappears when strong nucleophiles (X = *p*-CH_3O and *p*-CH_3) react with a substrate activated by a strong nucleofuge (Z = *p*-NO_2). The large magnitude of ρ_x (–1.7 to –2.5), ρ_z (3.4 to 4.3), and ρ_{xz} (1.4) values, and relatively large k_H/k_D (1.6 to 1.8) found for the uncatalyzed path (k_1) can be accounted for in terms of a stepwise mechanism with rate-limiting expulsion of the phenoxide leaving group. The catalyzed process (k_2) is characterized by the much smaller magnitude of ρ_x (–1.0 to –1.7), ρ_z (0.4 to 0.7), and ρ_{xz} (0.2), the larger k_H/k_D (2.1 to 2.5) values, and the lower $\Delta H^{\ddagger}$ values (1.8–1.9 kcal mol^{-1}) than those of the uncatalyzed process (k_1) with large negative $\Delta S^{\ddagger}$ values (–65 to –67 cal K^{-1} mol^{-1}). These results are consistent with four- and six-centered transition states for the two processes, k_1 and k_2, respectively.

Key words: ethyl aryl carbonates, aminolysis mechanism, base catalysis, stepwise mechanism, cross-interaction constant.

Résumé : On a étudié les réactions d'aminolyse des carbonates d'éthyle et d'aryle par les benzylamines, dans l'acétonitrile, à 25,0°C. La voie réactionnelle catalysée par les bases, k_2, disparaît lorsque des nucléophiles forts (X = *p*-CH_3O et *p*-CH_3) réagissent avec un substrat activé par un groupe fortement nucléofuge (Z = *p*-NO_2). Pour expliquer la grande amplitude des valeurs de ρ_x (de –1,7 à –2,5), ρ_z (3,4 à 4,3) et de ρ_{xz} (1,4) ainsi que de la valeur relativement importante observée pour k_H/k_D (1,6 à 1,8) observées pour la voie non catalysée, on peut imaginer un mécanisme par étapes impliquant une expulsion cinétiquement limitante du groupe phénolate partant. Le processus catalysé (k_2) est caractérisé par des amplitudes beaucoup plus faibles de ρ_x (de –1,0 à –1,7), ρ_z (0,4 à 0,7) et de ρ_{xz} (0,2), des valeurs beaucoup plus élevées de k_H/k_D (2,1 à 2,5) et des valeurs de $\Delta H^{\ddagger}$ (1,8 à 1,9 kcal mol^{-1}) beaucoup plus faibles que celles observées pour le processus non catalysé (k_1) avec des valeurs de $\Delta S^{\ddagger}$ très négatives (–65 à –67 cal K^{-1} mol^{-1}). Ces résultats sont en accord avec des états de transition à quatre et à six centres respectivement pour les deux processus k_1 et k_2.

Mots clés : carbonates d'éthyle et d'aryle, mécanisme d'aminolyse, catalyse par les bases, mécanisme par étape, constante d'interaction de croisement.

[Traduit par la rédaction]

Introduction

Aminolyses of sulfur analogs of ethyl aryl carbonates, **2**–**4** (1–4) have been shown to exhibit interesting mechanistic variations depending on sulfur substitution for oxygen and the reaction medium used. In the aminolysis of thiono compounds, **3** (3), a weaker π-bonding energy of the thio carbonyl (C═S) compared to the carbonyl (C═O) leads to the difficulty in forming the C═S bond to expel the nucleofuge, which results in a lowering of the nucleofugality (k_b in Scheme 1) of ArO^-. The change of O^- by S^- in $\mathbf{T}^{\pm}$ brings about therefore a mechanistic change in aqueous solution to a complex one in which the deprotonation step, k_d, can compete with k_{-a} and k_b (Scheme 1). The increased leaving ability (larger k_b) by introducing nitro groups (**3b**–**3d**) or suppressed proton transfer rate (smaller $k_d[RNH_2]$) by using an aprotic medium (5*a*) can, however, restore the mechanism to a simple rate-limiting breakdown (k_b) of the tetrahedral intermediate, $\mathbf{T}^{\pm}$, which is commonly observed in most of the aminolysis reactions of esters and carbonates (5). On the other hand, in the aminolysis of thiol compounds, **2** (2), the ethoxy group apparently destabilizes $\mathbf{T}^{\pm}$ and is known to enforce a concerted mechanism as a result of the enhanced leaving ability of 2,4-dinitro-, **2c**, and 2,4,6-trinitro-thiophenoxides, **2d** (relative to the corresponding phenoxides). This mechanistic change from a stepwise mechanism for oxyesters and oxycarbonates to a concerted mechanism for the thiol carbonate (**2**) has not been observed with acetates (EtO replaced by Me) (6), methyl aryl carbonates (EtO replaced by MeO) (3*b*), and benzoates (EtO replaced by Ph, in **1**–**4**) (7). The aminolyses of dithio (**4**) derivatives were

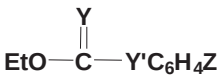

1 Y = Y′ = O (**a**) Z = H
2 Y = O, Y′ = S (**b**) Z = 4-NO_2
3 Y = S, Y′ = O (**c**) Z = 2,4-(NO_2)
4 Y = Y′ = S (**d**) Z = 2,4,6-(NO_2)$_3$

Received November 3, 1997.

This paper is dedicated to Professor Erwin Buncel in recognition of his contributions to Canadian chemistry.

H.J. Koh. Department of Science Education, Chonju National University of Education, Chonju, 560-757, Korea.
J.-W. Lee, H.W. Lee, and I. Lee.[1] Department of Chemistry, Inha University, Inchon, 402-751, Korea.

[1] Author to whom correspondence may be addressed. Telephone: (032) 860-7671. Fax: (032) 865-4855. E-mail: Ilee@dragon12.inha.ac.kr

© 1998 NRC Canada

Scheme 1.

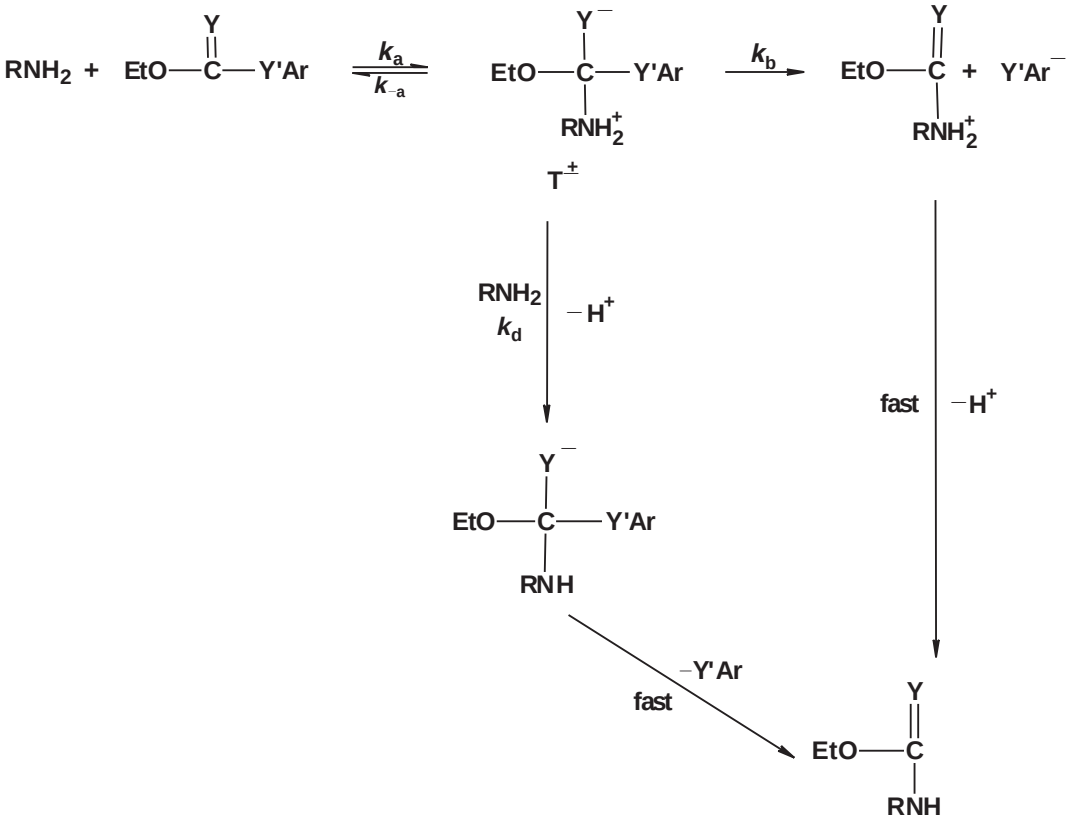

found, in general, to proceed by mechanisms similar to those for the thiono (**3**) series (4).

In this work, we carried out kinetic studies of the aminolysis of ethyl aryl carbonates, **1**, with benzylamines (BA, $XC_6H_4CH_2NH_2$) in acetonitrile at 25.0°C. We varied substituents X (X = *p*-CH_3O, *p*-CH_3, H, *p*-Cl, and *m*-Cl) in the nucleophile and Z (Z = *m*-NO_2, *p*-$COCH_3$, *p*-Cl + *m*-NO_2, *p*-CN, and *p*-NO_2) in the nucleofuge to probe the transition state (**TS**) structure through structure–reactivity correlation involving the cross-interaction constant, ρ_{XZ} in eqs. [1] (8). Our previous studies have shown that the sign and magnitude of ρ_{XZ} provide valuable mechanistic information (8).

$$[1a] \quad \log(k_{XZ}/k_{HH}) = \rho_X\sigma_X + \rho_Z\sigma_Z + \rho_{XZ}\sigma_X\sigma_Z$$

$$[1b] \quad \rho_{XZ} = \frac{\partial^2 \log k_{XZ}}{\partial \sigma_X \partial \sigma_Z} = \frac{\partial \rho_Z}{\partial \sigma_X} = \frac{\partial \rho_X}{\partial \sigma_Z}$$

In this work, we aim to test whether or not there is any mechanistic variation found in the aminolysis of thiono (**3**) and (or) thiol (**2**) derivatives, and to characterize the **TS** structure by determining the cross-interaction constant, ρ_{XZ}, and the secondary kinetic isotope effects (SKIEs) involving deuterated nucleophiles ($XC_6H_4CH_2ND_2$) (9).

Results and discussion

For all the carbonates investigated, solvolysis was not observed under the reaction conditions. The rates were measured with amine excesses, [BA] = 0.018–0.430 M and [Substrate] $\cong 1 \times 10^{-4}$ M, and pseudo-first-order rate constants (k_{obs}) were obtained at more than 10 amine concentrations, Figs. 1 and 2. The plots of k_{obs} versus amine concentration, [BA], were linear, eq. [2], for the reactions of substrate with a strong electron acceptor, Z = *p*-NO_2, and nucleophile with a strong electron donor, X = *p*-CH_3O and *p*-CH_3, Fig. 1.

$$[2] \quad k_{obs} = k_1[BA]$$

For all other reactions, the plots were curvilinear, which can be fitted to a second-order equation in benzylamine concentration, eq. [3] and Fig. 2.

$$[3] \quad k_{obs} = k_1[BA] + k_2[BA]^2$$

Because of this second-order term, accurate determinations of the rate constants, k_1 and k_2, required more than 10 k_{obs} data with varied amine concentrations. Plots of k_{obs}/[BA] versus [BA] gave k_1 and k_2 as the intercepts and slopes of the straight line. The k_1 and k_2 values obtained are summarized in Tables 1 and 2. The catalytic rate constants, k_2, are ca. 2 (X = *m*-Cl, Z = *p*-NO_2) to 170 (X = *m*-Cl, Z = *m*-NO_2) times greater than the corresponding uncatalyzed rate constants, k_1; this comparison is unjustified since k_1 and k_2 have different units, but we are making only numerical comparisons with other similar results reported. Similar trends are reported for the reactions of *p*-Cl-phenyl acetates with pyrrolidine (10) and for the reactions of phenyl phenoxyacetates with benzylamines (5*d*) in acetonitrile at 25.0°C. For the aminolysis of *p*-nitrophenyl acetates the k_2 term was absent, but both k_1 and k_2 terms were observed for chloro- and dichloroacetates in acetonitrile (11). This should be an indication that a strong acceptor aryl moiety (the Taft σ* values for CH_3, CH_2Cl, $CHCl_2$, $CH_2OC_6H_5$, and C_2H_5O are

© 1998 NRC Canada

Fig. 1. The plot of k_{obs} vs. concentration of *p*-methoxybenzylamine for the reaction of ethyl *p*-nitrobenzyl carbonate in MeCN at 25.0°C.

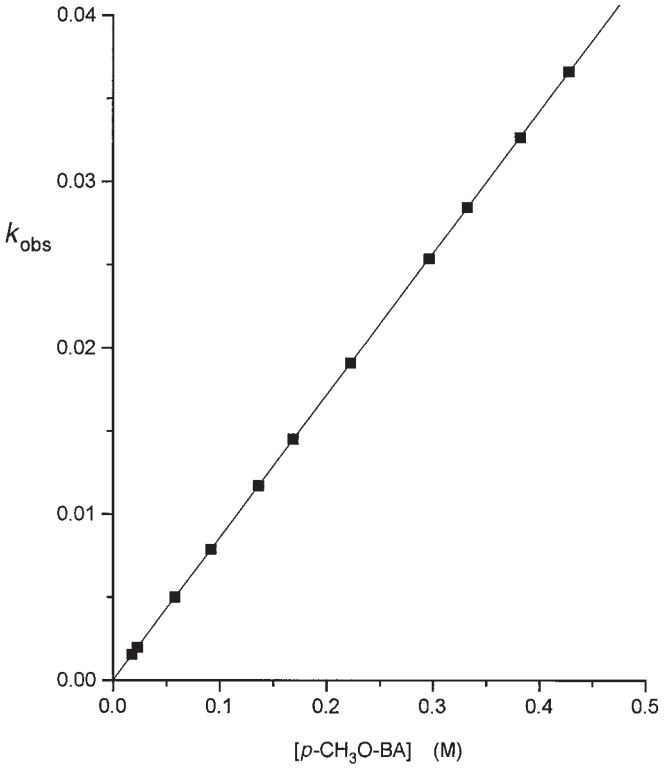

Fig. 2. The plot of k_{obs} vs. concentration of benzylamine for the reaction of ethyl *m*-nitrobenzyl carbonate in MeCN at 25.0°C

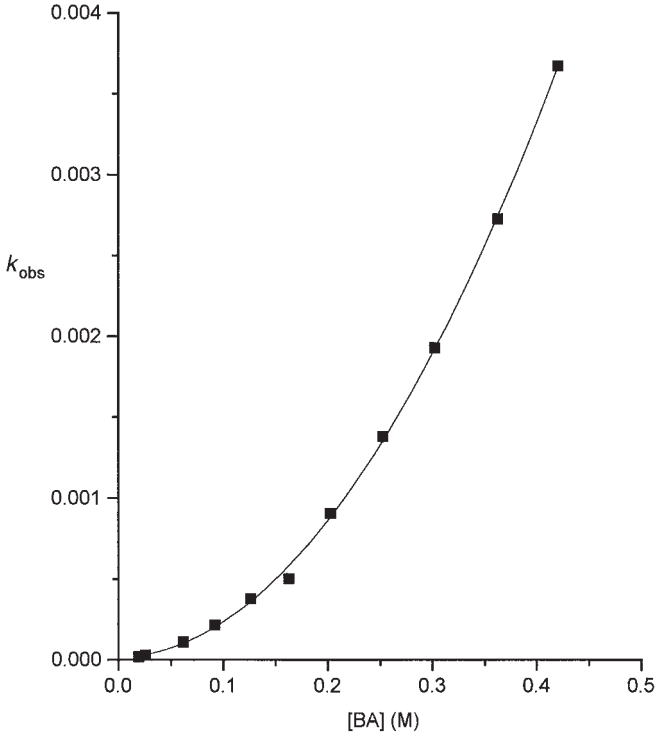

0.0, 1.05, 1.94, ca. 1.0, and 1.68, respectively) (5*d*, 12) requires general base catalysis, especially in aprotic solvents. Moreover, it has been well established that electron withdrawal from the acyl carbon favors amine expulsion relative to the negatively charged phenoxide expulsion from a tetrahedral intermediate, $\mathbf{T}^{\pm}$ (1*c*, 1*d*, 13). The results of the present work also show that the aminolysis of esters and carbonates can proceed without base catalysis even in aprotic solvents if the nucleophile and (or) nucleofuge are strong, i.e., for a strong donor X coupled with a strong acceptor Z. This is evident from the rate ratio (k_2/k_1) changes with the substituents X and Z. The k_2/k_1 ratio becomes smaller as the electron donor ability of X and acceptor power of Z increase: the k_2/k_1 values are 170, 32.4, 6.4, and 2.4 for X = *m*-Cl, Z = *m*-NO_2; X = *p*-Cl, Z = *p*-$COCH_3$; X = *p*-CH_3, Z = *p*-Cl + *m*-NO_2; and X = *p*-CH_3O, Z = *p*-CN, respectively, eventually reaching zero for X = *p*-CH_3O (and *p*-CH_3) with Z = *p*-NO_2. Thus when the aminolysis rate reaches a sufficiently large value by reacting a strong nucleophile with a strong nucleofuge, the base catalysis becomes redundant.

The Hammett ρ and Brönsted β values are listed in Tables 1 and 2. Examination of Table 1 reveals that magnitudes of ρ_X, ρ_Z, β_X, and β_Z values for the uncatalyzed path, k_1, are large and are much greater than the corresponding values for the catalyzed path (k_2). The large magnitudes of ρ_X (β_X) and ρ_Z (β_Z) are indicative of a stepwise mechanism with rate-limiting breakdown of a zwitterionic tetrahedral intermediate, $\mathbf{T}^{\pm}$ (1–5, 13). The importance of expulsion of the leaving group is reflected in the better Hammett correlations with σ_z^- than with σ_Z and in the large magnitude of ρ_Z, which suggests a strong negative charge development in the phenoxide leaving group.

For this mechanism, $k_1 = (k_a/k_{-a}) \times k_b = K \cdot k_b$. Such large ρ_z^- values reflect the importance of leaving group expulsion in the rate-determining step and are commonly found for the stepwise mechanism involving rate-limiting breakdown of $\mathbf{T}^{\pm}$. In acylation, when leaving group departure is kinetically important, substituent changes in leaving groups have a larger effect than do equivalent changes in the remaining group. Although β_X and β_Z values are also listed in Tables 1 and 2, they are less reliable since the pK_a values in water are used in the correlation instead of those in acetonitrile. However, the relative pK_a values ($\Delta pK_a = pK_{CH_3CN} - pK_{H_2O}$) remain constant for various conjugate acids of amines so that the solvent effect on β_X may be small (5*c*). The values of β_Z may be significantly smaller than those reported on the basis of aqueous acidities. We note that both ρ_X and ρ_Z are considerably greater in magnitude than the corresponding values for the reactions reported to proceed

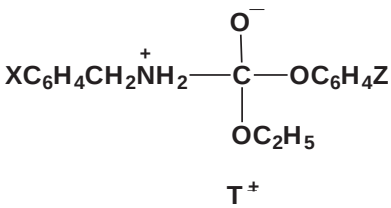

$\mathbf{T}^{\pm}$

by rate-limiting breakdown of $\mathbf{T}^{\pm}$ (2*c*, 3*b*, 4*c*, 4*d*). Another strong support for the proposed mechanism comes from a large positive cross-interaction constant ρ_{XZ} (= 1.35): both the positive sign and the large magnitude of ρ_{XZ} have been shown to be the necessary conditions for the rate-limiting breakdown of $\mathbf{T}^{\pm}$ (8, 9, 13). Since an electron acceptor in the nucleophile, $\delta\sigma_X > 0$ (in the nucleofuge, $\delta\sigma_Z > 0$), leads to an increase in ρ_Z, $\delta\rho_Z >$

© 1998 NRC Canada

Table 1. Second-order rate constants, k_1 ($\times 10^3$ dm^3 mol^{-1} s^{-1}), for the reactions of ethyl aryl carbonates with X-benzylamines in acetonitrile at 25.0°C.

	Z						
X	*m*-NO_2	*p*-OCH_3	*p*-Cl + *m*-NO_2	*p*-CN	*p*-NO_2	ρ_Z[c]	β_Z[d]
	1.10						
p-CH_3O	2.52[a]	3.89	7.41	13.8	85.7	3.40	–1.22
	5.77[b]						
p-CH_3	0.589	2.75	4.47	0.47	58.9	3.50	–1.58
H	0.17	0.813	1.58	2.24	24.5	3.81	–1.71
p-Cl	0.0575	0.275	0.525	0.933	11.8	4.12	–1.82
				0.477			
m-Cl	0.0295	0.138	0.269	1.02[a]	7.24	4.26	–1.90
				2.34[b]			
ρ_X[e]	–2.47	–2.33	–2.27	–2.26	–1.69	$\rho_{XZ} = 1.35$[g]	
β_X[f]	2.38	2.37	2.25	2.09	1.66		

[a] At 35.0°C.
[b] At 45.0°C.
[c] The σ-values were taken from ref. 21. Correlation coefficients were better than 0.997 in all cases.
[d] The pK_a (H_2O, 25.0°C) values were taken from ref. 22. Correlation coefficients were better than 0.974 in all cases. Z = *p*-$COCH_3$ and *p*-Cl and *m*-NO_2 were excluded.
[e] The σ values were taken from ref. 23. Correlation coefficients were better than 0.993 in all cases.
[f] The pK_a (H_2O, 25.0°C) values were taken from ref. 24. Correlation coefficients were better than 0.992 in all cases. X = *p*-CH_3O was excluded from the Brönsted plot for β_X (benzylamine) due to unreliable pK_a value listed.
[g] Correlation coefficient was better than 0.997.

Table 2. Third-order rate constants, k_2 ($\times 10^2$ dm^6 mol^{-2} s^{-1}), for the reactions of ethyl aryl carbonates with X-benzylamines in acetonitrile at 25.0°C.

	Z					
X	*m*-NO_2	*p*- $COCH_3$	*p*-Cl + *m*-NO_2	*p*-CN	*p*-NO_2	ρ_Z[c]
	2.14					
p-CH_3O	2.43[a]	2.75	3.16	3.38	—	0.70
	2.76[b]					
p-CH_3	1.91	2.51	2.88	3.16	—	0.77
H	1.22	1.50	1.66	1.76	7.93	0.56
p-Cl	0.708	0.891	1.02	1.13	3.61	0.69
				0.664		
m-Cl	0.501	0.575	0.631	0.757[a]	1.76	0.44
				0.863[b]		
ρ_X[d]	–1.02	–1.08	–1.11	–1.11	–1.73	$\rho_{XZ} = 0.16$[f]
β_X[e]	1.08	1.16	1.18	1.19	1.71	

[a] At 35.0°C.
[b] At 45.0°C.
[c] The σ^- values were taken from ref. 21. Correlation coefficients were better than 0.995 in all cases.
[d] The σ values were taken from ref. 23. Correlation coefficients were better than 0.944 in all cases.
[e] The pK_a (H_2O, 25.0°C) values were taken from ref. 24. Correlation coefficients were better than 0.990 in all cases. X = *p*-CH_3O was excluded from the Brönsted plot for β_X (benzylamine) due to unreliable pK_a value listed.
[f] Correlation coefficient was better than 0.971.

0 ($\delta\rho_X > 0$), ρ_{XZ} is positive, eq. [1*b*]. Since the rate increase is invariably accompanied by a decrease in the magnitude of ρ (ρ_X or ρ_z^-), the reactivity–selectivity principle (RSP) holds (14). Adherence to the RSP is considered another criterion for the stepwise mechanism with rate-limiting expulsion of the leaving group (phenoxides) (14).

For the third-order process, k_2, the RSP is violated and the ρ_X, ρ_z^-, and ρ_{XZ} values are considerably smaller in magnitude than the corresponding values for the uncatalyzed path (k_1). These can be accommodated with a rate-limiting deprotonation mechanism, $k_2 = (k_a/k_{-a})\cdot k_d[RNH_2]$ in Scheme 1. In this case, deprotonation of $\mathbf{T}^{\pm}$ leads to a decrease in the positive charge on the N atom (decrease in the magnitude of ρ_X) and also to a small increase in the negative charge on the O atom (small positive ρ_z^-) in the intermediate. Since the magnitudes of both ρ_X and ρ_z^- are reduced to much smaller values, the cross-interaction constant ρ_{XZ} also decreases to a smaller value than that for the uncatalyzed process, k_1.

Secondary kinetic isotope effects involving deuterated benzylamine nucleophiles are summarized in Tables 3 and 4. The k_H/k_D values in Table 3 are all greater than 1.0. This is consistent with the stepwise mechanism proposed (5*d*, 7*b*, 15), k_1 =

© 1998 NRC Canada

Table 3. Kinetic isotope effects on the second-order rate constants (k_1) for the reactions of ethyl aryl carbonates with deuterated X-benzylamines ($XC_6H_4CH_2ND_2$) in acetonitrile at 25.0°C.

X	Z	k_H($\times10^3$ dm^3 mol^{-1} s^{-1})	k_D($\times10^3$ dm^3 mol^{-1} s^{-1})	k_H/k_D
p-CH_3O	*m*-NO_2	1.10±0.03[a]	0.705±0.006	1.56±0.04[a]
p-CH_3O	*p*-$COCH_3$	3.89±0.04	1.82±0.03	1.59±0.03
p-CH_3O	*p*-CN	13.8±0.3	8.52±0.06	1.62±0.04
p-CH_3O	*p*-NO_2	85.7±0.6	50.7±0.3	1.69±0.02
m-Cl	*m*-NO_2	0.0295±0.0004	0.0178±0.0006	1.66±0.05
m-Cl	*p*-$COCH_3$	0.138±0.003	0.0812±0.0004	1.70±0.04
m-Cl	*p*-CN	0.447±0.006	0.254±0.003	1.76±0.03
m-Cl	*p*-NO_2	7.24±0.06	4.07±0.04	1.78±0.02

[a] Standard deviation.

Table 4. Kinetic isotope effects on the second-order rate constants (k_2) for the reactions of ethyl aryl carbonates with deuterated X-benzylamines ($XC_6H_4CH_2ND_2$) in acetonitrile at 25.0°C.

X	Z	k_H($\times10^2$ dm^6 mol^{-2} s^{-1})	k_D($\times10^2$ dm^6 mol^{-2} s^{-1})	k_H/k_D
p-CH_3O	*m*-NO_2	2.14±0.03[a]	1.02±0.02	2.10±0.04[a]
p-CH_3O	*p*-$COCH_3$	2.75±0.03	1.97±0.03	1.97±0.04
p-CH_3O	*p*-CN	3.38±0.05	1.90±0.02	1.90±0.04
m-Cl	*m*-NO_2	0.501±0.004	0.197±0.003	2.54±0.05
m-Cl	*p*-$COCH_3$	0.575±0.005	0.246±0.006	2.40±0.07
m-Cl	*p*-CN	0.664±0.004	0.284±0.003	2.34±0.02
m-Cl	*p*-NO_2	1.76±0.07	0.782±0.006	2.25±0.09

[a] Standard deviation.

Table 5. Activation parameters[a] for the reaction of ethyl aryl carbonates with X-benzylamines in acetonitrile at 25.0°C.

X	Z	Reaction path	$\Delta H^{\ddagger}$(kcal mol^{-1})	$-\Delta S^{\ddagger}$(cal mol^{-1} K^{-1})
p-CH_3O	*m*-NO_2	k_1	15.0±0.3	17±1
m-Cl	*p*-CN	k_1	14.4±0.7	21±2
p-CH_3O	*m*-NO_2	k_2	1.78±0.03	64.8±0.1
m-Cl	*p*-CN	k_2	1.85±0.04	66.9±0.1

[a] Calculated by the Eyring equation. Errors shown are standard deviations.

$(k_a/k_{-a})\cdot k_b = K\cdot k_b$. In this mechanism, the H-N-H moiety becomes sterically relieved in the rate-determining step of the leaving-group departure from $\mathbf{T}^{\pm}$. This will cause the decrease in the N–H vibration frequencies and the k_H/k_D values become greater than 1. In the equilibrium step, the effects of k_a and k_{-a} on the N–H vibrational frequencies approximately cancel out, leading to a k_H/k_D value of approximately 1.0 in the complex quantity of $k_1 = K\cdot k_b$ (5*d*, 7*b*, 15). We note, however, that the magnitude of the secondary kinetic isotope effects in Table 3 is somewhat larger with k_H/k_D = 1.6–1.8 than that found (k_H/k_D = 1.0–1.2) in most of the acyl transfer reactions (5*d*, 7*b*, 15) proceeding by a similar mechanism. We therefore suggest that there is weak deprotonation taking place through a four-center type **TS** (16), **5**. The cyclic proton transfer in **5** not only provides charge

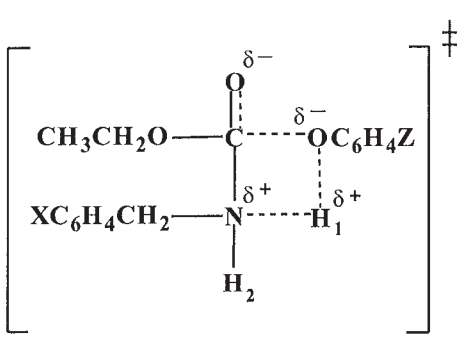

5

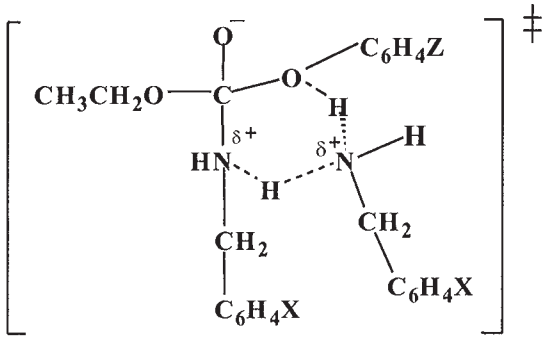

6

© 1998 NRC Canada

dispersion, but it also assists leaving-group departure (17). This assistance is particularly important in the second-order path, k_1, when the (aprotic) solvent cannot assist by hydrogen bonding (17).

For the catalyzed path, the k_H/k_D values are further increased to 2.0–2.5, reflecting correctly the partial bond cleavage of the N—H(D) bond in the rate-determining step, $k_d[RNH_2]$ in Scheme 1. Among several conceivable **TS** structures for the catalyzed path, the cyclic hydrogen bonded structure, **6**, is considered to be the most likely candidate. The larger k_H/k_D and smaller ρ_z^-, ρ_X, and ρ_{XZ} values for **6** than for **5** can be explained as follows. Two hydrogen bonds are involved so that k_H/k_D should increase, but positive charge on N and negative charge on O should be partially offset by partial deprotonation from N and partial protonation on O. The decrease in the two ρ values, ρ_X and ρ_z^-, should result in a substantial decrease in the intensity of interaction leading to a large decrease in the ρ_{XZ} values (18). The trends of change in the magnitude of k_H/k_D in Tables 3 and 4 are also in line with our proposed **TS** structures, **5** and **6**. In structure **5**, the greater the leaving ability ($\delta\sigma_Z > 0$) of the phenoxide, the greater will be the extent of deprotonation and consequently the larger is the k_H/k_D value (Table 3). However, in **6**, the stronger the electron acceptor in the phenoxide ($\delta\sigma_Z > 0$), the less will be the negative charge on O due to the greater delocalization, and hence the weaker is the hydrogen bond between O and the catalyst amine nitrogen. Thus the k_H/k_D value will decrease as the electron-withdrawing power of Z increases (Table 4). In both structures, an electron acceptor X ($\delta\sigma_X > 0$) should increase the acidity of a substituted benzylammonium cation, i.e., deprotonation becomes more facile, so that k_H/k_D increases.

The proposed mechanism is also supported by the activation parameters (Table 5) determined from rate data at three temperatures, 25.0, 35.0, and 45.0°C. The relatively low positive $\Delta H^{\ddagger}$ and large negative $\Delta S^{\ddagger}$ values are in accord with the stepwise mechanism proposed (11, 19). For the catalyzed path, the $\Delta H^{\ddagger}$ values are lower than those for the uncatalyzed path and the $\Delta S^{\ddagger}$ values are large and negative. This is consistent with a simple proton transfer process involved in **TS 6**, where there is a two-proton bridge that is highly structured but very little energy will be required for the deprotonation.

In summary, the aminolysis of ethyl aryl carbonates in acetonitrile proceeds by a stepwise mechanism with rate-limiting expulsion of the phenoxide leaving group from the zwitterionic tetrahedral intermediate, $\mathbf{T}^{\pm}$. Two reaction pathways, catalyzed and uncatalyzed paths, compete in most of the reactions; base catalysis is not required for the reactions involving strong nucleophiles (X = *p*-CH_3O, *p*-CH_3) with a strong nucleofuge (Z = *p*-NO_2). The proposed mechanism is based on (*i*) the large magnitude of ρ_X and especially of ρ_z^-, (*ii*) the relatively large normal kinetic isotope effects ($k_H/k_D > 1.0$) involving a deuterated benzylamine nucleophile, (*iii*) the greater k_H/k_D values for the catalyzed path, and (*iv*) the low $\Delta H^{\ddagger}$ and $\Delta S^{\ddagger}$ values for both pathways, but with lower values for the base-catalyzed path than for the uncatalyzed reaction.

Experimental

Materials

Merck GR acetonitrile was used after three distillations. The benzylamine nucleophiles, Aldrich GR, were used without further purification. Preparation of deuterated benzylamines was as described previously (5). The analysis (NMR and GC mass spectroscopy) of the deuterated benzylamines showed more than 99% deuterium content, so that no corrections to kinetic isotope effects for incomplete deuteration were made. Ethyl aryl carbonates were prepared by reacting phenols with ethyl chloroformates. The substrates synthesized were confirmed by IR, NMR, and mass spectral analyses as follows.

*$CH_3CH_2OC(O)OC_6H_4$–*p*-CN:* mp 40–42°C. ν_{max}: 3100 (C-H), 3000 (C-H, aromatic), 2250 (C≡N), 1760 (C═O). $\delta_H(CDCl_3)$: 7.2–7.7 (C_6H_4, 4H, m), 4.3 (CH_2, 2H, q), 1.3 (CH_3, 3H, t). m/z = 119 (M^+).

*$CH_3CH_2OC(O)OC_6H_4$–*p*-$COCH_3$:* mp 44–45°C. ν_{max}: 3100 (C-H), 3000 (C-H, aromatic), 1750 (C═O), 1680 ($COCH_3$). $\delta_H(CDCl_3)$: 7.2–8.0 (C_6H_4, 4H, m), 4.3 (CH_2, 2H, q), 2.6 ($COCH_3$, 3H, s), 1.3 (CH_3, 3H, t). m/z = 208 (M^+).

*$CH_3CH_2OC(O)OC_6H_4$–*m*-NO_2:* mp 50–52°C. ν_{max}: 3100 (C-H), 3000 (C-H, aromatic), 1750 (C═O), 1680 ($COCH_3$). $\delta_H(CDCl_3)$: 7.3–8.1 (C_6H_4, 4H, m), 4.3 (CH_2, 2H, q), 1.2 (CH_3, 3H, t). m/z = 208(M^+).

$CH_3CH_2OC(O)OC_6H_3$–(p-Cl, m-NO_2):* liquid. ν_{max}: 3100 (C-H), 3000 (C-H, aromatic), 1760 (C═O). $\delta_H(CDCl_3)$: 7.2–7.7 (C_6H_3, 3H, m), 4.2–4.4 (CH_2, 2H, q), 1.3 (CH_3, 3H, t). m/z = 245 (M^+).

*$CH_3CH_2OC(O)OC_6H_4$–*p*-NO_2:* mp 60–61°C. ν_{max}: 3100 (C-H), 3000 (C-H, aromatic), 1750 (C═O). $\delta_H(CDCl_3)$: 7.3–8.3 (C_6H_4, 4H, m), 4.2 (CH_2, 2H, q), 1.2 (CH_3, 3H, t). m/z = 211 (M^+).

Kinetic procedures

Rates were measured conductimetrically in acetonitrile. The conductivity bridge used in this work was a homemade computer-automatic A/D converter conductivity bridge. Pseudo-first-order rate constants, k_{obs}, were determined by the Guggenheim (20) method with a large excess of benzylamine. The k_1 and k_2 values were reproducible to ± 5%.

Product analysis

Ethyl *p*-nitrobenzyl carbonate was reacted with excess benzylamine with stirring for more than 15 half-lives at 25.0°C in acetonitrile, and the products were isolated by evaporating the solvent under reduced pressure. The product mixture was treated with column chromatography (silica gel, 20% ethyl acetate – n-hexane). Analysis of the product gave the following results.

$CH_3CH_2OC(O)NHCH_2C_6H_5$: Liquid. ν_{max}: 3300 (N-H), 3000 (C-H, aromatic), 1700 (C═O). $\delta_H(CDCl_3)$: 7.2–7.5 (C_6H_5, 5H, m), 5.2 (NH, 1H, s), 4.2 (CH_2, 2H, q), 4.4 (CH_2, 2H, s), 1.2 CH_3, 3H, t). m/z = 227 (M^+).

Acknowledgements

We thank the Korea Science and Engineering Foundation, Inha University, and Chonju National University of Education for support of this work.

© 1998 NRC Canada

References

1. (*a*) E.A. Castro and F.J. Gil. J. Am. Chem. Soc. **99**, 7611 (1977); (*b*) E.A. Castro and M. Freudenberg. J. Org. Chem. **45**, 906 (1980); (*c*) P. Bond and R.B. Moodie. J. Chem. Soc. Perkin Trans. 2, 679 (1976); (*d*) M.J. Gresser and W.P. Jencks. J. Am. Chem. Soc. **99**, 6970 (1977); (*e*) J. Am. Chem. Soc. **99**, 6963 (1977).
2. (*a*) E.A. Castro, F. Ibanez, M. Salas, and J.G. Santos. J. Org. Chem. **56**, 4819 (1991); (*b*) E.A. Castro, M. Salas, and J.G. Santos. J. Org. Chem. **59**, 30 (1994); (*c*) E.A. Castro, M.I. Pizarro, and J.G. Santos. J. Org. Chem. **61**, 5982 (1996).
3. (*a*) E.A. Castro, M. Cubillos,and J.G. Santos. J. Org. Chem. **61**, 3501 (1996); (*b*) E.A. Castro, M. Cubillos, J.G. Santos, and J. Tellez. J. Org. Chem. **62**, 2512 (1997).
4. (*a*) M. Cabrera, E.A. Castro, M. Salas, J.G. Santos, and P. Sepulveda. J. Org. Chem. **56**, 5324 (1991); (*b*) E.A. Castro, F. Ibanez, M. Salas, J.G. Santos, and P. Sepulveda. J. Org. Chem. **58**, 5400 (1993); (*c*) J. Org. Chem. **58**, 459 (1993); (*d*) E.A. Castro, C.A. Araneda, and J.G. Santos. J. Org. Chem. **62**, 126 (1997).
5. (*a*) H.K. Oh, C.H. Shin, and I. Lee. J. Chem. Soc. Perkin Trans. 2, 1169 (1995); (*b*) J. Korean Chem. Soc. **16**, 657 (1995); (*c*) H.K. Oh, S.Y. Woo, C.H. Oh, Y.S. Park, and I. Lee. J. Org. Chem. **62**, 5780 (1997); (*d*) H.J. Koh, T.H. Kim, B.S. Lee, and I. Lee. J. Chem. Res. (S), 482 (1996); J. Chem. Res. (M), 2741 (1996); (*e*) H.J. Koh, J.W. Lee, H.W. Lee, and I. Lee. New J. Chem. **21**, 447 (1997).
6. (*a*) E.A. Castro, F. Ibanez, J.G. Santos, and C. Ureta. J. Org. Chem. **58**, 4908 (1993); (*b*) E.A. Castro and C. Ureta. J. Org. Chem. **54**, 2153 (1989).
7. (*a*) P. Campbell and B.A. Lapinskas. J. Am. Chem. Soc. **99**, 5373 (1977); (*b*) I. Lee and H.J. Koh. New J. Chem. **20**, 131 (1996).
8. (*a*) I. Lee. Chem. Soc. Rev. **19**, 317 (1990); (*b*) Adv. Phys. Org. Chem. **27**, 57 (1992).
9. I. Lee. Chem. Soc. Rev. **24**, 223 (1995)
10. F.M. Menger and J.J. Smith. J. Am. Chem. Soc. **94**, 3824 (1972).
11. H. Neuvonen. J. Chem. Soc. Perkin Trans. 2, 951 (1995).
12. J.A. Dean. Handbook of organic chemistry. McGraw–Hill, New York. 1987. Table 7.
13. (*a*) D. Lee, C.K. Kim, B.S. Lee, and I. Lee. Bull. Korean Chem. Soc. **16**, 1203 (1995); (*b*) I. Lee. Bull. Korean Chem. Soc. **15,** 985 (1994).
14. (*a*) A. Pross. Adv. Phys. Org. Chem. **14**, 69 (1997); (*b*) O. Exner. J. Chem. Soc. Perkin Trans. 2, 973 (1993); (*c*) I. Lee, B.S. Lee, H.J. Koh, and B.D. Chang. Bull. Korean Chem. Soc. **16**, 277 (1995).
15. H.J. Koh, H.C. Lee, H.W. Lee, and I. Lee. Bull. Korean Chem. Soc. **16**, 839 (1995); (*b*) H.J. Koh, S.I. Kim, B.C. Lee, and I. Lee. J. Chem. Soc. Perkin Trans. 2, 1353 (1996); (*c*) Y.H. Kim, C. Huh, B.S. Lee, and I. Lee. J. Chem. Soc. Perkin Trans. 2, 2257 (1995); (*d*) H.K. Oh, C.H. Shin, and I. Lee. J. Chem. Soc. Perkin Trans. 2, 2411 (1993).
16. (*a*) I. Lee, H.Y. Kim, H.K. Kang, and H.W. Lee. J. Org. Chem. **53**, 2678 (1988); (*b*) I. Lee, H.J. Koh, and H.W. Lee. J. Chem. Res. (S), 282 (1990).
17. M. Jedrzejczak, R.E. Motie, D.P.N. Satchell, R.S. Satchell, and W.N. Wassef. J. Chem. Soc. Perkin Trans. *2,* 1471 (1994).
18. I. Lee. J. Phys. Org. Chem. **5**, 736 (1992).
19. (*a*) E.A. Castro and M. Freudenberg. J. Org. Chem. **45**, 906 (1980); (*b*) E.A. Castro and C.L. Santander. J. Org. Chem. **50**, 3595 (1985).
20. E.A. Guggenheim. Philos. Mag. **2**, 538 (1926).
21. H.H. Jaffe. Chem. Rev. **53**, 191 (1953).
22. A. Albert and E.P. Serjeant. The determination of ionization constants. 3rd ed. Chapman and Hall, London. 1984. p. 45.
23. D.H. McDaniel and H.C. Brown. J. Org. Chem. **23**, 420 (1958).
24. A. Fischer, W.J. Galloway, and J. Vaughan. J. Chem. Soc. 3588 (1964).

© 1998 NRC Canada

Skeletal vibrational circular dichroism of a series of bicyclic dilactones: the fingerprint region?

A. Rauk, J.L. McCann, H. Wieser, P. Bour, Yu.I. El'natanov, and R.G. Kostyanovsky

Abstract: The vibrational circular dichroism (VCD) spectra of 2,5-dioxabicyclo[2.2.1]heptane-3,6-dione **1** (R = H) and the 1,4-dialkyl derivatives, **1** (R = Me) and **1** (R = *t*-Bu), were calculated by the ab initio magnetic field perturbation (MFP) procedure with a B3LYP/6–31G* force field, and the VCD spectra of the dimethyl and di-*t*-butyl derivatives were measured in the region 800–1500 cm^{-1}. While the absolute configurations of **1** (R = Me) and **1** (R = *t*-Bu) could be assigned unambiguously by comparison of the experimental and predicted spectra, there is little obvious correspondence between the spectra of the series of compounds. The VCD spectra are analysed on the basis of operation of a coupled oscillator mechanism involving motions of the polar bonds. In the case of the parent dihydro system, bridgehead C—H bond motions appear to dominate contributions to the VCD of vibrational transitions into which they are mixed.

Key words: vibrational circular dichroism (VCD), 2,5-dioxabicyclo[2.2.1]heptane-3,6-dione, dilactones, optical activity.

Résumé : On a calculé les spectres de dichroïsme circulaire vibrationnel (DCV) de la 2,5-dioxabicyclo[2.2.1]heptane-3,6-dione **1** (R = H) et de ses dérivés 1,4-dialkyles **1** (R = Me ou R = *t*-Bu) grâce à la méthode ab initio de la perturbation du champ magnétique (PCM), en utilisant un champ de force B3LYP/6–31G*; on a aussi mesuré les spectres de DCV des dérivés diméthyle et di-*t*-butyle dans la région allant de 800 à 1500 cm^{-1}. Même si on a pu attribuer les configurations des composés **1** (R = Me) et **1** (R = *t*-Bu) en comparant les spectres expérimentaux à ceux qui avaient été prédits, il n'y a pas de correspondance évidente entre les spectres des séries de composés. On a analysé les spectres de DCV en se basant sur l'opération du mécanisme de l'oscillateur couplé impliquant des mouvements des liaisons polaires. Dans le cas du système dihydro parent, les mouvements de la liaison C–H en tête de pont semblent donner les contributions dominantes aux transitions de vibration du spectre de DCV dans lesquels ils sont mélangés.

Mots clés : dichroïsme circulaire vibrationnel (DCV), 2,5-dioxabicyclo[2.2.1]heptane-3,6-diones, dilactones, activité optique.

[Traduit par la rédaction]

Introduction

As a technique for studying the three-dimensional structures of molecules in solution, particularly in connection with handedness, vibrational circular dichroism (VCD) spectroscopy has matured over the last two decades (1–3). When coupled with ab initio theoretical calculations, it may be used to assign the absolute configuration of small molecules with complete confidence (4, 5). Solution conformation (6) and state of aggregation (7) may also be amenable to analysis by VCD spectroscopy. However, unlike its counterpart, electronic circular dichroism (ECD) spectroscopy, no simple rules of thumb analogous to sector rules like the octant rule in ECD have yet emerged. We examine here the VCD spectra of three structurally related rigid, C_2 symmetric bicyclo[2.2.1]heptane derivatives, **1** (R = H), **1** (R = Me), and **1** (R-*t*-Bu), and compare the theoretically derived spectra with the experimental VCD spectra of two of them. While obvious parallels are not expected in the IR spectra of the three dialkyl derivatives because of congestion in the mid-IR region, it is not immediately apparent that the inherent chirality of the identical rigid skeletons should not be evident in the VCD spectra. The C_2 symmetry permits separation of the vibrational modes into two groups of *A* and *B* symmetry, and the application of the simple coupled oscillator model to the set of molecules.

Received October 15, 1997.

A. Rauk,[1] J.L. McCann, and H. Wieser. Department of Chemistry, University of Calgary, Calgary, AB T2N 1N4, Canada.
P. Bour. Institute of Organic Chemistry and Biochemistry, Academy of Sciences of the Czech Republic, Flemingovo No. 2, 16610 Praha, Czech Republic.
I.V. Vystorop. Institute of Chemical Physics in Chernogolovka, Russian Academy of Sciences, 142432 Chernogolovka, Moscow Region, Russia.
Yu.I. El'natanov and R.G. Kostyanovsky. N.N. Semenov Institute of Chemical Physics, Russian Academy of Sciences, 4 u1. Kosygina, 117977 Moscow, Russia.

[1] Author to whom correspondence may be addressed. Telephone: (403) 220–5341. Fax: (403) 289–9488. E-mail: rauk@chem.ucalgary.ca

Methods

Theoretical

The structures of compounds **1** (R = H), **1** (R = Me), and **1** (R = *t*-Bu) were optimized at the B3LYP/6–31G* level using

© 1998 NRC Canada

Fig. 1. The experimental and calculated VCD and absorption spectra of (1*R*,4*R*)-**1** (R = Me) in the 800–1600 cm^{-1} spectral region.

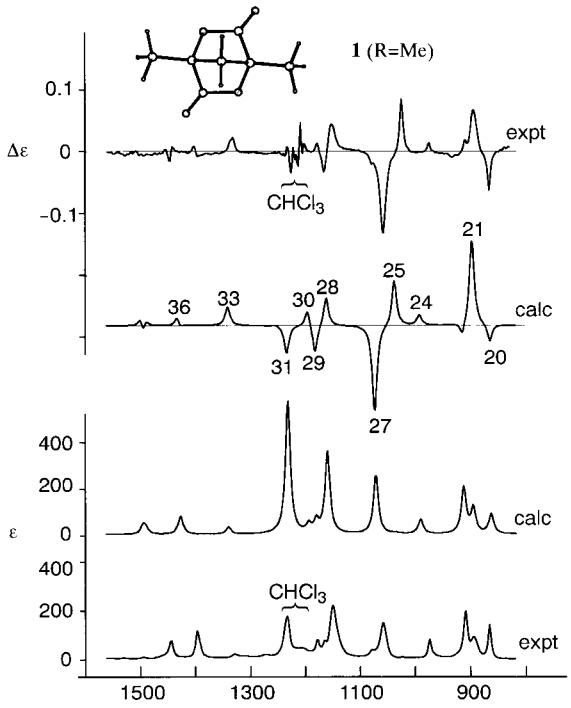

procedures implemented in the Gaussian 92 and 94 program packages (8). Harmonic vibrational analysis at the same level was used to determine the quantum mechanical force field. The VCD spectra were calculated using the MFP procedure (9), as implemented in CADPAC (10). The VCD calculation incorporated B3LYP/6–31G* atomic polar tensors and force field (11) and HF/6–31G atomic axial tensors (12–14).[2] For the purpose of the theoretical simulations, the calculated frequencies have been scaled by 0.98, and a constant line width at half height of 10 cm^{-1} has been adopted.

Experimental

The synthesis and resolution of **1** (R = Me)[3] and **1** (R = *t*-Bu) (15) has been described previously. Both enantiomers were obtained: (+)-**1** (R = Me), $[\alpha]_D^{20} = 130$ (*c* 0.3, $CHCl_3$); (–)-**1** (R = Me), $[\alpha]_D^{20} = -131$ (*c* 0.3, $CHCl_3$); (+)-**1** (R = *t*-Bu), $[\alpha]_D^{20} = 86.3$ (*c* 0.93, $CHCl_3$), (+)-CE ($n - \pi^*$) in CD spectrum (λ_{max} 232.5 nm, $\Delta\varepsilon$ + 5.791 (EtOH)); (–)-**1** (R = *t*-Bu), $[\alpha]_D^{20} = -84.5$ (*c* 1.01, $CHCl_3$), (–)-CE ($n - \pi^*$) in CD spectrum (λ_{max} 232.5 nm, $\Delta\varepsilon$ –5.603 (EtOH)). The absolute configuration of **1** (R = *t*-Bu) was assigned previously as (–)-(1*S*,4*S*)-**1** (R = *t*-Bu) on the basis of X-ray diffraction analysis of a diastereomeric intermediate (15).

The VCD spectra were obtained with a Bomem MB100 interferometer described in detail elsewhere (16). The VCD components included a KRS-5 polarizer (Cambridge Physical Sciences), a ZnSe photoelastic modulator operating at 37 kHz (Hinds Instruments), an f/1 ZnSe focussing lens (Infrared Optics), an MCT-A detector, the appropriate electronic filters, and an Ithaca Dynamic 391A Lock-in amplifier. The sample of **1** (R = Me) was contained in a 0.162 M solution in $CHCl_3$ in a 0.15 mm NaCl cell. In total, 5000 ac scans were collected at 4 cm^{-1} in one single block and ratioed against 500 dc scans. The total data accumulation time was about 2 h per spectrum. The raw VCD spectrum was corrected for artefacts by subtracting the VCD spectrum of the enantiomer, and then calibrated in the usual fashion (17). The sample of **1** (R = *t*-Bu), 0.0832 M in $CHCl_3$ was measured under the same conditions. Neither substance was soluble in CCl_4, our preferred solvent. Experimental IR and VCD spectra were analyzed using the Labcalc software (18).

Results and discussion

The measured IR and VCD spectra of (1*R*, 4*R*)-**1** (R = Me) and (1*S*, 4*S*)-**1** (R = *t*-Bu) in the 800–1600 cm^{-1} spectral region are shown in Figs. 1 and 2, respectively, where they are compared with the calculated spectra. Note that the two compounds are homochiral. The experimental data are listed in Tables 1 and 2, respectively, as are the calculated spectra (frequencies scaled by 0.98). Comparison of the theoretical simulations and the measured spectra for both compounds (Figs. 1 and 2) reveals an excellent correspondence. We discuss the assignments in the spectral region below 1500 cm^{-1} of each of the compounds separately.

(1*R*, 4*R*)-1 (R = Me)

The four asymmetric methyl deformation modes and the CH_2 scissoring mode appear as a single unresolved absorption at 1444 cm^{-1}, the latter contributing about 30% to the total absorption. The VCD spectrum in this region is very weak, consisting of a +, –, + pattern that is well-reproduced theoretically (Fig. 1 and Table 1). The remaining two methyl deformation modes, corresponding to umbrella motions, are also not resolved, at 1396 cm^{-1}. The in- and out-of-phase motions are predicted to be separated by only 4 cm^{-1}. The weak +, – pattern of the VCD signal observed experimentally is also reproduced computationally and is explained as due to the *A* symmetry mode (mode 36) with positive VCD, partly cancelled by a weaker negative VCD of the *B* symmetry mode.

Weak absorptions at 1328 and 1271 cm^{-1} originate from C–C stretching modes mixed with methylene twists and wags. An in-phase stretching motion of the bridgehead C—C bonds to the methyls and methylene (mode 33) gives rise to the moderately strong positive VCD signal at 1331 cm^{-1}. The 1271 cm^{-1} absorption is predicted to have only a very weak positive VCD signal. None is apparent in the experimental spectrum. The intensity of the strong absorption at 1233 cm^{-1} (mode 31) is overestimated somewhat by the calculations. It is predicted to arise from an antisymmetric ring deformation composed of C–O bond stretches and to have an intense negative VCD associated with it. Unfortunately, this region of the

[2] The necessity to use HF atomic axial tensors for calculations on large molecules has been circumvented. The use of correlated methods to derive the molecular force field and atomic polar tensors is essential for accurate VCD results, while extension of correlated methods to atomic axial tensors is desirable but less critical (12). Procedures have recently been developed for consistent VCD calculations at CASSCF (13) and B3LYP (14) levels with GIAO (gauge independent atomic orbitals) on molecules of the current size. The use of the GIAO basis removes origin dependence of the rotatory strengths and reduces basis-set dependence of the results.

[3] Dimethyl prep and optical activity. In preparation.

© 1998 NRC Canada

Table 1. Experimental spectra of dimethyl dilactone (–)-**1** (R = Me) and theoretical spectra of (1*R*,4*R*)-**1** (R = Me).

Expt.[a]				Calc.[a,b]					
Freq.	*D*	Freq.	*R*	Mode	Sym.	Freq.[c]	*D*	*R*	Assignment[d]
1808	vs			43	*A*	1873	300.0	+244	C═O sym str
				42	*B*	1862	1141.5	–266	C═O asym str
		1452	w+	41	*A*	1489	2.6	+15	CH_3 def
				40	*B*	1487	25.0	–8	CH_3 def
1444	67.4	1446	–9	39	*A*	1483	19.4	–9	CH_2 scissor
				38	*A*	1480	9.2	–5	CH_3 def
		1441	w+	37	*B*	1479	2.3	+11	CH_3 def
		1401	w+	36	*A*	1422	9.6	+11	CH_3 umb
1396	m	1395	w–	35	*B*	1418	71.3	–5	CH_3 umb
1328	16.3	1331	+22	34	*B*	1332	29.8	+1	CH_2 wag, C–C str
				33	*A*	1331	2.5	+20	C–C str
1271	21.4			32	*A*	1245	2.8	+2	CH_2 twist, C–C str
1233	237.6	[e]		31	*B*	1225	664.4	–36	ring def
1177	61.9	1177	+10	30	*B*	1187	41.9	+22	CH_2 wag
1164	10.1	1165	–29	29	*A*	1173	60.8	–39	ring def, CH_3 rock
1149	419.7	1151	–62	28	*B*	1153	435.7	+38	CH_2 wag
1078	47.2	1078	–38	26	*A*	1064	0.5	–9	CH_2 twist
1058	206.0	1057	–209	27	*B*	1065	341.1	–119	ring def, CH_3 rock
1024	3.6	1024	+82	25	*A*	1030	6.6	+68	ring def, CH_2 twist
974	78.7	974	+12	24	*B*	985	90.0	+16	CH_3 rock
909	254.4	909	+23	23	*B*	907.8	290.3	–28	CH_3 rock
				22	*A*	907.4	17.2	+5	CH_3 rock
895	134.7	894	+135	21	*A*	891	171.1	+149	C–O str, CH_3 rock
866	125.8	866	–67	20	*B*	859	139.9	–31	CH_3 rock

[a] Freq., cm^{-1}; *D*, $esu^2\ cm^2 \times 10^{40}$; *R*, $esu^2\ cm^2 \times 10^{44}$.
[b] MFP: structure, force field, and atomic polar tensors by B3LYP/6–31G*; atomic axial tensors by RHF/6–31G*.
[c] Scaled by 0.98.
[d] sym, symmetric; asym, asymmetric; str, stretch; def, deformation; umb, umbrella.
[e] Obscured by solvent.

VCD spectrum is obscured by solvent absorption. The absorption spectrum has a shoulder at 1207 cm^{-1}, which is attributed to solvent, as no IR band is predicted for this region.

The moderate absorption associated with a weak positive VCD signal at 1177 cm^{-1} (mode 30) is assigned as a wagging motion of the methylene group.

The pattern of the VCD absorptions at 1165 cm^{-1} (mode 29) and 1151 cm^{-1} (mode 28) is that of a highly conservative couplet indicative of a coupled oscillator mechanism (see below). The computed normal modes are complex mixtures of predominantly ring deformation (═C–C and C–O stretches) mixed with CH_2 wagging (*B* symmetry) or methyl rocking (*A* symmetry). The weak shoulder in the absorption spectrum, which appears to be associated with a weak negative VCD, is tentatively assigned as due to a twisting motion of the methylene group. This poorly defined mode is strongly mixed with other modes of *A* symmetry and is calculated to be virtually degenerate with a *B* symmetry ring deformation mode (mode 27). The latter is observed and calculated to have the strongest negative VCD amplitude in the 800–1600 cm^{-1} region. From the appearance of the experimental spectrum, one may infer that it (at 1058 cm^{-1}) is also a part of the bisignate pattern of a coupled pair of oscillators, the other component (mode 25) being the positive VCD absorption at 1024 cm^{-1}. The two modes are of *B* and *A* symmetry, respectively, and can be broadly described as ring deformations. However, the coupling (if it can be described as such) is of the nondegenerate kind, since the 1058 cm^{-1} mode largely involves stretching of the carbon bridgehead C—O bonds, while the 1024 cm^{-1} band is mostly a deformation of the six-membered ring, with carbonyl C–O stretching and C–O–C bending components.

Three of the remaining modes shown in Fig. 1, at 974 cm^{-1} (mode 24), 909 cm^{-1} (mode 23), and 866 cm^{-1} (mode 20), are due to the four methyl rocking modes, two of which are predicted to be within 0.4 cm^{-1} of each other. The fourth band, attributed to another combination (mode 21) involving the methyl rocking and bridgehead C–O stretching gives rise to the large positive VCD signal observed at 894 cm^{-1}. The positive VCD signal observed at 909 cm^{-1} is incorrectly predicted to be negative, while the strength of the negative circular dichroism at 866 cm^{-1} is underestimated. The mistake at 909 cm^{-1} is the only apparent error in sign in the entire mid-IR region.

(1*S*, 4*S*)-1 (R = *t*-Bu)

Although visually not more complex than that of the homochiral dimethyl dilactone, the vibrational spectra of the di-*tert*-butyl dilactone, shown in Fig. 2, are the resultant of many more normal modes, as is apparent from the assignments in Table 2. The calculations indicate that the 12 methyl deformation modes occur in four distinct groups, which correspond to the three unresolved absorption bands at 1485, 1466, and

© 1998 NRC Canada

Fig. 2. The experimental and calculated VCD and absorption spectra of (1*S*,4*S*)-**1** (R = *t*-Bu) in the 800–1600 cm^{-1} spectral region.

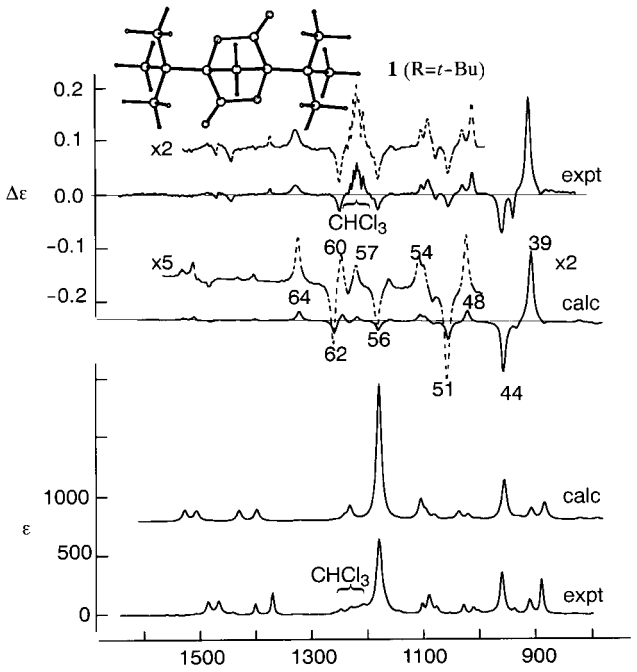

1441 cm^{-1}, the last of which also includes the CH_2 scissor mode. The first two groups are predicted to have moderate absorption intensity but negligible VCD. Experimentally, a weak negative VCD band is observed at 1469 cm^{-1} for the second group. The third and fourth groups are predicted to be negligibly weak in both absorption and circular dichroism. The weak signals observed at 1441 cm^{-1} are predicted to arise from the CH_2 scissor mode, which occurs at the same place. The six umbrella modes of the methyl groups also are predicted to separate into two groups, observed at 1401 and 1370 cm^{-1}. No VCD signal is predicted nor observed for the first of these. The second group is predicted and observed to have a net positive VCD band.

The 14 modes predicted for the middle portion of the IR and VCD spectra (1322–1054 cm^{-1}) are complex mixtures of ring deformations, deformations of the heavy atom skeleton of the *tert*-butyl groups, and wags and twists of the methylene group. They are predicted to occur in 12 groups. Ten absorptions are apparent in the IR spectrum and eight bands can be distinguished in the VCD spectrum. The solvent absorption obscures the range 1150–1230 cm^{-1}. The conspicuous positive VCD feature at 1322 cm^{-1} is assigned to a mixed CH_2 wag, C–C stretching combination of *B* symmetry (mode 64). On either side of the solvent-obscured region are two pronounced negative VCD features, at 1249 and 1180 cm^{-1}. The former must be assigned to another combination (mode 62) of the same two CH_2 wag, C–C stretching motions. This is the only mode predicted to have appreciable negative VCD intensity. It is calculated after scaling to be 11 cm^{-1} higher than observed. Under the solvent band are predicted to occur several of the asymmetric C–C stretching combinations of the *tert*-butyl groups (identified as "*t*-Bu def" in Table 2). The moderately intense negative VCD band at 1180 cm^{-1} is associated with the most intense IR absorption in this region and is assigned to a mixed mode of *B* symmetry (mode 56) comprised of some CH_2 wag and a deformation of the six-membered ring involving changes to C—C and C—O bonds terminating at the carbonyl group. This may alternatively be described as in-plane wagging of the C═O bond although in mass-weighted coordinates it is the carbon atom that does most of the moving.

The +, +, – VCD pattern of the bands at 1103, 1090, and 1077 cm^{-1} is nicely reproduced by the calculations, as is the pronounced negative band at 1054 cm^{-1} (assigned to mode 51) for which the absorption can barely be distinguished. All of these originate from various deformations of the bicyclic skeleton.

Nine of the 12 methyl rocking modes are fairly isolated from the bicyclic skeletal modes, and are assigned to the absorption bands observed in the range 940 –1029 cm^{-1}. The exception is the band at 961 cm^{-1}, which has a heavy admixture of, and derives its intensity from, a deformation mode (mode 44) of *B* symmetry of the six-membered ring involving stretching of the bridgehead C—O bonds. The negative VCD feature associated with this absorption is preceded on the high-frequency side by two weaker positive VCD bands, at 1028 cm^{-1} and 1012 cm^{-1}. A methyl rocking combination admixed with the CH_2 wag is predicted to have moderate intensity and is assigned to the 1028 cm^{-1} absorption feature, but its rotatory strength is calculated (two lines predicted) to be very small. The 1012 cm^{-1} feature is readily assigned on the basis of both the absorbance and VCD intensities, as is the weak band at 940 cm^{-1}. In this case, the negative VCD sign is correctly predicted but the intensity is underestimated.

The most intense VCD feature, at 912 cm^{-1} in this region of the spectrum is assigned to a ring deformation of *A* symmetry involving asymmetric stretching of the two C—O bonds to each of the ether oxygen atoms (mode 39). The *B* symmetry combination of the same asymmetric stretch, at 891 cm^{-1}, is correctly predicted to have even greater intensity in absorbance but negligible VCD strength.

Coupled oscillators?

The presence of the C_2 axis of symmetry and of the strongly polar components of the lactone group suggest that an exciton coupling mechanism may provide a simple assignment of absolute configuration and an explanation of features of the VCD spectrum. Electrostatic coupling of the electric dipole transition moments of two chromophores separated in space and chirally oriented relative to each other will give rise to predictable Cotton effects (CEs). If the orientation of the two dipoles has negative handedness ((*M*)-chirality), then the out-of-phase (*B* symmetry) coupling will have a negative CE. The in-phase (*A* symmetry) coupling will have positive rotatory strength. Exactly the reverse is true for a positive-handed ((*P*)-chirality) disposition of the dipoles. If the mechanism of coupling is purely dipole–dipole coupling, then the electrostatic interactions dictate that the out-of-phase combination of the oscillators (*B* symmetry) is lower in energy than the in-phase (*A* symmetry) combination. As a consequence, the pattern of signs, positive–negative or negative–positive, is intrinsically related to the handedness of the spatial arrangement of the chromophoric groups (19). Thus a negative handedness to the orientation of the chromophores ((*M*)-chirality) will be

© 1998 NRC Canada

Table 2. Experimental and theoretical spectra of the di-*tert*-butyl dilactone (–)-(1*S*,4*S*)-**1** (R = *t*-Bu).

Expt.[a]				Calc.[a,b]					
Freq.	*D*	Freq.	*R*	Mode	Sym.	Freq.[c]	D	R	Assignment[d]
				85	*A*	1855	264.1	+378	C═O asym str
				84	*B*	1845	1134.3	–389	C═O sym str
				83	*A*	1529	6.3	+3	CH_3 def
1485	97.9			82	*B*	1528	78.4	–0	CH_3 def
				81	*A*	1506	31.0	+13	CH_3 def
				80	*B*	1506	6.5	–1	CH_3 def
				79	*B*	1508	41.5	+3	CH_3 def
1466	114.6	1469	–5	78	*A*	1508	3.2	–10	CH_3 def
				77	*A*	1497	0.8	+1	CH_3 def
				76	*B*	1496	0.1	+1	CH_3 def
				75	*B*	1495	1.1	–1	CH_3 def
1441	26.1	1442	–21	74	*A*	1494	0.4	–3	CH_3 def
				73	*A*	1484	0.4	–1	CH_3 def
				72	*B*	1483	0.1	+1	CH_3 def
				71	*A*	1482	4.0	–5	CH_2 scissor
				70	*A*	1432	4.5	–0	CH_3 umb
1401	61.0			69	*B*	1431	80.5	+1	CH_3 umb
				68	*A*	1400	1.0	+7	CH_3 umb
1370	124.4	1372	+12	67	*B*	1400	41.6	+7	CH_3 umb
				66	*A*	1400	44.5	+4	CH_3 umb
				65	*B*	1400	8.3	–15	CH_3 umb
1322	vw	1327	+57	64	*B*	1323	6.9	+17	CH_2 wag, C–C str
				63	*A*	1322	0.2	+6	C–C str
1258	20.3			62	*B*	1259	5.5	–34	C–C str, CH_2 wag
1248	18.5	1249	–66	61	*A*	1251	0.1	+6	CH_2 twist, *t*-Bu def
		[e]		60	*A*	1244	13.1	+24	*t*-Bu def
		[e]		59	*B*	1243	23.1	–6	*t*-Bu def
1229	126.2	[e]		58	*B*	1233	127.8	–8	CH_2 wag, *t*-Bu def
1207	75.1	[e]		57	*A*	1219	1.8	+12	CH_2 twist
1180	952.1	1180	–71	56	*B*	1181	1367.0	–24	CH_2 wag, ring def
1157	38.6	1157	w+	55	*A*	1160	0.6	+7	ring def, CH_2 twist
1102	59.1	1103	+27	54	*B*	1107	211.0	+18	ring def, CH_2 wag
1091	197.5	1090	+56	53	*B*	1097	71.6	+12	ring def, CH_2 wag
1077	57.9	1077	–20	52	*A*	1082	44.4	–7	ring def
1054	9.2	1054	–61	51	*A*	1056	9.5	–56	ring def, CH_2 twist
1029	84.8	1028	+29	50	*B*	1039	93.5	+0	CH_3 rock, CH_2 wag
				49	*A*	1035	0.0	–3	CH_3 rock
1012	56.0	1012	+75	48	*B*	1022	57.7	+38	CH_3 rock
1004	24.0			47	*A*	1006	13.7	–0	CH_3 rock
				46	*B*	964	30.3	+22	CH_3 rock
				45	*A*	964	0.0	–0	CH_3 rock
961	485.7	959	–244	44	*B*	958	491.9	–182	ring def, CH_3 rock
				43	*A*	935	0.3	–3	CH_3 rock
940	31.6	939	–74	42	*B*	934	17.7	–21	CH_3 rock
				41	*B*	930	3.9	+12	CH_3 rock
				40	*A*	930	5.6	–11	CH_3 rock
912	157.7	912	+533	39	*A*	910	143.5	+256	ring def, CH_2 twist
891	299.5	890	w–	38	*B*	887	229.2	–13	ring def, CH_2 rock

[a] Freq., cm^{-1}; *D*, esu^2 cm$^2 \times 10^{40}$; *R*, esu^2 cm$^2 \times 10^{44}$.
[b] MFP: structure, force field, and atomic polar tensors by B3LYP/6–31G*; atomic axial tensors by RHF/6–31G*.
[c] Scaled by 0.98.
[d] sym, symmetric; asym, asymmetric; str, stretch; def, deformation; umb, umbrella.
[e] Obscured by solvent.

associated with a +, – pattern of VCD signal in the direction of increasing wavelength and vice versa for positive handedness. However, in their analysis of the VCD spectrum of *trans*-2,3-dideuteriooxirane, Freedman et al. (20), and subsequently Bour and Keiderling (21), showed that mechanical coupling of the oscillators (C—H and C—D bonds, in that case) may lead

© 1998 NRC Canada

Scheme 1.

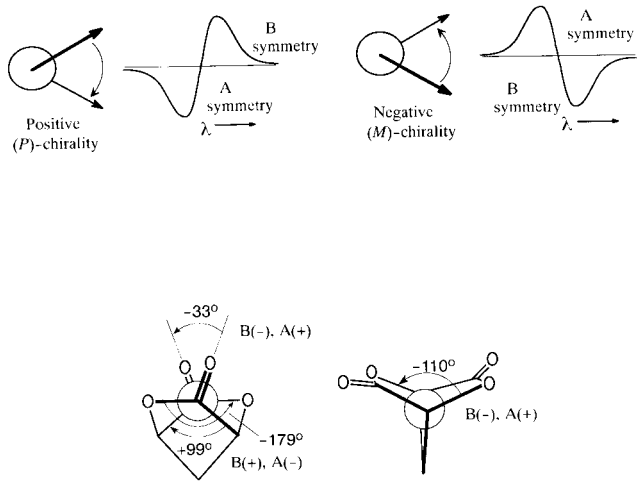

to nonconservative coupling patterns, possibly even of opposite sign. The "oscillators" most readily identified in **1** are the stretching vibrations of the polar bonds, C═O (carbonyl), C—O (bridgehead C to ether oxygen), ═C—O (carbonyl C to ether oxygen), and ═C—C (carbonyl C to bridgehead C). In (1*R*, 4*R*)-**1**, the symmetry-related pairs of these bonds have dihedral angles, –33°, –110°, –179°, and +99°, respectively, as shown in Scheme 1. The two C═O stretches form a pair of oscillators, which are most isolated from each other spatially and from other motions by virtue of frequency (no near degeneracies with other oscillators). For these, dipolar coupling should be the dominant mechanism. Indeed, the calculations predict a strong bisignate, conservative VCD pattern consistent with (*M*)-chirality (Tables 1, 2, and 3) in the vicinity of 1870 cm^{-1}. Unfortunately, this region of the VCD spectrum is not accessible to our instrument. The other polar C—O and C—C bonds are strongly coupled to each other as components of the modes identified in the tables as "ring deformations," and they fall in the congested region 900–1100 cm^{-1}. In the methyl and di-*tert*-butyl derivatives, they are also mixed and overlaid by C–C stretches and C-C-H angle deformations. In retrospect, it is not surprising that there are no recognizable coupled oscillator-derived patterns in the spectra of the two 1,4-dialkyl dilactones. Nevertheless, to the extent that one or the other of these degenerate pairs of stretching motions is a component of a particular normal mode, the sign of the CE should be determined by the handedness of the orientation of the bonds. One would not expect to see a VCD contribution from the ═C—O bonds (carbonyl C to ether O), since these are essentially coplanar (the projected dihedral angle is –179°, Scheme 1). However, modes of *A* and *B* symmetry that have a significant contribution from the stretching of the ═C—C bonds (carbonyl C to bridgehead C), which are oriented with positive chirality (+99°), should have negative and positive CEs, respectively. Conversely, the C—O bonds (bridgehead C to ether O) are oriented with negative chirality (–110°), and modes of *A* and *B* symmetry that incorporate the stretches of these bonds should have positive and negative CEs, respectively.

In the VCD spectrum of **1** (R = Me) shown in Fig. 1, a number of the fundamental modes have significant components of one or other of the polar bond stretches. Thus mode

Fig. 3. A comparison of the calculated VCD spectra of (1*R*,4*R*)-**1** (R = H), (1*R*,4*R*)-**1** (R = Me), and (1*S*,4*S*)-**1** (R = *t*-Bu) in the 500–1500 cm^{-1} spectral region.

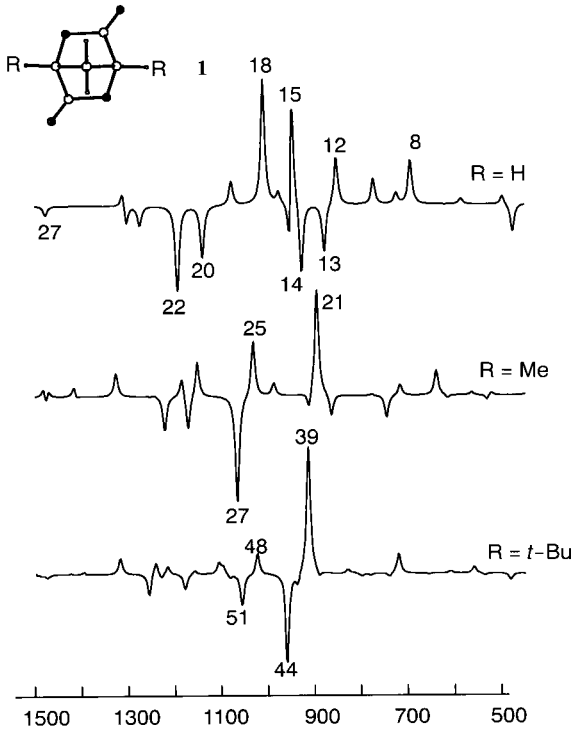

31 at 1233 cm^{-1} is predicted to arise from a *B* symmetry ring deformation composed of C–O bond stretches and to have an intense negative VCD associated with it, as expected from the (*M*)-chirality. The pattern of the VCD absorptions due to modes 29 and 28 is indicative of a coupled oscillator mechanism. These modes are complex mixtures of ring deformation (═C–C and C–O stretches) mixed with CH_2 wagging (*B* symmetry) or methyl rocking (*A* symmetry). The two polar bonds are disposed as two oppositely handed pairs. The observed and calculated signs are consistent with dominance of the ═C–C stretching mode, i.e., the pair with (*P*)-chirality. Similarly, modes 27 and 25 appear as a nonconservative couplet. The two modes are of *B* and *A* symmetry, respectively. Mode 27 involves stretching of the bridgehead C—O bonds, and the sign of the CE is consistent with the handedness. On the other hand, mode 25 is mostly a deformation of the six-membered ring, with carbonyl ═C–O stretching and ═C–O–C bending components. The ═C—O bonds are nearly coplanar and should not contribute to the CD. The origin of the positive rotatory strength of this band is obscure. Finally, mode 21 involves methyl rocking and bridgehead C–O stretching motions of *A* symmetry. The positive VCD signal is expected to arise from the C–O stretching components of the mode.

In the same vein, the CD signs of two of the fundamental modes of **1** (R = *t*-Bu), can be explained as originating from motions of the chirally disposed polar bonds. The band at 961 cm^{-1}, which is assigned to mode 44 with *B* symmetry, corresponds to a deformation of the six-membered ring involving stretching of the bridgehead C—O bonds. The observed and calculated negative CE is consistent with a coupled

© 1998 NRC Canada

Table 3. Theoretical[a,b] spectra of the dihydro dilactone (1*R*,4*R*)-**1** (R = H).

Mode	Sym.	Freq.[c]	*D*	*R*	Assignment[d]
29	*A*	1887	141.8	+200	C═O sym str
28	*B*	1875	572.2	–205	C═O asym str
27	*A*	1469	4.7	–4	CH_2 scissor
26	*A*	1310	0.2	+9	C–H ⊥ wag
25	*B*	1301	39.7	–11	C–H ⊥ wag
24	*B*	1271	5.1	–12	CH_2 wag
23	*A*	1266	0.1	–1	C–H ⊥ wag
22	*B*	1190	93.5	–36	C–H ∥ wag, CH_2 wag
21	*A*	1139	0.0	–0	C–H ⊥ wag, CH_2 twist
20	*B*	1138	132.7	–25	C–H ∥ wag, ═C–O str
19	*A*	1074	0.2	+16	CH_2 twist, ═C–O str
18	*B*	1001	37.8	+84	CH_2 rock
17	*A*	972	25.9	+3	C–O str
16	*B*	945	60.7	–50	C–O str, CH_2–C str
15	*A*	941	25.3	+94	CH_2–C str, C–H ∥ wag
14	*B*	921	66.0	–48	C–H ∥ wag, CH_2 wag, C–O str
13	*B*	872	29.9	–61	═C–O–C bend, C–H ⊥ wag
12	*A*	845	1.5	+38	═C–O str, C–H ∥ wag
11	*A*	772	0.2	–1	ring def, C═O out of plane, CH_2–C str
10	*B*	765	6.8	+6	ring def, C═O out of plane, CH_2 rock
9	*A*	715	8.7	+7	ring def, C═O out of plane, CH_2 twist
8	*B*	683	7.3	+52	ring angle def, C═O out of plane, CH_2–C str
7	*A*	574	0.1	+5	ring def, C═O out of plane, CH_2 twist
6	*B*	483	2.8	+16	CH_2 twist, O═C–O bend
5	*A*	462	6.0	–41	C═O wag

[a] Freq., cm^{-1}; *D*, esu^2 $cm^2 \times 10^{40}$; *R*, esu^2 $cm^2 \times 10^{44}$.

[b] MFP: structure, force field, and atomic polar tensors by B3LYP/6–31G*; atomic axial tensors by RHF/6–31G*.

[c] Scaled by 0.98.

[d] sym, symmetric; asym, asymmetric; str, stretch; z, perpendicular to the symmetry axis; ∥, parallel to the symmetry axis; def, deformation; umb, umbrella.

oscillator mechanism for the origin of the CD. Similarly, the most intense VCD feature, at 912 cm^{-1}, is assigned to mode 39, a ring deformation of *A* symmetry involving asymmetric stretching of the two C—O bonds to each of the ether oxygen atoms. Again, because the bonds terminating at the carbonyl C are achirally disposed, the VCD should arise from the bridgehead C–O component and have a positive sign according to the coupled oscillator mechanism.

(1*R*, 4*R*)-1 (R = H)

The parent bicyclic dilactone, **1** (R = H), has not been prepared in optically active form. In Fig. 3 is shown the theoretically predicted VCD spectrum together with the VCD spectra of the dimethyl and di-*tert*-butyl derivatives, which were discussed above. Both the predicted IR and VCD spectroscopic values are listed in Table 3. A cursory inspection of Fig. 3 does not reveal many obvious similarities between the VCD spectra of the three compounds in spite of the fact that they all have the same handedness of the same bicyclo[2.2.1]heptyl dilactone skeleton. We discuss below the assignments of the normal modes of the parent while seeking spectroscopic commonalities among the three compounds.

Lacking methyl groups, the first band of the 500–1500 cm^{-1} region of the spectrum is due to the CH_2 scissor (mode 27) at 1469 cm^{-1}. This mode is predicted to have a weak negative VCD in all three compounds and so is diagnostic of the skeletal chirality. Unfortunately, because of its weakness and the fact that it occurs in the methyl deformation region, it is difficult to identify in the dialkyl derivatives.

All of the remaining modes of the parent bicyclic dilactone are complex mixtures of C–H and CH_2 wags and twists with various deformations of the bicyclic skeleton. The assignments listed in Table 3 identify what appears to be the dominant contribution based on a visual inspection of the normal modes. We will discuss only the more intense VCD features.

The most intense VCD feature of **1** (R = H) is predicted to be a positive band at 1001 cm^{-1}, originating from a rocking motion of the methylene bridge (*B* symmetry, mode 18). This mode has a minor contribution from stretching of the bridgehead C—O bonds, but the sign is opposite to that expected for the contribution of an (*M*)-chirality bond array to a *B* symmetry mode. Mode 15 of *A* symmetry at 941 cm^{-1}, corresponding to a mixture of CH_2–C and C–O stretches and methine wag parallel to the C_2 axis, is predicted to have a high positive rotatory strength, which is partially cancelled by overlapping negative absorptions due to *B* symmetry modes (modes 14 and 16). The positive CE is consistent with a coupled oscillator mechanism operating for the C–O stretches as is the negative sign for the *B* symmetry mode 14, which also has a significant C–O stretching component.

It is not clear whether the polar bond motions of modes 14 and 15 are responsible for the signs of the CE or merely reinforce a dominant contribution from the methine motions. Mode 16, of *B* symmetry and negative rotatory strength, has a

© 1998 NRC Canada

Scheme 2.

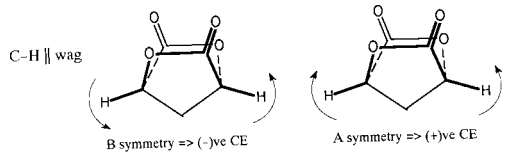

strong contribution of the parallel C–H wag, as do modes 20 and 22, at 1138 and 1190 cm^{-1}, respectively, both of which are also negative and of *B* symmetry. It is of interest that the major part of the ring deformation component of these last two modes appears to be stretching of the =C—C bonds whose (*P*)-chirality would contribute positive rotatory strength to modes of *B* symmetry. Since the observed and calculated signs are negative, the motion of the methine hydrogens must dominate the rotatory strength of the mode, as they apparently did in the case of mode 16. Mode 12, like mode 15, is in part the parallel C–H wag of *A* symmetry and has a positive CE. One may tentatively generalize that the in-phase (*A* symmetry) wag of the C—H bond is associated with a positive CE, and the out-of-phase (*B* symmetry) mode consistently has negative rotatory strength. The situation is summarized in Scheme 2. These contributions from motions of the C—H bonds may overwhelm the effects of other polar bonds in the molecule.

Conclusions

The experimental VCD spectra of 1,4-dimethyl- and 1,4-di-*tert*-butyl-2,5-dioxabicyclo[2.2.1]heptane-3,6-dione were measured in the mid-IR region (800–1500 cm^{-1}) and compared with spectra predicted by the ab initio magnetic field perturbation (MFP) theoretical method in conjunction with a B3LYP/6–31G* force field. The excellent agreement between calculated and experimental spectra permits the assignments not only of the absolute configuration but of all of the fundamental transitions. Although the absolute configuration of **1** (R = Me) was previously inferred from ab initio calculations of the ECD spectrum and comparison with the experimental ECD spectrum of (–)-(1*S*,4*S*)-**1** (R = *t*-Bu) (15), the present work provided an unambiguous confirmation of the assignment as (–)-(1*R*,4*R*)-**1** (R = Me).

The theoretical VCD spectrum of the parent 1,4-dihydro system is also presented and discussed. In spite of the homochirality and structural similarity of the bicyclic skeletons, there is little obvious correspondence among the three VCD spectra. Nevertheless, the analysis of the VCD spectra is greatly enhanced by the presence of the C_2 axis of symmetry. Many of the major VCD features of the two dialkyl compounds can be understood on the basis of the coupled oscillator mechanism where the oscillators are the chirally disposed pairs of equivalent polar bonds. Only the carbonyl stretching modes produce the characteristic bisignate couplet of VCD bands. However, the signs of the contributions to the rotatory strengths of individual fundamental transitions of *A* or *B* symmetry are predictable from the coupled oscillator mechanism if they have stretching of the polar C—O or C—C bonds as components. Surprisingly, VCD contributions due to motions of the C—H bonds in the parent dihydro system may dominate the contributions of the polar bonds. A general rule for the VCD sign of the *A* and *B* symmetry modes, which encompass wagging motions of the bridgehead C—H bonds, is deduced.

Acknowledgements

This work was sponsored by the Natural Sciences and Engineering Research Council of Canada and a NATO Linkage grant for which we express our gratitude. Yu.I.E. and R.G.K. also acknowledge funding from the Russian Foundation for Basic Research (grant no. 97-03-33021).

References

1. T.A. Keiderling. *In* Practical fourier transform spectroscopy. *Edited by* J.R. Ferraro and K. Krishnan. Academic Press, New York, N.Y. 1990. pp. 203–284.
2. T.B. Freedman and L.A. Nafie. *In* Modern nonlinear optics. Part 3. Advances in chemical physics series. Vol. 75. *Edited by* M. Evans and S. Kielich. J. Wiley & Sons, New York, N.Y. pp. 207–263 (1994).
3. D. Yang and A. Rauk. *In* Reviews of computational chemistry. Vol. 7. *Edited by* K.B. Lipkowitz and D.B. Boyd. VCH Publisher, Inc., New York, N.Y. 1996. pp. 261–301.
4. (*a*) A. Rauk, D. Yang, D. Tsankov, H. Wieser, Yu. Koltypin, A. Gedanken, and G.V. Shustov. J. Am. Chem. Soc. **117**, 4160 (1995); (*b*) S.T. Pickard, H.E. Smith, P.L. Polavarapu, T.M. Black, A. Rauk, and D. Yang. J. Am. Chem. Soc. **114**, 6850 (1992) (*Erratum*. J. Am. Chem. Soc. **116**, 4529 (1994)); (*c*) P.L. Polavarapu, S.T. Pickard, H.E. Smith, T.M. Black, A. Rauk, and D. Yang. J. Am. Chem. Soc. **113**, 9747 (1991).
5. (*a*) C.S. Ashvar, F.J. Devlin, K.L. Bak, P.R. Taylor, and P.J. Stephens. J. Phys. Chem. **100**, 9262 (1996); (*b*) F.J. Devlin and P.J. Stephens. J. Am. Chem. Soc. **116**, 5003 (1994).
6. (*a*) R. Dutler, R.A. Shaw, H. Wieser, and A. Rauk. J. Am. Chem. Soc. **112**, 5401 (1990); (*b*) A. Rauk, T. Eggimann, H. Wieser, G.V. Shustov, and D. Yang. Can. J. Chem. **72**, 506 (1994); (*c*) J.A. Nieman, B.A. Keay, M. Kubicki, D. Yang, A. Rauk, D. Tsankov, and H. Wieser. J. Org. Chem. **60**, 1918 (1995); (*d*) J.L. McCann, A. Rauk, and H. Wieser. Can. J. Chem. 1998. In press.
7. A. Rauk, D. Yang, G.V. Shustov, J. McCann, and H. Wieser. Appl. Spectrosc. **50**, 630 (1996).
8. (*a*) M.J., Frisch, G.W. Trucks, M. Head-Gordon, P.M.W. Gill, M.W. Wong, J.B. Foresman, B.G. Johnson, H.B. Schlegel, M.A. Robb, E.S. Replogle, R. Gomperts, J.L. Andres, K. Raghavachari, J.S. Binkley, C. Gonzalez, R.L. Martin, D.J. Fox, D.J. Defrees, J. Baker, J.J.P. Stewart, and J.A. Pople. Gaussian 92, Revision B. Gaussian, Inc., Pittsburgh Pa. 1992; (*b*) M.J. Frisch, G.W. Trucks, H.B. Schlegel, P.M.W. Gill, B.G. Johnson, M.A. Robb, J.R. Cheeseman, T.A. Keith, G.A. Petersson, J.A. Montgomery, K. Raghavachari, M.A. Al-Laham, V.G. Zakrewski, J.V. Ortiz, J.B. Foresman, J. Cioslowski, B.B. Stefanov, A. Nanayakkara, M. Challacombe, C.Y. Peng, P.Y. Ayala, W. Chen, M.W. Wong, J.L. Andres, E.S. Replogle, R. Gomperts, R.L. Martin, D.J. Fox, J.S. Binkley, D.J. Defrees, J. Baker, J.P. Stewart, M. Head-Gordon, C. Gonzalez, and J.A. Pople. Gaussian 94, (SGI-Revision B.3). Gaussian, Inc., Pittsburgh Pa. 1995.
9. P.J. Stephens. J. Phys. Chem. **89**, 748 (1985).
10. R.D. Amos. The Cambridge Analytical Derivatives Package 5.0. Cambridge University, Cambridge, U.K. 1992.
11. C.S. Ashvar, F.J. Devlin, K.L. Bak, P.R. Taylor, and P.J. Stephens. J. Phys. Chem. **100**, 9262 (1996).
12. D. Yang and A. Rauk. J. Chem. Phys. **100**, 7995 (1994).
13. K.L. Bak, P. Jorgensen, T. Helgaker, K. Ruud, and H.J.Aa. Jensen. J. Chem. Phys. **98**, 8873 (1993).

© 1998 NRC Canada

14. (*a*) J.R. Cheeseman, M.J. Frisch, F.J. Devlin, and P.J. Stephens. Chem. Phys. Lett. **252**, 211 (1996); (*b*) P.J. Stephens, C.S. Ashvar, F.J. Devlin, J.R. Cheeseman, and M.J. Frisch. Mol. Phys. **89**, 579–594 (1996); (*c*) F.J. Devlin, P.J. Stephens, J.R. Cheeseman, and M.J. Frisch. J. Am. Chem. Soc. **118**, 6328 (1996).
15. I.V. Vystorop, G.V. Shustov, A. Rauk. and R.G. Kostyanovsky. Mendeleev Commun. 97 (1994).
16. D. Tsankov, T. Eggimann, and H. Wieser. Appl. Spectrosc. **49**, 132 (1995).
17. L.A. Nafie and D.W. Vidrine. *In* Practical Fourier transform infrared spectroscopy. Vol. 3. *Edited by* J.R. Ferraro and L.J. Basile. Academic Press, New York, N.Y. 1982. p. 83.
18. (*a*) Labcalc. Galactic Industries Corp. 1992. (*b*) P. Bour, J. McCann, and H. Wieser. J. Phys. Chem. In press.
19. (*a*) J.G. Kirkwood. J. Chem. Phys. **5**, 479 (1937); (*b*) W. Moffitt. J. Chem. Phys. **25**, 467 (1956); (*c*) I. Tinoco, Jr. Adv. Chem. Phys. **4**, 113 (1962).
20. T.B. Freedman, K.M. Spencer, N. Ragunathan, L.A. Nafie, J.A. Moore, and J.M. Schwab. Can. J. Chem. **69**, 1619 (1991).
21. P. Bour and T.A. Keiderling. J. Am. Chem. Soc. **114**, 9100 (1992).

© 1998 NRC Canada

Microwave-enhanced metal- and acid-catalysed hydrogen isotope exchange reactions

Jean M. Barthez, Anton V. Filikov, Lottie B. Frederiksen, Marie-Loire Huguet, John R. Jones, and Shui-Yu Lu

Abstract: The benefits of using microwaves to accelerate the rates of hydrogen isotope exchange reactions are illustrated by reference to heterogeneous and homogeneous metal-catalysed reactions as well as to homogeneous acid-catalysed reactions. The results show that good incorporation of deuterium is obtained in very short time intervals, typically <20 min, and that the approach has considerable potential for the labeling of a wide range of compounds with both deuterium and, by implication, tritium.

Key words: microwave enhanced deuteriations, hydrogen isotope exchange.

Résumé : Faisant appel à des réactions hétérogènes et homogènes catalysées par les métaux ainsi qu'à des réactions homogènes catalysées par les acides, on montre les bénéfices de l'utilisation des microondes pour accélérer les vitesses de réaction d'échanges isotopiques de l'hydrogène. Les résultats montrent que l'on obtient une bonne incorporation de deutérium dans des intervalles de temps de réaction très courts, en général <20 min, et que cette approche présente un grand potentiel pour le marquage d'un grand nombre de produits tant avec du deutérium que, par implication, par le tritium.

Mots clés : deutérations facilitées par les microondes, échange isotopique d'hydrogène.

[Traduit par la rédaction]

The focus of our recent labeling studies with both ^{2}H and ^{3}H has been concerned with (*a*) developing one-step catalysed reactions (1–3) and (*b*) the use of polymer-supported acid (4) and base (5) catalysts, the former in order to achieve regiospecific incorporation and the latter in order to simplify the isolation of product, which is particularly important in the case of highly radioactive compounds. In both areas success has been achieved but only by using a combination of high temperatures and prolonged heating times, conditions that many pharmaceuticals find too harsh, leading to decomposition.

Forty years ago Wilzbach (6) reported on an apparently promising radiation-induced method for tritiating organic compounds, which stimulated a great deal of interest in the use of alternative sources of energy, such as microwaves (7), to enhance the attractions of hydrogen isotope exchange labeling procedures. However, it was only in 1986 that the potential of microwaves in organic synthesis (8, 9) was fully appreciated, since when the field has seen considerable expansion (10).

Microwaves have been used to synthesize radiopharmaceuticals containing the short-lived ^{11}C, ^{18}F isotopes (11–13) as well as tritiated peptides (14–17), steroids (18), carcinogens (19), and benzodiazepine-type compounds (20), but the overall picture is one in which relatively few studies have been reported. In the present paper we address this issue by investigating several metal-catalysed hydrogen isotope exchange reactions, both under homogeneous and heterogeneous conditions, as well as a high-temperature dilute acid catalysed exchange procedure that has previously been used with considerable success by Werstiuk (21). The extensive studies of Garnett (22), Garnett and Long (23), and Williams (24) on the use of transition metal catalysed hydrogen isotope exchange reactions show, that like Werstiuk's studies, both high temperatures and long periods of time are required in order to achieve good isotopic incorporation.

Received December 18, 1997.

This paper is dedicated to Professor Erwin Buncel in recognition of his contributions to Canadian chemistry.

J. M. Barthez, A.V. Filikov, L.B. Frederiksen, M.-L. Huguet, J.R. Jones,[1] and S.-Y. Lu. Chemistry Department, University of Surrey, Guildford, GU2 5XH, England.

[1] Author to whom correspondence may be addressed. Telephone: +44 (0) 1483 59313. Fax: +44 (0) 1483 259514. E-mail:J.R.Jones@surrey.ac.uk

Experimental

Three different microwave instruments (a CEM MDS system, a Scientific and Medical Products unit, and a Matsui M169BT unit) were used for the deuteriation studies of which the first two were of a commercial design and the third of a household kind. It was customary practice when using the commercial instruments to employ a fixed time whilst with the domestic version short pulses, typically of 2 min duration, interspersed by a cooling period, were used.

In the early studies the reagents were contained in a thick-walled glass tube sealed at the top but experience showed that a small conical flask (capacity 25 mL) containing a septum was equally satisfactory. The latter was placed in a beaker containing vermiculite and slowly rotated during the course of the irradiation. The procedure for isolating the labeled product depended on the kind of catalyst employed.

Heterogeneous metal-catalysed hydrogen isotope exchange

Known amounts of catalyst (pre-reduced PtO_2), D_2O (99.6%

© 1998 NRC Canada

Table 1. Deuteration of selected aromatics under microwave conditions (15 min irradiation at 160 W) using PtO_2 catalyst and D_2O (1 mL).

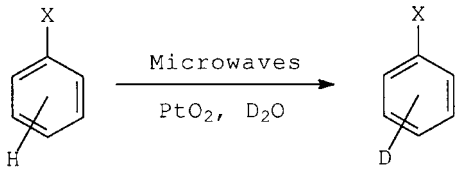

X	Amount	Catalyst (mg)	Deuteration orientation (relative %)		
CH_3	2 mL	34	*ortho* (29)	*meta* (57)	*para* (14)
COOH	307 mg	124		*meta* (100)	
NH_2	3 mL	130	*ortho* (95)	*meta* (5)	
OH	465 mg	95	*ortho* (54)	*meta* (19)	*para* (27)
$COCH_3$	3 mL	105	acetyl (25)	*meta* (50)	*para* (25)
2,6-Dimethoxy benzoic acid	290 mg	100		*meta* (5)	*para* (95)

isotopic abundance), and substrate were inserted in the reaction flask (Table 1). On completion of the irradiation the flask was allowed to cool, the catalyst filtered off, and the substrate extracted into an organic solvent (usually diethyl ether) and washed with water, before drying over anhydrous Na_2SO_4. The solvent was then removed by rotary evaporation.

Homogeneous metal-catalysed hydrogen isotope exchange

For these studies a 5% aqueous solution of sodium tetrachloroplatinate was used as the catalyst. On completion of the irradiation, solvent extraction, washing with water, and drying over anhydrous Na_2SO_4 were undertaken prior to removal of the solvent.

Homogeneous acid-catalysed hydrogen isotope exchange

Stock *o*-toluidine hydrochloride was prepared by mixing *o*-toluidine (8.57 g), 3 M HCl (27 mL), and activated charcoal (2 g) in a 100 mL flask at 70°C for 15 min. Removal of charcoal using filtration, then removal of water using rotary evaporation, afforded the salt as a grey solid. *o*-Toluidine hydrochloride (0.8 g) was stirred with D_2O (2 mL) at ambient temperature for 4 h and the D_2O was distilled off under vacuum. In each hydrogen isotope exchange reaction, the deuteriated salt (30 mg) was dissolved in fresh D_2O (300 mL) in the conical flask. On completion of the irradiation, the D_2O solution was used directly for NMR analysis. Deuteriated *o*-toluidine in the free amine form was also obtained by neutralizing the reaction mixture with NaOH (3 M), followed by extraction with chloroform, drying over anhydrous $MgSO_4$, and evaporation of the solvent.

In all three kinds of hydrogen isotope exchange the ^1H NMR spectra of a solution of the substrate in a deuteriated solvent were recorded, both before and after deuteriation has taken place; the ^2H NMR (^1H decoupled) spectra were also obtained. For this work a Bruker AC 300 instrument operating at 300 MHz for the ^1H spectra and at 46 MHz for the ^2H spectra was used. For both the heterogeneous and homogeneous metal-catalysed studies it was the orientation effects that were of interest whilst with the acid-catalysed exchange interest focused on the extent of deuteriation; the methyl group hydrogens, which do not undergo exchange, provide a convenient internal standard.

Table 2. Deuteration of selected aromatics under microwave conditions (15 min irradiation at 160 W) using Na_2PtCl_4 catalyst and D_2O (1 mL).

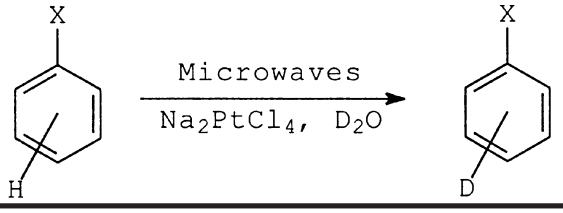

X	Amount	Catalyst[a] (mL)	Deuteration orientation (%)		
COOH	500 mg	0.5		*meta* (100)	
NH_2	3 mL	1	*ortho* (65)		*para* (35)
OH	445 mg	0.5	*ortho* (86)		*meta* (14)
$COCH_3$	3 mL	0.55	acetyl (100)		
2,6-Dimethoxy benzoic acid	260 mg	0.5		*meta* (100)	

[a] 5% aqueous solution.

Table 3. Deuteration of *o*-toluidine hydrochloride under microwave conditions.

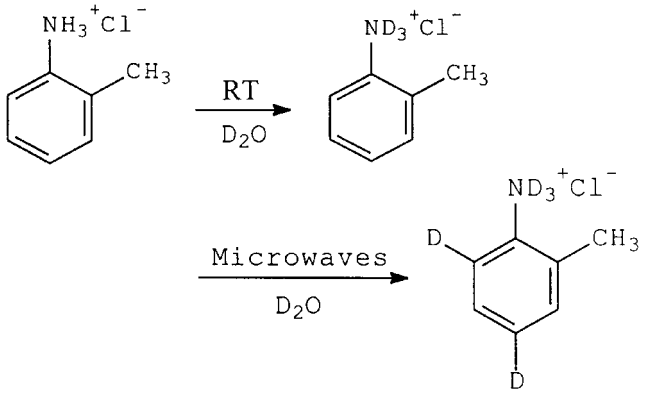

Number of 2 min pulses	% Deuterium incorporation in the *o* + *p* positions
1	6
2	14
5	23
10	62
15	100
25	100

Results and discussion

The most remarkable feature of all the results (Tables 1–3) is the very brief time that is necessary to obtain extensive deuteriation. What is achieved in a matter of a few minutes can be compared with what is customarily required under thermal conditions — temperatures in excess of 100°C for prolonged periods, sometimes of several days duration. Furthermore, the short irradiation times ensure that the reactions are cleaner and

© 1998 NRC Canada

lead to less by-product formation, findings that are similar to those reported by others (10).

Pre-reduced PtO_2 has long been considered (24) one of the most active and generally useful heterogeneous metal catalysts for hydrogen isotope exchange studies and the results in Table 1 show that in at least two cases (X = COOH, NH_2) a high degree of regioselectivity is observed. In the case of 2,6-dimethoxy benzoic acid steric hindrance ensures that but little deuterium is inserted in the *meta* positions, neither is deuterium incorporated into the *ortho* positions in acetophenone.

With the homogeneous sodium tetrachloroplatinate catalyst the pattern of labeling is the same as under heterogeneous conditions for benzoic acid but in other cases there are significant differences. Caution is required in interpreting these as there may well be instances, for example, in the case of acetophenone, where base catalysis is in direct competition with metal catalysis. However, the ease and rapidity with which the necessary data can now be obtained, as compared to thermal conditions, greatly increases the attractions of using deuterium orientation as an indicator of possible reaction mechanisms.

Finally the ease with which *o*-toluidine hydrochloride can be deuteriated can be compared with the conditions employed by Werstiuk (21) for deuteriating the structurally similar aniline hydrochloride — heating at 175–250°C for between 12 and 54 h. The hope must be that the present findings can be extended to include more sensitive pharmaceuticals, in which case the hope expressed by Wilzbach in his pioneering paper will have been achieved, albeit with a different kind of radiation. Its extension to the tritiation of organic compounds is currently being explored.

Acknowledgments

We are grateful to NATO and The Royal Society for financial support (A.V.F.) and the European Union for postdoctoral fellowships (J.M.B., L.B.F., and M.-L.H.). We are also grateful to Professor D.M P. Mingos, F.R.S. for useful discussions at the early stages of this work.

References

1. D. Hesk, J.R. Jones, W.J.S. Lockley, and D.J. Wilkinson. J. Labelled Comp. Radiopharm. **28**, 1309 (1990).
2. D. Hesk, J.R. Jones, and W.J.S. Lockley. J. Labelled Cmpd. Radiopharm. **28**, 1427 (1990).
3. D. Hesk, J.R. Jones, and W.J.S. Lockley. J. Pharm. Sci. **80**, 887 (1991).
4. J.R. Brewer, J.R. Jones, K.W.M. Lawrie, D. Saunders, and A. Simmonds. J. Labelled Cmpd. Radiopharm. **34**, 391 (1994).
5. J.R. Brewer, J.R. Jones, K.W.M. Lawrie, D. Saunders, and A. Simmonds. J. Labelled Cmpd. Radiopharm. **34**, 787 (1994).
6. K.E. Wilzbach. J. Am. Chem. Soc. **79**, 1013 (1957).
7. N.A. Ghanem and T. Westermark. J. Am. Chem. Soc. **82**, 4432 (1960).
8. R. Gedye, F. Smith, K. Westaway, A. Humera, L. Baldisera, L. Laberge, and L. Roussell. Tetrahedron Lett. **27**, 279 (1986).
9. R.J. Giguere, T.L. Bray, S.M. Duncan, and G. Majetich. Tetrahedron Lett. **27**, 4945 (1986).
10. S. Caddick. Tetrahedron, **51**, 10403 (1995).
11. D.R. Hwang, S.M. Moerlein, L. Lang, and M.J. Welch. J. Chem. Soc. Chem. Commun. 1799, (1987).
12. S.A. Stone-Elander, N. Elander, J.O. Thorell, G. Solas, and J. Svennebrink. J. Labelled Cmpd. Radiopharm. **34**, 949 (1994).
13. S.A. Stone-Elander and N. Elander. Proc. Int. Symp. Synthesis and Applications of Isotopically Labelled Compounds, 4th. Toronto, Ont., September 1991. *Edited by* E. Buncel and G.W. Kabalka. Elsevier, Amsterdam. 1992. pp. 648–651.
14. W.C. Hembree, R.L.E. Ehrenkaufer, S. Lieberman, and A.P. Wolf. J. Biol. Chem. **248**, 5532 (1973).
15. R.L.E. Ehrenkaufer, W.C. Hembree, S. Lieberman, and A.P. Wolf. J. Am. Chem. Soc. **99**, 5005 (1977).
16. R.L.E. Ehrenkaufer, A.P. Wolf, W.C. Hembree, and S. Lieberman. J. Labelled Cmpd. Radiopharm. **13**, 359 (1977).
17. R. Hua and C.T. Peng. J. Labelled Cmpd. Radiopharm. **24**, 1095 (1987).
18. G.Z. Tang and C.T. Peng. J. Labelled Cmpd. Radiopharm. **25**, 585 (1988).
19. C.T. Peng. To be published.
20. J. Koves. J. Labelled Cmpd. Radiopharm. **34**, 255 (1996).
21. N.H. Werstiuk. *In* Isotopes in the physical and biological sciences. Vol. 1A. *Edited by* E. Buncel and J.R. Jones. Elsevier, Amsterdam. 1987. pp. 124–155.
22. J.L. Garnett. Catal. Rev. **5**, 229 (1971).
23. J.L. Garnett and M.A. Long. *In* Isotopes in the physical and biological sciences. Vol. 1A. *Edited by* E. Buncel and J.R. Jones. Elsevier, Amsterdam. 1987. pp. 86–121.
24. P.G. Williams. *In* Isotopes in the physical and biological sciences. Vol. 2. *Edited by* E. Buncel and J.R. Jones. Elsevier, Amsterdam. 1991. pp. 55–98.

© 1998 NRC Canada

An unusual ground-state stabilization effect and origins of the α-effect in aminolyses of Y-substituted phenyl X-substituted benzoates

Ik-Hwan Um, Eun-Kyung Chung, and So-Mi Lee

Abstract: Second-order rate constants have been measured spectrophotometrically for the reactions of X-$C_6H_4CO_2C_6H_4$-Y with a series of primary amines in H_2O containing 20 mol% DMSO at 25.0 ± 0.1°C. The reactivity increases as the substituent (X and Y) becomes a stronger electron-withdrawing group. The σ^+ constants give better Hammett correlation than σ constants for the reactions of 4-nitrophenyl X-substituted benzoates with glycylglycine (glygly) and hydrazine (NH_2NH_2), indicating that the ground-state stabilization effect is unusually significant on the reaction rates. The reactions of X-$C_6H_4CO_2C_6H_4$-Y with glygly and NH_2NH_2 appear to proceed through the same mechanism, but the degree of leaving-group departure and the negative charge developed in the acyl moiety at the rate-determining TS is considered to be more significant for the glygly system than the NH_2NH_2 system based on $ß_{lg}$ and ρ_X values. The magnitude of the α-effect is observed to be not always dependent on the $ß_{nuc}$ value but dependent on the electronic nature of the substituent X and Y, i.e., an electron-donating substituent increases the α-effect, while an electron-withdrawing one decreases the α-effect. The present study has led to the conclusion that the ground-state effect is important for the reaction rates but it is not solely responsible for the α-effect, and the intramolecular H-bonding interactions (**4**) are proposed for the cause of the increasing or decreasing α-effect trends observed in the present system.

Key words: α-effect, intramolecular H-bonding interaction, ground-state stabilization effect.

Résumé : Faisant appel à la spectrophotométrie, on a mesuré les constantes de vitesse du deuxième ordre des réactions de X-$C_6H_4CO_2C_6H_4$-Y avec une série d'amines primaires, dans de l'eau contenant 20 mol% de DMSO, à 25,0 ± 0,1°C. La réactivité augmente lorsque les substituants (X et Y) de plus en plus électroaffinitaires. Pour les réactions des benzoates de 4-nitrophényle substitués par un groupe X avec la glycylglycine (glygly) et avec l'hydrazine (NH_2NH_2), les constantes σ^+ donnent une meilleure corrélation de Hammett que les constantes σ; ces résultats indiquent que l'effet de stabilisation dans l'état fondamental particulièrement important pour les vitesses de réaction. Les réactions des X-$C_6H_4CO_2C_6H_4$-Y avec la glygly et l'hydrazine semblent se produire par le même mécanisme; toutefois, si l'on se base sur les valeurs β_{lg} et ρ_x, il semble que le degré de séparation du groupe partant et le niveau de charge négative développé sur la partie acyle dans l'état de transition (ET) de l'étape cinétiquement limitante soient plus importants pour le système glygly que pour le système de l'hydrazine. On a observé que l'amplitude de l'effet α ne dépend pas toujours de la valeur β_{nuc}, mais qu'elle dépend de la nature électronique des substituants X et Y, c'est-à-dire qu'un substituant électrodonneur augmente l'effet α alors qu'un substituant électroattracteur diminue l'effet α. Le présent travail conduit à la conclusion que l'effet de l'état fondamental influence beaucoup les vitesses de réaction, mais qu'il n'est pas le seul responsable de l'effet α; on suggère que des interactions par liaisons hydrogènes intramoléculaires sont la cause de l'augmentation ou de la diminution des tendances dans les effets α observées dans le présent système.

Mots clés : effet α, interaction par liaison hydrogène intramoléculaire, effet de stabilisation de l'état fondamental.

[Traduit par la rédaction]

Introduction

The basicity of nucleophiles has been most commonly used to predict nucleophilicity (1). However abnormally higher nucleophilic reactivity than would be predicted from the basicity has been often observed in the reaction of nucleophiles containing an atom with one or more nonbonding electron pairs at the α-position of the reaction site, e.g., peroxides, oximates, hydroxamates, hydrazines, hydroxylamine, etc. The term α-effect was given to the abnormally enhanced nucleophilicity shown by these nucleophiles by Edwards and Pearson in 1962 (2). Since then, numerous studies have been performed to investigate the cause of the α-effect (3–10). The explanations suggested for the origin of the α-effect are: ground-state (GS) destabilization due to the repulsion of the nonbonding electrons (2), transition-state (TS) stabilization including intramolecular general acid–base catalysis (5), product stabilization (6), decreased solvation (7), etc. (3).

Received December 8, 1997.

This paper is dedicated to Professor Erwin Buncel in recognition of his numerous contributions to physical organic chemistry.

I.-H. Um,[1] E.-K. Chung, and S.-M. Lee. Department of Chemistry, Ewha Womans University, Seoul 120-750, Korea.

[1] Author to whom correspondence may be addressed. Telephone: 822) 360-2349. Fax: 822) 360-2844. E-mail: ihum@mm.ewha.ac.kr

© 1998 NRC Canada

Scheme 1.

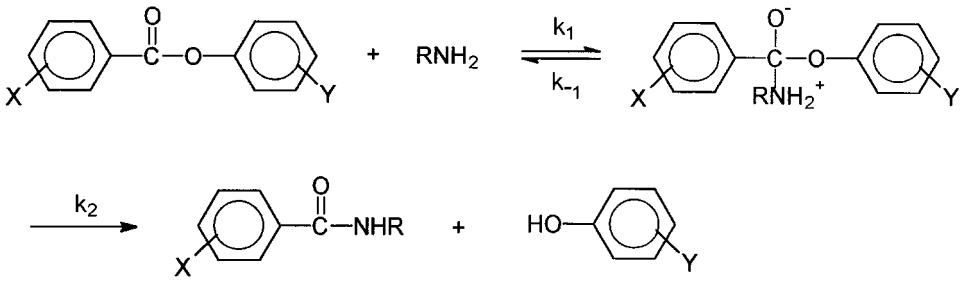

Table 1. Summary of apparent second-order rate constants, k (M^{-1} s^{-1}), for the reactions of 4-nitrophenyl X-substituted benzoates (X-$C_6H_4COOC_6H_4$-4-NO_2) with primary amines in water containing 20 mol% DMSO at 25.0 ± 0.1°C.

			k (M^{-1} s^{-1})		
No.	Primary amine	pK_a[a]	X = 4-CH_3O	X = H	X = 4-NO_2
1	Hydroxylamine	6.17[b]	0.0561	0.218	2.33
2	Glycine ethyl ester	7.68	0.00316	0.0106	0.0738
3	Hydrazine	8.20[b]	0.728	2.39	11.5
4	Glycylglycine	8.25[b]	0.00689	0.025	0.169
5	Benzylamine	9.46	0.0791	0.242	1.73
6	Ethanolamine	9.67	0.103	0.34	2.7
7	Glycine	10.06	0.164	0.604	4.03
8	Ethylamine	10.67	0.542	1.97	16.3

[a] The pK_a data were taken from ref. 25, unless noted otherwise.
[b] pK_a data were taken from ref. 11*b*.

Table 2. Summary of apparent second-order rate constants, k (M^{-1} s^{-1}), for the reactions of Y-substituted phenyl benzoates ($C_6H_5COOC_6H_4$-Y) with hydrazine (NH_2NH_2) and glycylglycine (glygly) in water containing 20 mol% DMSO at 25.0 ± 0.1°C.

			k (M^{-1} s^{-1})	
No.	Y	pK_a (YC_6H_4OH)[a]	NH_2NH_2	glygly
1	2,4-$(NO_2)_2$	4.11	39.2	1.02
2	4-Cl-2-NO_2	6.46	2.58	0.0369
3	4-NO_2	7.14	2.39	0.024
4	4-CHO	7.66	[b]	0.014
5	4-CN	7.95	0.538	0.00446
6	4-MeCO	8.05	0.201	0.00161
7	4-CO_2Et	8.50	0.0836	0.0006
8	4-Cl	9.38	0.0052	[c]

[a] pK_a data were taken from ref. 32.
[b] Rate constant not measured due to the addition reaction of NH_2NH_2 to the 4-CHO group in the leaving phenoxide.
[c] Rate constant not measured due to extremely slow reaction rate.

We have studied the reaction of 4-nitrophenyl acetate (PNPA) with butane-2,3-dione monoximate (Ox^-) and 4-chlorophenoxide (ArO^-) as an α-effect nucleophile and the corresponding normal nucleophile, respectively, in H_2O – dimethyl sulfoxide (DMSO) mixtures of varying compositions (8). The magnitude of the α-effect has been found to increase as the mol% DMSO increases up to near 50 mol% DMSO and then to decrease upon further additions of DMSO to give a bell-shaped α-effect trend. Such a bell-shaped α-effect trend has been also reported for the reaction of 4-nitrophenyl diphenylphosphinate (PNPDPP) with Ox^- and ArO^- in H_2O–DMSO mixtures (9). However, the reactions of PNPA with Ox^- and benzohydroxamates run in H_2O–acetonitrile (MeCN) mixtures have been observed to exhibit an increasing α-effect as the mol% MeCN increases, indicating that the solvent effect on the α-effect is significant (10).

We have now extended our study to the reactions of Y-substituted phenyl X-substituted benzoates with a series of primary amines including hydrazine and hydroxylamine as shown in Scheme 1. Aminolyses of esters have been intensively studied, and numerous data about the reaction mechanisms are available (11–13). Therefore, our systematic study would be expected to give us important information about the origin of the α-effect.

Results

All the kinetic reactions in the present study obeyed pseudo-first-order kinetics. Pseudo-first-order rate constants (k_{obs}) were measured spectrophotometrically for the aminolyses of X-$C_6H_4CO_2C_6H_4$-Y in H_2O containing 20 mol% DMSO at 25.0 ± 0.1°C, i.e., the k_{obs} value was obtained from the slope of the plot of $\ln(A_\infty - A_t)$ vs. time. Generally five different amine concentrations were used to obtain second-order rate constants from the slope of the linear plot of k_{obs} vs. amine concentration. Correlation coefficient of the plot was usually higher than 0.9995 except for the reactions of 4-chlorophenyl benzoate and 4-ethoxycarbonylphenyl benzoate with hydrazine and glygly, which exhibited an upward curvature as the amine concentration increased. Since the plots of k_{obs}/[amine] vs. [amine] were linear for these reactions, the second-order and third-order rate constants were obtained from the intercept and slope of the linear plots, respectively. It is estimated from replicate runs that the error in any particular measured rate constant is less than ±3%. The kinetic results including the carbonyl stretching bands for the substrates ($\nu_{C=O}$) are summarized in Tables 1–4, and demonstrated graphically in Figs. 1–7.

Discussion

Reaction mechanism

As shown in Table 1, the reactivity increases with increasing the basicity of amines except NH_2NH_2 and NH_2OH. Interestingly, NH_2NH_2 is much more reactive than glycylglycine (glygly), although the basicity of the two amines is comparable. NH_2OH also exhibits higher reactivity than would be expected from its basicity, i.e., NH_2OH is almost as reactive as benzylamine, although the former is about 3.5 pK_a units less basic than the latter. The dependence of reactivity on the basicity of amines is graphically demonstrated in Fig. 1. It is seen from the

© 1998 NRC Canada

Table 3. Summary of apparent second-order rate constants, k (M^{-1} s^{-1}), for the reactions of 4-nitrophenyl X-substituted benzoates (X-$C_6H_4COOC_6H_4$-4-NO_2) with hydrazine (NH_2NH_2) and glycylglycine (glygly) in water containing 20 mol% DMSO at 25.0 ± 0.1°C.

			k (M^{-1} s^{-1})	
No.	X	σ^+ (X)	NH_2NH_2	glygly
1	4-OMe	–0.78	0.728	0.00689
2	4-Me	–0.31	1.54	0.0153
3	3-Me	–0.07	2.05	0.0189
4	H	0	2.39	0.0250
5	4-Cl	0.11	3.60	0.0413
6	3-Cl	0.37	6.19	0.0688
7	4-CN	0.66	10.3	0.126
8	4-NO_2	0.78	11.5	0.169
9	4-Cl-3-NO_2	0.94	14.1	0.206
10	3,5-$(NO_2)_2$	1.42	27.3	0.523

figure that the logarithmic apparent second-order rate constant (log k) increases linearly with increasing the pK_a of the amines except NH_2NH_2 and NH_2OH, which exhibit positive deviations from the linear Brönsted-type plots. Since these two amines have been classified into the α-effect nucleophile, the positive deviation shown by them is apparently the α-effect.

To investigate the origin of the α-effect in the present system, it is necessary to understand the reaction mechanism and the structure of the transition state (TS). Aminolyses of carboxylic esters have been generally suggested to proceed via a stepwise mechanism in which the rate-determining step (RDS) is dependent on the basicity of the leaving group and the nucleophilic amine (11–13). A change in the RDS has been reported to accompany a significant decrease in the magnitude of $ß_{nuc}$ value, e.g., from 0.7–0.9 to 0.2–0.3 as the RDS changes from the breakdown of the addition intermediate (the k_2 step in Scheme 1) to the formation of the intermediate (the k_1 step in Scheme 1) (11–13). The $ß_{nuc}$ value for the present system has been calculated to be 0.76 ± 0.2, indicating that the RDS is the k_2 step.

It is interesting that the magnitude of $ß_{nuc}$ values in the present aminolysis appears to be independent on the electronic nature of the acyl substituent X, but remains almost constant within the experimental error. This is an unexpected result based on the reactivity–selectivity principle (RSP) (14). However failures of the RSP have been often reported (14). Lee et al. (15) have observed that the magnitude of $ß_{nuc}$ values increases with increasing electron-withdrawing ability of the acyl substituents for aminolyses of X-substituted benzoyl halides and their related compounds, although the reactivity increases with increasing electron-withdrawing ability of the substituent. We have also observed a larger $ß_{nuc}$ value for a stronger electron-withdrawing substituent in the acyl moiety for the nucleophilic substitution reaction of 4-nitrophenyl X-substituted benzoates with aryloxides in the same reaction condition as in the present system (16). Such anti-RSP behaviors have been often reported for the reactions that proceed via an associative S_N2 mechanism, or for the one in which nucleophilic attack is involved in the RDS (15, 16). Lee et al. (15) have attributed the anti-RSP behavior to more bond formation by the stronger electron-withdrawing substituent. For a stepwise reaction in which the breakdown of the intermediate is the RDS, bond formation between the nucleophile and the carbonyl group of the substrate would be complete at the rate-determining TS. In this case, the acyl substituent would no longer influence the magnitude of $ß_{nuc}$ value. Therefore, the constant $ß_{nuc}$ values also support that the present aminolysis proceeds via a rate-determining breakdown of the addition intermediate.

To get more information about the reaction mechanism and the α-effect, we have performed the reaction of Y-substituted phenyl benzoates with NH_2NH_2 and glygly as an α-effect nucleophile and the corresponding normal nucleophile, respectively. One can see from the kinetic data in Table 2 that NH_2NH_2 is more reactive than glygly for all the substrates studied, and the reactivity of the substrates increases with decreasing the basicity of the leaving aryloxide for both NH_2NH_2 and glygly systems. The dependence of the reactivity on the basicity of the leaving group is demonstrated in Fig. 2. The Brönsted-type plots are not as linear as the ones in Fig. 1. Besides, the points for the weakly basic leaving groups such as 4-chloro-2-nitrophenoxide and 2,4-dinitrophenoxide appear to deviate negatively from linearity for both NH_2NH_2 and glygly systems. Since a break or curvature in Brönsted-type plots has been understood as a change in the RDS or the reaction mechanism (17), one might consider that a change in the RDS occurs as the leaving group becomes weakly basic. However, it has been generally known that a change in the RDS for aminolyses of various carboxylic esters occurs when the nucleophilic amine becomes more basic than the leaving group by ~5 pK_a units (11–13). Although NH_2NH_2 and glygly are more basic than the leaving phenoxide (except 4-chlorophenoxide and 4-ethoxycarbonylphenoxide) in the present system, the basicity of these amines is not larger than that of the leaving aryloxides by ~5 pK_a units even for the least basic leaving group, 2,4-dinitrophenoxide. Therefore, the curvatures obtained in Fig. 2 are not considered to be a result of a change in the RDS.

Curvatures in Brönsted-type plots have been often observed for reactions whose mechanism does not change. Recently, Jencks and co-workers (18) have performed the reactions of 3- and 4-nitrophenyl formates with a series of substituted phenoxides and found nonlinear Brönsted-type plots. Interestingly, the phenoxides having a chlorine atom at the *ortho* position exhibit negative deviations from the linear Brönsted-type plots (18). Accordingly, the steric effect but not a change in mechanism has been suggested to be responsible for the deviations (18). As shown in Fig. 2, the substrates having an *ortho* substituent in the leaving group deviate negatively from the linear Brönsted-type plots. Therefore, one can consider that the present reactions of Y-substituted phenyl benzoates with NH_2NH_2 and glygly proceed through the same mechanism without changing the RDS.

The slopes ($ß_{lg}$) in Fig. 2 have been calculated to be –1.08 and –1.25 for the reaction with NH_2NH_2 and glygly, respectively. Since NH_2NH_2 is more reactive than glygly, the larger $ß_{lg}$ value for the less reactive glygly system appears to be in accordance with the RSP. The magnitude of $ß_{lg}$ has been also used as a measure of the leaving group departure at the rate-determining TS. Accordingly, one can consider that the degree of the leaving-group departure would be slightly more significant for the glygly than the NH_2NH_2 system. However, the shape of the Brönsted-type plots for the reactions of NH_2NH_2

© 1998 NRC Canada

Table 4. Summary of carbonyl stretching bands ($\nu_{C=O}$, cm^{-1}) and the magnitude of the α-effect (k^{NH2NH2}/k^{glygly}) for the reactions of Y-substituted phenyl X-substituted benzoates with hydrazine (NH_2NH_2) and glycylglycine (glygly) in water containing 20 mol% DMSO at 25.0 ± 0.1°C.

X	Y	$\nu_{C=O}$, cm^{-1}	α-Effect
4-OMe	4-NO_2	1737	106
4-Me	4-NO_2	1741	101
3-Me	4-NO_2	1740	108
H	4-NO_2	1741	95.6
4-Cl	4-NO_2	1744	87.2
3-Cl	4-NO_2	1745	90.0
4-CN	4-NO_2	1745	81.7
4-NO_2	4-NO_2	1747	68.1
4-Cl-4-NO_2	4-NO_2	1748	68.4
3,5-$(NO_2)_2$	4-NO_2	1749	52.2
H	2,4-$(NO_2)_2$	1753	38.4
H	4-Cl-2-NO_2	1742	69.9
H	4-CHO	1741	—
H	4-CN	1736	121
H	4-MeCO	1735	125

Fig. 1. Brönsted-type plots for the reactions of 4-nitrophenyl X-substituted benzoates (X-$C_6H_4COOC_6H_4$-4-NO_2) with primary amines in water containing 20 mol% DMSO at 25.0 ± 0.1°C. The numbers in the figure refer to the amines in Table 1.

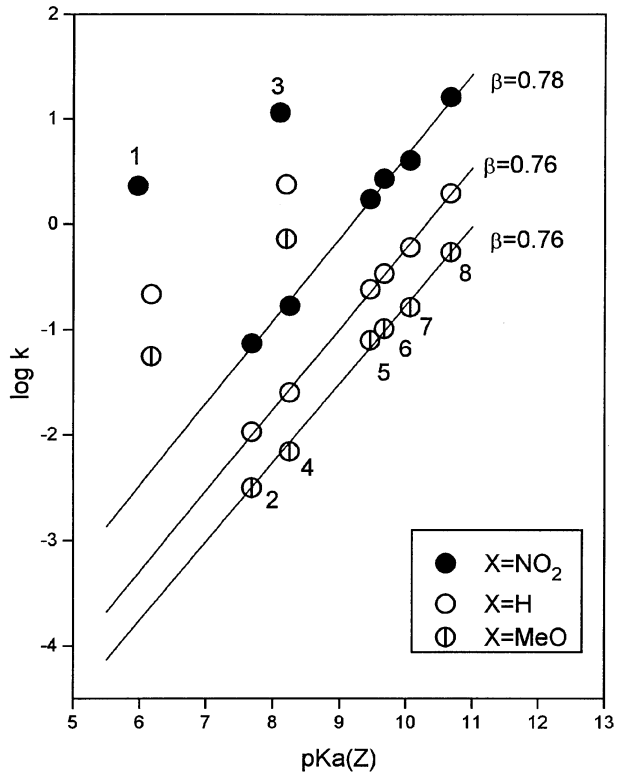

and glygly is similar to each other. Therefore, it is considered that the reaction of Y-substituted phenyl benzoates with NH_2NH_2 and glygly proceeds in a similar mechanism but the leaving group departure at the TS is slightly more advanced for the less reactive glygly system.

Fig. 2. Brönsted-type plots for the reactions of Y-substituted phenyl benzoates ($C_6H_4COOC_6H_4$-Y) with hydrazine (●) and glycylglycine (○) in water containing 20 mol% DMSO at 25.0 ± 0.1°C. The numbers in the figure refer to the substrates in Table 2.

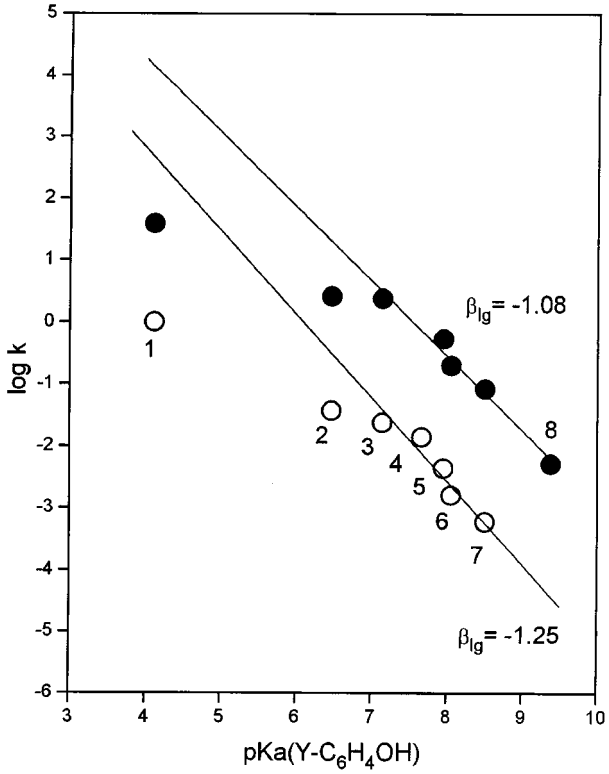

To get further information about the structure of the TS, we have performed the reactions of 4-nitrophenyl X-substituted benzoates with NH_2NH_2 and glygly. The kinetic results are summarized in Table 3. One can see that NH_2NH_2 is more reactive than glygly, and the reactivity of these benzoates increases with increasing electron-withdrawing ability of the acyl substituent (X). The dependence of reactivity on the electronic nature of the substituent is demonstrated in Fig. 3. Excellent linear Hammett plots have been obtained for both NH_2NH_2 and glygly systems, indicating that the variation of the acyl substituent does not cause any change in the mechanism or RDS in the aminolysis reaction.

The ρ_X values have been calculated to be +0.76 and +0.90 for the reaction with NH_2NH_2 and glygly, respectively. It has been known that the sign and the magnitude of the ρ_X value represent the type and the relative degree of the charge development at the acyl moiety at the TS, respectively (19). Therefore, the positive ρ_X value suggests that the negative charge is developing in the acyl moiety at the TS, and the degree is less significant for the NH_2NH_2 system than the glygly system based on the ρ_X values. The magnitude of ρ_X values in the present aminolyses (ρ_X = 0.76, 0.90) has been obtained to be much smaller than the one for the corresponding reactions with anionic nucleophiles, such as HO^- and aryloxides (ρ_X = 2.44–2.96) (20–22). Since the neutral nucleophile would share its electrons less significantly with the acyl moiety of the substrate than the anionic nucleophile, one can expect a smaller ρ_X value for the reaction with amines than for the one with the anionic nucleophiles. Therefore, one might consider the

© 1998 NRC Canada

Fig. 3. Hammett plots for the reactions of 4-nitrophenyl X-substituted benzoates (X-$C_6H_4COOC_6H_4$-4-NO_2) with hydrazine (●) and glycylglycine (○) in water containing 20 mol% DMSO at 25.0 ± 0.1°C. The numbers in the figure refer to the substrates in Table 3.

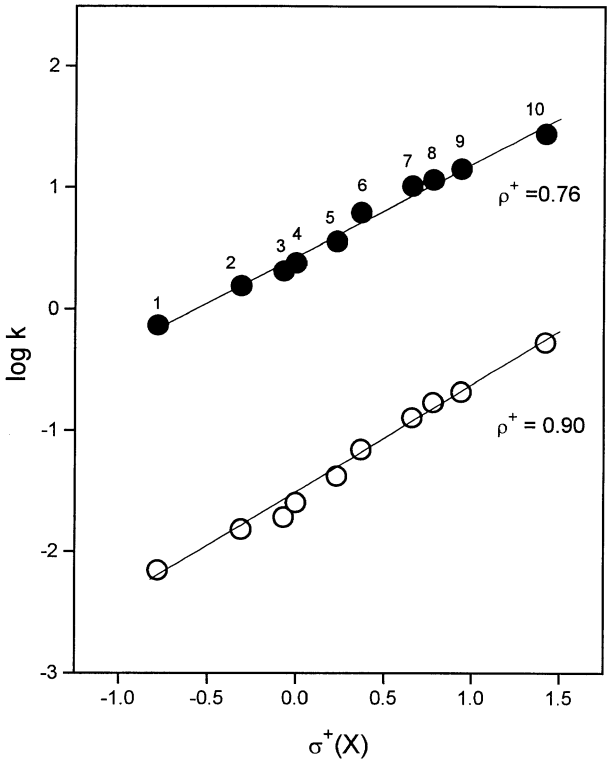

difference in the charge type between the neutral and anionic nucleophiles is responsible for the difference in the magnitude of the ρ_X values. However, the nature of the reaction mechanism is also considered to be responsible for the small ρ_X values in the aminolysis. For a stepwise mechanism (e.g., addition–elimination mechanism), the first step to form an addition intermediate would be accelerated by an electron-withdrawing substituent (EWS) but retarded by an electron-donating substituent (EDS), resulting in a large positive ρ_X value. On the contrary, the second step to break down the addition intermediate would be retarded by an EWS but accelerated by an EDS, yielding a negative ρ_X value. Accordingly, one would expect a small ρ_X value for the reaction that proceeds via a stepwise mechanism with rate-determining breakdown of the intermediate due to the opposite substituent effect. The small ρ_X values for the present aminolysis compared with the ones for the reactions with anionic nucleophiles also support that the aminolysis proceeds via a stepwise mechanism in which the breakdown of the intermediate is the RDS.

Interestingly, as shown in Fig. 3, σ^+ constants give better correlation than σ constants, and the sign of ρ_X is positive. The σ^+ constants have been derived from solvolysis of $ArCMe_2Cl$ in 90% acetone–water at 25°C (23) and used for the reactions in which a positive charge is formed at the reaction centre, which can resonate with an EDS because of the additional resonance transmission for these substituents. Accordingly, negative ρ_X values have been generally obtained. Therefore, the present result (e.g., positive ρ_X values with σ^+ constants) is quite unusual, and one can suggest that the polarization of the C═O bond by resonance (**1**) or by hyperconjugation (**2**) in the ground state (GS) is significantly reflected in the reaction rate for both NH_2NH_2 and glygly systems.

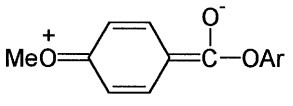

1 **2**

To investigate the contribution of the C═O bond polarization to the reactivity, carbonyl stretching bands of the substrates ($\nu_{C=O}$) have been correlated with log *k*. As shown in Fig. 4, log *k* is linearly correlated with $\nu_{C=O}$ for both NH_2NH_2 and glygly systems, i.e., the substituent that increases $\nu_{C=O}$ accelerates the rate, and the one that decreases $\nu_{C=O}$ retards the rate, whether it is on the acyl moiety (X) or on the leaving group (Y). Good linear correlations of log *k* vs. $\nu_{C=O}$ have been often reported, e.g., aminolyses of 2-furoyl chlorides and their related compounds (24). Therefore, one might consider that the linear correlations observed in Fig. 4 are not so significant. However, such a good linearity is not always available. In fact, we obtained nonlinear correlation for the corresponding reaction with anionic nucleophiles such as substituted phenoxides (25). Therefore, the linearity observed from the plot of log *k* vs. $\nu_{C=O}$ clearly suggests that the effect of the polarization of the C═O bond on rates is significant for both NH_2NH_2 and glygly systems, since $\nu_{C=O}$ is a measure of the force constant and the polarization of the C═O bond. This argument is consistent with the proceeding one based on the positive ρ_X value with σ^+ constant. Therefore, one can conclude that the reactions of $XC_6H_4CO_2C_6H_4Y$ with NH_2NH_2 and glygly proceed in the same mechanism with slightly different TS structures, i.e., the degree of the leaving-group departure and the negative charge developed in the acyl moiety at the rate-determining TS would be slightly more significant for the glygly system than for the NH_2NH_2 system based on the magnitude of $ß_{lg}$ and ρ_X values.

Origin of the α-effect

As shown in Table 2, NH_2NH_2 is more reactive than glygly toward all the Y-substituted phenyl benzoates studied. The ratio of the apparent second-order rate constant for NH_2NH_2 (k^{NH2NH2}) to the one for glygly (k^{glygly}) (the α-effect: k^{NH2NH2}/k^{glygly}) decreases as the leaving group becomes a weaker base. The dependence of the α-effect on the leaving group basicity has been demonstrated graphically in Fig. 5. One can see the magnitude of the α-effect is linearly correlated with the pK_a of the conjugate acid of the leaving group.

Many factors have been suggested to influence the magnitude of the α-effect. Four of them are the basicity of the α-effect nucleophile (26), the kind of solvent (8–10, 27), the type of the hybridization of the electrophilic centre (28), and the magnitude of $ß_{nuc}$ value (29, 30). Recently, Terrier and co-workers (26*a*) have observed that the magnitude of the α-effect becomes smaller as the basicity of the α-effect nucleophile increases for the reactions of 4-nitrophenyl acetate (PNPA) and phosphonate (PNPDPP) with various oximates. A similar result was also reported by Hudson and co-workers (26*b*). On the other hand, significant solvent-dependent α-effects have

© 1998 NRC Canada

Fig. 4. Plots showing dependence of rate constant on $\nu_{C=O}$ for the reactions of Y-substituted phenyl X-substituted benzoates with hydrazine (●, X; ◆, Y) and glycylglycine (○, X; ◇, Y) in water containing 20 mol% DMSO at 25.0 ± 0.1°C.

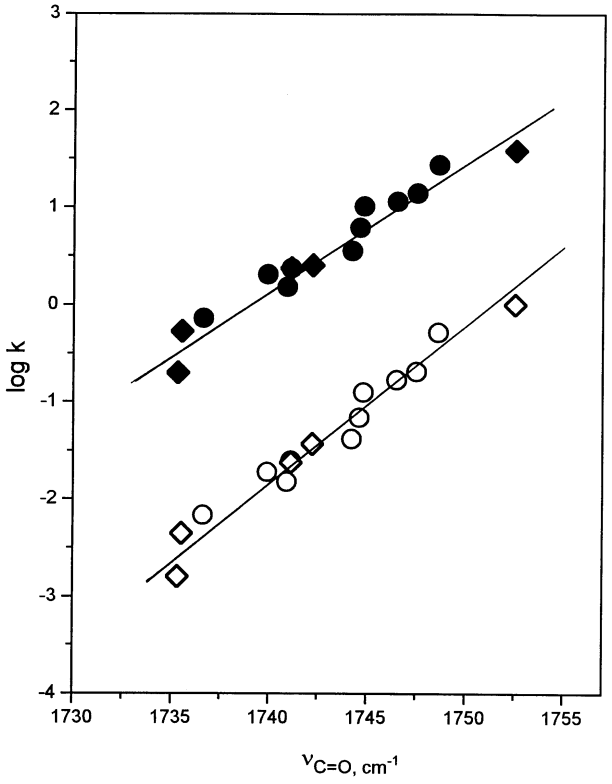

Fig. 5. A plot showing dependence of α-effect (k^{NH2NH2}/k^{glygly}) on the basicity of the leaving group for the reactions of Y-substituted phenyl benzoates ($C_6H_5COOC_6H_4$-Y) with hydrazine and glycylglycine in water containing 20 mol% DMSO at 25.0 ± 0.1°C. The numbers in the figure refer to the substrates in Table 2.

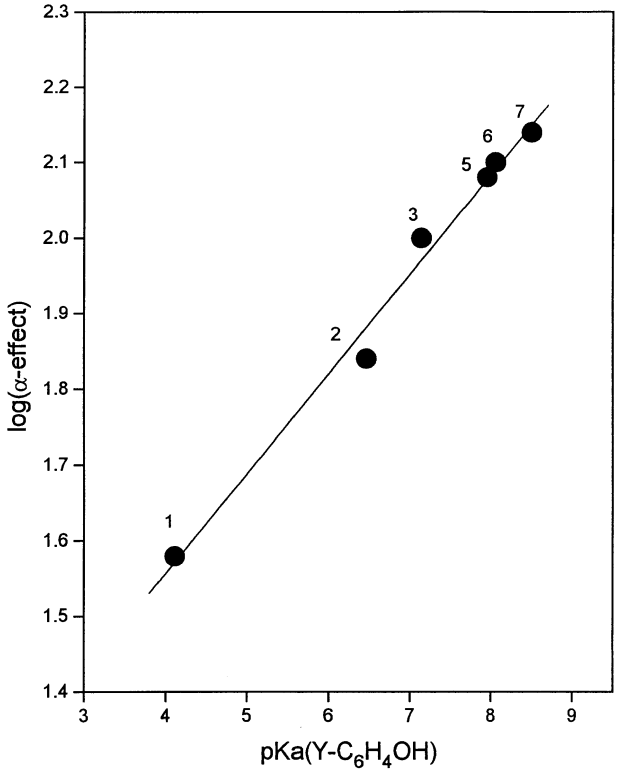

been reported (8–10, 27). Buncel and Um (8) and Tarkka and Buncel (9) have observed bell-shaped α-effect trends for the reactions of PNPA and PNPDPP with butane-2,3-dione monoximate (Ox^-) and 4-chlorophenoxide (ArO^-) in DMSO–H_2O mixtures of varying compositions. On the other hand, Um et al. (10) have reported increasing α-effect trends for the same reactions run in MeCN–H_2O mixtures as the concentration of MeCN increases in the medium. The magnitude of the α-effect has been also suggested to increase with increasing the *s* character of the hybridization of the electrophilic centre (eg., $sp > sp^2 > sp^3$) (28) and with increasing the magnitude of $ß_{nuc}$ value (29, 30). Since the basicity of the nucleophiles, solvent, and the type of the hybridization are kept constant in the present system, these factors are obiously not considered to be responsible for the α-effect trend in Fig. 5.

It has been generally observed that the magnitude of the $ß_{nuc}$ value increases with decreasing the leaving-group ability for the nucleophilic substitution reactions of aryl acetates and benzoates with neutral or anionic nucleophiles. For example, Dixon and Bruice (29) have reported that the magnitude of $ß_{nuc}$ value is 1.05, 0.83, and 0.57 for aminolysis of phenyl, 4-nitrophenyl, and 2,4-dinitrophenyl acetate, respectively. A similar result was reported for reactions of substituted phenyl acetates and benzoates (31). Therefore, one can consider that the α-effect and $ß_{nuc}$ value decrease in the same manner as the leaving group becomes less basic. This argument appears to be consistent with the proposal made by Bruice and Hoz (29, 30) that the magnitude of the α-effect is dependent on the $ß_{nuc}$ value.

In Fig. 6 is demonstrated the relationship of the α-effect with the σ constant for the reaction of 4-nitrophenyl X-substituted benzoates with NH_2NH_2 and glygly. One can see a good linear correlation in the figure, i.e., the magnitude of the α-effect decreases as the σ constant of the acyl substituent X increases. It has been shown from Fig. 1 that the $ß_{nuc}$ value is independent of the electronic nature of the acyl substituents but remains constant ($ß_{nuc}$ = 0.76 ± 0.02) when the leaving group is fixed to 4-nitrophenoxide. Interestingly, the magnitude of the α-effect has been observed to be dependent on the nature of the acyl substituents but $ß_{nuc}$ value is not, i.e., the α-effect is clearly not dependent on the $ß_{nuc}$ value. This is obviously inconsistent with the preceding result, eg., the increasing α-effect trend with increasing $ß_{nuc}$ value. Therefore, the proposal made by Bruice and Hoz appears to not always be true. However, a common feature in Figs. 5 and 6 is that the α-effect decreases as the reactivity of the substrates increases, indicating that the RSP is operative in the present system.

It is clear that the enhanced nucleophilic reactivity shown by the α-effect nucleophile should be determined by decreasing the free energy gap between the GS and the TS of the reaction. Therefore, among the theories suggested to explain the origin of the α-effect, two factors (GS destabilization and TS stabilization) will be considered. One can assume that the GS of the α-effect nucleophiles can be destabilized compared with their corresponding normal nucleophiles either by desolvation, repulsion between the nonbonding electrons, or

© 1998 NRC Canada

Fig. 6. A plot showing dependence of α-effect (k^{NH2NH2}/k^{glygly}) on the electronic nature of acyl substituents for the reactions of 4-nitrophenyl X-substituted benzoates (X-$C_6H_4COOC_6H_4$-4-NO_2) with hydrazine and glycylglycine in water containing 20 mol% DMSO at 25.0 ± 0.1°C.

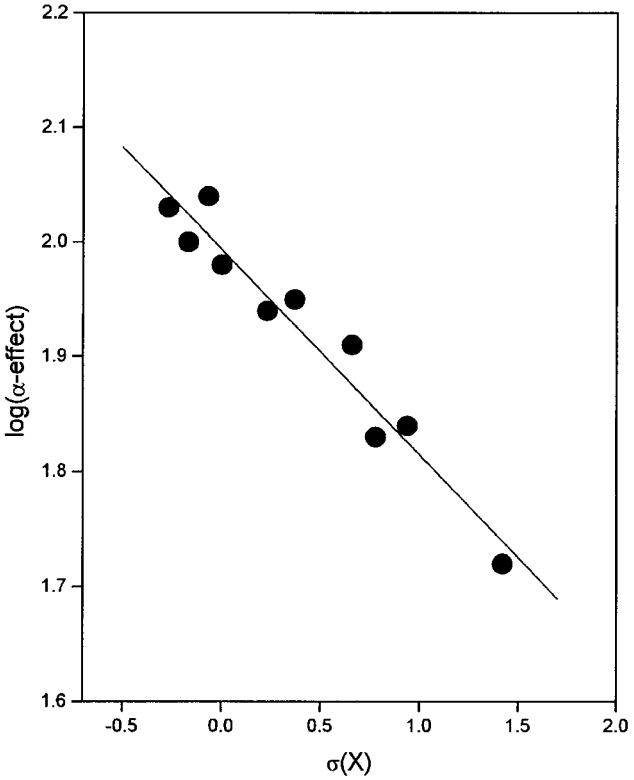

Fig. 7. A plot showing dependence of α-effect (k^{NH2NH2}/k^{glygly}) on $\nu_{C=O}$ for the reactions of Y-substitued phenyl X-substituted benzoates with hydrazine and glycylglycine in water containing 20 mol% DMSO at 25.0 ± 0.1°C (●, X; ○, Y).

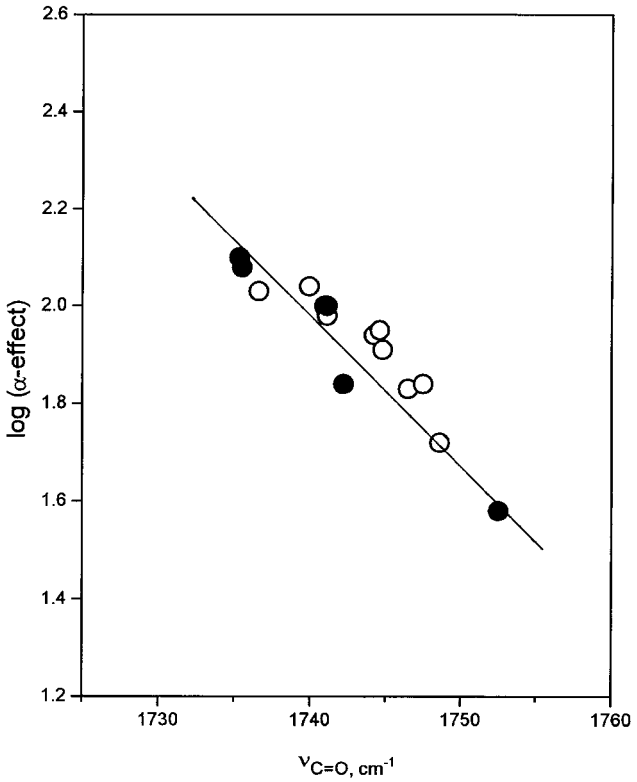

others. However, the difference in the GS energy (ΔE_{GS}) for a given set of nucleophiles (eg., NH_2NH_2/glygly or Ox^-/ArO^-) remains constant although the substrate changes. Therefore, the magnitude of the α-effect should have remained constant for the present aminolyses of X-$C_6H_4CO_2C_6H_4$-Y, if ΔE_{GS} were solely responsible for the α-effect. In fact, the magnitude of the α-effect has been observed to be nearly constant for the corresponding reaction with Ox^- and ArO^- (25), indicating that ΔE_{GS} is significantly responsible for the α-effect observed in the Ox^- system. Therefore, the decreasing or increasing α-effect trends in Figs. 5 and 6 clearly suggest that ΔE_{GS} is not solely responsible for the α-effect in the present NH_2NH_2 system.

Recently, Terrier et al. (26*a*) have explained the α-effect in terms of the TS stabilization by an intramolecular general base catalysis model (**3**). However, **3** is not possible in the present system. Instead, one can suggest an intramolecular general acid catalysis model (**4**). Such a model was probably one of the first explanations suggested for the α-effect shown by NH_2NH_2, NH_2OH, HOO^-, etc. (3). On the other hand, $MeONH_2$ has often exhibited a large α-effect although it cannot form such an intramolecular H-bonding structure. Therefore, the importance of structure **4** has been neglected. However, the origin of the α-effect shown by NH_2NH_2 and $MeONH_2$ would not necessarily be the same. In fact, Hengge and co-workers (4*i*) have recently suggested an intramolecular H-bonding structure **5** to explain the enhanced nucleophilic reactivity of $HONH_2$, from an intensive study of kinetic isotope effect for acyl-transfer reaction of PNPA with $HONH_2$.

The intramolecular H-bonding interaction as shown in **4** would be dependent on the degree of the polarization of the C═O bond, i.e., an EDS would increase both the H-bonding interaction and C═O bond polarization, while an EWS would decrease them whether the substituent is on the acyl moiety (X) or on the leaving group (Y). It is evident that the H-bonding interaction can stabilize the TS of the NH_2NH_2 system and result in increasing both the rate and the α-effect. In fact, as shown in Figs. 5 and 6, the α-effect increases as the substituent X or Y becomes a stronger EDS, but decreases with increasing electron-withdrawing ability of the substituent X and Y, indicating that the substituent that assists the C═O bond polarization or H-bonding increases the magnitude of the α-effect. Therefore, **4** is considered to be responsible for the α-effect trend obtained in the present system. This argument can be further supported from the linear correlation of the α-effect with $\nu_{C=O}$ as shown in Fig. 7. One can see that the magnitude of the α-effect is inversely correlated with $\nu_{C=O}$. Since $\nu_{C=O}$ represents the force constant of the C═O bond, the degree of polarization of the C═O bond would increase as the $\nu_{C=O}$ decreases. Therefore, the linear dependence of the α-effect on $\nu_{C=O}$ also indicates that the structure **4** plays an important role in the present α-effect trend (e.g., the increasing or decreasing α-effect trend).

Conclusions

The following conclusions have been drawn from the kinetic study for the reaction of X-$C_6H_4CO_2C_6H_4$-Y with a series of

© 1998 NRC Canada

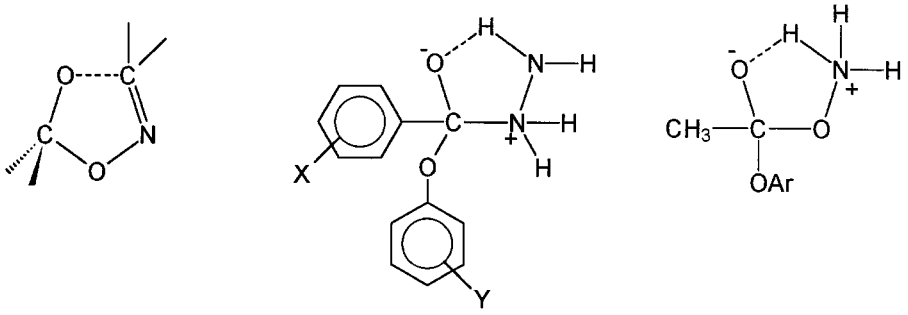

3 4 5

primary amines in H_2O containing 20 mol% DMSO at 25.0 ± 0.1°C. (*i*) The reactions of X-$C_6H_4CO_2C_6H_4$-Y with primary amines including glygly and NH_2NH_2 are considered to proceed through the same mechanism with slightly different TS structures, i.e., the degree of leaving-group departure and the negative charged in the acyl moiety at the rate-determining TS would be slightly more significant for the glygly system than for the NH_2NH_2 system based on the magnitude of β_{lg} and ρ_X values. (*ii*) The magnitude of the α-effect is not always dependent on the β_{nuc} value but dependent on the electronic nature of the substituent, i.e., an EDS increases the α-effect, while an EWS decreases the α-effect whether the substituent is in the acyl moiety (X) or in the leaving group (Y). (*iii*) The difference in the GS energy between NH_2NH_2 and glygly is not considered to be solely responsible for the α-effect. Instead, the intramolecular H-bonding structure **4** is proposed to be responsible for the α-effect, at least for the increasing or decreasing α-effect trends obtained in the present system.

Experimental

Materials

Aryl benzoates (X-$C_6H_4CO_2C_6H_4$-Y) were easily prepared from the reactions of X-substituted benzoyl chloride with Y-substituted phenol in the presence of triethylamine in methylene chloride as reported in literature (33). Their purity was checked by means of melting points and spectral data such as IR and ^1H NMR characteristics. The amines and other chemicals used were of the highest quality available (Aldrich) and recrystallized or distilled before use. Dimethyl sulfoxide (DMSO) was distilled over calcium hydride at a reduced pressure (bp 64–66°C at 6–7 mmHg) (1 mmHg = 133.3 Pa) and stored under nitrogen. Doubly glass distilled water was further boiled and cooled under a nitrogen atmosphere just before use.

Kinetics

The kinetic studies were performed with a Hitachi U-2000 model UV-vis spectrophotometer for slow reactions ($t_{1/2} \geq 10$ s) or with an Applied Photophysics SX 17MV stopped-flow spectrophotometer for fast reactions ($t_{1/2} < 10$ s) equipped with a Neslab RTE-110 model constant temperature circulating bath to keep the temperature of the reaction mixture at 25.0 ± 0.1°C. All the kinetics were performed in H_2O containing 20 mol% DMSO to eliminate a solubility problem. The reactions were followed by monitoring the appearance of the leaving phenoxides (or phenols) at a fixed wavelength corresponding to the maximum absorption (λ_{max}) of Y-$C_6H_4O^-$ (or Y-C_6H_4OH). All the reactions were carried out under pseudo-first-order conditions in which the concentration of amines was at least 20 times greater than that of the substrates. Amine stock solutions of ca. 0.2 M were prepared in a 25.0 mL volumetric flask under a nitrogen atmosphere by adding 2 equiv. of the amine hydrochloride to 1 equiv. of standardized NaOH solution in order to obtain a self-buffered solution. All the solutions were prepared freshly just before use under a nitrogen atmosphere and transferred by Hamiltom gas-tight syringes. Typically, reaction was initiated by adding 5 μL of ca. 0.02 M substrate solution to a 10 mm quartz cuvette containing the self-buffered amine solution. Generally, the concentration of the amines was varied over the range (5–50) × 10^{-3} M. The effect of ionic strength on rate was observed to be negligible in the present reaction condition. Usually, five different amine concentrations were employed and replicate values of k_{obs} were determined to obtain the second-order rate constants from the linear plot of k_{obs} vs. free amine concentration. Other details in kinetic methods were similar to the ones described previously (34).

Acknowledgement

The authors are grateful for the financial support from the Basic Science Research Institute Program of Ministry of Education of Korea (BSRI-97-3422) and the Korea Science and Engineering Foundation (KOSEF 94-0501-09-3).

References

1. T.H. Lowry and K.S. Richardson. *In* Mechanism and theory in organic chemistry. 3rd ed. Harper Collins Publishers, New York. 1987. pp. 289–290.
2. J.O. Edwards and R.G. Pearson. J. Am. Chem. Soc. **84**, 16 (1962).
3. (*a*) N.J. Fina and J.O. Edwards. Int. J. Chem. Kinet. **5**, 1 (1973); (*b*) A.P. Grekov and V.Y. Veselov. Usp. Khim. **47**, 1200 (1978); (*c*) E. Buncel and S. Hoz. Isr. J. Chem. **26**, 313 (1985).
4. (*a*) F. Terrier, G. Moutiers, L. Xiao, E.L. Guevel, and F. Guir. J. Org. Chem. **60**, 1974 (1995); (*b*) F. Terrier, P. MacCormack, E. Kizilian, J.C. Halle, P. Demerseman, F. Guir, and C. Lion. J. Chem. Soc. Perkin Trans. 2, 153 (1991); (*c*) F. Degorre, D. Kiffer, and F. Terrier. J. Med. Chem. **31**, 757 (1988); (*d*) K.R. Fountain, K.L. Hutchinson, D.C. Mulhearn, and Y.B. Xu. J. Org. Chem. **58**, 7883 (1993); (*e*) K.R. Fountain, D.P. Fountain, B. Michales, D.B. Myers, J.K. Salmon, D.A. Van Galen, and P. Yu. Can. J. Chem. **69**, 798 (1991); (*f*) K.R. Fountain and K.D. Patel. J. Org. Chem. **62**, 4795 (1997); (*g*) K.R. Fountain, T.W. Dunkin, and K.D. Patel. J. Org. Chem. **62**, 2738 (1997); (*h*) O.A. El Seoud and M.F. Martins. J. Phys. Org. Chem. **8**, 637 (1995); (*i*) R.A.

© 1998 NRC Canada

Hess, A.C. Hengge, and W.W. Cleland. J. Am. Chem. Soc. **119**, 6980 (1997).
5. (*a*) E. Buncel, C. Chuagui, and H. Wilson. Int. J. Chem. Kinet. **14**, 823 (1982); (*b*) E. Buncel, H. Wilson, and C. Chuagui. J. Am. Chem. Soc. **104**, 4896 (1982); (*c*) A.R. Fersht and Y. Requena. J. Am. Chem. Soc. **93**, 6592 (1971).
6. (*a*) J.E. Dixon and T.C. Bruice. J. Am. Chem. Soc. **93**, 3248 (1971); (*b*) J. Gerstein and W.P. Jencks. J. Am. Chem. Soc. **86**, 4655 (1964).
7. (*a*) C.H. DePuy, E.W. Della, J. Filley, J.J. Garbowski, and V.M. Bierbaum. J. Am. Chem. Soc. **105**, 2481 (1983); (*b*) S. Wolfe, D.J. Mitchell, H.B. Schlegel, C. Minot, and O. Eisenstein. Tetrahedron Lett. **23**, 615 (1982).
8. E. Buncel and I.H. Um. J. Chem. Soc. Chem. Commun. 595 (1986).
9. R.M. Tarkka and E. Buncel. J. Am. Chem. Soc. **117**, 1503 (1995).
10. (*a*) I.H. Um, H.W. Yoon, J.S. Lee, H.J. Moon, and D.S. Kwon. J. Org. Chem. **62**, 5939 (1997); (*b*) I.H. Um, G.J. Hahn, G.J. Lee, and D.S. Kwon. Bull. Korean Chem. Soc. **13**, 642 (1992); (*c*) D.S. Kwon, G.J. Lee, and I.H. Um. Bull. Korean Chem. Soc. **10**, 642 (1989).
11. (*a*) W.P. Jencks and M. Gilchrist. J. Am. Chem. Soc. **88**, 104 (1966); (*b*) J. Am. Chem. Soc. **90**, 2622 (1968); (*c*) D.J. Palling and W.P. Jencks. J. Am. Chem. Soc. **106**, 4869 (1984).
12. (*a*) E.A. Castro, M.I. Pizarro, and J.G. Santos. J. Org. Chem. **61**, 5982 (1996); (*b*) E.A. Castro, M. Cubillos, and J.G. Santos. J. Org. Chem. **62**, 4395 (1997); (*c*) E.A. Castro, J.G. Santos, J. Tellez, and M. Umana. J. Org. Chem. **62**, 6568 (1997).
13. (*a*) I.H. Um, H.J. Kwon, D.S. Kwon, and J.Y. Park. J. Chem. Res. Synop. 301, J. Chem. Res. Miniprint, 1801 (1995); (*b*) I.H. Um, M.J. Kim, J.S. Min, and D.S. Kwon. Bull. Korean Chem. Soc. **18**, 523 (1997); (*c*) I.H. Um, E.S. Yeom, and D.S. Kwon. Bull. Korean Chem. Soc. **18**, 865 (1997).
14. (*a*) C.D. Johnson. Tetrahedron, **36**, 3461 (1980); (*b*) A. Pross. Isr. J. Chem. **26**, 390 (1985).
15. (*a*) I. Lee, C.S. Shim, S.Y. Chung, H.Y. Kim, and H.W. Lee. J. Chem. Soc. Perkin Trans. 2, 1919 (1988); (*b*) K.H. Yew, H.J. Koh, H.W. Lee, and I. Lee. J. Chem. Soc. Perkin Trans. 2, 2263 (1995).
16. I.H. Um, J.S. Jeon, and D.S. Kwon. Bull. Korean Chem. Soc. **12**, 406 (1991).
17. N.B. Chapman and J. Shorter (*Editors*). Advances in linear free energy relationships. Plenum, London, 1972.
18. D. Stefanidis, S. Cho, S. Dhe-Paganon. and W.P. Jencks. J. Am. Chem. Soc. **115**, 1650 (1993).
19. R.A.Y. Jones. Physical and mechanistic organic chemistry. 2nd ed. 1984. pp. 38–67.
20. J.F. Kirsch, W. Chewell, and A. Simon. J. Org. Chem. **33**, 127 (1968).
21. I.H. Um, Y.J. Hong, and D.S. Kwon. Tetrahedron, **53**, 5073 (1997).
22. I.H. Um, E.K. Chung, and D.S. Kwon. Tetrahedron Lett. **38**, 4787 (1997).
23. H.C. Brown and Y. Okamoto. J. Am. Chem. Soc. **80**, 4979 (1958).
24. G. Alberghina and S. Fisichella. J. Chem. Soc. Perkin Trans. 2, 81 (1978).
25. E.K. Chung. M.S. thesis. Ewha Womans University, Seoul, Korea. 1997.
26. (*a*) G. Moutiers, E. Le Guevel, L. Villien, and F. Terrier. J. Chem. Soc. Perkin Trans. 2, 7 (1997); (*b*) J.D. Aubort, R.F. Hudson, and R.C. Woodcock. Teterahedron Lett. **24**, 2229 (1973).
27. (*a*) I.H. Um, S.J. Oh, and D.S. Kwon. Tetrahedron Lett. **36**, 6903 (1995); (*b*) R.A. Moss, S. Swarup, and S. Ganguri. J. Chem. Soc. Chem. Commun. 860 (1987); (*c*) R. Curci and F. Di Furia. Int. J. Chem. Kinet. **7**, 341 (1975).
28. E. Buncel, H. Wilson, and C. Chuagui. J. Am. Chem. Soc. **104**, 4896 (1982).
29. J.E. Dixon and T.C. Bruice. J. Am. Chem. Soc. **94**, 2052 (1972).
30. E. Buncel and S. Hoz. Tetrahedron Lett. **24**, 4777 (1983).
31. I.H. Um, G.J. Lee, and D.S. Kwon. Bull. Korean Chem. Soc. **11**, 262 (1990).
32. W.P. Jencks and F. Regenstein. *In* Handbook of biochemistry. Selected data for molecular biology. *Edited by* H.A. Sober. The Chemical Rubber Co., Cleveland, Ohio. 1968.
33. (*a*) J.F. Kirsch and C.D. Hubbard, Biochem. **13**, 2483 (1972). (*b*) A.A. Humffray and J.J. Ryan. J. Chem. Soc. (B). 468 (1967). (*c*) A.R. Katritsky, R.T. Langthorne, H.A. Muathin, and R.C. Patel. J. Chem. Soc. Perkin Trans. 1, 2601 (1983).
34. E. Buncel, I.H. Um, and S. Hoz. J. Am. Chem. Soc. **111**, 971 (1989).

© 1998 NRC Canada

The rhodium(II)-catalyzed aziridination of olefins with {[(4-nitrophenyl)sulfonyl]imino}phenyl-λ^3-iodane

Paul Müller, Corine Baud, and Yvan Jacquier

Abstract: The aziridination of olefins with {(4-nitrophenylsulfonyl)imino}phenyl-λ^3-iodane, NsN═IPh (**1c**), in the presence of $[Rh_2(OAc)_4]$ proceeds in yields of up to 85% when the olefin is used in large excess. Under optimized conditions, styrene (**4a**) is aziridinated with 1 equiv. of NsN═IPh (**1c**) in 64% yield with 2 mol% of catalyst. The aziridines derived from electron-rich olefins undergo ring-opening under the conditions of the aziridination and afford rearrangement products or pyrrolidines. The aziridination is sterospecific with 1,2-dialkyl- and 1,2-arylalkyl-disubstituted olefins, but nonstereospecific with stilbene.The ρ-value for aziridination of substituted styrenes is –0.61. No ring-opened products are observed upon aziridination of vinylcyclopropanes. In the presence of chiral Rh^{II} catalysts, the aziridination is enantioselective, affording an ee of 73% with *cis*-β-methylstyrene (**4k**) and Pirrungs $[Rh_2\{(R)\text{-}(-)\text{-bnp}\}_4]$ catalyst. The experimental results are consistent with a one-step mechanism for transfer of the nitrenoid moiety from the catalyst to the olefin.

Key words: aziridination, nitrene transfer, rhodium catalysis.

Résumé : Lorsqu'on utilise un grand excès d'oléfine, l'aziridination des oléfines par le {(4-nitrophénylsulfonyl)imino}phényl-λ^3-iodane, NsN═IPh (**1c**), en présence de $[Rh_2(OAc)_4]$, se produit avec des rendements allant jusqu'à 85%. Dans des conditions optimales, le rendement de l'aziridination du styrène (**4a**) par un équivalent de NsN═IPh (**1c**) et 2 mol% de catalyseur est de 64%. Les aziridines obtenues à partir d'oléfines riches en électrons subissent des ouvertures de cycle dans les conditions de l'aziridination et elles conduisent à des produits de réarrangement ou à des pyrrolidines. L'aziridination est stéréospécifique avec les oléfines disubstituées par des groupes alkyle ou arylalkyle en 1,2, mais elle n'est pas stéréospécifique avec le stilbène. La valeur de ρ pour l'aziridination des styrènes substitués est de –0,61. On n'observe pas de produits à cycles ouverts lors de l'aziridination de vinylcyclopropanes. En présence de catalyseurs de Rh^{II} chiraux, l'aziridination est énantiosélective, conduisant à un ee de 73% lors de la réaction du *cis*-β-méthylstyrène (**4k**) en présence du catalyseur de Pirrung $[Rh_2\{(R)\text{-}(-)\text{-bnp}\}_4]$. Les résultats expérimentaux sont en accord avec un mécanisme de transfer en une étape de la portion nitrénoïde du catalyseur à l'oléfine.

Mots clés : aziridination, transfert de nitrène, catalyseur au rhodium.

[Traduit par la rédaction]

1. Introduction

The possibility of generating sulfonylnitrenes from {(organosulfonyl)imino}-λ^3-iodanes has been the subject of different investigations in the past. While thermal reaction in benzene of the phenyliodonium ylid **1a** (MsN═IPh) derived from methane–sulfonamide provided no nitrene-derived decomposition products (1), the tosyl analogue **1b** (TsN═IPh) transferred the sulfonylnitrene moiety to acceptors such as thioanisole (100°C, 49%), triphenylphosphine (100°C, 87%), and dimethylsulfoxide (25°C, 100%) (2). The first reported transition-metal-catalyzed reactions of sulfonylnitrenes, derived from TsN═IPh (**1b**), concerned CH-bond insertions, which occurred in the presence of Mn^{III}- or Fe^{III}-porphyrinate or $[Rh_2(OAc)_4]$ catalysts (3). In connection with model studies on the transfer of oxygen by cytochrome P-450 and model iron or manganese complexes, the group of Mansuy (4) reported the aziridination of olefins with TsN═IPh and Mn^{III}- and Fe^{III}-porphyrinates. These systems were also efficient for formal insertion of sulfonylnitrene into CH bonds (5). The aziridinations and CH-bond insertions exhibited characteristics typical for radical reactions.

The metal-catalyzed nitrene transfer from TsN═IPh (**1b**) to olefins was developed to become an efficient method for aziridination by Evans et al. (6). Cu^{I} and Cu^{II} complexes proved to be the most efficient catalysts. With chiral bis-oxazoline ligands the aziridination became enantioselective, and inductions of up to 97% were reported with cinnamate esters as substrates. With simple olefins such as styrenes the enantiomeric excess was, however, only 63% (7). The aziridination with Jacobsens's (8) Cu-based catalysts having benzylidene derivatives of 1,2-diaminocyclohexane as ligands afforded enantioselectivities near to perfection with 6-cyano-2,2-dimethylchromene, but were less satisfactory with simple olefins (ee's varying from 58–87%). Applications and extensions of the Cu-catalyzed aziridination using TsN = IPh (**1b**) as nitrene

This paper is dedicated to Professor Erwin Buncel in recognition of his contributions to Canadian chemistry.

Received December 10, 1997.

P. Müller,[1] C. Baud, and Y. Jacquier. Département de Chimie Organique, Université de Genève, 30 Quai Ernest Ansermet, CH-1211 Genève 4, Switzerland.

[1] Author to whom correspondence may be addressed. Telephone: +41 22 702 6527. Fax: +41 22 328 7396. E-mail: Paul.muller@chiorg.unige.ch

© 1998 NRC Canada

Scheme 1.

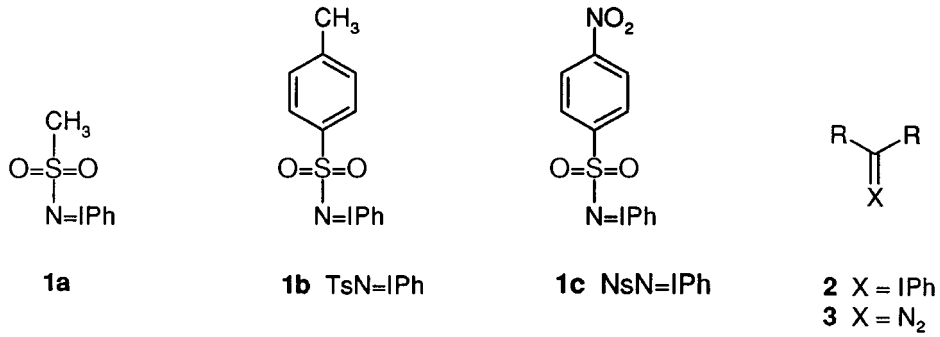

Table 1. Catalyzed aziridination of styrene (**4a**) with TsNXY (**6**), Scheme 2.[a]

Compd.	X, Y	Catalyst	Conditions	Yield of **5b** (%)
6a	N_2	Cu^0, 0.3 equiv.	MeCN, 80°C	3
6a	N_2	[CuCl], 0.13 equiv.	MeCN, 80ºC	0
6a	N_2	$[PdCl_2(PhCN)_2]$, 0.1 equiv.	MeCN, 80°C	0
6a	N_2	$[Rh_2(OAc)_4]$, 0.02 equiv.	CH_2Cl_2, 25°C	0
6b	Cl, $N(Bu)_4$	Cu^0, 1.0 equiv.	Styrene, 40 h, 25°C	36
6b	Cl, $N(Bu)_4$	[CuCl], 0.10 equiv.	Styrene, 40 h, 25°C	29
6b	Cl,$N(Bu)_4$	$[Cu(acac)_2]$, 0.10 equiv.	Styrene, 40 h, 25°C	16
6b	Cl,$(NBu)_4$	$[Cu(acac)_2]$, 0.10 equiv.	CH_2Cl_2, 14 h, 25°C	9
6b	Cl,$N(Bu)_4$	$[PdCl_2(PhCN)_2]$, 0.10 equiv.	MeCN, 14 h, 25°C	8
6b	Cl,$(NBu)_4$	$[Rh_2(OAc)_4]$, 0.10 equiv.	CH_2Cl_2, 14 h, 25°C	21
6b	Cl,$(NBu)_4$	$[Rh_2(OAc)_4]$, 0.10 equiv.	MeCN, 14 h, 25°C	8

[a] Conditions: slow addition of 1.00 mmol of TsNXY (**6**) in 5.0 mL of solvent to 5.0 mmol of styrene (**4a**) and catalyst (0.02–0.35 mmol) in 10.0 mL of solvent.

source have been reported in the literature with achiral (9) as well as chiral ligands (10). Several metal–salen complexes have been tried as catalysts for olefin aziridination with TsN═IPh, using Fe^{III}, Co^{II}, Cr^{III}, Ni^{II}, Mn^{III}, Pd^{II}, and Rh^{II}, but only {Mn(salen)Cl} was effective (11). An efficient chiral salen ligand for aziridination of styrenes with Mn^{III} has, however, been described recently by Katsuki and co-workers (12).

The observation that dimeric rhodium^{II} complexes having chiral carboxamidate ligands are highly efficient for asymmetric cyclopropanations of olefins (13) and cyclopropenations of terminal acetylenes (14) was the starting point of our own investigations on Rh^{II}-catalyzed asymmetric aziridinations. Owing to the formal analogy between TsN═IPh (**1b**) and alkylidene phenyliodonium ylides **2**, which are convenient substitutes for diazo compounds **3** in Rh^{II}-catalyzed carbenoid reactions (15), and the apparent similarity between carbene and nitrene transfer, we speculated that catalysis with chiral Rh^{II} carboxamidates would afford aziridines with enantioselectivities in the range of those reported for cyclopropanations. We therefore initiated a search for an efficient system for Rh^{II}-catalyzed generation and transfer of sulfonylnitrenes. Mechanistic aspects of the reaction were investigated, and a series of chiral Rh^{II}-based catalysts were tested. Some of the results of this investigation using {[(4-nitrophenyl)sulfonyl]imino}phenyl-λ^3-iodane (**1c**) have been reported previously (16).

2. Results and discussion

2.1. Nitrene precursors for aziridination of styrene

The aziridination of styrene (**4a**) was selected as model reaction for several systems, which, on the grounds of literature reports, appeared to have potential as precursors in metal-catalyzed nitrene transfer (17). The decomposition of tosyl azide (**6a**) (18) in the presence of Cu^I or Cu^{II} catalysts and styrene (**4a**) afforded none of the desired aziridine **5b**; however, a poor 3% yield of **5b** was isolated when the reaction was carried out in the presence of copper powder in acetonitrile at 80°C. Similarly, the use of $[PdCl_2(PhCN)_2]$ (19) or $[Rh_2(OAc)_4]$ afforded no **5b**. Exposure of chloramine-T ($TsNCl^-Na^+$) to copper powder in dimethylsulfoxide (DMSO) reportedly affords the corresponding sulfoximine in 80% yield (20), presumably via an intermediate Cu-complexed nitrene. However, application of this and related systems to aziridination of **4a** appears to be limited. In our hands, the best results were obtained with the tetrabutylammonium salt of $TsNCl^-$ (**6b**), which afforded a 36% yield of **5b** with 1 equiv. of Cu^0; [CuCl] (0.1 equiv.) in turn, gave a yield of 29% of **5b**, and the highest yield with $[Rh_2(OAc)_4]$ was 21%. The sulfonamide $TsNH_2$ (**7b**) was the major secondary product in these reactions. See Table 1 and Scheme 2.

2.2. Optimization of aziridination conditions

Selection of catalyst

Recently, Evans et al. (6, 7) reported the metal-catalyzed aziridination of styrene (**4a**) by TsN═IPh (**1b**) with a large variety of catalysts. The Cu^I and Cu^{II} complexes were the most suitable for olefin aziridination, and these catalysts were used later by other groups. $[Rh_2(OAc)_4]$ was also tested, but was found much less suitable than Cu catalysts. In view of the low

© 1998 NRC Canada

Scheme 2.

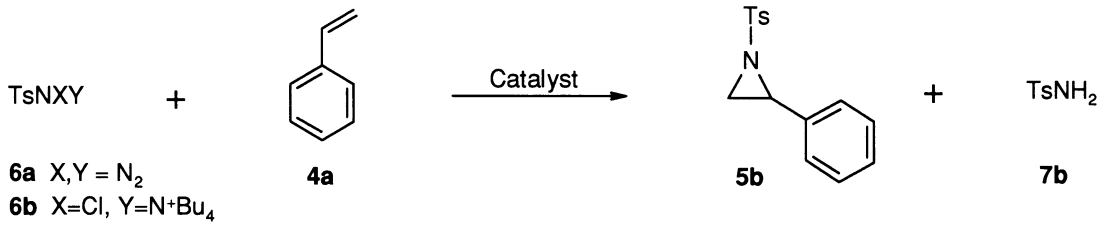

Table 2. Aziridination of styrene (**4a**) with TsN═IPh (**1b**) and Pd^{II} or Rh^{II} catalysts.[a]

Entry	Catalyst	Conditions	Yield of **5b** (%)
1	$[PdCl_2]$, 0.10 mmol	MeCN, 96 h	26
2	$[PdCl_2]$, 0.10 mmol	MeCN, 50°C, 3 h	22
3	$[PdCl_2]$, 0.10 mol	MeCN, 80°C, 3 h	12
4	$[PdCl_2(PhCN)_2]$, 0.10 mmol	MeCN, 96 h	37
5	$[PdCl_2(PhCN)_2]$, 0.10 mmol	MeCN, 50°C, 0.5 h	25
6	$[Pd(acac)_2]$, 0.10 mmol	MeCN, 20°C, 96 h	10
7	$[Rh_2(OAc)_4]$, 0.02 mmol	PhMe, 15 h	18
8	$[Rh_2(OAc)_4]$, 0.02 mmol	DMF, mol. sieves, 3 h	0
9	$[Rh_2(OAc)_4]$, 0.02 mmol	$MeNO_2$, mol. sieves,[b] 0.5 h	19
10	$[Rh_2(OAc)_4]$, 0.02 mmol	THF, 18 h	6
11	$[Rh_2(OAc)_4]$, 0.02 mmol	MeCN, 19 h	23
12	$[Rh_2(OAc)_4]$, 0.02 mmol	MeCN, mol. sieves,[b] 16 h	32
13	$[Rh_2(OAc)_4]$, 0.02 mmol	$CHCl_3$, mol. sieves,[b] 0.5 h	23
14	$[Rh_2(OAc)_4]$, 0.02 mmol	$C_2H_4Cl_2$, mol. sieves,[b] 0.5 h	34
15	$[Rh_2(OAc)_4]$, 0.02 mmol	CH_2Cl_2, 0.25 h	32
16	$[Rh_2(OAc)_4]$, 0.02 mmol	CH_2Cl_2, mol. sieves,[b] 1.0 h	43
17	$[Rh_2(OAc)_4]$, 0.02 mmol	as above, 16 h, 20 equiv. of styrene	59
18	$[Rh_2(OAc)_4]$, 0.02 mmol	as above, 16 h, 50 equiv. of styrene	59
19	$[Rh_2(OAc)_4]$, 0.02 mmol	as above, 40°C, mol. sieves,[b] 1.2 h	28
20	$[Rh_2(OAc)_4]$, 0.20 mmol	CH_2Cl_2, mol. sieves, 1.0 h	59
21	$[Rh_2\{(2S)\text{-mepy}\}_4]$, 0.02 mmol	CH_2Cl_2, mol. sieves, 1.0 h	11
22	$[Rh_2(pfb)_4]$, 0.02 mmol	CH_2Cl_2, mol. sieves, 1.0 h	20

[a] Conditions: 1.0 mmol of TsN═IPh (**1b**) suspended in the appropriate solvent (10.0 mL), stirred with 5.0 mmol of styrene (**4a**) and the catalyst at 20°C, unless otherwise indicated.
[b] Activated molecular sieves (6.0 g) added to solvent.

yields in our experiments with **6a**,**b**, we investigated the aziridination of styrene (**4a**) with TsN═IPh (**1b**) with Pd^{II} and Rh^{II} catalysts under a variety of conditions, but success was very limited. In the case of Pd^{II} the highest yield of **5b** (37%) was achieved with $[PdCl_2(PhCN)_2]$ (10%) with a five-fold excess of **4a** (Table 2). With $[Rh_2(OAc)_4]$, reaction in dry dichloromethane at 20°C produced the highest yield (43%) with a five-fold excess of **4a** and 2% of catalyst. When the excess of styrene (**4a**) was increased to 20-fold, the yield of (**5b**) increased to 59%. Other Rh^{II} catalysts, such as $[Rh_2\{(2S)\text{-mepy}\}_4]$ (mepy = methyl pyrrolidone-2-carboxylate) (21) or $[Rh_2(pfb)_4]$ (pfb = perfluorobutyrate) (22) resulted in reduced yields of **5b**.

Optimization of ylide structure

In the next step of the optimization procedure the nature of the sulfonamide group of the iodonium ylides was varied. The ylides **1a**–**g** were synthesized by the standard procedure described for TsN═IPh (**1b**), which consists in the reaction of the appropriate sulfonamide or carboxamide, respectively, **7a**–**g** with diacetoxy iodobenzene, $PhI(OAc)_2$ in MeOH in the presence of KOH (2). They were in general amorphous solids that could not be further purified, but were > 95% pure, except the 4-methoxy derivative **1d**, which was isolated as an unseparable 64:36 mixture of ylide and the starting sulfonamide **7d**. A comparative study was carried out for aziridination of styrene with $[Rh_2(OAc)_4]$ in CH_2Cl_2, (2% of catalyst) and $[Cu(acac)_2]$ in acetonitrile (5–10% of catalyst) and the ylides **1a**–**g** (Table 3, Scheme 3).

Efficient aziridine formation occurred only with the iodonium ylides derived from aromatic sulfonamides, while those derived from methanesulfonamide and trifluoroacetamide were either less effective or failed completely. Among the phenyl derivatives, the 4-nitro-compound (NsN═IPh, **1c**) afforded the highest yield of aziridine with $[Rh_2(OAc)_4]$. Cu catalysis, in turn, was more efficient for TsN═IPh (**1b**). A recent more detailed study revealed, however, that NsN═IPh (**1c**) is also more suitable than TsN═IPh (**1b**) in Cu-catalyzed aziridinations (23). We expected a still higher yield with the 2,4-dinitro derivative **1e**, but this ylide turned out to be significantly less suitable than the mono nitro derivative NsN═IPh (**1c**). The ylide **1f**, derived from pentafluorophenylsulfonamide **7f**, afforded no aziridine with either of the catalysts.

© 1998 NRC Canada

Scheme 3.

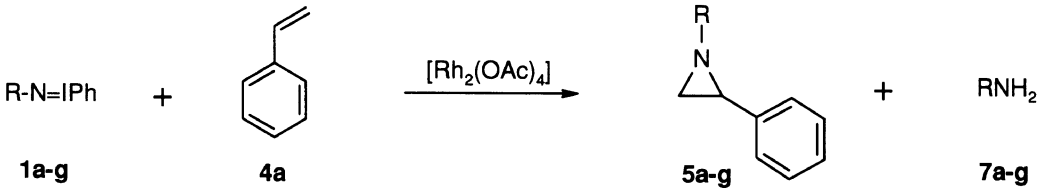

Table 3. Aziridination of styrene (**4a**) with ylides **1a**–**g** and $[Cu(acac)_2]$ or $[Rh_2(OAc)_4]$, Scheme 3.[a]

No.	R	Catalyst	Aziridine	Yield (%)
1a	$MeSO_2$	$[Cu(acac)_2]$	**5a**	7
1a	$MeSO_2$	$[Rh_2(OAc)_4]$	**5a**	0
1b	4-$MeC_6H_4SO_2$	$[Cu(acac)_2]$	**5b**	95[b]
1b	4-$MeC_6H_4SO_2$	$[Rh_2(OAc)_4]$	**5b**	59
1c	4-$NO_2C_6H_4SO_2$	$[Cu(acac)_2]$	**5c**	71
1c	4-$NO_2C_6H_4SO_2$	$[Rh_2(OAc)_4]$	**5c**	85
1c	4-$NO_2C_6H_4SO_2$	none	**5c**	0
1d	4-$MeOC_6H_4SO_2$	$[Cu(acac)_2]$	**5d**	60
1d	4-$MeOC_6H_4SO_2$	$[Rh_2(OAc)_4]$	**5d**	0
1e	2,4-$(NO_2)_2C_6H_3$	$[Cu(acac)_2]$	**5e**	58
1e	2,4-$(NO_2)_2C_6H_3$	$[Rh_2(OAc)_4]$	**5e**	48
1f	$C_6F_5SO_2$	$[Cu(acac)_2]$	**5f**	0
1f	$C_6F_5SO_2$	$[Rh_2(OAc)_4]$	**5f**	0
1g	CF_3CO	$[Cu(acac)_2]$	**5g**	0
1g	CF_3CO	$[Rh_2(OAc)_4]$	**5g**	0

[a] Conditions: at room temperature under N_2 and in presence of molecular sieves (6.0 g). $[Cu(acac)_2]$: 5.0 mmol of styrene in dry MeCN (10.0 mL), stirred with 1.0 mmol of ylide **1a**–**g** and 0.05–0.10 mmol of catalyst. $[Rh_2(OAc)_4]$: 5.0 mmol of styrene in CH_2Cl_2 (10.0 mL) containing molecular sieves, stirred with 1.0 mmol of ylide and 0.02 mmol of catalyst.
[b] References 6 and 7.

Table 4. Solvent effect on $[Rh_2(OAc)_4]$-catalyzed aziridination of styrene (**4a**) with 1 equiv. of NsN═IPh (**1c**).[a]

Solvent	Temp. (°C)	Time	Yield of aziridine **5c** (%)
Sulfolane	25	48 h	0
$MeNO_2$	25	21 h	0
CH_2Cl_2	25	20 h	9
CH_2Cl_2/sulfolane 2:1	25	64 h	47
CH_2Cl_2/sulfolane 95:5	25	2 h	51
CH_2Cl_2/sulfolane 99:1	25	2 h	59
CH_2Cl_2/sulfolane 99:1	25	2 h	43[b]
CH_2Cl_2/sulfolane 99.5:0.5	25	2 h	64
CH_2Cl_2/sulfolane 99.5:0.5	25	2 h	48[b]
CH_2Cl_2/sulfolane 99.9:0.1	25	2 h	45
CH_2Cl_2/sulfolane 99.5:0.5	50	2 h	49
CH_2Cl_2/sulfolane 99.5:0.5	–20	2 h	45
CH_2Cl_2/MeNO2 2:1	25	2 h	9
CH_2Cl_2/MeNO2 95:5	25	2 h	37

[a] Conditions: 0.02 mmol of $[Rh_2(OAc)_4]$ stirred in 10 mL of solvent (v/v) containing molecular sieves (6.0 g) with 1.0 mmol of styrene and 1.0 mmol of NsN═IPh (**1c**).
[b] 2.0 equiv. of **1c**.

The reasons for the absence of reactivity of the aliphatic ylides was not further investigated. Nevertheless, a difference in behavior was observed. All the ylides were almost or entirely insoluble in most of the conventional solvents. However, the ylides derived from arenesulfonamides dissolved in CH_2Cl_2 upon exposure to the catalyst and the substrate and produced aziridines or sulfonamides. In contrast, the ylides **1a** and **1f**, derived from methanesulfonamide (**7a**) and pentafluorobenzenesulfonamide (**7f**), respectively, remained suspended in the solvent and were recovered unchanged. The same observation applies to **1g**. The mechanism for formation of the sulfonamide **7** as the main secondary reaction product has yet to be established. In the case of the metallo-porphyrin-catalyzed aziridinations with TsN═IPh (**1c**) it has been proposed that $TsNH_2$ (**7b**) arises from hydrolysis of the intermediate metal nitrene complex; the resulting metal-oxo species, in turn, attacks olefins to afford epoxides. However, no epoxides were ever detected in the aziridinations using iminophenyliodinanes **1** catalyzed with Rh^{II}. In addition, control experiments revealed the absence of epoxide formation when *trans*-stilbene was exposed to iodosylbenzene in the presence of $[Rh_2(OAc)_4]$.

As a precautionary measure, all aziridinations with NsN═IPh (**1c**) were carried out in the presence of activated molecular sieves in order to avoid hydrolysis of NsN═IPh to $NsNH_2$ (**7c**). Despite this, sulfonamide formation could not be suppressed entirely. It became particularly important in the aziridination of electron-deficient or sterically hindered olefins. The reason for this is a catalyst-induced decomposition of NsN═IPh (**1c**), competitive with the aziridination, which ultimately, after work-up, affords $NsNH_2$ (**7c**). However, the nature of this secondary reaction could so far not be established.

Solvent effect

The Rh^{II}-catalyzed aziridination exhibits a peculiar solvent effect. Best results were obtained with chlorinated solvents such CH_2Cl_2. The dipolar nonprotogenic solvents sulfolane or $MeNO_2$, etc., were found inefficient. However, the addition of small quantities of sulfolane or, to a minor degree, $MeNO_2$ to CH_2Cl_2 resulted in an increase of yield of aziridine. Under optimized conditions, with a CH_2Cl_2/sulfolane ratio of 99.5:0.5 the aziridination of styrene (**4a**) with 1.0 equiv. of NsN═IPh (**1c**) proceeded in 64% yield. Smaller, but also larger, amounts of sulfolane resulted in reduced yields, however (see Table 4).

2.3. Scope and limitations of the aziridination

A series of olefins of different structure was examined in order to establish the scope of the reaction. The reaction conditions were optimized for styrene (**4a**) as follows: NsN═IPh (**1c** 1.0 mmol) was suspended in CH_2Cl_2 (20 mL) at room temperature under N_2. After addition of the olefin (20.0 mmol) and

© 1998 NRC Canada

Table 5. $[Rh_2(OAc)_4]$-catalyzed aziridination of olefins with NsN═IPh (**1c**), Scheme 4.[a]

No.	Olefin	Time (h)	No.	Aziridine yield (%)	Comment
4a	Styrene	2	**5c**	85	Reference 16*a*
4b	4-Acetoxystyrene	0.75	**8b**	82	
4c	4-Bromostyrene	1.3	**8c**	82	
4d	3-Chlorostyrene	0.30	**8d**	79	
4e	4-Methoxycarbonylstyrene	23	**8e**	17	
4f	4-Methylstyrene	0.50	**8f**	76	Reference 16*a*
4g	3-Nitrostyrene	19	**8g**	46	Reference 16*a*
4h	4-Methoxystyrene	0.75	**8h**	0	16% of pyrrolidine **12h**
4i	3-Methylbut-1-ene	91	**8i**	0	
4j	Buta-1,3-diene	1.0	**8j**	94	200 mmol of olefin
4k	*cis*-β-Methylstyrene	0.5	**8k**	82	Reference 16*a*
4l	*trans*-β-Methylstyrene	18	**8l**	68	Reference 16*a*
4m	Ethyl vinylether	0.5	**8m**	0	52% of pyrrolidine **12m** (16*a*)
4n	Vinyl acetate	4	**8n**	47	Reference 16*a*
4o	Ethyl acrylate	4.5	**8o**	7	
4p	Norbornene	0.7	**8p**	29	
4q	Indene	2.5	**8q**	40	
4r	Norbornadiene	91	**8r**	0	50% rearr. to **10**
4s	Ethyl sorbate	91	**8s**	0	

[a] Conditions: 20 mmol of olefin stirred with 1.0 mmol of NsN═IPh (**1c**) and 0.02 mmol of $[Rh_2(OAc)_4]$ in 10 mL of CH_2Cl_2 at room temperature in the presence of molecular sieve (6.0 g).

Scheme 4.

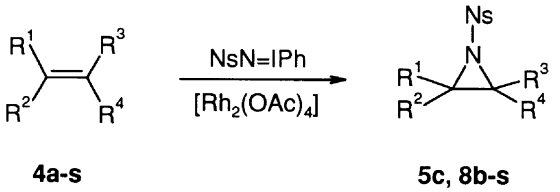

4a-s **5c, 8b-s**

$[Rh_2(OAc)_4]$ (0.02 mmol) the mixture was stirred until all of the ylide was dissolved (see Table 5, Scheme 4).

Inspection of Table 5 reveals that the reactivity of olefins towards NsN═IPh (**1c**) – $[Rh_2(OAc)_4]$ is determined by electronic and steric factors. Electron-deficient olefins such as 3-nitrostyrene (**4g**), 4-methoxycarbonylstyrene (**4e**), or ethyl acrylate (**4o**) afford lower yields of aziridines than the electron-rich substrates. Yields with *cis*-1,2-disubstituted olefins are slightly higher than with the *trans*-isomers (except in the case of stilbene) (16*a*). The low reactivity of 3-methylbut-1-ene (**4i**) and norbornene (**4p**) is best ascribed to steric hindrance. Ethyl sorbate (**4s**) produced no aziridination product with NsN═IPh (**1c**) – $[Rh_2(OAc)_4]$, probably owing to an unfavorable combination of steric and electronic factors, and the same applies to ethyl cinnamate, which is the best substrate in the Cu-catalyzed aziridination of Evans et al. (6). An attempt to extend the aziridination of olefins to acetylenes, a reaction well known in the series of carbenoid additions, failed with hex-1-yne.

Consecutive reactions with electron-rich olefins

With some of the electron-rich olefins complications owing to consecutive reactions of the originally formed aziridines arose. The isolation of rearranged products upon aziridination of 1,1-diphenylethene and *trans*-stilbene has been reported previously (16*a*). Similarly, aziridination of norbornadiene (**4r**) afforded none of the expected aziridine **8r** but a rearranged product **10**, presumably by a mechanism involving **9**, analogous to that proposed for reaction of norbornadiene with phenyl azide (24) (see Scheme 5).

The aziridine derived from 4-methoxystyrene (**4h**) underwent ring-opening under the aziridination conditions, which was followed by cycloaddition of the supposed intermediate dipolar species **11** to a second molecule of olefin to afford a *cis*/*trans* mixture of pyrrolidines **12h**. Analogous products have been isolated upon aziridination of ethyl vinylether (**4m**) and α-methylstyrene (16*a*). The structure of the pyrrolidines was deduced from the mass spectra, which showed the incorporation of a second olefin molecule in the product, and from detailed analysis of the ^1H NMR. Reinspection of the NMR data of the isomers of **12m** revealed that they are *cis*/*trans* isomers and that the previous structural assignement was incorrect (16*a*). The formation of regioisomeric adducts, which would have either C_2 or C_s symmetry, could be ruled out on the grounds of the spectra, but the assignment of relative configurations of the pyrrolidines proved impossible (17). Since no aziridines could be isolated in these reactions, it is not established whether the dipolar intermediate **11** is derived from direct attack of the NsN═IPh (**1c**) to the olefin or via ring-opening of the putative aziridines (see Scheme 6).

Intermolecular CH-bond insertion

The aziridination of olefins having alkyl substituents is usually accompanied by formal products of nitrene insertion into CH bonds. In the case of cyclohexene, the aziridine was formed in only 4% yield, while 70% of the allylic sulfonamide was isolated (16*a*). Subsequent work showed, however, that cyclohexene is an exception. Olefins react usually via aziridination, and CH insertion is only a secondary reaction, although it may occur with other compounds having activated CH bonds, such as arylalkanes and ethers. The reaction proceeds with retention

© 1998 NRC Canada

Scheme 5.

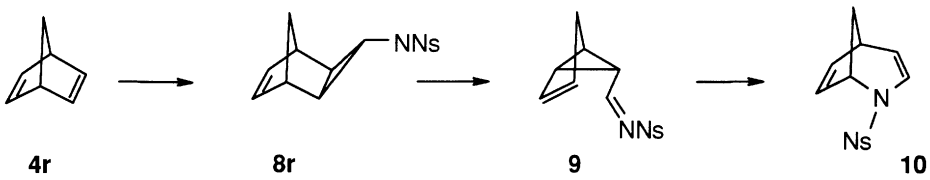

Scheme 6.

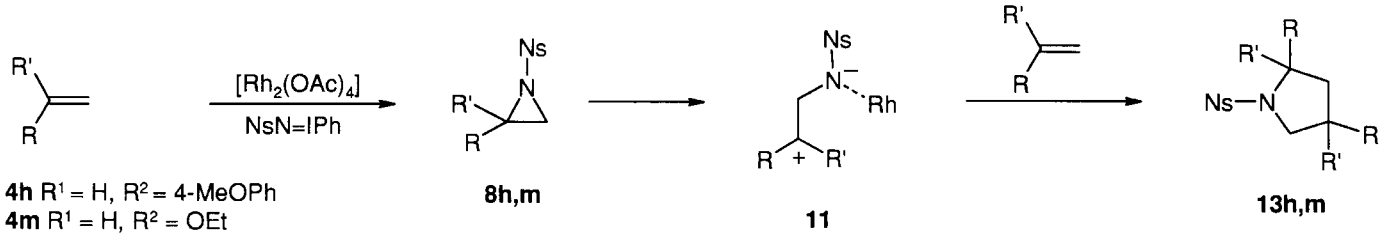

Scheme 7.

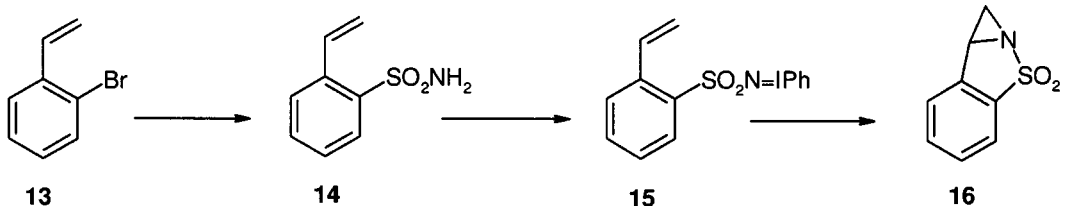

of configuration at the reacting carbon center (25) and most likely proceeds via a one-step mechanism (25).

Intramolecular aziridination

Since the presence of a large excess of olefin is necessary for efficient aziridination, an intramolecular aziridination was carried out in the hope that generation of the reacting species in the immediate vicinity of the double bond would compensate for the reduction of the 20:1 olefin/ylide ratio in the intermolecular reaction to 1:1 ratio in the intramolecular version. Since the preparation of iminophenyliodinanes from unsaturated aliphatic sulfonamides by the conventional methods failed, the aromatic derivative **15** was synthesized via metallation–sulfonation of 2-bromostyrene **13** (26) and treatment of the sulfonamide **14** with diacetoxyiodobenzene. The ylide was contaminated with unreacted **14**, which could not be separated. Treatment of **15** with $[Rh_2(OAc)_4]$ afforded **16** in only 20% yield together with much sulfonamide **12**. Apparently, the eventual advantage of carrying out the reaction intramolecularly is lost owing to a less favorable substitution pattern (absence of nitro substituent) on the aromatic moiety (see Scheme 7).

2.4. Mechanistic investigations

Stereochemistry of aziridination

The stereochemistry of the Rh^{II}-catalyzed aziridination with NsN═IPh (**1c**) was investigated with the *cis*- and *trans*-isomers of hex-2-ene, β-methylstyrene, and stilbene. Hex-2-ene and β-methylstyrene reacted stereospecifically, but *cis*-stilbene afforded a mixture of *cis*- and *trans* aziridines in low yield. In contrast, *trans*-stilbene reacted to a mixture of *trans*-aziridine and a rearranged enamide in 41% and 11% yield, respectively (16*a*).

The observation of stereospecificity upon aziridination of β-methylstyrene contrasts with that observed in the Cu-catalyzed aziridination where, with most ligands, the stereospecificity is lost. The loss of stereospecificity suggests a two-step mechanism for aziridination involving either an intermediate radical **17** or a zwitterionic species **18** in which bond rotation occurs faster than ring closure. The Rh^{II}-catalyzed aziridination, in turn, could be concerted or stepwise, but with the rate of ring closure faster than bond rotation. The loss of stereospecificity observed with *cis*-stilbene appears more consistent with a two-step mechanism, but it is not clear whether stilbene stands at the extreme end of a mechanistic continuum of a general two-step mechanism or whether the general mechanism is concerted and stilbene must be considered an exception (see Scheme 8).

Polar substituent effects

As mentioned above, the two-step mechanism for aziridination could involve either a radical intermediate **17** or a zwitterionic species **18**. To eliminate this latter possibility, the polar substituent effect on the reaction was examined by means of competition experiments using pairs of substituted styrenes **4a**–**g**. Relative reactivities of the styrenes were determined from the product ratios of the aziridines, as analyzed by NMR (Table 6, Figure 1).

The ρ-value for the aziridination with NsN═IPh (**1c**)/$[Rh_2(OAc)_4]$ of –0.61 is close to that measured for the Rh(II)-catalyzed cyclopropanation of styrenes with diazomalonate, and

© 1998 NRC Canada

Scheme 8.

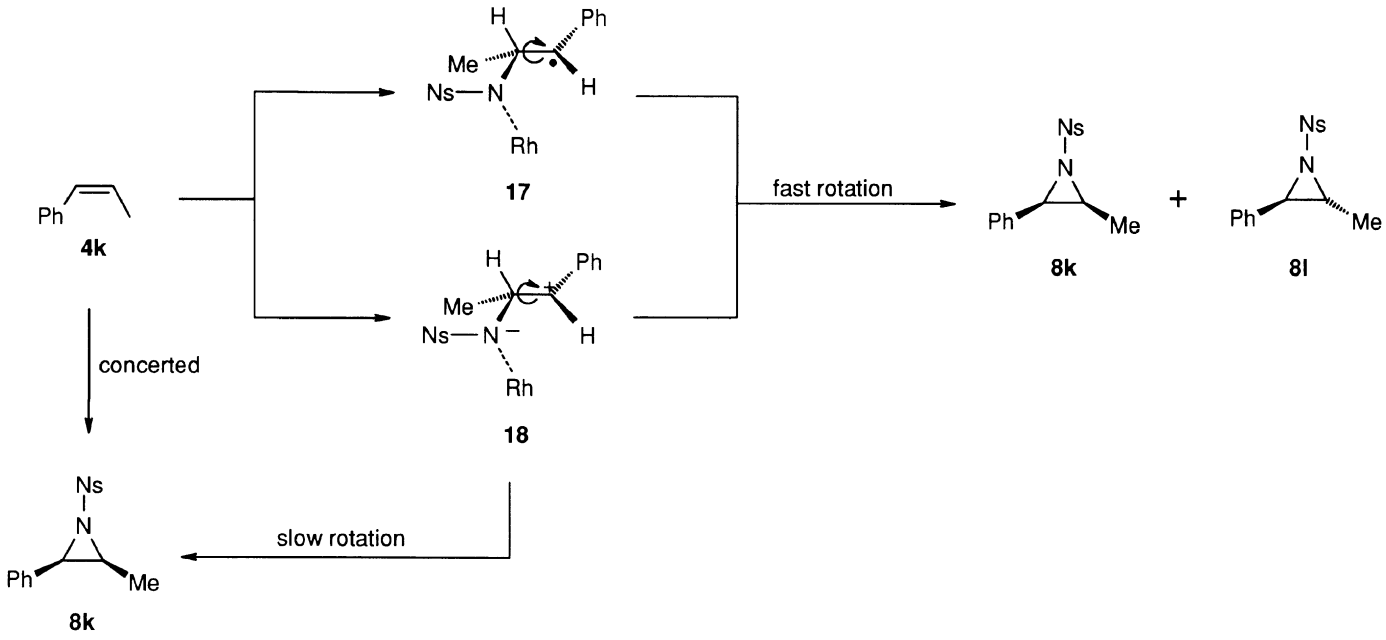

Fig. 1. Hammett plot (vs. σ^+) (27) for aziridination of styrenes with NsN═IPh (**1c**) and $[Rh_2(OAc)_4]$ ($\rho = -0.613$, $r = 0.984$) or $[Cu(acac)_2]$ ($\rho = -0.49$, $r = 0.999$) at 22°C.

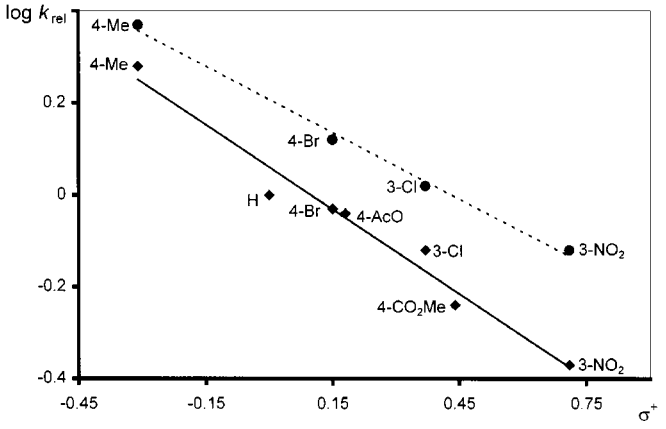

also close to the values reported for dichlorocarbene addition to styrene ($\rho = -0.62$, 80°C) (28) or to α-methylstyrene ($\rho = -0.38$, 0°C) (29). This is clearly too low for a dipolar intermediate with development of a positive charge at the benzylic position in the transition state. On the other hand, it is consistent with a concerted as well as with a radical mechanism. The Hammett ρ-constant for the $[Cu(acac)_2]$-catalyzed reaction is slightly lower (–0.49; $r = 0.991$). The plot of this latter reaction suffers from an anomaly, since it does not pass through the origin. The reasons for this anomaly are not clear, but have not been investigated yet.

Radical clocks in aziridination

The possible intervention of radicals in the aziridination pathway was tested with vinylcyclopropane **19a** and its *cis*-diphenyl-substituted derivative **19b**. The corresponding

Table 6. Competitive aziridination of styrenes **4a**–**g** with NsN═IPh (**1c**) and $[Rh_2(OAc)_4]$ or $[Cu(acac)_2]$.[a]

Compd.	Subst.	log $k_{rel}[Rh_2(OAc)_4]$	log $k_{rel}[Cu(acac)_2]$	σ^+, σ_m [b]
4a	H	0	0	0
4b	4-OAc	–0.029		0.18
4c	4-Br	–0.025	0.122	0.15
4d	3-Cl	–0.13	0.017	0.37
4e	4-CO_2Me	–0.243		0.44
4f	4-Me	0.268	0.367	–0.31
4g	3-NO_2	–0.365	–0.123	0.71

[a] Conditions: see Experimental.
[b] Reference 27.

secondary radicals **20a**,**b** ring-open to homoallylic radicals **21a**,**b** with rate constants of $> 2 \times 10^7$ s^{-1} and $> 2 \times 10^{10}$ s^{-1}, respectively (30). The olefins were synthesized via Wittig olefination of the corresponding aldehydes (31) (see Scheme 9).

Aziridination of vinylcyclopropane (**19a**) afforded the aziridine **22a** in ca. 43% yield (partial decomposition during work-up). The diphenyl derivative **19b** reacted only sluggishly to yield the aziridine **22b** in 35% yield. No products derived from ring-opening of an intermediate radical could be detected in the crude reaction mixture. It follows that the aziridination of mono-substituted olefins should proceed via a concerted mechanism or via a radical that undergoes cyclization with a rate constant significantly faster than 10^{12} s^{-1}. While this latter possibility cannot be ruled out, it has no consequences on the actual stereospecificity of the aziridination. On the other hand, the significance of this result with respect to the aziridination mechanism of disubstituted olefins, in particular to stilbene is open to debate.

Asymmetric aziridination

Styrene (**4a**) and *cis*-β-methylstyrene (**4j**) were aziridinated

© 1998 NRC Canada

Scheme 9.

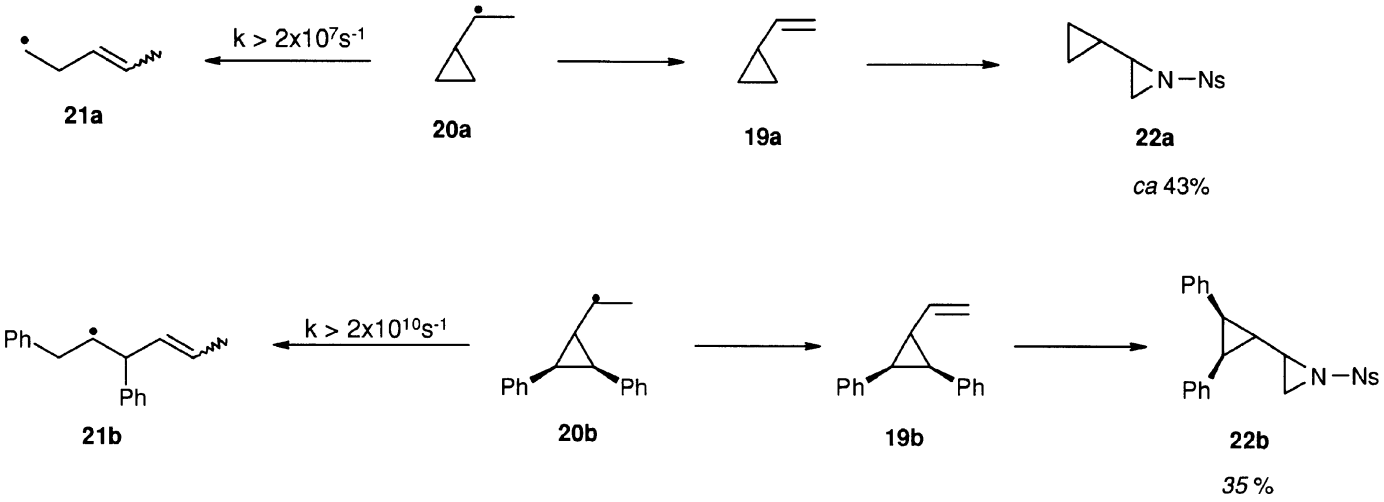

Scheme 10.

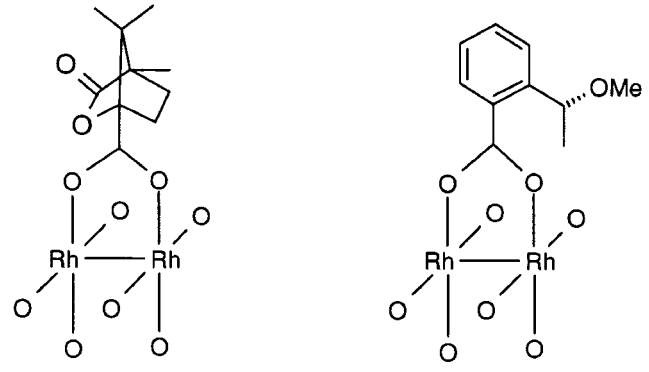

with NsN═IPh (**1c**) in the presence of the known Rh^{II} catalysts $[Rh_2\{(2S)\text{-mepy}\}_4]$ (22), $[Rh_2\{(4S)\text{-phox}\}_4]$ (32), $[Rh_2\{(2S)\text{-bepy}\}_4]$ (33), $[Rh_2\{(4S)\text{-macim}\}_4]$, $[Rh_2\{(S)\text{-ptpa}\}_4]$ (34), $[Rh_2\{(R)\text{-(–)-bnp}\}_4]$ (35), $[Rh_2\{(S)\text{-psp}\}_4]$ (36), and $[Rh_2\{(–)\text{-mpmt}\}_4]$ (37), which were prepared according to literature procedures. Two new Rh^{II} carboxylate catalysts, $[Rh_2\{(–)\text{-campha}\}_4]$ (**23**) and $[Rh_2\{(R)\text{-meba}\}_4]$ (**24**), were prepared via ligand exchange from $[Rh_2(OAc)_4]$ with camphanic acid, and with 2-(*R*-methoxyethyl)benzoic acid, respectively (38). The results are summarized in Table 6. The chemical yields of the reaction were usually satisfactory, but enantioselectivity has not yet reached levels useful for synthetic applications. Typically, the Rh^{II}-carboxamidate catalysts that have shown exceptional enantioselectivities in carbenoid reactions exhibit only modest selectivity in aziridination. At this time, the best results were obtained with Pirrungs $[Rh_2\{(R)\text{-(–)-bnp}\}_4]$ (bisnaphtholphosphate ligand), which afforded an ee of 55% with styrene (**4a**) and 73% with *cis*-β-methylstyrene (**4j**), respectively. No enantioselectivity was observed in the intramolecular aziridination with **16**.

Although these selectivities are still considerably below the desired level, they show unambiguously that the catalyst is not only involved in the decomposition of the NsN═IPh (**1c**), but that it is intimately associated in the transfer of the nitrene moiety to the olefin (see Scheme 10, Table 7).

Photochemical nitrene generation

Jacobsen (8) has shown that Cu catalysts are highly efficient in trapping 4-toluenesulfonylnitrene, generated by photolysis of the corresponding azide, TsN_3. In the presence of a chiral catalyst, aziridination proceeded with the same enantioselectivity as in the aziridination starting with TsN═IPh (**1b**) and the same catalyst. Analogous experiments have been carried out with the NsN═IPh/$[Rh_2\{(R)\text{-(–)-bnp}\}_4]$ system. The aziridination of styrene (**4a**) proceeds with 74% yield and 55% ee (Table 7). NsN_3 (**25**) is stable towards the catalyst at room temperature. Photolytic decomposition of NsN_3 (20 mmol) in the presence of $[Rh_2(R)\text{-(–)-bnp})_4]$ (1.0 mmol) afforded the aziridine **5c** in 9% yield and 17% ee. Since photolysis of sulfonylazides is known to produce sulfonylnitrenes (39), the observation of enantioselectivity implies that at least part of the reaction must proceed via a metal-complexed nitrene **26**. The trapping efficiency is, however, much lower than that of 100% observed by Jacobsen (8) in the Cu-catalyzed aziridination.

© 1998 NRC Canada

Table 7. Asymmetric aziridination of olefins with NsN═IPh (**1c**) and chiral Rh^{II} catalysts.[a]

Olefin	Catalyst	Time (h)	Aziridine Yield (%)	Aziridine ee (%)
Styrene (**4a**)	$[Rh_2\{(2S)\text{-mepy}\}_4]$	20	81	21
Styrene (**4a**)	$[Rh_2\{(2S)\text{-bepy}\}_4]$	3	71	27
Styrene (**4a**)	$[Rh_2\{(4S)\text{-phox}\}_4]$	23	56	22
Styrene (**4a**)	$[Rh_2\{(4S)\text{-macim}\}_4]$	2.5	50	<10
Styrene (**4a**)	$[Rh_2\{(S)\text{-ptpa}\}_4]$	0.2	92	0
Styrene (**4a**)	$[Rh_2\{(R)\text{-(–)-bnp}\}_4]$	1.5	74	55
cis-β-Methylstyrene (**4k**)	$[Rh_2\{(2S)\text{-bepy}\}_4]$	27	70	35
cis-β-Methylstyrene (**4k**)	$[Rh_2\{(R)\text{-(–)-bnp}\}_4]$	1.0	80	73
cis-β-Methylstyrene (**4k**)	$[Rh_2\{(S)\text{-psp}\}_4]$	48	70	<10
cis-β-Methylstyrene (**4k**)	$[Rh_2\{(–)\text{-mpmt}\}_4]$	1.5	73	0
cis-β-Methylstyrene (**4k**)	$[Rh_2\{(–)\text{-campha}\}_4]$	27.5	71	0
cis-β-Methylstyrene (**4k**)	$[Rh_2\{(R)\text{-meba}\}_4]$	1.5	78	15
15[b]	$[Rh_2\{(R)\text{-(–)-bnp}\}_4]$	0.75	30	0

[a] Conditions according to general procedure.
[b] {(2-Ethenylsulfonyl)imino}phenyl-λ^3-iodane (**15**), intramolecular reaction.

Scheme 11.

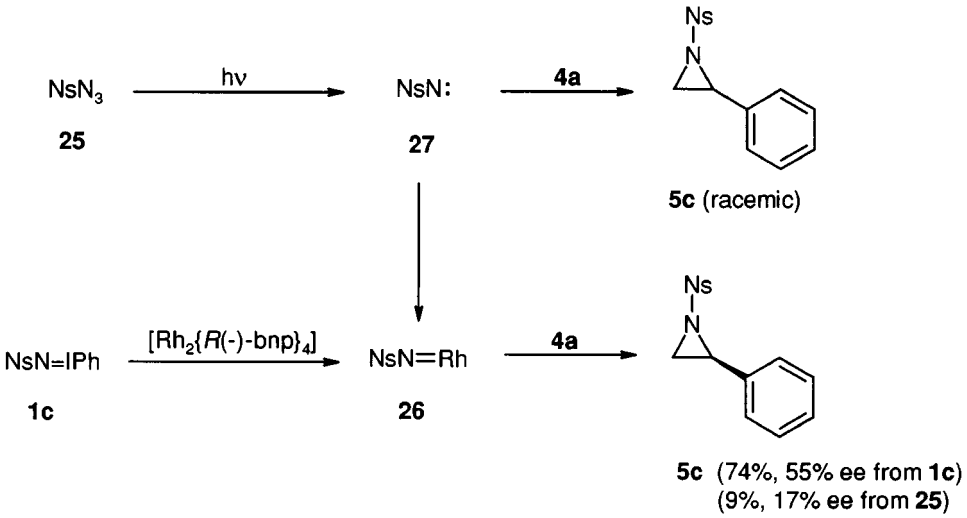

In our experiments, about two thirds of the reaction proceed directly from attack of the free nitrene **27** to produce racemic aziridine **5c**, and only a minor part is delivered via the metal-complexed species (see Scheme 11).

3. Conclusion

The Rh^{II}-catalyzed aziridination with NsN═IPh (**1c**) exhibits many similarities to the more established Cu^{I}-catalyzed reactions with TsN═IPh (**1b**). In both systems, a metal-complexed nitrene is probably involved. Both are stereospecific with alkyl-substituted olefins, but loss of stereospecificity may occur when the olefin carries one (Cu/TsN═IPh) or two (Rh/NsN═IPh) aryl substituents. Both systems suffer from limited efficiency, which may be overcome by the use of a large amount of catalyst (with Cu) or a large excess of olefin (with Rh). Further work will be directed towards a more efficient system for nitrene transfer and towards improvement of the enantioselectivity, in order to achieve a general method for enantioselective catalytic olefin aziridination.

4. Experimental

General

(See ref. 32.)

Synthesis of iminophenyl-λ^3-iodanes 1a–g

The syntheses of **1a** (1), **1b** (2), and **1g** (4) have been described in the literature.

*Preparation of {(4-nitrophenylsulfonyl)imino}phenyl-λ^3-iodane (**1c**)*

To a solution of *p*-nitrophenylsulfonamide **6c** (10.0 mmol) and KOH (25.0 mmol) in MeOH was added at 0°C diacetoxyiodobenzene (10.0 mmol) at once. The mixture was stirred at 0°C until the color had changed from colorless to pale yellow (25 min). The temperature was allowed to raise to 20°C, and stirring was

© 1998 NRC Canada

continued during 3.0 h. After addition of water (100 mL) the ylide **1c** precipitated upon standing at 0°C overnight. After filtration, the product was dried in vacuo to afford crude **1c** (98%), which was used without further purification. IR(KBr): 3100m, 1524vs, 1346s, 1274s, 1125s, 1080s, 878m, 853s, 736s. ^{1}H NMR (400 MHz, DMF-*d*7): 8.18 (d, *J* = 8.7 Hz, 2H), 7.92 (m, 4H), 7.51 (m, 1H), 7.39 (m, 2H). ^{13}C NMR (DMF-*d*7): 152.4 (s), 149.2 (s), 137.9 (d), 135.3 (d), 134.9 (d), 132.2 (d), 128.1 (d). MS: 404 (0.4, M^+), 204 (63), 186 (61), 122 (62), 77 (100). HR-MS: 403.9288 ($C_{12}H_9IN_2O_4S^+$; calc. 403.9328).

{(4-Methoxyphenylsulfonyl)imino}phenyl-λ^3*-iodane (**1d**)*
Same procedure; yield 41%; contaminated with sulfonamide. ^{1}H NMR (200 MHz, DMSO-*d*6): 7.75–7.66 (m, 2H), 7.48–7.17 (m, 4H), 6.76 (d, *J* = 8.9 Hz, 2H), 3.73 (s, 3H).

{(2,4-Dinitrophenylsulfonyl)imino}phenyl-λ^3*-iodane (**1e**)*
Same procedure; yield 98%. IR (KBr): 3093m, 1539vs, 1351s, 1286s, 1131s, 1097s, 880m. ^{1}H NMR (200 MHz, DMF-*d*7): 8.66 (d, *J* = 2 Hz, 1H), 8.33 (dd, *J* = 8.7, 2 Hz, 1H), 8.12 (d, *J* = 8.7 Hz, 1H), 7.99 (d, 7.6 Hz, 2H), 7.56–7.37 (m, 3H). ^{13}C NMR (DMF-*d*7): 149.1 (s), 148.1 (s), 143.5 (s), 134.5 (d), 132.2 (d), 131.8 (d), 131.1 (d), 126.4 (d), 119.5 (d), 118.1 (s). MS: 449 (1, M^+), 231 (72), 204 (100), 77 (41). HR-MS: 448.9216 ($C_{12}H_8IN_3O_6S^+$; calc. 448.9168).

{(Pentaflurophenylsulfonyl)imino}phenyl-λ^3*-iodane (**1f**)*
Same procedure; yield 32%. IR (KBr): 1641m, 1333s, 1095s. ^{1}H NMR (200 MHz, DMSO-*d*6): 7.79 (d, *J* = 7.5 Hz, 2H), 7.51–7.43 (tl, 1H), 7.29–7.37 (tl, 2H).

Synthesis and characterization of aziridines
The experimental details are summarized in the footnotes of Tables 1–6.

[$Rh_2(OAc)_4$]-catalyzed aziridination of olefins with {[(4-nitrophenyl)sulfonyl]imino}-λ^3*-phenyliodane (**1c**). General procedure*
To [$Rh_2(OAc)_4$] (9.2 mg, 0.02 mmol) in CH_2Cl_2 (10 mL) was added, under N_2, activated molecular sieves 4A (6.0 g) and the olefin (20 mmol), followed by NsN═IPh (**1c**) (404 mg, 1.0 mmol). The suspension was stirred at RT until all of **1c** had dissolved. The mixture was filtered through a plug of celite, which was washed exhaustively with CH_2Cl_2, and the filtrate was evaporated. The excess of olefin was removed by flash distillation under reduced pressure. The crude aziridine was purified by flash *chromatography* with silica gel and a mixture of hexane–ether as eluant, or by recrystallization.

*(*N*-Methanesulfonyl)-2-phenylaziridine (**5a**)*
IR ($CHCl_3$): 3019w, 1324m, 1154m, 1046w. ^{1}H NMR (400 MHz, $CDCl_3$): 7.38–7.30 (m, 5H), 3.73 (dd, *J* = 4.4, 7 Hz, 1H), 3.12 (s, 3H), 2.99 (d, *J* = 7 Hz, 1H), 2.45 (d, 4.4 Hz, 1H). ^{13}C NMR ($CDCl_3$): 134.9 (s), 128.7 (d), 128.6 (d), 126.5 (d), 40.8 (d), 39.8 (q), 35.4 (t). MS: 197 (< 1, M^+), 118 (53), 91 (100), 77 (12). HR-MS: 197.0526 ($C_9H_{11}NO_2S^+$; calc. 197.0510).

*(*N*-4-Toluenesulfonyl)-2-phenylaziridine (**5b**)*
See refs. 6 and 7.

*(*N*-4-Methoxyphenylsulfonyl)-2-phenylaziridine (**5d**)*
mp 75–77°C. IR ($CHCl_3$): 3020w, 2976m, 1522w, 1423w, 1224vs, 1157w, 1046m. ^{1}H NMR (400 MHz, $CDCl_3$): 7.92 (d, *J* = 8.8 Hz, 2H), 7.30–7.26 (m, 3H), 7.23–7.21 (m, 2H), 7 (d, *J* = 8.8 Hz, 2H), 3.87 (s, 3H), 3.75 (dd, *J* = 4.4, 7.4 Hz, 1H), 2.97 (d, *J* = 7 Hz, 1H), 2.38 (d, *J* = 4.4 Hz, 1H). ^{13}C NMR ($CDCl_3$): 163.7 (s), 135.2 (s), 130.2 (d), 129.5 (s), 128.6 (d), 128.3 (d), 126.6 (d), 114.4 (d), 55.7 (q), 41.0 (d), 35.9 (d). MS: 289 (23, M^+), 171 (12), 118 (84), 107 (18), 91 (89), 77 (29). HR-MS: 289.0771 ($C_{15}H_{15}NO_3S^+$; calc. 289.0772).

*(*N*-2,4-Dinitrophenylsulfonyl)-2-phenylaziridine (**5e**)*
IR ($CHCl_3$): 3018m, 1557vs, 1350s, 1216s, 1168s. ^{1}H NMR (400 MHz, $CDCl_3$): 8.56–8.52 (m, 2H), 8.46 (d, *J* = 8.4 Hz, 1H), 7.35–7.32 (m, 3H), 7.29–7.26 (m, 2H), 4.11 (dd, *J* = 4.8, 7.4 Hz, 1H), 3.32 (d, *J* = 7.4 Hz), 2.71 (d, *J* = 4.8 Hz). ^{13}C NMR ($CDCl_3$): 150.3 (s), 148.7 (s), 137.5 (s), 134.0 (s), 133.0 (d), 128.9 (d), 128.8 (d), 126.6 (d), 120.0 (d), 43.7 (d), 38.6 (t). MS: 349 (2, M^+), 231 (3), 118 (86), 91 (100). HR-MS: 349.0358 ($C_{14}H_{11}N_3O_6S^+$; calc. 349.0369).

*(*N*-4-Nitrophenylsulfonyl)-2-(4-acetoxyphenyl)aziridine (**8b**)*
mp 142–145°C. IR ($CHCl_3$): 3029m, 1754m, 1608w, 1595vs, 1349s, 1312m, 1224vs, 1198vs, 1166vs, 854m. ^{1}H NMR (400 MHz, $CDCl_3$): 8.40 (d, *J* = 9.0 Hz, 2H), 8.19 (d, *J* = 9.0 Hz, 2H), 7.24 (d, *J* = 8.4 Hz, 2H), 7.05 (d, *J* = 8.4 Hz, 2H), 3.9 (dd, *J* = 4.4, 7.2 Hz, 1H), 3.12 (d, *J* = 7.2 Hz, 1H), 2.49 (d, *J* = 4.4 Hz, 1H), 2.29 (s, 3H). ^{13}C NMR ($CDCl_3$): 169.3 (s), 151.0 (s), 150.8 (s), 131.8 (s), 129.2 (d), 127.6 (d), 124.4 (d), 122.1 (d), 41.3 (d), 36.7 (t), 21.1 (q). MS: 362 (1, M^+), 176 (32), 134 (100), 107 (78), 77 (16). HR-MS: 362.0565 ($C_{16}H_{15}NO_4S^+$; calc. 362.0572.

*(*N*-4-Nitrophenylsulfonyl)-2-(4-bromophenyl)aziridine (**8c**)*
mp 93–95°C. IR ($CHCl_3$): 3031w, 1609w, 1595vs, 1378s, 1216s, 1167vs, 1013m, 822 m. ^{1}H NMR (400 MHz, $CDCl_3$): 8.38 (d, *J* = 8.8 Hz, 2H), 8.18 (d, *J* = 8.8 Hz, 2H), 7.44 (d, *J* = 8.4 Hz, 2H), 7.10 (d, *J* = 8.4 Hz, 2H), 3.87 (dd, *J* = 4.5, 7.1 Hz, 1H), 3.10 (d, *J* = 7.1 Hz, 1H), 2.45 (d, *J* = 4.5 Hz, 1H). ^{13}C NMR ($CDCl_3$): 150.7 (s), 143,7 (s), 133.3 (s), 131.9 (d), 129.2 (d), 128.1 (d), 124.4 (d), 122.8 (s), 41.1 (d), 36.6 (t). MS: 384 (3, M^+), 382 (3, M^+), 198 (100), 196 (100), 171 (95), 169 (97), 117 (71), 90 (77), 76 (21). HR-MS: 381.9625 ($C_{14}H_{12}BrNO_2S^+$; calc. 381.9628).

*(*N*-4-Nitrophenylsulfonyl)-2-(3-chlorophenyl)aziridine (**8d**)*
mp 156–158°C. IR ($CHCl_3$): 3013w, 1555vs, 1348s, 1313m, 1223m, 1167vs, 856m. ^{1}H NMR (400 MHz, $CDCl_3$): 8.40 (d, *J* = 8.8 Hz, 2H), 8.19 (d, *J* = 8.8 Hz, 2H), 7.31–7.24 (m, 2H), 7.20 (sl, 1H), 7.15–7.12 (m, 1H), 3.87 (dd, *J* = 4.4, 7.3 Hz, 1H), 3.10 (d, *J* = 7.3 Hz, 1H), 2,47 (d, *J* = 4.4 Hz, 1H). ^{13}C NMR ($CDCl_3$): 152.0 (s), 143.7 (s), 136.3 (s), 134.8 (s), 130.1 (d), 129.3 (d), 129.0 (d), 126.5 (d), 124.8 (d), 124.4 (d), 40.9 (d), 36.8 (t). MS: 338 (< 1, M^+), 152 (93), 125 (100), 75 (12). HR-MS: 338.0168 ($C_{14}H_{12}ClNO_2S^+$; calc. 338.013).

*(*N*-4-Nitrophenylsulfonyl)-2-(4-methoxycarbonylphenyl)-aziridine (**8e**)*
mp 116–118°C. IR ($CHCl_3$): 3017m, 1718s, 1348s, 1284vs, 1167vs, 1113m. ^{1}H NMR (400 MHz, $CDCl_3$): 8.39 (d, *J* = 8.8 Hz, 2H), 8.20 (d, *J* = 8.8 Hz, 2H), 7.99 (d, *J* = 8.4 Hz, 2H),

© 1998 NRC Canada

7.31 (d, J = 8.4 Hz, 2H), 3.94 (dd, J = 4.4, 7.2 Hz, 1H), 3.91 (s, 3H), 3.15 (d, J = 7 Hz, 1H), 2.51 (d, J = 4.4 Hz, 1H). ^{13}C NMR ($CDCl_3$): 166.4 (s), 150.8 (s), 143.7 (s), 139.2 (s), 130.0 (d), 129.2 (d), 126.4 (d), 124,4 (d), 52.2 (q), 41.1 (d), 36.8 (t). MS: 362 (< 2, M^+), 331 (3), 176 (100). HR-MS: 362.0594 ($C_{16}H_{15}NO_4S^+$; calc. 362.0572).

*(*N*-4-Nitrophenylsulfonyl)-2-ethenylaziridine (**8j**)*
mp 138°C. IR ($CHCl_3$): 3029w, 1535 vs, 1351s, 1217s, 1092m, 936m. ^{1}H NMR (400 MHz, $CDCl_3$): 8.40 and 8.16 (AA′XX′, app. (app. = apparent) d, J = 9.1 Hz, 4H), 5.57–5.48 (m, 2H), 5.32–5.29 (m, 1H), 3.42–3.38 (m, 1H), 2.92 (d, J = 6.8 Hz), 2.34 (d, J = 4.8 Hz, 1H). ^{13}C NMR ($CDCl_3$): 150.7 (s), 144.1 (s), 132.2 (s), 129.1 (s), 124.3 (d), 121.2 (t), 41.9 (q), 34.8 (t). MS: 254 (0.5, M^+), 186 (2), 122 (8), 76 (20), 68 (100). HR-MS: 186.9935 ($C_6H_4O_4NS^+$; calc. 186.9939).

*(*N*-4-Nitrophenylsulfonyl)-2-ethoxycarbonylaziridine (**8o**)*
mp 96–98°C. IR ($CHCl_3$): 3106w, 3029m, 2927m, 2855w, 1745s, 1608m, 1535vs, 1403m, 1350vs, 1312m, 1229s, 1209vs, 1169vs, 1093s, 1014m, 934m, 882m, 856m. ^{1}H NMR (400 MHz, $CDCl_3$): 8.42 and 8.19 (AA′XX′, app. d, J = 8.8 Hz, 4H), 4.21 (q, J = 7 Hz, 2H), 3.45 (dd, J = 7.2, 4 Hz, 1H), 2.88 (d, J = 7 Hz), 2.66 (d, J = 4.4 Hz, 1H), 1.27 (t, J = 7 Hz, 3H). ^{13}C NMR ($CDCl_3$): 166.1 (s), 151.0 (s), 143.1(s), 129.5 (d), 124.4 (d), 62.4 (t), 36.4 (d), 32.4 (t), 14,0 (t). MS: 301(< 1, M^++1), 255 (2), 227 (3), 186 (5), 122 (9), 114 (37), 86 (100), 58 (33).

exo–(N-*4-Nitrophenylsulfonyl)-3-aza-tricyclo[3.2.1.0^{2,4}]-octane (**8p**)*
mp 133–136°C. IR ($CHCl_3$): 3105w, 3020m, 2968m, 2878m, 1633m, 1607m, 1534vs, 1474w, 1401m, 1350vs, 1330s, 1310s, 1159vs, 1127m, 1091s, 1034m, 977s, 913s, 855s. ^{1}H NMR (400 MHz, $CDCl_3$): 8.39 and 8.14 (AA′XX′, app. d, J = 8.8 Hz, 4H), 3.07 (s, 2H), 2.49 (s, 2H), 1.51–1.55 (m, 2H), 1.40–1.43 (m, 1H), 1.26–1.31 (m, 2H), 0.82 (d, J = 10.3 Hz, 1H). ^{13}C NMR ($CDCl_3$): 155.5 (s), 144.8 (s), 128.8 (d), 124.2 (d), 43.0 (d), 35.9 (d), 28.2 (t), 25.5 (t). MS: 294 (1, M^+), 265 (4), 186 (2), 108 (56), 81 (100), 67 (15). HR-MS: 294.0659 ($C_{13}H_{14}N_2O_4S^+$; calc. 294.0674).

*(*N*-4-Nitrophenylsulfonyl)-6-aza-benzobicyclo[3.1.0]hexene (**8q**)*
mp 139–140°C. IR ($CHCl_3$): 3105w, 3030m, 2920w, 1608m, 1534vs, 1476m, 1422m, 1402m, 1350vs, 1336s, 1311s, 1161vs, 1090s, 972s, 931s, 877s, 854s. ^{1}H NMR (400 MHz, $CDCl_3$): 8.38 and 8.15 (AA′XX′, app. d, J = 9.2 Hz, 4H), 7.42 (d, J = 7.7 Hz, 1H), 7.19–7.31 (m, 3H), 4.43 (d, J = 5.1 Hz, 1H), 4.06 (t, J = 4 Hz, 1H), 3.22 (app. ABX, dd, J = 18, 4 Hz, 1H), 3.16 (app. ABX, d, J = 18 Hz, 1H). ^{13}C NMR ($CDCl_3$): 150.6 (s), 144.4 (s), 143.3 (s), 137.5 (s), 129.1 (d), 129.0 (d), 127.0 (d), 125.7 (d), 125.1 (d), 124.3 (d), 51.1 (d), 45.7 (d), 34.7 (t). MS: 316 (4, M^+), 130 (100), 103 (27), 77 (18). HR-MS: 316.0527 ($C_{15}H_{12}N_2O_4S^+$; calc. 316.0518).

Data for rearrangement and cycloaddition products from aziridinations (Schemes 5, 6)

*2-(*N*-4-Nitrophenylsulfonyl)-azabicyclo[3.2.1]octa-3,6-diene (**10**)*
mp 123-125°C. ^{1}H NMR (400 MHz, $CDCl_3$): 8.37 and 8.01 (AA′XX′, app. d, J = 8.9 Hz, 4H), 6.30–6.28 (m, 1H), 6.20–6.18 (m, 1H), 5.39–5.35 (m, 1H), 5.24–5.22 (m, 1H), 4.80 (sl, 1H), 2.73–2.70 (m, 1H), 1.90–1.80 (m, 1H), 1.37 (d, J = 12 Hz, 1H). ^{13}C NMR ($CDCl_3$): 150.1 (s), 145.8 (s), 140.0 (d), 127.9 (d), 124.5 (d), 121.2 (d), 112.4 (d), 60.2 (d), 35.9 (d), 35.1 (t). MS: 292 (6, M^+), 106 (87), 79 (100). HR-MS: 292.0482 ($C_{13}H_{12}N_2O_4S^+$; calc. 292.0517).

cis- *and* trans-*(*N*-4-Nitrophenylsulfonyl)-2,4-di(4-methoxyphenylpyrrolidine (**12h**)*
Purified on aluminum oxide with ether – petroleum ether 3:2; separation of isomers by HPLC; first fraction (8%), oil. IR ($CHCl_3$): 3030vw, 2935vw, 2837vw, 1607w, 1531s, 1510vs, 1346s, 1248s, 1161m, 1035m, 856w. ^{1}H NMR (400 MHz, $CDCl_3$): 8.17 and 7.63 (AA′XX′, app. d, J = 8.8 Hz, 4H), 7.13 (d, J = 8.8 Hz, 2H), 7.11 (d, J = 8.8 Hz, 2H), 6.87 (d, J = 8.8 Hz, 2H), 6.74 (d, J = 8.8 Hz, 2H), 4.92 (dd, J = 9.9, 6.6 Hz, 1H), 4.30 (dd, J = 9.5, 7.7 Hz, 1H), 3.80 (s, 3H), 3.78 (s, 3H), 3.45 (app. t, J = 10.7 Hz, 1H), 3.31–3.25 (m, 1H), 2.76–2.70 (m, 1H), 2.15–2.06 (m, 1H). ^{13}C NMR ($CDCl_3$): 159.3 (s), 158.9 (s), 149.6 (s), 145.9 (s), 132.8 (s), 130.6 (s), 128.4 (d), 128.1 (d), 128.0 (d), 123.8 (d), 114.2 (d), 113.8 (d), 64.3 (q), 55.7 (t), 55.4 (d), 44.3 (t), 43.1 (d). MS: 468 (42, M^+), 281 (38), 254 (100), 121 (57), 91 (15). HR-MS: 468.1412 ($C_{24}H_{24}N_2O_6S^+$; calc. 468.1388).

Second fraction (8%), oil. IR ($CHCl_3$): 3030vw, 2935vw, 2837vw, 1607w, 1531w, 1510vw, 1346s, 1248s, 1161m, 1035m, 856w. ^{1}H NMR (400 MHz, $CDCl_3$): 8.28 and 7.86 (AA′XX′, app. d, J = 8.8 Hz, 4H), 7.18 (d, J = 8.8 Hz, 2H), 7.03 (d, J = 8.8 Hz, 2H), 6.83 (d, J = 8.8 Hz, 2H), 6.82 (d, J = 8.8 Hz, 2H), 5.05 (dd, J = 2.9, 8.1 Hz, 1H), 4.01 (dd, J = 7, 9.2 Hz, 1H), 3.81 (s, 3H), 3.78 (s, 3H), 3.57–3.48 (m, 1H), 3.44 (app. t, J = 9.2 Hz, 1H), 2.26–2.16 (m, 2H). ^{13}C NMR ($CDCl_3$): 159.1 (s), 158.8 (s), 149.9 (s), 144.4 (s), 133.9 (s), 131.3 (s), 128.4 (d), 127.9 (d), 127.5 (td), 124.1 (d), 114.2 (d), 113.9 (d), 63.0 (q), 55.3 (t), 55.3 (d), 42.6 (t), 41.0 (d). MS: 468 (42, M^+), 281 (38), 254 (100), 121 (57), 91 (15). HR-MS: 468.1412 ($C_{24}H_{24}N_2O_6S^+$; calc. 468.1388).

cis- *and* trans-*(*N*-4-Nitrophenylsulfonyl)-2,4-diethoxypyrrolidine (**12m**)*
Separated on silica gel with hexane – ethyl acetate 3:1; first fraction (36%), oil. IR ($CHCl_3$): 3104w, 2980m, 2942m, 2897m, 1606m, 1532vs, 1479w, 1444w, 1401m, 1350vs, 1312s, 1169vs, 1110s, 1062s, 1002m, 920m, 899s, 855m. ^{1}H NMR (400 MHz, $CDCl_3$): 8.35 and 8.05 (AA′XX′, app. d, J = 8.8 Hz, 4H), 5.29 (dd, J = 5.7, 1.8 Hz, 1H), 4.22–4.17 (m, 1H), 3.78–3.70 (m, 1H), 3.61–3.48 (m, 2H), 3.34–3.27 (m, 3H), 2.19 (ddd, J = 13.3, 6.2, 1.4 Hz, 1H), 1.80–1.73 (m, 1H), 1.18 (t, J = 7 Hz, 3H), 1.04 (t, J = 7 Hz, 3H). ^{13}C NMR ($CDCl_3$): 150.1 (s), 145.2 (s), 128.8 (d), 124.1 (d), 89.9 (d), 76.9 (d), 65.1 (t), 63.8 (t), 51.8 (t), 39.6 (t), 15.2 (q), 15. 0 (q). MS: (M^+, absent), 299 (100), 253 (33), 186 (20), 129 (19), 122 (32), 86 (55), 76 (25), 58 (28).

Second fraction (16%), oil. ^{1}H NMR (400 MHz, $CDCl_3$): 8.35 and 8.10 (AA′XX′, app. d, J = 9.2 Hz, 4H), 5.34 (dd, J = 6.2, 1.8 Hz, 1H), 4.06–3.98 (m, 1H), 3.77–3.25 (m, 6H), 2.19–2.12 (m, 1H), 2.06–2.00 (m, 1H), 1.15 (t, J = 7 Hz, 3H), 1.14 (t, J = 7 Hz, 3H). MS: 344 (M^+, 1), 299 (82), 252 (83), 186 (51), 129 (30), 122 (100), 112 (27), 86 (89), 76 (20), 58 (27).

© 1998 NRC Canada

Intramolecular aziridination

*{(2-Ethenylphenylsulfonyl)imino}-phenyl-λ³-iodane (**15**) 2-Ethenylphenylsulfonamide* (***14***)
See ref. 25. The ylide was prepared according to the general procedure and used without purification and characterization.

*1,1a-Dihydro-6-thia-6a-aza-cycloprop[a]inden-6,6-dioxide (**16**)*
The ylide **15** (1.00 mmol) was suspended under N_2 in dry CH_2Cl_2 (10.0 mL) containing [$Rh_2(OAc)_4$] (0.02 mmol) and molecular sieves (6.0 g) and stirred during 2 h. The mixture was filtered through celite, which was washed out with CH_2Cl_2 (100 mL). After evaporation of the solvent, the crude product was purified by flash chromatography on silica gel using hexane – ethyl acetate 2:1 as eluant to afford **16** as an oil. IR ($CHCl_3$): 3155w, 2927w, 1601w, 1552w, 1470w, 1340s, 1178vs, 1052w, 916vs, 738vs. ^{1}H NMR (400 MHz, $CDCl_3$): 7.81–7.54 (m, 4H), 4.14 (m, 1H), 2.88 (dd, J = 1.1, 4.8 Hz, 1H), 2.37 (dd, J = 1.1, 4 Hz, 1H). ^{13}C NMR ($CDCl_3$), 136.9 (s), 133.4 (d), 133.3 (s), 130.4 (d), 125.5 (d), 123.6 (d), 44.2 (t), 43.0 (t). MS: 181 (4, M^+), 167 (13), 117 (93), 103 (11), 90 (100), 76 (29). HR-MS: 167.0022 ($C_7H_5NO_2S^+$; calc. 167.0041).

Relative reactivity of substituted styrenes with respect to NsN═IPh

To a mixture of dry CH_2Cl_2 (10.0 mL), [$Rh_2(OAc)_4$] (0.02 mmol), styrene (**4a**, 5.0 mmol) and substituted styrene (**4b**–**g**, 5.0 mmol), and molecular sieves (6.0 g) was added NsN═IPh (**1c**, 1.00 mmol). The suspension was stirred at room temperature until all of the ylide was dissolved. The solution was filtered through celite, which was washed with CH_2Cl_2 (100 mL). The filtrate was evaporated, and the ratio of the aziridines was determined by ^{1}H NMR by comparison of the integrals of the protons of the aziridines. In the case of 4-methoxycarbonylstyrene (**4e**), 1.0 mmol of **4a** was used with 5.0 mol of **4e** and 0.5 mol of NsN═IPh (**1c**), and with 3-nitrostyrene (**4g**) 10.0 mol were used with 2.0 mol of **4a** and 1.0 mmol of **1c**.

The [Cu(acac)$_2$]-catalyzed reactions were carried out by the same procedure, using 1:1 mixtures of styrenes and 10% of catalyst.

Aziridination of vinylcyclopropanes (radical probes)

*(N-4-Nitrophenylsulfonyl)-2-cyclopropylaziridine (**22a**)*
The reaction was carried out according to the general procedure, using 20 mmol of cyclopropylethene (**19a**) (30*a*), 1.00 mmol of NsN═IPh (**1c**), molecular sieves, and 0.02 mmol of [$Rh_2(OAc)_4$]. After stirring during 10 min. the reaction was worked up as usual; crude yield of aziridine 43%. Part of the product decomposed upon purification (preparative TLC on silica gel, using hexane–ether 2:1 as solvent); colorless oil. IR ($CHCl_3$): 3029vw, 1534s, 1350m, 1166m, 856w. ^{1}H NMR (400 MHz, $CDCl_3$): 8.15 and 8.40 (AA′XX′, app. d, J = 8.6 Hz, 4H), 2.88–2.86 (m, 1H), 2.72 (d, J = 7 Hz, 1H), 2.21 (d, J = 4.8 Hz, 1H), 0.94–0.90 (m, 1H), 0.55–0.42 (m, 2H), 0.25–0.16 (m, 2H). ^{13}C NMR ($CDCl_3$): 151.0(s), 144.0 (s), 129.0 (d), 124.0 (d), 43.0 (d), 34.0 (t), 10.0 (t), 3.0 (t), 2.0 (t). MS: 268 (5, M^+), 186 (4), 82 (80). HR-MS: 268.0512 ($C_{11}H_{12}N_2O_4S^+$; calc. 268.0518).

*(N-4-Nitrophenylsulfonyl)-2-(2-trans-3-trans-diphenylcyclopropyl)aziridine (**22b**)*
Same conditions as above with 20 mmol of 2-*trans*-3-*trans*-diphenylvinylcyclopropane (**19b**) (30*b*). Reaction time three days; yield of aziridine 35% (oil). IR ($CHCl_3$): 3035m, 1604m, 1535vs, 1349s, 1220vs, 1166s, 1092w, 856m. ^{1}H NMR (400 MHz, $CDCl_3$): 8.41 and 8.20 (AA′XX′, app. d, J = 8.8 Hz, 4H), 7.08 (sl, 6H), 6.84–6.80 (m, 4H), 3.30–3.26 (m, 1H), 2.88 (d, J = 7.1, 1H), 2.41 (d, J = 4.9 Hz, 1H), 2.38–2.29 (m, 2H), 1.96–1.92 (m, 1H). ^{13}C NMR ($CDCl_3$): 151.0 (s), 143.9 (s), 136.2 (s), 136.1 (s), 129.3 (d), 128.9 (d), 128.6 (d), 127.9 (d), 126.3 (d), 126.2 (d), 124.4 (d), 41.5 (d), 34.2 (t), 29.6 (d), 27.7 (d), 24.2 (d). MS: 420 (0.3, M^+), 234 (10), 186 (15), 91 (100), 77 (20). HR-MS: 234.1277 ($C_{17}H_{16}N^+$; calc. 234.1283).

Synthesis of Rh^{II} carboxylate catalysts

*[Rh_2{(–)campha}$_4$] (**23**)*
In a flask fitted with a Soxhlet extractor containing ground Na_2CO_3 and sand was heated, under N_2 and with stirring, (–)-camphanic acid (2.19 mmol) and [$Rh_2(OAc)_4$] (0.21 mmol) in chlorobenzene (50 mL) to reflux during three days. The mixture was evaporated to dryness and the residue was purified by flash chromatography on silica gel, using a mixture of ethyl acetate – CH_2Cl2 1:5 containing 1% of MeOH. Yield 97% of amorphous powder. ^{1}H NMR (200 MHz, $CDCl_3$): 2.72–2.50 (d, 1H), 1.90–1.50 (m, 3H), 1.04 (s, 3H), 0.87 (s, 3H), 0.71 (s, 3H). ^{13}C NMR ($CDCl_3$): 186.8 (s), 179.1 (s), 91.5 (s), 54.7 (s), 54.0 (s), 30.7 (t), 28.7 (t), 16.9 (q), 16.8 (q), 9.7 (q). MS (electrospray): 1017.0 (M^+ + Na).

*[Rh_2{(1R)-meba}$_4$] (**24**)*
Same procedure with 2.19 mmol of 2-((1*R*)-methoxyethyl)benzoic acid prepared from 2(1*R*-methoxyethyl)bromobenzene via carbonation of the organomagnesium derivative (92% ee) and 0.21 mmol of [$Rh_2(OAc)_4$]. The crude product was dissolved in CH_2Cl_2 and extracted three times with 10% aq. $NaHCO_3$. The organic layer was dried ($MgSO_4$), filtered, and the filtrate was evaporated to afford the product as amorphous powder in 98%. ^{1}H NMR (400 MHz, $CDCl_3$): 7.49–7.45 (m, 2H), 7.38 (d, J = 7.6 Hz, 1H), 7.26–7.23 (m, 1H), 4.72 (q, J = 6.4 Hz, 1H), 2.81 (s, 2H), 1.15 (d, J = 6.4 Hz, 3H). ^{13}C NMR ($CDCl_3$, 187.9 (s), 143.1 (s), 131.6 (d), 131.4 (s), 128.5 (d), 126.8 (d), 125.4 (d), 75.2 (q), 55.6 (d), 23.8 (q). MS (electrospray): 945 (M^+ + Na). $[\alpha]_D^{22}$ = +21.3 ($CHCl_3$, c = 0.30).

Photochemical nitrene generation

A solution of styrene (**4a**, 20 mmol), [Rh_2{(*R*)-bnp}$_4$] (0.05 mmol), and NsN_3 (**25**, 1.00 mmol) (40) in dry CH_2Cl_2 (15 mL) was irradiated in a Quartz vessel, which was placed in a Rayonet photoreactor (λ_{max} = 254 nm), under N_2 and with stirring during 70 h at room temperature. The reaction mixture was filtered through celite, which was washed with EtOAc. The solvent was evaporated, and excess styrene was removed by flash distillation. The crude product was purified by flash chromatography (silica gel, hexane–ether 3:1) to yield the aziridine **5c** in 9% yield with an ee of 17%.

© 1998 NRC Canada

Acknowledgments

This work was supported by the Swiss National Science Foundation (grant nos. 20-38'907.93 and 20-44'144.95). The authors are indebted to Mr. J.-P. Larcinese and P. Nury for experimental work on aziridinations, to Mrs. J.-P. Saulnier and A. Pinto for the NMR spectra, and Ms. G. Klink for the mass spectra.

References

1. R.A. Abramovitch, T.D. Bailey, T. Takaya, and V. Uma. J. Org. Chem. **39**, 340 (1975).
2. Y. Yamada, T. Yamamoto, and M. Okawara. Chem. Lett. 361 (1975).
3. (*a*) R. Breslow and S.H. Gellman. J. Chem. Soc. Chem. Commun. 1400 (1982). (*b*) J. Am. Chem. Soc. **105**, 6728 (1983).
4. (*a*) J.-P. Mahy, P. Battioni, D. Mansuy, J. Fisher, R. Weiss, J. Mispelter, I. Morgenstern-Badarau, and P. Gans. J. Am. Chem. Soc. **106**, 1699 (1984); (*b*) D. Mansuy, P. Battioni, and J.-P. Mahy. J. Am. Chem. Soc. **104**, 4487 (1982); (*c*) D. Mansuy, J.-P. Mahy, A. Dureault, G. Bedi, and P. Battioni, J. Chem. Soc. Chem. Commun. 1161 (1984); (*d*) J.-P. Mahy, G. Bedi, P. Battioni, and D. Mansuy. J. Chem. Soc. Perkin Trans 2, 1517 (1988).
5. (*a*) J.-P. Mahy, G. Bedi, P. Battioni, and D. Mansuy. Tetrahedron Lett. **29**, 1927 (1988); (*b*) New. J. Chem. **13**, 651 (1989).
6. (*a*) D.A. Evans, M.M. Faul, and M.T. Bilodeau. J. Org. Chem. **56**, 6744 (1991); (*b*) J. Am. Chem. Soc. **116**, 2742 (1994).
7. D.A. Evans, M.M. Faul, M.T. Bilodeau, B.A. Anderson, and D.M. Barnes. J. Am. Chem. Soc. **115**, 5328 (1993).
8. (*a*) N.H. Lee, A.R. Muci, and E.N. Jacobsen. J. Am. Chem. Soc. **115**, 5326 (1993); (*b*) Z. Li, R.W. Quan, and E.N. Jacobsen. J. Am. Chem. Soc. **117**, 5889 (1995); (*c*) W. Zhang, N.H. Lee, and E.N. Jacobsen. J. Am. Chem. Soc. **116**, 425 (1994).
9. (*a*) N.N. Knight and M.P. Mudlowney. Synlett, 949 (1995); (*b*) T. Hudlicky, K.A. Abboud, J. Bolonick, M. Stanton, and A.J. Thorpe. J. Chem. Soc. Chem. Commun. 1717 (1996); T. Hudlicky, X. Tain, K. Konigsberger, and J. Rouden. J. Org. Chem. **59**, 4037 (1994); (*c*) P.J. Pérez, M. Brookhart, and J.L. Templeton. Organometallics, **12**, 261 (1993).
10. (*a*) A.M. Harm, J.G. Knight, and G. Stemp. Tetrahedron Lett. **37**, 6189 (1996); (*b*) E.W. Lowenthal and S. Masamune. Tetrahedron Lett. **32**, 7373 (1991); (*c*) D. Tanner, P.G. Andersson, A. Harden, and P. Somfai. Tetrahedron Lett. **35**, 4631 (1994); D. Tanner, A. Harden, F. Johansson, P. Wyatt, and P.G. Andersson. Acta Chem. Scand. **50**, 361 (1996).
11. K. J. O'Connor, S.-J. Wey, and C.J. Burrows. Tetrahedron Lett. **33**, 1001 (1992).
12. (*a*) K. Noda, N. Hosoya, R. Irie, Y. Ito, and T. Katsuki. Synlett, 463 (1993); (*b*) H. Nishikori and T. Katsuki. Tetrahedron Lett. **37**, 9245 (1996).
13. (*a*) M.P. Doyle, R.J. Pieters, S.F. Martin, R.E. Austin, C.J. Oalman, and P. Müller. J. Am. Chem. Soc. **113**, 1423 (1991); (*b*) M.P. Doyle, R.E. Austin, A.S. Bailey, M.P. Dwyer, A.B. Dyatkin, A.V. Kalinin, M.M.Y. Kwan, S. Liras, C.J. Oalman, R.J. Pieters, M. Protopopova, C.E. Raab, G.H.P. Roos, Q.-L. Zhou, and S.F. Martin. J. Am. Chem. Soc. **117**, 5763 (1995).
14. (*a*) M.P. Doyle, M. Protopopova, P. Müller, and D. Ene. J. Am. Chem. Soc. **116**, 8492 (1994); (*b*) M.N. Protopopova, M.P. Doyle, P. Müller, and D. Ene. J. Am. Chem. Soc. **114**, 2755 (1992).
15. P. Müller and D. Fernandez. Helv. Chim. Acta, **78**, 947 (1995).
16. (*a*) P. Müller, C. Baud, and Y. Jacquier. Tetrahedron, **52**, 1543 (1996); (*b*) P. Müller, C. Baud, Y. Jacquier, M. Moran, and I. Nägeli. J. Phys. Org. Chem. **9**, 341 (1996).
17. C. Baud. Ph.D. thesis, University of Geneva. 1997.
18. H. Kwart and A.A. Kahn. J. Am. Chem. Soc. **89**, 1950 (1967); H. Kwart and A.A. Kahn. J. Am. Chem. Soc. **89**, 1951 (1967).
19. G. Besenyei, S. Németh, and L.I. Simandi. Angew. Chem. Int. Ed. Engl. **29**, 1147 (1990); G. Besenyei, S. Németh, and L.I. Simandi. Tetrahedron Lett. **34**, 6105 (1993); G. Besenyei and L.I. Simandi. Tetrahedron Lett. **34**, 2839 (1993).
20. D. Carr, T.P. Seden, and R.W. Turner. Tetrahedron Lett. **6**, 477 (1969).
21. M.P. Doyle, W.R. Winchester, M.N. Protopopova, A.P. Kazala, and L.J. Westrum. Org. Synth. **73**, 13 (1995).
22. (*a*) R.S. Drago, J.R. Long, and R. Cosmano. Inorg. Chem. **21**, 2196 (1982); (*b*) M.P. Doyle, S.N. Mahapatro, A.C. Caughey, M.S. Chinn, M.R. Colsman, N.K. Harn, and A.E. Redwine. Inorg. Chem. **26**, 3070 (1987).
23. M.J. Södergren, D.A. Alonso, A.V. Bedekar, and P.G. Andersson. Tetrahedron Lett. **38**, 6897 (1997).
24. P. Barraclough, S. Bilgic, J.B. Pedley, A.J. Rogers, and D.W. Young. Tetrahedron, **35**, 99 (1979); A.C. Oehlschlager and L.H. Zalkow. J. Org. Chem. **30**, 4205 (1965).
25. I. Nägeli, C. Baud, G. Bernardinelli, Y. Jacquier, M. Moran, and P. Müller. Helv. Chim. Acta, **80**, 1087 (1997).
26. J.V. Hay, D.F. Zimmermann, D. Frieze, and B.A. Wexler. Eur. Pat. Appl. EP 187489.
27. F.A. Carey and R.J. Sundberg. *In* Chimie organique avancée. 3rd ed. DeBoeck, Paris. 1996. p. 201.
28. D. Seyferth, J. Yick-Pui Mui, and R. Damraner. J. Am. Chem. Soc. **90**, 6182 (1968).
29. I.H. Sadler. J. Chem. Soc. B, 1024 (1969).
30. (*a*) G.-H. He and T.C. Bruice. J. Am. Chem. Soc. **113**, 2747 (1991); (*b*) A.J. Castellino and T.C. Bruice J. Am. Chem. Soc. **110**, 1313 (1988).
31. (*a*) N.C. Rol and D.H. Clague. Org. Magn. Reson. **16**, 187 (1981); (*b*) R. Breslow, R. Winter, and M. Battiste. J. Org. Chem. **24**, 415 (1959); R. Breslow, J. Lockhart, and A. Small. J. Am. Chem. Soc. **84**, 2793 (1962); A.J. Castellino and T.C. Bruice. J. Am. Chem. Soc. **119**, 7512 (1988); S. Hibino, E. Sugino, Y. Adachi, K. Nomi, and K. Sato. Heterocycles, 275 (1989).
32. M.P. Doyle, W.R. Winchester, M.N. Protopopova, P. Müller, G. Bernardinelli, D. Ene, and S. Motallebi. Helv. Chim. Acta, **76**, 2227 (1993).
33. D. Ene. Ph.D. thesis (no. 2783), University of Geneva. 1995.
34. S. Hashimoto, W. Watanabe, and S. Ikegami. Synlett, 353 (1994); S. Hashimoto, N. Watanabe, K. Kawano, and S. Ikegami. Synth. Commun. 3277 (1994); N. Watanabe, M. Anada, S. Hashimoto, and S. Ikegami. Synlett, 1031 (1994).
35. M.C. Pirrung, J. Zhang, and A.T. McPhail. J. Org. Chem. **56**, 6269 (1991); M.C. Pirrung, M.C. Zhang, and A.T. Morehead. Tetrahedron Lett. **35**, 6229 (1994); M.C. Pirrung and Y.R. Lee. Tetrahedron Lett. **36**, 6373 (1995); Tetrahedron Lett. **35**, 6231 (1994); M.C. Pirrung and M.C. Zhang. Tetrahedron Lett. **33**, 5987 (1992).
36. M. Kennedy, M.A. McKervey, A.R. Maguire, and G.H.P. Roos. J. Chem. Soc. Chem. Commun. 361 (1990); M.A. McKervey and T. Ye. J. Chem. Soc. Chem. Commun. 823 (1992); T. Ye, M.A. McKervey, B.D. Brandes, and M.P. Doyle. Tetrahedron Lett. **35**, 7269 (1994).
37. L. Ferris, D. Haigh, and C.J. Moody. Tetrahedron Lett. **37**, 107 (1996).
38. K. Burgess and A.M. Porte. Angew. Chem. Int. Ed. Engl. **33**, 1182 (1994).
39. G. Smolinsky, E. Wasserman, and W.A. Yager. J. Am. Chem. Soc. **84**, 3220 (1962).
40. T. Curtius. J. Prakt. Chem. **125**, 303 (1930); W. von E. Doering and C.H. de Puy. J. Am. Chem. Soc. **75**, 5955 (1953); M. Regitz, J. Hocker, and A. Liedhegner. Org. Synth. **5**, 179 (1973).

© 1998 NRC Canada

Correlation of the rates of solvolysis of arylmethyl *p*-toluenesulfonates: application of the aromatic ring parameter and a discussion of similarity models

Dennis N. Kevill, Malcolm J. D'Souza, and Haobo Ren

Abstract: The specific rates of solvolysis of benzyl *p*-toluenesulfonate and nine benzylic-ring-substituted derivatives are satisfactorily correlated using N_T and Y_{OTs} scales within the extended Grunwald–Winstein equation. Addition of a third term, governed by the aromatic ring parameter, shows the additional term to be statistically significant. As one incorporates increasingly more electron-withdrawing substituents, the sensitivities towards changes in solvent nucleophilicity (*l*) increase, and those towards changes in ionizing power and changes in the aromatic ring parameter decrease. The trend of *l* values can be very nicely shown, with very precise correlations, using an internally generated scale of *Y* values. However, it is demonstrated that there is no overall advantage to use of an internally generated scale if one ultimately wishes to make a comparison with sensitivity values generated using an external scale of *Y* values.

Key words: Grunwald–Winstein equation, aromatic ring parameter, solvent nucleophilicity, solvolysis, arylmethyl *p*-toluenesulfonates.

Résumé : Utilisant les échelles N_T et Y_{OTs} dans le domaine d'application de l'équation étendue de Grunwald–Winstein, on peut obtenir une corrélation satisfaisante entre les vitesses spécifiques de solvolyse du *p*-toluènesulfonate de benzyle et de neuf dérivés benzyliques substitués sur le noyau. L'addition d'un troisième terme régit par le paramètre du noyau aromatique permet de montrer que ce terme additionnel est statistiquement important. Lorsqu'on incorpore des substituants de plus en plus électroattracteurs, les sensibilités vis-à-vis les changements dans le caractère nucléophile du solvant (*l*) augmentent et celles relatives au pouvoir ionisant ainsi que les changements dans le paramètre du noyau aromatique diminuent. On peut montrer la tendance des valeurs *l*, avec des corrélations très précises, en utilisant une échelle de valeurs *Y* générée d'une façon interne. Toutefois, on démontre qu'il n'y a pas d'avantage global à utiliser une échelle générée de façon interne si l'on veut éventuellement faire une comparaison avec des valeurs de sensibilité générées en utilisant une échelle externe de valeurs *Y*.

Mots clés : équation de Grunwald–Winstein, paramètre du noyau aromatique, caractère nucléophile du solvant, solvolyse, *p*-toluènesulfonates d'arylméthyles.

[Traduit par la rédaction]

Introduction

In a preliminary communication (1), we presented the analyses in terms of the extended Grunwald–Winstein equation (eq. [1]) of the specific rates of solvolysis of benzyl *p*-toluenesulfonate (tosylate, **1**, X = H) and six substituted derivatives (**1**, X ≠ H) in 11 solvents.

Received December 16, 1997.

This paper is dedicated to Professor Erwin Buncel in recognition of his many contributions to physical-organic chemistry.

D.N. Kevill[1] **and H. Ren**. Department of Chemistry and Biochemistry, Northern Illinois University, DeKalb, IL 60115-2862, U.S.A.
M.J. D'Souza. Department of Chemistry, University of Wisconsin-Waukesha, Waukesha, WI 53188-2799, U.S.A.

[1] Author to whom correspondence may be addressed. Telephone: (815) 753-6882. Fax: (815) 753-4802.

[1] $$\log (k/k_0)_{RX} = lN + mY + c$$

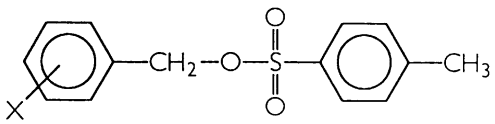

In eq. [1], k and k_0 are the specific rates of solvolysis of RX in a given solvent and in the standard solvent (80% ethanol), respectively; l is the sensitivity towards changes in solvent nucleophilicity (N); m is the sensitivity towards changes in ionizing power (Y); and c is a residual term (zero for ideally behaving solvolyses). Satisfactory analyses were obtained with use of either $N_{Et_3O^+}$ (2) or N_{OTs} (3) solvent nucleophilicity values, in conjunction with Y_{OTs} solvent ionizing power values (3–5); the sensitivities to changes in solvent nucleophilicity (l values) became larger as increasingly electron-withdrawing substituents were introduced.

Subsequently, reports of studies (with analyses in terms of N_{OTs} and Y_{OTs}) of the specific rates of solvolysis in 35–42

© 1998 NRC Canada

solvents of the parent compound (6) and derivatives with X = *m*-methyl (6), *m*-chloro (6), *p*-nitro (7), and 3,5-di(trifluoromethyl) (7) have appeared.

It has been suggested (8, 9) that the N_{OTs} scale is better based on an *m*-value of 0.55, rather than the chosen 0.3, in its derivation (3). The N'_{OTs} values, calculated in this way, are available (9). An even better approach is to use the RX^+-type scale based on the solvolyses of the *S*-methyldibenzothiophenium ion (9, 10). With this type of solvent nucleophilicity scale there is no need to incorporate an *mY* term into its derivation (2*c*, 11). The scale is termed the N_T scale, and the N'_{OTs} values are very similar, giving support to the premise that either of the two scales is giving a valid measure of solvent nucleophilicities. Several secondary N_T values (N''_T) are available (9, 12), based upon the specific rates of solvolysis of the *S*-methylthiophenium ion (13).

When the original N_{OTs} values are used in conjunction with Y_{OTs} values, the *l* value and its standard error and the correlation coefficient will be identical to those obtained using N'_{OTs} values, and the discrepancy will occur within the *m* value obtained, which can be corrected by the addition of 0.25*l* (8, 9). There is, however, no simple way to correct for errors introduced when N_{OTs} scales are used in the presence of leaving groups (X) differing appreciably from the tosylate.

Since the previous reports (1, 6, 7), a new type of scale has been developed for incorporation into the Grunwald–Winstein equations when the solvolyses involve benzylic derivatives (14). This scale is termed the aromatic ring parameter (*I*) and the sensitivity to changes in this value is termed *h*. The full equation is now represented by eq. [2]. The additional term has been found to make a significant contribution to the linear free energy relationship when there is appreciable development of

$$[2] \quad \log (k/k_o)_{RX} = lN_T + mY_X + hI + c$$

carbocationic character on the α-carbon at the transition state for solvolyses of benzylic derivatives (14–16). The *h* value has been found to increase with increase in the number of aromatic rings that can enter into conjugation with the carbocationic center. The origin of the *hI* term is believed (14, 17) to lie in a perturbation of the solvation changes in going to the transition state, relative to the changes observed for solvolyses of the standard adamantyl substrates used in establishment of Y_X scales. These effects may also be reflected in variations in the amounts of hidden internal return to substrate, which will perturb the detailed relationship with the Y_X scale (14).

As an alternative to the use of the *hI* term, numerous similarity models have been developed (18, 19). The use of similarity models has been reviewed (18*f*, 20). For example, the use of solvolyses of neophyl tosylate (Y_{neo}) (21), *p*-methoxyneophyl tosylate (Y_Δ) (21), and α-(*tert*-butyl)benzyl tosylate ($Y_{\alpha\text{-}t\text{-}Bu}$) (18*e*, 22) have been proposed as sources of improved scales for replacement of Y_{OTs}, when benzylic tosylates are being solvolyzed. It has been found, however, that these scales do not adequately correct for the perturbation involved when multiple aromatic rings are capable of entering into conjugation with the carbocationic center and the solvolysis of 2,2-dimethyl-1-(β-naphthyl)propyl tosylate was proposed as a similarity model (23). As a variant, multiple correlation analysis against a linear combination of both Y_Δ and Y_{OTs} terms has been proposed, primarily for ionizations proceeding with 1,2-aryl group migration (24) but also for the solvolyses of benzylic systems (25).

In the present report, we analyze the specific rates of solvolysis of several compounds of structure **1**, with varying identity of substituent X (1, 6, 7), in terms of both simple (eq. [1] without the *lN* term) and extended (eq. [1]) Grunwald–Winstein equations, and we also consider the extent to which the extended correlations are improved when the *hI* term is added (eq. [2]). An indication that it could be helpful to use eq. [2] comes from the study of Westaway and Waszczylo (26). These authors found evidence for appreciable electron deficiency at the α-carbon of benzylic substrates at the transition state, even in the presence of electron-withdrawing substituents and for bimolecular reaction with powerful nucleophiles, such as the thiophenoxide ion. Finally, for the solvolyses of substrates of type **1**, we consider the advantages and disadvantages of replacing the Y_{OTs} scale within eq. [1] by a similarity model scale (Y_{sim}) based on the specific rates of solvolysis of *p*-methylbenzyl *p*-toluenesulfonate (**1**, X = *p*-CH_3).

Results

The specific rates of solvolysis of the seven benzylic tosylates studied are reported in Table 1 for ethanol, methanol, acetic acid, formic acid, two aqueous ethanol compositions, three aqueous 2,2,2-trifluoroethanol (TFE) compositions, 95% acetone, and 60% TFE – 40% ethanol. The reported values (some extrapolated) are for solvolyses at 50.0°C, except for **1** (X = *p*-CH_3), which was studied at 0.0°C. The specific rates for **1** (X = H) were determined in this study only in the TFE–ethanol mixture, in 50% TFE, and in 95% acetone; the other values were available from an earlier publication (27). Also, contained within the footnotes to Table 1 are values determined at other temperatures, which were then extrapolated using the Arrhenius equation to get the corresponding values at 50.0°C.

The data for these substrates have been analyzed in terms of eq. [1], with and without the lN_T term, using the ABSTAT statistical package (Anderson-Bell, Arvada, Colorado, U.S.A.). The results of this analysis are contained within Table 2, together with identical analyses of the five more extensively studied (in terms of number of solvents) substrates, using the data of Fujio, Tsuno, and co-workers (6, 7). When values for solvolyses in acetonitrile–water mixtures are reported (6, 7), the appropriate secondary N''_T values (12) were used, in conjunction with the N_T values available (9, 10) for the other solvents. The Y_{OTs} values were as reported by Bentley and Llewellyn (5), except that those values based on 1-adamantyl tosylate solvolyses were corrected in the manner suggested by Allard and Casadevall (adjusted Y_{OTs} values of –1.75 for EtOH, –0.77 for MeOH, –0.74 for CH_3CO_2H, and –2.53 for 95% acetone, plus an interpolated value of 1.95 for 80% TFE) (4, 28). For the analyses of the literature data (6, 7), a full tabulation of Y_{OTs} values was available (6). For these analyses, several of the N_T values were interpolated values (–1.51 for 30% TFE, –1.68 for 40% TFE, –1.83 for 50% TFE, –2.31 for 80% TFE, and –2.77 for 50% 1,1,1,3,3,3-hexafluoro-2-propanol [HFIP], all mixtures prepared on a volume/volume basis). The N''_T value of –1.07 for 50% acetonitrile was also an interpolated value.

In Table 3, the correlations obtained upon addition of the *hI* term (eq. [2]) are reported. The number of solvents is fewer

© 1998 NRC Canada

Table 1. Specific rates of solvolysis of benzyl *p*-toluenesulfonates ($XC_6H_4CH_2OTs$) in pure and binary solvents, as a function of the X-substituent.

	10^4 *k*, s^{-1}						
Solvent[a]	*p*-Me[b]	H[c]	*p*-Cl[c]	*p*-Br[c]	*m*-F[c]	*p*-CF_3[c]	*p*-NO_2[c]
100% EtOH	0.230 ± 0.007	5.58[d]	3.51 ± 0.07	2.91 ± 0.07	1.17 ± 0.04	0.548 ± 0.0027	0.331 ± 0.014
80% EtOH	2.49 ± 0.10	28.1[d]	17.4 ± 1.1	11.3 ± 0.6	3.33 ± 0.07	2.01 ± 0.04	1.18 ± 0.04
60% EtOH	17.6 ± 1.4	86.0[d]	47.0 ± 3.2	30.1 ± 1.2	9.90 ± 0.55	3.85 ± 0.10	1.85 ± 0.11
100% MeOH	1.08 ± 0.04	18.1[d]	10.8 ± 0.6	8.00 ± 0.12	3.16 ± 0.10	1.33 ± 0.03	0.704 ± 0.019
97% TFE	81.4 ± 1.4	36.3[d]	21.3 ± 0.8	11.0 ± 0.3	0.554 ± 0.016	0.0807 ± 0.0007	0.0133 ± 0.0008
80% TFE	91.6 ± 5.4	81.1[d]	28.8 ± 1.0	31.7 ± 1.0	1.75 ± 0.02	0.763 ± 0.015	0.178 ± 0.007
50% TFE	98.2 ± 3.7	201[e, f]	94.8[e, g]	72.7 ± 2.6	7.15 ± 0.12	1.91 ± 0.07	0.542 ± 0.011
60T–40E	2.53 ± 0.08	12.7 ± 0.5	7.09 ± 0.30	4.45 ± 0.08	1.07 ± 0.03	0.421 ± 0.013	0.133 ± 0.005
95% Acetone	0.00279[e, h]	0.0636 ± 0.0024	0.0481 ± 0.0013	0.0497 ± 0.0012	0.0241 ± 0.0003	0.0110 ± 0.0002	0.00810 ± 0.00043
AcOH	0.0525[e, i]	0.462[d]	0.278 ± 0.021	0.103 ± 0.007	0.0300 ± 0.0006	0.00730 ± 0.00017	0.00493[e, j]
HCO_2H	[k]	530[d, e]	252[e, l]	164[e, m]	6.48 ± 0.21	0.873 ± 0.015	0.150 ± 0.006

[a] On a volume–volume basis (at 25.0°C), except for the three aqueous-TFE solvents, which are on a weight–weight basis; T–E are TFE–ethanol mixtures.
[b] At 0.0°C.
[c] At 50.0°C.
[d] From ref. 27.
[e] Extrapolated value, using the Arrhenius equation.
[f] Values of 0.977 ± 0.077 at 0.0°C, 10.5 ± 0.3 at 20.0°C, and 28.9 ± 0.6 at 30.0°C.
[g] Values of 12.4 ± 0.4 at 30.0°C and 35.5 ± 1.2 at 40.0°C.
[h] Values of 0.0595 ± 0.0006 at 25.0°C, 0.295 ± 0.008 at 40.0°C, and 0.793 ± 0.018 at 50.0°C.
[i] Values of 1.50 ± 0.07 at 25.0°C, 8.85 ± 0.17 at 40.0°C, and 25.7 ± 1.0 at 50.0°C.
[j] Values of 0.0294 ± 0.0007 at 70.0°C and 0.0663 ± 0.0010 at 80.0°C.
[k] Rates too fast to measure by technique employed at temperatures above freezing point of the solvent.
[l] Values of 14.6 ± 1.1 at 20.0°C and 39.9 ± 3.3 at 30.0°C.
[m] Values of 6.34 ± 0.23 at 20.0°C and 20.0 ± 1.4 at 30.0°C.

than in Table 2 because *I* scale values are not available for HCOOH, CH_3COOH, and the four aqueous acetonitrile mixtures. To allow a direct comparison with an analysis in terms of eq. [1], the eq. [1] analyses of Table 2 have been repeated with omission of these six solvents.

In Table 4 are presented analyses paralleling those of Table 2 but using Y_{sim} values defined as log (k/k_0) for **1** (X = *p*-CH_3) solvolyses in place of Y_{OTs} values.

For the analyses reported in Tables 2–4, the "goodness of fit" is considered in terms of the overall correlation coefficient, the *F*-test values, the probabilities that each individual term is statistically insignificant (reported if greater than 0.005), the standard error of the estimate (reported associated with the *c* value), and the standard errors associated with the calculated *l*, m, and *h* values. If multicollinearity had been a problem, a warning would have been issued to the effect that "the results may be spurious due to a high degree of multicollinearity."

Discussion

Our earlier claim (1), based on treatments in terms of eq. [1] of the seven substrates studied in 10 or 11 solvents, of an S_N1 mechanism involving appreciable nucleophilic solvation for *p*-methylbenzyl tosylate and an S_N2 mechanism (27, 29) with variable transition state structure for the solvolyses of the other six esters has been given very strong support (30) by a detailed correlation analysis of the effect of varying the substituent within a given solvolysis. A Yukawa–Tsuno treatment (31) indicated a gradual change in mechanism from S_N1 for electron-donating substituents, through a borderline region, to S_N2 as the substituents became increasingly electron withdrawing (30).

In Table 2, the earlier (1) treatments of seven of the substrates are now presented in terms of N_T and Y_{OTs} values; as well, the five substrates (three new) studied by Fujio, Tsuno and co-workers in 34–41 solvents (6, 7) are also now treated in terms of N_T and Y_{OTs}. The analyses in terms of the full eq. [1] all show an appreciable sensitivity towards changes in N_T values, even in the presence of an electron-donating methyl substituent. The sensitivities (*l* values) are, however, quite low in the presence of a methyl substituent and the *F*-test value falls slightly on incorporation of the lN_T term into the one-term equation. For **1** (X = *p*-CH_3) the *l* value of 0.34 ± 0.14 is accompanied by a 0.05 probability that the lN_T term is not statistically significant. For the solvolyses of **1** (X = *m*-Me), the study is in 41 solvents, and the *l* value of 0.24 ± 0.06 is associated with a very low probability that the lN_T term is statistically insignificant. The *m* values of 1.07 and 0.80, respectively, indicate appreciable carbocationic character at the transition state.

As one moves onward, in terms of σ^+ values (32), to the unsubstituted ester and then to the four halogenated derivatives (σ^+ of 0.11–0.40), there is a trend of gradually increasing *l* values (0.59–0.80) and gradually decreasing *m* values (0.82–0.67). These substrates appear to be solvolyzing by a mechanism that is S_N2 in character but with the bond breaking running ahead of the bond making, consistent with the picture for S_N2 reactions at benzylic carbon developed by Westaway and Waszczylo (26). The *F*-test values for these five solvolyses are all higher for the two-term treatment, significantly so for the halogenated derivatives.

The analyses for **1** (X = *p*-CF_3; $\sigma^+ = 0.61$), **1** (X = *p*-NO_2; $\sigma^+ = 0.79$), and **1** (X = 3,5-diCF_3; $\sigma^+ = 2 \times 0.52$) all show extremely poor one-term correlation against Y_{OTs}, with very

© 1998 NRC Canada

low correlation coefficients and *F*-test values. The correlations are enormously improved by use of the full eq. [1] and the *l* and *m* values stabilize at 0.94–1.04 and 0.70–0.61, respectively. It is proposed that these values reflect a fairly symmetrical S_N2 transition state, but still with bond breaking running a little ahead of the bond making (26). The values can be compared with those (9) for the typically S_N2 solvolyses of methyl tosylate of 0.96 ± 0.04 for *l* and 0.53 ± 0.04 for m.

The effect of adding an *hI* term to eq. [1], to give eq. [2], is demonstrated in Table 3, where a comparison is made of the applications of the two equations to solvolyses in the same sets of solvents. One cannot draw any firm conclusions from the application of a three-term equation to solvolyses in only nine solvents and, in these cases, the *h* values are associated with large standard errors and very high probabilities that the *hI* term is statistically insignificant; values are included only because the actual values (ignoring the large standard errors) are found to be consistent with those from parallel analyses for the five substrates using 28–35 solvents.

Concentrating on the investigations with 28–35 solvents (6, 7), we find that the *h* values fall as increasingly electron-withdrawing groups are introduced, from 0.79 ± 0.18 for *m*-CH_3, to 0.64 ± 0.18 for the unsubstituted substrate, to 0.50 ± 0.17 for *m*-Cl, to 0.25 ± 0.11 for *p*-NO_2, and to 0.28 ± 0.12 for the 3,5-diCF_3 substituent. Even for the two smallest values, there is only a 0.03 probability that the *hI* term is statistically insignificant. There is an appreciable increase in the correlation coefficient on addition of the *hI* term for the *m*-CH_3, H, and *m*-Cl substituents, but only small increases in the presence of *p*-NO_2 and 3,5-diCF_3 substituents. As regards *F*-test values, incorporation of the *hI* term leads to a slightly higher value for *m*-CH_3 and to slightly lower values for the other four substituents.

It can be concluded that the analyses reported in Table 3 give further support to the concept of carbocationic character for the benzylic carbon at the transition state of these solvolyses (26). The fairly large charge development in the solvolyses of the *m*-CH_3 derivative becomes very much smaller in the presence of the powerfully electron-withdrawing *p*-NO_2 and 3,5-diCF_3 substituents.

An alternative treatment to the incorporation of the *hI* term is to replace the Y_X scale by a similarity model scale, with the same leaving group but with the adamantyl group replaced by a group with a phenyl substituent either at the α-carbon or migrating, at the transition state, from a β-carbon to the α-carbon. In their consideration (6, 7) of benzyl tosylate and four derivatives, Fujio and Tsuno investigated the use within eq. [1] of not only the Y_{OTs} scale but also similarity models termed the $Y_{t\text{-Bu}}$ scale, the Y_{neo} scale, and the Y_Δ scale. It has been shown that the most important aspect of a good similarity model scale is that its h/*m* ratio is very similar to (ideally, identical to) that for the solvolysis under investigation (14, 15). It is instructive to consider the application of these three similarity models in terms of how well their *h*/*m* ratios match those for solvolyses of the five substrates under investigation. The relevant *h*/*m* ratios for the models are 0.82 (15*a*), 0.94 (15*d*), and 1.13 (15*d*), respectively. These values are all quite similar and, as one would expect, the three scales do about equally well when used as the *Y* scale within eq. [1] (6, 7).

Using the data of Table 3, we obtain *h*/*m* ratios of 0.95 with an *m*-Me substituent, 0.80 with no substituent, 0.72 with an *m*-Cl substituent, 0.37 with a *p*-NO_2 substituent, and 0.44 for the 3,5-diCF_3 derivative. The first three *h*/*m* ratios match well with those of the proposed similarity models and, accordingly, it is found (6) that one obtains considerably improved eq. [1] correlations when a similarity model *Y* scale replaces Y_{OTs}.

The finding (7), for each of the two substrates with highly electron-withdrawing substituents, that the Y_{OTs} scale and the three similarity model scales lead to almost identical eq. [1] correlation coefficients is also readily explained in terms of *h*/*m* ratios. The observed *h*/*m* ratios of about 0.4 are roughly half way between the 0.82–1.13 values for the proposed similarity models and the value of zero for solvolyses of 2-adamantyl tosylate. Accordingly, the error resulting from the undercorrection when the Y_{OTs} scale is incorporated is comparable to the error resulting from the overcorrection when one of the similarity models is employed.

For analyses of the specific rates of solvolyses of benzylic derivatives, incorporation of a similarity model scale, based on solvolyses of a substrate with similar structure, will usually lead to better correlations than those obtained using an adamantyl-based Y_X scale. There are several scales that have

Table 2. Correlation of the specific rates of solvolysis of ring-substituted benzyl *p*-toluenesulfonates ($XC_6H_4CH_2OTs$) using the simple and extended Grunwald–Winstein equations (eq. [1], with and without the lN_T term).

X (σ^+)	n^a	l^b	m^b	c^c	R^d	F^e
p-CH_3[f]	10		0.90 ± 0.10	–0.16 ± 0.48	0.9552	83
(–0.31)		0.34 ± 0.14	1.07 ± 0.11	0.16 ± 0.38	0.9752	68
m-CH_3[g]	41		0.66 ± 0.05	–0.37 ± 0.42	0.9055	173
(–0.07)		0.24 ± 0.06	0.80 ± 0.06	–0.23 ± 0.36	0.9326	124
H[h]	11		0.57 ± 0.11	–0.45 ± 0.59	0.8738	29
(0.00)		0.59 ± 0.11	0.86 ± 0.07	0.12 ± 0.29	0.9761	81
H[g]	41		0.60 ± 0.05	–0.42 ± 0.44	0.8784	132
(0.00)		0.33 ± 0.06	0.77 ± 0.05	–0.22 ± 0.33	0.9360	134
p-Cl[h]	11		0.53 ± 0.11	–0.48 ± 0.58	0.8600	26
(0.11)		0.59 ± 0.11	0.82 ± 0.07	0.08 ± 0.29	0.9714	67
p-Br[h]	11		0.52 ± 0.11	–0.45 ± 0.63	0.8387	21
(0.15)		0.63 ± 0.12	0.84 ± 0.08	0.16 ± 0.31	0.9676	59
m-F[h]	11		0.31 ± 0.13	–0.59 ± 0.74	0.6202	6
(0.35)		0.80 ± 0.09	0.71 ± 0.06	0.18 ± 0.23	0.9720	69
m-Cl[g]	41		0.35 ± 0.07	–0.52 ± 0.61	0.6212	25
(0.40)		0.59 ± 0.05	0.67 ± 0.04	–0.18 ± 0.29	0.9296	121
p-CF_3[h]	11		0.24 ± 0.15	–0.83 ± 0.85	0.4613	2
(0.61)		0.94 ± 0.09	0.70 ± 0.06	0.08 ± 0.23	0.9736	73
p-NO_2[h]	11		0.12 ± 0.16	–0.96 ± 0.90	0.2374	0.5
(0.79)		1.01 ± 0.07	0.62 ± 0.05	0.01 ± 0.19	0.9822	109
p-NO_2[i]	34		0.28 ± 0.09	–0.59 ± 0.71	0.4595	9
(0.79)		1.04 ± 0.03	0.65 ± 0.02	0.00 ± 0.13	0.9873	601
3,5-CF_3[i]	35		0.08 ± 0.11	–0.55 ± 0.85	0.1275	0.5
(2 × 0.52)		0.96 ± 0.03	0.61 ± 0.03	–0.04 ± 0.16	0.9831	462

[a] Number of solvents (data from Table 1 and refs. 6 and 7).
[b] With associated standard errors.
[c] Accompanied by the standard error of the estimate.
[d] Correlation coefficient.
[e] The *F*-test value.
[f] At 0.0°C.
[g] At 25.0°C, data from ref. 6.
[h] At 50.0°C.
[i] At 45.0°C, data from ref. 7.

© 1998 NRC Canada

Table 3. Correlation of the specific rates of solvolysis of ring-substituted benzyl *p*-toluenesulfonates ($XC_6H_4CH_2OTs$) using the extended Grunwald–Winstein equation, with and without addition of an aromatic ring parameter term (eqs. [1] and [2]).

X	n^a	l^b	m^b	h^b	c^c	R^d	F^e
p-CH_3[f]	9	0.22 ± 0.15	0.99 ± 0.11		0.12 ± 0.35	0.9795	71
		0.29 ± 0.14	1.00 ± 0.10	0.69 ± 0.45	0.05 ± 0.31	0.9861	59
m-CH_3[g]	34	0.16 ± 0.06	0.71 ± 0.05		–0.14 ± 0.30	0.9409	120
		0.37 ± 0.07	0.83 ± 0.05	0.79 ± 0.18	–0.10 ± 0.24	0.9643	133
H[h]	9	0.54 ± 0.13	0.83 ± 0.10		0.11 ± 0.30	0.9666	43
		0.60 ± 0.12	0.84 ± 0.09	0.61 ± 0.39	0.04 ± 0.27	0.9778	36
H[g]	35	0.26 ± 0.05	0.69 ± 0.05		–0.14 ± 0.28	0.9415	125
		0.43 ± 0.07	0.80 ± 0.05	0.64 ± 0.18	–0.10 ± 0.24	0.9588	118
p-Cl[h]	9	0.53 ± 0.13	0.78 ± 0.10		0.06 ± 0.31	0.9597	35
		0.58 ± 0.13	0.79 ± 0.09	0.59 ± 0.41	0.00 ± 0.29	0.9714	28
p-Br[h]	9	0.52 ± 0.12	0.75 ± 0.09		0.12 ± 0.27	0.9659	42
		0.56 ± 0.12	0.76 ± 0.08	0.46 ± 0.38	0.07 ± 0.27	0.9736	30
m-F[h]	9	0.73 ± 0.10	0.67 ± 0.07		0.16 ± 0.23	0.9676	44
		0.76 ± 0.10	0.68 ± 0.07	0.36 ± 0.32	0.12 ± 0.22	0.9744	31
m-Cl[g]	35	0.53 ± 0.05	0.61 ± 0.04		–0.12 ± 0.25	0.9292	101
		0.66 ± 0.06	0.69 ± 0.05	0.50 ± 0.17	–0.09 ± 0.23	0.9447	86
p-CF_3[h]	9	0.86 ± 0.07	0.68 ± 0.05		0.07 ± 0.16	0.9851	99
		0.88 ± 0.07	0.69 ± 0.05	0.29 ± 0.21	0.04 ± 0.15	0.9891	75
p-NO_2[h]	9	0.97 ± 0.05	0.63 ± 0.04		0.02 ± 0.13	0.9912	168
		0.98 ± 0.06	0.64 ± 0.04	0.05 ± 0.20	0.02 ± 0.14	0.9913	95
p-NO_2[i]	28	0.99 ± 0.04	0.63 ± 0.02		0.00 ± 0.12	0.9854	420
		1.06 ± 0.05	0.68 ± 0.03	0.25 ± 0.11	0.00 ± 0.11	0.9881	331
3,5-CF_3[i]	29	0.93 ± 0.03	0.58 ± 0.03		–0.03 ± 0.14	0.9847	414
		1.01 ± 0.05	0.64 ± 0.04	0.28 ± 0.12	–0.02 ± 0.13	0.9874	324

[a] Number of solvents (data from Table 1 and refs. 6 and 7; fewer than in Table 2 because of lack of *I* values for CH_3CO_2H, HCO_2H, and CH_3CN–H_2O mixtures).
[b–i] See footnotes to Table 2.

been proposed and, in principle, different scales will be needed for each leaving group.

We have considered above three similarity models that have been used for benzylic tosylates and another one has been proposed (23) for use when two aromatic rings enter into conjugation with the developing positive charge. Further, the high h/*m* ratio of 3.29 observed (15*b*) for the solvolyses of 1-(9-anthranyl)-2,2,2-trifluoroethyl methanesulfonate (33) suggests that yet another scale would be needed in the presence of three aromatic rings.

The concept of similarity models for correlations of specific rates of solvolysis can be considered as one example of the use of internally generated parameters for linear free energy analyses of a grouping of related data. We have recently discussed the advantages and disadvantages of internally generated scales of σ values (34) in a consideration of the importance of cross-interaction coefficients in Hammett treatments of reactions with two (35) or three (36) aromatic sites, each with varying substituents. In terms of evaluating the extent of cross interaction and obtaining calibrated values (37) for the coefficients, this is an excellent approach. The major disadvantage is that, in order to relate the values obtained to values determined using conventional σ scales, it is necessary to introduce the ρ values that are obtained by application of the appropriate conventional σ scale to the experimental data.

In Grunwald–Winstein equation considerations, if one is looking for a trend of relatively small variations in the *lN* term contribution within a series of related compounds, it can be advantageous to use an internally generated similarity model *Y* scale. For the consideration of solvolyses of compounds of type **1**, we have used the solvolyses of **1** (X = *p*-CH_3) to establish a Y_{sim} scale and we then applied the 10 values obtained,

Table 4. Correlation of the specific rates of solvolysis at 50.0°C of ring-substituted benzyl *p*-toluenesulfonates ($XC_6H_4CH_2OTs$) using the simple and extended Grunwald–Winstein equations (eq. [1], with and without the lN_T term) and incorporating Y_{sim} values (log (k/k_o) for *p*-$CH_3C_6H_4CH_2OTs$ solvolysis).

X	n^a	l^b	m^b	c^c	R^d	F^e
H	10		0.68 ± 0.08	–0.34 ± 0.36	0.9494	73
		0.32 ± 0.03	0.80 ± 0.02	–0.01 ± 0.10	0.9968	542
p-Cl	10		0.64 ± 0.08	–0.39 ± 0.37	0.9390	60
		0.33 ± 0.04	0.76 ± 0.03	–0.04 ± 0.12	0.9949	337
p-Br	10		0.64 ± 0.09	–0.36 ± 0.42	0.9259	48
		0.37 ± 0.03	0.78 ± 0.03	0.03 ± 0.11	0.9960	432
m-F	10		0.45 ± 0.14	–0.52 ± 0.63	0.7536	11
		0.57 ± 0.03	0.67 ± 0.03	0.07 ± 0.10	0.9952	358
p-CF_3	10		0.41 ± 0.17	–0.75 ± 0.77	0.6500	6
		0.70 ± 0.03	0.68 ± 0.02	–0.02 ± 0.09	0.9967	533
p-NO_2	10		0.29 ± 0.19	–0.90 ± 0.87	0.4691	2
		0.79 ± 0.04	0.59 ± 0.03	–0.08 ± 0.13	0.9919	214

[a] Number of solvents (data from Table 1; fewer than in Table 2 because of lack of Y_{sim} value for HCO_2H).
[b–e] See Table 2.

© 1998 NRC Canada

together with N_T values, to the specific rates of solvolysis of the other six compounds of type **1** that were studied in these solvents (Table 1). The results from correlations in terms of eq. [1], with and without the lN_T term, are reported in Table 4. In all cases, a comparison of both the correlation coefficients and *F*-test values shows considerably improved correlations when the lN_T term is included. The correlation coefficients and *F*-test values using the full equation are fairly constant except for **1** (X = *p*-NO_2), where lower values are obtained; this inferior correlation can be rationalized in terms of a much lower *h*/*m* ratio than is obtained in correlation of the Y_{sim} scale and the log (k/k_0) values for the other five substrates of Table 4 (*h* and *m* values from Table 3).

The values in Table 4 show a very clear trend of increasing *l* values as one increases the electron-withdrawing ability of the substituent. It must, however, be emphasized that these values are relative to the extent of nucleophilic participation involved in the solvolyses used to establish the Y_{sim} scale, where there is clear evidence (Tables 2 and 3) for a measure of nucleophilic participation. If one wishes to compare the values of Table 4 with others obtained using the Y_{OTs} scale in conjunction with N_T, it is necessary to know the correlation relationship between the log (k/k_0) values used to establish the Y_{sim} scale and the N_T and Y_{OTs} parameters. Further, not only the sensitivity values but also the associated standard errors will be required and, in particular, even if a sensitivity value should be found to be negligibly small, the associated standard error must still be applied.

If we should wish to compare the data obtained with use of N_T and Y_{sim} with data obtained using N_T and Y_{OTs}, we need the entry for **1** (X = *p*-Me) from Table 2. A general treatment is given below:

[3] $Y_{sim} = \log (k/k_0)_{sim}$ (definition)

[4] $= l_{sim}N_T + m_{sim}Y_{OTs}$

With a substituent X, we can correlate against N_T and Y_{sim}:

[5] $\log (k/k_0)_X = l_X N_T + m_X Y_{sim}$

and, substituting for Y_{sim} from eq. [4], we obtain:

[6] $\log (k/k_0)_X = (l_X + m_X l_{sim})N_T + m_X m_{sim} Y_{OTs}$

This is the same form as the correlation against N_T and Y_{OTs}:

[7] $\log (k/k_0)_X = lN_T + mY_{OTs}$

such that, comparing eqs. [6] and [7]:

[8] $l = l_X + m_X l_{sim}$

and

[9] $m = m_X m_{sim}$

If correlation is done first using internally generated Y_{sim} values and one wishes to compare these results with others obtained using the conventional (external) Y_X values, one must first adjust the l_X and m_X values as indicated. The end result is that the *l* and *m* values and their standard errors are essentially identical to those that would have been obtained by a direct one-step correlation against N_T and Y_X.

We can take, as an example, the correlation of the specific rates of solvolysis of **1** (X = *m*-F). The l_{sim} value is 0.34 ± 0.14 and the m_{sim} value is 1.07 ± 0.11 (from the **1** (X = *p*-Me) entry in Table 2). Using eq. [1] with N_T and Y_{sim} values, one obtains an l_X value of 0.57 ± 0.03 and an m_X value of 0.67 ± 0.03 (Table 4). Therefore, substituting in eqs. [8] and [9], the values corresponding to application of eq. [1] with N_T and Y_{OTs} values are

[10] $l = 0.57 \pm 0.03 + (0.67 \pm 0.03)(0.34 \pm 0.14)$
$= 0.80 \pm 0.10$

and

[11] $m = (0.67 \pm 0.03)(1.07 \pm 0.11) = 0.72 \pm 0.08$

with the values being essentially identical to the 0.80 ± 0.09 and 0.71 ± 0.06 obtained directly (Table 2).

Conclusions

The specific rates of solvolysis of the parent benzyl tosylate and ring-substituted derivatives are correlated with reasonable precision (correlation coefficient 0.930–0.987) using the two-term Grunwald–Winstein equation (eq. [1]), with incorporation of N_T and Y_{OTs} values. As one moves from substituents with negative σ^+ values to substituents with increasingly positive σ^+ values, the *l* values rise from 0.34 for *p*-Me to a value of close to unity for *p*-NO_2 and 3,5-diCF_3 and the *m* values fall from 1.07 to a value of 0.61–0.65. These changes in the values are believed (1) to represent a transition from an ionization mechanism with nucleophilic solvation to an S_N2 mechanism with varying transition state structure that, with strongly electron-withdrawing substituents, attains an *l* value identical to the 0.96 for methyl tosylate solvolysis and an *m* value only slightly higher than the 0.53 for methyl tosylate solvolysis.

For five of the substrates, a sufficiently large number of well-chosen solvents are available to carry out a meaningful investigation of the application of eq. [2], where a term governed by the aromatic ring parameter (*I*) is added to eq. [1]. The sensitivities (*h*) towards this parameter fall in an orderly fashion, from 0.79 ± 0.18 for *m*-Me to 0.25 ± 0.11 for *p*-NO_2. The observation of a meaningful (probability that the *hI* term is statistically insignificant of < 0.03) *h* value throughout the series of substrates, together with an *m* value always somewhat larger than for methyl tosylate solvolysis, is consistent with the previously expressed (26) view that S_N2 reactions of benzyl derivatives have some positive charge development on the α-carbon, even in the presence of powerfully electron-withdrawing ring-substituents.

Application of a similarity model for the *Y* scale, based on the solvolyses of *p*-methylbenzyl tosylate, demonstrates very clearly the well-defined trend of increasing *l* values with increasing σ^+ values, and very good *F*-test values and correlation coefficients (0.992–0.997) are observed. While this type of treatment, using an internally generated *Y* scale, is excellent for examining trends in *l* values within a series of closely related solvolyses, the goodness of fit is considerably diminished when one then applies the calibration factors (and their associated standard errors) needed prior to any comparison with sensitivities determined using N_T values and an external Y_X scale (for a leaving group X). Indeed, using one of the present analyses as an example, it is shown that one arrives at essentially identical sensitivity values and associated standard errors irrespective of whether one proceeds in two steps, use of N_T and Y_{sim} values being followed by adjustment of the *l* and *m* values, or by a one-step application of N_T and Y_{OTs} values.

© 1998 NRC Canada

Experimental

Solvents were purified and kinetic runs carried out as previously described (10).

The parent and six ring-substituted benzyl tosylates were prepared by the silver-salt method (38, 39). All seven substrates had previously been prepared, either by the silver-salt method or by the Schotten–Bauman method, and the melting points observed were in agreement with those initially reported (40–42). The procedure is illustrated for the parent compound as follows: Silver tosylate (Aldrich, 99+%, 3.07 g, 0.011 mol) was dissolved in 25 mL acetonitrile and benzyl bromide (Aldrich, 99%, 1.71 g, 0.010 mol) was added. The mixture was stirred overnight at room temperature and filtered. The filtrate was evaporated under reduced pressure and the residue was recrystallized from petroleum ether to give fine white needles of benzyl tosylate, mp 57.5–59°C (lit. (40) mp 58.5–58.9°C). Anal. calcd for $C_{14}H_{14}O_3S$: C 64.1, H 5.4; found: C 64.2, H 5.3. An identical procedure using commercially available (Aldrich, 95–99%) bromides or chlorides was used for the preparation of the ring-substituted derivatives.

Acknowledgment

M.J.D. thanks the University of Wisconsin Colleges Grant Program for financial support.

References

1. D.N. Kevill and H. Ren. J. Org. Chem. **54**, 5654 (1989).
2. (*a*) D.N. Kevill and G.M.L. Lin. J. Am. Chem. Soc. **101**, 3916 (1979); (*b*) D.N. Kevill and W.A. Kamil. J. Org. Chem. **47**, 3785 (1982); (*c*) D.N. Kevill and S.W. Anderson. J. Am. Chem. Soc. **108**, 1579 (1986).
3. F.L. Schadt, T.W. Bentley, and P.v.R. Schleyer. J. Am. Chem. Soc. **98**, 7667 (1976).
4. D.N. Kevill and D.C. Hawkinson. J. Org. Chem. **54**, 154 (1989).
5. T.W. Bentley and G. Llewellyn. Prog. Phys. Org. Chem. **17**, 121 (1990).
6. M. Fujio, T. Susuki, M. Goto, Y. Tsuji, K. Yatsugi, Y. Saeki, S.H. Kim, and Y. Tsuno. Bull. Chem. Soc. Jpn. **67**, 2233 (1994).
7. M. Fujio, T. Susuki, M. Goto, Y. Tsuji, K. Yatsugi, S.H. Kim, G.A-W. Ahmed, and Y. Tsuno. Bull Chem. Soc. Jpn. **68**, 673 (1995).
8. D.N. Kevill and T.J. Rissmann. J. Org. Chem. **50**, 3062 (1985).
9. D.N. Kevill. *In* Advances in quantitative structure–property relationships. Vol. 1. *Edited by* M. Charton. JAI Press, Greenwich, Conn. 1996. pp. 81–115.
10. D.N. Kevill and S.W. Anderson. J. Org. Chem. **56**, 1845 (1991).
11. D.N. Kevill, S.W. Anderson, N. HJ Ismail, and E.K. Fujimoto. Stud. Org. Chem. **31**, 311 (1987).
12. D.N. Kevill and S.W. Anderson. J. Chem. Res. (S), 356 (1991).
13. J.L. Kurz, J. Lee, M.E. Love, and S. Rhodes. J. Am. Chem. Soc. **108**, 2960 (1986).
14. D.N. Kevill, N.HJ Ismail, and M.J. D'Souza. J. Org. Chem. **59**, 6303 (1994).
15. D.N. Kevill and M.J. D'Souza. (*a*) J. Chem. Soc. Perkin Trans. 2, 973 (1995); (*b*) Org. React. (Tartu), **29**, 55 (1995); (*c*) J. Chem. Res. (S), 286 (1996); J. Chem. Res. (M), 1649 (1996); (*d*) J. Chem. Soc. Perkin Trans. 2, 257 (1997).
16. D.N. Kevill, S.W. Anderson, and N.HJ Ismail. J. Org. Chem. **61**, 7256 (1996).
17. (*a*) I. Lee, H.J. Koh, and B.D. Chang. Bull. Korean Chem. Soc. **16**, 1104 (1995); (*b*) H.K. Oh, Y.B. Kown, H.J. Koh, and I. Lee. New J. Chem. **20**, 579 (1996).
18. (*a*) K.-T. Liu, H.-C. Sheu, H.-I. Chen, P.-F. Chiu, and C.-R. Hu. Tetrahedron Lett. **31**, 3611 (1990); (*b*) K.-T. Liu and H.-C. Sheu. J. Org. Chem. **56**, 3021 (1991); (*c*) K.-T. Liu, H.-I. Chen, and C.-P. Chin. J. Phys. Org. Chem. **4**, 463 (1991); (*d*) K.-T. Liu and H.-C. Sheu. J. Chin. Chem. Soc. (Taipei), **38**, 29 (1991); (*e*) K.-T. Liu, J.-S. Yang, S.-M. Chang, Y.-S. Lin, H.-C. Sheu, and M.-L. Tsao. J. Org. Chem. **57**, 3041 (1992); (*f*) K.-T. Liu. J. Chin. Chem. Soc. (Taipei), **42**, 607 (1995).
19. T.W. Bentley, I.S. Koo, and S.J. Norman. J. Org. Chem. **56**, 1604 (1991).
20. D.N. Kevill and M.J. D'Souza. J. Phys. Org. Chem. **5**, 287 (1992).
21. M. Fujio, M. Goto, K. Funatsu, T. Yoshino, Y. Saeki, K. Yatsugi, and Y. Tsuno. Bull. Chem. Soc. Jpn. **65**, 46 (1992).
22. Y. Tsuji, M. Fujio, and Y. Tsuno. Tetrahedron Lett. **33**, 349 (1992).
23. K.-T. Liu, H.-Y. Hsu, and J.-S. Yang. Tetrahedron Lett. **33**, 3327 (1992).
24. M. Fujio, Y. Saeki, K. Nakamoto, K. Yatsugi, N. Goto, S.H. Kim, Y. Tsuji, Z. Rappoport, and Y. Tsuno. Bull. Chem. Soc. Jpn. **68**, 2603 (1995).
25. M. Fujio, T. Susuki, K. Yatsugi, Y. Saeki, M. Goto, S.H. Kim, Y. Tsuji, Z. Rappoport, and Y. Tsuno. Bull. Chem. Soc. Jpn. **68**, 2619 (1995).
26. K.C. Westaway and Z. Waszczylo. Can. J. Chem. **60**, 2500 (1982).
27. D.N. Kevill and T.J. Rissmann. J. Chem. Res. (S), 252 (1986).
28. B. Allard and E. Casadevall. Nouv. J. Chim. **9**, 565 (1985).
29 (*a*) V.J. Shiner, Jr., M.W. Rapp, and H. R. Pinnick, Jr. J. Am. Chem. Soc. **92**, 232 (1970); (*b*) J.M. Harris, S.G. Shafer, J.R. Moffatt, and A.R. Becker J. Am. Chem. Soc. **101**, 3295 (1979); (*c*) H. Maskill. J. Chem. Soc. Perkin Trans. 2, 1241 (1986).
30. (*a*) M. Fujio, M. Goto, T. Susuki, M. Mishima, and Y. Tsuno. Bull. Chem. Soc. Jpn. **63**, 1146 (1990); (*b*) J. Phys. Org. Chem. **3**, 449 (1990); (*c*) M. Fujio, I. Akasaka, S.H. Kim, M. Mishima, Y. Tsuji, and Y. Tsuno. Mem. Fac. Sci. Kyushu Univ. Ser. C: **18**, 131 (1991).
31. (*a*) Y. Yukawa and Y. Tsuno. Bull. Chem. Soc. Jpn. **32**, 971 (1959); (*b*) J. Shorter. Correlation analysis of organic reactivity. Wiley, New York. 1982. pp. 35–45.
32. H.C. Brown and Y. Okamoto. J. Am. Chem. Soc. **80**, 4979 (1958).
33. A.D. Allen, R. Girdhar, M.P. Jansen, J.D. Mayo, and T.T. Tidwell. J. Org. Chem. **51**, 1324 (1986).
34. O. Exner. Collect. Czech. Chem. Commun. **41**, 1516 (1976).
35. D.N. Kevill and M.J. D'Souza. J. Chem. Soc. Perkin Trans. 2, 945 (1994).
36. D.N. Kevill and M.J. D'Souza. J. Chem. Soc. Perkin Trans. 2, 2427 (1994).
37. V.A. Palm and B.I. Istomin. Org. React. (Tartu) (Engl. Transl.), **6**, 179 (1969).
38. W.D. Emmons and A.F. Ferris. J. Am. Chem. Soc. **75**, 2257 (1953).
39. D.N. Kevill. *In* The chemistry of the functional groups, supplement D: the chemistry of halides, pseudo-halides and azides. *Edited by* S. Patai and Z. Rappoport. Wiley, New York. 1983. pp. 948–950.
40. J.K. Kochi and G.S. Hammond. J. Am. Chem. Soc. **75**, 3443 (1953).
41. F.T. Fang, J.K. Kochi, and G.S. Hammond. J. Am. Chem. Soc. **80**, 563 (1958).
42. A. Streitwieser, Jr., H.A. Hammond, R.H. Jagow, R.M. Williams, R.G. Jesaitis, C.J. Chang, and R. Wolf. J. Am. Chem. Soc. **92**, 5141 (1970).

© 1998 NRC Canada

Isotope effects in nucleophilic substitution reactions X. The effect of changing the nucleophilic atom on ion-pairing in an S_N2 reaction

Yao-ren Fang, Zhu-gen Lai, and Kenneth Charles Westaway

Abstract: The effect of ion-pairing in an S_N2 reaction is very different when the nucleophilic atom is changed from sulfur to oxygen, i.e., changing the nucleophile from thiophenoxide ion to phenoxide ion. When the nucleophile is sodium thiophenoxide, ion-pairing markedly alters the secondary α-deuterium kinetic isotope effect (transition state structure) and the substituent effect found by changing the *para* substituent on the nucleophile. When the nucleophile is sodium phenoxide, ion-pairing does not significantly affect the secondary α-deuterium or the chlorine leaving group kinetic isotope effects (transition state structure) or the substituent effects found by changing a *para* substituent on the nucleophile or the substrate. The different effects of ion-pairing may occur because the electron density on the hard oxygen atom of the sodium phenoxide is not affected significantly by ion-pairing.

Key words: nucleophilic substitution, S_N2, kinetic isotope effect, transition state, substituent effects, ion-pair.

Résumé : L'effet de la formation de paires d'ions sur une réaction S_N2 est très différent si l'atome nucléophile est un soufre ou un oxygène, comme lorsque le nucléophile est un ion thiophénolate ou un ion phénolate. Lorsque le nucléophile est le thiophénolate de sodium, la formation de paires d'ions influence l'effet isotopique cinétique secondaire dû aux hydrogènes en α (structure de l'état de transition) ainsi que l'effet de substituant provoqué par le changement de substituants *para* sur le nucléophile. Lorsque le nucléophile est le phénolate de sodium, la formation de paires d'ions n'affecte pas de façon significative l'effet isotopique secondaire dû aux hydrogènes en α ou les effets isotopiques cinétiques du chlore comme groupe partant (structure de l'état de transition) ou les effets de substituants provoqués par le changement de substituants *para* sur le nucléophile ou le substrat. Les effets différents dus à la formation de paires d'ions peuvent être causés par la densité électronique sur l'atome d'oxygène dur du phénolate de sodium qui n'est pas affecté d'une façon significative par la formation de paires d'ions.

Mots clés : substitution nucléophile, S_N2, effet isotopique cinétique, état de transition, effets de substituants, paires d'ions.

[Traduit par la rédaction]

Introduction

Westaway and co-workers have shown that ion-pairing can have a significant effect on the magnitude of the secondary α-deuterium kinetic isotope effect (KIE) and transition state structure of an S_N2 reaction (1–4). For example, in the S_N2 reaction between sodium thiophenoxide and *n*-butyl chloride, eq. [1],

[1] $$C_6H_5\text{-}S^-(Na^+) + CH_3CH_2CH_2CL_2\text{-}Cl \rightarrow CH_3CH_2CH_2CL_2\text{-}S\text{-}C_6H_5 + Na^+ + Cl^-$$
(L = H, D)

in DMSO at 20.000°C, the secondary α-deuterium KIE changes from 1.116 ± 0.002, when the nucleophile reacts as a free ion, to 1.034 ± 0.002, when the nucleophile reacts as a solvent-separated ion-pair complex $[(Na^+)_y(solvent)_x(^-SC_6H_5)_y]$ (1, 2). Since the magnitude of the KIE is related to the nucleophile – leaving group distance in the S_N2 transition state (5, 6), the structure of the transition state for the free ion and the ion-pair reactions must also be different. The secondary α-deuterium KIE (transition state structure) for this reaction also changed, i.e., from 1.131 ± 0.002[2] to 1.07 ± 0.03 when the nucleophile changed from a solvent-separated ion-pair complex to a contact ion-pair in diglyme (3). Another study demonstrated that the substituent effects found by changing a *para* substituent on the nucleophile of an S_N2 reaction is also very different depending on whether the nucleophile is a free ion or a solvent-separated ion-pair complex (4). For example, changing the *para* substituent on the nucleophile from methoxy to

Received December 10, 1997.

This paper is dedicated to Professor Erwin Buncel in recognition of his contributions to Canadian chemistry.

Y.-r. Fang, Z.-g. Lai, and K.C. Westaway.[1] Chemistry Department, Laurentian University, Sudbury, ON P3E 2C6, Canada.

[1] Author to whom correspondence may be addressed. Fax: (705)-675-4844. E-mail: Kwestawa@Nickel.Laurentian.ca

[2] The secondary α-deuterium KIEs for the solvent-separated ion-pair complex reactions range from 1.034 in DMSO to 1.085 in DMF to 1.10 in methanol to 1.14 in diglyme. The secondary α- deuterium KIEs in the free ion reactions are 1.12 ± 0.01 in all solvents (2).

© 1998 NRC Canada

chloro in the S_N2 reaction between *para*-substituted thiophenoxide ions and benzyldimethylphenylammonium ion, eq. [2],

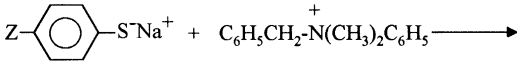

[2]

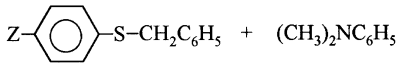

reduced the secondary α-deuterium KIE by 15%, i.e., from 1.27 to 1.12 when the nucleophile was a free ion but only from 1.22 to 1.15 (by 7%) when the nucleophile was a solvent-separated ion-pair complex. These findings are important because they demonstrate that the transition state and the substituent effects are different when the form of the reacting nucleophile is different. This means one must (*i*) determine the form of the nucleophile and (*ii*) ensure that it remains the same throughout a study where one is measuring the values of mechanistic criteria or substituent effects. The failure to do so could lead to significant errors when interpreting the results.

This study was undertaken to see if changing the nucleophilic atom from sulfur to oxygen affects how ion-pairing alters (*i*) the secondary α-deuterium KIE (transition state structure) and (*ii*) the substituent effects in an S_N2 reaction.

Results and discussion

The secondary α-deuterium KIEs for the S_N2 reactions between *para*-substituted benzyl chlorides and *para*-substituted sodium phenoxides, eq. [3]

[3] 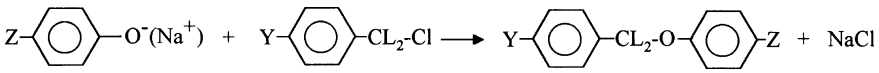

L = H, D

were measured to determine how ion-pairing (a change in the form of the reacting nucleophile) affects an S_N2 reaction when the nucleophilic atom is oxygen rather than sulfur.

Determining the concentrations where *para*-substituted sodium phenoxides exist as free ions and ion-pairs

Before one could determine how ion-pairing affects S_N2 reactions, it was necessary to determine the concentrations where the *para*-substituted sodium phenoxides exist as free ions and as ion-pairs in the organic solvents used in this study. The onset of ion-pairing in sodium *para*-substituted phenoxide solutions in DMSO, DMF, and methanol was identified by the downward curvature of the conductance versus concentration plot and (or) changes in λ_{max} in the UV spectrum as the concentration of the salt was increased (1). Although the concentration where ion-pairing of the *para*-substituted sodium phenoxides begins was determined by both methods in methanol, it was only determined by conductivity in DMF and DMSO. This was because both DMF and DMSO absorb strongly in the region where the *para*-substituted sodium phenoxide ion-pairs absorb. This is not thought to be a problem because, in those cases where conductivity and UV measurements were possible, the agreement between the two methods is good, Table 1.

Several observations are noteworthy. First, all the *para*-substituted sodium phenoxides exist as ion-pairs at high concentrations in methanol and in DMSO. Second, the substituent on the phenoxide ion does not significantly affect the concentration where ion-pairing occurs, i.e., all the *para*-substituted phenoxide salts begin forming ion-pairs in a very narrow concentration range between 5×10^{-4} and 2×10^{-3} M, Table 1. Third, the results also indicate that sodium phenoxide exists as free ions to a higher concentration than sodium thiophenoxide ions in methanol but forms ion-pairs at lower concentrations than sodium thiophenoxide in DMSO. This different behaviour in the dipolar aprotic and the protic solvents can be rationalized as follows. The higher concentration where ion-pairing begins in methanol is expected because the oxygen of the phenoxide ion has a higher negative charge density (vide infra) and would be more strongly solvated by hydrogen bonding to methanol than the sulfur of the thiophenoxide ion. As a result, the stabilization of the phenoxide ion by ion-pairing in methanol only begins when the concentration of the salt is high. In DMSO, on the other hand, the phenoxide ion forms ion-pairs at lower concentrations than the thiophenoxide ion. This is also reasonable because the negative charge density on the oxygen of the phenoxide ion is much higher than the negative charge density on the sulfur of the thiophenoxide ion. Therefore, phenoxide ion would be more strongly attracted to the sodium ion in these dipolar aprotic solvents, which do not solvate negative ions strongly (7, 8), and ion-pairing will occur at a lower concentration.

Another difference between the sodium phenoxide and sodium thiophenoxide salts is that the change in the form of the phenoxide ion with concentration is less abrupt than that of the thiophenoxide ions, which changed from free ions to a solvent-separated ion-pair complex when the concentration changed by a factor of two.

Finally, the change in the λ_{max} of the UV spectrum on ion-pairing is smaller for sodium phenoxide salt than for sodium thiophenoxide. The shift in the λ_{max} on ion-pairing was 32 nm, i.e., it increased from 235 to 267 nm in methanol when sodium thiophenoxide formed ion-pairs whereas it only increases by 7 nm, i.e., from 272 to 279 nm when sodium phenoxide changes from a free ion to an ion-pair. This indicates that the phenoxide ion chromophore is not altered significantly upon ion-pairing. This is interesting because it suggests that the effect of changing the form of the reacting nucleophile (ion-pairing) might be small when the nucleophile is the phenoxide ion.

The effect of ion-pairing of an oxygen nucleophile on the magnitude of the secondary α-deuterium KIE

The secondary α-deuterium KIE for the S_N2 reaction between sodium phenoxide and benzyl chloride was measured in methanol at 20.000 ± 0.002°C under conditions where (*i*) the

© 1998 NRC Canada

Table 1. The concentration at which sodium *para*-substituted phenoxides and thiophenoxides change from a solvent-separated ion-pair complex to free ions in methanol, DMSO, and DMF.

		Concentration at which the salt changes from an ion-pair to a free ion		
		Sodium phenoxide		Sodium thiophenoxide
para-Substituent	Solvent	By UV spectroscopy	By conductivity	By UV spectroscopy and conductivity [a]
CH_3O	CH_3OH	1×10^{-3}	1×10^{-3}	—
H	CH_3OH	1×10^{-3}	9×10^{-4}	1×10^{-4}
Cl	CH_3OH	3×10^{-4}	6×10^{-4}	—
H	DMSO	—	2×10^{-3}	2×10^{-2}
H	DMF	—	—	8×10^{-3}

[a] Reference 1.

Table 2. The second-order rate constants and secondary α-deuterium KIEs for the S_N2 reactions between sodium phenoxide and benzyl chloride in methanol at 20.000°C in the presence and absence of 15-crown-5 ether.

Nucleophile	[15-Crown-5 ether]	$k_H \times 10^6$ (L m^{-1} s^{-1})	$k_D \times 10^6$ (L m^{-1} s^{-1})	$(k_H/k_D)_\alpha$
Using the titrimetric method				
$C_6H_5O^-$ Na^+	None	8.0224 ± 0.0001[a]	7.8560 ± 0.0012[a]	1.0207 ± 0.0002[b]
$C_6H_5O^-$	0.05 M	9.049 ± 0.017	8.859 ± 0.0024	1.0215 ± 0.0019
Using the HPLC method				
$C_6H_5O^-$ Na^+	None	8.259	8.084	1.022
$C_6H_5O^-$	0.28 M	8.594	8.413	1.022

[a] The standard deviation of the mean for at least three different kinetic runs.

[b] The error in the isotope effect = $1/k_D[(\Delta k_H)^2 + (k_H/k_D)^2 \times (\Delta k_D)^2]^{1/2}$ where Δk_H and Δk_D are the standard deviations for the rate constants for the undeuterated and deuterated substrates, respectively.

phenoxide ion exists as an ion-pair and (*ii*) in the presence of 15-crown-5 ether where the nucleophile is the free phenoxide ion.[3] The second-order rate constants for the reactions of both the deuterated and undeuterated benzyl chloride and the secondary α-deuterium KIE found using two different methods of analysis[4] are presented in Table 2. The important observation is that the secondary α-deuterium KIEs are identical in these two reactions in spite of the fact that the form of the reacting nucleophile is different. This was surprising because the secondary α-deuterium KIEs were very different when the form of the nucleophile changed (ion-pairing occurred) in the S_N2 reaction when sodium thiophenoxide was the nucleophile; i.e., the KIE changed from 1.13 to 1.03 in DMSO, from 1.13 to 1.085 in DMF, and from 1.13 to 1.10 in methanol when the nucleophile changed from a free ion to a solvent-separated ion-pair complex in the S_N2 reaction between thiophenoxide ion and *n*-butyl chloride (1).

Because it was surprising that ion-pairing did not change the secondary α-deuterium KIE in the phenoxide ion – benzyl chloride reaction in methanol, it was important to learn whether this was a general phenomenon that occurred whenever oxygen nucleophiles were used in an S_N2 reaction. Therefore, the secondary α-deuterium KIEs were measured for two other S_N2 reactions where the form of the sodium phenoxide nucleophile was altered from an ion-pair to a free ion by adding 15-crown-5 ether. The results in Table 3 show that the different behaviour for the thiophenoxide and phenoxide ion nucleophiles is, indeed, real. Identical secondary α-deuterium KIEs were found for the free ion and the ion-pair phenoxide ion reactions with benzyl chloride in DMF and with *n*-butyl chloride in DMSO. It is important to note that these two reaction systems were chosen because the change in the secondary α-deuterium KIE on ion-pairing in the thiophenoxide ion reactions was greatest in DMF and DMSO. (1) However, changing the form of the oxygen nucleophile in two S_N2 reactions in three different solvents did not change the secondary α-deuterium KIE. Clearly, the effect of ion-pairing is very different when the nucleophilic atom in an S_N2 reaction is sulfur and oxygen.

The effect of ion-pairing of an oxygen nucleophile on the substituent effects and the magnitude of the secondary α-deuterium KIE

The different response to ion-pairing by oxygen nucleophiles was tested in another way. The substituent effects observed when the form of the thiophenoxide ion nucleophile changed in the S_N2 reactions between *para*-substituted sodium thiophenoxides and benzyldimethylphenylammonium ion in methanol, eq. [2], were significantly different (4). Changing the *para* substituent on the thiophenoxide ion from methoxy to chloro, when the nucleophile was the free ion, caused the secondary

[3] This method of converting the ion-pair into the free ion was chosen because when the phenoxide ion existed exclusively as a free ion, the phenoxide ion concentration was too low to measure the rate constants needed for the isotope effect accurately.

[4] The second method of analysis was used to ensure that the rate constants and isotope effects were not an artifact of the method.

© 1998 NRC Canada

Table 3. The second-order rate constants and secondary α-deuterium KIEs for the S_N2 reactions between sodium phenoxide and benzyl chloride in DMF and with *n*-butyl chloride in DMSO at 20.000°C in the presence and absence of 15-crown-5 ether.

Nucleophile	[15-Crown-5 ether]	$k_H \times 10^2$ (L m^{-1} s^{-1})	$k_D \times 10^2$ (L m^{-1} s^{-1})	$(k_H/k_D)_\alpha$
Benzyl chloride in DMF				
$C_6H_5O^-$ Na^+ [a]	None	4.145 ± 0.031[b]	4.073 ± 0.031[b]	1.018 ± 0.011[c]
$C_6H_5O^-$	0.032 M	5.640 ± 0.0004	5.526 ± 0.0002	1.021 ± 0.0008
***n*-Butyl chloride in DMSO**				
$C_6H_5O^-$ Na^+ [d]	None	0.1595 ± 0.009	0.1547 ± 0.0149	1.031 ± 0.012
$C_6H_5O^-$	0.014 M	0.1662 ± 0.013	0.1615 ± 0.0047	1.029 ± 0.008

[a] The sodium phenoxide ion concentrations in both the free ion and ion-pair reactions varied from 1.6×10^{-2} to 2.4×10^{-2} M.

[b] The standard deviation of the mean for at least three separate kinetic runs.

[c] The error in the isotope effect = $1/k_D[(\Delta k_H)^2 + (k_H/k_D)^2 \times (\Delta k_D)^2]^{1/2}$ where Δk_H and Δk_D are the standard deviations for the rate constants for the undeuterated and deuterated substrates, respectively.

[d] The sodium phenoxide ion concentrations in both the free ion and ion-pair reactions varied from 9.4×10^{-3} to 9.7×10^{-3} M.

Table 4. The secondary α-deuterium KIEs for the S_N2 reactions between sodium *para*-substituted thiophenoxides and benzyldimethylphenylammonium ion in methanol at 20.000°C in the presence and absence of 15-crown-5 ether.[a]

para-Substituent	$(k_H/k_D)_\alpha$	$(k_H/k_D)_\alpha$
	Free ion reactions with 15-crown-5 ether	**Ion-pair reactions no 15-crown-5 ether**
CH_3O	1.271 ± 0.013[a]	1.216 ± 0.012[a]
CH_3	1.237 ± 0.008	1.213 ± 0.013
H	1.222 ± 0.013	1.207 ± 0.008
Cl	1.121 ± 0.014	1.150 ± 0.009

[a] These isotope effects were taken from ref. 4. The error in the isotope effect equals $1/k_D[(\Delta k_H)^2 + (k_H/k_D)^2 \times (\Delta k_D)^2]^{1/2}$ where Δk_H and Δk_D are the standard deviations for the rate constants for the undeuterated and deuterated substrates, respectively.

α-deuterium KIE to decrease from 1.27 to 1.12, Table 4. When the *para* substituent on the nucleophile changed from methoxy to chloro and the nucleophile was the solvent-separated ion-pair complex, the secondary α-deuterium KIE decreased from 1.22 to 1.15. In fact, all but one of the secondary α-deuterium KIEs was larger for the free-ion reactions than for the ion-pair reactions. Also, changing the *para* substituent on the free ion changed the secondary α-deuterium KIE by 15% whereas the change in the secondary α-deuterium KIE with substituent was only 7% for the ion-pair reactions. The important observation, however, is that the substituent effects were significantly different when the form of the reacting nucleophile was different and the nucleophilic atom was sulfur.

The substituent effect caused by a change in the form of the reacting nucleophile when the nucleophilic atom is oxygen was determined in two ways. First, the effect of changing the *para* substituent on the nucleophile was determined for both the free ion and the ion-pair nucleophiles by measuring the secondary α-deuterium KIEs for a series of S_N2 reactions between *para*-substituted sodium phenoxides and benzyl chlorides, Table 5. In contrast to the large substituent effects observed when the nucleophilic atom was sulfur, Table 4, the results in Table 5 show that the substituent effect on the secondary α-deuterium KIE is very small (effectively zero) for both the free ion and the ion-pair reactions when the nucleophilic atom is oxygen. Moreover, ion-pairing does not affect the secondary α-deuterium KIE significantly for either the free ion or the ion-paired oxygen nucleophiles.

The substituent effect caused by changing a substituent on the substrate was also determined for both the free ion and ion-pair reactions by measuring the secondary α-deuterium KIEs for the S_N2 reactions between sodium phenoxide and several *para*-substituted benzyl chlorides, Table 6. Again, the substituent effect on the secondary α-deuterium KIE is very small. The effect of ion-pairing is also very small (zero, considering the errors in the KIEs).

The failure to detect a change in the secondary α-deuterium KIE when the form of the reacting nucleophile was changed in the reactions with the phenoxide ion nucleophile is an important discovery because both the substituent effect and the effect of ion-pairing on the KIE were significantly different when the form of the nucleophile was altered in the sodium thiophenoxide S_N2 reactions.

Two explanations are possible for the very different behaviour found with phenoxide ion. One explanation is that ion-pairing does not significantly affect the nucleophilic oxygen atom and, therefore, does not cause a change in transition state structure. In fact, CNDO/2 calculations, Table 7, have shown that ion-pairing affects the electron density on a nucleophilic sulfur and oxygen atom very differently. The change in the negative charge on the nucleophilic atom on forming the contact ion-pair is almost four times greater for the sulfur nucleophiles than for the oxygen nucleophiles. This probably occurs because oxygen is a hard nucleophile (9) and it is more difficult to reduce the electron density on the nucleophilic oxygen atom by bringing the sodium ion near the oxygen. When the nucleophilic atom is sulfur, on the other hand, the nucleophilic atom is soft (polarizable), and bringing the positive sodium ion near the sulfur pulls electron density towards the sodium ion, thereby reducing the electron density available for bond formation (the nucleophilicity) of the sulfur ion. As a result, the sulfur nucleophile is altered significantly when ion-pairing occurs and there is a significant change in the secondary α-deuterium KIE and in transition state structure. When the nucleophile is oxygen, the sodium ion does not significantly alter the tightly held electron density on the nucleophilic atom

© 1998 NRC Canada

Table 5. The second-order rate constants and secondary α-deuterium KIEs for the S_N2 reactions between sodium *para*-substituted phenoxides and benzyl chloride in methanol at 20.000°C in the presence and absence of 15-crown-5 ether.

para-Substituent	$k_H \times 10^6$ (L m^{-1} s^{-1})	$k_D \times 10^6$ (L m^{-1} s^{-1})	$(k_H/k_D)_\alpha$	$\Delta(k_H/k_D)_\alpha$ (Free ion – ion-pair)
Free ion reactions with 15-crown-5 ether				
CH_3O	10.519 ±0.056[a]	10.508 ± 0.049[a]	1.008 ± 0.004[b]	+0.011
CH_3	12.232 ± 0.018	12.207 ± 0.019	1.002 ± 0.001	–0.012
H	9.049 ± 0.017	8.858 ± 0.002	1.022 ± 0.002	+0.001
Cl	6.442 ± 0.002	6.283 ± 0.027	1.025 ± 0.002	+0.012
Ion-pair reactions — no 15-crown-5 ether				
CH_3O	12.510 ± 0.066	12.553 ± 0.064	0.997 ± 0.007	
CH_3	10.522 ± 0.006	10.379 ± 0.005	1.014 ± 0.005	
H	8.0224 ± 0.0001	7.860 ± 0.001	1.021 ± 0.0002	
Cl	6.111 ± 0.026	6.035 ± 0.012	1.013 ± 0.005	

[a] The standard deviations of the mean of between three and five different measurements.

[b] The error in the isotope effect equals $1/k_D[(\Delta k_H)^2 + (k_H/k_D)^2 \times (\Delta k_D)^2]^{1/2}$ where Δk_H and Δk_D are the standard deviations for the rate constants for the undeuterated and deuterated substrates, respectively.

Table 6. The second-order rate constants and secondary α-deuterium KIEs for the S_N2 reactions between sodium phenoxide and *para*-substituted benzyl chlorides in methanol at 20.000°C in the presence and absence of 15-crown-5 ether.

para-Substituent	$k_H \times 10^6$ (L m^{-1} s^{-1})	$k_D \times 10^6$ (L m^{-1} s^{-1})	$(k_H/k_D)_\alpha$	$(k_H/k_D)_\alpha$ (Free ion – ion-pair)
Free ion reactions with 15-crown-5 ether				
CH_3	17.806 ±0.006[a]	17.326 ± 0.081$_a$	1.028 ± 0.004[b]	–0.001
H	9.049 ± 0.017	8.859 ± 0.002	1.022 ± 0.002	+0.001
Cl	12.218 ± 0.027	12.097 ± 0.020	1.010 ± 0.002	–0.003
NO_2	12.143 ± 0.061	11.822 ± 0.001	1.027 ± 0.005	–0.003
Ion-pair reactions — no 15-crown-5 ether				
CH_3	14.87 ± 0.33	14.432 ± 0.004	1.029 ± 0.002	
H	8.0224 ± 0.0001	7.860 ± 0.001	1.021 ± 0.0002	
Cl	10.131 ± 0.012	10.006 ± 0.093	1.013 ± 0.010	
NO_2	8.990 ± 0.045	8.727 ± 0.017	1.030 ± 0.006	

[a] The standard deviations of the mean of between three and five different measurements.

[b] The error in the isotope effect equals $1/k_D[(\Delta k_H)^2 + (k_H/k_D)^2 \times (\Delta k_D)^2]^{1/2}$ where Δk_H and Δk_D are the standard deviations for the rate constants for the undeuterated and deuterated substrates, respectively.

and neither the secondary α-deuterium KIE nor the transition state structure changes significantly.

A second explanation for the constant secondary α-deuterium KIEs that are found when a substituent is altered in the nucleophile and in the substrate of the *para*-substituted phenoxide ion – *para*-substituted benzyl chloride reaction series is that the transition states for these reactions are unsymmetrical and product-like. Westaway et al. (10) recently suggested that a change in substituent would not change the secondary α-deuterium KIE in an S_N2 reaction significantly when the transition state is unsymmetrical. They also found that in all the S_N2 reactions with unsymmetrical transition states, the stronger reacting bond is short and the weaker reacting bond is long. In the *para*-substituted phenoxide ion – *para*-substituted benzyl chloride reaction series the O—C_α reacting bond is stronger than the C_α—Cl reacting bond (11). Therefore, if these transition states are unsymmetrical, they should have a short O—C_α bond and a long C_α—Cl bond. A second factor that is important in determining the substituent effects on S_N2 transition state structure is the Bond Strength Hypothesis (11), which predicts that a change in substituent in the nucleophile, the leaving group, or the substrate of an S_N2 reaction will alter the weaker (C_α—Cl) reacting bond but will not affect the stronger (O—C_α) reacting bond significantly. Thus, if the transition states for these reactions are unsymmetrical, they should have a short O—C_α bond that does not change significantly and a long C_α—Cl bond that changes significantly with a change in substituent in the nucleophile or the reactant. Because a change in substituent only changes the long, weak (C_α—Cl) reacting bond in the unsymmetrical (product-like) transition state, the change in transition state structure occurs too far away to affect the C_α–H(D) out-of-plane bending vibrations that determine the magnitude of the secondary α-deuterium KIE, Fig. 1 (10). Therefore, the secondary α-deuterium KIEs will not change with a change in substituent in the nucleophile or the substrate.

There are two possible explanations for the constant secondary α-deuterium KIEs found when the reacting nucleophile changes from a free ion to an ion-pair and when a substituent is altered in the nucleophile and in the substrate of the

© 1998 NRC Canada

Table 7. The change in the negative charge on the nucleophilic atom caused by ion-pairing and by a change in substituent when the nucleophilic atom is sulfur and oxygen.[a]

para-Substituent	Negative charge on the nucleophilic atom	
Free ion		
	$C_6H_5S^-$ $(CH_3OH)_2$	$C_6H_5O^-(CH_3OH)_2$
CH_3O	–0.5166[a]	–0.5625
CH_3	–0.5112	–0.5619
H	–0.5080	–0.5596
Cl	–0.4958	–0.5486
Ion-pair		
	$C_6H_5S^-$ Na^+ (CH_3OH)	$C_6H_5O^-$ Na^+ (CH_3OH)
CH_3O	–0.3088	–0.5076
CH_3	–0.3071	–0.5030
H	–0.2998	–0.4933
Cl	–0.2917	–0.4904
Average change in charge on ion-pairing	0.2061	0.0596

[a] Some of these data were taken from ref. 4.

para-substituted phenoxide ion – *para*-substituted benzyl chloride reactions. One is that ion-pairing does not change the structure of the S_N2 transition state. The second is that the transition states are unsymmetrical and product-like and that the transition state changes but that the only significant change is in the long and weak C_α—Cl transition state bond and this change does not affect the magnitude of the secondary α-deuterium KIE. One way to resolve this problem was to measure the chlorine leaving-group KIEs for these reactions. If ion-pairing does not affect the structure of the S_N2 transition state, identical chlorine KIEs should be found for both the free ion and the ion-pair reactions. If the constant secondary α- hydrogen/deuterium KIEs are the result of an unsymmetrical transition state with a short O—C_α bond that does not change significantly with a change in substituent and a long C_α—Cl bond that changes markedly with a change in substituent, the chlorine KIEs should be different for the ion-pair and the free ion reactions.

The chlorine (leaving group) KIEs for the free ion and ion-pair reactions between two different *para*-substituted phenoxide ions and benzyl chloride in methanol at 20.000°C and between *n*-butyl chloride and phenoxide ion in DMSO at 20.000°C are presented in Table 8. The obvious conclusion is that ion-pairing does not affect the chlorine KIE in three different S_N2 reactions. This means that ion-pairing does not alter the transition state of an S_N2 reaction when the nucleophilic atom is oxygen. These results are important because they suggest that ion-pairing will not alter transition state structure significantly when a hard nucleophile is used and that one need only worry about the effect of ion-pairing when a soft nucleophile is used.

Experimental

Preparation of reagents

All the *para*-substituted sodium phenoxides were prepared by reacting the appropriate phenol with a sodium methoxide – methanol solution, evaporating the solvent, removing the excess phenol by washing the salt with benzene and hexane, and drying under vacuum at 110°C. A typical synthesis involved preparing a 0.80 M solution of sodium methoxide in anhydrous methanol by adding 5.5 g of freshly cut sodium slowly to 300 mL of anhydrous methanol. Then, a 10% excess (20.6 g, 0.22 mol) of freshly distilled phenol was added to 250 mL of the 0.80 M solution of sodium methoxide. The methanol was evaporated under reduced pressure on a rotary evaporator and the solid was washed three times with 100 mL of dry benzene and finally with 100 mL of hexane under an atmosphere of dry nitrogen (Praxair) in a I^2R glove bag.[5] Finally, the salt was dried under vacuum in a sand bath at 110°C for 12 h. The yield of the purified salt was 15.6 g (67%).

Fig. 1. The unsymmetrical product-like S_N2 transition state where the magnitude of the secondary α-deuterium KIE would be determined by only the changes in the length of the O—C_α transition state bond.

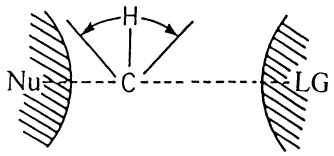

The preparation of the *para*-substituted (1,1-^{2}H) benzyl chlorides and the (1,1-^{2}H) butyl chloride used in this study is described in refs. 12 and 1, respectively. The methanol was ACS reagent grade that was redistilled before use.

A study of ion-pairing for sodium phenoxide in organic solvents

The concentrations at which sodium phenoxide solutions existed as ion-pairs and as free ions were determined by recording the UV spectrum and by determining the conductivity of various sodium phenoxide solutions ranging from 1.433×10^{-5} M to 3.239×10^{-2} M. The procedure used in this study was identical to those used to determine the UV spectrum and the conductivity of sodium thiophenoxide solutions (1).

[5] The 37 in. × 37 in. I^2R glove bags were purchased from Instruments for Research and Industry, I^2R, Inc., P.O. Box 159B, Cheltenham, PA 19012, U.S.A.

© 1998 NRC Canada

Table 8. The chlorine leaving-group KIEs for the S_N2 reactions between *para*-substituted phenoxide ions acting as a free ion and an ion-pair with benzyl chloride in methanol at 20.000°C or *n*-butyl chloride in DMSO at 20.000°C.

Substrate	Nucleophile	k^{35}/k^{37} Ion-pair	k^{35}/k^{37} Free ion
$C_6H_5CH_2$-Cl	C_6H_5ONa	1.00831 ± 0.00005[a]	1.00826 ± 0.00010[a]
$C_6H_5CH_2$-Cl	$CH_3OC_6H_4ONa$	1.00819 ± 0.00088	1.00822 ± 0.00014
$CH_3(CH_2)_3$-Cl	C_6H_5ONa	1.00806 ± 0.00009	1.00811 ± 0.00007

[a] The standard deviation of the mean for five different measurements of the isotope effect.

Secondary α-deuterium KIEs

Unless otherwise specified, the rate constants required for calculating the secondary α-deuterium KIEs were determined by titrating the chloride ion produced during the reaction with a standard silver nitrate solution using the electrochemical method described in ref. 1. The only differences between the kinetic procedure described in ref. 1 and that used in this study were that the initial concentrations of the *para*-substituted benzyl chloride, the sodium *para*-substituted phenoxide, and the 15-crown-5 ether were 0.051 M, 0.246 M, and 0.285 M, respectively, and that a 2.5 mL, rather than a 5.00 mL, aliquot from the reaction mixture was titrated.

The rate constants for the benzyl chloride reactions with the free phenoxide ion and the sodium phenoxide ion-pair determined by the HPLC method, Table 2, involved determining the concentration of the unreacted benzyl chloride at various times throughout the reaction with the internal standard method (13). The actual HPLC analysis involved removing a 1.00 mL sample of the reaction mixture at various times throughout the reaction with a Hamilton gas-tight syringe fitted with a 6 in. stainless steel needle. This sample was transferred to a 10 mL volumetric flask containing 1.00 mL of a benzylphenyl sulfide (the internal standard) solution. This mixture was diluted to the mark with methanol and 25 μL of the solution was injected into a Waters 600 HPLC fitted with a Waters 10 cm 5PAH 10 μm column using a 70:30 methanol–water mixture as the eluting solvent. The flow rate was 2 mL/min and the Waters 490 variable wavelength detector was set at 254 nm. The concentration of the unreacted benzyl chloride at different times was determined from a calibration curve and the rate constants for the second-order reaction were calculated in the usual way (14).

Chlorine leaving-group KIEs

The procedure used for measuring the chlorine KIEs has been described elsewhere (15, 16). There were only two differences between the reported procedure and that used in this study. One difference was that the reactions in this study were quenched by adding 100 mL of a 0.09 M nitric acid solution rather than 100 mL of water. The second change was that the unreacted substrate in the benzyl chloride reactions was extracted with two 200 mL portions of toluene and one 100 mL portion of heptane rather than with three 100 mL portions of hexane.

Acknowledgements

The authors gratefully acknowledge the financial assistance of the Natural Sciences and Engineering Research Council of Canada (NSERC) and the Laurentian University Research Fund.

References

1. K.C. Westaway and Z.G. Lai. Can. J. Chem. **66**, 1263 (1988).
2. K.C. Westaway and Z.G. Lai. Can. J. Chem. **67**, 345 (1989).
3. Y.-R. Fang and K.C. Westaway. Can. J. Chem. **69**, 1017 (1991).
4. K.C. Westaway and Z.G. Lai. Can. J. Chem. **67**, 21 (1989).
5. R.A. Poirier, Y.Wang, and K.C. Westaway. J. Am. Chem. Soc. **116**, 2526 (1994).
6. J.A. Barnes and I.H. Williams. J. Chem. Soc. Chem. Commun. 1286 (1993).
7. T.H. Lowry and K.S. Richardson. *In* Mechanism and theory in organic chemistry. 3rd ed. Harper and Row, New York. 1987. pp. 182–183.
8. A.J. Parker. Chem. Rev. **69**, 1 (1969).
9. J. March. *In* Advanced organic chemistry. 4th ed. J. Wiley and Sons, New York. 1992. pp. 260–263.
10. K.C. Westaway, T. Pham, and Y.-R. Fang. J. Am. Chem. Soc. **119**, 3670 (1997).
11. K.C. Westaway. Can. J. Chem. **71**, 2084 (1993).
12. K.C. Westaway and Z. Waszczylo. Can. J. Chem. **60**, 2500 (1982).
13. S. Dal Nogare and R.S. Juvet, Jr. *In* Gas–liquid chromatography. Interscience, New York. 1962. p. 256.
14. K.J. Laidler. *In* Chemical kinetics. 2nd ed. McGraw–Hill Book Co., New York. 1965. p. 9.
15. K.C. Westaway, T. Koerner, Y.-R. Fang, J. Rudziński, and P. Paneth. Anal. Chem. In press.
16. T. Koerner. M. Sc. Dissertation. Laurentian University, 1996. pp. 168–182.

© 1998 NRC Canada

Extended lithium ion pair indicator scale in tetrahydrofuran[1]

Andrew Streitwieser, Daniel Zerong Wang, Manolis Stratakis, Antonio Facchetti, Roustam Gareyev, Alessandro Abbotto, James A. Krom, and Kathleen V. Kilway

Abstract: The lithium p*K* scale has been extended to 25 indicators with a p*K* range of 9.7–24.4. The resulting scale is compared with the cesium ion pair acidities and to ionic p*K*'s in DMSO and aqueous DMSO.

Key words: ion pair acidity, organolithium compounds, indicator, acidity scale.

Résumé : On a étendu l'échelle p*K* du lithium à 25 indicateurs couvrant une plage de p*K* allant de 9,7 à 24,4. On a établi une comparaison entre l'échelle qui en résulte et les acidités des paires d'ion du césium et aux p*K* ioniques dans le DMSO et de DMSO aqueux.

Mots clés : acidité d'une paire d'ion, composés organolithium, indicateur, échelle d'acidité.

Several years ago we proposed a scale of proton transfer indicators in THF based on the solvent separated (SSIP) lithium ion pair salts of hydrocarbons whose UV–vis spectral characteristics are convenient (1). Equilibrium constants for the individual ion pair proton transfer equilibria in eq. [1] were converted to a numerical p*K* scale, eq. [2], by arbitrarily assigning to the lithium SSIP of fluorene its free ion p*K* value in DMSO of 22.90 (per hydrogen) (2).

$$[1] \quad RH + R'^{-}\,Li^{+} \overset{K}{\rightleftharpoons} R^{-}\,Li^{+} + R'H$$

$$[2] \quad pK(RH) = pK(R'H) - \log K$$

The resulting p*K* values were related to a corresponding scale involving the contact ion pairs (CIP) of the cesium salts by conductivity measurements of the dissociation of both the lithium and cesium ion pairs to the free ions in THF (3).

The resulting lithium scale has been used in a number of studies of the ion pair acidities of various substrates in THF, including fluorenes with chelating groups (4), dilithiated carboxylic acids (5), silanes (6), dithianes (7), dilithiated 9,9′-bifluorenyl (8), diphenylamine (9), acetylenes (10), polyhalobenzenes (11), ketones. (12–14), and carbazole (15). In the course of these and other studies we have added a number of new indicators to the lithium scale. The present paper presents a summary of the published and unpublished results in a convenient form.

Received January 5, 1998.

This paper is dedicated to Professor Erwin Buncel in recognition of his contributions to Canadian chemistry.

A. Streitwieser,[2] D.Z. Wang, M. Stratakis, A. Facchetti, R. Gareyev, A. Abbotto, J.A. Krom, and K.V. Kilway.
Department of Chemistry, University of California, Berkeley, CA 94720-1460, U.S.A.

[1] Carbon acidity. 99.

[2] Author to whom correspondence may be addressed. Telephone: (510) 642-2204. Fax: (510) 643-6232. E-mail: astreit@socrates.berkeley.edu

Other ion pair scales have been proposed in THF solution. Fraser et al. used NMR measurements of equilibria to determine the effective p*K*'s of a number of types of compounds (16–21). This work required measurements at high concentration and no account was taken of the possible role of ion pair aggregation; such aggregation is known to lower measured p*K* values (22). We have published an extended scale of cesium salts of indicators (23). Buncel and Menon used reactions of 18-crown-6 complexed potassium salts of indicators to determine the ion pair p*K* of dihydrogen in THF (24). Antipin et al. developed a scale of [2.1.1]-cryptated lithium salts of indicators in THF (25–27).

Results and discussion

The most precise measurements of the equilibria in eq. [1] are those of the so-called double-indicator method. In this approach, both lithium salts have conveniently measurable spectra and the concentrations of both are determined directly. Stoichiometry from the known starting amounts of RH and R′H then provides the equilibrium constant without interference from the traces of adventitious water generally present even with careful work. For example, we have found that with the use of Pyrex glassware the water content cannot be reduced below about 5×10^{-5} M because THF extracts water even from carefully dried and baked glassware. Lower water levels are possible with the use of quartz glassware and storage over molecular sieves in a glovebox. In many cases, the lithium salts were generated by adding 9-lithio-9,10,10-trimethyldihydroanthracene (LiTMDA) to the mixture. LiTMDA is a strong base that readily metallates the indicators on this scale.

UV–visible spectroscopic measurements of eq. [1] require that the two lithium salts have significantly different spectra. Moreover, good precision is not possible if *K* is too large or too small. These are the primary reasons for having a number of different indicators.

Table 1 summarizes the lithium indicator scale. Included in this table are the abbreviations for the indicators used in many of our papers, together with the absorption λ_{max} and the extinction

© 1998 NRC Canada

Table 1. The lithium indicator p*K* scale. All p*K*'s are on a per-hydrogen basis.

Symbol	Compound	p*K*	λ_{max}, nm	(ε)
PTFI	1-Phenyl-3-(2′,3′,5′,6′-tetrafluorophenyl)indene	9.66[a]	448	(37 900)
BBP	1,1,3,3-Bis(biphenylene)propene	10.38	557.5	(112 500)
PePC	1,2,3,4,5-Pentaphenyl-1,3-cyclopentadiene	11.07	346	(41 200)
DPI	1,3-Diphenylindene	12.32	450	(32 900)
			380	(22 000)
TeFPFl	9-(2′,3′,5′,6′-Tetrafluorophenyl)-fluorene	14.12	452	(21 000)
PDP	1,12-(*o*-Phenylene)-7,12-dihydropleiadene	14.44	401	(20 500)
TPI	1,2,3-Triphenylindene	14.67	436	(16 200)
			393.5	(17 500)
			325.5	(27 000)
Ph-3,4-BF	9-Phenyl-3,4-benzofluorene	14.84	418	(26 000)
			394	(23 900)
9-BpFl	9-Biphenylylfluorene	16.99	526	(25 600)
			498	(33 400)
			373	(14 300)
Ph-1,2-BF	9-Phenyl-1,2-benzofluorene	17.38	472	(11 500)
PhFl	9-Phenylfluorene[b]	17.6	411	(25 300)
Ph-2,3-BF	9-Phenyl-2,3-benzofluorene	17.84	442	(52 000)
DMAPhFl	9-(*p*-Dimethylaminophenyl)fluorene	19.02	383	(27 800)
3,4-BF	3,4-Benzofluorene[b]	19.29	410	(6 650)
			387	(7 740)
1,2-BF	1,2-Benzofluorene[b]	19.7	454	(8 530)
BA	Benzanthrene[b]	20.13	661	(800)
			447	(35 000)
BnMP	9-Benzyl-9*H*-benzo[*def*]fluorene[b]	21.35	535	(6 700)
BnFl	9-Benzylfluorene[b]	21.36	381	(15 400)
IPF	9-Isopropylidenefluorene	22.33	535	(1 730)
			498	(2 200)
			379	(27 700)
BFl	9-Butylfluorene[c]	22.4	387	(16 000)
MeFl	9-Methylfluorene	22.46	387	(16 200)
			517	(1 670)
DiBF	2:3,6:7-Dibenzofluorene[b]	22.68	497	(56 200)
Fl	Fluorene[b,d]	(22.90)	373	(9 300)
2,3-BF	2,3-Benzofluorene[b]	22.95	430	(25 500)
TBFl	9-*tert*-Butylfluorene	24.41	509	(1 350)
			387	(13 100)
BPDT	Biphenylyldithiane	29.30	485	(27 500)[e]

[a] Referred to the equilibrium mixture of the two indene isomers.
[b] References 1 and 3.
[c] Reference 4.
[d] The reference is taken as the Li SSIP salt of fluorene. Since fluorenyllithium in THF at 25°C is about 70% SSIP and 30% CIP the composite p*K*(SSIP+CIP) = 22.75 (3).
[e] CIP p*K* = 28.20, λ_{max} 388 nm (27 500) (7).

coefficient. The p*K* values are statistically corrected to be on a per-hydrogen basis; that is, the uncorrected p*K* of benzanthrene is lower by 0.30 (log 2), 1,3-diphenylindene is higher by 0.30 (the anion has two equivalent positions to which a proton can return), and 9-phenylfluorene is unchanged. The scale ends just below the p*K* value of 25. Above this value the proton transfer equilibria are inconveniently slow. The dithiane shown was measured by a special technique (7). The exchange rates of cesium salts are much higher and this scale goes up to pK's in the high 30s (23).

The indicators were generally compared with more than one reference. Agreement was generally a few parts in the second decimal. Accordingly, the assigned p*K*'s in Table 1 should be accurate to about ± 0.1 units.

The lithium and cesium scales in THF were interrelated by measuring the dissociation constants of several systems (3). The dissociation constants of the SSIP lithium salts of delocalized carbanions are relatively constant at 1×10^{-5} M; the cesium CIP dissociation constants show more variation with structure and are generally in the range $(1–20) \times 10^{-8}$ M. Accordingly, there is generally an excellent correlation between p*K*'s on the two ion pair scales (Fig. 1), but there is some scatter because of the variation in ion pair dissociation constants. Note that both scales are based on fluorene as a standard,

© 1998 NRC Canada

Fig. 1. Comparison of lithium SSIP and cesium CIP acidities in THF at 25°C. The equation of the line shown is p*K*(Li) = –1.984 + 1.080 p*K*(Cs); $R^2 = 0.993$.

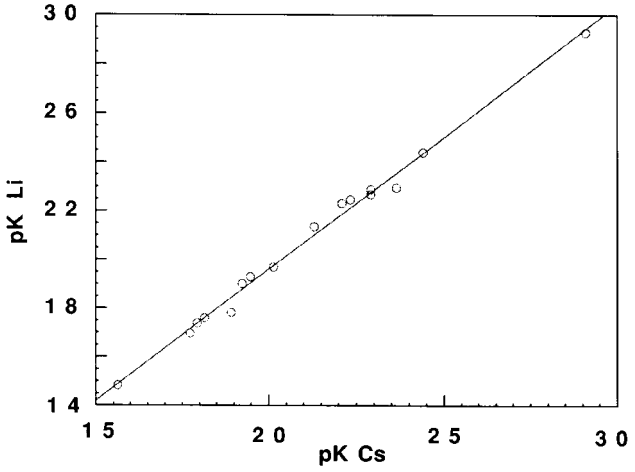

Fig. 2. Comparison of Li ion pair p*K*'s in THF with absolute p*K*'s in DMSO. The line shown is p*K*(Li) = –0.963 + 1.046 p*K*(DMSO); $R^2 = 0.998$.

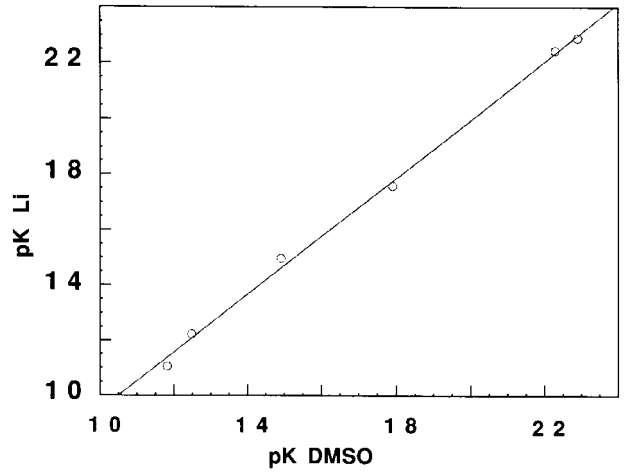

the Li SSIP in one case and the Cs CIP in the other. Because of the relative insensitivity to structural variation of the ion pair dissociation constants of the lithium salts of these delocalized carbanion indicators, the free ion acidities in THF should closely parallel the SSIP acidities. The slope of the correlation in Fig. 1, 1.08, shows that the Cs scale is slightly compressed compared to the Li scale; this result is probably due to the slightly higher electrostatic attraction of the carbanion to a cesium cation, which is effectively smaller than the solvent-separated lithium cation. There is an excellent correlation with the absolute p*K* as in DMSO with a slope close to unity (Fig. 2). This correlation shows that the choice of any other standard than fluorene would result in but little change in the lithium scale. Note that a number of compounds on the Li scale are not on the Cs and DMSO scales.

A number of the same compounds were studied in aqueous DMSO mixtures by the H_ method and should represent the p*K*'s for the dilute aqueous standard state (28). These values are also summarized in Table 2; a comparison with the lithium ion pair values in THF (Fig. 3) shows an excellent correlation but with a slope of only 0.70. The range of p*K*'s of these delocalized carbanions is highly attenuated in the aqueous medium.

Table 2. Comparison of p*K*'s.

Symbol	Li, THF	Cs, THF[a]	DMSO[b]	aq. DMSO[d]
PePC	11.07		11.8	
DPI	12.32		12.47[c]	
Ph-3,4-BF	14.84	15.62		16.60
TPI	14.67		14.60[c]	
9-BpFl	16.99	17.72		18.21
Ph-1,2-BF	17.38	17.94		
PhFl	17.60	18.15	17.9	18.59
Ph-2,3-BF	17.84	18.92		
DMAPhFl	19.02	19.23		19.61
3,4-BF	19.29	19.47		19.92
1,2-BF	19.70	20.13		
BnFl	21.36	21.30		21.20
IPF	22.33	22.08		
MeFl	22.46	22.32	22.3	21.80
DiBF	22.68	22.91		
Fl	(22.90)	(22.90)	22.90	22.40
2,3-BF	22.95	23.63		
TBFl	24.41	24.39		23.41
BPDT	29.30	29.1		

[a] Reference 23.
[b] Reference 2.
[c] Reference 29.
[d] Reference 28.

Some of the results show features of special interest. The powerful inductive effect of fluorine is shown by comparing PTFl with DPI and TeFPFl with PhFl. The four fluorine substituents increase acidity by 2.6–3.5 p*K* units. Steric hindrance to conjugation can play an important role. A phenyl substituent in the 9-fluorenyl position of 2,3-benzfluorene (11*H*-benzo[*b*]fluorene) and 3,4-benzfluorene (7*H*-benzo[*c*]fluorene) increases acidity by 4.5–5.1 p*K* units, but a similar substitution in 1,2-benzfluorene (7*H*-benzo[*a*]fluorene) has only a 2.3 p*K* unit effect, undoubtedly because of steric interaction between the benzo group and the phenyl ring. In agreement with the DMSO results of Bordwell and Drucker (30), triphenylindene (TPI) is 2.3 p*K* units less acidic than 1,3-diphenylindene (DPI), probably in part because the central phenyl substituent impedes conjugation of the terminal phenyls.

Conclusions

The lithium scale of SSIP indicators in THF has been extended to 25 compounds. This scale should find use in ion pair acidity measurements of lithium salts in THF, particularly in the region of convenient proton transfer rates below p*K* = 25.

Experimental section

The syntheses of many of the indicators have been reported previously (30–35) or were available from our past work or commercially. In general, the aromatic hydrocarbons were recrystallized from hexane or an ethanol–hexane mixture and

© 1998 NRC Canada

Fig. 3. Comparison of aqueous DMSO p*K*'s (H_ method) with lithium ion pair p*K*'s. The correlation line shown is p*K*(aq DMSO) = 6.26 + 0.701 p*K*(Li, THF); $R^2 = 0.998$.

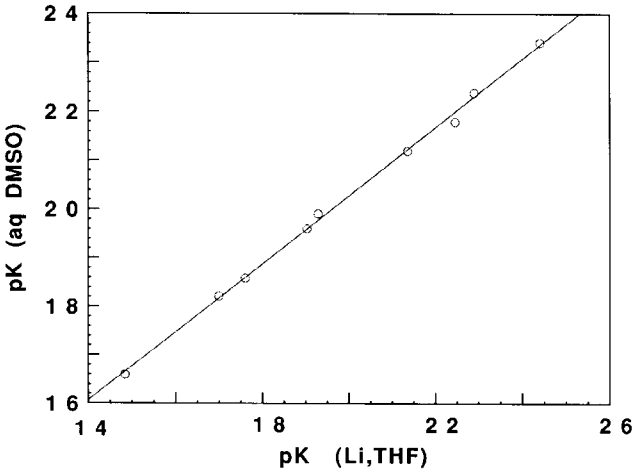

then vacuum sublimed. Purity was assessed by spectroscopic methods, melting point, and (or) elemental analysis as necessary. The details of the procedure of p*K* measurement have been described in previous publications.

1,1,3,3-Bis(biphenylene)propene (BBP)
This compound was prepared following Kuhn et al. (36) and was purified by multiple recrystallizations from benzene–hexane to remove the last traces of fluorene and, finally, from toluene. Sublimation afforded a white powder, mp 215–216°C (lit. (36) mp 205–206°C); ^{1}H NMR (300 MHz, $CDCl_3$) δ: 8.33 (d, J = 7.5 Hz, 1H), 7.20–7.85 (m, 15H), 6.51 (d, J = 10 Hz, 1H), 5.87 (d, J = 10 Hz, 1H).

1-Phenyl-3-(2′,3′,5′,6′-tetrafluorophenyl) indene (PTFI)
To a 250 mL flame-dried three-necked flask containing 100 mL of dry THF and 2 g (13.3 mmol) of 1,2,4,5-tetrafluorobenzene was added 5.7 mL of *n*-BuLi (2.1 M in hexanes) dropwise at –78°C. After 20 min, 2.08 g (10 mmol) of 3-phenylindanone was added. The solution was stirred for an additional 1 h at –50°C and then quenched with water. An NMR spectrum of the crude product showed a mixture of the desired carbinol and starting material (probably through enolization of the ketone by the tetrafluorophenyllithium) in a ratio of 60/40. The crude mixture of carbinol and ketone was dissolved in 60 mL of benzene and a few drops of concentrated H_2SO_4 were added. The mixture was refluxed for 5 h until TLC showed no carbinol remaining. The indene was isolated by flash column chromatography using hexane–ether in a ratio of 10/1 as an eluant, recrystallized from methanol, and finally sublimed; mp 104–106°C. ^{1}H NMR: 7.18–7.33 (m, 9H), 7.13 (tt, J_1 = 9.6 Hz, J_2 = 7.3 Hz), 6.81 (d, J = 1.8 Hz), 4.82 (d, J = 1.8 Hz). ^{19}F NMR (H-decoupled): –138.78 (m, 2F), –139.09 (m, 2F) relative to $CFCl_3$.HRMS, calcd.: 340.0882; found: 340.0875.

General procedure for the preparation of the lithium bases
Lithium diisopropylamide (LDA) was freshly prepared, twice sublimed under vacuum, and placed in the glovebox. The neutral indicator, 9,9,10-trimethyldihydroanthracene (5.3 mg, 0.024 mmol), was added to a vacuum-adapted storage flask. To this flask, THF (2 mL) and LDA (2.1 mg, 0.020 mmol) were added, resulting in an orange solution. The deprotonation reaction is slow and it was necessary for reaction to proceed for a minimum of 3 days with occasional stirring. The flask was then taken out of the glovebox and directly attached to a vacuum line. The THF was removed via vacuum and the flask was returned to the glovebox. The resulting red semi-solid was dissolved with an appropriate amount of THF to give a 0.1 M concentration. The resulting base was stored at –10°C and checked periodically for decomposition.

Acknowledgment

This work was supported by grants from the National Science Foundation (NSF) and the National Institutes of Health (NIH).

References

1. S. Gronert and A. Streitwieser. J. Am. Chem. Soc. **108**, 7016 (1986).
2. F.G. Bordwell. Acc. Chem. Res. **21**, 456 (1988).
3. M.J. Kaufman, S. Gronert, and A. Streitwieser. J. Am. Chem. Soc. **110**, 2829 (1988).
4. S. Gronert and A. Streitwieser. J. Am. Chem. Soc. **110**, 2836 (1988).
5. S. Gronert and A. Streitwieser. J. Am. Chem. Soc. **110**, 4418 (1988).
6. A. Streitwieser, L.F. Xie, P. Wang, and S.M. Bachrach. J. Org. Chem. **58**, 1778 (1993).
7. L.F. Xie and A. Streitwieser. J. Org. Chem. **60**, 1339 (1995).
8. M. Stratakis and A. Streitwieser. J. Org. Chem. **58**, 1989 (1993).
9. J.A. Krom, J.T. Petty, and A. Streitwieser. J. Am. Chem. Soc. **115**, 8024 (1993).
10. R. Gareyev and A. Streitwieser. J. Org. Chem. **61**, 1742 (1996).
11. M. Stratakis, P.G. Wang, and A. Streitwieser. J. Org. Chem. **61**, 3145 (1996).
12. A. Abbotto and A. Streitwieser. J. Am. Chem. Soc. **117**, 6358 (1995).
13. F. Abu-Hasanayn, M. Stratakis, and A. Streitwieser. J. Org. Chem. **60**, 4688 (1995).
14. R. Gareyev, J.C. Ciula, and A. Streitwieser. J. Org. Chem. **61**, 4589 (1996).
15. A. Abbotto, A. Streitwieser, M. Stratakis, and J.A. Krom. J. Am. Chem. Soc. **120**, 1718 (1998).
16. R.R. Fraser, M. Bresse, and T.S. Mansour. J. Chem. Soc. Chem. Commun. 620 (1983).
17. R.R. Fraser, M. Bresse, and T.S. Mansour. J. Am. Chem. Soc. **105**, 7790 (1983).
18. R.R. Fraser, M. Breese, and O. Chuaqui. Can. J. Chem. **61**, 2729 (1983).
19. R.R. Fraser and T.S. Mansour. J. Org. Chem. **49**, 3442 (1984).
20. R.R. Fraser, T.S. Mansour, and S. Savard. Can. J. Chem. **63**, 3505 (1985).
21. R.R. Fraser, T.S. Mansour, and S. Savard. J. Org. Chem. **50**, 3232 (1985).
22. M.J. Kaufman and A. Streitwieser, Jr. J. Am. Chem. Soc. **109**, 6092 (1987).
23. A. Streitwieser, J.C. Ciula, J.A. Krom, and G. Thiele. J. Org. Chem. **56**, 1074 (1991).
24. E. Buncel and B. Menon. J. Am. Chem. Soc. **99**, 4457 (1977).
25. I.S. Antipin, A.N. Vedernikov, and A.I. Konovalov. Zh. Org. Khim. **21**, 1355 (1985).

© 1998 NRC Canada

26. I.S. Antipin, R.F. Gareev, A.N. Vedernikov, and A.I. Konovalov. Zh. Org. Khim. **25**, 1153 (1989).
27. I.S. Antipin, A.N. Vedernikov, and A.I. Konovalov. Zh. Org. Khim. **25**, 3 (1989).
28. R.A. Cox and R. Stewart. J. Am. Chem. Soc. **98**, 488 (1976).
29. F.G. Bordwell and G.E. Drucker. J. Org. Chem. **45**, 3325 (1980).
30. S.H. Tucker and P. Maltland. J. Chem. Soc. 2559 (1929).
31. S. Patai and S. Dayagi. J. Chem. Soc. 716 (1962).
32. K. Bowden and A.F. Cockerill. J. Chem. Soc. B, 173 (1970).
33. A.F. Cockerill and J.E. Lamper. J. Chem. Soc. B, 503 (1971).
34. M. Dufour, F. Perin, and P. Jacquignon. Bull. Soc. Chim. Fr. 3166 (1973).
35. T.E. Nalesnik, J.H. Freudenberger, and M.J. Orchin. J. Organomet. Chem. **221**, 193 (1981).
36. R. Kuhn, H. Fischer, F.A. Neugebauer, and H. Fisher. Justus Liebigs Ann. Chem. **654**, 64 (1962).

© 1998 NRC Canada

Remarkable efficiency of iron(III) versus manganese(III) tetraphenylporphyrins as catalysts for fast and quantitative oxidation of sulfides into sulfones by hydrogen peroxide

Antonio Marques, Massimo di Matteo, and Marie-Françoise Ruasse

Abstract: The efficiency of various metallo-phtalocyanines (Pht) and -tetraphenylporphyrins (TPP) as catalysts for the H_2O_2 oxidations of dibenzylsulfide, phenylchloroethylsulfide, and thioanisole is investigated in ethanol and acetonitrile, using imidazole as a cocatalyst. Neither $PhtNi^{II}$ nor $TPPCo^{II}$ exhibits any catalytic activity. $PhtMn^{II}$ and $TPPMn^{III}Cl$ accelerate markedly these reactions but do not promote quantitative oxidations, at most 70% of the sulfides being transformed into sulfoxides. In contrast, with $PhtFe^{II}$ sulfoxides are obtained with a 100% yield from sulfides. Finally, the only catalyst able to oxidize sulfides rapidly (<5 min), completely and quantitatively (100% sulfone) is $TPPFe^{III}Cl$ in EtOH. The absence of any by-product, disulfide in particular, suggests that a free sulfenium radical cation is not an active intermediate in these reactions. The marked differences in the behaviour of $TPPMn^{III}Cl$ and $TPPFe^{III}$ Cl are analyzed by comparing the rates of the catalyst decomposition, of the sulfoxide and sulfone formation as a function of the hydrogen peroxide concentration. The results are discussed in terms of a competition between the several oxidative pathways and a possible mechanism for the oxygen transfer to sulfides.

Key words: sulfide, oxidation, H_2O_2, manganese(III) or iron(III) tetraphenylporphyrin.

Résumé : Opérant dans l'éthanol et l'acétonitrile et utilisant l'imidazole comme cocatalyseur, on a étudié l'efficacité de divers métallo-phtalocyanines (Pht) et de -tétraphénylporphyrines (TPP) comme catalyseurs des oxydations par le peroxyde d'hydrogène du sulfure de dibenzyle, du sulfure de chloroéthyle et de phényle et du thioanisole. Ni le $PhtNi^{II}$ ni le $TPPCo^{II}$ ne présente d'activité catalytique. Le $PhtMn^{II}$ et le $TPPMn^{III}Cl$ accélèrent beaucoup ces réactions, mais ils ne conduisent pas à des oxydations quantitatives; au mieux, 70% des sulfures sont transformés en sulfoxydes. Par ailleurs, avec le $PhtFe^{II}$, les sulfures conduisent aux sulfoxydes avec des rendements de 100%. Enfin, le $TPPFe^{III}Cl$ dans l'éthanol est le seul catalyseur à pouvoir oxyder les sulfures rapidement (moins de 5 min), complètement et quantitativement (100% de sulfone). L'absence de sous-produit, en particulier de disulfure, suggère que le cation radicalaire sulfénium libre n'est pas un intermédiaire actif dans ces réactions. On a analysé les différences marquées de comportement du $TPPMn^{III}Cl$ et $TPPFe^{III}Cl$ en procédant à une comparaison des vitesses de décomposition du catalyseur ainsi que les vitesses de formation du sulfoxyde et de la sulfone en fonction de la concentration du peroxyde d'hydrogène. On discute des résultats en fonction d'une compétition entre plusieurs voies d'oxydation et un mécanisme possible pour le transfert d'oxygène aux sulfures.

Mots clés : sulfure, oxydation, peroxyde d'hydrogène, manganèse(III) ou fer(III) tétraphénylporphyrine.

[Traduit par la rédaction]

Introduction

Toxic sulfides and, in particular, mustard $(ClCH_2\text{-}CH_2)_2S$, a warfare agent, are markedly detoxified by transforming them into their corresponding oxidized derivatives, sulfoxides, and sulfones (1). Therefore, strong oxidants, hypochlorite, or *N*-chloramines for

$$[1] \quad R_2S \overset{[O]}{\rightarrow} R_2SO \overset{[O]}{\rightarrow} R_2SO_2$$

example, were currently used[2] as decontaminants (1*b*, 2, 3). In contrast, hydrogen peroxide, a cheap, nonpolluting, and not strongly corrosive oxidant, has not been considered[3] until now for this objective (4). This is not surprising, since it is well known that uncatalyzed hydrogen peroxide oxidations[4] of

Received December 18, 1997.

This paper is dedicated to Professor Erwin Buncel in recognition of his contributions to Canadian chemistry.

A. Marques, M. di Matteo, and M.-F. Ruasse.[1] Institut de Topologie et de Dynamique des Systèmes de l'Université Paris 7, Denis Diderot, associé au CNRS, URA 34, 1, rue Guy de la Brosse, 75005 Paris, France.

[1] Author to whom correspondence may be addressed. Telephone: 33 1 44 27 68 05. Fax: 33 1 44 27 68 14. E-mail: ruasse@paris7.jussieu.fr

[2] For synthetic, mechanistic, and other purposes, oxidation of sulfides into sulfoxides but not sulfones by a large variety of oxidants is extensively investigated (3).

[3] In contrast, the reactivity of H_2O_2 under basic conditions towards VX, a toxic organophosphorous thioester, has been investigated (4) using the high nucleophilicity of the perhydroxyl anion.

[4] Sulfide half-lives of several hours for reagent concentrations in the 10 mmol range (5).

© 1998 NRC Canada

sulfides are slow (5) whereas decontamination procedures require very fast chemical transformations. Consequently, hydrogen peroxide can be viewed as an efficient oxidant only if its reaction is markedly catalyzed. Biomimetic catalysts and, in particular, metalloporphyrins have been extensively developed for olefin epoxidations and alkane hydroxylations (6). These catalysts should be efficient also for sulfide oxidations, since these latter are oxidized more readily than unsaturated and saturated hydrocarbons (7). However, with the currently investigated catalysts, strong oxidants (iodosobenzene, peracids, etc.) are generally preferred to hydrogen peroxide, in order to avoid the catalyst destruction by hydroxyl radicals readily released by homolytic H_2O_2 decomposition, itself catalyzed by metal complexes (8). Nevertheless, hydrogen peroxide can be used successfully using specially robust porphyrin ligands (9). More recently, metallo-phtalocyanines were shown to be also powerful catalysts for H_2O_2 oxidation of resistant chlorophenols (10). Moreover, depending on the substrate and on the objectives of the authors, iron or manganese or any other transition metal can be the most efficient for oxygen transfer (11).

With regards to sulfides, much less work has been carried out (3*b* and *c*, 12) and, to the best of our knowledge, there is no data that allows for a reasonable choice of a given catalyst (metal and ligand) for promoting their fast and quantitative oxidation into sulfones. In this paper, we report a preliminary investigation of the efficiency of various commercially available biomimetic catalysts for the hydrogen peroxide oxidation of some alkyl sulfides often used to simulate the reaction of mustard (2).

Results and discussion

In the two last columns of Table 1 are shown the yields in sulfoxide and sulfone obtained by oxidation of dibenzyl ($PhCH_2SCH_2Ph$), (2-chloroethyl)phenyl sulfides ($PhSCH_2CH_2Cl$), and thioanisole ($PhSCH_3$), **1**, **2**, and **3**, respectively, by hydrogen peroxide in ethanol and acetonitrile in the presence of catalysts with phtalocyanine, Pht, and meso-tetrakisphenylporphyrin, TPP, as ligands[5] complexing transition metals in various oxidation states, Co(II), Ni(II), Fe(II), Fe(III), Mn(II), Mn(III).

In all the experiments, the initial concentrations of sulfide and catalyst are 8.5×10^{-2} and 2×10^{-3} M, respectively (these values correspond to a substrate/catalyst molar ratio of 42.5). The catalyst concentration is significantly larger than those currently used to compensate for its decomposition, expected because of the well-known fragility of the ligands in the absence of particular substituents. As usual (6–9, 11–13), imidazol (Im) is employed as a cocatalyst in a [Im]:catalyst conc. ratio of 25. Five sulfide equivalents of hydrogen peroxide (35% in water) are added by small portions (10 μL every 5 min) to minimize dismutation of the oxidant and (or) the destruction of the catalyst by reaction of the active metallic species with H_2O_2. Five minutes after the completion of the addition, an aliquot of the reaction mixture is analyzed by GC. The products are identified by GC–MS analysis and (or) by comparison of their retention times to those of authentic samples that were commercially available. When sulfide is not completely consumed, aliquots of the reaction mixture are analyzed at regular time intervals until the sulfide disappearance does not progress significantly.

[5] On one hand, phtalocyanines, which are important industrial dyes, are very cheap. On the other hand, there is extensive work on metallo-porphyrins as biomimetic catalysts of oxidation (6–9, 11, 12).

Table 1. Sulfide oxidation[a] by hydrogen peroxide in the presence of metallo-phtalocyanines (Phth) and -tetraphenylporphyrins (TPP).[b]

Catalyst	Time (min)[c]	Sulfide	Solvent	%S[d]	%SO[a]	%SO_2[a]
None	2800	$(PhCH_2)_2S$	EtOH	5	95	[f]
$PhthNi^{II}$[e]	2760			5	95	[f]
$TPPCo^{II}$	2760			5	95	[f]
$PhthMn^{II}$	5			30	70	[f]
$PhthFe^{II}$	5			7	93	[f]
$TPPMn^{III}Cl$	5			30	70	[f]
$TPPFe^{III}Cl$	5			0	[f]	99
$TPPFe^{III}Cl$	5	$PhSCH_2CH_2Cl$		0	[f]	100
$TPPFe^{III}Cl$	5	$PhSCH_3$		0	[f]	100
$TPPMn^{III}Cl$	5	$(PhCH_2)_2S$	CH_3CN[g]	25	75	[f]
$TPPFe^{III}Cl$	5			0	0	99

[a] Sulfoxide, SO, and sulfone, SO_2, are the only products. Product yields are reproducible at ±3%.

[b] Catalyst conc., 2×10^{-3} M; [Im], 5×10^{-2} M; sulfide conc., 8.5×10^{-2} M; $[H_2O_2]_{Tot}$, 0.476 M, added by fraction of 10 μL; room temperature.

[c] Between the last addition of H_2O_2 and the end of the reaction.

[d] Unchanged sulfide.

[e] Catalyst conc., 5×10^{-4} M, because of the poor solubility of the catalyst in EtOH.

[f] This product is not detectable in the corresponding chromatogram.

[g] In this solvent, metallo-phthalocyanines are not soluble at the concentration used in ethanol.

As shown in the three first rows of Table 1, neither $Co^{II}TPP$ nor $Ni^{II}Pht$ catalyzes significantly the oxidation of **1**, since the time required for its almost complete disappearance is similar with and without these catalysts. In contrast, Mn(II) or Fe(II) phtalocyanines exhibit significant catalytic power; 5 min after the complete addition of H_2O_2, most of dibenzylsulfide is transformed into the corresponding sulfoxide. However, Mn(II) is less efficient than Fe(II), since with Mn(II) the reaction stops when 70% of sulfide is oxidized whereas 7% only subsists with Fe(II). The behavior of Mn(II) porphyrin is quite similar to that of the two metallo-phtalocyanines. Compound **1** is significantly oxidized into sulfoxide only. With all these catalysts, no sulfone was obtained. Finally, the only catalyst able to totally oxidize dibenzylsulfide into sulfone is $Fe^{III}TPPCl$. The reaction is very fast under the reaction conditions, sulfide being completely oxidized in less than 5 min. Moreover, oxidation products, other than sulfoxide and sulfone, are never observed.

In Table 1, are also shown results for (2-chloroethyl)phenyl sulfide **2** and thioanisole **3**. Again, $Fe^{III}TPPCl$ is able to promote the complete and quantitative transformation of these sulfides into the corresponding sulfones directly. At variance with dibenzylsulfide, $Mn^{III}TPPCl$ is not very efficient, **2** being oxidized at most 30% with this catalyst.

In these experiments, ethanol is preferred to acetonitrile in order to minimize sulfide oxidation by $OH^{\cdot}$ radicals, formed by metal-mediated homolysis of H_2O_2, which would lead to unwanted oxidation by-products. It is expected that these radicals react with ethanol more rapidly than with sulfide, since

© 1998 NRC Canada

ethanol is an $OH^{\cdot}$ trapping agent more efficient than acetonitrile (13). Nevertheless, when the catalyzed oxidations are carried out in acetonitrile (last rows of Table 1), the product distribution is essentially the same as that observed in ethanol. A reasonable conclusion is, therefore, that free $OH^{\cdot}$ radicals do not play a significant role in these sulfide oxidations under the present reaction conditions.

Another remarkable result of this investigation is the absence of any by-product arising from the cleavage of sulfide radical cations as potential intermediates,[6] namely aldehyde

[2] $R_2S \longrightarrow R_2S^{\bullet+} \longrightarrow R^+ + RS^{\bullet}$ → RS-SR / RCHO

or alcohol and disulfide (eq. [2]). These two latter products are currently obtained in sulfide oxidation by typical electron transfer (ET) oxidants but not when the H_2O_2 oxidation is catalyzed by metal porphyrins or cytochrome P-450 (14). In particular, our results agree fairly well with the conclusions of Baciocchi et al. (14) in their extensive comparison of sulfide oxidation by ET oxidants and by hydrogen peroxide in the presence of biomometic catalyst. Whereas biomometic oxidations give mainly sulfoxide and small amounts of sulfone, these two compounds are very minor products when the oxidant is a $Co^{III}W$ complex (3*c*).

These results are in contrast with previous observations of Oae et al. (12) who obtained some disulfide with an analogous catalytic system. However, disulfides were obtained, only when the starting sulfide ($PhSCH_2CN$ or $PhSCH_2COPh$) presents an α-acidic hydrogen favoring the cleavage of the carbon-sulfur bond and the formation of a phenylthiyl radical.

In agreement with Baciocchi results (14), a free sulfur-centered radical cation is not suggested as an active intermediate by our results. Therefore, a mechanism (eq. [3], route *a*) involving a direct oxygen transfer from oxene **4** (6*d*, 8, 15) to sulfide and then to sulfoxide, in a process similar to that for catalyzed epoxidation (9, 11), can be reasonably proposed when the catalyst is Fe^{III}TPPCl. Nevertheless, an oxygen transfer from metal-oxo radical **5** formed by homolysis of the perhydroxymetal species (9) (route *b* of eq. [3]):

[3] Por M → PorM-OOH $\xrightarrow{(a)}$ Por - $\overset{\bullet+}{M}$=O (**4**) $\xrightarrow{+R_2S}$ R_2SO; PorM-OOH $\xrightarrow{-OH^{\bullet}\ (b)}$ PorMO$^{\bullet}$ (**5**) $\xrightarrow{+R_2S}$ R_2SO; R_2SO $\xrightarrow{+\ 4}$ R_2SO_2

cannot be ruled out a priori, in particular when M is Mn(III). However, further results (vide supra) do not support necessarily route *b*.

The markedly different behavior of the Mn(III) and Fe(III) porphyrins is rather surprising, since these two catalysts behave quite similarly in olefin epoxidation (11). In the view of better understanding the origin of this difference, we investigated in more detail the progress of the oxidation of **1** as hydrogen peroxide is added. The results are shown in Figs. 1*a* and *b*. With Fe^{III}TPPCl, the very first additions of H_2O_2 quantitatively transform sulfide into sulfoxide. The further additions are still very efficient, since after the addition of 1 equiv. of H_2O_2, 75% of H_2O_2 is used in sulfide–sulfoxide oxidation, the remaining 25% of sulfide being unchanged. With 1.5 equiv. of H_2O_2, sulfide is totally consumed, the sulfoxide yield reaches

Fig. 1. The progress of the hydrogen peroxide oxidation of dibenzylsulfide with the oxidant addition in the presence of M(III) porphyrins; (*a*) M = Fe; (*b*) M = Mn; △, sulfide; □, sulfoxide; ●, sulfone. (Room temperature. Initial concentrations in ethanol: 0.085 M sulfide; 0.05 M imidazole; 0.002 M $TPPM^{III}$ Cl. 40 μL H_2O_2 (35% in water) corresponds to 1 sulfide conc. equiv.).

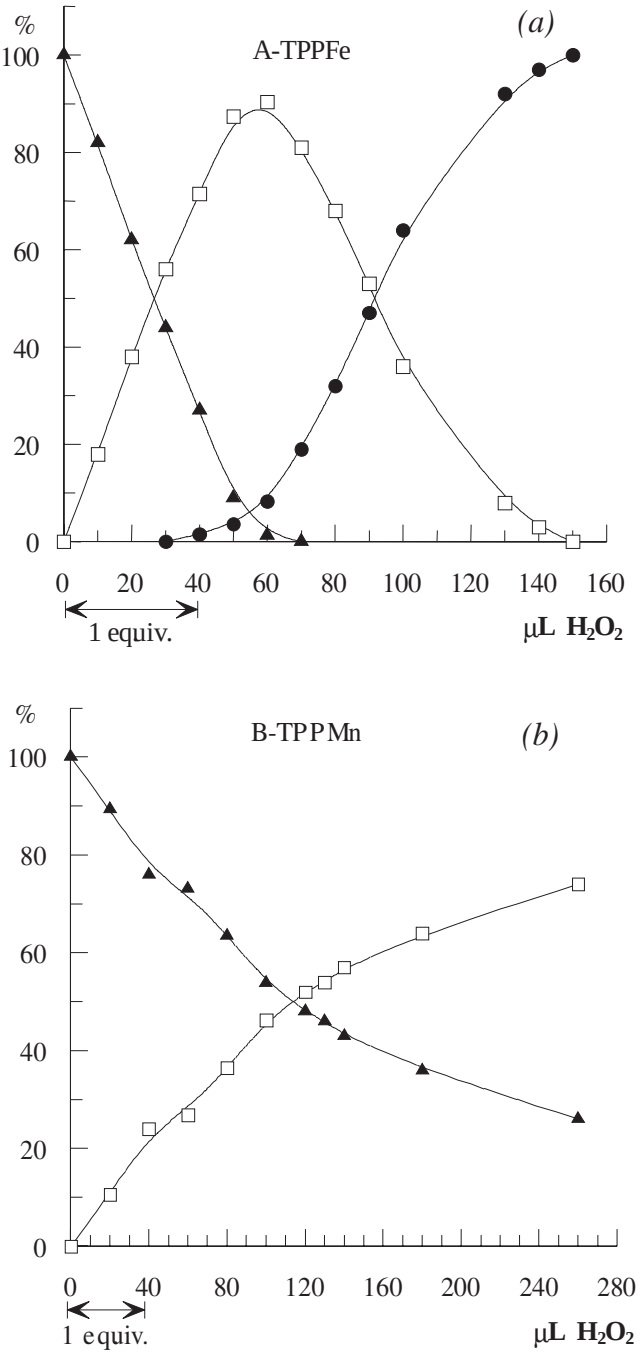

[6] However, the formation of this sulfur radical cation by electron transfer from oxene (eq. [3]) and its very fast recombination with **4** cannot be totally excluded.

© 1998 NRC Canada

Fig. 2. Catalyst decomposition during dibenzylsulfide oxidation with H_2O_2 addition: ●, TPPFe^{III}Cl; ▲, TPPMn^{III}Cl. The open marks (○ and △) are obtained by correcting the added H_2O_2 from the amount consumed by sulfide oxidation. Reaction conditions are identical to those in Fig. 1.

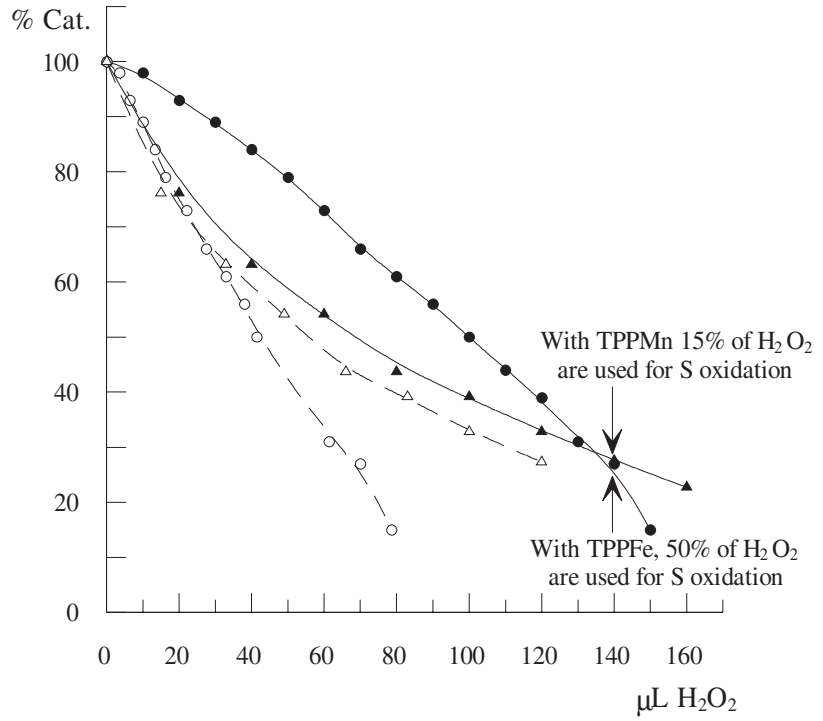

a maximum at about 95% whereas some sulfone is present. The last additions of H_2O_2 are used for sulfoxide oxidation into sulfone. Finally, after the incorporation of 4 equiv. of H_2O_2, the yield in sulfone is quantitative. There are several conclusions from this experiment. Firstly, oxidation of sulfide into sulfoxide and of sulfoxide into sulfone are consecutive reactions, sulfoxide being an intermediate. This implies that sulfoxide oxidation is slower than that of sulfide, so that sulfone appears only when sulfide is almost completely transformed into sulfoxide. Secondly, at every stage of the reaction progress, the transformation of sulfide and sulfoxide is quantitative, without formation of any other oxidation products. Thirdly, hydrogen peroxide is not quantitatively used for sulfide oxidation, since 4 equiv., as compared to sulfide, are necessary for the complete transformation in sulfone, which requires 2 equiv. only. Clearly, other H_2O_2-consuming processes are involved.

The results with Mn^{III}TPPCl are completely different (Fig. 1*b*). Sulfide is still exclusively transformed into sulfoxide but the efficiency of the oxidant is very small, since after the addition of 1 equiv. of H_2O_2, only 20% of the sulfide is oxidized. After a more and more rapid efficiency decrease, the reaction stops when about 30% of sulfide still subsists.

Therefore, the difference between the two metal porphyrins is that most of hydrogen peroxide is consumed by processes in which sulfide is not involved when Mn^{III}TPPCl is the catalyst whereas with Fe^{III}TPPCl, the H_2O_2 consumption by sulfide is an important route. This difference explains also why no sulfone is obtained with Mn^{III}TPPCl, since sulfoxide oxidation can start only when there is no more sulfide.

To gain some insights on the competing processes that consume hydrogen peroxide, the destruction of the catalysts was monitored spectroscopically at their Soret band (λ_{max} = 466 nm and 415 nm in ethanol for Mn(III) and Fe^{III}TPPCl, respectively), during oxidation of **1** under concentrations identical to those used in the previous experiments. In Fig. 2 is shown the decrease in the concentration of the two catalysts as the reaction progresses. Mn^{III}TPPCl is destroyed rapidly with the first H_2O_2 additions, and then its disappearance is progressively slowed down. Fe^{III}TPPCl is also consumed, although in the first H_2O_2 additions its concentration decreases less rapidly. With 140 μL of H_2O_2 (i.e., 3.5 sulfide equiv.), about 25% of the two catalysts are still preserved, i.e., the catalyst concentration is still 8×10^{-5} M with an initial concentration of 2×10^{-3} M. This remaining amount is enough to promote further substrate oxidation, since sulfide, added at this stage of the reaction, is transformed into sulfoxide. Nevertheless, there is a very large difference between the two catalysts insofar as after the addition of 140 μL H_2O_2, 57% of the added H_2O_2 has been consumed by sulfide, in the presence of Fe^{III}TPPCl, whereas with Mn^{III}TPPPCl, 17% of H_2O_2 has been used for this reaction. Figure 3 shows the disappearance of Fe^{III}TPPCl consecutive to successive additions of H_2O_2 in experiments similar to those of Figs. 1 and 2 but in the absence of sulfide. The comparison of Figs. 2 and 3 exhibits that the catalyst is markedly less consumed when sulfide is present. In other words, it seems that the presence of sulfide exerts some "protection" of the catalyst. However, this conclusion is artificial, since H_2O_2 is used partly in sulfide oxidation. When the amount of added H_2O_2 is corrected for the sulfide uptake, the rates of the ligand destruction by H_2O_2 are not markedly different with Mn(III) and Fe(III).

Therefore, the oxidative destruction of the two catalysts is promoted by hydrogen peroxide via similar processes,

© 1998 NRC Canada

Fig. 3. Comparison of TPPFe^{III}Cl decomposition by hydrogen peroxide in the presence (●) and in the absence (○) of dibenzylsulfide. Reaction conditions are identical to those in Fig. 1.

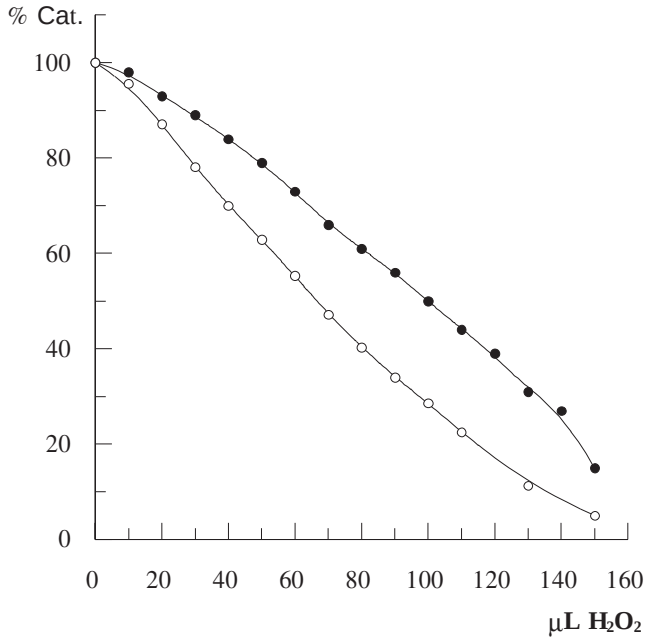

independently on the catalyzed sulfide oxidation route. Since the efficiencies of the two catalysts are very different, there must be a much more efficient route for the H_2O_2 consumption in the presence of Mn^{III}TPPCl than with Fe^{III}TPPCl. This route is most likely the dismutation of hydrogen peroxide, which is well known to be metal-catalyzed and which would be favoured, particularly by the Mn(III) catalyst. Our results suggest, therefore, that among the various possible fates of the oxene species, which is assumed to be the active form of the catalyst for sulfide oxidation as for alkene epoxydation (9, 11), route *c* (eq. [4]) is of comparable importance when M is Mn(III) or Fe(III).

[4]

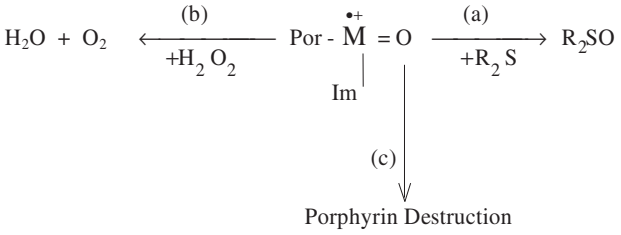

In contrast, route *a* is highly favoured as compared to route *b* with iron but not with manganese catalyst. There are two possible interpretations for the observed metal dependence of the competition between these two routes. The H_2O_2 dismutation could be catalyzed by manganese complex more efficiently than by iron complex. This is unlikely in the view of previous data on alkene epoxidation (6*a*), which show that H_2O_2 consumption is similarly fast with the two catalysts in the presence of imidazole, i.e., the rate of route *b* does not markedly depend on the nature of the metal. Since our results suggest that route *a* is favored with iron but not with manganese, a reasonable conclusion is that the oxygen transfer from the high-valent oxo complex to sulfides is probably faster with Fe(III) than with Mn(III) catalyst.

In conclusion, this preliminary work points out that among the investigated biomimetic catalysts, the most efficient catalyst for quantitative and fast oxidation of sulfide into sulfone by hydrogen peroxide is Fe^{III}TPPCl. The efficiency of the analogous Mn(III) complex is markedly smaller. Regarding the selective biomimetic oxidations of sulfide into sulfoxide, Fe(II) phtalocyanine can be used successfully. Therefore, with readily oxidizable sulfides, a significant role of both the metal and its ligand on the oxygen-transfer ability of these catalysts is evidenced. More work, in particular using more robust ligands (16) and aqueous media, is in progress with the objective of designing performant catalytic systems for toxic sulfide oxidation.

Experimental section

Physical measurements

The UV-vis spectra were recorded on a Perkin–Elmer lambda II spectrophotometer. Gas chromatography analysis was carried out on a Delsi–Nermag 200 gas chromatograph equipped with a fid detector and a CP-Sil 5 column. The products were identified by comparison of their retention times with authentic samples or by GC–MS (I.T.D. Finigan 800).

Materials

Acetonitrile and ethanol (HPLC grade, Prolabo) were used as received. Hydrogen peroxide (H_2O_2 35% in water, Acros) was stored at 5°C and titrated every month. Sulfides, sulfoxides, and sulfones were purchased from Aldrich or Acros and used as received. The absence of any oxidation product in the commercial sulfides was checked before use by GC. All the catalysts were commercial (Aldrich) and used without further purification.

Oxidation procedure

To 5 mL of a reaction mixture (0.085 M sulfide, 0.05 M imidazole, and 0.002 M catalyst, in ethanol or in CH_3CN) was added directly the commercial solution of hydrogen peroxide by small amounts with a microsyringe. The oxidant is added 10 μL per 10 μL with a delay of 5 min between each addition, to prevent hydrogen peroxide dismutation. The GC analysis was performed on aliquots withdrawn directly from the reaction mixture. Yields were measured by GC with the internal standard method. All the reactions were carried out at room temperature, without any buffer and under aerobic conditions.

Measurements of the catalyst destruction

The disappearance of the porphyrins were monitored by UV-vis spectrophotometry by the decrease of their Soret band (415 nm for TPPFe^{III}Cl, 466 nm for TPPMn^{III}Cl in ethanol). Eight microliters of the reaction mixture was taken with a microsyringe and diluted directly in the cell containing 2 mL of ethanol. The percentage of remaining catalyst was then calculated.

Acknowledgements

A.M. is indebted to DRET (Direction des Recherches et Études Techniques) for financial support (1996). The authors gratefully

© 1998 NRC Canada

acknowledge the fruitful suggestions of Dr. P. Battioni, Dr. E. Baciocchi, and Dr. C.L. Perrin.

References

1. (*a*) E.E. Reid. *In* Chemistry of bivalent sulfur. Chemical Publishing Co., New York. 1960. Chap. 5; (*b*) Y.C. Yang, J.A. Baker, and J.R. Ward. Chem. Rev. **92**, 1729 (1992).
2. (*a*) J.H. Ramsden, R.S. Drago, and R. Riley. J. Am. Chem. Soc. **111**, 3958 (1989); (*b*) Y.C. Yang, L.L. Szafraniec, and W.T. Beaudry. J. Org. Chem. **55**, 3664 (1990).
3. (*a*) M. Madesclaire. Tetrahedron, **42**, 5459 (1986); (*b*) F. Pautet, R. Barret, L. Favre, and M. Daudon. Pharmazie, **43**, 437 (1988); (*c*) V. Conte, F. Di Furia, and G. Modena. *In* Organic peroxides. *Edited by* W. Ando. Wiley, New York. 1992. p. 559; (*d*) E. Baciocchi, O. Lanzalunga, and B. Pirozzi. Tetrahedron, **53**, 12287 (1997).
4. Y.C. Yang, L.L. Szafraniec, W.T. Beaudry, and C.A. Bunton. J. Org. Chem. **58**, 6964 (1993).
5. M.A.P. Dankleff, R. Curci, J.O. Edwards, and H.Y. Pyun. J. Am. Chem. Soc. **90**, 3209 (1968), and refs. cited therein.
6. (*a*) P. Battioni, J.P. Renaud, J. Bartoli, M. Reina-Artiles, M. Fort, and D. Mansuy. J. Am. Chem. Soc. **110**, 8462 (1988); (*b*) T.C. Bruice. Acc. Chem. Res. **24**, 243 (1991); (*c*) B. Meunier. Chem. Rev. **92**, 1411 (1992); (*d*) T.G. Traylor, C. Kim, J.L. Richards, F. Xu, and C.L. Perrin. J. Am. Chem. Soc. **117**, 3468 (1995).
7. J.T. Groves and P. Viski. J. Org. Chem. **55**, 3628 (1990).
8. T.G. Traylor and F. Xu. J. Am. Chem. Soc. **112**, 178 (1990).
9. T.G. Traylor, S. Tsuchiya, Y.S. Byun, and C. Kim. J. Am. Chem. Soc. **115**, 2775 (1993).
10. A. Sorokin and B. Meunier. Chem. Eur. J. **2**, 1308 (1996).
11. D. Ostovic and T.C. Bruice. Acc. Chem. Res. **25**, 314 (1992).
12. (*a*) S. Oae, Y. Watanabe, and K. Fujimori. Tetrahedron Lett. **23**, 1189 (1982); (*b*) Y. Watanabe, T. Iyanagi, and S. Oae. Tetrahedron Lett. **23**, 533 (1982).
13. J.O. Edwards and R. Curci. *In* Catalytic Oxidation with hydrogen peroxide as oxidant. *Edited by* G. Strukul. Kluwer, Dordrecht. 1992. p. 112.
14. (*a*) E. Baciocchi, M. Crescenzi, E. Fasella, and M. Mattioli. J. Org. Chem. **57**, 4684 (1992); (*b*) E. Baciocchi, O. Lanzalunga, and F. Marconi. Tetrahedron Lett. **35**, 9771 (1994).
15. T.G. Traylor and J.P. Ciccone. J. Am. Chem. Soc. **111**, 8413 (1989).
16. D. Dolphin, T.G. Traylor, and L.Y. Xie. Acc. Chem. Res. **30**, 251 (1997).

© 1998 NRC Canada

Theoretical study of O → X (S, Se, Te) coordination in organic compounds

Ruslan M. Minyaev and Vladimir I. Minkin

Abstract: Ab initio (RHF/LanL2DZ, MP2(fc)/LanL2DZ, MP2(fc)/6-31G**, and MP2(fc)/6-311++G**) calculations were performed for a series of β-chalcogenovinylaldehydes, 1,6-dioxa-6a-chalcogenopentalenes, and bimolecular complexes of formaldehyde with chalcogen hydrides and chlorides. The calculations reproduce well the existence and experimentally observed structural peculiarities of the intra- and intermolecular O → chalcogen attractive interactions that stabilize the hypervalent T-shaped bond configuration at a chalcogen atom. These interactions increase in the order S, Se, Te and with the increasing electronegativity of a substituent attached to the chalcogen center. The ab initio calculations performed predict the existence of sufficiently stable bimolecular complexes $H_2CO\cdots XR_1R_2$ (X = S, Se, Te; R_1, R_2 = H, Cl) with a complexation energy comparable to the energy of a strong hydrogen bond.

Key words: ab initio calculations, chalcogen-containing compounds, intramolecular coordination.

Résumé : On a effectué des calculs ab initio (RHF/LanL2DZ, MP2(fc)/LanL2DZ, MP2(fc)/6-31G** et MP2(fc)/6-311++G**) sur une série de β-chalcogénovinylaldéhydes, de 1,6-dioxa-6a-chalcogénopentalènes et de complexes moléculaires du formaldéhyde avec des hydrures et des chlorures de chalcogènes. Les calculs permettent de bien reproduire l'existence et les particularités structurales observées expérimentalement des interactions attractives intra- et intermoléculaires O → chalcogène qui stabilisent la configuration de la liaison hypervalente en forme de T au niveau de l'atome de chalcogène. Ces interactions progressent dans l'ordre S, Se et Te et elles augmentent avec l'électronégativité du substituant attaché au centre chalcogène. Les calculs ab initio effectués permettent de prédire l'existence de complexes bimoléculaires $H_2CO\cdots XR_1R_2$ (X = S, Se, Te; R_1, R_2 = H, Cl) assez stables, avec des énergies de complexation comparables aux énergies de liaisons hydrogènes fortes.

Mots clés : calculs ab initio, composés contenant des chalcogènes, coordination intramoléculaire.

[Traduit par la rédaction]

Introduction

Intra- and intermolecular donor–acceptor interactions play a crucial role in defining the molecular structure of compounds with spatially suitably fitted functionalities, secondary and tertiary structures of biologically important macromolecules, and modes of packing of molecules in a crystal, i.e., solid-state structures as well. The most important types of donor–acceptor interactions involve hydrogen (1–6) and coordination or dative bonds formed by metal centers with ligands donating electrons from lone-pairs or π-orbitals (7–10). During the last two decades a third, less common, type of attractive interaction occurring between two electron-abundant main group 15–17 (VA–VIIA) element centers has become a topic of rapidly growing interest (11–14). Special attention has been given to intramolecular and intermolecular noncovalent attractive interactions existing between di- and tetracoordinated sulfur, selenium, and tellurium atoms from one side and oxygen or nitrogen atoms from another side (11–13, 15–18). When occurring within a molecule, interactions of this kind strongly affect the reactivity and enhance the stability of the chalcogen-containing compounds (13, 19, 20). These interactions are also responsible for the high biological activity of selenium, in particular selenoproteins and nucleoside analogues (21).

A peculiar feature of the chalcogen–oxygen and chalcogen–nitrogen bonds is the strong dependence of their strengths and lengths on the nature of chalcogen, its valence state, and the electronegativity of the attached substituent R (11–13). By varying these factors in a series of compounds with similar geometry it is possible to cover wide ranges of chalcogen–oxygen or chalcogen–nitrogen intramolecular distances, from those approaching values characteristic of covalent bonds to those close to van der Waals contacts. This trend is illustrated by excerpts of X-ray structural data for compounds with five-membered chelate rings formed by the intramolecular O → chalcogen coordination (Fig. 1).

Much effort has been devoted to gaining insight into the origin of the specific attractive forces between the electron-abundant main group centers in type **1–8** molecules. The terms "secondary bonding" (30), "fractional bonds" (31), "specific noncovalent contacts" (32), and "premature hypervalent bonds" (16) have been introduced to describe the tendency in non-metallic compounds to form short intra- and intermolecular contacts between the above centers. The theoretical work

Received February 12, 1998.

This paper is dedicated to Professor Erwin Buncel in recognition of his contributions to Canadian chemistry.

R.M. Minyaev and V.I. Minkin.[1] Institute of Physical and Organic Chemistry, Rostov State University, 194/2 Stachka Ave., Rostov-on-Don 344090, Russian Federation.

[1] Telephone: 7(8632)285700. Fax: 7(8632)285667. E-mail: minyaev@ipoc.rnd.runnet.ru and minkin@ipoc.rnd.runnet.ru

© 1998 NRC Canada

Fig. 1. X-ray structural data (O → chalcogen bond length, *d* in Å) and the covalency ratio factor, χ, calculated on the basis of Bondi (34) covalent (r_A, r_B), and vdW (R_A, R_B) radii.

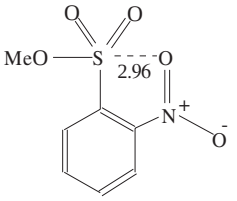

1 (22), χ=0.22

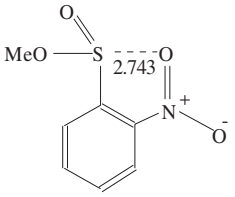

2 (22), χ=0.36

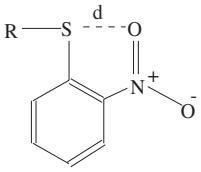

3a, R=OMe (22), d=2.46, χ=0.22
3b, R=Cl (22), d=2.38, χ=0.59

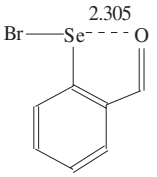

4 (23), χ=0.73

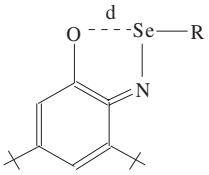

5a, R=Ph (18), d=2.476, χ=0.62
5b, R=Cl (24), d=2.079, χ=0.88

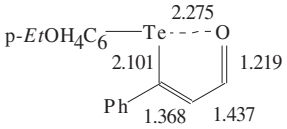

6a (25), χ=0.58

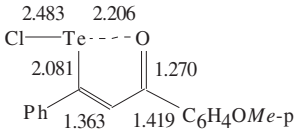

6b (15), χ=0.92

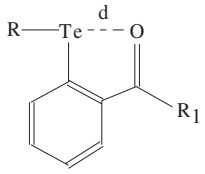

7a, R=Cl, R_1=NHMe (26), d=2.250, χ=0.89
7b, R=Br, R_1=NH_2 (26), d=2.237, χ=0.90
7c, R=I, R_1=CH_2CH_2I (27), d=2.368, χ=0.81

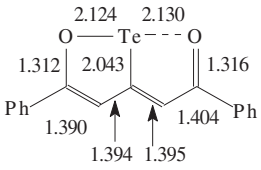

8 (28), χ=0.97

reveals that there exist several principal factors that account for this tendency (16, 18, 31, 33). These include an electrostatic effect, a *d*-orbital participation, and negative hyperconjugation, i.e., donation of an electron pair from the highest π- or *n*-orbitals of one center to the lowest lying σ*-orbital of the neighbouring center. The latter interaction, which corresponds to the n_0–$\sigma^*_{Ch\text{-}X}$ type in compounds **1–8**, has been found to be the principal factor responsible for the formation of additional bonds between the electron-abundant atomic centers associated with expansion of the valence shell of the chalcogen atoms. The degree of this expansion may be characterized by the so-called covalency ratio factor χ introduced by Weinhold and co-workers (34)

$$[1] \qquad \chi = \frac{(R_A + R_B) - d_{AB}}{(R_A + R_B) - (r_A + r_B)}$$

where R_A and R_B stand for van der Waals and r_A and r_B for covalent radii of the interacting centers, d_{AB} being the experimentally determined (or calculated) contact.

© 1998 NRC Canada

Table 1. Total (E_{tot}), relative (ΔE), and zero point vibration (ZPE) energies and relative enthalpies (ΔH) for the structures **9** and **11** calculated by RHF/LanL2DZ, MP2(fc)/LanL2DZ (numbers in parentheses), and MP2(fc)/6-311++G** (numbers in square brackets) methods.

Structure	E_{tot}	ΔE	ZPE	ΔH [b]
	au [a]	kcal/mol	au	kcal/mol
9, XR = SH	–200.569 06	0.	0.066 461	0.
	(–200.998 26)	(0.)	(0.060 53)	(0.)
	[–588.994 081]	[0.]	[0.062 93]	[0.]
11, XR = SH	–200.573 94	–3.60	0.065 56	–3.29
	(–201.000 18)	(–1.20)	(0.059 69)	(–1.38)
	[–588.994 59	[–0.32]	[0.061 92]	[–0.72]
9, XR = SCl	–214.677 94	0.	0.058 89	0.
	(–215.146 86)	(0.)	(0.053 57)	(0.)
	[–1048.008 16]	[0.]	[0.055 54]	[0.]
11, XR = SCl	–214.677 20	0.46	0.058 50	0.46
	(–215.138 97)	(4.95)	(0.052 83)	(4.89)
	[–1047.999 86]	[5.21]	[0.055 54]	[5.08]
9, XR = SeH	–199.694 29	0.	0.065 10	0.
	(–200.120 48)	(0.)	(0.059 44)	(0.)
11, XR = SeH	–199.696 02	–1.08	0.064 03	–1.32
	(–200.119 06)	(0.89)	(0.058 36)	(0.67)
9, XR = SeCl	–213.825 50	0.	0.058 24	0.
	(–214.288 74)	(0.)	(0.053 20)	(0.)
11, XR = SeCl	–213.815 88	6.03	0.057 33	5.33
	(–214.271 94)	(10.54)	(0.051 88)	(9.74)
9, XR = TeH	–198.531 14	0.	0.063 88	0.
	(–198.952 94)	(0.)	(0.058 27)	(0.)
11, XR = TeH	–198.528 05	1.94	0.062 58	1.70
	(–198.946 87)	(3.81)	(0.056 84)	(2.97)
9, XR = TeCl	–212.691 72	0.	0.058 04	0.
	(–213.145 59)	(0.)	(0.052 97)	(0.)
11, XR = TeCl	–212.671 11	12.93	0.057 02	12.85
	(–213.119 34)	(16.47)	(0.051 63)	(16.28)

[a] 1 au = 627.5095 kcal/mol.
[b] Thermochemistry at temperature 298.15 K and pressure 1 atm (101.3 kPa).

The χ values calculated on the basis of available experimental data for compounds **1–8** are given in Fig. 1. Although seemingly overestimated, these values clearly indicate a rather close similarity of the O $\rightarrow$ chalcogen bonds in compounds **1–8** to corresponding covalent bonds of this type. These values reveal also the trends discussed above of strengthening the O $\rightarrow$ chalcogen bonds (*i*) when passing from sulfur to selenium and tellurium and (*ii*) with increasing electronegativity of a substituent R to the chalcogen atom.

The present work is aimed at further elucidating these trends with the help of ab initio calculations of model compounds **9** and **10** containing intramolecular coordination O $\rightarrow$ chalcogen bonds included in conjugated five-membered rings common to the type **1–8** compounds. Apart from the structural information relevant to the intramolecular coordination O $\rightarrow$ chalcogen bonds, particular attention has been given to the energy of these bonds. The latter values were estimated as the difference between the full energies of the cyclic structures **9** and **10** and their *trans-s-trans* conformers (**11** and **12**) relieved of angle strain.

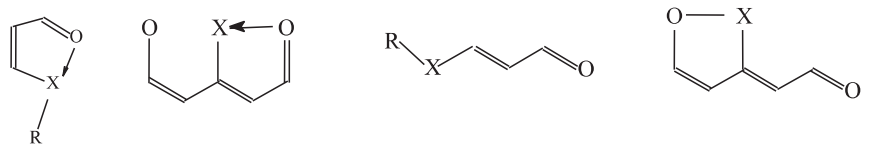

9 10 11 12

X=S,Se,Te; R=H, Cl X=S,Se,Te; R=H, Cl

© 1998 NRC Canada

Fig. 2. Geometrical parameters for *cis*-, **9**, and *trans*-,**11**, β-thiovinylaldehyde and β-chlorothiovinylaldehyde as predicted by the RHF/LanL2DZ, MP2(fc)/LanL2DZ (numbers in parentheses), and MP2(fc)/6-311++G** (numbers in square brackets) ab initio methods. Bond lengths and angles are given in Å and degrees, respectively.

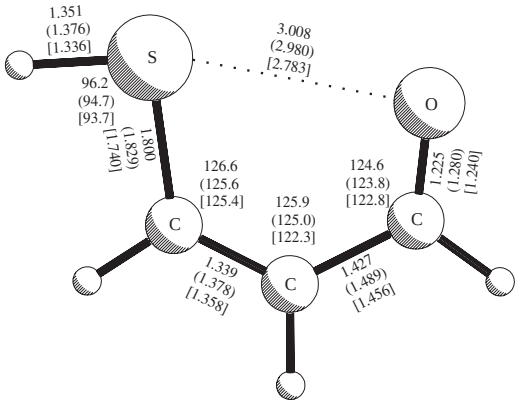

9 (X=S,R=H), C_s

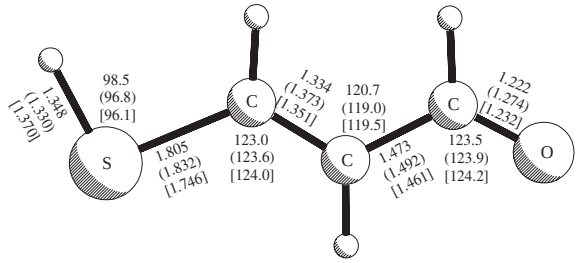

11, (X=S,R=H), C_s

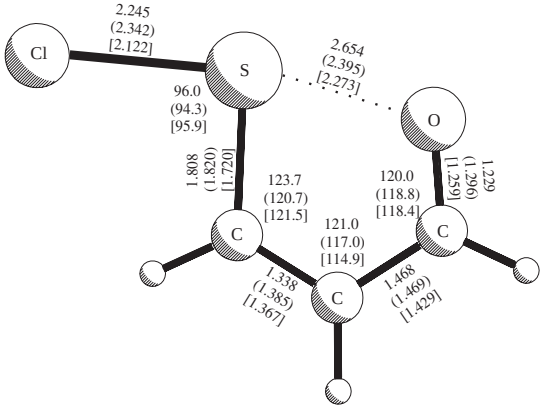

9, (X=S,R=Cl), C_s

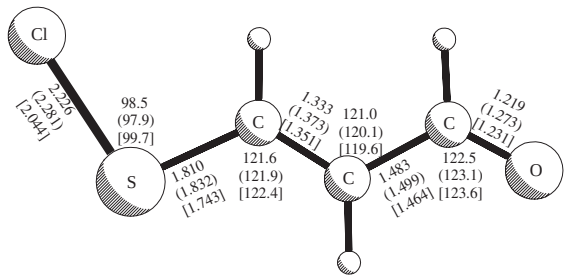

11, (X=S,R=Cl), C_1

Dihedral angle ClSCC = 130.7 (132.4) [151.2]

To compare the intramolecular O → chalcogen interactions with the intermolecular reactions we also studied the geometries and complexation energies of bimolecular complexes **13**.

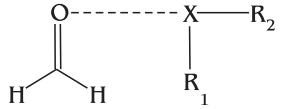

13

X=S,Se,Te; R_1,R_2=H, Cl

Several important ab initio calculations concerned with the problems addressed by the present work have previously been performed. For a series of β-thiovinylaldehydes **9** (X = S; R = F, OH, NH_2, SH, CH_3), it was found that the stability of the cyclic conformation that results through the intramolecular coordination O → S bond and the characteristic shortening of the O···S contact were well reproduced by calculations even at the moderate RHF/3-21G level of approximation (16). The same type of conclusion was reached by Barton et al. (18) in their MP2 calculations with DZ basis set on two simple selenoiminoquinones that model the compounds **5** (R = H, Cl). By studying

© 1998 NRC Canada

Fig. 3. Geometrical parameters for *cis*-, **9**, and *trans*-,**11**, β-hydroselenovinylaldehyde and β-chloroselenovinylaldehyde as predicted by the RHF/LanL2DZ and MP2(fc)/LanL2DZ (numbers in parentheses) ab initio methods. Bond lengths and angles are given in Å and degrees, respectively.

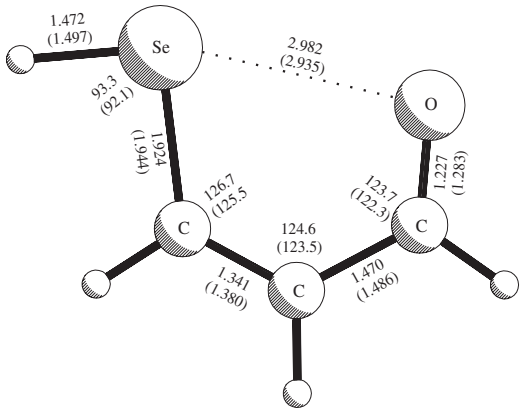

9 (X=Se,R=H), C_s

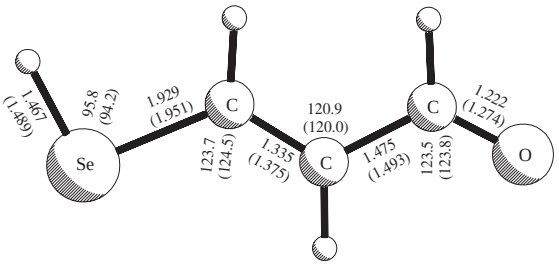

11 (X=Se,R=H), C_s

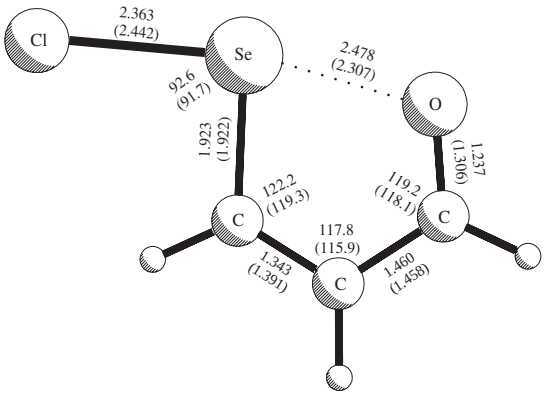

9 (X=Se,R=Cl), C_s

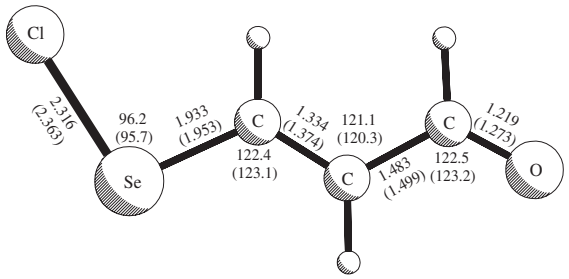

6, (X=Se,R=Cl), C_1

Dihedral angle ClSeCC = 130.7 (132.4)

the electron charge distribution around the Se atom with the use of Bader and Mulliken population analyses, the authors (18) qualitatively described the electronic structure of the O → Se-R triad in terms of the VSEPR model and a three-center, four-electron bond. In contrast with this conclusion are the results of the STO-3G* calculations (35) on the dimer formed by two anions of the ammonium trichloro(ethane-1,2-dithiolato-*O*,*O′*)tellurate (IV). The calculations performed at the geometry obtained from the X-ray study that displayed a short O–Te intradimeric distance of 2.764 Å pointed to the donation of a lone pair of an oxygen to the $\sigma^*_{Te\text{-}Cl}$-orbital as the main interaction, but did not reveal three-center orbitals in the O → Te-Cl unit of the dimer.

Methods

All the stationary point optimization calculations in this work were performed by standard RHF/LanL2DZ, MP2(fc)/LanL2DZ, MP2(fc)/6-31G**, and MP2(fc)/6-311++G** methods (36) using the Gaussian-94 (37) and GAMESS (38) packages of ab initio programs. Optimization of molecular geometry at stationary points at all levels of approximation was carried out with a "tight" convergence criterion for the force in the Gaussian program and a 10^{-5} convergence criterion for the RMS gradient in the GAMESS program in order to obtain accurate harmonic vibrational frequencies. Force constants at all levels of approximation were calculated by a numerical method.

© 1998 NRC Canada

Fig. 4. Geometrical parameters for *cis*-, **9**, and *trans*-, **11**, β-hydrotellurovinylaldehyde and β-chlorotellurovinylaldehyde as predicted by the RHF/LanL2DZ and MP2(fc)/LanL2DZ (numbers in parentheses) ab initio methods. Bond lengths and angles are given in Å and degrees, respectively.

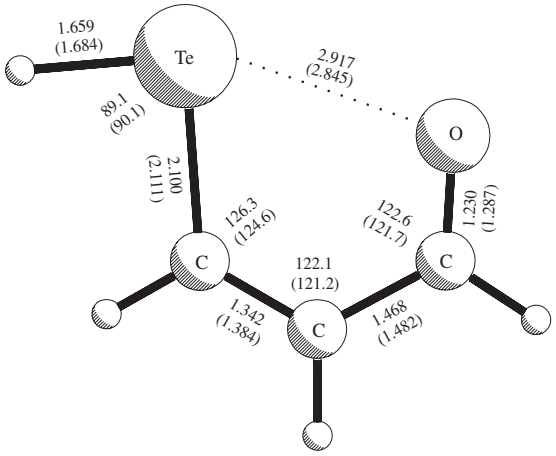

9 (X=Te,R=H), C_s

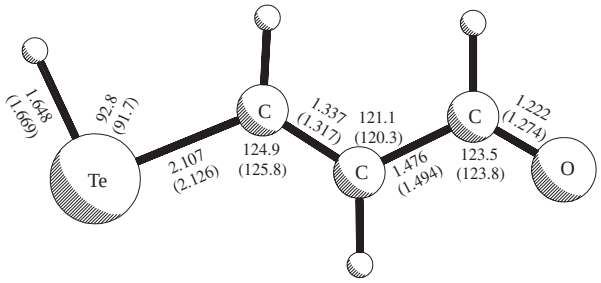

11 (X=Te,R=H), C_s

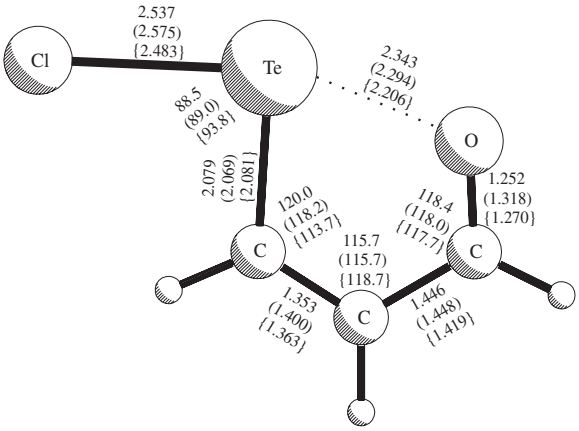

9 (X=Te,R=Cl), C_s

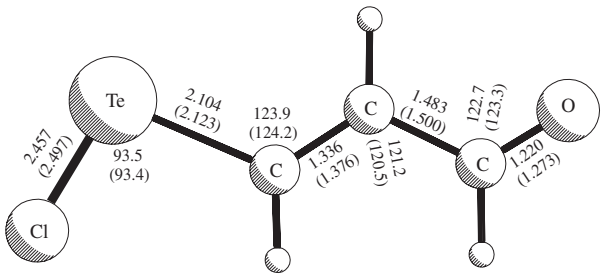

11 (X=Te,R=Cl), C_1

Dihedral angle ClTeCC = 138.1 (142.7)

No counterpoise corrections were made for the basis set superposition error (BSSE) (39) in calculations concerned with the dimer **13,** accounting for recent findings (40–44) that inclusion of BSSE often enormously decreases thermodynamic stability and binding energy in various multimolecular complexes. For example, the calculations of the alanine dimer give rise to an interaction energy of –19.7 kcal/mol, while including the BSSE affords a value of +14.4 kcal/mol (43).

All the results obtained relate to the gas phase. No attempts were made to take into account solution effects.

We are confident that for heavy elements like Se and Te the influence of relativistic effects on various chemical properties of the compounds under study becomes important. Although no relativistic effects were included in the calculations we expect that the results obtained describe the essential trends in the properties of the compounds under study.

Results and discussion

β-Chalcogenovinylaldehydes

According to the ab initio calculations performed, all β-chalcogenovinylaldehydes (X = S, Se, Te; R = H, Cl) in their

© 1998 NRC Canada

Table 2. Total (E_{tot}), relative (ΔE), and zero point vibration (ZPE) energies and relative enthalpies (ΔH) for the structures **10** and **12** calculated by RHF/LanL2DZ, MP2(fc)/LanL2DZ (numbers in parentheses) and MP2(fc)/6-311++G** (numbers in square brackets) methods.

Structure	E_{tot}	ΔE	ZPE	ΔH [b]
	au [a]	kcal/mol	au	kcal/mol
10, X = S	–351.092 90	0.	0.086 97	0.
C_s, C_{2v}	(–351.822 57)	(0.)	(0.079 11)	(0.)
	[–740.023 41]	[0.]	[0.082 04]	[0.]
12, X = S	–351.083 20	6.09	0.086 34	5.95
C_s	(–351.803 27)	(12.11)	(0.077 41)	(11.54)
	[–739.990 40)	[20.71]	[0.079 72]	[19.95]
10, X = Se	–350.242 10	0.	0.085 63	0.
C_{2v}	(–350.969 68)	(0.)	(0.078 77)	(0.)
12, X = Se	–350.221 38	13.00	0.085 31	13.07
C_s	(–350.938 19)	(19.76)	(0.076 61)	(19.02)
10, X = Te	–349.113 81	0.	0.085 85	0.
C_{2v}	(–349.828 62)	(0.)	(0.078 41)	(0.)
12, X = Te	–349.073 96	25.01	0.084 70	24.83
C_s	(–349.784 51)	(27.69)	(0.076 01)	(21.23)

[a] 1 au=627.5095 kcal/mol.
[b] Thermochemistry at temperature 298.15 K and pressure 1 atm.

cis-conformation **9** leading to the formation of the intramolecular O → chalcogen bond correspond to minima (the number of the negative Hessian eigenvalues at the corresponding stationary point is zero) on their potential energy surfaces (PES). The values of the total and relative energies of structures **9** and **11** are listed in Table 1. The optimized geometries of the isomers **9** and **11** are featured in Figs. 2–4.

It is worth noting that the results obtained at various levels of approximation are in good agreement with one another. All structures **9** are predicted to be planar with the O···chalcogen distances significantly shortened compared to respective van der Waals contacts (3.30 Å, 3.40 Å, and 3.60 Å for, respectively, O···S, O···Se, and O···Te). In accordance with the experimental data (Fig. 1), the degree of this shortening and, thus, the strength of the intramolecular coordination O → chalcogen bonds were found to be strongly affected by the electronegativity of the substituent R attached to the chalcogen atom. The O···chalcogen distance in **9** decreases by about 0.5 Å when substituent R = H is replaced by R = Cl. In compound **9** (X = Te, R = Cl) the calculated O···Te distance almost approaches the length of a normal covalent O—Te bond, 2.08–2.10 Å, whereas for the sulfur analogue (**9**: X = S, R = Cl) the difference between the calculated O···S contact and the length of a covalent S—O bond is substantially longer and reaches 0.5–0.9 Å depending on the level of approximation. This tendency is also in agreement with the experimental observations.

Not only the geometry calculated for the O···Te-R fragment but also that for the whole five-membered ring of compounds **9** reproduces the experimental data reasonably well. No direct comparisons are possible because no data are available on the compounds bearing no substituents at the carbon centers or containing a hydrogen atom attached to the chalcogen. However, there is good agreement of the corresponding calculated and experimentally determined bond lengths in the following pairs of compounds: **9** (X = Te, R = H) and **6a**, and **9** (X = Te, R = Cl) and **6b** (see Figs 1 and 4). Of special interest is the structure of the compound **9** (X = Te, R = Cl) with a very short O···Te contact and significantly equalized carbon–carbon bonds. A description of such a structure for the compound **6b** was given earlier (15) in terms of the resonance of several forms including those shown as **14a–d**.

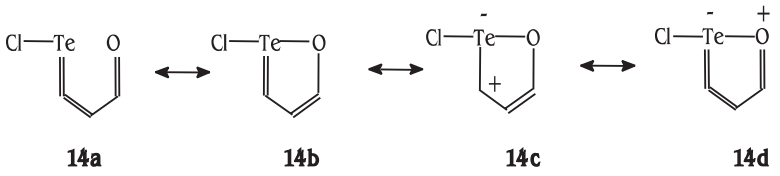

14a **14b** **14c** **14d**

A small contribution of the **14c** and **14d** resonance structures is demonstrated by a larger positive charge on the tellurium center in structures **9** as compared with that in its acyclic analogues **11**. For example, the Mulliken charge on the tellurium atom in **9** (X = Te, R = H) is equal to 0.546e and 0.491e, calculated by the RHF/LanL2DZ and MP2(fc)/LanL2DZ methods, respectively, whereas the same charge in the acyclic isomer **11** (X = Te, R = H) is, correspondingly, 0.491e and 0.390e.

Along with the geometrical characteristics of the compounds

© 1998 NRC Canada

Fig. 5. Structural parameters for 1,6-dioxa–6a-thia (selena and tellura) pentalenes **10** as calculated by the RHF/LanL2DZ, MP2(fc)/LanL2DZ (numbers in parentheses), and MP2(fc)/6-311++G** (number in square brackets) ab initio methods. Numbers in curved brackets are experimental data (28, 47). Bond lengths and angles are given in Å and degrees, respectively.

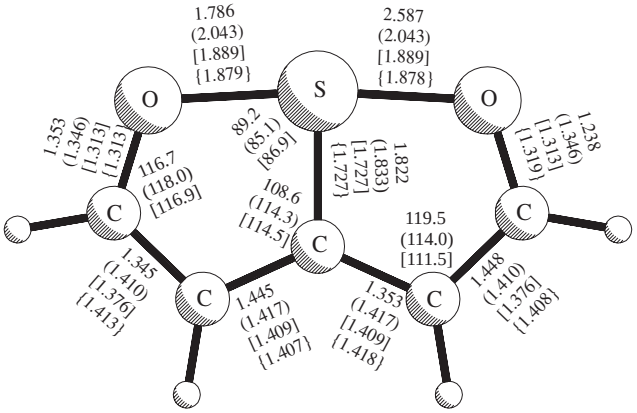

10 (X=S), C_{2v}

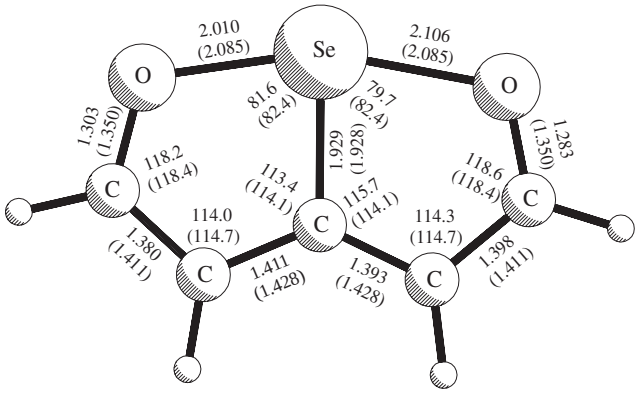

10 (X=Se), C_{2v}

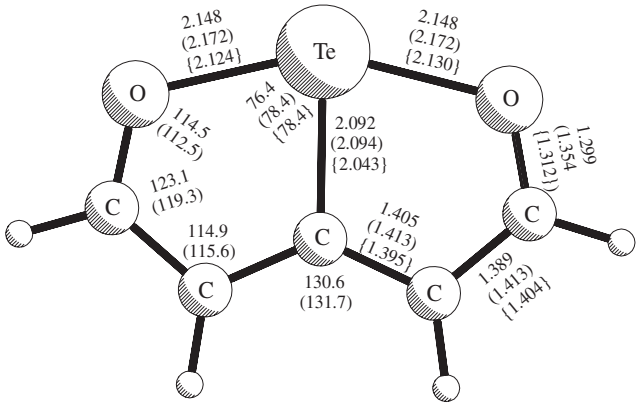

10 (X=S), C_{2v}

9, a clear manifestation of the existence and strength of the intramolecular O → chalcogen bonds is given by the values of

Fig. 6. Structural parameters for 3-formylmethylene-1,2-oxathiol (selenol and tellurol) -4,5-enes **12** as calculated by the RHF/LanL2DZ and MP2(fc)/LanL2DZ (numbers in parentheses) ab initio methods. Bond lengths and angles are given in Å and degrees, respectively.

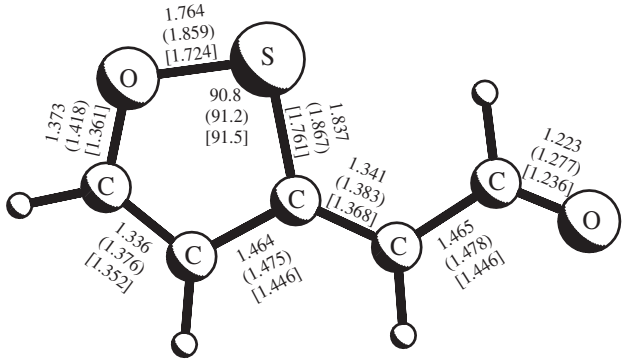

6, C_s (X=S)

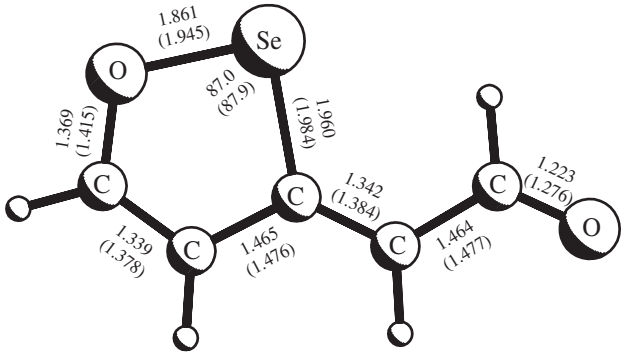

6, C_s (X=Se)

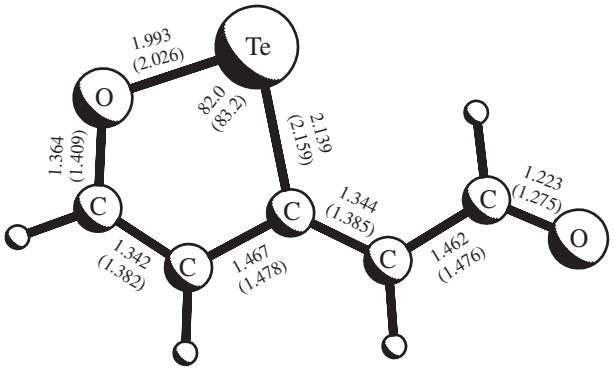

6, C_s (X=Te)

the relative energies of **9** with respect to their noncoordinated, free-of-strain, conformers **11**. As seen from the data of Table 1, in the case of β-thiovinylaldehydes (RX = HS) the

© 1998 NRC Canada

Table 3. Total (E_{tot}), relative (ΔE), and zero point vibration (ZPE) energies and relative enthalpies (ΔH) for the complexes **8** calculated by RHF/LanL2DZ, MP2(fc)/LanL2DZ (numbers in parentheses) and MP2(fc)/6-311++G** (numbers in square brackets) methods.

Structure	E_{tot} au [a]	ΔE [b] kcal/mol	ZPE au	ΔH [b,c] kcal/mol
13, X = SH_2	–124.866 46	–2.9	0.046 06	–1.5
	(–125.131 52)	(–3.3)	(0.042 97)	(–1.6)
	[–513.102 10]	[–7.9]	[0.044 55]	[–6.6]
13, X = SHCl	–138.969 13	–5.0	0.039 87	–1.0
	(–139.268 21)	(–5.4)	(0.037 01)	(–1.3)
	[–972.137 09]	[–7.8]	[0.038 38]	[–6.5]
13, X = SCl_2	–153.065 91	–4.4	0.033 01	–3.1.
	(–153.406 67)	(–5.7)	(0.030 51)	(–4.3.)
	[–1431.177 61]	[–7.5]	[0.030 96]	[–6.2]
13, X = SeH_2	–123.984 61	–1.7	0.044 34	–0.3
	(–124.243 95)	(–2.0)	(0.041 26)	(–0.7)
13, X = SeHCl	–138.108 65	–6.0	0.038 94	–4.5
	(–138.399 52)	(–6.7)	(0.036 13)	(–4.8)
13, X = $SeCl_2$	–152.226 46	–7.0	0.032 82	–5.6
	(–152.554 89)	(7.9)	(0.030 36)	(–6.4)
13, X = TeH_2	–122.814 04	–2.1	0.043 00	–0.7
	(–123.068 46)	(–2.5)	(0.039 92)	(–1.1)
13, X = TeHCl	–136.961 75	–7.7	0.038 12	–6.2.
	(–137.244 04)	(–7.7)	(0.035 52)	(–6.1)
13, X = TeClH	–136.957 00	–4.7	0.038 37	–3.3
	(–137.239 91)	(–5.1)	(0.035 44)	(–3.6)
13, X = $TeCl_2$	–151.104 73	–10.8	0.033 00	–9.3
	(–151.419 51)	(–10.6)	(0.030 50)	(–9.0)

[a] 1 au = 627.5095 kcal/mol.
[b] ΔE and ΔH are relative energies in respect to isolated molecules calculated without including BSSE.
[c] Thermochemistry at temperature 298.15 K and pressure 1 atm.

conformation **11** is preferable to **9** at all levels of approximation used. An attachment to the sulfur atom of the more electronegative substituent, chlorine, results in inversion of stability of the conformers. For the tellurium analogues, the conformers **9** with the intramolecular O → Te bond are predicted to be more stable than **11,** even for the case of R = H.

Accounting for the electron correlation energy leads to significant enhancement of the X···O hypervalent interactions in **9** and provides for additional delocalization of the electron density. Thus, correlation energy plays an important role in the stabilization of the complexes **9**. The difference between total energies of **9** and **11,** ΔE, can be considered as the energy of the X···O interaction. The value of ΔE for **9** (see Table 1) changes from repulsive for **9** (XR = SH) to slightly attractive for **9** (XR = TeH). At the same time, for the compounds **9** the X···O interaction energy remains strongly attractive, being increased (depending on the calculational method) from about 5 kcal/mol for XR = SCl to 10.5 kcal/mol for XR = SeCl and 16.5 kcal/mol for XR = TeCl. No experimental estimates of energies of the intramolecular O → chalcogen bonds are currently available. Attempts were made to assess the S···N (45) and Se···N (46) dissociation energies on the basis of dynamic NMR studies of the exchange processes that include dissociation of these bonds in one of the steps. Through detecting the energy barriers to mutual exchange of two benzylic protons in a series of 2-selenobenzylamines, **15**, the energies of the intramolecular N → Se bonds were found to lie in the range of 10.8 kcal/mol (R = SPh) to more than 18.8 kcal/mol (R = Cl, Br, OAc). Considering that N → chalcogen bonds are known to be stronger than O → chalcogen ones, the values ΔE and ΔH describing the strength of the O → Se bonds (Table 1) may be regarded as reasonable estimates.

15a **15b**

It appears that the pseudopotential basis set LanL2DZ underestimates the hypervalent bonding effects, as clearly seen from comparison of the geometries of **9** (X = S, R = H, Cl) calculated by the MP2(fc)/LanL2DZ and MP2(fc)/6-311++G(d,p) methods (see Fig. 2). For both structures the MP2(fc)/6-311++G(d,p) method predicts shorter S···O distances and S—H, S—Cl bond lengths than the MP2(fc)/LanL2DZ method. The same trend is revealed in calculations of the Se and Te analogues. This explains a small lengthening of the predicted O···Te distance and the Te—H, Te—Cl bonds (Fig. 4) compared to those experimentally determined for the compounds **6a** and **6b**.

1,6-Dioxa-6a-chalcogenopentalenes and their isomers

To elucidate the tendency of the chalcogen atoms to form

© 1998 NRC Canada

Fig. 7. Geometrical parameters of bimolecular complexes of formaldehyde with H_2Te, HTeCl, and $TeCl_2$ as calculated by the RHF/LanL2DZ and MP2(fc)/LanL2DZ (numbers in parentheses) ab initio methods. Bond lengths and angles are given in Å and degrees, respectively.

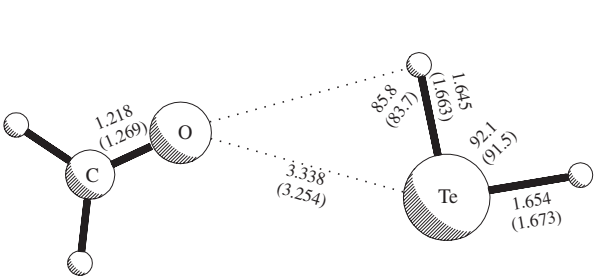

13 (X=TeH_2), C_s

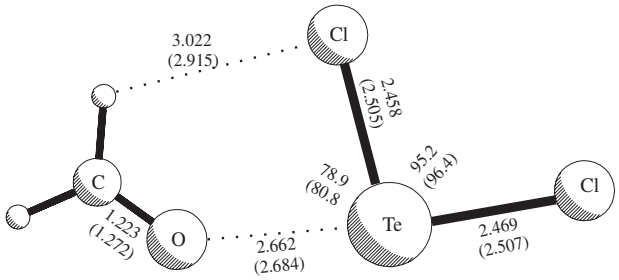

13 (X=$TeCl_2$), C_s

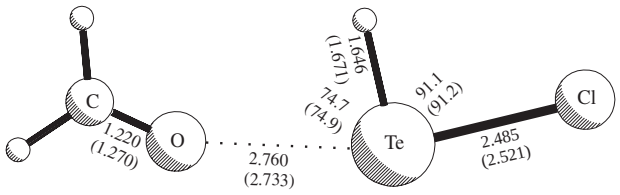

13 (X=TeHCl), C_s

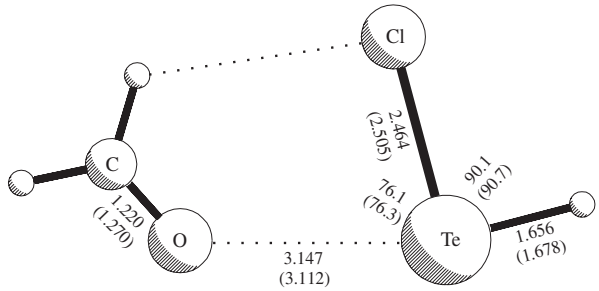

13 (X=TeClH), C_s

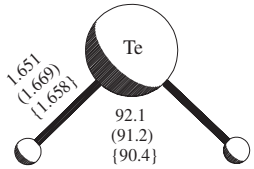

C_{2v}

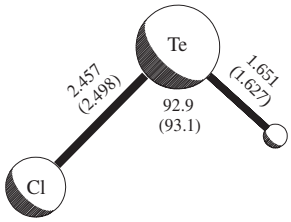

C_s

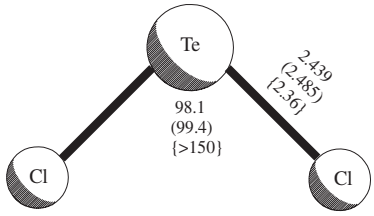

C_{2v}

hypervalent structures, we also calculated molecular structures and energies of the compounds **10** (X = S, Se, Te) and **12** (X = S, Se, Te). According to the ab initio calculations, all the structures **10** and **12** (X = S, Se, Te) correspond to minima on the relevant PES's. The values of total energies and optimized geometrical parameters of the structures **10** and **12** are presented in Table 2 and Figs. 5 and 6.

As seen from the data of Table 2, at all levels of approximation used, the bicyclic structures **10** are more stable than their isomers **12.** The trend to strengthening the intramolecular

© 1998 NRC Canada

Table 4. Total (E_{tot}), zero point vibration (ZPE) energies, and harmonic frequencies (ω_i) for chalcogen hydrides and chalcogen halogenides calculated by RHF/LanL2DZ, MP2(fc)/LanL2DZ (numbers in parentheses) and MP2(fc)/6-311++G** (numbers in square brackets) methods.

Structure	E_{tot} au [a]	ZPE au [a]	$\omega_1(A_1)$ cm^{-1}	$\omega_2(A_1)$ cm^{-1}	$\omega_3(B_2)$ cm^{-1}
SH_2	–11.031 26	0.015 41	1312.5	2704.9	2746.9
C_{2v}	(–11.083 58)	(0.014 61)	(1232.6)	(2564.9)	(2614.3)
	[–398.847 72]	[0.015 69]	[1233.3]	[2816.8]	[2836.0]
Exp. [b]			1182.7	2614.6	2625.0
SHCl	–25.130 62	0.009 32	478.7	909.7	2701.1
C_s	(–25.216 97)	(0.008 62)	(432.1)	(816.6)	(2533.9)
	[–857.892 83]	[0.009 74]	[532.2]	[938.2]	[2876.4]
SCl_2	–39.228 38	0.002 57	175.5	466.3	484.3
C_{2v}	(–39.354 84)	(0.002 24)	(150.1)	(409.8)	(423.5)
	[–1316.923 93]	[0.002 85]	[207.5]	[520.2]	[520.8]
Exp. [b]			205.0	525.5	528.0
SeH_2	10.151 37	0.013 92	1182.6	2439.8	2486.7
C_{2v}	(–10.198 08)	(0.013 21)	(1110.0)	(2318.9)	(2370.8)
Exp. [b]			1034.2	2344.5	2357.8
SeHCl	–24.268 59	0.008 31	390.8	813.4	2441.3
C_s	(–24.246 80)	(0.007 73)	(357.1)	(737.1)	(2299.4)
$SeCl_2$	–38.384 79	0.002 11	145.5	388.9	392.4
C_{2v}	(–38.499 70)	(0.001 88)	(126.3)	(348.4)	(351.0)
Exp [b]			153.0	377.0	415.0
TeH_2	–8.980 19	0.012 39	1016.0	2204.2	2217.2
C_{2v}	(–9.021 78)	(0.011 74)	(942.3)	(2094.9)	(2116.6)
Exp. [b]			860–765	2000	2000
TeClH	–23.118 95	0.007 42	350.6	696.8	2209.6
C_s	(–23.189 17)	(0.006 94)	(323.8)	(636.8)	(2086.5)
$TeCl_2$	–37.256 96	0.001 89	121.3	353.7	356.8
C_{2v}	(–37.359 91)	(0.001 72)	(107.6)	(323.1)	(324.0)
Exp. [b]			125.	377.	—

[a] 1 au = 627.5095 kcal/mol.

[b] Experimental data are taken from ref. 52.

O → X bonds when going from sulfur to tellurium is clearly expressed by the values of ΔE. An important structural feature of compounds **10** is further significant shortening of the O···chalcogen contacts, even compared to those occurring in their monocyclic analogues **9** with the electronegative substituents, R = Cl. For the dioxatellurapentalene **10** (X = Te), the length of this contact is almost equal to that of a normal covalent O → Te bond. For the whole set of the compounds **10** (X = S, Se, Te), the calculations in accord with the experimental data available (28, 47) predict equal bond lengths of both the O—X (X = S, Se, Te) bonds and the C_{2v} symmetry of dioxachalcogenopentalenes. Realization of the symmetrical structures in all of the compounds **10** (X = S, Se, Te) may be explained in terms of aromatic stabilization due to their 10π-electron systems. The only exception to this result is found in the RHF/LanL2DZ calculations of dioxathiapentalene **10** (X = S), which is predicted to be a monocyclic C_s structure with T-shaped bond configuration at the chalcogen atom. It should be noted that this result was obtained when using the lowest applied level of approximation and for the compound in the series with the weakest intramolecular O···X interaction.

As for the type **9** compounds, the use of the pseudopotential basis set LanL2DZ leads to underestimation of the hypervalent effects. This is seen in a comparison of the MP2(fc)/LanL2DZ and MP2(fc)/6-311++G(d,p) calculations (Fig. 5). The MP2(fc)/LanL2DZ method predicts all bonds to be longer than those obtained by the MP2(fc)/6-311++G(d,p) method, whose predictions on bond lengths and valence angles are in excellent agreement with the experimental data available on derivatives of dioxathiapentalenes (9, 47). The same tendency may, therefore, be expected for the Se and Te analogues **10** (X = Se, Te) for which the MP2(fc)/LanL2DZ method slightly overestimates bond lengths. As seen from the data of Table 2, accounting for the correlation energy results in additional stabilization of the delocalized structure with the hypervalent chalcogen centers. The difference in energy (ΔE) between total energies of the bicyclic **10** and monocyclic **12** structures, given in Table 2 according to the MP2(fc)/LanL2DZ calculations, are 12.1, 20.0, and 27.7 kcal/mol for X = S, Se, and Te, respectively. These should be considered as the lowest limits of the O → X energies. As follows from the comparison of results obtained by the MP2(fc)/LanL2DZ and MP2(fc)/6-311++G(d,p) methods for **10** (X = S), the former method predicts the S—O bond energy to be nearly 9 kcal/mol lower than the latter. Assuming that the same correction may be applied to the assessment of the O → Se and O → Te energies, these should amount to approximately 30 and 38 kcal/mol, respectively.

The Mulliken X—O bond populations in **10** (X = S, Se, Te)

© 1998 NRC Canada

calculated by the MP2/LanL2DZ method are equal to 0.063, 0.068, and 0.072, respectively. These values are three times larger than the corresponding values for compounds **9**. They reflect much stronger O···X (X = S, Se, Te) bonding in dioxachalcogenopentalenes. The χ values (0.81, 0.88, and 0.94) as well as the Pauling bond orders, n (48) (0.51, 0.65, and 0.81), as calculated by eq. [2]

$$[2] \quad d_{AB} = d(1) - 0.6 \log n$$

where $d(1)$ is the single bond distance, i.e., $(r_A + r_B)$, and d_{AB} is the O—X bond length in **10** (X = S, Se, Te) obtained in the MP2/LanL2DZ calculations, reflect very well the same trend in the strength of these bonds.

Bimolecular complexes with intermolecular O···chalcogen bonds

The tendency of chalcogen atoms towards attractive intermolecular donor–acceptor O → chalcogen interactions is manifested by calculations of molecular structures and energies of the bimolecular complexes **13** (X = S, Se, Te) formed by the parent carbonyl compound with dicoordinated chalcogen hydrides (R_1 = H; R_2 = H, Cl) or chlorides ($R_1 = R_2$ = Cl). According to the ab initio calculations all the dimers **13** correspond to minima on the relevant PES's. The total energies of the bimolecular complexes **13** (X = S, Se, Te) are listed in Table 3. Figure 7 displays the optimized geometrical parameters for the complexes **13** (X = Te).

Predicted geometrical parameters and harmonic frequencies for chalcogen hydrides XHR (R = H, Cl) or chlorides XCl_2 (Table 4 and Fig. 7) are in good agreement with the available experimental data.

The principal trends characteristic of intramolecular O → chalcogen coordination bonds revealed by calculations for compounds **9** and **11** hold true also for the case of the intermolecular interaction. The energy of the donor–acceptor intermolecular interaction increases approximately by 1.5–2 times when the correlation energy is taken into account. The stabilization energy, ΔE, for the complexes with chalcogen hydrides ($R_1 = R_2 = H$) is smaller than that for the complexes **13** in which one or both hydrogen atoms are substituted by the more electronegative chlorine. Worth noting is that the isomers **13** (R_1 = H, R_2 = Cl) with an (approximately) linear arrangement of the O···X-Cl fragment are preferable to their isomers in which the less electronegative hydrogen atom takes an axial position. This effect is particularly noticeable in the case of Te complexes for which the first isomer is about 3 kcal/mol more stable than **13** (X = TeClH) (see Table 3 and Fig. 7). As for the case of the intramolecular O → chalcogen interactions, the complexation energy monotonically increases in the order X = S, Se, Te (Table 3). To the authors' knowledge, no experimental data on the type **13** bimolecular complexes are currently available. However, stabilization of the bimolecular complexes $YF\cdots XH_2$ (Y = F, Cl; X = N, O, S) due to a similar type of weak Y···X interactions has recently been described (49–51). The results of the calculations presented suggest that the stability of the complexes **13** is sufficient for their possible experimental observation.

Conclusions

The ab initio calculations carried out showed that there exists a strong intra- and intermolecular donor–acceptor O → chalcogen interaction that stabilizes the hypervalent T-shaped bond configuration at the chalcogen atom. This interaction in chalcogen-containing compounds increases in the order S, Se, Te and with increasing electronegativity of a substituent attached to the chalcogen center. The ab initio calculations performed predict the existence of rather stable bimolecular complexes $H_2CO\cdots XR_1R_2$ (X = S, Se, Te; R_1, R_2 = H, Cl) with the complexation energy comparable to the energy of strong hydrogen bonds.

Acknowledgement

This work was supported by the Russian Foundation for Basic Research (grants 96-15-97476 and 98-03-33169a) and the Ministry of General and Professional Education of the Russian Federation (grant 9-288).

References

1. G.A. Jeffrey and W. Saenger. Hydrogen bonding in biological structures. Springer-Verlag, Berlin. 1991.
2. R. Desiraju. Acc. Chem. Res. **24**, 290 (1991).
3. C.L. Perrin and J.B. Nielsen. Annu. Rev. Phys. Chem. **48**, 511 (1997).
4. A.J. Kirby. Angew. Chem. Int. Ed. Engl. **35**, 707 (1996); Adv. Phys. Org. Chem. **29**, 87 (1994).
5. S. Sheiner. Acc. Chem. Res. **18**, 174 (1985); **27**, 402 (1994).
6. M.S. Gordon and J.H. Jensen. Acc. Chem. Res. **29**, 536 (1996).
7. G.R. Newcome, W.E. Puckett, and G.E. Kiefer. Chem. Ber. **86**, 451 (1986).
8. J. Omae. Coord. Chem. Rev. **83**, 137 (1988).
9. J.T.B.H. Jastrzebski and G. Van Vioten. Adv. Organomet. Chem. **35**, 241 (1993).
10. G.J. Gruter, G.P.M. van Kink, O.S. Akkerman, and F. Bickelhaupt. Chem. Rev. **95**, 2405 (1995).
11. V.I. Minkin, I.D. Sadekov, A.A. Maksimenko, O.E. Kompan, and Yu.T. Struchkov. J. Organomet. Chem. **402**, 331 (1991).
12. N. Sudha and H. Singh. Coord. Chem. Rev. **135/136**, 469 (1994).
13. W.R. McWhinnie, I.D. Sadekov, and V.I. Minkin. Sulfur Rep. **18**, 295 (1996).
14. V.R. Pedireddi, D.S. Goud, D.C. Craig, A.D. Rae, and G. Desiraju. J. Chem. Soc. Perkin Trans. 2, 2353 (1994).
15. M.R. Detty, B.J. Murray, D.L. Smith, and N. Zumbulyadis. J. Am. Chem. Soc. **105**, 875 (1983).
16. G. Angyan, R.A. Poirier, A. Kucsman, and I.G. Csizmadia. J. Am. Chem. Soc. **109**, 2237 (1987).
17. D. Szabo, I. Kapovits, G. Argay, M. Czugler, A. Kalman, and T. Koritsauszky. J. Chem. Soc. Perkin Trans. 2, 1045 (1997).
18. D.H.R. Barton, M.B. Hall, Z. Lin, S.I. Parekh, and J. Reibeuspies. J. Am. Chem. Soc. **115**, 5056 (1993).
19. I.D. Sadekov, A.A. Maksimenko, and V.I. Minkin. Sulfur Rep. **9**, 359 (1990).
20. I.D. Sadekov, and V.I. Minkin. Usp. Khim. **64**, 527 (1995); Russ. Chem. Rev. (Engl.), **64**, 491 (1995).
21. F.T. Burling and B.M. Goldstein. J.Am.Chem.Soc. **114**, 2313 (1992).
22. A. Kucsman, I. Kapovits, M. Czugler, L. Parkanui, and A. Kalman. J. Mol. Struct. (Theochem), **198**, 339 (1989).
23. I. Hargittai and B. Rozsondai. *In* The chemistry of organic selenium and tellurium compounds. Vol. 1. *Edited by* S. Patai and Z. Rappoport. J.Wiley, New York. 1986. p. 157.
24. W.W. Roesky, K.L. Weber, U. Seseke, W. Pinter, M. Noltemeyer,W. Clegg, and G.M. Sheldrick. J.Chem.Soc. Dalton Trans. 565 (1985).

© 1998 NRC Canada

25. V.I. Minkin, I.D. Sadekov, B.B. Rivkin, A.V. Zakharov, V.L. Nivorozhkin, O.E. Kompan, and Yu.T. Struchkov. J.O rganomet. Chem. **536–537**, 233 (1997).
26. P.I. Dupont, O. Dideberg, and J. Lamotte. Acta Crystallogr. Sect. B: Struct. Crystallogr. Cryst. Chem. **B35**, 849 (1979).
27. I.D. Sadekov, A.A. Ladatko, V.L. Nivorozhkin, O.E. Kompan, Yu.T. Struchkov, and V.I. Minkin. Zh. Obshch. Khim. **60**, 2764 (1990).
28. M.R. Detty and H.R. Luss. J. Org. Chem. **48**, 5149 (1983).
29. A. Bondi. J. Phys. Chem. **68**, 441 (1964).
30. N.M. Adcock. Adv. Inorg. Chem. Radiochem. **15**, 1 (1972).
31. H.-B. Burgi and J. Dunitz. J. Am. Chem. Soc. **109**, 2924 (1987).
32. A. Masunov and P.M. Zorky. Zh. Struct. Khim. **33**, 105 (1992).
33. A.E. Reed and P.v.R. Schleyer. J. Am. Chem. Soc. **112**, 1434 (1990).
34. A.E. Reed, L.A. Curtiss, and F. Weinhold. Chem. Rev. **88**, 899 (1988).
35. M. Sundberg, R. Uggla, T. Laitalainen, and J. Bergman. J. Chem. Soc. Dalton Trans. 3279 (1994).
36. J.B. Foresman and A. Frisch. Exploring chemistry with electronic structure methods. Gaussian, Inc., Pittsburg, Pa. 1996. pp. 302.
37. M.J. Frisch, G.W. Trucks, H.B. Schlegel, P.M.W. Gill, B.G. Johnson, M.A. Robb, J.R. Cheeseman, T.A. Keith, G.A. Petersson, J.A. Montgomery, K. Raghavachcri, M.A. Al-Laham, V.G. Zakrzewski, J.V. Ortiz, J.B. Foresman, C.Y. Peng, P.Y. Ayala, W. Chen, M.W. Wong, J.L. Andres, E.S. Replogle, R. Gomperts, R.L. Martin, D.J. Fox, J.S. Binkley, D.J. Defrees, J. Baker, J.P. Stewart, M. Head-Gordon, C. Gonzalez, and J.A. Pople. Gaussian-94, Revision B.3. Gaussian, Inc., Pittsburgh, Pa. 1995.
38. M.W. Schmidt, K.K. Baldridge, J.A. Boatz, S.T. Elbert, M.S. Gordon, J.H. Jensen, S. Koseki, N. Matsunaga, K.A. Nguyen, S.J. Su, T.L. Windus, M. Dupuis, and J.A. Montggomery. J. Comput. Chem. **14**, 1347 (1993). (Package of ab initio programs, "GAMESS," Version 1996).
39. R. Cammi, R. Bonaccorsi, and J. Tomasi. Theor. Chim. Acta, **68**, 271 (1985).
40. F.B. v. Duijnevelt, J.G.C.M. v. Dijneveld-van de Rijdt, and J.H. v. Lenthe. Chem. Rev. **94**, 1873 (1994).
41. F.F. Muguet and G.W. Robinson. J. Chem. Phys. **102**, 3643 (1995).
42. F. Jensen. Chem. Phys. Lett. **261**, 633 (1996).
43. D.B. Cook, T.L. Sordo, and J.A. Sordo. Chem. Commun. 185 (1990).
44. S. Simon, M. Duran, and J.J. Dannenberg. J. Chem. Phys. **105**, 11024 (1997), and references cited therein.
45. K.-Y. Akiba. Bull.Chem.Soc.Jpn. **62**, 479 (1989).
46. M. Iwaoka and S. Tomoda. J. Am. Chem. Soc. **118**, 8077 (1996).
47. R. Gleiter and R. Gygax. Top. Curr. Chem. **63**, 49 (1976).
48. L. Pauling. J. Am. Chem. Soc. **69**, 542 (1947).
49. A.G. Legon and D.J. Millen. *In* Principles of molecular recognition. *Edited by* A.D. Buckingham, A.C. Legon, and S.M. Roberts. Blackie Academic and Professional, London. 1993. pp. 16–42.
50. A.C. Legon. Chem. Commun. 109 (1996).
51. H. Bürger. Angew. Chem. Int. Ed. Engl. **36**, 718 (1997).
52. K.S. Krasnov (*Editor*). Molecular constants of inorganic compounds. Khimia, Leningrad. 1979.

© 1998 NRC Canada

The reaction of *S*-nitrosothiols with thiols at high thiol concentration

Andrew P. Dicks, E. Li, Andrew P. Munro, Helen R. Swift, and D. Lyn H. Williams

Abstract: Reactions of *S*-nitrosothiols (RSNO) with their corresponding thiols (RSH) present in a large excess (>20-fold) proceed readily to give the disulfide. Ammonia is formed together with some nitrite anion, and these constitute >90% of the "nitrogen" products. This is in marked contrast with the reaction at low thiol concentration, where nitric oxide is the major initial "nitrogen" product, which is rapidly converted in the presence of oxygen in water to nitrite anion. Also in marked contrast to the "low thiol concentration" reaction, the reaction at high thiol concentration is not affected by added Cu^{2+}, nor by the metal-ion scavenger EDTA. Kinetically all reactions were excellent first-order processes, and the reactions were also strictly first order in thiol concentration. A large range of nitrosothiols were studied and the generality of the reaction established. Some reactions of RSNO with other thiols (R′SH) were examined and the results readily interpreted in terms of a prior rapid equilibrium transnitrosation. The pH dependence for the reaction of *S*-nitrosocysteine with cysteine clearly showed that the reactive species is the cysteine thiolate anion. The results are discussed along with those of two other recent reports of these reactions, in terms of thiolate attack initially at the nitroso nitrogen atom, and subsequently at sulfur atoms, eliminating RSSR and yielding hydroxylamine, which is rapidly reduced by thiolate ion to ammonia. The results are also discussed in connection with the release of NO from nitrosothiols and with the important biological consequences, both for the in vivo reactions of NO and for the potential of nitrosothiols as NO-releasing drugs for medical use.

Key words: *S*-nitrosothiols, thiols, nitric oxide, ammonia, nitrous oxide.

Résumé : Les réactions de *S*-nitrosothiols (RSNO) avec un grand excès (>20 fois) des thiols correspondants (RSH) se produisent facilement et elles conduisent au disulfure. Il y a formation d'ammoniac ainsi que de faibles quantités de l'anion nitrite qui forment tous ensemble plus de 90% des produits «azotés.» Ce résultat est en opposition avec ce qui se passe lors de la réaction à faible concentration de thiol, alors que l'oxyde nitrique, le produit «azoté» principal, se transforme en anion nitrite en présence de l'oxygène présent dans l'eau. Le fait que la réaction à haute concentration de thiol ne soit pas affectée par la présence de Cu^{2+} ou d'EDTA, piège pour les ions métalliques, est une autre différence importante par rapport à la réaction à faible concentration de thiol. On a examiné un large éventail de nitrosothiols et on a démontré la généralité de la réaction. On a aussi examiné quelques réactions de RSNO avec d'autres thiols (R′SH) et on peut facilement interpréter les résultats en fonction d'une réaction d'équilibre rapide de transnitrosation. Le fait que la réaction de la *S*-nitrosocystéine sur la cystéine dépende du pH montre clairement que l'espèce réactive est l'anion thiolate de la cystéine. On discute des résultats, ainsi que ceux de deux rapports récents sur ces réactions, en fonction d'une attaque initiale de l'ion thiolate sur l'atome d'azote du nitroso et d'une attaque ultérieure au niveau des atomes de soufre conduisant à une élimination de RSSR avec formation d'hydroxylamine qui est rapidement réduit par l'ion thiolate en ammoniac. On discute aussi des résultats en relation avec l'élimination de NO à partir des nitrosothiols et de leurs conséquences biologiques importantes qui sont toutes les deux importantes pour les réactions in vivo du NO ainsi que pour le potentiel des nitrosothiols à agir comme médicaments dégageant du NO à des fins médicales.

Mots clés : *S*-nitrosothiols, thiols, oxyde nitrique, ammoniac, oxyde nitreux.

[Traduit par la rédaction]

Introduction

In recent years one of the principal discoveries that has excited biologists and other scientists has been the realisation that we (and other animals) synthesize nitric oxide (NO) in vivo from the amino acid L-arginine, and that NO is principally involved in the control of a number of our bodily functions, including vasodilation (1). These findings have generated a massive research effort worldwide, and there a number of review articles available (2). As part of the findings it was found that the drug widely used to treat angina and other circulatory problems, namely, glyceryl trinitrate (GTN), breaks down in vivo to give NO, which effects vasodilation, and hence gives relief to the patient (3). It is interesting to note that GTN had been used for over a hundred years simply on the basis of observation of the medical patterns of the work force in Nobel's factories, which

Received December 15, 1997.

This paper is dedicated to Professor Erwin Buncel in recognition of his contributions to Canadian chemistry.

A.P. Dicks, E. Li, A.P. Munro, H.R. Swift, and D.L.H. Williams.[1] Department of Chemistry, University of Durham, South Road, Durham DH1 3LE, U.K.

[1] Author to whom correspondence may be addressed. Telephone: (44) 191 374 3125. Fax: (44) 191 384 4737. E-mail: D.L.H.Williams@durham.ac.uk

© 1998 NRC Canada

were producing dynamite. GTN is not, however, a totally satisfactory drug, for although it is quick-acting, it is also "short-acting," and in some patients a tolerance to it is generated. Consequently there has been a major research effort directed at the production of an alternative to GTN. One group of compounds being closely looked at in this connection are *S*-nitrosothiols RSNO, i.e., the sulfur analogues of alkyl nitrites. It is known that *S*-nitrosothiols (sometimes called thionitrites) are readily formed from nitrous acid and thiols (4), and decompose thermally (5) and photochemically (6) generating initially NO, eq. [1]. In the presence of oxygen NO can react further.

[1] $2RSNO \rightarrow RSSR + 2NO$ ($h\nu$ or Δ)

We have recently (7) examined the reactions of many RSNO compounds (sometimes generated in situ by thiol nitrosation) in water, mostly at pH 7.4, and have found that reaction is brought about by catalytic amounts of Cu^+, formed by thiolate reduction of Cu^{2+}, present as an impurity (at ~ 10^{-6} M level), or specifically added; see eqs. [2] and [3].Thiolate ion is usually

[2] $2Cu^{2+} + 2RS^- = 2Cu^+ + RSSR$

[3] $RSNO + Cu^+ = RS^- + Cu^{2+} + NO$

[4] $4NO + 4OH^- + O_2 = 4NO_2^- + 2H_2O$

present as a low-level impurity, and also is present from the reversibility of RSNO formation (8). In water in the presence of oxygen at pH 7.4, NO is quantitatively converted to nitrite anion, eq. [4] (9, 10). From a biological point of view it is interesting to note that Cu^+ can also be generated (by thiolate reduction) from Cu^{2+} sources in which the copper is bound to amino acids, peptides, or proteins (11). Further, the copper reduction can also be brought about by other reducing agents, notably ascorbic acid (12). Reaction is virtually halted in the presence of the general metal-ion chelator EDTA or the specific Cu^+ chelator neocuproine, as the thermal reaction is generally very slow at 25°C. Increasing the thiol concentration in some cases promotes reaction by increasing the rate of Cu^+ formation, whilst in other cases (such as with *S*-nitroso penicillamine and added penicillamine) reaction is retarded when the thiol acts as a metal-ion chelator (12).

More recently three reports have shown that a different reaction of *S*-nitrosothiols occurs in the presence of higher concentrations of added thiols (typically in 10–100-fold excess over RSNO). Komiyama and Fujimori (13) reported the kinetics of the reaction of cysteine with *S*-nitroso cysteine under conditions where metal ions were carefully removed, and from initial rate measurements established the rate equation [5]. The first term represents the thermal reaction,

[5] $Rate = k_1[RSNO] + k_2[RSNO]\,[RSH]$

and the value of k_1 confirms the belief that the thermal reaction is negligibly slow at 25 or 37°C. Swift (14) independently found the same rate equation for the reactions of *S*-nitrosoglutathione (GSNO), *S*-nitroso-*N*-acetylcysteine, and *S*-nitrosocaptopril with their corresponding thiols, and showed that the rate constants were independent of added Cu^{2+} and also of added EDTA. In a detailed product study of the reaction of GSNO with glutathione (GSH), Singh et al.(15) showed that, apart from the disulfide, the end products were ammonia, nitrite anion, and nitrous oxide. A scheme was put forward to explain the product distribution, based on the formation of an *N*-hydroxysulfenamide and of radical intermediates.

Because of the intense interest in NO formation from RSNO species, we believed it important to establish details of the "high concentration of thiol" reaction, particularly given that in vivo it is likely that GSNO is likely to encounter intracellularly a large concentration excess of GSH.

Experimental section

Materials

All of the *S*-nitrosothiols (except GSNO) were generated in solution by nitrosation of the corresponding thiols in mildly acidic aqueous solution, immediately before use in the kinetic experiments. All (except GSNO) are too unstable to isolate and characterize in the pure state. Their concentration is taken to be the concentration of the thiol and sodium nitrite used (equimolar). This procedure works well when checked for the stable species GSNO, comparing spectra of solutions made up in this way with those in which the solid is dissolved in the buffer. GSNO was prepared by the literature method described by Hart (16). Thiols, buffer components, and all other materials were of the highest purity grade available, and were used as such. Some of the anaerobic experiments were carried out on N_2-purged solutions, whilst others used the glucose/glucose oxidase method (17). The two methods gave results that were in acceptable agreement. Nitrite anion was determined by the well-known Griess method (18). Ammonia was determined quantitatively with a standard diagnostic kit (Sigma) using the method of van Anken and Shiporst (19), based on the reductive amination of oxoglutarate by the enzymes glutamate dehydrogenase and NADPH. Reaction mixtures were left for ~10 h before the analyses were carried out, to ensure, as nearly as possible, complete decomposition of the *S*-nitrosothiol.

Kinetics

All rate measurements were carried out in water at 25°C mostly in phosphate buffer at pH 7.4. Reactions were followed spectrophotometrically at ~ 340 nm, noting the disappearence of the absorbance due to the RSNO. In all experiments the thiol was in at least a 20-fold excess over the nitrosothiol. Excellent first-order behaviour occurred throughout. The data were collected directly from the spectrophotometer to a PC and a kinetics program used to obtain values of the first-order rate constants k_0. Values of k_0 were reproducible to better than 5%.

Results

Kinetics

Our original work (14) looked at the reactions of GSNO, *S*-nitroso-*N*-acetylcysteine (SNAC), and *S*-nitrosocaptopril with their corresponding thiols. We have now extended the range of RSNO compounds in an attempt to establish the generality of the reaction. In all cases there was excellent first-order behaviour in the individual kinetic experiments when $[RSH]_0 >> [RSNO]_0$, and plots of the first-order rate constants vs. [RSH] were linear with, in many cases, a small positive intercept at [RSH] = 0 representing the thermal reaction. From the slopes of the lines, values of k_2 (eq. [5]) were easily obtained. These are presented in Table 1 for a range of RSNO structures. The

© 1998 NRC Canada

Table 1. Values of k_2 (from eq. [5]) for the reaction of RSH with RSNO.

RSH	$k_2/10^{-3}$ dm^3 mol^{-1} s^{-1} [a]
Penicillamine	262, 259[b]
2-Mercaptoimidazole	115
1-Thioglycerol	39.1, 38.9[c]
2-Mercaptoethane sulfonic acid	30.6
Captopril	27.3, 22.7[b]
Cysteamine	11.9
Cysteine	10.7, 10.9,[b] 11.7[c]
Cysteine ethyl ester	8.0
Glutathione	5.5, 4.8,[b] 5.1[b]
Mercaptosuccinic acid	0.6
Dithiothreitol	273
Dithioerythritol	135

[a] Rate constants generally were subject to a standard error of less than 5%.
[b] Duplicate measurements.
[c] Reactions carried out anaerobically.

Table 2. First-order rate constants (k_0) for the reaction of GSNO (5×10^{-4} mol dm^{-3}) with glutathione (1.5×10^{-2} mol dm^{-3}) as a function of added Cu^{2+}.

[Added Cu^{2+}]/10^{-5} mol dm^{-3}	$k_0/10^{-4}$ s^{-1} [a]
0	2.47
0.75	2.38
1.5	2.37
7.5	2.27
15	2.41

[a] Standard error less than 3%.

reaction is clearly quite general. Rate constants are independent of both added Cu^{2+} and added EDTA as shown in Tables 2 and 3. Further results (Table 4) were obtained for the reaction of *S*-nitrosocysteine (SNC). The contrast with the effect of metal ions when the reaction is carried out at low thiol concentration is very marked. For example, the addition of EDTA virtually stops reaction under these conditions completely, as shown in Fig. 1, which gives the absorbance–time plots for the decomposition of GSNO (5×10^{-4} M) in the presence of GSH (5×10^{-5} M), (*a*) without added EDTA and (*b*) with added EDTA (1×10^{-4} M). This behaviour is quite general for RSNO decomposition with no added RSH, or at low concentration of added RSH.

Some experiments were carried out using a thiol different from the parent thiol, i.e., for the reaction of RSNO with a large excess of R′SH. Results for two such pairs are given in Table 5.

In one case the effect of pH on reactivity was examined. Figure 2 shows the variation of k_2 for the reaction of SNC with cysteine in the pH range 1–14. The shape of the curve clearly shows that the reacting species is the thiolate anion. In two examples studied, there was no significant difference in the measured second-order rate constants when reaction was carried out anaerobically (see Table 1).

Product analyses

Nitrite anion was determined by the Griess method in the final reaction products of the decomposition of SNC as a function

Table 3. First-order rate constants (k_0) for the reaction of SNAC (5×10^{-4} mol dm^{-3}) with *N*-acetyl cysteine (2×10^{-2} mol dm^{-3}) as a function of added EDTA.

[EDTA] /10^{-4} mol dm^{-3}	$k_0/10^{-4}$ s^{-1} [a]
0	2.31
0.4	2.37
2.0	2.37
5.0	2.35
10.0	2.25

[a] Standard error less than 3%.

Table 4. First-order rate constants (k_0) for the reaction of *S*-nitrosocysteine, SNC, (1×10^{-3} mol dm^{-3}) with cysteine in the presence and absence of EDTA (1×10^{-4} mol dm^{-3}).

	$k_0/10^{-4}$ s^{-1} [a]	
[Cysteine]/mol dm^{-3}	with EDTA	without EDTA
0.01	1.19	1.04
0.025	2.58	2.66
0.05	5.40	4.97
0.075	8.27	7.94
0.10	11.4	11.0

[a] Standard error less than 2%.

Fig. 1. Absorbance–time plots for the reaction of GSNO (5×10^{-4} mol dm^{-3}) with glutathione (5×10^{-5} mol dm^{-3}) and Cu^{2+} (5×10^{-5} mol dm^{-3}), (*a*) without added EDTA, and (*b*) with added EDTA (1×10^{-4} mol dm^{-3}).

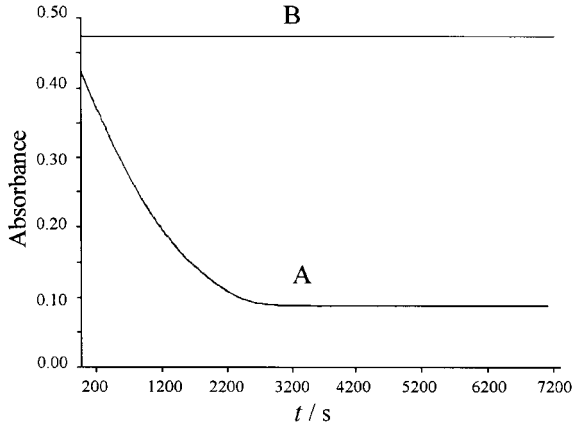

of added cysteine. The results are in Table 6. Without added cysteine we find 91% nitrite, i.e., almost quantitative formation. This confirms what we and others have observed on a number of occasions, namely that the Cu^+-promoted reaction is dominant, generating NO, which is rapidly converted to NO_2^- in aqueous aerated solution. However, as the concentration of cysteine is increased, the NO_2^- yield drops sharply, approaching 5% at high cysteine concentration.

Following the important and unexpected finding by Singh et al. (15) that ammonia was a major product in the reaction of GSNO with GSH, we analysed the reaction products for ammonia. The results for the reaction of SNC with cysteine are also given in Table 6. It is clear that ammonia is formed at the expense of nitrite ion and that the reaction leading to ammonia is totally dominant when the concentration of cysteine

© 1998 NRC Canada

Table 5. Values of k_2 (eq. [5]) for the "mixed" reaction RSNO + R′SH.

RSNO–R′SH	$k_2/10^{-4}$ dm^3 mol^{-1}s^{-1} [a]
S-Nitrosopenicillamine–penicillamine	2590
1-Thioglycerol SNO – 1-thioglycerol	389
S-Nitrosopenicillamine–1-thioglycerol	285
1-Thioglycerol SNO – penicillamine	1312

[a] Standard error less than 3%.

is greater than ~0.05 M. The product total $[NO_2^-]$ + $[NH_3]$ accounts for ~90% of the "nitrogen" product. Similar product distributions were obtained for the reactions of SNAC, and *S*-nitrosothioglycerol with their respective thiols. These analyses were repeated for the reaction of SNC with cysteine under anaerobic conditions. The nitrite analyses were approximately unchanged, within the experimental error, but the ammonia yield was reduced somewhat compared with the results obtained aerobically, rising only to 70% of the theoretical maximum, as compared with 85%.

We found that in some cases the disulfide product precipitated from solution at the end of the reaction, and was identified by its nmr or ir spectrum. In other cases (notably with the GSNO reaction) we identified the disulfide by addition of Cu^{2+} at the end of the reaction and observed the characteristic uv spectrum of the Cu^{2+} complex (20). Spectral measurements indicated that reaction was reasonably(>90%) quantitative.

Discussion

We have confirmed the observation by Singh et al. (15) that at reasonably high thiol concentrations there is a reaction between thiols and *S*-nitrosothiols (observed also kinetically by Komiyama and Fujimori (13)), leading to the disulfide formation, which is not catalysed by Cu^+ or any other metal ion, but which is first order in both reactants, and leads principally to the formation of ammonia and **not** nitric oxide. It is now well established that the reaction leading to nitric oxide formation is (in spite of a comment by Singh et al. (15) to the contrary) brought about by Cu^+ (from Cu^{2+} reduction), apart from a component due to the thermal decomposition, which for most *S*-nitrosothiols is very small.

Tables 2–4 show clearly that the reaction rate constants are quite unaffected by the removal of adventitious metal ions and also by the specific addition of Cu^{2+}. This behaviour is in marked contrast with the behaviour at low concentrations of thiol (either added or present in equilibrium concentrations from the preparation of the *S*-nitrosothiols from nitrous acid and thiols), when the addition of EDTA (Fig. 1) or the specific Cu^+ chelator neocuproine (11) completely suppresses reaction (apart from the small component due to the thermal reaction). There are also a large number of examples (e.g., ref. 20) where addition of Cu^{2+}, at low thiol concentrations, results in large rate increases. Again the contrast with the results in Table 2 is marked. The "high concentration of thiol" reaction appears to be quite general from the range of reactants examined (including dinitroso compounds), and rate constants are listed in Table 1. There was no attempt in this range to look for a structure–reactivity relationship; rather the choice reflects the *S*-nitrosothiols that might be of biological interest, including the possibility of their use as NO-releasing drugs. Our value

Fig. 2. Plot of k_2 (eq. [5]) vs. pH for the reaction of SNC with cysteine.

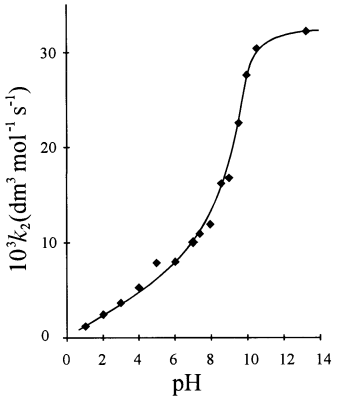

for the reaction of SNC is consistent with that found by Komiyama and Fujimori (13), who carried out their experiments at 37°C. Our duplicate values are also in acceptable agreement.

When a thiol (R′SH) different from that used to generate the *S*-nitrosothiol (RSNO) is taken, reaction still occurs and the results for two such experiments are given in Table 6. The rate constant for the reaction of penicillamine with *S*-nitrosopenicillamine (259×10^{-3} dm^3 mol^{-1} s^{-1}) is much reduced (to 28.5×10^{-3} dm^3 mol^{-1} s^{-1}) when the thiol is changed to thioglycerol, i.e., the value is much closer to that for the reaction of *S*-nitrosothioglycerol with thioglycerol. (However, it is not clear why the value is actually a little *less* than this.) Similarly, when S-nitrosothioglycerol reacts with penicillamine the rate constant is increased compared to the value for its reaction with thioglycerol. Qualitatively these results can be explained if we consider that the transnitrosation reaction, eq. [6], occurs, which then allows a number of reactions to take

[6] $$RSNO + R'SH = RSH + R'SNO$$

place in parallel, and what is measured is some averaged rate constant. Such transnitrosation reactions are well known, and take place by nucleophilic attack of RS^-. The rate then depends on the pK_a of the thiol, but usually takes place quite rapidly at pH 7.4 (21).

We have also confirmed the finding by Singh et al. (15) that ammonia and not nitric oxide is the main "nitrogen" product in RSNO decomposition at high concentration of RSH. Table 6 clearly shows the increasing ammonia yield as the RSH concentration is increased for the reaction of *S*-nitrosocysteine with cysteine. At the same time the nitrite ion (the NO-derived product) yield decreases towards ~5%.

The pattern appears to be general for RSNO species from similar product analyses using other reactants. If our product analyses are correct, then we appear to be "missing" ~10% of our nitrogen product. Singh et al. (15) detected small amounts of nitrous oxide (by mass spectrometry) in the reaction of GSNO with GSH. It is possible that our "missing" 10% is indeed nitrous oxide.

Consideration of the respective rate constants for RSNO reactions with Cu^{2+} and with RSH, e.g., for the reaction of SNC (see the values in Table 7), would suggest that at a Cu^{2+} concentration of 1×10^{-6}, and a thiol concentration of 0.01 mol dm^{-3}, the Cu^{2+} reaction should dominate. However, it is known (22) that at these high thiol concentrations copper

© 1998 NRC Canada

Table 6. Nitrite and ammonia yields from the reaction of SNC (1×10^{-3} mol dm^{-3}) with cysteine, as a function of the concentration of cysteine ([cysteine]).

[Cysteine]/ mol dm^{-3}	$\%NO_2^-$ *a*	$\%NO_2^-$ *b**	$\%NH_3$ *a*	$\%NH_3$ *b*
0	91	92	0.7	0
0.01	34	26	56	7
0.025	13	15	80	35
0.05	7	12	82	49
0.075	6	6	83	55
0.10	5	7	85	70

[a] Experiments carried out aerobically.
[b] Experiments carried out anaerobically.
[*] These values are not as reliable as the others, since they depend on the oxidation of any NO generated, over many hours, by leakage of oxygen into the solution.

can become complexed (forming either Cu^+ or Cu^{2+} complexes), reducing the rate of the copper reaction to a negligible level. Under these cirumstances there is no need to use EDTA or similar product as a metal-ion scavenger, since the thiol will perform that function.

As to the mechanism of the reaction leading principally to ammonia formation, our pH–rate profile strongly suggests that the thiolate anion is the reactive species. The enhanced reactivity of penicillamine and reduced reactivity of mercaptosuccinic acid (Table 1) can then be rationalized in terms of the inductive effects of the methyl and carboxylic acid groups, respectively, strengthening and weakening the nucleophilic activity of the thiolate anion.

The ammonia-forming reaction is clearly a thiolate-promoted reduction of the nitroso group, of which there are a number of other known examples and where the final product is often an amine (23). A reasonable sequence of reactions, based on the suggestion of Singh et al. and which are compatible with our findings, are given in eqs. [7]–[13]. Presumably the rate-limiting

[7] $RSNO + RS^- = RS(NO^-)SR$

[8] $RS(NO^-)SR + H_2O = RS(NOH)SR + OH^-$

[9] $RS(NOH)SR + RS^- = RSSR + RSN^-OH$

[10] $RSN^-OH + H_2O = RSNHOH + OH^-$

[11] $RSNHOH + RS^- = RSSR + {}^-NHOH$

[12] $^-NHOH + H_2O = NH_2OH + OH^-$

[13] $NH_2OH + RS^- \rightarrow NH_3$

step is the first reaction of RS^- at the nitrogen atom of the *S*-nitrosothiol, eq. [7], which is followed by other reactions of RS^- at the sulfur atom and various proton transfers, leading to the formation of hydroxylamine, which would be expected to undergo thiolate reduction to give ammonia. At the low end of the range of thiolate ion concentrations used in our work, this sequence of reactions is in competition with the copper ion promoted reaction that gives NO (measured in terms of NO_2^-), but as [RS^-] increases (and Cu^{2+} is progressively complexed) the ammonia reaction soon dominates, and at >0.025 mol dm^{-3} cysteine, for example, this pathway accounts for ~80% of the total for the reaction of *S*-nitrosocysteine.

The reaction rate constant is unchanged, within the error of measurement, when reaction is carried out anaerobically. However, the product distribution is somewhat changed, in that the ammonia yield is a little lower, whilst the nitrite level is approximately unchanged (though it is difficult to be precise about the anaerobic nitrite values), when compared with the results of the aerobic experiments. The undetected product (possibly nitrous oxide) yield appears to be higher anaerobically. This suggests that a partitioning of reaction pathways occurs (after the rate-limiting step), and that oxygen plays a part in one of these steps. A detailed mechanism of that part of the reaction awaits further study. Singh et al. (15) have proposed a scheme for nitrous oxide formation involving the radical RS-$\dot{N}$-OH, while Stamler (24) has suggested that earlier reports of nitrous oxide formation (25) can be explained in terms of a heterolytic mechanism involving attack of RS^- at the sulfur atom of RSNO, releasing NO^-, which would lead to nitrous oxide formation. Nitrous oxide has also been detected in the reaction products from sodium nitroprusside and glutathione (26) — a reaction formally similar to RSNO + RSH. We cannot at this time establish whether either of these suggestions is correct.

Table 7. Comparison of the copper-catalysed RSNO decomposition and the thiol–RSNO reaction.

RSNO	Copper reaction [a] k_2/dm^3 mol^{-1} s^{-1}	Thiol reaction [b] k_2/10^{-3} dm^3 mol^{-1} s^{-1}
S-Nitrosocysteine	24 500	10.7
S-Nitrosocysteine – ethyl ester	270 000	8.0

[a] k_2 in rate = k_2 [RSNO] [Cu^{2+}].
[b] k_2 in rate = k_2 [RSNO] [RSH].

The finding that *S*-nitrosothiols generally, in the presence of a large excess of thiol, decompose to give ammonia and not nitric oxide as the principal nitrogen product is, (*a*) surprising, and (*b*) potentially far-reaching, in considering RSNO compounds as possible in vivo NO donors. Hitherto it has been tacitly assumed that RSNO compounds act biologically by first breaking down to give nitric oxide. This is a reasonable assumption given that the biological poperties of RSNO (notably of effecting vasodilation and prevention of platelet aggregation) are much the same as those of nitric oxide itself. Indeed GSNO is currently undergoing clinical trials (*a*) for inhibition of platelet aggregation during coronary angioplasty (27), and (*b*) for the treatment of one form of pre-eclampsia (28), where its role is not so clear. Our results presented here, together with those of Komiyama and Fujimori (13) and of Singh et al. (15), show that in the presence of thiols at reasonably high concentration, the NO-forming reaction is replaced by the NH_3-forming reaction. Given that the the intracellular concentration of glutathione can be as high as 10 mmol dm^{-3} (29), the assumption of RSNO breakdown to NO as a prerequisite to effect the biological action must be reexamined. This is not so much due to the ammonia-forming reaction taking over (in a direct competition in the rate sense), since even at 10 mmol dm^{-3} glutathione concentration the half-life of this reaction is almost 4 h, but rather that under these conditions Cu^{2+} is effectively removed from solution, thus drastically reducing the rate of the NO-forming reaction. Other ways of NO delivery need to be considered, including the direct transfer of the NO group, possibly to an Fe atom in a heme complex, or to another sulfur

© 1998 NRC Canada

site, which could compete effectively with the reaction with the thiolate ion leading to ammonia formation.

Acknowledgement

We thank the Engineering and Physical Sciences Research Council (EPSRC) for research studentships to A.P.D. and A.P.M., and the University of Durham for a similar award to H.R.S.

References

1. S. Moncada, R.M.J. Palmer, and E.A. Higgs. Pharmacol. Rev. **43**, 109 (1991).
2. P.L. Feldman, O.W. Griffith, and D.J. Stuehr. Chem. Eng. News, December 20, 26 (1993); A.R. Butler and D.L.H.Williams. Chem. Soc. Rev. **22**, 233 (1993); M. Fontcave, and J.L. Pierre. Bull. Soc. Chim. Fr. **131**, 620 (1994).
3. M. Feelisch and E. Noack. Eur. J. Pharmacol. **139**, 19 (1987).
4. D.L.H. Williams. *In* Nitrosation. Cambridge University Press, Cambridge.1988. pp. 173–180.
5. L. Field, R.V. Dilts, R Ravichandran, P.G. Lenhert, and G.E. Carnahan. J. Chem. Soc. Chem. Commun. 249 (1978).
6. D.J. Sexton, A. Muruganandam, D.J. McKenny, and B. Mutus. Photochem. Photobiol. **59**, 463 (1994).
7. D.L.H. Williams. J. Chem. Soc. Chem. Commun. 1085 (1996).
8. P.H. Beloso, and D.LH. Williams. J. Chem. Soc. Chem. Commun. 89 (1997).
9. D.A. Wink, J.F. Darbyshire, R.W. Nims, J.E. Saavedra, and P.C. Ford. Chem. Res. Toxicol. **6**, 23 (1993).
10. H.H. Awad and D.M. Stanbury. Int. J. Chem. Kinet. **25**, 375 (1993).
11. A.P. Dicks and D.L.H. Williams. Chem. Biol. **3**, 655 (1996).
12. A.P. Dicks, P.H. Beloso, and D.L.H. Williams. J. Chem. Soc. Perkin Trans. 2, 1429 (1997).
13. T. Komiyama and K. Fujimori. Bioorg. Med. Chem. Lett. **7**, 175 (1997).
14. H.R. Swift. Ph. D. Thesis, University of Durham, U.K. 1996. pp. 80–98.
15. S.P. Singh, J.S. Wishnock, M. Keshive, W.M. Deen, and S.R. Tannenbaum. Proc. Natl. Acad. Sci. U.S.A. **93**, 14428 (1996).
16. T.W. Hart. Tetrahedron Lett. **26**, 2013 (1985).
17. A.C.F. Gorren, A. Schrammel, K. Schmidt, and B. Mayer. Arch. Biochem. Biophys. **330**, 219 (1996).
18. A. Vogel. *In* Textbook of quantitative inorganic analysis, 4th ed. Longman, London. 1978. p. 755.
19. H.C. van Anken and M.E. Schiporst. Clin. Chim. Acta, **56**, 151 (1974).
20. S.C. Askew, D.J. Barnett, J. McAninly, and D.L.H. Williams. J. Chem. Soc. Perkin Trans. 2, 741 (1995).
21. D.J. Barnett, A. Rios, and D.L.H. Williams. J. Chem. Soc. Perkin Trans. 2, 1279 (1995).
22. D. Cavallini, C. de Marco, S. Dupre, and G. Rotilio. Arch. Biochem. Biophys. **130**, 354 (1969); P. Hemmerich. *In* The biochemistry of copper. *Edited by* J. Peisach, P. Aisen, and W.E. Blumberg. Academic Press, New York. 1996. p. 15.
23. J.H. Boyer. *In* The chemistry of the nitro and nitroso groups, Part 1. *Edited by* H. Feuer. Wiley–Interscience, London. 1969. pp. 260–263.
24. J.S. Stamler. *In* Current topics in microbiology and immunology. *Edited by* H. Kopsowski and H. Maeda. Springer, Berlin. 1995. pp. 19–36.
25. J. W. Park. Biochem. Biophys. Res. Commun. **152**, 916 (1988); J. W. Park, G.E. Billman, and G.E. Means. Biochem. Mol. Biol. Int. **30**, 885 (1993).
26. V. Sampath, D.L. Rousseau, and W.S. Caughey *In* Methods in nitric oxide research. *Edited by* M. Feelisch and J.S. Stamler. Wiley, Chichester. 1996. pp. 415–417.
27. E.J. Langford, A.S. Brown, R.J. Wainwright, A.J. de Belder, M.R. Thomas, R.E.A. Smith, M.W. Radomski, J.F. Martin, and S. Moncada. Lancet, **344**, 1458 (1994).
28. A. de Belder, C. Lees, J. Martin, and S. Moncada. Lancet, **345**, 124 (1995).
29. H. Sies, R. Brigelius, and T.P.M. Akerboom. *In* Functions of glutathione: biochemical, physiological, and clinical aspects. *Edited by* A.L. Larsson, S. Orrenius, A. Holmgren, and B. Monnerik. Raven, New York. 1983. pp. 51–64.

© 1998 NRC Canada

Solvent-induced stereospecific isomerization of an allylic alcohol to a homoallylic alcohol catalyzed by a chiral lithium amide

Per I. Arvidsson, Maria Hansson, Agha Zul-Qarnain Khan, and Per Ahlberg

Abstract: Deprotonation of cyclohexene oxide, **1**, by lithium (*S*)-2-(1-pyrrolidinylmethyl)pyrrolidide, **2**-Li, on changing the solvent from tetrahydrofuran (THF) to, for example, 2,5-dimethyltetrahydrofuran (DMTHF) or diethyl ether (DEE) has been shown to yield, besides the lithium alkoxide of 2-cyclohexene-1-ol, **3**-Li, the lithium alkoxide of the homoallylic alcohol 3-cyclohexene-1-ol, **4**-Li. It was shown that compound **4**-Li is formed from **3**-Li. No such rearrangement has been observed in THF. We have now shown that the solvent-induced isomerization of the lithium alkoxide of (*S*)-3-methyl-2-cyclohexene-1-ol, (*S*)-**5**-Li, catalyzed by **2**-Li to the lithium alkoxide of (*S*)-3-methyl-3-cyclohexene-1-ol, (*S*)-**6**-Li, is 100% stereospecific. Furthermore, deuterium-labeling experiments suggest that the rearrangement of the proton is close to 100% intramolecular.

Key words: 1,3-proton transfer, chiral lithium amide, intramolecular, solvent-induced isomerization, stereospecific.

Résumé : On a montré que, lors de la déprotonation de l'oxyde de cyclohexène, **1**, par le (*S*)-2-(1-pyrrolidinylméthyl)pyrrolidure de lithium, **2**-Li, un changement de solvant du tétrahydrofurane (THF) au 2,5-diméthyltétrahydrofurane (DMTHF) ou à l'éthoxyéthane (EE) provoque la formation de l'alcoolate de lithium de l'alcool homoallylique cyclohex-3-én-1-ol, **4**-Li, en plus de celle de l'alcoolate de lithium du cyclohex-2-én-1-ol, **3**-Li, attendu. On n'observe pas ce réarrangement dans le THF. On a maintenant montré que l'isomérisation induite par le solvant de l'alcoolate de lithium du (*S*)-3-méthylcyclohex-2-én-1-ol, (*S*)-**5**-Li, catalysée par le **2**-Li, en alcoolate de lithium du (*S*)-3-méthylcyclohex-3-én-1-ol, (*S*)-**6**-Li, est 100% stéréospécifique. De plus, des expériences de marquage au deutérium suggèrent que le réarrangement du proton est presque 100% intramoléculaire.

Mots clés : transfert de proton-1,3, amide de lithium chiral, intramoléculaire, isomérisation induite par le solvant, stéréospécifique.

[Traduit par la rédaction]

Introduction

Despite the enormous usefulness of lithium organic reagents in synthesis, surprisingly little is known about their reaction mechanisms.

Special attention has been placed on the enantioselective deprotonation of a variety of epoxides to synthesize allylic alcohols in high yields and with high enantiomeric excess (ee) (1–4), for example, deprotonation of cyclohexene oxide, **1**, by lithium (*S*)-2-(1-pyrrolidinylmethyl)pyrrolidide, **2**-Li, in tetrahydrofuran (THF) yields (*S*)-2-cyclohexene-1-ol, (*S*)-**3**, after work-up in 80% enantiomeric excess (ee) (Scheme 1) (5–7). A number of pheromones and drugs may be prepared starting from such optically active alcohols (8–12).

Recently we reported that deprotonation of **1** by **2**-Li, on changing the solvent from THF to, for example, 2,5-dimethyltetrahydrofuran (DMTHF) or diethyl ether (DEE), gives, besides the lithium alkoxide of 2-cyclohexene-1-ol, **3**-Li, the lithium alkoxide of the homoallylic alcohol 3-cyclohexene-1-ol, **4**-Li (Scheme 2) (13).

It was shown that compound **4**-Li is formed from **3**-Li. No such rearrangement was observed in THF. In DMTHF, as in THF, (*S*)-**3**-Li was the enantiomer formed in excess but its ee decreased with time. One of the enantiomers of **4**-Li was also formed in excess but with lower ee than for **3**-Li and its ee decreased even more rapidly with time. The major stereoisomer of **4**-Li was proposed to be (*S*)-**4**-Li. The time dependence of the ee's of (*S*)-**3**-Li and (*S*)-**4**-Li was suggested to be either the result of further 1,3-proton transfers, which take (*S*)-**4**-Li into (*R*)-**4**-Li and (*R*)-**4**-Li into (*R*)-**3**-Li (Scheme 2), i.e., the racemizations may be caused by prototropic rearrangements. Other possibilities not shown in Scheme 2 are that the rearrangement is accompanied by inversion of the configurations of the stereogenic centers in **3**-Li and (or) **4**-Li.

We now wish to report some results on the detailed mechanism of the solvent- induced chiral amide-catalyzed rearrangement using 3-methyl-2-cyclohexene-1-ol, **5**, as substrate (Scheme 3). The results show that the rearrangement is highly stereospecific and that it takes place intramolecularly.

Results and discussion

For the mechanistic studies 3-methyl-2-cyclohexene-1-ol, **5**, a

Received January 28, 1998.

This paper is dedicated to Professor Erwin Buncel in recognition of his contributions to Canadian chemistry.

P.I. Arvidsson, M. Hansson, A.Z.-Q. Khan, and P. Ahlberg.[1] Department of Organic Chemistry, Göteborg University, S-412 96 Göteborg, Sweden.

[1] Author to whom correspondence may be addressed. Telephone: +46-31-772 2899. Fax: +46-31-772 2908. E-mail: Per.Ahlberg@oc.chalmers.se

© 1998 NRC Canada

Scheme 1.

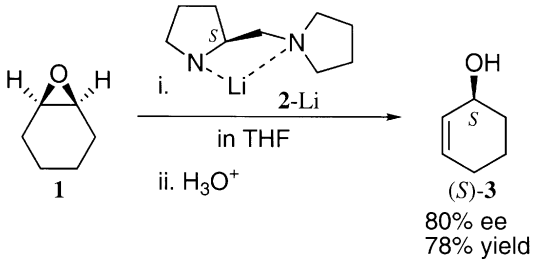

Scheme 2.

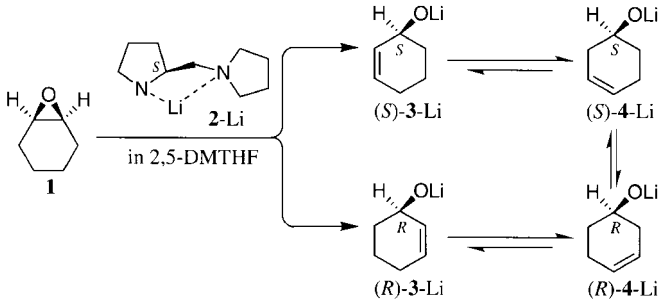

compound known as seudenol (a sex pheromone of the Douglas fire beetle), was chosen since the stabilization of **5**-Li and **6**-Li by their methyl groups was expected to make them thermodynamically more stable than their isomers, **7**-Li and **8**-Li (Scheme 3), respectively. As a consequence, further rearrangement to **7**-Li and **8**-Li is expected to be relatively slow, making it possible to study the reversible rearrangement of **5**-Li to **6**-Li without significant interference of further rearrangements.

Racemic **5** is commercially available and can be enzymatically resolved with high selectivity. This procedure was utilized to make a mixture of enantiomers with (*S*)-**5** in 76% ee as measured by chiral gas chromatography (14).

The lithium alkoxide of the enantiomerically enriched allylic alcohol, (*S*)-**5** (76% ee) was reacted with **2**-Li in DMTHF at 30.0°C. Quenching of the reaction and extraction of the mixture of products and remaining reactants followed by chiral gas chromatographic analysis showed that one of the enantiomers of **6** had been formed in 76% ee. The ee was studied as a function of time during the approach of the equilibrium. The equilibrium mixture contained 66% **5** and 34% **6**. The ee of **5** remained constant, within experimental error, at 76% during the whole reaction. That is, no significant racemization of either **5** nor **6** took place during the rearrangement. Obviously the methyl substitution had the predicted result of avoiding racemizations. Thus it is concluded that the rearrangement is 100% stereospecific (15). The results indicate that the racemizations observed upon the rearrangement of **3** into **4** are caused by consecutive 1,3-proton transfer reactions.

Assignment of the absolute configuration of the enantiomer of **6** formed in enantiomeric excess from (*S*)-**5** was investigated in the following way. If (*S*)-**6** is the product formed from (*S*)-**5**, then the chiral chromatogram of the mixture of the enantiomers of **5** and **6** (Fig. 1) shows that the elution order of the enantiomers of **5** and **6** must be unexpectedly different. Therefore, the absolute configuration of the enantiomer of **6** formed in enantiomeric excess was established in the following way. Racemic seudenol, **5**, was rearranged to the homoallylic alcohol **6** by amide **2**-Li in DMTHF. Chiral chromatographic analysis showed to our surprise that compound **5** remained racemic during the rearrangement, i.e., both enantiomers of **5** react with the chiral amide **2**-Li with equal rate constants. As a consequence, the product **6** was also found, within experimental error, to be racemic.

The isolated mixture of racemic **5** and **6** was used in enzymatic resolution of **6** employing the same enzyme that was used to resolve **5** to yield (*S*)-**5** in enantiomeric excess. The enantiomer of compound **6** remaining in excess was by analogy assumed to be (*S*)-**6** (16–19). Chiral chromatography showed that the elution order of the enantiomers of **6** indeed is the reverse of that of the enantiomers of **5**. Thus (*S*)-**5** isomerize exclusively to (*S*)-**6**.

Besides the stereospecificity, i.e., the configuration of the stereogenic carbon center remains intact in the rearrangement, the above results do not give any details of the mechanism of the 1,3-proton transfer reaction: Is the proton transfer intermolecular or intramolecular? Does it take place suprafacially or antarafacially? Is the rearrangement selective with respect to any one of the two protons in the 4-position of **5**? Is the proton delivered to the carbon *syn* or *anti* to the oxygen on the ring? Experiments are in progress to also answer these questions. The first problem has been solved in the following way.

To investigate whether the 1,3-proton transfer takes place intra- or intermolecularly the following experiment was carried out. Compound **5**-Li was isomerized in DMTHF into **6**-Li in the presence of **2**-Li and the N-deuterated amine, **2**-ND (Scheme 4). After ca. 10 half-lives the reaction was quenched and the mixture of the allylic alcohol **5** and product homoallylic alcohol **6** was isolated and analyzed by ^1H and ^2H NMR. Only traces of deuterium were detected in the product and the starting material, respectively. The absence of incorporation of deuterium in the starting material and product during the reaction indicates that the prototropic rearrangement is close to 100% intramolecular (Scheme 4).

In our system the 1,3-proton transfer might take place within a 1:1 complex of lithium alkoxide, e.g., **5**-Li and the lithium amide **2**-Li. Recently we carried out a computational investigation of a model system, i.e., the lithium amide catalyzed rearrangement of lithium allylic alkoxide to lithium homoallylic alkoxide. Pathways have been calculated using semiempirical (PM3), ab initio (HF, MP2), and DFT (B3LYP) methods. The rearrangement takes place in heterodimer complexes in which the two lithiums play different roles in different pathways via intermediates. In the calculated proton-transfer transition states the proton is about half transferred between carbon and nitrogen (20).

Experimental section

General

All glassware used for synthesis was, when needed, dried overnight in a 120°C oven. Glassware and syringes used for isomerization reactions were dried at 50°C in a vacuum oven before transfer into a glove box (Mecaplex GB 80 equipped with a gas purification system that removes oxygen and moisture) containing a nitrogen atmosphere. Typical moisture

© 1998 NRC Canada

Scheme 3.

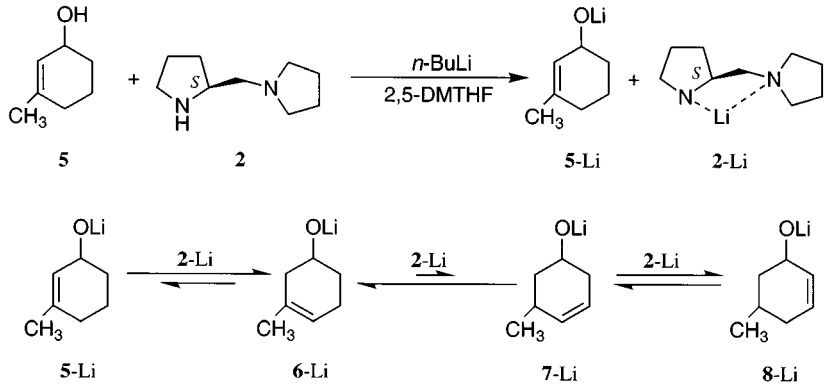

Scheme 4.

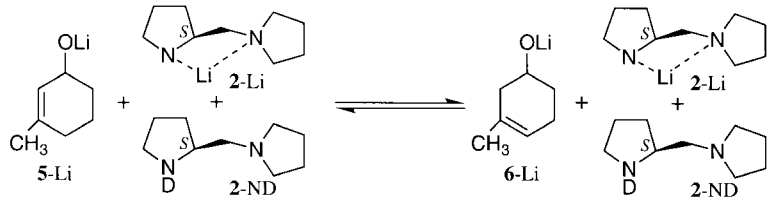

content was less than 0.5 ppm. All manipulations concerning the isomerization reactions were carried out in the glove box using gas-tight syringes. Etheral solvents, distilled under nitrogen from sodium and benzophenone, were kept over 4 Å molecular sieves in a septum-sealed flask inside the glove box. The concentrations of commercially available butyllithium solutions (*n*-BuLi 1.6 M or 2.5 M solution in hexanes, Aldrich) were determined by titration using biphenylmethanol (21).

Routine 1D ^{1}H and ^{2}H NMR spectra were recorded on a Varian Unity 400 MHz or a Varian Unity 500 MHz machine. Chromatographic analyses were carried out using a Varian Star 3400 CX gas chromatograph and a Varian 9012Q HPLC with Varian 9050 UV detector and Varian 9040 refractive index detector. All GC analyses were run on a chiral stationary-phase column (CP-Chirasil-DEX CB, 25 m, 0.32 mm) from Chrompack. All analyses were done at 95°C (injector 225°C, detector 250°C) using He (2 mL/min) as carrier gas.

Commercially available 3-methyl-2-cyclohexene-1-ol **5** (purity 96%) were obtained from Aldrich. ^{1}H NMR (400 MHz, $CDCl_3$) δ: 5.51 (m, 1 H), 4.18 (m, 1 H), 1.90 (m, 2 H), 1.77 (m, 2 H), 1.69 (s, 3 H), 1.59 (m, 2 H), 1.42 (br s, 1 H); ^{13}C{1H} NMR (100 MHz, $CDCl_3$) δ: 19.2, 23.8, 30.3, 31.9, 66.1, 124.4, 138.9.

(*S*)-2-(1-Pyrrolidinylmethyl)pyrrolidine **2** was synthesized as previously described (13). Commercially available 2,5-dimethyltetrahydrofuran was obtained from Lancaster. After distillation from sodium and benzophenone analysis by GC (J & W Scientific DB-5MS), **2** showed the composition 56% *cis*- and 44% *trans*-DMTHF.

Preparations

*(*S*)-3-Methyl-2-cyclohexene-1-ol ((*S*)-**5**)*

The method of Orrenius et al. (14) was used with some modifications; most importantly, the enzyme preparation was different.

All reagents and the toluene used as solvent were dried over 4 Å molecular sieves for several days prior to use. Racemic **5** (0.5 mL; 4.2 mmol) and vinyl acetate (1.17 mL; 12.6 mmol) were added to a magnetically stirred 50 mL flask containing 1 g of 4 Å molecular sieves and 12 mL of toluene. After a few minutes, the lipase *Candida antarctica* B (100 mg; preparation SP435, immobilized) was added and the flask was capped with a drying tube. The reaction was allowed to proceed for 3 h at room temperature, when gas chromatographic analysis showed that the remaining **5** contained (*S*)-**5** in 76% ee. The reaction mixture was filtered and the solvent evaporated. The remaining alcohol was separated from the ester by dry column flash chromatography using hexane – ethyl acetate (90:10) as eluent, yielding 80 μL (yield 16%) of (*S*)-**5**. Racemization was avoided by not subjecting (*S*)-**5** to acid.

*Racemic 3-methyl-3-cyclohexene-1-ol (**6**)*

Isomerization of racemic **5** into racemic 3-methyl-3-cyclohexene-1-ol, **6**, was performed in up to a half-gram scale according to the general protocol for isomerizations, cited below. For work-up, the organic layer was washed with a solution of NH_4Cl (1 M) followed by brine, prior to drying (Na_2SO_4) and evaporation of the solvent. The alcohol mixture was purified by silica gel flash chromatography (eluent 75/25 hexane/DEE), giving a pure mixture of **5** and **6** in 45% yield as shown by ^{1}H NMR and GC. The isomeric mixture can be separated on analytical and semi-preparative scale using HPLC (Dynamax silica column, solvent: 75/25 cyclohexane/EtOAc (analytical 1.2 mL/min, semipreparative 5.5 mL/min) with refractive index detection.

3-Methyl-3-cyclohexene-1-ol: ^{1}H NMR (500 MHz, $CDCl_3$) δ: 5.39 (m, 1 H), 3.99 (m, 1 H), 2.25 (m, 1 H), 2.16 (m, 1 H), 2.07 (m, 1 H), 1.96 (m, 1 H), 1.75 (m, 1 H), 1.67 (s, 3 H), 1.54 (m 1 H), 1.27 (br s, 1 H); ^{13}C{1H} NMR (100 MHz, $CDCl_3$) δ: 23.3, 23.8, 30.7, 39.3, 67.6, 120.7, 131.5.

© 1998 NRC Canada

Fig. 1. GC chromatogram (chiral stationary-phase column) of isolated product mixture after 72 h of reaction of (*S*)-**5** (76% ee) with **2**-Li in DMTHF at 30.0°C. The elution order of the enantiomers of **6** is reversed as compared to that of the enantiomers of **5.**

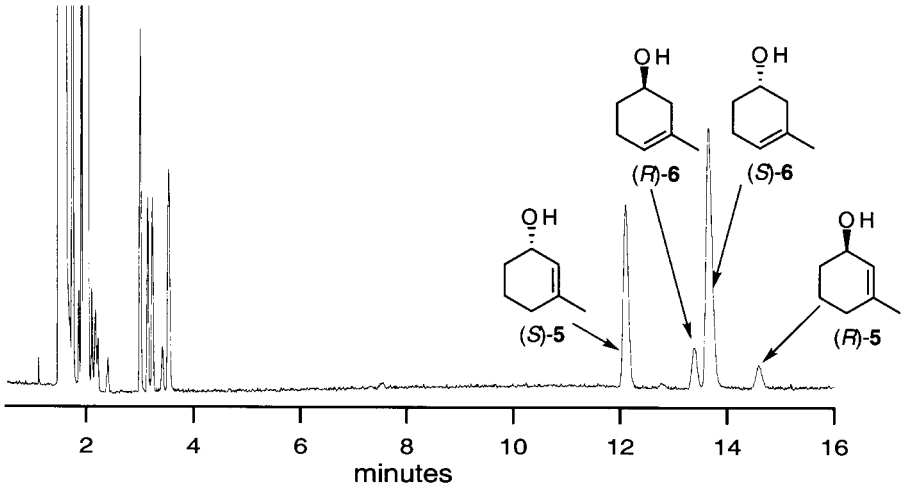

*Mixture of (*S*)-3-methyl-2-cyclohexene-1-ol (*S*)-***5** *and (*S*)-3-methyl-3-cyclohexene-1-ol (*S*)-***6***

An analytical-scale resolution of a mixture of **5** and **6** was performed in order to establish the reverse elution order of the **6** enantiomers, as compared to the **5** enantiomers, respectively, on the chiral column used for gas chromatographic analysis.

To the mixture of **5** and **6** (35/65 **5/6**; 20.0 μL; 0.17 mmol) in toluene (0.50 mL) was added vinyl acetate (47 μL; 0.51 mmol) and 10 mg *Candida antarctica* B (preparation SP435). The resolution was monitored by gas chromatographic analysis during approximately 3 h. Then only the peaks from (*S*)-**5** and (*S*)-**6** remained in the chromatogram.

*Oxygen deuterated 3-methyl-2-cyclohexene-1-ol (***5***-OD)*

3-Methyl-2-cyclohexene-1-ol (1 mL; 8.27 mmol) was dissolved in dry chloroform (4.0 mL). Deuterium oxide (800 μL; 44 mmol) was added and the mixture was stirred for 4 h. Separation of the layers and drying (Na_2SO_4) followed by evaporation of the solvent gave **5** in quantitative yield. The isotopomer fraction of **5**-OD was 66% as measured by ^{1}H NMR.

General protocol for the isomerizations

n-Butyllithium (1.5 M in hexane; 227 μL; 0.34 mmol) was added to a solution of 3-methyl-2-cyclohexene-1-ol **5** (20.0 μL; 0.17 mmol) and (*S*)-2-(1-pyrrolidinylmethyl)pyrrolidine **2** (28.0 μL; 0.17 mmol) in 2,5-dimethyltetrahydrofuran (1.00 mL) maintained at 0°C. The flask was then moved to a thermostat held at 30.0°C. The reaction was monitored by withdrawing 20.0 μL of the reaction mixture using a dry syringe while protecting the reaction mixture by a stream of argon. The sample was transferred to a vial containing diethyl ether (1.0 mL) and saturated NH_4Cl (0.50 mL), and the mixture was shaken. The aqueous layer was removed and the ether layer washed with one portion of brine (0.50 mL) and dried over Na_2SO_4 prior to gas chromatographic analysis. After 72 h the reaction mixture contained **6** and **5** in about a 65/35 ratio.

Intramolecularity of isomerization

(*S*)-2-(1-Pyrrolidinylmethyl)pyrrolidine **2** (584 μL; 3.58 mmol) in 2,5-dimethyltetrahydrofuran (4.0 mL) was cooled to 0°C prior to addition of *n*-butyllithium (1.57 M in hexane; 2280 μL; 3.58 mmol). After 30 min, **5**-OD (300 μL; 2.50 mmol) was added and, after another 10 min, the reaction flask was moved to a thermostat held at 30.0°C. After 192 h (ca. 10 $t_{1/2}$) the reaction was quenched by addition of 1 M NH_4Cl (2.0 mL). The organic layer was washed with 1 M HCl (0.5 mL) and brine (3 × 5 mL) before drying (Na_2SO_4) and evaporation of the solvent. The residue was silica gel flash chromatographed (eluent 75/25 hexane/DEE) giving a mixture of **5** and **6** (120 mg; 43% yield). The deuterium content in the isomers was analyzed by ^{1}H and ^{2}H NMR. Only traces of deuterium were found in position 4 and in the methyl group of **5**, and in the 2- and 5-positions and the methyl group of **6**.

Acknowledgment

We thank the Swedish Natural Research Council (NFR) for financial support and NOVO-Nordisk A/S Denmark for provision of enzyme.

References

1. P.J. Cox and N.S. Simpkins. Tetrahedron: Asymmetry, **2**, 1 (1991).
2. D.M. Hodgson, A.R. Gibbs, and G.P. Lee. Tetrahedron, **52**, 14361 (1996).
3. K. Koga. Pure Appl. Chem. **66**, 1487 (1994).
4. D. Bhuniya, A. DattaGupta, and V.K. Singh. J. Org. Chem. **61**, 6108 (1996).
5. M. Asami. Chem. Lett. 829 (1984).
6. M. Asami. Bull. Chem. Soc. Jpn. **63**, 721 (1990).
7. M. Asami. J. Synth. Org. Chem. (Jpn), **54**, 188 (1996).
8. T. Mukaiyama and M. Asami. Top. Curr. Chem. **127**, 133 (1985).
9. J.S. Sabol and R.J. Cregge. Tetrahedron Lett. **30**, 3377 (1989).
10. M. Asami, J. Takahashi, and S. Inoue. Tetrahedron: Asymmetry, **5**, 1649 (1994).
11. D.M. Hodgson, J. Witherington, and B.A. Moloney. Tetrahedron: Asymmetry, **5**, 337 (1994).
12. D.M. Hodgson and A.R. Gibbs. Tetrahedron: Asymmetry, **7**, 407 (1996).
13. A.Z.Q. Khan, P.I. Arvidsson, and P. Ahlberg. Tetrahedron: Asymmetry, **7**, 399 (1996).

© 1998 NRC Canada

14. C. Orrenius, T. Norin, K. Hult, and G. Carrea. Tetrahedron: Asymmetry, **6**, 3023 (1995).
15. IUPAC glossary of terms used in physical organic chemistry. Pure Appl. Chem. **166**, 1077 (1994).
16. C.S. Chen and C.J. Sih. Angew. Chem. Int. Ed. Engl. **28**, 695 (1989).
17. G. Carrea, B. Danieli, G. Palmisano, S. Riva, and M. Santagostino. Tetrahedron: Asymmetry, **3**, 775 (1992).
18. H. Hagiwara, T. Nakano, and H. Uda. Bull. Chem. Soc. Jpn. **66**, 3110 (1993).
19. A.B. Bueno, M.C. Carreno, J.L.G. Ruano, and C. Hamdouchi. Tetrahedron: Asymmetry, **6**, 1237 (1995).
20. S.O. Nilsson Lill, P.I. Arvidsson, and P. Ahlberg. Acta Chem. Scand. **52**, 280 (1998).
21. E. Juaristi and A. Martinez-Richa. J. Org. Chem. **48**, 2603 (1983).

© 1998 NRC Canada

Selective hydroboration of alkenes and alkynes in the presence of aldehydes and ketones

George W. Kabalka, Su Yu, and Nan-Sheng Li

Abstract: The reactions of terminal alkenes in the presence of ketones or aldehydes with a variety of borane reagents have been investigated. It was found that the selective hydroboration of a terminal alkene in the presence of a ketone or an aldehyde is most efficient when dicyclohexylborane is used as the hydroborating agent. The hydroboration of olefinic ketones and olefinic aldehydes with dicyclohexylborane generates the corresponding hydroxyaldehydes and hydroxyketones in good yields after oxidation with sodium perborate. The hydroboration of alkynyl ketones and alkynyl aldehydes with dicyclohexylborane yields the corresponding olefinic carbonyl compounds after protonation, or dicarbonyl compounds after oxidation.

Key words: hydroboration, reduction, dicyclohexylborane, hydroxyaldehyde, hydroxyketone.

Résumé : On a étudié les réactions des alcènes terminaux, en présence de cétones ou d'aldéhydes, avec une variété de boranes comme réactifs. On a trouvé que le dicyclohexylborane est le meilleur agent pour effectuer l'hydroboration sélective d'un alcène terminal en présence d'une cétone ou d'un aldéhyde. L'hydroboration des cétones ou des aldéhydes oléfiniques suivie d'une oxydation avec du perborate de sodium conduit aux hydroxyaldéhydes et aux hydroxycétones correspondants avec de bons rendements. L'hydroboration des alcynylcétones et des alcynylaldéhyes par le dicyclohexylborane conduit aux composés carbonylés oléfiniques correspondants après protonation ou aux composés dicarbonylés après oxydation.

Mots clés : hydroboration, réduction, dicyclohexylborane, hydroxyaldéhyde, hydroxycétone.

[Traduit par la rédaction]

Introduction

Boron hydride reagents have been utilized extensively in organic synthesis. They have proven to be valuable for the selective reduction of carbonyl compounds as well as for the stereoselective hydroboration of alkenes and alkynes (1, 2). Because of the effectiveness of borane reagents in reducing aldehydes and ketones, hydroboration reactions involving substrates containing these functional groups are often carried out by either converting the carbonyl group to a less reactive functionality (3, 4) or modifying the hydroborating agent (5). Otherwise, reduction of the carbonyl moiety might compete with the desired hydroboration reaction. For example, α,β-unsaturated aldehydes and ketones are reduced rapidly and quantitatively to the corresponding allylic alcohols by 9-BBN (6). Similarly, the hydroboration of allyl ketones with diisopinocampheyborane produces enantiomerically enriched 1,4-diols via an intramolecular reduction (7). Diols are also the final products (after oxidation) when olefinic ketones are reduced by either borane or thexylborane (8). These latter reports, and related examples such as one involving a hydroboration with catecholborane in the presence of Wilkinson's catalyst (9), indicate that it might be possible to selectively hydroborate alkenes in the presence of aldehydes and ketones. Recently, we reported the preliminary results of our studies, which focused on the selective hydroboration of alkenes (Fig. 1) and alkynes (Fig. 2) in the presence of ketones and aldehydes (10). We now wish to report the details of these studies.

Received February 12, 1998.

This paper is dedicated to Professor E. Buncel in recognition of his contributions to Canadian chemistry.

G.W. Kabalka,[1] S. Yu, and N.-S. Li. Departments of Chemistry and Radiology, The University of Tennessee, Knoxville, TN 37996-1600, U.S.A.

[1] Author to whom correspondence may be addressed. Telephone: (423) 974-3260. Fax: (423) 974-2997. E-mail: kabalka@utk.edu

Results and discussion

Brown and his co-workers (11) have carried out extensive research on the reactions of alkenes and carbonyl compounds with a variety of boron hydrides. Their kinetic data indicates that both the hydroboration of terminal alkenes as well as the reduction of most aldehydes and some ketones by 9-BBN follow first-order kinetics (12). Although they exhibit first-order rate constants when reduced by borane reagents, the aldehydes, ketones, and alkenes exhibit different overall reaction rates. For example, aldehydes are more reactive toward 9-BBN than alkenes but 9-BBN reacts faster with certain alkenes than with ketones. We felt that these reactivity differences might be amplified if more hindered borane reagents were utilized.

As a probe, we allowed a mixture of 1-octene and 2-heptanone to react with a variety of common borane reagents at various temperatures (0, 25, 68°C). The mixtures were then oxidized to the corresponding alcohols using sodium perborate (13); the results of the study are presented in Table 1.

Analysis of the data in Table 1 indicates that the reactivities of a terminal alkene and an acyclic aliphatic ketone toward boron hydrides are quite different; in fact, a terminal alkene

© 1998 NRC Canada

Fig. 1.

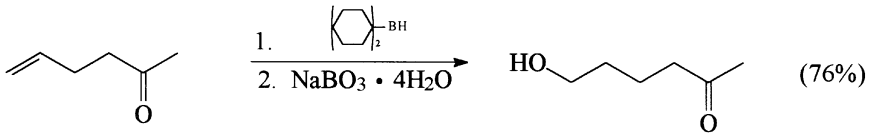

Fig. 2.

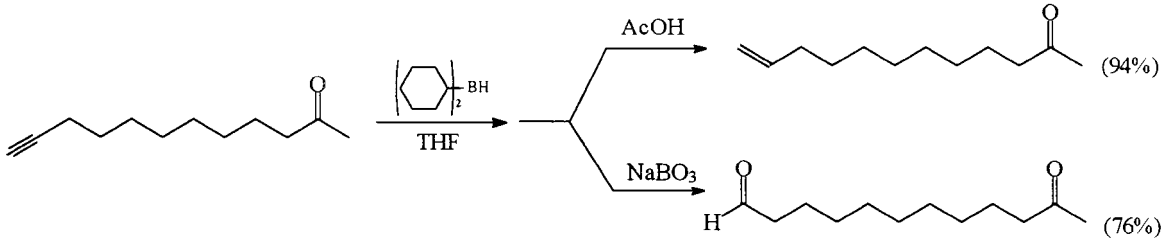

Table 1. The reaction of 1-octene and 2-heptanone with various borane reagents: a competitive study.[a]

Entry	Rxn. temp. (°C)	Borane reagent	Ratio of 1-octanol to 2-heptanol[b,c]
1	0	BH_3·THF	97:3[d]
2	25	BH_3·THF	99:1[d]
3	68	BH_3·THF	98:2[d]
4	0	BMS	96:4[d]
5	25	BMS	97:3[d]
6	25	9-BBN	93:7
7	68	9-BBN	89:11
8	0	(*c*-C_6H_{11})$_2$ BH	100:0
9	25	(*c*-C_6H_{11})$_2$ BH	100:0
10	0	Sia_2BH	96:4
11	25	Sia_2BH	97:3

[a] Reactions were carried out using 1 equiv. each of hydride, alkene, and ketone.
[b] Ratios obtained by GC analysis after aqueous sodium perborate oxidation.
[c] Overall combined yields ranged from 90 to 100%.
[d] 2-Octanol was also formed in small quantities.

Table 2. The reaction of 1-octene and cyclopentanone with various borane reagents.[a]

Entry	Borane reagent	Ratio of 1-octanol to cyclopentanol[b,c]
1	BH_3·THF	94:6[d]
2	BMS	89:11[d]
3	9-BBN	34:66
4	Sia_2BH	92:8
5	(*c*-C_6H_{11})$_2$BH	100:0

[a] Reactions were carried out using 1 equiv. each of hydride, alkene, and ketone.
[b] Ratios obtained by GC analysis after aqueous sodium perborate oxidation.
[c] Overall combined yields ranged from 90 to 100%.
[d] 2-Octanol was also formed in small quantities.

can be successfully hydroborated in the presence of a ketone utilizing essentially all of the common hydroborating agents. As anticipated from earlier studies, 9-BBN is less chemoselective than the more hindered hydroborating reagents (entries 6–11); but dicyclohexylborane is quite effective at hydroborating a terminal alkene in the presence of a ketone. Also noteworthy is the fact that temperature had little effect on the selectivity of the reagents.

Cyclic ketones are present in a number of important naturally occuring molecules. Since cyclic ketones are more reactive toward 9-BBN than acyclic ketones (11), they might compete more effectively with terminal alkenes. As a probe, we allowed 1-octene and cyclopentanone to react with a limited quantity of the various borane reagents. The mixtures were then oxidized with sodium perborate, and the results are presented in Table 2.

As shown in Table 2, cyclopentanone competes more effectively than 2-heptanone for the borane reagents. However, hydroboration is still the major reaction except when 9-BBN is used as the hydroborating reagent. Cyclopentanone is slightly more reactive than 1-octene toward 9-BBN. Dicyclohexylborane is the most effective at hydroborating a terminal alkene in the presence of a cyclic ketone.

We also carried out a competitive study of reactions of alkenes and an aromatic ketone using various borane reagents. The results of the study are presented in Table 3. The data indicate that a terminal alkene can be selectively hydroborated in the presence of an aromatic ketone. Consistent with the earlier studies, 9-BBN is the least chemoselective.

As noted earlier, aldehydes are more reactive than terminal alkenes toward 9-BBN (11). 1-Octene and heptanal were used as model substrates and allowed to react with a limited quantity of the borane reagent. The results are presented in Table 4. The data reveal that hydroboration is the major reaction when hindered borane reagents are utilized, while reduction predominates in reactions using unhindered borane reagents. Dicyclohexylborane is once again the most effective at hydroborating a terminal alkene in the presence of an aldehyde.

We then examined the ability of dicyclohexylborane to selectively hydroborate olefinic aldehydes and ketones (Table 5). The results indicate that hydroxyaldehydes and hydroxyketones can be prepared in good yields after oxidation. Interestingly, no "simple" reduction products (olefinic alcohols) were detectable in any of the reactions except when 11-undecylenic aldehyde was used as the substrate. However,

© 1998 NRC Canada

Table 3. The reaction of 1-octene and acetophenone with various borane reagents.[a]

Entry	Borane reagent	Ratio of 1-octanol to 1-phenylethanol[b,c]
1	BH_3·THF	100:0[d]
2	BMS	94:6[d]
3	9-BBN	76:24
4	Sia_2BH	100:0
5	$(c\text{-}C_6H_{11})_2BH$	100:0

[a] Reactions were carried out using 1 equiv. each of hydride, alkene, and ketone.
[b] Ratios obtained by GC analysis after aqueous sodium perborate oxidation.
[c] Overall combined yields ranged from 90 to 100%.
[d] 2-Octanol was also formed in small quantities.

Table 4. The reaction of 1-octene and heptanal with various borane reagents.[a]

Entry	Borane reagent	Ratio of 1-octanol to 1-heptanol[b,c]
1	BH_3·THF	45:55[d]
2	BMS	53:47[d]
3	9-BBN	16:84
4	Sia_2BH	71:29
5	$(c\text{-}C_6H_{11})_2BH$	82:18

[a] Reactions were carried out using 1 equiv. each of hydride, alkene, and ketone.
[b] Ratios obtained by GC analysis after aqueous sodium perborate oxidation.
[c] Overall combined yields ranged from 90 to 100%.
[d] 2-Octanol was also formed in small quantities.

overreduction to the diol product (up to 10%) was observed in some cases.

A variety of unconjugated alkynyl carbonyl compounds were then hydroborated with dicyclohexylborane to probe the ability of dicyclohexylborane to selectively hydroborate alkynes in the presence of both aldehydes and ketones. The results are summarized in Table 6. Both terminal and internal alkynyl carbonyl compounds can be hydroborated in the presence of the carbonyl group. The reaction affords the corresponding olefins in high yields (71–94%) after protonation, or dicarbonyl compounds in good yields (50–76%) after oxidation with sodium perborate.

Experimental section

Alkenyl ketones and alkenyl aldehydes, obtained from Aldrich Chemical Company, were used as received or purified by distillation prior to use. Alkynyl ketones and alkynyl aldehydes were synthesized from the alkynyl alcohols by oxidation with PCC (14). Alkynyl alcohols were either obtained commercially or prepared via Grignard reactions (14). ^{1}H NMR spectra and ^{13}C NMR spectra were run at 250 MHz. Elemental analyses were performed by Atlantic Microlab Inc., Atlanta, Ga.

General procedure for the preparation of hydroxyketones and hydroxyaldehydes

6-Hydroxy-2-hexanone
Borane tetrahydrofuran (5.0 mmol, 5.0 mL of a 1.0 M solution in THF) was placed in a dry, argon-flushed, round-bottomed flask, which was then immersed in an ice-water bath. Cyclohexene (10.0 mmol, 0.82 g, 1.0 mL) was added dropwise and the mixture stirred at 0°C for 1 h. 5-Hexen-2-one (5.0 mmol, 0.49 g, 0.58 mL) was then added to the slurry of dicyclohexylborane in THF. The cooling bath was removed and the mixture stirred for 2 h at room temperature. Oxidation was achieved by adding $NaBO_3$·$4H_2O$ (15 mmol, 2.3 g) and water (5 mL) and stirring the mixture at room temperature for 2 h. The product was extracted into ether (3 × 15 mL), the solvent removed under pressure, and 6-hydroxy-2-hexanone (15) (0.44g, 76% yield) was isolated by flash chromatography. ^{1}H NMR ($CDCl_3$/TMS), δ (ppm): 3.62 (t, J = 6.1 Hz, 2H), 2.59 (br s, 1H), 2.49 (t, J = 6.8 Hz, 2H), 2.16 (s, 3H), 1.73–1.50 (m, 4H); ^{13}C NMR ($CDCl_3$/TMS), δ (ppm): 209.38, 61.96, 43.15, 31.87, 19.73, 19.72.

2-Methyl-5-(1-methyl-2-hydroxylethyl)cyclohexanone (16)
Yield: 77%; ^{1}H NMR ($CDCl_3$/TMS), δ (ppm): 3.59–3.44 (m, 2H), 2.49–1.26 (m, 9H), 1.01 (d, J = 6.4 Hz, 2H), 0.94 (d, J = 6.9 Hz), 0.91 (d, J = 6.9 Hz) (total 3H); ^{13}C NMR ($CDCl_3$/TMS), δ (ppm): 213.72, 213.45, 65.45, 65.36, 46.17, 44.83 (44.83), 43.91, 41.57, 41.37, 40.19, 40.00, 34.97 (34.97), 29.71, 27.51, 14.20 (14.20), 13.05, 12.71.

1-Methoxy-2-oxabicyclo[4.4.0]decane (17)
Yield: 70%; ^{1}H NMR ($CDCl_3$/TMS), δ (ppm): 3.72–3.56 (m, 2H), 3.22–3.16 (m, 3H), 1.98–1.12 (m, 13H); ^{13}C NMR ($CDCl_3$/TMS), δ (ppm): 98.34, 60.87, 46.34, 44.44, 31.74, 29.45, 26.36, 25.88, 24.72, 22.67.

6-Hydroxy-5-methyl-2-hexanone
Yield 80%; a cyclic and acyclic mixture (50:50) of 6-hydroxy-5-methyl-2-hexanone was produced. ^{1}H NMR ($CDCl_3$/TMS), δ (ppm): 3.55–3.42 (m, 2H), 2.97 (br s, 0.5H) 2.61–2.46 (m, 1.5H), 2.16 (s, 1.5H), 1.81–1.35 (m, 5.5H), 0.91 (d, J = 6.6 Hz, 1.5H), 0.82 (d, J = 6.3 Hz, 1.5H); ^{13}C NMR ($CDCl_3$/TMS), δ (ppm): 209.58, 94.50, 67.18, 60.50, 41.06, 35.15, 34.85, 30.06, 29.94, 29.72, 27.56, 26.65, 17.05, 16.39. HRMS calcd. for $C_7H_{14}O_2$: 130.099; found: 130.096.

4-(2-Propenoxy)-2-hydroxybenzophenone
Yield 78%; ^{1}H NMR ($CDCl_3$/TMS), δ (ppm): 12.66 (s, 1H), 7.61–7.44 (m, 6H), 6.50 (d, J = 2.2 Hz, 1H), 6.38 (dd, J = 8.9, 2.2 Hz, 1H), 4.13 (t, J = 6.0 Hz, 2H), 3.80 (t, J = 6.0 Hz, 2H), 2.66 (s, 1H), 2.02 (p, J = 6.0 Hz, 2H); ^{13}C NMR ($CDCl_3$/TMS), δ (ppm): 199.85, 166.04, 165.40, 138.01, 135.13, 131.32, 128.64, 128.12, 112.93, 107.42, 101.53, 65.32, 59.14, 31.61. Anal. calcd. for $C_{16}H_{16}O_4$: C 70.57, H 5.92; found: C 70.66, H 5.91.

2-Acetyl-5-hydroxynorbornane and 2-acetyl-6-hydroxynorbornane (18)
Yield 68%; ^{1}H NMR ($CDCl_3$/TMS), δ (ppm): 3.85–3.62 (m, 1H), 3.05–1.12 (m, 13H); ^{13}C NMR ($CDCl_3$/TMS), δ (ppm): 209.79, 209.64, 209.28, 73.98, 73.68, 73.38, 69.72, 60.20, 53.39, 52.79, 51.43, 50.13, 47.30, 47.03, 44.65, 43.70, 41.70,

© 1998 NRC Canada

Table 5. The hydroboration of olefinic carbonyl compounds with dicyclohexylborane.

Entry	Substrate	Product[a]	Yield (%)[b]
1[c]	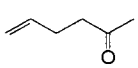	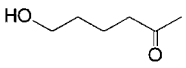	76
2[c]	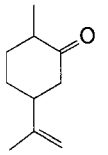	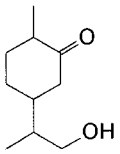	77
3[d]	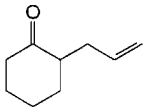	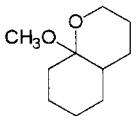	70
4	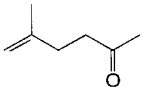	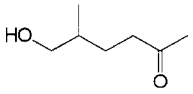	80
5[e]	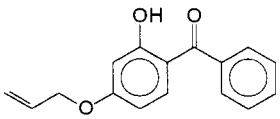	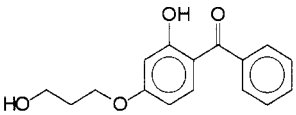	78
6[c]	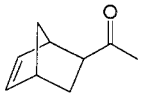	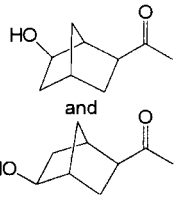	68
7[f]	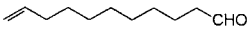	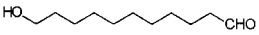	50

[a] Known compounds exhibited physical and spectral characteristics in accord with literature values, and new compounds were characterized by spectral and elemental analysis or HRMS.

[b] Isolated yield.

[c] Up to 10% of the corresponding diols were isolated.

[d] Acetal formed by the reaction of the crude product with methanol in the presence of TsOH.

[e] Two equiv. of dicyclohexylborane were utilized.

[f] A trace of 11-undecylenic alcohol was detected by TLC.

41.21, 39.17, 38.85, 36.27, 34.93, 32.07, 31.63, 31.17, 29.44, 29.23, 28.63, 28.42, 26.76, 25.06.

11-Hydroxyundecanal (19)

Yield 50%; ^{1}H NMR ($CDCl_3$/TMS), δ (ppm): 9.76 (t, J = 1.6 Hz, 1H), 3.61 (t, J = 6.6 Hz, 2H), 2.65 (s, 1H), 2.43 (dt, J = 7.3, 1.6 Hz, 2H), 1.65–1.53 (m, 4H), 1.29 (br s, 12H); ^{13}C NMR ($CDCl_3$/TMS), δ (ppm): 202.71, 62.47, 43.63, 32.51, 29.26, 29.11 (29.11), 28.90, 25.54, 21.82, 13.89.

General procedure for the preparation of alkenyl carbonyl compounds and dicarbonyl compounds

The hydroboration of 11-dodecyn-2-one is representative: BH_3·THF (2.0 mmol, 2.0 mL of a 1.0 M solution in THF) was placed in a dry, argon-flushed flask, which was then immersed in an ice-water bath. Cyclohexene (4.0 mmol, 0.33 g, 0.41 mL) was added dropwise and the mixture stirred at 0°C for 1 h. 11-Dodecyn-2-one (2.0 mmol, 0.36 g) was then added to the slurry of dicyclohexylborane in THF. The cooling bath was removed and the mixture stirred for 1 h at room temperature. Protonation was achieved by adding glacial acetic acid (1.0 mL) and stirring the mixture at room temperature for 1 h. 11-Dodecen-2-one (20) (0.34 g, 94% yield) was isolated after work-up. ^{1}H NMR, δ (ppm): 5.88–5.72 (m, 1H), 5.02–4.90 (m, 2H), 2.41 (t, J = 7.4 Hz, 2H), 2.13 (s, 3H), 2.03 (q, J = 6.8 Hz, 2H), 1.56 (m, 2H), 1.28 (m, 10H); ^{13}C NMR ($CDCl_3$/TMS), δ (ppm): 209.08, 139.05 114.06, 43.70, 33.71, 29.72, 29.25 (29.25), 29.09, 29.00, 28.83, 23.78. Alternatively, oxidation could be achieved by adding of $NaBO_3$·$4H_2O$ (6.0 mmol, 0.92 g) and water (2 mL) and stirring the mixture at room temperature for 2 h. 11-Oxododecanal (21) (0.30 g, 76% yield) was isolated after work-up. ^{1}H NMR, δ (ppm): 9.76

© 1998 NRC Canada

Table 6. Preparation of olefinic carbonyl compounds and dicarbonyl compounds.

Entry	Substrate	Work-up	Product[a]	Yield (%)[b]
1	$CH_3C{\equiv}C(CH_2)_8C(O)Ph$	Protonation	(*Z*)-$CH_3CH{=}CH(CH_2)_8C(O)Ph$	92
2	$CH_3C{\equiv}C(CH_2)_8C(O)CH_3$	Protonation	(*Z*)-$CH_3CH{=}CH(CH_2)_8C(O)CH_3$	88
3	$CH_3C{\equiv}C(CH_2)_8CHO$	Protonation	(*Z*)-$CH_3CH{=}CH(CH_2)_8$ CHO	71
4	$HC{\equiv}C(CH_2)_8C(O)CH_3$	Protonation	$CH_2{=}CH(CH_2)_8C(O)CH_3$	94
5	$HC{\equiv}C(CH_2)_8C(O)CH_3$	Oxidation	$HC(O)(CH_2)_9C(O)CH_3$	76
6	$HC{\equiv}C(CH_2)_8C(O)CH_2CH_3$	Protonation	$CH_2{=}CH(CH_2)_8C(O)CH_2CH_3$	83
7	$HC{\equiv}C(CH_2)_8C(O)CH_2CH_3$	Oxidation	$HC(O)(CH_2)_9C(O)CH_2CH_3$	68
8	$HC{\equiv}C(CH_2)_8CHO$	Protonation	$CH_2{=}CH(CH_2)_8CHO$	90
9	$HC{\equiv}C(CH_2)_8CHO$	Oxidation	$HC(O)(CH_2)_9CHO$	50
10	$HC{\equiv}C(CH_2)_3C(O)Ph$	Protonation	$CH_2{=}CH(CH_2)_3C(O)Ph$	85
11	$HC{\equiv}C(CH_2)_3C(O)Ph$	Oxidation	$HC(O)(CH_2)_4C(O)Ph$	66

[a] Products exhibited physical and spectral characteristics in accord with literature values or gave acceptable elemental analyses.
[b] Isolated yield.

(t, *J* = 1.9 Hz, 1H), 2.45–2.39 (m, 4H), 2.14 (s, 3H), 1.62–1.56 (m, 4H), 1.29 (m, 10H); ^{13}C NMR ($CDCl_3$/TMS), δ (ppm): 209.07, 202.64, 43.71, 43.58, 29.65, 29.10, 28.95, 23.65, 21.89.

1-Phenyl-(Z)-10-dodecen-1-one
Yield 92%; ^{1}H NMR ($CDCl_3$/TMS), δ (ppm): 7.98–7.94 (m, 2H), 7.58–7.41 (m, 3H), 5.47–5.35 (m, 2H), 2.96 (t, *J* = 7.2 Hz, 2H), 2.04–1.99 (m, 2H), 1.78–1.68 (m, 2H), 1.61–1.58 (m, 3H), 1.43–1.20 (m, 10H); ^{13}C NMR ($CDCl_3$/TMS), δ (ppm): 200.49, 137.07, 132.77, 130.77, 128.47, 127.99, 123.56, 38.55, 29.33 (29.33, 29.33), 29.18 (29.18), 26.77, 24.32, 12.50. Anal. calcd. for $C_{18}H_{26}O$: C 83.67, H 10.14; found: C 83.73, H 10.20.

(Z)-11-Tridecen-2-one
Yield 88%; ^{1}H NMR ($CDCl_3$/TMS), δ (ppm): 5.47–5.32 (m, 2H), 2.41 (t, *J* = 7.4 Hz, 2H), 2.13 (s, 3H), 2.03–1.98 (m, 2H), 1.61–1.54 (m, 5H), 1.28 (br s, 10H); ^{13}C NMR ($CDCl_3$/TMS), δ (ppm): 209.19, 130.72, 123.53, 43.70, 29.72, 29.42, 29.27 (29.27), 29.10 (29.10), 26.72, 23.78, 12.64. HRMS calcd. for $C_{13}H_{24}O$: 196.182; found: 196.182.

(Z)-10-Dodecenal
Yield 71%; ^{1}H NMR, δ (ppm): 9.76 (t, *J* = 1.9 Hz, 1H), 5.43–5.41 (m, 2H), 2.42 (dt, *J* = 7.3, 1.9 Hz, 2H), 2.07–1.98 (m, 2H), 1.78–1.53 (m, 5H), 1.30 (br s, 10H); ^{13}C NMR, δ (ppm): 202.82, 130.76, 123.63, 43.86, 29.45, 29.30 (29.30), 29.16, 26.79, 23.80, 22.06, 12.50. HRMS calcd. for $C_{12}H_{22}O$: 182.167; found: 182.167.

12-Tridecen-3-one (19)
Yield 83%; ^{1}H NMR ($CDCl_3$/TMS), δ (ppm): 5.85–5.72 (m, 1H), 5.03–4.90 (m, 2H), 2.46–2.36 (m, 4H), 2.03 (q, *J* = 6.9 Hz, 2H), 1.62–1.54 (m, 2H), 1.28 (m, 10H), 1.05 (t, *J* = 7.3 Hz, 3H); ^{13}C NMR ($CDCl_3$/TMS), δ (ppm): 211.81, 139.08, 114.06, 42.36, 35.78, 33.72, 29.23 (29.23), 29.00 (29.00), 28.84, 23.87, 7.77.

11-Oxotridecanal (22)
Yield 68%; ^{1}H NMR ($CDCl_3$/TMS), δ (ppm): 9.76 (t, *J* = 1.7 Hz, 1H) 2.46–2.37 (m, 6H), 1.59 (m, 4H), 1.29 (br s, 10H), 1.04 (t, *J* = 7.2 Hz, 3H); ^{13}C NMR ($CDCl_3$/TMS), δ (ppm): 211.52, 202.50, 43.64, 42.12, 35.58, 29.00, 23.66, 21.81, 7.58.

10-Undecenal (23)
Yield 90%; ^{1}H NMR ($CDCl_3$/TMS), δ (ppm): 9.76 (t, *J* = 1.9 Hz, 1H), 5.89–5.73 (m, 1H), 5.03–4.90 (m, 2H), 2.42 (dt, *J* = 7.3, 1.9 Hz, 2H), 2.08–2.00 (m, 2H), 1.66–1.57 (m, 2H), 1.30 (m, 10H); ^{13}C NMR ($CDCl_3$/TMS), δ (ppm): 202.80, 139.08, 114.12, 43.87, 33.73, 29.23 (29.23), 29.11, 29.00, 28.84, 22.03.

1,11-Undecanedial (24)
Yield 50%; ^{1}H NMR ($CDCl_3$/TMS), δ (ppm): 9.76 (t, *J* = 1.6 Hz, 2H), 2.42 (dt, *J* = 7.3, 1.6 Hz, 4H), 1.62 (m, 4H), 1.30 (br s, 10H); ^{13}C NMR ($CDCl_3$/TMS), δ (ppm): 202.74, 43.72, 29.10, 29.01, 28.97, 21.89.

1-Phenyl-5-hexen-1-one (25)
Yield 85%; ^{1}H NMR ($CDCl_3$/TMS), δ (ppm): 7.94 (m, 2H), 7.57–7.41 (m, 3H), 5.90–5.74 (m, 1H), 5.08–4.97 (m, 2H), 2.97 (t, *J* = 7.3 Hz, 2H), 2.15 (q, *J* = 7.3 Hz, 2H), 1.84 (p, *J* = 7.3 Hz, 2H); ^{13}C NMR ($CDCl_3$/TMS), δ (ppm): 200.07, 137.95, 136.98, 132.80, 128.46, 127.92, 115.18, 37.60, 33.10, 23.21.

6-Oxo-6-phenylhexanal (26)
Yield 66%; ^{1}H NMR ($CDCl_3$/TMS), δ (ppm): 9.78 (t, *J* = 1.4 Hz, 1H), 7.96–7.93 (m, 2H), 7.59–7.43 (m, 3H), 3.03 (t, *J* = 6.8 Hz, 2H), 2.53–2.48 (m, 2H), 1.76–1.72 (m, 4H); ^{13}C NMR ($CDCl_3$/TMS), δ (ppm): 202.19, 199.69, 136.77, 132.94, 128.49, 127.89, 43.61, 38.00, 23.50, 21.59.

Acknowledgement

We wish to thank the Department of Energy and the Robert H. Cole Foundation for support of this research.

References

1. H.C. Brown. *In* Organic syntheses via boranes. Wiley–Interscience, New York. 1975.
2. A. Pelter, K. Smith, and H.C. Brown. *In* Borane reagents. Academic Press, London. 1988.
3. A. Ruettimann, G. Englert, H. Mayer, G.P. Moss, and B.C.L. Weedon. Helv. Chim. Acta, **66**, 1939 (1983).
4. J.E. McMurry. J. Am. Chem. Soc. 6821 (1968).
5. G.P. Kim and N.M. Yoon. Bull. Korean Chem. Soc. **7**, 160 (1986).

© 1998 NRC Canada

6. (*a*) S. Krishnamurthy and H.C. Brown. J. Org. Chem. **40**, 1864 (1975); (*b*) J. Org. Chem. **42**, 1197 (1977).
7. G.A. Molander and K.L. Bobbitt. J. Org. Chem. **59**, 2676 (1994).
8. (*a*) T. Harada, Y. Matsuda, S. Imanaka, and A. Oku. J. Chem. Soc. Chem. Commun. 1641 (1990); (*b*) T. Harada, S. Imanaka, Y. Ohyama, Y. Matsuda, and A. Oku. Tetrahedron Lett. **33**, 5807 (1992).
9. D. Männig and H. Nöth. Angew. Chem. Int. Ed. Engl. **24**, 878 (1985).
10. (*a*) G.W. Kabalka, S. Yu, and N.-S. Li. Tetrahedron Lett. **38**, 5455 (1997); (*b*) Tetrahedron Lett. **38**, 7681 (1997).
11. (*a*) H.C. Brown, S. Krishnamurthy, and N.M. Yoon. J. Org. Chem. **41**, 1778 (1976); (*b*) H.C. Brown, C.G. Scouten, and K.K. Wang. J. Org. Chem. **44**, 2589 (1979); (*c*) K.K. Wang and H.C. Brown. J. Am. Chem. Soc. **104**, 7148 (1982); (*d*) H.C. Brown, D.J. Nelson, and C.G. Scouten. J. Org. Chem. **48**, 641 (1983); (*e*) H.C. Brown and J. Chandrasekharan. J. Org. Chem. **48**, 5080 (1983); (*f*) J. Org. Chem. **48**, 644 (1983); (*g*) H.C. Brown, J. Chandrasekharan, and D.J. Nelson. J. Am. Chem. Soc. **106**, 3768 (1984); (*h*) J. Chandrasekharan and H.C. Brown. J. Org. Chem. **50**, 518 (1985).
12. (*a*) K. K. Wang and H.C. Brown. J. Org. Chem. **45**, 5303 (1980); (*b*) H. C.Brown, K.K. Wang, and J. Chandrasekharan. J. Am. Chem. Soc. **105**, 2340 (1983).
13. (*a*) G.W. Kabalka, T.M. Shoup, and N.M. Goudgaon. J. Org. Chem. **54**, 5940 (1989); (*b*) D.S. Matteson and R. Moody. J. Org. Chem. **45**, 1091 (1980).
14. C.W. Subramanian, P.J. Thomas, V.R. Mandapur, and M.S. Chadha. J. Chem. Soc. Perkin Trans. 1, 2346 (1979).
15. G.F. Weber, and S.S. Hall. J. Org. Chem. **44**, 364 (1979).
16. V. Khanna and P.H. Ladwa. Indian J. Chem. **26B**, 816 (1987).
17. J. Colonge, J. Dreux, M. Thiers. Bull. Soc. Chim. Fr. 1459 (1959).
18. M. Lajunen and M.A. Hintsanen. Acta Chem. Scand. Ser. A, **A37**(7), 545 (1983).
19. B.M. Trost and R.J. Kulawiec. J. Am. Chem. Soc. **115**, 2027 (1993).
20. S.C. Sinha, A. Sinha-Bagchi, and E. Keinan. J. Org. Chem. **58**, 7789 (1993).
21. L. Cottier and G. Descotes. Bull. Soc. Chim. Fr. 1072 (1972).
22. G. Cahiez and B. Figadere. Tetrahedron Lett. **27**, 4445 (1986).
23. P. Four and F. Guide. J. Org. Chem. **46**, 4439 (1981).
24. K. Griesbaum, V. Ball, J. Beck, and K. McCullough. Liebigs Ann. Org. Bioorg. Chem. **11**, 1993 (1995).
25. G.A. Molander and J.A. McKie. J. Org. Chem. **60**, 872 (1995).
26. Y.-S. Hon, S.-W. Lin, L. Lu, and Y.-J. Chen. Tetrahedron, **51**, 5019 (1995).

© 1998 NRC Canada

Kinetics of thermal racemization of (2*S*,3*S*)-1-^{13}C-1,2,3-d_3-cyclopropane followed by vibrational circular dichroism spectroscopy

Teresa B. Freedman, Diane L. Hausch, Steven J. Cianciosi, and John E. Baldwin

Abstract: Vibrational circular dichoism spectra recorded for (2*S*,3*S*)-1-^{13}C-1,2,3-d_3-cyclopropane and for mixtures of it and the three related stereoisomers prepared through gas-phase thermal stereomutation reactions at 407°C lead to the rate constant for racemization: $k_\alpha = (4k_1 + 4k_{12}) = (3.12 \pm 0.04) \times 10^{-5}$ s^{-1}. This and the rate constant measured for geometrical equilibration between the two chiral and the two achiral stereoisomers of 1-^{13}C-1,2,3-d_3-cyclopropane, $k_i = (8k_1 + 4k_{12}) = (4.63 \pm 0.20) \times 10^{-5}$ s^{-1}, give two equations in two unknowns, and allow one to solve for one-center (k_1) and two-center (k_{12}) epimerization rate constants for cyclopropane stereomutations. They are nearly equal, a clear indication of closely competitive reaction pathways.

Key words: cyclopropane stereomutations, thermal epimerizations, chirality through deuterium and carbon-13 labeling, vibrational circular dichroism.

Résumé : On a enregistré les spectres de dichroïsme circulaire vibrationnel du (2*S*,3*S*)-1-^{13}C-1,2,3-d_3-cyclopropane et de son mélange avec les trois stéréoisomères apparentés préparés par stéréomutation thermique en phase gazeuse, à 407°C; ces données permettent de tirer la constante de vitesse de racémisation, $k_\alpha = (4k_1 + 4k_{12}) = (3{,}12 \pm 0{,}04) \times 10^{-5}$ s^{-1}. Cette valeur associée à la constante de vitesse mesurée pour l'équilibre géométrique entre les deux isomères chiraux et les deux isomères achiraux du 1-^{13}C-1,2,3-d_3-cyclopropane, $k_i = (8k_1 + 4k_{12}) = (4{,}63 \pm 0{,}20) \times 10^{-5}$ s^{-1}, fournit deux équations et deux inconnues qui peuvent être résolues pour les constantes de vitesse d'épimérisation à un centre (k_1) et à deux centres (k_{12}) pour les stéréomutations du cyclopropane. Ces valeurs sont presque normales; ceci est une indication claire que les voies réactionnelles compétitives sont très proches.

Mots clés : stéréomutations du cyclopropane, épimérisations thermiques, chiralité due au marquage au deutérium et au ^{13}C, dichroïsme circulaire vibrationnel.

[Traduit par la rédaction]

Vibrational circular dichroism (VCD), the differential interaction of a chiral molecule with left and right circularly polarized infrared radiation during vibrational excitation (1, 2) may be used as a sensitive spectroscopic method for assessing the optical purity of a compound. The method may be readily extended to determine enantiomeric excess (ee) values of a non-racemic compound in the presence of achiral isomers. The VCD spectroscopic method is particularly noteworthy when applied to molecules that cannot be probed for ee by chiral chromatographic techniques or by polarimetry or by chiroptical spectroscopic methods in the ultraviolet or visible regions of the electromagnetic spectrum. There is no other presently available direct method for determining ee values for compounds of this class, such as saturated hydrocarbons chiral only by virtue of isotopic labels.

Both enantiomers of *trans*-1,2-d_2-cyclopropane and both (2*S*,3*S*)-1-^{13}C-1,2,3-d_3-cyclopropane and (2*R*,3*R*)-1-^{13}C-1,2,3-d_3-cyclopropane (**(2*S*,3*S*)-1** and **(2*R*,3*R*)-1**) have been synthesized and have demonstrated the point (3–7). The VCD spectra of the optical antipodes in each case are related as mirror images, with excellent agreement between experimentally determined absolute stereochemistry, observed VCD spectra, and theoretically calculated VCD spectra (6).

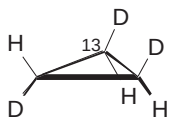

(2*S*,3*S*)-**1**

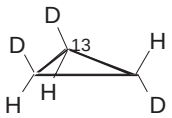

(2*R*,3*R*)-**1**

The first attempt to apply this spectroscopic analytical method to the determination of a rate constant for a thermal racemization reaction was made by Chickos, Annamalai, and Keiderling (8). They followed the loss of relative optical

Received January 5, 1997.

This paper is dedicated to Professor Erwin Buncel in recognition of his contributions to Canadian chemistry.

T.B. Freedman,[1] D.L. Hausch, S.J. Cianciosi,[2] and J.E. Baldwin.[1] Department of Chemistry, Syracuse University, Syracuse, NY 13244-4200, U.S.A.

[1] Authors to whom correspondence may be addressed. (J.E.B.) Telephone: (315) 443-3743. Fax: (315) 443-4070. E-mail: jbaldwin@syr.edu and (T.B.F.) Telephone: (315) 443-1134. E-mail: tbfreedm@syr.edu

[2] Current address: Merck & Co., PO Box 7, Elkton, VA 22827, U.S.A.

© 1998 NRC Canada

Scheme 1. Thermal stereomutations of 1-^{13}C-1,2,3-d_3-cyclopropanes.

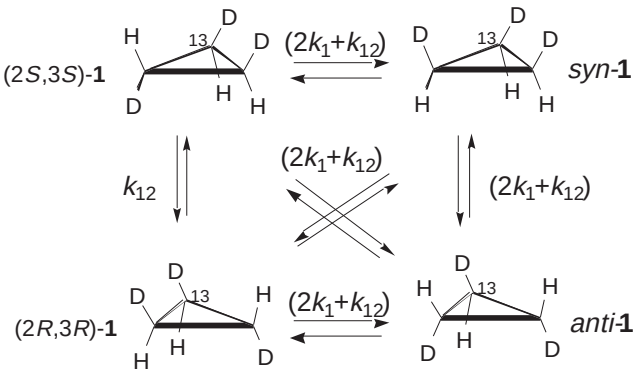

activity for a chiral *trans*-1,2-d_2-cyclobutane as it underwent reversible thermal stereomutations, forming the enantiomer and the achiral *cis* isomer, and dissociated to ethylene and deuterium-labeled ethylenes.[3]

In a second application of this approach, the thermal stereomutations of (1*R*,2*R*)-1,2-d_2-cyclopropane were followed by VCD, and the rate constant k_α for the first-order loss of optical activity through reversible formation of the *cis* isomer and of the (1*S*,2*S*) isomer at 422.5°C in the gas phase was reported to be 12.3×10^{-5} s^{-1} (10). In hindsight, however, it was recognized that the experimental uncertainties for k_α were too large for it to be of any mechanistically telling significance. The calculated rate constant was based on only three (time, α_{rel}) data points and a two-parameter nonlinear least-squares fit[4] of these three points to an exponential function; the calculated 95% confidence interval for k_α was $(3.9–20.8) \times 10^{-5}$ s^{-1}. This estimation of k_α was inadequate because too few kinetic points were determined and those few points were overinterpreted, not because of some inherent shortcoming in the VCD method itself.

In subsequent work, when the rate of loss of optical activity of **(2*S*,3*S*)-1** was followed by VCD spectroscopy, five well-spaced kinetic points were determined using enantiomerically pure **(2*S*,3*S*)-1** as the reference, and a substantially more precise value for k_α for this system was derived (5). The value of k_α at 407°C reported in a preliminary communication (5) was $(3.10 \pm 0.07) \times 10^{-5}$ s^{-1} (standard deviation) and the 95% confidence interval calculated for k_α was $(2.86–3.33) \times 10^{-5}$ s^{-1}. This k_α value ($k_\alpha = (4k_1 + 4k_{12})$) and the rate constant for geometrical isomerizations of the ^{13}C, d_3-labeled cyclopropanes determined by tunable diode laser spectroscopy (5, 11) ($k_i = (8k_1 + 4k_{12}) = (4.63 \pm 0.20) \times 10^{-5}$ s^{-1}) provided values of $k_1 = (0.38 \pm 0.05) \times 10^{-5}$ s^{-1} and $k_{12} = (0.39 \pm 0.05) \times 10^{-5}$ s^{-1}, thus demonstrating that the thermal stereomutations of isotopically labeled cyclopropanes occur as both one-center and two-center epimerizations and take place with comparable rate constants. This experimental result is now reflected in theoretical calculations and models from several laboratories (12–19).

The rate constants in Scheme 1 are defined so as to include symmetry considerations, for a one-center epimerization at C1 could follow upon cleavage of the C1—C2 bond or the C1—C3 bond. With this convention the rate constants k_1 and k_{12} reflect the competitive situation attendant upon breaking a single C—C bond. By symmetry, neglecting conceivable but surely minuscule carbon-13 kinetic isotope effects, $k_1 = k_2 = k_3$ and $k_{12} = k_{13} = k_{23}$.

The present report presents in full detail the VCD spectroscopic data from which a k_α value for **(2*S*,3*S*)-1** may be derived. While the method and instrumentation used have been detailed in print (4), and the VCD spectra have been available in a dissertation since 1991 (20), this account, prompted by colleagues and a recent renewal of interest in the cyclopropane stereomutation problem (12–23), offers a complete presentation of spectral data and an alternative, independent procedure for data reduction. It provides, in a still more readily accessible form, information necessary for judging the power of VCD spectroscopy applied to problems of this sort. The new derivation of the k_α value for thermal racemization of **(2*S*,3*S*)-1** from the primary spectral data confirms the original kinetic determination (5) and the conclusion that thermal stereomutations of cyclopropane take place with $k_1 \approx k_{12}$.

Experimental

The syntheses and characterizations of **(2*S*,3*S*)-1**, **(2*R*,3*R*)-1**, and of the racemic mixture of both enantiomers, **rac-1**, have been described in detail (7). The gas-phase thermal reactions at 407°C with pentane as a bath gas and the reisolation and purification of labeled cyclopropane samples have been described in a full paper (11). Samples of pure **(2*S*,3*S*)-1** and of preparative-GC purified mixtures of 1-^{13}C-1,2,3-d_3-cyclopropane isomers from thermal reaction mixtures were transferred to a gas infrared spectroscopy cell on a vacuum line, employing a constant volume manifold and a MKS Baritron high-accuracy capacitance manometer pressure-measuring device. The 5 cm path length Pyrex infrared cell, with ~20 mL volume, was equipped with KBr windows, a high-vacuum stopcock, and a cold-finger. The reference sample size was ~5 mg.

The gas-phase VCD spectra were recorded in the CH-stretching region (2900–3200 cm^{-1}) on a dispersive VCD spectrometer (4, 24–26) with a fresh Xenon arc source to maximize throughput, CaF_2 photoelastic modulator, liquid-nitrogen-cooled InSb detector, and computerized data acquisition (interfaced to SpectraCalc, Galactic Industries Corp., Salem, NH 03079). Three scans were recorded for each sample or reference at 8 cm^{-1} resolution and averaged. The noise level was ~1×10^{-6} in absorbance units, whereas the maximum VCD magnitude for the pure sample of **(2*S*,3*S*)-1** was ~2×10^{-5} absorbance units.

For each reaction time, three VCD spectra were measured: one for the kinetic sample from **(2*S*,3*S*)-1**, one for a "baseline" sample obtained from an equal-time thermal reaction of **rac-1**, and one for the pure **(2*S*,3*S*)-1** reference sample; the three VCD spectra were recorded consecutively without modification of instrument settings. Reference and baseline sample pressures (Table 1), which were approximately the same for all the kinetic points, corresponded to maximum sample absorbances below 0.5. Kinetic sample pressures were increased relative to the reference sample pressures to increase the VCD

[3] For recent theoretical work on these reactions and the tetramethylene diradical, see ref. 9.

[4] Calculated with software from the SAS Institute, Inc, Box 8000, Cary, NC 27511, U.S.A.

© 1998 NRC Canada

Table 1. Loss of optical activity for **(2S, 3S) -1** at 407°C determined by VCD spectroscopy.

Time (min)	Sample pressure (Torr)	Reference pressure (Torr)	Data points (number)	α_{rel} (mean)[a]	Standard deviation	Data points (number)	α_{rel} (mean)[a]	Standard deviation
			Determination 1			Determination 2		
181	56.30	43.98	54	0.7081	0.0189	53	0.7069	0.0177
360	81.30	53.59	76	0.5165	0.0233	67	0.5120	0.0216
600	75.50	43.35	28	0.3398	0.0177	56	0.3072	0.0489
960	85.40	44.72	60	0.1529	0.0162	63	0.1718	0.0198

[a] $\alpha_{rel} = [VCD_{sample} \times (\text{ref. (Torr)/sample (Torr)})/VCD_{reference}]_{mean}$.

Fig. 1. Gas-phase VCD spectra of **(2*S*,3*S*)-1**, **(2*R*,3*R*)-1**, and **rac-1** before any adjustments through baseline corrections or spectral subtractions or any other calculational manipulations.

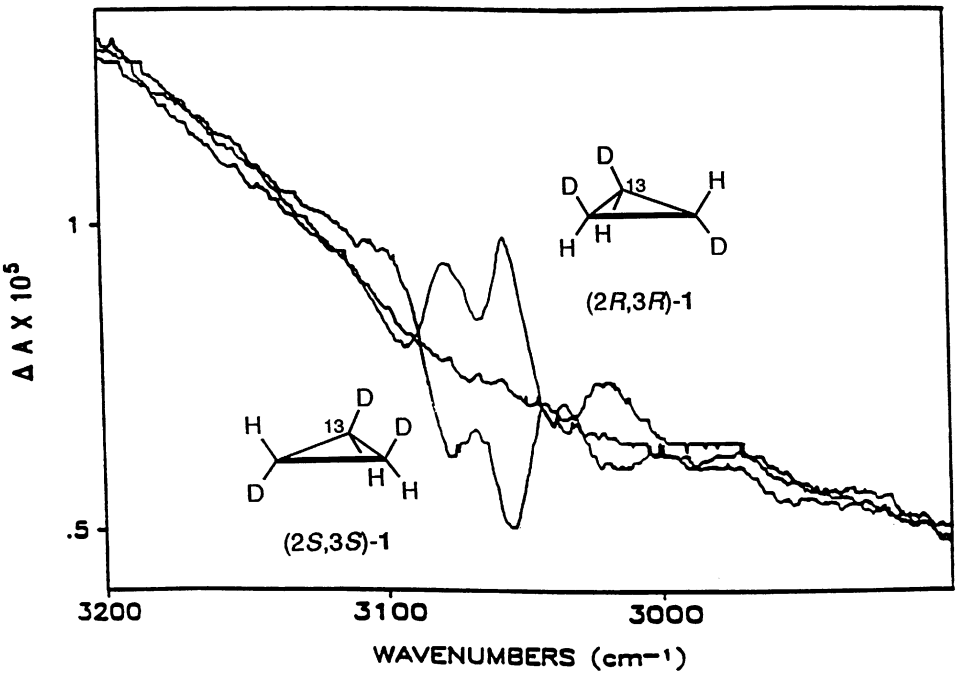

signal in the partially racemized samples, while maintaining maximum absorbance below 1, for higher absorbances degraded the VCD signal at the absorbance maxima.

The raw VCD spectra for **rac-1**, for **(2*S*,3*S*)-1**, and for **(2*R*,3*R*)-1**, displayed in Fig. 1, were recorded in March 1990; they provided the first experimental confirmation that VCD methods could be applied successfully to saturated hydrocarbons chiral only by virtue of a carbon-13 label.

The spectra of Fig. 1 show a consistent sloping instrumental baseline, an artifact that was readily corrected for spectra observed for the enantiomers or for thermal product mixtures. Subtracting the VCD spectrum recorded for **rac-1** from the VCD spectra for pure **(2*S*,3*S*)-1** and **(2*R*,3*R*)-1** gives nearly mirror image related spectra about $\Delta A = 0$ for the two ^{13}C, d_3 enantiomers (5, 6). Similarly, subtracting VCD spectra for samples obtained from thermolysis of **rac-1** from spectra obtained for the equal-time kinetic samples derived from **(2*S*,3*S*)-1** corrected for the sloping instrumental baseline.

Effects of any slight instrument baseline drift among the three raw spectra for each kinetic point were eliminated by linear offset of the racemic-baseline-corrected kinetic and reference data to zero ΔA (averaged over ~100 consecutive data points) in regions above and below the 3150–2950 cm^{-1} region of sample absorbance. In some cases the linear offset was preceded by a minor two-point baseline slope adjustment. For one sample (960 min) an anomalously large instrumental drift was encountered below 3000 cm^{-1}, a region beyond the data range employed in the ee determination.

The loss in optical activity of the kinetic samples was determined by first scaling the kinetic point VCD spectra by the pressure ratio (reference (Torr)/sample (Torr)) (1 Torr = 133.3 Pa) to correct for the difference in masses of sample and reference measured. The pressure and baseline corrected VCD spectra for the four pairs of kinetic non-racemic mixtures of isomers and the corresponding reference samples are displayed in Fig. 2.

For each kinetic sample, 30–80 data points in the vicinity of the two VCD maxima at 3077 and 3054 cm^{-1} were selected and the mean and standard deviation of the ratio $\alpha_{rel} = [VCD_{sample} \times (\text{ref. (Torr)/sample (Torr)})/VCD_{reference}]_{mean}$ were determined. These values, compiled in Table 1, were calculated in 1990 (determination 1) and derived independently from the original electronically stored VCD spectral data in 1996 (determination 2). The data for the latter analysis are plotted in Fig. 3.

The data were fit to a function of the form $A*\exp(-b*t)$ by

© 1998 NRC Canada

Fig. 2. Experimental pressure-corrected VCD spectra for thermal stereomutation product mixtures from **(2*S*,3*S*)-1** (——) and reference **(2*S*,3*S*)-1** samples (- - -) with data processing as described in text.

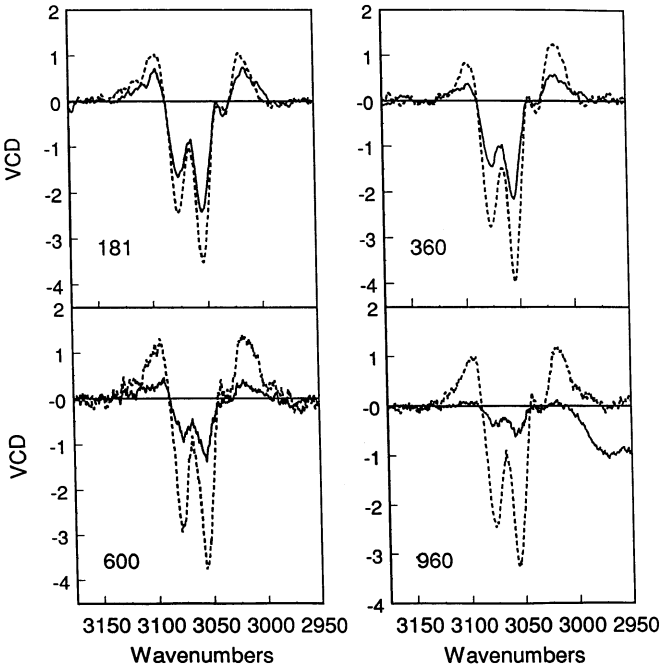

a weighted nonlinear least-squares procedure with the Axum graphics and data analysis software (MathSoft, Inc., Cambridge, MA 02142). Kinetic points were weighted by their inverse standard deviation, with the $t = 0$ point 100 times more heavily weighted. This procedure provides rate constant $k_\alpha = (3.10 \pm 0.06) \times 10^{-5}$ s^{-1} for determination 1, and $k_\alpha = (3.12 \pm 0.04) \times 10^{-5}$ s^{-1} for determination 2, with all five data points used in each calculation. Eliminating the 960 min data point, for which instrumental drift was encountered, does not significantly alter the rate constant ($k_\alpha = (3.15 \pm 0.04) \times 10^{-5}$ s^{-1} for four data points).

Mean values of α_{rel} obtained in determinations 1 and 2 are not significantly different. The newly calculated value of k_α was derived using a different weighting scheme and least-squares program than those originally employed (5), and is only very slightly larger. The redetermined value for $k_\alpha = (3.12 \pm 0.04) \times 10^{-5}$ s^{-1} is well within the originally defined 95% confidence interval, $(2.86–3.33) \times 10^{-5}$ s^{-1}.

Discussion

From $k_\alpha = (4k_1 + 4k_{12}) = (3.12 \pm 0.04) \times 10^{-5}$ s^{-1} and $k_i = (8k_1 + 4k_{12}) = (4.63 \pm 0.20) \times 10^{-5}$ s^{-1} one may calculate $k_1 = (0.38 \pm 0.05) \times 10^{-5}$ s^{-1}, $k_{12} = (0.40 \pm 0.05) \times 10^{-5}$ s^{-1}, $k_{12}:k_1 = 1.05 \pm 0.19$, and $k_i:k_\alpha = 1.48 \pm 0.07$. The determination that k_1 and k_{12} are equal within one-standard-deviation error estimates reinforces the essential experimental finding, $k_1 \approx k_{12}$, reported in the preliminary communication (5). The stereomutations that occur when a C—C bond in cyclopropane is broken are most frequently of the one-center variety, for $2k_1:k_{12}$ is 1.9. Some 66% of the initial stereomutation product mixture formed directly from **(2*S*,3*S*)-1** is ***cis*-1**. Since the ratios of rate

Fig. 3. Exponential kinetic plot for k_α based on determination 2 data in Table 1 and the VCD spectra of Fig. 2.

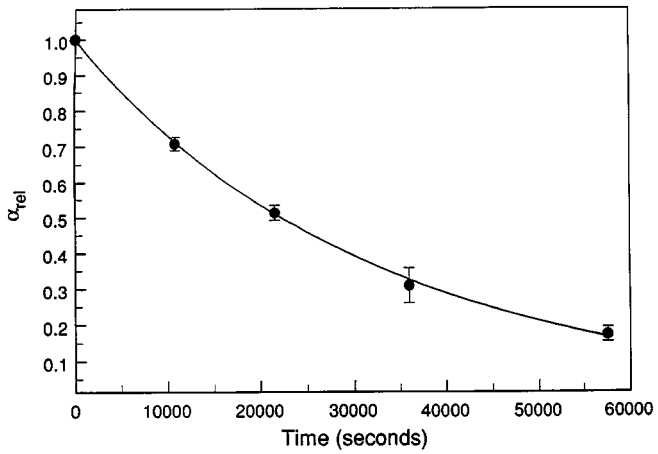

constants $(k_1 + k_2):k_{12}$ found experimentally for various 1,2-substituted cyclopropanes range from 1.4 to 4 (some 25 examples) (21), the balance between experimentally determined one-center versus two-center epimerization rate constants for 1-^{13}C-1,2,3-d_3-cyclopropanes is unexceptional.

Theoretical models for these stereomutations are still being evolved, and further work will surely be forthcoming. There remain important conceptual and calculational uncertainties to be resolved, especially regarding the detailed topography of the potential energy surface and the role of dynamic effects modeled through trajectory calculations (12–19). The present contribution may aid that ongoing effort and help provide for a measure of agreement between experimental and theoretical assessments of the stereomutations.

Acknowledgments

Support for this work from the National Institutes of Health (GM-23567) and the National Science Foundation (CHE 9532016) is gratefully acknowledged.

References

1. L.A. Nafie. Appl. Spectrosc. **50**, A14 (1996).
2. L.A. Nafie. Annu. Rev. Phys. Chem. **48**, 357 (1997).
3. S.J. Cianciosi, K.M. Spencer, T.B. Freedman, L.A. Nafie, and J.E. Baldwin. J. Am. Chem. Soc. **111**, 1913 (1989).
4. K.M. Spencer, S.J. Cianciosi, J.E. Baldwin, T.B. Freedman, and L.A. Nafie. Appl. Spectrosc. **44**, 235 (1990).
5. S.J. Cianciosi, N.Ragunathan, T.B. Freedman, L.A. Nafie, D.K. Lewis, D.A. Glenar, and J.E. Baldwin. J. Am. Chem. Soc. **113**, 1864 (1991).
6. T.B. Freedman, S.J. Cianciosi, N. Ragunathan, J.E. Baldwin, and L.A. Nafie. J. Am. Chem. Soc. **113**, 8298 (1991).
7. J.E. Baldwin and S.J. Cianciosi. J. Am. Chem. Soc. **114**, 9401 (1992).
8. J.S. Chickos, A. Annamalai, and T.A. Keiderling. J. Am. Chem. Soc. **108**, 4398 (1986).
9. C. Doubleday. J. Am. Chem. Soc. **115**, 11968 (1993); Chem. Phys. Lett. **233**, 509 (1995).
10. S.J. Cianciosi, N.Ragunathan, T.B. Freedman, L.A. Nafie, and J.E. Baldwin. J. Am. Chem. Soc. **112**, 8204 (1990).
11. J.E. Baldwin, S.J. Cianciosi, D.A. Glenar, G.J. Hoffman, I.-W. Wu, and D.K. Lewis. J. Am. Chem. Soc. **114**, 9408 (1992).

© 1998 NRC Canada

12. Y. Yamaguchi, H.F. Schaefer, and J.E. Baldwin. Chem. Phys. Lett. **185**, 143 (1991).
13. S.J. Getty, E.R. Davidson, and W.T. Borden.J. Am. Chem. Soc. **114**,2085 (1992).
14. J.E. Baldwin, Y. Yamaguchi, and H.F. Schaefer. J. Phys. Chem. **98**, 7513 (1994).
15. C. Doubleday. J. Phys. Chem. **100**, 3520 (1996).
16. C. Doubleday, K. Bolton, G.H. Peslherbe, and W.L. Hase. J. Am. Chem. Soc. **118**, 9922 (1996).
17. K. Bolton, W.L. Hase, and C. Doubleday. Ber. Bunsen-Ges. Phys. Chem. **101**, 414 (1997).
18. C. Doubleday, K. Bolton, and W.L. Hase. J. Am. Chem. Soc. **119**, 5251 (1997).
19. D.A. Hrovat, S. Fang, W.T. Borden, and B.K. Carpenter. J. Am. Chem. Soc. **119**, 5253 (1997).
20. S.J. Cianciosi. Ph. D. Dissertation, Syracuse University, 1990; Diss. Abstr. Int. B: **52**, 832 (1991).
21. J.E. Baldwin. *In* The chemistry of the cyclopropyl group. Vol. 2. *Edited by* Z. Rappoport. Wiley, Chichester. 1995. p. 469.
22. S. Petersen, J.L Herek, and A.H. Zewail. Science, **266**, 1359 (1994).
23. J.E. Baldwin, T.B. Freedman, Y.Yamaguchi, and H.F. Schaefer. J. Am. Chem. Soc. **118**, 10934 (1996).
24. M. Diem, P.J. Gotkin, J.M. Kupfer, A.G. Tindall, and L.A. Nafie. J. Am. Chem. Soc. **99**, 8103 (1977).
25. M. Diem, P.P. Gotkin, J.M. Kupfer, and L.A. Nafie. J. Am. Chem. Soc. **100**, 5644 (1978).
26. M. Diem, E. Photos, H. Khouri, and L.A. Nafie. J. Am. Chem. Soc. **101**, 6829 (1979).

© 1998 NRC Canada

The conformational equilibrium of *N*,*N*′-bis[(*S*)-1-phenylethyl]-thiourea and its solvent dependence, studied by NMR and CD spectra and by X-ray crystallography

Knut Rang, Jan Sandström, and Christer Svensson

Abstract: Favoured conformations of *N*,*N*′-bis[(*S*)-1-phenylethyl]thiourea (**1**) have been predicted by empirical force-field calculations, and the corresponding rotational strengths for the important transitions in the near UV region have been calculated. Experimental studies by ^{1}H NMR, IR, UV, and CD spectroscopy have permitted the assignment of a conformation denoted *E*,*Za* to the conformer, which dominates in nonpolar solvents, while hydroxylic solvents were found to favour conformations of *Z*,*Za* type. The *E*,*Za* conformer is also predicted by force-field calculations to be the most stable one.

Key words: circular dichroism, conformation, crystal structure, dynamic NMR spectroscopy, *N*,*N*′-bis[(*S*)-1-phenylethyl]thiourea.

Résumé : Faisant appel à des calculs empiriques de champs de force, on a prédit les conformations privilégiées de la *N*,*N*′-bis[(*S*)-1-phényléthyl]thiourée (**1**) et on a calculé les forces rotationnelles correspondantes des transitions importantes dans la région du proche UV. Des études expérimentales par spectroscopies IR, UV, de DC et RMN du ^{1}H on permis d'attribuer une conformation indiquée par *E*,*Za* au conformère prédominant dans les solvants non polaires; par ailleurs, dans les solvants hydroxyliques, les conformations favorisées sont du type *Z*,*Za*. Les calculs de champs de forces prédisent aussi que le conformère *E*,*Za* devrait être le plus stable.

Mots clés : dichroïsme circulaire, conformation, structure cristalline, spectroscopie RMN dynamique, *N*,*N*′-bis[(*S*)-1-phényléthyl]thiourée.

[Traduit par la rédaction]

Introduction

In 1970, Terent'ev and co-workers reported the ultraviolet spectra and the anomalous rotatory dispersion (ORD) curves of *N*,*N*′-bis[(*S*)-1-phenylethyl]-thiourea (**1**) and a number of analogues (1, 2). They observed positive Cotton effects at ca. 300 nm in chloroform and benzene solutions, but negative effects in ethanol. These observations were qualitatively explained by the solvent dependence of the *E*–*Z* equilibrium with respect to the N—C(═S) bonds (2).

Simple *N* -alkylamides (3, 4) and -thioamides (5) prefer the *Z* to the *E* conformation, but simple *N*,*N*′-dialkylthioureas have been shown by ^{1}H NMR (6, 7) and IR (7) spectroscopy to appear as mixtures of *E*,*Z* and *Z*,*Z* forms with the former dominating. The conformational situation becomes more complicated in thioureas substituted by secondary alkyl groups like isopropyl and 1-phenylethyl groups, since these can take up (at least) two different "bisected" orientations with respect to the thioamide plane (8–10). In combination with the *E* and *Z* conformations, this leads to (at least) 10 possible conformations for **1** (Scheme 1).

The early workers were confined by instrumental limitations to use only the ORD technique and to work in the wavelength region above 300 nm, which barely touches the absorption region of these compounds. To examine more closely the detailed conformational behaviour of **1**, we have performed a study of its NMR, IR, UV, and CD spectra in hydrogen bonding and non-hydrogen-bonding solvents. The crystal structure of **1** has also been studied, and the spectral data are interpreted with the aid of CNDO/S calculations and theoretical calculations of CD spectra. The calculations are based on geometries of minimum energy conformations obtained by empirical force-field calculations.

Experimental part

Materials

The synthesis of **1** has been described by Lovén and Ohlsson (11), by Kallenberg (12), and by Terent'ev and co-workers (1). In the present work **1** was prepared in 88% yield by heating an

This paper is dedicated to Professor Erwin Buncel in recognition of his contributions to Canadian chemistry.

Received January 6, 1998.

K. Rang and J. Sandström.[1] Division of Organic Chemistry 1, Center for Chemistry and Chemical Engineering, University of Lund, P.O. Box 124, SE-22100 Lund, Sweden.
C. Svensson. Inorganic Chemistry 2, Center for Chemistry and Chemical Engineering, University of Lund, P.O. Box 124, SE-22100 Lund, Sweden.

[1] Author to whom correspondence may be addressed. Telephone: +46-46-2228130. +46-46-2118911. Fax: +46-46-2224119. E-mail: jan.sandstrom@orgk1.lu.se

© 1998 NRC Canada

Scheme 1.

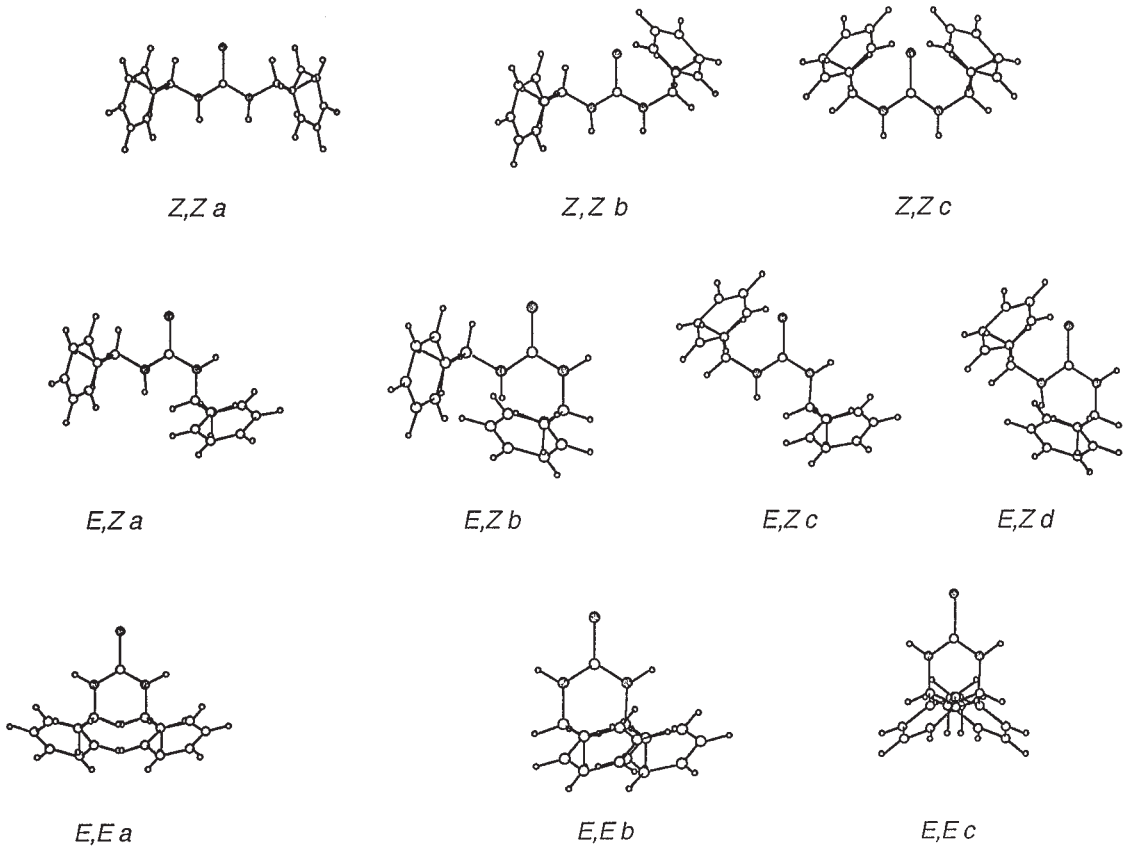

ethanol solution of (*S*)-1-phenylethylammonium (*S*)-*N*-1-phenylethyldithiocarbamate (13) to reflux; pale yellow crystals, mp 206–207°C (Kofler Heizbank) after recrystallization from 1-propanol. Previous authors have reported melting points of 195.5 (11), 195–197 (12), and 199–200°C (1).

Spectra

^1H *NMR spectra* were recorded with a Bruker ARX 500 NMR spectrometer operating at 500.14 MHz. *IR spectra* in chloroform-*d* solution and in KBr were recorded with a Perkin–Elmer Model 298 infrared spectrophotometer. *UV spectra* were recorded with a Cary Model 2290 spectrophotometer. By using 0.1 cm cells, it was possible to record spectra down to 190 nm. *CD spectra* were recorded with a JASCO Model J-500A spectropolarimeter. The experimental spectra were digitized and simulated by a set of Gaussians, using a least squares approach.[2] In all cases, quite good agreement with the experimental curves were obtained. From the Gaussians, the rotational strengths of the transitions (R_i, in Debye Bohr magnetons) were obtained by eq. [1], where Δ_e is half the band width at $\varepsilon = \Delta\varepsilon_{max}/e$.

[1] $$R_i = 0.4389\Delta\varepsilon_{max}\Delta e/\lambda_{max}$$

X-ray crystallography

Intensity data were collected at room temperature on a Siemens SMART (14) CCD diffractometer using a Rigaku rotating anode generator. The data collection covered, nominally, a hemisphere of reciprocal space, $\Theta_{max} = 46.5°$. Three

Table 1. Crystal data and structure refinement.

Empirical formula	$C_{17}H_{20}N_2S$
Formula weight	284.41
Temperature	298 (2) K
Wavelength	0.71073 Å
Crystal system	Trigonal
Space group	$P3_2$
Unit cell dimensions	$a = b = 10.33820$ (10) Å $c = 13.2001$ (3) Å
Volume	1221.79 (3) Å^3
Z	3
Density (calc.)	1.160 Mg/m^3
Absorption coefficient	0.191 mm^{-1}
F(000)	456
Crystal size	0.30 × 0.20 × 0.10 mm
Theta range for data collection	2.27–23.24°
Limiting indices	$-11 \le h \le 11, -6 \le k \le 11, -14 \le l \le 14$
Reflections collected	4791
Independent reflections	2206 [R(int) = 0.0623]
Absorption correction	None
Goodness-of-fit on F^2	1.067
Final R indices [$I > 2\sigma(I)$]	$R1 = 0.0409$, $wR2 = 0.1044$
R indices (all data)	$R1 = 0.0461$, $wR2 = 0.1123$
Absolute structure parameter	0.00 (9)
Extinction coefficient	0.013 (4)

[2] Deltagraph Pro 3. Copyright 1993. Delta Point, Inc., Harris Court, Monterey 93940, Calif., U.S.A.

© 1998 NRC Canada

Table 2. Input data for the theoretical calculation of the CD spectra of the significant conformations of **1**.[a]

Chromophore	ν (kK)[b]	μ,[c] m[d]	α (°)	Transition charges	Transition
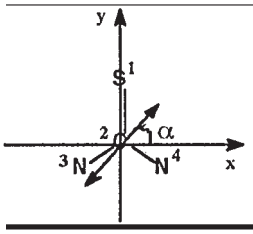	34.50	0.9547[d]	90	0.450 (x, y = ±0.660)[e]	$n\rightarrow\pi^*$ (A)
	40.35	3.58[c]	90	S(1): –0.1802 C(2): +0.0902 N(3), N(4): +0.0450	$(\pi\rightarrow\pi^*)_1$ (B)
	43.48	3.17[c]	0	N(3), N(4): ±0.1406	$(\pi\rightarrow\pi^*)_2$ (C)

[a] The charges are in units of the protonic charge.
[b] 1 kK = 10^3 cm^{-1}.
[c] Electric transition moment in D.
[d] Magnetic transition moment in Bohr magnetons.
[e] Transition quadrupole on the sulfur atom, in the x, y plane.

sets of exposures were taken, each with a different ϕ setting, and each exposure covered 0.3° in ω. The data reduction was performed by the program SAINT (15).

Space group $P3_2$ was assigned on the basis of the three-dimensional intensity distribution, the systematic extinctions, and the value of the absolute structure parameter. Cell dimensions were refined using the the spot positions determined from the data frames. SHELXTL[3] was used for the full-matrix least-squares structure refinement based on F^2. The final residual electron density was between 0.21 and –0.11 e/Å^3. A summary of the crystal data and structure refinement is given in Table 1.

Calculations

The empirical force-field calculations were performed with the MacMimic implementation[4] of the Allinger MM2–91 force field (16).[5] The atomic charges used were obtained by the semiempirical AM1 method (17). Nonstandard force-field parameters related to the thioamide group have been summarized earlier (18), and the small number of new parameters required for the thiourea group are available from the authors on request. The standard length of the C═S bond was changed from 162.6 pm, applicable for simple thioamides, to 169.2 pm as found in the crystal structure of **1** (vide infra).

The minimum energy conformations were found by systematic driving of the 1-phenylethyl groups and by energy minimization starting from a large number of feasible starting geometries, including a variety of torsion angles with respect to the phenyl groups.

CNDO/S calculations were performed with a program based on the original Jaffé formalism but modified for sulfur compounds by Pfister-Guillouzo and co-workers (19). Two-center repulsion integrals were calculated by the Nishimoto–Mataga formalism (20), and configuration interaction was performed with the 20 lowest singly excited states. Inclusion of a larger number of configurations was considered unnecessary, since it has only a moderate effect on the calculated transition energies and oscillator strengths, and it complicates the analysis of the transitions in terms of molecular orbitals.

Scheme 2.

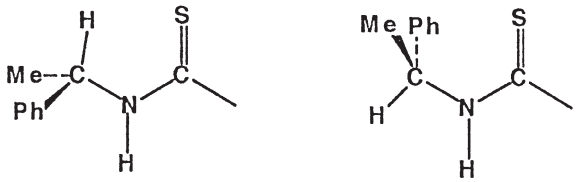

Za *Zb*

Theoretical calculations of the CD spectra were performed with the matrix technique devised by Schellman and co-workers (21–24). This method allows the use of the one-electron (Condon) (25), magnetic–electric coupling ($m\mu$) (26, 27), and coupled oscillator (Kirkwood) (28, 29) mechanisms. The required input is transition energies strengths and directions of electric and magnetic transition dipoles, transition monopoles and quadrupoles, and static charges. The methods for derivation of these data have recently been summarized (30). The input data for the thiourea chromophore are shown in Table 2 and those for the 1-phenylethyl group are taken from ref. 13.

Results and discussion

Conformations, crystal structure, and NMR spectra

A qualitative survey of the 10 conformations of **1** shown in Scheme 1 leads to the conclusion that several of them must be too high in energy to be considered as contributing significantly to observed spectra. No *E*,*E* forms have ever been observed in NMR spectra of *N*,*N*′-dialkylureas or -thioureas, which is explained by the steric repulsion between the alkyl groups. The same effect leads to the considerable nonplanarity found for tetramethylurea and -thiourea (31). Therefore, all *E*,*E* forms are neglected in the forthcoming discussion.

In previous studies of *N*-1-phenylethyl-thioamides (10, 13, 32) it was observed that 1-phenylethyl groups oriented *Z* to the thiocarbonyl group (Scheme 2) prefer the conformation (*Za*) in which the methine hydrogen points in the direction of the C═S group to the conformation (*Zb*) in which the phenyl group approaches the sulfur atom. This preference is not reproduced by force-field calculations in which the electrostatic

[3] G.M. Sheldrick. SHELXTL/PC Version 5. Siemens Analytical X-ray Instruments Inc., Madison, Wisconsin, U.S.A. 1994.
[4] The program is available from Instar Software, IDEON Research Park, SE 22370 Lund, Sweden.
[5] The program is available from the Quantum Chemistry Program Exchange, QCPE, University of Indiana, Bloomington 47405, Ind., and from Molecular Design Ltd., San Leandro, Calif.

© 1998 NRC Canada

Table 3. Relative strain energies and pertinent dihedral angles for various conformations of **1** calculated by the MM2–91 force field using the dipole model.

Conformer	Energy (kcal mol^{-1})	Φ_1 (°) C(1)-N(1)-C(2)-H(2)	Φ_2 (°) C(1)-N(1′)-C(2′)-H(2′)
Z,*Za*	+4.28	–37.0	–37.0
Z,*Za*$_1$	+6.02	+21.7	+30.3
Z,*Za*$_2$	+5.50	+24.5	–20.5
Z,*Zb*	+9.42	–140.1	–36.8
Z,*Zc*	+11.20	+171.6	+168.5
		(*E*)	**(*Z*)**
E,*Za*	0	+72.2	–32.3
E,*Zb*	+1.46	+162.9	–21.1
E,*Zc*	No energy minimum		
E,*Zd*	No energy minimum		
E,*Ea*	+8.80	–3.8	–2.4
E,*Eb*	+10.86	–26.1	135.3
E,*Ec*	637	Strongly deformed	

Fig. 1. Stereo picture of the *E*,*Za* conformer of **1**.

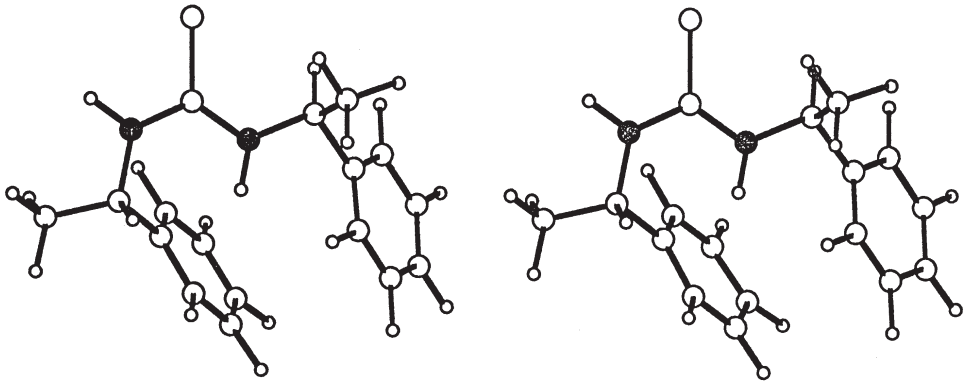

Fig. 2. Stereo picture of the unit cell of **1**.

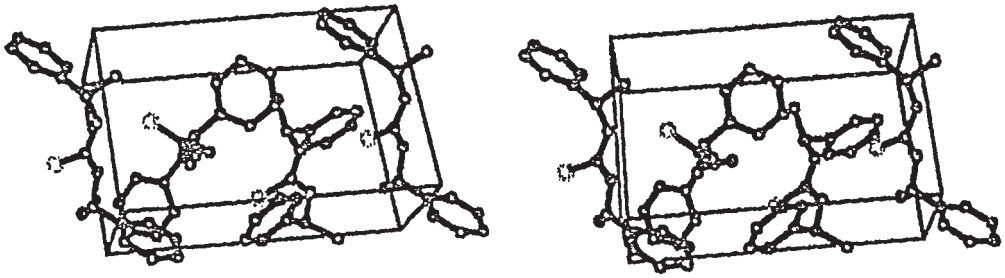

interactions are treated by the dipole model, while use of the point charge model (see ref. 16, p. 195) gives more realistic results (10). In our qualitative survey, this leads to the exclusion of *Z*,*Zb* and *Z*,*Zc* as important conformers. Similarly, the *E*,*Za* and *E*,*Zb* forms have to be considered, while *E*,*Zc* and *E*,*Zd* can be neglected.

As shown in Table 3, these qualitative deductions are corroborated by force-field calculations already by use of the dipole model. With the point charge model, the *Zb* type conformations do not appear as energy minima, but the energy minimization (Table 3) proceeds to *Za* type conformations. According to the calculations, which apply to isolated molecules, the *E*,*Za* and *E*,*Zb* forms are predicted to be much favoured. An analysis of the force-field contributions to the strain energy reveals that the *E*,*Z* forms are favoured in particular by a large number of small attractive van der Waals interactions. The other contributions are very similar for the *E*,*Z* and *Z*,*Z* forms.

The phenyl groups in the *E*,*Za* and *E*,*Zb* forms seem to be attracted by the atoms in the opposite half of the molecule. This leads to short $C_{ipso}\cdots H(\text{-}N)$ distances, *r* in Table 4, down to 219 pm in the *E* part of *E*,*Za*. This attraction leads to rotation of the 1-phenylethyl group out of the ideal bisected conformation (Fig. 1). It should be noted that the *E* phenyl groups approach the thiourea plane from opposite sides in *E*,*Za* and *E*,*Zb*, which has consequences for the predicted signs of the CD bands (vide infra).

© 1998 NRC Canada

Table 4. $^3J_{H\text{-}H}$ calculated by eq. [2] for the H-N-C_αH dihedral angle (α) and the corresponding[a] (N-)H···C_{ipso} distances (r) for the *E*,*Z* conformations of **1**.

	E part			*Z* part		
Conformer	α (°)	*J* (Hz)	*r* (pm)	α (°)	*J* (Hz)	*r* (pm)
E,*Za*	–104.9	2.89	219	146.2	7.01	245
E,*Zb*	–17.7	5.87	225	179.1	8.85	267

[a] The *E* distance is measured from C_{ipso} in the *E* part to (N-)H in the *Z* part, the *Z* distance from C_{ipso} in the *Z* part to (N-)H in the *Z* part.

Scheme 3.

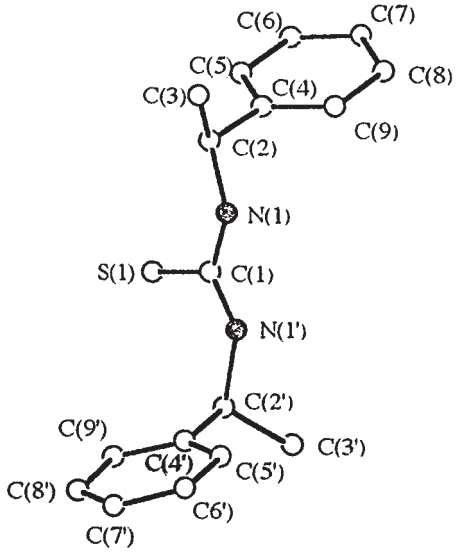

Scheme 4.

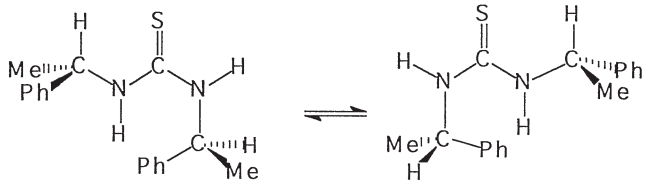

The angles called Φ_1 and Φ_2 (see Table 3) have rather high negative values in the *Za* forms (Fig. 1), i.e., the methine protons are rather far from eclipsing the C═S group (Table 4).

However, it was found in a study of *N*-(1-phenylethyl)-thiazoline-2-thiones (32) that the dominant conformer is of *Za* type, but that this corresponds to two conformers with similar energy, one with positive and one with negative Φ_1. A force-field exploration of the *Z*,*Za* region of **1** with positive values for Φ_1 and (or) Φ_2, using the dipole model, reveals further minimum energy conformations, denoted *Z*,Za_1 and *Z*,Za_2 in Table 3. However, these conformations have quite high energies, and when the point charge model is used, they revert to the *Z*,*Za* form.

The energy hypersurface with respect to variations in the *Z* part show several close-lying shallow energy minima with Φ_1

Table 5. Bond lengths, bond angles, and dihedral angles from the crystal structure of **1**.

Bond length (pm)	
S(1)—C(1)	169.2 (3)
C(1)—N(1)	134.0 (4)
C(1)—N(1′)	133.0 (4)
N(1)—C(2)	146.8 (4)
N(1′)—C(2′)	147.6 (4)
C(2)—C(3)	151.7 (4)
C(2′)—C(3′)	152.9 (6)
C(2)—C(4)	150.5 (5)
C(2′)—C(4′)	150.9 (4)
Bond angles (°)	
S(1)-C(1)-N(1)	121.8 (2)
S(1)-C(1)-N(1′)	124.6 (2)
N(1)-C(1)-N(1′)	113.6 (2)
C(1)-N(1)-C(2)	126.8 (2)
C(1)-N(1′)-C(2′)	127.0 (3)
N(1)-C(2)-C(3)	108.2 (3)
N(1′)-C(2′)-C(3′)	108.6 (3)
N(1)-C(2)-C(4)	112.5 (3)
N(1′)-C(2′)-C(4′)	109.7 (2)
C(3)-C(2)-C(4)	112.1 (3)
C(3′)-C(2′)-C(4′)	113.6 (3)
Dihedral angles (°)	
S(1)-C(1)-N(1)-C(2)	–4.5
S(1)-C(1)-N(1′)-C(2′)	–8.1
C(1)-N(1)-C(2)-C(3)	143.9
C(1)-N(1′)-C(2′)-C(3′)	126.6
C(1)-N(1)-C(2)-C(4)	–91.9
C(1)-N(1′)-C(2′)-C(4′)	–108.8
N(1)-C(2)-C(4)-C(5)	133.0
N(1′)-C(2′)-C(4′)-C(5′)	108.3

Fig. 3. Assignments of ^{1}H NMR shifts (δ) for **1** in chloroform-*d* solution at –40°C. Coupling constants (Hz) in parentheses.

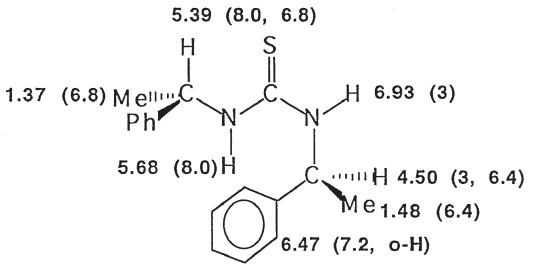

Fig. 4. The N-H···Ph hydrogen bond in *N*,*N*′-bis(α,α-dimethylbenzyl)-thiourea (45).

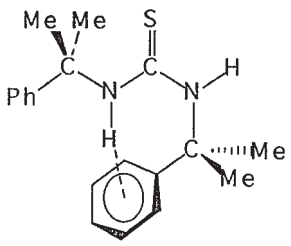

© 1998 NRC Canada

Table 6. The UV and CD spectra of *N*,*N*′-bis[(*S*)-1-phenylethyl]-thiourea (**1**).

Solvent	UV/CD	λ nm (ε, Δε M^{-1} cm^{-1})
Cyclohexane	UV	259 (10 700), 203 S[a] (28 500)
	CD	311 (+0.22), 269 (+3.44)*, 263 (+5.00)*, 257 (+3.2)*, 232 (+2.28), 217 (–4.4), 205 (+6.3), 197 (+14) Three sharp bands at 269, 263, and 257 nm (^1L_b, marked with an asterisk) are superimposed on a stronger and broader positive band, centered at ca. 262 nm (Fig. 5*a*).
Cyclohexane–dichloromethane 95:5 (v/v)	CD	297 (+0.83), 272 (+4.03)*, 267 (+5.76)*, 262 (+4.82)*, 234 (+3.1), 221 (–4.9)
Dichloromethane	CD	288 (+1.57), 269 (+3.35)*, 262 (+5.42)*, 257 (+5.45)*, 251 S (+4.11), 232 (+2.24), 220 (–3.3). Here the strong and broad positive band is centered at 258 nm.
Chloroform	CD	286 (+1.96)
Acetonitrile	UV	251 (13 300), 215 S (22 700), 205 S (26 000)
	CD	293 (+0.67), 268 (+2.96)*, 262 (+3.70)*, 247 (–6.7), 229 (+5.3), 205 (+9.2), 195 (+39)
Ethanol, abs.	UV	245 (12 100), 214 S (19 800), 203 S (23 800)
	CD	300 (+0.068), 275(–0.62). 269 (+0.52)*, 265.5 (–0.52),[b] 263 (–0.064)*, 257 (–1.52)*, 247 (–5.32), 210 (+4.4)
Ethanol–water, 3:1	UV	244 (12 600), 210 (24 300)
	CD	285 (+0.58), 268 (+1.60)*, 262 (+1.55)*, 256 (–0.27)*, 244 (–8.4), 228 (+3.5), 210 (+11.8)
Methanol	UV	244.5 (14 500), 203 S (29 000), 195 (31 000)
	CD	297 (+0.101), 277 (–0.37), 268 (+1.10)*, 262 (+1.24)*, 256 S (–1.60)*, 246 (–8.7), 226 (+5.9), 210 (+12), 194 (+20)

[a] Shoulder.
[b] Negative minimum.

values varying from ca. –20 to ca. –45°, constituting what may be referred to as a *Z*,*Za* "family."

In a protic and (or) basic solvent **1** can be expected to be involved in hydrogen bonding with solvent molecules and with other thiourea molecules both at the C═S and the NH groups, and this may change the populations considerably, but also under such circumstances only the conformations of *Z*,*Za*, *E*,*Za*, and *E*,*Zb* type need to be considered.

The conformation of **1** in the crystal (Scheme 3) was found to be of the *Z*,Za_1 type but without a C_2 axis. The molecules in the crystal form an infinite chain along the *c* axis with bifurcated hydrogen bonds between the sulfur atom in one molecule and the two NH protons in one of the neighbouring molecules (Fig. 2). The corresponding S···N distances are 341.6 and 354.2 pm, quite similar to the S···N distances related to bifurcated hydrogen bonds (335–343 pm) found in a neutron-diffraction study of thiourea (33). Crystal structures for a number of symmetrical *N*,*N*′-disubstituted thioureas have recently been reported. *N*,*N*′-diphenylthiourea (34) was found to have the *Z*,*Z* conformation with bifurcated hydrogen bonds similar to those in **1** but with C_s symmetry, while *N*,*N*′-diethyl- (34), -diisopropyl- (34), bis(2-chlorophenyl)- (35), dibenzyl- (36), and dicyclohexyl-thiourea (36) take up the *E*,*Z* conformation. The preference for this latter conformer in the crystals is ascribed to the formation of hydrogen-bonded cyclic dimers.

The C(1)-N(1)-C(2)-C(3), C(1)-N(1)-C(2)-C(4), C(1)-N(1′)-C(2′)-C(3′), and C(1)-N(1′)-C(2′)-C(4′) dihedral angles in the crystal of **1** are +126.1, –108.4, +143.5, and –91.5°, respectively. (The numbering of the heavy atoms follows from Scheme 3, and the hydrogen atoms are numbered as the attached heavy atoms.) Thus Φ_1 and Φ_2 have approximative values of +9 and +26°, to be compared with the negative dihedral angles predicted by the force-field calculations (Table 3). Pertinent bond lengths and angles are found in Table 5.

The ^{1}H NMR spectrum of **1** in chloroform-*d* solution at ambient temperature displays a doublet for the methyl protons at δ 1.42, a broad resonance for the methine protons at δ 4.95, and a similar resonance for the NH protons at δ 6.02. The aromatic resonance consists of one broad singlet (4H) at δ 7.0 and another (6H) at δ 7.2. When the temperature is lowered, the signals broaden and split. The methyl resonances appear at –40°C as two doublets of equal intensity at δ 1.37 (J = 6.8) and δ 1.48 (J = 6.4 Hz), the methine resonances as two multiplets, nearly quintets, at δ 4.50 (J = 3.0 and 6.4 Hz) and δ 5.39 (J = 6.8 and 8.0 Hz). The NH resonance splits into two doublets, at δ 5.68 (J = 8.0 Hz) and at δ 6.93 (J = 3.0 Hz). The high-field 4H aromatic resonance also splits. Part of it apprears as a doublet (2H) at δ 6.47 (J = 7 Hz), while the remainder is hidden in a 5H multiplet in the range δ 7.30–7.40. Besides, a 3H multiplet appears in the range δ 7.05–7.10.

This NMR spectrum can only be interpreted in terms of the complete dominance of one or more *E*,*Z* conformers, in the latter case rapidly equilibrating. The assignment of the chemical shifts shown in Fig. 4 is based on the following arguments: it has been observed in several studies (37–39) that the resonances of methine protons in *N*-alkylthioamides, which nearly eclipse the thiocarbonyl group, appear at unusually low field. Therefore the methine proton with the low-field shift δ 5.39

© 1998 NRC Canada

Fig. 5. (*a*) The CD spectrum of **1** in cyclohexane; (*b*) the CD spectrum of **1** in methanol.

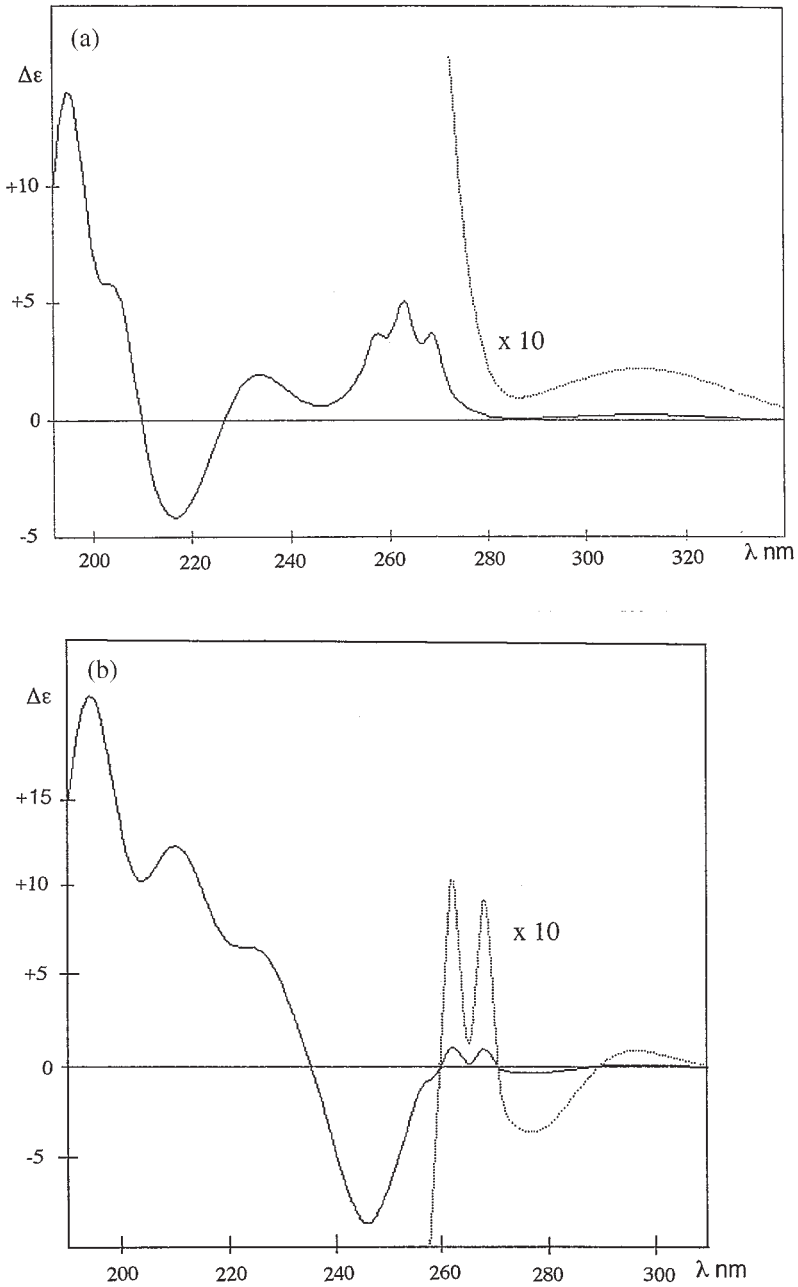

must be in a *Za* type 1-phenethyl group and nearly eclipse the thiocarbonyl group, which makes *E*,*Za* and *E*,*Zb* the prime candidates in the detailed conformational analysis. The couplings to this proton identify the corresponding methyl and NH protons. The vicinal HN–CH coupling constant is 8 Hz in the *Z* part and only 3 Hz in the *E* part. This kind of coupling has been much studied in peptides (40–42), and Demarco et al. (42) have proposed a version of the Karplus equation (eq. [2]), which describes ^3J(H-C_α-N-H) as a function of the dihedral angle α for a number of ferrichrome peptides reasonably well. Using this, equation and geometries for the conformers in Table 3,

[2] $$^3J(\alpha) = 5.4 \cos^2 \alpha - 1.3 \cos \alpha + 2.2 \text{ (Hz)}$$

α-values and ^3J values have been found for the relevant conformers (Table 4). The agreement between experimental and calculated ^3J values is much better for *E*,*Za* than for *E*,*Zb*. Consequently, the ^3J(H-C_α-N-H) values support the conclusion that the *E*,*Za* conformer dominates in chloroform and similar solvents.

The resonance of two aromatic protons (*ortho* protons according to the doublet structure with $J = 7$ Hz) falls at an unusually high field (δ 6.47). The *E* phenyl group falls in the shielding region of the thiocarbonyl group (37) both in the *E*,*Za* and the *E*,*Zb* conformation, as follows from the short (N-)H···C_{ipso} distances (Table 4).

The temperature-dependent broadenings observed are in agreement with those expected for an *E*,*Z* –*Z*,*E* exchange (Scheme 4), and complete band-shape analysis (43) of the

© 1998 NRC Canada

Table 7. Experimental and calculated rotational strengths (Debye Bohr magnetrons)

	Experimental		*Z,Za*				
Transition	Cyclohexane	Methanol	$\Phi_1 = +17°$	$\Phi_1 = -35°$	$\Phi_1 = -45°$	*E,Za*	*E,Zb*
n→π*	+0.008	+0.002	–0.150	+0.135	+0.018	+0.015	+0.090
(A)		–0.006					
^1L_b[a]	+0.013	+0.010	+0.005	–0.010	–0.012	+0.012	–0.010
B	+0.059	–0.124	–0.161	–0.723	–0.573	+0.026	–0.706
C	+0.043	+0.092	+0.700	+0.360	+0.240	+0.486	+1.158
^1L_a	–0.089[b]	+0.226	+0.015[b]	+1.247[b]	+0.981[b]	0.954b	+1.558[b]
	(12)		(5.6)	(6.3)	(6.6)	(5.2)	(5.8)
	+0.067		–0.388	–1.007	–0.642	+0.702	–1.082
^1B_b	+0.157	+0.317	+1.662[b]	+4.478[b]	–4.913[b]	+0.896[b]	–1.360[b]
			(1.3)	(1.0)	(0.3)	(10.0)	(5.2)
			–2.320	–4.600	+4.678	–0.575	+2.152

[a] Sum of all bands.
[b] Long-wavelength band of couplet. Δλ nm in parentheses.

methyl resonance at intermediate broadening leads to a free energy barrier to this exchange of 12.8 ± 0.1 kcal mol^{-1}. This agrees well with the barrier found for *N*,*N*′-dimethylthiourea: 12.5 kcal mol^{-1} in CD_3CN (7), 12.7 kcal mol^{-1} in pyridine-d_5 (6). The lower barrier, 11.1 kcal mol^{-1}, found for *N*,*N*′-di-*tert*-butylthiourea (7, 44) can be ascribed to ground-state strain.

The ^{1}H NMR spectrum of **1** in methanol-d_4 solution at ambient temperature shows only one methyl doublet, one broad methine resonance, and a narrow aromatic multiplet. The NH resonance coincides with the water signal, possibly because of fast exchange. On lowering the temperature, broadenings and splittings occur, but because of overlap with the solvent peaks and lack of fine structure, fewer resonances can be observed and identified at slow exchange than in chloroform-*d* solution. The methyl resonance appears as a single broad signal at –38°C, but the methine proton resonance appears split into two equally intense resonances at δ 4.94 and δ 5.59 and a single resonance at δ 5.53.The first two correspond to the *E*,*Z* form observed alone in chloroform-*d* solution, an assignment which is corroborated by NH signals at δ 5.36 and 7.05 and an aromatic 2H resonance at δ 6.63. The single methine resonance at δ 5.53 has a corresponding NH signal at δ 7.00, and these signals must be assigned to a conformer with C_2 symmetry. The low-field position of the methine resonance makes *Z*,*Za* the only likely candidate. The *Z*,*Z*:*E*,*Z* ratio is found to be 1.23:1.

Infrared, ultraviolet, and circular dichroism spectra

The infrared spectrum of **1** in the solid state (KBr tablet) shows NH stretching bands at 3235 and 3254 cm^{-1}, in agreement with the existence of two unequally hydrogen bonded NH groups in the crystal. In 10^{-2} M solution in chloroform-*d* likewise two bands appear, now at 3390 and 3416 cm^{-1}. Walter and Ruess (7, 45) have made an extensive study of the infrared spectra of mono- and symmetrically dialkyl-substituted thioureas, using 10^{-3}–10^{-5} M solutions in carbon tetrachloride. They assign a band at ca. 3450 cm^{-1} to the NH stretching in the *Z* oriented *N*-alkylamino group and another at ca. 3420 cm^{-1} to the *E* counterpart. However, in the spectrum of *N*,*N*′-bis(α,α-dimethylbenzyl)-thiourea, the former band is shifted to 3387 cm^{-1}, which is ascribed to the formation of an intramolecular "hydrogen bond" in the *E*,*Z* conformer (Fig. 5). This interpretation is evidently applicable also to **1** in chloroform-*d* solution for which a dominant *E*,*Za* conformer is inferred from NMR data.

The thioureas discussed above are undoubtedly largely monomeric at the reported measuring concentrations. Dunina et al. (46) report IR bands at 3250, 3400, and 3430 cm^{-1} in the infrared spectrum of **1** in a saturated $CHCl_3$ solution ($C \approx 0.15$ M). The 3250 cm^{-1} band is ascribed to an intermolecularly hydrogen-bonded species, and it disappears at 10-fold dilution. As mentioned below, the CD spectrum of **1** in chloroform and dichloromethane solution is independent of the concentration in the range 10^{-2}–10^{-4} M, which also supports the notion that **1** is largely unassociated in these solvents at concentrations of 10^{-2} M and lower.

Ultraviolet spectra of thiones and in particular of thioamides have been the subject of interest for a long time, among other things because they can be expected to show similarity with the oxygen analogues, albeit with the thione transitions giving rise to absorption bands at longer wavelengths and thus in more accessible spectral regions (47, 48). Thioureas have been studied by among others Janssen (49, 50), Hosoya et al. (51), Gosavi and Rao (52), and Ritchie and Spedding (53). Three bands are observed in the spectra of simple thioureas: a weak band at 280–300 nm, a strong band (ε = 10 000–12 000) at 236–250 nm, and a band of similar intensity at 195–210 nm. We will designate these three bands as due to transitions A, B, and C, respectively. Transition A is assigned to an *n*→π* transition (49, 51, 53). Analysis of transitions B and C by MO theory (51, 53) led to the classification of transition B as a regular π→π* transition, and transition C as a charge transfer transition of π→π* type in which an electron is excited from an MO described as the antisymmetric combination of the nitrogen *p* orbitals to a MO antibonding in the C═S bond. Polarized UV spectra of a thiourea crystal showed that transition B is polarized in the direction of the C_2 axis and transition C perpendicular to this direction and in the molecular plane, in agreement with the MO analysis (51).

Our CNDO/S calculations predict a forbidden *n*→π* transition at 371 nm, a π→π* transition at 271 nm (f = 0.122) polarized along the C═S bond, and another π→π* transition at 172 nm (f = 0.139) polarized perpendicular to the C═S bond. Analysis of the dominant MO:*s* involved in these

© 1998 NRC Canada

transitions shows a complete agreement with the conclusions reached for transitions B and C by the previous authors (51, 53).

The UV spectrum of **1** should be the result of overlap of the A, B, and C transitions with the aromatic ^1L_b, ^1L_a, ^1B_b, and ^1B_a transitions (54). The experimental UV spectrum (Table 5) does not display a $n\rightarrow\pi^*$ band even in cyclohexane solution. The first strong band, assigned to the B transition, appears at 259 nm in cyclohexane, at 251 nm in acetonitrile, and at 245 nm in ethanol. At shorter wavelengths shoulders appear at 215 and 205 nm, less sensitive to the solvent.

The CD spectra of **1** are quite complex and strongly solvent dependent. The spectrum in cyclohexane (Table 6 and Fig. 5*a*) shows a broad, weak positive band at 311 nm assigned to the $n\rightarrow\pi^*$ transition (transition A), followed by a stronger broad and positive band at 262 nm overlapped by three sharp positive bands of lower intensity with separations of 6 nm. The stronger band is assigned to transition B, and the three weaker bands to the aromatic ^1L_b transition. Next follows a positive band at 232 nm, tentatively assigned to the C transition. A negative band appears at 217 nm and a moderately strong positive one at 205 nm, and since model calculations indicate considerable couplings between the transitions in the aromatic rings in some conformations, the two latter bands may be seen as a negative ^1L_a couplet. A stronger positive band at 197 nm is assigned to a ^1B type transition.

Addition of a small amount (5% by volume) of dichloromethane to the cyclohexane solution does not affect the signs of the bands, but the $n\rightarrow\pi^*$ band is shifted to 297 nm and its intensity is increased nearly fourfold. In pure dichloromethane solution this development is further accentuated. In this solvent, the CD spectra at $C = 10^{-2}$ M and $C = 10^{-4}$ M are quite equal, which supports the notion that no dimerization occurs in this concentration range.

In chloroform solution only the $n\rightarrow\pi^*$, the first ^1L_b and the beginning of the B band can be observed. They have the same signs as in cyclohexane and dichloromethane solution, but the $n\rightarrow\pi^*$ band is now still stronger.

In methanol (Fig. 5*b*) and ethanol solutions two bands are observed in the 270–300 nm region, which are resolved into a weak positive band at 295 nm and a stronger negative one at 277 nm, both probably of $n\rightarrow\pi^*$ origin. The ^1L_b bands are unchanged but the stronger band B is now negative and shifted to 246–247 nm, and the following two bands are positive. This means that the ^1L_b and C band have the same signs in cyclohexane–dichloromethane and methanol–ethanol solutions but that the B band has opposite sign. The bands at 210 and 195 nm are both positive, and no couplet is observed in the ^1L_a region. The CD spectrum of **1** in methanol has been described earlier (55), but this spectrum differs in important respects from the one reported here.

The spectrum in acetonitrile is quite similar to those in methanol and ethanol, the main difference being that only one (positive) $n\rightarrow\pi^*$ band is observed and that the ^1L_b bands (positive) are unusually strong.

Dilution of the ethanol solution with water leads to the replacement of the negative $n\rightarrow\pi^*$ band by a positive band at 285 nm, the intensity of which increases with increasing concentration of water. The remainder of the spectrum is less affected by the water.

Rotational strengths for the relevant conformers of **1** (*Z*,*Za* with a selection of Φ_1 and Φ_2 values, *E*,*Za* and *E*,*Zb*) have been calculated using the geometries from the MM2 calculations and are presented in Table 7 together with the experimental data from spectra in cyclohexane and methanol solution, derived by use of eq. [1] (experimental section). The conformer, which dominates in cyclohexane, should give rise to positive A, B, C, and ^1L_b transitions, a negative ^1L_a couplet, and a positive long-wavelength band in the ^1B system. Inspection of Table 7 reveals that these conditions are fulfilled by the *E*,*Za* conformer, but not by any of the others. The predicted magnitudes of the A, B, and ^1L_b rotational strengths are of the same order of magnitude as the experimental ones, whereas the values predicted for the C,^1L_a, and ^1B transitions are vastly exaggerated. This deviation may be qualitatively explained by the low value for the dielectric constant, 1.5, used in these calculations. In any case, the agreement in sign is impressive and lends strong support to the conclusion from NMR spectra that the *E*,*Za* conformer dominates in nonpolar solvents.

The appearance of two bands of $n\rightarrow\pi^*$ type in the CD spectrum of **1** in methanol solution indicates the presence of more than one conformer, in agreement with the NMR results. Of all conformers in Table 7, only *Z*,*Za* with $\Phi_1, \Phi_2 = +17°$ (*Z*,Za_1 type) is predicted to have a negative $n\rightarrow\pi^*$ band. This conformer is similar to the one found in the crystal but idealized to C_2 symmetry, and it may owe its stabilization to favourable hydrogen bonding to solvent molecules. Such bonding evidently involves profound changes in the steric conditions around the NH and C═S groups, and conformers predicted on basis of MM2–91 calculations without solvent must be used with reserve.

The dominant conformer in ethanol should have positive ^1L_b bands and a negative B band, a combination only shown by *Z*,*Za* with $\Phi_1, \Phi_2 = +17°$. It should also have a positive C band, which is predicted for all five conformers. The methanol spectrum displays only one band, positive, in the ^1L_a region, which is not in complete agreement with the predictions for *Z*,*Za*, although the first ^1L_a band is predicted to be positive, as is the first 1B band.

The weak positive $n\rightarrow\pi^*$ band can be assigned to an *E*,*Z* conformer, which was also concluded from the NMR spectrum, but it must not necessarily be *E*,*Za*. The spectrum shows no sign of a positive B transition, which rather speaks for *E*,*Zb* for which a negative B transition is predicted.

The effect of adding water to an ethanol solution, the appearance of a gradually growing positive $n\rightarrow\pi^*$ band, is less readily explained. Replacement of methanol–ethanol by water around the NH and CS groups may change the steric conditions and favour *Z*,*Za* forms with different Φ_1 values. It follows from Table 7 that positive $n\rightarrow\pi^*$ bands are predicted for *Z*,*Za* forms with Φ_1 and Φ_2 equal to –35° and –45°, respectively, but no safe conclusion can be drawn.

Conclusions

Studies of **1** with ^1H NMR, IR, and CD spectroscopy in conjunction with semiempirical calculations of steric energies and rotational strengths show conclusively that the *E*,*Za* conformer dominates in nonpolar solvents. In hydroxylic solvents the equilibrium is shifted towards the *Z*,*Za* "family," and the form(s) dominating in methanol and ethanol may have $\Phi_1, \Phi_2 > 0$. The further changes in the CD spectrum caused by addition

© 1998 NRC Canada

of water to an ethanol solution may be ascribed to changes in Φ_1 within the *Z,Za* "family."

Acknowledgments

We are grateful to the Swedish Natural Science Research Council, the Knut and Alice Wallenberg Foundation, and the Royal Physiographic Society of Lund for for financial support, to Dr. Karl-Erik Bergquist for recording the NMR spectra, to Dr. Ulf Berg for performing the AM1 calculations, and to Dr. Åke Oscarsson for valuable discussions.

References

1. V.V. Dunina, E.G. Rukhadze, and A.P. Terent'ev. Zh. Obshch. Khim. **40**, 2278 (1970); J. Gen. Chem. U.S.S.R. 2266 (1971).
2. V.V. Dunina, E.G. Rukhadze, and A.P. Terent'ev. Zh. Obshch. Khim. **40**, 2285 (1970); J. Gen. Chem. U.S.S.R. 2273 (1971).
3. S. Mizushima. *In* Structure of molecules and internal rotation. Academic Press, New York. 1954. p. 118.
4. L. La Planche and M. Rogers. J. Am. Chem. Soc. **86**, 337 (1964).
5. J. Sandström and B.Uppström. Acta Chem. Scand. **21**, 2254 (1967).
6. R.H. Sullivan and E. Price. Org. Magn. Reson. **7**, 143 (1975).
7. W. Walter and K.-P. Ruess. Justus Liebigs Ann. Chem. **746**, 54 (1971).
8. U. Berg, T. Liljefors, C. Roussel, and J. Sandström. Acc. Chem. Res. **18**, 80 (1985).
9. U. Berg and J. Sandström. Adv. Phys. Org. Chem. **25**, 1 (1989).
10. M. Langgård and J. Sandström. J. Chem. Soc. Perkin Trans. 2, 435 (1996).
11. J.M. Lovén and E. Ohlsson. Ber. **47**, 1534 (1914).
12. S. Kallenberg. Ber. **52**, 2057 (1919).
13. K. Rang, F.-L. Liao, J. Sandström, and S.-L. Wang. Chirality, **9**, 568 (1997).
14. SMART Software Reference Manual. Siemens Analytical X-ray Instruments Inc., Madison, Wisconsin, U.S.A. 1996.
15. SAINT Software Reference Manual. Siemens Analytical X-ray-Instruments Inc., Madison, Wisconsin, U.S.A. 1996.
16. U. Burkert and N.L. Allinger. *In* Molecular mechanics. ACS Monograph 177. American Chemical Society, Washington, D.C. 1982.
17. M.J.S. Dewar, E.G. Zoebisch, E.F. Healy, and J.J.P. Stewart. J. Am. Chem. Soc. **107**, 3902 (1985).
18. I. Pettersson and J. Sandström. Acta Chem. Scand. Ser. B, **38**, 397 (1984).
19. C. Guimon, D. Gombeau, and G. Pfister-Guillouzo. Tetrahedron, **29**, 3399 (1973).
20. K. Nishimoto and N. Mataga. Z. Phys. Chem. (Munich), **12**, 335 (1957).
21. P.M. Bayley, E.B. Nielsen, and J.A. Schellman. J. Phys. Chem. **8**, 228 (1969).
22. E.B. Nielsen and J.A. Schellman. Biopolymers, **10**, 1559 (1971).
23. V. Madison and J.A. Schellman. Biopolymers, **11**, 1041 (1972).
24. V. Rizzo and J.A. Schellman. Biopolymers, **23**, 435 (1984).
25. E.U. Condon, W. Altar, and H. Eyring. J. Chem. Phys. **5**, 753 (1937).
26. I. Tinoco, Jr. Adv. Chem. Phys. **4**, 113 (1962).
27. J.A. Schellman. Acc. Chem. Res. **1**, 144 (1968).
28. J.G. Kirkwood. J. Chem. Phys. **5**, 479 (1937).
29. N. Harada and K. Nakanishi. *In* Circular dichroic spectroscopy - exciton coupling in organic stereochemistry. Oxford University Press, Oxford. 1983.
30. J. Sandström. *In* Circular dichroism, principles and applications. *Edited by* K. Nakanishi, N. Berova, and R.W. Woody. VCH Publishers, New York. 1994. p. 443.
31. L. Fernholt, S. Samdal, and R. Seip. J. Mol. Struct. **72**, 217 (1981).
32. J. Roschester, U. Berg, M. Pierrot, and J. Sandström. J. Am. Chem. Soc. **109**, 492 (1987).
33. M.M. Elcombe and J.C. Taylor. Acta Crystallogr. Sect. A: Cryst. Phys. Diffr. Theor. Gen. Crystallogr. **A24**, 410 (1968)
34. A. Ramnathan, K. Sivakumar, K. Subramanian. Acta Crystallogr. Sect. C: Cryst. Struct. Commun. **C51**, 2446 (1995).
35. A. Ramnathan, K. Sivakumar, K. Subramanian, N. Janarthanan, K. Ramadas, and H.- K. Fun. Acta Crystallogr. Sect. C: Cryst. Struct. Commun. **C52**, 134 (1996).
36. A. Ramnathan, K. Sivakumar, K. Subramanian, D. Merarani, and H.-K. Fun. Acta Crystallogr. Sect. C: Cryst. Struct. Commun. **C52**, 139 (1996).
37. W. Walter, E. Schaumann, and H. Paulsen. Justus Liebigs Ann. Chem. **727**, 61 (1969).
38. C. Roussel, A. Lidén, M. Chanon, J. Metzger, and J. Sandström. J. Am. Chem. Soc. **98**, 2847 (1976).
39. A. Lidén, C. Roussel, T. Liljefors, M. Chanon, R.E. Carter, J. Metzger, and J. Sandström. J. Am. Chem. Soc. **98**, 2853 (1976).
40. M. Barfield and H.L. Gearhart. J. Am. Chem. Soc. **95**, 641 (1973).
41. V.F. Bystrov, V.T. Ivanov, S.L. Portnov, T.A. Balashova, and Yu.A. Ovchinnikov. Tetrahedron, **29**, 873 (1974).
42. A. Demarco, M. Llinás, and K. Wütrich. Biopolymers, **17**, 637 (1978).
43. J. Sandström. *In* Dynamic NMR spectroscopy. Academic Press, New York. 1982. p. 86.
44. C.D. Freeman and D.L. Hooper. J. Phys. Chem. **78**, 961 (1974).
45. W. Walter and K.-P. Ruess. Justus Liebigs Ann. Chem. **743**, 167 (1971).
46. V.V. Dunina, E.G. Rukhadze, and A.P. Terent'ev. Zh. Obshch. Khim. **42**, 2565 (1972); J. Gen. Chem. U.S.S.R. 2556 (1973).
47. M. Kajtar, M. Hollosi, J. Kajtar, Z. Majer, and A. Vass-Lakatos. *In* F.E.C.S. Int. Conf. Circular Dichroism. Sofia, Bulgaria. Sept. 21–25, 1985. p. 126.
48. M. Hollosi, Z. Majer, M. Zewdu, F. Ruff, M. Kajtar, and K.E. Köver. Tetrahedron, **44**, 195 (1988).
49. M.J. Janssen. Rec. Trav. Chim. **79**, 454 (1960).
50. M.J. Janssen. Rec. Trav. Chim. **79**, 1066 (1960).
51. H. Hosoya, J. Tanaka, and S. Nagakura. Bull. Chem. Soc. Jpn. **33**, 850 (1960).
52. R.K. Gosavi and C.N.R. Rao. Can. J. Chem. **45**, 1897 (1967).
53. R.K. Ritchie and H. Spedding. Spectrochim. Acta Part A, **26A**, 9 (1970).
54. J.R.J. Platt. J. Chem. Phys. **17**, 484 (1949).
55. Z. Krawczyk and C. Belzecki. Pol. J. Chem. **53**, 631 (1979).

© 1998 NRC Canada

Identity-reaction proton transfers from nitrogen acids yielding localized vs. delocalized conjugate bases. An ab initio study

James E. Van Verth, William H. Saunders, Jr., and Thomas W. Kermis

Abstract: Identity-reaction proton transfers from a series of nitrogen acids to the corresponding conjugate bases have been studied by ab initio methods at the MP2/6-31+G*//MP2/6-31+G* level. The acids are NH_4^+, $H_2NNH_3^+$, $CH_3NH_3^+$, CH_2NH_2, $OCNH_2^+$, $OCHNH_3^+$, $H_2NCHNH_2^+$, $HNCHNH_3^+$, NH_3, CH_3NH_2, CH_2NH, OCNH, $OCHNH_2$,and $HNCHNH_2$. Gas-phase acidities were calculated at the G2(MP2) level where experimental values are not available in order to have benchmark values for all acidities. Barriers to proton transfer relative to the separated reactants, ΔH_{TS}, show a straight-line relation to acidity for all of the neutral acids and for all but four of the cationic acids. Three show ΔH_{TS} values well above the line: $HNCHNH_3^+$, $OCNH_2^+$, and $OCHNH_3^+$, in increasing order of positive deviation. One shows a small negative deviation: $H_2NNH_3^+$. The first three acids have localized π systems but can yield delocalized transition structures and conjugate bases. The barriers result from a lag in delocalization relative to proton transfer in the transition structures. All of the other acids give transition structures that can only be localized, or if they can be delocalized they prefer to adopt conformations in which the unshared pair on nitrogen delocalizes rather than the electrons of the N---H bond. The negative deviation for $H_2NNH_3^+$ is attributed to polarizability of the NH_2 group.

Key words: ab initio, nitrogen acids, proton transfer, acidity.

Résumé : Faisant appel à des méthodes ab initio au niveau MP2/6-31+G*//MP2/6-31+G*, on a étudié les réactions d'identité par transfert de proton d'une série d'acides azotés vers les bases conjuguées correspondantes. Les acides étudiés sont le NH_4^+, $H_2NNH_3^+$, $CH_3NH_3^+$, $CH_2NH_2^+$, $OCNH_2^+$, $OCHNH_3^+$, $H_2NCHNH_2^+$, $HNCHNH_3^+$, NH_3, CH_3NH_2, CH_2NH, OCNH, $OCHNH_2$ et $HNCHNH_2$. Dans les cas où les valeurs expérimentales des acidités ne sont pas disponibles, on a calculé les acidités en phase gazeuse au niveau G2(MP2) afin de disposer de valeurs de référence pour toutes les acidités. Les barrières au transfert de proton par rapport aux réactifs séparés, ΔH_{TS}, présentent une relation linéaire avec l'acidité pour tous les acides neutres ainsi que pour tous les acides cationiques à l'exception de quatre. Trois présentent des valeurs de ΔH_{TS} bien au-dessus de la ligne; il s'agit dans l'ordre d'augmentation de la déviation de $HNCHNH_3^+$, $OCHNH_2^+$ et $OCHNH_3^+$. Le $H_2NNH_3^+$ présente une légère déviation négative. Les trois premiers acides possèdent des systèmes π localisés, mais peuvent conduire à des structures de transition délocalisées et à des bases conjuguées. Les barrières résultent d'un retard dans la délocalisation relative au transfert de proton dans les structures de transition. Tous les autres acides conduisent à des structures de transition qui ne peuvent qu'être localisées ou, si elles peuvent être délocalisées, elles préfèrent adopter des conformations dans lesquelles la paire d'électron non partagés de l'azote se délocalise plutôt que les électrons de la liaison N---H. On attribue la déviation négative du $H_2NNH_3^+$ à la polarisabilité du groupe NH_2.

Mots clés : ab initio, acides de l'azote, transfert de proton, acidité.

[Traduit par la rédaction]

Introduction

Proton transfers to or from "normal" or Eigen acids usually occur at a diffusion-controlled (or close to diffusion controlled) rate when the proton transfer is exoergic (1). Slower deprotonation results when the reaction is endoergic, but essentially the only barrier is the endoergicity. Eigen acids are those in which the proton is bound to an electronegative atom such as nitrogen or oxygen. In contrast, carbon acids often deprotonate at much slower rates than Eigen acids of similar acidity. The factors contributing to these barriers have been examined in recent years by means of quantum-chemical calculations as well as experiment.

A clear distinction can be made between carbon acids that yield localized vs. delocalized conjugate bases. Although both, unlike Eigen acids, show significant barriers, the carbon acids yielding delocalized bases deprotonate more slowly than acids of similar acidity yielding localized bases. In general terms the need for heavy-atom reorganization during proton transfer is considered to raise the barrier to the reaction (2, 3). A more

Received December 17, 1997.

This paper is dedicated to Professor Erwin Buncel in recognition of his contributions to Canadian chemistry.

J.E. Van Verth and T.W. Kermis. Department of Chemistry, Canisius College, Buffalo, NY 14208, U.S.A.
W.H. Saunders, Jr.[1] Department of Chemistry, University of Rochester, Rochester, NY 14627, U.S.A.

[1] Author to whom correspondence may be addressed. Telephone: (716) 275-4235. Fax: (716) 473-6889. E-mail: saunders@chem.chem.rochester.edu

© 1998 NRC Canada

rigorous treatment called the principle of nonperfect synchronization (PNS) has been proposed by Bernasconi (4–6). He argues that charge delocalization lags behind charge transfer from the base, and that the resulting lag in development of resonance stabilization contributes to the intrinsic barrier to proton transfer.

The validity of the PNS can be most easily tested if contributions from solvent reorganization can be eliminated and the intrinsic barrier determined directly by employing identity reactions. It is not easy to accomplish experimentally, but ab initio calculations are ideally suited to this end. Pioneering work by Scheiner and his co-workers on simple systems (7–10) was followed by studies that treated mainly carbon acids yielding delocalized conjugate bases (11–15). From these studies it was clear that, even in the absence of solvent, intrinsic barriers to proton transfers from such carbon acids are higher than expected from their acidity. Furthermore, the charge distributions in the transition structures show that charge delocalization lags well behind proton transfer.

With these results in mind, a natural question to ask is whether the PNS would apply to Eigen acids as well as to carbon acids. Published work provides no guidance on this point. Identity reactions involving a number of neutral and positively charged nitrogen acids have been examined, but none of them has a delocalized conjugate base. The most extensively studied has been the ammonium ion to ammonia proton transfer (16). At the highest levels there is only a small barrier (ca. 1 kcal). The ammonia to amide ion proton transfer has also been studied by several groups (17). Again, the barrier is small (1.2 kcal using the G2+ method (17*b*)). Only a few examples could be found in which other nitrogen acids were used: simple alkylammonium ions to amines (16*e*); CH_2═NH to CH_2═N- (18); and CNH to NC- (19). In these cases the barriers were either small or negligible. There is thus little doubt that nitrogen acids with localized conjugate bases behave as Eigen acids.

Computational procedures

Ab initio calculations utilized the Gaussian 92 (20) and Gaussian 94 (21) programs with the standard basis sets 6-31+G* and 6-31+G** (22). Correlation corrections utilized the Møller–Plesset method (23). The enthalpies (ΔH) in the tables are corrected to constant pressure and, for zero-point-energy differences from MP2/6-31+G*//MP2/6-31+G* calculations, scaled to 0.95 to account for the overestimation of frequencies by Hartree–Fock methods (24). Enthalpies were further corrected to 298 K for the contributions of the translational, rotational, and vibrational partition functions (25). The vibrational correction is not based on scaled frequencies, for it is doubtful that low-lying frequencies (the only ones that contribute significantly to the vibrational partition function) bear a predictable relation to experimental values (26). Although many of the calculations were done up to the MP4SDTQ(frozen core)/6-31+G**//MP2/6-31+G* level, the results did not differ much from the complete set done at MP2/6-31+G*//MP2/6-31+G*, so only the latter are reported in Table 2. Where different stable conformations of a species are possible, the most stable one is listed in the tables. All reasonable conformations of reactants and transition structures were, however, optimized. In nearly all cases, the energy difference between the most stable and the next most stable conformation was large enough that the latter should make no significant contribution. No effort was made to locate all possible conformations of the ion–dipole complexes. Our experience with carbon acids has been that the complexes have several conformations very close in energy and easily interconvertible (11, 14). Since the energies of the complexes in the present context are useful only for establishing the magnitude of the central barrier, they were usually not explored exhaustively.

Z matrices of optimized structures in Cartesian or internal coordinates have been deposited as supplementary material.[2]

Results and discussion

As has been our practice, we compared calculated and experimental (27) gas-phase acidities to test the adequacy of the level of our calculations. The results are given in Table 1. There appear, unfortunately, to be no experimental data for the cationic acids except ammonium ion, where the agreement is excellent at all levels. Calculations by the G2(MP2) method (28) were done where experimental values were not available so as to provide benchmark values for all of the acids. In one case, the symmetrical formamidinium ion, a value was already available in the literature (29). There is only one bad disagreement among the neutral acids, HNCO. The G2(MP2) value is close to the experimental value, however, so the disagreement with values at lower levels is undoubtedly real. Comparison of the results at MP2/6-31+G*//MP2/6-31+G* with the benchmark values shows that the former are usually lower than the latter, but the difference exceeds 5 kcal mol^{-1} in only two cases. The agreement in the case of these nitrogen acids is not as good as for carbon acids (30), but is adequate for the semiquantitative purposes of our proton-transfer calculations.

Stationary points calculated for the identity-reaction proton transfers at MP2/6-31+G*//MP2/6-31+G* are given in Table 2. Enthalpies are relative to the separated reactants except as otherwise noted. Not all ion–dipole complexes were calculated. All of the proton transfers showed potential energy barriers with imaginary frequencies ranging from 600 to 1416i cm^{-1}. The frequencies ran higher for the neutral acids (839–1416i cm^{-1}) than for the cationic acids (600–1193i cm^{-1}). With exceptions to be discussed below, the enthalpic barriers, $\Delta H^{\ddagger}$, were small or even negative relative to the ion–dipole complexes, where these were calculated. The N···H bond lengths in the transition structures were relatively constant, from 1.26 to 1.30 Å for the positively charged acids and 1.25 to 1.31 Å for the neutral acids.

The best way of looking at the transition structure enthalpies is relative to the enthalpies of the corresponding separated reactants, ΔH_{TS}, which avoids complications from specific interactions affecting the enthalpies of the ion–dipole complexes. We have previously shown that for carbon acids yielding localized conjugate bases a plot of ΔH_{TS} vs. ΔH(acid) gives a straight-line relationship (14). An analogous plot in Fig. 1 for the neutral nitrogen acids shows some scatter but no points that are off the line by more than a few kcal in ΔH_{TS}. In fact, the three acids that can yield delocalized conjugate bases,

[2] Copies of this supplementary material may be purchased from: The Depository of Unpublished Data, Document Delivery, CISTI, National Research Council of Canada, Ottawa, Canada, K1A 0S2.

© 1998 NRC Canada

Table 1. Observed and calculated enthalpies[a] for $HA^+ \rightarrow H^+ + A$ and $HA \rightarrow H^+ + A^-$.

	ΔH(acid)			
	expt/G2(MP2)*a*	MP2/6–31+G*//6–31+G*	MP2/6–31+G*//MP2/6–31+G*	MP4/6-31+G*//MP2/6–31+G*
HA^+				
NH_4^+	204.1	204.2	204.4	205.4
$H_2NNH_3^+$	209.5[b]	204.7	204.9	206.6
$CH_3NH_3^+$	215.4[b]	214.5	214.7	215.7
$CH_2NH_2^+$	207.7[b]	205.7	205.1	205.9
$HCNH^+$	170.6[b]	165.0	164.4	165.8
$OCNH_2^+$	172.8[b]	168.7	169.4	170.5
$OCHNH_3^+$	182.6[b]	178.7	179.8	182.0
$H_2NCHNH_2^+$	226.8[c]	224.1	223.6	224.4
$HNCHNH_3^+$	197.1[b]	194.8	195.3	197.5
HA				
NH_3	403.6	402.5	402.6	404.1
CH_3NH_2	403.2	401.8	401.8	403.0
CH_2NH	388.3	385.7	386.2	387.1
OCNH	340.9[d]	332.2	331.7	334.1
OCHNH	359.8	355.3	355.4	356.3
$HNCHNH_2$	367.2[b]	363.2	363.1	364.3

[a] In kcal mol^{-1} at 298 K. Experimental values are given where available, G2(MP2) calculated values where they are not.
[b] Calculated by the G2(MP2) method.
[c] G2(MP2) value in ref. 29 is 225.3, which appears to be off by the enthalpy of H^+ at 298 K, 1.48 kcal mol^{-1}.
[d] G2(MP2) gives 341.6.

Table 2. Enthalpies[a] of stationary points in $AH^+ + A$ and $AH + A^-$ identity proton transfers at MP2/31+G*//MP2/6-31+G*.

	ΔH_{well}	$\Delta H^{\ddagger}$ [b]	ΔH_{TS} [c]
AH^+			
NH_4^+	[d]	[d]	–27.61
$H_2NNH_3^+$	[d]	[d]	–29.47
$CH_3NH_3^+$	–25.67	–0.91	–26.58
$CH_2NH_2^+$	–26.09	–0.94	–27.03
HCNH+	–28.15	–1.55	–29.69
$OCNH_2^+$	–17.99	–1.34	–19.33
$OCHNH_3^+$	–30.13	17.36	–12.76
$H_2NCHNH_2^+$	–27.00	0.91	–26.09
$HNCHNH_3^+$	[e]	[e]	–21.56
AH			
NH3	–14.61	2.82	–11.79
CH_3NH2	–16.02	1.53	–14.48
CH_2NH	–16.81	1.20	–15.61
OCNH	–24.63	–1.47	–26.10
OCHNH2	–21.78	–2.14	–23.92
HNCHNH2	–19.01	–1.39	–20.40

[a] In kcal mol–1 at 298 K.
[b] $H_{TS} - H$complex.
[c] $H_{TS} - H$reactants.
[d] The ion–dipole complexes were not examined.
[e] A stable low-energy ion–dipole complex could not be found. A spontaneous proton transfer to give $H_2NCHNH_2^+$ occurs. See discussion.

$O{=}CHNH_2$, $HN{=}CHNH_2$, and O=C=NH, show no greater deviations from the line than those that cannot.

The situation is different for the cationic acids. Plots including all of the data points show substantial scatter. Five of the acids, however, define a good straight line, shown in Fig. 2. Three of the remaining acids, $HN{=}CHNH_3^+$, $O{=}CHNH_3^+$, and $O{=}C{=}NH_2^+$, show large positive deviations (6–16 kcal) from the defining line, and one, $H_2NNH_3^+$, shows a smaller negative deviation. The three acids showing positive deviations are precisely those that can yield delocalized conjugate bases. The first two are isoelectronic with acetaldehyde, whose identity-reaction deprotonation also occurs with a substantial barrier (11, 12, 14*a*). In these cases the substrate is localized but the transition structure and product can be delocalized. If delocalization in the transition structure lags behind the proton transfer, as predicted by the PNS, the large barriers can be understood. The situation is a little less obvious with $O{=}C{=}NH_2^+$. Here there can be no interaction between the orthogonal π orbitals of the allene-like system. In the transition structure, however, the electrons of the breaking N---H bond can interact with the π electrons of the C=O group, and the product can be resonance stabilized by an analogous interaction of the unshared pair left behind with the C=O π electrons:

The negative deviation from the line shown by $H_2NNH_3^+$ may arise from the polarizability of the amino-group unshared pair. We have shown previously that the barrier to deprotonation of XCH_3, where X is halogen, is smaller the more polarizable the halogen (14*b*).

Why do the three neutral acids that yield delocalized bases, $O{=}CHNH_2$, $HN{=}CHNH_2$, and O=C=NH, *not* show high barriers to deprotonation like those for the corresponding cationic acids? Part of the answer is that the acids themselves are

© 1998 NRC Canada

Fig. 1. Calculated barriers, ΔH_{TS}, vs. calculated acidity at MP2/6-31+G*//MP2/6-31+G* for neutral acids reacting with their anionic conjugate bases.

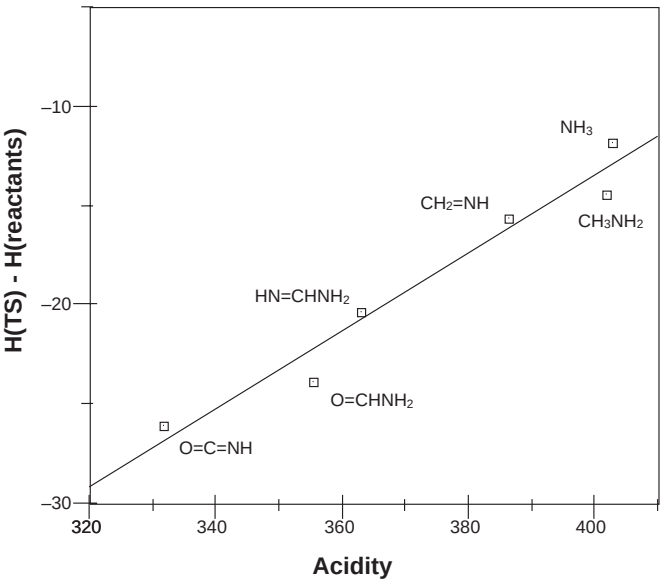

Fig. 2. Calculated barriers, ΔH_{TS}, vs. calculated acidity at MP2/6-31+G*//MP2/6-31+G* for cationic acids reacting with their neutral conjugate bases. Open squares, points included in least-squares fit; closed diamonds, outlying points.

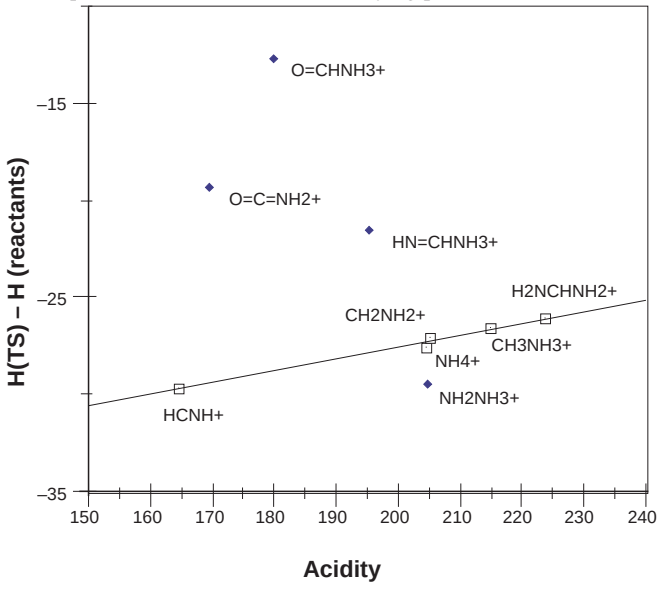

to a considerable degree delocalized. The resonance forms for OCNH are given above; those for the remaining two are

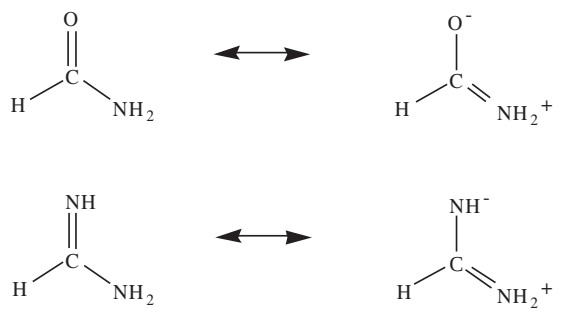

Fig. 3. Transition structures optimized at MP2/6-31+G*//MP2/6-31+G* for $HCONH_3^+$ reacting with $HCONH_2$ (*a*) and $HCONH_2$ reacting with $HCONH^-$ (*b*).

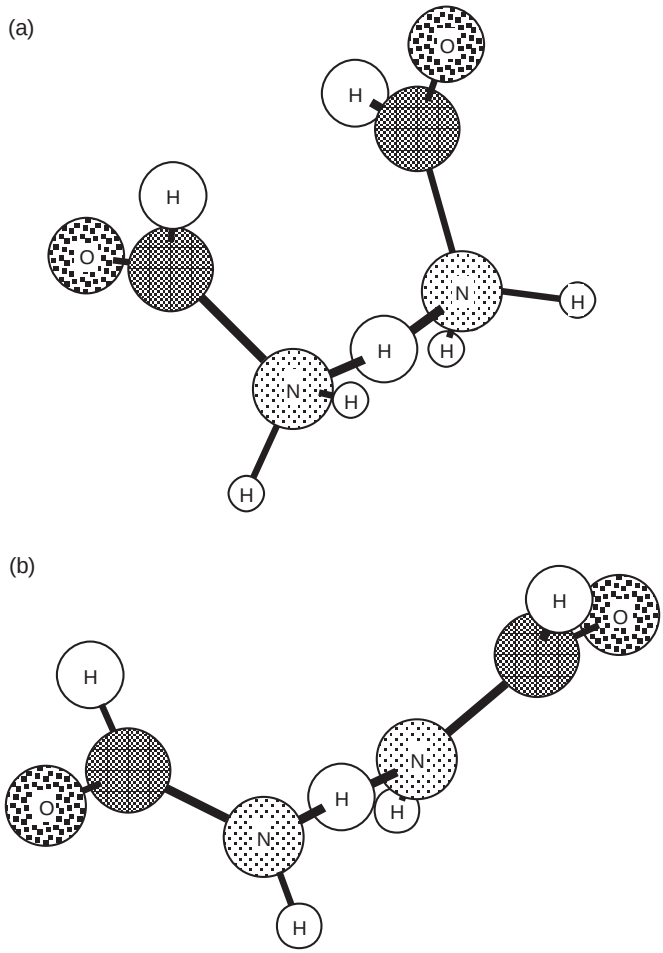

One possible rationalization would be that resonance stabilization is equal in the acid and its conjugate base and thus no delocalization occurs along the reaction coordinate. But there is another, and probably more important, reason for the low barriers shown by these three acids.

Examination of the transition structures shows clear differences between the cationic acids and the neutral acids. Figure 3*a* gives the transition structure for $HCONH_3^+ + HCONH_2$ and Fig. 3*b* the corresponding structure for $HCONH_2$ + $HCONH^-$. The first structure has the atoms aligned so that the N···H bonding electrons can interact with the C═O π orbitals. Thus the system is isoelectronic with and very similar to the transition structure of the $HCOCH_3$ + $HCOCH_2^-$ reaction, which was previously shown to possess a high barrier to deprotonation (11, 12). In contrast, the structure in Fig. 3*b* has the N---H bonding electrons in the N-C═O plane, which makes them orthogonal to and thus unable to interact with the C═O π orbitals. The principle of nonperfect synchronization (4–6) consequently applies to Fig. 3*a* but not to Fig. 3*b*.

Why should Figs. 3*a* and 3*b* be so different? There are two related reasons. In Fig. 3*b* there are unshared electrons on the two nitrogen atoms that can evidently interact more efficiently than the N---H bonding electrons with the C═O π orbitals. In addition, the system can in this way avoid the high-energy path

© 1998 NRC Canada

Fig. 4. Transition structures optimized at MP2/6-31+G*//MP2/6-31+G* for $HCNHNH_3^+$ reacting with $HCNHNH_2$ (*a*) and $HCNHNH_2$ reacting with $HCNHNH^-$ (*b*).

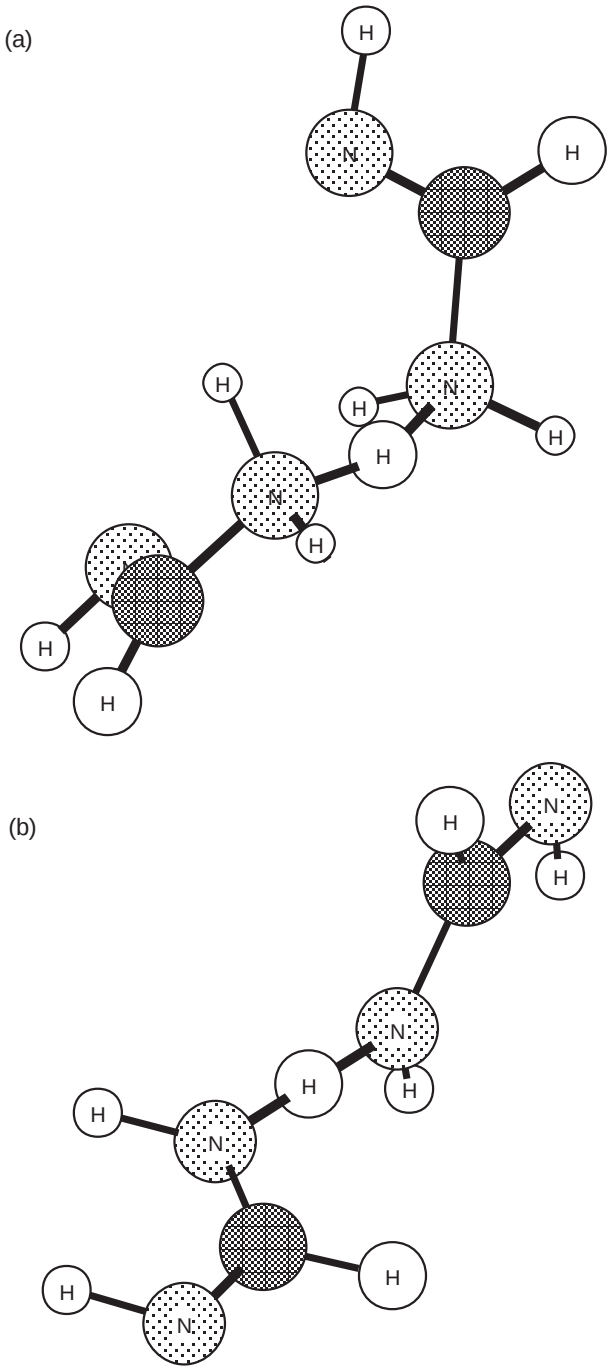

Fig. 5. Transition structures optimized at MP2/6-31+G*//MP2/6-31+G* for $OCNH_2^+$ reacting with OCNH (*a*) and OCNH reacting with OCN^- (*b*).

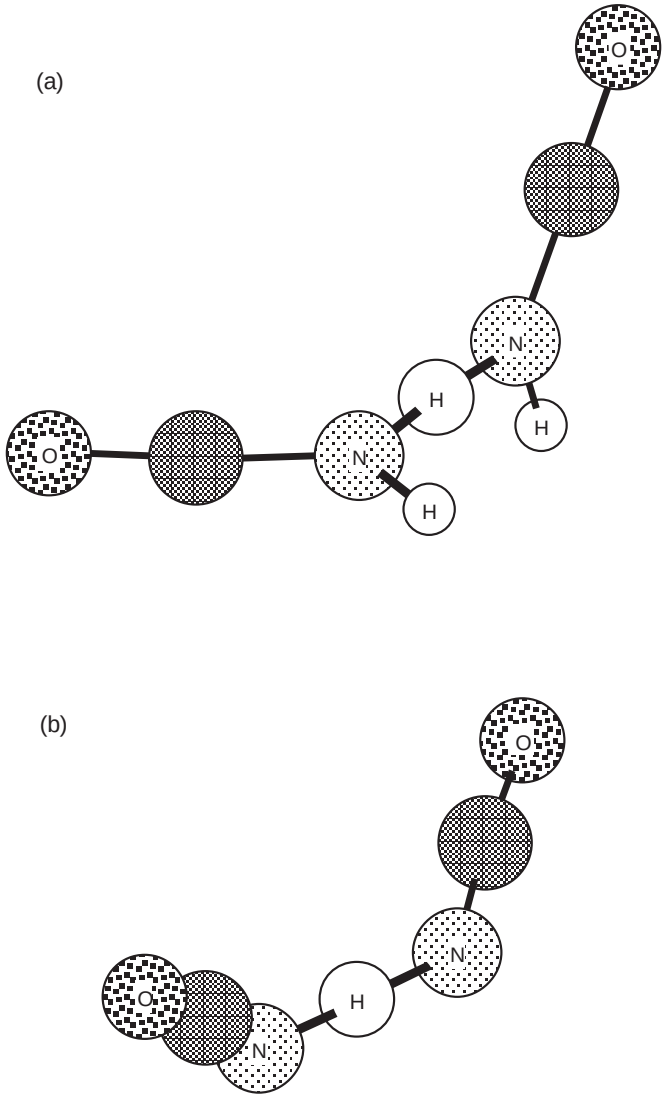

that results in Fig. 3*a* when the N---H electrons of the acid become only partly delocalized as the system proceeds along the reaction coordinate.

Figure 4 reveals an analogous situation in the comparison between the $HCNHNH_3^+$ + $HCNHNH_2$ (Fig. 4*a*) and the $HCNHNH_2$ + $HCNHNH^-$ (Fig. 4*b*) reactions. Again the N---H bonding electrons can interact with the C═N π electrons in Fig. 4*a* but cannot in Fig. 4*b* because the C═N π electrons are now orthogonal to the N---H bonding electrons. The reasons for this difference are clearly the same as in the case of Figs. 3*a* and 3*b*.

The situation is very similar but not completely analogous for the $OCNH_2^+$ + OCNH (Fig. 5*a*) and the OCNH + OCN^- (Fig. 5*b*) reactions. In Fig. 5*a* the N---H bonding electrons are in the H-N═C plane and thus able to interact with the π electrons of the C═O bond. In Fig. 5*b* it appears that the N---H bonding electrons could in principle interact with the C═O π electrons, but so can the unshared pair on nitrogen, and it evidently takes precedence. The structure in Fig. 5*b* shows more *sp* character at the nitrogen by virtue of an H---N═C angle of 146° compared to 123° in Fig. 5*a*. This provides further evidence for substantial delocalization of the unshared pair on nitrogen into the N═C bond in Fig. 5*b*.

The charge distributions in the transition structures also support the idea that the PNS applies to the reactions involving the cationic acids but not the neutral acids. For this purpose NPA (natural population analysis (31)) charges were used for reasons we have discussed previously (14*a*). Since charges are

© 1998 NRC Canada

influenced not only by π electron distributions but also by inductive effects, polarizabilities, and hybridization, an analysis that separates, as far as possible, π electron shifts from shifts due to these other factors is needed. If the PNS did not operate, π electron delocalization in the transition structure of an identity reaction should have proceeded exactly half way. Thus the shift of negative charge into the X of the donor species, XNH_2 or XNH_3^+,should be half completed in the transition structure and fully completed in the product. We therefore compare the change in q_x between the reactant acid and transition structure with the change between transition structure and the product base in Table 3.

Looking first at the reactions of neutral acids with anionic bases, we see that Δq(acid→ TS) and Δq(TS→ base) are close to each other, with a slight preference for the former to be somewhat larger than the latter. These small differences are in the opposite direction from those expected if the PNS were operating, because it predicts that electron shifts within the donor species should lag *behind* the extent of proton transfer. The reactions of cationic acids with neutral bases are definitely in accord with the PNS predictions, for in these cases Δq(acid→ TS) < Δq(TS→ base) for **3*a***, **4*a***, and **5*a*** (Figs. 3*a*, 4*a*, and 5*a*), and the differences are substantial in magnitude. Indeed, if the same factors that cause Δq(acid→ TS) > Δq(TS→ base) with the neutral acids operate, the actual π-electron differences with the cationic acids are even larger.

One would expect greater ionic character to the bonding in nitrogen acids than in carbon acids because nitrogen is more electronegative than carbon. The NPA charges for the cationic acids bear out this expectation. The proton in transit has a charge close to +0.5 in all cases. For the cationic acids this charge differs little (ca. ±0.01) from the charge on the proton in the acid. It does represent a significant increase from the charges on the protons in the neutral acids (+0.36 to +0.46). The neutral acids resemble the neutral carbon acids in this respect, where the charge on the proton goes from ca. +0.25 in the acid to +0.3 for the proton in transit. As an interesting aside, the intuitive picture most chemists have of the ammonium ion as a positive nitrogen surrounded by more or less neutral hydrogens is completely different from the NPA picture of four +0.5 hydrogens around a –1.0 nitrogen.

Of the three reactions that fall above the line in Fig. 2, only the proton transfer from $HCONH_3^+$ to $HCONH_2$ clearly shows a high central barrier, $\Delta H^‡$. A stable ion–dipole complex for $HNCHNH_3^+ + HNCHNH_2$ of lower energy than the transition structure could not be calculated because trial structures on full optimization collapsed to a complex of the products, $(H_2NCHNH_2)^+$ and $HNCHNH_2$, of the non-identity proton transfer, a reaction that can be calculated from the acidities (Table 1) to be nearly 30 kcal exothermic. The intrinsic barrier for this reaction can be estimated from Marcus theory (32) to be approximately the mean of the barriers for each of the corresponding identity reactions. If we assume that a barrier for the identity reaction giving $HNCHNH_3^+$ would be about its height above the line in Fig. 2, and average this with the barrier for the identity reaction giving $(H_2NCHNH_2)^+$ (0.91 kcal from Table 2), the result is a less than 4 kcal intrinsic barrier for the non-identity reaction. From Marcus' quadratic equation relating barrier height to intrinsic barrier and enthalpy of reaction, it becomes readily apparent that there should be no barrier for the actual reaction because $\Delta H^0/4\Delta H^‡ < -1$. Optimization of an ion–dipole complex with a hydrogen bond distance between the components fixed so as to prevent proton transfer did give a "virtual complex" below the transition structure by 7 kcal in potential energy. It was, however, not a stationary state.

Table 3. Group charges (NPA) at MP2/6-31+G*.

Species	X/q_x	Δq(acid→TS)	Δq(TS→base)
HCO			
$HCONH_2$	0.0854		
TS⁻(**3*b***)	–0.0996	–0.1850	–0.1811
$HCONH^-$	–0.2807		
$HCONH_3^+$	0.4139		
TS⁺(**3*a***)	0.2889	–0.1250	–0.2035
HCNH			
$HCNHNH_2$	0.0949		
TS⁻ (**4*b***)	–0.1050	–0.1999	–0.1504
$HCNHNH^-$	–0.2554		
$HCNHNH_3^+$	0.3620		
TS⁺(**4*a***)	0.2578	–0.1042	–0.1629
CO			
OCNH	0.4339		
TS⁻(**5*b***)	0.1526	–0.2813	–0.2668
OCN^-	–0.1142		
$OCNH_2^+$	0.8501		
TS⁺(**5*a***)	0.7195	–0.1306	–0.2856

The reason for a negligible central enthalpic barrier in the $OCNH_2^+ + OCNH$ reaction is not obvious (there is a potential energy barrier of 1.11 kcal). Consequently, we made an effort here also to determine whether we had missed a more stable ion–dipole complex, because ΔH_{well} for this reaction is considerably less negative than for the other reactions between positive and neutral species. The complex in Table 2 is a head-to-head species. Of the two possible head-to-tail species, only the one with a proton of NH_2^+ hydrogen bonded to the oxygen of the neutral component is stable, and it is actually 0.94 kcal *higher* in enthalpy than the head-to-head species when optimized at MP2/6-31+G*. In any event, other evidence for the operation of the PNS in this reaction is strong, and the apparent absence of a central enthalpic barrier at the higher level serves to underline the importance of using ΔH_{TS} rather than $\Delta H^‡$ in discussing such reactions. It is, of course, ΔH_{TS}, not $\Delta H^‡$, which constitutes the enthalpic contribution to measured efficiencies in experiments on gas-phase proton transfers.

Some speculation is desirable on why these identity-reaction proton transfers choose the paths they do. Evidently the preferred situation is one in which the path can involve little or no change in charge delocalization along the entire reaction coordinate. This is the case for the neutral acids reacting with their conjugate bases, where a transition structure conformation that shuts off delocalization is adopted. It is true that barriers are high when there is a lag in delocalization until after the transition state, but it does not, however, follow that the barrier would be lower if delocalization could become synchronous with progress along the reaction coordinate. The valence bond model pictures the transition structure of such a (hypothetical) synchronous reaction as a hybrid of reactant-like and product-like structures — a 1:1 hybrid for an identity

© 1998 NRC Canada

reaction. In the general case in which the PNS operates, a third contributor with charge localized on the proton donor atom is needed to describe the transition structure (33). For an identity reaction following the PNS, this contributor should also have charge localized on the proton acceptor atom. Admixture of this contributor has the effect of both stabilizing the transition structure and causing the observed lag in charge delocalization. In this view, the lag in delocalization is actually a strategy the system uses to achieve the lowest barrier possible under the circumstances.

The present results point up a problem with the conventional definition of Eigen acids. All of the acids in this study could be considered Eigen acids, but not all of them meet the criterion of a small or negligible barrier unless the proton transfer is endothermic. The proton transfer from $HCONH_3^+$ to $HCONH_2$ more closely resembles that from acetaldehyde to acetaldehyde enolate than it resembles the reactions of most of the other acids in this study. More thought needs to be given to definitions of the categories for classifying acids and their reactions.

Acknowledgments

This work was supported by the U.S. National Science Foundation Grants 9313657 and 9706242. J.E. Van Verth thanks the Dana Foundation for a fellowship, which made possible a sabbatical year at Rochester during 1993–1994. Thomas W. Kermis was an NSF REU (Research Experience for Undergraduates) student during the summer of 1994 at Rochester. We thank Professor Addy Pross for stimulating comments in his referee report.

References

1. M. Eigen. Angew. Chem. Int. Ed. Engl. **3**, 1 (1964).
2. A.J. Kresge. Chem. Soc. Rev. **2**, 475 (1973).
3. W.J. Albery, C.F. Bernasconi, and A.J. Kresge. J. Phys. Org. Chem. **1**, 29 (1988).
4. C.F. Bernasconi. Acc. Chem. Res. **20**, 301 (1987).
5. C.F. Bernasconi. Acc. Chem. Res. **25**, 9 (1992).
6. C.F. Bernasconi. Adv. Phys. Org. Chem. **27**, 119 (1992).
7. Z. Latajka and S. Scheiner. Int. J. Quantum Chem. **29**, 285 (1986).
8. S.M. Cybulski and S. Scheiner. J. Am. Chem. Soc. **109**, 4199 (1987).
9. S. Scheiner and L. Wang. J. Am. Chem. Soc. **114**, 3650 (1992).
10. S. Scheiner. J. Mol. Struct. (THEOCHEM), **307**, 65 (1994).
11. W.H. Saunders, Jr. J. Am. Chem. Soc. **116**, 5400 (1994).
12. C.F. Bernasconi and P.J. Wenzel. J. Am. Chem. Soc. **116**, 5404 (1994).
13. C.F. Bernasconi and P.J. Wenzel. J. Am. Chem. Soc. **118**, 10494 (1996).
14. (*a*) W.H. Saunders, Jr. and J.E. Van Verth. J. Org. Chem. **60**, 3452 (1995); (*b*) J.E. Van Verth and W.H. Saunders, Jr. J. Org. Chem. **62**, 5743 (1997).
15. C.F. Bernasconi, P.J. Wenzel, J.R. Keeffe, and S. Gronert. J. Am. Chem. Soc. **119**, 4008 (1997).
16. (*a*) S. Scheiner. J. Chem. Phys. **75**, 5791 (1981); (*b*) S. Scheiner. J. Chem. Phys. **86**, 376 (1982); (*c*) S. Scheiner, M.M. Szczesniak, and L.D. Bigham. Int. J. Quantum Chem. **23**, 739 (1983); (*d*) S. Scheiner. Acc. Chem. Res. **18**, 174 (1985); (*e*) S. Scheiner and P. Redfern. J. Phys. Chem. **90**, 2969 (1986); (*f*) J.E. Del Bene, M.J. Frisch, and J.A. Pople. J. Phys. Chem. **89**, 3669 (1985).
17. (*a*) H.Z. Cao, M. Allevena, O. Tapia, and E.M. Evleth. J. Phys. Chem. **89**, 1581 (1985); (*b*) S. Gronert. J. Am. Chem. Soc. **115**, 10258 (1993).
18. S. Scheiner and L. Wang. J. Am. Chem. Soc. **114**, 3650 (1992).
19. S.M. Cybulski and S. Scheiner. J. Am. Chem. Soc. **109**, 4199 (1987).
20. M.J. Frisch, G.W. Trucks, M. Head-Gordon, P.M.W. Gill, M.W. Wong, J.B. Foresman, B.G. Johnson, H.B. Schlegel, M. Robb, E.S. Replogle, R. Gomperts, J.L. Andres, K. Raghavachari, J. S. Binkley, C.Gonzalez, R.L. Martin, D.J. Fox, D.J. Defrees, J. Baker, J.J.P. Stewart, and J.A. Pople. Gaussian 92. Gaussian Inc., Pittsburgh, Pa. 1992.
21. M.J. Frisch, G.W. Trucks, H.B. Schlegel, P.M.W. Gill, B.G. Johnson, M.A. Robb, J.R. Cheeseman, T. Keith, G.A. Petersson, J.A. Montgomery, K. Raghavachari, M.A. Al-Laham, V. G. Zakrzewski, J.V. Ortiz, J.B. Foresman, J. Cioslowski, B.B. Stefanov, A. Nanayakkara, M. Challocombe, C.Y. Peng, P.Y. Ayala, W. Chen, M.W. Wong, J.L. Andres, E.S. Replogle, R. Gomperts, R.L. Martin, D.J. Fox, J.S. Binkley, D.J. Defrees, J. Baker, J.J.P. Stewart, M. Head-Gordon, C. Gonzalez, and J.A. Pople. Gaussian 94. Gaussian Inc., Pittsburgh, Pa. 1995.
22. (*a*) W.J. Hehre, R. Ditchfield, and J.A. Pople. J. Chem. Phys. **56**, 2257 (1972); (*b*) T. Clark, J. Chandrasekhar, G.W. Spitznagel, and P.v.R. Schleyer. J. Comput. Chem. **4**, 294 (1983).
23. (*a*) C. Møller and M.S. Plesset. Phys. Rev. **46**, 618 (1934); (*b*) M.J. Frisch, M. Head-Gordon, and J.A. Pople. Chem. Phys. Lett. **166**, 281 (1990); (*c*) J.A. Pople, R. Seeger, and R. Krishnan. Int. J. Quantum Chem. Symp. **11**, 149 (1978); (*d*) R. Krishnan and J.A. Pople. Int. J. Quantum Chem. **14**, 91 (1978); (*e*) R. Krishnan, M.J. Frisch, and J.A. Pople. J. Chem. Phys. **72**, 4244 (1980).
24. (*a*) J.A. Pople, H.B. Schlegel, R. Krishnan, D.J. Defrees, J.S. Binkley, M.J. Frisch, R.A. Whiteside, R.F. Hout, and W.J. Hehre. Int. J. Quantum Chem. Symp. **15**, 269 (1981); (*b*) D.J. Defrees and A.D. McLean. J. Chem. Phys. **82**, 333 (1985).
25. K.B. Wiberg. Physical organic chemistry. Wiley, New York. 1964. p. 218.
26. W.J. Hehre, L. Radom, P.v.R. Schleyer, and J.A. Pople. Ab initio molecular orbital theory. Wiley–Interscience, New York. 1986. p. 228.
27. S.G. Lias, J.E. Bartmess, J.L. Liebman, R.D Holmes, R.D. Levin, and W.G. Mallard. J. Phys. Chem. Ref. Data Suppl. 17 (1988) as updated by NIST Databases 19a and b, National Institute of Standards and Technology, Gaithersburg, MD 20889. The most up-to-date version of these databases is available at the web site http://webbook.nist.gov/chemistry.
28. L.A. Curtiss, K. Raghavachari, and J.A. Pople. J. Chem. Phys. **98**, 1293 (1994).
29. J. Tortajada, E. Leon, O.M. Luna, and M. Yanez. J. Phys. Chem. **98**, 12919 (1994).
30 (*a*) W.H. Saunders, Jr. J. Phys. Org. Chem. **7**, 268 (1994); (*b*) G.N. Merrill and S.R. Kass. J. Phys. Chem. **100**, 17465 (1996).
31. (*a*) E.D. Glendenning, A.E. Reed, E. Carpenter, and F. Weinhold. NBO Version 3.1 in Gaussian 92 and 94; (*b*) A.E. Reed, L.A. Curtiss, and F. Weinhold. Chem. Rev. **88**, 899 (1988).
32. R.A. Marcus. J. Phys. Chem. **72**, 891 (1968).
33. A. Pross and S.S. Shaik. J. Am. Chem. Soc. **104**, 1129 (1982).

© 1998 NRC Canada

1,3-Diphenylsulphonylcyclobutane: an unprecedented case of a higher stability of the *trans* isomer of 1,3-disubstituted cyclobutane

Ariel Sella, Shmuel Cohen, and Shmaryahu Hoz

Abstract: Equilibration of 1,3-diphenylsulphonylcyclobutane in *t*-BuOK/*t*-BuOH shows that the *trans* isomer is more stable than is the *cis* isomer by 2.1 kcal/mol. This is in contradistinction to the general case of 1,3-disubstituted cyclobutanes, where the bulky substituent prefers the *cis* geometry in order to avoid 1,3-diaxial interactions. The effect was found to be enthalpic in nature. Ab initio 3-21G calculations resulted in an energy difference of 2.6 kcal between the two isomers, in favor of the *trans* isomer. The cyclobutane rings were found to be nearly planar. While this may explain the higher stability of the *trans* isomer, it is not clear why the system avoids steric interaction this way, rather than by adopting the puckered conformation with the two bulky substituents at equatorial positions.

Key words: cyclobutanes, 1,3-diaxial interactions, equilibrium constant.

Résumé : L'équilibre du 1,3-diphenylsulfonylcyclobutane dans le *t*-BuOK/*t*-BuOH montre que la différence d'énergie favorisant l'isomère *trans* par rapport l'isomère *cis* est égale à 2,1 kcal/mol. Ce résultat est en contradiction avec le cas général des cyclobutanes 1,3-disubstitués dans lesquels les substituants encombrants se trouvent en général dans une géométrie *cis* de façons à éviter les interactions 1,3-diaxiales. On a trouvé que l'effet est de nature enthalpique. Des calculs ab initio 3-21G indiquent que la différence entre les deux isomères est de 2,6 kcal, en faveur de l'isomère *trans*. On a trouvé que les cyclobutanes sont pratiquement plans. Même si ce fait peut expliquer la stabilité plus grande de l'isomère *trans*, il est difficile d'expliquer pourquoi le système évite l'interaction stérique de cette façon plutôt que d'adopter la conformation plissée avec les deux substituants encombrants en positions équatoriales.

Mots clés : cyclobutanes, interactions 1,3-diaxiales, constante d'équilibre.

[Traduit par la rédaction]

Cyclobutane has been shown by various methods to be puckered (1) with a dihedral angle of 32° (2). Presumably, the relief in the strain, which results from the modest amount of puckering, outweighs the additional bond-angle distortion required by the puckering. As a result, geminal substituents become inequivalent, and axial/equatorial positions may be assumed. In monosubstituted cyclobutane, equatorial positioning of a substituent, such as F, was found (computationally) to be more stable than the planar geometry by 2 kcal/mol and from the axial conformer by 2.5 kcal/mol (3).

In general, in 1,3-disubstituted cyclobutanes, the *cis* isomer is found to be more stable than is the *trans* isomer (4). The explanation offered in the literature (4) is that in the *cis* isomer, the two substituents can simultaneously adopt equatorial positions, whereas in the *trans* isomer, one substituent will always assume an axial position, thus inflicting a destabilizing 1,3-diaxial interaction. To the best of our knowledge, of the many examples studied, the only exception to this rule is the dimethyl-1,3-cyclobutanedicarboxylate **1**. In this case, the *trans*/*cis* isomer ratio at equilibrium is 1.16 at 25°C (5).

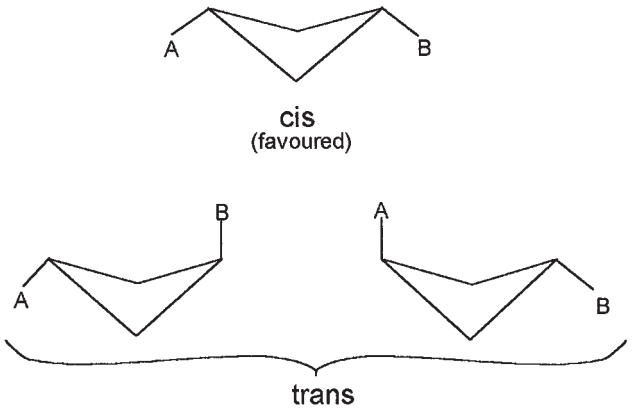

The present paper reports the second exception to the above rule, where the *trans*/*cis* ratio of the two isomers sets a record value of 35.5.

Synthesis

The two isomers of the disulfone **2** were synthesized from **3** (6)

Received November 3, 1997.

This paper is dedicated to Professor Erwin Buncel in recognition of his contributions to Canadian chemistry.

A. Sella and S. Hoz.[1] Department of Chemistry, Bar-Ilan University, Ramat-Gan 52900, Israel.
S. Cohen. Department of Inorganic and Analytical Chemistry, The Hebrew University, Jerusalem 91904, Israel.

[1] Author to whom correspondence may be addressed. Telephone: 972-3-5318822. Fax: 972-3-5353567. E-mail: shoz@mail.biu.ac.il

© 1998 NRC Canada

in the following reaction sequence. In the first step, **3** was reacted with PhS^- in MeOH for 2 h. The product **4** was obtained as a mixture of two isomers in a yield of 98% (eq. [1]).

Oxidation of the mixture with metachloroperbenzoic acid in dichloromethane yielded a mixture of the two isomers of **2** in an overall yield of 93% and a *cis*/*trans* (**2**c:**2**t) ratio of 1.16:1 (eq. [2]).

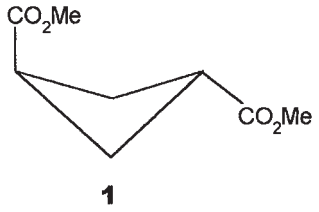

1

[1]

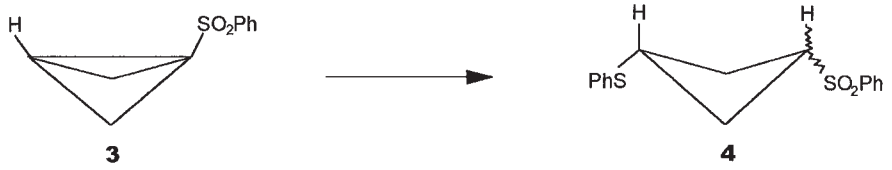

3 **4**

[2]

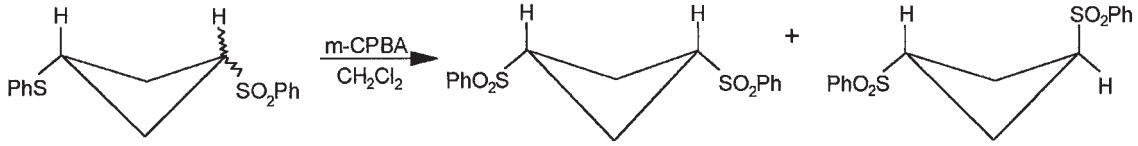

4 **2**c **2**t

The mixture was separated on a silica column, and the two isomers were obtained in a pure form in an 84% yield. The two isomers could be distinguished from each other by their melting points (**2**c, 236°C and **2**t, 204°C) and by their NMR spectra.

Structural assignment

Structural assignment can be easily made on the basis of two characteristic features of the NMR spectrum. The first one is the absorption of the methine protons on C1 and C3 (7). As a

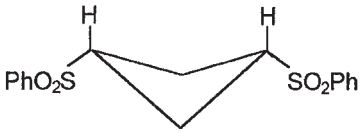

2c

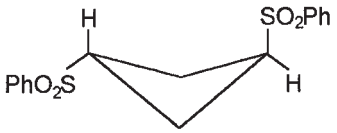

2t

rule, in a substituted cyclobutane when the substituent is electronegative, the absorption of the protons on the opposing carbon is shifted downfield when *syn* to the electronegative group. Therefore, the absorption of the methine protons in **2**t should be shifted downfield relative to that of **2**c. The second characteristic feature is that the NMR spectrum of the two methylene protons of the *trans* isomer should display a much higher symmetry than that of the *cis* isomer. The high symmetry results from a rapid ring flip, which equilibrates the *endo*- and *exo*-protons in positions 2 and 4 of the ring. The NMR spectra of the two isomers is shown in Fig. 1.

Because of the unexpected results of the equilibration experiment (see below), an X-ray crystallography analysis (Table 1) of **2**t was also made. The results (Fig. 2) show unambiguously that the NMR-based structural assignment is correct.

Equilibration experiments and theoretical analysis

A mixture of the two isomers was equilibrated by 0.154 M *t*-BuO^- in *t*-BuOH, both at room temperature (ca. 25°C) and at 50°C, and the composition of the mixture was analyzed by NMR (Table 2). The estimated error in the NMR determination is 5%. The data show that the **2**t/**2**c ratio is 35.5 ± 1.5 at both temperatures.

Thus, **2** is indeed a unique case, since in contradistinction to current knowledge (with a single exception (5)), the *trans* isomer is, by far, more stable than the *cis* isomer. The absence of a noticeable temperature effect on the equilibrium ratio shows that the difference in stability stems solely from enthalpic effects.

The energies of the two isomers were computed at the 3-21G level (8). The calculations have shown that **the *trans* isomer** (1700.29284 au) **is more stable than the *cis* isomer** (1700.28870 au) by 2.6 kcal, in surprisingly close resemblance to the experimental value of 2.1 kcal. For both isomers, the structure of the cyclobutane was found to be planar with a dihedral angle < 0.17°. The structures of the two isomers are shown in Fig. 3. The fact that similar results were obtained in the liquid phase as well as in the ab initio calculations, which simulate the gas phase, rules out the possibility that the higher stability of the *trans* isomer stems from solvation effect.

To further ensure that the higher stability of the *trans* isomer does not stem from a higher dipole and therefore a better solvation, a series of calculations was carried out at the AM1 level (9). The AM1 was chosen for this purpose because of economic reasons and in spite of the fact that starting at several

© 1998 NRC Canada

Fig. 1. The NMR spectra of **2**c and **2**t.

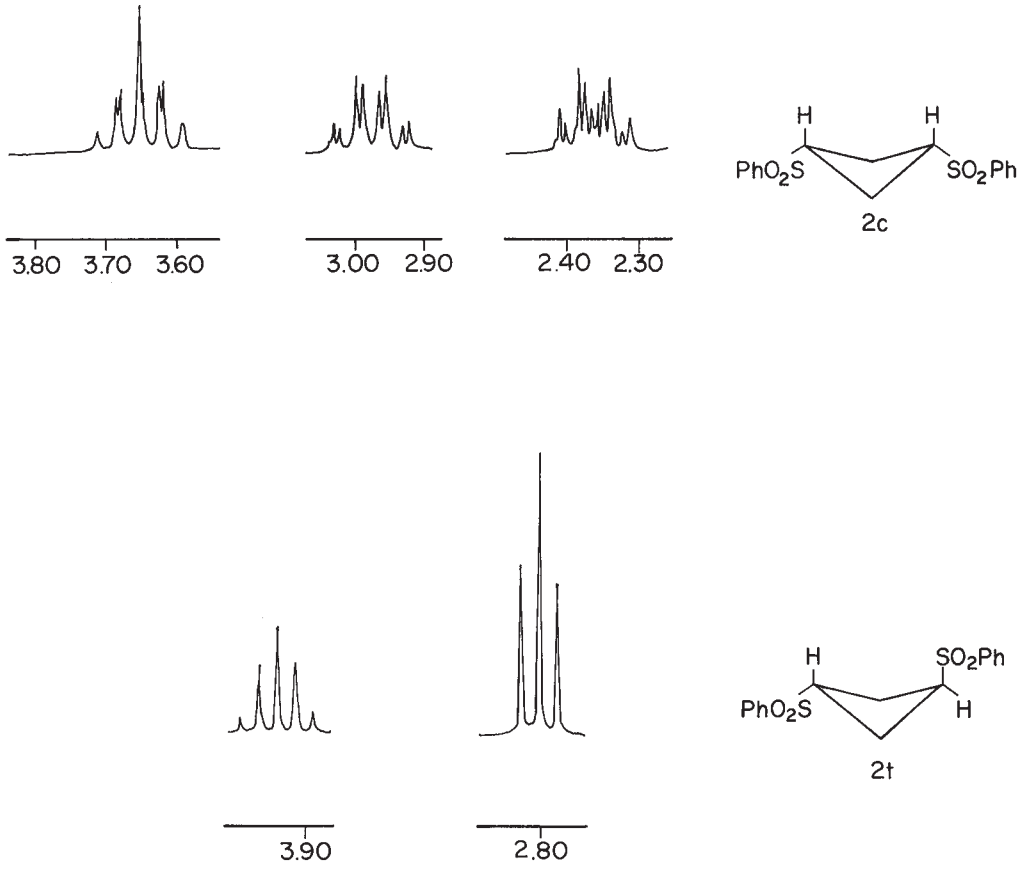

Table 1. Crystallographic data.

Formula	$C_{16}H_{16}O_4S_2$	Data collected	$\pm h, +k, +l$
Space group	$P2_1/c$	Scan type	θ–2θ
Crystal system	Monoclinic	Scan range, deg (θ)	0.80 + 0.15 tan θ
a, Å	10.259(4)	Scan rate, deg/min	1.27–8.24
b, Å	9.972(2)	$2\theta_{max}$, deg	140
c, Å	15.180(3)	Crystal decay	Negligible
β, deg	96.84(1)	Unique reflections	3071
		Reflections with	
V, Å^3	1541.9(2)	$I \geq 36(I)$	2703
Z	4	No. of variables	264
ρ_{calc}, g/cm^3	1.45	*R*	0.036
μ, cm^{-1}	32.12	*Rw*	0.059

[a] Temperature 293°K, Enraf–Nonius CAD4 diffractometer, CuKα radiation (λ = 1.5418 Å), graphite monochromator, function minimized $\Sigma w(|F_o| - |F_c|)^2$, $R = \Sigma||F_o| - |F_c||/\Sigma|F_o|$, and $Rw = [\Sigma w(|F_o| - |F_c|)^2/\Sigma w(|F_o|)^2]^{1/2}$.

Fig. 2. Structure **2**t, obtained from X-ray analysis.

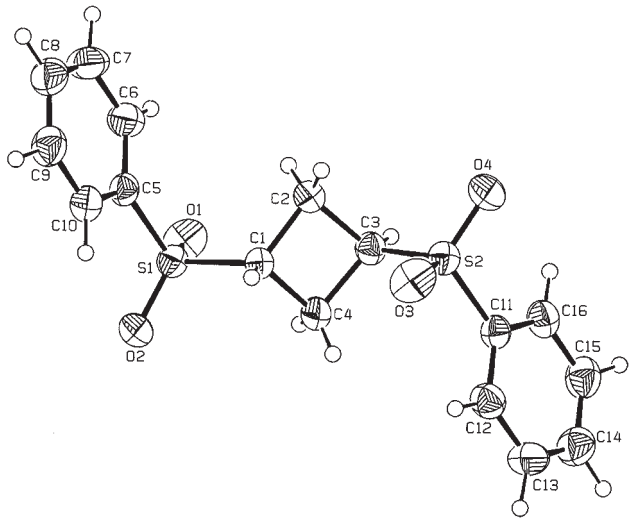

different initial geometries, **2**c was found to be more stable than **2**t by 0.9 kcal. The dipole moments of 12 different conformations, resulting from rotations around the C1-S and the C3-S bonds by 30° increments, were computed. In 9 conformations out of the 12, the dipole moment of the *cis* isomer was higher than that of the *trans*, by up to 4.4 D. In three conformations, the dipole moment of the *trans* isomer was higher (by only 0.4 D). This clearly rules out the possibility that solvent effects are responsible for the higher solution stability of **2**t. Thus, the sum total of the evidence gathered points to the unexpected higher stability of the *trans* isomer, as an intrinsic property of the isolated molecule.

The cyclobutane ring of the *trans* isomer was found to be nearly planar (X-ray (dihedral angle = 8°) and ab initio calculations (dihedral angle < 0.4°)). Calculations have shown that the cyclobutane is planar also in the *cis* isomer. No doubt, when the cyclobutane ring is planar, the *trans* isomer will be, as observed, more stable than the *cis* isomer. However, we were unable to explain, in classical interaction terms, why the

© 1998 NRC Canada

Table 2. Equilibration of the two isomers of **2** with *t*-BuO^- in *t*-BuOH.

Reaction time (h)	*T* (°C)	**2**t/**2**c Initial ratio	**2**t/**2**c Final ratio
18	~25[a]	0.63	37.5
51	~25[a]	0.6	35.6
72	~25[a]	0.63	36.0
120	25	0.63	37.1
48	25	34.6	35.1
96	25	34.6	34.1
72	50	0.63	33.6
120	50	0.63	34.6

[a] Room temperature.

system chose to adopt another stabilization mechanism, while discarding the more common puckering mechanism.

Experimental

General and instrumentation

General
The NMR spectra were recorded on a Bruker AC-200 spectrometer and measured in $CDCl_3$ solution. Mass spectra were taken with a VG AutoSpec mass spectrometer.

Syntheses

*3-Thiophenoxycyclobutanephenylsulphone (**4**)*
To a solution of 0.01 g (0.052 mmol) bicyclobutanephenylsulphone (**4**) in 0.5 mL MeOH was added 0.11 mL of PhSNa (0.5 M) solution in MeOH. After 2 h the reaction mixture was quenched with water, extracted by hexane, and dried over $MgSO_4$. The two isomers of **4** were obtained after evaporation of the solvent in 98% yield in a pure form in a ratio *trans*/*cis* of 4.8. **4**c: ^{1}H NMR (200 MHz) δ: 2.60 (4H, t, J = 9 Hz), 3.68 (1H, t, t, J = 10, 8 Hz), 3.67 (1H, t, t, J = 10, 8 Hz), 7.35–7.20 (5H, m), 7.70–7.45 (3H, m), 7.84 (2H, m); ^{13}C NMR δ: 30.22 t, 36.34 d, 54.87 d, 128.28 (o), 129.35 (m), 133.80 (p), 137.88 (ip), 129.86 (o), 129.09 (m), 126.70 (p), ipso AR C 135–130. **4**t: ^{1}H NMR (200 MHz) δ: 2.29 (2H, m), 3.03 (2H, m), 3.93 (1H, t, t, d, J = 10, 8, 1 Hz), 7.70–7.50 (3H, m), 7.88 (2H, m), 7.35–7.20 (5H, m), 4.05 (1H, t, t, d, J = 10, 8, 1 Hz); ^{13}C NMR δ: 36.29 t, 9.48 d, 57.16 d, 128.25 (o), 129.44 (m), 134.00 (p), 137.48 (ip). Anal. calcd. for **4**: C 63.13, H 5.30, S 21.06; found: C 63.27, H 5.41, S 21.18.

*1,3-Diphenylsulphonylcyclobutane (**2**)*
0.08 g (0.0263 mmol) of **4** were dissolved in 3 mL dichloromethane. To the solution, 0.1 g (0.576 mmol) *m*-CPBA were added. The reaction was quenched after 3 h at room temperature. Treating the reaction mixture with water and hexane gave a mixture of **2** and the reagent. Stirring of the mixture with 10% sodium bicarbonate solution for 5 h followed by extraction with dichloromethane gave, after evaporation of the solvent, 0.082 g (93% yield) of the two isomers in a ratio of 1:1.16 in favour of the *cis* isomer. The mixture of the two isomers was separated on a Kieselgel 60 column with dichloromethane as an eluent. The *cis* isomer (**2**c) is eluted first, mp 236°C, and

Fig. 3. Structures **2**c and **2**t, obtained by ab initio calculations (3-21G).

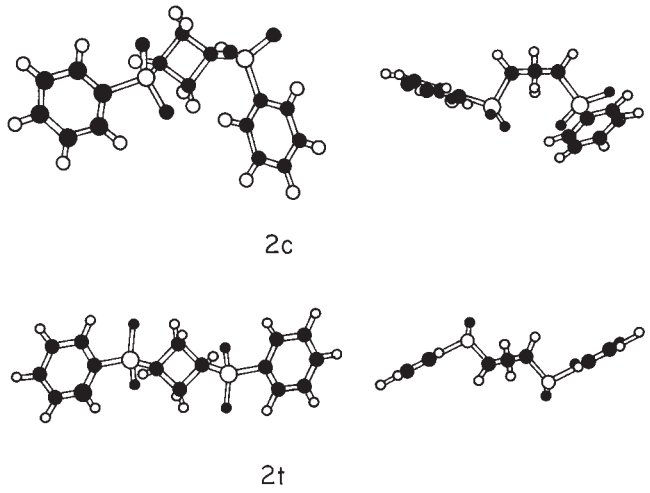

then the *trans* isomer (**2**t) with mp 204°C. **2**c: ^{1}H NMR (200 MHz) δ: 2.36 (2H, m), 2.98 (2H, m), 3.66 (2H, t, t, J = 8, 8 Hz), 7.59 (4H, m), 7.69 (2H, m), and 7.87 (4H, m); ^{13}C NMR δ: 25.10 t, 51.03 d, 128.47 (o), 129.47 (m), 134.14 (p), 137.12 (ip). **2**t: mp 204°C; ^{1}H NMR (200 MHz) δ: 2.80 (4H, t, J = 8 Hz), 3.94 (2H, t, t, J = 8, 8 Hz), 7.59 (4H, m), 7.69 (2H, m), and 7.87 (4H, m); ^{13}C NMR δ: 23.88 t, 53.44 d, 128.28 (o), 129.51 (m), 134.15 (p), 137.19 (ip).

Equilibration experiments
To a solution of ca. 0.02 g (0.06 mmol) **2** in 1.5 mL *t*-BuOH 0.04 g of *t*-BuOK was added. After incubation for the periods of time and temperatures indicated in Table 2, the reaction mixtures were quenched by 2 mL of water and extracted by 3 portions of 3 mL dichloromethane. The solvent was evaporated after drying over $MgSO_4$.

References

1. A. Almenningen, O. Eastiansen, and P.N. Skancke. Acta Chem. Scand. **15**, 711 (1961); J.D. Dunitz and V. Schomaker. J. Chem. Phys. **20**, 1703 (1952); G.W. Rathjens, Jr., N.K. Freeman, W.D. Gwinn, and K.S. Pitzer. J. Am. Chem. Soc. **75**, 5634 (1953).
2. J.L. Nelsen and A.A. Frost. J. Am. Chem. Soc. **94**, 3727 (1972); D. Cremer. J. Am. Chem. Soc. **99**, 1037 (1977).
3. T. Jonvik and J.E. Boggs. J. Mol. Struct. **85**, 293 (1981).
4. R.M. Moriarty. *In* Topics in sterochemistry. *Edited by* E.L. Eliel and N.L. Allinger. Vol. 8. Wiley, New York. 1974. See refs. cited therein.
5. N.L. Allinger and L.A. Tushaus. J. Org. Chem. **30**, 1945 (1965).
6. Y. Gaoni and A. Tomazic. J. Org. Chem. **50**, 2948 (1985).
7. S. Hoz, M. Liveneh, and D. Cohen. J. Am. Chem. Soc. **109**, 5149 (1987).
8. M.J. Frisch, G.W. Trucks, H.B. Schlegel, P.M.W. Gill, B.G. Johnson, M.A. Robb, J.R. Cheeseman, T. Keith, G.A. Petersson, J.A. Montgomery, K. Raghavachari, M.A. Al-Laham, V.G. Zakrzewski, J.V. Ortiz, J.B. Foresman, J. Cioslowski, B.B. Stefanov, A. Nanayakkara, M. Challacombe, C.Y. Peng, P.Y. Ayala, W. Chen, M.W. Wong, J.L. Andres, E.S. Replogle, R. Gomperts, R.L. Martin, D.J. Fox, J.S. Binkley, D.J. Defrees, J. Baker, J.P. Stewart, M. Head-Gordon, C. Gonzalez, and J.A. Pople. Gaussian 94, Revision C.2. Gaussian, Inc., Pittsburgh Pa. 1995.
9. (*a*) M.J.S. Dewar, E.G. Zoebisch, E.F. Healy, and J.J.P. Stewart. J. Am. Chem. Soc. **107**, 3902 (1985); (*b*) M.J.S. Dewar and H.S. Rzepa. J. Am. Chem. Soc. **100**, 58 (1978).

© 1998 NRC Canada

Concerted motion in bicyclobutane

Ariel Sella, Harold Basch, and Shmaryahu Hoz

Abstract: In bicyclobutane, the bridgehead substituents move inward as the bridge bond lengthens, and vice versa. The effect of BH_2, H, F, and OH as bridgehead substituents was investigated using quantum-mechanical calculations. The degree of invertedness of the bridgehead carbon was found to depend on the electronegativity of the substituent. It becomes more pronounced with electropositive substituents which, at the same time, also cause lengthening of the central bond (1.43 Å for F to 1.55 Å for BH_2). The oscillation phenomenon was found to be common to all the substituents regardless of their electronegativity. Substituent effects on the structure, energy, and electronics of the system are discussed.

Key words: bicyclobutanes, oscillation, geometry distortion.

Résumé : Dans le bicyclobutane, les substituants en tête de pont se déplacent vers l'intérieur lorsque la longueur de la liaison augmente et vice versa. Faisant appel à des calculs de mécanique quantique, on a étudié l'effet de BH_2, H, F et OH comme substituants en tête de pont. On a trouvé que le degré d'inversion au niveau du carbone en tête de pont dépend de l'électronégativité du substituant. Il devient plus prononcé avec des substituants électropositifs qui provoquent en même temps une élongation de la liaison centrale (1,43 Å pour le F à 1,55 Å pour le BH_2). On a trouvé que le phénomène d'oscillation est commun à tous les substituants quelle que soit leur électronégativité. On discute des effets de substituant sur la structure, l'énergie et l'électronique du système.

Mots clés : bicyclobutane, oscillation, distorsion de la géométrie.

[Traduit par la rédaction]

Introduction

When all the four valences of a carbon center are contained in a single hemisphere it is said to have an inverted geometry.

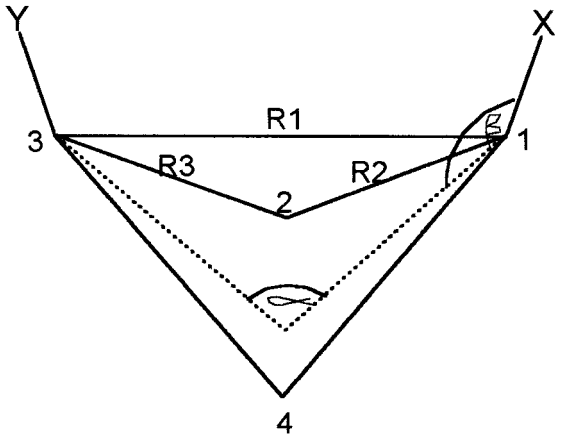

This phenomenon, which is rarely encountered in carbon compounds, was first identified in the bridgehead carbon of bicyclobutane (1). While in [1.1.1]-propellane the invertedness at the bridgehead carbons is constrained (2), in bicyclobutane there is no compelling reason why the geometry should be inverted since the hydrogen at either bridgehead is apparently free to move outward to give the "normal" geometry. This unique feature of bicyclobutane is probably also the cause for the equatorial direction being the common course of attack for both nucleophiles and electrophiles (3). Even more surprising is the correlation found between the length of the central bond and the degree of invertedness (4). The latter may be quantified as the inward angle (β) the bridgehead substituent forms with the C2C4C1 plane.

It turns out that as the central bond lengthens, this angle becomes smaller, thus magnifying the degree of invertedness. Likewise, shortening of the central bond results in an outward motion of the bridgehead substituent. In an extreme case, as in tricyclo[2.1.0.$0^{2,5}$] pentane, which has a very short bridge bond, the invertedness is lost (5).

The bond length – bond angle correlation has been demonstrated by X-ray analyses (4, 6) as well as by quantum-mechanical computations (4, 7). Theoretical calculations enable the study of structures in which the length of the bridge bond is varied beyond the constraints of the molecules in their ground state. Thus, (computationally) stretching the bridge bond of bicyclobutane, starting with its optimal geometry, causes the substituents to initially move inward. However, at a certain point the substituents will reverse direction and move outwards to form the final equilibrium geometry around the radical center resulting from homolytic cleavage of the central bond. Similarly, compressing the central bond will result in an outward motion of the substituents. In the case of the radical cation of bicyclobutane, a double oscillation has been observed (8). Namely, as the central bond is stretched, the substituent on the incipient radical center moves first inward and then outward as in the neutral bicyclobutane. However in the

This paper is dedicated to Professor Erwin Buncel in recognition of his contributions to Canadian chemistry.

Received December 17, 1997.

A. Sella, H. Basch, and S. Hoz.[1] Department of Chemistry, Bar-Ilan University, Ramat-Gan 52900, Israel.

[1] Author to whom correspondence may be addressed. Telephone: 972-3-5318822. Fax: 972-3-5353567. E-mail: shoz@gefen.cc.biu.ac.il

© 1998 NRC Canada

Scheme 1.

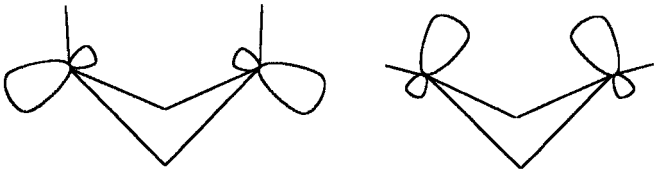

course of this outwards motion, the substituent passes by its final equilibrium position, and only at the final stages of the relaxation of the molecule to its open structure the substituent moves back inward. To the best of our knowledge, there is no proven explanation for the oscillation motion. At the intuitive level one can assume that the inward motion of the substituents is aimed at achieving a better alignment of the orbitals forming the central bond at the expense of some squeezing out of the inward lobes of these orbitals, as shown in Scheme 1.

At the point where the gain in energy is not sufficient, the substituents move backward in order to reach the normal geometry around the incipient radical center. In this paper we have examined the effect of various bridgehead substituents (Scheme 2) on the oscillation phenomenon, using quantum-mechanical calculations.

Methods

Ab initio RHF computations were performed with the Gaussian 92 package using the 6-31G* basis set (9) on IBM RS/6000 workstations. The geometries were optimized by gradient methods. After each equilibrium geometry was calculated, the angle α was varied by 10° steps both in the inward and outward direction.

Results and discussion

The various geometrical and electronic parameters are collected in Table 1. Since R1 increases nearly linearly with α (Fig. 1), increasing α (R1) beyond a certain limit could induce a diradicaloid state for which the closed shell method used here is inadequate. We have therefore computed the energy of the triplet and the singlet states (UHF) at α = 30° and 40°. The energies obtained for the triplet state were higher than that for the singlet by 33.7 and 16.1 kcal, respectively, showing that for the values of α used in this study the closed shell method is appropriate.

Geometrical parameters

In the optimum geometry, the degree of invertedness of the bridgehead carbon bearing the substituent depends on the electronegativity of the substituent. Thus, with the boron as a substituent, β decreases and the substituent is tilted more inwards. For BB this angle reaches nearly 160°. For F and O as bridgehead substituents, the invertedness of the carbon practically disappears as β reaches 180° and beyond (Table 1).

It is interesting to note that simultaneously with the lengthening of the central bond, shortening of the side bonds takes place. The sum of the bond lengths remains therefore nearly constant. This is in agreement with the observation made earlier by Eisenstein and Hirshfeld (10) and was confirmed for other systems as well (11, 12). It is correct mainly for the electronegative substituents, whereas for the electropositive ones, H and B, the deviation from a constant sum is as high as 0.1 Å. In addition, it was found that in the length of the central bond is a function of the electronegativity of the substituent. The more electronegative the substituent, the shorter the bond. This demonstrates again the dependence of β on R1 irrespective of the identity of the substituent that causes the variation.

Table 1. Variation of geometrical parameters, energies, and central bond overlap population as a function of α.

	α – 20	α – 10	α	α + 10	α + 20
			R1 (Å)		
HH	1.357	1.414	1.467	1.517	1.567
HF	1.345	1.397	1.442	1.486	1.532
FF	1.337	1.386	1.428	1.464	1.506
OOa	1.334	1.386	1.432	1.475	1.522
OOb	1.342	1.396	1.442	1.483	1.525
HB	1.385		1.515		1.624
BB	1.406		1.551		1.665
			R2 (Å)		
HH	1.533	1.504	1.488	1.48.0	1.477
HF[a]	1.505	1.484	1.470	1.463	1.460
	(1.562)	(1.526)	(1.507)	(1.496)	(1.491)
FF	1.536	1.507	1.489	1.48	1.473
OOa	1.548	1.514	1.495	1.484	1.478
OOb	1.530	1.499	1.481	1.471	1.465
HB[a]	1.553		1.507		1.498
	(1.505)		(1.474)		(1.468)
BB	1.530		1.494		1.487
			β (deg.)		
HH	190.7	181.8	172.2	162.2	152.9
HF[b]	191.5	184.4	176.5	167.6	158.4
	(195.2)	(186.4)	(176.5)	(165.4)	(154.2)
FF	193.2	187.31	180.1	171.2	159.1
OOa	190.1	183.5	175.6	166.4	156.2
OOb	195.4	189.9	183.22	175.1	164.3
HB[b]	187.3		163.7		151.0
	(183.4)		(165.7)		(148.6)
BB	181.8		161.1		148.1
			Energy (kcal)		
HH	13.8	2.7	0	1.8	6.2
HF	13.1	2.5	0	1.5	5.0
FF	13.7	2.6	0	1.4	3.8
OOa	14.3	2.7	0	1.6	5.1
OOb	14.5	2.8	0	1.6	5.4
HB	13.0		0		8.0
BB	14.1		0		9.6
			Overlap pop.		
HH	0.159	0.164	0.158	0.143	0.120
HF	0.098	0.119	0.130	0.126	0.109
FF	0.026	0.064	0.086	0.088	0.069
OOa	0.139	0.148	0.149	0.137	0.116
OOb	0.064	0.103	0.127	0.133	0.117
HB	0.133		0.113		0.081
BB	0.109		0.086		0.059

[a] Values in parentheses are for R3.
[b] Values in parentheses are for the angle of the bridgehead proton.

© 1998 NRC Canada

Scheme 2.

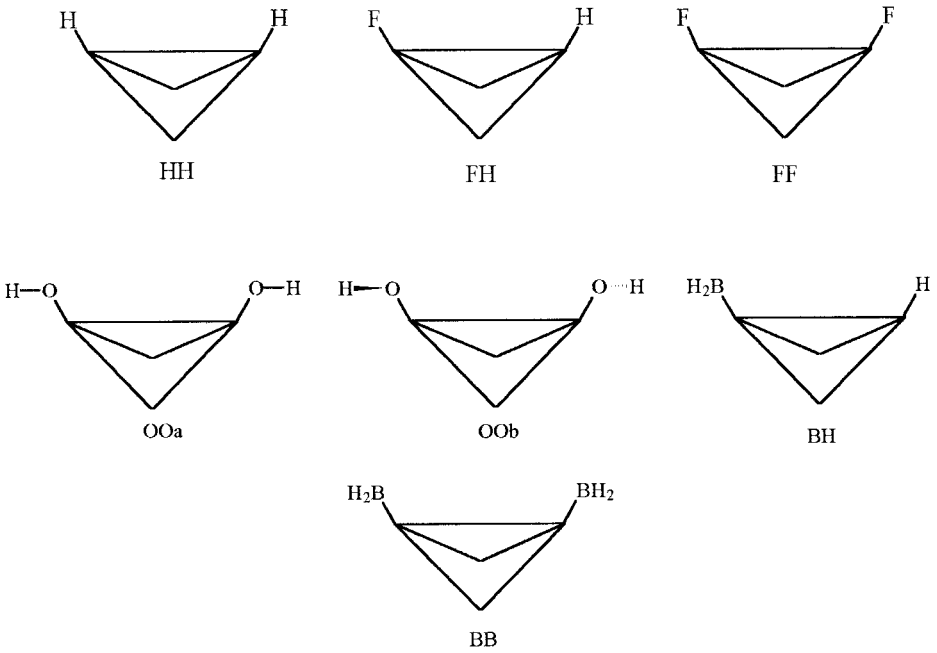

Fig. 1. Correlation between the bridge bond length R1 and α.

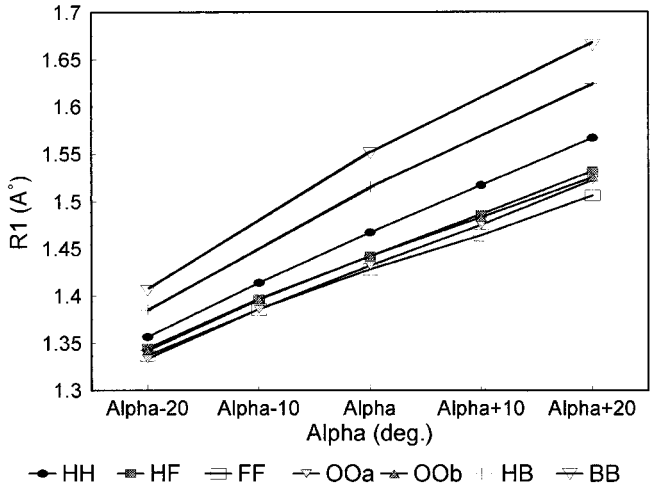

Fig. 2. Variation of *E* as a function of α for the various substituted bicyclobutanes.

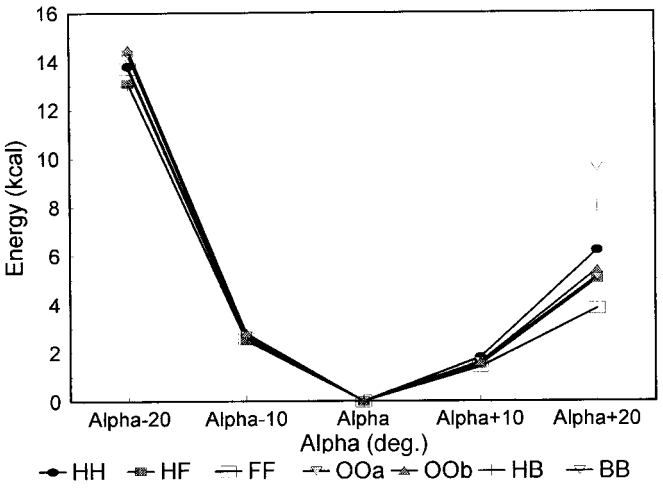

Fig. 3. Variation of β as a function of α for the various substituted bicyclobutanes.

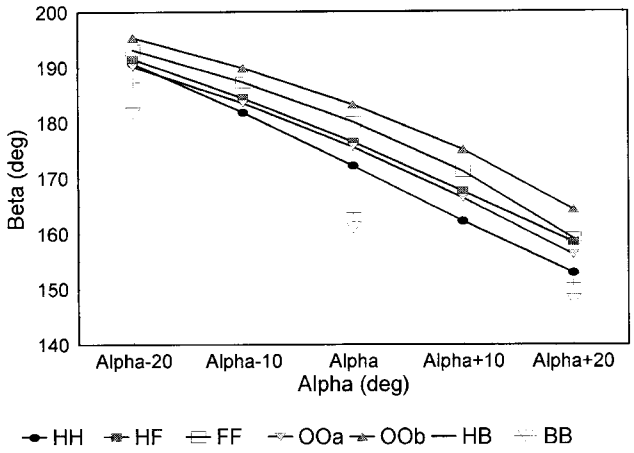

Energy and electronic structure

Figure 2 shows that decreasing α (shortening of the bridge bond) leads to a steeper increase in energy than increasing α. This effect, which is in line with the general form of a Morse curve (the RHF method is suitable for at small deviation from equilibrium, see below), is obviously more pronounced as the deviation from the minimum energy structure becomes larger. It is worth pointing out that the substituent differentiating effect is larger on the right-hand side of the diagram than on its left. In the latter, the increase of energy results probably mainly from an increase in the internal repulsion within the bicyclobutane unit, while the increase in energy associated with the motion to the right reflects, most likely, the incipient cleavage of the central bond. As the calculations used the closed shell HF method, it is clear that the differentiating substituent effect does not stem from the ability of the substituent to stabilize the incipient radical center on the bridgehead carbon. The differentiating effect probably reflects more the lowering of the

© 1998 NRC Canada

Fig. 4. Variation of the C1—C3 overlap population as a function of α for the various substituted bicyclobutanes.

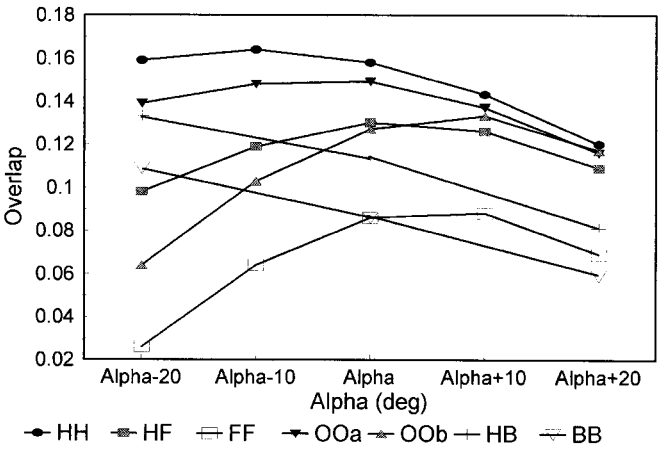

LUMO of the bicyclobutane moiety and the resulting enhanced interaction with the lone pair(s) on the F or O substituents. In spite of the nonequivalence of the two lone pairs on the oxygen in OOa and OOb, the two conformations have only a moderate effect on the energy rise upon increasing α; the reason being, as we have shown a while ago, that the lone pairs can interact with the LUMO associated with the central bond as well as with the antibonding orbital associated with the combination of the side σ bonds with nearly the same efficiency (13).

We expected that if the simplistic explanation offered in the introductory section for the correlation between the motion of the bridgehead substituents upon varying the central bond length is correct, varying the bridgehead substituents will have a dramatic effect on the phenomenon. However, in spite of the large range of substituents used, the same pattern of behavior is always exhibited. As can be seen from Table 1 and Fig. 3 it is clear that the concerted motion, i.e., coupling between β and α, is independent of the bridgehead substituent. Therefore, we examined the overlap population of the central bond as a function of the substituent. The data displayed in Table 1 and Fig. 4 show, not unexpectedly, a tendency for maximum overlap in the region of α optimum ±10°. It shows also that changing the value of α results in an increase in the overlap for some substituents, whereas for the others the overlap diminishes. Thus, the data at hand, while not allowing a complete rejection of the simplistic model mentioned in the introductory section, clearly does not support it.

References

1. K.W. Cox, M.D. Harmony, G. Nelson, and K.B. Wiberg. J. Chem. Phys. **50**, 1976 (1969).
2. K.B. Wiberg. Acc. Chem. Res. **17**, 379 (1984).
3. S. Hoz. *In* The chemistry of the cyclopropyl group. *Edited by* Z. Rappoport. Wiley, New York. 1987. Chap. 19.
4. P.G. Gassman, M.L. Greenlee, D.A. Dixon, S. Richtsmeier, and J.Z. Gougoutas. J. Am. Chem. Soc. **105**, 5865 (1983).
5. P.D. Dowd, P. Garner, R. Schappert, H. Irngartinger, and A. Goldman. J. Org. Chem. **47**, 4240 (1982).
6. H. Irngartinger and K.L. Lukas. Angew. Chem. Int. Ed. **18**, 694 (1979).
7. M.N. Paddon-Row, K.N. Houk, and P. Dowd. Tetrahedron Lett. **22**, 4799 (1981).
8. S. Hoz, H. Basch, and D. Cohen. J. Am. Chem. Soc. **109**, 6891 (1987).
9. M.J. Frisch, G.W. Trucks, M. Head-Gordon, P.M.W. Gill, M.W. Wong, J.B. Foresman, B.G. Johnson, H.B. Schlegel, M.A. Robb, E.S. Replogle, R. Gomperts, J.L. Andres, K. Raghavachari, J.S. Binkley, C. Gonzalez, R.L. Martin, D.J. Fox, D.J. Defrees, J. Baker, J.J.P. Stewart, and J.A. Pople. Gaussian 92, Revision C. Gaussian, Inc., Pittsburgh Pa. 1992.
10. M. Eisenstein and F.L. Hirshfeld. Acta Cryst. **B39**, 61 (1983).
11. R.D. Suenran and M.D. Harmony. J. Chem. Phys. **56**, 3837 (1972).
12. R.D. Suenran and M.D. Harmony. J. Am. Chem. Soc. **95**, 4506 (1973).
13. S. Hoz and R. Levy. J. Mol. Struct. Theochem. **121**, 93 (1985).

© 1998 NRC Canada

Reactions of benzyl methyl substituted-benzyl phosphites with *tert*-butyl hypochlorite: "balanced TS" validating reactivity/selectivity principle

Sung Soo Kim, Yu Zhu, In Seok Oh, and Chang Gyeong Lim

Abstract: Reactions of a series of several benzyl methyl substituted-benzyl phosphites with *tert*-butyl hypochlorite were investigated. The reactions produced phosphates, isobutene, alkyl chlorides, and benzyl chlorides via phosphonium chlorides as intermediates. Furthermore, the phosphates bearing a *tert*-butyl group underwent fragmentation to yield isobutene and another phosphates. Relative rates of formations of substituted benzyl and benzyl chloride (k_Y/k_H) were measured at the temperatures (–20, 0, 20, 40°C). Logarithms of the rates (log k_Y/k_H) were plotted against σ^+ and $1/T$, respectively. The former gave Hammett correlations to suggest a polar transition state (TS). The latter yielded differential activation parameters ($\Delta\Delta H^{\neq}_{Y-H}$ and $\Delta\Delta S^{\neq}_{Y-H}$), which indicate isokinetic relations and enthalpy control of rates. The selectivities (k_Y/k_H) decrease with higher temperatures and thereby follow the reactivity/selectivity principle.

Key words: phosphites, *tert*-butyl hypochlorite, Hammett correlations, differential activation terms, reactivity/selectivity principle.

Résumé : On a étudié les réactions de l'hypochlorite de *tert*-butyle avec une série de phosphites de benzyle substitués par des groupes méthyles. Les réactions conduisent à des phosphates, à l'isobutène, à des chlorures d'alkyle et à des chlorures de benzyle par le biais de chlorures de phosphonium comme intermédiaires. De plus, les phosphates portant un groupe *tert*-butyle subissent une fragmentation conduisant à de l'isobutène et à d'autres phosphates. On a mesuré les vitesses relatives de formation des chlorures de benzyle (et benzyle substitué) (k_Y/k_H) à diverses températures (–20, 0, 20 et 40°C). On a tracé les courbes des logarithmes des vitesses (log k_Y/k_H) en fonction respectivement de σ^+ et de $1/T$. La première courbe conduit à des relations de Hammett qui suggèrent un état de transition (ET) polaire. La deuxième fournit les paramètres différentiels d'activation ($\Delta\Delta H^{\neq}_{Y-H}$ et $\Delta\Delta S^{\neq}_{Y-H}$) qui indiquent des relations isocinétiques et un contrôle enthalpique des vitesses. Les sélectivités (k_Y/k_H) diminuent avec une augmentation de la température; elles suivent ainsi le principe de réactivité/sélectivité.

Mots clés : phosphites, hypochlorite de *tert*-butyle, corrélations de Hammett, termes différentiels d'activation, principe réactivité/sélectivité.

[Traduit par la rédaction]

Introduction

Trialkyl phosphites may react with *tert*-alkyl hypochlorites to yield trialkyl phosphates, *tert*-alkyl chlorides, and olefins as major products (1). Tetraalkoxyphosphonium chlorides were assigned as the key intermediates, which decompose to give the products. Previous studies (1) strongly excluded implication of radical intermediates (2, 3). Therefore **1** should undergo heterolytic bond fissions for the reactions to take place. Interestingly, olefins were also produced from the pyrolysis of arylethyl acetates (4). Trialkyl phosphites reacted with *N*-halosuccinimides (5) to give comparable product distributions as with the reactions of *tert*-alkyl hypochlorites (1). We would like to report the mechanism of decomposition of phosphonium chlorides derived from the title reactions.

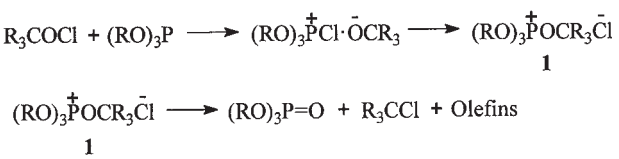

This paper is dedicated to Professor Erwin Buncel for his outstanding contributions to physical organic chemistry.

Received January 23, 1998.

S.S. Kim,[1] Y. Zhu,[2] I.S. Oh, and C.G. Lim. Department of Chemistry and Center for Chemical Dynamics, Inha University, Inchon 402-751, South Korea.

[1] Author to whom correspondence should be addressed. Telephone: 82-32-860-7678. Fax: 82-32-867-5604. E-mail: sungsoo@dragon.inha.ac.kr

[2] A visiting scholar under the programme of the Brain Pool (1996–1998) supported by the Korean Federation of Science and Technology Societies.

Results and discussion

Product studies

Benzyl methyl substituted-benzyl phosphites **2** reacted at –20–40°C in CCl_4 with *tert*-butyl hypochlorite **3** to give the products in Scheme 1. Phosphonium chloride 12 is an

© 1998 NRC Canada

Scheme 1.

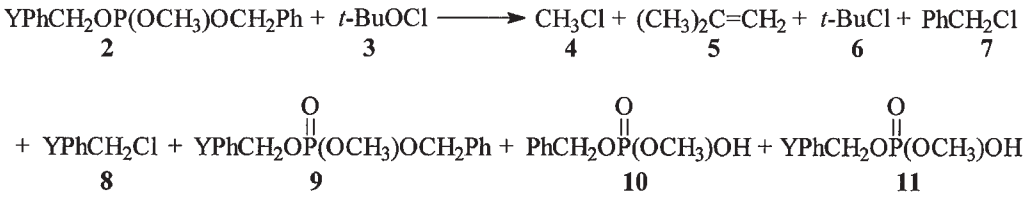

Scheme 2.

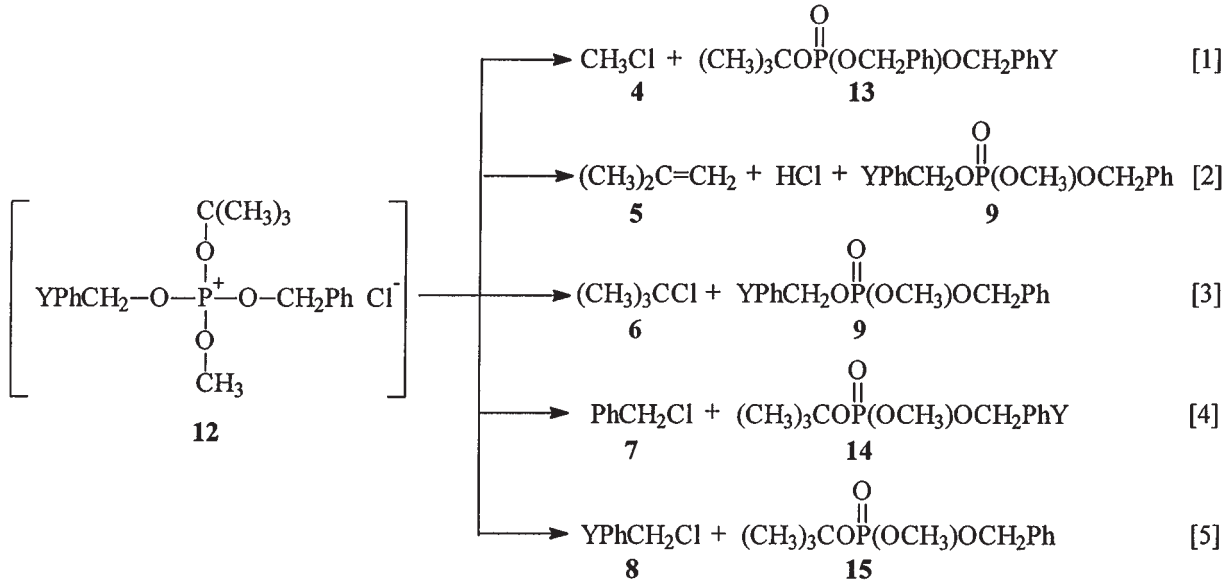

Scheme 3.

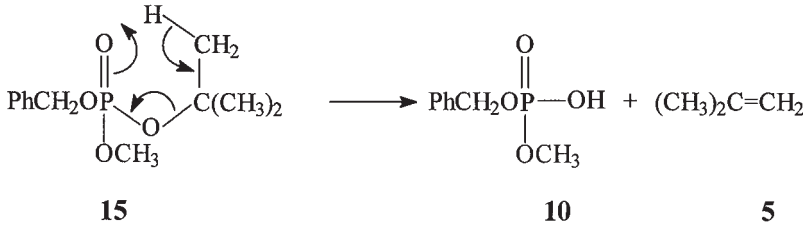

Table 1. Products and yields derived from reactions of phosphites with *tert*-butyl hypochlorite at 20°C.

	Yield (%)[a]				
Products	*p*-OCH_3	*p*-CH_3	*m*-CH_3	*p*-Cl	*p*-NO_2
MeCl	Trace	Trace	Trace	Trace	Trace
t-BuCl	11.6	48.6	47.3	43.9	50.7
$(CH_3)_2C{=}CH_2$	85.6	45.5	49.8	56.3	49.8
	(23.6)[b]	(12.6)[b]	(8.7)[b]	(12.0)[b]	(14.8)[b]
$PhCH_2Cl$	6.0	10.6	21.6	23.5	31.5
$YPhCH_2Cl$	58.8	28.2	22.4	20.6	3.0
t-BuCl + $(CH_3)_2C{=}CH_2$	**97.2**	**94.1**	**97.1**	**100.2**	**100.5**

[a] Measured by GLC using biphenyl as an internal standard.

[b] The yields indicate amount of isobutene formed from eq. [2] only. The yields have been obtained by subtracting total yield of *tert*-butyl chloride, benzyl chloride, and substituted benzyl chloride from 100%.

intermediate and undergoes heterolytic fragmentation in several pathways (Scheme 2).

Alkyl and benzyl chlorides (**4**, **6**, **7**, and **8**) were identified and quantified. Isobutene **5** has been produced by either eq. [2] or the intramolecular fragmentations of **13**–**15** as shown by Scheme 3. The pyrolysis of the acetates (4) underwent similar fragmentation to give olefins and carboxylic acids via a six-membered TS. Compound **9** with Y = *p*-CH_3 was isolated and identified by comparison with the authentic sample. Formation of **13** could be ignored because eq. [1] is a very minor pathway. Compounds **14** and **15** were not detected in the reaction mixtures. However **10** was isolated and the spectral data showed the consistency with the authentic structure. Table 1 contains yields of the products based on the amount of **2** consumed. According to Schemes 2 and 3, the total quantity of **5** and **6** should be equal to that of **12** undergoing decomposition. The material balances were calculated as (96 ± 3)% or better at the temperatures (40, 20, 0, and –20°C), which strongly supports

© 1998 NRC Canada

Table 2. Relative rates and Hammett correlations for reactions of the phosphites with *tert*-butyl hypochlorite in CCl_4.

Temp.	k_Y/k_H[a,b]						Hammett correlations	
(°C)	*p*-OCH_3	*p*-CH_3	*m*-CH_3	H	*p*-Cl	*p*-NO_2	ρ^{+}[c,d] (*r*)[e]	ρ[c,d] (*r*)[e]
40	8.43	2.40	1.03	1	0.91	0.118	–1.17 (0.995)	–1.46 (0.935)
20	9.73	2.61	1.05	1	0.88	0.087	–1.29 (0.995)	–1.63 (0.943)
0	14.4	2.93	1.07	1	0.88	0.068	–1.46 (0.996)	–1.83 (0.937)
–20	18.1	3.26	1.08	1	0.86	0.057	–1.58 (0.996)	–1.97 (0.936)

[a] Reaction times are less than 30 min.
[b] Average value of three runs. Error limits are within 5%.
[c] Substituent constants were taken from ref. 19.
[d] Plotted against σ^{+} for ρ^{+} and σ for ρ.
[e] Correlation coefficient.

the proposed reaction mechanism. Table 1 shows representative data at 20°C.

Substituent effects and temperature studies

Benzyl chloride **7** and substituted benzyl chloride **8** are products of reactions [4*a*] and [5*a*], respectively. The relative rates (k_Y/k_H) were measured from k_Y/k_H = [**8**]/[**7**] and correlated with Hammett equation using σ^{+} and σ values. Table 2 contains the rate data and Hammett ρ and ρ^{+} values.

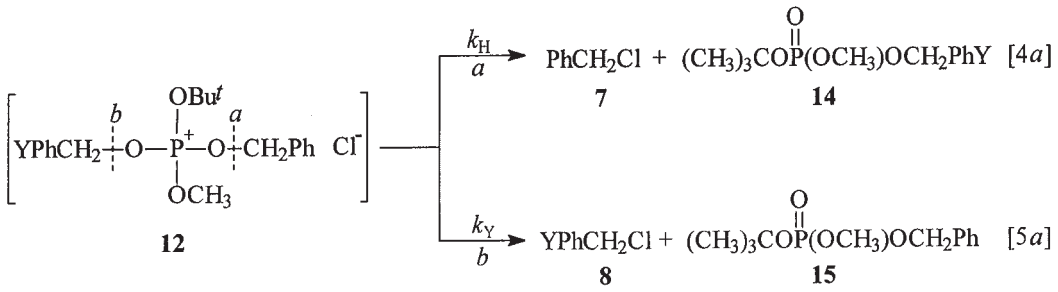

Negative sign of ρ^{+} and better correlations with σ^{+} indicate that cleavages of *a* and *b* involve polar TS with the positive charge enjoying conjugation with phenyl ring. Temperature studies employed the Eyring equation (6) and gave differential activation parameters from Fig. 1 (Table 3). Both terms ($\Delta\Delta H^{\neq}_{Y-H}$ and $\Delta\Delta S^{\neq}_{Y-H}$) were plotted against σ^{+} with good linear lines having positive slopes (Figs. 2 and 3).

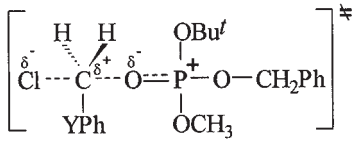

16

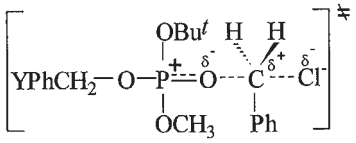

17

The chlorine anion Cl^- in **12** could act as a strong nucleophile in CCl_4 to promote S_N2-type decomposition. Relatively moderate ρ^{+} values (ρ^{+} = –1.17 to –1.58) should then be consistent with TS structures **16** and **17** for reactions [5*a*] and [4*a*], respectively. Accordingly a real carbocation may be developed in neither **16** nor **17**. The differential activation parameters correspond to increment of activation terms perturbed by the substituent effects. When Y is of electron withdrawing, the carbocationic character in **16** becomes destabilized so as to increase magnitude of enthalpy of activation ($\Delta H^{\neq}_{Y}$). The term $\Delta\Delta H^{\neq}_{Y}$ is equivalent to differential substituent effects. Figure 2 shows the systematic perturbation of $\Delta H^{\neq}_{Y}$ caused by substituent constant (σ^{+}). The destabilization by electron-attracting substituents (Y) could also function to reduce extent of the bond cleavage. The lesser bond cleavage could bring about correspondingly the lesser π-bond formation and the smaller charge separation in **16**. The double-bond character restricts the free rotations evolving rotational entropy. Since CCl_4 is nonpolar, the electrostrictions caused by solvent molecules could greatly reduce translational freedom of **16**. Therefore electron-withdrawing substituents could augment the rotational and translational freedoms of **16** so as to increase entropies of activation ($\Delta S^{\neq}_{Y}$) (7).

Figures 2 and 3 are empirical drawings to visualize substituent effects controlling structures of TSs **16** and **17**. The differential terms ($\Delta\Delta H^{\neq}_{Y-H}$ and $\Delta\Delta S^{\neq}_{Y-H}$) realize an excellent isokinetic relation (8) (Fig. 4). The isokinetic behavior (8) may imply that activation process is controlled by a single parameter,

© 1998 NRC Canada

Table 3. Differential activation parameters for reactions of the phosphites with *tert*-butyl hypochlorite in CCl_4.

	p-OCH3	*p*-CH_3	*m*-CH_3	H	*p*-Cl	*p*-NO_2
$\Delta\Delta H^{\neq}_{Y-H}$ (kcal/mol) [a]	–2.11 ± 0.08	–0.81 ± 0.06	–0.13 ± 0.04	0	0.13 ± 0.04	1.89 ± 0.08
$\Delta\Delta S^{\neq}_{Y-H}$ (eu) [b]	–2.54 ± 0.32	–0.86 ± 0.22	–0.33 ± 0.13	0	0.22 ± 0.13	1.67 ± 0.32

[a] $\Delta\Delta H^{\neq}_{Y-H} = \Delta H^{\neq}_{Y} - \Delta H^{\neq}_{H}$.
[b] $\Delta\Delta S^{\neq}_{Y-H} = \Delta S^{\neq}_{Y} - \Delta S^{\neq}_{H}$.

Fig. 1. Plot of log k_Y/k_H vs. $1/T$.

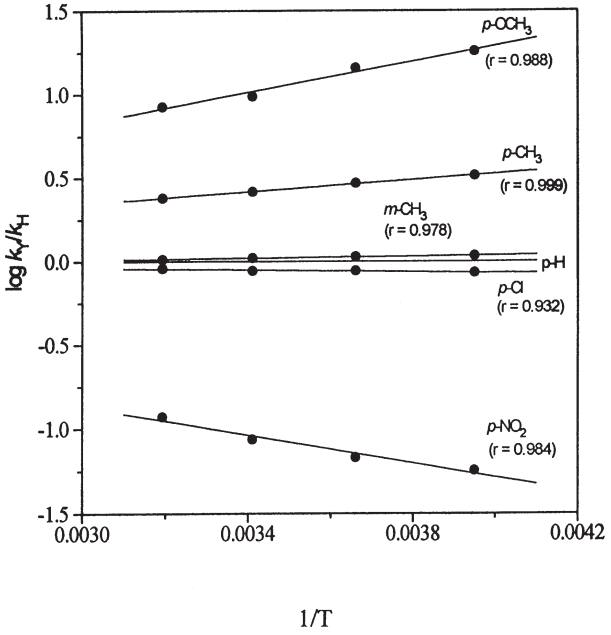

Fig. 2. Plot of $\Delta\Delta H^{\neq}_{Y-H}$ vs. σ^+.

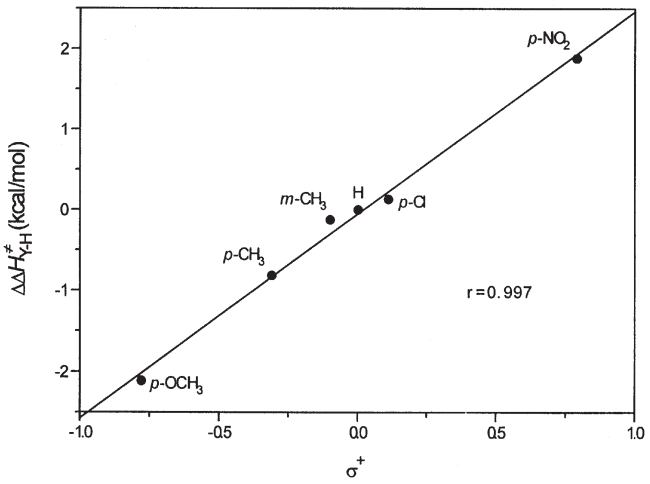

that is, substitutent constant (σ^+). The slope of line of Fig. 4 corresponds to isokinetic point (T_k = 937 K) where the rates become immune to substituent effects. The reaction temperatures are well below 937 K. Such high isokinetic point ($\Delta\Delta H^{\neq}_{Y-H}/\Delta\Delta S^{\neq}_{Y-H}$ = 937 K) indicates that increment of enthalpy term ($\Delta\Delta H^{\neq}_{Y-H}$) provoked by substituents far outweighs corresponding entropy change ($\Delta\Delta S^{\neq}_{Y-H}$). The rates

Fig. 3. Plot of $\Delta\Delta S^{\neq}_{Y-H}$ vs. σ^+.

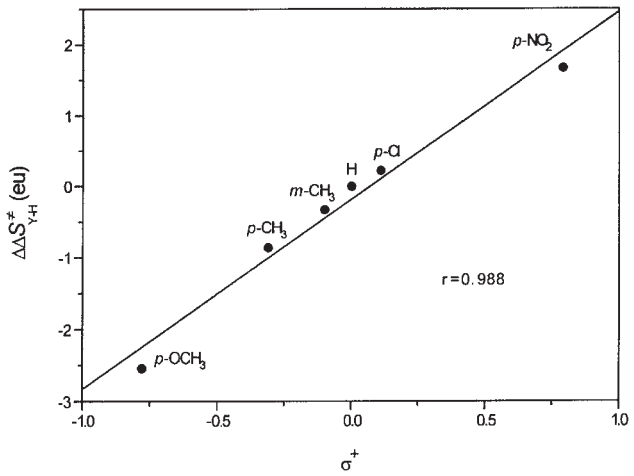

Fig. 4. Isokinetic relationship by the enthalpy–entropy compensation effect.

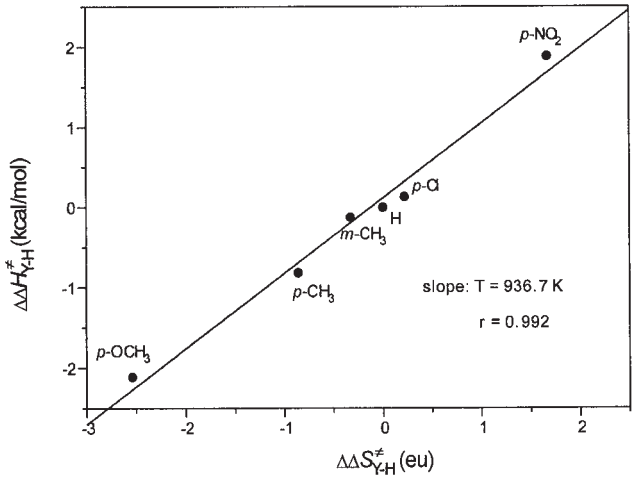

are accordingly determined by contribution of enthalpic term to engender enthalpy control of reactivities. The relative rates (k_Y/k_H) can be taken as selectivities caused by substituent constant (σ^+). The selectivities increase with lower temperatures thus obeying the reactivity/selectivity principle (RSP) (9) (Table 2). The obedience has been featured when rates are parallel with equilibria. The parallelism can be ascribed to a balanced TS such as **16** or **17**, which assumes an intermediate configuration between reactant and product. Polar TS in radical reactions (10, 11) has been however defined as an "imbalanced TS" (12) by us (11). The rates of various radical reactions (10, 11) were fitted to Hammett correlations and controlled by

© 1998 NRC Canada

Scheme 4.

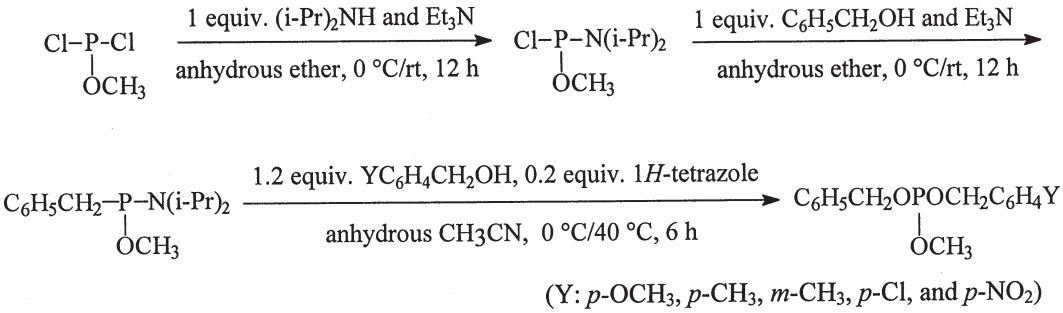

differential entropy term ($\Delta\Delta S^{\neq}_{Y-H}$). Entropy control of reactivities has been also observed very recently in thermal isomerizations of substituted benzyl isocyanides (13). The TS retains cyclic structure that resembles neither reactant (isonitrile) nor product (nitrile). The entropic dominance in a series of reactions (11, 13) confines validity of RSP (9) and Hammond postulate (14).

Selectivity Q can be defined as $Q = \ln(k_Y/k_H)$ and $\ln(k_Y/k_H) = -(\Delta G^{\neq}_Y - \Delta G^{\neq}_H)/RT = -\Delta\Delta G^{\neq}_{Y-H}/RT$. The equation $Q = -\Delta\Delta G^{\neq}_{Y-H}/RT$ can be divided into enthalpy and entropy terms.

[6] $$Q = \Delta\Delta S^{\neq}_{Y-H}/R - \Delta\Delta H^{\neq}_{Y-H}/RT$$

Due to an isokinetic relation (Fig. 4), two differential terms carry the same sign whether positive or negative. Accordingly, Q becomes the difference between the two terms of eq. [6]. Table 3 indicates $|\Delta\Delta H^{\neq}_{Y-H}/RT| > |\Delta\Delta S^{\neq}_{Y-H}/R|$. Therefore increase of temperature must reduce magnitude of Q to decrease selectivities. On the contrary, the radical reactions (11) and the isomerizations of substituted benzyl isocyanides (13) yielded $\Delta\Delta H^{\neq}_{Y-H}$ close to zero. Equation [6] reduces to $Q = \Delta\Delta S^{\neq}_{Y-H}/R$, which is independent of temperature. Constant selectivites (11, 13) were indeed observed against temperature gradient. A number of authors (15) including Professor Buncel (15*d*) have expressed serious concerns about the applicability of RSP to the numerous heterolytic reactions.

Conclusions

The structure of TS controls trend of the selectivities (k_Y/k_H) with variation of temperature. Balanced TS invites enthalpy control of rates to entertain Hammond postulate and reactivity/selectivity principle. The dominance of either term ($\Delta\Delta H^{\neq}_{Y-H}$ or $\Delta\Delta S^{\neq}_{Y-H}$) is due to structural feature of the TS.

Experimental section

Materials and methods

All reagents were purchased from major suppliers. Liquids were distilled with center-cut collection, and solids recrystallized according to the standard procedures (16) when necessary. Varian Vista 4600 gas chromatography, Varian Gemini 2000 NMR, and Fisions VG-Trio-2000 GC–MS spectrometer were used for identifications and analyses of the products.

Chloro diisopropylamino methyl phosphite

To a 2 L three-necked flask equipped with a 250 mL pressure-equalized addition funnel and an efficient magnetic stirrer were added dry ethyl ether (600 mL) and dichloro methyl phosphite (25.0 g, 0.188 mol). The solution was cooled in an ice bath. Ethyl ether solution (200 mL) containing diisopropylamine (19.0 g, 0.188 mol) and triethylamine (19.0 g, 0.188 mol) was added dropwise to the stirred solution over 1 h under nitrogen atmosphere. After completion of the addition, the ice bath was removed and the reaction mixture was allowed to continuously stir for 12 h at room temperature and then filtered. Excess amount of ether was removed by a rotary evaporator. The residue was distilled under reduced pressure to give 17.0 g (46%) of colorless liquid with bp 69–71°C/5 torr (1 torr = 133.3 Pa). ^{1}H NMR ($CDCl_3$, 200 MHz), δ (ppm): 1.24 (d, J = 6 Hz, 12H), 3.58 (d, J = 14 Hz, 3H), 3.83 (m, 2H).

Benzyl diisopropylamino methyl phosphite

To a 250 mL three-necked flask equipped with a 50 mL pressure-equalized addition funnel, an efficient magnetic stirrer, and a condenser were added dry ethyl ether (100 mL) and chloro diisopropylamino methyl phosphite (8.4 g, 0.042 mol) under nitrogen atmosphere. The solution was cooled in an ice bath. Ethyl ether solution (50 mL) containing benzyl alcohol (4.6 g, 0.042 mol) and triethylamine (4.3 g, 0.042 mol) was added dropwise to the stirred solution over 0.5 h under nitrogen atmosphere. After the addition was complete, the ice bath was removed, and the reaction mixture was allowed to continuously stir for 12 h at room temperature and then filtered. The excess amount of ether was removed by evaporation. The product was colorless liquid (9.8 g, 86%). ^{1}H NMR ($CDCl_3$, 200 MHz), δ (ppm): 1.19 (d, J = 2 Hz, 6H), 1.22 (d, J = 2 Hz, 6H), 3.40 (d, J = 13 Hz, 3H), 3.70 (m, 2H), 4.72 (t, J = 8 Hz, 2H), 7.34 (m, 5H).

Benzyl methyl substituted-benzyl phosphite

See Scheme 4 for synthesis of benzyl methyl substituted-benzyl phosphites (17).[3]

Typical run: to a 100 mL three-necked flask equipped with a 50 mL pressure-equalized addition funnel and an efficient magnetic stirrer were added dry acetonitrile (50 mL) and benzyl diisopropylamino methyl phosphite (4.0 g, 0.015 mol). The solution was cooled in an ice bath. Anhydrous acetonitrile solution (15 mL) containing *p*-methylbenzyl alcohol (2.0 g, 0.016 mol) and 1*H*-tetrazole (0.50 g, 0.007 mol) was added dropwise to the stirred solution over 0.5 h under nitrogen atmosphere. After addition was complete, the ice bath was removed, and the reaction mixture was allowed to continuously stir for 12 h at room temperature. The amino salt was formed,

[3] W.G. Bentrude. Private communication.

© 1998 NRC Canada

filtered off, and acetonitrile was removed by evaporation. The residue was separated by flash column chromatography on neutral alumina treated with 5% Et_3N/petroleum. The eluent was 15:1 petroleum ether – ethyl ether. Colorless liquid of benzyl methyl *p*-methylbenzyl phosphite was obtained (3.6 g, 83.5%).

^{1}H NMR ($CDCl_3$, 200 MHz), δ (ppm) data of benzyl methyl substituted-benzyl phosphites. *p*-OCH_3: 3.48 (d, J = 11 Hz, 3H), 4.84 (t, J = 7 Hz, 4H), 6.89 (d, J = 8 Hz, 2H), 7.24 (d, J = 8 Hz, 2H), 7.34 (m, 5H). *p*-CH_3: 2.34 (s, 3H), 3.48 (d, J = 11 Hz, 3H), 4.84 (t, J = 7 Hz, 4H), 7.16 (d, J = 8 Hz, 2H), 7.21 (d, J = 8 Hz, 2H), 7.32 (m, 5H). *m*-CH_3: 2.34 (s, 3H), 3.48 (d, 11 Hz, 3H), 4.84 (t, J = 7 Hz, 4H), 7.14 (m, 4H), 7.32 (m, 5H). *p*-Cl: 3.48 (d, J = 11 Hz, 3H), 4.84 (t, J = 8 Hz, 4H), 7.25 (d, J = 8 Hz, 2H), 7.27 (d, J = 8 Hz, 2H), 7.32 (m, 5H). *p*-NO_2: 3.54 (d, J = 11 Hz, 3H), 4.93 (t, J = 7 Hz, 4H), 7.34 (m, 5H), 7.49 (d, J = 8Hz, 2H), 8.21 (d, J = 8Hz, 2H). *p*-H: 3.49 (d, J = 11 Hz, 3H), 4.85 (d, J = 8 Hz, 4H), 7.33 (m, 9H).

tert-Butyl hypochlorite

Prepared according to a known method (18).

Identifications and isolations of the products

To a jacketed three-necked vessel through which water was circulated from a constant temperature bath operating at 20 ± 0.1°C was placed 2 mL CCl_4 solution containing benzyl methyl *p*-methylbenzyl phosphite (1.5 g, 4.99 mmol). A CCl_4 solution (1 mL) containing *tert*-butyl hypochlorite (0.541 g, 4.99 mmol) was added dropwise to the stirred solution over 3 min under nitrogen atmosphere. Then the reaction mixture was allowed to stir for 30 min. The CCl_4 was removed by evaporation. The residue was separated on neutral alumina (washed with 5% Et_3N/petroleum ether) with petroleum ether – ethyl ether as eluent. *tert*-Butyl chloride **6**, benzyl chloride **7**, *p*-methylbenzyl chloride **8**, and isobutene **5** were identified by comparison of GLC retention time with authentic samples. The molecular ions were also detected by GC–MS. Benzyl methyl *p*-methylbenzyl phosphate **9** was isolated and identified by NMR. Benzyl methyl phosphate **10** was isolated and identified by GC–MS and NMR.

Benzyl methyl *p*-methylbenzyl phosphate (**9**, Y = *p*-CH_3): ^{1}H NMR ($CDCl_3$, 200 MHz), δ (ppm): 2.35 (s, 3H), 3.66 (d, J = 11 Hz, 3H), 5.01 (t, J = 7 Hz, 4H), 7.18 (d, J = 8 Hz, 2H), 7.23 (d, J = 8 Hz, 2H), 7.35 (m, 5H). Dibenzyl methyl phosphate (**9**, Y = H): ^{1}H NMR ($CDCl_3$, 200 MHz), δ (ppm): 3.64 (d, J = 11 Hz, 3H), 5.00 (d, J = 8 Hz, 4H), 7.33 (m, 5H). Benzyl methyl phosphate (**10**): ^{1}H NMR ($CDCl_3$, 200 MHz), δ (ppm): 3.68 (d, J = 11 Hz, 3H), 5.03 (t, J = 10 Hz, 2H), 7.39 (m, 5H), 8.60 (s, 1H). GC–EIMS, *m/z* (rel. intensity): 186 $[M - CH_3 - 1]^+$ (27), 153 $[M - OCH_3 - 1]^+$ (1), 109 $[PhCH_2O]^+$ (100), 91 $[PhCH_2]^+$ (91), 77 $[Ph]^+$ (28).

Reactions of the phosphites with *tert*-butyl hypochlorite

Typical run: the kinetic runs were made using a three-necked jacketed vessel through which water was circulated from a constant temperature bath operating at –20, 0, 20, 40 ± 0.1°C. The CCl_4 solution (1 mL) containing benzyl methyl *p*-methylbenzyl phosphite (0.1449 g, 0.499 mmol) and biphenyl (0.0120 g, 0.0778 mmol, internal standard) was placed in the vessel and stirred to reach the desired temperature. The CCl_4 solution (1 mL) containing *tert*-butyl hypochlorite (0.0541 g, 0.499 mmol) was added dropwise to a stirred solution over 3 min under nitrogen atmosphere. The reaction mixture was allowed to stir for 30 min and was analyzed by GLC.

Analytical procedure

The reaction mixtures were analyzed on a 6 ft × 1/8 in. (1 in. = 25.4 mm) stainless-steel column packed with 10% OV-101 or 10% OV-17 on Chromosorb W with temperature programming from 28 to 250°C. The FID and CDS 401 data system were employed for the analysis.

Acknowledgments

This work has been supported by Non Directed Research Fund administered by the Korea Research Foundation (1994–1995). We are also very grateful to Professor Wesley G. Bentrude for the very careful and kind suggestions for the present investigations. Warm thanks are due to the editor and the reviewers for the kind instructions and comments. The editorial corrections were kindly performed by Professor Bong Rae Cho.

References

1. (*a*) D.B. Denny and R.R. Dilone. J. Am. Chem. Soc. **84**, 4737 (1962); (*b*) J.H. Finley, D.Z. Denny, and D.B. Denny. J. Am. Chem. Soc. **91**, 5826 (1969); (*c*) D.B. Denney and W. Hanifin, Jr. Tetrahedron Lett. 2177 (1963); (*d*) D.B. Denney, D.Z. Denny, and B.C. Chang. J. Am Chem. Soc. **90**, 6332 (1968); (*e*) J.H. Finley and D.B. Denney. J. Am. Chem. Soc. **92**, 362 (1970); (*f*) D.B. Denney, D.Z. Denney, and S.G. Schutzbank. Phosphorous and Sulfur, **8**, 369 (1980); (*g*) D.B. Denny, B.H. Garth, J.W. Hanifin, Jr., and H.M. Relles. Phosphorous and Sulfur, **8**, 275 (1980).
2. C. Walling and M.S. Pearson. J. Am. Chem. Soc. **86**, 2262 (1964).
3. W.G. Bentrude. *In* The chemistry of organophosphorous compounds. Vol. 1. *Edited by* F.R. Hartely. Wiley, New York. 1990. Chap. 14.
4. (*a*) G.G. Smith, F.D. Bagley, and R. Taylor. J. Am. Chem. Soc. **83**, 3647 (1961); (*b*) R. Taylor, G.G. Smith, and W.H. Wetzel. J. Am. Chem. Soc. **84**, 4817 (1962).
5. D.J. Scharf. J. Org. Chem. **39**, 922 (1974).
6. H. Eyring. J. Chem. Phys. **3**, 107 (1935).
7. L.L. Schaleger and F.A. Long. Adv. Phys. Org. Chem. **1**, 1 (1963).
8. J.E. Leffler. J. Org. Chem. **20**, 1202 (1955).
9. J.E. Leffler and E. Grunwald. Rates and equilibria of organic reactions. Wiley, New York. 1963.
10. G.A. Russell. *In* Free radicals. Vol. 1. *Edited by* J.K. Kochi. Wiley, New York. 1973. Chap. 7.
11. (*a*) S.S. Kim, H. Kim, and K.W. Yang. Tetrahedron Lett. **38**, 5303 (1997); (*b*) S.S. Kim, S.C. Im, and C.S. Lee. Gazz. Chim. Ital. **126**, 445 (1996); (*c*) S.S. Kim. Pure. Appl. Chem. **67**, 791 (1995); (*d*) S.S. Kim, H.R. Kim, H.B. Kim, S.J. Youn, and C.J. Kim. J. Am Chem. Soc. **116**, 2754 (1994); (*e*) S.S. Kim, S.Y. Choi, and C.H. Kang. J. Am. Chem. Soc. **107**, 4234 (1985).
12. D.A. Jencks and W.P. Jencks. J. Am. Chem. Soc. **99**, 7948 (1977).
13. S.S. Kim, W.J. Choi, Y. Zhu, and J.H. Kim J. Org. Chem. **63**, 1185 (1998).
14. G.S. Hammond. J. Am. Chem. Soc. **77**, 334 (1955).
15. (*a*) W.P. Jencks. Chem. Rev. **85**, 511 (1985); (*b*) C.F. Bernasconi. Acc. Chem. Res. **25**, 9 (1992); (*c*) S. Hoz. Acc. Chem. Res. **26**, 69 (1993); (*d*) E. Buncel. J. Chem. Educ. **64**, 475 (1987); (*e*) Israel J. Chem. **24**, the whole volume (1985); (*f*) C.D.

© 1998 NRC Canada

Johnson. Tetrahedron, **36**, 3461 (1980); (*g*) E.M. Arnett and K.E. Molter. Acc. Chem. Res. **18**, 339 (1985); (*h*) C.D. Ritchie. Acc. Chem. Res. **5**, 348 (1972); (*i*) B. Giese. Angew. Chem. Int. Engl. Ed. **16**, 125 (1977); (*j*) C.D. Johnson. Chem. Rev. **75**, 755 (1975).

16. D.D. Perrin, W.L.F. Armarego, and D.F. Perrin. Purification of laboratory chemicals. 2nd ed. Pergamon Press, Oxford, U.K. 1980.
17. (*a*) W.G. Bentrude, K.P. Dockery, S. Ganapathy, S.G. Lee, M. Tabet, Y.W. Wu, R.T. Cambron, and J.M. Harris. J. Am. Chem. Soc. **118**, 6192 (1996); (*b*) W.G. Bentrude, E.R. Hansen, W.A. Khan, T.B. Min, and P.E. Rogers. J. Am. Chem. Soc. **95**, 2286 (1973).
18. M.J. Mintz and C. Walling. *In* Org. synth. coll. vol. 5. Wiley, New York. 1973. p. 184.
19. J. March. Advanced organic chemistry. 4th ed. Wiley, New York. 1992. p. 280.

© 1998 NRC Canada

Kinetics of the self-assembly of α-cyclodextrin [2]pseudorotaxanes with polymethylene threads bearing quaternary ammonium and phosphonium end groups

Angela P. Lyon, Nicola J. Banton, and Donal H. Macartney

Abstract: The kinetics and mechanism of the formation and dissociation of a series of [2]pseudorotaxanes, comprised of α-cyclodextrin (α-CD) as the cyclic component and the ($[Me_3N(CH_2)_nNMe_3]^{2+}$ (n = 8–12), $[Me_2EtN(CH_2)_{10}NEtMe_2]^{2+}$, and $[Me_3P(CH_2)_{10}PMe_3]^{2+}$) dications as the threads, were determined by means of ^1H and ^{31}P NMR in aqueous solution. The length of the polymethylene chain (n) of the thread, which has a minor effect on the rate constant for pseudorotaxane formation, is important in the kinetics of the dissociation reactions, with the longer, more hydrophobic chains resulting in slower pseudorotaxane dissociation. The replacement of one methyl substitutent by an ethyl group in each of the end groups on the $[Me_3N(CH_2)_{10}NMe_3]^{2+}$ thread results in a 30-fold decrease in the formation rate constant. Replacements, by ethyls, of two or all of the methyl substitutents prevent the formation of the pseudorotaxane, even after prolonged heating. The pseudorotaxane containing the $\{Me_3P(CH_2)_{10}PMe_3{\cdot}\alpha\text{-CD}\}^{2+}$ thread forms only at elevated temperatures by a slippage mechanism, and the rate constant for its self-assembly at 75°C (8×10^{-5} M^{-1} s^{-1}) is more than 10^6 smaller than the rate constant at 75°C (200 M^{-1} s^{-1}) extrapolated for the corresponding $\{Me_3N(CH_2)_{10}NMe_3{\cdot}\alpha\text{-CD}\}^{2+}$ complex. The enthalpies and entropies of activation for the formation and dissociation of the [2]pseudorotaxanes decrease with an increase in the size and hydrophobicity of the end groups, suggesting a reduced role of desolvation of the quaternized atoms in the threading or dethreading processes.

Key words: pseudorotaxane, α-cyclodextrin, kinetics, self-assembly, slippage, supramolecular.

Résumé : Faisant appel à la RMN du ^1H et du ^{31}P en solutions aqueuses, on a déterminé la cinétique et le mécanisme de formation et de dissociation d'une série de [2]pseudorotaxanes formés d'α-cyclodextrine (α-CD) comme composant cyclique et des dications $[Me_3N(CH_2)_nNMe_3]^{2+}$ (n = 8–12), $[Me_2ETN(CH_2)_{10}NEtMe_2]^{2+}$ et $[Me_3P(CH_2)_{10}PMe_3]^{2+}$ comme fils. La longueur de la chaîne polyméthylénique (n) du fil, qui a un effet mineur sur la constante de vitesse de formation du pseudorotaxane, est importante dans la cinétique des réactions de dissociation; avec de longues chaînes hydrophobes, la dissociation des pseudorotaxane est ralentie. Le remplacement d'un substituant méthyle par un groupe éthyle dans chacun des groupes aux extrémités du fil $[Me_3N(CH_2)_{10}NMe_3]^{2+}$ provoque une diminution de 30 fois de la constante de la vitesse de formation. Les remplacements, par des groupes éthyles, de deux ou de tous les substituants méthyles empêchent la formation des pseudorotaxanes, même après un chauffage prolongé. Le pseudorotaxane contenant le fil $\{Me_3P(CH_2)_{10}PMe_3{\cdot}\alpha\text{-CD}\}^{2+}$ ne se forme qu'à des températures élevées par un mécanisme de glissement et la constante de vitesse pour cette autoassemblée, à 75°C, (8×10^{-5} M^{-1} s^{-1}) est 10^6 fois plus faible que la constante de vitesse, à 75°C (200 M^{-1} s^{-1}), extrapolée pour le complexe correspondant $\{Me_3N(CH_2)_{10}NMe_3{\cdot}\alpha\text{-CD}\}^{2+}$. Les enthalpies et les entropies d'activation pour la formation et la dissociation des [2]pseudorotaxanes diminuent avec une augmentation dans la taille et l'hydrophobicité des groupes terminaux; ceci suggère que la désolvatation des atomes quaternisés joue un rôle réduit dans les processus de formation et de déformation des fils.

Mots clés : pseudorotaxane, α-cyclodextrine, cinétique, autoassemblage, glissement, supramoléculaire.

[Traduit par la rédaction]

This paper is dedicated to Professor Erwin Buncel on the occasion of his 65th birthday and in recognition of his contributions to Canadian chemistry.

Received December 8, 1997.

A.P. Lyon, N.J. Banton, and D.H. Macartney.[1] Department of Chemistry, Queen's University, Kingston, ON K7L 3N6, Canada.

[1] Author to whom correspondence may be addressed. Telephone: (613) 545-2617. Fax: (613) 545-6669. E-mail: donal@chem.queensu.ca

Introduction

Rotaxanes are supramolecular species in which a cyclic molecular bead is threaded by a linear chain bearing sufficiently bulky end units such that the complex is prevented from dissociating into its cyclic and linear molecular components (1–15). If the end groups are not sufficiently bulky to prevent the dissociation of the complex, the supramolecular species is termed a pseudorotaxane. One of the most frequently used cyclic components in the assembly of rotaxanes and pseudorotaxanes (6–15) is the family of cyclodextrins (CD), a series of cyclic

© 1998 NRC Canada

Fig. 1. Schematic representations of (*a*) α-cyclodextrin and (*b*) the [2]pseudorotaxanes assembled in this study.

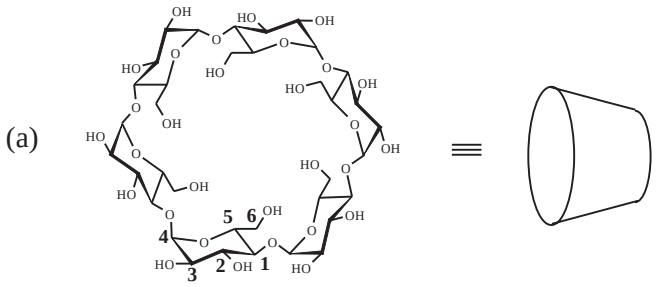

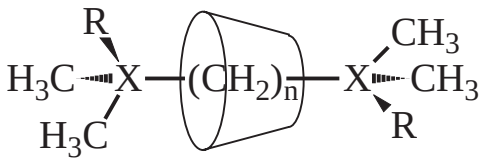

X = N; R = CH_3; n = 8-12
X = N; R = CH_2CH_3; n = 10
X = P; R = CH_3; n = 10

oligosaccharides normally consisting of six (α-CD), seven (β-CD), or eight (γ-CD) α-(1→4)-linked D-(+)-glucopyranose units (16). The smallest of the cyclodextrins, α-CD (Fig. 1), possesses a hydrophobic interior cavity with a diameter of about 5.5 Å and exhibits a strong affinity for polymethylene chains. A number of [2]pseudorotaxanes (the [2] refers to the total number of cyclic and linear components in the complex) have been prepared with α-CD and threads of the form $[L(CH_2)_nL]^{m+}$ (n = 8–12) in which the end groups (L) may be organic moieties such as amines (11), carboxylates (9), or substituted aromatic *N*-heterocycles (8, 10, 12). Coordination of the end groups to inert transition metal centres such as $[Fe(CN)_5]^{3-}$ (12) or $[Co(NH_3)_5]^{3+}$ (11) results in the formation of kinetically stable [2]rotaxanes.

The self-assembly of cyclodextrin rotaxanes and pseudorotaxanes may occur by one of several mechanisms (2, 3). The threading process for the assembly of rotaxanes involves the attachment of bulky groups to the ends of a pseudorotaxane, which has been formed by threading the cyclodextrin with the linear component. A second method involves the dissociation of a bulky group from one end of a linear chain, allowing threading through the cyclic bead (yielding a semirotaxane), followed by reattachment of the bulky group to yield a rotaxane. We have employed this method to generate a number of [2]rotaxanes with α-CD in which the bulky $[Fe(CN)_5]^{3-}$ ion is coordinated to terminal *N*-heterocycles (L = 4,4′-bipyridine (12*a*–*c*), pyrazine (12*c*), or 4-cyanopyridine (12*d*) on either end of a polymethylene chain ($[(NC)_5Fe\{L(CH_2)_nL{\cdot}\alpha\text{-CD}\}Fe(CN)_5]^{4-}$).

A third method of preparing rotaxanes, termed slippage (13, 14), occurs when the internal diameter of the cavity of the cyclic component and the diameter of the end units on the thread are comparable. In this situation the threading of the cyclic component occurs efficiently only at elevated temperatures. Stoddart and co-workers (15) have employed this method to synthesize a number of rotaxanes with tetracationic cyclophanes as the cyclic component. We have recently reported the very slow self-assembly of a [2]pseudorotaxane of α-cyclodextrin employing the 1,10-bis[4-*tert*-butylpyridinium]-decane dication ($[tbp(CH_2)_{10}tbp]^{2+}$) as the thread (10). The *tert*-butyl group has a similar diameter to that of the α-CD cavity, and the rate constant for the formation of the [2]pseudorotaxane was found to be significantly enhanced at elevated temperatures.

To more fully understand the effects of the nature of the end unit on the rate and activation parameters associated with the cyclodextrin pseudorotaxane self-assembly processes, systematic kinetic investigations, employing several series of linear thread components, have been undertaken. In this paper the results of a ^1H and ^{31}P NMR kinetic study of the self-assembly and dissociation of α-cyclodextrin [2]pseudorotaxanes (Fig. 1) containing the 1,10-bis(trimethylphosphonium)decane dication ($[Me_3P(CH_2)_{10}PMe_3]^{2+}$) and a series of α,ω-bis(trialkylammonium)alkane dications ($[Me_3N(CH_2)_nNMe_3]^{2+}$ (n = 8–12) and $[Et_mMe_{(3-m)}N(CH_2)_{10}NMe_{(3-m)}Et_m]^{2+}$ (m = 1–3) are presented. The rate and activation parameters are discussed in terms of the steric and electronic effects of varying the polymethylene chain length, the nature of the quaternized atom, and nature of the alkyl substituents.

Experimental

Materials

The α-cyclodextrin (Aldrich) was dried at 80°C under reduced pressure for at least 8 h prior to use. The 1,*n*-dibromoalkanes (n = 8–12), 1,12-diiododecane, trimethylphosphine, and decamethonium bromide ($[Me_3N(CH_2)_{10}NMe_3]Br_2$) were purchased from Aldrich and used as received.

The α,ω-bis(trimethylammonium)alkane dibromides ($[Me_3N(CH_2)_nNMe_3]Br_2$, n = 8, 9, 11, 12) were prepared by a modification of the method of Blomquist et al. (17). Trimethylamine hydrochloride (16 mmol) was dissolved in a minimum of methanol and 0.6 mol equiv. of potassium carbonate were added. This solution was stirred for 12 h at which time the appropriate α,ω-dibromoalkane (3.2 mmol) was added slowly to the reaction mixture. After the addition, the reaction mixture was left for approximately 7 days without stirring. The solution was then filtered to remove unreacted potassium carbonate, and the filtrate was reduced in vacuo to obtain the crude product in 41–72% yields. The products were recrystallized from methanol–acetone.

$[Me_3N(CH_2)_8NMe_3]Br_2$

mp 274–277°C. Anal. calcd. for $C_{14}H_{34}N_2Br_2{\cdot}H_2O$: C 41.19, H 8.89, N 6.86; found: C 41.56, H 9.15, N 6.85. ^1H NMR (D_2O), δ: 3.30 (m, 4H, H_α), 3.09 (s, 18H, H_{Me}), 1.78 (m, 4H, H_β), 1.38 (m, 8H, $H_{\gamma-\delta}$) ppm.

$[Me_3N(CH_2)_9NMe_3]Br_2$

mp 92–94°C. Anal calcd. for $C_{15}H_{36}N_2Br_2{\cdot}0.5H_2O$: C 43.59, H 9.02, N 6.78; found: C 44.16, H 9.83, N 6.84. ^1H NMR

© 1998 NRC Canada

(D_2O), δ: 3.30 (m, 4H, H_α), 3.09 (s, 18H, H_{Me}), 1.78 (m, 4H, H_β), 1.36 (m, 10H, $H_{\gamma-\varepsilon}$) ppm.

$[Me_3N(CH_2)_{11}NMe_3]Br_2$
mp 129–133°C. Anal calcd. for $C_{17}H_{40}N_2Br_2 \cdot 0.5H_2O$: C 46.27, H 9.36, N 6.35; found: C 46.60, H 9.20, N 6.27. ^{1}H NMR (D_2O), δ: 3.44 (m, 4H, H_α), 3.24 (s, 18H, H_{Me}), 1.92 (m, 4H, H_β), 1.47 (m, 14H, $H_{\gamma-\varepsilon}$) ppm.

$[Me_3N(CH_2)_{12}NMe_3]Br_2$
mp 209–212°C. Anal. calcd. for $C_{18}H_{42}N_2Br_2$: C 48.44, H 9.48, N 6.28; found: C 48.67, H 9.60, N 6.27. ^{1}H NMR (D_2O), δ: 3.30 (m, 4H, H_α), 3.10 (s, 18H, H_{Me}), 1.78 (m, 4H, H_β), 1.33 (m, 16H, $H_{\gamma-\xi}$) ppm.

$[Me_2EtN(CH_2)_{10}NEtMe_2]Br_2$
mp 261–263°C. Anal. calcd. for $C_{18}H_{42}N_2Br_2$: C 48.44, H 9.48, N 6.28; found: C 48.47, H 9.16, N 6.24. ^{1}H NMR (D_2O), δ: 3.26 (m, 4H, H_α), 2.37 (q, 4H, H_{CH2CH3}, J = 7.3 Hz), 3.03 (s, 12H, H_{Me}), 1.76 (m, 4H, H_β), 1.36 (m, 12H, $H_{\gamma-\varepsilon}$), 1.34 (t, 6H, H_{CH2CH3}) ppm.

The 1,10-bis(trimethylphosphonium)decane diiodide ($[Me_3P(CH_2)_{10}PMe_3]I_2$) was prepared by a modification of a reported procedure for related phosphonium cations (18). 1,10-Diiododecane (2 mmol) was added to 12.5 mL of a 1.0 M solution of trimethylphosphine in toluene. The solution was stirred under an atmosphere of N_2(g) at room temperature for 8 h. The product precipitated upon addition of 100 mL of diethyl ether to the reaction mixture.

$[Me_3P(CH_2)_{10}PMe_3]I_2$
mp 232–233°C. Anal. calcd. for $C_{16}H_{38}P_2I_2$: C 35.18, H 7.01; found: C 35.35, H 7.05. ^{1}H NMR (D_2O), δ: 2.18 (m, 4H, H_α), 1.84 (d, 18H, H_{Me}, J_{PH} = 14 Hz), 1.61 (m, 4H, H_β), 1.47 (m, 4H, H_γ), 1.33 (m, 8H, $H_{\delta,\epsilon}$) ppm.

Physical measurements

The ^{1}H, ^{13}C, and ^{31}P NMR spectra were recorded on a Bruker AM-400 instrument in D_2O, utilizing the residual solvent proton signal, external CH_3OH, and external 85% H_3PO_4 as the references, respectively. The stability constants for the α-CD pseudorotaxanes of the $[Me_3N(CH_2)_nNMe_3]^{2+}$ (where n = 8–12) series of threads and of the $[Me_2EtN(CH_2)_{10}NEtMe_2]^{2+}$ thread were determined by ^{1}H NMR titrations by the application of nonlinear least-squares and Simplex optimization programs to the equations for a 1:1 guest–host model, as described previously (12).

The kinetics of the formation of the α-CD pseudorotaxanes of the $[Me_3N(CH_2)_nNMe_3]^{2+}$ (n = 8–12) and $[Me_2EtN(CH_2)_{10}NEtMe_2]^{2+}$ threads at 25°C were determined by ^{1}H NMR spectra taken at timed intervals following the addition of an excess of α-CD, as described previously (10). The rate constants for the formation of the α-CD pseudorotaxane with the $[Me_3P(CH_2)_{10}PMe_3]^{2+}$ guest were determined, in the presence of an excess of α-CD (50–150 mM), at 75, 80, and 85°C by ^{31}P NMR, as described above. The extent of pseudorotaxane formation after 24 h was also determined at five degree temperature intervals between 50 and 70°C in the presence of 150 mM α-CD.

The kinetics of the dissociation of the α-CD pseudorotaxanes into their cyclic and linear components were studied in the case of the $[Me_3N(CH_2)_nNMe_3]^{2+}$ (n = 9–12) and $[Me_2EtN(CH_2)_{10}NEtMe_2]^{2+}$ guests by the addition of 1,12-bis(4,4′-bipyridinium)dodecane dibromide ($[bpy(CH_2)_{12}bpy]Br_2$, 10 mM) to the pseudorotaxane (1 mM) solution, monitoring the rate of formation of the $\{bpy(CH_2)_{12}bpy\cdot\alpha\text{-CD}\}^{2+}$ pseudorotaxane as described previously (10, 12*d*).

The mass spectra were obtained on a VG Quattro quadrupole mass spectrometer, with an atmospheric-pressure electrospray source. Samples of the pseudorotaxanes, as solutions in distilled water with excess α-cyclodextrin, were introduced into the source at a flow rate of 5 mL min^{-1}. Elemental analyses were performed by Canadian Microanalytical Services Ltd (Delta, B.C.).

Results

The additions of excess α-cyclodextrin to aqueous solutions of the $[Me_3N(CH_2)_nNMe_3]^{2+}$ (n = 8–12) and the $[Me_2EtN(CH_2)_{10}NEtMe_2]^{2+}$ dications result in the room-temperature formations of [2]pseudorotaxanes. Attempts to assemble the corresponding [2]pseudorotaxanes with the more sterically demanding $[Et_2MeN(CH_2)_{10}NMeEt_2]^{2+}$ and $[Et_3N(CH_2)_{10}NEt_3]^{2+}$ dications were unsuccessful, even upon heating the solutions at 70°C for prolonged periods (up to one week).

The symmetry-related proton resonances of the dicationic threads of the pseudorotaxanes are split into pairs of resonances upon the threading of the asymmetic α-CD cavity (Fig. 2). From 2-D ROESY spectra of α-CD pseudorotaxanes with related threads (A.P. Lyon and D.H. Macartney; A.C. Smith and D.H. Macartney),[2] we have determined that the upfield peak of the pairs of resonances for each of the aliphatic thread protons is located near the narrower end of the cyclodextrin. The chemical-shift differences (on a 400 MHz instrument) between the two methyl singlets decrease as the polymethylene chain length is increased (34 Hz (n = 8), 25 Hz (n = 9), 19 Hz (n = 10), 14 Hz (n = 11), and 10 Hz (n = 12)), and the trimethylammonium end groups are located further from the rims of the α-CD cavity. The proton resonances of the α-cyclodextrin also exhibit chemical-shift changes upon inclusion of the threads (Fig. 2). In the ^{13}C NMR spectrum of the pseudorotaxane with the $[Me_3N(CH_2)_{10}NMe_3]^{2+}$ thread the polymethylene resonances are split into pairs of peaks, while no splitting is observed in the methyl carbon resonance.

At higher concentrations of α-cyclodextrin (in excess of that needed for pseudorotaxane formation) there are no noticeable changes in the chemical shifts of the pairs of methyl proton resonances, which might be associated with inclusion of the methyl groups by additional α-CD hosts in solution. Such 1:1 and 2:1 α-CD adducts of the [2]pseudorotaxanes may be detected, however, in the gas phase by electrospray mass spectrometry. The $[Me_3N(CH_2)_{10}NMe_3]^{2+}$ dication in the presence of excess α-CD gives rise to peaks at m/z = 614.5 ($\{L(CH_2)_{10}L\cdot\alpha\text{-CD}\}^{2+}$ 100%), 1101.6 ($\{L(CH_2)_{10}L\cdot 2\alpha\text{-CD}\}^{2+}$ 30%), 1588.0 ($\{L(CH_2)_{10}L\cdot 3\alpha\text{-CD}\}^{2+}$ 7%).

The stability constants for the pseudorotaxanes (K_1) containing the $[Me_3N(CH_2)_{10}NMe_3]^{2+}$ (n = 8–12) dications were determined by a ^{1}H NMR titration of the threads with α-cyclodextrin at 25°C in D_2O (I = 0.10 M NaCl) and are presented in Table 1. The approaches to equilibrium for the pseudorotaxanes

[2] Unpublished results.

© 1998 NRC Canada

Fig. 2. The ^{1}H NMR spectra of (*a*) $[Me_3N(CH_2)_{10}NMe_3]^{2+}$ (5 mM), (*b*) α-CD (5 mM), (*c*) $[Me_3N(CH_2)_{10}NMe_3]^{2+}$ (5 mM) in the presence of α-CD (50 mM), and (*d*) α-CD (5 mM) in the presence of $[Me_3N(CH_2)_{10}NMe_3]^{2+}$ (50 mM) in D_2O. The polymethylene protons of the thread (spectrum (*a*)) are labelled α-ε according to their positions with respect to the quaternized N atoms, while the α-CD protons (spectrum (*b*)) are labelled as in Fig. 1. The resonance denoted by the asterisk is for the solvent HDO proton.

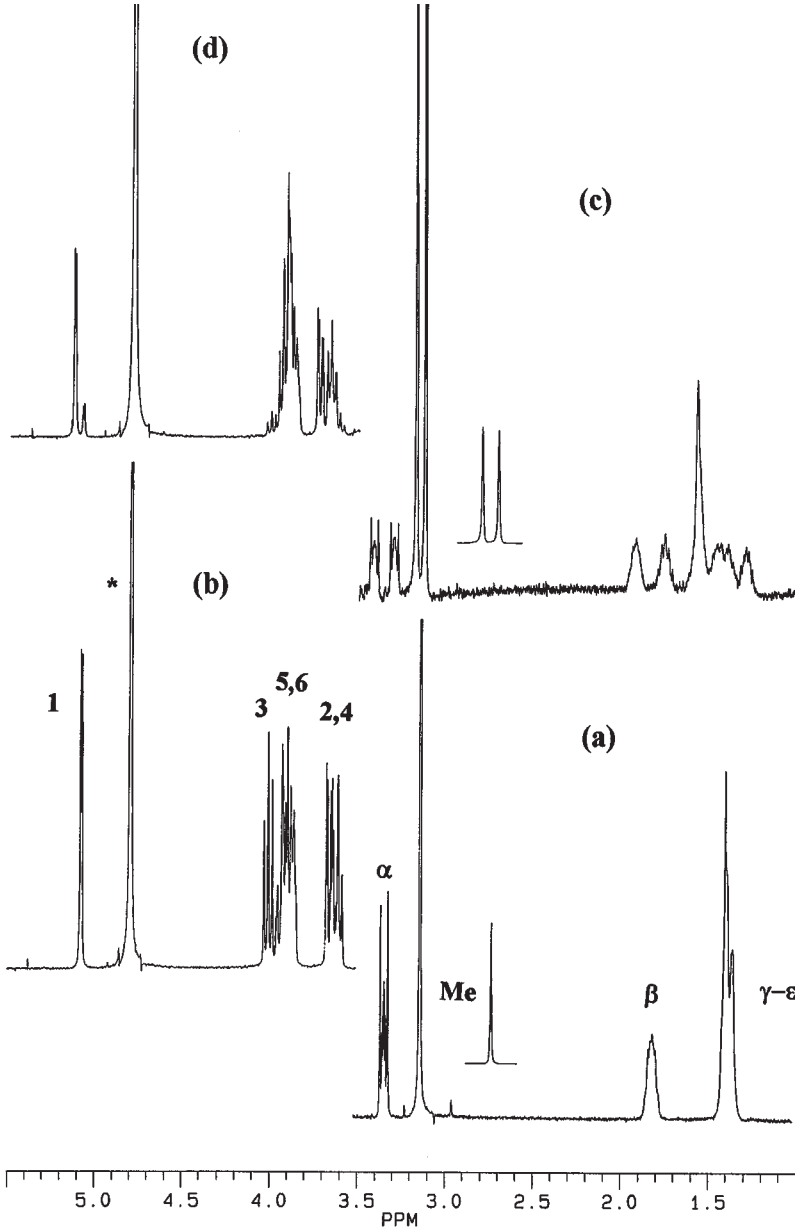

containing the $[Me_2EtN(CH_2)_{10}NEtMe_2]^{2+}$ and $[Me_3P(CH_2)_{10}PMe_3]^{2+}$ threads are too slow at 25°C to permit accurate determinations of K_1 by this titration method.

The kinetics of the formation of the [2]pseudorotaxanes from α-CD and the $[Me_3N(CH_2)_nNMe_3]^{2+}$ (n = 9–12) and $[Me_2EtN(CH_2)_{10}NEtMe_2]^{2+}$ dications were determined at 25°C in D_2O (I = 0.10 M NaCl) by monitoring the methyl proton resonances of the threads in the ^{1}H NMR spectra (Fig. 3).

$$[1] \quad [L(CH_2)_nL]^{2+} + \alpha\text{-CD} \xrightarrow{k_1} \{L(CH_2)_nL{\cdot}\alpha\text{-CD}\}^{2+}$$

The observed pseudo-first-order rate constants exhibited a first-order dependence on the concentration of α-CD (10–50 mmol) present in excess of the thread (1–2 mmol), as illustrated in Fig. 4.

The second-order rate constants k_1 are presented in Table 1. Activation parameters associated with k_1 were determined for the $[Me_3N(CH_2)_{10}NMe_3]^{2+}$ and $[Me_2EtN(CH_2)_{10}NEtMe_2]^{2+}$ dications and are also presented in Table 1, along with the rate and activation parameters for the $[tbp(CH_2)_{10}tbp]^{2+}$ (tbp = 4-*tert*-butylpyridinium) dication, determined in a previous study (10). It was not possible to accurately determine the formation rate constant for the pseudorotaxane with the $[Me_3N(CH_2)_8NMe_3]^{2+}$ thread by ^{1}H NMR, due to the low stability constant (K_1 = 44 M^{-1}) and the rapid approach to

© 1998 NRC Canada

Table 1. The rate, activation, and thermodynamic parameters for the formation of α-CD pseudorotaxanes $\{L(CH_2)_nL\cdot\alpha CD\}^{2+}$.[a]

Threads	$10^3 k_1$ (M^{-1} s^{-1})	$\Delta H^{\ddagger}_1$ (kJ mol^{-1})	$\Delta S^{\ddagger}_1$ (J K^{-1} mol^{-1})	K_1 (M^{-1})
$[Me_3N(CH_2)_8NMe_3]^{2+}$				44 ± 5
$[Me_3N(CH_2)_9NMe_3]^{2+}$	187 ± 15			240 ± 50
$[Me_3N(CH_2)_{10}NMe_3]^{2+}$	164 ± 22	117 ± 2	134 ± 6	1360 ± 290
$[Me_3N(CH_2)_{11}NMe_3]^{2+}$	104 ± 11			3170 ± 970
$[Me_3N(CH_2)_{12}NMe_3]^{2+}$	121 ± 13			6760 ± 850
$[Me_2EtN(CH_2)_{10}NEtMe_2]^{2+}$	5.83 ± 0.38	120 ± 6	114 ± 16	
$[Me_3P(CH_2)_{10}PMe_3]^{2+}$	0.079 ± 0.006[b]	95 ± 12	–53 ± 12	
$[tbp(CH_2)_{10}tpb]^{2+}$ [c]	7.6 ± 1.8	102 ± 10	58 ± 32	

[a] Determined by ^{1}H NMR studies at 25°C in D_2O (I = 0.10 M (NaCl)).
[b] At 75°C in 20% D_2O/80% H_2O ((I = 0.10 M (NaCl)).
[c] tbp = 4-*tert*-butylpyridinium, data from ref. 10.

Fig. 3. The ^{1}H NMR spectra (methyl resonance) of the $[Me_2EtN(CH_2)_{10}NEtMe_2]^{2+}$ dication (1 mM) (*a*) 1 min, (*b*) 15 min, (*c*) 28 min, (*d*) 55 min, (*e*) 81 min, (*f*) 108 min, (*g*) 211 min, and (*h*) 651 min after the addition of α-CD (30 mM) at 25°C in D_2O (I = 0.10 M (NaCl)).

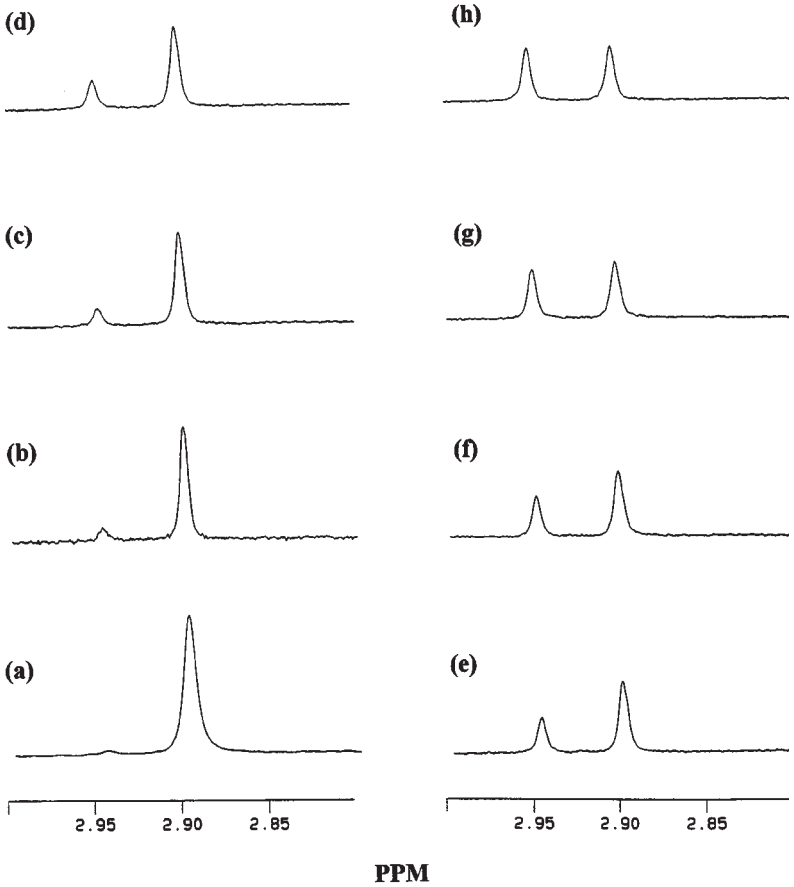

equilibrium (k_1[α-CD] + k_{-1}) at higher concentrations of α-CD. The rate constant for the formation of the pseudorotaxane with the $[Me_3N(CH_2)_{10}NMe_3]^{2+}$ thread at 25°C was observed to decrease with an increase in the ionic strength: k_1 = 0.215 M^{-1} s^{-1} (I = 0.003 M (no added NaCl), 0.164 M^{-1} s^{-1} (0.10 M), and 0.138 M^{-1} s^{-1} (1.0 M).

The kinetics of the dissociation of the [2]pseudorotaxanes were determined by ^{1}H NMR, following the addition of an excess of $[bpy(CH_2)_{12}bpy]^{2+}$ to the assembled pseudorotaxane. Upon pseudorotaxane dissociation, the $[bpy(CH_2)_{12}bpy]^{2+}$ dication rapidly traps the released α-CD, forming a stable pseudorotaxane (K_1 = 3700 M^{-1} at 25°C (12*b*)).

[2] $\{L(CH_2)_{10}L\cdot\alpha\text{-CD}\}^{2+} + [bpy(CH_2)_{12}bpy]^{2+} \underset{k_{-1}}{\rightarrow} \{bpy(CH_2)_{12}bpy\cdot\alpha\text{-CD}\}^{2+} + [L(CH_2)_nL]^{2+}$

The rate and activation parameters associated with the reaction in eq. [2] are presented in Table 2.

The formation of an α-cyclodextrin pseudorotaxane with the 1,10-bis(trimethyl-phosphonium)decane dication may be

© 1998 NRC Canada

Table 2. The rate and activation parameters for the dissociation of the α-CD pseudorotaxanes $\{L(CH_2)_nL\cdot\alpha CD\}^{2+}$.[a]

Threads	$10^5\ k_{-1}$ (s^{-1})	$\Delta H^{\ddagger}_{-1}$ (kJ mol^{-1})	$\Delta S^{\ddagger}_{-1}$ (J K^{-1} mol^{-1})	K_1[b] (M^{-1})
$[Me_3N(CH_2)_9NMe_3]^{2+}$	52.3 ± 1.4	144 ± 3	176 ± 10	360 ± 40
$[Me_3N(CH_2)_{10}NMe_3]^{2+}$	10.4 ± 0.1	136 ± 8	135 ± 25	1580 ± 220
$[Me_3N(CH_2)_{11}NMe_3]^{2+}$	3.41 ± 0.04			3050 ± 360
$[Me_3N(CH_2)_{12}NMe_3]^{2+}$	1.32 ± 0.04			9170 ± 1260
$[Me_2EtN(CH_2)_{10}NEtMe_2]^{2+}$	0.54 ± 0.02	120 ± 1	57 ± 4	1080 ± 110
$[tbp(CH_2)_{10}tbp]^{2+}$[c]	0.42 ± 0.02	99 ± 3	–17 ± 10	1800 ± 200

[a] Determined by ^1H NMR studies at 25°C in D_2O (I = 0.10 M (NaCl)) in the presence of $[bpy(CH_2)_{12}bpy]Br_2$.
[b] Calculated from $K_1 = k_1/k_{-1}$.
[c] tbp = 4-*tert*-butylpyridinium, data from ref. 10.

Fig. 4. The dependencies of the observed rate constants on [α-CD] for the formations of the [2]pseudorotaxanes with (●) $[Me_2EtN(CH_2)_{10}NEtMe_2]^{2+}$ (25°C), (■) $[Me_3P(CH_2)_{10}PMe_3]^{2+}$ (75°C), and (▼) $[Me_3N(CH_2)_{10}NMe_3]^{2+}$ (25°C).

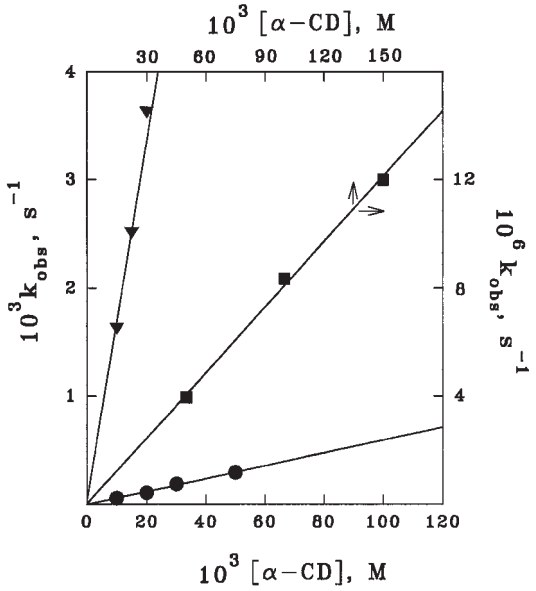

conveniently monitored by using $^{31}P\{^1H\}$ NMR, as the free guest exhibits a singlet at 26.45 ppm. The addition of dibromide salt of the dication (5 mM) to a large excess of α-CD (150 mM) in aqueous solution (20% D_2O, 80% H_2O, 0.10 M NaCl) at 25°C does not result in the formation of a pseudorotaxane, even after one week. At elevated temperatures, however, slow formation of the pseudorotaxane is indicated by the appearance of a pair of singlet resonances (26.79 and 26.50 ppm) and the disappearance of the free-guest resonance (Fig. 5). Similar splittings of the proton and carbon resonances of the methyl groups are observed in the ^1H and ^{13}C spectra of the pseudorotaxane, with proton doublets centred at 1.94 and 1.89 ppm (J_{PH} = 14 Hz) and carbon doublets centred at 7.22 and 7.21 ppm (J_{PC} = 52 Hz). The percent inclusion of the guest dication after 24 h in the presence of 150 mM α-CD was determined at five degree intervals over the temperature range of 50–70°C: 9% (50°C), 16% (55°C), 27% (60°C), 35% (65°C), 51% (70°C). A study of the formation rate constant as a function of α-CD concentration at 75°C (Fig. 4) revealed a first-order dependence on [α-CD] and a second-order rate constant of (7.9 ± 0.6) × 10^{-5} M^{-1} s^{-1}. The enthalpy and entropy of

Fig. 5. The $^{31}P\{^1H\}$ NMR spectra of the $[Me_3P(CH_2)_{10}PMe_3]^{2+}$ dication (5 mM) (*a*) 1 h, (*b*) 3.7 h, (*c*) 10 h, (*d*) 17 h, and (*e*) 30 h after the addition of α-CD (150 mM) in 20% D_2O/80% H_2O (I = 0.10 M (NaCl) at 80°C, and (*f*) a plot of ln(1 – I) versus time for this system.

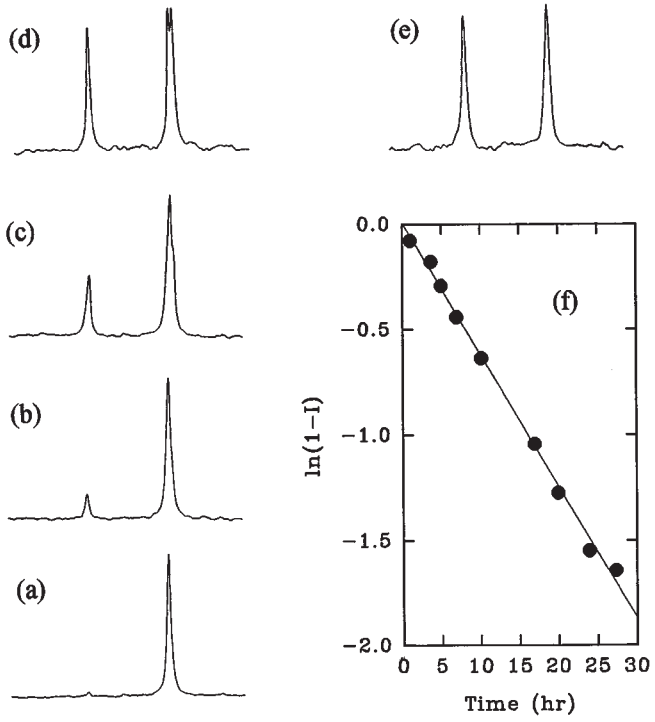

activation for the formation of the [2]pseudorotaxane were determined to be 96 ± 10 kJ mol^{-1} and –50 ± 30 J K^{-1} mol^{-1}, respectively. The electrospray mass spectrum of this pseudorotaxane in the presence of excess α-CD exhibits peaks at *m*/*z* = 632.3 ($\{L(CH_2)_{10}L\cdot\alpha\text{-CD}\}^{2+}$ 100%), 1118.5 ($\{L(CH_2)_{10}L\cdot2\alpha\text{-CD}\}^{2+}$ 43%), and 1605.0 ($\{L(CH_2)_{10}L\cdot3\alpha\text{-CD}\}^{2+}$ 5%), corresponding to the [2]pseudorotaxane and its 1:1 and 2:1 adducts, respectively, in the gas phase.

Discussion

The rate constants and activation parameters for the formation (k_1) and dissociation (k_{-1}) of α-cyclodextrin [2]pseudorotaxanes have been determined for series of dicationic threads $[Me_2RX(CH_2)_nXRMe_2]^{2+}$, varying the polymethylene chain length (n = 8–12), the quaternized atom X (N or P), and the

© 1998 NRC Canada

alkyl substituent R (Me or Et). The kinetic data obtained in this study indicated that the rate constants for the formation of the [2]pseudorotaxanes are very dependent on the size of the end group, but are relatively independent of the polymethylene chain length.

The results of this study indicate that α-CD is able to effectively discriminate between end groups on the basis of their size and shape as demonstrated by the slow formation of the pseudorotaxane with $[Me_2EtN(CH_2)_{10}NEtMe_2]^{2+}$, as compared to the inability to form pseudorotaxanes with threads containing the more sterically demanding diethylmethyl- and triethylammonium head groups. Extrapolation of the rate constant for the formation of the [2]pseudorotaxane with the $[Me_3N(CH_2)_{10}NMe_3]^{2+}$ dication to 75°C gives a value of 200 M^{-1} s^{-1}, which is 2.5×10^6 times greater than the rate constant for the $[Me_3P(CH_2)_{10}PMe_3]^{2+}$ dication. Using crystallographic data determined for $[(CH_3)_4N]I$ (19) and $[(CH_3)_4P][Cu_2Cl_5]$ (20), the diameter of the trimethylphosphonium end group is estimated to be 0.54 Å larger than the trimethylammonium end group. Therefore, the threading of the larger trimethylphosphonium end group must occur by the slippage mechanism at elevated temperatures.

In a separate study using dicationic threads bearing 4-(α-alkyl-α-methylmethanol)pyridinium (L) end groups, $[L(CH_2)_{12}L]^{2+}$, similar dependences of the pseudorotaxane formation constants on the steric bulk of the head groups were observed (A.C. Smith and D.H. Macartney)[2]. With these dications, however, the threading is preceded by inclusion of the end groups in the α-CD cavities. In the present study, there is no evidence, other than in the electrospray mass spectrum, of significant inclusion of the trialkylammonium or -phosphonium groups by the cyclodextrin. ^{1}H NMR studies of the proton chemical shifts of the tetramethylammonium and trimethylethylammonium ions in the presence of α-CD indicate that there is negligible inclusion of these cations. For this reason, the tetramethylammonium ion has been proposed as an internal reference for NMR titrations with cyclodextrins (21).

The rate constants for the dissociation of the [2]pseudorotaxanes into their cyclic and linear components indicate a dependence on both the size of the head group and the length of the polymethylene chain. The effects of the steric bulk of the head group have been discussed above, and the length of the polymethylene chain is related to its hydrophobicity and the degree of hydrophobic interactions with the cyclodextrin interior cavity. As a result, the stability constants for the pseudorotaxanes with the $[Me_3N(CH_2)_nNMe_3]^{2+}$ threads increase with the polymethylene chain length and are similar in magnitude to the corresponding values for other $[L(CH_2)_nL]^{2+}$ threads with *N*-heterocyclic head groups (8, 12). The stability constants were also calculated from the ratio of the formation and dissociation rate constants ($K_1 = k_1/k_{-1}$, Table 2) and are in reasonable agreement with the values determined by the ^{1}H NMR titrations. We have observed similar degrees of agreement in stability constants between kinetic and NMR measurements in previous studies (12).

The enthalpies of activation for the formation of these α-cyclodextrin [2]pseudorotaxanes are in the range of 95–120 kJ mol^{-1} and are likely associated the distortions required in the α-CD and the end group upon threading, along with desolvation of the end group. The entropies of activation are comprised of an unfavourable term associated with the combining of the cyclic and linear components and a favourable contribution from the release of water molecules solvating the quaternized atom. The $\Delta S^{\ddagger}_1$ values (and the values of $\Delta H^{\ddagger}_1$ to a lesser extent) determined in this study (Tables 1 and 2) tend to decrease with an increase in the bulk and hydrophobicity of the end groups. Upon replacing N by P as the quaternized atom, or replacing one methyl group by an ethyl, the hydrophobicity of the cationic end group is increased and the group is less strongly solvated, leading to decreases in both the entropy and enthalpy of activation associated with end group desolvation. The rate constants for pseudorotaxane formation (with $[Me_3N(CH_2)_{10}NMe_3]^{2+}$) were also found to decrease with increasing ionic strength, as ion pairing between the quaternized nitrogen and the chloride ion inhibited the threading of the α-CD by the end group. We have also recently observed that the rate constants for α-CD pseudorotaxane formation with these and other cationic threads are significantly increased in basic solution as a result of α-CD hydroxyl deprotonation. We are continuing to investigate this and other medium effects on the kinetics and mechanisms of pseudorotaxane self-assembly.

Acknowledgements

The financial support of this research by the Natural Sciences and Engineering Research Council of Canada, in the form of research and equipment grants, is gratefully acknowledged. The authors wish to thank Drs. R.S. Wylie and B.K. Hunter for helpful discussions.

References

1. G. Schill. Catenanes, rotaxanes and knots. Academic Press, New York. 1971.
2. H.W. Gibson, M.C. Bheda, and P.T. Engen. Prog. Polym. Sci. **19**, 843 (1994).
3. (*a*) D.B. Amabilino and J.F. Stoddart. Chem. Rev. **95**, 2725 (1995); (*b*) D. Philp and J.F. Stoddart. Angew. Chem. Int. Ed. Engl. **35**, 1154 (1996).
4. P.L. Anelli, P.R. Ashton, R. Ballardini, V. Balzani, M. Delgado, M.T. Gandolfi, T.T. Goodnow, A.E. Kaifer, D. Philp, M. Pietraszkiewicz, L. Prodi, M.V. Reddington, A.M.Z. Slawin, N. Spencer, J.F. Stoddart, C. Vicent, and D.J. Williams. J. Am. Chem. Soc. **114**, 193 (1992).
5. (*a*) J.F. Stoddart. Angew. Chem. Int. Ed. Engl. **31**, 846 (1992); (*b*) H. Ogino. New. J. Chem. **17**, 683 (1993).
6. (*a*) G.H. Wenz and B. Keller. Angew. Chem. Int. Ed. Engl. **31**, 197 (1992); (*b*) G. Wenz, E. van der Bey, and L. Schmidt. Angew. Chem. Int. Ed. Engl. **31**, 783 (1992); (*c*) G. Wenz. Angew. Chem. Int. Ed. Engl. **33**, 803 (1994).
7. (*a*) A. Harada, J. Li, and M. Kamachi. Nature (London), **356**, 325 (1992); (*b*) Nature (London), **364**, 516 (1992); (*c*) A. Harada. Coord. Chem. Rev. **148**, 115 (1996).
8. (*a*) H. Yonemura, H. Saito, S. Matsushima, H. Nakamura, and T. Matsuo. Tetrahedron Lett. **30**, 3143 (1989); (*b*) H. Saito, H. Yonemura, H. Nakamura, and T. Matsuo. Chem. Lett. 535 (1990); (*c*) H. Yonemura, M. Kasahara, H. Saito, H. Nakamura, and T. Matsuo. J. Phys. Chem. **96**, 5765 (1992).
9. M. Watanabe, H. Nakamura, and T. Matsuo. Bull. Chem. Soc. Jpn. **65**, 164 (1992).
10. D.H. Macartney. J. Chem. Soc. Perkin Trans. 2, 2775 (1996).
11. (*a*) H. Ogino. J. Am. Chem. Soc. **103**, 1303 (1981); (*b*) H. Ogino and K. Ohata. Inorg. Chem. **23**, 3312 (1984).
12. (*a*) R.S. Wylie and D.H. Macartney. J. Am. Chem. Soc. **114**,

© 1998 NRC Canada

3136 (1992); (*b*) Supramol. Chem. **3**, 29 (1993); (*c*) C.A. Waddling and D.H. Macartney. Inorg. Chem. **33**, 5912 (1994); (*d*) A.P. Lyon and D.H. Macartney. Inorg. Chem. **36**, 729 (1997).

13. (*a*) I.T. Harrison. J. Chem. Soc. Chem. Commun. 231 (1972); (*b*) J. Chem. Soc. Perkin Trans. 1, 301 (1974).
14. G. Schill, W. Beckmann, N. Schweickert, and H. Fritz. Chem. Ber. **119**, 2647(1986).
15. (*a*) P.R. Ashton, M. Belohradsky, D. Philp, and J.F. Stoddart. J. Chem. Soc. Chem. Commun. 1269 (1993); (*b*) P.R. Ashton, M. Belohradsky, D. Philp, N. Spencer, and J.F. Stoddart. J. Chem. Soc. Chem. Commun. 1274 (1993); (*c*) D.B. Amabilino, P.R. Ashton, M. Belohradsky, F.M. Raymo, and J.F. Stoddart. J. Chem. Soc. Chem. Commun. 747 (1995); J. Chem. Soc. Chem. Commun. 751 (1995); (*d*) P.R. Ashton, R. Ballardini, V. Balzani, M. Belohradsky, M.T. Gandolfi, D. Philp, L. Prodi, F.M. Raymo, M.V. Reedington, N. Spencer, J.F. Stoddart, M. Venturi, and D. J. Williams. J. Am. Chem. Soc. **118**, 4931 (1996).
16. K.A. Connors. Chem. Rev. **97**, 1325 (1997).
17. A.T. Blomquist, B.F. Hallam, and A.D. Josey. J. Am. Chem. Soc. **81**, 678 (1959).
18. (*a*) E. Renaud and M.C. Baird. J. Chem. Soc. Dalton Trans. 2905 (1992); (*b*) E. Renaud, R.B. Russell, S. Fortier, S.J. Brown, and M.C. Baird. J. Organomet. Chem. **419**, 403 (1991).
19. V.G. Herrschaft and H. Hartll. Acta Crystallogr. Sect. C: Cryst. Struct. Commun. **45**, 1021 (1989).
20. W.G. Haije, J.A.L. Dobbelaar, and W.J.A. Maaskant. Acta Crystallogr. Sect. C: Cryst. Struct. Commun. **42**, 1485 (1986).
21. Y. Matsui and S. Tokunaga. Bull. Chem. Soc. Jpn. **69**, 2477 (1996).

© 1998 NRC Canada

On the possibility of conversion of strained bridgehead alkenes into carbenes via 1,2 hydrogen and 1,2 carbon migrations. A theoretical study of the rearrangements in the adamantene and protoadamantene systems

Gennady V. Shustov and Michael T.H. Liu

Abstract: Rearrangements of 2-adamantene **3**, adamantylidene **4**, and 4-protoadamantylidene **5** have been studied theoretically using high level ab initio computations. Adamantene **3** and adamantylidene **4** have singlet ground states. The conversion of **3** into **4** via 1,2 hydrogen migration ($\Delta G^{\neq}$ = 69.1 kcal mol^{-1}) cannot compete with 1,2 carbon migration of **3** to **5** (30.3 kcal mol^{-1}). The singlet carbene **5** rearranges to 2,4-dehydroadamantane **6** and 4,5-protoadamantene **9** via 1,3H and 1,2H shifts, respectively, with identical activation barriers of 8.8 kcal mol^{-1}. The 1,2 migration of the bridge hydrogen in **5** leading to 3,4 protoadamantene **8** has a higher activation barrier (37.2 kcal mol^{-1}). A retro Diels–Alder cycloaddition of **3** to 5-allyl-3-methylenecyclohex-1-ene **7** is the main channel of the unimolecular conversion of **3** ($\Delta G^{\neq}$ = 20.5 kcal mol^{-1}). A predicted ratio of **7** > > **6** ≈ **9** of the products of thermolysis of **3** is in agreement with experimental data. The rearrangement of **4** into **6** via the 1,3H shift ($\Delta G^{\neq}$ = 11.8 kcal mol^{-1}) dominates over the 1,2C shift of **4** to **8** (13.5 kcal mol^{-1}), also in accord with experiment.

Key words: adamantene, protoadamantenes, carbenes, rearrangements, ab initio, computation.

Résumé : Faisant appel à des calculs ab initio à des niveaux élevés, on a étudié d'une façon théorique les réarrangements des adamant-2-ène (**3**), adamantylidène (**4**) et 4-protoadamantylidène (**5**). Les adamant-2-ène (**3**) et adamantylidène (**4**) possèdent des états fondamentaux singulets. La conversion de **3** en **4** par le biais d'une migration 1,2 d'hydrogène ($\Delta G^{\neq}$ = 69,1 kcal/mol) ne peut pas faire compétition à la migration 1,2 de carbone de **3** à **5** (30,3 kcal/mol). Le carbène singulet **5** se réarrange en 2,4-déhydroadamantane (**6**) et en 4,5-protoadamantène (**9**) par le biais de déplacements 1,3 et 1,2 d'hydrogène respectivement; les barrières initiales d'activation sont toutes les deux égales à 8,8 kcal/mol. La barrière d'activation pour la migration 1,2 de l'hydrogène de pont du composé **5** conduisant au 3,4-protoadamantène (**8**) est plus élevée (37,2 kcal/mol). Une rétrocycloaddition de Diels–Alder du composé **3** en 5-allyl-3-méthylènecyclohex-1-ène (**7**) correspond à la voie principale de la conversion unimoléculaire de **3** ($\Delta G^{\neq}$ = 20,5 kcal/mol). Un rapport prévu de **7** > > **6** ≈ **9** pour les produits de thermolyse de **3** est en bon accord avec les données expérimentales. Le réarrangement de **4** en **6** par le biais d'un déplacement 1,3 d'hydrogène ($\Delta G^{\neq}$ = 11,8 kcal/mol) est plus important que le déplacement 1,2 de carbone de **4** à **8** (13,5 kcal/mol); ces prédictions sont aussi en accord avec les données expérimentales.

Mots clés : adamantène, protoadamantènes, carbènes, réarrangements, ab initio, calculs théoriques.

[Traduit par la rédaction]

Introduction

Conversions of strained bridgehead alkenes (anti-Bredt alkenes) into the corresponding carbenes have been known for two decades (1–12). A "bridgehead alkene–carbene" isomerization has been thoroughly studied in the case of the homocubene system **1/2** (6–12) (Scheme 1).

The strain in anti-Bredt alkenes is one of the factors promoting their isomerization to carbenes because, owing to this strain, energy of the alkene energy approaches that of the carbene, or even exceeds it (6, 12). From the formation of "carbene products" under conditions of generation of the bridgehead alkenes, one can make judgements about the "alkene–carbene" conversion process (4–14).

As a rule, the isomerization process of anti-Bredt alkenes into the corresponding carbenes is described as a 1,2 carbon migration (4–11, 14). However, for adamantene **3**, Bian and Jones (13) proposed the possibility of its isomerization into adamantylidene **4** via a 1,2 hydrogen shift. They explained the

This paper is dedicated to Professor Erwin Buncel in recognition of his contributions to Canadian chemistry.

Received January 5, 1998.

G.V. Shustov.[1] Department of Chemistry, University of Calgary, Calgary, AB T2N 1N4, Canada.
M.T.H. Liu. Department of Chemistry, University of Prince Edward Island, Charlottetown, PE C1A 4P3, Canada.

[1] Author to whom correspondence may be addressed. Telephone: (403) 220–6905. Fax: (403) 289–9488. E-mail: gshustov@acs.ucalgary.ca

© 1998 NRC Canada

Scheme 1.

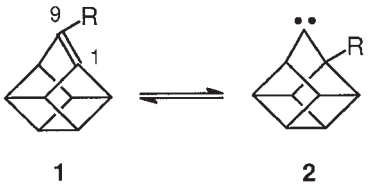

Scheme 2.

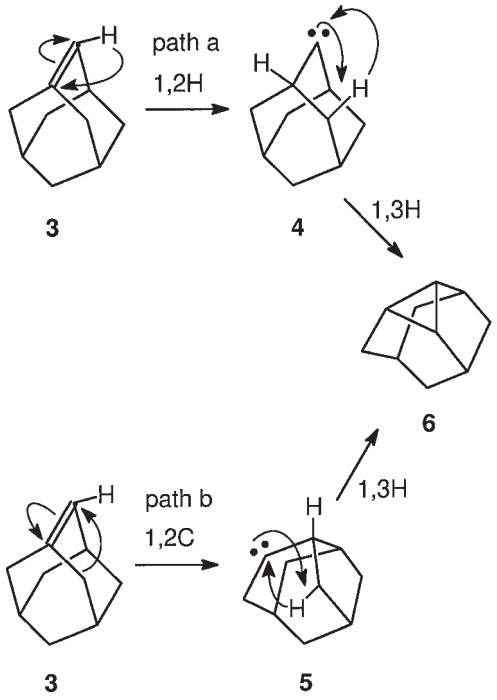

formation of 2,4-dehydroadamantane **6** under the conditions of the generation of adamantene **3** (vacuum flash pyrolysis of 1-noradamantyldiazomethane at 500°C) by consecutive rearrangements involving a 1,2H shift in **3** and a 1,3H shift in **4** (Scheme 2, path a).

It was shown earlier that dehydroadamantane **6** is the main product of vacuum pyrolysis of 2-diazoadamantane (15) and adamantane-2-spiro-3′-diazirine (16): the precursors of carbene **4**. Formation of **6** was also observed in photolysis of adamantane-2-spiro-3′-diazirine in β-cyclodextrin (17) and argon matrixes (18) and inside a zeolite (19). The possibility of 1,2 hydrogen migration in the pair **3/4** has been considered (17, 18), but no experimental proof for this process at low temperatures was found.

On the other hand, the formation of dehydroadamantane **6** under the conditions of the generation of adamantene **3** can be explained by a 1,2 carbon migration followed by a 1,3H shift in the intermediate protoadamantylidene **5** (Scheme 2, path b). This path was demonstrated in the rearrangement of 2-(1-adamantyl)-adamantene into 2-(1-adamantyl)-2,4-dehydroadamantane (14).

Thus, it is of interest to estimate quantitatively the possibility of rearrangement of adamantene **3** via 1,2 hydrogen and 1,2 carbon migrations. In the present work, we have undertaken a theoretical study of the paths a and b (Scheme 2), including

Scheme 3.

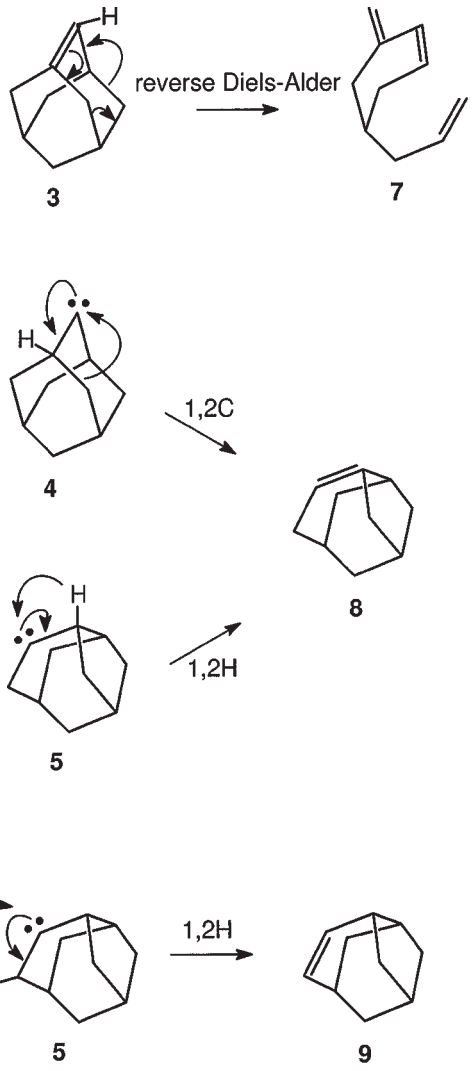

the corresponding transition states. In previous ab initio theoretical studies (12, 18) of the "anti-Bredt alkene–carbene" isomerization, transition structures connecting anti-Bredt alkenes with the corresponding carbenes were not considered.

For comparison with the experimental data (13–19), we have also studied a reverse Diels–Alder reaction, the 1,2C shift in **4**, and the 1,2H shifts in **5** (Scheme 3) as competitive conversion paths for adamantene **3**.

It is worthy of note that rearrangements of bi- and tricyclic carbenes, like **4** and **5,** themselves are a field of much current interest (20).

Computational methods

All ab initio calculations presented here were performed with the Gaussian 94 system of programs (21) on a Silicon Graphics Power Challenge computer with 18 R8000 processors. The geometry optimizations and frequency calculations were carried out at the RHF/6-31G(d) and B3LYP/6-31+G(d) (UB3LYP/6-31+G(d) for the triplets **3**, **4**) theoretical levels using procedures implemented in the Gaussian molecular orbital package. The (U)B3LYP/6-31+G(d) optimized structures

© 1998 NRC Canada

Fig. 1. (U)B3LYP/6-31+G(d), HF/6-31G(d) (in parentheses), and MP2(fc)/6-31G(d) (in square brackets) optimized structures of the singlet and triplet states of adamantene **3** and adamantylidene **4**; oop = out-of-plane angle. Bond lengths in angstroms, angles in degrees.

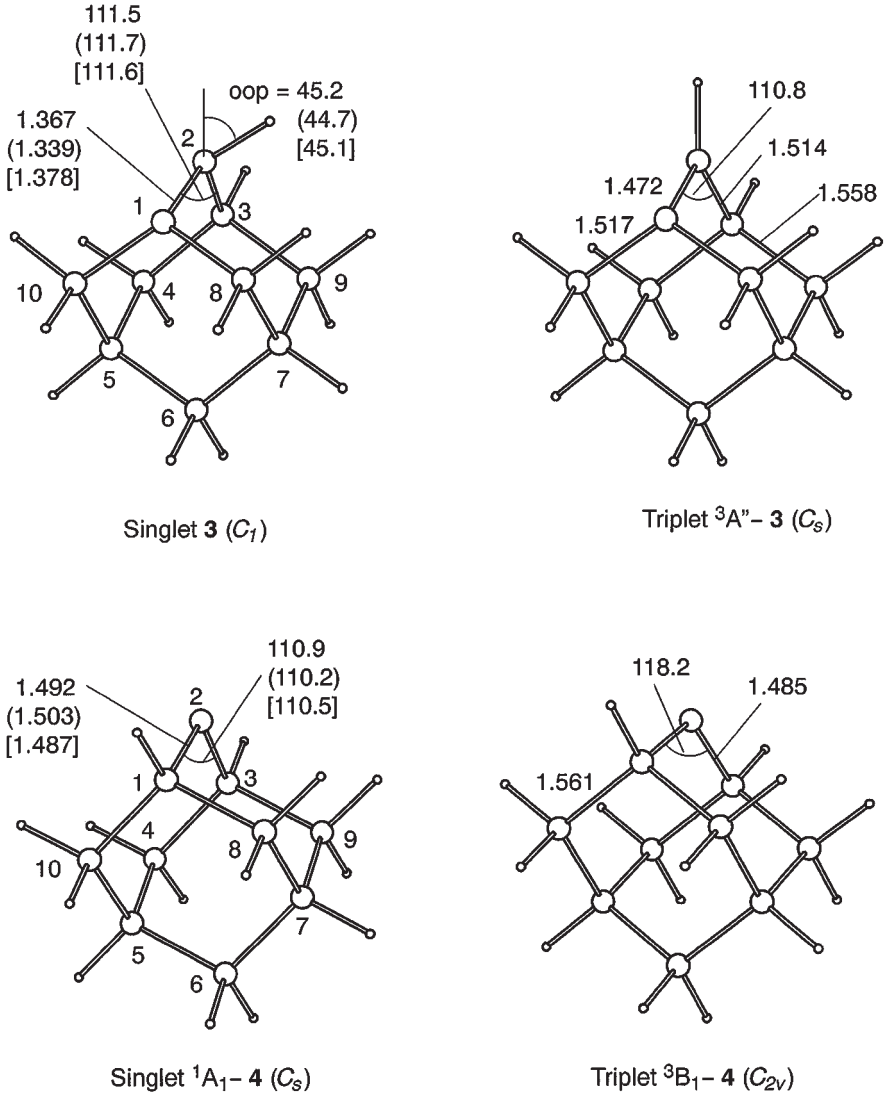

of $C_{10}H_{14}$ are drawn in Figs. 1–4 using a program written by Professor Arvi Rauk. The harmonic frequency analysis verified the nature of the stationary points as minima (all real frequencies) or as transition structures (one imaginary frequency) and was used to provide an estimate of the zero-point vibrational energies (ZPVE). Zero-point corrections (ΔZPVE) were scaled by a 0.91 factor for the RHF/6-31G(d) level and by a 0.98 factor for the (U)B3LYP/6-31+G(d) level (22). Final energies were obtained at the (U)B3LYP/6-311++G(3df, 2pd)//(U)B3LYP/6-31+G(d) level of theory (hereinafter referred to B3LYP). Geometries of the singlet species **3**, **4**, and **TS(3/4)** were also optimized at the MP2/6-31G(d) level with the frozen-core approximation. Table 1 shows total energies of $C_{10}H_{14}$ stationary structures along with ZPVEs. Schematic presentations of the relative energies of the $C_{10}H_{14}$ isomers are drawn in Figs. 5–7.

Heat capacities and entropy corrections were made using scaled (0.98) B3LYP/6-31+G(d) frequencies and standard statistical procedures within the rigid rotator – harmonic oscillator model (23) to determine enthalpies and free energies at 25 and 500°C (1 atm). Half-lives ($t_{1/2}$) of the reactions **3**→**4** and **3**→**5** were estimated ($t_{1/2}$ = (ln 2)/$k(T)$) using values of the first-order rate constants ($k(T)$). These constants were computed assuming that the transmission coefficient is equal to 1, as expressed by the following relation

$$k(T) = (kT/h)\exp(-\Delta G^{\neq}/RT)$$

which provides a direct relationship between the rate constant for an elementary reaction and its free energy of activation, $\Delta G^{\neq}$. In this equation, k and h are the Boltzmann and Planck constants, respectively.

It should be noted that density functional theory methods proved to be quite reliable for computing carbenes (20, 24), strained alkenes (24), "strained alkene-carbene" isomerizations (25- 29), and cycloaddition reactions (30).

Results and discussion

Relative energies and the singlet–triplet separations of 3 and 4

As in the case of the earlier studied pair of 1(9)-homocubene **1**

© 1998 NRC Canada

Fig. 2. B3LYP/6-31+G(d) and HF/6-31G(d) (in parentheses) optimized structures of 4-protoadamantylidene **5**, 3,4-protoadamantene **8**, and 4,5-protoadamantene **9**; oop = out-of-plane angle. Bond lengths in angstroms, angles in degrees.

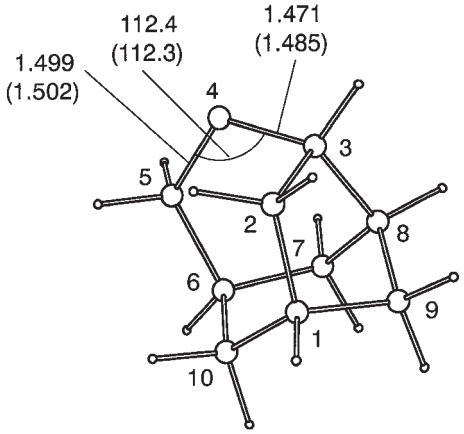

Singlet **5**

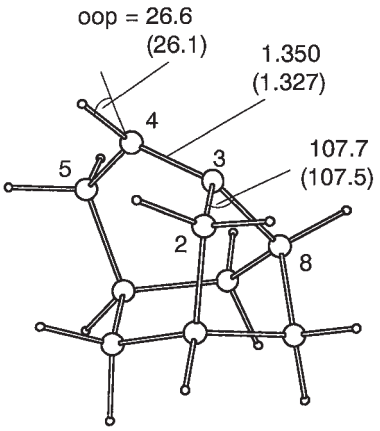

8

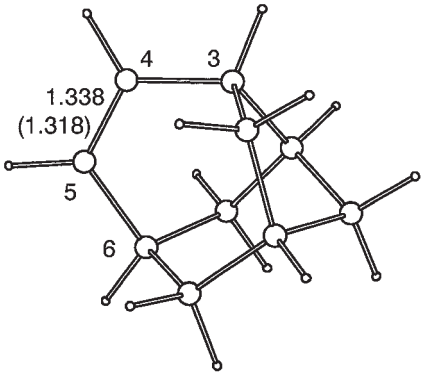

9

and 9-homocubylidene **2** (12) (Scheme 1), the ground states of the singlet adamantene **3** and adamantylidene $^1A_1$-**4** belong to the C_1 and C_s symmetries, respectively (Fig. 1).

The pyramidal configuration of the C2 atom in alkene **3** (out-of-plane angle for the hydrogen at C4 is 45.2°) provides a small but significant overlapping of the *p* atomic orbitals of the formally double C1—C2 bond, since these AOs are orthogonal in the planar configuration of the C2 atom (12). However, in the same time, pyramidalization of the C1 and C2 atoms decreases the *p* character of the lobes participating in the "π" bonding. Therefore, the pyramidalization of the bridgehead C1 atom, unlike the pyramidalization of the C2 atom, reduces double bonding between these atoms and has to be a destabilizing factor. The latter must bear on the relative energies of a strained alkene and the corresponding carbene. Evidently, the pyramidality of the bridgehead C1 atom in adamantene **3** is smaller than the pyramidality in homocubene **1**. According to GVB-PP(1)/6-31G(d) calculations (12), **1** is less stable than the isomeric singlet carbene **2**. For the pair **3/4**, the HF method predicts a small preference for carbene $^1A_1$-**4** (Fig. 5). However, taking into account the effects of electron correlation in the MP2 method leads to a substantial stabilization (24.2 kcal mol^{-1}) of adamantene **3** relative to the singlet adamantylidene **4**. A B3LYP energy difference between **3** and $^1A_1$-**4** is 17.4 kcal mol^{-1} in favor of **3** and is closer to the difference (ca. 12 kcal mol^{-1}) calculated earlier for this pair at the CASSCF/6-31G(d) level (18).

We also estimated the singlet–triplet separations for anti-Bredt alkene **3** and carbene **4** at the B3LYP level (Table 1, Fig. 5). The triplet states of **3** and **4** were optimized under C_s and C_{2v} symmetry constraints, respectively (Fig. 1), and were minima.

The triplet adamantene $^3A''$-**3** is characterized by a longer C1—C2 bond (1.472 Å) (1 Å = 0.1 nm) in comparison with the C1—C2 bond in the singlet **3,** and by the planar configuration of the C2 atom. A calculated destabilization of triplet **3** with respect to singlet **3** is 11.4 kcal mol^{-1} (ΔG°_{298} = 10.3 kcal mol^{-1}, ΔS°_{298} = 7.0 cal mol^{-1} K^{-1}).

The rigidity of the adamantane skeleton in the triplet $^3B_1$-**4** does not allow the valence angle at the carbene atom C2 to adopt the value (ca. 130°), which is typical for triplet carbenes (24, 31–33). Narrowing of the valence angle C1-C2-C3 to

© 1998 NRC Canada

Fig. 3. B3LYP/6-31+G(d), HF/6-31G(d) (in parentheses), and MP2(fc)/6-31G(d) (in square brackets) optimized structures of the transition states for 1,2 hydrogen migrations. Bond lengths in angstroms.

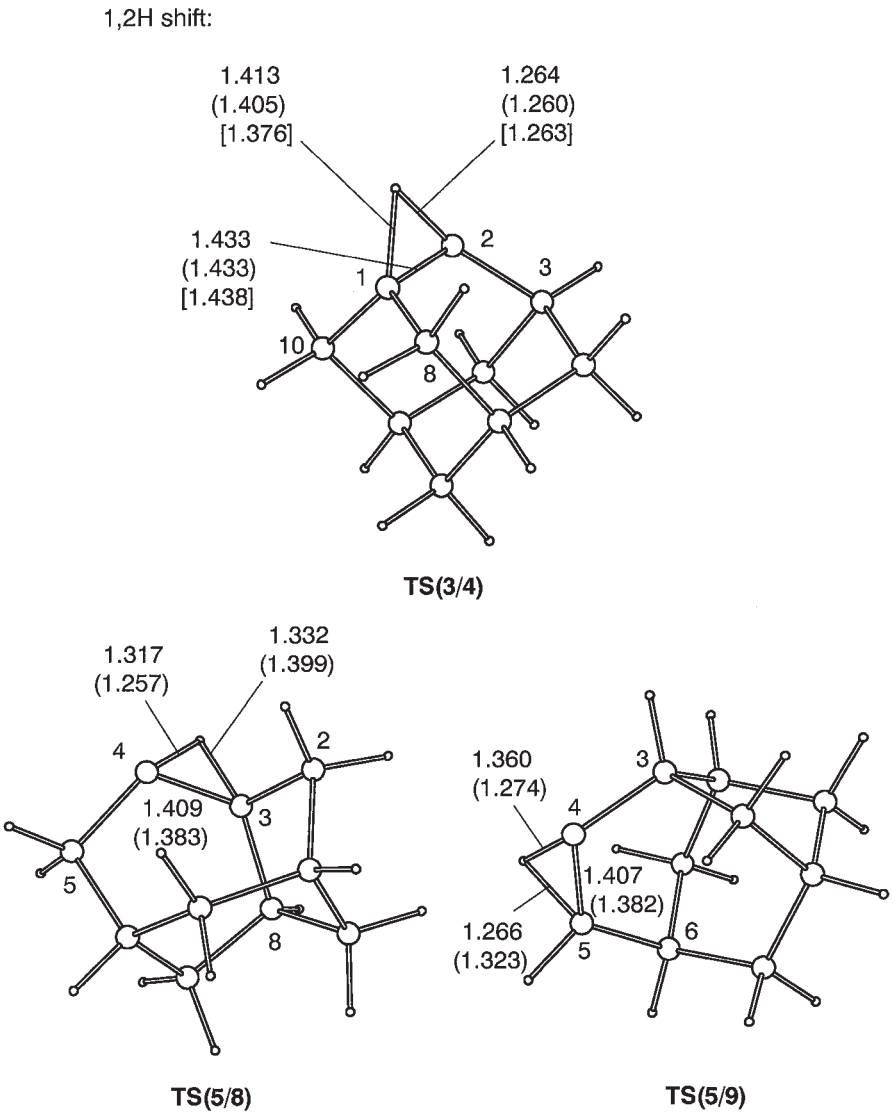

118.2° increases the *s* character in the nonbonding σ^1 orbital of the triplet, and reportedly leads to destabilization of this state (31). The B3LYP energy difference between $^3B_1$-**4** and $^1A_1$-**4** is 3.1 kcal mol^{-1} ($\Delta G°_{298}$ = 3.2 kcal mol^{-1}, $\Delta S°_{298}$ = –1.2 cal mol^{-1} K^{-1}) in favor of the latter. This value is close to an experimental estimate of the singlet–triplet gap in carbene **4** (–4.8 kcal mol^{-1}) (18, 34). Acyclic dialkyl carbenes are characterized by a smaller singlet–triplet splitting (–0.2/–1.6 kcal mol^{-1}) (24, 32, 33). The angle dependencies of singlet–triplet gaps in other strained carbenes and alkenes have recently been dealt with in detail by Bettinger et al. (27, 29) and Xie et al. (28).

Supposedly, the large singlet–triplet gap in **4** is also caused by the stabilizing effects of hybridization of the carbene atom C2 and hyperconjugation between the empty carbene *p* orbital and the σ orbitals of the proximal C—C bonds in $^1A_1$-**4** (Fig. 8*a*). Indeed, the valence angle at the carbene atom in $^1A_1$-**4** (110.9°) is smaller than it is in acyclic dialkyl carbenes (ca. 113°) (24, 32, 33), and the occupied σ^2 carbene orbital in $^1A_1$-**4** must have a larger *s* character. One can deduce there is enhanced σ–*p* hyperconjugation in $^1A_1$-**4** from the decrease of the C2-C1-C8 and C2-C3-C9 valence angles (103.7°), compared with the C2-C1-C10 and C2-C3-C4 angles (115.3°), as well as from the lengthening of the C1—C8 and C3—C9 bonds (1.567 Å) in comparison with the C1—C10 and C3—C4 bonds (1.555 Å) at the B3LYP level (for numbering see Figs. 1–4).

Owing to the substantial destabilization of the triplet states of adamantene **3** and adamantylidene **4**, we have limited our theoretical investigation of the rearrangements of these compounds to the singlet $C_{10}H_{14}$ potential energy surface.

1,2 Hydrogen migration

The HF and MP2 methods predict almost identical high relative energies for the transition state **TS(3/4)** of 1,2H migration in adamantene **3** (Table 1, Fig. 5). The B3LYP method gives a rather smaller relative energy for **TS(3/4)**, although the calculated activation barrier ($\Delta G^{\neq}_{773}$ = 69.1 kcal mol^{-1}, $\Delta S^{\neq}_{773}$ = 0.9

© 1998 NRC Canada

Fig. 4. B3LYP/6-31+G(d) optimized structures of the transition states for the retro Diels–Alder reaction, 1,2 carbon, and 1,2 hydrogen migrations. Bond lengths in angstroms.

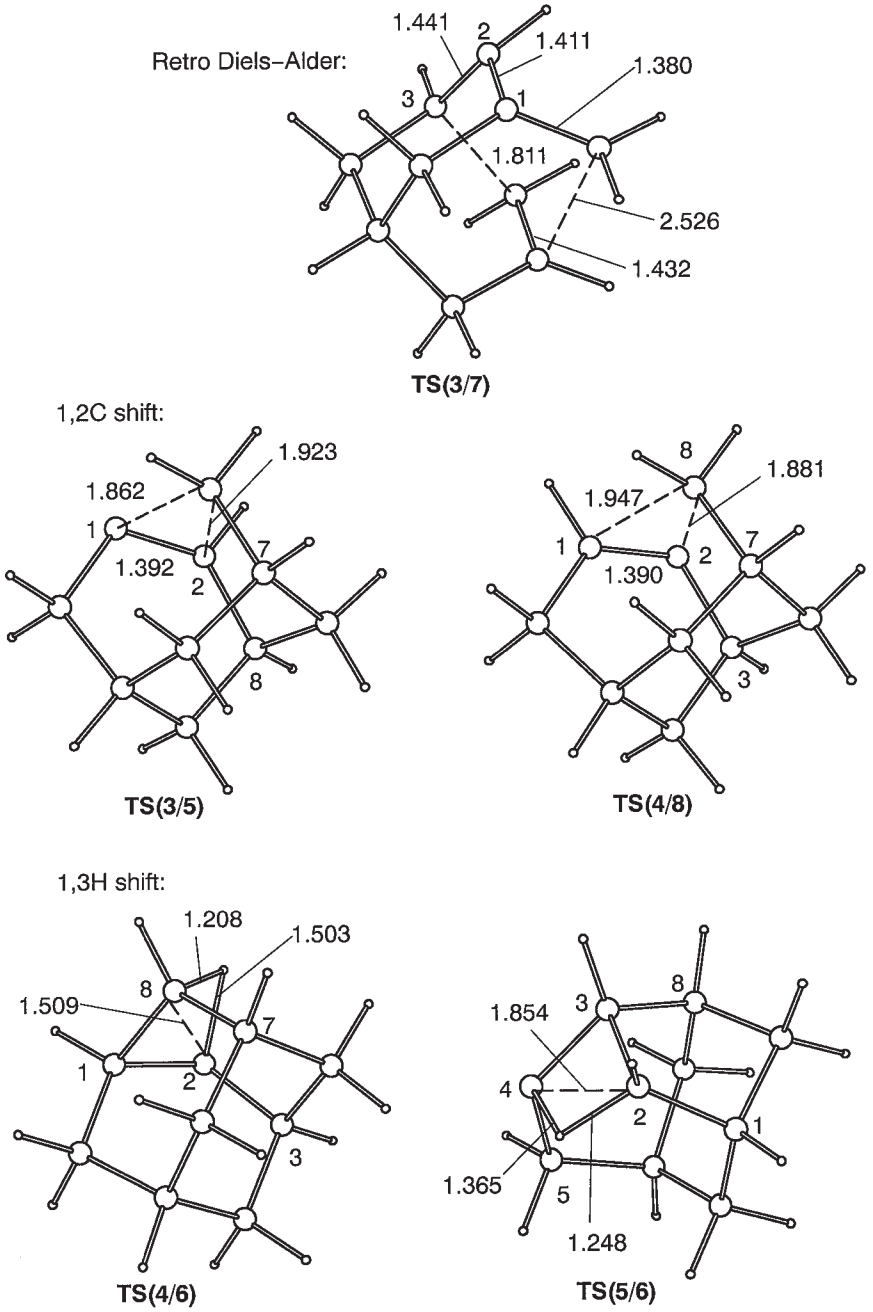

cal mol^{-1} K^{-1}) is predicted to be prohibitively high even at 500°C, the temperature at which the generation of adamantene **3** was carried out (13). The half-life of **3** with respect to 1,2 hydrogen migration is 402 h at 500°C, based on the B3LYP activation barrier.

It should be noted that the B3LYP relative energy of transition state **TS(3/4)** for the 1,2H shift in adamantene **3** (69.6 kcal mol^{-1}) is almost the same as for the less strained alkenes **8** and **9** –68.8 (**TS(5/8)**) and 69.5 kcal mol^{-1} (**TS(5/9)**), respectively (Fig. 6), although these barriers have different origins.In the case of planar alkenes like **9**, the migrating C—H bond is orthogonal to the *p* part of the π* orbital of the C═C bond. A high barrier for the 1,2H shift results from the necessity of breaking the double bond at turning the migrating C—H bond to an angle close to 90° from the initial plane of the C═C bond. In particular, this angle is 82° in the transition state **TS(5/9)** (Scheme 4). The other bonds of the alkene fragment in the transition state must remain close to the initial plane.

In the anti-Bredt alkene **3**, the migrating C—H bond is nonorthogonal to the corresponding lobe of the "π" orbital, i.e., the double bond itself has been broken in the ground state of **3**. However, the rigidity of the molecular skeleton does not allow the bridgehead C1 atom to be planar and retains the C2—C3 bond at almost bisector orientation with respect to the

© 1998 NRC Canada

Table 1. Total energies (hartrees) and zero-point vibrational energies[a] (kcal mol^{-1}) of $C_{10}H_{14}$ stationary structures.

	RHF/A[b]		(U)B3LYP/B[b]		(*U*)B3LYP/C//B[b]
Species	E_T	ZPVE	E_T	ZPVE	E_T
3, singlet[c]	–386.73225	147.2(0)	–389.41834	137.1(0)	–389.53230
3, triplet (C_s)			–389.39821	135.2(0)	–389.51128
4, singlet[d] (C_s)	–386.73231	146.5(0)	–389.39140	136.4(0)	–389.50392
4, triplet (C_{2v})			–389.38750	136.8(0)	–389.49953
5, singlet	–386.72143	146.2(0)	–389.38281	135.9(0)	–389.49606
6 (C_s)	–386.81264	148.2(0)	–389.47874	138.0(0)	–389.59226
7	–386.77833	143.5(0)	–389.45344	133.5(0)	–389.57422
8	–386.75653	147.5(0)	–389.43459	137.1(0)	–389.54953
9	–386.81405	147.9(0)	–389.48236	137.7(0)	–389.59765
TS(3/4)[e]	–386.60336	142.8(1)	–389.29878	132.8(1)	–389.41466
TS(3/5)	–386.68944	145.8(1)	–389.36766	135.6(1)	–389.48186
TS(3/7)	–386.65659	143.8(1)	–389.37183	133.7(1)	–389.48937
TS(4/6)	–386.69150	145.3(1)	–389.36900	135.2(1)	–389.48403
TS(4/8)	–386.68844	145.8(1)	–389.36718	135.5(1)	–389.48146
TS(5/6)	–386.68677	145.1(1)	–389.36767	134.7(1)	–389.48341
TS(5/8)	–386.63132	143.4(1)	–389.31704	133.2(1)	–389.43372
TS(5/9)	–386.69102	144.6(1)	–389.36608	134.5(1)	–389.48204

[a] Unscaled; number of imaginary frequencies in parentheses.
[b] Basis set "A" is 6-31G(d), "B" is 6-31+G(d), and "C" is 6-311++G(3df,2pd).
[c] E_T = –388.04999 hartree at the MP2(fc)/6-31G(d) level.
[d] E_T = –388.00930 hartree at the MP2(fc)/6-31G(d) level.
[e] E_T = –388.92188 hartree at the MP2(fc)/6-31G(d) level.

Fig. 5. Schematic presentation of the relative energies of the $C_{10}H_{14}$ isomers participating in rearrangements of adamantene **3** at (U)B3LYP/6-311++G(3df,2pd)//(U)B3LYP/6-31+G(d) + 0.98 × ΔZPVE, HF/6-31G(d) + 0.91 × ΔZPVE (in parentheses), and MP2(fc)/6-31G(d) + 0.98 × ΔZPVE (in square brackets) in kcal mol^{-1}.

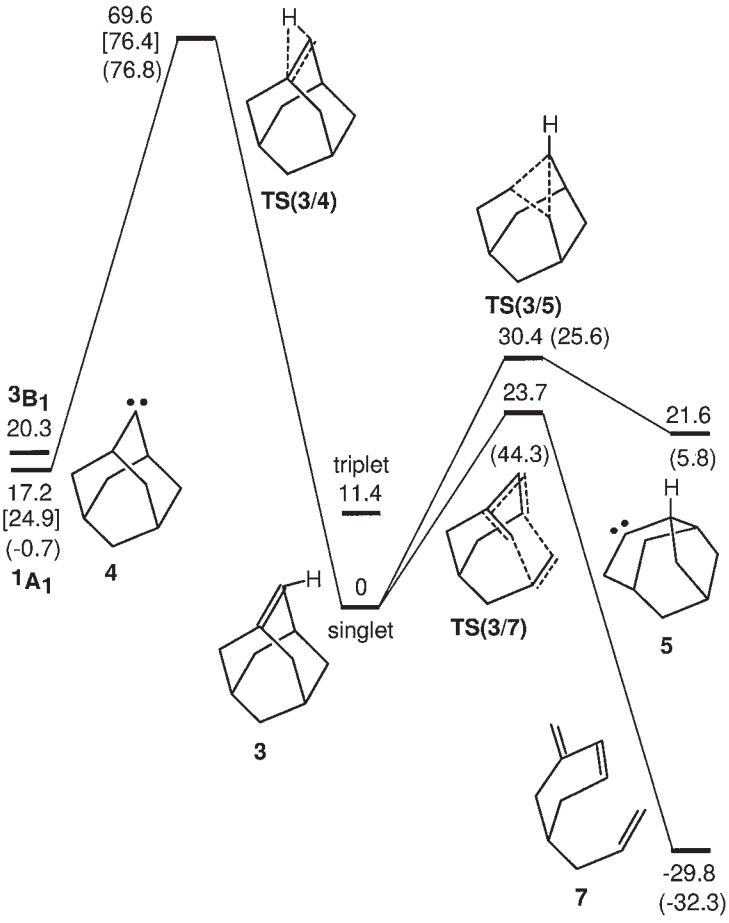

© 1998 NRC Canada

Fig. 6. Schematic presentation of the relative energies of the $C_{10}H_{14}$ isomers participating in rearrangements of singlet adamantylidene **5** at B3LYP/6-311++G(3df,2pd)//B3LYP/6-31+G(d) + 0.98 × ΔZPVE and HF/6-31G(d) + 0.91 × ΔZPVE (in parentheses) in kcal mol^{-1}.

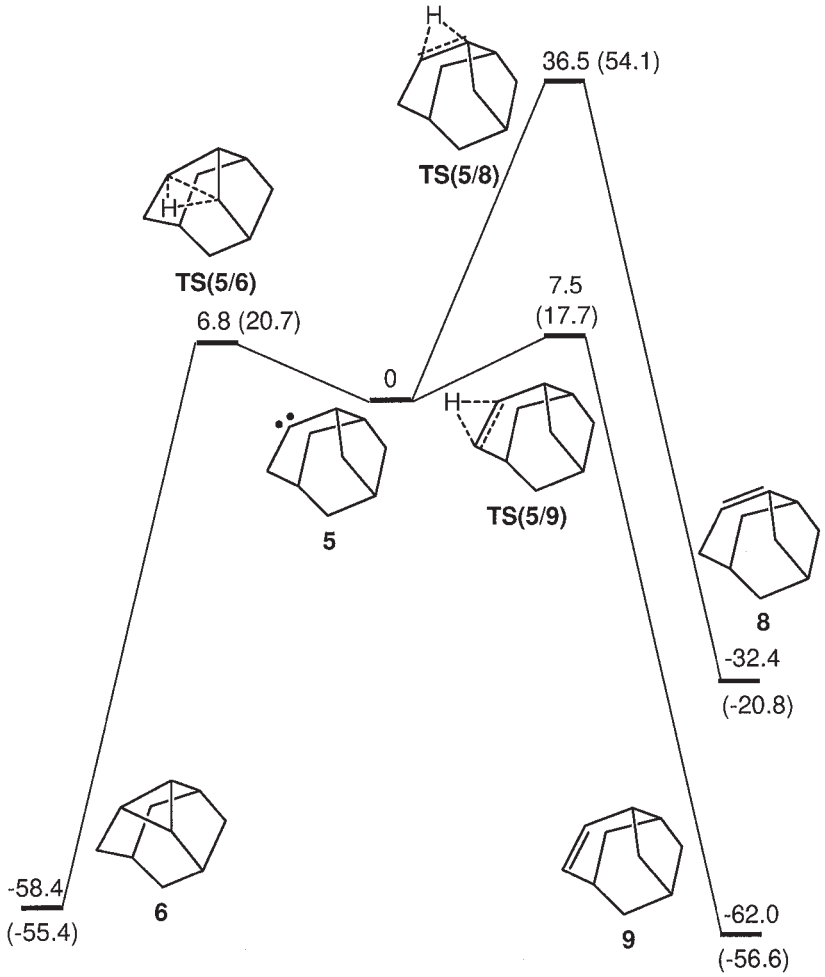

C8-C1-C10 angle (Scheme 4). Such a geometry provides a considerable strain in transition state **TS(3/4)**. The 1,2 H shift in the bridgehead, but less strained, alkene **8** (Scheme 4) can be considered as an intermediate case in which both factors (energy of breaking the C═C bond and the strain of the transition state) play their role.

If we consider the 1,2 hydrogen migration from the side of the singlet carbenes **4**, **5**, a different picture emerges. Substantial differences are seen in the free enthalpies of activation for the migration of the bridge hydrogens in **4** and **5** ($\Delta G^{\neq}_{773}$ = 53.5 and 37.2 kcal mol^{-1}, respectively) and of a nonbridge hydrogen at C4 in **5** ($\Delta G^{\neq}_{773}$ = 8.8 kcal mol^{-1}). This barrier ratio is caused entirely by the difference in the strain of the transition states **TS(3/4) > TS(5/8) > TS(5/9)**.

1,2 Carbon migration and other rearrangements

Examination of the ground-state orbital alignment in adamantene **3** implies that the lobes of the "π" and "π*" orbitals of the formally double C1—C2 bond overlap better with the σ orbitals of the proximal C—C bonds than with each other. Such "π"–σ* and σ–"π*" interactions (Fig. 8*b*) are revealed in the noticeable lengthening of the C3—C9 (1.593 Å) and C7—C8 (1.607 Å) bonds and in the shortening of the C1—C8 (1.509 Å) and C7—C9 (1.555 Å) bonds in comparison with the corresponding relatively unperturbed C3—C4 (1.536 Å), C5—C10 (1.542 Å), C1—C10 (1.518 Å), and C4—C5 (1.547 Å) bonds (Fig. 1, B3LYP level). The C2-C1-C8 (110.2°) and C2-C3-C9 (96.4°) valence angles are also substantially smaller than the C2-C1-C10 (119.1°) and C2-C3-C4 (115.2°) valence angles. Thus, in the ground state of adamantene **3**, an especially favorable stereoelectronic situation for breaking the C3—C9 and C7—C8 bonds, i.e., for a reverse Diels–Alder cycloaddition, has been created. The interaction of the C2 lobe of the "π*" orbital with the σ orbital of the C1—C8 bond, which promotes the 1,2 carbon migration, also should be pointed out in **3** (Fig. 8*c*). However, unlike the C3—C9 bond, the C1—C8 bond looks unperturbed because a stretching of this bond, as a result of the σ–"π*" interaction, is compensated for by its shortening, owing to the interaction of the C1 lobe with the C8—C7 bond (Fig. 8*b*).

The B3LYP method gives more realistic activation energies for the 1,2C shift and retro Diels–Alder reaction in adamantene **3** than does the HF method (Fig. 5). A B3LYP activation barrier of the 1,2 carbon migration ($\Delta G^{\neq}_{773}$ = 30.3 kcal mol^{-1}, $\Delta S^{\neq}_{773}$ = –0.9 cal mol^{-1} K^{-1}) is more than twice as low as the barrier of the 1,2 hydrogen migration. The calculated half-life of adamantene **3** for the 1,2C shift is 1.6 × 10^{-5} s at 500°C. The product of the 1,2 carbon migration, the singlet

© 1998 NRC Canada

Fig. 7. Schematic presentation of the relative energies of the $C_{10}H_{14}$ isomers participating in rearrangements of singlet adamantylidene **4** at B3LYP/6-311++G(3df,2pd)//B3LYP/6-31+G(d) + 0.98 × ΔZPVE and HF/6-31G(d) + 0.91 × ΔZPVE (in parentheses) in kcal mol^{-1}.

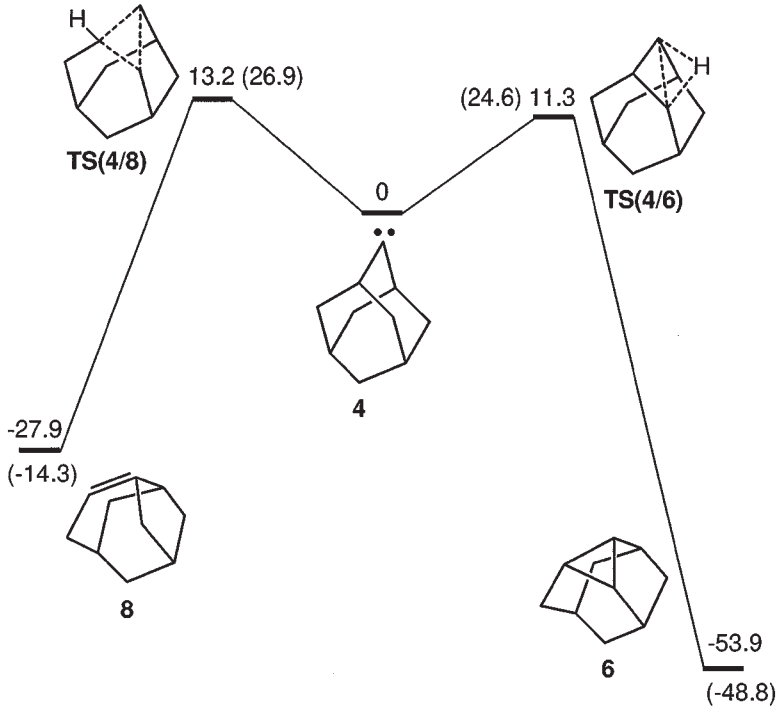

Scheme 4.

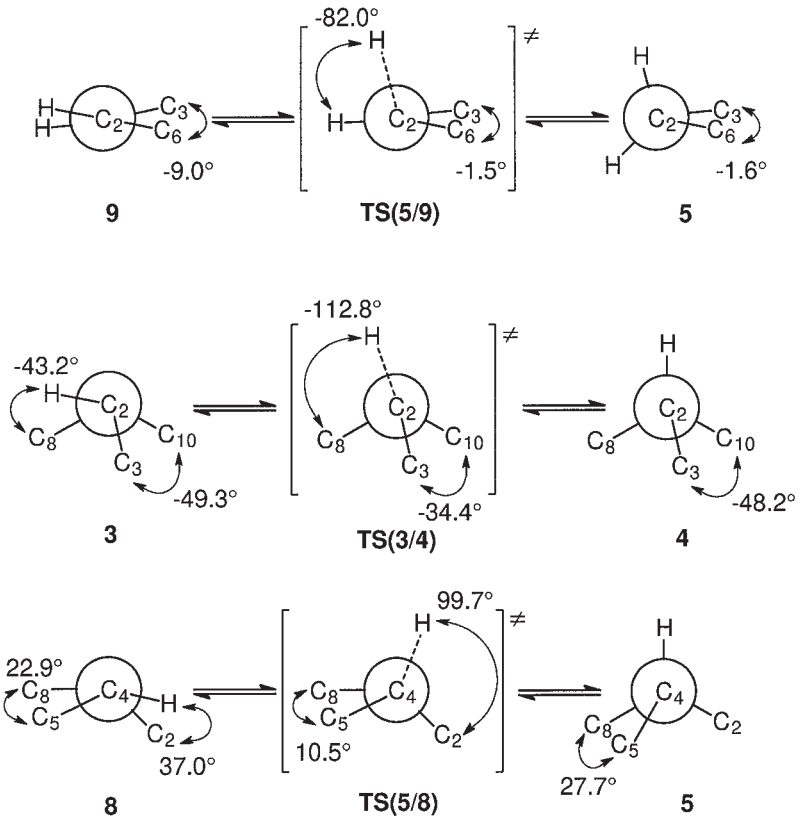

4-protoadamantylidene **5**, in its turn can rearrange in at least three ways: a 1,3 hydrogen migration with the formation of 2,4-dehydroadamantene **6**, and two 1,2H shifts, which lead to protoadamantenes **8**, **9** (Fig. 6). For the reason discussed above, the activation barrier ($\Delta G^{\neq}_{773}$ = 37.2 kcal mol^{-1}, $\Delta S^{\neq}_{773}$ = –1.6 cal mol^{-1} K^{-1}) for the bridge 1,2H migration is four

© 1998 NRC Canada

Fig. 8. Ground-state orbital alignments in the singlet adamantylidene **4** (*a*) and adamantene **3** (*b*, *c*).

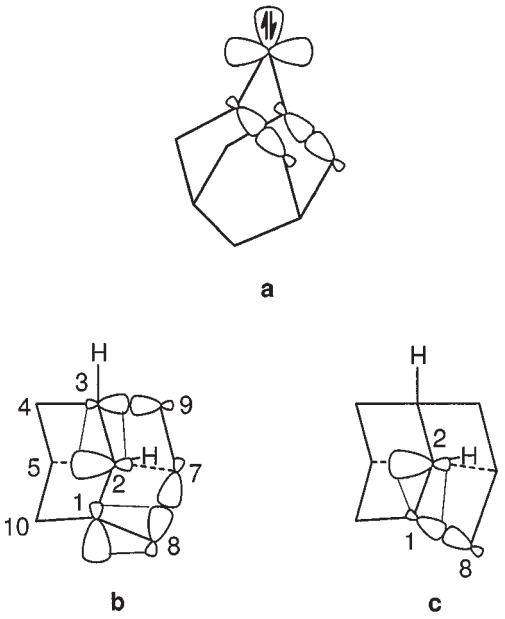

times higher than the barrier ($\Delta G^{\neq}_{773}$ = 8.8 kcal mol^{-1}, $\Delta S^{\neq}_{773}$ = –3.2 cal mol^{-1} K^{-1}) for migration of the nonbridge hydrogen at C4, which is identical to the barrier ($\Delta G^{\neq}_{773}$ = 8.8 kcal mol^{-1}, $\Delta S^{\neq}_{773}$ = –4.4 cal mol^{-1} K^{-1}) for the 1,3 hydrogen shift. Therefore, the bridge 1,2H shift in carbene **5** cannot compete with the two other rearrangements of this carbene. The products of these rearrangements (protoadamantene **9** and dehydroadamantane **6**) must be formed with almost identical yields.

According to the B3LYP calculations, the retro Diels–Alder reaction in adamantene **3** has a lower activation barrier ($\Delta G^{\neq}_{773}$ = 20.5 kcal mol^{-1}, $\Delta S^{\neq}_{773}$ = 5.3 cal mol^{-1} K^{-1}) than the 1,2 carbon migration. Therefore, this reaction is predicted to be the main channel of the gas-phase unimolecular conversion of adamantene **3**. It is feasible to assume 5-allyl-3-methylenecyclohexene **7** to be the major product of the vacuum flash thermolysis of **3**, and dehydroadamantane **6** and protoadamantene **9** — minor ones. The theoretical distribution of the products (**7** > > **6** ≈ **9**) is in good agreement with the experimental data (13).

The B3LYP activation energy for 1,2 hydrogen migration in singlet adamantylidene **4** ($\Delta G^{\neq}_{298}$ = 52.7 kcal mol^{-1}, $\Delta S^{\neq}_{298}$ = –1.7 cal mol^{-1} K^{-1}) is too high for this process to be considered as a real path of conversion of this carbene. For two other probable rearrangements of **4** (Fig. 7), low activation barriers were found: $\Delta G^{\neq}_{298}$ = 11.8 kcal mol^{-1}, $\Delta S^{\neq}_{298}$ = –3.2 cal mol^{-1} K^{-1} for the 1,3H shift (**TS(4/6)**), and $\Delta G^{\neq}_{298}$ = 3.2 kcal mol^{-1}, $\Delta S^{\neq}_{298}$ = –1.2 cal mol^{-1} K^{-1} for the 1,2C shift (**TS(4/8)**). The predicted domination of the 1,3 hydrogen migration in **4** is in accord with the experimental data (15–19).

The transition state **TS(4/8)** for the 1,2C shift in adamantylidene **4** lies only 0.2 kcal mol^{-1} lower than the transition state **TS(3/5)** for the 1,2C shift in adamantene **3**, whereas the activation barrier for the 1,2C shift in **4** is 16.8 kcal mol^{-1} lower than the barrier in **3**. Apparently, this difference in the barriers is due to destabilization of adamantylidene **4** with respect to adamantene **3**.

A similar situation is observed in the case of the 1,3 hydrogen migration in the singlet carbenes **4**, **5**. The energies of transition states **TS(4/6)** and **TS(5/6)** also differ by 0.2 kcal mol^{-1} at the B3LYP level (Figs. 6, 7). However, stabilization of carbene **4** with respect to **5** by the effects of hybridization and σ–π hyperconjugation results in the higher activation energy for the 1,3H shift in the former.

Conclusions

According to the B3LYP study of the singlet $C_{10}H_{14}$ potential energy surface, 2-adamantene **3** is more stable than the corresponding carbene, adamantylidene **4**. The activation barrier for conversion of **3** into **4** via the 1,2 hydrogen migration is prohibitively high even at 500°C ($\Delta G^{\neq}_{773}$ = 69.1 kcal mol^{-1}) and is almost identical to the barrier for the 1,2H shift in a planar alkene, 4,5-protoadamantene **9** ($\Delta G^{\neq}_{773}$ = 69.7 kcal mol^{-1}). The barrier in the latter is caused mainly by the necessity of breaking the C═C double bond, whereas in the anti-Bredt alkene **3** the origin of the barrier is connected with the strain of the transition state **TS(3/4)**. This is so because of the impossibility of forming a planar arrangement of the C—C bonds around the rearranging fragment. Anti-Bredt alkenes with a more rigid skeleton and a more pyramidal bridgehead carbon atom must have a higher barrier for 1,2 hydrogen migration.

The C1 and C2 lobes of the "π" and "π*" orbitals of the formally double C1—C2 bond in adamantene **3** overlap better with the σ orbitals of the proximal C—C bonds than with each other. Such a stereoelectronic situation favors the 1,2 carbon migration ($\Delta G^{\neq}_{773}$ = 30.3 kcal mol^{-1}) and especially the reverse Diels–Alder cycloaddition ($\Delta G^{\neq}_{773}$ = 20.5 kcal mol^{-1}), which leads to 5-allyl-3-methylenecyclohexene **7**. The products of the 1,2C shift, singlet 4-protoadamantylidene **5**, in its turn quickly rearranges into 2,4-dehydroadamantane **6** and 4,5-protoadamantene **9** via 1,3 and 1,2 hydrogen migrations with identical activation barriers ($\Delta G^{\neq}_{773}$ = 8.8 kcal mol^{-1}). The theoretical yield distribution of the products (**7** > > **6** ≈ **9**) is in accord with the experimental data (13). Thus, the calculations support the formation of 2,4-dehydroadamantane **6** through path b, shown in Scheme 2. The activation energy of the 1,2 carbon migration has to be lower in more strained bridgehead alkenes because of increased reactivity of the formally double bond and the better electron-donating ability of the more strained proximal C—C bonds.

The B3LYP calculations also properly predict the preference of the rearrangement of adamantylidene **4** into 2,4-dehydroadamantane **6** via 1,3 hydrogen migration ($\Delta G^{\neq}_{298}$ = 11.8 kcal mol^{-1}), as well as the greater stability of the singlet state of **4** with respect to the triplet state (ΔG°_{298} = 3.2 kcal mol^{-1}, ΔS°_{298} = –1.2 cal mol^{-1} K^{-1}).

Acknowledgement

We thank Professor Arvi Rauk for valuable comments and discussion and for providing access to the Gaussian 94 system of programs. We are also grateful to the University of Calgary for providing computational facilities. M.T.H.L. acknowledges financial support from the Natural Sciences and Engineering Research Council of Canada.

© 1998 NRC Canada

References

1. P.M. Warner. Chem. Rev. **89**, 1067 (1989).
2. W. Luef and R. Keese. *In* Topics in stereochemistry. Vol. 20. *Edited by* E.L. Eliel and SH. Wilen. Wiley, New York. 1991. pp. 231–318.
3. G. Szeimies. *In* Advances in strain in organic chemistry. Vol. 2. *Edited by* B. Halton. JAI Press Ltd., London. 1992. pp. 1–55.
4. T.H. Chan and D. Massuda. J. Am. Chem. Soc. **99**, 936 (1977).
5. T.J. Barton and M.-H. Yeh. Tetrahedron Lett. **28**, 6421 (1987).
6. P.E. Eaton and K.L. Hoffmann. J. Am. Chem. Soc. **109**, 5285 (1987).
7. M. Jones, Jr., and N. Chen. J. Phys. Org. Chem. **1**, 305 (1988).
8. N. Chen and M. Jones, Jr. Tetrahedron Lett. **30**, 6969 (1989).
9. P.E. Eaton and A.J. White. J. Org. Chem. **55**, 1321 (1990).
10. P.E. Eaton and R.B. Appel. J. Am. Chem. Soc. **112**, 4055 (1990).
11. N. Chen, M. Jones, Jr., W.R. White, and M. Platz. J. Am. Chem. Soc. **113**, 4981 (1991).
12. D.A. Hrovat and W.T. Borden. J. Am. Chem. Soc. **114**, 2719 (1992).
13. N. Bian and M. Jones, Jr. J. Am. Chem. Soc. **117**, 8957 (1995).
14. T. Okazaki, H. Isobe, T. Kitagawa, and K. Takeuchi. Bull. Chem. Soc. Jpn. **69**, 2053 (1996).
15. A.C. Udding, J. Strating, and H. Winberg. J. Chem. Soc. Chem. Commun. 657 (1966).
16. S.D. Isaev, A.G. Yurchenko, F.N. Stepanov, G.C. Kolyada, S.S. Novikov, and N.F. Karpenko. Zh. Org. Khim. **9**, 724 (1073); J. Org. Chem. U.S.S.R. **9**, 745 (1973) (English translation).
17. U.H. Brinker, R. Buchkremer, M. Kolodziejczyk, R. Kupfer, M. Rosenberg, M.D. Poliks, M. Orlando, and M. Gross. Angew. Chem. Int. Ed. Engl. **32**, 1344 (1993).
18. T. Bally, S. Matzinger, L. Truttmann, M.S. Platz, and S. Morgan. Angew. Chem. Int. Ed. Engl. **33**, 1964 (1994).
19. R. Kupfer, M.D. Poliks, and U.H. Brinker, J. Am. Chem. Soc. **116**, 7393 (1994).
20. H.M. Sulzbach, M.S. Platz, H.F. Schaefer III, and C.M. Hadad. J. Am. Chem. Soc. **119**, 5682 (1997), and refs. cited therein.
21. M.J. Frisch, G.W. Trucks, H.B. Schlegel, P.M.W. Gill, B.G. Johnson, M.A. Robb, J.R. Cheeseman, T. Keith, G.A. Petersson, J.A. Montgomery, K. Raghavachary, M.A. Al-Laham, U.G. Zakrzewski, J.V. Ortiz, J.B. Foresman, J. Cioslowski, B.B. Stefanov, A. Nanayakkara, M. Challacombe, C.Y. Peng, P.Y. Ayala, W. Chen, M.W. Wong, J.L. Andres, E.S. Replogle, R. Gomperts, R.L. Martin, D.J. Fox, J.S. Binkley, D.J. Defrees, J. Baker, J.P. Stewart, M. Head-Gordon, C. Gonzalez, and J.A. Pople. Gaussian 94 (Revision D.2). Gaussian, Inc., Pittsburgh, Pa. 1995.
22. A.P. Scott and L. Radom. J Phys. Chem. **100**, 16 502 (1996).
23. D.A. McQuarrie. Statistical thermodynamics. Harper & Row, New York. 1973. Chap. 8.
24. H.M. Sulzbach, E. Bolton, D. Lenoir, P.v.R. Schleyer, and H.F. Schaefer III. J. Am. Chem. Soc. **118**, 9908 (1996).
25. M.W. Wong and C. Wentrup. J. Org. Chem. **61**, 7022 (1996).
26. P.R. Schreiner, W.L. Karney, P.v.R. Schleyer, W.T. Borden, T.P. Hamilton, and H.F. Schaefer III. J. Org. Chem. **61**, 7030 (1996).
27. H.F. Bettinger, P.R. Schreiner, P.v.R. Schleyer, and H.F. Schaefer III. J. Phys. Chem. **100**, 16 147 (1996).
28. Y. Xie, P.R. Schreiner, P.v.R. Schleyer, and H.F. Schaefer III. J. Am. Chem. Soc. **119**, 1370 (1997).
29. H.F. Bettinger, P.v.R. Schleyer, P.R. Schreiner, and H.F. Schaefer III. J. Org. Chem. **62**, 9267 (1997).
30. B.S. Jursic. J. Org. Chem. **62**, 3046 (1997), and refs. cited therein.
31. S. Khodabandeh and E. Carter. J. Phys. Chem. **97**, 4360 (1993).
32. S. Matzinger and M.P. Fülscher. J. Phys. Chem. **99**, 10 747 (1995).
33. C.A. Richards, Jr., S.J. Kim, Y. Yamaguchi, and H.F. Schaefer III. J. Am. Chem. Soc. **117**, 10 104 (1995).
34. S. Morgan, J.E. Jackson, and M. Platz. J. Am. Chem. Soc. **113**, 2782 (1991).

© 1998 NRC Canada

The mechanism of solvolysis of 2-adamantyl azoxytosylate: isotopic labelling, medium effect, and attempted deoxygenation studies

John K. Conner, Johanna Haider, M.N. Stuart Hill, Howard Maskill, and Monique Pestman

Abstract: Rates of solvolysis of 2-adamantyl azoxytosylate (**1**) have been measured over a range of temperatures in ethanoic acid, methanoic acid, 50:50 (v/v) trifluoroethanol:water, 80:20 (v/v) trifluoroethanol:water, 97:3 (w/w) trifluoroethanol:water, and 70:30 (v/v) ethanol:water. For comparison, rates of solvolysis of 2-adamantyl tosylate (**2**) have also been measured in 50:50, 80:20, and 90:10 (v/v) trifluoroethanol:water, and for both compounds, activation parameters have been determined. These and results published earlier allow a correlation of the two reactions and indicate that the *m* value for 2-adamantyl azoxytosylate solvolysis is only 0.46. This is one of the lowest *m* values for a reaction that is unambiguously an S_N1 solvolysis. We have also recorded the ^{17}O NMR spectrum of the 2-adamantyl tosylate formed from ^{17}O-labelled 2-adamantyl azoxytosylate in deuteriochloroform, and the millimeter-wave spectrum of the nitrous oxide evolved in the hydrolysis of ^{18}O-labelled 2-adamantyl azoxytosylate. These labelling studies have provided more detailed knowledge of the S_N1 fragmentation mechanism of **1** and exclude a mechanism of reaction via rearrangement to *N*-nitroso,*N*-(2-adamantyl),*O*-(*p*-toluenesulfonyl)hydroxylamine (**5**). Attempted deoxygenation of **1** to give 2-adamantyl diazotosylate (**8**) and a subsequent fragmentation proved unsuccessful.

Key words: nitrous oxide, carbenium ion, isotopic labelling, solvolysis, *m* value.

Résumé : On a mesuré les vitesses de solvolyse de azoxytosylate d'adamant-2-yle (**1**) à diverses températures, dans l'acide éthanoïque, l'acide méthanoïque, le trifluoroéthanol:eau (50:50, v/v), le trifluoroéthanol:eau (80:20, v/v), le trifluoroéthanol:eau (97:3, p/p) et l'éthanol:eau (70:30, v/v). Pour fins de comparaison, on a aussi mesuré les vitesses de solvolyse du tosylate d'adamant-2-yle (**2**) dans des mélanges (50:50, 80:20 et 90:10, v/v) de trifluoroéthanol:eau et, dans les cas des deux composés, on a déterminé les paramètres d'activation. Ces résultats couplés à d'autres publiés antérieurement permettent d'établir une corrélation entre les deux réactions et ils indiquent que la valeur *m* pour la solvolyse de l'azoxytosylate d'adamant-2-yle n'est que 0,46. Ceci correspond à l'une des valeurs de *m* les plus faibles pour une réaction qui est sans ambiguïté S_N1. On a aussi déterminé le spectre RMN du ^{17}O du tosylate d'adamant-2-yle formé à partir de l'azoxytosylate d'adamant-2-yle marqué au ^{18}O lors d'une réaction dans le chloroforme deutéré ainsi que le spectre d'onde à un millimètre de l'oxyde nitreux qui se dégage lors de l'hydrolyse de l'azoxytosylate d'adamant-2-yle marqué au ^{17}O. Ces études de marquage ont fourni des connaissances plus détaillées du mécanisme de fragmentation S_N1 du composé **1** et elles ont permis d'exclure un mécanisme réactionnel impliquant un réarrangement en *N*-nitroso-*N*-(adamant-2-yl)-*O*-(*p*-toluènesulfonyl)hydroxylamine (**5**). Il a été impossible de provoquer une désoxygénation du composé **1** pour donner du diazotosylate d'adamant-2-yle (**8**) et provoquer une fragmentation subséquente.

Mots clés : oxyde nitreux, ion carbénium, marquage isotopique, solvolyse, valeur *m*.

[Traduit par la rédaction]

Introduction

Mechanisms of reactions involving intermediate carbenium ions are amongst the earliest to have been investigated, and early proposals that some of the most deep seated of molecular rearrangements (e.g., amongst terpenoids) occur via such intermediates were some of the boldest (1). These proposals were accepted only after fierce debate and overwhelming evidence, and much of current organic chemistry reaction mechanisms vernacular originates from that Olympian period earlier this century. However, even though the principal features of substitution and elimination reactions that involve carbenium ions are well known, some details of the natures of these intermediates have been inferred from only indirect evidence or still remain obscure.

According to a frequently encountered model for S_N1 reactions (2*a*), the carbenium ion is generated in an initial rate-limiting step, then is captured by a nucleophile (which could be a

This paper is dedicated to Professor Erwin Buncel in recognition of his contributions to Canadian chemistry.

Received October 7, 1997.

J.K. Conner. Chemistry Department, University of Stirling, Stirling FK9 4LA, United Kingdom.
J. Haider, H. Maskill,[1] M. Pestman, and M.N.S. Hill. Chemistry Department, University of Newcastle, Newcastle upon Tyne NE1 7RU, United Kingdom.

[1] Author to whom correspondence may be addressed. Telephone: 44-191-222-7088. Fax: 44-191-222-6929. E-mail: h.maskill@ncl.ac.uk

© 1998 NRC Canada

Scheme 1.

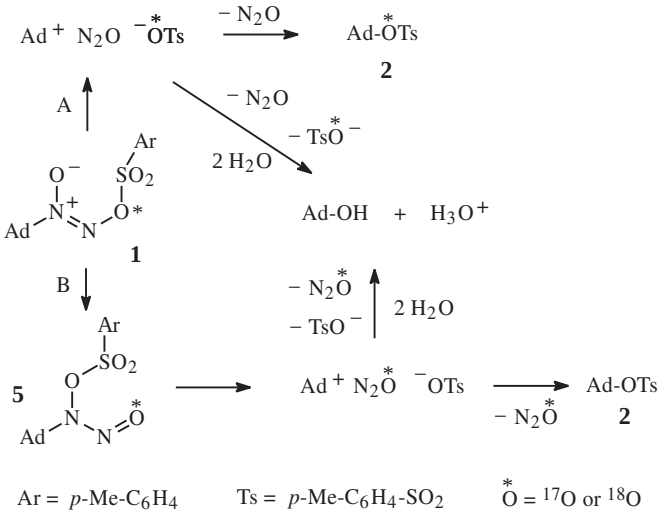

solvent molecule) in a subsequent product-forming step. In this simple model, the transition structure in the first step involves vestigial bonding between the developing trigonal electrophilic carbon and the nucleofuge. According to the more complete Winstein–Shiner ion-pair model (2*b*, 3), the rate-limiting step in the solvolysis of 2-adamantyl tosylate, for example, is not the initial ionization but the separation of the first-formed contact (or intimate) ion pair to give the solvent-separated ion pair. Clearly, this model requires that the contact ion pair undergoes internal return in competition with, but faster than, progression to the solvent-separated ion pair. In this model, the transition structure in the rate-limiting step of the solvolytic process involves a fully developed positive charge in the electrophilic fragment, and the solvent-separated ion pair is the main product-forming intermediate from 2-adamantyl tosylate.

Comparison of the effect of solvents upon the rate of solvolysis of a compound with the effect upon the rate of solvolysis of a standard compound may be quantified using the Winstein–Grunwald equation (4) (or an extended (5) or modified (6) version). An *m* value, the gradient of the $\log(k_{compound})$ versus $\log(k_{standard})$ correlation, close to unity means that the solvent effect for the solvolysis of the compound in question is the same as for the standard compound, and this is usually interpreted as evidence for very closely similar S_N1 solvolytic mechanisms. The original standard compound was *tert*-butyl chloride but 2-adamantyl tosylate is now regarded as more appropriate for substrates with arenesulfonate nucleofuges (7, 8). An *m* value appreciably lower than unity is usually interpreted as indicating that the reaction involves a low degree of charge separation in the transition structure (assuming there are other reasons for believing that the reaction is still an S_N1), or that the mechanism is not an S_N1 at all.

Recently, there has been an expansion in our knowledge of carbenium ion chemistry partly through developments in fast reaction methods pioneered by McClelland et al. (9), partly through new experimental techniques developed, for example, by Olah et al. (10) and Mayr and Patz (11) for preparing carbenium ions under nonnucleophilic conditions, partly through improved theoretical procedures for studying isolated carbenium ions themselves, for example, by Schleyer and co-workers (12), and partly due to better conceptual models for solvolytic and related reactions offered by Jencks and Richard (13). It is within this last context that the present project had its origins. Some years ago (14), we introduced the solvolysis of alkyl azoxyarenesulfonates as a heterolytic reaction, which is unambiguously unimolecular and allows the study of the S_N1 mechanism uncomplicated by competitive bimolecular substitution. The carbenium ions so formed are the same as when produced by other means, but their initial environment is different. We proposed a mechanism that is a link between the solvolysis of alkyl arenesulfonates on the one hand and nitrous acid induced deamination of primary alkylamines (and related reactions) on the other (14, 15). We also presented evidence that the initial fragmentation to give an ion pair and nitrous oxide is rate-determining (i.e., there is no internal

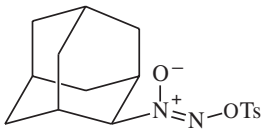

1

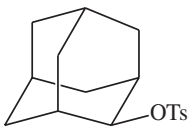

2

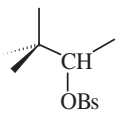

6

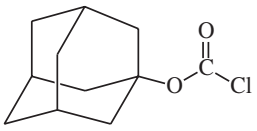

7

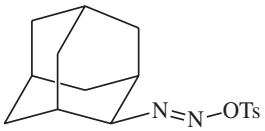

8

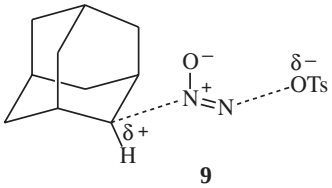

9

© 1998 NRC Canada

Scheme 2.

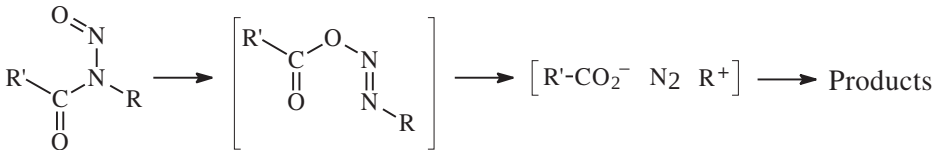

Scheme 3. (*i*) $NH_3OH^+Cl^-$, H_2SO_4, EtOH; (*ii*) NaH_3BCN, MeOH, HCl; (*iii*) $NaNO_2$, $H_3O^+Cl^-$, H_2O (using ordinary water or oxygen-labelled water as appropriate); (*iv*) TsCl, pyridine. The asterisk denotes the position of the ^{17}O or ^{18}O isotope when the nitrosation was carried out using labelled water.

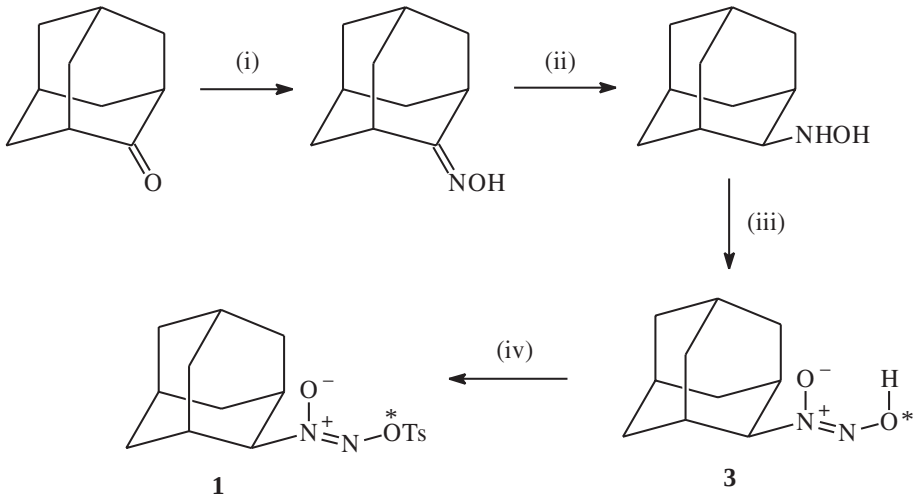

return) and concerted (14, 16). In nonnucleophilic, weakly ionizing solvents such as chloroform or toluene, the initially formed ion pair collapses to give the covalent alkyl arenesulfonate whereas in ionizing nucleophilic media such as water, the carbocation is captured by a solvent molecule to give a solvolytic substitution product (17). These possibilities are illustrated for 2-adamantyl azoxytosylate (**1**) in Scheme 1, path A. An alternative mechanism for the decomposition of **1** is included in Scheme 1 path B, which is based (in part, see later) upon the probable mechanism for the isomerization of *N*-alkyl,*N*-nitrosoamides into alkyl diazocarboxylates prior to fragmentation in the nitrosoamide method of deamination and related reactions, Scheme 2 (18). In this route, there is an initial rearrangement of the substrate to give *N*-nitroso,*N*-(2-adamantyl),*O*-(*p*-toluenesulfonyl)hydroxylamine (**5**), possibly but not necessarily through a concerted cyclic mechanism, followed by the fragmentation step.

We now report a comparison of the decompositions in a range of solvents of 2-adamantyl azoxytosylate (**1**) and 2-adamantyl tosylate (**2**), the latter long having been regarded as an archetypal S_N1 substrate (19); we also compare the solvolyses of **1** and pinacolyl brosylate (3,3-dimethyl-2-butyl *p*-bromobenzenesulfonate, **6**) (19, 20), an S_N1 substrate that reacts with rate-limiting ionization, i.e., with no internal return, and 1-adamantyl chloroformate (**7**), an S_N1 substrate that also solvolyzes with liberation of a gas molecule (21). Additionally, we present oxygen isotope labelling results, which allow us to refine our earlier mechanistic proposal for the solvolysis of **1**. Finally, attempts to remove the pendant oxygen from **1**, which would lead to the previously unknown but presumably more unstable 2-adamantyl diazotosylate (**8**), are described. Compound **8**, which is analogous to the alkyl diazocarboxylate in Scheme 2 should, if formed, fragment to give a nitrogen-separated ion pair and thence either 2-adamantyl tosylate or solvent-derived products.

Results

The two substrates **1** and **2** were made by literature methods, see Scheme 3 for **1**, and all solvolytic media were prepared in conventional ways. Rate constants were already known for 2-adamantyl tosylate in many solvents, but to allow comparison with all our results for 2-adamantyl azoxytosylate, some new values were required. Rates of reaction of both substrates in all solvolytic media were investigated by our normal UV spectrophotometric methods (see experimental section) and activation parameters were calculated using the Eyring equation from rate constants measured over a temperature range of at least 30°C. Our results are shown in Table 1; Fig. 1 is a correlation of the rate results for the solvolyses of **1** and **2** in 11 solvents (gradient = 0.46, $R = 0.96$), and Fig. 2 is a correlation of the rate results for the solvolyses of **1** and pinacolyl brosylate (**6**) in just six solvents (gradient = 0.53, $R = 0.96$).

We also prepared samples of 2-adamantyl azoxytosylate specifically enriched with ^{17}O and with ^{18}O in the oxygen marked with an asterisk in Scheme 3 by reaction of tosyl chloride (22) with a specifically labelled sample of *N*-(2-adamantyl)hydroxydiazenium oxide (**3**), which in turn had been prepared by nitrosation of *N*-(2-adamantyl)hydroxylamine by a method based upon earlier work by Dahn and Ung-Truong (23). The ^{17}O NMR spectrum of the 2-adamantyl tosylate from the reaction of the labelled 2-adamantyl azoxytosylate in deuteriochloroform after more than 10 half-lives at 65°C unambiguously showed enhancement of the signal at δ_O 158.4 ppm

© 1998 NRC Canada

Table 1. Rate constants at 25°C and enthalpies and entropies of activation for the solvolysis of 2-adamantyl azoxytosylate (**1**) and 2-adamantyl tosylate (**2**).[a]

Compound	Solvent	Y_{OTs}[b]	$10^6\,k_{25°C}$ (s^{-1})	$\Delta H^{\ddagger}$ (kJ mol^{-1})	$\Delta S^{\ddagger}$ (J K^{-1} mol^{-1})
1	50TFE	2.14	22.2	98	–5
	80TFE	1.95[c]	18.3	98	–6
	97TFE[d]	1.83	13.3	101	–1
	HCO_2H	3.04	19.4	105	16
	70E	0.47	3.56	107	10
	AcOH	–0.61	0.589	110	3
2	50TFE	2.14	2.98[e]	101	–12
	80TFE	1.95[c]	1.83	96	–32
	90TFE	1.9[c]	1.63	94	–41

[a] Rate constants at 25°C are by extrapolation from results at other temperatures, which in turn are means of several determinations and estimated to be reliable to 5%. The uncertainties in $\Delta H^{\ddagger}$ and $\Delta S^{\ddagger}$ are estimated to be 5 kJ mol^{-1} and 8 J K^{-1} mol^{-1}.

[b] Reference 8.

[c] Estimated from ref. 8.

[d] Less reliable results of $\Delta H^{\ddagger}$ = 89 kJ mol^{-1} and $\Delta S^{\ddagger}$ = –35 J K^{-1} mol^{-1} were reported earlier in ref. 14*b*.

[e] A result of 3.35×10^{-6} s^{-1} is reported in ref. 8.

Fig. 1. Graph of log k/s^{-1} for solvolysis of 2-adamantyl azoxytosylate **1** plotted against log k for solvolysis of 2-adamantyl tosylate **2**.

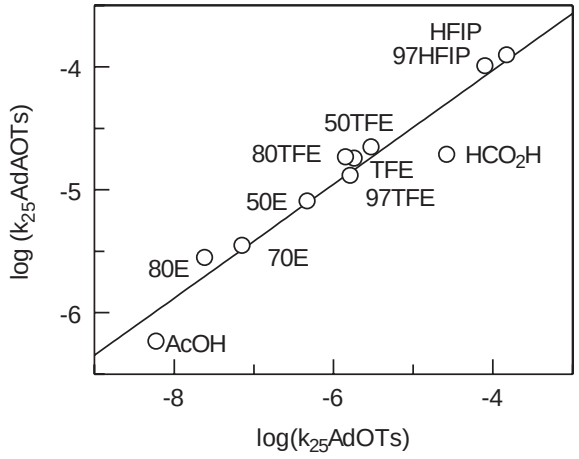

Fig. 2. Graph of log k/s^{-1} for solvolysis of 2-adamantyl azoxytosylate **1** plotted against log k for solvolysis of pinacolyl brosylate **6**.

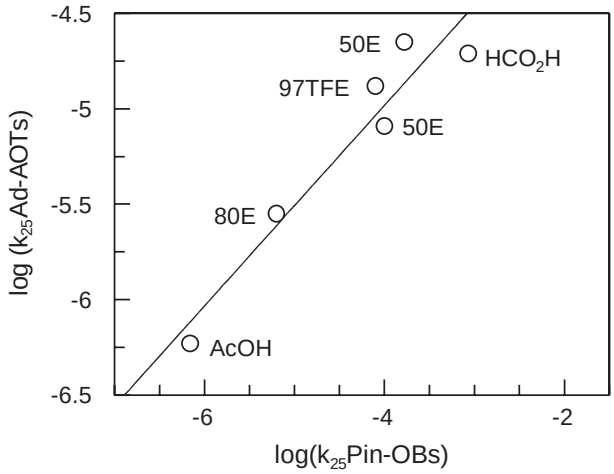

due to the sulfonyl oxygens; this compares with the signal at δ_O 157.5 ppm due to the sulfonyl bonded oxygens in the starting material. The millimeter-wave spectrum of the gas produced from the hydrolysis of the ^{18}O-labelled substrate was also recorded (24), which identified it unambiguously as nitrous oxide by the J 4←3 band at 96 512 MHz due to $N_2{}^{16}O$; there was no trace of the J 3←2 band at 71 155 MHz previously identified in the spectrum of N_2O containing the ^{18}O isotope (25).

Using a variety of reaction conditions and established deoxygenating agents (acetyl bromide (26), triethyl phosphite (27, 28), thionyl chloride (26), phosphorus trichloride (26, 29), triphenylphosphine (28), tri(*n*-butyl)phosphine (28*b*), and lithium metal (30)), we found no unambiguous evidence for the formation of 2-adamantyl tosylate from 2-adamantyl azoxytosylate under nonnucleophilic conditions.

Discussion

Isomerization of **3**, the product of nitrosation of *N*-(2-adamantyl)hydroxylamine, into **4** prior to the fragmentation in Scheme 4 has been identified as the first step in the mechanism of reaction of **3**; it involves a proton transfer either intermolecularly by protonation/deprotonation under the acidic conditions, or intramolecularly along a trajectory beginning in a strong hydrogen bond within **3** (25). In the next acid-catalysed step of this mechanism, the fragmentation is not concerted but stepwise via the oxodiazonium ion. In view of this preferred reaction of **3** via the *N*-nitroso tautomer, an intramolecular rearrangement of 2-adamantyl azoxytosylate (**1**) into the isomeric *N*-nitroso,*N*-(2-adamantyl),*O*-(*p*-toluenesulfonyl)hydroxylamine (**5**) via a cyclic transition structure is included as a preliminary to a credible alternative solvolytic mechanism for **1** in Scheme 1, path B. To distinguish between paths A and B in Scheme 1, we prepared 2-adamantyl azoxytosylate specifically labelled separately with ^{17}O and ^{18}O in the tosylated oxygen marked with an asterisk in Scheme 1. Clearly, if the mechanism follows path A, the labelled oxygen will end up in the 2-adamantyl tosylate in a nonnucleophilic medium whereas if the mechanism follows path B it will be lost as nitrous oxide. We have already shown that nitrous oxide

© 1998 NRC Canada

Scheme 4.

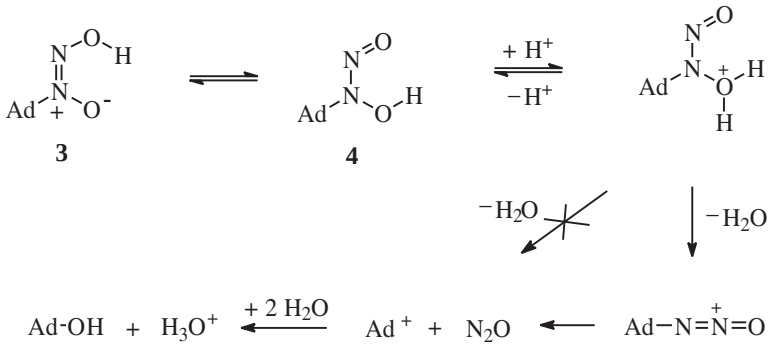

enriched with ^{18}O can be readily identified by observation of the J 3←2 rotational band at 71 155 MHz (25); its absence in the sample isolated in the present case established that the label is not in the nitrous oxide. To corroborate this negative evidence and now using ^{17}O enriched starting material **1** (25) we recorded an enhanced ^{17}O NMR signal at δ_O 158.4 ppm in the 2-adamantyl tosylate product (**2**). Clearly, the oxygen marked with an asterisk in 2-adamantyl azoxytosylate (**1**) in Scheme 1 ends up in the 2-adamantyl tosylate product (**2**), and not in the nitrous oxide, so path B via rearrangement to *N*-nitroso,*N*-(2-adamantyl),*O*-(*p*-toluenesulfonyl)hydroxylamine (**5**) in Scheme 1 may now be ruled out.

The logarithmic correlation of solvolytic rate constants at 25°C for 2-adamantyl azoxytosylate (**1**) and 2-adamantyl tosylate (**2**) is shown in Fig. 1. The nine points for aqueous alcoholic media constitute an excellent linear plot ($R > 0.99$), and the points for the two carboxylic acid solvents are noticeably off; omitting these two points has a negligible effect upon the gradient. Since 2-adamantyl tosylate is the standard compound for defining the solvent parameter Y(OTs), the gradient of this plot is the m value for 2-adamantyl azoxytosylate (**1**); the actual plot for **1** of log k/s^{-1} against Y(OTs) with the two carboxylic acid solvents omitted gives $m = 0.46$ ($R > 0.99$). Confidence in our earlier proposal that solvolysis of **1** involves rate-limiting fragmentation with formation of an ion pair separated by a molecule of nitrous oxide (14) is strengthened by our now having excluded the alternative mechanism for reaction of **1** via rearrangement through **5** (see above). Consequently, this very low m value for a reaction that is unambiguously an S_N1 indicates that the transition structure for this fragmentation has only a modest degree of dipolarity spread over four atoms, structure **9**. This is in accord with our conclusion from a double Hammett investigation of solvolyses of substituted benzyl azoxyarenesulfonates, i.e., that the bonds from the carbon to one nitrogen and from the other nitrogen to oxygen are about half broken in the transition structure (16). In contrast, the rate-limiting step in the solvolysis of **2** involves conversion of one type of ion pair into another (17, 31), i.e., ionization occurs in a prior (reversible) step, and the higher dipolarity in this transition structure arises from fully developed charges even though they are at only a small interionic separation. Our m value for **1** establishes that such a low result alone cannot be taken as a reliable indicator that a reaction of a simple secondary alkyl system is not an S_N1.

The deviations for the two carboxylic acids in the correlation of Fig. 1 indicate that the reactions of 2-adamantyl tosylate (**2**) in these solvents are faster than anticipated on the basis of their reactivity in aqueous alcohols. The most credible explanation on the basis of existing mechanistic understanding is that the bidentate carboxylic acid molecules are more effective than the aqueous alcohols at preventing internal return in the solvolysis of **2**. Internal return is also absent in the solvolysis of pinacolyl brosylate (**6**) but for a reason different to that for **1**. In the solvolysis of **6**, rearrangement is either concerted with the ionization or follows on so rapidly that internal return cannot compete (20). Consequently, in the correlation of pinacolyl brosylate with 2-adamantyl tosylate, points for carboxylic acids are also not on the line defined by reactions in aqueous ethanol (19). Low extents of internal return in the acetolysis and formolysis of 2-propyl brosylate (compared with trifluoroethanolysis) have been reported earlier (20). A fair correlation is obtained between the log k values for solvolyses of **1** and **6**, neither of which undergoes internal return, as shown in Fig. 2; the gradient (0.53) corresponds to an appreciably higher solvent effect for **6** than for **1**. This indicates a transition structure for the ionization of **6** with a higher degree of dipolarity than that in the ionization of **1**.

Another model for the reaction of **1** is 1-adamantyl chloroformate (**7**), although it is tertiary rather than secondary. A low m value determined over a wide range of solvents and appreciably positive $\Delta S^{\ddagger}$ values were reported by Kevill and colleagues (21); their solvolytic mechanism for **7** involves ionization to give the 1-adamantyl cation, carbon dixide, and chloride. Clearly, fragmentation in this system also cannot be followed by internal return to give covalent **7**, although the ions of the carbon dioxide separated ion pair can collapse to give 1-adamantyl chloride.

The newly determined activation parameters for the solvolysis of **1** shown in Table 1 are unexceptional except that they provide further supportive evidence that the reactions are S_N1 solvolyses, i.e., the enthalpies of activation are relatively high, and the entropies of activation are small (close to zero). In general terms, these and earlier results (14) show that the $\Delta S^{\ddagger}$ values are somewhat less negative than the corresponding results for **2**. We attribute this to a positive contribution to the overall entropy of activation arising from the nascent N_2O molecule in the reaction of **1** not found in the reaction of **2**. However, even this does not compensate in all cases for the substantial negative contribution to $\Delta S^{\ddagger}$ from the enhanced solvation that occurs due to the increased dipolarity in the transition state from **1**.

The original isolation of alkyl azoxyarenesulfonates as

© 1998 NRC Canada

stable compounds was initially surprising in view of the instability of analogous compounds prepared by White et al. (18, 32), which fragment at low temperatures into cation, stable molecule, and anion. We reasoned that abstraction of the pendant oxygen atom of azoxytosylates such as **1** would give the corresponding diazotosylate (**8**) and that fragmentation of **8** would now liberate nitrogen (rather than nitrous oxide), and consequently be an easier reaction. We anticipated that **8**, if formed, would be too unstable to isolate under the deoxygenation reaction conditions and sought its expected decomposition product under non nucleophilic conditions, i.e., 2-adamantyl tosylate (17). Using a range of deoxygenating reagents, we found no firm evidence by TLC or NMR for the formation of **2** and conclude that **1** does not undergo an easy deoxygenation.

Experimental

Ethanoic acid was heated under reflux for 12 h with ethanoic anhydride, then fractionally distilled; trifluoroethanol was either stirred over molecular sieves for several days, then fractionally distilled, or heated under reflux over calcium hydride for 2 h, then fractionally distilled; spectroscopic grade absolute ethanol was used as supplied; methanoic acid was purified by standing over boric anhydride (B_2O_3) for several days followed by successive distillation from fresh B_2O_3 under reduced pressure until the separation of the OH and the CH signals in the ^{1}H NMR spectrum of the neat distillate became constant at ca. 3.158 ppm. Aqueous solvolytic media were prepared by mixing appropriate volumes of glass distilled water with either ethanol or trifluoroethanol except 97TFE, which was prepared by weight; the ethanoic acid was buffered with 0.15 mol dm^{-3} anhydrous sodium ethanoate, but all other solvents were unbuffered. Isotopically enriched water was purchased from Goss (10% enriched with ^{17}O) and from Aldrich (10% enriched with ^{18}O).

2-Adamantyl azoxytosylate (1) and 2-adamantyl tosylate (2)

2-Adamantyl azoxytosylate (**1**) (mp 111–112°C, lit. (14) 111–113°C) and 2-adamantyl tosylate (**2**) (mp 82–83°C, lit. (33) 82.7–83.7°C; δ_O 159.3 ppm (S═O, natural abundance)) were prepared as described previously (14*b*).

Isotopically labelled *N*-(2-adamantyl)hydroxydiazenium oxide (3) and the corresponding azoxytosylates

An ice-cold solution of sodium nitrite (0.20 g) in water (10% enriched with ^{18}O, 0.5 cm^3) was added dropwise over about 10 min to an ice-cold stirred solution of conc. hydrochloric acid (37%, 0.20 cm^3), *N*-(2-adamantyl)hydroxylammonium chloride (170 mg), and water (10% enriched with ^{18}O, 0.5 cm^3) in ethanol (3 cm^3). After about 20 min, the white crystalline product was filtered at the pump, washed with cold water, and dried under vacuum (143 mg; mp 134–135°C, lit. (14*b*) (unlabelled material) 137–139°C; δ_H 1.60–2.10 (m, 14H), 4.29 (s, 1H), 12.1 (br, 1H)). The ^{17}O-labelled analogue (148 mg, mp 135–136°C) was made in the same way from *N*-(2-adamantyl)hydroxylammonium chloride (167 mg) using 10% ^{17}O-enriched water and had an identical ^{1}H NMR spectrum.

Specifically labelled 2-adamantyl azoxytosylate (**1**)-^{17}O (δ_O 157.5 (S═O), 291.6 (N-O-S), 452.4 ppm (N-O)) and (**1**)-^{18}O were then made by our usual Tipson (14*b*, 22) method from **3**-^{17}O and **3**-^{18}O; both had melting points and ^{1}H NMR spectra identical with the unlabelled compound.

Decomposition of ^{17}O-labelled 2-adamantyl azoxytosylate

A sample (85 mg) of ^{17}O-labelled 2-adamantyl azoxytosylate (δ_O 157.5 (S═O)) was dissolved in a 1:4 mixture of chloroform:deuteriochloroform (4 cm^3) in an NMR tube and maintained at ca. 50°C in an oil bath for 10 h. The ^{1}H NMR spectrum indicated only about 10% conversion, so the temperature of the oil bath was raised to about 60°C, and the reaction was continued for a further 15 h by which time the conversion was about 40% by ^{1}H NMR, and the ^{17}O NMR spectrum showed a single strong but broad band centred at 158 ppm. After 4 days at this temperature, the ^{1}H NMR spectrum showed complete conversion to 2-adamantyl tosylate; there was no trace of the starting material, and the product showed a strong ^{17}O NMR signal at δ_O 158.4 ppm (S═O).

Decomposition of ^{18}O-labelled 2-adamantyl azoxytosylate

A gentle flow of nitrogen was passed through a stirred solution made up from aqueous perchloric acid (70%, 6.1 cm^3), water (24 cm^3), and ^{18}O-labelled 2-adamantyl azoxytosylate (85 mg, 0.25 mmol) in a flask fitted with a reflux condenser. The reaction was maintained at 69°C for 6 h, then for another 30 min as the reaction mixture cooled down; the gas flow passed through a KOH drying tower and a gas trap immersed in liquid nitrogen. The contents of the gas trap were then transferred at room temperature to a millimeter-wave spectrometer using standard vacuum line procedures, and predetermined regions of the spectrum were scanned. An intense absorption was recorded at 96 512 MHz due to the J 4←3 transition of $N_2{}^{16}O$; no absorption was detected in the region of 71 155 MHz previously identified as due to the J 3←2 transition of $N_2{}^{18}O$ (25).

Kinetics

Rates of solvolytic reactions were measured using either a Pye–Unicam SP8-300 spectrophotometer connected to an Apple microcomputer with in-house software for data collection (34) or a Cecil CE 5502 spectrophotometer connected to an Elonex PC using commercial data collection software. In the former case, rate constants were calculated also using in-house software (34); in the latter case, GraFit version 3.0 (Erithacus Software Ltd.) was used. In both cases, cell holders for up to four cells were thermostatted by circulating water, the cell-holder block temperature being measured with a fitted platinum resistance thermometer, and the system was programmed to record absorbance data automatically at predetermined time intervals. Rate constants were calculated from absorbance–time data collected over about three or four half-lives using standard computational techniques.

Attempted deoxygenations

(*i*) Four drops of triethyl phosphite (27, 28) were added to a solution of compound **1** (10 mg) in toluene (0.5 cm^3), and the reaction was monitored by TLC for 24 h. The temperature was then raised to 40°C but TLC showed only starting material after several days.

(*ii*) A solution of **1** (26 mg) in phosphorus trichloride (26, 29) (2 cm^3) was stirred at room temperature under nitrogen and protected from atmospheric moisture (SiO_2 tube). No change

© 1998 NRC Canada

was detected by TLC after 24 h whereupon the reaction was worked up, and the isolated crystalline product was shown to be starting material by ^{1}H NMR and TLC. Further reactions with acetyl bromide (26) thionyl chloride (26), triphenylphosphine (28), tri(*n*-butyl)phosphine (28), and lithium wire (30), were also attempted but gave negative or ambiguous results.

Acknowledgement

We thank Dr. J.G. Smith for help with the millimeter-wave spectroscopy, the ERASMUS Bureau for grants to J.H. and M.P., the EPSRC for a grant to J.K.C., and Drs. J.S. Roberts (Stirling University) and C.I.F Watt (Manchester University) for helpful discussions.

References

1. C.D. Nenitzescu. *In* Carbonium ions. Vol. 1. *Edited by* G.A. Olah and P. von R. Schleyer. Wiley–Interscience, New York. 1968. pp. 1–75.
2. (*a*) T.H. Lowry and K.S. Richardson. *In* Mechanism and theory in organic chemistry. 3rd ed. Harper Collins, New York. 1987. p. 329; (*b*) *In* Mechanism and theory in organic chemistry. 3rd ed. Harper Collins, New York. 1987. pp. 335–349.
3. A.F. Diaz, I. Lazdins, and S. Winstein. J. Am. Chem. Soc. **90**, 1904 (1968); S. Winstein, B. Appel, R. Baker, and A. Diaz. *In* Organic reaction mechanisms. Special Publication No. 19. The Chemical Society, London. 1965. pp. 109–130; V.J. Shiner and W. Dowd. J. Am. Chem. Soc. **91**, 6528 (1969); V.J. Shiner, D.A. Nollen, and K. Humski. J. Org. Chem. **44**, 2108 (1979); A.D. Allen, T.T. Tidwell, and O.S. Tee. J. Am. Chem. Soc. **115**, 10 091 (1993).
4. E. Grunwald and S. Winstein. J. Am. Chem. Soc. **70**, 846 (1948).
5. S. Winstein, E. Grunwald, and H.W. Jones. J. Am. Chem. Soc. **73**, 2700 (1951).
6. D.N. Kevill. *In* Advances in Quantitative structure-property relationships. Vol. 1. *Edited by* M. Charton. Jai Press, Greenwich, Conn., U.S.A. 1996. pp. 81–115; D.N. Kevill and M.J. D'Souza. J. Chem. Soc. Perkin Trans. 2, 257 (1997).
7. T.W. Bentley, F.L. Schadt, and P. von R. Schleyer. J. Am. Chem. Soc. **94**, 992 (1972); F.L. Schadt and P. von R. Schleyer. J. Am. Chem. Soc. **95**, 7860 (1973).
8. F.L. Schadt, T.W. Bentley, and P. von R. Schleyer. J. Am. Chem. Soc. **98**, 7667 (1976).
9. R.A. McClelland, V.M. Kanagasabapathy, N.S. Banait, and S. Steenken. J. Am. Chem. Soc. **111**, 3966 (1989); J. Am. Chem. Soc. **114**, 1816 (1992).
10. G.A. Olah, M.D. Heagy, and G.K.S. Prakash. J. Org. Chem. **58**, 4851 (1993).
11. H. Mayr and M. Patz. Angew. Chem. Int. Ed. Engl. **33**, 938 (1994).
12. S. Sieber, P. von R. Schleyer, H. Vancik, M. Mesic, and D.E. Sunko. Angew. Chem. Int. Ed. Engl. **32**, 1604 (1993); S. Sieber, P. Buzek, P. von R. Schleyer, W. Koch, and J.W. de M. Carneiro. J. Am. Chem. Soc. **115**, 259 (1993).
13. W.P Jencks. Chem. Soc. Rev. **10**, 345 (1981); Chem. Rev. **85**, 511 (1985); R.D. Guthrie and W.P. Jencks. Acc. Chem. Res. **22**, 343 (1989); T.L. Amyes, I.W. Stevens, and J.P. Richard. J. Org. Chem. **58**, 6057 (1993); V. Jagannadham, T.L. Amyes, and J.P. Richard. J. Chem. Soc. Perkin Trans. 2, 171 (1993).
14. (*a*) H. Maskill, P. Murray-Rust, J.T. Thompson, and A.A. Wilson. J. Chem. Soc. Chem. Commun. 788 (1980); (*b*) H. Maskill, J.T. Thompson, and A.A. Wilson. J. Chem. Soc. Perkin Trans. 2, 1693 (1984).
15. J.K. Conner and H Maskill. Bull. Soc. Chim. Fr. 342 (1988).
16. I.M. Gordon and H Maskill. J. Chem. Soc. Chem. Commun. 1358 (1989).
17. H. Maskill, J.T. Thompson, and A.A. Wilson. J. Chem. Soc. Chem. Commun. 1239 (1981).
18. E.H. White and D.J. Woodcock. *In* The chemistry of the amino group. *Edited by* S. Patai. Interscience, New York. 1968. pp. 407–497.
19. T.W. Bentley and P. von R. Schleyer. J. Am. Chem. Soc. **98**, 7658 (1976).
20. V.J. Shiner, R.D. Fisher. and W Dowd. J. Am. Chem. Soc. **91**, 7748 (1969).
21. D.N. Kevill and F.L. Weitl. Tetrahedron Lett. 707 (1971); D.N. Kevill, J.B. Kyong, and F.L. Weitl. J. Org. Chem. **55**, 4304 (1990).
22. R.S Tipson. J. Org. Chem. **9**, 235 (1944).
23. H. Dahn and M-N. Ung-Truong. Helv. Chim. Acta, **71**, 241 (1988).
24. J.H. Carpenter, J.D. Cooper, J.B. Simpson, J.G. Smith, and D.H. Whiffen. J. Phys. E, **7**, 678 (1974).
25. J. Haider, M.N.S. Hill, I.D. Menneer, H. Maskill, and J.G. Smith. J. Chem. Soc. Chem. Commun. 1571 (1997).
26. J.F. Vozza. J. Org. Chem. **34**, 3219 (1969).
27. J.I.G. Cadogan, M. Cameron-Wood, R.K. Mackie, and R.J.G. Searle. J. Chem. Soc. 4831 (1965); T. Mukaiyama, H. Nambu, and M. Okamoto. J. Org. Chem. **27**, 3651 (1962).
28. (*a*) J.I.G. Cadogan. *In* Organophosphorus reagents in organic synthesis. *Edited by* J.I.G. Cadogan Academic Press, London and New York. 1979. pp. 269–294; (*b*) A.G Rowley. *In* Organophosphorus reagents in organic synthesis. *Edited by* J.I.G. Cadogan Academic Press, London and New York. 1979. pp. 295–350.
29. T.R. Emerson and C.W. Rees. J. Chem. Soc. 2319 (1964).
30. V. Kalyanaraman and M.V. George. J. Org. Chem. **38**, 507 (1973).
31. V.J. Shiner. *In* Isotope effects in chemical reactions. *Edited by* C.J. Collins and N.S. Bowman. A.C.S. Monograph 167. Van Nostrand-Reinhold, New York. 1970. pp. 90–159; V.J. Shiner and R.D. Fisher. J. Am. Chem. Soc. **93**, 2553 (1971).
32. E.H. White, H.P. Tiwari, and M.J. Todd. J. Am. Chem. Soc. **90**, 4734 (1968).
33. P. von R. Schleyer and R.D. Nicholas. J. Am. Chem. Soc. **83**, 182 (1961).
34. H. Maskill and J.T. Thompson. Lab. Microcomput. **1**, 11 (1982).

© 1998 NRC Canada

Are mesoionic compounds aromatic?

Alfredo Mayall Simas, Joseph Miller, and Petrônio Filgueiras de Athayde Filho

Abstract: We have evaluated the experimental evidence relevant to the structure and character of mesoionic compounds, accumulated for more than 100 years and including X-ray diffraction studies. We have also evaluated relevant theoretical studies. All these, including our own extensive work, lead us to conclude that mesoionic compounds are not aromatic. According to our recent definition "mesoionic compounds are planar five-membered heterocyclic betaines with at least one side chain whose α-atom is also in the ring plane and with dipole moments of the order of 5 D. Electrons are delocalized over two regions separated by what are essentially single bonds. One region, which includes the α-atom of the side chain is associated with the HOMO and negative π-charge whereas the other is associated with the LUMO and positive π-charge."

Key words: mesoionic compounds, betaines, aromaticity.

Résumé : On a évalué les données expérimentales accumulées au cours des cent dernières années, y compris les études de diffraction des rayons X, relatives à la structure et au caractère des composés mésoioniques. On a aussi évalué les études théoriques appropriées. Toutes ces données ainsi que nos propres travaux permettent de conclure que les composés mésoioniques ne sont pas aromatiques. Selon notre définition récente, « les composés mésoioniques sont des bétaïnes planaires d'hétérocycles à cinq chaînons portant au moins une chaîne latérale dont l'atome α est aussi dans le plan du noyau et dont les moments dipolaires sont de l'ordre de 5 D. Les électrons sont délocalisés sur deux régions séparées par ce qui essentiellement des liaisons simples. L'une des régions, qui comprend l'atome α de la chaîne latérale, est associée avec l'orbitale moléculaire HO et la charge π négative alors que l'autre est associée avec l'orbitale moléculaire BV et la charge π positive. »

Mots clés : composés mésoioniques, bétaïnes, aromaticité.

[Traduit par la rédaction]

Introduction

Compounds now classified as mesoionic have been known for more than 100 years (1, 2): many others have since been prepared. By 1976 several comprehensive reviews had appeared (3–10) and were followed soon afterwards by the extensive review of Ramsden et al. (11).

Their unusual character was indirectly illuminated by the improbable classical structures put forward in early studies. Later, recourse was made to both covalent and polar structures to represent mesoionic compounds.

The sydnones (vide infra) are perhaps the best known group of mesoionic compounds. They were first prepared in 1935 by Earl and Mackney (12), working in Sydney, hence the trivial name. They suggested the improbable bicyclic aza-β-lactone structure (**I**).

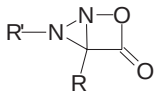

I

An important contribution was made by Schönberg in 1938. In his paper (13) he suggested that mesoionic compounds should be represented by resonance and charge hybrid structures. The designation mesoionic was launched by Baker et al. in 1949 (14): from "mesomeric" and "ionic." They also put forward the first definition, refined in 1976 by Ollis and Ramsden (15): "A compound may appropriately be called mesoionic if it is a five-membered heterocycle which cannot be satisfactorily represented by any one covalent or ionic structure and possesses a sextet of electrons in association with the five atoms comprising the ring."

While the word satisfactorily leaves a margin for uncertainty, there has in fact been little doubt as to which compounds should be called mesoionic.

The main general structures used at the time, are shown as **II**–**V**. Structure **V** clearly suggests that mesoionic compounds are aromatic.

It is important to note that there were dissenting voices. In 1955, Katritzky (15) wrote on "the representation of the

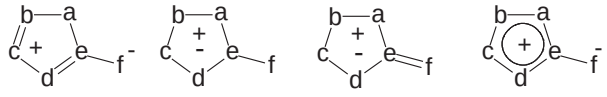

II III IV V

Received December 15, 1997.

This paper is dedicated to Professor Erwin Buncel in recognition of his contributions to Canadian chemistry.

A.M. Simas, J. Miller,[1] and P.F. de Athayde Filho.[2]
Departamento de Química Fundamental, CCEN, Universidade Federal de Pernambuco, Recife, PE 50.670-900, Brazil.

[1] Author to whom correspondence may be addressed. Telephone: (+) 55 83 216 7381. Fax: (+) 55 83 216 7511 (7502). E-mail: millerjo@vm.npd.ufpb.br
Current address: Departamento de Química, CCEN and Laboratório de Tecnológia Farmacêutica, CCS, Universidade Federal da Paraiba, Campus I, João Pessoa, PB 58.051-970, Brazil.

[2] Current address: Departamento de Química, Universidade Federal Rural de Pernambuco, Dois Irmãos, Recife, PE 52.171-030, Brazil.

© 1998 NRC Canada

so-called mesoionic compounds." He suggested that the ± representation should be discontinued as should the term mesoionic, to be substituted by mesomeric betaine.

While not directly relevant to the question of aromaticity, it is worth intercalating that Ollis and Ramsden (16) divided mesoionic compounds into two broad subclasses (so-called Type A and Type B) according to the degree to which each ring atom contributes to the total of eight π-electrons (ring plus α-atom with formal negative charge): most mesoionic compounds belong to Type A. It is worth adding further that Type B mesoionic compounds are 1,3-dipoles, and Type A mesoionic compounds are "masked" 1,3-dipoles. In any event 1,3-dipolar additions are common and important reactions of mesoionic compounds.

In 1978 Potts (16) suggested that "the term mesoionic should be restricted to five-membered heterocycles that cannot be satisfactorily represented by normal covalent structures but are better represented as a hybrid of all possible charged forms."

He added that this implies the presence of some degree of aromatic character ($(4n+2)\pi$ electrons) in the positively charged ring system, which is counterbalanced by a negatively charged atom.

A highly relevant contribution was made by Dewar and Turchi (17) in 1975 in their theoretical studies by the MINDO/3 molecular orbital method inter alia the 3-*N*-methyl-1,3-oxazolium-5-Y$^-$ system (**VI**). They also referred to a series of relevant earlier studies (18–23) of the sydnones (1,2,3-oxadiazolium-5-olates); as well as two more recent studies (24, 25) using CNDO/2, ab initio, and INDO molecular orbital methods (assumed geometries).

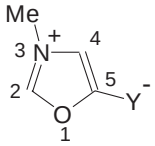

VI

They added that the results were in qualitative agreement with (*i*) X-ray crystallography data for 4,4′-dichloro-3,3′-ethylene-disydnone (24) and (*ii*) a ^{13}C NMR study of 3-methylsydnone (25).

Dewar and Turchi emphasized the large positive charge at C-2 and the large negative charge at C-4. This led them to suggest the nonaromatic structures **VII** and **VIII**.

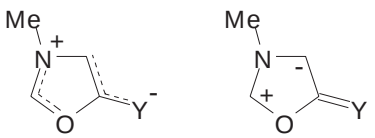

VII VIII

It is noteworthy that the authors of the crystallographic study (24) referred to "the unusually long endocyclic C—O bond," i.e., having little or no π-character.

The group of Miller and Simas have contributed an extensive sequence of experimental and theoretical studies (the latter more recent) following the pioneering study by Chan et al. (26) in 1964. These authors made a comparative kinetic study of the S_NAr reactions of 3-(4-chloro-3-nitrophenyl)-1,2,3-oxadiazolium-5-olate (**IX**) and of 1-chloro-2,4-dinitrobenzene with methanethiolate in methanol. This study was amplified much later by Braz et al. (27). By that time Echevarria and Miller (28) and Echevarria (29) had made kinetic studies of the S_NAr reactions of 5-(4-choro-3-nitrophenyl)-1,3-diphenyl-1,3,4-triazólium-2-thiolate (**X**) with a range of anionic and neutral nucleophiles in methanol comparing their data with those for 1-chloro-2,4-dinitrobenzene in the same solvent.

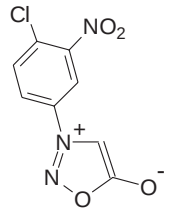

IX

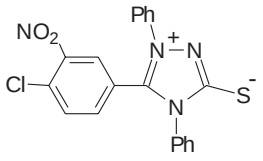

X

It is of special interest that in both cases the mesoionic ring as an activating substituent for S_NAr reactions in a benzenoid ring has an equivalent σ^- value (Hammett substituent constant appropriate for S_NAr reactions) ca. 0.7; recalling that in one case the benzene ring suffering nucleophilic attack was attached to the formally positively charged 3-nitrogen atom of the 1,2,3-oxadiazolium moiety and in the other case attached to the formally neutral 2-carbon atom of the 1,3,4-triazolium moiety.

An analysis of the enthalpies and entropies of activation for the reactions of 5-(4-chloro-3-nitrophenyl)-1,3,4-triazólium-2-thiolate with the wide range of nucleophiles used led Echevarria and Miller to conclude that in the mesoionic substrate the positive and negative regions were so well separated that it behaved as a *pair of ions* with respect to solvation.

Echevarria and Miller (28), having demonstrated that the positively charged region of the 1,3,4-triazolium-2-thiolate system served as an activating group for S_NAr reactions (vide supra), then showed that the negative region acted as a nucleophile (29), and that nucleophilic character was not confined to the formally negative thiolate function but was shared by the 3-nitrogen atom. They formed both mono- and dimethyl salts. Still more importantly, their study indicated that the *first* methyl group was linked to the 3-nitrogen atom.

It is relevant that early studies of the sydnones (3, 5, 9) showed that they react with electrophiles at the 4-carbon atom giving, e.g., a bromo derivative.

In contrast, protonation (30) occurs on the exocyclic olate oxygen. The similarity to the behaviour of enolate ions is noteworthy.

Very recently, the group of de Athayde Filho, Miller, and Simas (31) reported (*i*) the condensation of 1,4-diphenyl-5-(4-chloro-3-nitrophenyl)-1,3,4-triazolium-2-thiolate, acting as a nucleophile, with its hydrochloride acting as an electrophile; (*ii*) the cross-condensation of four different 1,4-diphenyl-5-aryl-1,3,4-triazolium-2-thiolates, acting as nucleophiles, with the hydrochloride of 1,4-diphenyl-5-(4-chloro-3-nitrophenyl)-1,3,4-triazolium-2-thiolate acting as an electrophile; (*iii*) the self-condensation of 1,4-diphenyl-5-(4-chloro-3-nitrophenyl)-1,3,4-triazolium-2-thiolate, acting as both nucleophile and electrophile, forming an oligomer.

We are currently studying systems in which the positive region of mesoionic compound acts directly as an electrophilic centre.

© 1998 NRC Canada

The combination of the synthetic and kinetic studies indicates clearly that the mesoionic systems studied have well-separated positive and negative regions able to act *independently* as electron-deficient and electron-rich functions. This is tantamount to indicating that mesoionic compounds should *not* be considered aromatic.

This conclusion has been further reinforced by our X-ray diffraction studies (32, 33). These indicated clearly the existence of two regions in each of which bond distances correspond to the existence of electron and charge delocalization and that *these two regions are separated by what are essentially single bonds*. In particular, we studied 2-*N*-piperidino-5-methyl-1,3-dithiolium-4-thiolate (**XI**), 2-*N*-morpholino-5-*n*-propyl-1,3-dithiolium-4-thiolate (**XII**), and the hydrochloride of 4-phenyl-5-(4-methoxyphenyl)-1,3,4-thiadiazolium-2-phenylaminide (**XIII**).

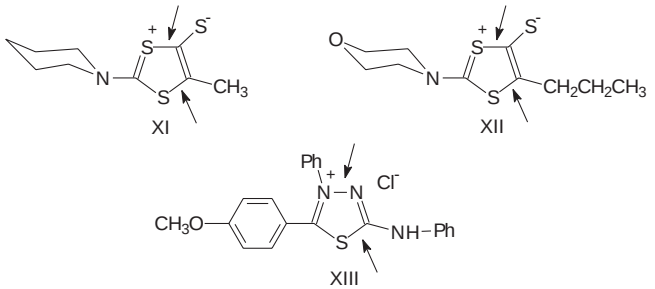

In these structures the single annular bonds are indicated by arrows. These studies clearly indicate that mesoionic compounds are not aromatic. Moura and Simas (34) carried out theoretical studies of 36 mesoionic systems with two heteroatoms in the five-membered ring. The structures were optimized by the semiempirical AM1 molecular orbital method, codified in the MOPAC 93 programme. Their results are fully coherent with X-ray and other studies. The positive and negative regions are separated by what are essentially single bonds; whereas the other annular bonds and that linking the five-membered ring to the α-atom, bearing a formal negative charge, have bond order between single and double bonds. This is illustrated in structure **XIV**.

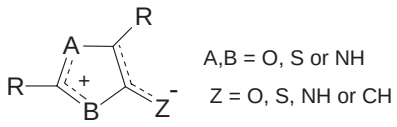

The existence of separate electron-rich and electron-deficient regions is well illustrated by ^{1}H NMR data.

In a series of 4-*N*-arylsydnones (**XV**) (35) the chemical shifts of the hydrogen atom attached to C-3, i.e., in the negative region, lie between 6.3–6.8 ppm, at higher field than otherwise similar five-membered aromatic heterocycles.

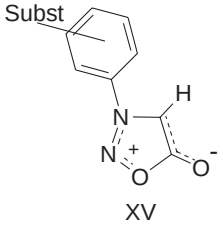

Calculations (36) indicate a fractional negative charge on the 3-carbon atom a clear contribution to diamagnetic protection.

In contrast, in mesoionic compounds of the classes 1,3,4-triazolium-2-thiolate, 1,3,4-thiadiazolium-2-thiolate, and 1,3,4-triazolium-2-olate, the hydrogen atoms linked to C-5 in each case have chemical shifts of 10.40 and 10.10 ppm, at lower field than otherwise similar five-membered aromatic heterocycles. Calculations (37, 38) indicate a fractional positive charge on the five-carbon atom, a clear contribution to diamagnetic deprotection (see structures **XVI**, **XVII**, and **XVIII**).

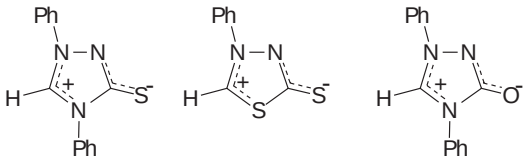

It is especially convenient at this point to refer to 1.4-diphenyl-1,4-diazolium-2-thiolate **XIX** (39). This has a hydrogen atom atached to the three-carbon atom in the negative region and another to the five-carbon atom in the positive region.

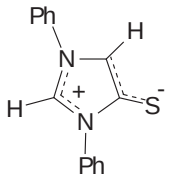

The hydrogen atom attached to C-3 has a chemical shift of 6.82 ppm, whereas that attached to C-5 has a chemical shift of 8.36 ppm.

Jaz´win´ski et al. (40) have published an extensive review of the structures and NMR parameters of mesoionic compounds.

They used ^{1}H, ^{13}C, ^{14}N, ^{15}N, ^{17}O, and ^{77}Se NMR; while the the systems they studied all have three or four hetero-atoms in the five-membered ring. However they simply assumed aromatic character and did not use their data to clarify this or otherwise; though they affirmed that the positive charge is delocalized over the ring atoms, while the negative charge is situated on the exocyclic atom.

It is convenient to present here the definition of mesoionic compounds by the group of Miller and Simas (41): "Mesoionic compounds are planar five-membered heterocyclic betaines with at least one side chain whose α-atom is also in the ring plane and with dipole moments of the order of 5 D. Electrons are delocalized over two regions separated by what are essentially single bonds. One region, which includes the α-atom of the side chain, is associated with the HOMO and negative π-charge whereas the other is associated with the LUMO and positive π-charge."

We add, finally, a quotation from Gilchrist's text on heterocyclic chemistry (42), revised in 1992. He states, "It does not therefore seem useful or appropriate to classify sydnones and

© 1998 NRC Canada

other mesoionic compounds as aromatic, despite the existence of a cyclic array of *p*-orbitals."

Conclusion

On the basis of the available evidence, accumulated for more than 100 years and summarized in this paper, we conclude that mesoionic compounds are not aromatic though well-stabilized in two separate regions by electron and charge delocalization.

Acknowledgment

The authors thank CNPq (The Brazilan National Research Council) for the doctoral bursary conceded to one of us (P.F. de A.F.).

References

1. E. Fischer and E. Besthorn. J. Liebigs Ann. **212**, 316 (1882).
2. (*a*) M. Busch. Ber. dt. Chem. Ges. **28**, 2635 (1895); (*b*) J. Prakt. Chem. **60**, 225 (1899); (*c*) Ber. dt. Chem. Ges. **38**, 856 (1905); Ber. dt. Chem. Ges. **38**, 4049 (1905); (*d*) J. Prakt. Chem. **74**, 533 (1906).
3. W. Baker and W.D. Ollis. Quart. Rev. **11**, 15 (1957).
4. Y. Noël. Bull. Soc. Chim. Fr. 173 (1964).
5. F.H.C. Stewart. Chem. Rev. **64**, 129 (1964).
6. R. Huisgen. Chem. Soc. Spec. Publ. **21**, 51 (1967).
7. L.B. Kier and E.B. Roche. J. Pharm. Sci. **56**, 149 (1969).
8. N. Sucia. Stud. Cercet. Chim. **16**, 117 (1968).
9. M. Ohta and H. Kato. *In* Nonbenzenoid aromatics. *Edited by* J.P. Snyder. Academic Press, New York. 1969.
10. W.D. Ollis and C.A. Ramsden. Adv. Heterocycl. Chem. **19**, 1 (1976).
11. (*a*) C.A. Ramsden. Compr. Org. Chem. **4**, 1171 (1979); (*b*) W.D. Ollis, S.P. Stanforth, and C.A. Ramsden. Tetrahedron, **41**, 2239 (1985).
12. J.C. Earl and A.W. Mackney. J. Chem Soc. 899 (1935).
13. A.J. Schönberg. J. Chem Soc. 824 (1938).
14. W. Baker, W.D. Ollis, and V.D. Poole. J. Chem Soc. 307 (1949).
15. A.R. Katritzky. Chem. Ind. (London), 521 (1955).
16. K.T. Potts. Lect. Heterocycl. Chem. **4**, 53 (1978).
17. M.J.S. Dewar and I.J. Turchi. J. Chem. Soc. Perkin Trans. **2**, 548 (1976).
18. L.E. Orgel, T.L. Cottrell, W. Dick, and L.E. Sutton. Trans. Faraday Soc. **47**, 113 (1951).
19. L. Paoloni. Gazz. Chim. Ital. **96**, 83 (1966).
20. D.A. Bochvar and A.A. Bagatur'yants. Zh. fiz. Khim. **39**, 1631 (1985); Chem. Abstr. **64**, 3328 (1966).
21. H.C. Longuet-Higgins. J. Chim. Phys. Phys.-Chim. Biol. **46**, 244 (1949).
22. L.B. Kier. Tetrahedron Lett. 1233 (1967).
23. L.B. Kier and E.B. Roche. J. Pharm. Sci. **55**, 807 (1968).
24. J.E. Bloor, B.R. Bilson, and F.P. Billlingsley. Theor. Chim. Acta, **12**, 360 (1968).
25. M. Barber, S.J. Broadbent, J.A. Connor, M.F. Guest, H. Hillier, and H.J. Paxley. J. Chem. Soc. Perkin Trans. 2, 1517 (1972).
26. T.L. Chan, J. Miller, and F. Stansfield. J. Chem. Soc. 1213 (1964).
27. V.R. Braz, A. Echevarria, and J. Miller. Heterocycl. Commun. **2**, 507 (1996).
28. A. Echevarria and J. Miller. J. Chem. Soc. Perkin Trans. 2, 1425 (1989).
29. A. Echevarria. Doctoral thesis, University of São Paulo, Brazil. 1986.
30. G.A. Olah, D.P. Kelly, and N. Sucia. J. Am. Chem. Soc. **92**, 3133 (1970).
31. P.F. de Athayde Filho, J. Miller, and A.M. Simas. Chimia, **51**, 453 (1997).
32. (*a*) K-K. Cheung, S.E. Galembeck, J. Miller, M.B. de Oliveira, A.B. Pereira, and A.M. Simas. Acta Crystallogr. Sect. C, **C47**, 2630 (1991); (*b*) Acta Crystallogr. Sect. C, **C48**, 523 (1992).
33. K-K. Cheung, A. Echevarria, S.E. Galembeck, M.A.M. Maciel, J. Miller, V.M. Rumjanek, and A.M. Simas. Acta Crystallogr. Sect. C, **C48**, 1471 (1992).
34. G.L.C. Moura. Masters thesis, Federal University of Pernambuco, Brazil. 1996.
35. F.H.C. Stewart and N. Danieli. Chem. Ind. (London), 1926 (1962).
36. G.H. Schmid. J. Mol. Struct. **5**, 236 (1970).
37. G.W. Evans and B. Milligan. Aust. J. Chem. **20**, 1779 (1967).
38. A.Ya. Lazaris and A.N. Egorochkin. Izv. Akad. Nauk SSSR Ser. Khim. **8**, 1870 (1979).
39. M. Begtrup. J. Chem Soc. Perkin Trans. 1, 1132 (1979).
40. (*a*) J. Jaz´win´ski, O. Staszewska, L. Stefaniak, and G.A. Webb. Magn. Reson. Chem. **33**, 134 (1995); (*b*) J. Mol Struct. **377**, 167 (1996).
41. J. Miller, M.B. de Oliveira, A.B. Pereira, S.E. Galembeck, G.L.C. Moura, and A.M. Simas. Phosphorus Sulfur Silicon Relat. Elem. **108**, 75 (1996).
42. G. Gilchrist. *In* Heterocyclic chemistry. 2nd ed. Wiley, N.Y. 1992. p. 329.

© 1998 NRC Canada

Regioselectivity and stereoelectronic effects in the reactions of the dinitroaniline herbicides trifluralin and benefin with nucleophiles

Michael T. Annandale, Gary W. vanLoon, and Erwin Buncel

Abstract: The reactions of two members of the dinitroaniline class of herbicides, *N*,*N*-di-*n*-propyl-2,6-dinitro-4-(trifluoromethyl)aniline (trifluralin; **1**) and *N*-ethyl-*N*-*n*-butyl-2,6-dinitro-4-(trifluoromethyl)aniline (benefin; **2**), along with their analogue, *N*-phenyl-2,6-dinitro-4-(trifluoromethyl)aniline (**3**), with the nucleophiles, OD^- and SO_3^{2-}, have been investigated using 400 MHz ^1H NMR spectroscopy. The reactions of both **1** and **2** with OD^- result in formation of Meisenheimer anionic σ-complexes according to a K3T1 (*kinetic* preference for formation of the C-3 adduct with *thermodynamic* preference for formation of the C-1 adduct) reaction sequence while the reaction of **3** with OD^- and that of **1** with SO_3^{2-} follow a K3T3 (*kinetic* and *thermodynamic* preference for formation of the C-3 adduct) sequence. There was no observation of the C-1 adducts of **1** and **2** with OD^-, but the products of S_NAr displacement at C-1 were observed as the final thermodynamic products. Geometry optimization calculations support our hypothesis of $n \rightarrow \sigma^*$ stabilization of the C-1 adduct leading to S_NAr displacement. In the reaction of **3** with OD^-, initial N-deprotonation to form the anion, **3a**, is followed by σ-complex formation. The final thermodynamic product observed in this system is 3,5-dinitro-4-(*N*-phenylamino)benzoic acid formed through hydrolysis of the trifluoromethyl group on the anion, **3a**. Aryl H–D exchange has been found for the systems of **1** and **2** with OD^-, but not for the SO_3^{2-} system and neither for the reaction of **3** with OD^-. Since dimethylpicramide showed significantly slower H–D exchange under identical conditions, it is argued that this discrepancy has as origin the ability of the amino N lone electron pair to interact with the π-system of the ring. With both **1** and **2** the larger size of the amino alkyl chains prevent the amino N lone pair from aligning with the π-system of the ring, thus hindering electron density donation to the electron-deficient ring carbons.

Key words: trifluralin, benefin, herbicides, Meisenheimer complexes, stereoelectronic effects.

Résumé : Faisant appel à la spectroscopie RMN du ^1H à 400 MHz, on a étudié les réactions de deux herbicides membres de la classe des dinitroanilines, soit la *N,N*-dipropyl-2,4-dinitro-4-(trifluorométhyl)aniline (trifluraline; **1**) et la *N*-éthyl-*N*-butyl-2,6-dinitro-4-(trifluorométhyl)aniline (bénéfine, **2**), et de leur analogue, la *N*-phényl-2,6-dinitro-4-(trifluorométhyl)aniline (**3**), avec les nucléophiles OD^- et SO_3^{2-}. Les réactions des composés **1** et **2** avec OD^- conduisent à la formation de complexes σ anioniques de Meisenheimer suivant une séquence réactionnelle K3T1 (préférence *cinétique* pour la formation de l'adduit C-3 avec préférence *thermodynamique* pour la formation de l'adduit C-1); par ailleurs, la réaction de **3** avec OD^- ainsi que celle de **1** avec SO_3^{2-} d'après une séquence K3T3 (préférences *cinétique* et *thermodynamique* pour la formation de l'adduit C-3). On n'a pas observé de formation d'adduits C-1 entre **1** et **2** et OD^-, mais les produits de substitution S_NAr en C-1 ont été observés comme produits thermodynamiques finals. Des calculs avec optimisation de la géométrie supportent notre hypothèse d'une stabilisation $n \rightarrow \sigma^*$ de l'adduit C-1 conduisant à une substitution S_NAr. Dans la réaction de **3** avec OD^-, la N-déprotonation initiale conduisant à la formation de l'anion **3a** est suivie de la formation d'un complexe σ. Le produit thermodynamique final observé dans ce système est l'acide 3,5-dinitro-4-(*N*-phenylamino)benzoïque formé par hydrolyse du groupe trifluorométhyle de l'anion **3a**. On a observé un échange H–D des protons aromatiques pour les systèmes de **1** et de **2** avec le OD^- ; on ne l'a toutefois pas observé ni pour le système avec SO_3^{2-} ni pour la réaction de **3** avec OD^-. Puisque l'échange H–D de la diméthylpicramide est beaucoup plus lent dans des conditions identiques, il a été suggéré que cette différence provient de l'habilité de la paire d'électrons non partagée de l'azote à interagir avec le système π du noyau. Avec les composés **1** et **2**, la taille plus grande des chaînes alkyles du groupe aminé empêche la paire d'électrons non partagée de l'azote de l'amine de s'aligner avec le système π du noyau et ceci empêche d'accroître la densité électronique sur les carbones électrodéficients du noyau.

Mots clés : trifluraline, bénéfine, herbicides, complexes de Meisenheimer, effets stéréoélectroniques.

[Traduit par la rédaction]

Received December 8, 1997.

This paper is dedicated to Professor Erwin Buncel in recognition of his contributions to Canadian chemistry.

M.T. Annandale, G.W. vanLoon, and Erwin Buncel.[1] Department of Chemistry, Queen's University, Kingston, ON K7L 3N6, Canada.

[1] Author to whom correspondence may be addressed. Telephone: (613) 545-2616. Fax: (613) 545-6669.

© 1998 NRC Canada

Introduction

Trifluralin (*N*,*N*-di-*n*-propyl-2,6-dinitro-4-(trifluoromethyl)-aniline; **1**) and benefin (*N*-ethyl-*N*-*n*-butyl-2,6-dinitro-4-(trifluoromethyl)aniline; **2**) are members of the dinitroaniline family of herbicides, widely used for the control of most grasses and broad-leafed weeds. They are selective pre-emergence soil-herbicides used on a variety of crops, including beans, carrots, tomatoes, potatoes, and strawberries. They are also used for the control of annual grasses and broad-leafed weeds in grain and cereal crops as well as in orchards and vineyards (1).

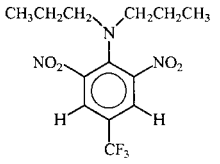

Trifluralin (1)

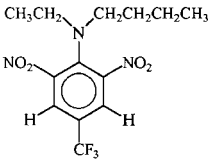

Benefin (2)

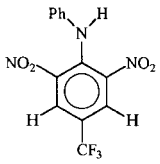

3

The mode of action of these herbicides is not fully understood at present. However, since dinitroanilines possess an electron-deficient aromatic ring, it has been postulated that the biological activity may arise from their ability to form stable covalent anionic adducts (Meisenheimer complexes) with nucleophiles (e.g., -NH_2 of lysine protein residues, -SH of cysteine residues, etc.) in plant cells (2–4).

The present study focuses on the reaction pathways of herbicides **1** and **2**, and their aryl analogue, *N*-phenyl-2,6-dinitro-4-(trifluoromethyl)aniline, **3**, with hydroxide and sulfite ions. The reactions were followed by ^{1}H NMR spectroscopy in order to eludicate the degradation products formed, and to identify any Meisenheimer complex intermediates that may lie along the reaction path.

^{1}H nuclear magnetic resonance (NMR) spectroscopy has proved to be the most useful tool in the determination of the structures of σ-complexes in solution (5–11). For example, in the reaction of 1,3,5-trinitrobenzene (TNB) with nucleophiles, the ring carbon (C-2) to which the nucleophile becomes attached, undergoes a change in hybridization from sp^2 to sp^3, which affects the shielding felt by the attached proton. The resonances of the C-4 and C-6 protons are also shifted upfield relative to uncomplexed TNB, but to a lesser extent than the C-2 proton, due to loss of aromaticity (reduction of ring current) in the trinitrocyclohexadienate moiety and the increased negative charge on the ring in the complex.

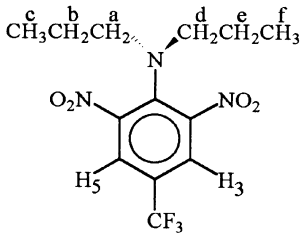

1

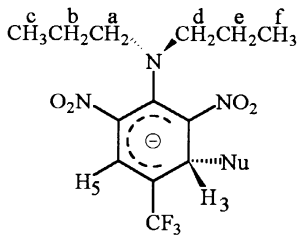

1a Nu = OD
1c Nu = NPr_2
1d Nu = SO_3^-

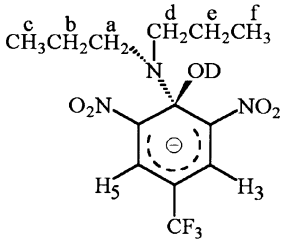

1b

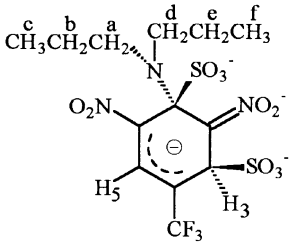

cis-**1e**

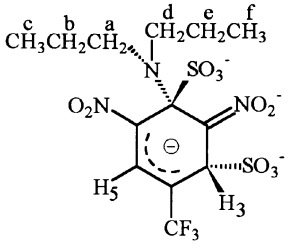

trans-**1e**

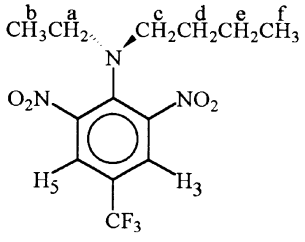

2

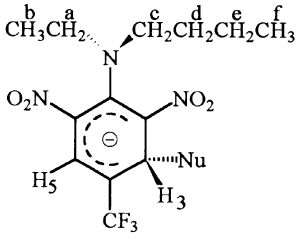

2a Nu = OD
2c Nu = N(Et)Bu

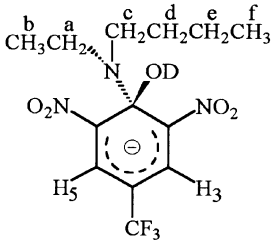

2b

© 1998 NRC Canada

Table 1. Proton NMR resonance shifts[a] of substrates, σ-complexes, and products observed for the reactions of **1–3** with deuteroxide and sulfite ion.

Compound	Chemical shift (ppm)							
	H_3	H_5	H_a	H_b	H_c	H_d	H_e	H_f
1[b]	8.39 (s)	8.39 (s)	2.89 (t)	1.45 (m)	0.75 (t)	2.89 (t)	1.45 (m)	0.75 (t)
1a[b]	5.77 (s)	7.43 (s)	3.35 (m), 2.64 (m)	1.55 (m), 1.36 (m)	0.75 (bt)	3.35 (m), 2.64 (m)	1.55 (m), 1.36 (m)	0.75 (bt)
1b[b]	Not observed							
1c[b]	Not obs.	Not obs.	3.53 (m)	2.05 (bm)	Obscured	3.53 (m)	2.05 (bm)	Obscured
1d[b]	5.50 (s)	7.28 (s)	3.39 (m), 2.62 (bm)	1.57 (m), 1.32 (bm)	0.75 (bt)	3.39 (m), 2.62 (bm)	1.57 (m), 1.32 (bm)	0.75 (bt)
cis-**1e**[b]	5.01 (d)	7.15 (d)	Obscured	Obscured	Obscured	Obscured	Obscured	Obscured
trans-**1e**[b]	5.01 (d)	7.68 (d)	Obscured	Obscured	Obscured	Obscured	Obscured	Obscured
2[c]	8.42 (s)	8.42 (s)	3.02 (q)	1.02 (t)	2.90 (t)	1.40 (m)	1.17 (m)	0.76 (t)
2a[c]	5.74 (s)	7.43 (s)	2.75 (m); 3.37 (m)	1.02 (t)	2.75 (m); 3.37 (m)	1.46 (bm)	1.17 (m)	0.76 (t)
2b[c]	Not observed							
2c[c]	Not obs.	Not obs.	Obscured	2.06 (m)	Obscured	Obscured	Obscured	Obscured
3[c]	8.53 (s)	8.53 (s)	7.09 (bm)	7.26 (bm)	7.09 (bm)	N/A	N/A	N/A
3a[c]	7.74 (s)	7.74 (s)	6.44 (d)	7.04 (t)	6.69 (t)	N/A	N/A	N/A
3b[c]	5.56 (s)	6.91 (s)	Obscured	Obscured	Obscured	N/A	N/A	N/A
4[b]	8.02 (s)	8.02 (s)	N/A	N/A	N/A	N/A	N/A	N/A
5[b]	8.34 (s)	8.34 (s)	N/A	N/A	N/A	N/A	N/A	N/A
6[b]	N/A	N/A	2.35 (t)	1.35 (m)	0.79 (t)	2.35 (t)	1.35 (m)	0.79 (t)
7[c]	N/A	N/A	2.44 (q)	0.94 (t)	2.39 (t)	1.35 (m)	1.35 (m)	0.81 (t)
8[c]	8.06 (s)	8.06 (s)	6.62 (d)	7.00 (t)	6.60 (t)	N/A	N/A	N/A

[a] Measurements obtained using a Bruker AM-400 spectrophotometer (^{1}H: 400.1 MHz). Residual DMSO-d_5H was used as a reference.
[b] 80% DMSO-d_6–20% D_2O (v/v) solvent.

Results

The proton chemical shifts of the observed Meisenheimer complexes, intermediates, and products for the reactions of the three dinitroaniline compounds (**1–3**) with deuteroxide nucleophile and for the reaction of **1** with sulfite ion are given in Table 1. Proton-labelled structures are shown in Chart 1.

Reaction of trifluralin (1) and benefin (2) with OD^-

Upon addition of the OD^- solution to the substrate solutions of **1** and **2** in DMSO-d_6 (final DMSO concentration 80% v/v), there was an immediate disappearance of the peak at 8.39 ppm (**1**) or 8.42 ppm (**2**) and, concurrently, the appearance of downfield peaks at 5.77 and 7.43 ppm (**1a**) and 5.74 and 7.43 ppm (**2a**) characteristic of formation of Meisenheimer adducts through addition of OD^- at C-3. Due to the asymmetry of **1a**, the *N*-propyl resonances appear to be in a pseudo-$ABMNX_3$ spin system, similar to the ABX_3 spin system described by Servis (12) for the C-3 σ-adduct of *N,N*-diethyl-2,4,6-trinitroaniline with MeO^-. The AB and MN methylene groups arise from the asymmetric environment induced by the OD^- group in a preferred conformation as shown in Fig. 1, where AB and MN represent the two protons on the N-bound methylene group and the two protons on the C-bound methylene group, respectively. The methylene protons of **1a**, H_a and H_d, are found at 3.35 (2H) and 2.64 (2H) ppm; H_b and H_e at 1.55 (2H) and 1.36 (2H) ppm; and the methyl protons, H_c and H_f, at 0.76 (6H) ppm (Fig. 2).

Homonuclear decoupling (13) experiments, leading to more specific assignments of the individual peaks, were performed. The decoupling results indicated that each of the four methylene protons on the individual propyl groups have significant chemical shift differences from one another, but have chemical shifts similar to the corresponding proton on the other propyl group. Therefore, one can assign the four multiplets to the following four pairs of protons: $H_{1,4}$, $H_{2,3}$, $H_{5,8}$, and $H_{6,7}$ (using the numbering scheme portrayed in Fig. 1). Specific assignments identifying the separate N-bound methylene proton multiplets or the C-bound methylene proton multiplets cannot be made at this time.

The initial formation of the C-3 Meisenheimer adduct (**1a**, **2a**) is followed by the appearance of aryloxide, **4**, and the amines, **6** and **7** (**6** from **1**; **7** from **2**). In time, **4** becomes hydrolyzed to **5** in the basic medium. Adducts **1c** and **2c** become observable as the concentration of **6** and **7** increases in their respective systems. However, as the reaction proceeds and the available substrate concentration decreases, the peaks assigned to **1c** and **2c** also decrease. The C-1 adducts (**1b** and **2b**) were not detected.

Reaction of both **1** and **2** with OD^- was accompanied by a notable decrease in the aromatic proton signals of **1** and **1a** (**2** and **2a**) as a result of H–D exchange, which was confirmed through product isolation and MS analysis.

Reaction of trifluralin (1) with SO_3^{2-}

Addition of the nucleophile (Na_2SO_3–D_2O) to **1** in DMSO-d_6 (final DMSO concentration 80% v/v) resulted in the immediate reduction of the peak at 8.39 ppm (**1**). This was accompanied by formation of the C-3 adduct (**1d**) with characteristic ring proton resonances at 5.50 and 7.28 ppm; however, no C-1 adduct or S_NAr displacement products were detected. With time, new peaks assignable to the *cis* and *trans* diadducts of **1e**

© 1998 NRC Canada

Chart 1.

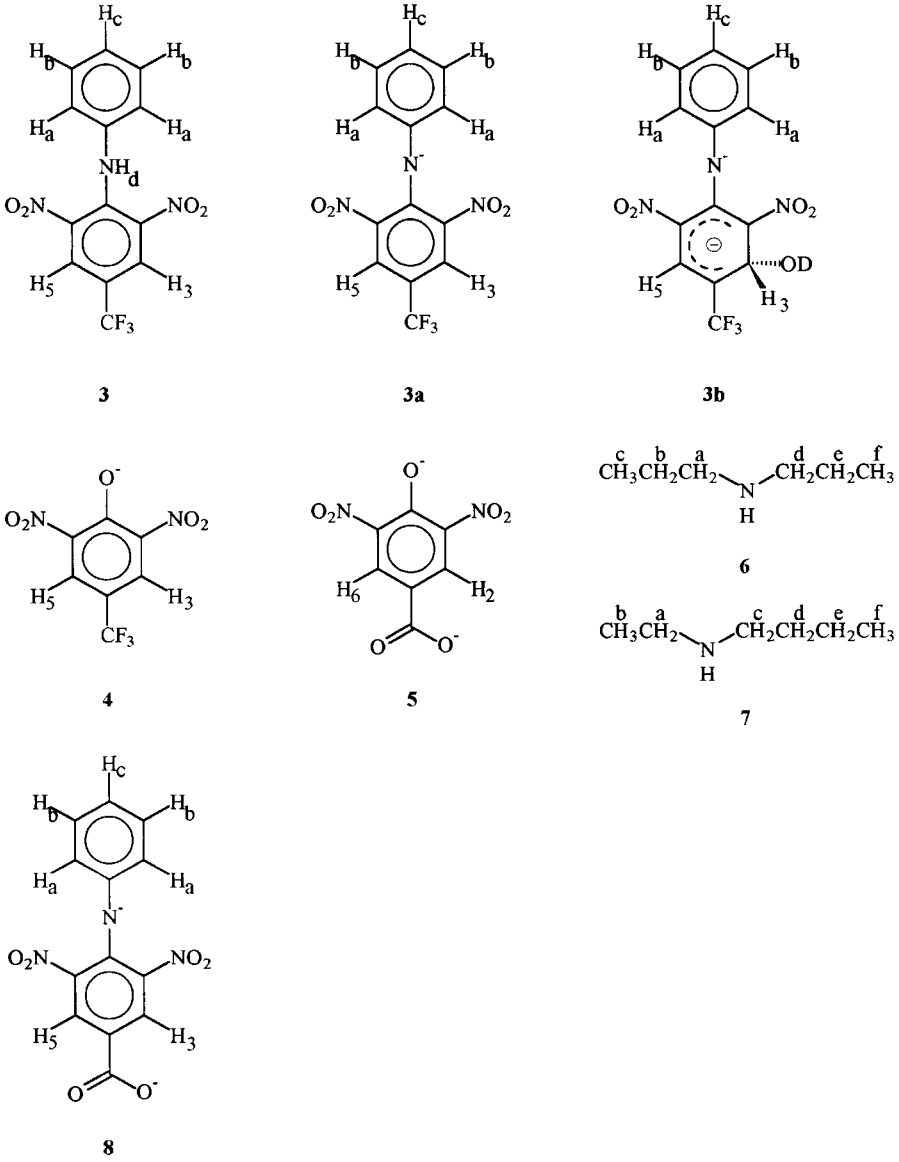

were observed at 5.01, 7.15, and 7.68 ppm. No aromatic proton exchange was observed for this system.

Reaction of *N*-phenyl-2,6-dinitro-4-(trifluoromethyl)-aniline (3) with OD^-

Upon the addition of the base (KOH–D_2O) to the solution of **3** in DMSO-d_6 (final DMSO concentration 85% v/v), there was an immediate distinct colour change from orange to deep purple. Concurrently the peak at 8.53 ppm (**3**) disappeared and was replaced by a singlet at 7.74 ppm assigned to the anion, **3a**. This deprotonation was followed by the appearance of a singlet at 8.06 ppm assignable to **8**, a hydrolysis product of **3a**. At low base:substrate ratios (ca. < 4:1 molar ratio) no σ-adduct formation was observed. Only with a large excess of base, specifically, 10:1 molar equivalents of OD^-:**3**, formation of the C-3 adduct (**3b**) was detected by the appearance of small peaks at 5.56 and 6.91 ppm. No aromatic proton exchange was observed for this system.

Discussion

Regioselectivity and stereoelectronic factors in reaction of trifluralin (1) and benefin (2) with OD^-

The reaction pathways for the reactions of trifluralin (**1**) and benefin (**2**) with OD^- are shown in Scheme 1. The reactions of both **1** and **2** with OD^- appear to follow a K3T1 sequence, i.e., *kinetic* preference for formation of the C-3 adduct with *thermodynamic* preference for formation of the C-1 adduct. This kind of behaviour has been observed with a number of oxygen nucleophiles (14). General qualitative free energy diagrams for common reaction sequences, including the K3T1 sequence, are shown in Fig. 3.

Although the products of nucleophilic aromatic substitution (S_NAr) at C-1 are predicted to be the final thermodynamic products, the C-1 adduct was not spectroscopically observed in the present system. Thus our assumption, that the C-1 adduct is thermodynamically more stable than the C-3 adduct and that

© 1998 NRC Canada

Fig. 1. The preferred conformation of **1a** showing the asymmetric environments yielding AB and MN methylene protons. (*A*) View with the aromatic ring in the *x*–*y* plane. The second propyl group is not shown in this view. This perspective shows how H_1, H_2, H_5, and H_6 on the same propyl group are all in chemically different environments due to their relative positions to the OD substituent. (*B*) View with the aromatic ring in the *y*–*z* plane showing the two propyl groups in different environments induced by the OD substituent. (*C*) View with down the amine-N—aromatic-C bond with the aromatic ring in the *x*–*z* plane. This perspective shows the eight methylene protons in chemically different environments arising from their relative position to the OD substituent.

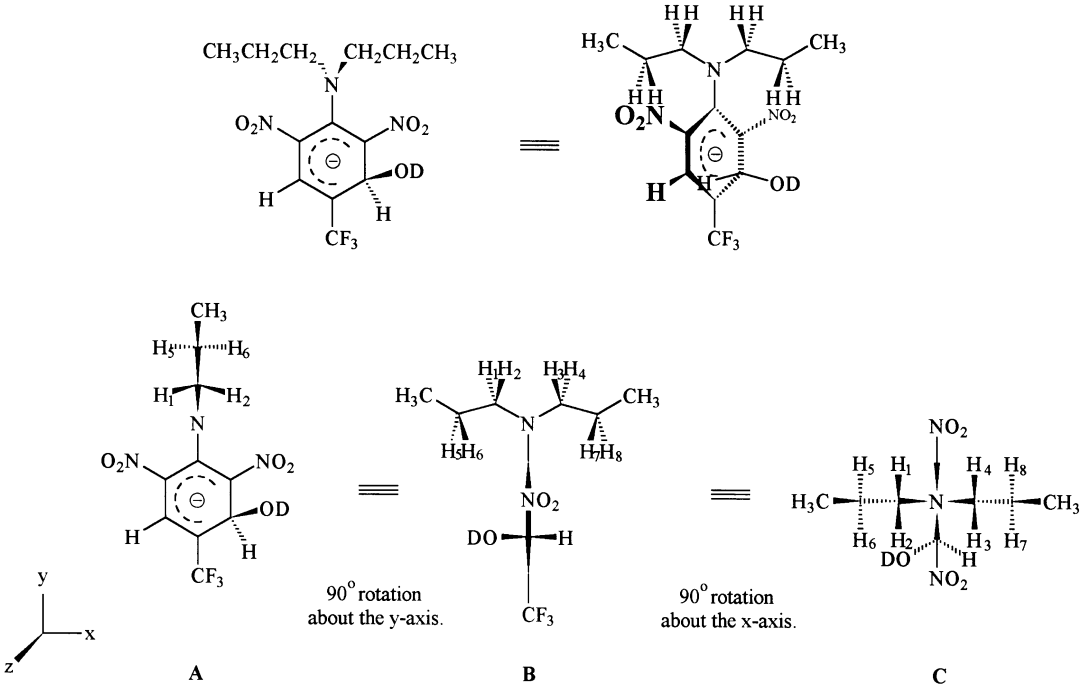

Fig. 2. 400 MHz ^{1}H NMR spectrum of **1a** in 80% DMSO-d_6 – 20% D_2O solution. Only the upfield aliphatic region is shown.

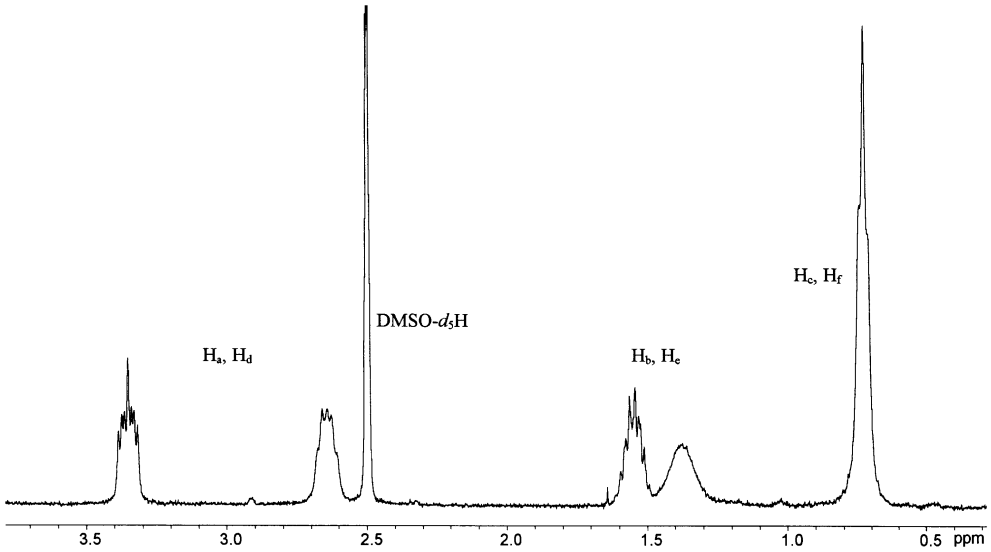

once formed the C-1 adduct rapidly decomposes with loss of a secondary amine (**6** from **1**, **7** from **2**) to yield the phenoxide **4**, is supported by past findings that C-1 OH^- adducts have not been observed in any system where the C-1 position is also substituted by an acceptable leaving group (15).

Since there is no direct observation of the C-1 adduct in the present system, one needs to consider the possibility that the C-3 adduct is actually more stable than the C-1 adduct. It has been documented in 1,3,5-trinitrobenzene (TNB) and other polynitroaromatics (16, 17), that the nitro group *para* to the site of attack plays an important role in stabilizing adduct formation through resonance. Since the adducts derived from **1** and **2** have a CF_3 group rather than NO_2 in the *para*-position, this kind of stabilization is reduced. However, there remains the possibility of stereoelectronic stabilization of the C-1 adduct (14, 18, 19) with lone pair electron density donated from

© 1998 NRC Canada

Scheme 1.

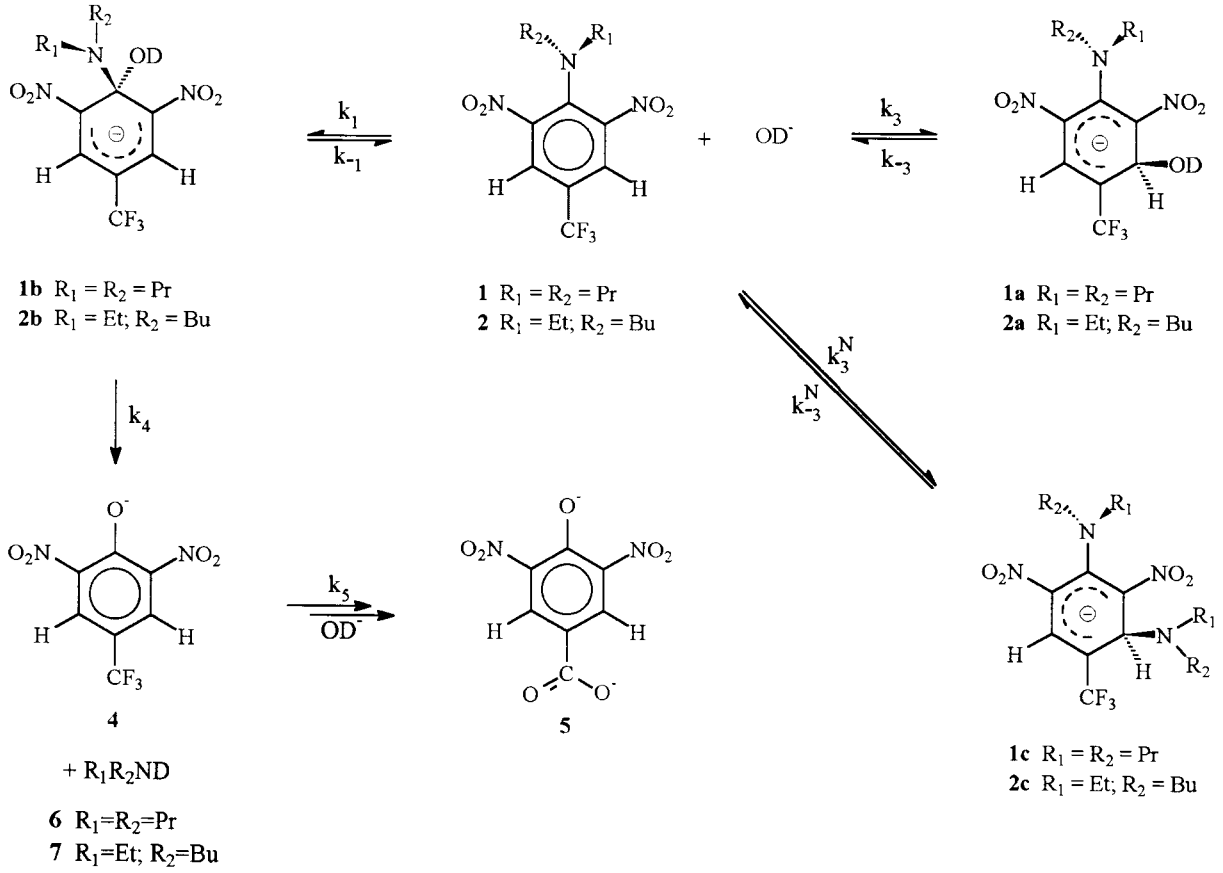

Fig. 3. Qualitative comparative energy – reaction coordinate profiles for the four general patterns of regioselectivity. Barrier heights and relative stabilities are exaggerated for clarity. K3T1 describes those systems in which formation of the C-3 adduct is the product of kinetic control, while the the C-1 adduct is the thermodynamic product. In the K1T1 profile the C-1 adduct is favoured by both kinetics and thermodynamics. Conversely, K3T3 represents the situation where the C-3 adduct is doubly preferred: by kinetics and thermodynamics. The K1T3 profile describes the inverse behaviour of that indicated by K3T1; now, the C-1 adduct is favoured kinetically, but the C-3 adduct is the most stable product (14).

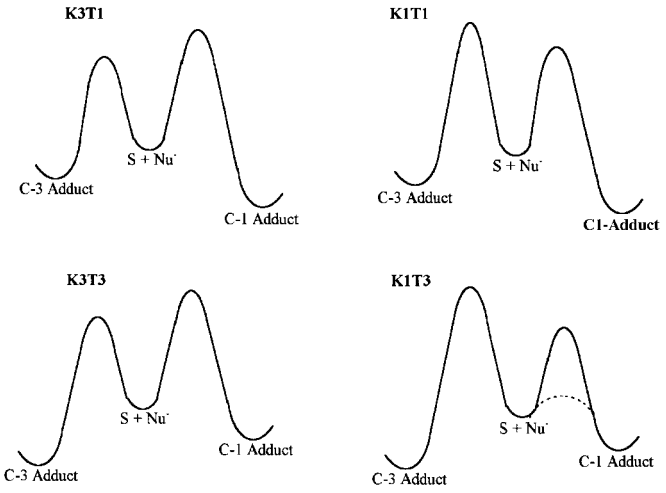

the oxygen of the OD moiety into the antibonding orbital of the C-1—NR_2 bond, and vice versa. Such $n \rightarrow \sigma^*$ interactions (20, 21) have previously been shown to be important in stabilizing structurally similar C-1 adducts (14, 18, 19, 22). The calculated (geometry optimized, PM3) structure supports the supposition of $n \rightarrow \sigma^*$ stabilization for the C-1 adduct **1b** (vide infra).

A further complexity in the reactions of **1** and **2** with OD^- results from the displacement of secondary amines (**6** from **1**; **7** from **2**); once liberated, these amines can act as nucleophiles and compete with OD^- for reaction with the substrates. From separate experiments in which **1** was reacted with **6** in the presence of OD^-, it was noted that **6** formed the C-3 adduct, **1c**, but no adduct resulting from attack at C-1 was seen, in accord with a K3T3 sequence. However, an important note of caution has been raised (14), namely, that if the rate constants are of vastly different magnitudes and the kinetic conditions $k_1 > k_3$ but $k_{-1} > > k_{-3}$ both apply (shown by the dotted lines in Fig. 3, K1T3 profile), then it may not be possible to observe the C-1 adduct owing to the time scale of the reaction. In the present system, it is unlikely that the C-1 adduct would be kinetically favoured because of the greater steric interactions associated with attack at the C-1 position (F-strain) (11, 18, 23–25).

Geometry optimization calculations on **1**, **1a,** and **1b** yield conformations that concur with the aforementioned hypotheses. The geometry-optimized structure of **1** (Fig. 4) has both nitro groups aligned perpendicular to the plane of the ring

© 1998 NRC Canada

Fig. 4. Geometry-optimized structure using SPARTAN for trifluralin (**1**) showing the alignment of the *N,N*-di-*n*-propyl groups such that the amine nitrogen lone electron pair is parallel with the plane of the ring and cannot interact with the ring π-system. The ChemWindow3 structure is shown in the centre.

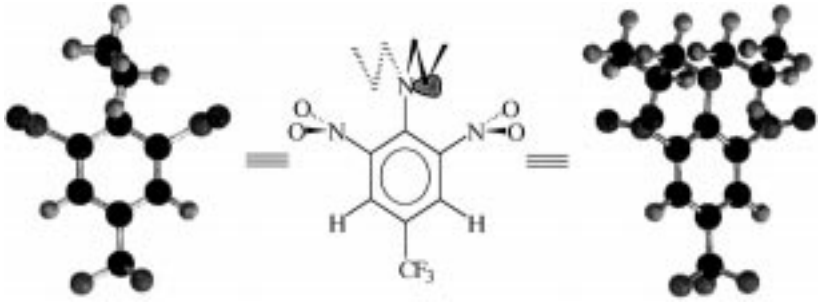

Fig. 5. Geometry-optimized structure using SPARTAN for *N,N*-dimethylpicramide (DMP) showing the alignment of the *N,N*-dimethyl groups such that the amine nitrogen lone electron pair is perpendicular to the plane of the ring and has maximum interaction with the ring π-system. The ChemWindow3 structure is shown in the centre.

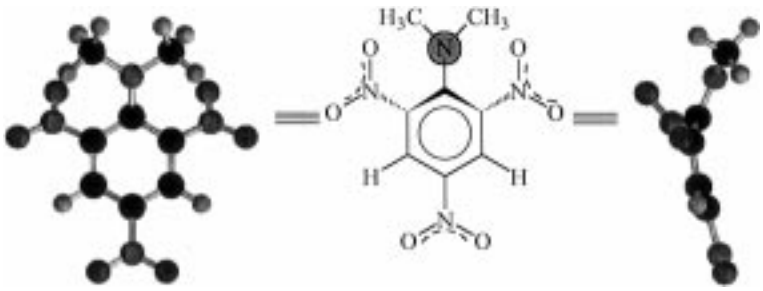

Fig. 6. Geometry-optimized structure using SPARTAN for **1a** showing the alignment of the nitro group *para* to the site of nucleophilic attack such that its π-system can interact with the π-system of the ring, allowing for greater charge stabilization of the anionic Meisenheimer adduct. The ChemWindow3 structure is shown in the centre.

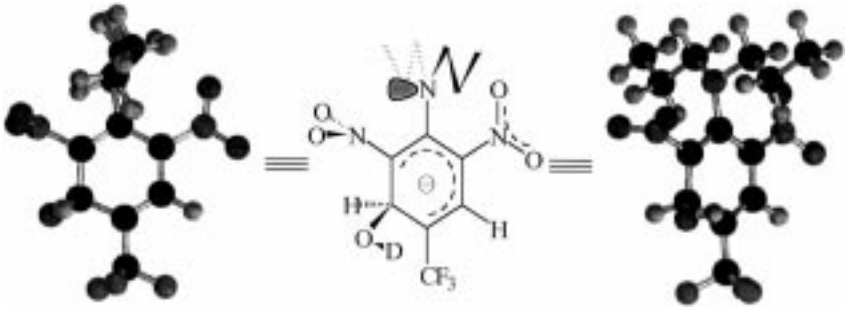

along with the two *N*-*n*-propyl groups. The orientation of the nitro groups perpendicular to the plane of the ring probably results from steric interactions with the two *N*-*n*-propyl groups. This may be expected since the optimized geometry for *N,N*-dimethylpicramide (DMP; Fig. 5) suggests significant ring strain (indicated by the displacement of C-1 from the plane of the ring) due to interaction between the *N*-methyl and the nitro groups.

The importance of the nitro group *para* to the sp^3 hybridized carbon (C-3) in **1a** can be seen in the geometry-optimized structure shown in Fig. 6; the *para*-NO_2 has become aligned with the ring for maximum π–π interaction while the *ortho*-NO_2 remains perpendicular to the plane of the ring. This conformation allows for greater delocalization of negative charge onto the *para*-NO_2 group, and such stabilization is unavailable to the C-1 adduct of **1**. However, the geometry-optimized structure for **1b** (Fig. 7) shows the -OH substituent aligned such that one of the oxygen lone pairs is approximately antiperiplanar to the C-1—NR_2 bond. This orientation is optimal for $n \rightarrow \sigma^*$ interactions where electron density is donated from the oxygen lone electron pair into the antibonding orbital of the C-1—NR_2 bond.

The $n \rightarrow \sigma^*$ stabilization indicated above provides support for the assumption that the C-1 adduct is more thermodynamically stable than the C-3 adduct in the reactions of both **1** and **2** with OD^-. This stereoelectronic stabilization does not appear to occur from the amine-N lone pair to the C-1—OH bond since the amine-N lone electron pair is not in an antiperiplanar alignment to the C-1—OH bond.

Aryl H–D exchange in trifluralin (1) and benefin (2)

It was noted in the Results that in the reaction of **1** and **2** with OD^- there is a significant decrease in the intensity of the resonances due to H_3 and H_5 on **1** and **1a**, as well as on **2** and **2a**,

© 1998 NRC Canada

Fig. 7. Geometry-optimized structure using SPARTAN for **1b** showing the alignment of the deuteroxide oxygen such that one of its lone electron pairs is aligned antiperiplanar to the ring-C—NR_2 bond allowing for $n \rightarrow \sigma^*$ stabilization. The antiperiplanar lone electron pair is shaded. The ChemWindow3 structure is shown on the right.

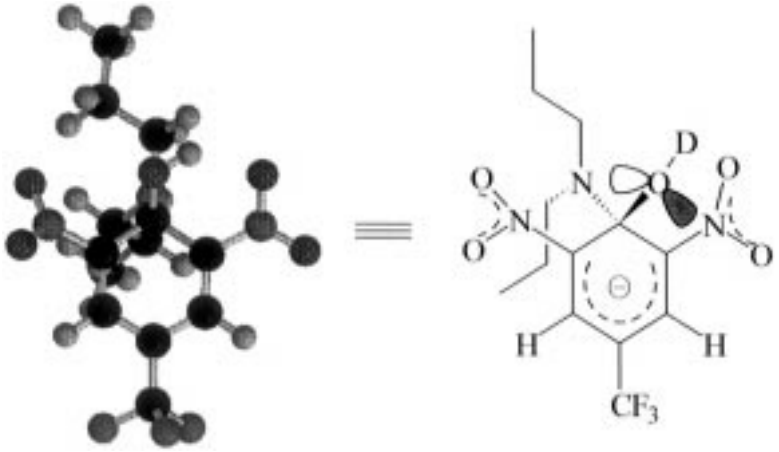

Scheme 2.

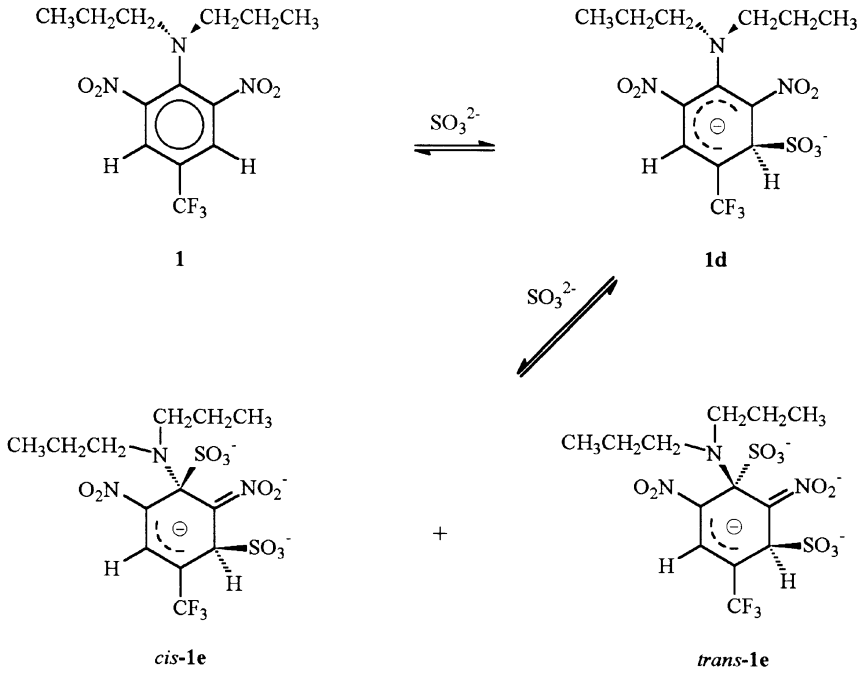

relative to their aliphatic signals, arising from aryl ring hydrogen–deuterium exchange. Exchange of polynitroaromatic ring hydrogen by deuterium is well known to compete with σ-complex formation (26–31). It has been documented that σ-complexes do not themselves undergo exchange (24, 26, 32), and neither do polynitroaryloxides (26, 33). Thus H–D exchange occurs in the uncomplexed trifluralin and benefin molecules.

Although exchange of aryl hydrogen is well documented, its observation in this system is unexpected for a number of reasons. First, aryl ring H–D exchange generally occurs preferentially at a position *ortho* to **two** nitro groups (26–31, 34), whereas with **1** and **2** the aryl hydrogens are *ortho* to one nitro group and a trifluoromethyl group. Equally important is the slower rate of aryl H–D exchange in *N,N*-dimethylpicramide (DMP) under identical conditions. Preliminary observations indicate that 100% H–D exchange of trifluralin aryl protons has occurred within 24 h whereas with DMP under the same conditions only ca. 50% H–D exchange was observed over a 48 h period. It is suggested that this reduced rate of exchange has as origin the electron-donating properties of the C-1 N substituent. The ability of the lone pair of electrons on the amine-nitrogen in DMP to donate electron density by aligning with the π-orbital system of the ring (π–π overlap) (21) will lead to an increase in the electron density of the ring carbons. In trifluralin and benefin, however, the increased steric interactions associated with the larger *N*-alkyl groups prevent the alignment of the amine-N lone electron pair for effective π–π overlap and, therefore, aryl proton abstraction leading to H–D exchange is facilitated.

Geometry optimization calculations (semi-empirical; AM1) support this hypothesis. The optimized configuration for **1** and **1a** with the *N*-propyl groups aligned perpendicular

© 1998 NRC Canada

Scheme 3.

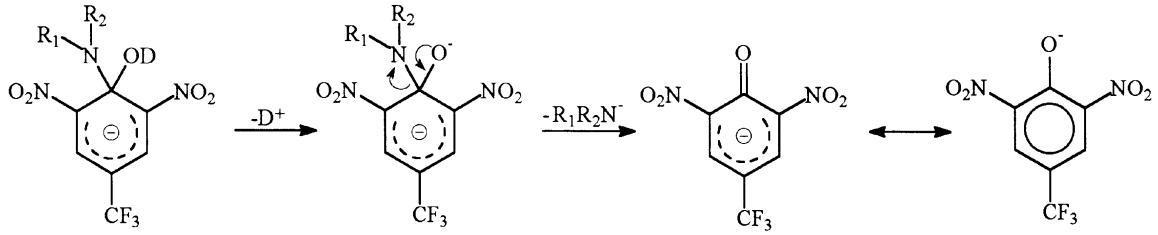

to the plane of the ring are displayed in Figs. 4 and 6, respectively. The same geometry optimization calculation performed for DMP (Fig. 5) yielded an optimized configuration with the *N*-methyl groups aligned with the plane of the ring, allowing for maximum interaction of the amine-N lone pair of electrons with the ring π-electron system. A comparison of partial atomic charges (semi-empirical; AM1; Mulliken population analysis) shows that the amine nitrogen of DMP is more positively charged than the amine nitrogen of **1**. This supports our arguement that there is significant overlap between the C-1 nitrogen lone pair of DMP with the ring π-system that is hindered in the sterically constrained molecules of trifluralin (**1**) and benefin (**2**).

Regioselectivity in reaction of trifluralin (1) with SO_3^{2-}

As shown in Scheme 2, reaction of SO_3^{2-} with **1** initially results in formation of the C-3 adduct. By analogy with the SO_3^{2-} adducts of picramides (5, 6, 9, 35–37), bonding to sulfite nucleophile is presumed to occur through the *S*-center. The C-1 adduct is not observed in the present system, presumably due to steric hindrance (F-strain) arising from the bulky *N,N*-di-*n*-propylamine substituent at the C-1 position. Nevertheless, further attack on **1d** by SO_3^{2-} occurs at the C-1 position, forming the *cis* and *trans* isomers of diadduct **1e**. Formation of the diadduct, **1e**, is thought to be stabilized by $n \rightarrow \sigma^*$ stabilization from the NR_2 lone electron pairs and the forming C-1—SO_3^{2-} bond. Due to the alignment of the NR_2 group in **1**, this stereoelectronic interaction is not present to help stabilize the formation of the C-1 monoadduct with SO_3^{2-}. Interestingly, a diadduct of **1** with the two -SO_3^{2-} groups at the C-3 and C-5 positions was not observed, even though such diadducts are seen with related picramides (35–37). This is probably due to the presence of the C-4 -CF_3 group in **1**, whereas in picramides with a -NO_2 substituent at C-4 negative charge can be delocalized onto the -NO_2 group. Since no C-1 monoadduct is observed in this system, we conclude that this reaction follows a K3T3 sequence.

The fact that there is no overall nucleophilic displacement of the dialkylamino group by sulfite, in contrast to the hydroxide reaction, is worthy of comment. One factor is the ease of formation and the stability of adduct **1d**, attack at the 3-position of **1** being favored over the 1-position for steric reasons as discussed above. Moreover, there is clearly no expulsion of the dialkylamino group from the *cis* and *trans* diadducts **1e**, i.e., in Scheme 2, **1e** may eject SO_3^{2-} but not R_2N^-. The much greater nucleofugality of sulfite relative to the dialkylamino group is readily evident on the basis of pK_a values but, as shown in Scheme 1, expulsion of the dialkylamino group does occur from **1b** and **2b** despite an unfavorable pK_a situation (though clearly not as unfavorable as in the sulfite case). However, another pathway is available for expulsion of R_2N^- in the case of **1b** and **2b**, namely, a prior ionization of the deuteroxide adduct followed by expulsion of R_2N^-, as shown in Scheme 3.

Proton abstraction versus σ-complex formation in the reaction of *N*-phenyl-2,6-dinitro-4-(trifluoromethyl)aniline (3) with OD^-

Since *N*-phenyl-2,6-dinitro-4-(trifluoromethyl)aniline (**3**) has only one substituent on the C-1 nitrogen, the interaction with base can, in principle, lead to N-deprotonation as well as σ-complex formation. Such behaviour has been reported for the reaction of *N*-methylpicramide (NMP) with MeO^- in DMSO–MeOH solutions, which was reported to undergo initial N-deprotonation upon the addition of 1 molar equivalent of MeO^-, with further reaction to the C-3 adduct upon addition of excess base (38). In fact this behaviour has also been found in the present study.

Scheme 4 shows the reaction pathway for the reaction of **3** with OD^-. It was found that, initially, reaction results in N-deprotonation to form the anion, **3a.** This is followed by the further reaction of **3a** with OD^- to form the C-3 adduct, **3b**, but only when a large excess of base is present. Of notable significance is the fact that with the NMP–MeO^- system, σ-complexation was reported for solutions containing 1.1 molar equivalents of MeO^- to NMP (38). However, in the present system σ-complexation required ca. 10 molar equivalents of OD^-. The origin of this contrasting behaviour is not clear at present, although a possible explanation is the decreased electron deficiency of **3** relative to the NMP system.

As in the reaction of **1** with SO_3^{2-}, there was no observation of a C-1 monoadduct, in accord with a K3T3 sequence. The final thermodynamic product of this reaction is the hydrolysis product of **3a**, 3,5-dinitro-4-(*N*-phenylamino)benzoic acid, **8**.

Experimental

N,N-Di-*n*-propyl-2,6-dinitro-4-(trifluoromethyl)aniline (trifluralin; **1**) was available from Chem Service, Inc. with a reported purity of 99.0% and was used without further purification. *N*-Ethyl-*N*-*n*-butyl-2,6-dinitro-4-(trifluoromethyl)-aniline (benefin; **2**) was prepared via a variation of method II reported by Marshall et al. (39) by adding ca. 4 molar equivalents of *N*-ethyl-*n*-butylamine to a solution of 2,6-dinitro-4-(trifluoromethyl)chlorobenzene in diethyl ether and acidifying the resulting solution with HCl (ca. 1 M). After removal of the colourless aqueous layer, the clear orange-yellow diethyl ether solution was washed with H_2O and dried over $MgSO_4$ followed by evaporation of the ether under reduced pressure. The resulting solid was further purified using flash chromatography

© 1998 NRC Canada

Scheme 4.

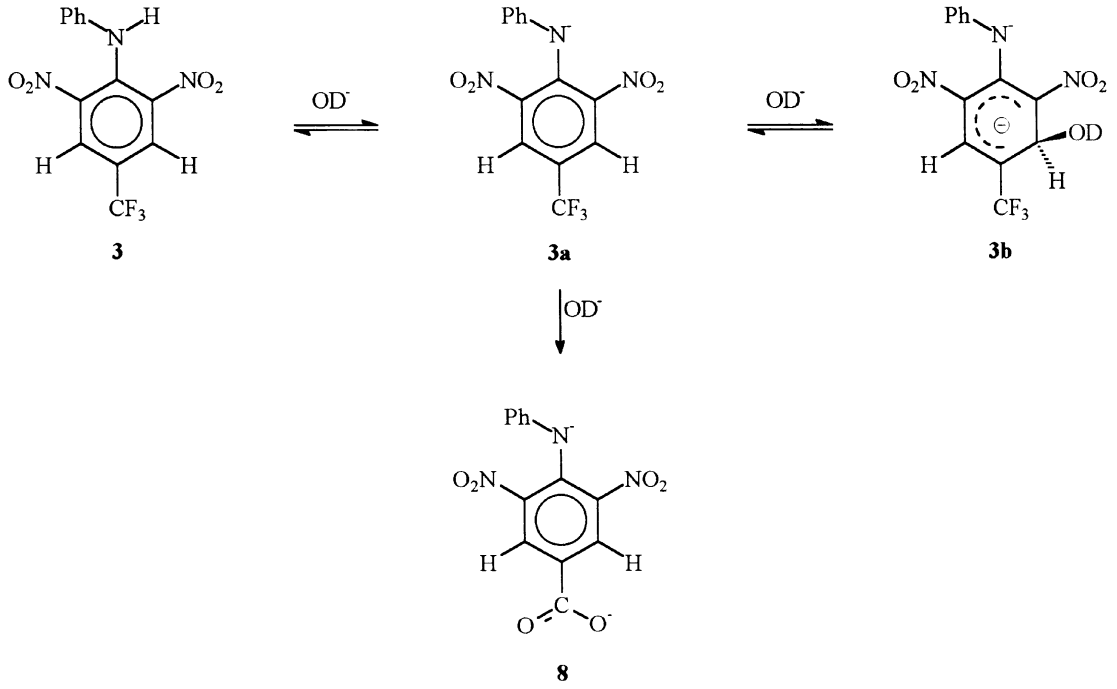

($CHCl_3$ eluent), yielding bright yellow crystals, mp 66–67°C (lit. (40) mp 67–68°C). *N*-Phenyl-2,6-dinitro-4-(trifluoromethyl)aniline (**3**) was prepared using the same procedure as described for **2** with the addition of aniline in place of *N*-ethyl-*n*-butylamine, yielding bright yellow crystals, mp 123°C (lit. (41) mp 119–121°C).

N,N-Di-*n*-propyl-2,6-dinitro-4-(trifluoromethyl)aniline-d_2 (trifluralin-d_2) was isolated by adding ca. 2 molar equivalents of NaOD (D_2O) to a solution of **1** in DMSO-d_6. The solution was let stand for ca. 24 h at which time ca. 3 molar equivalents of trifluoroacetic acid were added to quench the reaction. The reaction mixture was then added to H_2O and orange crystals were collected via vacuum filtration and dried under reduced pressure (< 0.1 Torr; 1 Torr = 133.3 Pa); mp = 48–49°C. ^{1}H NMR (DMSO-d_6) δ: 2.93 (4H, t, J_{H-H} = 7.3, $H_{c,c'}$), 1.50 (4H, tq, J_{H-H} = 7.3, $H_{b,b'}$), 0.80 (6H, t, J_{H-H} = 7.3, $H_{a,a'}$). ^{13}C NMR (DMSO-d_6) δ: 145.5 (1C, C_1), 140.3 (2C, $C_{2,6}$), 126.9 (2C, t, J_{C-D} = 23, $C_{3,5}$), 122.4 (1C, q, J_{C-F} = 270, C_7), 121.0 (1C, q, J_{C-F} = 36, C_4), 53.2 (2C, $C_{8,11}$), 20.4 (2C, $C_{9,12}$);,10.8 (6C, $C_{10,13}$). EI-MS: M = 337 m/z (calcd. for $C_{13}H_{14}D_2F_3N_3O_4$: 337.0 g/mol).

Sodium deuteroxide solutions were prepared by adding freshly cut sodium metal to D_2O (99.9% D) under a stream of N_2. Potassium deuteroxide solutions were prepared from a weighed amount of potassium hydroxide (AnalaR by BDH, Inc.), which was added to D_2O under N_2. The alkaline solutions were standardized against 0.108 M potassium hydrogen phthalate (KHP). Sodium sulfite solutions were prepared by dissolving a calculated amount of Na_2SO_3 (Aldrich Chemical Company, Inc.) in D_2O under N_2.

Stock solutions of substrate were prepared in DMSO-d_6 while stock solutions of nucleophile were prepared in D_2O. Solutions used in the reaction studies were prepared in clean dry NMR tubes by adding appropriate volumes of the stock solutions to a known volume of DMSO-d_6–D_2O such that the final concentration of DMSO-d_6 was 80% v/v. The reactions were then monitored at various intervals by ^{1}H NMR until completion. Nuclear magnetic resonance (NMR) measurements were obtained using a Bruker AM-400 spectrophotometer (^{1}H: 400.1 MHz) with DMSO-d_5H acting as reference (^{1}H: 2.50 ppm).

Acknowledgement

Financial support of this research by the Natural Sciences and Engineering Research Council of Canada and valuable discussions with Professor Julian Dust are gratefully acknowledged. Some preliminary experiments by Louisa Wong are also acknowledged with thanks.

References

1. D. Hartley and H. Kidd (*Editors*). The agrochemicals handbook. Royal Society of Chemistry, Nottingham, England. 1983.
2. F.M. Ashton and A.I. Crafts. Mode of action of herbicides. Wiley–Interscience, New York. 1973.
3. S.J. Parke and Q.F. Soper. Weed Sci. **25**, 79 (1977).
4. R.C. Hall and C.S. Giam. J. Agric. Food. Chem. **22**, 461 (1974).
5. M.J. Strauss. Chem. Rev. **70**, 667 (1970).
6. E. Buncel, M.R. Crampton, M.J. Strauss, and F. Terrier. Electron deficient aromatic– and heteroaromatic–base interactions: The chemistry of anionic σ-complexes. Elsevier Science Publishing Company, Inc., New York. 1984.
7. F. Terrier. Nucleophilic aromatic displacement: the influence of the nitro group. Organic Nitro Chemistry Series, VCH Publishers Inc., New York. 1991.
8. E. Buncel. The chemistry of functional groups. Supplement F: The chemistry of amino, nitro and nitroso compounds. Wiley, London. 1982.
9. F. Terrier. Chem. Rev. **82**, 77 (1982).
10. E. Buncel, J.M. Dust, and R.A. Manderville. J. Am. Chem. Soc. **118**, 2072 (1996).

© 1998 NRC Canada

11. E. Buncel, R.A. Manderville and J.M. Dust. J. Chem. Soc. Perkin Trans. 2, 1019 (1997).
12. (*a*) K.L. Servis. J. Am. Chem. Soc. **87**, 5495 (1965); (*b*) J. Am. Chem. Soc. **89**, 1508 (1967).
13. J.K.M. Sanders and B.K. Hunter. Modern NMR spectroscopy. Oxford University Press, London. 1987. pp. 56–62.
14. E. Buncel, J.M. Dust, and F. Terrier. Chem. Rev. **95**, 2261 (1995).
15. C.F. Bernasconi, J. Fassberg, R.B. Killion, D.F.Schuck, and Z. Rappaport. J. Am. Chem. Soc. **113**, 4937 (1991).
16. R.A. Manderville. Ph.D Thesis. Queen's University, Kingston, Ont. 1992. p. 46.
17. R.A. Manderville, J.M. Dust, and E. Buncel. J. Phys. Org. Chem. **9**, 515 (1996).
18. E. Buncel, J.M. Dust, A. Jo czyk, R.A. Manderville, and I. Onyido. J. Am. Chem. Soc. **114**, 5610 (1992).
19. E. Buncel, R.M. Tarkka, and J.M. Dust. Can. J. Chem. **72**, 1709 (1994).
20. (*a*) A.J. Kirby. The anomeric effect and related stereoelectronic effects at oxygen. Springer Verlag, Berlin. 1983; (*b*) Stereoelectronic effects. Oxford University Press Inc., New York. 1996.
21. W. Szarek and D. Horton. Anomeric effect. Origin and consequences. ACS Symp. Ser. **87**. American Chemical Society, Washington, D.C. 1979.
22. R.A. Manderville and E. Buncel. J. Am. Chem. Soc. **115**, 8985 (1993).
23. M.R. Crampton and V. Gold. J. Chem Soc. 4293 (1964).
24. M.R. Crampton and V. Gold. J. Chem Soc. B: 893 (1966).
25. A. Cooney and M.R. Crampton. J. Chem. Soc. Perkin Trans. 2, 1973 (1984).
26. J.M. Dust and M.D. Secord. J. Phys. Org. Chem. **8**, 810 (1995).
27. R. Foster and R.K. Mackie. Tetrahedron, **19**, 691 (1963).
28. E. Buncel and W.A. Zabel. J. Am. Chem. Soc. **89**, 3082 (1967).
29. E. Buncel, J.A. Elvidge, J.R. Jones, and K.T. Walkin. J. Chem. Res. 272 (1980).
30. E. Buncel and E.A. Symons. Can. J. Chem. **44**, 771 (1966).
31. E. Buncel and E.A. Symons. J. Chem. Soc. Chem. Commun. 771 (1967).
32. E. Buncel and E.A. Symons. J. Org. Chem. **38**, 1201 (1978).
33. R. Bacaloglu, C.A. Bunton, G. Cerichelli, and F. Ortega. J. Am. Chem. Soc. **110**, 3495 (1988).
34. R. Bacaloglu, A. Blasko, C. Bunton, E. Dorwin, F. Ortega, and C. Zucco. J. Am. Chem. Soc. **113**, 238 (1991).
35. N. Marendic and A.R. Norris. Can. J. Chem. **51**, 3927 (1973).
36. M.R. Crampton. J. Chem. Soc. B: 1208 (1968).
37. E. Buncel, A.R. Norris, K.E. Russell, and P.J. Sheridan. Can. J. Chem. **52**, 25 (1974).
38. (*a*) E. Buncel, M. Hamaguchi, and A.R. Norris. Can. J. Chem. **58**, 1615 (1980); (*b*) Can. J. Chem. **58**, 1609 (1980).
39. F.J. Marshall, R.E. McMahon, and R.G. Jones. J. Agric. Food. Chem. **14**, 498 (1966).
40. R.C. Hall and C-S. Giam. J. Agric. Food. Chem. **20**, 546, (1972).
41. B.F. Malichenko, E.M. Levchenko, and L.M. Yagupol'skii. Ukr. Khim. Zh. (Ukr. Ed.) **33**, 717, (1967).

© 1998 NRC Canada

Phenanthroimidazole dimers: structure and free radical reactivity; piezochromism, thermochromism, and photochromism

Yuehui Zhou, W.E. Baker, P.M. Kazmaier, and E. Buncel

Abstract: A series of 2-phenyl phenanthroimidazole dimers was synthesized by means of a two-phase preparative method, which allowed their isolation in pure form. Definitive proof of structure was obtained by means of ^{1}H and ^{13}C NMR spectroscopy; five of the six possible structural isomers of the dimer could thus be eliminated. The dimers exhibited thermochromic and piezochromic behavior, but not photochromic. The colored species were shown to be free radicals formed on dissociation of the dimers; this was confirmed through ESR measurements. The electronic absorption spectra of the radicals were influenced by substituents on the phenyl ring. The UV–VIS measurements allowed the evaluation of the dimer–radical equilibrium constants, which were also found to be dependent on substituents on the phenyl ring.

Key words: phenanthroimidazole dimers, free radical equilibrium, piezochromism, thermochromism, photochromism.

Résumé : Faisant appel à une méthode de synthèse en deux phases qui permet d'isoler les produits à l'état pur, on a synthétisé une série de dimères de la 2-phénylphénanthroimidazole. On a obtenu des preuves irréfutables de structure grâce à la spectroscopie RMN du ^{1}H et du ^{13}C; on a ainsi pu éliminer cinq des six structures isomères possibles du dimère. Les dimères présentent un comportement thermochromique et piézochromique, mais pas photochromique. Il a été démontré que les espèces colorées proviennent de radicaux libres formés lors de la dissociation des dimères; cette conclusion a été confirmée par des mesures RPE. Les spectres d'absorption électronique des radicaux sont influencés par les substituants présents sur les noyaux phényles. Les mesures UV–VIS ont permis d'évaluer les constantes d'équilibre dimère–radical; on a trouvé que celles-ci dépendent des substituants présents sur le noyau phényle.

Mots clés : dimères de la phénanthroimidazole, équilibre de radicaux libres, piézochromie, thermochromie, photochromie.

[Traduit par la rédaction]

Introduction

Nitrogen-containing heterocyclic compounds play an important role in many biological systems (1). It is known that certain dimeric nitrogen-containing heterocyclic compounds such as dimeric NAD (*N*-benzyldihydronicotinamide) are involved in some biological redox processes (2). On the other hand, triphenylimidazole dimers have also attracted attention because of the sensitivity of these compounds to light and heat, as well as to pressure. Hayashi and Maeda (3) observed that, upon oxidation with potassium ferricyanide in ethanolic solution, triphenylimidazole (**1**) gave rise to a violet color; the color then disappeared rapidly. The oxidation product was obtained as a pale violet-colored powder, which turned deep violet in solution under UV irradiation. The authors suggested (3) that the colored species was a free radical, and soon afterwards EPR evidence for the existence of the radical was presented (4).

It is now known that the oxidation product is a piezochromic dimer, which transforms to the photochromic dimer on dissolution in a solvent. In solution the photochromic dimer exists in a photostationary equilibrium with its radical form.

Radical stability in these systems has been investigated by a number of workers with respect to the influence of substituents (5). It was found that an electron-donating group on the phenyl ring will shift the photostationary state to the radical form. Interestingly, on replacing 1,4,5-triphenylimidazole by phenanthro[9,10-*d*]imidazole, so that the conjugation system is extended, the characteristics of the dimer changed dramatically. The electronic absorption of the radical form of the phenanthroimidazole dimers is shifted to longer wavelength (~600 nm) so that the solution appears blue or green, whereas the triphenylimidazole dimer solution is violet. Moreover, the dissociation of the phenanthroimidazole dimers becomes a thermal process and irradiation is no longer necessary. Various papers and patents have described the application of triphenylimidazole dimers in silver-free photographic processes (6); their application as initiators in polymerization has also been investigated (7). However, relatively few papers have elucidated problems inherent in the synthesis and characterization of the phenanthroimidazole dimer system (8). We

Received January 8, 1998.

This paper is dedicated to Professor Erwin Buncel in recognition of his contributions to Canadian chemistry.

Y. Zhou, W.E. Baker, and E. Buncel.[1] Department of Chemistry, Queen's University, Kingston, ON K7L 3N6, Canada.
P.M. Kazmaier. Xerox Research Center of Canada, Mississauga, ON L5K 2L1, Canada.

[1] Author to whom correspondence may be addressed. Telephone: (613) 545-2616. Fax: (613) 545-6669. E-mail: buncele@chem.queensu.ca

© 1998 NRC Canada

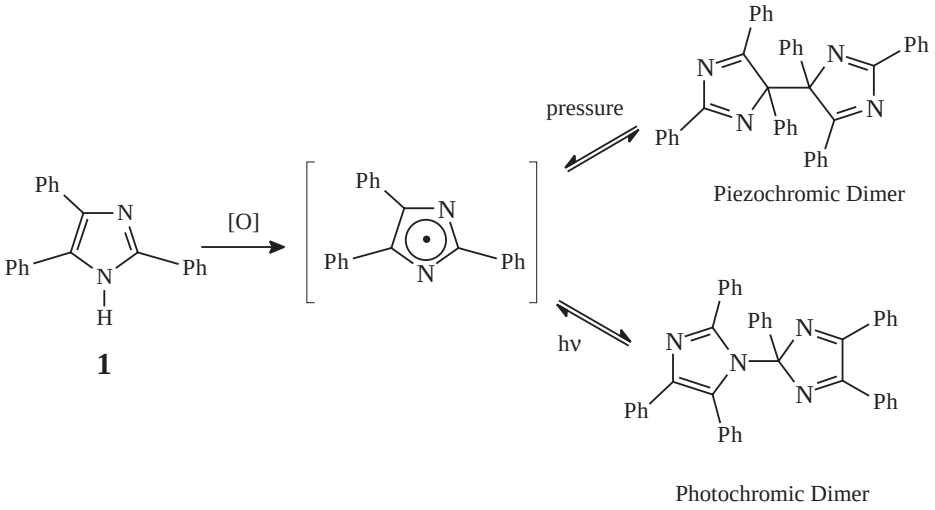

1

Scheme 1.

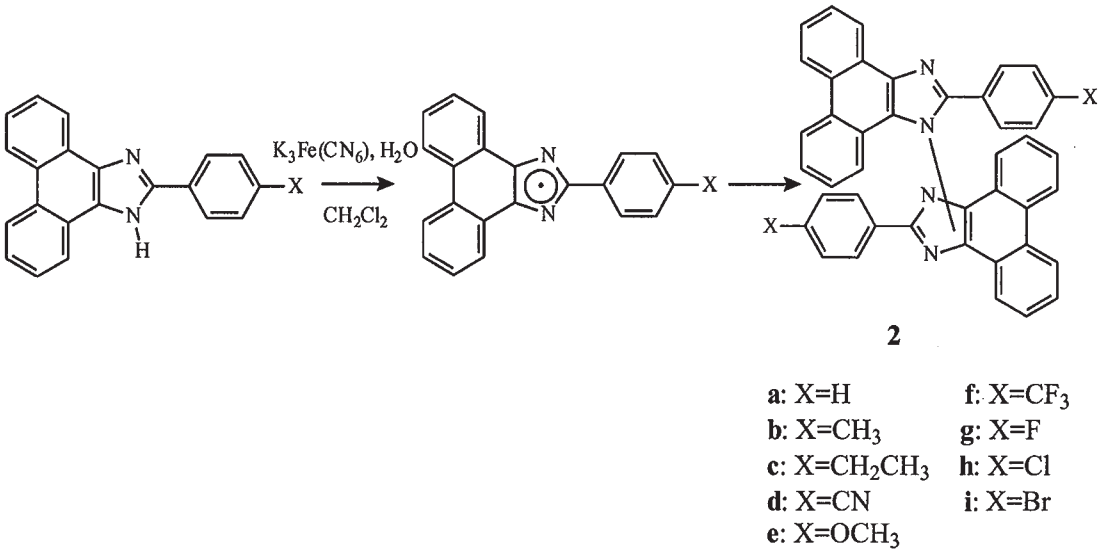

2

a: X=H
b: X=CH_3
c: X=CH_2CH_3
d: X=CN
e: X=OCH_3
f: X=CF_3
g: X=F
h: X=Cl
i: X=Br

report here our results concerning the synthesis and characterization of phenanthroimidazole dimers **2a–i**, using the oxidative synthesis method shown in Scheme 1. Compounds **2c**, **2d**, **2f**, **2g**, and **2i** have not been reported previously. Some comparisons are also made with corresponding dimer systems derived from triphenylimidazole (lophine), **1**. The original purpose of this work was to devise pressure- and sheer-sensitive dye molecules that could be used as sensors in polymer processing (9*a–d*)]; this is an extension of our studies on thermochromic and photochromic dye molecules and other photoactive pigments (9*e–r*).

Results and discussion

Synthesis

The synthesis of phenanthroimidazole dimers by the literature method used in the synthesis of triphenylimidazole dimers (10, 11), i.e., addition of an aqueous solution of potassium ferricyanide to a cold solution of the imidazole in ethanolic potassium hydroxide, proved to be unsuitable in the present work because of precipitation of reactants and isolation of impure products due to decomposition. In our experience, only dimer **2a** could be synthesized in pure form by the method used in the synthesis of triphenylimidazole dimers, probably because of its lower solubility in organic solvents, thus retarding decomposition. Coincidentally, this compound was the only one whose structure was fully elucidated by Sakaino et al. (8*a*).

Oxidation with potassium ferricyanide is of common use in organic synthesis, especially in oxidative coupling of phenols (12) and of amines (13), but, importantly, in both cases two-phase reaction conditions were used: inorganic reactant dissolved in water and the organic reactant in methylene chloride. A two-phase system (water–benzene) was used previously by Cescon et al. (5*a*) in the synthesis of triarylimidazole dimers and has been successfully applied to the synthesis of phenanthroimidazole dimers in the present work. The dimer product could be obtained in crystalline form from the organic phase after most of the solvent was evaporated; these products gave unambiguous NMR spectra. Dimer **2e** is an exception, since this gave the correct molecular peak corresponding to the dimer in the mass spectrum but failed to give a definitive NMR

© 1998 NRC Canada

Fig. 1. ^{13}C NMR spectra of representative phenanthroimidazole dimers **2a**, **2g**, and **2h**.

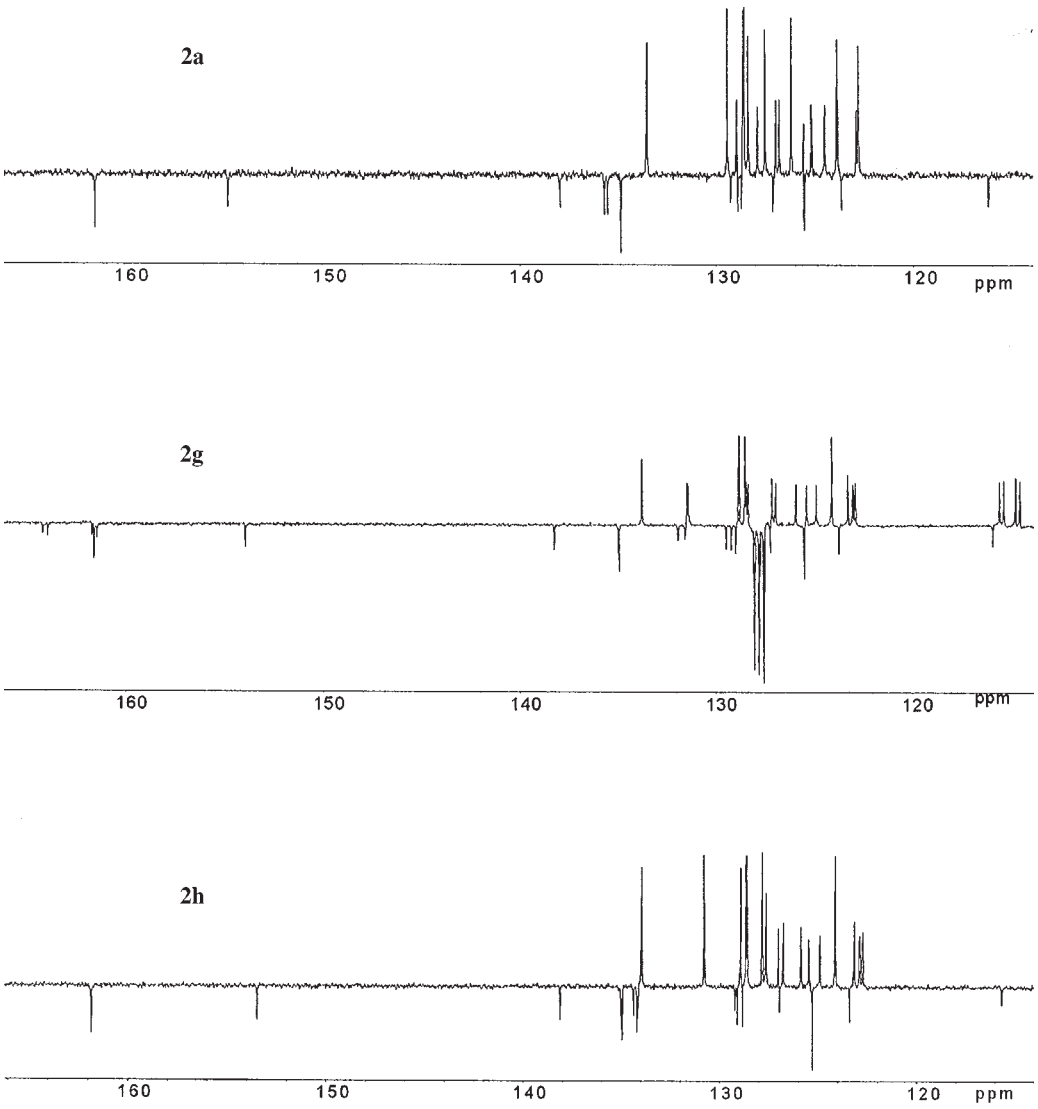

spectrum, probably because of decomposition, as indicated by the color change of the $CDCl_3$ solution. The other dimers were relatively more stable in $CDCl_3$ and allowed definitive characterization by NMR.

Structure elucidation by NMR

Triarylimidazole dimers can, in principle, exist in six structurally different isomeric forms (11). Since our work entailed a modified literature method, the structure suggested by Sakaino et al. (8*a*) for the phenanthroimidazole dimers in their work cannot be taken for granted in the case of dimers **2a–i**. Structure elucidation in the present work was based mainly on the use of NMR spectroscopy. Structures **5** and **6** can readily be excluded because of their symmetry, which would lead to a smaller number of signals of aromatic carbons than actually observed in the ^{13}C NMR spectra. Structures **7** and **8** could also be excluded, for the opposite reason, i.e., lower symmetry, which should give rise to more signals of aromatic carbons than actually observed in the ^{13}C NMR spectra. Only structures **3** and **4** satisfy the requirement of the observed number of ^{13}C NMR signals: 16 for the protonated aromatic carbons and 15 for nonprotonated aromatic carbons in the case of *para*-substituted dimers **2b–d**, **2h**, and **2i**. For the unsubstituted dimer **2a** the number of signals for protonated aromatic carbons is 18 and for nonprotonated aromatic carbons 13. However, due to overlap only 17 distinct signals were observed. In the case of the *p*-fluoro-substituted dimer **2g**, due to coupling between ^{19}F and ^{13}C (J_{CF} = 249.1 Hz, 247.7 Hz; $^1J_{CF}$ = 22.0 Hz, 21.9 Hz; $^2J_{CF}$ = 8.5 Hz, 8.3 Hz; $^3J_{CF}$ = 3.1 Hz, 3.0 Hz) the number of signals for protonated aromatic carbons increased to 20 and for nonprotonated aromatic carbons to 19 (Fig. 1). For **2f**, on the other hand, the three fluorines of the trifluoromethyl group split the signals of the vicinal carbons of the phenyl ring to a quartet ($^1J_{CF}$ = 32.5 Hz, 32.3 Hz), increasing the signal number of nonprotonated ring carbons to 21. Again, due to overlap only 15 protonated and 20 nonprotonated carbon signals were observed. The other eight signals corresponding to two quartets (J_{CF} = 272.3 Hz, 272.3 Hz) in the aromatic chemical shift region stem from the two trifluoromethyl carbons due to the deshielding and coupling with the three fluorines (Table 1).

© 1998 NRC Canada

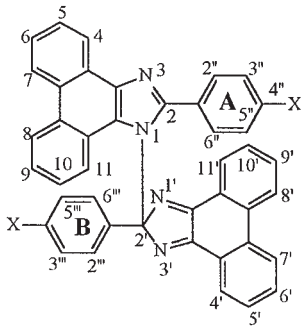

3

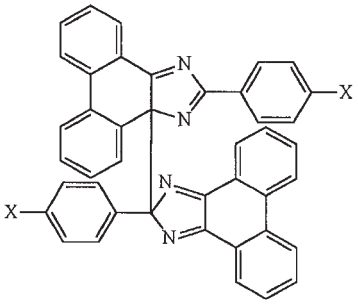

4

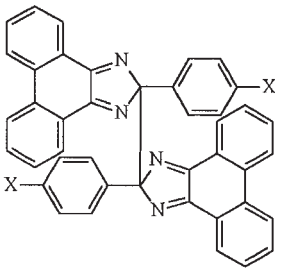

5

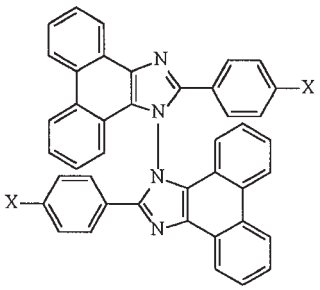

6

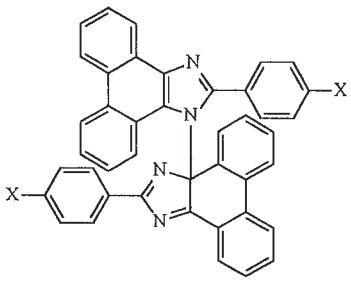

7

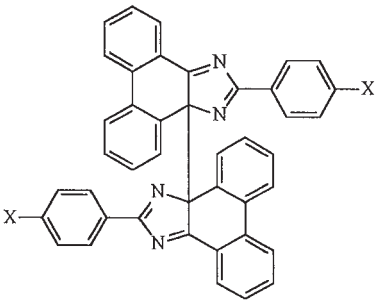

8

To distinguish between structures **3** and **4**, we have made use of the reference compounds **9**–**14** reported in the literature (8*a*, 14), which are good representatives of the half-dimer subunits. The ^{1}H NMR chemical shifts (in ppm) for the 2,6-protons on the 2-phenyl ring are as follows: <8.0 in **9**, **10**; 8.47, 8.18 in **11**; 7.50 in **12**; 7.85 in **13**; and 8.45 for **14**.

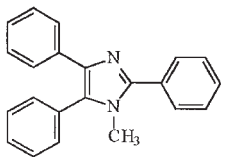

9

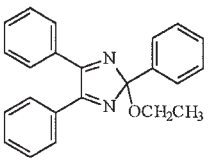

10

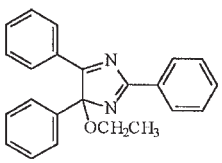

11

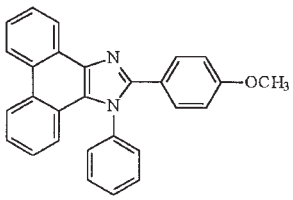

12

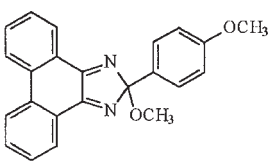

13

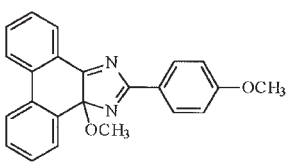

14

© 1998 NRC Canada

Table 1. Summary of ^{13}C NMR chemical shifts of ring carbons in phenanthroimidazole dimers (solvent $CDCl_3$, $CDCl_3$ + C_6D_6 (3:1 v/v) for **2g**, TMS as internal reference).

	Protonated carbons				Nonprotonated carbons			
2a	133.55	129.47	128.98	128.66	161.47	154.79	137.97	135.71
	128.61	128.43	127.94	127.55	135.55	134.89	129.28	128.92
	127.01	126.83	126.22	125.59	128.76	127.13	125.55	123.69
	125.19	124.52	123.89	122.96	116.21			
	122.81							
2b	133.39	129.36	129.11	128.72	161.20	154.93	138.87	138.01
	128.50	128.23	127.09	126.80	137.94	134.84	132.82	132.45
	126.18	125.51	125.22	124.43	129.21	128.86	128.76	127.20
	123.89	122.91	122.84	122.79	125.82	123,82	116.22	
2c	133.35	129.39	128.615	128.56	161.17	154.95	145.13	144.18
	127.92	127.08	127.03	126.80	137.92	134.81	132.91	132.53
	126.22	125.50	125.19	124.40	129.39	128.85	128.75	127.17
	123.86	122.85	122.81	122.79	125.74	123.80	116.25	
2d	134.65	132.19	131.33	130.05	162.71	152.78	140.88	139.97
	129.10	128.55	127.25	127.05	138.32	135.07	129.39	129.29
	126.36	126.22	125.60	125.39	128.90	126.74	124.93	122.94
	124.38	123.37	122.98	122.63	118.27	117.91	115.32	
2f	134.21	129.88	128.99	128.51	162.32	153.04	139.72	139.31
	127.13	126.60	126.04	125.55	138.27	135.02	131.20[a]	129.85[b]
	125.11	124.59	124.56	124.17	129.26	128.90	126.92	124.99
	123.27	122.92	122.75		123.19	115.57		115.57
2g	133.79	131.43[c]	128.82	128.52	162.94[g]	162.69[h]	161.61	153.97
	128.41[d]	127.14	126.97	125.92	138.26	134.96	131.94[i]	131.57[j]
	125.38	124.88	124.10	123.28	129.48	129.21	128.99	127.24
	123.02	122.91	115.44[e]	114.61[f]	125.50	123.74	115.88	
2h	133.98	130.80	128.94	128.67	161.83	153.50	138.13	135.03
	128.62	127.85	127.65	127.02	134.97	134.39	134.22	134.66
	126.79	125.88	125.48	124.92	129.23	129.11	128.86	126.97
	124.14	123.18	122.90	122.75	125.32	123.42	115.67	
2i	134.02	131.63	131.04	130.78	161.86	153.74	138.12	134.98
	129.01	128.68	127.89	127.05	134.76	134.61	129.20	129.14
	126.77	125.90	125.51	124.95	128.87	126.95	125.30	123.37
	124.15	123.20	122.90	122.73	123.31	122.75	155.71	

[a] Quartet, $J = 32.5$ Hz.
[b] Quartet, $J = 32.3$ Hz.
[c] Doublet, $J = 8.3$ Hz.
[d] Doublet, $J = 8.5$ Hz.
[e] Doublet, $J = 22.0$ Hz.
[f] Doublet, $J = 21.9$ Hz.
[g] Doublet, $J = 249.1$ Hz.
[h] Doublet, $J = 247.7$ Hz.
[i] Doublet, $J = 3.0$ Hz.
[j] Doublet, $J = 3.1$ Hz.

The reference compounds **9**–**14** fall into two structurally similar sets: the triaryl imidazole series **9**–**11** and the phenanthroimidazole series **12**–**14**. These structural parallels are reflected in parallel trends in the ^1H NMR chemical shifts of the 2-phenyl 2,6-protons. The COSY and ^1H NMR spectra of the synthesized dimers indicate that the resonance of the 2-phenyl 2,6-protons was lower than 8.00 ppm, the chemical shift values being <8.00 (**2a**); 7.31, 7.0 1(**2b**); 7.34, 7.05 (**2c**); 7.51, 7.19 (**2d**); 7.41, 7.25 (**2f**); 7.35, 7.06 (**2g**); 7.35, 7.05 (**2h**); and 7.28, 7.15 (**2i**), respectively (Table 2). This shows that the dimer structure must be made of two moieties that resemble the reference compounds **12** and **13**. Hence generic structure **3** is assigned to the synthesized dimers, which is consistent with the conclusions of the earlier work (8*a*). Moreover, by analysis of the COSY spectra on the dimers and the NOE results, we could make unambiguous assignment of the ^1H NMR spectra of the dimers (in the case of **2a**, only assignment for the phenanthryl rings was made) as shown in Table 2.

The assignment is made on the following basis: (*i*) the chemical shift values of protons in ring A bonded to the imidazole ring via an sp^2 carbon will be higher (further downfield) than those in the ring B bonded to the imidazole ring via an sp^3 carbon, because of more facile transmission of electronic effects in the former case. (*ii*) The protons on the asymmetric phenanthroimidazole ring at positions 4 and 11 have the same splitting pattern and integral values, but the higher chemical shift is assigned to position 11 since molecular models have shown that the proton at this position is the more "crowded."

© 1998 NRC Canada

Table 2. Assignment of ^{1}H NMR chemical shifts in structure **3** (*J* in Hz).

	3a	**3b**	**3c**	**3d**	**3f**	**3g**	**3h**	**3i**
4	8.89 (d, 7.5, 1H)	8.85 (d, 7.9, 1H)	8.85 (d, 7.9, 1H)	8.77 (d, 7.8, 1H)	8.81 (d, 7.9, 1H)	8.93 (d, 8.0, 1H)	8.81 (d, 7.9, 1H)	8.80 (d, 7.9, 1H)
5	7.71 (t, 7.4, 1H)	7.67 (t, 7.0, 1H)	7.65 (t, 7.4, 1H)	7.70 (t, 7.5, 1H)	7.70 (t, 7.3, 1H)	7.64 (t, 7.5, 1H)	7.69 (t, 7.3, 1H)	7.69 (t, 7.1, 1H)
6	7.64 (d, 6.9, 1H)	7.61 (t, 7.6, 1H)	7.59 (t, 9.0, 1H)	7.65 (d, 7.6, 1H)	7.64 (t, 7.3, 1H)	7.54 (t, 7.7, 1H)	7.62 (t, 8.0, 1H)	7.63 (t, 7.7, 1H)
7	8.69 (d, 8.1, 1H)	8.66 (d, 8.2, 1H)	8.65 (d, 7.9, 1H)	8.66 (d, 7.4, 1H)	8.67 (d, 8.2, 1H)	8.59 (d, 8.1, 1H)	8.66 (d, 8.2, 1H)	8.67 (d, 8.6, 1H)
8	8.70 (d, 8.2, 1H)	8.67 (d, 7.9, 1H)	8.65 (d, 7.9, 1H)	8.68 (d, 7.6, 1H)	8.69 (d, 7.9, 1H)	8.61 (d, 8.3, 1H)	8.68 (d, 8.1, 1H)	8.69 (d, 8.7, 1H)
9	7.49 (t, 7.8, 1H)	7.46 (t, 7.6. 1H)	7.44 (t, 7.5, 1H)	7.51 (t, 8.2, 1H)	7.50 (t, 7.6, 1H)	7.41 (t, 7.9, 1H)	7.49 (t, 7.6, 1H)	7.51 (t, 7.4, 1H)
10	7.41 (t, 7.6, 1H)	7.39 (t, 7.7, 1H)	7.36 (t, 7.6, 1H)	7.41 (t, 8.5, 1H)	7.40 (t, 7.9, 1H)	7.41 (t, 7.9, 1H)	7.41 (t, 7.5, 1H)	7.42 (t, 7.8, 1H)
11	9.37 (d, 8.4, 1H)	9.38 (d, 8.3, 1H)	9.32 (d, 8.4, 1H)	9.28 (d, 8.3, 1H)	9.30 (d, 8.3, 1H)	9.39 (d, 8.3, 1H)	9.35 (d, 8.4, 1H)	9.34 (d, 8.3, 1H)
4′(11′)	8.06 (d, 8.1, 2H)	8.09 (d, 8.1, 2H)	8.04 (d, 8.5, 2H)	8.16 (d, 8.1, 2H)	8.12 (d, 8.1, 2H)	8.02 (d, 7.7, 2H)	8.11 (d, 8.1, 2H)	8.14 (d, 8.1, 2H)
5′(10′)	7.60 (t, 7.4, 2H)	7.61 (t, 7.6, 2H)	7.30 (d, 8.0, 2H)	7.72 (t, 7.7, 2H)	7.67 (t, 7.7, 2H)	7.21 (t, 7.5, 2H)	7.65 (t, 8.2, 2H)	7.68 (t, 7.9, 2H)
6′(9′)	7.34 (t, 7.5, 2H)	7.35 (t, 7.5, 2H)	7.57 (d, 8.3, 2H)	7.45 (t, 7.5, 2H)	7.37 (t, 7.5, 2H)	7.42 (t, 7.9, 2H)	7.41 (t, 7.5, 2H)	7.44 (t, 7.7, 2H)
7′(8″)	8.03 (d, 7.7, 2H)	8.05 (d, 7.2, 2H)	8.02 (d, 8.0, 2H)	8.00 (d, 7.6, 2H)	7.96 (d, 7.5, 2H)	7.87 (d, 8.1, 2H)	8.04 (d, 7.7, 2H)	8.04 (d, 7.7, 2H)
2″(6″)		7.31 (d, 7.9, 2H)	7.34 (d, 8.0, 2H)	7.51 (d, 8.1, 2H)	7.41 (d, 8.2, 2H)	7.35 (q, 8.6, 2H)[a]	7.35 (d, 8.4, 2H)	7.28 (d, 8.7, 2H)
3″(5″)		6.90 (d, 7.8, 2H)	6.90 (d, 7.7, 2H)	7.40 (d, 8.4, 2H)	7.55 (d, 7.9, 2H)	6.69 (t, 8.7, 2H)[b]	7.10 (d, 8.5, 2H)	7.25 (d, 8.6, 2H)
2‴(6‴)		7.01 (d, 8.3, 2H)	7.05 (d, 8.2, 2H)	7.19 (d, 8.6, 2H)	7.25 (d, 8.6, 2H)	7.06 (q, 8.9, 2H)[c]	7.05 (d, 8.8, 2H)	7.15 (d, 8.6, 2H)
3‴(5‴)		6.81 (d, 8.2, 2H)	6.83 (d, 8.1, 2H)	7.30 (d, 8.6, 2H)	7.31 (d, 8.6, 2H)	6.57 (t, 8.6, 2H)[d]	6.99 (d, 8.8, 2H)	6.98 (d, 8.6, 2H)
		2.11 (s, CH_3)	2.41 (q, 8.0, CH_2)					
		2.09 (s, CH_3)	2.39 (q, 8.0, CH_2)					
			1.02 (t, 7.2, CH_3)					
			0.99 (t, 7.3, CH_3)					

[a] $J_{HF(meta)}$ = 5.4 Hz.
[b] $J_{HF(ortho)}$ = 8.7 Hz.
[c] $J_{HF(meta)}$ = 5.1 Hz.
[d] $J_{HF(ortho)}$ = 8.6 Hz.

© 1998 NRC Canada

Fig. 2. (*a*) Spectra of dimer **2h** in benzene (8.55×10^{-5} M) after UV irradiation for 20 s at 25°C, solid line: before irradiation; dotted line: after irradiation. (*b*) Spectra of lophine dimer in benzene (9.15×10^{-5} M) after UV irradiation for 20 s at 25°C, solid line: before irradiation; dotted line, after irradiation.

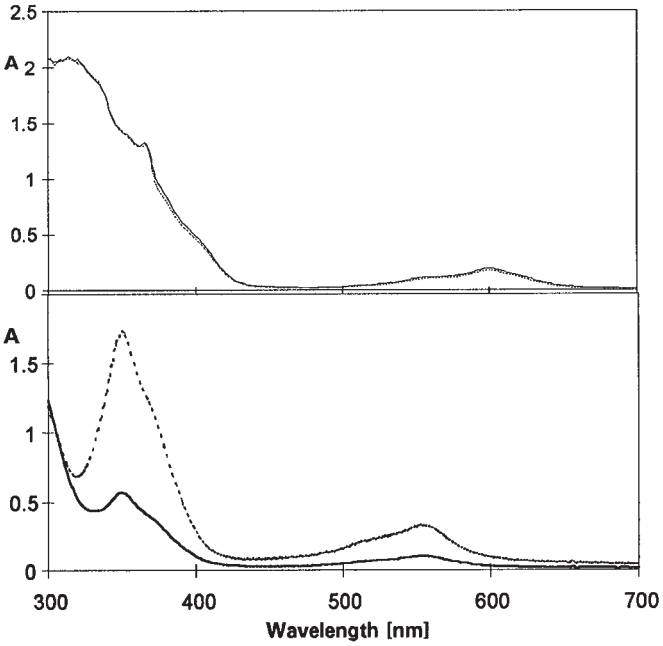

This crowding is also found in the optimized structure of dimer **2e** by the AM1 computational method.[2] Other cases have been recorded in the literature where "crowded" protons in aromatic compounds were found to have abnormally high chemical shifts (15). (*iii*) The protons at positions 4′(11′) and 7′(8′) on the symmetric phenanthroimidazole ring have the same splitting pattern and integral value, and the higher chemical shift value is assigned to position 4′(11′) due to proximity of the nitrogen in the imidazole ring. (4). Other assignments are based on results of COSY experiments with each dimer.

Features (*i*) and (*ii*) have been confirmed by means of an NOE experiment with dimer **2b**, the results of which show a strong Overhauser effect between protons having chemical shifts 9.38 and 7.01. These two values have been assigned to the protons at positions 11 and 6‴(2‴). The results of the AM1 optimization on dimer **2b** also reveal that the spatial distance between positions 11 and 6‴(2‴) is 2.81 Å,[2] which falls in the effective range of Overhauser effects (16). In the work of Sakaino et al. (8*a*), a chemical shift of 9.3 was also assigned to the proton at position 11 of dimer **2a**, though definitive proof for the assignment was not given.[3]

[2] S. Chen, Y. Zhou, and E. Buncel. Unpublished results.

[3] It has been pointed out by a referee that one can distinguish between structures **3** and **4** on the basis of symmetry. Structure **4** has a stereogenic centre at the dimer linkage to the top imidazole ring. Hence the lower phenanthroimidazole ring system does not have symmetry and will have the same carbon count in the ^{13}C NMR as the lower ring in **7**, which leaves the generic structure **3** as the only possible one. We thank the referee for this observation, which complements the structural assignment made on the basis of the experimental NMR evidence.

Fig. 3. (*a*) Spectra of dimer **2h** in benzene (8.67×10^{-5} M) on heating from 25°C (solid line) to 60°C (dotted line). (*b*) Spectra of lophine dimer in benzene (9.15×10^{-5} M) on heating from 25°C (solid line) to 60°C (dotted line).

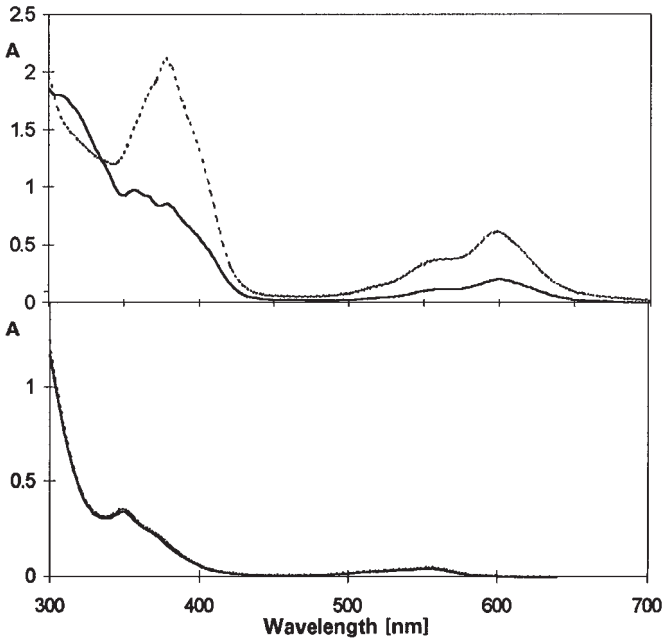

Photochromism

The synthesized phenanthroimidazole dimers are not photosensitive at room temperature. Thus the absorbance of the dimer solution in benzene remains constant under irradiation (Fig. 2*a*); in contrast the absorbance of the solution of lophine dimer in benzene increased 2–3 fold under identical irradiation conditions (Fig. 2*b*). Figure 2*a* shows the constant absorbance of the solution of dimer **2h** in benzene at 25°C after UV irradiation for 20 s. All other synthesized phenanthroimidazole dimers behave similarly to dimer **2h** toward UV irradiation.

Thermochromism

In contrast to the lack of an effect of UV irradiation on spectra in the phenanthroimidazole dimer series, the absorbance of the dimer solutions in benzene increased 2–3 fold when the temperature of the solutions was raised from 25°C to 60°C (Fig. 3*a*); on cooling the color faded again. The process of color development on heating and the subsequent fading of color on cooling could be repeated a number of times. However, a gradual decomposition took place on standing at a given temperature. This color fading followed a first-order process, but it was not possible to identify the products of decomposition. The triphenylimidazole dimers, in contrast, show little or no change in their UV–VIS spectra on heating (Fig. 3*b*), even though literature reports claim these compounds to also be thermochromic (10, 17).

Piezochromism

We have found that all synthesized phenanthroimidazole dimers are pressure sensitive: the originally brown or yellow crystals turned green or bluish green upon grinding. The colored ground dimers could be pressed to a transparent disc with potassium bromide and the absorption in the visible range

© 1998 NRC Canada

Fig. 4. Representative UV–vis spectra of dimers **2e** and **2h** in KBr disc after grinding and pressurization.

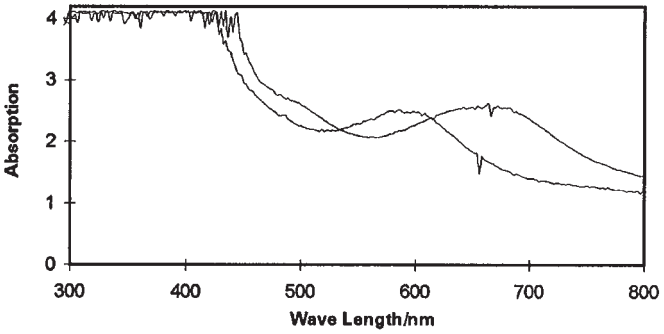

Table 3. Spectral characteristics of dimers in benzene solution and in KBr disc.

	λ_{max} (nm)	
	Benzene	KBr
2a	584	586
2b	612	594
2c	612	580
2d	552	552
2e	648	654
2f	570	570
2g	582	574
2h	600	588
2i	604	604

recorded (Fig. 4). After several days the color formed through grinding and pressurization faded. Interestingly, it was found that spectra recorded in this way displayed a bathochromic shift with electron-donating substituents such as OCH_3 and CH_3, similar to the observation with the benzene solutions of these dimers (Table 3).

It seems plausible that the observed color development on grinding and pressurization is due to dissociation of the dimers to free radicals, although it is not clear whether the dissociation is brought about by crystal deformation or rupture through external pressure, or as a result of a thermal effect from mechanical grinding. Both factors have been reported to cause color change through structural changes (18). In general, one expects formation of two radicals from a dimer to be accompanied by an increase in molecular volume, but in the present system the reverse situation may obtain since the radicals will be essentially planar and capable of stacking, which is clearly not the case with the dimer as shown by molecular models and AM1 calculations. The experiments described below prove conclusively that the colored species formed from the dimers are indeed free radicals.

Dimer–radical equilibrium

It was possible to investigate the dimer–radical thermal equilibrium for the phenanthroimidazole dimers and to determine the molar extinction coefficient as well as the equilibrium constant for formation of the radical species by means of the following derivations.

Consider the dissociation of the dimer to its radical form:

Table 4. Equilibrium constants and molar extinction coefficients calculated from the slope and intercept of A versus $[D]_o/A$ plots of dimer solutions in benzene at 25°C, and the fraction of dissociation, $\alpha = K^{1/2}$.

	$-\log K$	$10^{-3}\varepsilon$	$10^{3}\alpha$
2a	5.99±0.06	8.87±0.64	1.01±0.07
2b	5.19±0.04	10.10±0.06	2.58±0.08
2c	5.35±0.04	11.54±0.41	2.13±0.09
2g	5.88±0.07	13.43±1.11	1.16±0.10
2h	5.88±0.02	10.72±0.24	1.16±0.03
2i	5.84±0.04	8.95±0.49	1.21±0.06

Table 5. Influence of substituents (19) on λ_{max} of free radicals and on the dimer–radical dissociation constants in benzene at 25°C.

	σ_{para}	λ_{max} (nm)	$-\log K$
2e (OCH_3)	–0.27	648	
2b (CH_3)	–0.17	612	5.19
2c (CH_2CH_3)	–0.15	612	5.35
2a (H)	0	584	5.99
2g (F)	0.06	582	5.88
2h (Cl)	0.23	600	5.88
2i (Br)	0.23	604	
2f (CF_3)	0.54	570	[a]
2d (CN)	0.66	552	[a]

[a] K values too small to be measured accurately.

$$D \rightleftharpoons R + R$$

where D stands for the dimer and R for the radical formed from the dimer on dissociation. The equilibrium constant is given by

$$K = \frac{[R]^2}{4[D]} = \frac{[R]^2}{4[D]_0 - 2[R]}$$

where [D] and [R] refer to the equilibrium concentrations while $[D]_0$ is the initial dimer concentration. If the Lambert–Beer law is valid and the radical species is responsible for the color formation, then $[R] = A/\varepsilon l$, where A is absorbance, ε the molar extinction coefficient, and l, the light pathlength, equals 1. Hence

$$K = \frac{(A/\varepsilon)^2}{4[D]_0 - 2(A/\varepsilon)}$$

$$A = 4K\varepsilon^2 \frac{[D]_0}{A} - 2K\varepsilon = a\frac{[D]_0}{A} - b$$

It follows that a plot of A against $[D]_0/A$ will be linear with slope $a(= 4K\varepsilon^2)$ and intercept $b(= 2K\varepsilon)$. The molar extinction coefficient ε and equilibrium constant K can then be obtained: $\varepsilon = a/2b$ and $K = b^2/a$. The degree of dissociation is given by $\alpha = K^{1/2}$ (where $\alpha << 1$).

In Fig. 5 is shown the relevant plot of A vs. $[D]_o/A$ for the various substituted dimers and it is seen that satisfactory linearity is obtained. The resulting values of K, ε, and α are given in Table 4. Importantly, the results show that the fraction of dissociation of the phenanthroimidazole dimers to radical is of the order of 10^{-3}. This is consistent with the fact that the NMR spectra of the dimers appear to be free of paramagnetic

© 1998 NRC Canada

Fig. 5. Plot of A versus $[D_0]/A$ for dimer solutions in benzene at 25°C (correlation r^2: **2a** l, l; **2b** 0.9999, 0.9992; **2c** 0.9999, 0.9995; **2g** 0.9999, 0.9997; **2h** 0.9999, 0.9998; **2i** 0.9999, 0.9998).

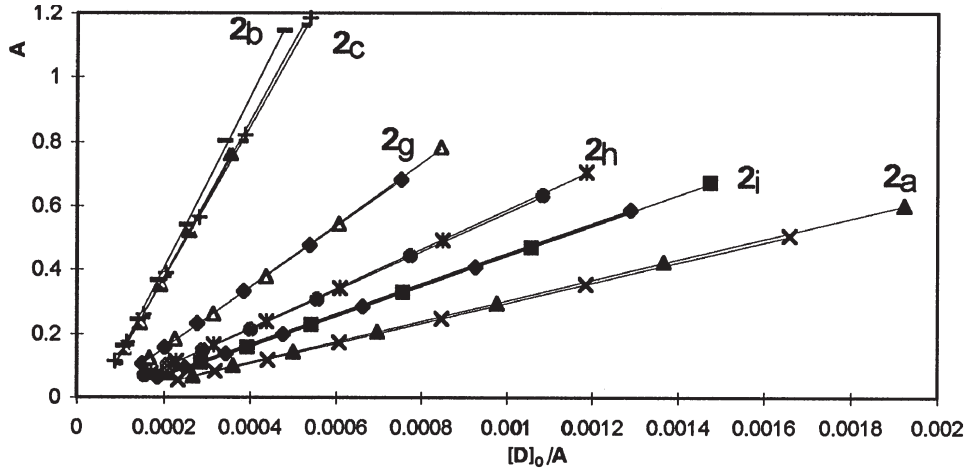

Fig. 6. (*a*) Hyperfine ESR spectrum of dimer **2b** in benzene (1.873×10^{-4} M) at room temperature, scale: 1.52 G/cm, scan range 25 G. (*b*) Hyperfine ESR spectrum of 2-*p*-methylphenyl-4,5-diphenylimadazole dimer in benzene (9.15×10^{-5} M) at room temperature, scale: 3.05 G/cm, scan range 50 G.

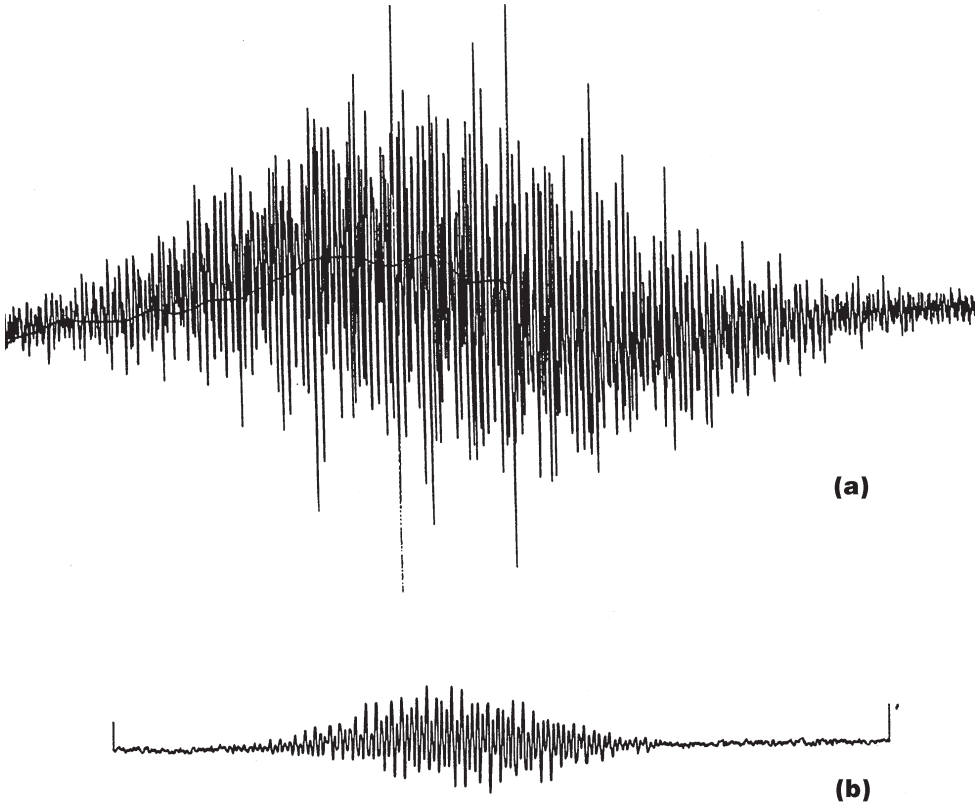

interference. In that regard, it is interesting that Maeda and Hayashi (10) reported a degree of dissociation, $\alpha = 0.3$, for triphenylimidazole dimers, although one might have expected α to be smaller for triphenylimidazole dimers than for phenanthroimidazole dimers.

The results in Table 5 indicate that the dimer–radical equilibrium constants increase as the *para* substituents on the 2-phenyl ring of the dimers become more electron donating (Table 5). This is consistent with the trend that electron-donating substituents stabilize the radicals, as was also found for dissociation of triphenylimidazole dimers (5). The halogenated phenanthroimidazole dimers do not show a clear trend, given the experimental error in measurement of K, though the λ_{max} values exhibit a reverse trend relative to the electron-donating substituents. The strong electron-withdrawing trifluoromethyl and cyano substituents both exhibit a hypsochromic effect on λ_{max} and decreased dissociation constants, which were in fact too small to be measured accurately.

© 1998 NRC Canada

Fig. 7. ESR spectra of lophine dimer in benzene (8.53×10^{-5} M) at room temperature, scale: 1.22 G/cm, scan range 20 G; (*a*) before irradiation; (*b*) after irradiation.

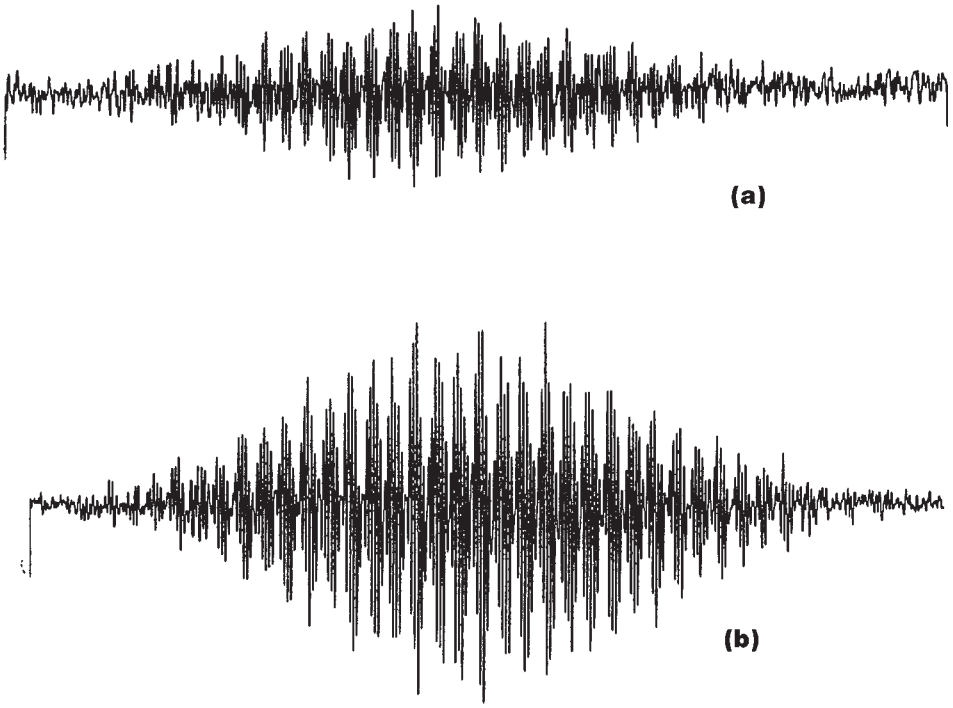

Fig. 8. ESR signals of dimer **2b** in benzene (1.173×10^{-4} M) at room temperature (left, signal gain 5×10^4) and at 65°C (right, signal gain 2×10^3), scale: 19.53 G/cm, scan range 500 G).

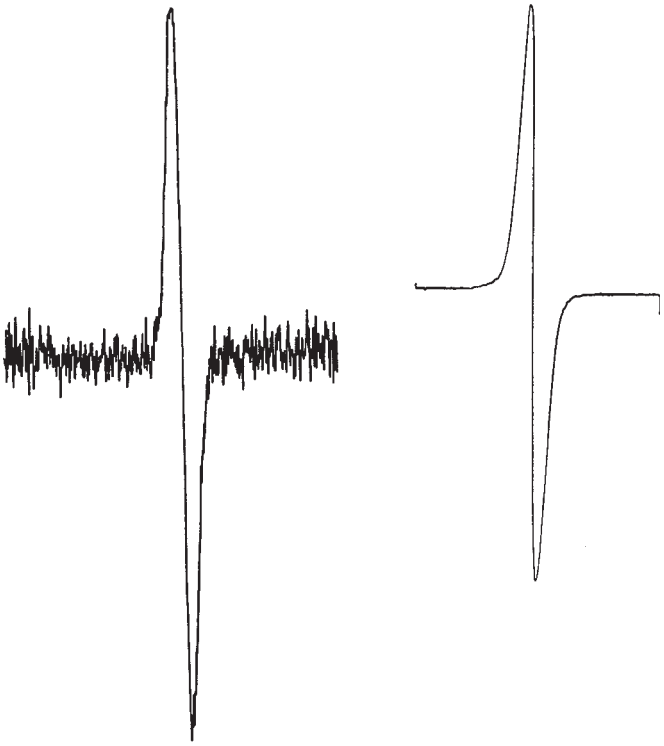

Fig. 9. ESR signals of dimer **2b** solid sample (weak) and its ground powder (strong) at room temperature, scale: 15.62 G/cm, scan range 400 G.

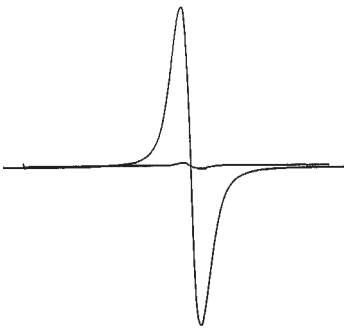

ESR spectra

Several studies have reported on the ESR hyperfine structure of the free radical derived from the lophine dimer (20, 21) and the radical anion derived from lophine (22). It was found that the free radical of the lophine dimer has spin density distributed in all three phenyl rings even though these are twisted out of the plane of the imidazole ring and also with respect to one another (21). One would expect that in the free radical derived from the phenanthroimidazole dimer the spin density would be more delocalized because of the extended conjugation, leading to more complex ESR hyperfine structure. We have, indeed, obtained a much more complex ESR hyperfine structure from dimer **2b** than from the corresponding 2-*p*-methylphenyl-4,5-diphenyl imidazole dimer (Fig. 6).

While the ESR signal of the lophine dimer in benzene is enhanced following UV irradiation (Fig. 7), the ESR signal of dimer **2b** in benzene becomes stronger on heating (Fig. 8). It is interesting to note that the ESR signal of dimer **2b** in the solid state is also enhanced on grinding (Fig. 9). These experiments confirm that the colored species obtained on UV

© 1998 NRC Canada

Fig. 10. Aromatic region of ^{1}H NMR spectrum of **2b** in $CDCl_3$.

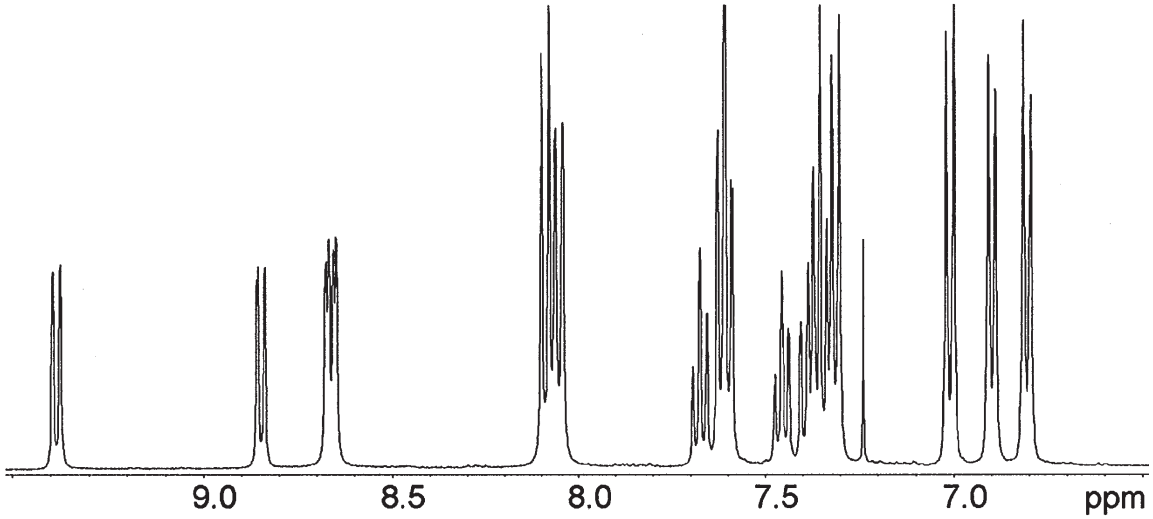

Table 6. MS data of dimers **2**.

	Melting point (lit.)	MS (*m*/*z*)
2a	200–203°C (8*a*)	(CI) 587.5(M^+), 295.3, 194.1
2b	170–173°C (8*a*)	(EI) 614.1(M^+), 308.1, 189.9, 163.0, 153.2, 82.8
2c		(EI) 642.2(M^+), 320.2, 189.8, 162.9, 116.8
2d		(EI) 636.1(M^+), 319.1, 189.8, 175.8, 162.6, 127.2, 116.8
2e		(EI) 646.4(M^+), 428.4, 324.3, 279.2, 235.2, 190.1, 176.0, 165.0, 149.0, 111.0
2f		(EI) 722.1(M^+), 362.1, 275.0, 198.7, 176.0, 162.6, 136.7, 128.6, 116.7
2g		(EI) 622.1(M^+), 312.1, 249.4, 235.9, 189.7, 175.8, 162.5,155.6, 130.8, 122.8, 116.7
2h	172–180°C (8*a*)	(EI) 654.1(M^+), 328.2, 189.9, 162.8, 136.9, 110.8
2i		(CI): 745.2(M^+), 667.3, 587.5, 373.3, 295.3, 194.1, 163.0

irradiation of the triphenylimidazole dimers, and also on heating the solutions of the phenanthroimidazole dimers or on grinding the phenanthroimidazole dimer, are free radical species. These qualitative observations on solutions of phenanthroimidazole dimers further validate the measurement of the molar extinction coefficient of the colored species as described above.

Experimental

The starting phenanthroimidazole compounds were synthesized according to the modification by Davidson et al. (23) of Radziszewski's imidazole synthesis (24). The dimers were synthesized by means of a two-phase reaction as described below.

To a solution of 1 g of the imidazole derivative in 250–350 mL methylene chloride was added a solution of potassium ferricyanide (5 g) and sodium hydroxide (5 g) in 100 mL water while cooling to 0°C and with vigorous stirring. The blue- or green-colored solution was stirred for 5 min at 0°C. The aqueous phase was separated and the organic phase was dried over sodium sulfate, and evaporated under reduced pressure to ca. 3 mL. After addition of ca. 3 mL ethyl acetate, the solution was placed in a refrigerator until crystals formed; these were filtered and washed with diethyl ether, yield over 90%. The MS data of the synthesized dimers are summarized in Table 6.

The UV–VIS spectroscopic measurements on the dimer solution in benzene were carried out by dissolution of ca. 20 mg of a dimer in 50 mL of benzene (BDH) freshly distilled from calcium hydride, followed by repetitive dilution to half concentration. UV–VIS spectra were recorded on an HP 8452A diode array spectrophotometer supported by HP89531A MS-DOS – UV–VIS operating software.The temperature of solutions in the cuvette (1 cm) was equilibrated to ± 0.1°C by means of a thermostatted water bath, RTE-210 (Neslab Instruments. Inc., Newington, NH 03801 U.S.A.). The UV light source for the irradiation was Spectroline, CX-Series (Spectronics Corporation, Westbury, New York).

NMR spectra were taken on a Bruker AM-400 NMR spectrometer operating at 400.134 MHz for ^{1}H and at 100.614 MHz for ^{13}C. The NMR solvents were purchased from CDN. The ESR spectra were recorded on a Varian E 104 ESR spectrometer and the UV light source for ESR measurement was a 1000-W Xe/Hg arc lamp. Sharp melting points could not be obtained; instead the sample in the capillary turned to a straw-colored resin-like material when the temperature was raised slowly (10°C/min). On raising the temperature quickly (>20°C/min) a transient blue or green color characteristic of the radical was observed; then the compound changed to the resin-like material. Purity was judged by the ^{1}H NMR spectra, which showed the absence of any extraneous peaks except for solvent (CH_2Cl_2 or EtOAc) of crystallization, which was difficult or impossible to remove, rendering

© 1998 NRC Canada

elemental analysis a poor criterion of purity. A typical ^{1}H NMR spectrum is shown in Fig. 10.

Acknowledgments

This research was supported by a grant from the Ontario Center for Materials Research. The authors are also grateful to Dr. L. Johnston, Dr. J. Lusztyk, and Dr. D. Shukla (National Research Council of Canada, Steacie Institute for Molecular Science) for assistance with the ESR measurements. We thank Prof. B.K. Hunter and Ms. S. Blake for helpful discussion on NMR data analysis.

References

1. H.C. van der Plas, M. Simonyi, F.C. Alderweireldt, and J.A. Lepoivre (*Editors*). Bio-organic heterocycles 1986. Elsevier, Amsterdam. 1986.
2. M. Patz, Y. Kuwahara, T. Suenobu, and S. Fukuzumi. Chem. Lett. 567 (1997).
3. T. Hayashi and K. Maeda. Bull. Chem. Soc. Jpn. **33**, 565 (1960).
4. T. Hayashi, K. Maeda, S. Shida, and K. Nakada. J. Chem. Phys. **32**, 1568 (1960).
5. (*a*) L.A. Cescon, G.R. Coraor, R. Dessauer, E.F. Silversmith, and E.J. Urban. J. Org. Chem. **36**, 2262 (1971); (*b*) B.S. Tanaseichuk, K.V. Stanovkina, A.N. Sunin, and L.G. Rezepova. Zh.Org. Khim. **5**, 2054 (1969); (*c*) B.S. Tanaseichuk and L.G. Rezepova. Zh. Org. Khim. **6**, 1065 (1970); (*d*) B.S. Tanaseichuk, A. A. Bardina, and V. A. Makskov. Zh. Org. Khim. 7, 1508 (1971). (*e*) B.S. Tanaseichuk, A.A. Bardina, and A.A. Khomenko. Khim. Geterotsikl. Soedin. **7**, 1255 (1971); (*f*) B.S. Tanaseichuk and S.V. Yartseva. Zh. Org. Khim. **7**, 1260 (1971); (*g*) Yu.A. Rozin, V.E. Blokhin, and Z.V. Pushreva. Khim. Geterotsikl. Soedin. **9**, 1105 (1973); (*h*) V.N. Shishkin, B.S. Tanashechuk, L.G. Tikhonova, and A.A. Bardina. Khim. Geterotsikl. Soedin. **9**, 387 (1973); (*i*) Yu.A. Rozin, V.E. Blokhin, Z.V. Pushreva, and V.I. Elin. Khim. Geterotsikl. Soedin. **10**, 990 (1974); (*j*) H. Baumgaertel and H. Zimmermann. Z. Naturforsch. B: Anorg. Chem. Org. Chem. Biochem. Biophys. Biol. **18B**, 406 (1961); (*k*) Chem. Ber. **99**, 843 (1966); (*l*) W. Suemmermann and H. Baumgaertel. Collect. Czech. Chem. Commun. **36**, 575 (1971); (*m*) Ber. Bunsen-Ges. Phys. Chem. **74**, 19 (1970).
6. (*a*) R.L. Mitchell, W.J. Nebe and W.M. Hardam. J. Imaging Sci. **30**, 215 (1986); (*b*) H.D. Hartzler (DuPont de Nemours & Co.). US Pat. 4,017,313 (1977); (*c*) Th.E. Duebner, B.M. Monroe (DuPont de Nemours & Co.). US Pat. 4,565,796 (1986); (*d*) H. Nagasaka (Mitsubishi Chem. Ind.). US Pat. 4,594,310 (1986).
7. L.A. Cescon, G.R. Coraor, R. Dessauer, A.S. Deutsch, H.L. Jackson, A. MacLachlan, K. Marcali, E.M. Potraftke, R.E. Read, E.F. Silversmith, and E.J. Urban. J. Org. Chem. **36**, 2267 (1971).
8. (*a*) Y. Sakaino, H. Kakisawa, and T. Kusumi. *J*. Chem. Soc. Perkin. Trans. 1, 2361 (1975); (*b*) J. Heterocycl. Chem. **12**, 953 (1975).
9. (*a*) B.M. Kosowski. CAMES sensor system, Plast. Technol. J. March, 1995; (*b*) A.C. Cordo and B.M. Kosowski. Int. Annu. Conf. ICT, 25th, 1994. p. 1; (*c*) D.C. Clark, W.E. Baker, A.C. Cordo, and B.M. Kosowski. Int. Polym. Process. Submitted; (*d*) D.C. Clark and W.E. Baker. Annu. Conf. Polym. Process. Soc. Secaucus, N.J. Paper 6, June 1997; (*e*) S.-R. Keum, S.-S. Hur, P.M. Kazmaier, and E. Buncel. Can. J. Chem. **69**, 1940 (1991); (*f*) S.-R. Keum, K.-B. Lee, P.M. Kazmaier, R.A. Manderville, and E. Buncel. Magn. Reson. Chem. **30**, 1128 (1992); (*g*) S.-R. Keum, K.-B. Lee, P.M. Kazmaier, and E. Buncel. Tetrahedron Lett. **35**, 1015 (1994); (*h*) S. Swansburg, Y.-K. Choi, S.-R. Keum, E. Buncel, and R.P. Lemieux. Liq. Cryst. **24**, 341 (1998); (*i*) S.-R. Keum,. M.J. Lee, S. Swansburg, E. Buncel, and R.P. Lemieux. Dyes Pigm. In press; (*j*) K.-S Cheon, R.A. Cox, S.-R. Keum, and E. Buncel. J. Chem. Soc. Perkin Trans. 2, 1231 (1998); (*k*) E. Buncel and K. -S Cheon. J. Chem. Soc. Perkin Trans. 2, 1241 (1998); (*l*) S.-R. Keum, P.M. Kazmaier, K.-S. Cheon. R.A. Manderville, and E. Buncel. Bull. Korean Chem. Soc. **17**, 391 (1996); (*m*) S.-R. Keum, S.S. Lim, B.H. Min, P.M. Kazmaier, and E. Buncel. Dyes Pigm. **30**, 225 (1996); (*n*) A. J. McKerrow, E. Buncel, and P.M. Kazmaier. Can. J. Chem. **73**, 1605 (1995); (*o*) E. Buncel, A.J. MacKerrow, and P.M. Kazmaier. J. Chem. Soc. Chem. Commun. 1242 (1992); (*p*) A.J. MacKerrow, E. Buncel, and P.M. Kazmaier. Can. J. Chem. **71**, 390 (1992); (*q*) P.M. Kazmaier, A.J. McKerrow, and E. Buncel. J. Imaging Sci. **36**, 373 (1992); (*r*) E. Buncel amd S. Rajagopal. Acc. Chem. Res. **23**, 226 (1990).
10. K. Maeda and T. Hayashi. Bull. Chem. Soc. Jpn. **43**, 429 (1970).
11. D.M. White and J. Sonnenberg. J. Am. Chem. Soc. **88**, 3825 (1966).
12. W.I. Talor and A.R. Battersby. Oxidative coupling of phenols. Marcel Dekker, Inc. New York. 1967.
13. D. Taub, C.H. Kuo, and N.L. Wendler. J. Org. Chem. **28**, 2752 (1963).
14. H. Tanino, T. Kondo, K. Okada, and T. Goto. Bull. Chem. Soc. Jpn. **45**, 1474 (1972).
15. J.D. Memory and N.K. Wilson. NMR of aromatic compounds. John Wiley &Sons, New York. 1982. p. 45.
16. D.H. Williams and I. Fleming. Spectroscopic methods in organic chemistry. 5th ed. McGraw–Hill Book Company, London. 1995. p. 112.
17. (*a*) Y. Sakaino, T. Takizawa, Y. Inouye, and H. Kakisawa. J. Chem. Soc. Perkin Trans. 2, 1623 (1986); (*b*) T. Hayashi, K. Maeda, and M. Morinaga. Bull. Chem. Soc. Jpn. **37**, 1563 (1964); (*c*) T. Hayashi, K. Maeda and T. Kanaji. Bull. Chem. Soc. Jpn. **38**, 857 (1965).
18. For pressure effects on organic compounds: (*a*) Z.A. Dreger and H.G. Drickamer. Chem. Phys. Lett. **179**, 199 (1991); (*b*) R.R. Birge, C.T. Berge, L.L. Noble, and R.C. Neuman, Jr. J. Am. Chem. Soc. **101**, 5162 (1979); (*c*) D.G. Wilson and H.G. Drickamer. J. Chem. Phys. 3649 (1975); (*d*) G. Kortuem and W. Zoller. Chem. Ber. **100**, 280 (1967); (*e*) S. Murphy. B. Sauerwein, H.G. Drickamer, and G.B. Schuster. J. Phys. Chem. **98**, 13476 (1994); (*f*) L. Comeford and E. Grunwald. J. Phys. Chem. **94**, 1105 (1990); (*g*) K. Song, R.D. Miller, and J.F. Rabolt. Macromolecules, **26**, 3232 (1993); (*h*) E. Orti, R. Crespo, and M.C. Piqueras. Synth. Met. **41**–**43**, 1575 (1991); (*i*) R.A. Nallicheri and M.F. Rubner. Macromolecules, **24**, 517 (1991). For pressure effects on metal complexes: (*j*) S. Alshehri, J. Burgess, G.H. Morgan, B. Patel, and M.S. Patel. Transition Met. Chem. (London), **18**, 619 (1993); (*k*) B. Scott and R.D. Willett. J. Am. Chem. Soc. **113**, 5253 (1991); (*l*) K.H. Drickamer and L. Bray. Acc. Chem. Res. **23**, 55 (1990); (*m*) M. Kotowski, R. van Edlik, R.B. Ali, J. Burgess, and S. Radulovic. Inorg. Chim. Acta, **131**, 225 (1987).
19. T.H. Lowry and K.S. Richardson. Mechanism and theory in organic chemistry. 3th ed. R.R. Donnelley & Sons, New York. 1987.
20. R.D. Allendoerfer and A.S. Pollock. Mol. Phys. **22**, 661(1971).
21. N. Cyr, M.A. Wilks, and M.R. Willis. J. Chem. Soc. B: 404 (1971).
22. H. Ueda. J. Phys. Chem. **68**, 1304 (1964).
23. D. Davidson, M. Weiss, and M. Jelling. J. Org. Chem. **2**, 319 (1937).
24. B. Radziszewski. Ber. Dtsch. Chem. Ges. **10**, 10 (1877).

© 1998 NRC Canada

Mechanism of the benzidine disproportionation of (arylhydrazo)pyridines. The reactions of 4-(4-chlorophenylazo)pyridine and -hydrazo)pyridine in acid media

Robin A. Cox, Kap-Soo Cheon, Sam-Rok Keum, and Erwin Buncel

Abstract: A kinetic and product analysis study of the reactions of 4-(4-chlorophenylhydrazo)pyridine (**1**) and 4-(4-chlorophenylazo)pyridine (**2**) in acid media is reported. The disproportionation of two moles of **1** in aqueous sulfuric acid gives one mole of the oxidized product **2**, and one mole each of the reduced products 4-chloroaniline and 4-aminopyridine. The azo compound **2**, a product of the reaction of **1**, undergoes a slower hydroxylation reaction in acid media, and this process was also investigated. The first-formed product in the reaction of **2** is probably 4-(4-hydroxyphenylazo)pyridine, the 4-chlorine being displaced. At the low substrate concentrations used for the kinetic measurements both reactions are straightforward, but at the much higher concentrations used for product isolation studies a complex product mixture results, one of the products being a dimer. The complexity is increased because **1** had to be used as its hydrochloride salt for reasons of stability, and the chloride ion can also react with the diprotonated substrates; chloride ion also accumulates in the system as it is displaced from **2** during the hydroxylation. Thus chloride ion competes with bisulfate ion (present in large excess) for the diprotonated substrates. Nevertheless, complete mechanistic schemes accounting for all of the observed products, including the dimer, could be derived and are presented. Values of $pK_{BH_2^{2+}}$ for **2** and two of the azo products, needed for the kinetic analysis, were measured using the excess acidity equilibrium method. The nucleophile reacting with protonated **2** in the rate-determining step of the hydroxylation was positively identified as being bisulfate ion by an excess acidity analysis. A comparison of the reaction of **1** with the equivalent reactions of two previously studied 4-(arylhydrazo)pyridines, **9** and **10**, reveals that the benzidine disproportionation of these molecules is an A1 process with the second protonation being a pre-equilibrium; $pK_{BH_2^{2+}}$ values for the hydrazo compounds could not be measured as they react too quickly, but they could be determined from the kinetic data, using the excess acidity method. The rate-determining step is a thermally allowed 10-electron electrocyclic process of the diprotonated substrate, giving rise to an intermediate that undergoes fast reaction with a molecule of protonated substrate in a thermally allowed 14-electron electrocyclic process to give the observed products.

Key words: azopyridines, benzidine, disproportionation, excess acidity, hydrazopyridines, hydroxylation, mechanism.

Résumé : On a réalisé une étude cinétique ainsi qu'une analyse des produits des réactions des 4-(4-chlorophénylhydrazo)pyridine (**1**) et 4-(4-chlorophénylazo)pyridine (**2**) en milieu acide. La dismutation de deux molécules de **1** dans de l'acide sulfurique conduit à une mole du produit oxydé **2** et à une mole chacun des produits réduits, 4-chloroaniline et 4-aminopyridine. En milieu acide, le composé azo **2**, un produit de la réaction de **1**, subit une réaction d'hydroxylation plus lente; on a aussi examiné ce processus. Le premier produit formé dans la réaction de **2** est probablement la 4-(4-hydroxyphénylhydrazo)pyridine (**1**) provenant d'un remplacement du chlore en position 4. Aux faibles concentrations utilisées dans les mesures cinétiques, les deux réactions sont simples; toutefois, aux concentrations plus élevées utilisées pour les études en vue d'isoler les produits, il y a formation d'un mélange complexe de produits comprenant un dimère. La complexité est accrue à cause du fait qu'il a été nécessaire, pour des raisons de stabilité, d'utiliser le chlorhydrate du composé **1** et que l'ion chlorure peut aussi réagir avec les substrats diprotonés; de plus, l'ion chlorure s'accumule aussi dans le système lorsqu'il est déplacé du composé **2** par hydroxylation. L'ion chlorure est donc en compétition avec l'ion bisulfate (présent en très grand excès) pour les substrats diprotonés. Malgré tout, on peut présenter des schémas mécanistiques complets permettant d'expliquer tous les produits observés, y compris le dimère. Utilisant la méthode d'équilibre d'acidité en excès, on a mesuré les valeurs de $pK_{BH_2^{2+}}$ du composé **2** et de deux produits azo nécessaires pour l'analyse cinétique. Faisant appel à l'analyse de

Received January 14, 1998.

This paper is dedicated to Professor Erwin Buncel in recognition of his contributions to Canadian chemistry.

R.A. Cox.[1] Department of Chemistry, University of Toronto, 80 St. George Street, Toronto, ON M5S 3H6, Canada.
K.-S. Cheon and E. Buncel.[2] Department of Chemistry, Queen's University, Kingston, ON K7L 3N6, Canada.
S.-R. Keum. Department of Chemistry, Graduate Studies of Korea University, Seoul, Korea 136-701.

[1] Mechanistic studies in strong acids, part 24. Part 23 is ref. 26. Telephone: (416) 978-4581. Fax: (416) 978-8775. E-mail: rcox@alchemy.chem.utoronto.ca
[2] Studies of azo and azoxy dyestuffs, part 25; part 24 is ref. 24. Telephone: (613) 545-2653. Fax: (613) 545-6669. E-mail: buncele@chem.queensu.ca

© 1998 NRC Canada

l'acidité en excès, il a été possible d'identifier sans ambiguïté que l'ion bisulfate est le nucléophile qui réagit avec la forme protonée de **2** dans l'étape cinétiquement limitante de l'hydroxylation. Une comparaison de la réaction de **1** avec les réactions équivalentes de deux 4-(arylhydrazo)pyridines (**9** et **10**) étudiées antérieurement révèle que la dismutation de la benzidine de ces molécules est un processus A1 dans lequel la deuxième protonation est un prééquilibre; il n'a pas été possible de mesuré les valeurs des $pK_{BH_2^{2+}}$ de ces composés hydrazo à cause de leur trop grande vitesse de réaction, mais il a été possible de les déterminer à partir de données cinétiques faisant appel à la méthode d'acidité en excès. L'étape cinétiquement limitante est un processus électrocyclique thermique permis, à 10 électrons, du substrat diprotoné qui conduit à un intermédiaire qui réagit rapidement avec une molécule de substrat protoné par le biais d'un processus électrocyclique thermique permis, à 14 électrons, conduisant aux produits observés.

Mots clés : azopyridines, benzidine, dismutation, acidité en excès, hydrazopyridines, hydroxylation, mécanisme.

[Traduit par la rédaction]

Introduction

Studies of azo and azoxy compounds have revealed a remarkable diversity of structure–reactivity relationships, and some challenging problems in mechanism. Our work in this area was originally concerned with the mechanism of the acid-catalyzed Wallach rearrangement of azoxyarenes (1–7). This has developed in recent years to encompass a variety of photoactive molecules and processes, including the synthesis (8) and electronic spectral characteristics (9) of novel azo merocyanine dyes, and their solvatochromism (9, 10), which led to the establishment of the π^*_{azo} solvent polarity scale (10). The photochemical and thermal interconversion of merocyanines and their spiro precursors (11–15) has led most recently to studies of the chiroptical properties of spiro molecules, with a view to developing a ferroelectric liquid crystal optical switch based on the principle of photoresolution (16, 17).

The present series of studies is an extension of the Wallach rearrangement studies of phenyl and naphthyl substrates (2–6) to the heteroaromatic series, with the observed $>10^4$ reactivity difference between the isomeric α- and β-phenylazoxypyridines involving di-and tri-protonation processes in the 95–100 wt.% H_2SO_4 acidity region (7). This led to the discovery of the remarkably facile hydrolysis of the aryl azo ethers in acid media, with protonation on nitrogen, oxygen or carbon centers occurring as fast equilibria or as the rate-determining step (18, 19). In the course of these studies it was discovered that phenylazopyridine is itself unstable in strong acid media, undergoing hydroxylation and disproportionation (20). Since this was reminiscent of the classical benzidine rearrangement (21–23), kinetic studies were extended to the surmised intermediate, 4-(4-hydroxyphenylhydrazo)pyridine (24). However, an excess acidity treatment of the results (25) led to uncertainties in the postulated reaction mechanism. This was unsatisfactory, since the excess acidity method (25) has proven to be very useful in the determination of the mechanisms of reactions that take place in strong acid media. For instance, lactam (26), alkylnitramine (27), *N*-nitro amide (28), and acylimidazole (29) hydrolyses, as well as imidazoline cyclizations (30), alkene hydrations (31), aromatic hydrogen exchange processes (32), and ether (19, 33) and thioacetal (34) hydrolyses have been studied using this approach.

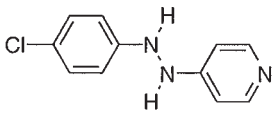

1

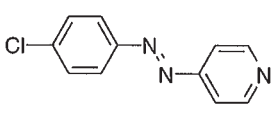

2

Thus, in our quest to resolve the mechanistic ambiguity in the benzidine-type disproportionations of the 4-(arylhydrazo)pyridines (24), we have extended these studies to include 4-(4-chlorophenylhydrazo)pyridine **1**. We also examined the azo analog **2**, the results for which can be compared with those previously obtained for other (arylazo)pyridines (20). These substrates form the subject of the present paper; it will be shown that while the results obtained using **1** and **2** are more complex in terms of reaction products, the kinetic data obtained do, in fact, allow the definitive resolution of the mechanism of this benzidine rearrangement-like process.

Experimental

The hydrochloride salt of 4-(4-chlorophenylhydrazo)pyridine **1** was obtained in 33.8% yield when 4-phenylazopyridine was simultaneously chlorinated and reduced (35), mp 241–242°C (lit. (35) mp 243°C). This compound was used as its hydrochloride salt rather than in the free base form, since the former proved to be much more air-stable. 4-(4-Chlorophenylazo)pyridine **2** resulted in 22.3% yield when **1** was oxidized (35), mp 97–98°C (lit. (35) mp 99–100°C). The synthesized compounds were characterized as before (20).

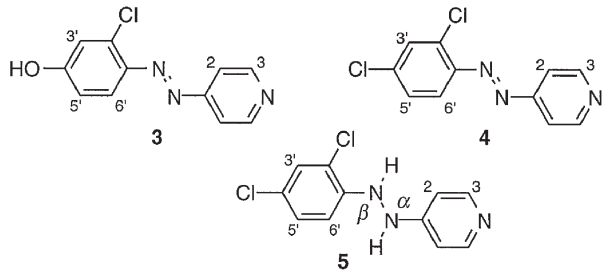

3 **4** **5**

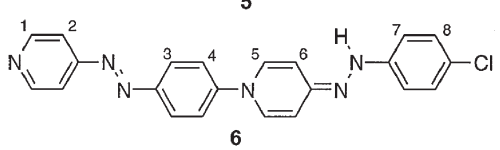

6

Substrates and isolated products were purified by several techniques, recrystallization, and column and thin-layer chromatography using silica gel 60 F_{254} plates (BDH) in various eluting solvent systems. The products of the reactions of **1** and **2** in 65 wt.% aqueous H_2SO_4 were identified by UV–vis, NMR, and GC–MS analysis following direct isolation as previously described (20); some of the isolated products, **3**–**6**, are shown above. The MS results were particularly useful for

© 1998 NRC Canada

Table 1. Isolated products and yields in the reactions of **1** and **2** in 65 wt.% H_2SO_4.

Substrate	Product	Yield, %	Total yield, % [a]
1	4-(4-Chlorophenylazo)pyridine **2**	22	48
(5 h)	4-Aminopyridine	23	
	4-Chloroaniline	21	
	4-(2,4-Dichlorophenylhydrazo)pyridine **5**	4	
1	4-(2,4-Dichlorophenylazo)pyridine **4**	21	50
(24 h)	4-Aminopyridine	25	
	2,4-Dichloroaniline	20	
	4-(4-Chlorophenylazo)pyridine **2**	5	
	4-Chloroaniline	3	
	Dimeric product **6**	Trace	
2	4-(2-Chloro-4-hydroxyphenylazo)pyridine **3**	15	57
	4-(2,4-Dichlorophenylazo)pyridine **4**	13	
	2-Chloro-4-hydroxyaniline	14	
	4-Aminopyridine	26	
	2,4-Dichloroaniline	10	
	4-(4-Hydroxyphenylazo)pyridine **7**	2	
	Dimeric product **6**	2	

[a] Since two aniline products result from one substrate molecule, their yields have to be averaged in calculating the overall yield, which is why the numbers in this column are not the simple sum of those in the previous column.

identifying the chlorine-containing products; for instance, the mass spectrum of **4** with its two chlorine atoms showed a characteristic intensity pattern of 100:65.3:10.6, in which each peak is separated by two mass units due to the natural abundance of the two chlorine isotopes, ^{35}Cl:^{37}Cl being 100:32.5. The structural identification of the products was achieved using ^1H NMR spectroscopy and MS. For **3**: δ_H (DMSO-d_6): 12.82 (OH), 8.79 (H^3), 7.83 (H^2), 7.68 ($H^{6'}$), 7.17 ($H^{3'}$), 6.98 ($H^{5'}$); *m/z*: 233.0 (M). For **4**: δ_H (DMSO-d_6): 8.86 (H^3), 7.96 ($H^{3'}$), 7.77 (H^2), 7.73 ($H^{6'}$), 7.60 ($H^{5'}$); *m/z*: 251.0 (M). For **5**: δ_H (DMSO-d_6): 8.90 (NH^{α}), 8.14 (H^3), 8.08 (NH^{β}), 7.48 ($H^{3'}$), 7.20 ($H^{5'}$), 6.74 ($H^{6'}$), 6.67 (H^2); *m/z*: 235.1 (M). For the dimer **6**: δ_H (DMSO-d_6): 9.98 (NH), 8.72 (H^1), 8.14 (H^5), 7.86 (H^3), 7.65 (H^2), 7.42 ($H^{7,8}$), 7.16 (H^4), 6.60 (H^6); *m/z*: 401.2 (M+1).

The $pK_{BH_2^{2+}}$ values of the azo substrate **2** and the azo products **3** and **4** were determined from the variation of the UV–vis spectra with sulfuric acid concentration as previously described (20); the acid concentration and extinction data are given here as supplementary information, Tables S1–S3.[3] The kinetic techniques used were similar to those used before (20).

Results

Products

The products formed when 4-(4-chlorophenylhydrazo)pyridine **1** is allowed to react in 65 wt.% H_2SO_4 for 5 h at a substrate concentration of 0.05 M are given in Table 1, and illustrated in Scheme 1. Under these conditions, and at the much lower substrate concentrations used for the kinetic runs (as determined from the UV–vis spectra after the kinetic runs), the reaction gives the three products shown, 4-(4-chlorophenylazo)pyridine **2**, 4-chloroaniline, and 4-aminopyridine. Trace amounts of 4-(2,4-dichlorophenylhydrazo)pyridine **5** were also present in the mixture analyzed.

Scheme 1.

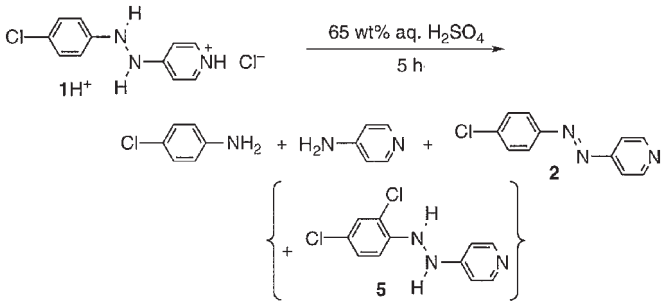

Scheme 2.

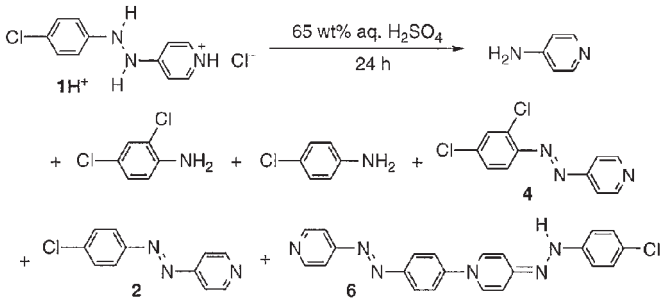

If the reaction of **1** is allowed to continue for longer periods the number of products increases, as shown in Table 1 and illustrated in Scheme 2. The products still include **2**, 4-chloroaniline, and 4-aminopyridine, but 4-(2,4-dichlorophenylazo)pyridine **4** and 2,4-dichloroaniline are also present, with trace amounts of the dimeric product **6**. There is no evidence for the presence of **5**, leading to the inference that at least some of the new products may have been formed from it. The presence of extra Cl^- (**1** had to be used as its hydrochloride salt)

[3] Tables S1–S3, supplementary material, may be purchased from: The Depository of Unpublished Data, Document Delivery, CISTI, National Research Council of Canada, Ottawa, Canada, K1A 0S2.

© 1998 NRC Canada

Scheme 3.

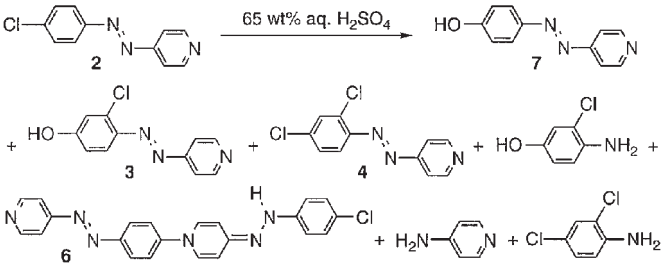

Scheme 4.

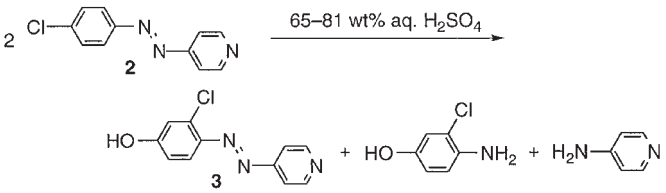

also complicates the situation. The product recovery in Table 1 is less than 100%, probably due to losses incurred during the TLC technique used for product separation (20).

The first-formed product **2** also reacts in aqueous H_2SO_4, albeit more slowly than does **1**, and the products of the reaction of **2** at 0.05 M substrate concentration were also investigated, see Table 1. A complex mixture of **4**, 4-(2-chloro-4-hydroxyphenylazo)pyridine **3**, 4-(4-hydroxyphenylazo)pyridine **7**, 2-chloro-4-hydroxyaniline, 2,4-dichloroaniline, 4-aminopyridine, and the dimeric product **6** was found, as shown in Scheme 3.

However, at the substrate concentrations typically used for the kinetic runs, ~8×10^{-5} M, the situation for **2** is much simpler, as shown in Scheme 4. The primary product is **3**, which could be identified by its UV–vis spectrum; the concentration of this product was shown not to depend on the medium acidity, averaging (46.8 ± 4.0)% over the 65–81 wt.% H_2SO_4 concentration range, as determined from the known extinction coefficients and the observed absorbances after 10 half-lives. The two aniline products also formed could not be directly identified, but undoubtedly form in equivalent amounts (20). Evidently the reaction is uncomplicated; according to Table 1 two moles of **2** give one mole of oxidized products (total 30% azo compounds) and one mole of reduced products with the N—N bond broken (total 24% anilines, 26% 4-aminopyridine).

$pK_{BH_2^{2+}}$ values

The azo compounds **2**–**4** are all protonated on the pyridine nitrogen in the pH range (8), so the protonation of interest in this work is the second protonation at the azo group. The $pK_{BH_2^{2+}}$ values were measured as described before (20). Extinction differences ($\delta\varepsilon = \varepsilon_{BH^+} - \varepsilon_{BH_2^{2+}}$) were obtained from UV–vis spectra measured in different sulfuric acid solutions at wavelengths appropriate for the peak maxima of the protonated and diprotonated forms; this is the Davis–Geissman method (36), preferred because errors due to small differences between the individual samples tend to cancel out when the difference is taken (these may cause irregular isosbestic point behaviour, for instance), and spectra of both forms contribute to the resulting $pK_{BH_2^{2+}}$ values. The data were treated according to the excess acidity method; for equilibria the relevant equation is $\log I - \log C_{H^+} = pK_{BH_2^{2+}} + m^*X$ (37), where C_{H^+} is the proton concentration in the sulfuric acid solution and X is the excess acidity, both obtained from published sources (37). The ionization ratio I is given in terms of $\delta\varepsilon$ by $I = (\delta\varepsilon_{BH^+} - \delta\varepsilon)/(\delta\varepsilon - \delta\varepsilon_{BH_2^{2+}})$ (38), where $\delta\varepsilon_{BH^+}$ and $\delta\varepsilon_{BH_2^{2+}}$ apply to the pure monoprotonated form and the pure diprotonated form, respectively. This expression was substituted in the excess acidity equation and the result recast in terms of $\delta\varepsilon$ and curve-fitted directly, as before (38); previous experience (39) shows that this method gives reliable protonation constants. The slope parameter m^* is characteristic of the substrate, having values of 1.0 for primary nitroanilines, 0.6 for amides and so on (37). The parameters given by the curve fit are $\delta\varepsilon_{H^+}$, $\delta\varepsilon_{BH_2^{2+}}$, $pK_{BH_2^{2+}}$, and m^*; the latter two are listed for **2**–**4** in Table 2. Also listed in Table 2 are the $pK_{BH_2^{2+}}$ and m^* values for 4-(4-hydroxyphenylazo)pyridine **7** and the parent compound **8**, already available (20), for comparison. The experimental data obtained and the values of X and $\log C_{H^+}$ used for **2**–**4** are given as supplementary material in Tables S1–S3,[3] together with the calculated $\delta\varepsilon_{BH^+}$ and $\delta\varepsilon_{BH_2^{2+}}$ values.

Table 2. Azo-compound $pK_{BH_2^{2+}}$ values obtained using the excess acidity method.[a]

Compound	Substituents	$pK_{BH_2^{2+}}$	m^*
2	4-Cl	–6.47 ± 0.37	0.991 ± 0.070
3	4-OH, 2-Cl	–4.15 ± 0.26	0.760 ± 0.063
4	2,4-Di-Cl	–6.61 ± 0.32	0.875 ± 0.053
7[b]	4-OH	–3.07 ± 0.21	0.994 ± 0.089
8[b]	H	–4.97 ± 0.22	0.807 ± 0.045

[a] Errors quoted are standard deviations.
[b] From ref. 20.

Kinetics

The kinetics of the reaction of 4-(4-chlorophenylazo)pyridine **2** (see Scheme 4) were monitored spectrophotometrically by following the disappearance of the reactant, in either its monoprotonated SH^+ form at 354 nm (up to 72 wt.% H_2SO_4), or its diprotonated SH_2^{2+} form at 444 nm (at the higher acidities). The observed pseudo-first-order rate constants as a function of acidity, k_ψ, and other parameters relevant to the kinetic analysis, are given in Table 3. All the kinetic plots showed excellent first-order linearity over the three half-lives for which the reaction was typically followed.

$$[1] \quad \log k_\psi - \log (C_{SH_2^{2+}} / (C_{SH^+} + C_{SH_2^{2+}})) - \log a_{Nu^-} = \log k_0 + (m^{\ddagger} - 1)m^* X$$

Previously it was found that eq. [1] describes the kinetic behaviour of 4-(phenylazo)pyridine (**8**) (and that of 2-(phenylazo)pyridine) at these acidities (20), and the behaviour of **2** was found to be very similar. Protonation of the substrate is a pre-equilibrium process (20), and so the $pK_{BH_2^{2+}}$ and m^* values given in Table 2 were used with the equilibrium excess acidity equation to calculate protonation correction terms (PCT) on the basis of full substrate protonation, $\log (C_{SH_2^{2+}} / (C_{SH^+} + C_{SH_2^{2+}}))$, or $\log (I/(1 + I))$ after division by C_{SH^+} (since the ionization ratio $I = C_{BH_2^{2+}} / C_{BH^+}$), which correct

© 1998 NRC Canada

Table 3. Kinetic data for the hydroxylation of 4-(4-chlorophenylazo)pyridine **2**.

H_2SO_4, wt.%	k_ψ [a]	X [b]	log C_{H^+} [b]	log $C_{HSO_4^-}$	PCT [c]	log k_ψ – PCT
64.99	2.01	3.793	1.078	0.932	–1.640	–3.057
	2.03					–3.053
68.22	2.90	4.208	1.100	0.975	–1.224	–3.314
	2.91					–3.312
71.67	7.32	4.708	1.122	1.020	–0.762	–3.373
	7.35					–3.372
75.86	9.12	5.397	1.144	1.071	–0.289	–3.751
	9.16					–3.749
78.28	7.99	5.830	1.154	1.096	–0.128	–3.969
	8.01					–3.968
81.36	3.91	6.407	1.157	1.118	–0.038	–4.370
	3.92					–4.369
85.98	0.81	7.274	1.118	1.102	–0.006	–5.086
	0.81					–5.086

[a] Observed pseudo-first-order rate constants, $\times 10^5$ s^{-1}. Both duplicate determinations given.

[b] From ref. 37.

[c] Protonation Correction Term; log ($C_{SH_2^{2+}}$ / (C_{SH^+} + $C_{SH_2^{2+}}$)). Calculated using p$K_{BH_2^{2+}}$ = –6.47 and m^* = 0.991 from Table 2.

for less than full substrate protonation at the acidity under investigation. The nucleophile involved at these acidities is bisulfate ion, and log bisulfate ion concentrations were used for log a_{Nu^-} as before (20). Log k_0 refers to the rate constant for the reaction in the hypothetical ideal 1 M acid solution which is the standard state (37), and $m^\ddagger$ refers to the transition state, having values of >1 for an A1 reaction, <1 for an A-S_E2 reaction, and probably ~1 for an A2 reaction with water (25). Plots according to eq. [1] are given in Fig. 1 for **2**, with that for the parent compound **8** for comparison (20). For the reaction of **8** with bisulfate, log $k_0 = 0.36 \pm 0.11$ and $m^*(m^\ddagger - 1) = -0.645 \pm 0.018$, i.e. $m^\ddagger = 0.201 \pm 0.050$ (20). In this work we find, for the reaction of **2** with bisulfate, log $k_0 = -1.60 \pm 0.13$ and $m^*(m^\ddagger - 1) = -0.612 \pm 0.024$, i.e. $m^\ddagger = 0.383 \pm 0.031$.

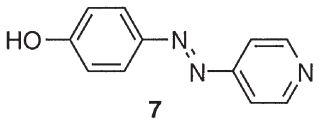

7

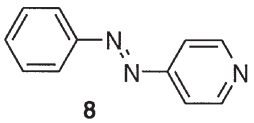

8

The kinetics of the disproportionation of **1** could be conveniently followed spectrophotometrically over the 60–86 wt.% H_2SO_4 range, by monitoring the formation of the azo product, 4-(4-chlorophenylazo)pyridine **2** (see Scheme 1) at either 354 nm (up to 72 wt.% H_2SO_4, monoprotonated form) or at 444 nm (at the higher acidities, diprotonated form). Reactions were generally followed over three half-lives, and all showed excellent first-order behaviour over this range. The observed pseudo-first-order rate constants, k_ψ, are given in Table 4, together with other pertinent information.

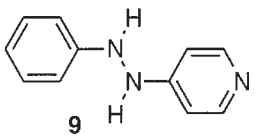

9

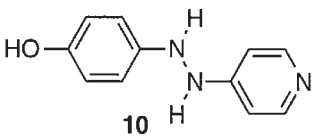

10

Fig. 1. Excess acidity plots for the reactions of **2** (open circles) and **8** (closed circles) (20) in aqueous sulfuric acid, assuming reaction with one bisulfate ion.

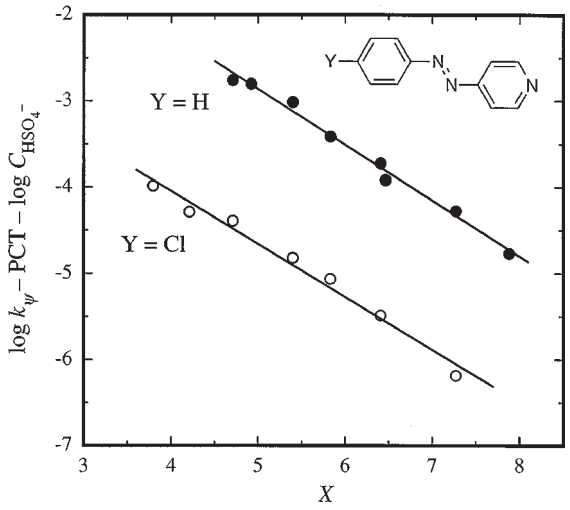

Table 4. Kinetic data for the disproportionation of 4-(4-chlorophenylhydrazo)pyridine **1**.

H_2SO_4, wt.%	k_ψ [a]	X [b]	log C_{H^+} [b]	PCT [c]	log k_ψ –PCT
59.96	0.0384	3.234	1.039	–0.644	–3.772
	0.0386				–3.769
64.99	0.162	3.793	1.078	–0.270	–3.520
	0.163				–3.518
68.22	0.362	4.208	1.100	–0.119	–3.322
	0.363				–3.321
71.67	0.839	4.708	1.122	–0.039	–3.037
	0.843				–3.035
75.86	2.02	5.397	1.144	–0.008	–2.687
	2.02				–2.687
78.28	3.01	5.830	1.154	–0.003	–2.518
	3.05				–2.513
81.36	5.44	6.407	1.157	–0.001	–2.263
	5.48				–2.260
85.98	16.7	7.274	1.118	0	–1.777
	16.9				–1.772

[a] Observed pseudo-first-order rate constants, $\times 10^3$ s^{-1}. Both duplicate determinations given.

[b] From ref. 37.

[c] Protonation Correction Term; log ($C_{BH_2^{2+}}$ / (C_{BH^+} + $C_{BH_2^{2+}}$)). Calculated using the p$K_{BH_2^{2+}}$ value of –4.806 (m^* = 1) given in Table 5.

These rate data were also treated according to the excess acidity method (25). To this end plots of log k_ψ – log C_{H^+} vs. X for **1**, together with the previously published equivalent plots for the parent 4-(phenylhydrazo)pyridine **9** and 4-(4-hydroxyphenylhydrazo)pyridine **10** for comparison (24), are shown here as Fig. 2. The observed downward curvature in Fig. 2 indicates (*a*) that the reaction is not an A-S_E2 process, as otherwise these plots would be straight, and (*b*) that the data go through a pK_a value (substrate titration) in an A1 reaction, which means that a protonation correction term has to be applied (25). Reaction with water in an A2 process would also

© 1998 NRC Canada

Fig. 2. Excess acidity plots of log k_ψ – log C_{H^+} vs. X for the reactions of **1** (open triangles), **9** (open circles) (24), and **10** (closed circles) (24) in aqueous sulfuric acid, illustrating the downward curvature due to substrate titration. The points are experimental and the curves theoretical, see text.

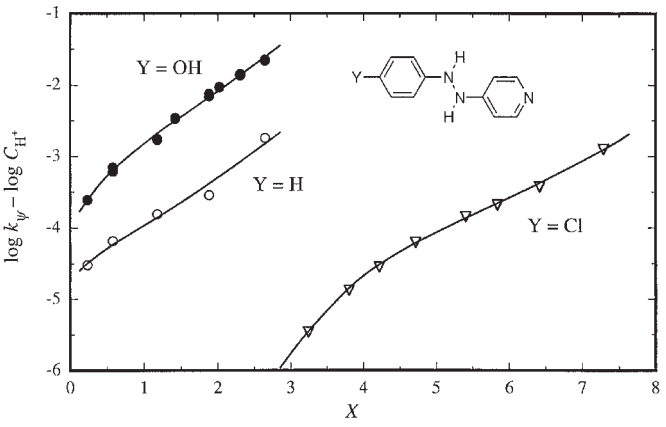

Table 5. Second basicities and excess acidity slopes and intercepts for the phenylhydrazopyridines **1**, **9**, and **10**.[a]

Substrate	Substituents	$pK_{BH_2^{2+}}$	log k_0	$m^\ddagger$
1	4-Cl	–4.806 ± 0.045	–5.371 ± 0.052	1.4915 ± 0.0092
9	H	–0.59 ± 0.45	–4.15 ± 0.52	1.87 ± 0.12
10	4-OH	–1.038 ± 0.090	–2.934 ± 0.098	1.872 ± 0.033

[a] Errors listed are standard deviations.

cause downward curvature in these plots (20, 27), but if that were the case here the curvature would be different for the different substrates, with much stronger curvature for **2** than for **10**, since the water activity decreases with acidity much faster at the higher acidities (4). The observed (Fig. 2) very similar curvature for **2** and **10** is much more likely to be due to a substrate titration; indeed, the Fig. 2 plots straighten out, as expected for a substrate protonation, rather than show the increasing curvature that would be expected for a reaction with water. This mechanistic distinction can now be made, with the addition of the data for **2**, whereas it could not without it (24).

The protonation involved is again the second one, undoubtedly on the hydrazo group, because these compounds are all already protonated on the pyridine ring, this process occurring in the pH range (8). The $pK_{BH_2^{2+}}$ values for these compounds are not known, and reaction is too fast to allow them to be measured, but $pK_{BH_2^{2+}}$ values can be estimated from the curvature of the kinetic plots in Fig. 2. It has recently been shown that quite precise values can be obtained in this way (29). The modified excess acidity equation for an A1 reaction that applies here, accounting for the changing state of protonation with acidity, is eq. [2] (25):

$$[2] \quad \log k_\psi - \log C_{H^+} - \log (C_{BH^+}/(C_{BH^+} + C_{BH_2^{2+}})) = \log (k_0/K_{BH_2^{2+}}) + m^\ddagger m^* X$$

where k_0 is the standard-state rate constant for the reaction. The protonation correction term in eq. [2], log $(C_{BH^+}/(C_{BH^+} + C_{BH_2^{2+}}))$, becomes log $(1/(1 + I))$ upon division by C_{BH^+}, and we can put $m^* = 1$ in the excess acidity equation

Fig. 3. Excess acidity plots of log k_ψ – log $(C_{BH_2^{2+}}/(C_{BH^+} + C_{BH_2^{2+}}))$ (PCT) vs. X for the reactions of **1** (open triangles), **9** (open circles), and **10** (closed circles) in aqueous sulfuric acid.

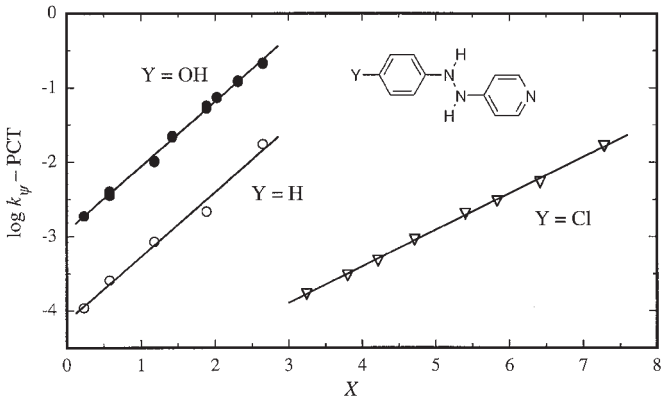

for equilibria (log $I = pK_{BH_2^{2+}} + m^*X + \log C_{H^+}$), because these hydrazo compounds are very similar to the H_0 primary aniline indicators, for which m^* is known to have the value 1.0 (37). Using eq. [2] means that we have three unknowns to calculate for each compound, slope ($m^\ddagger m^*$), intercept (log $(k_0/K_{BH_2^{2+}})$) and $pK_{BH_2^{2+}}$. A standard curve-fitting computer program was used (40), and the resulting, reasonably precise, $pK_{BH_2^{2+}}$ values are given in Table 5. These were then used to calculate protonation correction terms in the form log $(C_{BH_2^{2+}}/(C_{BH^+} + C_{BH_2^{2+}}))$. Subtraction of the latter from log k_ψ results in the very good straight lines in Fig. 3. This figure is drawn on the basis of full substrate protonation, which more accurately reflects the true situation at these acidities. The slope is $(m^\ddagger - 1)m^*$ and the intercept is log k_0 (25). These and the observed $m^\ddagger$ values, with their errors, are also given in Table 5. The $m^\ddagger$ values, all >1, are only consistent with an A1 mechanism (25). The Table 5 values were used to calculate the theoretical curves in Fig. 2.

Discussion

Reaction pathways

The products of the reactions of **1** and **2** in acid media, given in Table 1 and in Schemes 1–4, are quite complex. Although under kinetic conditions Schemes 1 and 4 prevail, it is nevertheless most convenient to begin with the elements that are common to several schemes. We have established previously (24) that 4-(phenylhydrazo)pyridines undergo a disproportionation in sulfuric acid media, for example, see Scheme 1, very similar to the processes undergone by other hydrazo compounds that have both 4-positions blocked (21, 41). Two substrate molecules give an azo compound (oxidized product) and two anilines (reduced products), as shown in Scheme 5. This disproportionation is much faster than any reaction undergone by the 4-(phenylazo)pyridine products (24); for the reactions of **1** and **2** this is readily apparent from a comparison of the rate constants in Tables 3 and 4. It is also very likely to be irreversible, since the reverse would be a termolecular process.

Deferring consideration of the mechanism until later, it is apparent that as soon as a hydrazo compound is formed it will react according to Scheme 5. The other products, apart from the dimer, can then be accounted for as shown in Scheme 6.

© 1998 NRC Canada

Scheme 5.

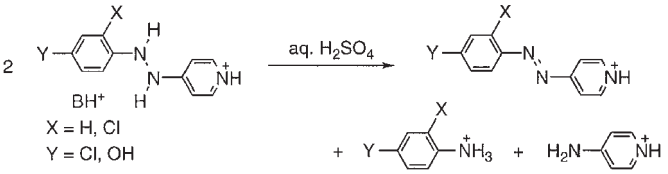

Scheme 6.

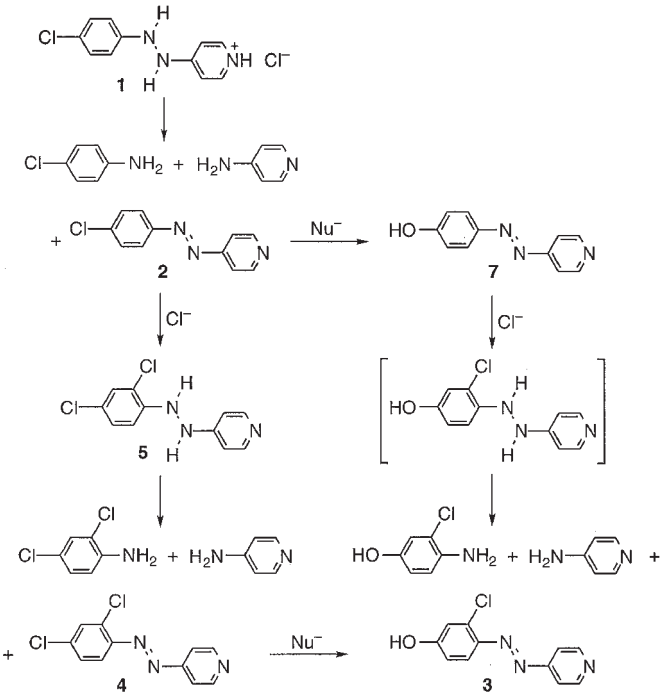

Scheme 7.

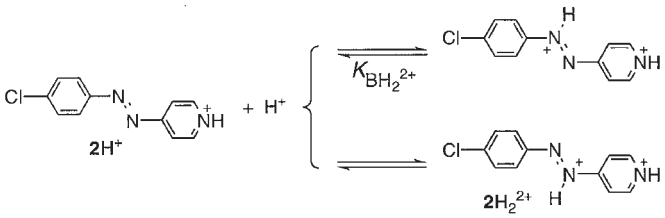

Scheme 8.

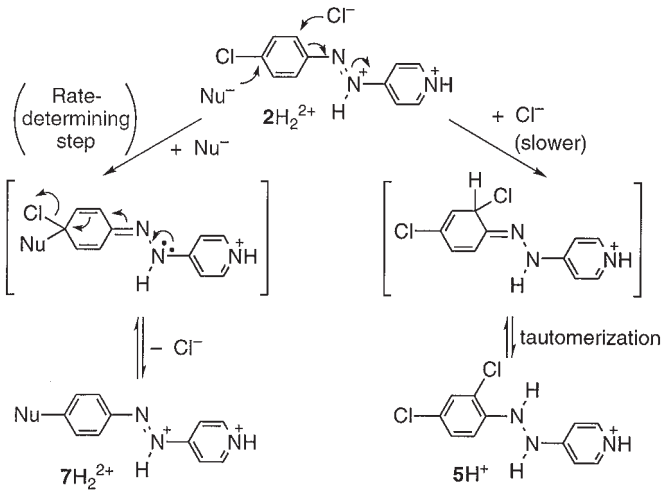

Starting with **1**, which has an equimolar amount of chloride ion present, product formation takes place from top to bottom on the left-hand side only, with no displacement by hydroxide occurring; products on the right are not observed if the starting material is **1**. On the other hand, if the starting material is **2** there is no free chloride ion present initially and the first reaction is **2** → **7**, with subsequent product formation taking place down both sides of Scheme 6, chloride ion accumulating as it is displaced. The hydrazo product in brackets is the only one we did not observe, presumably because it is too reactive.

The reaction of **2**H$^+$ begins with a second protonation (the reaction is acid catalyzed), undoubtedly on the azo group. There are two nitrogens that can be protonated, as shown in Scheme 7. It does not particularly matter which azo nitrogen bears the proton, since the nitrogen lone pairs do not form part of the π system, but it seems reasonable to place it on the nitrogen furthest from the pyridinium positive charge, and the p$K_{BH_2^{2+}}$ values quoted in Table 2 probably refer to this. However, it is easier to draw the mechanistic schemes for subsequent reactions with the proton on the other nitrogen, **2**H_2^{2+} in Scheme 7.

Two different mechanistic possibilities for **2**H_2^{2+} are given in Scheme 8. (In Scheme 8 and subsequently the attacking nucleophile is identified as either Cl^- or as Nu^-; the latter is actually HSO_4^- in these media, as shown by the kinetic analysis (see Fig. 1), but in the identified products it appears as OH, since these sulfate ester products hydrolyze very rapidly to phenols in more dilute acid, as we have shown previously (42), and this will occur during the product work-up.) Chloride ion is present during the reaction of **2** when it derives from **1**, since **1** had to be used as its hydrochloride salt, and it accumulates as Nu^- displaces it from **2**; it is the best nucleophile in the system, and can react at the 2-position of the phenyl group in **2**H_2^{2+} as shown on the right-hand side of Scheme 8. Tautomerization leads to the hydrazo compound **5**H$^+$, most of which will react according to Scheme 5, giving the observed product **4** (Schemes 2 and 3). However, in the initial reaction of **2** itself the chloride concentration is zero, and thus the rate-determining step involves diprotonated **2** and bisulfate ion, as shown by the kinetic analysis; this is the left-hand pathway in Scheme 8. Loss of chloride ion (a good leaving group) as shown gives **7**H_2^{2+}. With free chloride ion now present, the right-hand side of Scheme 8 can come into play, and **7**H_2^{2+} can also react further, as shown in Scheme 9. Presumably the better nucleophile Cl^- can react at the more crowded *ortho* site (Schemes 8 and 9), whereas the far worse (and much bigger) nucleophile HSO_4^- is limited to *para* attack.

The chlorination of **7**H_2^{2+}, shown in Scheme 9, will be faster than the chlorination of **2**H_2^{2+}, shown at the right of Scheme 8, because of the presence of the inductively electron-withdrawing oxygen in the Nu group encouraging nucleophilic attack. Again, fast tautomerization leads to a hydrazo compound, **11**H$^+$, which will immediately react via Scheme 5 to give the observed product **3** (Schemes 3 and 4); in fact this is the first-formed major product in the reaction of **2**, according to the kinetics and Scheme 4. There are other possibilities; for

© 1998 NRC Canada

Scheme 9.

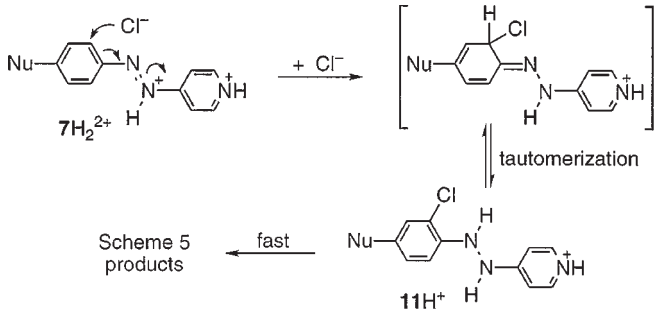

Scheme 10.

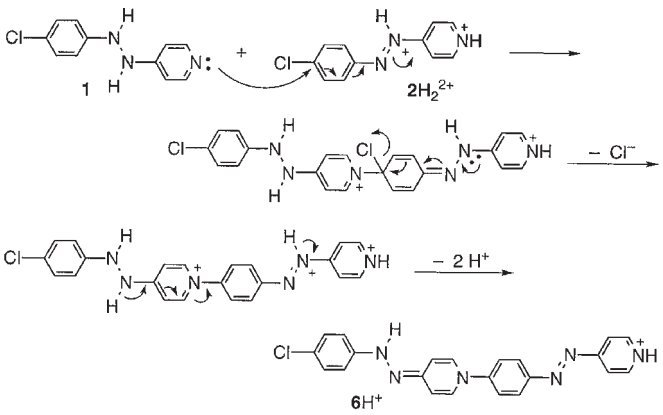

instance, it seems reasonable that $\mathbf{4}H_2^{2+}$ could undergo a chlorine displacement as in Scheme 8 to give $\mathbf{3}H_2^{2+}$ (and hence the isolated products should contain more **3** than **4**, see Table 1), and any two hydrazo compounds can take part in the disproportionation of Scheme 5. It is also possible (although probably less likely) that the 4-chloro- and 4-hydroxyanilinium ion products formed can be chlorinated at the 2-position by the free chloride ion (the presence of the $^+NH_3$ group increasing susceptibility to nucleophilic attack), perhaps giving rise to some of the observed 2,4-dichloro- and 2-chloro-4-hydroxyanilinium products.

The only remaining major product to be accounted for is the dimer **6**. It has been mentioned that chloride ion is the best nucleophile in the system, but if any starting material that is not protonated on the pyridine nitrogen is present, this will be quite nucleophilic as well. The simplest dimerization possibility is a nucleophilic attack by **1** on $\mathbf{2}H_2^{2+}$, as shown in Scheme 10. (It is likely that **1** will be protonated somewhere on the hydrazo group; for simplicity it is shown as being unprotonated in Scheme 10.) Loss of chloride ion from the resulting intermediate is straightforward, and simple loss of two more protons gives the observed dimer product **6**.

Another possibility results from an attack of $\mathbf{2}H^+$ on $\mathbf{2}H_2^{2+}$, as shown in Scheme 11. Essentially, chlorine has to be lost as Cl^+ in this scheme, but this has precedence in reactions of this type; Rhee and Shine have observed a similar Cl^+ loss during the benzidine rearrangement and disproportionation of 4,4′-dichlorohydrazobenzene (43). Whatever the dimerization mechanism may be, presumably dimerization will diminish in importance as the acidity increases, since the probability of

Scheme 11.

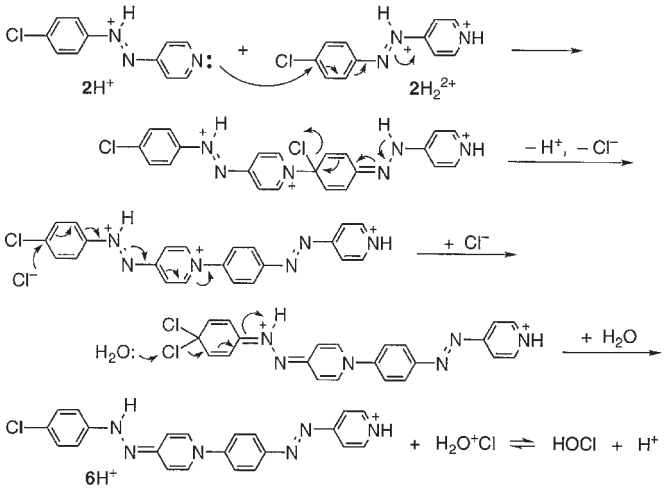

Scheme 12.

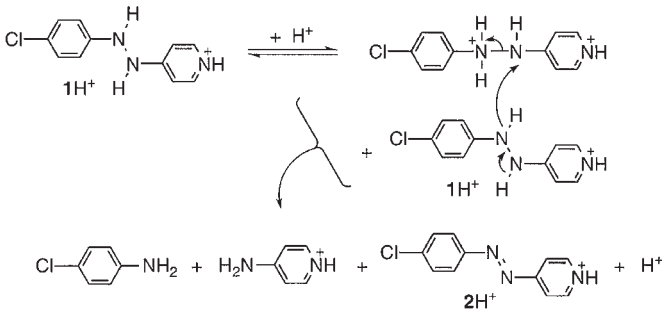

having an unprotonated pyridine nitrogen present decreases with increasing acidity, and, being bimolecular, the reaction will only occur at all at the high substrate concentrations used for the product analysis.

pK_a relationships

The $pK_{BH_{2^+}}$ values for the various 4-(arylphenylazo)pyridines listed in Table 2 seem reasonable, with compounds having electron-donating OH groups being easier to protonate on the azo group, and those with electron-withdrawing Cl being more difficult. There are insufficient data for a good linear free energy relationship (some of the substituents are *ortho* in any case), but a ρ^+ value of -2.9 ± 0.6 can be estimated. The m^* slopes show considerable variation, averaging 0.86 ± 0.09. The reactions undergone by **2** and **8** are not quite the same, that of **2** being an *ipso* substitution at a carbon already bearing a substituent but, as Fig. 1 shows, the kinetic behaviour is very similar, and reaction of the deactivated chloro compound is slower, by a factor of ~100 in the standard state according to the intercept difference.

The $m^‡$ values for both **2** and **8** are <0.5. At the moment

© 1998 NRC Canada

Scheme 13.

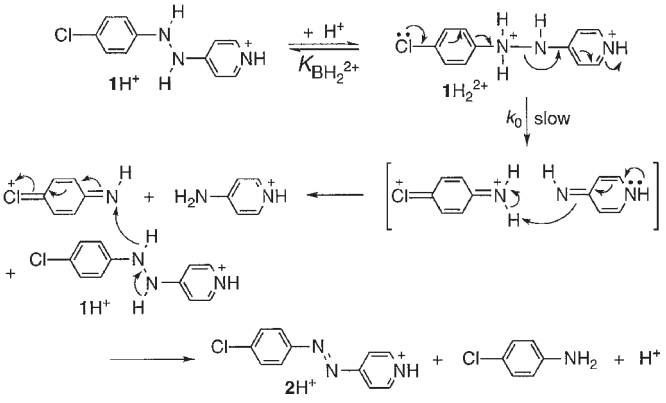

there are very few data for comparison, and so it is difficult to predict $m^{\ddagger}$ values for reaction with bisulfate. In the case of protonated benzamide a value of 1.1 was found for nucleophilic attack of bisulfate at the carbonyl group (44) (but this number is subject to revision (26)), and for several substituted alkylnitramines values of $m^{*}m^{\ddagger}$ between 0.9 and 1.2 were found for S_N2 displacement by bisulfate (27), the value of m^{*} unfortunately not being known. Neither case corresponds very well to the situation in the reaction under discussion here, nucleophilic attack on a benzene ring.

Benzidine disproportionation mechanism

Proposed mechanisms for the benzidine disproportionation of **1** (and the other 4-(phenylhydrazo)pyridines involved in this work) have to account for the observed kinetic behaviour, which is that the rate-determining step of these disproportionations is an A1 process involving the diprotonated substrate, as well as the reaction products. The second protonation is written as occurring on the hydrazo nitrogen away from the pyridinium ring. There are two reasons for this: apart from simple electrostatic repulsion of the two positive charges, the lone pair on the other nitrogen is occupied to some extent in resonance interaction with the pyridinium centre, as shown, and so is less available for protonation.

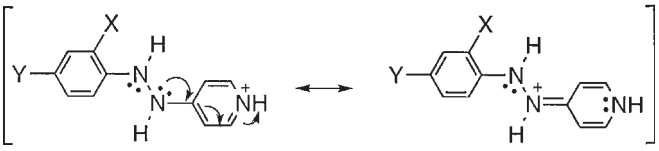

Processes such as the one shown in Scheme 12, although it gives the correct products, can be ruled out as Scheme 12 would result in second-order kinetics, and all of the observed kinetics were accurately first order, for **1** and also for **9** and **10** (24).

Scheme 13, involving rate-determining breakup of diprotonated $\mathbf{1}H_2^{2+}$, is a more plausible mechanism. Deriving an excess acidity rate equation based on Scheme 13 is straightforward (25). On the basis of full substrate diprotonation, the observed rate constants k_{ψ} can be equated with k_0 and the activities of the species present in the activated complex according to eq. [3].

$$[3] \quad k_{\psi}\,(C_{BH^+} + C_{BH_2^{2+}}) = k_0 a_{BH_2^{2+}}/f_{\ddagger}$$

Scheme 14.

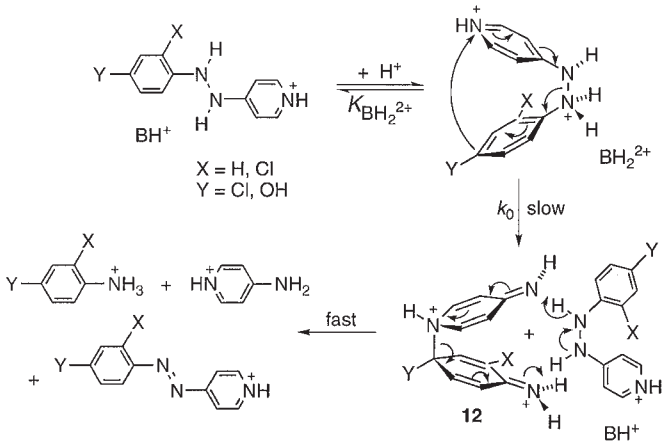

$$[4] \quad \log k_{\psi} - \log\,(C_{BH_2^{2+}}/(C_{BH^+} + C_{BH_2^{2+}})) = \log k_0 + (m^{\ddagger} - 1)m^{*}X$$

Upon replacing activity by concentration and activity coefficient, taking logs and rearranging, eq. [3] becomes eq. [4], since the log activity coefficient ratio term here is equal to $(m^{\ddagger} - 1)m^{*}$ (25), where the slope parameters m^{*} (= 1 in this case) and $m^{\ddagger}$ are defined above. This is the rate equation that gives the good straight lines in Fig. 3.

Although Scheme 13 explains the products and the kinetics, there is a problem with it. The proposed chloronium intermediate is actually a nitrenium ion:

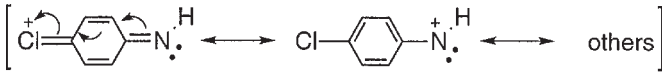

and these are highly reactive, with very short lifetimes (45). They have carbene-like properties, and would be expected to react almost instantly with the water present, probably on the aromatic ring (46). So Scheme 13 can be ruled out on the grounds that this nitrenium ion would not exist long enough for the suggested hydride transfer from another $\mathbf{1}H^+$ molecule to be possible.

Thus the most likely mechanism for the reaction of **1**, **9**, and **10**, and the other hydrazo compounds suggested as intermediates in this work, is the benzidine-type disproportionation mechanism shown in Scheme 14 for the general structure BH^+, as proposed previously (24). This would give the same kinetic behaviour as does Scheme 13, i.e., eq. [4] is followed. The rate-determining step is a thermally allowed 10-electron electrocyclic reaction involving the diprotonated substrate BH_2^{2+}, giving rise to intermediate **12**. This is now firmly established as being the key step in the rearrangement mechanism for hydrazobenzene and many other hydrazo aromatics, primarily by the application of heavy-atom isotope effect studies to these processes (21, 23). Also, for hydrazobenzene itself, an intermediate equivalent to **12** has been experimentally observed under stable-ion conditions (47). Regular hydrazo compounds can form benzidines by rearomatization of intermediates like **12**, but this cannot happen here because the pyridine nitrogen would have to acquire a permanent positive charge, and

© 1998 NRC Canada

because of the presence of the substituents. So disproportionation occurs instead, and reaction with another BH^+ molecule is proposed by analogy with a similar proposal made for the disproportionation of 4,4′-diiodohydrazobenzene (21, 41). This is likely to be quite a fast reaction, because (*a*) it is a highly favourable, thermally allowed 14-electron electrocyclic reaction, (*b*) it is energetically downhill because the aromatic protonated products formed are all much more stable than is **12** in the reaction medium, and (*c*) formation of three molecules from two counteracts the entropy factor involved in orienting **12** and BH^+ for reaction.

The benzidine rearrangement of hydrazobenzenes is a fast reaction (1). Our reactions are quite fast, but rate comparisons are difficult because most other kinetic studies have been performed in dilute acid media containing a cosolvent, and the acid used is usually HCl or $HClO_4$ rather than H_2SO_4 (1). The most recent study is that of Bunton and Rubin (48), who studied hydrazobenzene (i.e., 1,2-diphenylhydrazine) and two substituted hydrazobenzenes in pure aqueous HCl and $HClO_4$ to concentrations of about 1 M; their substrates were diprotonated (on both hydrazo nitrogens), and their reaction rates were much faster than ours, in the stopped-flow range.

Depending on the substrate, the hydrazo group may be diprotonated, monoprotonated, or even unprotonated during the rearrangement step, but the process is fastest for diprotonated substrates and slowest for unprotonated ones (1, 21, 48). Our substrates are diprotonated but one of the protons is on the pyridine nitrogen; because of this, protonation on the other hydrazo nitrogen (to give a triprotonated species) is expected to be very difficult, only occurring at acidities much higher than those used here. Diprotonation in hydrazobenzenes is assumed to speed reaction by encouraging N—N bond cleavage and the subsequent charge separation (1). Hydrazo group protonation presumably does that here too, but since the two positive charges are further apart in our case the reaction will not be accelerated nearly so much, which probably accounts for our rates being slower than those of Bunton and Rubin.

Mechanisms are sometimes suggested for the benzidine rearrangement in which the second proton transfer is part of the rate-determining step (A-S_E2 mechanism). For instance, rate-limiting ring carbon protonation followed by fast N—N bond cleavage (47) was a popular mechanism at one time (1), as was rate-determining formation of the $-\overset{+}{N}H_2 - \overset{+}{N}H_2-$ species with its subsequent rearrangement being a fast process (48). More recent heavy-atom isotope effect results (49) have rendered these mechanisms unlikely, however (21). For the disproportionations in this paper we have good evidence that the second protonation is a pre-equilibrium process (A1 mechanism) and not part of the rate-determining step: the excellent linearity of the Fig. 3 plots, and the fact that the $m^‡$ values (Table 5) are all much greater than one (25).

The log k_0 values in Table 5 fall in the expected order, electron-donor OH fastest, then H, with the electron-withdrawing Cl slowest. The observed $pK_{BH_2^{2+}}$ values (Table 5) are indicative of only inductive interaction with the positive charge on the hydrazo group; both OH and Cl are inductively electron withdrawing, and both **1** and **10** are more basic than **9**. Any attempted mesomeric interaction of the lone pairs on oxygen with the positive charge on the hydrazo nitrogen leads to cleavage of the N—N bond as shown at the top of Scheme 13, and this was not observed.

The $m^‡$ values in Table 5 are all quite large, 1.5–1.9, values that are only compatible with an A1 reaction mechanism (25), as discussed. However, they are not all the same; the value for **1**, with a *p*-Cl substituent, is smaller than the others. Variation of $m^‡$ with substituent is not unusual; for instance, a gradual increase with σ^* was observed in *N*-nitro amine decompositions in aqueous H_2SO_4 (27), a slow decrease with σ^+ was seen in some phenylpropiolic acid hydrations in these media (50), and slow increases or decreases with σ or σ^+ were found for some acylal and thioacylal hydrolyses (51), and some thiol- and thion-benzoate ester hydrolyses, in aqueous H_2SO_4 (52). What, if anything, these trends mean is not clear at present, although as data accumulate it may become possible to use them for mechanistic diagnosis. It is interesting that Marziano, Tomasin, and Tortato have commented upon similar trends in m^* value in a variety of aqueous acid systems (53), although it is not certain with the data available at present that the adduced variations are real.

Hydroxylation of the (arylazo)pyridines is an unusual reaction. Normal azobenzenes are stable in strong acid solution, indeed, acidity functions based on their protonation behaviour have been defined (54). Presumably the strongly electron-withdrawing pyridinium substituent in these molecules strongly activates the other ring to nucleophilic attack. The benzidine rearrangement and related processes have always fascinated chemists, and interest in them continues to be high (1, 21–24). For instance, an 18-electron thermally allowed electrocyclic reaction in a benzidine rearrangement has been described very recently (55), which complements the 10- and 14-electron processes discussed in this work. To our knowledge, the work in this paper is the first definitive delineation of the mechanism of the acid-catalyzed benzidine disproportionation reaction as an A1 process.

Acknowledgments

Financial support of this research through a grant by the Natural Sciences and Engineering Research Council of Canada (to E.B.) is gratefully acknowledged. We would also like to thank a referee for helpful comments.

References

1. R.A. Cox and E. Buncel. *In* The chemistry of the hydrazo, azo and azoxy groups. Vol. 1. *Edited by* S. Patai. Wiley, London. 1975. p. 775.
2. E. Buncel and B.T. Lawton. Can. J. Chem. **43**, 862 (1965).
3. E. Buncel and W.M.J. Strachan. Can. J. Chem. **48**, 377 (1970).
4. R.A. Cox. J. Am. Chem. Soc. **96**, 1059 (1974).
5. R.A. Cox and E. Buncel. J. Am. Chem. Soc. **97**, 1871 (1975); E. Buncel, R.A. Cox, and A.J. Dolenko. Tetrahedron Lett. 215 (1973); R.A. Cox, A.J. Dolenko, and E. Buncel. J. Chem. Soc. Perkin Trans. 2, 471 (1975).
6. E. Buncel. Acc. Chem. Res. **8**, 132 (1975).
7. E. Buncel and S.-R. Keum. J. Chem. Soc. Chem. Commun. 578 (1983).
8. E. Buncel and S.-R. Keum. Tetrahedron, **39**, 1091 (1983).
9. S. Rajagopal and E. Buncel. Dyes Pigm. **17**, 303 (1991).
10. E. Buncel and S. Rajagopal. J. Org. Chem. **54**, 798 (1989); Acc. Chem. Res. **23**, 226 (1990).

© 1998 NRC Canada

11. S.-R. Keum, S.-S. Hur, P.M. Kazmaier, and E. Buncel. Can. J. Chem. **69**, 1940 (1991).
12. S.-R. Keum, K.-B. Lee, P.M. Kazmaier, R.A. Manderville, and E. Buncel. Magn. Reson. Chem. **30**, 1128 (1992).
13. S.-R. Keum, K.-B. Lee, P.M. Kazmaier, and E. Buncel. Tetrahedron Lett. **35**, 1015 (1994).
14. S.-R. Keum, S.-S. Lim, B.-H. Min, P.M. Kazmaier, and E. Buncel. Dyes Pigm. **30**, 225 (1996).
15. S.-R. Keum, P.M. Kazmaier, K.-S. Cheon, R.A. Manderville, and E. Buncel. Bull. Korean Chem. Soc. **17**, 391 (1996).
16. S. Swansburg, Y.-K. Choi, S.-R. Keum, E. Buncel, and R.P. Lemieux. Liq. Cryst. In press (1998).
17. S.-R. Keum, M.-J. Lee, S. Swansburg, E. Buncel, and R.P. Lemieux. Dyes Pigm. In press (1998).
18. E. Buncel and I. Onyido. Can. J. Chem. **64**, 2115 (1986).
19. R. A. Cox, I. Onyido, and E. Buncel. J. Am. Chem. Soc. **114**, 1358 (1992).
20. K.-S. Cheon, R.A. Cox, S.-R. Keum, and E. Buncel. J. Chem. Soc. Perkin Trans. 2, 1231 (1998).
21. R.A. Cox and E. Buncel. *In* The chemistry of the hydrazo, azo and azoxy groups. Vol. 2. *Edited by* S. Patai. Wiley, London. 1997. p. 569.
22. D.V.Banthorpe, E.D. Hughes, and C.K. Ingold. J. Chem. Soc. 2864 (1964); D. V. Banthorpe. Top. Carbocycl. Chem. **1**, 1 (1969); H.J. Shine. Aromatic rearrangements. Elsevier, Amsterdam. 1967. p. 126; *In* Mechanisms of molecular migrations. Vol. 2. *Edited by* B.S. Thyagarajan. Wiley, New York. 1969. p. 191.
23. H.J. Shine. J. Phys. Org. Chem. **2**, 491 (1989); *In* Isotopes in organic chemistry. Vol. 8. *Edited by* E. Buncel and W.H. Saunders. Elsevier, Amsterdam. 1992. p. 1.
24. E. Buncel and K.-S. Cheon. J. Chem. Soc. Perkin Trans. 2, 1241 (1998).
25. R.A. Cox. Acc. Chem. Res. **20**, 27 (1987); R.A. Cox and K.Yates. Can. J. Chem. **57**, 2944 (1979).
26. R.A. Cox. Can. J. Chem. **76**, 649 (1998).
27. R.A. Cox. Can. J. Chem. **74**, 1774 (1996).
28. R.A. Cox. J. Chem. Soc. Perkin Trans. 2, 1743 (1997).
29. R.A. Cox. Can. J. Chem. **75**, 1093 (1997).
30. R.A. Cox, D.B. Moore, and R.S. McDonald. Can. J. Chem. **72**, 1910 (1994).
31. J.-P. Bégué, F. Benayoud, D. Bonnet-Delpon, A.D. Allen, R.A. Cox, and T.T. Tidwell. Gazz. Chim. Ital. **125**, 399 (1995); Y. Chiang, A.J. Kresge, P.A. Obraztsov, and J.B. Tobin. Croat. Chem. Acta, **65**, 615 (1992), and earlier papers; M. Lajunen, M. Virta, and O. Kylläinen. Acta Chem. Scand. **48**, 122 (1994), and earlier papers.
32. R.A. Cox. J. Phys. Org. Chem. **4**, 233 (1991).
33. M. Lajunen, R. Laine, and M. Aaltonen. Acta Chem. Scand. **51**, 1155 (1997), and earlier papers.
34. M. Ali and D.P.N. Satchell. J. Chem. Soc. Perkin Trans. 2, 167 (1995); J. Chem. Soc. Perkin Trans. 2, 1825 (1993).
35. E. Koenigs, W. Freigang, G. Lobmayer, and A. Zscharn. Ber. Dtsch. Chem. Ges. **59B**, 321 (1926).
36. C.T. Davis and T.A. Geissman. J. Am. Chem. Soc. **76**, 3507 (1954).
37. R.A. Cox and K. Yates. J. Am. Chem. Soc. **100**, 3861 (1978).
38. R A. Cox and K. Yates. Can. J. Chem. **59**, 1560 (1981).
39. R.A. Cox, L.M. Druet, A.E. Klausner, T.A. Modro, P. Wan, and K. Yates. Can. J. Chem. **59**, 1568 (1981); R.A. Cox and K. Yates. Can. J. Chem. **59**, 2116 (1981); Can. J. Chem. **62**, 2155 (1984).
40. P.R. Bevington. Data reduction and error analysis for the physical sciences. McGraw–Hill, New York. 1969. p. 237.
41. H.J. Shine, J. Habdas, H. Kwart, M. Brechbiel, A.G. Horgan, and J. San Filippo. J. Am. Chem. Soc. **105**, 2823 (1983).
42. E. Buncel and W.M.J. Strachan. Can. J. Chem. **47**, 911 (1969).
43. E.-S. Rhee and H.J. Shine. J. Am. Chem. Soc. **108**, 1000 (1986).
44. R.A. Cox and K. Yates. Can. J. Chem. **59**, 2853 (1981).
45. R.A. McClelland. Tetrahedron, **52**, 6823 (1996); J.C. Fishbein and R.A. McClelland. Can. J. Chem. **74**, 1321 (1996).
46. M. Novak, M.J. Kahley, J. Lin, S.A. Kennedy, and L.A. Swanegan. J. Am. Chem. Soc. **116**, 11626 (1994).
47. G.A. Olah, K. Dunne, D.P. Kelly, and Y.K. Mo. J. Am. Chem. Soc. **94**, 7438 (1972).
48. C.A. Bunton and R.J. Rubin. J. Am. Chem. Soc. **98**, 4236 (1976).
49. H.J. Shine, G.N. Henderson, A. Cu, and P. Schmid. J. Am. Chem. Soc. **99**, 3719 (1977).
50. R.A. Cox, E. Grant, T. Whitaker, and T.T. Tidwell. Can. J. Chem. **68**, 1876 (1990).
51. R.A. Cox and K. Yates. J. Org. Chem. **51**, 3619 (1986).
52. R.A. Cox and K. Yates. Can. J. Chem. **60**, 3061 (1982).
53. N.C. Marziano, A. Tomasin, and C. Tortato. Org. React. (Tartu), **30**, 39 (1996).
54. H.H. Jaffé and R.W. Gardner. J. Am. Chem. Soc. **80**, 319 (1958); S.-J. Yeh and H.H. Jaffé. J. Am. Chem. Soc. **81**, 3274 (1959); A.J. Kresge and H.-J. Chen. J. Am. Chem. Soc. **94**, 8192 (1972).
55. K.H. Park and J.S. Kang. J. Org. Chem. **62**, 3794 (1997).

© 1998 NRC Canada

On the role of copper and iron in DNA cleavage by ochratoxin A. Structure–activity relationships in metal binding and copper-mediated DNA cleavage

Jason A. Ardus, Ivan G. Gillman, and Richard A. Manderville

Abstract: Ochratoxin A (OTA, **1**: X = Cl) is a fungal carcinogen that facilitates single-strand DNA cleavage and DNA adduction when metabolically activated. To determine if redox-active transition metals induce OTA-mediated DNA damage, we have examined the toxin's ability to bind Cu(II) and Fe(III) in aqueous media and facilitate DNA cleavage in their presence using agarose gel electrophoresis and supercoiled plasmid DNA. Using fluorescence spectroscopy, **1** was found to bind Cu(II) readily at physiological pH, while acidic conditions (pH 2.6) were employed to study Fe(III) binding due to the formation of Fe-oxide precipitates at higher pH values. Structure–activity relationships employing synthetic derivatives of **1** implied that **1** binds both Cu(II) and Fe(III) by its phenolic oxygen, while the carboxylic acid of its phenylalanine moiety binds Cu(II), but does not appear to play a role in Fe(III) coordination at pH 2.6. In terms of metal-mediated DNA cleavage, no role for **1** could be detected in Fe-induced DNA strand scission. With Cu(II), DNA cleavage by the 1:1 copper-bound complex of **1** could only be initiated by addition of a suitable reducing agent (sodium ascorbate). However, **1** was found to facilitate DNA cleavage by the Cu(II) complex of 1,10-phenanthroline ($Cu(OP)_2$); a prototypical Cu-mediated nuclease system that cleaves DNA upon activation by an external reducing agent. Structure–activity relationships employing analogs lacking the chlorine atom, ochratoxin B (**2**: X = H), and the lactone (**12**), indicated that the chlorine atom is essential for activity of the OTA in potentiating DNA cleavage by $Cu(OP)_2$. The implications of our findings to the genotoxic properties of **1** are discussed.

Key words: ochratoxin, DNA cleavage, copper, iron, 1,10-phenanthroline.

Résumé : L'ochratoxine A (OTA, **1**; X = Cl) est un cancérigène de champignon qui, lorsqu'il est métaboliquement activé, facilite le clivage de l'ADN monobrin et l'adduction de l'ADN. Dans le but de déterminer si les métaux de transition actifs en oxydoréduction induisent des dommages à l'ADN sous l'influence de l'OTA, on a utilisé l'électrophorèse sur gel d'agarose et un plasmide d'ADN surtorsadé pour examiner l'habilité de la toxine à se lier au Cu(II) et au Fe(III) en milieu aqueux et à faciliter le clivage de l'ADN en leur présence. En utilisant la spectroscopie de fluorescence, on a trouvé que **1** se lie facilement au Cu(II) à pH physiologique alors que, à cause de la formation de précipités d'oxyde de Fe à des valeurs de pH plus élevées, des conditions acides sont nécessaires pour étudier la liaison avec le Fe(III). Des relations structure–activité développées à l'aide de dérivés synthétiques de **1** impliquent que **1** se lie au Cu(II) ainsi qu'au Fe(III) par son oxygène phénolique; par ailleurs, l'acide carboxylique de sa partie phénylalanine se lie au Cu(II), mais ne semble pas jouer de rôle dans la coordination du Fe(III) à un pH de 2,6. En termes de clivage de l'ADN sous l'influence des métaux, on n'a détecté aucun rôle pour **1** dans la scission de l'ADN catalysé par le Fe(III). Avec le Cu(II), le clivage de l'ADN par le complexe 1:1 de cuivre lié à **1** ne peut être initié que par l'addition d'un agent réducteur approprié (ascorbate de sodium). Toutefois, on a trouvé que **1** facilite le clivage de l'ADN par le complexe du Cu(II) avec la 1,10-phénanthroline, ($Cu(OP)_2$), un prototype de système de nucléase catalysée par le Cu qui clive l'ADN lors d'une activation par un agent réducteur externe. Les relations structure–activité utilisant des analogues ne comportant pas d'atome de chlore, ochratoxine B (**2**, X = H) et la lactone (**12**), indiquent que l'atome de chlore est essentiel pour l'activité de l'OTA pour potentialiser le clivage de l'ADN par le $Cu(OP)_2$. On discute des implications de nos observations en relation avec les propriétés génotoxiques de **1**.

Mots clés : ochratoxine, clivage d'ADN, cuivre, fer, 1,10-phénanthroline.

[Traduit par la rédaction]

This paper is dedicated to Professor Erwin Buncel, my mentor, who was the first to stimulate my interest in physical organic chemistry.

Received November 17, 1997.

J.A. Ardus, I.G. Gillman, and R.A. Manderville.[1] Department of Chemistry, Wake Forest University, Winston-Salem, NC 27109–7486, U.S.A.

[1] Author to whom correspondence may be addressed. Telephone: (336)-758–5513. Fax: (336)-758–4698. E-mail: manderra@wfu.edu

© 1998 NRC Canada

Scheme 1. Synthetic route used for the preparation of the dihydroisocoumarine.

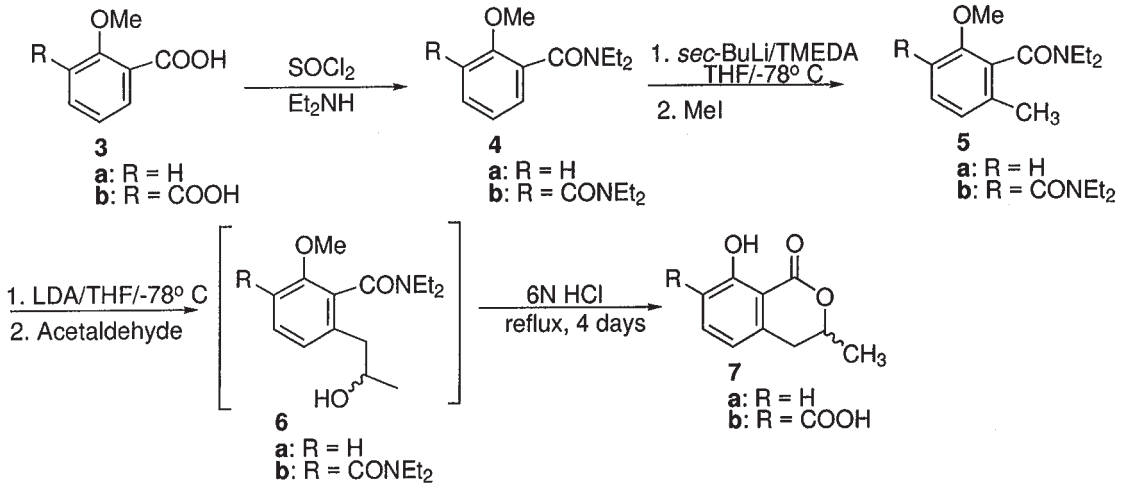

Ochratoxin A (OTA, **1**: X = Cl) is a fungal carcinogen produced by species of *Aspergillus* and *Penicillium* (1). Its occurrence in feed is widespread (2) and ingestion has been linked to the disease Balkan endemic nephropathy in which patients suffer from urinary tract tumors (3). The toxin consists of a phenolic dihydroisocoumarin, amide linked to L-phenylalanine, and has been shown to promote DNA adduction (4) and single-strand DNA cleavage (5); properties that establish a basis for its genotoxic action.

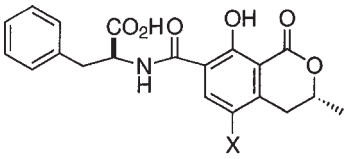

OTA, **1**: X = Cl
OTB, **2**: X = H

Although the mechanisms underlying the genotoxicity of OTA are uncertain, in vivo studies have established that the chlorine atom (6) and lactone (7) are essential and that activation may be mediated by cytochrome P-450 (8) with subsequent formation of activated oxygen species, such as superoxide (9) and (or) hydroxyl radicals (10, 11). The ability of **1** to bind Fe(III) has also been implicated as a possible source of reactive oxygen species that promote lipid peroxidation (12), and may facilitate DNA cleavage (10). Reports by Hecht et al. (13) and Li and Trush (14) that certain phenols and hydroquinones damage DNA by a copper-redox mechanism implies that Cu(II) ions may also play a role in OTA carcinogenicity.

Since OTA activation appears to be oxidative (3–11) and may involve participation of redox-active transition metals (9–14), we examined the toxin's ability to bind Cu(II) and Fe(III) in aqueous solutions and facilitate DNA cleavage in their presence using supercoiled plasmid DNA and agarose gel electrophoresis.

In the present article, we report that, although no role for **1** in Fe-mediated DNA cleavage could be detected, the toxin was found to bind Cu(II) to form a stable 1:1 complex that initiates DNA strand scission upon activation by a suitable reducing agent (sodium ascorbate). However, more importantly to the possible mechanism of OTA genotoxicity, the toxin was found to facilitate DNA cleavage by the Cu(II) complex of 1,10-phenanthroline ($Cu(OP)_2$), a well-known footprinting reagent (15) that requires an external reducing agent to convert Cu(II) → Cu(I). Structure–activity relationships employing synthetic derivatives of **1** that lack the chlorine atom, OTB (**2**, X = H), and the lactone functionality indicated that these components (especially the chlorine atom) facilitate the ability of **1** to potentiate DNA cleavage by $Cu(OP)_2$. This contrasting behavior for **1** in Cu-mediated DNA cleavage is discussed through consideration of the toxin's chelating versus redox properties.

Results

Synthesis of structural analogs

To derive structure–activity relationships for metal binding and DNA cleavage by ochratoxin A (OTA, **1**: X = Cl), we prepared analogs that lack the following: the chlorine atom, OTB, **2**: X = H; the dihydroisocoumarine (lactone), (**12**); and the phenylalanine moiety, (±)-mellein (**7a**) (16). Derivatives of **2** containing an altered phenylalanine side-chain, i.e., the methyl ester (**9a**) and the amide (**9b**), were also prepared.

Compounds containing the lactone ring system of **1** were synthesized according to methods outlined in Scheme 1. Using procedures described by Snieckus and co-workers (17), *o*-anisic acid (2-methoxybenzoic acid, **3a**) was converted into (±)-mellein (**7a**) (16), while 2-methoxyisophthalic acid (**3b**) yielded the carboxylic acid derivative **7b** (17).

To attach the L-β-phenylalanine side-chain moiety, the phenolic groups were initially protected as the acetate and then reacted with the requisite phenylalanine using a dicyclohexylcarbodiimide (DCC)/1-hydroxybenzotriazole (HOBT) peptide coupling procedure (18), as outlined in Scheme 2. The coupled products, **9a**, **9b**, and **11**, were isolated as the free phenols as the acetate protecting groups were lost in the work-up. Hydrolysis of the methyl ester derivatives (**9a** and **11**) into the corresponding free acids (**2** and **12**) was carried out under basic conditions. These strategies provided mixtures of stereoisomers for **2**, **9a**, and **9b** that were not separated.

© 1998 NRC Canada

Scheme 2. Synthetic route used for attachment of the phenylalanine moiety.

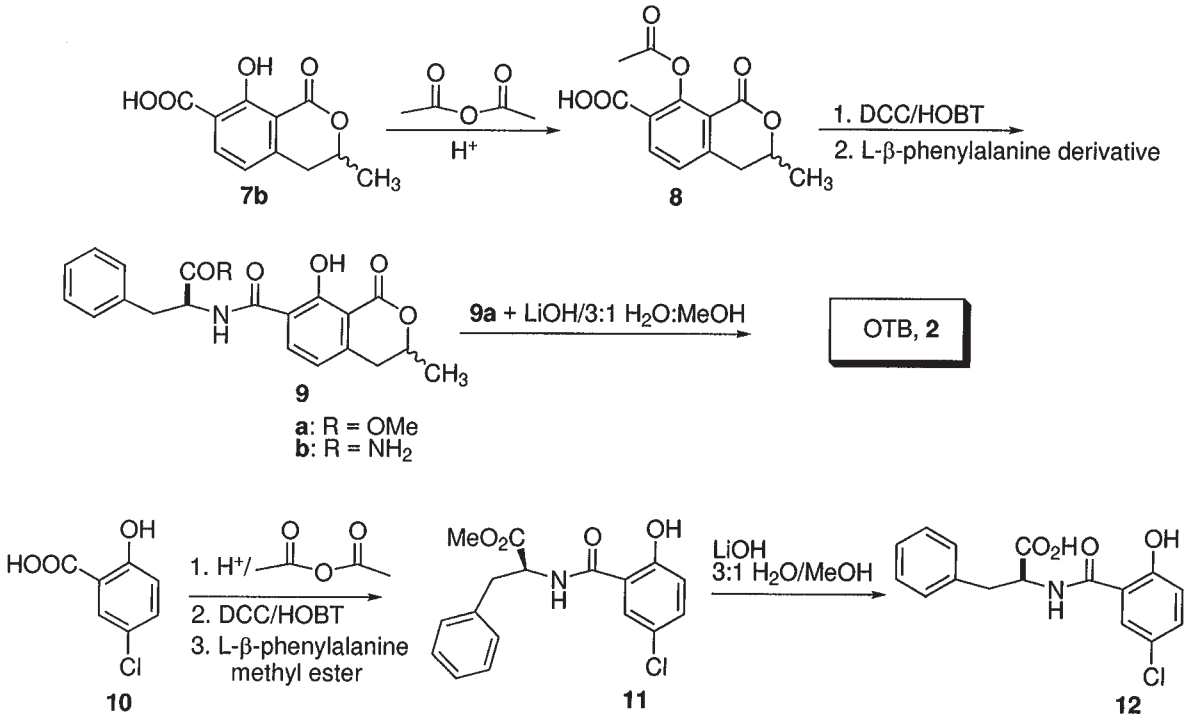

Fig. 1. The UV–absorption spectrum of **1** in ethanol (0.175 mM) in the absence (bold trace) and presence of 1 equiv. of $Cu(OAc)_2$. Inset: spectrum of Cu(II)·OTA complex at 1.75 mM highlighting the absorbance at 608 nm.

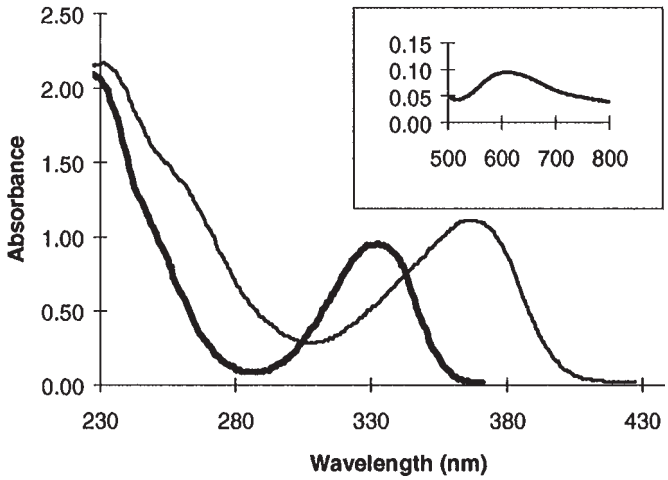

Copper and iron binding affinity

In ethanol, **1** exhibits an absorption spectrum with λ_{max} at 215 (ε = 28 000 M^{-1} cm^{-1}) and 333 nm (ε = 5500 M^{-1} cm^{-1}) (19). Addition of 1 equiv. of $Cu(OAc)_2$ yielded a pale green solution with λ_{max} at 222 (ε = 20 911 M^{-1} cm^{-1}), 258 (sh), 367 (ε = 6420), and 608 nm (ε = 55) (Fig. 1). Figure 2 shows the electrospray mass spectrum of the 1:1 mixture (in methanol) using negative ionization (ES^-). The copper complex was found to have $[M - H]^-$ = 463, which corresponds to a complex with molecular formula $CuC_{20}H_{16}NO_6Cl$ and suggests that complexation between **1** (*m*/*z* 403) and Cu(II) (*m*/*z* 63) leads to the loss of two protons. This observation strongly implies that the ligands bearing the two acidic groups of **1** (COOH and phenolic oxygen) participate in copper coordination. The OTA also forms a 1:1 complex with $FeCl_3$ that is pink in alcoholic solution (10). Generation of the complex in methanol followed by analysis by ES^- showed the presence of a single iron complex with $[M - H]^-$ = 563. This mass corresponds to a complex with molecular formula $FeC_{20}H_{18}NO_6Cl_4$ and indicates that $FeCl_3$ (*m*/*z* = 161) binding in methanol does not lead to deprotonation of **1**. Table 1 contains UV–absorption data in ethanol for the protonated and deprotonated forms of **1**, **2**, and **12**, along with their corresponding 1:1 Cu(II) and Fe(III) complexes.

The ability of **1** to bind Cu(II) and Fe(III) was determined in aqueous buffer at 25°C using fluorescence spectroscopy. Addition of Cu(II) and Fe(III) quenched the fluorescence of the toxin (10), which permitted determination of apparent equilibrium binding constants (log *K**). That the observed fluorescence quenching was due to metal binding was confirmed by performing the metal titration in the presence of excess EDTA. This metal chelator inhibited the fluorescence quenching if added prior to addition of the metal, and restored the fluorescence of OTA if added after the titration.

Figure 3*a* shows fluorescence quenching of the emission spectrum (λ_{em} = 441 nm) of **1** by $Cu(OAc)_2$ in 4-morpholineethanesulfonic acid (MES) buffer (pH 6.0), while the accompanying Scatchard analysis (20) is shown in Fig. 3*b*. From the negative slope in Fig. 3*b*, an apparent equilibrium binding constant of log *K** = 5.35 M^{-1} for formation of the 1:1 Cu(II)·OTA complex was determined. For Fe(III) binding by **1** (log *K** = 3.34 M^{-1}), aqueous HCl·KCl buffer (pH 2.6) was utilized due to the formation of Fe-oxide precipitates at higher pH values.

© 1998 NRC Canada

Fig. 2. Electrospray mass spectrum of the Cu(II)·OTA complex in methanol (m/z = 462.9). Also present is free **1** (m/z = 402.1).

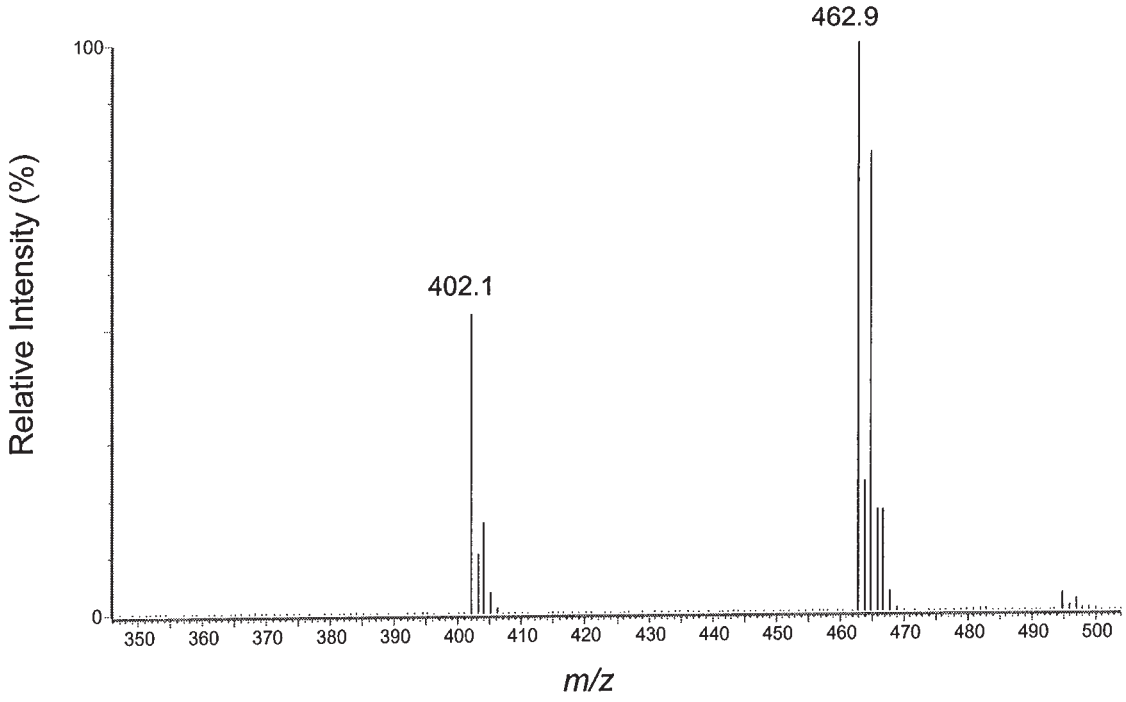

Table 1. The UV–absorption data in ethanol for ochratoxin A (OTA, **1**), OTB (**2**), and **12** in the absence (Free) and presence of base, and with 1 equiv. of Fe(III) and Cu(II).[a]

Compound	Free	+ Base[b]	+ Fe(III)[c]	+ Cu(II)[d]
OTA (**1**, X = Cl)	215 (28 000)	222 (20 300)	224, 342, 483	222 (21 000), 258 (sh),
	333 (5500)	383 (11 000)		367 (6420), 608 (55)
OTB (**2**, X = H)	218 (32 000)	230 (10 400)	241, 340, 508	235 (11 050), 331 (sh)
	320 (6900)	371 (10 200)		356 (6050), 620 (60)
12	214 (17 500)	222 (19 900)	215, 311	250 (19 600)
	312 (3600)	342 (5050)		322 (3700), 584 (130)

[a] Absorbance data are given in nm; extinction coefficients are in M^{-1} cm^{-1}.
[b] +2 equiv. of NaOH.
[c] +1 equiv. of $FeCl_3$.
[d] +1 equiv. of $Cu(OAc)_2$.

Apparent equilibrium binding constants (log K^*) for formation of 1:1 Cu(II) and Fe(III) complexes of **1** and our synthesized derivatives are listed in Table 2. Values in parentheses for Cu(II) binding represent the copper binding affinity of the anionic forms of the various derivatives (log $K_{1:1}$). For comparison to our synthesized sample of **2**, metal binding by the natural stereoisomer of **2** (purchased from Sigma) was determined, and as anticipated, the binding constants of the purchased **2** and our synthesized sample were nearly identical. The binding affinity of **1** for Zn(II) in 4-morpholinepropanesulfonic acid (MOPS) buffer (pH 7.4) was also measured to provide insight into Cu(I) binding, as both Zn(II) and Cu(I) are diamagnetic d^{10}-electron metals that favor a tetrahedral binding arrangement (21). Also presented are pK_a values for **1**, **2**, **7a**, and **12**. Values for **1** (7, 22) and **2** (7, 23) are from the literature, while pK_as for **7a** and **12** were measured at 25°C in 0.1 M aqueous buffer solutions using the recommended spectrophotometric procedure (24).

DNA cleavage

The ability of **1** to effect DNA cleavage in the presence of Fe and Cu was determined using supercoiled plasmid DNA and agarose gel electrophoresis. In our initial experiments, attempts were made to establish the toxin's ability to facilitate DNA cleavage in the presence of Fe. However, utilizing both Fe(III) and Fe(II) in the presence of excess **1** under various conditions (sodium ascorbate and HOOH as additives), no definitive role for **1** was determined, as control lanes in the gels for free Fe were equally efficient in promoting single-strand DNA cleavage (data not shown).

For DNA cleavage by Cu(II) ($Cu(OAc)_2$, 20 μM) admixture of **1** had very little effect on the extent of single-strand DNA cleavage (over a 15 h incubation period at 37°C in MOPS buffer, pH 7.4). Thus, the ability of the Cu(II)·OTA complex to facilitate DNA cleavage in the presence of sodium ascorbate was examined. For these experiments, 20 μM Cu(II) was premixed with 60 μM **1** prior to addition of plasmid DNA

© 1998 NRC Canada

Fig. 3. (*a*) Emission spectrum (λ_{ex} = 380 nm, λ_{em} = 440 nm) of fluorescence quenching of **1** (10 μM) at increasing $Cu(II)(OAc)_2$ concentrations in 10 mM MES (pH 6.0) and 100 mM $NaClO_4$ buffer solution at 25°C, and (*b*) Scatchard plot of the fluorescence quenching of part *a*.

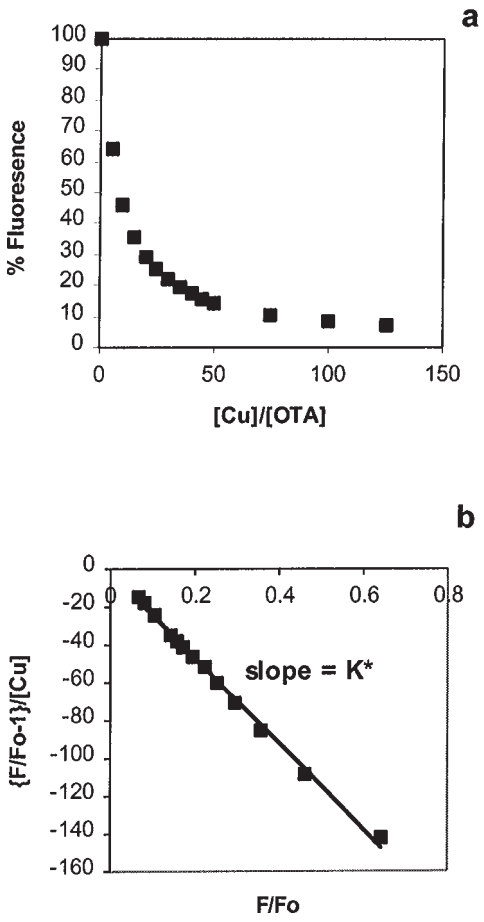

and sodium ascorbate. Under these conditions, approximately 99% of Cu(II) is bound by the toxin, determined from log *K** = 6.26 M^{-1} for formation of the 1:1 Cu(II)·OTA complex at pH 7.4. Figure 4 shows a representative gel highlighting that the Cu(II)·OTA complex is capable of redox cycling and thus inducing DNA cleavage in the presence of sodium ascorbate. Additional experiments showed the cleavage to be completely inhibited by the enzyme catalase (1000 units/mL) and sodium azide (100 mM), while the hydroxyl radical scavengers, dimethyl sulfoxide (1 M) and *tert*-butanol (1 M), provided only partial protection (data not shown). These results indicate a requirement for HOOH and favor the involvement of a copper-oxo species over a freely diffusible hydroxyl radical (15).

To further explore Cu-mediated DNA cleavage by **1**, its ability to induce DNA cleavage by Cu(II) prebound to 2 equiv. of 1,10-phenanthroline (OP) was examined. The OP ligand binds Cu(II) to form a $Cu(OP)_2$ complex that is a prototypical copper nuclease system and facilitates DNA cleavage in the presence of an external reducing agent (15). As reported by Sigman (15), reduction of $Cu(II)(OP)_2$ to $Cu(I)(OP)_2$ followed by HOOH oxidation produces a copper-oxo species that cleaves DNA through H1′-atom abstraction of the deoxyribose sugar. The utility of $Cu(OP)_2$ here was to test if **1** could facilitate the production of $Cu(I)(OP)_2$, the species necessary for DNA cleavage (15). Figure 5 shows that DNA cleavage by $Cu(OP)_2$ was potentiated by OTA in a concentration dependent fashion. Additional experiments showed that the reaction was completely inhibited by the enzyme catalase, which mimicked the findings observed by Sigman and co-workers (15) for $Cu(OP)_2$ cleavage in the presence of thiol. However, unlike thiol-potentiation, the cleavage reaction was also partially inhibited by superoxide dismutase (SOD) (ca. 70%, data not shown), which suggests that the reduction of $Cu(II)(OP)_2$ is also mediated by O_2^- (15).

Since in vivo studies on OTA genotoxicity suggest a role for the chlorine atom and lactone (6, 7, 11), we also examined $Cu(OP)_2$-mediated DNA cleavage in the presence of **2** and **12** (Scheme 2). Figure 6 shows that under conditions where **1** effectively potentiates DNA cleavage by $Cu(OP)_2$ (lane 4), the derivative **12** (lane 5) was only slightly less efficient, while **2** (lane 6) failed to induce DNA cleavage above background (lane 2). To test if differences in the phenolic pK_as for these species (Table 2) could account for these results, the experiment was repeated in 2-(cyclohexylamino)-ethanesulfonic acid (CHES) buffer at pH 8.6. Interestingly, no change in the extent of cleavage was detected for all species (data not shown), indicating that the presence of the phenoxy anion does not explain the differences noted in the gel.

The ability of **1** to induce DNA cleavage in the presence of Fe(III) prebound to the metal chelator EDTA (25) was also examined. At 20 μM Fe(III)·EDTA, additions of **1** up to 250 μM, followed by 30 min incubation time at 37°C, failed to induce DNA cleavage (data not shown). This result was contrasted by our findings with $Cu(OP)_2$ and by the reaction of Fe(III)·EDTA (20 μM) with sodium ascorbate (50 μM), which almost facilitated the complete conversion of Form I into Form II DNA after the 30 min incubation time.

Discussion

One of the major goals in the field of toxicology is to elucidate the mechanisms by which xenobiotics produce detrimental biological responses in an organism (26). This knowledge can be used to identify chemical structures that predispose a molecule to a sequence of events that leads to toxicity. In the present study, we have evaluated the role played by Fe(III) and Cu(II) ions in DNA cleavage by the fungal carcinogen ochratoxin A (OTA, **1**). Since it had been shown that an Fe(III) complex of **1** produces hydroxyl radicals to an extent greater than free iron (10), it was anticipated that **1** would facilitate Fe-mediated DNA cleavage. That **1** possesses a *para*-chlorophenolic group also suggested that copper ions may promote OTA-induced DNA damage, based on analogy to Cu-mediated DNA cleavage by hydroquinones (13, 14).

Initial studies focused on the ability of the toxin and several structural analogs (Schemes 1 and 2) to bind Fe(III) and Cu(II) using fluorescence spectroscopy (Table 2). Both metals were found to quench the fluorescence of the toxin, which permitted determination of apparent equilibrium binding constants (log *K**) for formation of the 1:1 complexes. Of particular relevance to the biological properties of these compounds was the ability to monitor Cu(II) binding at physiological pH, while acidic conditions (pH 2.6) were employed for Fe(III) binding due to the formation of Fe-oxide precipitates at higher

© 1998 NRC Canada

Table 2. Equilibrium binding data for ochratoxin A (OTA, **1**) and structural analogs in aqueous buffered solutions at 25°C.

Compound	pK_a COOH/PhOH	Cu(II)[e] log K^* (log $K_{1:1}$)[f]	Fe(III)[i] log K^*	Zn(II)[j] log K^*
OTA (**1**, X = Cl)	4.2/7.0[a]	5.35 (6.40)	3.34	3.92
OTB (**2**, X = H)	4.2/7.8[b]	4.42 (6.24)	3.49	
9a (R = OMe)	—	3.73 (5.52)[g]	3.24	
9b (R = NH_2)	—	3.65 (5.45)	3.28	
12	7.5[c]	5.17 (6.69)[h]	3.71	
(±)-Mellein (**7a**)	10.4[d]	2.55 (6.95)	3.93	

[a] Taken from refs. 7 and 22.
[b] Taken from refs. 7 and 23.
[c] Determined by UV-vis spectroscopy in 0.1 M phosphate buffers.
[d] Determined by UV-vis spectroscopy in 0.1 M carbonate buffers containing 20 vol.% 1,4-dioxane.
[e] Determined by fluorescence spectroscopy in 10 mM MES buffer (pH 6.0) containing 100 mM $NaClO_4$.
[f] log $K_{1:1}$ = [Cu(II)·OTA]/[Cu(II)][OTA^{2-}]; determined from log K^* by accounting for the percent anionic forms at pH 6.0.
[g] Phenolic pK_a of **9a** and **9b** has been taken as 7.8 to estimate log $K_{1:1}$.
[h] pK_a of COOH has been taken as 4.2 to estimate log $K_{1:1}$.
[i] Determined by fluorescence spectroscopy in 10 mM KCl·HCl (pH 2.6), 100 mM $NaClO_4$.
[j] Determined by fluorescence spectroscopy in 10 mM MOPS buffer (pH 7.4), 100 mM $NaClO_4$.

Fig. 4. The DNA cleavage by Cu(II)·OTA in the presence of sodium ascorbate. Cleavage was carried out at 37°C for 30 min in 10 mM MOPS (pH 7.4), 50 mM NaCl buffer solution. Lane 1: DNA alone; lane 2: 20 μM $Cu(OAc)_2$; lane 3: 20 Cu(II)·OTA; lane 4–7: 20 μM Cu(II)·OTA + 10, 20, 50, and 250 μM sodium ascorbate, respectively.

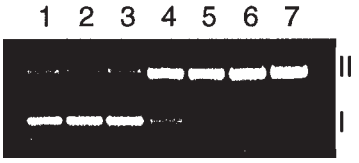

Fig. 5. The OTA–potentiation of Form I DNA cleavage by Cu(II)$(OP)_2$. Cleavage was carried out at 37°C for 30 min in 10 mM MOPS (pH 7.4), 50 mM NaCl buffer solution. Lane 1: DNA alone; lane 2: 20 μM Cu(II)$(OP)_2$; lane 3: 20 μM Cu(II)$(OP)_2$ + 10 μM sodium ascorbate; lane 4–7: 20 μM Cu(II)$(OP)_2$ + 50, 100, 150, and 250 μM **1**, respectively.

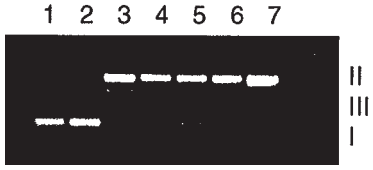

pH values. This finding indicates that **1** would be more efficient at binding Cu(II) than Fe(III) ions in biological systems.

Although we have not unequivocally determined the exact Cu(II) binding mode for **1**, that formation of the Cu(II)·OTA complex in methanol (Fig. 2) was accompanied by the loss of two protons suggests strongly that the two acidic groups of **1** (COOH and phenol) participate in Cu(II) coordination. Support for participation of the phenolic group stems from the fact that at pH 6, log $K^* = 5.35$ M^{-1} for **1**, while for **2** log $K^* = 4.42$ M^{-1} (Table 2). Clearly the binding affinity is sensitive to ionization of the phenolic group. Participation of the COOH group was supported by the finding that the OTB derivatives **9a** and **9b** (Scheme 2), which possess the methyl ester and amide

As demonstrated by Bredenkamp et al. (27), **1** adopts a β phenylalanine group respectively, showed diminished Cu(II) binding affinity when compared to the free acid **2**. The results presented in Table 2 also indicate that the dihydroisocoumarin moiety (lactone) of **1** is not important for formation of the 1:1 Cu·OTA complex. This hypothesis stems for the fact that the derivative **12**, which lacks the lactone moiety, has a greater affinity for Cu(II) than **1** (compare log $K_{1:1}$ values in Table 2).

For both the phenolic oxygen and the carboxylic acid of the phenylalanine moiety of **1** to participate in Cu(II) binding, it also appears that the amide nitrogen coordinates Cu(II). This hypothesis was derived from inspection of molecular models and from consideration of the conformation of the free toxin derived from single-crystal X-ray structural studies (27).

form (crystals obtained from benzene) conformation that

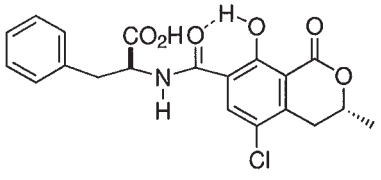

α form

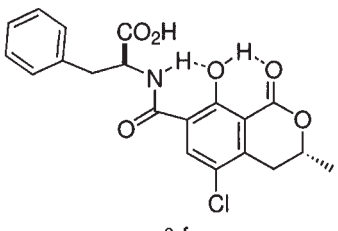

β form

© 1998 NRC Canada

Fig. 6. Structure–activity relationships in OTA–potentiation of Form I DNA cleavage by $Cu(II)(OP)_2$. Cleavage was carried out at 37°C for 30 min in 10 mM MOPS (pH 7.4), 50 mM NaCl buffer solution. Lane 1: DNA alone; lane 2: 20 μM $Cu(II)(OP)_2$; lane 3: 20 μM $Cu(II)(OP)_2$ + 10 μM sodium ascorbate; lane 4: 20 μM $Cu(II)(OP)_2$ + 50 μM OTA; lane 5: 20 μM $Cu(II)(OP)_2$ + 50 μM **12**; lane 6: 20 μM $Cu(II)(OP)_2$ + 50 μM **2**.

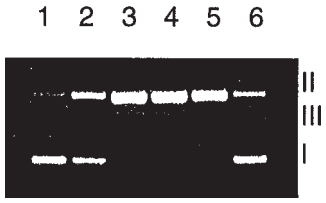

maximizes hydrogen bonding interactions between the amide, phenolic group, and lactone carbonyl. The alternative α form was not detected. Although the fully protonated form of **1** is not important for Cu(II) coordination, the orientation of the phenylalanine moiety in the β form appears to facilitate coordination to Cu(II) by the phenolic oxygen and carboxylic acid of the phenylalanine. This conformation also predicts that the amide nitrogen participates in Cu(II) binding, which is consistent with previous studies on Cu(II) binding by the amide group of peptides (28), and Cu(II)·phenylalanine complexes (29).

For Fe(III) binding the data in Table 2 indicates that all derivatives possess similar binding affinity at pH 2.6. These results are consistent with the mass spectral data obtained in methanol, which indicated that $FeCl_3$ binding by **1** is not accompanied by proton removal from the toxin. This suggests that $FeCl_3$ forms a coordinate bond with the phenolic oxygen. Consistent with this hypothesis, **7a**, which lacks both the electron-withdrawing chlorine atom and amide group ($pK_a = 10.4$), possesses the greatest affinity for $FeCl_3$ at pH 2.6 (Table 2). In contrast to Cu(II) binding, the derivatives **9a** and **9b** do not show significant differences in binding from **2**. This result appears to indicate that the carboxylic acid does not participate in Fe(III) binding at pH 2.6 and may suggest that these compounds bind Fe(III) by the phenolic oxygen (7, 10) and an *ortho*-carbonyl, either from the lactone (10) or the amide group (7, 30).

To define the role played by Fe(III) and Cu(II) in OTA-induced DNA cleavage, we examined the ability of **1** to facilitate DNA strand-scission in the presence of free iron and copper ions. Utilizing both Fe(III) and Fe(II) ions, no definitive role for the toxin could be identified. This result was surprising, given reports that **1** coordinates Fe(III), facilitates lipid peroxidation (12), and produces the hydroxyl radical via the Fenton reaction (10). However, results by Marquardt and co-workers (11*b*) on production of the hydroxyl radical in a microsomal-NADPH preparation, showed conclusively that addition of **1** and Fe(III) produces the hydroxyl radical in a lower yield than NADPH and Fe(III) alone. Our in vitro results are in accord with this finding and reaffirm that coordination of **1** to Fe(III) is not responsible for OTA genotoxicity.

For Cu-mediated DNA cleavage, **1** was found to form a 1:1 Cu(II)·OTA complex that induced DNA strand-scission only upon activation by a suitable reducing agent (Fig. 4). This result is in sharp contrast to the reports by Hecht and co-workers (13) and Li and Trush (14) on the ability of hydroquinones to induce copper-mediated DNA cleavage. They found that 30 min incubation time at 37°C was more than sufficient to cleave the DNA through reduction of Cu(II) to Cu(I) with concomitant oxidation of the hydroquinone to the respective benzoquinone (13, 14). The inability of **1** to induce Cu-mediated DNA cleavage in the absence of a reducing agent, however, can be rationalized by consideration of the toxin's chelating properties. Unlike *ortho*- or *para*-hydroquinone, which are not expected to coordinate Cu(II) with high binding affinity, **1** binds Cu(II) very efficiently (Table 2). If binding affinity of the OTA for Zn(II) ($\log K = 3.92\ M^{-1}$ at pH 7.4) is representative of the toxin's affinity for Cu(I) (both are d^{10}-electron metals that favor a tetrahedral binding arrangement (21)) then the Cu(II) complex is significantly more stable than the putative Cu(I) complex ($\log (K_{Cu}/K_{Zn})$ at pH 7.4 = 6.26/3.92 = 1.6). This finding would explain the inability of **1** to facilitate Cu-mediated DNA damage in the absence of a reducing agent, and is consistent with the fact that Cu(II) is much less efficient in reduction when it is bound to protein ligands than when it is free in solution (31). Studies by Marquardt and co-workers (11*a*) on hydroxyl radical production by **1** in bacteria also show that additions of divalent cations such as Fe(II) and Cu(II) ions fail to enhance hydroxyl radical production, which appears consistent with the findings presented here on the inability of **1** to cleave DNA in the presence of these metal ions free in solution. Furthermore, Cu(II)·OTA mediated DNA cleavage in the presence of sodium ascorbate is probably irrelevant to OTA genotoxicity, since antioxidants inhibit the toxicity of **1** (9).

To explore the role played by Cu(II) ions in OTA-induced DNA cleavage in more detail, we also examined the ability of **1** to potentiate DNA cleavage by the Cu(II) complex of 1,10-phenanthroline ($Cu(OP)_2$). As described by Sigman (15), the nuclease activity of $Cu(OP)_2$ proceeds by an obligatory, ordered mechanism, whereby the cupric complex $Cu(II)(OP)_2$ is reduced to the cuprous complex, $Cu(I)(OP)_2$, which is then oxidized by HOOH to generate the copper-oxo species directly responsible for strand-scission. Since the reaction is independent of the reductant used to potentiate it (15), we used the $Cu(OP)_2$ nuclease system to gain insight into redox properties of the OTA in DNA cleavage. Interestingly, **1** was found to potentiate DNA cleavage by $Cu(OP)_2$ (Fig. 5), presumably by reducing $Cu(II)(OP)_2 \rightarrow Cu(I)(OP)_2$ with the concomitant oxidation of **1**. Although the exact nature of OTA oxidation is uncertain, it is informative that the nonchlorinated derivative **2** failed to induce DNA cleavage by $Cu(OP)_2$. The derivative **12**, which lacks the lactone of **1**, showed only slightly diminished activity (Fig. 6), which indicates that the chlorine atom is more important than the lactone for OTA potentiation of $Cu(OP)_2$-mediated DNA cleavage.

To provide a rationale for the ability of **1** to induce DNA cleavage by $Cu(OP)_2$, it is informative to consider oxidation of phenols, where the oxidation takes place according to the routes presented in Scheme 3 (32). Under aprotic conditions, oxidation of phenol (**I**) produces the cation radical (**II**), which deprotonates to the neutral radical (**III**). For solutions containing the phenolate ion (**V**), oxidation to the phenoxyl radical (**III**) proceeds readily and the resulting phenoxyl radical (**III**) may be further oxidized to the phenoxonium ion (**IV**), or couple to yield a variety of products (32).

© 1998 NRC Canada

Scheme 3. Oxidation pathway for common phenols.

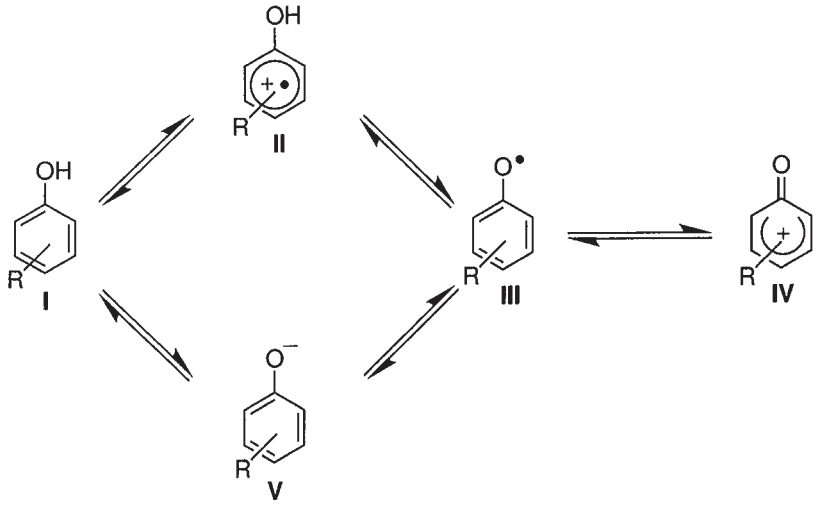

Insight from Scheme 3 suggests that single electron transfer from **1** to $Cu(II)(OP)_2$ would yield the OTA phenoxyl radical ($OTA^{\cdot}$) and $Cu(I)(OP)_2$ (eq. [1*a*]). For $Cu(I)(OP)_2$ to initiate DNA strand-scission, it must combine with hydrogen peroxide (HOOH) to generate a copper-oxo species (15). The finding that SOD inhibits the reaction (70%) suggests that the reduction of $Cu(II)(OP)_2$ is also mediated by $O_2^{\cdot-}$. Although oxidation of $Cu(I)(OP)_2$ by O_2 can yield $O_2^{\cdot-}$ (15), another possible source of superoxide is the oxidation of $OTA^{\cdot}$ by O_2 to yield the phenoxonium ion of OTA (OTA^+), eq. [1*b*]. The liberated $O_2^{\cdot-}$ could assist OTA in the reduction of $Cu(II)(OP)_2$ (eq. [1*c*]) and yield HOOH after disproportionation (eq. [1*d*]). Oxidation of $Cu(I)(OP)_2$ by HOOH would yield a copper-oxo species (eq. [1*e*]), that initiates DNA cleavage (eq. [1*f*]).

[1*a*] $OTA + Cu(II)(OP)_2 \rightarrow OTA^{\cdot} + Cu(I)(OP)_2$

[1*b*] $OTA^{\cdot} + O_2 \rightarrow OTA^+ + O_2^{\cdot-}$

[1*c*] $Cu(II)(OP)_2 + O_2^{\cdot-} \rightarrow Cu(I)(OP)_2 + O_2$

[1*d*] $2O_2^{\cdot-} + 2H^+ \rightarrow HOOH + O_2$

[1*e*] $Cu(I)(OP)_2 + HOOH \rightarrow$ copper-oxo species

[1*f*] Copper-oxo species + DNA $\rightarrow$ DNA cleavage

While we have yet to identify the products resulting from OTA oxidation, it is informative that the intermediacy of the OTA phenoxyl radical in the in vivo genotoxicity of **1** has been proposed by Malaveille et al. (6). Oxidation to the putative phenoxonium ion (OTA^+) may also provide a rationale for the toxin's ability to facilitate DNA adduction (4). A DNA-derived nucleophile could react directly with OTA^+, or reaction of OTA^+ with H_2O to furnish a quinone intermediate after loss of HCl could precede DNA adduction. In this regard, chlorinated phenols have been converted to the respective *para*-quinones with $CuCl_2$ and O_2 (33) and by enzymatic oxidative pathways (34), and quinones are Michael acceptors that have been implicated in DNA adduct formation (35).

Conclusions

The present study implies that the genotoxic properties of **1** may be attributable to the toxin's redox properties, instead of its ability to bind redox-active transition metals. The toxin does not facilitate DNA cleavage in the presence of free Fe, or Fe(III) bound to EDTA. With Cu(II), **1** forms a stable 1:1 Cu(II)·OTA complex that facilitates DNA cleavage upon activation by sodium ascorbate. However, since OTA toxicity is inhibited by antioxidants, this pathway is unlikely to play a role in the mechanism(s) of OTA genotoxicity. A more significant finding was the demonstrated ability of **1** to initiate DNA cleavage by $Cu(II)(OP)_2$. Here, **1** provides the reducing equivalents to convert $Cu(II)(OP)_2 \rightarrow Cu(I)(OP)_2$. The chlorine atom was found to be critical for this activity, which is consistent with in vivo studies on OTA genotoxicity (6). Currently, we are studying oxidation of **1** by electrochemical and chemical means in an effort to determine the nature of the oxidized OTA species and the potential of such a species to induce DNA adduction.

Experimental section

Materials

Ochratoxin A (OTA, **1**: X = Cl) was purchased from Dr. Ronald Marquardt, Department of Animal Sciences, University of Manitoba, and was used without further purification. Supercoiled plasmid (Form I) DNA was a gift from Dr. Fred W. Perrino, Department of Biochemistry, Bowman Gray School of Medicine, Wake Forest University. The plasmid was a derivative of pOXO4 (36) containing the dnaQ gene. The following enzymes and reagents were obtained commercially and used without further purification: 1,10-phenanthroline (OP), copper acetate ($Cu(OAc)_2$), ferric chloride ($FeCl_3$), sodium perchlorate ($NaClO_4$), 4-morpholinepropanesulfonic acid (MOPS), 4-morpholineethanesulfonic acid (MES), 2-(cyclohexylamino)ethanesulfonic acid (CHES), ethylenediaminetetraacetic acid (EDTA), 1,3-dicyclohexylcarbo-diimide (DCC), 1-hydroxybenzotriazole hydrate (HOBT), L-phenylalanine methyl ester hydrochloride, 5-chlorosalicylic acid, *sec*-butyllithium (*sec*-BuLi), *N*,*N*,*N*′,*N*′-tetramethylethylenediamine (TMEDA), methyl iodide (MeI), lithium diisopropyamide (LDA), acetaldehyde, and acetic anhydride

© 1998 NRC Canada

(Aldrich); ochratoxin B (**2**: X = H), catalase, superoxide dismutase (SOD), and L-β-phenylalanine amide (Sigma).

Methods

Elemental analyses were carried out by Atlantic Microlab, Inc. High-resolution mass spectral analyses were carried out by the Nebraska Center for Mass Spectrometry. Melting points were taken on a Mel-Temp apparatus and are not corrected. NMR spectra were recorded on a Varian VXR-200 spectrometer (^{1}H, 200 MHz; ^{13}C, 50 MHz). Chemical shifts are given in parts per million (ppm) relative to tetramethylsilane (TMS), and coupling constants (*J*) are reported in hertz (Hz). The following abbreviations are used: s, singlet; d, doublet; t, triplet; q, quartet; m, multiplet; br, broad. Absorption measurements were made on a Hitachi U-2001 UV-vis spectrophotometer, and fluorescence spectra were acquired with a Hitachi F-2000; both instruments were equipped with a thermostated cell compartment. Distilled, deionized water from a Milli-Q system was used for all aqueous solutions and manipulations. Other solvents were purified and dried according to standard procedures. Agarose gel electrophoresis was carried out in 40 mM Tris-acetate buffer (pH 8.0), containing 5 mM EDTA. Agarose gel loading buffer: 40 mM Tris-OAc (pH 8.0), 5 mM EDTA, 40% glycerol, 0.3% bromophenol blue.

Mass spectra were acquired using a Micromass Quattro II operating in the negative ion spray mode (ES^-). The system acquired signal over a *m*/*z* range of 200–1000 at 8 s/scan with a 0.06 step. Samples of **1** and Cu(II)·OTA (0.1mg/mL) were prepared in methanol and injected via syringe into a fixed loop injector port (100 μL volume) interfaced to the ion spray source. The Cu(II)·OTA sample was also prepared in 10 mM NH_4OAc (pH 7.0) buffer and subjected to reverse-phase high-pressure liquid chromatography (HPLC, Hewlett Packard (HP) 1100 series with photodiode array detection, 190–600 nm, using a gradient of MeOH in 2 mM ammonium acetate, pH 7.0), prior to analysis by ESI/MS. The sample of Fe(III)·OTA (0.1mg/mL) was prepared in methanol and was analyzed by ESI/MS without prior separation by HPLC.

N,N-Diethyl-2-methoxybenzamide (4a)

To prepare **4a** (37), 2-methoxybenzoic acid (1.00 g, 6.57 mmol) was reacted with excess thionyl chloride ($SOCl_2$) and diethylamine using standard conditions. After purification by silica-gel chromatography (1:1 EtOAc–hexane), **4a** was obtained as a colorless oil: yield 1.21 g (89%); ^{1}H NMR ($CDCl_3$), δ: 7.29 (m, 1H), 7.18 (m, 1H), 6.93 (m, 1H), 3.79 (s, 3H), 3.59–3.54 (m, 2H), 3.14 (q, 2H, *J* = 7.02), 1.24 (t, 3H, *J* = 7.02), 1.02 (t, 3H, *J* = 7.02); ^{13}C NMR ($CDCl_3$), δ: 168.3, 154.7, 129.5, 126.9, 126.5, 120.3, 110.5, 55.0, 42.4, 38.4, 13.6, 12.5.

N,N-Diethyl-2-methoxy-6-methylbenzamide (5a)

Using the procedure described by Snieckus and co-workers (17*a*), **5a** was obtained as a colorless oil: yield 0.191 g (80%); ^{1}H NMR ($CDCl_3$), δ: 7.13–6.66 (m, 3H), 3.78–3.68 (m, 1H), 3.72 (s, 3H), 3.39–3.29 (m, 1H), 3.05 (q, 2H, *J* = 7.19), 2.17 (s, 3H), 1.18 (t, 3H, *J* = 7.33), 0.95 (t, 3H, *J* = 7.19); ^{13}C NMR ($CDCl_3$), δ: 168.2, 155.1, 135.4, 128.9, 126.2, 122.3, 107.9, 55.3, 42.2, 38.3, 18.5, 13.6, 12.6.

8-Hydroxy-3-methyl-3,4-dihydroisocoumarin (Mellein) (7a)

To a stirred solution of **5a** (0.193 g, 0.873 mmol) in dry THF (75 mL) at –78°C under argon was added lithium diisopropylamide (LDA, 0.655 mL, 1.31 mmol, from 2.0 M solution in heptane–THF–ethylbenzene). After stirring for 1 h at –78°C, the resulting burgundy red mixture was quenched with acetaldehyde. The mixture was allowed to warm to room temperature, stirred for an additional 12 h, and then washed with 1 N HCl (50 mL) and extracted with EtOAc. The organic layer was dried over $MgSO_4$, filtered, and the solvent removed under reduced pressure. The resultant crude residue was then refluxed in 6 N aqueous 6 N HCl (50 mL) for 4 days. The mixture was filtered, washed with water, and dried under vacuum to afford **7a** as a light yellow solid. Recrystallization from acetone gave **7a** as a white solid: yield 0.080 g (52%); mp 38.0°C (lit. (17*b*) 38°C); ^{1}H NMR ($CDCl_3$), δ: 11.0 (s, 1H), 7.38 (m, 1H), 6.86 (m, 1H), 6.66 (m, 1H), 4.71 (m, 1H), 2.91 (m, 2H), 1.51 (d, 3H, *J* = 6.3 Hz); ^{13}C NMR ($CDCl_3$), δ: 162.9, 161.3, 142.1, 134.6, 119.3, 111.0, 74.2, 56.3, 36.2, 20.8.

N,N-Diethyl-2-methoxy-3-(diethylcarbamoyl)benzamide (4b)

The benzamide **4b** (17*c*) was prepared from 2-methoxyisophthalic acid (0.850 g, 4.33 mmol), excess $SOCl_2$ and diethylamine using standard conditions. After purification by silica-gel chromatography (elution with EtOAc), **4b** was obtained as a white solid: yield 1.13 g (85%); mp 82°C from Et_2O–hexane (lit. (17*c*) 82°C); ^{1}H NMR ($CDCl_3$), δ: 7.27 (m, 3H), 3.86 (s, 3H), 3.80–3.20 (br, 8H), 1.27 (t, 6H, *J* = 7.18 Hz), 1.06 (t, 6H, *J* = 7.14 Hz); ^{13}C NMR ($CDCl_3$), δ: 166.8, 150.6, 127.0, 42.0, 37.9, 12.8, 11.7.

N,N-Diethyl-2-methoxy-3-(diethylcarbamoyl)-6-methylbenzamide (5b)

To a stirred mixture of **4b** (0.304 g, 0.993 mmol) in dry THF (75 mL) at –78°C under argon, was added via syringe *sec*-BuLi (1.25 mL, 1.19 mmol, from 0.950 M in cyclohexanes) and TMEDA (0.138 g, 1.19 mmol). The resulting yellow solution was allowed to stir for 1 h at –78°C, and dry methyl iodide (0.423 g, 2.98 mmol) was added. The stirred mixture was allowed to warm to room temperature and stirred for an additional 12 h. The solution was then washed with 1 N HCl (100 mL) and extracted with EtOAc. The organic layer was separated, washed with three 20 mL portions of brine, then dried over $MgSO_4$. The solution was concentrated under reduced pressure to afford a crude product that was purified by silica-gel chromatography. Elution with ether (containing 1% triethylamine) afforded **5b** as a light yellow oil: yield 0.27 g (85%); ^{1}H NMR ($CDCl_3$), δ: 7.13 (d, 1H, *J* = 7.6), 7.00 (d, 1H, *J* = 7.6), 3.84 (s, 3H), 3.80–3.20 (br, 8H), 2.27 (s, 3H), 1.27 (m, 6H), 1.06 (t, 6H, *J* = 7.06 Hz); ^{13}C NMR ($CDCl_3$), δ: 167.9, 167.1, 151.3, 136.2, 127.2, 42.6, 42.3, 18.3, 13.5, 13.4, 12.3; mass spectrum (HREI), *m*/*z*: 320.209 ($C_{18}H_{28}N_2O_3$ requires 320.210).

3-Methyl-7-carboxy-8-hydroxy-2,3-dihydroisocoumarin (7b)

To a stirred solution of **5b** (1.20 g, 3.75 mmol) in dry THF (75 mL) at –78°C under argon was added LDA (2.25 mL, 4.50 mmol, from 2.0 M in heptane–THF–ethylbenzene). After

© 1998 NRC Canada

stirring for 1 h at –78°C, the resultant burgundy red solution was quenched with acetaldehyde. The mixture was allowed to warm to room temperature, stirred for an additional 12 h, washed with 1 N HCl (100 mL) and then extracted with EtOAc. The organic layer was separated, dried over $MgSO_4$, and then concentrated under reduced pressure. The crude residue was then refluxed in 6 N HCl for 4 days. The mixture was filtered, washed with water, and dried under vacuum, producing **7b** as a white solid: yield 0.528 g (63%); mp 233–235°C from acetone (lit. (17*c*) 234–236°C); ^{1}H NMR (DMSO-d_6), δ: 7.96 (d, 1H, J = 7.9), 6.88 (d, 1H, J = 7.9), 4.70 (br, 1H), 3.00 (m, 2H), 1.39 (d, 3H, J = 6.27); ^{13}C NMR (DMSO-d_6), δ: 168.9, 165.4, 161.9, 146.9, 136.6, 117.9, 115.7, 110.9, 74.8, 34.5, 20.2.

3-Methyl-7-carboxy-8-acetate-2,3-dihydroisocoumarin (8)
To a suspension of **7b** (0.200 g, 0.901 mmol) in acetic anhydride (10 mL) was added phosphoric acid (0.10 mL). The resulting solution was stirred for 24 h at 50°C. Concentration under reduced pressure, followed by purification by silica-gel chromatography (EtOAc) afforded **8** as a white solid: yield 0.233 g (98%); mp 136–137°C; ^{1}H NMR ($CDCl_3$), δ: 10.4 (br, 1H), 8.22 (d, 1H, J = 8.01), 7.24 (d, 2H, J = 8.01), 4.63 (m, 1H), 2.99 (m, 2H), 2.21 (s, 3H), 1.50 (d, 3H, J = 6.4); ^{13}C NMR ($CDCl_3$), δ: 169.3, 168.6, 161.0, 146.8, 136.7, 125.1, 123.3, 119.4, 77.2, 74.3, 35.8, 21.0, 20.6. Anal. calcd. for $C_{13}H_{12}O_6$: C 59.09; H 4.58; found: C 59.03; H 4.62.

Methyl ester of ochratoxin B (9a)
To a stirred solution of **8** (0.250 g, 0.87 mmol) in dry acetonitrile–DMF (10:3, 65 mL) at 0°C under argon was added DCC (0.217 g, 1.05 mmol) and HOBT (0.141 g, 1.05 mmol). The mixture was allowed to warm to room temperature and then stirred for an additional 1.5 h. L-Phenylalanine methyl ester (0.157 g, 0.87 mmol) in pyridine (2 mL) was then added in a dropwise fashion. After stirring for 12 h, the solvent was removed under reduced pressure. The resulting residue was redissolved in EtOAc (25 mL), washed with three 20 mL portions of brine, dried over $MgSO_4$, and concentrated under diminished pressure to yield a crude product. Purification by silica-gel column chromatography (elution with EtOAc–hexane, 80:20) afforded **9a** as a colorless residue: yield 0.276 g (83%); ^{1}H NMR ($CDCl_3$), δ: 12.7 (s, 1H), 8.53 (d, 1H, J = 6.4), 8.36 (d, 1H, J = 7.9), 7.27 (br, 5H), 6.84 (d, 1H, J = 7.9), 5.06 (m, 1H), 4.77 (m, 1H), 3.74(s, 3H), 3.24 (m, 2H), 2.99 (m, 2H), 1.56 (d, 3H, J = 6.4); ^{13}C NMR ($CDCl_3$), δ: 172.0, 170.3, 163.6, 160.5, 143.6, 139.0, 136.1, 129.3, 128.6, 127.1, 119.3, 118.4, 114.0, 108.7, 54.2, 52.3, 38.0, 34.6, 20.6; mass spectrum (HREI), *m*/*z*: 383.136 ($C_{21}H_{21}NO_6$ requires 383.137).

Ochratoxin B (2)
The hydrolysis of the methyl ester **9a** (0.383 g, 1.00 mmol) into the free acid, OTB (**2**), was achieved by reaction in a 3% LiOH solution in 3:1 H_2O–MeOH. Recrystallization from benzene afforded **2** as a white solid: yield 0.243 g (66%); mp 205–208°C (lit. (19) 220°C); ^{1}H NMR (DMSO-d_6), δ: 8.50 (d, 1H, J = 7.4), 8.06 (d, 1H, J = 7.9), 7.24 (m, 5H), 6.95 (d, 1H, J = 7.9), 4.81 (m, 2H), 3.16 (m, 2H), 1.41 (d, 3H, J = 6.1); ^{13}C NMR (DMSO-d_6), δ: 172.6, 169.1, 163.7, 159.6, 144.8, 137.0, 136.9, 129.3, 128.3, 126.7, 118.5, 118.3, 109.4, 76.1, 53.9, 36.7, 33.7, 20.2.

Amide of ochratoxin B (9b)
To a stirred solution of **8** (0.264 g, 0.379 mmol) in dry acetonitrile–DMF (8:1, 45 mL) at 0°C under argon was added DCC (0.094 g, 0.455 mmol) and *N*-hydroxysuccinimide (0.52 g, 0.455 mmol). The resulting mixture was allowed to warm to room temperature and then stirred for an additional 1.5 h under argon. L-Phenylalanineamide (0.062 g, 0.379 mmol) in pyridine (2 mL) was then added in a dropwise fashion. The mixture was stirred for an additional 12 h, then concentrated under reduced pressure to leave a residue that was resuspended in EtOAc (25 mL). The resulting solution was washed with three 20 mL portions of brine, dried over $MgSO_4$, then concentrated under diminished pressure to afford a crude product that was purified by silica-gel chromatography. Elution with 80/20 EtOAc–hexanes produced **9b** as a white residue: yield 0.027 g (20%); ^{1}H NMR ($CDCl_3$), δ: 12.4 (br, 1H), 8.53 (d, 1H, J = 7.1), 8.29 (d, 1H, J = 8.1), 7.24 (m, 5H), 6.82 (d, 1H, J = 8.1), 6.32 (s, 1H), 5.82 (s, 1H), 4.89 (m, 1H), 4.78 (m, 1H), 3.20 (m, 2H), 2.96 (m, 2H), 1.55 (d, 3H, J = 6.2); ^{13}C NMR ($CDCl_3$), δ: 173.3, 170.2, 164.0, 160.3, 143.7, 138.7, 136.6, 129.3, 128.6, 126.9, 118.9, 118.5, 108.7, 54.9, 37.8, 34.5, 20.6; mass spectrum (HREI), *m*/*z*: 368.13734 ($C_{20}H_{20}N_2O_5$ requires 368.1372).

5-Chloro-2-hydroxy-*N*-L-phenylalaninebenzamide methyl ester (11)
To a stirred solution of the acetate of 5-chloro-2-hydroxybenzoic acid (1.00 g, 4.66 mmol) in dry acetonitrile–DMF (5:1, 55 mL) at 0°C under argon was added DCC (1.15 g, 5.59 mmol) and HOBT (0.755 g, 5.59 mmol). The mixture was allowed to warm to room temperature, stirred for an additional 1.5 h, and then L-phenylalanine methyl ester (1.55 g, 4.66 mmol) in dry pyridine (3 mL) was added in a dropwise fashion. The resulting mixture was stirred for an additional 12 h and then concentrated under diminished pressure. The resulting residue was resuspended in EtOAc (25 mL), filtered, and then washed with three 20 mL portions of brine. The organic layer was collected, dried over $MgSO_4$, and concentrated under reduced pressure to afford a crude product that was purified by silica-gel chromatography. Elution with 40/60 EtOAc–hexanes afforded **11** as a white solid: yield 0.9 g (60%); mp 83–85°C. ^{1}H NMR ($CDCl_3$), δ: 11.9 (s, 1H), 7.40–6.60 (m, 9 H), 5.07 (m, 1H), 3.80 (s, 3H), 3.26 (m, 2H); ^{13}C NMR ($CDCl_3$), δ: 171.7, 168.4, 160.1, 135.3, 134.5, 129.2, 128.8, 127.5, 125.2, 123.5, 120.1, 114.7, 114.0, 53.3, 52.7, 37.8. Anal. calcd. for $C_{17}H_{16}ClNO_4$: C 61.18; H 4.83; N 4.20; found: C 61.07; H 4.87; N 4.16.

5-Chloro-2-hydroxy-*N*-L-phenylalaninebenzamide (12)
The hydrolysis of the methyl ester **11** (1.00 g, 3.00 mmol) into the free acid **12** was achieved by reaction in a 3% LiOH solution in 3:1 H_2O–MeOH (33). Recrystallization from MeOH–H_2O afforded **12** as a white solid: yield 0.67 g (70%); mp 172–173°C. ^{1}H NMR (acetone-d_6), δ: 12.3 (br, 1H), 8.62 (d, 1H, J = 7.9), 7.92 (m, 1H), 7.54–7.10 (m, 6H), 6.94 (d, 1H, J = 8.9), 5.01 (m, 1H), 3.4–3.1 (m, 2H); ^{13}C NMR (acetone-d_6), δ: 173.0, 169.2, 160.6, 138.3, 134.6, 130.0, 129.2, 127.7, 127.5, 123.7, 120.3, 116.7, 55.0, 37.7. Anal. calcd. for $C_{16}H_{14}ClNO_4$: C 60.10; H 4.41; N 4.38; found: C 60.02; H 4.47; N 4.39.

© 1998 NRC Canada

Metal binding

The ability of **1** and our synthesized derivatives to bind Fe(III) and Cu(II) was studied by fluorescence spectroscopy at 25°C. Stock solutions of the toxin samples were prepared in 1,4-dioxane. Concentrations were determined by UV-vis in ethanol using extinction coefficients for the phenolic absorptions, ca. 330 nm. For Cu(II) binding, a solution (2 mL) containing 10 mM MES (pH 6.0), 100 mM $NaClO_4$ buffer, or 10 mM MOPS (pH 7.4), 100 mM $NaClO_4$ buffer was utilized. Studies on Fe(III) binding were performed in buffer solutions (2 mL) containing 10 mM HCl·KCl (pH 2.6), 100 mM $NaClO_4$. In each case, 2 μL of the toxin dioxane stock solution was added for a final concentration of 10 μM. For determination of the metal binding constants, quenching of the toxin's emission spectrum (emission ca. 440 nm, excitation ca. 330–380 nm) was measured 5 min after each addition of $Cu(II)(OAc)_2$ or $Fe(III)Cl_3$ to allow binding equilibration. Scatchard analysis (20) of the quenching was performed using the following equation: $(F/F_o) - 1)/[L] = (k_{11}/k_s)K_{11} - K_{11}(F/F_o)$ where F_o is the fluorescence intensity of free toxin, [L] is the ligand concentration, and k_{11}/k_s are proportionality constants (20). From a plot of $(F/F_o) - 1/[L]$ versus F/F_o, an association constant was derived from the negative slope. For $Zn(OAc)_2$ binding at pH 7.4 (10 mM MOPS, 100 mM $NaClO_4$), emission spectra were recorded at 400 nm, and the data was analyzed by the Benesi–Hildebrand equation (20*b*, 38). Double-reciprocal plots of $1/\Delta A$ (change in emission) versus 1/[Zn] afforded straight lines from which the association constant (K_{11}) was determined from K_{11} = (*y*-intercept)/(slope) (20*b*).

pK_a determination

The pH measurements were obtained on a Fisher Scientific Accumet pH meter 910 using standard glass electrodes. Calibration was done using commercial buffers (BDH, pH 4.00, 7.00, and 10.00, all ± 0.01). The pK_a of **12** (Scheme 2) was determined using 0.1 M phosphate buffers, which were prepared by dilution of a stock (1 M K_2HPO_4) solution with deionized water. For (±)-mellein (**7a**), 0.1 M $NaHCO_3$–Na_2CO_3 buffer solutions were utilized. All UV-vis spectra were acquired at 25°C using a standard matched pair of 1 cm quartz cells. In the case of **12**, the sample and reference were filled with 1.00 mL of buffer solution, and to the sample cell was added 2 μL of a stock solution of **12** in 1,4-dioxane. For **7a**, 1 mL of carbonate buffer containing 20 vol.% 1,4-dioxane was used, and to the sample cell was added 2 μL of the stock solution of **7a** in 1,4-dioxane. The UV-visible spectra were recorded by the overlay method in the wavelength range of 250–500 nm.

Relaxation of supercoiled DNA by Fe and Cu in the presence of ochratoxin A

Reaction mixtures (20 μL total volume) contained 400 ng of Form I DNA, 10 mM MOPS (pH 7.4), 50 mM NaCl, and 20 μM each of OTA (**1**) and metal ion. The metal salts employed were $Cu(OAc)_2$, $Fe(Cl)_3$, and $Fe(NH_4)_2(SO_4)_2$. For reactions with iron, external reducing agents (200 μM sodium ascorbate) and oxidants (200 μM HOOH) were also employed. Reaction mixtures were incubated at 37°C for varying lengths of time, then quenched by the addition of 4 μL of loading buffer. Samples were loaded onto a 1% agarose gel containing ethidium bromide (1 ug/mL). The gel was run at 110 V for 2 h and visualized by UV illumination.

Densitometric quantitation was performed using a Microtek Scanmaker E_6 equipped with PhotoImpact and UTHSCSA Image Tool software. Supercoiled plasmid DNA values were corrected by a factor of 1.3, based on average literature estimates of lowering binding of ethidium to this structure (39).

Relaxation of supercoiled DNA by Cu(II)·ochratoxin A

Reaction mixtures (20 μL total volume) contained 400 ng of Form I DNA, 10 mM MOPS (pH 7.4), 50 mM NaCl, 20 μM $Cu(OAc)_2$, and 60 μM OTA. The OTA and $Cu(OAc)_2$ were premixed prior to addition of Form I DNA. Addition of sodium ascorbate 10–250 μM initiated the reaction, and mixtures were incubated at 37°C for 30 min, then quenched by the addition of 4 μL loading buffer. Samples were loaded onto a 1% agarose gel containing ethidium bromide (1 μg/mL). The gel was run at 110 V for 2 h and visualized by UV illumination. In a separate experiment, the quenching effect of catalase (1000 units/mL), sodium azide (100 mM), DMSO (1 M), and *tert*-butanol (1M) was examined.

Relaxation of supercoiled DNA by $Cu(OP)_2$ in the presence of ochratoxin A

Reaction mixtures (20 μL total volume) contained 400 ng of Form I DNA, 10 mM MOPS (pH 7.4), 50 mM NaCl, 20 μM $Cu(OAc)_2$, 40 μM OP, and either 10 μM sodium ascorbate or 50–250 μM OTA (**1**). Reaction mixtures were incubated at 37°C for 30 min, then quenched by the addition of 4 μL loading buffer. Samples were loaded onto a 1% agarose gel containing ethidium bromide (1 μg/mL). The gel was run at 110 V for 2 h and visualized by UV illumination. In a separate experiment, the quenching effect of catalase (1000 units/mL) and SOD (1000 units/mL) on the ability of 50 μM OTA to potentiate DNA cleavage by $Cu(II)(OP)_2$ was examined.

Relaxation of supercoiled DNA by $Cu(OP)_2$ in the presence of OTA, OTB, and 12

Reaction mixtures (20 μL total volume) contained 400 ng of Form I DNA, 10 mM MOPS (pH 7.4), 50 mM NaCl, 20 μM $Cu(OAc)_2$, 40 μM OP, and 50 μM OTA (**1**), OTB (**2**), or **12**. Reaction mixtures were incubated at 37°C for 30 min, then quenched by the addition of 4 μL loading buffer. Samples were loaded onto a 1% agarose gel containing ethidium bromide (1 μg/mL). The gel was run at 110 V for 2 h and visualized by UV illumination. In a separate experiment, the reactions described above were repeated, but in 10 mM CHES buffer, pH 8.6.

Relaxation of supercoiled DNA by Fe^{III}·EDTA in the presence of OTA

Reaction mixtures (20 μL total volume) contained 400 ng Form I DNA, 10 mM MOPS (pH 7.4), 50 mM NaCl, 20 μM $FeCl_3$, 20 μM EDTA, and either 50 μM sodium ascorbate or 50–250 μM OTA. Reaction mixtures were treated as described in the previous experiments.

Acknowledgment

We thank Dr. Fred W. Perrino (Department of Biochemistry, Wake Forest University School of Medicine) for the sample of

© 1998 NRC Canada

plasmid DNA, Dr. Gary Byrd (RJR Tobacco Co.) for acquisition of the mass spec data, and Mr. Sumit Borah, Mr. Keith Merritt, and Ms. Jennifer M. Yezek for preliminary experiments. This work was supported by grant no. IRG from the American Cancer Society and Wake Forest University.

References

1. K.J. van der Merwe, P.S. Steyn, L. Fourie, D.B. Scott, and J.J. Theron. Nature (London), **205**, 1112 (1965).
2. (*a*) T. Kuiper-Goodman and P.M. Scott. Biomed. Environ. Sci. **2**, 179 (1989); (*b*) A.E. Pohland, S. Nesheim, and L. Friedman. Pure Appl. Chem. **64**, 1029 (1992).
3. (*a*) A.M. Bendele, W.W. Carlton, P. Krogh, and E.B. Lillehoj. J. Natl. Cancer Inst. **75**, 733 (1985); (*b*) M. Castegnaro, R. Plestina, G. Dirheimer, I.N. Chernozemsky, and H. Bartsch. Mycotoxins, Endem. Nephropathy Urinary Tract Tumours. Vol. 115. IARC Sci. Publ., Oxford Univ. Press, Oxford, U.K. 1991; (*c*) R.R. Marquardt and A.A. Frohlich. J. Anim. Sci. **70**, 3968 (1992).
4. (*a*) Y. Grosse, I. Baudrimont, M. Castegnaro, A.-M. Betbeder, E.E. Creppy, G. Dirheimer, and L.A. Pfohl. Chem. Biol. Interact. **95**, 175 (1995); (*b*) P.S. Obrecht, Y. Grosse, L.A. Pfohl, and G. Dirheimer. Arch. Toxicol. **70**, 244 (1996).
5. (*a*) E.E. Creppy, A. Kane, G. Dirheimer, C. Lafarge-Frayssinet, S. Mousset, and C. Frayssinet. Toxicol. Lett. **28**, 29 (1985); (*b*) J.C. Seegers, L.H. Bohmer, M.C. Kruger, M.L. Lottering, and K.M. de A. Toxicol. Appl. Pharmacol. **129**, 1 (1994).
6. C. Malaveille, G. Brun, and H. Bartsch. Mutat. Res. **307**, 141 (1994).
7. H. Xiao, S. Madhyastha, R.R. Marquardt, S. Li, J.K. Vodela, A.A. Frohlich, and B.W. Kemppainen. Toxicol. Appl. Pharmacol. **137**, 182 (1996).
8. (*a*) G.E. de Groene, I.G. Hassing, M.J. Blom, W. Seinen, G.J. Fink, and G.J. Horbach. Cancer Res. **56**, 299 (1996); (*b*) R.F. Omar, H.V. Gelboin, and A.D. Rahimtula. Biochem. Pharmacol. **51**, 207 (1996).
9. I. Baudrimont, A.-M. Betbeder, A. Gharbi, L.A. Pfohl, G. Dirheimer, and E.E. Creppy. Toxicology, **89**, 101 (1994).
10. B.B. Hasinoff, A.D. Rahimtula, and R.F. Omar. Biochim. Biophys. Acta, **1036**, 78 (1990).
11. (*a*) D. Hoehler, R.R. Marquardt, A.R. McIntosh, and H. Xiao. J. Biol. Chem. **271**, 27 388 (1996); (*b*) D. Hoehler, R.R. Marquardt, A.R. McIntosh, and G.M. Hatch. Biochim. Biophys. Acta, **1357**, 225 (1997).
12. (*a*) A.D. Rahimtula, J.C. Bereziat, V. Bussacchini-Griot, and H. Bartsch. Biochem. Pharmacol. **37**, 4469 (1988); (*b*) R.F. Omar, A.D. Rahimtula, and H. Bartsh. J. Biochem. Toxicol. **6**, 203 (1991).
13. (*a*) R.T. Scannell, J.R. Barr, V.S. Murty, K.S. Reddy, and S.M. Hecht. J. Am. Chem. Soc. **110**, 3650 (1988); (*b*) U.S. Singh, R.T. Scannell, H. An, B.J. Carter, and S.M. Hecht. J. Am. Chem. Soc. **117**, 12 691 (1995).
14. (*a*) Y. Li and M.A. Trush. Carcinogenesis, **14**, 1303 (1993); (*b*) Cancer Res. **54**, 1895s (1994).
15. (*a*) D.S. Sigman. Acc. Chem. Res. **19**, 180 (1986); (*b*) T.B. Thederahn, M.D. Kuwabara, T.A. Larsen, and D.S. Sigman. J. Am. Chem. Soc. **111**, 4941 (1989).
16. J. Blair and G.T. Newbold. J. Chem. Soc. 2871 (1955).
17. (*a*) M. Watanabe, M. Sahara, M. Kubo, S. Furukawa, R.J. Billedeau, and V. Snieckus. J. Org. Chem. **49**, 742 (1984); (*b*) M.P. Sibi, S. Chattopadyyay, J.W. Dankwardt, and V. Snieckus. J. Am. Chem. Soc. **107**, 6312 (1985).
18. S. Terao, M. Shiraishi, K. Kato, S. Ohkawa, Y. Ashida, and Y. Maki. J. Chem. Soc. Perkin Trans. 1, 2909 (1982).
19. H. Xiao, R.R. Marquart, A.A. Frohlich, and Y.Z. Ling. J. Agric. Food Chem. **43**, 524 (1995).
20. (*a*) G. Scatchard. Ann. N.Y. Acad. Sci. **51**, 660 (1949); (*b*) K.A. Conners. Binding constants. The measurement of molecular complex stability. John Wiley & Sons, New York. 1987. pp. 339–343.
21. F.A. Cotton and G. Wilkinson. Advanced inorganic chemistry. A comprehensive text. 4th ed. John Wiley & Sons, New York. 1980.
22. F.S. Chu. Arch. Biochem. Biophys. **147**, 359 (1971).
23. F.S. Chu. CRC Crit. Rev. Toxicol. **2**, 499 (1974).
24. A. Albert and E.P. Sergeant. The determination of ionization constants. Chapman & Hall, London. 1962.
25. W. Knapp Pogozelski, T.J. McNeese, and T.D. Tullius. J. Am. Chem. Soc. **117**, 6428 (1995).
26. I.M.C.M. Rietjens, C. den Besten, R.P. Hanzlik, and P.J. van Bladeren. Chem. Res. Toxicol. **10**, 629 (1997).
27. M.W. Bredenkamp, J.L.M. Dillen, P.H. van Rooyen, and P.S. Steyn. J. Chem. Soc. Perkin Trans. 2, 1835 (1989).
28. H. Sigel and R.B. Martin. Chem. Rev. **82**, 385 (1982).
29. (*a*) J. Balla, P.V. Bernhardt, P. Buglyo, P. Comba, T.W. Hambley, R. Schmidlin, S. Stebler, and K. Varnagy. J. Chem. Soc. Dalton Trans. 277 (1991); (*b*) F.V Pamatong, C.A. Detmer III, and J.B. Bocarsly. J. Am. Chem. Soc. **118**, 5339 (1996).
30. A. Stassinopoulos, G. Schulte, G.C. Papaefthymiou, and J.P. Caradonna. J. Am. Chem. Soc. **113**, 8686 (1991).
31. (*a*) D.P. Mack, B.L. Iverson, and P.B. Dervan. J. Am. Chem. Soc. **110**, 7572 (1988); (*b*) C. Harford and B. Sarkar. Acc. Chem. Res. **30**, 123 (1997).
32. H. Lund and M.M Baizer (*Editors*). Organic electrochemistry, an introduction and a guide. 3rd ed. Revised and expanded. Marcel Dekker, Inc., New York. 1991. pp. 615–635.
33. (*a*) K. Takehira, M. Shimiza, Y. Watanabe, H. Orita, and T. Hayakawa. J. Chem. Soc. Chem. Commun. 1705 (1989); (*b*) Y. Takizawa, T. Munakata, Y. Iwasa, and T. Mitsuhashi. J. Org. Chem. **50**, 4383 (1985).
34. (*a*) T. Ohe, T. Mashino, and M. Hirobe. Tetrahedron Lett. **36**, 7681 (1995); (*b*) V.M. Samokyszyn, J.P. Freeman, K.R. Maddipati, and R. Lloyd. Chem. Res. Toxicol. **9**, 1368 (1996).
35. (*a*) Y.J. Abul-Hajj, K. Tabakovic, and I. Tabakovic. J. Am. Chem. Soc. **117**, 6144 (1995); (*b*) M.A. Lewis, D.G Yoerg, J.L. Bolton, and J.A. Thompson. Chem. Res. Toxicol. **9**, 1368 (1996).
36. D. Parsonage, H. Miller, R.P. Ross, and A. Claiborne. J. Biol. Chem. **268**, 3161 (1993).
37. S.O. de Silva, M. Watanabe, and V. Snieckus. J. Org. Chem. **44**, 4802 (1979).
38. H. Benesi and J.H. Hildebrand. J. Am. Chem. Soc. **71**, 2703 (1949).
39. C.K. Mirabelli, C.H. Huang, and S.T. Crooke. Cancer Res. **40**, 4173 (1980).

© 1998 NRC Canada

Mechanisms for the oxidation of secondary alcohols by dioxoruthenium(VI) complexes

Zhao Wang, W. David Chandler, and Donald G. Lee

Abstract: Possible mechanisms for the oxidation of alcohols by dioxoruthenium(VI) complexes are critically evaluated. Rate constants for the reduction of *trans*-$[(TMC)Ru^{VI}(O)_2]^{++}$ (TMC = 1,4,8,11-tetramethyl-1,4,8,11-tetraazacyclotetradecane) by substituted benzhydrols are correlated more satisfactorily with Hammett σ substituent constants ($\rho = -1.44 \pm 0.08$, $r^2 = 0.98$) than with σ^+ substituent constants ($\rho = -0.72 \pm 0.11$, $r^2 = 0.83$). Similar observations for the oxidation of substituted benzyl alcohols have recently been reported, confirming that the transition state for these reactions is not carbocation-like. Primary deuterium isotope effects indicate that cleavage of the α-C–H bond is rate-limiting. The lack of an observable O-D isotope effect and the ease of oxidation of ethers indicates that the presence of a hydroxyl is not essential. The previously reported observation that cyclobutanol is quantitatively converted into cyclobutanone by dioxoruthenium(VI) complexes eliminates free-radical intermediates from consideration as part of the mechanism, and negative entropies of activation ($-\Delta S^{\ddagger} = 96$–$137$ J mol^{-1} K^{-1}) suggest a structured transition state. Only two of eight possible reaction mechanisms considered were found to be consistent with the available data. A critical analysis of the available data indicates that a 2 + 2 (C—H + Ru═O) addition and a reaction initiated by ligand formation through the interaction of the reductant's HOMO with the oxidant's LUMO are the most likely reaction mechanisms.

Key words: oxidation, alcohols, ruthenium(VI), mechanism, substituent effects.

Résumé : On évalue d'une façon critique divers mécanismes possibles pour l'oxydation des alcools par des complexes de dioxoruthénium(VI). La corrélation entre les constantes de vitesse de réduction du *trans*-$[(TMC)Ru^{VI}(O)_2]^{++}$ (TMC = 1,4,8,11-tétraméthyl-1,4,8,11-tétraazacyclotétradécane) par des benzhydrols substitués est meilleure avec des constantes de substituants σ^+ de Hammett ($\rho = -1{,}44 \pm 0{,}08$; $r^2 = 0{,}98$) qu'avec des constantes de substituants σ^+ ($\rho = -0{,}72 \pm 0{,}11$; $r^2 = 0{,}83$). Des observations semblables ont été rapportées récemment pour l'oxydation d'alcools benzyliques substitués; elles confirment que l'état de transition de ces réactions ne ressemble pas à un carbocation. Les effets isotopiques primaires du deutérium indiquent que le clivage de la liaison C-H en α limite la vitesse. Le fait que l'on n'observe pas d'effet isotopique O-D et la facilité d'oxydation des éthers indiquent que la présence d'un groupe hydroxyle n'est pas essentielle. L'observation rapportée antérieurement à l'effet que le cyclobutanol peut être transformé quantitativement en cyclobutanone par les complexes de dioxoruthénium(VI) élimine la possibilité d'un mécanisme impliquant des intermédiaires radicalaires; par ailleurs, les entropies d'activation négatives ($-\Delta S^{\ddagger} = 96$ à 137 J mol^{-1} K^{-1}) suggèrent la présence d'un état de transition structuré. On a trouvé que seulement deux des huit mécanismes réactionnels possibles sont en accord avec les données disponibles. Une analyse critique des données disponibles indique qu'une addition 2 + 2 (C-H + Ru═O) et une réaction initiée par la formation de ligand par interaction des OMHO du réducteur avec les OMBV de l'oxydant sont les mécanismes réactionnels les plus probables.

Mots clés : oxydation, alcools, ruthénium(VI), mécanisme, effets de substituants.

[Traduit par la rédaction]

Introduction

A knowledge of the redox properties of dioxoruthenium(VI) complexes, $[LRu(O)_2]^{++}$, where L is a neutral macrocyclic ligand, is important because of their potential use as stoichiometric or catalytic oxidants. The chemical and physical properties of these complexes, which can exist as either *cis* or *trans* isomers, have been studied in several laboratories including those of Che (1), Meyer (2), Drago (3), James (4), Groves (5), Morishima (6), Hirobe (7), and Jorgensen (8).

It has been observed in these studies that dioxoruthenium(VI) complexes can be used as oxidants for alcohols, alkenes, arenes, sulfides, amines, and phosphines. The products obtained from the oxidation of primary and secondary alcohols are aldehydes (7, 9–13) and ketones (9–14) respectively; from alkanes the products are alcohols (3, 10, 12) or ketones (10, 12); from alkenes the products are α,β-unsaturated ketones (10–13, 15), epoxides (5, 7, 10–13, 16), or products derived from the oxidative cleavage of the double bond (10, 11, 16); from arenes the products are α-phenyl alcohols (10, 12, 13, 16), aldehydes (11, 16, 17), ketones (10, 12, 16), or carboxylic acids (10), depending on the nature of the side

This paper is dedicated to Professor Erwin Buncel in recognition of his contributions to Canadian chemistry.

Received November 3, 1997.

Z. Wang, W.D. Chandler, and D.G. Lee.[1] Department of Chemistry, University of Regina, Regina, SK S4S 0A2, Canada.

[1] Author to whom correspondence may be addressed. Telephone: (306) 585-4247. Fax: (306) 585-4894. E-mail: dglee@meena.cc.uregina.ca

© 1998 NRC Canada

Scheme 1.

Single-electron transfer:

$$R_2CHOH + [LRu^{VI}(O)_2]^{++} \longrightarrow R_2C\dot{O}H^{+} + [LRu^{V}(O)_2]^{+}$$

Hydrogen atom transfers:

$$R_2CHOH + [LRu^{VI}(O)_2]^{++} \longrightarrow R_2C\dot{O} + [LRu^{V}(OH)O]^{++}$$

$$R_2CHOH + [LRu^{VI}(O)_2]^{++} \longrightarrow R_2\dot{C}OH + [LRu^{V}(OH)O]^{++}$$

Hydride transfers:

$$R_2CHOH + [LRu^{VI}(O)_2]^{++} \longrightarrow R_2CHO^{+} + [LRu^{IV}(OH)O]^{+}$$

$$R_2CHOH + [LRu^{VI}(O)_2]^{++} \longrightarrow R_2\overset{+}{C}OH + [LRu^{IV}(OH)O]^{+}$$

2+2 (C-H + Ru=O) addition:

$$R_2CHOH + [LRu^{VI}(O)_2]^{++} \longrightarrow [L(R_2\overset{HO}{\overset{|}{C}})Ru^{VI}(OH)O]^{++}$$

2+2 (O-H + Ru=O) addition:

$$R_2CHOH + [LRu^{VI}(O)_2]^{++} \longrightarrow [L(R_2CHO)Ru^{VI}(OH)O]^{++}$$

Ligand Formation:

$$R_2CHOH + [LRu^{VI}(O)_2]^{++} \longrightarrow [L(R_2C\overset{+}{\underset{H}{\underset{|}{O}}})Ru^{VI}(O)_2]^{+}$$

chain; from cyclic ethers the products are lactones (10); from sulfides the products are the corresponding sulfoxides (6, 7) or sulfones (7); from amines, dehydrogenated products (primarily nitriles and imines) are obtained (18); and from phosphines the products are the corresponding phosphine oxides (2, 6, 19, 20).

This paper reports the results obtained from a variety of experiments designed to provide a better understanding of the mechanism of the reaction between secondary alcohols and a typical dioxoruthenium(VI) complex, *trans*-$[(TMC)Ru^{VI}(O)_2]^{++}$ (TMC = 1,4,8,11-tetramethyl-1,4,8,11-tetraazacyclotetradecane). Eight theoretically possible reaction mechanisms have been considered: direct single-electron transfer from the alcohol to the oxidant, hydrogen atom or hydride ion transfer from either oxygen or carbon, 2 + 2 addition of a ruthenium oxo (Ru═O) to either the O—H or the α-C—H bond of the alcohol and ligand formation followed by a cyclic transfer of hydrogen. These possibilities, derived from the discussion by March (21*a*) and the theoretical work of Deng and Ziegler (22), Mayer and co-workers (23), and Rappe and Goddard (24) on the reactions of high valent transition metal compounds, have been summarized in Scheme 1.

Each of the mechanistic possibilities outlined in Scheme 1 has been examined in light of the rather large amount of experimental evidence currently available with respect to the reactions of dioxoruthenium(VI) complexes and alcohols. From such an analysis it is possible to eliminate several potential processes and to arrive at the "most likely" mechanisms.

Fig. 1. Sequential scans for the oxidation of benzhydrol (0.485 M) by *trans*-$[(TMC)Ru(O)_2]^{++}$ (1.68×10^{-3} M) at 40.0 ± 0.1°C. Scans were taken at intervals of 5500 s.

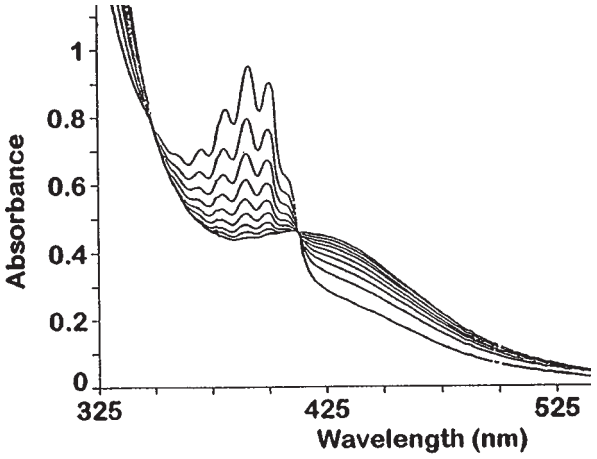

Experimental section

Materials

Benzhydrol (α-phenylbenzenemethanol), 4-methylbenzhydrol, 4-chlorobenzhydrol, and 4,4′-dichlorobenzhydrol were obtained commercially (Aldrich) and purified by repeated crystallizations from a mixture of diethyl ether and hexane until sharp melting points in agreement with literature values were obtained. 2-Propanol was purified by distillation from calcium oxide. A middle fraction (bp 80.5–81.0°C) was collected and analyzed by use of GLC. The results indicated a purity of at least 99.9%.

4-Bromobenzhydrol, 4,4′-dimethylbenzhydrol, 4-fluorobenzhydrol, and 4-methoxybenzhydrol were prepared by reduction of the corresponding benzophenones with lithium aluminum hydride (25). The benzophenones were obtained from Aldrich. In a typical procedure, a flame-dried 300 mL three-necked flask, fitted with a magnetic stirrer and a dropping funnel, was charged with 0.3 g (8 mmol) of lithium aluminum hydride (J.T. Baker) and 100 mL of anhydrous ether. A solution of benzophenone (24 mmol) in anhydrous ether (50 mL) was added dropwise. The mixture was stirred under gentle reflux until the reaction was complete. The solution was then treated with 50 mL of ice water while cooling the reaction flask in an ice bath. The organic layer was separated and the aqueous layer extracted with ether (2 × 30 mL). The combined organic layers were dried over $CaCl_2$, filtered, and evaporated to give the corresponding benzhydrol in 85–93% yield. The products were repeatedly recrystallized from a solution of diethyl ether and hexane until sharp melting points were obtained and then identified from physical and spectral data. 4-Bromobenzhydrol, mp 62–63°C, lit. (26) 63–65°C; ^{1}H NMR ($CDCl_3$), δ: 2.12 (d, 1H), 5.74 (d, 1H), 7.36 (m, 9H); ^{13}C NMR ($CDCl_3$), δ: 75.6, 121.4, 126.6, 127.9, 128.3, 128.7, 131.6, 142.8, 143.4. 4,4′-Dimethylbenzhydrol, mp 68.5–69.0°C, lit. (26) 69°C; ^{1}H NMR ($CDCl_3$), δ: 2.22 (d, 1H), 2.36 (s, 6H), 5.72 (s, 1H), 7.38 (M, 8H); ^{13}C NMR ($CDCl_3$), δ: 21.2, 76.0, 126.5, 129.2, 137.2, 141.2. 4-Fluorobenzhydrol, mp 47–48°C; ^{1}H NMR ($CDCl_3$), δ: 2.41 (d, 1H), 5.78 (d, 1H), 6.99 (t, 2H), 7.28 (m, 7H); ^{13}C NMR ($CDCl_3$), δ: 75.6, 115.5, 126.5, 127.8,

© 1998 NRC Canada

Fig. 2. Typical pseudo first-order plot for the oxidation of benzhydrol (0.670 M) by *trans*-[(TMC)Ru(O)$_2$]$^{++}$. Slope = 9.67 × 10^{-5} s^{-1}, r^2 = 0.999.

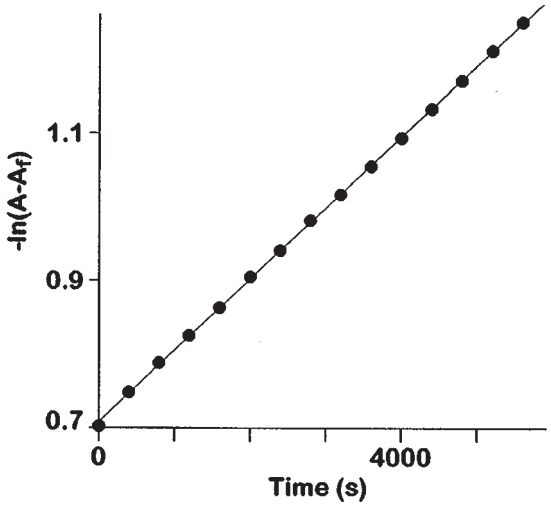

128.2, 128.3, 128.6, 139.5, 143.0. 4-Methoxybenzhydrol, mp 65–66°C; ^{1}H NMR ($CDCl_3$), δ: 2.65 (d, 1H), 3.81 (s, 3H), 5.74 (d, 1H), 6.88 (d, 2H), 7.33 (M, 7H); ^{13}C NMR ($CDCl_3$), δ: 55.3, 75.8, 113.9, 126.5, 128.0, 128.5, 136.0, 144.5, 159.5.

Benzhydrol-α-*d* and 2-propanol-α-*d* were prepared by the reduction of benzophenone and acetone with lithium aluminium deuteride (Aldrich). Benzhydrol-α-*d*, mp 67.5–68.0°C, was identified by use of NMR: ^{1}H NMR ($CDCl_3$), δ: 2.39 (s, 1H), 7.38 (m, 10H); ^{13}C NMR ($CDCl_3$), δ: 126.6, 127.6, 128.5, 144.5. 2-Propanol-α-*d* was purified by distillation from calcium oxide, bp 80.0–80.5°C, and identified by NMR: ^{1}H NMR ($CDCl_3$), δ: 1.11 (s, 6H), 2.66 (br, 1H). Only one peak was detected in a GLC analysis indicating at least 99.9% purity. From the NMR integrals, the incorporation of deuterium was calculated to be 98%. 2-Propanol-*O*-*d* was prepared by repeatedly treating 2-propanol with D_2O. The product was identified by NMR; the ^{1}H NMR integrals indicated 96.7% incorporation of deuterium.

The oxidant was prepared in two forms, [(TMC)-$Ru^{VI}(O)_2](ClO_4)_2$ and [(TMC)$Ru^{VI}(O)_2](BF_4)_2$ using procedures previously described in the literature (27). Both salts reacted with alcohols at the same rate under any particular set of conditions, indicating that the identity of the anion has little influence on the reaction rate. The initial work was done with the perchlorate salt; however, on two occasions small explosions occurred when it was being transferred as a dry solid from the reaction flask in which it had been prepared to a storage vial. The explosions were sufficiently violent to shatter glassware and cause minor cuts to the hand of one of us (Z.W.). The fluoroborate salt proved to be much safer to work with.

Both salts were prepared starting from $K_2[Ru^{III}(Cl)_5H_2O]$, obtained from either Johnson Matthey or Strem Chemicals. Initially, 1.056 g (2.82 mmol) of $K_2[Ru^{III}(Cl)_5(H_2O)]$ was suspended in 150 mL of absolute ethanol and heated under reflux with vigorous stirring for 15 min. 1,4,8,11-Tetramethyl-1,4,8,11-tetraazacyclotetradecane, TMC (Aldrich, 0.92 g, 3.59 mmol), dissolved in 280 mL of ethanol was added dropwise to the refluxing suspension over a period of 6 h. After refluxing for an additional 12 h (overnight), the solution was filtered hot, and the yellow filtrate evaporated to dryness. This product was redissolved in a minimum of hot 3 M HCl. Yellow crystals of *trans*-[(TMC)$Ru^{III}(Cl)_2$]Cl formed when the solution was allowed to slowly cool. After filtration and washing with cold 3 M HCl, a yellow crystalline product (0.70 g, 1.64 mmol, 58%) was obtained; λ_{max} = 370 nm, with a shoulder at 315 nm when dissolved in acetonitrile. A portion of this product (0.43 g, 0.95 mmol) and silver *p*-toluenesulfonate (0.77 g, 2.77 mmol) were heated at 60°C for 0.5 h in 35 mL of distilled water. A grey–white precipitate (AgCl), which formed immediately, was removed by filtration, and 50% H_2O_2 (9 mL) was added dropwise to the remaining yellow solution at 60°C. After 30 min the solution was cooled in an ice–water bath and an excess of $NaClO_4$ added. The compound *trans*-[(TMC)$Ru^{VI}(O)_2](ClO_4)_2$, which slowly precipitated, was collected and recrystallized from hot (60°C) 0.1 M $HClO_4$. Crystalline product (0.23 g, 43%) was obtained. The spectrum of this product dissolved in acetonitrile was similar to that reported in the literature for other dioxoruthenium(VI) complexes: λ_{max} = 228, 257, and 388 nm; lit. (13, 27) 223, 255, and 388 nm.

The compound *trans*-[(TMC)$Ru^{VI}(O)_2](BF_4)_2$ was prepared by first treating *trans*-[(TMC)$Ru^{III}(Cl)_2$]Cl (0.43 g, 0.95 mmol) with silver *p*-toluenesulfonate (0.77 g, 2.77 mmol) dissolved in 35 mL of distilled water and heating the mixture at 60°C for 0.5 h. The solution was filtered to remove AgCl, and 50% H_2O_2 (9 mL) was added dropwise to the yellow filtrate at 60°C. This solution was concentrated to two thirds of its volume and cooled in an ice-water bath. When an excess of saturated $NaBF_4$ solution was added, a precipitate formed slowly over several hours. Collection of the precipitate and recrystallization from hot (60°C) 0.1 M HBF_4 yielded *trans*-[(TMC)$Ru^{VI}(O)_2](BF_4)_2$ (0.12 g, 34%).

Plots of the concentration of this product in acetonitrile solutions vs. absorbance at 388 nm were precisely linear, as required by Beer's Law, with a slope of ε = 539 ± 5.

The solvent, acetonitrile, used in these experiments was purified by stirring with $KMnO_4$ overnight and simple distillation. The distillate was then carefully redistilled over CaH_2 in a nitrogen atmosphere.

Table 1. Rate constants for the oxidation of 2-propanol and benzhydrol by [*trans*-(TMC)$RuO_2]^{++}$ in acetonitrile at 40°C.

Reductant	Concentration (M)	k_1 ($s^{-1} \times 10^5$)[a]	k_2 (M^{-1} $s^{-1} \times 10^5$)[b]
2-Propanol	2.62	6.6 ± 0.6	2.5 ± 0.2
2-Propanol	2.84	7.0 ± 0.3	2.5 ± 0.1
2-Propanol	3.01	7.3 ± 0.1	2.4 ± 0.1
2-Propanol	3.26	8.1 ± 0.1	2.5 ± 0.1
2-Propanol	3.56	9.1 ± 0.1	2.6 ± 0.1
Benzhydrol	0.485	6.8 ± 0.3	14 ± 1
Benzhydrol	0.492	7.2 ± 0.5	15 ± 1
Benzhydrol	0.550	8.2 ± 0.1	15 ± 1
Benzhydrol	0.661	9.0 ± 0.6	15 ± 1
Benzhydrol	0.670	9.6 ± 0.2	14 ± 1

[a] Pseudo first-order rate constants.
[b] $k_2 = k_1$/[reductant].

Kinetic method

Reaction rates were determined by monitoring spectral

© 1998 NRC Canada

Table 2. Kinetic deuterium isotope effects for the oxidation of alcohols by *trans*-dioxoruthenium(VI) complexes.

Reductant	Oxidant[a]	Solvent	Temp. (°C)	k_H/k_D	Reference no.
$CH_3CDOHCH_3$	*trans*-$[LRu(O)_2]^{++}$	CH_3CN	40	7.8 ± 0.5	This work
Ph_2CDOH	*trans*-$[LRu(O)_2]^{++}$	CH_3CN	40	21 ± 2	This work
$PhCD_2OH$	*trans*-$[L'Ru(O)_2]^{++}$	CH_3CN	25	19 ± 2	9
CD_3OD	*trans*-$[L'Ru(O)_2]^{++}$	CH_3CN	25	8 ± 1	9
CD_3CD_2OD	*trans*-$[L'Ru(O)_2]^{++}$	CH_3CN	25	8 ± 1	9
$CD_3CDODCD_3$	*trans*-$[L'Ru(O)_2]^{++}$	CH_3CN	25	11 ± 1	9
$CH_3CHODCH_3$	*trans*-$[LRu(O)_2]^{++}$	CH_3CN	40	1.0 ± 0.1	This work
CH_3CH_2OD	*trans*-$[L'Ru(O)_2]^{++}$	CH_3CN	25	1.0 ± 0.1	9
CH_3CH_2OD	*trans*-$[L'Ru(O)_2]^{++}$	D_2O	25	1.0 ± 0.1	9

[a] L is 1,4,8,11-tetramethyl-1,4,8,11-tetraazacyclotetradecane (TMC). L′ is *N*,*N*′-dimethyl-6,7,8,9,10,11,17,18-octahydro-5*H*-dibenzo[en][1,4,8,12]dioxadiazacyclopentadecane.

Fig. 3. Hammett correlation, using σ substituent constants, for the oxidation of substituted benzhydrols by *trans*-$[(TMC)Ru(O)_2]^{++}$ at 40.0 ± 0.1°C. Slope = –1.44 ± 0.08, r^2 = 0.978. Substituent constants were taken from March (21*b*). The effects when substituents are present in both rings were taken to be additive.

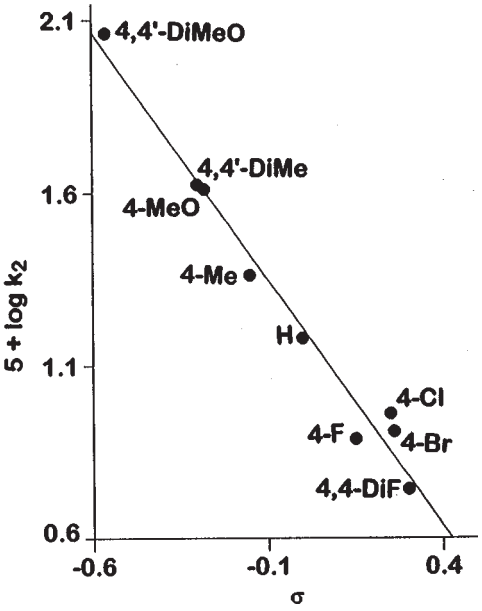

Fig. 4. Attempted Hammett correlation, using σ^+ substituent constants, for the oxidation of substituted benzhydrols by *trans*-$[(TMC)Ru(O)_2]^{++}$ at 40.0 ± 0.1°C. Slope = –0.72 ± 0.11, r^2 = 0.834. Substituent constants were taken from March (21*b*). The effects when substituents are present in both rings were taken to be additive.

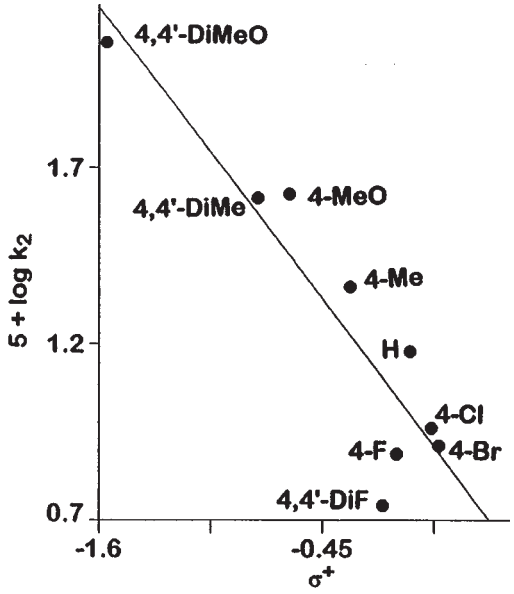

Table 3. Hammett correlations for the oxidation of alcohols by dioxoruthenium(VI) complexes in acetonitrile.[a]

Oxidant[b]	Reductant	Temp. (°C)	ρ(r^2)[c]	ρ$^+$(r^2)[d]	Reference
trans-$[LRu(O)_2]^{++}$	Ar_2CHOH	40	–1.44 (0.98)	–0.72 (0.83)	This work
trans-$[L'Ru(O)_2]^{++}$	$ArCH_2OH$	25	–1.51 (0.96)	–0.91 (0.87)	9[e]
cis-$[L''Ru(O)_2]^{++}$	$ArCH_2OH$	25	–1.24 (0.99)	–0.75 (0.90)	16[e]

[a] Substituent constants were taken from ref. 21*b*.

[b] L is 1,4,8,11-tetramethyl-1,4,8,11-tetraazacyclotetradecane (TMC). L′ is *N*,*N*′-dimethyl-6,7,8,9,10,11,17,18-octahydro-5*H*-dibenzo[en][1,4,8,12]dioxadiazacyclopentadecane. L″ is *N*,*N*,*N*′,*N*′-tetramethyl-3,6-dimethyl-3,6-diazaoctane-1,8-diamine.

[c] Hammett ρ value obtained using σ substituent constants (r^2 is the correlation coefficient).

[d] Hammett ρ value obtained using σ^+ substituent constants (r^2 is the correlation coefficient).

[e] Correlations were recalculated using rate-constant data reported in these references.

changes as the reaction progressed. All measurements were made under pseudo first-order conditions with alcohol concentrations at least 100 times that of the oxidant. Each rate constant reported is the average of at least three determinations that agreed within ± 10% or less. In a typical kinetic experiment, a quartz cuvette containing a 2.00 mL aliquot of

© 1998 NRC Canada

Fig. 5. Eyring plot for the oxidation of benzhydrol (0.504 M) by $[(TMC)Ru(O)_2]^{++}$. Slope = –6920 ± 370 K, intercept = 7.5 ± 1.2, $r^2 = 0.989$.

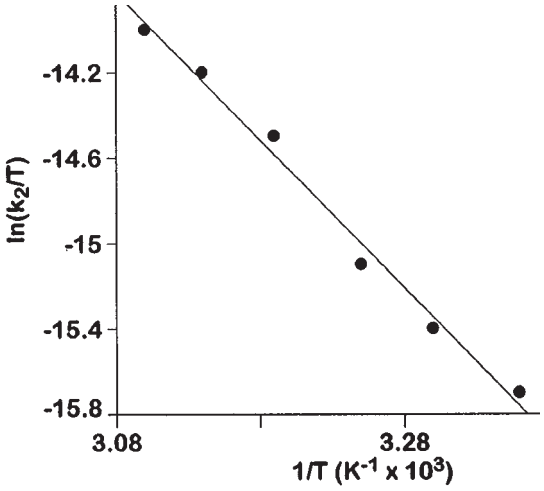

approximately 1×10^{-3} M $[(TMC)Ru^{VI}(O)_2]^{++}$ in acetonitrile was placed in the thermostated cell compartment of a Hewlett Packard 8450A diode array spectrophotometer and held there until thermal equilibrium had been established. An excess of the alcohol, also dissolved in acetonitrile and thermostated at the same temperature, was added from a microliter syringe and, after thorough mixing, spectra recorded at equal time intervals. Sequential scans exhibited sharp isosbestic points at 334 nm and 404 nm (Fig. 1). The final spectrum was identical to that reported for $[(TMC)Ru^{IV}O(CH_3CN)]^{++}$ (13).

Results

Rate law

Plots of ln(absorbance – final absorbance) at 388 nm were linear (Fig. 2), indicating that the reaction is first order in oxidant. Second-order rate constants, calculated by division of the pseudo first-order rate constants by alcohol concentration (Table 1), were observed to be constant, indicating that the reaction is also first order with respect to the reductant. The rate law is therefore given by eq. [1].

$$[1] \quad -d[Ru^{VI}]/dt = k_2[Ru^{VI}][alcohol]$$

Isotope effects

Kinetic isotope effects, determined for the oxidation of 2-propanol-2-*d*, 2-propanol-*O*-*d* and benzhydrol-α-*d* are summarized in Table 2. The results reported from other laboratories for the oxidation of isotopically substituted alcohols by dioxoruthenium(VI) complexes have also been included in Table 2 for comparison purposes.

Substituent effects

The second-order rate constants for the oxidation of substituted benzhydrols by $[(TMC)Ru^{VI}(O)_2]^{++}$ were found to correlate well with Hammett σ values (Fig. 3), but not with the corresponding σ^+ values (Fig. 4). The negative ρ value (–1.44) indicates that the electron density on the α-carbon has decreased in the transition state; however, the lack of correlation with σ^+ values, observed in this and other studies, indicates that the transition state is not carbocation-like. Table 3 contains a comparison of the Hammett correlations for similar reactions of dioxoruthenium(VI) complexes that have been reported from other laboratories.

Table 4. Activation parameters for the oxidation of alcohols by dioxoruthenium(VI) complexes in acetonitrile.

Reductant	Oxidant[b]	$\Delta H^{\ddagger}$ (kJ/mol)	$\Delta S^{\ddagger}$ (J/mol K)	Reference no.
Benzhydrol	*trans*-$[LRu(O)_2]^{++}$	58 ± 9	–137 ± 8	This work
2-Propanol	*trans*-$[LRu(O)_2]^{++}$	62 ± 5	–135 ± 2	This work
2-Propanol	*cis*-$[L'Ru(O)_2]^{++}$	54 ± 4	–109 ± 17	16
2-Propanol	*trans*-$[L''Ru(O)_2]^{++}$	50 ± 4	–117 ± 13	9
Cyclobutanol	*cis*-$[L'Ru(O)_2]^{++}$	59 ± 4	–92 ± 13	16
Benzyl alcohol	*cis*-$[L'Ru(O)_2]^{++}$	50 ± 4	–100 ± 13	16
Benzyl alcohol[a]	*trans*-$[L'''Ru(O)_2]^{++}$	35 ± 4	–96 ± 13	10
Benzyl alcohol	*trans*-$[L''Ru(O)_2]^{++}$	42 ± 4	–109 ± 13	9

[a] Solvent: CF_3SO_3H.

[b] L is 1,4,8,11-tetramethyl-1,4,8,11-tetraazacyclotetradecane (TMC). L′ is *N*,*N*,*N*′,*N*′-tetramethyl-3,6-dimethyl-3,6-diazaoctane-1,8-diamine. L″ is *N*,*N*′-dimethyl-6,7,8,9,10,11,17,18-octahydro-5*H*-dibenzao[en][1,4,8,112] dioxadiazacyclopentadecane. L‴ is 5,5-dimethyl-2,2′-bipyridine.

Activation parameters

The enthalpies and entropies of activation for the oxidation of 2-propanol and benzhydrol were determined from a study of the reaction rates at different temperatures. A typical Eyring plot has been reproduced in Fig. 5. The activation parameters that have been reported for other similar reactions are included in Table 4 for comparison purposes.

Discussion

There are at least two reasons why chemists wish to have a good understanding of reaction mechanisms: (*i*) a knowledge of the mechanism of a reaction provides an indication of the conditions that should be used to maximize the yield and rate of formation of a specific reaction product, and (*ii*) insights into the details of a particular reaction mechanism are often transferable to other reactions; i.e., there is a likelihood that all chemistry will ultimately be understandable in terms of a finite number of fundamental principles.

The reactions between high valent transition metal compounds (oxidants) and organic reductants are examples of important, often used processes for which the chemistry is not particularly well understood, despite a voluminous literature. The products obtained, in common with most redox reactions, could be produced via several possible mechanisms (21*a*), as summarized in Scheme 1 for the reaction under consideration. With such a multiplicity of viable mechanistic options available, it will likely be very difficult to "prove" that a particular mechanism is correct; the best that can be expected at this time is a critical evaluation of each possible mechanism in light of the available experimental evidence and the most current theoretical calculations. Using this approach several possibilities can be eliminated and the "most likely" mechanisms proposed. Ultimately, it is reasonable to expect that it may be possible to arrive at a unified mechanistic consensus that is applicable to a large number of redox reactions (28).

The observation made by Che and co-workers (12, 29), that

© 1998 NRC Canada

the only product obtained from the oxidation of cyclobutanol by dioxoruthenium(VI) complexes is cyclobutanone, indicates that free-radical intermediates are not involved. As discussed in detail elsewhere (16, 30–36), it is known that the internal strain of the cyclobutyl system causes it to open if free radical intermediates are formed. For example, acyclic products are obtained when cyclobutanol is oxidized by typical one-electron oxidants such as vanadium(V) (30, 31), manganese(III) (31), chromium(IV) (32), cerium(IV) (33), and ruthenium(VII) (34, 36), while cyclobutanone is obtained from typical two-electron oxidants such as ruthenium tetroxide (35), ruthenium(VI) (35, 36), chromium(VI) (32), and chromium(V) (32). The expected products from oxidations involving single-electron or hydrogen atom transfers would therefore be acyclic compounds (Scheme 2), while two-electron transfer reactions would result in the formation of cyclobutanone (Scheme 3).

Reaction mechanisms that involve cleavage of the O—H bond in the rate-limiting step are also eliminated from further consideration by the observation that there is no measurable kinetic deuterium isotope effect when the hydroxyl hydrogen is replaced by deuterium (Table 2). This would include both hydrogen atom and hydride ion transfers from oxygen, as well as 2 + 2 (O-H + Ru=O) additions. The report that ethers, such as tetrahydrofuran, are readily oxidized by dioxoruthenium(VI) complexes (10, 29, 37) indicates that the presence of O-H groups in the structure of the reductant is not essential, in contrast to chromic acid oxidations (for example see ref. 38).

A mechanism involving direct transfer of a hydride ion from the α-carbon would be in agreement with the observed isotope effects, but not with the Hammett studies reported here and elsewhere. The rate constants for such reactions (eq. [2]) should correlate better with σ^+ values (39), contrary to the experimental observations summarized in Table 3. In fact, any reaction in which the α-carbon is carbonyl-like (sp^2 hybridized) in the transition state should correlate better with σ^+ values. The correlation reported herein and those found in the literature are consistently better when σ values are used, the clear implication being that direct hydride transfer is not a likely mechanism.

[2] $$Ar_2CHOH + [(TMC)Ru^{VI}(O)_2]^{++} \longrightarrow Ar_2\overset{+}{C}OH + [(TMCRu^{IV}(OH)O]^{+}$$

A mechanism in which the reaction is initiated by a 2 + 2 addition of a ruthenium oxo to the α-C—H bond, as has been proposed for several other oxidation reactions (40–42), is in agreement with the isotope effects reported in Table 2 and the Hammett studies summarized in Table 3. In this reaction (eq. [3]) the α-carbon remains sp^3 hybridized, eliminating the possibility of a direct resonance contribution from the substituents and therefore a lack of correlation with σ^+ values.

[3] 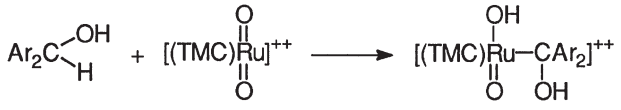

1

The observation (37) that the oxidation of tetrahydrofuran by dioxoruthenium(VI) complexes exhibits a primary isotope effect and activation parameters ($k_H/k_D = 20 \pm 2$, $\Delta H^{\ddagger} = 59 \pm 4$ kJ mol^{-1}, $\Delta S^{\ddagger} = -117 \pm 13$ J mol^{-1} K^{-1}) similar to those for the corresponding alcohol reactions (Tables 2 and 4) is also consistent with a possible 2 + 2 (C—H + Ru=O) addition mechanism. The α-hydrogens of ethers and alcohols are electronically similar and would therefore be expected to respond similarly to oxidants that cause C—H bond cleavage in the rate-limiting step.

It is also possible to consider a mechanism for conversion of the organometallic intermediate, **1**, into products. Two possibilities exist: (*i*) homolytic cleavage of the Ru—C bond would give a ruthenium(V) complex and a free radical that could subsequently undergo a hydrogen atom transfer as in eqs. [4] and [5], or (*ii*) heterolytic cleavage of the Ru—C bond to give a ruthenium(IV) complex and a cation that could transfer a proton to give the observed products as in eqs. [6] and [7].

[4] 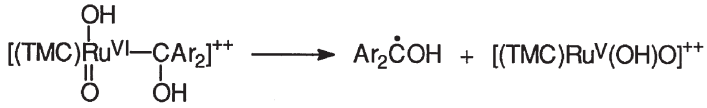

[5] $$Ar_2\dot{C}OH + [(TMC)Ru^{V}(OH)O]^{++} \longrightarrow Ar_2CO + [(TMC)Ru^{IV}(OH)_2]^{++}$$

[6] 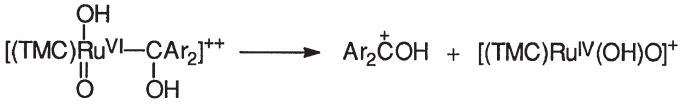

[7] $$Ar_2\overset{+}{C}OH \rightleftharpoons A_2CO + H^{+}$$

The reaction sequence in eqs. [4] and [5] involves formation of free-radical intermediates, which are considered to be unlikely because of the previously described observation that oxidation of cyclobutanol does not result in ring opening. It is,

© 1998 NRC Canada

Scheme 2.

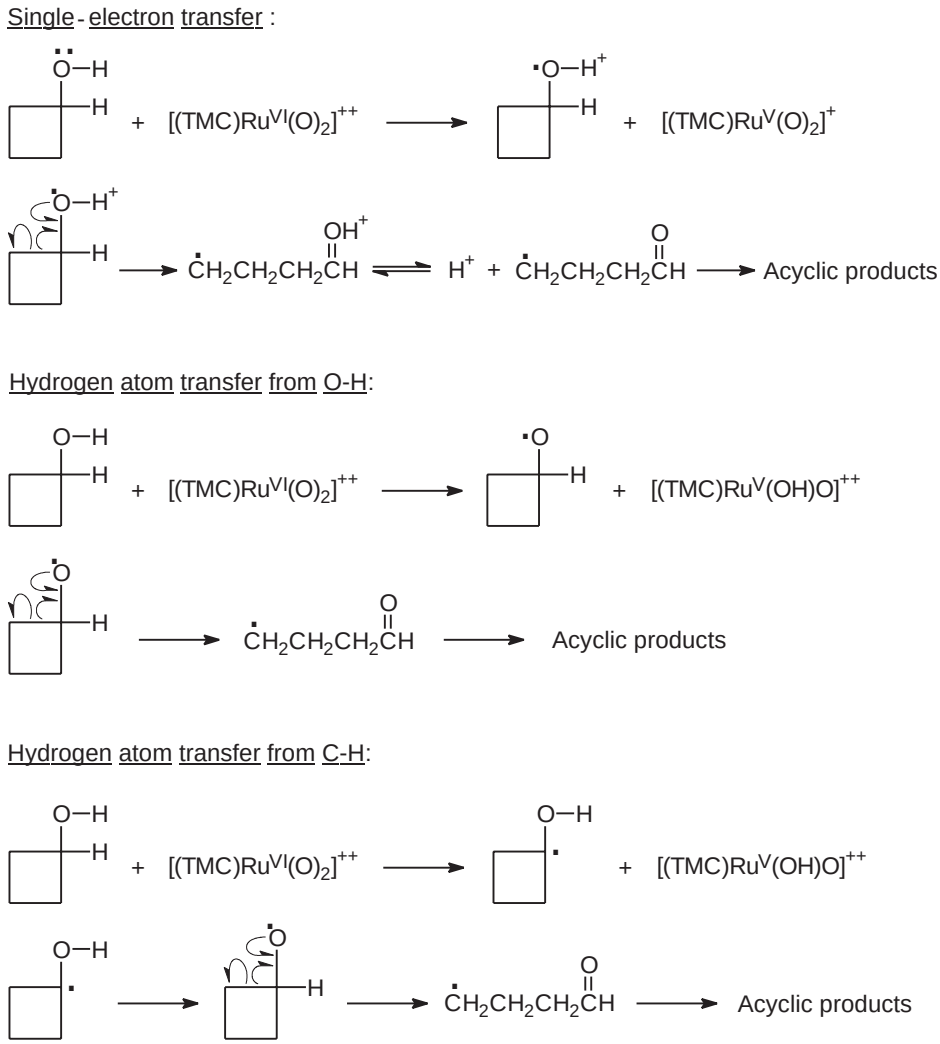

however, possible that the transfer of the hydrogen atom (eq. [5]) could occur more rapidly than ring opening, thereby precluding the formation of acyclic products. In such an event, the hydrogen atom transfer would have to take place rapidly before the free radical could diffuse out of the solvent cage enclosing it and the ruthenium(V) complex; diffusion out of the solvent cage would provide more than sufficient time for ring opening to occur.

A mechanism consisting of reaction [3], followed by either [4] and [5] or [6] and [7], is consistent with the observed rate law, the products from the oxidation of cyclobutanol, the isotope effects, and the Hammett study. It is also consistent with the observed activation parameters (Table 4). A 2 + 2 addition (eq. [3]) would be expected to exhibit a negative entropy of activation in common with most combination reactions that require an organized transition state and result in the loss of one translational degree of freedom. The low enthalpy of activation is also consistent with a 2 + 2 addition of a ruthenium oxo bond to a C—H bond because the energy required for bond cleavage would be partly compensated for by the concurrent formation of new O—H and Ru—C bonds.

There is, however, a theoretical difficulty associated with the 2 + 2 (C—H + Ru=O) mechanism. Frontier molecular orbital theory suggests that oxidation reactions of this type should involve an initial interaction between the reductant's HOMO and the oxidant's LUMO. The oxidant's LUMO in this case would be an Ru=O π^* antibonding orbital (28), while the reductant's HOMO would be an oxygen 2*p*-nonbonding orbital. Since the LUMO would be centered primarily on the metal, it is predicted on the basis of this theory that the initial reaction would involve ligand formation as in eq. [8].

[8] $Ar_2CHOH + [(TMC)Ru(O)_2]^{++} \longrightarrow (TMC)Ru(O)(O)-OCHAr_2 \rightleftharpoons (TMC)Ru(O)(OH)-OCHAr_2$

3 **4**

© 1998 NRC Canada

Scheme 3.

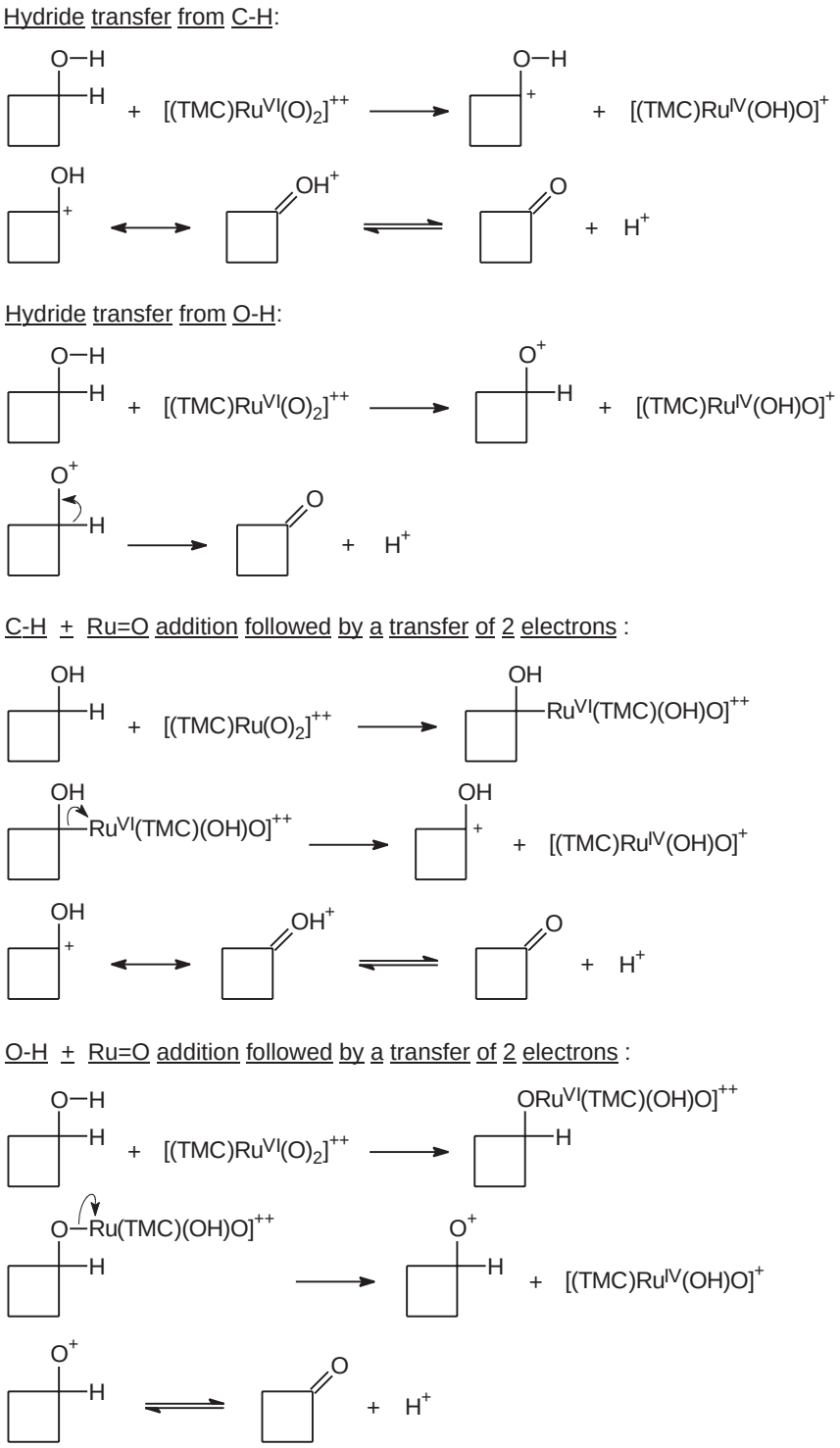

Ligand formation would be followed by proton transfer as in eq. [8] to give **4**, which is formally the 2 + 2 (O—H + Ru═O) addition product. The amounts of **3** and **4** present would be controlled by the relative pK_{BH^+} values for the two compounds. However, the lack of an observable O-D isotope effect (Table 2) suggests that **4** may not be part of the reaction sequence leading to product formation. The aforementioned fact that tetrahydrofuran is readily oxidized by dioxoruthenium(VI) complexes also indicates that a proton transfer would not be an essential part of the reaction if this is the correct mechanism.

The intermediates **3** and **5** for alcohol and ether oxidation, respectively, would decompose to yield oxidized products by a cyclic transfer of hydrogen as depicted in eqs. [9] or [10] and [11]. This mechanism is similar to one recently proposed by Espenson and co-workers (43) for the oxidation of alcohols by $[Cr = O]^{++}$. It is also in general agreement with the theoretical

© 1998 NRC Canada

description of the reaction between methanol and oxidants containing chromium or ruthenium oxos recently published by Deng and Ziegler (22).

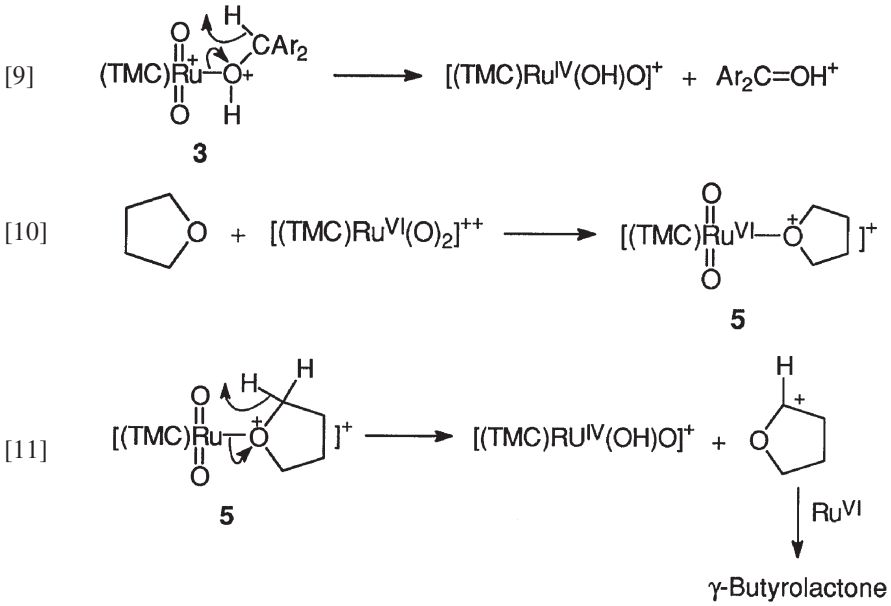

The electron flow in these reactions has been indicated as if it involved hydride transfer; however, for cyclic redox mechanisms it is not possible to specify the direction of electron flow, nor whether it occurs by single- or double-electron shifts. The assumption that the oxygen bears a positive charge in the transition state is consistent with the negative Hammett ρ value and with the observation that electronic substituent effects correlate with σ rather than σ^+ values. Since the positive charge is not located adjacent to the aromatic ring in intermediate **3**, direct resonance interactions are not possible.

In common with the 2 + 2 (C—H + Ru═O) reaction mechanism discussed previously, the mechanism defined by eqs. [8] and [9] would be consistent with the unfavorable entropies of activation and the low enthalpies of activation summarized in Table 4. The cyclic, well-organized transition state would be expected to result in an unfavorable entropy of activation and the simultaneous bond making and breaking would be consistent with a low enthalpy of activation. The significant C-D isotope effect and the lack of an observable O-D isotope effect are also consistent with this mechanism.

Both the 2 + 2 (C—H + Ru═O) addition mechanism (eq. [3]) and the ligand association mechanism (eq. [8]) require the introduction of a new ruthenium ligand into the octahedral complex, $[(TMC)Ru^{VI}(O)_2]^{++}$. In eq. [3] the new ligand is attached through carbon to give an organometallic intermediate, while in eq. [8] the new ligand is attached through oxygen giving a ruthenate ester intermediate. Whether these new ligands would be introduced by associative or dissociative mechanisms (44) cannot be determined conclusively on the basis of the experimental evidence currently available. However, the observation made by Che et al. (9) that complexes with more flexible acyclic tetraaza ligands react faster by several orders of magnitude than the corresponding cyclic tetraaza ligands suggests that a dissociative mechanism with loss of an *N*-donor ligand may be most likely (45).

Conclusions

The experimental and theoretical information available with respect to the oxidation of alcohols by dioxoruthenium(VI) complexes is not compatible with several possible redox mechanisms including a single-electron transfer and direct hydrogen atom or hydride ion transfers from either carbon or oxygen. The available information is consistent with both a 2 + 2 (C—H + Ru═O) mechanism (eqs. [3]–[7]) or attachment of the alcohol as a ligand on Ru, followed by a cyclic transfer of hydrogen from the reductant to the oxidant as in eqs. [8] and [9]. Currently available information does not permit a choice between these two possibilities; however, the latter appears to be more consistent with theoretical considerations.

Acknowledgment

Financial assistance from the Natural Sciences and Engineering Research Council of Canada is gratefully acknowledged.

References

1. C.M. Che and W.V.V. Yam. Adv. Inorg. Chem. **39**, 233 (1992), and refs. therein.
2. A. Dovletoglou and T.J. Meyer. J. Am. Chem. Soc. **116**, 215 (1994), and refs. therein.
3. A.S. Goldstein, R.H. Beer, and R.S. Drago. J. Am. Chem. Soc. **116**, 2424 (1994), and refs. therein.
4. T. Mlodnicka and B.R. James. *In* Metallorporphyrins catalyzed oxidations. *Edited by* F. Montanari and L. Casella. Kluwer Academic Publishers, Amsterdam. 1994. pp. 121–148, and refs. therein.
5. J.T. Groves and R. Quinn. J. Am. Chem. Soc. **107**, 5790 (1985), and refs. therein.
6. Y. Tokita, K. Yamguchi, Y. Watanabe, and I. Morishima. Inorg. Chem. **32**, 329 (1993).

© 1998 NRC Canada

7. T. Higuchi, H. Ohtake, and M. Hirobe. Tetrahedron Lett. **32**, 7435 (1991); **30**, 6545 (1989).
8. K.A. Jorgensen. *In* Metalloporphyrins catalyzed oxidations. *Edited by* F. Montanari and L. Casella. Kluwer Academic Publishers, Amsterdam. 1994. pp. 207–238.
9. C.M. Che, W.T. Tang, W.O. Lee, K.Y. Wong, and T.C. Lau. J. Chem. Soc. Dalton Trans. 1551 (1992).
10. C.M. Che, W.H. Leung, C.K. Li, and C.K. Poon. J. Chem. Soc. Dalton Trans. 379 (1991).
11. C.M. Che, W.T. Tang, W.O. Lee, W.T. Wong, and T.F. Lai. J. Chem. Soc. Dalton Trans. 2011 (1989).
12. C.M. Che, W.T. Tang, W.T. Wong, and T.F. Lai. J. Am. Chem. Soc. **111**, 9048 (1989).
13. C.M. Che, T.F. Lai, and K.Y. Wong. Inorg. Chem. **26**, 2289 (1987).
14. S.Y.S. Cheng, N. Rajapakse, S.J. Rettig, and B.R. James. J. Chem. Soc. Chem. Commun. 2669 (1994).
15. C.K. Li, C.M. Che, W.F. Tong, W.T. Tang, K.Y. Wong, and T.F. Lai. J. Chem. Soc. Dalton Trans. 2109 (1992).
16. W.C. Cheng, W.Y. Yu, C.K. Li, and C.M. Che. J. Org. Chem. **60**, 6840 (1995).
17. N. Rajapakse, B.R. James, and D. Dolphin. Catal. Lett. **2**, 219 (1989).
18. A.J. Bailey and B.R. James. J. Chem. Soc. Chem. Commun. 2343 (1996).
19. B.A. Moyer, B.K. Sipe, and T.J. Meyer. Inorg. Chem. **20**, 1475 (1981).
20. S.Y.S. Cheng and B.R. James. J. Mol. Catal. **117**, 91 (1997).
21. (*a*) J. March. Advanced organic chemistry. 4th ed. Wiley, New York. 1992. pp. 1158–1161, and refs. therein; (*b*) Advanced organic chemistry. 4th ed. Wiley, New York. 1992. p. 280.
22. L. Deng and T. Ziegler. Organometallics, **16**, 716 (1997), and refs. therein.
23. K.A. Gardner, L.L. Kuehnert, and J.M. Mayer. Inorg. Chem. **36**, 2069 (1997); G.K. Cook and J.M. Mayer. J. Am. Chem. Soc. **117**, 7139 (1995); J. Am. Chem. Soc. **116**, 1855 (1994); J. Am. Chem. Soc. **116**, 1868 (1994); K.A. Gardner and J.M. Mayer. Science (Washington, D.C.) **269**, 1849 (1995).
24. A.K. Rappe and W.A. Goddard. J. Am. Chem. Soc. **104**, 3287 (1982).
25. L.A. Paquette. Encyclopedia of reagents for organic synthesis. Vol. 5. *Edited by* L.A. Paquette. Wiley, New York. 1995. p. 3009; W.F. Gannon and H.O. House. Organic syntheses. Coll. vol. 5. Wiley, New York. 1973. p. 294.
26. C.W.N. Cumper and A.P. Thurston. J. Chem. Soc. Perkin Trans. 2, 106 (1972).
27. C.M. Che, K.Y. Wong, and C.K. Poon. Inorg. Chem. **24**, 1797 (1985); C.M. Che, T.W. Tang, and C.K. Poon. J. Chem. Soc. Chem. Commun. 641 (1984).
28. R.H. Holm. Chem. Rev. **87**, 1401 (1987).
29. C.M. Che, W.T. Tang, and C.K. Li. J. Chem. Soc. Dalton Trans. 3735 (1990).
30. J. Rocek and D.E. Aylward. J. Am. Chem. Soc. **97**, 5452 (1975).
31. J. Rocek and A.E. Radkowsky. J. Org. Chem. **38**, 89 (1973).
32. J. Rocek and A.E. Radkowsky. J. Am. Chem. Soc. **95**, 7123 (1973).
33. K. Meyer and J. Rocek. J. Am. Chem. Soc. **94**, 1209 (1972).
34. D.G. Lee and L.N. Congson. Can. J. Chem. **68**, 1774 (1990).
35. D.G. Lee, U.A. Spitzer, J. Cleland, and M.E. Olson. Can. J. Chem. **54**, 2124 (1976).
36. D.G. Lee, L.N. Congson, U.A. Spitzer, and M.E. Olson. Can. J. Chem. **62**, 1835 (1984).
37. C.M. Che, W.T. Tang, K.Y. Wong, and C.K. Li. J. Chem. Soc. Dalton Trans. 3277 (1991).
38. F.H. Westheimer. Chem. Rev. **45**, 419 (1948).
39. T.H. Lowry and K.S. Richardson. Mechanism and theory in organic chemistry. Harper and Row, New York. 1987. pp. 143–151.
40. D.G. Lee and T. Chen. J. Am. Chem. Soc. **115**, 11231 (1993).
41. D.G. Lee and T. Chen. J. Org. Chem. **56**, 5341 (1991).
42. D.G. Lee and H. Gai. Can. J. Chem. **71**, 1394 (1993).
43. S.L. Scott, A. Bakac, and J.H. Espenson. J. Am. Chem. Soc. **114**, 4205 (1992).
44. J.E. Huheey, E.A. Keiter, and R.L. Keiter. Inorganic chemistry principles of structure and reactivity. Harper Collins, New York. 1993. p. 540.
45. R.G. Wilkins. Kinetics and mechanisms of reactions of transition metal complexes. 2nd ed. VCH, New York. 1991. p. 224.

© 1998 NRC Canada

Thermodynamics of methanesulfonic acid, methanesulfonyl chloride, and methyl methanesulfonate

J. Peter Guthrie, Allan R. Stein, and Anthony P. Huntington

Abstract: The heat of formation of liquid methanesulfonic acid, –178.09 ± 1.48, was determined by measuring the heat of reaction of methyl thiolacetate with aqueous hypochlorite solution to give aqueous methanesulfonate and acetate. The heats of formation of liquid methanesulfonyl chloride, –126.91 ± 1.54, and methyl methanesulfonate, –164.34 ± 1.58, were determined by measuring the heats of reaction of methanesulfonyl chloride with water or methanol in the presence of a suitable basic catalyst. Heats of vaporization (based on vapor-pressure data), entropies (based on ab initio molecular orbital calculations), and free energies of transfer from gas phase to aqueous solution were calculated leading to values for the free energies of formation in aqueous solution. The free energies of formation so determined were methanesulfonic acid, –151.72 ± 2.68, methanesulfonyl chloride, –101.29 ± 1.96, and methyl methanesulfonate, –127.28 ± 2.08. From these values the free energies of hydrolysis (leading to unionized methanesulfonic acid) are methanesulfonyl chloride, –25.11 ± 3.04, and methyl methanesulfonate, –9.90 ± 2.48.

Key words: sulfonic acids, heat of formation, free energy of formation, hydrolysis.

Résumé : On a déterminé la chaleur de formation de l'acide méthanesulfonique liquide (–178,09 ± 1,48) en mesurant la chaleur de réaction du thiolacétate de méthyle avec une solution aqueuse d'hypochlorite qui conduit à la formation de méthanesulfonate et d'acétate aqueux. Les chaleurs de formation du chlorure de méthanesulfonyle liquide (–126,91 ± 1,54) et du méthanesulfonate de méthyle (–164,34 ± 1,58) ont aussi été déterminées en mesurant les chaleurs de réaction du chlorure de méthanesulfonyle avec l'eau ou le méthanol en présence d'un catalyseur basique approprié. On a calculé les chaleurs de vaporisation (en se basant sur des données de tension de vapeur), les entropies (en se basant sur des calculs d'orbitales moléculaires ab initio) et les énergies libres de transfert de la phase gazeuse à une solution aqueuse et on en a déduit les valeurs pour les énergies libres de formation en solution aqueuse. Les énergies libres de formation ainsi déterminées sont acide méthanesulfonique, –151,72 ± 2,68, chlorure de méthanesulfonyle, –101,29 ± 1,96, et méthanesulfonate de méthyle, –127,28 ± 2,08. À partir de ces valeurs, les énergies libres d'hydrolyse (conduisant à de l'acide méthanesulfonique non ionisé) sont: chlorure de méthanesulfonyle, –25,11 ± 3,04 et méthanesulfonate de méthyle, –9,90 ± 2,48.

Mots clés : acides sulfoniques, chaleur de formation, énergie libre de formation, hydrolyse.

[Traduit par la rédaction]

Introduction

Although sulfonic esters have been extensively studied as substrates for nucleophilic substitution reactions (1), and are frequently used either as activating or protecting groups in synthesis (2), there has been no direct information about the thermochemistry of these important compounds (3). Values for the thermodynamics of sulfonate ester hydrolysis have been estimated (4), and recently an indirect evaluation of the heats of formation of methanesulfonyl chloride and benzene sulfonyl chloride has been reported (3, 5).

We wish to report calorimetric determinations of the heats of formation of methanesulfonic acid, methanesulfonyl chloride, and methyl methanesulfonate. These are the first determinations of heats of formation of sulfonic acid derivatives based on calorimetric heats of reaction for conversion of a thiol derivative to the corresponding sulfonic acid derivative. Although less direct than a heat of combustion measurement, it is much less indirect than all previous attempts to determine such heats of formation. Although the values are in the same general range as previous estimates, there are substantial differences. We will show that our thermochemical data lead by way of values of the free energies of formation of the ester and acid to a free energy of hydrolysis close to the previous estimate of the free energy of hydrolysis from this laboratory (4). The new value differs by slightly more than the sum of the standard deviations from the old value.

The approach we have used could be applied to many other sulfonic acids and their derivatives so that thermochemical

This paper is dedicated to Professor Erwin Buncel in recognition of his contributions to Canadian chemistry.

Received December 8, 1997.

J.P. Guthrie[1] and A.P. Huntington. Department of Chemistry, University of Western Ontario, London, ON N6A 5B7, Canada.
A.R. Stein. Department of Chemistry, Memorial University of Newfoundland, St. John's, NF A1B 3X7, Canada.

[1] Author to whom correspondence may be addressed. Telephone: 519–679–2111–6352. Fax: 519–661–3022. E-mail: peter.guthrie@uwo.ca

© 1998 NRC Canada

Table 1. Heats of reaction and solution.[a]

Compound	ΔH
CH_3SCOCH_3	–241.08[b]
	–242.18[b]
	–241.19[b]
	–243.75[b]
	–239.95[b]
Avg.	–241.63 ± 1.42[b]
H_2O	0.00152[b,d]
CH_3SO_3H	–25.74[b]
	–25.64[b]
	–25.63[b]
	–25.59[b]
Avg.	–25.65 ± 0.06[b]
CH_3COOH	–14.05[b]
	–14.05[b]
	–14.12[b]
	–13.81[b]
Avg.	–14.01 ± 0.14[b]
CH_3SO_2Cl	–33.585[c]
	–33.635[c]
	–33.439[c]
Avg.	–33.55 ± 0.10[c]
CH_3OH	0.00074[c,d]
	0.00057[c,d]
	0.00090[c,d]
	0.0007 ±
	0.0002[c,d]
$CH_3CO_2CH_3$	0.878[c,d]
	0.869[c,d]
Avg.	+0.87 ± 0.01[c,d]
CH_3SO_2Cl	–39.873[e]
	–39.711[e]
	–40.184[e]
	–39.772[e]
Avg.	–39.89 ± 0.21[e]
CH_3COCl	–28.007[e]
	–28.442[e]
	–28.500[e]
Avg.	–28.32 ± 0.27[e]
CH_3SO_3H	–14.943[e]
	–14.798[e]
	–14.695[e]
	–14.610[e]
Avg.	–14.76 ± 0.14[e]
CH_3COOH	–3.839[e]
	–3.815[e]
	–3.860[e]
	–3.743[e]
Avg.	–3.81 ± 0.05[e]
CH_3COCl	–39.057[c]
	–39.019[c]
	–38.730[c]
	–38.528[c]
	–38.867[c]
Avg.	–38.84 ± 0.22[c]
$CH_3SO_3CH_3$	2.284[c,d]
	2.284[c,d]
	2.265[c,d]
	2.243[c,d]
Avg.	+2.27 ± 0.02[c,d]

[a] All at 25°C; units are kcal/mol; heat of reaction unless noted.
[b] In 0.235 M aqueous NaOCl.
[c] In methanol containing tributylamine, molar ratio 100:1.
[d] Heat of solution.
[e] In pH 10.2 carbonate buffer, 0.297 M in $NaHCO_3$, and 0.235 M inNaOH.

information about this large and important class of compounds should at last become available.

Results

S-Methyl thiolacetate was used as a (relatively) nonvolatile nonodoriferous equivalent of methanethiol. It reacted rapidly and quantitatively with aqueous sodium hypochlorite solution to give sodium acetate and sodium methanesulfonate. NMR analysis confirmed that no other products were observed and that the signals from acetate and methanesulfonate were in a 1:1 ratio. The observed heat of reaction corresponds to

[1] $$CH_3SCOCH_3(l) + 3NaOCl(soln) + H_2O(soln) \rightleftharpoons CH_3SO_3H(soln) + CH_3COOH(soln) + 3NaCl(soln)$$

By measuring heats of solution for the organic products we were able to derive the heat of reaction for the more convenient hypothetical process:

[2] $$CH_3SCOCH_3(l) + 3NaOCl(soln) + H_2O(soln) \rightleftharpoons CH_3SO_3H(l) + CH_3COOH(l) + 3NaCl(soln)$$

The relevant heats of reaction and solution are found in Table 1. Then from the heats of formation of all reactants and products except methanesulfonic acid we could calculate the heat of formation of methanesulfonic acid. In the case of the starting material, *S*-methyl thiolacetate, we had to estimate the heat of formation of both the gaseous and liquid forms, starting from the accurately known heat of formation of *S*-ethyl thiolacetate. The heat of formation of *S*-methyl thiolacetate could be calculated from that of *S*-ethyl thiolacetate by subtraction of the group contribution for $[CH_2(C)(S)]$. The heat of vaporization of *S*-methyl thiolacetate was estimated from the boiling point, using the correlation that we have reported (6). These literature data are summarized in Table 2, as is our value for the heat of formation of methanesulfonic acid.

The reaction of methanesulfonyl chloride with water required a basic catalyst in order to get sufficiently rapid reaction for calorimetry to be practical. With sodium hydroxide solution, however, the reaction was so rapid and exothermic that spattering of the solution and liquid acid chloride occurred when the ampoule broke, leading to scatter in the measured heat of reaction. Reaction in carbonate buffer, pH 10.2, led to a convenient rate of reaction. The observed heat of reaction refers to the process:

© 1998 NRC Canada

Table 2. Heats of formation.[a]

Compound	Phase	ΔH_f°
$CH_3CH_2SCOCH_3$	g	-54.54 ± 0.22[b]
CH_3SCOCH_3	g	-58.45 ± 0.22[c]
CH_3SCOCH_3	l	-66.99 ± 0.35[c]
CH_3COOH	l	-115.80 ± 0.12[d]
H_2O	l	-68.32 ± 0.01[b]
NaOCl	soln.	-82.79 ± 0.24[d]
NaCl	soln.	-97.25 ± 0.02[d]
CH_3OH	l	-57.14 ± 0.07[b]
CH_3COCl	l	-65.22 ± 0.17[b]
CH_3COOCH_3	l	-106.55 ± 0.17[b]
CH_3SO_3H	l	-178.09 ± 1.48[e]
CH_3SO_2Cl	l	-126.91 ± 1.54[e]
$CH_3SO_3CH_3$	l	-164.34 ± 1.58[e]

[a] All at 25°C; heats of formation in kcal/mol.
[b] Reference 28.
[c] Estimated as described in the text.
[d] Reference 29.
[e] This work.

[3] $CH_3SO_2Cl(l) + H_2O(soln) \rightleftharpoons CH_3SO_3H(soln) + HCl(soln)$

In this process HCl(soln) will actually be sodium bicarbonate, because carbonate buffer will be partially neutralized by the reaction. To bypass the problems of defining the heat of solution of HCl from some known state to the product solution, we used the analogous reaction of acetyl chloride for which the standard heat of formation is known.

[4] $CH_3COCl(l) + H_2O(soln) \rightleftharpoons CH_3CO_2H(soln) + HCl(soln)$

By combining these two reactions, and measuring heats of solution for the organic products, we obtain the convenient, if somewhat artificial process:

[5] $CH_3SO_2Cl(l) + CH_3CO_2H(l) \rightleftharpoons CH_3SO_3H(l) + CH_3COCl(l)$

where the only unknown heat of formation is that of $CH_3SO_2Cl(l)$.

The heat of reaction of methanesulfonyl chloride with methanol also required base catalysis in order to get an adequate rate of reaction. In this case we employed 1% tributylamine in methanol. The observed heat of reaction refers to the process:

[6] $CH_3SO_2Cl(l) + CH_3OH(soln) \rightleftharpoons CH_3SO_3CH_3(soln) + HCl(soln)$

Once again we bypass the problem of determining the heat of solution of HCl by measuring the heat of reaction for the process:

[7] $CH_3COCl(l) + CH_3OH(soln) \rightleftharpoons CH_3CO_2CH_3(soln) + HCl(soln)$

By combining reactions [6] and [7] and measuring heats of solution for the organic products we obtain the convenient process:

Table 3. Vapor pressures, heats of vaporization, and heat capacities of vaporization for compounds discussed in this work.

Compound	t (°C)	p (Torr)	ΔH_{vap} (kcal/mol)	$\Delta C_{p,vap}$ ($cal^{-1}\ deg^{-1}\ mol^{-1}$)
CH_3SO_3H	25	5.61×10^{-4}[a]	17.97[a]	
CH_3SO_2Cl	55[b]	12	11.63[c]	
	46[b]	9	11.41[c]	
	40[b]	4	11.93[c]	
	82[d]	50	11.42[c]	
	71[d]	30	11.45[c]	
	61[d]	21	11.31[c]	
	55[d]	11	11.74[c]	
	159[e]	754	11.30[c]	
	58[e]	17	11.39[c]	
	161[f]	730	11.45[c]	
	25	3.1[g]	11.50 ± 0.28[h]	–28.6[i]
$CH_3CH_2CH_2SO_2Cl$	78.5[j]	15	12.89[c]	
	67[j]	9	12.79[c]	
	77.3[k]	13	13.00[c]	
	75[l]	13	12.85[c]	
	–30[l]	0.00379	12.78[c]	
	–25[l]	0.00692	12.75[c]	
	–20[l]	0.0123	12.73[c]	
	–15[l]	0.0214	12.71[c]	
	–10[l]	0.0365	12.68[c]	
	–5[l]	0.0312	12.65[c]	
	0[l]	0.1	12.63[c]	
	25	0.67[m]	12.77 ± 0.28[h]	–30.7[i]
$CH_3SO_3CH_3$	97[n]	19	13.85[c]	
	91[n]	16	13.68[c]	
	75[n]	5	14.16[c]	
	59[n]	0.6	15.62[c]	
	202[o]	753	13.63[c]	
	101[o]	26	13.63[c]	
	198[o]	732	13.45[c]	
	101[o]	25	13.70[c]	
	25		13.96 ± 0.70[h]	–35.2[i]
$CH_3SO_2CH_3$	238	760	15.1 ± 0.3[p]	–28.1[i]
	109	8.59	18.4 ± 0.7[p]	–6.1[i]
	25	0.010[q]		

[a] Reference 7.
[b] Reference 30.
[c] Calculated following ref. 6; the uncertainty in ΔH_{vap} by this method is 0.28.
[d] Reference 31.
[e] Reference 32.
[f] Reference 33.
[g] Calculated from the boiling point at 12 Torr using ΔH_{vap} and $\Delta C_{p,vap}$, as described in the text.
[h] Average value.
[i] Estimated as described in the text.
[j] Reference 34.
[k] Reference 35.
[l] Reference 36.
[m] Calculated from the boiling point at 26 Torr using ΔH_{vap} and $\Delta C_{p,vap}$, as described in the text.
[n] Reference 37.
[o] Reference 38.
[p] Reference 14.
[q] Calculated from the boiling point at 760 Torr, and the melting point, using ΔH_{vap}, ΔH_{sub}, $\Delta C_{p,vap}$, and $\Delta C_{p,sub}$, as described in the text.

© 1998 NRC Canada

Table 4. Thermodynamic quantities for compound discussed in this paper.[a] Compounds for which ΔG_f(aq) (*a*) has not previously been reported; (*b*) has been reported.

(*a*) Compound	ΔH_f(l)	ΔH_{vap}	ΔH_f(g)	$S°$(g)	ΔG_f(g)	ΔG_t	ΔG_f(aq)	(*b*) Compound	ΔG_f(aq)[f]
CH_3SO_3H	–178.09 ± 1.48	17.97 ± 2.0	–160.12 ± 2.48	74.03 ± 2.0	–138.99 ± 2.56	–12.73 ± 0.79	–151.72 ± 2.68	H_2O	–56.69 ± 0.01
CH_3SO_2Cl	–126.91 ± 1.54	11.50 ± 0.28	–115.40 ± 1.57	74.76 ± 2.0	–98.50 ± 1.68	–2.97 ± 0.27	–101.48 ± 1.70	HCl	–31.36 ± 0.01
$CH_3SO_3CH_3$	–164.34 ± 1.58	13.96 ± 0.70	–150.37 ± 1.73	82.33 ± 2.0	–122.01 ± 1.83	–5.27 ± 0.18	–127.28 ± 1.83	HCN	28.61 ± 1.0
CH_3CN			15.37 ± 1.72[b]	58.19 ± 0.3[c]	19.61 ± 1.72	–2.00 ± 0.1[d]	17.61 ± 1.73	HSO_3^-	–126.13 ± 0.1
$(CH_3)_3N$			–5.66 ± 0.17[b]	69.02 ± 0.3[c]	23.67 ± 0.19	–1.34 ± 0.1[d]	22.33 ± 0.22	CH_3OH	–41.88 ± 0.15[g]
$CH_3CH_2SCH_3$			–14.24 ± 0.26[b]	79.62 ± 0.3[c]	2.73 ± 0.27	0.41 ± 0.5[e]	3.14 ± 0.57	$(CH_3)_2NH$	13.88 ± 0.1
								CH_3CH_2SH	–0.02 ± 0.21[h]
								CH_3OCH_3	–27.00 ± 0.18[g]

[a] All at 25°C; enthalpies and free energies are in kcal/mol, entropies are in cal^{-1} deg^{-1} mol^{-1}, standard states are the ideal gas at 1 atm and 1 M aqueous solution, with an infinitely dilute reference state. Standard entropies in the gas phase and free energies of transfer (from the gas at 1 atm to 1 M aqueous solution) were calculated as described in the text. Free energies of formation in the gas phase are calculated from the corresponding enthalpies of formation and the standard entropies, and free energies of formation in aqueous solution are calculated from the corresponding free energies of formation in the gas and free energies of transfer.

[b] Reference 28.

[c] Reference 39; uncertainty assigned as 0.3.

[d] Reference 40; uncertainty assigned as 0.1.

[e] Interpolated between values for dimethyl sulfide and diethyl sulfide from ref. 41; uncertainty assigned as 0.5 to allow for errors from this interpolation.

[f] Reference 29 unless otherwise noted.

[g] Reference 42.

[h] Reference 43

[8] $$CH_3SO_2Cl(l) + CH_3CO_2CH_3(l) \rightleftharpoons CH_3SO_3CH_3(l) + CH_3COCl(l)$$

where the only unknown heat of formation is that of $CH_3SO_3CH_3$(l).

For further thermodynamic calculations we wished to have the heats of vaporization for these compounds. For methane sulfonic acid we calculated the heat of vaporization from the Clausius–Clapeyron equation, which fits data including the vapor pressure at 25°C (7). This is based very heavily on one point, the value at 25°C. If we were to use the relationship between heat of vaporization at 25°C and the boiling point and pressure (6) (which is not really applicable, because it is based on non-hydrogen bonding liquids) we obtain an average value of 20 kcal/mol. We have used the Clausius–Clapeyron value of 18 kcal/mol, but assign an error of 2 kcal/mol. For methanesulfonyl chloride and methyl methanesulfonate we calculated the heats of vaporization from literature vapor-pressure data, using the correlation that we have reported (6). These data, and the derived heats of vaporization, are found in Table 3.

Given the heats of vaporization we can calculate the heats of formation of the gaseous compounds; these values are found in Table 4. Entropies were estimated by statistical mechanics, using vibrational frequencies from molecular orbital calculations using Gaussian 92 (8). We used the 6–31 G** Hamiltonian and the default scaling factors for vibrational frequencies from Gaussian 92. This procedure is approximately the E1 method of East and Radom (9). The experimental barrier to torsional rotation of the methyl in methanesulfonyl chloride is 2.1 kcal (10), safely over the 0.84 kcal which East and Radom suggest as the cutoff for using the harmonic oscillator approximation. Since we have not used the full E1 method of East and Radom we make a more pessimistic estimate of uncertainty, i.e., 2 cal deg^{-1} mol^{-1} in $S°$. With estimates in hand we could calculate the free energies of formation of the gaseous molecules: see Table 4.

We are most interested in free energies of formation in aqueous solution. Here the problem is to determine the free energies of transfer, which except in the case of methane sulfonic acid comes down to determining the solubilities.

We begin with methyl methanesulfonate for which the solubility in aqueous solution, 3.16 M, was determined in this work. The vapor pressure can be estimated as 0.331 ± 0.095 Torr (1 Torr = 133.3 Pa) (6) from the vapor pressure at 101°C (11), the heat of vaporization, 13.96 ± 0.70 kcal/mol, estimated as described (6), and the heat capacity of vaporization, –35.24 ± 1.5 cal deg^{-1} mol^{-1}, estimated as described (12). These values lead to a free energy of transfer for methyl methanesulfonate of –5.27 ± 0.18 kcal/mol, and a free energy of formation in aqueous solution of –127.28 ± 2.08.

To estimate the free energy of transfer for methanesulfonic acid, we first examined the relationship between the difference in free energies of transfer of acids and their methyl esters, and the pK_a of the acids. Our expectation was that the difference in free energy of transfer would be dominated by hydrogen bonding effects, which would be related to the pK_a. The available data, found in Table 5, led to the correlation equation $\Delta\Delta G_t = -(6.06 \pm 0.66) + (0.732 \pm 0.20)\ pK_a$, and a predicted value for methanesulfonic acid of $\Delta G_t = -12.73 \pm 0.79$ kcal/mol.

Alternatively we interpolate between dimethyl sulfone and

© 1998 NRC Canada

sulfuric acid. The vapor pressure of dimethyl sulfone can be estimated as 0.0100 ± 0.0024 Torr (6) from the boiling point at 1 atm (1 atm = 101.325 kPa) (13), the heat of vaporization, 15.10 ± 0.30 kcal/mol (14), the heat capacity of vaporization, –28.06 ± 1.5 cal deg^{-1} mol^{-1}, estimated as described (12), the heat of sublimation, 18.40 ± 0.67 kcal/mol (14), and the heat capacity of sublimation, –6.06 ± 1.5, calculated from the heat capacity of the gas estimated by Benson's additivity method (15), and the heat capacity of the solid estimated by Kopps law (16). The hypothetical ideal solubility of the supercooled liquid can be estimated as log s = 2.78 ± 0.04 (M) from the partition constant, log P = –1.34 (17), and the relation between log P and log s (18). Then using the heat of fusion, 3.3 ± 0.6 kcal/mol (14), we can calculate the hypothetical ideal solubility of the solid as log s = 2.25 ± 0.56. With these values in hand the free energy of transfer can be calculated as –9.74 ± 0.78 kcal/mol. The free energy of transfer for H_2SO_4 can be calculated from the free energy of formation in the gas, –156.20 ± 2.01 (19), and in aqueous solution, –176.84 ± 0.69, as –20.65 ± 2.13. By interpolation, which assumes simple group additivity, we obtain ΔG_t = –15.20, with an uncertainty of several kilocalories because the assumption of simple group additivity is unlikely to be exact. The two values seem to be in agreement. A similar estimation of the value (calculated above) for ΔG_t of methyl methanesulfonate can be made by interpolation between the value for dimethyl sulfate (–3.2 kcal/mol (4)) and that for dimethyl sulfone. The value so obtained is –6.47, again with an uncertainty of several kilocalories because the assumption of simple group additivity is unlikely to be exact. The agreement here is better.

We hoped to determine the solubility of methanesulfonyl chloride, despite its rapid hydrolysis, by determining the pseudo-zero order rate of reaction for a saturated solution (20), but the process proved to be too rapid to follow titrimetrically. Instead we determined the free energy of transfer of propanesulfonyl chloride and estimated that of methanesulfonyl chloride by group additivity. For propanesulfonyl chloride the zero order rate of hydrolysis, at a pH of approximately 2.7, was 2.57×10^{-5} M s^{-1}, while the rate constant for uncatalyzed hydrolysis is 3.93×10^{-4} s^{-1} (21). These values lead to a solubility of 0.065 M. From vapor-pressure data in Beilstein we could calculate (6) the heat of vaporization as 12.88 ± 0.09 kcal/mol. The heat capacity of vaporization was estimated from that of dimethyl sulfone by atomic additivity (12), as –30.67 cal deg^{-1} mol^{-1}. The vapor pressure can then be estimated (6) as 0.67 Torr. From the solubility and vapor pressure we obtain ΔG_t for propanesulfonyl chloride as –2.55 ± 0.23.

The free energy of transfer for methanesulfonyl chloride could be estimated from that for propanesulfonyl chloride by means of the group contribution for a CH_2 group (22); in this way we obtained ΔG_t = –2.97 ± 0.27.

Now we can calculate the free energy of formation of aqueous methanesulfonic acid as –151.72 ± 2.68, of aqueous methyl methanesulfonate as –127.28 ± 2.08, and of aqueous methanesulfonyl chloride as –101.29 ± 1.96.

With free energies of formation in hand we can calculate the free energy of hydrolysis for methyl mesylate:

$$CH_3SO_3CH_3(aq) + H_2O(l) \rightleftharpoons CH_3SO_3H(aq) + CH_3OH(aq)$$

as –9.90 ± 2.48 kcal/mol (4). We have previously estimated this quantity as –5.4 ± 1.6 kcal/mol. The agreement is not as good as might be desired, but the difference is only just outside the sum of the standard deviations.

Table 5. Difference in free energy of transfer between acids and methyl esters as a function of acid pK_a.[a]

Acid	pK_a	ΔG_t acid	ΔG_t ester	$\Delta\Delta G_t$
H_2SO_4	–2.8[b]	–19.96[b]	–3.2[b]	–8.38[c]
HNO_3	–1.3[b]	–6.79[b]	1.09[b]	–7.88
CH_3COOH	4.76[d]	–4.80[e]	–1.42[e]	–3.38
CF_3COOH	–0.78[f]	–4.88[g]	0.80[g]	–5.68
HCOOH	3.77[d]	–4.94[e]	–0.88[e]	–4.06
PhCOOH	4.17[d]	–5.80[e]	–1.88[e]	–3.92

[a] Free energies of transfer have units of kcal/mol for transfer from ideal gas at 1 atm to ideal 1 M aqueous solution with an infinitely dilute reference state.
[b] Reference 4.
[c] Corrected for the number of OH groups by dividing by two.
[d] Reference 44.
[e] Reference 42.
[f] References 45 and 46.
[g] Reference 47; both values involved some estimated quantities.

Similarly we can calculate the free-energy change for the hydrolysis of methanesulfonyl chloride:

$$CH_3SO_2Cl(aq) + H_2O(l) \rightleftharpoons CH_3SO_3H(aq) + HCl(aq)$$

as –25.11 ± 3.05 kcal/mol (calculated for undissociated methanesulfonic acid, but dissociated HCl).

Discussion

Liebman (3), in a thorough review of the literature on thermochemistry of sulfonic acid derivatives, estimated the heat of formation of liquid methanesulfonic acid as –147 kcal/mol, that of the liquid methyl ester as –135, and that of the liquid mesyl chloride as –101 kcal/mol. The corresponding values from this work are –178.09 ± 1.48, –164.34 ± 1.58, and –126.91 ± 1.54. Liebman's values ultimately all depend on the heat of reaction for the chlorosulfonation of *n*-dodecane to a mixture of primary and secondary dodecanesulfonyl chlorides (3*b*) from which he deduced the heat of formation of *n*-dodecanesulfonyl chloride and *n*-dodecanesulfonic acid, and then scaled to methanesulfonic acid and its chloride by a form of group additivity. It should be noted that the differences in heat of formation are in better agreement: ΔH_f(l) acid – ΔH_f(l) ester = 12 (ref. 3) or 15 (this work); ΔH_f(l) acid – ΔH_f(l) chloride = 46 (ref. 3), 51 (this work).

Chatgilialoglu et al. (5) derived, from photoacoustic calorimetry experiments, a bond dissociation energy for CH_3SO_2-Cl that leads to a heat of formation of gaseous methanesulfonyl chloride of –101.1, where our value is –115.37 ± 1.73. It should be noted that Chatgilialoglu et al. did not report a heat of formation for methanesulfonyl chloride, but they did calculate a heat of formation for benzenesulfonyl chloride; the only additional number needed to calculate a heat of formation of gaseous methanesulfonyl chloride was a heat of formation for methanesulfonyl radical for which a value is available in the literature (23). The difficulty may lie in the necessarily indirect determination of the heat of formation for methanesulfonyl radical. Thus our new values deviate significantly from the

© 1998 NRC Canada

Fig. 1. Free-energy change (kcal/mol) for reaction [9] as a function of Γ for the nucleophile. The line was determined by least squares to the points $\Delta G° = -(12.3 \pm 1.7) - (6.85 \pm 0.69)\Gamma$. The points (□) represent (from left to right) the reactions of CH_3OH, $(CH_3)_2NH$, CH_3CH_2SH, HCN, and HSO_3^- with CH_3OH. The error bars correspond to the estimated standard deviations; 95% confidence limits would be twice as large. The point (○) represents the reaction of HSO_3^- based on the heat of formation in ref. 3.

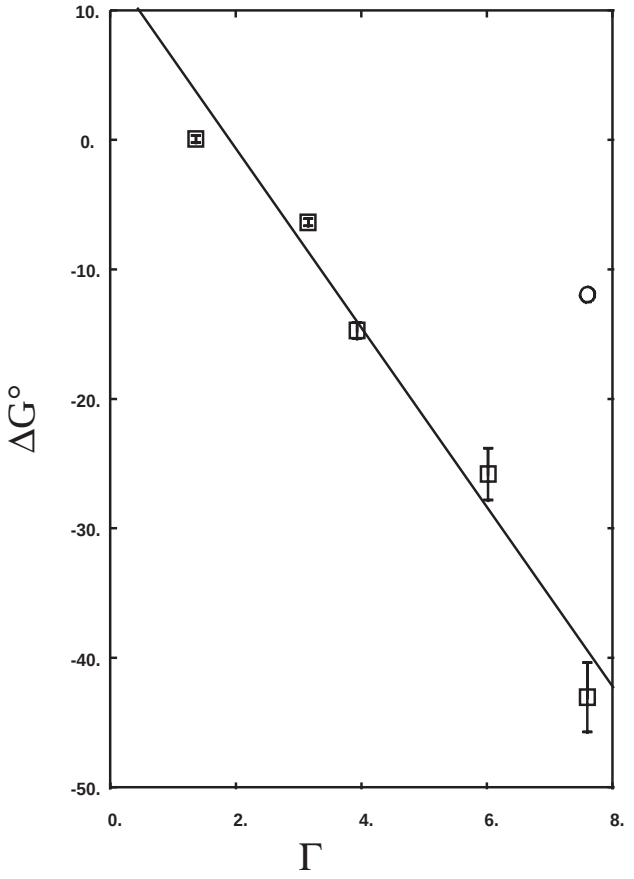

best previous estimates, which unavoidably involved extended arguments.

We believe that the new calorimetric technique reported in this paper will provide a convenient method for determining the heats of formation of sulfonic acids, for which there has been a surprising dearth in the literature (3). Further applications of this approach from this lab will be reported in due course. The principal limitations on the approach are as follows. (*i*) The heat of reaction is large so that even with a small relative error, 0.59% in this case, the absolute uncertainty in the heat of reaction is 1.4 kcal/mol. It will be difficult to improve this. (*ii*) The compound OCl^- is a powerful oxidant, which limits the other functional groups that can be present in the initial thiol or thiol equivalent. (*iii*) The heat of formation of the thiol (or thiol equivalent) used as starting material must be available. Since heats of formation for many of the simple thiols are available this is not a severe restriction.

Once the heat of formation of a sulfonic acid has been determined, heats of formation of other derivatives at the sulfonate level of oxidation can be determined by measurement of heats of reaction of the corresponding sulfonyl chloride, as we have demonstrated here.

Table 6. Free-energy changes for reaction [9].[a]

Nucleophile	Γ	$\Delta G°$
CH_3OH	1.36	0.07 ± 0.28
$(CH_3)_2NH$	3.15[b]	–6.36 ± 0.28
CH_3CH_2SH	3.93[c]	–11.65 ± 0.63
HCN	6.02	–25.81 ± 2.00
HSO_3^-	7.60	–43.03 ± 2.68[d]
		–11.93[e]

[a] In water at 25°C; free energies in kcal/mol; Γ values calculated from γ values from ref. 25 except as noted; $\Delta G°$ values calculated from data in Table 4.

[b] The value for morpholine (25) was used; morpholine, piperidine, and piperazine have very similar γ values (25).

[c] The value for β-mercaptoethanol (25) was used; β-mercaptoethanol, methoxyethanethiol, and ethanethiol have very similar equilibrium constants for addition to acetaldehyde or isobutyraldehyde (48).

[d] The equilibrium gives methanesulfonate anion; the free-energy change was calculated using the pK_a of methanesulfonic acid (49).

[e] Calculated using the value for $\Delta H°_f(l)$ for methanesulfonic acid from ref. 3.

As a further test of the consistency of our value for the free energy of formation of methanesulfonic acid, we have examined the (hypothetical) equlibrium processes

[9] $$CH_3OH + H\text{-}Nu \rightleftharpoons CH_3\text{-}Nu + H\text{-}OH$$

The free-energy change for such reactions can be calculated from the free energies of the four species involved. This free energy is expected to be linear in Γ (24) (where Γ is related to the Sander and Jencks γ values (25); $\Gamma = \gamma_{HNu} - \gamma_{H_2O}$) by analogy with carbonyl reactions, which can be expressed (24) as

$$R_1R_2C(OH)_2 + H\text{-}Nu \rightleftharpoons R_1R_2C(OH)(Nu) + H\text{-}OH$$

Data are available for five such reactions; the data are found in Table 6. Figure 1 shows that there is indeed an approximate relationship of the form expected; this suggests that the new thermodynamic data in this paper are indeed consistent with the body of existing information, and suggests a novel way to make approximate estimates of the free energy of formation in solution of other alkanesulfonate ions. The line in Fig. 1 was calculated by an unweighted least-squares fit to the points. One ought to use weighted least squares, but in this case the two points with the smallest calculated uncertainty are both at one end of the plot, and would essentially determine the slope. Because of the uncertainties in the points at high Γ this test is less rigorous than one would like, but it clearly shows that our value for methanesulfonate is in much better agreement with other thermodynamic data from the literature than the best previous estimate (3).

Experimental

Materials

S-Methyl thiolacetate, methanesulfonic acid, methanesulfonyl chloride, propanesulfonyl chloride, methyl methanesulfonate, acetyl chloride, and tributylamine were purchased as reagent grade; purity was checked and materials were redistilled as necessary. Sodium hypochlorite was purchased as a 5% analytical reagent solution (Malinckrodt). The sodium hypo-

© 1998 NRC Canada

chlorite solution used for calorimetry was made up by diluting 35 mL of 5% sodium hypochlorite to 100 mL with distilled water. Methanolic tributylamine was made up with a molar ratio of 100:1. Carbonate buffer for the hydrolysis of methanesulfonyl chloride was made by dissolving 22.35 g $NaHCO_3$ and 4.70 g NaOH in a total volume of 500 mL using CO_2-free distilled water.

Methods

Boiling points at reduced pressures were determined as previously described (26). Calorimetric measurements were carried out using a Tronac Model 458 isoperibol calorimeter. Data were captured by computer and analyzed using software from Tronac, as has been described (27).

The solubility of propanesulfonyl chloride was determined indirectly (20) by titrimetric kinetic measurements. Water (25 mL) was charged to a jacketed reaction vessel maintained at 25 ± 0.1°C by a circulating water bath. This was allowed to equilibrate for 10 min before initiation of the experiment by injection of 400 mL of propanesulfonyl chloride. The contents of the reaction vessel were stirred rapidly to ensure complete dispersion of the excess propanesulfonyl chloride throughout the solvent. The stirring rate was kept constant between replicate runs to ensure uniformity of the experimental conditions. The pH of the aqueous solution was monitored throughout the experiment using a Fisher Scientific Accumet pH meter and was allowed to fall uncontrolled for the first 2 min to allow the solution to reach saturation. After this time the pH was held constant at a convenient value (i.e., one where only water-catalyzed hydrolysis would take place) by titration with aqueous sodium hydroxide (0.297 M). The uptake of sodium hydroxide was measured as a function of time. Since the propanesulfonyl chloride was always in excess the concentration of the substrate dissolved in water is constant throughout the experiment. The uptake of sodium hydroxide is therefore a pseudo-zero order rate process. A plot of concentration of base versus time gave a straight line of slope $2k_0$. Each mole of hydrolyzed sulfonyl chloride produces two moles of acid. Therefore, the rate of uptake of base is twice the rate of hydrolysis. The solubility could then be calculated from the known rate constant for uncatalyzed hydrolysis (21).

The aqueous solubility of methyl methane sulfonate was determined by NMR analysis. A standard solution of sodium 3-trimethylsilylpropanesulfonate (DSS) (125.06 mg) in water (5 mL) was prepared. Four 5 mL volumetric flasks were filled with distilled water, which had been adjusted to pH = 5.67 with dilute HCl (to prevent hydrolysis of the ester). An excess of methyl methane sulfonate was then added to each of these flasks and the flasks shaken vigorously. They were then placed in a water bath maintained at 25 ± 0.1°C and allowed to stand, with periodic shaking, for 1 h. Four NMR tubes were then filled with 300 mL of the standard solution and 300 mL of the aqueous methyl methane sulfonate, which was carefully withdrawn from the top of each volumetric flask after they had been allowed to settle for a further 10 min. A sealed capillary tube containing D_2O was then placed inside each NMR tube (to provide a lock signal). The ^1H NMR was then run for each of the samples. The NMR spectra taken after 24 h confirmed that no hydrolysis had taken place. Integration of the signals from the methyl groups of methyl methanesulfonate and DSS were used to determine the solubility: the value so determined was 3.16 ± 0.25 M.

Acknowledgments

We thank the Natural Sciences and Engineering Research Council of Canada for financial support of this work. One of us (A.R.S.) also thanks Memorial University of Newfoundland for the sabbatical leave and financial assistance that made this work possible.

References

1. J. Hoyle. *In* The chemistry of sulphonic acids, esters and their derivatives. *Edited by* S. Patai and Z. Rappoport. John Wiley and Sons Ltd., Chichester. 1991. p. 351.
2. K. Tanaka. *In* The chemistry of sulphonic acids, esters and their derivatives. *Edited by* S. Patai and Z. Rappoport. John Wiley and Sons Ltd., Chichester. 1991. p. 401.
3. (*a*) J.F. Liebman. *In* The chemistry of sulphonic acids, esters and their derivatives. *Edited by* S. Patai and Z. Rappoport. John Wiley and Sons Ltd, Chichester. 1991. p. 283; (*b*) G. Geiseler and H.D. Nagel. Chem. Ber. **91**, 204 (1958).
4. J.P. Guthrie. Can. J. Chem. **56**, 2342 (1978).
5. C. Chatgilialoglu, D. Griller, J.M. Kanabus-Kaminska, and F.P. Lossing. J. Chem. Soc. Perkin Trans. 2, 357 (1994).
6. J.P. Guthrie. Can. J. Chem. **64**, 635 (1986).
7. I.N. Tang and H.R. Munkelwitz. J. Colloid Interface Sci. **141**, 109 (1991).
8. M.J. Frisch, G.W. Trucks, M. Head-Gordon, P.M.W. Gill, M.W. Wong, J.B. Foresman, B.G. Johnson, H.B. Schlegel, M.A. Robb, E.S. Replogle, R. Gomperts, J.L. Andres, K. Raghavachari, J.S. Binkley, C. Gonzalez, R.L. Martin, D.J. Fox, D.J. Defrees, J. Baker, J.J.P. Stewart, and J.A. Pople. Gaussian 92, Revision D.2. Gaussian, Inc., Pittsburgh, Pa. 1992.
9. A.L.L. East and L. Radom. J. Chem. Phys. **106**, 6655 (1997).
10. A. Sebestyen and B. Vizi. Acta Chim. Hung. **118**, 111 (1985).
11. Beilstein. Handbuch der organischen chemie. Vol. 4 III. p. 11.
12. J.P. Guthrie and K.F. Taylor. Can. J. Chem. **62**, 363 (1984).
13. Beilstein. Handbuch der organischen chemie. Vol. 1 H. p. 289.
14. H. Mackle and P.A.G. O'Hare. Trans. Faraday Soc. **57**, 1070 (1961).
15. S.W. Benson. Thermochemical kinetics. Wiley, New York. 1976.
16. J. Sturtevant. *In* Physical methods of chemistry. Vol. 1. Part 1. *Edited by* A. Weissberger. Interscience, London. 1959. p. 557.
17. C. Hansch and A. Leo. Exploring QSAR: fundamentals and applications in chemistry and biology. American Chemical Society, Washington. 1995.
18. C. Hansch, J.E. Quinlan, and G.L. Lawrence. J. Org. Chem. **33**, 347 (1968).
19. M.W. Chase. JANAF thermochemical tables. American Chemical Society and American Institute of Physics. Washington, D.C. 1986.
20. R. Ohnishi and K. Tanabe. Bull. Chem. Soc. Jpn. **41**, 2647 (1971).
21. J. King, J. Lam, and S. Skonieczny. J. Am. Chem. Soc. **114**, 1743 (1992).
22. J.P. Guthrie. Can. J. Chem. **69**, 1893 (1991).
23. J. Herron. *In* The chemistry of sulphones and sulphoxides. *Edited by* S. Patai, Z. Rappoport, and C. Stirling. Wiley, Chichester. 1988.
24. J.P. Guthrie. Can. J. Chem. **56**, 962 (1978).
25. E.G. Sander and W.P. Jencks. J. Am. Chem. Soc. **90**, 6154 (1968).
26. J.P. Guthrie and D.C. Pike. Can. J. Chem. **65**, 1951 (1987).

© 1998 NRC Canada

27. S. Taylor and R. Kluger. J. Am. Chem. Soc. **114**, 3067 (1992).
28. J.B. Pedley, R.D. Naylor, and S.P. Kirby. Thermochemical data of organic compounds. Chapman and Hall, London. 1986.
29. D.D. Wagman, W.H. Evans, V.B. Parker, R.H. Schumm, I. Halow, S.M. Bailey, K.L. Churney, and R.L. Nuttall. J. Phys. Chem. Ref. Data, **11**, Suppl. 2 (1982).
30. Beilstein. Handbuch der organischen chemie. Vol. 4 IV. p. 27.
31. Beilstein. Handbuch der organischen chemie. Vol. 4 III. p. 12.
32. Beilstein. Handbuch der organischen chemie. Vol. 4 II. p. 525.
33. Beilstein. Handbuch der organischen chemie. Vol. 4 H. p. 5.
34. Beilstein. Handbuch der organischen chemie. Vol. 4 III. p. 18.
35. Beilstein. Handbuch der organischen chemie. Vol. 4 H. p. 8.
36. K. Quitzsch, C. Nowak, P. Winkler, and G. Geiseler. J. Prakt. Chem. **20**, 92 (1963).
37. Beilstein. Handbuch der organischen chemie. Vol. 4 IV. p. 11.
38. Beilstein. Handbuch der organischen chemie. Vol. 4 III. p. 11.
39. D.R. Stull, E.F. Westrum, and G.C. Sinke. The chemical thermodynamics of organic compounds. Wiley, New York. 1967.
40. J. Hine and P.K. Mookerjee. J. Org. Chem. **40**, 292 (1975).
41. S. Cabani, P. Gianni, V. Mollica, and L. Lepori. J. Solution Chem. **10**, 563 (1981).
42. J.P. Guthrie. Can. J. Chem. **70**, 1042 (1992).
43. J.P. Guthrie. J. Am. Chem. Soc. **100**, 5892 (1978).
44. W.P. Jencks and J. Regenstein. *In* Handbook of biochemistry and molecular biology. Vol. 1. *Edited by* G. Fassman. Chemical Rubber Company, Cleveland. 1976. p. 305.
45. A. Covington, J. Freeman, and T. Lilley. J. Phys. Chem. **74**, 3773 (1970).
46. R. Hershfield and G.L. Schmir. J. Am. Chem. Soc. **95**, 3994 (1973).
47. J.P. Guthrie. Can. J. Chem. **54**, 202 (1976).
48. G. Lienhard and W. Jencks. J. Am. Chem. Soc. **88**, 3983 (1966).
49. A.K. Covington and R. Thompson. J. Solution Chem. **3**, 603, (1974).

© 1998 NRC Canada

Carbon–carbon coupling of 4,6-dinitrobenzofuroxan with 3-aminothiophenes: a kinetic and structural study

François Terrier, Marie-José Pouet, Khalid Gzouli, Jean-Claude Hallé, Francis Outurquin, and Claude Paulmier

Abstract: Potentiometric measurements carried out in a 50–50 (v/v) H_2O–Me_2SO mixture together with ^1H and ^{13}C NMR studies carried out in pure Me_2SO-d_6 reveal that 3-aminothiophene (**4a**), 3-*N*-(methylamino)thiophene (**4b**), and 3-*N*,*N*-dimethylaminothiophene (**4c**) undergo protonation exclusively at the amino groups in dilute acid solutions. The pK_a values of **4a**, **4b**, and **4c** are equal to 3.38, 3.65, and 3.53, respectively, at 25°C, comparing well with those for related anilines in the same aqueous Me_2SO mixtures. However, despite this similarity of the nitrogen basicities, compounds **4a**, **4b,** and **4c** are found to behave differently from anilines upon treatment with super-electrophilic 4,6-dinitrobenzofuroxan (DNBF). While anilines react to give first an N-bonded σ-adduct that subsequently decomposes to afford the thermodynamically more stable C-bonded adduct, the 3-aminothiophenes react only as carbon nucleophiles, giving rise directly to the corresponding C-adducts. Based on ^1H and ^{13}C NMR data as well as measurements of the rate constants (k_1^{DNBF}) for DNBF addition to **4a**, **4b,** and **4c**, it is demonstrated that 3-aminothiophenes possess such high negative charge density at C-2 that they can be regarded as strongly enaminic in nature. Estimates of the pK_a values for protonation at C-2 of **4a**, **4b**, and **4c** could be made: $pK_a^{\mathbf{4a}} \approx -0.4$; $pK_a^{\mathbf{4b}} \approx 0.2$; $pK_a^{\mathbf{4c}} \approx 0.8$. Thus, these compounds are more susceptible to electrophilic addition at this position than most of the five-membered ring heterocycles studied so far. Altogether, the results demonstrate the importance of the hyper-*ortho* relationship in the thiophene systems, accounting for the ease of both electrophilic and nucleophilic reactivity of 3-X-thiophenes in σ-complex formation processes.

Key words: aminothiophenes, enamines, superelectrophiles, dinitrobenzofuroxan, hyper-*ortho* relationship.

Résumé : Des mesures potentiométriques effectuées dans un mélange 50/50 (v/v) de H_2O/Me_2SO et des études de RMN du ^1H et du ^{13}C effectuées dans du Me_2SO-d_6 révèlent que, en solutions diluées d'acide, les 3-aminothiophène (**4a**), 3-*N*-méthylaminothiophène (**4b**) et 3-*N,N*-diméthylaminothiophène (**4c**) se protonent exclusivement au niveau des groupes aminés. À 25°C, les valeurs de pK_a des composés **4a**, **4b** et **4c** sont respectivement égales à 3,38, 3,65 et 3,53 et elles se comparent avantageusement à celles des anilines correspondantes dans les mêmes mélanges aqueux de Me_2SO. Toutefois, malgré cette similarité dans les basicités, on a observé que les composés **4a**, **4b** et **4c** ont des comportements différents de ceux des anilines lors de leur traitement par le 4,6-dinitrobenzofuroxane (DNBF) superélectrophile. Alors que les anilines réagissent pour donner en premier lieu un adduit-σ lié à l'azote qui se décompose ultérieurement pour conduire à l'adduit lié au carbone qui est thermodynamiquement plus stable, les 3-aminothiophènes ne réagissent que comme des nucléophiles carbonés conduisant directement aux adduits-C correspondants. Sur la base de données de RMN du ^1H et du ^{13}C ainsi que de mesures de constantes de vitesse (k_1^{DNBF}) pour l'addition de DNBF sur les composés **4a**, **4b** et **4c**, on peut démontrer que les 3-aminothiophènes portent une densité de charge négative tellement élevée en C-2 que l'on peut considérer qu'ils ressemblent fortement aux énamines. On a pu évaluer que les valeurs de pK_a pour la protonation en C-2 des composés **4a**, **4b** et **4c** sont respectivement –0,4, 0,2 et 0,8. Ces composés sont donc plus susceptibles à une réaction d'addition électrophile dans cette position que la plupart des composés hétérocycliques à cinq chaînons qui ont été étudiés jusqu'à maintenant. Dans l'ensemble, les résultats démontrent l'importance de la relation hyper-*ortho* dans les systèmes du thiophène; elle explique la réactivité tant électrophile que nucléophile des 3-X-thiophènes dans les processus de formation de complexes σ.

Mots clés : aminothiophènes, énamines, superélectrophiles, dinitrobenzofuroxane, relation hyper-*ortho*.

[Traduit par la rédaction]

Received January 13, 1998.

This paper is dedicated to Professor Erwin Buncel in recognition of his contributions to Canadian chemistry.

F. Terrier,[1] M.-J. Pouet, K. Gzouli, and J.-C. Hallé.[1] Laboratoire SIRCOB, CNRS EP 102, Department of Chemistry, The University of Versailles, 45, Avenue des États-Unis, F-78035 Versailles-Cedex, France.
F. Outurquin and C. Paulmier. Laboratoire de synthèse thio et sélénoorganique, IRCOF, UFR de Sciences, The University of Rouen, F-76821 Mont-Saint-Aignan Cedex, France.

[1] Authors to whom correspondence may be addressed. Telephone: 33-1-39-25-44-51. Fax: 33-1-39-25-44-52. E-mail: terrier@chimie.uvsq.fr

© 1998 NRC Canada

Scheme 1.

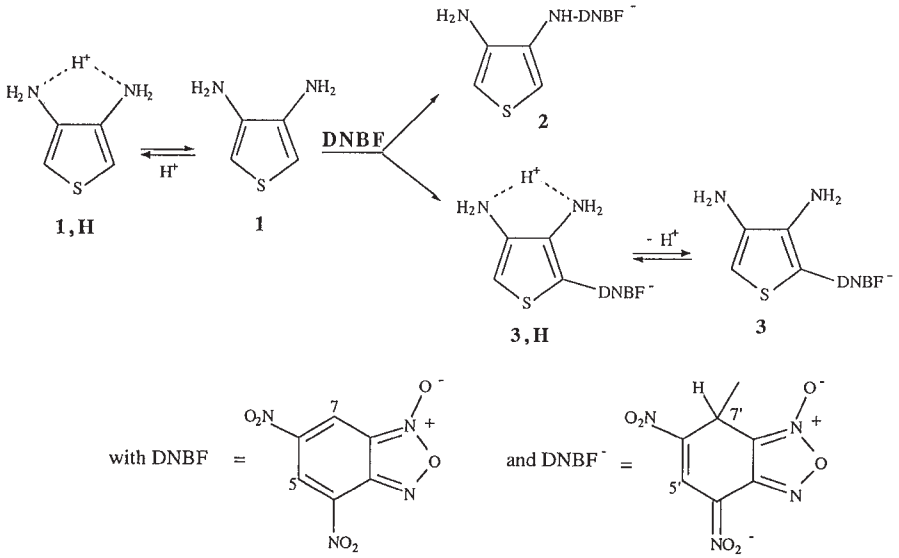

Various synthetic procedures have been described that have afforded facile access to a number of 3-amino and 3,4-diaminothiophene derivatives (1–3). A remarkable feature of these compounds is their ability to act as nitrogen as well as carbon nucleophiles towards a number of electrophiles (2, 4, 5). This ambident behaviour has proven to be especially useful for building certain fused ring systems; a prototype example is shown in eq. [1] (2).

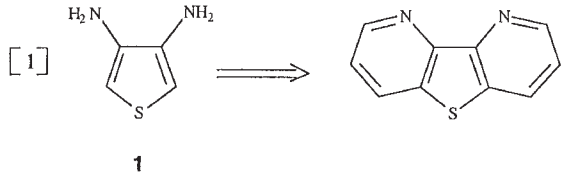

The increasing interest in the chemistry of aminothiophenes called for better understanding of the factors governing their reactivity (6–11). In this context, we have recently undertaken a potentiometric and NMR study of the protonation of 3,4-diaminothiophene **1** in water–Me_2SO mixtures and have investigated the kinetics of the reaction of this compound with 4,6-dinitrobenzofuroxan (DNBF), a super-electrophilic compound known to be a good probe for assessing the carbon nucleophilicity of very weak carbon bases (12–18). The results obtained have provided clear evidence that the proton affinity of the amino groups to give the cation **1,H** is considerably greater than that of the α-carbon but that the electrophilic coupling of DNBF at C-2 of **1** to give the carbon-bonded adduct **3,H** is both kinetically and thermodynamically favored compared to the coupling at the amino groups to give the N-adduct **2** (Scheme 1). On these grounds, we concluded that this behaviour of **1** must be the reflection of an appreciable enaminic character (12).

In the course of our NMR investigation of the reactivity of **1** towards H^+ and DNBF, we made the interesting observation that the resonances of the H_2 and C_2 atoms of **1** appear at considerably higher field than analogous resonances for common thiophene derivatives (19). Surprisingly, little attention was paid previously to this feature, and so we decided to

Scheme 2.

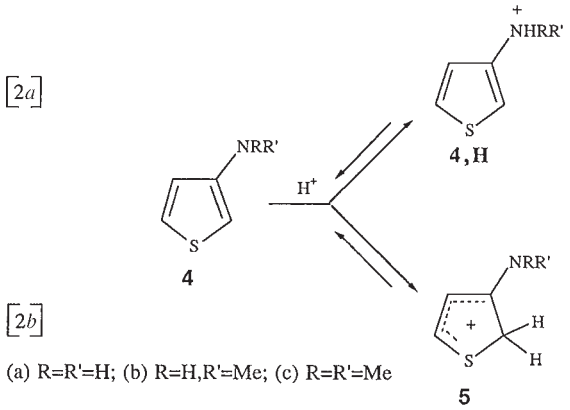

extend our measurements to a number of 3-aminothiophenes. In this paper, we report a detailed structural, thermodynamic, and kinetic investigation of the protonation (Scheme 2) and substitution by DNBF (Scheme 3) of the three monoamino compounds **4a–c** in 50:50 (v/v) H_2O–Me_2SO and (or) pure Me_2SO. As will be seen, our collected data support the idea that 3-aminothiophene derivatives exhibit a strong enaminic behaviour. Moreover, our results emphasize the extent to which the hyper-*ortho* relationship governs the reactivity of the 3-X-thiophene systems, especially in electrophilic and nucleophilic processes.

Results

Protonation of 4a–c

The protonation behaviour of **4a–c** was first studied by ^1H and ^{13}C NMR. Addition of increasing amounts of a strong acid, namely methanesulfonic acid, to a solution of **4a**, **4b,** or **4c** in Me_2SO-d_6 results in a progressive and significant deshielding of the AMX system representative of the H_2, H_4, and H_5 resonances of these compounds. This deshielding is essentially complete after addition of 1 equiv. CH_3SO_3H (Table 1), which

© 1998 NRC Canada

Scheme 3.

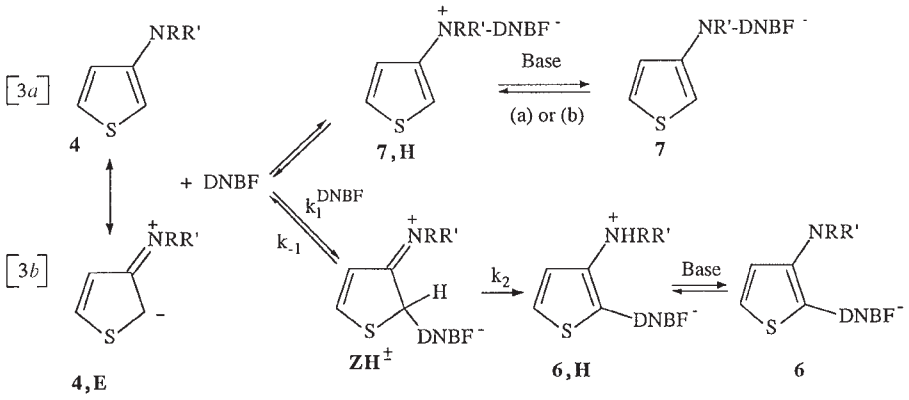

(a) R=R'=H; (b) R=H,R'=Me; (c) R=R'=Me

Table 1. ^{1}H NMR data for DNBF, 3-methoxythiophene, and the base and acid forms of 3-aminothiophenes and related DNBF adducts.[a,b]

Compounds	H_2	H_4	H_5	$H_{5'}$	$H_{7'}$	
DNBF	—	—	—	8.95	9.27	$J_{H_{5'}H_{7'}}$ = 1.9
4a	5.96	6.57	7.18	—	—	$J_{H_4H_5}$ = 5.0; $J_{H_2H_5}$ = 3.0; $J_{H_2H_4}$ = 1.5
4a,H	7.59	7.12	7.69	—	—	$J_{H_4H_5}$ = 5.1; $J_{H_2H_5}$ = 3.2; $J_{H_2H_4}$ = 1.5
6a,H	—	6.95	7.59	8.68	6.25	$J_{H_4H_5}$ = 5.7
4b	5.84	6.61	7.25	—	—	δ_{CH_3} = 2.65; $J_{H_4H_5}$ = 5.1; $J_{H_2H_5}$ = 3.0; $J_{H_2H_4}$ = 1.50
4b,H	7.78	7.28	7.73	—	—	δ_{CH_3} = 2.94; $J_{H_4H_5}$ = 5.2; $J_{H_2H_5}$ = 3.2; $J_{H_2H_4}$ = 1.40
6b,H	—	7.22	7.64	8.68	6.28	δ_{CH_3} = 3.06; $J_{H_4H_5}$ = 5.5
6b	—	6.68	7.18	8.62	5.79	δ_{CH_3} = 2.79
4c	6.06	6.86	7.34	—	—	δ_{CH_3} = 2.75; $J_{H_4H_5}$ = 5.2; $J_{H_2H_5}$ = 3.1; $J_{H_2H_4}$ = 1.6
4c,H	7.82	7.41	7.75	—	—	δ_{CH_3} = 3.16; $J_{H_4H_5}$ = 5.2; $J_{H_2H_5}$ = 3.1; $J_{H_2H_4}$ = 1.4
6c,H	—	7.57	7.74	8.68	6.36	δ_{CH_3} = 3.29; $J_{H_4H_5}$ = 5.6
1	5.83	—	5.83	—	—	
1,H	6.85	—	6.85			
3,H	—	—	7.09	8.66	5.98	
3	—	—	5.73	8.61	5.73	
10	6.55	6.76	7.40			δ_{CH_3} = 3.73 ; $J_{H_4H_5}$ = 5.15 ; $J_{H_2H_5}$ = 3.31; $J_{H_2H_4}$ = 1.47
11	—	6.94	7.33	8.62	5.63	δ_{CH_3} = 3.71 ; $J_{H_4H_5}$ = 5.52

[a] Relative to internal $SiMe_4$; solvent $(CD_3)_2SO$.
[b] This work except for 1, 3, 10 and 11; refs. 12 and 21*c*.

supports the quantitative formation of the cations **4a–c,H** (eq. [2*a*] in Scheme 2). No evidence for the appearance of new absorption patterns consistent with the occurrence of a protonation process at C-2 to give the C-adducts **5a–c** according to eq. [2*b*] could be found in the ^{1}H NMR spectra. Similar conclusions could be formulated on the basis of the chemical shift variations observed in the ^{13}C NMR spectra (Table 2). Clearly, the very large downfield shifts engendered by the C-2 carbons upon protonation of **4a–c** can only be accounted for in terms of the formation of the nitrogen cations **4a–c,H**.

Because of the poor solubility of **4a–c** in aqueous solution, we have measured the pK_a values associated with the equilibrium [2*a*] in Scheme 2 in a 50:50 (v/v) H_2O–Me_2SO mixture, using a standard potentiometric procedure (see Experimental section). The results obtained at 25°C (I = 0.1 M, KCl) are given in Table 3, together with those for nitrogen protonation of 3,4-diaminothiophene **1** and the corresponding anilines **8a–d** under equal or rather similar experimental conditions (12, 20).

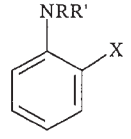

8

(a) X=R=R'=H
(b) X=R=H, R'=Me
(c) X=H, R=R'=Me
(d) X=NH_2, R=R'=H

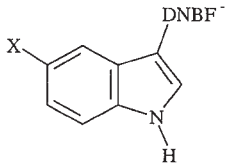

9

(a) X=CN; (b) X=Cl
(c) X=Br; (d) X=H
(e) X=Me; (f) X=OMe

DNBF complexation with 4a–c

Structural studies

The addition of 1 equiv. DNBF to a Me_2SO-d_6 solution of **4a**,

© 1998 NRC Canada

Table 2. ^{13}C NMR data for DNBF, 3-methoxythiophene, and the base and acid forms of 3-aminothiophenes and related DNBF adducts.[a,b]

Compound	C_2	C_3	C_4	C_5	$C_{4'}$	$C_{5'}$	$C_{6'}$	$C_{7'}$	$C_{8'}$	$C_{9'}$	CH_3
DNBF	—	—	—	—	136.72	126.52	144.83	120.80	116.64	145.02	—
4a	95.94	147.55	121.29	124.52	—	—	—	—	—	—	—
4a,H	119.15	128.96	123.39	128.34	—	—	—	—	—	—	—
6a,H	131.42	127.08	123.71	126.79	109.78	131.13	124.95	31.40	113.34	147.69	—
4b	92.37	150.80	120.02	124.90	—	—	—	—	—	—	32.00
4b,H	119.19	135.32	122.36	128.86	—	—	—	—	—	—	36.27
6b,H	131.64	133.20	122.41	127.69	109.97	131.21	125.12	31.47	113.46	147.67	37.75
6b	109.48	147.81	118.94	123.14	108.97	129.89	127.23	31.09	113.83	147.93	33.21
4c	97.11	153.01	125.55	119.84	—	—	—	—	—	—	42.17
4c,H	118.00	141.39	121.12	129.22							46.20
6c,H	131.29	138.89	120.48	128.40	110.09	131.14	125.04	31.44	113.62	147.51	47.43
1	95.85	138.60	138.60	95.85	—	—	—	—	—	—	
1,H	109.44	130.67	130.67	109.44	—	—	—	—	—	—	—
3,H	115.77	135.19	124.94	112.26	109.16	130.56	125.93	31.64	113.41	147.90	—
3	107.30	138.71	136.36	94.04	109.32	130.05	127.43	31.95	114.04	148.22	
10	97.19	158.42	119.13	125.34	—	—	—	—	—	—	57.11
11	115.12	155.16	117.18	123.35	109.60	130.17	126.45	31.09	113.11	148.43	59.03

[a] Relative to internal $SiMe_4$; solvent $(CD_3)_2SO$.
[b] This work except for **1**, **3**, **10**, and **11**; ref. 21*c*.

Table 3. pK_a values for protonation of 3-aminothiophenes and related anilines in 50%H_2O – 50% Me_2SO (v/v) at 25°C.

Amino compound	Numbering	pK_a
3-Aminothiophene	**4a**	3.38[a]
3-(Methylamino)thiophene	**4b**	3.65[a]
3-(Dimethylamino)thiophene	**4c**	3.53[a]
3,4-Diaminothiophene	**1**	3.96[b]
Aniline	**8a**	3.73[b]
N-Methylaniline	**8b**	3.06[c]
N,N-Dimethylaniline	**8c**	3.87[c]
1,2-Diaminobenzene	**8d**	4.17[c]

[a] This work.
[b] Reference 12.
[c] In 30% H2O – 70% Me2SO; see ref. 20.

4b, or **4c** at room temperature resulted in the immediate and quantitative formation of the zwitterionic C-bonded adducts **6a–c,H** (cf. Scheme 3). In addition to the presence of the AB systems expected for the H4 and H5 protons of the thiophenic ring, the ^1H NMR spectra showed the presence of AX systems typical of the negatively charged DNBF moieties of related carbon-bonded σ-complexes (H5′,H7′) (12, 13, 15–17, 21), e.g., $\delta_{H4} = 7.57$, $\delta_{H5} = 7.74$, $J_{H4-H5} = 5.6$, $\delta_{H5'} = 8.68$, $\delta_{H7'} = 6.36$ for the *N,N*-dimethyl adduct **6c,H**. A most noteworthy feature, however, derives from the ^{13}C NMR data, which reveal that substitution of **4a-c** by DNBF results in a significant downfield shift of the C-2 carbon of the thiophene ring ($\Delta\delta \approx 35$ ppm). Such a $\Delta\delta$ value is actually typical of formation of the zwitterionic structure **6,H**, being the reflection of two effects: (*i*) the fact that a negatively charged DNBF moiety still exerts a considerable *–I* effect (13, 14, 21); (*ii*) the presence of the positive charge at the amino group. Interestingly, lower values of the order of 12.5–13 ppm, consistent with those generally observed at the sites of substitution of aromatic or heteroaromatic positions by DNBF (e.g., $\Delta\delta \approx 10$ ppm for formation of the indole adducts **9** (21*a*)) are obtained when comparing δC_2 between **6a–c,H** and the related protonated thiophenes **4,H**. On the other hand, we have observed that use of an excess of the aminothiophene reagent over DNBF leads partially to the conversion of **6a–c,H** to the conjugate anionic bases **6a–c**. Complete conversion of **6b,H** to **6b** could be effected by adding 3 equiv. of triethylamine to a solution resulting on mixing equimolar amounts of DNBF and **4b**. As can be seen in Tables 1 and 2, the process is accompanied by significant upfield shifts of the proton and carbon resonances of the thiophenic ring but, because of the *–I* effect of the DNBF moiety, the C-2 resonance of **6b** still appears at lower field than in the parent thiophene. However, the observed shift ($\Delta\delta \approx 17$ ppm) is now reduced, comparing well with that found on formation of the 3-methoxythiophene σ-adduct **11** from the parent thiophene **10** ($\Delta\delta \approx 18$ ppm) (21*c*). As will be emphasized in our discussion, this finding of a greater value when comparing **4** and **6** rather than **4,H** and **6,H**,reflects the fact that the C-2 position of **4**, as well as that of 3-methoxythiophene, is markedly

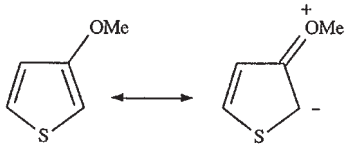

10 **10,E**

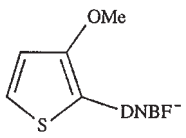

11

© 1998 NRC Canada

Table 4. Summary of rate parameters for formation of the adducts **6a,H**, **6b,H**, and **6c,H** according to eq. [3*b*] in 50% H_2O – 50% Me_2SO.[a]

	6a,H		6b,H		6c,H	
$[H^+]$, M	k, M^{-1} s^{-1}	k_1^{DNBF}, M^{-1} s^{-1} [c]	k, M^{-1} s^{-1}	k_1^{DNBF}, M^{-1} s^{-1} [c]	k, M^{-1} s^{-1}	k_1^{DNBF}, M^{-1} s^{-1} [c]
0.010	1345	3.22×10^4	—	—	—	—
0.020	770	3.69×10^4	3150	2.81×10^5	1095	7.42×10^4
	730 [b]	3.50×10^4 [b]	2950 [b]	2.63×10^5 [b]	1055 [b]	7.15×10^4 [b]
0.025	540	3.24×10^4	—	—	—	—
0.050	270	3.24×10^4	1155	2.58×10^5	530	8.98×10^4
	245 [b]	2.94×10^4 [b]	1030 [b]	2.30×10^5 [b]	—	—
0.100	145	3.48×10^4	570	2.54×10^5	305	1.03×10^5

[a] $T = 25°C$; $I = 0.1$ M KCl.
[b] Values for the corresponding 2-deuterio derivatives.
[c] Average k_1^{DNBF} values: 3.37×10^4 M^{-1} s^{-1} for **6a,H**; 2.58×10^5 M^{-1} s^{-1} for **6b,H**; 9.03×10^4 M^{-1} s^{-1} for **6c,H**.

Fig. 1. Influence of the concentration of 3-aminothiophene **4a** and pH on the observed first-order rate constant k_{obs} for addition of DNBF in 50:50 (v/v) H_2O–Me_2SO at $T = 25°C$.

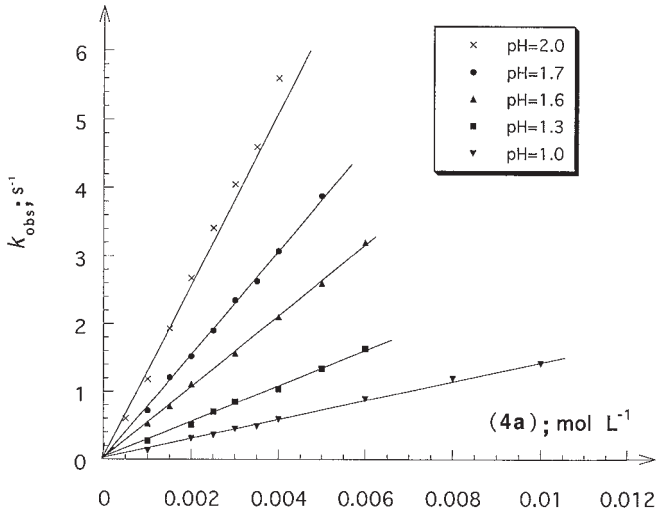

shielded as compared with that of other 3-X thiophenes, due to an especially strong +M effect of the NR_2 and OMe groups (structures **4,E** and **10,E**).

The three zwitterionic adducts **6a–c,H** could be isolated as crystalline solids from experiments carried out at –60°C in THF (see Experimental section). Dissolution of these compounds in Me_2SO-d_6 gave NMR spectra identical to those recorded in the in situ experiments. In any of the above NMR experiments, signals ascribable to the isomeric N-adducts **7,H** or **7** (Scheme 3) could be detected in the recorded spectra. The structures of **6a–c,H** were confirmed by mass spectral experiments. In addition, the visible spectra of **6a–c,H** recorded in 50:50 (v/v) H_2O–Me_2SO were typical of C-bonded σ-adducts of DNBF: $\lambda_{max} = 481$ nm for **6a,H** and **6b,H** and 479 nm for **6c,H** (12, 14–16, 21).

For purposes of comparison, Tables 1 and 2 contain the ^1H and ^{13}C NMR data for the **4a–c** – DNBF systems as well as those for the previously studied 3-methoxythiophene– and 3,4-diaminothiophene–DNBF systems (12, 21*c*).

Kinetic studies

The kinetics of reactions of **4a–c** with DNBF were studied at 25°C under pseudo-first-order conditions with respect to the thiophene reagents as the excess components in 50:50 (v/v) H_2O-Me_2SO. Experiments were carried out by mixing various HCl solutions of DNBF (3×10^{-5} M) with equal volumes of solutions of **4a–c** (10^{-3}–10^{-2} M) in a stopped-flow apparatus. The HCl concentrations of the DNBF solutions were chosen so as to afford, after mixing, H^+ concentrations in the range 0.01–0.1 M ($I = 0.1$ M KCl). Under these experimental conditions, the three aminothiophenes **4a–c** were present essentially in their protonated forms. Only one relaxation time corresponding to the quantitative formation of the C-adducts **6a–c,H** was observed in all cases. In particular, no interference between the formation of these adducts and that of the hydroxy adduct **12** according to eq. [4] was detected (17*a*, 22).

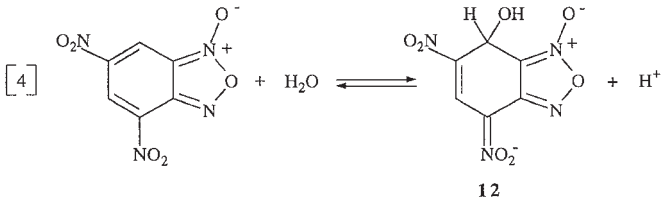

The most reasonable mechanism for the complexation process is described in eq. [3*b*] of Scheme 3, which involves the attack of DNBF by equilibrium concentrations of **4a–c**. The general expression for the observed first-order rate constants, k_{obs}, for the formation of the adducts **6,H**, as derived under the assumption that the "Wheland–Meisenheimer" zwitterion $ZH^{\pm}$ is a low concentration ("steady-state") intermediate, is given by

$$[5] \quad k_{obs} = \frac{k_1^{DNBF} k_2}{k_{-1} + k_2} \frac{K_a}{K_a + [H^+]} [\mathbf{4a–c}]_0$$

which reduces to

$$[6] \quad k_{obs} = \frac{k_1^{DNBF} k_2}{k_{-1} + k_2} \frac{K_a}{[H^+]} [\mathbf{4a–c}]_0 = k [\mathbf{4a–c}]_0$$

at the different pH's studied ($[H^+] >> K_a$).

In accord with eq.[6], excellent linear plots of k_{obs} vs. the total concentration of the aminothiophene reagent ($[\mathbf{4a–c}]_0 = [\mathbf{4a–c}] + [\mathbf{4a–c,H}]$) were obtained at each pH studied (Fig. 1). Table 4 summarizes the values of the second-order rate constants k, which were readily determined from the slopes of

© 1998 NRC Canada

Table 5. Comparison of the carbon nucleophilicity of aminothiophenes and 3-methoxythiophene with those of various pyrroles and indoles in 50% H_2O – 50% Me_2SO.

Compound	$pK_a^{H_2O}$	k_1^{DNBF}, M^{-1} s^{-1}
3,4-Diaminothiophene	≈1.5 [a]	9.58×10^5 [a]
3-(Methylamino)thiophene	≈0.8 [b]	2.58×10^5
3-(Dimethylamino)thiophene	≈0.2 [b]	9.03×10^4
3-Aminothiophene	≈ –0.40 [b]	3.37×10^4
1,2,5-Trimethylpyrrole	–0.49 [a]	2.4×10^4 [a]
2,5-Dimethylpyrrole	–1.07 [a]	7600 [a]
N-Methylindole	–2.32 [a]	3510 [a]
5-Methoxyindole	–2.90 [a]	2613 [a]
5-Methylindole	–3.30 [a]	2100 [a]
Indole	–3.46 [a]	555 [a]
Pyrrole	–3.79 [a]	520 [a]
N -Methylpyrrole	–3.88 [a]	100 [a]
5-Chloroindole	–4.53 [a]	52 [a]
5-Bromoindole	–4.30; –4.57 [a]	46.2 [a]
5-Cyanoindole	–6 [a]	1.14 [a]
3-Methoxythiophene	–6.5 [b]	0.49 [a]

[a] Data from refs. 12, 14, and 21*a*; p*K*a values taken from ref. 39.
[b] Values estimated in this work; see text.

these plots in the three DNBF–aminothiophene systems studied.

Also given in Table 4 are the *k* values corresponding to a series of experiments carried out with the 2-deuteriated-3-aminothiophenes. As can be seen, the results do not reveal a significant influence of the nature of the isotopic substitution at C-2 on the rates of formation of **6a–c,H**; the measured k_H/k_D ratios are 1.1 ± 0.1. This absence of a significant isotope effect shows that proton removal from the zwitterionic intermediate $ZH^{\pm}$ is rapid and that the rate-determining step of the complexation is the nucleophilic addition step, i.e., $k_2 >> k_{-1}$ in Scheme 3 (12,14, 21*a*, 21*c*). Accordingly, the expression of the second-order rate constant *k* takes on the simplified form of eq. [7]:

$$[7] \qquad k = \frac{k_1^{DNBF} K_a}{[H^+]}$$

from which values of the second-order rate constant k_1^{DNBF} for the addition of **4a–c** to DNBF could be readily calculated at each pH (Table 4). The average values of k_1^{DNBF} obtained for the three systems in 50:50 (v/v) H_2O–Me_2SO are compared in Table 5 with similar data previously reported for DNBF addition to 3,4-diaminothiophene **1**, 3-methoxythiophene **10**, and a number of 5-X substituted indoles (**9a–f**) as well as a few pyrrole derivatives (**13a–d**).

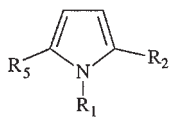

13 (a) R_1=R_2=R_5=H ;
(b) R_1=Me, R_2=R_5=H ;
(c) R_1=H, R_2=R_5=Me ;
(d) R_1=R_2=R_5=Me

Table 6. Effect of 3-X substituents on the H_2 and C_2 chemical shifts of thiophene.

X	$\Delta\delta H_2$	$\Delta\delta C_2$	σ^d
NO_2	0.95 [a]	—	1.27
CHO	0.79 [a]	12.7 [c]	1.03
CO_2Me	0.78 [a]	7.5 [c]	0.64
I	0.06 [a]	3.7 [c]	0.18
Br	–0.12 [a]	2.5 [c]	0.23
Me	–0.45 [a]	–4.3 [c]	–0.31
OMe	–1.10 [a]	–27.7 [c]	–0.78
NH_2	–1.52 [b]	–29.8 [b]	–1.30
NHMe	–1.63 [b]	–33.3 [b]	–1.81
NMe_2	–1.38 [b]	–28.6 [b]	–1.70

[a] Data in cyclohexane solution; ref. 19.
[b] This work in Me_2SO-d_6.
[c] Data in CS_2 solution; ref. 23.
[d] Substituent constants taken from ref. 27 with $\sigma = \sigma_{p-}$ for X = NO_2, CHO, CO_2Me; $\sigma = \sigma_p$ for X = I, Br; $\sigma = \sigma_{p+}$ for X = Me, OMe, NH_2, NHMe, NMe_2.

Discussion

Nitrogen vs. carbon basicity of 4a–c

As seen from the results in Table 3, the pK_a values associated with protonation of the three monoaminothiophenes **4a–c** in 50% H_2O–Me_2SO are very similar to those for the related 3,4-diamino compound **1** and the anilines **8a–d**. These results agree well with the NMR experiments carried out in pure Me_2SO, which show unambiguously that protonation of **4a–c**, as well as that of **1**, occurs exclusively on nitrogen in the presence of a strong acid such as methanesulfonic acid (Scheme 2). However, important information for understanding the reactivity of **4a–c** derives from comparison of the H_2 and C_2 chemical shifts of these compounds with those previously reported for a number of 3-X-substituted thiophenes (19, 23). These chemical shifts are collected in Table 6.

The first noteworthy feature in Table 6 is that introduction of an amino group at C-3 of the thiophene ring induces, as does that of a methoxy group, a large upfield shift of the H_2 and C_2 resonances, e.g., $\Delta\delta H_2$ = –1.52 ppm; $\Delta\delta C_2$ = –29.8 ppm for X = NH_2; $\Delta\delta H_2$ = –1.10 ppm, $\Delta\delta C_2$ = –27.7 ppm for X = OMe. For comparison, the $\Delta\delta H_2$ and $\Delta\delta C_2$ values are only –0.45 and –4.3 ppm, respectively, for X = Me. Obviously, such chemical shift variations favor the idea that the enaminic resonance contributor **4,E** is very important in determining the structure of the 3-aminothiophenes **4a–c**. In a similar way, Gronowitz and Hoffman (19) as well as Takahashi et al. (23) previously suggested that the vinyl ether structure **10,E** contributes significantly to the representation of **10**.

As previously emphasized by Spinelli and co-workers, the electron density at C-2 of a thiophene ring is greatly dependent on the nature of the X substituent at C-3 (24–26). This phenomenon, known as the hyper-*ortho* relationship, is commonly expressed through Hammett relationships based on use of the σ_{para} substituent constants defined in the benzene series (24–26). Although all available data do not refer to the same solvent, it can be seen in Fig. 2 that an approximately linear relationship is obtained on plotting the $\Delta\delta C_2$ ($= \delta C_{2(X)} - \delta C_{2(H)}$) value, measuring the shielding or deshielding effects exerted

© 1998 NRC Canada

Fig. 2. Effect of a 3-X substituent on (*a*) the H2 and (*b*) the C2 chemical shifts of a thiophene ring. See Table 6 for the data used to draw these plots.

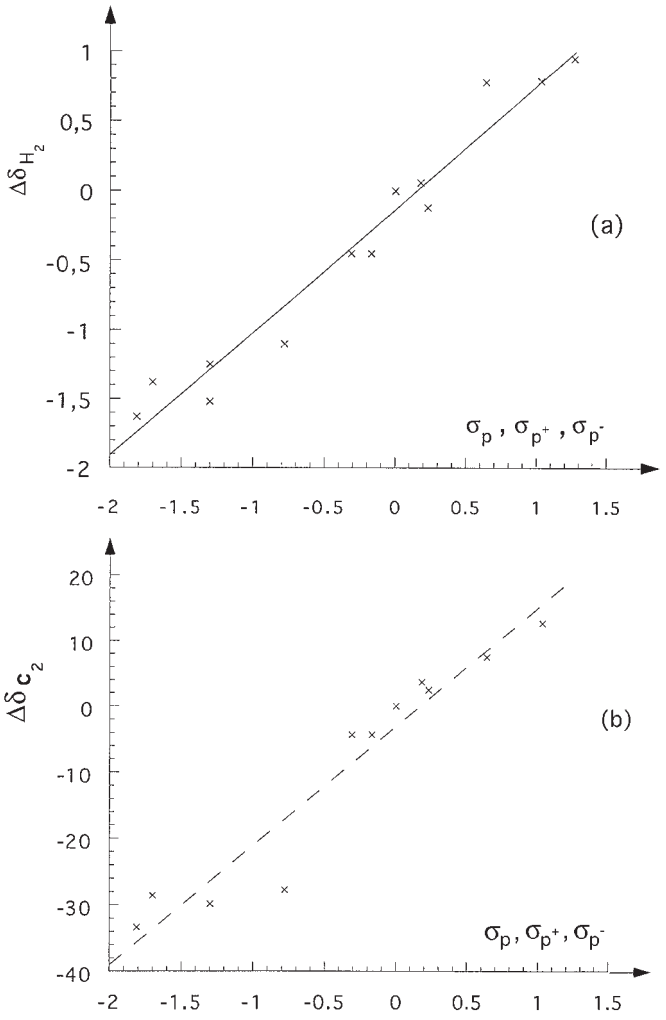

by the 3-X substituent, against σ_p (27). A similar correlation is obtained when considering the related $\Delta\delta H_2$ values, including that for 3-nitrothiophene. Interestingly, the above Hammett-type relationships require the use of the σ_{p+} and σ_{p-} values for substituents exhibiting strong +M or –M effects. Hence it is clear that the resonance structures **14** and **15** must primarily govern the reactivity of 3-X-thiophenes at the two extremes of the substituent spectrum. This conclusion fits well the experimental observation that **4a–c** and **1** are highly susceptible to electrophilic substitution at C-2 while 3-nitrothiophenes are highly prone to nucleophilic addition or substitution processes at this position.

14 (= **4,E** if X = NRR') **15**

A comparison of the rate constants k_1^{DNBF} for formation of the adducts **6a-c,H** and **3H** with those previously measured for the 3-methoxythiophene adduct **11** as well as the various indole and pyrrole adducts **9** and **13**, is useful both to assess the carbon nucleophilicity of **4a–c** and **1** and to estimate indirectly the basicities of these derivatives (14, 21*a*, 21*c*). As can be seen in Table 5, the k_1^{DNBF} values for C-2 substitution of **4a–c** and **1** by DNBF are by far the highest in the series of heterocycles studied, reaching 3×10^5 M^{-1} s^{-1} for 3-(methylamino)thiophene **4b** and nearly 10^6 M^{-1} s^{-1} for **1**. Even though a few faster carbon–carbon bond-forming reactions of this type have been reported, these k_1^{DNBF} values rank among the highest ever measured for σ-complexation processes by carbon nucleophiles (28, 29).

In the case of indoles **9** and pyrroles **13**, a roughly linear Brönsted-type relationship was found to describe the observed increase in k_1^{DNBF} with increasing carbon basicity of these derivatives (21*a*). If one assumes as a first approximation that this correlation will also fit the nucleophilic behaviour of related five-membered heterocycles, the pK_a^{CH} values for C-protonation of thiophene derivatives can be estimated. In fact, we have recently applied this treatment to the DNBF–3-methoxythiophene system and estimated a pK_a^{CH} value for **10** of –6.5, which compares well with an independent determination of ≈–7 (21*c*). In the case of **4a–c**, one thus obtains: $pK_a^{CH} \approx -0.4$ for **4a**; $pK_a^{CH} \approx +0.8$ for **4b**; $pK_a^{CH} \approx +0.2$ for **4c**, as compared with a pK_a^{CH} value ≈ +1.5 for **1** and a pK_a^{CH} value of –0.49 for the most basic nitrogen heterocycle in Table 5, namely 1,2,5-trimethylpyrrole.

In considering the carbon basicities of **1** and **4a–c**, it is first noteworthy that they are all lower by 2.5–3 p*K* units than the basicities of the related amino groups. This accounts very well for the acid–base behaviour observed in dilute HCl solutions in 50% H_2O – 50% Me_2SO or CH_3SO_3H solutions in Me_2SO. Recalling, however, that thiophene compounds are the five-membered ring heterocycles that are by far the least prone to electrophilic addition or substitution processes (30, 31), the above pK_a^{CH} values are in themselves convincing evidence that the C-2 position of **1** and **4a–c** bears an especially high electron density, further supporting the predominance of the enaminic representation **4,E** in the structure of **1** and **4a–c**. To be noted are the much higher k_1^{DNBF} and pK_a^{CH} values for the 3-aminothiophenes than for 3-methoxythiophene, a result that is perhaps unexpected in view of the similar shielding effects exerted by the NRR′ and OMe groups at C-2 of a thiophene ring.

DNBF–aniline systems vs. DNBF–aminothiophene systems

In view of the high k_1^{DNBF} values measured for reaction [3*b*] in Scheme 3, it seems reasonable to suggest that initial formation of the N-bonded adducts **7** is not observed because this is both kinetically and thermodynamically disfavored compared to the C-adducts **6,H**. The situation is therefore in marked contrast to that observed in the DNBF–aniline system (15, 16). In this case, Buncel et al. as well as Spear et al. have reported that the reaction involves first the reversible formation of the N-adduct **16a** under kinetic control. In a second and much slower step, similar to the one depicted in eq. [3*b*] for the aminothiophene systems, the formation of the zwitterionic C-adduct **17a,H** occurs irreversibly; hence **17a,H** was obtained quantitatively as

© 1998 NRC Canada

the thermodynamically favored product (15, 16). Similarly, the reaction of DNBF with 1,2-diaminobenzene **8d** afforded initially the N-adduct **16b** but it is the C-adduct **17b,H** which formed eventually as the stable product (21*a*).

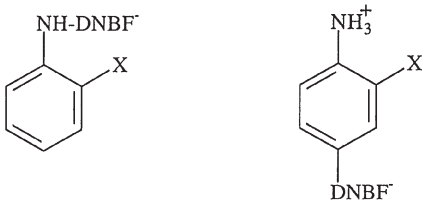

16 (a) X=H, (b) X=NH_2 **17,H**

The similarity of the nitrogen basicities of aminothiophenes and anilines implies that donation of the nitrogen lone pair to the respective aromatic or heteroaromatic ring is rather similar. On the other hand, formation of N-bonded adducts like **7** or **16** does not require major geometrical or electronic changes in these rings. Thus, it is difficult to understand why anilines should be intrinsically more efficient nucleophiles in forming the adducts **16** than aminothiophenes in forming the adducts **7**. Accordingly, we suggest that the initial formation of **16** in the aniline–DNBF system is made possible only because formation of the related C-adduct **17,H** is kinetically less favored than that of **6,H** in the thiophene system. In the formation of C-adducts such as **6,H** and **17,H**, the first step involves not only σ-complexation of the carbocyclic ring of DNBF but also that of the benzene or thiophene ring. In this regard, it is well known that σ-complex formation is a more favored process in the thiophene than in the benzene series (32, 33). According to Illuminati and co-workers (32, 34), two main factors would account for this behaviour: (*i*) a somewhat lower aromaticity of the heterocyclic ring system as compared with the benzene system; (*ii*) the fact that the σ-complexation process does not involve as much change in geometry in the five- as in the six-membered ring systems. The bond angle at the site of addition of a benzene derivative is almost 120° while the analogous angle at the reactive C_α center in a thiophene substrate is 111.5° (35). Since tetrahedral geometry must be achieved at the reaction site in all σ-complexes, it is clear that the complexation process must involve much greater bond strain in the benzene than in the five-membered ring system (34, 36, 37). It is this factor which would reduce the rate of formation of **17,H**, as compared to that of **6,H**, thus allowing the formation of **16** under kinetic control. Clearly, an additional factor will also be present, namely, that in the thiophene system delocalization of the nitrogen lone pair occurs solely at C-2 whereas in the aniline system dispersion of charge density occurs in part at the *ortho* position though predominantly at the *para* reaction center.

In conclusion, the enaminic character of 3-aminothiophenes is a feature of considerable importance in understanding the chemistry of these compounds, which are attractive synthons for the preparation of biologically active compounds (10). Interestingly, our finding that **4a**, **4b,** and **4c**, as well as the 3,4-diamino derivative **1**, act exclusively as carbon nucleophiles towards DNBF is also consistent with recent reports of a similar behaviour of these thiophenes in reactions with other types of electrophiles (11). Thus, alkylation of the thiophene ring occurs exclusively at C-2 upon treatment of 3-aminothiophenes with carbonyl derivatives in the presence of an acid catalyst and of selenophenol used as a reducing agent.

Experimental section

Materials

4,6-Dinitrobenzofuroxan (DNBF) was prepared according to the procedure of Drost: mp 172°C (lit. (12, 14–16, 38) mp 172–174.5°C). 3-Aminothiophene (**4a**), 3-*N*-(methylamino)thiophene (**4b**), and 3-*N,N*-dimethylaminothiophene (**4c**), were prepared as described previously (2, 4): Me_2SO was stirred with calcium hydride and distilled under vacuum. Me_2SO-d_6 was dried by storing over molecular sieves.

Deuteriation of **4a**, **4b,** or **4c** at C-2 to give 2-deuterio-3-*N,N*-dideuteriothiophene (**4a-*d*$_3$**), 2-deuterio-3-*N*-deuterio-*N*-methylthiophene **(4b-d$_2$)**, and 2-deuterio 3-*N,N*-dimethylaminothiophene (**4c-*d***) was effected according to the efficient H^+-catalyzed exchange process described by Paulmier and coworkers (4). Dissolution of **4a-*d*$_3$** or **4b-*d*$_2$** in 50% H_2O – 50% Me_2SO was found by NMR to restore only the signals assigned to the amino protons in a few minutes, as expected from the known ability of these hydrogen atoms. For this reason, the kinetic experiments carried out to measure the effect of isotopic substitution at C-2 on the rates of complexation of **4a**, **4b,** or **4c** by DNBF have been described in the Results as referring to reactions involving the 2-deuteriothiophenes **4a-*d***, **4b-*d,*** and **4c-*d*** as the starting deuteriated substrates. In fact, similar rates were obtained whether isolated samples of **4a-*d*** or **4a-*d*$_3$**, **4b-*d*** or **4b-*d*$_2$** were used as starting materials.

The zwitterionic DNBF σ-adducts of **4a**, **4b,** and **4c**, i.e., **6a,H**, **6b,H**, and **6c,H,** were prepared as follows: a solution of 0.2 mmol of a freshly prepared sample of the appropriate 3-aminothiophene compound in 2 cm^3 of dry THF was prepared in a small reactor equipped with a septum and cooled at –60°C with an acetone–CO_2 bath. To this solution was added dropwise by means of a syringe a solution of 45 mg DNBF (0.2 mmol) in 2 cm^3 of THF, which had previously been cooled at –60°C. A red-orange solution was thus obtained in each case, and was allowed to warm up slowly. At about –30°C, dark-orange solids began to precipitate, and were collected by filtration at room temperature. After washing with copious amounts of dry diethyl ether, the crystals were dried under vacuum and stored at –20°C under argon and in the dark; yields of 50–60% were obtained. As with most DNBF adducts studied so far, attempts to obtain satisfactory elemental analyses of the collected solids failed, but mass spectra experiments performed with the FAB technique left no doubt that we have isolated the expected zwitterions **6,H**. Thus, we have $m/z = 324$ for **6a,H**, m/z = 338 for **6b,H,** and m/z = 352 for **6c,H**. In addition, dissolution of the crystals in Me_2SO-d_6 gave NMR spectra identical to those recorded in the in situ generation of **6a,H**, **6b,H**, and **6c,H** in this solvent. Also, the strong maxima at λ_{max} = 480 nm observed in 50% H_2O – 50% Me_2SO were typical of the formation of C-bonded adducts of DNBF (12,16).

pK_a measurements

The pK_a values for protonation of the amino groups of **4a**, **4b,** and **4c** in 50% H_2O – 50% Me_2SO (v/v) were obtained from

© 1998 NRC Canada

potentiometric measurements carried out by using buffer solutions of these aminothiophenes with [**4**]/[**4,H**] ratios equal to 1:2, 1:1, and 2:1. These solutions were prepared so that the molarity of the cationic species, i.e., **4,H**, was always equal to 0.01 M. Under these experimental conditions, the pK_a values at $I = 0.01$ M (Table 3) were thus deduced from the measured pH values of the buffers by means of eq. [8]. The details of the cell and experimental procedure used were as described previously (12).

$$[8] \qquad pK = pH - \log \frac{[\mathbf{4}]}{[\mathbf{4,H}]}$$

Kinetic measurements

Stopped-flow determinations were performed on either a Durrum or a Tritech spectrophotometer, the cell compartments of which were maintained at 25 ± 0.3°C. All kinetic runs were carried out in triplicate under pseudo-first-order conditions with a DNBF concentration of ca. 3×10^{-5} M and aminothiophene concentrations in the range 5×10^{-4} to 0.01 M. In a given experiment, the rates were found to be very reproducible (to ± 2–3%) and to be similar whether the process was followed by monitoring the increase in absorbance at $\lambda_{max} = 480$ nm of the adduct **6,H** or the decrease in absorbance at $\lambda_{max} = 425$ nm of the parent DNBF substrate as a function of time.

Spectroscopy

The NMR, UV–visible, and mass spectrometers used in this study were as described in our previous work of σ-complexation of DNBF by indoles, pyrroles, and thiophenes. The FAB experiments were performed in triplicate with negative ion detection.

References

1. M.G. Reinecke, H.W. Adickes, and C. Pyun. J. Org. Chem. **36**, 2690 (1971).
2. (*a*) F. Outurquin and C. Paulmier. Bull. Soc. Chim. Fr. II, 153 (1983); 159 (1983); (*b*) Bull. Soc. Chim. Fr. II, 151 (1980).
3. J.M. Barker, P.M. Huddleston, and M.L. Wood. Synth. Commun. **25**, 3729 (1995).
4. F. Outurquin, P. Lerouge, and C. Paulmier. Bull. Soc. Chim. Fr. **259**, 267 (1986).
5. R.F. Abdulla and H.K. Fuhr. J. Heterocycl. Chem. **13**, 427 (1976).
6. S. Rault, M. Cugnon de Sevricourt, and M. Robba. Recl.: J. R. Neth. Chem. Soc. **101**, 205 (1982).
7. C. Paulmier and F. Outurquin. J. Chem. Res. (S), 318 (1977); (M), 3660 (1977).
8. W. Verboom, C. Berboom, I.M. Eissink, B.H.M. Lammerink, and D.N. Reinhoudt. Recl. Trav. Chim. Pays-Bas, **109**, 481 (1990).
9. (*a*) F. Outurquin and C. Paulmier. Tetrahedron Lett. **34**, 5715 (1993); **34**, 5719 (1993); (*b*) M. Berkaoui, F. Outurquin, and C. Paulmier. J. Heterocycl. Chem. **33**, 9 (1996).
10. C. Paulmier. Sulfur Rep. **19**, 215 (1996).
11. D. Brugier, F. Outurquin, and C. Paulmier. Tetrahedron, **53**, 103 (1997).
12. F. Terrier, M.-J. Pouet, E. Kizilian, J.-C. Hallé, F. Outurquin, and C. Paulmier. J. Org. Chem. **58**, 4696 (1993).
13. (*a*) F. Terrier. *In* Nucleophilic aromatic displacement. *Edited by* H.Feuer. VCH, New York. 1991. pp. 142, 262; (*b*) Chem. Rev. **82**, 77 (1982).
14. F. Terrier, E. Kizilian, J.-C. Hallé, and E. Buncel. J. Am. Chem. Soc. **114**, 1740 (1992).
15. (*a*) E. Buncel, R.A. Renfrow, and M.J. Strauss. J. Org. Chem., **52**, 488 (1987); (*b*) M.J. Strauss, R.A. Renfrow, and E. Buncel. J. Am. Chem. Soc. **105**, 2473 (1983).
16. (*a*) R.J. Spear, W.P. Norris, and R.W. Read. Tetrahedron Lett. **24**, 1555 (1983); (*b*) W.P. Norris, R.J. Spear, and R.W. Read. Aust. J. Chem. **36**, 297 (1983); (*c*) R.W. Read, R.J. Spear, and W.P. Norris. Aust. J. Chem. **37**, 985 (1984).
17. (*a*) F. Terrier, F. Millot, and W.P. Norris. J. Am. Chem. Soc. **98**, 5883 (1976); (*b*) F. Terrier, J.-C. Hallé, M.-P. Simonnin. and M.-J. Pouet. J. Org. Chem. **49**, 4363 (1984); (*c*) F. Terrier, M.-P. Simonnin, M.-J. Pouet, and M.J. Strauss. J. Org. Chem. **46**, 3537 (1981); (*d*) P. MacCormack, J.-C. Hallé, M.-J. Pouet, and F. Terrier. J. Org. Chem. **53**, 4407 (1988).
18. (*a*) J. Kund and H.J. Niclas. Synth. Commun. **23**, 1569 (1993); (*b*) H.J. Niclas, B. Göhrmann, and E. Gründemann. Synth. Commun. **21**, 909 (1991).
19. S. Gronowitz and R.A. Hoffman. Ark. Kemi, **16**, 515 (1960); **16**, 539 (1960).
20. K.Yates and G. Welch. Can. J. Chem. **50**, 474 (1972).
21. (*a*) F. Terrier, M.-J. Pouet, J.-C. Hallé, S. Hunt, J.R. Jones, and E. Buncel. J. Chem. Soc. Perkin Trans. 2, 1665 (1993); (*b*) F. Terrier, R. Goumont, M.-J. Pouet, and J-C. Hallé. J. Chem. Soc. Perkin Trans. 2, 1629 (1995); (*c*) E. Kizilian, F. Terrier, A.-P. Chatrousse, K. Gzouli, and J.-C. Hallé. J. Chem. Soc. Perkin Trans. 2, 2667 (1997).
22. F. Terrier, H.A. Sorkhabi, F. Millot, J.-C. Hallé, and R. Schaal. Can. J. Chem. **58**, 1155 (1980).
23. K. Takahashi, T. Sone, and K. Fujieda. J. Phys. Chem. **74**, 2765 (1970).
24. (*a*) D. Spinelli, G. Guanti, and C. Dell'Erba. J. Chem. Soc. Perkin Trans. 2, 441 (1972); (*b*) D. Spinelli, G. Consiglio, R. Noto, and A. Corrao. J. Chem. Soc. Perkin Trans. 2, 620 (1975); (*c*) D. Spinelli, G. Consiglio, and R. Noto. J. Chem. Soc. Perkin Trans. 2, 747 (1976); 1495 (1976).
25. G. Consiglio, C. Arnone, D. Spinelli, F. Saucassan, C. Dell'Erba, G. Leandri, and F. Terrier. Gazz. Chim. Ital. **117**, 267 (1987).
26. G. Consiglio, D. Spinelli, C. Arnone, F. Saucassan, C. Dell'Erba, R. Noto, and F. Terrier. J. Chem. Soc. Perkin Trans. 2, 317 (1984).
27. C. Hansch, A. Leo, and R.W. Taft. Chem. Rev. **91**, 165 (1991).
28. J.H. Atherton, M.R. Crampton, G.L. Duffield, and J.A. Stevens. J. Chem. Soc. Perkin Trans. 2, 443 (1995).
29. J.W. Bunting, C. Fu, and J.W. Tam. Can. J. Chem. **68**, 1762 (1990).
30. R.M. Kellog. *In* Comprehensive heterocyclic chemistry. Vol. 4. *Edited by* A.R. Katritzky and C.W. Rees. Pergamon, Oxford. 1982. Chap. 13, p. 713.
31. A.R. Katritzky and R. Taylor. Adv. Heterocycl. Chem. **47**, 87 (1990).
32. G. Baldini, G. Doddi, G. Illuminati, and F. Stegel. J. Org. Chem. **41**, 2153 (1976).
33. F. Terrier, A.-P. Chatrousse, and C. Paulmier. J. Org. Chem. **44**, 1634 (1979).
34. G. Illuminati and F. Stegel. Adv. Heterocycl. Chem. **34**, 305 (1983).
35. M. Nardelli, G. Fava, and G. Giraldi. Acta Crystallogr. **15**, 737 (1962).
36. F. Terrier. Chem. Rev. **82**, 77 (1982).
37. E. Buncel, M.R. Crampton, M.J. Strauss, and F. Terrier. *In* Electron-deficient aromatic– and heteroaromatic–base interactions. Elsevier, Amsterdam. 1984. pp. 161–166.
38. P. Drost. Justus Liebigs Ann. Chem. **307**, 49 (1899).
39. (*a*) B.C. Challis and E.M. Millar. J. Chem. Soc. Perkin Trans. 2, 1111 (1972); 1618 (1972); (*b*) Y. Chiang and E.B. Whipple. J. Am. Chem. Soc. **85**, 2736 (1963); (*c*) R.L. Hinman and J. Lang. J. Am. Chem. Soc. **86**, 3796 (1964).

© 1998 NRC Canada

Dephosphorylation and aromatic nucleophilic substitution in nonionic micelles. The importance of substrate location

Clifford A. Bunton, Houshang J. Foroudian, Nicholas D. Gillitt, and Christy R. Whiddon

Abstract: Reactions of OH^- and F^- with *p*-nitrophenyl diphenyl phosphate (pNPDPP) are inhibited by very dilute dodecyl (10) and (23) polyoxyethylene glycol ($C_{12}E_{10}$ and $C_{12}E_{23}$, respectively), but rate constants become independent of surfactant concentrations at concentrations above the critical micelle concentration. Low charge density anions, e.g., ClO_4^-, inhibit and low charge density cations, e.g., $(n\text{-}C_7H_{15})_4N^+$, accelerate reactions, probably by controlling concentrations of nucleophiles in the palisade layer. Diphenyl phosphorofluoridate, generated by attack of F^-, is not detected but is rapidly hydrolyzed to phenyl phosphorofluoridate or diphenyl phosphate ion with loss of phenol or F^-. The products are different in DMSO containing modest amounts (<15 vol%) of water and no surfactant and are phenyl phosphorofluoridate and difluorophosphate ions generated by attack of F^- on the initial phosphorofluoridate. These differences are consistent with the micellar palisade layer being water-rich. Although the nonionic surfactants do not intervene nucleophilically in reactions of pNPDPP, considerable amounts of ether are formed in the reaction of 2,4-dinitrochlorobenzene (DNCB), in $C_{12}E_{10}$ and $C_{12}E_{23}$ at high pH by attack of alkoxide ion with the relatively hydrophilic DNCB located close to the micellar surface. The differences in the chemistries of reactions of pNPDPP and DNCB appear to be associated largely with differences in locations of these substrates in the nonionic micelles.

Key words: fluoridates, *p*-nitrophenyl diphenyl phosphate, 2,4-dinitrochlorobenzene, nonionic micelles, palisade layer.

Résumé : Les réactions des ions OH^- et F^- avec le phosphate de *p*-nitrophényle et de diphényle (PpNPDP) est inhibée par des solutions très diluées de dodécyl (10) et (23) polyoxyéthylèneglycol (respectivement $C_{12}E_{10}$ et $C_{12}E_{23}$), mais les constantes de vitesse deviennent indépendantes de la concentration de l'agent tensioactif à des concentrations supérieures à la concentration micellaire critique. Les réactions sont inhibées par les anions de faible densité de charge, comme le ClO_4^-, et accélérées par les cations de faible densité de charge, comme le $(n\text{-}C_7H_{15})_4N^+$; ces effets sont probablement dus à un contrôle des concentrations de nucléophiles dans la couche palissade. On ne peut détecter la présence de phosphorofluoridate de diphényle, généré par une attaque du F^-; il est rapidement hydrolysé en phosphorofluoridate de phényle ou en ion phosphate de diphényle avec perte de phénol ou de F^-. Les produits sont différents dans le DMSO contenant de faibles quantités (<15% par volume) d'eau et aucun agent tensioactif; il s'agit de phosphorofluoridate de phényle et de l'ion difluorophosphate généré par l'attaque du F^- sur le phosphorofluoridate initial. Ces différences sont en accord avec une couche micellaire palissade riche en eau. Même si les agents tensioactifs non ioniques n'interviennent pas d'une façon nucléophile dans les réactions du PpNPDP, il se forme de grandes quantités d'éther lors de la réaction du 2,4-dinitrochlorobenzène (DNCB), dans $C_{12}E_{10}$ et $C_{12}E_{23}$, à pH élevé; elles proviennent d'une attaque de l'ion alcoolate sur le DNCB relativement hydrophile qui se trouve près de la surface micellaire. Les différences dans les chimies des réactions du PpNPDP et du DNCB semblent associées à des différences dans la situation de ces substrats dans les micelles non ioniques.

Mots clés : fluoridates, phosphate de *p*-nitrophényle et de diphényle, 2,4-dinitrochlorobenzène, micelles non ioniques, couche palissade.

[Traduit par la rédaction]

Phosphate esters with nitrophenoxy groups are often used in simulating detoxification of phosphonofluoridates, e.g., Sarin, GB, by nucleophilic attack (1), because formation of nitrophenoxide ion is readily followed spectrophotometrically. Many nucleophiles have been examined (1), especially such α-effect nucleophiles as HO_2^-, oximate and hydroxamate ions (2), metal complexes (3–6), and iodosobenzoate ion and its derivatives (7). Reactions are often carried out in micelles or microemulsions, which solubilize reactants and may accelerate reaction by concentrating reactants in the small volume of the association colloid. If this concentration effect is taken into account, second-order rate constants in the interfacial region of the association colloid are generally similar to those in water (5, 8, 9). Much of the work with anionic nucleophiles has involved

This paper is dedicated to Professor Erwin Buncel in recognition of his contributions to Canadian chemistry.

Received February 16, 1998.

C.A. Bunton,[1] H.J. Foroudian, N.D. Gillitt, and C.R. Whiddon. Department of Chemistry, University of California, Santa Barbara, CA 93106, U.S.A.

[1] Author to whom correspondence may be addressed. Telephone: (805) 893-2605. Fax: (805) 893-4120.

© 1998 NRC Canada

cationic micelles that concentrate anions, but nonionic micelles provide useful media for dephosphorylation by amphiphilic metal complexes (3, 6), and nonionic are better solubilizing agents than ionic micelles (10).

In his pioneering work Hartley (11) showed that nonionic micelles have little effect on acid–base equilibria, although they are sensitive to charges on ionic micelles. Subsequently rate constants of reactions of hydrophilic ions with polar, nonionic substrates were found to be generally similar to those in water, even though substrates were micellar-bound. These observations are summarized in monographs (12).

Many nonionic surfactants have apolar groups attached to polyoxyethylene chains, as in the Brij$^{(R)}$ family,

$$CH_3(CH_2)_{m-1}O(CH_2CH_2O)_{n-1}CH_2CH_2OH$$

designated C_mE_n. In aqueous micelles the ethylene oxide, palisade layer is extensively hydrated (13–16), although estimated hydration numbers depend upon structures of the apolar and hydrophilic groups, and probably also upon the method of determination. Evidence on hydration is summarized (16). Therefore hydrophilic ions should be able to penetrate the palisade layer, although there should be no coulombic micelle–ion interactions, as in ionic micelles. Depending upon values of *m* and *n* the volume of the palisade layer may be much greater than that of the apolar core, unlike the situation with ionic micelles (8, 9, 12). In addition, many nonionic surfactants, e.g., Brij$^{(R)}$35, $C_{12}E_{23}$, are of high molecular weight (ca. 10^3), and even at low molarities their micelles occupy a significant volume of the solution.

The similarity between rate constants in water and in nonionic micelles indicates that many substrates reside in an interfacial micellar region, where they are exposed to ionic reagents (9, 12). However, reactions of OH^- and F^- with *p*-nitrophenyl diphenyl phosphate (pNPDPP) are significantly inhibited by dilute Igepal (17), a nonyl phenol condensed with ca. 24 ethylene oxide residues (12). First-order rate constants, k_{obs},

$$(PhO)_2PO{\cdot}OC_6H_4NO_2(p) \xrightarrow{Nu^-} (PhO)_2PO{\cdot}Nu + O^-C_6H_4NO_2, \quad Nu = OH, F$$

(pNPDPP)

decrease sharply at Igepal concentration below the critical micelle concentration, cmc, and then become independent of the Igepal concentration (17). Physical evidence shows that pNPDPP is bound strongly to Igepal, even at low concentration, and it probably goes sufficiently deep into the micelle to be partially protected from OH^- or F^-. This behavior is different from that seen for reaction in an anionic micelle of sodium dodecyl sulfate, SDS, where there is little inhibition until micelles form and then k_{obs} decreases monotonically with increasing SDS concentration to very low, but non-zero, values (17, 18).

At high pH alkoxide ions generated by deprotonation of hydroxyl groups in micelles or microemulsions can be effective nucleophiles (19, 20). For example, 1-butoxide ion in microemulsions with 1-butanol as co-surfactant reacts with pNPDPP (20). The terminal OH of a nonionic surfactant should have an acidity similar to that of ethane diol ($pK_a = 14.8$ (21)), and its alkoxide residue should be an effective nucleophile. This reaction was considered, but excluded, for reaction of pNPDPP in $C_{12}E_{23}$ (3). However, this intervention may be feasible with a shorter polyoxyethylene residue, as in $C_{12}E_{10}$, or with a less hydrophobic substrate. So far as we know the only kinetic test of intervention is that with pNPDPP in $C_{12}E_{23}$ (3), although a very short-lived aryl cation generated by decomposition of an amphiphilic diazonium ion in micelles of $C_{12}E_6$ is trapped, albeitly weakly, by the terminal OH group (16).

Alkoxide ions compete with OH^- in reactions of 2,4-dinitrochlorobenzene (DNCB) in cationic micelles and microemulsions (19). This relatively hydrophilic substrate may bind at the surface of a nonionic micelle and react with an alkoxide ion generated by deprotonation of the terminal OH^-. The reaction with OH^-, followed by formation of 2,4-dinitrophenoxide appeared to be slightly faster in Igepal than in water (22), but intervention of the alkoxide ion was not examined, and we have now examined the products of this reaction in $C_{12}E_{10}$ and $C_{12}E_{23}$.

Reaction of F^- with pNPDPP probably involves initial formation of a fluoridate **1**, which should react further.

$$(PhO)_2PO{\cdot}OC_6H_4NO_2 \xrightarrow{F^-} (PhO)_2PO{\cdot}F + O^-C_6H_4NO_2$$

1

Attack of OH^- upon pNPDPP displaces *p*-nitrophenoxide ion, but there is a minor displacement of phenoxide ion (3, 20). We expected this minor reaction to be less important when the nucleophile is F^-, but so far as we know this possibility has not been tested.

The interfacial regions of ionic micelles have polarities, based largely on spectrophotometric probes, slightly lower than that of water (12), but the recent application of linear solvation free-energy relationships to solute–micelle interactions shows that micellar charge and head group structure are important (23). However, the kinetic implications of these treatments have not been explored extensively, nor have the effects of differences between volumes of the interfacial regions of ionic and nonionic micelles relative to total micellar volumes (8, 9, 12).

Experimental

Materials

The surfactants, $C_{12}E_{10}$ (Sigma) and $C_{12}E_{23}$ (Brij$^{(R)}$35) (Aldrich), were used as received but samples, purchased in both 1996 and 1997, gave similar rate data. Diphenyl phosphorochloridate (Aldrich) was redistilled, tetrabutylammonium fluoride (ACROS), sodium fluoride (Fisher), and ammonium fluoride (Aldrich) were used as received, and pNPDPP and DNCB had been used earlier (5, 22). Reactions were carried out in redistilled, CO_2-free deionized water or in DMSO or DMSO–H_2O without surfactants.

Kinetics

Reactions were followed spectrophotometrically in Beckman or HP 8450 spectrophotometers at 25.0°C as described (5, 17). Substrate was added in MeCN to give 2×10^{-5} M pNPDPP and 0.2 vol% MeCN in the kinetic solution. Solutions of the more concentrated surfactants were viscous, and then substrate was mixed by using a square plunger with small holes. Provided that the plunger did not break the surface we could mix reagents without introducing air bubbles. Freshly made up solutions

© 1998 NRC Canada

Table 1. Reactions of OH^- and F^- with *p*-NPDPP.[a]

	0.02 M KOH	0.1 M KOH		0.01 M NaF		0.1 M NaF	
10^3 [C_mE_n], M	$C_{12}E_{23}$	$C_{12}E_{10}$	$C_{12}E_{23}$	$C_{12}E_{10}$	$C_{12}E_{23}$	$C_{12}E_{10}$	$C_{12}E_{23}$
	10.1	48.3		1.05		10.5	
0.2	4.10				0.45		
0.25	3.75	16.7	18.2				
0.5	1.63	12.0	10.4	0.22	0.25	2.24	2.35
1.0	1.54	7.81	5.70	0.21	0.17	1.55	1.61
2.5	0.86	5.50	4.35		0.12	1.12	
3.0						0.92	
5.0	0.77	4.15	3.19	0.17	0.12	0.92	0.93
7.5	0.70						
10.0	0.63	4.25	3.47	0.13	0.12		0.86
25.0	0.61		2.75		0.12		
50.0		4.02	2.95	0.12	0.13	0.95	0.92
100	0.71	4.01		0.13	0.12	0.84	1.06
150				0.13			
200				0.13			

[a] Values of 10^3 k_{obs} (s^{-1}) at 25.0°C.

were always used. For reactions of NaF in nonionic micelles we added 0.01 M sodium borate to prevent build up of acidity (17).

NMR spectroscopy

Products of reactions at ca. 21.5°C were identified by their ^1H, ^{19}F, and ^{31}P NMR spectra, generally on a Varian Unity (Inova) instrument, 400 M Hz for ^1H. The ^{31}P chemical shifts were referred to external 85% H_3PO_4, ^1H chemical shifts were referred to TMS, TSP, or DMSO at 2.50 ppm as convenient, and ^{19}F chemical shifts were referred to CF_3Cl by using external CF_3CO_2H, $\delta_F = -76.55$ ppm.

We typically used 10^{-2} M substrate, except for $C_{12}E_{10}$ where we used 5×10^{-3} M pNPDPP. We generally used $d1$ = 1 s for ^1H and ^{19}F but increasing it to 5 s did not change the signals, and we used $d1 = 3$ s for ^{31}P, but increasing it to 20 s had no effect on the signals.

Most reactions went to completion, but in some experiments with pNPDPP and KOD in surfactants we stopped the reaction after about one half-life with DCl, and saw only signals of pNPDPP and the final products. There was considerable overlap of some ^1H signals in the aromatic region, and in some cases we used the COSY spectrum to identify products. Chemical shifts are medium dependent, but not so much so as to complicate product identification.

Chemical shifts of pNPDPP are δ_P –18.19 and –18.15 ppm in 0.1 M $C_{12}E_{10}$ and $C_{12}E_{23}$, respectively, and in 0.1 M $C_{12}E_{23}$ ^1H chemical shifts are phenyl group, *o*-H, 7.26 (d); *m*-H, ca. 7.48 (m); *p*-H, 7.35 (t), and for the nitrophenyl group are *o*-H, ca. 7.48 (m); *m*-H, 8.31 (d) ppm. For DNCB in $C_{12}E_{10}$ and $C_{12}E_{23}$ ^1H chemical shifts are δ (ppm): H-3, 8.75 (d), J = 2.7 Hz; H-5, 8.60 (dd), J = 2.8, 9.0 Hz; H-6, 8.11 (d), J = 8.8 Hz. There is a large, broad surfactant signal at ca. 3.7 ppm with shoulders to the main peak. Some of the ^1H signals of $C_{12}E_{10}$ in D_2O were identified. For the dodecyl group they are CH_2(1), 3.44; CH_2(2), 1.55; CH_2(3–11), 1.31; ω-CH_3, 0.89 ppm, numbering from the junction with the polyoxyethylene group. The ^1H NMR spectrum of $C_{12}E_{23}$ is similar to that of $C_{12}E_{10}$ except that the broad signal at ca. 3.7 ppm is much larger.

Table 2. Kinetic salt effects in $C_{12}E_{10}$ and $C_{12}E_{23}$.[a]

	0.1 M NaOH	0.1 M NaF	
Salt	$C_{12}E_{10}$	$C_{12}E_{10}$	$C_{12}E_{23}$
—	3.75	0.84[b]	1.06
0.1 M NaC1	3.89		
0.1 M NaBr	3.42	0.71	
0.1 M $NaClO_4$	1.81	0.32[c]	0.36
0.0025 M $(C_7H_{15})_4NBr$		1.30	
0.005 M $(C_7H_{15})_4NBr$			1.91

[a] Values of 10^3 k_{obs} (s^{-1}) at 25.0°C and 0.1 M C_mE_n unless specified.
[b] With 0.1 M CsF, 10^3 $k_{obs} = 0.87$ s^{-1}.
[c] In 0.05 M $C_{12}E_{10}$, 10^3 $k_{obs} = 0.31$ s^{-1}.

Results

Kinetics of dephosphorylation

Values of k_{obs}, monitored by formation of *p*-nitrophenoxide ion (Table 1) decrease sharply in very dilute surfactant and then level off, as found earlier for reactions in Igepal (17), and rate–surfactant profiles are similar for the three surfactants, when allowance is made for differences in concentrations of the nucleophiles. There is inhibition by Igepal well below its cmc, and we see significant inhibition near the cmc of the surfactants (ca. 10^{-4} M for $C_{12}E_{10}$ and 6×10^{-5} M for $C_{12}E_{23}$) (24), and values of k_{obs} for reaction of F^- with old and new samples agreed within ± 5%. Added inorganic salts inhibit the reactions (Table 2), and as with cationic micelles, inhibition increased with decreasing charge density of the anion (9), but tetra *n*-heptyl ammonium bromide increased k_{obs}. In agreement with earlier results (17) k_{obs} is greater by about one order of magnitude for OH^- relative to F^-.

Products of dephosphorylation by OD^-

In agreement with earlier work in $C_{12}E_{23}$ (3) and in microemulsions

© 1998 NRC Canada

Table 3. Chemical shifts of products of the reaction of KOD with *p*-NPDPP.[a]

Observed	Product		DMSO-D_2O [b]		$C_{12}E_{10}$ [c]		$C_{12}E_{23}$ [c]	
^1H	*p*-$O_2NC_6H_4O^-$	*o*-	6.24		6.50	(6.94)	6.49	(6.93)
		m-	7.88		8.02	(8.08)	8.01	(8.07)
^1H	$C_6H_5O^-$	*o*-	6.36	(6.60)	6.63	(6.84)	6.63	(6.82)
		m-	6.86	(7.03)	— [d]	(7.12)	— [d]	(7.18)
		p-	6.17	(6.48)	6.58	(6.79)	6.57	(6.77)
^1H	$(PhO)_2PO_2^-$	*o*-	7.18		7.21		7.21	
		m-	7.32		7.35		7.34	
		p-	7.08		7.14		7.13	
^{31}P	$(PhO)_2PO_2^-$		–11.68		–9.73		–10.00	
^{31}P	*p*-$O_2NC_6H_4OP(OPh)O^-$ [e]		–12.45		–11.45		–11.54	

[a] In 0.1 M KOD with 0.01 M *p*-NPDPP (0.005 M in $C_{12}E_{10}$); values in parentheses are for the protonated species.
[b] DMSO-d_6:D_2O 85:15 v/v.
[c] 0.1 M.
[d] Overlapped with signals of $(PhO)_2PO_2^-$.
[e] For *m*-H of the nitrophenyl group δ = 8.25, 8.22, and 8.21 ppm in the three media listed, respectively; there was also a multiplet at 7.42–7.44 ppm.

Table 4. Chemical shifts and coupling constants of the products of reaction of F^- with *p*-NPDPP.[a]

Observed	Product	DMSO	DMSO-D_2O	$C_{12}E_{10}$	$C_{12}E_{23}$
^1H	$PhOPO_2^-·F$	*o*- 7.10 (d)	7.26 (d)	— [b]	— [b]
		m- 7.25 (t)	ca. 7.07	7.41 (t)	7.41 (t)
		p- 7.00 (t)	ca. 7.04	— [b]	— [b]
^{31}P	$PhOPO_2^-·F$	–11.88 (940)	–12.75 (932)	–10.88 (945)	–11.02 (942)
^{19}F	$PhOPO_2^-·F$	–71.92 (933)	–73.48 (932)	–76.05 (942)	–75.91 (942)
^{31}P	$F_2PO_2^-$	–14.51 (953)	–15.62 (951)		
^{19}F	$F_2PO_2^-$	–78.81 (951)	–79.88 (951)		
^{31}P	FPO_3^{2-}		0.10 (864)		
^{19}F	FPO_3^{2-}		70.55 (865)		

[a] With 0.1 M KF in 0.1 M surfactant and 0.1 M Bu_4NF in DMSO, δ in ppm, and *J* in Hz in parentheses.
[b] Extensive overlap with signals of $(PhO)_2PO_2^-$.

with 1-butanol with co-surfactant (20) the major reaction at 21.5°C is loss of *p*-nitrophenoxide ion with minor loss of phenoxide ion (11 and 14 mol% in DMSO, 15 vol% D_2O and $C_{12}E_{10}$ or $C_{12}E_{23}$, respectively) and formation of the corresponding diarylphosphate ion (Table 3). There is some overlap of the ^1H NMR signals, but based on these and the ^{31}P NMR signals, there is no product of dephosphorylation by the alkoxide residue of $C_{12}E_{10}$ or $C_{12}E_{23}$ (cf. ref. 3). Trisubstituted phosphates react readily with OH^-, but if a phosphorylated derivative had been formed it would decompose with loss of phenoxide ion, and we would have seen additional NMR signals. These conclusions were confirmed by stopping reaction with DCl at about one half-life and by examining the ^1H NMR spectrum, which except for signals of unreacted pNPDPP was similar to that observed at complete reaction. Reaction of the terminal group of the surfactants is unimportant, consistent with the similar values of k_{obs} for reactions in $C_{12}E_{10}$ and $C_{12}E_{23}$ (Table 1).

Products of dephosphorylation by F^-

The products of reaction depend upon the reaction medium, and although phenol is formed (Table 4 and Scheme 1) we do not believe that it comes from the initial attack of F^-. A number of possible phosphorofluoridates were synthesized and their ^{19}F and ^{31}P NMR signals characterized by Reddy and Schmutzler (25) whose compilation was very useful in the identification, or exclusion, of intermediates and products.

Reaction in $C_{12}E_{10}$ and $C_{12}E_{23}$ (Scheme 1) gave phenol and *p*-nitrophenoxide ion, identified by their ^1H NMR signals, diphenyl phosphate ion, **2**, identified by its ^{31}P signal, and phenylphosphorofluoridate, **3**, identified largely by its ^{19}F and ^{31}P signals (Table 4). Addition of KOD at the end of reaction did not affect the NMR spectra, except by generating phenoxide ion from phenol. Reactions of the anions **2** and **3** with OD^- are slow, and NMR signals changed only slowly with time.

We saw no signals of diphenyl phosphorofluoridate, **1**, which has $\delta_P = -21.8$ ppm, d; $\delta_F = -78.4$ ppm, d; $J_{PF} = 1001$ Hz (25). A sample prepared by the original method (reaction of the chloridate with NH_4F in refluxing toluene (25)), but without purification, had $\delta_F = -77.9$ ppm, $J_{PF} = 999$ Hz in DMSO-d_6, the differences in the NMR data are due to the original values being obtained with the pure liquid (25).

The reactions and yields are shown in Scheme 1, and **1** is hydrolyzed with loss of either phenol or F^-. There were no products that could be ascribed to reaction of F^- with pNPDPP and direct displacement of phenol.

The products of the very rapid reaction in DMSO with or without added D_2O differ from those in water, probably because the increased nucleophilicity of F^- (26) allows it to attack the first-formed diphenyl phosphorofluoridate, **1** (Scheme 2). This reaction gives the difluoridate, **4**, which can

© 1998 NRC Canada

Scheme 1.

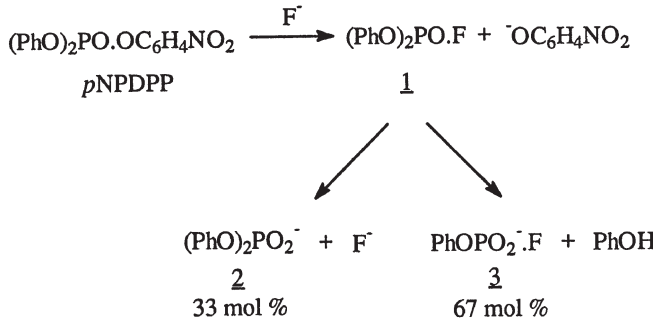

Scheme 2.

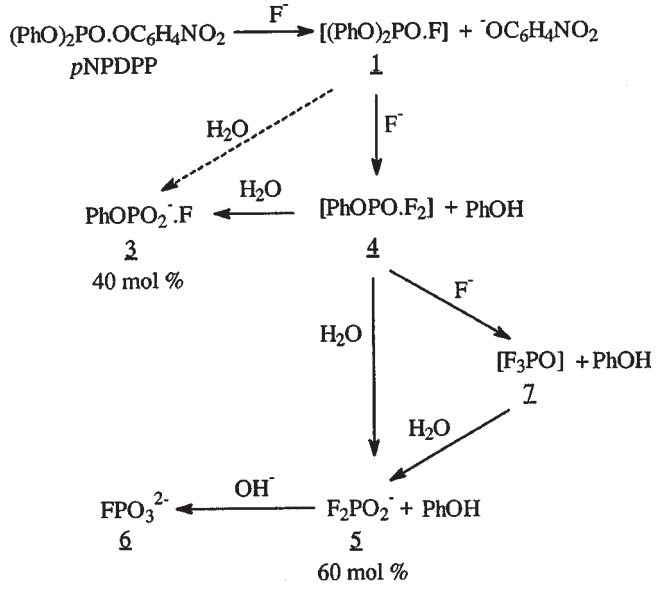

be hydrolyzed with loss of either phenol or F^-, giving **5** and **3**, respectively. Alternatively, displacement of phenol from **1** by water could give **3**, but we think that this reaction is improbable because in aqueous nonionic micelles it competes with displacement of F^-, giving diphenyl phosphate ion, **2** (Scheme 1), and we do not obtain **2** in DMSO. Both **3** and difluorophosphate ion, **5**, are relatively stable in the reaction conditions, but the latter is slowly converted into fluorophosphate dianion, **6**, on addition of KOD-D_2O, and **6** is hydrolyzed only in aqueous acid (27). Conversion of the difluoridate, **4**, into difluorophosphate ion, **5**, could occur via formation of trifluorophosphate, **7**, which should be very reactive in our conditions, and this alternate reaction path is also shown in Scheme 2. The NMR parameters are given in Table 4, and the differences from literature chemical shifts (25) are due to the use of pure liquids or concentrated solutions in the earlier work.

There are minor ^{19}F and ^{31}P signals (ca. 25% of the major signals) in the products of reaction in nominally dry DMSO-d_6 at δ_F = 54.85 ppm (d), J = 828 Hz and δ_P = –75.7 ppm (t), J = 828 Hz. The ^{31}P signal is not much above the noise level, and there are no corresponding ^1H signals in the aromatic region. We did not see these signals in DMSO-d_6:D_2O 85:15 v/v, and they disappear slowly (over a few hours at 21.5°C) due to reaction with small amounts of water in the DMSO and immediately on addition of D_2O to the reaction mixture. Our speculation is that they are formed by reaction of DMSO, acting as a nucleophile (28), towards a fluorophosphate, e.g., **7** (Scheme 2). These signals also appear in the products of reaction of tris(*p*-nitrophenyl) phosphate with Bu_4NF in DMSO-d_6; they also disappear on addition of D_2O, and there are no corresponding ^1H signals in the aromatic region. We carried out the reaction in 80% DMSO – 20% DMSO-d_6 in the hope of seeing new ^1H signals in the aromatic region, but without success. However, ^1H signals of a phosphorylated DMSO could have been obscured by those of Bu_4NF or DMSO. Formation of the pyrophosphate, $(F_2PO)_2O$, would explain the multiplicity of the signals, but this compound has δ_F = –85.7 ppm, δ_P = –22.1 ppm. J_{PF} = 980 Hz (25).

We see no signals of diphenyl phosphorofluoridate, **1**, even in DMSO-d_6, but the signals of **3** and **5** appear within the time required for running the NMR spectrum in DMSO.

Reaction of DNCB in nonionic micelles

The terminal OH group of a polyoxyethylene surfactant should be partially deprotonated at high pH, and based on examples of alkoxide ion reactions in micelles and microemulsions (19, 20, 29), there should be a reaction with DNCB if it is bound close to the micellar surface.

Reaction of 0.02 M DNCB and 0.15 M DNCB in 0.1 M $C_{12}E_{10}$ initially gives signals of an ether, **8a**, and weak signals of 2,4-dinitrophenoxide ion, **9** (Table 5). With time, signals of **8a** decrease and those of the phenoxide ion increase. Approximate half-lives for appearance of **8a** and its disappearance are 0.9 and 25 h, respectively, from inspection of the data in Table 5. There are also methylene signals of **8a** at 3.97 and 4.52 ppm whose areas are twice those of the aromatic ^1H signals. A third signal at 3.75 ppm appears to have a similar area to the first two, but it is too close to the large signal at ca. 3.7 ppm for estimation of its area.

The reactions shown in Scheme 3 are confirmed by taking the absorbance spectra of the NMR reaction mixture after 200-fold dilution (Fig. 1). Some plots are omitted for clarity but formation and subsequent reaction of **8a** are evident.

Some dinitrophenoxide ion may be formed by direct reaction with OH^- in the micelle, or in water, because DNCB is probably not fully micellar bound. Association constants with respect to micellized surfactant are 88, 75, and 44 M^{-1} in Igepal, CTABr, and SDS, respectively (22), and is probably similar in $C_{12}E_{10}$ and $C_{12}E_{23}$, indicating that ca. 10% DNCB will be in the water.

The reaction was carried out as above in 0.01 M DNCB with added 0.01 M 2,4-dinitrophenol, but there were no additional ^1H NMR signals, so we exclude formation of bis(2,4-dinitrophenyl) ether as an intermediate.

An ether, **8b**, is formed in the reaction in 0.1 M $C_{12}E_{23}$, and its ^1H NMR spectrum in the aromatic and aliphatic regions is very similar to that of **8a** (Table 5). However, formation and disappearance of this ether are not as well separated as in $C_{12}E_{10}$, and we did not examine this system in detail. The different behaviors could be due to differences in the contributions of a direct reaction with OD^- in water, or differences in relative rates of formation and reaction of the ethers in the two micellized surfactants. However, it has been known for many years that rates of aromatic nucleophilic substitutions are

© 1998 NRC Canada

Table 5. Products of reactions of DNCB in nonionic micelles.[a]

Time, h	0.08	0.45	1.00	2.13	4.25	8.08	16.0	19.8	92.5	141
Product										
Ether, **8**[b]	10	25	47 (22)	66	76	74	(43)	59	13	5
Phenoxide, **9**[c]	2	4	6 (12)	10	16	25	(57)	41	87	95

[a] Products, mol%, with 0.02 M DNCB, 0.15 M KOD, 0.1 M $C_{12}E_{10}$–D_2O (values in parentheses are with 0.1 M $C_{12}E_{23}$), $T = 21.5$°C.

[b] δ (ppm) for aromatic H; H-5, 8.58 (d); H-6, 7.69 (d). $J = 9.6$ Hz for all the signals.

[c] δ (ppm) for aromatic H; H-5, 8.03 (d); H-6, 6.72 (d) ppm.

Scheme 3.

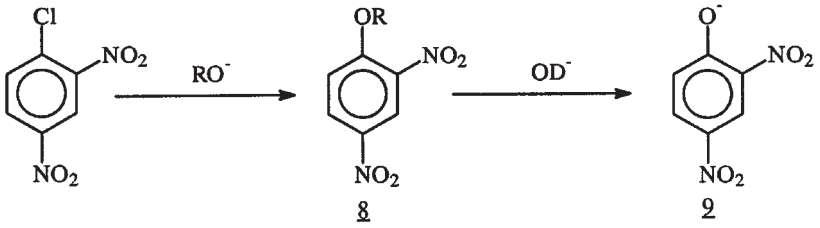

$R = C_{12}H_{25}O(CH_2CH_2O)_{n-1}\ CH_2CH_2$

typically not very sensitive to the nature of the leaving group (30) (fluoride is a major exception to this generalization).

There are overlaps in some of the ^{1}H NMR signals (Table 5), but chemical shifts of the ethers were determined from spectra taken after DNCB had disappeared. We did not see signals of H-3 due to H–D exchange in the reaction conditions (31).

Discussion

The fate of the putative phosphorofluoridate, **1** (Schemes 1 and 2), does not affect values of k_{obs} calculated from the rate of formation of *p*-nitrophenoxide ion, and they are insensitive to structures of the nonionic surfactants (Tables 1 and 2). The relative reactivities of OH^- and F^- are as expected (17, 32). Reactions are approximately first-order in nucleophile concentration, unlike kinetics in ionic micelles (9), indicating that transfer of ions into the micelles does not significantly deplete them in the aqueous pseudophase. The initial sharp decrease of k_{obs} in dilute surfactant at concentration close to the cmc (Table 1) is indicative of inhibition by monomeric surfactant or premicelles (9).

Inhibition of bimolecular reactions in ionic micelles by inert counterions is explained in terms of ionic competition at the micellar surface, which, in this respect, behaves like an ion-exchange resin (9, 33). The interactions are not solely coulombic, but depend on the charge densities of the ions, and the source of this ion specificity has been discussed (9, 33, 34). The salt order for inhibitions of dephosphorylation in nonionic micelles is that for reactions mediated by cationic (9, 33) (and sulfobetaine (35)) micelles, but effects are smaller, probably because there are no coulombic ion–micelle interactions. Cation effects are small, except that the bulky tetra-*n*-heptylammonium ion increases the reactivity of F^- (Table 2). Incorporation of ClO_4^- or $(C_7H_{15})_4N^+$ in the palisade layer generates charges that affect ionic transfer from water into this region. This subject will be covered in more detail elsewhere.

Based on the binding constant of pNPDPP to micellized Igepal, estimated by solubility (17), we assume that pNPDPP will be fully micellar-bound at 2×10^{-3} M surfactant. The constancy of k_{obs} over a range of $[C_{12}E_{10}]$ and $[C_{12}E_{23}]$ indicates that concentrations of OH^- and F^- in the palisade layer do not decrease with increasing surfactant concentration, as in ionic micelles (9, 33). We do not know the extent to which concentrations of OH^- and F^- in the "water-rich" palisade layer depend upon the length of the polyoxyethylene group, but the similarities of values of k_{obs} in micelles of $C_{12}E_{10}$ and $C_{12}E_{23}$ (Table 1) indicate that there is little effect.

If the acidity of the terminal OH group is similar to that of ethane diol (21), alkoxide ion should be generated at the micellar surface in dilute OH^-, but it does not react with pNPDPP, probably because eclipsing strains make it difficult for the terminal groups to reach the micellar interior, but see ref. 16 for different observations on $C_{12}E_6$. Therefore terminal alkoxide residues cannot compete with OH^- in reacting with pNPDPP, although in other situations alkoxide ions are effective dephosphorylating agents (19, 20, 36, 37).

Reactions of pNPDPP with anionic nucleophiles are inhibited by initial addition of organic solvents to water (38), due to a decrease in the activity coefficient of the substrate, although rate constants increase in the drier solvents due to decreased anion solvation (39). Therefore the inhibitions by nonionic micelles could be merely kinetic medium effects. We cannot exclude this possibility, but polyethylene glycol (PEG, MW 10^4) does not strongly inhibit the reaction of F^- with *p*-nitrophenyl diphenyl phosphinate,[2] and based on this surrogate for the micellar palisade layer, we conclude that the micellar inhibition of reactions of pNPDPP is due largely to depletion of OH^- and F^- in the palisade layer relative to water. This explanation is consistent with the kinetic salt effects (Table 2).

There is no simple and rigorous way of comparing ionic concentrations in aqueous and micellar pseudophases (9).

[2] H.J. Foroudian. Unpublished results.

© 1998 NRC Canada

Fig. 1. Time dependence of the absorbance spectrum of the reaction mixture of DNCB in $C_{12}E_{10}$: 0.08, 0.45, 1.00, 4.25, 19.8, 92.5, and 141 h in order of increasing absorbance at $\lambda > 340$ nm. For conditions see text and Table 5.

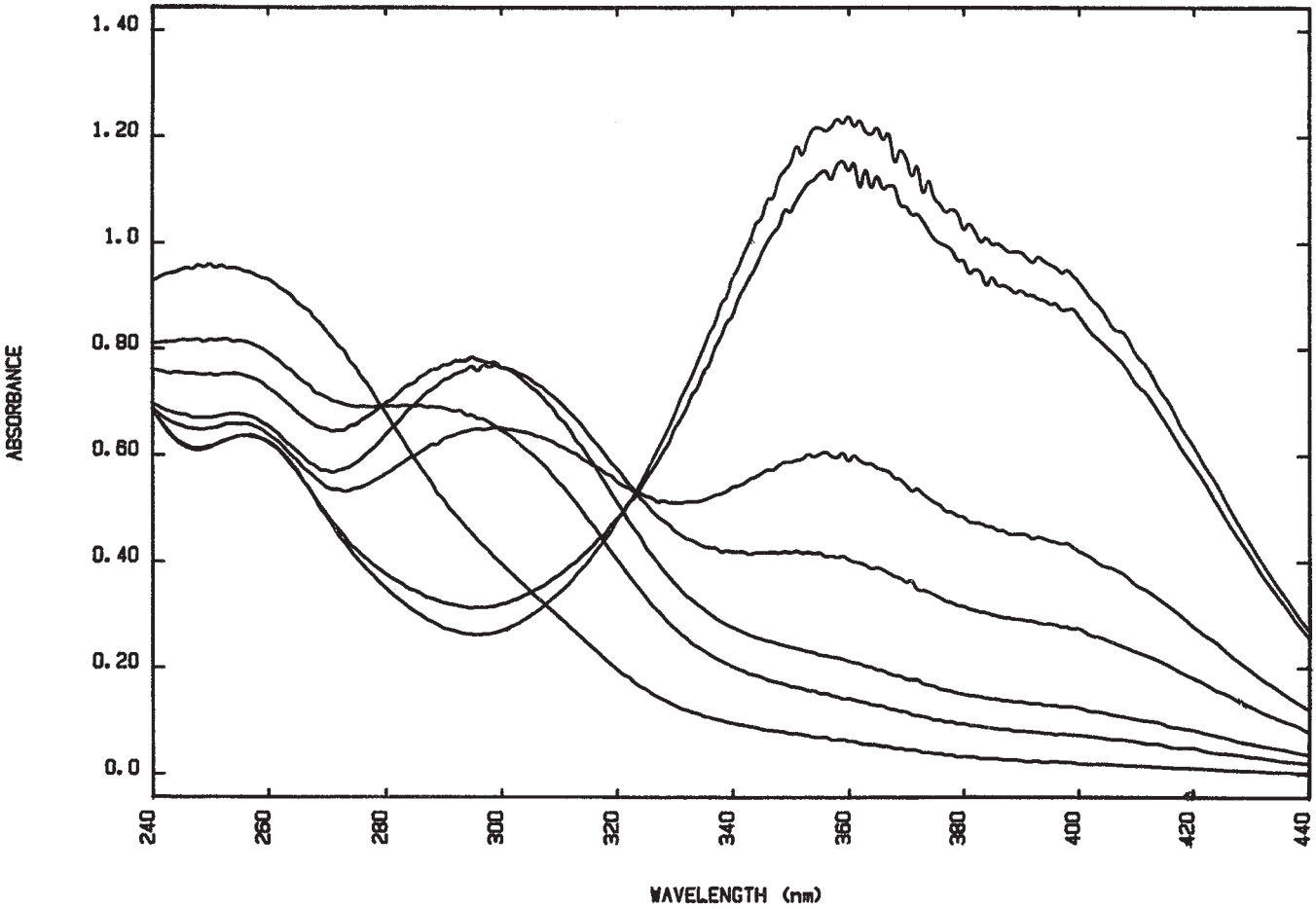

Concentrations in ionic micelles can be written in terms of the relative numbers of head groups and counterions in the interfacial region, but this measure of concentration is not readily comparable with concentration in a bulk solvent, written as molarity. There are various approaches for estimating local ionic molarities in the interfacial regions of association colloids (9), but they all depend on unverified assumptions. However, dediazonization is an experimental method for determining local molarities (40), and these values are similar to some values estimated theoretically for anions in cationic micelles (41). So far as we know, this method has not been applied to anionic nucleophiles in nonionic micelles. The volume of the palisade layer can be estimated from simple geometry for a spherical micelle, and if we assume a hydration number of three for each ethylene oxide residue (14–16) and the usual densities of water and alcohols or ethers, water will occupy approximately half the volume of the palisade layer.

Micellar reactivity and substrate location

Most kinetic work with aqueous association colloids has involved ionic surfactants, and it is generally accepted that both counterions and polar nonionic substrates bind largely in the interfacial region that encompasses the head groups (9, 12). This region is often identified with the micellar Stern layer. Most, but not all, quantitative treatments of rate effects involve the assumption that reactant composition is uniform in this region, although the dimensions of many substrates are greater than the thickness of this interfacial region, which is taken to be 2–5 Å. Despite the weaknesses of these assumptions the quantitative treatments indicate that for many bimolecular reactions second-order rate constants are similar in water and the association colloids (8, 9, 33). Minor failures of this generalization are understandable on the assumption that the concept of uniform location is merely a crude first approximation, and the few major deviations are understandable in terms of the dependence of kinetic medium effects on reaction mechanism (42).

These simplifying assumptions regarding reactant location are expected to be less useful for reactions in nonionic micelles where the interfacial region is the palisade layer, and its volume is usually very much larger than those of the Stern layers in ionic micelles. Nonetheless, local second-order rate constants of dephosphorylation of pNPDPP and tris(*p*-nitrophenyl) phosphate by amphiphilic metal complexes in nonionic micelles of $C_{12}E_{23}$(3) and Triton X-100 (6) are similar to those of monomeric complexes in water, on the assumption that the molar volume of the reaction region is somewhat larger than those of ionic micelles, viz. 0.5 M^{-1}.[3] However,

[3] We are indebted to Prof. P. Scrimin for his insight into this question of the source of rate enhancements by amphiphilic metal complexes in nonionic micelles.

© 1998 NRC Canada

these conclusions apply to reactions of relatively hydrophobic substrates with amphiphilic nucleophiles, which probably occur deeply in the palisade layer, close to the apolar core and may not apply when one reactant is hydrophobic and the other hydrophilic.

A referee made the interesting comment that transition-state geometries are different for aromatic nucleophilic substitution and dephosphorylation, which may affect the discrimination between reactions of hydroxide and alkoxide ion. However, in cationic and zwitterionic micelles with a functional alkoxide residue its reactions are dominant for both aromatic nucleophilic substitution and dephosphorylation (9, 29, 37).

The concentration of OH^- should be similar at the surface of a nonionic micelle to that in water, because there are no ion–micelle interactions. If we assume that the pK_a of the terminal OH group is 14.8, as for ethane diol (21), the mole fraction of alkoxide ion is 0.024 in 0.15 M OH^-, and the local molarity is $0.024/V_M$, where V_M is the molar volume of the reaction region at the micellar surface (9). We do not know the value of V_M, but values of 0.14–0.37 M^{-1} have been used in fitting rate data (8, 9, 33). The lower value gives the local molarity of alkoxide ion at the micellar surface as ca. 0.17 M, and in view of the higher nucleophilicities of alkoxide ions as compared with OH^- (36, 43) it is understandable that the dominant reaction at the micellar surface involves attack of the alkoxide ion. These estimates of local molarity apply to reactions in H_2O, but should be reasonable approximations to our systems in D_2O.

It appears that nonionic micelles can behave as functional micelles at high pH, provided that the substrate is bound at or near the micellar surface. This behavior will not be seen in reactions of very hydrophilic substrates that occur largely in the aqueous pseudophase, or of very hydrophobic substrates that bind deeply in the micelle.

It is difficult to give other than an approximate concentration of alkoxide ion in the micellar reaction region, because we do not know either the value of V_M or the precise location of DNCB in the micelle. Alkoxide ions compete effectively with OH^- in dephosphorylation and aromatic nucleophilic substitution in cationic micelles and microemulsions (19, 20, 29), because reactions occur in the compact interfacial region at the surface of the association colloid, regardless of substrate hydrophobicity. This simplifying generalization does not apply to nonionic micelles with very large palisade layers, which allow a very hydrophobic substrate, e.g., pNPDPP, to locate deeply in the micelle, while a less hydrophobic substrate, e.g., DNCB, stays closer to the surface. The kinetic significance of these differences in location depends also upon the nucleophile and its ability to reach various regions of the micelle or other association colloid.

Solute location may be concentration dependent if solutes are very hydrophobic; for example, distribution of a hydrophobic, bulky porphyrin between the apolar core and the palisade layer of a Triton micelle is concentration dependent (44).

Conclusions

Reactions of OH^- and F^- with pNPDPP in nonionic micelles occur in a region of the micelle from which nucleophilic ions are partially excluded, but which is not accessible to a terminal alkoxide residue of the surfactant. The initial reaction with F^- generates labile diphenyl phosphorofluoridate, which in the micelles is hydrolyzed with loss of either phenol or F^-. In DMSO with up to 15 vol% D_2O the first-formed fluoridate is converted into the relatively unreactive phenyl phosphorofluoridate ion and difluorophosphate ion by reactions with F^-. These differences in products indicate that the micellar reaction region is not behaving like a mixed solvent of low water content.

Reaction of DNCB with OH^- in $C_{12}E_{10}$ and $C_{12}E_{23}$ gives considerable amounts of the ether formed by attack of alkoxide ion on DNCB. This ether gradually forms 2,4-dinitrophenoxide ion by reaction with OH^-. Consideration of the probable pK_a of the terminal OH group indicates that the local concentration of alkoxide ion at the micellar surface will be higher than that given by deprotonation of a monomeric 1,2-diol monoether at the same stoichiometric $[OH^-]$ in water.

Acknowledgments

Support by the U.S. Army Research Office is gratefully acknowledged.

References

1. Y.-C. Yang, J.A. Baker, and J.R. Ward. Chem. Rev. **92**, 1729 (1992); Y.-C. Yang. Chem. Ind. (London), 334 (1995).
2. N.J. Fina and J.O. Edwards. Int. J. Chem. Kinet. **5**, 1 (1973); G. Hoz and E. Buncel. Isr. J. Chem. **26**, 313 (1985); R.M. Tarkka and E. Buncel. J. Am. Chem. Soc. **117**, 1503 (1995); Y.-C. Yang, F.J. Berg, L.L. Szfraniec, W.T. Beaudry, C.A. Bunton, and A. Kumar. J. Chem. Soc. Perkin Trans. 2, 607 (1997); K.R. Fountain, T.W. Dunkin, and K.D. Patel. J. Org. Chem. **62**, 2738 (1997).
3. S.H. Gellman, R. Petter, and R. Breslow. J. Am. Chem. Soc. **108**, 2388 (1986).
4. F.M. Menger, L.-H. Gan, E. Johnson, and D.H. Durst. J. Am. Chem. Soc. **109**, 2800 (1987).
5. C.A. Bunton, P. Scrimin, and P. Tecilla. J. Chem. Soc. Perkin Trans. 2, 419 (1996).
6. E. Kimura, H. Hashimoto, and T. Koike. J. Am. Chem. Soc. **118**, 10 963 (1996).
7. R.A. Moss, K.W. Alwis, and G.O. Bizzigotti. J. Am. Chem. Soc. **105**, 683 (1983); C.A. Bunton, M.M. Mhala, and J.R. Moffatt. J. Phys. Chem. **93**, 854 (1989).
8. K. Martinek, A.K. Yatsimirski, A.V. Levashov, and I.V. Berezin. *In* Micellization, solubilization and microemulsions. Vol. 2. *Edited by* K.L. Mittal. Plenum, New York. 1977. pp. 489–508.
9. C.A. Bunton and G. Savelli. Adv. Phys. Org. Chem. **22**, 213 (1986); C.A. Bunton, F. Nome, F.H. Quina, and L.S. Romsted. Acc. Chem. Res. **24**, 357 (1991); C.A. Bunton. J. Mol. Fluids, **72**, 231 (1997).
10. J.G. Weers, S.F. Rathman, F.U. Axe, C.A. Crichlow, L.D. Foland, D.R. Scheuing, R.J. Wiersema, and A.G. Zielske. Langmuir, **7**, 854 (1991).
11. G.S. Hartley. Q. Rev. Chem. Soc. **2**, 152 (1948).
12. J.H. Fendler and E.J. Fendler. Catalysis in micellar and macromolecular systems. Academic Press, New York. 1975; J.H. Fendler. Membrane mimetic chemistry. Wiley Interscience, New York. 1982.
13. P.H. Elworthy, A.T. Florence, and C.B. Macfarlane. Solubilization by surface-active agents. Chapman and Hall, London. 1968. Chap. 1.
14. M. Jonstomer, B. Jonsson, and B. Lindman. J. Phys. Chem. **95**, 3293 (1991).
15. G.D.J. Phillies and J.E. Yambert. Langmuir, **12**, 3431 (1996).

© 1998 NRC Canada

16. L.S. Romsted and J. Yao. Langmuir, **12**, 2425 (1996).
17. C.A. Bunton and L. Robinson. J. Org. Chem. **34**, 773 (1969).
18. F.H. Quina, M.J. Politi, I.M. Cuccovia, S.M. Martins-Franchetti, and H. Chaimovich. *In* Solution behavior of surfactants. Vol. 2. *Edited by* K.L. Mittal and E.J. Fendler. Plenum Press, New York. 1982. pp. 1125–1136; C.A. Bunton, M.M. Mhala, and J.R. Moffatt. J. Phys. Chem **93**, 7851 (1989).
19. C.A. Bunton, F. De Buzzaccarini, and F.H. Hamed. J. Org. Chem. **48**, 2461 (1983); V. Athanassakis, C.A. Bunton, and F. De Buzzaccarini. J. Phys. Chem. **86**, 5002 (1982); C.A. Bunton, L.-H. Gan, F.H. Hamed, and J.R. Moffatt. J. Phys. Chem. **87**, 336 (1983).
20. B.L. Knier, H.D. Durst, B.A. Burnside, R.A. Mackay, and F.R. Longo. J. Solution Chem. **17**, 77 (1988).
21. P. Ballinger and F.A. Long. J. Am. Chem. Soc. **82**, 795 (1960).
22. C.A. Bunton and L. Robinson. J. Am. Chem. Soc. **90**, 5972 (1968).
23. F.H. Quina, E.O. Alonso, and J.P.S. Farah. J. Phys. Chem. **99**, 11708 (1995); M.H. Abraham, H.S. Chadha, J.P. Dixon, C. Fafols, and C. Treiner. J. Chem. Soc. Perkin Trans. 2, 887 (1995): J. Chem. Soc. Perkin Trans. 2, 19 (1997).
24. F. Mukerjee and K.J. Mysels. Critical micelle concentrations of aqueous surfactant systems. Natl. Bur. Standards, Govt. Printing Office, Washington, D.C. 1970.
25. G.S. Reddy and R. Schmutzler. Z. Naturforsch. B: Anorg. Chem. Org. Chem. **25B**, 1199 (1970).
26. A.J. Parker. Chem. Rev. **69**, 1 (1969); T.H. Lowry and K.S. Richardson. Mechanism and theory in organic chemistry. 3rd ed. Harper and Row, New York. 1987. Chap. 4.
27. S. DiSabato and W.P. Jencks. J. Am. Chem. Soc. **83**, 4400 (1961); A.J. Kirby and A.G. Varvoglis. J. Chem. Soc. B, 135 (1968).
28. R. Ratz and O.J. Sweeting. J. Org. Chem. **28**, 1612 (1963); J.A. Cox and O.B. Ramsay. Chem. Rev. **64**, 317 (1964).
29. C.A. Bunton and S. Diaz. J. Am. Chem. Soc. **98**, 556 (1976).
30. J.F. Bunnett. Q. Rev. Chem. Soc. **12**, 1 (1958); J. Miller. Aromatic nucleophilic substitution. Elsevier, New York. 1968. Chap. 5.
31. R. Bacaloglu, A. Blasko, C.A. Bunton, E. Dorwin, F. Ortega, and C. Zucco. J. Am. Chem. Soc. **113**, 238 (1991).
32. R.F. Hudson. Structure and mechanism in organo-phosphorus chemistry. Academic Press, New York. 1965. Chap. 4.
33. L.S. Romsted. *In* Surfactants in solution. Vol. 2. *Edited by* K.L. Mittal and B. Lindman. Plenum Press, New York. 1984. pp. 1015–1068.
34. J.D. Morgan, D.H. Napper, and G.G. Warr. J. Phys. Chem. **99**, 9458 (1995).
35. C.A. Bunton, M.M. Mhala, and J.R. Moffatt. J. Org. Chem. **52**, 3832 (1987).
36. E.J. Dunn, R.V. Moir, E. Buncel, J.G. Purdon, and R.A.B. Bannard. Can. J. Chem. **68**, 1837 (1990).
37. C.A. Bunton, L.-H. Gan, and G. Savelli. J. Phys. Chem. **87**, 5491 (1983).
38. C.A. Bunton, N.D. Gillitt, and A. Kumar. J. Phys. Org. Chem. **9**, 145 (1996); J. Phys. Org. Chem. **10**, 221 (1997).
39. E. Buncel and H. Wilson. Acc. Chem. Res. **12**, 42 (1979).
40. A. Chaudhuri, J.A. Loughlin, L.S. Romsted, and J. Yao. J. Am. Chem. Soc. **115**, 8351 (1993).
41. A. Blasko, C.A. Bunton, G. Cerichelli, and D.C. Mckenzie. J. Phys. Chem. **97**, 11 324 (1993).
42. G. Cerichelli, C. Grande, L. Luchetti, and G. Mancini. J. Org. Chem. **56**, 3025 (1991); A. Blasko, C.A. Bunton, and H.J. Foroudian. J. Colloid Interface Sci. **175**, 122 (1995).
43. J.M. Harris and S.P. McManus. Nucleophilicity, Adv. Chem. Ser. 215. American Chemical Society, Washington, D.C. 1987.
44. D.M. Davies and N.D. Gillitt. J. Chem. Soc. Dalton Trans. 2819 (1977).

© 1998 NRC Canada

Catalysis by topologically anchored metal complexes. Liquid-phase hydroxylation of benzene by H_2O_2 in the presence of zeolite-supported Fe(II) phthalocyanine

Nikolai S. Zefirov and Alexandre N. Zakharov

Abstract: Fe(II) phthalocyanine topologically anchored on NaA zeolite has been prepared. The catalytic activity of zeolite-supported Fe(II) phthalocyanine has been studied in the liquid-phase hydroxylation of benzene by H_2O_2. The main product of the reaction at room temperature is phenol. By refluxing, the reaction proceeds to give the products of subsequent oxidation, i.e., hydroquinone and *p*-benzoquinone, in low yields.

Key words: topologically anchored Fe(II) phthalocyanine, catalysis, oxidation, benzene, phenol.

Résumé : On a preparé le phthalocyanine du Fe(II) ancré topologiquement sur le zeolite du NaA. On a étudié l'activité catalytique du phthalocyanine du Fe(II) supporté sur le zeolite dans l'hydroxylation du benzène par le H_2O_2 dans la phase liquide. Le phénol est le produit principal de la réaction à température ordinaire. La réaction dans les conditions refluées conduit à des produits consécutives de l'oxydation, i.e., l'hydroquinone et le *p*-benzoquinone, avec un rendement négligeable.

Mots clés : phthalocyanine du Fe(II) ancré topologiquement, catalyse, oxydation, benzène, phénol.

Introduction

The metal complexes of phthalocyanine are known to be active catalysts for a number of reactions. These compounds, however, are practically insoluble in most organic solvents, which restricts their application in homogeneous processes. Earlier (1–5), the synthesis of metal phthalocyanines in zeolites to produce supported heterogeneous catalysts was reported. Elsewhere (6) was suggested an alternative way of supporting these complexes via their incorporation into a system of crystallizing zeolite to get higher dispersion throughout the bulk of the porous material. However, the "inner" catalyst molecules hidden deep in a grain of crystallite were found (7, 8) to be inaccessible to the substrates as a result of a sieve effect and thus are excluded from the catalytic process even for small molecules such as CO, NO, NH_3, etc. Because of the above considerations these systems cannot be accepted as really advanced systems for catalysis, especially for sterically hindered organic substrates and products.

The external-surface catalyst molecules are species that really operate in heterogeneous processes. We have suggested withdrawing the metal complexes from the zeolite crystal structure without, however, losing any topologic linkage with the zeolite matrix (9). While that idea was first illustrated for metalloorganic compounds, the topologic bond with the support can also be realized for a number of organic molecules.

This work presents the results obtained by supporting Fe(II) phthalocyanine on the NaA zeolite via topologic anchoring of a backside fragment of the ligand, and the studies of the catalytic properties of the samples obtained in the liquid-phase hydroxylation of benzene by H_2O_2.

Experimental

The kinetics of the oxidation of benzene in the presence of Fe(II) phthalocyanine topologically anchored on NaA zeolite ($FePc^*$/NaA) were studied under liquid-phase conditions in the temperature range 20–80°C. In a typical experiment, a glass reactor was loaded with benzene, a sample of $FePc^*$/NaA containing 0.25 mg of iron per 1 g of calcined NaA, and an aqueous solution of 50% H_2O_2. Stirring of the mixture was carried out intensively with a magnetic stirring rod to provide the kinetic conditions. The oxidation of benzene by H_2O_2 proceeds neither in the absence of Fe(II) phthalocyanine derivative topologically anchored on the NaA zeolite nor in the presence of the calcined NaA at operating temperatures.

The reaction kinetics were monitored spectrophotometrically with a Specord UV–VIS spectrometer and verified chromatographically on a Chrom-5 instrument (Separon, 1.5 m × 3 mm). All solutions were prepared using reagent grade materials.

The NaA zeolite was dehydrated by calcination in air at 500°C for 5 h. The sample of $FePc^*$/NaA was prepared according to ref. 9, from (1-acetyl)phthalocyanine of Fe(II), zeolite containing diethyl ketone, and hexamethylene diamine, by refluxing in benzene under anaerobic conditions. The colored solid was extracted by warm benzene and characterized by

Received December 10, 1997.

This paper is dedicated to Professor Erwin Buncel in recognition of his contributions to Canadian chemistry.

N.S. Zefirov[1] and A.N. Zakharov. Department of Chemistry, Moscow State University, 119899 Moscow, Russia.

[1] Author to whom correspondence may be addressed. Telephone: (095) 939–1620. Fax: (095) 939–0290. E-mail: zefirov@synth.chem.msu.su

© 1998 NRC Canada

Fig. 1. Scheme of the anchoring of the metal complex **M** in supercage **B** of the NaA zeolite via the side fragment **A**. **C** is the entrance into the zeolite supercage.

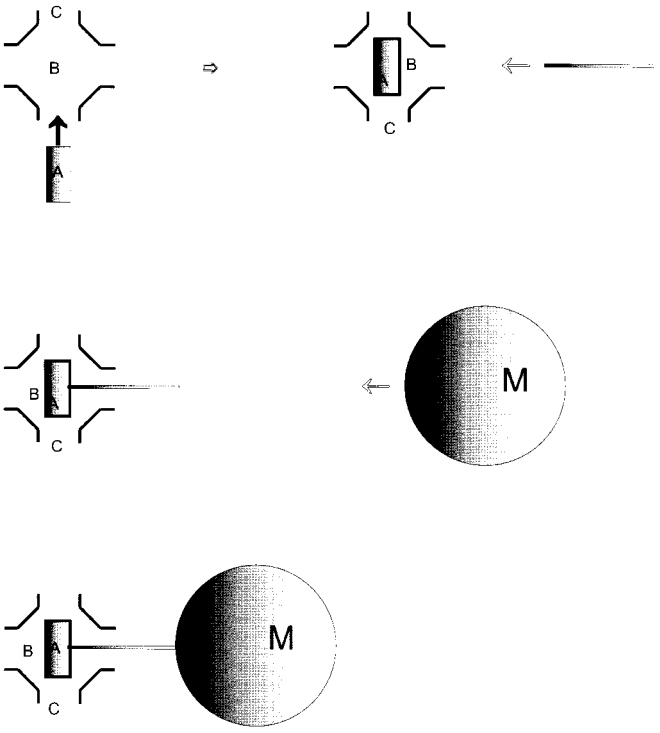

diffuse reflectance spectra, SEM technique, IR spectroscopy, and elemental analysis.

Results and discussion

The **zeolite-encapsulated** metal phthalocyanines are localized in supercages of the solid, which results in an increase in diffusion resistance for any substance penetrating the crystalline framework. Thus it is reasonable to expect a decrease in the adsorption capacity of the samples containing the guest molecules (3, 7, 8). The rate of the reaction in the presence of the intracrystalline metal complexes was found to be proportional to the covering only at low concentration of the catalyst (7, 8). There is a critical concentration of the zeolite-encapsulated metal complexes at which the "inner" active centers become inaccessible to the substrates. The values of the critical concentration for a stochastic distribution of the catalyst molecules usually depends on a number of factors, the main one being the size of reactants. The rate of the reaction is shown to become independent of the metal complex concentration at higher coverings. The absence of the concentration dependence of the reaction rate suggests that some of the active centers seem to be screened by the crystal framework of the support and so to be excluded from the catalytic process. **Thus, in the case of the zeolite-encapsulated metal complexes, the increase in covering does not result in an adequate enhancement of the corresponding rate of the reaction**. In fact, increasing the metal complex concentration in the zeolite further worsens the diffusion conditions, which makes this factor ineffective especially for reactions of organic molecules.

On the other hand, the above considerations show that the active molecules on the **external surface** are the only ones that work as operating catalysts. Taking this into account, we recently developed (9) a means of supporting metal complexes on porous materials. The main thrust of the new approach consists in the application of the zeolite or other porous material as a support only for that part of the molecular complex which is located far away from the center of the catalysis. This part may be a side fragment of the ligand that does not affect dramatically the donor–acceptor properties of the coordinated atoms.

The side fragment of the ligand is connected by some available means with an "anchor," a molecule topologically entrapped by the zeolite. The scheme of the anchoring is depicted in Fig. 1.

The anchor fragment **A** may either be synthesized inside a large cavity of the zeolite according to the usual scheme for topologically encapsulated metal complexes or remain as the starting molecule having lost one degree of the freedom for movement within the supercage of the zeolite. In this work, we suceeded in anchoring the Fe(II) phthalocyanine derivative by means of diethyl ketone, the carbon-chain precursor that played the role of anchor fragment **A**. Although the effective diameter of the entrance into the supercage of the zeolite crystal lattice is somewhat greater than the linear size of this compound, it is the asymmetric shape of diethyl ketone that permits it to penetrate the large cavities of the NaA zeolite. Thus, the anchoring is possible if a starting material is a linear compound and bears a function group in the middle of the chain. Diethyl ketone is shown to satisfy all of these requirements.

The above scheme demonstrates the anchoring via a linear molecule **A** as precursor. Normally, the linear compound is reversibly adsorbed in the large cavity of the NaA zeolite. This means that desorption occurs in the same manner, i.e., the precursor can abandon the supercage along the axis of the chain, while, on the contrary, the removal of the adsorbate in the direction perpendicular to the axis of the chain is impossible. So if the molecule possesses only one possibility for removal from the supercage of the NaA zeolite it becomes sterically retained. It is this mode of retention that we applied to the supporting of the Fe(II) complex of (1-acetyl)phthalocyanine on the NaA zeolite. The resulting sample, $FePc^{*}$/NaA, containing a zeolite-supported complex of Fe(II) is shown in Scheme 1.

The treatment of the sample $FePc^{*}$/NaA (Scheme 1) containing the Fe(II) phthalocyanine derivative topologically anchored via a diethyl ketone fragment with organic solvents results in no extraction of the metal complexes. Thus, the retention of the catalyst on the support indicates that there are certain restrictions for the motion of the anchor inside the large cavity of the NaA zeolite. Such behavior of the supported catalyst confirms the conclusion that the Fe(II) phthalocyanine derivative is linked to the anchor fragment, which in turn, after formation of the bond with the ligand, becomes sterically hindered.

Characterization of the sample

The effective diameter of the starting complex of Fe(II) is greater than the size required for entering the supercage of the

© 1998 NRC Canada

Scheme 1.

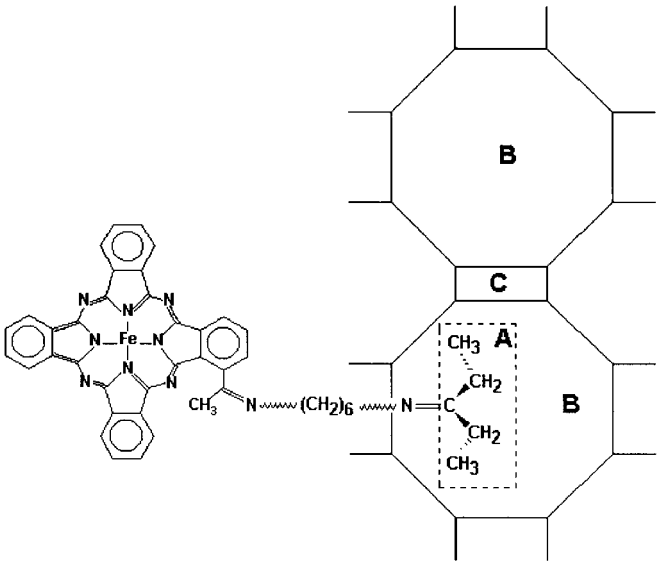

NaA zeolite so that it cannot penetrate the crystal structure. On the other hand, the anchor fragment also is shown to be sterically entrapped by the supercage of the NaA zeolite as it could not be dragged out of the framework by the same route followed on adsorption, i.e., along the main axis of the carbon chain. The sample of FePc*/NaA obtained did not lose the metal complex by multiple extraction with DMF, which is known to dissolve metal phthalocyanines. At the same time, the diffuse reflectance spectrum of FePc*/NaA revealed a band at 660–780 nm (Fig. 2), which is consistent with the data obtained for the initial complex and for Fe(II) phthalocyanine supported on the zeolite (2, 5). This result provides evidence that the introduction of the anchor fragment into the backside of the phthalocyanine ligand does not appreciably disturb the electron configuration of the compound.

IR spectroscopy is known to provide no information on the samples of Fe(II) phthalocyanine embedded in the zeolite except for the regions of 1500–1300 and 800–700 cm^{-1} (10). In these regions the zeolite absorption is practically absent; however, bands appear at 1290, 1340, 1390, 1420, 1460, 1500, and 732 cm^{-1} (10) that are characteristic of stretching and deformation vibrations in the phthalocyanine ligand. Opposite to the absorption of the zeolite, the sample FePc*/NaA exhibits an asymmetric doublet at 700–800 cm^{-1} consistent with the intensive band at 740–730 cm^{-1} assigned to the stretching vibrations of benzopyrrole CH fragments of the ligand. As we found previously for the zeolite-encapsulated Fe(II) phthalocyanine (10), most of these bands also appear in the IR spectrum of the FePc*/NaA sample.

According to the SEM data obtained for FePc*/NaA, the sample contains 0.24 mg of Fe per 1 g of NaA, which is consistent with an elemental analysis within 3–5%. This result indicates that the metal complexes are quantitatively deposited on the external surface of the zeolite crystals.

Fig. 2. Diffuse reflectance spectra for FePc*/NaA (1) and the mixture of the initial complex and zeolite (2).

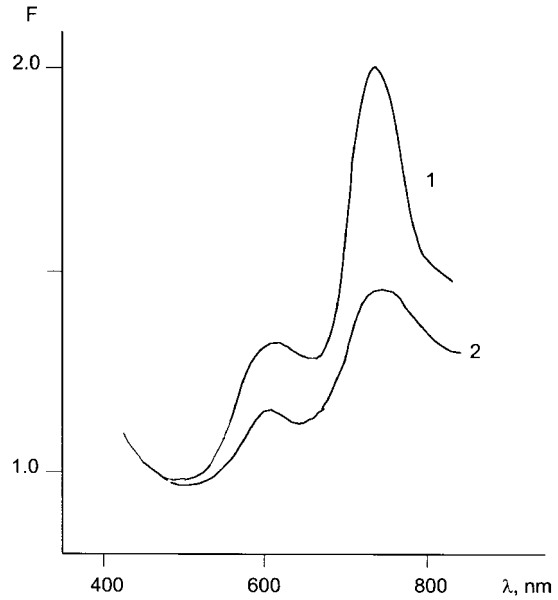

Catalytic properties of FePc*/NaA

No reaction between benzene and H_2O_2 occurs in the absence of topologically anchored Fe(II) (1-acetyl)phthalocyanine. As mentioned, free Fe(II) phthalocyanine is of low solubility in benzene (less than 10^{-7}–10^{-8} mol/L), which makes its use in homogeneous processes impractical. The acylated derivative, Fe(II) (1-acetyl)phthalocyanine, also is practically insoluble in benzene and exhibits no catalytic activity on being suspended in the benzene – 50% H_2O_2 heterogeneous mixture either at room temperature or upon refluxing. On the contrary, the topologically anchored FePc* complex shows remarkable catalytic activity in reaction [1].

[1] 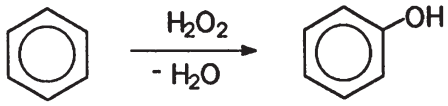

The hydroxylation of benzene by H_2O_2 in the presence of FePc*/NaA occurred even at room temperature. Under these conditions, the substrate gave quantitatively the only product of the reaction, which is phenol. As the process at 20°C was sluggish, it needed some days for the reaction to be complete. At small conversions, the initial rate of the hydroxylation of benzene was constant with time. A plot of the concentration of phenol vs. time is shown in Fig. 3.

The rate of the hydroxylation of benzene by H_2O_2 proved to be dependent on the amount of the sample of the catalyst used. As the mass of the sample was proportional to the concentration of the active molecules within a statistical deviation, the above-mentioned dependence reflects the influence of the Fe(II) (1-acetyl)phthalocyanine derivative on the observed rate of the reaction. A similar result was obtained with respect to the proportionality between the observed rate of the hydroxylation of benzene and the amount of H_2O_2. These data are presented in Fig. 4.

Thus, according to these facts, the observed rate of the reaction, r_{obs}, is as follows:

© 1998 NRC Canada

Fig. 3. A plot of phenol concentration vs. time for the hydroxylation of benzene by H_2O_2 (mole ratio is 100:1) at 20°C in the presence of FePc*/NaA: 0.45 (1), 0.80 (2), and 1.0 (3) g.

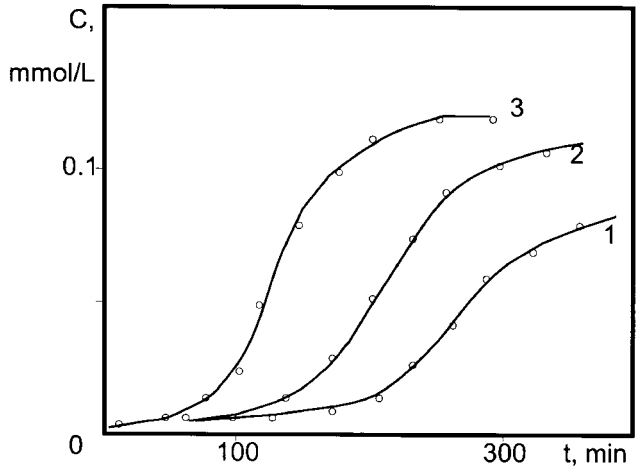

Fig. 4. A plot of phenol concentration vs. time for the hydroxylation of benzene at 20°C in the presence of 0.5 g of FePc*/NaA and varying amounts of H_2O_2: 0.6 (1), 1.1 (2), and 1.8 (3) mmol/L. The arrows indicate when the additional amount of H_2O_2 was introduced into the system.

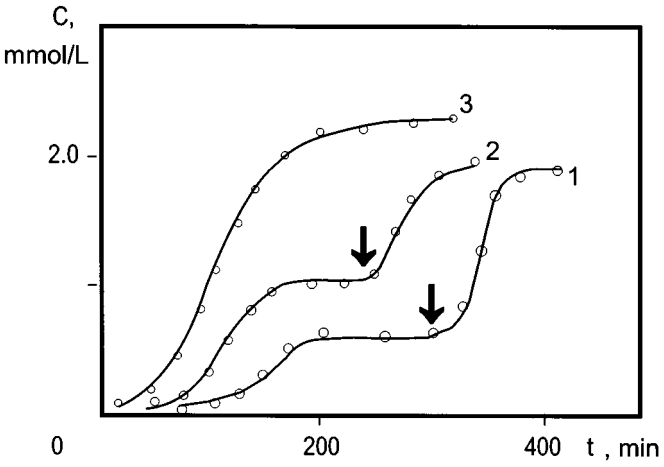

[2] $r_{obs} = k_{eff}[H_2O_2][Cat]$

where k_{eff} is the effective rate constant, and $[H_2O_2]$, and [Cat] are the current concentration of hydroperoxide and the total concentration of the catalyst, respectively.

In fact, eq. [2] also remains operative at elevated temperatures. However, during reflux of the heterogeneous mixture, the side processes become noticeable. It was found that the excess of H_2O_2 on refluxing of benzene in the presence of the topologically supported phthalocyanine derivative of Fe(II) gives the products of further hydroxylation and oxidation of the phenol formed. Semi-quinone and *p*-benzoquinone were detected chromatographically. The former obviously appears as a by-product of the interaction of hydroquinone and *p*-benzoquinone (Scheme 2, reaction [5]), which in turn are formed by the side reactions [3] and [4], respectively.

Scheme 2.

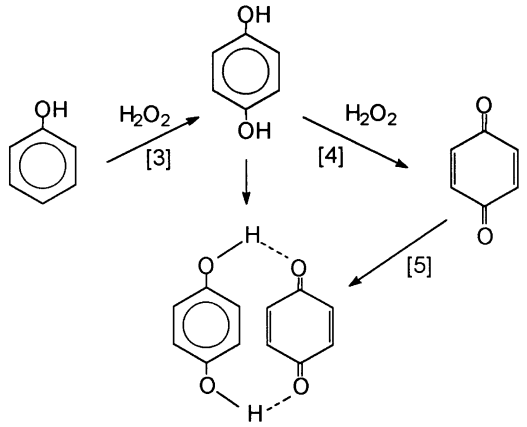

However, it should be noted that semi-quinone and *p*-benzoquinone are also formed on reflux with low yields (no more than 2 and 5%, respectively).

The variation in effective rate constants with temperature between 20 and 80°C calculated according to eq. [2] is presented graphically in Fig. 5. The effective activation energy for the formation of phenol determined from these data using the Arrhenius equation is 12.6 (0.5) kJ/mol, a value that is too small for molecular or ionic reactions.

Also, the reaction stops when a certain amount of radical traps (e.g., $HNPh_2$ and others) is introduced into the system This result is consistent with a radical chain mechanism, which is typical of oxidation by H_2O_2 in the presence of Fe(II) complexes of chelating ligands and phthalocyanine.

Thus, according to refs. 11 and 12, the proposed mechanism for the hydroxylation of benzene by H_2O_2 in the presence of topologically anchored Fe(II) (1-acetyl)phthalocyanine may be as follows:

$$FePc + H_2O_2 = (HO)FePc + HO^{\bullet}$$

$$(HO)FePc + C_6H_6 = FePc + C_6H_5^{\bullet} + H_2O$$

$$HO^{\bullet} + C_6H_6 = H_2O + C_6H_5^{\bullet}$$

$$(HO)FePc + C_6H_5^{\bullet} = FePc + C_6H_5OH$$

$$H_2O_2 + C_6H_5^{\bullet} = C_6H_5OH + HO^{\bullet}$$

$$HO^{\bullet} + C_6H_5^{\bullet} = C_6H_5OH$$

$$HO^{\bullet} + HO^{\bullet} = H_2O_2$$

Therefore the homolytic cleavage of H_2O_2 within the coordination sphere of Fe(II) is considered to produce free radicals, giving rise to a chain process in the liquid phase.

Conclusions

The topologic anchoring of the Fe(II) phthalocyanine derivative on the NaA zeolite provides for a more effective application of chelate–metal complexes to heterogeneous catalysis. The topologically anchored metal complexes differ from zeolite-encapsulated chelates, which are known to become nonoperative as catalysts for sterically hindered substrates.

There have also been some difficulties for the intracrystalline synthesis of metal complexes using ligands or precursors unable to penetrate the cavities of the solids. In that sense,

© 1998 NRC Canada

Fig. 5. A plot of ln k_{eff} against $1/T$ for the hydroxylation of benzene by H_2O_2 in the presence of zeolite-anchored FePc*/NaA.

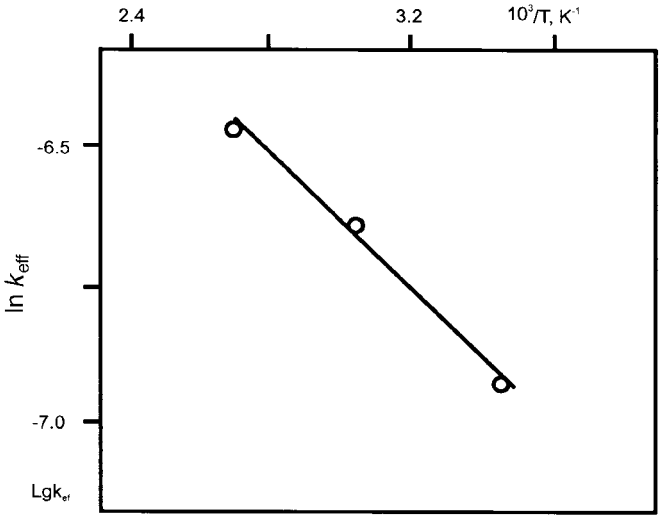

the topologic anchoring by the side fragment of the ligand is shown to be applicable to the supporting of coordination compounds of any dimension and shape.

The high affinity of the NaA zeolite for water obviously results in an increase in the efficiency of the anchoring. Indeed, the water, after the process of anchoring (9), fills up the free space of the large cavities. This additionally hinders the moving of the anchor in the supercage of the zeolite and makes negligible any extraction of the entrapped fragment of the ligand by the liquid reaction medium.

Thus, the example of the liquid-phase hydroxylation of benzene by H_2O_2 in the presence of the topologically anchored derivative of Fe(II) (1-acetyl)phthalocyanine shows higher catalytic efficiency of the samples obtained in comparison with the patterns containing the intracrystalline complexes. This confirms that, in any case, it is unreasonable to attempt to obtain more effective molecular dispersion of the catalytically active species throughout the bulk of the support.

References

1. V.Yu. Zakharov and B.V. Romanovskii. Vestn. Mosk. Univ. Ser. 2. Khim. **20**, 78 (1979).
2. T.V. Korolkova, A.N. Zakharov, and B.V. Romanovskii. Vestn. Mosk. Univ. Ser. 2. Khim. **25**, 362 (1984).
3. G. Meyer, D. Wöhrle, M. Mohl, and G. Schulz-Ekloff. Zeolites, **4**, 30 (1984).
4. A.N. Zakharov and B.V. Romanovskii. J. Inclusion Phenom. **3**, 389 (1985).
5. A.N. Zakharov, T.V. Korolkova, and B.V. Romanovskii. Koord. Khim. **12**, 94 (1986).
6. K.J. Balkus, A.G. Gabrielov, S.L. Bell, T. Bedioui, L. Roue, and J. Devynck. Inorg. Chem. **31**, 67 (1994).
7. A.N. Zakharov, D. Louca, B.V. Romanovskii, and V.I. Sokolov. Metalloorg. Soedin. **1**, 119 (1998).
8. A.N. Zakharov. Kinet. Katal. **32**, 1377 (1991).
9. A.N. Zakharov and N.S. Zefirov. Dokl. Ross. Akad. Nauk Ser. Khim. **357**, 60 (1997).
10. A.N. Zakharov, L.N. Burenkova, and V.A. Voblikova. Zh. Prikl. Khim. (S. Peterburg), **65**, 2211 (1992).
11. F. Haber and J. Weiss. Naturwissenschaften, **20**, 948 (1932).
12. R.A. Sheldon and J.K. Kochi. Adv. Catal. **25**, 272 (1976).

© 1998 NRC Canada

Kinetic effects induced by cellulose on water-catalyzed reactions. Hydrolysis of 2,4-dinitrophenyl cellulose xanthate and some sugar xanthate ester analogues

Eduardo Humeres, Luiz Fernando Sequinel, Mauricéa Nunes, Célia M.S. Oliveira, and Patrick J. Barrie

Abstract: The hydrolysis of 2,4-dinitrophenyl cellulose xanthate (CelXDNP) was studied in 10% v/v aqueous ethanol at 25°C and $\mu = 0.1$ (KCl). The water-catalyzed hydrolysis showed that, as for *p*-nitrobenzyl cellulose xanthate, it occurs through two parallel reactions with rate constants $k'_{H2O} = 4.40 \times 10^{-3}$ s^{-1} for the fast hydrolysis, and $k''_{H2O} = 6.90 \times 10^{-5}$ s^{-1} for the slow hydrolysis. The entropy of activation of the fast hydrolysis was 0.7 ± 1.8 cal K^{-1} mol^{-1}. External nucleophiles such as hydroxide and simple amines show simple first-order kinetics. The spontaneous hydrolysis of CelXDNP in acetone–water mixtures indicates that the fast reaction does not occur through water polymers and that for water molarity higher than 30 M there are no acetone molecules (or very few) in the highly ordered cybotactic region of cellulose. The spontaneous hydrolysis of methyl 4,6-*O*-benzylidene-α-D-glucopyranoside 3-(*S*-*p*-nitrobenzyl-xanthate) although is faster than the 6-isomer, it is slower than the fast hydrolysis of *p*-nitrobenzyl cellulose xanthate (CelXNB). Also $\Delta S^{\neq}$ is highly negative (–41.0 cal K^{-1} mol^{-1}), as it is for alkyl and sugar analogues. Only for the fast hydrolyses of CelXDNP and CelXNB is the entropy of activation almost zero. It is concluded that there is no neighbouring OH effect on the fast hydrolysis of cellulose xanthate esters.

Key words: hydrolysis, water catalysis, cellulose xanthate esters, methyl glucose, xanthate esters, neighbouring OH effect.

Résumé : On a étudié l'hydrolyse du xanthate de 2,4-dinitrophénylcellulose (CelXDNP) en opérant à 25°C, en solutions aqueuses d'éthanol à 10% v/v et à $\mu = 0,1$ (KCl). L'hydrolyse catalysée par l'eau montre que, comme dans le cas du xanthate de *p*-nitrobenzylcellulose, celle-ci se produit par le biais de deux réactions parallèles avec des constantes de vitesse de $k'_{H2O} = 4,40 \times 10^{-3}$ s^{-1} pour l'hydrolyse rapide et de $k''_{H2O} = 6,90 \times 10^{-5}$ s^{-1} pour l'hydrolyse lente. L'entropie d'activation de l'hydrolyse rapide est égale à $0,7 \pm 1,8$ cal K^{-1} M^{-1}. Les nucléophiles externes, tels l'hydroxyde et les amines simples, réagissent avec une cinétique du premier ordre simple. L'hydrolyse spontanée du CelXDNP dans des mélanges eau–acétone indique que la réaction rapide ne se produit pas avec des polymères-eau et que, à des molarités d'eau supérieures à 30 M, il n'y a pas (ou très peu) de molécules d'acétone dans la région cybotactique bien organisée de la cellulose. L'hydrolyse spontanée du 3-(*S*-*p*-nitrobenzylxanthate) de 4,6-*O*-benzylidène-α-D-glucopyranoside de méthyle, même si elle est plus rapide que celle de son isomère en position 6, est plus lente que l'hydrolyse rapide du xanthate de la *p*-nitrobenzylcellulose (CelXNB). Les $\Delta S^{\neq}$ est très négatif (–41,0 cal K^{-1} mol^{-1}), comme c'est le cas avec les analogues alkylés ou avec les sucres. Ce n'est que dans le cas des hydrolyses rapides des CelXDNP et CelXNB que l'entropie d'activation est pratiquement égale à zéro. On en conclut qu'il n'y a pas d'effet avoisinant de OH sur l'hydrolyse rapide des esters xanthiques de la cellulose.

Mots clés : hydrolyse, catalyse par l'eau, esters xanthiques de la cellulose, esters xanthiques de glucosides de méthyle, effet avoisinant de OH.

[Traduit par la rédaction]

Received December 9, 1997.

This paper is dedicated to Professor Erwin Buncel in recognition of his important contribution to physical organic chemistry.

E. Humeres,[1] L.F. Sequinel, M. Nunes, and C.M.S. Oliveira. Departamento de Química, Universidade Federal de Santa Catarina, Florianópolis, SC 88040-900, Brazil.
P.J. Barrie. Department of Chemistry, University College London, 20 Gordon Street, London WC1H OAJ, U.K.

[1] Author to whom correspondence may be addressed. Telephone: 55 48 331 9219. Fax: 55 48 331 9711. E-mail: humeres@mbox1.ufsc.br; humeres@qmc.ufsc.br

Introduction

The nonbonding interactions of carbohydrates with water depend on their stereochemistry and have been the subject of numerous studies (1). Kinetic medium effects induced by carbohydrates give some insight into the specificity of the stereochemical interaction with water (2) and are important to the understanding of their role in the sugar–protein recognition involved in carbohydrate transport (3).

The study of the reactivity of a moiety covalently bound to a polysaccharide system showed that the reaction of water was much faster compared to small analogue molecules (4). The water-catalyzed hydrolysis of *p*-nitrobenzyl cellulose xanthate

© 1998 NRC Canada

(CelXNB) occurred through a fast reaction and a slower parallel reaction. The faster hydrolysis was ascribed to the reaction of the C-2 + C-3 isomers and the slower hydrolysis to the C-6 isomer. The acceleration observed in the fast hydrolysis was attributed to an entropic effect due to a well-oriented water molecule, catalyzed by a second water molecule that acts as a general base as shown by proton inventory. However, it was also recognized that instead of a second water molecule, a neighbouring OH was able to act as a general base. External nucleophiles such as hydroxide ions and amines do not discriminate between the isomers and react like small analogue molecules (5).

This paper deals with the hydrolysis of 2,4-dinitrophenyl cellulose xanthate (CelXDNP), a cellulose ester with a good leaving group, in order to characterize the spontaneous reaction in comparison to CelXNB (eq. [1]).

[1] 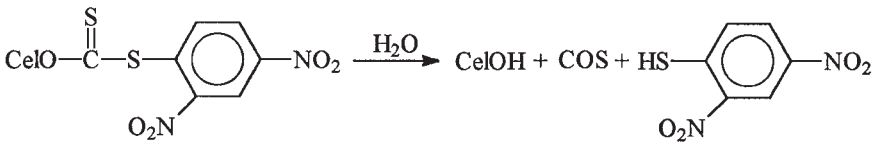

The hydrolysis of the 3- and 2,3-*p*-nitrobenzyl methyl glucose xanthate esters was studied to determine if there was a neighbouring OH group involved in the rate acceleration observed in the spontaneous hydrolysis of CelXNB.

Experimental

All chemicals and solvents were of analytical grade and were used as received, except the amines, which were previously distilled.

The solid-state ^{13}C NMR measurements were obtained using cross polarization (CP), magic angle spinning (MAS), and total sideband suppression (TOSS), and were performed using a Bruker MSL-300 spectrometer. The NMR spectra in solution were obtained with Bruker AC-200, WM-250, and AMX-400 equipment.

2,4-Dinitrophenyl cellulose xanthate (CelXDNP)

Commercial cotton tissue (2.2 g) was washed with 1 M HCl for 1 h and then several times with water. The sample was mechanically shaken in 100 mL of 2 M NaOH for 1 h. Half of the basic solution was taken away, a solution of 30 mL of CS_2 in 20 mL of *p*-dioxane was added, and the suspension was shaken for 2 h. The cellulose xanthate was filtered and treated with 0.1 M phosphate buffered solution at pH 8.0, then washed with dried acetone, and allowed to react with a solution of 3 g of 2,4-dinitro-1-fluorobenzene dissolved in 100 mL of dried acetone for 72 h with mechanical shaking. The cellulose xanthate ester was filtered, washed rapidly with 0.1 M HCl, then with acetone and finally with diethyl ether, and dried under vacuum for 10 h at room temperature over P_2O_5. The degree of substitution (DS, number of xanthate ester groups per 100 glucoanhydropyranose units) was 4.6 determined as described previously (4), measuring the number of moles of 2,4-dinitrothiophenol liberated in the ethylaminolysis, observed at 410 nm, using the extinction coefficient of 1.38×10^4 (6).

The CelXDNP was characterized from the ^{13}C NMR spectra with 12 h acquisition time, 2 ms contact time, 4 s recycle delay between scans, using CP/MAS TOSS (Table 1).

The thiocarbonyl signal of CelXDNP appears at 195 ppm, about 19 ppm at higher field than for the *p*-nitrobenzyl cellulose xanthate (CelXNB) where there is a methylene bridge between the xanthate group and the phenyl ring. All the signals

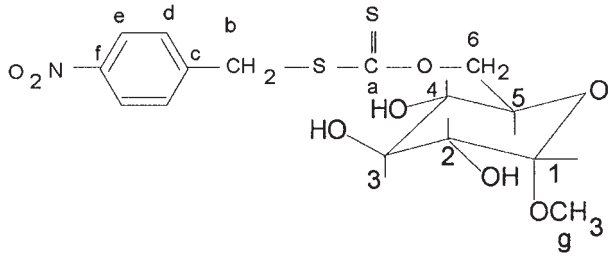

MGX - 6

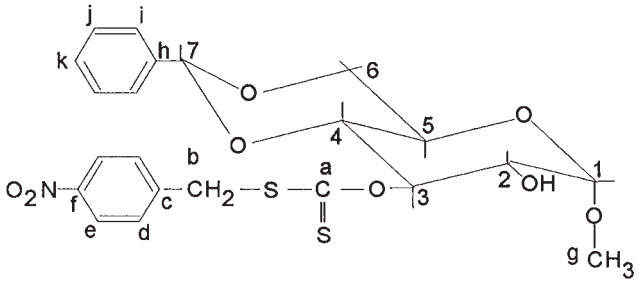

MGX - 3

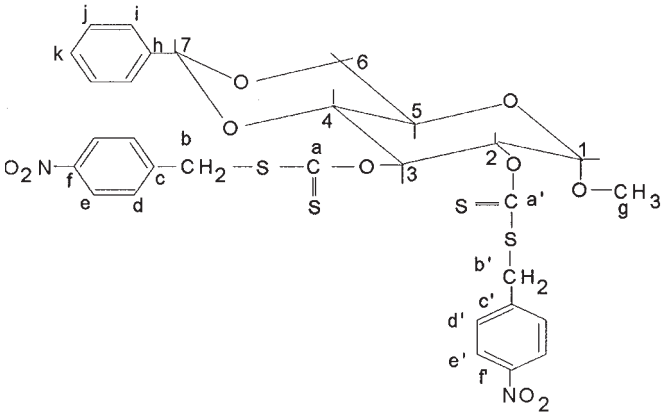

MGX - 2,3

© 1998 NRC Canada

Table 1. ^{13}C chemical shifts of CelXDNP.[a]

Carbon	Chemical shift (ppm)		
	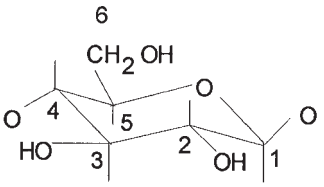		
C-1	104.5[b]	98.1[b]	
C-4	89.2[b]	83.4[c]	
C-2,-3,-5	75.2[b]	73.0[b]	71.8[c]
C-6	65.4[b]	62.7[c]	
	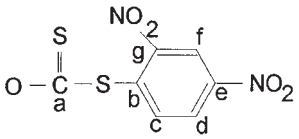		
C-*a*	195.0		
C-*b*	140.6 (140)		
C-*c*	129.0 (128)		
C-*d*	129.0 (130)		
C-*e*	155.7 (146)		
C-*f*	122.4 (119)		
C-*g*	155.7 (147)		

[a] CP/MAS TOSS.

[b] From crystalline components.

[c] From noncrystalline components (refs. 7 and 8). Values in parentheses are calculated (ref. 9).

for the 2,4-dinitrophenyl ring in the 120–150 ppm region agreed with the calculated values (9). Considering the area of the signals due to the 2,4-dinitrophenyl ring with respect to that of C-1, the DS was 5.1, reasonably close to that calculated by ethylaminolysis.

After *n*-butylaminolysis of CelXDNP, the NMR spectrum of *n*-butyl cellulose thioncarbamate showed that the signal at 195 ppm disappeared, producing a signal at 189.6 ppm assigned to the thioncarbamate group [O-C(S)-N] and the calculated signals for the *n*-butyl group at 45.1, 30.6, 20.6, and 14.5 ppm. This spectrum was identical to that obtained from CelXNB after *n*-butylaminolysis.

Methyl-D-glucopyranoside 6-(*S*-*p*-nitrobenzyl xanthate) (MGX-6)

In a solution of 20 g of methyl-α-D-glucopyranoside in 20 mL of water, 4.5 g of sodium hydroxide was slowly added, and when it was completely dissolved, 3.1 mL of carbon disulfide was mixed dropwise with constant stirring for 3 h at room temperature. The mixture was then neutralized with cooled acetic acid. A solution of 11.02 g of *p*-nitrobenzyl bromide in methylene chloride (20 mL) was added slowly while stirring, and the mixture was allowed to react for 2 h. The solution was concentrated under vacuum. The solid product was dissolved in 90% v/v aqueous ethanol and allowed to crystallize. Upon recrystallization in the same solvent, the white crystals were dried under vacuum over phosphorus pentoxide. The product gave positive test of carbohydrate, showing only one spot of TLC on alumina with ethyl acetate (R_f 0.75); mp 70–71°C; λ_{max} 283 nm; $[\alpha]_D^{25}$ +72.3 (*c* 0.41, chloroform). Anal. calcd. for $C_{15}H_{19}NO_8S_2$: C 44.4, N 3.4, H 4.7, S 15.8; found: C 43.1, N 3.4, H 4.8, S 15.5.

Table 2. ^{13}C chemical shifts (ppm) for some sugar xanthate esters.

Carbon	MGX-6[a]		MGX-3[b]	MGX-2,3[b,c]	
1	99.9	(100.0)	100.2	99.9	(99.9)
2	72.4	(72.2)	72.0	77.5	(72.4)
3	74.7	(74.1)	78.9	78.6	(70.5)
4	70.6	(70.6)	81.2	79.2	(80.8)
5	73.5	(72.5)	62.7	62.4	(62.0)
6	69.6	(61.6)	68.9	68.7	(68.5)
7			101.5	101.6	(101.5)
a	213.6		214.3	211.7; 212.7	(200)[d]
b	40.0		39.6	39.2; 39.4	
c	147.7		143.6	143.5; 143.2	(144.4)[e]
d	130.4		129.8	129.6; 129.9	(129.8)[e]
e	124.1		123.8	123.7; 123.8	(125.5)[e]
f	147.7		143.6	147.27; 147.29	(146.8)[e]
g	55.7	(55.9)	55.8	55.4	(54.9)
h			136.8	136.5	(137.7)[e]
i			129.2	129.3	(129.2)[e]
j			128.3	128.3	(128.4)[e]
k			126.1	126.0	(125.5)[e]

[a] In CD_2Cl_2. Values in parentheses for methyl α-D-glucopyranoside (ref. 11).

[b] In $CDCl_3$.

[c] Values in parentheses for methyl 4,6-*O*-benzylidene-α-D-glucopyranoside unless indicated (ref. 10).

[d] For CS_2 in solution.

[e] Calculated values (ref. 9).

^{13}C NMR (Table 2); ^1H NMR (400 MHz, CD_2Cl_2), δ: 8.13 (d, *J* = 6.7 Hz, 2H, C_e-H), 7.54 (d, *J* = 6.7 Hz, 2H, C_d-H), 5.08 (s, 1H, OH), 4.85 (dd, *J* = 11.7, 2.0 Hz, 1H, C_6-H), 4.73 (d, *J* = 3.6 Hz, 1H, C_1-H, dd, *J* = 11.7, 6.0, 1H, C_6-H′), 4.46 (s, 3H, C_b-H2, H_2O?), 4.1 (d, *J* = 7.2, 1H, OH), 3.89 (ddd, *J* = 9.7, 5.8, 1.9, 1H, C_5-H), 3.73 (t, *J* = 9.2, 1H, C_3-H), 3.52 (m, 1H, C_2-H), 3.43 (ddd, *J* = 9.5, 9.5, 7.0, 1H, C_4-H), 3.37 (s, 3H, OMe). Couplings between C_6-H and C_5-H are not equal (2.0 and 6.0 Hz), showing that the side chain is in a preferred conformation.

Methyl 4,6-*O*-benzylidene-α-D-glucopyranoside 3- and 2,3-(*S*-*p*-nitrobenzyl-xanthate) (MGX-3 and MGX-2,3)

Twenty five milliliters of CS_2 and 10 mL of 5 N NaOH were added to a solution of 10 g of methyl 4,6-*O*-benzylidene-α-D-glucopyranoside in 25 mL of *p*-dioxane, and the reaction mixture was stirred for 30 min at room temperature. Then it was neutralized with acetic acid at 5°C. *p*-Nitrobenzyl bromide (7.6 g) was slowly added, and the mixture was stirred for 5 h. The layers were separated, and the organic layer was concentrated under vacuum to a solid that was extracted with diethyl ether. After evaporation, the solid was recrystallized several times with dried 2-propanol, giving white crystals of MGX-3: TLC, alumina, 2-propanol, R_f 0.74; mp 176°C; λ_{max} 283; $[\alpha]_D^{22}$ + 51.9 (*c* 0.03, chloroform). Anal. calcd. for $C_{22}H_{23}NO_2S_2$: C 53.6, H 4.6, N 2.8, S 12.9; found: C 53.3, H 4.6, N 2.9, S 13.0.

IR (KBr): 3448 cm^{-1} (sharp, C_2-OH); ^{13}C NMR (Table 2); ^1H NMR (250 MHz, $CDCl_3$), δ: 8.10 (d, *J* = 7.7 Hz, 2H, C_e-H),

© 1998 NRC Canada

Fig. 1. pH–rate profile of the hydrolysis of CelXDNP at 25°C, in 10% v/v aqueous ethanol, μ = 0.1 (KCl).

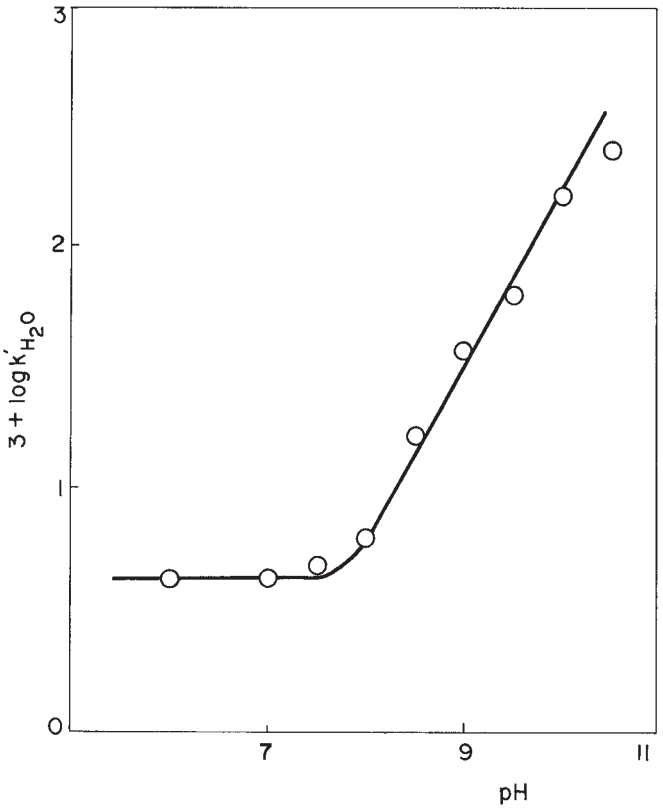

7.48 (d, *J* = 7.7 Hz, 2H, C_d-H), 7.35 (m, 5H, Ar-H), 6.31 (dd, *J* = 9.7, 9.7 Hz, 1H, C_3-H), 5.46 (s, 1H, C_7-H), 4.86 (d, *J* = 3.9, 1H, C_1-H), 4.47 (ab, *J* = 14.6 Hz, 2H, C_b-H), 4.32 (dd, *J* = 10.1, 4.5 Hz, 1H, C_6-H), 3.91 (ddd, *J* = 9.9, 9.9, 4.3 Hz, 1H, C_5-H), 3.85 (ddd, *J* = 11.6, 9.5, 3.7 Hz, 1H, C_2-H), 3.76 (dd, *J* = 10.0, 10.0 Hz, 1H, C_6-H′), 3.70 (dd, *J* = 9.5, 9.5 Hz, 1H, C_4-H), 3.50 (s, 3H, OMe), 2.21 (d, *J* = 11.5 Hz, 1H, C_2-OH).

The solid left after the extraction with diethyl ether was then extracted with chloroform, concentrated, and crystallized in chloroform–hexane, giving white crystals of MGX-2,3: TLC on alumina producing one spot in chloroform:acetone (19:1), R_f 0.76; mp 72°C; λ_{max} 283 nm; $[\alpha]_D^{25}$ +64.1 (*c* 0.07, $CHCl_3$). Anal. calcd. for $C_{30}H_{28}N_2O_{10}S_4$: C 51.1, H 3.9, N 3.9, S 18.2; found: C 51.0, H 3.9, N 3.7, S 18.5.

^{13}C NMR (Table 2); ^{1}H NMR (400 MHz, $CDCl_3$), δ: 8.18 (d, *J* = 8.8 Hz, 2H, C_e-H), 8.04 (d, *J* = 8.7 Hz, 2H, $C_{e'}$-H), 7.51 (d, *J* = 8.7 Hz, 2H, C_d-H), 7.46 (d, *J* = 8.7 Hz, 2H, $C_{d'}$-H), 7.38 (m, 5H, Ar-H), 6.70 (dd, *J* = 9.6, 9.6 Hz, 1H, C_3-H), 5.90 (dd, *J* = 9.8, 3.8 Hz, 1H, C_2-H), 5.46 (s, 1H, C_7-H), 5.10 (d, *J* = 3.7 Hz, 1H, C_1-H), 4.46 (d, *J* = 14.6 Hz, 1H, C_b-H), 4.45 (d, *J* = 15.0 Hz, 1H, $C_{b'}$-H), 4.37 (d, *J* = 15.0 Hz, 1H, $C_{b'}$-H″), 4.34 (dd, *J* = 10.5, 5.0 Hz, 1H, C_6-H), 4.17 (d, *J* = 14.6 Hz, 1H, C_b-H′), 4.01 (dt, *J* = 9.9, 4.9 Hz, 1H, C_5-H), 3.82 (dd, *J* = 10.4, 4.1 Hz, 1H, C_4-H), 3.80 (dd, *J* = 10.2, 4.9 Hz, 1H, C_6-H′), 3.38 (s, 3H, OMe).

For MGX-3 the C_2-OH proton couples to the C_2-H proton, which is also coupled to the anomeric proton. This coupling can only be due to a *trans*-CH-OH conformation. Thus, the hydroxyl is not hydrogen-bonding to either of the neighbouring methoxy or xanthate groups. The IR spectrum confirmed this, showing a sharp OH band. The other proton couplings are consistent with a rigid chair–chair conformation.

For the MGX-2,3, the assignment fits with the chair–chair conformation.

Table 3. Rate constant for the hydrolysis of some sugar xanthates in 10% v/v aqueous ethanol at 25°C.[a]

Ester		k_{H2O}, s^{-1}	k_{OH}, M^{-1} s^{-1}[b]
CelXDNP	k'_{H2O}	4.40×10^{-3}	9.25×10^{-2}
	k''_{H2O}	6.90×10^{-5}	
EtXDNP		3.85×10^{-6}[c]	5.22[c]
CelXNB[d]	k'_{H2O}	0.82×10^{-3}[e]	1.40×10^{-3}[b]
	k''_{H2O}	1.4×10^{-5}[e]	
EXNB		1.36×10^{-6}[c]	4.16×10^{-2}[c]
MGX-6		1.01×10^{-7}[c]	2.05[c]
MGX-3		1.87×10^{-5}[b]	43.10[b]
MGX-2,3	k_1	3.27×10^{-4}[b]	
	k_2	1.94×10^{-5}[b]	

[a] μ = 0.1 (KCl).
[b] μ = 1.0 (KCl).
[c] 20% v/v aqueous methanol (ref. 11).
[d] Reference 5.
[e] μ = 0.6 (KCl).

Kinetics

The hydrolysis of CelXDNP was studied in a continous-flow system, with mechanical stirring, under inert atmosphere, using deoxygenated water as described previously (5), following the appearance of 2,4-dinitrothiophenol at 410 nm. The basic hydrolysis was pseudo-first order. The spontaneous hydrolysis of CelXDNP showed a biphasic plot of ln Δ*A* vs. time similar to that observed for CelXNB, due to two parallel reactions with rate constants k'_{H2O} (fast) and k''_{H2O} (slow) (5).

In the range of pH 4–12 all the hydrolyses were carried out at three different buffer concentrations, and the rate constants were extrapolated to zero buffer concentration.

Hydrolyses of the methylglucose xanthates were followed by the disappearance of the xanthate at 283 nm. The spontaneous hydrolysis of MGX-2,3 showed also a biphasic plot as a consequence of the consecutive hydrolyses of the two xanthate groups with rate constants k_1 and k_2.

Activation parameters were calculated from the Eyring equations at four temperatures.

Results

Hydrolysis of sugar xanthates

The spontaneous hydrolysis of CelXDNP occurs through two parallel reactions with rate constants k'_{H2O} for the fast hydrolysis and k''_{H2O} for the slow hydrolysis. At high pH where the hydroxide catalyzed reaction predominates, kinetics become simple first-order.

The pH–rate profile of the fast spontaneuos hydrolysis of CelXDNP is shown in Fig. 1. It is similar to other xanthate esters and can be represented by eq. [2], where k_{obs} is the rate constant extrapolated to zero buffer concentration; k'_{H2O} and k_{OH} are

$$[2] \quad k_{obs} = k'_{H2O} + k_{OH}[OH^-]$$

© 1998 NRC Canada

Fig. 2. Hydrolysis of CelXDNP in aqueous acetone at 25°C; (*a*) fast hydrolysis (k'_{H2O}); (*b*) slow hydrolysis (k''_{H2O}).

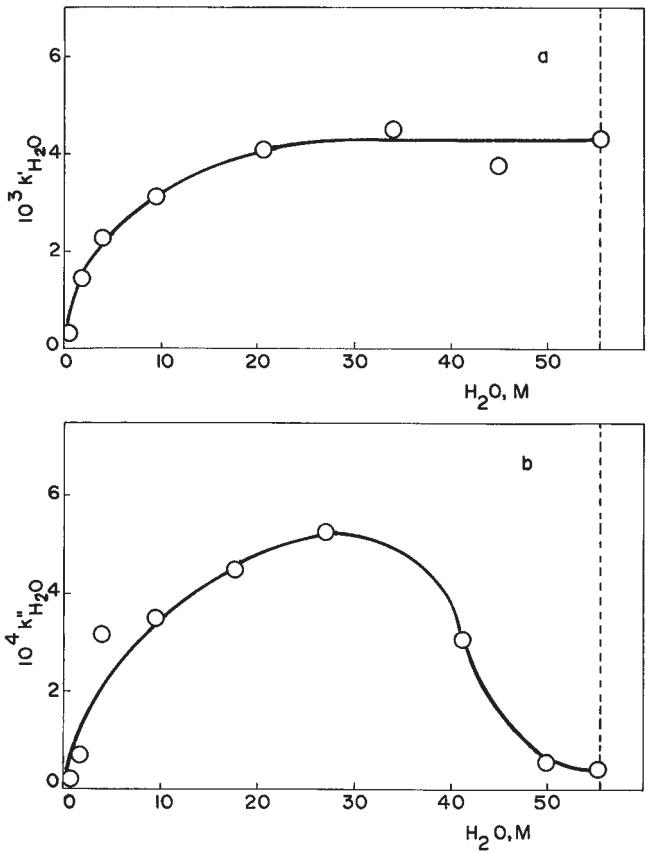

the rate constants for the water-catalyzed fast reaction and hydroxide-catalyzed reaction, respectively. In Table 3 are shown k'_{H2O}, k''_{H2O}, and k_{OH} for CelXDNP and some sugar xanthates. The rate constants for the ethylxanthate ester analogues are also included for comparison. All sugar xanthates, except the 6-substituted methylglucose xanthates (MGXB and MG-6), hydrolyze faster than the ethyl analogues. The rate constant k_2 for MG-2,3 is the same as that for MG-3.

Hydrolysis in aqueous acetone

To observe if the active species involved in the spontaneous hydrolysis were water polymers, the reaction of CelXDNP in acetone with increasing molarity of water was studied. The rate constants showed a downward curve for both the fast and slow spontaneous hydrolysis (Fig. 2), which is the reverse of the type of the curve expected when water polymers are involved in the transition state of the spontaneous hydrolysis (12). Both rate constants k'_{H2O} and k''_{H2O} increase with water molarity, following the change of dielectric constant of the medium, up to ca. 30 M water, whereas k'_{H2O} remains approximately constant with further increase while k''_{H2O} decreases rapidly in pure water.

Activation parameters

The activation parameters for the hydrolysis of sugar xanthates are shown in Table 4. The average value of $\Delta G^{\neq}$ was obtained from four temperatures, and $\Delta H^{\neq}$ was obtained from the least-squares fit of ln(k/T) vs. 1/T. It is important to note that only

Table 4. Activation parameters for the hydrolysis of sugar xanthates in 10% v/v aqueous ethanol, μ = 1.0 (KCl).

Ester	Nucleophile	$\Delta G^{\neq}$, kcal mol^{-1}	$\Delta H^{\neq}$, kcal mol^{-1}	$\Delta S^{\neq}$, cal K^{-1} mol^{-1}[a]
CelXDNP	H_2O (fast)[b]	20.68 ± 0.22	20.87 ± 0.43	0.7 ± 1.8
	OH-	18.56 ± 0.18	7.50 ± 0.23	–37.1 ± 0.8
CelXNB	H_2O (fast)[c]	21.67 ± 0.03	22.68 ± 0.20	3.3 ± 0.8
	OH-	21.17 ± 0.06	11.20 ± 0.30	–33.4 ± 0.8
MGX-3	H_2O	24.13 ± 0.12	11.90 ± 0.01	–41.0 ± 0.4
	OH-	18.15 ± 0.12	4.35 ± 0.15	–46.3 ± 0.6
MGX-2,3 (k_1)	H_2O	22.23 ± 0.12	14.65 ± 1.06	–25.4 ± 3.7
(k_2)	H_2O	23.52 ± 0.29	12.10 ± 0.97	–38.3 ± 1.0

[a] 1 M, 25°C.
[b] μ = 0.1 (KCl).
[c] μ = 0.6 (KCl), ref. 5.

for the spontaneous hydrolysis of the cellulose esters is the entropy of activation near zero. For the other sugar xanthates, MGX-3 and MGX-2,3 (k_1 and k_2), the values of $\Delta S^{\neq}$ are highly negative, as they also are for all the hydroxide ion-catalyzed reactions.

Discussion

The spontaneous hydrolysis of cellulose esters is faster than it is for ethyl xanthates. For CelXDNP, k'_{H2O} is more than 1000 times the rate constant of 2,4-dinitrophenyl ethylxanthate (EXDNP), and the ratio k'_{H2O}/ k''_{H2O} is about 60. Therefore the kinetic behaviour of the spontaneous hydrolysis CelXDNP is similar to that of CelXNB. For CelXNB it was found that the water molecule acting as a nucleophile is general-base catalyzed by a second water molecule (5). The fast hydrolysis has been attributed to the reaction of isomers C-2 + C-3. The reaction of CelXDNP in aqueous acetone showed that k'_{H2O} is insensitive to the increase of the molarity of water higher than 30 M (Fig. 2), suggesting that the cybotactic region is tight enough to expulse the cosolvent. The slow hydrolysis (k''_{H2O}) due to C-6 isomer is more sensitive to the composition of the medium because C-6 might be in a looser region.

We then addressed the question as to whether the observed acceleration of the fast hydrolysis of cellulose esters, such as CelXNB, could be a consequence of the

neighbouring effect of the OH in the C-2 or C-3 positions. The effect was expected to be the same for the 2- or 3-substituted ester. The spontaneous hydrolysis of the 3-isomer is indeed about 200 times faster than the 6-isomer (Table 3). However, it is still slower than the fast hydrolysis of CelXNB. The ratios of the rate constants for CelXNB (k'_{H2O}):MGX-3:EXNB are 603:14:1, and for CelXNB (k''_{H2O}):MGX-6:EXNB they are 10:0.1:1. The fast hydrolysis of CelXNB is much faster than expected from the 3-isomer. In addition, the acceleration of the spontaneous hydrolysis is due not only to the sugar moiety, because the 6-isomer is slower than EXNB. The ratio k'_{H2O}/k''_{H2O} for CelXNB is 64, also very different to the ratio MGX-3:MG-6 of 185.

The main argument against the anchimeric assistance of the hydroxyl group comes from the activation parameters. In Table 4 is shown that only for the fast hydrolyses of CelXDNP and CelXNB is the entropy of activation almost zero. For the other water- and hydroxide ion-catalyzed hydrolyses, $\Delta S^{\neq}$ is

© 1998 NRC Canada

highly negative, supporting the theory that the rate acceleration observed for the cellulose esters is due to the ordered water around the cellulose matrix.

The spontaneous hydrolysis of the first xanthate group of MG-2,3 might be faster than the second due to steric compression that is relieved in that step. The hydrolysis of MGX-2,3 raises the possibility that k'_{H2O} and k''_{H2O} correspond to the rate constants of the hydrolysis of dixanthated anhydroglucopyranose rings in CelXNB. The ratios k'_{H2O}/k_1 and k''_{H2O}/k_2 for the rate constants of CelXNB and the hydrolysis of MGX-2,3 are 2,5 and 0.7, respectively. However, there are two pieces of evidence against this alternative. In the first place, the C-6 isomer should predominate over the C-2 + C-3 isomers, because the xanthation of methylglucose in alkaline solution produces mainly the C-6 isomer (13, 14). Therefore, if k'_{H2O} and k''_{H2O} correspond to the hydrolysis of di- and monoxanthated rings, the reactivity of the C-6 isomer should be the same as the C-2 or C-3 isomer, when actually it is about 100 times slower than MGX-3 (Table 3). The second piece of evidence comes again from the negative entropies of activation of the water catalyzed hydrolysis of MG-2,3 (Table 4).

As for the CelXNB, the hydroxide ion-catalyzed hydrolysis of CelXDNP follows simple first-order kinetics, and this reaction is slower than that of the ethylxanthate analogue, as can be observed in Table 3. The slower rates might be due to a diffusion effect of the bulky hydrated OH- through the cybotactic region of cellulose.

Acknowledgements

The solid-state NMR spectra were obtained through the ULIRS Solid State NMR Service at University College London. The NMR spectra of the sugar xanthates were obtained from the Chemistry Department of the University of Liverpool. We are grateful to Prof. Raymond J. Abraham for advice in the assignments and comments.

References

1. (*a*) A.Suggett. *In* Water, a comprehensive treatise. Vol. 4. *Edited by* F. Franks. Plenum, New York. 1975. Chap. 6; (*b*) F. Franks. Pure Appl. Chem. **59**, 1189 (1987).
2. (*a*) S.A. Galema, M.J. Blandamer, and J.B.F.N. Engberts. J. Am. Chem. Soc. **112**, 9665 (1990); (*b*) J. Org. Chem. **57**, 1995 (1992).
3. F.A. Quiocho and N.K. Vyas. Nature (London), **310**, 381 (1984).
4. E. Humeres, C.M.S. Oliveira, V.T. Osellame, and I. de Souza. J. Phys. Org. Chem. **4**, 573 (1991).
5. E. Humeres, L.F. Sequinel, M. Nunes, C.M.S. Oliveira, and P.J. Barrie. J. Phys. Org. Chem. **7**, 287 (1994).
6. M. Sokolovsky, T. Sadeh, and A. Patchornik. J. Am. Chem. Soc. **86**, 1212 (1964).
7. D.W. Sindorf, V.J. Bartuska, and G.E. Maciel. J. Am. Chem. Soc. **102**, 3249 (1980).
8. A. Hirai, F. Horii, and R. Kitamaru. Bull. Inst. Chem. Res. Kyoto Univ. **63**, 340 (1985).
9. E. Pretsch, T. Clerc, J. Seibl, and W. Simon. Tables of spectral data for structure determination of organic compounds. 2nd ed. Springer, Berlin. 1989.
10. K. Bock and C. Pedersen. *In* Advances in carbohydrate chemistry and biology. *Edited by* R.S. Tipson and D. Horton. Vol. 41. Academic, New York. 1983.
11. E. Humeres, M. Klug, and V. Soldi. Atual. Fis.-Quim. Org. Conf. 2nd, 136 (1984).
12. B.M. Allen, A.F. Hegarty, P.O. Neill, and M.T. Naguyen. J. Chem. Soc. Perkin Trans. 3, 927 (1992).
13. D. Trimmel, W.M. Doane, C.R. Russel, and C.E. Rist. Carbohydr. Res. **5**, 166 (1967).
14. K. Kamide, K. Kowsaka, and K. Okajima. Polym. J. **19**, 231 (1987).

© 1998 NRC Canada

COMMUNICATION

Effects of superoxide anion generated from aromatic radical anions produced in nucleophilic aromatic photosubstitution reactions

Maria Cervera and Jordi Marquet

Abstract: Superoxide anion is generated from aromatic radical anions produced in nucleophilic aromatic photosubstitutions when the reactions are carried out in non-deoxygenated solutions of polar aprotic solvents. Superoxide anion thus generated displaces cyanide anion from acetonitrile and benzyl cyanide, ethoxide anion from ethyl acetate, and methanesulfenate anion from dimethyl sulfoxide. Hence, non-deoxygenated polar aprotic solvents should be avoided in nucleophilic aromatic photosubstitution reactions.

Key words: superoxide, fluoride, nucleophilic aromatic photosubstitution.

Résumé : Lorsqu'on effectue des photosubstitutions aromatiques nucléophiliques dans des solutions non désoxygénées de solvants aromatiques polaires, on génère l'anion superoxyde à partir des anions radicaux aromatiques alors produits. L'anion superoxyde ainsi produit déplace l'anion cyanure de l'acétonitrile et du cyanure de benzyle, l'anion éthylate de l'acétate d'éthyle et l'anion méthanesulfonate du diméthylsulfoxyde. Lorsqu'on effectue des réactions de photosubstitution aromatiques nucléophiles, on doit donc éviter les solvants aprotiques polaires non désoxygénés.

Mots clés : superoxyde, fluorure, photosubstitution aromatique nucléophilique.

[Traduit par la rédaction]

Nucleophilic aromatic photosubstitutions have been the object of intense research since their discovery in 1956 (1). A mechanistic borderline between polar S_N2Ar^* (2) and S_N2Ar^*-SET (reactions that take place through single electron transfer from the nucleophile to the excited nitroaromatic substrate) has been well established (3, 4). These photoreactions are normally carried out in protic solvents (water is the more common) and without any precautions with regard to the presence of oxygen since its effect on the photoreaction is generally negligible. This has been attributed to the very short lifetime of the nitroaromatic excited states (5) and to the fact that the S_N2Ar^*-SET reactions involve a collapse of radicals in the solvent cage (6).

Fluorinated aromatics nowadays constitute an important class of compounds because of their wide applications, especially in medicinal chemistry (7). The most common way of introducing a fluorine atom into an aromatic nucleus is based on the use of nucleophilic fluoride anion through nucleophilic aromatic substitution reactions (known as the "Halex method") (8). The efficiency of this method has been much improved by the use of tetralkylammonium fluorides (9). Fluoride anion is strongly solvated in protic solvents, its reactivity being very reduced in these media. Therefore, reactions with fluoride anion are normally carried out in anhydrous polar aprotic solvents where fluoride behaves as a very strong base and nucleophile (10).

Nucleophilic aromatic photosubstitutions show in many cases a different regioselectivity when compared with the corresponding ground state reaction. Moreover, inefficient leaving groups in thermal reactions, such as alkoxy groups, are operative in the photochemical version. Therefore, we decided to explore the nucleophilic aromatic photosubstitution of 4-nitroveratrole (NVT), a typical nitrophenyl ether for which the regioselectivity of the photoreaction can be established, with fluoride anion in non-deoxygenated polar aprotic solvents such as acetonitrile (ACN). However, no fluorinated products were obtained. In Scheme 1 the results of the photoreactions carried out in acetonitrile are described. There is no precedent in the literature for the reaction reported in the Scheme 1.

Received December 15, 1997.

This paper is dedicated to Professor Erwin Buncel in recognition of his contributions to Canadian chemistry.

M. Cervera and J. Marquet.[1] Departament de Química, Universitat Autònoma de Barcelona. 08193 Bellaterra, Barcelona. Spain.

[1] Author to whom correspondence may be addressed. Telephone: (3) 581-1029 / (3) 581-1265. Fax:(3) 581-1265 / (3) 581-2477. e-mail: iqor3@cc.uab.es

© 1998 NRC Canada

Scheme 1.

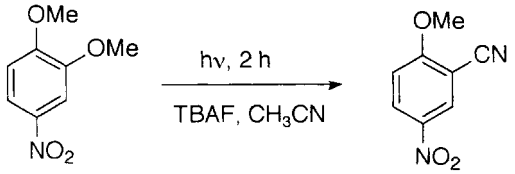

	Yield (%)[a]
air bubbling	67
normal air pressure	17
inert atmosphere	0

[a] Medium-pressure Hg lamp (Pyrex filter, λ > 290 nm). Room temperature. The products were characterized by comparison with authentic samples. Absolute preparative yields based on nonrecovered starting material. Blank irradiations in the absence of fluoride led in all cases to recovery of the starting material.

Scheme 2.

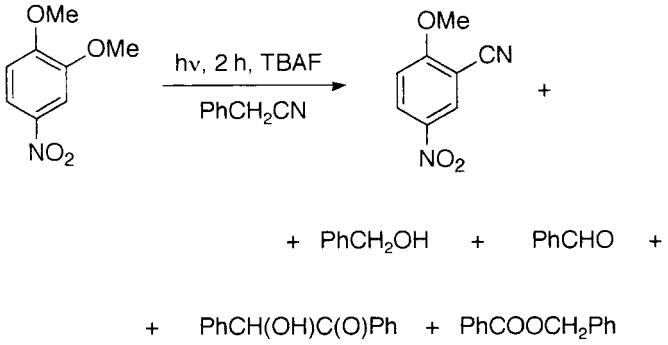

Scheme 3.

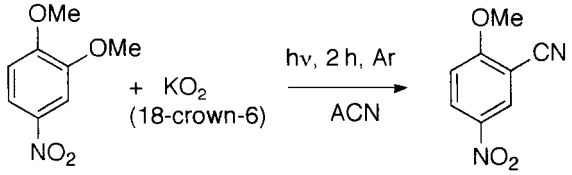

For the sake of comparison, we carried out the photoreaction of NVT with sodium cyanide in ACN–H_2O (1 h), obtaining the same photosubstitution product, 2-cyano-4-nitroanisole (46% yield), as the only cyanide substitution product, indicating complete *meta* regioselectivity. Therefore, it seems that the photoreaction described in Scheme 1 involves the fragmentation of the solvent. However, the only related cases described in the literature refer to reductive cleavage of tertiary or secondary alkylnitriles (11) promoted either electrochemically or by solvated electrons, and to photoinduced reductive cleavage of benzylnitriles (12). In these cases the resulting free radical would be stabilized by conjugative or hyperconjugative effects. No such effects are present in the methyl radical and, in addition, our photoreactions proved to be very sensitive to the presence of oxygen. Thus, the photoreaction in non-deoxygenated ACN led to 17% yield of photosubstitution product, but this yield was increased to 67% by bubbling air into the solution. The photoreaction in the absence of oxygen led to

Scheme 4.

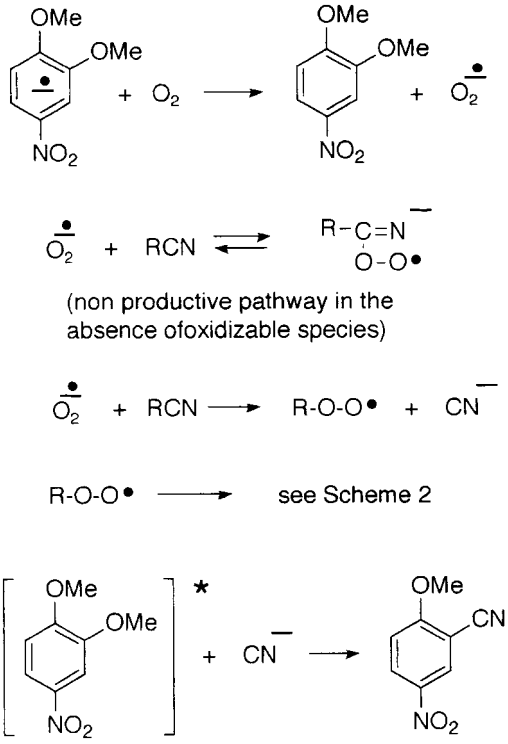

complete recovery of the starting material. These results rule out the hypothesis of a reductive cleavage in the mechanism for the photoreactions described in Scheme 1.

To investigate the evolution of the alkyl fragment, the photoreaction was carried out in benzyl cyanide (instead of ACN) and with air bubbling. The reaction crude was directly analyzed by GC–MS and the products detected are described in the Scheme 2.

From the results reported in Scheme 2 it was clear that the photofragmentation of alkylnitriles is a general process under our conditions, and that the agent responsible for it is an oxidizing species with nucleophilic properties. All products derived from the benzyl moiety are easily justified by considering the radical $PhCH_2OO^{\bullet}$ as a key intermediate (13). These results led us to the hypothesis that the "oxidizing species with nucleophilic properties" was the superoxide anion ($O2^{-\bullet}$) (14). The excellent nucleophilic properties of superoxide anion in polar aprotic solvents are well documented (it reacts with alkyl halides (15) or carbonylic compounds (16)); however, as far as we know no displacement of cyanide from nitriles has been reported (Sawyer and co-workers (18) describe the action of superoxide as a base with acetonitrile, obtaining condensation products). On the contrary, acetonitrile has been used as a solvent in fundamental studies on the reactivity of superoxide anion and its derivatives (18); however, it has been noted that the reactivity of $O2^{-\bullet}$ in acetonitrile is different from that in other solvents (for example, ref. 19), the lifetime of $O2^{-\bullet}$ being typically 10 times shorter in the nitrile.

Sawaki and Ogaka (20) reported the reaction between superoxide and acetonitrile in the presence of an easily oxidizable species such as dimethyl sulfoxide as leading to acetamide and dimethylsulfone through the attack of superoxide on the nitrile. However, when the reaction was carried out

© 1998 NRC Canada

Scheme 5.

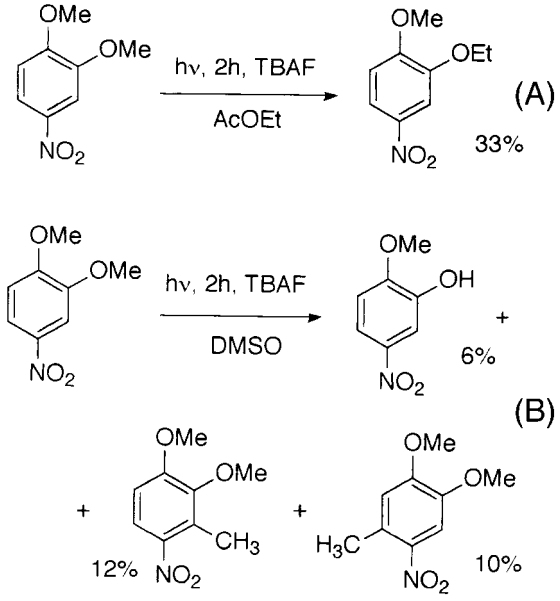

Scheme 6.

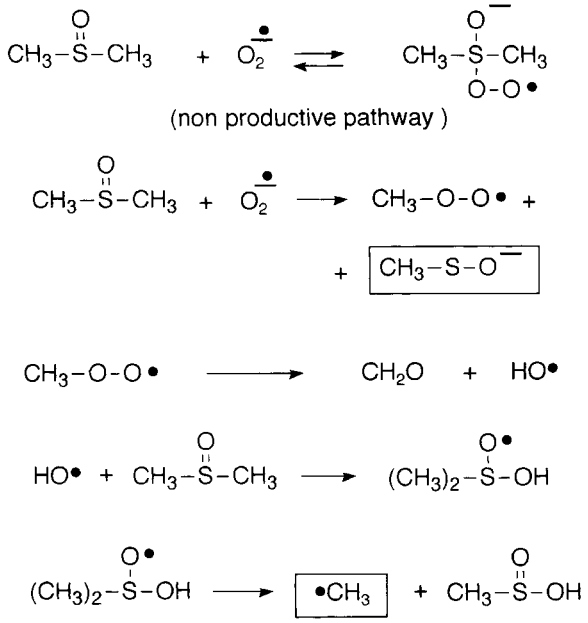

in the absence of the oxidizable species, these authors described the disappearance of the superoxide anion. No explanation was advanced for this behavior.

We have confirmed the role played by the superoxide anion in our reactions by carrying out the photoreaction of NVT with potassium superoxide in acetonitrile and in inert atmosphere, in the presence of the 18-crown-6 (Scheme 3). Direct analysis of the reaction crude by GC showed only the presence of starting NVT and 2-cyano-4-nitroanisole. The displacement of cyanide from acetonitrile in the presence of superoxide anion seems to be a ground state reaction, and this was shown by the detection of cyanide anion (Prussian blue test) in a solution of potassium superoxide and 18-crown-6 in acetonitrile.

After the identification of the agent responsible for our photoreactions an immediate question arises: how is the superoxide anion produced? A still unsolved paradox in ground state aromatic chemistry is the fact that when an electronically poor aromatic (e.g., polynitrobenzenes) substrate is placed in the presence of not easily oxidizable anions such as alkoxy or cyanide, not only the Meisenheimer complexes, but also the corresponding radical anions, can be detected (21). It is known that the concentration of radical anions depends on the concentration and nature of the nucleophile, and on the concentration of Meisenheimer complexes present in the solution (normally very low in ground state chemistry) (22). Therefore, the simplest hypothesis is that production of significant amounts of superoxide anion in our photochemical reactions originates by interaction of dioxygen with the radical anion of the aromatic substrate (NVT), and that this radical anion is present in a significant concentration under our photochemical conditions due to the enhanced reactivity of the nucleophile (fluoride) versus the excited state of the aromatic substrate (NVT is not a very electronically poor substrate), affording a sufficiently large concentration of Meisenheimer complexes. The dependence of the photoreaction upon the nature of the nucleophile and on the concentration of Meisenheimer complexes is demonstrated by the fact that the reactions of Scheme 1 fail when attempted with bromide (a weaker nucleophile in anhydrous acetonitrile) instead of fluoride. In addition, the radical anion of NVT (23) was detected by UV–vis spectroscopy when NVT was irradiated in the presence of TBAF in acetonitrile, under inert atmosphere, but this radical anion could not be detected when bromide was used. These results strongly support our hypothesis. In Scheme 4 a simplified mechanistic proposal is described.

As expected, this behavior was not restricted to nitriles. The photoreaction of NVT in the presence of TBAF·$3H_2O$ in ethyl acetate gave rise to 2-ethoxy-4-nitroanisole (Scheme 5*A*), whereas in dimethyl sulfoxide (DMSO), 1,2-dimethoxy-3-methyl-4-nitrobenzene, 1,2-dimethoxy-4-methyl-5-nitrobenzene, and 2-methoxy-5-nitrophenol were obtained (Scheme 5*B*). These results support our previous conclusions and can also be justified by considering the superoxide anion as responsible. Thus, and for the case of ethyl acetate, it is well known that superoxide anion reacts with esters producing alkoxy anions (17). Here, the ethoxy anion would act as a nucleophile towards NVT in a nucleophilic aromatic photosubstitution reaction (last step of Scheme 4, RO^- instead of CN^-). In the case of the photoreaction carried out in DMSO, the main photoreaction corresponds to the methylation of the aromatic ring. This result suggests the operation of methyl radicals as reaction intermediates. It is known (24) that hydroxyl radicals (•OH) add to DMSO producing methyl radicals through decomposition of intermediate species such as $Me_2S(O^•)OH$. The presence of hydroxyl radicals can be justified by assuming that superoxide anion behaves towards DMSO in a similar way as towards ACN (Scheme 6), through nucleophilic displacement of, in this case, methanesulfenate anion. The methanesulfenate anion thus produced would be responsible for the observed 2-methoxy-5-nitrophenol through a nucleophilic attack upon the excited state of NVT and subsequent hydrolysis, probably at work-up, since no phenol was observed in the photoreactions carried out in ACN, either in ethyl acetate or in a blank irradiation in the absence of fluoride anion.

© 1998 NRC Canada

Acknowledgements

Financial support from the Ministerio de Educación y Culture (M.E.C.) of Spain through project DGES PB96–1145 and from the Generalitat de Catalunya through project 1995SGR00469 is gratefully acknowledged.

References

1. J. Cornelisse and E. Havinga. Chem. Rev. **75**, 353 (1975), and references therein.
2. H.C.H.A. Van Riel, G. Lodder, and E. Havinga. J. Am. Chem. Soc. **103**, 7257 (1981).
3. (*a*) K. Mutai, K. Kobayashi, and K. Yokoyama. Tetrahedron, **40**, 1755 (1984); (*b*) N.J. Bunce, S.R. Cater, J.C. Scaiano, and L.J. Johnston. J. Org. Chem. **52**, 4214 (1987).
4. (*a*) A. Cantos, J. Marquet, M. Moreno-Mañas, and A. Castelló. Tetrahedron, **44**, 2607 (1988); (*b*) A. Cantos, J. Marquet, M. Moreno-Mañas, A. González-Lafont, J.M. Lluch, and J. Bertrán. J. Org. Chem. **55**, 3303 (1990).
5. (*a*) J. Cornelisse, G.P. De Gunst, and E. Havinga. Adv. Phys. Org. Chem. **11**, 225 (1975); (*b*) P.H.M. Van Zeijl, A.M.J. van Eijk, and C.A.G.O. Varma. J. Photochem. **29**, 415 (1985).
6. A.M.J. Van Eijk, H. Huizer, C.A.G.O. Varma, and J. Marquet. J. Am. Chem. Soc. **111**, 88 (1989).
7. J. Mann. Chem. Soc. Rev. **16**, 381 (1987), and references therein.
8. S. Brown and M. Bowden. Chem. Ind. (London), 143 (1993), and references therein.
9. J.H. Clark and D.K. Smith. Tetrahedron Lett. **26**, 2233 (1985).
10. J.H. Clark. Chem. Rev. **80**, 429 (1980).
11. (*a*) P.B. Arapakos. J. Am. Chem. Soc. **89**, 6917 (1967); (*b*) P.G. Arapakos and M.K. Scott. Tetrahedron Lett. 1975 (1968); (*c*) P.G. Arapakos, M.K. Scott, and F.E. Huber, Jr. J. Am. Chem. Soc. **91**, 6425 (1969).
12. P. Maslak and J. Kula. Tetrahedron Lett. **31**, 4969 (1990).
13. J.R. Kanofsky, M. Matsumoto, H. Sugimoto, and D.T. Sawyer. J. Am. Chem. Soc. **110**, 5193 (1988).
14. (*a*) D.T. Sawyer and J.S. Valentine. Acc. Chem. Res. **14**, 393 (1981); (*b*) M. Chanon, M. Julliard, J. Santamaria, and F. Chanon. New J. Chem. **16**, 171 (1992).
15. (*a*) J.L. Roberts, Jr., T.S. Calderwood, and D.T. Sawyer. J. Am. Chem. Soc. **105**, 3337 (1983); (*b*) T.S. Calderwood and D.T. Sawyer. J. Am. Chem. Soc. **106**, 7185 (1984); (*c*) H. Sugimoto, S. Matsumoto, D.T. Sawyer, J.R. Kanofsky, A.K. Chowdhury, and C.L. Wilkins. J. Am. Chem. Soc. **110**, 5193 (1988).
16. (*a*) J.L. Roberts, Jr. and D.T. Sawyer. J. Am. Chem. Soc. **106**, 4667 (1984); (*b*) F. Magno and G. Bontempelli. J. Electroanal. Chem. **68**, 337 (1976); (*c*) D.T. Sawyer, J.J. Stamp, and K.A. Menton. J. Org. Chem. **48**, 3733 (1983).
17. M.J. Gibian, D.T. Sawyer, T. Ungermann, R. Tangpoonpholvivat, and M.M. Morrison. J. Am. Chem. Soc. **101**, 640 (1979).
18. (*a*) J.W. Peter and C.S. Foote. J. Am. Chem. Soc. **98**, 875 (1976); (*b*) H. Sugimoto, S. Matsumoto, and D.T. Sawyer. J. Am. Chem. Soc. **109**, 8081 (1987).
19. (*a*) D.B. Denney and J.D. Rosen. Tetrahedron, **20**, 271 (1964); (*b*) M.J Gibian and T. Ungermann. J. Am. Chem. Soc. **101**, 1291 (1979); (*c*) M. Tezuka, H. Hamada, Y. Ohkatsu, and T. Osa. Denki Kagaku, **44**, 17 (1976).
20. Y. Sawaki and Y. Ogata. Bull. Chem. Soc. Jpn. **54**, 793 (1981).
21. S.M. Shein, L.V. Bryukhovetskaya, F.V. Pishchugin, V.F. Starichenko, V.N. Panfilov, and V.V. Voevodskii. J. Struct. Chem. **11**, 228 (1970).
22. (*a*) C. Mariani, G. Modena, G.P. Pizzo, and G. Scorrano. J. Chem. Soc. Perkin Trans. 2, 1187 (1979); (*b*) A. Sauer, F. Wasgestian, and B. Barbasch. J. Chem. Soc. Perkin Trans. 2, 1317 (1990).
23. K. Mutai, K. Yokoyama, S. Kanno, and K. Kobayashi. Bull. Chem. Soc. Jpn. **55**, 1112 (1982).
24. B.C. Gilbert, R.O.C. Norman, and R.C. Sealy. J. Chem. Soc. Perkin Trans. 2, 303 (1975).

© 1998 NRC Canada

COMMUNICATION

Formation of *cis*-[R_f(CO)Re(CO)$_4$Hal]Na complexes as an evidence of halogen–metal exchange between [Re(CO)$_5$]Na and polyfluorinated aryl and vinyl halides

Galina A. Artamkina, Petr K. Sazonov, Vasily A. Ivushkin, and Irina P. Beletskaya

Abstract: Halo(acyl)rhenate complexes *cis*-[R_f(CO)Re(CO)$_4$Hal]Na (Hal = Cl, Br; R_f = C_6F_5, *trans*-$(CF_3)_3$CCF═CF) are the primary products of the reactions of [Re(CO)$_5$]Na with the corresponding aryl or vinyl halides R_fHal.

Key words: pentacarbonylrhenate anion, carbonylmetallates, halogen–metal exchange, nucleophilic aromatic substitution, nucleophilic vinylic substitution.

Résumé : Les complexes d'halo(acyl)rhénate du type *cis*-[R_f(CO)Re(CO)$_4$Hal]Na (Hal = Cl, Br; R_f = C_6F_5, *trans*-$(CF_3)_3$CCF═CF) sont les produits primaires des réactions du [Re(CO)$_5$]Na avec les halogénures d'aryle ou de vinyle correspondants, R_fHal.

Mots clés : anion pentacarbonylrhénate, carbonylmétallates, échange halogène–métal, substitution aromatique nucléophile, substitution vinylique nucléophile.

[Traduit par la rédaction]

Nucleophilic aromatic and vinylic substitution with metal carbonyl anions in perfluorinated arenes and alkenes is a well-established synthetic approach to σ-aryl– and σ-vinyl–metal complexes (1, 2). Polyfluorinated aryl and vinyl halides bearing heavier halogens (Cl, Br, I) were shown to be much more reactive than their totally fluorinated analogues in the few cases that have been examined (2–4). It was even possible to likewise obtain the substitution products with the metal carbonyl anions that were unreactive towards the corresponding perfluoroarene or alkene (5). Up until now the reactions of carbonylmetallates with halopolyfluoroarenes and alkenes were treated as ordinary nucleophilic substitution in the framework of the classic addition–elimination mechanism, even though the yields of substitution products often were poor (2–4). We show in this paper that halogen–metal exchange can be the actual reaction pathway in the case of substrates containing the heavier halogens. The reactions of [Re(CO)$_5$]Na with C_6F_5Hal and $(CF_3)_3$CCF═CFHal (Hal = Cl, Br) taken as a model in our study do not yield the nucleophilic substitution products at all; instead the *cis*-[R_f(CO)Re(CO)$_4$Hal]Na complexes are observed, the first example of halo(acyl)carbonylmetallate formed in the reaction of metal carbonyl anion with organic halide.

The reaction of [Re(CO)$_5$]Na with C_6F_5Cl and C_6F_5Br in THF at room temperature occurs within the time of mixing of the reactants. The ^{19}F NMR spectrum of the resulting light yellow solution shows that in both cases only one reaction product is formed quantitatively. The chemical shifts of three resonances belonging to these products are typical of a C_6F_5 group bound to a carbonyl in transition metal – acyl complexes (6). The metal-coordinated acyl group is also evidenced by a band in the IR spectrum at ≈1610 cm^{-1} (7, 8) and a ^{13}C NMR resonance observed at 256–258 ppm (9). The IR spectrum in the metal–carbonyl stretching region shows a characteristic pattern of three bands, and the ^{13}C NMR spectrum displays three resonances due to metal carbonyls with the expected 1:2:1 intensity ratio,[2] both spectra being similar to that of the known *cis*-[R(CO)Re(CO)$_4$X]M complexes (7–9). The structure of *cis*-[C_6F_5(CO)Re(CO)$_4$Cl]Na was also confirmed by the FAB-MS spectrum.[3]

Various (acyl)carbonylmetallates, known as precursors to neutral metal carbene complexes, can be readily obtained via

Received December 19, 1997.

This paper is dedicated to Professor Erwin Buncel in recognition of his contributions to Canadian chemistry.

G.A. Artamkina, P.K. Sazonov, V.A. Ivushkin, and I.P. Beletskaya.[1] Department of Chemistry, Moscow State University, B-234, Vorob'yovy Gory, 119899 Moscow, Russia.

[1] Author to whom correspondence may be addressed. Fax: 7 + (095)-938-18-44. E-mail: Beletska@elorg1.chem.msu.su

[2] The ^{13}C NMR spectrum of [C_6F_5(CO)$_4$Br]Na in the metal carbonyl region consists only of two signals at 187.69 and 189.71 with intensity ratio 3:1, indicating that chemical shifts of two different carbons happened to coincide.

© 1998 NRC Canada

Scheme 1.

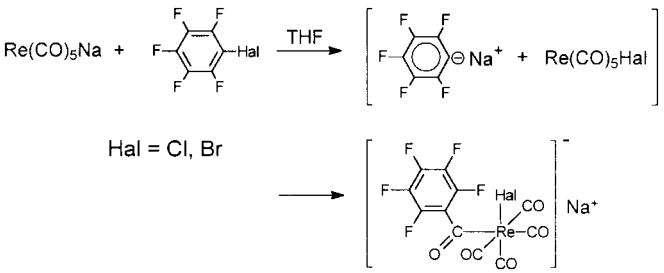

Scheme 2.

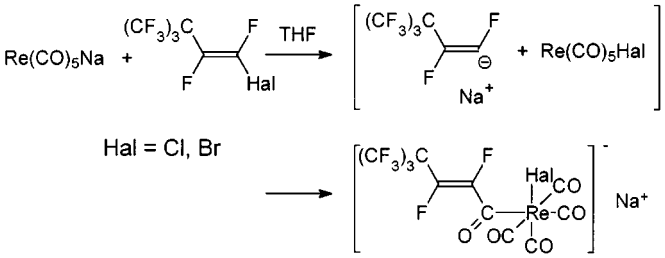

nucleophilic addition of carbanionic species such as organolithiums to the carbonyl coordinated to transition metal (10). It was reported that methyllithium does not displace halogen in $Re(CO)_5Hal$ but attacks the carbonyl ligand, producing the corresponding halo(acyl)rhenate (7). In the reaction studied the products are apparently formed by a similar pathway, which seems to have no reasonable alternatives. Any mechanistic hypothesis involving migratory insertion of C═O should be rejected, since with perfluorinated organic ligands the migratory insertion reactions are considered infeasible (11). Moreover, lithium bromide failed to induce CO insertion even in $Re(CO)_5Me$ (7) and, further still, in our case NaCl is almost insoluble in THF. In the proposed mechanism, halogen transfer between $[Re(CO)_5]Na$ and C_6F_5Hal is required to produce $Re(CO)_5Hal$ and C_6F_5Na intermediates (Scheme 1). Thus the formation of such a product as halo(acyl)rhenate may be considered as "autotrapping" of these intermediates, and is a strong argument for the halogen–metal exchange being the primary process in the reaction of metal carbonyl anion and halopolyfluoroarene.

The complexes obtained are unstable; C_6F_5H builds up in solution after several hours at room temperature (yield 4%) as a result of their decomposition.

Analogous products are observed in the reaction of $[Re(CO)_5]Na$ with *trans*-1-chloroundecafluoro-2-*tert*-butylethylene and the corresponding bromide (Scheme 2). Their structure was assigned on the basis of IR and ^{19}F and ^{13}C NMR spectra, which are very similar to the spectra of corresponding aryl complexes.[4] Also formed in these reactions are $Re_2(CO)_{10}$ (20–30%) with chloroalkene and a small amount of $Re(CO)_5Br$ (≈10%) with bromoalkene. Halopolyfluoroalkenes turned out to be less reactive than the aryl halides C_6F_5Hal; the reaction of $[Re(CO)_5]Na$ is completed within 1 h with the chloroalkene and in less than 4 min with the corresponding bromide, indicating that the reactivity of organic halide increases in the same order (Br > Cl) as in the halophilic reactions (12).

The formation of halo(acyl)rhenate complexes demonstrates that $[Re(CO)_5]Na$ attacks halogen rather than the carbon atom in both polyfluorinated aryl and vinyl halides studied. In the reactions of other metal carbonyl anions such as $[CpFe(CO)_2]^-$ with C_6F_5Cl, the halo(acyl)metallate complexes are not observed among the final products; nevertheless in that case other products including $C_6F_5Fe(CO)_2Cp$ are formed via the halogen–metal exchange mechanism (13).

[3] Spectral properties of *cis*-$[C_6F_5(CO)Re(CO)_4Cl]Na$ are IR (THF), ν cm^{-1}: 1927 (vs), 1998 (vs), 2101 (m) (C≡O); 1607 (m) (acyl); ^{19}F NMR (376.3 MHz, THF-d_8) δ: –150.24 (m, 2F, *ortho*), –161.88 (m, 2F, *meta*), –160.06 (t, 1F, *para*); ^{13}C NMR (100.58 MHz, THF-d_8): 185.45 (1C), 187.65 (2C), 188.18 (1C) (C≡O), 256 (C═O); FAB MS (*m*-nitrobenzyl alcohol, NBA, matrix, beam of Xe atoms at 8 kV and 4 mA) m/z^+: 761 (M + 2Na, +NBA), 728 (M + Na, +NBA), 633 (M + 2Na, +NaCl), 625 (M + H, +THF), 575 (M + Na).

[4] Spectral properties of *cis*-[*trans*-$(CF_3)_3CCF^{\alpha}$═CF^{β}(CO)-$Re(CO)_4Br]Na$; IR (THF), ν cm^{-1}: 1937 (vs), 1997 (vs), 2100 (m) (C≡O); 1593 (m) (acyl); ^{19}F NMR (376.3 MHz, THF-d_8) δ: –62.00 (dd, J = 12.5 Hz, J = 17 Hz, 9F, CF_3),–128.62 (d of m, $J_d(F^{\alpha},F^{\beta})$ = 135 Hz, 1F, CF═), –166.09 (d of m, 1F, CF═); ^{13}C NMR (100.58 MHz, THF-d_8): 187.09 (d, J ≈ 5 Hz), 189.45 (d, J ≈ 3.5 Hz), 189.52 (s) (C≡O).

Acknowledgements

We gratefully acknowledge financial support from the Russian Fundamental Science Foundation (Grants 97-03-33161a and 96-15-97484) and from the program "Integration of High School with the Russian Academy of Sciences" (Grant 234). We thank Dr. Olga S. Anisimova for obtaining the FAB mass spectra.

References

1. (*a*) R.B. King. Acc. Chem. Res. **3**, 417 (1970) (*b*) R.Chukwa, A.D. Hunter, and B.D. Santarsiero. Organometallics, **10**, 2141 (1991); (*c*) R.P. Hughes, R.T. Carl, S.J. Daig, R.C. Hemond, and D.E. Samkoff. Organometallics, **9**, 2732 (1990).
2. M.I. Bruce and F.G.A. Stone. Angew. Chem. **80**, 835 (1968).
3. (*a*) M.I. Bruce and F.G.A. Stone. J. Chem. Soc. A: 1837 (1966); (*b*) N.J. Ishikawa and S. Ibuki. Bull. Chem. Soc. Jpn. **47**, 2621 (1974); (*c*) M.I. Bruce, P.W. Jolly, and F.G.A. Stone. J. Chem. Soc. A: 1602 (1966).
4. (*a*) I.P. Beletskaya, G.A. Artamkina, A.Yu. Mil'chenko, P.K. Sazonov, and M.M. Shtern. J. Phys. Org. Chem. **9**, 319 (1996); (*b*) G.A. Artamkina, A. Yu. Mil'chenko, I.P. Beletskaya, and O.A. Reutov. Dokl. Akad. Nauk, **304**, 616 (1989).
5. (*a*) M.I. Bruce, D.N. Sharrocs, and F.G.A. Stone. J. Chem. Soc. A: 680 (1970); (*b*) O.E. Fenton and A.G. Murrey. Tetrahedron, **21**, 3005 (1965).
6. T.V. Magdesieva, I.I. Kukhareva, D.P. Krut'ko, K.P. Butin, and I.P. Beletskaya. Russ. Chem. Bul. **43**, 881 (1994).
7. K.P. Darst and C.M. Lukehart. J. Organomet. Chem. **171**, 65 (1979).
8. C.P. Casey and D.M. Scheck. J. Am. Chem. Soc. **102**, 2723 (1980).
9. (*a*) C.P. Casey, C.J. Czerwinski, and R.K Hayashi. Organometallics, **15**, 4362 (1996); (*b*) K.P. Darst and C.M. Lukehart. J. Organomet. Chem. **161**, 1 (1978).
10. H. Fisher. *In* Transition metal carbene complexes. VCH, Weinheim, Germany. 1983. pp. 1–68.
11. J.P. Collman, L.S. Hegedus, J.R. Norton, and R.G. Finke.

© 1998 NRC Canada

Principles and applications of organotransition metal chemistry. University Science Books, Mill Valley, Calif. 1987. Chap. 7.

12. (*a*) N.S.. Zefirov and D.I. Makhon'kov. Chem. Rev. **82**, 615 (1982); (*b*) T.V. Talalaeva and K.A. Kocheshkov. Methods of organometallic chemistry. Vol. 1. Nauka, Moscow. 1971. pp. 215–251 (in Russian).
13. G.A. Artamkina, P.K. Sazonov, V.A. Ivushkin, and I.P. Beletskaya. Chemistry — Euro. J. **4**, 1167 (1998).

© 1998 NRC Canada

1997 Polanyi Award Lecture
Why are there atoms in chemistry?[1]

R.F.W. Bader

Abstract: Dalton made a bold assumption in his atomic hypothesis by stating that atoms retained their mass and their identity in chemical combination. Its vindication had to await Rutherford's nuclear model of the atom. The continuing evolution of chemistry led to the realization that atoms exhibit not only a unique mass but also characteristic additive properties, thereby making it possible to recognize their presence in a molecule and to predict the molecule's static and reactive properties. The theoretical vindication of the model of a functional group as the carrier of chemical information had to await the work of Feynman and Schwinger. Their generalization of physics leads to a unique definition of an atom as an open quantum system and makes possible the renormalization that is required to account for the short-range nature of the forces that enable one to identify a given group in any environment. The lecture will demonstrate that the proper open systems predicted by the quantum action principle define the atom and that this definition accounts for the retention of an atom's chemical identity by enabling one to replace the quantum mechanical observables for force and energy with dressed, real space density distributions whose forms parallel the transferable topology of the electron density distribution.

Key words: atom, action principle, atoms in molecules, functional groups.

Résumé : Dalton, dans son hypothèse atomique, a posé un postulat audacieux lorsqu'il a affirmé que les atomes gardent leur masse et leur identité dans les combinaisons chimiques. Il a fallu attendre le développement du modèle de l'atome de Rutherford pour le justifier. L'évolution continuelle de la chimie a permis de réaliser que les atomes ne présentent pas uniquement une masse qui est spécifique, mais aussi des propriétés additives caractéristiques qui permettent de reconnaître leur présence dans une molécule et de prédire les propriétés statiques et réactives de la molécule. La justification théorique du modèle d'après lequel le groupe fonctionnel est porteur de l'information chimique a dû attendre les travaux de Feynman et Schwinger. Leur généralisation de la physique a conduit à une définition unique d'un atome d'après laquelle il s'agit d'un système quantique ouvert et elle permet la renormalisation requise pour tenir compte de la nature à courte portée des forces qui permettent d'identifier un groupe donné dans tous les environnements. Dans cette conférence, on démontrera que les systèmes ouverts appropriés prédits par le principe de l'action quantique permettent de définir l'atome et que cette définition permet de tenir compte de la rétention de l'identité chimique d'un atome en permettant de remplacer les données observables de la mécanique quantique pour la force et l'énergie par des distributions de densité d'espace réel dont les formes sont parallèles à la topologie transférable de la distribution de la densité électronique.

Mots clés : atome, principe d'action, atomes dans les molécules, groupes fonctionnels.

[Traduit par la Rédaction]

How to define an atom in a molecule

It is almost 200 years since Dalton put forth his atomic hypothesis and we are approaching the centennial of Rutherford's experimental vindication of Dalton's hypothesis regarding the constancy of the atomic mass and identity throughout chemical combination in terms of the nuclear model. Not only does the nuclear model account for the conservation of the atomic mass, but it also stamps each atom with its own chemical identity. The force of attraction between the positive charge concentrated at the nucleus and the diffuse distribution of electronic charge is the single most dominant force operative in an atom, molecule, or solid. This force determines the atom's fundamental form and endows it with a set of characteristic and measurable properties, properties that underlie the cornerstone of chemical thinking, the concept of a functional group. We shall show in this lecture that because of an atom's fundamental form, all of the molecular structure hypotheses, that is, all of the concepts of chemistry, follow from physics.

In the past there have been many failed attempts to define an atom in a molecule and its contributions, or those of a functional group, to the properties of the molecule. There was and, for some, there remains a prevailing belief that a unique definition is not possible. Consider for example the following statement that appeared in the Journal of the

Received March 6, 1998.

R.F.W. Bader.[2] Department of Chemistry, McMaster University, Hamilton, ON L8S 4M1, Canada.

[1]This is an invited review article based on the 1997 Polanyi Award Lecture presented by Professor Bader at the 80th Annual Conference of the Canadian Society for Chemistry, held in Windsor, Ontario, in June 1997.

[2]Telephone: (905) 525-9140, ext. 23499. Fax: (905) 522-2509.

© 1998 NRC Canada

PROOF/ÉPREUVE

Fig. 1. The electron density for the cyclopropane molecule in the form of a relief map and a contour plot together with a display of its gradient vector field in two planes: LHS in plane of carbon nuclei, RHS in symmetry plane containing one carbon nucleus and two attached protons. The density is a local maximum at each nucleus with the result that space is partitioned into atomic basins, each basin being defined by the set of trajectories traced out by $\nabla\rho(\boldsymbol{r})$, the gradient vectors of the density, that terminate at a given nucleus. Shown in bold are the pairs of trajectories in each indicated plane that terminate at the positions of (3,–1) or bond critical points (bcps). These cps, whose positions are denoted by dots, are found only between certain pairs of nuclei. Each such pair of trajectories is part of a set of trajectories defining a two-dimensional manifold embedded in three-dimensional space, which terminate at each bcp and define an interatomic surface. The set of trajectories defining the C | C interatomic surface between two out-of-plane carbon nuclei, for example, is represented by the trajectories that terminate at the bcp in the lower portion of the gradient map on the RHS. The interatomic surfaces defined in this manner are not crossed by any trajectories of the gradient vector field of the density — they are "zero-flux surfaces." Unique pairs of trajectories, also shown in bold, originate at each bcp, and define a bond path — a line of maximum electron density linking the neighboring nuclei. Trajectories originate at the ring or (3,+1) cp in the bottom LH diagram and a pair of trajectories originate at this point in the RH diagram. The outer contour has the value 0.001 au and the remaining contours increase in value in the order 2×10^n, 4×10^n, and 8×10^n with n beginning at –3 and increasing in steps of unity. The same contours are used in all density diagrams.

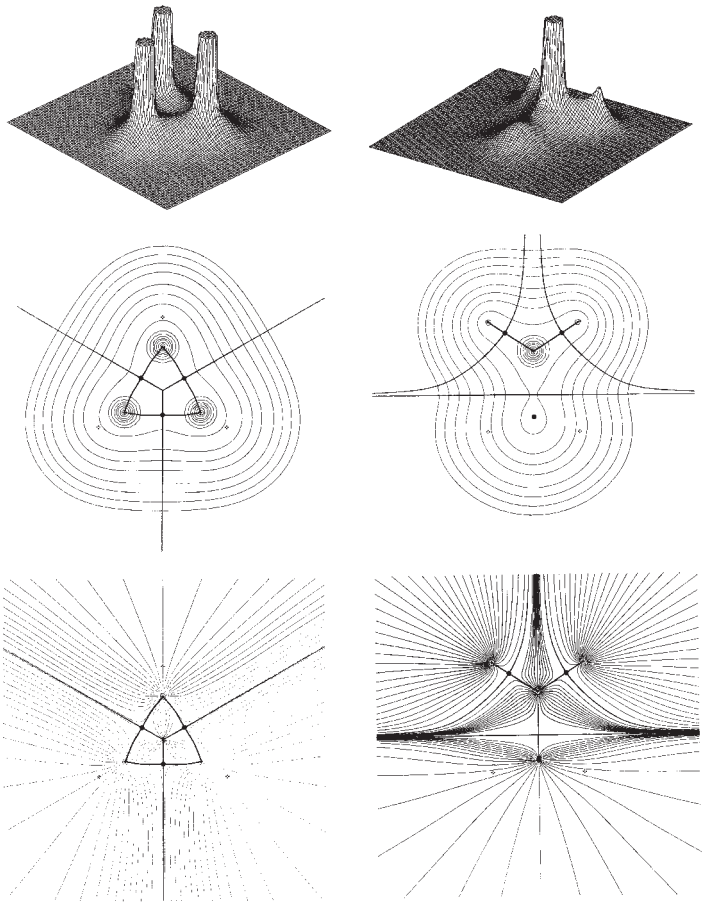

American Chemical Society in 1994: "The atom (or functional group) in a molecule is not easily defined. There are always subjective factors for any definition, or strict partition of the molecule. What model one chooses is subject to one's particular needs." The remark that how one defines an atom is a matter of expediency is at variance with the practice of science wherein one's attempts at definition and understanding are necessarily guided by observation and by theory. Any definition that does not recover the essential observations that are associated with the concept of an atom in a molecule serves no useful purpose. Any definition that does not ultimately allow for the quantum definition of the atom's properties cannot be a physically admissible one. We shall, in turn, consider the chemical and theoretical constraints on the definition of an atom.

Chemical constraints

There are three essential requirements imposed upon the definition of an atom in a molecule by the observations of chemistry. (*i*) The first stems from the necessity that two identical pieces of matter exhibit identical properties. Since the form of matter is determined by the distribution of charge throughout real space, two objects are identical only if they possess identical charge distributions. This parallelism of properties with form exists not only at the macroscopic level but, in accordance with Dalton's assumption that atoms of a given element are alike in all respects, is assumed to exist at the atomic level as well. It demands that an atom be a function of its form in real space, requiring that it be defined in terms of the charge distribution. It follows that if an atom exhibits the same form in the real space of two

© 1998 NRC Canada

PROOF/ÉPREUVE

systems, or at two different sites within a crystal, it must contribute identical amounts to the total value of every property in each case. (*ii*) This requirement of property following form as described in (*i*) demands in turn that the atomic contributions sum to yield the total value for the system. That is, that the atomic contributions to some property must sum to yield the value of the property for the molecule. Only atoms meeting these two requirements can account for the existence of so-called additivity schemes wherein the atomic properties appear to be transferable as well as additive. (*iii*) Finally, the boundary defining an atom or functional group must be such as to maximally preserve its form and thereby maximize the transfer of chemical information from one system to another.

Quantum constraints

The only subjectivity one can exercise in "a strict partition of a molecule" is to decide whether or not to adhere to the constraints imposed by physics or to ignore them, thereby abandoning physics as "subject to one's particular needs." The constraints imposed by quantum mechanics on the definition of an atom are best stated in the form of two questions: (*a*) Does the state function, the function that contains all of the information that can be known about a system, predict a unique partitioning of the molecule into atoms? and (*b*) Does quantum mechanics provide a complete description of the atoms so defined? Affirmative answers to these two questions in effect require that quantum mechanics be extended to properly bounded open systems, that is, that one define the physics of a piece of a total system.

The extension of quantum mechanics to obtain the definition of a class of open systems with such a unique set of properties is indeed possible. It is based on the reformulation of quantum physics provided by the work of Feynman (1) and Schwinger (2). Their approach is based on the Lagrangian as opposed to the Hamiltonian formalism of quantum mechanics and makes possible the asking and answering of questions not possible within the traditional Hamiltonian framework. Indeed, Schwinger's generalization of the action principle provides a unifying description of quantum and classical physics. That the answers to chemistry would be found within the physics formulated to "provide a framework capable of admitting fundamentally new physical ideas" into the general theory of quantum field dynamics (2) is not something that was or is immediately obvious, certainly not to someone like myself, trained as an experimental chemist. It is the purpose of this paper to trace out the path of the research that led to this conclusion, and to emphasize in particular how it evolved from a search for the conceptual basis of chemistry in terms of the observable properties of a system.

Observational basis for the definition of an atom

Through a collaboration with the Mulliken–Roothaan laboratory in the 1960s, my group had access to near Hartree–Fock quality wave functions, before their publication (3), for nearly 300 diatomic molecules, in both ground and excited states, and these were used to study the properties of the electron density, $\rho(\boldsymbol{r})$. I consider these studies (4) to be "theoretical" experiments in the study of $\rho(\boldsymbol{r})$. The general properties we found for the density in these diatomic molecules could now be observed in the densities obtained experimentally for solids (5, 6), but at that time the experimental techniques and methods had not been perfected to the degree needed to obtain reliable electron density distributions.

These studies led to the realization that the topology of $\rho(\boldsymbol{r})$ provided a unique partitioning of the space of a molecule or a crystal into mononuclear regions that I shall refer to as atoms (7). Equally important, it soon became apparent that the resulting regions were transferable to varying extents between molecules. Indeed, if one insisted that the pieces transferred had to exhaust the system, they had the property of maximizing any transferability that was present.

This atomic form imposed on the structure of matter is a consequence of the principal topological form exhibited by the charge density — that, in general, it exhibits maxima only at the positions of the nuclei (7, 8). In a manner now well documented in terms of the topology of the electron density, as revealed by its associated gradient vector field (9) and illustrated in Fig. 1, this property results in an exhaustive partitioning of real space into a set of non-overlapping atomic domains Ω, each of which is bounded by a surface $S(\Omega,\boldsymbol{r})$ characterized by a local zero-flux in the gradient vector field of the electron density, eq. [1],

$$[1] \qquad \nabla\rho(\boldsymbol{r}) \cdot \boldsymbol{n}(\boldsymbol{r}) = 0 \ \forall \ \boldsymbol{r} \in \boldsymbol{S}(\Omega, \boldsymbol{r})$$

where $\rho(\boldsymbol{r})$ for a system of N electrons is defined as

$$[2] \qquad \rho(\boldsymbol{r}) = N \int d\tau' \psi^* \psi$$

The manner of integration implied by the symbol $\int d\tau'$ occurs throughout the theory and denotes a sum over all spins and an integration over the spatial coordinates of all electrons but the one whose position vector is denoted by $\boldsymbol{r}$. Examples of atoms bounded by a surface defined by eq. [1] whose density distributions changed little upon substitution of the neighboring atom are provided by the Li atoms in the set of diatomic molecules illustrated in Fig. 2 (7). One must regard the observed similarity in form of the Li atoms so defined as no less than remarkable when one considers the very different natures of its bonded neighbors in the three systems. The electron populations of the Li atom are obtained by integration of $\rho(\boldsymbol{r})$ over its basin and yield similar net charges of +0.94, +0.93, and +0.91 e for LiF, LiO, and LiH, respectively (7).

In addition to $\rho(\boldsymbol{r})$, we were also studying the properties of the electronic kinetic energy density (10). An important point of this parallel study is that the zero-flux defining condition stated in eq. [1] ensures that the average electronic kinetic energy of the atom is uniquely determined (7). One may define the kinetic energy density using the usual Schrödinger or Laplacian form for the operator as

$$[3] \qquad K(\boldsymbol{r}) = (-\hbar^2/4m)N \int d\tau'\{\psi^* \nabla^2\psi + (\nabla^2\psi^*)\psi\}$$

or in its eminently real form as

$$[4] \qquad G(\boldsymbol{r}) = (\hbar^2/2m)\, N \int d\tau' \nabla\psi^* \cdot \nabla\psi$$

© 1998 NRC Canada

PROOF/ÉPREUVE

Fig. 2. Contour plots of the ground state electron density distributions in the plane of the nuclei for LiH ($^1\Sigma^+$), LiO ($^2\Pi$), and LiF ($^1\Sigma^+$) in descending order in the diagram. The intersections with this plane of the zero-flux interatomic surfaces defining the Li atom and its bonded neighbor are also indicated. The reader is asked to note the high degree of similarity in the distribution of the density over the basins of the Li atom defined in this manner and to contrast this with the very different distributions of the density found within the basins of its neighbors, differences that extend up to the interatomic surface. Any other choice of surface would either include a portion of the neighboring density, which changes radically in each case, or assign to the neighbor a portion of the density that is similar for the Li atom in all three molecules. These results are for Hartree–Fock calculations (7).

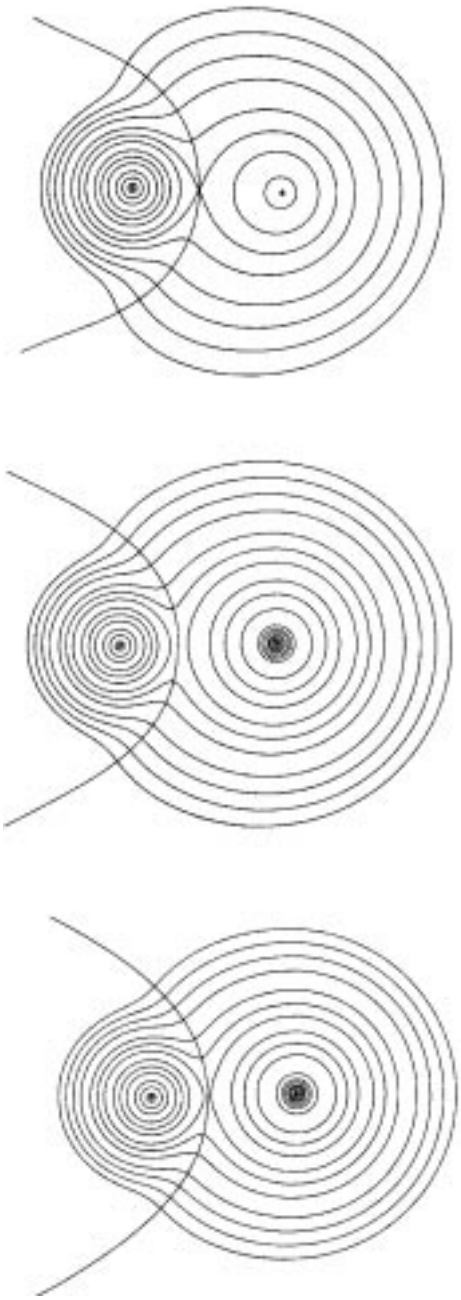

Since operators are not necessarily Hermitian over a subsystem, one must always consider a quantity plus its complex conjugate to ensure a real quantity in taking an average, as is done in eq. [3]. These two kinetic energy densities differ by a function of the electron density, its Laplacian, as given by eq. [5]:

$$[5] \qquad K(r) - G(r) = (-\hbar^2/4m)\nabla^2\rho(r)$$

Thus the two forms for the kinetic energy density differ locally, as will their average values when the densities are integrated over an arbitrary region of space Ω. Their integrated values are related by

$$[6] \qquad K(\Omega) - G(\Omega) = (-\hbar^2/4m)\int_{\Omega} d\boldsymbol{r}\nabla\cdot\nabla\rho(\boldsymbol{r}) = (-\hbar^2/4m)\oint dS(\Omega, \boldsymbol{r})\nabla\rho(\boldsymbol{r})\cdot\boldsymbol{n}(\boldsymbol{r})$$

Gauss' theorem enables one to rewrite the volume integral of $\nabla^2\rho = \nabla\cdot\nabla\rho$ in eq. [6] as an integral of the flux in $\nabla\rho$ through the surface of Ω. Clearly this integral vanishes for an atom, as it does for the total system, because of the defining condition given in eq. [1]. Thus, as indicated below in eq. [7], the average electronic kinetic energy of an atom in a molecule, $T(\Omega)$, is well defined,

$$[7] \qquad T(\Omega) = K(\Omega) = G(\Omega)$$

One notes that the average electronic kinetic energy defined in this manner is necessarily additive to yield the total value T over any set of disjoint regions such as the atoms that exhaust the space of the system

$$[8] \qquad T = \sum_{\Omega} T(\Omega)$$

The paralleling behavior of the electron and kinetic energy densities

These studies of the kinetic energy density resulted in a most important observation — that both $K(\boldsymbol{r})$ and $G(\boldsymbol{r})$ exhibit the same degree of transferability over the basin of an atom up to its zero-flux surface as does the electron density $\rho(\boldsymbol{r})$. Thus the conservation in the form of $\rho(\boldsymbol{r})$ and, consequently in its integrated electron population on transfer, was paralleled by a conservation in the electronic kinetic energy density and its atomic average. The average kinetic energies of the Li atoms in the three molecules fall within 8 kcal/mol (7). The paralleling transferability of $\rho(\boldsymbol{r})$ and $G(\boldsymbol{r})$ is further illustrated in Fig. 3 for the methylene group adjacent to a methyl group in butane in one case and pentane in the other. This paralleling behavior is the crucial observation that leads to the theory of atoms in molecules, as deduced from the following chain of reasoning.

The virial theorem for a system with Coulombic forces states that the total energy of a set of particles equals the negative of their average kinetic energy, $E = -T$. In our case, it states that the total electronic energy equals the negative of the average electronic kinetic energy. If one could show that there is a virial theorem for an atom in a molecule — that is, for a region of space bounded by a zero-flux surface — then one could use this theorem to define the energy of atom in a molecule $E(\Omega)$ in terms of its electronic kinetic energy $T(\Omega)$, as shown in eq. [9],

© 1998 NRC Canada

PROOF/ÉPREUVE

Fig. 3. Contour plots for the methylene group adjacent to a methyl group in butane (LHS) and in pentane (RHS): (*a*) the electron density $\rho(\boldsymbol{r})$, eq. [2]; (*b*) the kinetic energy density $G(\boldsymbol{r})$, eq. [4]; and (*c*) the virial field or potential energy density $\mathcal{V}(\boldsymbol{r})$, eq. [67]. The plane shown is the symmetry plane containing the carbon nucleus and two protons. Also shown in the electron density maps are the intersections of the C–H interatomic surfaces and the C—H bond paths, which intersect at a bcp, denoted by a dot. The virial paths, the lines of maximally negative potential energy density, are also indicated on the maps of the virial field. Every bond path is mirrored by such a virial path. The results are from MP2/6-311++G(2d,2p) calculations. Each map is superimposable on its counterpart for the two molecules. All three fields are equally transferable between the normal hydrocarbons, but only the electron density and the virial field are homeomorphic (33).

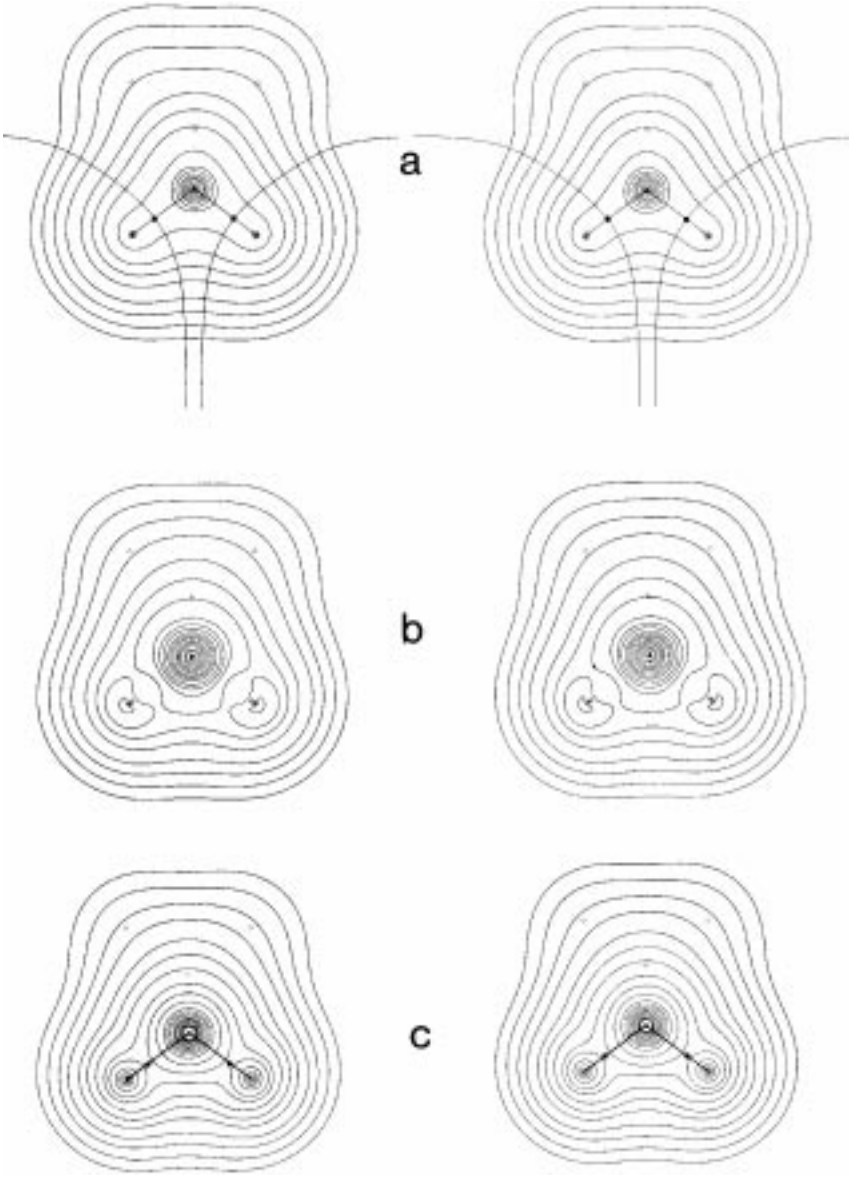

[9] $$T(\Omega) = -E(\Omega)$$

Since $T(\Omega)$ is additive, this definition of the energy of an atom would necessarily be additive as well, and the total electronic energy of a molecule would be the sum of its atomic contributions $E(\Omega)$,

[10] $$E = \sum_{\Omega} E(\Omega)$$

Most important, because of the paralleling behavior of $\rho(\boldsymbol{r})$ and $G(\boldsymbol{r})$, one would know that when the form of the atom in real space remains unchanged on transfer between systems, so does its contribution to the total energy. That is, by observation, the energy of an atom would be transferable to the same extent as is its distribution of charge. Thus the topological atoms, those defined by eq. [1], meet the very observational requirements of additivity and transferability that, as discussed above, are essential for the definition of an atom in a molecule.

A spatial partitioning of the total energy is not a trivial problem, because it requires a partitioning of the potential energy contributions. How does one spatially partition the

© 1998 NRC Canada

PROOF/ÉPREUVE

energy of repulsion between the nuclei and between the electrons or partition the energy of attraction of each nucleus for all of the electrons? We shall return to this in detail later, but the underlying physics is readily understood. The answer is provided by the virial theorem, which identifies the potential energy as the virial of the forces exerted on the electrons. One can write down the operator that determines the force exerted on one electron at a given point in space by all of the remaining particles in the system. This is the Ehrenfest force (11). Knowing the force exerted on an electron, and hence on the electron density at a point in space, enables one to determine the potential energy of that element of density by taking the virial of the force, that is, by forming the scalar product of the force with the position vector of the point. Integration of the resulting potential energy density or virial field $\mathcal{V}(\boldsymbol{r})$ over the basin of the atom yields its average potential energy, $\mathcal{V}(\Omega)$. The energy $E(\Omega)$ of the atom can, by the virial theorem, be alternatively expressed as the sum of $T(\Omega)$ and $\mathcal{V}(\Omega)$. Furthermore, Fig. 3 shows that this virial field is as transferable for the methylene groups in butane and pentane as are the electron and kinetic energy densities. Thus the total energy defined as the sum of $T(\Omega)$ and $\mathcal{V}(\Omega)$ would be as transferable as is $\rho(\boldsymbol{r})$. The average numbers of electrons in the two methylene groups obtained by integration of $\rho(\boldsymbol{r})$ differ by 0.0005 e, and their total energies, obtained by integration of $G(\boldsymbol{r})$, by less than one kcal/mol.

Thus with these observations we have reformulated the question of "how does one define an atom in a molecule?" into "can one show that the virial theorem applies to a spatial region bounded by a zero flux surface?." It is clear that if the virial theorem applies to such a region then all the theorems of quantum mechanics should apply, and one is, therefore, asking whether regions bounded by zero-flux surfaces and their properties are defined by quantum mechanics. To answer this question we initially turned to Schrödinger and his original derivation of "wave mechanics" (12). In retracing Schrödinger's steps to extend quantum mechanics to an open system bounded by a surface of zero flux (13) one is led to a statement of Schwinger's principle of stationary action for a time-independent system, a principle that completely determines the physics of a system in a stationary or time-dependent state (2).

From Schrödinger to atoms in molecules

Derivation of the hypervirial theorem for an open system

Before giving the derivation of Schwinger's principle for a stationary state, we introduce ourselves to the quantum mechanics of an open system and the manner in which it differs from the quantum mechanics for the total system. This difference is a result of operators no longer necessarily being Hermitian when averaged over an open system. This has the important result of introducing fluxes in property currents through the surface of the open system when deriving the Heisenberg equation of motion for an observable $\hat{\boldsymbol{A}}$. In the Schrödinger representation this most important equation determines the time rate-of-change of the average value of the observable

$$\mathrm{d}\langle\hat{A}\rangle/\mathrm{d}t = (i/\hbar)\langle\Psi[\hat{H},\hat{A}]\Psi\rangle$$

For each choice of the operator $\hat{A}$, one obtains a corresponding theorem. For example, the virial theorem is obtained by setting $\hat{A} = \boldsymbol{r}\cdot\boldsymbol{p}$, the product of the position and momentum coordinates of an electron. In the case of a stationary state the equation is referred to as the hypervirial theorem, and is of the form

$$[11] \quad \langle\psi,[\hat{H},\hat{A}]\psi\rangle = 0$$

This result is easily proved independently of setting the time derivative of $\langle\hat{A}\rangle$ equal to zero by (*a*) expanding the commutator, (*b*) making use of the fact that $\hat{H}$ is Hermitian, that is, one makes use of the identity

$$[12] \quad \langle\psi,\hat{H}\hat{A}\psi\rangle = \langle\hat{H}\psi,\hat{A}\psi\rangle$$

and (*c*) recognizing that ψ is a solution to the stationary state equation $\hat{H}\psi = E\psi$.

We shall, without any loss in generality, consider a single-electron case in deriving the theorem for an open system Ω. To ensure a real quantity, one must consider the sum of $\langle\psi,[\hat{H},\hat{A}]\psi\rangle_\Omega$ and its complex conjugate (cc). In addition, one can no longer assume that $\langle\psi,\hat{H}\hat{A}\psi\rangle_\Omega = \langle\hat{H}\psi,\hat{A}\psi\rangle_\Omega$, as is done in eq. [12]. We shall detail the derivation for just the term $\langle\psi,[\hat{H},\hat{A}]\psi\rangle_\Omega$. One adds and subtracts the term $\langle\hat{H}\psi,\hat{A}\psi\rangle_\Omega$ to the terms obtained by averaging the expanded commutator over the open system to obtain

$$[13] \quad \langle\psi,[\hat{H},\hat{A}]\psi\rangle_\Omega = \langle\psi,\hat{H}\hat{A}\psi\rangle_\Omega - \langle\hat{H}\psi,\hat{A}\psi\rangle_\Omega + \langle\hat{H}\psi,\hat{A}\psi\rangle_\Omega - \langle\psi,\hat{A}\hat{H}\psi\rangle_\Omega$$

Making use of Schrödinger's equation $\hat{H}\psi = E\psi$ results in cancellation of the last two terms on the RHS. The terms $\hat{V}\psi^*\psi$ cancel in taking the difference between the two remaining terms, where $\hat{V}$ is the potential energy operator in $\hat{H}$. Writing out the explicit form for an open system average denoted by $\langle\ \rangle_\Omega$ for the difference between the two remaining terms yields

$$[14] \quad \langle\psi,[\hat{H},\hat{A}]\psi\rangle_\Omega = (\hbar^2/2m)\int_\Omega \mathrm{d}\boldsymbol{r}\{(\nabla^2\psi^*)\hat{A}\psi - \psi^*\nabla^2(\hat{A}\psi)\}$$

$$[15] \quad \langle\psi,[\hat{H},\hat{A}]\psi\rangle_\Omega = (\hbar^2/2m) \times \int_\Omega \mathrm{d}\boldsymbol{r}\nabla\cdot\{(\nabla\psi^*)\hat{A}\psi - \psi^*\nabla(\hat{A}\psi)\}$$

Making use of Gauss' theorem for transforming the volume integral of a divergence into a surface integral, one has

$$[16] \quad \langle\psi,[\hat{H},\hat{A}]\psi\rangle_\Omega = (\hbar^2/2m) \times \oint \mathrm{d}S(\Omega,r)\{(\nabla\psi^*)\hat{A}\psi - \psi^*\nabla(\hat{A}\psi)\}$$

The surface term represents the flux in vector current density for the observable $\hat{A}(\boldsymbol{r})$ through the surface of the open system, as can be seen by comparing the bracketed term in the surface integral with the expression for the current density of property A given in eq. [17]:

$$[17] \quad \boldsymbol{j}_A(\boldsymbol{r}) = (\hbar/2mi)\{\psi^*\nabla(\hat{A}\psi) - (\nabla\psi^*)\hat{A}\psi\}$$

© 1998 NRC Canada

PROOF/ÉPREUVE

Thus unlike the total system, the average of the commutator $[\hat{H},\hat{A}]$ does not vanish for an open system but is given by the flux in the property density of A through the surface of the subsystem,

$$[18] \quad (1/2)\{(i/\hbar)\langle\psi,[\hat{H},\hat{A}]\psi\rangle_\Omega + \text{cc}\} = (1/2)\oint dS(\Omega,\boldsymbol{r})\,\boldsymbol{j}_A\cdot\boldsymbol{n}(\boldsymbol{r}) + \text{cc}$$

The presence of the flux term is essential to describe the properties of an open system. When $\hat{H}$ and $\hat{A}$ do not commute, there is a property flux across the surface bounding the atom, a contribution that is necessarily equal and opposite to the average of the corresponding commutator for an open system in a stationary state. In the time-dependent case, the difference between the two terms in eq. [18] determines the time rate of change of the average value of the property A for an open system.

The surface term in eq. [18] determines the net outflow of the property A in terms of the flux in the property's current density through surface bounding the open system. Thus the quantum description of a property and its time rate of change are determined only for bounded regions of space including the total system that is bounded at infinity. An essential part of this description for an open system is provided by the surface flux of the associated current density. An important consequence of this result is that one must forego all definitions of an atom based on the orbital model or on partitionings of the basis set used in its construction, as these definitions assume the atom to be without boundaries and to extend over all space.

The generalization of the result in eq. [18] to the many-electron case is straightforward, as one simply modifies all of the integrals by inserting the symbol $N\int d\tau'$ denoting a summation over all spins and an integration over all coordinates save those denoted by the vector $\boldsymbol{r}$, the coordinate of the electron whose integration is restricted to the open system Ω followed by multiplication by N, the number of electrons. Thus for example, the general definition of the current density for property A for the many-electron case obtained from eq. [17] becomes

$$[19] \quad \boldsymbol{j}_A(\boldsymbol{r}) = (\hbar/2mi)N\int d\tau'\{\psi^*\nabla(\hat{A}(\boldsymbol{r})\psi) - (\psi^*\nabla)\hat{A}(\boldsymbol{r})\psi\}$$

where the gradient operator ∇ is a function of the coordinate $\boldsymbol{r}$, as is explicitly indicated for the operator $\hat{A}(\boldsymbol{r})$. When $\hat{A}(\boldsymbol{r})$ equals the unit operator, one obtains the definition for the current $\boldsymbol{j}(\boldsymbol{r})$ that describes the flow of the electron density through space:

$$[20] \quad \boldsymbol{j}(\boldsymbol{r}) = (\hbar/2mi)N\int d\tau'\{\psi^*\nabla\psi - (\psi^*\nabla)\psi\}$$

This is the same mode of integration used to define the electron density, eq. [2], and through its use one obtains a spatial and current density for any property. The mode of integration denoted by $N\int d\tau'$ is not arbitrary but, as demonstrated later, follows directly from the field theoretic derivation of the principle of stationary action wherein every operator $\hat{A}(\boldsymbol{r})$ is identified with a generator that acts on a single field point.

In what follows we shall consider a one-electron system with the understanding that the many-electron case is trivially obtained from it by the insertion of $N\int d\tau'$. Or alternatively, one can consider what follows to be in the language of field theory with $\psi \equiv \hat{\Psi}(\boldsymbol{r})$ and $\psi^* \equiv \hat{\Psi}^+(\boldsymbol{r})^*$ describing the Schrödinger matter field, an interpretation underscored by a quotation from Schwinger (14): "The essence of field theory is to provide a conceptually simpler and more fundamental description by depending on the particle as the basic entity."

We have used Schrödinger's equation to derive the hypervirial theorem for an open system without placing any restrictions on its form other than that it be bounded. The question remaining is whether any and all regions Ω have physical significance, or whether there is a special class of open systems, special in the sense that they and their properties would be defined and determined by the same physics that determines the properties of the total system of which they are a part?

Schrödinger revisited

In his first paper, Schrödinger (12) demonstrated that making the energy functional $\mathcal{J}[\psi]$ stationary with respect to first-order variations in the wave function ψ, where

$$[21] \quad \mathcal{J}[\psi] = \int d\tau\{(\hbar^2/2m)\nabla\psi^*\cdot\nabla\psi + V\psi^*\psi\}$$

and subject to the constraint that ψ remain normalized, yields $\hat{H}\psi = E\psi$ as the Euler equation. The constant E is introduced as the Lagrange multiplier required for the normalization constraint on ψ. The functional $\mathcal{J}[\psi]$, which he termed the "Hamilton integral,"is the total energy expressed in a manifestly real form, with the kinetic energy expressed as $(1/2m)\,\langle\hat{\boldsymbol{p}}\psi,\hat{\boldsymbol{p}}\psi\rangle$, see eq. [4]. Thus the function ψ, which makes the energy stationary (and a minimum) through the condition $\delta\mathcal{J}[\psi] = 0$, is the same function that satisfies Schrödinger's equation. In his first paper Schrödinger considered the hydrogen atom and showed that the solutions to his equation yielded quantization of the energy and angular momentum, as opposed to previous work in which such quantization was imposed in the form of "quantum conditions." The manner in which the variation of eq. [21] is carried out is outlined in the next section for those unfamiliar with the calculus of variations. The actual procedure is quite simple. Someone interested in more detail can refer to my book (15) or to one particular Feynman lecture (16).

Schrödinger's energy functional for an open system Ω, $\mathcal{G}[\psi,\Omega]$, is defined as (13)

$$[22] \quad \mathcal{G}[\psi,\Omega] = \int_\Omega d\tau\{(\hbar^2/2m)\nabla\psi^*\cdot\nabla\psi + (\hat{V}-E)\psi^*\psi\}$$

where the undetermined multiplier for normalization is incorporated into the expression and identified with $-E$, the negative of the total energy. The variation of $\mathcal{G}[\psi,\Omega]$ must include a variation of the surface bounding Ω if one is to obtain a non-arbitrary definition of Ω and its properties. Using the usual recipe for the variation of some functional, as described in my book (15), one obtains the result given in eq. [23]. The integrand of the functional $\mathcal{G}[\psi,\Omega]$, denoted by f, depends upon ψ and $\nabla\psi$ (and their complex conjugates; ψ

© 1998 NRC Canada

PROOF/ÉPREUVE

is treated independently of ψ^* in the variation) and the variation of $\mathcal{G}[\psi,\Omega]$, including a variation of its surface, assumes the form

$$[23]\quad \delta\mathcal{G}[\psi,\Omega] = \int_\Omega d\tau\{(\partial f/\partial\psi)\delta\psi + (\partial f/\partial\nabla\psi)\partial\nabla\psi\} + \oint dS(\Omega,\boldsymbol{r}) f(\psi,\nabla\psi)\delta S(\Omega,\boldsymbol{r}) + cc$$

where $\delta\psi$ and $\delta\nabla\psi$ denote variations (infinitesimal changes) in ψ and its gradient. The surface bounding the open system is denoted by $S(\Omega,\boldsymbol{r})$, a function of the coordinate $\boldsymbol{r}$, and δS denotes a variation of S through its dependence on ψ. Carrying out the steps indicated above one obtains

$$[24]\quad \delta\mathcal{G}[\psi,\Omega] = \int_\Omega d\tau\{\hat{H}\psi^* - E\psi^*\}\delta\psi + \oint dS(\Omega,\boldsymbol{r})\{(\hbar^2/2m)\nabla\psi^*\cdot\boldsymbol{n}(\boldsymbol{r})\delta\psi + \delta S(\Omega,\boldsymbol{r}) f(\psi,\nabla\psi)\} + cc$$

where the Hamiltonian appearing in eq. [24] is

$$[25]\quad \hat{H} = -(\hbar^2/2m)\nabla^2 + \hat{V}$$

An integration by parts is used to obtain eq. [24] by ridding the original expression of variations in $\nabla\psi$ that arise from the second term on the RHS of eq. [23]. The identity in eq. [26]

$$[26]\quad \nabla\cdot(\nabla\psi^*\delta\psi) = (\nabla^2\psi^*)\delta\psi + \nabla\psi^*\cdot(\delta\nabla\psi)$$

enables one to replace the resulting troublesome term $\nabla\psi^*\cdot(\delta\nabla\psi)$ with the term $-(\nabla^2\psi^*)\delta\psi$, the kinetic energy operator as it appears in $\hat{H}$ together with the divergence term appearing on the LHS. The integral of this latter term is replaced with the first of the surface terms appearing in eq. [24] using Gauss' theorem.

When Ω refers to the total system, the surface $S(\boldsymbol{r})$ then occurs infinitely remote from the attractors of the system and the surface terms vanish either by demanding that $\delta\psi = 0$ when any $\boldsymbol{r} = \infty$ or by imposing the so-called natural boundary condition, that

$$[27]\quad \nabla\psi\cdot\boldsymbol{n}(\boldsymbol{r}) = 0 \text{ and } \nabla\psi^*\cdot\boldsymbol{n}(\boldsymbol{r}) = 0 \qquad \forall\boldsymbol{r} = \infty$$

In this case, the variation in eq. [24] becomes the variation in $\mathcal{G}[\psi]$, the functional used by Schrödinger, see eq. [21], and eq. [24] reduces to eq. [28]

$$[28]\quad \delta\mathcal{G}[\psi] = \int d\tau\{\hat{H}\psi^* - E\psi^*\}\delta\psi + cc = 0$$

The variation $\delta\mathcal{G}[\psi]$ is equated to zero, making the functional stationary with respect to arbitrary variations in ψ, as postulated by Schrödinger (12). The condition that $\delta\mathcal{G}[\psi]$ be stationary for *any* and *all* arbitrary variations $\delta\psi$ or $\delta\psi^*$ (which are considered to be independent), can be satisfied only if the quantity multiplied by the variation $\delta\psi$ or $\delta\psi^*$ in eq. [28] vanishes. This yields the so-called Euler equations of the variation, which in this case is Schrödinger's equation and its complex conjugate,

$$[29]\quad \hat{H}\psi^* - E\psi^* = 0 \text{ and } \hat{H}\psi - E\psi = 0$$

If eq. [24] for the variation in $\mathcal{G}[\psi,\Omega]$ is to be obtained for all variations and for all regions, then it necessarily holds for the case $\Omega = \boldsymbol{R}^3$, which, as demonstrated above, yields Schrödinger's equations as the Euler equations. Thus at the point of variation, Schrödinger's equations apply and the variation of Schrödinger's energy functional generalized to any open system reduces, at the point of variation, to

$$[30]\quad \delta\mathcal{G}[\psi,\Omega] = \oint dS(\Omega,\boldsymbol{r})\{(\hbar^2/2m)\nabla\psi^*\cdot\boldsymbol{n}(\boldsymbol{r})\delta\psi + \delta S(\Omega,\boldsymbol{r}) f(\psi,\nabla\psi)\} + cc$$

Thus, unlike the case for the total system where $\delta\mathcal{G}[\psi] = 0$, the variation in $\mathcal{G}[\psi,\Omega]$ does not vanish but rather equals a sum of two surface terms. One is proportional to the variation of ψ on the boundary, the other to the variation of the boundary itself. It is clear that the surface term proportional to $\delta\psi$ does not vanish, for the boundary of Ω involves finite values of $\boldsymbol{r}$ where the natural boundary condition does not apply and the variations of ψ on such a boundary must remain arbitrary and cannot be set equal to zero.

As we were later to discover, this generalization of the variation principle that we obtained by retaining the variations in ψ on the boundary of the system and of varying the boundary itself, a procedure followed out of necessity in the variation of $\mathcal{G}[\psi,\Omega]$, is precisely the step that Schwinger purposely introduces in his generalization of the variation of the action integral to obtain the principle of stationary action (2).

Equation [30] is not an operational result because of the appearance of the variation of the surface $S(\Omega,\boldsymbol{r})$, which prevents one from relating the result to the physics governing the system. Further progress is possible only through the replacement of this term. It is this step which limits the final result to a particular class of open systems. One first notes that when Schrödinger's equations apply, the integrand of $\mathcal{G}[\psi]$ or $\mathcal{G}[\psi,\Omega]$ reduces in the manner shown in eq. [31]:

$$[31]\quad f(\psi,\nabla\psi) = (\hbar^2/4m)\nabla^2(\psi^*\psi) = (\hbar^2/4m)\nabla^2\rho(\boldsymbol{r})$$

This result, and an identical one for the complex conjugate, is obtained using the identity relating the alternative expressions for the kinetic energy densities as previously discussed in eq. [5]. Equation [31] is a remarkable result. It states that Schrödinger's energy functional reduces to a term proportional to the Laplacian of the electron density at the point of variation, that is, when $\hat{H}\psi = E\psi$. This same reduction occurs in the many-electron case for both stationary and time-dependent states. In the latter case, the functional becomes the many-particle Lagrangian density, including that appropriate to the presence of an electromagnetic field. For this reason there is a parallel in the development given here for a stationary state and that for the generalized variation of the action integral. By Gauss' theorem, the integral of $\nabla^2\rho$ over Ω reduces to the flux in $\nabla\rho$ through its surface, eq. [6], a term that vanishes for an atom because of the zero-flux condition, eq. [1]. Thus the atomic average of the energy functional $\mathcal{G}[\psi,\Omega]$, of the Lagrangian and of the action integral vanish, as they do for the total system.

Using the result given in eq. [31], the variation of $\mathcal{G}[\psi,\Omega]$ as given in eq. [30] reduces to

© 1998 NRC Canada

PROOF/ÉPREUVE

[32] $$\delta\mathcal{G}[\psi,\Omega] = \oint dS(\Omega,\boldsymbol{r})(\hbar^2/4m)\{2\nabla\psi^*\cdot\boldsymbol{n}(\boldsymbol{r})\delta\psi + \delta S(\Omega,\boldsymbol{r})\nabla^2\rho(\boldsymbol{r})\} + cc$$

an expression that makes possible the elimination of the surface variation term by the imposition of a constraint on the form of the open system. One considers the entire variation to be carried out using a trial function Φ, which, at the point of variation, reduces to the state function ψ. One imposes, at all stages of the variational procedure, the constraint that the region $\Omega(\Phi)$, defined in terms of the trial function Φ, be bounded by a "zero-flux surface," one such that

[33] $$\nabla\rho_\Phi(\boldsymbol{r})\cdot\boldsymbol{n}(\boldsymbol{r}) = 0 \quad \forall\boldsymbol{r}\in S(\Omega,\boldsymbol{r})$$

where ρ_Φ is the trial density. The region $\Omega(\Phi)$ represents the open system in the varied total system described by the trial function Φ just as $\Omega(\psi)$ represents the open system in the state described by ψ. Requiring the fulfillment of eq. [33] amounts to imposing the variational constraint that the divergence of $\nabla\rho_\Phi = \nabla\cdot\nabla\rho_\Phi$ integrates to zero at all stages of the variation, i.e.,

[34] $$\int_\Omega \nabla^2\rho_\Phi(\boldsymbol{r})\,d\tau = 0$$

for all admissible Φ, which in turn implies that

[35] $$\delta\{\int_\Omega \nabla^2\rho(\boldsymbol{r})\,d\tau\} = 0$$

The variation denoted in eq. [35] requires a variation of the surface as well as a variation of the integrand, as in eq. [23]. Since the sum of these two terms must vanish as a result of the constraint, one is able to equate the integral of the variation in the surface to the negative of the variation of the integrand to obtain

[36] $$(\hbar^2/4m)\oint dS(\Omega,\boldsymbol{r})\delta S(\Omega,\boldsymbol{r})\nabla^2\rho(\boldsymbol{r}) = -(\hbar^2/4m)\int_\Omega \delta\{\nabla^2\rho(\boldsymbol{r})\}\,d\tau$$

and the RHS of this constraint equation can be substituted for the term involving the variation of the surface appearing in eq. [32]. The RHS is easily evaluated to yield

[37] $$\int_\Omega \delta\{\nabla^2\rho(\boldsymbol{r})\}d\tau = \int_\Omega d\tau\nabla\cdot\{\nabla\psi^*\delta\psi + \psi^*\nabla\delta\psi\} = \int_\Omega dS(\Omega,\boldsymbol{r})\{\nabla\psi^*\delta\psi + \psi^*\nabla\delta\psi\}\cdot\boldsymbol{n}(\boldsymbol{r})$$

where the final step uses Gauss' theorem to replace the volume integral of a divergence with a surface integral. This is a most important step for, because of it, the imposition of the variational constraint yields only surface terms and thus Schrödinger's equations are still obtained as the Euler equations from the volume variations. Using eqs. [36] and [37], the expression for the constrained variation obtained from eq. [32] is

[38] $$\delta\mathcal{G}[\psi,\Omega] = (\hbar^2/4m)\times\oint dS(\Omega,\boldsymbol{r})\{\nabla\psi^*\delta\psi - \psi^*\delta\nabla\psi\}\cdot\boldsymbol{n}(\boldsymbol{r})$$

Equation [38] is a physical result because, as is now demonstrated, it expresses the variation of the energy functional for an open system in terms of the flux in the infinitesimal change in the vector current density through its surface. The single-particle vector current density is defined in eq. [20] and the infinitesimal change in $\boldsymbol{j}(\boldsymbol{r})$ caused by a variation in ψ is

[39] $$\delta\boldsymbol{j}(\boldsymbol{r}) = (\hbar/2mi)\{\psi^*\delta(\nabla\psi) - (\nabla\psi^*)\delta\psi\}$$

The expression for the variation of the open system energy functional constrained to a region bounded a zero-flux surface in the gradient vector field of the electron density can thus be expressed as (13)

[40] $$\delta\mathcal{G}[\psi,\Omega] = -(i\hbar/2)\oint dS(\Omega,\boldsymbol{r})\delta\boldsymbol{j}(\boldsymbol{r})\cdot\boldsymbol{n}(\boldsymbol{r}) + cc$$

Equation [40] is obtained as a result of taking two distinct steps: (*a*) generalizing the variation so as to retain the variation in ψ on the system's boundary together with a variation of the boundary, and (*b*) restricting the system to one bounded by a zero-flux surface in $\nabla\rho$. It provides the basis for the formulation of the principle of stationary action for an open system in a stationary state. This is accomplished by identifying the variations in ψ appearing in the surface term of eq. [40] with the generators of infinitesimal unitary transformations, the procedure introduced by Schwinger (2).

The transformations of quantum mechanics are unitary transformations and Schwinger makes use of the fact that *infinitesimal unitary transformations, acting separately on the state function or observables, can be used to generate any and all possible changes in the dynamical variables of a quantum system*. The transformations are introduced into the theory by identifying them with the variations of the state function obtained in the generalized variation of Schrödinger's energy functional.

The operator for an infinitesimal unitary transformation and its inverse, its Hermitian conjugate, are given by

[41] $$\hat{U} = \hat{\imath} - (i\varepsilon/\hbar)\hat{G} \text{ and } \hat{U}^{-1} = \hat{\imath} + (i\varepsilon/\hbar)\hat{G}$$

where ε denotes an infinitesimal and $\hat{G}$, referred to as the generator of the transformation, is any linear Hermitian operator, i.e., any observable. The first-order changes in ψ and ψ^* are equated to the action of the generator $\hat{G}$ on ψ and ψ^* according to

[42] $$\delta\psi = -(i\varepsilon/\hbar)\hat{G}\psi \text{ and } \delta\psi^* = (i\varepsilon/\hbar)\hat{G}\psi^*$$

The generator of an infinitesimal temporal change is $-\hat{H}\,\delta\boldsymbol{t}$ while the generators of all possible spatial changes are functions of the coordinate and (or) momentum operators. A generator $\hat{G}$ that is a function only of the position operator $\hat{\mathbf{r}}$ will generate a gauge transformation while one which is linear in the momentum $\hat{\boldsymbol{p}}$ will generate a coordinate translation.

Replacing the variations $\delta\psi$ and $\delta\psi^*$ in eq. [40], as they appear in the expression for the variation of the current in eq. [39], by the action of infinitesimal generators defined in eq. [42] yields

[43] $$\delta\mathcal{G}[\psi,\Omega] = -(\varepsilon/2)\{\oint dS(\Omega,\boldsymbol{r})\boldsymbol{j}_G(\boldsymbol{r})\cdot\boldsymbol{n}(\boldsymbol{r}) + cc\}$$

© 1998 NRC Canada

PROOF/ÉPREUVE

using the definition of a property current density given in eq. [19]. Thus the variation in Schrödinger's energy functional for an open system bounded by a zero-flux surface is proportional to the surface flux of the current density of the infinitesimal generator causing the change in the system. An alternative and final form for the variation of the functional is obtained by using the statement of the hypervirial theorem for an open system, eq. [18], to substitute for the surface terms. This yields (13)

$$[44] \quad \delta\mathcal{G}[\psi,\Omega] = -(\varepsilon/2)\{(i/\hbar)\langle\psi\,|\,[\hat{H},\hat{G}]\,|\,\psi\rangle_{\Omega} + \text{cc}\}$$

It will be demonstrated below that eq. [44] is a statement of the principle of stationary action for a system in a stationary a state. It determines the physics of an atom in a molecule. It applies only to a region of real space Ω bounded by a surface of zero flux in the gradient vector field of the electron density, eq. [1], a condition fulfilled by the total system as well. *Thus a single principle provides the quantum mechanical description of the total system and of its constituent atoms*. Open systems defined by the principle of stationary action are called *proper open systems.*

The derivation of the theorems that govern the behavior of atoms in molecules using eq. [44], the atomic virial theorem for example, is preceded with a condensed account of how Dirac's work laid the groundwork for the ideas of Schwinger and Feynman and of how and why Schwinger's principle of stationary action reduces to eq. [44] for a proper open system in a stationary state.

From Dirac to Schwinger

Dirac's work set the stage for the work of Feynman and Schwinger. First and foremost, he introduced transformation theory into quantum mechanics (17). This is the underlying mathematical formalism of this new physics, which consists of the general mathematical scheme of linear operators and state vectors with its associated probability interpretation. In doing so, he stressed how the theory of infinitesimal unitary transformations in quantum mechanics parallels the infinitesimal canonical transformations of classical theory, as is made clear in the quotation given in the endnote.[3]

In particular, in 1933 these arguments led Dirac to write what was to be a paper of singular importance (18). In it he posed the question of what would correspond to the limiting classical expression for the quantum probability amplitude for the passage of a system with a set of coordinates denoted collectively by q at time t to another state with coordinates q' at t', a quantity denoted by the transformation amplitude $\langle q,t\,|\,q',t'\rangle$. In effect, Dirac was asking for the correspondence of quantum mechanics with the Lagrangian method of classical mechanics, a formulation he considered to be more fundamental than the one based on Hamiltonian theory.

In the Lagrangian approach, the equation of motion (Lagrange's or Newton's) that determines how a system proceeds from one classical state (q,t) to another (q',t') is

Fig. 4. A diagram illustrating the correct space-time trajectory linking an initial position q_1 at time t_1 to the final position q_2 at t_2 and a second possible trajectory obtained from it by a variation of the position q at each time t along the path. The correct path is the one that minimizes the action integral W_{tt}'. Note that the variations in q are set to zero at each time end point, a limitation that is removed in Schwinger's generalization of the variation of the action integral.

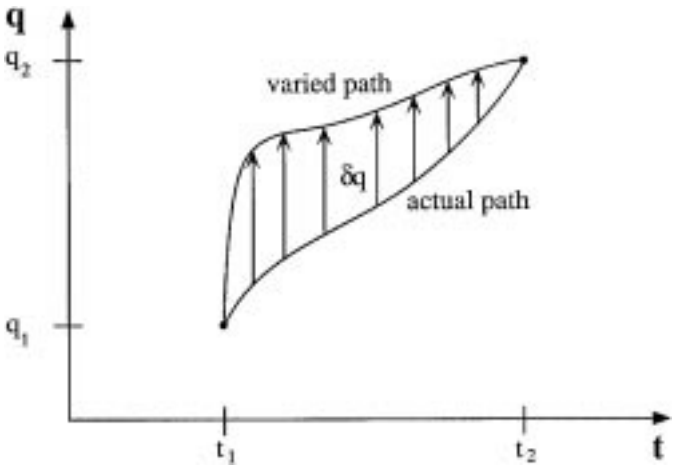

obtained from the principle of least action. In this principle the space-time trajectory connecting the two classical states, as illustrated in Fig. 4, is the one that minimizes a quantity called the action, the time integral of the system's Lagrangian and denoted by $W_{tt'}$. The Lagrangian has the dimensions of energy, and the action, of energy multiplied by time. The classical Lagrangian is a function of the coordinates, their velocities, and the time, $L(q,\dot{q},t)$, and is expressed as the difference between the kinetic and potential energies. The action is expressed as a double integral of the Lagrangian: once over the space interval q to q' and again over the time interval t to t', as shown in eq. [45]:

$$[45] \quad W_{tt'} = \int \mathrm{d}t \int \mathrm{d}q\; L(q,\dot{q},t)$$

Minimizing the action integral through a variation of the coordinates defining the path followed by the system through time, that is, setting the variation in $W_{tt'}$ equal to zero, yields the classical equation of motion as the Euler equation in the same manner that the variation of the wave function in Schrödinger's functional $\mathcal{G}[\psi]$ yielded Schrödinger's equation by setting $\delta\mathcal{G}[\psi] = 0$, eq. [28]. The particular form for the Lagrangian is chosen so as to yield the correct equation of motion in the minimization of the action, as described above. Taking the Lagrangian as given, whether it be classical, quantal, or relativistic, enables one to derive the corresponding equation of motion using this "principle of least action."

The limiting classical expression for the quantum probability amplitude proposed by Dirac is

[3] "The variation with time of the Heisenberg dynamical variables may thus be looked upon as the continuous unfolding of a unitary transformation. In classical mechanics the dynamical variables at time $t + \mathrm{d}t$ are connected with their values at time t by an infinitesimal contact transformation and the whole motion may be looked upon as a continuous unfolding of a contact transformation. We have here the mathematical foundation of the analogy between the classical and quantum equations of motion, and can develop it to bring out the quantum analogue of all the main features of the classical theory of dynamics." Dirac, see ref. 17, p. 125.

© 1998 NRC Canada

PROOF/ÉPREUVE

[46] $\langle q,t \mid q',t'\rangle = \exp\,(i\,W_{tt'}/\hbar)$

where $W_{tt'}$ is the classical action evaluated along the unique path the causes it to assume its minimum value, that is, the path that causes $\delta W_{tt'} = 0$. Equation [46] set the stage for the reformulation of quantum mechanics by Feynman and Schwinger.

The classical concept of a system following a uniquely defined trajectory must be abandoned in a quantum description. Thus Feynman, in 1948, replaced the expression given by Dirac for the single classically allowed path, by a corresponding sum over all possible paths $q(t)$ connecting the two space-time points to obtain the path integral expression for the quantum probability amplitude $\langle q,t \mid q',t'\rangle$ (1). (The sum is replaced by an integral in eq. [47] in the limit of a continuum of possible paths $\delta q(t)$, and N is a normalizing factor.)

[47] $\langle q,t \mid q',t'\rangle = (1/N)\int \exp\,(i\,W/\hbar)\delta q(t)$

Each contributing path has the same modulus, but its phase is proportional to the classical action along the path, as given in Dirac's expression. Feynman went on to show that the path integral expression yields Schrödinger's equation and the commutation relations (1).

Schwinger, in a related but separate derivation given in 1951, showed how one can obtain all the laws of physics by combining the action principle with Dirac's transformation theory (2). Schwinger realized that infinitesimal unitary transformations can be used to provide a differential characterization of a transformation function such as $\langle q,t \mid q',t'\rangle$ and this led him to postulate his new dynamical principle, eq. [48], that is in effect a differential form of Feynman's expression

[48] $\delta\langle q,t \mid q',t'\rangle = (i/\hbar)\langle q,t \mid \delta\hat{W}_{tt'} \mid q',t'\rangle$

The corresponding expression for $\delta\langle q,t \mid q',t'\rangle$ obtained from Dirac's transformation theory in terms of infinitesimal generators $\hat{G}(t)$ acting at the two time end points is given by (the infinitesimal ε is absorbed in the symbol for the generator in eqs. [49] and [50])

[49] $\delta\langle q,t \mid q',t'\rangle = (i/\hbar)\langle q,t \mid \hat{G}(t) - \hat{G}(t') \mid q',t'\rangle$

A comparison of these two expressions leads to the principle of stationary action, eq. [50],

[50] $\delta\hat{W}_{tt'} = \hat{G}(t) - \hat{G}(t')$

that is, the variation of the action integral does not vanish, as it does in the principle of least action, but instead equals the difference in the values of the generators acting at the two time end points. This principle, like Feynman's, yields Schrödinger's equation and the commutation relations (2).

What Schwinger has done is to identify the variations in the state vectors at the two time end points with generators of infinitesimal unitary transformations. The time evolution of an open system will sweep out a space-time volume and, in the general formulation of his principle, Schwinger allows for the generators to act not only at the time end points, but also on the spatial boundaries of an open system by retaining the variations both on and of its surface at each time. Thus in Schwinger's general formulation, one retains the variations at the time-like surface that is created by the temporal evolution of the spatial boundary, as well as at the space-like surfaces that represent the system at the two time end points, and identifies them with the generators of infinitesimal unitary transformations.

In our generalization of the variation of Schrödinger's energy functional to an open system to obtain eq. [44] we necessarily retained the variations in ψ on its spatial boundary, but for just a single time, and then identified them with the action of infinitesimal generators. Schwinger on the other hand recognized that, by making such an identification at both the time-like and space-like surfaces bounding the space-time volume swept out by the action integral, he could incorporate all of physics into a single dynamical principle, the principle of stationary action. Clearly, if one desires a fundamental definition of an atom based on the action principle, its motion through time must sweep out a piece of space-time and its boundaries must therefore, be defined in real space, the same conclusion arrived at earlier using the equation of motion for an observable.

Having realized that eq. [44] was a stationary state embodiment of the ideas used by Schwinger in his principle of stationary action, we were faced with the challenge of deriving the corresponding expression for the time-dependent case through a variation of the action integral for an open system (19, 20). While Schwinger's paper gives the general expression for the variation of both the time-like and space-like surfaces of the action integral, he limits his use of this result to variations at the two time endpoints of a total system, to obtain the result given in eq. [50].

The generalization of eq. [50] to a proper open system through a variation of the action integral follows, step for step, the variation of Schrödinger's energy functional for an open system in a stationary state. To show this correspondence we shall reproduce two important steps in the derivation and, to make them particularly clear, state them in the form of a variation for an infinitesimal time interval, that is, as variations of the Lagrange integral rather than of the action integral (21). Equation [51] comes at the point corresponding to that of eq. [30] in the stationary state case,

[51] $$\delta\hat{\mathscr{L}}[\hat{\Psi},\Omega] = (\varepsilon/2)\int_{\Omega} d\boldsymbol{r}\partial\{\hat{\Psi}^{+}(\hat{G}\hat{\Psi}) + \text{cc}\}/\partial t + \oint dS(\Omega,\boldsymbol{r})\cdot\{(-\hbar^2/2m)(\nabla\hat{\Psi}^{+}\delta\Psi + \text{cc} + \boldsymbol{n}\hat{\boldsymbol{L}}\delta S(\Omega,\boldsymbol{r}))\}$$

At this point, the appropriate Schrödinger equation has been obtained from the variation of the action over the space-time volume corresponding to the variation of $\mathscr{G}[\psi,\Omega]$ over the interior of the system in the stationary state case, leaving variations on the boundaries in both cases. For $\delta\mathscr{G}[\psi,\Omega]$ this yields only the surface integral, but eq. [51] contains a time-dependent term resulting from the variation of $\hat{\Psi}$, as represented by the action of a generator, over the open system Ω at each time end point, that is, over the space-like surfaces of the open system. The surface integrals in eqs. [30] and [51] are identical in form and content and one proceeds, from this point on, in an identical manner. The troublesome term involving the variation of the surface is treated as before, by recognizing that at the point of variation, the Lagrange

© 1998 NRC Canada

PROOF/ÉPREUVE

density $\hat{L}(\hat{\Psi},\nabla\hat{\Psi},t)$ in eq. [51] reduces to $-(\hbar^2/4m)\nabla^2\,\hat{\rho}$. Aside from a sign change, this is the same property exhibited by Schrödinger's functional $f(\Psi,\nabla\Psi)$, eq. [31]. Because of this property of $\hat{L}(\hat{\Psi},\nabla\hat{\Psi},t)$ one may impose the variational constraint on the boundary of the open system given in eq. [35] and thereby replace the term $\boldsymbol{n}\cdot\hat{L}\delta\boldsymbol{S}(\boldsymbol{r}_s)$ with one proportional to the variation of $\nabla\rho\cdot\boldsymbol{n}$, as done in eqs. [36] and [37]. Combining this result with the first of the surface terms in eq. [51] and replacing the variations in $\hat{\Psi}$ with the action of infinitesimal generators, transforms the surface integral into an integral of the flux in the current of the generator though the surface of the open system, eq. [52],

$$[52]\qquad \delta\hat{\mathscr{L}}[\hat{\Psi},\Omega] = (\varepsilon/2)\int_{\Omega} d\boldsymbol{r}\partial\{\hat{\Psi}^{+}(\hat{G}\hat{\Psi}) + cc\}/\partial t + (\varepsilon/2)\oint dS(\Omega,\boldsymbol{r})\cdot\{\boldsymbol{J}_G(\boldsymbol{r}) + cc\}$$

the identical surface term to that obtained in the generalization of Schrödinger's variation principle, eq. [43]. Indeed, eq. [52] reduces to eq. [43] when applied to a stationary state. Finally, through the use of the Heisenberg equation of motion for a generator $\hat{G}$, eq. [52] is transformed into eq. [53] (19–21):

$$[53]\qquad \delta\hat{\mathscr{L}}[\hat{\Psi},\Omega] = (\varepsilon/2)\{(i/\hbar)\langle\hat{\Psi}\,|[\hat{H},\hat{G}(\boldsymbol{r})]\,|\,\hat{\Psi}\rangle_{\Omega} + cc\}$$

Thus the form of the principle of stationary action obtained from a variation of the action integral operator is in complete correspondence with the expression obtained for a stationary state, eq. [44]. Like eq. [44], eq. [53] applies only to systems bounded by a surface satisfying eq. [1], that is, to the total system and its proper open systems. This principle, in addition to yielding Schrödinger's equation, defines the observables, their equations of motion, and their expectation values. These are the properties that must be established and defined for an open system if one wishes to obtain a quantum description of an atom in a molecule.

The physics of an atom in a molecule

The atomic theorems are obtained by setting the generator $\hat{G}$ in eq. [53] equal to the observable of interest, as done for a number of important cases to obtain the theorems listed in Table 1 (22). Each term on the LHS in Table 1 is the time-rate-of change of $\rho_G(\boldsymbol{r})$, the density of property G. This term and the surface term on the RHS are obtained from eq. [52], giving the variation of $\hat{\mathscr{L}}[\hat{\Psi},\Omega]$ as caused by the generator $\hat{G}(\boldsymbol{r})$ for a proper open system. The first term on the RHS is the atomic average of the commutator in eq. [53]. For a total system, the surface integral in each theorem vanishes and one obtains the usual Heisenberg equation of motion for $\hat{G}(\boldsymbol{r})$. For a total system in a stationary state, one obtains the hypervirial theorem wherein the commutator average is equated to zero. For an open system in a stationary state, the commutator average is equated to and balanced by the negative of the flux of the corresponding current through the surface of the open system.

The commutator average is obtained in the manner previously described by the notation $N\int d\tau'$ and illustrated in the definition of the electron density, eq. [2], and its current, eq. [20]. As pointed out in the latter case, this mode of integration follows directly from the field theoretic derivation of eq. [53], as consequence of each generator $\hat{G}(\boldsymbol{r})$ acting at a single field point. It is this feature of the theory that yields a spatial density $\rho_G(\boldsymbol{r})$ and a current $\boldsymbol{j}_G(\boldsymbol{r})$ describing its flow for every property G and leads to the renormalization of the mechanics underlying chemistry referred to in the Abstract. The resulting densities and currents account for the short-range nature of the forces that enable one to identify a given atom or group in any environment. This transformation from field theory, which "depends on the particle as the basic entity" (14), to the Schrödinger representation employed in Table 1 is indicated in eq. [54]

$$[54]\qquad \{(i/\hbar)\langle\hat{\Psi}\,|[\hat{H},\hat{G}(\boldsymbol{r})]\,|\,\hat{\Psi}\rangle_{\Omega} + cc\} \Rightarrow \{(i/\hbar)N\int_{\Omega} d\boldsymbol{r}\int d\tau'\{\psi^*[\hat{H},\hat{G}(\boldsymbol{r})]\psi\} + cc\}$$

Atomic force theorem

To illustrate the use of the atomic principle of stationary action, we derive the atomic force theorem, obtained when $\hat{G}(\boldsymbol{r})$ is set equal to $\hat{\boldsymbol{p}}\,(\boldsymbol{r}) = -i\hbar\nabla$, the momentum operator for an electron. The time-rate-of change of $\hat{\boldsymbol{p}}(\boldsymbol{r})$ is force and the commutator yields, the force acting on the electron. Since $(i/\hbar)[\hat{\boldsymbol{H}},\hat{\boldsymbol{p}}(\boldsymbol{r})] = -\nabla\hat{\boldsymbol{V}}$ where $\hat{\boldsymbol{V}}$ is the total potential energy operator, the commutator determines the force exerted on the electron at $\boldsymbol{r}$ by all of the remaining particles in the system and the averaging of this operator over the coordinates of the remaining electrons yields a force density $\boldsymbol{F}(\boldsymbol{r})$

$$[55]\qquad \boldsymbol{F}(\boldsymbol{r}) = N\int d\tau'\{\psi^*(-\nabla\hat{\boldsymbol{V}})\psi\}$$

While the operator $-\nabla\hat{\boldsymbol{V}}$ determines the force acting on the electron at the point $\boldsymbol{r}$ for one configuration of the system, the averaging denoted in eq. [55] yields the force acting on the electron at $\boldsymbol{r}$ for all possible configurations of the remaining electrons. The result is a "dressed particle," one whose density is determined by its interactions with the remainder of the system. Note that the definition of the force density differs from the definition of the electron density in eq. [2] only by the inclusion of the force operator between the state functions. In this manner, any property, even one involving many-particle interactions, is reduced to a corresponding real space density and this is how physics recovers real space chemistry. The integration of $\boldsymbol{F}(\boldsymbol{r})$ over the atomic basin then yields $\boldsymbol{F}(\Omega)$, the force acting on the electron density within the atomic basin,

$$[56]\qquad \boldsymbol{F}(\Omega) = \int_{\Omega} d\boldsymbol{r}\boldsymbol{F}(\boldsymbol{r}) = \int_{\Omega} N d\boldsymbol{r}\int d\tau'\{\psi^*(-\nabla\hat{\boldsymbol{V}})\psi\}$$

The current for $\hat{G}(\boldsymbol{r}) = \hat{\boldsymbol{p}}(\boldsymbol{r})$ appearing in eq. [52] is of particular importance. Its real part defines the quantum stress tensor $\boldsymbol{\sigma}(\boldsymbol{r})$,

$$[57]\qquad \boldsymbol{\sigma}(\boldsymbol{r}) = (N\hbar^2/4m)\int d\tau'\{(\nabla\nabla\psi^*)\psi - \nabla\psi^*\nabla\psi - \nabla\psi\nabla\psi^* + \psi^*\nabla\nabla\psi\} = -\mathrm{Re}\{\boldsymbol{j}_p(\boldsymbol{r})\}$$

© 1998 NRC Canada

PROOF/ÉPREUVE

Table 1. Atomic theorems for molecules and crystals.

Atomic force theorem $\hat{G} = \hat{\boldsymbol{p}}$

$$m\int d\boldsymbol{r}\, \partial \boldsymbol{j}(\boldsymbol{r})/\partial t = \int d\boldsymbol{r}\int d\tau'\, \Psi^*(-\nabla\hat{V})\Psi + \oint dS(\boldsymbol{r})\, \boldsymbol{\sigma}(\boldsymbol{r})\cdot \boldsymbol{n}(\boldsymbol{r})$$

Atomic virial theorem $\hat{G} = \hat{\boldsymbol{r}}\cdot\hat{\boldsymbol{p}}$

$$m\int_{\Omega} d\boldsymbol{r}\; \boldsymbol{r}\cdot\partial \boldsymbol{j}(\boldsymbol{r})/\partial t = 2T(\Omega) + \int_{\Omega} d\boldsymbol{r}\int d\tau'\, \Psi^*(-\boldsymbol{r}\cdot\nabla\hat{V})\Psi + \oint dS(\boldsymbol{r})\, \boldsymbol{r}\cdot\boldsymbol{\sigma}(\boldsymbol{r})\cdot\boldsymbol{n}(\boldsymbol{r})$$

Atomic torque theorem $\hat{G} = \hat{\boldsymbol{r}}\times\hat{\boldsymbol{p}}$

$$m\int_{\Omega} d\boldsymbol{r}\; \boldsymbol{r}\times\partial \boldsymbol{j}(\boldsymbol{r})/\partial t = \int_{\Omega} d\boldsymbol{r}\int d\tau'\, \Psi^*(-\boldsymbol{r}\times\nabla\hat{V})\Psi - \oint dS\; \boldsymbol{\sigma}(\boldsymbol{r})\times\boldsymbol{r}\cdot\boldsymbol{n}$$

Atomic current theorem $\hat{G} = \hat{\boldsymbol{r}}$

$$\int_{\Omega} d\boldsymbol{r}\; \boldsymbol{r}\, \partial\rho(\boldsymbol{r})/\partial t = \int_{\Omega} d\boldsymbol{r}\;\; \boldsymbol{j}(\boldsymbol{r}) - \oint dS\; \boldsymbol{n}(\boldsymbol{r})\cdot\; \boldsymbol{j}(\boldsymbol{r})\boldsymbol{r}$$

Atomic continuity theorem $\hat{G} = \hat{N}$

$$\int_{\Omega} d\boldsymbol{r}\, \partial\rho(\boldsymbol{r})/\partial t = -\oint dS\;\; \boldsymbol{j}(\boldsymbol{r})\cdot\boldsymbol{n}(\boldsymbol{r})$$

Atomic power theorem $\hat{G} = \hat{\boldsymbol{p}}^2/2m$, written without $1/2\; m$

$$\int_{\Omega} d\boldsymbol{r}\, \partial\rho_{\mathrm{p}^2}(\boldsymbol{r})/\partial t = \int_{\Omega} d\boldsymbol{r}\int d\tau'\,(\hbar/i)\{\Psi\nabla\Psi^* - \Psi^*\nabla\Psi)\cdot\nabla\hat{V}\} + \oint d\boldsymbol{S}\mathrm{Re}\{\boldsymbol{j}_{\mathrm{P}^2}(\boldsymbol{r})\}$$

Quantum stress tensor density

$$\boldsymbol{\sigma}(\boldsymbol{r}) = (\hbar^2/4m)\int d\tau'\,\{(\nabla\nabla\Psi^*)\Psi - \nabla\Psi^*\nabla\Psi - \nabla\Psi\nabla\Psi^* + \Psi^*\nabla\nabla\Psi\}$$

Quantum vector current density

$$\boldsymbol{j}(\boldsymbol{r}) = (\hbar/2mi)\int d\tau'\,\{\Psi^*\nabla\Psi - \Psi\nabla\Psi^*\}$$

which is expressible in terms of the one-electron density matrix. Thus the surface term in eq. [52], like the commutator, yields a density, the stress tensor having the dimensions of an energy density or pressure, force per unit area. For an open system in a stationary state, the atomic force theorem, eq. [58], equates the force acting over the basin of the atom to the momentum flux through its surface, that is, to the pressure acting on each of its surface elements $d\boldsymbol{S}$,

$$[58]\qquad \boldsymbol{F}(\Omega) = N\int_{\Omega} d\boldsymbol{r}\int d\tau'\,\{\psi^*(-\nabla\hat{V})\psi\} = -\oint dS(\Omega,\boldsymbol{r})\boldsymbol{\sigma}(\boldsymbol{r})\cdot\boldsymbol{n}(\boldsymbol{r})$$

Equation [58] states that the force acting on the electron density in an atomic basin is completely determined by the momentum flux through its surface, and is otherwise independent of the nature of the remainder of the system. That is, no knowledge of the remainder of the system is required over and above the pressure it exerts on the surface of the atom. The interdependence of basin and surface properties for an open system in a stationary state is a general result and is a consequence of the variational principle stated in eq. [40] (23). For example, if the two amidic surfaces of zero flux bounding an amino acid residue remain unchanged on its transfer from one polypeptide environment to another, then the residue and all of its properties remain unaffected by the transfer. When this behavior is found, one can construct polypeptides from amino acid residues defined as the central residue in tripepetides (23, 24).

Atomic virial theorem

The virial operator $\hat{\boldsymbol{r}}\cdot\hat{\boldsymbol{p}}$ has the dimensions of action and its time derivative is energy. Setting the generator equal to $\hat{\boldsymbol{r}}\cdot\hat{\boldsymbol{p}}$ yields the atomic statement of the virial theorem (13, 20). The commutator average yields twice the average electronic kinetic energy and the basin virial

$$[59]\qquad (1/2)\{(i/\hbar)\langle\psi|[\hat{H},\hat{\boldsymbol{r}}\cdot\hat{\boldsymbol{p}}]|\psi\rangle_{\Omega} + \mathrm{cc}\} = 2\boldsymbol{T}(\Omega) + \mathscr{V}_{\mathrm{b}}(\Omega)$$

The basin virial is the virial of the Ehrenfest forces acting over the basin of the atom (compare eq. [58])

$$[60]\qquad \mathscr{V}_{\mathrm{b}}(\Omega) = N\int_{\Omega} d\boldsymbol{r}\int d\tau'\,\psi^*(-\boldsymbol{r}\cdot\nabla\hat{V})\psi = -\int_{\Omega} d\boldsymbol{r}\;\boldsymbol{r}\cdot\nabla\cdot\boldsymbol{\sigma}$$

The surface term is determined by $\mathrm{Re}\{\boldsymbol{j}_{\mathrm{r}\cdot\mathrm{p}}\}$ and yields the contribution $-\mathscr{V}_{\mathrm{s}}(\Omega)$, the virial of the forces exerted on the surface of the atom (compare with the surface term in eq. [58])

© 1998 NRC Canada

PROOF/ÉPREUVE

$$[61]\quad (1/2)\oint dS(\Omega, \boldsymbol{r})\{\boldsymbol{j}_{r\cdot p}(\boldsymbol{r}) \cdot \boldsymbol{n}(\boldsymbol{r}) + cc\} = -\mathcal{V}_s(\Omega) - (\hbar^2/4m)\oint dS \nabla\rho(\boldsymbol{r}) \cdot \boldsymbol{n}(\boldsymbol{r})$$

where

$$[62]\quad \mathcal{V}_s(\Omega) = \oint dS(\Omega, \boldsymbol{r})\boldsymbol{r} \cdot \boldsymbol{\sigma}(\boldsymbol{r}) \cdot \boldsymbol{n}(\boldsymbol{r})$$

The final surface integral in eq. [61] vanishes because of the zero-flux boundary condition, eq. [1]. The surface integral $\mathcal{V}_s(\Omega)$ has been shown to be proportional to the pressure volume product for the atom Ω and it enables one to determine the pressure acting on an atom in any environment (25).

Equating the commutator and surface integrals for a stationary state followed by some rearrangement, yields the atomic statement of the virial theorem

$$[63]\quad -2T(\Omega) = \mathcal{V}_b(\Omega) + \mathcal{V}_s(\Omega) = \mathcal{V}(\Omega)$$

where the atomic virial $\mathcal{V}(\Omega)$ is the sum of the basin and surface contributions. By equating the electronic potential energy to the virial, the electronic energy of an atom in a molecule $E(\Omega)$ is defined as

$$[64]\quad E(\Omega) = T(\Omega) + \mathcal{V}(\Omega) = -T(\Omega)$$

where the final identity comes from the use of eq. [63]. This is precisely the form of the virial theorem that was postulated to hold for an atom in a molecule based on the studies of the charge and kinetic energy densities in 1972 (7). When there are no external (Hellmann–Feynman) forces acting on the nuclei, the virial $\mathcal{V}$ equals the average potential energy of the molecule and $E = T + \mathcal{V}$ then equals the total energy of the molecule. Equation [64] is as remarkable as it is unique. It uses a theorem of quantum mechanics to spatially partition all of the interactions in a molecule, electron–nuclear, electron–electron, and nuclear–nuclear, into a sum of atomic contributions, and the total energy of the molecule, as are all molecular properties, is given by a sum of atomic contributions as previously surmised in eq. [10].

Remarkable as this definition of the energy of an atom in a molecule is, it would be of no practical use if it did not exhibit the same degree of transferability from one molecule to another as does the atom itself, as previously illustrated for the methylene group in Fig. 3. As stated in the section listing the chemical constraints on the definition of an atom, if the atom appears the same in two different systems, that is, if its distribution of charge remains unchanged on transfer, then all its properties must exhibit the same invariance, the property exhibited by the methyl and methylene groups both experimentally and theoretically, when defined as proper open systems.

Atomic properties

The atomic theorems make possible the definition of all properties of an atom in a molecule and in every case, the sum of the atomic contributions $\boldsymbol{A}(\Omega)$ to property A equals the molecular value

$$[65]\quad \langle\hat{\boldsymbol{A}}\rangle = \sum_{\Omega} \boldsymbol{A}(\Omega)$$

The atomic current theorem, for example, enables one to define the atomic contributions to magnetically induced properties such as the magnetic susceptibility (26) and NMR shielding constants (27). As a consequence of the atomic statement of the principle of stationary action, the properties of an atom are determined by its distribution of charge, changing only in response to changes to its form in real space, and because of the zero-flux boundary condition, atoms are consequently the most transferable pieces that can be defined in an exhaustive partitioning of real space. Thus atoms maximize the transfer of chemical information from one system to another. In those limiting cases where an atom can be transferred from one molecule to another without apparent change to its charge distribution, the atom contributes the same amount to every property in both systems and the result, experimentally, is a so-called additivity scheme. The theory of atoms in molecules recovers the experimentally observed additivity of volume (28), of heats of formation (29), of moments and of polarizability (30), and of magnetic susceptibility (26). The theory recovers all nuances of the experimental additivity schemes, including the measured change in the energy of the transferable methylene group found in small ring systems, the so-called strain energy, and the exaltation in the magnetic susceptibility of a carbon atom when in an aromatic ring.

Chemistry and the short-sighted nature of the one-matrix

With the atomic theorems at hand, we are in a position to understand the presence of functional groups in chemistry — linked groupings of atoms in molecules or crystals that exhibit characteristic and measurable sets of properties. All of the atomic theorems have corresponding local expressions that integrate term for term to give the atomic expressions. The local statement of the virial theorem (31) given in eq. [66]

$$[66]\quad -2G(\boldsymbol{r}) = \mathcal{V}(\boldsymbol{r}) - (\hbar^2/4m)\nabla^2\rho(\boldsymbol{r})$$

defines the virial field $\mathcal{V}(\boldsymbol{r})$ in terms of the stress tensor in two equivalent ways:

$$[67]\quad \mathcal{V}(\boldsymbol{r}) = \{-\boldsymbol{r} \cdot \nabla\boldsymbol{\sigma}(\boldsymbol{r}) + \nabla \cdot (\boldsymbol{r} \cdot \boldsymbol{\sigma}(\boldsymbol{r}))\} = \text{Trace } \boldsymbol{\sigma}(r)$$

The virial field $\mathcal{V}(\boldsymbol{r})$ is the potential energy density of an electron at $\boldsymbol{r}$ (7, 15, 20). For a system with no net forces exerted on the nuclei as denoted by the symbol $\mathcal{V}_{eq}$, it integrates to the total potential energy of a system, including the nuclear–nuclear repulsions V_{nn},

$$[68]\quad \mathcal{V}_{eq} = \int \mathcal{V}(\boldsymbol{r})d\boldsymbol{r} = V_{ne} + V_{ee} + V_{nn}$$

Like the other property densities defined within the theory, it is a "dressed" density, one that determines the effective potential field experienced by a single electron in a many-particle system. All of the complex interactions between the electrons and the nuclei that are determined by the many-electron wave function are representable in real three-dimensional space by the density of the virial field. It provides the most short-range possible description of the interactions experienced by an element of the density (32). This is a consequence of the electronic virial containing the contribution from the nuclear–nuclear forces of repulsion that are described locally as the virial of the Hellmann–Feynman forces exerted on the electron density by the nuclei. Not

© 1998 NRC Canada

PROOF/ÉPREUVE

only does $\mathcal{V}(\boldsymbol{r})$ mimic the transferable nature of $\rho(\boldsymbol{r})$, as first noted in the 1972 paper that established the observational basis for the theory, $-\mathcal{V}(\boldsymbol{r})$ is found to be structurally homeomorphic with $\rho(\boldsymbol{r})$, exhibiting the same number and type of critical points and yielding the same structures (33). Thus a density, which has the appearance of a scaled version of $\rho(\boldsymbol{r})$, has the property of integrating to twice the total energy of the system. The homeomorphism has the important consequence of mirroring each bond path, the line of maximum electron density linking neighbouring nuclei, with a virial path, a line of maximally negative potential energy linking the same nuclei (33).

When an atom is transferred between molecules, the individual contributions to $\mathcal{V}(\boldsymbol{r})$, since they are individually long-range interactions, will in general exhibit large changes, of the order of thousands of kcal/mol when integrated over the atom, even in those cases where the integrated value of $\mathcal{V}(\boldsymbol{r})$ changes by only a few kcal/mol. The exchange and correlation energy densities of density functional theory also exhibit long-range behavior (34). The virial field, on the other hand, exhibits only the resultant change, one that reflects the corresponding chemical changes in the form of the atom, as reflected in the behavior of $\rho(\boldsymbol{r})$. It is not generally appreciated how small these changes can be. It is an experimental observation that, throughout most of chemistry, a group changes by amounts small enough so as to stamp it with a set of characteristic properties. These changes in $\rho(\boldsymbol{r})$, as now demonstrated in many cases, frequently translate into relatively small energy changes and can approach zero, as exhibited by the examples given in Fig. 3. The transferable nature of functional groups defined as proper open systems is currently being exploited through the determination of transferable amino acid residues that are to be used as building blocks in the construction of polypeptides or portions thereof (23, 24). These groups are prepared by sandwiching the residue between two glycyl groups in a tripeptide.

The stress tensor, even though it contains all of the two-electron information required for the determination of the electronic force and energy, is completely determined by just the one-electron density matrix. The one-matrix determines the kinetic energy density and its diagonal elements determine $\rho(\boldsymbol{r})$. Thus chemistry is a consequence of the shortsighted nature of the one-matrix as reflected in the paralleling shortsighted behavior of $\rho(\boldsymbol{r})$, $G(\boldsymbol{r})$, and $\mathcal{V}(\boldsymbol{r})$ exemplified in Fig. 3 (15, 32). Density functional theory demonstrates that the ground state energy is a unique functional of the electron density and does so by establishing the existence of a one-to-one correspondence between the density and the external potential (35). Thus, this theory does not account for the underlying observation of the theory of atoms in molecules: that what are apparently identical distributions of charge can be observed for a group in systems with differing external potentials, leaving one unprepared for the fundamental observation of chemistry — the existence of functional groups that exhibit characteristic properties in spite of changes in their environment. The two methylene groups whose properties are displayed in Fig. 3, for example, are from molecules that have very different external potentials and should, by the basic tenet of the theorem of Hohenberg and Kohn (35), have different distributions of charge. While differences necessarily do exist (36), they appear in this case to be vanishingly small.

The observations of chemistry, as interpreted by the theory of atoms in molecules, require the existence of a local relationship between the electron density and the virial field (7) while in density functional theory one searches for the functional relating the density to the total energy. The above comments on density functional theory are offered not as a criticism but rather to illustrate how the differing relationships between the density and the energy demanded by the two theories complement one another, a complementarity that could aid in the search for the complete understanding of the relationship between the energy and the density.

Conclusions

This account has focused on how the mapping of chemical concepts onto the observed topology of the electron density leads to the development of the statement of the principle of stationary action for a proper open system, the quantum mechanics underlying the definition of an atom in a molecule. In addition to defining the quantum boundary condition for the atom, eq. [1], the topology of this real, measurable field (5, 6) also provides the basis for a theory of molecular structure and structural stability (9, 15). Since both the quantum and structural aspects of the theory are determined by the topology of a common field, the two components of the theory are intimately coupled and provide the basis for a unified theory of molecular structure, one that demonstrates that chemistry follows from physics.

The description of a system provided by physics is unique. When alternative formulations are provided, such as the Heisenberg and Schrödinger representations of quantum mechanics, they are found to be equivalent. Thus there are no other definitions of a group that will yield the energies and other properties that are defined by quantum mechanics for a proper open system. It is these values that are found to be in agreement with the experimentally measured group properties, measurements that are possible in those cases where the properties of a group are found to be transferable, as well as additive. The definition of functional groups as quantum mechanical proper open systems is unique and no other definition can recover their observed properties.

Acknowledgement

I wish to thank Mr. D. Bayles for help with the preparation of the manuscript and Dr. G.L. Heard for assistance with the diagrams.

References

1. R.P. Feynman. Rev. Mod. Phys. **20**, 367 (1948).
2. J. Schwinger. Phys. Rev. **82,** 914 (1951).
3. P.E. Cade and W.M. Huo. At. Data Nucl. Data Tables, **12**, 415 (1973); **15**, 1 (1975); P.E. Cade and A.C. Wahl. At. Data Nucl. Data Tables, **13**, 339 (1974).
4. R.F.W. Bader, W.H. Henneker, and P.E. Cade. J. Chem. Phys. **46**, 3341 (1967); R.F.W. Bader, I. Keaveny, and P.E. Cade. J. Chem. Phys. **47**, 3381 (1967); R.F.W. Bader and A.D. Bandrauk. J. Chem. Phys. **49**, 1666 (1969); R.F.W. Bader, P.E. Cade, W.H. Henneker, and I. Keaveny. J. Chem. Phys. **50**,

© 1998 NRC Canada

PROOF/ÉPREUVE

5313 (1969); P.E. Cade, R.F.W. Bader, and J. Pelletier. J. Chem. Phys. **54**, 3517 (1971); R.F.W. Bader, P.M. Beddall, and P.E. Cade. J. Am. Chem. Soc. **93**, 3095 (1971).
5. P. Coppens. X-ray charge densities and chemical bonding. IUCr Oxford Science, Oxford University Press, Oxford. 1997.
6. V.G. Tsirelson and R.P. Ozerov. Electron density and bonding in crystals. IOP Publishing, Bristol. 1996.
7. R.F.W. Bader and P.M. Beddall. J. Chem. Phys. **56**, 3320 (1972).
8. R.F.W. Bader, S.G. Anderson, and A.J. Duke. J. Am. Chem. Soc. **101**, 1389 (1979).
9. R.F.W. Bader, T.T. Nguyen-Dang, and Y. Tal. Rep. Prog. Phys. **44**, 893 (1981).
10. R.F.W. Bader and H.J.T. Preston. Int. J. Quantum Chem. **3**, 327 (1969).
11. P. Ehrenfest. Z. Phys. **45**, 455 (1927).
12. E. Schrödinger. Ann. Phys. **79**, 361 (1926).
13. S. Srebrenik and R.F.W. Bader. J. Chem. Phys. **63**, 3945 (1975).
14. J. Schwinger. Lect. Part. Field Theory, Brandeis Summer Inst. Theor. Phys. **2**, 157 (1964).
15. R.F.W. Bader. Atoms in molecules: a quantum theory. Oxford University Press, Oxford. 1990.
16. R.P. Feynman, R.B. Leighton, and M. Sands. The Feynman lectures on physics. Vol. II. Addison–Wesley, Reading, Mass. 1964.
17. P.A.M. Dirac. The principles of quantum mechanics. Oxford University Press, Oxford. 1958.
18. P.A.M. Dirac. Phys. Z. Sowjetunion, **3**, 64 (1933).
19. S. Srebrenik, R.F.W. Bader, and T.T. Nguyen-Dang. J. Chem. Phys. **68**, 3667 (1978); R.F.W. Bader, S. Srebrenik, and T.T. Nguyen-Dang. J. Chem. Phys. **68**, 3680 (1978).
20. R.F.W. Bader and T.T. Nguyen-Dang. Adv. Quantum Chem. **14**, 63 (1981).
21. R.F.W. Bader. Phys. Rev. B: Condens. Matter, **49**, 13348 (1994).
22. R.F.W. Bader and P.A.L. Popelier. Int. J. Quantum Chem. **45**, 189 (1993).
23. R.F.W. Bader and F. Martín. Can. J. Chem. **76**, 284 (1998).
24. C. Chang and R.F. W.Bader. J. Phys. Chem. **96**, 1654 (1992); P.L.A. Popelier and R.F.W. Bader. J. Phys. Chem. **98**, 4473 (1994).
25. R.F.W. Bader and M. Austen. J. Chem. Phys. **107**, 4271 (1997).
26. R.F.W. Bader and T.A. Keith. J. Chem. Phys. **99**, 3669 (1993).
27. T.A. Keith and R.F.W. Bader. Can. J. Chem. **74**, 185 (1996).
28. R.F.W. Bader, M.T. Carroll, J.R. Cheeseman, and C. Chang. J. Am. Chem. Soc. **109**, 7968 (1987).
29. K.B. Wiberg, R.F.W. Bader, and C.D.H. Lau. J. Am. Chem. Soc. **109**, 1001 (1987).
30. R.F.W. Bader, K.M. Gough, K.E. Laidig, and T.A. Keith. Mol. Phys. **75**, 1167 (1992).
31. R.F.W. Bader. J. Chem. Phys. **73**, 2871 (1980).
32. R.F.W. Bader. Int. J. Quantum Chem. **56**, 409 (1995).
33. T.A. Keith, R.F.W. Bader, and Y. Aray. Int. J. Quantum Chem. **57**, 183 (1996).
34. J.P Perdew. *In* Density functional theory. *Edited by* E.K.U. Gross and R.. Dreizler. Plenum Press, New York. NATO ASI Ser. Ser. B: **337**, 51 (1995).
35. P. Hohenberg and W. Kohn. Phys. Rev. [Sect.] B, **136**, 864 (1964).
36. R.F.W. Bader and P. Becker. Chem. Phys. Lett. **148**, 452 (1988).

© 1998 NRC Canada

Synthesis, conformational studies, and inclusion properties of tris[(2-pyridylmethyl)oxy]hexahomotrioxacalix[3]arenes

Takehiko Yamato, Mitsuteru Haraguchi, Jun-Ichi Nishikawa, Seiji Ide, and Hirohisa Tsuzuki

Abstract: *O*-Alkylation of the flexible macrocycle **1** with 2-(chloromethyl)pyridine in the presence of Cs_2CO_3 resulted in the preferential formation of partial-cone-**2**. The cone-to-partial-cone ratio of **2** increased in the presence of K_2CO_3, and led to almost equal in the presence of NaH. The template effect of the alkali metal cations plays an important role in this *O*-alkylation reaction. The structural characterization of these products is also discussed. The two-phase solvent extraction data indicated that tris[(2-pyridylmethyl)oxy]hexahomotrioxacalix[3]arenes **2** show moderate extractability for *n*-butylammonium ion and high extractability for Ag^+. The ^1H NMR titration of cone-**2** with $AgSO_3CF_3$ clearly demonstrates that a 1:1 complex is formed, which is stable on the NMR time scale. Thus, the synergism of cyclophane moiety and two or three lower-rim side chains with pyridyl groups play a significant role on the complexation of tris[(2-pyridylmethyl)oxy] derivatives cone-**2** and partial-cone-**2** with Ag^+ ion and *n*-butylammonium ion.

Key words: macrocycles, calixarenes, *O*-alkylation, ionophores, cation–N interaction.

Résumé : La *O*-alkylation du macrocycle flexible **1** par de la 2-(chlorométhyl)pyridine en présence de Cs_2CO_3 conduit à la formation préférentielle du cône-partiel **2**. Le rapport de cône à cône-partiel augmente en présence de K_2CO_3 et, en présence de NaH, les quantités sont pratiquement égales. L'effet de gabarit des cations des métaux alcalins joue un rôle important dans cette réaction de *O*-alkylation. On discute de la caractérisation des structures de ces produits. Des données d'extractions par deux phases de solvants indiquent que les tris[(2-pyridylméthyl)oxy]hexahomotrioxacalix-[3]arènes, **2**, peuvent être extraits relativement facilement par l'ion butylammonium et très facilement par Ag^+. Un titrage par RMN du ^1H du cône-**2** par du $AgSO_3CF_3$ démontre sans ambiguïté qu'il se forme un complexe 1:1 qui est stable à l'échelle de temps de la RMN. La synergie entre la portion cyclophane et deux ou trois des chaînes latérales de la portion inférieure portant des groupes pyridyles joue un rôle important dans la complexation des dérivés tris[(2-pyridylméthyl)oxy] cône-**2** et cône-partiel-**2** avec l'ion Ag^+ et l'ion *n*-butylammonium.

Mots clés : macrocyles, calixarènes, *O*-alkylation, ionophores, interaction N–cation.

[Traduit par la Rédaction]

Introduction

Calixarene and related macrocycles have received considerable attention for their host–guest chemistry as ionophoric receptors (1–4; for a comprehensive review of all aspects of calixarene chemistry see ref. 1) and potential enzyme mimics in biology (5). Chemical modification of calixarene represents an effective and versatile way of producing receptors with high selective cation binding properties (6–10). Even minor changes in the regioselective functionalization (11) or conformation (12) of the chemically modified calixarene can be associated with drastic changes in the complexation properties.

Recently, Shinkai and co-workers (13, 14) have reported the complexation of alkali metals with the *O*-alkylated hexahomotrioxacalix[3]arene derivatives, e.g., tris[(ethoxycarbonyl)methoxy]hexahomotrioxacalix[3]arene and tris-[(N,N-diethylaminocarbonyl)methoxy]hexahomotrioxacalix-[3]arene. However, satisfied high selectivities for alkali metal ions or alkyl ammonium ions have not been established so far. On the other hand, Pappalardo et al. (15) reported on the synthesis of calix[4]arenes bearing pedant pyridine groups at the lower rim as potential ligands for transition metals. Thus, hexahomotrioxacalix[3]arene derivatives bearing 2-picolyl groups on the phenolic oxygens are also supposed to selectively bind with soft metal ions, such as transition metal ions, Ag^+, or alkyl ammonium ions and should exhibit some superior to ester or amide derivatives because of a high stability in a wide pH range (16, 17).

Received February 19, 1998.

T. Yamato,[1] M. Haraguchi, and J.-I. Nishikawa. Department of Applied Chemistry, Faculty of Science and Engineering, Saga University, Honjo-machi 1, Saga-shi, Saga 840, Japan.
Seiji Ide. Biotechnology and Food Research Institute, Fukuoka Industrial Technology Center, 1465–5 Aikawa, Kurume City, Fukuoka 839, Japan.
H. Tsuzuki. Center of Advanced Instrumental Analysis, Kyushu University, 6–1, Kasuga-kohen, Kasuga-shi, Fukuoka 816, Japan.

[1] Author to whom correspondence may be addressed. Telephone: (0952)28-8679. Fax: (0952)28–8591. E-mail: yamatot@cc.saga-u.ac.jp

© 1998 NRC Canada

Scheme 1.

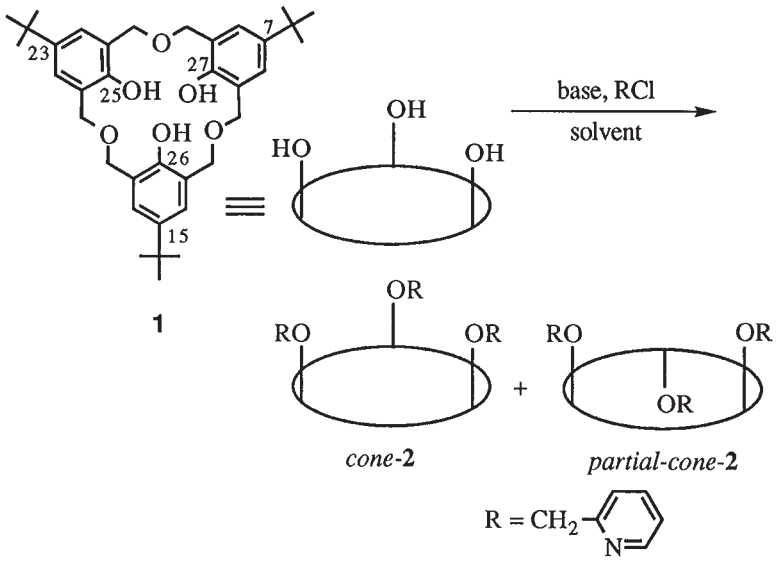

Table 1. *O*-Substitution reaction of triol **1** with 2-(chloromethyl)pyridine.

			Distribution (%)[a,b]	
Run	Base	Solvent	Cone	Partial-cone
1	NaH[c]	THF–DMF	25 [10]	30 [21]
2	K_2CO_3[d]	Acetone	24 [20]	71 [50]
3	Cs_2CO_3	Acetone	12 [8]	88 [62]

[a] Relative yields determined by ^{1}H NMR spectra.
[b] Isolated yields are shown in square brackets.
[c] Starting compound **1** was recovered in 45% yield.
[d] Starting compound **1** was recovered in 5% yield.

In this paper, we describe the synthesis, structures, and metal and ammonium ion complexation properties of tris[(2-pyridylmethyl)oxy]hexahomotrioxacalix[3]arenes with cone and partial-cone conformations, which are supposed to have encapsuled ionophilic cavities. Crystallographic data, structural report, bond distances and angles, and data collection have been deposited.[2]

Results and discussion

Hexahomotrioxacalix[3]arene **1** (18–20) was *O*-alkylated with 2-(chloromethyl)pyridine in the presence of Cs_2CO_3 to yield a mixture of two conformers of tri-*O*-alkylated product **2** in a ratio of 12:88 (cone-**2**:partial-cone-**2**) in 70% yield. The cone-to-partial-cone ratio of **2** increased in the presence of K_2CO_3 to 24:71 (cone-**2**:partial-cone-**2**), and led to almost equal in the presence of NaH in the *O*-substitution of triol **1**. However, Na_2CO_3 is employed, only the starting compound **1** was recovered in quantitative yield. (See Scheme 1 and Table 1.)

Fig. 1. Ring inversion of *O*-alkylation intermediate of triol **1** and immobilization by metal template.

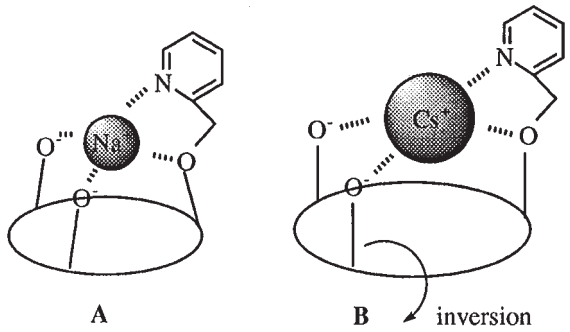

The ratio of the products cone-**2** and partial-cone-**2** is governed by the nature of alkali metal carbonates or NaH used as a base. Thus, when Cs_2CO_3 is used in this reaction, partial-cone-**2** was obtained as a major product in 62% yield. On the other hand, when K_2CO_3 or NaH is employed, the increased formation of cone conformer was observed. Although the much larger contribution of Cs^+ to the template effect than Na^+, as reported by Harrowfield et al. (21), can be expected; the larger Cs^+ might enlarge the cyclophane ring (e.g., the intermediate **B**) to form a sufficient space for ring inversion to afford thermodynamically stable partial-cone conformer. In contrast, the smaller Na^+ or K^+ might increase the contribution of the metal template effect, which can hold the 2-pyridylmethyl group(s) and the oxide group(s) on the same side of the hexahomotrioxacalix[3]arene through the cation–O and cation–N interactions (Fig. 1(*a*)).

The ^{1}H NMR spectrum of cone-**2** shows a singlet for the *tert*-butyl protons at δ 1.12 and a singlet for ArO*CH*$_2$Py and the aromatic protons at δ 4.73 and 7.05, respectively,

[2] Supplementary material may be purchased from: The Depository of Unpublished Data, Document Delivery, CISTI, National Research Council of Canada, Ottawa, Canada, K1A 0S2. Crystal data, structural refinements, bond distances and angles, and data collection have also been deposited with the Cambridge Crystallographic Data Centre and can be obtained on request from: The Director, Cambridge Crystallographic Data Centre, University Chemical Laboratory, 12 Union Road, Cambridge, CB2 1EZ, U.K.

© 1998 NRC Canada

Table 2. Chemical shifts of pyridine protons in cone-**2** and reference compound **4**.[a]

	Chemical shifts, δ (ppm)			
Compd.	H_6	H_5	H_4	H_3
Cone-**2**	8.49	7.09[c]	7.33	7.50
4	8.58	7.20	7.74	7.74
$\Delta\delta$[b]	+0.09	–0.11	–0.41	–0.24

[a] $\Delta\delta$ value is the difference of the chemical shift between cone-**2** and reference compound **4** in $CDC1_3$ at 27°C.
[b] A plus sign (+) denotes a shift to lower magnetic field, whereas a negative sign (–) denotes a shift to higher magnetic field.
[c] The midpoint value of multiplet.

indicating a C_3 symmmetric structure of cone-**2**. Interestingly, the heteroaromatic protons of the pyridine rings of cone-**2** are exposed to the ring current shielding effect (22, 23) operated by the opposing pyridine ring among the dibenzyl ether linkage, and resonate at higher fields with respect to those of the reference compound **4**, which was prepared by *O*-alkylation of 4-*tert*-butyl-2,6-dimethylphenol with 2-(chloromethyl)pyridine in the presence of NaH. Table 2 shows that the magnitude of this shielding, computed as the difference between pertinent pyridine protons of cone-**2** and reference compound **4**, increases significantly on H_3 and H_4 protons. The remarkable shielding effect experienced by H_4 (–0.41 ppm) and H_3 (–0.24 ppm) protons of the pyridine suggests that these protons are located in much closer environment toward the opposing pyridine ring than H_5 and H_6 protons due to the repulsion among the nitrogen atoms in the pyridine rings between the dibenzyl ether linkage. Thus, nitrogens in all of the pyridine rings were oriented outwards the cyclophane cavity as shown in Fig. 2.

In contrast, the ^{1}H NMR spectrum of partial-cone-**2** shows two singlets for the *tert*-butyl protons at δ 0.99, 1.14 (relative intensity 2:1), a singlet and a pair of doublets at δ 7.37 and 7.17, 7.24 for the aromatic protons. Furthermore, the resonance for the ArOCH_2Py methylene protons appeared as a singlet at δ 4.12 and a pair of doublets at δ 4.65, 4.74 (J_{AB} = 12.7 Hz). Upfield shifts for the inverted pyridine ring protons were observed, especially at δ 6.45 for $H_{3'}$ proton. These signals correspond to C_s symmetric structure. On the basis of the ^{1}H NMR studies and the consideration of CPK model of partial-cone-**2**, two 2-pyridylmethyl groups in the compound point upwards and the another one folded into the π-cavity formed by two benzene rings and are thus shifted stronger upfield. Furthermore, two *tert*-butyl groups are located on the pyridine ring of the inverted 2-pyridylmethyl group in spite of the sterically crowded enviroment. This finding might be attributed to the C-H-π interaction (24) between methyl groups of the *tert*-butyl group and the pyridine ring.

It was also found that ring inversion by oxygen-through-the-annulus rotation is inhibited for tris[(2-pyridylmethyl)oxy] derivatives cone-**2** and partial-cone-**2** because of the observation of no change of spectrum pattern for the ArCH_2OCH_2Ar methylene protons below 150°C in DMSO-d_6.

Although cone- (cone-**2**) and partial-cone-tris[(2-pyridylmethyl)oxy]hexahomotrioxacalix[3]arene (partial-cone-**2**) both

Fig. 2. Reference compound **4** and orientation of the pyridine N atoms in cone-**2**.

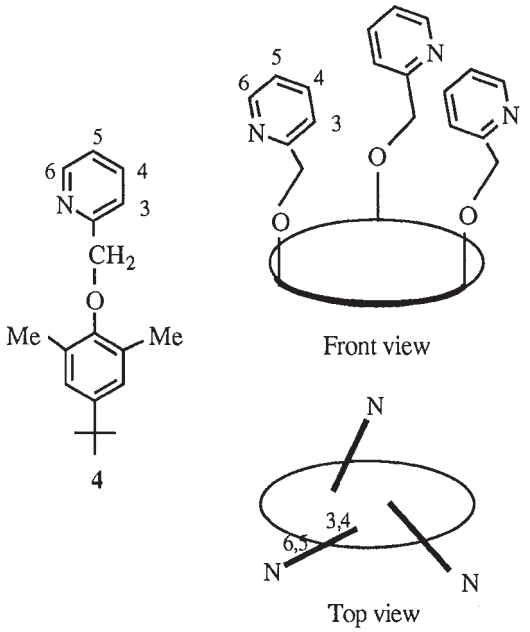

hardly extracted alkali metal cations in the present experimental system (2, 3, 9, 25–27), moderate extractability for *n*-butylammonium ion and high extractability for Ag^+ was observed (Table 3). The presently developed ionophores exhibit not only more superior extractabilities for Ag^+ (% extraction: 84% for cone-**2** and 80% for partial-cone-**2**) but also high selectivities for Ag^+ and *n*-butylammonium ion than those of commercially available dibenzopyridino-18-crown-6 (% extraction: 65%) (28) or other Ag^+ ionophores.

To obtain quantitative insights into the metal affinity of tris[(2-pyridylmethyl)oxy]hexahomotrioxacalix[3]arene **2** and to compare it with that of the partial confomer of tris(benzyloxy)hexahomotrioxacalix[3]arene **3**, which was prepared by *O*-benzylation of triol **1** in the presence of Cs_2CO_3 in 95% yield (Scheme 2), we have determined the association constants by absorption spectroscopy.

Interestingly, tris[(2-pyridylmethyl)oxy] derivatives cone- and partial-cone-**2** show higher association constants K ($\times 10^3$) for both Ag^+ ion and *n*-butylammonium ion as 29.4–42.4, respectively, than those for tris(benzyloxy) derivative partial-cone-**3**, i.e., the association constants for Ag^+ ion and *n*-butylammonium ion are 2.6 and 12.5, respectively (Table 4). Therefore, the synergism of cyclophane moiety and two or three lower-rim side chains having pyridyl groups play a significant role on the complexation of tris[(2-pyridylmethyl)oxy] derivatives cone-**2** and partial-cone-**2** with Ag^+ ion and *n*-butylammonium ion. Although cone-**2** with C_3 symmetry might serve as an efficient receptor for alkylammonium ions (14, 29), the significant increase of the association constants by the introduction of pyridyl groups was observed in complexation of partial-cone-**2** with *n*-butylammonium ion. This finding might be attributable to not only the contribution of the inverted pyridyl group but also to the much larger ionophilic cavity in partial-cone conformer than that in cone conformer from the consideration of molecular model.

© 1998 NRC Canada

Table 3. Extraction (%) of metal picrates in CH_2C1_2.[a]

	Ionophore	
Cation	Cone-**2**	Partial-cone-**2**
Li^+	0.6	1.1
Na^+	8.4	1.8
K^+	4.0	5.0
Cs^+	0	0
n-$BuNH_3^+$	23.4	13.5
Ag^+	84.4	80.0

[a] Extraction (%) of alkali metal picrates by ionophores **2** in CH_2C1_2. Extraction conditions: 2.5×10^{-4} M of ionophore in CH_2C1_2; 2.5×10^{-4} M of picric acid in 0.1 M of alkaline hydroxide at 25°C. Ionophore solution (5.0 mL) was shaken for 2 h with picrate solution (5.0 mL) and % extraction was measured by the absorbance of picrate in CH_2C1_2. Experimental error was ±2%.

Recently, Shinkai and co-workers (30) reported that the 1,3-alternate conformer of calix[4]arene tetraester can form both a 1:1 and a 2:1 metal–calixarene complex, and the two metal-binding sites display negative allostericity by ^{1}H NMR titration experiment. In the present systems, due to the existence of three metal-binding sites of pyridine moiety there are several possibilities for metal complexation mode. Thus, a 1:1 and a 2:1 metal complexation of cone-**2** might be possible. As shown in Fig. 3, the percent extractions reach maximum at 0.5 mol fraction for this cation. This fact clearly indicates that Ag^+ forms 1:1 complex with cone-**2**. Thus we could prove the synergism of the cyclophane moiety and three pyridine arms at the complexation.

To prove the synergism between cyclophane moiety and three lower-rim side chains with pyridyl groups in more detail, we examined the ^{1}H NMR chemical-shift differences between those before and after the addition of an equimolar $AgSO_3CF_3$, and the composition of the ion–ionophore complex. In fact, the chemical shifts of the aromatic protons of cone-**2** were altered by titration with $AgSO_3CF_3$ in $CDCl_3/CD_3OD$ (1:1 v/v): i.e., 1:1 mixture of cone-**2** and $AgSO_3CF_3$ showed a completely different ^{1}H NMR spectrum, with sharp lines becoming evident for these protons. The methylene proton peak ArO*CH*$_2$Py resonates at lower field at δ 5.07 (Δδ = +0.40 ppm) in comparison to that in the metal-free spectrum. Particularly, as shown Fig. 4, the pyridine moieties show considerable shifts lower field (Δδ = +0.52 ppm for H_4, +0.38 ppm for H_5, and +0.50 ppm for H_6), just as the reported one composed by two pyridine arms, one crown ether ring, and one Ag^+ ion (28*b*). In contrast to these observations, the signals for the aromatic protons and *tert*-butyl protons did not appear separately (Δδ = –0.10 and +0.01 ppm, respectively).

More detailed examination of the chemical-shift change suggests that Ag^+ should be bound to the lower rim of the cavity, which is composed of three phenolic oxygens and three nitrogens of pyridine rings, because the large downfield shifts were observed for H_4, H_5, and H_6 protons on a pyridine ring due to the inductive effect arising from the N---Ag^+ interaction present around this cavity. The similar downfield shift of methylene protons of ArO*CH*$_2$Py was also observed (Δδ = +0.40 ppm) due to the interaction of the

Scheme 2.

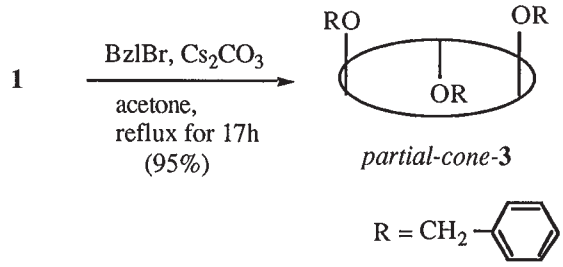

Table 4. Association constants (*K*)[a] in THF:$CHC1_3$ = 1:1 (v/v) at 25°C.

	K (× 10^3)	
Ionophore	Ag^+	*n*-$BuNH_3^+$
Cone-**2**	42.4	29.4
Partial-cone-**2**	35.2	40.4
Partial-cone-**3**	2.6	12.5

[a] K = [M^+Pic^-, ionophore]/[M^+Pic^-][ionophore].

oxygen atoms in these phenyl units with Ag^+. Another interesting feature is the upfield shift observed for the Ar*CH*$_2$O*CH*$_2$Ar methylene protons (Δδ from –0.11 to –0.35 ppm). In calix[4]arenes, the Ar*CH*$_2$Ar methylene protons serve as a measure of the "flattening" of each phenyl unit: $\Delta\delta_H$ is generally 0.9 ppm for a system in the regular cone conformation, and in the "flattened" conformation $\Delta\delta_H$ is significantly decreased (1). In the absence of Ag^+ $\Delta\delta_H$ is 0.09 ppm, whereas in the presence of Ag^+ $\Delta\delta_H$ becomes 0.32 ppm. Provided that the concept established in calix[4]arenes is also applicable to the hexahomotrioxacalix[3]arenes, it follows that the phenyl groups in cone-**2** are more flattened than those in cone-calix[4]arenes and stand up when Ag^+ enters into the ionophoric cavity. This finding is also supported by the upfield shift observed for the aromatic protons attributable to the ring current shielding effect (22, 23) operated by the opposing benzene rings (Δδ = –0.10 ppm). Thus the conformational changes of the cyclophane moiety of *cone*-**2** also exists after Ag^+ ion complexation in the present system. Consequently, these results are explicable only by the "interaction" of Ag^+ with the pyridine rings: that is, Ag^+ is trapped in a cavity composed of three phenolic oxygens and three nitrogens of pyridine rings, by both metal–oxygen electrostatic interactions and metal–nitrogen interactions.

In partial-cone-**2**–Ag^+ complex, the ArO*CH*$_2$Py methylene protons and the pyridine ring protons (H_4, H_5, H_6) in the ordinary phenyl units shift to lower magnetic field (by +0.15 and from +0.35 to +0.38 ppm), whereas those in the one inverted phenyl unit shift to higher magnetic field (by –0.06 and from –0.03 to –0.14 ppm). This fact suggests that Ag^+ ion is mainly bound to the phenolic oxygens and nirogens of pyridine rings in the two ordinary phenyl units, and the picolyl group in the inverted phenyl unit rotates into the cavity. Probably, this rotation is induced by steric repulsion between bound Ag^+ ion and the *tert*-butyl group in the inverted phenyl unit. In this complex the splitting pattern for the Ar*CH*$_2$O*CH*$_2$Ar methylene protons is very complicated.

© 1998 NRC Canada

Fig. 3. Job plots of the extractions of Ag^+ with host cone-**2**.

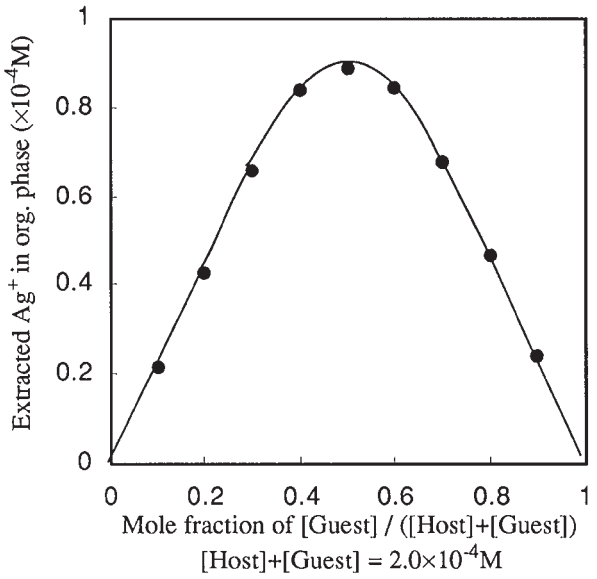

Hence, it is difficult to obtain useful information from the δ values for the propane bridged protons.

The conformational changes of pyridine moiety from the original outward orientation of the ring nitrogen to the inside orientation toward the cyclophane cavity was observed in the process of Ag^+ complexation. This result strongly suggests that the original C_3 and C_s symmetry might remain after the complete metal-cation complexation. Further experiments on these metal complexations are currently in progress in our laboratory.

Conclusions

An interesting result was obtained by introduction of 2-picolyl groups into the hydroxy groups of triol **1**. We have demonstrated for the first time that *O*-alkylation of the flexible macrocycle **1** with 2-(chloromethyl)pyridine gave tri-*O*-alkylated products with cone or partial-cone conformation. The alkali metal cation can play an important role for the confomer distribution based on the template effect. The two-phase solvent extraction data indicated that tris[(2-pyridylmethyl)oxy]hexahomotrioxacalix[3]arenes **2** show strong Ag^+ ion and *n*-butylammonium ion affinity. The ^1H NMR titration of cone- and partial-cone-**2** with $AgSO_3CF_3$ clearly demonstrates that a 1:1 complex is formed with retention of the original symmetry. The conformational changes of pyridine moiety from the original outward orientation of the ring nitrogen to the inside orientation toward the cyclophane cavity was observed in the process of Ag^+ complexation.

Experimental

All melting points (Yanagimoto MP-S1) were uncorrected. Proton nuclear magnetic resonance (^1H NMR) spectra were recorded on a Nippon Denshi JEOL FT-270 spectrometer. Chemical shifts are reported as δ values (ppm) relative to internal Me_4Si. Mass spectra were obtained on a Nippon Denshi JMS-01SA-2 mass spectrometer at an ionization energy of 70 eV; *m*/*z* values reported include the parent ion peak. Infrared (ir) spectra were obtained on a Nippon Denshi JIR-AQ2OM spectrophotometer as KBr disks. Elemental analyses were performed by Yanaco MT-5. The GLC analyses were performed by Shimadzu gas chromatograph, GC-14A; Silicone OV-1, 2 m; programmed temperature rise, 12°C/min; carrier gas nitrogen, 25 cm^3/min.

Fig. 4. Chemical-shift changes of cone-**2** and partial-cone-**2** induced in the presence of $AgSO_3CF_3$; a plus sign (+) denotes the downfield, and a negative sign (–) denotes the upfield shift.

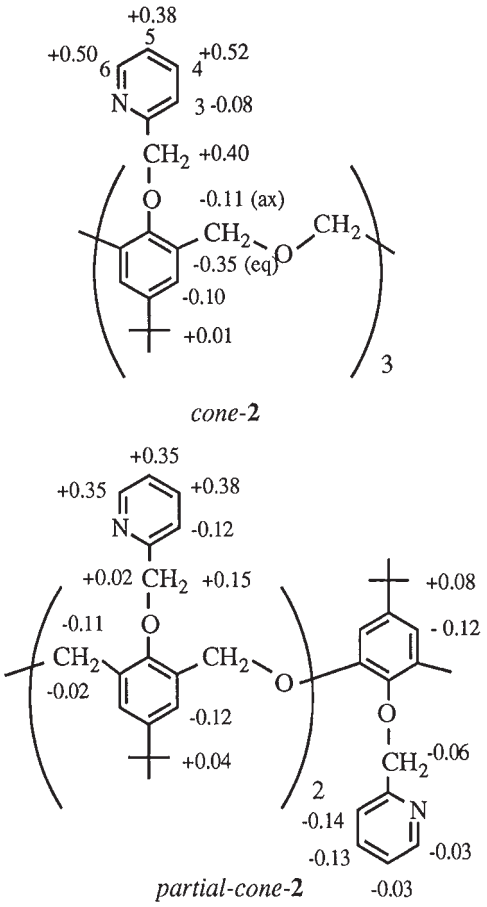

Materials

7,15,23-Tri-*tert*-butyl-25,26,27-trihydroxy-2,3,10,11,18,19-hexahomo-3,11,19-trioxacalix[3]arene **1** was prepared according to the literature (18).

Alkylation of 1 with 2-(chloromethyl)pyridine in the presence of NaH

A mixture of **1** (600 mg, 1.04 mmol) and NaH (400 mg, 10.0 mmol, 60%) in dry tetrahydrofuran (THF) (12 mL) was heated at reflux for 1 h under N_2. Then a solution of 2-(chloromethyl)pyridine (10.4 mmol)(prepared by neutralization of 2-(chloromethyl)pyridine hydrochloride (1.71 g, 10.4 mmol) in DMF (10 mL) with a solution of triethylamine (1.45 mL, 10.4 mmol) in THF (20 mL) at room temperature) was added and the mixture heated at reflux for an additional 17 h. After cooling the reaction mixture to room

© 1998 NRC Canada

temperature, it was acidified with 1 M HCl (10 mL) and extracted with CH_2Cl_2 (100 mL × 2). The combined extracts were washed with water (50 mL × 2), dried (Na_2SO_4), and condensed under reduced pressure to give a yellow oil. The yellow precipitate was obtained by adding Et_2O (5 mL), which was recrystallized from methanol to give partial-cone-**2** (184 mg, 21%). The ethereal filtrate was condensed in vacuo to leave a residue, which was chromatographed on silica gel with methanol as an eluent to give cone-**2** (88 mg, 10%).

Partial-cone-7,15,23-tri-*tert*-butyl-25,26,27-tris[(2-pyridylmethyl)oxy]-2,3,10,11,18,19-hexahomo-3,11,19-trioxacalix[3]arene (partial-cone-2)

Colorless prisms [MeOH/$CHCl_3$ (3:1)]; mp 172–173°C; ^{1}H NMR ($CDCl_3$): 0.99 (18 H, s), 1.14 (9 H, s), 4.12 (2 H, s, O*CH*$_2$Py), 4.14 (2 H, d, *J* 11.2), 4.22 (d, 2 H, *J* 12.2), 4.27 (d, 2 H, *J* 10.7), 4.53 (d, 2 H, *J* 10.7), 4.65 (d, 2 H, *J* 12.7, O*CH*$_2$Py), 4.74 (d, 2 H, *J* 12.7, O*CH*$_2$Py), 4.83 (d, 2 H, *J* 12.2), 4.97 (d, 2 H, *J* 11.2), 6.45 (d, 1 H, *J* 7.8, $H_{3'}$), 6.96 (m, 2 H, H_5), 7.00 (d, 2 H, *J* 7.8, H_3), 7.06 (m, 1 H, $H_{5'}$), 7.17 (d, 2 H, *J* 2.4), 7.24 (d, 2 H, *J* 2.4), 7.34 (ddd, 2 H, *J* 2.0, 7.3, 7.8, H_4), 7.37 (s, 2 H), 7.56 (ddd, 1 H, *J* 2.0, 7.3, 7.8, $H_{4'}$), 8.31 (d, 1 H, *J* 4.9, $H_{6'}$), 7.34 (d, 2 H, *J* 4.9, H_6); MS, *m/z*: M^+ 850. Anal. calcd. for $C_{54}H_{63}N_3O_6$: C 76.3, H 7.47, N 4.94; found: C 75.95, H 7.28, N 4.86.

The splitting pattern in ^{1}H NMR shows that the isolated compound is partial-cone-**2**.

Cone-7,15,23-tri-*tert*-butyl-25,26,27-tris[(2-pyridylmethyl)oxy]-2,3,10,11,18,19-hexahomo-3,11,19-trioxacalix[3]arene (cone-2)

Colorless prisms (MeOH/$CHCl_3$ (3:1)); mp 166–168°C; ^{1}H NMR ($CDCl_3$): 1.12 (s, 27 H), 4.63 (d, 6 H, *J* 13.2, *CH*$_2$O*CH*$_2$, eq), 4.65 (d, 6 H, *J* 13.2, *CH*$_2$O*CH*$_2$, ax), 4.73 (s, 6 H, O*CH*$_2$Py), 7.05 (s, 6 H, ArH), 7.09 (m, 3 H, H_5), 7.33 (ddd, 3 H, *J* 2.0, 7.3, 7.8, H_4), 7.50 (d, 3 H, *J* 7.8, H_3), 8.49 (d, 3 H, *J* 4.9, H_6); MS, *m/z*: M^+ 850. Anal. calcd. for $C_{54}H_{63}N_3O_6$: C 76.3, H 7.47, N 4.94; found: C 76.13, H 7.29, N 4.80.

The splitting pattern in ^{1}H NMR shows that the isolated compound is cone-**2**.

Alkylation of 1 with 2-(chloromethyl)pyridine in the presence of Cs_2CO_3

A mixture of **1** (600 mg, 1.04 mmol) and Cs_2CO_3 (3.39 g, 10.4 mmol) in dry THF (12 mL) was heated at reflux for 2 h under N_2. Then a solution of 2-(chloromethyl)pyridine (10.4 mmol) (prepared by neutralization of 2-(chloromethyl)pyridine hydrochloride (1.71 g, 10.4 mmol) in DMF (10 mL) with a solution of triethylamine (1.45 mL, 10.4 mmol) in THF (20 mL) at room temperature) was added and the mixture heated at reflux for an additional 17 h. After cooling the reaction mixture to room temperature, it was filtered. The filtrate was concentrated, and the residue was extracted with CH_2Cl_2 (2 × 100 mL) and washed with water (2 × 50 mL), dried (Na_2SO_4), and condensed under reduced pressure. The ^{1}H NMR analyses of the residue was in accord with its being a mixture of cone-**2** and partial-cone-**2** in the ratio of 12:88. The yellow precipitate was obtained by adding Et_2O (10 mL), which was recrystallized from methanol to give partial-cone-**2** (552 mg, 62%). The ethereal filtrate was condensed in vacuo to leave a residue, which was chromatographed on silica gel with methanol as an eluent to give cone-**2** (70 mg, 8%).

Benzylation of 1 with benzyl bromide in the presence of Cs_2CO_3

A mixture of **1** (100 mg, 0.174 mmol) and Cs_2CO_3 (567 mg, 1.74 mmol) in acetone (10 mL) was heated at reflux for 1 h. Then benzyl bromide (0.21 mL, 1.74 mmol) was added and the mixture heated at reflux for 17 h. After cooling the reaction mixture to room temperature, it was filtered. The filtrate was concentrated, and the residue was extracted with CH_2Cl_2 (2 × 100 mL) and washed with water (2 × 50 mL), dried (Na_2SO_4), and condensed under reduced pressure. The residue was washed with methanol to give the crude partial-cone-**3** (139 mg, 95%) as a colorless solid. Recrystallization from methanol/$CHCl_3$ (3:1) gave partial-cone-7,15,23-tri-*tert*-butyl-25,26,27-tris(benzyloxy)-2,3,10,11,18,19-hexahomo-3,11,19-trioxacalix[3]arene (partial-cone-**3**) as colorless prisms (MeOH/$CHCl_3$ (3:1)); mp 180–185°C; ^{1}H NMR ($CDCl_3$): 0.93 (s, 18 H), 1.20 (s, 9 H,), 3.40 (s, 2 H, O*CH*$_2$Ph), 4.07 (d, 2 H, *J* 12.7), 4.15 (d, 2 H, *J* 12.2, O*CH*$_2$Ph), 4.19 (d, 2 H, *J* 12.2, O*CH*$_2$Ph), 4.27 (d, 2 H, *J* 9.3), 4.28 (d, 2 H, *J* 12.7), 4.46 (d, 2 H, *J* 12.7), 4.53 (d, 2 H, *J* 12.7), 4.54 (d, 2 H, *J* 9.3), 6.72–6.78 (m, 2 H), 7.01–7.14 (m, 17 H), 7.29 (s, 2 H); MS, *m/z*: M^+ 846. Anal. calcd. for $C_{57}H_{66}O_6$: C 80.82, H 7.85; found: C 80.53, H 7.73.

The splitting pattern in ^{1}H NMR shows that the isolated compound is partial-cone-**3**.

Preparation of 4-*tert*-butyl-2,6-dimethyl[(2-pyridylmethyl)oxy]benzene 4

A mixture of 4-*tert*-butyl-2,6-dimethylphenol (400 mg, 2.25 mmol) and NaH (580 mg, 14.5 mmol, 60%) in dry THF (20 mL) was heated at reflux for 1 h under N_2. Then a solution of 2-(chloromethyl)pyridine (14.5 mmol) (prepared by neutralization of 2-(chloromethyl)pyridine hydrochloride (2.38 g, 14.5 mmol) in DMF (15 mL) with a solution of triethylamine (2.02 mL, 14.52 mmol) in THF (25 mL) at room temperature) was added and the mixture heated at reflux for an additional 17 h. After cooling the reaction mixture to room temperature, it was acidified with 1 M HCl (10 mL) and extracted with CH_2Cl_2 (100 mL × 2). The combined extracts were washed with water (50 mL × 2), dried (Na_2SO_4), and condensed under reduced pressure to give a yellow oil. The residue was chromatographed on silica gel with methanol as an eluent to give the title compound **4** (380 mg, 63%) as a colorless oil; ^{1}H NMR ($CDCl_3$): 1.30 (s, 9 H), 2.31 (s, 6 H), 4.95 (s, 2 H), 7.05 (s, 2 H), 7.20 (m, 1 H, H_5), 7.74 (m, 2 H, H_3 and H_4), 8.58 (dd, 1 H, *J* 0.9, 4.9, H_6); MS, *m/z*: M^+ 269. Anal. calcd. for $C_{18}H_{23}NO$: C 80.26, H 8.61, N 5.2; found: C 80.55, H 8.49, N 4.98.

Picrate extraction measurements

Alkali metal picrates (2.5×10^{-4} M) were prepared in situ by dissolving the alkali metal hydroxide in 2.5×10^{-4} M picric acid; triply distilled water was used for all aqueous solutions. Similarly, silver picrate was prepared in situ by

© 1998 NRC Canada

dissolving silver nitrate in 2.5×10^{-4} M picric acid. Two-phase solvent extraction was carried out between water (5 mL, alkali picrate conc. = 2.5×10^{-4} M) and CH_2Cl_2 (5 mL, ionophore conc. = 2.5×10^{-4} M). The two-phase mixture was shaken in a stoppered flask for 2 h at 25°C. We confirmed that this period is sufficient to attain the distribution equilibrium. This was repeated three times, and the solutions were left standing until phase separation was complete. The extractability was determined spectrophotochemically from the decrease in the absorbance of the picrate ion in the aqueous phase as described by Pedersen (31).

^{1}H NMR complexation experiment

To a $CDCl_3$ solution (5×10^{-4} M) of cone-**2** in the NMR tube was added a [D_4]methanol solution (5×10^{-4} M) of $AgSO_3CF_3$. The spectrum was registered after addition and the temperature of NMR probe kept constant at 27°C.

Cone-7,15,23-tri-*tert*-butyl-25,26,27-tris[(2-pyridylmethyl)oxy]-2,3,10,11,18,19-hexahomo-3,11,19-trioxacalix[3]arene (cone-2)

^{1}H NMR ($CDCl_3$:[D_4]methanol, 1:1 v/v): 1.08 (s, 27 H), 4.51 (d, 6 H, *J* 13.2, CH_2OCH_2, eq), 4.60 (d, 6 H, *J* 13.2, CH_2OCH_2, ax), 4.67 (s, 6 H, OCH_2Py), 6.95 (s, 6 H, ArH), 7.03 (m, 3 H, H_5), 7.29 (ddd, 3 H, *J* 2.0,7.3,7.8, H_4), 7.45 (d, 3 H, *J* 7.8, H_3), 8.43 (d, 3 H, *J* 4.9, H_6).

Cone-2–$AgSO_3CF_3$ complex

δ_H ($CDCl_3$:[D_4]methanol, 1:1 v/v): 1.09 (s, 27 H), 4.16 (d, 6 H, *J* 13.2, CH_2OCH_2, eq), 4.48 (d, 6 H, *J* 13.2, CH_2OCH_2, ax), 5.07 (s, 6 H, OCH_2Py), 6.85 (s, 6 H, ArH), 7.41 (m, 3 H, H_5), 7.82 (ddd, 3 H, *J* 2.0, 7.3, 7.8, H_4), 7.37 (d, 3 H, *J* 7.8, H_3), 8.93 (d, 3 H, *J* 4.9, H_6).

References

1. (*a*) C.D. Gutsche. Calixarenes. Royal Society of Chemistry, Cambridge. 1989; (*b*) J. Vicens and V. Böhmer. Calixarenes: a versatile class of macrocyclic compounds. Kluwer Academic Publishers, Cambridge. 1990; (*c*) C.D. Gutsche. Acc. Chem. Res. **16**, 161 (1983).
2. (*a*) S.G. Bott, A.W. Coleman, and J.L. Atwood. J. Chem. Soc. Chem. Commun. 610 (1986); (*b*) A. Arduini, A. Pochini, S. Reverber, R. Ungaro, G.D. Andreetti, and F. Ugozzoli. Tetrahedron, **42**, 2089 (1986).
3. S.-K. Chang and I. Cho. J. Chem. Soc. Perkin Trans. 1, 211 (1986).
4. (*a*) P. Zerr, M. Mussrabi, and J. Vicens. Tetrahedron Lett. **32**, 1879 (1991); (*b*) C.D. Gutsche and L.J. Bauer. J. Am. Chem. Soc. **107**, 6052 (1985).
5. (*a*) S. Shinkai. Tetrahedron, **49**, 8933 (1993); (*b*) J.-M. Lehn. Angew. Chem. **100**, 91 (1988); Angew. Chem. Int. Ed. Engl. **27**, 89 (1988); (*c*) D.J. Cram. Angew. Chem. **100**, 1041 (1988); Angew. Chem. Int. Ed. Engl. **27**, 1009 (1988).
6. V. Bocchi, D. Foina, A. Pochini, and R. Ungaro. Tetrahedron, **38**, 373 (1982).
7. G. Ferguson, B. Kaitner, M.A. McKervey, and E.M. Seward. J. Chem. Soc. Chem. Commun. 584 (1987).
8. F. Arnaud-Neu, M.-J. Schwing-Weill, K. Ziat, S. Cremin, S.J. Harris, and M.A. McKervey. New J. Chem. **15**, 33 (1991).
9. G.D. Andreetti, G. Calestani, F. Ugozzoli, A. Arduini, E. Ghidini, A. Pochini, and R. Ungaro. J. Inclusion Phenom. **5**, 123 (1987).
10. (*a*) E. Ghidini, F. Ugozzoli, R. Ungaro, S. Harkema, A. Abu El-Fadl, and D.N. Reinhoudt. J. Am. Chem. Soc. **112**, 6979 (1990); (*b*) A. Arduini, E. Ghidini, A. Pochini, R. Ungaro, G.D. Andreetti, G. Calestani, and F. Ugozzoli. J. Inclusion Phenom. **6**, 119 (1988).
11. J.A.J. Brunink, W. Verboom, J.F.J. Engbersen, S. Harkema, and D.N. Reinhoudt. Recl. Trav. Chim. Pays-Bas, **111**, 511 (1992).
12. R. Ungaro, A. Casnati, F. Ugozzoli, A. Pochini, J. F. Dozol, C. Hill, and H. Rouquette. Angew. Chem. Int. Ed. Engl. **33**, 1506 (1994).
13. K. Araki, K. Inada, H. Otsuka, and S. Shinkai. Tetrahedron, **49**, 9465 (1993).
14. (*a*) K. Araki, N. Hashimoto, H. Otsuka, and S. Shinkai. J. Org. Chem. **58**, 5958 (1993); (*b*) M. Takeshita and S. Shinkai. Chem. Lett. 125 (1994); (*c*) M. Takeshita, F. Inokuchi, and S. Shinkai. Tetrahedron Lett. **36**, 3341 (1994); (*d*) H. Matsumoto, S. Nishio, M. Takeshita, and S. Shinkai. Tetrahedron**, 51**, 4647 (1995).
15. (*a*) S. Pappalardo, L. Giunta, M. Foti, G. Ferguson, J.F. *Gallagher, and B. Kaitner. J. Org. Chem.* **57**, 2611 (1992); (*b*) G. Ferguson, J.F. Gallagher, L. Giunta, P. Neri, S. Pappalardo, and M. Parisi. J. Org. Chem. **59**, 42 (1994); (*b*) S. Pappalardo, G. Ferguson, P. Neri, and C. Rocco. J. Org. Chem. **60**, 4576 (1995); (*b*) S. Pappalardo. New J. Chem. 465 (1996).
16. C. Canevet, J. Libman, and A. Shanzer. Angew. Chem. Int. Ed. Engl. **35**, 2657 (1996).
17. K. Kita, T. Kida, Y. Nakatsuji, I. Ikeda. Chem. Lett. 405 (1997).
18. H. Ninagawa and H. Matsuda. Makromol. Chem. Rapid Commun. **3**, 65 (1982).
19. B. Dhawan and C.D. Gutsche. J. Org. Chem. **48**, 1536 (1983).
20. (*a*) P.D. Hampton, Z. Bencze, W. Tong, and C.E. Daitch. J. Org. Chem. **59**, 4838 (1994); (*b*) C.E. Daitch, P.D. Hampton, E.N. Duesler, and T.M. Alam. J. Am. Chem. Soc. **118**, 7769 (1996).
21. J.M. Harrowfield, M.I. Ogden, W.R. Richmond, and A.H. White. J. Chem. Soc. Chem. Commun. 1159 (1991).
22. (*a*) B.H. Smith. *In* Bridged aromatic compounds. Academic Press, New York. 1964; (*b*) F. Vögtle and P. Neumann. Angew. Chem. **84**, 75 (1972); Angew. Chem. Int. Ed. Engl. **11**, 73 (1972); (*c*) F. Vögtle and P. Neumann. Synthesis, 85 (1973); (*d*) F. Vögtle and G. Höhner. Top. Curr. Chem. **74**, 1 (1978); (*e*) P.M. Keehn and S.M. Rosenfield. Cyclophanes. Vol. 1. Academic Press, New York. 1983; (*f*) F. Vögtle. Cyclophane chemistry. John Wiley & Sons Ltd., Chichester. 1993.
23. (*a*) M. Tashiro and T. Yamato. J. Org. Chem. **46**, 4556 (1981); *(b)* J. Org. Chem. **48**, 1461 (1983).
24. (*a*) M. Nishio and M. Horita. Tetrahedron, **45**, 7201 (1989); (*b*) C.D. Andreetti, R. Ungaro, and A. Pochini. J. Chem. Soc. Chem. Commun. 1005 (1979); (*c*) R. Ungaro, A. Pochini, C.D. Andreetti, and O. Domiano. J. Chem. Soc. Perkin Trans. 2, 197 (1985); (*d*) M.A. McKervey, E.M. Seward, G. Ferguson, and B.L. Ruhl. J. Org. Chem. **51**, 3581 (1986); (*e*) D.J. Cram, S. Karbach, H.-E. Kim, C.B. Knobler, E.F. Marverick, J.L. Ericson, and R.C. Helgeson. J. Am. Chem. Soc. **110**, 2229 (1988); (*f*) P. Soncini, S. Bonsignore, E. Dalcanale, and F. Ugozzoli. J. Org. Chem. **57**, 4608 (1992); (*g*) J.L. Atwood, S.G. Bott, C. Jones, and C.L. Raston. J. Chem. Soc. Chem. Commun. 1349 (1992); (*h*) K. Kobayashi, Y. Asakawa, Y. Kikuchi, H. Toi, and Y. Aoyama. J. Am. Chem. Soc. **115**, 2648

© 1998 NRC Canada

(1993); (*i*) T. Yamato, A. Miyazawa, and M. Tashiro. J. Chem. Soc. Perkin Trans. 1, 3127 (1993).
25. (*a*) M.A. McKervey, E.M. Seward, G. Ferguson, B. Ruhl, and S. Harris. J. Chem. Soc. Chem. Commun. 388 (1985); (*b*) F. Arnaud-Neu, E.M. Collins, M. Deasy, G. Ferguson, S.J. Harris, B. Kaitner, A.J. Lough, M.A. McKervey, E. Marques, B. Ruhl, M.J. Schwing-Weill, and E.M. Seward. J. Am. Chem. Soc. **111**, 8681 (1989).
26. (*a*) S.-K. Chang, S.-K. Kwon, and I. Cho. Chem. Lett. 947 (1987); (*b*) G. Calestani, F. Ugozzoli, A. Arduini, E. Ghidini, and R. Ungaro. J. Chem. Soc. Chem. Commun. 344 (1987); (*c*) A. Arduini, E. Ghidini, A. Pochini, R. Ungaro, G.D. Andreetti, G. Calestani, and F. Ugozzoli. J. Incl. Phenom. **6**, 119 (1988).
27. (*a*) T. Arimura, M. Kubota, T. Matsuda, O. Manabe, and S. *Shinkai. Bull. Chem. Soc. Jpn.* **62**, 1674 (1989); (*b*) K. Iwamoto and S. Shinkai. J. Org. Chem. **57**, 7066 (1992); (*c*) N. Sato and S. Shinkai. J. Chem Soc. Perkin Trans. 1, 2621 (1993).
28. (*a*) S. Inokuma, S. Yasuda, S. Araki, S. Sakai, and J. Nishimura. Chem. Lett. 201 (1994); (*b*) H. Tsukube, T. Yamashita, M. Iwashido, and M. Zenki. J. Org. Chem. **56**, 268 (1991).
29. K. Araki, K. Inada, and S. Shinkai. Angew. Chem. Int. Ed. Engl. **35**, 72 (1996).
30. (*a*) A. Ikeda and S. Shinkai. J. Am. Chem. Soc. **116**, 3102 (1994); (*b*) V. Böhmer. Angew. Chem. Int. Ed. Engl. **34**, 713 (1995); (*c*) M. Takeshita and S. Shinkai. Bull. Chem. Soc. Jpn. **68**, 1088 (1995); (*d*) A. Ikeda and S. Shinkai. Chem. Rev. **97**, 1713 (1997).
31. C.J. Pedersen. J. Am. Chem. Soc. **89**, 2495 (1967).

© 1998 NRC Canada

ipso-Nitration of *tert*-butyl[*n*.2]metacyclophanes; through-space electronic interactions between two benzene rings

Takehiko Yamato, Hideo Kamimura, and Hirohisa Tsuzuki

Abstract: The selective introduction of one or two nitro groups by direct replacement of *tert*-butyl groups via the *ipso* aromatic nitration of the meta-bridged aromatic compounds having two arene rings is described. The *ipso*-nitration at the *tert*-butyl groups of *syn*- and *anti*-di-*tert*-butyl-dimethoxy[*n*.2]metacyclophanes **1** is attributed to the highly activated character of the aryl ring and the increased stabilization of a σ-complex intermediate arising from the dienone-type σ-complex intermediate possible in the case of an internally methoxy substituent. However, only one *tert*-butyl group is *ipso*-nitrated in the mild reaction conditions such as copper(II) nitrate in an acetic anhydride solution because of deactivation of the second aromatic ring by the introduced nitro group. A first σ-complex intermediate would be stabilized by two types of the through-space electronic interaction, i.e., face-to-face overlapping and intra-annular interaction with the opposing benzene ring, thus accelerating the reaction. The higher yields of mononitrated product are obtained in syn-conformer than in anti-conformer. Therefore, face-to-face overlapping might be much more favourable to stabilize the first σ-complex intermediate than the intra-annular interaction. On the other hand, nitration of **1** with fuming nitric acid afforded the two-fold *ipso*-nitration product **3** in quantitative yield. Thus, the number of *ipso*-nitration at the *tert*-butyl groups of **1** was strongly affected by the reactivity of the nitration reagent.

Key words: cyclophanes, electrophilic aromatic substitutions, *ipso*-nitration, σ-complex intermediates, through-space electronic interactions.

Résumé : On décrit l'introduction sélective d'un ou de deux groupes nitro par le remplacement direct de groupes *tert*-butyles par le biais d'une nitration aromatique *ipso* de composés aromatiques comportant deux noyaux arènes portant des ponts en méta. La nitration *ipso* au niveau des groupes *tert*-butyles des *syn*- et *anti*-di-*tert*-butyl-diméthoxy-[*n*.2]métacyclophanes, **1**, est attribuée au caractère hautement activé du noyau aryle et à une stabilisation accrue d'un complexe-σ intermédiaire découlant d'un complexe-σ intermédiaire de type diénone qui serait possible dans le cas d'un substituant méthoxy interne. Toutefois, dans des conditions douces comme celles rencontrées avec du nitrate de cuivre(II), un seul des groupes *tert*-butyles donne lieu à une nitration *ipso* à cause de la désactivation du deuxième noyau aromatique par le groupe nitro qui a été introduit. Un premier complexe-σ intermédiaire serait stabilisé par deux types d'interactions électroniques à travers l'espace, à savoir un recouvrement face à face et une interaction intraannullaire avec le noyau benzénique opposé, et conduirait à une accélération de la réaction. On obtient de meilleurs rendements de produit mononitré avec le conformère syn qu'avec le conformère anti. Le recouvrement face à face semble donc plus favorable que l'interaction intraannullaire pour stabiliser le premier complexe-σ intermédiaire. Par ailleurs, la nitration du produit **1** à l'aide d'acide nitrique fumant conduit au produit **3**, découlant d'une double nitration *ipso*, avec un rendement quantitatif. Le nombre de nitrations *ipso* au niveau de groupes *tert*-butyles du composé **1** est donc fortement affecté par la réactivité du réactif de nitration.

Mots clés : cyclophanes, substitutions aromatiques électrophiles, nitration *ipso*, complexe-σ intermédiaire, interactions électroniques à travers l'espace.

[Traduit par la Rédaction]

Introduction

Although the replacement of a *tert*-butyl group by a nitro group in electrophilic aromatic substitutions has frequently been described in the literature (1, 2), generally the yields are mostly modest because of the accompanying side reactions (3). Only in activated compounds are better yields obtained. However, there have been only a few investigations on the *ipso*-electrophilic aromatic substitution of *tert*-butylarenes having more than two benzene rings (4, 5). Recently, we have reported (6) that *ipso* aromatic nitration of 1,n-bis(5-*tert*-butyl-2-methoxyphenyl)alkanes leads to the direct introduction of one or two nitro groups, depending on

Received November 12, 1997.

Takehiko Yamato[1] and Hideo Kamimura. Department of Applied Chemistry, Faculty of Science and Engineering, Saga University, Honjo-machi 1, Saga-shi, Saga 840, Japan. **Hirohisa Tsuzuki.** Center of Advanced Instrumental Analysis, Kyushu University, 6–1, Kasuga-kohen, Kasuga-shi, Fukuoka 816, Japan.

[1]Author to whom correspondence may be addressed. Telephone: (0952)28-8679. Fax: (0952)28–8591. E-mail: yamatot@cc.saga-u.ac.jp

© 1998 NRC Canada

Scheme 1.

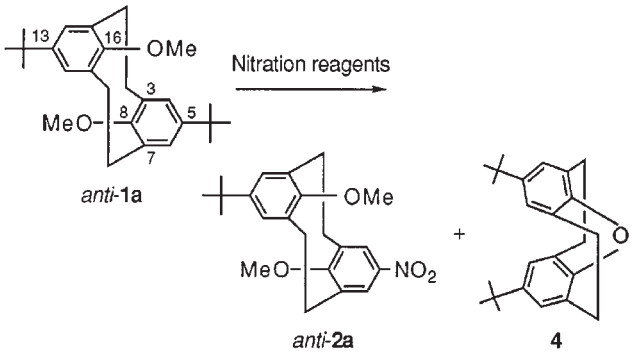

the nitration reagents. However, the mechanistic aspects of *ipso*-attack in electrophilic aromatic substitutions having more than two aromatic rings are still not clear because of the possibility of through-space electronic interactions occurring among the other benzene rings.

Subsequently, we reported (7) that nitration of 5,13-di-*tert*-butyl-8,16-dimethoxy[2.2]MCP (MCP = metacyclophane) *anti*-**1a** with various nitrating reagents led to *ipso*-nitration at the *tert*-butyl group to give 5-*tert*-butyl-8,16-dimethoxy-13-nitro[2.2]MCP *anti*-**2a** as well as the corresponding 8,16-epoxy[2.2]MCP **4** arising from intramolecular condensation reaction via *anti*-*syn*-ring inversion of the nitration intermediate. The latter novel product was found to be obtained, owing to the release of the strain in these systems (Scheme 1).

In contrast, nitration of 5,13-di-*tert*-butyl-8,16-dimethyl-[2.2]MCP with fuming HNO_3 afforded a different type of product, 2,7-di-*tert*-butyl-4,9-dinitro-*trans*-10b,10c-dimethyl-10b,10c-dihydropyrene (8). This novel transannular reaction might be attributed to the electronic interaction between two benzene rings, the proximity of 8,16-positions and the release of the considerable strain energy to form the more stable annulene π-electron system, 10b,10c-dihydropyrene. Thus there is substantial interest in systematically investigating the effect of substituents on the *ipso*-attack and the relationship between neighbouring benzene rings in electrophilic aromatic substitutions of larger ring-sized *tert*-butyl-[*n*.2]MCPs, which might only afford the *ipso*-nitration product at the *tert*-butyl group because of not only the formation of the intramolecular condensation product via *anti*-*syn*-ring inversion of the nitration intermediate but also the formation of 14π dihydropyrene derivatives being impossible.

In this paper we describe the selective introduction of one or two nitro groups by direct replacement of *tert*-butyl groups via the *ipso* aromatic nitration of the meta-bridged aromatic compounds having two arene rings to investigate the through-space electronic interactions occurring among other benzene rings.

Results and discussion

Attempted nitration of *anti*-6,14-di-*tert*-butyl-9,17-dimethoxy[3.2]MCP *anti*-**1b** (9) with copper(II) nitrate at room temperature for 24 h gave *anti*-6-*tert*-butyl-9,17-dimethoxy-14-nitro[3.2]MCP *anti*-**2b** in 56% yield as a major product along with *anti*-9,17-dimethoxy-6,14-dinitro[3.2]MCP

Scheme 2.

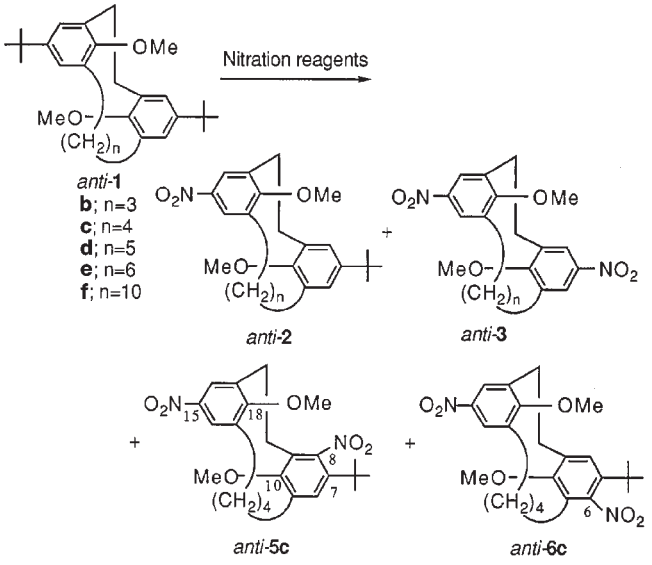

Table 1. Nitration of *anti*-di-*tert*-butyl-dimethoxy-[*n*.2]metacyclophanes *anti*-**1**.

Substrate	Number of methylene units, *n*	Reagent[a]	Products (%, yield)[b]
anti-**lb**	3	A	*anti*-**2b** (56), *anti*-**3b** (25)
anti-**lc**	4	A	ann-**2c** (58), *anti*-**5c** (10), *anti*-**6c** (15)
anti-**ld**	5	A	*anti*-**2d** (10)[c]
anti-**le**	6	A	*anti*-**2e** (30)[c]
anti-**1f**	10	A	*anti*-**2f** (31)[c]
anti-**lb**	3	B	*anti*-**3b** (89)
anti-**lc**	4	B	*anti*-**3c** (91)
anti-**ld**	5	B	*anti*-**3d** (93)
anti-**le**	6	B	*anti*-**3e** (88)
anti-**lf**	10	B	*anti*-**3f** (91)

[a]A, $Cu(NO_3)_2$ in Ac_2O, room temp. for 24 h; B, fuming HNO_3 in CH_2Cl_2/HOAc, room temp. for 30 min.
[b]Isolated yields are shown.
[c]Starting compounds, *anti*-**ld**, *anti*-**le**, and *anti*-**lf**, were recovered in 75, 53, and 55% yields, respectively.

anti-**3b** in 25% yield. No formation of the corresponding 9,17-epoxy[3.2]MCP arising from intramolecular condensation reaction via *anti*-*syn*-ring inversion like 8,16-dimethoxy[2.2]MCP *anti*-**1a** was observed. While in the nitration of *anti*-[4.2]MCP *anti*-**1c**, mono *ipso*-nitrated product *anti*-**2c** was also obtained in 58% yield; two other different dinitrated products *anti*-**5c** and *anti*-**6c** were obtained in 10 and 15% yields, respectively. The formation of a two-fold *ipso*-nitration product, i.e., *anti*-10,18-dimethoxy-7,15-dinitro[4.2]MCP *anti*-**3c**, was not observed under the reaction conditions used (Scheme 2, Table 1).

In fact, nitration of mono *ipso*-nitrated product *anti*-**2c** carried out under the same conditions afforded almost same ratio of dinitrated products *anti*-**5c** and *anti*-**6c** along with recovery of starting compound. This result strongly suggests

© 1998 NRC Canada

Scheme 3.

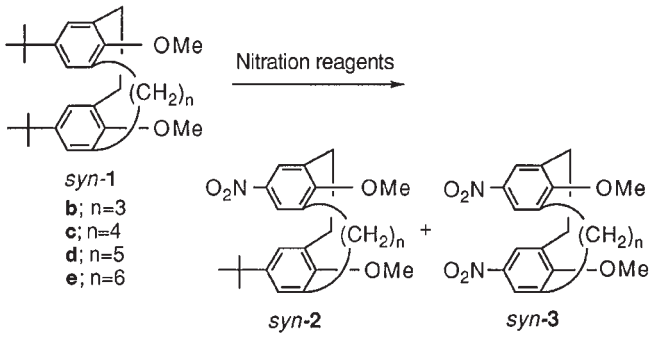

that in the first step the *ipso*-nitration at the *tert*-butyl group must occur. In the second step, the different regioselectivity was then observed exclusively to complete nitration at positions 6 or 8 *ortho* to the *tert*-butyl group, because of deactivation of the second aromatic ring by the nitro group. It was also found that nitration of *anti*-**5c** and *anti*-**6c** with copper(II) nitrate resulted in only the recovery of the starting compound. Thus, an attempted nitration with fuming HNO_3 of *anti*-**5c** and *anti*-**6c** also failed. Only the starting compound was recovered in quantitative yield. Formation of a two-fold *ipso*-nitration product, i.e., *anti*-10,18-dimethoxy-7,15-dinitro[4.2]MCP *anti*-**3c**, was not observed under the reaction conditions. These results suggest that *anti*-**5c** and *anti*-**6c** are not the intermediates for the formation of two-fold *ipso*-nitration product *anti*-**3c**, as discussed later.The structures of *anti*-**5c** and *anti*-**6c** were assigned on the basis of elemental analyses and spectral data. The ^{1}H NMR spectrum of *anti*-**5c** in $CDCl_3$ shows three singlets at δ 1.38 for *tert*-butyl protons, at δ 3.23 and 3.34 for methoxy protons, respectively, and a set of doublets (J = 2.9 Hz) at δ 7.76 and 8.02 for aromatic protons in a strongly deshielded region due to the nitro group. It was also found that one of the ethano-bridge protons has been observed in a deshielded region (δ 3.30–3.34) due to the nitro group at position 8. As a result *anti*-**5c** has been assigned to 7-*tert*-butyl-10,18-dimethoxy-8,15-dinitro[4.2]MCP. Similar spectrum was observed in *anti*-**6c** and assigned to 7-*tert*-butyl-10,18-dimethoxy-6,15-dinitro[4.2]MCP.

We have reported (8) that nitration of *anti*-8,16-dimethyl[2.2]MCP exclusively afforded mononitrated product because of deactivation of the second aromatic ring by nitro group introduced. Thus, one *tert*-butyl group is *ipso*-nitrated because of deactivation of the second aromatic ring by nitro group by a through-space electronic interaction through the intra-annular 8,16 positions. However, this effect is much as a tendency to decrease as a number of bridged methylene group increases. Interestingly, in the case of higher methylene bridged *anti*-[*n*.2]MCPs, only mononitrated products were obtained along with recovery of the starting compounds. In the MCP system a first σ-complex intermediate would be stabilized by a through-space electronic interaction with the opposing benzene ring, thus accelerating the reaction. The order of reactivity of *anti*-[*n*.2]MCPs for nitration is estimated from the above results to be [3.2] > [4.2] > [5.2]MCP, and almost same reactivites are observed in [6.2] and [10.2]MCPs similar to those for 1,n-bis(5-*tert*-butyl-2-methoxyphenyl)alkanes (6). This finding

Table 2. Nitration of *syn*-di-*tert*-butyl-dimethoxy-[*n*.2]metacyclophanes *syn*-**1**.

Substrate	Number of methylene units, *n*	Reagent[a]	Products (%, yield)[b]
syn-**1b**	3	A	Complex mixture
syn-**lc**	4	A	*syn*-**2c** (65), *syn*-**3c** (20)
syn-**1d**	5	A	*syn*-**2d** (81), *syn*-**3d** (trace)[c]
syn-**1e**	6	A	*syn*-**2e** (73), *syn*-**3e** (10)[c]
syn-**1b**	3	B	Complex mixture
syn-**1c**	4	B	*syn*-**3c** (92)
syn-**1d**	5	B	*syn*-**3d** (90)
syn-**1e**	6	B	*syn*-**3e** (93)

[a]A, $Cu(NO_3)_2$ in Ac_2O, room temp. for 24 h; B, fuming HNO_3 in CH_2Cl_2/AcOH, room temp. for 30 min.
[b]Isolated yields are shown.
[c]Starting compounds, *syn*-**1d** and *syn*-**1e**, were recovered in 7 and 3% yields, respectively.

suggests that the stability of the cation intermediate, which may be due to a through-space electronic interaction with the opposing benzene ring through the intra-annular positions, decreases as the size of the polymethylene bridge increases.

Cram et al. (10) reported that the rate of the acetolysis of [2.2]paracyclophane tosylates was accelerated by the through-space electronic interactions with the opposite aromatic ring. This phenomenon was explained by the stability of the cationic intermediates, which should arise from the through-space electronic interaction with the benzene ring located on the opposite side. The rate increases as the degree of the overlapping with benzene ring increases. In the present [*n*.2]MCPs there are two possible conformers, anti- and syn-conformer. The through-space electronic interaction could be performed through the intra-annular positions in the former conformer, but through face-to-face overlapping among the two benzene rings in the latter conformer. Therefore, there is substantial interest to investigate the different behaviour on the nitration of *anti*- and *syn*-[*n*.2]MCPs and which conformer contributes more strongly to the through-space electronic interaction (Scheme 3, Table 2).

Nitration of *syn*-6,14-di-*tert*-butyl-9,17-dimethoxy-[3.2]MCP *syn*-**1b** (9) with copper(II) nitrate at room temperature for 24 h gave only a complex mixture of nonvolatile materials. But formation of the desired nitro compound *syn*-**2b** was not detected. This result might be attributable to a highly strained structure of *syn*-[3.2]MCP. In contrast, nitration of *syn*-[4.2]MCP *syn*-**1c** afforded mononitrated product *syn*-**2c** in 65% yield as a major product along with *syn*-10,18-dimethoxy-7,15-dinitro[4.2]MCP *syn*-**3c** in 20% yield. The same result was obtained in the nitration of *syn*-[5.2]MCP (*syn*-**1d**) and *syn*-[6.2]MCP (*syn*-**1e**) to afford a mixture of mononitrated product *syn*-**2d** and *syn*-**2e** in 81 and 73% yields along with the dinitrated product *syn*-**3d** and *syn*-**3e**. The higher yields of mononitrated product are obtained in syn-conformer than in anti-conformer. A first σ-complex intermediate would be stabilized by the through-space electronic interaction through face-to-face overlapping with the opposing benzene ring (**A**), thus accelerating the reaction. Therefore, face-to-face overlapping might be much

© 1998 NRC Canada

Fig. 1. Two possible through-space electronic interactions of [*n*.2]metacyclophanes.

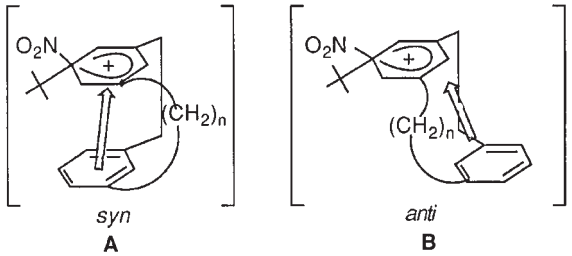

more favourable to stabilize the first σ-complex intermediate than the intra-annular interaction (**B**) (Fig. 1).

Interestingly, with varying reactivity of the nitrating reagents the ratio of the product arising from mono *ipso*-nitration **2** to the product arising from two-fold *ipso*-nitration at the *tert*-butyl groups **3** changed. When the nitration reagent was changed from copper(II) nitrate or 61% HNO_3 to the more reactive fuming HNO_3 the yield of di-*ipso*-nitrated products **3** increased from 5 to 35% to quantitative yields. Thus, the number of *ipso*-nitration at the *tert*-butyl groups of **1** was strongly affected by the reactivity of the nitration reagent, as has been reported for nitration in normal aromatic systems (11).

It should be noted that the present *ipso*-nitration of **1** is quite different from the results of the nitration of the corresponding internally methyl substituted *anti*-di-*tert*-butyl-[*n*.2]MCPs. For example, *anti*-6,14-di-*tert*-butyl-9,17-dimethyl[3.2]MCP *anti*-**7** (12) with fuming HNO_3 did not afford the desired *anti*-dinitro[3.2]MCPs *anti*-**8**, instead only intractable mixture was obtained. This result seems to indicate that the methoxy group in **1** plays an important role in the present *ipso*-nitration reaction. The *ipso*-nitration of **1** is attributed to the highly activated character of the aryl ring and the increased stabilization of the σ-complex intermediate arising from a dienone-type σ-complex intermediate, which is possible in the case of a methoxy substituent (Scheme 4).

Recently, we have reported (7) that similar treatment of 4-*tert*-butyl-2,6-dimethylanisole **9** with excess copper(II) nitrate in an acetic anhydride solution at room temperature only gave a quantitative recovery of starting compound. Raising the reaction temperature to 50°C afforded 2,6-dimethyl-4-nitroanisole **10** from *ipso*-nitration at the *tert*-butyl group in 40% yield, along with the starting compound **9**.

In contrast, as mentioned previously, nitration of [*n*.2]MCPs **1** with excess copper(II) nitrate in an acetic anhydride solution led to *ipso*-nitration at only one of the *tert*-butyl groups to give **2** in moderate yields along with dinitrated product **3**, thus differing from the nitration of **9** under the same conditions, which afforded only the starting compound. Recently, Cacace et al. (13) reported an intramolecular proton shift, namely, a ring-to-ring proton migration, in (β-phenylethyl)arenium ions during the cationic alkylation of 1,2-diphenylethanes, which occurs at a faster rate than the same reaction conducted with toluene in the gas phase. In the present system, an initial σ-complex intermediate would be stabilized by a through-space electronic interaction with the opposing benzene ring, therefore

Scheme 4.

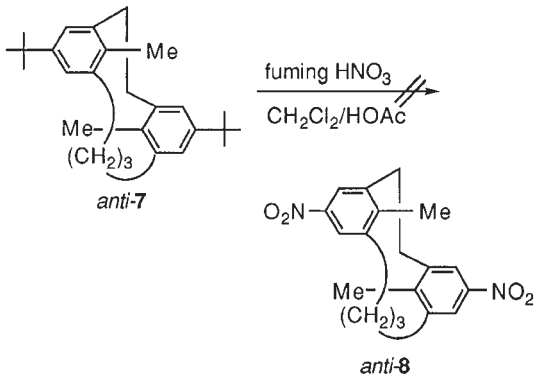

accelerating the reaction, as in the formylation of *tert*-butyl[*n*.2]MCPs (4*c*).

We previously reported the crystal structure of *anti*-[6.2]MCP *anti*-**1e** (9). Although the two benzene rings are located on different sides, but a longer distance was estimated in *anti*-**1d** than that for *anti*-[3.2]MCP *anti*-**1b** (14). Thus when the rings are *anti*, an increased bridge length increases the ring separation and decreases the ring–ring electronic interaction. In contrast, from consideration of the crystal structure of *syn*-[5.2]MCP *syn*-**3d** as shown in Fig. 2, in the *syn* series the through-space electronic interaction through face-to-face overlapping with the opposing benzene ring can still be large, even the larger bridge length. Therefore, the initial σ-complex intermediate could be much more stabilized by a through-space electronic interaction with other benzene rings through the face-to-face overlapping, and thus higher reactivity for syn-conformer than that for anti-conformer in the present *ipso*-nitration was observed.

Interestingly, the bridged methylene protons for $CH_2CH_2\mathit{CH_2}CH_2CH_2$ in the compound *syn*-**3d** are located in different spaces, with one of them folded into the π-cavity formed by two benzene rings. Thus, a higher field signal at δ –0.90–0.10 ppm was observed. The individual peaks of the methylene protons for middle $\mathit{CH_2}$ in the pentane bridge do not coalesce below 140°C in DMSO-d_6, and the energy barrier to conformational wobbling is above 25 kcal/mol.

The presently developed procedure was further applied to the direct removal of a *tert*-butyl group of *O*-(ethoxycarbonyl)methoxy derivative. Thus, nitration of *syn*-16,24-bis[(ethoxycarbonyl)methoxy]-13,21-di-*tert*-butyl[10.2]MCP *syn*-**12**, which was prepared by di-*O*-alkylation of 13,21-di-*tert*-butyl-16,24-dihydroxy[10.2]MCP **11** (15) with ethyl bromoacetate in the presence of NaH (16), with fuming HNO_3, afforded the desired 16,24-bis[(ethoxycarbonyl)-methoxy]-13,21-dinitro[10.2]MCP *syn*-**13** in 91% yield. No cleavage of the ester groups of *syn*-**12** was observed under the condition used as previously observed in the *ipso*-nitration of tetrakis[(ethoxycarbonyl)methoxy]-*tert*-butylcalix-[4]arene (5*c*) (Scheme 5).

We conclude that the selective *ipso*-nitration of *syn*- and *anti*-di-*tert*-buty[*n*.2]MCPs **1** led to the direct introduction of one or two nitro group(s) due to a through-space electronic interaction with the opposing benzene ring, similar to the electrophilic aromatic substitution of MCPs. The number of *ipso*-nitration of **1** has been controlled by the reactivity of the nitration reagent. Especially, the present two-fold

© 1998 NRC Canada

Fig. 2. Molecular structure of *syn*-11,19-dimethoxy-8,16-dinitro[5.2]metacyclophane *syn*-**3d**.

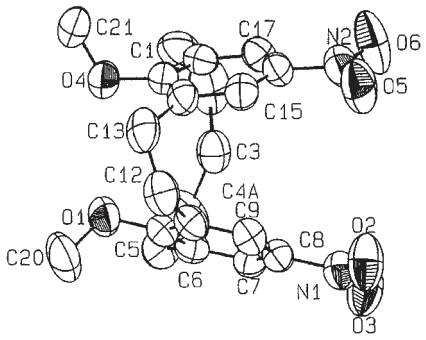

ipso-nitration with fuming HNO_3 provides excellent yields and easy isolation of the products. Further studies on *ipso*-nitration are currently in progress in our laboratory.

Experimental

All melting points (Yanagimoto MP-S1) were uncorrected. Proton nuclear magnetic resonance (^{1}H nmr) spectra were recorded on a Nippon Denshi JEOL FT-270 spectrometer. Chemical shifts are reported as δ values (ppm) relative to internal Me_4Si. Mass spectra were obtained on a Nippon Denshi JMS-01SA-2 mass spectrometer at an ionization energy of 70 eV; *m/z* values reported include the parent ion peak. Infrared (ir) spectra were obtained on a Nippon Denshi JIR-AQ2OM spectrophotometer as KBr disks. Elemental analyses were performed by Yanaco MT-5. The GLC analyses were performed by Shimadzu gas chromatograph, GC-14A; Silicone OV-1, 2 m; programmed temperature rise, 12°C/min; carrier gas nitrogen, 25 cm^3/min.

Materials

The preparations of *anti*-dimethoxy[*n*.2]MCPs *anti*-**1b**–**f** (9), *syn*-dimethoxy[*n*.2]MCPs *syn*-**1b**–**e** (9), 13,21-di-*tert*-butyl-16,24-dihydroxy[10.2]MCP **11** (15*a*), and *anti*-6,14-di-*tert*-butyl-9,17-dimethyl[3.2]MCP *anti*-**7** (12) were previously described.

Nitration of 1 with copper(II) nitrate in acetic anhydride. Typical procedure

To a solution of 7,15-di-*tert*-butyl-10,18-dimethoxy-[4.2]metacyclophane (*anti*-**1c**) (118.1 mg, 0.289 mmol) in a mixture of CH_2Cl_2 (2.5 mL) and acetic anhydride (50 mL) was added $Cu(NO_3)_2{\cdot}3H_2O$ (150 mg, 0.62 mmol) at 0°C. After the mixture had been stirred at room temperature for 24 h, the reaction mixture was poured into ice-water and then extracted with CH_2Cl_2, washed with water and 10% aqueous sodium hydrogen carbonate. The extract was dried over anhydrous sodium sulfate and concentrated. The GLC analyses of the residue was accord with its being a mixture of *anti*-**2c**, *anti*-**5c**, and *anti*-**6c** in the ratio of 65:14:21. The residue was subjected to silica-gel (Wako, C-300; 100 g) column chromatography using as eluent hexane/benzene (2:1), hexane/benzene (1:1), and benzene to give 7-*tert*-butyl-10,18-dimethoxy-6,15-dinitro[4.2]metacyclophane (*anti*-**6c**) (19.2 mg, 15%), 7-*tert*-butyl-10,18-dimethoxy-15-nitro[4.2]metacyclophane (*anti*-**2c**) (66.7 mg, 58%), and 7-*tert*-butyl-10,18-dimethoxy-8,15-dinitro[4.2]metacyclophane (*anti*-**5c**) (13.0 mg, 10%), respectively.

Scheme 5.

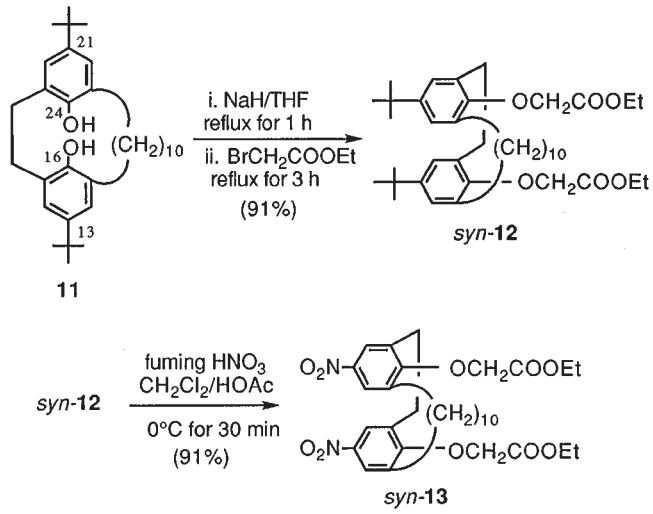

anti-7-*tert*-Butyl-10,18-dimethoxy-15-nitro[4.2]metacyclophane (*anti*-2c)

Pale-yellow prisms (hexane/benzene (2:1)); mp 165–166°C; ir (KBr): 2967, 2928, 1870, 2830, 1519, 1484, 1455, 1345, 1266, 1229, 1208, 1110, 1092, 1013, 1001, 904, 870, 751 cm^{-1}; ^{1}H nmr ($CDCl_3$): 1.22–1.31 (m, 2 H), 1.32 (s, 9 H), 1.34–1.47 (m, 2 H), 2.02–2.28 (m, 2 H), 2.72–2.84 (m, 6 H), 3.18 (s, 3 H), 3.26 (s, 3 H), 6.81 (d, 1 H, *J* 2.4), 7.08 (d, 1 H, *J* 2.4), 7.74 (d, 1 H, *J* 2.9), 8.02 (d, 1 H, *J* 2.9); MS, *m/z*: M^+ 397. Anal. calcd. for $C_{24}H_{31}NO_4$: C 72.52, H 7.86, N 3.52; found: C 72.32, H 7.75, N 3.17.

anti-7-*tert*-Butyl-10,18-dimethoxy-8,15-dinitro[4.2]metacyclophane (*anti*-5c)

Pale-yellow prisms (hexane/benzene (2:1)); mp 183–185°C; ir (KBr): 2931, 2873, 1584, 1529, 1474, 1456, 1424, 1398, 1371, 1338, 1287, 1267, 1210, 1171, 1092, 1061, 1035, 1000, 967, 899, 875, 852, 806, 795, 787, 749, 695 cm^{-1}; ^{1}H nmr ($CDCl_3$): 1.25–1.47 (m, 4 H), 1.38 (s, 9 H), 1.88–2.31 (m, 2 H), 2.45–2.91 (m, 5 H), 3.23 (s, 3 H), 3.30–3.34 (m, 1 H), 3.34 (s, 3 H), 6.96 (s, 1 H), 7.76 (d, 1 H, *J* 2.9), 8.02 (d, 1 H, *J* 2.9). MS, *m/z*: M^+ 442. Anal. calcd. for $C_{24}H_{30}N_2O_6$: C 65.14, H 6.83, N 6.33; found: C 65.28, H 6.66, N 6.14.

anti-7-*tert*-Butyl-10,18-dimethoxy-6,15-dinitro[4.2]metacyclophane (*anti*-6c)

Pale-yellow prisms (hexane/benzene (2:1)); mp 127–129°C; ir (KBr): 2956, 2928, 2866, 1587, 1524, 1476, 1456, 1424, 1398, 1371, 1346, 1287, 1268, 1217, 1097, 1032, 1016, 990, 960, 872, 838, 808, 797, 754, 746, 695 cm^{-1}; ^{1}H nmr ($CDCl_3$): 1.14–1.31 (m, 2 H), 1.38 (s, 9 H), 1.43–1.52 (m, 2 H), 2.04–2.31 (m, 2 H), 2.67–2.89 (m, 6 H), 3.22 (s, 3 H), 3.40 (s, 3 H), 7.00 (s, 1 H), 7.76 (d, 1 H, *J* 2.9), 8.00 (d, 1 H, *J* 2.9); MS, *m/z*: M^+ 442. Anal. calcd. for $C_{24}H_{30}N_2O_6$: C 65.14, H 6.83, N 6.33; found: C 65.35, H 6.75, N 6.07.

© 1998 NRC Canada

Reaction of *anti*-**1b**, *anti*-**1d–1f**, and *syn*-**1b**–**1e** with copper(II) nitrate in acetic anhydride was carried out using the same procedure as described above, and details of the products and yields are compiled in Tables 1 and 2.

***anti*-6-*tert*-Butyl-9,17-dimethoxy-14-nitro[3.2]metacyclophane (*anti*-2b)**

Pale-yellow oil; ir (NaCl): 2953, 2824, 1584, 1552, 1514, 1482, 1463, 1392, 1341, 1295, 1265, 1202, 1171, 1108, 1089, 1015, 899, 797, 779, 748 cm^{-1}; ^1H nmr ($CDCl_3$): 1.32 (s, 9 H), 2.00–2.07 (m, 2 H), 2.46–2.82 (m, 8 H), 3.05 (s, 3 H), 3.12 (s, 3 H), 6.99 (d, 1 H, *J* 2.4), 7.03 (d, 1 H, *J* 2.4), 7.91 (s, 2 H); MS, *m*/*z*: M^+ 383. Anal. calcd. for $C_{23}H_{29}NO_4$: C 72.04, H 7.62, N 3.65; found: C 71.86, H 7.49, N 3.52.

***anti*-8-*tert*-Butyl-11,19-dimethoxy-16-nitro[5.2]metacyclophane (*anti*-2d)**

Pale-yellow prisms (hexane/benzene (2:1)); mp 85–87°C; ir (KBr): 2930, 2860, 2824, 1588, 1516, 1482, 1460, 1347, 1295, 1266, 1224, 1205, 1171, 1110, 1091, 1006, 901, 794, 748 cm^{-1}; ^1H nmr ($CDCl_3$): 0.85–1.08 (m, 1 H), 1.21–1.32 (m, 4 H), 1.32 (s, 9 H), 1.34–1.46 (m, 1 H), 2.10–2.21 (m, 2 H), 2.48–2.66 (m, 2 H), 2.81–2.95 (m, 4 H), 3.26 (s, 3 H), 3.33 (s, 3 H), 6.90 (d, 1 H, *J* 2.4), 7.12 (d, 1 H, *J* 2.4), 7.77 (d, 1 H, *J* 2.9), 8.05 (d, 1 H, *J* 2.9); MS, *m*/*z*: M^+ 411. Anal. calcd. for $C_{25}H_{33}NO_4$: C 72.96, H 8.08, N 3.40; found: C 72.76, H 8.19, N 3.49.

***anti*-9-*tert*-Butyl-12,20-dimethoxy-17-nitro[6.2]metacyclophane (*anti*-2e)**

Pale-yellow prisms (hexane/benzene (1:1)); mp 133–134°C; ir (KBr): 2965, 2923, 1859, 1521, 1481, 1461, 1450, 1426, 1346, 1330, 1295, 1268, 1205, 1170, 1089, 1011, 904, 769, 748 cm^{-1}; ^1H nmr ($CDCl_3$): 0.78–0.86 (m, 2 H), 0.91–1.02 (m, 2 H), 1.32 (s, 9 H), 1.56–1.72 (m, 4 H), 2.23–2.42 (m, 2 H), 2.42–2.66 (m, 2 H), 2.82–2.98 (m, 4 H), 3.26 (s, 3 H), 3.27 (s, 3 H), 6.97 (d, 1 H, *J* 2.4), 7.11 (d, 1 H, *J* 2.4), 7.88 (d, 1 H, *J* 2.9), 8.05 (d, 1 H, *J* 2.9); MS, *m*/*z*: M^+ 425. Anal. calcd. for $C_{26}H_{35}NO_4$: C 73.38, H 8.29, N 3.29; found: C 73.31, H 8.36, N 3.14.

***anti*-13-*tert*-Butyl-16,24-dimethoxy-21-nitro[10.2]metacyclophane (*anti*-2f)**

Pale-yellow oil; ^1H nmr ($CDCl_3$): 1.12–1.35 (m, 12 H), 1.19 (s, 9 H), 1.40–1.47 (m, 4 H), 2.50 (broad s, 4 H), 2.99 (broad s, 4 H), 3.55 (s, 3 H), 3.59 (s, 3 H), 6.80 (broad d, 1 H, *J* 2.4), 6.90 (d, 1 H, *J* 2.4), 7.63 (broad d, 1 H, *J* 2.9), 8.02 (d, 1 H, *J* 2.9); MS, *m*/*z*: M^+ 481. Anal. calcd. for $C_{30}H_{43}NO_4$: C 74.81, H 9.0, N 2.91; found: C 74.98, H 8.85, N 3.17.

***syn*-7-*tert*-Butyl-10,18-dimethoxy-15-nitro[4.2]metacyclophane (*syn*-2c)**

Pale-yellow prisms (hexane/benzene (5:1)); mp 116–118°C; ir (KBr): 2931, 2871, 2824, 1514, 1483, 1464, 1445, 1346, 1265, 1232, 1220, 1208, 1085, 1013, 996, 896, 748 cm^{-1}; ^1H nmr ($CDCl_3$): 0.82–0.96 (m, 1 H), 1.05 (s, 9 H), 1.22–1.36 (m, 2 H), 1.94–2.18 (m, 4 H), 2.65–2.82 (m, 4 H), 3.41–3.57 (m, 1 H), 3.58 (s, 3 H), 3.64 (s, 3 H), 6.49 (d, 1 H, *J* 2.4), 6.52 (d, 1 H, *J* 2.4), 7.40 (d, 1 H, *J* 2.9), 7.54 (d, 1 H, *J* 2.9); MS, *m*/*z*: M^+ 397. Anal. calcd. for $C_{24}H_{31}NO_4$: C 72.52, H 7.86, N 3.52; found: C 72.20, H 7.84, N 3.25.

***syn*-8-*tert*-Butyl-11,19-dimethoxy-16-nitro[5.2]metacyclophane (*syn*-2d)**

Pale-yellow prisms (hexane/benzene (1:1)); mp 121–123°C; ir (KBr): 2952, 2926, 2857, 1586, 1516, 1484, 1337, 1266, 1218, 1200, 1086, 1013, 998, 899, 748 cm^{-1}; ^1H nmr ($CDCl_3$): 0.02–0.20 (m, 1 H), 0.78–0.92 (m, 1 H), 1.07 (s, 9 H), 1.21–1.25 (m, 2 H), 1.26–1.31 (m, 2 H), 1.32–1.39 (m, 2 H), 2.06–2.25 (m, 2 H), 2.82–2.86 (m, 1 H), 2.86–3.01 (m, 2 H), 3.22–3.34 (m, 1 H), 3.60 (s, 3 H), 3.67 (s, 3 H), 6.60 (d, 1 H, *J* 2.4), 6.67 (d, 1 H, *J* 2.4), 7.51 (d, 1 H, *J* 2.9), 7.65 (d, 1 H, *J* 2.9); MS, *m*/*z*: M^+ 411. Anal. calcd. for $C_{25}H_{33}NO_4$: C 72.96, H 8.08, N 3.40; found: C 73.35, H 8.30, N 3.22.

***syn*-9-*tert*-Butyl-12,20-dimethoxy-17-nitro[6.2]metacyclophane (*syn*-2e)**

Pale-yellow prisms (hexane/benzene (1:1)); mp 139–140°C; ir (KBr): 2947, 2856, 2826, 1516, 1484, 1466, 1442, 1365, 1341, 1308, 1294, 1268, 1245, 1216, 1208, 1171, 1132, 1114, 1089, 1014, 1000, 901, 781, 748, 731, 707 cm^{-1}; ^1H nmr ($CDCl_3$): 0.44–0.92 (m, 2 H), 1.08 (s, 9 H), 1.21–1.45 (m, 4 H), 1.69–1.92 (m, 2 H), 2.17–2.36 (m, 2 H), 2.73–2.92 (m, 4 H), 3.50–3.74 (m, 2 H), 3.64 (s, 3 H), 3.68 (s, 3 H), 6.69 (d, 1 H, *J* 2.4), 6.73 (d, 1 H, *J* 2.4), 7.59 (d, 1 H, *J* 2.9), 7.79 (d, 1 H, *J* 2.9); MS, *m*/*z*: M^+ 425. Anal. calcd. for $C_{26}H_{35}NO_4$: C 73.38, H 8.29, N 3.29; found: C 73.49, H 8.31, N 3.45.

Nitration of 1 with fuming HNO_3. Typical procedure

To a solution of *anti*-6,14-di-*tert*-butyl-9,17-dimethoxy-[3.2]metacyclophane (*anti*-**1b**) (98.5 mg, 0.25 mmol) in a mixture of CH_2Cl_2 (2.5 mL) and glacial acetic acid (2.5 mL) was added fuming HNO_3 (0.83 mL) at 0°C. After the mixture had been stirred at room temperature for 30 min, it was poured into ice-water, extracted with CH_2Cl_2, washed with water and 10% aqueous sodium hydrogen carbonate. The extract was dried over anhydrous sodium sulfate and concentrated. The residue was subjected to silica-gel (Wako, C-300; 100 g) column chromatography using as eluent benzene to give *anti*-9,17-dimethoxy-6,14-dinitro[3.2]metacyclophane (*anti*-**3b**) (86 mg, 89%) as pale-yellow prisms (hexane/benzene (4:1)); mp 266–268°C; ir (KBr): 2935, 2860, 2825, 1585, 1505, 1466, 1447, 1429, 1337, 1307, 1263, 1215, 1185, 1089, 1008, 931, 907, 806, 791, 748, 699 cm^{-1}; ^1H nmr ($CDCl_3$): 2.04–2.14 (m, 2 H), 2.55–2.74 (m, 6 H), 2.87–2.90 (m, 2 H), 3.14 (s, 6 H), 7.95 (d, 2 H, *J* 2.9), 7.98 (d, 2 H, *J* 2.9); MS, *m*/*z*: M^+ 372. Anal. calcd. for $C_{19}H_{20}N_2O_6$: C 61.28, H 5.41, N 7.52; found: C 61.16, H 5.59, N 7.42.

Reaction of *anti*-**1c–f** and *syn*-**1b–e** with fuming HNO_3 was carried out using the same procedure as described above, and details of the products and yields are compiled in Tables 1 and 2.

***anti*-10,18-Dimethoxy-7,15-dinitro[4.2]metacyclophane (*anti*-3c)**

Pale-yellow prisms (hexane/benzene (1:1)); mp 224–226°C; ir (KBr): 2936, 2872, 2828, 1587, 1513, 1471, 1456,

© 1998 NRC Canada

1431, 1333, 1265, 1220, 1095, 1006, 971, 957, 911, 801, 782 cm^{-1}; ^1H nmr ($CDCl_3$): 1.16–1.37 (m, 2 H), 1.46–1.56 (m, 2 H), 2.19–2.32 (m, 2 H), 2.79–2.89 (m, 4 H), 2.92–2.96 (m, 2 H), 3.28 (s, 6 H), 7.78 (d, 2 H, *J* 2.93), 8.05 (d, 2 H, *J* 2.93); MS, *m*/*z*: M^+ 386. Anal. calcd. for $C_{20}H_{22}N_2O_6$: C 62.17, H 5.74, N 7.25; found: C 62.24, H 5.83, N 7.48.

anti-11,19-Dimethoxy-8,16-dinitro[5.2]metacyclophane (*anti*-3d)

Pale-yellow prisms (hexane/benzene (1:1)); mp 222–223°C; ir (KBr): 2965, 2933, 2865, 1587, 1516, 1468, 1459, 1432, 1424, 1339, 1295, 1266, 1226, 1210, 1195, 1172, 1000, 943, 909, 974, 772, 749, 697 cm^{-1}; ^1H nmr ($CDCl_3$): 0.91–1.02 (m, 2 H), 1.29–1.44 (m, 4 H), 2.21–2.30 (m, 2 H), 2.57–2.67 (m, 2 H), 2.96 (s, 4 H), 3.36 (s, 6 H), 7.83 (d, 2 H, *J* 2.9), 8.07 (d, 2 H, *J* 2.9); MS, *m*/*z*: M^+ 400. Anal. calcd. for $C_{21}H_{24}N_2O_6$: C 62.99, H 6.04, N 7.0; found: C 63.18, H 6.18, N 6.63.

anti-12,20-Dimethoxy-9,17-dinitro[6.2]metacyclophane (*anti*-3e)

Pale-yellow prisms (hexane/benzene (1:1)); mp 242–243°C; ir (KBr): 2976, 2940, 2926, 2857, 1521, 1471, 1463, 1342, 1303, 1286, 1265, 1227, 1215, 1177, 1089, 1005, 938, 904, 894, 803, 769, 748, 696 cm^{-1}; ^1H nmr ($CDCl_3$): 0.86–0.95 (m, 4 H), 1.69–1.74 (m, 4 H), 2.37–2.45 (m, 2 H), 2.55–2.66 (m, 2 H), 2.98 (s, 4 H), 3.35 (s, 6 H), 7.92 (d, 2 H, *J* 2.9), 8.06 (d, 2 H, *J* 2.9); MS, *m*/*z*: M^+ 414. Anal. calcd. for $C_{22}H_{26}N_2O_6$: C 63.76, H 6.32, N 6.76; found: C 63.78, H 6.39, N 6.44.

anti-16,24-Dimethoxy-13,21-dinitro[10.2]metacyclophane (*anti*-3f)

Pale-yellow prisms (hexane/benzene (1:1)); mp 170–172°C; ir (KBr): 2931, 2860, 1586, 1514, 1466, 1443, 1423, 1348, 1295, 1265, 1241, 1228, 1219, 1198, 1169, 1104, 1089, 1000, 914, 798, 789, 749 cm^{-1}; ^1H nmr ($CDCl_3$): 1.14–1.37 (m, 12 H), 1.40–1.48 (m, 4 H), 2.55 (broad s, 4 H), 3.05 (broad s, 4 H), 3.63 (s, 6 H), 7.63 (broad d, 2 H, *J* 2.9), 7.88 (d, 2 H, *J* 2.9); MS, *m*/*z*: M^+ 470. Anal. calcd. for $C_{26}H_{34}N_2O_6$: C 66.36, H 7.28, N 5.95; found: C 66.43, H 7.51, N 6.02.

syn-10,18-Dimethoxy-7,15-dinitro[4.2]metacyclophane (*syn*-3c)

Pale-yellow prisms (hexane/benzene (1:1)); mp 141–143°C; ir (KBr): 2939, 2859, 1585, 1517, 1474, 1457, 1429, 1347, 1269, 1232, 1090, 1006, 901, 802, 748, 697, 668 cm^{-1}; ^1H nmr ($CDCl_3$): 1.02–1.11 (m, 2 H), 2.09–2.18 (m, 4 H), 2.70–2.94 (m, 4 H), 3.48–3.61 (m, 2 H), 3.67 (s, 6 H), 7.42 (d, 2 H, *J* 2.9), 7.53 (d, 2 H, *J* 2.9); MS, *m*/*z*: M^+ 386. Anal. calcd. for $C_{20}H_{22}N_2O_6$: C 62.17, H 5.74, N 7.25; found: C 61.86, H 5.65, N 6.95.

syn-11,19-Dimethoxy-8,16-dinitro[5.2]metacyclophane (*syn*-3d)

Pale-yellow prisms (hexane/benzene (1:1)); mp 234–236°C; ir (KBr): 2991, 2940, 2861, 2832, 1586, 1516, 1474, 1456, 1431, 1349, 1287, 1269, 1230, 1200, 1176, 1096, 1005, 940, 911, 894, 747, 711 cm^{-1}; ^1H nmr ($CDCl_3$): – 0.90–0.10 (m, 1 H), 0.79–0.96 (m, 1 H), 1.21–1.31 (m, 1 H), 1.30–1.44 (m, 2 H), 1.61–1.78 (m, 2 H), 2.21–2.36 (m, 2 H), 2.88–3.02 (m, 4 H), 3.62–3.70 (m, 1 H), 3.69 (s, 6 H), 7.55 (d, 2 H, *J* 2.9), 7.67 (d, 2 H, *J* 2.9); MS, *m*/*z*: M^+ 400. Anal. calcd. for $C_{21}H_{24}N_2O_6$: C 62.99, H 6.04, N 7.0; found: C 62.86, H 6.27, N 6.80.

Table 3. Fractional atomic coordinates for the non-hydrogen atoms, with estimated standard deviations in parentheses, for *syn*-11,19-dimethoxy-8,16-dinitro[5.2]metacyclophane *syn*-**3d** and the isotropic equivalent displacement parameter defined as $B_{eq} = 4/3[a^2B_{11} + b^2B_{22} + c^2B_{33} + ab(\cos\gamma)B_{12} + ac(\cos\beta)B_{13} + bc(\cos\alpha)B_{23}]$.

Atom	*x*	*y*	*z*	B_{eq}
01	0.0318(3)	0.2856(3)	0.6913(4)	6.23(8)
02	0.6058(4)	0.1817(3)	0.4202(5)	8.7(1)
03	0.5861(3)	0.3631(3)	0.4665(5)	8.0(1)
04	0.0962(3)	0.2281(3)	1.0187(4)	6.61(8)
O5	0.6767(4)	0.0389(4)	0.7984(5)	9.4(1)
06	0.7248(4)	0.1670(4)	0.9968(6)	11.0(1)
N1	0.5418(4)	0.2740(3)	0.4672(4)	5.68(9)
N2	0.6439(4)	0.1149(4)	0.9076(5)	6.9(1)
C1	0.2749(6)	0.3848(5)	1.1812(6)	6.9(1)
C2A	0.3236(9)	0.4912(9)	1.145(1)	9.5(3)
C2B	0.201(1)	0.4669(9)	1.070(1)	4.4(2)
C3	0.3031(5)	0.5024(4)	0.9748(6)	6.2(1)
C4B	0.1604(8)	0.5018(7)	0.918(1)	4.0(2)
C4A	0.208(1)	0.5617(9)	0.851(1)	9.1(3)
C5	0.1383(5)	0.4967(4)	0.7276(6)	6.0(1)
C6	0.2123(4)	0.3840(3)	0.6460(5)	4.66(9)
C7	0.3395(4)	0.3801(3)	0.5895(5)	4.75(9)
C8	0.4072(4)	0.2764(3)	0.5262(5)	4.43(9)
C9	0.3542(4)	0.1749(4)	0.5186(5)	5.0(1)
C10	0.2280(4)	0.1746(3)	0.5747(5)	4.9(1)
C11	0.1560(4)	0.2814(4)	0.6328(5)	4.66(9)
C12	0.1785(5)	0.0626(4)	0.5883(6)	6.2(1)
C13	0.1661(5)	0.0483(4)	0.7519(6)	6.4(1)
C14	0.2688(4)	0.1086(4)	0.8673(5)	5.2(1)
C15	0.4070(4)	0.0794(4)	0.8451(5)	5.4(1)
C16	0.4981(4)	0.1454(4)	0.9378(5)	5.2(1)
C17	0.4600(4)	0.2418(4)	1.0476(5)	5.5(1)
C18	0.3239(5)	0.2733(4)	1.0733(5)	5.4(1)
C19	0.2321(4)	0.2010(4)	0.9877(5)	5.2(1)
C20	–0.0798(5)	0.2713(6)	0.5849(7)	8.7(2)
C21	0.0546(5)	0.1736(5)	1.1321(6)	8.3(1)

syn-12,20-Dimethoxy-9,17-dinitro[6.2]metacyclophane (*syn*-3e)

Pale-yellow prisms (hexane/benzene (1:1)); mp 143–144°C; ir (KBr): 2936, 2860, 2833, 1516, 1468, 1446, 1344, 1303, 1270, 1231, 1218, 1086, 1008, 914, 904, 792, 747, 702 cm^{-1}; ^1H nmr ($CDCl_3$): 0.58–0.66 (m, 1 H), 0.81–0.92 (m, 1 H), 1.21–1.48 (m, 4 H), 1.74–1.89 (m, 2 H), 2.34–2.46 (m, 2 H), 2.80–2.95 (m, 4 H), 3.63–3.69 (m, 2 H), 3.71 (s, 6 H), 7.66 (d, 2 H, *J* 2.9), 7.74 (d, 2 H, *J* 2.9); MS, *m*/*z*: M^+ 414. Anal. calcd. for $C_{22}H_{26}N_2O_6$: C 63.76, H 6.32, N 6.76; found: C 63.58, H 6.32, N 6.76.

© 1998 NRC Canada

Alkylation of 11 with bromoethylacetate in the presence of NaH to afford *syn*-13,21-di-*tert*-butyl-16,24-bis[(ethoxycarbonyl)methoxy][10.2]metacyclophane (*syn*-12)

A mixture of **11** (81 mg, 0.175 mmol) and NaH (28.0 mg, 0.700 mmol, about 60% in oil) in dry tetrahydrofuran (9 mL) was heated at reflux for 1 h under N_2. Then ethyl bromoacetate (0.1 mL, 0.902 mmol) was added and the mixture heated at reflux for an additional 3 h. After cooling the reaction mixture to room temperature, it was filtered. The filtrate was concentrated to give a yellow oil, which was then distilled under the reduced pressure to remove the excess unreacted ethyl bromoacetate using a kugelrohr apparatus. The residue was recrystallized from hexane/benzene (1:1) affording the *title compound syn*-**12** (101 mg, 91%) as colorless prisms; mp 38–40°C; ir (KBr): 2931, 2860, 1741 (C=O), 1480, 1461, 1371, 1284, 1195, 1142, 1059, 1039, 949, 863, 777, 745, 667 cm^{-1}; ^1H nmr ($CDCl_3$): 0.81–0.92 (m, 8 H), 1.16 (s, 18 H), 1.21–1.30 (m, 2 H), 1.27–1.35 (m, 6 H), 1.38–1.47 (m, 4 H), 2.17–2.29 (m, 2 H), 2.62–2.74 (m, 2 H), 2.77–2.89 (m, 2 H), 3.32–3.44 (m, 2 H), 4.19–4.31 (m, 4 H), 4.38 (s, 4 H), 6.73 (d, 2 H, *J* 2.4), 6.89 (d, 2 H, *J* 2.4); MS, *m/z*: M^+ 636. Anal. calcd. for $C_{40}H_{60}O_6$: C 75.43, H 9.5; found: C 75.26, H 9.59.

Nitration of *syn*-12 with fuming HNO_3

To a solution of *syn*-**12** (38.0 mg, 0.06 mmol) in a mixture of CH_2Cl_2 (1.0 mL) and glacial acetic acid (1.0 mL) was added fuming HNO_3 (0.25 mL) at 0°C. After the mixture had been stirred at room temperature for 30 min, it was poured into ice-water, extracted with CH_2Cl_2, washed with water and 10% aqueous sodium hydrogen carbonate. The extract was dried over anhydrous sodium sulfate and concentrated. The residue was subjected to silica-gel (Wako, C-300; 100 g) column chromatography using as eluent chloroform to give *syn*-16,24-bis[(ethoxycarbonyl)methoxy]13,21-dinitro[10.2]metacyclophane (*syn*-**13**) (33 mg, 91%) as pale-yellow prisms (hexane/benzene (1:1)); mp 72–74°C; ir (KBr): 2933, 2854, 1765, 1728 (C=O), 1619, 1448, 1371, 1342, 1310, 1283, 1265, 1198, 1184, 1105, 1086, 1056, 1042, 1030, 944, 920, 886, 865, 746 cm^{-1}; ^1H nmr ($CDCl_3$): 0.79–0.92 (m, 8 H), 1.15–1.55 (m, 8 H), 1.30 (t, 6 H, *J* 7.3), 2.29–2.43 (m, 2 H), 2.69–2.83 (m, 2 H), 2.86–2.98 (m, 2 H), 3.52–3.67 (m, 2 H), 4.26 (q, 4 H, *J* 7.3), 4.44 (s, 4 H), 7.57 (d, 2 H, *J* 2.9), 7.88 (d, 2 H, *J* 2.9). – MS (75 eV); MS, *m/z*: M^+ 614. Anal. calcd. for $C_{32}H_{42}N_2O_{10}$: C 62.53, H 6.89, N 4.56; found: C 62.35, H 6.68, N 4.36.

Crystallographic data for *syn*-11,19-dimethoxy-8,16-dinitro[5.2]metacyclophane (*syn*-3d)

Crystal data: $C_{21}H_{24}N_2O_6$; M = 400.44; triclinic; a = 996.28 (8), b = 1200.77 (6), c = 875.12 (5) pm; α = 102.604 (5), β = 94.445 (6), γ = 83.340 (6)°; V (m^3) = 1745.5 (4) × 10^{-30} (by least-squares refinement on diffractometer angles for 25 automatically centered reflections); λ (Å) = 1.54184; space group P-1 (no. 2); Z = 2; D_x (g/cm^3) = 1.312; pale-yellow prism; crystal size (mm) 0.3 × 0.25 × 0.2; μ(Cu-K_α) (cm^{-1}) = 7.65.

Data correction and procedure

Enraf–Nonius CAD4 FR586 diffractometer, $\omega/2\theta$ mode with ω scan width of 0.8 + 0.140 tan θ, scan speed 1.0–7.0 deg min^{-1}, graphite-monochromated Cu-K_α radiation; 4250 reflections were measured ($2.31 \leq \theta \leq 64.92$, $-h$, k, l); 3702 unique (merging R = 0.0260, no absorption correction); linear and approx. isotopic crystal decay, ca. –3.8% corrected during procedure.

Structure analysis and refinement

The structure was solved by direct method (SIR88 (17)). Full-matrix least-squares refinement on F with all non-hydrogen atoms anisotropic and hydrogens isotropic fixed at B_{eq} 4.0 Å^2. The weighting scheme is $\omega = 4F_o^2/[(\sigma I_o)^2 + 0.0016F_o^4]$. Final R and Rw values are 0.083 and 0.121 (refined on F). All calculations were performed on a Micro VAX3100 using MolEN (18).

The non-hydrogen atoms were refined anisotropically, but it was considered that C2A and C4A were disordered with their counterparts C2B and C4B in a ratio of 0.64:0.36 and 0.57:0.43, respectively. The 14 independent hydrogen atoms except for C(2A), C(2B), C(3), C(4A), and C(4B) were located in the calculated positions at thermally fixed B_{iso} 5.0 Å^2 and included in the refinement, but restrained to ride on the atoms to which they are bonded.

The refined non-hydrogen atomic coordinates are listed in Table 3, whilst the hydrogen coordinates, temperature factors (anisotropic for carbon atoms), scale factor, secondary estimation coefficient, bond distances and angles, and crystal data have been deposited.[2]

References

1. R.B. Moodie and K. Schofield. Acc. Chem. Res. **9**, 287 (1976).
2. (*a*) A. Fischer and R. Röderer. Can. J. Chem. **54**, 3978 (1976); (*b*) A. Fischer and K.C. Teo. Can. J. Chem. **56**, 258 (1978); (*c*) Can. J. Chem. **56**, 1758 (1978).
3. (*a*) H. Suzuki. Synthesis, 217 (1977); (*b*) P.C. Myhre and M. Beug. J. Am. Chem. Soc. **88**, 1568 (1966); (*c*) P.C. Myhre, M. Beug, and L.L. James. J. Am. Chem. Soc. **90**, 2105 (1968); (*d*) P.C. Myhre, M. Beug, K.S. Brown, and B. Östman. J. Am. Chem. Soc. **93**, 3452 (1971).
4. (*a*) T. Yamato, J. Matsumoto, K. Tokuhisa, Y. Takezaki, and M. Tashiro. Chem. Express, **6**, 663 (1991); (*b*) T. Yamato, J. Matsumoto, M. Shigekuni, and M. Tashiro. J. Chem. Res. Synop. 198 (1993); (*c*) T. Yamato, J. Matsumoto, S. Kabu, Y. Takezaki, and M. Tashiro. J. Chem. Res. Synop. 44 (1993); (*d*) T. Yamato, K. Maeda, H. Kamimura, K. Noda, and M. Tashiro. J. Chem. Res. Synop. 310 (1995); J. Chem. Res. Miniprint, 1865 (1995).
5. (*a*) A. Fischer and R. Röderer. J. Chem. Soc. Chem. Commun. 798 (1975); (*b*) G.A. Olah and S.J. Kuhn. J. Am. Chem. Soc. **86**, 1067 (1964); (*c*) W. Verboom, A. Durie, R.J.M. Egberink,

[2] Supplementary material may be purchased from: The Depository of Unpublished Data, Document Delivery, CISTI, National Research Council of Canada, Ottawa, Canada, K1A 0S2. Crystal data, refinement data, and bond distances and angles have also been deposited with the Cambridge Crystallographic Data Centre and can be obtained on request from: The Director, Cambridge Crystallographic Data Centre, University Chemical Laboratory, 12 Union Road, Cambridge, CB2 1EZ, U.K.

© 1998 NRC Canada

Z. Asfari, and D.N. Reinhoudt. J. Org. Chem. **57**, 1313 (1992); (*d*) E. Kelderman, L. Derhaeg, G.J.T. Heesink, W. Verboom, J.F.J. Engbersen, N.F. van Hulst, A. Persoons, and D.N. Reinhoudt. Angew. Chem. Int. Ed. Engl. **31**, 1075 (1992).
6. T. Yamato, H. Kamimura, K. Noda, and M. Tashiro. J. Chem. Res. Synop. 210 (1994); J. Chem. Res. Miniprint, 1152 (1994).
7. T. Yamato, H. Kamimura, and T. Furukawa. J. Org. Chem. **62**, 7560 (1997).
8. M. Tashiro, S. Mataka, Y. Takezaki, M. Takeshita, T. Arimura, A. Tsuge, and T. Yamato. J. Org. Chem. **54**, 451 (1989).
9. T. Yamato, J. Matsumoto, K. Tokuhisa, M. Kajihara, K. Suehiro, and M. Tashiro. Chem. Ber. **125**, 2443 (1992).
10. (*a*) R.E. Singer and D.J. Cram. J. Am. Chem. Soc. **93**, 4443 (1971); (*b*) J. Am. Chem. Soc. **94**, 3512 (1972); (*c*) D.J. Cram, R.B. Hornby, E.A. Truesdale, H.J. Reich, M.H. Delton, and J.M. Cram. Tetrahedron, **30**, 1757 (1977).
11. G.A. Olah. Acc. Chem. Res. **4**, 240 (1971).
12. T. Yamato, J. Matsumoto, S. Ide, K. Tokuhisa, K. Suehiro, and M. Tashiro. J. Org. Chem. **57**, 5243 (1992).
13. F. Cacace, M.E. Crestoni, S. Fornarini, and D. Kuck. J. Am. Chem. Soc. **115**, 1024 (1993).
14. A. Tsuge, M. Yasumatsu. T. Moriguchi, K. Sakata, T. Yamato, S. Mataka, and M. Tashiro. Chem. Lett. 413 (1997).
15. (*a*) T. Yamato, J. Matsumoto, M. Sato, K. Noda, and M. Tashiro. J. Chem. Soc. Perkin Trans. 1, 1299 (1995); (*b*) T. Yamato, J. Matsumoto, M. Sato, K. Noda, T. Moriguchi, and M. Tashiro. Liebigs Ann. Chem. 995 (1995).
16. (*a*) K. Iwamoto, K. Araki, and S. Shinkai. J. Org. Chem. **56**, 4955 (1991); (*b*) S. Shinkai, K. Fujimoto, T. Otsuka, and H.L. Ammon. J. Org. Chem. **57**, 1516 (1992); (*c*) K. Araki, N. Hashimoto, H. Otsuka, and S. Shinkai. J. Org. Chem. **58**, 5958 (1993); (*d*) K. Araki, K. Inada, H. Otsuka, and S. Shinkai. Tetrahedron, **49**, 9465 (1993).
17. M.C. Burla, M. Camalli, G. Cascarano, C. Giacovazzo, G. Polidori, R. Spagna, and D. Viterbo. J. Appl. Crystallogr. **22**, 389 (1989).
18. MolEN, an interactive structure solution procedure. Enraf-Nonius, Delft, The Netherlands. 1990.

© 1998 NRC Canada

A comparative theoretical study of the electronic structure of some nickel(II) azides, thiocyanates, and isothiocyanates

R.H. Abu-Eittah, M. El-Esawy, N. Ghoneim, and A.T. Aly

Abstract: The electronic structure, conformation, and molecular orbitals of some nickel(II) azides, thiocyanates, and isothiocyanates have been studied. Three different basis sets: split valence (SV), split valence with six *d*-Gaussians (SV6D), and double zeta (DZ) sets, were used to find the best ground state for nickel. It has been found that the combination, DZ-^3F, gives results closest to the experimental values. The electronic structures of the nickel azides studied were completely different from those of the nickel thiocyanates. On the other hand, the electronic structures of the nickel thiocyanates studied were highly comparable to those of the corresponding nickel isothiocyanates. Molecular orbitals were computed for the complexes studied and the types of electronic transitions expected were identified and discussed.

Key words: Ni(II) azides, thiocyanates, and isothiocyanates: ab initio SCF calculations; MO calculations on some Ni(II) complexes; theoretical treatment of some Ni(II) ions and salts; geometry and energetics of some nickel(II) azides, thiocyanates, and isothiocyanates.

Résumé : On a étudié la structure électronique, la conformation et les orbitales moléculaires de quelques azotures, thiocyanates et isothiocyanates de nickel(II). On a utilisé trois ensembles de base (ensembles de valence scindée (VS), de valence scindée avec six gaussiennes-*d* (VS6G) et de double zêta (DZ)) pour déterminer le meilleur état fondamental du nickel. On a trouvé que la combinaison DZ-^3F conduit aux résultats qui se rapprochent le plus des valeurs expérimentales. Les structures électroniques des azotures de nickel étudiés sont complètement différentes de celles des thiocyanates de nickel. Par ailleurs, les structures électroniques des thiocyanates étudiés se comparent avantageusement avec celles des isothiocyanates de nickel correspondants. On a calculé les orbitales moléculaires des complexes étudiés, on a identifié et on discute des types de transitions électroniques attendues.

Mots clés : azotures de nickel(II), thiocyanates et isothiocyanates : calculs ab initio autocohérents, calculs d'OM, géométrie, énergies.

[Traduit par la Rédaction]

1. Introduction

Theoretical calculations on the compounds of third-row and higher elements are still scarce in the literature due both to the problems faced with parameterization of these elements in semiempirical calculations and to the need for fast computers for ab initio calculations. A theoretical study of transition metals and their compounds is important. There have been several studies on the role of transition metals in catalytic dehydrogenation and their mode of interaction with hydrocarbons. Rappe and Goddard (1) studied the electronic states of $NiCH_2$ and $NiCH_3$ using effective core potentials(ECPs) instead of all-electron calculations. The results obtained for the ^3F and ^3D states were very illustrative.

Kitaura et al. (2) used ab initio MO calculations on the complexes of nickel with phosphines whereas Lin and Hall (3) investigated the stability of hydrides. Simpson and Hall (4) studied the carbonyls and discussed the possibilities of bridging as well as metal–metal bonding.

The complexes of nickel with azide ion and different phosphines have been studied (5). Sensie et al. (6) used polarographic and potentiometric methods in their study of nickel azide. The formation of azido nickel complexes was studied by Egghart (7) while a study in nonaqueous media was carried out by Gutmann and Bardy (8). The formation of Ni(II) and Co(II) azides as well as the electronic absorption spectra of the complexes formed have been studied (9, 10).

The thiocyanate ion, having S and N atoms on its ends, has the ability to bond through either of them, thus producing the so-called thiocyanates and isothiocyanates. The bonding of thiocyanate ion through the nitrogen atom has been widely reported (11–15) and bond lengths were determined from single-crystal X-ray measurements.

Received July 25, 1997.[1]

R.H. Abu-Eittah,[2] M. El-Esawy, N. Ghoneim, and A.T. Aly. Department of Chemistry, Faculty of Science, University of Cairo, Giza, Egypt.

[1]Revision received April 28, 1998.
[2]Author to whom correspondence may be addressed. E-mail: HILAL2@FRCU.EUN.EG

2. Computational methods

2.i. Electronic state of Ni

Computations throughout this work were carried out using the GAMESS program (16) distributed free of charge by Mike Schmidt. Smaller programs were developed for fine

© 1998 NRC Canada

analysis of the outputs without incorporation into the original GAMESS code.

When dealing with a system of $2n$ electrons occupying n double-occupied molecular orbitals, the restricted Hartree–Fock state function is a product of the antisymmetrized spin orbitals

$$[1] \qquad \Psi^{\mathrm{RHF}} = \left|\phi_1 \ldots \bar{\phi}_1 \phi_n \bar{\phi}_n\right|$$

The LCAO approximation involves expanding ϕ_i as a finite series of simpler basis functions (which roughly correspond to atomic orbitals), i.e.,

$$[2] \qquad \phi_i = \sum_{p=1}^{m} C_{ip} \chi_p$$

Roothaan's equations (17) give

$$[3] \qquad \sum_{p=1}^{m} C_{ip} \left\langle \chi_p \left| \hat{H}^{\mathrm{HF}} \right| \chi_p \right\rangle = \sum_{p=1}^{m} \varepsilon_i C_{ip} \left\langle \chi_q \middle| \chi_p \right\rangle$$

or

$$[4] \qquad \sum_{p} C_{iq} (h_{pq}^{\mathrm{HF}} - \varepsilon_i S_{pq}) = 0$$

For a given basis set, the Hartree–Fock operator is

$$[5] \qquad h_{pq}^{\mathrm{HF}} = \left\langle \chi_p(1) \left| -\frac{\nabla^2}{2} \right| \chi_q(1) \right\rangle + \left\langle \chi_p(1) \left| -\frac{Z_j}{r_{ij}} \right| \chi_q(1) \right\rangle + \sum_j \sum_r \sum_s C_{jr} C_{js} \left[\left\langle \chi_p(1)\chi_q(1) \left| \frac{1}{r_{12}} \right| \chi_r(2)\chi_s(2) \right\rangle + \left\langle \chi_p(1)\chi_r(1) \left| \frac{1}{r_{12}} \right| \chi_q(2)\chi_s(2) \right\rangle \right]$$

which is written as

$$[6] \qquad h_{pq}^{\mathrm{HF}} = h_{pq}^{\mathrm{N}} + \sum_r \sum_s D_{rs} (2\langle pq | rs \rangle - \langle pr | qs \rangle)$$

where

$$[7] \qquad D_{rs} = \sum_j C_{jr} C_{js}$$

With an open-shell system, two treatments will be used. The first is that proposed by Roothaan (18) and is called restricted open-shell Hartree–Fock (ROHF) where the wave function is partitioned into a closed-shell part describing the doubly occupied MOs and an open-shell part for the rest of the occupied MOs. Thus, for a doublet system with $2n + 1$ electrons the ROHF wave function is

$$[8] \qquad \Psi^{\mathrm{RHF}} = \left|\phi_1 \bar{\phi} \ldots \phi_n \bar{\phi}_n \phi_{n+1}\right|$$

The second treatment is that proposed by Pople and Nebest (19) and is called the unrestricted Hartree–Fock (UHF) method. It is based on the fact that, since the number of electrons of spin *a* differs from the number of electrons of spin *b* and the repulsion between electrons depends on their spin, the state function for $2n + 1$ electrons is

$$[9] \qquad \Psi^{\mathrm{UHF}} = |a_1(1) \ldots a_n(n) a_{n+1}(n+1) b_1(1) \ldots b_n(2n+1)|$$

where the a_i and b_i are the α and β spin orbitals. The energy of this system is given by

$$[10] \qquad E = \sum_{i}^{\alpha+\beta} h_i^{\mathrm{N}} + \frac{1}{2} \sum_{i}^{\alpha+\beta} \sum_{j}^{\alpha+\beta} J_{ij} - \frac{1}{2} \left[\sum_{i}^{\alpha} \sum_{j}^{\alpha} + \sum_{i}^{\beta} \sum_{j}^{\beta} \right] K_{ij}$$

where J_{ij} and K_{ij} are the conventional Coulomb and exchange integrals. The Ψ^{UHF} is not an eigen function of the spin operator $\hat{s}^2$ and the resulting states are spin contaminated and are difficult to interpret.

Most molecular calculations begin with the choice of a basis set. The success of the calculations is dependent on the use of an adequate basis set. In the LCAO method each molecular orbital is expressed as a finite sum of Slater-type orbitals (STOs) or Gaussian-type functions (GTFs). Instead of using individual Gaussian functions as basis functions, contracted Gaussian-type functions are used. The latter consist of a linear combination of a small number of primitive Gaussians, which are Cartesian Gaussians centered on the same atom but have different orbital exponents.

Transition metals are hard to deal with because of their peculiar electronic structure. The partially filled and closely spaced *d*-orbitals allow the transition metal to have more than one ground state with little energy difference (20).

Several trials have been attempted to obtain a consistent theoretical description of the electronic states that arise from the s^2d^n, $s\ d^{n+1}$, and d^{n+2} configurations of the transition metal atoms (21–23). It has been generally accepted that for the first-row transition metal atoms the ground state is s^2d^n; experimentally this was not always true. The Hartree–Fock calculations give inadequate results, since a difference of up to 1.3 eV is found between the experimental results and the Hartree–Fock calculations.

Botch et al. (24) considered the differential correlation effects within the lowest-lying states arising from s^2d^n, $s\ d^{n+1}$, and d^{n+2} of the first-row transition metal atoms using multiconfiguration SCF and non-relativistic procedures. For nickel, the experimental results indicate that the ^3F ($4s^23d^8$) state lies 0.03 eV above the ^3D ($4s3d^9$) state (24). The numerical HF calculations result in a ^3F state that is of 1.3 eV lower energy than the ^3D state. Theoretical attempts could not predict this order; for example, the excitation energy $^3F \rightarrow {}^3D$ calculated by Botch et al. was 0.42 eV using Wachters' basis set. It turned out that a ^3F state is not a good ground state (lowest energy) for $Ni(CO)_4$ whereas a ^1S ($3d^{10}$) is a good one. On the other hand, a ^3D state is a good ground state for nickel atom in NiH and Ni_2 (25).

2.ii. Basis sets

The split valence 3-21G (26) basis set was used for carbon, nitrogen, and hydrogen atoms. For sulphur atom an extra *d*-function was added to the 3-21G basis set.

Several attempts have been applied to building basis sets for transition metals. Wachters (27) and Viellard (28) used fairly large basis sets (14*s*9*p*5*d*). Basch et al. (29) introduced a 15*s* 8*p* 5*d* basis set whereas Roos et al. (30) introduced a smaller basis set (12*s*6*p*4*d*). In an attempt to improve the description of the different ground state configurations of the

© 1998 NRC Canada

Table 1. Structural parameters of the different ground states of $Ni(H_2O)_6^{2+}$ using different basis sets.

Basis set	State	Ni—O bond length[a] (Å)	Total energy (au)	Ni–O overlap population	Charge on Ni
DZ	^1S	2.0312	–1960.120 630	0.021 5560	1.593 392
	^3D	2.0319	–1960.143 061	0.037 6069	1.534 599
	^3F	2.0313	–1960.153 038	0.038 0042	1.585 239
SV6D	^1S	2.0111	–1959.968 546	0.039 2026	1.595 101
	^3D	2.0244	–1960.000 675	0.034 1761	1.574 622
	^3F	2.0241	–1960.011 269	0.032 5569	1.586 016
SV	^1S	2.0172	–1959.933 931	0.0201479	1.622 209
	^3D	2.0199	–1959.970 042	0.0294804	1.579 350
	^3F	2.021	–1959.983 533	0.0320140	1.614 842
Ref. 41		2.108	–1962.799 521		1.51
Ref. 42		2.11			

[a] Experimental bond length = 2.06 Å (43, 44).

transition metals, Hay (31) modified the representation of the 3*d* atomic orbitals and used diffuse functions for more extension of the basis sets. Many other attempts have been made (32–34).

Recently, Schaefer et al. (35) published a collection of reoptimized basis sets. For the nickel atom, a collection of basis sets of different sizes: split valence (SV), split valence with six *d*-Gaussian functions (SV6D), and double zeta (DZ) were reported. Each basis set was optimized for three possible ground states for the Ni atom, namely, the ^3F, ^3D, and ^1S states. In this work these sets were tested and the best was adopted for use throughout. The size of each basis set differs according to the electronic state under consideration. For the singlet *S*-state, $^1S = 3d^{10}$, the split valence basis set is SV = (12s8*p* 5*d)* contracted to [2*p* 2*d* 3s] = {633/53/41} whereas for the ^3D state, the basis set is SV = (14*s* 8*p* 5*d*) contracted to [5*s* 2*p* 2*d*] = {633 11/53/41}. For the ^3F state the basis set is the same as that of the ^3D state. The split valence with six *d*-functions basis set for the ^1S state of nickel is SV6D = (12*s* 8*p* 6*d*) contracted to [3*s* 2*p* 2*d*] = {633 /53/51}; for the ^3D state it is SV6D = (14*s* 8*p* 6*d*) contracted to [5*s* 2*p* 2*d*] = {633 11/53/51} and is also used for the ^3F state. The double zeta basis set for the nickel ^1S state is denoted by DZ = (12*s* 9*p* 5*d*) contracted to [6*s* 5*p* 3*d*] = {62 1111/33 111/3 11} whereas that used for the ^3D state is (14*s* 9*p* 5*d*) contracted to [8*s* 5*p* 2*d*] = {62 111111/33 111/41}; the ^3F DZ basis set is (14*s* 9*p* 5*d*) contracted to [8*s* 5*p* 2*d*] = {62 111111/33 111/3 11}.

2.iii. Testing the basis sets on $Ni(H_2O)_6^{2+}$

Three basis sets were used for MO calculations on the $Ni(H_2O)_6^{2+}$ ion. Geometry optimization was performed using gradient methods assuming a T_h symmetry. The Ni—O bond was considered as the judging parameter since it was found that the energy dependence on the O—H bond is insignificant; results are given in Table 1. The observation of Antolovic and Davidson (36) that the SCF geometry overestimates the ligand bond lengths and underestimates the metal–ligand bond length is confirmed in this work; the results show that the Ni—O bond length of the ^3F state was closer to the experimental value with SV and SV6D basis sets, whereas the ^3D state gave closer agreement with the DZ basis set.

The results for the total energy are given in Table 1. The ^3F ground state has the lowest energy, especially with the DZ basis sets.

It is worthwhile to investigate other parameters such as Mulliken overlap population and transition energies. In this work the numerical value of atomic overlap population is taken as a criterion for the type of bonding between atoms. The calculated overlap populations between Ni and O atoms in $Ni(H_2O)_6^{2+}$ using the different basis sets are given in Table 1. The highest overlap population is obtained for the ^3F ground state using both the DZ and SV basis sets. However, using the SV6D sets, where the *d*-orbitals are represented by a large number of basis functions, the highest population was obtained for a ^1S ground state. Atomic population is represented by the net charge on the atom, Table 1; the smaller sets give a high accumulation of positive charge on the Ni atom.

The UV–VIS spectrum (37) of aqueous Ni^{2+} ions shows a band at 8500 cm^{-1} and at about 13800 cm^{-1}. Configuration interaction calculations (38), CIS, were carried out on $Ni(H_2O)_6^{2+}$ using the different basis sets. The results of DZ-^3F calculations were closest to the experimental (Table 1). The above results indicate that the ground state for nickel in $Ni(H_2O)_6^{2+}$ is the ^3F state and the best basis set is the DZ. This combination, DZ-^3F, is used in all subsequent calculations.

3. Results and discussion

3.i. Monoazidonickel (II) ion; $[Ni(N_3)]^+$

Azide ion is a linear ion, it remains so when attached to metal ions and most probably when attached to an organic moiety such as CH_3N_3 or phenyl azide (38–40). An extensive structural study of transition-metal-ion azides is not found in the literature. In this work ab initio procedures were applied to Ni(II) mono- and diazides. The singlet states were calculated at the RHF-SCF level whereas the triplets were calculated at the ROHF and UHF-SCF levels. During geometry optimization, the azide ion was allowed to bend by imposing C_1 symmetry but the resulting optimum geometry was linear.

The optimized geometry of monoazidonickel(II) is given in Table 2. The linear molecule follows the $C_{\infty v}$ point group; a reduced symmetry C_{4v} was adopted throughout the MO calculations, but the reduction in symmetry had no effect on the energetics of the ion.

Nickel(II) ion, d^8 configuration, exists in a high-spin triplet state when placed in an O_h field, while it exists in a low-

© 1998 NRC Canada

spin singlet state if placed in a D_{4h} field. The energetics and geometry of $Ni(N_3)^+$ have been calculated for both singlet and triplet states. The RHF-SCF procedures were used for singlet calculations, which resulted in a total energy of –1668.701 19 au with a binding energy of –0.609 681 au (–392 kcal mol^{-1}). As can be seen, $Ni(N_3)^+$ is significantly stable; the distribution of charge density is given in Table 3.

Table 2. Optimized geometry of nickel(II)-azides, thiocyanates, and isothiocyanates ions.

Ion	Bond length, Å		
Nickel azides	Ni—N_1	N_1—N_2	N_2—N_3
Ni N_3^+	1.724	1.196	1.112
Ni $(N_3)_2$	1.799	1.185	1.126
Nickel thiocyanates	Ni—S	S—C	C—N
$Ni(SCN)^+$	2.019	1.630	1.150
$Ni(SCN)_2$	2.064	1.647	1.147
Nickel isothiocyanates	Ni—N	N—C	C—S
$Ni(NCS)^+$	1.743	1.573	1.176
$Ni(NCS)_2$	1.775	1.173	1.598

In this work, Mulliken overlap population is taken as an indication of bonding between atoms. The calculated Mulliken overlap population is 0.2418 between nickel atom and the adjacent nitrogen and is analyzed to 0.3092 for σ overlap and –0.0674 for π overlap. The overlap between N_1 and N_2 is 0.9058 whereas that between N_2 and N_3 is 0.4196; the σ overlap between Ni and N_1 is of the same order of magnitude as that between N_2 and N_3 in the $Ni(N_3)^+$ ion. This result indicates the existence of an apparent covalent bonding between Ni^{2+} and N_3^- and shows the absence of π-bonding between Ni^{2+} and azide ion.

The singlet ground state of $Ni(N_3)^+$ has the electronic configuration $\ldots 1e^4 1a_1^2 2e^4 2a_1^0 3a_1^0 4a_1^0 3e^0$. A molecular orbital energy level diagram is shown in Fig. 1 and an analysis of the molecular orbitals is given in Table 4. The four highest occupied MOs are localized on the azide ion whereas the three lowest unoccupied MOs are metal ion orbitals. These results mean that the electronic transitions of $Ni(N_3)^+$ must be very intense and result from azide → nickel (ligand → metal) charge transfer transitions.

The electronic population of nickel in $Ni(N_3)^+$ is found to be $\ldots 3d^{7.98}4s^{0.32}4p^{0.02}$, which is evidence for covalent bonding between nickel and azide in $Ni(N_3)^+$.

The triplet ground state of $Ni(N_3)^+$ was calculated using the UHF-SCF procedures with 25 α-spin electrons and 23 β-spin electrons. The total energy is –1668.707 316 au, giving a –0.616 148 au (–386 kcal mol^{-1}) binding energy. It is more stable than the singlet state by 4 kcal mol^{-1}. The charge distribution has changed significantly (Table 3) from that in the singlet state. A buildup of electron density on nickel in the triplet state of $Ni(N_3)^+$ is indicated by the results of the electronic configuration, which is $\ldots 3d^{8.70}4s^{0.26}4p^{0.004}$. Thus in the triplet state, back-donation of electrons from N_3^- to Ni^{2+} is more pronounced than in the singlet state. Consequently, covalent bonding between Ni^{2+} and N_3^- in $Ni(N_3)^+$ is more pronounced in the triplet than in the singlet state. Analysis of the MO energy level diagram of the triplet state of $Ni(N_3)^+$ indicated that the lowest electronic transition is a *d*–*d* transition, a result that was not obtained in the singlet state.

Fig. 1. A MOED for the ground singlet state of $Ni(N_3)^+$.

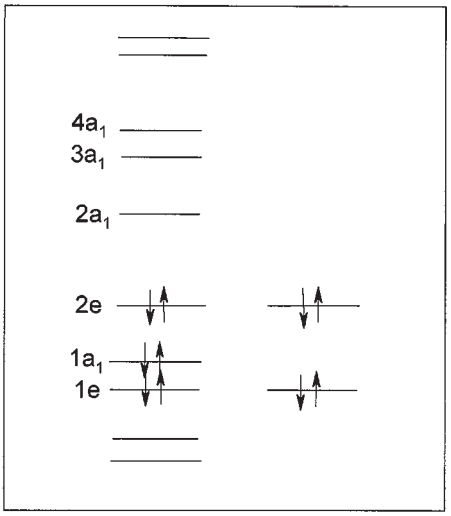

3.ii. Diazidonickel(II) ion; $Ni(N_3)_2$

Geometry optimization has shown that the molecule is linear; D_{4h} symmetry was imposed on the molecule. The singlet ground state energy gave a binding energy of –615 kcal mol^{-1}, which reflects an extra stability of the molecule relative to its components. The charge density on nickel is lower in $Ni(N_3)_2$ than it is in $Ni(N_3)^+$, Table 3.

The total atomic overlap population between Ni and the nearest N atom in $Ni(N_3)_2$ is 0.2244, which is analyzed to give 0.254 for σ overlap and –0.0296 for π overlap, i.e., the aabsence of π-bonding between nickel and azide in $Ni(N_3)_2$. This result is confirmed by the calculated electronic configuration of Ni in $Ni(N_3)_2$, which is $\ldots 3d^{8.00}4s^{0.41}4p^{0.03}$; back-donation to the 4*s*-orbital results in σ- and not π-bonding. It is found that covalent bonding between nickel and azide is stronger in $Ni(N_3)^+$ than it is in $Ni(N_3)_2$.

The electronic configuration of the singlet ground state of $Ni(N_3)_2$ is $\ldots a_u^2 1e_u^4 1e_g^4 1a_g^0 2a_g^0 2e_u^0 2e_g^0$. A MO energy level diagram is shown in Fig. 2 and a MO analysis is given in Table 4. One observes a large energy separation between the occupied and vacant MOs compared to the situation in $Ni(N_3)^+$, in addition to the fact that the lowest electronic transitions in $Ni(N_3)_2$ are charge transfer and not *d*–*d* transitions.

The ground triplet state of $Ni(N_3)_2$ was investigated using ROHF-SCF procedures. The binding energy is –637 kcal mol^{-1} compared to –615 kcal mol^{-1} for the singlet state. The charge distribution is shown in Table 3 where one can observe a lower charge density on the different atoms than is the case for the singlet state. Mulliken population analysis for nickel in the triplet ground state of $Ni(N_3)_2$ gives the population $3d^{7.87}4s^{0.62}4p^{0.02}$. The *s*-orbital becomes populated and σ-bonding predominates between the 4*s* atomic orbital of nickel and the appropriate orbital of the nitrogen atom.

A MO energy level diagram is shown in Fig. 3 and an analysis is given in Table 4. Here, the highest occupied and lowest vacant MOs are mainly metal orbitals. The lowest transition, $d_g \rightarrow s_g$, is both Laporte and angular momentum forbidden. On the other hand, a strong symmetry-allowed

© 1998 NRC Canada

Table 3. Distribution of charge density in nickel azides.

Molecule	Ground state	Ni	N_1	N_2	N_3
$[Ni(N_3)]^+$	Singlet (RHF-SCF)	1.6927	–0.7427	0.0059	0.0440
	Triplet (UHF-SCF)	1.0303	–0.2104	–0.0307	0.2107
$[Ni(N_3)]_2$	Singlet (RHF-SCF)	1.5638	–0.6809	–0.0237	–0.0772
	Triplet (ROHF-SCF)	1.4868	–0.6722	–0.0197	–0.0514

Table 4. Analysis of the MOs of the ground states of some of the nickel azides, thiocyanates, and isothiocyanates studied.

Molecule	Energy (au)	MO	%Metal, (type)	Molecule	Energy (au)	MO	%Metal, (type)
$[Ni(N_3)]^+$	–0.8354	$1e$	1.40	**$[Ni(SCN)]^+$**	–0.7422	$1e$	4.90
Singlet	–0.7590	$1a_1$	0.51	Singlet	–0.7353	$1a_1$	64.81 d
ground	–0.5074	$2e$	1.58	ground	–0.6327	$2e$	41.47 d
state	–0.2526	$2a_1$	82.83 s	state	–0.4342	$3e$	40.42 d
using	–0.1438	$3a_1$	65.45 d, s	using	–0.1787	$2a_1$	69.98 s
RHF SCF	–0.0060	$4a_1$	98.67 s	RHF SCF	–0.0213	$3a_1$	71.43 s
	0.0817	$3e$	0.53		0.0222	$4e$	0.69
$[Ni(N_3)_2]$	–0.6045	$1a_{2u}$	0.20	**$[Ni(N_3)_2]$**	–0.3518	$1e_g$	2.15
Singlet	–0.3517	$1e_u$	0.34	Triplet	–0.3484	$1e_u$	0.39
ground	–0.3385	$1e_g$	2.56	ground	–0.2650	$2e_g$	93.31 d
state	–0.0006	$1a_{1g}$	90.05 d, s	state	0.0691	$1a_{1g}$	88.08 s
using	0.1487	$2a_{1g}$	97.76 s	using	0.2159	$2e_u$	0.37
RHF SCF	0.2258	$2e_u$	0.32	ROHF SCF	0.2179	$2e_g$	0.66
	0.2323	$2e_g$	0.56				
$[Ni(NCS)]^+$	–0.7274	$1b_1$	100 d	**$[Ni(NCS)_2]$**	–0.3955	$1e_g$	24.69 d
Singlet	–0.7274	$1b_2$	100 d	Singlet	–0.3506	$1e_u$	0.12
ground	–0.7011	$1a_1$	78.58 d	ground	–0.2203	$2e_g$	48.72 d
state	–0.5677	$1e$	33.70 d	state	0.0841	$1a_{1g}$	96.18 s
using	0.4071	$2e$	44.58 d	using	0.1640	$2e_u$	0.30
RHF SCF	0.1427	$2a_1$	81.91 s	RHF SCF	0.1948	$3e_g$	3.01
	0.0014	$3e$	2.03		0.2506	$2a_{1g}$	17.97 s
	0.0592	$3a_1$	92.60 s				

Fig. 2. A MOED for the ground singlet state of $Ni(N_3)_2$.

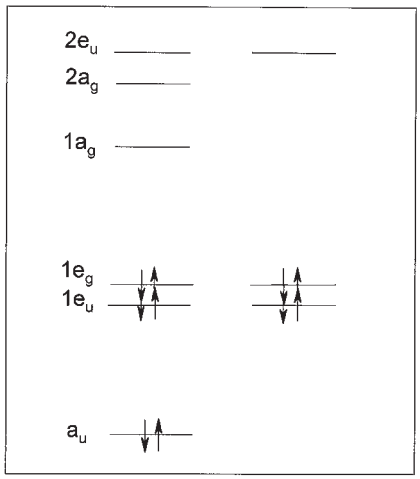

Fig. 3. A MOED for the ground triplet state of $Ni(N_3)_2$.

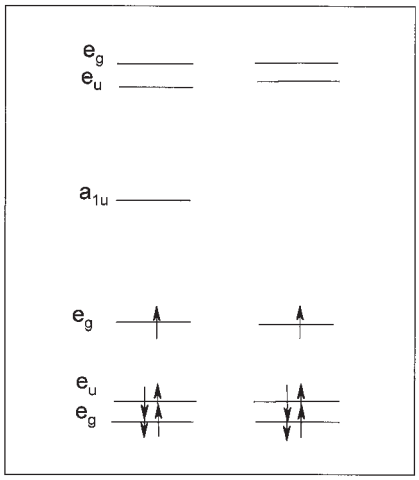

metal-to-azide charge transfer, $e_g \rightarrow e_u$, is expected to predominate.

The overlap population between the different atoms of $Ni(N_3)_2$ in the ground triplet state gives

$Ni–N_1 = 0.2674$, $N_1–N_2 = 0.7412$, and $N_2–N_3 = 0.4494$

One observes a larger overlap between the metal ion and the azide ion in the triplet than in the singlet state.

Computations on the triplet state of $Ni(N_3)_2$ using the UHF procedures led to results that are less favourable than those obtained with the ROHF procedures. Lower binding

© 1998 NRC Canada

Table 5. Charge for each atom in the nickel thiocyanates and isothiocyanates studied.

Molecule	Ground state	Ni	S	C	N
$[Ni(SCN)]^+$	Singlet (RHF-SCF)	0.9718	0.1835	0.1017	–0.2751
	Triplet (UHF-SCF)	1.6337	–0.4430	0.1449	–0.3356
$[Ni(SCN)_2]$	Singlet (RHF-SCF)	0.8533	–0.0861	0.0773	–0.4178
	Triplet (UHF-SCF)	1.5594	–0.4868	0.15067	–0.4434
$[Ni(NCS)]^+$	Singlet (RHF-SCF)	0.8784	0.5791	0.3872	–0.8448

energy and lower overlap population were obtained with UHF procedures.

3.iii. Monothiocyanatonickel(II) ion, $Ni(SCN)^+$

Ab initio MO calculations adopting full geometry optimization were performed and results showed the linearity of the $Ni(SCN)^+$ ion. Further computations adopted the C_{4v} point group instead of the $C_{\infty v}$ point group. The optimized geometry is given in Table 2. The binding energy (heat of formation) is –56 kcal mol^{-1} compared to –392 kcal mol^{-1} for $Ni(N_3)^+$. The population of nickel in $Ni(SCN)^+$ is $\ldots 3d^{8.81}4s^{0.22}4p^{0.01}$ whereby a unit of charge has been transferred from the SCN^- ion to the Ni^{2+} ion. The distribution of charge density is given in Table 5.

The Mulliken overlap population gives

N–S: 0.1514; S–C: 0.4594, and C–N: 1.4376

The existence of a covalent bond between nickel and sulphur is quite evident. Analysis of Mulliken overlap gives 0.0844 for σ overlap and 0.2358 for π overlap. Thus, the character of Ni—S π-bonding is more than twice that of the σ-bonding. Comparing these results with the corresponding overlap in $Ni(N_3)^+$, one finds a value of 0.3090 for σ overlap between Ni and N atoms and a value of –0.0673 for π overlap. In other words, no π overlap exists between Ni and N in $Ni(N_3)^+$ in contrast to the situation between Ni and S in $Ni(SCN)^+$.

A comparison of the electron population of the nickel atom in the ground singlet states of the two ions gives

$Ni(SCN)^+$:$\ldots 3d^{8.81}4s^{0.22}4p^{0.01}$

$Ni(N_3)^+$:$\ldots . 3d^{7.89}4s^{0.32}4p^{0.02}$

The SCN^- ion is a stronger electron donor than is the $(N_3)^-$ ion.

A MO energy level diagram for the ground singlet state of $Ni(SCN)^+$ is shown in Fig. 4 and an analysis of these MOs is given in Table 4. A pronounced mixing between the orbitals of metal and thiocyanate ion is observed. The four highest occupied MOs and the lowest three vacant MOs span the whole ion $Ni(SCN)^+$ and none of the low-energy transitions can be assigned to metal → metal, ligand → ligand, metal → ligand, or ligand → metal transitions. At least the lowest five electronic transitions are between MOs extending over the whole $Ni(SCN)^+$ ion. Consequently one expects to observe intense electronic transition and the weak $d \rightarrow d$ transitions would not be observed.

Computations on the ground triplet state of $Ni(SCN)^+$ were performed using UHF procedures. The binding energy of such a state is –272 kcal mol^{-1} compared to –56 kcal mol^{-1} for the singlet state. The charge density distribution varies more in the triplet state than in the singlet as shown in Table 5 whereby a buildup of positive charge is encountered on nickel and a buildup of negative charge is encountered on the S and N atoms. Analysis of atomic overlap population indicated an extensive π-bonding between Ni and S atoms and the following configuration is obtained for Ni in the triplet ground state of $NiSCN^+$: $3d^{8.07}4s^{0.27}4p^{0.02}$. In the triplet state, the highest occupied MOs are ligand (SCN^-) orbitals whereas the lowest vacant MOs are almost metal-ion orbitals. The lowest electronic transition should be ligand → metal charge transfer transitions. Mixing between metal and ligand orbitals is highly decreased as compared to the case in $Ni(N_3)^+$ or in the triplet state in $NiSCN^+$.

3.iv. Dithiocyanatonickel(II): $Ni(SCN)_2$

Geometry optimization proved that the molecule is linear. D_{4h} symmetry was imposed on the structure of the molecule. The optimized geometry is given in Table 2. The binding energy of the singlet ground state is –212 kcal mol^{-1}, which is much less negative than the binding energy of $Ni(N_3)_2$, –615 kcal mol^{-1}. The charge distribution is given in Table 5 and the configuration of the nickel atom is $3d^{8.73}4s^{0.40}4p^{0.01}$. Both the population and charge density on the nickel atom are different in $Ni(SCN)_2$ than in $Ni(N_3)_2$. In the latter, the positive charge on nickel is higher than in $Ni(SCN)_2$. Hence, electron back-donation (metal → ligand) is stronger when the ligand is the azide than when it is the thiocyanate ion. One can say that the π* molecular orbitals on the $(N_3)^-$ ion are of lower energy and act as electron acceptors.

The singlet ground state configuration of $Ni(SCN)_2$ is $\ldots 1a_g^2 1e_g^4 1e_u^4 2e_g^2 2a_{1g}^0 3a_{1g}^0 2e_u^0$. A MO energy level diagram is shown, Fig. 5, and an analysis of the MOs is given in Table 4. The lowest electronic transition, $1e_u \rightarrow 2e_g$, possesses a large contribution from an L → M charge transfer configuration.

The binding energy of the ground triplet state of $Ni(SCN)_2$ is –440 kcal mol^{-1}. The distribution of charge density is given in Table 5 and is different than is observed in the singlet state. One observes a buildup of positive charge density on the metal atom, indicating an electron back-donation from metal atom (ion) to the ligand, SCN^- ion. The electronic population of nickel in the ground triplet state of $Ni(SCN)_2$ is $\ldots 3d^{7.97}4s^{0.45}4p^{0.03}$. The Mulliken overlap population indicates the existence of σ as well as π overlap between the Ni and S atoms. The MO energy level diagram is given in Fig. 6 and the analysis of MOs is given in Table 6. The lowest-lying electronic transitions are L → M charge transfer transitions.

The above results indicate the following conclusions: the ground state of $Ni(SCN)_2$ is the triplet state; mixing between metal and ligand orbitals is not pronounced, and covalency between Ni^{2+} and SCN^- is more apparent than is the case for $Ni(SCN)^+$.

3.v. Monoisothiocyanatonickel(II) ion: $Ni(NCS)^+$

Computations showed that $Ni(NSC)^+$ is linear; the optimized geometry is shown in Table 2. The binding energy is

© 1998 NRC Canada

Fig. 4. A MOED for the ground singlet state of $Ni(SCN)^+$.

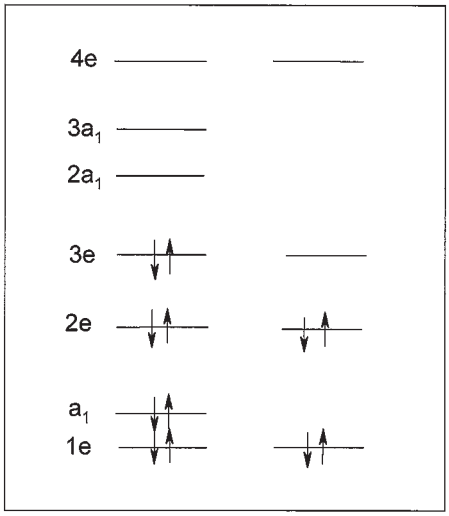

Fig. 5. A MOED for the ground singlet state of $Ni(SCN)_2$.

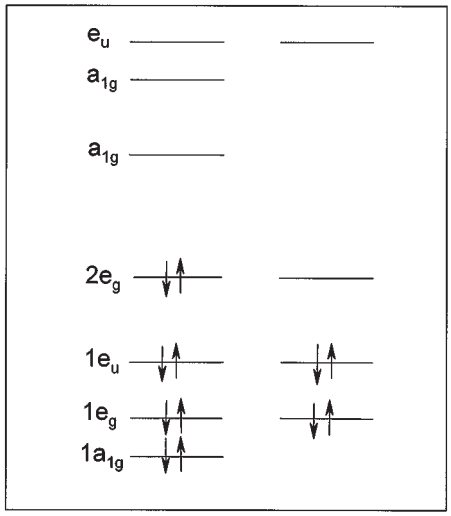

–90 kcal mol^{-1}, which is more negative than that of $Ni(SCN)^+$ but is much higher than that of $Ni(N_3)^+$, –392 kcal mol^{-1}. The distribution of charge is given in Table 5 whereas the electronic population of nickel is $3d^{8.58}4s^{0.36}4p^{0.01}$, which is significantly different from the population in $Ni(SCN)^+$.

It is important to compare bonding between the metal and SCN^- with that between the metal and NCS^-. Mulliken overlap population analysis for the ground singlet state of $Ni(NCS)^+$ gives

Ni–N = 0.1844; Ni–C = 1.0944; and C–S = 0.6224

Analysis of the Ni–N overlap gives –0.0518 for σ overlap (no σ bond) and 0.2362 for π overlap. The same behaviour was observed with $Ni(SCN)^+$.

The electronic configuration of the ground singlet state of $Ni(NCS)^+$ is $\ldots 1b_1^2 1b_2^2 1a_1^2 1e^2 2e^0 2a_1^0 3a_1^0$. A molecular orbital energy level diagram is shown, Fig. 7, and the weight percent of atomic orbitals in the different MOs is given in Table 4. The following observations are noted:

1. The energy of HOMO is –0.4071 au compared to –0.4342 au for N $(SCN)^+$.
2. The lowest electronic transition: $2e \rightarrow 3e$, is neither a *d–d* transition, localized on the metal ion, nor an L–L transition localized on the NCS^- ligand, nor a charge transfer transition.
3. The four HOMOs and the two LUMOs are delocalized over the whole ion, $Ni(NCS)^+$, which indicates a good mixing between the orbitals of the metal and the NCS^- ions.
4. The HOMO, $1e^2$, should result in a high-spin state.

Mulliken population analysis gives the following configurations for metal ion in $Ni(NCS)^+$: $\ldots 3d^{7.91}4s^{0.42}4p^{0.01}$ compared to $\ldots 3d^{8.08}4s^{0.27}4p^{0.02}$ for the metal ion in $Ni(SCN)^+$. The overlap population between Ni and N atoms in the triplet ground state of $Ni(NCS)^+$ is mainly π overlap, although the σ overlap is not zero.

3.vi. Diisothiocyanatonickel(II): $Ni(NCS)_2$

The ground singlet state of $Ni(NCS)_2$ has a binding energy of –278 kcal mol^{-1} and the optimum geometry is given in Table 2. The electronic configuration of the singlet

Fig. 6. A MOED for the ground triplet state of $Ni(SCN)_2$.

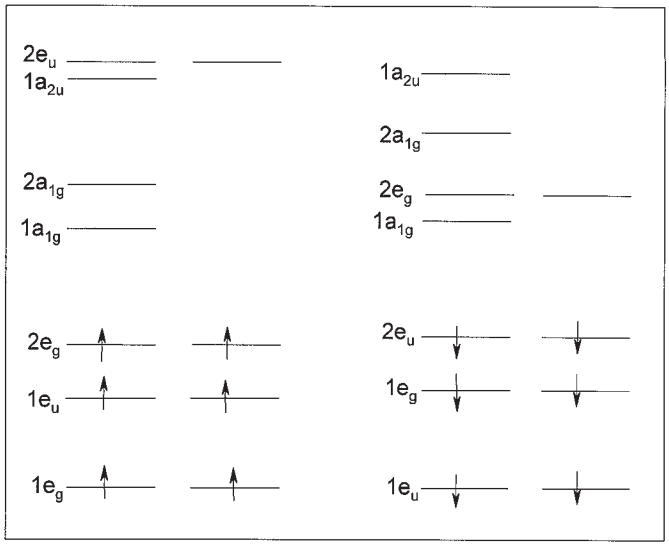

ground state of $Ni(NCS)_2$ is $\ldots 1e_g^4 1e_u^4 2e_g^2 a_{1g}^0 2e_u^0 3e_g^0$. A molecular orbital energy level diagram is shown in Fig. 8 and the analyses of the wave function of the MOs are given in Table 4, which indicates the following:

$1e_g$: MO spanning metal and ligand atoms; $1e_u$: pure ligand orbitals; $1a_{1g}$: pure metal ion orbitals;

$2e_g$: MO spanning metal and ligand atoms and $2e_u$: pure ligand orbitals.

The lowest electronic transition, $1e_u \rightarrow 2e_g$, has a contribution of charge transfer configuration and must be intense.

The Mulliken population of nickel in $Ni(NCS)_2$ is $3d^{8.31}4s^{0.67}4p^{0.02}$ compared to $3d^{8.73}4s^{0.4}4p^{0.01}$ in $Ni(SCN)_2$. The atomic overlap populations give

Ni–N = 0.2730; N–C = 1.2604; and C–S = 0.5306

Analysing the overlap to σ and π overlaps yields results that are very comparable to the situation in $Ni(SCN)_2$. The triplet state of $Ni(SCN)_2$ is of much lower energy than the singlet state. The population of nickel atomic orbitals and the extent and type of overlap between the AOs were very comparable

© 1998 NRC Canada

Table 6. Analysis of the MOs of the ground states of $Ni(SCN)_2$.

Molecule	Energy (au)	MO	%Metal, (type)	Molecule	Energy (au)	MO	%Metal, (type)
$[Ni(SCN)_2]$	–0.5433	$1e_u$	0.07	$[Ni(SCN)_2]$	–0.5330	$1a_{1g}$	69.09 d
Triplet	–0.5417	$1e_g$	0.39	Singlet	–0.4676	$1e_g$	39.97 d
ground	–0.4119	$2e_u$	0.33	ground	–0.3886	$1e_u$	0.27
state	–0.4021	$2e_g$	1.16	state	–0.2420	$1e_g$	40.22 d
using	–0.0229	$1a_{1g}$	45.00 s	using	0.0451	$2a_{1g}$	58.23 s
UHF SCF	0.0884	$2a_{1g}$	96.17 s	RHF SCF	0.1294	$3a_{1g}$	90.86 s
-set	0.1716	$1a_{2u}$	0.61		0.1985	$2e_u$	0.17
	0.2079	$3e_u$	0.24		0.2096	$1a_{2u}$	0.40
-set	–0.5395	$1e_u$	0.07	-set	0.0555	$2e_g$	76.01 d
	–0.4099	$1e_g$	3.94		0.0923	$2a_{1g}$	95.96 s
	–0.3943	$2e_u$	0.39		0.1757	$1a_{2u}$	0.52
	–0.0175	$1a_{1g}$	45.34 s		0.2157	$3e_u$	0.20

Fig. 7. A MOED for the ground singlet state of $Ni(NCS)^+$.

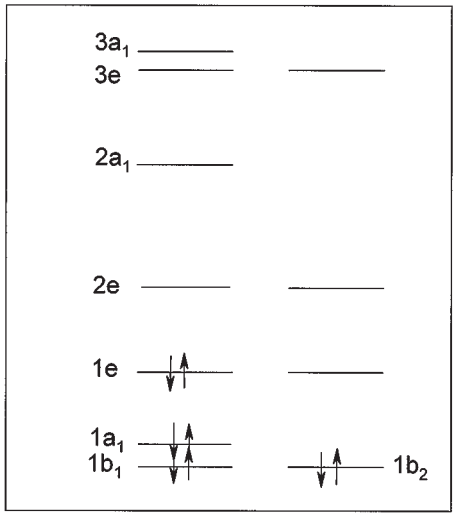

Fig. 8. A MOED for the ground singlet state of $Ni(NCS)_2$.

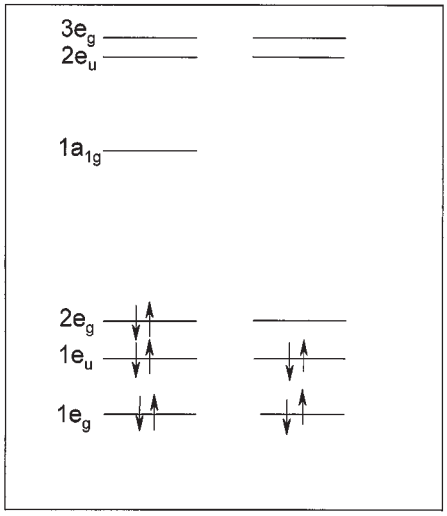

to their values in $Ni(SCN)_2$. One concludes that the electronic structures are similar in the two molecules, $Ni(SCN)_2$ and $Ni(NCS)_2$. However, the latter has a binding energy of 278 kcal mol^{-1}, whereas the former has a binding energy of 212 kcal mol^{-1}.

Conclusions

A controversy exists between experimental values and the theoretical predictions for the ground state of the nickel atom. Experimentally, the ^3F state lies 0.03 eV above the ^3D state, whereas HF calculations indicate that the ^3F state is not a good ground state for $Ni(CO)_4$ but that the ^1S state is a good one. In this work three different basis sets, namely, split valence (SV), split valence with six *d*-Gaussian functions (SV6D), and double zeta (DZ) basis sets, were used to predict the ground state of nickel in $Ni(H_2O)_6^{2}$. Geometry optimization was performed assuming a T_h symmetry. The three basis sets were applied to the three possible ground states: ^3F, ^3D, and ^1S; the calculations showed that the combination DZ-^3F gave results closest to the experimental values. Using the combination DZ-^3F, calculations were performed on $Ni(N_3)^+$, $Ni(N_3)_2$, $Ni(SCN)^+$, $Ni(SCN)_2$, Ni(NCS), and $Ni(NCS)_2$.

Table 7. A comparison between the binding energies of the compounds studied.

	Binding energy (kcal mol^{-1})	
Compound	Singlet state	Triplet state
$Ni(N_3)^+$	–392	–386
$Ni(N_3)_2$	–615	–637
$Ni(SCN)^+$	–56	–272
$Ni(SCN)_2$	–212	–440
$Ni(NCS)^+$	–90	–310
$Ni(NCS)_2$	–278	–229

The ion $Ni(N_3)^+$ is of significant stability with a binding energy of –392 kcal mol^{-1}. Bonding between nickel and azide ions has an apparent covalent character. The lowest electronic transitions are of charge transfer character. Computations on diazidonickel(II) showed that the molecule is linear, as is the case in $Ni(N_3)^+$, and is of significant stability (bonding energy is –615 kcal mol^{-1} for the ground singlet state). The character of covalent bonding in $Ni(N_3)_2$ is less than it is in $Ni(N_3)^+$.

The binding energy of $Ni(SCN)^+$, –56 kcal mol^{-1}, is much less than that of $Ni(N_3)^+$, –392 kcal mol^{-1}. Also, the

© 1998 NRC Canada

electronic population of nickel in $Ni(SCN)^+$ is $\ldots 3d^{8.81}4s^{0.22}4p^{0.01}$, which is totally different than in $Ni(N_3)^+$, $\ldots 3d^{7.98}4s^{0.32}4p0.02$, a result indicating that the SCN^- ion is a stronger electron donor than N_3^- ion. Another important and significant difference between the electronic structure of $Ni(N_3)^+$ and $Ni(SCN)^+$ is the existence of pronounced mixing of AOs to build the MOs in the latter ion. In addition, more extensive π-bonding is found between nickel and thiocyanate in $Ni(SCN)^+$ than between nickel and azide in $Ni(N_3)^+$. The Mulliken overlap population between atoms in $Ni(SCN)^+$ differs significantly from that between the corresponding atoms in $Ni(N_3)^+$. The covalent bonding between nickel and sulfur in $Ni(SCN)^+$ is of significant π character, whereas that between nickel and nitrogen in $Ni(N_3)^+$ is of significant σ character. A comparison between the binding energies of the different compounds studied is given in Table 7.

The binding energy of $Ni(SCN)_2$ is –212 kcal mol^{-1}, which is less negative than that of $Ni(N_3)_2$, –615 kcal mol^{-1}. The charge distribution as well as the atomic overlap population is different in the two compounds. Electron back-donation, metal → ligand, is stronger when the ligand is azide ion than when it is thiocyanate ion.

Computations on nickel isothiocyanates showed that their electronic structure is highly comparable to the structure of the corresponding thiocyanate complexes.

References

1. K. Rappe and W.A. Goddard III. J. Am. Chem. Soc. **99**, 3966 (1977).
2. K. Kitaura, S. Sakaki, and K. Morokuma. Inorg. Chem. **20**, 2292 (1981).
3. Z. Lin and M.B. Hall. J. Am. Chem. Soc. **114**, 6102 (1992).
4. C.Q. Simpson II and M. B. Hall. J. Am. Chem. Soc. **114**, 1641 (1992).
5. K. Bowman and Z. Dori. Inorg. Chem. **9**, 395 (1970).
6. P. Sensie, N. Almeida, and F. Eduardo. An. Acad. Bras. Cienc. **41**, 333 (1969).
7. H.C. Egghart. Inorg. Nucl. Chem. **31**, 1538 (1969).
8. V. Gutmann and H. Bardy. Z. Anorg. Allg. Chem. **361**,213 (1968).
9. R. Abu-Eittah and G. Arafa. J. Inorg. Nucl. Chem. **32**, 3337 (1970).
10. R. Abu-Eittah and S. El-Makabaty. Bull Chem. Soc. Jpn. **46**, 3427 (1973).
11. T.T. Bamgboye and D.B. Sowergy. Polyhedron, **5**, 1487 (1986).
12. J. Dille, A.T.H. Lenstra, J.G. Haasnoot, and J. Reedijk. Polyhedron, **2**, 195 (1983).
13. P.P. Singh and D.S. Gupta. Polyhedron, **5**, 1941 (1986).
14. C.W.G. Ansell, M. McPartlin, and P.A. Tasker. Polyhedron, **2**, 83 (1983).
15. K.W. Hipps and U. Mazur. J. Phys. Chem. **91**, 5218 (1987).
16. M.W. Schmidt, K.K. Baldridge, J.A. Boatz, S.T. Elbert, M.S. Gordon, J.H. Jensen, S. Koseki, N. Matsunaga, K.A. Nguyen, S.J. Su, T.L. Windus, together with M. Dupuis and J.A. Montgomery. J. Comput.Chem. **14**, 1347 (1993).
17. C.C.J. Roothan. Rev. Mod. Phys. **23**, 69 (1951).
18. C.C.J. Roothan. Rev. Mod. Phys. **32**, 179 (1960).
19. J.A. Pople and R.K. Nebest. J. Chem. Phys. **22**, 571 (1954).
20. M. Goodgame, D.M.L. Goodgame, and F.A. Cotton. J. Am. Chem. Soc. **83**, 4161 (1961).
21. T.H. Dunning, Jr., B.H. Botch, and J.F. Harrison. J. Chem. Phys. **72**, 3491 (1980).
22. R.L. Martin. Chem. Phys. Lett. **75**,290 (1980).
23. M. Guse, N.S. Ostlund, and G.D. Blyholder. Chem. Phys. Lett. **61**, 526 (1979).
24. B.H. Botch, T.H. Dunning, Jr., and J.F. Harrison. J. Chem. Phys. **75**, 3466 (1981).
25. C.F. Melius, B.D. Olafson, and W.A. Goddard III. Chem. Phys. Lett. **28**, 457 (1974).
26. For H, C, N: J.S. Binkley, J.A. Pople, and W.J. Hehre. J. Am. Chem. Soc. **102**, 939 (1980); for S: M.S. Gordon, J.S. Binkley, J.A. Pople, W.J. Pietro, and W.J. Hehre. J. Am. Chem. Soc. **104**, 2797 (1982); W.J. Pietro, M.M. Francl, W.J. Hehre, D.J. Defrees, J.A. Pople, and J.S. Binkley. J. Am. Chem. Soc. **104**, 5039 (1982).
27. A.J.. Watchers. J. Chem. Phys. **52**, 1033 (1970).
28. A. Veillard. Theor. Chem. Acta (Berlin), **12**, 405 (1968).
29. H. Basch, C.J. Hornback, and J.W. Moskowitz. J. Chem. Phys. **51**, 1311 (1969).
30. B. Roos, A. Veillard, and G. Vinot. Theor. Chem. Acta, **20**, 1 (1971).
31. J. Hay. J. Chem. Phys. **66**, 4377 (1977).
32. I. Hyla-Kryspin, J. Demuync, A. Strich, and M. Bernard. J. Chem. Phys. **75**, 3954 (1981).
33. J.O. Noell, M.D. Newton, P.J. Hay, R.L. Martin, and F.W. Bobrowicz. J. Chem. Phys. **73**, 2360 (1980).
34. R. Poirier, R. Kari, and I.G. Csizmada (*Editors*). Handbook of Gaussian basis sets. Elsevier, New York. 1985.
35. A. Schaefer, H. Horn, and R. Ahlrichs. J. Chem. Phys. **97**, 2571 (1992).
36. D. Antolovic and E.R. Davidson. J. Am. Chem. Soc. **109**, 5828 (1987).
37. C.K. Jorgensen. Adv. Chem. Phys. **5**, 642 (1963).
38. I. Shavitt. *In* Application of electronic structure theory. *Edited by* H.F. Schaefer. Plenum, New York. 1977. p. 255.
39. A.L. Companion and M.A. Komarynsky. J. Chem. Educ. **41**, 257 (1964).
40. R. Abu-Eittah and A. El-Shahawy. Appl. Spectrosc. **25**, 90 (1971).
41. R. Akesson, L.G.M. Pettersson, M. Samdstrom, P.E.M. Siegbahn, and U. Wahlgren. J. Phys. Chem. **26**, 10773 (1992).
42. F.P. Rotzinger. J. Am. Chem. Soc. **118**, 6760 (1996).
43. M. Magini, G. Licheri, G. Paschina, G. Piccalnga, and G. Pinna. X-ray diffraction of ions inaqueous solutions. Hydration and complex formation. CRC Press, Boca Raton, Fla. 1988. pp. 127–133.
44. Y. Marcus. Chem. Rev. **88**, 1475 (1988).

© 1998 NRC Canada

Ion channels based on bis-macrocyclic bolaamphiphiles: effects of hydrophobic substitutions

T.M. Fyles, D. Loock, and X. Zhou

Abstract: Four new bis-macrocyclic bolaamphiphiles were prepared to explore the effects of hydrophobic substitutions on ion transport. In bilayer vesicles the new compounds were remarkably similar to more hydrophilic derivatives prepared previously. Planar bilayer conductance experiments showed the new compounds induced an unique current–time signal consisting of a rapid rise time, followed by a slower decay time. Signal shape was cation dependent and was related to a modest selectivity between cations. Cation–anion selectivity was very high, approaching an ideal cation selectivity. One compound also showed voltage dependence of the signal shape and duration. Qualitative changes in signal shape, duration, and voltage dependence were provoked by variation in the electrolyte pH and by masking the head-group electrostatic interactions with low levels of barium ions. A model for the signal shape is proposed, involving a rapid current rise due to aggregate restructuring, followed by slower decay due to development of the local Donnan potential that results from the high cation–anion selectivity.

Key words: ion channel, synthesis, bilayer membrane, bilayer clamp, mechanism.

Résumé : On a préparé quatre nouveaux bolaamphiphiles bis-macrocycliques dans le but d'examiner les effets des substituants hydrophobes sur le transport ionique. Dans les vésicules à doubles couches, le comportement des nouveaux composés est remarquablement semblable à celui de dérivés plus hydrophobes préparés antérieurement. Des expériences de conductance de doubles couches planaires ont permis de montrer que les nouveaux produits induisent un signal unique de courant–temps qui consiste en un temps rapide d'augmentation du temps, suivie d'un temps de décroissante plus lent. La forme du signal dépend du cation et elle est reliée à une modeste sélectivité entre les cations. La sélectivité cation–anion est très élevée; elle approche une sélectivité idéale pour les cations. Pour un composé la forme et la durée du signal dépendent aussi du voltage. Une variation du pH de l'électrolyte provoque aussi des changements qualitatifs dans la forme du signal, sa durée et sa dépendance sur le voltage; ces mêmes effets sont aussi obtenus en masquant les interactions électrostatiques du groupe de tête par de faibles quantités d'ions baryum. On propose un modèle pour la forme du signal qui implique une augmentation rapide du courant résultant d'une restructuration de l'agrégat, suivie d'une décroissance plus lente provoquée par le développement du potentiel de Donnan qui résulte de la grande sélectivité cation–anion.

Mots clés : canal ionique, synthèse, membrane à double couche, champ de double couche, mécanisme.

[Traduit par la Rédaction]

Synthetic and naturally occurring peptides provide some of the best small-molecule models of ion channel proteins, yet even with relatively low molecular weights and precise sequence information, the structural and functional details of the models themselves remain complex (1, 2). "Channel engineering," or the site-specific modification of individual amino acid residues of active peptide ion channels, has emerged as a productive strategy for exploring structure–function relationships and for generating new channel behaviors (3). It is increasingly evident that non-peptide compounds can also mimic both natural channels and peptides, that specific activities can be as high as natural examples, and that a large range of structural types can promote ion translocation across bilayer membranes (4, 5). Relatively few non-peptide systems have been the object of channel engineering, either as a probe of mechanism, or to optimize activity. A notable exception is the extensive work of Gokel and co-workers on a very active tris-macrocyclic channel, which shows that structural variations at the core and at the head-group region can critically control activity (4*b*, 6).

Our own efforts with bis-macrocyclic bolaamphiphiles have shown that specific activity is related to the core regions of the molecule (7*a*), while ion selectivity (7*a*, 7*b*) and, ultimately, voltage switching (7*c*) are controlled by the polar head groups. As for ion stabilization during transit and the role of the channel walls, neither the Gokel system nor our bis-macrocyclic bolaamphiphiles is dramatically improved by additional donor atoms in these locations, as assessed by vesicle techniques for determining transport. The Gokel system activity actually *decreases* tenfold on substitution

Received January 20, 1998.

T.M. Fyles,[1] D. Loock, and X. Zhou. Department of Chemistry, University of Victoria, Victoria, BC V8W 3P6, Canada.

[1] Author to whom correspondence may be addressed. Telephone: (250) 721-7184. Fax: (250) 721-7147. E-mail: tmf@uvic.ca

© 1998 NRC Canada

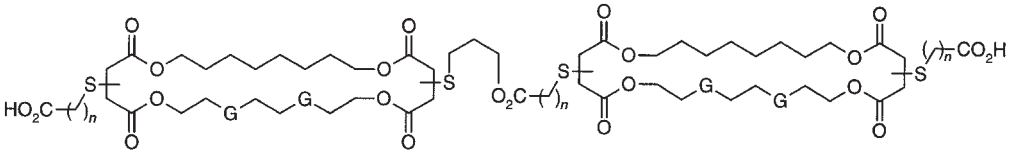

1 G = O, *n* = 1 **2** G = CH_2, *n* = 1 **3** G = CH_2, *n* = 2

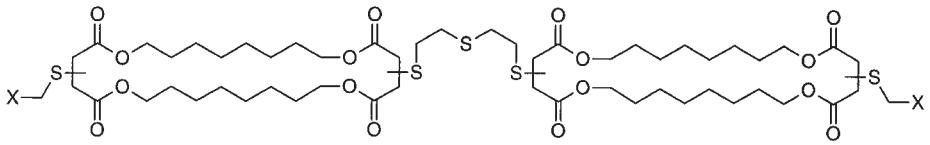

4 X = CO_2H **5** X = CH_2NMe_2

of a polymethylene segment by an oligoethylene oxide segment (6*a*). A similar type of substitution in our system makes only a small difference, albeit in the expected sense of increased activity (7*a*).

The channel "walls" must interact in some way with the ions as they pass through the channel, and the counter-intuitive results from vesicle experiments require resolution. We report here a new suite of compounds related to the active bis-macrocycle **1** and show, via a combination of vesicle and planar bilayer techniques, that minor hydrophobic substitutions provoke substantial mechanistic changes and give unique ion conduction behaviors.

Relative to the "parent" compound **1**, compounds **2**–**5** offer three significant structural variations. The first is the substitution of oxygen donor atoms in the macrocycle by methylene groups (Y = O to Y = CH_2). This will reduce the number of direct donor interactions with a cation in transit. As a secondary consequence, compound **2** will be more hydrophobic than **1**.[2] A similar effect due to hydrophobicity differences is expected for the substitution of ester by thioether as in the comparison of **1** or **2** and **4**. A second major structural variation is the effect of overall length; **3** is three atoms longer than **2** measured from the terminal carboxyl groups, while **4** is one atom shorter. More significant than the length difference between **2** and **4** is the marked difference in conformation expected for a thioether compared to an ester. Exploration of this problem by molecular mechanics (gas phase) showed a very large number of low-energy conformers for **1–5.**[3] Despite numerous small differences, compounds **1–3** adopted extended conformations with distances between the terminal carboxyl groups of about 3.1 nm for **1** and **2** and about 3.3 nm for **3**. Conversely, both **4** and **5** adopted a family of "U-shaped" conformations with a through-space carboxyl separation of about 1.9 nm. This reveals a third structural variation in the series, namely, shape. Previous work from Regen's group (9), confirmed by our subsequent explorations (10), has established that U-shaped conformations can lead to membrane disruption.

Results and discussion

Synthesis

The syntheses are based on routes described previously (7, 11), as outlined in Schemes 1 (**2** and **3**) and 2 (**4** and **5**). The starting material in both cases is the diene tetraester **6**, available from maleic anhydride and 1,8-octanediol in good yield (11). Michael addition of two equivalents of mercapto acetic acid gave the diacid **7a** in quantitative yield. One equivalent of the previously reported mesylate **8** (11) and one equivalent of the tetramethyl ammonium salt of **7a** were then coupled in DMF. Preparative gel permeation chromatography of the product mixture gave fractions enriched in the expected product **9a**, but successive separation steps consistently failed to produce high-purity samples. The NMR spectra were equivocal, but a relatively broad peak by analytical gel permeation analysis and a persistent ion at 1253 *m*/*z* in the negative LSIMS spectra eventually convinced us that we had an inseparable mixture of **9a** and **2**. This was confirmed by conversion of the mixture to **2** with mercapto acetic acid. The target **2** was fully characterized by NMR, showed a sharp analytical gel permeation peak, and a strong molecular ion by negative LSIMS at 1253 *m*/*e*.

The formation of **2** in the coupling of **7a** and **8** suggests that base-catalysed retro-Michael reaction of **7a** has occurred, leading to free mercapto acetate, which indiscriminately adds to available maleate diesters, including **9a**. It is possible to sketch an intramolecular elimination via a cyclic transition state in which the carboxylate abstracts the proton β to the sulfur. If this were occurring to a significant extent, we would expect that the longer homologue **7b** (from **6** and mercapto propionic acid) would undergo significantly less of this undesirable side reaction. In the event, **7b** and **8** again produced **9b** mixed with **3**, suggesting that intermolecular decomposition (not intra-) is the major source of the retro-Michael process. The proportion of contaminating **3** in **9b** was somewhat less than the corresponding **2** in **9a**. As previously, the **9b** mixture was treated with mercapto propionic

[2] Each substitution of O to CH_2 corresponds to an increase in log P_{ow} of approximately 1.1, thus log P_{ow} **(1)** + 4.4 = log P_{ow} (**2**), etc. (ref. 8).

[3] Energies of macrocycles were minimized using molecular mechanics from four initial nonplanar geometries. Thereafter, each minimized structure was subjected to molecular dynamics annealing to generate additional candidate geometries. A set of 10–20 geometries lying within 10 kJ of the lowest minimum found were examined and two "typical" examples were selected. Bis-macrocycles were then built from these two "typical" macrocycles, and the process of mechanics–dynamics–selection was repeated for the bolaamphiphiles; CAChe Ver 3.7, CAChe Scientific Inc.

© 1998 NRC Canada

Scheme 1.

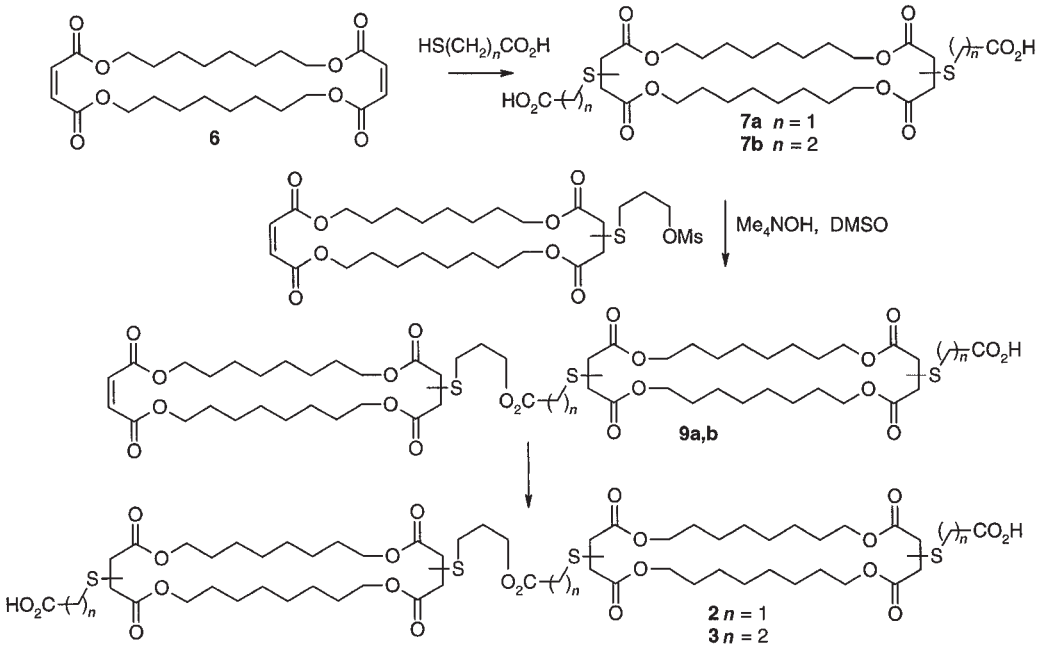

Scheme 2.

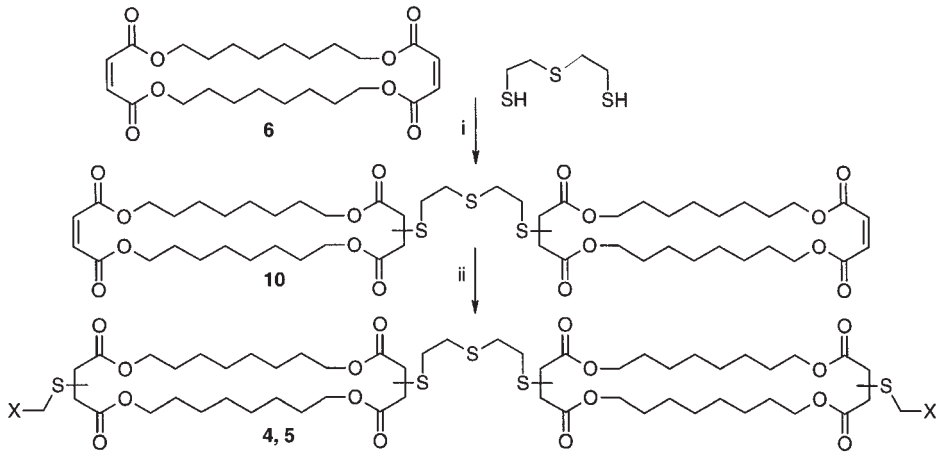

acid to produce a pure sample of **3** with the expected spectroscopic properties.

The synthesis of **4** and **5** used a common diene precursor **10** (Scheme 2), a strategy we reported previously (7*b*) Thus equivalent amounts of the macrocycle **6** and 2-mercaptoethyl sulfide were reacted, and the product mixture was repeatedly chromatographed on a preparative gel permeation column. Each fraction was inspected by analytical gel permeation and mass spectroscopy to ensure that a homogeneous sample of the expected mass was isolated. The main impurities are unreacted **6**, a product of mono-reaction of **6** and the sulfide, and higher oligomers. The latter were very obvious in the analytical gel permeation traces and give clear molecular ions in negative LSIMS. The addition of carboxylic acid and amino head groups proceeded as in previous cases (7, 11), and pure samples of **4** and **5** were isolated and characterized.

Vesicle experiments

The activities of compounds **2**–**5** were surveyed using the pH-stat vesicle assay used previously (7, 12). Vesicles containing an entrapped buffer at pH 6.6 were suspended in unbuffered medium held at pH 7.6 by automatic addition of base under pH-stat control. Addition of alkali metal sulfates to the solution created an additional cation concentration gradient, but no transport occurred until solutions of **2**–**5** in methanol were added. In each case, a rapid burst of activity immediately followed addition of the compound. We previously ascribed this to vesicle lysis due to high local concentrations of bolaamphiphile. After 1–2 min, the proton efflux occurred in a steady manner that could be fit using a first-order analysis to derive a rate. As previously, the transport rate depended on initial transporter concentration and an apparent kinetic order in transporter was determined. The results are given in Table 1, together with previously reported data for **1**.

© 1998 NRC Canada

Table 1. Transport of alkali metal cations by pore formers.

Transporter	Kinetic order	[Tr] (mM)	Rate × 10^{10}, mol $H^+.s^{-1}$ [a]					Normalized rate for K^+ (× 10^{10} mol H^+ s^{-1}) [b]
			Li^+	Na^+	K^+	Rb^+	Cs^+	
2	0.94	21	2.8	1.6	11	19	5.1	11
3	1	21	2.4	1.5	5.1	6.5	3.6	5.1
4	1.1	32	1.1	0.8	2.2	1.6	1.1	1.4
5	1	32	1.7	1.8	2.5	3.1	2.0	1.6
1	1.8	21	4.4	5.1	10	7.2	5.3	10

[a]. Uncertainty in rate, ±10%, transport at 298 K in the presence of 1.7×10^{-6} M FCCP and 2.1×10^{-2} M M_2SO_4.
[b] Normalized to [Tr] = 2.1×10^{-5} M, corresponding to 4 mol% Tr in lipid; normalized rate = $(2.1 \times 10^{-5}/[Tr])^{\text{kinetic order}}$ × rate in the presence of K_2SO_4.

Fig. 1. Current–time recordings showing typical "shark-fin" signals: (*a*) 75 nmol **2,** 38 min after first addition, data acquired at 2 kHz, and filtered at 500 Hz; (*b*) 78 nmol **3**, 30 min after first addition, data acquired at 10 kHz and filtered at 100 Hz. Both experiments used 1 M KCl electrolyte, diphytanoyl phosphatidyl choline membrane, +120 mV applied potential.

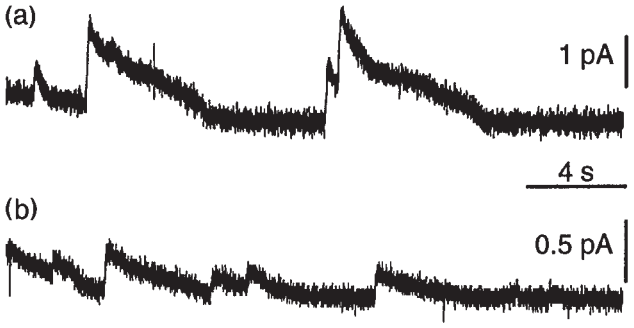

Fig. 2. Cation dependence of "shark-fin" signal for **2**: 1 M electrolyte, other conditions as in Fig. 1(*a*).

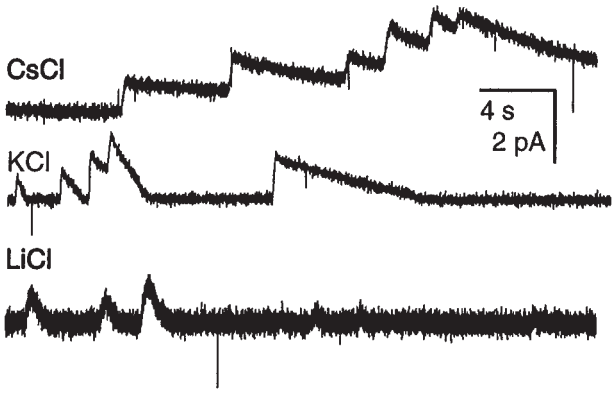

Apart from some modest differences in ion selectivity, the substitution of four oxygens in **1** by four methylenes in **2** has remarkably little influence on the transport of the alkali metal cations. Other structural variables, such as overall length (compare **2** and **3**) and shape (compare **2** with **4** or **5**) apparently play a much larger role in controlling the transport. Similar conclusions were previously drawn both for bolaamphiphiles and for more complex crown ether channels bearing similar macrocycles (12). The most significant difference between compounds **2–5** and **1** is in the apparent kinetic order: the former are all close to one, while the latter is nearly two. This suggests that the initiation of transport involves some unimolecular process rather than the slow formation of dimers or aggregates as suggested by previous work. We return to this issue below.

Bilayer clamp experiments

The ionic conductance behavior of channels formed by **2–5** in bilayer membranes was examined in a bilayer clamp experiment (time dependence of current carried at an applied potential). The presence of an ion channel is typically revealed as a series of "square-topped" peaks in the current–time record due to the abrupt shift from the "off" to the "on" state of the channel (13). As previously, bilayers were formed by painting a lipid solution in decane over a small hole in a polystyrene barrier between two aqueous electrolytes (7*a*). Transmembrane potential was imposed across the bilayer via two Ag/AgCl electrodes directly immersed in the separated electrolytes. The liquid junction potential of the cell was "backed-off" to zero prior to membrane formation. Each bilayer used was monitored at a range of applied potentials over 30–60 min to ensure stability and low conductance in the absence of added transporter. Bilayers showing "leaky" or "erratic" events at any point in this monitoring period were rejected.

The typical conductance behaviour of **2** and **3** in bilayer membranes is illustrated in Fig. 1. The odd-shaped conductance events were observed throughout the current–time records for six independent replicates, and subsequently through the records of experiments to be described below. The odd-shaped conductance events persisted throughout experiments lasting up to 2 h, without sign of diminishing in frequency. To ensure that the unusual signal shape was not due to some impurity or decomposition product, an independent sample of **2** was prepared and found to show the same behaviour. Given the reproducibility of the signals over long periods of time, in a variety of experiments, it is unlikely that they are due to transient experimental artefacts. They are the "normal" behaviour of this system. About twice the amount of compounds **2** or **3**, compared to **1,** is required to induce conductance events, contrary to the expectation of increased partition to the lipid. It is evident that **2** and **3** act in a fundamentally different fashion to **1**.

The characteristic conductance events consist of a relatively rapid increase in current flow, followed by a slower decay over a few seconds. The rise amplitudes vary between 1 and 6 pA and vary within a single experiment. The rise times, typically tens of milliseconds, are at least three orders of magnitude slower than the step-conductance changes

© 1998 NRC Canada

observed for **1** (microseconds or less). Occasionally a second rise occurred, superimposed on a preceding decay, suggesting more than one active species. Each conductance event for **2** apparently carries more current than does the comparable event for **3** even though the characteristic signal shapes are similar. Reversal of the applied potential reversed the sign of the current flow but did not alter the rise amplitudes or the decay times of the conductance events. As the experiments progress in time, the current amplitudes and decay durations of the conductance events increase, but retain the characteristic signal shape. To distinguish these conductance events from typical "square-topped" step conductance changes typically observed for channels, with **1** as an example, we refer to the characteristic signal shape illustrated in Fig. 1 as a "shark-fin" conductance event.

The shark-fin behaviour is cation dependent as illustrated in Fig. 2 for compound **2** and three electrolytes. The opening rise time and amplitudes are independent of the cation, but the decay times are progressively shorter for K^+ and Li^+ relative to Cs^+. Typical durations were 4–10 s for CsCl, 2–6 s for KCl, and 1–2 s for LiCl. The differences between electrolytes is less marked with **3**, consistent with the lower cation selectivity observed in the vesicle experiments.

The charge selectivities of channels are typically determined from the reversal potential for two ions in competition. The reversal potential is the applied potential at which there is no net ion flux with different electrolyte solutions on either side of the membrane. If the channel is permeable to multiple ionic species then the system is not at a thermodynamic equilibrium but at a steady state. The Goldmann–Hodgkin–Katz equation (13) applies to the steady state, and is given in eq. [1] for mixed cesium and sodium chlorides:

$$[1] \qquad V_{\text{rev}} = \frac{RT}{F} 1\text{n}\left(\frac{P_{\text{Na}}\gamma_{\text{Na}}[\text{Na}^+]_{trans} + P_{\text{Cs}}\gamma_{\text{Cs}}[\text{Cs}^+]_{trans} + P_{Cl}\gamma_{Cl}[\text{Cl}^-]_{cis}}{P_{\text{Na}}\gamma_{Na}[\text{Na}^+]_{cis} + P_{\text{Cs}}\gamma_{\text{Cs}}[\text{Cs}^+]_{cis} + P_{Cl}\gamma_{Cl}[\text{Cl}^-]_{trans}} \right)$$

where V_{rev} is the reversal potential, P_x and γ_x are the permeability and activity coefficients of the species x, respectively, R is the gas constant, T the absolute temperature, and F is the Faraday constant. Other cations can be substituted and the cation–anion selectivity can be obtained from the dilution potential for single electrolyte at two concentrations across the membrane (13).

The reversal potentials were determined manually by changing the holding potential and monitoring currents over periods up to one minute per potential. The initial liquid junction potential was "backed-off" to zero before the membrane was formed. A reversal potential of –50 mV was obtained for **2** with a gradient of 0.5 M KCl_{cis} : 0.1 M KCl_{trans}, and a potential of –56 mV was obtained for the same gradient of LiCl solutions. In a similar experiment a reversal potential of –36 mV was obtained for **3** under a gradient of 0.5 M KCl_{cis} : 0.1 M KCl_{trans}. These values can be compared to the equilibrium potentials for the cations of –37.6 mV for KCl and –39.9 mV for LiCl. The observed values are more negative than these limiting values, giving unrealistic negative values of $P_{\text{M:}}P_{\text{Cl}}$. These experiments were additionally complicated by a varying junction potential: although initially set to zero, small amounts of transport will alter the electrolyte compositions and the initial zeroing process will be inadequate to correct for these changes. If we assume a linear correlation between the change in junction potential, then the corrected reversal potentials approach the theoretical values for a perfectly cation-selective channel. An additional factor is a variable reference potential due to direct insertion of the reference electrodes into the electrolyte. Neither of these effects previously interfered with determination of the selectivities of **1** and related compounds (7), or with the determination of cation selectivity for these compounds (below). We conclude that the problems we encountered with our experimental procedure are a result of a very high cation–anion selectivity of **3**. The selectivity of two cations in competition was not complicated by junction potential problems, and a value of –20 mV for the reversal potential was observed for 1 M $CsCl_{cis}$: 1 M KCl_{trans}, which corresponds to P_{K}:P_{Cs} = 2.2. Similar results were obtained for the CsCl : LiCl system, indicating a weak selectivity among the cations.

The relatively slow opening process suggests that several molecules are involved. We consider some mechanistic alternatives below, but our working hypothesis is that several bolaamphiphiles are involved in the formation of an active aggregate. A number of additional observations are consistent with this hypothesis. Firstly, the activity of **2** depends markedly on the ionic strength. More compound is required at lower ionic strength, the currents carried per opening are smaller, and the decay times are faster. Ionic strength will affect partitioning of the amphiphile into the bilayer, and will assist in masking head-group electrostatic repulsions leading to aggregate stabilization. More direct control of head-group repulsion is available through partial protonation of the head groups by lowering the electrolyte pH. Figure 3 shows the effect of lowering the pH to 4.75, where approximately 50% of the head-groups will be protonated.[4] These two segments of an experiment show the typical features that extend over much longer periods (tens of minutes). "Shark-fin" events such as D are occasionally observed, and in some cases have very long decay times (up to 50 s). More interesting are the "square-top" openings, evident at C and E with amplitudes of about 2.7 pA, and at F with an amplitude of 0.6 pA. Some erratic or very short-lived square-top openings are also observed throughout the record, including a cluster of events at A, which consist of numerous short openings of about 0.8 pA amplitude. Short high-amplitude openings, such as the truncated one at B, occur occasionally.

The main conclusion from Fig. 3 is that the active transporter species formed from **2** are very sensitive to the external conditions. Although less active, compound **3** behaves in

[4] Assuming the pK_a is similar to acetic acid (4.75).

© 1998 NRC Canada

Fig. 3. Current–time recording for **2** at pH 4.75: 80 nmol of **2**, 1 M KCl, diPhyPC bilayer, +120 mV, data acquired at 20 kHz and filtered at 2 kHz.

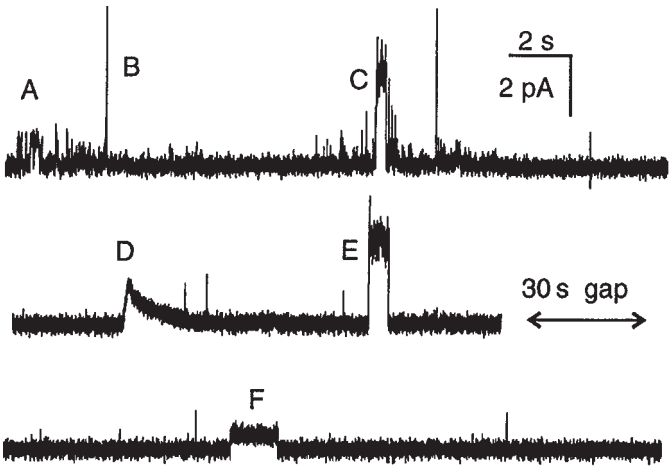

a similar fashion. The results are consistent with our hypothesis of some type of aggregate structure. The aggregates of **1** responsible for its square top conductance behaviour were previously assigned to a fixed stoichiometry, probably a dimer (7*a*). If aggregates are implicated here, they must be larger as the rise times are significantly longer. Large aggregates would be consistent with the different levels observed, corresponding to aggregates with different numbers of monomers, or different organizations of the same number of monomers.

What is the origin of the "shark-fin" signal? The different time scales of the opening and closing processes indicate different underlying physical processes. They are too long for conformational changes (picoseconds) or lateral diffusion processes (nano- to micro-seconds) (14). Whatever the opening process, transport via highly cation-selective channels will develop a Donnan potential, due to excluded anions, which opposes the applied transmembrane potential (13). In the absence of anion translocation, this opposing potential will build until it is locally equal to the applied potential and no net current flow would be observed. Development of the Donnan potential will depend on the probability that transported cations remain near the aggregate after transport, and this could lead to the cation dependence observed. Before developing these mechanistic ideas more fully, the behaviour of **4** and **5** must be considered.

Compounds **4** and **5** proved to be difficult to study. Compound **5** is inactive below a threshold of about 90 nmol added (1.8 μM concentration in the aqueous phase), and above this threshold inevitably provokes bilayer breakage (2–4 replicates for each of 1 M NaCl, KCl, RbCl electrolytes). Typically, a few current spikes of 1–3 ms duration and amplitudes greater than 10 pA were observed in the 60–90 s preceding breakage. The threshold concentration dependence might implicate aqueous phase aggregates as the membrane-disrupting species. Compound **4** also provokes bilayer breakage above a threshold of 70 nmol for 1.0 M NaCl and CsCl electrolytes. In KCl electrolyte, however, **4** resembled **2** and **3** in its ability to produce "shark-fin" conductance events. Figure 4 shows data at a range of applied

Fig. 4. Voltage-dependent "shark-fin" behaviour of **4**: 77 nmol **4**, other conditions as in Fig. 1(*a*).

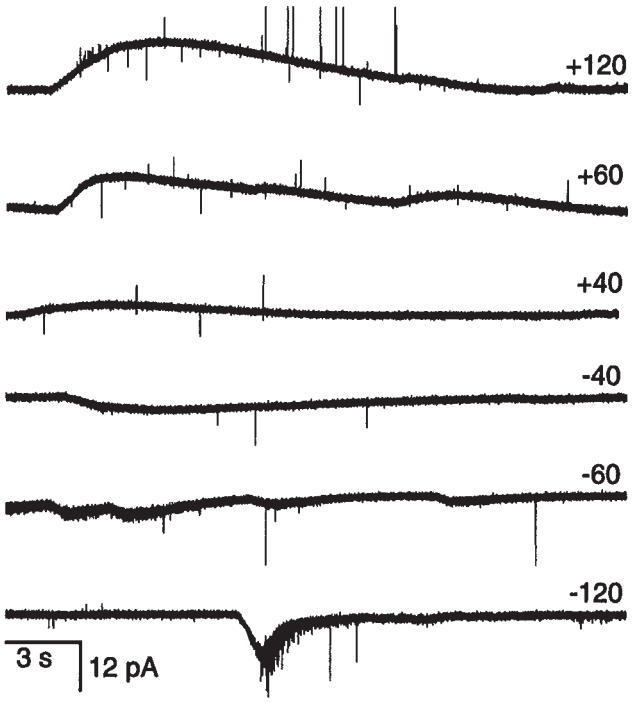

potentials. The "shark-fins" produced by **4** have current amplitudes of up to 15 pA, substantially larger than were observed with **2** under similar conditions (Fig. 1). The "shark-fin" amplitudes vary throughout the experiment, implying aggregates of variable stoichiometry or structure. In addition to the dominating "shark-fin" signals, brief (2–5 ms) openings of varying amplitude (10–1000 pA) were observed in all records. These brief events occurred with other compounds, but are much more frequent with **4** (compare Figs. 1, 2, and 4).

The remarkable feature of Fig. 4 is that the "shark-fin" shape was voltage dependent. Not only did the total duration of each event became progressively shorter as the potential was changed from positive to negative, the opening rise time of the signal decreased. The illustrated events are representative of at least 10 events at each potential, and the effect was replicated in three independent experiments. An additional feature of the replicate experiments is that the maximum amplitude varied between experiments from a low of 4 pA to the high of 15 pA illustrated in Fig. 4. Within a single experiment the amplitude varied only a few pA for a given potential.

As discussed above, our working hypothesis for the "shark-fin" signal is based upon aggregates formed by **4**. The propensity for membrane disruption except under limited conditions suggests that U-shaped monomers are present (9, 10) Combining these two ideas suggests an aggregate involving U-shaped molecules. If the hypothesis is correct, the local Donnan potential must develop more rapidly and decay more quickly at *cis*-negative potentials than at *cis*-positive potentials in order to result in the observed voltage dependence. The transporter **4** has no marked asymmetry, hence the voltage dependence must arise from some asymmetry in the aggregate itself. Suppose that **4** has a propensity

© 1998 NRC Canada

Fig. 5. (*a*) Current–time record for **4** in the presence of added barium: 100 nmol **4** added, 1 M KCl plus 1.6 mM $BaCl_2$ electrolyte, other conditions as in Fig. 1(*a*); (*b*) charge carried by **4** during a 2 min period as a function of applied potential: in the presence of barium (triangles), and the absence of barium (circles).

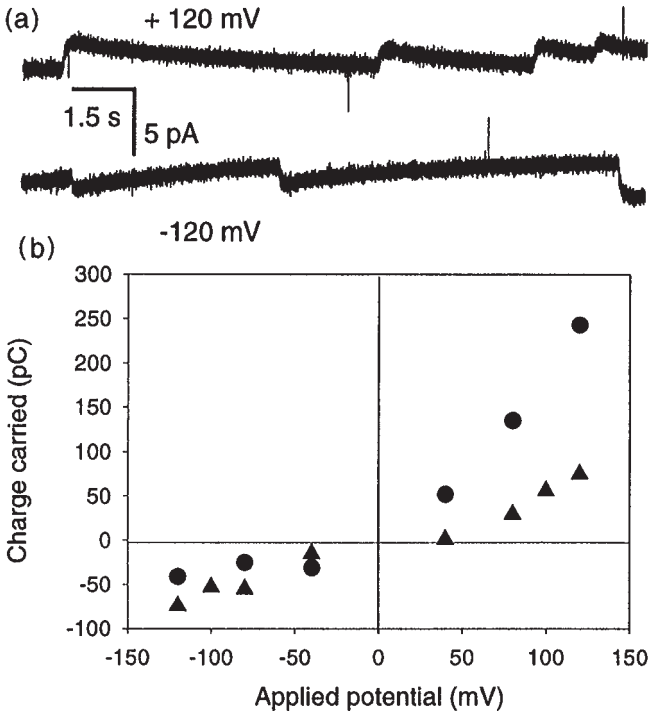

for a U-shaped conformation that limits its ability to flip-flop across the membrane. In this case fewer molecules of **4** would be available on the side of the bilayer opposite to the side of the addition, and an aggregate containing U-shaped conformations would form with fewer molecules on the *trans* side of the bilayer. The aggregate would therefore contain an asymmetric distribution of anionic head groups and this would offer the possibility of asymmetric interactions with the applied electric field. The decay of the signal was related to the stability of the aggregate in the case of **2** (above), so the prediction would be that asymmetric aggregates should be stabilized to a greater extent at *cis*-positive potentials. Fundamentally, the transmembrane potential directs the cation flow (cations flow from *cis* to *trans* at *cis* positive potentials). A larger number of monomers in the aggregate at the *cis* face of the bilayer than at the *trans* face would imply that head-group repulsions would be more important on the *cis* face. The flow of cations under positive potentials could thus stabilize the aggregate by masking head-group repulsions. The longer decay times at positive potentials would be consistent with this analysis. The voltage dependence of the rise times could also be related to the cation flux through the aggregate. The slow buildup of the opposing Donnan potential at *cis*-positive potentials would allow for more extensive restructuring of the aggregate during the rise period. Conversely, less restructuring of the aggregate would occur in the shorter-lived aggregates formed at *cis*-negative potentials.

If the working hypothesis discussed above is correct, then the voltage-dependent behaviour should be eliminated by factors that reduce the energy barrier to flip-flop of **4**. Addition of divalent cations could potentially produce a formally neutral U-shaped salt. This would accelerate flip-flop, lead to formally neutral divalent cation–transporter complexes equally distributed across the membrane, and the local Donnan potential would develop at the same rate for either sign of the applied potential. Alternatively, neutralized head groups would experience smaller repulsive interactions, larger aggregates would be expected, and the differences between the two faces of the bilayer would be reduced. Thus, for addition of a divalent cation such as barium, the working hypothesis predicts that the "shark-fin" signal should persist, but the voltage dependence should vanish. The result of this experiment is illustrated in Fig. 5. Part (*a*) shows that the prediction is qualitatively supported: at either potential the rise times and decay times are similar. The current carried was integrated over a 2 min period at several applied potentials to determine the total charge carried, and the results are displayed in part (*b*) of Fig. 5. In the absence of barium, substantially more charge is carried at positive applied potentials, due to the prolonged decay times under these conditions. In the presence of barium, the charge carried is significantly reduced at positive potentials, leading to a nearly symmetric dependence on applied potential in accord with the prediction.

Partial protonation of the head groups by lowering the pH would be predicted to achieve a similar attenuation in the voltage-dependent behaviour of **4**. At pH 4.75, typical "shark-fin" signals were observed at all potentials examined and no "square-top" step conductance changes were observed. Parts of the current–time traces were similar at both positive and negative potentials, but the negative potential records included examples of rapid rise, and of short- duration "shark-fins" as well. This could be due to a mixed population of symmetric and asymmetric aggregates as a result of incomplete equilibration of monomers across the membrane.

Mechanism

The "shark-fin" signal shape for an ion channel is unprecedented. It is unlikely that the signals are just experimental artefacts given the level of reproducibility over the range of experimental conditions explored. The slow time course of signal evolution would be consistent with some slower diffusional process such as a carrier of some type. We think a carrier mechanism of any type is unlikely since freely diffusing species would simply increase the "zero conductance" level over time, not periodically reverse direction as is observed. A referee sees parallels between the signal shapes reported here and the distorted single-channel currents observed with vesicles attached to a patch-clamp pipette immediately following removal of the membrane patch from the cell (13*a*).[5] The signal shape in these examples is due to the modulating effect of the membrane capacitance of the attached vesicle on the single-channel currents. Any vesicle attachment should also perturb the signal shape of the capacitance test function routinely used to monitor the

[5] For examples see Figs. 10 A–D and 11 A,B of ref. 13*a*, pp. 490–491.

© 1998 NRC Canada

Fig. 6. Schematic mechanism: upper section shows membrane-bound monomers; lower sections shows candidate aggregates. See text.

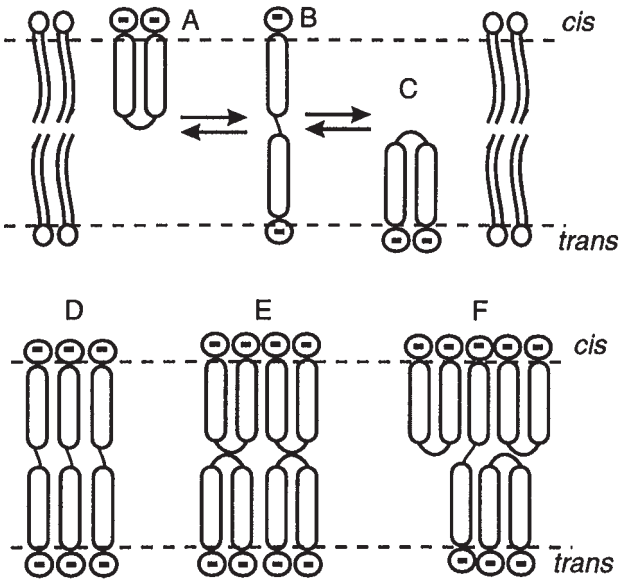

membrane; no such changes were seen. Also, the effect of the vesicle attached to a patch-clamp pipette diminishes over a few minutes. Attached vesicles, if formed in our system, would need to be constant over periods of a few hours. It is difficult to see how the "shark-fin" signal and the "square-topped" signal could follow one another as illustrated in Fig. 3 if the former were due to a long-lived vesicle.

We conclude that the "shark-fin" signal must be related to some type of channel opening and closing process. Some aspects of the working hypothesis were discussed above. Overall, the mechanism needs to account for the "shark-fin" signal shape and its voltage dependence with **4**, the origin of the high cation selectivity, the structural effects of length and shape, and the apparent discrepancy between the aggregates invoked by the working hypothesis and the rate-limiting unimolecular process of the vesicle experiments. It should also bear close resemblance to the well-supported mechanism derived for **1** and other compounds containing ether oxygen in the macrocyclic units (*7a*) and should explain the differences between **1** and **2–5**.

To assist discussion of the alternatives, Fig. 6 sketches some structures of bolaamphiphile aggregates in a bilayer. We assume, as previously, that the bolaamphiphile diffuses to the membrane and inserts in a stepwise process involving both U-shaped (A) and spanning (B) conformations. A flip-flop process would generate a second U-shaped conformation on the *trans* side of the bilayer (C). These states were previously assumed to be in rapid equilibrium, and must be electrically silent. Thereafter, the monomer states (A–C) can aggregate to form a variety of structures. For example, several spanning molecules could cluster to form a bundle (D), several U-shaped molecules in states A and C could associate (E), or mixed aggregates involving A–C could form (F).

The structures of **2–5** are devoid of specific complementary sites for intermolecular interactions and the head groups are charged at the pH of the experiments. So what drives the aggregation? Aggregates D–F are akin to phase separation within the bilayer. Overall lipid ordering will tend to push transporter molecules to defect areas where they eventually form the aggregates envisaged. Depending on the external conditions of concentration, electrolyte, and pH, the aggregates will vary both in the number and the packing of the monomers. The aggregates are "leaky" relative to the bulk bilayer phase, but still offer some control over the transport of ions.

We view hydration differences as the central difference between channels formed by **1** and related oxygenated bolaamphiphiles, and compounds **2–5**. The former can support a predominantly aqueous channel due to association of water with the walls of the channel, while the latter cannot. One consequence is the high cation–anion selectivity observed. Typically, anions are much more highly solvated than cations; the free energy of hydration of K^+ is –306 kJ mol^{-1} while it is –356 kJ mol^{-1} for Cl^- (15). Hydrated chloride ion is also somewhat larger than hydrated potassium (16), and partial dehydration of potassium ion in the gas-phase is more endothermic than for chloride for all extents of dehydration (17). As a result, the migration of a partially desolvated ion, or of an ion that requires additional solvation from the channel, will be more difficult for an anion than for a cation.

The high cation–anion selectivity is the root cause of the "shark-fin" signal shape, since the initial flow of cations in response to the transmembrane potential is not accompanied by a neutralizing flow of anions. Compound **1** is already cation-selective (P_K:P_{Cl} = 25 ± 4) (7), and the enhancement of this selectivity in **2–5** poses severe restrictions on charge balance during transport. The result is a Donnan potential, which opposes the transmembrane electric field gradient. The driving force for cation translocation is diminished and the ionic flux eventually falls off to zero. This accounts for the decay of the signal over periods of seconds and for its cation dependence. The relatively slow rise time of the "shark-fin" signal could be due to reorganization processes within the aggregate in response to the flow of cations and their associated waters of hydration. Suppose that nonconducting aggregates form. As a result of thermal motions, a transient aqueous defect could form in the aggregate. Once this "seed" defect forms, it could be stabilized by reorientations to eventually produce an efficient channel. During the reorganization time, the current observed would rise. Subsequently, the retarding effect of the Donnan potential would predominate and the current would fall off as discussed above.

The molecular structures of **2–5** control the type of aggregates formed. The small increase in the length of the bolaamphiphile (from **2** to **3**) is destabilizing, and the channels formed by **3** are less efficient than those formed by **2**. This suggests that the aggregates of **2** and **3** are of similar type. The absence of voltage dependence in these cases implies the aggregate is symmetrical, hence a cluster of spanning molecules is likely, such as illustrated in Fig. 6 D. Substitution in the central linker as in **4** and **5** results in a greater proportion of U-shaped states (A and C), so the aggregates formed are more likely to be as sketched in Fig. 6 E and F. An asymmetric structure involving a greater head-group charge on the *cis* face of the bilayer is required to rationalize the voltage-dependent behaviour of **4** as discussed

© 1998 NRC Canada

above. Compound **5** apparently does not form stable aggregates of any of the types sketched in Fig. 6. Aggregates of U-shaped monomers have been previously implicated as essential for membrane disruption by a mechanism involving aggregation in only the *cis* leaflet of the bilayer (9, 10). If the proportion of the molecules in state A (Fig. 6) was high for compound **5**, then disruption would proceed in preference to the subsequent aggregation steps illustrated.

The mechanism of Fig. 6 is inconsistent with the apparent kinetic order of approximately one, determined in the vesicle experiment. Another puzzling feature of the vesicle experiments is the apparent lack of membrane-disrupting activity by **4,** and especially **5,** for a range of cations. There are a number of possible ways to deal with these discrepancies. One is simply to refute the mechanism presented above (at least for vesicles) and assert that only monomeric species are involved. We think this is unlikely due to the very slow time scales involved. The molecular events of conformational change and diffusion have characteristic times that are many orders of magnitude faster than the "shark-fin" signal evolution (14). A more appealing rationalization is that the vesicle experiment probes a particular subset of the proposed mechanism, which in fact involves a unimolecular slow step. The central difference between the vesicle and planar bilayers is the curvature of the former. The lipid packing densities in the two leaflets of the bilayer differ and there is greater free volume in the outer leaflet (18). The symmetrical processes illustrated for states A–C in Fig. 6 will be biased by this curvature, with state C particularly disfavoured. Suppose that mixed aggregates such as state F are the dominant active species in vesicles. Consider a simple case of a trimer of two state B molecules and a state C molecule. If the transition from state B to C were slow, then the formation of the active aggregate would be controlled by a unimolecular step and would appear in the overall kinetics as a first-order process. The processes discussed here are strongly influenced by environmental factors. The shift of the rate-limiting step is just another example, this time involving membrane curvature. Curvature also accounts for the differences in membrane-disrupting ability. The outer leaflet of a vesicle can accommodate a certain proportion of U-shaped molecules due to the available free volume. The *cis* leaflet of a planar bilayer cannot. Compounds **4** and **5** lie close to the tolerance level for vesicles and they largely exceed the tolerance of planar bilayers.

Experimental section

^{1}H NMR spectra were recorded with 300 MHz spectrometers in $CDCl_3$ as solvent referenced to the residual $CHCl_3$ line (7.24 ppm relative to TMS). ^{13}C NMR spectra were recorded with 75.47 MHz spectrometers in $CDCl_3$ as solvent referenced to the central solvent line (77.0 ppm relative to TMS). Complete ^{1}H and ^{13}C NMR spectra of all new compounds (**2**, **3**, **4**, **5**, **7a**, **7b**, and **10**) have been deposited as supplementary material.[6] LSIMS spectra and Exact Mass were recorded with a sector mass spectrometer in *meta*-nitrobenzyl alcohol as matrix. In addition to the data reported, all samples ran as single sharp peaks on an analytical gel permeation column (mixed polydivinylbenzene, 10 mm i.d. × 25 cm) with $CHCl_3$ as eluent. The gel permeation column can resolve products differing by >50 g mol^{-1}. THF was dried by refluxing over, then distilling from, potassium metal under a dry nitrogen atmosphere.

Bis[3- or 4-, 17- or 18-(2-carboxy-1-thiaethyl)]-1,6,15,20-tetraoxa-2,5,16,19-tetraoxocyclooctacosane (7a)

Macrocycle **6** (2.00 g, 4.42 mmol) and 2-mercaptoacetic acid (2.04 g, 22.1 mmol, 5 equiv.) were dissolved in THF (150 mL). 2,2,6,6-Tetramethylpiperidine (6 mL) was added and the mixture was stirred at 64°C under nitrogen for 26 h. The THF was removed under reduced pressure. The pale yellow mixture was dissolved in dichloromethane (200 mL), and washed with 1 M hydrochloric acid (4 × 100 mL). After drying with sodium sulfate and removal of dichloromethane, the compound **7a** was collected as a pale yellow oil (2.81 g, quantitative).

^{1}H NMR 300 MHz (δ, $CDCl_3$): 9.14 (br s, 2H), 4.16–3.96 (m, 8H), 3.79 (dd, J_1 = 10.7 Hz, J_2 = 3.2 Hz), 3.47 (dd, J_1 = 56.6 Hz, J_2 = 16.2 Hz), 2.94, 2.70 (dd, J_1 = 16.9 Hz, J_2 = 11.0 Hz, J_1' = 16.9 Hz, J_2' = 4.4 Hz, 4H), 1.60–1.56 (m, 8H), 1.27 (br s, 16H). ^{13}C NMR 75.47 MHz (δ, $CDCl_3$): 174.9, 174.8, 174.7, 170.9, 170.1, 65.7, 65.2, 41.8, 41.7, 41.6, 36.1, 33.0, 29.0, 28.9, 28.4, 25.6. MS (–LSIMS, mNBA): 635.2 $(M - H)^-$ 100%. Exact Mass calcd. for $(M - H)^-$, $C_{28}H_{43}O_{12}S_2$, *m/e:* 635.2196; found: 635.2188.

3- or 4-[8′-[17″- or 18″-(2‴-Carboxy-1‴-thiaethyl)-1″,6″,15″,20″-tetraoxa-2″,5″,16″,19″-tetraoxocyclooctacos-3″- or 4″-yl]-6′-oxo-5′,1′,8′-oxadithiaoctyl]-17- or 18-(2-carboxy-1-thiaethyl)-1,6,15,20-tetraoxa-2,5,16,19-tetraoxocyclooctacosane (2)

Tetramethylammonium hydroxide pentahydrate (0.29 g, 1.60 mmol) was dissolved in dimethyl sulfoxide (2 mL) at 55°C under nitrogen, and mixed with **7a** (1.02 g, 1.60 mmol, 1 equiv.) in dimethyl sulfoxide (4 mL). Compound **8** (1.00 g, 1.61 mmol, 1 equiv.) in dimethyl sulfoxide (6 mL) was added dropwise and the solution was stirred at 50°C under nitrogen for 7.5 h. The dimethyl sulfoxide was removed under reduced pressure. The yellow mixture was dissolved in dichloromethane (200 mL), and washed with 1 M hydrochloric acid (3 × 100 mL). It was dried over magnesium sulfate and the solvent was removed. The yellow oil was chromatographed on a gel permeation column (LH-20, 3 × 60 cm) eluted with a mixed solvent of 2-propanol:chloroform (3:4). The desired compound **9a** was obtained in the middle fractions, and the product-containing fractions were evaporated to give compound **9a** as a light yellow oil (0.10 g, 0.086 mmol, 5.4%). The –LSIMS indicated **9a** was contaminated by compound **2** due to the retro-Michael addition discussed in the text.

A mixture of **9a** and **2** (0.101 g, 0.087mmol) and 2-mercaptoacetic acid (0.079 g, 0.86 mmol, 9.9 equiv.) were dissolved in THF (10 mL). 2,2,6,6-Tetramethylpiperidine (1.5 mL) was added and the solution was stirred for 39 h at 60°C under nitrogen. The THF was removed under reduced

[6] Copies of the spectra on deposit may be purchased from: The Depository of Unpublished Data, Document Delivery, CISTI, National Research Council Canada, Ottawa, Canada K1A 0S2.

© 1998 NRC Canada

pressure. The light yellow mixture was dissolved in dichloromethane (150 mL), and washed with 1 M hydrochloric acid (4 × 100 mL) and distilled water (3 × 70 mL). It was dried over magnesium sulfate and the solvent was removed to give a light yellow oil. The crude product was chromatographed on a gel permeation column (LH-20, 3 × 20 cm) eluted with a solvent of 2-propanol:chloroform (3:4). The middle fractions contained the expected product **2**, and the early and later fractions contained unidentified by-products. The product-containing fractions were evaporated to give **2** as a light yellow oil (0.037 g, 0.030 mmol, 34%). ^{1}H NMR 300 MHz (δ, $CDCl_3$): 9.05 (br s, 2H), 4.19–3.93 (m, 18H), 3.84–3.31 (m, 10H), 2.98–2.59 (m, 10H), 1.94–1.87 (m, 2H), 1.59–1.56 (m, 16H), 1.27 (br s, 32H). ^{13}C NMR 75.47 MHz (δ, $CDCl_3$): 174.3, 171.3, 170.8, 170.4, 170.1, 170.0, 169.5, 65.6, 65.5, 65.1, 63.9, 41.7, 41.5, 36.5, 36.2, 36.1, 33.1, 33.0, 29.1, 29.0, 28.4, 28.0, 27.8, 25.7, 25.6. MS (–LSIMS, mNBA): 1253.5 $(M - H)^-$ 100%, 1275.5 $(M + Na - 2H)^-$ 4.0%. Exact Mass calcd. for $(M - H)^-$, $C_{57}H_{89}O_{22}S_4$, *m*/*e*: 1253.4728; found: 1253.4706.

Bis[3- or 4-, 17- or 18-(3-carboxy-1-thiapropyl)]-1,6,15,20-tetraoxa-2,5,16,19-tetraoxocyclooctacosane (7b)

Macrocycle **6** (1.00 g, 2.21 mmol) and 3-mercaptopropionic acid (1.17 g, 11.0 mmol, 5 equiv.) were dissolved in THF (40 mL). 2,2,6,6-Tetramethylpiperidine (3 mL) then was added to the solution, and it was kept to reflux for 47 h under nitrogen. The THF was removed under reduced pressure, and the residual oil was dissolved in dichloromethane (200 mL) and washed with 1 M hydrochloric acid (6 × 100 mL). The solution was dried over magnesium sulfate, and solvent was removed to give a acidic mixture. It was chromatographed with a silica column (50 g silica) and eluted by the following solvent gradient: 30% ethyl acetate – hexanes (300 mL), 50% ethyl acetate – hexanes (200 mL), and 100% ethyl acetate (200 mL). The early fractions were unreacted **6**, the middle fractions were the mono adduct, and the later fractions were the desired double adduct **7b**. Product-containing fractions were combined to give **7b** as an oily solid (0.44 g, 0.66 mmol, 30%); by-product, mono adduct, as an oily solid (0.20 g, 0.36 mmol, 16%); and recovered **6** as a white solid (0.28 g, 0.62 mmol, 28%). ^{1}H NMR 300 MHz (δ, $CDCl_3$): 9.91 (br s, 2H),; 4.14–3.94 (m, 8H), 3.40 (d d, J_1 = 11.0 Hz, J_2 = 4.4 Hz, 2H), 2.98–2.60 (m, 12H), 1.60–1.57 (m, 8H), 1.28 (br s, 16H). ^{13}C NMR 75.47 MHz (δ, $CDCl_3$): 177.3, 171.3, 171.2, 170.2, 65.5, 65.0, 41.7, 36.5, 34.1, 29.1, 29.0, 28.4, 26.1, 25.7, 25.6. MS (–LSIMS, mNBA): 485.2 $(M - CH_2CH_2CO_2H)^-$ 9.3%, 663.2 $(M - H)^-$ 100%. Exact Mass calcd. for $(M - H)^-$, $C_{30}H_{47}O_{12}S_2$, *m*/*e* 663.2509; found: 663.2522.

3- or 4-[9′-[17″- or 18″-(3‴-Carboxy-1‴-thiapropyl)-1″,6″,15″,20″-tetraoxa-2″,5″,16″,19″-tetraoxocyclooctacos-3″- or 4″-yl]-6′-oxo-5′,1′,9′-oxadithianonyl]-17- or 18-(3-carboxy-1-thiapropyl)-1,6,15,20-tetraoxa-2,5,16,19-tetraoxocyclooctacosane (3)

Tetramethylammonium hydroxide pentahydrate (0.072 g, 0.40 mmol) was dissolved in DMSO (2 mL) at 60°C under nitrogen, and mixed with compound **7b** (0.24 g, 0.39 mmol, 1 equiv.) in DMSO (4 mL). Compound **8** (0.26 g, 0.39 mmol, 1 equiv.) in DMSO (6 mL) was added dropwise and the solution was stirred for 22 h at 62–65°C under nitrogen protection. After DMSO was removed under reduced pressure, the yellowish mixture was dissolved in dichloromethane (200 mL) and washed with 1 M hydrochloric acid (4 × 100 mL). The organic layer was dried over sodium sulfate and the dichloromethane was removed. The crude oil was chromatographed on a gel permeation column (LH-20, 3 × 60 cm) and eluted with a mixed solvent of 2-propanol:chloroform (3:4). The desired compound **9b** was obtained in the middle fractions, and the product-containing fractions were evaporated to give the compound **9b** as a pale yellow oil (0.14 g, 0.12 mmol, 31%). The negative LSIMS indicated **9b** was contaminated by compound **3** due to the retro-Michael addition discussed in the text.

A mixture of **7b** and **3** (0.12 g, 0.10 mmol) and 3-mercaptopropionic acid were dissolved in THF (10 mL). 2,2,6,6-Tetramethylpiperidine (0.7 mL) was added to the solution, and it was refluxed for 18 h under nitrogen protection. After THF was removed under reduced pressure, the yellowish solution was dissolved in dichloromethane (150 mL), and washed with 1 M hydrochloric acid (3 × 100 mL). The organic layer was dried over sodium sulfate and dichloromethane was removed. The crude oil was chromatographed on a gel permeation column (LH-20, 3 × 60 cm) and eluted with a mixed solvent, 2-propanol:chloroform (3:4). The desired compound **3** was in the middle fractions, and the product-containing fractions were evaporated to give the compound **3** as a pale yellow oil (0.080 g, 0.062 mmol, 62%). ^{1}H NMR 300 MHz (δ, $CDCl_3$): 8.38 (br s, 2H), 4.14–3.97 (m, 18H), 3.66–3.57 (m, 4H), 2.98–2.60 (m, 22H), 1.89 (m, 2H), 1.58–1.56 (m, 16H), 1.27 (br s, 32H). ^{13}C NMR 75.47 MHz (δ, $CDCl_3$): 176.6, 171.4, 171.2, 170.3, 170.2, 170.1, 65.5, 65.0, 63.1, 41.7, 41.5, 36.5, 34.2, 34.0, 29.6, 29.0, 28.4, 28.1, 27.9, 26.4, 26.1, 25.7. MS (–LSIMS, mNBA): 1295.4 $(M - H)^-$ 100%, 1334.7 $(M + K - H)^-$ 4.3%. Exact Mass calcd. for $(M - H)^-$, $C_{60}H_{95}O_{22}S_4$, *m*/*e* 1295.5198; found: 1295.5187.

3- or 4-[7′-(1″,6″,15″,20″-tetraoxa-2″,5″,16″,19″-tetraoxocyclooctacos-17-enyl-3″- or 4″-yl)]-1′,4′,7′-trithiahepta]-1,6,15,20-tetraoxa-2,5,16,19-tetraoxocyclooctacosa -17-ene (10)

Macrocycle **6** (3.53 g, 7.8 mmol) and 2,2,6,6-tetramethylpiperidine (8 drops) were dissolved in THF (15 mL). 2-Mercaptoethyl sulfide (0.30 g, 1.95 mmol, 0.25 equiv.) in THF (7 mL) was added dropwise for 1 h and 45 min at 63–68°C under nitrogen. The solution was then kept at reflux for 23 h. After removal of THF under reduced pressure, the crude product was added to a column of silica gel (50 g) prepared in 20% ethyl acetate – hexanes as a slurry. A solvent gradient was used to elute the column: 20% ethyl acetate – hexanes (400 mL), 35% ethyl acetate – hexanes (250 mL), 50% ethyl acetate – hexanes (400 mL), 100% ethyl acetate – hexanes (200 mL). Two cycles of separation were applied following the same procedures, and the unreacted **6** was eventually separated from the mixture. The rest of the mixture was put on a Lipophilic Sephadex gel permeation column (LH-20, 3 × 60 cm), and eluted with 2-propanol: chloroform (3:4). After two cycles of purification, the expected compound **10** came out in the middle fractions. The analytical gel permeation column indicated it was a

© 1998 NRC Canada

single sharp peak. The combined product-containing fractions were evaporated to give compound **10** as colorless oil (0.50 g, 0.47 mmol, 24%). ^{1}H NMR 300 MHz (δ, $CDCl_3$): 6.76, 6.17 (s, 4H), 4.16–3.90 (m, 16H), 3.65–3.60 (m, 2H), 2.95–2.58 (m, 12H), 1.60–1.56 (m, 16H), 1.27 (br s, 32H). ^{13}C NMR 75.47 MHz (δ, $CDCl_3$): 171.0, 170.0, 165.2, 165.1, 133.4, 129.6, 129.4, 65.4, 65.2, 64.9, 41.5, 36.5, 31.5, 29.1, 29.0, 28.8, 28.4, 28.3, 25.7, 25.6. MS (–LSIMS, mNBA): 1058.4 $(M - H)^-$ 70.0%. Exact Mass calcd. for $(M - H)^-$, $C_{52}H_{81}O_{16}S_3$, *m/e*: 1057.4687; found: 1057.4737.

3- or 4-[7′-[17″- or 18″-(2‴-Carboxy-1‴-thiaethyl)-1″,6″,15″,20″-tetraoxa-2″,5″,16″,19″-tetraoxocyclooctacos-3″- or 4″-yl]-1′,4′,7′-trithiahepta]-17- or 18-(2-carboxy-1-thiaethyl)-1,6,15,20-tetraoxa-2,5,16,19-tetraoxocyclooctacosane (4)

Compound **10** (0.20 g, 0.19 mmol) and 2-mercaptoacetic acid were dissolved in THF (15 mL), and 2,2,6,6-tetramethylpiperidine (0.5 mL) was added to the solution. The mixture was refluxed for 36 h under nitrogen. After evaporation of THF under reduced pressure, the crude product was dissolved in dichloromethane (150 mL) and washed with 1 M hydrochloric acid (5 × 100 mL). Drying with magnesium sulfate and evaporation gave a colorless oil. Gel permeation (LH-20, 3 × 60 cm) of the product eluted with 2-propanol:chloroform (3:4) gave the desired product **4** in the middle fractions. The combined product-containing fractions were evaporated to give compound **4** as a colorless oil (0.15 g, 0.12 mmol, 63%).^{1}H NMR 300 MHz (δ, $CDCl_3$): 7.61 (br s, 2H), 4.12–3.93 (m, 16H), 3.81, 3.65 (dd, $J_1 = J_1' = 4.4$ Hz, $J_2 = J_2' = 11.1$ Hz, 4H), 3.46 (dd, $J_1 = 16.2$ Hz, $J_2 = 56.6$ Hz), 2.97–2.60 (m, 16H), 1.57 (br s, 16H), 1.27 (br s, 32H). ^{13}C NMR 75.47 MHz (δ, $CDCl_3$): 174.1, 171.2, 170.8, 170.3, 170.0, 65.6, 65.5, 65.1, 41.7, 41.5, 36.5, 36.1, 33.0, 31.6, 31.5, 29.1, 29.0, 28.4, 25.7, 25.6. MS (–LSIMS, mNBA): 1241.4 $(M - H)^-$ 100%. Exact Mass calcd. for $(M - H)^-$, $C_{56}H_{89}O_{20}S_5$, *m/e:* 1241.4551; found: 1241.4549.

3- or 4-[7′-[17″- or 18″-(*N*,*N*-Dimethyl-3‴,1‴-azathiapropyl)-1′,6″,15″,20″-tetraoxa-2″,5″,16″,19″-tetraoxocyclooctacos-3″- or 4″-yl]-1′,4′,7′-trithiahepta]-17- or 18-(*N*,*N*-dimethyl-3,1-azathiapropyl)-1,6,15,20-tetraoxa-2,5,16,19-tetraoxocyclooctacosane (5)

Compound **10** (0.20 g, 0.19 mmol) and 2-dimethylaminoethanethiol (0.11 g, 0.78 mmol, 4.1 equiv.) were dissolved in 2-propanol (15 mL), and 2,2,6,6-tetramethylpiperidine (0.5 mL) was added. The solution was refluxed for 4 h under nitrogen. After solvent evaporation, the crude product was dissolved in chloroform (150 mL), washed with 1 M hydrochloric acid (5 × 100 mL), and dried over magnesium sulfate. Following evaporation of chloroform, the crude product was chromatographed by a gel permeation column (LH-20, 3 ×60 cm) eluted with 2-propanol:chloroform (3:4). The desired compound **5** was in the middle fractions. The combined product-containing fractions were evaporated to give compound **5** as a colorless oil (0.18 g, 0.14 mmol, 74%). ^{1}H NMR 300 MHz (δ, $CDCl_3$): 4.01–3.83 (m, 16H), 3.61–3.53 (m, 4H), 2.91–2.52 (m, 36H), 1.48 (br s, 16H), 1.18 (br s, 32H). ^{13}C NMR 75.47 MHz (δ, $CDCl_3$): 170.8, 170.7, 169.8, 65.4, 65.2, 64.8, 64.7, 57.1, 43.4, 41.5, 41.3, 36.3, 36.1, 31.4, 31.3, 28.9, 28.8, 28.2, 28.7, 26.6, 25.5, 25.4. MS (+LSIMS, mNBA): 1269.4 $(M + H)^+$ 100%. Exact Mass calcd. for $(M - H)^-$, $C_{60}H_{103}O_{16}N_2S_4$, *m/e:* 1267.5911; found: 1267.6014.

Vesicle experiments

The general procedures for vesicle preparation and pH-stat titration have previously been reported (7, 12) Compounds **2–5** were dissolved in methanol (5.0 mM) and were directly added to the vesicle suspension to initiate transport. All experiments gave good (r^2 >0.98) fits to a first-order expression for consumption of titrant as a function of time for the period of the experiment where the pH-stat controlled the pH.

Bilayer clamp experiments

All electrolytes were analytical grade or better. The apparatus and general procedures for single-channel recording and analysis have been reported (7*a*). In experiments with two cations in competition, 1 M chloride salts of the ions in question were employed. The dilution potentials were determined from 0.1 M and 0.5 M salts. Liquid junction potentials were "backed-off" to zero before the membrane was formed. In cases of moderate selectivity, the junction potential after membrane rupture was still at the zero set point. High-selectivity cases are discussed in the text; the change in junction potential over an experiment was less than 20 mV in all cases. Enough transporter was added to ensure macroscopic (nA) currents across the bilayer to avoid artifacts from periods of low channel activity. Usually a potential of ±100 mV was applied initially until channel activity was established. The reversal potential was then manually approached from both directions. Following this estimation, a voltage ramp crossing the region of interest, typically with a rate of 2–13 mV s^{-1}, was applied using the Clampex data acquisition program. A current–voltage diagram was constructed as an average of 10–20 cycles and the reversal potential was determined from the voltage intercept. The manual and averaged values generally agreed within ±2 mV.

Acknowledgement

The ongoing support of the Natural Sciences and Engineering Research Council of Canada, and of the University of Victoria, is gratefully acknowledged.

References

1. (*a*) K.S. Åkerfeldt, J.D. Lear, Z.R. Wasserman, L.A. Chung, and W.F. DeGrado. Acc. Chem. Res. **26**, 191(1993); (*b*) K.S. Åkerfeldt, P.K. Kienker, J.D. Lear, and W.F. DeGrado. *In* Comprehensive supramolecular chemistry. Vol. 10. *Edited by* D.N. Reinhoudt. Pergammon, Oxford. 1996. p. 659.
2. (*a*) M.S.P. Sansom. Prog. Biophys. Mol. Biol. **55**, 139 (1991); (*b*) G.A. Wooley and B.A. Wallace. J. Membr. Biol. **129**, 109 (1992); (*c*) D.S. Cafiso. Annu. Rev. Biophys. Biolmol. Struct. **23**, 141 (1994); (*d*) B.J. Bechinger. Membr. Biol. **156**, 197 (1997).
3. (*a*) R.E. Koeppe II and O.S. Andersen. Annu. Rev. Biophys. Biomol. Struct. **25**, 231 (1996); (*b*) S. You, S. Peng, L. Lien, J. Breed, M.S.P. Sansom, and G.A. Wooley. Biochemistry, **35**, 6225 (1996); (*c*) G. Molle, J.-Y. Dugast, G. Spach, and H. Duclohier. Biophys. J. **70**, 1669 (1996); (*d*) A. Matsubara, K. Asami, A. Akagi, and N. Nishino. J. Chem. Soc. Chem.

© 1998 NRC Canada

Commun. 2069 (1996); (*e*) J.D. Lear, J.P. Schneider, P.K. Keinker, and W.F. DeGrado. J. Am. Chem. Soc. **119**, 3212 (1997).

4. (*a*) T.M. Fyles and W.F. van Straaten-Nijenhuis. *In* Comprehensive supramolecular chemistry. Vol. 10. *Edited by* D.N. Reinhoudt. Pergammon, Oxford. 1996. p. 53; (*b*) G.W. Gokel and O. Murillo. Acc. Chem. Res. **29**, 425 (1996).
5. (*a*) D. Seebach, A. Brunner, H.M. Bürger, R.N. Reusch, and L.L. Bramble. Helv. Chim. Acta, **79**, 509 (1996); (*b*) G. Deng, M. Merritt, K. Yamashita, V. Janout, A. Sadownik, and S.L. Regen. J. Am. Chem. Soc. **118**, 3307 (1996); (*c*) G. Deng, T. Dewa, and S.L. Regen. J. Am. Chem. Soc. **118**, 8975 (1996); (*d*) H. Wagner, K. Harms, U. Koert, S. Meder, and G. Boheim. Angew. Chem. Int. Ed. Engl. **35**, 2643 (1996); (*e*) J.-C. Meillon and N. Voyer. Angew. Chem. Int. Ed. Engl. **36**, 967 (1997).
6. (*a*) O. Murillo, S. Watanabe, A. Nakano, and G.W. Gokel. J. Am. Chem. Soc. **117**, 7665 (1995); (*b*) O. Murillo, I. Suzuki, E. Abel, and G.W. Gokel. J. Am. Chem. Soc. **118**, 7628 (1996); (*c*) O. Murillo, E. Abel, G.E.M. Maguire, and G.W. Gokel. J. Chem. Soc. Chem. Commun. 2147 (1996); (*d*) O. Murillo, I. Suzuki, E. Abel, C.L. Murray, E.S. Meadows, T. Jin, and G.W. Gokel. J. Am. Chem. Soc. **119**, 5540 (1997).
7. (*a*) T.M. Fyles, D. Loock, W.F. van Straaten-Nijenhuis, and X. Zhou. J. Org. Chem. **61**, 8866 (1996); (*b*) T.M. Fyles, K.C. Kaye, A. Pryhitka, J. Tweddell, and M. Zojaji. Supramol. Chem. **3**, 197 (1994); (*c*) T.M. Fyles, D. Loock, and X. Zhou. J. Am. Chem. Soc. **120**, 7997 (1998).
8. C. Hansch and A. Leo. Substituent constants for correlation analysis in chemistry and biology. John Wiley and Sons, New York. 1979. p. 22.
9. N. Jayasuriya, S. Bosak, and S.L. Regen. J. Am. Chem. Soc. **112**, 5844 (1990).
10. T.M. Fyles and B. Zeng. Chem. Soc. Chem. Commun. 2295 (1996).
11. T.M. Fyles, T.D. James, A. Pryhitka, and M. Zojaji. J. Org. Chem. **58**, 7456 (1993).
12. T.M. Fyles, T.D. James, and K.C. Kaye. J. Am. Chem. Soc. **115**, 12315 (1993).
13. (*a*) B. Sakmann and E. Neher. Single-channel recording. Plenum, New York. 1983; (*b*) B. Hille. Ionic channels of excitable membranes. Sinauer, Sunderland. 1984.
14. S. König and E. Sackmann. Curr. Opin. Colloid Interface Sci. **1**, 78 (1996).
15. W.E. Dasent. Inorganic energetics. Penguin Books, Hammondsworth. 1970.
16. Y. Marcus. Chem. Rev. **88**, 1475 (1988).
17. M. Arshadi, R. Yamdagni, and P. Kebarle. J. Phys. Chem. **74**, 1475 (1970).
18. J.T. Mason and C. Huang. Ann. N. Y. Acad. Sci. **308**, 29 (1978).

© 1998 NRC Canada

Effect of the hydrogen bond network in carbonic anhydrase II zinc binding site. A theoretical study

Silvia Álvarez-Santos, Àngels González-Lafont, and José M. Lluch

Abstract: The hydrogen bond network influence on the carbonic anhydrase II (CAII) zinc binding site has been studied theoretically by using the semiempirical AM1 method. To this aim, quantum mechanical reduced models of wild-type CAII and several CAII variants have been constructed. We have shown that, when a direct metal ligand donates a hydrogen bond to an indirect metal ligand, the first-shell residues enhance their electrostatic interaction with the zinc cation. Thus, the hydrogen-bond network is able to modulate the zinc binding affinity and the zinc–water pK_a.

Key words: hydrogen bond network, carbonic anhydrase II, Zn^{2+} metalloenzyme ligands.

Résumé : Faisant appel à la méthode semi-empirique AM1, on a effectué une étude théorique de l'influence du réseau de liaisons hydrogènes sur le site de fixation du zinc de l'anhydrase carbonique (ACII). À cet effet, on a construit plusieurs modèles (de mécanique quantique) réduits de l'ACII de type sauvage et de ses variantes. On a montré que, lorsqu'un ligand métallique direct donne une liaison hydrogène à un ligand métallique indirect, les résidus de la première couche augmentent leur interaction électrostatique avec le cation zinc. Il en résulte donc que le réseau de liaisons hydrogènes peut moduler l'affinité de fixation du zinc et le pK_a du complexe zinc–eau.

Mots clés : réseau de liaisons hydrogènes, anhydrase carbonique II, ligands métalloenzyme du Zn^{2+}.

Introduction

The design of proteins with predictable structure and function is one of the objectives of protein engineering. Knowledge of the ligand geometry and stereochemistry of many metalloenzymes, which are well characterized structurally, has been used to redesign some metal sites with different protein scaffoldings (1–4). However, these sites cannot reproduce the catalytic activity and the avid metal binding of natural metalloenzymes (5).

An important point that has to be considered is that the side chains that ligate the metal ion in metalloenzymes are nested in a hydrogen-bonding network with other protein residues. Hydrogen bonding interactions with metal ligands are proposed to orient the ligands for optimal metal coordination, enhancing the electrostatic interaction between the ligands and the metal ion (6). These hydrogen bond networks with metal ligands could be important for the structure and function of metalloenzymes.

Zinc metalloenzymes, such as carbonic anhydrase II (CAII) (7), carboxypeptidase A (CPA) (8), or termolysin (TLN) (9), generally have a water molecule (solvent) bound to the zinc ion. Hydrogen-bonding networks with zinc ligands could also modulate the pK_a and reactivity of the zinc-bound water molecule (10, 11), which is implicated in the catalytic mechanism of the enzyme. The residues that establish hydrogen-bonding interactions with direct metal ligands (first-shell residues) are referred to as "indirect metal ligands" and build a second shell of residues surrounding protein–metal binding sites.

Recently, carbonic anhydrase II (CAII) has been used as the most appropriate zinc enzyme paradigm to analyze the structural and functional roles of hydrogen-bond networks between "indirect ligands" and direct metal ligands (12, 13). In CAII, the zinc ion is coordinated to three histidine residues (94, 96, and 119) and a water molecule. Those direct ligands interact through a hydrogen-bond network with a second shell of residues of the enzyme as shown schematically in Fig. 1.

To investigate the functional role of these hydrogen bonds, Kiefer et al. (12) have determined experimentally the effects of varying the structure of the side chain of indirect ligands on zinc binding and catalysis. The authors conclude that weakening the hydrogen bonds to the zinc ligands should increase the mobility of the histidine residues and decrease the metal ion affinity due to the increased entropic cost of metal binding. Removing two indirect ligands has an additive effect on zinc affinity, leading to a decrease in zinc binding energy of 2.2 kcal/mol. It seems that the role of indirect ligands is to preorganize the direct ligands for optimal metal coordination, and increase the electrostatic interaction between the ligands and metal ion, so enhancing metal affinity. Moreover, the authors suggest that the indirect ligand interacting with His-119 plays an essential role in slow zinc dissociation.

The zinc–water pK_a is also perturbed when the indirect ligands are altered in carbonic anhydrase II (12). Altering

Received September 9, 1997.[1]

S. Álvarez-Santos, À. González-Lafont, and J.M. Lluch.[2]
Departament de Química, Universitat Autònoma de Barcelona, 08193 Bellaterra, Barcelona, Spain.

[1]Revision received April 2, 1998.
[2]Author to whom correspondence may be addressed. Telephone: 34-93-5812138. Fax: 34-93-5812920. E-mail: lluch@klingon.uab.es

© 1998 NRC Canada

Fig. 1. Scheme of the active site of wild-type CAII.

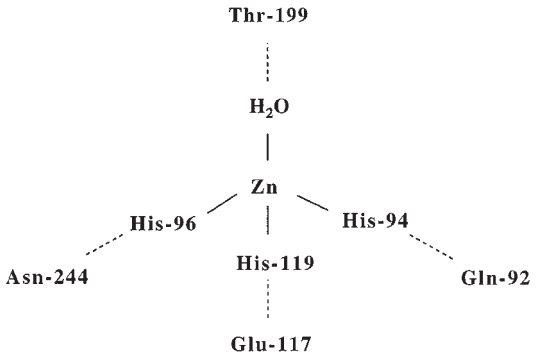

the hydrogen-bonding interactions with zinc ligands provokes changes in the electrostatic environment of zinc. Then the ability of zinc to polarize its bound water molecule is modified, which confirms that the indirect ligands do modulate the catalytic efficiency of zinc in CAII, beginning with alterations to the pK_a of the zinc–water ligand.

X-ray crystallographic studies on several recombinant CAIIs (13) confirm the importance of indirect ligands modulating the pK_a of zinc-bound water and the zinc binding affinity, which leads us to conclude that in the structure-assisted design of protein–metal binding sites, not only direct ligands, but also the indirect ligands involved in the hydrogen-bond network, must be included.

The purpose of the present paper is to theoretically analyze the hydrogen-bond network influence on the zinc binding affinity and the zinc–water pK_a in carbonic anhydrase II. To this end we will use a quantum mechanical reduced model of that enzyme.

Method of calculation

The reduced quantum mechanical model of wild-type CAII, which we designed in order to reproduce the hydrogen-bond networks on the active site of the enzyme, consisted of the following key elements: a zinc ion coordinated to its four direct ligands (a water molecule and three histidines) and the second shell of residues that hydrogen bond to those zinc ligands (glutamine, glutamate, threonine, and asparagine) (see Fig. 1). The protonated nitrogen atom in the imidazole ring of His-94 donates a hydrogen bond to the carboxamide side chain of Gln-92, His-119 donates a hydrogen bond to the carboxylate side chain of Glu-117, zinc-bound water donates a hydrogen bond to the hydroxyl side chain of Thr-199, and His-96 donates a hydrogen bond to the backbone carbonyl oxygen of Asn-244.

Unlike proline, all the amino acids commonly found in proteins contain a primary amino group (-NH_2) on the α-carbon atom (the one attached to the carboxyl group). The rest of the molecule, the side chain, is also bonded to the α-carbon atom and characterizes the different amino acids. In this paper, we are interested in second-shell hydrogen bonds between residues that ligate zinc and the side chains of indirect ligands. To reduce computational requirements, histidines were modeled by imidazole rings. In modeling the three indirect ligands that are hydrogen bonded to the first-shell residues through their side chains, the substituents bonded to the α-carbon atom were simplified by substituting the $NH_2C^{\alpha}HCOOH$ terminal group by a CH_3 group, but the chemical structure of the side chains was maintained in the quantum mechanical model. As for the fourth indirect ligand, the backbone fragment corresponding to Asn-244 has been modeled by a propanamide. A three-dimensional picture of the model compound that we have used in our calculations for the wild-type CAII is displayed in Fig. 2. We have also modeled some enzymatic variants of CAII by replacing wild-type CAII indirect ligands with other amino acid side chains. Those new indirect ligands have also been simplified in our

Fig. 2. Three-dimensional picture of the model compound for wild type CAII.

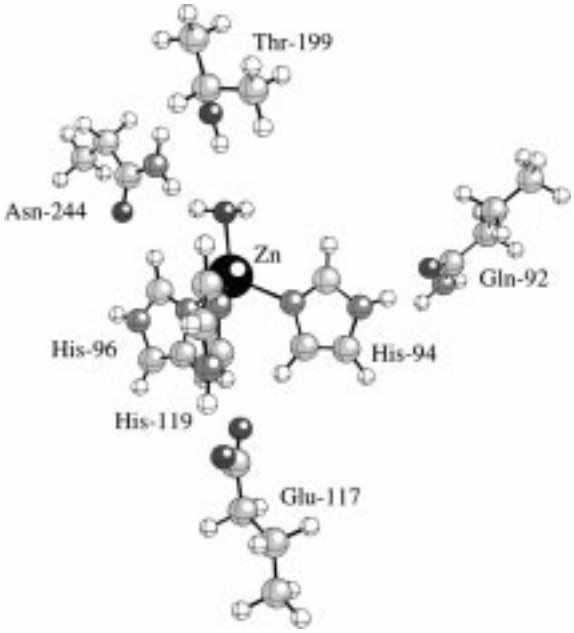

Fig. 3. Three-dimensional pictures of the model compounds for alanine, leucine, and aspartate.

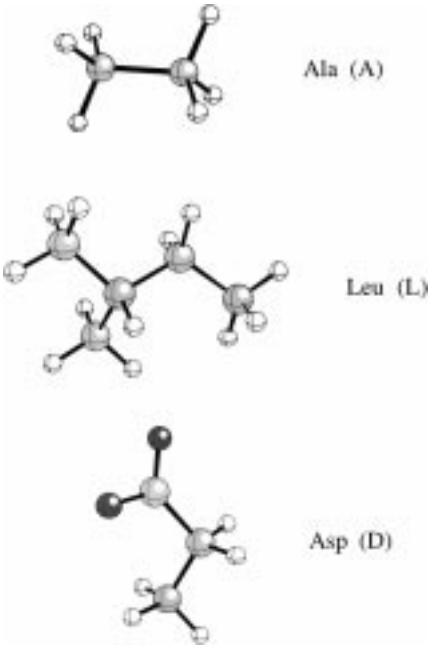

© 1998 NRC Canada

quantum mechanical model by substituting the $NH_2C^{\alpha}HCOOH$ terminal group by a CH_3 group but maintaining the chemical structure of their side chains. A three-dimensional picture of the model compounds used in our calculations to represent the new residues (alanine, leucine, and aspartate) is shown in Fig. 3.

In spite of those reductions, the calculations carried out in this work involved systems containing up to 85 atoms. Due to the size of those systems, the use of ab initio or DFT methods is quite beyond our computational capabilities. Thus, calculations were performed using the standard AM1 (14) semiempirical procedure, as implemented in the AMPAC (15) package of computer programs. It must be noted that the AM1 semiempirical method has provided good theoretical results in several recent Zn^{2+} metalloenzyme simulations (16–18) although it does not reproduce the geometry of hydrogen bonds properly (19). Geometry minima on the semiempirical hypersurface were located by minimizing the energy with respect to all geometrical variables using the Davidon–Fletcher–Powell (DFP) method (20, 21). In any event, it must be kept in mind that the full geometry optimization of our reduced model can move some groups away from the position that they occupy in the real entire enzyme. In some cases (indicated below), several internal coordinates were kept frozen in the optimization run. The stationary points (that is, when no constraint is introduced) found on the complete hypersurface were characterized as minima by diagonalizing their Hessian (force constant) matrices and looking for all positive eigenvalues.

Results and discussion

First, we present our results concerning the influence of the CAII hydrogen-bond network on the zinc binding affinity, between zinc first-shell and second-shell residues. Secondly, the effect of the hydrogen-bond network on the pK_a of the zinc–water ligand is analyzed.

To theoretically estimate the zinc binding affinity in CAII, several complexation enthalpies within our quantum mechanical model have been calculated. Those enthalpy values are presented in Table 1. In this work, complexation enthalpies are defined as enthalpy differences between each fully optimized complex (zinc plus residues) and a set of different fragments of that complex. We have distinguished between two main kinds of complexation enthalpies. The first will be called the fragment complexation enthalpy (first column in Table 1) and it comes from putting together five different fragments. These five fragments are, on the one hand, zinc ion and, on the other hand, each one of its four direct ligands, which are hydrogen bonded to a second-shell ligand depending on whether the indirect ligand is present in the final complex. In these enthalpy calculations, each fragment and the complete complex were fully optimized. The second complexation enthalpy that we have calculated will be called zinc complexation enthalpy (second column in Table 1). These zinc complexation enthalpies correspond to enthalpy differences between each optimized complex and two different fragments: zinc ion, on the one hand, and, on the other hand, the whole set of ligands present in the final complex. In the calculation of these zinc complexation enthalpies the set of residues are held fixed at their optimized disposition in the final system, that is, when binding to zinc ion. The first row in Table 1 gives fragment and zinc complexation enthalpy values when only the first-shell ligands are present in the final complex. In the rest of the rows, the corresponding complexation enthalpies are given for those systems formed when the different indirect ligands are successively included at the locations indicated in Fig. 1. In this paper, amino acids will be designated using either the well-known three-letter or the one-letter abbreviations. That is: His or H, Thr or T, Asn or N, Glu or E, Gln or Q, Ala or A, Leu or L, and Asp or D. Here, Glu and Asp refer to negatively charged glutamate and aspartate species, respectively.

Table 1. Complexation enthalpies. From top to bottom the different indirect ligands are successively introduced in going from the first shell up to the wild-type model (TNEQ).

Model	Fragment complexation (kcal/mol)	Zn complexation (kcal/mol)
First shell	–395.2	–411.1
T	–404.6	–421.4
TN	–416.7	–438.5
TNE	–534.5	–570.9
TNEQ	–540.4	–582.9

The calculated fragment complexation enthalpies presented in Table 1 (first column) become more negative as the complex size increases, as a result of progressively including the indirect ligands, until completing the second shell of residues. A more significant stabilization is observed when the indirect ligand being added is Glu-117 or E117, in good agreement with previous experimental results where the carboxylate–histidine–zinc triad was classified as stronger than, for instance, the carboxamide–histidine–zinc triad (10, 11). Zinc complexation enthalpies (second column of Table 1) show the same above-mentioned trends with increasing number of hydrogen bonds, but this magnitude compares better with the experimental measurement of zinc binding affinity in CAII, because the experimental process only consists of zinc dissociation, without dismantling the rest of the structure of the enzyme. The difference between the values in the two columns of Table 1 comes from the destabilization energy that results from the approach of the four fragments different from zinc from infinity to their final location in the complex. As can be seen, this destabilization effect becomes more significant as the number of indirect ligands increases.

The role of indirect ligands in the enhancement of metal affinity in metalloenzymes has been attributed to two different factors: the capability of indirect ligands to orient first-shell ligands for optimal metal coordination, and the increase of electrostatic interaction between direct ligands and the metal ion due to the presence of second-shell residues. In our quantum-mechanical calculations only the electrostatic effect is introduced because we have included in our model just two shells of amino acids. This electrostatic effect is due to both the through-space charge interactions and the formation of the hydrogen bond. As for the contribution of the hydrogen bond, when a first-shell residue donates a hydrogen bond to a second-shell residue, the net effect is equivalent to

© 1998 NRC Canada

Table 2. Complexation enthalpies for the wild-type CAII and different CAII variants. For the sake of comparison, experimental zinc K_D dissociation constants are shown in the last column.

Model	Fragment complexation (kcal/mol)	Zn complexation (kcal/mol)	Zinc K_D [a] (pM)
Wild-type	–540.4	–582.9	4.0 ± 1
Q92A	–485.4	–548.2	18 ± 2
Q92L	–533.4	–566.8	30 ± 8
Q92N	–538.2	–579.5	5 ± 1
Q92E	–610.7	–678.7	5 ± 1
E117D	–540.9	–583.0	12 ± 2
E117D/Q92A	–535.7	–570.3	
E117D/Q92L	–534.1	–568.4	
E117D/Q92N	–539.0	–579.5	
E117D/Q92E	–623.3	–700.2	
E117A	–429.0	–452.5	40 ± 15
E117A/Q92A	–418.5	–438.6	160 ± 35

[a] From ref. 12.

a negative charge transfer in the reverse direction, that is, from the second to the first shell, which enhances its electrostatic interaction with the metal cation. As already noted, this electrostatic contribution to metal binding affinity is particularly important when Glu-117 (with a negatively charged side chain) is added in the second shell. Experimentally it has been shown that about 1.4 kcal/mol of zinc binding energy is conferred per hydrogen bond for up to 5 kcal/mol increase in zinc affinity for four hydrogen bonds (12). Our calculations in vacuo show the qualitative trends although they are quantitatively exaggerated because Zn^{2+} becomes free when dissociated in our quantum-mechanical model. As a matter of fact, Weinhold (22) has recently shown that a simple ab initio gas-phase cluster model is able to qualitatively reproduce the H-bond network of an enzyme active site. It could be expected that adding solvent molecules would decrease zinc binding energy per hydrogen bond, progressively approaching the corresponding experimental value in solution.

The experimental conclusions on the function of the hydrogen bond network of CAII in zinc binding affinity have been assessed from the study of several CAII variants (12, 13). We have also modeled those enzymatic variants by replacing hydrogen bond acceptors with other amino acid side chains. The criteria for choosing CAII variants have been the following: (*a*) removal of the entire side chain functionality that forms a hydrogen bond with the first-shell ligands by substituting the hydrogen bond acceptor amino acid with Ala or Leu; (*b*) the change of size or charge of the hydrogen-bonded second-shell residues. In addition, several double variants have been considered in order to study combined effects. The different CAII variants that we have modeled theoretically are listed in the first column of Table 2 using one-letter abbreviations. The first one-letter symbol (followed by the location numbering) indicates the wild-type hydrogen acceptor residue while the second one-letter abbreviation refers to the amino acid used for substitution in the enzyme variant. Double substitution variants are individually specified in the same way and separated by a slash. For each of the modeled CAII variants, fragment complexation enthalpies of the entire system (i.e.,with the second shell of residues completed) were calculated relative to the five fragments: zinc ion, on the one hand, and, on the other hand, the four pairs of direct–indirect ligands. Zinc complexation enthalpies have also been calculated for each variant relative to zinc ion, on the one hand, and, on the other hand, relative to the whole set of ligands frozen at their optimized location in the final complex. The results are presented in Table 2 along with the corresponding wild-type values for the sake of comparison. Fragment and zinc complexation enthalpies present very similar trends along the series of CAII variants. For that reason, in this section we will comment only on zinc complexation enthalpy values, which are, in addition, more comparable to experimental data as we have previously observed.

The series of CAII variants that we modeled can be classified in three different groups. In the first group, Q92 was changed by four different residues. In the Q92A and the Q92L variants, the existing hydrogen bond with His-94 is eliminated in both cases, although those two new residues maintain a weak interaction with the imidazole ring of the first shell. Our calculations show that in both the Q92A and the Q92L variants, the system is destabilized relative to wild-type CAII in agreement with the electrostatic effect explained in the previous paragraphs. It has to be noted at this point that additional geometry constraints were needed in the calculations for optimizing the Q92A variant. Concretely, the hydrogen forming the hydrogen bond between His-119 and Glu-117 was fixed in such a way that both the hydrogen-acceptor atom and the hydrogen-donor atom distances were kept frozen. In the absence of this constraint, a proton transfer from His-119 to E117 occurs in our model, which has nothing to do with the elimination of the hydrogen bond in the system.

Zinc avidity is not very sensitive to the length of the side chain of the acceptor residue as long as the potential for forming a hydrogen bond is maintained. This can be seen by the insignificant change in the complexation enthalpy when going from wild-type CAII to the Q92N variant, in which a methylene group of the side chain of the acceptor residue has been eliminated. On the contrary, when a net negative charge is introduced at the 92 location in the Q92E variant, the complexation enthalpy decreases nearly 100 kcal/mol, confirming the important role played by carboxylate–histidine–zinc triads (10).

In the second group of CAII variants that we modeled, Glu-117 was substituted by Asp in the wild-type enzyme and, as well, in the four CAII variants described in the previous paragraph. Altering the length of the acceptor residue in the E117D variant does not modify metal affinity for its ligands, as we had already inferred from substitution at location 92. The series of double substitution variants modeled by changing Gln-92 for Ala, Leu, Asn, and Glu in the E117D variant show trends similar to our first group of variants. The only difference worth noting concerns Q92A substitution. In the E117D variant, when a hydrogen bond is eliminated by introducing Ala at location 92, there is no proton transfer from H119 to D117 and the destabilization effect of removing a hydrogen bond can be observed.

The third group of variants were modeled to analyze the energetic effects of removing the hydrogen bond network at

© 1998 NRC Canada

position 117. The great increase in the complexation enthalpy obtained for the E117A and E117A/Q92A variants indicates that the indirect ligand at position 117 anchors the zinc ion more tightly than any other indirect ligand, in particular, the Gln at position 92. In other words, our calculations confirm again that the carboxylate–histidine–zinc triad is stronger than the carboxamide–histidine–zinc triad.

Kiefer et al. (12) assessed the effects of altering the indirect ligands on metal binding by measuring zinc dissociation constants at pH 7 for the different CAII variants. Those dissociation constants were obtained by establishing the relationship between unbound zinc concentration (metal ion outside the active site) and the concentration of bound zinc (metal ion inside the active site) in an equilibrium dialysis experiment. In Table 2 (third column) the experimental dissociation constants values are given. When Ala or Leu is used for substitution either at position 92 or at position 117, larger zinc K_D values are experimentally measured, indicating that in those variants zinc affinity has decreased relative to wild-type CAII. This increase is particularly important in the E117A variant and in E117A/Q92A CAII, where the effect is found to be additive. In any case, these zinc K_D values are somewhat underestimated because, even in those variants where the hydrophobicity of the indirect ligand was changed to disrupt the hydrogen-bond network, a hydrogen bond is always experimentally maintained by the unexpected recruitment of new hydrogen-bond partners from the protein or from the solvent. In two variants, Q92A and E117A, a compensatory hydrogen bond is experimentally formed between the histidine zinc ligand and either an inserted water molecule or a chloride ion. In the Q92L variant an alternative amino acid side chain moves to form a poorly oriented hydrogen bond with H94. Our theoretical complexation enthalpies qualitatively agree with the trends observed for the zinc K_D dissociation constants. That is, when the zinc dissociation constant increases, the zinc complexation enthalpy relative to wild-type CAII is less negative. In particular, our theoretical results reproduce the high destabilization of the E117A and E117A/Q92A variants, which experimentally present 10-fold and 40-fold larger zinc K_D dissociation constants than wild-type CAII. Moreover, the greater effect on weakening protein–zinc affinity at position 117 than at position 92 can be seen from a comparison of the zinc complexation enthalpies in the E117A and Q92A variants. Kiefer et al. (12) also indicate that shortening the side chain of the acceptor residue has no major effect on the zinc dissociation constants, in agreement with the calculated values for the corresponding (Q92N and E117D) zinc complexation enthalpies that do not significantly differ from wild-type CAII. Taking all this into account, the large experimental zinc K_D value in the E117D variant appears rather surprising. In the Q92E variant another disagreement is found between experimental and theoretical results. Altering the charge of the hydrogen-bond acceptor does not significantly modify the experimentally determined zinc dissociation constant, leading the authors to conclude that the charge of the indirect ligand at position 92 is not a primary determinant of metal affinity. In contrast, our calculations show a particular stabilization of the system when neutral glutamine is substituted by negatively charged glutamate at position 92. This theoretical result agrees better with the changes in the zinc electrostatic environment in the Q92E variant compared to the wild-type CAII that we have already described, because a negatively charged acceptor side chain increases the electrostatic interaction between the ligands and the metal ion. This discrepancy in the experimental results may be attributed to the influence of certain factors in the experimental measurements that have not been included in the quantum mechanical model. In any case, the experimental value for the zinc dissociation constant in Q92E CAII is rather surprising and contradicts the result of the rate dissociation constant for the same system given by the authors, which decreases 6-fold relative to wild-type CAII (12). Thus, the experimental half-time for dissociation ($t_{1/2}$) of zinc from CAII appears to be 31.7 days for Q92E whereas it is 5.2 days for wild-type CAII. In addition, the reported value for $t_{1/2}$ in the Q92N variant is only 1.1 days while, according to the experimental results, the Q92N and Q92E variants present identical dissociation rate constants.

Table 3. Deprotonation enthalpy differences relative to the wild-type CAII and experimental zinc–water pK_a values.

Model	$\Delta\Delta H^0$ (cal/mol)	pK_a [a]
First shell	–425.1	—
Wild type	0	6.8
Q92A	55.8	6.8
Q92L	–47.9	6.4
Q92N	36.5	6.9
Q92E	683.1	7.7

[a] From ref. 12.

As for the second subject under consideration in this paper, the pK_a of zinc-bound water affords a convenient means of quantifying the electrostatic contributions, including hydrogen bonding to the metal ligands, with respect to the ability of zinc to polarize its bound water molecule. In other words, changes in the electrostatic environment of the zinc in CAII should be reflected in the pK_a of the zinc–water ligand since this measures the ability of zinc to stabilize a negatively charged hydroxide ion. We have studied theoretically the acid–base equilibrium of removing a proton from the zinc-bound water by calculating the corresponding standard deprotonation enthalpy in some of our quantum mechanical models of the CAII active site. The differences in those reaction enthalpies with respect to wild-type CAII ($\Delta\Delta H^0$) are listed in Table 3 along with the experimental pK_a's reported by Kiefer et al. (12). The hydrogen-bond network between zinc first-shell and second-shell residues contributes to diminishing the effective positive charge of the zinc ion and thereby one would expect an increase in the water-bound pK_a. In agreement, the $\Delta\Delta H^0$ value for the first-shell model (with no indirect ligand included) is negative. This is indicative of the more acidic character of the water-bound molecule in the model where none of the metal direct ligands is hydrogen bonded to indirect ligands. With only first-shell residues, the zinc ion supports more positive charge and it is able to better stabilize a negatively charged hydroxide ion. The opposite effect is observed in Q92E CAII: the substitution of neutral glutamine with negatively charged glutamate at position 92 increases the electron density on zinc and, consequently, its water ligand is less

© 1998 NRC Canada

polarized and has significantly less acidic character. This accounts for the positive $\Delta\Delta H^0$ value listed in Table 3. In good agreement, the experimental pK_a increases by almost one pH unit. When, instead, a hydrogen bond to a histidine zinc ligand in wild-type CAII is eliminated, the pK_a of zinc-bound water should decrease. In Q92L CAII, the aliphatic side chain of Leu cannot accept a hydrogen bond from H94, although, as we have already explained, a compensatory hydrogen bond is formed in the experimental system between an alternative amino acid side chain and H94. In any case, that new hydrogen bond is not well oriented and, consequently, the effective positive charge on zinc increases. This explains the experimental decrease by 0.4 pK_a units of the wild-type pK_a. In the theoretical model, no alternative hydrogen bond is formed and we obtain a negative $\Delta\Delta H^0$ value. At first glance, it could seem surprising that the experimental pK_a's in wild-type CAII and in the Q92A variant are identical. Kiefer et al. (12) explain that in this substitution there is no net change in the electrostatic environment of zinc because the void created on the active site of Q92A CAII allows for the entrance of a water molecule, which forms a compensatory hydrogen bond with the histidine zinc ligand. The theoretical $\Delta\Delta H^0$ value is slightly positive. However, this theoretical value cannot be used for comparison because of the above-mentioned constraint used to avoid the proton transfer between His-119 and E117. The perturbation of this constraint is much too strong in the scale of cal/mol of the computed $\Delta\Delta H^0$. Finally, the effect of shortening the side chain of the acceptor residue in the Q92N variant leads to a slight increase of the experimental pK_a and, in agreement, of a positive theoretical $\Delta\Delta H^0$ value.

To summarize, in this paper we have shown theoretically that the hydrogen bond network, in which the direct zinc ligands are nested in CAII, modulates the zinc binding affinity and the zinc–water pK_a. These results, which confirm previous experimental findings, prove the importance of hydrogen bonds in determining the structure and reactivity of metalloenzymes. As a matter of fact, the role of these hydrogen bonds between direct and indirect ligands of the metal ion is to create a hydrogen-bonding network of residues on the active site. The energetic stabilization achieved once the hydrogen-bond network is formed comes from several contributions: those arising from the hydrogen bond itself and those due to electrostatic interactions at longer distances.

Finally we have to note again that the calculations presented in this paper correspond to in vacuo supermolecules, whereas the experimental quantities were obtained in solution. Although no quantitative comparison can be made between both sets of results, our theoretical gas-phase model is able to qualitatively reproduce the main trends of the different ligands in a real hydrogen-bond network.

Acknowledgements

Financial support from Dirección General de Enseñanza Superior (DGES) through project PB95–0637 and the use of computational facilities of the Centre de Computació i de Comunicacions de Catalunya are gratefully acknowledged.

References

1. L. Regan, and N.D. Clark. Biochemistry, **29**, 10878 (1990).
2. W.S. Wade, J.S. Koh, N. Han, D.M. Hoekstra, and R.A. Lerner. J. Am. Chem. Soc. **115**, 4449 (1993).
3. M.E. McGrath, B.L. Haymore, N.L. Summers, C.S. Craik, and R.J. Fletterick. Biochemistry, **32**, 1914 (1993).
4. J.D. Stewart, V.A. Roberts, M.W. Crowder, E.D. Getzoff, and S.J. Benkovic. J. Am. Chem. Soc. **116**, 415 (1994).
5. D.W. Christianson. Adv. Protein Chem. **42**, 281 (1991).
6. P. Argos, R.M. Garauito, W. Eventoff, M.G. Rossman, and C.I. Branden. J. Mol. Biol. **126**, 141 (1978).
7. K. Håkansson, M. Carlsson, L.A. Svensson, and A. Liljas. J. Mol. Biol. **227**, 1192 (1992).
8. D.C. Rees, M. Lewis, and W.N. Lipscomb. J. Mol. Biol. **168**, 367 (1983).
9. M.A. Holmes and B.W. Matthews. J. Mol. Biol. **160**, 623 (1982).
10. D.W. Christianson and R.S. Alexander. J. Am. Chem. Soc. **111**, 6412 (1989).
11. D.W. Christianson and R.S. Alexander. Nature, **346**, 225 (1990).
12. L.L. Kiefer, S.A. Paterno, and C.A. Fierke. J. Am. Chem. Soc. **117**, 6831 (1995).
13. C.A. Lesburg and D.W. Christianson. J. Am. Chem. Soc. **117**, 6838 (1995).
14. M.J.S. Dewar, E.G. Zoebisch, E.F. Healy, and J.J.P. Stewart. J. Am. Chem. Soc. **107**, 13 (1985).
15. D.A. Liotard, E.F. Healy, J.M. Ruiz,and M.J.S. Dewar, AMPAC version 2.1. Quantum Chemistry Program Exchange, Program 506, QCPE Bull. **9**, 123 (1989).
16. A. Alex and T. Clark. J. Comput. Chem. **13**, 704 (1992).
17. S. Alvarez-Santos, A. González-Lafont, J.M. Lluch, B. Oliva, and F.X. Avilés. Can. J. Chem. **72**, 2077 (1994).
18. S. Alvarez-Santos, A. González-Lafont, J.M. Lluch, B. Oliva, and F.X. Avilés. New. J. Chem. **20**, 979 (1996).
19. S. Galera, J.M. Lluch, A.Oliva, and J. Bertrán. J. Mol. Struct. (Theochem), **163**, 101 (1988).
20. R. Fletcher and M.J.D. Powell. Comput. J. **6**, 163 (1963).
21. W.C. Davidon. Comput. J. **10**, 406 (1968).
22. F. Weinhold. J. Mol. Struct. (Theochem), **398**, 181 (1997).

© 1998 NRC Canada

Heteroleptic gold complexes with 4,5-diselenolate-1,3-dithiole-2-thione ($C_3S_3Se_2^{2-}$, dsit)

Elena Cerrada and Mariano Laguna

Abstract: The reaction of $(NBu_4)_2[Zn(dsit)_2]$ (dsit = 4,5-diselenolate-1,3-dithiole-2-thione) with AuClL in a 1:4 ratio leads to $[Au_2(dsit)L_2]$ (L = PPh_3 (**1**), PPh_2Me (**2**)), transferring the diselenolate group. Complex **2** reacts further with equimolar amounts of $[Au(OClO_3)L]$, affording the trinuclear complex $[Au_3(dsit)(PPh_2Me)_3]ClO_4$ (**3**). When the reaction of $(NBu_4)_2[Zn(dsit)_2]$ with $[Au_2Cl_2(P\text{-}P)]$ was carried out in a 1:2 ratio, complexes $[Au_2(dsit)(P\text{-}P)]_n$ (P-P = dppe (1,2-bis(diphenylphosphine)ethane), n = 1 (**4**); P-P = dppm (bis(diphenylphosphine)methane), n = 2 (**5**)) are obtained. Anionic derivatives such as $(NBu_4)[Au(dsit)_2]$ (**6**) could be obtained by reaction of the zinc complex with $(NBu_4)[AuBr_4]$ in a 1:1 ratio while other gold complexes require a tin complex as ligand transfer. So $[Sn(dsit)Me_2]$ (**7**), obtained from the zinc complex and $[SnCl_2Me_2]$, reacts with $PPN[Au(C_6F_5)Cl]$ (PPN = bis(triphenylphosphine)iminium) or $[AuBr_2(S_2CNR_2)]$ affording $[Au(dsit)(S_2CNR_2)]$ (R = Me (**8**); R = Bz (**9**)) or $(PPN)_2[Au_2(dsit)(C_6F_5)_2]$ (**10**), respectively. Electrochemical oxidation of **6** gives $(NBu_4)_{0.4}[Au(dsit)_2]$ (**11**) and the reaction with $(TTF)_3(BF_4)_2$ (TTF = tetrathiafulvalene) affords $(TTF)[Au(dsit)_2]$ (**12**). Electrical conductivities of these complexes at room temperature in compacted pellets are 3×10^{-8} (**11**) and 5×10^{-3} (**12**) S cm^{-1}.

Key words: diselenolate, dsit, gold complexes, tin complexes.

Résumé : La réaction du $(NBu_4)_2[Zn(dsit)_2]$ (dsit = 4,5-disélénaloate-1,3-dithiole-2-thione) avec le AuClL dans un rapport de 1 : 4 conduit au $[Au_2(dsit)L_2]$ (L = PPh_3 (**1**), PPh_2Me (**2**)) avec transfert du groupe disélénolate. Le complexe **2** réagit ultérieurement avec des quantités équimolaires de $[Au(OClO_3)L]$ pour conduire au complexe trinucléaire $[Au_3(dsit)(PPh_2Me)_3]ClO_4$ (**3**). Lorsqu'on fait réagir le $(NBu_4)_2[Zn(dsit)_2]$ avec du $[Au_2Cl_2(P\text{-}P)]$ dans un rapport de 1 : 2, on obtient des complexes $[Au_2(dsit)(P\text{-}P)]_n$ (P-P = dppe [1,2-bis(diphénylphosphine)éthane], n = 1 (**4**); P-P = dppm [bis(diphénylphosphine)méthane], n = 2 (**5**)). On peut obtenir des dérivés anioniques, tel que le $(NBu_4)[Au(dsit)_2]$ (**6**), en faisant réagir le complexe de zinc avec du $(NBu_4)[AuBr_4]$ dans un rapport de 1 : 1; pour la préparation d'autres complexes de l'or, il est nécessaire d'utiliser un complexe d'étain comme ligand de transfert. Ainsi, le complexe $[Sn(dsit)Me_2]$ (**7**), obtenu à partir du complexe de zinc et du $[SnCl_2Me_2]$, réagit avec le $PPN[Au(C_6F_5)Cl]$ (PPN = bis(triphénylphosphine)iminium) ou le $[AuBr_2(S_2CNR_2)]$ pour conduire respectivement au $[Au(dsit)(S_2CNR_2)]$ (R = Me (**8**); R = Bz (**9**)) et au $(PPN)_2[Au_2(dsit)(C_6F_5)_2]$ (**10**). L'oxydation électrochimique du composé **6** conduit au $(NBu_4)_{0,4}[Au(dsit)_2]$ (**11**) alors que sa réaction avec le $(TTF)_3(BF_4)_2$ (TTF = tétrathiafulvalène) mène au $(TTF)[Au(dsit)_2]$ (**12**). Les conductivités électriques de ces complexes, à la température ambiante, sous la forme de pastilles, sont 3×10^{-8} (**11**) et 5×10^{-3} (**12**) S cm^{-1}.

Mots clés : disélénolate, dsit, complexes d'or, complexes d'étain.

[Traduit par la Rédaction]

Introduction

Metal complexes containing 4,5-dithiolate-1,3-dithiole-2-thione ($C_3S_5^{2-}$, dmit) have been investigated because of the high conductivity reported in certain of them (1, 2). Since the discovery in 1986 of the first formally inorganic molecular superconductor (3) $(TTF)[Ni(dmit)_2]_2$ (TTF = tetrathiafulvalene), a great number of $(cation)_x[M(dmit)_2]$ (M = Ni, Pd, and Pt; cation = TTF or NMe_4 and $0 \leq x \leq 2$) have been synthesized (4–10), including the recently reported α-EDT-TTF$[Ni(dmit)_2]$, which is superconducting at ambient pressure (4). The dmit ligand acts in all these complexes as a bidentate chelate but the coordination chemistry of this ligand is very rich, at least in gold chemistry, where coordination as μ_2 (11–13) and μ_3 (12) bridging modes in di-, tri-, and tetra-nuclear complexes have been described.

Substituting selenium atoms for sulphur atoms in dmit has led to a number of new ligands such as dsit ($C_3S_3Se_2$), dsise (C_3S_4Se), dmise ($C_3S_2Se_3$), and dsis (C_3Se_5) (14–17) (Fig. 1). They have been investigated because they are expected to enable more effective molecular interaction through the selenium–selenium contacts due to the more diffuse and spatially extended *p* and *d* orbitals of the selenium atom as compared with sulphur. However, to date only a few complexes of these ligands have been reported and those with metallic behaviour are scarce, namely, $[NHMe_3][Ni(dmise)_2]_2$ (18), $[NMe_4][Ni(dmise)_2]_2$ (19), and $[NMe_4][Pd(dsise)_2]_2$ (20).

Received October 10, 1997.

E. Cerrada and M. Laguna.[1] Departamento de Química Inorgánica, Instituto de Ciencia de Materiales de Aragón, Universidad de Zaragoza-C.S.I.C., 50009 Zaragoza, Spain.

[1] Author to whom correspondence may be addressed. Telephone: 34-976-761181. Fax: 34-976-761187. E-mail: mlaguna@posta.unizar.es

© 1998 NRC Canada

Fig. 1.

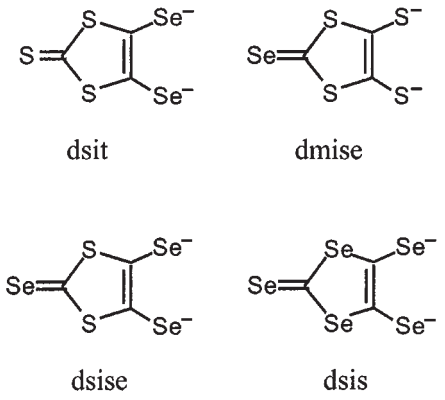

This paper reports a systematic study of the coordination properties of dsit as a ligand in gold(I) and gold(III) chemistry, giving rise to novel bridging coordination modes, through the useful transfer of dsit from zinc and tin complexes, such as $[NBu_4]_2[Zn(dsit)_2]$ and $[Sn(dsit)Me_2]$. Gold complexes with the dsit acting as μ_2 (e.g., $[Au_2(dsit)(PPh_2Me)_2]$) or μ_3 (e.g., $[Au_3(dsit)(PPh_2Me)_3]ClO_4$) bridging ligand are reported among others, with the dsit acting in a chelate form (e.g., $[Au(dsit)(S_2CNMe_2)]$). Complex $[Bu_4N][Au(dsit)_2]$ undergoes oxidation to give fractional oxidation state complexes $[NBu_4]_{0.4}[Au(dsit)_2]$ or reacts with $(TTF)_3(BF_4)_2$ affording $[TTF][Au(dsit)_2]$ (TTF = tetrathiafulvalene). Both gold complexes show low electrical conductivity in compacted pellets, 3×10^{-8} and 5×10^{-3} S cm^{-1}, respectively.

Experimental

$Q_2[Zn(dsit)_2]$ (Q = NBu_4, NEt_4) (21), $[AuCl(PPh_3)]$ (22), $[AuCl(PPh_2Me)]$ (22), $[Au_2(\mu\text{-dppe})Cl_2]$ (dppe = 1,2-bis(diphenylphosphine)ethane) (23), $[Au_2(\mu\text{-dppm})Cl_2]$ (dppm = bis(diphenylphosphine)methane) (23), $PPN[Au(C_6F_5)Cl]$ (PPN = bis(triphenylphosphine)iminium) (24), $[AuBr_2(S_2CNR_2)]$ (25), and $(TTF)_3(BF_4)_2$ (26) were prepared by literature procedures. $[Au(OClO_3)(PPh_2Me)]$ was synthesized from $[AuCl(PPh_2Me)]$ with $AgClO_4$ in dichloromethane. All other reagents were commercially available.

IR spectra were recorded on a Perkin–Elmer 559 or 883 spectrophotometer, over the range 4000–250 cm^{-1}, using Nujol mulls between polyethylene sheets, and Raman spectra were recorded using a Dilor XY spectrometer with a multichannel diode array detector and λ (Ar^+) = 514.5 nm. NMR spectra were recorded on a Varian Unity 300 spectrometer in $CDCl_3$ solutions (^1H (300 MHz), $^{31}P\{^1H\}$ (121.4 MHz), and ^{19}F (282.2 MHz)) using tetramethylsilane, H_3PO_4 (85%, external), and $CFCl_3$ as references. Mass spectra were recorded with the VG Autospec LSIMS technique using 3-nitrobenzylalcohol as matrix and a cesium gun. The C, H, N, and S analyses were performed with a Perkin–Elmer 2400 microanalyser; Au was determined by ashing the samples with an aqueous solution of hydrazine. Conductivities were measured in acetone with a Philips PW 9509 apparatus. Electrical conductivities were measured in compacted pressed pellets at room temperature.

$[Au_2(dsit)L_2]$ (L = PPh_3 (1), PPh_2Me (2)), $[Au_2(dsit)(P\text{-}P)]_n$ (P-P = dppe, n = 1 (4); P-P = dppm, n = 2 (5)), $(NBu_4)[Au(dsit)_2]$ (6), $[Sn(C_3S_3Se_2)Me_2]$ (7)

To an acetone (20 mL) solution of $(NBu_4)_2[Zn(dsit)_2]$ (56 mg, 0.05 mmol) under a dinitrogen atmosphere was added $[AuCl(PPh_3)]$ (98 mg, 0.2 mmol), $[AuCl(Ph_2Me)]$ (86 mg, 0.2 mmol), $[Au_2(\mu\text{-dppe})Cl_2]$ (86 mg, 0.1 mmol), or $[Au_2(\mu\text{-dppm})Cl_2]$ (85 mg, 0.1 mmol). Orange solids precipitated immediately in the case of **4** and **5**; these were filtered off, washed with acetone, and dried under vacuum. In the other cases orange solutions were obtained. After stirring for 1 h, the solutions were concentrated to 1 mL. Addition of diethyl ether (15 mL) gave a pale solid, which was filtered off. The resulting solution was concentrated to 5 mL. Addition of *n*-hexane (10 mL) led to precipitation of **1** and **2** as yellow solids The solids were filtered off, washed with water, and recrystallized with diethyl ether – hexane. Formation of **7** was accomplished similarly, but starting from $(NEt_4)_2[Zn(dsit)_2]$ (45 mg, 0.05 mmol) and $SnCl_2Me_2$ (22 mg, 0.1 mmol).

Complex **6** was formed similarly but starting from $NBu_4[AuBr_4]$ (38 mg, 0.05 mmol) and $(NBu_4)_2[Zn(dsit)_2]$ (56 mg, 0.05 mmol) and using diethyl ether to precipitate a garnet solid, which was filtered off, washed with water, and recrystallized from dichloromethane – diethyl ether.

$[Au_3(dsit)(PPh_2Me)_3]ClO_4$ (3)

To a dichloromethane (20 mL) solution of $[AuCl(PPh_2Me)]$ (43 mg, 0.1 mmol) was added $AgClO_4$ (21 mg, 0.1 mmol). After 1 h of stirring the suspension was filtered through a 1 cm layer of Celite. $[Au_2(dsit)(PPh_2Me)_2]$ (110 mg, 0.1 mmol) was added to the resulting solution. After being stirred for 2 h, the solution was concentrated to 2 mL. Addition of *n*-hexane led to precipitation of an orange solid. Λ_M in acetone (5×10^{-4} M) 107 Ω^{-1} cm^2 mol^{-1}.

$[Au(dsit)(S_2CNR_2)]$ (R = Me (8), CH_2Ph (Bz) (9)), $(PPN)_2[Au_2(dsit)(C_6F_5)_2]$ (10)

To an acetone (20 mL) solution of $[Sn(dsit)Me_2]$ (39 mg, 0.1 mmol) under a dinitrogen atmosphere was added $[AuBr_2(S_2CNMe_2)]$ (47 mg, 0.1 mmol), $[AuBr_2(S_2CNBz_2)]$ (63 mg, 0.1 mmol), or $PPN[Au(C_6F_5)Cl]$ (180 mg, 0.2 mmol). Dark brown (**8**) and green (**9**) solids inmediately appeared and were filtered off and dried under vacuum. In the other case, the solution was concentrated to 1 mL. Addition of *n*-hexane (15 mL) gave a brown solid (**10**), which was filtered off.

$(NBu_4)_{0.4}[Au(dsit)_2]$ (11)

An acetonitrile solution (10 mL) containing $(NBu_4)[Au(dsit)_2]$ (24 mg, 24 mmol) and NBu_4ClO_4 (27 mg, 80 mmol) was subjected to controlled-current (1.2 μA) electrolysis for 15 days in an H-type glass cell consisting of platinum wires (27). Black microcrystals (7 mg) of complex **11** produced on the anode were collected and washed with acetonitrile.

$(TTF)[Au(dsit)_2]$ (12)

To an acetonitrile (20 mL) solution of $NBu_4[Au(dsit)_2]$ (101 mg, 0.1 mmol) was added $(TTF)_3(BF_4)_2$ (102 mg,

© 1998 NRC Canada

Scheme 1.

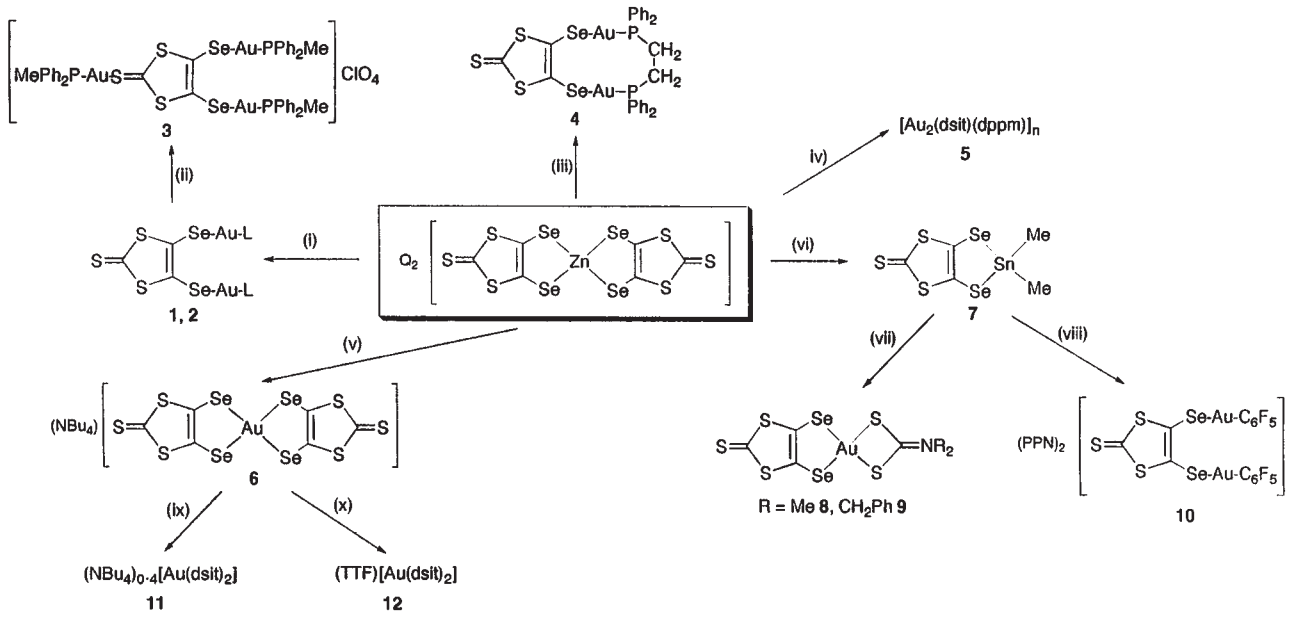

0.13 mmol). A dark garnet solid precipitated immediately and was filtered off and dried under vacuum.

Results and discussion

The syntheses of dmit and dsit complexes reported to date have been carried out mainly from the COPh protected derivatives, $C_3S_5(COPh)_2$ and $C_3S_3Se_2(COPh)_2$, respectively. The reaction of these stable derivatives with ethanol solutions of EtONa yields fresh solutions of $C_3S_5Na_2$ or $C_3S_3Se_2Na_2$, which further react with the corresponding halo–metal complexes (17, 28, 29). This method does not yield good results with the dsit and gold(I) complexes [AuClL] (L = PPh_3, PPh_2Me). The preparation of $[Au_2(dsit)L_2]$ (L = PPh_3, **1**; PPh_2Me, **2**) can be achieved through the use of the zinc derivative $(NBu_4)_2[Zn(dsit)_2]$ with the corresponding [AuClL] complexes in a 1:4 ratio in acetone solutions (reaction (i), Scheme 1) in a similar way to those reported for dmit derivatives (30). The reaction works in very mild conditions such as 1 h reaction time at room temperature. The lack of solubility of the by-product $(NBu_4)_2[ZnCl_4]$ in diethyl ether permits the separation of complexes **1** and **2** in good yields (Table 1).

The spectroscopic properties of these complexes are in agreement with their formulation, showing one singlet in the $^{31}P\{^1H\}$ NMR spectrum, displaced slightly low field with respect to the $[Au_2(dmit)L_2]$ derivatives (31). The mass spectra (LSIMS +) are very informative, showing the parent peak M^+ at *m/z* (%) 1210 (15), **1,** and 1086 (12), **2**, with the expected isotopic distributions, which in this case are illustrative because of the presence of six isotopes of selenium. It is noteworthy that, as happened in the dithiolate mass spectra (30, 31), there are signals assignable to $[M + Au\ L]^+$ at *m/z* (%): 1669 (9), **1**, and 1483 (8), **2**. The trinuclear gold(I) complex $[Au_3(dsit)(PPh_2Me)_3](ClO_4)$ (**3**) can be obtained by reaction of complex **2** with a fresh solution of $[Au(OClO_3)(PPh_2Me)]$. The corresponding PPh_3 derivative is not obtained in a pure form. Complex **3** shows conductivity in acetone solution (5×10^{-4} M) corresponding to a 1:1 electrolyte, in agreement with its formulation (32). The mass spectrum shows the parent ion peak with the lack of the ClO_4 anion at *m/z* 1483 (17%). The ^1H NMR spectrum shows a CH_3 doublet at 2.4 ppm ($^2J_{P-H}$ = 7.8 Hz) and the $^{31}P\{^1H\}$ NMR spectrum consists of a broad singlet at room temperature, which is resolved into two singlets with a 2:1 intensity ratio at –80°C, as did the dmit complex $[Au_3(dmit)(PPh_2Me)_3](ClO_4)$ (31). In accordance with all these data we believe that complexes **1–3** have similar structures as those reported for the dmit derivatives with the dsit acting as μ_2 and μ_3 bridging ligands as represented in Scheme 1.

The zinc derivative $(NBu_4)_2[Zn(dsit)_2]$ reacts with $[Au_2Cl_2(P\text{-}P)_2]$ (P-P = dppm, dppe) in a 1:2 ratio with the transfer of a diselenolate group. New complexes $[Au_2(dsit)(P\text{-}P)]_n$ (P-P = dppe, n = 1, **4** ; P-P = dppm, n = 2, **5**) appear as insoluble yellow solids in the reaction solvent, acetone. The $^{31}P\{^1H\}$ NMR spectra show a single resonance at δ 33.7 ppm for **4** and an AA′XX′ system for **5**: δ_A = 36.7 ppm, δ_X = 27.1 ppm, $^2J_{AA}$ = 112 Hz, $^2J_{AX} = {}^2J_{A'X}$ = 46 Hz. All these values are very close to those reported for the dmit derivatives (12, 13) and are displaced slightly low field with respect to them with the exception of δ_A. It is noteworthy that although the differences are small (one CH_2 group) between the diphosphines used, dppm and dppe, the spectroscopic properties of complexes **4** and **5** are very different. Similar $^{31}P\{^1H\}$ NMR spectral patterns have been

© 1998 NRC Canada

Table 1. Analytical and spectroscopic data for complexes **1**–**12**.

Complex	Yield (%)	Anal. found (calcd.)(%) C	H	S	N	^{31}P {^{1}H}	^{1}H NMR CH_3 or CH_2
1[Au_2(dsit)(PPh_3)$_2$]	70	39.5 (38.8)	2.6 (2.5)	8.15 (8.0)	—	37.1(s)	—
2[Au_2(dsit)(PPh_2Me)$_2$]	68	33.3 (33.1)	2.3 (2.3)	8.8 (8.9)	—	20.9(s)	1.92(^2J(PH) 4 Hz)
3[Au_3(dsit)(PPh_2Me)$_3$]ClO_4	65	31.5 (31.9)	2.1 (2.5)	6.6 (6.1)	—	20.2(s,br)[a]	2.46(^2J(PH) 7.8 Hz)
4[Au_2(dsit)(dppe)]	75	32.2 (32.4)	2.0 (2.2)	8.4 (8.9)	—	33.7(s)	2.62(s)
5 [Au_4(dsit)$_2$(dppm)$_2$]	85	32.0 (31.5)	2.1 (2.1)	8.7 (9.0)	—	36.7(m) 27.1(m)	4.45(m), 4.25(m)
7 [Sn(dsit)Me_2]	90	15.5 (15.0)	1.3 (1.5)	24.3 (24.1)		—	1.27(^2J(SnH) 60 Hz)
8 [Au(dsit)(S_2CNMe_2)]	90	12.3 (11.9)	0.9 (1.0)	26.5 (26.4)	2.6 (2.3)	—	[b]
9 [Au(dsit)(S_2CNBz_2)]	72	28.5 (28.1)	1.6 (1.7)	20.6 (21.1)	1.8 (1.9)	—	[b]
10 (PPN)$_2$[Au_2(dsit)(C_6F_5)$_2$]	50	50.5 (49.9)	3.4 (2.9)	4.8 (4.6)	1.5 (1.3)	—	—
11 (NBu_4)$_{0.4}$[Au(dsit)$_2$][c]	—	17.2 (17.0)	1.8 (1.7)	21.4 (22.0)	0.6 (0.7)	—	—
12 (TTF)[Au(dsit)$_2$][d]	65	13.9 (14.7)	0.3 (0.4)	33.2 (32.7)	—	—	—

[a] In $(CD_3)_2CO$ at room temp. At –80°C: 20.7(s) and 18.5(s).
[b] Insoluble.
[c] Au: Anal. found 23.1, calcd. 22.5.
[d] Au: Anal. found 20.6, calcd. 20.1.

observed in the dmit derivatives and in fact their structures [Au_2(dmit)(dppe)] (13) and [Au_2(dmit)(dppm)]$_2$ (12) are very different. The spectroscopic properties indicate a similar structure for the dmit and dsit derivatives, dinuclear for **4** and tetranuclear for **5**, although other polynuclear structures are not ruled out (Scheme 1). The mass spectra of these complexes are not helpful because only Au(dsit) and Au(P-P) fragments appear.

The use of the zinc derivative as the diselenolate transferring group can be extended to the preparation of gold(III) complexes, but in this case only the reaction with (NBu_4)[$AuBr_4$] works in a clean way to give the previously described (NBu_4)[Au(dsit)$_2$] (**6**) (33) in a very good yield. Because of the square planar coordination of gold(III), the dsit ligand acts as a bidentate chelate ligand in this complex. The preparation of anionic gold(I) complexes or gold(III) derivatives requires other transferring metal complexes. For this reason we tested the preparation of the dsit–tin derivative, which can be obtained from the reaction of (NBu_4)$_2$[Zn(dsit)$_2$] with [$SnCl_2Me_2$] (reaction (vi)). The resulting tin [Sn(dsit)Me_2] **7** and the zinc by-product (NBu_4)$_2$[$ZnCl_4$] complexes can be easily separated because of their different solubilities in diethyl ether. The ^{1}H NMR spectrum of **7** shows a singlet for methyl groups bonded to tin flanked by a broad pair of satellite peaks ($^2J_{Sn–H}$ = 60.0 Hz). Although there are two active tin isotopes, ^{117}Sn and ^{119}Sn, the different coupling constants are not resolved in this case.

Complex **7** is a suitable reagent for transferring the dsit to different dithiocarbamate gold(III) complexes [$AuBr_2$(S_2CNR_2)] or to the anionic gold(I) derivative (PPN)[Au(C_6F_5)Cl] (PPN = $Ph_3P{=}N{=}PPh_3$), affording the mononuclear [Au(dsit)(S_2CNR_2)] (R = Me, **8**; CH_2Ph (Bz), **9**) or the dinuclear gold(I) complex (PPN)$_2$[Au_2(dsit)(C_6F_5)$_2$] (**10**). In both cases the reaction by-product [$SnCl_2Me_2$] can be separated from the reaction mixture because of its solubility in acetone or hexane, respectively. Due to the insolubility of complexes **8** and **9**, data from measurements in solution were not available. Complex **10** shows three signals in the ^{19}F NMR spectrum: –115.4 (m, F_o), –163.3 (t, F_p), –164.6 (m, F_m) in accordance with two equivalent C_6F_5 groups. Complex **10** shows in the mass spectrum (LSIMS–) a signal corresponding to the anion at *m/z* 821 (3%). The coordination of dsit ligand in compounds **6**, **8**, and **9** should be as bidentate chelate because of the preferred square planar arrangement of the gold(III) center, whereas the prefered linear array at gold(I) centers induces a coordination of dsit as μ_2- or μ_3-bridge as proposed for compounds **1–5** and **10**.Unfortunately, all attempts to obtain crystals of good quality for X-ray studies of the new complexes were unsuccessful and do not permit us to confirm the proposed coordination properties of the dsit ligand in gold chemistry.

The preparation of fractional charge complexes has usually been achieved by starting from anionic complexes. In our case neither gold(I) anionic **10**, nor neutral derivatives, **1** and **2,** give non-integral derivatives. On the contrary, the electrochemical oxidation of an acetonitrile solution of (NBu_4)[Au(dsit)$_2$] **6** in the presence of NBu_4ClO_4 affords black microcrystals of complex: (NBu_4)$_{0.4}$[Au(dsit)$_2$] **11**,

© 1998 NRC Canada

which has been characterized by elemental analyses and the electrical conductivities measured from compacted pellets of 3×10^{-8} S cm^{-1} at room temperature.

The reaction of complex **6** with $(TTF)_3(BF_4)_2$ gives complex (TTF)[Au(dsit)$_2$] (**12**) in which no oxidation has taken place. Complex **12** shows IR (KBr pellets) absorption at 1050 and 1025 cm^{-1} corresponding to the ν(C=S) band and a Raman spectrum with a band at 1415 cm^{-1} due to the C=C of the TTF molecule in accordance with a formulation as TTF^+ (34), so the metal atom remains as gold(III) in the complex. The solid shows a conductivity in a compacted pellet of 5×10^{-3} S cm^{-1} at room temperature.

Conclusions

In conclusion, the complexes $(NBu_4)_2[Zn(dsit)_2]$ and [Sn(dsit)Me$_2$] are able to transfer the dsit group to gold centers under very mild conditions, allowing the synthesis of dsit gold compounds that cannot be obtained using fresh solutions of $C_3S_3Se_2Na_2$. Remarkably, the NMR spectra of the new complexes show similar patterns to those of the dmit gold compounds; therefore the structures of the dsit derivatives should be similar to those reported on dmit analogues. We are interested in the study of the generality of this synthetic strategy to transfer the dsit and related selenium ligands to other metal centers, because the mild conditions should permit a more effective control of the final products.

Acknowledgement

We thank the Dirección General de Investigación Científica y Técnica (Grant PB95–0140) for financial support.

References

1. P. Cassoux, L. Valade, H. Kobayashi, A. Kobayashi, R.A. Clark, and A.E. Underhill. Coord. Chem. Rev. **110**, 115 (1991).
2. R.M. Olk, B. Olk, W. Dietzsch, R. Kirmse, and E. Hoyer. Coord. Chem. Rev. **117**, 99 (1992).
3. L. Brossard, M. Ribault, M. Bousseau, L. Valade, and P.C. Cassoux. R. Acad. Sci. Paris, Ser 2, **302**, 205 (1986).
4. H. Tajima, M. Inokuchi, A. Kobayashi, T. Ohta, R. Kato, H. Kobayashi, and H. Kuroda. Chem Lett. 1235 (1993).
5. L. Brossard, M. Ribault, M. Bousseau, L. Valade, and P.C. Cassoux. R. Acad. Sci. Paris, Ser 2. **302**, 205 (1986).
6. A. Kobayashi, H. Kim, Y. Sasaka, R. Kato, K. Kobayashi, S. Moriyama, Y. Nishio, K. Kajita, and W. Sasaki. Chem. Lett. 1819 (1987).
7. L. Brossard, H. Hundequint, M. Ribault, L. Valade, J.P. Legros, and P. Cassoux. Synth. Met. **27**, B157 (1988)
8. L. Brossard, M. Ribault, L. Valade, and P. Cassoux. J. Phys. (Paris), **50**, 1521 (1989).
9. A. Kobayashi, H. Kobayashi, A. Miyamoto, R. Kato, R.A. Clark, and A.E. Underhill. Chem. Lett. 2163 (1991).
10. H. Kobayashi, K. Bun, T. Naito, R. Kato, and A. Kobayashi. Chem Lett. 1909 (1992).
11. E. Fritsch, K. Polborn, C. Robl, K. Sünkel, and W. Beck. Z. Anorg. Allg. Chem. **619**, 2050 (1993).
12. E. Cerrada, A. Laguna, M. Laguna, and P.G. Jones. J. Chem. Soc. Dalton Trans. 1325 (1994).
13. E. Cerrada, P.G. Jones, A. Laguna, and M. Laguna. Inorg. Chim. Acta, **24**9 163 (1996).
14. J.P. Cornelissen, J.-G. Haasnoot, J. Reedjik, C. Faulmann, J-P Legros, P. Cassoux, and P.J. Nigrey. Inorg. Chim. Acta, **202**, 131 (1992).
15. B. Olk, R.M. Olk, J. Sieler, and E. Hoyer. Synth. Met. **41–43**, 2585 (1991).
16. R.M. Olk, C. Semmelmann, R. Kirmse, K. Köhler, E. Hoyer, and B. Olk. Z. Anorg. Allg. Chem. **581**, 59 (1990).
17. R.M. Olk, A. Röhr, J. Sieler, K. Köhler, R. Kirmse, W. Dietzsch, E. Hoyer, and B. Olk. Z. Anorg. Allg. Chem. **577**, 206 (1989).
18. T. Naito, A. Sato, K. Kawano, A. Tateno, H. Kobayashi, and A. Kobayashi. J. Chem. Soc. Chem. Commun. 351 (1995).
19. J.P. Cornelissen, B. Pomarède, A.L. Spek, D. Reefman, J.G. Haasnoot, and J. Reedjik. Inorg. Chem. **32**, 3720 (1993).
20. C. Faulmann, J.-P Legros, P. Cassoux, J. Cornelissen, L. Brossard, M. Inokuchi, H. Tajima, and M. Tokumoto. J. Chem. Soc. Dalton Trans. 249 (1994).
21. H. Poleschner, R. Radeglia, and J. Fuchs. J. Organomet. Chem. **427**, 213 (1992).
22. R. Usón and A. Laguna. Inorg. Synth. **21**, 71 (1982).
23. H. Schmidbaur, A. Wohlleben, F. Wagner, O. Orama, and G. Huttner. Chem. Ber. **110**, 1748 (1977).
24. R. Usón and A. Laguna. Organomet. Synth. **3**, 322 (1989).
25. R. Usón, A. Laguna, and B. Bergareche. J. Organomet. Chem. **184**, 411 (1980).
26. F. Wudl. J. Am. Chem. Soc. **110**, 1748 (1977).
27. H. Anzai, T. Moriya, K. Nozaki, T. Ukachi, and G. Saito. J. Phys. Colloq. 1195 (1983).
28. R. Kirmse, R.M. Olk, K. Köhler, W. Dietszsch, E. Hoyer, and G. Zwanenburg. Inorg.Chem. **29**, 4073 (1990).
29. R.M. Olk, B. Olk, J. Rohloff, J. Reinhold, J. Sieler, K. Trübenbach, R. Kirmse, and E. Hoyer Z. Anorg. Allg. Chem. **609**, 103 (1992).
30. E. Cerrada, E.J. Fernández, M.C. Gimeno, A. Laguna, M. Laguna, R. Terroba, and M.D. Villacampa J. Organomet. Chem. **492**, 105 (1995).
31. E. Cerrada, A. Laguna, and M. Laguna. Inorg. Chem. **35**, 2995 (1996).
32. G. Geary. Coord. Chem. Rev. **7**, 81 (1971).
33. R.M. Olk, W. Dietzsch, J. Mattusch, J. Stach, C. Nieke, E. Hoyer, W. Meiler, and W. Robien. Z. Anorg. Allg. Chem. **544**, 199 (1987).
34. S. Matsuzaki, T. Moriyama, and K. Toyoda. Solid State Commun. **34**, 857 (1980).

© 1998 NRC Canada

Studies with polyfunctionally substituted heteroaromatics: synthesis of new heterocyclic aromatic amines as potential intermediates for preparation of dyes for thermal diffusion printing

Ayman Wahba Erian, Ebtisam Abdul Aziz Hafez, Elham Sayed Darwish, and Mohamed Hilmy Elnagdi

Abstract: Several new dibenzopyrans as well as novel thiadiazaacenaphthenes are obtained via 4 + 2 addition of the thienocoumarins (1) and thienopyridazines (2) to electron-poor olefins.

Key words : pyridazines, thienopyridazines, phthalazines, coumarines, thiadiazaacenaphthenes.

Résumé : L'addition 4 + 2 de thiénocoumarines (1) et de thiénopyridazines (2) sur des oléfines pauvres en électron permet d'obtenir plusieurs dibenzopyranes et thiadiazaacénaphtènes nouveaux.

Mots clés : pyridazines, thiénopyridazines, phtalazines, coumarines, thiadiazaacénaphtènes.

[Traduit par la Rédaction]

Introduction

Heterocyclic aromatic amines are interesting compounds because of considerable utility as intermediates in both the pharmaceutical and dye industries (1–6). In the last years we were involved in a program to develop new polyfunctional substituted heterocyclic amines for use as agrochemicals and as intermediates in the dye industry (7–9). During this phase of our research we have developed a synthesis of benzo-fused azines via addition of electron-poor olefins and acetylenes to aminothienoazines. It is well documented that thiophene and its derivatives are reluctant partners in [4+2] cycloadditions with dienophiles containing a double bond in general and with dimethyl fumarate in particular. For instance, Gaertner and Tonkyn (10) failed to add maleic anhydride to tetramethylthiophene even when the reaction was carried out in boiling nitrobenzene (bp 211°C). A similar failure was also reported by Clapp (11), who attempted to induce tetraphenylthiophene to react with maleic anhydride. Similarly, thiophene fails to undergo [4+2] cycloaddition with dienophiles (12) such as dimethyl maleate, dimethyl fumarate, methyl acrylate, acrylonitrile, or acrylaldehyde, even under high pressure. A Diels–Alder adduct was obtained, however, with maleic anhydride (100°C, 15 kbar, 3 h) (1 bar = 100 kPa) (12). However, it should be noted that at atmospheric pressure diene reactivity towards compounds containing a double bond has been observed with 2,5-dimethoxythiophene (13), 2,4-bis-(*N*-isopropyl-*N*-phenylamino)thiophene (14), and 2,3,4,5-di(naphthalene-1,8-diyl)thiophene (15). However, aminothienopyridazines, being both electron-rich and strained molecules, add readily to electron-poor olefins to yield aminophthalazines via [4+2] cycloaddition reaction followed by ring opening and aromatization through loss of hydrogen sulfide or elimination of hydrogen depending on the nature of the reagent and applied reaction condition (15, 16). To our knowledge this was the first reported addition of an electron-rich strained thiophene to an electron-poor olefin. Recently Dopp and coworkers (17) have reported the addition of dimethyl fumarate and dimethyl acetylenedicarboxylate to 3-amino-4-imino-4H-thieno[3,4-*c*]-benzopyran. Although the reaction of dimethyl fumarate afforded dibenzopyran via a reaction sequence similar to that observed earlier by us (15), the cycloadduct from reaction with dimethyl acetylene dicarboxylate underwent a novel type of rearrangement that afforded benzopyrano-thiepine (17). In conjunction of this work we reported here synthesis of 3-aminothieno[3,4-*c*]coumarin (1) and thieno[3,4-*d*]pyridazin-1-carboxylates (2) and their reactivity toward electron-poor olefins.

Received July 2, 1997.

A.W. Erian,[1] E.A.A. Hafez, and E.S. Darwish. Department of Chemistry, Faculty of Science, Cairo University, Giza, Egypt.
M.H. Elnagdi. Department of Chemistry, Faculty of Science, University of Kuwait, P.O. Box 5965, Safat 13060, Kuwait.

[1]Author to whom correspondence may be addressed. Telephone: 5932216. Fax: 3601614.

Results and discussion

Thus, we have found that 4-methylcoumarin-3-carbonitrile (3) reacts readily with sulfur in refluxing dimethylformamide in the presence of ethanolic piperidine to yield the thienobenzopyran derivative **1** via the intermediate **4**. This compound readily added *N*-phenylmaleimide and

© 1998 NRC Canada

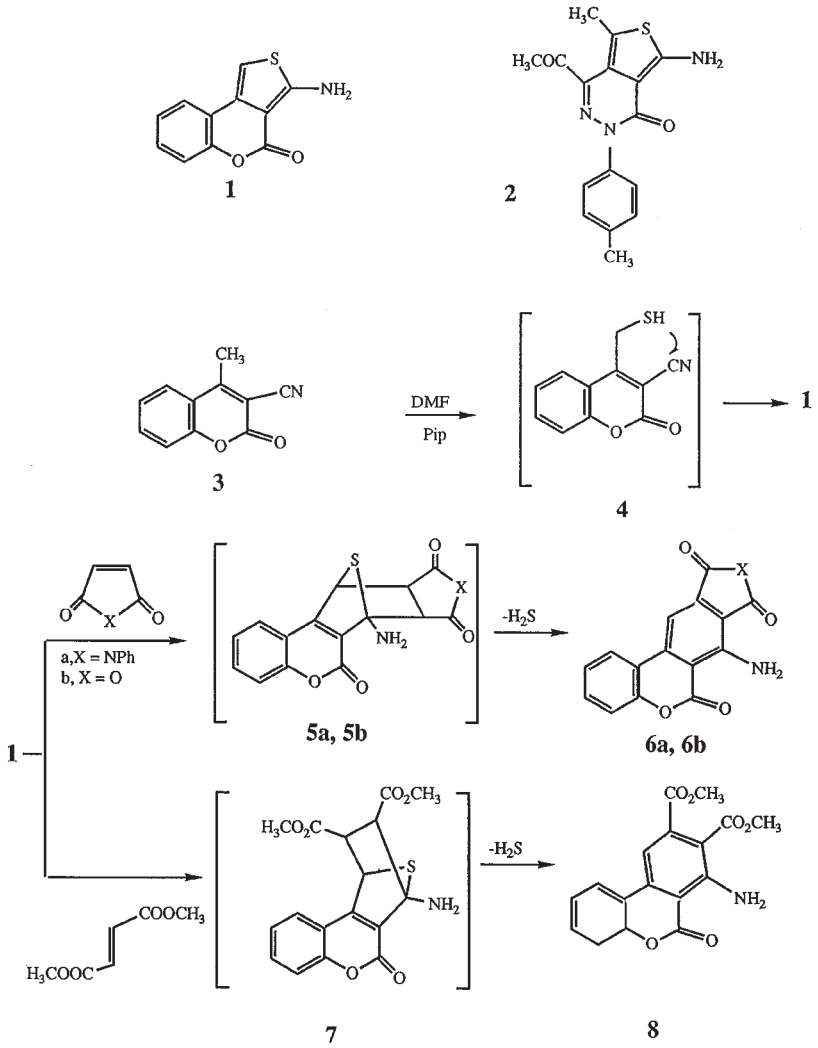

maleic anhydride to yield the condensed dibenzopyran **6a**,**b**. Formation of **6** is assumed to proceed via initial [4+2] cycloaddition of the olefinic double bond to diene system of **1**, yielding intermediate cycloadducts **5a** and **5b** that then loses hydrogen sulfide to yield the final isolable product. This is similar to the recently reported (17) behaviour of 3-amino-4-imino-4H-thieno[3,4-*c*][1]benzopyran toward dimethyl fumarate. Similar to this, it has also found that **1** reacts with dimethyl fumarate to yield the dibenzopyrane derivative **8,** most likely via the intermediate of the cycloadduct **7**.

Compound **2** reacted with methyl acrylate when refluxed in dioxane containing few drops of acetic acid to yield products of addition and methanol elimination. These are assigned structure **11** and are assumed to be formed via rearrangement of the initially formed cycloadduct **9** to **10** in presence of acid medium. The latter cyclized via loss of methanol to give **11**. If **10** would lose hydrogen sulphide to yield a phthalazine, the methyl and ester function in this product would experience large steric interactions. The structure proposed for compound **11** was established with ^{13}C NMR. Furthermore ^{1}H NMR showed an AB multiplet near δ 3.00 ppm for CH_2 protons at position C-8. Similarly, the reaction of maleic anhydride with **2** afforded **12**. It is believed that the methanol eliminated during formation of **12** effects ring opening of the anhydride ring.

Compound **2** reacted with benzoyl isothiocyanate to yield a 1:1 adduct. The ^{1}H NMR of this adduct revealed the presence of two lower field D_2O exchangeable hydrogen atoms at δ 12.10 and 15.20 ppm. The absence of any amino hydrogens excludes the possibility that the cycloadduct **14** was formed. It is most likely that this product is the benzoyl thiourea derivative **13**. This assumption is further supported by ^{13}C NMR data, which did not show any signals for sp^3 hybridized besides carbons those of the methyl and methoxy group (further detail cf. experimentat section).

Experimental

All melting points are uncorrected, IR spectra were obtained on a Pye Unicam SP 1000 spectrophotometer using KBr discs. The ^{1}H NMR were recorded on a varian EM 390-90 MHz, and Bruker WM 300 MHz using TMS as internal reference. The chemical shifts were expressed as a δ ppm GCMS-QP 1000-EX Shimadzu, Japan. Analytical data were obtained from the microanalytical data unit at Cairo University.

© 1998 NRC Canada

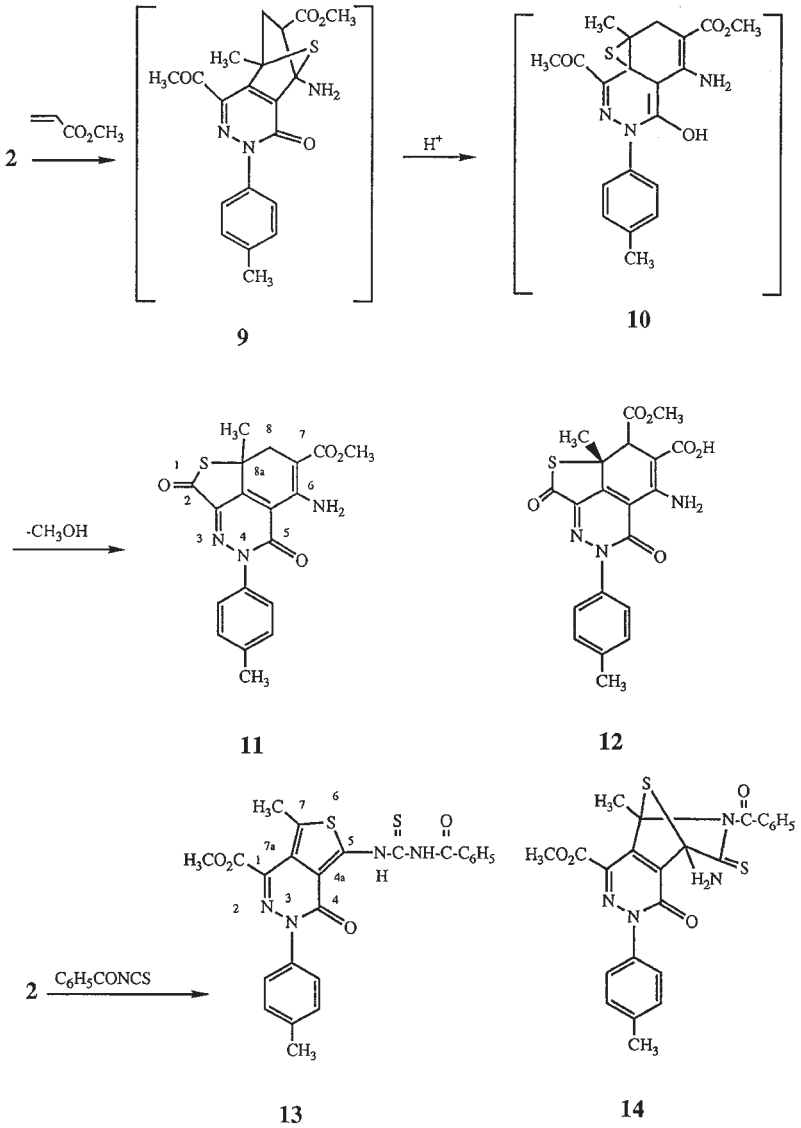

3-Aminothieno[3,4-*c*]coumarin (1)

To a solution of **3** (1.8 g, 0.01 mol) in DMF (15 mL) containing few drops of piperidine was added elemental sulfur (0.32 g, 0.01 mol). The reaction mixture was heated under reflux for 5 h, then left to cool. The resulting solution was poured on ice water and acidified with few drops of hydrochloric acid. The resulting precipitate was collected by filtration and crystallized from ethanol to give yellow plates (1.9 g, 87%), mp 195°C. IR, ν (KBr): 3400–3300 (NH_2) and 1680 cm^{-1} (C=O). ^1H NMR (DMSO), δ: 3.45 (br, 2H, NH_2), 6.9–8.15 ppm (M, 5H, Ar-H, and thiophene H). Anal. calcd. for $C_{11}H_7NO_2S$ (217): C 60.8, H 3.2, N 6.4, S 14.7; found: C 60.7, H 3.1, N 6.2, S 14.5.

4-Methylcoumarin-3-carbonitrile (3)

In a flask fitted with a Dean–Stark trap, a solution of *o*-hydroxy-acetophenone (1.36 g, 0.01 mol) in a mixture of acetic acid (10 mL) and toluene (10 mL), ammonium acetate (2 g), and malononitrile (0.66 g, 0.01 mol) was refluxed for 6 h. The solvents were evaporated in vacuo, and the remaining solid was collected and crystallized from acetic acid to give yellow needles, mp 184°C.

9-(*N*-Phenyl)-8,10-dioxoisoindolo[5,6-*c*]coumarin-7-amine (6a)

A solution of **1** (2.17 g, 0.01 mol) in a mixture of acetic acid (10 mL) and dioxane (10 mL) was treated with *N*-phenylmaleimide (1.7 g, 0.01 mol) and refluxed for 8 h. After evaporation of the solvents the solid product was collected by filtration and crystallized from dioxane to give yellow needles (3.3 g, 94%), mp > 300°C. IR, ν (KBr): 3440–3322 (NH_2), 3043 (CH aromatic), 1760–1709 (3 C=O), and 1630 cm^{-1} (C=C). ^1H NMR (DMSO), δ: 7.74–7.39 (m, 9H, Ar-H), 8.06 (s, 1H, H-11), and 8.60 ppm (br, 2H, NH_2). Anal. calcd. for $C_{21}H_{12}N_2O_4$ (356): C 70.7, H 3.3, N 7.8; found: C 70.7, H 3.2, N 7.5. Mass, *m*/*z*: 356 (M^+).

8,10-Dioxoisobenzofuro[5,6-*c*]coumarin-7-amine (6b)

A solution of **1** (2.17 g, 0.01 mol) in a mixture of acetic acid (10 mL) was treated with maleic anhydride (0.98 g, 0.01 mol) and refluxed for 3 h. The solvents were evaporated, and the solid product was washed with ethanol, collected by filtration, and crystallized from ethanol to give yellow needles (2.2 g, 78%), mp 194°C. IR, ν (KBr): 3433–3340 (NH_2), 3084 (CH aromatic), 1835–1763(3 C=O), and

© 1998 NRC Canada

1630 cm^{-1} (C=C). ^1H NMR (DMSO), δ: 7.20–7.82 (m, 4H, Ar-H), 8.00 (s, 1H, H-11), and 8.50 ppm (br, 2H, NH_2). Anal. calcd. for $C_{15}H_7NO_5$ (281): C 64.0, H 2.4, N 4.9; found: C 63.9, H 2.3, N 4.7. Mass, *m*/*z*: 281 (M^+).

Dimethyl 4-aminobenzo[c]coumarin-2,3-dicarboxylate (8)

A mixture of **1** (2.17 g, 0.01 mol) and dimethyl fumarate (1.44 g, 0.01 mol) was heated in an oil bath at 170°C for 4 h. The reaction mixture was cooled, then triturated with ethanol. The solid product, so formed, was collected by filtration and crystallized from dioxane as brown needles, (2.5 g, 76%), mp > 300°C. IR, ν (KBr): 3464–3351 (NH_2), 3095 (CH aromatic), and 1721–1608 cm^{-1} (3 C=O). ^1H NMR (300 MHz, $CDCl_3$), δ: 3.68 (3 H, s, CO_2Me), 3.74 (3H, s, CO_2Me), 6.69–7.06 (1H, dd, *J* = 8.19 and 1.15, 7-H), 7.02 (1H, s, 1-H), 7.05–7.15 (1H, ddd, *J* = 7.91, 7.69, and 1.18, 9-H), 7.27–7.36 (1H, ddd, *J* = 8.16, 7.75, and 1.47, 8-H), 7.74–7.78 (1H, dd, *J* = 8.11 and 1.41, 10-H), 9.05 (2H, br s, NH_2). Anal. calcd. for $C_{17}H_{13}NO_6$ (327): C 62.3, H 3.9, N 4.2; found: C 62.2, H 3.8, N 4.1. Mass, *m*/*z*: 327 (M^+).

Methyl 6-amino-8,8a-dihydro-2,5-dioxo-8a-methyl-4-(*p*-tolyl)-1,3,4-thiadiazaacenaphthene-7-carboxylate (11)

A solution of **2** (3.2 g, 0.01 mol) in dioxane (20 mL) and few drops of acetic acid was treated with methyl acrylate (0.86 g, 0.01 mol). The reaction mixture was refluxed for 10 h, then evaporated in vacuo. The remaining product was triturated with water, and the resulting solid product was collected by filtration and crystallized from dioxane as red needles (3 g, 79%), mp 201°C. IR, ν (KBr): 3402–3292 (NH_2), 2987 (CH_3), 1711 (C=O), 1676 (ring CO), 1675 (CO), and 1620 cm^{-1} (C=C). ^1H NMR (300 MHz, DMSO), δ: 1.82 (s, 3H, CH_3), 2.40 (s, 3H, CH_3), 2.95 and 3.16 (AB system, 2H, CH_2, JAB = 15.7 Hz), 3.70 (s, 3H, OCH_3), 7.31–7.68 (m, 4H, aromatic protons), and 8.10 ppm (br, 2H, NH_2); ^{13}C NMR, δ: 194.20 (C-2), 171.35 (C=O ester), 163.29 (C-5), 153.07 (C-2a), 146.01 (C-6), 144.22, 133.11, 131.20, 129.42 (aromatic ring), 124.35 (C-5a), 104.0 (C-7), 80.56 (C-8a), 50.91 (C-8), 54.82 (CH_3), 15.48 (CH_3). Anal. calcd. for $C_{19}H_{17}N_3O_4S$ (383): C 59.5, H 4.4, N 10.9, S 8.3; found: C 59.3, H 4.2, N 10.8, S 8.2. Mass, *m*/*z*: 383 (M^+).

Methyl 6-amino-8,8a-dihydro-2,5-dioxo-8a-methyl-4-(*p*-tolyl)-1,3,4-thiadiazaacenaphthene-7-carboxy-8-carboxylate (12)

A solution of **2** (3.2 g, 0.01 mol) in a mixture of acetic acid (10 mL) and dioxane (10 mL) was treated with maleic anhydride (0.98 g, 0.01 mol). The reaction mixture was refluxed for 10 h. The reaction mixture was evaporated, then washed with ethanol. The solid product, so formed, was collected by filtration and crystallized from ethanol–dioxane as orange needles (3 g, 71%), mp 280°C. IR, ν (KBr): 3446–3251 (NH_2), 3035 (CH aromatic), 2953 (CH_3), 1830–1731–1673 (4 C=O), and 1637 cm^{-1} (C=C). ^1H NMR (DMSO), δ: 2.40 (s, 3H, CH_3), 2.79 (s, 3H, CH_3), 3.40 (s, 3H, OCH_3), 3.98 (s, 1H, C-8), 7.3–7.7 (m, 4H, Ar-H), 8.88 (br, protons of NH_2), and 11.70 ppm (s, 1H, COOH) (the downfield shift of the amino group due to the effect of the amino acid moiety). Anal. calcd. for $C_{20}H_{17}N_3O_6S$ (427): C 56.2, H 3.9, N 9.8, S 7.4; found: C 56.0, H 3.6, N 9.5, S 7.1. Mass, *m*/*z*: 427 (M^+).

1-Benzyl-5-[7-methyl-3,4-dihydro-7-methyl-3-(*p*-tolyl)-4-oxo-thieno[3,4-*d*]pyridazin-1-carboxylate]-3-ylthiourea (13)

To a suspension of ammonium thiocyanate (0.76 g, 0.01 mol) in dry acetone (20 mL), benzoyl chloride (1.4 g, 0.01 mol) was added. The reaction mixture was refluxed for 5 min then treated with **2** (3.2 g, 0.01 mol). The reaction mixture was refluxed for 3 h, then left to cool. The resulting solution was poured onto ice water. The solid product, so formed, was collected by filtration and crystallized from dioxane as yellow needles (4.8 g, 97%), mp 270°C. IR, ν (KBr): 3350–3220 (2 NH), 2948 (CH_3), 1732 (ester CO), 1675 (2 C=O), and 1641 cm^{-1} (C=C). ^1H NMR (DMSO), δ: 2.40 (s, 3H, CH_3), 3.30 (s, 3H, CH_3), 3.98 (s, 3H, OCH_3), 7.3–7.7 (m, 9H, Ar-H), 12.10 (br, 1H, NH), and 15.20 ppm (br, 1H, NH). ^{13}C NMR, δ: 177.08 (C=O), 174.32 (C=O), 169.26 (C=S), 165.71 (ring C=O), 159.12 (C-1), 147.95 (C-5), 139.31–125.65 (phenyl ring), 121.96 (C-7), 117.38 (C-7a), 106.42 (C-4a), 54.65 (CH_3), 22.26 (CH_3), 14.92 (CH_3). Anal. calcd. for $C_{24}H_{20}N_4S_2O_4$(492): C 58.5, H 4.0, N 11.3, S 13.0; found: C 58.2, H 3.9, N 11.1, S 12.6. Mass, *m*/*z*: 492(M^+).

References

1. A.G. Gilman and L.S. Goodman. The pharmaceutical basis of therapeutics. Macmillan, New York. 1985. p. 1109.
2. J.M. Domagala and P. Peterson. J. Heterocycl. Chem. **26**, 1147 (1989), and refs. cited therein.
3 W.F. von Oettingen. The therapeutic agents of the quinoline group. Chemical Catalog Co., New York. 1933.
4. R.B. Woodward and W.E. Doering. J. Am. Chem. Soc. **67**, 860 (1945).
5. E. Hahn. *In* Lectures in heterocyclic chemistry IX. *Edited by* R.N. Castle. 1990. p. 13.
6. F. Fanger, S. Nicklen, and A.R. Coulson. Proc. Natl. Acad. Sci. U.S.A. **74**, 5463 (1977).
7. M.H. Elnagdi, M.R.H. Elmoghayar, and G.E.H. Elgemeie. Chemistry of pyrazolopyrimidines. *In* Advances in heterocyclic chemistry. Vol. 41. *Edited by* A.R. Katritzky. Academic Press, New York. 1987. p. 319.
8. M.H. Elnagdi, N.S. Ibrahim, F.M. Abdelrazek, and A.W. Erian. Liebigs Ann. Chem. 909 (1988).
9. M.H. Elnagdi and K.U. Sadek. Synthesis, 483 (1988).
10. R. Gaertner and R.G. Tonkyn. J. Am. Chem. Soc. **73**, 5872 (1951).
11. D.B. Clapp. J. Am. Chem. Soc. **61**, 2733 (1939).
12. H. Kotsuki, S. Kitagawa, H. Nishizawa, and T. Tokoroyama. J. Org. Chem. **43**, 1471 (1978).
13. J.M. Barker, P.R. Huddleston, and S.W. Shutler. J. Chem. Soc. Perkin Trans. 1, 2483 (1975).
14. J.P. Chupp. J. Heterocycl. Chem. **7**, 285 (1970).
15. M.H. Elnagdi, A.M. Negm, and K.U. Sadek. Synlett, 27 (1994).
16. M.H. Elnagdi, R.M. Mohareb, F.A. Abdel Aal, and H.A. Mohamed. Phosphorus and sulfur. **82**, 195 (1993).
17. E. Nyiondi-Bonguen, F.E. Sopbue, F.Z. Tanee, and D. Dopp. J. Chem. Soc. Perkin Trans. 1, 2191 (1994).

© 1998 NRC Canada

On the influence of secondary structure on the α-C—H bond dissociation energy of proline residues in proteins: a theoretical study

D.A. Block, D. Yu, D.A. Armstrong, and A. Rauk

Abstract: Ab initio computations (B3LYP/6-31G(D), coupled with isodesmic reactions) were used to predict $^{\alpha}$C—H bond dissociation energies (BDEs) for proline as a residue in a model peptide, intended to mimic the environment in proteins. The environment was further constrained to mimic common proline positions in β turns of different types. The BDEs were found to be very dependent on the structural constraints imposed by the β turn type, implying different structure-mediated susceptibilities to free radical damage to proline residues. Unnatural repair of proline (inversion of chirality) was found to be thermodynamically unfavourable. The predicted BDEs for the proline $^{\alpha}$C—H bond, in kJ mol^{-1}, to an estimated accuracy of ±10 kJ mol^{-1} are as follows: fully optimized *trans* rotamer, 368.6; fully optimized *cis* rotamer, 357.7; β turn type I, 380.7; β turn type II, 397.8; β turn type II′, 385.4; β turn type VIa, 374.0; β turn type VIb, 355.0.

Key words: proline, β-turns, free radical, bond dissociation energy, molecular structure, oxidative damage.

Résumé : On a utilisé des calculs ab initio (B3LYP/6-31G(D) couplés à des réactions isodesmiques) pour prédire les énergies de dissociations des liaisons (EDL) $^{\alpha}$C—H de la proline comme résidu d'un modèle de proline qui devrait servir de modèle pour l'environnement des protéines. On a restreint encore plus l'environnement de façon à reproduire les positions habituelles de la proline dans divers types d'orientations β. On a trouvé que les EDL dépendent fortement des contraintes structurales imposées par le type d'orientation β; ceci implique que, suivant leur structure, les résidus prolines ont des susceptibilités différentes aux dommages causés par les radicaux libres. On a trouvé que les réparations non naturelles de la proline (inversion de chiralité) sont thermodynamiquement défavorisées. Les EDL de la liaison $^{\alpha}$C—H de la proline (en kJ mol^{-1}, à une précision évaluée à ±10 kJ mol^{-1}) sont les suivantes : rotamère *trans* complètement optimisé, 368,6; rotamère *cis* complètement optimisé, 357,7; orientation β de type I, 380,7; orientation β de type II, 397,8; orientation β de type II', 385,4; orientation β de type VIa, 374,0; orientation β de type VIb, 355,0.

Mots clés : proline, orientations β, énergie de dissociation des liaisons, structure moléculaire, dommage oxidatif.

[Traduit par la Rédaction]

Introduction

Oxidative damage to proteins is an everyday event, and inadequate cellular response to oxidative stress can lead to disease states. Proteins damaged by oxidation are normally marked for degradation, but buildup of such proteins has been shown to be a mark of aging (1). Oxidative damage to proteins has also been implicated in various disorders, including inflammatory diseases, atherosclerosis, ischemia–reperfusion tissue damage, and various neurologic disorders (1, 2). The damage to proteins is a poorly understood process, both in its mechanism and in its selectivity. It often occurs on the side chains of amino acids in the protein, but it can also occur by the removal of the hydrogen on the α-carbon of amino acids. The strength of the $^{\alpha}$C—H bond will be influenced by the chemical nature of the side chains of the amino acids.

Proline (**1**) is a unique amino acid because it contains a five-membered ring on the peptide backbone (see Fig. 1). The presence of the ring creates a tertiary amide as opposed to the secondary amides in the other amino acids. This means that there is no proton on the amide nitrogen to form hydrogen bonds. It constrains the Ramachandran Φ dihedral angle in proline peptides to around 60°, where in other amino acids there is much more flexibility. Whereas the peptide linkage of all other amino acid residues has the *trans* relationship between the $^{\alpha}$C centres (3), the proline ring allows the *cis* rotamer to exist as perhaps 10% of the population of proline residues in nature (see eq. [1]).

[1]

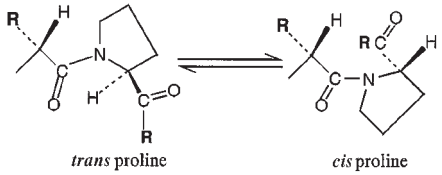

The above properties lead to proline's unique role in protein structure. Proline is the preferred residue at the second of

Received April 16, 1998.

D.A. Block, D. Yu, D.A. Armstrong,[1] and A. Rauk.[1]
Department of Chemistry, University of Calgary, Calgary, AB T2N 1N4, Canada.

[1]Authors to whom correspondence may be addressed.
Telephone: (403) 220-6247. Fax: (403) 289-9488. E-mail: rauk@acs.ucalgary.ca

© 1998 NRC Canada

Fig. 1. The 3-dimensional structure of proline, **1**. Small white circles represent hydrogen atoms, larger white circles represent carbon atoms, gray circles represent nitrogen atoms, and black circles represent oxygen atoms.

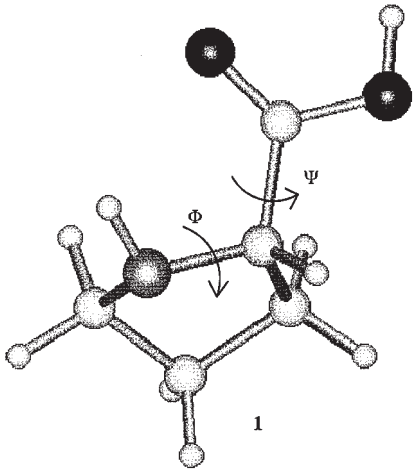

1

four positions in β turns of type I, II, and III (4). It is also the preferred residue at the third of four positions in a β turn of type II′ (5). The *cis* rotamer is the third of four residues by definition in type VI turns (5). Proline is also common on the first turn of an α-helix, and is also seen just following the end of the helix. It is commonly found on the outside edge of β sheets, and is the cause of β bulges in the interior of β sheets (5). It is a crucial structural member of collagen, in which it is on the outside of a unique triple helical structure.

These properties make proline, although a hydrophobic residue, usually the most exposed residue in proteins (3). Its position in β turns, on the edge of sheets, at the beginning of helices, and just following both helices and sheets, leaves it exposed to solvent and the environment. β turns, in particular, have been postulated to be important in molecular recognition because they are almost exclusively on the exterior of globular proteins, and they are highly conserved (3, 6).

Proline has been found to be sensitive to oxidation, both by radiolysis (7) and in metal- catalyzed systems (8). The hydroxyl radical can produce hydroxyproline, or it can abstract the $^{\alpha}$C hydrogen, leaving a neutral radical. This radical can spontaneously cleave the peptide backbone (see Scheme 1*a*) (7), or it can be further attacked by O_2, also resulting in peptide cleavage (Scheme 1*b*) (9). Radiolysis can result in the cleavage of the C—N bond, leading to unnatural flexibility in the peptide backbone, and possibly further radical damage within the protein (Scheme 1*c*) (9). All of these results are expected to occur in vivo.

The combination of a crucial role in protein structure, general exposure of proline to the environment, and a C—H bond that is easily oxidized leads to the importance of this study. We continue the work done earlier on the bond dissociation energies (BDEs) of the $^{\alpha}$C—H bond of peptide models of the amino acids (10–14). The BDE of the $^{\alpha}$C—H bond of a proline peptide model, $D_{\alpha CH}$ (pro), has been calculated, as well as the equivalent BDEs for a number of constrained systems, simulating the constraints placed on the proline residue in various secondary structural environments.

Computation

The minimum energy structure and constrained minima were calculated at the 6-31G(D) level of theory, using the B3LYP hybrid HF-DFT procedure as implemented in the Gaussian 94 suite of programs (15), with the keyword INT = FINEGRID. Preliminary minimizations were performed at the AM1 semiempirical level using the Spartan (16) program.

The $^{\alpha}$C—H bond dissociation energies (BDEs), $D_{\alpha CH}$, are defined as the heat of reaction [2], $\Delta H^{\circ}_{(2)}$:

[2] 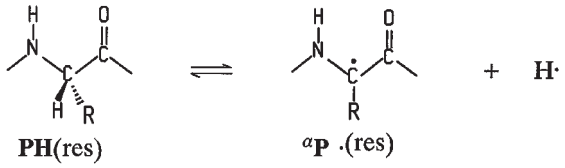

where **PH**(res) represents a mid-chain amino acid residue of a polypeptide chain, and $^{\alpha}$**P**$^{\bullet}$(res) the corresponding α-carbon centred radical.

In the present case, as a means of reducing residual errors due to basis set and correlation effects, they were derived from the heats of isodesmic reactions (10). These reactions can be represented by eq. [3]:

[3] $^{\alpha}\mathbf{P}^{\bullet}(\text{res}) + \text{AH} \leftrightarrow \mathbf{PH}(\text{res}) + \text{A}^{\bullet}$

AH is a reference molecule for which the BDE, D_{CH}(AH), is known accurately. For each **PH**(res) the heat of reaction (3), $\Delta H^{\circ}_{(3)}$, was evaluated from the energies obtained in the ab initio calculations at the B3LYP/6-31G(D) level, which was shown to give reliable results for the glycine model peptides (11). In the context of BDEs, D_{CH}(**PH**) is then given by

[4] $$D_{CH}(\mathbf{PH}) = D_{CH}(\text{AH}) - \Delta H^{\circ}_{(3)}$$

To obtain the most effective cancellation of residual errors, the structures of the reference molecule and radical used in reaction [3] should be related as closely as possible to those of **PH**(res) and $^{\alpha}$**P**$^{\bullet}$(res), respectively. Ideally AH should have both an adjacent amino group and a carbonyl group so that the special feature of the captodative effect can be taken into account. Previous studies have shown (11, 17) that H_2NCH_2COOH (glycine) is the most suitable reference molecule to give reliable values of $D_{\alpha CH}$. The magnitude of $D_{\alpha CH}$ for glycine itself (331.0 kJ mol^{-1}) (12), was not directly available from experiment. However, it has been derived from a number of isodesmic reactions with heats of reaction based on G2(MP2) calculations (12).

Frequency calculations were not undertaken in this study, as the presence of constraints in nearly every structure leads to imaginary frequencies and difficulty in calculating the zero point energy. Fortuitously, the zero point energies and thermal corrections ($H^{\circ}_{298} - H^{\circ}_{0}$) approximately cancel each other out, as seen in this group's previous work (10). The error introduced by not adding the zero point energy and the thermal correction is estimated to be less than 2 kJ mol^{-1}, whereas the estimated error in the BDEs calculated by the isodesmic reaction procedure is approximately ±10 kJ mol^{-1}. This cancellation, and the approximations involved in doing frequency analysis of constrained systems, led us to decide

© 1998 NRC Canada

Scheme 1.

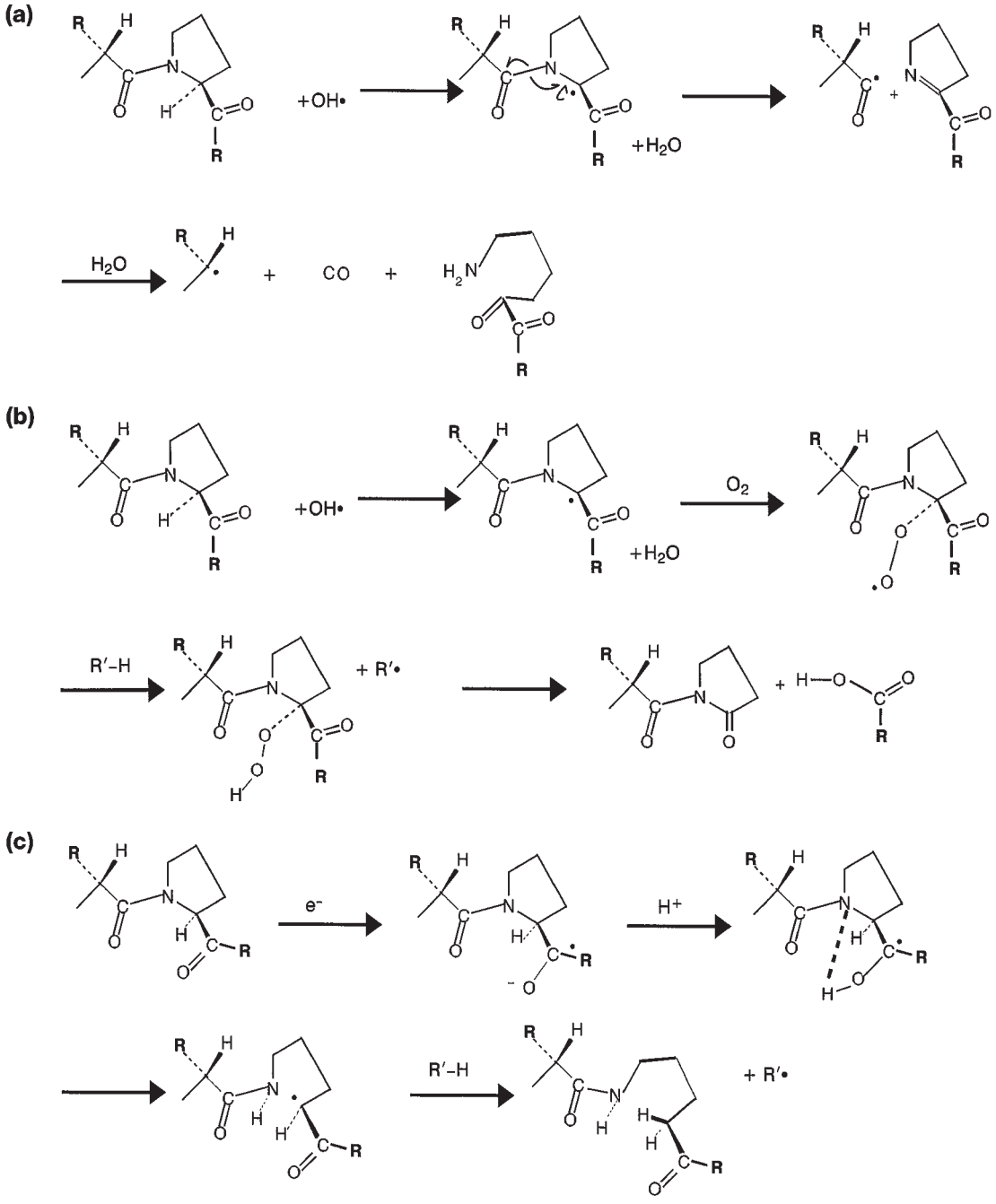

that frequency calculations were not justified. The structures presented are all converged geometries according to the default convergence criteria of Gaussian 94 (15).

In previous studies of $^{\alpha}$C—H BDEs, an *N*-formyl amino acid amide was adopted as the model of the mid-chain residue (10, 11). In this model, the next $^{\alpha}$C site is replaced by the formyl hydrogen atom. It was shown that use of *N*-acetyl glycine amine rather than the *N*-formyl analogue resulted in only a 3 kJ mol^{-1} difference in the calculated $^{\alpha}$C—H BDE (11). However, the higher steric requirements imposed by the five-membered ring of proline, particularly for the *cis* rotamer, dictated the use of the larger *N*-acetyl proline amide (**2, 3)** (see Fig. 2) as the peptide model for the present work since the steric requirements of the next $^{\alpha}$C site are better modelled by a methyl group than by a hydrogen atom. The *N*-formyl proline amide model **(4)** will be briefly touched upon in the discussion.

Constrained geometries

It has been estimated that one third of amino acid residues in globular proteins are involved in turns (5). As noted earlier, proline is frequently found in turns, the most common of which is the β turn (**5**), which allows the reversal of direction of the peptide chain within four residues (see Fig. 3). The convention is to number the residues relative to the first one, calling the first *i*, the second *i*+1, etc. The β turns have

© 1998 NRC Canada

Fig. 2. The *N*-acetyl proline peptide model, **2** (*trans*) and **3** (*cis*). The methyl group of the *N*-acetyl models the α-carbon of the next amino acid in the chain. Small white circles represent hydrogen atoms, larger white circles represent carbon atoms, gray circles represent nitrogen atoms, and black circles represent oxygen atoms.

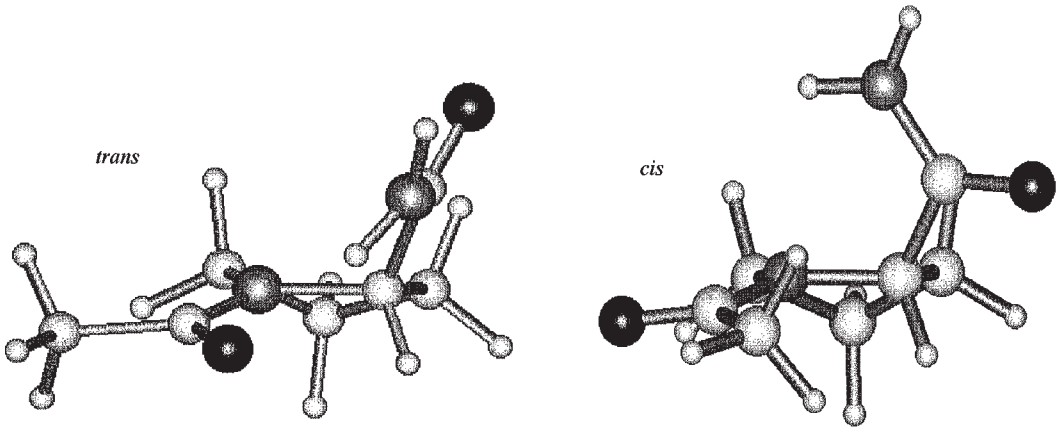

Fig. 3. A tetrapeptide *(gly-pro-gly-gly),* **5,** showing a type II β turn.

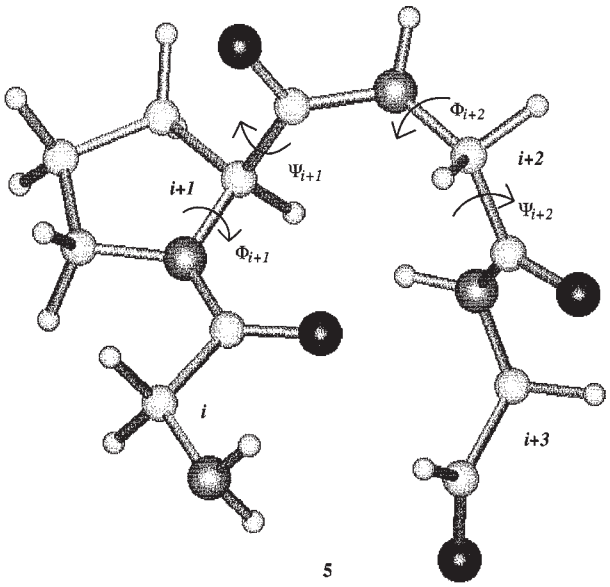

Table 1. β Turn *types.*[a]

	Position *i+1*		Position *i+2*	
β Turn type	Φ_{i+1} (°)	Ψ_{i+1} (°)	Φ_{i+2} (°)	Ψ_{i+2} (°)
I	*–60	*–30	–90	0
I′	60	30	90	0
II	*–60	*120	80	0
II′	60	–120	*–80	*0
VIa	–60	120	*–90	*0
VIb	–120	120	*–60	*0

[a] For a visual depiction of the locations of the dihedral angles, see Fig. 3 (* indicates common proline positions).

Table 2. Proline conformations optimized in this study.[a]

Structure label	β Turn type	Position	Rotamer	Φ (°)	Ψ (°)
6	I	*i+1*	trans	–60	–30
7	II	*i+1*	trans	–60	120
8	II′	*i+2*	trans	–80	0
9	VIa	*i+2*	cis	–90	0
10	VIb	*i+2*	cis	–60	0

[a] For a visual depiction of the locations of the dihedral angles, see Fig. 3.

been classified in terms of the Φ and Ψ angles of the *i*+1 and *i*+2 residues. The major types are summarized, with asterisks indicating common proline positions, in Table 1 (4).

Type I and II turns contain proline most often in the *i*+1 position. It can be noted that type III turns are identical to type I turns at the *i*+1 position (5), where proline is the most common residue (4). Proline is the most common residue at the *i*+2 position of type II′ β turns (5), where the prime indicates a mirror image of the unprimed β turn types in terms of the Ramachandran dihedral angles Φ and Ψ of the peptides in the *i*+1 and *i*+2 positions. Both types VIa and VIb are defined as having a *cis* proline residue in the *i*+2 position (5).

Proline residues in the first turn of an α-helix will have structural constraints very similar to type II′ β turns (3). Prolines are proportionately rare in β sheets due to their lack of an N-H for hydrogen bonding (3); typical Ψ values in β sheets are not favorable for the five-membered ring of proline.

Collagens form the most common protein type by mass in the vertebrate body. They are made up primarily of repeats of the three peptides (Gly-X-Y) where X and Y are predominantly proline or lysine. The proline and lysine residues may or may not be oxidatively modified by the addition of a hydroxyl group to one of the side-chain carbons. The rigidity of proline (and hydroxyproline) is crucial in stabilizing the unique left-handed helical structure of collagen. Because three strands wind together, the small glycine unit is needed in the middle of the braid. This forces proline in collagen to be exposed to the solvent (18).

Proline's conformation in collagen is very similar to proline in residue *i*+1 in a type II β turn, with Φ and Ψ angles of about –60° and +160°, respectively (19), as compared with –60° and +120° for a type II turn. The energetics of radical damage to collagen at the proline α-centre is modelled adequately by our β turn type II model. Damage to

© 1998 NRC Canada

Table 3. Calculated energies and BDEs of various proline model conformations.

Structure label	Molecule description	Energy (hartrees)	Bond dissociation energy (kJ mol^{-1})
	Glycine	–284.423 45[a]	
	Glycine radical	–283.790 39[a]	**331.0**[a]
2	Proline model *trans*	–533.959 38	**368.6**
2rad	Proline model *trans* radical	–533.312 01	
3	Proline model *cis*	–533.952 19	**357.7**
3rad	Proline model *cis* radical	–533.308 96	
6	Proline model β turn type I	–533.951 08	**380.7**
6rad	Proline model β turn type I radical	–533.299 11	
6R	Proline model β turn type I *R* isomer	–533.934 13	336.2
7	Proline model β turn type II	–533.954 93	**397.8**
7rad	Proline model β turn type II radical	–533.296 41	
7R	Proline model β turn type II *R* isomer	–533.932 34	338.5
8	Proline model β turn type II′	–533.953 47	**385.4**
8rad	Proline model β turn type II′ radical	–533.299 67	
8R	Proline model β turn type II′ *R* isomer	–533.924 13	308.4
9	Proline model β turn type VIa	–533.951 53	**374.0**
9rad	Proline model β turn type VIa radical	–533.302 10	
9R	Proline model β turn type VIa *R* isomer	–533.916 76	282.7
10	Proline model β turn type VIb	–533.948 69	**355.0**
10rad	Proline model β turn type VIb radical	–533.306 46	
10R	Proline model β turn type VIb *R* isomer	–533.923 28	288.3

[a]Data from ref. 11.

proline at this site can be expected to lead to cleavage of the peptide bond (7) (see Scheme 1*b*).

In this study, proline was constrained in geometries corresponding to β turns of type I, II, II′, VIa, and VIb (Table 2). Proline was assumed to be the $i+1$ residue for turn types I and II, and the $i+2$ residue for types II′, VIa, and VIb. In types VIa and VIb, the proline model was constrained to be a *cis* residue.

For each natural constraint the minimum energy geometry was calculated. The α-radical was created by removing the hydrogen attached to the α-carbon. This structure was then optimized as well, maintaining the existing constraints on the Ramachandran angles. The radical $^{\alpha}$C centre thus created was nearly planar and sp^2-hybridized. A hydrogen atom was then added to the opposite side of the α-carbon to create the unnatural *R* isomer of proline. This was also optimized, while maintaining the constraints on the system. This procedure allows the examination of the thermodynamics of unnatural repair of an amino acid radical in the peptide backbone.

Results

The results of our calculations are shown in Table 3. The corresponding structures of the natural (*S*) isomers, the unnatural (*R*) isomers, and the radicals are shown in Fig. 4. All represent minimum energy geometries subject only to secondary structural constraints (on Φ and Ψ). All Φ and Ψ angle measurements are indicated. The bond dissociation energies were calculated using the isodesmic reaction described above, with glycine and the glycine α-radical as the known components of the reaction, and the value of glycine's BDE taken as 331.0 kJ mol^{-1} (10).

Discussion

Stabilizing β turns is the most significant role for proline in protein secondary structure. Damage to the proline α-carbon can result in peptide bond scission, modification into glutamic acid, or formation of other carbonyl-containing derivatives. Any of these results could lead to the loss of local secondary structure about the proline residue, and perhaps loss of tertiary structure as well. The oxidation of proline would thus initiate a cascade of events that may lead to pathological processes (7, 8, 20). The most common pathway for the oxidation of amino acids generally is the abstraction of the hydrogen from the α-carbon by a hydroxy radical (9). Understanding the impact of the structural environment on the strength of the $^{\alpha}$C—H bond is important in order to predict the likelihood of oxidative damage to proline.

$^{\alpha}$C—H bonds

The BDE of the $^{\alpha}$C—H bond in fully optimized *trans*- and *cis*-proline residues (**2**, 368.6 kJ mol^{-1}, and **3**, 357.7 kJ mol^{-1}, respectively, Fig. 4*a* and Table 3, column four) are higher than the corresponding bonds of glycine (348 kJ mol^{-1}), alanine (344 kJ mol^{-1}), serine (348 kJ mol^{-1}), threonine (356 kJ mol^{-1}) (10), or any of the other residues studied thus far (21). This is because structural requirements of the five-membered ring result in increased steric repulsion from the groups of neighbouring residues and the $^{\alpha}$C-centered radical cannot achieve the planar geometry required for maximum captodative stabilization. That this is the case is dramatically illustrated in the *N*-formyl model (**4**) in which the next α-carbon is replaced by a hydrogen atom. There the $^{\alpha}$C-centered radical is able to achieve a planar geometry and the BDE is calculated to be 321 kJ mol^{-1}. The additional

© 1998 NRC Canada

Fig. 4. B3LYP/6-31G(D)-optimized structures of the parent molecule, the $^{\alpha}$C-radical, and the unnatural (R) isomer of the proline conformers in Table 3. The view selected is edge-on to the proline's five-membered ring, which allows one to see the variations in the orientations of the backbone amide groups with respect to changes in the $^{\alpha}$C—H bond. Also shown is the *N*-formyl *cis* unconstrained conformer and its $^{\alpha}$C-radical.

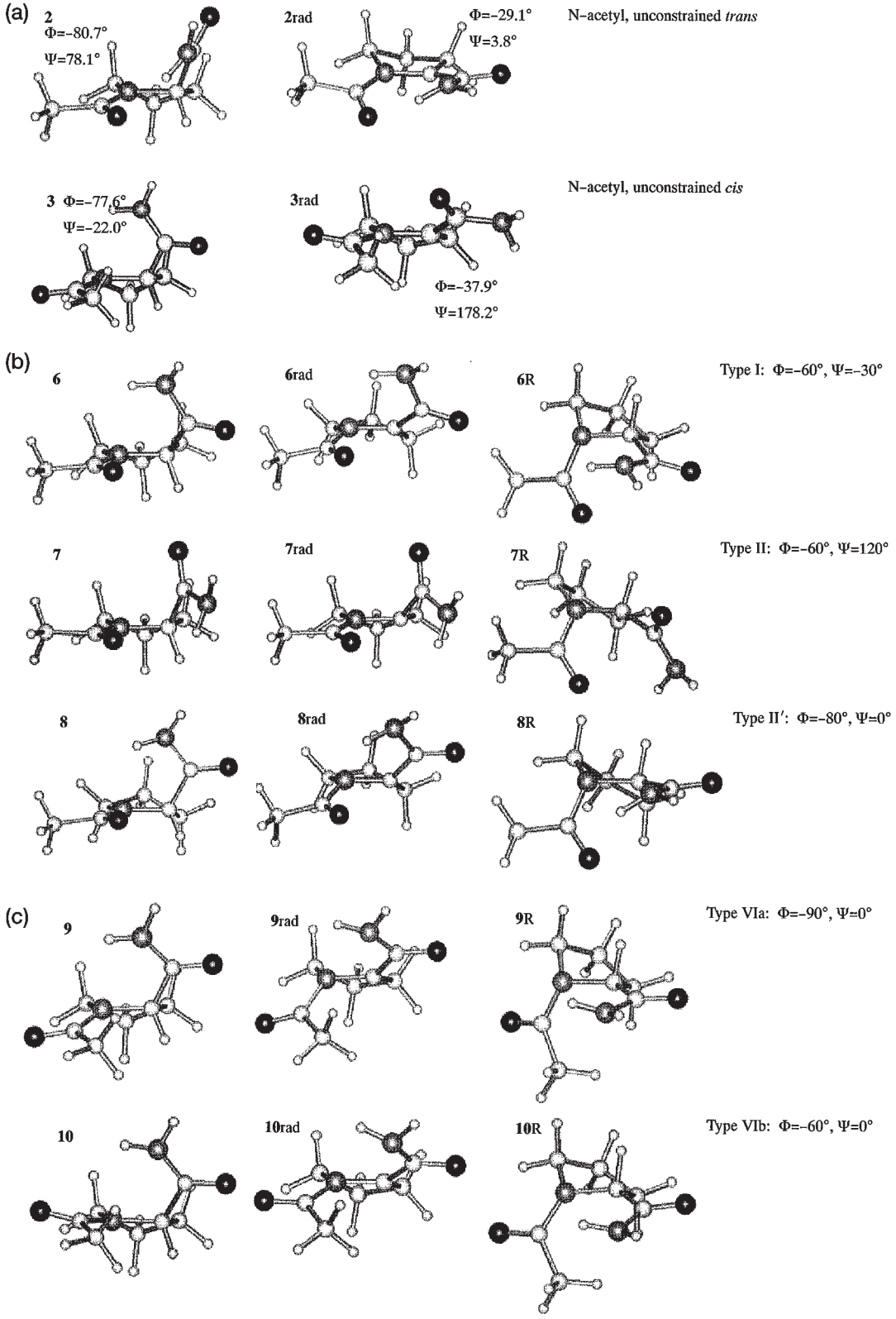

© 1998 NRC Canada

steric hindrance manifests itself primarily in the parent system — the optimized *trans* conformer **2** is 18.9 kJ mol^{-1} more stable than the *cis* conformer **3**, while the difference in the respective radicals is 8.0 kJ mol^{-1}.

The high $^{\alpha}$C—H BDEs are significant because they are close to the BDE of an alkyl sulfhydryl bond, 370 kJ mol^{-1}, as occurs in cysteine, cysteine residues (22), or glutathione (GSH) (23). $^{\alpha}$C—H bonds that are weaker than 370 kJ mol^{-1} are liable to be damaged by thiyl radicals, such as GS$^{\bullet}$, or conversely, the corresponding $^{\alpha}$C-centered radicals would not be repairable by, for example, GSH.

The constraints imposed by secondary structure on this system prevent any of the α-carbon radicals from achieving planarity, and cause a concomitant rise in BDE. Other than β turn type VIb (**10**), all of the constrained systems have BDEs higher than 370 kJ mol^{-1}. This indicates that the sulfur radical of glutathione, GS$^{\bullet}$, is not able to abstract hydrogens from the α-carbon of proline, and glutathione would be able to repair damage at this site. Given proline's position at the "hinge" of turns, the loss of a proline residue's $^{\alpha}$C—H bond may be expected to result in the destruction of the protein's tertiary structure and therefore its function. The high $^{\alpha}$C—H BDEs confer some protection against weaker oxidizing species such as thiyl radicals, ROO$^{\bullet}$, or superoxide ($O_2^{\bullet-}$).

The $^{\alpha}$C—H BDE of proline residues in the type II β turn (**7**) is higher than the corresponding BDE of proline in type I turns (**6**). The natural type II conformation is lower in energy, and the type II radical higher in energy, than the type I equivalents. The difference is in the rotation of the C-terminal amide group: the type II conformation does not allow the α-carbon radical to link its π orbitals with those of the amide system, which are perpendicular to it. The type I system allows some limited mixing of the π systems, which accounts for the lower BDE.

The BDE of proline residues in type II′ turns (**8**) is similar to that of residues in type I turns. This is to be expected, as their structures differ by only 20° and 30° at the Φ and Ψ angles, respectively. The molecule's attempt at planarity is blocked by the angle constraints, but the α-carbon and the nitrogen are each individually almost planar. Because proline residues in the first turn of an α-helix will have similar structural constraints, these results can be also applied to proline in that environment. Proline residues in an α-helix are thus protected against GS$^{\bullet}$ attack.

Turn types VIa (**9**) and VIb (**10**) are similar, and have similar BDEs for proline residues. Type VIb (**10**) has, as mentioned previously, the weakest $^{\alpha}$C—H bond among the constrained systems. It appears that the α-carbon is able to achieve planarity in these systems, at the expense of the planarity of the neighbouring nitrogen. This means that the amide system including the proline nitrogen is unable to delocalize electrons, but the amide system on the other side is able to delocalize electrons all the way to the radical centre. This strategy appears to be the most successful in stabilizing the radical.

It is evident from Table 3 that the BDEs of the unnatural *(R)* isomers are much lower than those of the natural *(S)* isomers. Loss of the hydrogen from the *(S)* isomer does not induce much change in conformation outside of the α-carbon. Addition of a hydrogen to the radical on the pro-*R* face of the α-carbon forces the proline ring to pucker the opposite way, leading to a higher energy conformation. Thermodynamics will thus favor formation of the natural (*S*) isomers, when prolyl radical residues are repaired by hydrogen transfer agents such as glutathione.

C—H bonds of the proline ring

We have not explicitly examined the BDEs of the remaining six C—H bonds of the proline ring. The two C—H bonds that are adjacent to the N atom will have BDEs similar to the corresponding bonds in pyrrolidone, 377 kJ mol^{-1} (24). The remaining four C—H bonds should have BDEs similar to those of cyclopentane, 398 ± 5 kJ mol^{-1} (25). Thus C—H BDEs of the methylene groups of proline are higher than the $^{\alpha}$C—H BDE of unconstrained proline, similar to the highest $^{\alpha}$C—H BDEs among the proline β-turn conformations, and substantially higher than the parent BDEs of the weaker oxidizing radicals, ROO$^{\bullet}$ and RS$^{\bullet}$.

Enzyme-controlled oxidation of the 3- and 4-carbon of the five-membered ring occurs only in collagen and collagen-like proteins. Prolyl 4-hydroxylase selectively and stereospecifically hydroxylates the inactivated carbon β to the nitrogen on the pyrrole ring. The peptide must contain an X-Pro-Gly triplet for the hydroxylation to proceed. The reaction consumes one O_2 and one 2-oxoglutarate, and occurs at an active site containing an Fe^{2+} atom. Prolyl 3-hydroxylase uses a similar active site and set of cosubstrates, but requires a Pro-4-hydroxyproline-Gly triplet. The purpose of 3-hydroxyproline is unknown, but the hydroxyl group of 4-hydroxyproline is important in hydrogen-bonding to other peptide residues in the formation of the unique collagen triple helix (26).

Ascorbate is required to regenerate the Fe^{2+} after an uncoupled decarboxylation of the 2-oxoglutarate. Without ascorbic acid (Vitamin C), the enzyme will decarboxylate a 2-oxoglutarate molecule and be deactivated, leading to collagen without hydroxyproline. This reduces the strength of the collagen helices, leading to scurvy (the breakdown of the body's connective tissues) (26).

Significance for oxidative damage

The most striking result from the present work is that the $^{\alpha}$C—H BDEs of all the natural proline residues in Table 3 are appreciably larger than those of glycine and the residues of the other common amino acids thus far examined. While they are much lower than the O—H BDE of water (499 ± 1 kJ mol^{-1} (25)), and thus still susceptible to oxidative damage by the exothermic hydrogen abstraction reaction, eq. [5],

$$[5] \qquad \mathbf{PH}(\text{res}) + OH^{\bullet} \leftrightarrows {}^{\alpha}\mathbf{P}^{\bullet}(\text{res}) + H_2O$$

the proline $^{\alpha}$C-centres will not be preferred sites of attack by OH$^{\bullet}$; they are less exposed than the C—H bonds on the ring. Nor will they be susceptible to oxidative damage by the weaker oxidants like peroxy (ROO$^{\bullet}$) and thiyl (RS$^{\bullet}$) radicals, which may be present in cellular systems and whose parent precursors have BDEs near 370 kJ mol^{-1} (23, 27). At the same time, the repair reaction, eq. [6],

$$[6] \qquad {}^{\alpha}\mathbf{P}^{\bullet}(\text{res}) + GSH \leftrightarrows \mathbf{PH}(\text{res}) + GS^{\bullet}$$

© 1998 NRC Canada

would be exothermic and they should be repairable by the natural protector glutathione, GSH, which has a BDE of ~370 kJ mol^{-1} (23). As noted above, this repair will give preference to the natural isomer. The only radical potentially not repairable by GSH is the proline β turn type VIb, **10**, which has a relatively low BDE (355 kJ mol^{-1}) near to that of the glycine residue.

Inspection of the β-turn conformation (Fig. 3) indicates that the ring carbons are more exposed to solvent than the α-carbon. The comparable C—H BDEs of the ring carbons indicate that accidental oxidation of these C—H bonds is perhaps more likely than attack at the $^{\alpha}$C—H bond, given the structural constraints of the protein environment. Accidental oxidation of these bonds will create a C-centred radical that could abstract a hydrogen from a nearby carbon, propagating damage into the peptide backbone or onto another amino acid side chain. However, oxidation of the ring carbon is itself not likely to be damaging to a protein's secondary or tertiary structure, or its function.

Conclusions

Proline is vulnerable to oxidative damage at the $^{\alpha}$C—H bond when it is unconstrained; rigid constraints, such as would exist in nature, serve to protect the bond from damage. The degree of planarity at the radical centre seems to be a good visual indicator of the stabilization of the radical; better stabilization indicates a lower BDE and a weaker $^{\alpha}$C—H bond. Proline residues in β turns of type VIb are expected to have sufficiently weak $^{\alpha}$C—H bonds to allow attack by weaker oxidizing agents, like $ROO^{\bullet}$ and thiyl radicals, whereas other turn types should protect the $^{\alpha}$C—H bond from all but the strongest oxidizers.

Damage to the $^{\alpha}$C—H bond of proline may be expected to lead to the degradation of the parent protein. This is a common event for many proteins, but may lead to pathological states if the damaged protein is not removed and replaced quickly. Thus pathology will result if damage occurs in structural proteins such as collagen, which have a high proline content. This long-lasting damage can be seen, for example, in the breakdown of the vitreous humour of the eye during aging (28).

This work extends our investigation of the BDEs of the amino acids in proteins (10–12), both unconstrained and in specific secondary structural environments. These calculations support earlier experimental work (7, 8, 20, 29) and will be crucial in the goal of predicting the site specificity of oxidative damage to proteins.

Acknowledgements

The financial support of the Natural Sciences and Engineering Research Council of Canada and the University of Calgary is gratefully acknowledged.

References

1. E.R. Stadman and C.N. Oliver. J. Biol. Chem. **266**, 2005 (1991).
2. E.R. Stadman. Annu. Rev. Biochem. **62**, 797 (1993).
3. M.W. MacArthur and J.M. Thornton, J. Mol. Biol. **218**, 397 (1991).
4. C.M. Wilmot and J.M. Thornton, J. Mol. Biol. **203**, 221 (1988).
5. J.S. Richardson. Adv. Protein Chem. **34**, 116 (1981).
6. G.D. Rose, L.M. Gierasch, and J.A. Smith. Adv. Protein Chem. **37**, 1 (1985).
7. K. Uchida, Y. Kato, and S. Kawakishi. Biochem. Biophys. Res. Commun. **169**, 265 (1990).
8. A. Amici, R.L. Levine, L. Tsai, and E.R. Stadman. J. Biol. Chem. **264**, 3341 (1989).
9. V.A. Sharpatyi. High Energy Chem. **29**, 2 (1995).
10. A.Rauk, D. Yu, and D.A. Armstrong. J. Am. Chem. Soc. **119**, 208 (1997).
11. D.A. Armstrong, A. Rauk, and D. Yu. Can. J. Chem. **74**, 1192 (1996).
12. D. Yu, A. Rauk, and D.A. Armstrong. J. Am. Chem. Soc. **117**, 1789 (1995).
13. D.A. Armstrong, A. Rauk, and D. Yu. J. Chem. Soc. Perkin Trans. 2, 553 (1995).
14. D. Yu, D.A. Armstrong, and A. Rauk. Can. J. Chem. **70**, 1762 (1992).
15. M.J. Frisch, G.W. Trucks, H.B. Schlegel, P.M.W. Gill, B.G. Johnson, M.A. Robb, J.R. Cheeseman, T. Keith, G.A. Petersson, J.A. Montgomery, K. Raghavachari, M.A. Al-Laham, V.G. Zakrzewski, J.V. Ortiz, J.B. Foresman, J. Cioslowski, B.B. Stefanov, A. Nanayakkara, M. Challacombe, C.Y. Peng, P.Y. Ayala, W. Chen, M.W. Wong, J.L. Andres, E.S. Replogle, R. Gomperts, R.L. Martin, D.J. Fox, J.S. Binkley, D.J. Defrees, J. Baker, J.P. Stewart, M. Head-Gordon, C. Gonzalez, and J.A. Pople. Gaussian 94, Revision D.2. Gaussian, Inc., Pittsburg, Pa. 1995.
16. PC Spartan v. 1.1. Wavefunction, Inc., Irving, Calif. 1996.
17. M. Jonsson, D.D.M. Wayner, D.A. Armstrong, D. Yu, and A. Rauk. J. Chem. Soc. Perkin Trans. 2, 1967 (1998).
18. S.L. Wolfe, Molecular and Cellular Biology. Wadsworth, Belmont, Calif. 1993. p. 274.
19. A.L. Lehninger, D.L. Nelson, and M.M. Cox. Principles of biochemistry. 2nd ed. Worth, New York. 1993. p. 171.
20. J.M. Creeth, B. Cooper, A.S.R. Donald, and J.R. Clamp. Biochem. J. **211**, 323 (1983).
21. D. Yu, A. Rauk, G.V. Shustov, D.A. Block, and D.A. Armstrong. Results communicated at Fifth North American Chemical Congress, Cancun, Mexico, November 11–15, 1997. To be published
22. A. Rauk, D. Yu, and D.A. Armstrong. J. Am. Chem. Soc. **129**, 8842 (1998).
23. D. Griller, J.A.M. Simoes, and D.D.M. Wayner. *In* Sulfur-centered reactive intermediates in chemistry and biology. *Edited by* C. Chatgilialoglu and K.-D. Asmus. NATO ASI Ser. Plenum Press, New York. 1990. p. 37.
24. D.D.M. Wayner, I.B. Clark, A. Rauk, D. Yu, and D.A. Armstrong. J. Am. Chem. Soc. **119**, 8925 (1997).
25. S.G. Lias, J.E. Bartness, J.F. Liebman, J.L. Holmes, R.D. Levin, and W.G. Mallard. J. Phys. Chem Ref. Data, **17**, Suppl. 1 (1988).
26. K.I. Kivirkko and R. Myllylä. Proc. N.Y. Acad. Sci. **460**, 187 (1985).
27. J.L. Holmes, F.P. Lossing, and P).M. Mayer. J. Am. Chem. Soc. **113**, 9723 (1991).
28. M. Goss-Sampson, A.J. Vivian, and F.J. Kelly. *In* Immunopharmacology of free radical species. *Edited by* D. Blake and P.G. Winyard. Academic Press, Toronto. 1995. pp. 133–134.
29. B. Cooper, J.M. Creeth, and A.S.R. Donald. Biochem. J. **228**, 615 (1983).

© 1998 NRC Canada

The preparation, X-ray crystal structure, and spectroscopic characterization of pentafluorophenyl-bis(pentafluorophenylthio)sulfonium hexafluoroarsenate, $[(C_6F_5S)_2SC_6F_5][AsF_6]$

Scott Brownridge, T. Stanley Cameron, Jack Passmore, Gabriele Schatte, and George W. Sutherland

Abstract: Pentafluorophenyl-bis(pentafluorophenylthio)sulfonium hexafluoroarsenate, $[(C_6F_5S)_2SC_6F_5][AsF_6]$, was prepared by the reaction of $(C_6F_5)_2S_2$ and AsF_5 in liquid SO_2 at room temperature. The compound has been characterized by single-crystal X-ray and powder diffraction, and IR and FT-Raman spectroscopy. Crystals of $[(C_6F_5S)_2SC_6F_5][AsF_6]$ are orthorhombic, space group $P2_12_12_1$ (cell dimensions measured at room temperature in brackets): a = 13.132(3) [13.157(2)] Å, b = 21.477(4) [21.575(3)] Å, c = 8.770(2) [8.775(1)] Å, α = ß = γ = 90.00°; V = 2473.3(9) Å^3, Z = 4, temperature = 181 ± 1 K. The structure consists of $[AsF_6]^-$ anions and $[(C_6F_5S)_2SC_6F_5]^+$ cations that have a different structure than the related $[X_2MMMX]^+$ cations (M = S, Se; X = Cl, Br), which contain a trichalcogen chain with a pronounced chalcogen–chalcogen bond alternation. Ab initio calculations suggest the observed $[(C_6F_5S)_2SC_6F_5]^+$ geometry is due to steric and solid state effects. Comparison of the Raman spectra of $[(C_6F_5)S_2SC_6F_5][AsF_6]$, $[Cl_2SSSCl][AsF_6]$, and $[(CH_3)_2ClS_3]^+$ implies that $[(CH_3)_2ClS_3]^+$ has a structure with equal sulfur–sulfur distances, and therefore the structure is likely $[(CH_3S)_2SCl]^+$ and probably not the previously reported $[(CH_3)_2SSSCl]^+$.

Key words: $[R_3X_3]^+$ cations, X-ray crystal structure, FT-Raman spectroscopy, $[(C_6F_5S)_2SC_6F_5]^+$, pentafluorophenyl-bis(pentafluorophenylthio)sulfonium cation, hexafluoroarsenate.

Résumé : On a préparé l'hexafluoroarsénate de pentafluorométhyl-bis(pentafluorophénylthio)sulfonium $[(C_6F_5S)_2SC_6F_5][AsF_6]$ en faisant réagir le $(C_6F_5)_2S$ avec du AsF_5, dans du SO_2 liquide, à la température ambiante. On a caractérisé le composé par son spectre de diffraction des rayons X de poudre et de cristal unique ainsi que par spectroscopies IR et Raman à transformée de Fournier. Les cristaux de $[(C_6F_5S)_2SC_6F_5][AsF_6]$ sont orthorhombiques, groupe d'espace $P2_12_12_1$ (les dimensions cellulaires mesurées à la température ambiante apparaissent entre parenthèses carrées) : a = 13,132(3) [13,157(2)], b = 21,477(4) [21,575(3)] et c = 8,770(2) [8,775(1)] Å, α = β = γ = 90,00°, V = 2473,3(9) Å^3, Z = 4, à une température de 181 ± 1 K. La structure est formée d'anions $[AsF_6]^-$ et de cations $[(C_6F_5S)_2C_6F_5]^+$ dont la structure est différente de celle des cations apparentés $[X_2MMMX]^+$ (M = S, Se; X = Cl, Br) qui contiennent une chaîne de trichalcogène avec une forte alternance de liaison chalcogène–chalcogène. Des calculs ab initio suggèrent que la géométrie observée pour le cation $[(C_6F_5S)_2C_6F_5]^+$ résulte d'effets stériques et d'état solide. Une comparaison des spectres Raman des composés $[(C_6F_5S)_2C_6F_5][AsF_6]$, $[Cl_2SSSCl][AsF_6]$ et $[(CH_3)_2ClS_3]^+$ implique que, dans ce dernier, les distances soufre–soufre sont égales et que, en conséquence, la structure correspond à $[(CH_3S)_2SCl]^+$ plutôt qu'à la structure $[(CH_3)_2ClS_3]^+$ proposée antérieurement.

Mots clés : cations $[R_3X_3]^+$, structure cristalline par diffusion des rayons X, spectroscopie Raman à TF, $[(C_6F_5S)_2C_6F_5]^+$, cation pentafluorométhyl-bis[pentafluorophénylthio]sulfonium, hexafluoroarsénate.

[Traduit par la Rédaction]

Introduction

The $[(MeS)_2SMe]^+$ (Me = CH_3) (1, 2) and $[(PhS)_2SPh]^+$ (3) cations ($[SbCl_6]^-$ or $[BF_4]^-$ salts) are useful electrophilic reagents in organic and pharmaceutical chemistry (4). Their structures, and those of related species, are of interest in the context of sulfur–sulfur bonding, both in simple polysulfur-containing molecules, e.g., neutral sulfur oxides

Received October 10, 1997.

S. Brownridge, J. Passmore,[1] G. Schatte,[2] and G.W. Sutherland. Department of Chemistry, University of New Brunswick, Fredericton, NB E3B 6E2, Canada.
T.S. Cameron. Department of Chemistry, Dalhousie University, Halifax, NS B3H 4J3, Canada.

[1] Author to whom correspondence may be addressed. Telephone: (506) 453-4781. Fax: (506) 453-4981. E-mail: passmore@unb.ca

[2] Present address: Department of Chemistry, University of Calgary, Calgary, AB T2N 1N4, Canada.

 © 1998 NRC Canada

S_nO (5*a*), sulfur homopolyatomic cations (5*b*), and polysulfur halogen cations (5*c*). The X-ray crystal structures of $[(MeS)_2SMe][A]$ (A = $[SbCl_6^-]$ (1), $[AsF_6]^-$ (2)) show the cations to adopt the configuration **1** with equal S—S bond distances. In contrast, the structures (X-ray) of $[M_3X_3][AsF_6]$ (M = S, Se; X = Cl, Br) contain isomeric $[X_2MMMX]^+$ cations **2** with alternating chalcogen–chalcogen bonds (5*d*–5*g*). In an attempt to understand the factors governing the difference in the geometries of these $[S_3X_3]^+$ cations (X = univalent group) we prepared and determined the X-ray structure of $[(Ph_FS)_2SPh_F][AsF_6]$($Ph_F = C_6H_5$) (with cation geometry **3**), containing the C_6F_5 substituent, which has an electronegativity between those of chlorine and bromine (5*h*) and also has back-bonding capability. The preparation of $[(Ph_FS)_2SPh_F][AsF_6]$ by the reaction of Ph_FSSPh_F and arsenic pentafluoride, the IR and FT-Raman spectra and X-ray crystal structure, and theoretical ab initio (RHF/6-31G*) calculations on isomers of $[S_3H_3]^+$ are reported below.

Experimental

General aspects

General techniques and apparatus are described in ref. 6. All reactions were carried out in a carefully dried one-piece apparatus consisting of two thick-walled round-bottom flasks (V = 25 mL) linked by a glass tube (o.d. 10 mm) incorporating a sintered glass filter disk (medium porosity). Both bulbs were fitted with Pyrex glass valves with PTFE pistons (J. Young, London, U.K.). All apparatus were carefully dried prior to use. Moisture-sensitive materials, crystals suitable for X-ray analysis, and all solid products were manipulated in a Vacuum Atmospheres Dri-Lab using dry nitrogen and equipped with a Dri-Train (HE-493) and an internal circulating drying unit containing 1 kg of 3 Å molecular sieves. Sulfur dioxide (Matheson) was vacuum distilled onto and stored over CaH_2. SO_2ClF (Ozark–Mahoning) was vacuum distilled onto and stored over molecular sieves. AsF_5 (Ozark–Mahoning) was used as received. Sulfur (precipitated; Fisher Scientific) was vacuum dried prior to use. The compound Ph_FSSPh_F was a gift from Dr. M. Peach and was characterized by FT-Raman[3] and IR (7) spectroscopy. Elemental analyses were carried out by Beller Mikroanalytisches Laboratorium, Göttingen, Germany.

Infrared and FT-Raman spectroscopy

Infrared spectra of Nujol mulls of $[(Ph_FS)_2SPh_F][AsF_6]$ between CsI plates were recorded using a Perkin–Elmer model 683 grating spectrometer in the range 4200–200 cm^{-1}. FT-Raman spectra were obtained from neat samples, sealed under nitrogen atmosphere in melting point tubes, using an FT-IR spectrometer (Bruker IFS66) equipped with an FT-Raman accessory (Bruker FRA 106) using a Nd-YAG laser (emission wavelength: 1064 nm; maximum laser power: 300 mW). The data were collected in the backscattering mode (180° excitation; resolution: 4 cm^{-1}) at room temperature in the range 4200–70 cm^{-1}.

Preparation of $[(Ph_FS)_2SPh_F][AsF_6]$ from Ph_FSSPh_F and arsenic pentafluoride (eq. [1])

Sulfur dioxide (7.2 g) and AsF_5 (0.500 g, 2.9 mmol) were successively condensed onto Ph_FSSPh_F (1.33 g, 3.34 mmol) placed into one bulb of a two-bulb reaction vessel. A pale green homogeneous solution was observed immediately on warming the reaction mixture to room temperature. Slow removal of 2/3 of the solvent into the second bulb cooled to 15°C (ΔT = 5°C), filtration of the last portion (ca. 2 mL) of solution, and removal of the volatiles by brief evacuation resulted in large plate-like yellow-orange crystals and small amounts of a noncrystalline green product from the soluble fraction that likely contained the slight excess (0.43 mmol) of Ph_FSSPh_F. The total weight of product was 1.73 g. The estimated weight of product according to eq. [1] with limiting reagent AsF_5, and unreacted Ph_FSSPh_F: 1.70 g. In another experiment, an excess of AsF_5 (1.015 g, 5.97 mmol) was reacted with Ph_FSSPh_F (0.771g, 1.93 mmol) in AsF_3 (10.9275 g) to give $[(Ph_FS)_2SPh_F][AsF_6]$ (Raman) (1.628 g, 2.04 mmol, 105% yield based on eq. [1]) containing some AsF_3 (Raman).

The FT-Raman spectra of crystalline $[(Ph_FS)_2SPh_F][AsF_6]$ and Ph_FSSPh_F[3] are shown in Fig. 1. FT-Raman of $[(Ph_FS)_2SPh_F][AsF_6]$, ν cm^{-1} (peak height): 1644 (100), 1593 (4), 1584 (4), 1526 (4), 1517 (4), 1430 (6), 1421 (53), 1403 (86), 1309 (10), 1298 (42), 1279 (8), 1263 (3), 1162 (3), 1109 (sh, 5), 1099 (8), 869 (77), 861 (58), 680 (21) $[AsF_6]^-$, 640 (6), 639 (sh, 2), 590 (43), 577 (3) $[AsF_6]^-$, 521 (34), 471 (87), 442 (29), 416 (93), 388 (42), 369 (26) $[AsF_6]^-$, 334 (15), 316 (15), 277 (18), 231 (sh, 12), 208 (br, 42), 177 (26), 149 (8), 120 (44), 103 (54). IR of $[(Ph_FS)_2SPh_F][AsF_6]$, ν cm^{-1} : 1638 m, 1513 vs, 1488 vs, 1413 m, 1403 s, 1312 m, 1298 s, 1279 m, 1263 m, 1163 m, 1099 sh, 1095 vs, 1043 w, 1020 m, 980 vs, 865 m, 854 m, 720 s, 695 s $[AsF_6]^-$, 635 sh, 629 m, 590 w, 573 w $[AsF_6]^-$, 518 m, 473 w, 395 m $[AsF_6]^-$, 310 m. The actual spectra have been deposited.[4] Crystals suitable for single-crystal X-ray diffraction were obtained by recrystallization of the yellow-orange crystals (0.68 g) in SO_2–SO_2ClF solution (molar ratio 5:1; 5.36 g SO_2–SO_2ClF). Elemental analysis (found (calcd.) for $[(Ph_FS)_2SPh_F][AsF_6]$): C 27.97 (27.50); S 12.69 (12.23); As 9.30 (9.53); F 49.70 (50.74)}.

X-ray analysis

Crystals of $[(Ph_FS)_2SPh_F][AsF_6]$ were examined, in a Dri-Lab filled with very dry nitrogen, using a Wild M3 microscope of long focal length mounted outside the dry box. A number of crystals were inserted into rigorously dried

[3] Chemistry Department, Acadia University, Wolfville, NS B0P 1X0, Canada. FT-Raman ν cm^{-1} (peak height): 1639 (55), 1402 (33), 1291 (10), 1272 (3), 1252 (2), 859 (35), 636 (4), 590 (26), 515 (33), 489 (100), 444 (23), 420 (2), 386 (29), 375 (sh, 15), 317 (10), 310 (sh, 6), 278 (5), 239 (22), 219 (5), 203 (3), 155 (7), 106 (5), 83 (10).

[4] Copies of material on deposit may be purchased from: The Depository of Unpublished Data, Document Delivery, CISTI, National Research Council Canada, Ottawa, Canada K1A 0S2. The data have been also deposited with the Cambridge Crystallographic Data Centre and can be obtained on request from The Director, Cambridge Crystallographic Data Centre, University Chemical Laboratory, 12 Union Road, Cambridge, CB2 1EZ, U.K. Structure factor tables are no longer being deposited and may be obtained directly from the author.

© 1998 NRC Canada

Fig. 1. FT-Raman spectra of (*a*) Ph_FSSPh_F and (*b*) $[(Ph_FS)_2SPh_F][AsF_6]$. The parameters for laser power, temperature, and number of scans are: (*a*) 16 mW, –147°C, 300 scans; (*b*) 66 mW, 22°C, 300 scans.

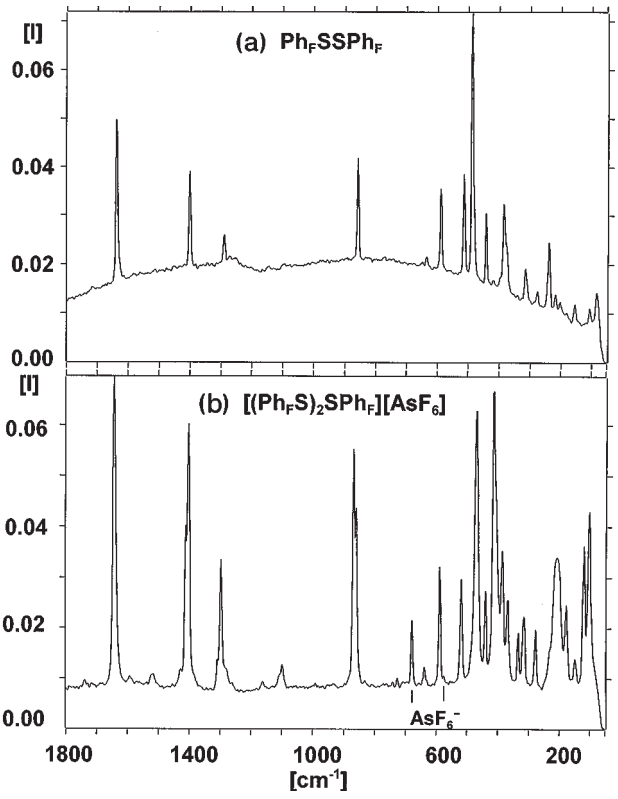

hand-drawn Pyrex glass capillaries under dry nitrogen atmosphere and then flame sealed.

Space group and cell dimensions

The yellow-orange crystals of $[(Ph_FS)_2SPh_F][AsF_6]$ were orthorhombic, space group $P2_12_12_1$ (cell dimensions measured at room temperature in brackets): a = 13.132(3) [13.157(2)] Å, b = 21.477(4) [21.575(3)] Å, c = 8.770(2) [8.775(1)] Å, $\alpha = \beta = \gamma = 90.00°$; V = 2473.3(9) Å^3, Z = 4, and D_{calc} = 2.111 g cm^{-3}. Temperature: 181 ± 1 K. Crystal size: 0.10 × 0.17 × 0.40 mm. Empirical formula: $AsC_{18}F_{21}S_3$. FW = 786.27. $\lambda(MoK_\alpha)$ = 0.71069 Å. $\mu(MoK_\alpha)$ = 17.96 cm^{-1}.

Data collection, structure solution, and refinement

The data for $[(Ph_FS)_2SPh_F][AsF_6]$ were collected on a Rigaku AFC5R diffractometer with graphite monochromated Mo-K_α radiation at a temperature of 181 ± 1 K using ω–2θ scans ($2\theta_{max}$ of 50°). The ω scan width was (0.84 + 0.35 tan θ)° and the ω scan speed was 4° min^{-1}. The weak reflections ($I < 15\sigma(I)$) were rescanned up to a maximum of six scans and the counts were accumulated. Stationary background counts were recorded on each side of the reflection with a peak/background counting time ratio of 2:1.

Cell constants and an orientation matrix for the data collection were obtained from a least-squares refinement using the setting angles of 21 carefully centred reflections in the range 22.13° < 2θ < 30.61°. All of the 2513 reflections collected were unique. The structure was determined by direct methods (8) and the data were corrected for Lorentz and polarization effects and for absorption using the program ψ-scan corrections, which resulted in absorption coefficients ranging from 0.9055 to 1.0000. Over the course of data collection the standards increased by 1.1%; a linear correction factor was applied to the data to account for this phenomenon. The $[AsF_6]^-$ group was disordered, and was refined with all the fluorine atoms having isotropic thermal parameters. Initially these fluorine atoms were restrained to have reasonable As—F distances and F-As-F interbond angles and were subsequently refined, riding on the As position. This $[AsF_6]^-$ was badly disordered and, unless extraordinarily fierce restraints are applied to the As–F distances, they spread over the range 1.68–1.80 Å. It is not clear whether this is an artifact of the disorder or a consequence of the F···F interactions. The three SC_6F_5 were also originally restrained to give a reasonable geometry to the C_6F_5 groups, and they were subsequently refined with the group riding on the sulfur position. The final cycle of full-matrix least-squares refinement was based on 1221 observed reflections ($I > 3\sigma(I)$)

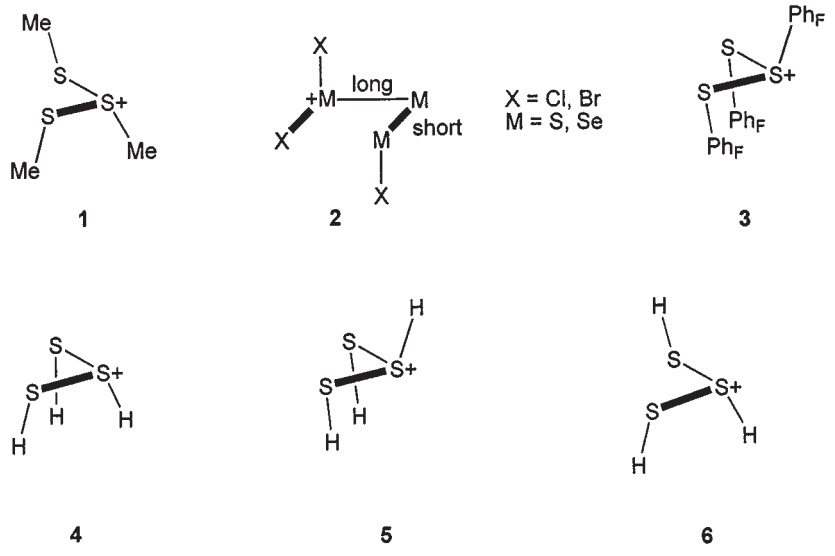

© 1998 NRC Canada

and 257 variable parameters and resulted in the final residuals $R = \Sigma\Delta F^2/\Sigma|F|^2 = 0.058$ and $R_w = \Sigma(w\Delta F)^2/\Sigma w^2|F|^2 = 0.063$. The standard deviation of an observation of unit weight (goodness-of-fit factor) was 1.93. The weighting scheme was based on counting statistics and included a factor ($p = 0.0266$) to downweight the intense reflections. A correction for secondary extinction was not applied. The maximum and minimum peaks in the final difference Fourier map correspond to 0.74 and –0.63 $e^- Å^{-3}$, respectively. All calculations were performed using the teXsan crystallographic software package of Molecular Structure Corporation.[5] Scattering factors for the structure determinations were taken from ref. 9 and effects of anomalous dispersion were included in F_{calc} (10); the values for $\Delta f'$ and $\Delta f''$ were those of Creagh and McAuley (11).

The final atomic coordinates are listed in Table 1. Available as supplementary material are a complete listing of thermal parameters, distances, angles, and the X-ray powder diffraction data.[4]

Theoretical methods

A series of RHF/6–31G* geometry optimizations were carried out on isomers of $[(HS)_2SH]^+$ (**4–6**) using the GAUSSIAN 92/DFT suite of programs (12), with **4** having all H atoms arranged *cis* to each other, and **5** and **6** having the starting geometries of $[(Ph_FS)_2SPh_F]^+$ and $[(MeS)_2SMe]^+$, respectively.

Discussion

Preparation

The yellow salt $[(Ph_FS)_2SPh_F][AsF_6]$ was prepared quantitatively from Ph_FSSPh_F and AsF_5 (in slight deficit or large excess) according to eq. [1].

$$[1] \quad 3\,Ph_FSSPh_F + 3\,AsF_5 \xrightarrow{SO_2(l)} 2[(Ph_FS)_2SPh_F][AsF_6] + AsF_3$$

The identity of $[(Ph_FS)_2SPh_F][AsF_6]$ was supported by elemental analyses of all elements and vibrational spectra (Raman spectra shown in Fig. 1, IR spectra deposited), and confirmed by single-crystal X-ray analysis. The bulk material was shown to be the same as the single crystal by the similarity of the intensities of the observed reflections given in an X-ray powder diffraction photograph with intensities calculated from the single-crystal data (details included in the supplementary material).

The $SbCl_6^-$ salts of related hydrocarbon derivatives have been prepared according to eq. [2]. $[(MeS)_2SMe][AsF_6]$ was obtained in a more complex synthesis (eq. [3]) from $[MeSCl_2][AsF_6]$, which was prepared from MeSCl, Cl_2, and AsF_5 (2).

$$[2] \quad 3\,(RS)_2 + 3\,SbCl_5 \xrightarrow[0\,^\circ C \text{ or } -60\,^\circ C]{CH_2Cl_2 \text{ or } SO_2} [(RS)_2SR][SbCl_6] + SbCl_3$$

(R = Me, Ph, 4-MeC_6H_4, 4-ClC_6H_4, 2,4,6-$Me_3C_6H_2$)

Table 1. Fractional atomic positional parameters for $[(Ph_FS)_2SPh_F][AsF_6]$ with estimated standard deviations (esd's) in parentheses.

Atom	*x*	*y*	*z*	B_{eq} [a]
As(1)	0.5896(1)	0.37363(7)	0.0812(1)	3.56(3)
F(1)[b]	0.672(1)	0.3618(8)	–0.054(1)	6.4(4)
F(2)[b]	0.494(1)	0.3787(9)	0.227(2)	6.7(4)
F(3)[b]	0.5947(8)	0.4487(5)	0.030(1)	8.2(3)
F(4)[b]	0.5827(8)	0.2993(4)	0.131(1)	7.1(2)
F(5)[b]	0.480(1)	0.3590(8)	–0.040(2)	6.4(4)
F(6)[b]	0.681(1)	0.3818(9)	0.202(2)	6.9(4)
F(22)[c]	0.559(2)	0.413(1)	0.245(3)	10.5(7)
F(23)[c]	0.636(1)	0.3403(8)	–0.091(2)	4.5(4)
F(24)[c]	0.724(2)	0.369(1)	0.137(2)	6.7(5)
F(25)[c]	0.476(2)	0.386(1)	0.017(2)	6.2(5)
S(1)	0.6372(3)	0.6334(2)	0.2035(4)	3.47(2)
C(1)	0.524(1)	0.5903(6)	0.171(2)	3.51(9)
C(2)	0.4647(8)	0.5963(6)	0.039(1)	2.87(8)
C(3)	0.3830(9)	0.5603(6)	0.020(1)	3.3(3)
C(4)	0.355(1)	0.5164(1)	0.129(2)	3.4(3)
C(5)	0.413(1)	0.5107(6)	0.266(2)	4.4(3)
C(6)	0.498(1)	0.5467(6)	0.280(1)	3.1(3)
F(7)	0.4926(5)	0.6397(3)	–0.0629(8)	4.2(2)
F(8)	0.3258(6)	0.5646(4)	–0.1078(9)	4.9(2)
F(9)	0.2776(6)	0.4780(4)	0.105(1)	5.3(2)
F(10)	0.3839(6)	0.4683(4)	0.3636(9)	5.5(2)
F(11)	0.5530(6)	0.5414(4)	0.4057(9)	5.0(2)
S(2)	0.7155(3)	0.6222(2)	–0.0028(4)	4.79(9)
C(7)	0.8376(9)	0.6048(6)	0.074(1)	3.0(3)
C(8)	0.860(1)	0.5490(6)	0.140(1)	3.7(3)
C(9)	0.956(2)	0.5380(9)	0.192(2)	8.4(5)
C(10)	1.030(2)	0.574(2)	0.172(2)	11.9(8)
C(11)	1.010(1)	0.635(1)	0.104(2)	7.5(3)
C(12)	0.916(1)	0.6503(7)	0.054(1)	5.0(4)
F(12)	0.780(1)	0.5080(4)	0.165(1)	9.2(3)
F(13)	0.9666(9)	0.4777(5)	0.258(1)	9.5(3)
F(14)	1.1209(8)	0.5599(9)	0.217(1)	16.1(5)
F(15)	1.0876(9)	0.6699(8)	0.083(1)	14.7(4)
F(16)	0.8974(9)	0.7047(4)	0.000(1)	8.2(3)
S(3)	0.5803(4)	0.7239(2)	0.2176(5)	5.9(1)
C(13)	0.652(1)	0.7520(6)	0.370(2)	3.6(3)
C(14)	0.731(1)	0.7947(6)	0.334(2)	4.2(4)
C(15)	0.782(1)	0.8202(8)	0.460(2)	6.1(5)
C(16)	0.762(1)	0.8025(7)	0.601(2)	7.8(5)
C(17)	0.694(1)	0.7604(9)	0.635(2)	6.4(5)
C(18)	0.638(1)	0.7339(6)	0.519(2)	4.7(4)
F(17)	0.7471(9)	0.8156(4)	0.198(1)	7.8(3)
F(18)	0.8522(7)	0.8654(4)	0.433(2)	10.8(3)
F(19)	0.821(1)	0.8271(5)	0.719(1)	13.1(4)
F(20)	0.674(1)	0.7369(5)	0.774(1)	13.1(4)
F(21)	0.5668(8)	0.6890(4)	0.539(1)	6.6(2)

[a] B_{eq} is the mean of the principal axes of the thermal ellipsoids.
[b] Occupancy 55.5%.
[c] Occupancy 45.5%.

[5] teXsan for Windows: Crystal Structure Analysis Package, Molecular Structure Corporation, The Woodlands, Texas, 1997.

© 1998 NRC Canada

Fig. 2. A PLUTO view of the structure $[(Ph_FS)_2SPh_F][AsF_6]$ including nine $[(Ph_FS)_2SPh_F]^+$ and six $[AsF_6]^-$ (only F(1)–F(6) included). Fluorine atoms attached to carbons have been omitted for clarity.

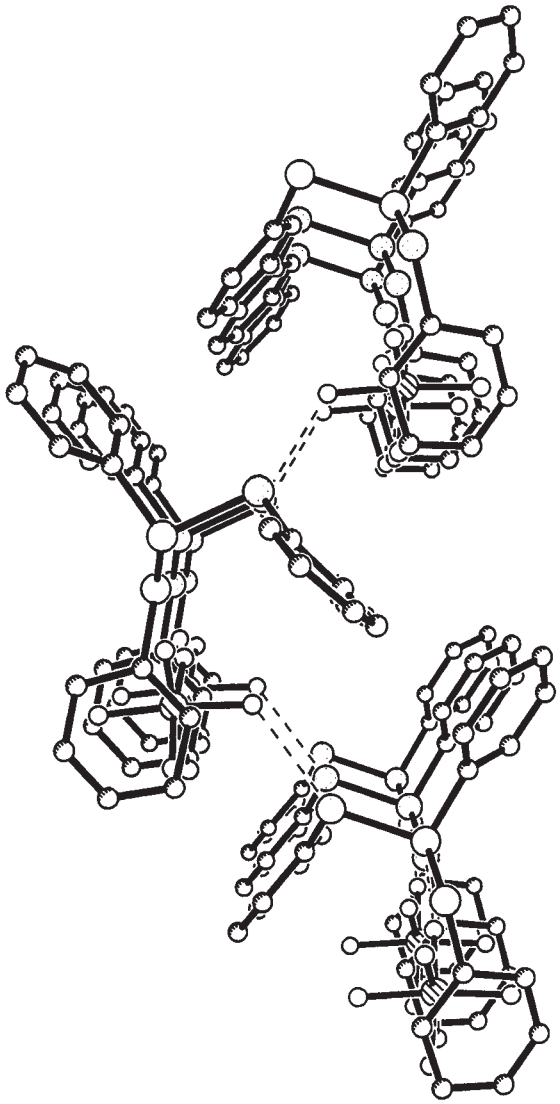

[3] $[MeSCl_2][A] + 2\ (MeS)_2 \xrightarrow[-65°C]{CH_2Cl_2} [(MeS)_2SMe][A] + 2\ MeSCl$

$(A = [AsF_6]^-, [SbCl_6]^-)$

The X-ray crystal structure of $[(Ph_FS)_2SPh_F][AsF_6]$

Figure 2 includes a portion of the crystal structure illustrating the packing and the presence of discrete $[(Ph_FS)_2SPh_F]^+$ cations with stacking of perfluorophenyl rings, $[AsF_6]^-$ anions, and some weak cation–anion contacts (broken lines). The cation and the disordered $[AsF_6]^-$ are illustrated in Fig. 3. Table 2 lists intercation–anion and intracation contacts, and related intraionic angles are given in Table 3. The minor set of four fluorine atoms used to model the observed $[AsF_6]^-$ electron density has not been included in Fig. 2 for clarity.

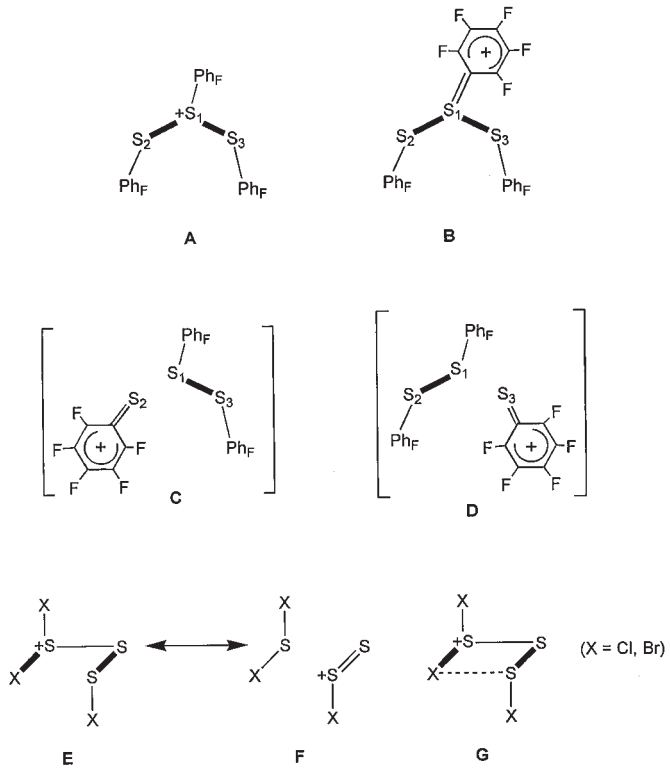

The bond distances, corresponding bond orders, and angles in the cations $[(Ph_FS)_2SPh_F]^+$ and $[(MeS)_2SMe]^+$, and Ph_FSSPh_F (13) are compared in Table 4, and the geometries of $[(Ph_FS)_2SPh_F]^+$ and $[(MeS)_2SMe]^+$ compared in Fig. 4. The C—F and C—C distances and angles are very similar in all three C_6F_5 rings in $[(Ph_FS)_2SPh_F]^+$, and similar to those in Ph_FSSPh_F (13). To a first-order approximation, the structure of $[(Ph_FS)_2SPh_F]^+$ may be represented by valence bond structure **A**. The S—S bond orders (Table 5) are less than one and longer than in $[(MeS)_2SMe]^+$ and Ph_FSSPh_F, whereas the C—S bond orders are shorter and slighty greater than one. This can be accounted for by some contribution of the resonance structures **B, C,** and **D** as well as **A**, with positive charge delocalization into the C_6F_5 ring. Consistently, there are several weak C···F interionic contacts that are less than the sum of the anisotropic van der Waals radii[6] (see Table 2). Alternatively, polarization of positive charge from tricoordinate S(1) to dicoordinate S(2) and S(3), rendering all sulfur atoms positively charged, and delocalization of electron density from the C_6F_5 ring into the S—S antibonding orbitals leads to the observed C—S bond strengthening and S—S bond weakening. Interestingly, there is only one S···F interionic contact to S(1) (see Table 2) which is formally positively charged, (S(1)···F(1*a*), 3.29(2) Å (0.06 v.u.)), whereas there are stronger contacts to formally neutral S(2) and S(3): (S(2)···F(6*b*), 2.92(3) Å (0.09 v.u.); S(2)···F(20*d*), 3.19(2) Å (0.06 v.u.); S(2)···F(24*a*), 3.26(3) Å (0.06 v.u.); S(3)···F(4*c*), 2.99(2) Å (0.08 v.u.)).

[6] Sum of the van der Waals radii: C···F, 3.17 Å; S···F, 3.27 Å (see ref. 14).

© 1998 NRC Canada

Fig. 3. An ORTEP view of $[(Ph_FS)_2SPh_F]^+$ and $[AsF_6]^-$ ions (F(1)–F(6) have occupancy 55.5%, F(22)–F(25) at 45.5%). The ORTEP program is included in the NRCVAX program package (28), and the thermal ellipsoids are scaled to 30% of the probability density. Inter- and intraionic contacts are listed in Table 2.

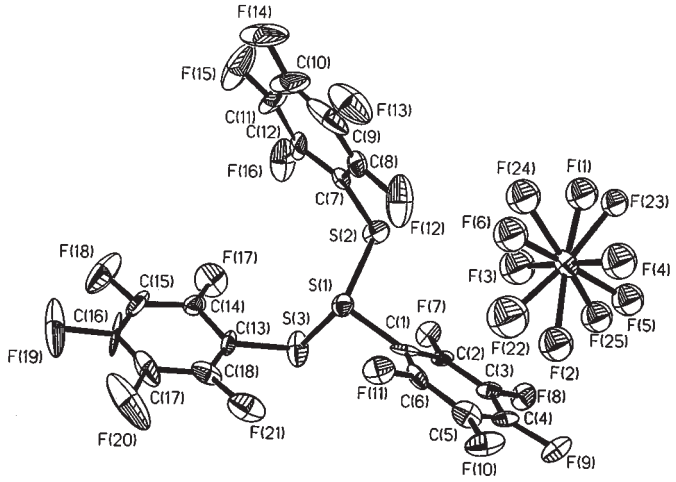

Table 2. Selected bond distances in angstroms (esd's in parentheses).

Bond	Distance	Bond	Distance	Bond	Distance
		$[(Ph_FS)_2S(Ph_F)]^+$			
S(1)—S(2)	2.095(7)	S(1)—C(1)	1.77(2)	S(3)—C(13)	1.75(2)
S(1)—S(3)	2.086(7)	S(2)—C(7)	1.78(2)		
		$[AsF_6]^-$			
As(1)—F(1)	1.62(2)	As(1)—F(5)	1.81(2)	As(1)—F(24)	1.84(3)
As(1)—F(2)	1.80(3)	As(1)—F(6)	1.61(2)	As(1)—F(25)	1.62(3)
As(1)—F(3)	1.68(1)	As(1)—F(22)	1.72(4)		
As(1)—F(4)	1.66(1)	As(1)—F(23)	1.78(3)		
		Interionic distances [a,b]			
S(1)···F(1*a*)	3.29(2)	C(6)···F(22)	2.99(4)	C(11)···F(5*i*)	3.13(3)
S(2)···F(6*b*)	2.92(3)	C(7)···F(22*a*)	3.21(4)	C(12)···F(2*b*)	3.16(3)
S(2)···F(20*d*)	3.19(2)	C(7)···F(23*b*)	3.19(3)	C(12)···F(22*a*)	3.05(4)
S(2)···F(24*a*)	3.26(3)	C(8)···F(11*b*)	3.05(2)	C(12)···F(23*b*)	3.19(3)
S(3)···F(4*c*)	2.99(2)	C(9)···F(3*a*)	3.05(3)	C(16)···F(4*a*)	3.00(3)
C(2)···F(13*a*)	3.07(2)	C(9)···F(11*b*)	3.04(3)	C(17)···F(4*c*)	3.20(3)
C(3)···F(13*a*)	3.14(2)	C(10)···F(5*a*)	2.91(4)	C(17)···F(24*b*)	2.99(4)
C(5)···F(2)	3.05(3)	C(10)···F(10*b*)	3.07(3)	C(18)···F(5*c*)	3.11(3)
C(5)···F(22)	2.85(4)	C(10)···F(25*b*)	3.15(4)	C(18)···F(24*b*)	3.04(4)

[a] Includes all interionic contacts less than the sum of the isotropic van der Waals radii for S···F ≤ 3.27 Å and C···F ≤ 3.17 Å; van der Waals radii: C, 1.70 Å; F, 1.47 Å; S, 1.80 Å (14).

[b] The letters *a*, *b*, *c*, and *d* indicate symmetry equivalent atoms: *a*, 1.5 – *x*, 1.0 – *y*, –0.5 + *z*; *b*, 1.5 – *x*, 1.0 – *y*, 0.5 – *z*; *c*, 1.0 – *x*, –0.5 + *y*, 0.5 – *z*; *d*, *x*, *y*, –1 + *z*.

Intracationic S—F contacts are similar to all three sulfur atoms. The relative strength of these contacts supports the view that all three sulfur atoms are positively charged. The cation–anion contacts are slightly stronger than those in monoclinic $[(MeS)_2SMe][AsF_6]$ (S(1)···F(6*i*), 3.137 Å (0.07 v.u.); S(2)···F(6*c*), 3.244 Å (0.06 v.u.); S(3)···F(1*j*), 3.061 Å (0.07 v.u.); see ref. 2).[7]

The average As—F distance (1.68 Å) in the $[AsF_6]^-$ anions of the $[(Ph_FS)_2SPh_F][AsF_6]$ salt is slightly shorter than the one in $KAsF_6$ (1.719(3) Å (16)), likely reflecting greater cation–anion contacts in the potassium salt.

A comparison of the geometries of $[(Ph_FS)_2SPh_F]^+$ and $[(MeS)_2SMe]^+$

The geometries of $[(Ph_FS)_2SPh_F]^+$ and $[(MeS)_2SMe]^+$ are not identical and are compared in Fig. 4. The

[7] It has been shown that the strength of the S(IV)···F contacts can be assessed by the relative magnitude of the bond valences (*S*) in valency units (v.u.) and is directly correlated to the localization of positive charge. An increase of positive charge on an atom leads to an increase in the sum of bond valences around the atom and this is accompanied by the formation of additional bonds and contacts (interionic and (or) intracationic) equal to the charge on the atom. The bond valence *S* in valence units (v.u.) is given by: $S = (R/R_0)^{-N}$, where *R* is the observed bond distance (Å), R_0 = 1.55 Å, and N = 3.8 (see ref. 15).

© 1998 NRC Canada

Table 3. Selected bond angles in degrees (esd's in parentheses).

	Angle		Angle		Angle
		$[(Ph_FS)_2S(Ph_F)]^+$			
C(1)-S(1)-S(2)	102.2(6)	C(1)-S(1)-S(3)	101.3(6)		
S(2)-S(1)-S(3)	109.5(3)	S(1)-S(2)-C(7)	98.1(5)	S(1)-S(3)-C (13)	100.0(7)
S(1)-C(1)-C(2)	124(1)	S(2)-C(7)-C(8)	123(2)	S(3)-C(13)-C(14)	116(2)
S(1)-C(1)-C(6)	117(2)	S(2)-C(7)-C(12)	118(1)	S(3)-C(13)-C(18)	124(2)
		$[AsF_6]^-$			
F(1)-As(1)-F(2)	174(1)	F(2)-As(1)-F(5)	83(1)	F(5)-As(1)-F(6)	174(1)
F(1)-As(1)-F(3)	86(1)	F(2)-As(1)-F(6)	93(1)	F(22)-As(1)-F(23)	172(2)
F(1)-As(1)-F(4)	95(1)	F(3)-As(1)-F(4)	179.1(7)	F(22)-As(1)-F(24)	91(2)
F(1)-As(1)-F(5)	94(1)	F(3)-As(1)-F(5)	92.3(9)	F(22)-As(1)-F(25)	90(2)
F(1)-As(1)-F(6)	90(1)	F(3)-As(1)-F(6)	92(1)	F(23)-As(1)-F(24)	83(1)
F(2)-As(1)-F(3)	99(1)	F(4)-As(1)-F(5)	86.8(9)	F(23)-As(1)-F(25)	95(1)
F(2)-As(1)-F(4)	80(1)	F(4)-As(1)-F(6)	88(1)	F(24)-As(1)-F(25)	172(2)

Table 4. Comparison of bond distances (Å) and angles (°), and bond orders (in brackets)[a] in Ph_FSSPh_F (12), $[(Ph_FS)_2SPh_F][AsF_6]$, $[(MeS)_2SMe][AsF_6]$ (1, 2), and those calculated for isomers **5** and **6** of $[(HS)_2SH]^+$ (see Fig. 3 for labelling of the atoms).

Ph_FSSPh_F orthorhombic	$[(Ph_FS)_2SPh_F][AsF_6]$ orthorhombic	$[(HS)_2SH]^+$ (**5**)	$[(MeS)_2SMe][AsF_6]$ monoclinic[b]	$[(HS)_2SH]^+$ (**6**)	Bond distances / bond angles[c]
2.059(4) [0.95]	2.095(7) [0.81]	2.073 [0.90]	2.048(3) [1.00]	2.068 [0.92]	S(1)—S(2)
	2.086(4) [0.85]	2.073 [0.90]	2.054(3) [0.98]	2.072 [0.91]	S(1)—S(3)
	1.77(2) [1.03]	1.325 [1.05]	1.808(8) [1.01]	1.326 [1.05]	S(1)—C(1)/H
1.770(7) [1.03]	1.78(2) [1.00]	1.327 [1.04]	1.794(7) [1.06]	1.328 [1.04]	S(2)—C(7)/H
1.771(7) [1.03]	1.75(2) [1.10]	1.327 [1.04]	1.799(9) [1.04]	1.327 [1.04]	S(3)—C(13)/H
	109.5(3)	109.4	107.6(1)	111.1	S(2)-S(1)-S(3)
	102.2(6)	99.7	106.8(3)	103.3	C(1)/H-S(1)-S(2)
	101.3(6)	93.8	97.6(2)	99.3	C(1)/H-S(1)-S(3)
	98.1(5)	93.8	103.3(3)	97.6	S(1)-S(2)-C(7)/H
	100.0(7)	93.8	98.8(3)	94	S(1)-S(3)-C(13)/H
	118.8(6)	114.5	56.8(3)	53.6	S(3)-S(1)-S(2)-C(7)/H
	–114.0(7)	–118.8	71.4(3)	109.8	S(2)-S(1)-S(3)-C(13)/H
	–134.3(8)	–137.3	–47.2(4)	–55	C/H(1)-S(1)-S(2)-C(7)/H
	138.5(9)	137.2	–178.3(4)	–141.9	C/H(1)-S(1)-S(3)-C(13)/H

[a] Bond orders were estimated using a variation of Pauling's bond distance – bond order relationship (22*a*), $D(n') = D_1 - b \log n'$, where n' is the bond order, $D(n')$ is the observed bond length, D_1 is the single bond distance, and b is a constant. Carbon–sulfur bond orders were estimated using the relationship $D(n') = D_1 - 0.71 \log n'$, where $D_1 = 1.82$ Å is the length of a C—S single bond with an sp^3 hybridized carbon, and $D_1 = 1.78$ Å for an sp^2 hybridized carbon (22*b*). Similarly, sulfur–hydrogen bond orders were estimated using the relationship $D(n') = 1.34 - 0.71 \log n'$, where 1.34 Å is the length of a S—H single bond (22*b*). Sulfur–sulfur bond orders were estimated using the relationship $D(n') = 2.05 - 0.526 \log n'$, given in ref. 23.

[b] Bond distances, bond orders, and angles for $[(MeS)_2SMe][AsF_6]$ triclinic (2): S(1)—S(2) 2.036(5) [1.05], S(1)—S(3) 2.057(7) [0.96], S(1)—C(1) 1.813(13) [1.00], S(2)—C(7) 1.793(16) [1.06], S(3)—C(13) 1.818(17) [0.98]; S(2)-S(1)-S(3) 108.5(3), C(1)-S(1)-S(2) 105.9(6), C(1)-S(1)-S(3) 97.0(6), S(1)-S(2)-S(7) 103.7(5), S(1)-S(3)-S(13) 99.0(6), S(3)-S(1)-S(2)-C(7) 53.3(7), S(2)-S(1)-S(3)-C(13) 68.2(7), C(1)-S(1)-S(2)-C(7) –49.9(8), C(1)-S(1)-S(3)-C(13) –177.6(9). Bond distances, bond orders, and angles for $[(MeS)_2SMe][SbCl_6]$ monoclinic (2): S(1)—S(2) 2.041(2) [1.03], S(1)—S(3) 2.056(2) [0.96], S(1)—C(1) 1.778(5) [1.12], S(2)—C(7) 1.806(6) [1.02], S(3)—C(13) 1.792(5) [1.07]; S(2)-S(1)-S(3) 108.0(1), C(1)-S(1)-S(2) 104.5(2), C(1)-S(1)-S(3) 102.2(2), S(1)-S(2)-S(7) 101.9(2), S(1)-S(3)-S(13) 97.4(2), S(3)-S(1)-S(2)-C(7) 52.5(2), S(2)-S(1)-S(3)-C(13) 90.5(2), C(1)-S(1)-S(2)-C(7) –55.8(3), C(1)-S(1)-S(3)-C(13) –159.6(3).

[c] Atom labelling is for $[(Ph_FS)_2SPh_F][AsF_6]$.

orientation of perfluorophenyl groups to S(1)—S(2) and S(1)—S(3) are *trans* and face to face with an angle of 60.1° (best planes through the carbon atoms of each ring attached to S(2) and S(3)), whereas those of the methyl groups are *cis* to S(1)—S(3) and *trans* to S(1)—S(2). There are three possible isomers (**4–6**) for $[(HS)_2SH]^+$ with $3p^2$ lone pairs on the terminal dicoordinate sulfur atoms approximately in the S(3)S(1)S(2) plane, with **5** having the structure of $[(Ph_FS)_2SPh_F]^+$ and **6** the structure of $[(MeS)_2SMe]^+$. The $3p^2$ lone pairs perpendicular to the S(3)S(1)S(2) plane will have high repulsion with the S(1)—X substituent (17) as well as any S(1) sp^3 lone pair if it has any existence, therefore isomers including them have been omitted. The optimized geometries and electronic energies of **4–6** (**5** and **6** included in Table 4) were calculated by ab initio methods using the GAUSSIAN 92/DFT suite of programs at the

© 1998 NRC Canada

Fig. 4. A comparison of the geometries of $[(XS)_2SX]^+$: (*a*) X = Me, (*b*) X = Ph_F.

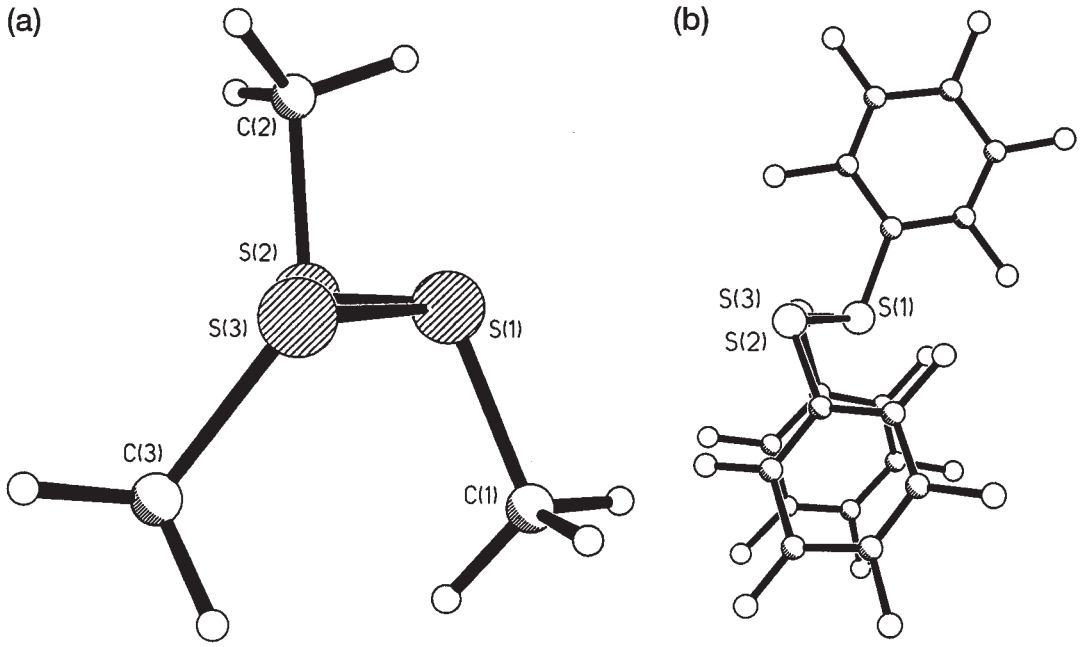

Table 5. C–S and S–S stretching frequencies (cm^{-1}) and bond distances (Å) with corresponding bond orders[a] (in brackets) for selected neutral and cationic species

Compound	C—S bond distance	ν (C–S) (sym., asym.)	S—S bond distance	ν(S–S) (sym., asym.)	Reference
H_2S_3			2.048 [1.01]	488, 470	24
$[(HS)_2SH]^+$ (**5**)			2.073 [0.90]	499, 434	This work
$[(HS)_2SH]^+$ (**6**)			2.072 [0.90], 2.068 [0.92]	502, 433	This work
Ph_FSH		865			21, 25
Ph_2S_2	1.789(3) [0.97]	662, 689	2.023(1) [1.13]	523	21, 26
$(Ph_F)_2S_2$	1.770(7) [1.03]	860	2.059(4) [0.96]	486	21
$(Ph_F)_2S$	1.75(1) [1.10]	875			21
$[(Ph_FS)_2S(Ph_F)]^+$ [b]	1.77(2) [1.03], 1.78(2) [1.00], 1.75(2) [1.10]	869, 861	2.095(7) [0.82], 2.086(7) [0.85]	471, 416	This work
$(C_2H_5)_2S_3$		668, 644		499, 486	27*a*
$(C_2F_5)_2S_3$		455, 435		516, 490	27*b*
Me_2S_3	1.78(4) [1.14]	694	2.04(2) [1.04]	486	27*a*
Me_2S_2	1.802(2) [1.06]	742, 692	2.022(3) [1.13]	509	21
Me_2S	1.806(2) [1.05]	694, 691			21
$[(MeS)_2S(Me)]^+$ [c]	1.778(5) [1.12], 1.792(5) [1.07], 1.806(6) [1.02]	690, 684	2.056(2) [0.97], 2.041(2) [1.04]	498, 461	1

[a] See footnote *a* of Table 4 for definition of bond order.
[b] As $[AsF_6]^-$ salt.
[c] The C–S stretching vibration is hidden underneath the stretching vibration of the $[AsF_6]^-$ anion in $[(MeS)_2SMe][AsF_6]$, so the values for the $SbCl_6^-$ salt are given. The frequencies for the S–S stretching vibration are observed at 501 and 455 cm^{-1} for the $[AsF_6]^-$ salt (see ref. 2*a*.

RHF/6–31G* level (12). In each case, the optimization led to a stationary point geometry. The energies of all isomers were similar (**6** and **4** were 2.1 and 9.3 kJ/mol higher in energy than **5**, respectively), suggesting steric and solid state effects (e.g., inter- and intraionic contacts, maximization of dipolar and van der Waals interactions, and the electrostatic[8] and repulsion components of the lattice energies) determine the relative energies of the isomers of $[(Ph_FS)_2SPh_F]^+$ and $[(MeS)_2SMe]^+$.

[8] The geometry of the dithionite anion was similarly shown to be very dependent on the electrostatic environment (18).

© 1998 NRC Canada

The structure of $[(Ph_FS)_2SPh_F]^+$ as an aid to an understanding of the structure of the $[X_2MMMX]^+$ cations (refs. 5*d*–5*g*)

The overall geometry of $[(Ph_FS)_2SPh_F]^+$ is symmetrical with essentially equal sulfur–sulfur bond distances, similar to that of $[(MeS)_2SMe]^+$ and dissimilar to the $[X_2MMMX]^+$ cations (M = S, Se; X = Cl, Br) (5*d*–5*g*). We have proposed that the $[X_2MMMX]^+$ cations (M = S, Se; X = Cl, Br) and related cations (5*b*, 5*c*) are stabilized by M—M bond alternation and charge delocalization (as shown for the $[X_2MMMX]^+$ cations in **E** and **F**), as well as intracationic and intercationic M···X contacts (**G**). Replacement of X (X = Cl, Br) by C_6F_5, with a similar electronegativity to Cl and Br (5*h*), allows the stabilization of the cation by bond alternation (i.e., **E** and **F**) and back-donation accompanied by further positive charge delocalization, but inter- and intracationic X···M contacts would not be possible (e.g., as in **G**). This supports the view that inter- and intracation X···M contacts are an important factor in determining the geometry of the $[X_2MMMX]^+$ (M = S, Se; X = Cl, Br) and related cations (5*b*, 5*c*, 19) in the solid state (5g).

The vibrational spectrum of $[(Ph_FS)_2SPh_F][AsF_6]$, and implications of the Raman spectra of $[(Ph_FS)_2SPh_F]^+$ and related cations for the structure of $[Me_2ClS_3]^+$ (ref. 20)

The IR and FT-Raman spectra of $[(Ph_FS)_2SPh_F][AsF_6]$ (see Fig. 1) contain bands attributable to the $[AsF_6]^-$ anion as well as to the Ph_FS group and the S_3 chain of the cation. The bands at 471 and 416 cm^{-1} in the FT-Raman spectrum were assigned to the asymmetric and symmetric SS stretching vibrations by comparison with the stretching vibrations for related species and those calculated for **5** and **6** (see Table 5). Similarly, the bands at 869 and 861 cm^{-1} were assigned to the asymmetric and symmetric CS vibrations (Table 5). The wide range of observed CS vibrations is attributed to the electronic effects of different substituents (21).

The Raman spectrum of $[Me_2ClS_3][SbF_6]$ has been reported (20) but not the X-ray structure. The S–S stretching vibrations are reported at 456(29) and 435(100) cm^{-1}. These frequencies are similar to those of the S–S stretches found for $[(MeS)_2SMe][AsF_6]$, $[(Ph_FS)_2SPh_F][AsF_6]$, and other related symmetrical S_3-containing cations (Table 5), but very different from the S–S stretches (223(100), 614(7, br) cm^{-1}) observed (5*e*, 5*g*) in the asymmetric $[Cl_2SSSCl]^+$. This implies that $[Me_2ClS_3]^+$ has a structure with equal sulfur–sulfur distances, and therefore the structure is likely $[(MeS)_2SCl]^+$ and probably not $[Me_2SSSCl]^+$ as previously suggested (20).

Acknowledgements

We wish to thank the Natural Sciences and Engineering Research Council of Canada for operating grants (J.P. and T.S.C.) and a graduate fellowship (S.B.), Dr. M. Peach for the sample of Ph_FSSPh_F, Dr. A. Decken for discussions, Figs. 2–4, and for improving the manuscript, and Mr. T. Way for his experimental results on the preparation of $[(Ph_FS)_2SPh_F][AsF_6]$ using an excess of AsF_5.

References

1. R. Laitinen, R. Steudel, and R. Weiss. J. Chem. Soc. Dalton Trans. 1095 (1986).
2. (*a*) R. Minkwitz, V. Gerhard, R. Krause, H. Prenzel, and H. Preut. Z. Anorg. Allg. Chem. **559**, 154 (1988); (*b*) R. Minkwitz, R. Krause, and H. Preut. Z. Anorg. Allg. Chem. **571**, 133 (1989).
3. A.S. Gybin, W.A. Smit, V.S. Bogdanov, M.Z. Krimer, and J.B. Kalyan. Tetrahedron Lett. **21**, 383 (1980).
4. S. Ramesh, N. Kaila, G. Grewal, and R.W. Franck. J. Org. Chem. **55**, 5 (1990).
5. (*a*) R. Steudel. Phosphorous Sulfur, **23**, 33 (1985); (*b*) N. Burford, J. Passmore, and J.C.P. Sanders. *In* From atoms to polymers: isoelectronic analogies. *Edited by* J.F. Liebman and A. Greenberg. VCH Publishers, New York. 1989. Chap. 2; (*c*) J. Passmore. *In* The chemistry of inorganic ring systems. *Edited by* R. Steudel. Elsevier Science Publishers, New York. 1992. Chap. 19; (*d*) J. Passmore, M. Tajik, and P.S. White. J. Chem. Soc. Chem. Commun. 175 (1988); (*e*) P. Bakshi, P.D. Boyle, T.S. Cameron, J. Passmore, G. Schatte, and G.W. Sutherland. Inorg. Chem. **33**, 3849 (1994); (*f*) P.D. Boyle, T.S. Cameron, J. Passmore, G. Schatte, and G.W. Sutherland. J. Fluorine Chem. **71**, 217 (1995); (*g*) S. Brownridge, T.S. Cameron, J. Passmore, G. Schatte, and T.C. Way. J. Chem. Soc. Dalton Trans. 2553 (1996); (*h*) J.A.J. Thompson and W.A.G. Graham. Inorg. Chem. **6**, 1875 (1967).
6. (*a*) M. Murchie and J. Passmore. Inorg. Synth. **24**, 76 (1986); (*b*) M. P. Murchie, R. Kapoor, J. Passmore, G. Schatte, and T. Way. Inorg. Synth. **31**, 102 (1997).
7. M.E. Peach. Can. J. Chem. **46**, 2699 (1968).
8. W.R. Busing, K.O. Martin, and H.A. Levi. ORFLS, a Fortran crystallographic least squares program. Report ORNL-TM-305, Oak Ridge National Laboratory, Oak Ridge, Tenn. 1962.
9. D.T. Cromer and J.T. Waber. International tables for X-ray crystallography. Vol. IV. Kynoch Press, Birmingham, England. 1974. Table 2.2A.
10. J.A. Ibers and W.C. Hamilton. Acta Crystallogr. **17**, 781 (1964).
11. D.C. Creagh and W.J. McAuley. International tables for X-ray crystallography. Vol. C. Kluwer Academic Publishers, Boston. 1992. Table 4.2.6.8.
12. M.J. Frisch, G.W. Trucks, H.B. Schlegel, P M.W. Gill, B.G. Johnson, M.W. Wong, J.B. Foresman, M.A. Robb, M. Head-Gordon, E.S. Replogle, R. Gomperts, J.L. Andres, K. Raghavachari, J.S. Binkley, C. Gonzalez, R.L. Martin, D.J. Fox, D.J. Defrees, J. Baker, J.J.P. Stewart, and J.A. Pople. GAUSSIAN 92/DFT, Revision G.3. Gaussian, Inc., Pittsburgh, Pa. 1993.
13. C.M. Woodard, D.S. Brown, J.D. Lee, and A.G. Massey. J. Organomet. Chem. **121,** 333 (1976).
14. A. Bondi. J. Phys. Chem. **68**, 441 (1964).
15. I.D. Brown. *In* Structure and bonding in crystals. Vol.2. *Edited by* M. O'Keeffe and A. Navrotsky. Academic Press, London. 1981. p. 1.
16. G. Gafner, and G.J. Kruger. Acta Crystallogr. Sect. B: Struct. Crystallogr. Cryst. Chem. **B30**, 250 (1974).
17. R. Steudel. Angew. Chem. Int. Ed. Engl. **14**, 655 (1975).
18. K.L. Carter, J.B. Weinrach, and D.W. Bennett. J. Am. Chem. Soc. **115**, 10981 (1993).
19. T. Klaplötke and J. Passmore. Acc. Chem. Res. **22**, 234 (1989).

© 1998 NRC Canada

20. R. Minkwitz, A. Kornath, R. Krause, and H. Preut. Z. Naturforsch. B: Chem. Sci. **45**, 1637 (1990).
21. R. Minkwitz, H. Preut, and J. Sawatzki. Z. Anorg. Allg. Chem. **569,** 158 (1989), and refs. therein.
22. (*a*) L. Pauling. The nature of the chemical bond. 3rd ed. Cornell University Press, Ithaca, N.Y. 1960; (*b*) J.E. Huheey, E.A. Keiter, and R.L. Keiter. Inorganic chemistry: principles of structure and reactivity. 4th ed. Harper Collins, New York. 1993.
23. M.P. Murchie, J.P. Johnson, J. Passmore, G.W. Sutherland, M. Tajik, T.K. Whidden, P.S. White, and F. Grein. Inorg. Chem. **31**, 273 (1992).
24. H. Wieser, P.J. Krueger, E. Muller, and J.B. Hyne. Can. J. Chem. **47**, 1633 (1969).
25. J.H.S. Green, D.J. Harrison, and C.P. Stockley. Spectrochim. Acta, **33A,** 423 (1977).
26. M.E. Peach. Int. J. Sulfur Chem. **8,** 27 (1973).
27. (*a*) F. Fehér, G. Krause, and K. Vogelbruch. Chem. Ber. **90**, 1570 (1957); (*b*) C.D. Desjardins and J. Passmore. J. Fluorine Chem. **9**, 53 (1977).
28. E.J. Gabe, Y. Le Page, J.-P. Charland, F.L. Lee, and P.S. White. J. Appl. Crystallogr. **22**, 384 (1989).

© 1998 NRC Canada

Crystal structure of the spirophosphorane $(OCMe_2C(O)O)_2PH$

Craig D. Montgomery, Steven J. Rettig, and Bryn Shurmer

Abstract: The crystal structure of the spirobicyclic phosphorane $(OCMe_2C(O)O)_2PH$, **1**, has been determined. Crystals of $C_8H_{13}O_6P$, **1**, are orthorhombic, a = 10.515(2), b = 10.623(2), c = 20.552(2) Å, Z = 8, space group $Pca2_1$. The structure was solved by direct methods and refined by full-matrix least-squares procedures to R = 0.037 (R_w = 0.033) for 1616 reflections with $I > 3\sigma(I)$. The structure consists of two independent molecules each displaying a distorted trigonal bipyramidal geometry; the distortion follows closely the Berry pseudorotation coordinate.

Key words: crystal structure, phosphorane, Berry pseudorotation, trigonal bipyramid.

Résumé : On a déterminé la structure cristalline du phosphorane spirobicyclique $(OCMe_2C(O)O)_2PH$, **1**. Les cristaux de $C_8H_{13}O_6P$, **1**, sont orthorhombiques, groupe d'espace $Pca2_1$, avec a = 10,515(2), b = 10,623(2) et c = 20,552(2) Å et Z = 8. On a résolu la structure par des méthodes directes et on l'a affinée par la méthode des moindres carrés (matrice entière) jusqu'à des valeurs de R = 0,037 (R_w = 0,033) pour 1616 réflexions avec $I > 3\sigma(I)$. La structure est formée de deux molécules indépendantes que présentent chacune une géométrie trigonale bipyramidale déformée; la déformation suit d'assez près la coordonnée de pseudorotation de Berry.

Mots clés : structure cristalline, phosphorane, pseudorotation de Berry, bipyramide trigonale.

[Traduit par la rédaction]

Introduction

Koenig et al. (1) have shown that a number of spirobicyclic hydrophosphoranes, including $(OCMe_2C(O)O)_2PH$, **1**, could be prepared by reaction of PCl_3 with the appropriate α-hydroxycarboxylic acid in the presence of NEt_3, eq. [1].

[1] 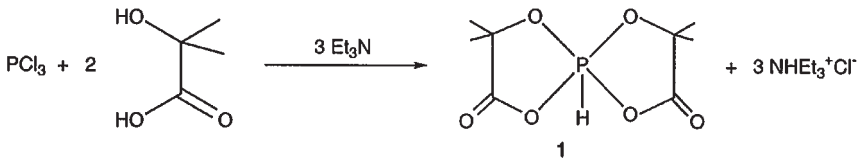

1

We have chosen compound **1** as a starting material in the synthesis of metallophosphoranes $L_nM\text{-}PR_5$, as shown in eq. [2] (2). In this study, we report the X-ray crystal structure of the starting material **1**.

[2] 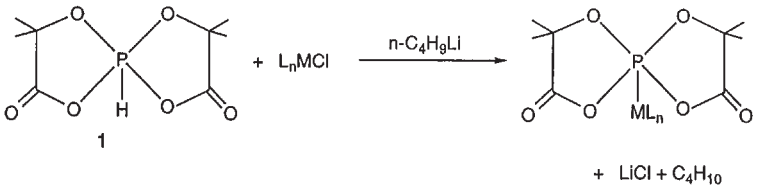

1

In addition, interest has been shown recently in the application of phosphoranes in the Wittig reaction (3, 4); compound **1** may be useful as an entry point into this chemistry. For this reason also, knowledge of the stereochemistry of **1** is desirable.

Received February 11, 1998.

C.D. Montgomery[1] and B. Shurmer. Dept. of Chemistry, Trinity Western University, Langley, BC V2Y 1Y1, Canada.
S.J. Rettig. Dept. of Chemistry, Structural Chemistry Laboratory, University of British Columbia, 2036 Main Mall, Vancouver, BC V6T 1Z1, Canada.

[1]Author to whom correspondence may be addressed. Telephone: (604) 888–7511. Fax: (604) 513–2018. E-mail: <montgome@twu.ca>

 © 1998 NRC Canada

Table 1. Crystallographic data.[a]

Compound	**1**
Formula	$C_8H_{13}O_6P$
fw	236.16
Crystal system	Orthorhombic
Space group	$Pca2_1$ (no. 29)
a, Å	10.515(2)
b, Å	10.623(2)
c, Å	20.552(2)
V, Å^3	2295.7(5)
Z	8 (two independent molecules)
ρ_{calc}, g/cm^3	1.366
F(000)	992
μ(Cu K_α), cm^{-1}	22.46
Crystal size, mm	0.15 × 0.35 × 0.45
Transmission factors	0.74–1.00
Scan type	ω-2θ
Scan range, deg in ω	0.89 + 0.20 tan θ
Scan speed, deg/min	16 (up to 9 scans)
Data collected	$+h, +k, +l$
$2\theta_{max}$, deg	155
Crystal decay, %	Negligible
Total reflections	2701
Total unique reflections	2422 (excluding systematic absences)
Reflections with $I > 3\sigma(I)$	1616
No. of variables	279
R	0.037
R_w	0.033
gof	2.16
Max Δ/σ (final cycle)	0.001
Residual density e/Å^3	–0.17–0.13

[a] Temperature 294 K, Rigaku AFC6S diffractometer, Cu K_α radiation (λ = 1.54178 Å), graphite monochromator, takeoff angle 6.0°, aperture 6.0 × 6.0 mm at a distance of 285 mm from the crystal, stationary background counts at each end of the scan (scan/background time ratio 2:1), $\sigma^2(F^2) = [S^2(C + 4B)]/Lp^2$ (S = scan rate, C = scan count, B = normalized background count), function minimized $\Sigma w(|F_o| - |F_c|)^2$ where $w = 4F_o^2/\sigma^2(F_o^2)$, $R = \Sigma||F_o| - |F_c||/\Sigma|F_o|$, $R_w = (\Sigma w(|F_o| - F_c|)^2/\Sigma w|F_o|^2)^{1/2}$, and gof = $[\Sigma w(|F_o| - |F_c|)^2/(m - n)]^{1/2}$. Values given for *R*, R_w, and gof are based on those reflections with $I > 3\sigma(I)$.

Table 2. Final atomic coordinates (fractional) and B_{eq} (10^3 Å^2).[a]

Atom	*x*	y	z	B_{eq}
P(1)	0.6330(2)	0.6814(2)	0.7264	4.21(4)
P(2)	0.6083(2)	0.8247(2)	0.38665(9)	4.25(4)
O(1)	0.7312(4)	0.7683(4)	0.6786(2)	5.19(11)
O(2)	0.7303(6)	0.9310(5)	0.6110(3)	7.7(2)
O(3)	0.5158(4)	0.7700(4)	0.7109(2)	4.65(10)
O(4)	0.5324(5)	0.5941(5)	0.7761(3)	5.30(14)
O(5)	0.4470(5)	0.4038(5)	0.7841(3)	7.1(2)
O(6)	0.6634(4)	0.5626(4)	0.6832(3)	4.47(12)
O(7)	0.5107(4)	0.7388(4)	0.4358(2)	5.21(12)
O(8)	0.5094(6)	0.5711(5)	0.5010(4)	7.7(2)
O(9)	0.7248(4)	0.7348(4)	0.4018(2)	4.53(10)
O(10)	0.7095(5)	0.9097(5)	0.3370(3)	4.99(12)
O(11)	0.7971(6)	1.0998(5)	0.3274(3)	6.9(2)
O(12)	0.5810(4)	0.9447(4)	0.4296(3)	4.16(11)
C(1)	0.6763(7)	0.8640(6)	0.6470(4)	5.5(2)
C(2)	0.5373(7)	0.8707(6)	0.6644(4)	5.1(2)
C(3)	0.4553(8)	0.8452(7)	0.6057(4)	6.1(2)
C(4)	0.5035(13)	0.9948(7)	0.6933(7)	7.2(3)
C(5)	0.5188(9)	0.4756(9)	0.7580(5)	5.2(2)
C(6)	0.5994(7)	0.4456(7)	0.7001(4)	4.6(2)
C(7)	0.5206(8)	0.4055(8)	0.6422(4)	7.1(2)
C(8)	0.7002(9)	0.3500(7)	0.7185(6)	8.1(3)
C(9)	0.5647(7)	0.6417(7)	0.4648(4)	5.1(2)
C(10)	0.7033(7)	0.6324(6)	0.4483(4)	4.9(2)
C(11)	0.7846(8)	0.6570(8)	0.5081(4)	6.5(2)
C(12)	0.7361(12)	0.5083(5)	0.4115(7)	6.0(2)
C(13)	0.7271(8)	1.0284(8)	0.3552(5)	4.7(2)
C(14)	0.6439(7)	1.0617(6)	0.4123(4)	4.1(2)
C(15)	0.7234(8)	1.1030(7)	0.4694(4)	6.5(2)
C(16)	0.5411(8)	1.1548(6)	0.3929(5)	6.5(2)

[a] $B_{eq} = (8/3)\pi^2\Sigma\Sigma(U_{ij}a_i^*a_j^*(\mathbf{a}_i\mathbf{a}_j))$.

Experimental

General

All manipulations were performed under prepurified nitrogen in a Vacuum Atmospheres HE 553–2 glovebox equipped with a MO-40 2H purifier or in standard Schlenk type glassware.

Solvents were dried by refluxing first over calcium hydride and then over sodium benzophenone followed by distillation under Ar. Deuterated benzene was purchased from Aldrich Chemicals and dried over 4 Å molecular sieves and vacuum-transferred prior to use.

The compound $(OCMe_2C(O)O)_2PH$, **1**, was prepared by literature method (1).

The ^1H NMR spectra were recorded on a Bruker WH-400 (400 MHz). The $^{31}P\{^1H\}$ NMR were recorded on a Varian XL-300 (121.42 MHz) and were referenced to external $P(OMe)_3$, set to +141.0 ppm relative to 85% H_3PO_4.

X-ray crystal structure determination of 1

Crystals suitable for X-ray crystallography were obtained by recrystallization in toluene. Crystallographic data appear in Table 1. The final unit-cell parameters were obtained by least-squares on the setting angles for 25 reflections with 2θ = 35.0–62.8°. The intensities of three standard reflections, measured every 200 reflections throughout the data collection, showed only small random fluctuations. The data were processed (5), corrected for Lorentz and polarization effects, and absorption (based on azimuthal scans).

The structure was solved by direct methods, the coordinates of the non-hydrogen atoms being determined from *E*-maps or from subsequent difference Fourier syntheses. The asymmetric unit contains two independent molecules, related by a pseudo-inversion centre. As a result, the *E*-statistics are centrosymmetric. The structure cannot be refined in the centrosymmetric space group *Pbcm* because the pseudocentre in $Pca2_1$ is not correctly located in the *xy* plane for conversion to the higher symmetry space group. All non-hydrogen atoms were refined with anisotropic thermal parameters. The P-H hydrogen atoms were refined

© 1998 NRC Canada

Table 3. Bond lengths (Å) with estimated standard deviations in parentheses.

Bond	Length	Bond	Length
P(1)—O(1)	1.698(4)	P(2)—O(7)	1.704(4)
P(1)—O(3)	1.583(4)	P(2)—O(9)	1.584(4)
P(1)—O(4)	1.739(5)	P(2)—O(10)	1.729(5)
P(1)—O(6)	1.574(5)	P(2)—O(12)	1.576(5)
O(1)—C(1)	1.337(8)	O(7)—C(9)	1.321(8)
O(2)—C(1)	1.173(8)	O(8)—C(9)	1.205(9)
O(3)—C(2)	1.453(8)	O(9)—C(10)	1.466(7)
O(4)—C(5)	1.321(9)	O(10)—C(13)	1.328(8)
O(5)—C(5)	1.199(10)	O(11)—C(13)	1.201(10)
O(6)—C(6)	1.456(8)	O(12)—C(14)	1.452(7)

Table 4. Bond angles (deg) with estimated standard deviations in parentheses.

Bond	Angle (deg)	Bond	Angle (deg)
O(1)-P(1)-O(3)	92.0(2)	O(7)-P(2)-O(9)	91.5(2)
O(1)-P(1)-O(4)	179.2(3)	O(7)-P(2)-O(10)	178.9(3)
O(1)-P(1)-O(6)	89.2(2)	O(7)-P(2)-O(12)	89.5(2)
O(3)-P(1)-O(4)	87.8(2)	O(9)-P(2)-O(10)	87.4(2)
O(3)-P(1)-O(6)	121.4(3)	O(9)-P(2)-O(12)	121.2(3)
O(4)-P(1)-O(6)	91.6(3)	O(10)-P(2)-O(12)	91.1(3)
P(1)-O(1)-C(1)	115.6(4)	P(2)-O(7)-C(9)	115.3(5)
P(1)-O(3)-C(2)	116.7(4)	P(2)-O(9)-C(10)	117.2(4)
P(1)-O(4)-C(5)	114.2(6)	P(2)-O(10)-C(13)	114.6(6)
P(1)-O(6)-C(6)	117.1(5)	P(2)-O(12)-C(14)	118.2(4)

isotropically, and the remaining hydrogen atoms were fixed in calculated positions with C—H = 0.98 Å and B_H = 1.2 $B_{\text{bonded atom}}$. A correction for secondary extinction was applied (Zachariasen type, isotropic, Gaussian), the final value of the extinction coefficient being 2.04(6) × 10^{-6}. Neutral atom scattering factors for all atoms and anomalous dispersion corrections for the non-hydrogen atoms were taken from the *International Tables for X-Ray Crystallography* (6). A parallel refinement of the opposite polarity gave slightly higher residuals, the R and R_w factor ratios being 1.017 and 1.010, respectively. Refinement of the Flack parameter (final value 0.046(6)) indicates that the polarity is correct, and the crystal is not a racemic twin. Final atomic coordinates and equivalent isotropic thermal parameters, selected bond lengths, and selected bond angles appear in Tables 2–4, respectively. Other tabulated data have been deposited.[2]

Results and discussion

In this study, **1** was first characterized by ^{1}H and ^{31}P{^{1}H} NMR. The ^{31}P{^{1}H} NMR spectrum is identical to that reported by Koenig et al. (1) with one singlet appearing at –53.4 ppm. In addition we report that the ^{1}H NMR spectrum displays a doublet at 6.85 ppm (^1J(H,P) = 915 Hz), which is comparable to that reported by Koenig et al. (7). However Koenig et al. reported a singlet at 1.2 ppm due to the methyl protons whereas we found two closely spaced singlets at 1.07 and 1.08 ppm. This observation is consistent with the different chemical environments of the methyl groups.

Bond lengths and angles for the two crystallographically independent molecules of **1** (one of which is shown in Fig. 1) are not significantly different. The two independent molecules have opposite chiralities, and the mirror images of both are also present in the crystal lattice as a result of the glide planes. The chiral nature of **1** enhances its value as a ligand.

Fig. 1. Stereoview of one of the two crystallographically independent molecules of **1**; 33% probability thermal ellipsoids are shown for the non-hydrogen atoms.

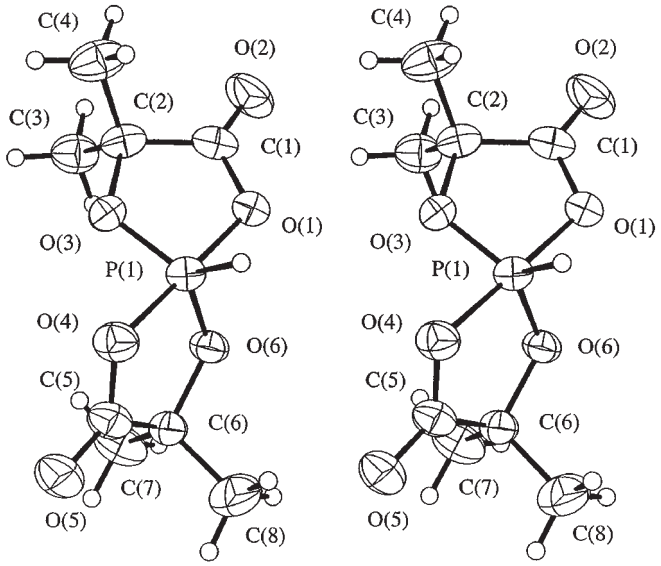

Both molecules display a distorted trigonal bipyramidal geometry (TBP) about the phosphorus atoms with the more strongly electron-withdrawing acyloxy groups occupying the axial positions. The distortion from an idealized TBP towards a rectangular pyramid (RP), as measured by the method of Holmes & Deiters (8) is l8.6% for molecule 1 (with P1) and 26.2% for molecule 2 (with P2). However this decreases to 7.3% and 4.3%, respectively, when unit bond lengths are used, suggesting that there is little angular distortion. This is true in spite of the presence of three of the five factors that Holmes has listed as favouring distortion towards a rectangular pyramid in cyclic phosphoranes: the presence of two rings as opposed to one, the presence of like atoms bonded to the phosphorus in any one ring and an

[2] Supplementary materials include a complete table of crystallographic data, complete tables of bond distances and bond angles, tables of hydrogen atom parameters, anisotropic thermal parameters, bond lengths involving hydrogen atoms, bond angles involving hydrogen atoms, torsion angles, intermolecular contacts, and least-squares planes. Copies of material on deposit may be purchased from: The Depository of Unpublished Data, Document Delivery, CISTI, National Research Council of Canada, Ottawa, Canada, K1A 0S2. With the exception of anisotropic parameters, torsion angles, and least-squares planes, these data have also been deposited with the Cambridge Crystallographic Data Centre and can be obtained on request from: The Director, Cambridge Crystallographic Data Centre, University Chemical Laboratory, 12 Union Road, Cambridge, CB2 1EZ, U.K.

© 1998 NRC Canada

acyclic, electropositive, sterically demanding fifth substituent in a spirobicyclic compound, all of which are present in **1**. However Holmes also stresses the importance of steric bulk in this last factor before it becomes operative and this is confirmed by the structure of **1**.

That the nature of the distortion is via the Berry pseudorotation mechanism is confirmed by the fact that the percentage distortions from an RP towards a TBP (when unit bond lengths are used) are 98.2% and 97.4%, respectively. Thus when the percentage distortions of **1** in each direction are added together, the sum is close to 100% (105.5% and 101.7%, respectively). Furthermore the equatorial O-P-O angles are greater than 120° (121.4(3)° and 121.2(3)°, respectively).

While crystal structures are known for a number of other hydrophosphoranes (see ref. 9 for examples), $(C_6H_4O_2)_2PH$ is the only one which, like **1**, is a tetraoxohydrophosphorane (10). Like **1**, $(C_6H_4O_2)_2PH$ also exhibits a near ideal TBP geometry with the hydrogen in an equatorial position. The work reported here on compound **1** further extends this class of structures.

Conclusions

The crystal structure of $(OCMe_2C(O)O)_2PH$ displays a distorted trigonal bipyramidal geometry with the acyloxy groups in the axial positions. The small amount of distortion from an idealized TBP structure follows the Berry pseudorotation coordinate towards a rectangular pyramidal geometry.

Acknowledgements

C.D.M. wishes to thank Professor Michael D. Fryzuk of the Department of Chemistry, University of British Columbia, in whose laboratory C.D.M. performed a portion of this work as an honorary visiting scientist. C.D.M. also acknowledges the support of Trinity Western University.

References

1. M. Koenig, A. Munoz, and R. Wolf. Bull. Soc. Chim. **11**, 4185 (1971).
2. R. Faw, C.D. Montgomery, S.J. Rettig, and B. Shurmer. Inorg. Chem. **37**, 4136 (1998).
3. M.L. Bojin, S. Barkallah, and S.A. Evans. J. Am. Chem. Soc. **118**, 1549 (1996).
4. S. Kojima, R. Takagi, and K. Akiba. J. Am. Chem. Soc. **119**, 5970 (1997).
5. teXsan: Crystal structure analysis package. Unix version 1.7. Molecular Structure Corporation, The Woodlands, Tex., U.S.A. 1995.
6. (*a*) International Tables for X-Ray Crystallography. Vol. IV. Kynoch Press, Birmingham, U.K. (present distributor Kluwer Academic Publishers, Boston, Mass., U.S.A.). 1974. pp. 99–102; (*b*) International Tables for Crystallography. Vol. C. Kluwer Academic Publishers, Boston, Mass., U.S.A. 1992. pp. 200–206.
7. M. Koenig, A. Munoz, and R. Wolf. Phosphorus Sulfur Relat. Elem. **6**, 435 (1979).
8. R.R. Holmes and J.A. Deiters. J. Am. Chem. Soc. **99**, 3318 (1977).
9. (*a*) M.G. Newton, J.E. Collier, and R. Wolf. J. Am. Chem. Soc. **96**, 6888 (1974); (*b*) M.A.H. Laramay and J.G. Verkade. J. Am. Chem. Soc. **112**, 9421 (1990); (*c*) M. Lattman, M.M. Olmstead, P.P. Power, D.W.H. Rankin, and H.E. Robertson. Inorg. Chem. **27**, 3012 (1988); (*d*) G.-V. Roschenthaler, R. Bohlen, and D. Schomburg. Z. Naturforsch. B: Anorg. Chem. Org. Chem. **B40**, 1593 (1985); (*e*) S. Kojima, M. Nakamoto, K. Kajiyama, and K. Akiba. Tetrahedron Lett. **36**, 2261 (1995).
10 H. Wunderlich and H.-G. Wussow. Acta Crystallogr. Sect. B: Struct. Sci. **B34**, 2663 (1978).

© 1998 NRC Canada

Decomposition of peracetic acid catalyzed by cobalt(II) and vanadium(V)

X.-Z. Zhang, R.C. Francis, D.B. Dutton, and R.T. Hill

Abstract: Peracetic acid (Pa) is now being used for totally chlorine-free delignification and bleaching of wood pulps. During the process, metals desorb from the pulp fibers into the aqueous solution. Of the relevant metals in bleaching systems, cobalt(II) and vanadium(V) are the most potent in wastefully decomposing Pa to O_2. In the present study, radical scavenging by *N*,*N*′-(5-nitro-1,3-phenylene)-bisglutaramide (GAMID) indicates that free-radical mechanisms are operative. Kinetic data support a free-radical decomposition mechanism previously described for Co(II). A similar type of mechanism, involving $VO(OH)_{2(aq)}$ and $VO(OH)_{3(aq)}$, is postulated to partially explain catalysis by vanadium.

Key words: peracetic acid, peroxymonosulfuric acid, transition metals, free radicals, acetoxy radical, peracetoxy radical.

Résumé : L'acide peracétique (aP) est maintenant utilisé pour la délignification et le blanchiment de pulpes de bois en absence totale de chlore. Durant ce processus, les métaux se désorbent des fibres de la pulpe et se retrouvent dans la solution aqueuse. De tous les métaux les plus importants pour les systèmes de blanchiment, le cobalt(II) et le vanadium(V) sont les plus puissants pour la décomposition inutile de l'aP en O_2. Dans le présent travail, des piégeages de radicaux à l'aide de *N*,*N*′-(5-nitro-1,3-phénylène)-bisglutaramide (GAMID) indiquent que des mécanismes radicalaires sont impliqués. Les données cinétiques sont en accord avec le mécanisme de décomposition radicalaire décrit antérieurement pour le Co(II). Pour expliquer la catalyse par le vanadium, on suggère un mécanisme semblable impliquant du $VO(OH)_{2(aq)}$ et $VO(OH)_{3(aq)}$.

Mots clés : acide peracétique, acide peroxymonosulfurique, métaux de transition, radicaux libres, radical acétoxy, radical peracétoxy.

[Traduit par la rédaction]

Introduction

The pulp and paper industry is under great pressure to delignify and bleach kraft pulps without using chlorine-containing chemicals. Peracids, peroxymonosulfuric acid (H_2SO_5), and peracetic acid (CH_3CO_3H) are being investigated as replacement oxidants. European mills are now using peracetic acid in TCF (totally chlorine-free) production runs (1).

The effects of transition metal ions on the decomposition of both peracids have been previously investigated (2–10). The metals that are most relevant to pulp delignification are Mn, Fe, Cu, V, and Co (8, 9). These metals are present in wood that is converted to pulp by high temperature, alkaline extraction of approximately 90% of the original lignin. Delignification and bleaching (whitening) involve the degradation and solubilization of the residual lignin in the fibers. Oxidation of phenolic and alcoholic groups to carboxylic groups followed by alkaline extraction is the usual approach. Peracid delignification is generally conducted in an aqueous slurry (1 kg pulp fibers in 9 L of solution) at an initial pH in the range of 2.0–6.0. Some of the transition metals desorb from the pulp under the mildly acidic conditions.

Under pulp bleaching conditions, cobalt(II) is the only reported active catalyst for HSO_5^- (8), while both cobalt(II) and vanadium(V) are potent catalysts for peracetic acid (Pa) (9). The free-radical mechanism by which Co(II) decomposes H_2SO_5 or HSO_5^- is well established (4–6). However, its role in Pa decomposition has not been fully elucidated (2, 3, 11). As for V species and Pa, the only reference found was one showing VO_3^- to be a highly catalytic anion but no reaction mechanism was postulated (12).

The objective of this research was to investigate the free-radical reactions associated with cobalt(II) and vanadium(V) catalysis of Pa decomposition. Free-radical reactions are particularly important because, in addition to giving rise to wasteful decomposition of Pa to O_2 (which is unreactive in the pH 2–6 range), free radicals cause random chain scission of the cellulose leading to a weaker fiber and ultimately to paper products having lower strength properties.

Received November 3, 1997.

X.-Z. Zhang and R.C. Francis.[1] Faculty of Paper Science and Engineering, State University of New York, College of Environmental Science and Forestry, Syracuse, NY 13210-2778, U.S.A.
D.B. Dutton and R.T. Hill. Solvay Interox Laboratories, Deer Park, TX 77536, U.S.A.

[1]Author to whom correspondence may be addressed. Telephone: (315) 470-6525. Fax: (315) 470-6945 or (315) 470-6593. E-mail: francis@syr.edu

Experimental

Materials

Reagent grade $CoSO_4 \cdot H_2O$, $VOSO_4 \cdot 3H_2O$ and V_2O_5 (dissolved in H_2SO_4 to yield VO_2^+) were supplied by Aldrich.

© 1998 NRC Canada

Fig. 1. First-order plots for peracetic acid decomposition at pH 4.8. Conditions: $[Pa]_0$ = 33 mM, $[Co(II)]_0$ = 3. 4 × 10^{-6} M, $[V(IV)]_0 = [V(V)]_0$ = 2.0 × 10^{-5} M, 60°C.

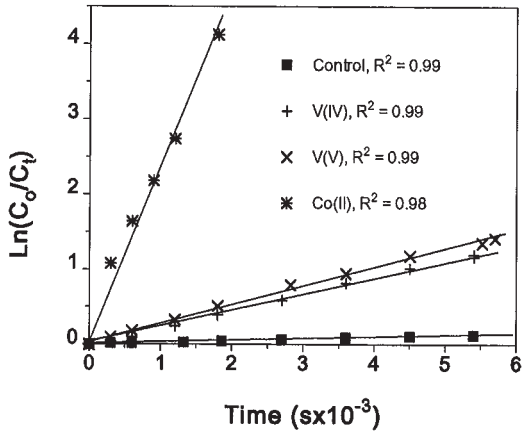

Fig. 2. First-order plots for peracetic acid decomposition at pH 2.4. See Fig. 1 caption for conditions.

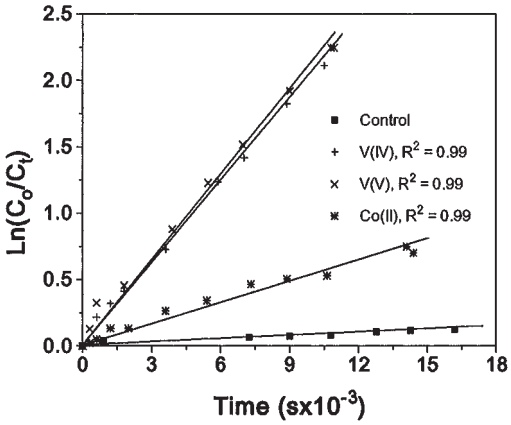

Fig. 3. *N*,*N*′-(5-Nitro-1,3-phenylene)-bisglutaramide, an effective scavenger for hydroxyl and other free radicals.

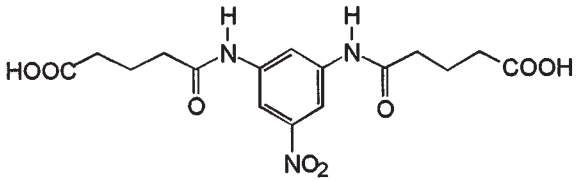

Dilute solutions of the cations were standardized by ICP spectroscopy. Ultrapure NaOH was obtained from Alfa Chemicals. *N*,*N*′-(5-Nitro-1,3-phenylene)-bisglutaramide was synthesized as described by Singh and Hider (13). Equilibrium peracetic acid, that is, peracetic acid formed in the equilibrium reaction shown in eq. [1], was obtained from Aldrich; distilled peracetic acid was obtained following treatment of acetic acid with H_2O_2 (both at ~20 wt.%) in dilute H_2SO_4 solution at ~40°C and ~60 torr (1 torr = 133.3 Pa). Peracetic acid and water are the most volatile products and are distilled off in an apparatus specially designed to avoid peracetic acid concentrations >40 wt.%.

Peracetic acid decomposition

The cations were preheated in acid-washed polyethylene bottles. An aliquot of concentrated Pa was added and a zero-time sample taken after pH adjustment. The pH was continuously monitored and controlled to ±0.1 unit by the addition of one or two drops of concentrated NaOH. When GAMID was used, crystals were added to give an initial concentration of 10 mM just prior to Pa addition. Residual Pa was determined by iodometric titration; while ceric sulfate titration was used to determine H_2O_2. Solutions containing hydroxylated GAMID were made alkaline and diluted 10-fold. Their UV-vis spectra were measured against a solution 1 mM in GAMID and 30 mM in Pa. The water used for all experiments had no transition-metal concentrations higher than 10 ppb.

Gas analysis

The Pa decomposition gases were collected in a Tedlar gas sampling bag. A sample was injected into a GC fitted with two columns in series and equipped with a thermal conductivity detector. The first column was packed with 80–100 mesh Columpak ^{TM}PQ and the second with 60–80 mesh Molecular Sieve 13X. Helium was the carrier gas.

Results and discussion

Peracetic acid is generated by the reaction in eq. [1]. An equilibrium product mixture or a distilled product mixture can be obtained. The latter is used in the paper industry and was used in all of the previous research (9) and in most of the present research.

$$[1] \qquad CH_3COOH + H_2O_2 \xleftrightarrow{H^+} CH_3COOOH + H_2O$$

In the preparation of distilled Pa, dilute solutions of CH_3COOH and H_2O_2 are allowed to react. Water and Pa are the most volatile components and are distilled from the reaction mixture. Equilibrium Pa can be prepared by treating concentrated solutions of CH_3COOH with H_2O_2. A product mixture containing ~34 wt.% Pa and ~5 wt.% H_2O_2 is normally obtained. Experiments conducted with equilibrium Pa are identified.

Catalysis by Co(II)

Research was initiated with Co(II) because free-radical mechanisms were already postulated to explain its catalytic effect (2, 3). Also, this ion catalyzed the depolymerization of cellulose more severely than V species (9). The secondary alcohols in cellulose can be oxidized to carbonyl groups by successive abstraction of hydrogen atoms (14). During alkaline extraction of depolymerized and oxidized lignin, the ketols in the cellulose undergo alkali-induced β-alkoxy elimination reactions causing cleavage of the glycosidic linkages (15).

Koubek and Edwards (2) investigated the decomposition of distilled Pa catalyzed by low concentrations of Co(II) at pH 5.4. They observed that the rate equation was first order in both Pa and Co(II) concentrations and postulated a free-radical mechanism involving acetoxy (AcO·) and peracetoxy (AcOO·) radicals. We observed that at pH 4.8 the rate equation was first order in Pa and approximately first order in Co(II) (an order of 1.1 was actually obtained, results are not included). The precision of the first-order fits (in terms of Pa concentration) is summarized in Figs. 1 and 2 for pH 4.8 and 2.4 with no added catalyst (control), and

© 1998 NRC Canada

Fig. 4. Log of observed first-order rate constant for Pa decomposition as a function of the log of vanadium(V) concentration. Conditions: $[Pa]_0$ = 33 mM, pH 2.4, 60°C.

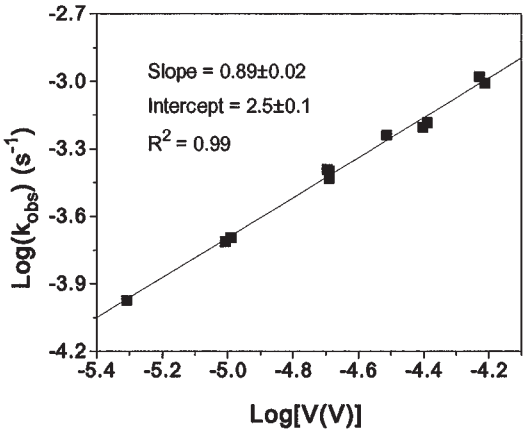

with 3.4 × 10^{-6} M Co(II) and 2.0 × 10^{-5} M V(IV) or V(V) solutions. The R^2 value consistenctly exceeded 0.985.

N,*N*′-(5-Nitro-1,3-phenylene)-bisglutaramide (GAMID) (see Fig. 3) was used to test for free radicals. This molecule was specifically designed to scavenge ·OH by ring hydroxylation (13). The resulting phenols are unreactive, and their phenolates can be quantified by UV-vis spectroscopy. We have observed that for a wide range of reaction conditions, GAMID is not degraded by H_2O_2, H_2SO_5, or Pa. It has also been observed that, when it scavenges ·OH, GAMID disrupts the free-radical mechanism with the result that peroxide decomposition is retarded (8, 16). GAMID was chosen because it is effective in scavenging the sulfate radical anion ($SO_4^{\cdot-}$) generated during HSO_5^- decomposition (hydroxylated products are not formed). It has been conclusively demonstrated (4–6) that $SO_4^{\cdot-}$ is generated by HSO_5^- decomposition catalyzed by Co(II) in the pH range 1.0–2.0. When GAMID was added to HSO_5^-–Co(II) reaction systems at a concentration of 1 mM, decomposition rates decreased by ~90% (8). When GAMID was added to the Co(II)–Pa system at 10 mM concentration, the decomposition rate decreased by ~70%, and there was no significant hydroxylation, indicating that ·OH was not involved. The possibility that hydroxylation occurred but that the resulting phenols were then oxidized by Pa was examined. Peracetic acid was added to the HSO_5^-–Cu(II) system, which is known to cause significant hydroxylation of GAMID (16). The result was a slight increase in hydroxylated products as compared to HSO_5^-–Cu(II).

We accepted the conclusion of Edwards (2, 6) and co-workers that eqs. [2] and [3] were key to the generation of free radicals and discontinued research with Co(II).

[2] $\quad Co(II) + AcOOH \rightarrow Co(III) + AcO\cdot + OH^-$

[3] $\quad Co(III) + AcOOH \rightarrow Co(II) + AcOO\cdot + H^+$

Catalysis by vandium species

The first experiments with V(IV) and V(V) were conducted at pH 4.8 and 2.4 with the results shown in Figs. 1 and 2. If a free-radical mechanism involving V(IV) and V(V) was operative, it is likely that the rate equation would

Fig. 5. Effect of radical scavenger on the decomposition of peracetic acid catalyzed by V(V). Plotted in accordance with 1.1 order in peracetic acid. Conditions: $[Pa]_0$ = 33 mM, $[V(V)]_0$ = 1.0 × 10^{-5} M, 60°C.

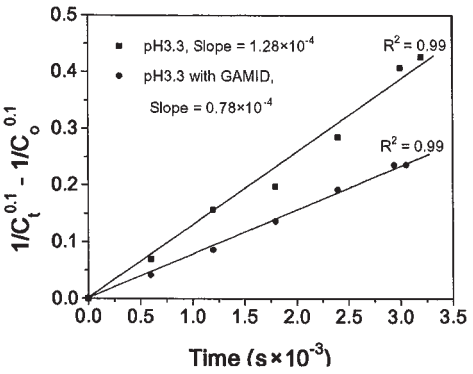

be first order in both [V(V)] and [Pa] (6). The [V(V)] concentration was varied at pH 2.4, and the results reported in Fig. 4 were obtained. The order for [V(V)] was 0.9. For mechanistic purposes the rate equation was assumed to be first order in both [V(V)] and [Pa] (eq. [4]).

$$[4] \qquad -\frac{d[Pa]}{dt} = k[V(V)][Pa]$$

Vanadium species caused less depolymerization of cellulose than Co(II) (9). Therefore, GAMID was used to determine if catalysis by V species was dominated by free-radical reactions. The first-order rate constant (in terms of [Pa], $k_{obs} = k[V(V)]$) was determined with and without GAMID addition at pH 4.8 and in the pH range of 3.0–3.5 ($[V(V)] = 2.0 \times 10^{-5}$ M). Multiple experiments were performed in the pH 3.0–3.5 range because it was difficult to maintain the pH to ±0.1. The decomposition rate was very sensitive to pH, particularly in this range. The control of pH was less tedious at values <2.5 and >4.0. The radical scavenger decreased the rate constant by 30–50% in the pH range of 3.0–3.5 and by ~10% at pH 4.8. It appears that a free-radical mechanism was operative but was not as dominant as in Co(II) catalysis.

The rate of Pa decomposition was found to be proportional to $[V(V)]^{0.9}$. It would then be expected that the reaction order in [Pa] should be slightly more than 1.0, i.e., about 1.1. In some experiments the R^2 values were slightly better for the 1.1 order fit as compared to 1.0. Such was the case for the results in Fig. 5 where the effect of GAMID on vanadium-induced decomposition is demonstrated. It can be seen that the radical scavenger decreased the rate constant (slope) by 39%.

The pH range of 3.0–3.5 was used instead of pH 2.4 to provide increased GAMID solubility. One interesting observation is that the decomposition rate increased in going from pH 4.8 to pH 3.0–3.5 but decreased when the pH was lowered from 3.0–3.5 to 2.4 ($[V(V)] = 2.0 \times 10^{-5}$ M, no GAMID). Several other pH levels were investigated in the 2.0–6.0 range. Also, literature on the variation of vanadium(V) species with pH was reviewed. Vanadium(IV) is known to be rapidly oxidized to V(V) by HSO_5^- (7). It is assumed that the case is similar for Pa solutions and that only V(V) is present at a detectable concentration. Other than the

© 1998 NRC Canada

Fig. 6. Variation of $[VO(OH)_3]$ at 25°C and log of observed first-order rate constant for Pa decomposition (60°C) with pH (total $[V(V)] = 2.0 \times 10^{-5}$ M).

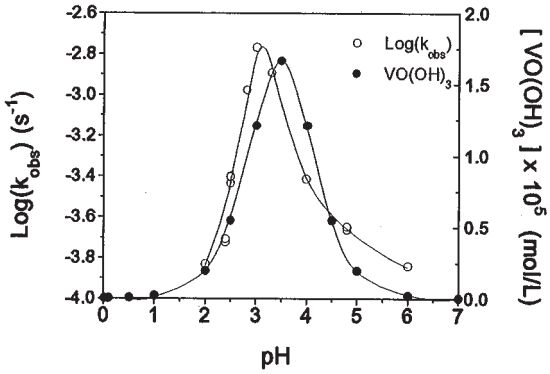

experiments in Fig. 4, the highest [V(V)] used was 2.0×10^{-5} M. At these low concentrations, only mononuclear V(V) species are present in solution (17). If the equilibrium relationship in eqs. [5] and [6] (17) are used to calculate the concentrations of VO_2^+, $VO(OH)_{3(aq)}$, and $VO_2(OH)_2^-$ at different pHs, the variation of $[VO(OH)_3]$ is as shown in Fig. 6 (concentration of total V species = 2.0×10^{-5} M). This hydroxide is soluble up to a concentration of 6.3×10^{-5} M (17). The variation of Pa decomposition rate with pH is also shown in Fig. 6. The similarity in the shape of the two curves suggests that $VO(OH)_3$ is the active vanadium(V) species.

[5] $VO_2^+ + 2H_2O \leftrightarrow VO(OH)_{3(aq)} + H^+, \quad \log K = -3.2$

[6] $VO_2^+ + 2H_2O \leftrightarrow VO_2(OH)_2^- + 2H^+, \quad \log K = 7.0$

Gas analysis

In alkali- or metal-induced H_2O_2 decomposition, 1 mol of O_2 is generated from every 2 mol of peroxide decomposed. For a wide range of decomposition mechanisms it appears that nearly 1.0 mol of O_2 is generated from 2 mol of HSO_5^- (6). These two peroxides have very few side reactions, and eq. [7] is obeyed. On the other hand, many side reactions have been reported for Pa decomposition catalyzed by Co(II) (2, 3). In one study, the evolution of CO_2 was found equal to that of O_2 (2), and a substantial amount of CH_4 was detected in the other (3). Both publications discussed the possible side reactions (2, 3). Interestingly, the above results conflict with each other and with earlier results showing O_2 to be the only gas generated by Co(II) catalysis (11). However, pH was not controlled in this earlier study (11).

[7] $2ROOH \rightarrow 2ROH + O_2$

It appears that reaction conditions, particularly pH, have a great influence on these side reactions. In a recent investigation on Pa decomposition catalyzed by Mn(II), the gas evolved at pH 8.2 was primarily O_2, and only a negligible amount of CO_2 was detected. However, a significant amount of CO_2 was generated at pH 5 (10). The aim of the present research was not to clarify the situation for Co(II) and Mn(II) but to collect data for V(V) so that a more detailed reaction mechanism could be postulated.

Fig. 7. Gas chromatograms for the analysis of gases from Pa decomposition: 0 min (top) and 60 min (bottom).

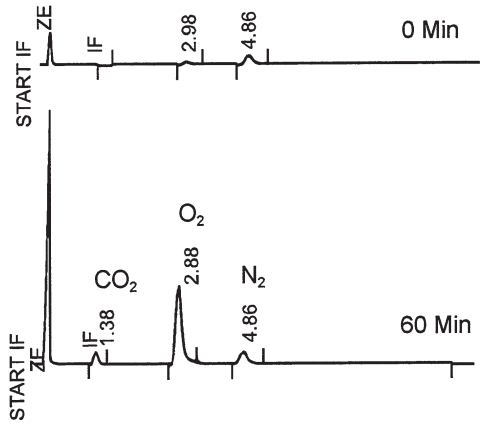

An equilibrium Pa solution was used for this experiment. Unconverted acetic acid (eq. [1]) does not affect the rate of V-induced decomposition. Distilled Pa solutions contain only a small amount of acetic acid (~4 wt.%), and when a 1:1, 2:1, or 4:1 mole ratio of acetic acid to Pa was used, the rate of Pa decomposition catalyzed by V(V) was unaffected. The small amount of H_2O_2 in distilled Pa solutions was rapidly decomposed by V species (9). An equilibrium Pa solution containing 49 mM Pa, 17 mM H_2O_2, and 2.0×10^{-5} M V(V) was allowed to decompose at pH 2.5 and 60°C for 40 min. The residual peroxide concentrations were 19 mM Pa and 0.5 mM H_2O_2. The solution was cooled, adjusted to pH 3.0, and poured into a gas bag that was then sealed. The bag was flushed with He at atmospheric pressure without it being inflated. The bag was then placed in a 60°C water bath and the gases analyzed after a given retention time. The bag was appropriately sized so that the final pressure was approximately atmospheric. The experiment was done twice (different degrees of Pa decomposition), and for every 2 mol of Pa decomposed, an average of 0.96 mol of O_2 was detected. The chromatograms corresponding to one of the gas mixtures at 0 and 60 min are shown in Fig. 7. Only a small amount of CO_2 was generated, and CH_4, whose retention time was ~7.2 min, was not detected.

Proposed free-radical mechanism

The following mechanism consists of likely reactions and is consistent with all of the data obtained in the pH 3 range. The rate equation for Pa decomposition was first order in [Pa] and approximately first order (0.9) in [V(V)] at pH 2.4. Based on Pa decomposition catalyzed by 1.0×10^{-5} M and 2.0×10^{-5} M V(V), it was concluded that the rate equation did not change in going from pH 2.4 to ~3.0. Reactions similar to those in eqs. [8]–[10] are frequently observed in peroxide decomposition chemistry (6), and eqs. [11] and [12] are found in the literature for metal-catalyzed decomposition of Pa (2, 3). Equations that support this data have been deposited.[2]

[2] Supplementary material may be purchased from: The Depository of Unpublished Data, Document Delivery, CISTI, National Research Council of Canada, Ottawa, Canada, K1A 0S2.

© 1998 NRC Canada

[8] $VO(OH)_{3(aq)} + AcOOH \xrightarrow{k_{1a}} VO(OH)_{2(aq)} + AcOO\cdot + H_2O$

[9] $VO(OH)_{2(aq)} + AcOOH \xrightarrow{k_{1b}} VO(OH)_{3(aq)} + AcO\cdot$

[10] $AcO\cdot + AcOOH \xrightarrow{k_{2a}} AcOH + AcOO\cdot$

[11] $AcOO\cdot + AcOOH \xrightarrow{k_{2b}} AcOH + AcO\cdot + O_2$

[12] $2\ AcOO\cdot \xrightarrow{k_3} O_2 + \text{other products}$

The first reaction (eq. [8]) is the rate-determining step. Using the steady-state approximation for the concentrations of $VO(OH)_2$, AcOO·, and AcO·, the rate law (eq. [24]) for the reaction scheme can be derived as follows.

[13] $$\frac{d[AcOOH]}{dt} = -k_{1a}[VO(OH)_3][AcOOH] - k_{1b}[VO(OH)_2][AcOOH] - k_{2a}[AcO\cdot][AcOOH] - k_{2b}[AcOO\cdot][AcOOH]$$

[14] $$\frac{d[VO(OH)_2]}{dt} = 0 = k_{1a}[VO(OH)_3][AcOOH] - k_{1b}[VO(OH)_2][AcOOH]$$

[15] $$k_{1b}[VO(OH)_2] = k_{1a}[VO(OH)_3]$$

[16] $$\frac{d[AcO\cdot]}{dt} = 0 = k_{1b}[VO(OH)_2][AcOOH] + k_{2b}[AcOO\cdot][AcOOH] - k_{2a}[AcO\cdot][AcOOH]$$

Substitute eq. [15] into eq. [16]:

[17] $$[AcO\cdot] = \frac{k_{1a}[VO(OH)_3] + k_{2b}[AcOO\cdot]}{k_{2a}}$$

[18] $$\frac{d[AcOO\cdot]}{dt} = 0 = k_{1a}[VO(OH)_3][AcOOH] + k_{2a}[AcO\cdot][AcOOH] - k_{2b}[AcOO\cdot][AcOOH] - k_3[AcOO\cdot]^2$$

Substitute eq. [17] into eq. [18]:

[19] $$\frac{d[AcOO\cdot]}{dt} = 0 = k_{1a}[VO(OH)_3][AcOOH] + \frac{k_{2a}}{k_{2a}}(k_{1a}[VO(OH)_3] + k_{2b}[ACOO\cdot])[AcOOH] - k_{2b}[AcOO\cdot][AcOOH] - k_3[AcOO\cdot]^2$$

[20] $$\frac{d[AcOO\cdot]}{dt} = 0 = 2k_{1a}[VO(OH)_3][AcOOH] - k_3[AcOO\cdot]^2$$

[21] $$[AcOO\cdot] = \left(\frac{2k_{1a}}{k_3}[VO(OH)_3][AcOOH]\right)^{1/2}$$

Substitute eq. [21] into eq. [17]:

[22] $$[AcO\cdot] = \frac{k_{1a}}{k_{2a}}[VO(OH)_3] + \frac{k_{2b}}{k_{2a}}\left(\frac{2k_{1a}}{k_3}[VO(OH)_3][AcOOH]\right)^{1/2}$$

Substitute eqs. [15], [21], and [22] into eq. [13]:

[23] $$\frac{d[AcOOH]}{dt} = -k_{1a}[VO(OH)_3][AcOOH] - k_{1a}[VO(OH)_3][AcOOH] - \frac{k_{2a}}{k_{2a}}[k_{1a}[VO(OH)_3][AcOOH]] - \frac{k_{2a}k_{2b}}{k_{2a}}\left(\frac{2k_{1a}}{k_3}[VO(OH)_3][AcOOH]\right)^{1/2}[AcOOH] - k_{2b}\left(\frac{2k_{1a}}{k_3}[VO(OH)_3][AcOOH]\right)^{1/2}[AcOOH]$$

Equation [23] simplifies to:

[24] $$\frac{d[AcOOH]}{dt} = -3k_{1a}[VO(OH)_3][AcOOH] - 2k_{2b}\left(\frac{2k_{1a}}{k_3}[VO(OH)_3]\right)^{1/2}[AcOOH]^{3/2}$$

The second term on the right-hand side (RHS) of eq. [24] is likely to be much less than the first term. Therefore, the theoretical rate law is approximately first order in both [V(V)] and [Pa]. The second term on the RHS of eq. [24] can be approximated at pH 3.3 where the free-radical mechanism is most significant. At a $[VO(OH)_3]$ of ~1.5×10^{-5} M, the first-order rate constant, k_{obs}, is ~1×10^{-3} s^{-1} (Fig. 6). The second-order rate constant, k', for eq. [25] would equal to 5×10^{-4} s^{-1} (one-half of the total rate) divided by 1.5×10^{-5} M or 33.3 M^{-1} s^{-1}. If the second term on the RHS of eq. [24] is assumed to be much less than the first term then $k' = 3k_{1a}$. The rate constant k_3 is reported to be ~1×10^8 M^{-1} s^{-1} (18) so that the term $(2k_{1a}/k_3[VO(OH)_3])^{1/2}$ is equal to ~1.82×10^{-6} $M^{0.5}$. At [AcOOH] of 0.03 M, the term $(2k_{1a}/k_3[VO(OH)_3])^{1/2}[AcOOH]^{1/2}$ would be equal to ~3.15×10^{-7} M, which is lower than $1.5 \times 10^{-5}([VO(OH)_3])$ by a factor of 48. Therefore, the second term on the RHS is significant only if $2k_{2b} > > 3k_{1a}$. Allen and Aguilo (3) proposed eq. [11] only because a similar reaction is known in H_2O_2 chemistry. However, the rate constant for that reaction ($HOO\cdot/H_2O_2$) is <1.0 M^{-1} s^{-1} (19). Acylperoxy radicals are known to be more reactive than HOO· (18), but even if 50 M^{-1} s^{-1} is assumed for k_{2b}, the second term on the RHS would be lower than the first term by a factor of ~16.

[25] $$-\frac{d[AcOOH]}{dt} = k'[VO(OH)_3][AcOOH]$$

If it is assumed that GAMID is efficient at scavenging AcO· and (or) AcOO· then approximately 50% of the decomposition of Pa can be explained by the mechanism

© 1998 NRC Canada

above. Ionic mechanisms have been postulated for H_2O_2 decomposition catalyzed by V(V) (20, 21) and may be responsible for additional decomposition of Pa. Since the rate laws for the proposed free-radical mechanism and total decomposition (eq. [4]) are both first order in [V(V)] and [Pa], it would be expected that the rate law for heterolytic decomposition is similar.

Conclusions

Peracetic acid (Pa) is now being used for totally chlorine-free delignification and bleaching of wood pulps. The Pa stage is normally conducted in the pH range of 2.0–6.0, and some transition metals desorb from the pulp fibers to the aqueous phase.

Of the metals likely to be present in bleaching systems, Co(II) and V(V) are the most potent catalysts for the wasteful decomposition of Pa to O_2. Radical scavenging by *N*,*N*′-(5-nitro-1,3-phenylene)-bisglutaramide (GAMID) indicated that free-radical mechanisms were operative. Kinetic data supported a free-radical mechanism previously published for Co(II). A similar type mechanism, involving $VO(OH)_{2(aq)}$ and $VO(OH)_{3(aq)}$, was postulated to partially explain catalysis by vanadium. The variation of $VO(OH)_3$ concentration with pH (total [V(V)] = 2.0×10^{-5} M) was obtained from the literature (17). The shape of the curve was very similar to that for decomposition rate with pH.

Acknowledgements

The authors gratefully acknowledge the financial support from the National Science Foundation through grant CHE 9412985. Besides their financial support, we are also grateful to Solvay Interox for allowing us to use their peracetic acid generation unit. We are further indebted to Dr. A.R.P. van Heiningen who made available to us the use of the gas analysis system at the Limerick Pulp and Paper Centre, University of New Brunswick, Fredericton.

References

1. B. Strandell and L.-E. Myhrman. Sven. Papperstidn. **93**(3), 36 (1996).
2. E. Koubek and J.O. Edwards. J. Inorg. Nucl. Chem. **25**, 1401 (1963).
3. G.C. Allen and A. Aguilo. Adv. Chem. Ser. **76**, 363 (1968).
4. V.A. Lunenok-Burmakina, G.G. Lezina, V.B. Emel'yanov, and A.G. Miroshnichenko. Russ. J. Phys. Chem. (Transl. of Zh. Fiz. Khim.) **51**, 1650 (1977).
5. R.C. Thompson. Inorg. Chem. **20**, 1005 (1981).
6. C. Marsh and J.O. Edwards. Prog. React. Kinet. **15**, 35 (1989).
7. Z. Zhang. Ph.D. thesis, Brown University, Providence, R.I. 1990.
8. R.C. Francis, X.Z. Zhang, P.M. Froass, and O. Tamer. Tappi J. **77**(6), 133 (1994).
9. X-Z. Zhang, R.C. Francis, D.B. Dutton, and R.T. Hill. J. Wood Chem. Technol. **18**, 253 (1998).
10. Z. Yuan. Ph.D. thesis, University of New Brunswick, Fredericton. 1997.
11. T. Vrbaski and I. Brihta. Arh. Kem. **26**, 267 (1954).
12. Ya.M. Vasyutyn, V.O. Garenko, I.A. Garbuzyuk, O.P. Ivanchishin, and R.G. Makitra. Soviet Prog. Chem. **55**(6), 25 (1989) (transl. from Ukr. Khim. Zh. (Russ. Ed.) **55**(6), 584 (1989)).
13. S. Singh and R.C. Hider. Anal. Biochem. **171**, 47 (1988).
14. H. Hingorani, H.C. Goal, G. Chandra, and S.N. Srivastava. Z. Phys. Chem. (Liepzig), **271**, 823 (1990)
15. C.W. Dence. *In* Pulp bleaching: principles and practice. *Edited by* C.W. Dence and D.W. Reeve. TAPPI Press, Atlanta. 1996. pp. 150–151.
16. A.R. Negri, G. Gimenez, R.T. Hill, and R.C. Francis. Tappi J. **81**, 241 (1998).
17. C.F. Baes and R.E. Mesmer. The hydrolysis of cations. Wiley, N.Y. 1976. p. 206.
18. G.E. Zaikov, J.A. Howard, and K.U. Ingold. Can. J. Chem. **47**, 3017 (1969).
19. B.H.J. Bielski, D.E. Cabelli, and R.L. Arudi. J. Phys. Chem. Ref. Data, **14**, 1041 (1985).
20. P. Flood, T.J. Lewis, and D.H. Richards. J. Chem. Soc. 5024 (1963).
21. G.A. Dean. Can. J. Chem. **39**, 1174 (1961).

© 1998 NRC Canada

Highly diastereoselective synthesis of 1,2-amino alcohols via nucleophilic addition of organocerium reagents to 4- and 5-oxazolidinonecarbaldehydes

Andrew G.H. Wee and Fuxing Tang

Abstract: The reaction of chiral, non-racemic 4- and 5-oxazolidinonecarbaldehydes, **6** and **13**, with organocerium reagents proceeds efficiently with good to excellent diastereoselectivity to give *syn* and *anti* alcohols, respectively. A model to explain the observed diastereoselectivity of the reaction of **6** and **13** is provided. The utility of this method for the synthesis of amino alcohols is exemplified by the synthesis of C-18-D-*ribo*-phytosphingosine from the *anti* alcohol **14f**.

Key words: oxazolidinonecarbaldehydes, organocerium, diastereoselective, amino alcohols, C-18-*ribo*-phytospingosine.

Résumé : La réaction de réactifs organiques du cérium avec les 4- et 5-oxazolidinonecarbaldéhydes chiraux et non racémiques, **6** et **13**, s'effectuent d'une façon efficace, avec des diastéréosélectivités allant de bonnes à excellentes, et elles conduisent aux alcools *syn* et *anti* respectivement. On propose un modèle pour expliquer la diastéréosélectivité de la réaction des produits **6** et **13**. Comme exemple pour démontrer l'utilité de cette méthode pour la synthèse d'aminoalcools, on propose la synthèse de la C-18-D-*ribo*-phytosphingosine à partir de l'alcool *anti*, **14f**.

Mots clés : oxazolidinonecarbaldéhydes, organocérium, diastéréosélectif, aminoalcools, C-18-*ribo*-phytosphingosine.

[Traduit par la Rédaction]

Introduction

The 1,2-amino alcohol moiety is a common subunit that is found in many naturally occurring and medicinally important compounds such as sphingolipids (1*a*), hydroxylated alkaloids (1*b*, 1*c*), amino acids (1*d*, 1*e*), HIV-enzyme inhibitors (1*f*, 1*g*), and amino sugars (1*h*). As well, chiral auxiliaries (2*a*) and ligands (2*b*) that are widely employed in asymmetric synthesis possess the 1,2-amino alcohol unit as a key structural feature. Much effort has, therefore, been devoted towards developing new strategies (for reviews, see ref. 3) for the synthesis of 1,2-amino alcohols. The most widely used method involves the nucleophilic addition of C-centred nucleophiles to α-amino aldehydes (3*a*, 3*c)* However, some limitations of the method have been noted; for example, the α-amino aldehyde is prone to racemization under the reaction conditions (3*a*, 4). As well, the diastereoselectivity of the nucleophilic addition reaction is usually not as high as expected although, recently, methods (3*c*) have been devised to overcome this problem.

In comparison, the use of 2-oxazolidinones for the synthesis of 1,2-amino alcohols has not been extensively investigated (5). Two aspects that make them attractive synthetic intermediates are (*a*) the 2-oxazolidinone moiety can be considered as a protected amino alcohol synthon, which can be subsequently unmasked to reveal the 1,2-amino alcohol unit, and (*b*) the reactions carried out on oxazolidinone derivatives are usually highly stereoselective (5).

Herein, we report our studies on the nucleophilic addition of organocerium reagents to chiral, non-racemic 4- and 5-oxazolidinonecarbaldehydes (**6** and **13**, respectively) (for a preliminary communication, see ref. 6). The addition was found to proceed with good to excellent diastereoselectivity to give *syn* or *anti* alcohol products in moderate to good chemical yields. We also developed a procedure for the generation and in situ reaction of 4-oxazolidinonecarbaldehyde **6** with organocerium reagents.

Received February 4, 1998.

A.G.H. Wee[1] and F. Tang. Department of Chemistry, University of Regina, Regina, SK S4S 0A2, Canada.

[1] Author to whom correspondence may be addressed. Telephone: (306) 585-4767. Fax: (306) 585-4894. E-mail: andreghw@meena.cc.uregina.ca

Results and discussion

Preparation of iodophenylsulfone (5) and benzylether (8)

The iodo phenylsulfone **5** serves as a convenient and shelf-stable precursor of the aldehyde **6**. The preparation of **5** is summarized in Scheme 1 and began with the oxidation of the known phenylsulfide **1** (7*a*) (α:β ratio 8.5:1.5 based on integration of H-1) with mCPBA to give a separable mixture of α,β-anomers (8:2)[2,3] of **2**. The slightly light-sensitive **2** were then treated with *n*-butyllithium in the presence of HMPA as a cosolvent to effect 1,2-elimination of a molecule of acetone to give the ene alcohol **3** (for the use of

 © 1998 NRC Canada

Scheme 1.

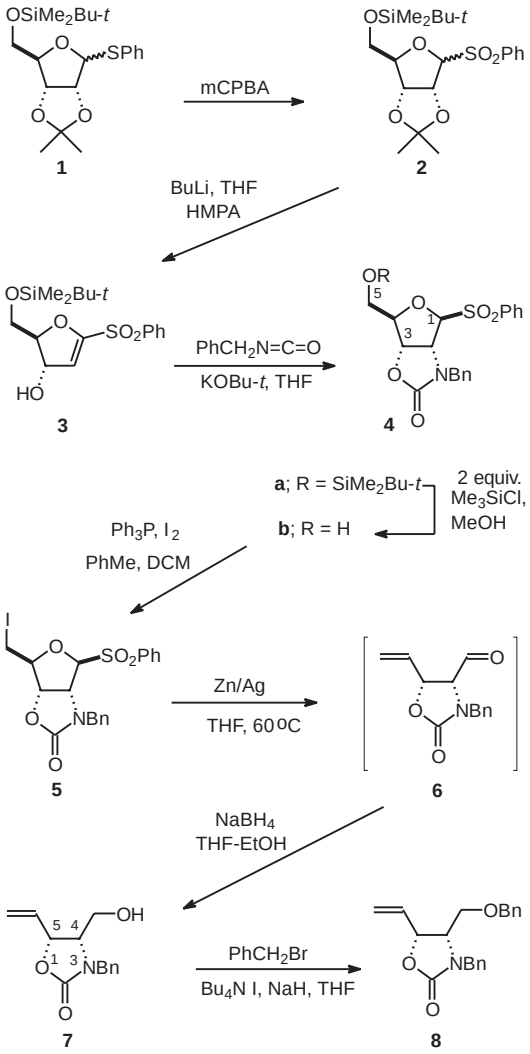

organosulfones in synthesis, see ref. 8). We found it unnecessary to treat α-**2** and β-**2** separately in this elimination reaction since both anomers lead to the same ene alcohol with no loss in yield. Compound **3** was found to be unstable during storage (~ 3 d) and was utilized immediately in the carbamation step. Base-catalyzed reaction of **3** with benzylisocyanate afforded *cis*-bicycle **4a** as a single diastereomer in good yield.

It was found that the use of KOBu-*t* is essential for efficient carbamation. With NaH as the base only a low yield of the **4a** was obtained; the uncyclized urethane, which had resulted from the nucleophilic addition of only the alcohol unit to the benzylisocyanate, was the major product. A likely explanation for the lack of intramolecular Michael addition is that, with NaH, the phenylsulfonyl-stabilized carbanion (8*b*) intermediate is prone to undergo a retro-Michael reaction. This pathway is absent in the *tert*-butoxide-catalyzed reaction because the phenylsulfone-stabilized carbanion is protonated by the *tert*-butyl alcohol that is present.

Desilylation of **4a** to the primary alcohol **4b** was accomplished using Me_3SiCl in MeOH and was followed by reaction of **4b** with $Ph_3P–I_2$ (9) to give the iodo phenylsulfone **5**.

We were not able to ascertain from the ^{1}H NMR spectra of **4a,b** whether the stereochemistry of the 1-phenylsulfonyl group is α or β because of the overlap of the H-1, H-2, and PhCHN resonances. However, the ^{1}H NMR of **5** was better resolved and showed H-1 as a doublet centred at δ 4.82 with a vicinal coupling constant, $J_{1,2}$, of 1.8 Hz. This small *J* value[3] suggests that the 1-phenylsulfonyl group has the β-configuration. This outcome is unexpected when the conversion of **3** to **4a** is considered and it suggests that the phenylsulfone-stabilized carbanion intermediate that is generated during the intramolecular carbamation reaction is protonated from the more hindered, concave side of the bicycle to give **4a**. It should be noted that protonation from the less hindered, convex side of the bicycle should, in principle, be more favoured; however, this would lead to a sterically congested product wherein the α-phenylsulfonyl moiety is engaged in severe nonbonded interactions with the *syn* oxazolidinone moiety.

The next step was the Zn–Ag[4] (10) mediated reductive elimination of **5** in dry THF at 60°C to afford the olefinic aldehyde **6**. Subsequent reduction of **6** with $NaBH_4$ proceeded uneventfully to give crystalline primary alcohol **7** ($[\alpha]_D^{23}$ –15.2 (*c* 0.98, $CHCl_3$))[5] in high yield. Alcohol **7** was then benzylated to give **8**, which served as the precursor for the 5-oxazolidinonecarbaldehyde **13**.

The formation of **6** deserves some comments. The ^{1}H and ^{13}C NMR spectra of the primary alcohol **7** that is derived from **6** are in accord with the assigned structure. The salient feature in the ^{1}H NMR spectrum is the pseudo triplet due to H-5 that was centred at δ 4.92. It has a $J_{4,5}$ of 7.4 Hz[6] that is characteristic of a *cis* stereochemistry (11). This indicates that no epimerization of the aldehyde to the *trans* diastereomer had occurred under the reaction conditions used in the reductive elimination step.

Formation and reaction of 4-oxazolidinonecarbaldehyde (6) with $RCeCl_2$

It is well documented (3*a*, 4) that amino aldehydes (except for a serine-derived aldehyde (12)) are, in general, unstable and are not amenable to isolation. To avoid potential difficulties associated with the isolation of **6**, we decided to investigate its generation and in situ reaction with the preformed organocerium reagent (13*a*, 13*b*) (hereafter referred to as $RCeCl_2$; the exact speciation of the organocerium reagent is not known. See ref. 13*c*) as depicted in eq. [1]. The

[2] Ratio is based on isolated yields. Decoupling of the H-3 multiplet (δ 4.72–4.81) in α-2 simplified the H-1,H-2 multiplet at δ 5.02–5.10; H-2 collapsed to a singlet at δ 5.9. H-1 was observed as a doublet centred at δ 5.7 and has a $J_{1,2}$ of 3.8 Hz.

[3] Typically, H-1 in the α-anomer shows a $J_{1,2}$ in the range 3.8–4.4 Hz, and in the β-anomer $J_{1,2}$ is in the range of 1.8–2.0 Hz (7).

[4] We have also examined other Zn-based methods such as Zn dust, EtOH; Zn/Cu, THF; and $ZnCl_2–C_8K$, THF. These methods either gave low yields of 6 and a substantial amount of the reduced product or decomposition products.

[5] We have prepared ent-**7** from D-mannose and it has $[\alpha]_D^{23}$ = +14.8 (c 1.01, $CHCl_3$).

[6] Decoupling of the alkene methine multiplet at δ 5.99–6.19 collapsed the H-5 "triplet" to a broad doublet centred at δ 4.92. Typically, J_{trans} = 3.3–4.5 Hz and J_{cis} = 6.2–7.5 Hz (11).

© 1998 NRC Canada

Table 1. Reaction of **6** with $RCeCl_2$ according to method A.

Entry	$RCeCl_2$	T,°C/h	*syn*-**9**:*anti*-**10** [b]	Yield (%)
1	**a**; MeLi	–78/5	95:5	85
2	MeLi[a]	–78/5	89:11	35
3	**b**; CH_2=CHMgBr	–78/5	>99:1	85
4	CH_2=CHMgBr[a]	–78/5	83:17	40
5	**c**; CH_2=C(OBu-*t*)O$^-$ Li^+	–78/5	86:14[c]	92
6	**d**; PhC≡CLi	–78/5	>99:1	94
7	**e**; 2-Furanyl Li	–78/5	>99:1	85
8	**f**; PhMgBr	–78/5; 0/1	88:12	52
9	PhMgBr	–78/5	88:12	29

[a]Reaction was performed without $CeCl_3$.
[b]Alcohols were inseparable. Ratio was based on the integration of Me resonance in the ^{1}H NMR of acetate derivatives.
[c]Ratio was based on the integration of the *t*-Bu singlet.

use of dry THF for the reductive elimination step was essential for the success of this procedure.

[1]

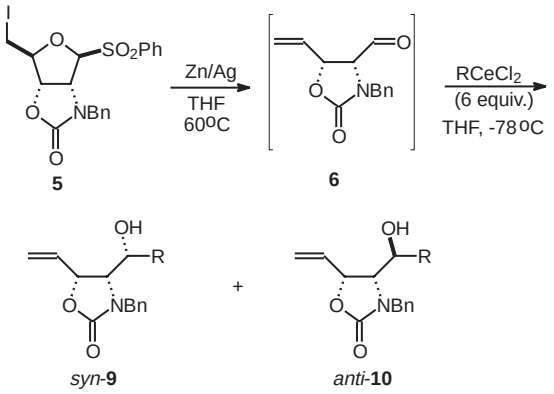

As shown in Table 1, Grignard-derived and organolithium-derived organocerium reagents reacted well with **6**. The nucleophilic addition reaction produced a crystalline, diastereomeric mixture of alcohols *syn*-**9** and *anti*-**10** in which the former was present as the predominant or exclusive product. For reactions in which Grignard-derived $RCeCl_2$ reagents were used, it was advantageous to warm the reaction mixture to 0°C and to maintain the reaction at 0°C for at least 1 h. Thus, quenching the $PhCeCl_2$ reaction after 5 h at –78°C yielded 29% of a mixture of **9f** and **10f** (entry 9). However, a 52% yield of **9f**, **10f** was obtained when the mixture was warmed to and maintained at 0°C for 1 h (entry 8). For the CH_2=$CHCeCl_2$ reaction, the reaction mixture must be conducted at –78°C because the organocerium reagent is unstable at 0°C (13*b*, 14). The use of Grignard and organolithium reagents alone resulted in lower diastereoselectivity and poorer chemical yields of products (compare entries 1, 2 and 3, 4).

The relative stereochemistry of the hydroxyl group and the benzylamino moiety of the oxazolidinone unit in **9** was assigned as *syn* on the basis of the data obtained from proton decoupling and NOE experiments performed on **12**. Compound **12** was synthesized from **9a,10a** using standard functional group manipulations as summarized in eq. [2]. Decoupling of the C-5 methyl doublet (δ 1.25) in **12** collapsed the H-5 quintet (br, δ 4.42) to a doublet, $J_{5,4}$ = 4.4 Hz. Similarly, irradiation of the H-4′ multiplet (δ 4.00–4.18) simplified the H-4 triplet (δ 3.11) to a doublet, $J_{4,5}$ = 4.4 Hz. Based on this small vicinal coupling constant (11) the relative stereochemistry of the methyl and dioxalanyl groups was, therefore, assigned as *trans*. This result was confirmed by the observation of a strong NOE enhancement (6.7%) for the H-4 proton upon irradiation of the C-5 methyl doublet.

[2]

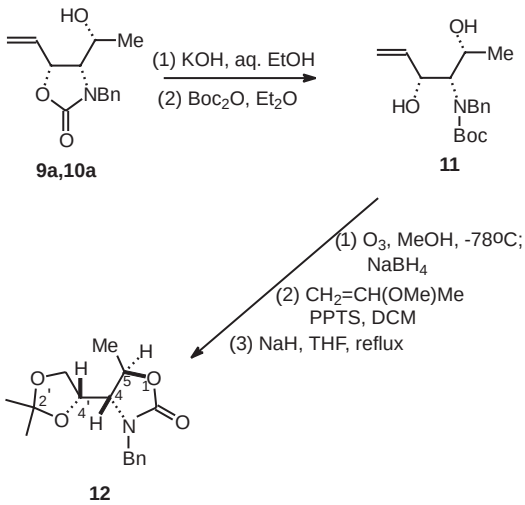

Formation and reaction of 5-oxazolidinonecarbaldehyde (13) with $RCeCl_2$

Aldehyde **13** was prepared by ozonolysis of the benzyl ether **8** in DCM followed by replacement of the DCM with dry THF. The THF solution of crude **13** was then added to $RCeCl_2$ (4 equiv.) at –78°C (eq. [3]). Again, we found that it

[3]

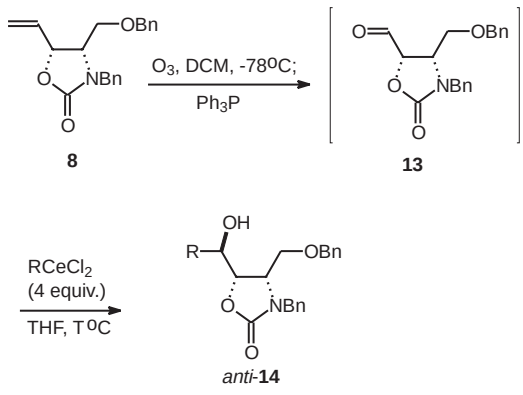

© 1998 NRC Canada

Table 2. Reaction of **13** with $RCeCl_2$ according to method B.

Entry	$RCeCl_2$	T,°C/h	*anti*-**14**	Yield (%)[b]
1	**a**; MeLi	–78/5	>99:1	62
2	MeLi[a]	–78/5	Dec.	0
3	**b**; CH_2=CHMgBr	–78/5	>99:1	59
4	CH_2=CHMgBr[a]	–78/5	>99:1	21
5	**c**; PhC≡CLi	–78/5	>99:1	85
6	**d**; CH_2=C(OBu-*t*)O$^-$ Li^+	–78/5	>99:1	84
7	**e**; 2-Furanyl Li	–78/5	>99:1	64
8	**f**; $C_{14}H_{29}MgBr$	–78/5; 0/1	>99:1	69
9	$C_{14}H_{29}MgBr$	–78/5	>99:1	40

[a]Reaction was performed in the absence of $CeCl_3$.
[b]Isolated yields.

was advantageous to warm the reactions involving Grignard-derived $RCeCl_2$ to 0°C before being quenched (Table 2, entries 8 and 9). In all cases, the alcohol product **14** was obtained as an oil, and in moderate to good overall yields. Only one diastereomer was produced as evidenced by ^1H and ^{13}C NMR analysis of the crude product: the other epimer was not detected.

The use of $CeCl_3$ is essential for the success of the reaction. For example, the use of MeLi only resulted in the complete decomposition of **13** (Table 2, compare entries 1 and 2) and the use of only CH_2=CHMgBr gave a lower yield of **14** (compare entries 3 and 4). The relative stereochemistry between the hydroxyl and the oxygen atom of the oxazolidinone unit was assigned as *anti* on the basis of the conversion of compound **14f** to C-18-D-*ribo*-phytosphingosine **18** (see later).

It was also of interest to examine the diastereoselectivity of nucleophilic addition reaction of **6** and **13** with $MeTi(OPr\text{-}i)_3$. It is well documented (15) that this nucleophilic reagent reacts with α-alkoxy aldehydes in a non-chelation controlled pathway because of the reduced Lewis acidity of the titanium centre. Unfortunately, the reaction of $MeTi(OPr\text{-}i)_3$ with **6** (using the same procedure developed for the conversion of **5** → **9**, **10**) resulted only in decomposition products. On the other hand, the reaction of $MeTi(OPr\text{-}i)_3$ with **13** (eq. [4]) gave a good yield (72%) of the addition product **15**. The ^1H NMR spectrum of **15** was very similar to that of *anti*-**14a**. We therefore prepared the

[4]

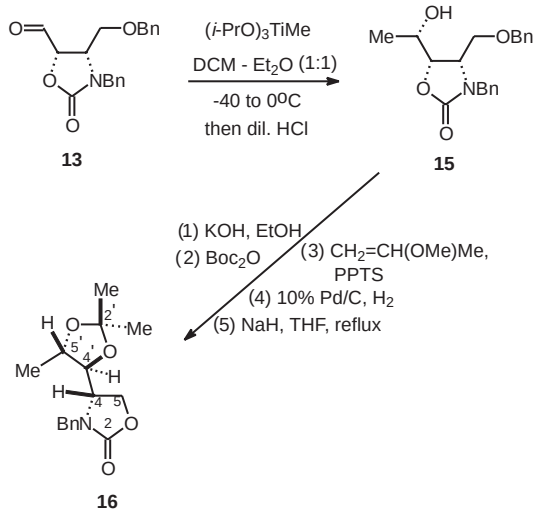

Chart 1.

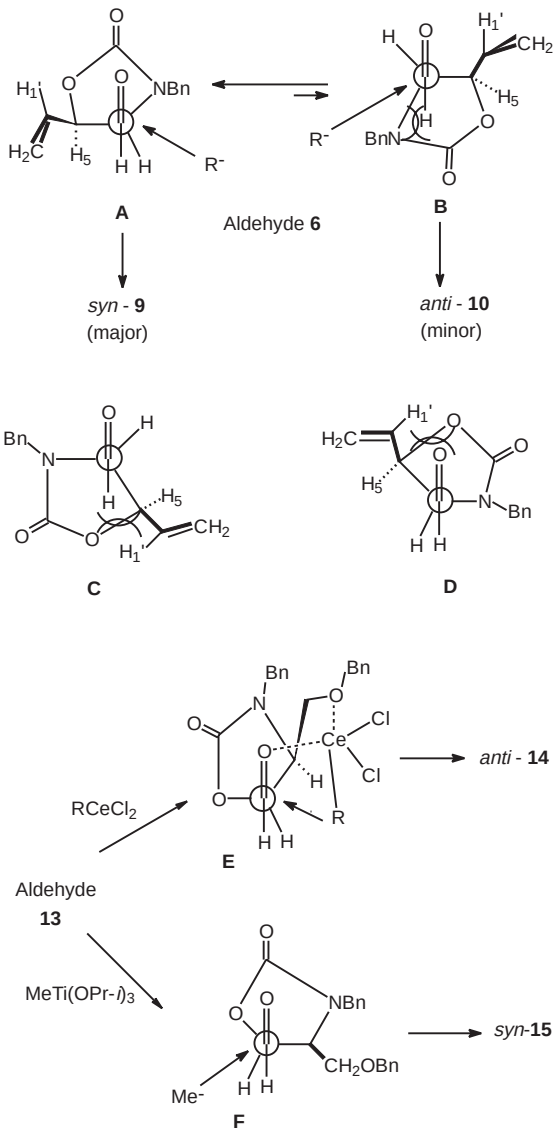

oxazolidinone derivative **16** (eq. [4]), which was subjected to NOE analysis. In particular, irradiation of the C-5′ methyl doublet centred at δ 1.05 resulted in a 3% enhancement of the H-4′ double doublet centred at δ 4.44. On the basis of this result, the configuration of the newly created carbinol

© 1998 NRC Canada

Scheme 2.

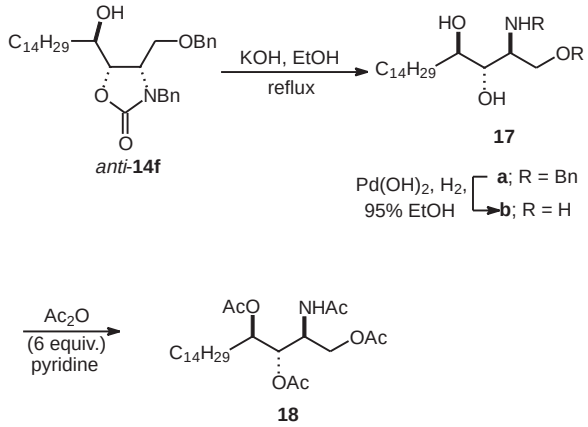

centre was assigned as *S*. That is, the addition reaction has proceeded with *syn* diastereoselectivity.

Reaction pathway

The diastereoselectivity observed in the reaction of aldehyde **6** can be understood if we consider the two reactive conformers **A** and **B** (Chart 1). In each of the conformers, the preferred orientation of the C-5-vinyl substituent with respect to the rigid, planar oxazolidinone unit is the one in which the vinyl H-1′ hydrogen is aligned antiperiplanar to the oxazolidinone H-5 hydrogen. This arrangement is adopted in order to relieve $A^{1,3}$ strain (16). Conformer **A** (17*a*) is more stable than **B** because in the latter a destabilizing interaction is present. Preferential nucleophilic attack via the sterically less hindered side in **A** leads to the major *syn* diastereomer **9** whereas attack via the sterically encumbered side in **B** results in the minor *anti* diastereomer **10**. The conformers **C** and **D** correspond to the Felkin–Anh-type model (17) but are considered less stable than **A** and **B** because of the presence of destabilizing steric interactions. **C** is destabilized by the steric interaction between the aldehydic hydrogen and the *cis*-vinyl group and especially H-1′. Similarly, steric interaction between the *cis*-vinyl group/H-1′ and the oxygen of the carbonyl function in **D** results in its destabilization.

The involvement of a five-membered chelate intermediate resulting from coordination of the carbonyl oxygen and the nitrogen atom of the NBn moiety to Lewis acidic Ce(III) (13*a*) is not likely because of the reduced basicity of the nitrogen atom resulting from conjugation of the nitrogen lone pair of electrons with the π-bond of the carbonyl group of the oxazolidinone unit.

In the case of **13**, a possible explanation for the unexpectedly high diastereoselectivity is the involvement of a seven-membered Ce(III) chelate **E** (Chart 1) (for the involvement of 7-membered chelates, see ref. 18). Its formation is entropically favoured because of the *cis* relationship of the aldehyde and $BnOCH_2$ moieties. Also, it is well documented that the oxygen atom in benzyl ethers shows a propensity to coordinate to Lewis acids (15*a*). The chelate can also accommodate a Felkin–Anh (17) arrangement. Thus, both chelation control and stereoelectronic effects reinforce one another in controlling the diastereoselectivity of the reaction. Intramolecular or intermolecular delivery of R′ will occur from the less hindered side of the carbonyl function, leading to *anti*-**14**. This line of reasoning is further supported by the result from the reaction of **13** with $MeTi(OPr\text{-}i)_3$. In the absence of any chelation to the titanium centre in the reagent, nucleophilic addition would proceed via **F** to give the *syn* diastereomer **15**.

Synthesis of C-18-D-*ribo*-phytosphingosine.

The oxazolidinone alcohol *anti*-**14f** ($[\alpha]_D^{22}$ +35.0 (*c* 1.50, $CHCl_3$)) was hydrolyzed in alcoholic 2 M aqueous KOH to provide **17a** in 83% yield (Scheme 2). Hydrogenolysis of the N,O-benzyl protecting groups in **17a** using Pearlman's catalyst afforded phytosphingosine **17b** as a powdery solid, which was subsequently peracetylated to give the crystalline tetraacetate derivative **18**. The spectroscopic data and specific rotations of **17b** and **18** are in excellent agreement with those reported (19).

Conclusions

The reactions of oxazolidinonecarbaldehydes **6** and **13** with organocerium reagents were found to proceed efficiently and with good to excellent diastereoselectivity to afford the corresponding secondary alcohol products. Compounds **6** reacted to give *syn* alcohols **9** as the major or exclusive products. With compounds **13**, the *anti* alcohols **14** were formed as the exclusive products. The results suggest that oxazolidinonecarbaldehyde **6** reacted with $RCeCl_2$ in a non-chelation pathway but with **13** a cerium chelate is involved. The method was applied to the synthesis of naturally occurring amino alcohol C18-D-*ribo*-phytosphingosine. Further application of this method and use of chiral, non-racemic 2-oxazolidinonecarbaldehydes in synthesis are in progress.

Experimental

General

Melting points are uncorrected and were measured on a Kofler hot-stage melting point apparatus. Infrared spectra were recorded using a Perkin Elmer 1600FT spectrophotometer: only diagnostic absorptions in the infrared spectrum are reported. ^1H (200 MHz) and ^{13}C (50.3 MHz) NMR spectra were recorded in $CDCl_3$ (unless otherwise stated), using a Bruker 200QNP spectrometer. Tetramethylsilane (δ_H = 0.00) and the $CDCl_3$ resonance (δ_C = 77.0) were used as references. Multiplicities "t", "q", and "quintet" represent pseudo triplet, quartet, and quintet, respectively, and are quoted as they appear in the ^1H NMR spectra. Where applicable, the signals of minor diastereomers are given within square brackets. Proton assignments were made using double irradiation experiments and, where necessary, 2D-COSY-45 experiments. Numberings in compounds **2–5** follow sugar numberings and, in compounds **6** onwards, numberings follow 2-oxazolidinone numberings. Elemental analyses and high-resolution electron impact (70 eV) and chemical ionization mass spectral analyses were performed at the Chemistry Department, University of Saskatchewan. Optical rotations were measured using an Optical Activity AA-5 polarimeter.

© 1998 NRC Canada

Reaction progress was monitored by thin-layer chromatography on Merck silica gel $60F_{254}$ precoated (0.25 mm) on aluminum backed sheets. Air- and moisture-sensitive reactions were conducted under a static pressure of argon. All organic extracts were dried over anhydrous Na_2SO_4. Flash chromatography (20) was performed on Merck silica gel 60 (230–400 mesh). Unless stated otherwise, the eluent is a mixture of petroleum ether:EtOAc in v/v ratio as follows: solvent A, 1:1; solvent B, 2:1; solvent C, 3:1; solvent D, 4:1; solvent E, 5:1. Abbreviations of solvents used: petroleum ether (PE, bp 35–60°C), ethyl acetate (EtOAc), diethyl ether (Et_2O), tetrahydrofuran (THF), and dichloromethane (DCM). THF and Et_2O were distilled from sodium-benzophenone, and DCM was distilled from CaH_2.

Organometallic reagents

Simple Grignard and organolithium reagents were purchased from Aldrich. Tetradecylmagnesium bromide was prepared from tetradecylbromide and magnesium metal as a 0.5 M solution in THF. Lithium phenylacetylide (21*a*), 2-lithiofuran (21*b*), and $CH_2 = C(OBu\text{-}t)O^- Li^+$ (21*c*) were prepared according to literature procedures. Organometallic reagents were standardized before use by titration using either 1,3-diphenylacetone *p*-tosylhydrazone (22*a*) (RLi) or pyreneacetic acid (22*b*) (RMgBr) as indicators.

Phenyl 5-*O*-(*tert*-butyldimethylsilyl)-2,3-*O*-isopropylidene-α,β-D-ribofuranosyl sulfone (2)

The phenylthio furanoside (7 g, 18 mmol) was dissolved in DCM (100 mL) and saturated aqueous $NaHCO_3$ (200 mL) was added. The biphasic mixture was cooled to 0°C in an ice-bath and mCPBA (11 g, 39 mmol, 60% tech.) was added portionwise. Then the mixture was stirred at room temperature (rt) for 20 h. The mixture was recooled to 0°C and 10% aqueous $NaHSO_3$ was added to destroy unreacted mCPBA. The mixture was stirred at rt for 1 h, and the aqueous phase was separated and back-extracted with DCM (50 mL). The combined organic phases were washed with saturated $NaHCO_3$ (2 × 50 mL), dried, filtered, and evaporated. The crude oil was chromatographed (solvent E) to give the desired sulfone (6.2 g, 85%) as a thick, viscous oil. β-**2**: ^{1}H NMR, δ: 0.00 (s, 6H, $SiMe_2$), 0.80 (s, 9H, *t*-Bu), 1.28 (s, 3H, Me), 1.40 (s, 3H, Me), 3.66 (dd, 1H, *J* = 10.3, 7.6 Hz, H-5), 3.76 (dd, 1H, *J* = 10.3, 6.5 Hz, H-5′), 4.23 (dt, 1H, *J* = 6.5, 2.1 Hz, H-4), 4.65 (dd, 1H, *J* = 6.5, 2.1 Hz, H-3), 4.82 (d, 1H, *J* = 2.1 Hz, H-1), 5.24 (dd, 1H, *J* = 6.5, 2.1 Hz, H-2), 7.40–7.62 (m, 3H, PhH), 7.76–7.87 (m, 2H, PhH). α-**2**: ^{1}H NMR, δ: –0.06 (s, 3H, SiMe), –0.02 (s, 3H, SiMe), 0.70 (s, 9H, *t*-Bu), 1.15 (s, 3H, Me), 1.26 (s, 3H, Me), 3.63 (dd, 1H, *J* = 11.4, 2.2 Hz, H-5), 3.75 (dd, 1H, *J* = 11.4, 2.2 H, H-5′), 4.27–4.32 (m, 1H, H-4), 4.72–4.81 (m, 1H, H-3), 5.02–5.13 (m, 2H, H-1, H-2), 7.42–7.62 (m, 3H, PhH), 7.94 (d, 2H, J = 7.5 Hz, PhH). ^{13}C NMR, δ: –5.4, 17.9, 24.2, 25.1, 25.7, 65.0, 81.0, 82.1, 86.1, 96.3, 114.3, 128.5, 129.4, 133.4, 139.1. Anal. calcd. for $C_{20}H_{32}O_6SSi \cdot ¼H_2O$: C 55.46, H 7.57; found: C 55.41, H 7.52.

Phenyl 2-benzylamino-5-*O*-(*tert*-butyldimethylsilyl)-2-deoxy-α-D-ribofuranosyl sulfone (4a)

The phenylsulfone **2** (6.2 g, 14.5 mmol) was dissolved in a mixture of dry THF (77 mL) containing dry HMPA (3.2 mL) under Ar. The solution was cooled to –78°C and *n*-BuLi (10.8 mL, 21.7 mmol, 2.1 M in hexanes) was added dropwise via syringe to the mixture. A deep yellow-orange solution resulted, which was stirred at –78°C for 1 h and then the cooling bath was removed. The mixture was allowed to warm slowly to rt, stirred at rt for 2 h, and then recooled to 0°C. Saturated aqueous NH_4Cl (15 mL) was added, followed by EtOAc (50 mL). The organic layer was removed and the aqueous phase was reextracted with EtOAc (2 × 50 mL). The combined organic phases were washed with saturated aqueous NaCl (70 mL), dried, filtered, and evaporated. The residual yellow oil was chromatographed (solvent C) to give **3** as a pale yellow oil (3.8 g, 71%) that slowly crystallized on standing. The product was found to be unstable and is best kept in the freezer for prolonged storage. IR, ν_{max}: 3575–3275 cm^{-1}. ^{1}H NMR, δ: –0.02 (s, 3H, SiMe), –0.05 (s, 3H, SiMe), 0.78 (s, 9H, *t*-Bu), 2.08–2.20 (br hump, 1H, OH), 3.57 (dd, 1H, *J* = 11.5, 4.8 Hz, H-5), 3.69 (dd, 1H, *J* = 11.5, 4.8 Hz, H-5′), 4.50 (q, 1H, *J* = 4.9 Hz, H-4), 4.92–5.2 (m, 1H, H-3), 5.98 (d, 1H, *J* = 2.6 Hz, H-2), 7.46–7.71 (m, 3H, PhH), 7.92–8.01 (m, 2H, PhH). ^{13}C NMR, δ: –5.4, 18.2, 25.7, 62.5, 74.9, 92.7, 109.6, 128.7, 129.2, 134.3, 137.9, 157.9.

The above ene alcohol (3.8 g, 10.3 mmol) was dissolved in dry THF (37 mL), under Ar. Benzyl isocyanate (1.4 mL, 11.4 mmol) was added and the reaction mixture was cooled to 0°C. Potassium *tert*-butoxide (0.24 g, 2.2 mmol) was added in one portion and the brown reaction mixture was stirred at 0°C for 1 h and at rt for 20 h. Then saturated NH_4Cl (20 mL) and EtOAc (20 mL) were added. The organic phase was separated and the aqueous phase was reextracted with EtOAc (3 × 30 mL). The combined organic extracts were washed with brine (50 mL), dried, filtered, and evaporated. The crude product was chromatographed (solvent E) to give the bicyclic oxazolidinone **4a** (4.6 g, 89%) as a pale yellow, viscous oil. IR, ν_{max}: 1766, 1585 cm^{-1}. ^{1}H NMR, δ: 0.30 (s, 6H, SiMe), 1.10 (s, 9H, *t*-Bu), 4.02 (dd, 1H, *J* = 10.9, 7.7 Hz, H-5), 4.08 (dd, 1H, *J* = 10.9, 6.0 Hz, H-5′), 4.55–4.65 (m, 1H, H-4), 4.57 (d, 1H, *J* = 14.6 Hz, PhCHN), 4.95 (d, 1H, *J* = 14.6 Hz, PhCHN), 4.98–5.05 (m, 2H, H-1, H-2), 5.09–5.18 (m, 1H, H-3), 7.50–8.10 (m, 10H, PhH). ^{13}C NMR, δ: –5.5, 18.1, 25.7, 47.2, 60.3, 62.0, 78.0, 89.1, 97.5, 128.3, 128.9, 129.2, 134.6, 135.0, 135.5, 156.6. Anal. calcd. for $C_{25}H_{33}NO_6SSi$: C 59.62, H 6.60, N 2.78; found: C 59.71, H 6.77, N 2.81.

Phenyl 2-benzylamino-2*N*,3*O*-carbamoyl-2-deoxy-α-D-ribofuranosyl sulfone (4b)

Compound **4a** (6.7 g, 13.4 mmol) was dissolved in dry MeOH (100 mL) under Ar, and the solution was cooled to 0°C. Freshly distilled Me_3SiCl (3.4 mL, 27 mmol) was added dropwise, via syringe, and the mixture was stirred at 0°C for 1 h. During this time, the white, fluffy, alcohol product precipitated out of solution. The solid product was filtered off and the filtrate was concentrated. The residue was triturated with solvent D and the resulting white, fluffy, product was filtered off. The filtrate was concentrated and chromatographed (solvent A) to obtain more product. The combined yield of **4b** was 4.5 g (88%); mp 172–174°C. IR,

© 1998 NRC Canada

ν_{max}: 3565–3307, 1754 cm^{-1}. ^1H NMR, δ: 3.30–3.40 (m, 1H, OH), 3.66–3.84 (m, 1H, H-5′), 3.86–3.99 (m, 1H, H-5), 4.36 (d, 1H, *J* = 14.4 Hz, PhCHN), 4.57–4.63 (m, 1H, H-4), 4.73 (d, 1H, *J* = 14.4 Hz, PhCHN), 4.77–4.87 (m, 2H, H-1, H-2), 5.03–5.12 (m, 1H, H-3), 7.30–7.85 (m, 10H, PhH). ^{13}C NMR, δ: 47.1, 61.2, 62.8, 78.6, 89.9, 98.5, 128.3, 128.7, 128.9, 128.9, 129.4, 134.8, 135.2, 135.5, 156.2. Anal. calcd. for $C_{19}H_{19}NO_6S$: C 58.60, H 4.92, N 3.60; found: C 58.53, H 5.13. N 3.67.

Phenyl 2-benzylamino-2*N*,3*O*-carbamoyl-2,5-dideoxy-5-iodo-α-D-ribofuranosyl sulfone (5)

The alcohol **4b** (2.9 g, 7.5 mmol) was dissolved in a mixture of dry toluene (60 mL), dry DCM (28 mL), and dry pyridine (1.8 mL, 26 mmol), under Ar. In a separate flask, Ph_3P (2.5 g, 9.4 mmol) was dissolved in dry toluene (30 mL) and iodine (2 g, 7.9 mmol) was added. The mixture was heated at 60°C for 30 min and then the temperature was raised to 80°C. The solution of the alcohol was added dropwise, via cannula, to the $Ph_3P–I_2$ mixture. After addition was complete, the mixture was heated at 80°C (oil bath) for 4 h, during which time the reddish brown precipitate was consumed and a white precipitate was formed. The reaction mixture was cooled to rt, filtered through a Florisil pad, and the solid residue was washed with EtOAc (2 × 30 mL). The combined filtrates were evaporated to leave a thick oil. Chromatographic purification (30:1 DCM:acetone) gave the desired iodide **5** (3.6 g, 95%) as a white solid; mp 188–190°C. IR, ν_{max}: 1747, 1584 cm^{-1}. ^1H NMR, δ : 3.43 (dd, 1H, *J* = 10.1, 6.3 Hz, H-5), 3.52 (dd, 1H, *J* = 10.1, 8.2 Hz, H-5′), 4.37 (d, 1H, *J* = 14.6 Hz, PhCH), 4.64 (dq, 1H, *J* = 8.5, 6.1, 2.2 Hz, H-4), 4.71 (d, 1H, *J* = 14.6 Hz, PhCH), 4.82 (d, 1H, *J* = 1.8 Hz, H-1), 4.89 (dd, 1H, *J* = 8.4, 1.8 Hz, H-2), 4.96 (dd, 1H, *J* = 8.4, 2.2 Hz, H-3), 7.30–7.40 (m, 5H, PhH), 7.50–7.80 (m, 3H, PhH), 7.80–7.90 (m, 2H, PhH). ^{13}C NMR, δ: 2.9, 47.5, 60.9, 79.9, 89.4, 97.8, 128.5, 128.9, 129.0, 129.4, 134.7 134.8, 135.1, 155.9. Anal. calcd. for $C_{19}H_{18}INO_5S$: C 45.70, H 3.63, N 2.81; found: C 45.70, H 3.59, N 2.82.

(4*S*,5*R*)-3-Benzyl-4-(hydroxymethyl)-5-vinyl-2-oxazolidinone (7)

Activated Zn dust (0.73g, 0.011 g atoms) was added to a solution of AgOAc (0.29 g, 1.77 mmol) in glacial AcOH (87 mL) at 110°C (oil bath). The mixture was stirred at 110°C for

35–40 s and then was allowed to cool slightly. Glacial AcOH was decanted off and the Zn/Ag couple was washed thoroughly with dry THF (4 × 10 mL) and then was covered with dry THF (10 mL). The slurry of the Zn/Ag couple in dry THF was heated to 60°C and a solution of the iodosulfone **5** (0.250 g, 0.50 mmol) was added dropwise via cannula to the Zn/Ag couple. The reaction mixture was heated at 60°C for 1 h, allowed to cool to rt, and the THF supernatant containing the aldehyde **6** was filtered through glass wool plug into a clean flask. The reaction flask was rinsed with THF (2 × 5 mL) and the washings filtered into the flask. The THF filtrate was cooled to 0°C and 95% ethanol (10 mL) was added, at which time the reaction mixture turned cloudy. Sodium borohydride (0.19 g, 5 mmol) was added, portionwise, to the mixture and the reaction mixture was stirred at 0°C for 2 h and then at rt overnight. The reaction mixture was recooled to 0°C and glacial AcOH (0.5 mL) was carefully added to destroy excess $NaBH_4$. After effervescence had subsided, the reaction mixture was evaporated and the residual oil was taken into EtOAc (15 mL). The organic phase was washed with water (10 mL), saturated aqueous $NaHCO_3$ (3 × 10 mL), and brine and then dried. The filtered solution was evaporated to give the crude crystalline primary alcohol. Chromatographic purification of the alcohol **7** (40:1 DCM:acetone) yielded white, fine needles (106 mg, 90%); mp 138–140°C. IR ν_{max}: 3518–3330, 1724, 1713 cm^{-1}. ^1H NMR, δ ($CDCl_3$-CD_3CN): 2.87 (t, 1H, *J* = 5.1 Hz, OH), 3.50–3.76 (m, 3H, H-4, CH_2O), 4.20 (d, 1H, *J* = 14.4 Hz, PhCH), 4.80 (d, 1H, *J* = 14.4 Hz, PhCH), 4.95 (“t”, 1H, *J* = 8.2 Hz, H-5), 5.32–5.51 (m, 2H, CH_2=), 5.99–6.19 (m, 1H, =CH). ^{13}C NMR, δ ($CDCl_3$-CD_3CN): 45.7, 57.8, 58.1, 77.1, 116.5, 119.8, 127.1, 127.3, 128.1, 131.1, 135.9, 157.9. Anal. calcd. for $C_{13}H_{15}NO_3$: C 66.94, H 6.48, N 6.00; found: C 66.70, H 6.68, N 5.89.

(4*S*,5*R*,)-3-Benzyl-4-(benzyloxymethyl)-5-vinyl-2-oxazolidinone (8)

The primary alcohol **7** (106 mg, 0.455 mmol) was dissolved in dry THF (5 mL), under Ar. The solution was added to a suspension of NaH (66 mg, 50% dispersion in mineral oil) in dry THF (10 mL) containing benzyl bromide (70 µL, 0.59 mmol) at 0°C. The mixture was stirred at 0°C to rt overnight (20 h). Then saturated NH_4Cl (5 mL), followed by saturated NaCl (5 mL) and EtOAc (10 mL), was added. The aqueous phase was separated and reextracted with EtOAc (5 mL). The combined organic phases were washed with water (10 mL), saturated NaCl (10 mL), dried, filtered, and evaporated. The crude oil was chromatographed (solvent C) to give the benzyl ether **8** as a pale yellow oil (127 mg, 86%). $[\alpha]_D^{21}$ –8.8 (*c* 1.70, $CHCl_3$). IR, ν_{max}: 3086, 3063, 3031, 1760 cm^{-1}. ^1H NMR, δ: 3.43 (dd, 1H, *J* = 14.7, 5.3 Hz, CHOBn), 3.51 (dd, 1H, *J* = 14.7, 3.5 Hz, CHOBn), 3.75 (“quintet”, 1H, *J* = 4.4 Hz, H-4), 4.12 (d, 1H, *J* = 14.3 Hz, PhCHN), 4.39 (d, 1H, *J* = 14.1 Hz, PhCHO), 4.47 (d, 1H, *J* = 14.1 Hz, PhCHO), 4.81 (d, 1H, *J* = 14.3 Hz, PhCHN), 4.93 (“t”, 1H, *J* = 8.5 Hz, H-5), 5.30–5.53 (m, 2H, $=CH_2$), 5.87–6.06 (m, 1H, =CH), 7.15–7.45 (m, 10H, PhH). ^{13}C NMR, δ: 46.6, 57.1, 66.6, 73.2, 77.1, 120.3, 127.7, 127.8, 128.0, 126.4, 128.6, 131.1, 136.2, 137.2, 157.9. HRMS, calcd. for $C_{20}H_{21}NO_3(M^+)$: 323.1521; found: 323.1525. Anal. calcd. for $C_{20}H_{21}NO_3$: C 74.28, H 6.55 N 4.33; found: C 73.99, H 6.43, N 4.35.

General procedure for the preparation of $RCeCl_2$ and reaction with oxazolidinonecarbaldehydes (6) and (13)

Anhydrous $CeCl_3$ (see also ref. 23)

Powdered $CeCl_3 \cdot 7H_2O$ (3 g) was placed in a 100 mL round-bottom flask containing a stir bar. The flask was fitted with an outlet tap and then connected to a high-vacuum pump (0.01–0.015 Torr; 1 Torr = 133.3 Pa). The flask was carefully evacuated, during which time a small amount of water was removed, and the salt had a whitish appearance. The flask was immersed in an oil bath that was heated at between 60 and 70°C and the salt was vigorously stirred. The

© 1998 NRC Canada

salt was heated at 60–70°C for 6 h and then the temperature of the bath was raised to 80–90° C and heating was continued for 2 h. After this period, the temperature was raised slowly, over a period of 1 h, to 140°C and the salt was stirred at this temperature for 18 h. The salt was cooled slowly to rt and then stored under Ar. The salt has an off-white appearance.

Method A: Dry THF (5 mL, at rt) was added to anhydrous $CeCl_3$ (1.2 mmol) under Ar and the mixture was stirred briefly. Then the suspension was sonicated for 1 h and allowed to stir at rt for 18 h. The white suspension was cooled to –78°C and RLi or RMgBr reagent (1.2 mmol) was added slowly. After addition was complete, the mixture assumed a light yellow or yellow-orange colour. The organometallic reagent was allowed to stir at –78°C for 1.5 h before use. The aldehyde **6** was generated from iodosulfone **5** (0.2 mmol) using a Zn/Ag couple (prepared using 292 mg Zn dust and 119 mg AgOAc) in dry THF (5 mL) according to the procedure used in the preparation of **7**. The THF supernatant was filtered (5 mL THF rinse) under Ar into a clean flask. This solution of **6** was transferred via cannula to the $RCeCl_2$ and the mixture was stirred at –78°C for the specified time (see Table 1). Then the mixture was quenched by addition of saturated NH_4Cl (5 mL) and stirred at rt for 20 min. The mixture was filtered through Florisil, and the residue washed with THF (2 × 10 mL). The combined filtrates were concentrated and the aqueous mixture was extracted with EtOAc (3 × 10 mL). The combined organic extracts were washed with brine, dried, filtered, and evaporated. The residual product was purified by chromatography.

Method B: The organocerium reagent was prepared as described in Method A except that 4 mol- equiv. of $RCeCl_2$ (0.62 mmol dry $CeCl_3$ and 0.62 mmol RLi or RMgBr) was used. The aldehyde **13** was generated by ozonolysis of olefin **8** (0.16 mmol) in dry DCM (5 mL) at –78°C. Ph_3P (0.19 mmol) was added and the mixture was slowly warmed to rt, under Ar, and stirred at rt for 18 h. The DCM was removed at rt under high vacuum and dry THF (5 mL) was added under Ar. The THF solution of **13** was added to the organocerium reagent and the mixture was stirred at –78°C for the specified time (see Table 2). The reaction mixture was processed as described in Method A.

(4*S*,5*R*)-3-Benzyl-4-[(1*RS*)-1-(hydroxyethyl)]-5-vinyl-2-oxazolidinone (9a,10a)

Method A: Solvent B: Yield, 85%; mp 95–97°C. IR, ν_{max}: 3600–3250, 1731 cm^{-1}. ^1H NMR, δ: 1.22 (d, *J* = 6.6 Hz, Me) and [1.48, d, *J* = 6.6 Hz, Me](3H), 2.46 (d, 1H, *J* = 5.6 Hz, OH), 3.52 (dd, *J* = 8, 4.8 Hz, H-4) and [3.71, dd, *J* = 8, 2.1 Hz, H-4](1H), 3.85–4.05 (m, 1H, CHOH), 4.41 (d, 1H, *J* = 15.2 Hz, PhCH), 4.85 ("t", 1H, *J* = 7.5 Hz, H-5), 4.93 (d, 1H, *J* = 15.2 Hz, PhCH), 5.36–5.54 (m, 2H, $=CH_2$), 5.90–6.12 (m, 1H, =CH), 7.24–7.42 (m, 5H, PhH). ^{13}C NMR, δ: 21.1, 48.4, 62.3, 66.6, 78.4, 121.0, 127.8, 128.0, 128.9, 131.4, 136.6, 159.3. LRMS-CI, NH_3 (*m*/*z*, rel. intensity): 265 (M + 18, 7.4), 248 (M + 1, 100), 202 (M – MeCHOH, 32), 91 ($PhCH_2^+$, 57). HRMS, calcd. for $C_{14}H_{17}NO_3$ (M^+): 247.1208; found: 247.1207.

(4*S*,5*R*)-3-Benzyl-4-[(1*R*)-1-(hydroxy-2-propenyl)]-5-vinyl-2-oxazolidinone (9b)

Method A: Solvent B: Yield, 85%; mp 157–159°C. IR, ν_{max}: 3471–3213, 1715, 1704 cm^{-1}. ^1H NMR, δ: 2.08 (d, 1H, *J* = 7.7 Hz, OH), 3.70 (dd, 1H, *J* = 8.5, 2.5 Hz, H-4), 4.25 (d, 1H, *J* = 15.4 Hz, PhCHN), 4.27–4.35 (m, 1H, CHOH), 4.90 ("t", 1H, *J* = 8.5 Hz, H-5), 4.95 (d, 1H, *J* = 15.4 Hz, PhCHN), 5.24–5.58 (m, 4H, 2× $=CH_2$), 5.81–6.00 (m, 1H, =CH), 6.08–6.23 (m, 1H, =CH), 7.16–7.40 (m, 5H, PhH). ^{13}C NMR, δ: 47.2, 60.7, 70.5, 78.3, 116.6, 121.1, 127.9, 128.0, 128.8, 131.6, 136.2, 137.9, 158.7. LRMS-CI, NH_3 (*m*/*z*, rel. intensity): 277 (M + 18, 8.4), 260 (M + 1, 100), 202 (M – CH_2=CHCHOH, 45), 91 ($PhCH_2^+$, 70). HRMS, calcd. for $C_{15}H_{18}NO_3$ (M + 1): 260.1286; found: 260.1275.

(4*S*,5*R*)-3-Benzyl-4-[(1*R*,*S*)-2-(*tert*-butyloxycarbonyl)-1-(hydroxyethyl)]-5-vinyl-2-oxazolidinone (9c,10c)

Method A: Solvent C: Yield, 92%; mp: 97–99°C. IR, ν_{max}: 3618–3131, 1726 cm^{-1}. ^1H NMR, δ: 1.40 (s, *t*-Bu) and [1.43, s, *t*-Bu](9H), 2.31 (dd, *J* = 15.4, 3.8 Hz) and 2.40–2.58 (m)(2H, CH_2CO), 3.14 (d, *J* = 5.1 Hz, OH) and [3.49, d, *J* = 5.1 Hz, OH](1H), 3.60 (dd, *J* = 7.7, 5.1 Hz, H-4) and [3.76, dd, *J* = 7.7, 2.3 Hz, H-4], 4.08–4.21 (m, 1H, CHOH), 4.31 (d, *J* = 14.9 Hz, PhCHN) and [4.33, d, *J* = 14.9 Hz, PhCHN](1H), 4.85 ("t", 1H, *J* = 7.7 Hz, H-5), 4.91 (d, 1H, *J* = 14.9 Hz, PhCHN), 5.34–5.55 (m, 2H, $=CH_2$), [5.80–5.97, m, =CH] and 5.98–6.17 (m, =CH)(1H), 7.20–7.35 (m, 5H, PhH). ^{13}C NMR, δ: 28.0, [30.0], [37.0], 39.1, [47.3], 48.0, 60.0, [60.6], 67.0, [68.1], 77.9, [81.2], 82.2, [85.2], [120.6], 120.8, 127.8, 128.0, [128.4], 128.7, 128.8, [128.9], [129.3], [130.6], 131.6, [134.6], 136.2, [157.5], 158.8, 171.5, [172.0]. Anal. calcd. for $C_{19}H_{25}NO_5$: C 65.69, H 7.25, N 4.03; found: C 65.59, H 7.38, N 3.95.

(4*S*,5*R*)-3-Benzyl-4-[(1*R*)-1-hydroxy-(3-phenyl-2-propynyl)]-5-vinyl-2-oxazolidinone (9d)

Method A: Solvent C: Yield, 94%; mp 119–121°C. IR, ν_{max}: 3550–3125, 2212, 1743, 1725, 1595, 1500 cm^{-1}. ^1H NMR, δ: 2.90–3.20 (br hump, 1H, OH), 3.90 (dd, 1H, *J* = 8.2, 3.3 Hz, H-4), 4.60 (d, 1H, *J* = 15.2 Hz, PhCHN), 4.75 (d, 1H, *J* = 3.1 Hz, CHOH), 4.94 ("t", 1H, *J* = 8 Hz, H-5), 5.02 (d, 1H, *J* = 15.2 Hz, PhCHN), 5.38–5.56 (m, 2H, $=CH_2$), 6.10–6.33 (m, 1H, =CH), 7.23–7.44 (m, 10H, PhH). ^{13}C NMR, δ: 47.4, 61.0, 61.2, 78.2, 87.3, 121.8, 128.0, 128.2, 128.5, 128.8, 129.0, 131.2, 131.6, 136.4, 158.4. LRMS-CI, NH_3 (*m*/*z*, rel. intensity): 351 (M + 18, 12), 334 (M + 1, 100), 202 (M – PhCCHOH, 52), 91 ($PhCH_2^+$, 66). HRMS, calcd. for $C_{21}H_{20}NO_3$(M + 1): 334.1443; found: 334.1426.

(4*S*,5*R*)-3-Benzyl-4-[(1*S*)-1-(2-furanyl)-1-(hydroxymethyl)]-5-vinyl-2-oxazolidinone (9e)

Method A: Solvent C: Yield, 85%; mp 137–139°C. IR ν_{max}: 3500–3150, 1715, 1703 cm^{-1}. ^1H NMR, δ (CD_3CN): 3.75 (d, 1H, *J* = 15 Hz, PhCHN), 3.93 (d, 1H, *J* = 6 Hz, OH), 4.08 (dd, 1H, *J* = 7.2, 3.6 Hz, H-4), 4.73 (d, 1H, *J* = 15 Hz, PhCHN), 4.75–4.85 (m, 1H, CHOH), 4.95 ("t", 1H, *J* = 7.2 Hz, H-5), 5.30–5.46 (m, 2H, $=CH_2$), 5.95–6.18 (m, 1H, =CH), 6.28–6.45 (m, 2H, furan-H), 7.05 (dd, 1H, *J* = 6.6,

© 1998 NRC Canada

2.4 Hz, furan-H), 7.20–7.45 (m, 5H, PhH). ^{13}C NMR, δ (CD_3CN): 48.2, 60.7, 67.0, 78.9, 107.9, 112.1, 121.9, 128.2, 128.9, 129.5, 133.0, 143.2, 157.0, 160.6. LRMS-CI, NH_3 (*m/z*, rel. intensity): 300 (M + 1, 100), 202 (M – furan-CHOH, 22), 91 ($PhCH_2^+$, 56). HRMS, calcd. for $C_{17}H_{17}NO_4$ (M^+): 299.1157; found: 299.1152.

(4*S*,5*R*)-3-Benzyl-4-[(1*R*,*S*)-1-hydroxy-1-phenylmethyl]-5-vinyl-2-oxazolidinone (9f,10f)

Method A: Solvent B: Yield, 52%; mp 142–144°C. IR ν_{max}: 3600–3283, 3075, 3025, 1751 cm^{-1}. ^{1}H NMR, δ: [2.28, d, *J* = 4.4 Hz, OH] and 2.47 (d, *J* = 4.4 Hz, OH)(1H), 3.56 (d, 1H, *J* = 15.4 Hz, PhCHN), 3.90 (dd, 1H, *J* = 8, 2.2 Hz, H-4), 4.80 (d, 1H, *J* = 15.2 Hz, PhCHN), 4.85–5.00 (m, 2H, CHOH, H-5), 5.30–5.70 (m, 2H, $=CH_2$), 6.00–6.27 (m, 1H, =CH), 7.12–7.50 (m, 10H, PhH). ^{13}C NMR, δ: 47.7, [48.1], 60.7, 62.6, 71.3, 78.1, 118.7, 121.3, 125.7, [126.9], 127.8, 128.1, 128.5, 128.6, [128.7], 131.2, 136.2, 140.7, 158.2. LRMS-CI, NH_3 (*m/z*, rel. intensity): 310 (M + 1, 100), 232 (M – Ph, 10), 202 (M – PhCHOH, 30), 91 ($PhCH_2^+$, 90). HRMS, calcd. for $C_{19}H_{20}NO_3$ (M + 1): 310.1443; found: 310.1453.

(4*R*,5*R*)-3-Benzyl-5-methyl-4-[(4*S*)-4-(2,2-dimethyl-1,3-dioxolanyl)]-2-oxazolidinone (12)

Compound **9a,10a** (111 mg. 0.45 mmol) was hydrolyzed using 2 M aqueous KOH (2.6 mL) in 95% EtOH (6.4 mL) at reflux for 20 h. The cooled reaction mixture was evaporated to dryness and distilled water (1 mL) was added followed by DCM (2 mL). The mixture was cooled to 0°C and Boc_2O (108 mg, 0.49 mmol) was added and the mixture was stirred under Ar for 20 h. The DCM layer was separated and saturated aqueous NaCl and solid NaCl were added to the aqueous layer. The mixture was stirred for 1 h and extracted with DCM (2 × 5 mL). The combined organic phases were dried, filtered, and evaporated to give the crude diol as a thick oil. Chromatographic separation (solvent B) gave 81 mg (59%) of diol **11.** IR ν_{max}: 3680–3113, 1690, 1660 cm^{-1}. ^{1}H NMR, δ: 0.80 (d, 3H, *J* = 7 Hz, Me), 1.50 (s, 9H, *t*-Bu), 2.90–3.10 (m, 1H), 3.25–3.42 (m, 1H), 3.95–4.25 (m, 1H), 4.65 (d, 1H, *J* = 12.6 Hz, PhCHN), 4.65–4.78 (m, 1H), 4.95–5.30 (m, 3H), 5.67–5.90 (m, 1H, =CH), 7.15–7.35 (m, 5H, PhH).

The diol **11** (40 mg) was dissolved in dry MeOH (3 mL) and was ozonized at –78°C until the blue color of ozone is visible. Argon was bubbled into the cold mixture and then $NaBH_4$ (25 mg, 0.65 mmol) was added. The mixture was allowed to stir at –78°C for 15 min and then warmed slowly to rt and stirred at rt for 20 h. Glacial AcOH (4 drops) was added to destroy unreacted $NaBH_4$. The mixture was concentrated and saturated aqueous $NaHCO_3$ (5 mL) was added. The mixture was thoroughly extracted with DCM (2 × 10 mL), the combined organic phases were dried, filtered, and evaporated to furnish crude triol (40 mg). Without further purification, the triol was treated with 2,2-dimethoxypropane (20 µL, 0.16 mmol) in dry DCM (2 mL) in the presence of *p*-$TSO_3H\cdot H_2O$ (1 crystal). After reaction was complete, dry Et_3N was added, the mixture was evaporated, and the residue was chromatographed (solvent C) to give the ketal (26 mg, 55%) as an oil. IR, ν_{max}: 3577–3224, 1691, 1675 cm^{-1}. ^{1}H NMR, δ: 1.08 (d, 3H, *J* = 7.1 Hz, Me), 1.25 and [1.32] (s, 3H, Me), 1.35 and [1.42] (s, 3H, Me), 1.49 (s, 9H, *t*-Bu), 3.42–3.95 (m, 3H), 4.05–5.85 (m, 5H), 7.18–7.40 (m, 5H, PhH).

The ketal (26 mg, 0.071 mmol) was dissolved in dry THF (2 mL) and was transferred, via cannula, to a suspension of NaH (2.5 mg, 0.11 mmol, 50% dispersion in mineral oil) in dry THF (2 mL). The mixture was refluxed under Ar for 2 h and then cooled to rt. Saturated NH_4Cl (4 drops) was added and the mixture was concentrated in vacuo. EtOAc (5 mL) and saturated NaCl (4 mL) were added and the organic layer was separated. The aqueous layer was reextracted with EtOAc (3 mL) and the combined organic extracts were dried, filtered, and evaporated to crude ketal oxazolidinone. Chromatographic purification (solvent C) furnished crystalline 2-oxazolidinone **12** (16 mg, 77%); mp 88–90°C. IR, ν_{max}: 1745 cm^{-1}. ^{1}H NMR, δ: 1.25 (s, 3H, Me), 1.27 (d, 3H, *J* = 7.0 Hz, Me), 1.35 (s, 3H, Me), 3.11 (t, 1H, *J* = 4.2 Hz, H-4), 3.51 (dd, 1H, *J* = 7.9, 5.5 Hz, H-4′), 3.90 (br "t", 1H, *J* = 7.9 Hz, H-5′), 4.07 (d, 1H, *J* = 14.3 Hz, PhCHN), 4.06–4.16 (m, 1H, H-5′), 4.42 (br "quintet", 1H, *J* = 4.2 Hz, H-5), 4.82 (d, 1H, *J* = 14.3 Hz, PhCHN), 7.10–7.40 (m, 5H, PhH). Anal. calcd. for $C_{16}H_{21}NO_4$: C 65.96, H 7.27, N 4.81; found: C 66.14, H 7.46, N 4.62.

(4*S*,5*S*)-3-Benzyl-4-benzyloxymethyl-5-[(1*R*)-1-(hydroxyethyl)]-2-oxazolidinone (14a)

Method B: Solvent A: Yield, 62%. IR, ν_{max}: 3450–3000, 1735 cm^{-1}. ^{1}H NMR, δ: 1.32 (d, 3H, *J* = 5.7 Hz, Me), 3.23–3.32 (br hump, 1H, OH), 3.53 (dd, 1H, *J* = 8.9, 4.3 Hz, CHOBn), 3.62 (t, 1H, *J* = 8.9 Hz, CHOBn), 3.78 (td, 1H, *J* = 8.9, 8.9, 4.3 Hz, H-4), 3.70–4.70 (m, 1H, CHOH), 4.00 (d, 1H, *J* = 15.2 Hz, PhCHN), 4.14 (dd, 1H, *J* = 8.9, 6.6 Hz, H-5), 4.51 (s, 2H, OCH_2Ph), 4.76 (d, 1H, *J* = 15.2 Hz, PhCHN), 7.14–7.45 (m, 10H, PhH). ^{13}C NMR, δ: 20.1, 45.5, 55.9, 64.5, 64.6, 73.8, 80.5, 127.9, 128.0, 128.1, 128.4, 128.7, 128.8, 135.4, 136.1, 157.1. Anal. calcd. for $C_{20}H_{23}NO_4\cdot\frac{1}{4}H_2O$: C 69.43, H 6.85, N 4.05; found: C 69.46, H 6.90, N 4.02.

(4*S*,5*S*)-3-Benzyl-4-(benzyloxymethyl)-5-[(1*R*)-(1-hydroxy-2-propenyl)]-2-oxazolidinone (14b)

Method B: Solvent B: Yield, 59%. IR, ν_{max}: 3550–3000, 1727, 1644 cm^{-1}. ^{1}H NMR, δ: 3.24 (d, 1H, *J* = 4.1 Hz, OH), 3.55–3.66 (m, 2H, CH_2OBn), 3.68–3.82 (m, 1H, H-4), 3.99 (d, 1H, *J* = 14.8 Hz, PhCHN), 4.24 (dd, 1H, *J* = 9.1, 6.8 Hz, H-5), 4.33–4.43 (m, 1H, CHOH), 4.45 (d, 1H, *J* = 12.5 Hz, PhCHO), 4.55 (d, 1H, *J* = 12.5 Hz, PhCHO), 4.77 (d, 1H, *J* = 14.8 Hz, PhCHN), 5.22–5.46 (m, 2H, $=CH_2$), 5.87–6.07 (m, 1H, =CH), 7.12–7.45 (m, 10H, PhH). ^{13}C NMR, δ: 45.5, 56.1, 64.8, 69.3, 73.8, 78.6, 117.2, 127.9, 128.1, 128.4, 128.7, 128.9, 136.1, 136.4, 157.5. Anal. calcd. for $C_{21}H_{23}NO_4$: C 71.37, H 6.56, N 3.96; found: C 71.40, H 6.77, N 3.90.

(4*S*,5*S*)-3-Benzyl-4-(benzyloxymethyl)-5-[(1*R*)-1-hydroxy-(3-phenyl-2-propynyl)]-2-oxazolidinone (14c)

Method B: Solvent B: Yield, 85%. IR, ν_{max}: 3575–3175, 3060, 3025, 2212, 1743, 1738, 1581, 1500 cm^{-1}. ^{1}H NMR, δ: 3.69–4.00 (m, 4H, CH_2OBn, OH, H-4), 4.05 (d, 1H, *J* =

© 1998 NRC Canada

15.4 Hz, PhCHN), 4.39 (d, 1H, *J* = 12 Hz, PhCHO), 4.55 (d, 1H, *J* = 12 Hz, PhCHO), 4.62 (dd, 1H, *J* = 7.7, 5.1 Hz, H-5), 4.75 (d, 1H, *J* = 15.4 Hz, PhCHN), 4.92 (dd, 1H, *J* = 7.7, 5.1 Hz, CHO), 7.05–7.45 (m, 15H, PhH). ^{13}C NMR, δ: 46.5, 56.1, 61.7, 65.0, 73.7, 77.4, 86.0, 86.8, 122.0, 127.9, 128.0, 128.1, 128.3, 128.4, 128.7, 128.8, 128.9, 131.7, 131.8, 135.9, 136.4, 157.8. Anal. calcd. for $C_{27}H_{25}NO_4$: C 75.86, H 5.89, N 3.28; found: C 75.78, H 5.95, N 3.20.

(4*S*,5*S*)-3-Benzyl-4-(benzyloxymethyl)-5-[(1*R*)-2-(*tert*-butyloxycarbonyl)-1-(hydroxyethyl)]-2-oxazolidinone (14d)

Method B: Solvent B: Yield, 84%. IR, ν_{max}: 3575–3275, 3075, 3030, 1748, 1731, 1625, 1587, 1520. 1500 cm^{-1}. ^{1}H NMR, δ: 1.50 (s, 9H, *t*-Bu), 2.43 (dd, 1H, *J* = 16.7, 7.5 Hz, $CHCO_2$), 2.79 (dd, 1H, *J* = 16.7, 2 Hz, $CHCO_2$), 3.57–3.84 (m, 4H, H-4, CH_2OBn, OH), 3.95 (d, 1H, *J* = 14.9 Hz, PhCHN), 4.20–4.39 (m, 2H, H-5, CHO), 4.45 (d, 1H, *J* = 11.5 Hz, PhCHO), 4.54 (d, 1H, *J* = 11.5 Hz, PhCHO), 4.78 (d, 1H, *J* = 14.7 Hz, PhCHN), 7.10–7.45 (m, 10H, PhH). ^{13}C NMR, δ: 28.0, 38.8, 46.3, 56.1, 64.8, 65.8, 73.4, 76.9, 81.6, 127.8, 127.9, 127.9, 128.0, 128.5, 128.7, 135.9, 136.9, 157.3, 171.8. Anal. calcd. for $C_{25}H_{31}NO_6$: C 67.99, H 7.08, N 3.17; found: C 67.68, H 7.32, N 3.48.

(4*S*,5*S*)-3-Benzyl-4-(benzyloxymethyl)-5-[(1*S*)-1-(2-furanyl)-1-(hydroxymethyl)]-2-oxazolidinone (14e)

Method B: Solvent B: Yield, 64%. IR, ν_{max}: 3637–3125, 3100, 3050, 1731, 1606, 1581, 1500 cm^{-1}. ^{1}H NMR, δ: 3.43 (d, 1H, *J* = 5.6 Hz, OH), 3.64 ("d" 2H, *J* = 4.3 Hz, CH_2OBn), 3.82 (dt, 1H, *J* = 7.5, 4.1 Hz, H-4), 3.96 (d, 1H, *J* = 15 Hz, PhCHN), 4.45 (d, 1H, *J* = 11.6 Hz, PhCHO), 4.55 (d, 1H, *J* = 11.6 Hz, PhCHO), 4.78 ("t", 1H, *J* = 7.5 Hz, H-5), 4.78 (d, 1H, *J* = 15 Hz, PhCHN), 4.98 (dd, 1H, *J* = 8.5, 5.6 Hz, CHO), 6.31–6.39 (m, 2H, furan-H), 7.12–7.45 (m, 11H, PhH, furan-H). ^{13}C NMR, δ: 45.3, 56.0, 64.6, 65.2, 73.6, 76.5, 108.5, 110.4, 127.9, 128.1, 128.3, 128.7, 128.8, 135.9, 136.1, 142.6, 152.2, 157.4. Anal. calcd. for $C_{23}H_{23}NO_5$: C 70.21, H 5.89, N 3.56; found: C 69.97, H 6.02, N 3.51.

(4*S*,5*S*)-3-Benzyl-4-(benzyloxymethyl)-5-[(1*R*)-1-(hydroxytetradecyl)]-2-oxazolidinone (14f)

Method B: Solvent D: Yield, 69%. IR, ν_{max}: 3600–3150, 1737, 1500 cm^{-1}. ^{1}H NMR, δ: 0.90 (t, 3H, *J* = 6.5 Hz, Me), 1.12–1.55 (m, 25H, CH_2), 1.65–1.85 (m, 1H, CH), 3.23 (d, 1H, *J* = 3.6 Hz, OH), 3.52 (dd, 1H, *J* = 9.7, 3.4 Hz, CHOBn), 3.60 ("t", 1H, *J* = 9.7 Hz, CHOBn), 3.70–3.85 (m, 2H, H-4, CHO), 3.99 (d, 1H, *J* = 15.4 Hz, PhCHN), 4.17 (dd, 1H, *J* = 9.5, 6.8 Hz, H-5), 4.46 (d, 1H, *J* = 12 Hz, PhCHO), 4.55 (d, 1H, *J* = 12 Hz, PhCHO), 4.75 (d, 1H, *J* = 15.4 Hz, PhCHN), 7.15–7.40 (m, 10H, PhH). ^{13}C NMR, δ: 14.1, 22.6, 24.8, 29.3, 29.6, 29.6, 31.9, 33.5, 46.4, 56.0, 64.5, 68.1, 73.8, 79.1, 127.6, 127.9, 128.0, 128.1, 128.4, 128.7, 128.8, 135.9, 136.1, 157.4. Anal. calcd. for $C_{33}H_{49}NO_4$: C 75.60, H 9.44, N 2.68; found: C 75.68, H 9.59, N 2.94.

(4*S*,5*S*)-3-Benzyl-4-(benzyloxymethyl)-5-[(1*S*)-1-(hydroxyethyl)]-2-oxazolidinone (15)

The MeTi(OPr-i)$_3$ reagent was prepared by treatment of ClTi(OPr-i)$_3$ (0.22 mL, 0.90 mmol) with MeLi (0.90 mL, 0.90 mmol) in dry ether (5 mL) at –40°C. Then the mixture was warmed slowly to rt and stirred at rt for 1.5 h. The mixture turned cloudy and a yellow precipitate was formed. In a separate flask the olefin **8** was dissolved in dry DCM (5 mL) and then oxidized (O_3; Pah_3) as described in Method B to provide **13**. The solution of **13** was added to the ethereal solution of MeTi(OPr-i)$_3$ at –40°C and the mixture was stirred at –40°C for 1 h. After this time, the reaction mixture was warmed slowly to rt and stirred at rt for 1.5 h. The reaction mixture was quenched by addition of aqueous 1 M HCl (10 mL) followed by DCM (10 mL). The aqueous phase was separated and reextracted with DCM (10 mL). The combined organic extracts were washed with brine, dried, filtered, and evaporated. Chromatographic purification (solvent B) of the residual oil gave **15** (57 mg, 74%). IR, ν_{max}: 3450–3050, 1735 cm^{-1}. ^{1}H NMR, δ: 1.29 (d, 3H, *J* = 5.7 Hz, Me), 3.34 (d, 1H, *J* = 8.5, 3.6 Hz, CHOBn), 3.62 (t, 1H, *J* = 8.5 Hz, CHOBn), 3.78 (td, *J* = 8.5, 8.5, 3.6 Hz, H-4), 3.92–4.06 (m, 1H, CHOH), 3.99 (d, 1H, *J* = 15.4 Hz, PhCHN), 4.14 (dd, 1H, *J* = 8.5, 6.8 Hz, H-5), 4.50 (s, 2H, OCH_2Ph), 4.76 (d, 1H, *J* = 15.4 Hz, PhCHN), 7.10–7.48 (m, 10H, PhH). ^{13}C NMR, δ: 20.1, 46.4, 55.9, 64.5, 64.6, 73.8, 80.5, 127.9, 127.9, 128.0, 128.4, 128.7, 128.8, 135.8, 136.1, 157.4. Anal. calcd. for $C_{20}H_{23}NO_4$: C 70.36, H 6.79, N 4.10; found: C 70.17, H 7.00, N 3.90.

(4*R*)-3-Benzyl-4-[(4*S*,5*R*)-4-(2,2,5-trimethyl-1,3-dioxolanyl)]-2-oxazolidinone (16)

2-Oxazolidinone **15** (33 mg, 0.097 mmol) was dissolved in a mixture of 95% EtOH (5 mL) and 2 M aqueous KOH (2 mL). The mixture was refluxed under Ar for 20 h. The cooled reaction mixture was evaporated to dryness and distilled water (2 mL) was added. Then Et_2O (4 mL) and Boc_2O (25 mg, 0.12 mmol) were added and the mixture stirred at rt, under Ar, for 4 h. The aqueous phase was removed and solid NaCl (1 g) was added. The mixture was stirred for 1 h; the aqueous phase was removed and then back-extracted with Et_2O (3 × 5 mL). The combined ether extracts were dried, filtered, and evaporated to leave crude diol as an oil (34 mg). Without further purification, the diol (34 mg) was dissolved in dry DCM (3 mL), and PPTS (11 mg) and 2-methoxypropene (0.2 mL) were added. The mixture was stirred under Ar for 3 h and then dry Et_3N (0.5 mL) was added. The mixture was evaporated to dryness and the crude residue was chromatographed (PE:EtOAc, 10:1) to give the ketal (30 mg).

The ketal (30 mg) was dissolved in dry MeOH (2 mL) and was hydrogenated (H_2, 1 atm (101.3 kPa), balloon) over 10% Pd/C (15 mg) for 4 h. The mixture was filtered through a Celite pad, the residue washed with dry MeOH (4 mL), and the combined filtrate was evaporated to leave an oil. The crude oil was dried under high vacuum for 2 h and then dissolved in dry THF (2 mL). The solution was added to a suspension of hexane-washed NaH (7 mg, 50% dispersion in mineral oil) in dry THF (2 mL). The mixture was refluxed for 45 min, cooled, and saturated NH_4Cl (4 drops) was added. The mixture was evaporated, and EtOAc (5 mL) and

© 1998 NRC Canada

saturated aqueous NaCl were added. The aqueous phase was separated and reextracted with EtOAc (4 mL). The combined organic phases were dried, filtered, and evaporated to give crude **16**. Chromatographic purification (solvent C) gave crystalline **16** (17 mg, 89%); mp 134–135°C. IR, ν_{max}: 1748 cm^{-1}. ^1H NMR, δ: 1.05 (d, 3H, *J* = 6.3 Hz, Me), 1.34 (s, 3H, Me), 1.50 (s, 3H, Me), 3.57 (dq, 1H, *J* = 8.9, 5.6, 2.1 Hz, H-4), 4.13 (d, 1H, *J* = 15.9 Hz, PhCHN), 4.25 ("t", 1H, *J* = 8.2 Hz, H-5), 4.27 (dd, 1H, *J* = 8.2, 2.1 Hz, H-5), 4.37 ("q", 1H, *J* = 6.3 Hz, H-5′), 4.44 (dd, 1H, *J* = 8.9, 5.2 Hz, H-4′), 4.93 (d, 1H, *J* = 15.9 Hz, PhCHN), 7.25–7.50 (m, 5H, PhH). ^{13}C NMR, δ: 15.2, 24.48, 26.4, 45.7, 54.8, 63.0, 71.6, 73.3, 108.4, 127.8, 127.9, 128.9, 135.7, 158.5. Anal. calcd. for $C_{16}H_{21}NO_4$: C 65.96, H 7.27, N 4.81; found: C 65.97, H 7.40, N 4.60.

(2*S*,3*S*,4*R*)-2-Benzylamino-1,3,4-dihydroxyoctadecane (17a)

The 2-oxazolidinone **14f** (270 mg, 0.528 mmol) was dissolved in 95% EtOH (10 mL) and aqueous 2 M KOH (4 mL) was added. The mixture was refluxed under Ar for 20 h, then cooled to rt, at which time a fluffy white precipitate was formed. The reaction mixture was concentrated and saturated NaCl (10 mL) was added. The mixture was thoroughly extracted with DCM (3 × 10 mL), the combined organic extracts were dried, filtered, and evaporated. The crude solid was chromatographed (DCM:MeOH, 190:2) to give crystalline **17a** (256 mg, 83%); mp 75–77°C. $[\alpha]_D^{23}$ +21.4 (*c* 1.75, $CHCl_3$). IR, ν_{max}: 3154–3448 cm^{-1}. ^1H NMR, δ: 0.90 (t, 3H, *J* = 6.5 Hz, Me), 1.15–1.75 (m, 26H, CH_2), 2.92 (dt, 1H, *J* = 6.8, 4 Hz), 3.10–3.30 (br hump, 3H), 3.47 ("t", 1H, *J* = 6.8 Hz), 3.55–3.85 (m, 5H), 4.49 (d, 1H, *J* = 13 Hz, PhCHO), 4.56 (d, 1H, *J* = 13 Hz, PhCHO), 7.20–7.42 (m, 10H, PhH). ^{13}C NMR, δ: 14.1, 22.7, 25.3, 29.3, 29.7, 29.8, 31.9, 33.9, 51.3, 60.3, 67.1, 72.1, 73.3, 74.4, 76.4, 77.0, 77.6, 127.3, 127.8, 127.9, 128.2, 128.5, 137.7, 139.1. HRMS, calcd. for $C_{32}H_{51}NO_3$ (M^+): 497.3869; found: 497.3868.

Synthetic (2*S*,3*S*,4*R*)-2-Amino-1,2,3-trihydroxyoctadecane (phytosphingosine) (17b)

The amino alcohol **17a** (256 mg) was dissolved in 95% EtOH (15 mL) and $Pd(OH)_2$ (281 mg) was added. The mixture was hydrogenated (H_2 at 50 psi (1 psi = 6.9 kPa)) for 16 h using a Parr apparatus. The mixture was filtered through Celite and the residue washed with 95% EtOH (3 × 2 mL). The combined filtrate was concentrated to about 8 mL, distilled water was added until the mixture was slightly turbid, and the mixture was placed in the freezer. The white powdery solid was filtered off and dried. Yield of **17b** was 130 mg (80%); mp 99–100°C (lit. (19*b*) mp 98–100°C; (19*c*) mp 103°C). $[\alpha]_D^{21}$ +8.3 (*c* 1.2, pyridine) (lit. (19*a*) $[\alpha]_D^{24}$ +8.7 (*c* 0.80, pyridine); (19*c*) $[\alpha]_D^{20}$ +7.9 (*c* 1.0, pyridine)). ^1H NMR, δ (DMSO-d_6): 0.85 (t, 3H, *J* = 6.5 Hz, Me), 1.15–1.35 (m, 24H, CH_2), 1.40–1.65 (m, 2H, CH_2), 2.60–2.75 (m, 1H, CHO), 3.05 (t, 1H, *J* = 6.7 Hz, CHO), 3.20–3.40 (m, 5H), 3.52 (dd, 1H, *J* = 9.6, 3.6 Hz), 4.40–4.60 (m, 1H).

Synthetic phytosphingosine tetraacetate (18)

Phytosphingosine **17b** (84 mg, 0.27 mmol) was dissolved in dry pyridine (2 mL) containing DMAP (30 mg), and Ac_2O (150 μL, 1.60 mmol) was added. The mixture was kept at rt for 18 h and then diluted with EtOAc (15 mL). The organic layer was washed twice with aqueous 1 N H_2SO_4 (10 mL), water (10 mL), and saturated $NaHCO_3$, then dried, filtered, and evaporated. The crude product was chromatographed (solvent B) to give **18** (126 mg, 98%); mp 46–48°C (lit. (19*c*) mp 48°C; (19*a*) mp 34–37°C).$[\alpha]_D^{21}$ +28.9 (*c* 0.95, $CHCl_3$), $[\alpha]_D^{21}$ +4 (*c* 1.25, DMF) (lit. (19*a*) $[\alpha]_D^{24}$ +28 (*c*, 1.30, $CHCl_3$); (19*b*) $[\alpha]_D^{30}$ +4.4 (*c* 1.12, DMF)). IR, ν_{max}: 3236–3342, 1746, 1660 cm^{-1}. ^1H NMR, δ: 0.87 (t, 3H, *J* = 6.8 Hz, Me), 1.18–1.33 (m, 24H, CH_2), 1.55–1.75 (m, 2H, CH_2), 2.20 (s, 3H, OAc), 2.50 (s, 6H, OAc), 2.80 (s, 3H, OAc), 4.00 (dd, 1H, *J* = 10.9, 2.8 Hz, CHOAc), 4.29 (dd, 1H, *J* = 10.9, 4.2 Hz, CHOAc), 4.40–4.55 (m, 1H), 4.94 (dt, 1H, *J* = 8.3, 3.4 Hz), 5.11 (dd, 1H, *J* = 8.0, 3.1 Hz), 6.05 (d, 1H, *J* = 8.3 Hz). ^{13}C NMR, δ: 14.1, 20.6, 20.7, 21.0, 22.6, 23.2, 25.5, 28.1, 29.2, 29.3, 29.4, 29.5, 29.6, 29.6, 31.9, 47.5, 62.8, 71.9, 72.9, 76.4, 76.9, 77.6, 169.7, 170.0, 170.8, 171.1. HRMS, calcd. for $C_{23}H_{42}NO_5$ (M – CH_2OAc): 412.3063; found: 412.3056.

Acknowledgements

Financial support from the Natural Sciences and Engineering Research Council of Canada and the University of Regina is gratefully acknowledged. We thank Dr. R. Kirk Marat of the Prairie Regional High-Field NMR Centre, Winnipeg, for the NOE experiments and Mr. K. Thoms for performing high-resolution mass spectral and elemental analyses.

References

1. Sphingolipids: (*a*) C.C. Sweeley. *In* Biochemistry of lipids and membranes. *Edited by* D.E. Vance and J.E. Vance. Benjamin/Cummings, Menlo Park, Calif. 1985. Chap. 12. Hydroxylated alkaloids: (*b*) G.R. Cook, L.G. Beholz, and J.R. Stille. J. Org. Chem. **59**, 3575 (1994), and references cited; (*c*) G.W.J. Fleet and D.R. Witty. Tetrahedron: Asymmetry, **1**, 119 (1990). Amino acids: (*d*) R. Duthaler. Tetrahedron, **50**, 1539 (1994); (*e*) C.N.C. Drey. *In* Chemistry and biochemistry of the amino acids. HIV protease inhibitors. *Edited by* G.C. Barrett. Chapman and Hall, New York. 1985.Chap. 3: HIV protease inhibitors; (*f*) P. Remuzon, C. Dussy, J.-P. Jacquet, P. Roty, and D. Bouzard. Tetrahedron: Asymmetry, **7**, 1181 (1996); (*g*) M.A. Schwindt, D.T. Belmont, M. Carlson, L.C. Franklin, V.S. Hendrickson, G.L. Farrick, R.W. Poe, D.M. Sobieray, and J. Van De Vusse. J. Org. Chem. **61**, 9564 (1996). Amino sugars: (*h*) F.M. Hauser and S.R. Ellenberger. Chem. Rev. **86**, 35 (1986).
2. (*a*) Oxazolidinone-based chiral auxiliaries: D.J. Ager, I. Prakash, and D.R. Schaad. Chem. Rev. **96**, 835 (1996). (*b*) Chiral oxazoline ligands: A.V. Bedekar, E.B. Koroleva, and P.G. Andersson. J. Org. Chem. **62**, 2518 (1997), and refs. cited.
3. (*a*) J. Jurczak and A. Golebiowski. Chem. Rev. **89**, 149 (1989); (*b*) G. Cardillo and M. Orena. Tetrahedron, **46**, 3321 (1990); (*c*) M.T. Reetz. Angew. Chem. Int. Ed. Engl. **30**, 1531 (1991); (*d*) A. Dondoni and D. Perrone. Aldrichimica Acta, **30**, 35 (1997). Recent approaches: (*e*) D.R. Williams, M.H. Osterhout, and J.P. Reddy. Tetrahedron Lett. **34**, 3271 (1993);

© 1998 NRC Canada

(*f*) R. Muller, T. Leibold, M. Patzel, and V. Jager. Angew. Chem. Int. Ed. Engl. **33**, 1295 (1994); (*g*) H.Y. Chang and K.B. Sharpless. Tetrahedron Lett. **37**, 3219 (1996); (*h*) A.G.M. Barrett, M.A. Seefeld, A.J.P. White, and D.J. Williams. J. Org. Chem. **61**, 2677 (1996).

4. (*a*) J.S. Ng, C.A. Przybyla, C. Liu, J.C. Yen, F.W. Muellner, and C.L. Weyker. Tetrahedron, **51**, 6397 (1995); (*b*) R. Polt, M.A. Peterson, and L. De Young. J. Org. Chem. **57**, 5469 (1992).
5. (*a*) Review: T. Yokomatsu, Y. Yuasa, and S. Shibuya. Heterocycles, **33**, 1051 (1992); (*b*) R.W. Friesen and A.E. Kolaczewska. J. Org. Chem. **56**, 4888 (1991); (*c*) M. Kimura, K. Fugami, S. Tanaka, and Y. Tamaru. J. Org. Chem. **57**, 6377 (1992); (*d*) T. Ishizuka, S. Ishibushi, and T. Kuneida. Tetrahedron, **49**, 1841 (1993); (*e*) M.P. Sibi, D. Rutherford, and R. Sharma. J. Chem. Soc. Perkin Trans. 1, 1675 (1994); (*f*) J.C. Carretero and E. Dominguez. Tetrahedron Lett. **35**, 4603 (1994); (*g*) A.B. Bueno, M.C. Carreno, J.L.G. Ruano, R.G. Arrayas, and M.M. Zarzuelo. J. Org. Chem. **6**2 2139 (1997); (*h*) S.C. Bergmeier and D.M. Stachina. J. Org. Chem. **62**, 4449 (1997).
6. A.G.H. Wee and F. Tang. Tetrahedron Lett. **37**, 6677 (1996).
7. (*a*) A. Furstner. Liebigs Ann. Chem. 1211 (1993); (*b*) P.M. Collins and B.R. Whitton. Carbohydr. Res. **36**, 293 (1974).
8. (*a*) N.S. Simpkins. Tetrahedron, **46**, 6951 (1990); (*b*) B.M. Trost. Bull. Soc. Chem. Jpn. **61**, 107 (1988).
9. R.S. Coleman and A.J. Carpenter. J. Org. Chem. **57**, 5813 (1992).
10. J.M. Denis, C. Girard, and J.M. Conia. Synthesis, 549 (1972).
11. T. Tsunada, K. Fujiwara, Y. Yamamoto, and S. Ito. Tetrahedron Lett. **32**, 1975 (1991).
12. P. Garner and J.M. Park. J. Org. Chem. **52**, 2361 (1987).
13. (*a*) T. Imamoto *In* Comprehensive organic chemistry. Vol. 1. *Edited by* B.M. Trost and I. Fleming. Pergamon Press, New York. 1991. Chap. 1.8. p. 231; (*b*) T. Imamoto, N. Takiyama, K. Nakamura, T. Hatajima, and T. Kanuya. J. Am. Chem. Soc. **111**, 4392 (1989); (*c*) P.M.J. Jung, A. Burger, and J.F. Biellmann. J. Org. Chem. **62**, 8309 (1997), and refs. cited
14. T. Imamoto, T. Hatajima, and K. Ogata. Tetrahedron Lett. **32**, 2787 (1991).
15. (*a*) M.T. Reetz. Angew. Chem. Int. Ed. Engl. **23**, 556 (1984); (*b*) M.T. Reetz, J. Westermann, R. Steinbach, B. Wenderoth, R. Peter, R. Ostanek, and S. Maus. Chem. Ber. **118**, 1421 (1985).
16. T. Ibuka, K. Suzuki, H. Habashita, A. Otaka, H. Tamamura, N. Mimura, Y. Miwa, T. Taga, and N. Fujii. Chem. Commun. 2151, (1994).
17. (*a*) M. Cherest, H. Felkin, and N. Prudent. Tetrahedron Lett. 2199 (1968); (*b*) N.T. Anh. Top. Curr. Chem. **88**, 145 (1980).
18. P. Munier, A. Krusinski, D. Picq, and D. Anker. Tetrahedron, **51**, 1229 (1995).
19. (*a*) T. Murakami, H. Minamikawa, and M. Hato. Tetrahedron Lett. **35**, 745 (1994); (*b*) A. Dondoni, G. Fantin, M. Fogagnolo, and P. Pedrini. J. Org. Chem. **55**, 1439 (1990); (*c*) J. Mulzer and C. Brand. Tetrahedron, **42**, 5961 (1986).
20. W.C. Still, M. Kahn, and A. Mitra. J. Org. Chem. **43**, 2923 (1978).
21. (*a*) J. Wardell. *In* Inorganic reactions and methods. Vol 11. *Edited by* J.J. Zuckerman. VCH, New York. 1988. p. 107; (*b*) V. Ramanathan and R. Levine. J. Org. Chem. **27**, 1316 (1962); (*c*) M.W. Rathke and D.F. Sullivan. J. Am. Chem. Soc. **75**, 3050 (1973).
22. (*a*) M.F. Lipton, C.M. Sorenson, A.C. Sadler, and R.H. Shapiro. J. Organomet. Chem. **186**, 155 (1980); (*b*) H. Kiljunen and T.H. Hase. J. Org. Chem. **56**, 6950 (1991).
23. V. Dimitrov, K. Kostova, and M. Genov. Tetrahedron Lett. **37**, 6787 (1996), and refs. cited.

© 1998 NRC Canada

C-(2-Hydroxyaryl)-*N*-(2-hydroxyphenylmethyl)nitrones as regioselective bidentate ligands in boron chelate formation. Crystal and molecular structures of a diphenylboron complex and its parent ligand[1]

Wolfgang Kliegel, Jörg Metge, Steven J. Rettig, and James Trotter

Abstract: The *C*-(2-hydroxyaryl)-*N*-(2-hydroxyphenylmethyl)nitrones **5** are synthesized by the condensation of variously substituted salicylaldehydes with *N*-(2-hydroxyphenylmethyl)-hydroxylamine. These nitrones react with diphenylborinic acid anhydride to form seven-membered diphenylboron chelates **6**. Crystals of *C*-(4-diethylamino-2-hydroxyphenyl)-*N*-(2-hydroxyphenylmethyl)nitrone, **5***d*, are monoclinic, a = 6.911(2), b = 10.663(2), c = 22.951(1) Å, β = 97.33(1)°, Z = 4, space group $P2_1/n$, and those of 4-dimethylamino-8-(2-hydroxyphenylmethyl)-6,6-diphenyl-5,7-dioxa-8-azonia-6-borata-6,7-dihydro-5*H*-benzocyclohepten e–ethanol, **6***d*·EtOH, are monoclinic, a = 9.069(2), b = 29.881(1), c = 11.1883(6) Å, β = 109.426(9)°, Z = 4, space group $P2_1/n$. The structures were solved by direct methods and refined by full-matrix least-squares procedures to R = 0.032 and 0.039 (R_w = 0.031 and 0.036) for 2510 and 4162 reflections with $I > 3\sigma(I)$, respectively.

Key words: *C*-(2-hydroxyaryl)-*N*-(2-hydroxyphenylmethyl)nitrones, organoboron compounds, crystal structures.

Résumé : La condensation de divers salicylaldéhydes substitués avec de la *N*-(2-hydroxyphénylméthyl)hydroxylamine conduit aux *C*-(2-hydroxyaryl)-*N*-(2-hydroxyphénylméthyl)nitrones (**5**). Ces nitrones réagissent avec l'anhydride de l'acide diphénylborinique pour former les chélates à sept chaînons du diphénylbore (**6**). Les cristaux de la *C*-(4-diéthylamino-2-hydroxyphényl)-*N*-(2-hydroxyphénylméthyl)nitrone (**5***d*) sont monocliniques, groupe d'espace $P2_1/n$, avec a = 6,911(2), b = 10,663(2) et c = 22,951(1) Å, β = 97,33(1)° et Z = 4 alors que ceux du 4-dimethylamino-8-(2-hydroxyphénylméthyl)-6,6-diphényl-5,7-dioxa-8-azonia-6-borata-6,7-dihydro-5*H*-benzocycloheptèn e–éthanol, **6***d*·EtOH, sont monocliniques, groupe d'espace $P2_1/n$, avec a = 9,069(2), b = 29,881(1) et c = 11,1883(6) Å, β = 109,426(9)° et Z = 4. On a résolu les structures par des méthodes directes et on les a affinées par la méthode des moindres carrés jusqu'à des valeurs de R = 0,032 et 0,039 (R_w = 0,031 et 0,036) pour respectivement 2510 et 4162 réflexions avec $I > 3\sigma(I)$.

Mots clés : *C*-(2-hydroxyaryl)-*N*-(2-hydroxyphénylméthyl)nitrones, composés organiques du bore, structures cristallines.

[Traduit par la Rédaction]

Introduction

Various boron chelates of *N*-alkyl or *N*-aryl salicylaldehyde nitrones **1** (1) provide relatively rare examples of seven-membered chelate complexes. An X-ray crystallographic analysis of the diphenylboron chelate **2** (R = Me) established the seven-membered ring structure (2). Chelates of the same ring size could also be obtained from aromatic aldonitrones of *N*-(2-hydroxyphenylmethyl)hydroxylamine **3**, provided that the nitrone basicity was enhanced by electron-donating substituents on the aromatic aldehyde moiety. The structure of the diphenylboron chelate **4** (Ar = 4-$Me_2NC_6H_4$) was also determined by an X-ray analysis (3). Continuing this investigation we have now synthesized a new class of nitrones, which offer both of the bidentate ligand systems **1** and **3**, combined in the same molecule, **5**, for the purpose of determining which of the two competing ligand moieties would be involved in the boron chelate formation. Based on the above-mentioned results it could generally be expected that chelates of type **6** should possess a greater stability compared to the (also) seven-membered chelates of type **7**. In the case of the *para*-dialkylamino substituted salicylaldehyde nitrone **5***d* ($R^2 = Et_2N$), however, the formation of both type **6** and (or) type **7** chelates had to be considered.

Received March 3, 1998.

W. Kliegel and J. Metge. Institut für Pharmazeutische Chemie der Technischen Universität Braunschweig, Beethovenstrasse 55, 38106 Braunschweig, Germany.
S.J. Rettig and J. Trotter.[2] Department of Chemistry, University of British Columbia, 2036 Main Mall, Vancouver, BC V6T 1Z1, Canada.

[1]Structural studies of organoboron compounds LXVIII. Previous paper in this series: ref. 9.

[2]Author to whom correspondence may be addressed. Telephone: (604) 822-4865. Fax: (604) 822-2847. E-mail: jtrt@xray4.chem.ubc.ca

© 1998 NRC Canada

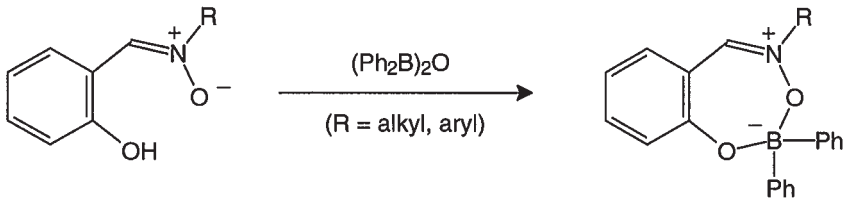

1 2

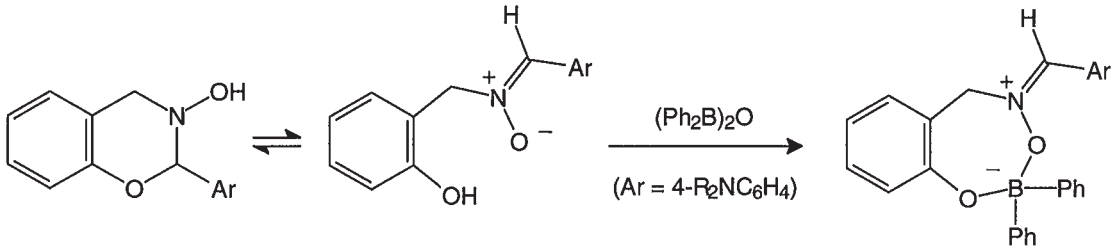

3' 3 4

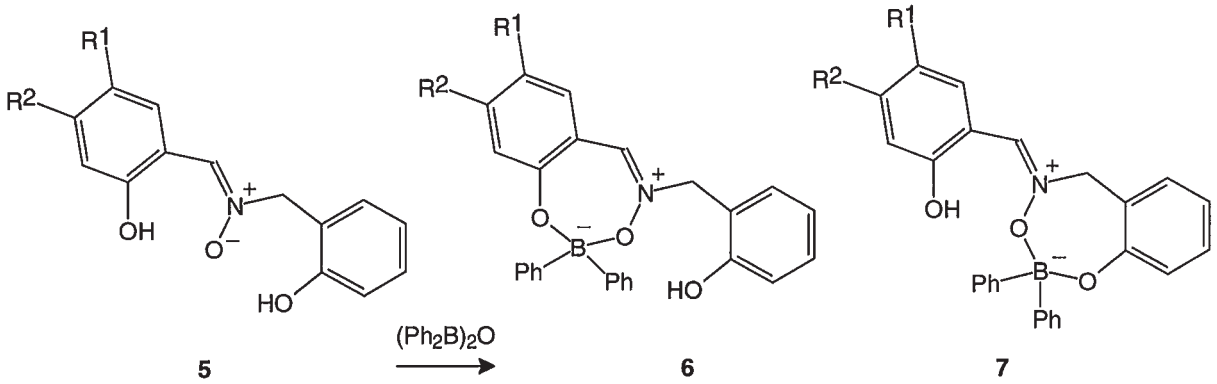

5 6 7

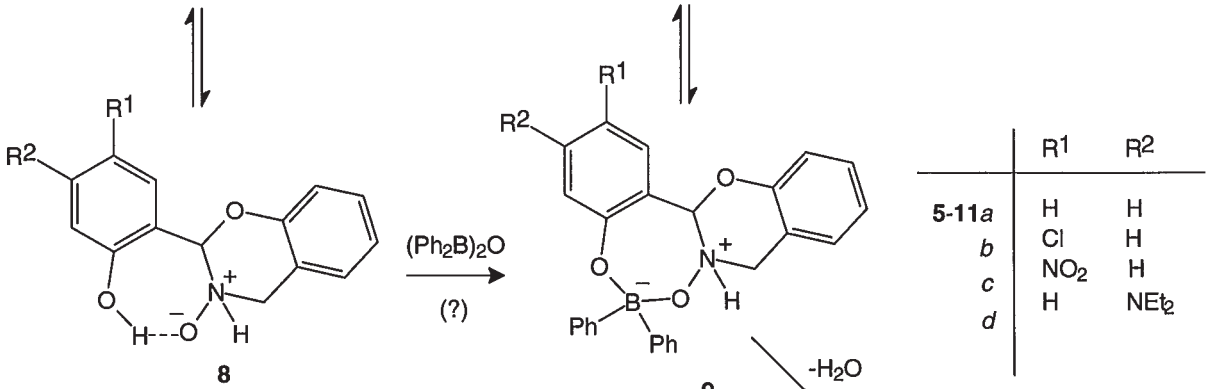

8 9

	R1	R2
5-11*a*	H	H
b	Cl	H
c	NO_2	H
d	H	NEt_2

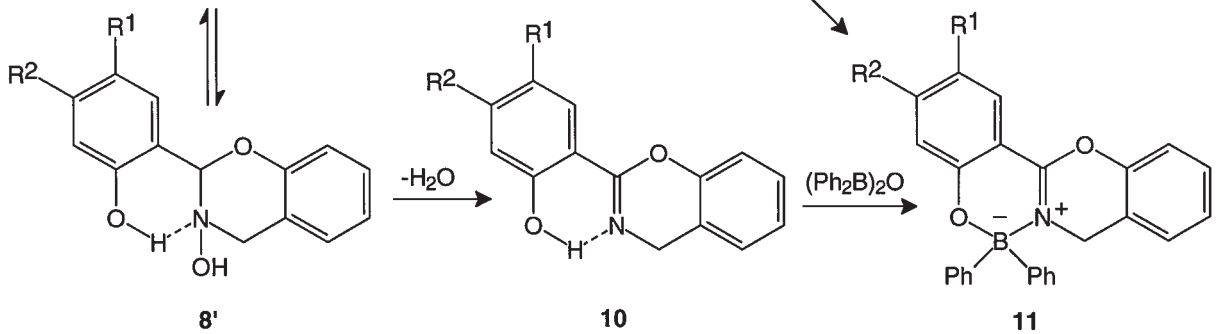

8' 10 11

© 1998 NRC Canada

Experimental

General procedures

All preparations and reactions were carried out under normal conditions, without protective gas atmosphere. Commercial solvents and reagents were used as supplied. Oxybis(diphenylborane) was prepared according to literature methods (4). Melting points were measured on a Linström SPA-1 apparatus and are uncorrected. Elemental analyses: (C, H, N) Carlo Erba elemental analyzer 1106; (B) oxidative disintegration (Schöninger), and potentiometric titration. Infrared spectra: Phillips PU 9800 FT-IR spectrometer, V 3.00, and Mattson Genesis Series FTIR Rev. I (ATI Unicam). ^{1}H nmr: Varian EM 390. ^{11}B nmr: Bruker AC 200. Mass spectra: Finnigan MAT 8430.

C-(2-Hydroxyphenyl)-*N*-(2-hydroxyphenylmethyl)nitrone, 5*a*[3]

According to the general procedure for the synthesis of *C*-aryl-*N*-(2-hydroxyphenylmethyl)nitrones **3** from *N*-(2-hydroxyphenylmethyl)hydroxylamine (3) **5***a* is obtained using salicylaldehyde (3.36 g, 30.0 mmol) as the aromatic aldehyde component. Yield: 5.0 g (69%) of orange-yellow crystals; mp 140°C (from ethanol). Infrared (KBr, cm^{-1}): 3000–1800 ("curtain" O-H), 1661 (C=N), 1609, (C=N), 1586 (C=C); ^{1}H nmr (90 MHz, $CDCl_3$–TMS), δ (ppm): 1.75 (s, broad, exchangeable, 65% of 1H, N-OH or $^+$NH-O$^-$), 3.2–4.9 (m, 65% of 3H, CH_2, and N-CH-O), 5.10 (s, 35% of 2H, CH_2), 6.60–7.86 (m, 8 aromatic H), 7.73 (s, 35% of 1H, N=CH), 9.83 (s, broad, exchangeable, 35% of 1H, phenolic OH), 11.83 (s, exchangeable, 35% of 1H, phenolic OH). Anal. calcd. for $C_{14}H_{13}NO_3$: C 69.13, H 5.39, N 5.76; found: C 69.14, H 5.13, N 5.78. The reaction of **5***a* in ethanolic solution with triphenyltetrazolium chloride (TTC) spontaneously gives a deep red color upon addition of 2 N NaOH solution, indicating the reductive potency (5) of an *N*-hydroxylamine grouping present in one of the possible tautomers of **5***a*.

C-(5-Chloro-2-hydroxyphenyl)-*N*-(2-hydroxyphenylmethyl)nitrone, 5*b*[4]

The compound is prepared as described for **5***a*, using 5-chloro-2-hydroxybenzaldehyde (4.70 g, 30.0 mmol). Yield: 6.3 g (75%) of a yellow powder; mp 177°C (from ethanol). Infrared (KBr, cm^{-1}): 3000–1800 (curtain O-H), 1602 (C=N), 1577 (C=C); ^{1}H nmr (90 MHz, DMSO-d_6–TMS), δ (ppm): 5.12 (s, CH_2), 6.73–7.46 (m, 6 aromatic H), 8.08 (d, ^4J = 3 Hz, 1 aromatic H), 8.16 (s, N=CH), 10.08 (s, broad, exchangeable, phenolic OH), 11.88 (s, broad, exchangeable, phenolic OH). Anal. calcd. for $C_{14}H_{12}ClNO_3$: C 60.55, H 4.36, Cl 12.77, N 5.04; found: C 60.80, H 4.43, Cl 12.03, N 4.96. The TTC test, carried out as with 5a, gives no red coloring of the solution.

C-(2-Hydroxy-5-nitrophenyl)-*N*-(2-hydroxyphenylmethyl)nitrone, 5*c*[5]

The compound is prepared as described for **5***a*, using 2-hydroxy-5-nitrobenzaldehyde (5.01 g, 30.0 mmol). Yield: 6.0 g (69%) of yellow crystals; mp 213°C (from ethanol). Infrared (KBr, cm^{-1}): 3421 (O-H), 3000–2000 (curtain O-H), 1602 (C=N), 1579 (C=C); ^{1}H nmr (90 MHz, DMSO-d_6–TMS), δ (ppm): 5.20 (s, CH_2), 6.76–7.53 (m, 5 aromatic H), 8.23 (dd, ^3J = 9 Hz, ^4J = 3 Hz, 1 aromatic H), 8.36 (s, N=CH), 9.23 (d, ^4J = 3 Hz, 1 aromatic H), 10.06 (s, broad, exchangeable, phenolic OH), 13.33 (s, broad, exchangeable, phenolic OH). Anal. calcd. for $C_{14}H_{12}N_2O_5$: C 58.33, H 4.20, N 9.72; found: C 58.32, H 4.25, N 9.57. The TTC test, carried out as with **5***a*, gives no red coloring of the solution.

C-(4-Diethylamino-2-hydroxyphenyl)-*N*-(2-hydroxyphenylmethyl)nitrone, 5*d*[6]

The compound is prepared as described for **5***a*, using 4-diethylamino-2-hydroxybenzaldehyde (5.80 g, 30.0 mmol). Yield: 4.7 g (50%) of pale-yellow crystals; mp 143°C (from ethanol). Infrared (KBr, cm^{-1}): 3100–1800 (curtain O-H), 1624 (C=N), 1600 (C=C); ^{1}H nmr (90 MHz, DMSO-d_6–TMS), δ (ppm): 1.10 (t, J = 7 Hz, 2 CH_3), 3.35 (q, J = 7 Hz, $N(CH_2)_2$), 5.00 (s, CH_2), 5.98 (d, ^4J = 3 Hz, 1 aromatic H), 6.21 (dd, ^3J = 9 Hz, ^4J = 3 Hz, 1 aromatic H), 6.73–7.43 (m, 5 aromatic H), 7.86 (s, N=CH), 10.30 (s, exchangeable, phenolic OH), 13.83 (s, exchangeable, phenolic OH); ^{1}H nmr (90 MHz, $CDCl_3$–TMS), δ (ppm): 1.15 (t, J = 7 Hz, 2 CH_3), 3.33 (q, J = 7 Hz, $N(CH_2)_2$), 4.93 (s, CH_2), 6.00–7.43 (m, 7 aromatic H), 7.33 (s, N=CH), 10.63 (s, broad, exchangeable, phenolic OH), 13.23 (s, exchangeable, phenolic OH). Anal. calcd. for $C_{18}H_{22}N_2O_3$: C 68.77, H 7.05, N 8.91; found: C 68.82, H 7.48, N 8.94. The TTC test, carried out as with **5***a*, gives no red coloring of the solution. Crystals suitable for X-ray analysis were obtained by slow cooling of a solution of **5***d* in absolute ethanol. A stereoview of **5***d* is shown in Fig. 1.

2-Chloro-8-(2-hydroxyphenylmethyl)-6,6-diphenyl-5,7-dioxa-8-azonia-6-borata-6,7-dihydro-5*H*-benzocycloheptene, 6*b*[7]

The compounds **5***b* (0.28 g, 1.0 mmol) and oxybis(diphenylborane) (0.17 g, 0.5 mmol) are dissolved separately, each in 20 mL of ethanol, with slight warming if necessary. After mixing the two solutions crystallization commences rapidly and gives an analytically pure product in most instances. Yield: 0.33 g (68%) of pale-yellow needles; mp 164°C (from ethanol). Infrared (KBr, cm^{-1}): 3430 (O-H), 1636 (C=N), 1615 (C=C); ^{1}H nmr (90 MHz, DMSO-d_6–TMS), δ (ppm): 1.06 (t, J = 6 Hz, CH_3), 3.45 (q, J = 6 Hz, OCH_2), 3.6 (s, broad, exchangeable, associated OH), 5.26 (s, NCH_2), 6.76–7.70 (m, 17 aromatic H), 8.53 (s, N=CH), 10.03 (s, exchangeable, phenolic OH); ^{11}B nmr (64 MHz, DMSO-d_6–Et_2OBF_3), δ (ppm): 8.0 (broad, very

[3] Alternative nomenclature: 2-[(2-hydroxyphenylmethylenamino)methyl]phenol *N*-oxide.
[4] Alternative nomenclature: 4-chloro-2-[(2-hydroxyphenylmethylimino)methyl]phenol *N*-oxide.
[5] Alternative nomenclature: 2-[(2-hydroxyphenylmethylimino)methyl]-4-nitrophenol *N*-oxide.
[6] Alternative nomenclature: 5-diethylamino^1-2-[(2-hydroxyphenylmethylimino^2)methyl]phenol N^3-oxide.
[7] The compound crystallizes with 1 mol of ethanol.

© 1998 NRC Canada

Fig. 1. Stereoview of **5***d*; 33% probability thermal ellipsoids are shown for the non-hydrogen atoms.

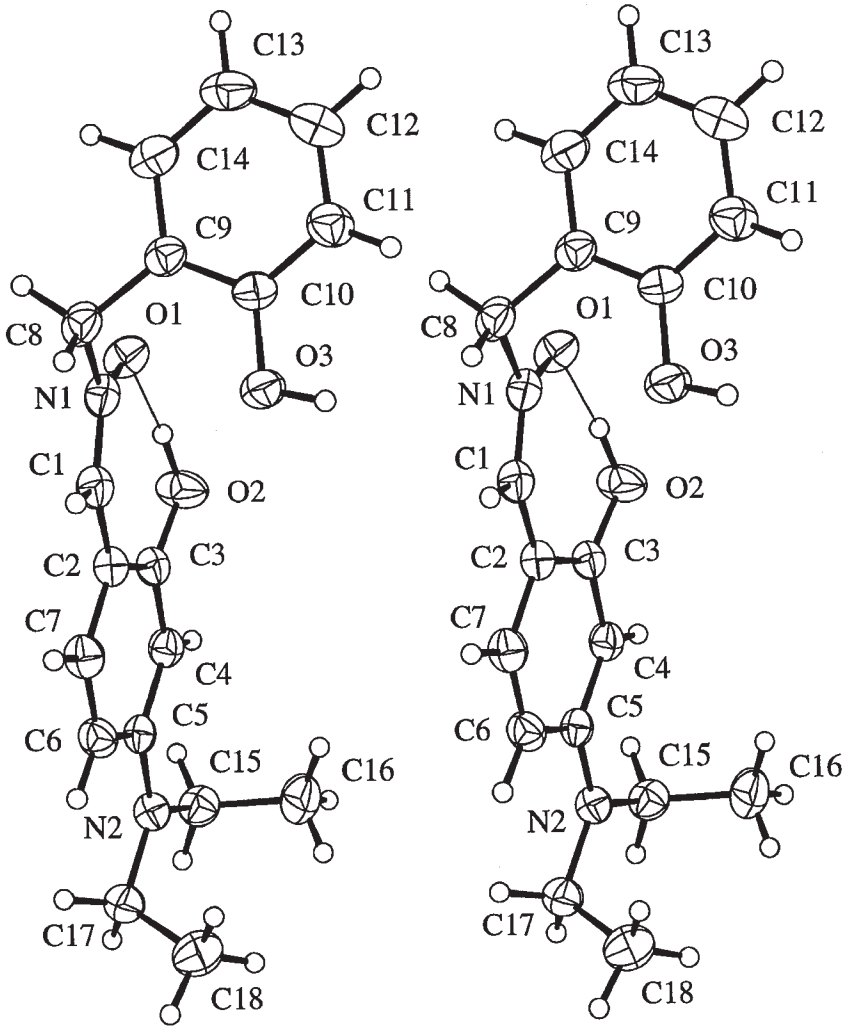

weak signal due to poor solubility). Anal. calcd. for $C_{26}H_{21}BClNO_3 \cdot C_2H_5OH$ ($C_{28}H_{27}BClNO_4$): C 68.95, H 5.58, B 2.22, Cl 7.27, N 2.87; found: C 69.20, H 5.67, B 2.33, Cl 7.04, N 2.79. The product gives a blue-colored solution in ethanol upon addition of diphenylcarbazone, indicating the presence of the chelated diphenylborenium (Ph_2B^+) ion (6).

8-(2-Hydroxyphenylmethyl)-2-nitro-6,6-diphenyl-5,7-dioxa-8-azonia-6-borata-6,7-dihydro-5*H*-benzocycloheptene, 6*c*

The compound **5***c* (0.29 g, 1.0 mmol) is reacted with oxybis(diphenylborane) (0.17 g, 0.5 mmol) as described for **6***b*. Yield: 0.25 g (55%) of a pale-yellow powder; mp (dec.) 295°C; very poor solubility in the usual solvents (alkanols, alkanes, $CHCl_3$, CH_2Cl_2, Me_2SO, benzene, toluene, and water). Infrared (KBr, cm^{-1}): 3460 (O-H), 1651 (C=N), 1615 (C=C); mass spectrum (EI, 170°C, 70 eV), *m*/*z* (%): 452 (0.8) [M^+], 357 (100) [$M^+ - H_2O - C_6H_5$], 311 (22) [$M^+ - H_2O - C_6H_5 - NO_2$]; (CI, 170°C, NH_3, pos), *m*/*z* (%): 452 (58) [M^+], 435 (100) [M^+ – OH], 357 (56) [$M^+ - H_2O - C_6H_5$], 311 (5) [$M^+ - H_2O - C_6H_5 - NO_2$], 271 (24) [$M^+ - (C_6H_5)_2BO$]; (CI, 170°C, NH_3, neg), *m*/*z* (%): 434 (100) [$M^+ - H_2O$]. Anal. calcd. for $C_{26}H_{21}BN_2O_5$: C 69.05, H 4.86, B 2.39, N 6.19; found: C 69.09, H 4.73, B 2.33, N 6.10. The product gives a blue-color reaction with diphenylcarbazone, as described for **6***b*.

4-Diethylamino-8-(2-hydroxyphenylmethyl)-6,6-diphenyl-5,7-dioxa-8-azonia-6-borata-6,7-dihydro-5*H*-benzocycloheptene, 6*d*[7]

The compound **5***d* (0.31 g, 1.0 mmol) is reacted with oxybis(diphenylborane) (0.17 g, 0.5 mmol) as described for **6***b*. Yield: 0.40 g (76%) of yellow crystals; mp 118°C (from ethanol). Infrared (KBr, cm^{-1}): 3400 (O-H), 1605 (C=N/C=C); ^{1}H nmr (90 MHz, $CDCl_3$–TMS), δ (ppm): 1.18 (t, J = 6 Hz, 2 CH_3), 1.20 (t, J = 6 Hz, CH_3), 1.73 (s, broad, exchangeable, OH), 3.35 (q, J = 6 Hz, $N(CH_2)_2$), 3.65 (q, J = 6 Hz, OCH_2), 4.86 (s, NCH_2), 6.00–7.60 (m, 17 aromatic H and possibly phenolic OH), 7.48 (s, N=CH); ^{11}B nmr (64 MHz, $CDCl_3$–Et_2OBF_3), δ (ppm): 7.4 ($W_{1/2}$ = 430 Hz) and 45.4 ($W_{1/2}$ = 340 Hz), ratio of peak areas: 20:1. Anal. calcd. for $C_{30}H_{31}BN_2O_3 \cdot C_2H_5OH$ ($C_{32}H_{37}BN_2O_4$): C 73.28, H 7.11, B 2.06, N 5.34; found: C 72.96, H 7.27, B

© 1998 NRC Canada

Fig. 2. Stereoview of **6***d*; 33% probability thermal ellipsoids are shown for the non-hydrogen atoms.

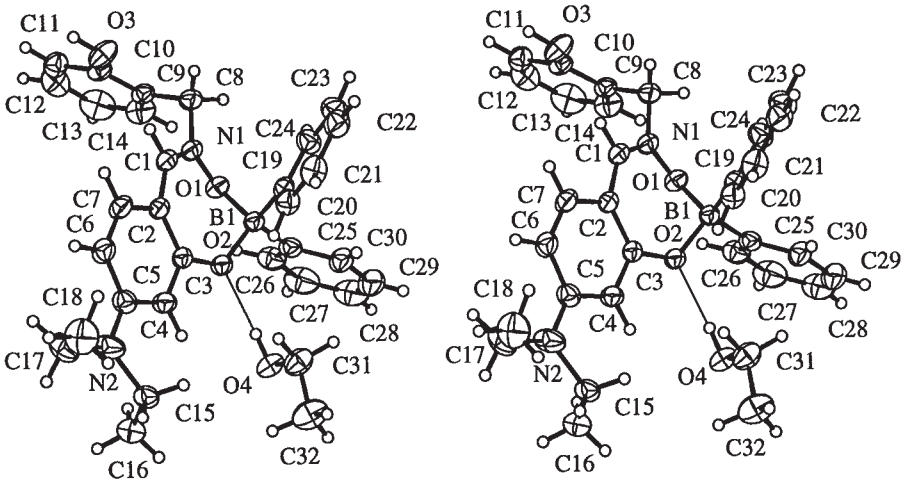

1.93, N 5.25. The product gives a blue-color reaction with diphenylcarbazone as described for **6***b*. Crystals suitable for X-ray analysis were obtained by slow cooling of a solution of **6***d* in absolute ethanol. A stereoview of **6***d* is shown in Fig. 2.

2-(2-Hydroxyphenyl)-4*H*-1,3-benzoxazine, 10*a*

The compound **5***a* (0.24 g, 1.0 mmol) is refluxed for 30 min in 30 mL of benzene using a Dean–Stark trap for continuous removal of water. After evaporation in vacuo the residue is recrystallized from ethanol. Yield: 0.21 g (93%) of colorless crystals; mp 155°C (from ethanol). Infrared (KBr, cm^{-1}): 3000–2000 (curtain O-H), 1661 (C=N), 1607 (C=C); ^{1}H nmr (90 MHz, $CDCl_3$–TMS), δ (ppm): 4.80 (s, CH_2), 6.80–7.50 (m, 7 aromatic H), 7.86–8.00 (m, 1 aromatic H), 13.13 (s, exchangeable, OH). Anal. calcd. for $C_{14}H_{11}NO_2$: C 74.65, H 4.92, N 6.22; found: C 74.63, H 4.86, N 6.11. The TTC test, carried out as with **5***a*, gives no red coloring of the solution.

6,6-Diphenyl-5,12-dioxa-6a-azonia-6-borata-5,6,7,12-tetrahydrobenz[a]anthracene, 11*a*[8]

The compound **5***a* (0.24 g, 1.0 mmol) is reacted with oxybis(diphenylborane) as described for the synthesis of **6***b*. Yield: 0.28 g (72%) of colorless crystals, mp 234°C (from ethanol). Infrared (KBr, cm^{-1}): 1651 (C=N), 1604 and 1591 (C=C); ^{1}H nmr (90 MHz, DMSO-d_6–TMS), δ (ppm): 4.38 (s, CH_2), 6.80–8.03 (m, 18 aromatic H); ^{1}H nmr (400 MHz, $CDCl_3$–TMS), δ (ppm): 4.33 (s, CH_2), 6.00 (dt, ^3J = 7 Hz, ^4J = 1 Hz, 1 aromatic H), 7.01 (s, 1 aromatic H), 7.03 (s, 1 aromatic H), 7.20–7.28 (m, 8 aromatic H), 7.33–7.37 (m, 1 aromatic H), 7.41–7.49 (m, 5 aromatic H), 7.79 (dd, ^3J = 8 Hz, ^4J = 1.5 Hz, 1 aromatic H); mass spectrum (EI, 125°C, 70 eV), *m*/*z* (%): 312 (100) [$M^+ - C_6H_5$]; (CI, 150°C, NH_3, neg), *m*/*z* (%): 389 (100) [M^+]. The product gives a blue-color reaction with diphenylcarbazone as described for **6***b*.

The compound **11***a* is also obtained in quantitative yield by the reaction of **10***a* (0.23 g, 1.0 mmol) with oxybis(diphenylborane) (0.17 g, 0.5 mmol) in ethanol. The spontaneously crystallizing substance is identical (by mp and IR) with **11***a* obtained from the reaction of **5***a* with oxybis(diphenylborane).

X-ray crystallographic analyses of 5*d* and 6*d*

Crystallographic data appear in Table 1. The final unit-cell parameters were obtained by least-squares on the setting angles for 25 reflections with 2θ = 93.8–107.8° for **5***d* and 76.5–90.7° for **6***d*. The intensities of three standard reflections, measured every 200 reflections throughout the data collections, showed only small random fluctuations for both compounds. The data were processed,[9] corrected for Lorentz and polarization effects, and absorption (based on azimuthal scans).

The structures were both solved by direct methods, the coordinates of the non-hydrogen atoms being determined from *E*-maps or from subsequent difference Fourier syntheses. A two-fold disordering of one of the NEt groups of **6***d* was modeled by split-atom refinement. A constrained group occupancy factor was refined. All non-hydrogen atoms were refined with anisotropic thermal parameters. For **6***d* the hydrogen atoms associated with the disordered ethyl group were fixed in calculated positions with C-H = 0.98 Å and $B_H = 1.2B_{\text{bonded atom}}$, and all remaining hydrogen atoms for both structures were refined with isotropic thermal parameters. Corrections for secondary extinction were applied (Zachariasen type, isotropic, Gaussian), the final values of the extinction coefficients being $6.88(6) \times 10^{-6}$ for **5***d* and $3.18(13) \times 10^{-6}$ for **6***d*. Neutral atom scattering factors for all atoms and anomalous dispersion corrections for the non-hydrogen atoms were taken from the *International Tables for X-Ray Crystallography* (7). Final atomic coordinates and equivalent isotropic thermal parameters, bond lengths, bond angles, and intra-annular torsion angles appear in Tables 2–5, respectively. Hydrogen atom parameters, anisotropic thermal parameters, torsion angles,

[8] Alternative nomenclature: 2-(2-diphenylboryloxyphenyl)-4*H*-1,3-benzoxazine (*N*→*B*).
[9] teXsan: Crystal structure analysis package. Unix version 1.7. Molecular Structure Corporation. The Woodlands, Tex., U.S.A. 1995.

© 1998 NRC Canada

Table 1. Crystallographic data.[a]

Compound	**5***d*	**6***d*·EtOH
Formula	$C_{18}H_{22}N_2O_3$	$C_{32}H_{37}BN_2O_4$
fw	314.38	459.15
Crystal system	Monoclinic	Monoclinic
Space group	$P2_1/n$ (no. 14)	$P2_1/n$ (no. 14)
a, Å	6.911(2)	9.069(2)
b, Å	10.663(2)	29.881(1)
c, Å	22.951(1)	11.1883(6)
β, °	97.33(1)	109.426(9)
V, Å^3	1677.5(5)	2859.5(6)
Z	4	4
ρ_{calc}, g/cm^3	1.245	1.218
F(000)	672	1120
μ(Cu K_α), cm^{-1}	6.53	6.31
Crystal size, mm	0.27 × 0.30 × 0.35	0.15 × 0.40 × 0.45
Transmission factors	0.93–1.00	0.79–1.00
Scan type	ω-2θ	ω-2θ
Scan range, deg in ω	1.21 + 0.20 tan θ	1.05 + 0.20 tan θ
Scan speed, deg/min	32 (up to 9 scans)	16 (up to 9 scans)
Data collected		$+h$, $+k$, $\pm l$
$2\theta_{max}$, deg	155	155
Crystal decay, %	Negligible	Negligible
Total reflections	3889	6378
Total unique reflections	3575	6066
R_{merge}	0.015	0.023
Reflections with $I > 3\sigma(I)$	2510	4162
No. of variables	297	500
R	0.032	0.039
R_w	0.031	0.036
gof	2.58	3.00
Max Δ/σ (final cycle)	0.002	0.02
Residual density e/Å^3	–0.14–0.13	–0.12–0.19

[a]Temperature 294 K, Rigaku AFC6S diffractometer, Cu K_α radiation (λ = 1.54178 Å), graphite monochromator, take-off angle 6.0°, aperture 6.0 × 6.0 mm at a distance of 285 mm from the crystal, stationary background counts at each end of the scan (scan/background time ratio 2:1), $\sigma^2(F^2) = [S^2(C + 4B)]/Lp^2$ (S = scan rate, C = scan count, B = normalized background count), function minimized $\Sigma w(|F_o| - |F_c|)^2$ where $w = 4F_o^2/\sigma^2(F_o^2)$, $R = \Sigma||F_o| - |F_c||/\Sigma|F_o|$, $R_w = (\Sigma w(|F_o| - |F_c|)^2/\Sigma w|F_o|^2)^{1/2}$, and gof = $[\Sigma w(|F_o| - |F_c|)^2/(m - n)]^{1/2}$. Values given for *R*, R_w, and gof are based on those reflections with $I > 3\sigma(I)$.

intermolecular contacts, and least-squares planes are included as supplementary material.[10]

Results and discussion

The nitrones 5 are synthesized by the condensation of variously substituted salicylaldehydes with *N*-(2-hydroxyphenylmethyl)hydroxylamine. The infrared and ^{1}H nmr spectra generally confirm the supposed nitrone structure via C=N absorption frequencies between 1602 and 1624 cm^{-1} and broad O-H "association" bands between 1800 and 3100 cm^{-1} or the ^{1}H nmr signals of the N=CH methine protons between δ = 7.73 and 8.36 ppm, respectively. Moreover, two OH signals of two different phenolic groups are found in the ^{1}H nmr spectra, one around 10 ppm, and the other between 11.8 and 13.8 ppm. Comparable shift data have been reported for δ (N=CH) and δ (OH) of the *N*-*tert*-butylsalicylaldonitrone **1** (R = *t*-C_4H_9) (8): 7.72 and 12.37 ppm, respectively.

Only compound **5***a* displays additional bands in the infrared and additional signals in the ^{1}H nmr spectrum. The infrared spectrum of **5***a* shows a distinct second band in the C=N absorption region at 1661 cm^{-1} in addition to the expected nitrone C=N band at 1609 cm^{-1}. A probable explanation for the higher frequency band might be the formation of a dehydration product, **10***a*, during the preparation of the KBr pellet (high pressure and vacuum). The dehydration pathway via the cyclotautomeric forms **8** and (or) **8′** is suggested by the discovery of additional signals indicating the cyclotautomers **8***a* or **8′***a* in the ^{1}H nmr spectrum of **5***a* in $CDCl_3$ solution. The presence of a cyclic form like **8′***a* in the solid state cannot be excluded, considering that a nitrone of type **3** (Ar = 4-$MeOC_6H_4$) has been shown by X-ray analysis to

[10] Copies of material on deposit may be purchased from the Depository of Unpublished Data, Document Delivery, CISTI, National Research Council Canada, Ottawa, Canada K1A 0S2. Tables of hydrogen atom coordinates and bond lengths and angles involving hydrogen atoms have also been deposited with the Cambridge Crystallographic Data Centre and can be obtained on request from The Director, Cambridge Crystallographic Data Centre, University Chemical Laboratory, 12 Union Road, Cambridge CB2 1EZ, U.K.

© 1998 NRC Canada

Table 2. Final atomic coordinates (fractional) and B_{eq} (10^3 Å^2).[a]

Atom	*x*	*y*	*z*	B_{eq}	Occupancy factor
			5*d*		
O(1)	0.6883(2)	0.61576(10)	0.18943(5)	4.66(3)	
O(2)	0.5615(2)	0.5089(1)	0.09552(5)	5.75(3)	
O(3)	0.7123(2)	0.3572(1)	0.29706(5)	5.03(3)	
N(1)	0.5682(2)	0.5791(1)	0.22783(5)	3.90(3)	
N(2)	–0.0276(2)	0.3268(1)	0.00847(5)	3.88(3)	
C(1)	0.4044(2)	0.5209(1)	0.21374(7)	3.96(3)	
C(2)	0.3085(2)	0.4779(1)	0.15854(6)	3.57(3)	
C(3)	0.3823(2)	0.4702(1)	0.10360(6)	3.68(3)	
C(4)	0.2706(2)	0.4195(1)	0.05530(6)	3.62(3)	
C(5)	0.0812(2)	0.3742(1)	0.05729(6)	3.44(3)	
C(6)	0.0069(2)	0.3815(1)	0.11185(7)	3.98(3)	
C(7)	0.1177(2)	0.4313(1)	0.15955(7)	4.11(3)	
C(8)	0.6379(2)	0.6134(2)	0.28919(7)	4.49(4)	
C(9)	0.8357(2)	0.5615(1)	0.31104(6)	3.85(3)	
C(10)	0.8661(2)	0.4327(1)	0.31571(6)	3.96(3)	
C(11)	1.0470(2)	0.3871(2)	0.33939(7)	4.88(4)	
C(12)	1.1955(3)	0.4682(2)	0.35928(8)	5.61(5)	
C(13)	1.1667(3)	0.5956(2)	0.35530(9)	5.78(5)	
C(14)	0.9880(3)	0.6415(2)	0.33072(8)	5.03(4)	
C(15)	0.0566(3)	0.3112(2)	–0.04597(7)	4.49(4)	
C(16)	0.1908(4)	0.1996(2)	–0.0466(1)	6.24(6)	
C(17)	–0.2257(2)	0.2804(2)	0.01012(8)	4.54(4)	
C(18)	–0.2347(4)	0.1447(2)	0.0293(1)	6.16(6)	
			6*d*		
O(1)	0.2331(1)	0.34155(4)	0.4099(1)	4.15(3)	
O(2)	0.2299(1)	0.40361(3)	0.2679(1)	3.89(3)	
O(3)	0.2340(2)	0.36878(5)	0.8183(1)	5.65(4)	
O(4)	0.2548(2)	0.41851(4)	0.0235(1)	4.93(3)	
N(1)	0.1926(2)	0.35824(5)	0.5077(1)	4.14(3)	
N(2)	0.3493(2)	0.55724(5)	0.3244(2)	6.63(5)	
C(1)	0.1839(2)	0.40088(6)	0.5271(2)	4.26(4)	
C(2)	0.2138(2)	0.43834(5)	0.4606(1)	3.84(4)	
C(3)	0.2454(2)	0.43908(5)	0.3445(1)	3.54(3)	
C(4)	0.2920(2)	0.47857(5)	0.3033(2)	4.16(4)	
C(5)	0.3048(2)	0.51916(5)	0.3689(2)	4.38(4)	
C(6)	0.2638(2)	0.51893(6)	0.4801(2)	4.71(5)	
C(7)	0.2207(2)	0.48016(6)	0.5218(2)	4.69(5)	
C(8)	0.1759(3)	0.32313(7)	0.5957(2)	4.76(5)	
C(9)	0.3245(2)	0.31644(5)	0.7039(2)	3.85(4)	
C(10)	0.3492(2)	0.34021(5)	0.8156(2)	3.92(4)	
C(11)	0.4850(3)	0.33468(6)	0.9171(2)	5.00(5)	
C(12)	0.5966(3)	0.30559(8)	0.9081(3)	6.46(6)	
C(13)	0.5750(3)	0.28182(9)	0.7984(3)	7.52(8)	
C(14)	0.4395(3)	0.28728(6)	0.6976(2)	5.84(6)	
C(15)	0.3319(6)	0.5599(1)	0.1801(5)	4.42(10)	0.595(8)
C(15a)	0.4504(8)	0.5548(2)	0.2471(6)	5.3(2)	0.405
C(16)	0.4855(5)	0.5463(1)	0.1659(5)	5.6(1)	0.595
C(16a)	0.338(1)	0.5613(3)	0.1166(8)	7.6(2)	0.405
C(17)	0.3705(3)	0.59954(7)	0.3938(3)	6.30(7)	
C(18)	0.2230(4)	0.6264(1)	0.3642(4)	8.09(9)	
C(19)	–0.0346(2)	0.37002(5)	0.2660(1)	3.76(4)	
C(20)	–0.1133(2)	0.41010(6)	0.2260(2)	4.72(4)	
C(21)	–0.2678(3)	0.41623(8)	0.2173(2)	5.68(6)	
C(22)	–0.3494(3)	0.38215(9)	0.2486(2)	5.87(6)	
C(23)	–0.2768(3)	0.34160(9)	0.2852(2)	6.01(6)	

© 1998 NRC Canada

Table 2 (*concluded*).

Atom	*x*	*y*	*z*	B_{eq}	Occupancy factor
C(24)	–0.1231(2)	0.33599(7)	0.2936(2)	4.87(5)	
C(25)	0.1732(2)	0.32659(5)	0.1801(2)	4.09(4)	
C(26)	0.3124(3)	0.30250(7)	0.2084(2)	5.42(6)	
C(27)	0.3382(4)	0.27263(8)	0.1234(3)	7.71(9)	
C(28)	0.2256(5)	0.26618(9)	0.0067(3)	8.7(1)	
C(29)	0.0888(5)	0.28923(10)	–0.0238(3)	7.64(8)	
C(30)	0.0617(3)	0.31940(7)	0.0617(2)	5.54(6)	
C(31)	0.1078(3)	0.44009(9)	–0.0318(2)	5.77(6)	
C(32)	0.1110(5)	0.4684(1)	–0.1371(3)	7.44(8)	
B(1)	0.1452(2)	0.36147(6)	0.2798(2)	3.57(4)	

[a] $B_{eq} = (8/3)\pi^2\Sigma\Sigma(U_{ij}a_i a_j(\mathbf{a}_i\mathbf{a}_j))$.

exist as its cycloisomer **3′** in the crystalline state (9). If **5***a*/**8′***a* is refluxed in benzene with continuous removal of water by a Dean–Stark trap, compound **10***a*, a hitherto (apparently) unknown 4*H*-1,3-benzoxazine derivative, is obtained in nearly quantitative yield. Furthermore, of all type **5** nitrones only **5***a* reacts spontaneously with triphenyltetrazolium chloride in alkaline solution, indicating the oxidizable N-OH function of the cyclic form **8′***a*, as demonstrated for other *N*-hydroxyl amines (6). This strongly supports the facile formation of the cycloisomer in solution, and also its probable existence in the solid state. The other type **5** nitrones, however, seem to be stable enough in their open-chain nitrone form and display no observable tendency to isomerize.

The X-ray analysis of **5***d* establishes the nitrone structure **5** for the crystalline state. Molecules of **5***d* feature an intramolecular hydrogen bond from the phenol group of the salicylaldehyde moiety to the nitrone *N*-oxide oxygen atom. This O(2)-H···O(1) bond is another example of a very strong intramolecular hydrogen bridge within a seven-membered "proton chelate" and has metrical parameters similar to those found in a similar salicylaldonitrone, **1** (R = *t*-C_4H_9) (8). The second phenol group, originating from the *N*-(2-hydroxyphenyl)hydroxylamine moiety, does not form an intramolecular hydrogen bond to the nitrone *N*-oxide group but rather links to the nitrone group of a neighboring molecule via intermolecular hydrogen bonding, thus forming infinite chains of **5***d* molecules about the two-fold screw axis. As a consequence, the nitrone oxygen atom serves as the nucleophilic center for bifurcated intra- and intermolecular hydrogen bonding to both of the phenol groups of **5***d*. In the nitrone **3** (Ar = 4-$Me_2NC_6H_4$) (3) the phenol group of the hydroxylamine moiety is engaged in a metrically similar intramolecular hydrogen bond to the *N*-oxide group, the O···O distance lying between those for the "chelate" and "chain" types found in **5***d*. Hydrogen-bonding parameters (O···O, O···H, H—O (Å), O···H-O (°)) are as follows: 2.473(4), 1.53(5), 0.96(5), 171(4) for **1**; 2.496(2), 1.53(2), 0.97(2), 170(2) for **5***d* (intramolecular H^+-chelate); 2.673(2), 1.75(2), 0.93(2), 172(2) for **5***d* (intermolecular "chain associate"); and 2.521(3), 1.40(3), 1.13(3), 174(2) for **3** (Ar = 4-$Me_2NC_6H_4$).

The N(1)—O(1) bond in **5***d* (1.343(2) Å) is significantly longer than the corresponding N—O bonds in **3** (Ar = 4-$Me_2NC_6H_4$) (1.324(2) Å) and related nitrones (3). One reason for this might be the two-fold demand on the nitrone oxygen atom by both intra- and intermolecular hydrogen bonds. In the nitrone **3** there is only a weak intramolecular C-H···O interaction in addition to the intramolecular O-H···O proton chelate bridge. The C=N bond of **5***d* (1.296(2) Å) does not differ significantly from the C=N double bond lengths of other nitrones (3).

An approximate coplanarity is seen, as in other *p*-dialkylaminosalicylaldehyde nitrone derivatives (3, 9), between the planes of the salicylaldehyde moiety, the dialkylaminophenyl moiety, and the nitrone function. The nature of the mesomeric resonance system is evinced by shortened bonds within the conjugated double-bond arrangement: N(2)—C(5) = 1.364(2) Å, C(3)—C(4) = 1.378(2) Å, C(6)—C(7) = 1.362(2) Å, and C(1)—C(2) = 1.429(2) Å.

Reaction of the nitrones **5** with diphenylborinic acid anhydride gives crystalline compounds containing an intact diphenylboron moiety shown by the blue-color reaction with diphenylcarbazone, which indicates the presence of the diphenylborenium (Ph_2B^+) moiety (5). The infrared, ^{1}H nmr, and ^{11}B nmr spectra, as well as the elemental analyses point to the alternative structures **6** and **7**. In the unique case of **5***a* the diphenylboron chelate has an elemental composition consistent with the elimination of one water molecule. Considering the missing O-H bands in the infrared spectrum, the missing phenolic proton, and the observed N=CH methine proton in the ^{1}H nmr spectrum; the chelate structure **11** seems most probable for this reaction product of **5***a*, especially since the above mentioned dehydration product of **5***a*, compound **10***a*, is easily formed. A simple confirmation comes from the reaction of **10***a* with diphenylborinic acid that results in **11***a*, an apparently new type of boron chelate.[11]

The diphenylboron chelates deriving from **5***b–d*, however, possess the spectroscopic properties of a seven-membered chelate of type **6** or **7**. The ^{1}H nmr spectra of **6***b* and **6***d* (the solubility of **6***c* was too low to record spectra) both display signals for the N=CH methine proton of the nitrone group and a phenolic OH proton. This precludes, at least for **6***b* and **6***d*, the isomeric structure **9** representing the

[11] Several boron chelates deriving from 2-(2-hydroxyphenyl)benzoxazole and other heteroanalogs of the benzazole series have been described in the literature (10) and are structurally similar to the diphenylboron chelate **11***a*.

© 1998 NRC Canada

Table 3. Bond lengths (Å) with estimated standard deviations in parentheses.

Bond	Length	Bond	Length
		5*d*	
O(1)—N(1)	1.343(2)	O(2)—C(3)	1.341(2)
O(3)—C(10)	1.358(2)	N(1)—C(1)	1.296(2)
N(1)—C(8)	1.475(2)	N(2)—C(5)	1.364(2)
N(2)—C(15)	1.453(2)	N(2)—C(17)	1.461(2)
C(1)—C(2)	1.429(2)	C(2)—C(3)	1.421(2)
C(2)—C(7)	1.412(2)	C(3)—C(4)	1.378(2)
C(4)—C(5)	1.402(2)	C(5)—C(6)	1.415(2)
C(6)—C(7)	1.362(2)	C(8)—C(9)	1.501(2)
C(9)—C(10)	1.392(2)	C(9)—C(14)	1.385(2)
C(10)—C(11)	1.386(2)	C(11)—C(12)	1.375(2)
C(12)—C(13)	1.373(3)	C(13)—C(14)	1.381(3)
C(15)—C(16)	1.511(3)	C(17)—C(18)	1.516(3)
		6*d*	
O(1)—N(1)	1.360(2)	O(1)—B(1)	1.528(2)
O(2)—C(3)	1.341(2)	O(2)—B(1)	1.504(2)
O(3)—C(10)	1.357(2)	O(4)—C(31)	1.424(2)
N(1)—C(1)	1.299(2)	N(1)—C(8)	1.480(2)
N(2)—C(5)	1.356(2)	N(2)—C(15)	1.571(5)
N(2)—C(15a)	1.456(7)	N(2)—C(17)	1.463(3)
C(1)—C(2)	1.419(2)	C(2)—C(3)	1.421(2)
C(2)—C(7)	1.417(2)	C(3)—C(4)	1.383(2)
C(4)—C(5)	1.402(2)	C(5)—C(6)	1.412(2)
C(6)—C(7)	1.354(2)	C(8)—C(9)	1.496(3)
C(9)—C(10)	1.390(2)	C(9)—C(14)	1.379(3)
C(10)—C(11)	1.380(3)	C(11)—C(12)	1.363(3)
C(12)—C(13)	1.374(4)	C(13)—C(14)	1.374(4)
C(15)—C(16)	1.509(7)	C(15a)—C(16a)	1.49(1)
C(17)—C(18)	1.499(4)	C(19)—C(20)	1.390(2)
C(19)—C(24)	1.392(2)	C(19)—B(1)	1.607(3)
C(20)—C(21)	1.384(3)	C(21)—C(22)	1.371(3)
C(22)—C(23)	1.375(3)	C(23)—C(24)	1.376(3)
C(25)—C(26)	1.395(3)	C(25)—C(30)	1.390(3)
C(25)—B(1)	1.607(2)	C(26)—C(27)	1.380(3)
C(27)—C(28)	1.378(4)	C(28)—C(29)	1.359(4)
C(29)—C(30)	1.395(3)	C(31)—C(32)	1.459(3)

Table 4. Bond angles (deg) with estimated standard deviations in parentheses.

Bonds	Angle (deg)	Bonds	Angle (deg)
		5*d*	
O(1)-N(1)-C(1)	124.7(1)	O(1)-N(1)-C(8)	113.6(1)
C(1)-N(1)-C(8)	121.7(1)	C(5)-N(2)-C(15)	120.6(1)
C(5)-N(2)-C(17)	121.6(1)	C(15)-N(2)-C(17)	117.6(1)
N(1)-C(1)-C(2)	131.9(1)	C(1)-C(2)-C(3)	128.8(1)
C(1)-C(2)-C(7)	115.3(1)	C(3)-C(2)-C(7)	115.8(1)
O(2)-C(3)-C(2)	123.2(1)	O(2)-C(3)-C(4)	116.2(1)
C(2)-C(3)-C(4)	120.6(1)	C(3)-C(4)-C(5)	122.6(1)
N(2)-C(5)-C(4)	121.3(1)	N(2)-C(5)-C(6)	121.5(1)
C(4)-C(5)-C(6)	117.1(1)	C(5)-C(6)-C(7)	120.2(1)
C(2)-C(7)-C(6)	123.7(1)	N(1)-C(8)-C(9)	113.6(1)
C(8)-C(9)-C(10)	120.8(1)	C(8)-C(9)-C(14)	120.3(1)
C(10)-C(9)-C(14)	118.8(1)	O(3)-C(10)-C(9)	117.1(1)
O(3)-C(10)-C(11)	123.1(1)	C(9)-C(10)-C(11)	119.7(1)
C(10)-C(11)-C(12)	120.5(2)	C(11)-C(12)-C(13)	120.3(2)
C(12)-C(13)-C(14)	119.5(2)	C(9)-C(14)-C(13)	121.2(2)
N(2)-C(15)-C(16)	114.3(2)	N(2)-C(17)-C(18)	113.8(1)
		6*d*	
N(1)-O(1)-B(1)	115.4(1)	C(3)-O(2)-B(1)	123.6(1)
O(1)-N(1)-C(1)	122.8(1)	O(1)-N(1)-C(8)	113.0(1)
C(1)-N(1)-C(8)	124.0(2)	C(5)-N(2)-C(15)	118.6(2)
C(5)-N(2)-C(15a)	120.0(2)	C(5)-N(2)-C(17)	122.2(2)
C(15)-N(2)-C(17)	117.0(2)	C(15a)-N(2)-C(17)	111.1(3)
N(1)-C(1)-C(2)	130.8(2)	C(1)-C(2)-C(3)	128.6(2)
C(1)-C(2)-C(7)	115.3(1)	C(3)-C(2)-C(7)	116.0(1)
O(2)-C(3)-C(2)	124.2(1)	O(2)-C(3)-C(4)	116.1(1)
C(2)-C(3)-C(4)	119.7(1)	C(3)-C(4)-C(5)	123.0(2)
N(2)-C(5)-C(4)	121.1(2)	N(2)-C(5)-C(6)	121.7(2)
C(4)-C(5)-C(6)	117.2(2)	C(5)-C(6)-C(7)	119.9(2)
C(2)-C(7)-C(6)	124.0(2)	N(1)-C(8)-C(9)	111.6(2)
C(8)-C(9)-C(10)	119.5(2)	C(8)-C(9)-C(14)	122.4(2)
C(10)-C(9)-C(14)	118.1(2)	O(3)-C(10)-C(9)	116.5(2)
O(3)-C(10)-C(11)	122.7(2)	C(9)-C(10)-C(11)	120.8(2)
C(10)-C(11)-C(12)	119.8(2)	C(11)-C(12)-C(13)	120.5(2)
C(12)-C(13)-C(14)	119.7(2)	C(9)-C(14)-C(13)	121.2(2)
N(2)-C(15)-C(16)	108.3(4)	N(2)-C(15a)-C(16a)	102.3(6)
N(2)-C(17)-C(18)	113.2(2)	C(20)-C(19)-C(24)	115.4(2)
C(20)-C(19)-B(1)	124.3(2)	C(24)-C(19)-B(1)	120.3(2)
C(19)-C(20)-C(21)	122.4(2)	C(20)-C(21)-C(22)	120.2(2)
C(21)-C(22)-C(23)	119.0(2)	C(22)-C(23)-C(24)	120.1(2)
C(19)-C(24)-C(23)	122.8(2)	C(26)-C(25)-C(30)	117.0(2)
C(26)-C(25)-B(1)	121.1(2)	C(30)-C(25)-B(1)	121.9(2)
C(25)-C(26)-C(27)	121.7(3)	C(26)-C(27)-C(28)	120.1(3)
C(27)-C(28)-C(29)	119.6(3)	C(28)-C(29)-C(30)	120.7(3)
C(25)-C(30)-C(29)	121.0(3)	O(4)-C(31)-C(32)	110.3(2)
O(1)-B(1)-O(2)	106.9(1)	O(1)-B(1)-C(19)	110.1(1)
O(1)-B(1)-C(25)	104.8(1)	O(2)-B(1)-C(19)	113.0(1)
O(2)-B(1)-C(25)	106.2(1)	C(19)-B(1)-C(25)	115.2(1)

diphenylboron chelate of the ring-isomeric form **8**. A compound of type **9** should display an acetalic O-CH-N proton in the ^{1}H nmr spectrum instead of the N=CH proton. No such signal is found. There still remains the problem of the assignment to one of the chelate structures **6** or **7**. As mentioned in the introduction, the seven-membered chelate **6** (employing the phenol group of the salicylaldehyde moiety) might be expected to be more stable; but, particularly in the case of the *p*-diethylamino substituted salicylaldehyde nitrone, the isomeric seven-membered chelate **7** could have formed. This ring system has already been established for the diphenylboron chelate **4** derived from a *p*-dimethylamino substituted benzaldehyde nitrone (3). For unambiguous proof of the molecular structure, an X-ray crystallographic analysis of the diphenylboron chelate of **5***d* was carried out. The diphenylboron chelates of both **5***b* and **5***d* crystallize as 1:1 ethanol solvates.

The X-ray analysis establishes the molecular structure **6***d* and thus shows that the chelate ring system of type **2** is favored, although the *p*-diethylamino substituent ($R^2 = NEt_2$) would allow the formation of a type **4** chelate ring, leading to the molecular structure **7***d*. It is reasonable to conclude that the structures of **6***b* and **6***c* are analogous to that of **6***d*, especially in view of the fact that there are no

© 1998 NRC Canada

Table 5. Intra-annular torsion angles (deg) for **6***d* with standard deviations in parentheses.

Atoms	Value (deg)
B(1)-O(1)-N(1)-C(1)	–49.2(2)
O(1)-N(1)-C(1)-C(2)	–1.3(3)
N(1)-C(1)-C(2)-C(3)	7.8(3)
C(1)-C(2)-C(3)-O(2)	10.1(3)
C(2)-C(3)-O(2)-B(1)	13.6(2)
C(3)-O(2)-B(1)-O(1)	–62.1(2)
O(2)-B(1)-O(1)-N(1)	84.8(2)

p-dialkylamino substituents present in the aldehyde moieties of the ligands (**5***b* and **5***c*) increasing the basicities of the respective nitrone groups. Due to the poor solubility of **6***c* it was not possible obtain an ^{1}H nmr spectrum, thus confirmation of the nitrone structure by the presence of the N=CH methine proton signal is lacking. The mass spectra of **6***c* give different fragmentation patterns depending on the method. In the EI mode only a very weak molecular ion peak (0.8%) is found, and the most prominent peak corresponds to a ($M^+ - H_2O - C_6H_5$) fragment showing the formation of the above-mentioned 1,3-benzoxazine derivative via the elimination of water and dephenylation. The CI mass spectrum gives a ($M^+ - H_2O$) parent peak in the negative mode and a ($M^+ - OH$) parent peak in the positive mode, which could be identical to (**11***c*)$^+$ and (**11***c* + H)$^+$, respectively. The latter dephenylates to the ($M^+ - H_2O - C_6H_5$) fragment, as in the EI mass spectrum, identical to (**11***c* – C_6H_5)$^+$. The loss of NO_2 is also observed in both the EI and CI mass spectra. The molecular ion peak is observed at 58% in the CI (positive mode) spectrum. It might be concluded from the mass spectra that the cyclized isomer **9***c* is the educt, or perhaps an intermediate in the fragmentation of **6***c*. It would be premature at this point to present a definitive decomposition pathway, since we were not able to produce crystals of the educt (**6***c* or **9***c*) suitable for X-ray crystallographic analysis. The occurrence of **11***c* and its dephenylation product in the mass spectra is in accordance with the above-mentioned facile dehydration reactions and the formation of the 1,3-benzoxazine derivative and its diphenylboron chelate **11***a*.

In the crystal lattice of **6***d*·EtOH the ethanol connects two of the **6***d* molecules via hydrogen bonds. The ethanolic hydroxyl group associates with the phenolic oxygen atom O(2) in the boron chelate ring of **6***d*, and the ethanol oxygen atom donates electrons to the phenol group O(3)-H(2) of a neighboring molecule. Hydrogen-bonding parameters (O···O, O···H, H—O (Å), O-H···O(°)) are as follows: 2.852(2), 1.97(2), 0.90(2), 166(2) for O(2)···H(1)-O(4); and 2.689(2), 1.82(2), 0.90(2), 161(2) for O(4)(x, y, 1 + z)···H(2)-O(3).

The seven-membered ring in **6***d* has a somewhat distorted "envelope" (or "sofa") conformation with the boron atom on the "flap," displaced 1.00 Å from the mean plane of the O(1)-N(1)-C(1)-C(2)-C(3)-O(2) ring segment (see Table 5). One of the *B*-phenyl groups is oriented above the mean plane of the coplanar fused-ring system, and closely resembles the chelate ring system of compound **2** (R = Me) in its overall geometry (2). The difference between the two O—B bonds in **6***d* (0.024 Å), however, is smaller than the corresponding value of 0.054 Å in **2** (R = Me) (2). This is primarily a result of the relatively short (N)O—B bond in **6***d*, reflecting the enhanced basicity of the *N*-oxide group via the inductive and (or) mesomeric influence of the dialkylamino substituent *para* to the nitrone group. The mean O—B (1.516 Å) and C—B distances (1.607 Å) are both slightly shorter than the corresponding mean bond lengths in **2** (1.528 and 1.610 Å, respectively) (2), and the mean C—B/mean O—B bond length ratio of 1.060 is slightly larger than the value of 1.054 for **2** (R = Me) (2). This might point to a slightly increased overall binding strength (11) of the ligand with respect to the Ph_2B^+ nucleus in **6***d* relative to that in **2**, but there should be additional stabilizing factors in effect because the overall binding strength in the Ph_2BO_2 moiety of the seven-membered chelate system of **4** (Ar = 4-$Me_2NC_6H_4$) is roughly the same, if not slightly greater (mean C—B/mean O—B bond length ratio = 1.063) (3). Thus the preference of the seven-membered chelate ring type **6** to the isomeric type **7** cannot be rationalized in terms of ligand–BPh_2 binding strength alone. It is possible that steric factors, or even differences in solubility between **6** and **7**, may cause the preferential formation–precipitation of **6** out of an equilibrium mixture of the possible chelate forms **6** and **7**.

The C=N and N—O bond lengths of the nitrone group in **6***d* (1.299(2) and 1.360(2) Å) are very similar to those reported for the chelate **2** (R = Me) (1.286(4)[12] and 1.360(3) Å), and the phenolate C—O distances in these two compounds are equal within experimental error (C(3)—O(2) = 1.342(2) Å for **6***d* and 1.334(7) Å for **2**). The most conspicuous difference can be seen at the bond between the nitrone carbonyl carbon atom and the aryl residue of the salicylaldehyde moiety: in **6***d* the C(1)—C(2) bond (1.419(2) Å) is distinctly shorter than the corresponding (N)C—C(aryl) bond (1.466(4) Å) in compound **2** (2). This can be easily explained by a +M effect of the *para*-diethylamino group in **6***d*, which increases the double-bond character of the C(1)—C(2) bond. This is further supported by the approximate coplanarity (within ±0.06 Å) of the dialkylaminoaryl system. Relative to the free ligand **5***d*, both the C(1)—C(2) and N(2)—C(5) bonds show increased double-bond character in the boron chelate **6***d* with decreases in the bond lengths of about 0.01 Å, pointing to an influence of the electron-withdrawing effect of the Lewis-acid diphenylborenium (Ph_2B^+) nucleus over the entire resonance system.

Acknowledgments

We thank the Natural Sciences and Engineering Research Council of Canada and the Fonds der Chemischen Industrie, Frankfurt am Main, for financial support. We are grateful to the spectroscopy laboratory of the Chemische Institute der Technischen Universität, Braunschweig, for running the ^{11}B nmr and mass spectra.

[12]All values reported for **2** (R = Me) correspond to average uncorrected values for the two independent molecules. The esd given is the individual value standard deviation or the rms deviation from the mean, whichever is larger.

© 1998 NRC Canada

References

1. W. Kliegel and D. Nanninga. J. Organomet. Chem. **243**, 373 (1983).
2. W. Kliegel, U. Lauterbach, S.J. Rettig, and J. Trotter. Can. J. Chem. **65**, 1457 (1987).
3. W. Kliegel, J. Metge, S.J. Rettig, and J. Trotter. Can. J. Chem. **75**, 1830 (1997).
4. (*a*) R. Neu. Chem. Ber. **87**, 802 (1954); (*b*) G.N. Chremos, H. Weidmann, and H.K. Zimmerman. J. Org. Chem. **26**, 1683 (1961).
5. (*a*) R. Neu. Z. Anal. Chem. **176**, 334 (1960); (*b*) B. Friese and F. Umland. Anal. Chim. Acta, **96**, 303 (1978).
6. (*a*) G.A. Snow. J. Chem. Soc. 2588 (1954); (*b*) A.W. Nineham. Chem. Rev. **55**, 355 (1955).
7. (*a*) International Tables for X-Ray Crystallography. Vol. IV. Kynoch Press, Birmingham, U.K. (present distributor Kluwer Academic Publishers, Boston, Mass., U.S.A.). 1974. pp. 99–102; (*b*) International Tables for Crystallography. Vol. C. Kluwer Academic Publishers, Boston, Mass., U.S.A. 1992. pp. 200–206.
8. D. Christensen, K.A. Jørgensen, and R. Hazell. J. Chem. Soc. Perkin Trans. 1, 2391 (1990).
9. W. Kliegel, J. Metge, S.J. Rettig, and J. Trotter. Can. J. Chem. **76**, 389 (1998).
10. (*a*) F. Umland and E. Hohaus. Angew. Chem. **79**, 1072 (1967); (*b*) Forschungsber. Landes Nordrhein-Westfalen, 2538 (1976).
11. W.R. Cullen, S.J. Rettig, J. Trotter, and E.B. Wickenheiser. Can. J. Chem. **66**, 2007 (1988).

© 1998 NRC Canada

Conformational isomers of 1,2,5,6-tetrathiocins and the photoisomerization of a 1,2,5,6-tetrathiocin into a 1,2,3,6-tetrathiocin: X-ray structures of $(C_6X_4S_2)_2$ (X = F, Cl) and $C_6F_4SSSC_6F_4S$

Tristram Chivers, Masood Parvez, Ignacio Vargas-Baca, and Gabriele Schatte

Abstract: The 1,2,5,6-tetrathiocins $(C_6X_4S_2)_2$ (**3a**, X = F; **3b**, X = Cl) are obtained in high yields by the oxidation of the dithiols 1,2-$C_6X_4(SH)_2$ (X = F, Cl) with I_2 or SO_2Cl_2, respectively. In the solid state **3a** has the C_{2h} (chair) conformation and crystallizes in two different phases: α-$(C_6F_4S_2)_2$, monoclinic, $P2_1/a$, a = 9.351(2), b = 6.465(2), and c = 11.546(2) Å, β = 95.60(1)°, V = 694.6(2) Å^3, Z = 2; and β-$(C_6F_4S_2)_2$, monoclinic, $P2_1/c$, a = 4.825(2), b = 11.302(2), and c = 12.453(2) Å, β = 91.45(3)°, V = 678.8(3) Å^3, Z = 2. By contrast, **3b** displays a D_2 (twist-boat) structure and crystallizes in the $C2/c$ space group with a = 15.243(3), b = 8.703(2), and c = 27.010(14) Å, β = 92.81(4)°, V = 3578(1) Å^3, and Z = 8. The derivative **3a** exists as an equilibrium mixture of two conformational isomers in toluene solution. The VT ^{19}F NMR data afford the thermodynamic parameters $\Delta H°$ = 9.9 ± 0.4 kJ mol^{-1} and $\Delta S°$ = 14 ± 1 J K^{-1} mol^{-1}. Density functional theory calculations for **3a** indicate that the D_2 conformation is lower in energy than the C_{2h} isomer by 4.6 kJ mol^{-1}. The photolysis of **3a** in benzene promotes a transannular sulfur migration to give the 1,2,3,6-tetrathiocin, $C_6F_4SSSC_6F_4S$ (**6**), which exists in a chair conformation with respect to antipodal sulfur atoms. Crystal structure of **6**: orthorhombic, space group *Pnma*, a = 8.652(6), b = 19.084(4), and c = 8.301(6) Å, V = 1370.6(14) Å^3, and Z = 4. The isomers **3a** and **6** were also characterized by EI mass spectrometry, ^{19}F NMR, FTIR, and Raman spectroscopies.

Key words: tetrathiocins, conformational isomers, photoisomerization.

Résumé : Les oxydations des dithiols 1,2-$C_6X_4(SH)_2$ (X = F, Cl) par I_2 ou SO_2Cl_2 conduisent aux 1,2,5,6-tétrathiocines $(C_6X_4S_2)_2$ (**3a**, X = F; **3b**, X = Cl) avec des rendements élevés. À l'état solide, le composé **3a** adopte la conformation C_{2h} (chaise) et cristallise dans deux phases différentes: α-$(C_6F_4S_2)_2$, monoclinique, $P2_1/a$, a = 9,351(2), b = 6,465(2) et c = 11,546(2) Å, β = 95,60(1)°, V = 694,6(2) Å^3, Z = 2 et β-$(C_6F_4S_2)_2$, monoclinique, $P2_1/c$, a = 4,825(2), b = 11,302(2) et c = 12,453(2) Å, β = 91,45(3)°, V = 678,8(3) Å^3, Z = 2. Par opposition, le composé **3b** existe sous la forme D_2 (bateau-croisé) et cristallise dans le groupe d'espace $C2/c$ avec a = 15,243(3), b = 8,703(2) et c = 27,010(14) Å, β = 92,81(4)°, V = 3578(1) Å^3, Z = 8. En solution dans le toluène, le dérivé **3a** existe sous la forme d'un mélange à l'équilibre de deux isomères conformationnels. Des données de RMN du ^{19}F à TV permettent de déterminer les paramètres thermodynamiques suivants: ΔH^0 = 9,9 ± 0,4 kJ mol^{-1} et ΔS^0 = 14 ± 1 J K^{-1} mol^{-1}. Des calculs de densité fonctionnelle sur le composé **3a** indiquent que l'énergie de la conformation D_2 est 4,6 kJ mol^{-1} plus faible que celle de l'isomère C_{2h}. La photolyse du composé **3a** dans le benzène provoque une migration transannulaire du soufre conduisant à la formation de la 1,2,3,6-tétrathiocine, $C_6F_4SSSC_6F_4S$ (**6**), qui existe dans une conformation chaise par rapport aux atomes de soufre antipodaux. Structure cristalline du composé **6**: orthorhombique, groupe d'espace *Pnma*, a = 8,652(6), b = 19,084(4) et c = 8,301(6) Å, V = 1370,6(14) Å^3, Z = 4. Les isomères **3a** et **6** ont aussi été caractérisés par spectrométrie de masse sous IE, par RMN du ^{19}F et par spectroscopies FTIR et Raman.

Mots clés : tétrathiocines, isomères conformationnels, photoisomérisation.

[Traduit par la Rédaction]

Introduction

A sulfur atom (-S-) and a -CH_2- group can be viewed as isoelectronic with the important difference that, in a ring system, the exocyclic electron pairs are nonbonding for -S- but bonding for -CH_2-. Consequently, the effect that the replacement of some of the -CH_2- groups by -S- linkages has

Received February 2, 1998.

T. Chivers,[1] M. Parvez, I. Vargas-Baca, and G. Schatte. Department of Chemistry, The University of Calgary, 2500 University Drive NW, Calgary, AB T2N 1N4, Canada.

[1]Author to whom correspondence may be addressed. Telephone: (403) 220-5741. Fax: (403) 289-9488. E-mail: chivers@ucalgary.ca

 © 1998 NRC Canada

Scheme 1.

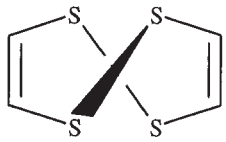

D_2

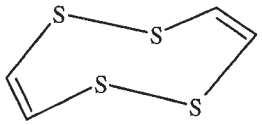

C_{2h}

on the structures and conformational barriers of organic ring systems is of interest. This substitution generally facilitates the observation of interconversion by increasing the magnitude of the inversion barriers (1). Since the number of degrees of freedom and the complexity of the system increase with the number of atoms in the ring, the majority of conformational investigations has been concerned with six-membered heterocycles (2).

The study of larger rings is simplified when some atoms are constrained to remain in a plane, e.g., 1,2,5,6-tetrathiocin **1**.[2] Although 3,4,7,8-tetrakis(trifluoromethyl)-1,2,5,6-tetrathiocin has been known since 1960 (3), it has not been structurally characterized. The parent ring system **1** was synthesized for the first time in 1996 (4). As in the case of cycloocta-1,5-diene (5), 1,2,5,6-tetrathiocin (**1**) should exhibit several conformers. Recent ab initio molecular orbital calculations predict that a (*Z*,*Z*) twist form of **1** (approximately D_2 symmetry) represents a global minimum (6) and that structure has been found in the solid state by an X-ray crystallographic analysis (Scheme 1) (4). By contrast the twist-boat form (C_2 symmetry) was calculated to be the global minimum for cycloocta-1,5-diene (5). The calculations also predict that the chair (*Z*,*Z*) conformation of **1** (C_{2h} symmetry) (Scheme 1) is only 22.2 kJ mol^{-1} higher in energy than the D_2 isomer (6), and consequently, this alternative geometry should be readily accessible. Indeed the chair conformation of the C_4S_4 ring has been established for C_6S_{10} (**2a**) (7) and the related derivative (**2b**) (8).

In this article we describe the synthesis and X-ray structures of the octahalogenated derivatives **3a** and **3b**. The fluoro derivative **3a** exists as an equilibrium mixture of two conformational isomers in solution. The thermodynamic parameters for this interconversion process, obtained from variable temperature ^{19}F NMR data, are compared with the values calculated by density functional theory (DFT) calculations. In view of the photochemical sensitivity of the parent system **1** (4), the photolysis of **3a** was also investigated.

Experimental section

Reagents and general procedures

All solvents were dried by treatment with the appropriate drying agent and freshly distilled before use. 1,2,3,4-Tetrafluorobenzene, C_6Cl_6, *n*-BuLi (2.5 M solution in hexanes), $Na_2S\cdot 9H_2O$, and I_2 were commercial reagents used as received. The SO_2Cl_2 was distilled under an N_2 atmosphere before use. Sulfur was recrystallized from CS_2. Tetrafluorobenzene-1,2-dithiol, C_6F_4-1,2-$(SH)_2$ (bp 50°C, 5 × 10^{-2} Torr (1 Torr = 133.3 Pa); ^{1}H NMR ($CDCl_3$), δ: 3.82; ^{19}F NMR ($CDCl_3$): –131.7 (m) and –158.5 (m)) was obtained in 70% yield by the literature method (9). The C_6Cl_4-1,2-$(SH)_2$ was prepared by a modification (vide infra) of the literature method (10). The $(C_6F_4S)_2$ was also synthesized by a known procedure (11).

Instrumentation

The ^{1}H NMR spectra were obtained on a Bruker ACE 200 MHz spectrometer, and chemical shifts are reported in ppm relative to Me_4Si. The ^{19}F NMR spectra were recorded on a Bruker AMX 300 spectrometer; chemical shifts are reported relative to $CFCl_3$ and were measured with an external standard of C_6F_6 (δ –162.9 ppm). Electron impact mass spectra were obtained by using a VG Micromass spectrometer (VG 7070) set at 70 eV. The FTIR spectra were recorded as Nujol mulls (KBr plates) on a Mattson 4030 FTIR spectrometer in the range 4000–300 cm^{-1} (resolution: 4 cm^{-1}; number of scans: 128). Raman spectra were recorded using a Jarrell–Ash model 25-100 monochromator interfaced to a microcomputer. A Coherent Radiation Model 540 argon laser fitted with an Innova 70 plasma tube was used as the exciting source (emission wavelength: 514.5 nm; laser power: 100 mW; laser current: 30 A). Scattered radiation was collected at 90° to the incident light. The Raman spectra were obtained from neat samples sealed in melting point tubes and measured in the range 2500–100 cm^{-1} at room temperature. The frequencies are believed accurate to ±2 cm^{-1}. Elemental analyses were performed by Canadian Microanalytical Service Ltd., Vancouver, B.C., and by Galbraith Laboratories Inc., Knoxville, Tennessee.

Preparation of C_6Cl_4-1,2-$(SH)_2$

In a typical preparation C_6Cl_6 (32.7 g, 0.11 mol), Fe powder (6.2 g, 0.11 mol) and $Na_2S\cdot 9H_2O$ (54 g, 0.22 mol) were heated at reflux in DMF (1 L) for 48 h. **Caution**: a wide-necked condenser and vigorous reflux are necessary to prevent sublimed C_6Cl_6 from plugging the condenser and

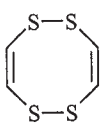

1

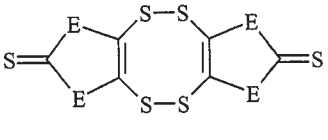

2a, E = S
2b, E = N^{i}Pr

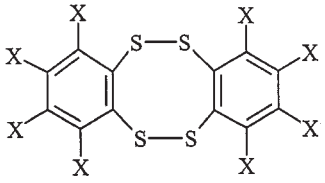

3a, X = F
3b, X = Cl

[2] 1,2,5,6-Tetrathiacycloocta-3,7-diene.

© 1998 NRC Canada

causing a pressure build-up. The mixture was allowed to cool to 23°C and then 2 L of NaOH (0.75 M) were added with vigorous stirring. The mixture was allowed to settle (48 h) and then centrifuged to separate the solid, which was dissolved in 300 mL of MeOH and refluxed for 3 h with ZnO (8 g) and NaOH (150 mL, 0.75 M). The hot slurry was filtered, and the solution was acidified to a neutral pH with H_2SO_4. A pale-yellow precipitate was filtered and dried with an air stream in the filtration funnel. This product was extracted (Soxhlet apparatus) with Et_2O to remove a dark-green insoluble material. The solvent was evaporated from the solution to leave 11.3 g of a yellow solid. This crude product was shown by EIMS to consist of a mixture of C_6Cl_5SH and C_6Cl_4-1,2-$(SH)_2$ (yield ~36%). Recrystallization from toluene and subsequent sublimation (140°C, 5×10^{-2} torr) produced C_6Cl_4-1,2-$(SH)_2$ containing only traces of C_6Cl_5SH.

Preparation of $(C_6F_4S_2)_2$ (3a)

A solution of C_6F_4-1,2-$(SH)_2$ (1.66 g, 7.70 mmol) in methanol (50 mL) was treated with a solution of I_2 (1.97 g, 7.70 mmol) in methanol (50 mL). A pale-yellow, microcrystalline product was formed. The crude product was filtered, rinsed with cold methanol, and recrystallized from Et_2O to give $(C_6F_4S_2)_2$ (**3a**) (1.42 g, 3.32 mmol, 86%); mp 193°C. Anal. calcd. for $C_6F_4S_2$: C 33.96, F 35.82, S 30.23; found: C 33.81, F 33.85, S 30.55.[3]

EIMS (*m*/*z*, %): 424, 40 (M^+), 328, 15 ($C_{12}F_8S^+$), 212, 100 ($C_6F_4S_2^+$), 168, 38 ($C_5F_4S^+$). ^{19}F NMR ($CDCl_3$, δ): two sets of resonances at –130.1 (m), –154.4 (m) and –122.1 (m), –147.4 (m) with approximate relative intensities 1:4. IR (Nujol, cm^{-1}): 1594 m, 1307 s, 1237 s, 1038 s, 973 m, 872 s, 818 s, 724 s, 483 w, 414 s.

Preparation of $(C_6Cl_4S_2)_2$ (3b)

A solution of SO_2Cl_2 (0.67 g, 5.0 mmol) in benzene (10 mL) was added to a solution of C_6Cl_4-1,2-$(SH)_2$ (1.33 g, 4.75 mmol) in benzene (50 mL). After 1 h the solvent was decanted by cannula to leave a yellow solid, which was rinsed with pentane (2 × 10 mL) to give $(C_6Cl_4S_2)_2$ (**3b**) (1.18 g, 2.12 mmol, 90%); mp 290°C (dec.). Anal. calcd. for $C_6Cl_4S_2$: C 25.92, Cl 51.01, S 23.07; found: C 26.30, Cl 48.88, S 23.27.[3] EIMS (*m*/*z*): 556 (M^+). IR (Nujol, cm^{-1}): 1377 s, 1335 m, 1303 s, 1095 m, 869 m.

Photoisomerization of 3a

A solution of **3a** (0.60 g, 1.41 mmol) in benzene (50 mL) in a Pyrex vessel at 23°C was irradiated with a Hg lamp. The progress of the reaction was monitored by ^{19}F NMR spectroscopy. After 7 h, solvent was removed under vacuum and the pale-yellow product was recrystallized from CH_2Cl_2–hexane to give $C_6F_4SSSC_6F_4S$ (**6**) (0.35 g) contaminated with **3a** (^{19}F NMR). A pure sample of **6** was obtained as a white solid by vacuum sublimation at 90°C and 10^{-3} Torr; mp 116–117°C. Anal. calcd. for $C_6F_4S_2$: C 33.96, S 30.23; found: C 33.53, S 32.10.[3] EIMS (*m*/*z* %): 424, 30 (M^+), 392, 26 ($C_{12}F_8S_3^+$), 360, 40 ($C_{12}F_8S_2^+$), 328, 100 ($C_{12}F_8S^+$), 244, 20 ($C_6F_4S_3^+$), 212, 100 ($C_6F_4S_2^+$), 180, 37 ($C_6F_4S^+$), 168, 40 ($C_5F_4S^+$); ^{19}F NMR ($CDCl_3$, δ): –117.3 (m), –122.9 (m), –147.5 (m), –147.8 (m). IR (Nujol, cm^{-1}): 1600 (s), 1487 (vs), 1305 (s), 1237 (s), 1163 (s), 1115 (s), 1042 (vs), 970 (m), 951 (m, sh), 866 (s), 817 (s), 771 (m), 724 (s), 491 (m), 446 (m).

X-ray diffraction studies

All measurements were made on a Rigaku AFC6S diffractometer using graphite monochromated Mo-K_α radiation. Crystallographic data for α-**3a**, β-**3a**, **3b**, and **6** are given in Table 1.[4]

α-3a

A yellow hexagonal-plate crystal of α-$(C_6F_4S_2)_2$ was mounted on a glass fibre. Cell constants and an orientation matrix for data collection, obtained from a least-squares refinement using the setting angles of 17 carefully centred reflections in the range $30.00 < 2\theta < 50.00°$, corresponded to a primitive monoclinic cell. The data were corrected for Lorentz, polarization, and empirical absorption effects (12). The structure was solved by direct methods (13) and expanded using Fourier techniques (14). All non-hydrogen atoms were refined anisotropically. All calculations were performed using the teXsan crystallographic software package (15).

β-3a

A yellow prismatic crystal of β-$(C_6F_4S_2)_2$ was mounted on a glass fibre. Cell constants and an orientation matrix for data collection, obtained from a least-squares refinement using the setting angles of 13 carefully centred reflections in the range $40.00 < 2\theta < 50.00°$, corresponded to a primitive monoclinic cell. The structure was solved by direct methods (16) and expanded using Fourier techniques (14). The rest of the calculations involving data processing and structure refinement followed the same procedures as described for α-**3a**.

3b

An orange prismatic crystal of $(C_6Cl_4S_2)_2$ was mounted on a glass fibre. Cell constants and an orientation matrix for data collection, obtained from a least-squares refinement using the setting angles of 25 carefully centred reflections in the range $15.00 < 2\theta < 30.00°$, corresponded to a C-centred monoclinic cell. Based on the systematic absences *hkl*, $h + k \neq 2n$ and *h*0l, $l \neq 2n$, packing considerations, a statistical analysis of intensity distribution, and the successful solution and refinement of the structure, the space group was deter-

[3] Consistently low analyses for halogens were obtained for both **3a** and **3b** by two different commercial analysts. Low analyses for fluorine were also obtained for **6**.

[4] Crystal data, tables of atomic coordinates and displacement parameters, complete listings of bond lengths and angles, and other refinement data may be purchased from: The Depository of Unpublished Data, Document Delivery, CISTI, National Research Council of Canada, Ottawa, Canada, K1A 0S2. Crystal data, atomic coordinates, and bond lengths and angles have also been deposited with the Cambridge Crystallographic Data Centre and can be obtained on request from: The Director, Cambridge Crystallographic Data Centre, University Chemical Laboratory, 12 Union Road, Cambridge, CB2 1EZ, U.K.

© 1998 NRC Canada

Table 1. Crystallographic data for $(C_6X_4S_2)_2$ (X = F, Cl) and $\overline{C_6F_4SSSC_6F_4S}$.

	α-**3a**	β-**3a**	**3b**	**6**
Dimensions (mm)	0.60 × 0.50 × 0.15	0.50 × 0.27 × 0.24	0.30 × 0.27 × 0.10	0.40 × 0.30 × 0.20
Formula	α-$C_{12}F_8S_4$	β-$C_{12}F_8S_4$	$C_{12}Cl_8S_4$	$C_{12}F_8S_4$
fw	424.36	424.36	556.00	424.36
Space group	$P2_1/a$	$P2_1/c$	$C2/c$	*Pnma*
a (Å)	9.351(2)	4.825(2)	15.243(3)	8.652(6)
b (Å)	6.465(2)	11.302(2)	8.703(2)	19.084(4)
c (Å)	11.546(2)	12.453(2)	27.010(14)	8.301(6)
β (°)	95.60(1)	91.45(3)	92.81(4)	—
V (Å^3)	694.6(2)	678.8(3)	3578(1)	1370.6(14)
Z	2	2	8	4
T (°C)	–103.0	–123.0	–103.0	–103.0
λ (Å)	0.71069	0.71069	0.71069	0.71069
ρ_{calcd} (g cm^{-3})	2.029	2.076	2.064	2.056
μ (cm^{-1})	7.42	7.89	17.17	7.81
Reflections: Collected	1440	1427	3557	1443
Unique	1356	1272	3413	1443
Observed	1022	912	1666	1252
Criteria	$I > 3.0\sigma(I)$	$I > 3.0\sigma(I)$	$I > 3.0\sigma(I)$	$I > 2.0\sigma(I)$
Transmission factors	0.803–1.00	0.972–1.00	0.786–1.000	0.918–1.000
Coefficients used	*F*	*F*	*F*	F_2
R, R_w	0.033,[a] 0.033[b]	0.025,[a] 0.024[b]	0.047,[a] 0.045[b]	0.032,[a] 0.077[c]
p-Factor	0.005	0.010	0.008	—
Goodness of fit, *S*	3.84	1.88	1.82	1.22
Max shift/error	0.00	0.00	0.17	0.00
Max and min peaks	0.37	0.26	0.65	0.37
In final diff. map	–0.25	–0.25	–0.52	–0.33

[a] $R = \Sigma||F_o| - |F_c||/\Sigma|F_o|$.

[b] $R_w = [\Sigma w(|F_o| - |F_c|)_2/\Sigma wF_o^2]^{1/2}$, where $w = 1/\sigma^2(F_o) = 4F_o^2/\sigma^2(F_o^2)$ and $\sigma^2(F_o^2) = \{S^2(C+R^2B) + (pF_o^2)^2\}/Lp^2$, *S* = scan rate, *C* = total integrated peak count, *R* = ratio of scan time to background counting time, *B* = total background count, Lp = Lorentz-polarization factor, *p* = *p*-factor.

[c] $R_w = [\Sigma w(|F_o| - |F_c|)^2/\Sigma wF_o^2]^{1/2}$, where $w = 1/[\sigma_2(F_o)^2 + (0.037P)^2 + 0.610P]$, $P = (F_o^2 + 2F_c^2)/3$.

mined to be *C*2/*c* (no. 15). The data processing, structure solution, and refinement followed the same procedures as described for α-**3a**.

6

A colourless, plate-like crystal of $\overline{C_6F_4SSSC_6F_4S}$ was mounted on a glass fibre. Cell constants and an orientation matrix for data collection, obtained from a least-squares refinement using the setting angles of 25 carefully centred reflections in the range $18.21 < 2\theta < 21.43°$, corresponded to a primitive orthorhombic cell. Based on the systematic absences of 0*kl*, $k + 1 = 2n + 1$ and *hk*0, $h = 2n + 1$, packing considerations, a statistical analysis of intensity distribution, and the successful solution and refinement of the structure, the space group was determined to be *Pnma* (no. 62). The structure was solved by direct methods (16) and expanded using Fourier techniques (14). The structure was refined with the aid of SHELX93 (17). Other details of the structure refinement were similar to those described for β-**3a**.

Computational details

Details of the methods used for the DFT calculations can be found in ref. 18.

Results and discussion

Synthesis and X-ray structures of dibenzotetrathiocins 3a and 3b

The tetrathiocins $(C_6F_4S_2)_2$ (**3a**) and $(C_6Cl_4S_2)_2$ (**3b**) were prepared by the oxidation of the corresponding dithiols with I_2 or SO_2Cl_2, respectively, in >85% yields. Compounds **3a** and **3b** are air stable, pale-yellow solids with high thermal stability. They are also stable in polar solvents, e.g., acetonitrile or chloroform. For comparison, the parent tetrathiocin (**1**), which is obtained in only 14% yield by the oxidation of *cis*-disodium ethene-1,2-dithiolate, is converted to the tetramer $(-CH{=}CH-S-S-)_4$ in acetonitrile at room temperature (4).

Single crystals of **3a** were grown from a diethyl ether solution. Two different crystalline phases, which could be separated manually, were apparent. The most abundant (α-**3a**) consists of hexagonal plates, while the other phase (β-**3a**) forms rectangular prisms. X-ray diffraction analysis reveals that the chair conformer (C_{2h}) of the 1,2,5,6-tetrathiocin ring pertains in both types of crystals (see Fig. 1). The difference between the α and β phases is caused by distinctive packing arrangements (see Figs. 2 and 3). A chair conformation for the 1,2,5,6-tetrathiocin ring has also been observed for **2a** (7) and **2b** (8). By contrast, crystals of **3b**, obtained by slow evaporation of a very dilute THF solution, provided an

© 1998 NRC Canada

Fig. 1. The ORTEP diagram for $(C_6F_4S_2)_2$ (**3a**).

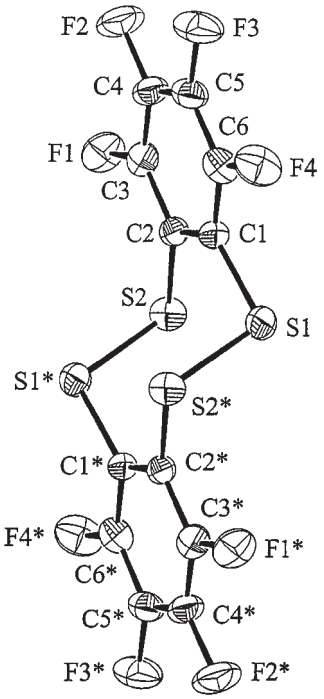

Fig. 2. Packing diagram for the α crystalline phase of $(C_6F_4S_2)_2$ (**3a**).

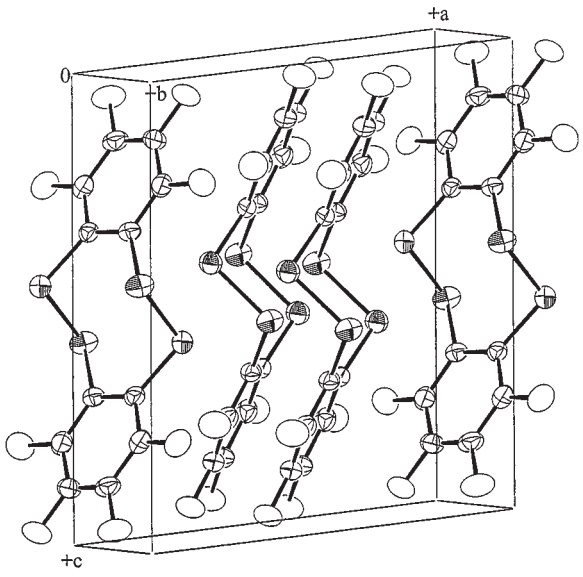

X-ray structure corresponding to the known twist-boat conformation (D_2) of the tetrathiocin ring **1** (4)) (see Fig. 4).

Relevant molecular dimensions for **3a** and **3b** are summarized in Tables 2 and 3. The mean bond distances and bond angles in the two dibenzotetrathiocins are very similar (|*d*(C—C)| = 1.40 Å, *d*|(C—S)| = 1.77 Å, *d*|(S—S)| = 2.05 Å, |angle CCS| = 124.3°, |angle CSS| = 103.8°). For comparison, the corresponding values for the parent compound **1** are 1.33 Å, 1.75 Å, 2.06 Å, 129.0°, and 104.8°(4). The benzo-dithiolato units in **3a** and **3b** are nearly planar, with S-C-C-S and S-C-C-C torsion angles close to 0° and 180°,

Fig. 3. Packing diagram for the β crystalline phase of $(C_6F_4S_2)_2$ (**3a**).

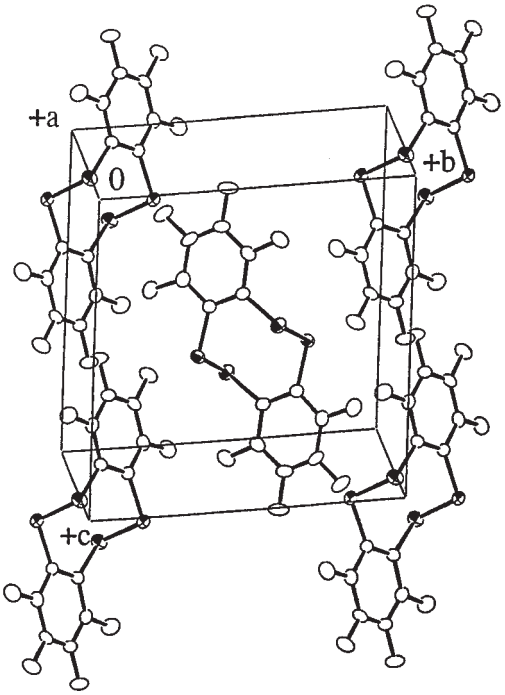

respectively. The C-S-S-C torsion angles are ca. 111° for **3a** and 115.3(4)° and 118.2(4)° for **3b**. The major disparity resulting from the different ring conformations of **3a** and **3b** is in the S-S-C-C torsion angles, which are 79.9° for **3a** and 42.3-52.2° for **3b**.

Conformational isomers of 3a

The ^{19}F NMR spectrum of **3a** in toluene solution at 300 K displays four resonances. These can be separated into two pairs, on the basis of their relative intensities. The less intense pair of AA′XX′ multiplets is centred at δ –130.7 and –154.7 ppm, while the more intense pair appears at δ –123.3 and –148.3 ppm. These observations suggest that **3a** exists as a mixture of the C_{2h} and D_2 conformers in solution (see Table 4). The interconversion of these two conformational isomers in toluene solution was investigated by variable temperature ^{19}F NMR spectroscopy. The relative intensity of the two pairs of resonances changes reversibly within the temperature range 300–380 K, as a result of the equilibrium between the two conformers. However, no significant line broadening or chemical-shift changes were observed, indicating that the fluxional process is too slow to be observed on the NMR time scale. The equilibrium constants at different temperatures were obtained from the intensity ratios for the two pairs of resonance (see Table 5) and a plot of ln *K* vs. T^{-1} (see Fig. 5) was used to determine $\Delta H°$ and $\Delta S°$ for this process. The experimental value of $\Delta H°$ is 9.9 ± kJ mol^{-1}. The $\Delta S°$ value of 14 ± 1 J K^{-1} can be attributed primarily to changes in solvation.

In view of the apparent inversion of the order of stability of the C_{2h} and D_2 conformers for **3a** compared to that calculated for **1** (6), the energies of these two conformers were determined by density functional theory calculations. The structure of **3a** was fully optimised for both C_{2h} and D_2 sym-

© 1998 NRC Canada

Fig. 4. The ORTEP diagram for $(C_6Cl_4S_2)_2$ (**3b**).

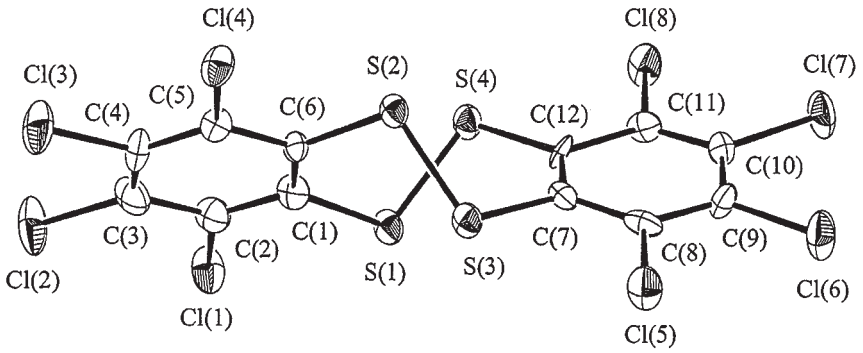

Table 2. Selected bond distances (Å), bond angles (°), and torsion angles (°) for $(C_6F_4S_2)_2$ (**3a**).[a]

	α	β
S(1)—S(2)*	2.057(1)	2.064(1)
S(1)—C(1)	1.771(3)	1.771(3)
C(1)—C(2)	1.403(4)	1.409(4)
S(2)—C(2)	1.771(3)	1.772(3)
S(2)*-S(1)-C(1)	103.0(1)	102.73(9)
S(1)-C(1)-C(2)	123.1(2)	123.1(2)
S(1)*-S(2)-C(2)	102.8(1)	102.97(9)
S(2)-C(2)-C(1)	123.5(3)	123.6(2)
S(1)*-S(2)-C(2)-C(1)	83.1 (3)	79.9(2)
S(1)-C(1)-C(2)-C(3)	–177.9(3)	176.1(2)
C(1)-S(1)-S*(2)-C*(2)	111.4(2)	–111.3(1)
S(1)-C(1)-C(2)-S(2)	–2.1(4)	–1.8(3)
S(2)-C(2)-C(1)-C(6)	174.7(3)	–179.6(2)

[a] Starred atoms are related to the unstarred atoms by symmetry operation: *x*, 1/2 – *y*, *z*.

Table 3. Selected bond distances (Å), bond angles (°), and torsion angles (°) for $(C_6Cl_4S_2)_2$ (**3b**).

S(1)—S(4)	2.033(3)	S(2)—S(3)	2.042(3)
S(1)—C(1)	1.782(8)	S(2)—C(6)	1.783(9)
S(3)—C(7)	1.799(8)	S(4)—C(12)	1.772(8)
C(1)—C(6)	1.40(1)	C(7)—C(12)	1.40(1)
S(1)-C(1)-C(6)	125.2(7)	S(2)-C(6)-C(1)	124.8(6)
S(3)-C(7)-C(12)	123.5(7)	S(4)-C(12)-S(7)	127.3(6)
S(4)-S(1)-C(1)	104.7(3)	S(3)-S(2)-C(6)	102.7(3)
S(1)-S(4)-C(12)	104.5(3)	S(2)-S(3)-C(7)	104.4(3)
S(4)-S(1)-C(1)-C(6)	–48.7(9)	S(3)-S(2)-C(6)-C(1)	–52.2(8)
S(2)-S(3)-C(7)-C(12)	–42.3(8)	S(1)-S(4)-C(12)-C(7)	–42.4(9)
S(1)-C(1)-C(6)-S(2)	3(1)	S(3)-C(7)-C(12)-S(4)	–7(1)
S(1)-C(1)-C(6)-C(5)	–178.1(7)	S(2)-C(6)-C(1)-C(2)	–178.8(7)
S(3)-C(7)-C(12)-C(11)	171.9(7)	S(4)-C(12)-C(7)-C(8)	171.9(7)
C(1)-S(1)-S(4)-C(12)	115.3(4)	C(6)-S(2)-S(3)-C(7)	118.2(4)

metries. The molecular dimensions were in agreement with the experimental values for **3a** and **3b** to within 0.01 Å for bond distances, 1° for bond angles, and 5° for torsional angles. The calculations indicate that the D_2 conformer should be the most stable in this case, but the difference of total energies of the two conformers is only 4.6 kJ mol^{-1}, significantly less than the value of 22.2 kJ mol^{-1} estimated for **1** (6).

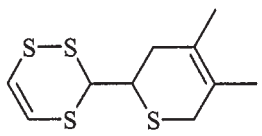

4

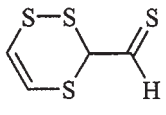

5

Photolysis of octafluorodibenzo-1,2,5,6-tetrathiocin (3a)

The parent ring system **1** is photochemically sensitive even towards daylight (4). The photolysis of **1** in benzene solution in the presence of excess 2,3-dimethylbutadine

© 1998 NRC Canada

Table 4. The ^{19}F NMR chemical shifts (in ppm) for $(C_6F_4S)_2$ and $(C_6F_4S_2)_2$ isomers.

	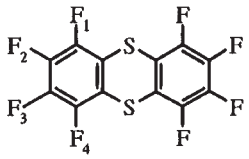	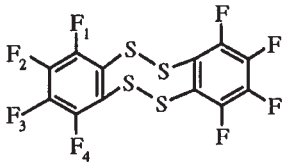	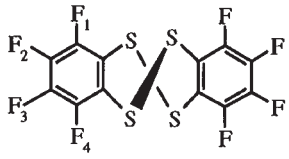	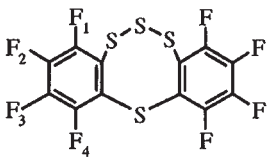
		3a	**3b**	**6**
F_1:	–134	–130.1	–122.1	–117.3
F_2:	–155	–154.4	–147.4	–147.5
F_3:	–155	–154.4	–147.4	–147.8
F_4:	–134	–130.1	–122.1	–122.9
Reference:	11	This work	This work	This work

Table 5. Measured conformation equilibrium constant for $(C_6F_4S_2)_2$ (**3a**) at different temperatures.

T (K)	*K*
300	9.99
310	8.55
320	8.16
330	6.55
340	6.38
350	5.51
360	4.98
370	4.65
380	4.42

Fig. 5. Temperature dependence of the conformational equilibrium constant for $(C_6F_4S_2)_2$ (**3a**).

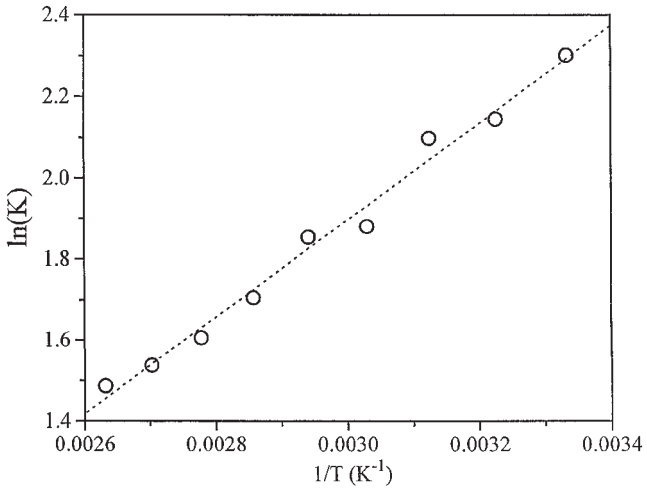

produced the bicyclic product **4** in 62% yield, suggesting the intermediate formation of the thioaldehyde **5**.

In view of these observations it was of interest to determine the influence of the rigid benzo substituents in **3a** on the outcome of the photochemical transformation. A solution of **3a** in benzene in a Pyrex vessel was irradiated with a medium-pressure mercury lamp through a Pyrex filter. The reaction was monitored by ^{19}F NMR, which revealed the formation of an intermediate with resonances at δ –121.8, –123.3, –146.7, and –147.1. The final product was identified as octafluorodibenzo-1,2,3,6-tetrathiocin (**6**) by elemental analysis, EIMS, ^{19}F NMR, IR, and Raman spectra, and by an X-ray structure (vide infra).

The photoisomerized product **6** is readily distinguished from the isomers of **3a** by the ^{19}F NMR spectrum, which exhibits an AMXY pattern (Table 4). The multiplets attributed to the inequivalent *ortho*-fluorine atoms have significantly different chemical shifts whereas those assigned to the other pair of inequivalent fluorine atoms differ by only 0.3 ppm. The mass spectra of **3a** and **6** show major differences. Both compounds exhibit the molecular ion $C_{12}F_8S_4^+$ with similar intensities. However, the mass spectrum of **6** also exhibits increasingly high abundances of the ions $[C_{12}F_8S_3]^+$ and $[C_{12}F_8S_2]^+$, suggesting that loss of sulfur (from the S_3 chain) is the dominant fragmentation process, which leads to the parent ion $[C_{12}F_8S^+]$. By contrast, the parent ion for **3a** is the monomeric fragment $C_6F_4S_2^+$, indicating that cleavage of *both* disulfide bonds occurs predominantly in this case.

Raman spectroscopy is a diagnostic technique for the identification of SS vibrations, which are normally observed in the 450–550 cm^{-1} region (19). In the present work, the photoisomerized product **6** should be readily distinguished by the presence of both asymmetric and symmetric stretching vibrations for the trisulfide (S_3) unit, whereas the precursor **3a** will exhibit only ν_s(SS). Consistently, the Raman spectrum of **6** shows bands at 492 and 469 cm^{-1}. On the basis of its stronger intensity, the former is attributed to ν_s(SSS) (cf. HSSSH (20)). The Raman spectrum of **3a** exhibits only one band in the 450–550 cm^{-1} region at 497 cm^{-1}, which is assigned to ν_s(SS) (cf. 489 cm^{-1} for $C_6F_5SSC_6F_5$ (21)).

[1] 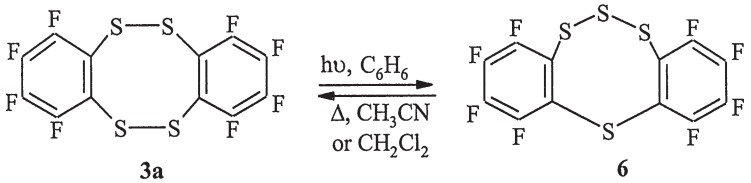

3a **6**

© 1998 NRC Canada

Fig. 6. The ORTEP diagram for $\overline{C_6F_4SSSC_6F_4S}$ (**6**).

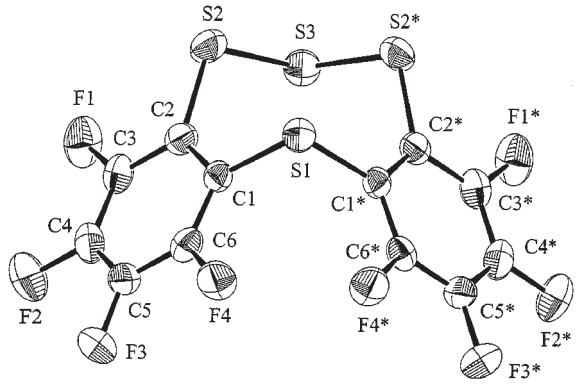

The photochemical transformation of **3a** into **6** (eq. [1]) formally involves a transannular migration of a sulfur atom. In view of the similarity of the ^{19}F NMR spectra of **6** and the intermediate observed in this process (vide supra), it is suggested that this intermediate is a conformational isomer of **6**. A similar isomerization of a C_4S_4 ring has been reported for C_6S_{10} (**2a**) but, in that example, the transformation from a 1,2,5,6- to a 1,2,3,6-tetrathiocin involves a Hg^{2+}-promoted hydrolysis to give $C_6S_8O_2$ (22*a*). A mechanism involving a thiosulfoxide intermediate has been proposed for the sulfur transfer process (22*b*). Although organic

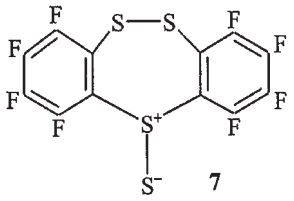

7

thiosulfoxides R_2SS have not characterized, the SS double bond is known to be stabilized by electronegative groups (23). For example, the cyclic thiosulfite ROS(=S)OR (R = cyclohexylidene) is stable at 20°C (24). In the case of the transformation represented by eq. [1], the proposed intermediate **7** may be stabilized by the electronegative perfluoroaryl groups attached to sulfur. Finally, we note that **6** is unstable in solution in polar solvents and slowly reverts to **3a**.

X-ray structure of octafluorodibenzo-1,2,3,6-tetrathiocin (6)

The structure of **6** was established by X-ray crystallography. An ORTEP diagram is represented in Fig. 6, and relevant structural parameters are given in Table 6. The S—S bond length of 2.047(1) Å is, as expected, a typical single-bond value. The bond angle S-S-S = 107.2(1)° is close to the mean value of 107.9° reported for *cyclo*-octasulfur (21). However, the mean bond distance, *d*|(C—S)| = 1.79 Å, and mean bond angles, |angle CCS| = 122.6°, |angle CSS| = 103.1°, show small, but significant, differences from the corresponding values for **3a** and **3b**, possibly owing to slightly greater ring strain in **6**. The small bond angle C(1)-S(1)-S(1)* of 102.81(1)° is perhaps indicative of some ring strain. The C_4S_4 ring in **6** adopts a chair conformation with respect to the sulfur atoms S(1) and S(3). The value of

Table 6. Selected bond distances (Å), bond angles (°), and torsion angles (°) for $\overline{C_6F_4SSSC_6F_4S}$ (**6**).[a]

S(1)—C(1)	1.799(2)
S(2)—C(2)	1.782(2)
S(2)—S(3)	2.047(1)
S(1)-C(1)-C(2)	121.7(1)
C(1)-C(2)-S(2)	123.5(1)
C(2)-S(2)-S(3)	103.1(1)
S(2)-S(3)-S(2)*	107.2(1)
C(1)-S(1)-C(1)*	102.8 (1)
C(2)-S(2)-S(3)-S(2)*	–93.78(10)
C(1)*-S(1)-C(1)-C(2)	–94.94(13)
C(1)*-S(1)-C(1)-C(6)	85.01(14)
S(1)-C(1)-C(2)-C(3)	179.95(15)
S(1)-C(1)-C(2)-S(2)	–6.0(2)
S(3)-S(2)-C(2)-C(3)	–103.79(11)
S(3)-S(2)-C(2)-C(1)	81.97(14)
S(2)-C(2)-C(3)-C(4)	–174.5(2)
S(1)-C(1)-C(6)-S(5)	–179.95(14)

[a] Starred atoms are related to the unstarred atoms by symmetry operation: *x*, 1/2 – *y*, *z*.

93.8(1)° for the torsion angle C-S-S-S in **6** is significantly smaller than the corresponding values for the torsion angles involving a central disulfide linkage in **3a** or **3b**, which are in the range 111–118°. We tentatively suggest that the intermediate detected by ^{19}F NMR in the photochemical transformation of **3a** into **6** is the corresponding boat conformer of **6**.

Conclusions

The 1,2,5,6-tetrathiocins $(C_6F_4S_2)_2$ (**3a**) and $(C_6Cl_4S_2)_2$ (**3b**) adopt chair (C_{2h}) and twist-boat (D_2) conformations of the C_4S_4 ring, respectively. The difference in the energies of the two conformers for **3a** is very small (<5 kJ mol^{-1}), and this derivative undergoes a slow conformational isomerization in solution. The photolysis of **3a** promotes a reversible, transannular sulfur migration to give the 1,2,3,6-isomer (**6**).

Acknowledgements

We thank NSERC (Canada) for financial support, Dr. T. Shimizu for a preprint of ref. 6, and Prof. T.B. Rauchfuss for helpful correspondence and a copy of the Ph.D. thesis of C.P. Galloway in which the possible rearrangement pathway for the transformation of C_6S_{10} into $C_6S_8O_2$ is presented. We also thank Professor C. Langford for the use of photochemical equipment and Professor R. Kydd for his assistance with the measurement of Raman spectra.

References

1. Z.S. Herman and K. Weiss. Inorg. Chem. **14**, 1592 (1974).
2. F.G. Riddell. *In* The chemistry of sulphur-containing functional groups. *Edited by* S. Patai and Z. Rappoport. John Wiley and Sons, Chichester, U.K. 1993. Chap. 9.

© 1998 NRC Canada

3. (*a*) C.G. Krespan, B.C. McKusick, and T.L. Cairns. J. Am. Chem. Soc. **82**, 1515 (1960); (*b*) C.G. Krespan. J. Am. Chem. Soc. **83**, 3434 (1961).
4. T. Shimizu, K. Iwata, and N. Kamigata. Angew. Chem. Int. Ed. Engl. **35**, 2357 (1996).
5. T. Shimizu, K. Iwata, N. Kamigata, and S. Ikuta. J. Chem. Res. Synop. 436 (1994).
6. T. Shimizu, K. Iwata, N. Kamigata, and S. Ikuta. J. Chem. Res. Miniprint, (1997). In press.
7. X. Yang, T.B. Rauchfuss, and S. Wilson. J. Chem. Soc. Chem. Commun. 34 (1990).
8. F. Bigoli, P. Deplano, F.A. Devillanova, J.R. Ferraro, V. Lippolis, P.J. Lukes, M.L. Mercuri, M.A. Pellinghelli, E.F. Trogu, and J.M. Williams. Inorg. Chem. **36**, 1218 (1997).
9. (*a*) G.H. Brooke, B.S. Furniss, W.K.R. Musgrave, and Md.A. Quasem. Tetrahedron Lett. 2991 (1965); (*b*) A. Callaghan, A.J. Layton, and R.S. Nyholm. J. Chem. Soc. Chem. Commun. 399 (1969).
10. M.J. Baker-Hawkes, E. Billings, and H.B. Gray. J. Am. Chem. Soc. **88**, 21 (1996).
11. R.D. Chambers and D.J. Spring. Tetrahedron, **27**, 669 (1971).
12. A.C.T. North, D.C. Phillips, and F.S. Mathews. Acta Crystallogr. Sect. A: Cryst. Phys. Diffr. Theor. Gen. Crystallogr. **24**, 351 (1968).
13. A. Altomare, M. Cascarano, C. Giacovazzo, and A. Guagliardi. SIR92: J. Appl. Crystallogr. **26**, 343 (1993).
14. P.T. Beurskens, G. Admiraal, G. Beurskens, W.P. Bosman, R. de Gelder, R. Israel, and J.M.M. Smits. DIRDIF 94: Technical Report of the Crystallography Laboratory. University of Nijmegen, The Netherlands. 1994.
15. teXsan: Crystal Structure Analysis Package. Molecular Structure Corp., The Woodlands, Texas, U.S.A. 1985 and 1992.
16. F. Hai-Fu. SAPI91: Structure Analysis Program with Intelligent Control. Rigaku Corp., Tokyo. 1991.
17. G.M. Sheldrick. SHELXL-93: Program for the Refinement of Crystal Structures. University of Göttingen, Germany. 1993.
18. T. Chivers, I. Krouse, M. Parvez, I. Vargas-Baca, T. Ziegler, and P. Zoricak. Inorg. Chem. **35**, 5836 (1996).
19. R. Steudel. Angew. Chem. Int. Ed. Engl. **14**, 655 (1975).
20. H. Wieser, P.J. Krueger, M. Muller, and J.B. Hyne. Can. J. Chem. **47**, 1633 (1969).
21. S. Brownridge, T.S. Cameron, J. Passmore, G. Schatte, G.W. Sutherland, and T. Way. Can. J. Chem. In press.
22. (*a*) C.P. Galloway, D.D. Doxsee, D. Fenske, T.B. Rauchfuss, S.R. Wilson, and X. Yang. Inorg. Chem. **33**, 4537 (1994); (*b*) C.P. Galloway. Ph.D. thesis, University of Illinois at Urbana-Champaign. 1994.
23. R. Steudel, Y. Drozdova, K. Miaskiewicz, R.H. Hertwig, and W. Koch. J. Am. Chem. Soc. **119**, 1990 (1997).
24. D.N. Harpp, K. Steliou, and C.J. Cheer. J. Chem. Soc. Chem. Commun. 825 (1980).
25. (*a*) L.K. Templeton, D.H. Templeton, and A. Zalkin. Inorg. Chem. **15**, 1999 (1976); (*b*) L.M. Goldsmith and C.E. Strouse. J. Am. Chem. Soc. **99**, 7580 (1977).

© 1998 NRC Canada

A new one-dimensional thiocyanato-bridged bimetallic compound $[Cu(en)_2Mn(NCS)_4(H_2O)_2]_n$. Synthesis, crystal structure, and magnetic properties

Hui-Zhong Kou, Dai-Zheng Liao, Peng Cheng, Zong-Hui Jiang, Shi-Ping Yan, Geng-Lin Wang, Xin-Kan Yao, and Hong-Gen Wang

Abstract: A bimetallic compound $[Cu(en)_2Mn(NCS)_4(H2O)_2]_n$ (en = ethylenediamine) has been prepared and its structure determined. It crystallizes in space group $P\bar{1}$, with a = 7.432(1), b = 7.492(1), c = 9.751(2) Å, α = 91.00(3)°, β = 99.14(3)°, γ = 112.51(3)°, and Z = 1. The structure consists of one-dimensional chains in which alternating Mn(II) and Cu(II) ions are bridged by NCS ligands. The coordination environment is octahedral for Mn(II) and elongated octahedral for Cu(II). From magnetic susceptibility measurements the compound was found to exhibit a ground state of low-spin multiplicity. Comparison between theory and experimental has been made using 1-D model and taking into account the zero-field splitting effect. The decrease in $\chi_m T$ observed at low temperature for the compound is attributed to a dominant zero-field splitting of the single Mn(II) ions with a weak antiferromagnetic interaction superimposed between the Mn(II) ions via the NCS-Cu-SCN pathway within each chain.

Key words: crystal structure, copper(II) complexes, manganese(II) complexes, thiocyanate bridges, bimetallic complexes.

Résumé : On a préparé un composé bimétallique $[Cu(en)_2Mn(NCS)_4(H_2O)_2]_n$ (en = éthylènediamine) et on a déterminé sa structure. Il cristallise dans le groupe d'espace $P\bar{1}$, avec a = 7,432(1), b = 7,492(1) et c = 9,751(2) Å, α = 91,00(3), β = 99,14(3) et γ = 112,51(3)° et Z = 1. La structure comporte des chaînes unidimensionnelles dans lesquelles les ions Mn(II) et Cu(II) qui alternent sont reliés par des ponts de ligands NCS. L'environnement de coordination est octaédrique pour le Mn(II) et octaédrique allongé pour le Cu(II). Sur la base de mesures de susceptibilité magnétique, on a trouvé que l'état fondamental du composé présente une multiplicité à faible spin. On a effectué une comparaison entre les résultats expérimentaux et les valeurs théoriques obtenues à l'aide d'un modèle 1-D, en tenant compte de l'effet de couplage à champ nul. La diminution dans la valeur de $\chi_m T$ observée pour le composé à basse température est attribuée à un couplage à champ nul dominant des ions Mn(II) individuels avec une faible interaction antiferromagnétique superposée entre les ions Mn(II) par le biais d'une voie NCS-Cu-SCN dans chaque chaîne.

Mots clés : structure cristalline, complexes du Cu(II), complexes du Mn(II), ponts thiocyanates, complexes bimétalliques.

[Traduit par la rédaction]

Introduction

The first molecular-based magnet emerged a decade ago (1), and during the last period a number of new compounds of this type have been reported (2–8). To obtain molecular-based ferromagnets, several means have been used (9–11). Among them, the exchange couplings of low-dimensional bimetallic Cu(S = 1/2)-Mn(S = 5/2) compounds have been paid much attention (12–15). Kahn and co-workers (3, 13) have suggested that such compounds may exhibit ferrimagnetic behavior at low temperatures. The Kahn concept is based on the following assumptions. In theory, provided that the Mn(II) and Cu(II) ions are antiferromagnetically coupled in all cases, an ordered alternation of the Mn and Cu ions is required throughout the crystal lattice. If so, below certain transition temperature the intrinsic antiferromagnetic interactions between the adjacent metal ions make the S_{Mn} and S_{Cu} antiparallel, and the material retains a net spin ($S = S_{Mn} - S_{Cu} = 2$) because the two sublattices are not equivalent (15).

However, it should be noted that some Cu(II)-Mn(II) compounds assume different magnetic properties. Very recently, Chiari et al. (16) reported that a bimetallic chain compound $Cu(en)_2MnCl_4$, exhibiting a ground state of low-spin multiplicity, does not conform to the above expectation.

Received January 27, 1998.

H.-Z. Kou, D.-Z. Liao,[1] P. Cheng, Z.-H. Jiang, S.-P. Yan, and G.-L. Wang. Department of Chemistry, Nankai University, Tianjin 300071, P.R. China.
X.-K. Yao and H.-G. Wang. Central Laboratory, Nankai University, Tianjin 300071, P.R. China.

[1]Author to whom correspondence may be addressed. Fax: (086) 022-23502458. E-mail: chemczl@sun.nankai.edu.cn

© 1998 NRC Canada

Table 1. Crystallographic data and data-collection parameters for $[Cu(en)_2Mn(NCS)_4(H_2O)_2]_n$.[a]

Formula	$C_8H_{20}CuMnN_8O_2S_4$
M	507.032
Colour, habit	Blue, prismatic
Temperature	299(1) K
Diffractometer	Enraf–Nonius CAD4
Crystal system	Triclinic
Space group	$P\bar{1}$
a, Å	7.432(1)
b, Å	7.492(1)
c, Å	9.751(2)
α, deg	91.00(3)
β, deg	99.14(3)
γ, deg	112.51(3)
V, Å^3	493.4(4)
Z	1
ρ_{calc}, g/cm^3	1.706
ρ_m, g/cm^3	1.69(1)
h, *k*, *l* limits	–8–8, –8–8, 0–10
F(000)	258
Agreement factor (on *I*)	0.031
No. variables	112
Largest shift/e.s.d. in final cycle	0.001
Residual density (min, max) (e Å^3)	–0.44, 0.53
*R*1	0.040
*wR*2	0.049
Goodness of fit	1.04

[a] Some equations of interest: $R1 = \Sigma||Fo| - |F_c||/\Sigma|F_o|$, $wR2 = [\Sigma(w|F_o| - |F_c|)^2/\Sigma w|F_o|^2]^{1/2}$ where $w = 1$, GoF = $s = [\Sigma w(|F_o - F_c|)^2/(N_{obs} - N_{para})]^{1/2}$.

Table 2. Atomic coordinates (×10^4) and equivalent isotropic displacement parameters (Å × 10^3) for $[Cu(en)_2Mn(NCS)_4(H_2O)_2]_n$.[a]

Atom	*x*	*y*	*z*	*U*(eq)
Cu(1)	0	0	0	34(1)
Mn(2)	0	–5000	–5000	34(1)
S(2)	3789(3)	–8625(3)	–3191(2)	48(1)
S(1)	2459(3)	–2469(3)	–75(2)	50(1)
O(1)	2127(7)	–2220(6)	–5619(5)	51(2)
N(11)	1034(8)	354(7)	2061(6)	41(2)
N(12)	2365(8)	2423(7)	–59(6)	43(2)
N(1)	882(10)	–3875(10)	–2830(8)	61(3)
C(1)	1527(9)	–3315(9)	–1675(8)	35(3)
C(12)	3345(10)	3301(10)	1380(8)	50(3)
C(11)	3164(10)	1725(10)	2305(8)	48(3)
N(2)	2225(10)	–6273(10)	–4667(8)	66(3)
C(2)	2887(10)	–7253(10)	–4052(7)	38(3)

[a] *U*(eq) is defined as one third of the trace of the orthogonalized U_{ij} tensor. The site occupancy factor (SOF) is 0.5 for the Cu and Mn atoms.

Table 3. Selected interatomic bond distances (Å) and angles (°).

Bond	Length
Cu(1)—N(11)	2.008(5)
Cu(1)—N(12)	1.995(5)
Mn(2)—N(1)	2.166(7)
N(1)—C(1)	1.154(10)
N(2)—C(2)	1.157(11)
Cu(1)—S(1)	3.065(10)
Mn(2)—O(1)	2.242(4)
Mn(2)—N(2)	2.190(9)
C(1)—S(1)	1.613(7)
C(2)—S(2)	1.609(8)
Bond	**Angle**
S(1)-Cu(1)-N(11)	84.3(8)
C(1)-S(1)-Cu(1)	94.3(8)
Mn(2)-N(2)-C(2)	149.5(7)
N(2)-C(2)-S(2)	179.5(7)
S(1)-Cu(1)-N(12)	91.2(8)
Mn(2)-N(1)-C(1)	172.9(7)
N(1)-C(1)-S(1)	178.3(6)

The unexpected cancellation of the spins has been attributed to the presence of either a dominant Mn(II)···(Mn(II) antiferromagnetic interaction within the chain or, alternately, cooperative intrachain and interchain Mn···Cu interactions of opposite signs. Some other compounds of this type show similar magnetic behaviours; however, the zero-field splitting effects were introduced to interpret the phenomenon (17, 18). Obviously, more such examples are needed in order to determine the relationship between the magnetic properties and molecular structures.

In this paper, we report a new compound, $[Cu(en)_2Mn(NCS)_4(H_2O)_2]_n$ (en = ethylenediamine). The compound has bimetallic chains with alternating copper(II) and manganese(II) ions within each chain, and shows magnetic properties quite different from those expected but similar to those of $Cu(en)_2MnCl_4$ (16).

Experimental

Synthesis of $[Cu(en)_2Mn(NCS)_4(H_2O)_2]_n$

To an aqueous solution of $MnSO_4 \cdot H_2O$ was added KSCN dissolved in water in a Mn:SCN molar ratio of 1:4. To the resulting solution was added ethanol (95%), then filtered. The filtrate was evaporated in a water bath giving rise to light pink microcrystals of $K_2[Mn(NCS)_4(H_2O)_2]$.

Equimolar amounts of $K_2[Mn(NCS)_4(H_2O)_2]$ and $Cu(en)_2Cl_2$ were mixed in aqueous solution to give rise to blue microcrystals. Crystals of large size for X-ray analysis and magnetic studies were obtained by recrystallization of the material from water. The yield is almost quantitative; mp 162–163°C. Anal. calcd for $C_8H_{20}N_8O_2S_4CuMn$: C 18.95, H 3.9, N 22.1; found: C 19.3, H 3.8, N 22.0%.

Physical measurements

Elemental analyses of carbon, hydrogen, and nitrogen were carried out with a Perkin–Elmer analyzer model 240. The electronic spectrum was measured with a Perkin–Elmer Hitachi-240 spectrophotometer. The infrared spectroscopy using a KBr pellet was performed on a Nicolet 5DX FT-IR spectrophotometer in the 4000–400 cm^{-1} region. Using the flotation method (carbontetrachloride and 1,3-dibromopropane), the density of the compound was determined. Magnetic susceptibility measurement of a crystalline sample was

© 1998 NRC Canada

Fig. 1. The ORTEP (35) drawing of $[Cu(en)_2Mn(NCS)_4(H_2O)_2]_n$, showing thermal ellipsoids drawn at the 30% probability level.

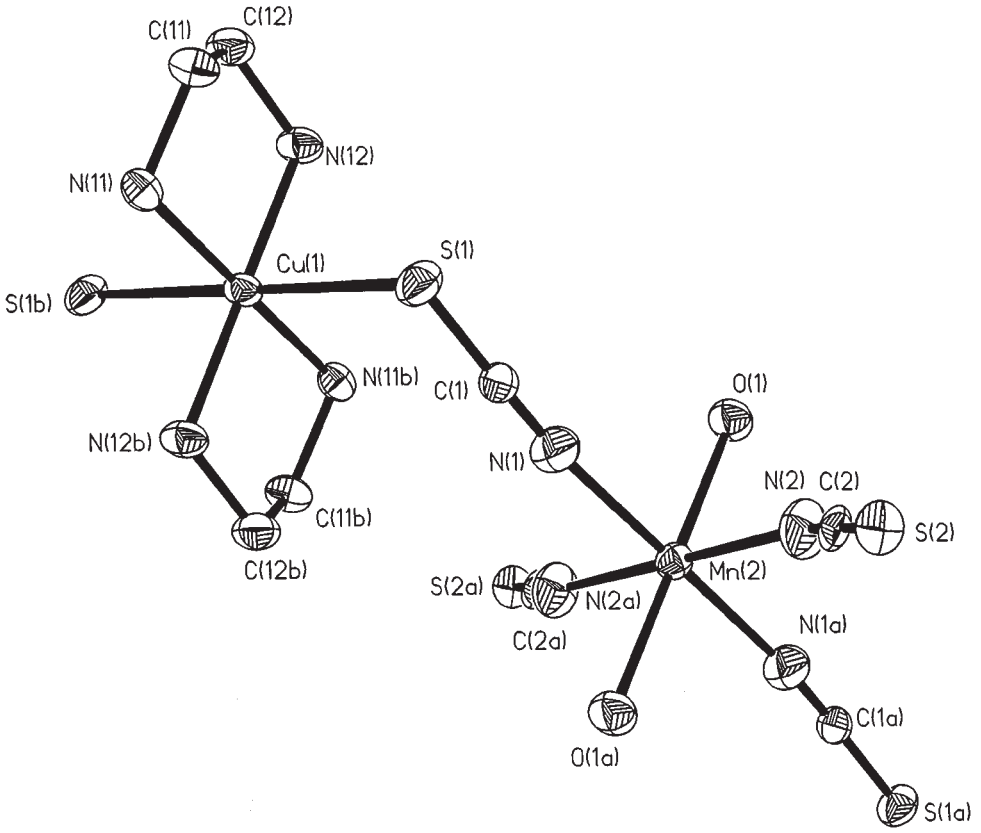

carried out in the temperature range 1.5–296 K on a vibrating sample magnetometer, model CF-1. The experimental susceptibilities were corrected for the diamagnetism of the constituent atoms (Pascal's tables).

Crystallographic data collection and structure determination

A blue prismatic crystal with dimensions 0.2 × 0.3 × 0.4 mm^3 was mounted on a computer-controlled Enraf–Nonius CAD4 diffractometer equipped with a graphite-monochromatized $M_oK\alpha$ radiation. Cell parameters were determined by least-squares calculations based on the setting angles and 25 reflections with 2θ angles ranging from 15 to 27° at 299(1) K. Cell dimensions and additional crystal data are listed in Table 1. The intensities of the ±*hkl* reflections were measured up to θ_{max} = 23°; the ω-2θ scan technique was employed, the ω-scan width equal to (0.65 + 0.35 tan θ)°, and the scan speed 0.92–5.49° min^{-1}. A total of 1313 independent reflections was measured giving 1121 observed reflections ($I > 3\sigma(I)$) used in the refinement. Three standard reflections monitored every 60 min showed no intensity variation during the data collection. No absorption correction was made during processing.

The structure was solved by direct method (MULTAN 82) using SDP-PLUS program (19). Atomic scattering factors were taken from ref. 20. The hydrogen atoms attached to the oxygen atoms were found in the Δ*F* map, and the other hydrogen atoms were added theoretically. All hydrogen atoms were refined with riding model and fixed isotropic thermal parameters.

Final atomic coordinates and equivalent isotropic displacement parameters are given in Table 2 and selected bond distances and angles appear in Table 3. Crystal data, data collection, solution and refinement, anisotropic displacement coefficients, bond lengths and angles, and atomic coordinates have been deposited.[2]

Results and discussion

Crystal structure

The structure has an inversion center and consists of chains in which alternating $Cu(en)_2^{2+}$ and $Mn(NCS)_4(H_2O)_2^{2-}$ entities are bridged by thiocyanate ligands. The molecular arrangement with an atom numbering scheme is shown in Fig. 1. The chains are generated by unit cell translation of the $Cu(en)_2Mn(NCS)_4(H_2O)_2$ unit as shown in Fig. 1.

The Mn coordination environment can be considered as a slightly distorted octahedral, with two oxygen atoms occupying the axial positions (Mn(2) – O(1) = 2.242(4) Å) and four nitrogen atoms from two bridging NCS groups (Mn(2) – N(1) = 2.166(7) Å) and two terminal ones (Mn(2) – N(2) = 2.190(9) Å) forming the basal plane. The NCS groups are

[2] Supplementary material may be purchased from: The Depository of Unpublished Data, Document Delivery, CISTI, National Research Council of Canada, Ottawa, Canada, K1A 0S2. With the exception of the anisotropic displacement coefficients, these have also been deposited with the Cambridge Crystallographic Data Centre and can be obtained on request from: The Director, Cambridge Crystallographic Data Centre, University Chemical Laboratory, 12 Union Road, Cambridge, CB2 1EZ, U.K.

© 1998 NRC Canada

Fig. 2. View of the crystal cell of $[Cu(en)_2Mn(NCS)_4(H_2O)_2]_n$.

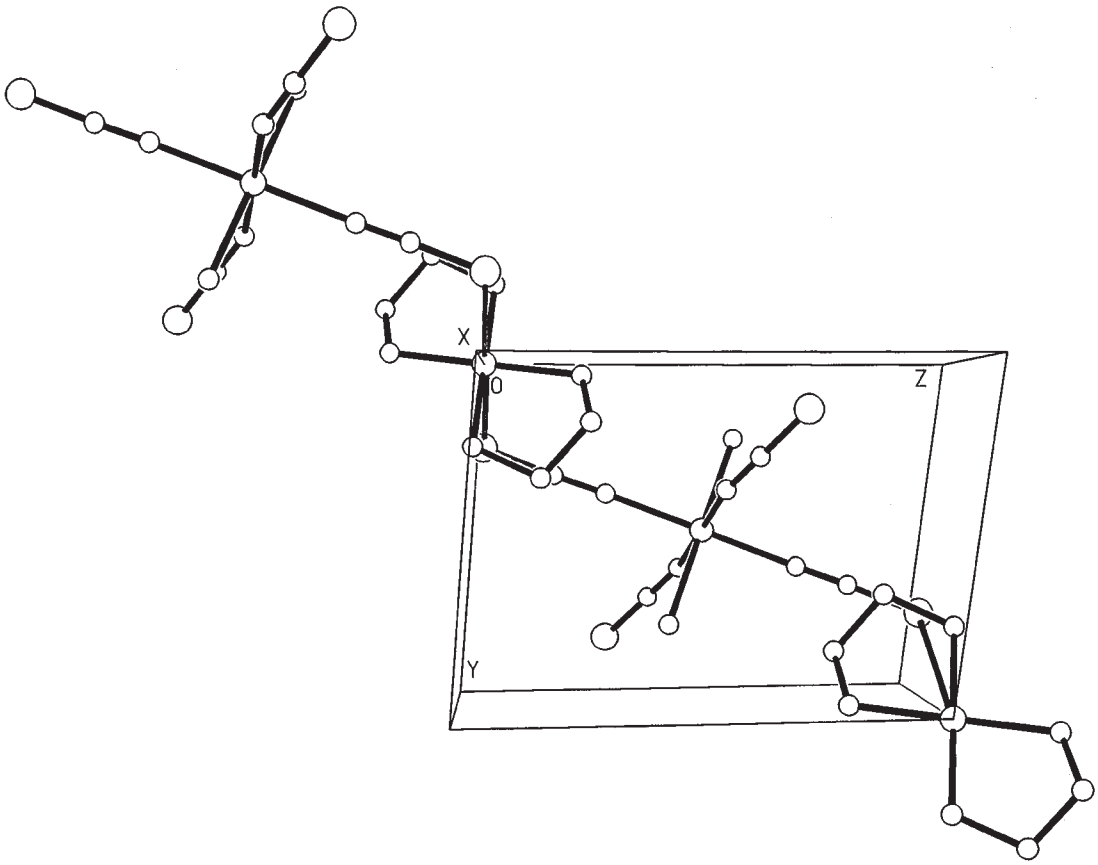

almost linear with the bond angles of 179.5(7)° for N(2)-C(2)-S(2) and 178.3(7)° for N(1)-C(1)-S(1). Also, the bond distances of C≡N (average value: 1.157 Å) and C—S (average value: 1.606 Å) fall within the normal ranges. The Mn-N-C linkages are bent with angles ranging from 149.5(7)° for Mn(2)-N(2)-C(2) to 172.9(7)° for Mn(2)-N(1)-C(1).

The copper ion has elongated octahedral surroundings: the equatorial positions are occupied by the four nitrogen atoms from two en ligands with the Cu—N distances of 1.995(5) Å to 2.008(5) Å and the axial positions by the sulfur atoms from the bridging NCS ligands. The bond distances of Cu—S, 3.065(10) Å, are shorter than the sum of van der Waals radii of Cu and S atom, 3.4 Å (21), and similar to the values reported for related axially S-thiocyanate copper(II) compounds (22–27). The adjacent Cu···Mn intrachain separations are 6.096 Å. It is worth mentioning that as far as the copper coordination environment is concerned, it is similar to that of a monomeric compound, $Cu(en)_2(SCN)_2$, whose molecular structure was determined three decades ago (27). The significant difference lies in the Cu—S bond length, considering that $Cu(en)_2(SCN)_2$ possesses a Cu—S distance of 3.27(1) Å, much longer than that of the present compound (3.065(10) Å).

The chain arrangement within the lattice cell is shown in Fig. 2. The shortest interchain metal–metal separations are Cu···Mn = 6.200 Å and Cu···Cu = Mn···Mn = 7.432 Å and 7.492 Å along the *a* and *c* directions, respectively. The interchain intermolecular contacts of S and O are 3.261, and 3.269 Å, slightly shorter than the sum of van der Waals radii of S and O atoms, 3.30 Å (21).

Spectroscopic properties

The interest in the IR spectrum of the compound lies mainly in the bands due to the NCS groups. A sharp and strong band at 2092 cm^{-1} and a shoulder at 2100 cm^{-1} are attributed to the asymmetric stretching vibration ν(CN). The weak band corresponding to ν(CS) vibration appears at 771 cm^{-1}, and the δ(NCS) bending mode is observed at 480 cm^{-1} as a shoulder.

The reflectance electronic spectrum on a crystalline sample exhibits a broad band centred at 543 nm, which can be assigned to the copper *d-d* transitions. This value is greater than that of $Cu(en)_2(SCN)_2$ (525 nm) with analogous CuN_4S_2 chromophores (28, 29). As stated by Lever et al. (29), the crystal field strengths of the coordinating axial ligands remarkably influence the value of ΔDq (the difference in in-plane and out-of-plane field strengths); in other words, the more strongly the axial ligands coordinate, the smaller ΔDq is. This gives rise to a red shift of *d-d* bands. Comparing with $Cu(en)_2(SCN)_2$, $[Cu(en)_2Mn(NCS)_4(H_2O)_2]_n$ has a much shorter Cu—S bond (3.066(10) Å) that can be considered a stronger one to afford a smaller ΔDq value. Therefore, a greater λ_{max} value compared with $Cu(en)_2(SCN)_2$ is obtained.

The electronic spectrum of the compound in an aqueous solution affords the same band at 543 nm, which suggests that no dissociation takes place upon dissolution.

Magnetic properties

The magnetic behaviour of the compound is represented in Fig. 3, in the form of $\chi_m T$ vs. *T*. At room temperature, the

© 1998 NRC Canada

Fig. 3. Plots of the product $\chi_m T$ vs. temperature for $[Cu(en)_2Mn(NCS)_4(H_2O)_2]_n$. The dotted, dashed, and solid lines represent the theoretical values based on the eqs. [2], [3], and [4], respectively.

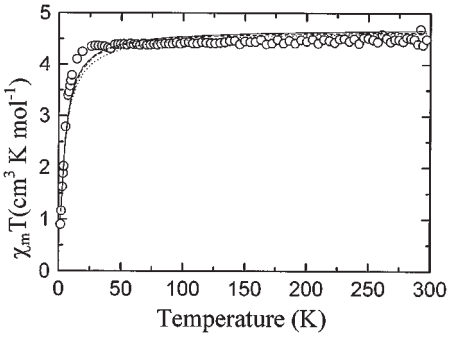

$\chi_m T$ value is 4.40 cm^3 K mol^{-1}, close to expected for isolated $S = 5/2$ and $S = 1/2$ spins (4.75 cm^3 K mol^{-1} for $g_{Mn} = g_{Cu} = 2$). When the temperature is lowered, $\chi_m T$ remains constant until 20 K and then decreases sharply to 1.14 cm^3 K mol^{-1} at 1.5 K.

According to Kahn's theory, in an antiferromagnetic exchange ($J < 0$) within an alternating Mn(II)-Cu(II) chain, the net spins ($S = S_{Mn} - S_{Cu} = 2$) are parallel to each other in the ground state, and $\chi_m T$ should diverge below a critical temperature. Two different results may be obtained (Fig. 4): first, the antiferromagnetic interchain interaction between the nearest manganese and copper ions gives rise to a ferrimagnetic behaviour (Fig. 4*a*); second, on the contrary, a cancellation of the spins (Fig. 4*b*) occurs (30–32). Although the crystal structure of $[Cu(en)_2Mn(NCS)_4(H_2O)_2]_n$ shows that the arrangements of Cu and Mn ions meet the former case, the fact that the spin density in an *xy*-like orbital delocalized from the copper ion to the sulphur atoms situated at the axial positions in the copper coordination sphere is negligibly small prevents us from drawing the above conclusion.

Under the circumstances, the Mn···Mn (ca. 11.7 Å) superexchange within the chain propagated by the filled d_{z^2} -like orbital of the NCS-Cu-SCN pathway may prevail over the Mn···Cu and, certainly, Cu···Cu interactions. A similar situation has been found in $Cu(en)_2MnCl_4$ (16). On the basis of the above hypothesis, the magnetic susceptibility of the chain χ_{chain} was calculated by eq. [1], where the first term describes an infinite Mn(II) chain according to the polynomial expression of Hiller et al. (18), and the second term is a temperature independent contribution from Cu(II).

$$[1] \qquad \chi_{chain} = \frac{Ng_{Mn}{}^2\beta^2}{KT}[A + Bx^2][1 + Cx + Dx^3] + \frac{Ng_{Cu}{}^2\beta^2}{3KT} S_{Cu}(S_{Cu} + 1) + TIP$$

where $x = |J|/KT$, $A = 2.9167$, $B = 208.04$, $C = 15.543$, and $D = 2707.2$, J is the exchange coupling constant, and TIP is the temperature-independent paramagnetism (60×10^{-6} cm^3 mol^{-1}).

Taking into account the 2-D interactions, we modified the molar magnetic susceptibility χ_m employing eq. [2], where J' is the interchain coupling constant and $z = 2$, the number of nearest Mn(II) neighbors. Other symbols have the usual meanings.

Fig. 4. Schematic representation of two modes of interchain metal–metal magnetic interactions: (*a*) antiferromagnetic interchain interaction between the nearest manganese and copper ions, giving rise to a ferrimagnetic behaviour; and (*b*) on the contrary, a cancellation of the spins.

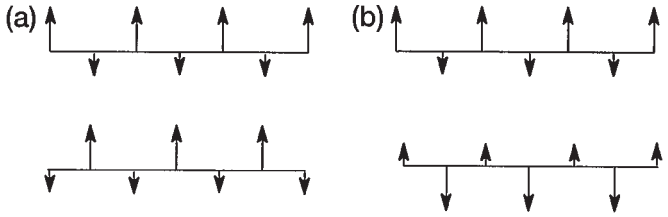

$$[2] \qquad \chi_m = \chi_{chain}/[1 - \chi_{chain}(2zJ'/Ng^2\beta^2)]$$

The least-squares fit from eq. [2] to the data was found with $J = -0.22(1)$ cm^{-1}, $g_{Mn} = g_{Cu} = 1.98$ and $zJ' = -0.004$ cm^{-1}, and the agreement factor, defined as $F = \Sigma_i(\chi_i{}^{obs} - \chi_i{}^{calcd})^2/\chi_i{}^{obs}$, was 1.95×10^{-3} for all of the 94 observations. On the basis of the above results, it can be concluded that a small antiferromagnetic intrachain interaction (J) between the nearest Mn(II) ions and a smaller antiferromagnetic interchain interaction (J') are present.

Alternatively, we attempted to interpret the phenomenon employing the zero-field splitting effect within the $S = 5/2$ local ground states of the Mn(II) ions. The theoretical expression of χ_{zfs} (33) is then

$$[3] \qquad \chi_{zfs} = \frac{Ng_{Mn}{}^2\beta^2}{4KT}\left[\frac{1 + 9\exp(2D/KT) + 25\exp(6D/KT)}{1 + \exp(2D/KT) + \exp(6D/KT)}\right]$$

$$\chi_m = \chi_{zfs} + \frac{Ng_{Cu}{}^2\beta^2}{3KT} S_{Cu}(S_{Cu} + 1) + TIP$$

where D is the axial zero-field splitting parameter for Mn(II). Least-squares fitting gave rise to $g_{Mn} = 1.99$, $g_{Cu} = 1.99$, and $D = 1.16$ cm^{-1}. The agreement factor F is equal to 2.5×10^{-3}.

Both analyses seem satisfactory, considering, however, the fact is that both situations usually concur in the case of Mn(II) and Mn(III) compounds. Therefore, the magnetic susceptibility expressed as a combination of the Mn···Mn interaction and the zero-field splitting may be more reasonable. The expression of Hiller (12) then was modified by replacing the $NS(S+1)g_{Mn}^2\beta^2/3KT$ term with χ_{zfs}, which is represented by eq. [3] (34). The final expression is as follows:

$$[4] \qquad \chi_{chain} = \frac{12}{35}\chi_{zfs}[A + Bx^2][1 + Cx + Dx^3] + \frac{Ng_{Cu}{}^2\beta^2}{3KT} S_{Cu}(S_{Cu} + 1) + TIP$$

$$\chi_m = \chi_{chain}/[1 - \chi_{chain}(2zJ'/Ng^2\beta^2)]$$

This led to the parameters $g_{Cu} = g_{Mn} = 1.99$, $J = -0.062$ cm^{-1}, $D = 0.73$ cm^{-1} and $zJ' = -0.005$ cm^{-1}. The agreement factor F is equal to 1.3×10^{-3}. The result that the D value is much larger than the absolute J value indicates

© 1998 NRC Canada

the presence of a very weak antiferromagnetic interaction between the Mn(II) ions within the chain and a dominant zero-field splitting within the $S = 5/2$ local ground states of the Mn(II) ions.

Conclusions

A new 1-D thiocyanate-bridged bimetallic compound $[Cu(en)_2Mn(NCS)_4(H_2O)_2]_n$ has been synthesized and structurally and magnetically characterized. The theoretical models presented fit the experimental data quantitatively, based on a vanishingly small interaction between the adjacent Cu(II) and Mn(II) ions, which leads to a weak intrachain AF coupling of manganese ions and a dominant zero-field splitting of the single Mn(II) ions. Apparently, similar examples or variations of such Cu-Mn compounds would help confirm and clarify the magnetic exchanges. The studies along this end are in progress.

Acknowledgements

This work was supported by the National Natural Science Foundation of China and State Key Laboratory of Structural Chemistry.

References

1. J.S. Miller, J.C. Calabrese, A.J. Epstein, R.W. Bigelow, J.H. Zang, and W.M. Reiff. J. Chem. Soc. Chem. Commun. 1026 (1986).
2. Y. Pei, M. Verdaguer, O. Kahn, J. Sletten, and J.P. Renard. J. Am. Chem. Soc. **108**, 428 (1986).
3. O. Kahn, Y. Pei, M. Verdaguer, J.P. Renard, and J. Sletten. J. Am. Chem. Soc. **110**, 782 (1988).
4. J.S. Miller and A.J. Epstein. Angew. Chem. Int. Ed. Engl. **33**, 385 (1994).
5. O. Kahn. *In* Molecular magnetism. VCH, New York. 1993.
6. T. Mallah, S. Thiebaut, M. Verdaguer, and P. Veillet. Science (Washington, D.C.) **262**, 1554 (1993).
7. D. Gatteschi. Adv. Mater. **6**, 635 (1994).
8. M.S. El Fallah, E. Rentschler, A. Caneschi, R. Sessoli, and D. Gatteschi. Angew. Chem. Int. Ed. Engl. **35**, 1947 (1996).
9. K. Nakatani, J.Y. Carriat, Y. Journaux, O. Kahn, F. Lloret, J.P. Renard, Y. Pei, J. Sletten, and M. Verdaguer. J. Am. Chem. Soc. **111**, 5739 (1989).
10. F. Sapina, E. Coronado, D.Beltran, and R. Burriel. J. Am. Chem. Soc. **116**, 11 566 (1994).
11. M. Ohba, N. Maruone, H. Okawa, T. Enoki, and J.-M. Latour. J. Am. Chem. Soc. **116**, 11 566 (1994).
12. D. Gatteschi, O. Kahn, J.S. Miller, and F. Palacio (*Editors*). NATO ASI Series, Ser. E. Kluwer, Dordrecht. 1991.
13. H.O. Stumpf, Y. Pei, O. Kahn, J. Sletten, and J.P. Renard. J. Am. Chem. Soc. **115**, 6738 (1993).
14. J. Kim, J.M. Lim, Y.-K. Choi, and Y. Do. Angew. Chem. Int. Ed. Engl. **35**, 998 (1996).
15. O. Kahn. Struct. Bonding (Berlin), **68**, 89 (1987).
16. B. Chiari, A. Cinti, O. Piovesana, and P.F. Zanazzi. Inorg. Chem. **34**, 2652 (1995).
17. M. Fettouhi, L. Ouahab, A. Boukhari, O. Cador, C. Mathoniere, and O. Kahn. Inorg. Chem. **35**, 4932 (1996).
18. W. Hiller, J. Strahle, A. Datz, M. Hanack, W.E. Hatfield, L.W. der Haar, and P. Gutlich. J. Am. Chem. Soc. **106**, 329 (1984).
19. SDP-PLUS. Enraf-Nonius, Delft, The Netherlands. 1985.
20. International tables for X-ray crystallography. Vol. 4. The Kynoch Press, Birmingham, England. 1974.
21. L. Pauling. *In* The nature of the chemical bonds. 3rd ed. *Edited by* Cornell University Press, Ithaca, New York. 1960. p. 260.
22. J. Ribas, C. Diaz, X. Solans, and M. Font-Bardia. Inorg. Chim. Acta, **231**, 229 (1995).
23. W. Haase, R. Mergehenn, and W. Krell. Z. Naturforsch. B: Anorg. Chem. Org. Chem. **31B**, 85 (1976).
24. J. Garaj. Inorg. Chem. **8**, 304 (1969).
25. J. Soldanova, M. Kabesova, and J. Gazo. Inorg. Chim. Acta, **76**, L203 (1983), and refs. therein.
26. K. Vicent, A. Esouer, E. Penalba, X. Solans, and M.F.-Badia. Inorg. Chim. Acta, **255**, 7 (1997).
27. B.W. Brown and E.C. Lingafelter. Acta Crystallogr. **17**, 1145 (1964).
28. J.M. Proctor, B.J. Hathaway, and P. Nicholls. J. Chem. Soc. A, 1678 (1968).
29. A.B.P. Lever and E. Mantovani. Inorg. Chem. **10**, 817 (1971).
30. M. Verdaguer, M. Julve, A. Michalowicz, and O. Kahn. Inorg. Chem. **22**, 2624 (1983).
31. Y. Pei, M. Verdaguer, O. Kahn, J. Sletten, and J.P. Renard. Inorg. Chem. **26**, 138 (1987).
32. A. Gleizes and M. Verdaguer. J. Am. Chem. Soc. **106**, 3727 (1984).
33. C.J. Oconnor. Prog. Inorg. Chem. **29**, 203 (1982).
34. M.L. Kirk, M.S. Lah, C. Raptopoulou, D.P. Kessissoglou, W.E. Hatfield, and L. Pecoraro. Inorg. Chem. **30**, 3900 (1991).

© 1998 NRC Canada

Synthesis and characterization of polyethylene glycol polyacrylamide copolymer (PEGA) resins containing carbohydrate ligands. Evaluation as supports for affinity chromatography

France-Isabelle Auzanneau, Mette Knak Christensen, Shannon L. Harris, Morten Meldal, and B. Mario Pinto

Can. J. Chem. Downloaded from www.nrcresearchpress.com by China University of Science and Technology on 09/05/12
For personal use only.

Abstract: The PEGA resin, a beaded polyethylene glycol dimethylacrylamide copolymer, was evaluated as an affinity support for the purification of carbohydrate-binding macromolecules, namely, the cation-independent mannosyl phosphate receptor (CI-MPR) and a polyclonal antibody directed against a *Streptococcus* Group A oligosaccharide. Two polyethylene glycol (PEG) derivatives, a di-acryloylated PEG_{1900} derivative or a longer di-acryloylated PEG_{4000} derivative, were used as cross-linkers. The longer cross-linker was synthesized in four steps from polyethylene glycol 4000. The mannosyl 6-phosphate (M6P)-containing immunoaffinity columns were prepared through the inverse suspension radical copolymerization of the corresponding allyl glycoside with acrylamide and the PEG cross-linker. The resin with the shorter cross-linker (PEG_{1900} derivative) had a 6.3% molar cross-linking while that with the longer cross-linker (PEG_{4000} derivative) had a 3.8% molar cross-linking. For the *Streptococcus* Group A trisaccharide-containing immunoaffinity columns, three PEGA affinity supports bearing free amino groups were prepared and subsequently substituted with a trisaccharide activated as its squarate adduct. While one resin contained the shorter cross-linker PEG_{1900} and had a 3% molar cross-linking, the other two resins contained the longer cross-linker PEG_{4000} with a molar cross-linking of 5% and 3%, respectively. In affinity chromatographic studies, the M6P-containing columns were ineffective in retaining the cation-independent mannosyl phosphate receptor (CI-MPR, ~ 215 kDa), whereas antibody (~ 150 kDa) retention was observed with two of the three *Streptococcus* Group A trisaccharide-containing immunoaffinity columns.

Key words: PEGA resins, immunoaffinity supports, carbohydrate ligands, antibody purification.

Résumé : On a évalué la résine PEGA, un copolymère en perle de polyéthylèneglycol et de diméthylacrylamide, comme support d'affinité pour la purification de macromolécules se liant aux carbohydrates, à savoir, le récepteur phosphate de mannosyle indépendant du cation («CI-MPR») et un anticorps polyclonal orienté vers un oligosaccharide d'un *Streptococcus* du groupe A. Pour la réticulation, on a utilisé deux dérivés du polyéthylèneglycol (PEG), un dérivé diacryloylé du PEG_{1900} ou un dérivé diacryloylé du PEG_{4000}. On a synthétisé le dérivé le plus long en quatre étapes à partir du polyéthylèneglycol 4000. On a préparé les colonnes d'immunoaffinité contenant du 6-phosphate de mannosyle (6PM) par le biais d'une copolymérisation radicalaire en suspension inverse du glucoside d'allyle correspondant avec de l'acrylamide et l'agent de réticulation du PEG. Dans le cas de la résine incorporant l'agent de réticulation le plus court (dérivé du PEG_{1900}), le niveau de réticulation est de 6,3 mol%; il est de 3,8 mol% dans le cas de l'agent de réticulation le plus long. Pour les colonnes d'immunoaffinité contenant le trisaccharide du *Streptococcus* du Groupe A, on a préparé trois supports d'affinité PEGA portant des groupes aminés libres qui ont été ultérieurement substitués par un trisaccharide activé sous la forme d'adduit. Alors qu'une résine contenait l'agent de réticulation le plus court, PEG_{1900}, et un taux de réticulation de 3 mol%, les deux autres contenaient l'agent plus long, PEG_{4000}, avec des taux de réticulations respectifs de 5 et 3 mol%. Lors des études de chromatographie d'affinité, les colonnes contenant du 6PM n'ont pas été efficaces pour retenir le récepteur phosphate de mannosyle cation indépendant (CI-MPR, ~215 kDa) alors que l'on a observé une rétention de l'anticorps (~ 150 kDa) avec deux des trois colonnes d'immunoaffinité contenant du trisaccharide de *Streptococcus* du Groupe A.

Mots clés : résines de PEGA, supports d'immunoaffinité, ligands carbohydrates, purification d'anticorps.

[Traduit par la Rédaction]

Received January 20, 1998.

F.-I. Auzanneau,[1] S.L. Harris, and B. M. Pinto.[2] Department of Chemistry, Simon Fraser University, Burnaby, BC V5A 1S6, Canada.
M.K. Christensen and M. Meldal. Department of Chemistry, Carlsberg Laboratory, Gamle Carlsberg Vej 10, DK 2500 Valby-Copenhagen, Denmark.

[1]Present address: Pasteur Mérieux Connaught, 1755 Steeles Ave. W., Toronto, ON M2R 3T4, Canada.
[2]Author to whom correspondence may be addressed. Telephone: (604) 291-4327. Fax: (604) 291-3765. E-mail: bpinto@sfu.ca

 © 1998 NRC Canada

Can. J. Chem. Downloaded from www.nrcresearchpress.com by China University of Science and Technology on 09/05/12
For personal use only.

Fig. 1. Schematic representation of immunoaffinity columns **15** and **16**.

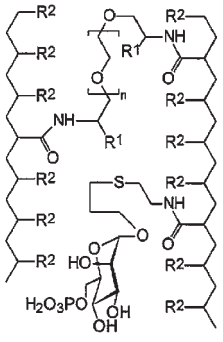

15 $R^1 = CH_3$, $R^2 = CONH_2$, n = 43-45
16 $R^1 = H$, $R^2 = CONH_2$, n = 77-100

Introduction

Affinity chromatography is a method of choice to purify enzymes, antibodies, lectins, and other macromolecules by binding selectively to a well-defined ligand. Methods to prepare affinity columns using carbohydrate-bearing adsorbents have been reviewed (1). The materials used for the preparation of affinity adsorbents are carbohydrate polymers such as agarose or cellulose (1, 2), polyacrylamide polymers (2–5), or porous glass beads (1). An ideal support material should have good permeability to and be compatible with biological molecules; it should be stable to chemical reagents and resistant to microbial and enzymic degradation. The PEGA resin, a beaded polyethylene glycol dimethylacrylamide copolymer (6–8), has been developed for solid phase peptide synthesis and has shown a very high permeability to chemicals. It has also been used in biochemical assays in which a protease (9) and a glycosyltransferase enzyme (10) have been tested for their ability to enter the polymer network. While this highly cross-linked resin (25% molar cross-linking) was shown to be permeable to the 27 kDa protease, the 50 kDa glycosyltransferase was not able to enter the resin network. However, an analogous PEGA resin, in which acrylamide replaced dimethylacrylamide and which had a lower degree of cross-linking (5%), was highly permeable to the glycosyltransferase (10) as well as to globular proteins of up to 66 kDa (8). The compatibility and permeability of the PEGA resins to biological macromolecules prompted us to evaluate the resins as affinity supports for the purification of carbohydrate-binding macromolecules such as the cation-independent mannosyl phosphate receptors (CI-MPRs) and the *Streptococcus* Group A-specific anti-carbohydrate polyclonal antibodies.

Results and discussion

The CI-MPRs are membrane glycoproteins with an apparent molecular weight of 215 kDa and whose binding to lysosomal enzymes bearing terminal mannosyl 6-phosphate residues (M6P) is partly reponsible for intracellular transport and binding of the enzyme to the cell surface (11–17). To attempt the purification of CI-MPRs using a PEGA-based immunoaffinity column, we prepared an M6P derivative containing a reactive double bond that allowed its copolymerization with the other constituents of the resin. Allyl α-D-mannopyranoside (18, 19) was trimethylsilylated to give the persilylated derivative **1**, which was then selectively hydrolyzed (20, 21) to give the alcohol **2**. Phosphorylation of **2** with phosphorus oxychloride followed by hydrolysis gave the phosphate **3**. To introduce a spacer-arm between the oligosaccharide and the solid support, the phosphate **3** was converted directly to the corresponding cysteamine adduct **4** by addition of cysteamine hydrochloride to the allyl group (22). The aminated derivative **4** was obtained in 73% yield after RP-HPLC purification and it was subsequently acryloylated to give the monomer **5**. The acryloylation of **4** using acryloyl chloride as the acylating agent gave only low yields of the desired acryloylated derivative **5**, together with side products resulting from the acryloylation of the phosphate group. Thus, the less reactive 3,4-dihydro-4-oxo-1,2,3-benzotriazin-3-yl acrylate **6**, prepared in situ from the reaction of 3,4-dihydro-4-oxo-1,2,3-benzotriazine (DhbtOH) with acryloyl chloride in the presence of *N*-ethylmorpholine, was reacted with the phosphate

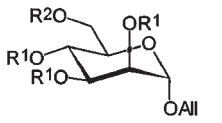

1 $R^1 = R^2 = SiMe_3$
2 $R^1 = SiMe_3$, $R^2 = H$
3 $R^1 = H$, $R^2 = PO_3H_2$

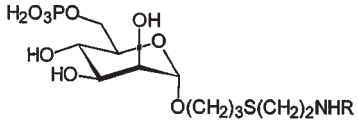

4 R= H
5 R = COCH=CH_2

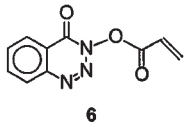

6

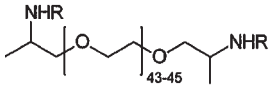

7 R = $COCHCH_2$
8 R = 0.5 $COCHCH_2$, 0.5 H

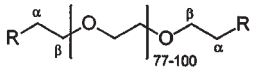

9 R = OH
10 R = Cl
11 R = N_3
12 R = NH_2
13 R = $NHCOCHCH_2$
14 R = 0.8 $NHCOCHCH_2$, 0.2 NH_2

4. The acryloylated monomer **5** was obtained in 77% yield and was used for the preparation of the immunoaffinity columns **15** and **16** (see Fig. 1). Since it was shown that the permeability of the PEGA resins depended on the degree of molar cross-linking as well as the length of the cross-linker (8), we prepared two affinity columns in which the cross-linker was either the di-acryloylated PEG_{1900} derivative **7** (8) or the longer di-acryloylated PEG_{4000} derivative **13**. The latter cross-linker was synthesized in four steps from polyethylene glycol 4000 **9** (PEG_{4000}). Thus, treatment of **9** with

© 1998 NRC Canada

Can. J. Chem. Downloaded from www.nrcresearchpress.com by China University of Science and Technology on 09/05/12
For personal use only.

Fig. 2. ^{13}C NMR spectra of PEG derivatives **9–13**.

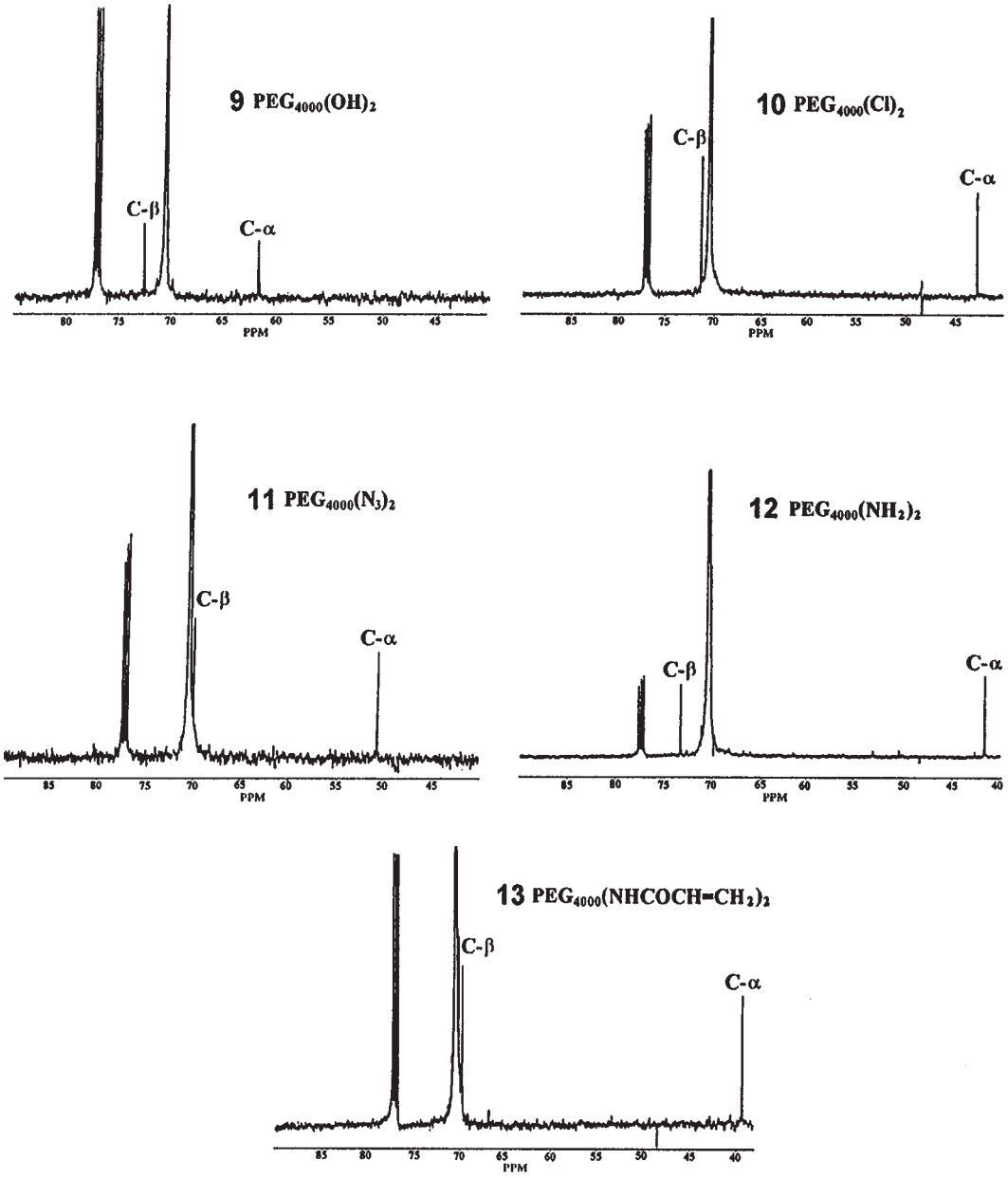

thionyl chloride gave the corresponding dichloride **10**, which was converted into the diazide **11** with sodium azide. The diazide **11** was, in turn, submitted to high-pressure hydrogenation in the presence of palladium-on-carbon catalyst to give the diamine **12**, which was acryloylated to yield the cross-linker **13**. Since separation of these PEG derivatives was not possible by common purification means, the reactions were monitored by ^{13}C NMR spectroscopy and driven to completion. Figure 2 shows that the signals corresponding to the α and β carbons of the PEG chains could be easily identified for each of compounds **9–13** and appear at very different chemical shifts depending on the subtitution of C-α. Therefore, the purity and integrity of these derivatives were assessed by ^{13}C NMR spectroscopy. Copolymerization of the M6P derivative **5** with acrylamide and the cross-linkers **7** or **13** was performed, as previously described (8), by inverse suspension radical polymerization (23), using sorbitan monolaurate as a droplet stabilizer, ammonium persulfate as the initiator, and *N*,*N*,*N*′,*N*′-tetramethylethylene diamine (TMEDA) as a promoter. The resin **15**, which used the shorter cross-linker **7**, was prepared to have a 6.3% molar cross-linking while the resin **16**, which used the longer cross-linker **13**, was designed to have a 3.8% molar cross-linking. These differences resulted in very different swelling abilities of the resins **15** and **16**, which were 13 mL and 22 mL per gram of resin, respectively. The incorporation of the sugar into resins **15** and **16** was confirmed by the ^{13}C NMR spectra in which the anomeric carbon atom gave a signal at 102 ppm (see Fig. 3 for resin **15**).

Purification of the receptor, CI-MPR, on these affinity columns was then attempted, as described previously (24); however, the receptor was not retained on either resin. Since

© 1998 NRC Canada

Can. J. Chem. Downloaded from www.nrcresearchpress.com by China University of Science and Technology on 09/05/12
For personal use only.

Fig. 3. ^{13}C NMR spectrum of resin **15**.

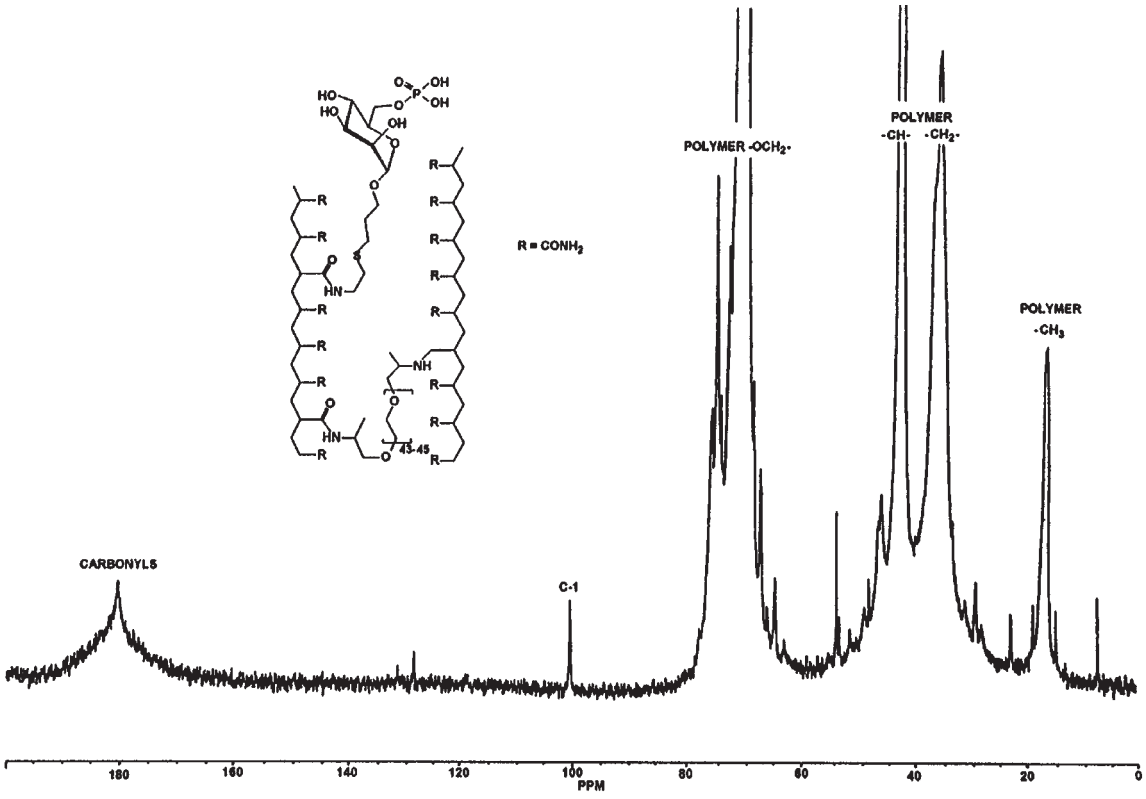

Table 1. Characteristics of PEGA resins **17–19** and immunoaffinity columns **22–24**.

PEGA resin	**17**	**18**	**19**
$[NH_2]$ mmol/g	0.15	0.08	0.09
Cross-linker	PEG_{1900}	PEG_{4000}	PEG_{4000}
Molar cross-linking (%)	3	6	3.5
Swelling in water (mL/g)	34	35	35
Immunoaffinity column	**22**	**23**	**24**
Yield of sugar coupling (%)	59	52	57
Sugar content (μmol)	4.45	2.1	2.8
Sugar loading (μmol/mL)	2.5	1.1	1.5
Weight of protein retained (μg)	71.2	0	90.1
Ratio of protein retained (%)	3	0	6

purification of the CI-MPR had been achieved by Sahagian et al. (25), using the M6P derivative **4** coupled to cyanogen bromide activated Sepharose, we concluded that the M6P unit was inaccessible to the binding site of the CI-MPR either because the spacer-arm was too short or because the receptor was too big (~ 215 kDa) to enter the resin beads of either **15** or **16**. To investigate the latter hypothesis we then attempted the purification of a smaller protein: a polyclonal IgG antibody (~ 150 kDa), using a similar solid support.

The β-hemolytic *Streptococcus* Group A is a common infective agent in humans, causing streptococcal pharyngitis, some forms of pneumonia, and toxic shock-like syndrome (26, 27). It can also act as a trigger of acute rheumatic fever, heart valve diseases, or glomerulonephritis (26, 28) resulting from an autoimmune reaction in which antibodies directed against streptococcal antigens lead an attack against the host tissues (29–33). To characterize these autoimmune responses, mono- and polyclonal antibodies have been raised against oligosaccharide portions of the *Streptococcus* Group A polysaccharide and it has been shown that the branched trisaccharide α-L-Rha*p*-(1→2)-[β-D-GlcNAc*p*-(1→3)]-α-L-Rha*p* was the smallest oligosaccharide recognized distinctly by the antibodies (34, 35). Since this trisaccharide **20** had been prepared previously (5, 36), we decided to prepare three PEGA affinity supports bearing free amino groups and to subsequently couple the activated trisaccharide to these supports. As described previously (8), the molar cross-linking of such resins as well as the amount of free amino groups incorporated in the network depends on both the degree of acryloylation of the PEG monomer used in the copolymerization and the ratio of the monomer to diluent used. Thus, we prepared resins **17–19** using the partially acryloylated monomers **8** and **14**. While resin **17** contained the shorter cross-linker PEG_{1900} and had a 3% molar cross-linking, resins **18** and **19** contained the longer cross-linker PEG_{4000} with a molar cross-linking of 5% and 3%, respectively. The swelling abilities of these copolymers in water were shown to be very similar (~ 35 mL/g). The number of free amino groups per gram of resin was measured for resins **17–19** by the bromophenol blue method (8) and the results are reported in Table 1. The trisaccharide **20** was coupled to the PEGA copolymers **17–19** using the method recently developed by Hindsgaul and co-workers (37) to give the immunoaffinity columns **22–24**, respectively. Thus, aliquots of the aminated oligosaccharide **20** were reacted with one equivalent of 3,4-diethoxy-3-cyclobutene-1,2-dione (diethyl squarate) and the reactions were followed by TLC, which

© 1998 NRC Canada

Can. J. Chem. Downloaded from www.nrcresearchpress.com by China University of Science and Technology on 09/05/12
For personal use only.

Fig. 4. Schematic representation of immunoaffinity columns **22–24**.

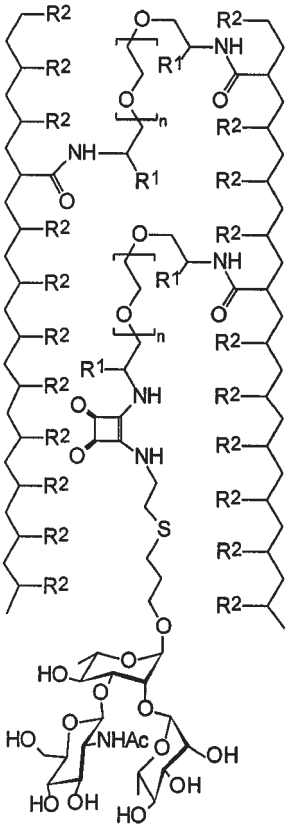

22 $R^1 = CH_3$, $R^2 = CONH_2$, n = 43-45
23, **24** $R^1 = H$, $R^2 = CONH_2$, n = 77-100

showed the complete disappearance of the starting material and the appearance of a less polar, UV-absorbent compound that was assumed to be the oligosaccharide–squarate adduct **21**. The reaction mixtures were concentrated to dryness and the crude adducts were coupled directly to the PEGA supports in a pH 10 buffer. After draining, the columns were washed until no more unreacted sugar could be detected (38) in the eluent. The amount of unreacted sugar was measured for each column using the method of Dubois et al. (38) and, by difference, the amount of trisaccharide incorporated into each column was calculated. Whether the trisaccharide was used in excess or not, the yield of the coupling reaction was greater than 50% (Table 1). The remaining free amino groups were capped by acetylation, thus giving the three immunoaffinity columns **22–24** (Fig. 4), which had the same swelling abilities as the copolymers from which they were obtained. Since resin **17** contained a higher number of free amino groups than resins **18** or **19**, the immunoaffinity column **22** presented the highest sugar loading (Table 1).

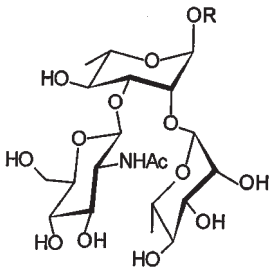

20 $R = (CH_2)_3S(CH_2)_2NH_2$
21 $R = (CH_2)_3S(CH_2)_2NH$ OEt

The availability of the immobilized trisaccharide **20** to antibodies (Abs) was investigated by using the immunoaffinity reagents **22** and **24** to purify the trisaccharide **20**-reactive Abs from polyclonal Abs raised against a pentasaccharide portion of the *Streptococcus* Group A polysaccharide (35). Trisaccharide **20**-reactive Abs are present in the polyclonal Abs since the latter were shown to react with the trisaccharide **20** (35).

For affinity reagent **23**, none of the fractions eluted with GlcNAc exhibited an absorbance at 280 nm. Moreover, the amount of protein collected during the initial TBS wash was equal to the total amount of protein added to the column. Therefore, no Ab was bound. However, fractions eluted with GlcNAc from affinity reagents **22** and **24** did contain 70 mg and 90 mg of protein, respectively, corresponding to 3% and 6%, respectively, of the total protein added to the columns. The columns could be reused without loss of binding, suggesting that all bound protein had been eluted. Thus, PEGA **18**, which was used to make affinity reagents **23**, does not appear to be permeable to Abs. Presumably, the higher degree of molar cross-linking found in PEGA **18** results in a pore opening that is too small to allow the passage of Abs. In contrast, the lower degree of molar cross-linking in PEGAs **17** and **19** results in a resin that is permeable to Abs.

The Abs that were eluted with GlcNAc from the affinity reagents **22** and **24** were compared to the Abs purified by caprylic acid precipitation alone or those obtained by sequential purification on protein A and BSA affinity columns (35). The binding of the different Ab preparations to a linear trisaccharide–BSA conjugate (Lin Tri-BSA) (35), the trisaccharide **20**–BSA conjugate, a pentasaccharide–BSA conjugate, and *Streptococcus* Group A bacteria was determined by ELISA and the data are shown in Table 2 (the cross-reaction of the different oligosaccharides with the polyclonal antibody against the pentasaccharide conjugate was demonstrated previously (35)). While purification with the affinity reagents **22** and **24** does decrease the background binding to BSA as compared to caprylic acid precipitation alone, the binding to BSA is still above the signal for binding to *Streptococcus* Group A and Lin Tri-BSA; however, signals for binding to trisaccharide **20** and the pentasaccharide could be detected. By way of comparison, purification with a pentasaccharide-UltraLinkTM reagent (5) yields a greater reduction in background binding to BSA as compared to the PEGA reagents, and gives signals above background for all antigens tested (data not shown). Abs purified with protein A and BSA affinity columns still have lower background binding to BSA. Thus, while the trisaccharide **20** immobilized on affinity reagents **22** and **24** was available for Ab binding, it appears that purification on protein A and BSA affinity columns is a more efficient

© 1998 NRC Canada

Can. J. Chem. Downloaded from www.nrcresearchpress.com by China University of Science and Technology on 09/05/12
For personal use only.

Table 2. Binding of anti-pentasaccharide polyclonal Abs, purified by four different methods, to carbohydrate antigens.

	Polyclonal Ab preparation			
Immobilized antigen	Purified with **22**	Purified with **24**	Caprylic acid precipitation	Protein A and BSA columns
Pentasaccharide–BSA[35]	1354[a]	1364	1190	1185
BSA	696	724	1192	39
Blotto	26	14	22	14
Lin Tri-BSA[35]	341	334	319	354
BSA	338	332	452	26
Blotto	14	10	13	8
Trisaccharide **20**–BSA[35]	418	418	368	380
BSA	276	284	362	22
Blotto	14	10	14	11
Streptococcus Group A	122	117	116	202
BSA	658	676	1017	47
Blotto	37	26	20	16

[a] $(A_{405} - A_{490}) \times 1000$.

Table 3. Selected ^{1}H and ^{13}C NMR shifts (ppm) for compounds **2–6**.

	2[a]	**3**[a]	**4**[b]	**5**[b]	**6**[b]
			^{1}H NMR (500 MHz)		
H-1	4.66	4.67	4.88	4.83	4.83
H-2	3.82	3.83	3.92	3.91	3.92
H-3	3.82	3.83	3.78	3.77	3.80
H-4	3.85	3.91	3.70	3.68	3.74
H-5	3.52	3.61	3.76	3.74	3.74
H-6	3.74	3.72	4.11	4.08	4.09
H-6′	3.79	3.79	4.17	4.17	4.09
-OCH_2-	3.98, 4.21	3.99, 4.20	4.05, 4.21	3.57, 3.80	3.58, 3.81
-CH=	5.86	5.92	5.95		6.26
CH_2=	5.19, 5.29	5.21, 5.30	5.25, 5.33		5.77, 6.18
-CH_2-CH_2- CH_2-S				1.86	1.88
-CH_2-CH_2- CH_2-S				2.63	2.65
-S-CH_2-CH_2-N				2.72	2.73
-S-CH_2-CH_2-N				3.18	3.48
			^{13}C NMR (125.77 MHz)		
C-1	99.88	100.13	101.63	102.37	102.36
C-2	72.77[c]	72.47[c]	72.96[c]	72.47	72.49
C-3	73.52[c]	73.62[c]	73.97[c]	72.98	72.98
C-4	67.45	68.11	68.72	68.80	68.74
C-5	74.81	73.94	74.00	74.20	73.98
C-6	62.60	62.23	67.26	64.40	67.36
-OCH_2-	68.42	67.80	70.80	68.80	68.74
-CH=	134.47	134.10	135.71		132.29
CH_2=	116.39	116.72	121.11		129.97
-CH_2-CH_2-CH_2-S				30.77	30.95
-CH_2-CH_2-CH_2-S				30.07	30.35
-S-CH_2-CH_2-N				30.77	32.91
-S-CH_2-CH_2-N				40.85	41.25

[a] For solutions in $CDCl_3$.
[b] For solutions in D_2O.
[c] Assignments may be reversed.

© 1998 NRC Canada

Can. J. Chem. Downloaded from www.nrcresearchpress.com by China University of Science and Technology on 09/05/12
For personal use only.

method for preparing polyclonal Abs with low binding to BSA.

The ratio of eluted protein to total immobilized carbohydrate can be used to compare the different affinity reagents. This ratio is 16 µg protein per µmol of immobilized carbohydrate for reagent **22** and 33 µg protein per µmol of immobilized carbohydrate for the reagent **24**. Thus, PEGA resins with 3% molar cross-linking are permeable to Abs. Moreover, the affinity reagent **24**, made from the PEGA containing the longer linker arm PEG_{4000}, provided the best access to immobilized carbohydrate.

Experimental section

General procedures

TLC was performed on Merck Silica Gel 60 F_{254} aluminum sheets with detection by charring with sulfuric acid, and by UV light. Vacuum liquid chromatography (VLC) (39) was performed on Merck Silica Gel 60 H (0.040–0.060 mm), and VLC under dry conditions was performed on dried silica gel (120°C; >24 h) with solvents dried over molecular sieves. Solvents were distilled and dried according to standard procedures (40). Concentrations were performed under reduced pressure at temperatures <40°C. Commercially available zinc was "activated" by washing with 1 M HCl and water and drying at 120°C overnight. Hydrogenation was performed in a Parr 4842 apparatus. Preparative HPLC reverse-phase separations were performed on a Waters HPLC system using a Delta PAK C-18 column (300 Å, 25 mm × 200 mm) with a flow rate of 10 cm^3 min^{-1} and detection at 215 nm with a photodiode array detector (Waters M 991); solvent system A: 0.1% TFA; B: 0.1% TFA in 90% acetonitrile – 10% water. Gel filtrations were performed on Sephadex G-10 (Pharmacia) with a flow rate of 1 mL/min and detection at 230 nm. ^{1}H NMR spectra were recorded on a Bruker AM500 spectrometer operating at 500.13 MHz. ^{13}C NMR spectra were recorded on DRX 250 or AM 500 Bruker spectrometers operating at 62.90 and 125.76 MHz, respectively. Chemical shifts are given in ppm and referenced to internal $SiMe_4$ (δ_H, δ_C 0.00) for solutions in $CDCl_3$ at 300 K, and to external dioxane (δ_H 3.76, δ_C 67.40) for solutions in D_2O at 300 K. For the assignment of signals, proton–proton and carbon–proton shift correlation spectroscopy were used. Optical rotations were recorded on a Perkin–Elmer 241 polarimeter. Elemental analysis was carried out at LEO Pharmaceutical Products, Denmark. Electrospray mass spectrometry was performed in the negative mode for deprotected carbohydrates on a VG Fisions Quattro instrument. Polymerizations were performed, as described previously (8), in a 250 mL or 850 mL laboratory-scale suspension polymerization apparatus (23) equipped with a four-blade stirrer.

Measurement of swelling

A weighed amount of dry resin was placed in a syringe equipped with a sintered Teflon filter and was allowed to swell in water. The excess solvent was drained, and the bed volume was measured and related to the sample weight to obtain the swelling ability.

Allyl 2,3,4,6-tetra-*O*-(trimethylsilyl)-α-D-mannopyranoside (1)

Chlorotrimethylsilane (35 mL, 279.3 mmol) was added dropwise over a period of 30 min to a solution of allyl α-D-mannopyranoside (19) (12.3 g, 55.8 mmol) in pyridine (50 mL). The mixture was stirred for 1 h, diluted with CH_2Cl_2 (50 mL), and left overnight at room temperature. The solids were removed by filtration, washed with toluene, and the combined filtrate and washings were concentrated. The residue was diluted with toluene (100 mL), filtered, and concentrated to give **1** (25.2 g, 89%), $[\alpha]_D^{25}$ +55° (*c* 3, CH_2Cl_2). Anal. calcd. for $C_{21}H_{48}O_6Si_4$: C 49.56, H 9.50; found: C 49.37, H 9.27.

Allyl 2,3,4-tri-*O*-(trimethylsilyl)-α-D-mannopyranoside (2)

Compound **1** (18.4 g, 36.2 mmol) was dissolved in methanol (100 mL) and a saturated solution of potassium carbonate in anhydrous methanol (1 mL) was added. The mixture was stirred for 1 h at room temperature, toluene (100 mL) was added, and the mixture was concentrated. Purification by VLC (light petroleum) and crystallization from acetonitrile yielded the *title compound* **2** (9.55 g, 60%); $[\alpha]_D^{25}$ +55° (*c* 1.3, CH_2Cl_2); mp 66–67°C. ^{1}H and ^{13}C NMR data are presented in Table 3. Anal. calcd. for $C_{18}H_{40}O_6Si_3$: C 49.50, H 9.23; found: C 49.27, H 9.25.

3-(2-Aminoethylthio)propyl α-D-mannopyranoside 6-phosphate (4)

$POCl_3$ (1.07 cm^3, 11.5 mmol) was added to a solution of the alcohol **2** (5 g, 11.4 mmol) and *N*-ethylmorpholine (1.6 mL, 12.65 mmol) in dry CH_2Cl_2 (25 mL), and the mixture was stirred overnight at room temperature. After concentration to half volume the mixture was diluted with hexane (13 mL) and stirred for 10 min at 0°C. Solids were removed by filtration and the filtrate was concentrated. The residue was dissolved in CH_2Cl_2 (25 mL) and washed with an ice-water HCl solution (0.4%, 30 mL) and with water. The organic phase was concentrated, and the resulting crude chlorophosphate ester was hydrolyzed by concentration with water (3 × 100 mL) at 40°C to give the phosphate **3** (3.0 g, 88%), which was characterized by ^{1}H and ^{13}C NMR (Table 3) and used directly in the next step. The crude allyl glycoside **3** (3.0 g, 10.0 mmol) was dissolved in degassed water (25 mL), cysteamine hydrochloride (12.6 g, 10.9 mmol) was added, and the solution, kept under Ar atmosphere, was irradiated with UV light for 4 h and then left standing at room temperature for 2 days. The cysteamine adduct **4** was purified by preparative RP-HPLC using solvent A (t_r 45 min) to yield the *title compound* **4** (2.76 g, 73%) as a hygroscopic syrup. $[\alpha]_D^{25}$ +36° (*c* 2.2, water). ^{1}H and ^{13}C NMR data are presented in Table 3. MS, *m/z*, M calcd. for $C_{11}H_{24}NO_9PS$: 377.09; found (M – H^+): 376.3.

3-[(2-Acrylamido)ethylthio]propyl α-D-mannopyranoside 6-phosphate (5)

Dhbt-OH (0.82 g, 5 mmol) and *N*-ethylmorpholine (640 µL, 5 mmol) were dissolved in DMF (5 mL) and acryloyl chloride (450 µL, 5.5 mmol) was added. After 30 min, 2 mL of this mixture was added to a solution of compound **4** (0.51 g, 1.4 mmol) in water (2 mL, degassed)

© 1998 NRC Canada

Can. J. Chem. Downloaded from www.nrcresearchpress.com by China University of Science and Technology on 09/05/12
For personal use only.

and DMF (3 mL). *N*-Ethylmorpholine (0.17 mL, 1.4 mmol) was then added in small portions. After 3.5 h, water (10 mL) was added to the reaction mixture, which was then cooled to 0°C (10 min) and filtered. The water was evaporated and the mixture was directly purified by preparative RP-HPLC using, first, solvent A (100%) for 60 min, then the linear gradient 0–100% solvent B for 100 min (t_r 92 min) to yield the *title compound* **5** (0.45 g, 77%) as a hygroscopic syrup. $[\alpha]_D^{25}$ +46° (*c* 1.7, water). ^{1}H and ^{13}C NMR data are presented in Table 3. MS, *m/z*, M calcd. for $C_{14}H_{26}NO_{10}PS$: 431.40; found ($M - H^+$): 430.4.

Bis-chloro-polyethylene glycol 4000 (10)

PEG_{4000} **9** (50 g, ~12.5 mmol) was melted by heating in an oil bath. Thionyl chloride (3.65 cm^3, 50 mmol) was added with stirring at 100°C over a period of 30 min. The mixture was stirred at 100°C overnight, and then slowly poured into cold (0°C) stirred diethyl ether (200 mL). The resulting white powder was filtered off, washed three times with diethyl ether, and dried to yield the *title compound* **10** (47.1 g, 93%). ^{13}C NMR (125.76 MHz, $CDCl_3$) δ_C: 42.59 (Cl-*C*H_2-CH_2-), 71.33 (Cl-CH_2-*C*H_2-). For compound **9** δ_C: 61.73 (HO-*C*H_2-CH_2-), 72.54 (HO-CH_2-*C*H_2-).

Bis-azido-polyethylene glycol 4000 (11)

Compound **10** (46.07 g, ~11.4 mmol) was suspended in DMF (75 mL), and sodium azide (1.63 g, 25.1 mmol) was added. The suspension was slowly heated to 50°C, tetradecyl trimethylammonium bromide (150 mg) was added, and the mixture was heated to 110°C. After 4 h, the reaction mixture was cooled to room temperature, filtered, and concentrated. The residue was dried under high vacuum for 2 days to give **11** (46.2 g, 100%). ^{13}C NMR (125.76 MHz, $CDCl_3$) δ_C: 50.62 (N_3-*C*H_2-CH_2-), 69.91 (N_3-CH_2-*C*H_2-).

Bis-amino-polyethylene glycol 4000 (12)

Compound **11** (45.7 g, ~11.3 mmol) was dissolved in DMF (25 mL), and the solution was transferred to a Parr apparatus. Palladium-on-charcoal (10%, 200 mg) was added and the mixture was hydrogenated overnight at 80 bar (1 bar = 100 kPa). The suspension was diluted with CH_2Cl_2, filtered through Celite, and concentrated. The residue was taken up in water, the remaining Pd/C was precipitated by centrifugation at 13 000 rpm for 10 min, and the supernatant was filtered through Celite. The filtrate was lyophilized to give compound **12** (36.6 g, 81%) as a colorless syrup. ^{13}C NMR (125.76 MHz, $CDCl_3$) δ_C: 41.65 (H_2N-*C*H_2-CH_2-), 73.23 (H_2N-CH_2-*C*H_2-).

Bis-acrylamido-polyethylene glycol 4000 (13)

Compound **12** (36.2 g, ~9.1 mmol) was dissolved in CH_2Cl_2 (20 mL), the solution was cooled to 0°C, and triethylamine (2.5 mL, 18.2 mmol) was added, followed by acryloyl chloride (1.48 mL, 18.2 mmol). The reaction mixture was stirred at 0°C for 2 h, filtered, and concentrated. The residue was dissolved in CH_2Cl_2, filtered, concentrated, and dried under high vacuum to give **13** (35.0 g, 94%). ^{13}C NMR (125.76 MHz, $CDCl_3$) δ_C: 39.28 (($CH_2CHCONH)_2$-*C*H_2-CH_2-), 69.75 (($CH_2CHCONH)_2$-CH_2-*C*H_2-), 126.05 (CH_2=), 131.07 (=CH-).

Partially acryloylated bis-amino-polyethylene glycol 4000 (14)

A solution of acryloyl chloride (275 µL, 3.38 mmol) in anhydrous CH_2Cl_2 (10 mL) was added dropwise to a solution of the diaminated PEG_{4000} **12** (17 g, 4.25 mmol) in anhydrous CH_2Cl_2 (12 mL) stirred at 0°C. The mixture was stirred at room temperature for 30 min, concentrated, and dried under high vacuum to give crude $PEG_{4000}(Acr)_{0.8}$ **14** (17.5 g), which was used directly in the preparation of resin **18**. A second portion of **12** (17 g, 4.25 mmol) was acryloylated under the same conditions as described above and the resulting partially acryloylated monomer **14** was used in the preparation of resin **19**.

Preparation of the immunoaffinity column (15)

A mixture of *n*-heptane–CCl_4 (6:4, v/v, 140 mL) was purged with argon for 30 min in the 250 mL polymerization flask. The solution was warmed to 70°C and the stirring speed adjusted to 650 rpm. A mixture of the monomers **7** (9.8 g, 4.64 mmol) (8), **5** (100 mg, 0.23 mmol), and acrylamide (4.9 g, 69 mmol) in water (27 mL) was purged with argon for 30 min. Solutions of sorbitan monolaurate (166 mg) in DMF (750 mL) and ammonium persulfate (205 mg) in water (750 mL) were added to the monomer mixture that was, in turn, quickly poured into the polymerization flask. After 4 min, tetramethylethylenediamine (TMEDA, 600 mL) was added and the sticky point was reached within 30 s. The reaction was allowed to proceed for 4 h at 650 rpm and 70°C and the mixture was cooled to room temperature. The resin was filtered off, washed with ethanol and water, and sieved through a steel net (1 mm^2 holes). It was transferred back to the filter, washed with ethanol, and dried successively under low vacuum (water pump), then high vacuum (freeze-dryer) for 2 days to give 11.3 g of resin **15** (76%). Molar cross-linking: 6.5%. Swelling ability in water: 13 mL/g. ^{13}C NMR is shown in Fig. 3.

Preparation of the immunoaffinity column (16)

Copolymerization of compound **5** (500 mg, 1.16 mmol), bis-2-acrylamido-PEG_{4000} **13** (9.3 g, 2.25 mmol), and acrylamide (4.0 g, 56.3 mmol) was performed as described for the preparation of the resin **15**, and gave 10.4 g of resin **16** (75%). Molar cross-linking: 4%. Swelling ability in water: 22 mL/g.

Preparation of the PEGA resin (17)

Copolymerization of partially acryloylated PEG_{1900} **8** (8) (60 g, 29 mmol) and acrylamide (10 g, 140 mmol) was performed in the 850 mL polymerization flask essentially as described for the preparation of resin **15**. The volumes and weights of the reagents and solvents were as follows: 470 mL of *n*-heptane–CCl_4 (6:4, v/v), 90 mL of water to dissolve the monomers, 1 g of sorbitan monolaurate in 2.5 mL of DMF, 700 mg of ammonium persulfate in 2.5 mL of water, 2 mL of TMEDA. The polymerization was performed with stirring at 1800 rpm and gave 27.4 g of the resin **17** (91%). Loading, as measured by the bromophenol blue test (8), [NH_2, HCl] = 0.15 mmol/g. Molar cross-linking: 3.5%. Swelling ability in water: 34 mL/g.

© 1998 NRC Canada

Can. J. Chem. Downloaded from www.nrcresearchpress.com by China University of Science and Technology on 09/05/12
For personal use only.

Preparation of the PEGA resin (18)

Copolymerization of partially acryloylated PEG_{4000} **14** (4.25 mmol) and acrylamide (1.43 g, 20.1 mmol) was performed in the 250 mL polymerization flask essentially as described for the preparation of resin **15**. The volumes and weights of the reagents and solvents were as follows: 138 mL of *n*-heptane–CCl_4 (6:4, v/v), 28 mL of water to dissolve the monomers, 350 g of sorbitan monolaurate in 730 µL of DMF, 250 mg of ammonium persulfate in 730 µL of water, 700 µL of TMEDA. The polymerization was performed with stirring at 1800 rpm and gave 7.9 g of the resin **18** (79%). Loading as measured by the bromophenol blue test (8), [NH_2, HCl] = 0.08 mmol/g. Molar cross-linking: 6%. Swelling ability in water: 35 mL/g.

Preparation of the PEGA resin (19)

Copolymerization of partially acryloylated PEG_{4000} **14** (4.25 mmol) and acrylamide (2.21 g, 31.1 mmol) was performed in the 250 mL polymerization flask essentially as described for the preparation of the resin **15**. The volumes and weights of the reagents and solvents used as well as the stirring speed were identical to those used in the preparation of the resin **18**. The polymerization gave 8.9 g of the resin **19** (79%). Loading, as measured by the bromophenol blue test (8), [NH_2, HCl] = 0.09 mmol/g. Molar cross-linking: 3.5%. Swelling ability in water: 35 mL/g.

3-[2-*N*-(3,4-Dione-2-ethoxycyclobutene)aminoethylthio]propyl 3-*O*-(2-acetamido-2-deoxy-β-D-glucopyranosyl)-2-*O*-(α-L-rhamnopyranosyl)-α-L-rhamnopyranoside (21)

The trisaccharide **20** (36) (4.7 mg, 7.45 µmol) was dissolved in freshly distilled MeOH (500 µL) and a solution (10 µL/mL, 110 µL, 7.45 µmol) of 3,4-diethoxy-3-cyclobutene-1,2-dione (diethyl squarate) in freshly distilled methanol was added. The reaction mixture was left standing at room temperature for 3 h, after which time TLC (EtOAc–MeOH–H_2O, 6:3:1) showed that the starting amine had been quantitatively converted to one homogeneous spot that was assumed to be the trisaccharide **21** ($R_f = 0 \rightarrow 0.61$). The reaction mixture was concentrated to dryness and the trisaccharide **21** was used without further purification in the conjugation to the PEGA columns **17** to give the immunoaffinity column **22**. Aliquots of the trisaccharide **20** (5.95 µmol and 6.66 µmol) were treated with diethyl squarate under the same conditions as described above and the resulting squarate adducts were used for coupling to the PEGA resins **18**, **19** to give the immunoaffinity columns **23**, **24**, respectively.

Preparation of the immunoaffinity column (22)

The crude squarate adduct **21** (7.45 µmol) was dissolved in a 0.1 M carbonate buffer pH 10 (1 mL) and added to the PEGA resin **17** (52.7 mg, 7.8 µmol of NH_2 groups); the flask that contained **21** was rinsed with more buffer (2 × 500 µL) and the washings were added to the reaction mixture. After 7 days at room temperature, the slurry (2 mL) was transferred to a syringe equipped with a sintered Teflon filter, the solvent was drained, and the resin was washed with water. The eluate was collected in a volumetric flask that was made up to a volume of 10 mL with the washings. Further washings with water were collected in a second volumetric flask (5 mL). These solutions were saved for quantitative analyses of the non-incorporated sugar. The column was subsequently washed with MeOH (10 mL), anhydrous MeOH (10 mL), 10% Ac_2O in MeOH (3 mL), and the resin was treated for 1 h with 5 mL 10% Ac_2O in MeOH. The solution was drained and the resin washed with EtOH (20 mL), 20% aqueous EtOH (20 mL), capped, and stored at 4°C until use for immunoaffinity purifications. Quantitation of non-incorporated sugar, fully recovered in the eluate and first washings, was accomplished using the method of Dubois et al. (38) and gave, by difference, the level of sugar incorporation. The immunoaffinity column **22** contained 4.45 µmol of trisaccharide (84 µmol/g or ≈2.5 µmol/mL of gel), corresponding to a 59% yield of incorporation of the trisaccharide.

Preparation of the immunoaffinity column (23)

Coupling of the squarate adduct **21** (4 µmol) to the PEGA resin **18** (54 mg, ~4.3 µmol of NH_2 groups), followed by acetylation of the unreacted amino groups, was performed under the same conditions as described for the preparation of column **22**. Quantitation of the non-incorporated trisaccharide (38) showed, by difference, that the immunoaffinity column **23** contained 2.1 µmol of sugar incorporated (39 µmol/g or ~1.1 µmol/mL of gel), corresponding to a 52% yield of incorporation of the trisaccharide.

Preparation of the immunoaffinity column (24)

Coupling of the squarate adduct **21** (6.66 µmol) to the PEGA resin **19** (54 mg, ~ 4.9 µmol of NH_2 groups), followed by acetylation of the unreacted amino groups, was performed under the same conditions as described for the preparation of column **22**. Quantitation of the non-incorporated trisaccharide (38) showed, by difference, that the immunoaffinity column **24** contained 2.8 µmol of sugar incorporated (52 µmol/g or ≈1.5 µmol/mL of gel), corresponding to a 57% yield for the coupling reaction.

Caprylic acid precipitation of IgG's

Four parts of sodium acetate (60 mM, pH 4) were added to one part of serum (35). The pH was adjusted to 4.5 with sodium hydroxide (5 N) and caprylic acid was slowly added with vigorous stirring until 2.5% (volume/volume) had been added. The mixture was stirred for 30 min at room temperature and then centrifuged (10 000 × *g*) for 30 min at less than 10°C. The supernatant was carefully collected and filtered through a 45 µm filter. One part of 10× phosphate buffered saline was added to 10 parts of filtered supernatant and the pH was adjusted to 7.4 with sodium hydroxide. The supernatant was cooled to 4°C and ammonium sulfate (saturated) was added until 45% saturation. The mixture was stirred for 30 min at 4°C and then centrifuged (7000 × *g*) for 15 min at 4°C. The pellet was collected and resuspended in the original volume of phosphate-buffered saline (PBS). The solution was dialyzed against PBS at 4°C overnight. The dialzylate was heated at 50°C for 20 min and cent

ELISA

Microwells were coated with the BSA glycoconjugates (1 µg/well, diluted in TBS, 40 µL/well), or *Streptococcus* Group A (4×10^7 bacteria/well, diluted in TBS, 40 µL/well),

© 1998 NRC Canada

BSA (2% in TBS) or blotto (5% milk powder in TBS) and incubated overnight at 4°C. The wells were washed three times with TBS and were blocked with blotto (200 µL) for 2 h at room temperature. After three washes with TBS, caprylic acid precipitated polyclonal Abs were added (approximately 0.5 µg in 35 mL of TBS with 0.2% BSA) and incubated for 4 h at room temperature. The wells were washed six times with TBS and bound Abs were detected with a secondary Ab conjugated to horseradish peroxidase (Pierce, Rockford, Ill.). Optical densities are reported as $(A_{405} - A_{490}) \times 1000$.

Affinity purification of polyclonal antibodies

Caprylic acid purified polyclonal Abs (2.3 mg, 1.1 mg, or 1.4 mg) were added to columns containing affinity reagents **22**, **23**, or **24**, respectively. After washing away unbound protein, bound Abs were eluted with 1 M GlcNAc in Tris buffered saline (TBS). The protein content was assessed by absorbance readings at 280 nm.

References

1. J.H. Pazur. Adv. Carbohydr. Chem. Biochem. **39**, 405 (1981).
2. P. Cuatrecasas. J. Biol. Chem. **245**, 3059 (1970).
3. L. Blomberg, J. Wieslander, and T. Norberg. J. Carbohydr. Chem. **12**, 265 (1993).
4. T. Ziegler, E. Eckhardt, J. Strayle, and H. Herzog. Carbohydr. Res. **253**, 167 (1994).
5. F.-I. Auzanneau and B.M. Pinto. Bioorg. Med. Chem. **4**, 2003 (1996).
6. M. Meldal. Tetrahedron Lett. **33**, 3077 (1992).
7. M. Meldal, F.-I. Auzanneau, and K. Bock. *In* Innovation and perspectives in solid phase synthesis. *Edited by* R. Epton. ESCOM, Leiden. 1993. pp. 259–266.
8. F.-I. Auzanneau, M. Meldal, and K. Bock. J. Pept. Sci. **1**, 31 (1995).
9. M. Meldal, L.I. Svendsen, K. Breddam, and F.-I. Auzanneau. Proc. Natl. Acad. Sci. U.S.A. **91**, 3314 (1994).
10. M. Meldal, F.-I. Auzanneau, O. Hindsgaul, and M.M. Palcic. J. Chem. Soc. Chem. Commun. 1849 (1994).
11. F. Mainferme, R. Wattiaux, and K.von Figura. Biochemistry, **153**, 211 (1985).
12. K. von Figura and A. Hasilik. Annu. Rev. Biochem. **55**, 167 (1986).
13. S.R. Pfeffer. J. Cell Biol. **105**, 229 (1987).
14. D.O. Willenborg, C.R. Parish, and W.B. Cowden. FASEB J. **3**, 1968 (1989).
15. A. Hille, A.Waheed, and K. von Figura. J. Biol. Chem. **264**, 13460 (1989).
16. M. Wendland, A. Hille, G. Nagel, A. Waheed, K. von Figura, and R. Pohlmann. Biochem. J. **260**, 201 (1989).
17. R. Einstein and C.A. Gabel. J. Cell Biol. **112**, 81 (1991).
18. V. Horejsí and J. Kocourek. Biochem. Biophys. Acta, **297**, 346 (1973).
19. F.M. Winnik, J.P. Carver, and J.J. Krepinsky. J. Org. Chem. **47**, 2701 (1982).
20. A.G. McInnes. Can. J. Chem. **43**, 1998 (1965).
21. D.T. Hurst and A.G. McInnes. Can. J. Chem. **43**, 2004 (1965).
22. R.T. Lee and Y.C. Lee. Carbohydr. Res. **37**, 193 (1974).
23. P. Kanda, R.C. Kennedy, and J.T. Sparrow. Int. J. Pept. Protein Res. **38**, 385 (1991).
24. M.K. Christensen, M. Meldal, K. Bock, H. Cordes, S. Mouritsen, and H. Elsner. J. Chem. Soc. Perkin Trans. 1, 1299 (1994).
25. G.G. Sahagian, J.J. Distler, and G.W. Jourdian. Methods Enzymol. **83**, 392 (1982).
26. A.L. Bisno. *In* Principles and practice of infectious diseases. 2nd ed. *Edited by* G.L. Mandell, R.G. Douglas, and J.E. Benett. Wiley, New York. 1985. pp. 1133–1142.
27. V.A. Fischetti. Sci. Am. 59 (1991).
28. J. Rotta. *In* Towards better carbohydrate vaccines. *Edited by* R. Bell and G. Torrigiani. John Wiley & Sons, New York. 1986. pp. 203–218.
29. M.W. Cunningham, S.M. Antone, J.M. Guliza, M.B. McManus, V.A. Fischetti, and C.J. Gauntt. Proc. Natl. Acad. Sci. U.S.A. **89**, 1320 (1992).
30. V.A. Fischetti. Clin. Microbiol. Rev. 285 (1989).
31. J.B. Dale and E.H. Beachey. J. Exp. Med. **162**, 583 (1985).
32. I. Goldstein, I. P. Rebeyrotte, J. Parlebas, and B. Halpern. Nature, **219**, 866 (1968).
33. I. Goldstein, L. Scebat, J. Renais, P. Hadjinsky, and J. Durartre. Isr. J. Med. Sci. **19**, 483 (1983).
34. B.M. Pinto. ACS Symp. Ser. **519**, 111 (1992).
35. K.B. Reimer, M.A.J. Gidney, D.R. Bundle, and B.M. Pinto. Carbohydr. Res. **232**, 131 (1992).
36. F.-I. Auzanneau, F. Forooghian, and B.M. Pinto. Carbohydr. Res. **291**, 21 (1996).
37. V.P. Kamath, P. Diedrich, and O. Hindsgaul. Glycoconjugate J. **13**, 315 (1996).
38. M. Dubois, K.H. Gilles, J.K. Hamilton, P.A. Rebers, and F. Smith. Anal. Chem. **28**, 350 (1956).
39. N.M. Targett, J.P. Kilcoyne, and B. Green. J. Org. Chem. **44**, 4962 (1979).
40. D.D. Perrin and W.L.F. Armarego. Purification of laboratory chemicals. 3rd ed. Pergamon Press, London. 1988.

Can. J. Chem. Downloaded from www.nrcresearchpress.com by China University of Science and Technology on 09/05/12
For personal use only.

© 1998 NRC Canada

Aqueous nonelectrolyte solutions. Part XV. The deuterium sulfide – deuterium oxide system and the deuterium sulfide D-hydrate

Colin W. Clarke and David N. Glew

Abstract: The univariant (l_1l_2g) saturation vapor pressure of liquid deuterium oxide (phase l_1) with liquid deuterium sulfide (phase l_2) in equilibrium with a gas phase (g) has been measured in a stirred titanium reaction vessel at 19 temperatures from 33.003 to 18.905°C and at total pressures from 2.4500 to 1.7428 MPa. The univariant (hl_1g) saturation vapor pressure of deuterium sulfide D-hydrate (phase h) in equilibrium with liquid deuterium oxide and a gas phase has been measured at 58 temperatures from 30.666 to 2.798°C and at pressures from 2.2959 to 0.11629 MPa. The maximum temperature for deuterium sulfide D-hydrate with a gas phase, the invariant quadruple point $Q(hl_1l_2g)$, has been determined from the cut of the (hl_1g) and the (l_1l_2g) curves at temperature 30.770°C with standard error 0.0043°C and at pressure 2.3263 MPa with standard error 0.00018 MPa. The univariant (s_1l_1g) equilibrium of D-ice (phase s_1) with liquid deuterium oxide and a gas phase containing deuterium sulfide has been measured at 11 temperatures from 3.8061 to 3.4540°C and at pressures between 0.00242 and 0.10542 MPa. The lowest temperature for stability of deuterium sulfide D-hydrate with liquid deuterium oxide, the invariant quadruple point $Q(hs_1l_1g)$, has been determined directly at 3.3917°C with standard error 0.0009°C and at pressure 0.12364 MPa with standard error 0.000011 MPa. This quadruple point $Q(hs_1l_1g)$ has also been defined by the cut of the (hl_1g) and the (s_1l_1g) curves at temperature 3.3912°C with standard error 0.0006°C and at pressure 0.12363 MPa with standard error 0.000002 MPa. The deuterium sulfide – deuterium oxide gas mixture, represented by a Redlich–Kwong equation of state, has been used to evaluate the fugacities and compositions of the gaseous and liquid deuterium oxide phases for all equilibria. Raoult's law using fugacities has been used to evaluate the saturation mole fraction of deuterium oxide in liquid deuterium sulfide and the Henry's law constant for deuterium oxide solubility in liquid deuterium sulfide between 33.003 and 18.905°C. Data for the (l_1l_2g) and (s_1l_1g) equilibria have been accurately represented by simple two-parameter equations. Data for the (hl_1g) equilibrium have required a model with seven significant parameters for proper representation betweem 30.666 and 2.798°C.

Key words: deuterium sulfide – deuterium oxide system, clathrate D-hydrate of deuterium sulfide, deuterium sulfide D-hydrate stability, freezing of deuterium oxide – deuterium sulfide, phase equilibria of deuterium sulfide – deuterium oxide.

Résumé : Opérant dans une cuve réactionnelle de titane sous agitation, à 19 températures allant de 33,003 à 18,905°C et à des pressions totales allant de 2,4500 à 1,7428 MPa, on a mesuré la tension de vapeur de saturation à une variable (1_11_2g) de l'oxyde de deutérium liquide (phase 1_1) avec du sulfure de deutérium liquide (phase 1_2) en équilibre avec une phase gazeuse (g). Opérant à 58 températures allant de 30,666 à 2,798°C et à des pressions allant de 2,2959 à 0,11629 MPa, on a aussi mesuré la tension de vapeur de saturation à une variable ($h1_1g$) du D-hydrate de sulfure de deutérium (phase h) en équilibre avec de l'oxyde de deutérium liquide et une phase gazeuse. En se basant sur le point de jonction des courbes ($h1_1g$) et (1_11_2g) à une température de 30,770°C avec une erreur-type de 0,0043°C et à une pression de 2,3263 MPa avec une erreur-type de 0,00018 MPa, on a déterminé la température maximale du D-hydrate du sulfure de deutérium, le point quadruple invariant $Q(h1_11_2g)$. Opérant à 11 températures allant de 3,8061 à 3,4540°C et à des pressions allant de 0,00242 à 0,10542 MPa, on a mesure l'équilibre à une variable (s_11_1g) de la glace-D (phase s_1) avec de l'oxyde de deutérium liquide et une phase gazeuse contenant du sulfure de deutérium. Opérant à 3,3917°C avec une erreur-type de 0,0009°C et à une pression de 0,12364 MPa avec une erreur-type de 0,000011 MPa, on a déterminé directement la température minimale pour la stabilité du D-hydrate de sulfure de deutérium avec de l'oxyde deutérium liquide, le point quadruple invariant $Q(hs_11_1g)$. Ce point quadruple, $Q(hs_11_1g)$, a aussi été défini par le point de rencontre des courbes ($h1_1g$) et (s_11_1g) à la température de 3,3912°C avec une erreur-type de 0,0006°C et à une pression de 0,12363 MPa avec une erreur type de 0,000002 MPa. On a utilisé le mélange gazeux sulfure de deutérium – oxyde de deutérium représenté par l'équation d'état de Redlich–Kwong pour évaluer les fugacités et les compositions des phases gazeuses et liquides de l'oxyde de deutérium de tous les équilibres. On a fait appel à la loi de Raoult utilisant des fugacités pour évaluer la fraction molaire de saturation de l'oxyde deutérium dans

Received January 26, 1998.

C.W. Clarke and D.N. Glew.[1] Exploratory Research Laboratory, Dow Chemical Canada Inc., Sarnia, ON N7T 7M1, Canada.

[1]Retired. Author to whom correspondence may be addressed. Telephone: (519) 337-3136. Present address: 536 Highbury Park, Sarnia, ON N7V 2J9, Canada.

© 1998 NRC Canada

le sulfure de deutérium liquide et on a utilisé la constante de la loi de Henry pour évaluer la solubilité de l'oxyde de deutérium dans le sulfure de deutérium liquide entre 33,003 et 18,905°C. On peut donner une représentation graphique correcte des données des équilibres ($1_1 1_2 g$) et ($s_1 1_1 g$) en faisant appel à des équations simples à deux paramètres. Pour donner une représentation adéquate des données pour l'équilibre ($h1_1 g$) entre 30,666 et 2,798°C, on doit faire appel à un modèle à sept paramètres significatifs.

Mots clés : système sulfure de deutérium – oxyde de deutérium, clathrate du D-hydrate de sulfure de deutérium, stabilité du D-hydrate du sulfure de deutérium, congélation de l'oxyde de deutérium – sulfure de deutérium, équilibre de phase du sulfure de deutérium – oxyde de deutérium.

[Traduit par la Rédaction]

Introduction

As part of a continuing study (1, 2) of the structural and thermodynamic properties of aqueous nonelectrolyte solutions and of their solid clathrate hydrate solutions, it became of interest to compare the thermodynamic properties of nonelectrolyte solutions in deuterium oxide with their solid clathrate D-hydrate solutions. The properties of aqueous hydrogen sulfide solutions (3, 4) and of the hydrogen sulfide gas hydrate (5–7) were well known, but the properties of deuterium sulfide solutions in deuterium oxide and of the deuterium sulfide D-hydrate had not been reported in the literature. Due to the importance in Canada of the hydrogen sulfide – water dual temperature exchange process (8, 9) for the initial extraction of deuterium oxide from water, it was desirable to know the equilibrium properties of deuterium sulfide with deuterium oxide and of deuterium sulfide D-hydrate.

The present experimental study, performed between 1963 and 1966, defines part of the deuterium sulfide – deuterium oxide system up to 33°C and the conditions for formation of deuterium sulfide D-hydrate with liquid deuterium oxide.

Experimental

Materials

Deuterium oxide was 99.75% pure with 0.25 wt.% protium oxide as supplied by Atomic Energy of Canada Limited: a complete isotopic analysis of this deuterium oxide has been reported earlier (10). Deuterium sulfide was prepared by the reaction of deuterium oxide with CP grade aluminum sulfide as described previously (11, 12).

Apparatus

The deuterium oxide – deuterium sulfide system was studied in a continuously stirred titanium pressure vessel, which was suspended in an enclosed and insulated water thermostat bath. The vessel was constructed of titanium to resist corrosion and was stirred continuously by an impellor operated by magnetic induction. All metal fittings, valves, and tubing used to connect the titanium vessel to the pressure gauge and to the vacuum filling system were of type-316 stainless steel, which was completely resistant to corrosion by wet deuterium sulfide.

Titanium pressure vessel

The titanium pressure vessel, shown in Fig. 1, was axially symmetric and 360 mm high, and was constructed from three machined titanium bodies, which were aligned vertically on top of each other by two pairs of flanges F1 and F2. The upper motor body was 90 mm high with a lower flange F1, the middle shaft body was 170 mm high with an upper flange F1 and a lower flange F2, and the lower impellor body was 100 mm high with an upper flange F2. Each pair of flanges was drawn together by six hexagonal nuts on 9.5 mm lug-bolts and was sealed by compression of an enclosed 1.6 mm thick gasket of polytetrafluoroethylene.

The central stirrer shaft, 336 mm long, 6.35 mm o.d., was of type-316 stainless steel and carried the rotor of the induction motor at its upper end and a two-blade titanium impellor at its lower end. The bearing at the bottom of the stirrer shaft was polytetrafluoroethylene and at the top a nylon sleeve. The induction rotor, 51 mm high × 32 mm o.d., was protected from corrosion by an epoxy resin coating that had been baked to enhance its chemical resistance. The upper motor body was 41.5 mm o.d. and carried the external stator of the induction motor (not shown) and enclosed the internal rotor with a clearance of 1.6 mm. The underside of the upper flange pair F1 was supported 14 mm above the insulated top cover of the thermostat tank (not shown) and was about 36 mm above the level of the thermostat water. The lower 220 mm of the titanium vessel, comprised of the shaft body, the lower flange pair F2, and the impellor body, was immersed in the thermostat water. The shaft body was 15.9 mm o.d. and enclosed the drive shaft with a radial clearance of 1.6 mm.

The lower impellor body was 63.5 mm o.d. and enclosed a stirred internal cell space, 80 mm high × 50.8 mm i.d., this provided a maximum cell volume of ~158 cm^3 of which 90 cm^3 was occupied by deuterium oxide. A titanium thermowell, 6.35 mm o.d., containing a 10-junction copper-constantan thermocouple, was located 5 mm from the cell wall and extended 64 mm from the top of the cell to 16 mm above the bottom. The lower end of the drive shaft was reduced to 4.76 mm o.d. and was threaded enabling two nuts to fix the position of the upper collar, 14 mm high × 9.5 mm o.d., 4.77 mm i.d., of the impellor. The titanium impellor was composed of two vertically aligned, symmetrically opposed blades, 42 mm × 6 mm × 1.6 mm, welded along the upper collar. The impellor was located centrally within the cell and its blades swept out a cylinder, >30 mm high × 16 mm o.d., within the stirred liquid sample.

Temperature measurement

The original experimental temperatures were measured on the International Practical Temperature Scale of 1948 (IPTS-48), and these have been converted to the International Temperature Scale of 1990 (ITS-90), using the approximate differences given in Table 4 of Goldberg and Weir (13). This

© 1998 NRC Canada

Fig. 1. Titanium pressure vessel.

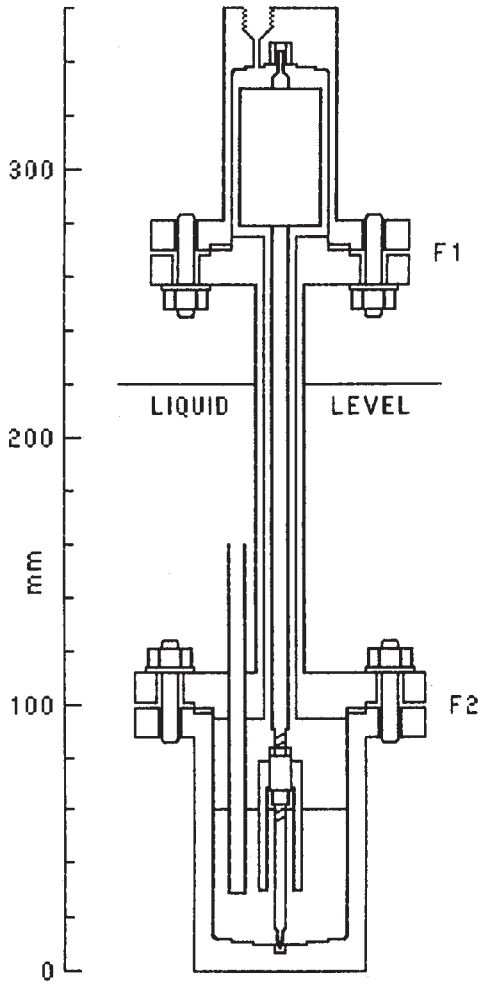

conversion has a root mean squared bias of less than 0.0003°C in the range zero to 40°C, of slightly smaller magnitude than the accuracy of our most precise measurements. All temperatures and equations are based on the units degree Celsius (ITS-90), with (t°C + 273.15) = T K.

Temperatures were measured on the (IPTS-48) scale using a standardized 25 ohm platinum resistance thermometer with a Leeds and Northrup G-2 Mueller bridge, nanovolt amplifier, and galvonometer (11). Resistances were measured to within 1×10^{-5} ohm, corresponding to about 0.0001°C. The resistance at the triple point of water was checked regularly using Jarrett triple-point cells, by Trans-Sonics Incorporated, maintained in an insulated ice-packed chest (14). The thermostat temperature was controlled to within 0.001°C and was measured with the platinum resistance thermometer mounted in a cavity in a submerged stainless-steel block located within the rapidly recirculating water of the thermostat bath. The temperature difference between the titanium thermowell and the stainless-steel block was measured by a 10-junction copper-constantan thermocouple with the off-balance signal detected by a nanovolt amplifier and galvonometer. With this arrangement the temperature of the stirred liquid sample within the reaction cell could be readily determined with a precision of 0.0005°C.

Pressure measurement

The top of the motor body of the titanium vessel was connected via Swagelok fittings to small-bore high-pressure tubing, 1.6 mm i.d., 6.35 mm o.d., and high-pressure bonnet bar stock valves to (*i*) the quartz pressure gauge, (*ii*) the deuterium sulfide storage cylinder, and (*iii*) the high-vacuum system. For pressure measurements with the titanium vessel above 25°C the high-pressure tubing was heated electrically to about 40°C using a thermally and electrically insulated external winding of a flat, 3.2 mm in width nichrome heating ribbon: the motor body and the high-pressure valves were heated by infra-red lamps.

Pressure was measured using fused quartz spiral precision Bourdon gauges manufactured by Texas Instruments Incorporated, which were completely resistant to corrosion. The temperature of the compartment containing the capsule of the quartz spiral was controlled at 35°C, and the gauge was capable of measuring absolute pressure with an accuracy of 0.020% at low pressure and 0.030% at high pressures (11): the precision of pressure measurement was better by a factor of two. An electrical output from the quartz gauge was recorded continuously to follow the attainment of equilibrium. All pressures have been corrected to the standard acceleration due to gravity, 9.80665 m s^{-2}.

Over the wide range of pressure exhibited by the deuterium sulfide D-hydrate, pressure was measured using three different capsules containing quartz spirals of different sensitivity: (*i*) the 16 psi capsule was used for pressures between 0.1163 and 0.1980 MPa, (*ii*) the 200 psi capsule between 0.1323 and 1.4449 MPa, and (*iii*) the 500 psi capsule between 1.1510 and 2.2959 MPa. The saturation pressure of the binary mixture of liquid deuterium sulfide and liquid deuterium oxide was measured using the 500 psi capsule. The pressure of the deuterium sulfide solutions in deuterium oxide with D-ice was measured using the 16 psi capsule.

Experimental method

Late in 1963 the 200 psi gauge was used for our initial measurements of the pressure. Approximately 90 cm^3 deuterium oxide liquid (l_1) was placed in the titanium cell and, with continuous stirring, was thoroughly degassed using the vacuum system. The thermostat was set at about 5°C, and deuterium sulfide from its storage cylinder was admitted to give a gas (g) pressure of about 100 psig in the cell. Rapid formation of solid deuterium sulfide D-hydrate (h) ensued as shown by a steady drop in pressure. After about 16 h, when it was evident that the three-phase (hl_1g) equilibrium had been attained, data sets of 14–37 pairs of pressure–temperature measurements were made over periods of 2–5 days: the determinations reported are the means of these data sets. The thermostat temperature was then raised by about 1°C and the measurement procedure repeated. In 1965, when the pressure exceeded 1.4449 MPa the 200 psi gauge was replaced by the 500 psi gauge. Temperature was increased incrementally, with further additions of deuterium sulfide to maintain the D-hydrate phase at higher pressures, up to the temperature of the quadruple point $Q(hl_1l_2g)$, about 30.77°C, above which the solid deuterium sulfide D-hydrate (h) became unstable and decomposed into its two liquid

© 1998 NRC Canada

Table 1. Vapor pressure of mixed liquids deuterium oxide and deuterium sulfide.

Temperature (°C)	$P(l_1l_2g)$		Difference (%)	Error on calculated pressure(%)
	Observed (MPa)	Calculated (MPa)		
33.003	2.4500	2.4501	–0.003	0.010
32.984	2.4494	2.4490	0.017	0.010
31.981	2.3924	2.3929	–0.019	0.009
31.503	2.3656	2.3664	–0.035	0.008
30.983	2.3380	2.3379	0.003	0.008
30.505	2.3123	2.3119	0.017	0.007
29.959	2.2831	2.2825	0.028	0.007
28.930	2.2274	2.2277	–0.016	0.006
27.916	2.1746	2.1747	–0.005	0.006
27.850	2.1708	2.1712	–0.019	0.006
26.853	2.1210	2.1201	0.041	0.006
25.862	2.0702	2.0701	0.006	0.006
24.877	2.0208	2.0212	–0.022	0.006
23.874	1.9730	1.9724	0.031	0.007
22.859	1.9242	1.9237	0.022	0.008
21.881	1.8772	1.8778	–0.031	0.009
20.887	1.8310	1.8318	–0.043	0.010
19.866	1.7860	1.7855	0.024	0.011
18.905	1.7428	1.7427	0.004	0.012

components, liquid deuterium oxide (l_1) and liquid deuterium sulfide (l_2).

At higher temperatures, where the three-phase (l_1l_2g) system was stable, total equilibrium pressures were determined for the stirred, mutually saturated, partially miscible liquids. Measurements began at highest temperatures ~33°C, and data sets of exactly 18 equilibrium pressure–temperature measurements were collected for each temperature at intervals of 2–3 days. The temperature was decreased and the process repeated. In this manner the equilibrium pressure was most rapidly attained by the removal of super-saturation from the two liquid phases: attainment of equilibrium from lower temperatures and from undersaturated conditions required up to 7 days. The (l_1l_2g) equilibrium was also measured with continuous stirring below the quadruple point in the metastable region down to 18.9°C: below this temperature the stirred, two-liquid system spontaneously reformed the stable deuterium sulfide D-hydrate. Three high temperatures were finally remeasured for the (l_1l_2g) system to check the hysteresis and reproducibility of the 500 psi gauge. Equilibrium total pressures for the mutually saturated deuterium oxide and deuterium sulfide liquids are listed in Table 1.

In 1966, to define the (hl_1g) system at lower temperatures with better accuracy, the 16 psi gauge was used (11), the stirred reactor temperature was reduced to 7.961°C, and some deuterium sulfide was removed so that excess solid D-hydrate did not impede the stirrer. Again data sets of exactly 18 equilibrium pressure–temperature measurements were collected at each temperature over periods of 3–4 days: the mean values are reported. The temperature was decreased and the process repeated down to 2.798°C. The seven measurements listed between 3.383 and 2.798°C are metastable relative to freezing of D-ice. Table 2 lists the equilibrium pressures for deuterium sulfide D-hydrate.

The pressure and temperature of the invariant lower quadruple point $Q(hs_1l_1g)$ were determined directly from equilibrium measurements of the (hs_1l_1g) system with the thermostat temperature controlled so that (*i*) the stirred D-hydrate (h) was neither forming nor decomposing, as shown by a constant observed pressure and (*ii*) the stirred D-ice (s_1) was neither freezing nor melting, as shown by a zero signal from the 10-junction thermocouple. To confirm equilibrium conditions the impressed thermostat temperature was bracketed, with decreasing temperature differences, slightly above and slightly below the temperature of the stirred reactor at the quadruple point for a period of 15 days.

In our final study in 1966 the (s_1l_1g) system was measured at preselected total pressures of deuterium sulfide. The equilibrium temperature for the (s_1l_1g) system was measured directly for a period of 2 days, by bracketing the thermostat temperature to equal the thermowell temperature, so that the D-ice (s_1) was in equilibrium (neither freezing nor melting) with the stirred deuterium oxide (l_1) saturated with deuterium sulfide (g) at the pre-defined total pressure. Table 3 lists the total pressures and temperatures found for the (s_1l_1g) equilibrium.

All pressures and temperatures listed as determinations for the various equilibria are the mean values of the sets of repeated single measurements. All regression equations have been evaluated using the method of least squares (15). Standard error, abbreviated to SE, is to be understood to mean the statistical estimate of the standard error.

Results and discussion

Equation of state

Following our earlier work (11, 12) gas-phase imperfections have been represented by the Redlich–Kwong equation of state (16), using the extension to mixtures by Spear et al. (17). The a_{22} and b_{22} parameters used for deuterium sulfide vapor are those derived from the high temperature (h.t.) measurements from –30 to +30°C (11): the a_{11} and b_{11} for

© 1998 NRC Canada

Table 2. Pressure of deuterium sulfide D-hydrate with deuterium oxide liquid.

Temperature (°C)	Gauge	$w^{1/2}$	$P(hl_1g)$		Difference (%)	Error on calculated pressure (%)
			Observed (MPa)	Calculated (MPa)		
30.666	500	0.4	2.2959	2.2953	0.027	0.021
30.462	500	0.4	2.2338	2.2348	–0.046	0.018
29.940	500	0.4	2.0903	2.0902	0.003	0.013
29.883	500	0.4	2.0763	2.0752	0.053	0.013
29.375	500	0.4	1.9476	1.9472	0.017	0.011
28.945	500	0.4	1.8461	1.8469	–0.043	0.011
28.932	500	0.4	1.8431	1.8440	–0.048	0.011
28.378	500	0.4	1.7244	1.7245	–0.002	0.011
27.967	500	0.4	1.6425	1.6419	0.041	0.010
27.967	500	0.4	1.6408	1.6419	–0.065	0.010
27.957	500	0.4	1.6400	1.6399	0.003	0.010
26.985	500	0.4	1.4638	1.4640	–0.014	0.008
26.869	200	0.5	1.4449	1.4446	0.021	0.007
26.845	200	0.5	1.4406	1.4406	–0.002	0.007
25.873	200	0.5	1.2903	1.2899	0.031	0.005
25.853	500	0.4	1.2862	1.2870	–0.065	0.005
25.000	500	0.4	1.1702	1.1701	0.003	0.004
24.879	200	0.5	1.1548	1.1546	0.017	0.003
24.862	500	0.2	1.1510	1.1524	–0.126	0.009
23.997	200	0.5	1.0482	1.0481	0.011	0.005
23.003	200	0.5	0.9411	0.9410	0.005	0.007
21.961	200	0.5	0.8419	0.8417	0.017	0.008
20.980	200	0.5	0.7585	0.7585	–0.005	0.009
19.971	200	0.5	0.6821	0.6821	0.001	0.010
18.981	200	0.5	0.6149	0.6150	–0.012	0.010
17.972	200	0.5	0.5537	0.5538	–0.017	0.010
16.972	200	0.5	0.4991	0.4993	–0.033	0.010
15.968	200	0.5	0.4500	0.4502	–0.029	0.010
14.987	200	0.5	0.4070	0.4069	0.012	0.010
13.963	200	0.5	0.3664	0.3664	–0.003	0.010
13.383	200	0.5	0.3452	0.3452	–0.004	0.010
12.975	200	0.5	0.3311	0.3311	0.012	0.010
12.381	200	0.5	0.3116	0.3115	0.021	0.010
11.980	200	0.5	0.2990	0.2990	0.010	0.010
11.379	200	0.282	0.2813	0.2811	0.063	0.012
10.983	200	0.162	0.2703	0.2700	0.115	0.015
9.977	200	0.078	0.2438	0.2435	0.136	0.024
9.144	200	0.054	0.2238	0.2236	0.117	0.033
7.998	200	0.04	0.19899	0.19874	0.129	0.044
7.997	200	0.04	0.19907	0.19872	0.180	0.044
7.961	16	1	0.19798	0.19798	–0.002	0.008
6.993	200	0.04	0.17952	0.17922	0.167	0.044
6.974	16	1	0.17883	0.17887	–0.022	0.007
5.936	200	0.04	0.16111	0.16071	0.246	0.044
5.895	16	1	0.16002	0.16003	–0.007	0.007
5.068	200	0.04	0.14728	0.14694	0.229	0.044
5.014	16	1	0.14610	0.14612	–0.016	0.007
4.032	200	0.04	0.13231	0.13206	0.191	0.044
3.987	16	1	0.13148	0.13145	0.024	0.006
3.485	16	1	0.12481	0.12482	–0.003	0.005
3.392	16	1	0.12364	0.12363	0.007	0.004
3.383	16	1	0.12353	0.12351	0.009	0.004
3.284	16	1	0.12227	0.12226	0.004	0.004
3.190	16	1	0.12109	0.12109	0.004	0.005
3.097	16	1	0.11994	0.11994	0.000	0.005
2.998	16	1	0.11872	0.11873	–0.003	0.005
2.895	16	1	0.11746	0.11748	–0.019	0.006
2.798	16	1	0.11629	0.11632	–0.021	0.007

© 1998 NRC Canada

Table 3. Freezing point of deuterium oxide solutions of deuterium sulfide.

$P(s_1l_1g)$ (MPa)	$t(s_1l_1g)$ Observed (°C)	$t(s_1l_1g)$ Calculated (°C)	Difference (°C)	Error on calculated temperature (°C)
0.00066	—	3.8125	—	0.00047
0.00242	3.8061	3.8064	–0.00029	0.00047
0.00563	3.7967	3.7954	0.00132	0.00045
0.01552	3.7614	3.7615	–0.00018	0.00040
0.02836	3.7160	3.7176	–0.00157	0.00035
0.04150	3.6741	3.6725	0.00158	0.00031
0.05402	3.6291	3.6297	–0.00062	0.00029
0.06655	3.5866	3.5867	–0.00015	0.00029
0.08341	3.5285	3.5290	–0.00045	0.00033
0.08408	3.5264	3.5267	–0.00026	0.00033
0.09313	3.4953	3.4957	–0.00034	0.00037
0.10542	3.4540	3.4536	0.00039	0.00042
0.12364	3.3917	3.3912	0.00055	0.00052

deuterium oxide vapor are those derived for the solubility measurements (12).

Method of evaluating compositions of aqueous and gaseous phases

The iterative process used to evaluate the intensive properties of the liquid deuterium oxide solution and of the binary gaseous phase at equilibrium with deuterium sulfide is similar in principle but different in method from that briefly outlined for the solubility (12). Modern values (*i*) for $p_1°$, the saturation vapor pressure of deuterium oxide, are from Hill and MacMillan (18) and (*ii*) for V_1^{l1}, the molar volume of liquid deuterium oxide, are from Kell (19), evaluated with proper allowance for the difference of the IPTS-48 and the IPTS-68 scales of temperature.

Consider the equilibrium evaporation at a total pressure P and temperature T of 1 g molar mass of deuterium oxide from its liquid solution with mole fraction x_1^{l1} deuterium oxide into its binary gas phase with mole fraction y_1 deuterium oxide as formally represented by the reaction equation:

$$[1] \qquad \begin{array}{ccc} D_2O(l_1) & \rightleftharpoons & D_2O(g) \\ P, x_1^{l1} & & P, y_1 \\ G_1^{l1}(P, x_1^{l1}) & & G_1^{g}(P, y_1) \end{array}$$

The molar Gibbs energy for deuterium oxide in the liquid and in the gas phases are defined as $G_1^{l1}(P, x_1^{l1})$ and $G_1^{g}(P, y_1)$, respectively. For the system in thermodynamic equilibrium at constant T and P the molar Gibbs energy of deuterium oxide is the same in both the liquid and the gas phases so that

$$[2] \qquad G_1^{l1}(P, x_1^{l1}) = G_1^{g}(P, y_1)$$

For the equilibrium evaporation of pure deuterium oxide with $x_1^{l1} = 1$, $y_1 = 1$, and $P = p_1°$, eq. [2] yields the relations:

$$[3] \qquad G_1^{l1}(p_1°, 1) = G_1^{*l1} = G_1^{g}(p_1°, 1) = G_1^{°g} + RT \ln f_1°$$

where G_1^{*l1} is the molar Gibbs energy of pure liquid deuterium oxide at its saturation vapor pressure $p_1°$, and where $f_1°$ is its saturation fugacity, and $G_1^{°g}$ is the standard molar Gibbs energy of gaseous deuterium oxide at unit pressure.

For pure liquid deuterium oxide at a total pressure $P(>p_1°)$ the molar Gibbs energy $G_1^{l1}(P, 1)$ is

$$[4] \qquad G_1^{l1}(P, 1) = G_1^{*l1} + (P - p_1°)V_1^{l1} = G_1^{*l1} + RT \ln f_1(\text{Poynting})$$

where $f_1(\text{Poynting}) = \exp((P - p_1°)V_1^{l1}/RT)$ is the Poynting pressure coefficient, and V_1^{l1} is the molar volume of the liquid.

For dilute solutions of deuterium sulfide in deuterium oxide with mole fraction x_1^{l1} of deuterium oxide at pressure P the molar Gibbs energy for deuterium oxide is taken as

$$[5] \qquad G_1^{l1}(P, x_1^{l1}) = G_1^{l1}(P, 1) + RT \ln x_1^{l1}$$

where the liquid is assumed to obey Raoult's law.

The sum of eqs. [3]–[5] gives

$$[6a] \qquad G_1^{l1}(P, x_1^{l1}) = G_1^{og} + RT \ln f_1° + RT \ln f_1(\text{Poynting}) + RT \ln x_1^{l1}$$

$$[6b] \qquad G_1^{l1}(P, x_1^{l1}) = G_1^{og} + RT \ln [f_1° \cdot f_1(\text{Poynting}) \cdot x_1^{l1}]$$

expressing the molar Gibbs energy of deuterium oxide $G_1^{l1}(P, x_1^{l1})$ at P and x_1^{l1} in eq. [6*a*] in terms of the molar Gibbs energy for the pure liquid at its saturation vapor pressure with fugacity $f_1°$, plus the Poynting molar Gibbs energy change with activity coefficient $f_1(\text{Poynting})$, plus the Raoult-law molar Gibbs energy change with activity coefficient x_1^{l1}. Alternately eq. [6*b*] expresses the same molar Gibbs energy in terms of the fugacity product within the square brackets.

The Redlich–Kwong equation of state for gas mixtures (12, 16, 17) provides an independent expression for the fugacity f_1 of deuterium oxide at mole fraction y_1 in a gas mixture with deuterium sulfide at total pressure P. Under

© 1998 NRC Canada

Table 4. Properties of gas and liquid phases in the (l_1l_2g) equilibrium.

Temperature (°C)	$f_2°$ (MPa)	f_2 (MPa)	f_1 (MPa)	y_1 (× 10^3)	x_2^{l1} (× 10^3)	x_3^{l1} (× 10^6)	x_1^{l2} (× 10^3)
33.003	2.0306	2.0039	0.00435	4.11	28.85	4.1	13.1
32.984	2.0298	2.0034	0.00435	4.10	28.85	4.1	13.0
31.981	1.9883	1.9626	0.00410	3.90	28.90	4.1	12.9
31.503	1.9687	1.9434	0.00399	3.81	28.92	4.0	12.8
30.983	1.9475	1.9234	0.00387	3.71	28.96	4.0	12.3
30.505	1.9281	1.9049	0.00376	3.62	28.99	4.0	12.1
29.959	1.9061	1.8837	0.00364	3.52	29.03	4.0	11.8
28.930	1.8652	1.8433	0.00342	3.34	29.09	3.9	11.8
27.916	1.8253	1.8047	0.00322	3.17	29.16	3.9	11.3
27.850	1.8228	1.8020	0.00321	3.16	29.16	3.9	11.4
26.853	1.7842	1.7653	0.00302	3.01	29.26	3.8	10.6
25.862	1.7463	1.7280	0.00284	2.86	29.33	3.8	10.5
24.877	1.7092	1.6914	0.00267	2.72	29.42	3.7	10.4
23.874	1.6719	1.6558	0.00251	2.58	29.53	3.7	9.6
22.859	1.6346	1.6193	0.00236	2.45	29.63	3.6	9.3
21.881	1.5992	1.5842	0.00221	2.33	29.72	3.6	9.4
20.887	1.5638	1.5494	0.00208	2.21	29.84	3.5	9.2
19.866	1.5279	1.5152	0.00195	2.10	29.98	3.5	8.3
18.905	1.4945	1.4824	0.00183	1.99	30.10	3.4	8.1

these conditions the molar Gibbs energy for deuterium oxide in the gas phase $G_1^g(P, y_1)$ is given by

$$[7] \qquad G_1^{\,g}(P, y_1) = G_1^{\,og} + RT \ln f_1$$

Returning to the equilibrium of the binary aqueous phase with the binary gaseous phase, eqs. [6*b*] and [7] are substituted into eq. [2] to obtain the equilibrium relationship

$$[8] \qquad f_1 = [f_1° \cdot f_1(\text{Poynting}) \cdot x_1^{\,l1}]$$

where the fugacity f_1 of deuterium oxide from the Redlich–Kwong equation is equal to the saturation fugacity $f_1°$ of the pure liquid corrected for the effects of pressure and of solution mole fraction. The equilibrium values for f_1 and x_1^{l1} are obtained by successive approximations to evaluate eq. [8] as follows.

As a first approximation the gas-phase mole fraction of deuterium oxide y_1' at total pressure P is taken as

$$[9] \qquad y_1' = p_1°/P$$

with $p_1°$ evaluated from the equation of Hill and MacMillan (18). This y_1' is used at P and T in the Redlich–Kwong (R–K) equation for gas mixtures (12, 16, 17) to obtain V' the molar volume of the gas mixture, and thence to evaluate the first approximations f_1' and f_2' for the R–K fugacities of deuterium oxide and of deuterium sulfide, respectively. This f_2' is used with the Henry's law solubility constant (12) and its Poynting correction to evaluate $x_2^{l1\prime}$, the mole fraction of undissociated deuterium sulfide dissolved in deuterium oxide.

The Poynting correction for the deuterium sulfide solute is $f_2(\text{Poynting}) = \exp((P - p_1°)V_2^{l1}/RT)$, where V_2^{l1} is the partial molar volume of deuterium sulfide in deuterium oxide. Values of V_2^{l1} for deuterium sulfide are estimated from the measurements for hydrogen sulfide in water by Barbero et al. (20).

The $x_2^{l1\prime}$ is used with the ionization constant for deuterium sulfide in deuterium oxide (12) to evaluate $x_3^{l1\prime}$, the dissolved mole fraction of the deuterium sulfide anion. In the first approximation $x_1^{l1\prime}$, the solution mole fraction of deuterium oxide, is given by $(1 - x_2^{l1\prime} - 2x_3^{l1\prime}) = x_1^{l1\prime}$.

The fugacity of deuterium oxide evaluated for the compressed solution using eq. [6*b*] is $[f_1° \cdot f_1(\text{Poynting}) \cdot x_1^{l1\prime}]$, which is greater than the fugacity f_1' evaluated from the Redlich–Kwong equation using y_1'. The reason that the R–K fugacity f_1' is too small is because our first approximation of y_1', using partial pressures, is too small: thus, in our second approximation we multiply y_1' by a converging factor greater than unity.

In the second approximation the gas-phase mole fraction of deuterium oxide y_1'' at total pressure P is taken as

$$[10] \qquad y_1'' = y_1'[f_1° \cdot f_1(\text{Poynting}) \cdot x_1^{\,l1\prime}] / f_1'$$

giving the second sequence of approximations, $y_1'' \rightarrow V'' \rightarrow f_1'', f_2'' \rightarrow x_2^{\,l1\prime\prime}, x_3^{\,l1\prime\prime} \rightarrow x_1^{\,l1\prime\prime} \rightarrow y_1''[f_1° \cdot f_1(\text{Poynting}) \cdot x_1^{\,l1\prime\prime}]/f_1'' = y_1$ (3rd approximation), and so on. The approximations converge rapidly to give equilibrium values after six cycles of iteration, satisfying eq. [8] within the limits of single precision arithmetic.

Liquid D_2O – liquid D_2S – gas (l_1l_2g) equilibrium

Table 1 presents 19 determinations of $P(l_1l_2g)$, the saturation vapor pressure of the partially miscible liquids deuterium oxide and deuterium sulfide between 33.003 and 18.905°C, together with calculated values from the best (21) representative equation

$$[11] \qquad \ln P(l_1l_2g) = 7.95368 - 2160.7 / T$$

with $P(l_1l_2g)$ in MPa and absolute temperature T in Kelvin. The percentage differences between observed and calculated pressures, shown in the fourth column, indicate a SE of 0.025% on a single determination: this precision properly

© 1998 NRC Canada

Table 5. Properties of gas and aqueous phases in the (hl_1g) equilibrium.

Temperature (°C)	f_2 (MPa)	f_1 (MPa)	y_1 (× 10^3)	x_2^{l1} (× 10^3)	x_3^{l1} (× 10^6)
30.666	1.8946	0.00380	3.65	28.74	4.0
30.462	1.8527	0.00375	3.62	28.25	3.9
29.940	1.7539	0.00364	3.55	27.11	3.8
29.883	1.7441	0.00363	3.54	27.00	3.8
29.375	1.6530	0.00352	3.49	25.93	3.7
28.945	1.5796	0.00343	3.46	25.05	3.6
28.932	1.5774	0.00343	3.46	25.02	3.6
28.378	1.4899	0.00332	3.42	23.97	3.5
27.967	1.4284	0.00324	3.41	23.23	3.4
27.967	1.4271	0.00324	3.41	23.21	3.4
27.957	1.4265	0.00323	3.41	23.20	3.4
26.985	1.2911	0.00305	3.39	21.53	3.3
26.869	1.2764	0.00303	3.38	21.35	3.2
26.845	1.2730	0.00303	3.38	21.30	3.2
25.873	1.1539	0.00285	3.39	19.80	3.1
25.853	1.1506	0.00285	3.39	19.75	3.1
25.000	1.0564	0.00271	3.40	18.54	2.9
24.879	1.0438	0.00269	3.40	18.38	2.9
24.862	1.0406	0.00268	3.41	18.33	2.9
23.997	0.9555	0.00254	3.43	17.21	2.8
23.003	0.8651	0.00239	3.47	15.99	2.6
21.961	0.7800	0.00224	3.52	14.82	2.5
20.980	0.7074	0.00211	3.57	13.80	2.4
19.971	0.6401	0.00198	3.64	12.83	2.2
18.981	0.5802	0.00186	3.71	11.95	2.1
17.972	0.5250	0.00174	3.78	11.12	2.0
16.972	0.4753	0.00163	3.87	10.35	1.9
15.968	0.4303	0.00153	3.95	9.640	1.8
14.987	0.3905	0.00143	4.04	8.998	1.7
13.963	0.3527	0.00134	4.14	8.372	1.6
13.383	0.3329	0.00129	4.20	8.038	1.6
12.975	0.3197	0.00125	4.24	7.813	1.6
12.381	0.3013	0.00120	4.30	7.496	1.5
11.980	0.2895	0.00117	4.34	7.289	1.5
11.379	0.2727	0.00112	4.40	6.993	1.4
10.983	0.2622	0.00109	4.44	6.806	1.4
9.977	0.2371	0.00102	4.56	6.348	1.3
9.144	0.2180	0.00096	4.65	5.990	1.3
7.998	0.19422	0.00089	4.79	5.534	1.2
7.997	0.19429	0.00089	4.79	5.536	1.2
7.961	0.19324	0.00089	4.80	5.513	1.2
6.993	0.17549	0.00083	4.92	5.165	1.1
6.974	0.17483	0.00083	4.93	5.148	1.1
5.936	0.15773	0.00077	5.05	4.805	1.1
5.895	0.15668	0.00077	5.07	4.780	1.1
5.068	0.14436	0.00072	5.17	4.526	1.0
5.014	0.14322	0.00072	5.19	4.499	1.0
4.032	0.12985	0.00067	5.31	4.216	1.0
3.987	0.12904	0.00067	5.32	4.196	1.0
3.485	0.12256	0.00064	5.39	4.054	0.93
3.392	0.12142	0.00064	5.41	4.029	0.93
3.383	0.12131	0.00064	5.41	4.027	0.93
3.284	0.12009	0.00063	5.42	4.000	0.92
3.190	0.11895	0.00063	5.43	3.975	0.92
3.097	0.11782	0.00062	5.45	3.950	0.91
2.998	0.11664	0.00062	5.46	3.923	0.91
2.895	0.11541	0.00062	5.48	3.896	0.90
2.798	0.11427	0.00061	5.49	3.870	0.90

© 1998 NRC Canada

Table 6. Properties of gas and aqueous phases in the (s_1l_1g) equilibrium.

Temperature (°C)	f_2 (MPa)	f_1 (MPa)	y_1 (× 10^3)	x_2^{l1} (× 10^3)	x_3^{l1} (× 10^6)
3.8061	0.00176	0.00066	273.0	0.058	0.11
3.7967	0.00497	0.00066	117.0	0.163	0.19
3.7614	0.01484	0.00066	42.6	0.487	0.32
3.7160	0.02762	0.00066	23.4	0.908	0.44
3.6741	0.04067	0.00065	16.0	1.338	0.54
3.6291	0.05306	0.00065	12.3	1.748	0.61
3.5866	0.06544	0.00065	10.0	2.159	0.68
3.5285	0.08204	0.00065	7.98	2.711	0.76
3.5264	0.08270	0.00065	7.92	2.733	0.76
3.4953	0.09158	0.00064	7.16	3.030	0.80
3.4540	0.10363	0.00064	6.33	3.432	0.86
3.3917	0.12142	0.00064	5.41	4.029	0.93

corresponds with the 0.030% accuracy of the 500 psi gauge (11). The parameter –2160.7 has SE 1.2 K. The fifth column shows the SE on the pressure calculated from eq. [11].

The vapor pressure of the mixed liquids, $P(l_1l_2g)$, is less than that of pure deuterium sulfide (11), $p_2°$, and the ratio of pressures in this temperature range is best represented by

$$[12] \quad \ln [P(l_1l_2g) / p_2°] = -0.09553 + 25.7 / T$$

where $p_2°$ has been evaluated using eq. [2] from ref. 11 and has a SE of 0.027%. The combined SE on an observed single ratio of pressure is 0.037%, and the parameter 25.7 has SE 1.7 K.

At 25°C the computed ratio of $P(l_1l_2g)/p_2°$ is 0.99074 with SE 0.000088 and 17 degrees of freedom; this gives the deviation (1 – 0.99074), a student t ratio of 106, which confirms that $P(l_1l_2g)/p_2°$ is significantly less than unity at a very high level of probability.

Table 4 presents values for the intensive properties of the equilibrium (l_1l_2g) phases under the conditions of Table 1. Values in columns three to seven are, respectively, for the fugacities f_2 of deuterium sulfide and f_1 of deuterium oxide, for the gas-phase mole fraction y_1 of deuterium oxide, for the mole fractions x_2^{l1} of undissociated deuterium sulfide and x_3^{l1} of deuterium sulfide anion in the liquid deuterium oxide phase l_1. In column eight the saturation mole fraction x_1^{l2} of deuterium oxide in the liquid deuterium sulfide phase l_2 has been evaluated as $(1 - (f_2/f_2°))$, using fugacities assuming the deuterium sulfide solvent obeys Raoult's law. Column two provides the required Redlich–Kwong fugacity $f_2°$ for pure deuterium sulfide at its saturation vapor pressure $p_2°$ (11).

The saturation solubility x_1^{l2} of deuterium oxide in liquid deuterium sulfide l_2 is best discussed in terms of the Henry's law constant, $H_1^{l2} = f_1/x_1^{l2}$ MPa, for transfer of deuterium oxide from phase l_2 into the gas phase. Comparison of our 19 estimates of f_1/x_1^{l2} for deuterium oxide in liquid deuterium sulfide with 27 similar estimates of f_1/x_1^{l2} for water in liquid hydrogen sulfide, derived from the vapor pressure data of Scheffer (6), shows that f_1/x_1^{l2} for deuterium oxide in deuterium sulfide and for water in hydrogen sulfide are equal within experimental error at the same temperature between 33 and 19°C.

Combination of our 19 estimates of f_1/x_1^{l2} for deuterium oxide in deuterium sulfide with five estimates of f_1/x_1^{l2} for water in hydrogen sulfide, derived from the direct phase analyses of x_1^{l2} between 40 and 105°C by Carroll (22), gives the best representative equation

$$[13] \quad \ln [f_1/x_1^{l2}] = 9.0634 - 3102/T$$

for the Henry's law constant of deuterium oxide in liquid deuterium sulfide with SE of 3.6% on a single determination between 33 and 19°C: the parameter –3102 has SE 67 K. At 25°C the Henry's law constant H_1^{l2} for deuterium oxide in deuterium sulfide is 0.261 with SE 0.0022 MPa, that evaluated from ref. 6 for water in hydrogen sulfide is 0.261 with SE 0.0073 MPa.

The temperature dependence of x_1^{l2}, the saturation mole fraction of deuterium oxide in liquid deuterium sulfide between 33 and 19°C, is best represented by

$$[14] \quad \ln x_1^{l2} = 2.7474 - 2182/T$$

with SE of 4.6% on a single determination: the parameter –2182 has SE 70 K. At 25°C x_1^{l2} for deuterium oxide in deuterium sulfide is 0.0103 with SE 0.00011, that evaluated from (6) for water in hydrogen sulfide is 0.0119 with SE 0.00034: the difference 0.0016 of x_1^{l2} is significant.

D_2S D-hydrate – liquid D_2O – gas (hl_1g) equilibrium

Table 2 presents 58 equilibrium determinations of $P(hl_1g)$, the saturation vapor pressure of deuterium sulfide D-hydrate in contact with liquid deuterium oxide between 30.666 and 2.798°C. The seven determinations below 3.392°C are in metastable equilibrium.

The second column denotes the pressure gauge used, data marked 500, 200, and 16 used the 500 psi, 200 psi, and 16 psi gauges, respectively. The third column gives the square root of the weights used to combine the data from the various gauges into a properly weighted least-squares regression of the logarithm of pressure as a function of temperature.

The fourth column lists the observed $P(hl_1g)$, the fifth gives $P(hl_1g)$ calculated from the best model of the form (21)

© 1998 NRC Canada

$$[15a] \quad \ln P(\mathrm{hl_1g}) = b0 + b1{\cdot}u1 + b2{\cdot}u2 + b3{\cdot}u3 + b4{\cdot}u4 + b5{\cdot}u5 + b6{\cdot}u6$$

which is mathematically equivalent to

$$[15b] \quad \ln P(\mathrm{hl_1g}) = A + B/T + C \ln T + DT + ET^2 + FT^3 + GT^4$$

and which required seven parameters for a proper representation of the 58 data. The percentage differences between observed and calculated pressures, shown in the sixth column, yield an overall SE of 0.013% for a single determination of unit weight with 51 degrees of freedom. The seventh column shows the percentage error on the pressure estimated from the weighted regression model.

The 14 residuals using the 16 psi gauge indicate a SE of 0.013%, the 19 residuals at highest pressure using the 200 psi gauge indicate a SE of 0.018%, and the 14 residuals at highest pressure using the 500 psi gauge indicate a SE of 0.039%. Comparison of these SE estimates with the gauge accuracies (11) shows that (*i*) the data at low pressure are properly represented with SE 0.013% and a 0.020% accuracy of 16 psi gauge calibration, (*ii*) the data at intermediate pressure with SE 0.018% are somewhat more precise than the 0.030% accuracy of 200 psi gauge calibration, and (*iii*) the high-pressure data with SE 0.039% are slightly more variable than the 0.030% accuracy of 500 psi gauge calibration.

The six temperature variables $u1$–$u6$ in eq. [15*a*] are defined in ref. 21 with $x = (T - 298.15)/298.15$, and the parameters $b0$–$b6$ with their (SEs) are $b0$ = 0.157129 (0.000090), $b1$ = 33.0126 (0.010), $b2$ = 232.179 (1.2), $b3$ = 5590.55 (84), $b4$ = 121 174 (5900), $b5$ = 1 619 360 (130 000), and $b6$ = 8 860 000 (890 000). We note that the deuterium sulfide D-hydrate pressures properly define six temperature parameters $b1$–$b6$ at 25°C, that all parameters are positive with no alternation of sign, and that the value of the least significant parameter $b6$ could arise by pure chance at a probability level of less than one in 10^{15} times.

Regression of the 58 data, each assumed equally probable with unit weight, (*i*) gave an unrealistic poor fit of the 14 most accurate determinations at low pressure by the 16 psi gauge and (*ii*) indicated an unrealistic high SE estimate of 0.057% for a single determination, but (*iii*) still required a seven-parameter model (21) with $b1$–$b6$ all positive and highly significant.

The requirement of a seven-parameter model together with the unusually large positive values of $b1$–$b3$ show that the $P(\mathrm{hl_1g})$ data contain information of significant composition change with temperature for deuterium sulfide D-hydrate between 2.8 and 30.7°C.

Table 5 presents values for the intensive properties of the equilibrium $\mathrm{l_1}$ and g phases under the conditions of Table 2. The values listed under f_2, f_1, y_1, x_2^{l1}, and x_3^{l1} have the same meaning as in Table 4.

The saturation vapor pressure $P(\mathrm{hl_1g})$ of deuterium sulfide D-hydrate is about 88% of that for hydrogen sulfide hydrate (6, 7) at the same temperature. This ratio of $P(\mathrm{hl_1g})$ is similar to the ratio of 81% exhibited by the Structure I cyclopropane D-hydrate relative to its cyclopropane hydrate (23) at the same temperature between 6 and 16°C.

D-Ice – liquid D_2O – gas ($\mathrm{s_1l_1g}$) equilibrium

Table 3 presents 11 determinations of $t(\mathrm{s_1l_1g})$, the equilibrium temperature of D-ice with a deuterium oxide solution saturated with deuterium sulfide at total pressure $P(\mathrm{s_1l_1g})$ between 0.00242 and 0.10542 MPa. The final row presents the temperature $t(\mathrm{hs_1l_1g})$ determined at the total pressure $P(\mathrm{hs_1l_1g})$ 0.12364 MPa. The third column shows calculated temperatures from the representative equation

$$[16] \quad t(\mathrm{s_1l_1g}) = \underset{(0.00047)}{3.81473} - \underset{(0.0067)}{3.4258}\, P(\mathrm{s_1l_1g})$$

with $t(\mathrm{s_1l_1g})$ in °C and $P(\mathrm{s_1l_1g})$ in MPa: the SEs are shown in parenthesis below the parameters. Differences between observed and calculated temperatures, shown in the fourth column, indicate a SE of 0.00090°C on a single temperature determination, with 10 degrees of freedom. The fifth column shows the SE estimate on the temperature evaluated from eq. [16].

The first row of Table 3 shows an estimated triple-point temperature of 3.8125 with SE 0.00047°C: this disagrees significantly with our first direct measurement of the triple-point at 3.800 with SE 0.0005°C in a preliminary experiment in 1963. We suggest in that first experiment, where we were unaware of the need to bracket the thermostat temperature both above and below the stirred reactor temperature, we unwittingly had applied a "too large" cooling differential to the stirred reactor, and that had caused the negative bias –0.0125°C on the observed temperature. We note that the 12 determinations presented in Table 3 were made at the end of our study in 1966, with more experience and with temperature bracketing, and therefore probably with less bias.

Table 6 presents values for the intensive properties of the equilibrium $\mathrm{l_1}$ and g phases under the conditions of Table 3.

Upper quadruple point $Q(\mathrm{hl_1l_2g})$

The upper quadruple point $Q(\mathrm{hl_1l_2g})$ is the invariant four-phase point at the highest temperature where the D-hydrate can coexist in equilibrium with a gas phase: it is located at the cut of the two univariant three-phase curves $(\mathrm{hl_1g})$ and $(\mathrm{l_1l_2g})$. The $(\mathrm{hl_1g})$ curve has been defined by the upper 14 determinations using the 500 psi gauge between 25.000 and 30.666°C and indicated a SE of 0.042% on a single pressure determination with 10 degrees of freedom. The $(\mathrm{l_1l_2g})$ curve has been defined by eq. [11]. The quadruple-point temperature $t(\mathrm{hl_1l_2g})$ is 30.770 with SE 0.0043°C and the quadruple-point pressure $P(\mathrm{hl_1l_2g})$ is 2.3263 with SE 0.00018 MPa.

Comparison of $Q(\mathrm{hl_1l_2g})$ for deuterium sulfide D-hydrate with that for hydrogen sulfide hydrate, reported by Scheffer (6) at 29.5°C and at 2.24 MPa, shows a difference of temperature of 1.27°C and a difference of pressure of 0.09 MPa.

Lower quadruple point $Q(\mathrm{hs_1l_1g})$

The lower quadruple point $Q(\mathrm{hs_1l_1g})$ is the invariant four-phase point at the lowest temperature where the D-hydrate coexists in stable equilibrium with a liquid deuterium oxide phase: it is located at the cut of the two univariant three-phase curves $(\mathrm{hl_1g})$ and $(\mathrm{s_1l_1g})$. The $(\mathrm{hl_1g})$ curve has been defined by the lower 10 determinations using the 16 psi gauge between 3.987 and 2.798°C and indicated a SE of 0.0072% on a single pressure determination with 8 degrees

© 1998 NRC Canada

of freedom. The (s_1l_1g) curve has been defined by eq. [16]. The lower quadruple-point temperature $t(hs_1l_1g)$ has been evaluated at 3.3912 with SE 0.00057°C and the quadruple-point pressure $P(hs_1l_1g)$ at 0.12363 with SE 0.000002 MPa.

The lower quadruple point, determined directly, has given the temperature $t(hs_1l_1g)$ at 3.3917 with SE 0.00090°C and the pressure $P(hs_1l_1g)$ at 0.12364 with SE 0.000011 MPa.

Comparison of $Q(hs_1l_1g)$ for deuterium sulfide D-hydrate with that for hydrogen sulfide hydrate evaluated by Scheffer and Meyer (7) at –0.4°C and at about 0.094 MPa, indicates a difference of temperature of 3.79°C and of pressure of about 0.030 MPa. The ratio of $P(hs_1l_1g)$ for deuterium sulfide D-hydrate relative to hydrogen sulfide hydrate at their quadruple points is equal to that 1.31 ratio exhibited by Structure I cyclopropane D-hydrate (23) relative to cyclopropane hydrate at their quadruple points.

Acknowledgments

We wish to thank Dr. Howard K. Rae of Atomic Energy of Canada Limited for his assistance in obtaining isotope analysis for our deuterium oxide sample. This work was supported in part by grants under the National Research Council of Canada, Industrial Research Assistance Program, for 1963–1966.

References

1. D.N. Glew. Can. J. Chem. **38**, 208 (1960).
2. D.N. Glew. J. Phys. Chem. **66**, 605 (1962).
3. R.H. Wright and O. Maass. Can. J. Res. **6B**, 94 (1932).
4. F.T. Selleck, L.T. Carmichael, and B.H. Sage. Ind. Eng. Chem. **44**, 2219 (1952).
5. R. de Forcrand and P. Villard. Compt. Rend. **106**, 849 (1888).
6. F.E.C. Scheffer. Proc. R. Acad. Sci. Amsterdam, **13**, 829 (1911).
7. F.E.C. Scheffer and G. Meyer. Proc. R. Acad. Sci. Amsterdam, **21**, 1338 (1919).
8. F.T. Barr and W.P. Drews. Chem. Eng. Progr. **56**(3), 49 (1960).
9. J.S. Drury. Progr. Nucl. Energy, **4**, 308 (1961).
10. D.N. Glew, H.D. Mak, and N.S. Rath. Can. J. Chem. **45**, 3059 (1967).
11. E.C.W. Clarke and D.N. Glew. Can. J. Chem. **48**, 764 (1970).
12. E.C.W. Clarke and D.N. Glew. Can. J. Chem. **49**, 691 (1971).
13. R.N. Goldberg and R.D. Weir. Pure Appl. Chem. **10**, 1545 (1992).
14. R.J. Berry. Can. J. Phys. **37**, 1230 (1959).
15. N.R. Draper and H. Smith. Applied regression analysis. 2nd ed. John Wiley & Sons, Inc., New York. 1981.
16. O. Redlich and J.N.S. Kwong. Chem. Rev. **44**, 233 (1949).
17. R.R. Spear, R.L. Robinson, Jr., and K.C. Chao. Ind. Eng. Chem. Fundam. **8**, 2 (1969).
18. P.G. Hill and R.D.C. MacMillan. Ind. Eng. Chem. Fundam. **18**, 412 (1979).
19. G.S. Kell. J. Phys. Chem. Ref. Data, **6**, 1109 (1977).
20. J.A. Barbero, K.G. McCurdy, and P.R. Tremaine. Can. J. Chem. **60**, 1872 (1982).
21. E.C.W. Clarke and D.N. Glew. Trans. Faraday Soc. **62**, 539 (1966).
22. J.J. Carroll. Ph.D thesis, University of Alberta, Edmonton, 1990.
23. D.R. Hafemann and S.L. Miller. J. Phys. Chem. **73**, 1392, (1969); **73**, 1398 (1969).

© 1998 NRC Canada

Transition metal azolates from metallocenes. Part 3: Polymeric manganese(II) and nickel(II) pyrazolates; synthesis, characterization, and magnetochemistry

Alan Storr, David A. Summers, and Robert C. Thompson

Abstract: Direct reactions of nickelocene and manganocene with molten pyrazoles in an inert atmosphere or under vacuum have led to the isolation of the following metal pyrazolate compounds: $[Ni(4\text{-}Xpz)_2]_x$ (where X = H, Cl and pz = pyrazolate); $[M(4\text{-}Xdmpz)_2]_x$ (where X = H, CH_3, Cl, Br and M = Ni, Mn and dmpz = 3,5-dimethylpyazolate); and $[Mn(4\text{-}Xpz)_2(4\text{-}XpzH)]_x$ (where X = Cl, Br and pzH = pyrazole). On the basis of indirect evidence all compounds are considered to have extended chain structures with metal ions linked in chains by double bridging pyrazolates. The two $[Ni(4\text{-}Xpz)_2]_x$ compounds are diamagnetic while all others are paramagnetic. Variable temperature magnetic susceptibility studies on the paramagnetic compounds reveal antiferromagnetic coupling between neighbouring metal ions. Analysis of the magnetic data (Hamiltonian of the form $H = -2J \Sigma S_i \cdot S_j$) yields values of the exchange coupling constant J of -14 to -17 cm^{-1} for the $[Ni(4\text{-}Xdmpz)_2]_x$ compounds, –1.2 to –2.1 cm^{-1} for the $[Mn(4\text{-}Xdmpz)_2]_x$ compounds, and –0.41 cm^{-1} for the $[Mn(4\text{-}Xpz)_2(4\text{-}XpzH)]_x$ compounds.

Key words: nickel, manganese, manganocene, nickelocene, pyrazolates, antiferromagnetic exchange.

Résumé : Par réactions directes du nickelocène et du manganocène avec des pyrazoles fondus, dans une atmosphère inerte ou sous vide, on a isolé les pyrazolates de métal suivants: $[Ni(4\text{-}Xpz)_2]_x$ (dans lesquels X = H, Cl et pz = pyrazolate); $[M(4\text{-}XpzH)]_x$ (dans lesquels X = H, CH_3, Cl, Br et M = Ni, Mn et dpmz = 3,5-diméthylpyrazolate) et $[Mn(4\text{-}Xpz)_2(4\text{-}XpzH)]_x$ (dans lesquels X = Cl, Br et pzH = pyrazole). Sur la base de données indirectes, on considère que tous les composés comportent des structures en chaînes étendues avec des ions métalliques liés aux chaînes par des pyrazolates agissant comme doubles ponts. Les deux composés $[Ni(4\text{-}Xpz)_2]_x$ sont diamagnétiques alors que tous les autres sont paramagnétiques. Des études de susceptibilité magnétique à température variable sur les composés paramagnétiques mettent en évidence la présence d'un couplage antiferromagnétique entre les ions métalliques voisins. L'analyse de données magnétiques (hamiltonien de la forme $H = -2J \Sigma S_i \cdot S_j$) conduit à des constantes de couplage d'échange, J, qui vont de –14 à –17 cm^{-1} pour les composés $[Ni(4\text{-}Xdmpz)_2]_x$, de –1,2 à –2,1 cm^{-1} pour les composés $[Mn(4\text{-}Xdmpz)_2]_x$ et de –0,41 cm^{-1} pour les composés $[Mn(4\text{-}Xpz)_2(4\text{-}XpzH)]_x$.

Mots clés : nickel, manganèse, manganocène, nickelocène, pyrazolates, échange antiferromagnétique.

[Traduit par la Rédaction]

Introduction

Pyrazole and pyrazolate containing transition metal coordination complexes have been extensively investigated and several review papers have been devoted to the topic (1–4). Our interest in pyrazolate ligands stems from their tendency (*i*) to bind metal ions in an exobidentate fashion and hence to form oligo- and poly-metallic compounds and (*ii*) to act as efficient mediators of magnetic exchange interactions. In previous studies we have synthesized several transition metal azolate complexes and investigated their magnetic properties (5–11). The main objectives in this research have been to gain a better understanding of the factors that influence the nature and magnitude of magnetic exchange between the transition metal centers in these materials. To achieve this and explore both electronic and steric effects it is necessary to study a variety of systems involving different C-substituted pyrazolates and different metals. To date our research has involved investigations on copper(II) and cobalt(II) systems (7–11) and the work described here complements these earlier studies.

Several synthetic approaches to generate linear chain transition metal pyrazolate polymers have been reported. Seel and Sperber described the preparation of $[Fe(pz)_2]_x$ and $[Fe(pz)_3]_x$ (where pz = pyrazolate) from a variety of iron derivatives such as $Fe(CO)_5$ or $[CpFe(CO)_2]_2$ (12). Bagley et al. prepared $[Co(dmpz)_2]_x$ (where dmpz = 3,5-dimethylpyrazolate) from Co(II) acetylacetonate and hydrazine in

Received May 8, 1998.

A. Storr,[1] D.A. Summers, and R.C. Thompson.[1]
Department of Chemistry, The University of British Columbia, Vancouver, BC V6T 1Z1, Canada.

[1]Authors to whom correspondence may be addressed. Telephone: R.C. Thompson: (604) 822-4979, A. Storr: (604) 822-3962. Fax: (604) 822-2847. E-mail: thompson@chem.ubc.ca and storr@chem.ubc.ca

© 1998 NRC Canada

isopropanol (13) and synthesized several other cobalt(II) C-substituted pyrazolate analogues by reacting cobalt(II) salts with the appropriate pyrazole in basic solutions. Trofimenko reported, as unpublished results, the preparation of nickel(II) and copper(II) pyrazolates by pyrolysis of the appropriate $M(pzH)_4(OAc)_2$ (OAc = acetate) complexes or by reacting pyrazole with metal salts in basic solutions (1). The preparation of $[Co(dmpz)_2]_x$, and $[Ni(dmpz)_2 \cdot 2H_2O]_x$, by the reaction of the appropriate bis-acetylacetonato metal(II) complex with hydrazine, was described by Singh et al. (14). A series of reports by Vos and Groeneveld described the synthesis and characterization of metal pyrazolate complexes of Mn, Co, Ni, Cu, Zn, and Cd with 4-Xpz and 4-Xdmpz (X = H, CH_3, Cl, Br, I, NO_2) (15, 16). The materials were prepared by reacting aqueous solutions of metal salts with basic aqueous solutions of pyrazoles. It should be noted that in many cases the reported purity of the materials described in this latter work was based on metal analysis alone, and attempts in this laboratory to reproduce much of this work led, at best, to the formation of impure products. The synthesis of $[Fe(pz)_2]_x$ from $FeCl_2$ and lithium pyrazolate in toluene has been described by Strahle et al. (17) and recently Vecchio-Sadus described an electrochemical synthesis route to a series of transition metal pyrazolates (18).

A novel synthetic approach, detailed in our previous reports, involving the reaction between metal shot (Cu or Co) and molten pyrazoles under a dioxygen atmosphere led not only to transition metal pyrazolates of high purity but also, in some cases, afforded crystalline materials (8*a*, 8*d*). In addition, three $[Cu(4\text{-}Xdmpz)_2]_x$ complexes (X = Cl, Br, CH_3) were prepared by reacting the corresponding trimetallic copper(I) complex, $[Cu(4\text{-}Xdmpz)]_3$, again with the appropriate molten pyrazole under an atmosphere of dioxygen (9*a*). Another method of producing binary metal pyrazolates, $[M(pz^*)_2]_x$ (M = Zn, Pt, Pd and pz^* = substituted pyrazolates), involves removing thermally the neutral coordinated pz^*H from complexes of formulation $[M(pz^*)_2(pz^*H)]_2$ (8*c*, 19–21).

Our attempts to prepare pyrazolate complexes of nickel(II) by the metal – molten azole method yielded pure samples only for $[Ni(pz)_2]_x$. In an earlier report we described an alternative synthetic approach involving nickelocene that led to the preparation of diamagnetic oligometallic nickel(II) pyrazolate complexes (6). The present report details the use of metallocenes to obtain several paramagnetic linear chain polymers containing either nickel(II) or manganese(II). The idea to synthesize pyrazolates via this pathway came from a 1977 article by Blake et al. in which two diamagnetic nickel(II) pyrazolate polymers, prepared by reacting nickelocene with the appropriate azole in benzene solvent, were reported (22). In the current work, eight paramagnetic complexes of composition $[M(4\text{-}Xdmpz)_2]_x$ (where M = Ni(II), Mn(II) and X = H, Cl, Br, CH_3), two paramagnetic complexes of composition $[Mn(4\text{-}Xpz)_2(4\text{-}XpzH)]_x$ (where X = Br, Cl), and two diamagnetic complexes of composition $[Ni(4\text{-}Xpz)_2]_x$ (where X = H, Cl) were obtained. We report here variable temperature (2–300 K) magnetic susceptibilities and other studies on these systems. The materials prepared in the present work were not obtained in a form suitable for single crystal X-ray diffraction studies; however, on the basis of indirect spectroscopic and other evidence they are proposed to have structures involving extended chains of metal ions doubly bridged by pyrazolate ligands. The polymeric copper(II) and cobalt(II) pyrazolates, previously studied, have been shown to exhibit this structural motif, with the structures of three of the copper compounds having been determined by single crystal X-ray diffraction studies (8*a*, 8*d*).

Experimental

Syntheses

Nickelocene and manganocene were prepared using the method of R.B. King (23). $Ni(Cp)_2$ was prepared from nickel powder, bromine, and cyclopentadiene while $Mn(Cp)_2$ was prepared from manganese powder, bromine, and sodium cyclopentadienide. Pyrazoles were used as supplied (Aldrich) or prepared as described previously (8*d*, 24). Solvents used were reagent grade and were dried and distilled under an atmosphere of dry dinitrogen before use.

$[Ni(4\text{-}Hpz)_2]_x$

$[Ni(4\text{-}Hpz)_2]_x$ was prepared using two different synthetic approaches. The complex was first produced by heating (110°C) nickel powder (0.24 g, 4.1 mmol) with an excess of molten pyrazole (1.25 g, 18 mmol) under normal atmosphere conditions for 48 h. The mixture was allowed to cool and the excess pyrazole was removed by washing with dichloromethane. The pure product was isolated as an insoluble orange powder by physical separation, using a magnet to remove the unreacted nickel powder. Anal. calcd. for $NiC_6H_6N_4$: C 37.4, H 3.1, N 29.1; found: C 37.4, H 3.4, N 28.9.

$[Ni(4\text{-}Hpz)_2]_x$ was also prepared by reacting a mixture of freshly sublimed nickelocene (0.5 g, 2.6 mmol) with an excess of molten pyrazole (4.5 g, 65 mmol) at 100°C under a dry nitrogen atmosphere for 24 h. After cooling, the excess pyrazole was dissolved in dichloromethane and the insoluble orange powder was isolated by vacuum filtration. TGA: 61% weight loss between 400°C and 515°C. Anal. calcd. for $NiC_6H_6N_4$: C 37.4, H 3.1, N 29.1; found: C 37.2, H 3.2, N 29.2.

$[Ni(4\text{-}CIpz)_2]_x$

This compound was prepared in a manner analogous to the latter method described above for the preparation of $[Ni(4\text{-}Hpz)_2]_x$. TGA: 70% weight loss between 360°C and 545°C. Anal. calcd. for $NiC_6H_4N_4Cl_2$: C 27.5, H 1.5, N 21.4; found: C 27.8, H 1.4, N 21.2.

$[Ni(4\text{-}Hdmpz)_2]_x$

The synthesis of $[Ni(4\text{-}Hdmpz)_2]_x$ was attempted, without success, using the nickel metal in molten pyrazole reaction that was employed in the $[Ni(4\text{-}Hpz)_2]_x$ preparation described above. The target compound was successfully prepared, however, using nickelocene and 3,5-dimethylpyrazole under inert atmosphere conditions. Freshly sublimed $Ni(Cp)_2$ (0.25 g, 1.3 mmol) was mixed intimately with an excess of 3,5-dimethylpyrazole (1.34 g, 19 mmol) and placed in a dry and oxygen-free glass Carius tube. The tube was flame-sealed under vacuum and placed in an oven (140°C) for 48 h. Following the initial melting of the 3,5-dimethylpyrazole a green solution, presumably of

© 1998 NRC Canada

nickelocene dissolved in the molten pyrazole, was observed. After approximately 10 min the colour of the solution had changed to a deep red and a few hours later a puce powder had begun to precipitate out. After 48 h the amount of puce solid had increased considerably and the intensity of the colour in the solution had diminished. At this point the tube was allowed to cool and the insoluble product (0.31 g, 94.3%) was purified by removal of the excess 3,5-dimethylpyrazole by dissolution in dry and oxygen-free THF. TGA: 70% weight loss between 380°C and 520°C. Anal. calcd. for $NiC_{10}H_{14}N_4$: C 48.2, H 5.7, N 22.5; found: C 48.1, H 5.7, N 22.3.

$[Ni(4\text{-}Xdmpz)_2]_x$ (where X = Br, Cl, or CH_3)

These polymers were prepared from nickelocene and an excess of the appropriate pyrazole as described above for the synthesis of $[Ni(4\text{-}Hdmpz)_2]_x$. $[Ni(4\text{-}Brdmpz)_2]_x$; TGA: 82% weight loss between 315°C and 595°C. Anal. calcd. for $NiC_{10}H_{l2}N_4Br_2$: C 29.5, H 3.0, N 13.8; found: C 29.9, H 3.0, N 14.1. $[Ni(4\text{-}Cldmpz)_2]_x$; TGA: 76% weight loss between 300°C and 495°C. Anal. calcd. for $NiC_{10}H_{12}N_4Cl_2$: C 37.8, H 3.8, N 17.6; found: C 38.1, H 3.9, N 17.5. $[Ni(4\text{-}CH_3dmpz)_2]_x$; TGA: 73% weight loss between 335°C and 480°C. Anal. calcd. for $NiC_{12}H_{18}N_4$: C 52.0, H 6.6, N 20.2; found: C 52.3, H 6.4, N 20.1.

$[Mn(4\text{-}Hdmpz)_2]_x$

Manganocene (1.1 g, 5.9 mmol) and 3,5-dimethylpyrazole (5.19 g, 54 mmol) were intimately mixed and placed in a Carius tube. The tube was flame-sealed under vacuum and placed in an oven (150°C). The 4-HdmpzH melted after a few minutes resulting in a mixture of molten ligand and solid manganocene. It was not possible to determine the extent of the reaction by visual means as both the manganocene and desired product appear as beige solids in the colourless and clear molten 4-HdmpzH. After 2 weeks the tube was allowed to cool, and the excess ligand to solidify, prior to the tube being opened under a dinitrogen atmosphere. The beige solid product was isolated by dissolving the excess 3,5-dimethylpyrazole in THF, benzene, and hexanes. The slurry was vacuum filtered and the $[Mn(4\text{-}Hdmpz)_2]_x$ collected on the filter. The product was dried, and any remaining volatile starting materials removed, under vacuum for 48 h, yielding 0.74 g (52%) of $[Mn(4\text{-}Hdmpz)_2]_x$ as a beige powder. Anal. calcd. for $C_{10}H_{14}N_4Mn$: C 49.0, H 5.8, N 22.9; found: C 49.0, H 5.7, N 23.0.

$[Mn(4\text{-}Xdmpz)_2]_x$ (where X = Br, Cl, or CH_3) and $[Mn(4\text{-}Xpz)_2(4\text{-}XpzH)]_x$ (where X = Br or Cl)

These polymers were prepared from manganocene and an excess of the appropriate pyrazole as described above for the synthesis of $[Mn(4\text{-}Hdmpz)_2]_x$. $[Mn(4\text{-}Brdmpz)_2]_x$; TGA: 76% weight loss between 265°C and 660°C. Anal. calcd. for $C_{10}H_{12}N_4Br_2Mn$: C 29.8, H 3.0, N 13.9; found: C 30.0, H 3.0, N 14.0. $[Mn(4\text{-}Cldmpz)_2]_x$; TGA: 75% weight loss between 250°C and 480°C. Anal. calcd. for $C_{10}H_{12}N_4Cl_2Mn$: C 38.2, H 3.9, N 17.8; found: C 38.5, H 3.8, N 17.7. $[Mn(4\text{-}CH_3dmpz)_2]_x$; TGA: 65% weight loss between 250°C and 505°C. Anal. calcd. for $C_{12}H_{18}N_4Mn$: C 52.8, H 6.6, N 20.5; found: C 52.7, H 6.6, N 20.3. $[Mn(4\text{-}Brpz)_2(4\text{-}BrpzH)]_x$; Anal. calcd. for $C_9H_7N_6Br_3Mn$: C 21.9, H 1.4, N 17.1; found: C 21.6, H 1.2, N 16.8. $[Mn(4\text{-}Clpz)_2(4\text{-}ClpzH)]_x$; TGA: 78% weight loss between 250°C and 700°C. Anal. calcd. for $C_9H_7N_6Cl_3Mn$: C 30.0, H 2.0, N 23.3; found: C 29.5, H 2.0, N 23.0.

Physical characterization

All compounds characterized here were found to be insoluble in common solvents and to decompose upon dissolution in acid. Differential scanning calorimetry (DSC; 35–600°C) and thermal gravimetric analysis (TGA; 35–800°C) measurements were made using a TA Instruments DSC 910S cell and a TA Instruments TGA 51 unit, respectively.

Electronic spectra (200–3000 nm) were obtained at room temperature on Nujol mulls pressed between quartz plates using a Varian Cary 5 UV–Vis-NIR spectrophotometer. Infrared spectra (4000–400 cm^{-1}) were recorded at room temperature on a Bomen FTIR spectrophotometer. Samples were prepared by compressing a powdered mixture of compound and KBr between portions of pure powdered KBr.

Magnetic susceptibilities were measured over the temperature range 2–300 K using a Quantum Design (MPMS) SQUID magnetometer (applied field = 10 000 G). A specially designed sample holder, as described previously (8*f*), was used to minimize the background signal. Magnetic susceptibilities were corrected for diamagnetism: nickel, –11; manganese, –14; $C_3H_3N_2$, –40; $C_3H_2N_2Br$, –72; $C_3H_2N_2Cl$, –61; $C_3H_3N_2Br$, –75; $C_3H_3N_2Cl$, –64; $C_5H_7N_2$, –62; $C_5H_6N_2Br$, –90; $C_5H_6N_2Cl$, –79; $C_6H_9N_2$, –74 (values in 10^{-6} cm^3 mol^{-1}). Data reported here are on a per mole of metal center basis.

Molecular modeling

Molecular models of $[Ni(4\text{-}Xdmpz)_2]_x$ in which the nickel(II) ions are present in either a square planar or tetrahedral NiN_4 chromophore geometry were generated by utilizing single crystal X-ray diffraction data from the related trimetallic complex $[CpNi(4\text{-}Cldmpz)_2]_2Ni$ (6). The crystallographic data of this trimetallic complex were manipulated to produce two different linear chain structures: one in which all of the nickel(II) centers are present in square planar NiN_4 chromophore geometries and the other in which the nickel ions are present in ideal tetrahedral geometries. To generate these models the internal bond lengths and angles in the pyrazolate rings were assumed to be identical to those found in the trimetallic system. In addition, the nickel to nitrogen bond lengths determined in $[CpNi(4\text{-}Cldmpz)_2]_2Ni$ were used in both of the modeled structures.

Results and discussion

Syntheses and stabilities

Following largely unsuccessful attempts to prepare manganese(II) and nickel(II) binary metal pyrazolates by reacting pure metal with molten pyrazoles, a synthetic method employed with success in the preparation of many copper(II) and cobalt(II) derivatives, an alternate approach was developed. This approach, involving the direct reaction of a metallocene with an excess of the appropriate pyrazole in an inert atmosphere or under vacuum gave, in the case of nickelocene, either oligometallic cyclopentadienyl nickel(II) pyrazolates (6) or, depending on conditions, binary nickel(II)

© 1998 NRC Canada

Fig. 1. Electronic spectra: (*a*) and (b), $[Ni(4\text{-}Hpz)_2]_x$ at high and low mull concentrations respectively; (*c*) and (d), $[Ni(4\text{-}Hdmpz)_2]_x$ at high and low mull concentrations respectively.

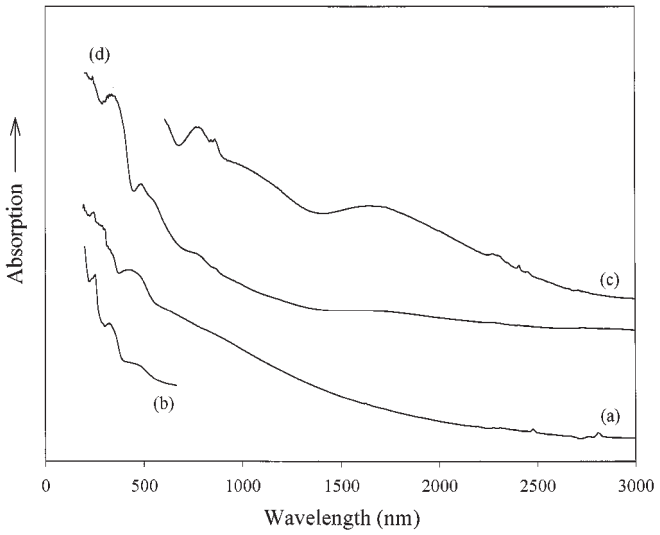

pyrazolates of composition $[Ni(4\text{-}Xpz)_2]_x$ (X = H or Cl) and $[Ni(4\text{-}Xdmpz)_2]_x$ (X = H, CH_3, Cl, or Br). The corresponding reactions with manganocene yielded manganese(II) pyrazolates of composition $[Mn(4\text{-}Xdmpz)_2]_x$ (X = H, CH_3, Cl, or Br) and $[Mn(4\text{-}Xpz)_2(4\text{-}XpzH)]_x$ (X = Cl, Br).

The six nickel(II) compounds reported here were all characterized as being air stable and thermally robust. TGA experiments showed decomposition at temperatures above 300°C. That decomposition occurs without melting was shown by DSC measurements that revealed no thermal events at temperatures below the onset of thermal decomposition. In addition to being thermally robust, all six of the nickel complexes were found to be insoluble in both polar and nonpolar solvents.

The manganese(II) complexes were also found to be thermally robust. TGA and DSC experiments on four of these compounds ($[Mn(4\text{-}Xdmpz)_2]_x$, (X = CH_3, Cl, Br) and $[Mn(4\text{-}Clpz)_2(4\text{-}ClpzH)]_x$) show them to decompose without melting at temperatures above 250°C. All six manganese compounds were also found to be insoluble in polar and nonpolar solvents: however, unlike the nickel compounds, the manganese derivatives decompose on exposure to air. The sensitivity to air is somewhat variable, with the four $[Mn(4\text{-}Xdmpz)_2]_x$ complexes being more sensitive than the two $[Mn(4\text{-}Xpz)_2(4\text{-}XpzH)]_x$ compounds. The presence of the additional neutral pyrazole appears to be responsible for the added stability of the latter complexes.

Electronic spectra

The nickel compounds can be divided into two groups, the four $[Ni(4\text{-}Xdmpz)_2]_x$ derivatives in the first and the two $[Ni(4\text{-}Xpz)_2]_x$ forming the second. Electronic spectra of powdered (mulled) samples revealed distinct spectral characteristics for each group. The electronic spectra of the X = H derivatives of the two groups are shown in Fig. 1. The $[Ni(4\text{-}Xpz)_2]_x$ spectra comprise a single strong band attributed to a *d–d* transition at 440 nm, consistent with square planar NiN_4 chromophores (25). Two higher energy bands, centered at 250 and 350 nm, are clearly visible in the spectra

Fig. 2. Modeled polymer segment for $[Ni(4\text{-}Hdmpz)_2]_x$ in which the metal centers are present in a square planar geometry.

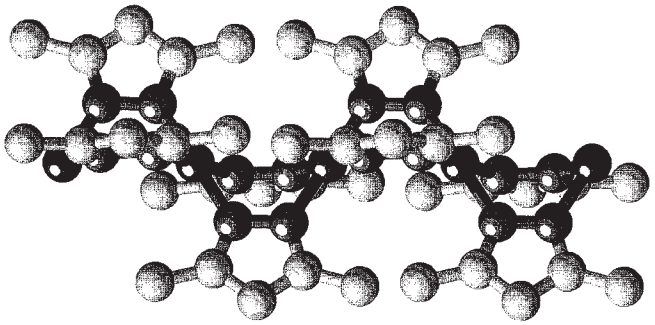

of samples run at lower mulled concentrations (Fig. 1(*b*) and 1(*d*)) and are likely charge transfer in origin. The $[Ni(4\text{-}Xdmpz)_2]_x$ compounds have spectra with three observable spin-allowed *d–d* transitions as is expected for tetrahedral Ni(II), and one observable spin-forbidden *d–d* transition. The three spin-allowed transitions, ν_1: $^3T_1(F) \rightarrow {}^3T_2(F)$, ν_2: $^3T_1(F) \rightarrow {}^3A_2(F)$, and ν_3: $^3T_1(F) \rightarrow {}^3T_1(P)$ are observed in the ranges of 1670–1700 nm, 770–780 nm, and 520–530 nm, respectively. The remaining observed transition has been assigned as $^3T_1(F) \rightarrow {}^1D$ and lies in the range 860–870 nm. Employing ν_1 and ν_2 values of 6000 and 13 000 cm^{-1} and the appropriate energy level expressions (26), ligand field parameter Dq, and *B* values of 700 and 970 cm^{-1}, respectively, were obtained. Employing these parameter values, ν_3 is calculated to be at 19 600 cm^{-1} (510 nm), in good agreement with experiment. Spectra obtained on highly concentrated mulls showed a broad feature in the 1000 nm region. It seems unlikely that a single feature of this nature is due to an additional nickel(II) chromophore. It is possibly part of the strong background signal that arises due to light scattering from mulled samples.

We were unable to obtain electronic spectra of solid samples of the manganese compounds. These are high-spin d^5 complexes and the resulting low-intensity spin-forbidden electronic transitions could not be observed on our mulled samples.

Structural considerations

The high thermal stabilities and low solubilities of the binary nickel(II) pyrazolates are properties consistent with polymeric structures for these materials. Moreover, extended-chain double pyrazolate-bridged structures are supported by the stoichiometry, the evidence from electronic spectroscopy that the metals are four coordinate, and by the fact that pyrazolate ligands tend to bind to metal centers in an exobidentate rather than endobidentate fashion (1–3). We note, though, that large ring structures as described, for example, by Ardizzoia et al. (27), cannot be ruled out.

Further support for a tetrahedral NiN_4 chromophore in the case of $[Ni(4\text{-}Hdmpz)_2]_x$ came from X-ray powder diffraction studies. These showed the compound to be isomorphous with the cobalt analogue $[Co(4\text{-}Hdmpz)_2]_x$ (28) for which strong evidence in favour of a linear chain polymer with tetrahedral metal centers has been presented (9*b*).

Magnetic studies on the nickel compounds, to be described in detail below, provide further evidence in support

© 1998 NRC Canada

Fig. 3. Magnetic susceptibility versus temperature plots: (*a*) for $[Ni(4\text{-}Hdmpz)_2]_x$ and (*b*) for $[Ni(4\text{-}CH_3dmpz)_2]_x$. Circles are experimental data and lines are calculated from theory as described in the text.

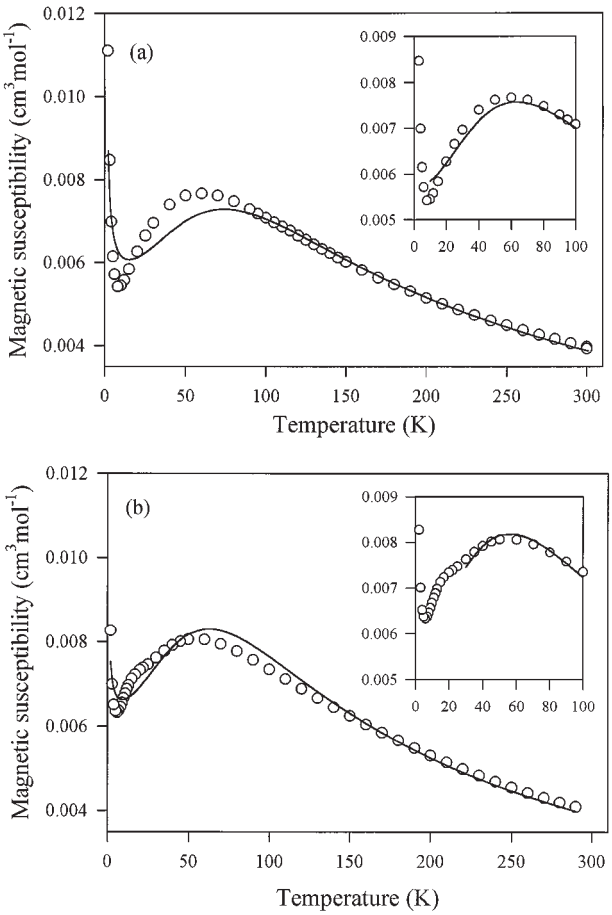

Fig. 4. Magnetic susceptibility versus temperature plots: (*a*) for $[Mn(4\text{-}Hdmpz)_2]_x$ and (*b*) for $[Mn(4\text{-}Clpz)_2(4\text{-}ClpzH)]_x$. Circles are experimental data and lines are calculated from theory as described in the text.

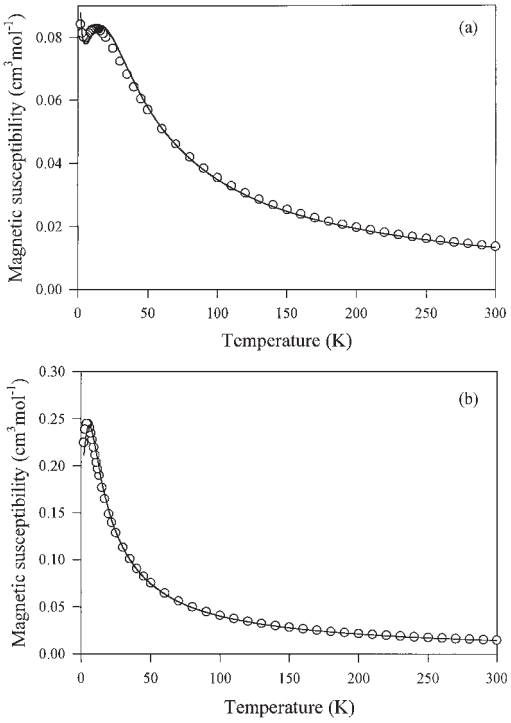

of the NiN_4 chromophore geometries proposed above. As expected, the complexes proposed to have square planar nickel ions are diamagnetic while those with tetrahedral geometry are paramagnetic. It thus appears that while both groups of nickel(II) polymers have similar extended-chain double pyrazolate-bridged structures, each group has a distinctive NiN_4 chromophore. For the polymers incorporating the 4-Xpz ligands the nickel is able to obtain the coordination geometry preferred for four-coordinate Ni(II), namely, square planar. However, in polymers incorporating the relatively bulky 4-Xdmpz ligands, it appears the nickel is forced into a distorted tetrahedral geometry due to steric interactions.

The geometry-related steric interaction, with nickel(II) in a square planar environment, is illustrated in Fig. 2. This diagram, which models a portion of the chain, was generated using X-ray crystallographic data from the related trimetallic compound $[CpNi(4\text{-}Cldmpz)_2]_2Ni$ (6). Steric crowding between the methyl groups in the 3 and 5 positions on neighbouring, translationally equivalent, pyrazolates is evident in the figure. The $C(CH_3)\cdots C(CH_3)$ distances in this structure are calculated to be 1.24 Å. Allowing the chromophores to become regular tetrahedral while keeping N—N and Ni—N distances the same as in the model structure generates a less sterically crowded structure and a calculated $C(CH_3)\cdots C(CH_3)$ distance of 1.88 Å. Hence, with methyl substituents in the 3,5 positions, the less sterically crowded tetrahedral geometry is obtained while in the absence of the two methyl substituents this steric interaction is eliminated and electronic effects control the nickel geometry, generating square planar nickel(II) centers.

Interestingly, no linear chain polymeric materials have been successfully prepared involving any of the metals Cu, Co, Mn, or Ni with the even bulkier 3,5-bis(trifluoromethyl)-pyrazolate ligand (7). This suggests that the additional steric bulkiness of the CF_3 groups is sufficient to prevent polymer formation.

The thermal stabilities and solubility properties of the manganese compounds studied here are similar to those of the nickel compounds and it seems likely that they also have linear- chain double pyrazolate-bridged structures. In the absence of definitive spectral or magnetic criteria to identify the geometry about the metal centers in the manganese systems, however, it is not possible to determine the nature of the MnN_x (x = 4,5) chromophore. Nonetheless, it is evident from the stoichiometry that, depending on the nature of the bridging ligands, there are at least two distinct manganese chromophore geometries. In the $[Mn(4\text{-}Xdmpz)_2]_x$ materials the metal centers are likely present in a tetrahedral geometry due to similar steric requirements to the ones discussed above. The $[Mn(4\text{-}Xpz)_2(4\text{-}XpzH)]_x$ materials, on the other hand, likely possess either 5-coordinate Mn(II) ions or an equal mixture of 4-coordinate and 6-coordinate metal centers with neutral 4-Xpyrazole ligands occupying the additional sites. The presence of neutral pyrazole molecules is

© 1998 NRC Canada

Table 1. Magnetic parameters for the $[Ni(4\text{-}Xdmpz)_2]_x$ polymers.

Compound	Temperature range (K)	J (cm^{-1})	g	P	F
$[Ni(4\text{-}Hdmpz)_2]_x$	2–300	– 19.3(7)	2.48(3)	0.0043(6)	0.062
	10–100	– 16.2(8)	2.33(6)	0 (fixed)	0.031
$[Ni(4\text{-}CH_3\text{-}dmpz)_2]_x$	2–300	– 16.2(3)	2.43(2)	0.0018(3)	0.028
	30–100	– 14.5(3)	2.28(2)	0 (fixed)	0.0073
$[Ni(4\text{-}Brdmpz)_2]_x$	2–300	– 16.4(2)	2.41(1)	0.0032(2)	0.027
	10–100	– 14.2(2)	2.28(1)	0 (fixed)	0.0095
$[Ni(4\text{-}Cldmpz)_2]_x$	2–300	– 18.9[a]	2.50[a]	0.0010[a]	0.058
	10–100	– 16.6(2)	2.40(1)	0 (fixed)	0.055

[a] Interdependencies of the three parameters prevented estimation of individual errors in this instance.

evident from both the stoichiometry and from IR spectroscopy. Unlike the $[Mn(4\text{-}Xdmpz)_2]_x$ materials or the nickel(II) polymers, the $[Mn(4\text{-}Xpz)_2(4XpzH)]_x$ complexes exhibit a strong and sharp IR band at ~3340 cm^{-1}, consistent with an N–H stretch. Evidence supporting coordinated neutral pyrazole, rather than lattice pyrazole, comes from the thermal studies performed on $[Mn(4\text{-}Clpz)_2(4\text{-}ClpzH)]_x$. This compound is thermally stable to 250°C, a temperature above the melting temperature of the neutral pyrazole (76°C).

Magnetic properties

All four $[Ni(4\text{-}Xdmpz)_2]_x$ complexes exhibit strong antiferromagnetic exchange, as evidenced by susceptibility maxima at T = 55 K for X = Br and at T = 60 K for the other three. Representative plots are shown in Fig. 3. Each compound shows an increase in susceptibility as temperature is decreased at very low temperatures, indicating the presence of small amounts of paramagnetic impurity. There is an observable discontinuity at 30 K in the data for $[Ni(4\text{-}CH_3\text{-}dmpz)_2]_x$ (Fig. 3*b*), suggesting a structural phase change for this polymer. Similar discontinuities were observed previously in related copper systems (8*d*).

The magnetic susceptibility data for the nickel complexes were modeled based on the linear chain structures proposed for these materials. This was accomplished using the isotropic Heisenberg model ($H = -2J \Sigma S_i \cdot S_j$) for exchange-coupled linear chains of S = 1 metal centers developed by Weng (29) and Hiller et al. (30). The model incorporates two parameters: J, the exchange coupling constant, and g, the Landé splitting factor. The theoretical expression was modified, in the manner described recently (31), to incorporate a third parameter P, the fraction of paramagnetic impurity present in the sample. The calculated susceptibilities were obtained by treating J, g, and P as variable parameters and minimizing the fitting function F, where:

$$F = \left[\frac{1}{n} \sum_{j=1}^{n} \left[\frac{\chi^i_{calc} - \chi^i_{obs}}{\chi^i_{obs}} \right]^2 \right]^{1/2}$$

The parameters J, g, P, and the values of F for the best fits are shown in Table 1. It is obvious from the plots comparing the experimental and calculated magnetic susceptibilities (Fig. 3), as well as by considering the values of F (Table 1), that the agreement between the observed and calculated data is not good. The primary difficulty in modeling these systems involves the orbitally degenerate ground state of the tetrahedral nickel(II) centers. There have been no models developed for extended chain systems that can simultaneously predict the effects (on magnetic properties) of spin-orbit coupling in orbitally degenerate ground term configurations and magnetic exchange coupling between metal centers as a function of temperature. For this reason, the magnetic data have also been analyzed employing data restricted to the region of the susceptibility maxima. As is evident from the fits (Fig. 3 (insets)) and from the F values listed in Table 1, this gives better agreement between the experimental and calculated data.

Table 2. Magnetic parameters for the $[Mn(4\text{-}Xdmpz)_2]_x$ and $[Mn(4\text{-}Xpz)_2(4\text{-}XpzH)]_x$ polymers.

Compound	J (cm^{-1})	P	F
$[Mn(4\text{-}Hdmpz)_2]_x$	–1.206(8)	0.0097(8)	0.023
$[Mn(4\text{-}CH_3\text{-}dmpz)_2]_x$	–2.12(2)	0.0051(5)	0.028
$[Mn(4\text{-}Cldmpz)_2]_x$	–1.53(3)	0.090(3)	0.045
$[Mn(4\text{-}Brdmpz)_2]_x$	–1.64(1)	0 (fixed)	0.031
$[Mn(4\text{-}Brpz)_2(4\text{-}BrpzH)]_x$	–0.412(4)	0 (fixed)	0.028
$[Mn(4\text{-}Clpz)_2(4\text{-}ClpzH)]_x$	–0.408(4)	0 (fixed)	0.030

The observed room temperature magnetic moments for the six manganese complexes show the presence of high-spin Mn(II) and the decrease in moment with decreasing temperature, in all cases, indicates antiferromagnetic exchange. Plots of χ_m versus temperature reveal susceptibility maxima at 5 K for $[Mn(4\text{-}Xpz)_2(4\text{-}XpzH)]_x$ (X = Cl, Br) and at 13 K, 20 K, and 25 K for the $[Mn(4\text{-}Xdmpz)_2]_x$ complexes (X = H, Br, CH_3, respectively). The maximum in the χ_m versus T plot for $[Mn(4\text{-}Cldmpz)_2]_x$ is less obvious due to the presence of a relatively large amount of paramagnetic impurity. For this compound, only an inflection point is seen at approximately 20 K. The abnormally large amount of impurity in this sample suggests the average chain length may be relatively small. Representative plots are given for $[Mn(4\text{-}Hdmpz)_2]_x$ and $[Mn(4\text{-}Clpz)_2(4\text{-}ClpzH)]_x$ in Fig. 4.

The magnetic data were modeled as described above using the equation for exchange-coupled linear chains of S = 5/2 metal centers developed by Weng (29) and Hiller et al. (30). Calculated magnetic susceptibilities were obtained by fixing g at 2.00, treating J and P as variable parameters, and minimizing the value of F. The resulting best-fit parameters with corresponding values of F are listed in Table 2.

© 1998 NRC Canada

Table 3. $|J|$ and $|4\ JS^2|$ ranges for polymeric transition metal (Ni(II), Cu(II), Co(II), Mn(II)) C-substituted pyrazolates.

Metal	Bridge type	S	$\|J\|$ values (cm^{-1})	$\|4\ JS^2\|$ values (cm^{-1})
Ni(II)	4-Xpz	0	–	–
	4-Xdmpz	1	14–16	56–64
Mn(II)	4-Xpz	5/2	0.4	10
	4-Xdmpz	5/2	1–2	25–50
Cu(II)	4-Xpz	½	81–105[a]	81–105
	4-Xdmpz	½	58–67[b]	58–67
Co(II)	4-Xpz	3/2	4–6[c]	36–54
	4-Xdmpz	3/2	2[c]	18

[a] References 8*a*, 8*d*.
[b] Reference 9*a*.
[c] Reference 9*b*.

An examination of J values obtained for the eight $[M(4\text{-}Xdmpz)_2]_x$ complexes shows very little dependence of the magnitude of exchange on electronic contributions from the 4-X substituents. In the case of the nickel complexes, the more highly electron-withdrawing Cl and Br substituents do not produce significantly different J values from those obtained for the X = H or CH_3 compounds (Table 1). For the manganese compounds, the J values for the X = Cl and Br derivatives are intermediate between those obtained for the other two (Table 2). The exchange coupling in the two $[Mn(4\text{-}Xpz)_2(4\text{-}XpzH)]_x$ materials is significantly weaker than in the corresponding $[Mn(4\text{-}Xdmpz)_2]_x$ compounds (Table 2). The presence of coordinated non-bridging pyrazole ligands in the former compounds presumably weakens the metal to bridging ligand interactions, resulting in a decrease in the magnitude of the magnetic exchange.

It is now possible to compare the magnitude of exchange in pyrazolate-bridged polymeric systems of four different metals, Ni(II) and Mn(II) studied here and Cu(II) and Co(II) studied in earlier work (9*a*, 9*b*). To compare the magnitude of exchange coupling in systems with different total spin, S, it is appropriate to compare $|4JS^2|$ values (32) instead of simply comparing values of J. Therefore, the range of $|J|$ and $|4JS^2|$ values for the four metal systems have been tabulated (Table 3). For both Co (II) and Cu(II) the exchange coupling is stronger for the 4-Xpz complexes than for the 4-Xdmpz complexes. This may be a consequence of steric interactions involving the methyl substituents in the 3,5 positions leading to weaker bridge bonding and hence weaker exchange. Similar comparisons cannot be made for the Ni(II) and Mn(II) systems since, as described earlier, the $Ni(4\text{-}Xpz)_2]_x$ complexes are diamagnetic due to the presence of a square planar NiN_4 chromophore, while in the case of manganese the 4-Xpz complexes are not simple binary pyrazolates. The best comparison among the four metals involves the 4-Xdmpz derivatives. In all of these a tetrahedral or distorted tetrahedral MN_4 chromophore is assumed. Based on the $|4JS^2|$ values, the strength of the exchange coupling is very similar for the Cu(II) and Ni(II) complexes and greater than that seen in either of the Mn(II) or Co(II) systems. Assuming tetrahedrally coordinated metal centers, the magnetic orbitals for all four metal systems are of t_2 symmetry (also of e symmetry for manganese). Interestingly, increasing the number of unpaired electrons in these orbitals does not lead to stronger exchange. Instead it appears that the coupling strength is more closely related to the total number of electrons, suggesting that the covalent character of the bridging ligand – metal ion bond is an important factor.

Acknowledgements

Funding for the project was provided by the Natural Sciences and Engineering Research Council of Canada. P. Borda of this department is thanked for the C, H, N analyses.

References

1. S. Trofimenko. Chem. Rev. **72**, 497 (1972).
2. S. Trofimenko. Prog. Inorg. Chem. **34**, 115 (1986).
3. G. La-Monica and G.A. Ardizzoia. Prog. Inorg. Chem. **46**, 151 (1997).
4. P.J. Steele. Coord. Chem. Rev. **106**, 227 (1990).
5. S.J. Rettig, A. Storr, D.A. Summers, R.C. Thompson, and J. Trotter. J. Am. Chem. Soc. **119**, 8675 (1997).
6. S.J. Rettig, A. Storr, D.A. Summers, R.C. Thompson, and J. Trotter. Can. J. Chem. **75**, 949 (1997).
7. M.K. Ehlert, A. Storr, D.A. Summers, and R.C. Thompson. Can. J. Chem. **75**, 491 (1997).
8. M.K. Ehlert, S.J. Rettig, A. Storr, R.C. Thompson, and J. Trotter. Can. J. Chem. (*a*) **67**, 1970 (1989); (*b*) **68**, 1444 (1990); (*c*) **68**, 1494 (1990); (*d*) **69**, 432 (1991); (*e*) **70**, 2161 (1992); (*f*) **71**, 1425 (1993).
9. M.K. Ehlert, A. Storr, and R.C. Thompson. Can. J. Chem. (*a*) **70**, 1121 (1992); (*b*) **71**, 1412 (1993).
10. M.K. Ehlert, S.J. Rettig, A. Storr, R.C. Thompson, F.W.B. Einstein, and R.J. Batchelor. Can. J. Chem. **71**, 331 (1993).
11. M.K. Ehlert, S.J. Rettig, A. Storr, R.C. Thompson, and J. Trotter. Acta. Crystallogr. Sect C: Cryst. Struct. Commun. **C50**, 1023 (1994).
12. F. Seel and V. Sperber. Angew Chem. Int. Ed. Engl. **7**, 70 (1968).
13. M.J. Bagley, D. Nicholls, and B.A. Warburton. J. Chem. Soc. (A), 2694 (1970).
14. C.B. Singh, S. Satpathy, and B. Sahoo. J. Inorg. Nucl. Chem. **35**, 3947 (1973).
15. J.G. Vos and W.L. Groeneveld. Transition Met. Chem. **4**, 137 (1979).
16. J.G. Vos and W.L. Groeneveld. Inorg. Chim. Acta, (*a*) **24**, 123 (1977); (*b*) **27**, 173 (1978); (*c*) **26**, 71 (1978); (*d*) **29**, 117 (1978).

© 1998 NRC Canada

17. J. Strahle, F. Kubel, W. Mller, and R. Dantona. Mol. Cryst. Liq. Cryst. **81**, 265 (1982).
18. A.M. Vecchio-Sadus. Transition Met. Chem. **20**, 46 (1995).
19. W. Burger and J. Strahle. Z. Anorg. Allg. Chem. **539**, 27 (1986).
20. W. Burger and J. Strahle. Z. Anorg. Allg. Chem. **529**, 111 (1984).
21. G.A. Ardizzola, G. La Monica, S. Cenini, M. Moret, and N. Masciocchi. J. Chem. Soc. Dalton Trans. 1351 (1996).
22. A.B. Blake, D.F. Ewing, J.E. Hamlin, and J.M. Lockyer. J. Chem. Soc. Dalton Trans. 1987 (1977).
23. B.R. King. Organometallic synthesis. Academic Press, New York. 1965. p. 71.
24. G.T. Morgan and I. Ackerman. J. Chem. Soc. **123**, 1308 (1923).
25. D. Nicholls. Comprehensive inorganic chemistry. Vol. 3. *Edited by* J.C. Bailar, H.J. Emeleus, R. Nyholm, and A.F. Trotman-Dickenson. Pergamon Press, New York. 1973.
26. A.P.B. Lever. Inorganic electronic spectroscopy. Elsevier, Amsterdam. 1984.
27. G.A. Ardizzoia, M.A. Angaroni, G. La Monica, F. Caiati, S. Cenini, M. Moret, and M. Masciocchi. Inorg. Chem. **30**, 4347 (1991).
28. M.K. Ehlert. Ph.D. Thesis, University of British Columbia, Vancouver. 1992.
29. C.H. Weng. Ph.D. Thesis, Carnegie-Mellon University, Pittsburgh, Pa. 1968.
30. W. Hiller, J. Strahle, A. Datz, M. Hanack, W.F. Hatfield, and P. Gutlich. J. Am. Chem. Soc. **106**, 329 (1984).
31. M. Ardon, A. Bino, K. Michelsen, E. Pedersen and R.C. Thompson. Inorg. Chem. **36**, 4147 (1997).
32. S.L. Lambert and D.N. Hendrickson. Inorg. Chem. **18**, 2683 (1979).

© 1998 NRC Canada

Noble gas catalysed 1,2-migrations in N_2H^+ and $N_2CH_3^+$

Alwin Cunje, Christopher F. Rodriquez, Diethard K. Bohme, and Alan C. Hopkinson

Abstract: Molecular orbital calculations are reported for N_2H^+ and $N_2CH_3^+$ and for the transition structures for the rearrangement of these ions by 1,2-shifts of H and CH_3. All reaction profiles were also calculated with one atom of noble gas, M, present (M = Ne, Ar, Kr). Structure optimizations were performed at B3LYP/6-311++G(d,p) and, in the case of $N_2H^+\cdots M$, single point calculations were also performed at QCISD(T)(full)/6-311++G(2df,p). For N_2H^+, inclusion of one noble gas atom reduces the barrier to rearrangement from 46.6 kcal mol^{-1} for the uncatalysed reaction to 42.6 kcal mol^{-1} (by Ne), to 21.4 kcal mol^{-1} (by Ar), and to 11.0 kcal mol^{-1} (by Kr). For $N_2CH_3^+$, the barrier of 36.4 kcal mol^{-1} is reduced to 35.1 kcal mol^{-1} by Ne, to 27.4 kcal mol^{-1} by Ar, and to 18.4 kcal mol^{-1} by Kr.

Key words: catalysis, molecular orbital theory, argon, krypton.

Résumé : On a effectué des calculs d'orbitales moléculaires pour N_2H^+ et $N_2CH_3^+$ et pour les structures de transition des réarrangements de ces ions par des déplacements 1,2 de H et de CH_3. On a aussi calculé tous les profils de réactions avec un atome de gaz rare, M (M = Ne, Ar, Kr). On a réalisé les optimisations de structure au niveau B3LYP/6-311++G(d,p) et, dans le cas de $N_2H^+\cdots M$, on a aussi effectué des calculs au niveau QCISD(T)(full)/6-311++G(2df,p). Dans le cas de N_2H^+, l'inclusion d'un atome de gaz rare réduit la barrière au réarrangement de 46,6 kcal mol^{-1} pour la réaction non catalysée à 42,6 kcal mol^{-1} (par le Ne), à 21,4 kcal mol^{-1} (par le Ar) et à 11,0 kcal mol^{-1} (par le Kr). Dans le cas de $N_2CH_3^+$, la barrière de 36,4 kcal mol^{-1} est réduite à 35,1 kcal mol^{-1} (par le Ne), à 27,4 kcal mol^{-1} (par le Ar) et à 18,4 kcal mol^{-1} (par le Kr).

Mots clés : catalyse, théorie des orbitales moléculaires, argon, krypton.

[Traduit par la Rédaction]

Introduction

Protonated dinitrogen, N_2H^+, has been observed in the gas phase (1) and has also been detected in interstellar clouds (2). The methyl analogue, $N_2CH_3^+$, has also been observed in the gas phase and this ion has been used as the primary standard in the construction of a methyl cation affinity scale (3, 4).

There have been several high-level theoretical studies of N_2H^+ and $N_2CH_3^+$, with emphasis on structure determination and on calculating proton affinities and methyl cation affinities (4–16). Recently, detailed calculations on N_2H^+ using the CCSD(T) method with a large basis set have been used to provide a potential energy surface for an intramolecular dynamics and density of states study (17). Both H^+ and CH_3^+ add end-on to one nitrogen atom, i.e., N_2H^+ is linear and $N_2CH_3^+$ has C_{3v} symmetry. Bending at the central N is a high-energy process and the barrier to a 1,2-proton shift in N_2H^+ is calculated to be 47.1 kcal mol^{-1} at MP2(full)/6-31G(d,p) (11). The barrier to 1,2-methyl migration in $N_2CH_3^+$ is lower and has been calculated to be 36.8 kcal mol^{-1} at MP4(SDTQ)/6-311G(d,p)//MP2(full)/6-31G(d) (13).

In solution, barriers to proton migration are often reduced by the solvent. The mechanism involves proton transfer to a solvent molecule followed by reprotonation at a different site on the substrate. A similar proton-switching mechanism has been proposed for gas-phase reactions. Here diatomic molecule AB can, in principle, protonate at either A or B and conversion of the higher energy isomer ABH^+ into the lower energy isomer BAH^+ can be achieved in a collision with a molecule, M, that has a proton affinity intermediate between those of atoms A and B in molecule AB. The overall reaction can be described as follows (18):

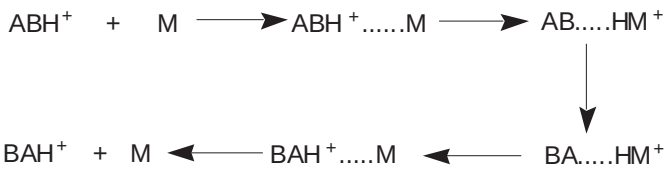

Here the proton is transferred from atom B to M and then in the third step the fragment AB in the hydrogen-bonded complex $AB\cdots HM^+$ rotates and subsequently the proton is transferred back to A. This "forth and back" mechanism, first proposed by Ferguson (19) to explain how $HNNO^+$

Received February 2, 1998.

A. Cunje, C.F. Rodriquez, D.K. Bohme, and A.C. Hopkinson.[1] Department of Chemistry, York University, North York, ON M3J 1P3, Canada.

[1]Author to whom correspondence may be addressed. Telephone: (416) 736-2100, ext. 77839.

© 1998 NRC Canada

reacts with NO in a charge transfer reaction to give NO^+, N_2, and OH, has also been invoked to explain the isomerization reactions of COH^+ catalysed by H_2 (20) and of HCN^+.catalysed by CO and CO_2 (21). By contrast, rearrangement of $HSiO^+$ to the lower energy isomer $SiOH^+$ is not catalysed by H_2 and this has been attributed to the high energy of the intermediate complex $OSi\cdots H_3^+$ (18, 22).

The barriers to 1,2-methyl migration in cations can also be high and recently inert gases Xe and N_2 have been shown to catalyse the conversion of ion $CH_3NO_2^+$ into the lower energy isomer, $ONOCH_3^+$, prior to dissociation into CH_3O and NO^+ (23). Molecular orbital calculations have also shown that the barrier to rearrangement of COH^+ to HCO^+ can be reduced substantially by the presence of one molecule of catalyst (24, 25).

These observations encouraged us to examine the effect of inert gases on the barrier to 1,2-proton and methyl shifts. For simplicity we have chosen here a system in which there are large barriers and where both the reactant and product are identical, namely, the migration of R from one nitrogen atom to the other in N_2R^+. In the presence of a potential catalyst, M, the overall barrier is given by the energy difference between the separated reactants N_2R^+ plus M and the complexed transition state, **3**.

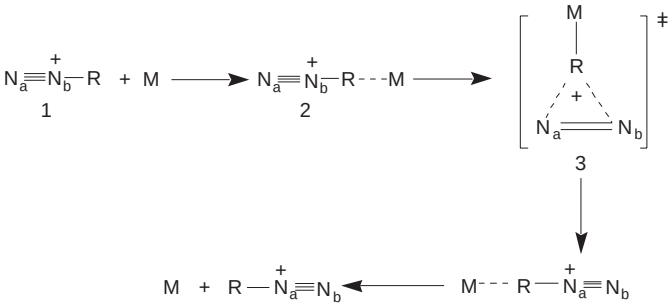

The choice of a diatomic with identical basicity sites means that any molecule M that has a larger R^+ affinity than N_2 will simply remove R^+. Only molecules with R^+ affinities *less* than that of N_2 can act as a catalyst to assist in transporting R^+ from one nitrogen atom to the other. In the current study we examine the noble gas atoms Ne, Ar, and Kr as catalysts for the rearrangements of ions N_2H^+ and $N_2CH_3^+$.

Computational methods

All molecular orbital calculations were performed using Gaussian 94 (26). Structure optimizations were carried out using the CALCALL routine along with molecular orbital calculations employing Density Functional Theory (DFT) at the B3LYP level (27, 28). The 6-311++G(d,p) basis set (29–33) was used for all structure optimizations and then for the N_2H^+ and $N_2H^+\cdots M$ systems these geometries were used for single-point calculations at QCISD(T)(full)/6-311++G(2df,p) (34, 35). For each transition state, Intrinsic Reaction Coordinate (IRC) calculations (36) were performed to establish that the structure was indeed for the migration of R^+ from one N atom to the other and not for transferring R^+ from N_2 to the catalyst. For all structures at critical points the calculations were corrected to 298 K by inclusion of zero-point and thermal energies.

Table 1. Total energies (hartrees) and zero-point energies (kcal mol^{-1}).

Molecule	B3LYP[a]	Zero-Point	QCI[b]
Ne	–128.960 40	—	–128.815 89
Ar	–527.553 87	—	–527.098 22
Kr	–2753.753 69	—	–2752.511 30
N_2	–109.559 69	3.5	–109.411 52
CH_3^+	–39.491 47	19.6	–39.415 75
N_2H^+	–109.753 50	10.0	–109.607 16
N_2H^+(ts)	–109.67564	6.3	–109.527 40
$N_2H^+\cdots$Ne	–238.717 61	10.7	–238.427 17
$N_2H^+\cdots$Ne(ts)	–238.643 17	7.0	–238.349 82
$N_2H^+\cdots$Ar	–637.318 84	10.3	–636.717 25
$N_2H^+\cdots$Ar(ts)	–637.267 44	7.4	–636.666 03
$N_2H^+\cdots$Kr	–2863.524 46	9.7	–2862.134 03
$N_2H^+\cdots$Kr(ts)	–2863.483 77	7.4	–2862.095 90
$N_2CH_3^+$	–149.124 97	28.3	–148.901 80
$N_2CH_3^+$(ts)	–149.063 03	25.3	–148.838 69
$N_2CH_3^+\cdots$Ne	–278.085 94	28.5	—
$N_2CH_3^+\cdots$Ne(ts)	–278.025 32	25.6	—
$N_2CH_3^+\cdots$Ar	–676.679 72	28.6	—
$N_2CH_3^+\cdots$Ar(ts)	–676.632 71	26.4	—
$N_2CH_3^+\cdots$Kr	–2902.880 51	28.5	—
$N_2CH_3^+\cdots$Kr(ts)	–2902.847 11	26.4	—

[a]B3LYP/6-311++G(d,p).
[b]QCISD(T)(full)/6-311++G(2df,p).

The overall conclusions on the relative energies of reactants and transition states from the two different levels of theory for $N_2H^+\cdots M$ were very similar and consequently we decided that it was unnecessary to perform QCI calculations on the larger $N_2CH_3^+\cdots M$ ions. All the computed energies are given in Table 1 and the optimized structures are given in Figs. 1 and 2.

Results and discussion

(a) Structures

(i) Ions $N_2H^+\cdots M$ (where M = Ne, Ar, and Kr)

The B3LYP/6-311++G(d,p) level calculations gave N_2H^+ to be linear with N—N and N—H distances of 1.090 and 1.040 Å, respectively. These compare with experimental equilibrium values of 1.093 and 1.033 Å (37). Protonation of N_2 is calculated to result in a slight shortening of the N—N distance from 1.096 to 1.090 Å. In the transition state for the 1,2-rearrangement the N—N distance is lengthened to 1.120 Å and the N—H distances are considerably longer than in the structure at the minimum (1.295 Å compared with 1.040 Å).

Noble gas atoms interact with N_2H^+ by attachment to the hydrogen atom along the N-N-H axis. Neon has little effect on the structure of N_2H^+, producing an increase in the N—H distance of only 0.001 Å, and the Ne—H distance in the complexed ion is 1.777 Å compared with a distance of 1.006 Å in the isolated NeH^+ ion. This interaction between Ne and N_2H^+ is calculated to be stabilizing by only 1.8 kcal mol^{-1} at B3LYP/6-311++G(d,p) and by only 2.1 kcal mol^{-1} at QCISD(T)(full)/6-311++G(2df,p). Interactions with argon and with krypton result in elongations of the N—H bond to

© 1998 NRC Canada

Fig. 1. Geometric parameters for $N_2H^+\cdots M$ ions. Bond lengths are in Ångstroms and angles are in degrees.

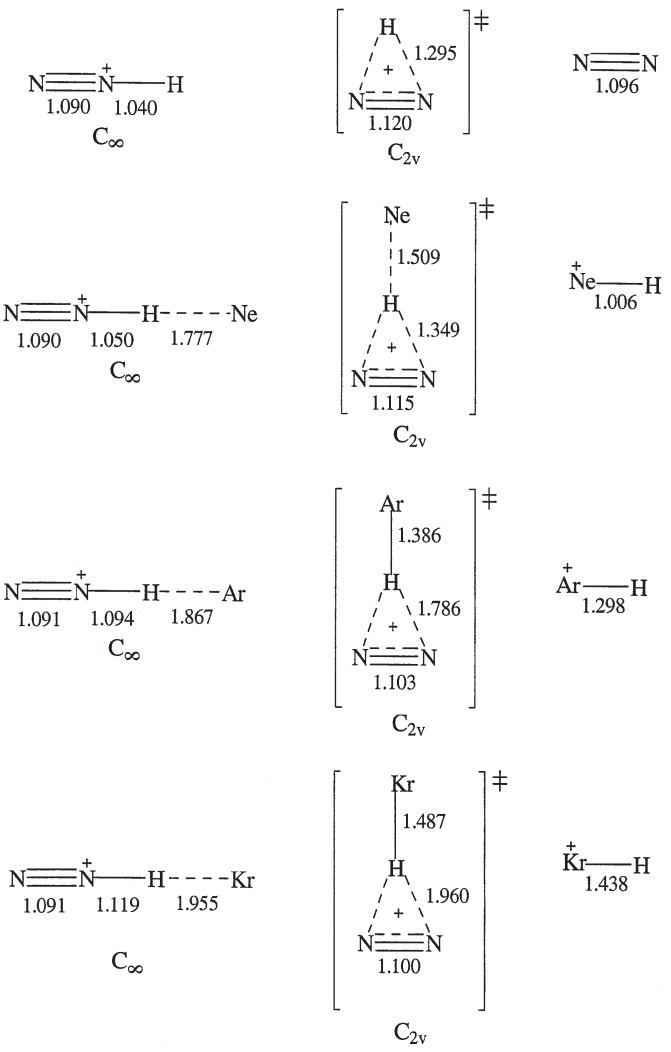

Fig. 2. Geometric parameters for $N_2CH_3^+\cdots M$ ions. Bond lengths are in Ångstroms and angles are in degrees.

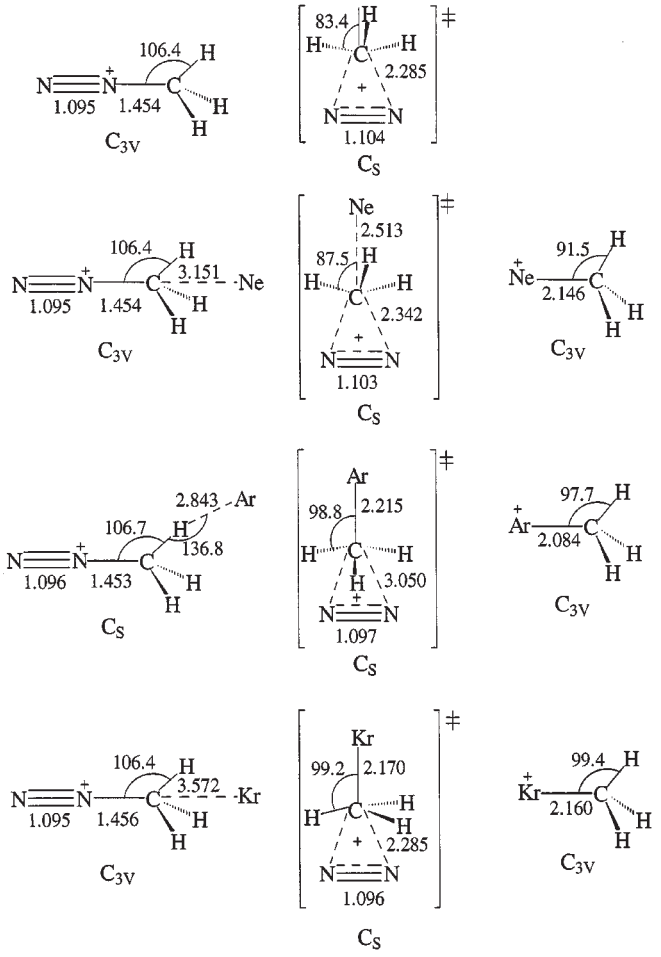

1.094 and 1.119 Å, respectively (from 1.004 Å), and, while the H—Ar and H—Kr distances of 1.867 and 1.955 Å are both more than 0.5 Å longer than in the isolated ArH^+ and KrH^+ ions, there is considerable interaction with the noble gases as shown by stabilization energies of 7.3 and 7.5 kcal mol^{-1} for Ar at the two levels of theory, and of 11.6 and 10.5 kcal mol^{-1} for Kr. Counterpoise calculations (38) on the fragments of dissociation, N_2H^+ and Kr, at the geometry of the complex $N_2H^+\cdots Kr$, gave a correction factor of only 0.2 kcal mol^{-1} for the basis set superposition error at B3LYP/6-311++G(d,p). In this complex the combination of a large basis set and the long distance between the two fragments in the complex that dissociate both contribute to a small counterpoise correction.

The geometric parameters for the transition structure for the 1,2-proton shift are heavily dependent upon which noble gas atom is present. The smallest structural changes are again produced by interaction with neon. Here the N—H distance of 1.349 Å is 0.054 Å longer than that in the transition state for the uncatalysed reaction and the Ne—H^+ distance of 1.509 Å is much longer than that in NeH^+ (1.006 Å), i.e., Ne interacts more strongly with the transition structure than with the structure at the minimum, but even in the the transition structure the proton is still firmly attached to N_2. This is most easily demonstrated by the stabilization resulting from interaction between Ne and N_2H^+. For the linear N_2H^+, i.e., the structure at the minimum, the interaction energy is calculated to be 3.1 and 3.4 kcal mol^{-1} at B3LYP/6-311++G(d,p) and QCISD(T)(full)/6-311++G(2df,p), respectively, while for the transition structure the interaction energies are 5.3 and 4.9 kcal mol^{-1}, respectively. Furthermore, dissociation of the transition structure into N_2 and NeH^+ is endothermic by approximately 30 kcal mol^{-1} at both levels of theory.

Interaction with argon produces a dramatic change in the transition structure. The N—N distance is decreased to 1.103 Å and the N—H increased to 1.786 Å. The Ar—H distance of 1.386 Å is only 0.088 Å longer than that in the isolated ArH^+ ion and this structure is best described as being ArH^+ solvated by attachment of the proton to the -bond of N_2. Interaction of the N_2H^+ transition structure with krypton results in an even larger N—H distance (1.960 Å) and the Kr—H distance of 1.487 Å is only 0.049 Å longer than that in KrH^+. Both the N_2HM^+ transition structures (where M = Ar and Kr) have energies just below those of the

© 1998 NRC Canada

Table 2. Barriers [a] to the 1,2-migration of R^+ in $N_2R^{+\cdot}$

Molecule	B3LYP[b]	QCI[c]
(*a*) Proton (R = H^+)		
(*i*) *From $N_2H^+\cdots M$*		
No catalyst	45.4	46.6
$N_2H^+\cdots$Ne	42.9	44.7
$N_2H^+\cdots$Ar	29.1	28.9
$N_2H^+\cdots$Kr	23.1	21.5
(*ii*)*From N_2H^+ + M*		
No catalyst	45.4	46.6
N_2H^+ + Ne	41.1	42.6
N_2H^+ + Ar	21.8	21.4
N_2H^+ + Kr	11.6	11.0
(*b*) Methyl cation (R = CH_3^+)		
(i) *From $N_2CH_3^+\cdots M$*		
No catalyst	36.4	37.1
$N_2CH_3^+\cdots$Ne	35.2	—
$N_2CH_3^+\cdots$Ar	27.7	—
$N_2CH_3^+\cdots$Kr	19.3	—
(ii)From $N_2CH_3^+$ + M		
$N_2CH_3^+$ + Ne	35.1	—
N_2CH_3+ + Ar	27.7	—
N_2CH_3+ + Kr	19.3	—

[a]In kcal mol^{-1} at 298 K.
[b]B3LYP/6-311++G(d,p).
[c]QCISD(T)(full)/6-311++G(2df,p).

Fig. 3. Reaction profile for N_2H^+ plus Kr. Upper numbers are for B3LYP/6-311++G(d,p) and lower ones for QCISD(T)(full)/6-311++G(2df,p).

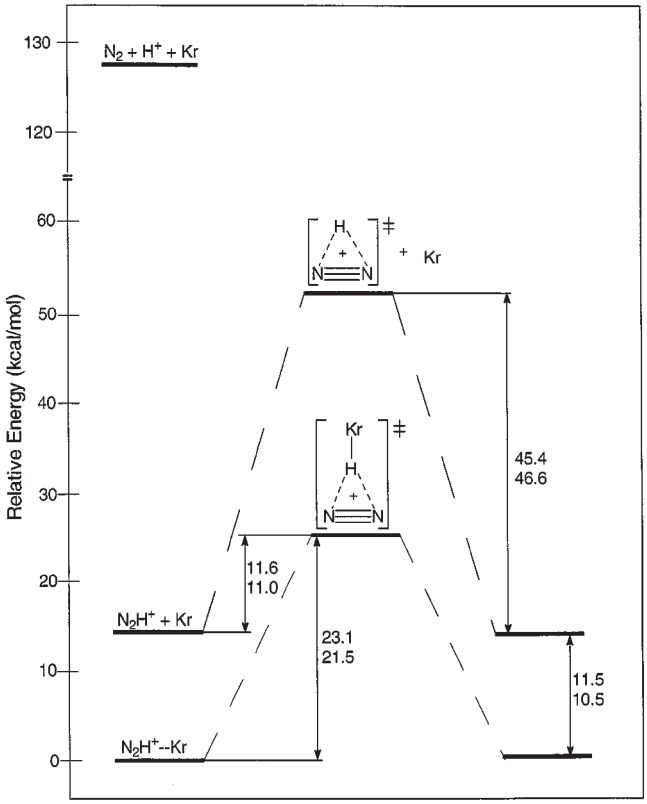

dissociation products MH^+ and N_2 (6.6 kcal mol^{-1} for Ar and 3.5 kcal mol^{-1} for Kr, where both calculations are at B3LYP/6-311++G(d,p)). Here again the basis set superposition errors are small and counterpoise calculations reduced the dissociation energy of the Kr-containing transition structure by 0.3 kcal mol^{-1} to 3.2 kcal mol^{-1}.

(ii) Ions $N_2CH_3^+\cdots M$ (where M = Ne, Ar, and Kr)

For the structure at the minimum for $N_2CH_3^+$, addition of an atom of Ne, Ar, or Kr produces essentially no geometric changes in the $N_2CH_3^+$ fragment and the noble gas atom is approximately 3 Å away from the methyl group. The exothermicities for formation of these weak association complexes, uncorrected for BSSE effects, are 0.1 kcal mol^{-1} for Ne, 0.3 kcal mol^{-1} for Ar, and 0.9 kcal mol^{-1} for Kr.

The transition structure for the 1,2-methyl migration in $N_2CH_3^+$ is characterized by long N—C distances and, as with the $N_2H^+\cdots$Ne transition structure, attaching a neon atom elongates the N—R distance slightly but overall there is little geometric change. The CH_3 group remains slightly pyramidal with the carbon atom pointing towards the N_2.

Attachment of argon and krypton both have a more profound effect on the geometry of the transition structure. The N—C distances of over 3 Å are much larger than those in the transition structure for the uncatalysed process (2.285 Å), the M—C distances are close to those in isolated $ArCH_3^+$ and $KrCH_3^+$ ions, and the methyl group has inverted so that the carbon atom is directed towards M and the hydrogen atoms are directed towards N_2. These geometric parameters are consistent with the transition structure being best described as MCH_3^+ stabilized by the -bond of N_2. Here there are close similarities with the $N_2H^+\cdots M$ transition structures. Despite the structural similarities to MR^+ plus N_2, however, it is important to realize that on both the N_2HM^+ and $N_2CH_3M^+$ (M = Ar or Kr) energy hypersurfaces the transition structures are indeed for the 1,2-migration of either the proton or the methyl cation. On both surfaces this was confirmed by Intrinsic Reaction Coordinate calculations.

(*b*) Barriers to rearrangement

(i) Proton migration

There is a substantial barrier to the migration of a proton from one nitrogen atom to the other in N_2H^+. At 298 K the barrier to this rearrangement is 45.4 kcal mol^{-1} at B3LYP/6-311++G(d,p) and 46.6 kcal mol^{-1} at QCISD(T)(full)/6-311++G(2df,p). When N_2H^+ is complexed by an inert gas atom M, then both the reactant and the transition structure are stabilized. As indicated by the change in structural parameters, the effect is much larger for the transition structure and the result is a pronounced lowering of the barrier to the 1,2-migration. Neon, the noble gas that is the least effective at "solvating" N_2H^+, has the smallest effect and reduces the barrier by only 2.5 and 1.9 kcal mol^{-1} at B3LYP/6-311++G(d,p) and QCISD(T)(full)/6-311++G(2df,p), respectively. At the same levels of theory, argon produces lowerings of 16.3 and 17.7 kcal mol^{-1} to give barriers of 29.1 and 28.9 kcal mol^{-1}, and krypton produces a lowering

© 1998 NRC Canada

of 22.3 and 25.1 kcal mol^{-1} to give values of 23.1 and 21.5 kcal mol^{-1} (see Table 2).

The barriers discussed in the preceding paragraph are for the rearrangement of an ion stabilized by attachment to one noble gas atom. Only one complexing or "solvating" molecule is considered in this treatment, but as the proton in the transition structure is essentially transferred to the "solvent" when M = Ar and Kr, inclusion of this one molecule is likely to be the major factor in reducing the barrier in solution. These calculations then give a crude upper estimate of the barrier height in solvent M. In the gas phase, when N_2H^+ collides with M, then the resulting complex rearranges via the same "solvated" transition structure and, as the energy of the reactants is that of the separated N_2H^+ and M, then the barrier to rearrangement is reduced even further. Thus the barrier to the krypton-catalysed rearrangement of N_2H^+, which is 23.1 and 21.5 kcal mol^{-1} respectively, at B3LYP/6-311++G(d,p) and QCISD(T)(full)/6-311++G(2df,p) starting from the "solvated" ion, is reduced further by 11.5 and 10.5 kcal mol^{-1} when starting from the unsolvated ion (see Fig. 3). For the purely gas-phase process, then, the barrier for the 1,2-proton migration in N_2H^+ is 46.6 kcal mol^{-1} in the absence of a catalyst and this is reduced to 42.6 kcal mol^{-1} by neon, to 21.4 kcal mol^{-1} by argon, and to 11.0 kcal mol^{-1} by krypton (all calculations at QCISD(T)(full)/6-311++G(2df,p)).

(ii) Methyl cation migration

Comparison of geometric parameters on the transition structures for the uncatalysed reactions revealed that the migrating CH_3^+ ion in $N_2CH_3^+$ is less firmly attached to N_2 than is the migrating H^+ in N_2H^+. This is a consequence of the greater ability of the CH_3 group to carry a substantial amount of the charge in cations. A population study on the structure at the minimum for $N_2CH_3^+$ using Bader's atoms in molecules method (39) showed that the methyl group carries the majority of the positive charge (+0.83 at MP2(full)/6-31G(d)) (13). In the present study a Mulliken population analysis (40) at B3LYP/6-311++G(d,p) showed that in the structure at the minimum on the $N_2CH_3^+$ surface the CH_3 group has a charge of +0.525 and that in the transition structure it is increased to +0.703. This enhanced ability of the migrating group to carry the positive charge results in the barrier to CH_3^+ shift being lower than that for proton migration in N_2H^+ by 9.0 kcal mol^{-1} at B3LYP/6-311++G(d,p) and by 9.5 kcal mol^{-1} at QCISD(T)(full)/6-311++G(2df,p).

More effective delocalization of the charge in $N_2CH_3^+$, as compared to that in N_2H^+, is expected to result in "solvation" by noble gases playing a smaller role in the rearrangement reaction. For the reactant ion at its equilibrium configuration there is little or no interaction with noble gas atoms and, in the presence of Ne, Ar, and Kr, both the complexed and uncomplexed ions have essentially the same barriers to rearrangement. "Solvation" of the transition structure then provides the major difference in the reaction profiles for the different noble gas atoms. At B3LYP/6-311++G(d,p), in the absence of catalyst, the barrier to migration in $N_2CH_3^+$ is 36.4 kcal mol^{-1} and this is reduced to 35.1 kcal mol^{-1} by neon, to 27.4 kcal mol^{-1} by argon, and to 19.3 kcal mol^{-1} by krypton.

Conclusions

The barriers to 1,2-migration in N_2R^+ (R = H, CH_3) are substantial, but are reduced considerably by inclusion of a single noble gas atom. Of the three noble gases studied, neon has the lowest affinity for R^+ and it displays only a small catalytic effect, reducing the barrier to rearrangement by approximately 4.0 kcal mol^{-1} in N_2H^+ and by only 1.3 kcal mol^{-1} in $N_2CH_3^+$. By contrast, both argon and krypton essentially form M—R bonds in the transition structure and the resulting stabilization leads to large reductions in the barriers. The largest catalytic effect is for the Kr-assisted migration of H^+ where the barrier is reduced from 46.6 to 11.0 kcal mol^{-1}.

The symmetric rearrangement that we have chosen here to illustrate the catalytic effect of noble gases establishes that preferential stabilization of the transition structure leads in some examples to a substantial reduction in the barriers to 1,2-migration. This discovery has important implications for rearrangements in cations formed from molecules that have two different sites for addition of R^+. Noble gas atoms are frequently used to thermalize the products of ion–molecule reactions. If the product ion has a lower energy isomer, then our calculations suggest that the noble gas atom may catalyse the rearrangement of the ion rather than simply thermalize the products. We are currently using theory to examine the rearrangements of several such ions.

Acknowledgements

We thank Steve Quan for much technical assistance in our computational work. Continued financial support from the Natural Sciences and Engineering Council of Canada is much appreciated.

References

1. (*a*) H. Kenso. Bull. Chem. Soc. Jpn. 578 (1979); (*b*) Y.-H. Li and A.G. Harrison. Int. J. Mass Spectrom. Ion Phys., **28**, 289 (1978); (*c*) C.S. Gudeman, J.P. Begemann, J. Pfaff, and R.J. Saykally. J. Chem. Phys. **78**, 5837 (1983); (*d*) R.J. Saykally, T.A. Dixon, T.G. Anderson, P.G. Sammis, and R.C. Woods. Astrophys. J. **205**, L101 (1976); (*e*) S.C. Foster and A.R.W. McKellar. J. Chem. Phys. **81**, 3424 (1984); (*f*) F.C. van den Heuvel and A.D. Dynamus. Chem. Phys. Lett. **92**, 219 (1982); (*g*) K.V.L.N. Sastry, P. Helminger, E. Herbst, and F.C. DeLucia. Chem. Phys. Lett. **84**, 286 (1981); (*h*) J.C. Owrutsky, C.S. Gudeman, C.C. Martner, L.M. Tack, H.H. Rosenbaum, and R.J. Saykally. J. Chem. Phys. **84**, 605(1986); (*i*) Y Kabbadj, T.R Huet, B.D. Rehfuss, C.M. Gabrys, and T. Oka. J. Mol. Spectrosc.**163**, 180 (1994).
2. (*a*) B.E. Turner. Astrophys. J. Lett. **193**, L83 (1974); (*b*) P. Thaddeus and B.E. Turner. Astrophys. J. Lett. **201**, L25 (1975); (*c*) L.E. Snyder, J.M. Hollis, D. Buhl, and W.D. Watson. Astrophys. J. Lett. **205**, 101 (1976); (*d*) R.J. Saykally and R.J. Woods. Annu. Rev. Chem. **32**, 403 (1981).
3. T.B. McMahon, T. Heinis, T. Nicol, J.K. Hovey, and P.J. Kebarle. J. Am. Chem. Soc. **110**, 7591 (1988).
4. M.N. Glukhovtsev, J.E. Szulejko, T.B. McMahon, J.W. Gauld, A.P. Scott, B.J. Smith, A. Pross, and L. Radom. J. Phys. Chem. **98**, 13099 (1994).
5. P. Botschwina. Chem. Phys. Lett. **107**, 535 (1984).
6. G. Forsen and B. Roos. Chem. Phys. Lett. **6**, 128 (1970).

© 1998 NRC Canada

7. D.J. DeFrees and A.D. McLean. J. Chem. Phys. **82**, 333 (1985).
8. J.E. Del Bene, M.J. Frisch, K. Raghavachari, and J.A. Pople. J. Phys. Chem. **86**,1529 (1982).
9. S. Ikuta. Chem. Phys. Lett. **109**, 550 (1984).
10. W.P. Kraemer, A. Korminicki, and D.A. Dixon. Chem. Phys. **105**, 87 (1986).
11. G. Rasul, G.K.S. Prakash, and G.A. Olah. J. Am. Chem. Soc. **116**, 8985 (1994).
12. M.A. Vincent and L. Radom. J. Am. Chem. Soc. **100**, 3306 (1978).
13. R.Glaser, G.S.-C. Choy, and M.K. Hall. J. Am. Chem. Soc. **113**, 1109 (1991).
14. R.Glaser, C.J. Horan, G.S.-C. Choy, and B.I. Harris. J. Phys. Chem. **96**, 3689 (1992).
15. S. Ikuta. J. Chem. Phys. **91**, 1376 (1989).
16. C.J. Horan and R. Glaser. J. Phys. Chem. **98**, 3989 (1994).
17. S. Schmatz and M. Mladenovic. Ber. Bunsen-Ges. Phys. Chem. **101**, 372 (1997).
18 D.K Bohme. Int J. Mass Spectrom. Ion Processes, **115**, 95 (1992).
19. E.E. Ferguson. Chem. Phys. Lett. **156**, 319 (1989).
20. S. Petrie, C.G. Freeman, M. Naut-Ner, M.J. McEwan, and E.E. Ferguson. J. Am. Chem. Soc. **112**, 7121 (1990).
21. M.J. McEwan. *In* Advances in gas phase ion chemistry. Vol 1. *Edited by* N.G. Adams and L.M. Babcock. JAI Press Inc., Greenwich, Conn. 1992.
22. A. Fox and D.K. Bohme. Chem. Phys. Lett. **187**, 541 (1991).
23. V Baranov, S. Petrie, and D.K. Bohme. J. Am. Chem. Soc. **118**, 4500 (1996).
24. A.J. Chalk and L. Radom. J. Am. Chem. Soc. **119**, 7573 (1997).
25. A. Cunje, C.F. Rodriquez, D.K. Bohme, and A.C. Hopkinson. J. Phys. Chem. A. **102**, 478 (1998).
26. M.J. Frisch, G.W. Trucks, H.B. Schlegel, P.M.W. Gill, B.G. Johnson, M.A. Robb, J.R. Cheeseman, T. Keith, G.A. Petersson, J.A. Montgomery, K. Raghavachari, M.A. Al-Laham, V.G. Zakrzewski, J.V. Ortiz, J.B. Foresman, J. Cioslowski, B.B. Stevanov, A. Nanayakkara, M. Challacombe, C.Y. Peng, P.Y. Ayala, W. Chen, M.W. Wong, J.L. Andres, E.S. Repogle, R. Gomperts, R.L. Martin, D.J. Fox, J.S. Binkley, D.J. Defrees, J. Baker, J.P. Stewart, M. Head-Gordon, C. Gonzalez, and J.A. Pople. Gaussian Inc., Pittsburgh, Pa. 1995.
27. A.D. Becke. J. Chem. Phys. **93**, 5648 (1993).
28. (*a*)C. Lee, W. Yang, and R.G. Parr. Phys. Rev. B: Condens. Matter, **37**, 785 (1988); (*b*) B. Miehlich, A. Savin, H. Stoll, and H. Preuss. Chem. Phys. Lett. **157**, 200 (1989).
29. R. Krishnan, J.S. Binkley, R. Seeger, and J.A. Pople. J. Chem. Phys. **72**, 650 (1980).
30. A.D. McLean and G.S. Chandler. J. Chem. Phys. **72**, 5639 (1980).
31. J. Chandrasekhar, J.G. Andrade, and P.v.R. Schleyer. J. Am. Chem. Soc. **103**, 5609 (1981).
32. J. Chandrasekhar, G.W. Spitznagel, and P.v.R. Schleyer. J. Comput. Chem. **4**, 294 (1983).
33. L.A. Curtiss, M.P. McGrath, J.P. Blaudeau, N. E. Davis, R.C. Binning, Jr., and L. Radom. J. Chem. Phys. **103**, 6104 (1995).
34. (*a*) J.A. Pople, M. Head-Gordon, and K. Raghavachari. J. Chem. Phys. **87**, 5968 (1987); (*b*) J. Chem. Phys. **90**, 4635 (1989); (*c*) K. Raghavachari, M. Head-Gordon, and J.A. Pople. J. Chem. Phys. **93**, 1486 (1990).
35. M.J. Frisch, J.A.Pople, and J.S. Binkley. J. Chem. Phys. **80**, 3265 (1984).
36. C. Gonzalez and H.B. Schlegel. J. Chem. Phys. **90**, 2154 (1989).
37. B. Ruscic and J. Berkowitz. J. Chem. Phys. **95**, 4378 (1991).
38. S.F. Boys and F. Bernardi. Mol. Phys. **19**, 553 (1970).
39. R.F.W. Bader. Atoms in Molecules. A quantum theory. Clarendon Press, Oxford. 1994.
40. R.S. Mulliken. J. Chem. Phys. **23**, 1833 (1955); **23**, 1841 (1955); **23**, 2338 (1955); **23**, 2243 (1955).

© 1998 NRC Canada

Direct optimization of self-modeling curve resolution: application to the kinetics of the permanganate – oxalic acid reaction

Peter D. Wentzell, Ji-Hong Wang, Leon F. Loucks, and Kelli M. Miller

Abstract: A new procedure to extract spectral and concentration information for unknown components in a series of mixture spectra is described. The algorithm, a form of self-modeling curve resolution (SMCR), requires no assumptions about the mixture data except for linear additivity and non-negativity of component spectra, and non-negativity of concentrations. It provides permissible bands for the spectra and concentration profiles of individual components in the mixtures and is applicable to problems in chromatography, equilibrium studies, and kinetics, among others. The new method employs a nonlinear optimization procedure and is substantially more efficient than similar methods that have been previously reported. The SMCR algorithm is demonstrated by applying it to the autocatalytic oxidation of oxalic acid by permanganate in the presence of sulfuric acid. The reaction was monitored spectroscopically between 200 and 1000 nm under four different reaction conditions. Results verified the presence of two reaction intermediates previously proposed in the literature and confirmed their spectral properties. Concentration profiles for the intermediates are described.

Key words: curve resolution, kinetics, chemometrics, permanganate, oxalic acid.

Résumé : On décrit une nouvelle procédure pour extraire des informations relatives aux spectres et à la concentration de composants inconnus présents dans une série de spectres de mélanges. L'algorithme, une forme de résolution de courbes automodélisante (RCAM), ne nécessite aucune hypothèse concernant les données des mélanges si ce n'est que les concentrations ne sont pas négatives et que les composantes spectrales donnent une additivité linéaire et non négative. Il conduit aux bandes permises des spectres et aux profils de concentration de composants individuels dans les mélanges et il est applicable, entre autres, aux problèmes de chromatographie, d'études d'équilibre et de cinétique. La nouvelle méthode fait appel à une procédure d'optimisation non linéaire et elle est sensiblement plus efficace que les méthodes similaires proposées antérieurement. On a démontré l'utilité de l'algorithme RCAM en l'appliquant à l'oxydation autocatalytique de l'acide oxalique par le permanganate en présence d'acide sulfurique. On a suivi la réaction spectroscopiquement entre 200 et 1000 nm dans quatre conditions réactionnelles différentes. Les résultats ont permis de vérifier la présence de deux intermédiaires réactionnels proposés antérieurement dans la littérature et de confirmer leurs propriétés spectrales. On décrit les profils de concentration des intermédiaires.

Mots clés : résolution de courbe, cinétique, chimimétrie, permanganate, acide oxalique.

[Traduit par la Rédaction]

Introduction

The use of multichannel detectors to study chemical phenomena has become commonplace in recent years. Such detectors are known as *first-order* detectors in the vernacular of chemometrics and the most common examples are multiwavelength absorption or emission spectrometers and mass spectrometers. When coupled with an experiment that presents a time series of mixtures varying in composition, such as in chromatographic or kinetics studies, a first-order detector produces a sequence of vectors that can be combined to form a matrix, or *second-order* data set. Even if the detector is not completely selective for each chemical species of interest, such a data matrix can significantly enhance the quality of information available to the investigator over that obtained with a single-channel detector.

The most common model assumed for a data matrix of this type is second-order bilinear, represented mathematically as

$$[1] \qquad \mathbf{D} = \mathbf{C}\mathbf{S}^{T} + \mathbf{E}$$

Here **D** is the $m \times n$ matrix of responses measured at n detector channels for the m samples in the time series (i.e., each row of **D** is a vector of responses for a single mixture). The $m \times p$ matrix **C** is the matrix of concentrations of each of p observable components in the m mixtures, and the $n \times p$ matrix **S** consists of the sensitivities of each of the components

Received January 5, 1998.

P.D. Wentzell[1] and J.-H. Wang. Trace Analysis Research Centre, Department of Chemistry, Dalhousie University, Halifax, NS B3H 4J3, Canada.
L.F. Loucks and K.M. Miller. Department of Chemistry, University of Prince Edward Island, Charlottetown, PE C1A 4P3, Canada.

[1]Author to whom correspondence may be addressed. Telephone: (902) 494-3305. Fax: (902) 494-1310. E-mail: wentzell@ac.dal.ca

 © 1998 NRC Canada

Table 1. Glossary of symbols used.

Symbol	Description
$\mathbf{C}$	True or estimated $m \times p$ matrix of component concentration profiles
$\tilde{\mathbf{C}}$	Estimate of $\mathbf{C}$ with negative values set to zero
$\mathbf{D}$	$m \times n$ data matrix of mixture spectra as a function of time
$\hat{\mathbf{D}}$	Truncated PCA estimate of $\mathbf{D}$
$\tilde{\mathbf{D}}$	Estimate of $\mathbf{D}$ from $\tilde{\mathbf{C}}$ and $\tilde{\mathbf{S}}$
$\mathbf{E}$	$m \times n$ residual error matrix for $\mathbf{D}$
H	Inverse Heaviside (step) function to penalize negative values
m	Number of mixture spectra in the time series
n	Number of wavelength channels for the spectra
P	Penalty function used in Sasaki algorithm
P', P'', P'''	Objective/penalty functions for new algorithm
p	Number of observable components in mixtures; pseudorank of $\mathbf{D}$
q	Number of factors retained in PCA/SVD truncation
$\mathbf{R}$, $\hat{\mathbf{R}}$	Scores matrix from PCA ("^" indicates truncation)
$\mathbf{S}$	True or estimated $n \times p$ matrix of pure component spectra
$\tilde{\mathbf{S}}$	Estimated matrix $\mathbf{S}$ with negative values set to zero
$\mathbf{s}_i$	Estimated or true $n \times 1$ spectrum for component i
$\mathbf{s}_i^0, \mathbf{s}_i'', \mathbf{s}_i'''$	Initial estimate and boundary estimates of spectrum for component i
s_{ik}	An element of the spectrum for component k at channel j
$\mathbf{T}$	$p \times p$ transformation matrix for converting eigenvectors ($\mathbf{V}$) to pure component spectra
$\mathbf{T}^\circ$	Initial estimate of $\mathbf{T}$
$\mathbf{t}_i$	$p \times 1$ transformation vector to estimate spectrum of component i
Δt	Step size for simplex optimization
$\mathbf{U}$, $\hat{\mathbf{U}}$	Left singular matrix from SVD ("^" indicates truncation)
$U_{jk}^{(+)}, U_{jk}^{(-)}$	Objective functions used in Sasaki algorithm
$\mathbf{V}$, $\hat{\mathbf{V}}$	Right singular matrix (eigenvectors) from SVD ("^" indicates truncation)
w	Weighting factor used in penalty function
γ	Scale factor for penalty functions
Λ, $\hat{\Lambda}$	Diagonal matrix of eigenvalues from PCA ("^" indicates truncation)
λ_i	Diagonal element i of $\mathbf{L}$ (eigenvalue i)
σ_1	Root-mean-square difference between $\mathbf{D}$ and $\hat{\mathbf{D}}$
σ_2	Root-mean-square difference between and $\tilde{\mathbf{D}}$

at each of the n detector channels (i.e., the columns of $\mathbf{S}$ represent the "spectra" of individual components at unit concentration). The superscript "T" indicates the transpose of the matrix. Finally, $\mathbf{E}$ is the $m \times n$ matrix of residuals (errors) for the measurements. (A complete list of symbols used is given in Table 1.)

Given a multivariate data set of this type, it is generally the objective of the chemist to extract the matrices $\mathbf{C}$ and $\mathbf{S}$ from the matrix $\mathbf{D}$, thereby obtaining the concentration profiles and spectra of the species of interest. Such information can be extremely valuable, for example, in the identification of unknown species or the elucidation of a reaction mechanism. If either $\mathbf{C}$ or $\mathbf{S}$ is completely known, computation of the companion matrix is straightforward, but more often this information is incomplete. This is the case, for example, in a kinetics experiment where one or more unidentified intermediates may be present, or in chromatography where component peaks may be unresolved, or in equilibrium studies where several unknown species may coexist. In some of these cases, it may be possible to extract spectra and concentration profiles for the individual components if there are regions of the data (spectral channels or samples) that are uniquely associated with particular components, but in many instances this will not be true. In these cases, it is usually impossible to obtain unique solutions for the profiles of interest. However, by imposing some simple general constraints, it is often possible to define upper and lower boundaries for the component spectra (and concentration profiles) in the mixtures, thereby providing some information about what is happening in the mixtures. This procedure is known as self-modeling curve resolution (SMCR).

The principles of SMCR were introduced in 1971 by Lawton and Sylvestre (1), who applied the method to two-component mixtures. There are only three basic constraints applied in the original method: (*i*) pure component spectra cannot be negative, (*ii*) component concentrations cannot be negative, and (*iii*) pure component spectra (and concentration profiles) must lie in the p-dimensional subspace defined by the mixture spectra, where p is the number of mixture components. Since the original work, many applications and extensions of the method have appeared, with a substantial amount of effort directed to devising algorithms applicable to more than two components. Unfortunately, SMCR becomes more difficult as the number of components becomes large, and these methods have had mixed success.

This paper describes a new approach to SMCR for mixtures of more than two components. The new method is

© 1998 NRC Canada

illustrated through its application to an interesting autocatalytic reaction, the oxidation of oxalic acid by permanganate. Like virtually all SMCR methods, this new approach is based on principal component analysis, which will be introduced first.

Principal component analysis

The first step in applying SMCR to a second-order bilinear data set is usually the determination of the number of observable components present (note that the term "observable" is used here to indicate that a chemical species must have a measurable response and have concentration and spectral profiles that are sufficiently different from other species in the mixture). This determination is typically carried out using principal component analysis (PCA) (2), normally implemented through singular value decomposition (SVD):

$$[2] \qquad \mathbf{D} = \mathbf{U}\Lambda^{1/2}\mathbf{V}^{\mathrm{T}} = \mathbf{R}\mathbf{V}^{\mathrm{T}}$$

If $\mathbf{D}$ is $m \times n$ and $m \leq n$, then $\mathbf{U}$ and $\mathbf{R}$ are $m \times m$, Λ is $m \times m$ diagonal matrix of eigenvalues ($\Lambda^{1/2}$ is called the matrix of singular values), and $\mathbf{V}$ is $n \times m$. The matrix $\mathbf{R}$ ($= \mathbf{U}\,\Lambda^{1/2}$) is sometimes called the scores matrix and the columns of $\mathbf{V}$ are called the eigenvectors or loadings. The columns of $\mathbf{U}$ and $\mathbf{V}$ are orthonormal. If the measurements in $\mathbf{D}$ were error-free, then the rank of $\mathbf{D}$ would be equal to p, the number of independently observable components in the linear system, and the last $(m - p)$ eigenvalues would be zero. In practice, the presence of experimental errors means that the numerical rank of $\mathbf{D}$ is normally full ($min(m,n)$), so an estimate of the "pseudorank" (also called the chemical rank) of the data matrix is needed in order to determine the number of components. To do this, the SVD results are truncated to the first q principal components and then used to reconstruct the data matrix:

$$[3] \qquad \hat{\mathbf{D}} = \hat{\mathbf{U}}\hat{\Lambda}^{1/2}\hat{\mathbf{V}}^{\mathrm{T}} = \hat{\mathbf{R}}\hat{\mathbf{V}}^{\mathrm{T}}$$

In this equation, $\hat{\mathbf{U}}$ and $\hat{\mathbf{R}}$ are $m \times q$, $\hat{\Lambda}$ is $q \times q$, and $\mathbf{V}$ is $n \times q$. Although there are a variety of methods to estimate the pseudorank of $\mathbf{D}$, most are typically based on increasing q from unity until $\mathbf{D}$ reproduces $\mathbf{D}$ within experimental error (2). At this point, q is taken to be equal to p, the pseudorank of the data matrix.

Two-component mixtures

Although PCA is useful for estimating the number of components in a series of mixtures, it does not generally provide the concentration or spectral profiles of those components. In the context of eq. [1], the p columns of $\mathbf{V}$ are sometimes called "abstract spectra" and will define the p-dimensional subspace of the n-dimensional spectral space containing the pure component spectra. However, the abstract spectra are orthonormal, whereas the real spectra usually are not, and therefore the p-dimensional subspace can theoretically be defined by an infinite number of combinations of p vectors. The same arguments hold for the relationship between $\hat{\mathbf{U}}$ (or $\hat{\mathbf{R}}$) and the concentration profiles of each component.

A solution to this dilemma was provided by Lawton and Sylvestre (1) who proposed SMCR for two-component mixtures. In addition to the restrictions imposed by the SVD, these authors reasoned that most linearly additive spectroscopic methods were bound by two additional constraints: non-negative concentration and spectral profiles for the pure components. Although these constraints do not generally specify unique solutions, they do define boundaries for spectra and concentration profiles that are useful in certain circumstances. By normalizing pure component spectra to unit area, Lawton and Sylvestre were able to describe a simple mathematical procedure to identify the high and low limits of pure component spectra.

One unavoidable problem with this approach, and others like it, is that the absolute scales of the spectra and concentration profiles have no meaning. This "ambiguity of scale" is a consequence of the fact that a spectral response is a product of concentration and sensitivity, and a change in scale for one can be offset by a reciprocal change in scale for the other. Nevertheless, the shape of a spectrum or concentration profile for a given component is consistent for that component and these can be very useful for identifying unknown mixture components or modeling their behaviour. Some applications of this approach have been reviewed by Hamilton and Gemperline (3).

More than two components

Although the SMCR method of Lawton and Sylvestre has been widely used, it does not easily extend itself to more than two components. The principles of the method are quite general and it is essentially a problem in linear programming, but the practical difficulties of encoding the constraints become difficult to manage as the number of components increases (4, 5). For this reason, several alternative strategies to the problem have been adopted. These have been reviewed by Hamilton and Gemperline (3) and will be treated only briefly here.

One of the problems in extending SMCR to more than two components is that the technique must define a region of feasible solutions for each component, and this is not as straightforward as in the two-component case, since a higher dimensional space means more boundaries to define. One approach to the problem has been to attempt to define unique solutions by adding additional constraints. These constraints may be based on physical requirements, such as the existence of pure component responses (6, 7) or the presence of the component in a spectral library (8), or may be more general, such as requirements for maximum dissimilarity among spectra (9) or maximum spectral simplicity (10).

One of the most popular methods of generating "unique" solutions by curve resolution is iterative target-transformation factor analysis (ITTFA) (11, 12), which is also known as alternating least squares (ALS). With this method, the spectral or concentration profiles of one of the components is first estimated using some independent method. This estimation can be as simple as choosing a delta function to represent a chromatographic peak (11), or may involve a technique such as varimax rotation (12) or evolving factor analysis (13). The estimate is then projected into the SVD subspace and iteratively refined with its companion

© 1998 NRC Canada

Fig. 1. Visual representation of optimization problem for a three-component system and the step size (Δt) used in simplex optimization.

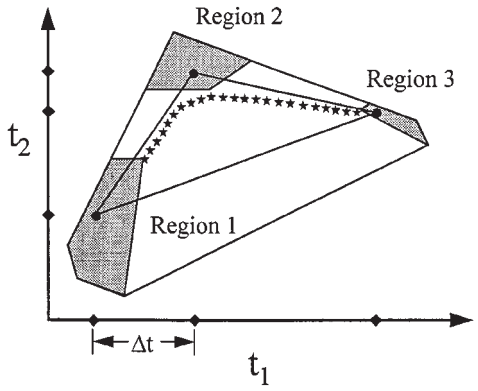

profile by setting negative values to zero until the process converges on positive solutions. The principle advantages of ITTFA are its speed and simplicity. Among its drawbacks, however, is a sensitivity to the initial estimate of the concentration profile or spectrum and a susceptibility to poorly defined convergence (14). Furthermore, the ITTFA procedure produces a single solution, ignoring the fact that there are usually a range of solutions.

True SMCR methods will generate a range of feasible solutions for component spectra and concentration profiles where no unique solutions exist. A direct extension of the original two-component approach can be used (4, 5), but solutions can become complex, especially if there are no additional constraints or the number of components is greater than three. Ohta (15) developed a Monte Carlo method to search for feasible solutions for the spectra that should be generally applicable, but is also likely to be slow. Nonlinear optimization has also been used to address the problem (16, 17) and this is the strategy used in this work. Since the method presented in this paper is derived from the work of Sasaki et al. (16), a brief description of this approach will be given.

The first step in this procedure developed by Sasaki et al. is decomposition of the data matrix **D** by SVD followed by truncation of the solution to rank *p*. Since the pure component spectra must lie in the subspace defined by the eigenvectors, each of these spectra can be represented as a linear combination of eigenvectors, that is:

$$\mathbf{S} = \mathbf{VT} \quad [4]$$

or,

$$\mathbf{s}_i = \mathbf{V}\,\mathbf{t}_i \quad [5]$$

Here **V** is the $n\times p$ matrix of eigenvectors (although this is the truncated matrix, the "^" has been removed for notational convenience), **S** is the $n\times p$ matrix of pure component spectral vectors, and $\mathbf{s}_i$ is the $n\times 1$ spectral vector for component *i* ($\mathbf{S} = [\mathbf{s}_1\ \mathbf{s}_2\ \cdots \mathbf{s}_p]$). The $p\times p$ matrix **T** (or alternatively the $p\times 1$ vectors **t**) describes the linear combinations of the eigenvectors in **V** needed to give the pure component spectra. Of course, the elements of **T** are unknown and are the parameters sought by the optimization. As was the case with two-component methods, the pure component spectra are normalized to unit area, i.e.,

$$\sum_{i=1}^{n} s_{ij} = 1 \quad [6]$$

This places a consequential restriction on **T** such that, for the *k*th component,

$$t_{pk} = \frac{1 - \sum_{i=1}^{p-1}\left(t_{ik}\sum_{j=1}^{n} v_{ji}\right)}{\sum_{j=1}^{n} v_{jp}} \quad [7]$$

In other words, the last row of **T** is defined by the first ($p-1$) rows and only $p\times(p-1)$ parameters need to be optimized.

With the Sasaki method (16), the optimization proceeds as follows for each component and each spectral channel. First, a set of t_{ij}'s is selected to define **T** and, therefore, the pure component spectra in accordance with eq. [4]. The matrix **S** is then used to estimate the concentration profile according to

$$\mathbf{C} = \mathbf{DS}(\mathbf{S}^{\mathrm{T}}\mathbf{S})^{-1} = \mathbf{DV}(\mathbf{T}^{-1})^{\mathrm{T}} \quad [8]$$

Note that this calculation can only be performed if **T** is non-singular, ensuring that the spectral profiles are not linear combinations of one another.

Once the spectral and concentration profiles have been calculated, the Sasaki algorithm minimizes the following functions with respect to the t_{ij}'s:

$$U_{jk}^{(+)} = +s_{jk} + P \quad [9]$$

$$U_{jk}^{(-)} = -s_{jk} + P \quad [10]$$

where the penalty function, *P*, is given by:

$$P(\mathbf{T}) = \gamma\left[\sum_{j=1}^{n}\sum_{k=1}^{p} H(s_{jk})s_{jk}^2 + \sum_{i=1}^{m}\sum_{k=1}^{p} H(c_{ik})c_{ik}^2\right] \quad [11]$$

and,

$$H(y) = \begin{cases} 0 & (y \geq 0) \\ 1 & (y < 0) \end{cases} \quad [12]$$

The functions $U_{jk}^{(+)}$ and $U_{jk}^{(-)}$, which are optimized separately for each component and spectral channel, represent the optimization functions for the upper and lower boundaries. The penalty function, *P*, ensures that no negative spectral or concentration values are tolerated if the scaling factor, γ, is set to a very large value. This function will be zero for non-negative solutions, allowing eqs. [9] and [10] to seek the highest and lowest allowed values for the spectral profiles.

It is useful to provide a visual interpretation of the Sasaki algorithm for a three-component system. In this case, the acceptable solutions can be regarded as being confined (by the unit area constraint) to three regions of the t_1–t_2 plane as shown in Fig. 1. (The diagram is not intended to represent an actual mixture problem, but is included for pedagogical

© 1998 NRC Canada

purposes.) The shaded regions indicate those cases which give $P = 0$ (i.e., they satisfy the non-negativity constraints) and therefore represent candidate spectra for the three components. The stars represent spectra obtained for the mixtures and in this case are shown as a smoothly varying sequence such as that which might be observed in a kinetics experiment or a chromatography run. Note that a selected combination of pure component spectra, such as that indicated by the points connected by the triangle, must encompass all of the mixture spectra. Because of this, it is not possible to simply choose a spectrum from each region arbitrarily, and the three spectra are mathematically interdependent, as suggested by the triangle. For each spectral channel, the Sasaki method seeks to find the points in each component region that give the highest and lowest response values. For more components, the process is essentially the same, except that the feasible regions become volumes and hyper-volumes instead of surfaces.

The Sasaki method is a useful, general approach to the problem of SMCR with more than two components, but it has some drawbacks as well. Some of these are listed below.

1. The discontinuous nature of the penalty function can make the optimization difficult and inhibits the use of gradient techniques.
2. The optimization is done twice for each spectral channel and each component, requiring $2np$ repetitions of the process. To further compound this problem, the original work (16) suggests an iterative procedure in which the value of the scaling factor, γ, is increased by a factor of 10 at the end of each run. Thus, the proposed procedure can be very computationally demanding, and becomes more so as the number of components is increased.
3. The search strategy needs to be able to locate local optima. The optimization is carried out one component at a time, with the intention of locating a pair of points within each region corresponding to the spectral boundaries for that component. However, it is possible for the search to "jump" to a different region and locate the optima for a different component. This problem can lead to redundant solutions and becomes more serious as the regions in Fig. 1 move closer together and, in some circumstances, overlap. Therefore, any optimization procedure used must be able to locate local optima associated with each component.
4. In some instances, there is no region in which the penalty function, P, is equal to zero. With experimental data, measurement errors can lead to negative values for some responses, which in turn may create a situation that forces either the concentration or spectral profiles to have negative values. If this is the case, the penalty function dominates the optimization and generates a single solution (i.e., no upper and lower bands) for each component. Furthermore, the nature of the solution depends on the scale of the measurements. This is because the spectra in eq. [11] are scaled to unit area, whereas the magnitude of the concentration values will depend on the magnitude of the measurements. The relative magnitudes of the concentration and spectral values will determine which is more likely to be forced to negative values during the course of the optimization, and therefore the shape of the extracted profile.
5. Because each spectral channel is separately optimized, the final bands produced to define the spectral boundaries do not necessarily represent contiguous spectra. In other words, the maximum value found for component 1 at wavelength 1 is not necessarily derived from the same spectrum as the maximum found at wavelength 2. Because of this, the resulting bands may show the limits, but do not themselves represent a spectrum. This may cause problems. For example, the resulting spectra will not necessarily have unit area.

In this work, the algorithm originally proposed by Sasaki et al. has been refined in an attempt to overcome some of these weaknesses.

A new approach

The procedure developed in this paper for treating mixtures of more than two components by SMCR is substantially faster than the Sasaki algorithm discussed in the previous section and, furthermore, helps minimize the influence of negative observations. The first step in the new algorithm is the same as for the Sasaki algorithm: decomposition of the original data matrix by SVD and estimation of the number of components present. Following this, the residual variance is calculated from

$$[13] \qquad \sigma_1^2 = \frac{\sum_{i=1}^{m}\sum_{j=1}^{n}(d_{ij} - \hat{d}_{ij})^2}{(m-p)(n-p)} = \frac{\sum_{i=p+1}^{min(m,n)}\lambda_i}{(m-p)(n-p)}$$

In this equation, d_{ij} and $\hat{d}_{ij}$ are elements of the original and reconstructed data matrices, λ represents an eigenvalue, p is the number of components, and m and n are the number of rows and columns in the data matrix. In this work, the residual variance is used as an estimate of the measurement variance.

The second stage of the modified algorithm involves the optimization of a function similar to eq. [11] that was used in the Sasaki algorithm. In this work, the objective function has been modified to

$$[14] \qquad P'(\mathbf{T}) = \sum_{j=1}^{n}\sum_{k=1}^{p} H(s_{jk}) s_{jk}^2 + \frac{1}{w^2}\sum_{i=1}^{m}\sum_{k=1}^{p} H(c_{ik}) c_{ik}^2$$

where the weighting factor, w, is given by

$$[15] \qquad w = \frac{max_{i=1,\ldots,m}(|u_{i1}|)\lambda_1^{1/2}\left(\sum_{i=1}^{n} v_{i1}\right)^2}{max_{i=1,\ldots,n}(|v_{i1}|)}$$

The purpose of the weighting factor in eq. [14] is to compensate for scale differences between the spectra and concentration profiles. Because the spectra are normalized to unit area, elements of the concentration vectors can be much larger or much smaller than the elements of the spectral vectors, depending on the magnitude of the observations. Although this will not be a problem when it is possible for all of the elements of **S** and **C** to be positive, some data sets will require negative elements and the disproportionate weighting of the two terms can cause difficulties (i.e., the

© 1998 NRC Canada

contribution of negative values is not equally balanced between the two parts). The weighting factor is calculated assuming that the first eigenvector is a reasonably good approximation for the "average" spectrum ($= \mathbf{v}_1/\Sigma v_{i1}$) and the first scores vector estimates the "average" concentration profile ($= \mathbf{u}_1\lambda_1^{1/2}\Sigma\ v_{i1}$). An approximate normalization factor is obtained from the ratio of the maxima of these two profiles.

The optimization of eq. [14] with respect to the elements of **T** is carried out using a simplex procedure because of the discontinuities in the objective function. In cases where there are feasible non-negative solutions for **S** and **C**, there is no unique solution for **T**, but this is not important. The purpose of this step is to locate the general region of potential solutions so that local optimization procedures can be used. The optimization of P' results in a solution that will be designated as **T**°, and this serves as an initial guess for the local optimization procedures.

The third stage of the algorithm uses **T**° as a starting point and attempts to locate one of the boundary solutions for each of the components in turn. Again, simplex optimization is used, but care must be taken to ensure that the search for one component does not stray into the local minimum corresponding to another component (see Fig. 1) or else redundant solutions will result. To reduce the chances of this happening, **T**° is used to gauge the distance between the component regions in "t"-space and set the step size for the simplex optimization. This could be done in a variety of ways (for example, taking the average distance between the components), but we have found it useful to set the step size to the largest value of the smallest differences among coordinate pairs, i.e.,

$$[16] \quad \Delta t = max_{i=1,\ldots,p}\{min_{j,k=1,\ldots,p:\, j\neq k}(|t_{ij} - t_{ik}|)\}$$

Because this equation is somewhat confusing, a visual example is presented in Fig. 1, although only the two dimensions t_1 and t_2 are considered, since the t_3 axis is not shown. Imagining the points shown to represent **T**°, it is clear that the smallest separation on the t_1 axis is between components 1 and 2, i.e., $(t_{12} - t_{11})$, and the minimum separation on the t_2 axis is between components 2 and 3, i.e., $(t_{22} - t_{23})$. Since the former of these two minimum distances is larger, it is chosen as the step size for the simplex optimization, Δt, as shown in Fig. 1 (again, this ignores the t_3 axis simply for purposes of illustration). The rationale for this defintion is that this is the largest step size that is still likely to confine the search to a particular region. The value of this step size is not critical, however, as long as it sufficiently restricts the search space.

For each of the components present, the initial guess for the simplex optimization is provided by **T**° and this is adjusted to find an optimum **T** by the following procedure. First, the spectra are calculated from the trial solution using eq. [4] (subject to the constraints in eqs. [6] and [7]. Any negative values in the calculated spectra are then set to zero:

$$[17] \quad \tilde{s}_{ij} = max(s_{ij},0)$$

Here s_{ij} is an element of the calculated matrix of spectra and $\tilde{s}_{ij}$ is an element of the adjusted spectra. The adjusted spectra are normalized to unit area as before and then used to calculate the concentration profiles according to:

$$[18] \quad \mathbf{C} = \mathbf{D}\tilde{\mathbf{S}}(\tilde{\mathbf{S}}^T\tilde{\mathbf{S}})^{-1}$$

As with the spectra, negative concentration values are set to zero, giving the new matrix, $\tilde{\mathbf{C}}$. The result is then used to calculate a new estimate for the data matrix:

$$[19] \quad \tilde{\mathbf{D}} = \tilde{\mathbf{C}}\tilde{\mathbf{S}}^T$$

The purpose of this procedure is to ensure that negative values are removed from the concentration and spectral profiles. Obviously, if negative values are present, the space spanned by $\tilde{\mathbf{C}}$ and $\tilde{\mathbf{S}}$ will not be the same as the original described by **U** and **V**, which could result in a poor reconstruction by eq. [19]. However, if the negative values are small, resulting only from measurement errors, the perturbations introduced should also be small and may result in an acceptable solution. Following the reconstruction, a new residual variance is calculated from the difference between the spectra reconstructed from eq. [19] ($\tilde{\mathbf{D}}$) and the PCA reproduced spectra ($\hat{\mathbf{D}}$):

$$[20] \quad \sigma_2^2 = \frac{\sum_{i=1}^{m}\sum_{j=1}^{n}(\tilde{d}_{ij} - \hat{d}_{ij})^2}{mn}$$

The quantity σ_2 is analogous to what Malinowski refers to as "imbedded" error, giving the difference between the proposed "pure" data and the PCA reconstructed data. If there were no negative values in the calculated spectra or concentration profiles, $\tilde{\mathbf{D}}$ should equal $\hat{\mathbf{D}}$ and therefore σ_2 will be zero. If adjustments for negative values were made, $\tilde{\mathbf{D}}$ and $\hat{\mathbf{D}}$ will not be equal and the question is whether $\tilde{\mathbf{D}}$ is an acceptable estimate of **D**. To answer this question, we simply examine the ratio

$$[21] \quad \alpha = \sigma_2^2/\sigma_1^2$$

In Malinowski's treatment of errors in PCA (2), the imbedded error should always be less than the real error (estimated by σ_1), so the solution is considered feasible if α is less than unity. Because the imbedded error for the correct solution is usually significantly smaller than the real error, this criterion is likely to provide slightly wider boundaries than should be the case, but in practice the boundaries predicted are not particularly sensitive to the critical value of α.

At this stage of the procedure, the actual objective function minimized is

$$[22] \quad P''(\mathbf{T}) = -\|\mathbf{s}_i - \mathbf{s}_i^{\circ}\| + \gamma\, H(\sigma_1^2 - \sigma_2^2)$$

where $\mathbf{s}_i$ is the trial spectrum for component i, $\mathbf{s}_i^{\circ}$ is the spectrum for component i computed from **T**°, and γ is a large constant. The second term of this expression ensures that only solutions that produce reasonable estimates of the original data are accepted. The first term attempts to maximize the difference between the trial spectrum and $\mathbf{s}_i^{\circ}$, thereby pushing the solution towards one of the boundaries of the acceptable range. This procedure is carried out for each component, in each case resulting in a solution which will be designated as $\mathbf{s}_i'$.

The final stage of the procedure is similar to the one just described except that the function minimized in this case is

© 1998 NRC Canada

Table 2. Conditions used for permanganate/oxalic acid reaction.

Run	$[H_2SO_4]$ (M)	$[H_2C_2O_4]$ (M)	$[KMnO_4]$ (M)	Time interval (s)	Delay + run time (s)
1	0.27	0.200	0.00050	10	30+600
2	0.27	0.025	0.00050	8	25+480
3	0.27	0.0013	0.00050	4	20+180
4	0.09	0.0013	0.00050	6	20+360

[23] $$P'''(\mathbf{T}) = -\| \mathbf{s}_i - \mathbf{s}_i' \| + \gamma H(\sigma_1^2 - \sigma_2^2)$$

This will seek an acceptable solution that is as far as possible from the first solution, thereby defining the other boundary for spectrum *i*. This solution will be designated as $\mathbf{s}_i''\}$, and the pairs $\mathbf{s}_i'$ and $\mathbf{s}_i''$ define the boundaries of the spectrum for component *i*.

It should be noted that the procedure described here differs from many other approaches to SMCR in one important respect — it allows the component spectral and concentration vectors to exist outside the subspace determined by PCA. This is a particularly useful feature when dealing with real data that have measurement errors since it allows some flexibility in adapting to negative values.

Although the procedure described here appears more complex than the original algorithm described by Sasaki et al. (16), we have found it to be less prone to numerical problems and much more efficient. Because it follows the initial optimization with more localized search procedures, it is less likely to generate redundant solutions. The new method is also more tolerant of negative values that arise from measurement error. Furthermore, there is a substantial reduction in computation time resulting from the fact that only $2p + 1$ optimizations are required as opposed to $2pn$ in the original work. This can save a significant amount of time as the number of channels becomes large. Finally, the boundaries determined by this method define mathematically feasible spectra, which is not necessarily the case for the Sasaki algorithm, since it does a separate calculation for each wavelength rather than considering each spectrum as a single entity.

Experimental

Data sets

Five sets of data were used to test the new algorithm in this work. The first was that originally given by Lawton and Sylvestre in their initial description of SMCR (1). These data consist of spectra measured for 5 mixtures of 2 dyes at 30 wavelength channels and were used to compare the new algorithm to the original procedure for two-component mixtures. The remaining four data sets were recorded for the autocatalytic reaction between permanganate and oxalic acid in a sulfuric acid medium. The conditions for these reactions were intended to duplicate those used by Pimienta et al. (18) in an earlier study. Further experimental details on the procedures used in obtaining these data are given below.

Procedure

All chemicals used were ACS Reagent Grade or better and solutions were prepared in deionized water. Solutions of oxalate were prepared from the disodium salt (Fisher, primary standard) and were acidified by adding the required amount of 1.000 M sulfuric acid (Caledon). Volumetric transfers were carried out using Class A glassware and Eppendorf pipettes (10–100 µL and 1–10 mL).

The permanganate – oxalic acid reaction was carried out by first adding 2.50 mL of a solution containing sodium oxalate and sulfuric acid to a standard 1 cm quartz cuvette (Hellma). To initiate the reaction, a 60.6 µL aliquot of potassium permanganate solution (0.02113 M) was added to the cuvette to give a starting concentration of 5.00×10^{-4} M for all of the reaction mixtures. Following this addition, timing was initiated and the solution was mixed by inverting it twice before placing it in the optical path of an HP8453 diode array spectrophotometer (Hewlett-Packard, Palo Alto, Calif.). Spectra were recorded at 1 nm intervals between 200 and 1000 nm with an integration time of 0.5 s and the shutter closed between measurements. The initial reagent concentrations, interval between measurements, and total run time for each of the four data sets are given in Table 2. A blank consisting of 5.00×10^{-4} M sulfuric acid was recorded prior to each kinetic run. All solutions were brought to 25°C prior to initiating the runs and the thermostatted cell holder of the spectrometer was maintained at 25.0°C. No stirring was done during the run.

Computational aspects

All calculations were carried out using programs written in Matlab 5.0 (The MathWorks, Natick, Mass.) on a Sun Microsystems SparcServer 1000 with 230 MB of memory and four 50 MHz SuperSPARC CPUs.

Results and discussion

Two-component data

The algorithm developed in this work was initially applied to the two-component data of Lawton and Sylvestre (1). Although the two-component case is easily solved analytically, these data were included here to validate the new method. Figure 2 shows the spectral boundaries obtained by the Lawton and Sylvestre (LS) method and the new method for both components in the mixture. From the figure, it is clear that there is excellent agreement between the two methods at the crossover points and the shapes of the spectral profiles are very similar, but the boundaries obtained by the new method are somewhat outside of those found by the LS technique. This is as expected, since the new SMCR method assumes a certain level of experimental error and therefore permits a wider range of solutions. In fact, it should be noted that the LS boundaries, so often employed for two-component SMCR problems, are actually too

© 1998 NRC Canada

Fig. 2. Comparison of spectral boundaries of a two-component system determined by (*a*) the Lawton–Sylvestre method, and (*b*) the new SMCR method.

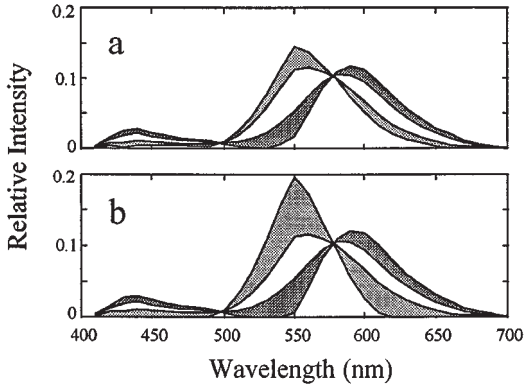

narrow. We were able to generate, with relatively little effort, realistic cases of simulated chromatographic/spectroscopic data in which the true spectra were outside of the LS boundaries, but inside the boundaries found by the new algorithm. This suggests that the results provided by the new algorithm may be more reliable than those based solely on a linear programming approach.

Permanganate – oxalic acid reaction

Figure 3 shows a three-dimensional mesh plot typical of the kinetic data obtained in this work. The example chosen is run number 3, the same as that shown in the earlier work of Pimienta et al. (18), and this figure exhibits virtually identical features. Characteristic of this reaction are the accelerating decay of the permanganate peak between 450 and 650 nm due to the autocatalytic reduction of permanganate by oxalic acid to form Mn(II), and the transient absorbance between 300 and 400 nm, which rises to a maximum before finally decaying to zero. This latter feature is attributed to the presence of one or more intermediates. Pimienta et al. (18) have proposed two intermediates, the first a well-recognized Mn(III) species (bis(oxalato)manganate (III), $[Mn(C_2O_4)_2]^-$), and the second a soluble Mn(IV) species. The aim of the present work was to use this autocatalytic reaction system to test the new SMCR algorithm and, if possible, confirm the presence of the two intermediates with the spectral characteristics reported by Pimienta.

The kinetics of this system are characterized by several isosbestic points that occur in the early to middle part of the reaction and then disappear. Some of these are evident in Fig. 4, which shows superimposed spectra for run number 3. Pimienta et al. (18) reported and used the isosbestic point around 450 nm, and its presence was confirmed in this work, along with similar isosbestic points around 335 nm and 390 nm. All of these points shift somewhat with reaction conditions. In addition, measurements made above 700 nm in this work established an additional early isosbestic point around 730 nm (710–740 nm, depending on reaction conditions). This is shown in the enlarged portion of Fig. 4. The isosbestic points arise at wavelengths where permanganate and the intermediate complexes of Mn(III) and Mn(IV) switch roles as the strongest absorbers. Permanganate is the stronger absorber between 335 and 390 nm and between 450 and 730 nm; the complexes are the stronger absorbers below 335 nm, between 390 and 450 nm, and above 730 nm. The shift in isosbestic points has been used to suggest the presence of more than one intermediate.

The analysis of the kinetic data began by removing measurements at wavelengths below 320 nm. This was done for two reasons. First, it eliminated possible absorbance by oxalic acid in the UV region, thereby reducing the number of components by one and simplifying the problem. Second, the absorbances at shorter wavelengths tended to be high, introducing problems with nonlinear response and larger noise levels, both of which complicated the mathematical analysis. Although component spectra generated by including wavelengths below 320 nm were of the same general shape as those generated when these wavelengths were excluded, the spectral boundaries were wider and sometimes truncated to zero due to excursions to negative values. Because of this, they were regarded as less reliable.

The next step in preparing for SMCR was to build one large "augmented" array from the four kinetic runs available. This was done by first appending the data matrix from the second run (61 time channels × 680 wavelength channels) to the bottom of the matrix from the first run (same dimensions). Runs 3 and 4 were then appended to this in the same way. This is a common practice (see, for example, ref. 13) that can be used whenever all data sets have the same wavelength channels. Although each of the four data matrices were also treated independently by SMCR, there are certain advantages to using the augmented matrix. First, the number of measurements is increased, providing more reliable results from PCA. Second, because several systems (encompassing different conditions) are analyzed simultaneously, the restrictions of non-negativity constrained solutions to narrower (and probably more reliable) regions than when single runs were analyzed. Finally, the use of the augmented data set results in one set of spectral boundaries, whereas four separate runs produce four sets of spectral boundaries for each component. Although these should be consistent with one another, they are likely to have broader limits and differ somewhat from run to run, making their interpretation more difficult. Of course, the use of an augmented array makes the implicit assumption that the spectra are independent of the kinetic run, which does not seem unreasonable in this study.

The SMCR analysis of the augmented data matrix was carried out assuming that there were four components present. Although only permanganate and two intermediates were expected, the assumption of four components allowed for the possibility of an additional intermediate, which, if not present, would result in a meaningless spectrum. The spectral boundaries for each of the four components extracted by SMCR are shown in Fig. 5. As noted earlier, SMCR produces an ambiguity of scale, so all of the spectra are normalized to unit area and there is no significance to the absolute scale of the *y* axis. The first spectrum is clearly that of the permanganate ion and the upper and lower bounds are so close together as to be indistinguishable, indicating very little ambiguity in the shape of this spectrum. The second spectrum, labeled "Intermediate 1," corresponds very closely to the spectrum of the Mn(III) complex

© 1998 NRC Canada

Fig. 3. Mesh plot of absorbance data from permanganate – oxalic acid reaction (run number 3).

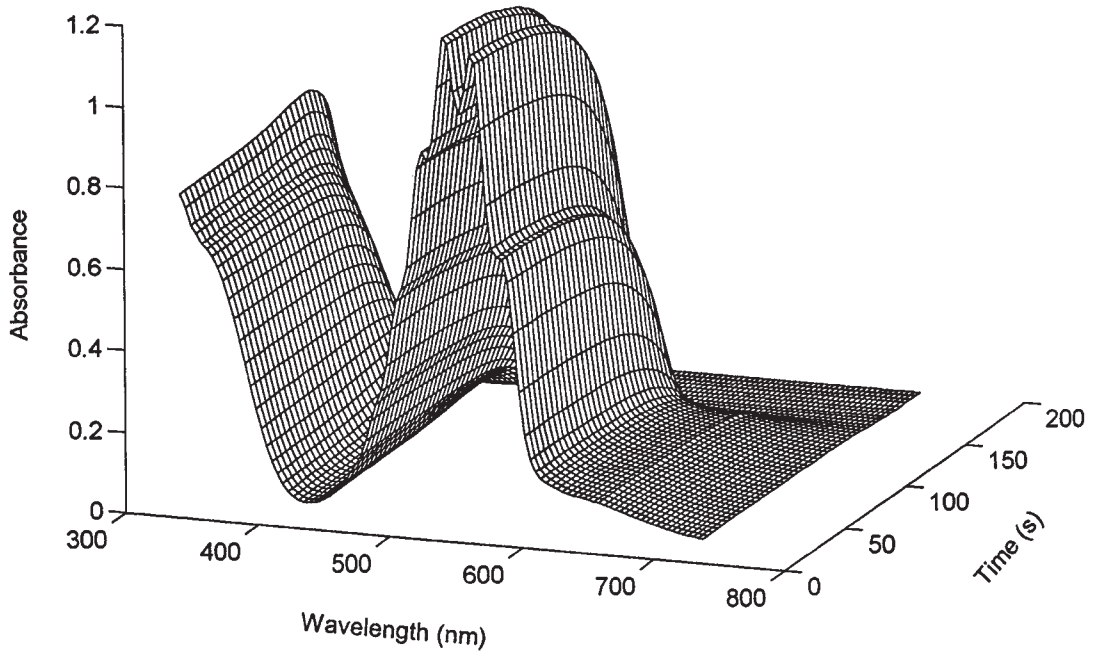

Fig. 4. Time series of spectra from the permanganate – oxalic acid reaction (run number 3). The region above 700 nm has been enlarged and offset to show the detail.

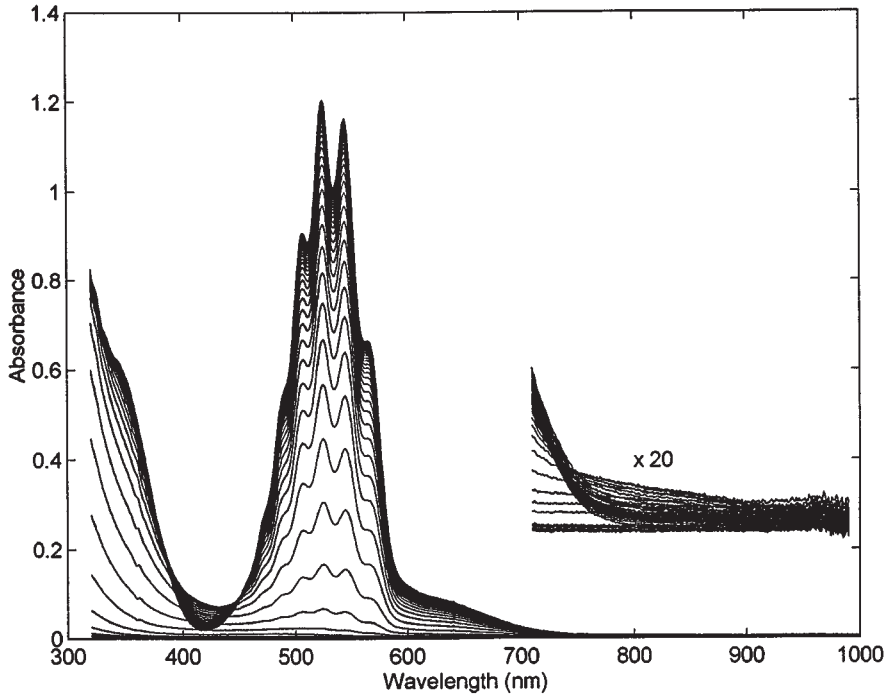

reported by Pimienta et al. (18) and has fairly tight boundaries as well. This is consistent with the fact that this species is a well-recognized intermediate. The third spectrum represents the second intermediate, which has been attributed to a soluble Mn(IV) species. Again, this spectrum is in good agreement with the spectrum reported in the literature (18), although the spectral bands are substantially wider than for the Mn(III) species, particularly at shorter wavelengths. This indicates that there is a fair amount of difficulty determining the spectrum of this species, probably because its contribution is dominated by other absorbing species (although it is also possible that the spectrum is sensitive to reaction conditions). The fourth spectrum in the series, although it exhibits some systematic features, is not considered to support the presence of an additional intermediate. Ideally, this spectrum should appear completely random in the absence of another component, but the features observed, which occur mainly in high-absorbance regions, are likely compensating for

© 1998 NRC Canada

Fig. 5. Spectral boundaries of four components extracted by SMCR.

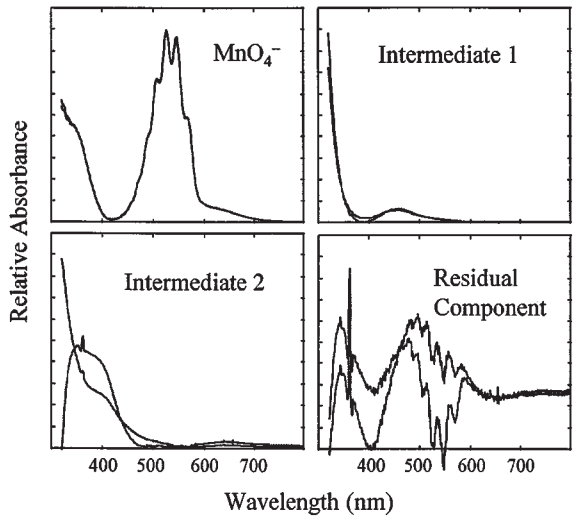

small amounts of nonlinearity in the response. In PCA it is not unusual to see this type of behaviour when the nonideal characteristics of the instrument are compensated for by additional eigenvectors. Similar structure in the residual spectra was observed when the system was modeled with five components, consistent with non-chemical artifacts.

To facilitate a better comparison between the spectral boundaries obtained for the intermediates and those reported by Pimienta et al. (18), the latter results were digitized and the two sets of spectra were scaled to a common area. The results are compared in Fig. 6. It is clear that there is excellent agreement between the two sets of results, with the spectra reported by Pimienta (indicated by the open circles) closely matching one of the spectral boundaries (solid lines) in both cases. Since the results of Pimienta et al. were obtained through an alternative approach, assuming the presence of only two intermediates and making use of isosbestic point data, this serves as validation of the SMCR results. The difference is that the latter results were obtained without any assumptions other than the non-negativity of spectral and concentration profiles.

Also shown in the figure are spectral boundaries obtained by the Sasaki algorithm (dotted lines). For both species, the upper and lower boundaries extracted by the Sasaki algorithm are completely overlapped and so appear as a single line. This demonstrates one of the weaknesses of this algorithm when even small negative values remain in the data after PCA. Because the penalty function in the Sasaki algorithm is essentially absolute in its rejection of negative values, the optimization routine ignores the spectral contribution to the objective functions in eqs. [9] and [10] and simply minimizes the penalty, giving the same result for both boundaries. In other words, whenever negative spectral and concentration contributions cannot be removed, regardless of how small they are, a single solution results. In this case, the Sasaki solutions match one of the boundaries from our algorithm for both species, but it is clear that there is a discrepancy with Pimienta's reults for the first intermediate.

The concentration profiles extracted by SMCR for each of the three species are shown in Fig. 7. As with the spectra, the concentration profiles extracted by SMCR normally have an ambiguity of scale, so while comparisons can be made for the same species in different runs, interspecies comparisons are not generally possible. In this case, however, the spectra reported by Pimienta et al. (18) were used to bring the concentration profiles for the intermediates to an approximately comparable scale. This means that the relative magnitudes of the concentration profiles in the last two columns of Fig. 7 can be compared directly. The concentration profiles for MnO_4^- are on a separate scale, however, and can only be compared within the column.

As in the case of the spectral profiles, the concentration profiles for MnO_4^- show very tight boundaries, to the point of being indistinguishable. These show a very clear picture of the autocatalytic reduction under different reaction conditions. The concentration profiles for the intermediates show generally wider bands and exhibit differing contributions from each species under different reaction conditions. In an attempt to quantify the relative contribution of each species for each run, Pimienta et al. (18) reported the percentage of intermediate 2 (Mn(IV)) to the total intermediate contribution in each run. This assumed a constant ratio of the intermediates, which is probably approximately valid for a significant portion of the reaction. They reported values of 9, 31, 60, and 68% Mn(IV) in runs 1 through 4, respectively. By integrating the mean concentration profiles for our results, we obtained values of 7, 29, 50, and 54%. Given the approximate nature of both calculations, this agreement is quite good. More importantly, however, the results presented in Fig. 7 give a picture of what is happening to species in solution, allowing a better visualization of reaction dynamics.

Conclusions

The principal objective of this work has been to introduce and demonstrate a modified SMCR procedure based on nonlinear optimization. The new procedure is substantially faster than the former procedure on which it is based, requiring many fewer steps in the optimization. In addition, the new method handles experimental measurement error in a more logical way and, unlike other SMCR methods, allows small departures of the solutions from the PCA subspace if these are warranted by measurement uncertainty. The new method requires no pure component regions or constraints other than non-negativity. Application of the method to the two-component data of Lawton and Sylvestre (1) led to results consistent with the analytical solution, but with broader boundaries, as expected when accounting for experimental error. Furthermore, the new method works in certain cases where the analytical solution fails because of the presence of measurement uncertainty. The new method was also applied to kinetic data for the permanganate oxidation of oxalic acid. This was an excellent case study, since (*i*) there were no clear pure component regions, (*ii*) there were a wide range of signal amplitudes, and (*iii*) results from an alternative approach were available for comparison. Results confirmed the presence of the two intermediates proposed by Pimienta et al. (18) and the spectra extracted by SMCR were in excellent agreement with those reported earlier. This clearly indicates the potential for SMCR in kinetic studies. In addition,

© 1998 NRC Canada

Fig. 6. Comparison of spectra of intermediates reported by Pimienta et al. (18) (open circles) with spectral boundaries extracted by the SMCR method in the present work (solid lines) and that used by Sasaki et al. (16) (dotted lines): (*a*) intermediate 1 (proposed Mn(III) species), (*b*) intermediate 2 (proposed Mn(IV) species).

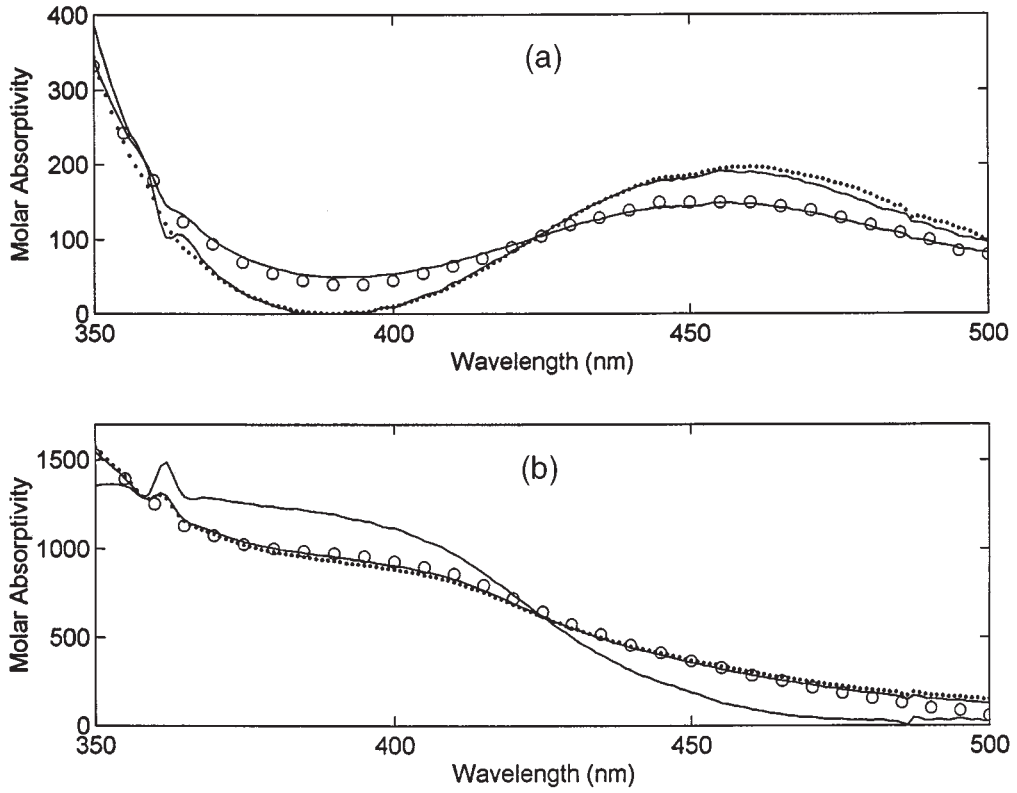

Fig. 7. SMCR-extracted concentration boundaries for permanganate and two intermediates for each of the four reaction conditions used. The horizontal axis runs from 0 to 700 s in all cases. Vertical scales are relative only. Permanganate profiles are on comparable scales, as are the profiles for all of the intermediates.

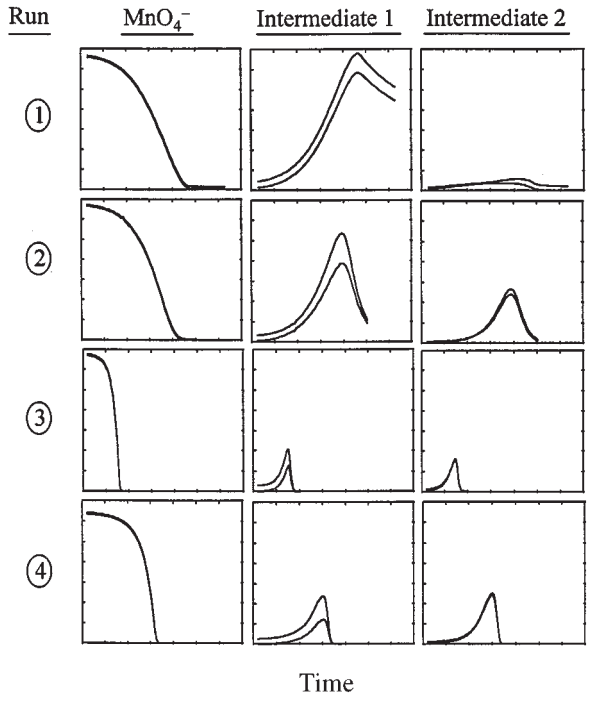

our laboratory has applied this algorithm to chromatography with multiwavelength fluorescence detection and to environmental receptor modeling. Given the wide range of studies now producing second-order data, tools such as this are likely to become more important in the future.

Acknowledgments

The authors gratefully acknowledge the financial support of the Natural Sciences and Engineering Research Council of Canada and helpful discussions with Prof. T.S. Cameron.

References

1. W.H. Lawton and E.A. Sylvestre. Technometrics, **13**, 617 (1971).
2. E.R. Malinowski. *In* Factor analysis in chemistry. 2nd ed. Wiley, New York. 1991.
3. J.C. Hamilton and P.J. Gemperline. J. Chemomet. **4**, 1 (1990).
4. O.S. Borgen and B.R. Kowalski. Anal. Chim. Acta, **174**, 1 (1985).
5. R.C. Henry and B.M. Kim. Chemom. Intell. Lab Syst. **8**, 205 (1990).
6. J. Chen and L. Hwang. Anal. Chim. Acta, **133**, 271 (1981).
7. Y. Sun, D.F. Sears, and J. Saltiel. Anal. Chem. **59**, 2515 (1987).
8. M.F. Delaney and D.M. Mauro. Anal. Chim. Acta, **172**, 193 (1985).
9. A. Meister. Anal. Chim. Acta, **161**, 149 (1984).
10. B. Vandeginste, R. Essers, T. Bosman, J. Reijnen, and G. Kateman. Anal. Chem. **57**, 971 (1985).

© 1998 NRC Canada

11. P.J. Gemperline. J. Chem. Inf. Comput. Sci. **24**, 206 (1984).
12. B.G.M. Vandeginste, W. Derks, and G. Kateman. Anal. Chim. Acta, **173**, 253 (1985).
13. R. Tauler, A.K. Smilde, J.M. Henshaw, L.W. Burgess, and B.R. Kowalski. Anal. Chem. **66**, 3337 (1994).
14. P.J. Gemperline. Anal. Chem. **58**, 2656 (1986).
15. N. Ohta. Anal. Chem. **45**, 553 (1973).
16. K. Sasaki, S. Kawata, and S. Minami. Appl. Opt. **22**, 3599 (1983).
17. K. Sasaki, S. Kawata, and S. Minami. Appl. Opt. **23**, 1955 (1984).
18. V. Pimienta, D. Lavabre, G. Levy, and J.C. Micheau. J. Phys. Chem. **98**, 13294 (1994).

© 1998 NRC Canada

Electrochemical behaviour of silver in aqueous chromate solutions

Sayed S. Abd El Rehim, Magdy A.M. Ibrahim, Hamdy H. Hassan, and Mohammed A. Amin

Abstract: The electrochemical behaviour of silver was studied under cyclic voltammetry and chronoamperometry conditions in aqueous K_2CrO_4 solutions. The forward cyclic voltammograms exhibited one oxidation peak, A_1, due to the formation of Ag_2CrO_4. The height of the anodic peak, A_1, increases with increasing chromate concentration, temperature, and scan rate. The solid films formed on the anode surface have been examined by X-ray diffractometry. The reverse voltammograms exhibited two reduction peaks, C_1 and C_2, indicating the formation of two distinct surface layers of Ag_2CrO_4, an inner compact layer reduced in peak C_1 and an outer powdery layer reduced in peak C_2.

Key words: silver electrode, cyclic voltammetry, K_2CrO_4 solutions.

Résumé : Faisant appel à la voltampérométrie cyclique et à la chronoampérométrie, on a étudié le comportement électrochimique de l'argent en solutions aqueuses de K_2CrO_4. Les voltampérogrammes cycliques de la réaction directe présentent un pic d'oxydation, A_1, dû à la formation de Ag_2CrO_4. La hauteur du pic anodique A_1 augmente avec une augmentation de la concentration du chromate, de la température et de la vitesse de balayage. Faisant appel à la diffraction des rayons X, on a examiné les films solides qui se forment à la surface anodique. Les voltampérogrammes inverses présentent deux pics de réduction, C_1 et C_2, qui indiquent qu'il y a formation de deux couches superficielles de Ag_2CrO_4 distinctes, une couche compacte intérieure réduite dans le pic C_1 et une couche extérieure en poudre qui est réduite dans le pic C_2.

Mots clés: électrode d'argent, voltampérométrie cyclique, solutions de K_2CrO_4.

[Traduit par la Rédaction]

Introduction

Very little work has been reported on the electrochemical behaviour of Ag in aqueous chromate solutions. However, the reduction of Ag_2CrO_4 was investigated in a number of nonaqueous electrolytes because Ag_2CrO_4 was used as a cathode in various lithium batteries (1–3). The system $Ag(s)–Ag_2CrO_4(s)–CrO_4^{2-}(aq)$ is a second kind of electrode, which is common and easy to use as a reference electrode (4). Druskovich et al. (4) studied the electrochemical behaviour of Ag in a solution containing sodium perchlorate and sodium chromate. In the absence of any chromate, only silver dissolution and deposition are observed. In the presence of low chromate ion concentrations ($<10^{-2}$ M), a film of silver chromate was observed. This Ag_2CrO_4 film did not suppress the silver dissolution reaction. However, the dissolution of silver was suppressed when the film of Ag_2CrO_4 was formed in more concentrated chromate solutions.

In the present work, an attempt is made to throw more light on the electrochemical behaviour of Ag in chromate solutions and the effect of chromate concentration, scan rate, temperature, repetitive cycling, and current transients on the voltammetric response of Ag electrode.

Received April 30, 1997.

S.S. Abd El Rehim,[1] M.A.M. Ibrahim, H.H. Hassan, and M.A. Amin. Faculty of Science, Ain Shams University, Cairo, Egypt.

[1]Author to whom correspondence may be addressed. Fax: (202)-4831-836. E-mail: imagdy@asunet.shams.eun.eg

Experimental

The working electrode employed in the present study was made of pure polycrystalline silver (99.99%, Koch light laboratories, Colnbrook Bucks England) axially embedded in an Araldite holder to offer an active flat disc-shaped surface of area 0.1256 cm^2. Prior to each experiment, the working electrode was mechanically polished with different grade emery papers, i.e., 600, 800, 1000, and finally 1200, and then the polished metal surface was rinsed with acetone, distilled water, and finally dipped in a conventional three-electrode cell. A platinum wire was used as the counter electrode. All potentials were measured against the saturated **c**alomel electrode (vs. SCE). To avoid contamination, the reference electrode was connected to the working electrode through a bridge with a Luggin capillary filled with the test solution. The capillary tip was put very close to the electrode surface to minimize the ohmic drop of the solution. All solutions were freshly made using doubly distilled water and analytical grade chemicals. All measurements were conducted at constant temperature ±1°C with the help of an air thermostat.

Electrochemical measurements were performed using a Potentiostat–Galvanostat Model 273 EG & G. The *E*/*i* curves were recorded using an X-Y recorder (series 2000, Omnigraphic).

 © 1998 NRC Canada

Fig. 1. Cyclic voltammograms for polycrystalline Ag electrode in 0.5 M K_2CrO_4 at 25°C and at a scan rate of 100 mV s^{-1} starting from $E_{s,c}$ = –1600 mV and reversed at various anodic potentials.

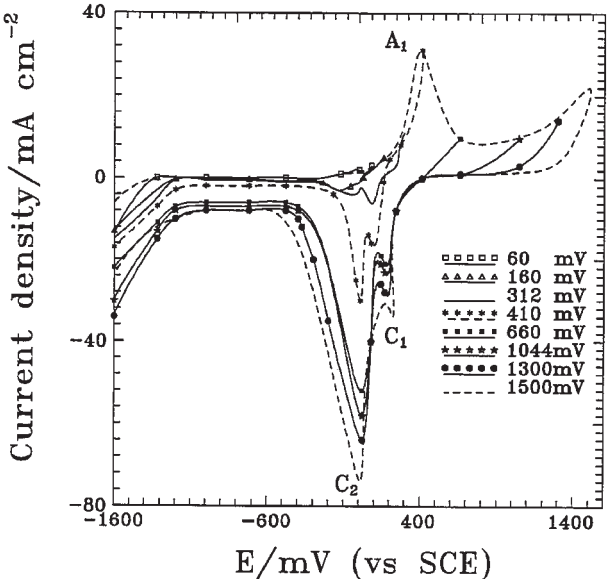

The current–time transients (constant anodic step potential limits, $E_{s,a}$) were recorded in the following way. The silver electrode was first held at the starting potential $E_{s,c}$ = –1600 mV for 60 s to attain a reproducible reduced silver surface, and then, the electrode was scanned potentiodynamically from –1600 mV in the positive direction with a constant scan rate of 100 mV s^{-1} to a potential limit $E_{s,a}$ at which the current–time transients were recorded for 100 s.

The composition and structure of the passive film formed on the silver electrode surface was examined by X-ray diffraction analysis. The X-ray diffraction system used for this analysis was a Philips P.W. model no. 1730 with a Cu-K_α radiation and nickel filter. The scanning speed was 1°/min. The X-ray diffraction measurements were performed on the electrode surface potentiodynamically polarized from –1600 mV up to 500 mV (with scan rate of 100 mV s^{-1}) and then held for 10 min at the potential 500 mV before withdrawing the electrode from the solution.

Results and discussion

Cyclic voltammetry

In Fig. 1, the dotted curve represents a typical cyclic voltammogram recorded in 0.5 M K_2CrO_4 at 25°C between the hydrogen and oxygen evolution reactions at a scan rate of 100 mV s^{-1}. The anodic response exhibits a well-defined anodic peak, A_1, followed by a passive region prior to oxygen evolution. This anodic peak is due to the formation of Ag_2CrO_4, since its potential range covers the potentials of the formation of Ag_2CrO_4 ($E°$ = 0.446 V for $Ag–Ag_2CrO_4–CrO_4^{2-}$) (4). The formation of solid phase Ag_2CrO_4 on the surface can be explained as follows:

$$2Ag + CrO_4^{2-} = Ag_2CrO_4 + 2e$$

Fig. 2. X-ray diffraction pattern for Ag anode potentiodynamically polarized from –1600 mV up to 500 mV (within the potential range of peak A_1) in 0.5 M K_2CrO_4 at a scan rate of 100 mV s^{-1}.

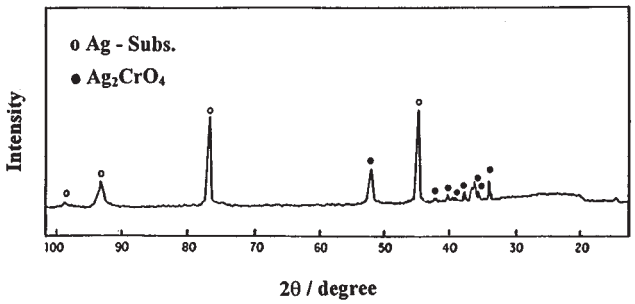

When the concentration of Ag_2CrO_4 at the anode surface exceeds its solubility product, precipitation of solid Ag_2CrO_4 occurs on the electrode surface, suggesting that the formation of solid Ag_2CrO_4 takes place via a dissolution–precipitation mechanism (4). When the surface is entirely covered with Ag_2CrO_4 passive film, the anodic current density falls sharply to a low value, i_{pass}, indicating the onset of passivation, which extends up to the oxygen evolution potential. The films formed were subsequently analyzed by X-ray diffraction. The diffraction analysis detected only Ag_2CrO_4, as shown in Fig. 2.

The cathodic response exhibits two distinct reduction peaks, C_1 and C_2, prior to hydrogen evolution. The existence of two reduction peaks suggests that two distinct films or phases are formed on silver surface during the anodic potential scan. Druskovich et al. (4) reported that the passivity of the silver anode in chromate solutions is due to the formation of compact layer of Ag_2CrO_4 containing a number of paths or flaws. However, in the passive region, the passive current density is involved in the formation and growth of a powdery layer of Ag_2CrO_4 on top of the inner compact layer. The authors proposed that, the formation of the powdery layer can be achieved by Ag^+ ions traveling rapidly along the paths and flaws of the compact layer to the chromate–solution interface. Therefore, it can be concluded that the peak, C_1, is assigned to the reduction of the compact layer, while the cathodic peak, C_2, is related to the reduction of the powdery layer. It seems that the difference in reduction potential between peaks C_1 and C_2 is due to the difference in morphology, which might exist between the silver formed during the reduction of the two solid layers (4). It is probable that the compact layer reduces more easily than the powdery layer because it is in good electrical contact with the underlying metal.

The solid curves of Fig. 1 show a series of voltammograms reversed at various anodic limits, $E_{s,a}$. The data reveal that, if the anodic potential is reversed at 60 mV, the reversing scan retraces itself and does not display any cathodic peaks, indicating the absence of any solid product. When $E_{s,a}$ is 160 mV, the reverse scan retraces part of the forward scan and then yields the reduction peak, C_1, corresponding to the reduction of the compact layer. When $E_{s,a}$ is 312 mV, the reverse scan shows hysteresis between the forward and the return scan and then yields two reduction peaks, C_1 and C_2, indicating that the two layers are formed

© 1998 NRC Canada

Fig. 3. Cathodic stripping voltammograms recorded for polycrystalline Ag electrode in 0.5 M K_2CrO_4 at 25°C and at a scan rate of 100 mV s^{-1} after potentiostatic oxidation at 840 mV for various times.

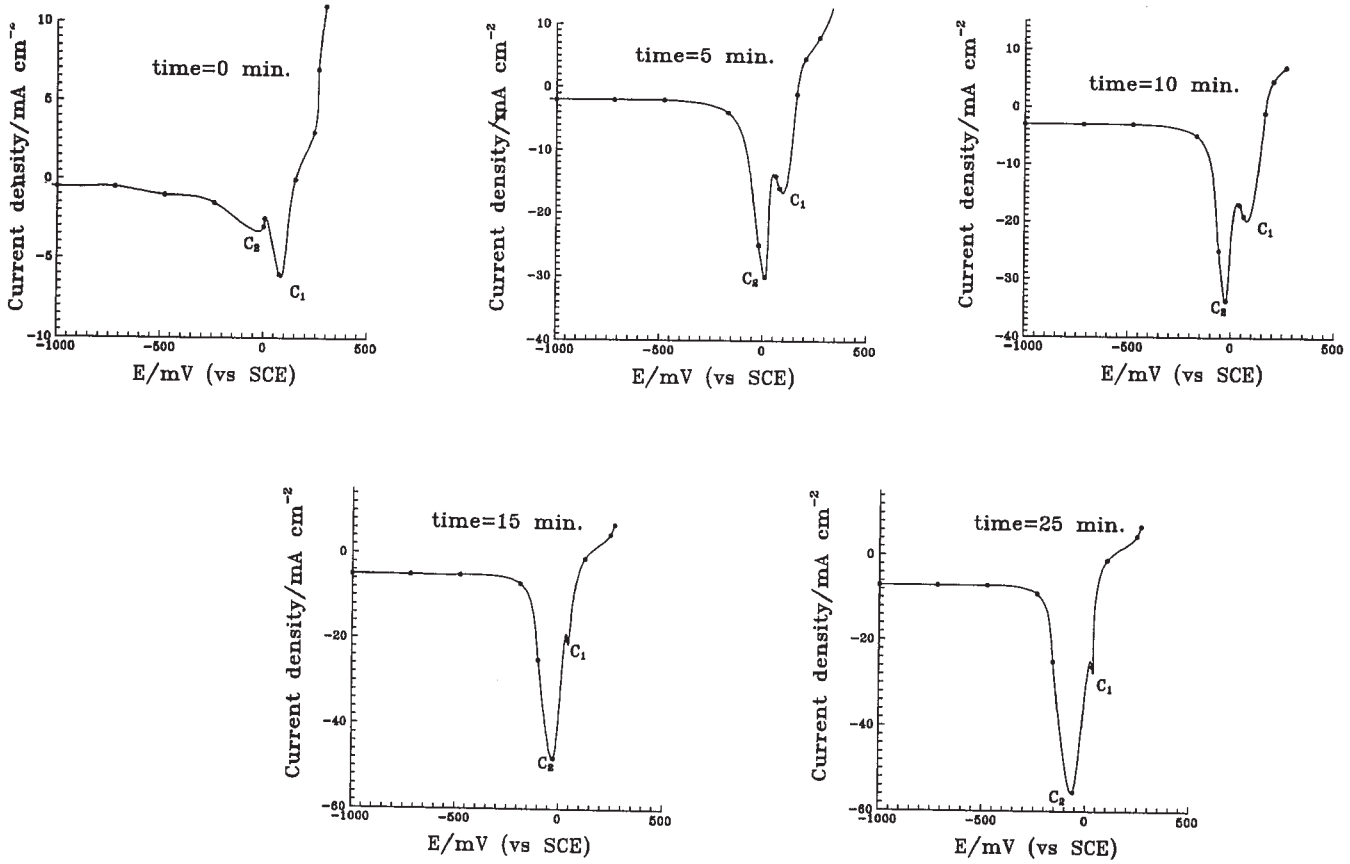

Fig. 4. Cyclic voltammograms for polycrystalline Ag electrode in 0.50 M K_2CrO_4 solution between $E_{s,c}$ = –1600 mV and $E_{s,a}$ = 1500 mV at 25°C and at different scan rates.

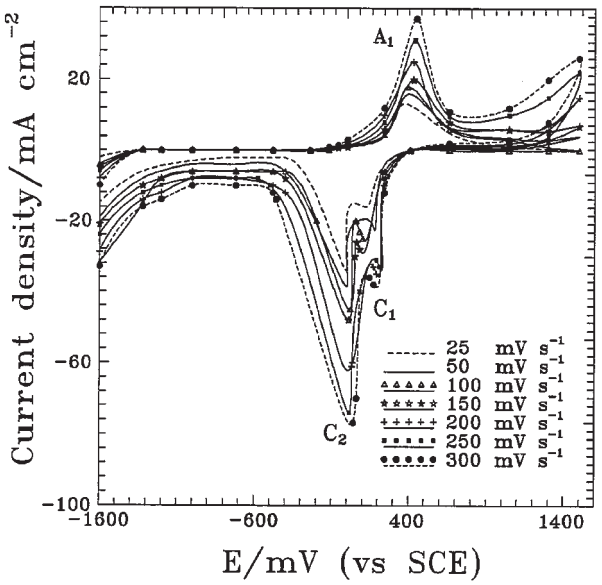

on the cathodic side of the anodic peak. It is seen that the cathodic peak height (i_{PC2}) is highly affected by increasing the anodic limit, while that of C_1 (i.e., i_{PC1}) increases slightly with increasing $E_{s,a}$, indicating that the thickness of the Ag_2CrO_4 powdery layer increases, while that of the compact layer remains nearly constant, as the scan progresses to more positive potentials.

It is interesting to note that i_{PC2} increases, not only by increasing $E_{s,a}$ within the passive region, but also by holding $E_{s,a}$ constant for some time before reversing the scan, as shown in Fig. 3. This figure shows a series of cathodic stripping voltammograms recorded after scanning the potentials up to $E_{s,a}$ = 840 mV and then holding $E_{s,a}$ constant for various periods of time before reversing the scan. The data reveal that the areas of both reduction peaks increase with increasing holding time as a result of increasing thickness of the two layers, but peak C_2 increases more significantly than peak C_1.

In Fig. 4 are presented cyclic voltammograms obtained at various sweep rates. It is seen that, current densities i_{PA1} (peak current for the process A_1), i_{pass} (current for the passivation process), i_{PC1} (peak current for the process C_1), and i_{PC2} (peak current for the process C_2) increase with increasing scan rate, ν. It is seen from Fig. 4 that the sweep rate is more effective on the powdery layer, than on the compact layer, indicating the formation of greater number of flaws and paths in the compact layer. The plots of i_{PA1}, i_{PC1}, and i_{PC2} against the square root of ν were straight lines with ordinates at their origins, as shown in Fig. 5. This is in accordance with the following equation (5):

$$i_p = abz^{1/2}CD^{1/2}\nu^{1/2}$$

© 1998 NRC Canada

Fig. 5. Dependence of the peak current density, i_p, on the square root of the potential scan rate $\nu^{1/2}$ for Ag electrode in 0.50 M K_2CrO_4 solution at 25°C.

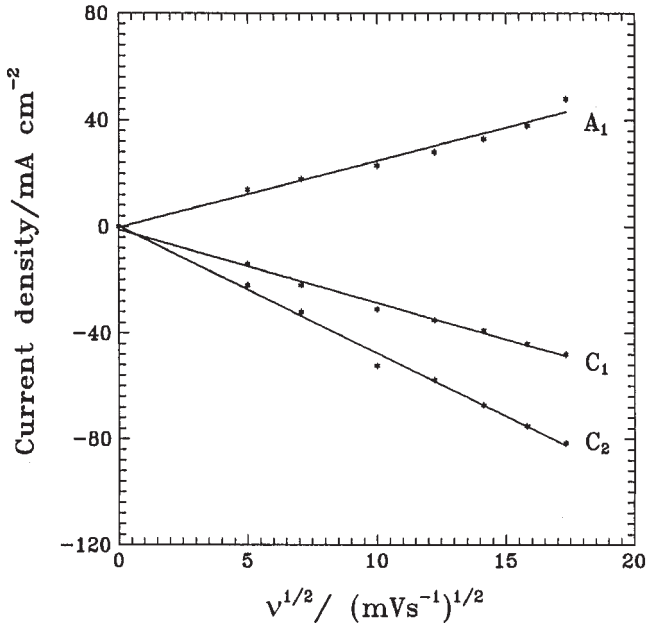

Fig. 6. Cyclic voltammograms for polycrystalline Ag electrode in K_2CrO_4 solutions of various concentrations (0.10–1.25 M) between $E_{s,c}$ = –1600 mV and $E_{s,a}$ = 1500 mV at 25°C and at a scan rate of 100 mV s^{-1}.

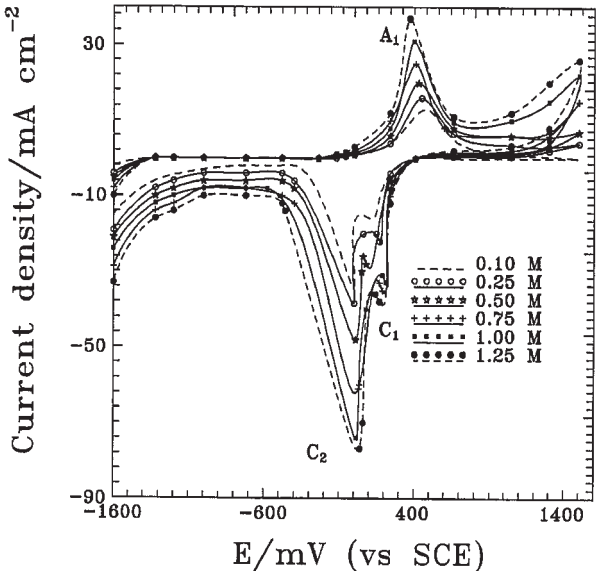

where a and b are constants, z is the number of exchanged electrons, C is the concentration, and D is the diffusion coefficients of the diffusing species. These results suggest that the formation of Ag_2CrO_4 passive layers and their subsequent reduction are under diffusion control.

Figure 6 shows the effect of chromate concentration on the cyclic voltammogram curves obtained at the silver electrode. The data reveal that the charges involved in the formation of both compact and powdery Ag_2CrO_4 layers increase with an increase in CrO_4^{2-} concentration. The peak

Fig. 7. Cyclic voltammograms for polycrystalline Ag electrode in 0.50 M K_2CrO_4 solution between $E_{s,c}$ = –1680 mV and $E_{s,a}$ = 1500 mV at different temperatures (10–60°C) and at a scan rate of 100 mV s^{-1}.

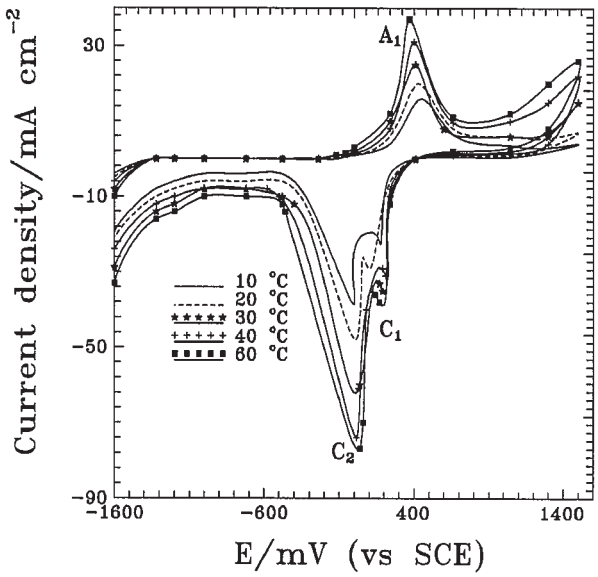

Fig. 8. Dependence of log i_p on $1/T$ (K) for Ag electrode in 0.5 M K_2CrO_4 solution at a scan rate of 100 mV s^{-1}.

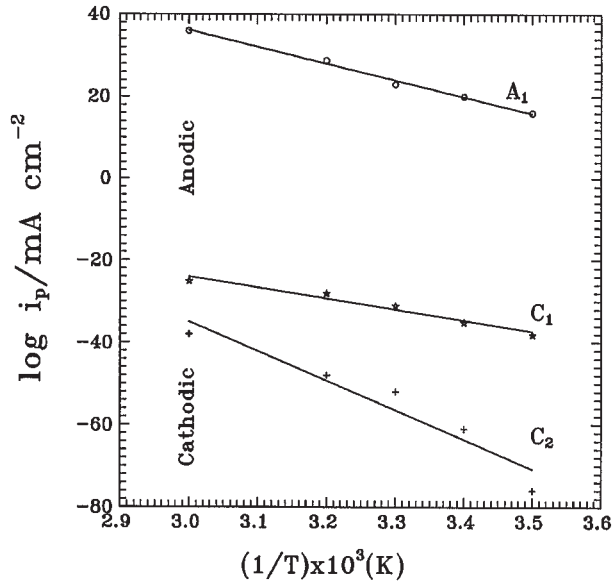

potential of the anodic peak, A_1, shifts to more negative potentials, while those of both C_1 and C_2 shift positively with increasing chromate concentration. The dissolution acceleration effect of CrO_4^{2-} ion may be due to its direct participation in the elementary act of Ag ionization and also to the increase of the rate of its transport through the flaws and paths of the compact layer.

Figure 7 shows the influence of solution temperature on the cyclic voltammograms obtained at the Ag electrode in 0.5 M K_2CrO_4 with a scan rate of 100 mV s^{-1}. The heights of the A_1, C_1, and C_2 peaks increase with rising temperature. The peak potential of peak A_1 shifts in the negative

© 1998 NRC Canada

Fig. 9. Current transients at constant step potential, $E_{s,a}$, recorded for a polycrystalline Ag electrode in 1.0 M K_2CrO_4 at 25°C after applying to the electrode the pretreatments mentioned before. $E_{s,a}$ = 300, 400, 500, 600, 700, 800, 900, 1000, 1300, and 1500 mV.

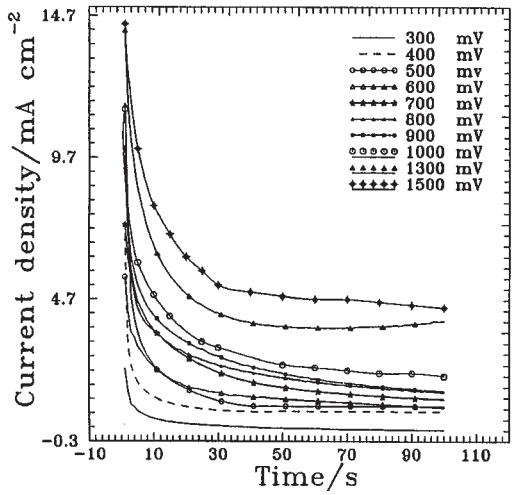

direction, while those of the two reduction peaks, C_1 and C_2, shift towards more positive potentials. The value log i_p of the A_1, C_1, and C_2 peaks for various temperatures was plotted as a function of $1/T$ (K) in Fig. 8. The apparent activation energies, E^*, for the formation of the compact powdery layers and their reduction were calculated from the slopes of the Arrhenuis plots, according to the equation:

$$i_p = A \exp(-E^*/RT)$$

and they are 6.4, 4.1, and 8.3 kJ mol^{-1} for peaks A_1, C_1, and C_2, respectively. The stimulation effect of temperature for the formation of Ag_2CrO_4 may be attributed to an increase in the solubility of the silver salt with temperature. In addition, an increase in temperature accelerates the diffusion rate of the diffusing species.

Current transient

A series of current–time transients at constant anodic step potentials, $E_{s,a}$, in the potential range $300 \le E_{s,a} \le 1500$ mV for a Ag electrode in 0.5 M K_2CrO_4 at 25°C were recorded after a two-step procedure. The Ag electrode was first held at $E_{s,c}$ = –1680 mV for 60 s to attain a reproducible reduced Ag surface, and then the electrode was potentiodynamically polarized in the positive direction with a scan rate of 100 mV s^{-1} to a potential limit $E_{s,a}$ at which the current transient was recorded. Figure 9 shows the current–time relationship for different anodic step potentials, $E_{s,a}$. The transient current decreases monotonically with time to reach a steady-state value. As $E_{s,a}$ is made more positive, the values of the instantaneous and steady-state currents increase, indicating an increase in the thickness of the anodically formed Ag_2CrO_4 layers. No peak is observed in the current transients, indicating that a phase nucleation and growth process is not involved. The continuously falling current was linear versus $t^{-1/2}$, as shown in Fig. 10. The slope of these lines depends on the value of $E_{s,a}$. This type of linear relationship suggests that the growth of the Ag_2CrO_4 layers is a

Fig. 10. Dependence of the current density on $t^{-1/2}$ for the descending portions of the current transients for Ag electrode in 0.5 M K_2CrO_4 at 25°C recorded in the potential range (300 mV $\le E_{s,a} \le$ 1500 mV) at a scan rate of 100 mV s^{-1}.

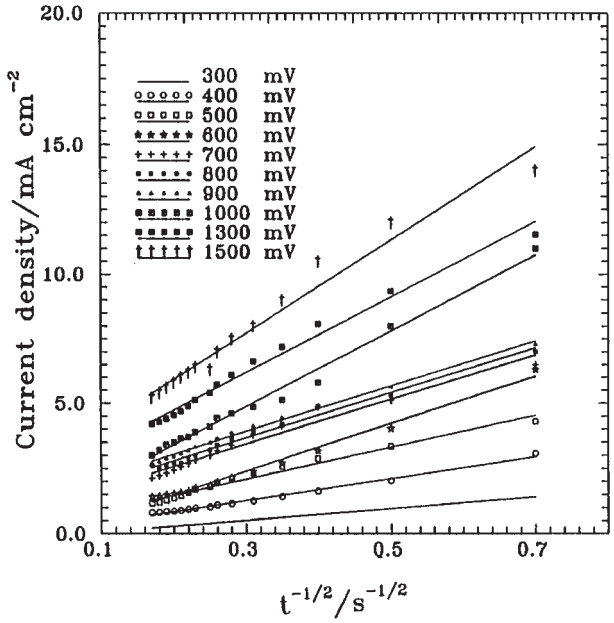

diffusion-controlled process and obeys the following equation (6):

$$i = P/t^{1/2}$$

where $P = zCD^{1/2}/\pi^{1/2}$ and z is the number of exchanged electrons, C is the concentration, and D is the diffusion coefficient of the diffusing species.

Conclusion

The electrochemical behaviour of silver in aqueous K_2CrO_4 solutions was studied using both cyclic voltammetry and chronoamperometry techniques. The cyclic voltammograms showed one oxidation peak, A_1 (due to the formation of solid Ag_2CrO_4 on the electrode surface), and two reduction peaks, C_1 and C_2. The presence of these two reduction peaks is an indication of two distinct layers of Ag_2CrO_4, an inner compact layer (peak C_1) and an outer powdery layer (peak C_2). The powdery layer is formed via the transport of Ag^+ ions through flaws and paths in the compact layer to the chromate–solution interface. The relative thickness of the powdery layer increases markedly with increasing applied potential, the holding time at a given potential, electrolyte concentration, scan rate, and temperature. On the other hand, the relative thickness of the compact layer is only slightly affected by these parameters. Current–time transients showed that the values of the instantaneous and steady-state currents increase with increasing anodic potential limit, $E_{s,a}$, indicating an increase in the thickness of the anodically formed Ag_2CrO_4 layers.

References

1. R. Messina, J. Perichon, M. Broussely, and G. Gerbier, J. Appl. Electrochem. **8**, 405 (1978).

© 1998 NRC Canada

2. G. Gerbier, G. Lehmann, P. Lenfant, and J.P. Rivault. Power sources, **6**, 483 (1977).
3. N. Margalit. U.S. Patent, 4, 11, 3929 (1978).
4. D.M. Druskovich, I.M. Ritchie, P. Singh, and Z. Hong-Guang. Electrochim. Acta, **34**, 409, (1989).
5. P. Delahay. New instrumental methods in electrochemistry. Interscience Publ., New York. 1954. p. 124.
6. R.C. Salvarezza, J. Gomez Becerra, and A.J. Arvia. Electrochim. Acta, **33**, 1753 (1988).

© 1998 NRC Canada

A study of the vacuum pyrolysis of *para*-substituted diazoacetophenones with He(I) ultraviolet photoelectron spectroscopy

Nick H. Werstiuk, Heidi M. Muchall, Jiagong Ma, and Michael T.H. Liu

Abstract: An ultraviolet photoelectron (PE) spectrometer apparatus that utilizes a tuneable 50 W CW CO_2 laser as a directed heat source was used to study the vacuum pyrolysis of diazoacetophenone (**1a**) and its *p*-methyl, *p*-methoxy, *p*-chloro, and *p*-nitro analogues **1b**, **1c**, **1d**, and **1e**. Analysis of the pyrolysate with He(I) ultraviolet PE spectroscopy shows that at a laser power level of 26 W (500 ± 50°C) **1a**, **1b**, **1c**, and **1d**, cleanly yield the corresponding phenylketenes **2a**, **2b**, **2c**, and **2d**, respectively, the products of the Wolff rearrangement of the incipient ketocarbenes. Of this group of highly reactive ketenes, which cannot be isolated in the condensed phase at ambient temperature, only **2a** has been the subject of a previous PE spectroscopic study. But our work indicates that the sample of **2a** prepared in the earlier study was impure. The low volatility of *p*-nitrodiazoacetophenone (**1e**) thwarted our attempts to generate **2e** and obtain its spectrum. Calculations at semiempirical (AM1) and ab inito (HF/6-31G(d)) levels of theory established that the diazoacetophenones prefer to adopt twisted *syn* conformations. That the calculated ionization potentials (HAM/3 and Becke3LYP/6-31+G(d)//HF/6-31G(d)) of **1a**–**1d** and the synthesized PE spectra of **1a**, **1b**, and **1c** correlate well with the PE spectroscopic data supports this finding. Shifts observed in the three low-energy ionizations of ketenes **2b, 2c**, and **2d** induced by the *para*-substitution can be related to the character of the corresponding occupied molecular orbitals of phenylketene (**2a**).

Key words: diazoacetophenones, phenylketenes, He(I) photoelectron spectroscopy, thermolysis, quantum chemical calculations.

Résumé : On a fait appel à un spectromètre photoélectronique (PE) ultraviolet, qui utilise comme source de chaleur un laser à CO_2 de 50 W ajustable et à VC, pour étudier la pyrolyse sous vide de la diazoacétophénone (**1a**) et de ses analogues *p*-méthyl-, *p*-méthoxy-, *p*-chloro- et *p*-nitro- (**1b, 1c, 1d** et **1e**). L'analyse des pyrolysats par spectroscopie PE ultraviolette à He(I) montre que, à une puissance de laser de 26 W (500 ± 50°C), les composés **1a, 1b, 1c** et **1d** conduisent proprement aux phénylcétènes correspondants, soit les produits **2a, 2b, 2c** et **2d** respectivement, qui correspondent aux produits de réarrangement de Wolff des cétocarbènes qui se forment. De ce groupe de cétènes hautement réactifs qui ne peuvent pas être isolés sous forme condensée à la température ambiante, seul le composé **2a** avait fait l'objet d'une étude antérieure par spectroscopie PE. Les résultats obtenus au cours de ce travail indiquent toutefois que le composé **2a** préparé antérieurement n'était pas pur. La faible volatilité de la *p*-nitrodiazoacétophénone (**1e**) nous a empêché de générer le produit **2e** et d'en obtenir un spectre. Des calculs théories aux niveaux semiempirique (AM1) et ab initio (HF/6-31G(d)) ont permis de déterminer que les diazoacétophénones adoptent préférentiellement les conformations *syn* déformées. Le fait que les potentiels d'ionisation calculés (HAM/3 et Becke3LYP/6-31+G(d)//HF/6-31G(d)) pour les composés **1a–1d** et que les spectres PE synthétisés des produits **1a**, **1b** et **1c** donnent une excellente corrélation avec les données de spectroscopie PE est en accord avec cette conclusion. Les déplacements observés dans les trois ionisations de faible énergie des cétènes **2b, 2c** et **2d** sont induits par les substituants en *para* et on peut les relier au caractère des orbitales molécules occupées correspondantes du phénylcétène (**2a**).

Mots clés : diazoacétophénones, phénylcétènes, spectroscopie photoélectronique He(I), thermolyse, calculs théoriques par chimie quantique.

[Traduit par la Rédaction]

Received March 26, 1998.

N.H. Werstiuk,[1] H.M. Muchall,[1] and J. Ma. Department of Chemistry, McMaster University, Hamilton, ON L8S 4M1, Canada. **M.T.H. Liu.** Department of Chemistry, University of Prince Edward Island, Charlottetown, PE C1A 4P3, Canada.

[1]Authors to whom correspondence may be addressed. Telephone: (905) 525-9140. Fax: (905) 522-2509. E-mail: werstiuk@mcmaster.ca; muchall@mcmaster.ca

 © 1998 NRC Canada

Fig. 1. Optimized structures of (*a*) **1a**–**1e** obtained with AM1 and (*b*) **1a**–**1d** obtained with HF/6-31G(d).

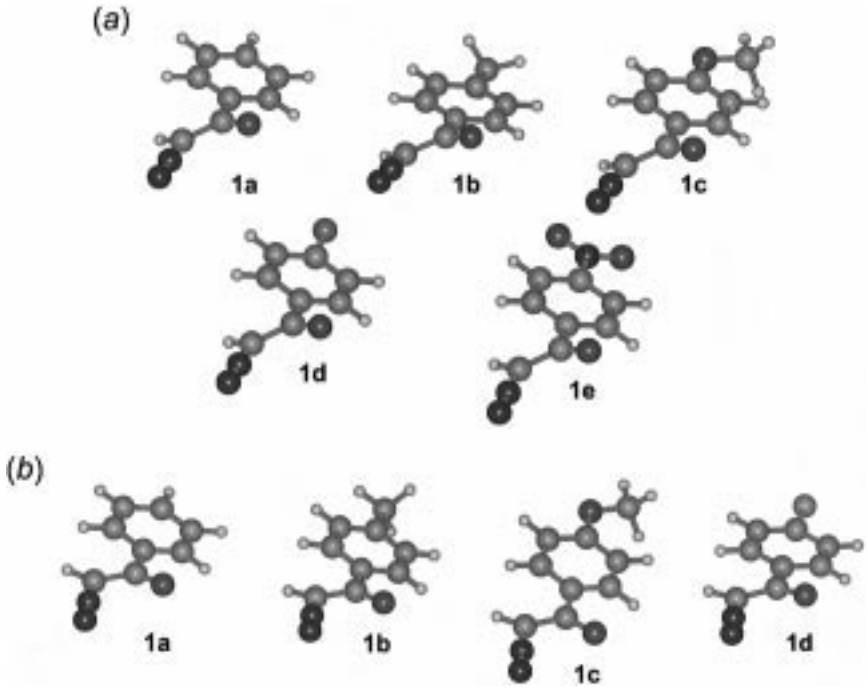

Fig. 2. Potential energy surface (AM1) of **1a** for the torsion of N=C—C=O and phenyl—C=O dihedral angles.

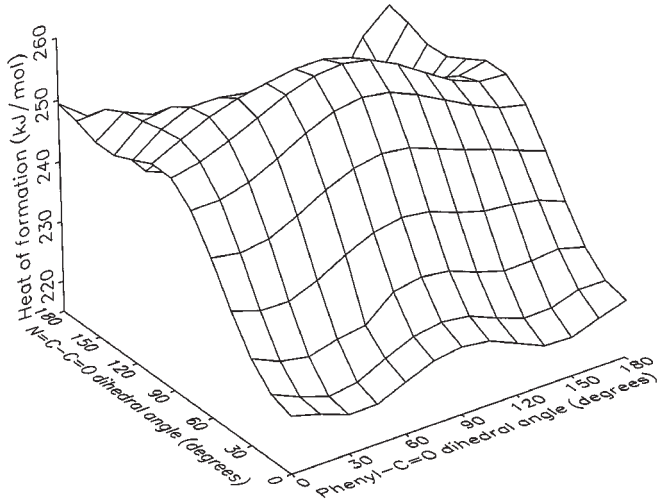

Introduction

To facilitate the preparation and detection of highly reactive transients in the gas phase, we developed a He(I) ultraviolet photoelectron (PE) spectrometer-CW CO_2 laser apparatus and used it successfully to study the vacuum pyrolysis of 6,6-dihalobicyclo[3.1.0]hexanes (1), 1,2,3-benzotriazines (2), 4-diazoisochroman-3-one (3), and 4-diazoisothiochroman-3-one (4), 11-oxatricyclo[6.2.1.$0^{2,7}$]-undeca-2,9-diene (5), and 2,2-dimethoxy-5,5-dimethyl-Δ^3-1,3,4-oxadiazoline (6). To widen our research in this field, we undertook a study of the vacuum pyrolysis of diazoacetophenone (**1a**), *p*-methyldiazoacetophenone (**1b**), *p*-methoxydiazoacetophenone (**1c**), *p*-chlorodiazoacetophenone (**1d**), and *p*-nitrodiazoacetophenone (**1e**) that are potential precursors of ketocarbenes and the corresponding *para*-substituted phenylketenes, which are the Wolff rearrangement products (7). Only a limited number of ketenes which cannot be isolated in the condensed phase at ambient temperature have been studied in the gas phase with PE spectroscopy (5, 8–13), and there is comparatively little experimental data available on the vacuum pyrolysis of α-diazocarbonyl compounds (see, for example, ref.14) in contrast to the large body of work that has been accumulated on the photochemistry of this class of compounds (14–21). Given that a wide variety of diazocarbonyl compounds can be synthesized (14) and, as our studies have shown, easily pyrolyzed in the gas phase, we expected PE spectroscopic and calculational studies to provide fundamental information on aspects of the electronic structure and reactivity of this group of compounds and the products derived from the incipient ketocarbenes (4, 5). We undertook a study of **1a**, **1b**, **1c**, **1d**, and **1e** specifically (*i*) to gain information about the nature of the frontier molecular orbitals (MOs), (*ii*) to study the conformational properties of these compounds in the gas phase, (*iii*) to establish whether our instrument is generally useful for preparing and studying ketenes in the gas phase (five new *para*-substituted phenylketenes were to be prepared), and (*iv*) to determine the effect of the *para*-substituents on the ionization potentials of **2a** with the goal of characterizing its highest occupied molecular orbitals. This paper documents the results of a PE spectroscopic study of the pyrolysis of diazoacetophenones **1a**, **1b**, **1c**, and **1d** and a computational study of the conformational properties and molecular orbitals of this group of compounds, the nitro analogue **1e**, and the corresponding ketenes (Scheme 1).

© 1998 NRC Canada

Table 1. The AM1 heats of formation ΔH_f (kJ mol^{-1}) and HF/6-31G(d) total energies E_T of two conformations of diazoacetophenones **1a**–**1e** and of phenylketenes **2a**–**2d**.

Compound	ΔH_f	$\Delta\Delta H_f$	E_T (hartrees)	ΔE_T (kJ mol^{-1})
syn-**1a**	221.42		–490.141 659[a]	
anti-**1a**	232.55	11.13	–490.135 222[a]	16.88
syn-**1b**	188.87		–529.179 538	
anti-**1b**	199.95	11.08	–529.173 039	17.05
syn-**1c**	60.54[b]		–604.023 915	
anti-**1c**	72.68	12.13	–604.017 046	18.02
syn-**1d**	192.67		–949.041 019	
anti-**1d**	205.06	12.38		
syn-**1e**	240.75			
anti-**1e**	253.05	12.30		
2a	72.22		–381.274 201	
2b	40.25		–420.311 107	
2c	–85.40[b]		–495.153 149	
2d	42.55		–840.173 832	

[a] The total energies obtained with the keyword TIGHT are identical within 10^{-6} hartrees to the values given.
[b] The stereoisomer with the methoxy group orientated *anti* to the C=O group is marginally higher in energy (**1c**: ΔH_f = 61.17 kJ mol^{-1}; **2c**: ΔH_f = –85.23 kJ mol^{-1}) than the correponding *syn* isomer.

Table 2. Selected calculated[a] dihedral angles (degrees) of two conformations of diazoacetophenones **1a**–**1e**.

	Dihedral	
Compound	N=C—C=O	phenyl—C=O
syn-**1a**	4.1(2.2)[b](1.6)[c]	31.6(17.0)[b](17.3)[c]
anti-**1a**	179.9(165.2)[b](165.2)[c]	58.6(36.8)[b](36.7)[c]
syn-**1b**	4.1(2.1)[b]	30.0(15.0)[b]
anti-**1b**	173.4(164.6)[b]	53.9(35.1)[b]
syn-**1c**	4.3(1.7)[b]	31.3(10.3)[b]
anti-**1c**	172.1(163.3)[b]	52.3(32.2)[b]
syn-**1d**	2.9	35.9
anti-**1d**	178.9	81.2
syn-**1e**	2.4	38.1
anti-**1e**	175.7	60.3

[a]Unless stated otherwise the values listed were calculated with AM1.
[b]Calculated at the HF/6-31G(d) level of theory.
[c]Calculated at the HF/6-31G(d) level of theory with the keyword TIGHT.

Scheme 1.

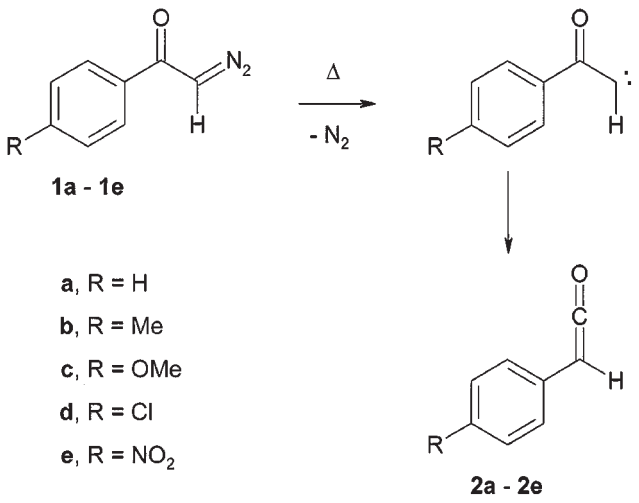

Experimental

Calculations

Calculations at the semiempirical level of theory were carried out with AM1 of HyperChem 4.0 (22), AMPAC 2.0 (23), or MOPAC 6.0 (24), with the latter two programs running on IBM RS/6000 model 320H, 350, and 530 computers. An RMS gradient of 0.02 was used to obtain optimized geometries with HyperChem 4.0, and the keyword PRECISE was used in the case of AMPAC and MOPAC calculations to tighten the convergence criteria. Ab initio HF (25) and Becke3LYP (26) calculations were carried out with GAUSSIAN 94 (27) running on IBM RS/6000 model 350, 530, 39H, and SP2 and SGI R10000 Impact computers. Optimized geometries were shown to be minima by frequency calculations; total energies are uncorrected for zero-point energies. The semiempirical method HAM/3 (28) was used to compute the ionization potentials. The acronyms HAM/3//AM1 and HAM/3//HF/6-31G(d) indicate that HAM/3 calculations were carried out on AM1 and HF/6-31G(d) optimized equilibrium geometries, respectively. Synthetic spectra were calculated from the MO results with a FORTRAN program PESPEC (29). Spectra were synthesized from the 10 lowest IPs (HAM/3), with a Gaussian convolution of 0.4 and the temperature set at 300 K. Graphical representations of the computationally determined eigenvectors (AM1//HF/6-31G(d)) were plotted from HyperChem 4.0.

PE spectroscopic studies

The locally built PE spectrometer-CW CO_2 infrared laser apparatus (the laser is used as a directed heat source) employed in this study is described in our earlier publications (1–5). To obtain the PE spectra of the diazoacetophenones (**1a**, mp 51–52; **1b**, mp 57–58; **1c**, mp 87–88; **1d**, mp 115–116; **1e**, mp 116–117°C), which were prepared by established methods (30), a 20 mg sample was placed in a bottle-shaped quartz reaction vessel that was inserted into the tip of a heated probe. The temperature was slowly ramped up (a

© 1998 NRC Canada

Table 3. Calculated vertical ionization potentials IP (eV) and orbital energies ε (eV) for diazoacetophenones[a] **1a**–**1d** and phenylketenes **2a**–**2d**.

1a	HAM3[b]	IP	8.60	9.09	9.53	9.60	11.74	11.96	12.33	12.72	13.22	13.83
	HAM3[c]	IP	8.72	9.47	9.58	9.66	11.87	12.15	12.49	13.10	13.68	13.88
	B3LYP[d]	–ε	6.87	7.21	7.41	7.47	9.82	10.17	10.24	11.37	11.61	12.01
		IP[e]	8.8	9.1	9.3	9.4	11.7	12.1	12.1	13.3	13.5	13.9
1b	HAM3[b]	IP	8.41	9.07	9.24	9.39	11.39	11.86	12.14	12.46	12.71	12.90
	HAM3[c]	IP	8.55	9.28	9.36	9.38	11.51	11.98	12.19	12.82	12.95	13.34
	B3LYP[d]	–ε	6.77	7.05	7.27	7.34	9.62	9.89	9.96	10.85	11.49	11.88
		IP[e]	8.6	8.9	9.1	9.1	11.4	11.7	11.8	12.7	13.3	13.7
1c	HAM3[b]	IP	8.28	8.75	8.95	9.43	10.84	11.27	12.05	12.24	12.43	12.64
	HAM3[c]	IP	8.35	8.77	9.28	9.42	10.95	11.46	12.33	12.45	12.83	12.91
	B3LYP[d]	–ε	6.46	6.80	7.16	7.43	9.13	9.32	10.24	10.63	10.87	11.32
		IP[e]	8.2	8.5	8.9	9.1	10.8	11.0	11.9	12.3	12.6	13.0
1d	B3LYP[d]	–ε	7.00	7.25	7.51	7.77	8.93	9.46	10.32	10.76	11.04	11.69
		IP[e]	8.8	9.1	9.3	9.6	10.7	11.3	12.1	12.6	12.8	13.5
2a	HAM3[b]	IP	8.17	9.36	10.19	11.99	12.03	12.27	13.35	13.80	14.04	14.21
	B3LYP[d]	–ε	5.97	7.15	8.20	9.62	9.86	10.47	11.45	11.74	12.14	12.55
		IP[e]	7.9	9.1	10.1	11.5	11.8	12.4	13.4	13.6	14.0	14.5
2b	HAM3[b]	IP	7.93	9.20	9.83	11.73	11.84	12.10	12.56	13.01	13.54	13.74
	B3LYP[d]	–ε	5.79	7.07	7.93	9.43	9.66	10.18	10.63	11.23	11.61	11.65
		IP[e]	7.7	9.0	9.8	11.3	11.6	12.1	12.5	13.1	13.5	13.6
2c	HAM3[b]	IP	7.67	9.17	9.33	11.13	11.25	12.15	12.21	12.60	13.25	13.35
	B3LYP[d]	–ε	5.52	7.15	7.46	9.11	9.35	10.03	10.48	10.68	11.48	11.81
		IP[e]	7.4	9.1	9.4	11.0	11.3	11.9	12.4	12.6	13.4	13.7
2d	B3LYP[d]	–ε	6.08	7.53	7.97	8.70	9.68	10.18	10.47	11.18	11.75	12.15
		IP[e]	7.9	9.3	9.8	10.5	11.5	12.0	12.3	13.0	13.6	14.0

[a]Twisted *syn* conformers.
[b]At the HAM/3//AM1 level of theory.
[c]At the HAM/3//HF/6-31G(d) level of theory.
[d]At the Becke3LYP/6-31+G(d)//HF/6-31G(d) level of theory.
[e]Orbital energies shifted uniformly, so that the HOMO energy[d] equals the calculated first IP_v as given in Table 4.

maximum temperature of 80°C was used) until a suitable source pressure in the region of (3×10^{-3})–(8×10^{-3}) Torr (1 Torr = 133.3 Pa) was obtained. In the case of **1b**, **1c**, and **1d**, which exhibited low volatilities, N_2 was used as a pressure make-up gas to improve the signal to noise.[2] Consequently, vertical expansions of the spectra were required in the region of 8–15 eV.

Spectra were obtained by averaging 20–35 scans and calibrated with the 15.6 eV band of N_2. Linearity of the scale was ensured through calibrations with methyl iodide (9.54 and 10.16 eV) and O_2 (12.30 eV) performed prior to the experiments. Vertical ionization potentials are accurate to ± 0.05 eV. Pyrolyses of the diazoacetophenones were carried out in a hot zone 1–2 mm in length obtained by focusing the laser beam (power levels of 26, 42, and 47 W were used) on the tip (2–3 mm inner diameter) of the bottle-shaped quartz sample vessel. Due to the very low volatility of **1e** we were not able to obtain its spectrum and study its pyrolysis even in the presence of the pressure make-up gas. Hatched bands in the PE spectra are due to traces of H_2O (12.6 eV) and a shadow peak (13.6 eV) of N_2.

Results and discussion

Calculations

1. Conformational properties of diazoacetophenones and phenylketenes

Figure 1(*a*) shows the AM1 optimized geometrical structures of the *syn* forms of **1a**–**1e**. The gas-phase torsional potential energy surfaces of **1a**, **1b**, and **1c** were calculated with AM1 by varying the N=C—C=O and phenyl—C=O dihedral angles from 0° to 180° in 15° increments. At the AM1 level, **1a** prefers a twisted *syn* rather than an *anti* conformation of the N=C—C=O group, and the conformer with the N=C—C=O and phenyl—C=O dihedral angles fixed at 90° is the highest energy species. Because the potential energy surfaces of **1a**–**1c** exhibit very similar topologies we report only the surface obtained for diazoacetophenone (**1a**) as Fig. 2. That the surfaces of **1b** and **1c** (not shown) are virtually identical to the surface of **1a** indicates that **1a**, **1b**, and **1c** have similar conformational properties in the gas phase. That twisted *syn* conformers are

[2] Although He(I) PE spectra of **1a**, **1b**, and **1d** already have been reported by Modelli et al. (31) they are presented again for two reasons: (*i*) the spectra reported earlier contain bands of nitrogen — and along with these, bands of further products — due to decomposition of the compounds, and (*ii*) the different analyzer transmission functions of the spectrometers used in the previous and in this study lead to PE spectra that differ in intensities of the bands. As we planned to record pyrolyses spectra, knowledge of the actual appearance of the spectra of the starting compounds taken with our instrument was essential.

© 1998 NRC Canada

Table 4. Total energies (hartrees) of diazoacetophenones[a] **1a**–**1d** and phenylketenes **2a**–**2d** (N electrons) and their radical cations[b] (N – 1 electrons) as well as derived first vertical ionization potentials IP_v (eV).

	Number of electrons	B3LYP/6-31+G(d)//HF/6-31G(d) Total energy	IP_v
1a	N	–493.149 931	8.81
	N–1	–492.826 329	
1b	N	–532.468 968	8.56
	N–1	–532.154 406	
1c	N	–607.677 699	8.17
	N–1	–607.377 936	
1d	N	–952.745 171	8.75
	N–1	–952.423 728	
2a	N	–383.668 080	7.93
	N–1	–383.376 646	
2b	N	–422.986 065	7.68
	N–1	–422.703 768	
2c	N	–498.192 693	7.36
	N–1	–497.922 314	
2d	N	–843.263 383	7.94
	N–1	–842.971 686	

[a] Twisted *syn* conformers.
[b] Single-point energy calculations on the optimized molecule (N electrons) geometries.

Table 5. Selected experimental vertical ionization potentials IP (eV) of diazoacetophenones **1a**–**1d** and phenylketenes **2a**–**2d**.

Compound	IP				
1a	9.10		9.6[a]		11.86
1b	8.78	9.00	9.19	9.41	11.62
1c	8.71	9.12		9.6[b]	11.01
1d	9.14	9.33	9.59	9.78	11.24
2a	8.23	9.34	10.41	11.78	
2b	8.22	9.36	10.17	11.38	
2c	7.91	9.22	9.56	11.09	
2d	8.29	9.25	9.74	10.55	

[a] Consists of three overlapping bands.
[b] Consists of two overlapping bands.

the low-energy structures in the cases of **1d** and **1e** as well indicates that the diazoacetophenones which are the subject of this study prefer to adopt twisted *syn* conformations in the gas phase.

At the AM1 level, the twisted *syn* isomers of **1a**–**1e** (the N=C—C=O twist angles are 4.1, 4.1, 4.3, 2.9, and 2.4°; the phenyl—C=O dihedral angles are 31.6, 30.0, 31.3, 35.9, and 38.1°, respectively) are 11.08–12.38 kJ mol^{-1} lower in energy than the twisted *anti* isomers (Table 1). The *syn* and *anti* isomers of **1a**, **1b**, and **1c** were also studied at the HF/6-31G(d) level of theory. Selected geometrical parameters are collected in Table 2, and the optimized equilibrium geometries of the *syn* isomers of **1a**–**1d** are displayed in Fig. 1(*b*). At the HF/6-31G(d) level, we find that the twisted *syn* isomers of **1a**, **1b**, and **1c** are 16.88, 17.05, and 18.02 kJ mol^{-1} lower in energy than the twisted *anti* isomers, and the N=C—C=O and phenyl—C=O twist angles are

Fig. 3. The He(I) PE spectra of (*a*) **1a**, (*b*) the pyrolysate of **1a** obtained at a laser power level of 26 W, and (*c*) the pyrolysate of **1a** obtained at a laser power level of 42 W. The HAM/3//AM1 (vertical solid lines) and HAM/3//HF/6-31G(d) (vertical broken lines) calculated IPs are given in (*a*) for **1a** and (*b*) for **2a**.

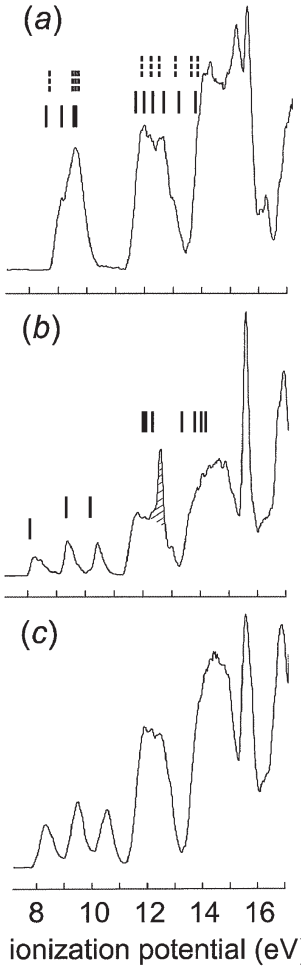

approximately one-half the values calculated with AM1 (Table 2). This is most likely a result of the fact that the ab initio calculations more accurately recover the stabilizing phenyl—C=O–π interaction, which would act to decrease the twist angle. When the geometries of the *syn* and *anti* isomers of **1a** were reoptimized — the geometries obtained with the default convergence limits were used as input — at the HF/6-31G(d) level of theory with the keyword TIGHT to tighten the convergence criteria, the total energies (E_Ts) obtained were identical within 10^{-6} hartree to E_Ts calculated with the default convergence limits, and the geometries differed little from the input geometries (Table 2). These results are in accord with published experimental data: 1,4-bisdiazo-2,3-butanedione adopts a bis-*syn* conformation in the solid state (32), and variable-temperature solution ^1H NMR studies in the temperature range of +30 to –40°C showed that diazoketones of the type $RCOCHN_2$ (R=H, CH_3, C_2H_5, *t*-C_4H_9, $C_6H_5CH_2$, CH_3O, and C_2H_5O) adopt *syn* and *anti* conformations with the *syn* forms being preferred (33). In the case of **1a**, **1c**, and **1e**, single stereoisomers identified as the *syn* forms were detected down to –40°C, but

© 1998 NRC Canada

Fig. 4. The He(I) PE spectra of (*a*) **1b**, (*b*) the pyrolysate of **1b** obtained at a laser power level of 26 W, and (*c*) the pyrolysate of **1b** obtained at a laser power level of 47 W. The HAM/3//AM1 (vertical solid lines) and HAM/3//HF/6-31G(d) (vertical broken lines) calculated IPs are given in (*a*) for **1b** and (*b*) for **2b**.

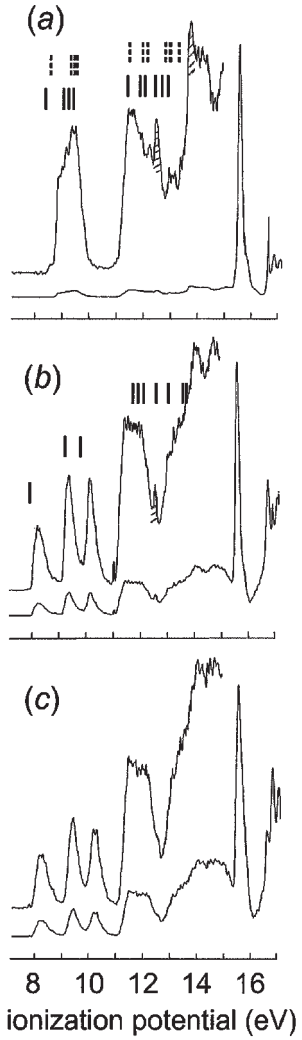

Fig. 5. The He(I) PE spectra of (*a*) **1c**, (*b*) the pyrolysate of **1c** obtained at a laser power level of 26 W, and (*c*) the pyrolysate of **1c** obtained at a laser power level of 42 W. The HAM/3//AM1 (vertical solid lines) and HAM/3//HF/6-31G(d) (vertical broken lines) calculated IPs are given in (*a*) for **1c** and (*b*) for **2c**.

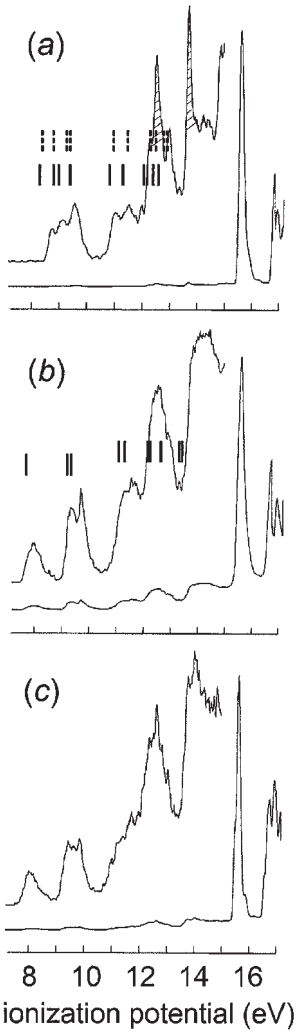

N=C—C=O and phenyl—C=O twist angles were not determined (33).

Phenylketenes **2a**–**2e** are found to adopt planar conformations with AM1, in accordance with previous findings for **2a** (13). This also holds at the ab initio level, **2a**–**2e** are planar with HF/6-31G(d). The AM1 heats of formation and ab initio total energies of **2a**–**2e** are listed in Table 1. According to AM1, the 90° conformation of **2a** is destabilized by 9.04 kJ mol^{-1}.

2. Ionization potentials

We have repeatedly demonstrated that the use of calculated ionization potentials (IPs) instead of orbital energies for the interpretation of PE spectra leads to excellent correlations between theory and experiment (2–4, 6, 34). This is especially important where a good agreement between absolute energy values is needed, as is the case for highly reactive or transient species which are generated in the PE spectrometer itself. The semiempirical HAM/3 method gives IPs directly, and both semiempirical and ab initio optimized geometries can be employed. The HAM/3//AM1 and HAM/3//HF/6-31G(d) results for diazoacetophenones **1a**–**1c** are given in Table 3. Although AM1 and HF/6-31G(d) geometries for **1a**–**1c** are distinctly different, IP values from the two levels of theory differ little. We therefore report HAM/3//AM1 results only for phenylketenes **2a**–**2c**. Because HAM/3 is not parameterized for chlorine, we also use the routine we developed in previous publications (6, 34): orbital energies calculated with the hybrid HF/DFT Becke3LYP method[3] are shifted uniformly so that the

[3] The successful application of the Koopmans' theory-like (35) interpretation of orbital energies obtained at the DFT level of theory in PE spectroscopic studies of numerous compounds has been shown and commented on (6, 34, 36–38).

© 1998 NRC Canada

Fig. 6. The He(I) PE spectra of (*a*) **1d**, (*b*) the pyrolysate of **1d** obtained at a laser power level of 26 W, and (*c*) the pyrolysate of **1d** obtained at a laser power level of 42 W. The Becke3LYP/6-31+G(d)//HF/6-31G(d) (vertical solid lines) calculated IPs are given in (*a*) for **1d** and (*b*) for **2d**.

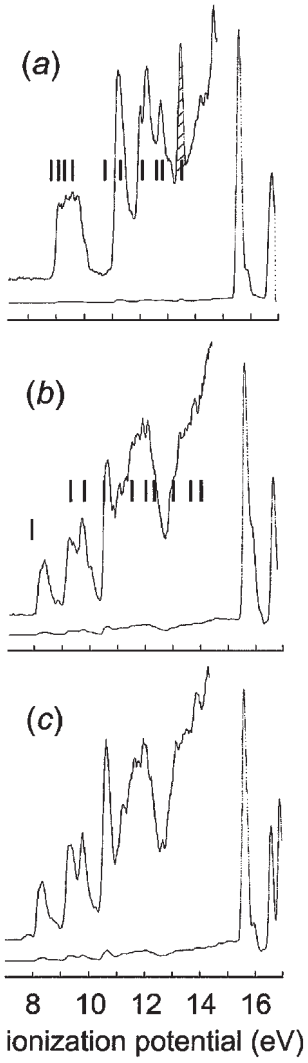

HOMO energy equals that of the calculated first vertical ionization potential IP_v. The IP_v is determined from the energy difference between the neutral (N electrons) and its radical cation (N – 1 electrons, geometry of the neutral) obtained using Becke3LYP/6-31+G(d)//HF/6-31G(d) (Table 4). Orbital energies and ionization potentials derived from the shift are reported in Table 3 for **1a**–**1d** and **2a**–**2d**. This level of theory is sufficient as could be concluded from virtually identical IP_vs and orbital energies of **2a**–**2d** obtained with Becke3LYP/6-31+G(d)//Becke3LYP/6-31+G(d) (not given).

Fig. 7. (*a*) Synthetic partial PE spectrum (from HAM/3//AM1 IPs) and (*b*) torsional potential (AM1) of **2a**.

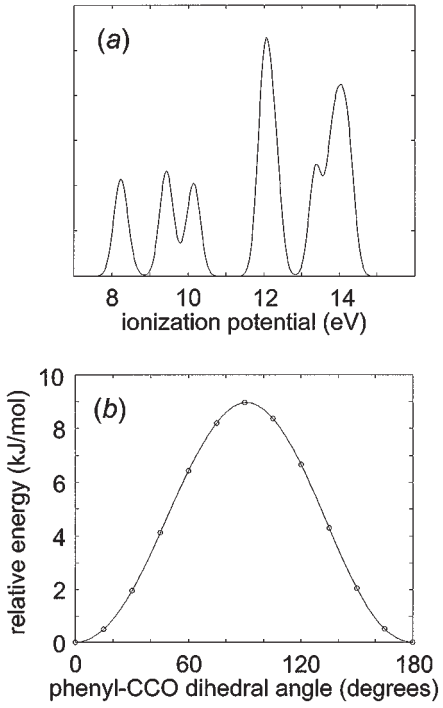

Photoelectron spectroscopic studies

1. Experimental PE spectra

The spectrum of **1a** (20 mg; source pressure 2.2×10^{-3} Torr) displayed as Fig. 3(*a*) was obtained at a probe temperature of 50°C. The vertical solid lines and vertical broken lines on the spectrum correspond to the 10 lowest HAM/3//AM1 and HAM/3//HF/6-31G(d) IPs (values in Table 3), respectively, and show that the experimental spectrum of this diazoacetophenone can be reproduced nicely with HAM/3. Figure 3(*b*) is a display of the spectrum of the pyrolysate of **1a** obtained at a laser power of 26 W (~500 ± 50°C). Based on the 1:1:1 relative intensities of the bands at 8.2, 9.3, and 10.4 eV and excellent correlation between the experimental vertical IPs and the IPs of phenylketene (**2a**) calculated with HAM/3//AM1 (vertical solid lines), the conversion of **1a** to **2a** is complete at a laser power level of 26 W. The IPs for **1a** and **2a** calculated with Becke3LYP/6-31+G(d)//HF/6-31G(d) (Table 3, compare to experimental IPs in Table 5) give an equally good representation of both spectra and therefore support this. That there was no significant change in the spectrum of the pyrolysate (Fig. 3(*c*)) and no CO (it exhibits a sharp band at 14.01 eV (39)) was formed when the laser power was increased from 26 W to 42 W (~850 ± 50°C) indicates that the loss of CO from **2a** is subject to a high activation energy.[4] This observation is in keeping with the results of our previous calculational study (5). The spectrum of **2a** obtained in this study differs to

[4] A comprehensive computational study of the decomposition of **1a**, **1c**, and **1e** (loss of nitrogen) and **2a**, **2c**, and **2e** (loss of CO) as well as the rearrangement of the ketocarbenes derived from **1a**, **1c**, **1d**, and **1e** will be the subject of a following publication. As shown in Scheme 1, the pyrolyses of the diazoacetophenones are expected to proceed via the respective intermediate ketocarbenes, even though thermolysis spectra provide no evidence for this. Alternatively, extrusion of nitrogen and rearrangement could be a concerted process.

© 1998 NRC Canada

Fig. 8. (*a*) Synthetic partial PE spectrum (HAM/3//AM1), (*b*) surface for the torsion of the phenyl—C=O dihedral angle (AM1), (*c*) synthetic spectrum (HAM/3//HF/6-31G(d)), (*d*) torsional potential (HF/6-31G(d)), and (*e*) angular dependences of the four lowest HAM/3//HF/6-31G(d) IPs of **1a**.

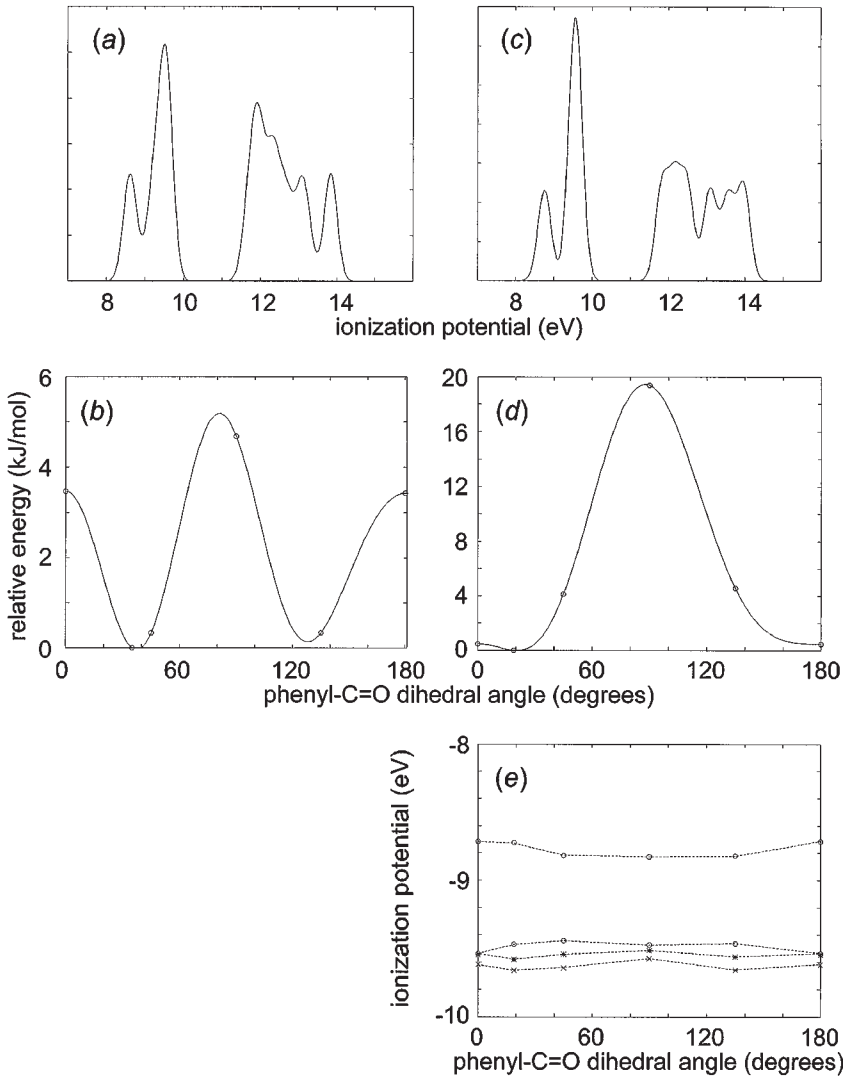

some degree from the published spectrum of phenylketene that was prepared by the zinc-induced dechlorination of 2-chloro-2-phenylacetyl chloride (13). While we find the relative areas of the first three bands to be 1:1:1 (Fig. 3(*b*)) in line with HAM/3//AM1 and Becke3LYP/6-31+G(d)//HF/6-31G(d) (Table 3) results, the relative areas of the first three bands of the previously published spectrum are approximately 1:2:1, an indication that phenylketene was not the sole product of the dechlorination reaction.

The spectrum of **1b** (20 mg; probe temperature 65°C), obtained with nitrogen added as a make-up gas to maintain the total pressure in the source at 3×10^{-3} Torr, is displayed along with the HAM/3//AM1 and HAM/3//HF/6-31G(d) IPs as Fig. 4(*a*). Again, HAM/3 values mirror experimental IPs. Figure 4(*b*) is a display of the spectrum of the pyrolysate of **1b** obtained at a laser power of 26 W and the calculated IPs of ketene **2b**. As in the case of the unsubstituted ketene **2a**, the experimental IPs in this spectrum are accurately reproduced by the computed values for **2b**, which shows that **1b** cleanly yields *p*-methylphenylketene (**2b**). The IPs for **1b** and **2b** calculated using Becke3LYP (Table 3) agree with this finding. Figure 4(*c*) displays the PE spectrum of the pyrolysate of **1b** obtained at a laser power of 47 W (>900°C). That spectra in Figs. 4(*b*) and 4(*c*) are virtually identical and no CO is formed indicates that the activation energy for decarbonylating ketene **2b**, as in the case of **2a**, is significantly higher than the activation energy for loss of nitrogen from the respective diazoacetophenones.

Figure 5(*a*) displays the PE spectrum of **1c** obtained at a probe temperature of 76°C along with its HAM/3//AM1 and HAM/3//HF/6-31G(d) IPs. As in the case of **1b**, N_2 was used as a make-up gas to maintain the source pressure at 3×10^{-3} Torr. HAM/3 once more correctly predicts the experimental spectrum. The spectra displayed as Figs. 5(*b*) and (*c*) were obtained when **1c** was pyrolyzed at laser power levels of 26 and 42 W, respectively. These spectra show that **1c** cleanly affords *p*-methoxyphenylketene (**2c**), which does not undergo pyrolysis at a nozzle-tip temperature in the region

© 1998 NRC Canada

Fig. 9. The four highest occupied molecular orbitals of **1a**.

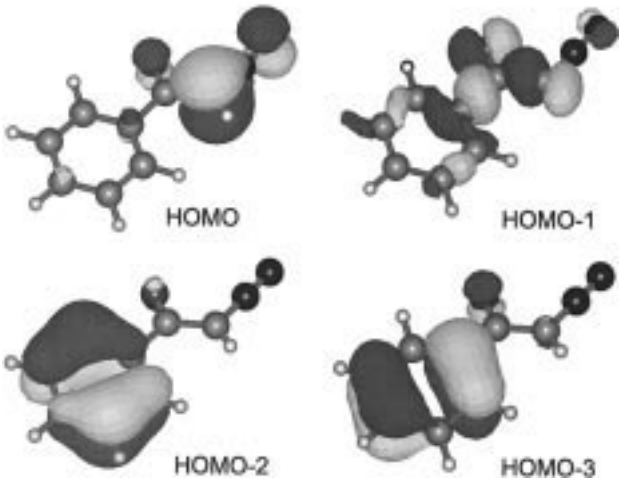

of 850 ± 50°C. Again, HAM/3 and Becke3LYP IPs for **1c** and **2c** do not differ much, which shows the validity of our Becke3LYP approach.

Figure 6(*a*) displays the PE spectrum of **1d** obtained at a probe temperature of 55°C with N_2 added as a make-up gas to maintain the source pressure at 3×10^{-3} Torr. Figures 6(*b*) and (*c*) display spectra of the pyrolysate of **1d** obtained at laser power levels of 26 and 42 W, respectively. As HAM/3 is not parameterized for chlorine, Figs. 6(*a*) and (*b*) include the 10 lowest ionization potentials of **1d** and **2d** as calculated with Becke3LYP/6-31+G(d)//HF/6-31G(d) and described above. As expected from the encouraging results of the pyrolyses of **1a**–**1c** with respect to this approach, the correlation between predicted spectra (vertical bars) and experimental spectra is excellent. These spectra show that **1d** yields *p*-chlorophenylketene (**2d**), which also appears to be stable at a nozzle-tip temperature in the region of 850 ± 50°C. The spectrum in Fig. 6(*c*) also exhibits a feature at 7.8 eV. A calculational study on *p*-chlorophenyloxirene, which is a second rearrangement product from the ketocarbene derived from **1d**, at the Becke3LYP/6-31+G(d)//HF/6-31G(d) level of theory established that the five lowest IPs of this compound should be 7.5, 9.6, 9.9, 11.0, and 11.7 eV. While the calculated first IP for *p*-chlorophenyloxirene is close to the first IP in the pyrolysis spectrum, at this point we cannot say with certainty whether it actually is a pyrolysis product of **1d**.[5]

The low volatility of **1e** thwarted our attempts to obtain its spectrum and study its pyrolysis. Even heating a relatively large sample (40 mg) of **1e** at 94°C near its melting point of 116°C in a 4 mm outer diameter tube inserted into the probe did not yield an acceptable spectrum. Selected experimental vertical ionization potentials of the diazoacetophenones **1a**–**1d** and the corresponding ketenes are collected in Table 5.

2. Synthesis of PE spectra

We have already demonstrated in several previous studies that PE spectra synthesized from torsional potential energy surfaces and the angle dependence of ab initio or semiempirical orbital energies as well as IPs calculated with HAM/3 using PESPEC correlate well with experimental spectra and can be used to obtain information about the conformational properties of molecules in the gas phase (29, 40–42). Additional support for this finding is seen in the excellent correlation between the experimental spectrum of phenylketene (**2a**) given in Figs. 3(*b*) and (*c*) and the synthesized spectrum displayed as Fig. 7(*a*). The synthetic spectrum of **2a** (with a Gaussian convolution of 0.4, temperature is 300 K) was obtained from the AM1 potential energy surface for the rotation of the ketene group given in Fig. 7(*b*) and the angle dependence of the 10 lowest HAM/3//AM1 ionization potentials (not shown).

Fig. 10. (*a*) Synthetic partial PE spectrum (HAM/3//HF/6-31G(d)) and (*b*) surface for the torsion of the phenyl—C=O dihedral angle (HF/6-31G(d)) of **1b**.

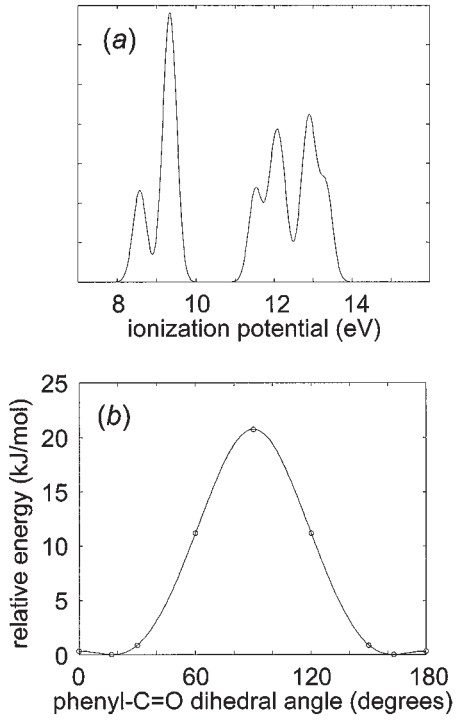

While Modelli et al. (31) do not offer an interpretation of the spectra of **1a**, **1b**, and **1d** with respect to orbital interactions or conformational considerations, for **1a** Vorob'ev et al. (43) report only weak π–π interactions both in the heterobutadiene group due to a large energy gap between interacting MOs and between diazo group and phenyl ring because of inefficient spatial overlap. Figure 8(*a*) is the PE spectrum of diazoacetophenone (**1a**) synthesized from the angle dependence of the HAM/3//AM1 IPs (not shown) and the AM1 potential energy surface displayed as Fig. 8(*b*) that corresponds to the 0–180° trajectory (the N=C—C=O dihedral angle is fixed at 0°) of Fig. 2. The synthetic spectrum recovers the general features of the experimental spectrum. Figure 8(*c*) is the synthetic spectrum of **1a** obtained from the

[5] While from the first IP *p*-chlorophenyloxirene is a likely candidate, it will only be present in the pyrolysis gas mixture if there is a reasonable barrier to the reverse reaction, the ring opening of the three-membered ring to give the ketocarbene. Calculations for the rearrangement of ketocarbenes derived from diazoacetophenones **1a**, **1c**, and **1e** to the corresponding oxirenes have shown no significant barrier.[4]

© 1998 NRC Canada

Fig. 11. (*a*) Synthetic partial PE spectrum (HAM/3//AM1), (*b*) surface for the torsion of the phenyl—C=O dihedral angle (AM1), (*c*) synthetic spectrum (HAM/3//HF/6-31G(d)), (*d*) torsional potential (HF/6-31G(d)), and (*e*) angular dependences of the four lowest HAM/3//HF/6-31G(d) IPs of **1c**.

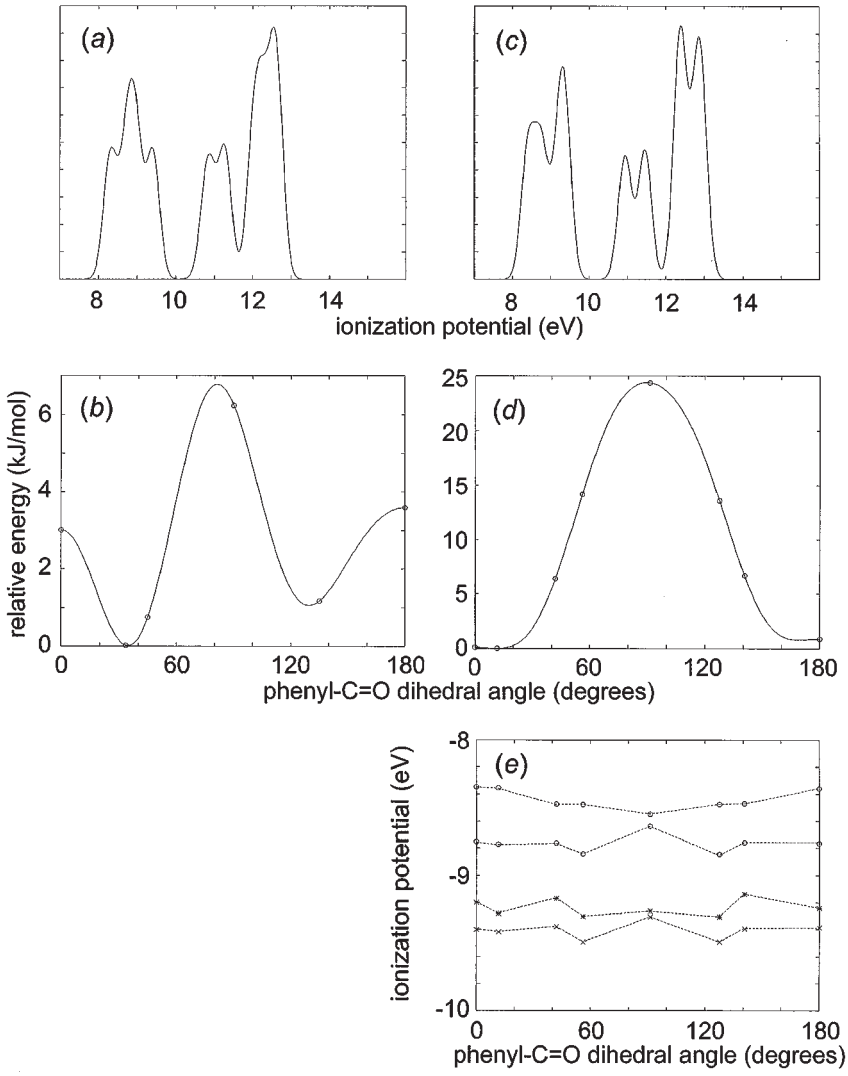

HF/6-31G(d) torsional potential (Fig. 8(*d*)) and the angular dependence of 10 HAM/3//HF/6-31G(d) IPs of which four are displayed in Fig. 8(*e*). Even though the rotational barrier at this level of theory is substantially higher than the AM1 barrier and the twisted *syn* conformer is only marginally lower in energy than the planar structure, the synthetic spectrum closely resembles the one obtained from the AM1 potential energy surface. This result derives from the fact that the low-energy IPs show a low sensitivity to the twist angle in both cases, as can be seen in Fig. 8(*e*). An explanation for this is given by the corresponding molecular orbitals (Fig. 9), which show that phenyl and diazoketo groups are present as separate units that do not interact at this energy level, a fact that was hinted at by Vorob'ev et al. (43). According to Becke3LYP/6-31+G(d)//HF/6-31G(d),[6] the HOMO is a π-type orbital with coefficients mainly on the diazo group ($\pi_{C=N}$), HOMO – 1 is a σ-type orbital, which represents an oxygen lone pair (n_O), and HOMO – 2 and HOMO – 3 are mostly phenyl π-type MOs (π) with small coefficients on the oxygen atom. This orbital sequence is in accord with the one given by Modelli et al. (31), while Vorob'ev et al. (43) give $\pi_{C=N} > \pi > n_O > \pi$ from MNDO calculations. Thus in **1a**, which can be considered to be the parent of this class of compounds, the low lying occupied MOs of the carbonyl group effectively function as an insulator for phenyl and diazo moieties.

Figure 10(*a*) displays the synthetic spectrum of **1b** obtained from the torsional potential obtained at the HF/6-

[6] Even though there is "no physical relevance" to Kohn–Sham orbitals, we have found eigenvectors obtained at the Becke3LYP/6-31+G(d)//HF/6-31G(d) level of theory to be similar to those computed with HF/6-31G(d)//HF/6-31G(d) or AM1//HF/6-31G(d). Yet for a number of diazoketones and diazo acyl esters containing an aromatic ring the predicted orbital sequence differs at the above-mentioned levels of theory. In a following paper (44) we will show that in these cases the orbital sequence as determined with the Becke3LYP method should be taken. For this reason, the orbitals displayed in Fig. 9 are arranged according to the Becke3LYP/6-31+G(d)//HF/6-31G(d) calculated sequence.

© 1998 NRC Canada

Fig. 12. The three highest occupied molecular orbitals of **2a**.

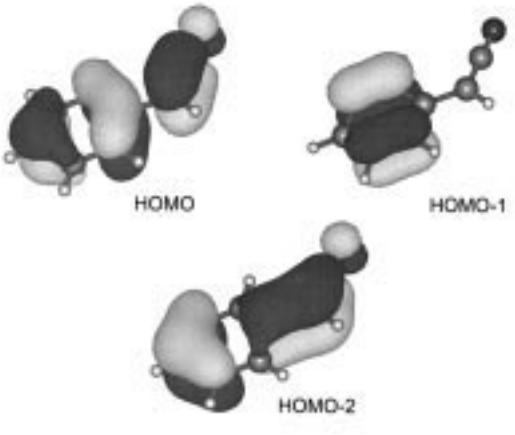

31G(d) level (Fig. 10(*b*)) and the HAM/3//HF/6-31G(d) IPs (not shown). The torsional dependence of the IPs as well as the corresponding molecular orbitals are similar to what we found for **1a**. On the whole, the general features of the experimental spectrum are reproduced in the synthethic spectrum with reasonable accuracy even though there is baseline separation of one band from three overlapping bands. Figure 11(*a*) is the synthetic spectrum of **1c** obtained from the AM1 potential energy surface shown as Fig. 11(*b*). While the general features of band structure correlate with the PE spectrum, the relative intensities of the peaks of the low-IP band are at variance with the experimental data. On the other hand, the synthetic spectrum of **1c (**Fig. 11(*c*)) obtained from the HF/6-31G(d) torsional potential (Fig. 11(*d*)) and the angular dependence of 10 HAM/3//HF/6-31G(d) ionization potentials of which four are displayed in Fig. 11(*e*) closely resembles the experimental spectrum. In contrast to **1a** and **1b**, the HOMO of **1c** is a phenyl π-type orbital that is raised in energy above the $\pi_{C=N}$ because of a substantial coefficent on the methoxy oxygen atom. This antibonding combination (π^-) is followed by $\pi_{C=N}$, n_O, π, and the corresponding bonding combination (π^+). As a consequence of this change in orbital sequence a phenyl π-type orbital (π^-) and the $\pi_{C=N}$ are closer in energy in **1c** than the respective orbitals in **1a**, which results in electron density on the diazo group being mixed into the HOMO of **1c**. Despite the presence of electron density on diazo group and aromatic ring, it is clear from Fig. 11(*e*) that the rotation of the ring does not affect the HOMO energy significantly, which again shows the insulating effect of the low-lying carbonyl orbitals. Our study shows that when compared to spectra synthesized on the basis of torsional potentials obtained at the HF/6-31G(d) level, experimental PE spectra provide support that diazoacetophenones **1a**–**1d** prefer twisted *syn* conformations in the gas phase.

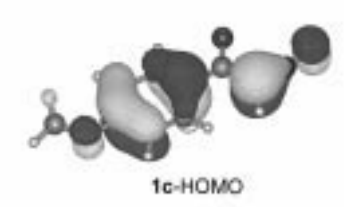

Substituent effects on ionization potentials of phenylketenes

Figure 12 displays the HOMO, HOMO – 1, and HOMO – 2 of phenylketene (**2a**) obtained at the AM1//HF/6-31G(d) level. The HOMO is a π-type MO characterized by substantial antibonding mixing of the ketene and phenyl π systems, with the latter exhibiting a large p_z coefficient at C-4. The HOMO – 1 is a pure phenyl π-type MO, which does not mix with the ketene π system and which has no p_z component at C-4. The HOMO – 2 is the bonding π-type MO that, like the HOMO, has contributions from the ketene and phenyl groups. Nevertheless, it has a larger p_z coefficient at C-4 than the HOMO. The nature of these frontier MOs indicates that the HOMO and HOMO – 2 should be affected more strongly than HOMO – 1 by *para*-substituents, which interact with the phenyl ring via π conjugation. That this is the case is seen in the PE spectra of **2a** (Figs. 3(*b*) and (*c*)), **2b** (Figs. 4(*b*) and (*c*)), and **2c** (Figs. 5(*b*) and (*c*)), and the data in Table 5, which clearly show that HOMO and HOMO – 2 are destabilized by the introduction of π donors at C-4. That HOMO – 2 appears to be more sensitive to substitution at C-4 is a consequence of the size of the p_z component at C-4 and its proximity in energy to the other filled orbitals of lower energy with which it interacts.

Conclusions

The gas-phase thermolysis of diazoacetophenones **1a**–**1d** at a laser power level of 26 W (500 ± 50°C) gave the corresponding phenylketenes **2a**–**2d**, which do not decompose at higher laser power levels. A comparison of our PE spectrum of **2a** with the one published earlier indicates that the sample prepared in the previous study was impure. The low volatility of **1e** made the recording of its PE spectrum and the generation of **2e** impossible. According to AM1 and HF/6-31G(d) calculations, diazoacetophenones prefer twisted *syn* conformations in the gas phase. This is supported by excellent correlations between calculated ionization potentials of **1a**–**1d** at the HAM/3 and Becke3LYP/6-31+G(d)//HF/6-31G(d) levels of theory as well as simulated PE spectra of **1a**–**1c** and experimental spectra.

Acknowledgments

We gratefully acknowledge the usage of the IBM SP2 computer at Queen's University granted under the auspices of an IBM Canada – Queen's University collaborative project as well as the usage of the SGI computing installation in the Geochemistry Labs at McMaster funded by NSERC. We thank Ms. O. Donini for assistance with operational aspects of parallel GAUSSIAN 94 and the Natural Sciences and Engineering Research Council of Canada for financial support.

References

1. N.H. Werstiuk, C.D. Roy, and J. Ma. Can. J. Chem. **72**, 2537 (1994).
2. N.H. Werstiuk, C.D. Roy, and J. Ma. Can. J. Chem. **73**, 146 (1995).

© 1998 NRC Canada

3. N.H. Werstiuk, J. Ma, C.D. Roy, A.J. Kresge, and E.A. Jefferson. Can. J. Chem. **73**, 1738 (1995).
4. N.H. Werstiuk, C.D. Roy, and J. Ma. Can. J. Chem. **74**, 1903 (1996).
5. N.H. Werstiuk, J. Ma, C.D. Roy, A.J. Kresge, and E. Jefferson. Can. J. Chem. **74**, 2536 (1996).
6. H.M. Muchall, N.H. Werstiuk, B. Choudhury, J. Ma, J. Warkentin, and J.P. Pezacki. Can. J. Chem. **76**, 238 (1998).
7. L. Wolff. Justus Liebigs Ann. Chem. **394**, 23 (1912).
8. D. Colbourne, D.C. Frost, C.A. McDowell, and N.P.C. Westwood. J. Chem Soc. Chem. Commun. 250 (1980).
9. A. Hotzel, R. Neidlein, R. Schultz, and A. Schweig. Angew. Chem. Int. Ed. Engl. **19**, 739 (1980).
10. S. Mohmand, T. Hirabayashi, and H. Bock. Chem. Ber. **114**, 2595 (1981).
11. D.P. Chong, N.P.C. Westwood, and S.R. Langhoff. J. Phys. Chem. **88**, 1479 (1984).
12. D. Colbourne and N.P.C. Westwood. J. Chem. Soc. Perkin Trans. II, 2049 (1985).
13. R. Sammynaiken and N.P.C. Westwood. J. Chem. Soc. Perkin Trans. II, 1987 (1989).
14. The chemistry of the diazonium and diazo groups. Parts 1 and 2. *Edited by* S. Patai. John Wiley and Sons, New York. 1978.
15. W. Kirmse. *In* Advances in carbene chemistry. Vol. 1. *Edited by* U.H. Brinker. JAI Press Inc., Greenwich, Conn. 1994.
16. B.M. Trost and P.L. Kinson. J. Am. Chem. Soc. **97**, 2438 (1975).
17. R.J. McMahon, O.L. Chapman, R.A. Hayes, T.C. Hess, and H.-P. Krimmer. J. Am. Chem. Soc. **107**, 597 (1985).
18. A. Allen, A.J. Kresge, N.P. Schepp, and T.T. Tidwell. Can. J. Chem. **65**, 1719 (1987).
19. R.J. McMahon, C.J. Abelt, O.L. Chapman, J.W. Johnson, C.L. Kreil, J.-P. LeRoux, A.M. Mooring, and P.R. West. J. Am. Chem. Soc. **109**, 2456 (1987).
20. C. Bachman, T.Y. N'Guessan, F. Debû, M. Monnier, J. Pourcin, J.-P. Aycard, and H. Bodot. J. Am. Chem. Soc. **112**, 7488 (1990).
21. J. Andraos and A.J. Kresge. J. Photochem. Photobiol. A, **57**, 165 (1991).
22. HYPERCHEM 4.0. Hypercube Inc., 419 Philip Street, Waterloo, Ont. 1994.
23. Dewar Research Group and J.J.P. Stewart. Austin Model 1 Package 1.0 (AMPAC). QCPE, 506 (1986).
24. J.J.P. Stewart. MOPAC, a semiempirical molecular orbital program. QCPE, 455 (1983).
25. W.J. Hehre, L. Radom, P.v.R. Schleyer, and J.A. Pople. Ab initio molecular orbital theory. John Wiley & Sons, New York. 1986.
26. A.D. Becke. J. Chem. Phys. **98**, 5648 (1993); C. Lee, W. Yang, and R.G. Parr. Phys. Rev. B: Condens. Matter, **37**, 785 (1988).
27. M.J. Frisch, G.W. Trucks, H.B. Schlegel, P.M.W. Gill, B.G. Johnson, M.A. Robb, J.R. Cheeseman, T. Keith, G.A. Petersson, J.A. Montgomery, K. Raghavachari, M.A. Al-Laham, V.G. Zakrzewski, J.V. Ortiz, J.B. Foresman, C.Y. Peng, P.Y. Ayala, W. Chen, M.W. Wong, J.L. Andres, E.S. Replogle, R. Gomperts, R.L. Martin, D.J. Fox, J.S. Binkley, D.J. Defrees, J. Baker, J.P. Stewart, M. Head-Gordon, C. Gonzalez, and J.A. Pople. Gaussian 94, Revision B.3. Gaussian, Inc., Pittsburgh Pa. 1995.
28. L. Åsbrink, C. Fridh, and E. Lindholm. HAM/3, QCPE Bull. **13**, 393 (1981).
29. N.H. Werstiuk, G. Timmins, G. Ma, and T.A. Wildman. Can. J. Chem. **70**, 1971 (1992).
30. M. Regitz and F. Menz. Chem. Ber. **101**, 2622 (1968).
31. A. Modelli, G. Innorta, and S. Torroni. J. Electron Spectrosc. Relat. Phenom. **18**, 359 (1980).
32. H. Hope and K.T. Black. Acta Crystallogr. Sect. B: Struct. Crystallogr. Cryst. Chem. **28**, 3632 (1972).
33. F. Kaplan and G.K. Meloy. J. Am. Chem. Soc. **88**, 950 (1966).
34. H.M. Muchall, N.H. Werstiuk, and B. Choudhury. Can. J. Chem. **76**, 221 (1998).
35. T. Koopmans. Physica, **1**, 104 (1933).
36. A.J. Arduengo, III, H. Bock, H. Chen, M. Denk, D.A. Dixon, J.C. Green, W.A. Herrmann, N.L. Jones, M. Wagner, and R. West. J. Am. Chem. Soc. **116**, 6641 (1994).
37. H.M. Muchall and P. Rademacher. J. Mol. Struct. **435**, 157 (1997).
38. N.H. Werstiuk, H.M. Muchall, C.D. Roy, J. Ma, and R.S. Brown. Can. J. Chem. **76**, 672 (1998).
39. K. Kimura, K. Katsumata, Y. Achiba, T. Yamazaki, and S. Iwata. Handbook of HeI photoelectron spectra of fundamental organic molecules. Japan Scientific Societies Press, Tokyo, and Halsted Press, New York. 1981.
40. N.H. Werstiuk, J. Ma, M.A. McAllister, T.T. Tidwell, and D.-C. Zhao. Trans. Faraday Soc. **90**, 3383 (1994).
41. D. Chmielewski, N.H. Werstiuk, and T.A. Wildman. Can. J. Chem. **71**, 1741 (1993).
42. H.M. Muchall, N.H. Werstiuk, J. Ma, T.T. Tidwell, and K. Sung. Can. J. Chem. **75**, 1851 (1997).
43. A.S. Vorob'ev, I.I. Furlei, Yu.Z. Ekov, A.M. Nazarov, G.A. Yamilova, U.M. Dzhemilev, and V.A. Dokichev. Russ. Chem. Bull. **42**, 281 (1993).
44. H.M. Muchall, N.H. Werstiuk, J.L. Pitters, and M.S. Workentin. Tetrahedron. In press.

© 1998 NRC Canada

A new diaza heteroaromatic crown of 3,5-disubstituted 1*H*-pyrazole which forms solid dinuclear complexes with lipophilic phenethylamines

Ana M. Sanz, Pilar Navarro, Fernando Gomez-Contreras, Mercedes Pardo, Gèrard Pèpe, and André Samat

Abstract: The cyclic stannoxane obtained from *N*-methyldiethanolamine and dibutyltin oxide reacts with 1*H*-pyrazole-3,5-dicarbonyl dichloride to afford the new 26-membered diaza tetraester crown **3**. In neutral medium, the above crown forms 1:2 solid dinuclear complexes with phenethylamine (**3a**) and homoveratrylamine (**3b**), which, after crystallization from acetonitrile, were isolated in high yield (90% and 85%, respectively). The **3**, **3a**, and **3b** structures were identified from their analytical and spectroscopic (^{1}H, ^{13}C NMR, and MS (FAB)) data. The spectroscopic properties of **3a** and **3b** are demonstrating that, in each complexation centre, simultaneously to the strong participation of the four pyrazole nitrogens, an additional weaker interaction between the aliphatic nitrogen of the side chain and the amine is involved. Comparison of the total interaction energies calculated (GenMol software) for phenethylamine-derived complex (**3a**) and homoveratrylamine-derived one (**3b**) suggests that the *o*-dimethoxy substitution of the guest aromatic ring could be improving the stability of **3b** in relation to **3a**.

Key words: diazacrown, 1*H*-pyrazole, dinuclear, complexes, phenethylamines.

Résumé : Le stannoxane cyclique obtenu à partir du *N*-méthyldiéthanolamine et de l'oxyde de dibutylétain réagit avec le dichlorure de 1*H*-pyrazole-3,5-dicarbonyle pour conduire à un nouvel éther diazacouronne tétraester à 26 chaînons (**3**). En milieu neutre, cette couronne forme des complexes dinucléaires solide 1:2 avec la phénéthylamine (**3a**) et l'homovératrylamine (**3b**) qui ont été isolés avec d'excellents rendements (90 et 85% respectivement) après cristallisation dans l'acétonitrile. On a identifié les structures **3**, **3a** et **3b** à partir de leurs données analytiques et spectroscopiques (RMN du ^{1}H et du ^{13}C et SM (FAB)). Les propriétés spectroscopiques des composés **3a** et **3b** démontrent que, pour chaque centre de complexation, en plus de la forte participation des quatre azotes des pyrazoles, il existe une faible interaction entre l'azote aliphatique de la chaîne latérale et celui de l'amine. Une comparaison des énergies totales d'interaction (calculées à l'aide du programme GenMol) des complexes dérivés de la phénéthylamine (**3a**) et de l'homovératrylamine (**3b**) suggère que le substituant *o*-diméthoxy du noyau aromatique de l'invité améliore la stabilité du composé **3b** par rapport à **3a**.

Mots clés : diazacouronne, 1*H*-pyrazole, dinucléaire, complexes, phénéthylamines.

[Traduit par la Rédaction]

Introduction

One of the two main categories of psychedelic drugs that produce perceptual distortions (hallucinations, illusions, and disorders of thinking such as paranoia) are hallucinogen phenethylamines methoxy and (or) methylenedioxy substituted at the aromatic ring (1).

The selective complexation of such hallucinogen substrates by adequately arranged synthetic receptors, in relation to neurotransmitter catecholamines, is an important but difficult target due to the similarity of their structures. Thus, dopamine and norepinephrine, involved in the normal emotional and autonomic control of humans, have in common a hydrophilic 3,4-dihydroxyphenethylamine nucleus, while its 3,4-dimethoxy substituted analogue (homoveratrylamine) of higher lipophilic character shows hallucinogen effects (2).

It is well known that synthetic oxaaza and polyaza macrocycles containing a trigonal symmetrical arrangement of NH binding sites are able to selectively complex ammonium and catecholammonium ions (3). In this way, we have previously synthesized and studied the transport properties of different series of synthetic heteroaromatic receptors

Received January 28, 1998.

A.M. Sanz and P. Navarro.[1] Instituto de Química Médica, Centro Nacional de Química Orgánica, Manuel Lora Tamayo, C.S.I.C., c/ Juan de la Cierva 3, 28006 Madrid, Spain.
F. Gomez-Contreras and M. Pardo. Departamento de Química Orgánica I, Facultad de Química, Universidad Complutense, 28040 Madrid, Spain.
G. Pèpe and A. Samat. UERS CNRS 158, Faculté des Sciences de Luminy, Université de la Méditerranée, Case 901, Cedex 9, 13288 Marseille, France.

[1]Author to whom correspondence may be addressed. Telephone: 34 91 5622900. Fax: 34 91 5644853. E-mail: iqmnt38@fresno.csic.es

© 1998 NRC Canada

Fig. 1.

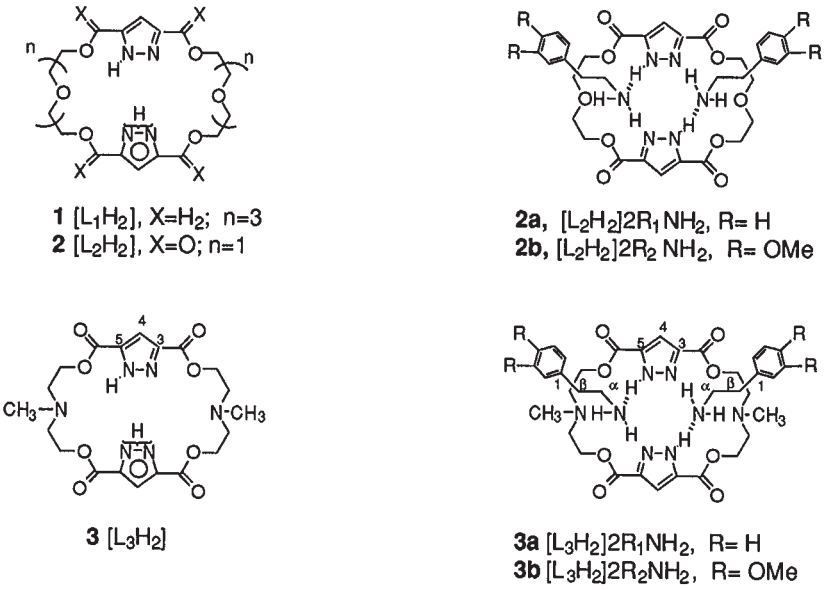

Scheme 1.

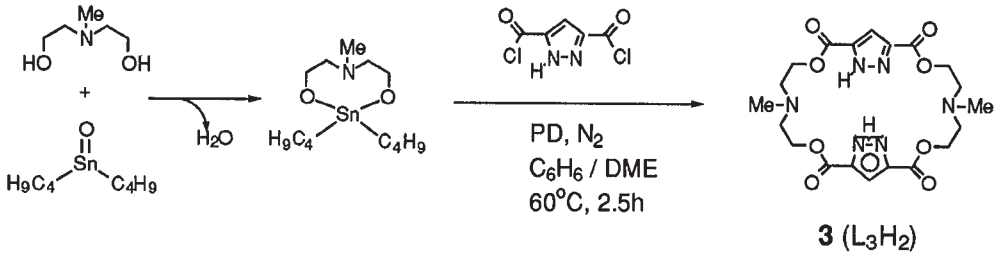

containing one to three 1,3,5- or 3,5-substituted pyrazole units (4). As the result of the above studies, we discovered a dinuclear receptor of 1*H*- pyrazole of similar size to that of valinomycin (36-membered) **1** [L_1H_2] (X = H_2; *n* = 3) (Fig. 1), which behaves as an effective and selective carrier of NH_4^+ (5). Furthermore, it has been recently discovered that such crown is able to form dinuclear complexes with lipophilic phenethylamine R-NH_3^+ ions of higher stability than those formed with those of hydrophilic phenethylamines.[2]

On the other side, we have also synthesized an analogous dinuclear receptor of 1*H*- pyrazole **2** [L_2H_2] of smaller size (26-membered), which strongly interacts with neutral lipophilic R-NH_2 phenethylamines, affording dinuclear complexes **2a** R = H; phenethylamine) and **2b** R = OMe;

homoveratrylamine), which were isolated in the solid state (6). Besides, the theoretical calculations (GenMol software) together with a careful ^{1}H and ^{13}C NMR study has recently demonstrated that in both complexes, the two sp^2 pyrazole nitrogens and the two N*H* pyrazole protons are involved in the complexation of the two guest amine molecules, affording a molecular association mainly stabilized by symmetrical hydrogen bonds (7), while other hydrogen bonds with ether oxygens belonging to the receptor side chains were discarded.

Considering the strong insoluble character of the above dioxa substituted coronand **2**, and taking into account that N···HN hydrogen bonds are more effective than O···HN ones, in this paper we have synthesized a more convenient diazatetraester crown of 1*H*-pyrazole **3**, [L_3H_2], which is soluble in common lipophilic organic solvents. This new diazacoronand is containing a double trigonal symmetrical arrangement of NH binding sites in which the two basic nitrogens incorporated to the side chains are improving the complexing properties of **3** toward phenethylamine and homoveratrylamine.

Results and discussion

The synthesis of the **3** has been achieved as depicted in Scheme 1.

N-Methyldiethanolamine was heated to reflux in benzene with dibutyltin oxide to give the corresponding cyclic stannoxane (8), which was reacted with 1*H*-pyrazole-3,5-dicarbonyl dichloride to afford crown **3** (mp 190–192°C; $C_{20}H_{26}N_6O_8 \cdot 2H_2O$; MH^+ 479) in a 10% overall yield.

In the FAB mass spectrum of the diaza tetraester crown **3**, the expected molecular ion MH^+ corresponds to the base peak (*m/z* 479, 100%). From MH^+, the fragmentation is mainly governed by usual ruptures of amine and ester bonds,

[2] M.I. Rodriguez-Franco, B. Gonzalez, A. Sanz, P. Navarro, C. Ochoa, A. Doménech, and E. García-España. 1998. Unpublished results.

© 1998 NRC Canada

Table 1. The ^{13}C NMR spectral data (75 MHz, Cl_3CD, δ) of complexes **3a** and **3b** compared with those of the free guests (phenethylamine(Ph), homoveratrylamine (Ho)) and host (**3**).

Compd.	Ph	**3a**	$\Delta\delta_{\mathbf{3a}\text{-Ph}}$	Ho	**3b**	$\Delta\delta_{\mathbf{3b}\text{-Ho}}$
Cα	43.35	42.95	–0.40	43.33	42.73	–0.60
Cβ	39.93	39.38	–0.55	39.20	38.06	–1.14
C_1-Ar	139.62	139.40	–0.22	132.07	131,48	–0.59

Compd.	**3**	**3a**	$\Delta\delta_{\mathbf{3a}\text{-}\mathbf{3}}$	**3**	**3b**	$\Delta\delta_{\mathbf{3b}\text{-}\mathbf{3}}$
C(3,5)	139.36	139.56	+0.20	139.36	139.93	+0.57
C(4)	111.70	111.52	–0.18	111.70	111.59	–0.11
CO	159.60	159.57	–0.03	159.60	160.07	+0.47
CH_2O	59.74	59.41	–0.33	59.74	59.37	–0.37
CH_2N	55.91	55.79	–0.12	55.91	56.07	+0.16
NMe	40.01	39.74	–0.27	40.01	39.82	–0.19

responsible for sequential losses of a = C_3H_7N (57) and b = C_5H_9N (83) fragments belonging to the host flexible chain, as well as c = $C_5H_2N_2O_2$ (122) and d = $C_5H_2N_2O_3$ (138) fragments corresponding to the losses of one of the two diceto pyrazolo moieties. Furthermore, as usually occurs with tetraester and polyether crowns of dimmer structure (5), from M^+ other important decompositions give rise to the characteristic $(M/2 + H)^+$ species (m/z 240, 7%).

The complexing ability of crown **3** [L_3H_2] was tested by stirring for 15 min with phenethylamine or homoveratrylamine in a 1:2 molar ratio using chloroform as solvent. In both cases, after concentration, the diaza substituted complexes were isolated as white solids and crystallized from acetonitrile. Their analytical and spectroscopic data were consistent with neutral dinuclear complexes **3a** (mp 140–142°C; $C_{36}H_{48}N_8O_8 \cdot 3H_2O$; $MH^+ - C_3H_7N$ 664) and **3b** (mp 170–172°C; $C_{40}H_{56}N_8O_{12} \cdot H_2O$; $MH^+ - C_3H_7N$ 684), which were obtained in 90% and 85% yield, respectively (Fig. 1).

The FAB mass spectra of both dinuclear complexes are clearly demonstrating the strong interaction of the two amino groups with both pyrazole rings. The phenethylamine complex **3a** shows a pattern in which two a = C_3H_7N (57), b = C_4H_9N (71), or c = $C_5H_{11}N$ (85) fragments belonging to the host flexible side chain, as well as two d = C_6H_5 (77) aromatic fragments belonging to the amine guest, are simultaneously lost giving up a series of peaks of m/z: 606 ($M^+ - 2(C_3H_7N)$) (0.1); 578 ($M^+ - 2(C_4H_9N)$) (1.9); 567 ($MH^+ - 2(C_6H_5)$) (0.6); 551 ($MH^+ - 2(C_5H_{11}N)$) (11.0); 550 ($M^+ - 2(C_5H_{11}N)$) (26.3). In a similar way, the homoveratrylamine complex **3b** show a pattern in which one or two host flexible side chain fragments (a = C_3H_7N (57); b = C_4H_9N (71); c = $C_5H_{10}N$ (84); and d = $C_5H_{11}NO_2$ (117)) and one or two homoveratrylamine fragments (e = $C_8H_9O_2$ (137) and f = $C_8H_9O_2$ (138)) are successively or simultaneously lost from the $MH^+(H_2O)$, $M^+(H_2O)$, MH^+, and M^+ molecular ions, affording different series of peaks of m/z: 801 ($M^+(H_2O) - C_3H_7N$) (0.2); 744 ($M^+(H_2O) - 2(C_3H_7N)$) (0.2); 788 ($MH^+(H_2O) - C_4H_9N$) (0.2); 716 ($MH^+(H_2O) - 2(C_4H_9N)$) (0.1); 703 ($M^+ - C_8H_9O_2$) (0.5); 566 ($M^+ - 2(C_8H_9O_2)$) (0.5); 606 ($M^+ - 2(C_5H_{11}NO_2)$) (0.1); 565 ($M^+ - (C_8H_9O_2) - (C_8H_{10}O_2)$) (0.46); 373 ($MH^+ - 2\ (C_5H_{10}N) - 2(C_9H_{10}O_2)$) (11.0).

As could be expected in the formation of strong NH···N hydrogen bonds (9), in the ^1H NMR spectra of **3a** and **3b** registered in Cl_3CD, the complexation strongly affects the amine RNH···N= signals, which are deshielded by 3.55 and 3.07 ppm in relation to the free phenethylamine and homoveratrylamine respectively.

Comparison of the ^{13}C NMR spectral data of these complexes with those corresponding to the free guests and host (Table 1) affords some relevant structural information. The two methylene carbons closer to the complexation centre, as well as the *ipso* aromatic carbons of the guest amines experience considerable upfield shifts, which are larger for the β than for the α and C_1-Ar carbons (Table 1*a*). This behaviour agree with a reduction of electronic density at the sp^3 nitrogen, which takes place when the complex is formed (10). Furthermore, it may be noted that shieldings measured are much higher for homoveratrylamine (Δδ **3b**-Ho) than for phenethylamine (Δδ **3a**-Ph).

On the other hand, the comparison of the ^{13}C NMR data of **3a** and **3b** and those of the free host **3** (Table 1*b*) shows that the signals belonging to the pyrazole ring undergo in both complexes chemical shifts to downfield carbons C(3,5) and highfield carbons C(4), which are much more smaller but of identical sign to those previously observed in the formation of dipyrazolate anions by deprotonation of 26-membered dinuclear 1*H*-pyrazole macrocycles (6*b*). Furthermore, the pyrazole carbons C(3,5), which in **3** appear as a broad signal due to the pyrazole prototropic equilibrium, collapse after complexation to a sharp singlet. As it was previously observed from dioxa tetraester crown-derived complexes(7), the above behaviour confirms that in complexes **3a** and **3b**, the NH pyrazole protons are not ambigously located but fastened to the guest amines. The above situation agrees with a molecular association mainly stabilized by symmetric RN·HN(Pz) and RNH···N=(Pz) hydrogen bonds. On the other hand, taking as reference the basic nitrogens located in middle of the host flexible side chains, it can be observed that after complexation, the β methylene carbons (CH_2O) as well as the a methyl ones (MeN) experience in both complexes upfield shifts, which suggest an additional interaction between the sp^3 nitrogens and the guest amines.

Theoretical approach of the stability of diaza tetraester crown-derived complexes 3a and 3b

The stability of the complexes has been evaluated using molecular modelling GenMol software (11). This program based on molecular mechanics calculations is designed to build molecules and to find their preferred conformations (12). It also allows to model molecular interactions and to find the minimum energy of complex molecular systems (13).

We have previously shown that, for dinuclear complexes obtained from the dioxa tetraester crown **2** [L_2H_2] with phenethylamine (**2a**) and homoveratrylamine (**2b**), *syn*- conformations (both amines on the same face of the crown) were more stable than the *anti*-conformations (amines on the opposite faces of the crown) (7).

Now, starting from the *syn*-conformation of the diaza tetraester crown **3** [L_3H_2], we have calculated the interaction energy between the host (crown) and the guest (both

© 1998 NRC Canada

Table 2. Relative stability of dinuclear cyclic complexes **3a** and **3b** modelled from diaza substituted coronand **3**. (E_I, E_H, E_{vdw}, E_C are, respectively, the interaction, hydrogen bond, van der Waals, and coulombic energies (kcal mol^{-1}).)

Compound	E_I	E_H	E_{vdw}	E_C
3a (Ph)	–18.4	–5.3	–13.2	–0.01
3b (Ho)	–22.1	–5.8	–16.2	–0.12

molecules of amine), which is directly connected to the association constants.

In Table 2 are reported the interaction energies (E_I, kcal mol^{-1}) and the hydrogen bond energies (E_H, kcal mol^{-1}) corresponding to the new dinuclear complexes obtained from the diaza substituted receptor **3** [L_3H_2] with phenethylamine (**3a**) and homoveratrylamine (**3b**).

The value E_I is the sum of classic nonbond interactions occurring between the crown and the amines:

$$E_I = E_{vdw} + E_C + E_H$$

in which E_{vdw}, E_c, and E_H are, respectively, van der Waals, coulombic, and hydrogen bond energies. The more E_I is negative, the more the complex is stable.

Regarding the geometries of the most stable complexes obtained for **3a** and **3b** it seems that hydrogen bonds exist really between the guest amine nitrogen atoms and the host pyrazole nitrogen ones (the distance is close to 2.9 Å), while the distances with nitrogen atoms of the NMe groups (3.2 Å) may correspond to weaker hydrogen bonds.

Comparison of the total interaction energies suggest that the theoretical stability of the homoveratrylamine complex **3b** is higher than that of the phenethylamine **3a**. Detail of the interaction energies (Table 2) shows that this increase is due at once to hydrogen bonding and van der Waals type interactions.

The more stable conformations of the diaza tetraester crown-derived homoveratrylamine complex **3b** is shown in Fig. 2.

Conclusions

(*i*) The synthesis of a new proton ionizable ester crown **3** (mp 190–92°C) has been performed in 10% yield by direct cyclization of 1*H*-pyrazole-3,5 dicarbonyl dichloride and 2,2-dibutyl-6-methyl-6-aza-1,3-dioxa-2-stannocyclooctane. (*ii*) Using chloroform as solvent, the reaction of crown **3** with phenethylamine and homoveratrylamine (molar ratio 1:2) affords solid dinuclear complexes, which after being crystallized from acetonitrile were obtained in high yield (**3a**, mp 140–142°C, 90%; **3b**, mp 170–72°C, 85%). (*iii*) The structure of the new compounds **3**, **3a**, and **3b** have been identified from their analytical and spectroscopic (FAB MS, IR, ^{1}H, and ^{13}C NMR) data. (*iv*) The ^{13}C NMR study is demonstrating that, in the new diaza substituted complexes **3a** and **3b**, simultaneously to a strong molecular association through NH···N=(Pz) and N·HN(Pz) hydrogen bonds, an additional weaker interaction between the host sp^3 nitrogens and the guest amines is contributing to the formation of these new solid complexes. (*v*) Comparison of the total interaction energies calculated for phenethylamine-derived

Fig. 2.

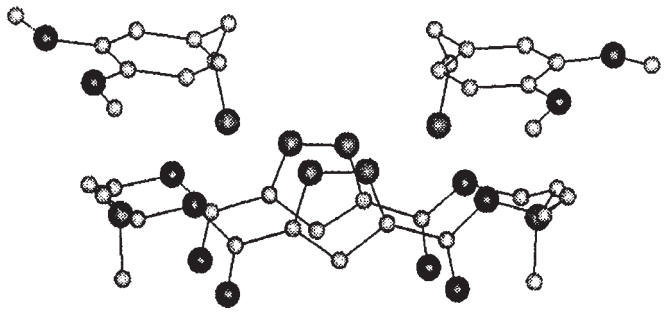

complexes (**3a**) and homoveratrylamine-derived ones (**3b**) is suggesting that the *o*-dimethoxy substitution of the guest aromatic ring could be improving the stability of **3b** in relation to **3a**. Now, work is in progress in order to evaluate the experimental stability constants of phenethylamine and homoveratrylamine dinuclear complexes **2a**, **2b** and **3a**, **3b**, as well as those formed from mescaline, amphetamine, and neurotransmitter catecholamines (dopamine and norepinephrine).

Experimental section

The IR spectra were recorded in KBr, and the NMR spectra in $CDCl_3$ solution, taking Me_4Si as internal reference. Analytical TLC and flash column chromatography were performed using silica gel 60 PF254 (Merck) and silica gel (Merck), 200–400 mesh, respectively. All reagents were of commercial quality from freshly opened containers. Thionyl chloride (Scharlau) was freshly purified prior to use as follows: distilled from quinoline (to remove acid impurities) followed by distillation from boiled linseed oil under argon. Pyrazole-3,5-dicarboxylic acid monohydrate (Aldrich), *N*-methyldiethanolamine (Aldrich), dibutyltin oxide (Merck), homoveratrylamine (Aldrich), phenethylamine (Aldrich), and reagent quality solvents were used without further purification.

1*H*-Pyrazole-3,5-dicarbonyl dichloride

Thionyl chloride freshly purified (350 mL) was slowly added to 1*H*-pyrazole-3,5-dicarboxylic acid monohydrate (2 g, 11.49 mmol) by stirring and heating until all the acid was completely dissolved. Then, the temperature was allowed to 140°C over 2 h. The hot reaction mixture was filtered, and the resulting solution evaporated to dryness to give the title compound (2 g, 10.3 mmol) as a white solid (mp 72–74°C) in 93% yield.

2,2-Dibutyl-6-methyl-6-aza-1,3-dioxa-2-stannocyclooctane (8)

To a solution of *N*-methyl diethanolamine (1.36 g, 11.46 mmol) in benzene (200 mL), solid dibutyltin oxide (2.85 g, 11.49 mmol) was slowly added. The reaction mixture was refluxed for 2 h, and the water formed in the cyclocondensation was removed by azeotropic distillation. The resulting suspension was diluted into dry toluene (260 mL) and collected to be used in the following step.

© 1998 NRC Canada

6,18-Dimethyl-25(26),27(28)-*H*,*H*-3,9,15,21-tetraoxa-6,18,25,26,27,28-hexaazatricycle[21.2.1.2^{11,13}]-octacosa-1(26),13(28),11,23-tetraen-2,10,14,22-tetraone 3

The suspension obtained above was heated to 60°C under nitrogen, and a solution of pyrazole-3,5-dicarbonyl chloride (21 g, 11.46 mmol) in dry dimethoxyethane (80 mL) was added dropwise. The reaction mixture was kept at 60°C under nitrogen for 24 h. After that, the solvent was removed in vacuo to give a syrup that was purified by flash column chromatography, eluting with an ethyl acetate – ethanol – ammonium hydroxide (5:1:0.15 v/v) mixture. From the fraction of R_f = 0.36, compound **3** was isolated as a pure solid compound (mp 190–92°C) in 10% yield. IR (KBr, cm^{-1}): 3360, 2950, 1725, 1750, 1600, 1250, 1000, 760. ^{1}H NMR (300 MHz, Cl_3CD (after treated with D_2O)), δ (ppm): 7.36 (s, 2H, Pz-H), 4.48 (t, 8H, $COOCH_2$), 2.79 (t, 8H, C*H*$_2$-NMe), 2.42 (s, 6H, MeN). MS (FAB): 479 (MH^+) (100), 435 ($MH^+ - C_2H_4O$) (1.0), 422 ($MH^+ - C_3H_7N$) (3.0), 396 ($MH^+ - C_5H_9N$) (5.2), 359 ($MH^+ - C_5H_2N_2O_2$) (2.0), 341($MH^+ - C_5H_2N_2O_3$) (8.0), 240 ($M^+/2 + 1$) (7.0), 139 $(C_5H_3N_2O_3)^+$ (5.4), 122 $(C_5H_3N_2O_2)^+$ (5.4). Anal. calcd. for $C_{20}H_{26}N_6O_8\cdot 2H_2O$: C 46.69, H 5.83, N 16.34; found: C 46.36, H 5.42, N 16.69.

Cyclic dinuclear complex 3a

Crown **3** (18 mg, 0.037 mmol) was dissolved at rt in chloroform (5 mL), and a solution of phenethylamine (9.11 mg, 0.075 mmol) in chloroform (2 mL) was added dropwise under stirring. After that, the solvent was removed in vacuo to give a residue, which was crystallized from acetonitrile, affording the pure dinuclear complex **3a** as a white solid (mp 140–142°C) in 90% yield. IR (KBr, cm^{-1}): 3400–3100, 1720, 1630, 1265, 1220, 1035, 795, 760. ^{1}H NMR (300 MHz, Cl_3CD), δ (ppm): 7.31 (s, 2H, Pz-H), 4.40 (m, 8H, $COOCH_2$), 2.70 (m, 8H, C*H*$_2$-NMe), 2.31 (s, 6H, MeN), 4.70 (brs, 6H, NH), 3.00 (t, 4H, C*H*$_2$-NH_2), 2.80 (t, 4H, C*H*$_2$-C_6H_5), 7.18 (m, 10H, C_6H_5). MS (FAB): 664 ($MH^+ - C_3H_7N$) (0.1), 663 ($M^+ - C_3H_7N$) (0.2), 606 ($M^+ - 2(C_3H_7N)$) (0.1), 600 ($MH^+ - C_8H_{11}N$) (0.8), 578 ($M^+ - 2(C_4H_9N)$) (1.9), 567 ($MH^+ - 2(C_6H_5)$) (0.6), 551 ($MH^+ - 2(C_5H_{11}N)$) (11.0), 550 ($M^+ - 2(C_5H_{11}N)$) (26.3), 479 ($MH^+ - 2(C_8H_{11}N)$) (63.0), 122 $(C_5H_2N_2O_2)^+$ (100), 121 $(C_8H_{11}N)^+$ (14.0), 77 $(C_6H_5)^+$ (31.0), 85 $(C_5H_{11}N)^+$ (8.0), 71 $(C_4H_9N)^+$ (14.0), 57 $(C_3H_7N)^+$ (31.0). Anal. calcd. for $C_{36}H_{48}N_8O_8\cdot 3H_2O$: C 55.81, H 7.02, N 14.47; found: C 56.12, H 6.62, N 14.32.

Free phenethylamine; ^{1}H NMR (300 MHz, Cl_3CD), δ (ppm): 1.13 (brs, 2H, NH), 2.94 (t, 2H, C*H*$_2$$NH_2$), 2.72 (t, 2H, C*H*$_2$$C_6H_5$), 7.15 (m, 5H, C_6H_5).

Cyclic dinuclear complex 3b

Crown **3** (18 mg, 0.037 mmol) was dissolved at rt in chloroform (5 mL), and a solution of homoveratrylamine (13.63 mg, 0.075 mmol) in chloroform (2 mL) was added dropwise under stirring. After that, the solvent was removed in vacuo to give a residue, which was crystallized from acetonitrile, affording the pure complex **3b** in 85% yield as a white solid (mp 170–172°C). IR (KBr, cm^{-1}): 3480–3200, 2920, 1720, 1635, 1260, 1235, 1035, 785, 760. ^{1}H NMR (300 MHz, Cl_3CD), δ (ppm): 7.37 (s, 2H, Pz-H), 4.47 (m, 8H, $COOCH_2$), 2.78 (m, 8H, C*H*$_2$-NMe), 2.38 (s, 6H, MeN), 6.78 (brs, 6H, NH), 3.04 (t, 4H, C*H*$_2$-NH_2), 2.80 (t, 4H, C*H*$_2$-$C_6H_3(OMe)_2$), 6.76 (m, 6H, $C_6H_3(OMe)_2$), 3.87 (s, 6H, MeO), 3.85 (s, 6H, MeO). MS (FAB): 801 ($M^+(H_2O) - C_3H_7N$)) (0.2); 788 ($MH^+(H_2O) - (C_4H_9N)$) (0.2), 684 ($MH^+ - (C_3H_7N)$) (0.1), 744 ($M^+(H_2O) - 2(C_3H_7N)$) (0.2), 716 ($M^+(H_2O) - 2(C_4H_9N)$) (0.1), 703 ($M^+ - (C_8H_9O_2)$) (0.5), 702 ($M^+ - (C_8H_{10}O_2)$) (1.0), 660 ($MH^+ - (C_{10}H_{15}NO_2)$) (0.3), 606 ($M^+ - 2(C_5H_{11}NO_2)$) (0.1), 566 ($M^+ - 2(C_8H_9O_2)$) (0.5); 565 ($M^+ - (C_8H_9O_2) - (C_8H_{10}O_2)$) (0.5), 551 ($M^+ - (C_8H_{10}O_2) - (C_9H_{11}O_2)$) (8.0), 550 ($M^+ - (C_8H_{10}O_2) - (C_9H_{11}O_2)$) (18.0), 479 ($MH^+ - 2(C_{10}H_{15}NO_2)$) (39.0), 373 ($MH^+ - 2(C_9H_{10}O_2) - 2(C_5H_{10}N)$) (11.0), 181 $(C_{10}H_{15}NO_2)^+$ (9.0), 165 $(C_{10}H_{13}O_2)^+$ (66.0), 164 $(C_{10}H_{12}O_2)^+$ (31.0), 150 $(C_9H_{10}O_2)^+$ (11.0), 151 $(C_9H_{11}O_2)^+$ (21.0), 138 $(C_8H_{10}O_2)^+$ (17.0), 137 $(C_8H_9O_2)^+$ (31.0), 117 $(C_5H_{11}NO_2)^+$ (9.0), 73 $(C_4H_{11}N)^+$ (100%), 71 $(C_4H_9N)^+$ (36.0), 57 $(C_3H_7N)^+$ (70.0). Anal. calcd. for $C_{40}H_{56}N_8O_{12}\cdot H_2O$: C 55.94, H 6.75, N 13.05; found: C 56.33, H 6.49, N 12.94.

Free homoveratrylamine; ^{1}H NMR (300 MHz, Cl_3CD), δ (ppm): 1.38 (brs, 2H, NH), 2.92 (t, 2H, C*H*$_2$$NH_2$), 2.66 (t, 2H, C*H*$_2$$C_6H_3(OMe)_2$), 6.75 (m, 3H, $C_6H_3(OMe)_2$), 3.85 (s, 3H, OMe), 3.83, (s, 3H, OMe).

Molecular modelling

GenMol (11) is a molecular mechanics software including some specificities, able to treat atomic and molecular systems till 10^5 atoms of 96 types: (*i*) The program uses local stretching and bending parameters, which depend not only on the chemical neighbourhood (nature of the bonded atoms, which is the case in all molecular mechanic programs), but also of the geometrical neighbourhood. This concept allows to win an order of magnitude in the geometry accuracy if compared to X-ray data. (*ii*) An original algorithm deforming the molecule by rotation around the bonds, and based on empirical rules deduced from X-ray observations, allow to very quickly find the most probable conformation of a molecule. (*iii*) The π systems are taken into account. The program calculates the atomic charges.

For the design of the complex, different packing of molecules were tested, and the most stable corresponding to the minimum of the nonbonded energy (van der Waals, coulombic, and hydrogen bond) was considered. Then in a first step, a calculation imposing all the possible hydrogen bonds was performed, and in a second step these constraints were removed in order to find the true hydrogen bonds and the more stable assemblage of the molecules.

Acknowledgement

Financial support of this work by the Spanish *Comision Interministerial de Ciencia y Tecnología* (CICYT, Coordinated Project SAF-96–0242-CO2) is gratefully acknowledged.

References

1. C.D. Klaassen and C.P. O'Brien. *In* Goodman and Gilman's The pharmacological basis of therapeutics. *Edited by* J.G. Hardman, L.E. Limbird, P.B. Molinoff, and R.W. Ruddon. McGraw–Hill, New York. 1996. Chap. 4. p. 63; Chap. 24. p. 557.

© 1998 NRC Canada

2. (*a*) J. Pearson. *In* An introduction to neurotransmission in health and disease. *Edited by* P. Riederer, N. Kopp, and J. Pearson. University press, Oxford. 1990. Chap. 21 and 26; (*b*) The reaction of living cells. Biochemistry. *Edited by* D.E. Metzler. Academic Press, New York. 1977. Chap. 16, p. 1017.
3. (*a*) J.M. Lehn. Angew. Chem. Int. Ed. Engl. **27**, 89 (1988); (*b*) I.O. Sutherland. Chem. Soc. Rev. **15**, 63 (1986).
4. (*a*). J. Elguero, P. Navarro, and M.I. Rodriguez-Franco. Chem. Lett. 425 (1984); (*b*) J. Elguero, P. Navarro, M.I. Rodriguez-Franco, F.H. Cano, C. Foces-Foces, and A. Samat. J. Chem. Res. Synop. 312 (1985); J. Chem. Res. Miniprint, 3401 (1985); (*c*) P. Navarro, M.I. Rodriguez-Franco, and A. Samat. Synth. Commun. **17**, 105 (1987); (*d*) P. Navarro and M.I. Rodriguez-Franco. J. Chem. Soc. Chem. Commun. 1365 (1988); (*e*) P. Navarro, M.I. Rodriguez-Franco, C. Foces-Foces, F.H. Cano, and A. Samat. J. Org. Chem. **54**, 1391 (1989); (*f*) P. Navarro, E. Pueyo, M.I. Rodriguez-Franco, and A. Samat. Tetrahedron, **46**, 2917 (1990); (*g*) J.M. Bueno, P. Navarro, M.I. Rodriguez-Franco, and A. Samat. J. Chem. Res. Synop. 126 (1991); J. Chem. Res. Miniprint, 1101 (1991); (*h*) M. Fierros, S. Conde, A. Martinez, P. Navarro, M.I. Rodriguez-Franco. Tetrahedron, **51**, 2417 (1995); (*i*) M.I. Rodriguez-Franco, M. Fierros, A. Martinez, P. Navarro, and S. Conde. Bioorg. Med. Chem. **5**, 363 (1997).
5. P. Navarro and M.I. Rodriguez-Franco. Trends Org. Chem. **4**, 69 (1993).
6. (*a*) L. Campayo, J.M. Bueno, C. Ochoa, P. Navarro, and A. Samat. Tetrahedron Lett. **34**, 7299 (1993). (*b*) C. Acerete, J.M. Bueno, L. Campayo, P. Navarro, M.I. Rodriguez-Franco, and A. Samat. Tetrahedron, **50**, 4765 (1994).
7. J.M. Bueno, L. Campayo, P. Navarro, C. Ochoa, J. Jimenez-Barbero, A. Samat, and G. Pèpe. J. Org. Chem. **62**, 2684 (1997).
8. H. Shanser, J. Libman, H.E. Gottlieb. J. Org. Chem. **48**, 4612 (1983).
9. F. Hibbert. *In* Advances in physical organic chemistry. Vol. 22. *Edited by* V. Gold and D. Bethell. Academic Press, London. 1986. p. 138.
10. A.D. Hamilton. Tetrahedron Lett. **31**, 2401 (1990).
11. G. Pèpe and D. Siri. Stud. Phys. Theor. Chem. **71**, 93 (1990).
12. F. Cavelier-Frontin, G. Pèpe, J. Verducci, D. Siri, and R. Jacquier. J. Am. Chem. Soc. **114**, 8885 (1992).
13. (*a*) G. Pèpe, D. Siri, A. Samat, E. Pottier, and R. Guglielmetti. Mol. Cryst. Liq. Cryst. **246**, 247 (1994); (*b*) F. Vila, P. Tordo, D. Siri, and G. Pèpe. Free Radical Res. Commun. **19**, 517 (1993); (*c*) F. Cavelier-Frontin, A. Sadijah, G. Pèpe, J. Verducci, and R. Jacquier. THEOCHEM, **286**, 125 (1993).

© 1998 NRC Canada

Preparation, properties, and reductive alkylation of arylhydrazides

Giancarlo Verardo, Nicoletta Toniutti, and Angelo G. Giumanini

Abstract: 1-Acyl-2-arylhydrazines (**1**), readily obtained in high yield from the condensation of arylhydrazines and the appropriate liquid carboxylic acid (**2**), underwent reductive alkylation with the same or different liquid carboxylic acids (**2**) and $NaBH_4$ to give 1-acyl-2-alkyl-2-arylhydrazines (**3**) in good to moderate yields. The carboxylic acid has both the role of supplying the entering alkyl group and of acting as solvent. Most likely, it also modifies the BH_4^- anion to an active reducing agent under those conditions. The ^1H NMR criteria for identifying the location of acylation of hydrazines and *E* and *Z* isomers are given. The MS spectra of the prepared hydrazides were analyzed in order to identify relevant structural features leading to specific fragmentations.

Key words: 1-acyl-2-arylhydrazine, 1-acyl-2-alkyl-2-arylhydrazine, reductive alkylation, sodium tetrahydroborate, carboxylic acid.

Résumé : La condensation d'arylhydrazines et d'acides carboxyliques liquides appropriés (**2**) conduit facilement aux 1-acyl-2-arylhydrazines (**1**) avec d'excellents rendements; celles-ci, par alkylation réductrice avec les mêmes (ou d'autres) acides carboxyliques (**2**) liquides et du $NaBH_4$, conduisent aux 1-acyl-2-alkyl-2-arylhydrazines (**3**) avec des rendements qui vont de bons à moyens. L'acide carboxylique joue à la fois le rôle de source du groupe méthyle qui entre et de solvant. Il est probable qu'il modifie aussi l'anion BH_4^- afin qu'il devienne un agent réducteur actif dans ces conditions. On présente les critères de RMN du ^1H permettant d'identifier la position de l'acylation des hydrazines et les isomères *E* et *Z*. On a analysé les SM des hydrazides préparés dans le but d'identifier les caractéristiques structurales pertinentes aux fragmentations spécifiques.

Mots clés : 1-acyl-2-arylhydrazine, 1-acyl-2-alkyl-2-arylhydrazine, alkylation réductrice, tétrahydroborate de sodium, acide carboxylique.

[Traduit par la Rédaction]

Introduction

The use of carboxylic acids in combination with $NaBH_4$ was found to effect *N*-alkylation of aliphatic as well as aromatic amines (1), nevertheless, the synthetic utility of this method was never developed to date on hydrazines and derivatives. The direct reductive alkylation of phenylhydrazine with carboxylic acid and $NaBH_4$ gave a mixture of products resulting from different multiple alkylations as well as acylation of the hydrazine.[2] In fact, it is well established that alkylation of alkyl- or arylhydrazines occurs preferentially on the substituted nitrogen atom (2), however, this reaction usually requires the use of protecting groups to limit or avoid multiple alkylations. For this reason, it has been performed on hydrazones or acylhydrazines. The resulting alkyl derivatives could be either hydrolyzed to remove the protecting group and give 1,1-disubstituted hydrazines or reduced to yield trisubstituted hydrazines (3). Herein, we focused our attention on arylhydrazides as better substrates for selective alkylation.

Hydrazides are an important class of compounds not only in organic synthesis, but also for industrial applications. Arylhydrazides (**1**) and 1-acyl-2-alkyl-2-arylhydrazines (**3**) were used in the preparation of herbicides (4), antiinflammatory indoles (5), derivatives with antimicrobial (6) or antimycotic activity (7, 8).

We now report the preparation and full characterization of some arylhydrazides (**1**) and their reductive alkylation with carboxylic acids and $NaBH_4$ combination as the method of choice for preparation of 1-acyl-2-alkyl-2-arylhydrazines (**3**). This simple, inexpensive, high-yielding method is also proposed as a one-pot procedure in which the carboxylic acid acts as acylating as well as alkylating agent. The MS and NMR spectra of these hydrazides were carefully discussed because literature data were sparse and scattered.

Received January 2, 1998.

G. Verardo, N. Toniutti, and A.G. Giumanini.[1] Department of Chemical Sciences and Technologies, University of Udine, I-33100 Udine, Italy.

[1] Author to whom correspondence may be addressed. Telephone: +39-432-558 870. Fax: +39-432-558 803. E-mail: gverardo@tin.dstc.uniud.it

[2] G. Verardo et al. Unpublished results.

Results and discussion

1-Acyl-2-arylhydrazines (**1a**–**f**) were readily obtained by heating the corresponding carboxylic acid and arylhydrazines without any condensing agent (9). This direct approach seems scarcely known and even less attended (10, 11). In producing 1-acyl-2-arylhydrazine instead of its isomer 1-acyl-1-arylhydrazine, the carboxylic acid here behaves in the same way as other acylating agents, frequently

© 1998 NRC Canada

Table 1. Physical data of 1-acyl-2-aryl-hydrazines (**1**).

Compound[a]	R	R_1	Yield[b]	mp (°C)[c]
1a	H	H	50%	144[d]
1b	H	Me	85%	129[e]
1c	H	Et	80%	157[f]
1d	H	Pr	75%	110[g]
1e	NO_2	Me	81%	213
1f	Me	Me	75%	132

[a]All solid compounds were analyzed for C, H, and N, and results agreed to ±0.5% of theoretical values.
[b]Yield of isolated product.
[c]Midpoint of narrow range.
[d]Literature (4) 145°C.
[e]Literature (5) 129°C.
[f]Literature (5) 157°C.
[g]Literature (5) 96°C.

used for hydrazines, such as esters, anhydrides, and acyl chlorides (12).

All the starting hydrazides **1a–f** were characterized and their properties compared with literature data (Tables 1 and 2). The correct structural identification of the arylhydrazides **1a–f** was essentially based on their ^{1}H NMR features. Upon accurate examination of the available literature data, we made the following observation. Although 1-acyl-1-substituted-hydrazines usually exhibit the *E*/*Z* amide isomerism (Fig. 1), which doubles all the hydrogen resonances, their primary amino group hydrogens appear as singlets at ca. 3.8–4.8 ppm in $CDCl_3$ and 4.2–5.3 ppm in DMSO-d_6 (13).

Completely different NMR features are recognized when the acyl and the aryl (or alkyl) groups are located on different nitrogens (that is, for 1-acyl-2-substituted derivatives). The hydrogen belonging to the amide function shows up as two unequal resonances with a separation of ca. 0.3–0.7 ppm both in $CDCl_3$ (at ca. 7.4 ppm) and in DMSO-d_6 (at ca. 9.0 ppm) (13). Interestingly, the amino proton also reflects

Fig 1.

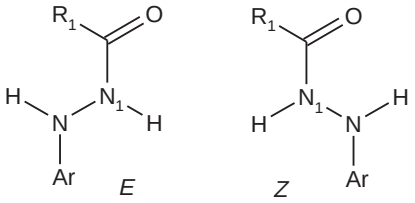

the different environment by showing two peaks at ca. 6.0 ppm in $CDCl_3$ and ca. 8.0 in DMSO-d_6 (13). After comparing these data with the spectra of our 1-acyl-2-arylhydrazines (1) (see Table 2), we confirmed their identification.

Of all the hydrazides **1a–f**, only 1-acetyl-2-(4-nitrophenyl)hydrazine (**1e)** did not show the *E*/*Z* isomerism in the NMR. The H-decoupled ^{13}C-NMR spectra of **1a–f** showed extensive doubling of the several peaks, but again **1e** did not exhibit this feature, a good indication that it was present in a single conformation.

The mass spectra of **1a–f** and of their 1,1-isomers **1a′–f′** differed in a number of features (Table 2 and experimental part). The latter showed weaker parent ions, which underwent extensive fragmentations to the RCO^+ acyl ions and the R^+ ions (likely in a rearranged form, whenever possible). Intense peaks at *m*/*z* 77 and 78 (corresponding to peaks at *m*/*z* 122, 123 for **1e′** and 91, 92 for **1f′** deriving from the substituted phenyl group) were detected. But their most impressive feature was the production of an outstanding peak at *m*/*z* 105 for PhN_2^+ (or the corresponding charged fragment from **1e′** and **1f′**), always accompanied by a weak peak at *m*/*z* 108 for the formula of phenylhydrazine (or the corresponding substituted phenylhydrazine from the parent ions **1e′** and **1f′**). A possible mechanism for the formation of ArN_2^+ involves a few rearrangements before cleavage of the parent ion of **1a′–f′**, eq. [1].

[1]

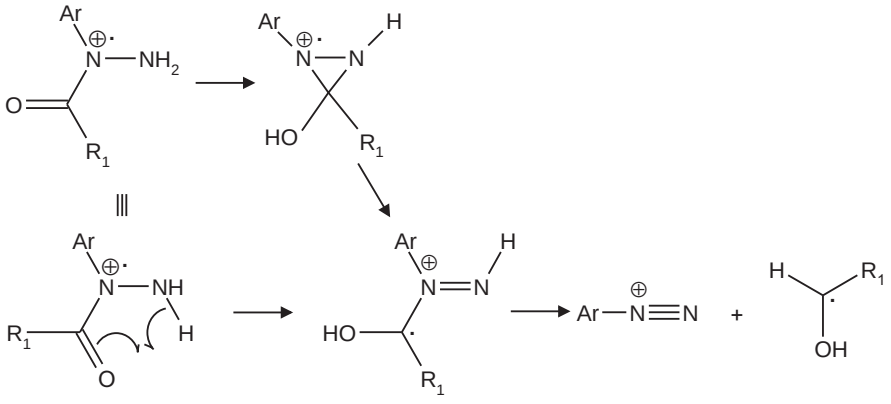

The 1,2-isomers **1b–f** also yielded all these ions, with the relevant difference that the ion at *m*/*z* 105 (or the corresponding charged fragment from **1e** and **1f**) was hardly discernible and that the ion at *m*/*z* 108 (or the corresponding peak for the formula of substituted phenylhydrazine from the parent ions **1e** and **1f**), due to the loss of ketene from the parent ion, was the base peak. The mass spectrum of **1a** is quite different from **1b–f** as the first most intense peak was the molecular ion (*m*/*z* 136), and the second one was the peak at *m*/*z* 107 ($PhN_2H_2^+$). On the contrary, the ion at *m*/*z* 108 was scarcely present.

© 1998 NRC Canada

Table 2. Spectroscopic and MS data of 1-acyl-2-arylhydrazines (**1**).

Product	IR (KBr) ν (cm^{-1})	^{1}H NMR δ, *J* (Hz)	^{13}C NMR δ	MS (70 eV) *m*/z (%)
1a	3310 s, 3204 s, 3072 s, 3026 s, 2907 m, 1690 vs, 1663 vs, 1604 s, 1505 s, 1394 vs, 1200 m, 874 s, 755 vs, 702 vs	6.65–6.85 (m, 3H, H_{arom}), 7.10–7.25 (m, 2H, H_{arom}), 8.11 (d, 1H, HC=O, *J* = 10.5, rotamer A), 8.13 (s, 1H, HC=O, rotamer B), 7.80 (app d, 1H, N-H, *J* = 2.7, rotamer A), 8.01 (s, 1H, N-H, rotamer B), 9.45 (d, 1H, N-H, *J* = 10.8, rotamer A), 9.72 (app d, 1H, N-H, *J* = 2.2, rotamer B)[b]	149.3, 149.4, 155.8, 156.6, 165.8, 166.1, 185.8, 186.5, 197.7, 204.8[b]	136 (M^+, 100), 108 (12), 107 (73), 92 (12), 91 (16), 78 (10), 77 (50), 65 (19), 64 (10), 51 (20), 39 (10)
1b	3270 s, 3072 m, 1670 vs, 1617 vs, 1500 s, 1485 vs, 1437 vs, 1372 s, 1300 s, 1250 s, 1010 s, 766 vs, 700 vs	2.03 (s, 3H, CH_3, rotamer A), 2.09 (s, 3H, CH_3, rotamer B), 5.84 (br s, 1H, N-H, rotamer A), 6.18 (app d, 1H, N-H, *J* = 3.9, rotamer B), 6.72–6.96 (m, 3H, H_{arom}), 7.15 (br s, 1H, N-H, rotamer A), 7.19–7.33 (m, 2H, H_{arom}), 7.63 (s, 1H, N-H, rotamer B)[a]	19.1, 20.9, 112.4, 113.48, 121.2, 121.2, 129.1, 129.5, 147.0, 147.8, 170.2, 176.9[a]	150 (M^+, 62), 108 (100), 107 (37), 93 (27), 92 (28), 91 (12), 78 (13), 77 (43), 65 (12), 51 (14), 43 (19), 39 (10)
1c	3310 vs, 3270 vs, 3039 s, 2980 s, 2940 s, 1650 vs, 1609 vs, 1557 vs, 1497 vs, 1464 vs, 1227 s, 1150 s, 1043 s, 944 s, 760 vs, 694 vs	1.05–1.25 (m, 3H, CH_3), 2.27 (q, 2H, CH_2, *J* = 7.5, rotamer A), 2.45 (q, 2H, CH_2, *J* = 7.5, rotamer B), 5.80 (br s, 1H, N-H, rotamer A), 6.15 (br s, 1H, N-H, rotamer B), 6.70–6.95 (m, 3H, H_{arom}), 7.03 (br s, 1H, N-H, rotamer A), 7.15–7.30 (m, 2H, H_{arom}), 7.50 (br s, 1H, N-H, rotamer B)[a]	8.0, 8.9, 23.9, 26.9, 111.7, 112.9, 120.6, 128.5, 128.8, 146.5, 147.4, 173.2[a]	164 (M^+, 68), 108 (100), 107 (31), 93 (50), 92 (18), 78 (19), 77 (37), 66 (17), 65 (15), 57 (16), 54 (19), 51 (14), 39 (11)
1d	3296 vs, 3236 vs, 3085 s, 3045 s, 2966 s, 2940 s, 2880 m, 1681 vs, 1642 vs, 1622 vs, 1576 vs, 1510 vs, 1445 s, 1120 s, 957 s, 760 vs, 694 vs, 502 vs	0.89 (t, 3H, CH_3, *J* = 7.3), 1.50–1.85 (m, 2H, CH_2), 2.10 (t, 2H, CH_2, *J* = 7.5, rotamer A), 2.33 (t, 2H, CH_2, *J* = 7.5, rotamer B), 5.85 (br s, 1H, N-H, rotamer A), 6.30 (br s, 1H, N-H, rotamer B) 6.60–6.90 (m, 3H, H_{arom}), 7.10–7.30 (m, 2H, H_{arom}), 7.38 (br s, 1H, N-H, rotamer A), 8.15 (br s, 1H, N-H, rotamer B)[a]	14.9, 19.3, 20.2, 34.3, 37.3, 113.6, 114.6, 122.1, 130.3, 130.5, 148.6, 149.3, 174.7, 180.8[a]	178 (M^+, 27), 108 (100), 107 (18), 93 (78), 92 (20), 78 (13), 77 (30), 71 (16), 66 (28), 65 (20), 51 (12), 43 (35), 41 (66), 39 (25)
1e	3315 vs, 3290 vs, 3091 m, 3006 m, 2933 m, 1655 vs, 1592 vs, 1504 vs, 1320 vs, 1257 vs, 1115 vs, 1008 s, 837 vs, 749 s	1.98 (s, 3H, CH_3), 6.79 (app d, 2H, H_{arom}, *J* = 8.7), 8.08 (app d, 2H, H_{arom}, *J* = 8.7), 9.01 (s, 1H, N-H), 9.97 (s, 1H, N-H)[b]	20.5, 110.5, 125.8, 138.0, 154.9, 169.2[b]	195 (M^+, 26), 154 (8), 153 (100), 123 (9), 108 (10), 107 (10), 106 (12), 43 (32)
1f	3289 vs, 3252 vs, 3026 s, 1666 vs, 1600 vs, 1547 vs, 1520 vs, 1381 vs, 1241s, 1150 m, 1000 s, 824 vs, 751 vs	1.90 (s, 3H, CH_3, rotamer A), 2.02 (s, 3H, CH_3, rotamer B), 2.23 (s, 3H, CH_3, rotamer A), 2.24 (s, 3H, CH_3, rotamer B), 5.85 (br s, 1H, N-H, rotamer A), 6.19 (br s, 1H, N-H, rotamer B), 6.50–6.70 (m, 2H, H_{arom}), 6.85–7.00 (m, 2H, H_{arom}), 7.46 (br s, 1H, N-H, rotamer A), 8.26 (br s, 1H, N-H, rotamer B)[a]	19.7, 21.1, 21.3, 113.1, 114.2, 130.2, 130.4, 130.9, 145.5, 146.2, 171.2, 177.9[a]	164 (M^+, 90), 121 (64), 122 (100), 121 (91), 107 (27), 106 (62), 91 (30), 77 (32), 65 (13), 43 (18)

[a]Solvent:$CDCl_3$.
[b]Solvent: DMSO-d_6.

The GC–MS analysis of the intact reaction mixtures, after removal of excess acid, showed that the 1,1-isomer was usually present in small concentrations (<5%). In the course of the GC analyses we observed that 1-acyl-2-arylhydrazines (**1**) isomerized extensively to the 1,1-isomer when they were injected using CH_2Cl_2 as solvent. We assumed that this was the result of the formation of HCl in the injector, kept at 250°C, which catalyzed the 1,2-migration of the acyl group.

We submitted the 1-acyl-2-arylhydrazines **1b–f** to reductive alkylation using an excess of either the same (R_1 = R_2, eq. [2]), or different ($R_1 \neq R_2$, eq. [2]) carboxylic acids and $NaBH_4$.

[2]

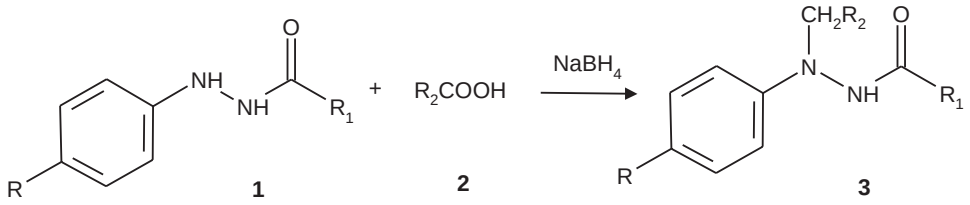

© 1998 NRC Canada

Table 3. Physical data of 1-acyl-2-alkyl-2-aryl-hydrazines (**3**).

Compound[a]	R	R_1	R_2	Yield[b]	mp (°C)[c]
3a	H	Me	H	15%	94[d]
3b	H	Me	Me	76%	87
3c	H	Me	Et	77%	93
3d	H	Me	Pr	80%	94
3e	H	Et	H	20%	80
3f	H	Et	Et	76%	72
3g	H	Pr	Pr	70%	90[e]
3h	NO_2	Me	Me	67%	144[f]
3i	Me	Me	Me	71%	100

[a]All solid compounds were analyzed for C, H, and N, and results agreed to ±0.5% of theoretical values.
[b]Yield of isolated product.
[c]Midpoint of narrow range.
[d]Literature (8) 94°C.
[e]Recrystallized at –20°C.
[f]Literature (11) 144°C.

In the former case the reaction can be easily carried out in a stepwise, one-pot procedure. The synthetic route reported herein promised to be an easy way to obtain monoalkylated arylhydrazides compared to previously described methods, mostly affording fair yields of impure products (14–18). Most of the alkylated products (**3**), prepared and characterized herein, were never synthesized before. The results are summarized in Table 3, and the spectroscopic and MS properties are collected in Table 4.

The structural identification of products **3a**–**i** were based both on chemical degradation and spectroscopic investigations. It was reported that treatment of azo compounds with Zn in aqueous HCl effected the reductive cleavage of the NN double bond (19). It is reasonable to conclude that the conversion went through the intermediacy of hydrazines. We applied this treatment to **3b** and **3d** and obtained *N*-ethyl and *N*-butylaniline, respectively, as the only aromatic amines, as determined by GC–MS analysis. The ^{1}H NMR spectra of **3b** and **3d** showed two relatively sharp singlets each at 7.66, 8.32 ppm and 7.50, 8.10 ppm, respectively, in $CDCl_3$ for the *E* and *Z* amide hydrogens. This assignment turned out to be correct upon comparison with the range for this proton in the spectra of **1a**–**f** (7.03–7.46 ppm and 7.50–8.26 ppm in $CDCl_3$). The ^{13}C NMR spectra were consistent with the data obtained from the proton spectra. As expected, the IR spectra for **3b** and **3d** showed single NH bands. The common features in the mass spectra of **3b** and **3d** are illustrated in Scheme 1. The outlined patterns of fragmentations were found in all other *N*-alkyl arylhydrazides **3a**, **c**, **e**–**i**. Analogously, the ^{1}H and ^{13}C NMR spectra of these compounds repeated quite consistently the features outlined above for **3b** and **3d**.

A likely mechanism of the reductive alkylation of 1-acyl-2-arylhydrazines **1** with the carboxylic acids **2** implies the reduction of **2** to aldehydes **4** by the action of some borohydride species formed in solution (20) and subsequent condensation of aldehydes with **1** to an easily reducible iminium ion **5** (Scheme 2). This rationale is consistent with the formation of traces of ethanal-phenylhydrazone from the reaction of phenylhydrazine with acetic acid and $NaBH_4$ (see footnote 2) as detected by GC–MS and confirmed the observation made by Gribble et al. (1). The proposed mechanism turned out to be correct when we tested the reaction between 1-acyl-2-phenylhydrazine (**1b**) and butanal in the presence of $NaBH_4$ (21) (see experimental part). The reaction afforded 1-acyl-2-butyl-2-phenylhydrazine (**3d**) in 50% yield together with some unreacted 1-acyl-2-phenylhydrazine.

The reductive alkylation of 1-aryl-2-acylhydrazines with carboxylic acids and $NaBH_4$ is a valid alternative method to the usual reductive alkylation with carbonyl compounds due to the high yields and easy procedure. The reaction implied the use of few and readily available reagents. The carboxylic acid plays the role of solvent, acylating agent, source of entering alkyl group, modifier of $NaBH_4$ reactivity, and acid catalyst.

When we applied our procedure of reductive alkylation with carboxylic acids and $NaBH_4$ to phenylhydrazine hydrochloride, after neutralization with the minimum amount of 10% aqueous NaOH, we observed the formation of the corresponding 1-acyl-2-phenylhydrazine only, but no formation of the alkylated product. This result was consistent with decomposition of acyloxyborohydride species in the presence of water as reported in literature (22).

Moreover, $NaBH_4$ is a mild and selective reagent. The GC–MS analysis revealed that neither any amide was reduced nor N—N bond was cleaved by $NaBH_4$. Even in 6 M H_2SO_4 at 80°C, sodium borohydride left 1-acetyl-2-butyl-2-phenylhydrazine (**3d**) unchanged; only some 2-butyl-2-phenylhydrazine was detected as the usual hydrolysis product obtainable under acidic conditions.

While the reductive alkylation of *N*-acyl-*N*′-arylhydrazines was applicable to **1b**–**f**, the only exception was **1a**, which resisted *N*′-ethylation by acetic acid – $NaBH_4$ under the standard condition.

Experimental

Phenylhydrazine hydrochloride, (4-methylphenyl)hydrazine hydrochloride, phenylhydrazine, (4-nitrophenyl)hydrazine, and $NaBH_4$ pellets were purchased from Aldrich, Italy, Milan. Solvents were used as received. The GC–MS analyses were performed with a Fisons Trio 2000 mass spectrometer, working in the positive ion 70 eV electron impact mode. Spectra were recorded in the range 35–500 u. Injector temperature was kept at 250°C, and the column (Supelco SPB^{TM}-5, 30 m long, 0.32 mm i.d.) temperature was programmed from 60 to 300°C with a gradient of 10°C/min. The GC analyses performed, keeping the injector at 250°C on pure 1-acyl-2-arylhydrazines (**1**), showed, at times, the formation of isomeric 1-acyl-1-arylhydrazines; the reaction was relevant when very dilute CH_2Cl_2 solutions were used, but did not occur with other solvents. The IR spectra were obtained with a Nicolet FT-IR Magna 550 spectrophotometer using KBr technique for solids in the range 4000–400 cm^{-1}. The ^{1}H and ^{13}C NMR spectra were recorded in $CDCl_3$ or DMSO-d_6 at room temperature on a Bruker AC-F 200 spectrometer at 200 and 50 MHz, respectively. The NMR peak locations are reported as δ-values from TMS (^{1}H NMR) and the central peak of $CDCl_3$ or DMSO-d_6 (^{13}C NMR). Some ^{1}H multiplets are characterized by the term app (apparent): this refers only to their

© 1998 NRC Canada

Table 4. Spectroscopic and MS data of 1-acyl-2-alkyl-2-arylhydrazines (**3**).

Product	IR (KBr) ν (cm^{-1})	^{1}H NMR δ, *J* (Hz)	^{13}C NMR δ	MS (70 eV) *m/z* (%)
3a	3256 vs, 3019 s, 2880 m, 2808 m, 1675 vs, 1605 vs, 1530 vs, 1504 vs, 1377 s, 1281 vs, 1220 s, 1120 s, 1038 s, 756 vs, 694 vs	1.93 (s, 3H, CH_3, rotamer A), 2.01 (s, 3H, CH_3, rotamer B), 3.03 (s, 3H, N-CH_3, rotamer A), 3.08 (s, 3H, N-CH_3, rotamer B), 6.65–6.95 (m, 3H, H_{arom}), 7.13–7.31 (m, 3H, $2H_{arom}$ + N-H, rotamer A), 8.05 (br s, 1H, N-H, rotamer B)[a]	18.9, 20.8, 40.5, 41.9, 112.9, 113.2, 119.5, 120.5, 128.9, 129.2, 149.1, 149.2, 169.2, 176.9[a]	164 (M^+, 42), 122 (45), 121 (100), 107 (33), 106 (19), 105 (60), 104 (12), 93 (8), 92 (33), 78 (9), 77 (60), 65 (8), 51 (16), 43 (16)
3b	3263 vs, 3032 m, 2986 m, 2940 m, 2861 m, 1683 vs, 1598 vs, 1551 s, 1499 vs, 1387 vs, 1295 s, 1269 s, 1144 m, 1045 m, 755 vs, 702 vs	1.05–1.22 (m, 3H, CH_3), 1.94 (s, 3H, CH_3, rotamer A), 1.98 (s, 3H, CH_3, rotamer B), 3.33–3.55 (m, 2H, N-CH_2), 6.70–6.95 (m, 3H, H_{arom}), 7.10–7.35 (m, 2H, H_{arom}), 7.66 (br s, 1H, N-H, rotamer A), 8.32 (br s, 1H, N-H, rotamer B)[a]	11.8, 12.4, 20.3, 21.8, 47.3, 49.8, 114.3, 115.2, 120.4, 121.7, 130.1, 130.5, 149.6, 149.9, 170.9, 177.9[a]	178 (M^+, 44), 136 (21), 135 (85), 121 (51), 120 (15), 119 (100), 107 (91), 105 (10), 104 (24), 79 (11), 78 (12), 77 (96), 51 (24), 43 (22)
3c	3270 vs, 3030 m, 2964 s, 2935 s, 2880 m, 1665 vs, 1600 vs,1532 vs, 1500 vs, 1370 vs, 1288 vs, 1236 m, 1194 m, 1140 m, 1045 m, 756 vs, 670 vs	0.95 (t, 3H, CH_3, *J* = 7.4, rotamer A), 0.97 (t, 3H, CH_3, *J* = 7.4, rotamer B), 1.55–1.70 (m, 2H, CH_2), 2.01 (s, 3H, CH_3, rotamer A), 2.03 (s, 3H, CH_3, rotamer B), 3.32–3.47 (m, 2H, N-CH_2), 6.75–6.92 (m, 3H, H_{arom}), 7.21–7.35 (m, 3H, $2H_{arom}$ + N-H)[a]	11.3, 19.0, 19.1, 19.7, 20.9, 54.0, 56.6, 112.9, 113.7, 119.4, 120.5, 129.1, 129.3, 148.5, 148.9, 169.2, 176.4[a]	192 (M^+, 43), 163 (13), 150 (8), 149 (33), 134 (12), 133 (75), 132 (30), 122 (11), 121 (100), 108 (7), 107 (54), 106 (25), 105 (14), 104 (36), 91 (10), 79 (9), 78 (10), 77 (68), 51 (14), 43 (30), 41 (11)
3d	3235 s, 3035 m, 2964 m, 2923 m, 1654 vs, 1602 s, 1542 vs, 1496 vs, 1458 s, 1374 s, 1291 s, 1219 m, 994 m, 746 s	0.91–1.00 (m, 3H, CH_3), 1.25–1.45 (m, 2H, CH_2, rotamer A), 1.47–1.63 (m, 2H, CH_2, rotamer B), 1.97 (s, 3H, CH_3, rotamer A), 2.00 (s, 3H, CH_3, rotamer B), 3.35–3.45 (m, 2H, N-CH_2), 6.72–6.95 (m, 3H, H_{arom}), 7.15–7.45 (m, 2H, H_{arom}), 7.50 (br s, 1H, N-H, rotamer A), 8.10 (br s, 1H, N-H, rotamer B)[a]	13.8, 13.8, 19.1, 20.1, 20.6, 20.7, 27.7, 28.4, 51.9, 54.6, 112.8, 113.7, 119.1, 120.4, 129.0, 129.2, 148.5, 148.9, 169.4, 176.4[a]	206 (M^+, 19), 163 (17), 132 (15), 122 (10), 121 (100), 120 (15), 119 (55), 118 (10), 107 (24), 106 (33), 105 (12), 104 (27), 91 (10), 78 (10), 77 (65), 51 (14), 43 (20), 41 (18)
3e	3256 s, 3052 m, 2992 m, 1675 vs, 1616 vs, 1543 s, 1510 vs, 1346 s, 1273 s, 1194 m, 1128 m, 766 s, 707 s	1.05–1.25 (m, 3H, CH_3), 2.30 (q, 2H, CH_2, *J* = 7.5, rotamer A), 2.41 (q, 2H, CH_2, *J* = 7.5, rotamer B), 3.10 (s, 3H, N-CH_3, rotamer A), 3.11 (s, 3H, N-CH_3, rotamer B), 6.70–6.95 (m, 3H, H_{arom}), 7.05 (br s, 1H, N-H, rotamer A), 7.15–7.40 (m, 2H, H_{arom}), 7.95 (br s, 1H, N-H, rotamer B)[a]	8.5, 9., 24.4, 27.4, 40.6, 42.2, 112.8, 113.2, 119.5, 120.5, 129.0, 129.3, 149.3, 149.5, 172.9, 179.0[a]	178 (M^+, 38), 122 (70), 121 (100), 107 (43), 106 (32), 105 (63), 104 (23), 93 (9), 92 (26), 79 (10), 78 (14), 77 (71), 65 (8), 52 (8), 51 (22), 39 (8)
3f	3210 s, 3040 s, 2980 s, 2887 m, 1675 vs, 1602 vs, 1504 vs, 1471 vs, 1379 s, 1240 s, 1194 s, 1148 m, 930 m, 753 vs, 687 s	0.93 (t, 3H, CH_3, *J* = 7.4, rotamer A), 0.94 (t, 3H, CH_3, *J* = 7.4, rotamer B), 1.06 (t, 3H, CH_3, *J* = 7.4, rotamer A), 1.18 (t, 3H, CH_3, *J* = 7.4, rotamer B), 1.52–1.70 (m, 2H, CH_2), 2.13–2.43 (m, 2H, CH_2), 3.20–3.45 (m, 2H, N-CH_2), 6.73–6.95 (m, 3H, H_{arom}), 7.10–7.30 (m, 3H, $2H_{arom}$ + N-H, rotamer A), 7.70 (br s, 1H, N-H, rotamer B)[a]	8.4, 9.7, 11.3, 11.4, 18.9, 19.8, 24.3, 27.4, 54.0, 56.7, 112.8, 113.7, 119.1, 120.4, 129.0, 129.3, 148.7, 150.0, 172.9, 179.3[a]	206 (M^+, 24), 150 (12), 149 (30), 133 (68), 122 (10), 121 (100), 120 (16), 107 (40), 106 (43), 105 (12), 104 (32), 91 (11), 78 (12), 77 (74), 57 (9), 51 (15), 43 (15), 41 (12)
3g	3243 s, 3045 m, 2973 s, 2947 s, 2887 s, 1675 vs, 1609 vs, 1550 s, 1510 vs, 1458 s, 1379 s, 1300 m, 1227 m, 1150 m, 1100 m, 977 m, 750 vs	0.80–1.00 (m, 6H, CH_3), 1.20–1.80 (m, 6H, CH_3), 2.05–2.35 (m, 2H, CH_2), 3.25–3.45 (m, 2H, N-CH_2), 6.65–6–95 (m, 3H, H_{arom}), 7.05–7.30 (m, 3H, H_{arom} + N-H, rotamer A), 8.00 (br s, 1H, N-H, rotamer B)[a]	13.8, 17.7, 19.0, 20.1, 27.5, 28.5, 32.8, 36.0, 51.9, 54.7, 112.8, 113.8, 119.0, 120.4, 128.9, 129.3, 148.7, 149.0, 172.3, 178.6[a]	234 (M^+, 16), 191 (10), 164 (19), 147 (10), 132 (13), 122 (9), 121 (100), 120 (10), 119 (47), 107 (12), 106 (27), 104 (11), 77 (32), 43 (10), 41 (12)

© 1998 NRC Canada

Table 4 (*concluded*).

Product	IR (KBr) ν (cm^{-1})	^{1}H NMR δ, *J* (Hz)	^{13}C NMR δ	MS (70 eV) *m/z* (%)
3h	3270 s, 3091 m, 2990 m, 2947 m, 1682 vs, 1590 vs, 1504 vs, 1326 vs, 1280 vs, 1201 s, 1128 vs, 825 s, 746 s, 687 s	1.16 (app t, 3H, CH_3, *J* = 7.0), 1.96 (s, 3H, CH_3, rotamer A), 1.99 (s, 3H, CH_3, rotamer B), 3.50–3.78 (m, 2H, N-CH_2), 6.76 (app d, 2H, H_{arom}, *J* = 9.3, rotamer A), 6.84 (app d, 2H, H_{arom}, *J* = 9.5), 10.4 (br s, 1H,N-H)[b]	11.4, 20.3, 45.9, 110.4, 110.6, 125.6, 137.3, 137.8, 153.4, 154.8, 168.4, 169.0[b]	223 (M^+, 15), 181 (35), 180 (30), 166 (62), 164 (100), 152 (46), 149 (11), 134 (22), 122 (11), 121 (11), 106 (13), 77 (11), 43 (20)
3i	3197 m, 3086 m, 2987 s, 2931 s, 1695 vs, 1616 vs, 1520 vs, 1403 vs, 1340 vs, 1256 vs, 1194 s, 1137 m, 1083 s, 1026 m, 822 vs, 762 s	1.05 (t, 3H, CH_3, *J* = 7.1, rotamer A), 1.06 (t, 3H, CH_3, *J* = 7.1, rotamer B), 1.89 (s, 3H, CH_3, rotamer A), 1.91 (s, 3H, CH_3, rotamer B), 2.10 (s, 3H, CH_3, rotamer A), 2.15 (s, 3H, CH_3, rotamer B), 3.25–3.40 (m, 2H, N-CH_2), 6.55–6.75 (m, 2H, H_{arom}), 6.85–7.00 (m, 2H, H_{arom}), 7.45 (br s, 1H, N-H, rotamer A), 8.05 (br s, 1H, N-H, rotamer B)[a]	11.2, 11.7, 19.8, 20.8, 21.3, 47.0, 49.5, 114.2, 114.9, 129.4, 130.1, 130.4, 130.7, 146.9, 147.1, 170.2, 177.2[a]	192 (62), 150 (20), 149 (100), 135 (40), 134 (17), 133 (98), 121 (92), 120 (20), 118 (28), 91 (81), 77 (41), 65 (20), 43 (18)

[a]Solvent: $CDCl_3$.
[b]Solvent: DMSO-d_6.

Scheme 1.

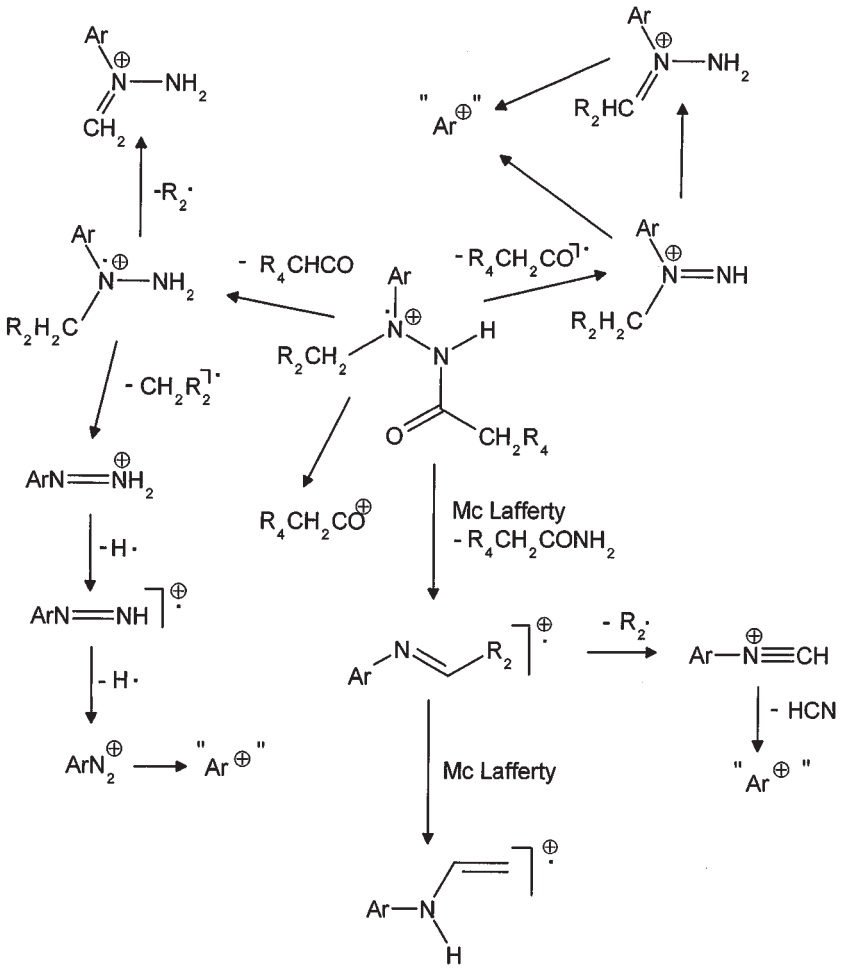

appearance and may be an oversimplification. Elemental analysis were performed with a Carlo Erba Mod. 1106 elemental analyzer.

Preparation of 1-formyl-2-phenylhydrazine (1a)

1-Formyl-2-phenylhydrazine (**1a**) was prepared as described procedure (9) by heating a mixture of

© 1998 NRC Canada

Scheme 2.

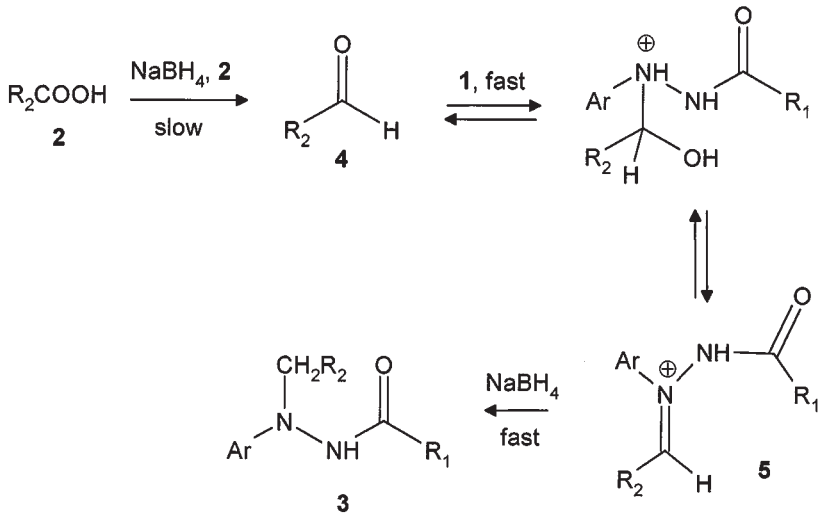

phenylhydrazine (5 mL, 46 mmol) and 50% HCOOH (18 mL, 240 mmol) at 120°C for 15 min. After the mixture was allowed to stand at rt, crystals of product precipitated; the resulting solid was recrystallized from EtOH and hexane.

Preparation of 1-acyl-2-arylhydrazines (1b–e)

The arylhydrazine (30 mmol) was added at rt to the appropriate carboxylic acid (**2**, 750 mmol), and the resulting mixture was stirred at 80°C for 1.5 h. Most of the acid was distilled off; the warm residue was treated with Et_2O or hexane and the crystals of the desired products **1b**–**e** precipitated. The products were further purified by recrystallization from hexane and the minimum amount of EtOH. Their physical and spectroscopic data are collected in Tables 1 and 2.

Procedure A

*Preparation of 1-acyl-2-alkyl-2-arylhydrazines (**3b**–**d**, **3f**–**i**)*

Sodium borohydride (pellets, 1.5 g, 40 mmol) was added portionwise to a mixture of 1-acyl-2-phenylhydrazine (**1**, 13 mmol) in carboxylic acid (**2**, 200 mmol) at ca. 60°C under vigorous stirring. The reaction usually required about 1 h for completion and could be considered completed soon after the sodium borohydride pellets were completely dissolved. The solvent was then partly distilled off under reduced pressure and, after neutralization of the residue with $NaOH–Na_2CO_3$ solution at ca. 0°C, the product was extracted with CH_2Cl_2 (20 mL × 5). Whenever after addition of $NaBH_4$ a too dense mixture resulted, distillation of the solvent was avoided and only a treatment with $NaOH–Na_2CO_3$ solution followed by CH_2Cl_2 extraction was performed. After the combined organic extracts were dried (Na_2SO_4) and the solvent was removed under reduced pressure, the product was crystallized from hexane by the addition of the minimum amount of EtOH. The physical and spectroscopic data of **3** are shown in Tables 3 and 4.

*Preparation of 1-acyl-2-methyl-2-phenylhydrazine (**3a**, **3e**)*

Procedure A was followed except that warming was prevented, keeping the temperature at 0–5°C, and that the amounts of reagents used were 13 mmol of 1-acyl-2-phenylhydrazine (**3**), 400 mmol of HCOOH, and 70 mmol of $NaBH_4$ (pellets). In the case of **3a**, twice crystallization from hot Et_2O was necessary to purify the desired product impure of 1-acetyl-2-formyl-2-phenylhydrazine.

In the case of **3e**, the reaction mixture containing 30% of unreacted reagent, was isolated in neutral form as explained in Procedure A and treated again with HCOOH and $NaBH_4$. At the end of reaction GC–MS analysis revealed the presence of product **3e** and a trace of unreacted **1c**. The reaction mixture was treated as in Procedure A. The physical and spectroscopic data of **3a** and **3e** are reported in Tables 3 and 4.

Procedure B

*One-pot preparation of 1-acetyl-2-ethyl-2-(4-methylphenyl)hydrazine (**3i**). Preparation of 1-acetyl-2-(4-methylphenyl)hydrazine (**1f**)*

(4-Methylphenyl)hydrazine hydrochloride (2.1 g, 13 mmol) was heated at 80°C for 15 h in acetic acid (20 mL, 320 mmol) with sodium acetate (1.1 g, 14 mmol) to allow the formation of 1-acetyl-2-(4-methylphenyl)hydrazine (**1f**), as revealed by GC–MS. The temperature was allowed to decrease to 60°C when $NaBH_4$ pellets (2.2 g, 58 mmol) were added portionwise. After all pellets were dissolved, GC–MS analysis revealed 1-acetyl-2-ethyl-2-(4-methylphenyl)-hydrazine (**3i**) as the sole volatile product. The reaction mixture was treated as described in Procedure A. Procedure B was repeated, obviously without the addition of $NaBH_4$, in order to obtain 1-acetyl-2-(4-methylphenyl)hydrazine (**1f**); it was recrystallized from EtOH and hexane. The physical and spectroscopic data of **1f** are reported in Tables 1 and 2 and **3i** in Tables 3 and 4.

*Reductive alkylation of 1-acyl-2-phenylhydrazine (**1b**) with butanal and $NaBH_4$*

A solution of aqueous 3 M H_2SO_4 (1.4 mL, 0.46 mmol) and butanal (0.18 mL, 2 mmol) in THF (3 mL) was slowly added to an open vessel containing a solution of 1-acetyl-2-phenylhydrazine (**1b**, 0.2 g, 1.33 mmol) in THF (10 mL) and MeOH (1.3 mL), while $NaBH_4$ pellets (0.17 g, 4.5 mmol) were added portionwise at 0°C (±5°C) under magnetic

© 1998 NRC Canada

stirring. The mixture was stirred for an additional hour at rt, diluted with H_2O, made strongly alkaline with NaOH (cooling), and extracted with CH_2Cl_2. After solvents were distilled off, 1-acetyl-2-butyl-2-phenylhydrazine (**3d**, 40% yield) and 1-acetyl-2-phenylhydrazine (**1b**, 43% yield) were separated by crystallization from Et_2O.

*Reductive cleavage of 1-acetyl-2-ethyl-2-phenylhydrazine (**3b**) and of 1-acetyl-2-butyl-2-phenylhydrazine (**3d**)*

Treatment of 0.22 mmol of either 1-acetyl-2-ethyl-2-phenylhydrazine (**3b**) or of 1-acetyl-2-butyl-2-phenylhydrazine (**3d**) in 37% HCl (3 mL) with Zn dust (0.6 g, 9.2 mmol) at 70°C for ca. 16 h gave *N*-ethylaniline and *N*-butylaniline, respectively, as the sole GC–MS products. The original products were completely transformed.

Mass spectra of 1-acyl-1-arylhydrazines

1-Formyl-1-phenylhydrazine (**1a′**), MS, *m*/*z*: 136 (M^+, 16), 107 (11), 106 (13), 105 (80), 93 (26), 92 (8), 91 (8), 78 (20), 77 (100), 66 (7), 51 (19), 39 (7); 1-acetyl-1-phenylhydrazine (**1b′**), MS, *m*/*z*: 150 (M^+, 10), 108 (18), 107 (7), 105 (49), 93 (18), 92 (6), 78 (13), 77 (64), 51 (23), 43 (100); 1-propionyl-1-phenylhydrazine (**1c′**), MS, *m*/*z*: 164 (M^+, 4), 119 (5), 108 (10), 105 (53), 93 (25), 78 (41), 77 (100), 66 (10), 57 (93), 52 (14), 51 (39), 50 (16), 39 (11); 1-butyril-1-phenylhydrazine (**1d′**), MS, *m*/*z*: 178 (M^+, 7), 108 (21), 105 (26), 93 (27), 78 (18), 77 (68), 71 (89), 66 (9), 51 (25), 43 (100), 41 (77), 39 (21); 1-acetyl-1-(4-nitrophenyl)hydrazine (**1e′**), MS, *m*/*z*: 195 (M^+, 6), 153 (20), 123 (4), 122 (6), 76 (13), 74 (6), 50 (14), 43 (100), 41 (12); 1-acetyl-1-(4-methylphenyl)hydrazine (**1f′**), MS, *m*/*z*: 164 (M^+, 10), 122 (13), 119 (96), 107 (9), 106 (15), 92 (13), 91 (100), 77 (8), 65 (25), 43 (99).

Acknowledgement

Financial support was obtained from the Italian National Research Council (95.01044.CT03, 96.027420.CT03 to AGG) and Italian Ministry of University, Sciences and Technology (MURST 40% and 60% 1993–95 to AGG, MURST 60% 1994–96, and MURST 40% 1995 to GV). The authors are grateful to Dr. P. Martinuzzi for recording ^1H and ^{13}C NMR spectra and Mr. P. Padovani for expert instrumental maintenance.

References

1. G.W. Gribble, P.D. Lord, J. Skotnicki, S.E. Dietz, J.T.J. Eaton, and J.L. Johnson. J. Am. Chem. Soc. **96**, 7812 (1974).
2. A.F. Hegarty. *In* The chemistry of the hydrazo, azo and azoxy groups. *Edited by* S. Patai. John Wiley & Sons, London, New York, Sydney, and Toronto. 1975. pp. 647–651.
3. J.W. Timberlake and J.C. Stowell. *In* The chemistry of the hydrazo, azo and azoxy groups. *Edited by* S. Patai. John Wiley & Sons, London, New York, Sydney, and Toronto. 1975. pp. 69–79.
4. A. Go, M. Ito, K. Endo, and H. Mukoda. Japanese patent JP 04005282 A2 920109 (C.A. 116, 168361, 1992).
5. G. Winters and N. Di Mola. German patent DE 2442667 750313 (C.A. 83, 28096, 1975).
6. Zh.V. Molodykh, B.I. Buzykin, M.A. Kudrina, L.P. Sysoeva, N.G. Gazetdinova, I.D. Neklesova, and Yu.P. Kitaev. Khim.-Farm. Zh. **14**, 33 (1980) (C.A. 93, 94943, 1980).
7. T. Zsolnai. Zentralbl. Bakteriol. Parasitenkd. Infektionskrankh. Hyg. Abt. 1: Orig. Reihe A, **232**, 119 (1975) (C.A. 83, 72591, 1975).
8. Y. Usui and C. Matsumura. Yakugaku Zasshi, **87**, 43 (1967) (C.A. 67, 32382, 1967).
9. E. Müller. *In* Methoden der organischen chemie. Vol. 10/2. *Edited by* Houben-Weyl. George Verlag, Stuttgart. 1967. pp. 355–357.
10. M.J. Hearn and J.E. Grimwade. Org. Prep. Proced. Int. **12**, 249 (1980).
11. M.J. Kornet, T.T. Tita, and A.P. Thio. Synth. Commun. **16**, 1261 (1986).
12. B.C. Challis and J.A. Challis. *In* Comprehensive organic chemistry. Vol. 2. *Edited by* I.O. Sutherland. Pergamon Press, Oxford, New York, Toronto, Sydney, Paris, and Frankfurt. 1979. p. 1047.
13. P. Bouchet, J. Elguero, and J. Pereillo. Bull. Soc. Chim. Fr. **6**, 2264 **(**1972).
14. W. Stühmer and E.A. Elbrächter. Arch. Pharm. **285**, 161 (1952).
15. D.H.R. Barton and E. Doris. Tetrahedron Lett. **37**, 3295 (1996).
16. V.N. Barinova, V.G. Voronin, V.P. Zhestkov, and Yu.N. Portnov. Zh. Org. Khim. **20**, 1765 (1984).
17. G. Barattini. Gazz. Chim. Ital. **58**, 821 (1926).
18. B.C. Challis and J.A. Challis. *In* Comprehensive organic chemistry. Vol. 2. *Edited by* I.O. Sutherland. Pergamon Press, Oxford, New York, Toronto, Sydney, Paris, and Frankfurt. 1979. pp. 1051–1052.
19. J. March. *In* Advanced organic chemistry. John Wiley & Sons, New York, Chichester, Brisbane, Toronto, and Singapore. 1992. p. 1224.
20. P. Marchini, G. Liso, A. Reho, F. Liberatore, and F.M. Moracci. J. Org. Chem. **40**, 3453 (1975).
21. G. Verardo, A.G. Giumanini, P. Strazzolini, and M. Poiana. Synthesis, 121 (1993).
22. G.W. Gribble and C.F. Nutaitis. Org. Prep. Proced. Int. **17**, 317 (1985).

© 1998 NRC Canada

Importance de la présence de magnésie dans le stockage de la chaux : carbonatation de l'oxyde et de l'hydroxyde de magnésium

Rose-Marie Dheilly, Yahya Sebaibi, Joseph Tudo et Michèle Queneudec

Résumé : L'influence de l'humidité relative de l'air, de la température et de la concentration en CO_2 sur la carbonatation de MgO et $Mg(OH)_2$ a été examinée dans des domaines compatibles avec des conditions climatiques courantes. L'oxyde et l'hydroxyde de magnésium purs utilisés pour cette étude originale étaient à l'état pulvérulent. Les espèces apparaissant au cours du processus de carbonatation ont été mises en évidence et la forme la plus stable dans les conditions usuelles de stockage a été identifiée. De plus l'étude des différents facteurs climatiques a montré que la carbonatation n'est jamais totale même après une exposition prolongée.

Mots clés : carbonatation, oxyde de magnésium, hydroxyde de magnésium, stockage, conditions climatiques.

Abstract: The influence of relative air moisture, temperature, and concentration of carbon dioxide on the carbonation of magnesium oxide and hydroxide have been studied in normal climatic conditions. The MgO and $Mg(OH)_2$ used for this original work are pure granular materials. The different species that appear during the process of carbonation and the most stable form in usual conditions of storage were identified. Moreover, the study of the different climatic factors showed that the carbonation is never complete even after a prolonged exposure.

Key words: carbonation, magnesium oxide, magnesium hydroxide, storage, climatic conditions.

1. Introduction

Dans des travaux publiés antérieurement (1) nous avons montré l'influence des conditions climatiques sur la carbonatation de l'oxyde de calcium et l'hydroxyde de calcium pulvérulents. Toutefois les roches calcaires utilisées pour la préparation de la chaux contiennent parfois du carbonate de magnésium. La cuisson à une température supérieure à 900°C conduit alors à un mélange de MgO et CaO : chaux magnésienne ou dolomitique. Le mécanisme de la carbonatation de CaO à l'état pulvérulent a déjà été élucidé (1). L'étude du stockage des chaux magnésiennes nécessite donc une seconde étape qui est l'étude du comportement de MgO dans différentes conditions atmosphériques et hygrothermiques.

La carbonatation de MgO a déjà fait l'objet de nombreux travaux. En particulier Evans et Saint Claire (2), Horiguchi et Yoshikazu (3) et Kataev et Kulikov (4) ont étudié la réaction avec le dioxyde de carbone de MgO en solution dans de l'eau afin de déterminer les conditions optimales d'obtention d'une solution saturée en hydrogénocarbonate. Smithson et Bakshi (5) ainsi que Xiangting et al. (6) ont étudié la préparation de $MgCO_3 \cdot 3H_2O$ à partir des pâtes de MgO en vue de la production de $MgCO_3 \cdot KHCO_3 \cdot 4H_2O$. Medvinskii et al. (7) ont relié le mécanisme de la carbonatation à la surface spécifique de l'hydroxyde $Mg(OH)_2$. Afin de réduire les émissions de dioxyde de carbone dans l'atmosphère Lackner et al. (8) se sont intéressé à la réaction de CO_2 avec des minéraux contenant de l'oxyde de magnésium. Ils ont travaillé sur la possibilité de fixer chimiquement CO_2 dans une forme carbonatée stable, en utilisant deux procédés différents de carbonatation : directe à haute température ou en solution aqueuse. Butt et al. (9) ont étudié les cinétiques des réactions simultanées de déshydroxylation et de carbonatation de $Mg(OH)_2$ pulvérulent à haute température. De nombreux carbonates de magnésium neutres ou basiques ont été identifiés mais souvent leurs compositions chimiques ont été contestées. Citons en particulier la nesquehonite $MgCO_3 \cdot 3H_2O$ (10–15), l'hydromagnésite $Mg_5(CO_3)_4(OH)_2 \cdot 4H_2O$ (15, 16) et la giorgiosite $Mg_5(CO_3)_4(OH)_2 \cdot 5H_2O$ (17). En ce qui concerne les carbonates basiques il semblerait qu'il soit possible de préparer toute une gamme de formule générale $a\mathrm{MgO} \cdot b\mathrm{CO_2} \cdot c\mathrm{H_2O}$ avec a = 5,4 ou 3, b = 4,3 ou 2 et c = 4–11. Pour l'hydromagnésite deux compositions sont le plus souvent formulées : $Mg_5(CO_3)_4(OH)_2 \cdot 4H_2O$ ($5MgO \cdot 4CO_2 \cdot 5H_2O$) et $Mg_4(CO_3)_3(OH)_2 \cdot 3H_2O$ ($4MgO \cdot 3CO_2 \cdot 4H_2O$). Les travaux les plus récents (15) confirmeraient la première formule. Par ailleurs Langmuir (18) présente les domaines de stabilité de ces différents carbonates en étudiant les équilibres dans le système CO_2–H_2O–$MgCO_3$ en fonction de la température (0–100°C) et de la pression de CO_2 (0–100 atm (1 atm = 101,3 kPa)).

Received Reçu le 5 août 1997.[1]

R.-M. Dheilly,[2] Y. Sebaibi, J. Tudo et M. Queneudec.[2] Equipe C.E.P.S.C.O. (Conception et Evaluation des Procédés et Systèmes de la Construction), Laboratoire matériaux, structure, thermique. Université de Picardie – Institut Universitaire de Technologie, Avenue des Facultés - 80025, Amiens Cedex 1, France.

1. Revision reçue le 30 avril 1998.

2. Auteurs à qui adresser toute correspondance. Tél./Téléc. : (33) 03-22-53-40-16.

© 1998 NRC Canada

Fig. 1. Image en électrons secondaires (microscopie électronique à balayage) de l'oxyde de magnésium (G = 3500).

Enfin, depuis les 10 dernières années, l'interaction de MgO avec le dioxyde de carbone a fait l'objet d'un intérêt grandissant dans le domaine de la catalyse hétérogène. Ces travaux se sont particulièrement intéressés aux phénomènes d'adsorption–désorption de molécules de gaz en surface de l'oxyde (19–25). Les essais sont essentiellement réalisés à basse température (T voisine de 100 K) sur le plan (100) du cristal isolé de MgO. Seuls Beruto et al. (26) et Yanagisawa et al. (27) ont étudié l'adsorption–désorption de CO_2 sur MgO à haute température (entre 400 et 1000 K).

Toutefois aucun de ces auteurs ne s'est intéressé à l'oxyde de magnésium pulvérulent à des températures voisines de 20°C et sous pression atmosphérique. Le présent travail s'intéresse donc à l'étude de l'influence des trois facteurs : température, humidité relative et concentration en CO_2 de l'atmosphère sur les réactions d'hydratation et de carbonatation de MgO et $Mg(OH)_2$ pulvérulents à des températures voisines de 20°C et sous pression atmosphérique.

2. Matériaux et techniques expérimentales

L'oxyde et l'hydroxyde de magnésium sont des produits du commerce purs «pour analyse». Sur les images en électrons secondaires faites au microscope électronique à balayage, l'oxyde de magnésium apparaît comme un amas sphérique de fines plaquettes de 1 à 2 × 10^3 nm de long, dont l'enchevêtrement ne permet pas de définir la forme exacte (fig. 1). L'hydroxyde de magnésium se présente sous la forme d'amas de plaquettes hexagonales de 200 à 300 nm d'épaisseur et de 0.5 à 1 × 10^3 nm de long (fig. 2).

Le dispositif expérimental utilisé pour la carbonatation est donné en fig. 3. La première enceinte thermostatée (1), régulée électroniquement, permet de maintenir l'ensemble de la chambre atmosphérique (2) et du système de saturation (3) à la température voulue. Ceci permet d'éviter tout point froid susceptible de modifier la pression de H_2O recherchée. L'atmosphère dans la chambre atmosphérique (2) est maintenue aux caractéristiques désirées par une circulation des gaz provenant du système de saturation (3). L'humidité relative souhaitée, 30 ou 60%, est obtenue grâce à des mélanges, toujours renouvelés, d'eau et d'acide sulfurique (17,82 M), dans les concentrations respectives suivantes : 775 et 495 g d'acide par litre de solution. Dans tous les cas les débits d'air et de gaz carbonique sont contrôlés par des débitmètres de façon à maintenir des conditions expérimentales constantes. Compte tenu de la forme de la nacelle dans laquelle est déposé l'échantillon, pour avoir une couche très fine de matériau pulvérulent le nombre de moles initial est fixé à 8,93 × 10^{-3} soit en masse 357 mg d'oxyde de magnésium ou 518 mg d'hydroxyde de magnésium.

Au cours de chaque expérience, les échantillons sont suivis par : (*i*) analyse gravimétrique : l'échantillon est pesé, en général, toutes les douze heures et replacé rapidement dans la chambre atmosphérique; (*ii*) analyse par diffraction des rayons X, effectuée sur un deuxième échantillon identique à celui pesé, placé dans les mêmes conditions. Le générateur utilisé est un Siemens Kristalloflex 700.

Pour déterminer rapidement le pourcentage de MgO, $Mg(OH)_2$ et d'espèce carbonatée présente dans l'échantillon nous avons défini un protocole de dosage par analyse thermogravimétrique, menée sur une microthermobalance Setaram 92, sous oxygène sec à la vitesse de chauffage de 40° par heure. Les différents constituants qui peuvent entrer dans la composition d'un échantillon sont repérés et dosés grâce aux étapes observées lors de la dégradation thermique de l'échantillon :

(*i*) L'hydroxyde de magnésium perd son eau pour donner MgO entre 270 et 370°C.

(*ii*) La nesquéhonite ($MgCO_3 \cdot 3H_2O$) se dégrade à partir de 80°C avec une perte de deux molécules d'eau pour donner à 280°C un composé qu'il faut globalement écrire

© 1998 NRC Canada

Fig. 2. Image en électrons secondaires (microscopie électronique à balayage) de l'hydroxyde de magnésium (G = 7500).

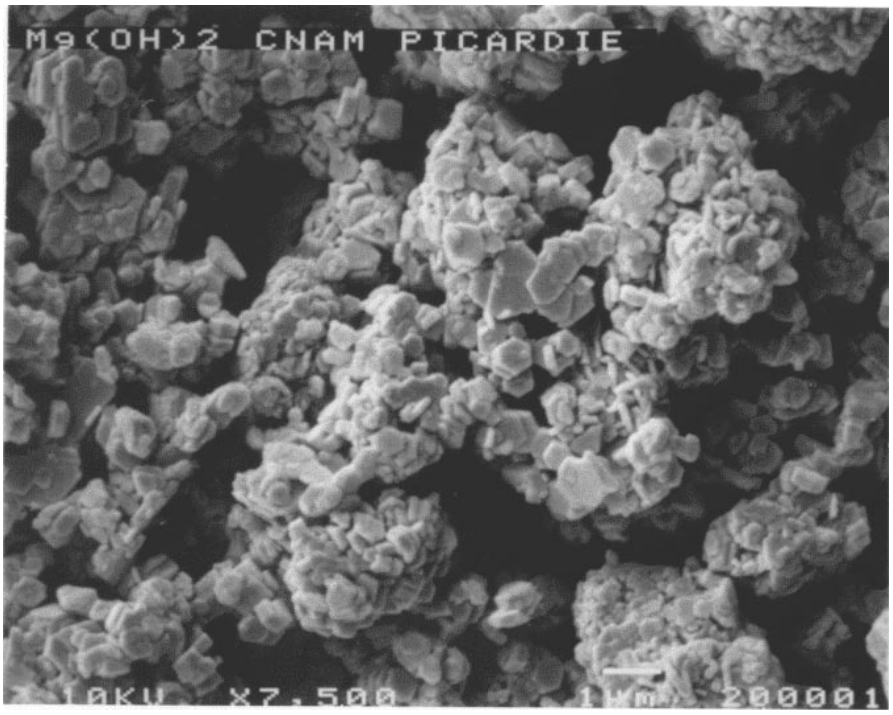

Fig. 3. Dispositif expérimental.

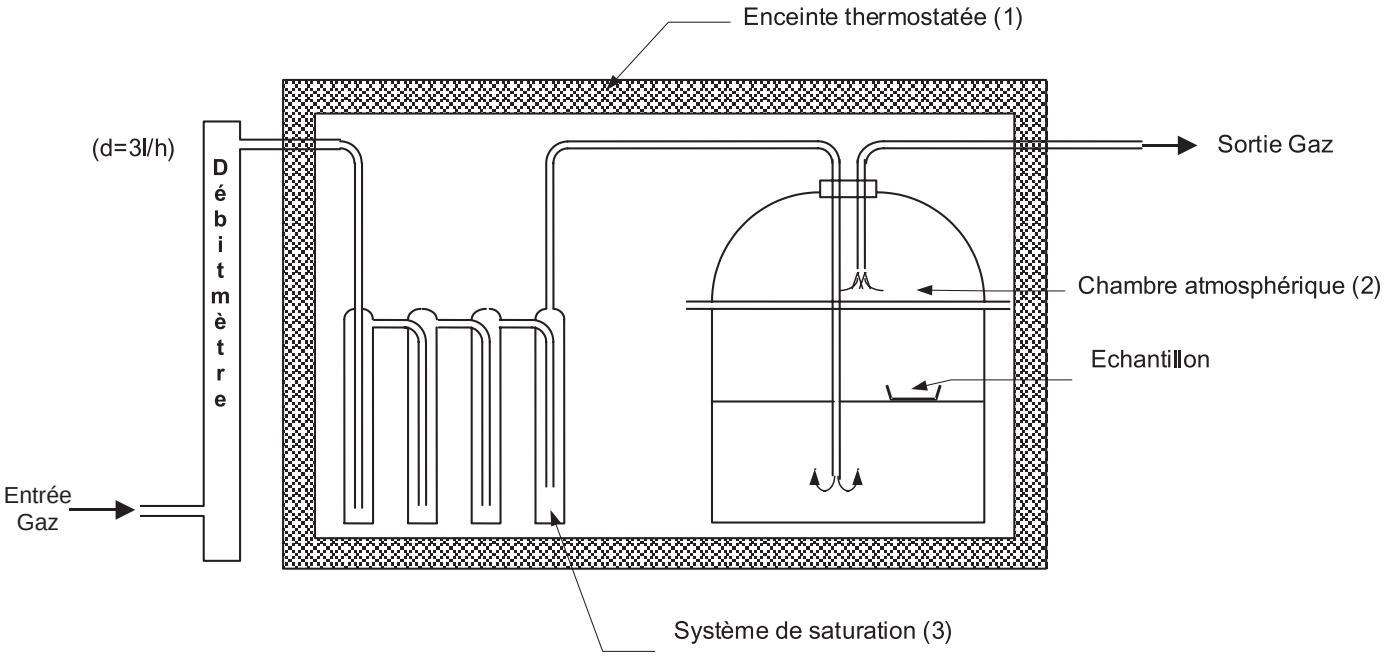

$MgCO_3 \cdot H_2O$. Entre 340 et 415°C celui-ci donne MgO avec départ simultané d'une molécule de H_2O et d'une molécule de CO_2.

(*iii*) L'hydromagnésite ($Mg_5(CO_3)_4(OH)_2 \cdot 4H_2O$) se dégrade à partir de 160°C pour donner à 295°C un palier, qui en masse correspondrait au produit anhydre $Mg_5(CO_3)_4(OH)_2$ amorphe aux rayons X. La dégradation se poursuit à partir de 335°C pour obtenir MgO à 420°C.

(*iv*) Quant à la giorgiosite ($Mg_5(CO_3)_4(OH)_2 \cdot 5\ H_2O$), nous ne l'avons jamais isolée pure mais toujours mélangée avec de l'hydromagnésite et de la brucite ($Mg(OH)_2$). Sa dégradation thermique est très voisine de celle de l'hydromagnésite.

(*v*) La présence de perte de masse à des températures inférieures à 100°C montre que les échantillons possèdent de l'eau « libre » ou faiblement liée.

© 1998 NRC Canada

Fig. 4. Analyse gravimétrique d'échantillons de MgO placés pendant 10 jours sous atmosphère pauvre en CO_2 avec HR = 60%. (◇) T = 10°C; (□) T = 20°C; (△) T = 40°C; (---) $Mg(OH)_2$ théorique.

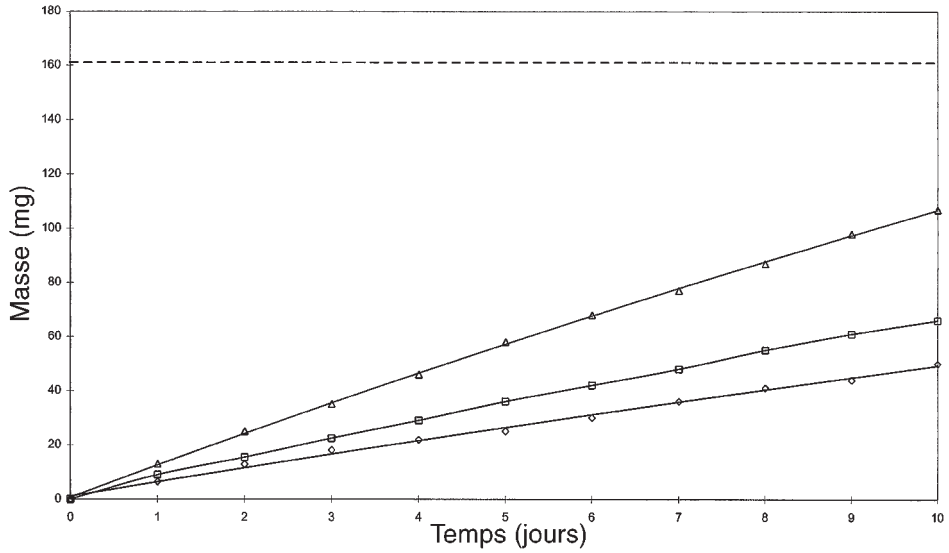

Il faut cependant reconnaître que si l'identification des espèces par analyse thermogravimétrique est aisée dans le cas des échantillons composés de mélanges $Mg(OH)_2$–$MgCO_3{\cdot}3H_2O$ ou $Mg(OH)_2$–$Mg_5(CO_3)_4(OH)_2{\cdot}4H_2O$, elle est plus difficile lorsque l'échantillon est un mélange des trois composés précédents ou des deux phases hydromagnésite et giorgiosite, même si les spectres obtenus par diffraction des rayons X sont différents.

3. Résultats expérimentaux et analyse

L'influence de la température et de l'hygrométrie a été étudiée pour des concentrations « extrêmes » en CO_2. La teneur minimum correspond à un air peu pollué soit 0.03% de CO_2, et la teneur maximum à une atmosphère carbonique. Les températures choisies sont des températures types d'un climat tempéré. L'humidité relative de 60% est une moyenne typique de ce type de climat. Les humidités de 30 et 100% correspondent à des états extrêmes qu'on peut rapprocher respectivement des conditions de stockage en silo et de périodes humides.

Sur les figures représentatives de cette étude nous avons indiqué la masse théorique de l'échantillon totalement transformé en $Mg(OH)_2$ et $MgCO_3{\cdot}3H_2O$.

L'étude des paramètres : température, hygrométrie, teneur en dioxyde de carbone de l'atmosphère, a permis les observations suivantes :

(*i*) Pour une humidité relative égale à 30%, quelles que soient la température d'étude et l'atmosphère sous laquelle est conservé l'échantillon, l'oxyde et l'hydroxyde de magnésium n'évoluent pas. La masse de l'échantillon ne varie pas et l'analyse par diffraction des rayons X décèle uniquement la présence de l'espèce initiale.

(*ii*) Lorsque l'humidité relative est de 60%, quel que soit le pourcentage de CO_2 de l'atmosphère, MgO se transforme lentement en $Mg(OH)_2$. L'examen en microscopie électronique et l'analyse thermogravimétrique montrent qu'il n'y a pas d'évolution vers le carbonate mais une fixation d'eau (fig. 4), la réaction étant plus rapide à 40°C.

(*iii*) Quel que soit le pourcentage de CO_2 de l'atmosphère, pour une humidité relative supérieure (HR = 100%) on remarque aussi que la variation de masse de MgO ou de $Mg(OH)_2$, est d'autant plus importante que la température est plus élevée (figs. 5 et 7).

En première lecture des courbes de la fig. 5*a*, sous atmosphère pauvre en CO_2 avec HR = 100% la transformation de l'oxyde en hydroxyde semble totale, quelle que soit la température. Les résultats des analyses radiocristallographique et thermogravimétrique confirment bien la formation de $Mg(OH)_2$, mais elles indiquent toujours la présence de magnésie. L'importance du gain de masse, enregistré pour 10 jours, s'explique différemment suivant la valeur de la température. À 40°C les analyses révèlent la présence dans l'échantillon des espèces carbonatées : hydromagnésite et giorgiosite en plus de celles de MgO et $Mg(OH)_2$. Alors que lorsque la température est inférieure ou égale à 20°C, l'analyse thermogravimétrique de l'échantillon met en évidence la présence d'eau « libre » en plus de celles de l'oxyde et l'hydroxyde de magnésium (fig. 6).

Le gain de masse de l'hydroxyde, sous atmosphère humide pauvre en CO_2 et pendant 10 jours (fig 7*a*), est aussi dû uniquement à un apport d'eau libre : $Mg(OH)_2$ s'humidifie, mais n'évolue pas en carbonate.

Sous atmosphère carbonique humide, que ce soit pour l'oxyde ou l'hydroxyde de magnésium, le gain de masse est plus grand que celui observé sous atmosphère pauvre en CO_2. Ce qui a été observé sous atmosphère pauvre en CO_2 est toujours valable : MgO évolue en $Mg(OH)_2$, qui fixe des molécules d'eau par adsorption. Mais sous atmosphère carbonique, l'analyse thermogravimétrique des produits obtenus enregistre aussi des pertes qu'il faut attribuer à l'existence d'une phase carbonatée dans l'échantillon en plus de la présence de MgO et $Mg(OH)_2$. La nature du carbonate qui se forme dépend de la température.

Pour une humidité relative de 100%, nous avons pu mettre en évidence, en maintenant l'échantillon plus

© 1998 NRC Canada

Fig. 5. Analyses gravimétriques d'échantillons de MgO placés pendant 10 jours sous une humidité relative égale à 100% : (*a*) atmosphère pauvre en CO_2; (*b*) atmosphère carbonique (◇) T = 10°C; (□) T = 20°C; (△) T = 40°C; (—-) $Mg(OH)_2$ théorique; (– - – -) $MgCO_3 \cdot 3H_2O$ théorique.

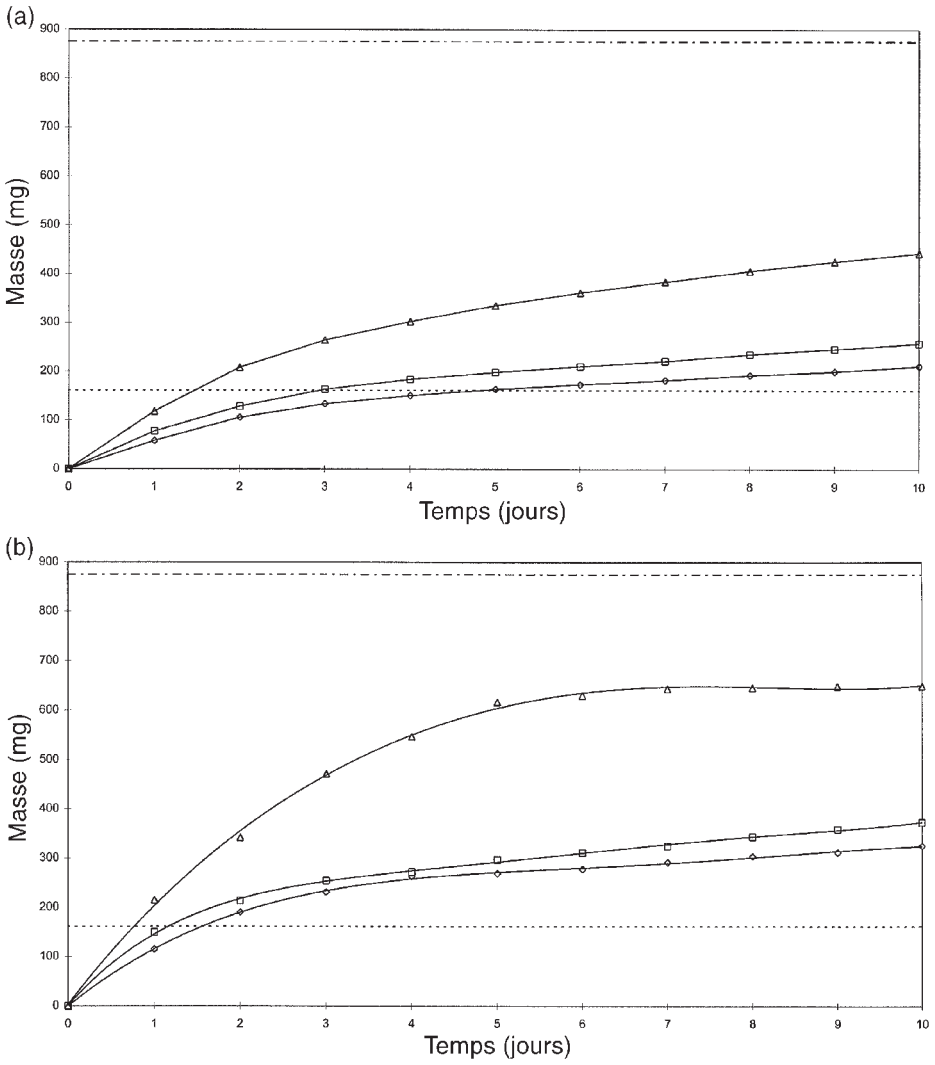

Fig. 6. Analyse thermogravimétrique d'un échantillon de MgO conservé 10 jours sous atmosphère pauvre en CO_2 avec HR = 100% et T = 20°C.

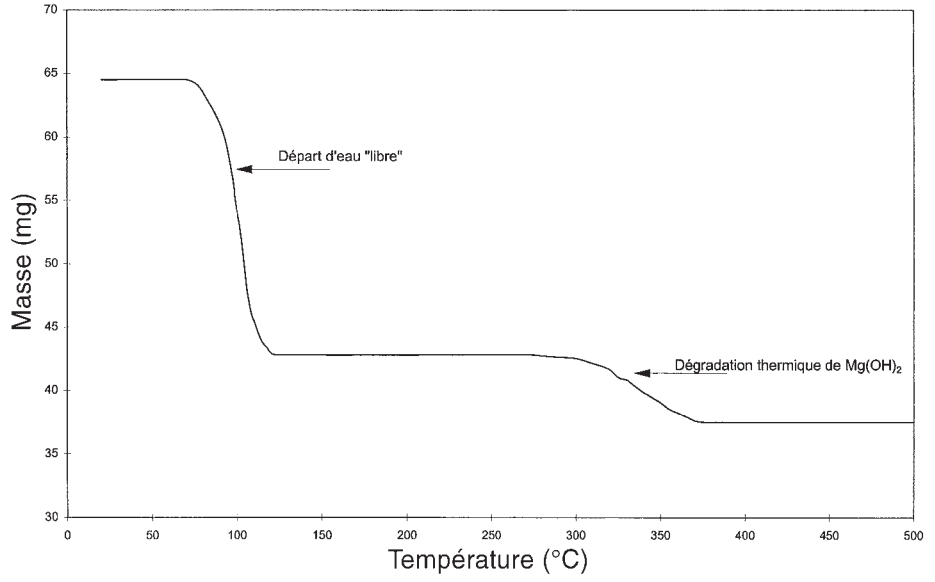

© 1998 NRC Canada

Fig. 7. Analyses gravimétriques d'échantillons de $Mg(OH)_2$ placés 10 jours sous une humidité relative égale à 100% : (*a*) atmosphère pauvre en CO_2; (*b*) atmosphère carbonique. (◇) T = 10°C; (□) T = 20°C; (△) T = 40°C; (—) $MgCO_3 \cdot 3H_2O$ théorique.

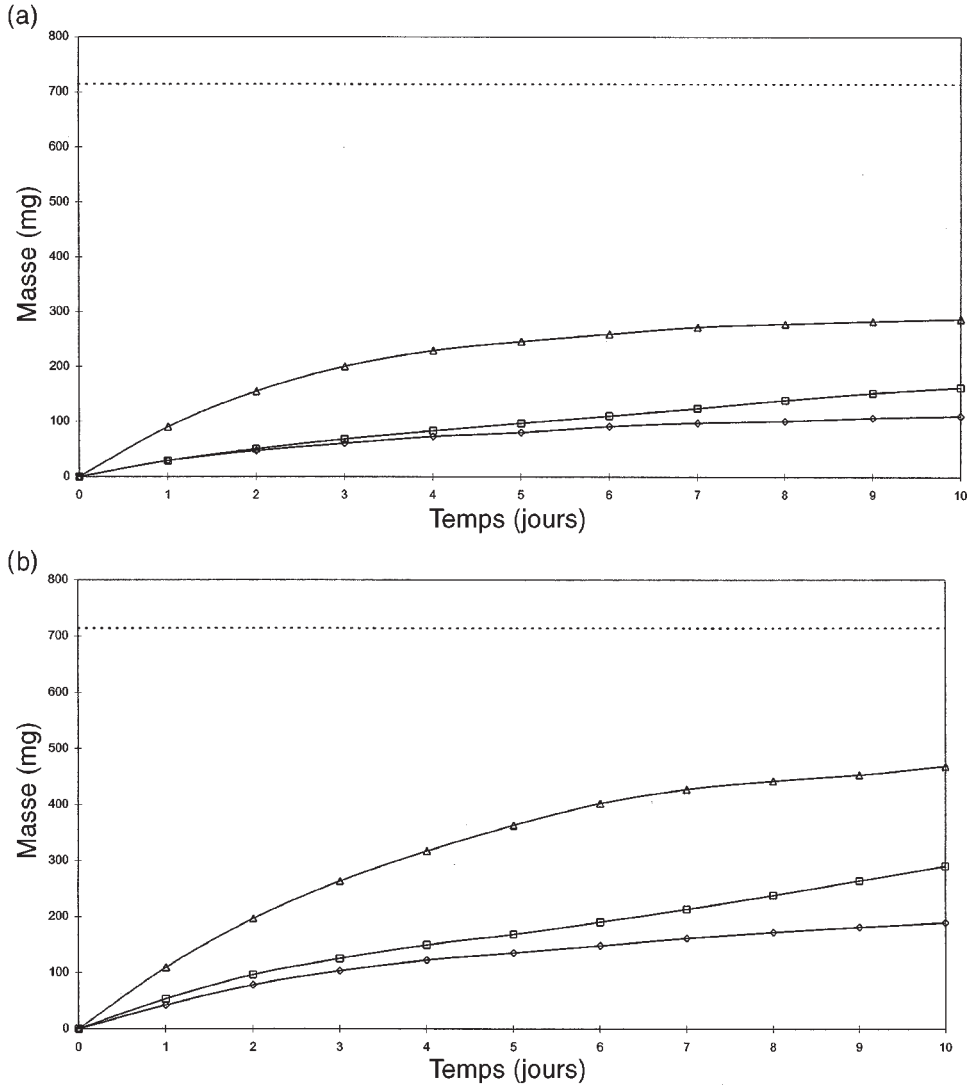

longtemps sous cette humidité, que le processus de carbonatation dépendait de la température et de la pression de CO_2.

Trois réactions ont pu être proposées suivant les conditions hygrothermiques et atmosphériques :

$$MgO \quad Mg(OH)_2 \quad MgCO_3 \quad 3H_2O$$
(Nesquéhonite)

si l'atmosphère est riche en CO_2 et la température inférieure ou égale à 20°C (conditions 1).

$$MgO \quad Mg(OH)_2 \quad Mg_5(CO_3)_4(OH)_2 \quad 4H_2O$$
(Hydromagnésite)

$$+ MgCO_3 \quad 3H_2O + Mg_5(CO_3)_4(OH)_2, 5H_2O$$
(Nesquéhonite) (Giorgiosite)

si l'atmosphère est riche en CO_2 et la température égale à 40°C (conditions 2).

$$MgO \quad Mg(OH)_2 \quad Mg_5(CO_3)_4(OH)_2 \quad 4H_2O$$
(Hydromagnésite)

$$+ Mg_5(CO_3)_4(OH)_2 \quad 5H_2O$$
(Giorgiosite)

si l'atmosphère est pauvre en CO_2, quelle que soit la température (conditions 3).

Il faut remarquer que le carbonate de magnésium $MgCO_3$ ne se forme pas.

Ces résultats ne sont pas en contradiction avec ceux de Langmuir (16). Pour lui, pour p_{CO_2} 1 atm, la nesquéhonite est la forme stable entre 10 et 50°C. Dans nos expériences il semble effectivement que 40°C soit la température limite, car un essai rapide à 50°C nous a montré que $MgCO_3 \cdot 3H_2O$ ne se formait pas. Dans le même diagramme sous atmosphère pauvre en CO_2 la phase hydromagnésite est la seule signalée au dessus de 5–10°C.

Nos travaux nous permettent aussi de noter que, quels que soient la température et le pourcentage de CO_2 contenu dans l'atmosphère, la conversion de l'oxyde, ou de l'hydroxyde,

© 1998 NRC Canada

Fig. 8. Image en électrons secondaires (microscopie électronique à balayage) de l'oxyde de magnésium conservé 80 jours sous atmosphère carbonique avec HR = 100% et T = 20°C (G = 3500).

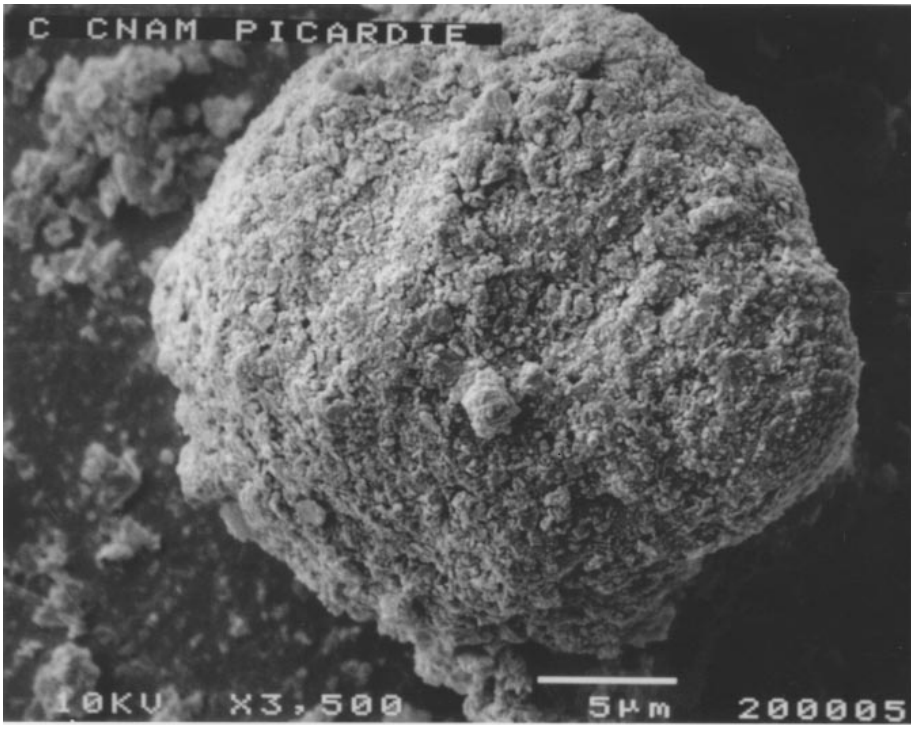

Fig. 9. Image en électrons secondaires (microscopie électronique à balayage) de l'oxyde de magnésium conservé 80 jours sous air avec HR = 100% et T = 20°C (G = 3500).

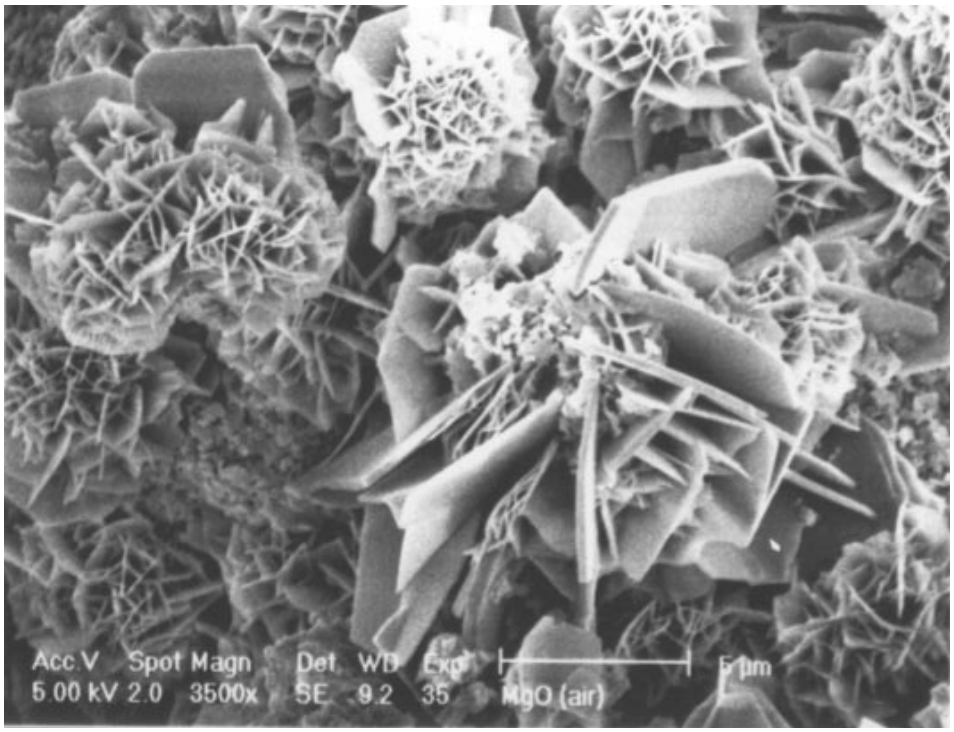

en espèce carbonatée n'est pas totale même après 80 jours d'expérimentation. Les analyses le confirment et, en particulier, l'analyse radiocristallographique qui révèle, à côté de la forme carbonatée formée, la présence dans l'échantillon de l'espèce $Mg(OH)_2$ sous atmosphère humide pauvre en CO_2 ou des espèces MgO et $Mg(OH)_2$ sous atmosphère

© 1998 NRC Canada

Fig. 10. Image en électrons secondaires (microscopie électronique à balayage) de l'oxyde de magnésium conservé 80 jours sous atmosphère carbonique avec HR = 100% et T = 40°C (G = 3500).

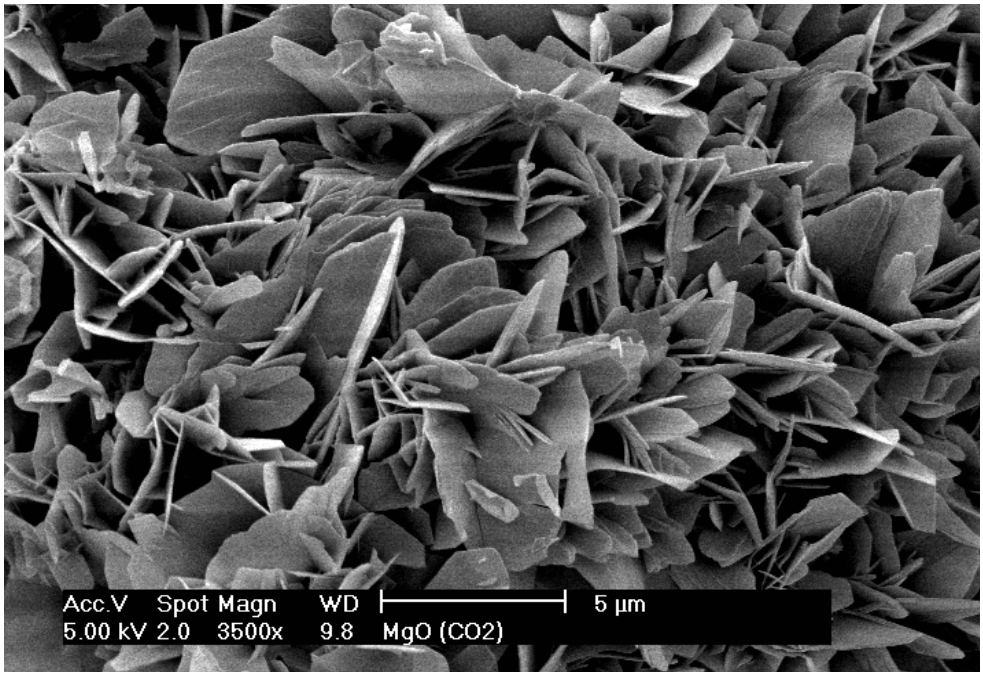

Tableau 1. Surfaces spécifiques BET mesurées après 80 jours de traitement et exprimées en m^2/g.

	Espèces chimiques de départ	
Conditions de conservation	MgO	$Mg(OH)_2$
Sans traitement	39,04	6,31
Sous CO_2, T 20°C HR = 100%	12,27	4,77
Sous CO_2, T = 40°C HR = 100%	6,51	3,79
Sous air, quelle que soit T HR = 100%	35,15	5,38

carbonique. La diffusion de H_2O et de CO_2 est probablement freinée par la formation des espèces carbonatées, quelle que soit leur nature.

Ces différentes espèces carbonatées obtenues présentent cependant des structures différentes. En effet lorsque l'oxyde de magnésium est placé pendant 80 jours sous atmosphère carbonique avec HR = 100% et T = 20°C l'échantillon conserve sa forme pulvérulente, mais l'image en électrons secondaires (fig. 8) montre qu'une couche de carbonate $MgCO_3 \cdot 3H_2O$ se forme sur la surface de l'oxyde de magnésium. Butt et al. (9) ont observé le même phénomène lors de leur étude de la carbonatation de $Mg(OH)_2$ sous CO_2 sec à haute température : un film de $MgCO_3$ se formait à la surface des cristaux de $Mg(OH)_2$ et, selon eux, freinait la diffusion interne de CO_2.

Nous avons précédemment montré qu'en atmosphère saturée en humidité la carbonatation présente une étape intermédiaire correspondant à la formation de l'hydroxyde $Mg(OH)_2$. L'évolution structurelle de l'échantillon après maintien pendant 80 jours dans les conditions 2 et 3 a donc été étudiée pour MgO et $Mg(OH)_2$. Dans les deux cas l'aspect pulvérulent disparaît. L'échantillon apparaît à l'œil nu comme une couche solide cohérente. L'analyse par microscopie électronique à balayage montre (figs. 9 et 10) la formation de touffes de fines plaquettes enchevêtrées qui peuvent être identifiées comme du $Mg_5(CO_3)_4(OH)_2$ cristallisé avec quatre molécules d'eau (15), soit un rapport CO_2 / MgO égal à 4/5 et inférieur à celui de la nesquéhonite (CO_2 / MgO = 1) obtenu dans les conditions 1.

Cette limitation dans la carbonatation peut s'expliquer, étant donnée l'évolution structurelle, par un blocage de la diffusion du dioxyde de carbone au sein de l'échantillon. Cette hypothèse a pu être confortée par la détermination de la surface spécifique BET.

On peut constater dans le tableau 1 que la surface spécifique évolue de façon considérable avec les conditions du traitement de MgO. Dans le cas de $Mg(OH)_2$ la surface spécifique de l'hydrate non traité est faible par rapport à celle de MgO et l'évolution est moins importante.

Cette diminution de la surface spécifique de l'oxyde, ou de l'hydroxyde, de magnésium semble être la cause du blocage de la diffusion de CO_2 au sein de l'échantillon, qui se traduit, quels que soient la température et le pourcentage de CO_2 contenu dans l'atmosphère, par une conversion non totale de l'oxyde, ou de l'hydroxyde, en espèce carbonatée.

4. Conclusion

L'objectif de ce travail était de déterminer l'influence des conditions climatiques sur la carbonatation de MgO et $Mg(OH)_2$. L'étude des différents facteurs : humidité relative et teneur en dioxyde de carbone de l'ambiance, a permis de montrer que quelles que soient les conditions expérimentales la transformation en espèce carbonatée n'est pas totale même après 80 jours. De plus, la forme la plus stable dans les conditions usuelles de stockage serait l'hydromagnésite.

© 1998 NRC Canada

Ce travail avait pour but de préparer l'étude du stockage des chaux magnésiennes ou dolomitiques dans lesquelles la quantité de magnésie peut atteindre des proportions relativement importantes. Toutefois la présence simultanée de composés calciques et magnésiens ne permet pas d'éloigner l'hypothèse d'un processus de carbonatation préférentiel pour l'une des espèces. C'est pourquoi actuellement une étude s'intéressant à la carbonatation de mélanges des espèces précédentes dans des proportions variables est en cours.

Remerciements

Que la Société LHOIST Europe trouve ici l'expression de nos sincères remerciements pour sa contribution technique et professionnelle et pour l'intérêt qu'elle porte à nos travaux.

Bibliographie

1. R.M. Dheilly. Thèse, Amiens. 1995.
2. R.L Evans et H.W. Saint Claire. Ind. Eng. Chem. **41**, 2814 (1949).
3. Y. Horiguchi J. Sci. Res. Inst. Tokyo, **48**, 27 (1954).
4. G.A. Kataev et B.A. Kulikov. Tr. Tomsk. Gos. Univ. Ser. Khim. **154**, 78 (1962).
5. G.L. Smithson et N.N. Bakshi. Ind. Eng. Chem. Process Des. Dev. **12**, 99 (1973).
6. Z. Xiangting, L. Bainian, L. Zhixian et T. Jigang. Youse Jinshu, **43**, 49 (1991).
7. A.A. Medvinskii, G.G. Saveliv, N.F. Stas, O.V. Tyunina, V.V. Nakhalov, I.A. Kononova, et P.D. Khalfina. React. Kinet. Catal. Lett. **6**, 139 (1977).
8. K.S. Lackner, C.H. Wendt, D.P. Butt, E.L. Joyce et D.H. Sharp. Energy, **20,** 1153 (1995).
9. D.P. Butt, K. S. Lackner, C.H. Wendt, S.D. Conzone, H. Kung, Y.C. Lu et J.K. Bremser. J. Am. Ceram. Soc. **79**, 1892 (1996).
10. J. Johnston. J. Am. Chem. Soc. **37**, 2001 (1915).
11. W.D. Klimev. J. Am. Chem. Soc. **51**, 2093 (1929).
12. W. Lévy. Thèse, Caen. 1937.
13. H.S. Hepbrun. J. Chem. Soc. **96**, (1937).
14. R.A. Robie et B.S. Hemingway. J. Res. U.S. Geol. Surv. **1**, 543 (1973).
15. B. Fritz. Thèse d'état n° 41, Strasbourg. 1975.
16. P. Bariand, F. Cesbron, H. Vachey et M. Sadrzadeh. Mineral. Rec. **4**, 18 (1973).
17. B. Friedel. Neues Jahrb. Mineral. **126**, 187 (1975).
18. D. Langmuir. J. Geol. **73**, 730 (1965).
19. D.L. Meixner, D.A. Arthur et S.M. George. Surf. Sci. **261**, 141 (1992).
20. J. Heidberg, D. Meine et B. Redlich. J. Electron Spectrosc. Relat. Phenom. **64**, 599 (1993).
21. G. Pacchioni. Surf. Sci. **281**, 207 (1993).
22. C. Girardet. S. Picaud et P.N.M. Hoang. Europhys. Lett. **25**, 131 (1994).
23. J. Heidberg et B. Redlich. Surf. Sci. **368**, 140 (1996).
24. J.V. Stark, D.G. Park, I. Lagadic et K.J. Klabunde. Chem. Mater. **8**, 1904 (1996).
25. K. Jug et G. Geudtner. J. Mol. Catal. A : Chem. **119**, 143 (1997).
26. D. Beruto, R. Botter et A.W. Searcy. J. Phys. Chem. **91**, 3578 (1987).
27. Y.Yanagisawa, H Shimodama et A. Ito. J. Chem. Soc. Chem. Commun. 610 (1993).

© 1998 NRC Canada

Method for the differentiation of leaf litter extracts and study of their interaction with Cu(II) by molecular fluorescence

Joaquim C.G. Esteves da Silva, Adélio A.S.C. Machado, Miguel A. Ferreira, and Francisco Rey

Abstract: Six leaf litter extracts (LLE) (eucalyptus (*Eucaliptus globulus*), fern (*Pteridium aquilinium*), oak (*Quercus robur*), chestnut (*Castanea sátiva*), laurel (*Laurus nobilis*), and ulex (*Ulex europoeus*) canopies) were isolated following an extraction procedure similar to that used for fulvic acids (FA) and were characterized by elemental analysis and UV–Vis, FT-IR, and synchronous molecular fluorescence (SyF) spectroscopies. Moreover, information about their interaction with the Cu(II) ion in aqueous solution (100 mg/L of LLE in 0.1 M KNO_3 at pH = 6) was obtained from the measurement of SyF spectra at increasing concentrations of Cu(II). These spectral sets were treated by a self-modeling mixture analysis method (SIMPLISMA) to obtain improved quenching profiles to be used in the estimation by the method of Ryan and Weber of the conditional stability constants (K_c), concentration of binding sites, and percentage of fluorescent binding sites accessible for complexation. For comparison purposes, two samples of FA extracted from two horizons of an oak forest soil (0–5 cm and 5–15 cm) were also studied. The spectroscopic data obtained for LLE and FA were different. The results suggest that LLE are characterized by relatively high concentrations of individualized simple molecules and include reactive structures (alkene and protein residues). The ratio of aliphatic/aromatic structures was higher in LLE than for FA. Both LLE and soil FA form stable complexes with Cu(II), but the logarithm of the conditional stability constant of the 1:1 complexes is larger for LLE (about 5) than for the soil FA (about 4.5).

Key words: leaf litter extracts, soil fulvic acids, synchronous fluorescence, Cu(II) complexation, SIMPLISMA, spectral pattern recognition.

Résumé : On a isolé les extraits de six litières feuillues (ELF) (couvertes d'eucalyptus (*Eucaliptus golbulus*), fougère (*Pteridum aquilinium*), chêne (*Quercus robur*), châtaignier (*Castanea sâtiva*), laurier (*Laurus nobilis*) et ajonc (*Ulex europoeus*)) par une méthode d'extraction semblable à celle utilisée pour les acides fulviques (AF) et on les a caractérisés par analyse élémentaire et par spectroscopies UV–Vis, FT-IR et de fluorescence moléculaire synchrone (FSy). De plus, faisant appel à des mesures de spectre de FSy à des concentrations de plus en plus élevées de Cu(II), on a obtenu des informations relatives à leur interaction avec des solutions aqueuses d'ion Cu(II) (100 mg/L d'ELF dans 0,1 M KNO_3, à un pH = 6). Ces ensembles de spectres ont été traités par une méthode d'analyse de mélanges automodelante (SIMPLISMA) pour d'obtenir des profils améliorés d'extinction pouvant être utilisés dans l'évaluation par la méthode de Ryan et Weber des constantes de stabilité conditionnelles (K_c), de la concentration des sites de fixation et du pourcentage de sites de liaison fluorescents accessibles à la complexation. Pour fins de comparaison, on a aussi étudié deux échantillons d'AF extraits de deux horizons de sol d'une forêt de chêne (0–5 et 5–15 cm). Les données spectroscopiques obtenues pour l'ELF et l'AF sont différentes. Les données suggèrent que les ELF sont caractérisés par des concentrations relativement élevées de molécules simples individualisées et qu'elles contiennent des structures réactives (résidus d'alcène et de protéine). Le rapport des structures aliphatique/aromatique est plus élevé dans les ELF que dans les AF. Les ELF et les AF forment des complexes stables avec le Cu(II); toutefois, le logarithme de la constante de stabilité conditionnelle des complexes 1 : 1 est plus élevé pour les ELF (environ 5) que pour les AF des sols (environ 4,5).

Mots clés : extraits de litières feuillues, acides fulviques de sols, fluorescence synchrone, complexation du Cu(II), SIMPLISMA, reconnaissance du patron de spectre.

[Traduit par la Rédaction]

Received August 7, 1997.[1]

J.C.G. Esteves da Silva, M.A. Ferreira, [2] and A.A.S.C. Machado. [3] LAQUIPAI, Chemistry Department, Faculdade de Ciências, R. Campo Alegre 687, P4150 Porto, Portugal.
F. Rey. Area de Química Física, Universidade de Vigo, Spain.

[1]Revision received June 11, 1998.
[2]Permanent address: Area de Química Física, Universidade de Vigo, Spain.
[3]Author to whom correspondence may be addressed. Telephone: 351-2-608-2874. Fax: 351-2-608-2959. E-mail: amachado@fc.up.pt

 © 1998 NRC Canada

Introduction

Soil organic matter (SOM) plays an important role in the capacity of soils to retain metal ions (1, 2). One of the most important fractions of SOM, of concern to the chemistry of soils, is humic substances (HS), and particularly its most soluble material, the fulvic acids (FA). These play an important part in the movement of metals down into the soil because of their strong complexing properties. As well as HS embedded in soils, there exists at the soil surface another SOM fraction, constituted by the leaf litter (LL), which can be considered as a precursor to HS. Aqueous extracts of LL have been shown to complex metal ions (3–7) and therefore must also have a role in their movement into the soil.

Aqueous extracts of LL are a mixture of simpler and easily assimilated compounds and other, more stable, chemical and biochemical complex molecules. To obtain further information about this less reactive fraction of LL, extracts can be isolated by an extraction procedure similar to that usually used for the extraction of soil FA (8–12), instead of the aqueous extracts studied previously. One of the properties of FA, employed in their extraction from soils, is the ability of FA to be adsorbed in a hydrophobic resin when they are in the acid form and to be desorbed when they are in the ionized (base neutralized) form (13). This property allows their isolation from other soluble soil constituents and their subsequent extraction. LL extracted by this procedure (LLE) are expected to present structural affinities to FA and have been shown to complex metal ions, but further information about them remains limited (9–12). Therefore, it was decided to continue our previous studies on FA with research addressed to this type of extracts.

The characterization of HS and like substances is a quite difficult problem because classical analytical techniques, such as elemental and spectroscopic analysis (UV–Vis and FT-IR, for example), show little variability and, consequently, are not suitable for exploratory studies and (or) classification of this type of substance. Recently, synchronous molecular fluorescence (SyF) spectroscopy has been found to give a large amount of information about FA and LLE, opening new perspectives for their study (14–18). Besides fingerprinting, further information can be generated, for example, about the complexation properties of the samples, by monitoring the SyF spectra as a function of metal ion concentration. If the metal ion (e.g., Cu(II)) provokes quenching of the fluorescence, it is possible to obtain quantitative equilibrium parameters for the complexation reaction (17–20). However, useful information can be extracted from these sets of SyF spectra if suitable chemometric techniques are employed for data reduction. This data treatment requires two levels of implementation: (*i*) the raw spectral data are reduced to the number of components, their spectra, and SyF fluorescent intensity profiles, by self-modeling mixture analysis, such as SIMPLISMA (21, 22); and (*ii*) when several samples are studied simultaneously, the comparison and classification of their spectra is best accomplished by pattern recognition techniques (23, 24).

The main objective of the present work was to develop a method for the differentiation of FA and similar substances based on the use of SyF spectra quenching initiated by Cu(II). As multiwavelength data sets are analyzed, chemometric methods for multidimensional reduction are necessary and three types of techniques are used: (*i*) SIMPLISMA, to detect different components in SyF spectral data sets collected at increasing concentrations of Cu(II) ion, and to obtain their spectra and SyF intensity profiles; (*ii*) pattern recognition methods, namely, cluster analysis and multidimensional scaling, to compare the previously calculated spectra for the samples under analysis; and (*iii*) least-squares adjustment by SIMPLEX of the SyF quenching profiles detected by SIMPLISMA, to determine the conditional equilibrium parameters for the Cu(II) complexation by the method of Ryan and Weber (19, 20). A secondary objective of this work was to obtain information about LLE samples. In addition, well-known methods of HS characterization, namely, elemental analysis and UV–Vis and FT-IR spectroscopy, were also used for comparative proposes.

The procedures described above were tested in the discrimination of six LLE obtained from the following canopies: eucalyptus (*Eucaliptus globulus*), designated feu; fern (*Pteridium aquilinium*) — fer; oak (*Quercus robur*) — foa; chestnut (*Castanea sátiva*) — fch; laurel (*Laurus nobilis*) — fla; and ulex (*Ulex europoeus*) — ful. For comparison purposes, two samples of FA extracted from the soil of an oak forest (0–5 cm, fuao1, and 5–15 cm, fuao2) were also obtained and characterized.

Methodology

Reagents

Materials were extracted from LL collected in Pontevedra (Galicia, Spain) (feu, fer, and foa), Forcarey (Galicia, Spain) (fch), Mugardos (La Corunã, Spain) (fla), and Guitiriz (Lugo, Spain) (ful), and from an oak forest soil collected in Salvatierra de Miño (Galicia, Spain) (fuao1 and fuao2). Solid samples were isolated by the procedure recommended by the IHSS (19). This, briefly, involves mixing the powdered LL or soil with hydrogen chloride (until pH = 1) followed by adsorption of the materials to be extracted on an XAD-8 resin (Fluka AG, Bucks, Switzerland). The extract is then recovered using sodium hydroxide, followed by acidification with a cation exchanger (Amberlite IR-120, Fluka AG, Bucks, Switzerland) in the acid form and freeze-drying.

Solutions (100 mg/L FA) were prepared in 0.1 M potassium nitrate. For adjusting the titrated solutions to constant pH = 6.0 (± 0.1 pH units), a 0.05 M decarbonated potassium hydroxide solution was used. A standard $Cu(NO_3)_2$ was used as titrant and the range of Cu(II) concentration covered in the titrated solutions was always between 0 and about 0.3 mM.

Equipment

The UV–Vis spectra of 20 mg/L of the samples in sodium hydrogen carbonate (0.05 M) were recorded between 250 and 800 nm, with a Hewlett-Packard 8452A spectrometer (0.5 s accumulation time and 2 nm resolution) using 1 cm quartz cells and with a background of 0.05 M sodium hydrogen carbonate.

The FT-IR spectra of solid FA samples (5% in KBr) were recorded between 500 and 4000 cm^{-1} with a Nicolet Magna 550 FT-IR spectrophotometer (200 scans and 2 cm^{-1}

© 1998 NRC Canada

Table 1. Elemental composition (mass %) and atomic ratios of elements of the LLE and FA samples.

Sample	Origin	N	C	H	H/C	N/C
feu	Eucaliptus	0.06	49.34	3.97	0.96	0.001
fer	Fern	0.11	53.76	4.46	1.00	0.002
foa	Oak	0.34	46.62	3.99	1.03	0.006
fch	Chestnut	0.36	45.56	3.75	0.99	0.007
fla	Laurel	0.15	48.32	4.00	0.99	0.003
ful	Ulex	0.58	51.56	4.86	1.13	0.010
fuao1	Oak(0–5 cm)	1.27	46.18	4.22	1.09	0.024
fuao2	Oak(5–15 cm)	0.75	44.55	3.95	1.02	0.014

resolution), using a microsampling diffuse reflectance (DRIFT) accessory (Baseline Nicolet).

Potentiometric and SyF measurements were made as previously described (16–18). SyF spectra were acquired between 250 and 550 nm excitation wavelength using a 20 nm wavelength interval between excitation and emission monochromators (each with 7.5 nm slit). The raw SyF spectra were reduced to the 270–500 nm wavelength range with a 5 nm resolution between points (47 points per spectrum) to be used in the data analysis.

Self-modeling mixture analysis

SIMPLISMA (21, 22) is a three-step self-modeling mixture analysis method. After analysis of the SyF spectra collected as a function of the Cu(II) concentration, the first step allows the calculation of the number of components that show linearly independent SyF quenching with an increase in Cu(II) concentration. In the second and third steps, the spectra and improved quenching profiles of the detected components, respectively, are calculated. The SIMPLISMA procedure used in this work is similar to that previously reported (17).

Spectral pattern recognition

Analysis of the spectral similarity was done using cluster analysis and multidimensional scaling. These methods are part of the statistical package SPSS for Windows 5.0 (SPSS Inc., Chicago). In these analyses each spectrum represents a point in the hyperspace of 47 dimensions (wavelengths).

Estimation of equilibrium parameters

If the interaction of Cu(II) with a FA (L) follows a 1:1 stoichiometry for complex formation, it can be schematically represented by

$$[1] \qquad L + Cu(II) \Leftrightarrow CuL$$

and the respective conditional stability constant (K_c), at fixed pH value, is defined by

$$[2] \qquad K_c = [CuL]/([Cu(II)][L])$$

where [CuL] is the concentration of the complex, [Cu(II)] is that of the total uncomplexed metal ion, and [L] is the total concentration of the uncomplexed FA (charges are omitted for sake of simplicity).

To obtain the complexation parameters from fluorescence intensity measurements, a procedure similar to that previously reported (17, 18) was used. The procedure involves several variables: experimental fluorescence intensity (I); fluorescence intensity due to the free FA (I_L); residual fluorescence intensity due to the bound ligand or fluorescent structure not accessible for complexation (I_{CuL}); conditional stability constant (K_c); total ligand concentration (C_L); and total metal concentration (C_{Cu}). The fraction of the total FA bound (= [CuL]/C_L) is given by (19, 20)

$$[3] \qquad [CuL]/C_L = (I_L - I)/(I_L - I_{CuL})$$

and, after setting I_L = 100, the relationship between the calculated SyF intensity profiles I, K_c, I_{CuL}, C_L, and C_M is given by

$$[4] \qquad I = [I_{CuL} - 100/(2K_cC_L)]\{(K_cC_L + K_cC_{Cu} + 1) - [(K_cC_L + K_cC_{Cu} + 1)^2 - 4K_c^2C_LC_{Cu}]^{1/2}\} + 100$$

This equation can be solved for K_c, C_L, and I_{CuL} by nonlinear regression analysis using the quenching profiles previously detected and calculated with SIMPLISMA by a SIMPLEX method previously described (17). The quality of the fitting of this equation to the experimental data can be assessed by the average deviation (ΔE) and sum of the squares of the residuals (SSR) functions.

Fig. 1. Typical UV–Vis spectra of (*a*) fch and (*b*) fuao2 samples.

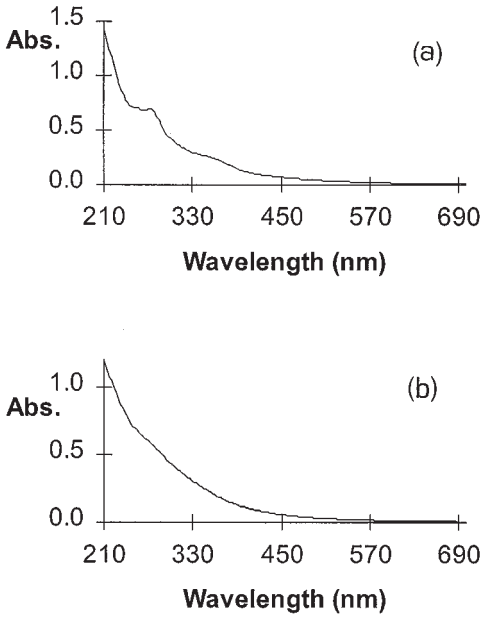

Results and discussion

Characterization

Elemental analysis

The elemental composition (N, C, and H) and the atomic ratios H/C and N/C of the LLE and FA samples are shown in Table 1. These percentages are within the ranges expected for HS (25) but not for nitrogen, where somewhat lower values were obtained. Although the carbon and nitrogen mass percentages show some variation, respectively, between about 44–54% and 0.06–1.27%, the atomic ratios are almost invariant. Indeed, the H/C ratio is 1.00 ± 0.04 for all

© 1998 NRC Canada

Table 2. UV–Vis spectral characteristics of the LLE and FA samples.[a]

Sample	E_4/E_6	ε_{280nm}
feu	4.04	401
fer	6.04	716
foa	8.53	616
fch	5.43	590
fla	8.83	323
ful	3.89	344
fuao1	10.12	491
fuao2	7.40	609

samples except ful (1.13) and fuao1 (1.09). The N/C ratio is less than or equal to 0.010 for the LLE samples but shows higher values for the two FA samples.

Comparison of the N/C ratio for the two soil FA samples shows that nitrogen is lost by mineralization in the upper layer of the soil, the N/C ratio of fuao1 (0–5 cm) being nearly double that for fuao2 (5–15 cm). A similar trend in the N/C ratio was previously observed for FA samples extracted from a pinewood soil (11).

UV–Vis spectra

All the UV–Vis spectra of the LLE samples (Fig. 1*a* shows that of fch) have a particular feature when compared to those of soil FA samples (Fig. 1*b* shows that of fuao1), i.e., a more or less well-defined band at about 280 nm. Moreover, some LLE samples show further fine details, namely, a narrow shoulder at about 260 nm (feu and fch samples) and a wider shoulder at about 350 nm (feu, fch, and ful samples). The band at about 280 nm may be due to π–π* electronic transitions for phenolic substances and benzoic-type acids (26), suggesting that a relatively high concentration of these structures is present in the LLE. These simple compounds undergo chemical transformation and are incorporated into the FA macromolecules during humification and therefore FA show no characteristic bands of the π–π* electronic transitions due to them in the LLE.

Table 2 presents semiquantitative information obtained from the UV–Vis spectra, namely, the E_4/E_6 ratio (an indicator of humification) and the molar absorptivity at 280 nm (26). The E_4/E_6 ratio for the LLE has the following sequence: 3.89 (ful) < 4.04 (feu) < 5.43 (fch) < 6.04 (fer) < 8.53 (foa) < 8.83 (fla), which may be related to a decrease of the molecular weight or particle size of the extracts (27). The E_4/E_6 ratios for the FA samples (fuao1, 10.12, and fuao2, 7.40) are in the same range as, or above, the highest values found for the LLE and are similar to those for other FA samples (28). The smaller E_4/E_6 ratios of the LLE samples (within 3–5) fall in the range of those usually found for the humic acids (28).

The molar absorptivity at 280 nm for the LLE and FA samples varied from about 300 to about 700 L (mol of carbon)$^{-1}$ cm^{-1}, within the range of values found for other HS samples (26).

Fig. 2. Typical diffuse reflectance FT-IR spectra (1900–600 cm^{-1}) of (*a*) fer and (*b*) fuao1 samples.

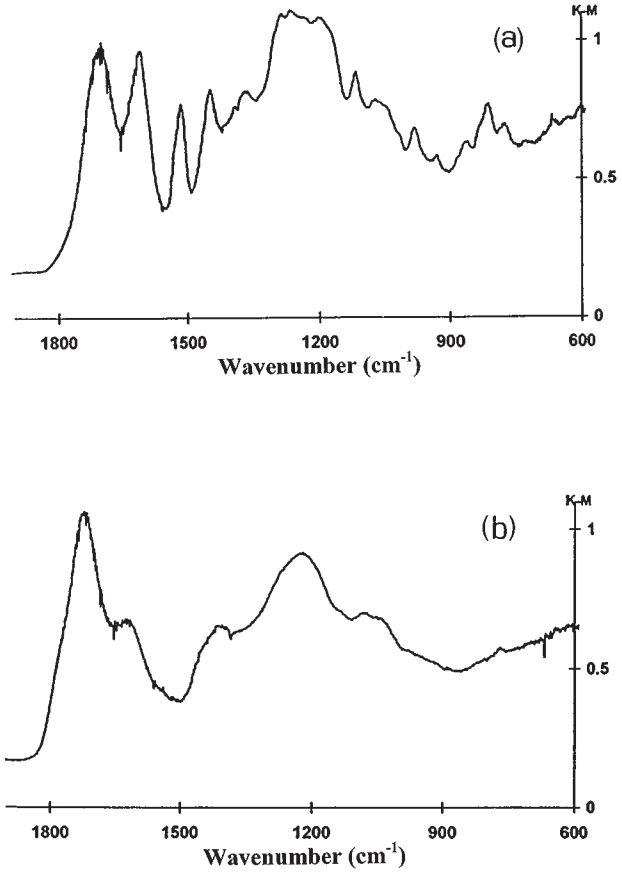

FT-IR spectra

Although infrared spectra are very powerful for the classification of organic materials, in the case of HS this type of spectra is characterized by a remarkably low dependence on sample origin, which limits the use of this technique for classification proposes (29–31). Nevertheless, some information can be obtained from these spectra. Two spectral regions, 4000–2500 cm^{-1} and 1900–600 cm^{-1}, can be considered separately.

The 4000–2500 cm^{-1} range of the FT-IR spectra shows little difference for all samples and is characterized by two bands: a broad band centered at about 3300 cm^{-1}, which is attributed to the O–H stretch; and a narrower band centered at about 2950 cm^{-1}, attributed to the C–H stretch. As these bands are always present in the FT-IR spectra of HS, they are useless for the classification of samples from different origins.

In contrast, the 1900–600 cm^{-1} FT-IR spectra show differences between the six LLE and the two FA samples, as exemplified by Fig. 2, where the spectra for fer (Fig. 2*a*) and fuao1 (Fig. 2*b*) are included. Table 3 indicates the position of the bands detected in this range of the FT-IR spectra, with some assignments based on literature information (29–31).

Comparison of the two spectral types (Fig. 2) shows that the spectra of LLE (Fig. 2*a*) are characterized by a much larger number of well-defined bands than those of the FA (Fig. 2*b*), as expected from the smaller extent of

© 1998 NRC Canada

Table 3. Characteristics of the FT-IR spectra (1900–600 cm^{-1}) of the LLE and FA samples.[a]

Band[b]	Sample								Assignment[c]
	feu	fer	foa	fch	fla	ful	fuao1	fuao2	
1716	x	x	x	x	x	x	x	x	C=O stretch (carboxylic groups)
1614	x	x	x	x	x	x	x	x	C=C stretch
1516	x	x	x	x	x	x	–	–	Substituted phenols (protein residues)
C–H bending spectral region									
1450	x	x	x	–	x	x	–	–	CH_2 and CH_3 bend
1428	–	–	–	–	–	x	–	–	
1412	–	x	–	x	–	–	x	x	O–H bend (carboxylic groups) C–O stretch (phenolic OH)
1366	–	x	–	–	x	x	–	–	C–(CH_3) bend
1333	x	–	–	–	–	x	–	–	
1279	–	x	–	–	x	–	–	x	
1264	–	x	–	–	–	–	–	–	
C–O stretch and C-O-H bend spectral region (carboxylic groups, alcohols, carbohydrates, ...)									
1224	x	–	x	x	x	x	x	x	
1174	–	–	–	–	–	x	–	–	
1116	x	x	x	x	x	x	–	–	
1078	x	x	x	x	x	x	x	x	
1042	x	–	x	x	x	x	x	$\bar{\nu}$	C–O stretch (ether and carbohydrates)
Fingerprint spectral region									
985	–	x	–	–	x	–	–	–	
920	x	x	–	x	–	–	–	–	
880	x	x	–	–	x	x	–	–	
826	x	x	x	x	x	x	–	x	
772	x	x	x	x	x	x	x	x	

[a]x: band detected; –: no band detected.
[b]Average wave number of the maximum of the most important bands (cm^{-1}) detected in the spectra: wave numbers in bold (italic) are characteristic only of the LLE samples (of one FA sample).
[c]Possible assignments according to the literature $\bar{\nu}$ (29, 31).

humification. Particularly well-defined bands observed in the spectra of the LLE (Fig. 2*b*) are those at 1716, 1614, 1518, and 1450 cm^{-1}. The following information can be obtained from these bands:

(*i*) The first two bands, 1716 and 1614 cm^{-1}, which are due to the C=O stretch (mainly carboxyl groups, esters, ketones, and aldehydes) and C=C stretch, respectively, are also present in the FT-IR spectra of the FA, although in different relative proportions. Indeed, while in the spectra of the FA the 1614 cm^{-1} band is very weak, in those of the LLE the intensity of this band is similar to that at 1716 cm^{-1}. This result shows that the LLE have a larger proportion of alkene structures and a smaller proportion of carbonyl compounds than the soil FA.

(*ii*) The 1518 cm^{-1} band, which occurs only in the spectra of the LLE, is assigned to protein residues (29). The presence of these molecular fragments confirms that decaying biological material is still present in these substances. This type of structure is not found in the FA, because protein fragments are transformed almost completely and mixed with other complex structures in the following stages of the humification process.

(*iii*) The 1450 cm^{-1} band, due to the bending of CH_2 and CH_3 structures, is only detected in the LLE. The presence of this well-defined band, together with those assigned to C–H bending (1366 and 1280 cm^{-1}), shows that these samples contain a relatively high proportion of aliphatic branches.

Besides these marked differences between the two types of spectra, analysis of Table 3 shows the existence of common bands in the C–O stretch and O–H bend spectral ranges, suggesting the existence of qualitatively similar structures in LLE and FA.

In conclusion, the FT-IR spectra allowed the identification of particularly reactive structures in the LLE, namely, alkene groups and protein fragments, that were not detected in the FA. These reactive structures play an important role in the decaying process of biomass in soil and in the humification process.

SyF spectra

The SyF spectra of the LLE and FA samples as a function of the Cu(II) concentration are shown in Fig. 3. These spectral sets show a major difference between LLE and FA. Indeed, while the SyF spectra of the LLE (Fig. 3*a–f*) are characterized by a strong and well-defined band around 280 nm, for FA (Fig. 3*g–h*) this band does not appear in the fuao1 spectra (extracted from the upper horizon (0–5 cm)) and is relatively weak in the fuao2 (from the lowest horizon (5–15 cm)). Monoaromatic phenolic structures and (or)

© 1998 NRC Canada

some fluorescent protein residues (tryptophan, tyrosine, and phenylalanine amino acid residuals) may be responsible for the 280 nm band (32) and the present results confirm the UV–Vis results and suggest that these types of structures are destroyed in the humification process of the LLE. Moreover, the shape of the SyF spectra of the LLE is simpler than for FA, i.e., the SyF bands are better defined in these spectra (Fig. 3*a*–*f*) than in those for FA (Fig. 3*g*–*h*), which show a high degree of overlapping.

The effect of Cu(II) on the SyF properties of the eight samples is different and the eight spectral sets can be classified into three classes according to the observed variations (quenching of fluorescence): (*i*) little variation is observed for ful and foa (Fig. 3*c*, *f*); (*ii*) marked quenching is observed in only one band of the spectra for feu, fer, fch, and fla (Fig. 3*a*, *b*, *d*, *e*); and (*iii*) marked quenching is observed in several bands or over a wide range of wavelengths for the FA samples (Fig. 3*g*, *h*). This shows that only some of the fluorescent structures that exist in the samples interact with Cu(II) at pH = 6, i.e., those that show quenching.

Further information about the LLE and FA can be obtained from the spectra shown in Fig. 3 as discussed in the following section.

Table 4. Main bands of the SyF spectra of the components of the LLE and FA detected by SIMPLISMA listed by decreasing relative intensity.

			Band position (nm)	
Sample	N [a]	Fig.	1	2
feu	1	4*a*	350	300
	2	4*b*	280	395
fer	1	4*c*	335	
	2	4*d*	285	
foa	1	4*e*	350	
	2	4*f*	280	390
fch	1	4*g*	350	
	2	4*h*	280	390
fla	1	4*i*	355	
	2	4*j*	285	
ful	1	4*k*	280	335
fuao1	1	4*l*	395	
	2	4*m*	465	
fuao2	1	4*n*	285	390
	2	4*o*	470	

[a]Component number.

Interaction with the Cu(II) ion

Self-modeling mixture analysis

The bands of each spectral data show different sensitivity towards the Cu(II) ion, owing to different complexation properties of the corresponding fluorescent structures. Any attempted detailed visual analysis of the observed spectral variations is useless, because of the large number of samples and different types of variations in the spectra. To overcome this difficulty, the three-dimensional spectral sets were analyzed by SIMPLISMA to reduce the information to a small number of components, each one characterized by a spectrum and a quenching profile (17, 21, 22). The quenching profile of the component (resulting from complex formation) that corresponds to the largest variation in each case permits an estimation of the respective equilibrium parameters (conditional stability constant and binding site concentration).

For all samples except ful, the SIMPLISMA analysis of the spectral sets, using criteria similar to those described previously (17), showed the existence of two components with linearly independent variations as the concentration of Cu(II) is increased. For ful, only one component was detected. The first of the two components is associated with the quenching provoked by the Cu(II) ion and the second to a non-varying (or showing a small variation) SyF spectrum. The first component is due to the binding structures that form stable complexes with Cu(II), while the second refers to structures that are not involved in the complexation, i.e., not accessible to the metal ion, or that form weak complexes with it.

The calculated spectra of the components for the eight samples are shown in Fig. 4 and, as examples, the concentration profiles for the feu and fuao2 samples are presented in Fig. 5. Table 4 shows the main bands of the SyF spectra of Fig. 4.

Inspection of Fig. 4 and Table 4 shows the following: (*i*) the main band of the first component, located at 350–355 nm, is observed in the feu, foa, fch, and fla samples; (*ii*) the main band of the second component, located at 280–285 nm, is observed in all the LLE samples and in fuao1; a second band, located at 390–395 nm, is present in the feu, foa, fch, and fuao1 samples. This result shows the existence of similarities both in the intrinsic SyF properties of the samples under analysis and in the variations imposed on those properties by the Cu(II) ion. Although the variations observed in the SyF spectra for each sample upon Cu(II) addition are now explained by a small number of spectra instead of the original set, this number is still too high to allow a detailed overall visual comparison. Therefore multidimensional pattern recognition techniques were applied to detect the similarities between them, as discussed below.

Figure 5*a* shows typical quenching profiles, i.e., the quenching of fluorescence as a function of the Cu(II) concentration, calculated for the two components of the feu sample. The curve corresponding to the first component shows the characteristic quenching, provoked by the Cu(II) ion, on the fluorescence of a binding site (17–20), while that for the second component shows little variation, indicating that the corresponding fluorescent structures are not involved in complexation reactions. The same observations can be made for the concentration profiles of the FA (Fig. 5*b* shows the profile for the fuao1 sample), but the curve for the second component is characterized by a larger quenching than for the LLE. This suggests that some of the structures that correspond to the second component of the soil FA samples compete with those of the first component for the complexation of Cu(II) ion.

Similarity analysis of the spectra of the detected components

Figure 6 shows typical dendrograms obtained in the cluster analysis (23) of the spectra of Fig. 4 (the variables are

© 1998 NRC Canada

Fig. 3. SyF spectra of the LLE and FA samples as function of the Cu(II) concentration: (*a*) feu; (*b*) fer; (*c*) foa; (*d*) fch; (*e*) fla; (*f*) ful; (*g*) fuao1; and (*h*) fuao2.

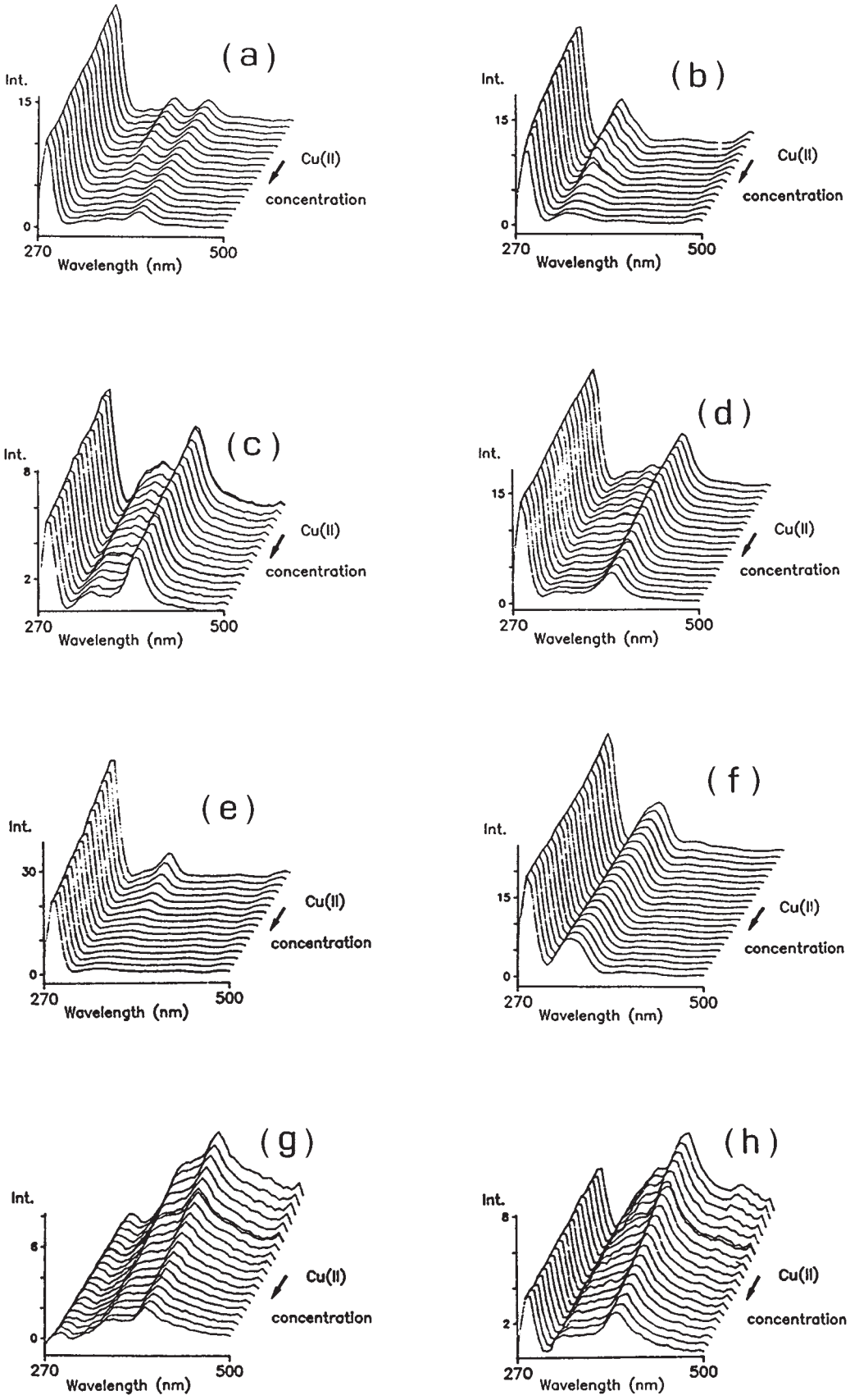

© 1998 NRC Canada

Fig. 4. SyF spectra of the detected components of the LLE and FA samples: (*a*, *b*) feu; (*c*, *d*) fer; (*e*, *f*) foa; (*g*, h) fch; (*i*, *j*) fla; (*k*) ful; (*l*, m) fuao1; (*n*, *o*) fuao2. Table 4 shows the position (nm) of the main bands.

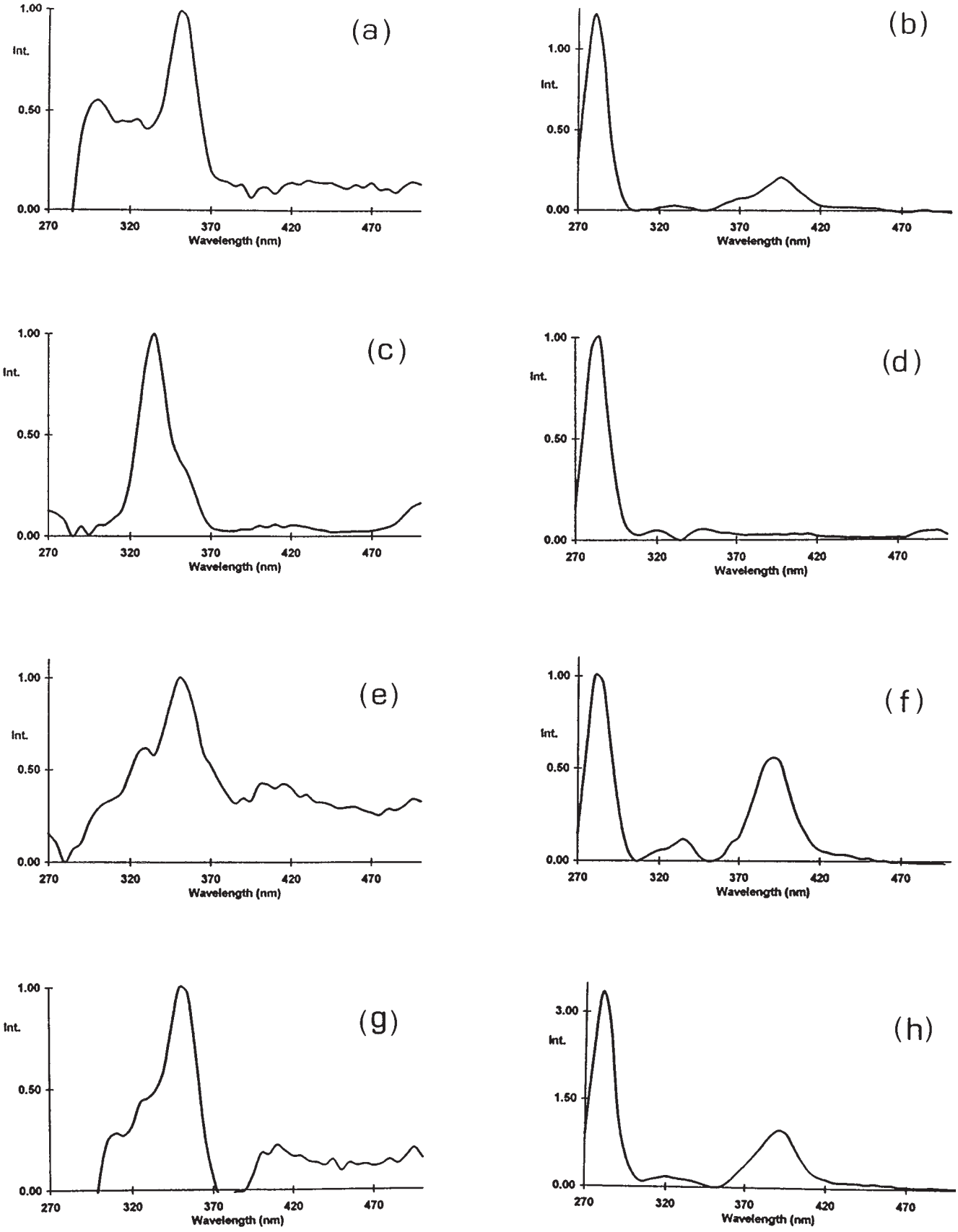

© 1998 NRC Canada

Fig. 4 (*concluded*).

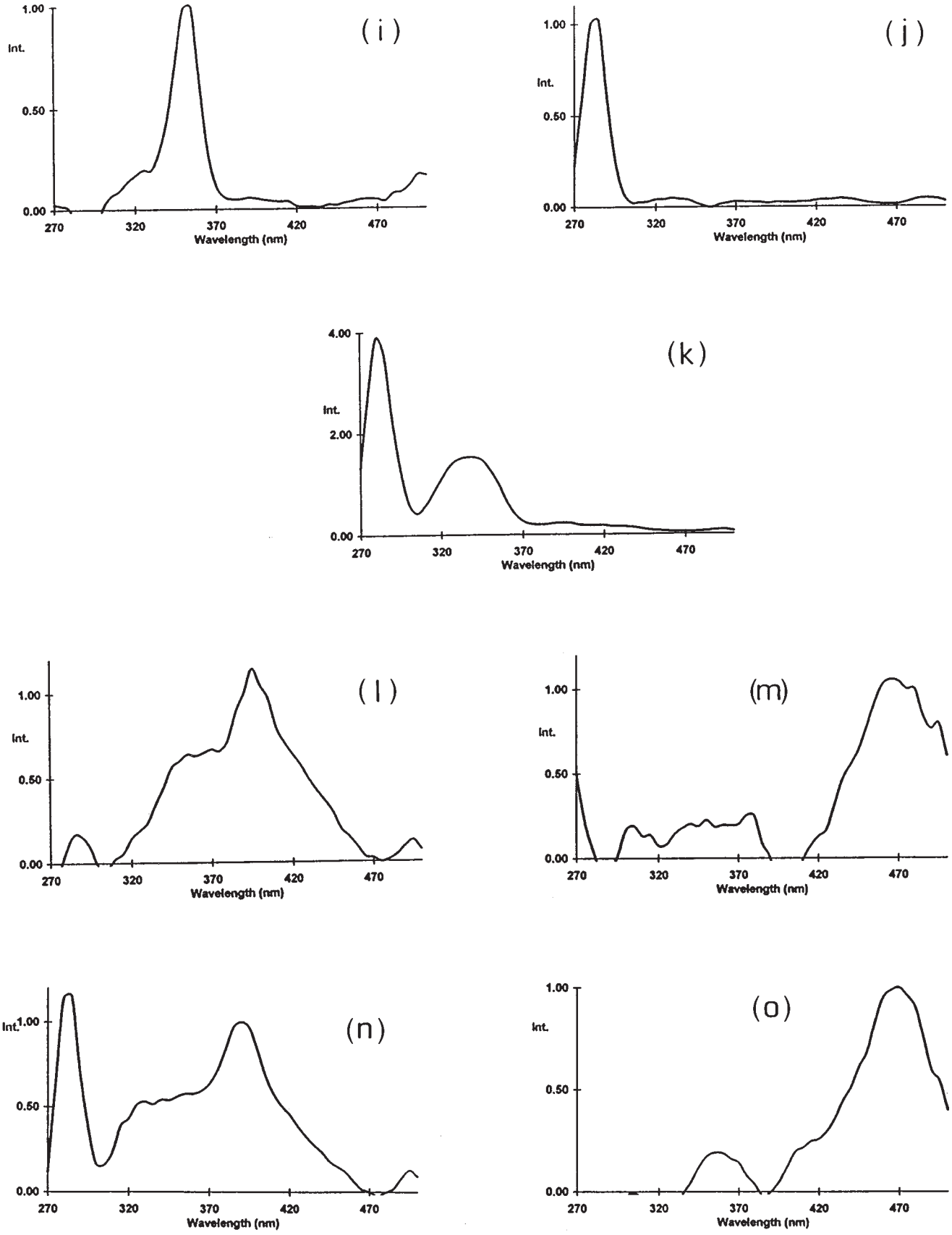

© 1998 NRC Canada

Fig. 5. Concentration profiles of the (▲) first and (■) second components of (*a*) feu and (*b*) fuao1.

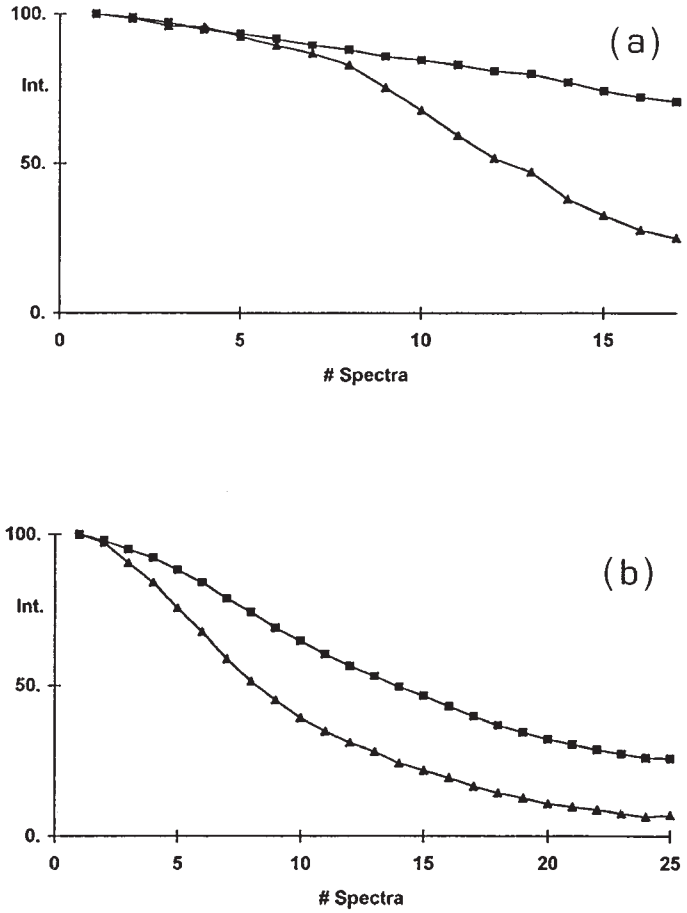

the wavelengths) and Fig. 7 the nonlinear map resulting from their multidimensional scaling (24).

The shape of the dendrograms (Fig. 6) indicates that several well-defined clusters of spectra occur, because quite a number of agglomerations are observed in the high similarity zone. Using the similarity slit for cluster identification included in the dendrogram obtained when the average linkage (between groups) method was used (Fig. 6*a*), which is less than 1/5 of the total similarity scale, seven clusters are detected, named from I to VII. The composition of these seven classes is presented in Table 5. Using the same approach for the analysis of the dendrogram obtained by the Ward method, shown in Fig. 6*b* (now with a similarity slit of about 1/10 of the total similarity scale), the same seven clusters are detected.

Figure 7 shows the nonlinear map obtained from the multidimensional scaling of the calculated spectra of the components and includes schematic borders to indicate the previously detected classes. The goodness-of-fit of this scaling, given by the stress value, is 0.063. The distribution observed in Fig. 7 is compatible with the results of the cluster analysis and confirms that the elements within clusters I–IV are very similar, particularly those of clusters I and III. The analysis of Fig. 7 also shows that the one-element clusters V–VII are very dissimilar from all the others.

By considering the similarity of the clusters and their composition (Table 5), the following conclusions can be drawn: (*i*) the nature of the fluorescent structures and that of the qualitative composition of the binding site are very similar in the feu, fer, foa, and fla LLE but quite different from all the others; (*ii*) the same situation is observed for the soil FA samples, fuao1 and fuao2; (*iii*) the fch and ful LLE have unique fluorescent structures and qualitative compositions of the binding site. The dissimilarity of the ful sample agrees with the differences detected in its elemental analysis (relatively high H/C and N/C ratios).

Table 5. Composition of the classes detected in the cluster analysis.

Class	Classification	Elements
I	LLE	feu(2); fer(2); foa(2); fla(2)
II	FA	fuao2(1); fuao1(1)
III	LLE	feu(1); fer(1); foa(1); fla(1)
IV	FA	fuao2(2); fuao1(2)
V		fch(1)
VI		fch(2)
VII		ful(1)

Calculation of the equilibrium parameters

Table 6 presents the results of the nonlinear fitting to eq. [4] above of the observed quenching profiles for the component of each sample that shows larger quenching. The values of the parameters ΔE and SSR indicate that the quality of the fitting is quite good for all cases. Indeed, these

© 1998 NRC Canada

Fig. 6. Dendograms from the cluster analysis of the spectra shown in Fig. 4: (*a*) average linkage (between groups) method; and (*b*) Ward's method.

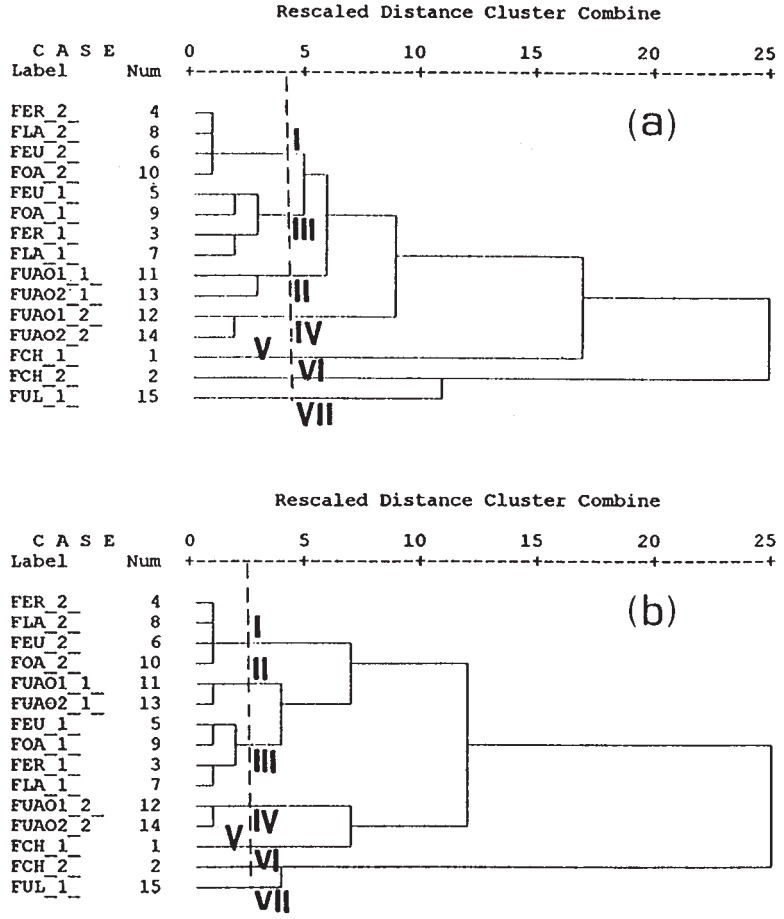

Fig. 7. Nonlinear map of the spectra shown in Fig. 4. The composition of the classes detected is shown in Table 5.

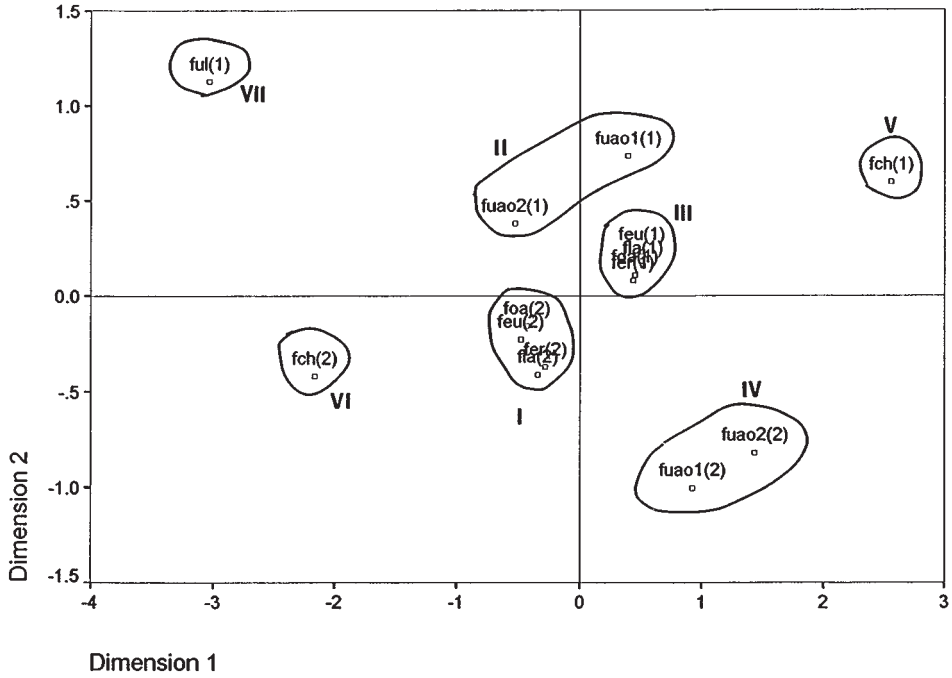

© 1998 NRC Canada

Table 6. Equilibrium parameters for the complexation of Cu(II) by LLE and FA. [a]

Sample	log K_c	Conc	I_{CuL}	N_p	ΔE	SSR	ΔCu
feu	5.35(1)	0.11(2)	35(4)	13	0.30	2.1	0.008–0.1
fer	5.8(2)	0.057(9)	20(3)	9	0.30	1.6	0.007–0.09
foa	4.5(1)	0.13(2)	20(6)	17	0.36	3.2	0.01–0.1
fch	5.05(7)	0.13(1)	22(4)	12	0.45	4.1	0.008–0.2
fla	5.0(2)	0.04(1)	9(3)	13	0.36	2.9	0.005–0.1
ful	4.1(1)	[b]	77(2)	18	0.22	1.4	0.03–0.3
fuao1	4.43(7)	0.03(2)	1(1)	21	0.41	5.1	0.005–0.3
fuao2	4.6(2)	0.04(1)	4(2)	21	0.22	1.8	0.004–0.3

[a]log K_c: logarithm of the conditional stability constant; Conc.: concentration of the ligand (mM); I_{CuL}: fluorescence intensity value at the end of the titration; N_p: number of points used in calculations; ΔE: average deviation of the estimates; SSR: sum of squares of residuals; ΔCu: Cu(II) concentration range used in calculations (mM). Average and average deviations of three independent experiments in parentheses for log K_c, Conc., and I_{CuL} and typical values for the other parameters.
[b]No convergence within reasonable values was observed.

parameters are always relatively small (SSR < 6 and ΔE < 0.5), particularly ΔE, because the experimental error of the SyF measurement is about one fluorescence intensity unit.

I_{CuL} is the lower limit of fluorescence achieved when all the corresponding binding sites are bounded to Cu(II) and, because the complex is usually nonfluorescent (17, 18), corresponds to the percentage of fluorescent structures not accessible for complexation. Data in Table 6 show that this parameter depends on the sample and ranges from zero (fuao2) to 77 (ful). Four of the LL samples (feu, fer, foa, and fch) have values ranging between ca. 20 and 30 units, while the fla and ful samples have, respectively, a relatively lower (I_{CuL} = 9) and a much higher (I_{CuL} = 77) value. The soil FA samples have values of I_{CuL} near zero. This and the existence of other SyF bands with quite small quenching show that the LLE have a relatively higher percentage than soil FA of fluorescent material that does not interact with Cu(II).

Comparison of the conditional stability constants shows that most of the LLE samples have higher values (log K_c > 5), but two (foa and ful) have log K_c close to those of soil FA (log K_c around 4.5). The log K_c values for fuao1 and fuao2 are similar to those of other samples of the same type found in the literature (17–19).

Although the methodology used for equilibrium parameter estimation provides only rough estimates of the concentration of binding sites (17–20), the values of C_L in Table 6 provide semiquantitative information about the number of binding sites for Cu(II) present in the samples. While feu, foa, and fch have a higher concentration of binding sites (C_L > 0.1 mM) than the soil FA samples (C_L around 0.04 mM), fer and fla have lower. No value for C_L could be obtained for the ful sample, probably because it is much smaller than the remainder.

The differences in the complexation properties (K_c and C_L) and in the percentage of fluorescent structures not accessible for complexation (I_{CuL}) observed between LLE and FA are related to structural differences in the two materials. LLE include a wide range of aliphatic and aromatic, amine, carboxylic, and hydroxylic molecules with low molecular weight. The carboxylic acid structures, probably together with hydroxylic groups, form relatively stable complexes with Cu(II), contributing to relatively high stability constants and C_L values. Fluorescent structures without Cu(II) binding capacity remain uncomplexed, contributing to relatively high I_{CuL} values, i.e., the percentage of fluorescent structures not accessible for complexation is relatively high. Conversely, the FA are constituted by relatively high molecular weight molecules containing "humified" conjugates with carbonyl, ester, and hydroxyl groups having a lower binding constant (K_c), but if these groups are more evenly distributed, a larger fraction would be available for quenching (providing relatively lower I_{CuL} values).

The global analysis of the equilibrium parameters shown in Table 6 shows that these are compatible with the clusters found in the similarity analysis of the SyF spectra, with two exceptions: (*i*) the stability constant of the foa sample is somewhat smaller than those for the other members of clusters I and III (feu, fer, and fla); and (*ii*) the equilibrium parameters obtained for the fch sample are similar to those of the other LLE, but no similarity was observed in the analysis of the SyF spectra of the components.

Conclusion

The methodology for the study of FA and like substances presented in this paper proved to be useful for the classification of this type of substance and permits the detection of fine details.

With reference to the characterization of the LLE, this study provided comparative information on structural features and quantitative data about the complexation of Cu(II) by these substances. From a qualitative point of view, different materials originate in similar LLE (feu, fer, foa, and fla), which proved to be different from the soil FA. Spectroscopic results (FT-IR and SyF) suggest a higher ratio of aliphatic/aromatic structures for the LLE than for soil FA. Because LLE contain such reactive structures as alkene and protein residues, they are expected to undergo chemical transformations to HS in a relatively short time. Moreover, the binding sites for Cu(II) that exist in LLE are mainly composed of one type of structure, while those in soil FA show a higher degree of mixture.

The LLE (with the exception of ful) show an overall larger complexation capacity for Cu(II) than soil FA samples. This result confirms that these substances may play an important role in the retention of metal ions in the superficial soil horizons and may be active participants in their transport into the soil.

© 1998 NRC Canada

Acknowledgments

A Praxis XXI Nr 2/2.1/QUI/294/94 project grant from JNICT (Lisbon) is acknowledged. Researcher exchange grants AILE E35/95, from CRUP (Portugal), and B13/95, from MEC (Spain), are also acknowledged.

References

1. F.J. Stevenson. *In* Humic substances in soil, sediment and water. *Edited by* G.R. Aiken, D.M. McKnight, R.L. Wershaw, and P. MacCarthy.Wiley, New York. 1985. Chap. 2.
2. L.J. Evans. Environ. Sci. Technol. **23**, 1046 (1989).
3. P. Blaser and G. Sposito. Soil Sci. Soc. Am. J. **51**, 612 (1987).
4. W. Shotyk and G. Sposito. Soil Sci. Soc. Am. J. **52**, 1293 (1988).
5. N. Senesi, G. Sposito, and G.R. Bradford. Forest Sci. **35**, 1040 (1989).
6. W. Shotyk and G. Sposito. Soil Sci. Soc. Am. J. **54**, 1305 (1990).
7. G. Sposito, N. Senesi, and K.M. Holtzclaw. Soil Sci. Soc. Am. J. **52**, 632 (1988).
8. E.M. Thurman. *In* Humic substances and their role in the environment. *Edited by* F.H. Frimmel and R.F. Christman. Wiley, New York. 1988. pp. 31–43.
9. C.S.P.C.O. Silva, J.C.G. Esteves da Silva, and A.A.S.C. Machado. Appl. Spectrosc. **48**, 363 (1994).
10. J.C.G. Esteves da Silva, A.A.S.C. Machado, and T.M. Garcia. Appl. Spectrosc. **49**, 1500 (1995).
11. J.C.G. Esteves da Silva, A.A.S.C. Machado, and C.S.P.C.O. Silva. Anal. Chim. Acta, **318**, 365 (1996).
12. J.C.G. Esteves da Silva, M.A. Ferreira, A.A.S.C. Machado, and F. Rey. Anal. Chim. Acta, **333**, 71 (1996).
13. G.R.Aiken. *In* Humic substances in soil, sediment and water. *Edited by* G.R. Aiken, D.M. McKnight, R.L. Wershaw, and P. MacCarthy. Wiley, New York. 1985. Chap. 14.
14. N. Senesi, T.M. Miano, and M.R. Provenzano. *In* Humic substances in the aquatic and terrestral environment. *Edited by* B. Allard, H. Borén, and A. Grimvall. Springer, Berlin. 1991. pp. 63–73.
15. S.E. Cabaniss. Environ. Sci. Technol. **26**, 1133 (1993).
16. A.A.S.C. Machado and J.C.G. Esteves da Silva. Chemom. Intell. Lab. Syst. **19**, 155 (1993).
17. A.A.S.C. Machado, J.C.G. Esteves da Silva, and J.A.C. Maia. Anal.Chim. Acta, **292**, 121 (1994).
18. J.C.G. Esteves da Silva and A.A.S.C. Machado. Chemom. Intell. Lab. Syst. **27**, 115 (1995).
19. D.K. Ryan and J.H. Weber. Anal. Chem. **54**, 986 (1982).
20. D.K. Ryan and J.H. Weber. Environ. Sci. Technol. **16**, 866 (1982).
21. W. Windig and J. Guilment. Anal. Chem. **63**, 1425 (1991).
22. W. Windig, C.E. Heckler, F.A. Agblevor, and R.J. Evans. Chemom. Intell. Lab. Syst. **14**, 195 (1992).
23. A.K. Jain and R.C. Dubes. *In* Algorithms for clustering data. Prentice Hall, New Jersey. 1988. Chap. 3.
24. S.J. Press. *In* Applied multivariate analysis. Holt, Rinehart and Winston, Inc., New York. 1972. Chap. 15.
25. C. Steelink. *In* Humic substances in soil, sediment and water. *Edited by* G.A. Aiken, D.M. McKnight, R.L. Wershaw, and P. MacCarthy. Wiley, New York. 1985. Chap. 18.
26. Y.P. Chin, G. Aiken, and E. O'Loughlin. Environ. Sci. Technol. **28**, 1853 (1994).
27. N. Belzile, H.A. Joly, and H. Li. Can. J. Chem. **75**, 14 (1997).
28. F.J. Stevenson. *In* Humus chemistry: genesis, composition, reactions. Wiley, New York. 1982. pp. 264–266.
29. W.V. Gerasimowicz, D.M. Byler, and S. Susi. Appl. Spectrosc. **40**, 504 (1986).
30. P. MacCarthy and J.A. Rice. *In* Humic substances in soil, sediment and water. *Edited by* G.A. Aiken, D.M. McKnight, R.L. Wershaw, and P. MacCarthy. Wiley, New York. 1985. Chap. 21.
31. F.J. Stevenson. *In* Humus chemistry: genesis, composition, reactions. Wiley, New York. 1982. pp. 267–277.
32. J.C.G. Esteves da Silva and A.A.S.C. Machado. Analyst, **120**, 2553 (1995).

© 1998 NRC Canada

Solubilité de la β-cyclodextrine dans les mélanges eau – nitrate d'éthylammonium à 25°C

Stéphane Duvivier, Mireille Turmine et Pierre Letellier

Can. J. Chem. Downloaded from www.nrcresearchpress.com by China University of Science and Technology on 09/05/12
For personal use only.

Résumé : Les solubilités de la β-cyclodextrine ont été déterminées dans les mélanges eau – nitrate d'éthylammonium (NEA) à 25°C. Le NEA est un sel fondu à la température ambiante (θ_f = 14°C) miscible à l'eau en toutes proportions. Contrairement aux solvants moléculaires, l'ajout du NEA à l'eau a pour effet de diminuer la solubilité de la β-cyclodextrine. Pour les milieux riches en sel, cette solubilité augmente à nouveau pour atteindre dans le sel fondu pur, environ 20 fois celle de l'eau. Le comportement de la β-cyclodextrine dans les mélanges eau–NEA peut être décrit simplement dès lors que l'on suppose la présence en solution d'un ion complexe associant deux molécules de β-cyclodextrine à un ion éthylammonium, susceptible de précipiter avec l'ion nitrate. La solubilité de la β-cyclodextrine dans les mélanges eau–NEA a été comparée à celle d'autres composés moléculaires (la 3-nitroaniline et la 2,4-dinitrodiphénylamine) et au comportement d'un composé ionique (le bromure de dodécyltriméthylammonium).

Mots clés : nitrate d'éthylammonium, β-cyclodextrine, solubilité, produit de solubilité, complexe d'inclusion.

Abstract : β-Cyclodextrin solubilities were determined in water – ethylammonium nitrate (EAN) mixtures at 25°C. EAN is a molten salt at room temperature (θ_f = 14°C). It is miscible with water in the whole range of mixtures. Unlike molecular solvents, addition of EAN to water involves a decrease of β-cyclodextrin solubility. In mixtures rich in salt, this solubility increases anew. β-Cyclodextrin solubility in pure salt is about 20 times the value in pure water. β-Cyclodextrin behavior in water–EAN mixtures can be easily described by assuming the presence in solution of a complex ion linking two molecules of β-cyclodextrin to one ethylammonium ion, which precipitates with nitrate ion.

Key words: ethylammonium nitrate, β-cyclodextrin, solubility, solubility product, inclusion compounds.

Introduction

Le nitrate d'éthylammonium (NEA) est un sel fondu à température ambiante (température de fusion θ_f = 14°C), miscible en toutes proportions à l'eau (1–3) et à d'autres solvants comme le méthanol (4), ou l'acétonitrile (5). Il démixte partiellement avec le *n*-octanol (6, 7). Les mélanges eau–NEA peuvent être utilisés comme milieux réactionnels. Ils possèdent un produit d'autoprotolyse élevé de l'ordre de 10 qui permet de fixer l'acidité de ces milieux au moyen de solutions tampons (8). Les propriétés redox dans le sel pur ont été également explorées. Le domaine très large d'électroactivité du sel (supérieur à 2 V), et sa conductivité importante, permettent d'envisager son utilisation comme solvant pour la synthèse électrochimique (9). Evans et al. ont montré que le sel pur possédait curieusement des propriétés physicochimiques très comparables à celles de l'eau (10). Ainsi, les amphiphiles ioniques peuvent former des édifices micellaires à des concentrations critiques 5–10 fois supérieures à celles observées en milieu aqueux (11, 12). D'autres types de structures organisées, telles que des bicouches phospholipidiques ou des cristaux liquides (13) ont pu être mises en évidence dans ce milieu salin. L'activité enzymatique de la phosphatase alcaline se conserve dans les mélanges eau–NEA jusqu'à plus de 60% en volume de sel (14). Cette ressemblance de comportement entre l'eau et le sel pur a été attribuée à la capacité de celui-ci de former des structures tridimensionnelles, entre le cation en configuration tétraédrique avec ses trois atomes d'hydrogène donneurs et l'anion plan et ses trois sites accepteurs. Cette structure est différente de celle, également tridimensionnelle, de l'eau qui ne fait intervenir que deux sites d'interaction donneur–accepteur de liaison hydrogène par molécule. Le passage de l'eau au NEA s'accompagne ainsi d'une modification de la structure du milieu. Les variations des grandeurs thermodynamiques (activités, volumes molaires partiels...) entre l'eau et le NEA pur traduisent cette évolution. Il a été ainsi montré que le nitrate d'éthylammonium se comportait comme un «briseur de structure» envers l'eau (5). Par ailleurs, les mélanges eau–NEA se caractérisent par un pouvoir solubilisant important envers les composés moléculaires. Ainsi, les solubilités de la 3-nitroaniline et de la 2,4-dinitrodiphénylamine dans le NEA pur sont de l'ordre de celles que l'on détermine dans un solvant hydro-organique à 70% en masse de méthanol ou encore à 45% en masse de dioxanne (8). Le NEA pur possède, sur ce plan, des propriétés qui le font ressembler à un solvant organique. Ce comportement ambivalent se traduit par la modification des propriétés physicochimiques d'un certain nombre de systèmes lorsqu'on les met en présence de NEA. Il en est ainsi des concentrations micellaires critiques des

Reçu le 26 janvier 1998.

S. Duvivier, M. Turmine et P. Letellier.[1] Laboratoire énergétique et réactivité aux interfaces, EA 1519, Université P. et M. Curie, case 39, 4 place Jussieu, 75252 Paris Cedex 05, France.

1.Auteur à qui adresser toute correspondance. Tél. : 33 1 44 27 36 76. Téléc. : 33 1 44 27 30 35. Mél. : letel@ccr.jussieu.fr

© 1998 NRC Canada

Can. J. Chem. Downloaded from www.nrcresearchpress.com by China University of Science and Technology on 09/05/12
For personal use only.

tensioactifs cationiques qui diminuent tout d'abord lors de l'ajout de sel à l'eau (effet de sel sur les micelles en milieu aqueux), puis qui augmentent fortement pour les milieux les plus riches en sel (stabilisation de l'amphiphile par le milieu).

Un autre exemple, qui fait l'objet de cet article, peut être trouvé avec les variations de la solubilité de la β-cyclodextrine (CD) dans les milieux eau–NEA à 298 K. La β-cyclodextrine est un oligosaccharide cyclique susceptible de fixer, dans l'eau (15–18) et dans les solvants mixtes (19), un certain nombre de composés dans sa cavité interne hydrophobe. Cette propriété est mise à profit dans de nombreux domaines de l'industrie pharmaceutique et cosmétique (20). Malgré la présence à la surface de cette molécule, de groupements hydroxyles susceptibles d'interagir avec le milieu environnant, la solubilité de la β-cyclodextrine est anormalement basse dans l'eau ($C_{sat.}$ = $1{,}6 \times 10^{-2}$ mol L^{-1}) (21). Ce comportement est attribué à l'auto-agrégation par liaisons hydrogènes des molécules de β-cyclodextrine. La méthylation de la cyclodextrine a pour effet d'augmenter la solubilité de ce composé sans pour cela modifier ses propriétés de complexation (22). L'ajout à l'eau d'additifs qui la destructurent, comme le propanol, le DMSO (23), l'urée (24) ou différents sels (25) comme $Ca(NO_3)_2$ et $CaCl_2$, se traduit également par une augmentation de la solubilité de la β-cyclodextrine. Il apparaît ainsi que la solubilité de la β-cyclodextrine est un paramètre directement lié à la structure de l'eau dans le milieu réactionnel. Il était intéressant d'étudier cette grandeur dans les mélanges eau–NEA.

I. Partie expérimentale

I.1. Matériel

Le nitrate d'éthylammonium a été préparé selon une procédure décrite dans une publication antérieure (2). La β-cyclodextrine est un produit commercial de la société Ringdex, Orsan (France). Sa masse molaire est égale à 1135 g mol^{-1}. Le bromure de dodécyltriméthylammonium est un produit Aldrich.

I.2. Procédures

Les mélanges eau–NEA ont été préparés volumétriquement dans des fioles jaugées de 50 mL et versés dans des flacons bouchés. Une quantité suffisante de β-cyclodextrine est introduite dans chaque flacon contenant les mélanges et le NEA pur, de manière à ce que la limite de solubilité soit largement dépassée (100–200 mg de phase solide restent présents dans le milieu). Les solutions sont portées à 40°C, puis mises à agiter en thermostat pendant 48 h à 25°C. De la β-cyclodextrine solide est éventuellement ajoutée à la solution lorsque la quantité initiale s'avère insuffisante. La concentration de β-cyclodextrine saturée est déterminée par dosage potentiométrique en prenant le bromure de dodécyltriméthylammonium comme réactif selon une procédure très générale de dosage par ajout, utilisée par ailleurs pour le dosage des tensioactifs neutres (26) ou l'établissement d'isothermes d'adsorption (27). L'électrode indicatrice de l'ion amphiphile est préparée au laboratoire selon une technique précédemment exposée (20). Les opérations de dosage sont réalisées directement dans le milieu lui-même. La précision du dosage est de l'ordre de 5%.

II. Résultats expérimentaux

Les valeurs des solubilités de la β-cyclodextrine obtenues dans les mélanges eau–NEA sont reportées dans le tableau 1. On constate que la solubilité de la β-cyclodextrine décroît très fortement dès les premiers ajouts de sel. Elle passe par un minimum pour une concentration en NEA de l'ordre de 7 mol L^{-1}, puis augmente à nouveau très fortement. Dans le sel pur, la solubilité de la β-cyclodextrine est environ 20 fois celle de l'eau. Ce comportement de la cyclodextrine diffère également de celui observé dans la plupart des autres solvants (28) dans lesquels la solubilité de la β-cyclodextrine croît dès l'addition du co-solvant.

Le comportement de la β-cyclodextrine diffère également, pour les mélanges eau–NEA, de celui observé pour la plupart des autres molécules. Pour la 3-nitroaniline et la 2,4-dinitrodiphénylamine, la solubilité moléculaire croît dès l'addition du NEA, comme on peut le constater sur le tableau 2 qui regroupe des résultats antérieurs (8) obtenus dans les mêmes milieux. Ce type de variation est caractéristique de la non-spécificité des interactions entre le solvant et les composés moléculaires. Afin de comparer les amplitudes de ces variations nous avons reporté sur la figure 1 les enthalpies libres standard de transfert entre l'eau (E) et la solution saline (S) de la β-cyclodextrine et des deux anilines subtituées. On rappelle que, pour le composé *i*, lorsque sa concentration est suffisamment faible pour identifier les valeurs des concentrations à celles des activités, l'enthalpie libre standard de transfert entre l'eau et le solvant S s'écrit :

$$[1] \qquad \Delta_t G^o_{E\to S}(i) = {}^S\mu_i^\theta - {}^E\mu_i^\theta = RT \ln \frac{{}^E C_{sat}(i)}{{}^S C_{sat}(i)}$$

${}^S\mu_i^\theta$ et ${}^E\mu_i^\theta$ étant les potentiels chimiques standard de *i* en prenant comme référence l'état infiniment dilué.

Nous avons également illustré sur la figure 1, le comportement du bromure de dodécyltriméthylammonium (M^+) (12) en reportant la quantité

$$[2] \qquad Y = \Delta_t G^o_{E\to S}(M^+_{mic.}) - \Delta_t G^o_{E\to S}(M^+_{mono.}) = RT \ln \frac{{}^E cmc}{{}^S cmc}$$

correspondant à la différence des enthalpies libres standard de transfert du cation sous ses formes micellisée et monomère en fonction de la fraction molaire en sel du milieu. La cmc du tensioactif diminue fortement dès l'ajout du NEA à la solution, ce qui correspond au maximum de *Y*. Puis la cmc augmente à nouveau pour les fortes concentrations en sel, ce qui se traduit par une diminution continue de *Y*.

III. Interprétation des résultats

Les mesures de grandeurs d'excès (volume, enthalpies libres) sur les mélanges eau–NEA montrent que, pour des concentrations en sel inférieures à 2 mol L^{-1}, le NEA se comporte essentiellement comme un sel dissocié (2). Ce

© 1998 NRC Canada

Tableau 1. Solubilités et enthalpies libres de transfert de la β-cyclodextrine dans les mélanges eau–NEA.

C_{NEA} (mol L^{-1})	0	1	2	4	6	8	10	11,2
x_{NEA}	0	0,019	0,042	0,1	0,18	0,32	0,60	1
${}^{S}C_{sat}$(CD) (mol L^{-1})	$1,6\cdot10^{-2}$	$1,7\cdot10^{-3}$	$8,4\cdot10^{-4}$	$5,0\cdot10^{-4}$	$4,2\cdot10^{-4}$	$1,0\cdot10^{-3}$	$5,3\cdot10^{-3}$	0,29
$\Delta_t G^o_{E\rightarrow S}$ (J mol^{-1})	0	5555	7301	8587	9019	6869	2737	–7178

Tableau 2. Solubilités de la 3-nitroaniline et de la 2,4-dinitrodiphénylamine et valeurs des concentrations micellaires critiques du bromure de dodécyltriméthylammonium dans les mélanges eau-NEA.

x_{NEA}	C_{sat} (mol L^{-1}) 3-Nitroaniline [a]	C_{sat} (mol L^{-1}) 2,4-Dinitrodiphénylamine [a]	cmc / mol L^{-1} DTA Br [b]
0	$1,26 \times 10^{-2}$	$6,80 \times 10^{-6}$	$1,38 \times 10^{-2}$
0,1	$2,96 \times 10^{-2}$	$3,32 \times 10^{-5}$	$3,60 \times 10^{-3}$
0,2	$7,04 \times 10^{-2}$	$1,38 \times 10^{-4}$	$1,60 \times 10^{-2}$
0,3	0,129	$3,25 \times 10^{-4}$	$3,00 \times 10^{-2}$
0,4	0,194	$6,01 \times 10^{-4}$	$4,40 \times 10^{-2}$
0,5	0,26	$8,49 \times 10^{-4}$	$5,70 \times 10^{-2}$
0,6	0,318	$1,30 \times 10^{-3}$	$7,20 \times 10^{-2}$
0,7	0,355	$1,96 \times 10^{-3}$	$8,50 \times 10^{-2}$
0,8	0,378	$1,99 \times 10^{-3}$	$0,97 \times 10^{-2}$
0,9	0,420	$2,47 \times 10^{-3}$	$1,11 \times 10^{-1}$
0,95	0,430	$2,82 \times 10^{-3}$	$1,18 \times 10^{-1}$
1	0,475	$2,96 \times 10^{-3}$	$1,25 \times 10^{-1}$

[a] Référence 8.
[b] Valeurs interpolées de la réf. 12.

domaine correspond à celui de la très forte diminution de la solubilité de la cyclodextrine. Coleman et al. (28) suggèrent que les additifs qui déstructurent l'eau augmentent la solubilité de la β-cyclodextrine par destruction des agrégats. Si l'on adoptait cette seule hypothèse, pour interpréter les présents résultats, il faudrait en conclure que le NEA renforce la structure de l'eau jusqu'à une fraction molaire x = 0,2 en NEA. Cette affirmation serait en contradiction avec les résultats de Perron et al. (5) qui démontrent qu'au contraire le NEA possède un caractère destructurant affirmé (5, 29).

Le comportement de la β-cyclodextrine s'apparente à celui des tensioactifs ioniques dont la concentration micellaire critique passe par un minimum lorsque l'on ajoute le NEA dans l'eau (voir tableau 2 et figure 1). La diminution de cmc correspond à une stabilisation de l'agrégat micellaire par diminution des interactions électrostatiques entre les têtes polaires de même signe lors de l'augmentation de la densité de charges dans la solution. La relation de Corrin–Harkins (30) rend compte de ces variations. Ceci suggère l'intervention d'une ou plusieurs espèces chargées dans l'équilibre de solubilisation de la β-cyclodextrine. La possibilité pour la β-cyclodextrine d'interagir avec des ions minéraux, comme NO_3^-, ClO_4^- a été évoquée dans plusieurs travaux (31, 32).

Supposons que la β-cyclodextrine (CD) forme, en solution, un complexe d'inclusion (C = $CD(EtA)_n$) avec n ions éthylammonium (E),

$$CD + nE \rightleftharpoons C$$

La constante de cet équilibre fait intervenir les activités des différentes espèces, référées à la solution infiniment diluée dans l'eau pour la β-cyclodextrine et le complexe, et au NEA pur pour l'ion éthylammonium.

$$[3] \qquad K = \frac{a_{CD}\cdot a_E^n}{a_C}$$

Supposons que le complexe intervienne dans un équilibre de solubilité (P = $CD(EtA)_n(NO_3)_n$) avec les ions nitrate (N) du milieu, selon

$$P \rightleftharpoons C + nN$$

Cette écriture suppose que le cation précipité possède une même stoechiométrie que l'ion complexe. Le produit de solubilité s'écrit :

$$[4] \qquad K_S = a_C a_N^n$$

L'activité de l'ion nitrate est également référée au sel pur.

La solubilité de la cyclodextrine, s, s'exprime en fonction des concentrations de CD et C :

$$s = [CD] + [C]$$

On peut considérer que pour les milieux les plus proches de l'eau, la solubilité est suffisamment faible pour que les valeurs des concentrations des cyclodextrines moléculaire et complexée s'identifient à leur activité et que les valeurs des potentiels chimiques standard de ces espèces sont encore peu affectées par la présence de sel (faible effet de solubilisation ou de relargage).

On peut alors écrire :

$$[5] \qquad s = [C]\left(1 + \frac{K}{a_E^n}\right)$$

© 1998 NRC Canada

Can. J. Chem. Downloaded from www.nrcresearchpress.com by China University of Science and Technology on 09/05/12
For personal use only.

Can. J. Chem. Downloaded from www.nrcresearchpress.com by China University of Science and Technology on 09/05/12
For personal use only.

Fig. 1. Enthalpies libres standard de transfert de la β-cyclodextrine (*A*), de la 3-nitroaniline (*C*), de la 2,4-dinitrodiphénylamine (*D*) et enthalpie libre de transfert standard pour la micellisation (grandeur *Y* de l'équation [2]) du bromure de dodécyltriméthylammonium (*B*).

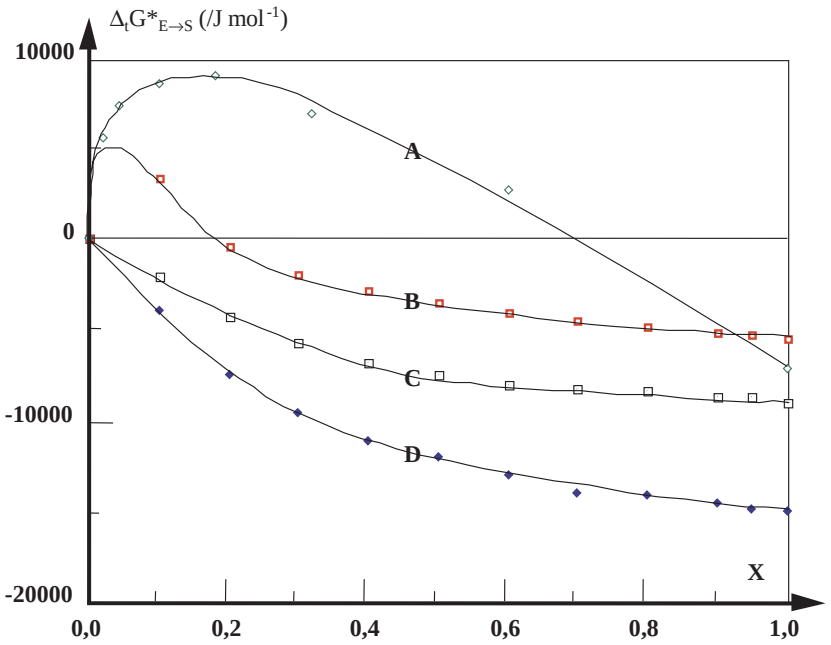

Tableau 3. Valeurs du logarithme de la solubilité de la β-cyclodextrine expérimentale et calculée (relation [9]), et des logarithmes des coefficients d'activité et de l'activité du NEA pour différentes compositions du milieu.

x_{NEA}	ln γ_{NEA}	ln a_{NEA}	ln $s_{exp.}$	ln $s_{calc.}$
0,019	–1,106	–5,07	–6,38	–6,51
0,042	–0,820	–3,99	–7,08	–7,05
0,1	–0,520	–2,82	–7,60	–7,64

soit

$$[6] \qquad K_s = s\left(\frac{a_N^n}{1+\frac{K}{a_E^n}}\right)$$

soit

$$[7] \qquad s = \frac{K_s(a_E^n + K)}{(a_E a_N)^n} = \frac{K_s(a_E^n + K)}{(a_{NEA})^n}$$

l'activité du NEA étant liée à celle de ses ions par la relation :

$$[8] \qquad a_{NEA} = a_E a_N = \gamma_{NEA} X$$

Les valeurs du coefficient d'activité du NEA pur peuvent être calculées au moyen de la relation suivante (3) :

$$[9] \qquad \ln \gamma_{NEA} = -\frac{\Delta_d G_E^\theta}{RT}(\ln x + 1 - x)$$

où $\Delta_d G_E^\theta$ ($\Delta_d G_E^\theta = -919$ J mol^{-1}) est l'enthalpie libre standard de dilution de l'eau pure à dilution infinie dans le sel.

Les valeurs de l'activité du NEA ont été déterminées pour les milieux les plus dilués en sel et reportées dans le tableau 3.

La relation [7] admet plusieurs cas limites selon l'importance de la complexation de l'ion éthylammonium par la β-cyclodextrine dans la solution. Dans le cas particulier où l'on considère un complexe en solution très peu formé, le précipté $CD(EtA)_n(NO_3)_n$ est en équilibre avec la β-cyclodextrine et le nitrate d'éthylammonium selon :

$$CD(EtA)_n\,(NO_3)_n \rightleftharpoons CD + n\,NEA$$

La relation [7] devient alors

$$[10] \qquad s = \frac{K\,K_s}{(a_E\,a_N)^n} = \frac{K}{(a_E\,a_N)^n}$$

K est le produit du complexe de la β-cyclodextrine et du NEA dans le milieu considéré. La relation [10] peut encore être écrite

$$[11] \qquad \ln s = \ln K\,K_s - n \ln a_{NEA}$$

Le tracé de la courbe représentative de ln *s* en fonction de ln a_{NEA} conduit à une droite d'équation :

$$\ln s = -9{,}05 - 0{,}5 \ln a_{NEA}$$

On a reporté dans le tableau 3 les solubilités calculées par cette équation. Elles sont en excellent accord avec les valeurs expérimentales.

Il apparaît ainsi, que le comportement de la β-cyclodextrine dans les mélanges eau–NEA peut être convenablement décrit en supposant qu'il se forme un édifice insoluble associant deux molécules de β-cyclodextrine pour une molécule de NEA en équilibre avec de la β-cyclodextrine en solution et du nitrate d'éthylammonium.

© 1998 NRC Canada

Can. J. Chem. Downloaded from www.nrcresearchpress.com by China University of Science and Technology on 09/05/12
For personal use only.

Le produit des deux constantes est alors égal à :

$$P = KK_s = 1{,}2 \times 10^{-4}$$

Cette valeur relativement petite montre que les associations entre la cyclodextrine et le NEA sont relativement faibles et que la précipitation ne survient que parce que le sel est en forte concentration en solution. Nous avons pu vérifier, au cours des procédures de dosage que la β-cyclodextrine conservait ses propriétés complexantes, même dans le sel pur, envers l'ion dodécyltriméthylammonium. La diminution de la solubilité de la β-cyclodextrine avec l'ajout de nitrate d'éthylammonium à l'eau relève donc d'un effet de sel sur la solubilité et non pas d'un effet de solvant.

Pour les fortes concentrations en sel, le nitrate d'éthylammonium se comporte comme un solvant moléculaire. Celui-ci stabilise la β-cyclodextrine dont la solubilité croît à nouveau malgré l'enrichissement de la solution en ions nitrate. Le phénomène est patent près du sel pur.

Contrairement aux additifs moléculaires, la modification de la structure du milieu ne semble pas jouer un rôle déterminant dans le cas présent sur la solubilité de la β-cyclodextrine.

Conclusions

Contrairement à l'ensemble des solvants moléculaires étudiés par Coleman et al. (28) l'ajout du nitrate d'éthylammonium à l'eau a pour effet de diminuer la solubilité de la β-cyclodextrine. Cette solubilité passe par un minimum puis augmente lorsque le milieu s'enrichit en sel fondu. La solubilité dans le sel fondu pur est importante et comparable à celle déterminée dans des solvants organiques comme le diméthylformamide (28). Les variations de la solubilité de la β-cyclodextrine dans les mélanges eau–NEA peuvent être interprétées simplement dès lors que l'on suppose la formation d'un cation complexe associant deux molécules de β-cyclodextrine à une d'éthylammonium, susceptible de précipiter sous la forme d'un nitrate.

Pour les faibles concentrations en sel, la diminution de la solubilité s'explique alors par un simple effet de sel. Ce cas particulier est complémentaire de celui étudié par Sanemasa et al. (18) qui ont examiné les solubilités de la β-cyclodextrine en présence d'additifs moléculaires. Lorsque le milieu s'enrichit en NEA, le solvant obtenu possède un comportement qui le rapproche des milieux hydro-organiques. Son pouvoir solubilisant augmente par rapport aux espèces moléculaires comme la 3-nitroaniline et la 2,4-dinitrodiphénylamine. La β-cyclodextrine est stabilisée. La valeur de sa solubilité augmente alors continûment jusqu'au sel pur.

Bibliographie

1. M. Allen, D.F. Evans et R. Lumry. J. Solution Chem. **14**, 549 (1985).
2. M. Hadded, M. Biquard, P. Letellier et R. Schaal. Can. J. Chem. **63**, 565 (1985).
3. M. Biquard, P. Letellier et M. Fromon. Can. J. Chem. **63**, 3587 (1985).
4. H. Hadded, A. Mayaffre et P. Letellier. J. Chim. Phys. **86**, 525 (1989).
5. G. Perron, A. Hardy, J.C. Justice et J.E. Desnoyers. J. Solution Chem. **22**, 1159 (1993).
6. M. Bonetti, A. Oleinikova et C. Bervillier. J. Phys. Chem. B, **101**, 2164 (1997).
7. M. Bonetti, C. Bagnuls et C. Bervillier. J. Chem. Phys. **107**, 550 (1997).
8. N. Benlhima, D. Lemordant et P. Letellier. J. Chim. Phys. **86**, 1919 (1989).
9. N. Benlhima, M. Turmine, P. Letellier, R. Naejus et D. Lemordant. J. Chim. Phys. **95**, 25 (1998).
10. D.F. Evans, A. Yamauchi, R. Roman et E.Z. Casassa. J. Colloid Interface Sci. **86**, 89 (1982).
11. D.F. Evans, A. Yamauchi, G.J. Wei et V.A. Bloomfield. J. Phys. Chem. **87**, 3537 (1983).
12. D. Jezequel, A. Mayaffre et P.Letellier. J. Chim. Phys. **88**, 391 (1991).
13. D.F. Evans, E.W. Kaler et J. Benton. J Phys. Chem. **87**, 533 (1983).
14. D.K. Magnuson, J.W. Bodley et D.F. Evans. J. Solution Chem. **13**, 583 (1984).
15. W. Saenger. Angew. Chem. Int. Ed. Engl. **19**, 344 (1980).
16. R. Lu, J. Hao, H. Wang et L. Tong. J. Colloid Interface Sci. **192**, 37 (1997).
17. D. Jezequel, A. Mayaffre et P. Letellier. Can. J. Chem. **69**, 1865 (1991).
18. I. Sanemasa, J.S. Wu et K. Toda. Bull. Chem. Soc. Jpn. **70**, 365 (1997).
19. J.V. Martin, M. Turmine, P. Letellier et P. Hemery. Electrochim. Acta, **40**, 2749 (1995).
20. J.L. Mesens, P. Putteman et P. Verheyen. *Dans* New trends in cyclodextrins and derivatives. *Édité par* D. Duchêne. Éditions de Santé, Paris. 1991. pp.369–408; D. Duchêne, E. Wouessidjewe et M.C. Poelman. *Dans* New trends in cyclodextrins and derivatives. *Édité par* D. Duchêne. Éditions de Santé, Paris. 1991. pp. 447–482.
21. A.W. Coleman, I. Nicolis, N. Keller et J.P. Dalbiez. J. Inclusion Phenom. **13**, 139 (1992).
22. M. Mokus, R. Gaboriaud, P. Letellier, J. Lelièvre et J.F. Letavernier. J. Chim. Phys. **93**, 1974 (1996).
23. A.K. Chatjigakis, C. Donzé, A.W. Coleman et Ph. Cardot. Anal. Chem. **64**, 1632 (1992).
24. D.Y. Pharr, Z.S. Fu, T.K. Smith et W.L. Hinze. Anal. Chem. **61**, 275 (1989).
25. A. Buvari et I. Barcza. J. Inclusion Phenom. **7**, 379 (1989).
26. M. Turmine, C. Macé, F. Millot et P. Letellier. Anal. Chem. Soumis.
27. M.P. Gloton, A. Mayaffre, M. Turmine, P. Letellier et H. Suquet. J. Colloid Interface Sci. **172**, 56 (1995).
28. A.W. Coleman, M. Munoz, A.K. Chatjigakis et Ph. Cardot. J. Phys. Org. Chem. **6**, 651 (1993).
29.- J.F. Côté, J.E. Desnoyers et J.C. Justice. J. Solution Chem. **25**, 113 (1996).
30. M.L. Corrin et W.D. Harkins. J. Am. Chem. Soc. **69**, 683 (1947).
31. H. von Dietrich et F. Cramer. Chem. Ber. **87**, 806 (1954).
32. E.A. Lewis et L.D. Hansen. J. Chem. Soc. Perkin Trans. 2, 2081 (1973).

© 1998 NRC Canada

vic-Diacrylic ester porphyrins as starting materials for monobenzoporphyrin and *opp*-dibenzoporphyrin syntheses

Arezki Boudif, Sandrine Gimenez, Bernard Loock, and Michel Momenteau

Abstract : Synthesis of a bis(*vic*-diacrylic ester) porphyrin using the "3+1" methodology is described. A two-step procedure is used to convert the *vic*-diacrylic ester porphyrin and the bis(*vic*-diacrylic ester) porphyrin to the monobenzoporphyrin and the *opp*-dibenzoporphyrin, respectively. Characterization of the compounds by ^{1}H NMR and UV–visible spectroscopies is also discussed.

Key words: tripyrrane, diformylpyrrole, *vic*-diacrylic ester porphyrin, "3+1" synthesis methodology, monobenzoporphyrin, *opp*-dibenzoporphyrin, photosensitizer.

Résumé : Nous décrivons la synthèse de la tétra (acrylate d'éthyle) porphyrine, également appelée bis(*vic*-diacrylate de diéthyle) porphyrine, en utilisant la méthode « 3+1 » de synthèse des porphyrines. Une séquence réactionnelle comportant deux étapes est ensuite utilisée pour convertir les groupes acryliques de la *vic*-(acrylate d'éthyle) porphyrine et de la bis(*vic*-diacrylate de diéthyle) porphyrine, et obtenir une monobenzoporphyrine et une dibenzoporphyrine, respectivement. La caractérisation des composés, par RMN du proton et par spectroscopie UV–visible, est rapportée et discutée.

Mots clés : tripyrrane, diformylpyrrole, *vic*-di(acrylate d'éthyle) porphyrine, méthode de synthèse « 3+1 », monobenzoporphyrine, dibenzoporphyrine, photosensibilisateur.

Introduction

Benzoporphyrins, especially the lower analog mono- and dibenzoporphyrins, are interesting chromophores that may find application as photosensitizers in photodynamic therapies (PDT). Indeed, a new generation of photosensitizers is needed to accompany the development of this new therapy. In this regard, criteria for an efficient photosensitizer have been established (1, 2): (*i*) a well-defined structure with large absorption coefficients in the red region; (*ii*) a high yield in the energy transfer process leading to $^1O_2$ and (or) $(O_2)^-$ reactive species; (*iii*) no toxicity in the absence of light; (*iv*) a preferential retention in tumor tissues and rapid evacuation from normal tissues.

Our objective in this work is to design porphyrins with expanded aromatic systems and bearing substitutents that could be easily converted to permit water solubility. Herein is reported the development of a short route for the synthesis of a monobenzoporphyrin **1** and an *opp*-dibenzoporphyrin **2**, in which the benzene isocycles are substituted by two ester groups. The starting material for the synthesis of **1** (Scheme 1) is the *vic*-diacrylic ester porphyrin **3**, whereas **2** (Scheme 2) was obtained from the bis(*vic*-diacrylic ester) porphyrin **4**.

Work on monobenzoporphyrins was initially motivated by the desire to determine a common structure (and to confirm some structural assumptions) of a series of petroporphyrins showing a rhodo-type electronic absorption spectrum. In pursuit of this aim, Clezy et al. (3) reported the preparation of monobenzoporphyrins using two different routes (Scheme 3, routes a and b). In the first approach, the starting material was a free-base porphyrin bearing a six-membered ring as a precursor of the isocycle (Scheme 3, route a). The second approach involved the formation of the benzene isocycle on a preformed zinc porphyrin. This was achieved through a Dieckmann cyclization on a pyrrole subunit conveniently substituted by propionic and acetic side chains (Scheme 3, route b). Investigating the ring-closure process, Chaudhry and Clezy (4) reported unsuccessful attempts to cyclize divinyl porphyrins in order to obtain monobenzoporphyrins. In contrast, di-(2-chloroethyl)porphyrins undergo a cyclization process to lead to a very low yield (about 1%) of monobenzoporphyrin. However, the aromatization of a cyclohexenylporphyrin isolated as a minor product (about 5%) in the basic treatment of the *vic*-divinylporphyrin afforded the desired monobenzoporphyrin.

Extension of the macrocycle π-system is one of the approaches to increase absorption in the red. Thus Bonnett and McManus (5) reported the synthesis of *opp*-dibenzoporphyrins by self-condensation of benzopyrromethene hydrobromides and later Smith and co-workers (6) also reported synthesis of an *opp*-dibenzoporhyrin in which the two benzo isocycles had been generated by aromatization of cyclohexyl moieties. In addition to purpurins in which a

Received January 26, 1998.

A. Boudif. [1] The University of Iowa, Department of Chemistry, Iowa City, IA 52242-1294, U.S.A.
S. Gimenez, B. Loock, and M. Momenteau. Institut Curie-Recherche, Unité Mixte de Recherche 176 du Centre national de la recherche scientifique, Bat. 112, Université Paris Sud, 91405 Orsay, France.

[1]Author to whom correspondence may be addressed. Fax: (319) 335-1333. E-mail: barezki@blue.weeg.uiowa.edu

© 1998 NRC Canada

Scheme 1.

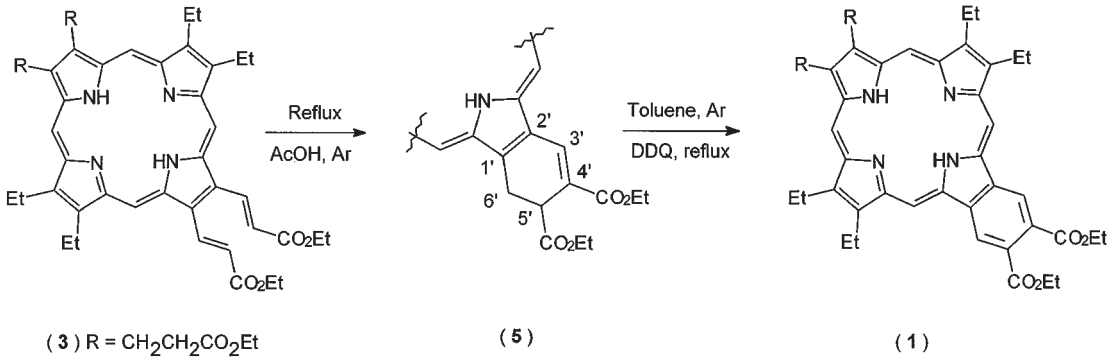

Scheme 2.

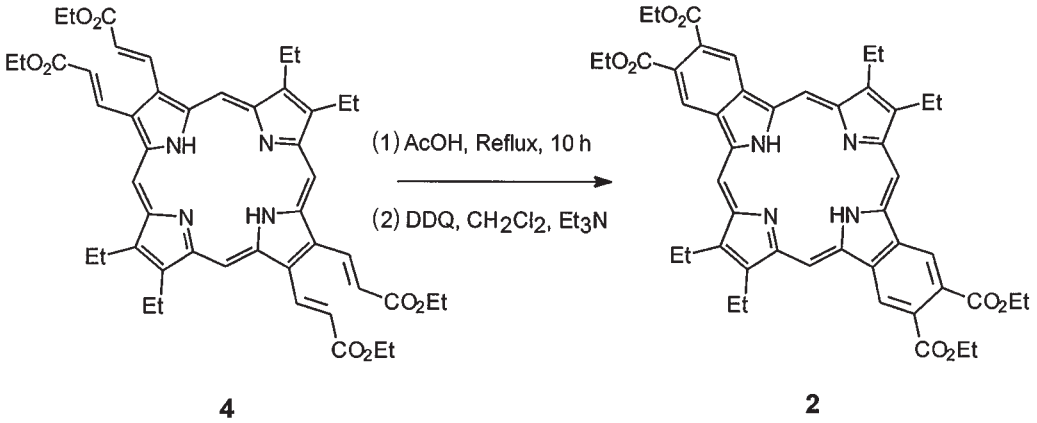

Scheme 3.

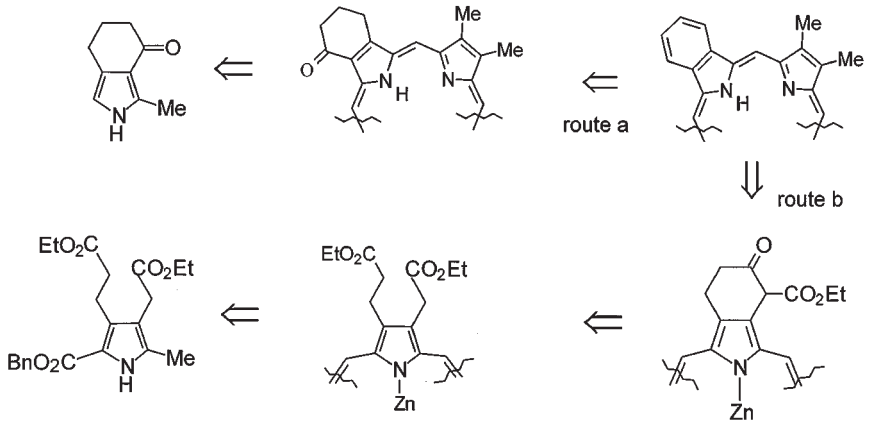

fused conjugated five-membered isocycle provides an interesting absorption feature (7), synthesis and evaluation of other types of photosensitizers have been reported in the literature. Among these are benzochlorins (8–10), which combine the extension of the π-system of the macrocycle and the absorption pattern of chlorins for a promising approach.

Results and discussion

In previous reports, we have described the preparation of vicinal diacrylic ester porphyrins using the "3+1" methodology, including the porphyrin **3** (Scheme 1) (11, 12). The same strategy was applied to the synthesis of the tetra acrylic ester porphyrin **4** (Scheme 2), also designated as the bis(*vic*-diacrylic ester) porphyrin. Starting from the 3,4-di(ethoxycarbonylvinyl)-2,5-dimethylpyrrole **6** (Scheme 4), the α- and α′-methyl groups have been oxidized either to obtain the 2,5-diacetoxymethylpyrrole **7** or the 2,5-diformylpyrrole **8**. We have described the preparation of these two compounds in a previous publication (12). However, in order to improve the yield of the reaction leading to the diformylpyrrole **8**, we have undertaken a modification of the procedure. Indeed, when the dimethyl derivative **6** was heated in the presence of 4 equivalents of $Pb(OAc)_4$ in glacial acetic acid, followed by the hydrolysis of the intermediate (probably the dihemiacetal pyrrole), the diformyl pyrrole

© 1998 NRC Canada

Scheme 4.

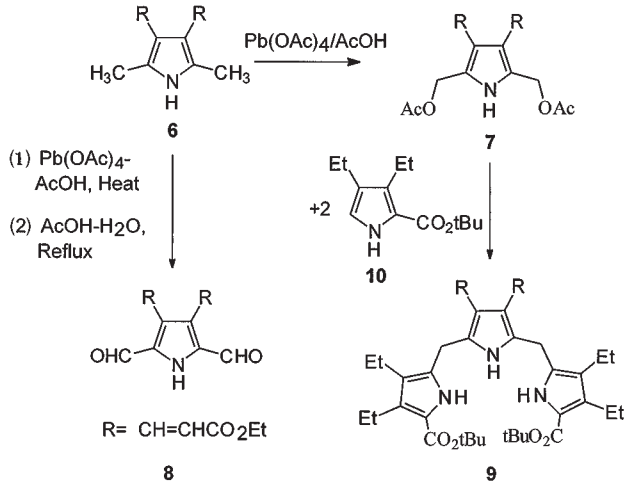

8 was isolated in 30% yield. Synthesis of the tripyrrane **9** (Scheme 4) was achieved by condensation of 2 equivalents of the α-free position pyrrole **10** with the 2,5-diacetoxymethylpyrrole **7**, catalyzed by an acidic clay (Montmorillonite K 10). The pyrrole **10** was prepared according to the procedure reported by Zard, Barton, and co-workers (13). Protection of the 1- and 14-positions of the tripyrrane **9** by *tert*-butyl esters, instead of benzyl esters, allowed us to remove these moieties without reducing the acrylic double bonds. Tripyrrane **9** was then treated with TFA and stirred for 4 h at room temperature before adding the diformylpyrrole **8** in dry methylene chloride. This mixture was then stirred for 16 h in the dark. Addition of 2,3-dichloro-5,6-dicyano-1,4-benzoquinone (DDQ) completed the oxidation of the resulting porphyrinogen and the bis(*vic*-diacrylic ester) porphyrin **4** was isolated in 40% yield. When the porphyrin **3** in acetic acid solution was heated at reflux under argon, the ring closure occurred to afford quantitatively the cyclohexenylporphyrin **5** (Scheme 1). However, it is unlikely that acetic acid could protonate the acrylic double bonds under these conditions. Therefore, the formation of the cyclohexenyl ring could result from a thermal intramolecular Diels–Alder reaction followed by a rearrangement of the π-system. Porphyrin **5** was then refluxed in toluene, in the presence of 4 equivalents of DDQ. The oxidation–aromatization process led to the monobenzoporphyrin **1** (Scheme 1) in 64% yield.

A second product of this reaction was identified as the diacrylic ester porphyrin **3** resulting from a retro Diels–Alder process. The same procedure as described above was applied to convert the porphyrin **4** into a bis(cyclohexenyl) porphyrin. As expected, this reaction gave a mixture of intermediate isomers that was used in the following step without further purification. During the oxidation–aromatization step, triethylamine was added to minimize the six-membered ring opening, as mentioned in the case of **5**. The *opp*-dibenzoporphyrin **2** was then isolated in 40% yield (Scheme 2). Identification of porphyrins **1**, **2**, **4**, and **5** was achieved by ^{1}H NMR in $CDCl_3$. In the case of the cyclohexenylporphyrin **5**, the *meso* protons are magnetically nonequivalent since they give four singlets near 10 ppm. One can note the disappearance of the doublets at 9.28 and

Fig. 1. UV–visible absorption spectra of **1** (——) and **2** (——) in CH_2Cl_2.

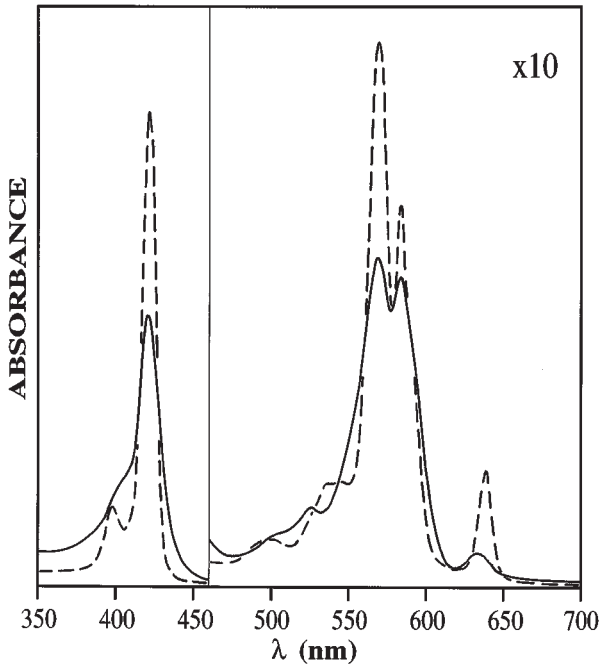

7.05 ppm, corresponding to acrylic protons of compound **3**. These were replaced by weakly coupled doublets at 5.03 and 5.12 ppm attributable to protons borne by the 5′-asymmetric carbon. Protons at the 6′-position appear as a multiplet at 5.48 ppm. The proton NMR spectrum of porphyrin **1** showed two singlets at 10.2 and 10.3 ppm for the *meso* protons and a singlet at 9.62 ppm for the 3′- and 6′-protons of the isocycle, suggesting the presence of a plane of symmetry and thus confirming the aromatization of the six-membered isocycle. NMR spectra of **2** and **4** were even simpler because of the presence of two planes of symmetry. Indeed, *meso* proton signals for each of these porphyrins were seen as singlets at 9.66 and 9.84 ppm, respectively. One should note the striking influence of the substituted benzene groups on the NH resonances, resulting in an upfield shift (–5.93 ppm in $CDCl_3$), in comparison to the shifts of the same groups in the 7,8,17,18-dibenzo-2,3,12,13-tetraethylporphyrin (δ, –2.65 ppm) reported by Smith and co-workers (5).

UV–visible electronic spectra (Fig. 1) of compounds **1** and **5** in dichloromethane show oxorhodo-type spectra. This spectral type is generally obtained when substituents in appropriate relative positions exercise a strong electron-withdrawing effect on the porphyrin macrocycle. Although monobenzoporphyrins reported by Clezy et al. (3) show a rhodo-type spectrum, the absorption feature shown by **1** seems to be consistent with the proposed structure since the electronic effect exercised by the two carboxyl groups is still evident due to the extension of the conjugated system. The same general absorption feature was observed in the case of the dibenzoporphyrin **2**.

From the synthetic point of view, this reaction sequence is an advantageous route allowing conversion of two peripheral acrylic groups, at the vicinal β-pyrrolic positions on porphyrins, into a six-membered conjugated isocycle. The route

© 1998 NRC Canada

will be of interest to chemists wishing to develop a new generation of chromophores as potent photosensitizers for photodynamic therapies.

Experimental section

3,4-Di(ethoxycarbonyl vinyl)-2,5-diformyl pyrrole 8

A suspension of lead tetraacetate (9.75 g, 22 mmol) and the 3,4-di(ethoxycarbonyl vinyl)-2,5-dimethyl pyrrole (1.45 g, 5 mmol) in glacial acetic acid (75 mL) was heated at 80–90°C for 2 h. Afterwards, the resulting solution was concentrated under vacuum, diluted with CH_2Cl_2, washed with water, neutralized with aqueous $NaHCO_3$ solution, and washed again with water. The organic layer was ultimately dried over Na_2SO_4 and the solvent was evaporated. The purpose of this first work-up was to remove lead salts. The solid was dissolved again in acetic acid (50 mL). An equal volume of H_2O was added and the mixture was heated at 80°C, for an hour. The solvent was evaporated under vacuum and the residue was dissolved in dichloromethane. This organic phase was treated with an aqueous solution of $NaHCO_3$, washed with water, and dried over Na_2SO_4. The drying agent was removed by filtration and the concentrated solution of the crude product was chromatographed on a silica gel column eluting with CH_2Cl_2/Et_2O (10/1, v/v), then (10/2, v/v). After evaporation of the solvent, the diformylpyrrole **8** (0.48 g, 30%) was obtained as a white solid. ^{1}H NMR ($CDCl_3$, 200 MHz), δ, ppm: 10.62 (1H, br, NH), 9.96 (2H, s, CHO), 7.85 (2H, d, $J_{HH\ trans}$ = 16 Hz, CH=), 6.28 (2H, d, $J_{HH\ trans}$ = 16 Hz, =CH), 4.25 (4H, q, CH_2CH_3), 1.3 (6H, t, CH_2CH_3). Anal. calcd. for $C_{16}H_{17}NO_6$: C 60.18%, H 5.33%, N 4.38%; found: C 59.22%, H 5.78%, N 3.91%.

1,4-Di(*tert*-butoxycarbonyl)-7,8-diethoxycarbonylvinyl-2,3,12,13-tetraethyl tripyrrane 9

Montmorillonite K-10 clay (1 g) was added to a solution of pyrroles **7** (0.5 g, 1.2 mmol) and **10** (0.630 g, 2 equiv.) in CH_2Cl_2 and the mixture was stirred at room temperature for 6 h. The reaction was monitored by TLC. The clay was removed by filtration and the organic phase was neutralized with aqueous $NaHCO_3$ solution, washed with water, and dried over Na_2SO_4. The crude product was chromatographed over a silica gel column with elution by mixtures of CH_2Cl_2/Et_2O (100/3, v/v) then (100/5, v/v). The desired tripyrrane **9** (0.566 g, 63%) was collected. ^{1}H NMR ($CDCl_3$, 200 MHz), δ, ppm: 8.39 (2H, br, 15- and 17-NH), 7.78 (2H, d, $J_{HH\ trans}$ = 16 Hz, CH=), 7.55 (1H, br, 16-NH), 5.99 (2H, d, $J_{HH\ trans}$ = 16 Hz, =CH), 4.25 (4H, q, OCH_2CH_3), 3.91 (4H, s, bridge CH_2), 2.6 and 2.25 (8H, q, CH_2CH_3), 1.5 (18H, s, $C(CH_3)_3$), 1.3 (6H, t, OCH_2CH_3), 1.1 and 0.85 (6H, t, CH_2CH_3). Anal. calcd. for $C_{46}H_{51}N_3O_8$: C 71.41%, H 6.59%, N 5.43%; found: C 71.31%, H 6.71%, N 5.18%.

[2,3]-(4′,5′-Diethoxycarbonyl cyclohex-3′-enyl)-12,13-di(ethoxycarbonyl ethyl)-7,8,17,18-tetraethyl porphyrin 5

Porphyrin **3** (50 mg, 0.06 mmol) was dissolved in glacial acetic acid (20 mL) and refluxed under nitrogen for 10 h. After the solvent was evaporated under reduced pressure, the crude product was dissolved in CH_2Cl_2 and the organic phase was neutralized, washed with H_2O, and dried over Na_2SO_4. Evaporation of the solvent led to the porphyrin **2** in quantitative yield after recrystallization from methanol. UV–visible (in CH_2Cl_2), λ_{max} (nm)(ε 10^{-3} M^{-1} cm^{-1}): 414 (198.9), 513 (10.1), 555 (27.8), 574 (15.6), 641 (2.5). ^{1}H NMR ($CDCl_3$, 200 MHz), δ, ppm: 10.09, 10.05, 10.02, 10.0(4H, 4s, *meso* H), 9.28 (1H, s, 2′-CH=), 5.1 (1H, dd, J_{HH} = 17.5 Hz, 4′-H), 4.6 (2H, m, 5′-CH_2), 4.41 (4H, t, $CH_2CH_2CO_2$), 4.20 (16H, m, CH_2CH_3 and 4 OCH_2CH_3), 1.93, 1.55, 1.18 (24H, 3m, 4 OCH_2CH_3 and 4 CH_2CH_3), –3.69 (2H, s, NH). Anal. calcd. for $C_{48}H_{58}N_4O_8 \cdot CH_3OH$: C 69.15%, H 7.34%, N 6.58%; found: C 69.41%, H 7.08%, N 6.71%.

[2,3]-(4′,5′-Diethoxycarbonyl benzo)-12,13-di(ethoxycarbonyl ethyl)-7,8,17,18-tetraethyl porphyrin 1

The cyclohexenylporphyrin **5** (50 mg, 0.06 mmol) in dry toluene (20 mL) was refluxed under nitrogen, for 24 h, in the presence of DDQ (55 mg, 4 equiv.). The solution was allowed to cool to room temperature and was washed several times with water to remove the oxidizing agent. The organic layer was then dried over Na_2SO_4. TLC analysis revealed the presence of two compounds with very close polarities. Nevertheless, the two porphyrins could be separated on preparative silica gel plates, after several elutions with CH_2Cl_2/Et_2O (10/2, v/v). The more polar band was the diacrylic porphyrin **3**. The slightly less polar band weighing 32 mg (64%) was found to be the monobenzoporphyrin **1.** It was recrystallized from methanol. UV–visible (in CH_2Cl_2), λ_{max} (nm)(ε 10^{-3} M^{-1} cm^{-1}): 421 (276.4), 498 (shoulder), 531 (7.8), 567 (33.4), 580 (31.4), 632 (2.8). ^{1}H NMR ($CDCl_3$, 200 MHz), δ, ppm: 10.29, 10.19 (4H, 2s, *meso* H), 9.62 (2H, s, benzo-H), 4.6 and 4.2 (16H, 2m, 4 OCH_2CH_3 and 4 CH_2CH_3), 4.54 (4H, t, $CH_2CH_2CO_2$), 3.26 (4H, t, $CH_2CH_2CO_2$), 1.9, 1.5, and 1.3 (24H, 3m, CH_2CH_3 and OCH_2CH_3), –3.76 (2H, s, NH). Anal. calcd. for $C_{48}H_{58}N_4O_8.CH_3OH$: C 69.33%, H 7.07%, N 6.60%; found: C 69.47%, H 6.61%, N 6.73%.

2,3,12,13-Tetraethoxycarbonyl vinyl-7,8,17,18-tetraethyl porphyrin 4

Tripyrrane **9** (88 mg, 0.12 mmol) was treated with trifluoroacetic acid (1 mL) and stirred under argon for 4 h. Dry methylene chloride (7 mL) was added followed by a solution of 2,5-diformyl pyrrole **8** (38 mg, 0.12 mmol) in CH_2Cl_2. The reaction mixture was stirred at room temperature, in the dark, for 16 h and the reaction progress was monitored by UV–visible spectroscopy. The solution was cooled with an ice-water bath during neutralization by addition of 2.5 mL of triethylamine. Oxidation of the porphyrinogen intermediate was completed by addition of DDQ (55 mg, 0.24 mmol) as a solution in THF (1.5 mL) with subsequent reflux of the mixture for 1 h. After being diluted with 30 mL of CH_2Cl_2, the solution was treated with dilute aqueous sodium hydroxide and then washed with water to neutral pH. After drying over Na_2SO_4 the organic layer was filtered and the solvent was evaporated. The crude product was chromatographed on a silica gel column with elution by mixtures of CH_2Cl_2–Et_2O with increasing ratios of diethyl ether from 100/1 to 100/3 (v/v). Recrystallization

© 1998 NRC Canada

from CH_2Cl_2–MeOH gave 39 mg, 40% of the desired porphyrin **4**. UV–visible (in CH_2Cl_2), λ_{max} (nm) (ε 10^{-3} M^{-1} cm^{-1}): 407 (shoulder), 431 (205), 536 (5), 591 (31.4), 614 (38.5). ^1H NMR ($CDCl_3$, 200 MHz), δ, ppm: 9.84 (4H, s, *meso* H), 9.07 (4H, d, J_{HH} = 16 Hz, CH=), 6.95 (4H, d, J_{HH} = 16 Hz, =CH), 4.59 (8H, q, OCH_2CH_3), 4.00 (8H, q, CH_2CH_3), 1.84 (12H, t, CH_2CH_3), 1.58 (12H, t, OCH_2CH_3), -4.57 (2H, s, NH). Anal. calcd. for $C_{48}H_{54}N_4O_8$: C 70.74%, H 6.68%, N 6.87%; found: C 69.85%, H 6.64%, N 6.76%.

***opp*-Di [4′,5′-(diethoxycarbonyl) benzo]-2,3,12,13-tetraethyl porphyrin 2**

Porphyrin **4** (82 mg, 0.1 mmol) was dissolved in glacial acetic acid (30 mL) and refluxed under inert atmosphere for 10 h. The solvent was then evaporated and the product of the reaction was redissolved in CH_2Cl_2. The solution was neutralized with an aqueous solution of $NaHCO_3$, washed with water, and dried over Na_2SO_4. The drying agent was removed by filtration and the solvent was evaporated. Recrystallization from methanol afforded 80 mg (98%) of the dicyclohexenylporphyrin isomeric mixture. This latter compound (40 mg, 0.05 mmol), along with DDQ (45 mg, 4 equiv.) and triethylamine (28 ml, 4 equiv.), was dissolved in toluene (15 mL) and refluxed for 24 h. The reaction was cooled to room temperature, washed once with H_2O, and then with a 10% aqueous NaOH solution. The organic phase was then dried over Na_2SO_4 and the drying agent was removed by filtration. The solution was concentrated and chromatographed over a silica gel column with elution by mixtures of CH_2Cl_2/Et_2O 100/2 (v/v) and 100/5 (v/v). Recrystallization from methanol afforded the dibenzoporphyrin **2** (20 mg, 45%) as purple crystals. UV–visible (in CH_2Cl_2), λ_{max} (nm)(ε 10^{-3} M^{-1} cm^{-1}): 398 (79), 421 (487), 498 (shoulder), 544 (10.6), 569 (55.8), 582 (39.1), 638 (11.8). ^1H NMR ($CDCl_3$, 200 MHz), δ, ppm: 9.66 (4H, s, *meso* H), 9.43 (4H, s, benzo-H), 4.8 (8H, q, OCH_2CH_3), 3.9 (8H, q, CH_2CH_3), 1.6 and 1.3 (24H, m, OCH_2CH_3 and CH_2CH_3), –5.93(2H, s, NH). Anal. calcd. for $C_{46}H_{51}N_4O_8$: C 71.09%, H 6.21%, N 6.91%; found: C 69.78%, H 6.17%, N 6.79%.

Acknowledgments

We would like to thank Prof. Harold Goff (University of Iowa, Department of Chemistry, Iowa City) for useful discussions and for his assistance with the revision of this paper. We would like also to express our gratitude to Dr. Philippe Maillard (UMR 176 du CNRS, Institut Curie-Recherche, Université Paris-Sud, Orsay, France) for his constant encouragement and helpful suggestions.

References

1. T.J. Dougherty. Photochem. Photobiol. **45**, 879 (1987); C. Gomer. J. Photochem. Photobiol. **54**, 1093 (1991); R. Bonnett and M.C. Berenbaum. Adv. Exp. Med. Biol. **160**, 241 (1983).
2. M. Momenteau, D. Oulmi, Ph. Maillard, and A. Croisy. Proc. SPIE – Int. Soc. Opt. Eng. **2325**, 13 (1994).
3. P.S. Clezy, C.J.R. Fookes, and A.H. Mirza. Aust. J. Chem. **30**, 1337 (1977).
4. I.A. Chaudhry and P.S. Clezy. Aust. J. Chem. **35**, 1185 (1982)
5. R. Bonett and K.A. McManus. J. Chem. Soc. Chem. Commun. 1129 (1994).
6. L T. Nguyen, M.O. Senge, and K.M. Smith. J. Org. Chem. **61**, 998 (1996).
7. A.R. Morgan and N.C. Tertel. J. Org. Chem. **51**, 1347 (1986).
8. W. Boyle and D. Dolphin. J. Chem. Soc. Chem. Commun. 2463 (1994).
9. Ph. Maillard, C. Hery, and M. Momenteau. Tetrahedron Lett. **38**, 3731 (1997).
10. M.G.H. Vincente, I.N. Rezzano, and K.M. Smith. Tetrahedron Lett. **31**, 1365 (1990); M.J. Gunter, B.C. Robinson, J.M.Gulbis, and E.R.T. Tiekink. Tetrahedron, **47**, 7853 (1991).
11. A. Boudif and M. Momenteau. J. Chem. Soc. Chem. Commun. 2069 (1994).
12. A. Boudif and M. Momenteau. J. Chem. Soc. Perkin Trans 1, 1235 (1996).
13 D.H.R. Barton, J. Kervagoret, and S.Z. Zard. Tetrahedron, **46**, 7587 (1990).

© 1998 NRC Canada

The electrophilic substitution reaction of the dithionitronium cation $[SNS]^+$ with benzene

Scott Brownridge, Jack Passmore, and Xiaoping Sun

Can. J. Chem. Downloaded from www.nrcresearchpress.com by China University of Science and Technology on 09/05/12
For personal use only.

Abstract: The compound $[SNS]^+$ ($[SNS][AsF_6]$) reacts with benzene in liquid sulfur dioxide to give orange-, blue-, and then purple-colored solutions. The assignment of the orange color to a molecule–ion charge-transfer complex $[C_6H_6{\cdot}SNS]^+$ is supported by the linear dependence of the ionization potential of the arenes (C_6H_6, C_6H_5Me, $C_6H_5Bu^t$, C_6HMe_5) and the energy of the charge-transfer absorption of freshly prepared arene–$[SNS][AsF_6]$ mixtures in liquid SO_2 solution. Variable-temperature multinuclear NMR studies of the reactions of $[SNS][AsF_6]$ and $[SNS][Sb_2F_{11}]$ with benzene are consistent with the blue color being due to a sulfur protonated substitution product $[C_6H_5(S_2N)H]^+$, providing the first example of a CH electrophilic substitution reaction of SNS^+. The geometries calculated at the RHF/6-31G* level for $[C_6H_5(SNS)H]^+$, the isomeric $[C_6H_5NSSH]^+$, and $[C_6H_5N(S)SH]^+$, together with NMR data, support $[C_6H_5(SNS)H]^+$ (i.e., suggest S, not N, is attached to the ring) as the structure of the cation. The electrophilic aromatic substitution reaction of $[SNS]^+$ and benzene is also supported by NMR studies of $[SNS][AsF_6]$ and other arenes (e.g., C_6HMe_5) in SO_2 solution. The UV-visible spectrum of $[SNS]^+$ ($[SNS][AsF_6]$) in liquid SO_2 is reported, and the absorption (λ = 406 nm, ϵ = 80) responsible for the yellow color is assigned to the $[SNS]^+$ HOMO–LUMO transition. Evidence is also presented for the formation of a molecule–ion charge-transfer complex between 5-methyl-1,3,2,4-dithiadiazolium and hexamethylbenzene in liquid SO_2, the first dithiadiazolium charge-transfer complex.

Key words: UV-visible, charge transfer, dithionitronium, benzene, electrophilic substitution.

Résumé : Le $[SNS]^+$ ($[SNS][AsF_6]$) réagit avec le benzène dans le dioxyde de soufre liquide pour donner des solutions colorées successivement en orange, bleu et finalement violet. L'attribution de la couleur orange à un complexe de transfert de charge molécule–ion $[C_6H_6{\cdot}SNS]^+$ découle de la dépendance linéaire du potentiel d'ionisation des arènes (C_6H_6, C_6H_5Me, *t*-BuC_6H_5, C_6HMe_5) et l'énergie de l'absorption de transfert de charge de mélanges fraîchement préparés d'arène–$[SNS][AsF_6]$ en solution dans le SO_2 liquide. Des études RMN multinucléaires à températures variables des réactions du $[SNS][AsF_6]$ et du $[SNS][Sb_2F_{11}]$ avec le benzène seraient en accord avec le fait que la couleur bleue est due à un produit de substitution protoné du soufre $[C_6H_5(S_2N)H]^+$; ceci constituerait le premier exemple de réaction de substitution électrophile de SNS^+ par un CH. Les géométries calculées au niveau RHF/6-31G* pour le $[C_6H_5(SNS)H]^+$ et les formes isomères $[C_6H_5(NSSH]^+$ et $[C_6H_5N(S)SH]^+$ considérées avec les données de la RMN sont en accord avec une structure $[C_6H_5(SNS)H]^+$ (c'est-à-dire que le S, et non pas le N, est attaché au noyau) pour le cation. La réaction de substitution aromatique électrophile du $[SNS]^+$ et du benzène est aussi appuyée par des études RMN du $[SNS][AsF_6]$ et d'autres arènes (comme le C_6HMe_5) en solution dans le SO_2 liquide. On a mesuré le spectre UV-visible du $[SNS]^+$ ($[SNS][AsF_6]$) dans le SO_2 liquide et l'absorption (λ = 406 nm, ϵ = 80) responsable de la couleur jaune est attribuée à la transition des OM HO et BV du $[SNS]^+$. On présente aussi des données relatives à la formation d'un complexe de transfert de charge molécule–ion entre le 5-méthyl-1,3,2,4-dithiadiazolium et l'hexaméthylbenzène dans le SO_2 liquide; il s'agirait du premier complexe de charge du dithiadiazolium.

Mots clés : UV-visible, transfert de charge, dithionitronium, benzene, substitution électrophile.

[Traduit par la rédaction]

Introduction

Aromatic nitration has been of interest in organic chemistry for many years (1). It was shown by Ingold and co-workers (2) in 1946 that nitronium $[ONO]^+$ was the reactive intermediate in the nitration of benzene by a mixture of sulfuric and nitric acids. Since then many reactions of salts of $[ONO]^+$ with arenes have been investigated. Spectroscopic and other evidence indicate that nitration of arenes proceeds in essentially two steps: first the formation of a charge-transfer complex (eq. [1]), followed by the formation of the Wheland complex **1** as shown in eq. [2] (1, 3).

[1] $$C_6H_6 + [ONO]^+ \rightarrow [C_6H_6{\cdot}NO_2]^+$$

[2] $$[C_6H_6{\cdot}NO_2]^+ \rightarrow \mathbf{1} \rightarrow C_6H_5NO_2 + \text{“}H^+\text{”}$$

The sulfur analog of nitric acid HNS_3 is unknown. However, dithionitronium $[SNS]^+$, the analog of $[ONO]^+$, can be

Received April 6, 1998.

S. Brownridge, J. Passmore,[1] and X. Sun. Department of Chemistry, University of New Brunswick, Fredericton, NB E3B 6E2, Canada.

[1]Author to whom correspondence may be addressed. Telephone: (506) 453-4781. Fax: (506) 453-4981. E-mail: passmore@unb.ca

 © 1998 NRC Canada

Can. J. Chem. Downloaded from www.nrcresearchpress.com by China University of Science and Technology on 09/05/12
For personal use only.

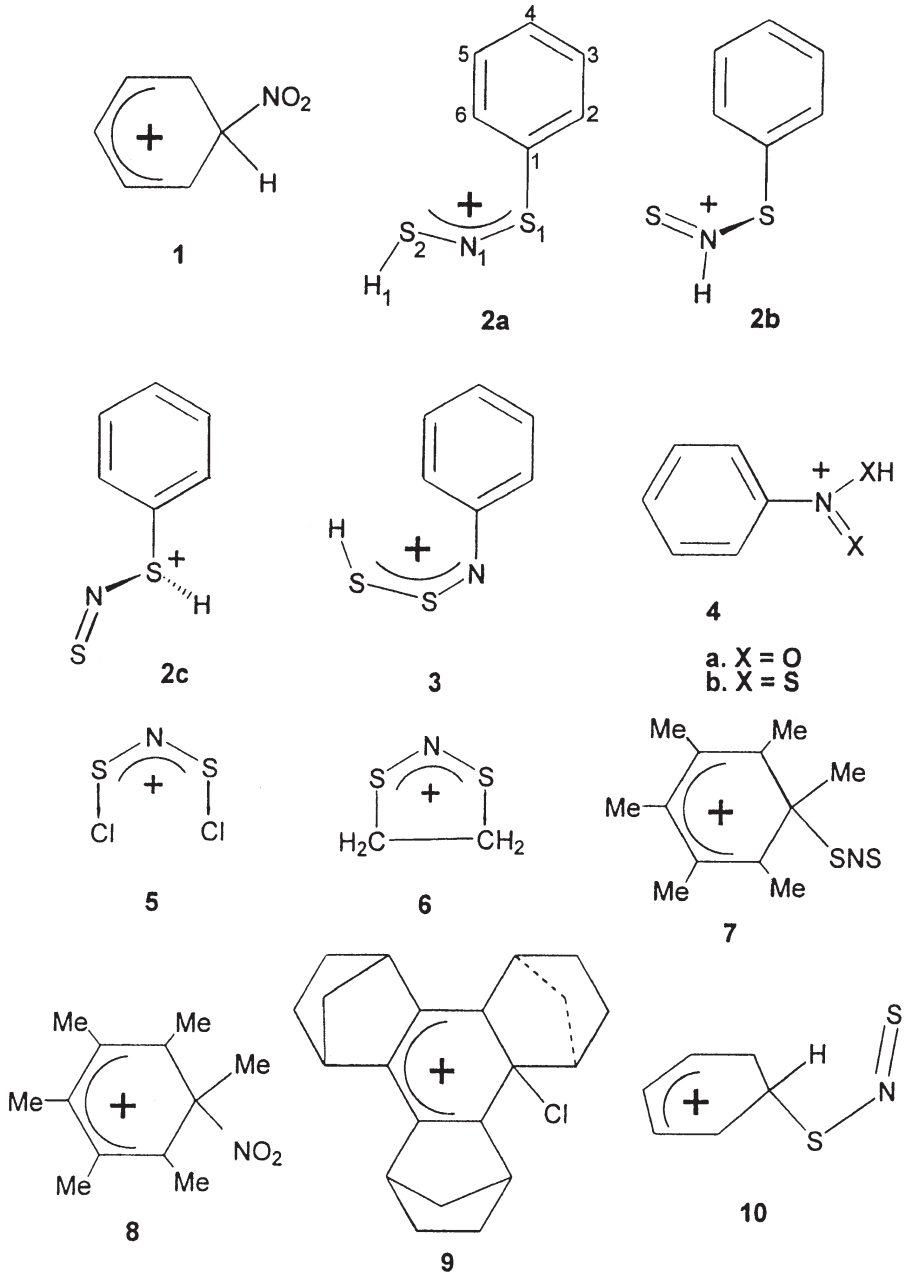

readily synthesized as the hexafluoroarsenate $[AsF_6]^-$ salt (4). We have shown (5) that $[SNS]^+$ (as $[SNS][AsF_6]$ in liquid sulfur dioxide) has an extensive symmetry allowed concerted cycloaddition chemistry with a wide range of multiple bonds including C≡N (5*a–e*), C≡C (5*a–e*), C=C (5*d–g*), C≡P (5*h*), and S≡N (5*i*). Analogous reactions of $[ONO]^+$ generally lead to nitration (1). Therefore it was of interest to investigate the reactions of $[SNS]^+$ with benzene and related arenes.

Preliminary experiments showed that $[SNS]^+$ reacted with benzene in liquid sulfur dioxide to give an orange solution, which changed to blue then purple with time (5*d*). In this work we present evidence that the color of the orange solution is due to a π–π^* molecular (more formally a molecule–ion) charge-transfer complex $[C_6H_6 \cdot SNS]^+$, and that the blue species is the sulfur protonated substitution product $[Ph(S_2N)H]^+$ (Ph = C_6H_5) (i.e., **2**, **3**, or **4b**). A preliminary account of this work has been reported (6).

Experimental

Benzene and C_6H_5Me were purchased from Anachemia, $C_6H_5Bu^t$ from Aldrich, and were dried over CaH_2. The C_6HMe_5 and C_6Me_6 were purchased from Anachemia and were used as received. Sulfur dioxide was obtained from Matheson and dried over CaH_2. The preparation of $[SNS][AsF_6]$ and general techniques were as previously described (4). The $[SNS][AsF_6]$ often contained a very small amount of brown impurities, and further purification was carried out for the spectroscopic studies. The UV-visible spectra were recorded using a Hewlett–Packard 8452A spectrophotometer. The acquisition of FT–Raman (5*c*, *f*) and NMR (^1H, ^{13}C, ^{14}N) (5*g*) spectra are described elsewhere.

The preparation of high-purity $[SNS][AsF_6]$

The SO_2 (2.90 g) was condensed at –196°C onto yellow

© 1998 NRC Canada

Can. J. Chem. Downloaded from www.nrcresearchpress.com by China University of Science and Technology on 09/05/12
For personal use only.

Fig. 1. The UV-visible spectrum of $[SNS][AsF_6]$ in liquid SO_2.

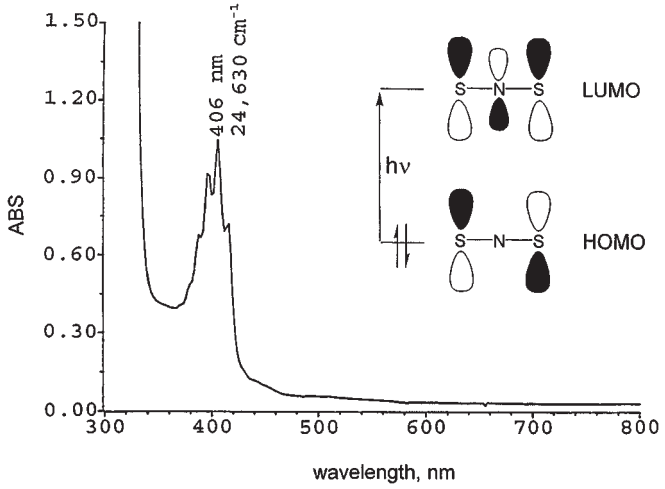

Fig. 2. The UV-visible spectra of the initial mixtures of arenes and $[SNS][AsF_6]$ in liquid SO_2, showing the absorption of the charge-transfer complex $[C_6H_6 \cdot SNS]^+$.

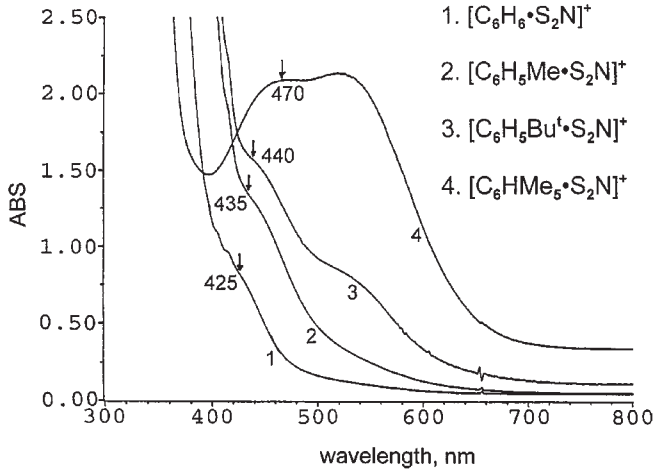

crystalline $[SNS][AsF_6]$ (2.90 g, 10.9 mmol) placed in a two-bulb vessel (7). The contents were warmed to room temperature, giving a very light brown solution over a yellow solid. The solution and solid were swirled, and all the solubles were then poured through a glass frit into the second bulb. The solid was washed again with an aliquot of SO_2 and all the resulting solution again poured into the second bulb. Part of the SO_2 was then condensed onto the yellow solid, giving a clean yellow solution, indicating the brown impurities had been extracted. All the SO_2 was then removed by evacuation, giving very yellow $[SNS][AsF_6]$ (1.83 g, 6.85 mmol) in 63% recovered yield. This product was used for all UV-visible spectroscopic measurements.

The preparation of $[SNS][Sb_2F_{11}]$

The $[SNS][Sb_2F_{11}]$ was prepared by reacting $[SNS][AsF_6]$ with SbF_5 (Ozark–Mahoning, triple distilled (7)) in a one-bulb vessel. The SO_2 (5.25 g) and SbF_5 (2.536 g, 11.7 mmol) were condensed successively onto $[SNS][AsF_6]$ (1.407 g, 5.27 mmol) at –196°C. The contents were warmed to room temperature, giving a homogeneous light brown solution, which was then stirred for 20 h. The volatiles were removed by evacuation, giving a brown tarry product. The product was heated with a heat-gun under dynamic vacuum until no further weight loss was observed. The final weight of the product $[SNS][Sb_2F_{11}]$ was 2.93 g (expected 2.80 g, 5.27 mmol). FT–Raman: 699.9 (s, $[SNS]^+$), 678.7 (s), 657 (m, sh), 646.5 (s), 599.4 (m), 576.3 (w), 299.0 (w), and 293.9 (w) cm^{-1}. The vibrations other than that at 699.9 cm^{-1} are attributable to $[Sb_2F_{11}]^-$.

The measurements of UV-visible spectra of $[SNS][AsF_6]$ and of $[SNS][AsF_6]$ with arenes (C_6H_6, C_6H_5Me, $C_6H_5Bu^t$, and C_6HMe_5)

The samples were prepared in a vessel constructed with a glass bulb (10 cm^3), incorporating a medium porosity sintered glass frit and a UV-vis cell (0.1 cm, Hellma). The SO_2 (0.89 g) was condensed onto high-purity $[SNS][AsF_6]$ (0.020 g, 0.15 mmol) in the bulb at –196°C. The contents were warmed to room temperature, giving a yellow solution (0.13 M). Part of the solution was poured into the UV cell, and a UV-visible spectrum was recorded at room temperature between 200 and 800 nm (Fig. 1).

For the measurements of mixtures of $[SNS][AsF_6]$ with arenes (C_6H_6, C_6H_5Me, $C_6H_5Bu^t$, and C_6HMe_5), preweighed SO_2 and the arenes were successively condensed onto preweighed high-purity $[SNS][AsF_6]$ (ca. 0.1 M) in the bulb at –196°C. The mixtures were quickly warmed to room temperature, giving orange solutions for C_6H_6 and C_6H_5Me, and reddish solutions for $C_6H_5Bu^t$ and C_6HMe_5 mixtures. The UV-visible spectra (Fig. 2) were recorded after 5 min. Another mixture of $[SNS][AsF_6]$ (0.042 g, 0.16 mmol) and C_6H_6 (0.05 g, 0.64 mmol) in liquid SO_2 (2.08 g) was examined by UV-visible spectroscopy as a function of time (Fig. 3), showing the disappearance of the band at 425 nm and the emergence of a new band at 500 nm, the center of which shifted to lower energies over time. Similarly for the $[SNS]^+$–$C_6H_5Bu^t$ mixture, the initial band at 440 nm disappeared after 30 min and a new band emerged at 520 nm. The strong absorption below 340 nm in all the spectra originated from the absorption of the SO_2 solvent.

The NMR (^1H, ^{13}C, ^{14}N) spectroscopic studies of the reaction of $[SNS][AsF_6]$ with C_6H_6

^1H spectra

The SO_2 (0.775 g) and excess of C_6H_6 (0.0159 g, 0.204 mmol) were condensed onto $[SNS][AsF_6]$ (0.0416 g, 0.156 mmol) in a 5 mm NMR tube at –196°C, and the tube was then flame sealed. The reactants were quickly warmed to room temperature, and the color of the solution turned to orange immediately, then gradually turned to blue after 30 min. Some colorless crystalline needles of $[NH_4][AsF_6]$ (see footnote 2) formed after a few hours; nevertheless, the

[2] The colorless crystalline by-product was identified to be $[NH_4][AsF_6]$ by ^1H NMR (6.0 ppm, 1:1:1 triplet, $^1J(^1H\text{-}^{14}N)$ = 54 Hz, attributable to the resonance of $[NH_4]^+$) and IR (695 s, br, and 398 s cm^{-1}, attributable to vibrations of $[AsF_6]^-$). Crystallographic parameters: rhombohedral, $a = b = c = 5.019(2)$, $\alpha = \beta = \gamma = 96.72(3)°$ (8).

© 1998 NRC Canada

Can. J. Chem. Downloaded from www.nrcresearchpress.com by China University of Science and Technology on 09/05/12
For personal use only.

Fig. 3. The UV-visible spectra of the $[SNS][AsF_6]$–C_6H_6 mixture in liquid SO_2 as a function of time. **1**, 5 min; **2**, 41 min; **3**, 78 min; **4**, 108 min; **5**, 258 min; **6**, 380 min; and **7**, 12 h. The color of the solution changed with time: orange (0–40 min), blueish (50–200 min), and purple (after 250 min).

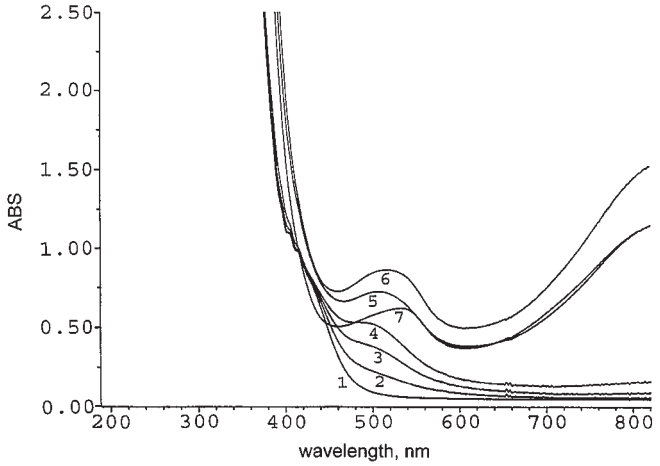

blue color of the solution remained unchanged after one day. The solid was then transferred to the top of the tube, and a ^1H spectrum of the solution was recorded at room temperature (Fig. 4(*a*)). δ (ppm) and assignments: 7.4–7.9 (very broad band, $\Delta\nu_{1/2}$ = 40 Hz, intensity (int) 100%, aromatic H's of $[Ph(S_2N)H]^+$) (**2**, **3**, or **4b**), 7.3 (singlet, int 55%, C_6H_6), and 5.8 (1:1:1 triplet, $^1J(^1H\text{-}^{14}N)$ = 54 Hz, int 3%, $[NH_4]^+$). The ^1H spectrum at –60°C was essentially identical. At both temperatures, resonances attributable to $-(S_2N)\mathbf{H}^+$ were not observed. On the basis of the stoichiometry and NMR integrations, ca. 90% $[SNS]^+$ had reacted at this stage, leading to $[Ph(S_2N)H]^+$. After one week, the color of the solution changed to purple,[3] and a ^1H spectrum was recorded again at room temperature (Fig. 4(*b*)). δ (ppm) and assignments: 7.45–7.88 (multiplet, int 100%, unknown[3]), 7.3 (singlet, int 36%, C_6H_6), and 5.8 (1:1:1 triplet, $^1J(^1H\text{-}^{14}N)$ = 54 Hz, int 2%, $[NH_4]^+$). On the basis of the stoichiometry and NMR integrations, the reaction was complete (100%) after one week. The weak $[NH_4]^+$ resonances are not shown in Fig. 4. A ^1H spectrum of C_6H_6 in liquid SO_2 was recorded (7.3 ppm, singlet) for comparison.

^{13}C and ^{14}N spectra

The SO_2 (3.28 g) and excess C_6H_6 (0.380 g, 4.87 mmol) were condensed onto $[SNS][AsF_6]$ (0.608 g, 2.28 mmol) in a 10 mm NMR tube at –196°C. The reactants were quickly warmed to room temperature, and the observations of the color changes and the formation of the colorless crystals of $[NH_4][AsF_6]$ (see footnote 2) were similar to those observed in the reactions in the 5 mm tube. After one day, the insoluble solid was transferred to the top of the tube, the ^{14}N spectrum was recorded on the solution (blue), and a broad band (–5 ppm, $\Delta\nu_{1/2}$ = 540 Hz, $[Ph(S_2N)H]^+$) was observed. After one week, the color of the solution became purple, and ^{14}N and ^{13}C spectra were recorded.[3] ^{14}N spectral data: δ = –255 ppm, $\Delta\nu_{1/2}$ = 180 Hz. ^{13}C spectral data (δ (ppm) and assignment): 135.5 (C_1), 133.4 (C_4), 132.2 ($C_{3,5}$), 131.3 ($C_{2,6}$), and 129.2 (C_6H_6). In addition, several very weak peaks were also observed in the ^{13}C spectrum at 209, 143,

Fig. 4. The ^1H NMR spectra of the blue product from the reaction of $[SNS][AsF_6]$ with C_6H_6 in liquid SO_2 (*a*) after 1 day and (*b*) after 2 weeks. Benzene was present as the internal standard.

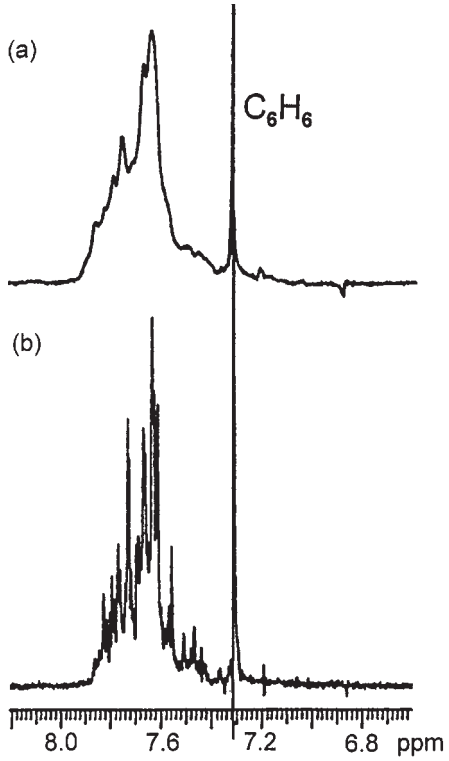

[3] The NMR (^1H, ^{13}C) spectra of the purple species are identical to those of the isolated product formed on an in situ neutralization (with Na_2CO_3) of the blue intermediate $[C_6H_5(S_2N)H]^+$ from the substitution reaction: $[C_6H_5(S_2N)H][AsF_6] + Na_2CO_3 \rightarrow X + NaHCO_3 + Na[AsF_6]$. Without Na_2CO_3 the purple species may be formed as shown by equilibria between **A**, **B**, and **C** (see text). The HF and AsF_5 may then react with the organic material, displacing the equilibrium to **C**. The mass spectrum of X contains peaks attributable to $[C_6H_5]^+$ (77, 20%), $[SNS]^+$ (78, 100%), and a small (4.5%) S_2^+ peak. Other evidence related to the neutral product has been deposited.[4] Several attempted preparations of single crystals were unsuccessful. The nature of X, which is possibly $[C_6H_5(S_2N)]_x$,[5] is as yet undetermined and will be the subject of further investigations.

[4] Copies of material on deposit may be purchased from: The Depository of Unpublished Data, Document Delivery, CISTI, National Research Council of Canada, Ottawa, Canada, K1A 0S2. Interatomic distances and angles have also been deposited with the Cambridge Crystallographic Data Centre and can be obtained on request from: The Director, Cambridge Crystallographic Data Centre, University Chemical Laboratory, 12 Union Road, Cambridge, CB2 1EZ, U.K.

[5] Related purple (for some R) RNSS compounds have been isolated and characterized (25, 26), and the crystal structure has been determined for 2,4-di-*tert*-butyl-6-methyl-*N*-thiosulfinylaniline (26*c*). The compound C_6H_5NSS has not been cited in the literature since first reported in 1921 (26*d*), although it has been reported as an intermediate (25).

© 1998 NRC Canada

Can. J. Chem. Downloaded from www.nrcresearchpress.com by China University of Science and Technology on 09/05/12
For personal use only.

Fig. 5. The ^{1}H NMR spectra of the product from the reaction of $[SNS][Sb_2F_{11}]$ with C_6H_6 in liquid SO_2 at various temperatures.

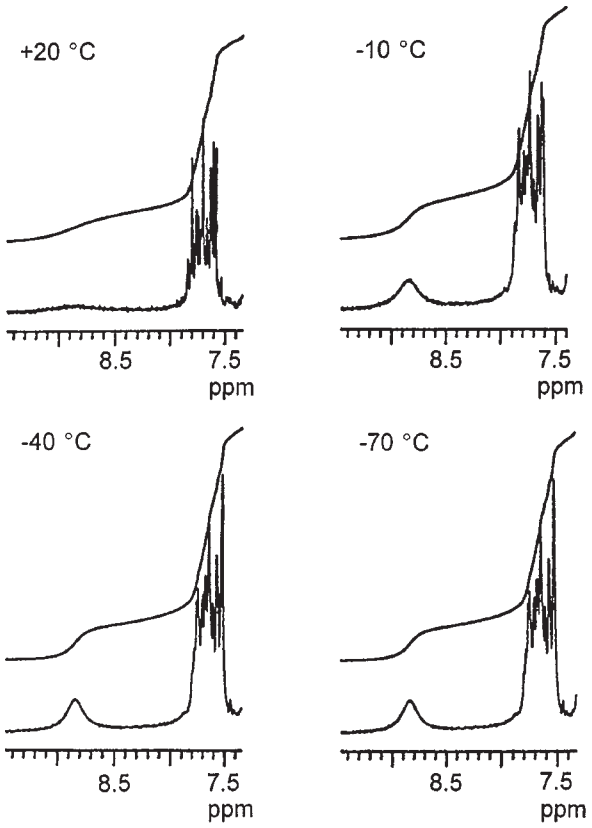

and 124 ppm. The carbon atoms are numbered in accordance with IUPAC rules (see **2a**). The actual spectra have been deposited with the supplementary material (Figs. S1 and S2).[4] A ^{13}C spectrum of C_6H_6 (129.2 ppm, singlet) and an ^{14}N spectrum of $[SNS][AsF_6]$ (δ = –91 ppm, $\Delta\nu_{1/2}$ = 6 Hz) in liquid SO_2 were recorded for comparison.

The reaction of C_6H_6 with $[SNS][Sb_2F_{11}]$, and ^{1}H (variable temperature) and ^{13}C NMR spectroscopic studies of $[Ph(SNS)H]^+$

The SO_2 (0.81 g) and C_6H_6 (0.0103 g, 0.132 mmol) were condensed successively onto $[SNS][Sb_2F_{11}]$ (0.0424 g, 0.0800 mmol) in a 5 mm NMR tube at –196°C. The contents were warmed to room temperature, and the color changes were observed, which were similar to those described for the reactions with $[SNS][AsF_6]$. After 1 h, the color turned to blue, indicating formation of $[Ph(SNS)H]^+$ (cf. the $[SNS][AsF_6]$ reaction), and this blue color remained unchanged for more than 10 h. The ^{1}H NMR spectra (Fig. 5) were then recorded at various temperatures (+20, +6, –10, –25, –40, –55, and –70°C), showing a multiplet at 7.5–7.9 ppm at all temperatures attributable to the C_6H_5 protons and a broad band at 8.8 ppm attributable to the $–(S_2N)\mathbf{H}^+$ proton, which were confirmed by the ratios of the integrations of the two resonances at various temperatures: 4.8:1 (+20°C), 5.2:1 (+6°C), 4.8:1 (–10°C), 5.0:1 (–25°C), 5.1:1 (–40°C), 5.2:1 (–55°C), and 4.8:1 (–70°C), an average of 5.0:1. A ^{13}C NMR spectrum was recorded at room temperature on a similarly prepared sample by reaction of $[SNS][Sb_2F_{11}]$ (0.101 g, 0.191 mmol) with C_6H_6 (0.0201 g, 0.257 mmol) in liquid SO_2 (0.742 g), leading to $[Ph(S_2N)H]^+$. Spectral data (δ (ppm) and assignment): 135.4 (C_1), 133.2 (C_4), 132.1 ($C_{3,5}$), 131.1 ($C_{2,6}$), and 129.3 (C_6H_6). In addition, several weak unassigned peaks were also observed between 135 and 124 ppm. The actual spectrum is deposited (Fig. S3).[4] The carbon atoms of $[Ph(S_2N)H]^+$ are numbered in accordance with IUPAC rules (see **2a**).

The reaction of the 5-methyl-1,3,2,4-dithiadiazolium cation with hexamethylbenzene

The SO_2 (3.71 g) was condensed onto a mixture of colorless $[MeCNSNS][AsF_6]$ (0.821 g, 2.67 mmol) and C_6Me_6 (0.430 g, 2.65 mmol) in a 10 mm NMR tube at –196°C. The contents were warmed to room temperature, and the color of the solution immediately turned to deep red. The NMR (^{13}C, ^{14}N) spectra were then recorded. The ^{13}C spectral data (δ(ppm)): 207.8, 134.0, 18.1, and 16.4 are almost the same as those for the individual two components, i.e., $[MeCNSNS]^+$ (208 (C_{ring}) and 18 (C_{Me})) (5*b*) and C_6Me_6 (135.6 (C_{ring}) and 18.0 (C_{Me})). The ^{14}N spectral data (δ (ppm), $\Delta\nu_{1/2}$ (Hz)): 21 (1600) and –32 (1070) (cf. ^{14}N spectral data (ppm) for $[MeCN'SN'S]^+$: 126 (550, N′) and –27 (500, N′) (5*b*). The average ^{14}N chemical shift for $[MeCN'SN'S]^+$ (75.5) becomes more shielded in the charge-transfer complex $[MeCN'SN'S]^+ \cdot C_6Me_6$ (–5.5). It is surprising that the ^{14}N′ chemical shift remains the same in the cation and complex, since the LUMO of $[MeCN'SN'S]^+$ is largely based on SN′S (5*a*, *j*).

Theoretical calculations

A series of possible geometries for $[Ph(SNS)H]^+$, **2a–c**, involving variation of the angles within the –(SNS)H group and variation of the dihedral angle between the planes of the benzene ring and the –(SNS)H group, were optimized at the RHF/6-31G* level with the GAUSSIAN 92/DFT suite of programs (9). Similar optimized geometries were also obtained for the isomer $[PhNSSH]^+$ **3**, since there is evidence for the neutral PhNSS as an intermediate,[5] and the isomer $[PhN(S)SH]^+$ **4b**.

Vibrational frequencies for **2a–c** and **3** were calculated at the RHF/6-31G* level from the optimized geometries and were scaled by the usual correction factor of 0.89 (10).

Results and discussion

The UV-visible spectrum of $[SNS]^+$ ($[SNS][AsF_6]$) in liquid sulfur dioxide

The UV-vis spectrum (Fig. 1) of high-purity $[SNS][AsF_6]$ (0.13 M) in liquid SO_2 exhibited an absorption band at 370–430 nm (extinction coefficient at 406 nm (maximum) ca. 80), consistent with its yellow color. The strong absorption below 340 nm was due to the SO_2 solvent. The broad absorption at 370–430 nm can be reasonably assigned to the HOMO (π) – LUMO (π^*) transition (3.05 eV (294 kJ/mol), the absorption maximum 406 nm) of the linear $[SNS]^+$ cation, and the fine structure (poorly resolved) of this band is attributable to the vibrational structure in the excited state of $[SNS]^+$. Previous studies (11) showed that the linear triatomic CO_2 and CS_2 molecules possess a bent lowest

© 1998 NRC Canada

Can. J. Chem. Downloaded from www.nrcresearchpress.com by China University of Science and Technology on 09/05/12
For personal use only.

Table 1. The charge-transfer energies ($h\nu_{CT}$) of $[ArH{\cdot}SNS]^+$ (ArH = C_6H_6, C_6H_5Me, $C_6H_5Bu^t$, C_6HMe_5) and ionization potentials (IP) of arene substrates.

	IP (eV)	λ_{CT} (nm)[a]	$h\nu_{CT}$ (cm^{-1})
C_6H_6	9.25	425	23 500
C_6H_5Me	8.82	435	23 000
$C_6H_5Bu^t$	8.68	440	22 700
C_6HMe_5	8.15	470	21 300

[a] Wavelength of maximum absorption. The errors are not estimated.

excited state ($^1B_2$ or $^3B_2$ symmetry). By analogy, the triatomic linear $[SNS]^+$ cation is also expected to have a similar bent lowest excited state ($^1B_2$ or $^3B_2$ symmetry). As expected, the observed electronic transition of $[SNS]^+$ has very low extinction coefficient (80), because the geometry change from a linear to a nonlinear configuration decreases the transition moment (11*b*).

The identification of the intermolecular charge-transfer complexes $[ArH{\cdot}SNS]^+$ as the first intermediates in the electrophilic substitution reactions of $[SNS]^+$ with arenes

On mixing C_6H_6 with $[SNS][AsF_6]$ (yellow) in liquid SO_2 at room temperature, the color of the solution immediately changed from yellow ($[SNS]^+$) to orange (425 nm), then gradually to blue (50–200 min) (500 nm), proposed to be $[Ph(S_2N)H]^+$ (i.e., **2**, **3**, or **4b**) (see below), and finally to purple[3] (after 250 min), as monitored visually and by UV-visible spectroscopy (Fig. 3). Previous investigations showed that the first step of aromatic nitration is the formation of a charge-transfer complex (eq. [1]). By analogy, we expected the formation of a charge-transfer complex $[C_6H_6{\cdot}SNS]^+$ in the initial stage of the reaction of $[SNS]^+$ and C_6H_6, which was implied by the orange color.

To obtain further evidence, we studied the reaction of $[SNS]^+$ with a series of arenes. The initial mixtures were characterized by UV-visible spectroscopy (Fig. 2), showing new broad absorption bands at 400–480 nm (maximum 425 nm, extinction coefficient ca. 70) for C_6H_6; 425–500 nm (maximum 435 nm, extinction coefficient ca. 130) for C_6H_5Me; 430–490 nm (maximum 440 nm, extinction coefficient ca. 150) for $C_6H_5Bu^t$; and 420–490 nm (maximum 470 nm, extinction coefficient ca. 210) for C_6HMe_5. All these bands appeared at lower energy regions relative to that of $[SNS]^+$ (370–430 nm, maximum 406 nm), and the original absorption band of $[SNS]^+$ disappeared or only a residual amount was observed (C_6H_6 case). The strong second absorptions observed at lower energies for the $[SNS]^+$–$C_6H_5Bu^t$ (522 nm) and $[SNS]^+$–C_6HMe_5–$[SNS]^+$ (540 nm) mixtures in the initial stages are likely attributable to the electrophilic substitution products related to $[Ph(S_2N)H]^+$ (see below).

Fig. 6. The relationship between charge-transfer energies of $[ArH{\cdot}SNS]^+$ and ionization potentials of the corresponding arenes.

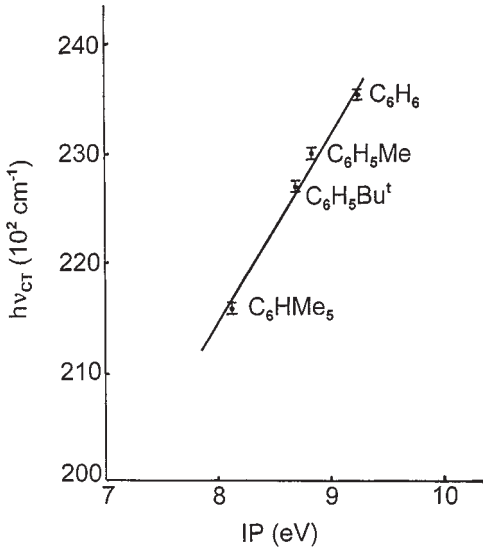

The UV-visible spectroscopic studies showed that the absorption energies of the initial $[SNS]^+$–arene mixtures assigned to the charge-transfer complexes are directly proportional to the ionization potentials of the arenes (Table 1 and Figs. 2 and 6). Kochi has previously shown (3, 12) that for the reactions of arenes (ArH) with various "nitrating agents" NO_2Y (Y = $[OH]^-$, $[OAc]^-$, $[NO_3]^-$, $[Cl]^-$, Py, $[C(NO_2)_3]^-$, etc.) the first step is the formation of a transitory weak intermolecular charge-transfer complex $[ArH{\cdot}NO_2Y]$. For a given NO_2Y, the charge-transfer energy was shown to be directly proportional to the ionization potential of the arene. Thus by analogy, the absorptions at 425, 435, 440, and 470 nm in Fig. 2 reasonably originate from similar molecule–ion charge-transfer complexes $[ArH{\cdot}SNS]^+$ formed between $[SNS]^+$ and the arenes (C_6H_6, C_6H_5Me, $C_6H_5Bu^t$, and C_6HMe_5) through the weak interaction between the arene HOMO (E_{HOMO} = –IP) (donor) and $[SNS]^+$ LUMO (acceptor) in the initial stage of the reactions. Therefore, the greater the ionization potential of an arene, the higher the energy of the charge-transfer absorption, consistent with the observed linear relationship in Fig. 6 and with the observation that the absorptions of all the $[ArH{\cdot}SNS]^+$ appeared at lower energies than that of $[SNS]^+$.[6] Kochi (3) showed that the charge-transfer complexes $[Ar{\cdot}C_7H_7]^+$ formed between arenes and the tropylium $[C_7H_7]^+$ cation exhibit strong absorptions the extinction coefficients of which increased with increase of the number of electron donating groups on the arenes. Similarly, the extinction coefficients of the charge-transfer bands of $[ArH{\cdot}SNS]^+$ (ArH = C_6H_6 (70), C_6H_5Me (130), $C_6H_5Bu^t$ (150), and C_6HMe_5 (210)) become larger with an increase in the electron donating abilities of arenes. The aromatic charge-transfer complexes of $[ONO]^+$ were not directly experimentally observed due to the subsequent very fast electrophilic displacement (i.e., the

[6] The HOMO level of an arene is presumably higher than the HOMO of $[SNS]^+$ because of the positive charge and therefore high ionization potential of the $[SNS]^+$ cation.

© 1998 NRC Canada

Can. J. Chem. Downloaded from www.nrcresearchpress.com by China University of Science and Technology on 09/05/12
For personal use only.

Table 2. The ^{1}H and ^{13}C NMR data for $[C_6H_5\text{-}(S_2N)H]^+$ (**2**, **3**, or **4b**), $[C_6H_5\text{-}N(OH)O]^+$ **4a**, and selected neutral species. All values rounded to the nearest 0.1 ppm.

	^{1}H (ppm)	^{13}C (ppm)[a]
$[C_6H_5\text{-}(S_2N)H]^+$ **2**[b]	Multiplet 7.6–7.9	135.4, 131.1, 132.1, 133.2
C_6H_6[c]	7.3	128.3
$C_6H_5\text{-}SH$[c]	Multiplet 7.1–7.3	130.7, 129.3, 129.0, 125.5
$C_6H_5\text{-}NH_2$[c]	6.6 ($H_{2,6}$), 6.7 ($H_{3,5}$), 7.1 (H_4)	146.4, 129.2, 118.4, 115.0
$C_6H_5\text{-}NO_2$[c]	7.5 ($H_{3,5}$), 7.7 (H_4), 8.2 ($H_{2,6}$)	148.2, 123.4, 129.3, 134.5
$[C_6H_5\text{-}N(OH)O]^+$ **4a**[d]	8.0 ($H_{3,5}$), 8.5 (H_4), 8.8 ($H_{2,6}$)	

[a] Resonances listed in the order: C_1, $C_{2,6}$, $C_{3,5}$, C_4, C_6.
[b] This work (^{1}H spectra recorded at 400 MHz).
[c] ^{1}H spectrum recorded at 300 Mhz; see ref. 19 for actual spectrum.
[d] See also ref. 14.

formation of **1** in eq. [2] above), followed by formation of nitroarene.[7] The reaction of the heterocyclic 5-methyl-1,3,2,4-dithiadiazolium $[MeCNSNS]^+$ cation (electron acceptor) with hexamethylbenzene C_6Me_6 (electron donor) gave a deep red molecule–cation charge-transfer complex $[MeCNSNS{\cdot}C_6Me_6]^+$. Related charge-transfer complexes have been reported to form between arenes and $[SN]^+$ (13).

Spectroscopic evidence for the formation of the blue protonated $[C_6H_5(S_2N)H]^+$ cation

Olah and co-workers (14) identified the protonated nitrobenzene $[C_6H_5NO_2H]^+$ **4a** in a mixture of $C_6H_5NO_2$ with "magic acid" $FSO_3H\text{–}SbF_5\text{–}SO_3$ by ^{1}H NMR spectroscopy.[8] In this work, the reaction of $[SNS][Sb_2F_{11}]$ and C_6H_6 was performed in liquid SO_2 at room temperature. The ^{1}H NMR spectra of the product at various temperatures (Fig. 5) showed a multiplet centered at 7.7 ppm (lower field than that of C_6H_6 (7.3 ppm)) attributable to the resonance of the C_6H_5 protons, confirmed by the ^{13}C NMR data. In addition, another resonance, although observed at all studied temperatures, was clearly resolved as a broad band at 8.8 ppm below –10°C. Its line width ($\Delta\nu_{1/2}$ = 35 Hz) and chemical shift remained essentially unchanged below –40°C. This band at 8.8 ppm is attributable to the $-(S_2N)\mathbf{H}^+$ proton of a protonated substitution product $[Ph(S_2N)H]^+$. The assignments of the resonances to $C_6\mathbf{H}_5$ and $-(S_2N)\mathbf{H}^+$ protons are consistent with the ratio of their NMR integration (ca. 5:1). The temperature invariance of the proton chemical shift implies that the blue species is not in equilibrium with a dimer (as would likely be the case for **4b**, and possibly for **2c**). The ^{14}N resonance of $[Ph(S_2N)H]^+$ (δ = –5 ppm, $\Delta\nu_{1/2}$ = 540 Hz) is comparable to those of the related **5** (15) (δ = 19 ppm, $\Delta\nu_{1/2}$ = 450 Hz) and **6** (5*f*) (δ = –134 ppm, $\Delta\nu_{1/2}$ = 680 Hz)). The ^{1}H NMR spectrum of the blue reaction product of $[SNS][AsF_6]$ and C_6H_6 in liquid SO_2 showed a broad band at 7.5–7.9 ppm (centered at 7.7 ppm, attributable to the C_6H_5 group) with poorly resolved fine structure (Fig. 4*a*). However, the $-(S_2N)\mathbf{H}^+$ proton was not observable at temperatures down to –60°C, implying a proton exchange between $[Ph(S_2N)H]^+$ and the counterion $[AsF_6]^-$. The $-(S_2N)\mathbf{H}^+$ proton in $[Ph(S_2N)H][AsF_6]$ is more labile than that in $[Ph(S_2N)H][Sb_2F_{11}]$ due to the greater basicity of $[AsF_6]^-$ (16).

The range of ^{1}H and ^{13}C chemical shifts for the C_6H_5 group in $[Ph(S_2N)H]^+$ are more similar to those of neutral sulfur monosubstituted benzenes than those of the related nitrogen monosubstituted aryls (17) (see Table 2). The proton resonances are a complex multiplet, in contrast to those in **4a** (14), which show good resolution of *meta*, *ortho*, and *para* protons at a lower field (8.0–8.8 ppm) than those of $C_6H_5NO_2$ (7.5–8.2 ppm). This implies that there is little charge delocalization into the aryl ring in $[Ph(S_2N)H]^+$. A similar trend is observed in the ^{13}C spectra (Table 2). The structure of $[Ph(S_2N)H]^+$ could be **2a**, which may be represented by resonance structures **A** and **B** in equilibrium with **C**, accounting for the high lability of the $-(S_2N)\mathbf{H}^+$ proton. The presence of positive charge on atoms directly bonded to the aryl ring in isomers **2c** and **4b**, and the extensive charge delocalization into the ring expected for **3** (see resonance structures **D** and **E**) implies that the blue protonated species does not adopt these structures. However we cannot rule out isomer **2b** on these grounds.

We have estimated, based on bond energies and a very simple view of charge redistribution, that the formation of **2**, **3**, and **4b** from $[SNS]^+$ and C_6H_6 is thermodynamically allowed.[9,10] Other less likely possibilities include $[C_6H_5\text{-}N(H)SS]^+$ **3′**[11] and dimers or oligomers of **2**, **3**, and **4b**.[12] Kinetic factors would favor formation of bonds to sulfur in the product as the LUMO of $[SNS]^+$ is sulfur based (5*e*, *j*). So far the products of reactions of $[SNS]^+$ do not include bonds to nitrogen, but are solely formed with sulfur (5*j*).

The reaction of $[SNS][AsF_6]$ and C_6Me_6

The ^{13}C NMR spectrum of the product for the reaction of $[SNS]^+$ with hexamethylbenzene C_6Me_6 in liquid SO_2 at room temperature exhibited complex resonances,[13] indicating the formation of a mixture. Part of the ^{13}C resonances may be tentatively assignable to a stable σ-type complex

[7] The reactions of benzene with $[ONO]^+$ salts are too fast (very fast even at –40°C) to monitor the intermediates. The nitration can be slowed down by combining a base Y (Y = $[OH]^-$, $[OAc]^-$, $[NO_3]^-$, Cl^-, Py, $[C(NO_2)_3]^-$, etc.) to $[ONO]^+$, forming an alternative nitrating agent NO_2Y. These NO_2Y are electron deficient and thus capable of serving as electron acceptors, forming charge-transfer complexes $[ArH{\cdot}NO_2Y]$ with electron-donating aromatics in the first step of the reactions (11).

[8] For the formation of protonated nitrobenzene **4a**, see ref. 14. The ^{1}H NMR data of **4a** were given in the reference as follows: $\delta H_2 = \delta H_6 = 8.76$, $\delta H_3 = \delta H_5 = 7.99$, $\delta H_4 = 8.46$; $J_{23} = J_{56} = 8.00$, $J_{24} = J_{46} = 1.00$; $J_{25} = J_{36} = 0.50$, $J_{26} = J_{35} = 1.00$, $J_{34} = J_{45} = 7.50$. The hydrogen atoms are numbered in accordance with IUPAC rules, i.e., H_2 and H_6 are *ortho* protons; H_3 and H_5 are *meta* protons; and H_4 is a *para* proton.

© 1998 NRC Canada

Can. J. Chem. Downloaded from www.nrcresearchpress.com by China University of Science and Technology on 09/05/12
For personal use only.

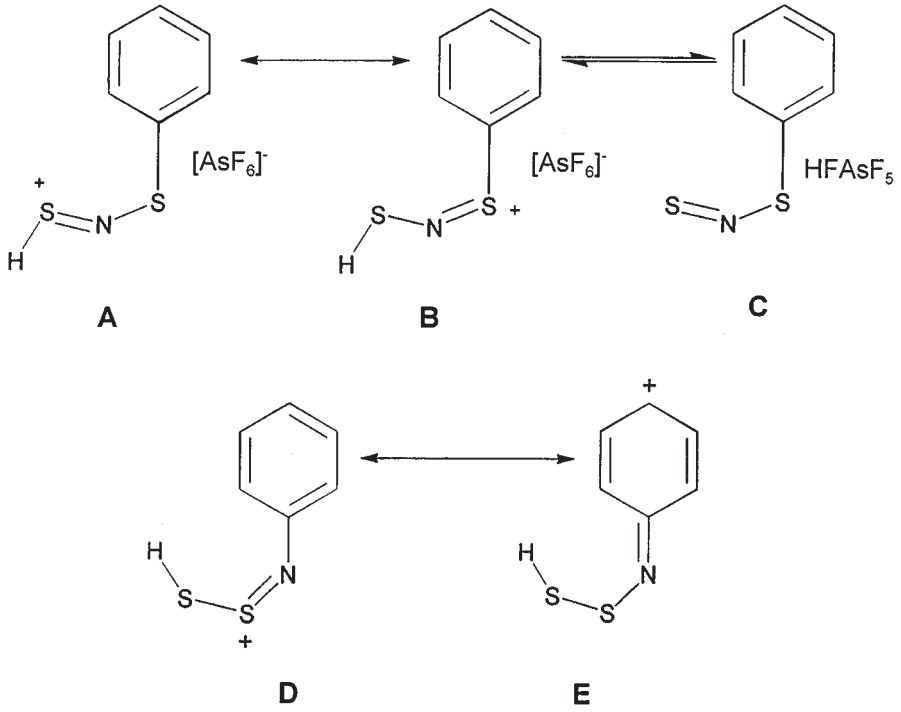

hexamethylbenzenium cation **7** in the mixture (Fig. 7). A similar σ-complex nitrohexamethylbenzenium cation **8** has been identified from the reaction of $[ONO]^+$ and C_6Me_6 by ^{13}C NMR spectroscopy (22). Concurrent with this work, Kochi and co-workers (23) very recently reported the isolation and structural characterization of a related novel σ-type chloro-arenium cation **9**.

Theoretical calculations

The geometries of the isomers **2a**, **2b**, **2c**, **3**, and **4b** were optimized at the RHF/6-31G* level. Relative energies and selected bond distances, bond angles, and dihedral angles are listed in Table 3. Isomer **4b** is the thio analogue of the known product of the reaction of ONO^+ and benzene, **4a** (14). The structure **4b** is higher in relative energy (428 kJ/mol) than **2a** (51 kJ/mol), **2b** (37 kJ/mol), **2c** (134 kJ/mol), or **3** (0 kJ/mol). This suggests that the isomers **2** and **3** are favored over **4b**. However energies may well not be the same in solution as in the gas phase, and dimers or polymers of the isomers are also possibilities.[12]

Notwithstanding these considerations, **4b** is likely the least favored isomer energetically, both from theoretical calculations and simple bond energy estimates.[9,10] The isomer **2c** is likely less favored than **2a**, **2b**, or **3**.

The calculated geometries are consistent with **2a** represented by resonance structures **A** and **B**, with **3** by resonance structures **D**, **E**, and those related to **E**, and with **2b, 2c**, and **4b** as depicted. The calculated carbon—carbon bond

[9] The standard enthalpy change ($\Delta H°$) of the reaction $C_6H_6 + [S = N = S]^+ \rightarrow C_6H_5\text{-}S\text{-}N = S^+H$ is simply estimated from the energy change in the related bond formation versus bond broken, which is formulated as $\Delta H° = D_{C—H}° + D_{S=N}° - D_{C—S}° - D_{S—N}° - D_{S—H}°$ The bond dissociation energies ($D°$) of C—H, C—S, and S—H bonds are taken as 411, 272, and 363 kJ/mol, respectively (18). The S = N and S—N bond energies were calculated as 335 and 245 kJ/mol, respectively, from the bond lengths (Å) according to the equation $E(SN) = 2143.3 - 1126.4d_{SN}$ (19). Thus, $\Delta H° = -134$ kJ/mol. Similarly, the $\Delta H°$ of the formation of **4b** from C_6H_6 and $[SNS]^+$ is estimated to be –167 kJ/mol by replacing $D_{C—S}°$ (272 kJ/mol) with $D_{C—N}°$ (305 kJ/mol) in the above equation. In this thermodynamic analysis, the following terms are neglected: the energy of charge delocalization in $[SNS]^+$, solvation energy change, entropy change, and charge redistribution from N^+ (in $[SNS]^+$; i.e., of N: 1402 kJ/mol (20)) to S^+ (e.g., in **2a**; i.e., of S: 999 kJ/mol (20)). The inclusion of energy of positive charge redistribution from N^+ to S^+ gives a new ΔH of –537 kJ/mol for **2a**.

[10] Using a similar approach as in footnote 9, the energy difference between **2a** and **3** may be estimated. The structure **3** is favored over **2a** by 14 kJ/mol, with the bond dissociation energies ($D°$) of the C—N, S—S, C—S, and S—N bonds taken as 305, 226, 272, and 245 kJ/mol, respectively (18, 19). Similarly, **3** is favored over **2b** by 394 kJ/mol and over **4b** by 384 kJ/mol, considering the bond dissociation energies of S—H (363 kJ/mol) and N—H (386 kJ/mol) bonds.

[11] The structure **3′**, i.e., $C_6H_5N(H)S^+ = S$, is an isomer of **3**. However, **3′** would contain a sulfur–sulfur double bond in the absence of bulky groups (e.g., 2,4-di-*tert*-butyl-6-methyl-*N*-thiosulfinylaniline (28*c*)). The dimer $(\mathbf{3'})_2$ is also without precendent (21). These and other oligomers containing C_6H_5– are expected to have ^{13}C and ^1H NMR spectra that would be different from that of the blue species **2**, as nitrogen, not sulfur, is attached to the phenyl ring (see text and Table 2).

[12] There are no precedents for dimers or oligomers of **2**, **3**, or **4b** (hydrogen-bonded dimers excluded), e.g., the known $RSNSR^+$ (e.g., **5** (15) and **6** (5*f*)) are monomers (5*j*, 21).

[13] The reaction of $[SNS][AsF_6]$ (0.543 g, 2.03 mmol) and C_6Me_6 (0.345 g, 2.13 mmol) in liquid SO_2 (3.27 g) at room temperature immediately gave a dark red solution, which was characterized by ^{13}C NMR spectroscopy. The ^{13}C resonances (ppm, referenced to TMS in SO_2) are 209, 168.6, 147, 144, 140, 138.5, 135, 126.5, 125, 124.5, 122.7, 54.1, 49.5, 48, 41.8, 24.5, 20.1, 18.1, 16.5.

© 1998 NRC Canada

Table 3. The RHF/6-31G* optimized geometry comparisons (bond lengths in Å, bond orders[a] in parentheses, bond angles in degrees). Atoms are numbered in accordance with IUPAC rules.[b]

	$[C_6H_5$-S1N1S2H1$]^+$		$[C_6H_5$-S1N1(H1)S2$]^+$		$[C_6H_5$-S1(H1)N1S2$]^+$		$[C_6H_5$-N1S1S2H1$]^+$		$[C_6H_5$-N1(S2)S1H1$]^+$
Parameter	**2a**	Parameter	**2b**	Parameter	**2c**	Parameter	**3**	Parameter	**4b**
C1—C6	1.400 (1.57)	C1—C6	1.394 (1.50)	C1—C6	1.393 (1.61)	C1—C6	1.425 (1.45)	C1—C6	1.390 (1.63)
C1—C2	1.397 (1.59)	C1—C2	1.394 (1.50)	C1—C2	1.388 (1.64)	C1—C2	1.429 (1.43)	C1—C2	1.360 (1.79)
C2—C3	1.379 (1.69)	C2—C3	1.381 (1.55)	C2—C3	1.384 (1.66)	C2—C3	1.363 (1.78)	C2—C3	1.372 (1.72)
C3—C4	1.391 (1.62)	C3—C4	1.388 (1.52)	C3—C4	1.384 (1.66)	C3—C4	1.405 (1.55)	C3—C4	1.382 (1.67)
C4—C5	1.387 (1.64)	C4—C5	1.388 (1.52)	C4—C5	1.392 (1.62)	C4—C5	1.393 (1.61)	C4—C5	1.409 (1.53)
C5—C6	1.380 (1.68)	C5—C6	1.381 (1.55)	C5—C6	1.377 (1.70)	C5—C6	1.370 (1.74)	C5—C6	1.380 (1.68)
C1—S1	1.745 (1.28)	C1—S1	1.757 (1.23)	C1—S1	1.762 (1.21)	C1—N1	1.323 (1.61)	C1—N1	1.357 (1.44)
S1—N1	1.517 (2.13)	S1—N1	1.732 (1.06)	S1—N1	1.718 (1.11)	N1—S1	1.536 (2.00)	N1—S1	1.786 (0.89)
N1—S2	1.622 (1.51)	N1—S2	1.544 (1.95)	N1—S2	1.530 (2.04)	S1—S2	2.077 (0.92)	N1—S2	1.727 (1.08)
S2—H1	1.323 (1.06)	N1—H1	1.013 (0.99)	S1—H1	1.333 (1.02)	S2—H1	1.328 (1.04)	S1—H1	1.324 (1.05)
S2···H2	2.61	S2···H2	3.92	S2···H2	3.826	S2···H2	2.574	S2···H2	1.852
H1-S2-N1	95.4	H1-N1-S1	110	H1-S1-N1	102.7	H1-S2-S1	92.9	H1-S1-N1	90
S1-N1-S2	137.9	S1-N1-S2	132.8	S1-N1-S2	120.8	S2-S1-N1	111.8	S1-N1-S2	126.8
N1-S1-C1	116.7	N1-S1-C1	102.8	N1-S1-C1	104.3	S1-N1-C1	142.8	S2-N1-C1	124.6
N1-S1-C1-C6	0	N1-S1-C1-C6	90	N1-S1-C1-C6	90	S1-N1-C1-C6	0	S1-N1-C1-C6	0
S2-N1-S1-C1	0	S2-N1-S1-C1	0	S2-N1-S1-C1	180	S2-S1-N1-C1	0	S2-N1-C1-C6	180
H1-S2-N1-S2	180	H1-N1-S1-C1	180	H1-S1-C1-C6	–90	H1-S2-S1-N1	0	H1-S1-N1-C1	180
Relative energy (kJ/mol)	51		37		134		0		387

[a] Bond orders were determined using the relation $D_b = D_1 - 0.71 \log b$ (ref. 27), where D_b is the bond length of bond order equal to 1 (18); D_1 is the observed bond length.
[b] See **2a**.

Can. J. Chem. Downloaded from www.nrcresearchpress.com by China University of Science and Technology on 09/05/12
For personal use only.

© 1998 NRC Canada

Can. J. Chem. Downloaded from www.nrcresearchpress.com by China University of Science and Technology on 09/05/12
For personal use only.

Fig. 7. The ^{13}C chemical shifts (ppm, referenced to TMS in liquid SO_2) of the ring and methyl carbons in $[C_6Me_5{\cdot}SNS]^+$ **7**[13] and $[C_6Me_5{\cdot}NO_2]^+$ **8**.

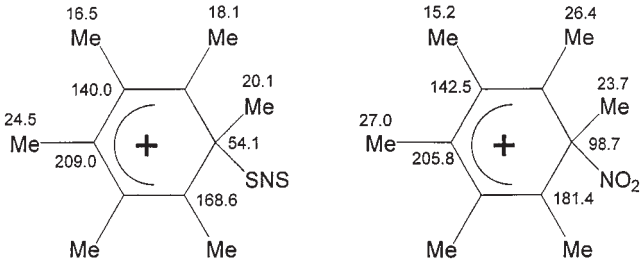

distances vary for **3** and **4b**, implying significant charge delocalization into the aryl ring in these isomers. In contrast, carbon—carbon distances are all similar in the **2** isomers. The NMR results imply little positive charge delocalization into the aryl ring consistent with the structures of **2**, but not **3** or **4b**.[14] Therefore **4b** is ruled out on thermodynamic grounds, and it does not fit the observed NMR data. The structure **3** is calculated to have the lowest energy of the isomers but does not fit the NMR data and is also kinetically not favored. All **2** isomers fit the NMR data, but **2a** and **2b** are marginally lower in energy than **2c**. The isomer **2a** has a similar structure to the known **5** (15) and **6** (5*f*) and therefore is likely the blue reaction product of benzene and $[SNS]^+$, although we cannot rule out **2b** and we have not calculated the energies of dimers and oligomers (11, 12). The Raman spectra of **2a**, **2b**, **2c**, and **3** were calculated from their stationary point geometries.[15] Unfortunately the spectrum of $[C_6H_5(S_2N)H][Sb_2F_{11}]$ is weak, and we cannot unambiguously distinguish between the isomers **2a–c** and **3**. A complete list of optimized geometries and calculated vibrational frequencies for **2a–c** and **3**, and the observed FT–Raman spectrum of $[C_6H_5(S_2N)H][Sb_2F_{11}]$ have been deposited.[4]

In conclusion the experimental results and the theoretical calculations show that $[SNS]^+$ has undergone an insertion reaction into the C—H bond of benzene to give a product that is different from that of $[ONO]^+$ **4a**, and can be reasonably formulated as $[C_6H_5(SNS)H]^+$ **2**.

The electrophilic aromatic substitution reactions of $[SNS]^+$

The electrophilic aromatic substitution reactions of $[ONO]^+$ have been extensively investigated (1, 3) and are one of the best known and most important studied organic reactions. In this work, the NMR (^1H, ^{13}C, ^{14}N) spectroscopic studies unambiguously show that the $[SNS]^+$ cation, the sulfur analogue of $[ONO]^+$, undergoes a related electrophilic substitution reaction with benzene. This type of electrophilic aromatic substitution is supported by a ^1H NMR spectroscopic study of the reaction of $[SNS]^+$ with C_6HMe_5 (26). Resonances attributable to an aromatic proton were absent in the spectrum, implying that the original aromatic proton (6.8 ppm) of C_6HMe_5 had been substituted by $[SNS]^+$.

The electrophilic reactions of both $[ONO]^+$ and $[SNS]^+$ and benzene can be viewed as proceeding by donation of electron density from the HOMO to the LUMO's of $[ONO]^+$ and $[SNS]^+$. The LUMO of $[ONO]^+$ is lower in energy that of $[SNS]^+$ (5*d*), and consistently the rate of the $[ONO]^+$–benzene reaction is very fast even at –40°C (12), whereas the rate of reaction of $[SNS]^+$ is slow even at room temperature. Consistently, the rate of the reaction of arenes with $[SNS]^+$ increases with decrease of IP of the arene.

A proposed mechanism of the electrophilic substitution of $[SNS]^+$ with benzene

The substitution of C_6H_6 with $[ONO]^+$ (1, 3) proceeds via a transient intermediate charge-transfer complex $[C_6H_6{\cdot}NO_2]^+$ (eq. [1])], which then leads to nitrobenzene via another transient intermediate, the Wheland complex **1** (eq. [2]). We have presented evidence for a relatively stable π–π^* charge-transfer complex $[C_6H_6{\cdot}SNS]^+$ (eq. [3]). We propose that $[C_6H_6{\cdot}SNS]^+$ transforms into a transient σ-type complex **10** (cf. the Wheland complex **1** (eq. [2]), which undergoes an intramolecular hydrogen transfer to give **2** (eq. [4]).

[3] $$C_6H_6 + SNS^+ \rightleftarrows [C_6H_6{\cdot}SNS]^+$$

[4] $$[C_6H_6{\cdot}SNS]^+ \rightarrow \mathbf{10} \rightarrow \mathbf{2}$$

There is evidence that **2** deprotonates to give an unidentified purple neutral species X, which is possibly $[C_6H_5(S_2N)]_x$.[2]

Conclusions

The $[SNS]^+$ cation (cf. $[ONO]^+$) has been previously shown (5) to undergo concerted, symmetry allowed reverse electron demand type cycloaddition reactions with various multiply π-bonded species. This work is the first study of the CH substitution reactions of $[SNS]^+$ opening up a new chapter in the diverse chemistry of this important cationic reagent. Both the cycloaddition and substitution reactions of $[SNS]^+$, as the $[AsF_6]^-$ salt, involve the interactions of the HOMO's of the organic substrates and the LUMO of $[SNS]^+$. The transition between the HOMO and LUMO of $[SNS]^+$ (λ = 406 nm, ϵ = 80, corresponding to 294 kJ/mol) has been observed for the first time in the UV-visible spectrum of $[SNS][AsF_6]$ in liquid SO_2 solution. The initial step of the reaction of $[SNS]^+$ with benzene is the formation of an identified weak molecule–cation charge-transfer complex $[C_6H_6{\cdot}SNS]^+$ (orange). Other arenes also formed charge-transfer complexes with the energy of the absorption of the charge-transfer band in the UV-visible spectrum being

[14]The calculated charges are in agreement with the calculated geometries and valence-bond representations given above, but it is known that charges obtained with this method are unreliable (24).

[15]The FT–Raman frequencies (ν(cm^{-1}), (relative integration, assignment)) were calculated for the lowest energy geometries of **2a** (2979 (12, CH), 2579 (83, SH), 1550 (100, ring CC), 1063 (50, CS), 788 (52, SNS)), **2b** (3264 (41, NH), 1577 (23, ring CC), 1053 (100, SN), 1040 (29, CS)), **2c** (2520 (100, SH), 1543 (49, ring CC), 1132 (29, SNS)), and **3** (3010 (19, CH), 2562 (70, SH), 1554 (100, ring CC), 1252 (35, CN), 960 (29, SN), 450 (5, SS)).

© 1998 NRC Canada

Can. J. Chem. Downloaded from www.nrcresearchpress.com by China University of Science and Technology on 09/05/12
For personal use only.

linearly related to the ionization energy of the arene. Thus the charge-transfer complex is formed by interaction of the HOMO of the arene and the LUMO of $[SNS]^+$. The analogous charge-transfer complex in the reaction of $[ONO]^+$ with benzene is a transient intermediate. A subsequent substitution of $[SNS]^+$ to benzene likely occurs on the terminal sulfur, forming a blue species, which we propose is $[C_6H_5(SNS)H]^+$ **2** supported by NMR spectroscopic evidence and theoretical calculations at the RHF/6-31G* level. This is in contrast to the aromatic nitration with $[ONO]^+$, which occurs on the central nitrogen. The difference reasonably relates to both kinetic (FMO's) and thermodynamic (lower IP of S relative to N) factors. The related protonated nitrobenzene **4a**, although identified (14) in a mixture of $C_6H_5NO_2$ with $FSO_3H–SbF_5–SO_3$ (a strong acid system), is not observed in the reaction of benzene with $[ONO]^+$ under similar conditions. The formation of **2** may occur by an intramolecular hydrogen transfer (eq. [5]) via an intermediate σ-complex **10** (cf. **1** for nitrations(1, 3)). The rate of reaction of $[SNS]^+$ with C≡N, C≡C, and other related multiple bonds (5*b*, *c*, *f*, *j*) as well as aryl rings is inversely proportional to the ionization energy of the unsaturated moiety. The $[SNS]^+$ reacts with aryl nitriles and diphenylacetylene to give 99% cycloaddition products on the C≡N and C≡C bonds with small amounts of colored impurities (5*c*, *e*), which are likely derived from attack on the aryl rings. The results imply that $[SNS]^+$ will preferential react with the C≡N and C≡C substituents of an aryl containing molecule with non-electropositive substituents. A purple colored species[2] is formed from the blue **2**, which has yet to be identified.

Evidence is presented for the first example of a dithiadiazolium charge-transfer complex $[MeCNSNS\cdot C_6H_6]^+$.

Acknowledgements

We would like to thank Dr. M.J. Schriver for his initial observations on the color changes during reaction of C_6H_6 with $[SNS]^+$ (5*d*), Dr. F. Grein for discussion on the UV-visible spectrum of $[SNS]^+$, the referees, Dr. A.J. Banister for very helpful comments on the manuscript and possible dimers and oligomers of **2**, and Dr. G. Villemure for use of the Hewlett–Packard UV-visible spectrophotometer. We also thank the Natural Sciences and Engineering Research Council (Canada) for a graduate fellowship (S.B.) and The University of New Brunswick (X.S.) for financial support.

References

1. G.A. Olah, R. Malhotra, and S.C. Narang. Nitration: methods and mechanisms. VCH, New York. 1989, and refs. therein.
2. R.J. Gillespie, J. Graham, E.D. Hughes, C.K. Ingold, and E.R.A. Peeling. Nature (London), **158**, 480 (1946).
3. J.K. Kochi. Acc. Chem. Res. **25**, 39 (1992), and refs. therein; Acta Chem. Scand. **44**, 409 (1990).
4. (*a*) E.G. Awere and J. Passmore. J. Chem. Soc. Dalton Trans. 1343 (1992), and refs. therein; (*b*) A.J. Banister, R.G. Hey, G.K. MacLean, and J. Passmore. Inorg. Chem. **21**, 1679 (1982).
5. (*a*) G.K. MacLean, J. Passmore, M.N.S. Rao, M.J. Schriver, P.S. White, D. Bethell, R.S. Pilkington, and L.H. Sutcliffe. J. Chem. Soc. Dalton Trans. 1405 (1985); G.K. MacLean, J. Passmore, M.J. Schriver, P.S. White, D. Bethell, R.S. Pilkington, and L.H. Sutcliffe. J. Chem. Soc. Chem. Commun. 807 (1983); N. Burford, J. Passmore, and M.J. Schriver. J. Chem. Soc. Chem. Commun. 140 (1986); (*b*) S. Parsons, J. Passmore, M.J. Schriver, and P.S. White. J. Chem. Soc. Chem. Commun. 369 (1991); S. Parsons, J. Passmore, M.J. Schriver, and X. Sun. Inorg. Chem. **30**, 3342 (1991); (*c*) J. Passmore, X. Sun, and S. Parsons. Can. J. Chem. **70**, 2972 (1992); (*d*) M.J. Schriver. Ph.D thesis. University of New Brunswick. 1989; (*e*) X. Sun. Ph.D thesis. University of New Brunswick. 1995; (*f*) N. Burford, J.P. Johnson, J. Passmore, M.J. Schriver, and P.S. White. J. Chem. Soc. Chem. Commun. 966 (1986); W.V.F. Brooks, S. Brownridge, J. Passmore, M.J. Schriver, and X. Sun. J. Chem. Soc. Dalton Trans. 1997 (1996); (*g*) S. Parsons, J. Passmore, M.J. Schriver, and P.S. White. Can. J. Chem. **68**, 852 (1990); (*h*) S. Parsons, J. Passmore, and X. Sun. Phosphorus Sulfur Silicon, **93**/**94**, 435 (1994); S. Parsons, J. Passmore, X. Sun, and M. Regitz. Can. J. Chem. **73**, 1312 (1995); (*i*) J. Passmore and M.J. Schriver. Inorg. Chem. **27**, 2749 (1988); W.V.F. Brooks, T.S. Cameron, S. Parsons, J. Passmore, and M.J. Schriver. Inorg. Chem. **33**, 6230 (1994); (*j*) S. Parsons and J. Passmore. Acc. Chem. Res. **27**, 101 (1994), and refs. therein.
6. J. Passmore and X. Sun. Abstr. no. 343, 76th Chem. Inst. Can. Conf. Sherbrooke, Quebec. May 30–June 3, 1993.
7. M.P. Murchie, R. Kapoor, J. Passmore, G. Schatte, and T. Way. Inorg. Synth. **31**, 102 (1996).
8. A. Wells. Structural inorganic chemistry. 5th ed. Clarendon Press, Oxford. 1984. p. 457.
9. M.J. Frisch, G.W. Trucks, H.B. Schlegel, P.M.W. Gill, B. G. Johnson, M.W. Wong, J.B. Foresman, M.A. Robb, M. Head-Gordon, E.S. Replogle, R. Gomperts, J.L. Andres, K. Raghavachari, J.S. Binkley, C. Gonzalez, R.L. Martin, D.J. Fox, D.J. Defrees, J. Baker, J.J.P. Stewart, and J.A. Pople. GAUSSIAN 92/DFT, Revision G.3. Gaussian, Inc., Pittsburgh, Pa. 1993.
10. J.B. Foresman and A. Frisch. Exploring chemistry with electronic structure methods: a guide to using Gaussian. Gaussian Inc., Pittsburgh, Pa. 1993.
11. (*a*) B. Kleman. Can. J. Phys. **41**, 2034 (1963); (*b*) R.S. Mulliken and W.C. Ermler. Polyatomic molecules. Academic Press, New York. 1981. pp. 111–117; G. Herzberg. Molecular spectra and molecular structure. III. Electronic spectra and electronic structure of polyatomic molecules. Van Nostrand, Princeton, N.J. 1967. pp. 500–505.
12. E.K. Kim, T.M. Bockman, and J.K. Kochi. J. Am. Chem. Soc. **115**, 3091 (1993); T.M. Bockman, Z.J. Karpinski, S. Sankararaman, and J.K. Kochi. J. Am. Chem. Soc. **114**, 1970 (1992); E.K. Kim, K.Y. Lee, and J.K. Kochi. J. Am. Chem. Soc. **114**, 1756 (1992).
13. S. Brownstein and B. Louie. Can. J. Chem. **65**, 1361 (1987).
14. G.A. Olah and T.E. Kiovsky. J. Am. Chem. Soc. **90**, 6461 (1968).
15. O. Glemser, E. Kindler, B. Krebs, R. Mews, F.M. Schnepel, and J. Wegener. Z. Naturforsch B: Anorg. Chem. Org. Chem. **35**, 657 (1980).
16. T.A. O'Donnell. Superacids and acidic melts as inorganic chemical reaction media. VCH, New York. 1993. Chap. 3, and refs. therein.
17. C.J. Pouchert and J. Behnke. The Aldrich library of ^1H and ^{13}C NMR spectra. Vol. 2. 1st ed. Aldrich Chemical Company, Inc., Milwaukee. 1993.
18. J.E. Huheey, E.A. Keiter, and R.L. Keiter. Inorganic chemistry; principles of structure and reactivity. Harper Collins, New York. 1993. pp. 21–34.

© 1998 NRC Canada

19. S. Parsons and J. Passmore. Inorg. Chem. **31**, 526 (1992).
20. F.A. Cotton and G. Wilkinson. Advanced inorganic chemistry. 5th ed. Wiley–Interscience, New York. 1988. p. 1381.
21. A.R. Katritzky, C.W. Rees, and E.F.V. Scriven (*Editors*). Comprehensive heterocyclic chemistry II. Pergamon, Oxford, U.K. 1996.
22. G.A. Olah, H.C. Lin, and D.A. Forsyth. J. Am. Chem. Soc. **96**, 6908 (1974).
23. R. Rathore, S.H. Loyd, and J.K. Kochi. J. Am. Chem. Soc. **116**, 8414 (1994).
24. S. Fliszár, A. Goursot, and H. Dugas. J. Am. Chem. Soc. **96**, 4358 (1974).
25. R. Mayer. Phosphorus Sulfur Relat. Elem. **23**, 277 (1985).
26. (*a*) D.H.R. Barton and M.J. Robson. J. Chem. Soc. Perkin Trans. I, 1245 (1974); (*b*) Y. Inagaki, T. Hosogai, R. Okazaki, and N. Inamoto. Bull. Chem. Soc. Jpn. **53**, 205 (1980); (*c*) F. Iwasaki. Acta Cryst. B, **35**, 2099 (1979); (*d*) S. Coffey. Rec. Trav. Chim. Pays-Bas, **40**, 747 (1921).
27. L. Pauling. The nature of the chemical bond. 3rd ed. Cornell University Press, Ithaca. 1960. p. 239.

Can. J. Chem. Downloaded from www.nrcresearchpress.com by China University of Science and Technology on 09/05/12
For personal use only.

© 1998 NRC Canada

The first reagent-controlled asymmetric halolactonizations. Dihydroquinidine–halogen complexes as chiral sources of positive halogen ion

Robert B. Grossman and Robert J. Trupp

Abstract: The first reagent-controlled asymmetric halolactonizations are described. Complexes of I^+ with *O*-acyl- and *O*-aryldihydroquinidines are used to promote the asymmetric halolactonization of prochiral γ,δ-unsaturated carboxylic acids with low but measurable and reproducible enantioselectivity. Experimental factors affecting the ee's are described.

Key words: halocyclization, halogenation, halonium ions, chiral, stereoselective.

Résumé : On décrit les premières réactions d'halogénolactonisations contrôlées par le réactif. On utilise des complexes de I^+ avec des *O*-acyl- et *O*-aryldihydroquinidines pour favoriser l'halogénolactonisation d'acides carboxyliques γ,δ-insaturés prochiraux avec une énantiosélectivité faible, mais mesurable et reproductible. On décrit les facteurs influençant les ee.

Mots clés : halogénocyclisation, halogénation, ions halogénium, chiral, stéréosélectif.

[Traduit par la Rédaction]

The development of efficient processes for the transformation of achiral starting materials into chiral, enantiopure products continues to be an important goal in organic synthesis (1). Two basic approaches to asymmetric synthesis have been studied. In *substrate-controlled* asymmetric synthesis, an achiral compound is rendered chiral and enantiopure by attachment of a chiral auxiliary, allowing diastereoselective transformations to be executed. The chiral auxiliary is then removed. In *reagent-controlled* asymmetric synthesis, a chiral, enantiopure reagent causes one enantioface or enantiotopic group of a prochiral compound to be selectively transformed. The main disadvantages of substrate-controlled asymmetric synthesis are that the substrate must have a suitable functional group (usually a carboxylic acid) to which the chiral auxiliary can be attached, and that addition and removal of the auxiliary usually requires two extra synthetic steps. Reagent-controlled asymmetric synthesis does not have these problems, but finding reagents with which high enantioselectivities can be achieved is very challenging. The epitome of reagent-controlled asymmetric synthesis is reached when the chiral component can be used in catalytic quantities (2), as in enzyme-mediated organic synthesis (3).

Reactions of alkenes, especially oxidation reactions such as epoxidations and dihydroxylations, have been popular targets for asymmetric modification, and some of the most widely used reagent-controlled catalytic asymmetric transformations have been derived therefrom (4–6). Halogenation reactions (including cohalogenations and halocyclizations) represent another class of widely used alkene oxidation reactions (7–10), but although examples of *substrate-controlled* asymmetric halogenations are abundant in the literature (11–15), there are few or no examples of *reagent-controlled* asymmetric halogenations. The asymmetric addition of Br_2 to cyclohexene in the presence of chiral quaternary ammonium salts has been investigated. Of course the halonium ion derived from cyclohexene is achiral, so the enantiomer-determining step in this reaction is nucleophilic attack of Br^- on the halonium ion (16). A very efficient catalytic asymmetric iodocarbocyclization of unsaturated malonates has also been demonstrated recently: a chiral Ti catalyst reacts with the malonate portion of the substrate, giving a chiral enolate, and a diastereoselective halocyclization ensues (17). The *seleno*cyclization of prochiral unsaturated nucleophiles mediated by chiral, enantiopure diselenides proceeds with very high diastereoselectivities (18, 19). Very good ee's were very recently reported for a Pd-catalyzed hydroxychlorination of alkenes (20), and it should be relatively easy to modify this system to accomplish halocyclization, instead.

We envisioned a reagent-controlled asymmetric cohalogenation reaction in which a *chiral source of* X^+ would be used to deliver X^+ selectively to one enantioface of a prochiral alkene to give a chiral, enantioenriched halonium ion (eq. [1]). Stereospecific nucleophilic attack at one of the

[1] 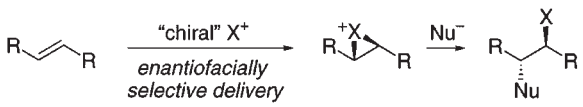

Received March 16, 1998.

R.B. Grossman[1] and R.J. Trupp. Department of Chemistry, University of Kentucky, Lexington, KY 40506–0055, U.S.A.

[1]Author to whom correspondence may be addressed. Telephone: (606) 257-1285. Fax: (606) 323-1069. E-mail: rbgros1@pop.uky.edu

© 1998 NRC Canada

Scheme 1.

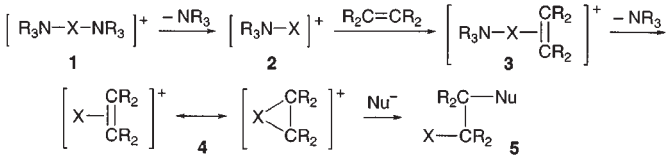

Scheme 2.

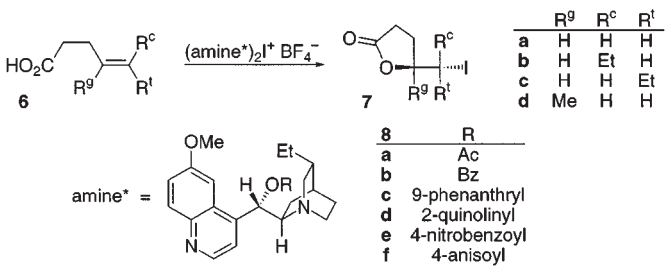

	R^g	R^c	R^t
a	H	H	H
b	H	Et	H
c	H	H	Et
d	Me	H	H

8	R
a	Ac
b	Bz
c	9-phenanthryl
d	2-quinolinyl
e	4-nitrobenzoyl
f	4-anisoyl

electrophilic carbon atoms would then give a chiral, enantioenriched product.

A reagent-controlled asymmetric cohalogenation requires a chiral source of X^+. Halogen complexes $(amine)_2X^+$ Y^- have seen increasing use in organic synthesis in recent years as mild sources of X^+ (21, 22). Recent work (15, 23) has shown that $(amine)_2X^+$ complexes **1** react with alkenes by dissociation of an amine to give $(amine)X^+$ complex **2** (Scheme 1), association of an alkene with nascent **2** to give the $[(amine)X(alkene)]^+$ complex **3**, and dissociation of the second amine from **3** to give the halonium ion, **4**. Attack of a nucleophile Nu^- on **4** then provides the isolable species, **5**. Loss of the second amine may also be concerted with nucleophilic attack on one of the electrophilic C atoms; in other words, Nu^- may attack **3** directly to give **5**, and intermediate **4** may not have an independent existence at all.

It occurred to us that if a *chiral, enantiopure amine* were used to form the $(amine)_2X^+$ complex, the association of a prochiral alkene with the nascent $(amine)X^+$ complex might proceed with enantiofacial selectivity to provide, after amine dissociation, a *chiral, enantioenriched halonium ion*, which could be captured by a nucleophile to give enantioenriched products. To test the hypothesis, we decided to study the iodolactonization of γ,δ-unsaturated carboxylic acids (**6**) to give δ-iodo-γ-lactones (**7**) using complexes $(amine^*)_2I^+$ BF_4^-, where amine* = *O*-acyl- or *O*-aryldihydroquinidine (**8**) (Scheme 2). This particular reaction was chosen for study for the following reasons.

(*i*) A cyclization reaction was chosen because it involved *intramolecular* nucleophilic capture of the iodonium ion. The rates of racemization processes such as alkene-to-alkene or alkene-to-amine transfer of I^+, which were shown to occur at perceptible rates in other systems (24, 25), were expected to decrease relative to nucleophilic capture if the latter occurred in an intramolecular fashion. The intramolecular reaction was also expected to give fewer regioisomeric complications for unsymmetrically substituted alkenes (7–9).

(*ii*) Iodolactonization was chosen over bromolactonization because the cyclization of an $(alkene)_2I^+$ complex is much faster than the cyclization of a $(alkene)_2Br^+$ complex (24). A longer lifetime for the $(alkene)_2X^+$ complex could lead to enantiomer equilibration and a decrease in the ee of the product.

(*iii*) *O*-Acyl- and *O*-aryldihydroquinidines were chosen as the chiral amine component of $(amine)_2I^+$ BF_4^- because a large number of them were known (6), they were easily prepared, and they had a long and venerable history in asymmetric synthesis (4, 26). Moreover, quinuclidine complexes of I^+ and Br^+ were well-known (27, 28).

(*iv*) The BF_4^- counterion for the $(amine)_2I^+$ complex was chosen because, unlike I^-, this non-nucleophilic counterion was not expected to equilibrate iodonium ion enantiomers by displacing I^+ from the alkene (7–9).

(*v*) Acids **6** were known compounds, and their halocyclizations to give γ-lactones **7** were thoroughly studied (7–9).

We are pleased to report the first reagent-controlled asymmetric halolactonizations of prochiral unsaturated carboxylic acids.

Table 1. Effect of substrate and amine structures on enantioselectivity of iodolactonizations.[a]

Acid **6**	Amine **8**	% Yield **7**	% ee **7**	% Recovery **8**
6a	**8a**	62	0	85
6b	**8a**	70	0	80
6c	**8a**	44	0	91
6d	**8a**	53	0	80
6a	**8b**	54	0	70
6b	**8b**	80	7	80
6c	**8b**	70	0	77
6d	**8b**	88	3	89

[a] See Scheme 3 for reaction and definitions. Neat **6** was added to a 25 mM solution of iodinating agent in CH_2Cl_2.

Results and discussion

The cyclizations of four γ,δ-unsaturated carboxylic acids with different substitution patterns around the alkene (terminal (**6a**), *cis*-disubstituted (**6b**) (29), *trans*-disubstituted (**6c**) (29), and geminally disubstituted (**6d**) (30)) were studied. In our initial experiments, the active halogenating agent was prepared in situ by sequential addition of 1.08 equiv. $AgBF_4$ and 1.00 equiv. I_2 to 2.16 equiv. **8a** or **8b** in CH_3CN, respectively (21). The solvent was replaced with CH_2Cl_2, the solution was cooled to –78°C, and 1.08 equiv. unsaturated acid **6** were added. The mixture was maintained at –78°C for 30 min, then allowed to warm to room temperature over 30 min. After filtration through Celite and quenching with aqueous Na_2SO_3, the products were isolated and purified by standard techniques. The reactions proceeded regioselectively in all cases to give only the γ-lactones **7** and no δ-lactones, as shown by the IR spectra of the products. Compounds **6b** and **6c** stereospecifically gave **7b** and **7c**, respectively. Yields of **7** and recoveries of **8** were good to excellent. The ee's of **7** were assessed by capillary GC on a chiral column (Table 1). We were disappointed to find that in most cases racemic **7** was obtained. However, iodolactonization of **6b** mediated by **8b** gave **7b** in 7% ee,

© 1998 NRC Canada

Table 2. Effect of concentration on enantioselectivity of iodolactonization of **6b**.[a]

[**8b**]	[**6b**] [b]	% Yield **7b**	% ee **7b**	% Recovery **8b**
54 mM	neat	80	7	80
27 mM	neat	90	15	84
13.5 mM	neat	92	15	80
27 mM	108 mM	86	14	77
27 mM	27 mM	85	8	82
27 mM	108 mM [c]	89	7	84

[a] See Scheme 1 for reaction and definitions.
[b] Before addition to the reaction mixture.
[c] Also 108 mM in AcOH.

and iodolactonization of **6d** in the presence of the same amine gave **7d** in 3% ee.

We decided to investigate whether the ee of **7b** could be increased by modification of the reaction conditions. If the halonium ion formed with a higher ee initially, one way in which the ee might be degraded was by displacement of I^+ from an iodonium ion by an alkene or an amine, a phenomenon discovered and investigated by Brown and Fraser-Reid and co-workers (24, 25). We hypothesized that dilution of the reaction mixture might increase the ee, and in fact this effect was observed (Table 2). With 54 mM **8b**, the iodolactonization of **6b** gave **7b** in 7% ee. *Halving the concentration doubled the ee to 15%.* Alas, halving the concentration again did not lead to further improvement. A high local concentration of acid at the point of addition of the alkene to the reagent solution may have led to deterioration of the ee, so the **6b** was diluted with CH_2Cl_2 before it was added to the reagent solution. The ee of **7b** remained substantially unchanged at 14%. Further dilution of **6b**, however, degraded the ee to 8%. To decrease the amount of free amine that was present in the solution, one equivalent of AcOH was combined with **7b** prior to its addition to the reaction mixture. Under these conditions the ee was degraded even further, to 7%. (The ee's were reproducible to within 0–2 percentage points, both for each sample and for samples obtained in different runs under identical conditions.) It should be noted that the yield of **7b** and recovery of **8b** remained substantially unchanged by all changes in reaction conditions.

Several other quinidines were investigated for their ability to induce enantioselective cyclization of **6b**. Quinidines **8c** and **8d** were examined in the hope that their greater steric bulk might communicate the asymmetry of the amine better to the approaching alkene, and quinidines **8e** and **8f** were examined to see whether varying the electronic nature of the aroyl group could affect the ee positively. Under the same conditions under which the reagent derived from **8b** gave a 14% ee of **7b**, though, the analogous reagents derived from compounds **8c–8f** gave **7b** with ee's of 3%, 4%, 3%, and 11%, respectively.

The N—Br bond (ca. 2.15 Å) (27) is slightly shorter than the N—I bond (ca. 2.3 Å) (28), so it was hypothesized that an **8b**–Br^+ complex might show higher enantiofacial discrimination toward **6b** than an **8b**–I^+ complex. When Br_2 replaced I_2 in the procedure that gave **7b** in 14% ee, compound **9**, the bromo analog of **7b**, was obtained in only 2% ee. Apparently the longer lifetime of bromonium ions, and the thereby enhanced opportunity to racemize, was more important to the outcome of the reaction than the shorter N—Br bond (24).

Several reasons for the low enantioselectivity can be adduced.

(*i*) The long N—I bond and the linear nature of the (amine)I^+(alkene) complex conspire to diminish the influence of the shape of the amine on the selectivity of approach of the two enantiofaces of the alkene. (The I^+ atom probably coordinates to the more basic of the two N atoms in **8b**, viz. the quinuclidine N, as does OsO_4.)

(*ii*) I^+ transfer to the alkene occurs from the carboxylate, i.e., via an acyl hypoiodite, and not directly from the amine.

(*iii*) The amine **8b** remains associated with the two iodonium ions (**6b**)I^+, either as the (amine)I^+(alkene) complex (**8b**)I^+(**6b**) (23), or as the carboxylate salt **8b**·H^+ (**6b**$^-$)I^+, where **6b**$^-$ is deprotonated **6b**. If this is the case, the two iodonium ions formed upon coordination of one or the other enantioface of **6b** to I^+ are *diastereomers*, not enantiomers. It is therefore possible that the two iodonium ions are in rapid equilibrium with one another, and that the observed enantioselectivities are due to *kinetic resolution* upon cyclization. However, if such a process were occurring, dilution should have a detrimental effect on the ee by retarding the equilibration of the diastereomeric iodonium ions, a prediction that is contrary to our observations.

In conclusion, we have demonstrated for the first time that chiral amines can induce asymmetry in halolactonization reactions. Future work from this laboratory will explore other substrate classes and other chiral amines in a continuing quest for a synthetically useful reagent-controlled asymmetric halolactonization reaction.

Experimental section

General

Acids **6b** and **6c** were prepared by homologation of the corresponding 3-hexen-1-ols, while **6d** was prepared by the literature procedure (29, 30). The latter compound was stored as its Na^+ salt because of its tendency to undergo spontaneous cyclization. Quinidines **8a–8f** were prepared by literature techniques (31–33). The ee's of lactones **7a–7d** and **9** were measured by capillary GC on a 25 m Lipodex E (50% octakis(3-*O*-butyryl-2,6-di-*O*-pentyl)-γ-cyclodextrin) chiral column purchased from Prof. Dr. W.A. König, Universität Hamburg; α values are collected in Table 3. New

© 1998 NRC Canada

compounds **7b**, **7c**, and **9** were prepared in racemic form using standard methods (7–9) and were characterized fully.

Best procedure for asymmetric iodolactonization of 6b

Compound **8b** (464 mg, 1.08 mmol) was dissolved in CH_3CN (20 mL), $AgBF_4$ (106 mg, 0.54 mmol) was added, and the solution allowed to stir for 10 min. A color change from yellow to brown was observed. The solvent was removed under reduced pressure to afford a brown solid. The flask was filled with N_2, and the solid was redissolved in freshly distilled CH_2Cl_2 (10 mL). Iodine (127 mg, 0.50 mmol) was dissolved in CH_2Cl_2 (30 mL) and added to the flask by syringe. The precipitation of a light gray solid was observed, and the reaction was allowed to continue for 10 min. The flask was then cooled to –78°C, and a solution of **6b** (73 μL, 0.54 mmol) in dry CH_2Cl_2 (5 mL) was added dropwise by addition funnel. The solution was allowed to stir for 30 min. The flask was allowed to warm to room temperature, with stirring, for an additional 30 min. The reaction was then filtered through Celite® and quenched with saturated aqueous Na_2SO_3. The organic layer was washed three times with 1 M H_2SO_4 and three times with saturated aqueous $NaHCO_3$, dried over anhydrous $MgSO_4$, filtered, and evaporated to afford **7b** (108 mg, 0.43 mmol, 86% yield) as a clear yellow oil, 14% ee, $[\alpha]_D^{22} = -4.09$ (*c* 1.74, CH_2Cl_2), absolute configuration not determined.

The aqueous acidic washes were made basic with 3 M NaOH and extracted with ether. The organic layer was dried over $MgSO_4$, filtered, and evaporated to give recovered **8b** (380 mg, 0.88 mmol, 82% recovery) as a white foam-like solid.

*5-Iodo-γ-valerolactone (**7a**) (ref. 34):* IR (neat): 2955, 1770, 1456, 1417, 1336, 1299, 1278, 1165, 1078, 1016, 982, 910, 874, 814, 795, 652, 611 cm^{-1}. ^1H NMR (200 MHz, $CDCl_3$), δ: 4.58 (m, 1H), 3.39 (m, 2H), 2.60 (m, 3H), 2.05 (m, 1H). $^{13}C\{H\}$ NMR (50 MHz, $CDCl_3$), δ: 176.5, 78.6, 29.0, 28.2, 8.0.

threo-*5-Iodo-γ-heptanolactone (**7b**):* After Kugelrohr distillation, 100% pure by GC–MS, 19:1 **7b**:**7c**. IR (neat): 2971, 2982, 2853, 1778, 1459, 1421, 1383, 1360, 1265, 1188, 1172, 1151, 1036, 1015, 986, 912, 896, 738, 704 cm^{-1}. ^1H NMR (200 MHz, $CDCl_3$), δ: 4.40 (m, 1H), 4.10 (m, 1H), 2.65 (m, 2H), 2.45 (m, 1H), 2.15 (m, 1H), 1.90 (m, 2H), 1.10 (t, 7.2 Hz, 3H). $^{13}C\{H\}$ NMR (50 MHz, $CDCl_3$), δ: 128.1, 81.9, 41.3, 29.3, 28.8, 27.0, 14.6.

erythro-*5-Iodo-γ-heptanolactone (**7c**):* After Kugelrohr distillation, 100% pure by GC–MS, 19:1 **7c**:**7b**. IR (neat): 2971, 2927, 1782, 1459, 1421, 1382, 1331, 1265, 1187, 1169, 1036, 1008, 986, 912, 896, 737, 704 cm^{-1}. ^1H NMR (200 MHz, $CDCl_3$), δ: 4.42 (m, 1H), 4.10 (dt, 1H), 2.59 (m, 3H), 1.98 (m, 3H), 1.10 (t, 7.2 Hz, 3H). 13C{H} NMR (50 MHz, $CDCl_3$), δ: 176.1, 81.8, 41.4, 29.2, 28.8, 28.6, 13.6.

*5-Iodo-4-methyl-γ-valerolactone (**7d**) (ref. 35):* IR (neat): 2977, 2933, 1770, 1456, 1417, 1381, 1273, 1254, 1159, 1124, 1083, 1065, 1002, 975, 949, 933, 909, 820, 800, 773, 643, 612 cm^{-1}. ^1H NMR (200 MHz, $CDCl_3$), δ: 3.41 (s, 2H), 2.72 (dt, 2H), 2.25 (m, 2H), 1.15 (s, 3H). $^{13}C\{H\}$ NMR (50 MHz, $CDCl_3$), δ: 175.8, 84.0, 33.1, 29.6, 26.1, 14.3.

Table 3. Separation of lactone enantiomers by chiral capillary GC.[a]

Lactone	α
7a	1.08
7b	1.22
7c	1.08
7d	1.18
9	1.27

[a]Lipodex E column, 25 m, 150°C to 170°C ramp, 1°C min^{-1}, FID detection.

threo-*5-Bromo-γ-heptanolactone (**9**):* After Kugelrohr distillation, 99% pure by GC–MS. IR (neat): 2970, 2878, 1760, 1460, 1362, 1337, 1284, 1180, 1106, 915 cm^{-1}. ^1H NMR (200 MHz, $CDCl_3$), δ: 4.18 (m, 1H), 4.00 (m, 1H), 2.65 (m, 2H), 2.45 (m, 1H), 2.23 (m, 1H), 1.95 (m, 2H), 1.12 (t, 7.2 Hz, 3H). $^{13}C\{H\}$ NMR (50 MHz, $CDCl_3$), δ: 175.2, 80.7, 59.6, 28.2, 27.9, 25.3, 12.3.

Acknowledgements

The authors gratefully acknowledge the financial support of the University of Kentucky and the donors of the Petroleum Research Fund, administered by the American Chemical Society. We thank Professor Greg Fu for helpful comments on the manuscript and Professor Stan Brown for useful discussions.

References

1. D.J. Ager and M.B. East. Asymmetric synthetic methodology. CRC Press, New York. 1996.
2. R. Noyori. Asymmetric catalysis in organic synthesis. Wiley, New York. 1994.
3. K. Faber. Biotransformations in organic chemistry — A textbook. Springer-Verlag, Berlin. 1995.
4. S. Chang, J.M. Galvin, and E.N. Jacobsen. J. Am. Chem. Soc. **116**, 6937 (1994), and refs. therein.
5. R.A. Johnson and K.B. Sharpless. *In* Comprehensive organic synthesis. Vol. 7. *Edited by* B.M. Trost and I. Fleming. Pergamon Press, Oxford. 1991. p. 389.
6. H.C. Kolb, M.S. VanNieuwenhze, and K.B. Sharpless. Chem. Rev. **94**, 2483 (1994).
7. M.D. Dowle and D.I. Davies. Chem. Soc. Rev. 171 (1979).
8. P. Bartlett. *In* Asymmetric synthesis. Vol. 3. *Edited by* J.D. Morrison. Academic Press, Orlando, Fla. 1984.
9. G. Cardillo and M. Orena. Tetrahedron, **46**, 3321 (1990).
10. J. Rodriguez and J.-P. Dulcère. Synthesis, 1177 (1993).
11. S. Jew, S. Terashima, and K. Koga. Tetrahedron, **35**, 2345 (1979).
12. S. Najdi, D. Reichlin, and M.J. Kurth. J. Org. Chem **55**, 6241 (1990).
13. S. Shibuya, T. Yokomatsu, and H. Iwasawa. J. Chem. Soc. Chem. Commun. 728 (1992).
14. H. Moon, S.W.E. Eisenberg, M.E. Wilson, N.E. Schore and M.J. Kurth. J. Org. Chem. **59**, 6504 (1994).
15. A.A. Neverov, T.L. Muise, and R.S. Brown. Can. J. Chem. **75**, 1844 (1997).

© 1998 NRC Canada

16. G. Bellucci, G. Berti, R. Bianchini, and L. Orsini. Gazz. Chim. Ital. **116**, 77 (1986), and refs. therein.
17. T. Inoue, O. Kitagawa, O. Ochiai, M. Shiro, and T. Taguchi. Tetrahedron Lett. **36**, 9333 (1995).
18. T. Wirth. Liebigs Ann./ Recl. 2189 (1997).
19. R. Déziel, E. Malenfant, C. Thibault, S. Fréchette, and M. Gravel. Tetrahedron Lett. **38**, 4753 (1997), and refs. therein.
20. A. El-Qisairi, O. Hamed, and P.M. Henry. J. Org. Chem. **63**, 2790 (1998).
21. R. Lemieux and A. Morgan. Can. J. Chem. **43**, 2190 (1965), and papers following.
22. T. Ray. *In* Encyclopedia of reagents for organic synthesis. Vol. 4. *Edited by* L.A. Paquette. John Wiley & Sons, Chichester. 1995. p. 2839.
23. A.A. Neverov and R.S. Brown. J. Org. Chem. **63**, 5997 (1998).
24. A.A. Neverov and R.S. Brown. J. Org. Chem. **61**, 962 (1996).
25. R. Rodebaugh and B. Fraser-Reid. Tetrahedron, **52**, 7663 (1996).
26. H.U. Blaser. Chem. Rev. **92**, 935 (1992).
27. L.K. Blair, K.D. Parris, P.S. Hii, and C.P. Brock. J. Am. Chem. Soc. **105**, 3649 (1983).
28. C.P. Brock, Y. Fu, L.K. Blair, P. Chen, and M. Lovell. Acta Crystallogr. Sect. C: Cryst. Struct. Commun. **C44**, 1582 (1988), and refs. therein.
29. L. Crombie, S.H. Harper, R.E. Stedman, and D. Thompson. J. Chem. Soc. 2445 (1951).
30. L. Crombie, A.J.B. Edgar, S.H. Harper, M.W. Lowe, and D. Thompson. J. Chem. Soc. 3552 (1950).
31. K.B. Sharpless, W. Amberg, M. Beller, H. Chen, J. Hartung, Y. Kawanami, D. Lübben, E. Manoury, Y. Ogino, T. Shibata, and T. Ukita. J. Org. Chem. **56**, 4585 (1991).
32. H.C. Kolb, P.G. Andersson, and K.B. Sharpless. J. Am. Chem. Soc. **116**, 1278 (1994).
33. J. Hartung and K.B. Sharpless. World Patent 9 307 142. 1993.
34. E.E. van Tamelen and M. Shamma. J. Am. Chem. Soc. **76**, 2315 (1954).
35. T. Tabuchi, J. Inanga, and M. Yamaguchi. Tetrahedron Lett. **27**, 3891 (1986).

© 1998 NRC Canada

Photochemical nucleophile–olefin combination, aromatic substitution (photo-NOCAS) reaction: methanol, β-myrcene, and 1,4-dicyanobenzene. Intramolecular cyclization of an ene–diene radical cation[1]

Donald R. Arnold and Kimberly A. McManus

Abstract: The photochemical nucleophile–olefin combination, aromatic substitution (photo-NOCAS) reaction of methanol, 7-methyl-3-methylene-1,6-octadiene (β-myrcene, **1**), and 1,4-dicyanobenzene yields five 1:1:1 adducts: *cis*-2-(4-cyanophenyl)-4-(1-methoxy-1-methylethyl)-1-methylenecyclohexane (**15**), *trans*-2-(4-cyanophenyl)-4-(1-methoxy-1-methylethyl)-1-methylenecyclohexane (**16**), 1-(4-cyanophenylmethyl)-4-(1-methoxy-1-methylethyl)cyclohexene (**17**), 4-[4-methoxy-3,3-dimethylcyclohex-(*E*)-1-ylidenyl]methylbenzonitrile (**18**), and 4-(1-vinyl-4-*trans*-methoxy-3,3-dimethylcyclohexyl)benzonitrile (**19**). All of these adducts are cyclic; variation in the product ratio as a function of methanol concentration indicates cyclization is occurring, 1,6-*endo*, with both the initially formed radical cation and with the intermediate β-alkoxyalkyl radicals. Evidence based upon comparison of the ionization and oxidation potential of β-myrcene with model alkenes and with conjugated dienes indicates the initial electron transfer involves the trisubstituted mono alkene moiety; the diene moiety, mono-substituted at a nodal position, has a higher oxidation potential. High-level ab initio molecular orbital calculations (MP2/6-31G*//HF/6-31G*) provide useful information regarding the nature (relative energies and charge and spin distribution) of the intermediate radical cations, which supports the proposed reaction mechanism.

Key words: photoinduced electron transfer, radicals, radical cations, β-myrcene, cyclization.

Résumé : La réaction photochimique de combinaison nucléophile–oléfine avec substitution aromatique (photo-NOCAS) entre le méthanol, le 7-méthyl-3-méthylène-octa-1,6-diène (β-myrcène, **1**) et le 1,4-dicyanobenzène fournit cinq adduits 1:1:1: *cis*-2-(4-cyanophényl)-4-(1-méthoxy-1-méthyléthyl)-1-méthylènecyclohexane (**15**), *trans*-2-(4-cyanophényl)-4-(1-méthoxy-1-méthyléthyl)-1-méthylènecyclohexane (**16**), 1-(4-cyanophénylméthyl)-4-(1-méthoxy-1-méthyléthyl)cyclohexène (**17**), 4-[4-méthoxy-3,3-diméthylcyclohex-(*E*)-1-ylidényl]méthylbenzonitrile (**18**) et le 4-(1-vinyl-4-*trans*-méthoxy-3,3-diméthylcyclohexyl)benzonitrile (**19**). Tous ces produits sont cycliques; les variations dans les rapports de produits en fonction de la concentration de méthanol indiquent que la cyclisation se produit, 1,6-*endo*, tant avec le cation radical formé initialement qu'avec les radicaux β-alkoxyalkyles intermédiaires. Des données obtenues sur la base d'une comparaison des potentiels d'ionisation et d'oxydation du β-myrcène avec ceux d'alcènes et de dienes conjugués indiquent que le transfert initial d'électron implique la portion trisubstituée du monoalcène; le potentiel d'oxydation de la portion diénique monosubstituée en position nodale est supérieur. Des calculs ab initio d'orbitales moléculaires à un niveau élevé (MP2/6-31G*//HF/6-31G*) fournissent des informations utiles relatives à la nature (énergies relatives et distributions de charge et de spin) des cations radicaux intermédiaires qui supportent le mécanisme réactionnel proposé.

Mots clés : transfert d'électron photoinduit, radicaux, cations radicaux, β-myrcène, cyclisation.

[Traduit par la Rédaction]

Introduction

The definition of the scope and limitations of the photochemical nucleophile–olefin combination, aromatic substitution (photo-NOCAS) reaction has received considerable attention (1–3). This reaction has synthetic utility; yields of the nucleophile, olefin, aromatic (1:1:1) adducts can be high. The reaction is general for mono alkenes, and dienes, both conjugated and nonconjugated, and the reaction can incorporate a variety of nucleophiles; e.g., methanol, fluoride anion, cyanide anion, acetonitrile. Our understanding of the mechanism of this reaction has progressed to the point where the

Received April 27, 1998.

D.R. Arnold[2] and K.A. McManus. Department of Chemistry, Dalhousie University, Halifax, NS B3H 4J3, Canada.

[1]See refs. 1 and 2 for preceding parts of this series.

[2]Author to whom correspondence may be addressed. Telephone: (902) 494-3714. Fax: (902) 494-1310. E-mail: Donald.Arnold@dal.ca

© 1998 NRC Canada

results from a new reaction can now provide useful fundamental information regarding the reactivity of the intermediates, i.e., radical cation, radical anion, and radical. A main objective of this project was to determine the probability and regiochemistry of intramolecular cyclization of the intermediate(s) involved during the reaction of a nonconjugated alkene – conjugated diene, 7-methyl-3-methylene-1,6-octadiene (β-myrcene, **1**).

Relevant examples of this reaction are shown in reactions [1]–[4] (2). The irradiation of an acetonitrile–methanol solution of 1,4-dicyanobenzene (2) and the unsymmetric mono alkene, 2-methyl-2-butene (**3**), yields both regioisomeric 1:1:1 adducts (**4**, **5**) in 70% yield (reaction [1]) (2*a*). The mechanism proposed for formation of the major (6:1) isomer, 3-(4-cyanophenyl)-2-methoxy-3-methylbutane (**4**), involves rapid equilibration of the initially formed distonic radical cation intermediates, followed by irreversible deprotonation, with preferential formation of the more stable β-alkoxyalkyl radical (2*a*, *b*).

Similar irradiation of an acetonitrile–methanol solution of 1,4-dicyanobenzene and 2-methyl-1,3-butadiene (**6**) gave four isomeric 1:1:1 adducts (reaction [2]) (2*c*). The major

[1]

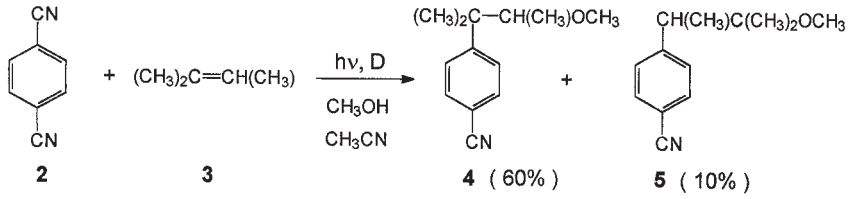

D (codonor) = biphenyl

[2]

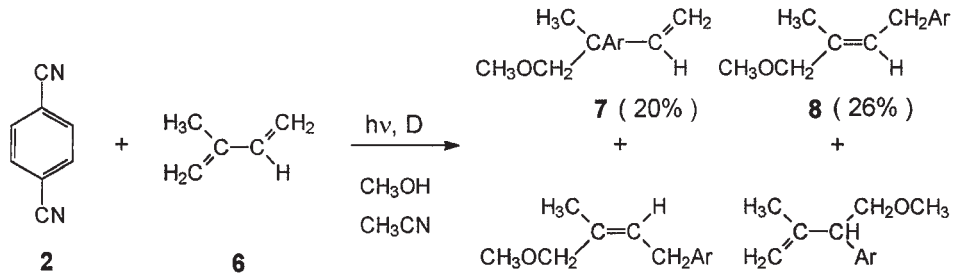

D (codonor) = biphenyl
Ar = 4-cyanophenyl

[3]

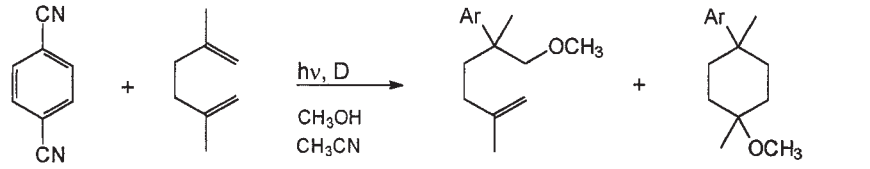

D (codonor) = biphenyl
Ar = 4-cyanophenyl

[4]

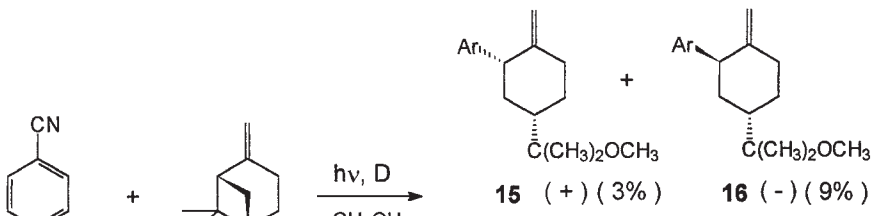

D (codonor) = biphenyl
Ar = 4-cyanophenyl

© 1998 NRC Canada

Table 1. The dependence of the product ratio [(**18** + **19**)/(**16** + **17**)] from reaction [5] on the concentration of methanol.

[CH_3OH] (M)	Product ratio
0.25	0.64 (0.03)[a]
0.50	0.64 (0.04)
1.00	0.89 (0.02)
1.50	1.01 (0.03)
2.00	1.02 (0.01)

[a]Population standard deviation.

(8:1) adducts (**7**, **8**, **9**) result from combination of methanol with the diene radical cation at C-1, which again leads ultimately to the more stable allylic radical (2*b*).

The irradiation of an acetonitrile–methanol solution of 1,4-dicyanobenzene and 2,5-dimethyl-1,5-hexadiene (**11**) provides an example of cyclization of the intermediate radical cation (reaction [3]) (2*d*). The ratio of 1:1:1 adducts is dependent upon the methanol concentration; lowering the concentration of methanol favours radical cation cyclization, increasing the yield of **13**. Cyclization, 1,6-*endo*, *endo*, of the initially formed alkene radical cation yields the more heavily substituted, more stable, 1,4-distonic radical cation intermediate, leading to the formation of **13**.

A particularly interesting example of the photo-NOCAS reaction involves irradiation of an acetonitrile–methanol solution of 1,4-dicyanobenzene and 6,6-dimethyl-2-methylenebicyclo[3.1.1]heptane (β-pinene) (**14**) (reaction [4]) (2*e*). In this case, the initially formed alkene radical cation cleaves an allylic cyclobutyl bond to give the distonic radical cation. The structures of the three 1:1:1 adducts (**15**, **16**, **17**) are consistent with reaction of this intermediate; no other 1:1:1 adducts were obtained. The adducts maintain optical activity, hence, the distonic radical cation does not cleave; cleavage of this distonic radical cation would yield the achiral radical cation of β-myrcene ($\mathbf{1}^{+\cdot}$).

Results

An acetonitrile–methanol (3:1) solution of 1,4-dicyanobenzene (**2**), biphenyl, serving as a codonor, and β-myrcene (1) was irradiated with a medium-pressure mercury vapour lamp through Pyrex. Progress of the reaction was monitored by capillary column gas chromatography with a flame ionization detector (GC–fid). The reaction produced five 1:1:1 (methanol, **1**, **2**) photo-NOCAS adducts (reaction [5]). The yields were based upon complete conversion of 1,4-dicyanobenzene as the limiting reagent (β-myrcene (1) was present in excess) and were calculated from the total weight of the combined products and the ratio of isomers determined by integrated peak (GC–fid) area. The ratio of adducts was not dependent upon the extent of conversion; these ratios remained constant during the irradiation.

Fig. 1. Variation in the product ratio [(**18** + **19**)/(**16** + **17**)] from reaction [5] as a function of the concentration of methanol.

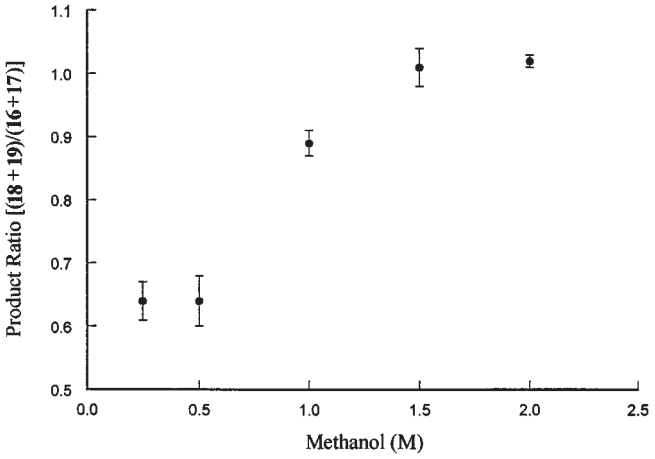

Three of the adducts, *cis*-2-(4-cyanophenyl)-4-(1-methoxy-1-methylethyl)-1-methylenecyclohexane (**15**), *trans*-2-(4-cyanophenyl)-4-(1-methoxy-1-methylethyl)-1-methylenecyclohexane (**16**), and 1-(4-cyanophenylmethyl)-4-(1-methoxy-1-methylethyl)cyclohexene (**17**), were racemic mixtures of the enantiomeric adducts previously characterized from the reaction involving β-pinene (**14**) (reaction [4]) (2*e*). The major adducts were the new compounds: 4-[4-methoxy-3,3-dimethylcyclohex-(*E*)-1-ylidenyl]methylbenzonitrile (**18**) and 4-(1-vinyl-4-*trans*-methoxy-3,3-dimethylcyclohexyl)-benzonitrile (**19**).

The ratio of products [(**18** + **19**)/(**16** + **17**)] was dependent upon the initial concentration of methanol. (The yield of **15** was too low for an accurate measurement.) Irradiations were carried out in Pyrex tubes (5 mm) under conditions similar to those used for the preparative scale reaction described above. The concentration of methanol was varied (0.25–2.0 M). The concentrations of the other reactants were the same as in the preparative scale reaction. The ratio [(**18** + **19**)/(**16** + **17**)] of products was determined from the corresponding integrated peak (GC–fid) areas (Table 1 and Fig. 1). An increase in methanol concentration caused an increase in the yield of **18** and **19** relative to **16** and **17**. At the lower range of methanol concentration (≤ 0.5 M) the ratio of

[5]

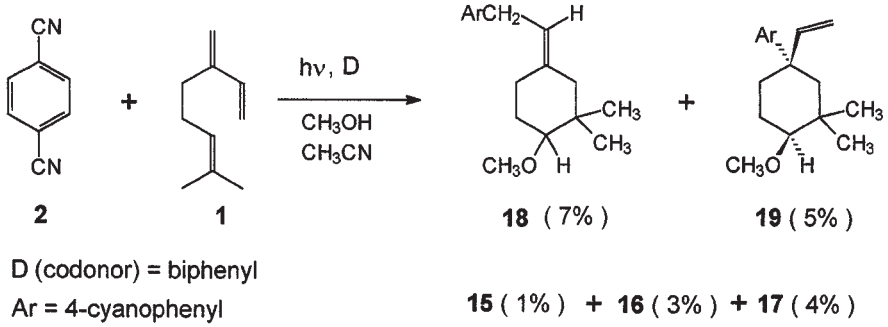

© 1998 NRC Canada

Fig. 2. The X-ray crystal structure of 4-[4-methoxy-3,3-dimethylcyclohex-(*E*)-1-ylidenyl]methylbenzoic acid (**18a**).[3]

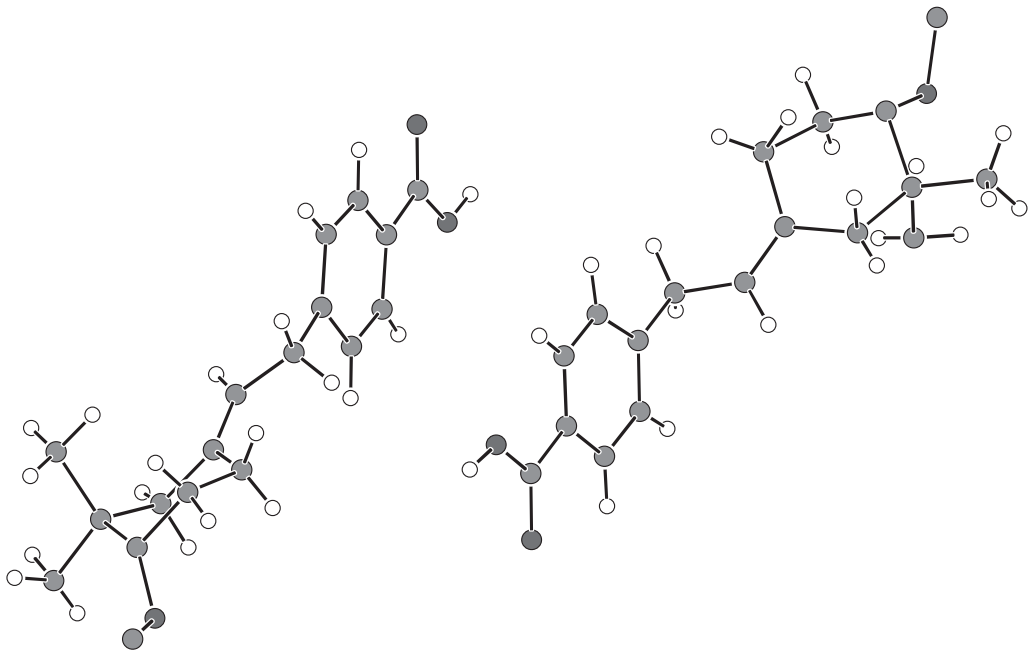

products remained constant. The ratios (**18**/**19**) and (**16**/**17**) were independent of methanol concentration.

Structural assignments

Products **15**, **16**, and **17** were shown to have identical gas chromatographic retention times and mass spectra as the previously characterized adducts (2*e*).

Compound **18** was identified as 4-[4-methoxy-3,3-dimethylcyclohex-(*E*)-1-ylidenyl]-methylbenzonitrile. The typical AA′XX′ pattern in the aromatic region of the ^{1}H nmr spectrum is indicative of the 4-cyanophenyl group. The presence of the trisubstituted alkene is supported by a triplet (5.20 ppm), representing a vinyl proton with typical coupling (7.3 Hz) to a geminal methylene, and a doublet (3.43 ppm), representing this geminal methylene, aryl-substituted. The doublet of doublets at 2.93 ppm represents the axial proton of the methoxy-substituted methine ($^3J_{4ax–5ax}$ = 8.5 Hz, $^3J_{4ax–5eq}$ = 3.7 Hz). The ^{1}H nmr also exhibits two singlets at 0.84 and 0.94 ppm indicative of two nonequivalent methyl groups.

The ^{13}C nmr spectrum of **18** exhibits a doublet (85.91 ppm), which indicates a methine group substituted by the methoxy group. There is a lower field triplet (47.93 ppm), which is consistent with an aryl-substituted methylene group (carbons adjacent to the 4-cyanophenyl group tend to occur between 37–55 ppm (1, 2)). The ^{13}C nmr spectrum also exhibits a doublet (120.12 ppm) for the vinyl methine and a singlet (138.77 ppm) for the quaternary vinyl carbon, further supporting the existence of the trisubstituted alkene.

The assigned overall structure and stereochemistry of **18** was substantiated by X-ray crystallography. The nitrile group in compound **18** was converted to a carboxylic acid; 4-[4-methoxy-3,3-dimethylcyclohex-(*E*)-1-ylidenyl]methylbenzoic acid (**18a**). The ^{1}H nmr spectrum of the nitrile (**18**) and this carboxylic acid (**18a**) are almost identical; the X-ray analysis of **18a** (Fig. 2) provides firm evidence for the structure of the initial product (**18**).[3]

Compound **19** was identified as 4-(1-vinyl-4-*trans*-methoxy-3,3-dimethylcyclohexyl)benzonitrile. The typical AA′XX′ pattern in the aromatic region of the ^{1}H nmr spectrum is indicative of the 4-cyanophenyl group. The presence of the terminal alkene is supported by two doublets and a doublet of doublets (4.87, 5.03, and 5.86 ppm) in the vinyl proton region. The distorted four-line multiplet at 2.81 ppm represents the axial proton of the methoxy-substituted methine. Individual coupling constants were not obtained; however, based on the width of the multiplet at half-height (13 Hz), this proton is axial. Typical equatorial–axial and equatorial–equatorial couplings range from 0 to 3 Hz; if this proton were equatorial, the separation of the outer lines of a four-line multiplet would be, at most, 6 Hz. The ^{1}H nmr spectrum also exhibits two singlets at 0.72 and 0.96 ppm indicative of two nonequivalent methyl groups.

A nuclear Overhauser enhancement (NOE) experiment proved the aryl group was *trans* to the methoxy group on the cyclohexyl ring. When the methyl protons at 0.72 ppm were irradiated, a NOE was observed for the proton of the methoxy-substituted methine, the methoxy–methyl protons, and the methyl protons (0.96 ppm). When the methyl protons at 0.96 ppm were irradiated, a NOE was observed for

[3] X-ray crystallographic data for **18a** may be purchased from: The Depository of Unpublished Data, Document Delivery, CISTI, National Research Council of Canada, Ottawa, Canada, K1A 0S2. Details of data collection, structural analysis and refinement, and tables of interatomic distances and bond angles have also been deposited with the Cambridge Crystallographic Data Centre and can be obtained on request from: The Director, Cambridge Crystallographic Data Centre, University Chemical Laboratory, 12 Union Road, Cambridge, CB2 1EZ, U.K.

© 1998 NRC Canada

the methoxy–methyl protons, the vinyl protons, and the methyl protons (0.72 ppm). Based on the evidence that the proton of the methoxy-substituted methine is axial, vide supra, the methoxy group is equatorial, the aryl group is equatorial, i.e., the *trans* configuration.

The ^{13}C nmr spectrum of compound **19** exhibits a doublet (85.58 ppm) indicative of a methine group substituted by the methoxy group. There is a lower field singlet (44.31 ppm), which is consistent with an aryl-substituted quaternary carbon. This spectrum also exhibits a triplet (112.52 ppm) for the vinyl methylene and a doublet (146.73 ppm) for the vinyl methine, thus further supporting the existence of the terminal mono-substituted alkene.

Calculations

Ab initio molecular orbital calculations were carried out, using the GAUSSIAN 94 package of programs (4), to obtain fully optimized structures (HF/6-31G*) of β-myrcene (1) and the radical cations $\mathbf{1}^{+\cdot}$, $\mathbf{1a}^{+\cdot}$, and $\mathbf{1b}^{+\cdot}$. The results of these calculations, optimized structures, and spin and charge density distribution obtained from Mulliken population analysis, are listed in Tables 2 and 3. The total energies, corrected for spin contamination, were obtained from single point calculations with Møller–Plesset perturbation theory (MP2) using the HF/6-31G* optimized structures (5). The results of an extensive stochastic search, using the molecular mechanics program (MM3-94 (6)), identified 24 conformers of β-myrcene (**1**); the more stable conformers are described in Table 4.

Discussion

A mechanism for the formation of **15**, **16**, and **17** involves cyclization of the initially formed radical cation of myrcene ($\mathbf{1}^{+\cdot}$) to the distonic radical cation ($\mathbf{1a}^{+\cdot}$) (Scheme 1). This distonic radical cation is identical to that formed upon cleavage of the β-pinene radical cation ($\mathbf{14}^{+\cdot}$). An alternative mode of cyclization of $\mathbf{1}^{+\cdot}$ yields the distonic radical cation $\mathbf{1b}^{+\cdot}$, which leads to formation of **18** and **19**. The regiochemistry of these adducts requires reaction of these distonic radical cations — tertiary or secondary alkyl cation with methanol and the allylic radical with the radical anion of 1,4-dicyanobenzene ($\mathbf{2}^{-\cdot}$). At lower methanol concentrations (≤0.5 M) cyclization of the radical cation dominates, the product ratio [(**18** + **19**)/(**16** + **17**)] is relatively small (0.64), 1,6-*endo*, *exo* cyclization of $\mathbf{1}^{+\cdot}$ to $\mathbf{1a}^{+\cdot}$ is favoured.

The results from the molecular orbital calculations are consistent with these observations (Table 3). The distonic radical cation $\mathbf{1a}^{+\cdot}$ has most of the positive charge density on the tertiary carbocation (C7, C8, and C9), while the spin density is delocalized over the allylic radical (C2 and C10). Similarly, the distonic radical cation $\mathbf{1b}^{+\cdot}$ has greatest positive charge on C6, and the spin density is delocalized over the allylic radical (C1 and C3). It seems likely that the alternative modes of cyclization of the initially formed β-myrcene radical cation, $\mathbf{1}^{+\cdot}$, are dependent upon conformational factors. The rate of the intermolecular reaction of a diene radical cation with the precursor diene is rapid, 10^8–10^9 M^{-1} s^{-1} (3*a*). Nevertheless, the molecular orbital calculations indicate that the major mode of cyclization of $\mathbf{1}^{+\cdot}$ yields the more stable distonic radical cation $\mathbf{1a}^{+\cdot}$. The calculations also indicate that cyclization is significantly exothermic, –21.6 kcal mol^{-1} for $\mathbf{1}^{+\cdot}$ to $\mathbf{1a}^{+\cdot}$ and –11.3 kcal mol^{-1} for $\mathbf{1}^{+\cdot}$ to $\mathbf{1b}^{+\cdot}$, consistent with the lack of reversibility.

At higher methanol concentrations the product ratio [(**18** + **19**)/(**16** + **17**)] increases; for the preparative runs (6 M methanol) this ratio becomes 1.7. Under these conditions, reaction of the radical cation ($\mathbf{1}^{+\cdot}$) with methanol competes with cyclization; the measured bimolecular rate constant for reaction of diene radical cations with methanol (>10^9 M^{-1} s^{-1}) is consistent (3*a*). Now the product ratio is controlled by the addition of methanol to the radical cation $\mathbf{1}^{+\cdot}$ at the alternative sites, C7 or C6, to yield the β-alkoxyalkyl radicals, $\mathbf{1c}^{\cdot}$ or $\mathbf{1d}^{\cdot}$ (Scheme 2). As expected, based upon the product ratio from reaction (1), addition of methanol to the alkene radical cation at C6, with subsequent formation of the more stable tertiary radical ($\mathbf{1d}^{\cdot}$), is favoured, relative to addition at C7, to give the secondary radical ($\mathbf{1c}^{\cdot}$). Both of these β-alkoxyalkyl radicals then cyclize 1,6-*endo* on the way to the observed products.

Adduct **18** results from cyclization of the radical cation (Scheme 1) or radical (Scheme 2) at C10 of the diene moiety. The *E*-configuration of this adduct (**18**) clearly indicates this diene had the s-*trans* conformation. The result of an extensive stochastic search for conformers of β-myrcene (**1**), using the molecular mechanics program (MM3-94 (6)), is consistent with reaction of this conformation (Table 4). Conformer 3 has close approach between C7 and C10, required for cyclization to $\mathbf{1b}^{+\cdot}$, and the s-*trans* conformation of the diene. Conformers 6 and 8 have close approach between C1 and C6 required for cyclization to $\mathbf{1a}^{+\cdot}$. None of the low-energy conformers have the s-*cis* conformation and close approach of C7-C10 or C1-C6. The fully optimized (ab initio) structures of β-myrcene (1) and of the β-myrcene radical cation ($\mathbf{1}^{+\cdot}$) are similar (Table 4).

Clearly, none of the products from reaction 5 involve initial addition of the nucleophile, methanol, to the conjugated diene moiety. This was, at first, a surprise; however, there is convincing evidence that formation of the trialkyl-substituted mono-ene radical cation (C6, C7) is energetically favoured (1*b*). The oxidation potentials and the ionization potentials of β-myrcene (1) and of the model compounds 2-methyl-2-butene (3) and 2-methyl-1,3-butadiene (**6**) are summarized in Table 5. The radical cation of the trialkyl-substituted mono-ene moiety (C5, C6, C7, C8, C9) is more stable than that at the conjugated diene moiety (C1, C2, C3, C10, C4). The molecular orbital calculations support this conclusion; the charge density of radical cation, $\mathbf{1}^{+\cdot}$, is largely on C6, C7, C8, and C9, while the spin density is on C6 and C7 (Table 3).

Conclusions

Photoinduced electron transfer, from 7-methyl-3-methylene-1,6-octadiene (β-myrcene, **1**) to 1,4-dicyanobenzene, in acetonitrile–methanol, leads to formation of five 1:1:1 (photo-NOCAS) adducts (**15**–**19**). All of these adducts are cyclic; both the initially formed radical cation and the intermediate β-alkoxyalkyl radicals cyclize. The preferred modes of cyclization are for the radical cation $\mathbf{1}^{+\cdot}$, 1,6-*endo*, *exo* and 1,6-*endo*, *endo*, and for the radicals, $\mathbf{1c}^{\cdot}$ and $\mathbf{1d}^{\cdot}$, 1,6-*endo*. The observed products, the measured oxidation and ionization potentials, and the molecular orbital

© 1998 NRC Canada

Table 2. Optimized (HF/6-31G*) structures for β-myrcene (**1**), β-myrcene radical cation (**1**$^{+\bullet}$), β-myrcene cyclized, distonic, radical cations (**1a**$^{+\bullet}$ and **1b**$^{+\bullet}$).

Bond length (Å)		Bond angle (deg)		Dihedral angle (deg)	
		β-Myrcene (1)			
C1—C2	1.323	C1-C2-C3	126.8	C4-C3-C2-C1	–0.1
C2—C3	1.480	C2-C3-C4	117.5	C5-C4-C3-C2	–180.0
C3—C10	1.326	C2-C3-C10	118.6	C6-C5-C4-C3	177.1
C3—C4	1.515	C3-C4-C5	116.4	C7-C6-C5-C4	114.0
C4—C5	1.534	C4-C5-C6	111.4	C8-C7-C6-C5	–180.0
C5—C6	1.507	C5-C6-C7	128.9	C9-C7-C6-C5	0.1
C6—C7	1.325	C6-C7-C8	120.8	C10-C3-C2-C1	179.8
C7—C8	1.511	C6-C7-C9	125.4		
C7—C9	1.510				
		β-Myrcene radical cation (1$^{+\cdot}$**)**			
C1—C2	1.322	C1-C2-C3	126.8	C4-C3-C2-C1	–0.7
C2—C3	1.479	C2-C3-C4	116.5	C5-C4-C3-C2	–178.1
C3—C10	1.325	C2-C3-C10	119.7	C5-C4-C3-C10	2.1
C3—C4	1.515	C3-C4-C5	114.4	C6-C5-C4-C3	–177.6
C4—C5	1.547	C4-C5-C6	110.0	C7-C6-C5-C4	–115.3
C5—C6	1.485	C4-C3-C10	123.8	C8-C7-C6-C5	–177.6
C6—C7	1.414	C5-C6-C7	127.0	C9-C7-C6-C5	1.8
C7—C8	1.488	C6-C7-C8	120.1	C10-C3-C2-C1	179.1
C7—C9	1.492	C6-C7-C9	121.5		
		C8-C7-C9	118.4		
		β-Myrcene cyclized, distonic, radical cation (1a$^{+\cdot}$**)**			
C1—C2	1.507	C1-C2-C3	125.3	C1-C6-C5-C4	66.0
C1—C6	1.577	C1-C6-C5	109.8	C2-C1-C6-C5	–46.9
C2—C3	1.389	C1-C6-C7	103.7	C2-C1-C6-C7	–173.2
C3—C4	1.519	C2-C1-C6	110.0	C2-C3-C4-C5	19.8
C3—C10	1.398	C2-C3-C4	120.1	C3-C2-C1-C6	15.9
C4—C5	1.529	C2-C3-C10	120.9	C3-C4-C5-C6	–51.2
C5—C6	1.534	C3-C4-C5	112.7	C4-C3-C2-C1	–2.2
C6—C7	1.469	C4-C5-C6	109.1	C7-C6-C5-C4	–175.9
C7—C8	1.478	C4-C3-C10	118.9	C8-C7-C6-C1	94.7
C7—C9	1.477	C5-C6-C7	117.4	C8-C7-C6-C5	–26.6
		C6-C7-C8	121.6	C9-C7-C6-C1	–85.5
		C6-C7-C9	119.9	C9-C7-C6-C5	153.2
		C8-C7-C9	118.5	C10-C3-C2-C1	179.0
				C10-C3-C4-C5	–161.4
		β-Myrcene cyclized, distonic, radical cation (1b$^{+\cdot}$**)**			
C1—C2	1.386	C1-C2-C3	126.7	C1-C2-C3-C10	–1.2
C2—C3	1.400	C2-C3-C10	121.5	C2-C3-C10-C7	163.6
C3—C4	1.513	C3-C4-C5	113.1	C3-C10-C7-C6	39.0
C3—C10	1.515	C3-C10-C7	115.5	C4-C3-C10-C7	–17.7
C4—C5	1.533	C4-C3-C10	119.4	C5-C4-C3-C10	–22.0
C6—C7	1.447	C6-C7-C10	113.2	C8-C7-C10-C6	–108.1
C7—C8	1.594	C8-C7-C10	111.2	C9-C7-C10-C6	129.8
C7—C9	1.536	C9-C7-C10	112.4		
C7—C10	1.540				

calculations all indicate the trisubstituted mono alkene moiety is the site of the initially formed radical cation **1**$^{+\cdot}$, not the conjugated diene. Cyclization of this radical cation is significantly exothermic and is irreversible. The observed products and the molecular orbital calculations indicate that on the cyclized, distonic radical cation intermediates, **1a**$^{+\cdot}$ and **1b**$^{+\cdot}$, the positive charge density is largely on the tertiary and secondary alkyl moiety, and the spin density is delocalized on the allylic radical. The addition of methanol to the initially formed radical cation follows the established pattern for alcohol addition to mono alkenes; addition occurs preferentially to ultimately yield the more heavily substituted, more stable, β-alkoxyalkyl radical. Cyclization of these radicals, **1c**$^{\cdot}$ and **1d**$^{\cdot}$, occur 1,6-*endo*.

© 1998 NRC Canada

Table 3. Charge and spin density distribution on the radical cations $\mathbf{1}^{+\bullet}$, $\mathbf{1a}^{+\bullet}$, and $\mathbf{1b}^{+\bullet}$.[a]

	Atom	Charge density	Spin density
β-Myrcene radical cation, $\mathbf{1}^{+\cdot}$ (E = –388.919 12)			
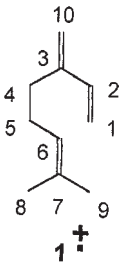 **1**	1	–0.026	–0.000
	2	0.065	0.002
	3	0.102	0.005
	4	0.043	0.030
	5	0.058	–0.068
	6	0.253	0.610
	7	0.187	0.451
	8	0.183	–0.015
	9	0.187	–0.014
	10	–0.051	–0.000
β-Myrcene cyclized, distonic, radical cation, $\mathbf{1a}^{+\cdot}$ (E = –388.953 51)			
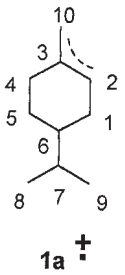 **1a**	1	0.060	–0.068
	2	0.029	0.914
	3	0.073	–0.788
	4	0.066	0.049
	5	0.059	–0.008
	6	–0.050	0.010
	7	0.323	–0.001
	8	0.211	0.000
	9	0.211	0.000
	10	0.017	0.892
β-Myrcene cyclized, distonic, radical cation, $\mathbf{1b}^{+\cdot}$ (E = –388.937 18)			
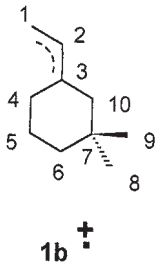 **1b**	1	0.023	0.854
	2	0.040	–0.787
	3	0.016	1.027
	4	0.092	–0.072
	5	0.110	0.012
	6	0.476	0.001
	7	–0.198	0.011
	8	0.180	–0.002
	9	0.151	–0.000
	10	0.110	–0.073

[a]Spin and charge densities include hydrogens summed into heavy atoms.

Experimental

General information

The ^{1}H and ^{13}C nmr spectra were obtained from a Bruker AC 250 F spectrometer. Spectra were recorded in parts per million and frequencies are relative to tetramethylsilane. Infrared spectra (ir) were recorded on a Nicolet 205 FTIR and are reported in wave numbers (cm^{-1}). Elemental analyses were performed by Canadian Microanalytical Service Ltd., B.C. Exact mass determinations were obtained using a CEC 21-110 mass spectrometer at Dalhousie University, Halifax, NS. Melting points were determined using a Cybron Corporation Thermolyne apparatus with a digital thermocouple and are corrected. Product yields and progress of the reactions were determined using a Hewlett–Packard (HP) 5890 gas chromatograph with a DB-1701 fused silica WCOT column (30 m × 0.25 mm, 0.25 μm film thickness) and a calibrated flame ionization detector (GC–fid) and are based upon 1,4-dicyanobenzene (2) as the limiting reagent. An HP 3392A integrator was interfaced with the GC–fid to obtain peak areas. An HP 5890 gas chromatograph with a 5% phenyl methyl silicone fused silica WCOT column (25 m × 0.20 mm, 0.33 μm film thickness) interfaced with an HP 5970 mass selective detector (GC–MS) was also used for product analyses. Mass spectra are reported as m/z (relative intensity). Separation of product mixtures was generally carried out using preparative medium-pressure liquid chromatography (mplc) (1*a*). The mplc consists of a 2.5 cm × 1 m column packed with thin-layer chromatography (TLC) grade silica gel (without binder) (Rose Scientific Ltd., cat. 81632) at a pressure of 19 psi using helium (1 psi = 6.9 kPa). Connected to the mplc was a uv spectrophotometer – fraction collector collecting ca. 10 mL fractions.

Materials

Acetonitrile (Fisher ACS grade) was distilled twice, first from sodium hydride and then from phosphorus pentoxide. It was then passed through a column of basic alumina,

© 1998 NRC Canada

Table 4. β-Myrcene (**1**) conformers.

Conformer	Energy diff. (kJ/mol)	C1—C6 (Å)	C7—C10 (Å)	C1—C7 (Å)	C6—C10 (Å)	C1-C2-C3-C10 (°)
Stochastic search, molecular mechanics (MM3, 94 (6))						
1	0.000	4.74	5.81	5.10	4.66	177.44
2	0.371	4.73	5.34	6.01	4.67	176.85
3	3.687	4.66	3.63	4.96	3.38	177.45
4	3.932	6.00	5.77	6.65	4.65	2.54
5	4.014	6.01	5.31	7.12	4.64	2.73
6	4.417	3.41	5.25	3.83	4.01	176.30
7	4.432	4.62	4.19	5.91	3.37	178.30
8	4.990	3.44	4.31	3.72	4.06	177.47
9	6.716	4.49	4.34	4.36	4.08	3.34
Ab initio molecular orbital theory (UHF/6-31G*) (4)						
		5.34	5.43	6.28	4.44	179.8
β-Myrcene radical cation ($\mathbf{1}^{+\cdot}$), ab initio molecular orbital theory (UHF/6-31G*) (4)						
		5.30	5.42	6.30	4.38	179.1

Scheme 1. Cyclization of the initially formed β-myrcene radical cation, to give the distonic radical cation, followed by reaction of the distonic radical cation with nucleophile (methanol) and with the aromatic radical anion.

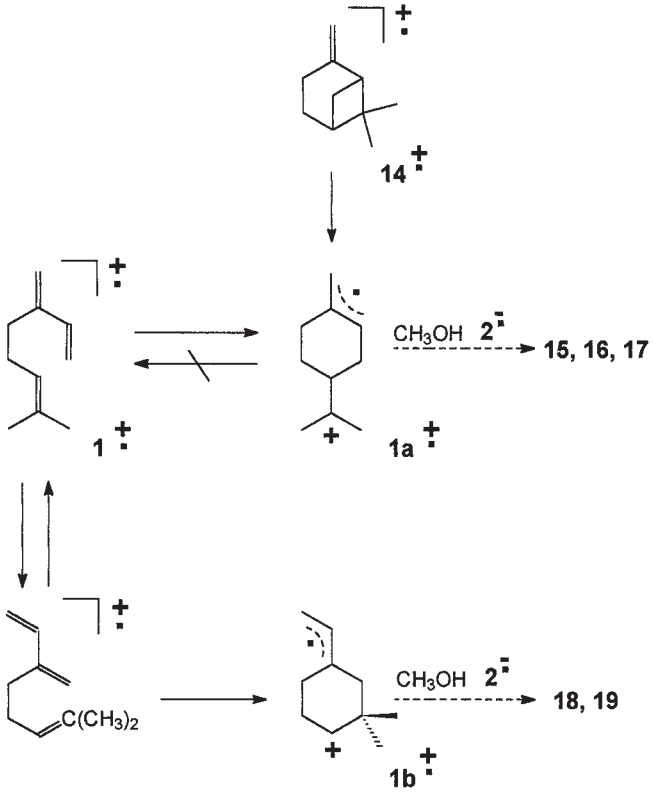

refluxed over calcium hydride for 24 h (under a nitrogen atmosphere), fractionally distilled (under nitrogen), and stored over molecular sieves (3 Å) (7). Methanol was distilled and then stored over molecular sieves (4 Å). 1,4-Dicyanobenzene (2) (Aldrich) was purified by treatment with Norite in methylene chloride, followed by recrystallization from 95% ethanol. Tetraethylammonium perchlorate (TEAP) (Aldrich) was recrystallized three times from water and then dried in a vacuum oven for 15 h, 70°C, 0.25 Torr (1 Torr = 133.3 Pa). Myrcene (1) (technical grade) was obtained from the Aldrich Chemical Co. and purified by vacuum distillation. Biphenyl (Eastman Kodak Co.) was recrystallized from methanol.

Irradiation

The irradiation was carried out on an acetonitrile–methanol (3:1) solution consisting of myrcene (**1**), 1,4-dicyanobenzene (**2**), and biphenyl. Solutions were irradiated in either 2 cm i.d. Pyrex tubes or 5 mm Pyrex nmr tubes, which were degassed by nitrogen ebullition. These samples were irradiated at 10°C using a CGE 1 MW medium-pressure mercury vapour lamp contained in a water-cooled quartz immersion well.

Cyclic voltammetric measurements

Cyclic voltammetry was used to obtain the oxidation potential of myrcene (**1**). The apparatus has been described (8). The working electrode was a platinum sphere (1 mm diameter), and the counter electrode was a platinum wire. The reference electrode was a saturated calomel electrode (sce), which was connected to the solution (TEAP 0.1 M, acetonitrile) through a Luggin capillary. The alkene concentration was ca. 0.005 M. Since the anodic wave was irreversible, the half-wave potential was taken as 0.028 V before the anodic peak potential (9).

Formation of the methanol, β-myrcene (1), 1,4-dicyanobenzene (2) photo-NOCAS adducts 15, 16, 17, 18, and 19: reaction [5]

A solution of β-myrcene (1) (10.0 mL, 8.0 g, 0.059 mol), 1,4-dicyanobenzene (2) (3.7 g, 0.029 mol), and biphenyl (2.3 g, 0.015 mol) in acetonitrile–methanol (3:1) (240 mL) was degassed by nitrogen ebullition and irradiated for 9 days using a 1 kW lamp at 10°C. The solvent was removed to yield a crude photolysate. The crude photolysate was chromatographed (mplc) using a linear solvent gradient (hexanes – 10% diethyl ether, 90% hexanes). Isolation of the adducts was achieved via further chromatography using mplc and a linear solvent gradient (hexanes – 1% diethyl ether, 99% hexanes). The five 1:1:1 adducts were eluted in

© 1998 NRC Canada

Scheme 2. Reaction of the initially formed β-myrcene radical cation with nucleophile (methanol), to give the radical, followed by cyclization of the radical and reaction with the aromatic radical anion.

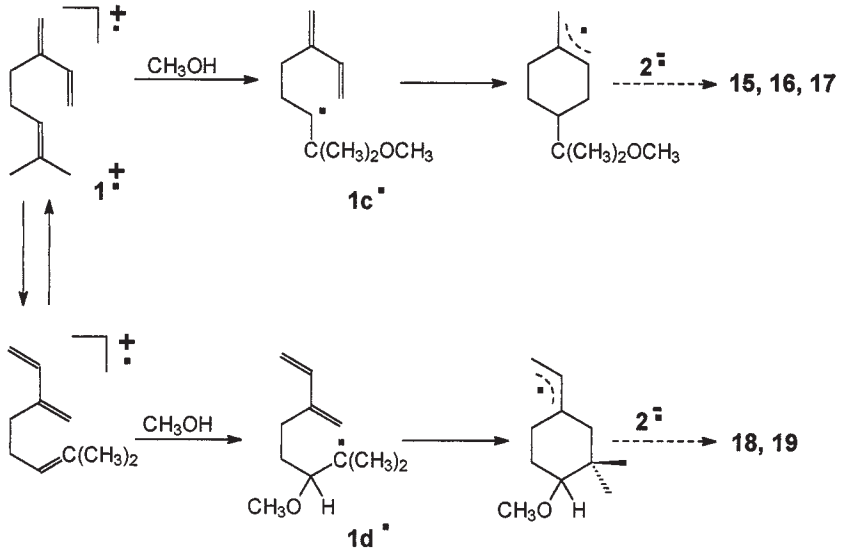

Table 5. Calculated and experimental oxidation potentials and ionization potentials of β-myrcene (**1**) and model systems.

	IP v (calcd.)[a]	IP a (calcd.)[b]	$E^{OX}_{1/2}$ (V)[c]
2-Methyl-2-butene (**3**)	8.68[d] (8.93)	(8.27)	2.03[e]
2-Methyl-1,3-butadiene (**6**)	8.89[d] (8.67)	(8.45)	2.25[f]
β-Myrcene (**1**)	8.68[g] (8.65) 8.92[h]	8.36 (8.24)	2.12

[a] Experimental vertical ionization potential; calculated vertical ionization potential in parentheses, taken from the eigenvalue of the HOMO.
[b] Experimental adiabatic ionization potential; calculated adiabatic ionization potential in parentheses, taken as the difference between the calculated total energy of the minimized neutral molecule and the minimized radical cation.
[c] Measured (CV) oxidation potential (vs. sce).
[d] Reference 10.
[e] Reference 2*a*.
[f] Reference 2*c*.
[g] HOMO.
[h] The second band.

the order **19**, **18**, **16**, **17**, and **15**. Adducts **15**–**17** were found to be identical, mass spectra and GC retention times, with photo-NOCAS adducts previously characterized from β-pinene (**14**) (2*e*), *cis*-2-(4-cyanophenyl)-4-(1-methoxy-1-methylethyl)-1-methylenecyclohexane (**15**, 1%), *trans*-2-(4-cyanophenyl)-4-(1-methoxy-1-methylethyl)-1-methylenecyclohexane (**16**, 3%), 1-(4-cyanophenylmethyl)-4-(1-methoxy-1-methylethyl)cyclohexene (**17**, 4%).

*4-(1-Vinyl-4-*trans*-methoxy-3,3-dimethylcyclohexyl]-benzonitrile (**19**)*

The yield of **19** was 5%; infrared (Nicolet 205) ν: 3082 (w), 2930 (s), 2875 (m), 2822 (m), 2228 (s), 1632 (w), 1605 (m), 1504 (m), 1461 (m), 1408 (w), 1388 (w), 1363 (m), 1186 (m), 1101 (s), 1040 (w), 1019 (w), 997 (w), 915 (m), 835 (m); ^{1}H nmr (250.13 MHz, $CDCl_3$), δ_{TMS}: 0.72 (s, 3H, CH_3), 0.96 (s, 3H, CH_3), 1.71–1.97 (m, 5H, cyclohexyl H's), 2.20 (m, 1H, cyclohexyl H), 2.81 (m, 1H, H of methoxy-substituted carbon (4-H)), 3.36 (s, 3H, OCH_3), 4.87 (d, 1H, $^3J_{1'-2'trans}$ = 17.7 Hz, vinyl H (2′*trans*-H)), 5.03 (d, 1H, $^3J_{1'-2'cis}$ = 10.7 Hz, vinyl H (2′*cis*-H)), 5.86 (dd, 1H, $^3J_{1'-2'trans}$ = 17.7 Hz, $^3J_{1'-2'cis}$ = 10.7 Hz, vinyl H (1′-H)), 7.45 (d, 2H, $^3J_{2'-3'}$ = 8.5 Hz, $^3J_{5'-6'}$ = 8.5 Hz, H's adjacent to alkyl-substituted aryl carbon (2′-H, 6′-H)), 7.58 (d, 2H, $^3J_{2'-3'}$ = 8.5 Hz, $^3J_{5'-6'}$ = 8.5 Hz, H's adjacent to cyano-substituted aryl carbon (3′-H, 5′-H)). The NOE experiment: the methyl protons at 0.72 and 0.96 ppm were irradiated. When the methyl protons at 0.72 ppm were irradiated, an NOE was observed for the proton of the methoxy-substituted methine, the methoxy–methyl protons, and the methyl protons (0.96 ppm). When the methyl protons at 0.96 ppm were irradiated, an NOE was observed for the methoxy–methyl protons, the vinyl protons, and the methyl protons (0.72 ppm). ^{13}C nmr (62.90 MHz, $CDCl_3$), δ: 22.12 (t), 24.03 (q), 29.44 (q), 30.17 (t), 36.17 (s), 44.31 (s), 47.42 (t), 57.37 (q, OCH_3), 85.58 (d, CH, methoxy-substituted), 109.50 (s, quaternary aryl carbon, cyano-substituted), 112.52 (t, alkene CH_2), 119.06 (s, CN), 127.27 (d, aromatic CH adjacent to alkyl-substituted aryl carbon), 131.98 (d, aromatic CH adjacent to cyano-substituted carbon), 146.73 (d, alkene CH), 153.38 (s, quaternary aryl carbon, alkyl-substituted); MS, *m*/*z*: 55(14), 58(22), 71(100), 115(15), 116(19), 121(17), 127(16), 140(18), 154(22), 155(13), 166(20), 181(13), 194(52), 195(13), 237(17). Exact mass calcd. for $C_{18}H_{23}NO$: 269.1780; found: 269.1773.

*4-[4-Methoxy-3,3-dimethylcyclohex-(*E*)-1-ylidenyl]-methylbenzonitrile (**18**)*

The yield of **18** was 7%; infrared (Nicolet 205) ν: 2969 (s), 2950 (s), 2870 (m), 2822 (m), 2228 (s), 1607 (m), 1504 (m), 1452 (m), 1184 (m), 1101 (s), 823 (m); ^{1}H nmr (250.13 MHz, $CDCl_3$), δ_{TMS}: 0.84 (s, 3H, CH_3), 0.94 (s, 3H, CH_3), 1.38–1.55 (m, 1H, $^3J_{4ax-5ax}$ = 8.5 Hz, $^3J_{5ax-6eq}$ = 5.5 Hz, axial H of methylene group (5ax-H)), 1.77–2.08 (m, 4H, $^2J_{6ax-6eq}$ = 13.7 Hz, $^2J_{2ax-2eq}$ = 13.4 Hz, $^3J_{5eq-6eq}$ = 5.5 Hz, $^3J_{4ax-5eq}$ = 3.7 Hz, H of methylene groups on ring (2ax-, 2eq-, 5eq-, 6ax-H)), 2.46 (dt, 1H, $^2J_{6ax-6eq}$ = 13.7 Hz,

© 1998 NRC Canada

$^3J_{5ax–6eq}$ = 5.5 Hz, $^3J_{5eq–6eq}$ = 5.5 Hz, equatorial H of methylene group on ring (6eq-H)), 2.93 (dd, 1H, $^3J_{4ax–5ax}$ = 8.5 Hz, $^3J_{4ax–5eq}$ = 3.7 Hz, CH group, methoxy-substituted (4ax-H)), 3.37 (s, 3H, OCH_3), 3.43 (d, 2H, $^3J_{7–8}$ = 7.3 Hz, CH_2 group, aryl-substituted (8-H)), 5.20 (t, 1H, $^3J_{7–8}$ = 7.3 Hz, vinyl H (7-H)), 7.27 (d, 2H, $^3J_{2'–3'}$ = 8.5 Hz, $^3J_{5'–6'}$ = 8.5 Hz, H's adjacent to alkyl-substituted aryl carbon (2′-H, 6′-H)), 7.56 (d, 2H, $^3J_{2'–3'}$ = 8.5 Hz, $^3J_{5'–6'}$ = 8.5 Hz, H's adjacent to cyano-substituted aryl carbon (3′-H, 5′-H)); ^{13}C nmr (62.90 MHz, $CDCl_3$), δ: 21.61 (q), 25.00 (t), 25.78 (t), 27.52 (q), 33.87 (t), 37.17 (s), 47.93 (t, CH_2, aryl-substituted), 57.52 (q, OCH_3), 85.91 (d, CH, methoxy-substituted), 109.59 (s, quaternary aryl carbon, cyano-substituted), 119.18 (s, CN), 120.12 (d, vinyl CH), 129.08 (d, aromatic CH adjacent to alkyl-substituted aryl carbon), 132.22 (d, aromatic CH adjacent to cyano-substituted carbon), 138.77 (s), 147.53 (s); MS, *m*/*z*: 55(27), 67(26), 71(25), 77(22), 79(23), 93(34), 116(55), 121(83), 154(44), 167(23), 180(22), 194(64), 195(24), 237(100). Anal. calcd. for $C_{18}H_{23}NO$: C 80.26, H 8.61, N 5.20; found: C 79.90, H 8.78, N 4.91.

Preparation of 4-[4-methoxy-3,3-dimethylcyclohex-(*E*)-1-ylidenyl]methylbenzoic acid (18a)

4-[4-Methoxy-3,3-dimethylcyclohex-(*E*)-1-ylidenyl]methylbenzonitrile (**18**) (0.041 g, 0.15 mmol) and 4 mL of a 40% sodium hydroxide solution was refluxed for 2 days. This mixture was cooled and extracted with dichloromethane. The aqueous layer was acidified with hydrochloric acid (conc.) and extracted twice with benzene. Evaporation of the solvent left a white solid (0.026 g, 0.090 mmol), which was recrystallized from hexanes.

*4-[4-Methoxy-3,3-dimethylcyclohex-(*E*)-1-ylidenyl]-methylbenzoic acid (**18a**)*

The yield of **18a** was 60%: the melting point was 112–113°C; infrared (Nicolet 205) ν: 2967 (s), 2938 (s), 2900 (m), 2871 (m), 2821 (m), 2674 (w), 2544 (w), 1682 (s), 1608 (m), 1572 (w), 1425 (s), 1318 (m), 1290 (s), 1182 (m), 1101 (s), 951 (w); ^{1}H nmr (250.13 MHz, $CDCl_3$), δ_{TMS}: 0.86 (s, 3H, CH_3), 0.95 (s, 3H, CH_3), 1.39–1.56 (m, 1H, $^3J_{4ax–5ax}$ = 8.6 Hz, $^3J_{5ax–6eq}$ = 5.5 Hz, axial H of methylene group (5ax-H)), 1.80–2.06 (m, 4H, $^2J_{6ax–6eq}$ = 13.7 Hz, $^2J_{2ax–2eq}$ = 13.6 Hz, $^3J_{5eq–6eq}$ = 5.5 Hz, $^3J_{4ax–5eq}$ = 3.7 Hz, H of methylene groups on ring (2ax-, 2eq-, 5eq-, 6ax-H)), 2.49 (m, 1H, $^2J_{6ax–6eq}$ = 13.7 Hz, $^3J_{5ax–6eq}$ = 5.5 Hz, $^3J_{5eq–6eq}$ = 5.5 Hz, equatorial H of methylene group on ring (6eq-H)), 2.94 (dd, 1H, $^3J_{4ax–5ax}$ = 8.6 Hz, $^3J_{4ax–5eq}$ = 3.7 Hz, CH group, methoxy-substituted (4ax-H)), 3.38 (s, 3H, OCH_3), 3.44 (d, 2H, $^3J_{7–8}$ = 7.3 Hz, CH_2 group, aryl-substituted (8-H)), 5.24 (t, 1H, $^3J_{7–8}$ = 7.3 Hz, vinyl H (7-H)), 7.27 (d, 2H, $^3J_{2'–3'}$ = 8.1 Hz, $^3J_{5'–6'}$ = 8.1 Hz, H's adjacent to alkyl-substituted aryl carbon (2′-H, 6′-H)), 8.02 (d, 2H, $^3J_{2'–3'}$ = 8.1 Hz, $^3J_{5'–6'}$ = 8.1 Hz, H's adjacent to cyano-substituted aryl carbon (3′-H, 5′-H)); ^{13}C nmr (62.90 MHz, $CDCl_3$), δ: 21.52 (q), 25.06 (t), 25.83 (t), 27.58 (q), 33.90 (t), 37.19 (s), 48.04 (t, CH_2, aryl-substituted), 57.53 (q, OCH_3), 86.14 (d, CH, methoxy-substituted), 120.79 (d, vinyl CH), 126.90 (s, quaternary aryl carbon, COOH-substituted), 128.46 (d, aromatic CH adjacent to alkyl-substituted aryl carbon), 130.41 (d, aromatic CH adjacent to COOH-substituted carbon), 138.13 (s), 148.43 (s), 172.13 (s, C=O of COOH); MS, *m*/*z*: 55(26), 77(35), 79(27), 91(36), 93(36), 107(31), 121(78), 128(37), 129(50), 135(30), 141(41), 211(30), 213(50), 256(100). X-ray data: see footnote 3.

Acknowledgement

This work was supported by grants from the Natural Sciences and Engineering Research Council of Canada. We thank Dr. D.L. Hooper, Atlantic Region Magnetic Resonance Centre at Dalhousie University, for help in the preparation of the manuscript, Dr. T.S. Cameron, Dalhousie University, for the X-ray crystal structure of **18a**, and Dr. T.B. Grindley and Dr. M.S.W. Chan, Dalhousie University, for assistance with the molecular mechanics calculations. We also wish to thank Dr. D. Klapstein, St. Francis Xavier University, for the photoelectron spectra of **1**.

References

1. (*a*) D.R. Arnold and M.S. Snow. Can. J. Chem. **66**, 3012 (1988); (*b*) D.R. Arnold and X. Du. J. Am. Chem. Soc. **111**, 7666 (1989); (*c*) X. Du, D.R. Arnold, R.J. Boyd, and Z. Shi. Can. J. Chem. **69**, 1365 (1991); (*d*) K. McMahon and D.R. Arnold. Can. J. Chem. **71**, 450 (1993); (*e*) D.A. Connor, D.R. Arnold, P.K. Bakshi, and T.S. Cameron. Can. J. Chem. **73**, 762 (1995); (*f*) D.R. Arnold, X. Du, and H.J.P. de Lijser. Can. J. Chem. **73**, 522 (1995); (*g*) D.R Arnold, D.A. Connor, K.A. McManus, P.K. Bakshi, and T.S. Cameron. Can. J. Chem. **74**, 602 (1996); (*h*) H.J.P. de Lijser, T.S. Cameron, and D.R. Arnold. Can. J. Chem. **75**, 1795 (1997); (*i*) M.S.W. Chan and D.R. Arnold. Can. J. Chem. **75**, 1810 (1997); (*j*) D.R. Arnold, K.A. McManus, and M.S.W. Chan. Can. J. Chem. **75**, 1055 (1997); (*k*) H.J.P. de Lijser and D.R. Arnold. J. Org. Chem. **62**, 8432 (1997); (*l*) J. Phys. Chem. **100**, 3996 (1996).
2. (*a*) K.A. McManus and D.R. Arnold. Can. J. Chem. **73**, 2158 (1995); (*b*) D.R. Arnold, M.S.W. Chan, and K.A. McManus. Can. J. Chem. **74**, 2143 (1996); (*c*) K.A. McManus and D.R. Arnold. Can. J. Chem. **72**, 2291 (1994); (*d*) D.R. Arnold, K.A. McManus, and X. Du. Can. J. Chem. **72**, 415 (1994); (*e*) D.R. Arnold and X. Du. Can. J. Chem. **72**, 403 (1994).
3. (*a*) C.S.Q. Lew, J.R. Brisson, and L.J. Johnston. J. Org. Chem. **62**, 4047 (1997); (*b*) R. Torriani, M. Mella, E. Fasani, and A. Albini. Tetrahedron, **53**, 2573 (1997); (*c*) H.X. Weng, C. Scarlata, and H.D. Roth. J. Am. Chem. Soc. **118**, 10 947 (1996); (*d*) M. Schmittel and A. Burghart. Angew. Chem. Int. Ed. Engl. **36**, 2551 (1997).
4. M.J. Frisch, G.W. Trucks, H.B. Schlegel, P.M.W. Gill, B.G. Johnson, M.A. Robb, J.R. Cheeseman, T. Keith, G.A. Petersson, J.A. Montgomery, K. Raghavachari, M.A. Al-Laham, V.G. Zakrzewski, J.V. Ortiz, J.B. Foresman, J. Cioslowski, B.B. Stefanov, A. Nanayakkara, N. Challacombe, C.Y. Peng, P.Y. Ayala, W. Chen, M.W. Wong, J.L. Andres, E.S. Repogle, R. Gomperts, R.L. Martin, D.J. Fox, J.S. Binkley, D.J. Defrees, J. Baker, J.P. Stewart, M. Head-Gordon, C. Gonzalez, and J.A. Pople. Gaussian 94, Revision B.2. Gaussian, Inc., Pittsburgh, Pa. 1995.
5. (*a*) C. Møller and M.S. Plesset. Phys. Rev. **46**, 618 (1934); (*b*) W.J. Hehre, L. Radom, P.v.R. Schelyer, and J.A. Pople. Ab initio molecular orbital theory. Wiley–Interscience, New York. 1987; (*c*) R.S. Mulliken. J. Chem. Phys. **23**, 1983 (1955).
6. (*a*) N.L. Allinger, Y.H. Yuh, and J.-H. Lii. J. Am. Chem. Soc. **111**, 8551 (1989); (*b*) J.-H. Lii and N.L. Allinger. J. Am.

© 1998 NRC Canada

Chem. Soc. **111**, 8566 (1989); (*c*) J. Am. Chem. Soc. **111**, 8576 (1989).
7. A. Okamoto, M.S. Snow, and D.R. Arnold. Tetrahedron, **42**, 6175 (1986).
8. D.D.M. Wayner and D.R. Arnold. Can. J. Chem. **64**, 100 (1986).
9. (*a*) R.S. Nicholson and I. Shain. Anal. Chem. **36**, 706 (1964); (*b*) Anal. Chem. **37**, 178 (1965).
10. (*a*) G. Bieri, F. Burger, E. Heilbronner, and J.P. Maier. Helv. Chim. Acta, **60**, 2213 (1977); (*b*) M. Beez, G. Bieri, H. Bock, and E. Heilbronner. Helv. Chim. Acta, **56**, 1028 (1973); (*c*) P. Mosclet, D. Grosjean, G. Mocivier, and J. Dubois. J. Electron Spectrosc. **2**, 225 (1973).

© 1998 NRC Canada

Ketone coordination chemistry of the diborane *t*-BuCH=C[B(C_6F_5)$_2$]$_2$

Katrin Köhler and Warren E. Piers

Abstract: Reactions of the bifunctional borane *t*-BuCH=C[B(C_6F_5)$_2$]$_2$, **1**, with simple Lewis bases were investigated to probe its Lewis acidity. Ethereal bases (Et_2O, THF) bind very weakly, if at all, as no adducts were detectable in solution. Certain ketones, however, were observed to bind to **1**. Acetone forms an adduct, **2**, reversibly in solution (K_{eq} at 293 K = 69.1), and the temperature dependence of this equilibrium yield thermodynamic parameters of $\Delta H°$ = –59.5 ± 2.0 kJ mol^{-1}; $\Delta S°$ = –167 ± 4 J K^{-1} mol^{-1}. Low temperature NMR spectroscopy suggests that the acetone binds to the more sterically accessible boron center *trans* to the *t*-Bu group. Ketone binding is strengthened when 2,3-diphenylcyclopropenone is reacted with **1**, irreversibly forming an isolable adduct, **4**, in high yield (95%). The availability of a resonance form incorporating the aromatic cyclopropenyl cation contributes to the added stability of this adduct in comparison to **2**.

Key words: organoboranes, diboranes, ketone complexes.

Résumé : Afin d'évaluer son acidité de Lewis, on a étudié les réactions du borane bifonctionnel *t*-BuCH=C[B(C_6F_5)$_2$]$_2$, **1**, avec des bases de Lewis simples. Au mieux, les bases éthérées (Et_2O, THF) ne s'y lient que faiblement puisqu'on ne peut détecter la présence d'adduits en solution. Toutefois, on a observé que certaines cétones se lient à **1**. En solution, l'acétone forme d'une façon réversible l'adduit **2** ($K_{éq}$ = 69,1, à 293 K) et la dépendance de cet équilibre sur la température permet de déterminer les paramètres thermodynamiques suivants: $\Delta H°$ = –59,5 ± 2,0 kJ mol^{-1} et $\Delta S°$ = –167 ± 4 J K^{-1} mol^{-1}. Les résultats d'expériences de RMN à basse température suggèrent que l'acétone se lie au bore stériquement le plus accessible, *trans* par rapport au groupe *tert*-butyle. La liaison avec la cétone est plus forte lorsqu'on fait réagir de la 2,3-diphénylcyclopropénone avec **1**; on peut alors isoler l'adduit **4**, formé d'une façon irréversible avec un rendement de 95%. La disponibilité d'une forme de résonance comportant le cation aromatique cyclopropényle contribue à la stabilité accrue de cet adduit par comparaison avec l'adduit **2**.

Mots clés : boranes organiques, diboranes, complexes de cétones.

[Traduit par la Rédaction]

Highly electrophilic pentafluorophenyl boranes and boronic acids have recently been applied as Lewis acids in organic synthesis (1). Much less attention has been given to *bis*-boryl compounds incorporating B(C_6F_5)$_2$ units (**I**) (2), which in principle could offer several advantages over the monofunction boranes in this regard (3).

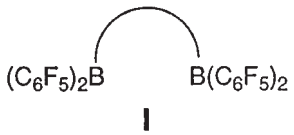

I

We (4) and others (5) have been interested in the activation of carbonyl functions by pentafluorophenyl substituted boranes. A variety of 1,1-*bis*(pentafluorophenyl)borane substituted alkyl derivatives are available via hydroboration of terminal alkynes with HB(C_6F_5)$_2$ (6). Reactions of the resulting bifunctional boranes with simple Lewis bases such as acetone reveal a problem with these systems, namely the facility of retrohydroboration. Instead of observing adducts, the product mixture shown in Scheme 1 was observed. Although the diborane dominates the equilibrium, ketones such as acetone react preferentially with the small amounts of HB(C_6F_5)$_2$, which are present via retrohydroboration. We judged that in order to study the coordination chemistry of diboranes incorporating the -B(C_6F_5)$_2$ functional group, compounds without β-hydrogens (or at least systems in which elimination of HB(C_6F_5)$_2$ is kinetically and (or) thermodynamically prohibitive) would be required.

To this end, we prepared some 1,1-*bis*-boryl alkenes RCH=C[B(C_6F_5)$_2$]$_2$, which by virtue of the unsaturation in the linker group do not undergo retrohydroboration. These bifunctional Lewis acids were prepared by regioselective hydroboration of boraalkynes with general formula RC≡CB(C_6F_5)$_2$, using HB(C_6F_5)$_2$; their complete characterization, including their molecular structures, have been reported elsewhere (7). Since diborane **1** is sufficiently Lewis acidic to abstract methyl groups from Cp_2ZrMe_2 (7) and generate active olefin polymerization catalysts, we have examined its reactivity with simple Lewis bases to probe its potential for applications in organic synthesis.

Received June 19, 1998.

K. Köhler and W.E. Piers.[1] Department of Chemistry, University of Calgary, 2500 University Drive N.W., Calgary, AB T2N 1N4, Canada.

[1]Author to whom correspondence may be addressed. Fellow of the Alfred P. Sloan Foundation, 1996–1998. Telephone: (403) 220-5746. Fax: (403) 289-9488. E-mail: wpiers@chem.ucalgary.ca

© 1998 NRC Canada

Scheme 1.

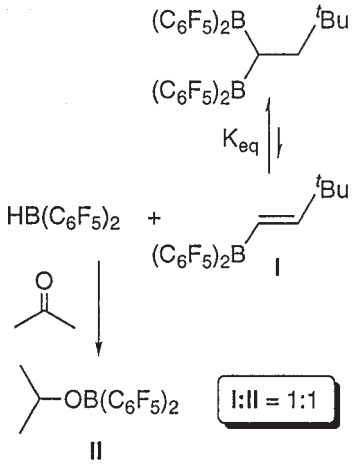

Results and discussion

Preliminary experiments were directed at exploring the ability of compound **1** to bind simple ethers, such as Et_2O or THF, since the parent Lewis acid $B(C_6F_5)_3$ strongly binds these solvents. In contrast, bidentate **1** does not form an isolable complex with either of these two bases. Dissolution of **1** in Et_2O or THF, followed by removal of the solvent in vacuo results in complete recovery of base-free **1**. Indeed, ^{1}H NMR experiments suggest that binding of THF in solution is minimal; a 1:1 mixture of THF and **1** in C_6D_6 gives a nearly identical spectrum to that obtained for THF in the absence of **1**, suggesting that the equilibrium does not favor adduct formation. In light of the favorable binding of THF by the related boranes $HB(C_6F_5)_2$ and $CH_3B(C_6F_5)_2$, it is likely that THF coordination to **1** is discouraged by the steric crowding in the molecule (7). Also, the most accessible boron center is the one *trans* to the *t*-Bu group, which is in conjugation with the carbon—carbon double bond (7) and is therefore less Lewis acidic on electronic grounds than, for example, $CH_3B(C_6F_5)_2$.

Sterically less demanding Lewis bases can, however, access the boron centers in **1**. Water reacts rapidly with **1** to liberate Bu-*t*-CH=CH_2 and 2 equiv. of the known boronic acid $HOB(C_6F_5)_2$ (8). Steric differentiation is also observed in ketone binding studies involving benzophenone and acetone (eq. [1]).

Whereas no binding is observed for benzophenone at room temperature (i.e., $K_{eq} \approx 0$), the smaller and more basic acetone coordinates reversibly to **1** as shown (K_{eq} = 69.1 at 293 K). Attempts to isolate acetone adduct **2** as a solid were unsuccessful; removal of solvent from solutions containing **2** resulted in complete loss of acetone and recovery of uncomplexed **1**.

It was possible, however, to perform detailed spectroscopic studies on adduct **2**. The temperature dependence of the equilibrium involving adduct formation was examined by ^{1}H NMR spectroscopy. Using the signal for the olefinic hydrogen atom as a probe, the equilibrium constant at various temperatures was calculated (9; see also ref. 4*b*) after the requisite chemical shifts for free **1** (7.17 ppm) and fully bound **2** (6.03 ppm)[2] were measured in d_8-toluene. A van't Hoff plot of ln K_{eq} vs. $1/T$ (Fig. 1, Table 1) allowed for extraction of the thermodynamic parameters associated with this equilibrium: $\Delta H° = -59.5 \pm 2.0$ kJ mol^{-1}; $\Delta S° = -167 \pm 4$ J K^{-1} mol^{-1}. Thus, binding is only slightly favored at 298 K ($\Delta G° = -9.7 \pm 2.2$ kJ mol^{-1}) due to a relatively low enthalpic contribution to adduct formation.

At temperatures below ≈–30°C, however, **2** is essentially the only species in solution and can be probed by various multinuclear NMR experiments. Interpretation of the spectra resulting from these experiments is complicated somewhat by the fluxionality observed in **2**, arising from -C_6F_5 ring rotations, which are frozen out at ≈–80°C. In this temperature regime, however, spectral changes can be assumed to be due to the dynamic behavior of **2** and not rapid exchange between free and bound acetone as is observed at higher temperatures.

Since ^{11}B chemical shifts are quite sensitive to the coordination environment about the boron center (10), this technique would seem to be ideal for addressing the question of whether the acetone is bound by one or both of the Lewis acid centers. Unfortunately, ^{11}B NMR spectroscopy gave ambiguous results in this regard. At room temperature, a strong signal centered around 39.0 ppm (fwhh = 650 ± 10 Hz) represents an average of the signals from **1** (7) and **2**. Upon cooling to temperatures at which **2** should dominate in solution (vide supra), this signal broadens considerably into two featureless humps centered around 32 ± 4 and –4 ± 4 ppm. Although this is a pattern that might be expected for a compound with one neutral three-coordinate and one neutral four-coordinate boron center, the rather poor signal-to-noise obtained in this experiment necessitates caution in this interpretation of the data. Attempts to improve the quality of the data were hampered by the fact that these are high molecular weight compounds with poor solubility at low temperature. Since ^{11}B is a quadrupolar nucleus, each boron has

[1]

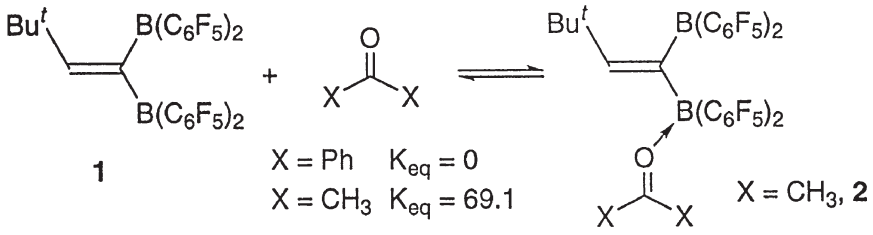

[2] This was measured at room temperature by adding an excess of acetone in 5 equiv. increments until the chemical shift of the C*H*= resonance did not change upon further addition.

© 1998 NRC Canada

Fig. 1. A van't Hoff plot for the equilibrium between **1** and acetone and the adduct **2**.

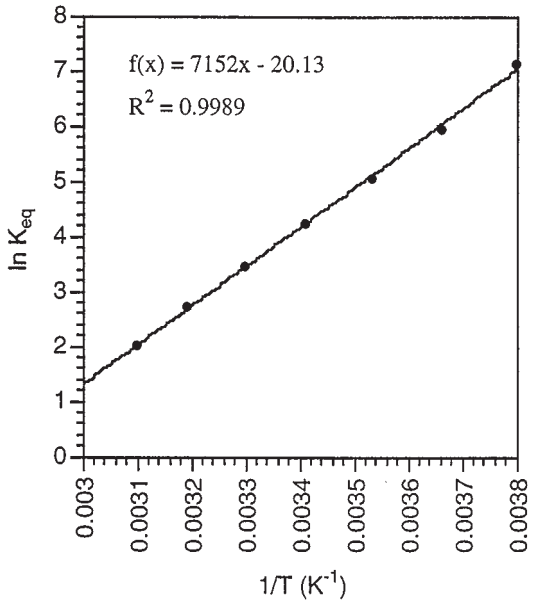

a broadening effect on the other; furthermore, the two boron nuclei are chemically inequivalent and therefore coupled to eachother. Together these factors conspire to severely broaden the signals, accounting for the poor quality of the data.

Fluorine-19 NMR spectroscopy was more useful in probing the solution structure of **2**. At room temperature, two sets of signals are observed; as the sample is cooled, these peaks broaden and shift until at –80°C, separate resonances for each of the 20 fluorine atoms present are observed. The resulting spectrum is shown in Fig. 2. To help assign this spectrum, a ^{19}F–^{19}F COSY experiment was performed at –80°C, allowing the signals to be grouped into four sets of resonances arising from each C_6F_5 ring. These assignments are given in Table 2, and the full COSY correlation map is included as supplementary information.[3] Precise assignment of the four different C_6F_5 rings was not possible, but the data indicates that two of the rings are associated with a four-coordinate boron center (**A**, **A′**), while the other two are bonded to tricoordinate boron (**B**, **B′**). The primary evidence for this lies in the observed absolute difference between the chemical shifts of the *para*- and *meta*-fluorines ($\Delta\delta_{m,p}$) in each ring.

Horton et al. (11) has noted the fact that $\Delta\delta_{m,p}$ is sensitive to the coordination environment about boron in pentafluorophenyl substituted borates and boranes. A relatively large $\Delta\delta_{m,p}$ is suggestive of three-coordinate boron, while smaller values of $\Delta\delta_{m,p}$ imply a coordination number of four. In **2**, two of the rings exhibit $\Delta\delta_{m,p}$ values of <10 ppm, while the other two range from 12.5 to 17.1 ppm (Table 2). For comparison, $\Delta\delta_{m,p}$ for free diborane **1**, $B(C_6F_5)_3$ and the acetophenone adduct of $B(C_6F_5)_3$ (*4b*) are also given. These

Table 1. Equilibrium data for acetone coordination to diborane **1** ($[\mathbf{1}]_0 = [CH_3COCH_3]_0 = 0.058$ M).

T (K)	δ_{obs}[a] (ppm)	N_1[b]	N_2[c]	K_{eq}[d]	ln K_{eq}	$1/T$ ($\times 10^{-3}$ K^{-1})
263	6.15	0.11	0.89	1268	7.14	3.80
273	6.25	0.19	0.81	387	5.96	3.66
283	6.35	0.28	0.72	158	5.06	3.53
293	6.47	0.39	0.61	69.1	4.24	3.41
303	6.61	0.51	0.49	32.5	3.48	3.30
313	6.76	0.64	0.36	15.2	2.72	3.19
323	6.89	0.75	0.25	7.66	2.04	3.10

[a]Chemical shift of the olefinic proton.
[b]Mole fraction of **1** = $(\delta_{obs} - \delta_2)/(\delta_1 - \delta_2)$. δ_1 = 7.17 ppm; δ_2 = 6.03 ppm.
[c]Mole fraction of **2**.
[d]$K_{eq} = (N_2 \times 0.058)/(N_1 \times 0.058)^2$.

data suggest, therefore, that only one borane moiety in adduct **2** is engaged in bonding with acetone and that rings **A** and **A′** belong to the ligated four-coordinate boron center. Based on the observation that it is the boron center *trans* to the *t*-Bu group, which abstracts CH_3^- from Cp_2ZrMe_2 (*7*), we presume that it is this more accessible center that is involved in acetone binding. Although this boron center is conjugated with the double bond (note the smaller $\Delta\delta_{m,p}$ for this $B(C_6F_5)_2$ unit compared to the one *cis* to the *t*-Bu group), it is the preferred site of attack for Lewis bases on steric grounds.

A striking feature of the low-temperature ^{19}F NMR spectrum of **2** is the rather large coupling observed between two of the *ortho*-F atoms in the molecule. This coupling is evident also in the ^{19}F–^{19}F COSY spectrum; the *ortho*-F region of this spectrum is shown in Fig. 3. The magnitude (183.5 ± 1.0 Hz)[4] of the coupling, combined with the the fact that the two F atoms in question are on different C_6F_5 rings leads to the conclusion that this is a "through-space" coupling rather than a more common "through-bond" coupling. Indeed, close inspection of the COSY map reveals that there are several inter-ring couplings observable in this complex; the *ortho*-F region of the COSY (Fig. 3) shows three such couplings, and there are others evident in the full spectrum as well (supplementary information[3]).

Ample precident exists for through space coupling between proximal ^{19}F nuclei and, while the phenomenon has been investigated most thoroughly in organic systems (12), instances have recently been observed in organometallic compounds as well (13). The coupling is thought to arise when two ^{19}F nuclei get close enough for the lone pair orbitals to overlap, although couplings between atoms separated by more than the sum of two ^{19}F van der Waals radii have been observed (14). As such, the magnitude of the coupling is directly related to the separation between the two nuclei, with stronger couplings observed between closer contacts. Several quantitative expressions have been developed to relate the coupling constant to the intranuclear distance (15), the most recent and accurate being put forward

[3] Copies of material on deposit may be purchased from: The Depository of Unpublished Data, Document Delivery, CISTI, National Research Council of Canada, Ottawa, Canada, K1A 0S2.
[4] The coupling constant of 183.5 Hz was observed at 282.37 MHz. To confirm that this was a genuine coupling constant, the ^{19}F NMR spectrum of **2** at –60°C was also acquired at 376.50 MHz. A coupling constant of 188.2 ± 1.0 Hz was observed in this experiment.

© 1998 NRC Canada

Fig. 2. A 282 MHz ^{19}F NMR spectrum of adduct **2** at –80°C. The *ortho*-, *para*-, and *meta*- fluorines are assigned as indicated; peaks marked by an asterisk (*) are minor impurities.

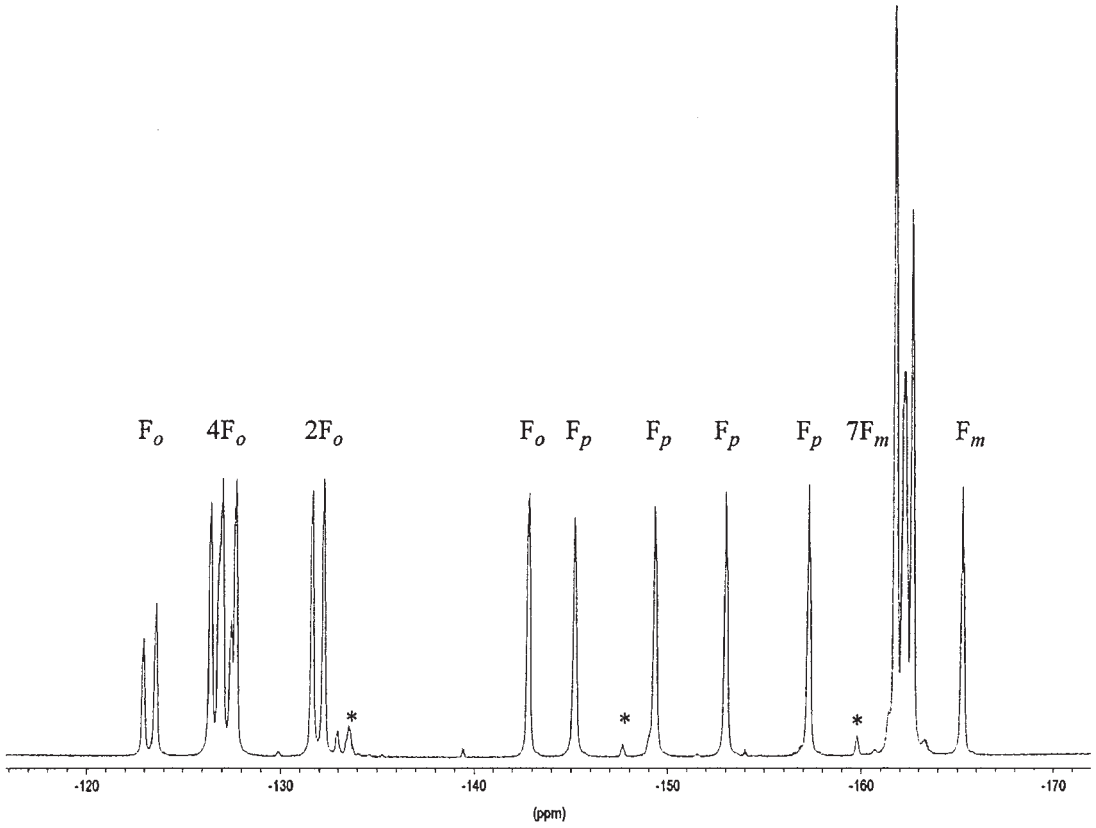

Table 2. The ^{19}F NMR data for **2** (–80°C), **1**, $B(C_6F_5)_3$, and $C_6H_5C(O)CH_3 \cdot B(C_6F_5)_3$, **3** (25°C).

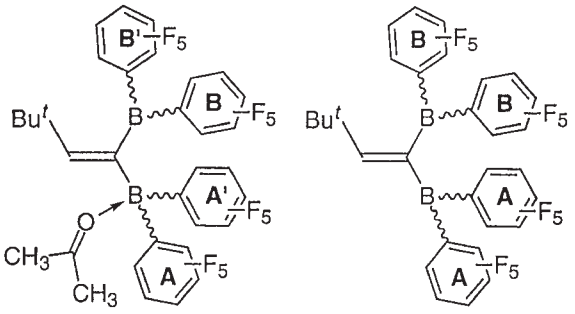

	A	**A′**	**B**	**B′**	**A**[b]	**B**[b]	**B(C$_6$F$_5$)$_3$**	**3**[c]
ortho	–126.4	–123.3[a]	–127.2[a]	–127.0	–130.1	–126.5	–128.8	–136.0
ortho	–142.9	–131.6	–127.7	–132.3				
para	–157.4	–153.1	–145.2	–149.3	–148.7	–143.3	–141.9	–157.0
meta	–162.7	–161.8	–161.8	–161.8				
meta	–163.4	–162.3	–162.3	–162.3	–160.5	160.6	–160.1	–164.6
$\Delta\delta_{m,p}$	5.3	8.7	16.6	12.5	11.8	17.3	18.2	7.6
$\Delta\delta_{m,p}$	6.0	9.2	17.1	13.0				

[a]Doublet, J_{FF} = 183.5 Hz.
[b]Taken from ref. 7. Assignment of the upfield *para* resonance to the rings **A** is based on the fact that this boron center is conjugated with the double bond.
[c]Taken from ref. 4*b*.

© 1998 NRC Canada

Fig. 3. The *ortho*-fluorine region of the ^{19}F–^{19}F COSY map for **2** at –80°C (excluding the resonance at –142.9 ppm to which no correlations to other *ortho*-F nuclei were observed). Arrows indicate the three "through-space" couplings revealed in the COSY experiment.

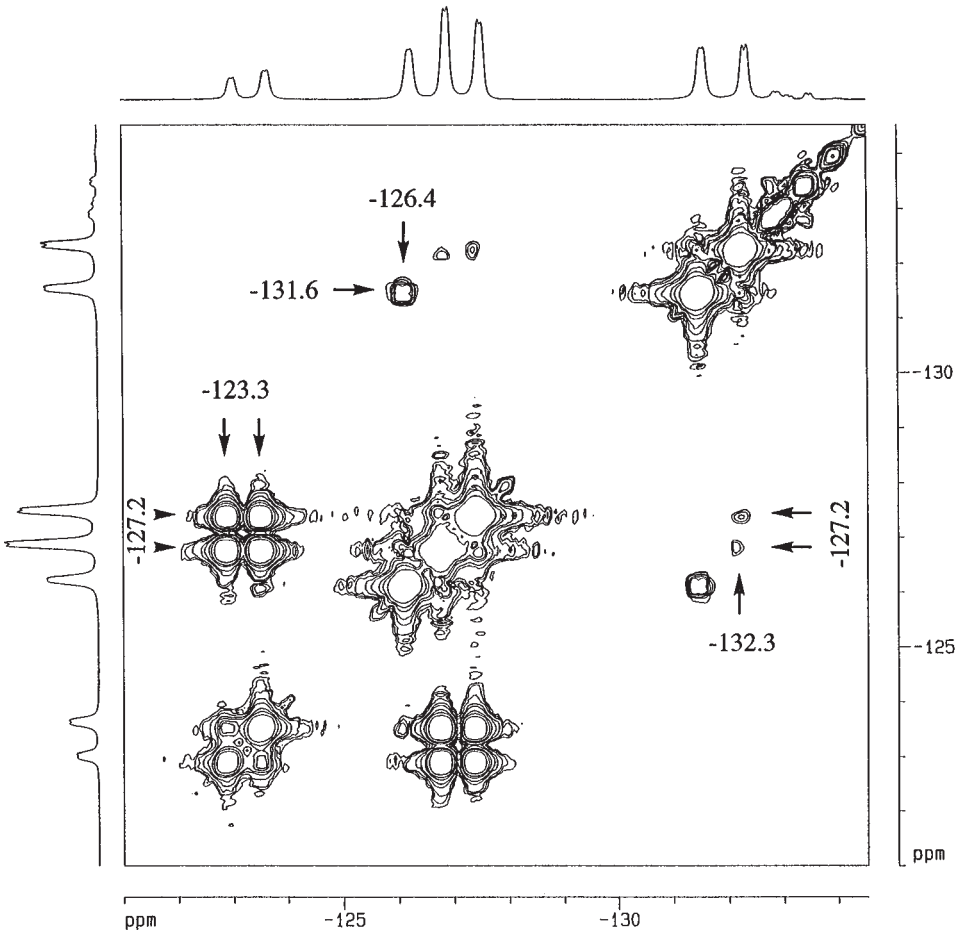

Scheme 2.

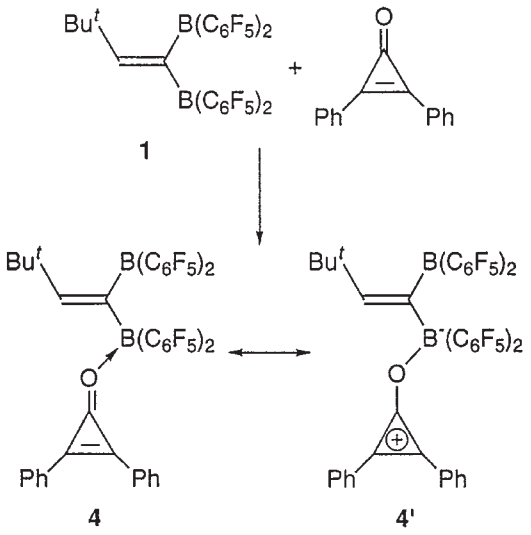

by Ernst and Ibrom (16) (J_{FF} = 275 000 $e^{-0.03211d_{FF}}$ (d_{FF} = nonbonding distance)). Using this expression, a distance of 2.28 ± 0.02 Å may be computed for two coupling *ortho*-^{19}F nuclei in **2**, well within the sum of the van der Waals radii of two fluorine atoms (2.70 Å). Molecular models of **2** built and minimized with MacSpartan Plus software (MM2) suggest that the closest contacts between *ortho*-F atoms exist between the "inner" rings (labelled **A′** and **B** in the graphic for Table 2), although none were as close as the coupling constant would indicate. The data does, however, suggest that coordination of a Lewis base (in this case, acetone) to **1**, crowds the molecule further and causes several close contacts between C_6F_5 rings on opposing boron nuclei. A variable temperature ^{19}F NMR study on **1** itself showed some broadening due to the onset of restricted C_6F_5 rotation, but the low-temperature limit was not imminent even at –80°C. It is therefore hard to say to whether similar close F–F contacts exist in free **1**, but the more facile C_6F_5 rotation would argue against this notion. This exacerbation of steric congestion upon Lewis base coordination to **1** accounts for the weak nature of the bonding of acetone to **1** and the apparent lack of bonding by more sterically demanding bases such as THF or Et_2O (vide supra).

In an attempt to strengthen the interaction, the reaction of **1** with 2,3-diphenylcyclopropenone was studied (Scheme 2), the assumption being that a significant contribution from the resonance form depicted as ***4′***, since cyclopropenyl cations are aromatic (17), would help to stabilize the adduct (a similar strategy for encouraging ketone binding to 1,8-naphthalenediylbis(dichloroborane) using 2,6-dimethylpyranone has

© 1998 NRC Canada

been employed; see ref. 18). Indeed, **4** is isolated analytically pure in 95% yield from 1:1 mixtures of the reagents in hexanes. Spectroscopic evidence in favor of the structure as shown in Scheme 2 follows along the same lines as that described above for the acetone adduct of **1**. Again, ^{11}B NMR spectroscopy was ambiguous, giving only one signal 9.4 ppm, implying that the resonance for the three-coordinate boron nucleus is too broad to be readily observed. The $\Delta\delta_{m,p}$ values of 12.6 and 7.1 ppm are consistent with the presence of both three and four coordinate boron nuclei, respectively. Finally, the ^{13}C chemical shifts for the carbon nuclei of the ketone are shifted significantly downfield with respect to the free ketone, consistant with the transfer of electron density from the ketone to the borane upon coordination. For example, the two carbon nuclei associated with the cyclopropenyl ring shift from 154.6 and 149.6 ppm in the free ketone to 158.1 and 157.3 ppm in **4**.

Conclusions

Although diborane **1** is an effective initiator of olefin polymerization reactions (7), it is a relatively poor Lewis acid for activating organic Lewis bases. This can be attributed to the steric properties of the molecule, which renders only one of the borane centers readily accessible to incoming nucleophiles. Although the $B(C_6F_5)_2$ group is quite bulky, the steric problems of the 1,1-alkenyl diboranes would likely be alleviated to a degree by incorporating longer linkers, possibly allowing for more interesting coordination chemistry directly involving both highly electrophilic boron centers. These studies are currently underway.

Experimental section

General

All manipulations of air- and moisture-sensitive materials were undertaken using standard vacuum and Schlenk techniques (19) or in a glove-box under an atmosphere of nitrogen. All solvents were dried and purified by passing through suitable drying agents (alumina and Q5) (20). The NMR spectra were recorded in C_6D_6 at room temperature or in C_7D_8 for low temperature experiments. Data are given in ppm relative to solvent signals for ^{1}H and ^{13}C spectra or relative to external standards for ^{11}B ($BF_3{\cdot}OEt_2$, 0.0 ppm) and ^{19}F ($CFCl_3$ at 0.0 ppm) experiments. Elemental analyses were performed by Mrs. Dorothy Fox in the microanalytical laboratory of the Department of Chemistry at the University of Calgary. Complex **1** was prepared as described previously (7). Acetone was dried over activated molecular sieves and distilled prior to use; ketones benzophenone and 2,3-diphenylcyclopropenone were purchased from Aldrich and used as received.

Reaction of 1 with Et_2O and THF

A small amount of **1** (≈30–40 mg) was dissolved in Et_2O or THF. Upon full dissolution, the solvent was removed in vacuo and the residue subjected to full vacuum for at least 1 h. The resulting solid was then dissolved in C_6D_6 and examined by ^{1}H NMR. Alternatively, **1** (50 mg, 0.064 mmol) was loaded into a 5 mm NMR tube and dissolved in C_6D_6. Dry, degassed THF (5.2 mL, 0.064 mmol) was introduced via syringe and the sample assayed by ^{1}H NMR spectroscopy.

Reaction of 1 with water

Diborane **1** (50 mg, 0.064 mmol) was loaded into a 5 mm NMR tube and dissolved in C_6D_6 (≈0.7 mL). The tube was capped with a rubber septum. Degassed, deionized water (1.2 mL, 0.064 mmol) was added by syringe and the sample assayed by ^{1}H NMR spectroscopy.

Reaction of 1 with benzophenone

Diborane **1** (70 mg, 0.090 mmol) and benzophenone (17 mg, 0.093 mmol) were loaded into a 5 mm NMR, dissolved in C_6D_6 and assayed by ^{1}H NMR spectroscopy.

Equilibrium studies concerning 1, acetone, and 2

Samples for study by a variety of NMR techniques were prepared as follows. Diborane **1**, (45 mg, 0.058 mmol) was dissolved in d_8-toluene (1 mL) and acetone (4.3 mL, 0.058 mmol) was added at 25°C. A portion of this solution ([**1**] = [CH_3COCH_3] = 0.058 M) was loaded into a 5 mm NMR tube and sealed for analysis with a septum wrapped with parafilm. The following data is for room temperature NMR spectra. ^{1}H NMR: 6.61 (s, 1H, *H*C=), 1.49 (s, 6H, OCC*H*$_3$), 0.98 (s, 9H, CC*H*$_3$). ^{13}C{^{1}H} NMR: 215.4 (O*C*CH$_3$), 171.9 (H*C*=), 37.9 (*C*CH$_3$), 29.9 (OC*C*H$_3$), 29.4 (CCH$_3$). ^{11}B NMR: 39.0. ^{19}F NMR: –127.0 (m, 4F, *o*-F), –130.4 (s, br, 4F, *o*-F), –145.6 (t, 2F, *p*-F), –151.2 (t, 2F, *p*-F), –161.5 (m, 4F, *m*-F), –161.8 (m, 4F,*m*-F). See Table 2 and text for low-temperature NMR data on **2**.

Preparation of Bu-*t*-(H)C=C[B(C_6F_5)$_2$]$_2$[OC(CC_6H_5)$_2$], 4

Compound **1**, (150 mg, 0.194 mmol) was dissolved in hexane (20 mL), and a solution of OC(CC_6H_5)$_2$ (40 mg, 0.194 mmol) in hexane (5 mL) was added at –78°C. After stirring for 1 h at –78°C the reaction solution was warmed to 25°C. A white precipitate was formed; a portion of the solvent was removed, the solid was separated by filtration and washed with hexane. Crystallization at –30°C in benzene/hexane (5:1) yielded **4** (180 mg, 95%). ^{1}H NMR: 6.95 (m, 4H, C_6H_5), 6.84 (m, 6H, C_6H_5), 6.16 (s, 1H, *H*C=), 1.08 (s, 9H, Bu-*t*). ^{13}C{^{1}H} NMR: 158.1 (O=*C*); 157.3 (H*C*=); 145.5 (C_{ipso}); 135.8, 132.3, 129.8 (C_6H_5); 120.6 (CC_6H_5); 37.1 (*C*CH$_3$); 30.6 (C*C*H$_3$). ^{11}B NMR: 9.4. ^{19}F NMR: –127.9 (m, 4F, *o*-F), –130.9 (m, 4F, *o*-F), –149.8 (m, 2F, *p*-F), –156.7 (m, 2F, *p*-F), –162.4 (m, 4F, *m*-F), –163.8 (m, 4F, *m*-F). Anal. calcd. for $C_{45}H_{20}B_2F_{20}O$: C 55.25, H 2.06; found: C 55.26, H 1.72.

Acknowledgments

Funding for this work from the Natural Sciences and Engineering Research Council of Canada is gratefully acknowledged. K.K. acknowledges the D.F.G. for a postdoctoral fellowship. W.E.P. also thanks the Alfred P. Sloan Foundation for a Research Fellowship (1996–2000). The authors thank Dr. Raghav Yamdagni and Mrs. Qiao Wu for assistance with NMR experiments and the preparation of Figs. 2 and 3.

© 1998 NRC Canada

References

1. W.E. Piers and T. Chivers. Chem. Soc. Rev. 345 (1997).
2. L. Jia, X. Yang, C.L. Stern, and T.J. Marks. Organometallics, **13**, 3755 (1994).
3. (*a*) J. Vaugeois, M. Simard, and J.D. Wuest. Coord. Chem. Rev. **145**, 55 (1995); (*b*) O. Saied, M. Simard, and J.D. Wuest. Organometallics, **17**, 1128 (1998), and refs. therein; (*c*) J. Vaugeois, M. Simard, and J.D. Wuest. Organometallics, **17**, 1215 (1998).
4. (*a*) D.J. Parks and W.E. Piers. J. Am. Chem. Soc. **118**, 9440 (1996); (*b*) D.J. Parks, W.E. Piers, M. Parvez, D.C. MacQuarrie, and M.J. Zaworotko. Organometallics, **17**, 1369 (1998).
5. (*a*) K. Ishihara, N. Hanaki, and H. Yamamoto. Synlett, 577 (1993); (*b*) K. Ishihara, M. Funahasi, N. Hanaki, M. Miyata, and H. Yamamoto. Synlett, 963 (1994); (*c*) K. Ishihara, N. Hanaki, and H. Yamamoto. Synlett, 721 (1995); (*d*) K. Ishihara, N. Hanaki, M. Funahasi, M. Miyata, and H. Yamamoto. Bull. Chem. Soc. Jpn. **68**, 1721 (1995).
6. D.J. Parks, R.E.v.H. Spence, and W.E. Piers. Angew. Chem. Int. Ed. Engl. **34**, 809 (1995).
7. K. Köhler, W.E. Piers, S. Xin, Y. Feng, A.M. Bravakis, A.P. Jarvis, S. Collins, W. Clegg, G.P.A. Yap, and T.B. Marder. Organometallics, **17**, 3557 (1998).
8. K. Ishihara, H. Kurihara, and H. Yamamoto. J. Org. Chem. **62**, 5664 (1997).
9. R.S. Drago. Physical methods for chemists. 2nd ed. Saunders, New York. 1992. p. 257.
10. R.G. Kidd. *In* NMR of newly accessible nuclei. Vol. 2. *Edited by* P. Laszlo. Academic Press, New York. 1983.
11. (*a*) A.D. Horton, J. de With, A.J. van der Linden, and H. van de Weg. Organometallics, **15**, 2672 (1996); (*b*) A.D. Horton and J. de With. Chem. Commun. 1375 (1996); (*c*) Organometallics, **16**, 5424 (1997).
12. (*a*) J. Hilton and L.H. Sutcliffe. Prog. NMR Spectrosc. **10**, 27 (1975); (*b*) F.B. Mallory, C.W. Mallory, and W.M. Ricker. J. Am. Chem. Soc. **97**, 4770 (1975); (*c*) L. Ernst, K. Ibrom, R. Marat, R.H. Mitchell, G.J. Bodwell, and G.W. Bushnell. Chem. Ber. **127**, 1119 (1994), and refs. therein.
13. A.C. Albeniz, A.L. Casado, and P. Espinet. Organometallics, **16**, 5417 (1997).
14. F.B. Mallory. J. Am. Chem. Soc. **95**, 7747 (1973).
15. (*a*) A.D. Buckingham and J.E. Cordle. J. Chem. Soc. Faraday Trans. 2, **70**, 994 (1974); (*b*) J. Hilton and L.H. Sutcliffe. Spectrochim. Acta Part A, **32**, 201 (1976); (*c*) V.I. Bakhmutov, M.V. Galakhov, and E.I. Fedin. Magn. Reson. Chem. **23**, 971 (1985).
16. L. Ernst and K. Ibrom. Angew. Chem. Int. Ed. Engl. **34**, 1881 (1995).
17. T. Eicher and J.L. Weber. Top. Curr. Chem. **57**, 1 (1975).
18. M. Reilly and T. Oh. Tetrahedron Lett. **36**, 217 (1995).
19. D.F. Shriver and M.A. Drezdzon. The manipulation of air-sensitive compounds. 2nd ed. Wiley, New York. 1986.
20. A.B. Pangborn, M.A. Giardello, R.H. Grubbs, R.K. Rosen, and F.J. Timmers. Organometallics, **15**, 1518 (1996).

© 1998 NRC Canada

The ultra high pressure conjugate addition of indoles to electron-deficient olefins

Paul Harrington and Michael A. Kerr

Abstract: The addition of indole and methyl indole at both high and ambient pressures to a series of Michael acceptors under the influence of ytterbium triflate was investigated. Under ambient pressure the more reactive and less sterically hindered electrophiles gave the expected 3-alkylated indoles in good to excellent yields. The more problematic Michael acceptors were subjected to pressures of 13 kbar. In all cases a dramatic reduction in reaction time and a significant improvement in yields was observed. In the cases involving 3-methylcyclohex-2-en-1-one, a by-product was formed and was characterized by single crystal X-ray diffraction. α,β-Unsaturated ketones gave the best yields. Enals tended to polymerize while enoates proved to be much too unreactive. A particularly reactive malonate derived ester and β-nitrostyrene gave good yields at ambient pressures.

Key words: hapalindole, indole, Michael addition, high pressure, ytterbium triflate, Lewis acid.

Résumé : On a étudié la réaction d'addition de l'indole et du méthylindole sur une série d'accepteurs de Michael sous l'influence de triflate d'ytterbium et à des pressions tant ambiante qu'élevée. À la pression ambiante, les électrophiles les plus réactifs présentant le moins d'encombrement stérique conduisent, avec des rendements allant de bons à excellents, aux indoles alkylés en position 3 attendus. Les accepteurs de Michael plus problématiques ont été soumis à des pressions de 13 kbar. Dans tous les cas, on a observé une réduction dramatique du temps de réaction et une amélioration significative des rendements. Dans les cas impliquant la 3-méthylcyclohex-2-én-1-one, il se forme un sous-produit qui a été caractérisé par diffraction des rayons X par un cristal unique. Les cétones α,β-insaturées donnent les meilleurs rendements. Les énals tendent à se polymériser alors que les énolates se sont avérés beaucoup moins réactifs. Un malonate particulièrement réactif, obtenu à partir de l'ester et du β-nitrostyrène, donne de bons rendements à des pressions ambiantes.

Mots clés : hapaindole, indole, addition de Michael, pression élevée, triflate d'ytterbium, acide de Lewis.

[Traduit par la Rédaction]

Introduction

We have recently been involved in studies directed towards the total synthesis of a class of bioactive indole alkaloids known as the hapalindoles. These cytotoxic compounds are a class of at least 20 members, isolated from the blue-green algae *Hapalosiphon fontinalis* by Moore et (1). The algae were isolated from soil samples collected from the Marshall Islands in 1981 and showed antibacterial, antimycotic, and antialgal activities. Initial reports disclosed the presence of two related compounds, hapalindole A and B (1*a*). Hapalindole A is responsible for the bulk of the biological activity. Three years later, the same group reported the structures of an additional 18 related compounds isolated from the same organism (1*b*). The structures possess either the tetracyclic framework present in hapalindole A and B or a tricyclic skeleton (possibly a biogenetic precursor) represented by hapalindoles C and D. There is large variation in the stereochemistry of the compounds; many have a diastereomeric relationship. This class of compounds provides an excellent opportunity for both stereochemical confirmation of the reported structures by synthesis and for the preparation of certain members for biochemical studies.

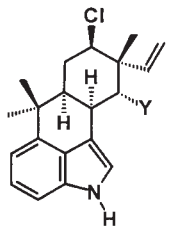

1 hapalindole A: Y = NC
2 hapalindole B: Y = NCS

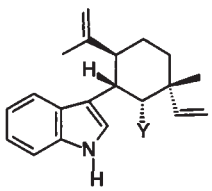

3 hapalindole C: Y = NC
4 hapalindole D: Y = NCS

The study of the chemistry of these compounds (2) as well as activity towards the synthesis of interesting natural products has been steady. There have been several syntheses of a few members of this class of compounds to date (3). Our retrosynthesis of hapalindole C (Scheme 1) centers around the nucleophilic addition of an indole moiety **6** to a suitable terpenoid fragment **7** to produce the key intermediate **5**. Subsequent conversion to the target molecule **3** would involve only the addition of the geminally disposed vinyl

Received November 6, 1996.[1]

P. Harrington and M.A. Kerr.[2] Department of Chemistry, Acadia University, Wolfville, NS B0P 1X0, Canada.

[1]Revision received July 8, 1998.
[2]Author to whom correspondence may be addressed. Telephone: (902) 585-1109. Fax: (902) 542-1454. E-mail: michael.kerr@acadiau.ca

© 1998 NRC Canada

Scheme 1. Proposed retrosynthesis of hapalindole C.

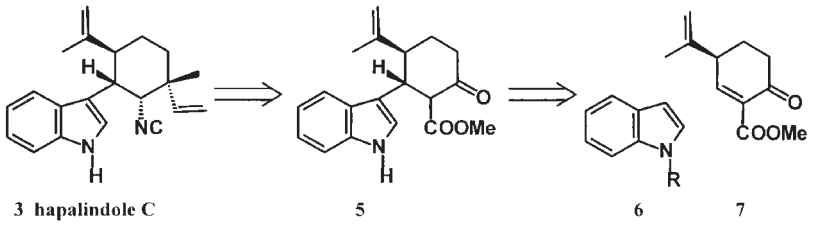

3 hapalindole C 5 6 7

Table 1. Ambient pressure alkylations of indoles with α,β-unsaturated ketones catalyzed by $Yb(OTf)_3$.

Entry	Indole	Enone	Time	Product(Yield)	Recovered Indole
	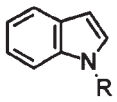	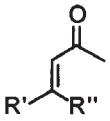		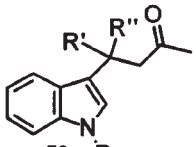	
1	R = H	R' = R'' = H	22h	72	0
2	R = Me	R' = R'' = H	7h	73	10
3	R = H	R' = Me, R'' = H	14h	85	0
4	R = Me	R' = Me, R'' = H	10h	95	0
5	R = H	R' = Me, R'' = Me	7d	19	63
6	R = Me	R' = Me, R'' = Me	7d	38	8
7	R = Me	R' = i-Pr, R'' = H	4d	77	0
		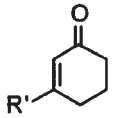		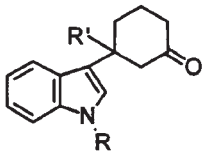	
8	R = H	R' = H	7d	44	3
9	R = Me	R' = H	7d	37	4
10	R = Me	R' = Me	7d	3	54
		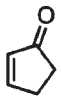		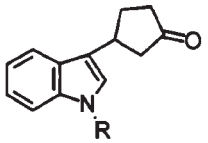	
11	R = Me		4d	95	2
		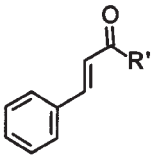		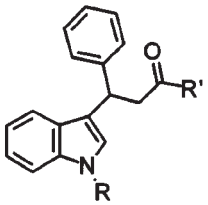	
12	R = H	R' = Me	7d	16	44
13	R = Me	R' = Me	7d	10	40
14	R = H	R' = Ph	7d	52	32
15	R = Me	R' = Ph	7d	93	4

© 1998 NRC Canada

[1]

and methyl substituents and conversion of the ester to an isonitrile. The use of the menthane class of terpenes as starting materials would imply that this approach has the potential to provide homochiral material.

While one could envision the addition of the indole fragment via an organometallic species such as a Grignard reagent or a copper derivative (via the readily available 3-haloindole), we were intrigued by the natural enamine character, which is present in indoles and imparts a relatively high degree of nucleophilicity to the 3-position (4). Because of our interest in the use of hyperbaric conditions to promote useful chemical reactions, we were curious as to whether or not the nucleophilicity of the indole would be sufficient to add to Michael acceptors and whether the nucleophilicity would be enhanced at ultra high pressures.

The addition of indole to electron-deficient olefins is not a new reaction; however, the utility of this process is restricted in that only highly reactive Michael acceptors can be used with acceptable results (5). Recently Kotsuki et al. disclosed their results of a study that investigated the addition of indoles to epoxides at ultra high pressures using catalysts such as ytterbium triflate and silica gel (6). At almost the same time, we reported our preliminary results (7), which showed that indoles add in a 1,4-fashion to α,β-unsaturated ketones under the influence of ytterbium triflate (eq. [1]). In this paper we wish to provide details of the preliminary study as well as report the results of our work involving the ultra high pressure variant of this reaction.

Ytterbium triflate has become, in recent years, a widely used Lewis acid in organic synthesis (8). While researching Lewis acids for use at elevated pressures, a report by Jenner indicated that ytterbium triflate might be a suitable candidate (9). The reaction in eq. [1] may also be considered to be a type of Friedel–Crafts alkylation, a class of reactions that has seen the use of lanthanide triflates (10).

Results and discussion

When investigating the effects of pressure on a reaction it is prudent to run the reaction at ambient pressure in order to isolate and quantify the effects of pressure on the reaction course. During such a reaction it was noticed that indoles added to many of the Michael acceptors under the influence of ytterbium triflate *at ambient pressures*. Table 1 summarizes the results of the addition of indole and 1-methylindole to a series of α,β-unsaturated ketones under ambient pressure. A methyl group was chosen as a simple model for alkyl-derived protecting groups for the nitrogen (i.e., benzyl, methoxymethyl, etc.). The use of an electron-withdrawing substitiuent (i.e., a *p*-toluenesulphonyl group) on the indole nitrogen greatly attenuated the nucleophilic character of the indole and the reactions with the Michael acceptors were suppressed. The 1-triisopropylsilyl derivative underwent the conjugate addition but at a slower rate and with the concomitant loss of the silyl protecting group. The absence of catalyst resulted in low yields of addition with only the most reactive Michael acceptors (methyl vinyl ketone, β-nitrostyrene).

Several trends from Table 1 are worthy of note. As expected, steric hindrance plays an important role in the success or failure of the reaction; an increase in steric bulk on the Michael acceptor generally impedes the reaction. A single β-substituent on the enone does little to slow the reaction (entries 3 and 4) while a second β-substituent greatly reduces the reactivity of the olefin towards the indole (entries 5 and 6 and entry 10). The fact that reactions involving *trans*-3-pentene-2-one (entries 3 and 4) provide improved yields over methyl vinyl ketone (entries 1 and 2) may be due to the fact that the former enone is much less prone to polymerization as a side reaction. Overall, the reactions were quite clean with the only major contaminant being the unreacted starting materials. If this methodology is to be truly useful for the synthesis of the hapalindoles, substrates such as cyclohexenone must work well. Under ambient pressures, the cyclohexenones gave surprisingly low yields with relatively little starting material recovered. An interesting by-product was formed in 6% yield in the reaction of 1-methylindole with 3-methyl-2-cyclohexenone. The ^{1}H and ^{13}C NMR spectra of this by-product were complicated and the structure remained a mystery for some time. The identity of the compound was ultimately found to be the triindolyl cyclohexane **8** using single crystal X-ray diffraction. A complete set of crystallographic data for compound **8** is available as supplementary material.[3] The ORTEP representation is shown in Fig. 1.[4,5] In hindsight, the formation of this material is not surprising. The addition of a single molecule of the indole in a 1,4-fashion would afford a ketone that may undergo what may be considered a vinylogous ketalization reaction.

The fact that a simple ketone can undergo such a reaction under these conditions was confirmed by the fact that when two equivalents of indole were combined with one equivalent of cyclohexanone, **9** was formed as the sole product (eq. [2]). This type of reaction catalyzed by protic acid has

[3] Supplementary material may be purchased from: The Depository of Unpublished Data, Document Delivery, CISTI, National Research Council of Canada, Ottawa, Canada, K1A 0S2. Tables of atomic coordinates and bond lengths and angles have also been deposited with the Cambridge Crystallographic Data Centre and can be obtained on request from: The Director, Cambridge Crystallographic Data Centre, University Chemical Laboratory, 12 Union Road, Cambridge, CB2 1EZ, U.K. Tables of structure factors are no longer being deposited, and may be obtained on request from the author.

[4] The figure shows one molecule of acetonitrile, which was co-crystallized.

[5] Empirical formula: $C_{36}H_{38}N_4$ (acetonitrile included): fw = 526.70, space group $P2_1/n$, a = 13.893(3) Å, b = 8.213(2) Å, c = 26.097(5) Å, V = 2969.3(11) Å^3, ρ_c = 1.178 mg/m^3, T = 293 K, λ = 1.54178 Å.

© 1998 NRC Canada

[2]

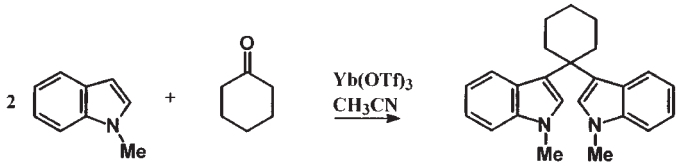

Fig. 1. ORTEP representation of by-product **8**.

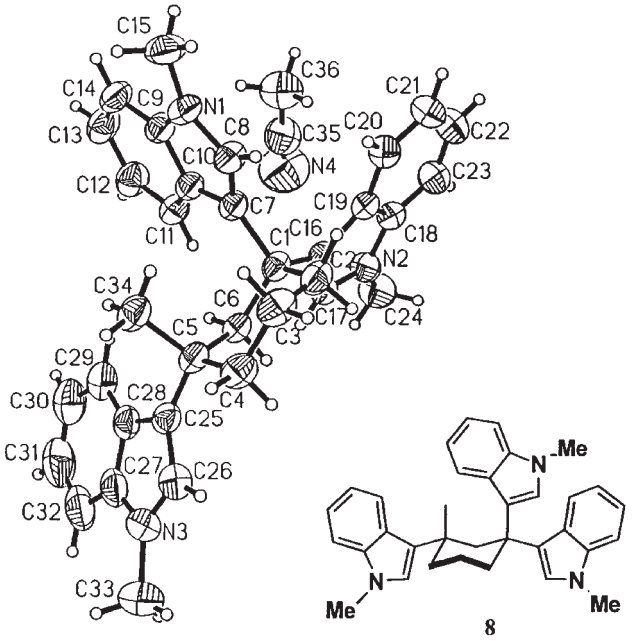

Table 2. $Yb(OTf)_3$ catalyzed alkylations of 1-methylindole with α,β-unsaturated ketones at 13 kbar.

Entry	Enone	Time	Product	Yield
1	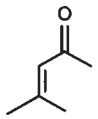	2d	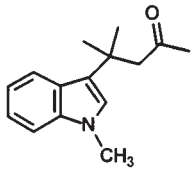	72
2	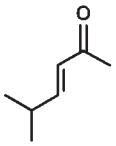	18h	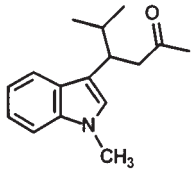	84
3	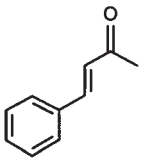	26h	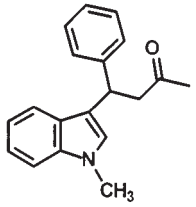	67
4	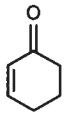	2d	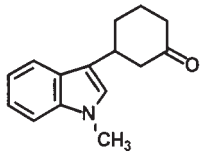	56
5	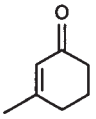	7d	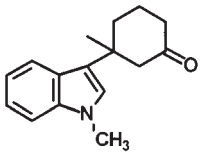	11
6	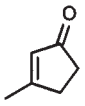	5d	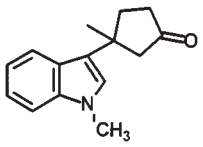	3

been reported (11). In addition, Wang and co-workers disclosed formally this same observation using a host of lanthanide triflates (12).

Cyclopent-2-en-1-one underwent addition in 95% yield; significantly higher than cyclohex-2-ene-1-one (entry 9). Finally, note that even when the β-substituent on the enone is a rather bulky isopropyl group (entry 7), the yield is still quite high.

The most notable limitation apparent from the results in Table 1 is that in cases where steric hindrance is significant, this methodology fails to produce useful amounts of adducts. In an effort to overcome this difficulty, reactions using these substrates were subjected to hyperbaric conditions (Table 2). In general, the reactions were performed at 13 kbar (1 bar = 100 kPa) using acetonitrile as the solvent.[6] In all cases, there was a notable reduction in reaction time and an increase in the yield of adduct. The most dramatic increase in isolated yield was observed with 4-phenyl-3-buten-2-one as the Michael acceptor (67% compared to 10% under ambient conditions, entry 3). Also of note is the fact that under these conditions, *N*-methyl indole added to cyclohex-2-en-1-one in 56% yield, an improvement from the 37% yield observed under ambient conditions. The same enones bearing an additional β-substituent proved extremely unreactive even under high-pressure conditions; however, small amounts of the expected adducts were isolated and characterized. The fact that high pressure facilitates the addition of indoles to enones is not surprising since formation of the transition state should result in a significant reduction in molar volume. (13). The use of high pressures to promote conjugate additions is not new and has been reported (14).

[6] Although a thorough screening of solvents was not performed, a brief experimental survey revealed that acetonitrile is the solvent of choice for these reactions.

© 1998 NRC Canada

Table 3. $Yb(OTf)_3$ catalyzed alkylations of indoles with other Michael acceptors.

Entry	Indole	Electrophile	Conditions	Product	Yield
1	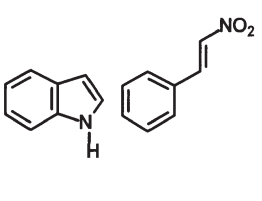		2d 1 atm	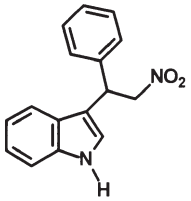	89
2	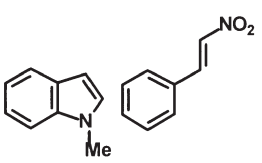		18h 1 atm	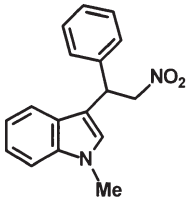	39
3	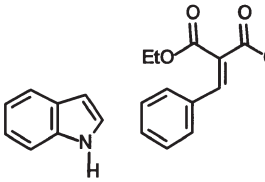		26h 1 atm	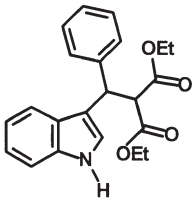	77
4	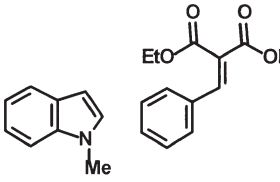		2d 1 atm	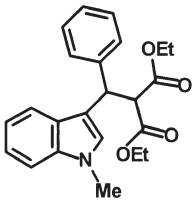	68
5	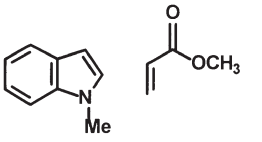		7d 13 kbar	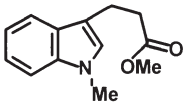	8

For the sake of exploring the general scope of this reaction, other electrophiles were also subjected to the above conditions and with some success. While many common electron-deficient olefins (phenyl vinyl sulphone, acrylonitrile, ethyl cinnamate, methyl propiolate, crotonaldehyde, and cinnnamaldehyde) failed to give satisfactory results, several reactive Michael acceptors proceeded to give the expected products (Table 3). As expected, β-nitrostyrene (entries 1 and 2) was quite reactive at ambient pressure. The fact that 1-methylindole gave an abnormally low yield is curious and may be due to the formation of a series of by-products that were not characterized. Note that even the reaction with a highly reactive diester such as diethyl benzalmalonate (entries 3 and 4) was sluggish and took several days to go to completion, albeit in good yield. Methyl acrylate was unreactive at ambient pressure but gave an isolable amount of material under hyperbaric conditions.

Finally, it should be noted that when 2-carbomethoxy-2-cyclohexenone was treated with indole in the presence of $Yb(OTf)_3$, a small amount of the desired Michael adduct was formed. The low yield may be attributed to the tendency of these types of compounds to exist, to a large degree, in the enol form.

In summary, we have shown that the use of ytterbium triflate to catalyze the addition of indoles to α,β-unsaturated ketones provides a useful complement to the existing methods available for the 3-alkylation of indole. Of interst to us for the synthesis of hapalindole alkaloids is the fact that cyclohexenones can be made to undergo reaction in acceptable yields under hyperbaric conditions, in contrast to more disappointing results using ambient conditions. Using this methodology, we intend to pursue as targets the interesting class of hapalindole alkaloids. Progress towards this end will be reported in due course.

Experimental section

General

Melting points were determined using a MEL-TEMP II melting point apparatus and are uncorrected. NMR spectra were obtained using a Bruker AM250 spectrometer in $CDCl_3$ as the solvent and are recorded in parts per million downfield from tetramethylsilane. ^1H NMR spectra were recorded at 250 MHz and ^{13}C NMR spectra were recorded at 63 MHz. Infrared spectra were measured on a Perkin–Elmer model 683 infrared spectrophotometer using a thin film of the compound on a sodium chloride plate. Mass spectra were recorded using a CEC model 21-11-B double-focusing mass spectrometer using a heated quartz direct-introduction probe with an 8000 V accelerating voltage. Crystallographic analysis was performed using a Rigaku AAFC5R diffractometer with a 12 MW rotating anode X-ray generator. Thin-layer chromatography was performed on E. Merck precoated TLC plates (Silica gel 60 F-254). Flash column chromatography was performed with EM Science Silica gel 60 (230–400 mesh). High-pressure reactions were performed in a LECO Tem-Pres HPC-200 chemical reactor in heat shrinkable Teflon® tubes. Samples for melting point determination were recrystallized from methylene chloride and hexanes. Commercial reagents and solvents were used as supplied without further purification.

Typical procedure for the ambient pressure reaction of indoles with α,β-unsaturated ketones

To a solution of the indole in acetonitrile was added the enone as a solid or a neat liquid. Ytterbium trifluoromethanesulphonate trihydrate was added and the mixture was stirred in a capped flask for the required amount of time. After thin-layer chromatography indicated the disappearance of starting material or after 1 week, which ever came first, the solvent was removed in vacuo and the residue was taken up in diethyl ether. Filtration of the ether suspension through a pad of Celite® followed by removal of the solvent in vacuo yielded the crude reaction product, which was purified by flash chromatography on a column of silica gel (elution with an appropriate mixture of ethyl acetate and hexanes).

4-(3-Indolyl)-2-butanone (Table 1, entry 1)

Standard procedure: indole (263 mg, 2.24 mmol), methyl vinyl ketone (500 μL, 6.11 mmol), $Yb(OTf)_3 \cdot 3H_2O$ (28 mg, 42 μmol), acetonitrile (2 mL). The mixture was stirred for

© 1998 NRC Canada

4 h after which time an additional 300 μL of methyl vinyl ketone (3.66 mmol) was added. After a total time of 22 h, the mixture was worked up in the usual way. Flash chromatography using gradient elution (20–50% EtOAc – hexanes) afforded 304 mg pure material (72%) as a white solid, mp 95–96°C. R_f = 0.31 (30% EtOAc – hexanes). IR (thin film), ν: 3315, 1700 cm^{-1}. ^{1}H NMR (250 MHz, $CDCl_3$), δ: 2.14 (s, 3H), 2.84 (t, *J* = 7.3 Hz, 2H), 3.05 (tm, *J* = 7.3 Hz, 2H), 6.98 (dm, *J* = 2.4 Hz, 1H), 7.12 (td, *J* = 7.0, 1.2 Hz, 1H), 7.19 (td, *J* = 7.0, 1.2 Hz, 1H), 7.35 (d, *J* = 7.6 Hz, 1H), 7.59 (d, *J* = 7.0 Hz, 1H), 7.98 (bs, 1H). ^{13}C NMR (63 MHz, $CDCl_3$), δ: 19.4, 30.1, 44.1, 111.3, 115.1, 118.7, 119.3, 121.6, 122.1, 127.2, 136.4, 209.0. MS (70 eV), *m*/*e*: 188 (M+1), 187 (M$^+$), 131, 130(100), 117, 115, 42. HRMS (for $C_{12}H_{13}NO$): 187.0997 (calcd.); 187.1008 (found).

4-(3-(1-Methylindolyl))-2-butanone (Table 1, entry 2)

Standard procedure: 1-methylindole (273 mg, 2.08 mmol), methyl vinyl ketone (500 μL, 6.11 mmol), $Yb(OTf)_3 \cdot 3H_2O$ (31 mg, 46 μmol), acetonitrile (2 mL). The mixture was stirred for 7 h and worked up in the usual way. Flash chromatography using gradient elution (10–30% EtOAc – hexanes) afforded 307 mg pure material (73%) as a white solid. R_f = 0.33 (30% EtOAc – hexanes). IR (neat), ν: 3040, 2905, 1700, 1475, 1460, 735 cm^{-1}. ^{1}H NMR (250 MHz, $CDCl_3$), δ: 2.13 (s, 3H), 2.82 (t, *J* = 7.6 Hz, 2H), 3.03 (tm, *J* = 7.6 Hz, 2H), 3.72 (s, 3H), 6.83 (s, 1H), 7.10 (ddd, *J* = 8.2, 6.7, 1.5 Hz, 1H), 7.22 (td, *J* = 7.9, 6.7, 1.5 Hz, 1H), 7.28 (dm, *J* = 7.9 Hz, 1H), 7.57 (dm, *J* = 7.6 Hz, 1H). ^{13}C NMR (63 MHz, $CDCl_3$), δ: 19.1, 30.0, 32.5, 44.2, 109.1, 113.5, 118.7 (two carbons), 121.5, 126.3, 127.5, 136.9, 208.9. MS (70 eV), *m/e*: 202(M+1), 201(M$^+$), 158, 145, 144(100), 143, 115. HRMS (for $C_{13}H_{15}NO$): 201.1154 (calcd.); 201.1123 (found).

4-(3-Indolyl)-2-pentanone (Table 1, entry 3)

Standard procedure: indole (258 mg, 2.20 mmol), 3-penten-2-one (500 μL, 5.12 mmol), $Yb(OTf)_3 \cdot 3H_2O$ (33 mg, 49 μmol), acetonitrile (2 mL). The mixture was stirred for 14 h and worked up in the usual way. Flash chromatography using gradient elution (20–50% EtOAc – hexanes) afforded 375 mg pure material (85%) as a white solid. R_f = 0.33 (30% EtOAc – hexanes). IR (neat), ν: 3400, 3045, 2950, 2915, 1705, 1610, 735 cm^{-1}. ^{1}H NMR (250 MHz, $CDCl_3$), δ: 1.38 (d, *J* = 7.0 Hz, 3H), 2.08 (s, 3H), 2.70 (dd, *J* = 16.2, 8.2 Hz, 1H), 2.93 (dd, *J* = 16.2, 6.1 Hz, 1H), 3.63 (m, 1H), 6.93 (d, *J* = 2.1 Hz, 1H), 7.11 (ddd, *J* = 8.2, 7.3, 1.5 Hz, 1H), 7.18 (ddd, *J* = 8.2, 7.0, 1.5 Hz, 1H), 7.33 (d, *J* = 7.9 Hz, 1H), 7.64 (d, *J* = 7.6 Hz, 1H), 8.02 (bs, 1H). ^{13}C NMR (63 MHz, $CDCl_3$), δ: 21.3, 27.1, 30.4, 51.5, 111.4, 119.1, 119.3, 120.2, 121.0, 122.1, 126.3, 136.6, 208.9. MS (70 eV), *m/e*: 201 (M$^+$), 158, 145, 144(100), 143, 42. HRMS (for $C_{13}H_{15}NO$): 201.1154 (calcd.); 201.1190 (found).

4-(3-(1-Methylindolyl))-2-pentanone (Table 1, entry 4)

Standard procedure: 1-methylindole (295 mg, 2.25 mmol), 3-penten-2-one (500 μL, 5.12 mmol), $Yb(OTf)_3 \cdot 3H_2O$ (33 mg, 49 μmol), acetonitrile (2 mL). The mixture was stirred for 10 h and worked up in the usual way. Flash chromatography using gradient elution (5–20% EtOAc – hexanes) afforded 461 mg pure material (95%) as a yellow oil. R_f = 0.41 (30% EtOAc – hexanes). IR (neat), ν: 3040, 2950, 2870, 1700, 1605, 1540, 1475, 1415, 1345, 1320, 1260, 1220, 1145, 1125, 1095, 1005, 755, 735 cm^{-1}. ^{1}H NMR (250 MHz, $CDCl_3$), δ: 1.36 (d, *J* = 7.0 Hz, 3H), 2.08 (s, 3H), 2.68 (dd, *J* = 16.2, 8.2 Hz, 1H), 2.91 (dd, *J* = 15.9, 6.1 Hz, 1H), 3.61 (m, 1H), 3.70 (s, 3H), 6.81 (s, 1H), 7.09 (tm, *J* = 7.3 Hz, 1H), 7.21 (tm, *J* = 7.5 Hz, 1H), 7.27 (dm, *J* = 7.6 Hz, 1H), 7.62 (dm, *J* = 7.6 Hz, 1H). ^{13}C NMR (63 MHz, $CDCl_3$), δ: 21.5, 27.0, 30.4, 32.6, 51.6, 109.3, 118.7, 119.2, 119.5, 121.6, 125.0, 126.6, 137.2, 208.6. MS (70 eV), *m/e:* 215(M$^+$), 172, 159, 158(100), 115. HRMS (for $C_{14}H_{17}NO$): 215.1310 (calcd.); 215.1309 (found).

4-(3-Indolyl)-4-methyl-2-pentanone (Table 1, entry 5)

Standard procedure: indole (263 mg, 2.24 mmol), mesityl oxide (500 μL, 4.36 mmol), $Yb(OTf)_3 \cdot 3H_2O$ (32 mg, 47 μmol), acetonitrile (2 mL). The mixture was stirred for 7 d and worked up in the usual way. Flash chromatography using gradient elution (10–20% EtOAc – hexanes) afforded 91 mg pure material (19%) as a yellow oil. R_f = 0.37 (30% EtOAc – hexanes). IR (neat), ν: 3400, 2950, 2915, 1685, 1450, 1410, 1345, 1325, 1235, 1200, 1115, 1100, 1005, 760, 735 cm^{-1}. ^{1}H NMR (250 MHz, $CDCl_3$), δ: 1.53 (s, 6H), 1.72 (s, 3H), 2.95 (s, 2H), 6.89 (d, *J* = 2.4 Hz, 1H), 7.08–7.21 (m, 2H), 7.34 (dm, *J* = 7.3 Hz, 1H), 7.80 (dm, *J* = 7.9 Hz, 1H), 8.01 (bs, 1H). ^{13}C NMR (63 MHz, $CDCl_3$), δ: 28.9, 29.7, 31.8, 34.5, 55.1, 111.7, 119.1, 120.6, 120.7, 121.7, 123.5, 125.5, 137.2, 209.5. MS (70 eV), *m/e*: 216 (M+1), 215(M$^+$), 200, 159, 158(100), 157, 143, 142, 115, 42. HRMS (for $C_{14}H_{17}NO$): 215.1310 (calcd.); 215.1324 (found).

4-(3-(1-Methylindolyl))-4-methyl-2-pentanone (Table 1, entry 6)

Standard procedure: 1-methylindole (290 mg, 2.21 mmol), mesityl oxide (500 μL, 4.36 mmol), $Yb(OTf)_3 \cdot 3H_2O$ (31 mg, 46 μmol), acetonitrile (2 mL). The mixture was stirred for 7 d and worked up in the usual way. Flash chromatography using gradient elution (10–20% ethyl acetate – hexanes) afforded 195 mg pure material (38%) as a yellow oil. R_f = 0.49 (30% EtOAc – hexanes). IR (neat), ν: 3020, 2940, 1700, 1605, 1535, 1475, 1415, 1350, 1230, 1145, 1100, 1010, 980, 760, 730 cm^{-1}. ^{1}H NMR (250 MHz, $CDCl_3$), δ: 1.53 (s, 6H), 1.73 (s, 3H), 2.94 (s, 2H), 3.73 (s, 3H), 6.79 (s, 1H), 7.11 (ddd, *J* = 8.2, 7.0, 1.2, 1H), 7.22 (ddd, *J* = 7.9, 7.0, 1.2 Hz, 1H), 7.30 (d, *J* = 8.2 Hz, 1H), 7.79 (dd, *J* = 7.9, 1.2 Hz, 1H). ^{13}C NMR (63 MHz, $CDCl_3$), δ: 29.0, 31.9, 32.7, 34.5, 55.2, 109.7, 118.7, 120.9, 121.3, 122.2, 125.4, 126.0, 137.8, 209.2. MS (70 eV), *m/e*: 230 (M+1), 229 (M$^+$), 173, 172 (100), 130, 115. HRMS (for $C_{15}H_{19}NO$): 229.1467 (calcd.); 229.1473 (found).

4-(3-(1-Methylindolyl))-5-methyl-2-hexanone (Table 1, entry 7)

Standard procedure: 1-methylindole (307 mg, 2.34 mmol), 5-methyl-3-hexen-2-one (500 μL, 3.79 mmol), $Yb(OTf)_3 \cdot 3H_2O$ (30 mg, 44 μmol), acetonitrile (2 mL). The mixture was stirred for 4 d and worked up in the usual way. Flash chromatography using gradient elution (5–20% EtOAc – hexanes) afforded 438 mg pure material (77%) as a low-melting solid. R_f = 0.50 (30% EtOAc – hexanes). IR (neat), ν: 2940, 2915, 2860, 1700, 1475, 1460, 1415, 1360, 1345, 1320, 1250, 1225, 1150, 1125, 1005, 730 cm^{-1}. ^{1}H NMR (250 MHz, $CDCl_3$), δ: 0.86 (d, *J* = 6.7 Hz, 3H), 0.91 (d, *J* =

© 1998 NRC Canada

6.7 Hz, 3H), 1.96 (s, 3H), 2.05 (m, 1H), 2.78–2.86 (m, 2H), 3.30 (td, *J* = 6.7, 6.4 Hz, 1H), 3.71 (s, 3H), 6.79 (s, 1H), 7.08 (ddd, *J* = 7.5, 6.7, 1.3, 1H), 7.19 (td, *J* = 7.4, 1.0 Hz, 1H), 7.26 (dm, *J* = 7.9 Hz, 1H), 7.63 (dm, *J* = 7.9 Hz, 1H). ^{13}C NMR (63 MHz, $CDCl_3$), δ: 20.4, 20.6, 30.1, 32.7, 32.8, 39.2, 47.2, 109.2, 115.9, 118.6, 119.5, 121.3, 126.7, 127.7, 136.9, 209.3. MS (70 eV), *m*/*e*: 244 (M+1), 243 (M^+), 201, 200 (100), 186, 158, 157, 143, 69. HRMS (for $C_{16}H_{21}NO$): 243.1623 (calcd.); 243.1626 (found).

3-(3-Indolyl)cyclohexanone (Table 1, entry 8)

Standard procedure: indole (241 mg, 2.06 mmol), 2-cyclohexen-1-one (500 μL, 5.16 mmol), $Yb(OTf)_3 \cdot 3H_2O$ (30 mg, 44 μmol), acetonitrile (2 mL). The mixture was stirred for 2 d and an additional 9 mg (15 μmol) of catalyst was added. The mixture was stirred for an additional 5 d and worked up in the usual way. Flash chromatography using gradient elution (10–30% EtOAc – hexanes) afforded 192 mg pure material (44%) as a pale yellow solid, mp 106–107°C. R_f = 0.26 (30% EtOAc – hexanes). IR (neat), ν: 3270, 2940, 2860, 1695, 1610, 1485, 1440, 1420, 1330, 1255, 1210, 1175, 1100, 1050, 1020, 1000, 870, 800, 755, 730 cm^{-1}. ^{1}H NMR (250 MHz, $CDCl_3$), δ: 1.78–2.08 (m, 3H), 2.25 (m, 1H), 2.38–2.46 (m, 2H), 2.62 (ddd, *J* = 14.0, 10.5, 1.1 Hz, 1H), 2.79 (ddt, *J* = 14.0, 4.6, 1.5 Hz, 1H), 3.42 (m, 1H), 6.95 (dd, *J* = 2.4, 0.6 Hz, 1H), 7.11 (ddd, *J* = 7.8, 7.0, 1.2 Hz, 1H), 7.19 (ddd, *J* = 7.8, 6.9, 1.5 Hz, 1H), 7.35 (dm, *J* = 7.9 Hz, 1H), 7.61 (dm, *J* = 7.9 Hz, 1H), 8.12 (bs, 1H). ^{13}C NMR (63 MHz, $CDCl_3$), δ: 24.9, 31.8, 36.0, 41.6, 48.1, 111.4, 119.0, 119.4, 119.6, 120.5, 122.2, 126.2, 136.5, 212.1. MS (70 eV), *m*/*e*: 214 (M+1), 213 (M^+), 170, 157, 156(100), 144, 143, 130, 128, 117. HRMS (for $C_{14}H_{15}NO$): 213.1154 (calcd.); 213.1166 (found).

3-(3-(1-Methylindolyl))cyclohexanone (Table 1, entry 9)

Standard procedure: 1-methylindole (268 mg, 2.04 mmol), 2-cyclohexen-1-one (500 μL, 5.16 mmol), $Yb(OTf)_3 \cdot 3H_2O$ (34 mg, 50 μmol), acetonitrile (2 mL). The mixture was stirred for 7 d and worked up in the usual way. Flash chromatography using gradient elution (10–30% EtOAc – hexanes) afforded 171 mg pure material (37%) as a yellow oil. R_f = 0.37 (30% EtOAc – hexanes). IR (neat), ν: 3040, 2920, 2855, 1700, 1605, 1540, 1460, 1415, 1365, 1305, 1250, 1210, 1145, 1120, 1045, 1005, 795, 730 cm^{-1}. ^{1}H NMR (250 MHz, $CDCl_3$), δ: 1.78–2.08 (m, 3H), 2.23 (m, 1H), 2.38–2.46 (m, 2H), 2.60 (ddd, *J* = 14.0, 10.4, 1.2 Hz, 1H), 2.78 (ddt, *J* = 14.0, 4.6, 1.5 Hz, 1H), 3.43 (m, 1H), 3.73 (s, 3H), 6.82 (d, *J* = 0.6 Hz, 1H), 7.10 (ddd, *J* = 7.9, 7.3, 1.2 Hz, 1H), 7.22 (ddd, *J* = 8.2, 7.5, 1.2 Hz, 1H), 7.29 (td, *J* = 8.2, 1.1 Hz, 1H), 7.60 (td, *J* = 7.9, 0.9 Hz, 1H). ^{13}C NMR (63 MHz, $CDCl_3$), δ: 24.9, 32.0, 32.7, 35.9, 41.6, 48.3, 109.4, 118.2, 118.9, 119.1, 121.8, 125.3, 126.6, 137.2, 211.9. MS (70 eV), *m*/*e*: 228 (M+1), 227 (M^+,100), 184, 170, 157, 144, 115. HRMS (for $C_{15}H_{17}NO$): 227.1311 (calcd.); 227.1302 (found).

3-Methyl-3-(3-(1-methylindolyl))cyclohexanone (Table 1, entry 10)

Standard procedure: 1-methylindole (292 mg, 2.23 mmol), 3-methyl-2-cyclohexen-1-one (400 μL, 3.53 mmol), $Yb(OTf)_3 \cdot 3H_2O$ (37 mg, 55 μmol), acetonitrile (2 mL). The mixture was stirred for 7 d and worked up in the usual way. Flash chromatography using gradient elution (10– 30% EtOAc – hexanes) afforded 16 mg pure material (3%) as a yellow oil. R_f = 0.36 (30% EtOAc – hexanes). IR (neat), ν: 3030, 2920, 1690, 1535, 1475, 1410, 1365, 1320, 1300, 1275, 1235, 1215, 1140, 1130, 1100, 1010, 730 cm^{-1}. ^{1}H NMR (250 MHz, $CDCl_3$), δ: 1.41–1.59 (m, 1H), 1.53 (s, 3H), 1.76–1.94 (m, 2H), 2.24–2.32 (m, 2H), 2.46 (d, *J* = 14.4 Hz, 1H), 2.58 (m, 1H), 2.89 (dd, *J* = 14.4, 1.5 Hz, 1H), 3.70 (s, 3H), 6.80 (s, 1H), 7.08 (ddd, *J* = 8.3, 7.3, 1.2 Hz, 1H), 7.21 (tm, *J* = 7.3 Hz, 1H), 7.29 (d, *J* = 8.2, Hz, 1H), 7.74 (d, *J* = 7.9 Hz, 1H). ^{13}C NMR (63 MHz, $CDCl_3$), δ: 22.4, 29.6, 32.7, 36.8, 40.0, 41.0, 54.4, 109.6, 118.5, 120.3, 120.9, 121.5, 125.4, 126.9, 137.8, 212.5. MS (70 eV), *m*/*e*: 242 (M+1), 241 (M^+,100), 226, 198, 184, 171, 131(100), 130, 42. HRMS (for $C_{16}H_{19}NO$): 241.1467 (calcd.); 241.1488 (found).

3-(3-(1-Methylindolyl))cyclopentanone (Table 1, entry 11)

Standard procedure: 1-methylindole (322 mg, 2.45 mmol), 2-cyclopenten-1-one (500 μL, 6.18 mmol), $Yb(OTf)_3 \cdot 3H_2O$ (32 mg, 47 μmol), acetonitrile (2 mL). The mixture was stirred for 4 d and worked up in the usual way. Flash chromatography using gradient elution (20–30% EtOAc – hexanes) afforded 496 mg pure material (95%) as a yellow oil. R_f = 0.38 (30% EtOAc – hexanes). IR (neat), ν: 3040, 2945, 2920, 2870, 1730, 1605, 1475, 1415, 1395, 1365, 1320, 1310, 1235, 1145, 1125, 1005, 730 cm^{-1}. ^{1}H NMR (250 MHz, $CDCl_3$), δ: 2.03–2.52 (m, 5H), 2.71 (dd, *J* = 18.3, 7.6 Hz, 1H), 3.67 (m, 1H), 3.70 (s, 3H), 6.80 (d, *J* = 0.6 Hz, 1H), 7.11 (ddd, *J* = 7.9, 6.7, 1.5 Hz, 1H), 7.23 (td, *J* = 7.3, 1.2 Hz, 1H), 7.29 (dm, *J* = 8.1 Hz, 1H), 7.59 (td, *J* = 7.9, 0.9 Hz, 1H). ^{13}C NMR (63 MHz, $CDCl_3$), δ: 30.0, 32.6, 33.6, 38.1, 45.4, 109.4, 116.9, 118.8, 119.1, 121.8, 124.7, 126.9, 137.3, 219.3. MS (70 eV), *m*/*e:* 214 (M+1), 213 (M^+,100), 184, 170, 158 157, 156 144. HRMS (for $C_{15}H_{17}NO$): 213.1154 (calcd.); 213.1167 (found).

4-(3-Indolyl)-4-phenyl-2-butanone (Table 1, entry 12)

Standard procedure: indole (250 mg, 2.13 mmol), benzalacetone (370 mg, 2.53 mmol), $Yb(OTf)_3 \cdot 3H_2O$ (31 mg, 46 μmol), acetonitrile (2 mL). The mixture was stirred for 7 d and worked up in the usual way. Flash chromatography using gradient elution (10–50% EtOAc – hexanes) afforded 89 mg pure material (16%) as a white solid, mp 98–99°C. R_f = 0.27 (30% EtOAc – hexanes). IR (neat), ν: 3400, 3050, 3020, 2910, 1695, 1590, 1485, 1445, 1405, 1345, 1330, 1230, 1215, 1150, 1090, 1000, 735, 695 cm^{-1}. ^{1}H NMR (250 MHz, $CDCl_3$), δ: 2.09 (s, 3H), 3.17 (dd, *J* = 16.2, 7.9 Hz, 1H), 3.27 (dd, *J* = 16.2, 7.3 Hz, 1H), 4.85 (bt, *J* = 7.6 Hz, 1H), 6.98 (dd, *J* = 2.4, 0.6 Hz, 1H), 7.03 (ddd, *J* = 7.9, 7.0, 1.2 Hz, 1H), 7.13–7.35 (m, 7H), 7.44 (dd, *J* = 7.0, 1.2 Hz, 1H), 8.04 (bs, 1H). ^{13}C NMR (63 MHz, $CDCl_3$), δ: 30.4, 38.4, 50.4, 111.2, 118.8, 119.4, 121.4, 122.2, 126.4, 126.5, 127.7, 128.5, 136.6, 144.0, 207.8. MS (70 eV), *m*/*e*: 264 (M+1), 263 (M^+,100), 221, 220, 207, 206, 42. HRMS (for $C_{18}H_{17}NO$): 263.1310 (calcd.); 263.1312 (found).

4-(3-(1-Methylindolyl))-4-phenyl-2-butanone (Table 1, entry 13)

Standard procedure: 1-methylindole (290 mg, 2.21 mmol), benzalacetone (386 mg, 2.64 mmol), $Yb(OTf)_3 \cdot 3H_2O$

© 1998 NRC Canada

(34 mg, 50 μmol), acetonitrile (2 mL). The mixture was stirred for 7 d and was worked up in the usual way. Flash chromatography using gradient elution (10–30% EtOAc – hexanes) afforded 63 mg pure material (10%) as a yellow oil. R_f = 0.31 (30% EtOAc – hexanes). IR (neat), ν: 3045, 3015, 2920, 1700, 1590, 1540, 1475, 1410, 1360, 1345, 1320, 1235, 1145, 1070, 1005, 730, 695 cm^{-1}. ^1H NMR (250 MHz, $CDCl_3$), δ: 2.07 (s, 3H), 3.14 (dd, *J* = 16.2, 7.9 Hz, 1H), 3.25 (dd, *J* = 16.2, 7.3 Hz, 1H), 3.73 (s, 3H), 4.85 (bt, *J* = 7.6 Hz, 1H), 6.80 (s, 1H), 7.00 (tm, *J* = 7.5 Hz, 1H), 7.11–7.32 (m, 7H), 7.42 (dm, *J* = 7.9 Hz, 1H). ^{13}C NMR (63 MHz, $CDCl_3$), δ: 30.3, 32.7, 38.3, 50.4, 109.2, 117.3, 118.9, 119.5, 121.7. 126.3, 126.9, 127.7, 128.5, 137.3, 144.1, 207.5. MS (70 eV), *m*/*e*: 278 (M+1), 277 (M^+,100), 221, 220, 218, 204. HRMS (for $C_{19}H_{19}NO$): 277.1467 (calcd.); 277.1464 (found).

3-(3-Indolyl)-3-phenylpropiophenone (Table 1, entry 14)

Standard procedure: indole (253 mg, 2.16 mmol), chalcone (528, 2.54 mmol), $Yb(OTf)_3{\cdot}H_2O$ (34 mg, 50 μmol), acetonitrile (2 mL). The mixture was stirred for 7 d and was worked up in the usual way. Flash chromatography using gradient elution (10–30% EtOAc – hexanes) afforded 366 mg pure material (52%) as a white solid, mp 131–132°C. R_f = 0.36 (30% EtOAc – hexanes). IR (neat), ν: 3410, 3045, 3020, 1670, 1590, 1570, 1485, 1440, 1405, 1325, 1255, 1195, 1090, 1010, 995, 970, 735, 690 cm^{-1}. ^1H NMR (250 MHz, $CDCl_3$), δ: 3.71 (dd, *J* = 16.8, 7.6 Hz, 1H), 3.81 (dd, *J* = 16.8, 6.7 Hz, 1H), 5.06 (bt, *J* = 7.3 Hz, 1H), 6.95 (d, *J* = 2.4 Hz, 1H), 7.00 (td, *J* = 7.5. 0.9 Hz, 1H), 7.10–7.55 (m, 12H), 7.92 (dm, *J* = 7.0 Hz, 1H), 7.97 (bs, 1H). ^{13}C NMR (63 MHz, $CDCl_3$), δ: 38.2, 45.2, 111.2, 119.3, 119.4, 119.6, 121.5, 122.1, 126.3, 126.6, 127.7, 128.1, 128.5, 128.6, 133.1, 136.6, 137.1, 144.3, 198.6. MS (70 eV), *m*/*e*: 326 (M+1), 325 (M^+), 220, 207, 206 (100), 178, 105, 77. HRMS (for $C_{23}H_{19}NO$): 325.1467 (calcd.); 325.1472 (found).

3-(3-(1-Methylindolyl))-3-phenylpropiophenone (Table 1, entry 15)

Standard procedure: 1-methylindole (287 mg, 2.19 mmol), chalcone (535, 2.57 mmol), $Yb(OTf)_3{\cdot}3H_2O$ (32 mg, 47 μmol), acetonitrile (2 mL). The mixture was stirred for 7 d and was worked up in the usual way. Flash chromatography using gradient elution (5–70% EtOAc – hexanes) afforded 687 mg pure material (93%) as a pale yellow solid, mp 181–182°C. R_f = 0.41 (30% EtOAc – hexanes). IR (neat), ν: 3050, 2910, 1665, 1590, 1560, 1535, 1475, 1440, 1405, 1360, 1325, 1305, 1290, 1235, 1145, 730, 690 cm^{-1}. ^1H NMR (250 MHz, $CDCl_3$), δ: 3.69 (s, 3H), 3.74–3.79 (m, 2H), 5.06 (bt, *J* = 7.3 Hz, 1H), 6.83 (s, 1H), 7.00 (td, *J* = 6.7, 1.2 Hz, 1H), 7.14–7.52 (m, 12H), 7.93 (dm, *J* = 7.0 Hz, 1H). ^{13}C NMR (63 MHz, $CDCl_3$), δ: 37.2, 38.2, 45.4, 109.2, 117.8, 118.9, 119.6, 121.7, 126.3, 127.0, 127.9, 128.1, 128.5, 128.6, 133.0, 137.2, 137.4, 144.4, 198.5. MS (70 eV), *m*/*e:* 340 (M+1), 339 (M^+), 234, 221, 220 (100). HRMS (for $C_{24}H_{21}NO$): 339.1623 (calcd.); 339.1628 (found).

2-(3-Indolyl)-2-phenylnitroethane (Table 3, entry 1)

Standard procedure: Indole (295 mg, 2.52 mmol), β-nitrostyrene (468 mg, 3.14 mmol), $Yb(OTf)_3{\cdot}3H_2O$ (31 mg, 46 μmol), acetonitrile (2 mL). The mixture was stirred for 30 h and was worked up in the usual way. Flash chromatography using gradient elution (10–30% EtOAc – hexanes) afforded 596 mg pure material (89%) as a pale yellow solid, mp 102–103°C. R_f = 0.34 (30% EtOAc – hexanes). IR (neat), ν: 3420, 3050, 3020, 1595, 1545, 1485, 1445, 1415, 1370, 1330, 1255, 1215, 1090, 1000, 965, 740, 695 cm^{-1}. ^1H NMR (250 MHz, $CDCl_3$), δ: 4.92 (dd, *J* = 12.4, 8.4 Hz, 1H), 5.04 (dd, *J* = 12.4, 7.5 Hz, 1H), 5.17 (bt, *J* = 7.9 Hz, 1H), 6.98 (d, *J* = 2.8 Hz, 1H), 7.06 (td, *J* = 7.5, 0.9 Hz, 1H), 7.15–7.35 (m, 7H), 7.43 (dm, *J* = 7.9 Hz, 1H), 8.03 (bs, 1H). ^{13}C NMR (63 MHz, $CDCl_3$), δ: 41.6, 79.6, 111.4, 119.0, 120.0, 121.7, 122.7, 126.1, 127.6, 127.8, 129.0, 136.5, 139.2. MS (70 eV), *m*/*e*: 267 (M+1), 266 (M^+, 100), 220, 219, 218, 217, 206, 204, 42. HRMS (for $C_{16}H_{14}N_2O_2$): 266.1055 (calcd.); 266.1055 (found).

2-(3-(1-Methyl-indolyl))-2-phenylnitroethane (Table 3, entry 2)

Standard procedure: 1-methylindole (287 mg, 2.19 mmol), β-nitrostyrene (387 mg, 2.59 mmol), $Yb(OTf)_3{\cdot}3H_2O$ (37 mg, 55 μmol), acetonitrile (2 mL). The mixture was stirred for 19 h and was worked up in the usual way. Flash chromatography using gradient elution (10–50% EtOAc – hexanes) afforded 241 mg pure material (39%) as a white solid, mp 94–95°C. R_f = 0.38 (30% EtOAc – hexanes). IR (neat), ν: 3050, 3020, 2910, 1595, 1540, 1465, 1445, 1415, 1370, 1325, 1240, 1150, 1120, 1075, 1005, 735, 695 cm^{-1}. ^1H NMR (250 MHz, $CDCl_3$), δ: 3.71 (s, 3H), 4.91 (dd, *J* = 12.5, 8.6 Hz, 1H), 5.03 (dd, *J* = 12.4, 7.5 Hz, 1H), 5.17 (bt, *J* = 7.9 Hz, 1H), 6.84 (d, *J* = 0.6 Hz, 1H), 7.06 (ddd, *J* = 7.9, 6.6, 1.5 Hz, 1H), 7.18–7.33 (m, 7H), 7.44 (td, *J* = 7.9, 0.9 Hz, 1H). ^{13}C NMR (63 MHz, $CDCl_3$), δ: 32.9, 41.6, 79.6, 109.6, 112.8, 119.0, 119.5, 122.3, 126.4, 126.6, 127.5, 127.8, 128.9, 137.3, 139.4. MS (70 eV), *m*/*e*: 281 (M+1), 280 (M^+, 100), 235, 234, 233, 221, 220, 218, 217, 157, 146, 115, 77, 50. HRMS (for $C_{17}H_{16}N_2O_2$): 280.1212 (calcd.); 280.1204 (found).

Ethyl 2-ethoxycarbonyl-3-(3-indolyl)-3-phenyl propanoate (Table 3, entry 3)

Standard procedure: indole (255 mg, 2.18 mmol), diethyl benzalmalonate (600 mg, 2.68 mmol), $Yb(OTf)_3{\cdot}3H_2O$ (32 mg, 47 μmol), acetonitrile (2 mL). The mixture was stirred for 4 d and was worked up in the usual way. Flash chromatography using gradient elution (20–50% EtOAc – hexanes) afforded 610 mg pure material (77%) as a white solid, mp 164–165°C. R_f = 0.30 (30% EtOAc – hexanes). IR (neat), ν: 3440, 1735, 1705, 1445, 1360, 1310, 1260, 1240, 1180, 1165, 1145, 1085, 740, 695 cm^{-1}. ^1H NMR (250 MHz, $CDCl_3$), δ: 0.97 (t, *J* = 7.0 Hz, 3H), 1.00 (t, *J* = 7.0 Hz, 3H), 3.97 (q, *J* = 7.1 Hz, 2H), 4.00 (q, *J* = 7.1 Hz, 2H), 4.29 (d, *J* = 11.9 Hz, 1H), 5.08 (d, *J* = 11.6 Hz, 1H), 7.02 (ddd, *J* = 7.8, 7.0, 0.9 Hz, 1H), 7.09–7.30 (m, 6H), 7.34–7.38 (m, 2H), 7.54 (dd, *J* = 7.9, 0.6 Hz, 1H), 8.05 (bs, 1H). ^{13}C NMR (63 MHz, $CDCl_3$), δ: 13.8 (two carbons), 42.9, 58.4, 61.5 (two carbons), 111.0, 116.9, 119.4, 119.5, 129.9, 122.2, 126.8, 128.2, 128.4, 136.2, 141.4, 167.9, 168.1. MS (70 eV), *m*/*e:* 366 (M+1), 365 (M^+), 246, 207, 206 (100). HRMS (for $C_{22}H_{23}NO_4$): 365.1627 (calcd.); 365.1660 (found).

© 1998 NRC Canada

Ethyl 2-ethoxycarbonyl-3-(3-(1-methylindolyl))-3-phenyl propanoate (Table 3, entry 4)

Standard procedure: 1-methylindole (270 mg, 2.06 mmol), diethyl benzalmalonate (600 mg, 2.68 mmol), $Yb(OTf)_3 \cdot 3H_2O$ (35 mg, 52 μmol), acetonitrile (2 mL). The mixture was stirred for 2 d and was worked up in the usual way. Flash chromatography using gradient elution (10–30% EtOAc – hexanes) afforded 530 mg pure material (68%) as a white solid, mp 87–88°C. R_f = 0.37 (30% EtOAc – hexanes). IR (neat), ν: 2925, 2870, 1735, 1695, 1605, 1535, 1460, 1415, 1360, 1020, 860, 735, 695 cm^{-1}. ^1H NMR (250 MHz, $CDCl_3$), δ: 0.98 (t, *J* = 7.2 Hz, 3H), 0.99 (t, *J* = 7.0 Hz, 3H), 3.71 (s, 3H), 3.97 (q, *J* = 7.2 Hz, 2H), 3.99 (q, *J* = 7.0 Hz, 2H), 4.27 (d, *J* = 11.6 Hz, 1H), 5.06 (d, *J* = 11.9 Hz, 1H), 7.01 (s, 1H), 7.02 (td, *J* = 7.3, 1.4 Hz, 1H), 7.09–7.25 (m, 6H), 7.36 (dm, *J* = 7.0 Hz, 1H), 7.55 (dt, *J* = 7.9, 0.6 Hz, 1H). ^{13}C NMR (63 MHz, $CDCl_3$), δ: 13.7 (two carbons), 32.7, 42.8, 58.4, 61.3, 61.4, 109.0, 115.3, 118.9, 119.4, 121.7, 125.6, 126.6, 127.1, 128.1, 129.4, 136.9, 141.6, 167.8, 168.0. MS (70 eV), *m*/*e*: 380 (M+1), 379 (M^+), 233, 221, 200 (100), 218, 217, 206. HRMS (for $C_{23}H_{25}NO_4$): 379.1783 (calcd.); 379.1811 (found).

Typical procedure for the high-pressure reaction of indoles with α,β-unsaturated ketones

The indole and the enone were dissolved in acetonitrile in a length of 1 cm diameter heat- shrinkable Teflon® tubing (about 10 cm in length) that had been clamped at one end using a brass clamp. The catalyst was added and the contents of the tube were mixed. Excess air was squeezed from the reaction vessel and the tube was then sealed with another brass clamp. The vessel was placed in the high-pressure reactor and was subjected to 1.2 GPa (13 kbar) for an appropriate period of time. The solvent was removed in vacuo and the crude residue was purified by flash chromatography on a column of silica gel (elution with an appropriate mixture of ethyl acetate and hexanes).

4-(3-(1-Methylindolyl))-4-methyl-2-pentanone (Table 2, entry 1)

Standard procedure: 1-methylindole (288 mg, 2.20 mmol), mesityl oxide (500 μL, 4.36 mmol), $Yb(OTf)_3 \cdot 3H_2O$ (33 mg, 49 μmol), acetonitrile (2 mL). The mixture was pressurized for 2 d and was worked up in the usual way. Flash chromatography using gradient elution (10–20% EtOAc – hexanes) afforded 360 mg pure material (72%) as a yellow oil. The material was identical in all respects to the compound prepared under ambient pressure (Table 1, entry 6).

4-(3-(1-Methylindolyl))-5-methyl-2-hexanone (Table 2, entry 2)

Standard procedure: 1-methylindole (2.92 mg, 2.23 mmol), 5-methyl-3-hexen-2-one (500 μL, 3.79 mmol), $Yb(OTf)_3 \cdot 3H_2O$ (33 mg, 49 μmol), acetonitrile (2 mL). The mixture was pressurized for 18 h and was worked up in the usual way. Flash chromatography using gradient elution (5–20% EtOAc – hexanes) afforded 455 mg pure material (84%) as a low-melting solid, identical in all respects to the compound prepared under ambient pressure (Table 1, entry 7).

4-(3-(1-Methylindolyl))-4-phenyl-2-butanone (Table 2, entry 3)

Standard procedure: 1-methylindole (295 mg, 2.25 mmol), benzalacetone (547 mg, 3.74 mmol), $Yb(OTf)_3 \cdot 3H_2O$ (33 mg, 49 μmol), acetonitrile (2 mL). The mixture was pressurized for 26 h and was worked up in the usual way. Flash chromatography using gradient elution (20– 30% EtOAc – hexanes) afforded 417 mg pure material (67%) as a yellow oil, identical in all respects to the compound prepared under ambient pressure (Table 1, entry 13).

3-(3-Indolyl)cyclohexanone (Table 2, entry 4)

Standard procedure: indole (276 mg, 2.36 mmol), 2-cyclohexen-1-one (500 μL, 5.16 mmol), $Yb(OTf)_3 \cdot 3H_2O$ (33 mg, 49 μmol), acetonitrile (2 mL). The mixture was pressurized for 2 d and was worked up in the usual way. Flash chromatography using gradient elution (20–30% EtOAc – hexanes) afforded 263 mg pure material (52%) as a pale yellow solid, identical in all respects to the compound prepared under ambient pressure (Table 1, entry 8).

3-Methyl-3-(3-(1-methylindolyl))cyclohexanone (Table 2, entry 5)

Standard procedure: 1-methylindole (292 mg, 2.23 mmol), 3-methyl-2-cyclohexen-1-one (400 μL, 3.53 mmol), $Yb(OTf)_3 \cdot 3H_2O$ (32 mg, 47 μmol), acetonitrile (2 mL). The mixture was pressurized for 7 d and was worked up in the usual way. Flash chromatography using gradient elution (10–30% EtOAc – hexanes) afforded 59 mg pure material (11%) as a yellow oil, identical in all respects to the compound prepared under ambient pressure (Table 1, entry 9).

3-Methyl-3-(3-(1-methylindolyl))cyclopentanone (Table 2, entry 6)

Standard procedure: 1-methylindole (316 mg, 2.41 mmol), 3-methyl-2-cyclopenten-1-one (500 μL, 5.05 mmol), $Yb(OTf)_3 \cdot 3H_2O$ (31 mg, 46 μmol), acetonitrile (2 mL). The mixture was pressurized for 5 d and was worked up in the usual way. Flash chromatography using gradient elution (10–30% EtOAc – hexanes) afforded 17 mg pure material (3%) as a yellow oil. IR (thin film), ν: 2940, 2910, 2860, 1730, 1600, 1475. 1455, 1410, 1390, 1365, 1320, 1230, 1145, 1120, 730 cm^{-1}. ^1H NMR (250 MHz, $CDCl_3$), δ: 1.60 (s, 3H), 2.13–2.37 (m, 3H), 2.44 (d, *J* = 17.7 Hz, 1H), 2.58 (m, 1H), 2.80 (d, *J* = 17.7 Hz, 1H), 3.73 (s, 3H), 6.78 (s, 1H), 7.11 (ddd, *J* = 8.1, 6.7, 1.4 Hz, 1H), 7.24 (tm, *J* = 7.5 Hz, 1H), 7.32 (dm, *J* = 7.9 Hz, 1H), 7.71 (dd, *J* = 7.9, 0.9 Hz, 1H). ^{13}C NMR (63 MHz, $CDCl_3$), δ: 28.0, 32.7, 35.8, 36.9, 39.9, 51.9, 109.7, 118.7, 119.8, 120.6, 121.7, 125.0, 126.5, 135.5, 200.9. MS (70 eV), *m*/*e*: 227 (M^+,100), 212, 198, 184, 172, 171 (100), 156, 144. HRMS (for $C_{15}H_{17}NO$): 227.1311 (calcd.); 227.1315 (found).

Methyl 3-(3-(1-methylindolyl))-propanoate (Table 3, entry 5)

Standard procedure: 1-methylindole (322 mg, 2.45 mmol), methyl acrylate (500 μL, 5.55 mmol), $Yb(OTf)_3 \cdot 3H_2O$ (36 mg, 53 μmol), acetonitrile (2 mL). The mixture was pressurized for 7 d and was worked up in the usual way. Flash chromatography using gradient elution (5–30% EtOAc – hexanes) afforded 40 mg pure material (8%) as a yellow

© 1998 NRC Canada

oil. R_f = 0.49 (30% EtOAc – hexanes). IR (neat), ν: 2935, 2910, 2840, 1730, 1545, 1460, 1425, 1370, 1315, 1180, 1155, 1125, 1110, 1060, 730 cm^{-1}. ^1H NMR (250 MHz, $CDCl_3$), δ: 2.73 (t, *J* = 7.6 Hz, 2H), 3.11 (t, *J* = 7.6 Hz, 2H), 3.69 (s, 3H), 3.74 (s, 3H), 6.88 (s, 1H), 7.13 (ddd, *J* = 7.8, 6.7, 1.2 Hz, 1H), 7.25 (td, *J* = 7.3, 1.2 Hz, 1H), 7.31 (dm, *J* = 7.2 Hz, 1H), 7.61 (d, *J* = 7.6 Hz, 1H). ^{13}C NMR (63 MHz, $CDCl_3$), δ: 20.5, 32.6, 35.0, 51.6, 109.2, 113.4, 118.8 (two carbons), 121.6, 126.3, 127.5, 137.0, 173.9. MS (70 eV), *m*/*e*: 217 (M^+), 145, 144 (100), 143, 131, 130, 77. HRMS (for $C_{13}H_{15}NO_2$): 217.1103 (calcd.); 217.1107 (found).

Acknowledgments

This research has been financially supported by the Natural Sciences and Engineering Research Council (NSERC), Sepracor Canada Ltd., and Acadia University. We are grateful to Drs. Don Hooper and Michael Lumsden of the Atlantic Region Magnetic Resonance Centre and Dr. Stuart Grossert of the Dalhousie University mass spectrometry facility for their technical assistance. We thank Drs. Stanley Cameron and Witek Kwiatkowski of Dalhousie University for crystallographic analyses. Paul Harrington thanks NSERC for a summer assistantship.

References

1. (*a*) R.E. Moore, C. Cheuk, X.–Q. Yang, G.M.L. Patterson, R. Bonjouklian, T.A. Smitka, J. Mynderse, R.S. Foster, N.D. Jones, J.K. Swartzendruber, and J.B. Deeter. J. Org. Chem. **52**, 1036 (1987); (*b*) R.E. Moore, C. Cheuk, and G.M.L. Patterson. J. Am. Chem. Soc. **106**, 6456 (1984).
2. R. Bonjouklian, R.E. Moore, and G.M.L. Patterson. J. Org. Chem. **53**, 5866 (1988).
3. (*a*) M. Sakagami, H. Muratake, and M. Natsume. Chem. Pharm. Bull. **42**, 1393 (1994); (*b*) T. Fukuyama and X. Chen. J. Am. Chem. Soc. **116**, 3125 (1994); (*c*) V. Vaillancouirt and K.F. Albizati. J. Am. Chem. Soc. **115**, 3499 (1993); (*d*) H. Muratake, H. Kumagami, and M. Natsume. Tetrahedron, **46**, 6351 (1990); (*e*) H. Muratake and M. Natsume. Tetrahedron, **46**, 6331 (1990); (*f*) H. Muratake and M. Natsume. Tetrahedron Lett. 1815 (1989).
4. R.J. Sunnberg. The chemistry of indoles. Academic Press, New York. 1970.
5. (*a*) J. Szmuszkovic. J. Am. Chem. Soc. **79**, 2819 (1957); (*b*) W.E. Noland, G,M. Christensen, G.L. Sauer, and G.G.S. Dutton. J. Am. Chem. Soc. **77**, 456 (1955); (*c*) R.L. Garnick, S.B. Levery, and P.W. Le Quesne. J. Org. Chem. **43**, 1226 (1978), and refs. cited therein; (*d*) Z. Iqbal, A.H. Jackson, and K.R.N. Rao. Tetrahedron Lett. 2577 (1988); (*e*) G. Dujardin and J.–M. Poirer. Bull. Soc. Chim. Fr. **131**, 900 (1994).
6. H. Kotsuki, M. Teraguchi, N. Shimomoto, and M. Ochi. Tetrahedron Lett. 3727 (1996).
7. P.E. Harrington and M.A. Kerr. Synlett, 1047 (1996).
8. (*a*) R.W. Marshman. Aldrichimica Acta, **28**, 77 (1995); (*b*) S. Kobayashi. Synlett, 689 (1994).
9. G. Jenner. Tetrahedron Lett. 233 (1995).
10. (*a*) S. Kobayashi, M. Moriwaki, and I. Hachiya. Synlett, 1153 (1995); (*b*) S. Kobayashi, S. Mitamura, and A. Kawada. Chem. Commun. 1157 (1993).
11. (*a*) K. Freter. J. Org. Chem. **37**, 2010 (1972); (*b*) J. Org. Chem. **40**, 2525 (1975).
12. D. Chen, L. Yu, and P.G. Wang. Tetrahedron Lett. 4467 (1996).
13. (*a*) N.S. Isaacs. High pressure techniques in chemistry and physics: a practical approach. *Edited by* W.B. Holzapfel and N.S. Isaacs. Oxford University Press, New York. 1997. p. 307; (*b*) F.-G. Klarner, M.K. Diedrich, and A.E. Wigger. Chemistry under extreme or non-classical conditions. *Edited by* R. van Eldik and C.D. Hubbard. John Wiley and Sons, New York. 1997. p. 53.
14. (*a*) R.A. Bounce, M.F. Schlecht, W.G. Dauben, and C.H. Heathcock. Tetrahedron Lett. 4943 (1983); (*b*) W.G. Dauben and J.M. Gerdes. Tetrahedron Lett. 3841 (1983); (*c*) W.G. Dauben and R.A. Bounce. J. Org. Chem. **48**, 4642 (1983); (*d*) W.G. Dauben and H.O. Krabbenhoft. J. Org. Chem. **42**, 282 (1977).

© 1998 NRC Canada

A nuclear magnetic resonance investigation of the micellar properties of two-headed surfactant systems: the disodium 4-alkyl-3-sulfonatosuccinates. 1. Equilibrium micellar properties

Gregory D. Boucher, Aaron C. MacDonald, Brent E. Hawrylak, and D. Gerrard Marangoni

Abstract: A family of two-headed surfactants, the disodium 4-alkyl-3-sulfonatosuccinates, has been synthesized by the monoesterification of maleic anhydride and the addition of sodium bisulfite to the corresponding monoester. The properties the micelles formed by these compounds in aqueous solution, and the conformations of the chains comprising the micellar interior, have been investigated using a combination of 1-D nmr experiments and homonuclear and heteronuclear 2-D nmr techniques. The critical micelle concentrations (cmc's) and the aggregation numbers determined from the nmr experiments indicate that, in agreement with the earlier literature on other two-headed surfactant systems, these amphiphiles have high cmc's and low aggregation numbers when compared to single-headed surfactants of comparable chain length. All these results are interpreted in terms of the effect of adding a second headgroup to a single-headed, single-tailed surfactant.

Key words: micelles, surfactants, nmr spectroscopy, chemical shifts, aggregation numbers.

Résumé : Procédant à une monoestérification de l'anhydride maléique suivie d'une addition de bisulfite de sodium au monoester correspondant, on a synthétisé une famille d'agents de surface à deux têtes, les 4-alkyl-3-sulfonatosuccinates de disodium. Faisant appel à une combinaison d'expériences de RMN en 1-D et à de techniques RMN homonucléaires et hétéronucléaires en 2-D, on a étudié les propriétés des micelles formées par ces composés en solutions aqueuses ainsi que les conformations des chaînes formant l'intérieur des micelles. Les concentrations micellaires critiques (cmc) et les nombres d'agrégation déterminés par les expériences de RMN indiquent que, en accord avec les données antérieures sur d'autres systèmes d'agents de surface à deux têtes, ces amphiphiles présentent des cmc élevées et des nombres d'agrégation faibles comparés aux valeurs correspondantes d'agents de surface à une seule tête de longueur de chaîne comparable. On interprète tous ces résultats en fonction de l'effet provoqué par l'addition d'une deuxième tête à un agent de surface portant une tête et une queue.

Mots clés : micelles, agents de surface, spectroscopie RMN, déplacements chimiques, nombres d'agrégation.

[Traduit par la Rédaction]

Introduction

The class of compounds known as surfactants (for surface active agents) displays a number of distinct solution properties in water and consist, in their most common form, of a polar or ionic headgroup (e.g., sulfate, carboxylate) and a linear or branched hydrocarbon or fluorocarbon chain. The application of surfactant technology to a number of important industrial and pharmaceutical processes has been intensely investigated in the literature (1).

The unusual properties of aqueous surfactant solutions can be ascribed to the presence of the hydrophilic head group and the hydrophobic chain (or tail) in the molecule. The polar or ionic headgroup usually interacts strongly with its aqueous environment and is solvated via dipole–dipole or ion–dipole interactions, whereas the nonpolar chains interact only very weakly with water, resulting in the formation of ordered water molecules in the vicinity of the nonpolar chain (the hydrophobic effect). Due to the presence of the hydrophobic effect, surfactant molecules (amphiphiles) adsorb at the air–water interface, even at low surfactant concentrations, reducing the surface tension. At a specific amphiphile concentration, the critical micelle concentration, or *cmc*, molecular aggregates known as micelles are formed (2). In fact, a large number of experimental observations can

Received October 31, 1997.

G.D. Boucher, A.C. MacDonald, B.E. Hawrylak, and D.G. Marangoni.[1] Dept. of Chemistry, St. Francis Xavier University, P.O. Box 5000, Antigonish, NS B2G 2W5, Canada.

[1]Author to whom correspondence may be addressed. Telephone: (902) 867–2324. Fax: (902) 867–2414. E-mail: gmarango@stfx.ca

 © 1998 NRC Canada

be summed up in a single statement: almost all physicochemical properties vs. concentration plots for a given surfactant–solvent system will show an abrupt change in slope in a narrow concentration range (the cmc).

The most commonly held view of a surfactant micelle at concentrations slightly above the cmc value of the surfactant is not much different than that published by Hartley in 1936 (3). At surfactant concentrations slightly above the cmc, amphiphiles tend to associate into spherical micelles, of about 50–100 monomers, with a radius similar to that of the length of an extended hydrocarbon chain. The micellar interior, being composed essentially of hydrocarbon chains, has properties closely related to the liquid hydrocarbon (4).

Nuclear magnetic resonance (nmr) spectroscopy is well recognized as powerful tool with which the physicochemical properties of micellar systems can be investigated. It is an inherently useful technique for studying micellar solutions, since the transfer of a monomer from the bulk solution to the micellar phase is generally accompanied by changes in a large number of nmr parameters (e.g., chemical shifts and relaxation rates). Nmr studies of surfactant solutions include the following: (*i*) cmc values and conformational changes upon micelle formation from ^{13}C chemical-shift measurements (5–8); (*ii*) counterion binding using counterion relaxation rates, e.g., ^{23}Na and ^{35}Cl (9–11); (*iii*) solubilization, counterion binding, and phase diagrams using the Fourier-transform, pulsed-gradient spin echo (FT-PGSE) method (12–22); (*iv*) the study of micellar structure and the determination of the *p*-value of solubilizates using ^{1}H and (or) ^{13}C paramagnetic relaxation experiments (23–26); (*iv*) reorientation and segmental motions of amphiphiles in lamellar or other ordered phases using ^{13}C, ^{31}P, ^{2}H, and ^{14}N relaxation experiments (27–32). The strength of the nmr technique, in general, lies in its multi-nuclear, multiparameter approach. As such, nmr experiments have been shown to provide important insight into the nature of the micellization process. A number of excellent reviews have been published recently on the application of nmr spectroscopy to the investigation of micellar and mixed micellar systems (33–36).

In view of the increasing and varied number of applications of surfactant technology, it is somewhat surprising that the surfactants usually used are long chain hydrocarbons with typical head groups like sulfate, trimethylammonium, carboxylate, and phosphate. In fact, the bulk of the work in all areas of surfactant technology, including how surfactants aggregate into simple micelles, has been limited to systems similar to those described above. Recently, however, the synthesis of novel surfactants, in particular surfactants possessing multiple or unusual headgroups has been gaining attention in the literature (37–40). As an example, Jobe and Reinsborough (37) have studied the properties of micelles formed by some of the C-6, C-8, and the C-10 members of the disodium 4-alkyl-3-sulfonatosuccinates (i.e., cmc's, aggregation numbers, and degrees of counterions binding) as a function of the alkyl chain length, using conductance, viscosity measurements, and dye solubilization techniques. These authors concluded that the addition of the second polar head group made it more difficult for the surfactant molecules to cluster together to form micelles; hence, these two-headed surfactants have relatively high cmc's and small aggregation numbers. However, the degrees of counterion binding appeared to be in the range most often quoted for single-headed surfactants. Kooreman and Engberts (38) and Beck and co-workers (39) have investigated the synthesis and characterization of the micellar properties of two different families of disulfate surfactants; the results from both groups also indicate that the addition of the second sulfate group affects greatly the properties of the alkanedisulfate micelles (the cmc's, degrees of counterion binding) when compared to the well-known alkanesulfate amphiphiles. In fact, Kooreman and Engberts (38) have demonstrated that two-headed sulfate surfactants are extremely stable towards precipitation by hard water ions (e.g., Ca^{2+}). The purpose of the present paper is to completely characterize the equilibrium properties of the micelles formed by a complete series (C-6 to C-10) of two-headed surfactants, the disodium 4-alkyl-3-sulfonatosuccinates, as a function of the chain length of the surfactant. These surfactants have the following structural formula.

The ^{1}H, ^{13}C, and ^{23}Na chemical shifts will be used to obtain estimates of the cmc values, the surfactant aggregation

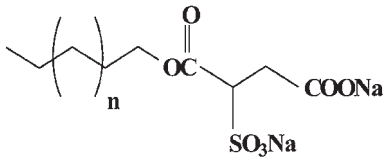

number, and examine the environment of the counterion in two-headed surfactant micelles. All these results will be discussed in terms of the change in the equilibrium micellar properties brought about by the addition of the second charged headgroup to a single-headed surfactant monomer.

Experimental

The monoester of maleic anhydride was synthesized by heating together an equimolar amount of maleic anhydride with the appropriate alcohol (1-hexanol-1-decanol, Aldrich Chemical Company, 99% purity, used as received). The monoester was diluted with water, neutralized with 6 M NaOH, and the reaction mixture was refluxed with an aqueous solution of sodium bisulfite (Aldrich Chemical Company, 99% purity) for a period of 24–48 h. The progress of the reaction was monitored by UV spectroscopy; the reflux was stopped when an aliquot of the reaction mixture did not exhibit a peak in the UV spectrum at 300 nm, which is the UV absorption peak for the monoester of maleic anhydride. The mixture was allowed to cool to room temperature, and the solvent was carefully removed under vacuum. The solid surfactants were collected and washed with a cold methanol–water or ethanol–water mixture and two portions of diethyl ether to remove any residual alcohol. The final product was purified via Soxhlet extraction from diethyl ether and (or) ethanol. The overall yield of product was about 65–70%. The purified surfactants were characterized by nmr and FT–IR spectroscopy, and by a two-phase surfactant titration. It was found that the surface tension vs. log (c_{surf}) plots

© 1998 NRC Canada

Fig. 1. The ^{13}C nmr spectrum of disodium 4-octyl-3-sulfonatosuccinate (C_8SS).

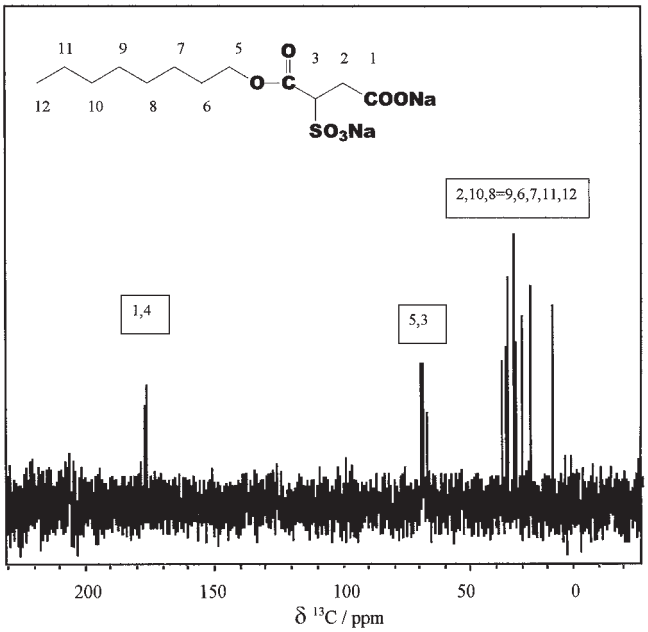

Fig. 2. The ^{13}C chemical shifts (ppm) vs. the inverse of the surfactant concentration for the methyl carbon of C_8SS.

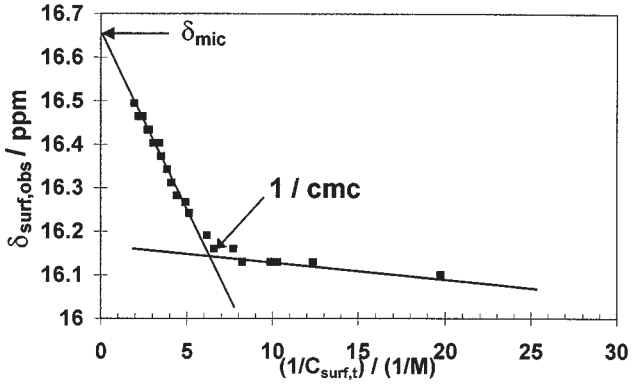

were free of any minima, indicating that the final product had no surface-active impurities.

The nmr spectra (^1H and proton decoupled ^{13}C) for our sulfosuccinate surfactants were obtained on a Bruker AC-200 at St. F.X. University and a Bruker AC-250 nmr at the Atlantic Region Magnetic Resonance Centre (ARMRC) at Dalhousie University. A typical ^{13}C nmr spectrum for the C_8 sulfosuccinate is presented in Fig. 1. The ^{23}Na chemical shifts were obtained on a Bruker AMX-400 nmr spectrometer at the ARMRC. Homonuclear 2-D nmr spectra (COSY and NOESY) were obtained on both the AC-200 spectrometer at St. F.X. and the AC-250 nmr at Dalhousie University, using the standard pulse programmes from the Bruker software library. The ^{13}C-detected HETCORR experiments were performed on the Bruker AC-200 nmr spectrometer at St. F.X. University. The compound D_2O was used as the solvent for all the nmr experiments. The ^1H spectra were referenced to the HOD peak (δ = 4.81 ppm), while the ^{13}C chemical shifts were referenced to the deuterium lock signal using the method of Söderman (41). The ^{23}Na chemical shifts are reported relative to a 1.00 M solution of NaCl.

Table 1. Micellar properties of disodium 4-alkyl-3-sulfanatosuccinate surfactants as a function of the alkyl chain length.

Alkyl chain length	cmc's[a] (M)	$\beta\delta_{Na,mic}$[b]	$\delta_{Na,mic}$	N_s
6	0.351	–0.34	–0.87	N/A
7	0.256	–0.30	–0.77	13 ± 4
8	0.154	–0.28	–0.65	20 ± 5
9	0.0798	–0.24	–0.60	29 ± 4
10	0.0369	–0.25	–0.59	42 ± 5

[a]The cmc value for the C_6SS is from ^{23}Na chemical-shift measurements. [b]β values from refs. 37, 42, and 46.

Results and discussion

A. The cmc values

The cmc values for the sulfosuccinate surfactants were obtained from the ^{13}C and ^{23}Na chemical-shift measurements as described below. Under the assumption of a two-site model for the surfactant ions and the counterions, i.e., the surfactant and counterions exist as "free" (in the aqueous phase) and "bound" (in the micellar phase), the observed ^{13}C or counterion chemical shifts can be written as follows.

$$[1] \qquad \delta_{s,obs} = p\delta_{s,mic} + (1-p)\delta_{s,aq}$$

where $\delta_{s,obs}$ is the averaged chemical shift of the surfactant or counterion, $\delta_{s,aq}$ is the nmr chemical shift of the surfactant ion or counterion in the aqueous phase, and $\delta_{s,mic}$ is the nmr parameter of the surfactant ion or counterion in the micellar phase. For the surfactant ion, if we define the *p*-value of the surfactant ion as

$$[2] \qquad p = \frac{C_{surf,mic}}{C_{surf,t}}$$

and substituting the definition of the *p*-value into the two-site model, we obtain the following for the ^{13}C chemical shifts.

$$[3] \qquad \delta_{s,obs} = \left(\frac{C_{surf,mic}}{C_{surf,t}}\right)\delta_{surf,mic} + \left(\frac{C_{surf,aq}}{C_{surf,t}}\right)\delta_{surf,aq}$$

where $\delta_{surf,mic}$ and $\delta_{surf,aq}$ are the ^{13}C chemical shifts of the surfactant carbon in the micellar phase and aqueous phase, respectively, and $C_{surf,mic}$, $C_{surf,aq}$ are the concentrations of surfactant in the micellar phase and in the aqueous phase, respectively. A plot of the observed ^{13}C chemical shift vs. the inverse of the total surfactant concentration should yield two linear regions intersecting at the inverse of the cmc value of the surfactant. An example plot of the ^{13}C chemical shifts versus the inverse surfactant concentration is given in Fig. 2 for the methyl carbon of the C_8 sulfosuccinate. The averaged cmc values of the sulfosuccinate surfactants were obtained from the breaks in the ^{13}C δ values vs. the inverse of the surfactant concentration for each of the carbon resonances for the C_7–C_{10} sulfosuccinates. All these values are given in Table 1. As there were no discernible changes in the ^{13}C chemical shifts for the C_6 sulfosuccinate, the cmc

© 1998 NRC Canada

Fig. 3. The ^{23}Na chemical shifts (ppm) vs. the inverse of the surfactant concentration. ●, C_6SS; ◆, C_7SS; ■, C_8SS; ▲, C_9SS; ×, C_{10}SS.

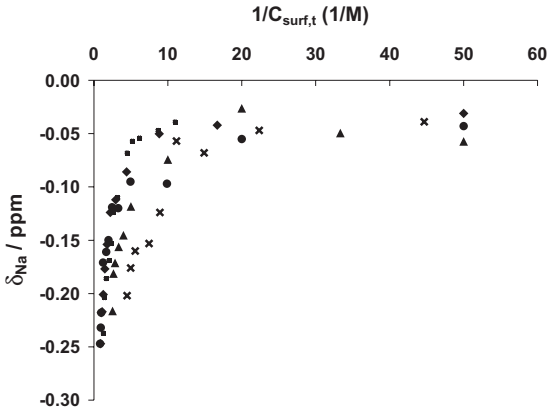

value reported in Table 1 for that surfactant is the cmc value obtained from a plot of the ^{23}Na δ values vs. $1/(C_{Na,t})$. We should point out that the cmc values obtained in this paper are in excellent agreement with the cmc values from a number of different techniques in the work of Jobe and Reinsborough (37) and the work of Wiseman et al. (42).

The degree of counterion binding of a surfactant (the β value) is defined as

$$[4] \qquad \beta = \frac{C_{c,mic}}{C_{surf,mic}}$$

Hence, when the definition of the β value is applied to the two-site model, the counterion nmr chemical shifts can be written as follows.

$$[5] \qquad \delta_{c,obs} = \delta_{c,aq} + \beta(\delta_{c,mic} - \delta_{c,aq})\left(1 - \frac{cmc}{c_{c,t}}\right)$$

A plot of the observed ^{23}Na chemical shifts vs. the inverse of the total counterion concentration should yield two linear regions intersecting at the inverse of the cmc value of the surfactant. With an estimate of the degree of counterion binding (e.g., from conductance measurements), the counterion nmr chemical shift in the micellar phase, $\delta_{c,mic}$, can be estimated from eq. [5]. In all our ^{23}Na spectra for the sulfosuccinates, only a single peak is observed for the counterion, which indicates that fast exchange of the counterion is occurring between the aqueous phase and the micellar phase. The ^{23}Na chemical-shift data for all the sulfosuccinate surfactants are presented in Fig. 3. The slopes and the intercepts of the plots of the counterion chemical shift vs. inverse counterion concentration above the cmc value yield the product of $\beta\delta_{Na,mic}$; these are also reported in Table 1. It appears that from Table 1 that the product $\beta\delta_{Na,mic}$ does not change significantly as the chain length of the carbon atom in the surfactant is increased. This is also the case for single-headed surfactants of comparable chain length. In the work of Gustavsson and Lindman (10, 11), the $\beta\delta_{Na,mic}$ values of alkyl sulfates were observed to be constant (–0.28 ± 0.04) as the chain length of the surfactant increases. Since the counterion binding values of ionic surfactants are not particularly sensitive to the increasing carbon chain length (2, 4), Gustavsson and Lindman (10, 11) estimated the $\delta_{Na,mic}$ values from the observed ^{23}Na chemical-shift plots for a number of different surfactant headgroups using the counterion binding values from tracer self-diffusion measurements. We have calculated our values of $\delta_{Na,mic}$ for the sulfosuccinate micelles using the counterion binding values derived from conductance measurements (37, 42, 46). It is clear from Table 1 that as the chain length of the surfactant increases, the electronic environment of the ^{23}Na counterion does not change significantly, as evidenced by the relatively constant value of the chemical shift of the sodium ion at the micellar surface (–0.70 ± 0.12). This value for the chemical shift of the sodium ion at the surface of a sulfosuccinate micelle is significantly different than the $\delta_{Na,mic}$ values of a sodium ion at the surface of either carboxylate micelles or sulfonate micelles (0.70 ppm and –0.13 ppm, respectively) (10, 11). It is generally assumed that the chemical-shift changes of the counterion are dominated by changes in the paramagnetic shielding term of the ion at infinite dilution. For a hydrated, monatomic counterion, the paramagnetic shielding term is mostly due to the overlap of the outer orbitals of the sodium counterion and the oxygen of the hydrating water molecule (i.e., direct ion–ion interactions are usually unimportant). In the case of the sulfosuccinates, the difference in the electronic environment of the head group must lead to significant differences in the hydration of the sodium counterions at the surface of these micelles than at the surface of either carboxylate or sulfonate micelles. The large, positive $\delta_{Na,mic}$ for the sodium ion bound to the carboxylate micelle indicates that there is a significant amount of polarization of the counterions due to the possibility of H-bonding between the negatively charged O atom in the carboxylate anion and the protons on the water molecules. The oxygen atoms on the sulfonate anion are significantly less polarizing, and the shielding of the Na^+ counterion increases. With the combination of a carboxylate group and a sulfonate group in the headgroup region of the sulfosuccinate micelles, it appears that the headgroup becomes less polarizing. It is clear that there are structural and electronic changes that occur in the headgroup region of the two-headed surfactant micelles, due to the addition of the second charged headgroup, that affect significantly the shielding of the sodium ion at the micellar surface. These effects are largely absent when we examine the ^{23}Na chemical-shift data for single-headed surfactants of Gustavsson and Lindman (11). We will return to the subject of conformational and structural changes when we examine the ^{13}C chemical-shift changes upon micelle formation below.

Using the nmr cmc values and the β values of these surfactants from our conductance measurements (42), the Gibbs energy of micellization ($\Delta_{mic}G°$ values) have been calculated using the equations of Zana (43), which for a two-headed surfactant with monovalent counterions is calculated as follows.

$$[6] \qquad \Delta_{mic}G° = RT(1 + 2\beta)\ln X_{cmc} + 2RT\beta\ln 2$$

The $\Delta_{mic}G°$ values for the sulfosuccinate surfactants are plotted in Fig. 4 as a function of the surfactant chain length. The slope of the plot of the $\Delta_{mic}G°$ values vs. surfactant chain length yields an estimate of –3.2 kJ/mol for the Gibbs

© 1998 NRC Canada

Fig. 4. The $\Delta_{mic}G°$ values for some families of one-headed and two-headed surfactant systems. ●, alkanedisulfates; ◆, alkyl carboxylates; ■, alkyl sulfates; ▲, SASA; ×, SASS.

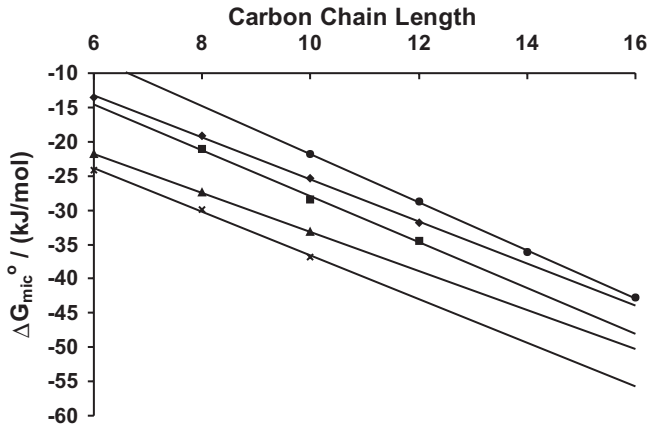

energy of transfer of a CH_2 group from the aqueous phase to the sulfosuccinate micellar phase, in excellent agreement with the literature (2, 43). In Table 2, we have calculated the $\Delta_{mic}G°$ values of the sodium alkylcarboxylates, the sodium alkylsulfates, the sodium alkyl sulfoacetates, and the disodium 1,2-alkanedisulfates (44–46); we have also plotted these Gibbs energies in Fig. 4. The sodium alkyl sulfoacetate surfactants are of interest, since they are structurally related to the sulfosuccinate surfactant family. It is clear that the $\Delta_{mic}G°$ values for the two-headed surfactants are higher than for the single-headed surfactants of comparable chain length, indicating that it is thermodynamically less favourable for the two headed surfactants to form micelles.

B. Surfactant aggregation numbers

The mean aggregation numbers of the surfactants were estimated from the ^{13}C chemical-shift data, using the method outlined by Lang (47) and Gao et al. (48). The N_s values of surfactants can be estimated from the application of the mass-action model of micelle formation to the ^{13}C nmr chemical shifts. Under the assumption of a single aggregation number, the equilibrium between the surfactant monomers (S) in the aqueous phase and the micellar phase (S_{N_s}) can be written as follows.

$$[7] \qquad N_s S \rightleftarrows S_{N_s}$$

The equilibrium constant for the above reaction is written (neglecting activity corrections):

$$[8] \qquad K = \frac{C_{mic}}{C_{surf,aq}^{N_s}}$$

where C_{mic} is the concentration of micelles having an aggregation number N_s (i.e., $C_{mic} = C_{surf,mic}/N_s$), and $C_{surf,aq}$ is the concentration of the free monomer in solution. Since the free-monomer concentration can be written in terms of the total surfactant concentration, $C_{surf,t}$, the equilibrium constant can then be written as

$$[9] \qquad K = \frac{C_{surf,t} - C_{surf,aq}}{N_s C_{surf,aq}^{N_s}}$$

Table 2. The $\Delta_{mic}G°$ values (kJ/mol) for different families of one-headed and two-headed surfactants.

Chain length	Alkyl carboxylates	Alkyl sulfates	SASA	SASS	Disulfates
6	–14.0	—	–21.8	–24.1	—
8	–19.9	–21.1	–27.4	–29.9	—
10	–24.7	–28.4	–33.2	–36.8	–21.8
12	–31.3	–34.5	—	—	–28.8
14	—	—	—	—	–36.1
16	—	—	—	—	–42.8

Fig. 5. Plot of the calculated chemical shifts (from eq. [10]) as a function of the inverse surfactant concentration for the methyl carbon of C_8SS.

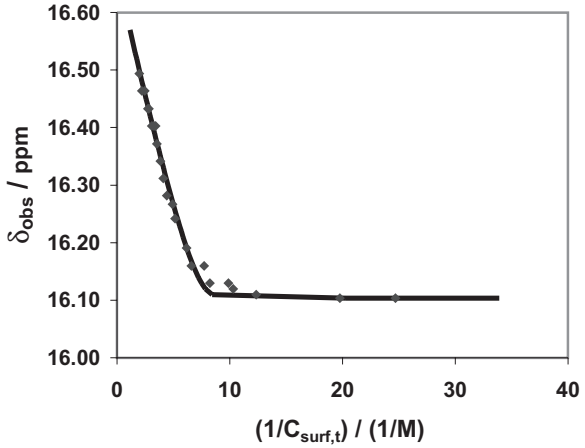

The observed chemical shift is written in terms of the total surfactant concentration according to eq. [3]. Hence, substituting for $C_{surf,aq}$ in eq. [8] yields

$$[10] \qquad \frac{1}{C_{surf,t}} = (KN_s)^{\frac{1}{N_s-1}}(\delta_{surf,mic} - \delta_{surf,aq})^{-1} (\delta_{surf,mic} - \delta_{surf,obs})^{\frac{N_s}{N_s-1}}(\delta_{surf,obs} - \delta_{surf,aq})^{\frac{1}{1-N_s}}$$

The aggregation numbers were estimated from fitting the ^{13}C chemical-shift data as a function of surfactant concentration to eq. [10]. A plot of the calculated and experimental chemical shifts as a function of the inverse surfactant concentration is presented in Fig. 5 for the methyl carbon of the C_8SS. The aggregation numbers are also presented in Table 1. The use of ^{13}C nmr chemical shifts to obtain the surfactant aggregation number from the application of the mass action model has been criticized by several authors as yielding low estimates of the surfactants aggregation number for typical anionic surfactants like SDS (41); however, as a function of the carbon chain length, it should at least qualitatively predict the trends in the aggregation number of the carbon chain length. With this in mind, the aggregation numbers range from a value of 13 for the C_7 sulfosuccinate to 42 for the C_{10} sulfosuccinate. These number are in very good agreement with the viscosity and conductivity determination of the aggregation numbers from the work of Jobe and Reinsborough, and for the higher chain lengths, are in

© 1998 NRC Canada

Table 3. A comparison of the micellar properties of structurally related one-headed (sodium alkyl sulfoacetate, SASA) and two-headed (disodium 4-alkyl-3-sulfanatosuccinate, SASS) surfactants.

	cmc's (M)		$\Delta_{mic}G°$ values (kJ/mol)		N_s	
Chain length	SASA	SASS	SASA	SASS	SASA	SASS
6	0.17	0.351	–21.8	–24.1	20	—
8	0.066	0.150	–27.4	–29.9	42	29
10	0.022	0.0369	–33.2	–36.8	70	42

reasonable agreement with the fluorescence quenching data of Hawrylak et al.[2] In Table 3, we compare the cmc values, Gibbs energies of micelle formation, and the aggregation numbers for the structurally related two-headed surfactants vs. the single-headed surfactants. It is quite evident that the addition of the second negatively charged headgroup has an effect on the micellar properties of the two-headed surfactants vs. the single-headed surfactants of the same alkyl chain length. Therefore, in agreement with our earlier paper on the cmc values of the disulfate surfactants (39) and the work of Jobe and Reinsborough (37), these surfactants have relatively high critical micelle concentrations reflecting a shift in the hydrophilic–lipophilic balance. It should be noted that a shift in the HLB of the surfactant also affects a number of other important solution and micellar properties of surfactants (37, 39, 42).

C. Chemical-shift changes upon micelle formation

The ^{13}C chemical-shift changes upon micellization can give qualitative information about conformational changes that surfactant molecules undergo when forming micelles. Generally, a high frequency shift is associated with an increase in the number of *trans* conformers, whereas a low frequency shift is interpreted in terms of an increasing probability of *gauche* configurations (5–8). It should be noted that there are other contributions to the chemical-shift changes upon micelle formation including headgroup interactions and hydration changes (49), but that the conformational arguments appear for the chemical-shift changes upon micelle formation to be supported by other experimental techniques (50, 51). The ^{13}C chemical-shift changes upon micelle formation, $\delta_{surf,mic} - \delta_{surf,aq}$, are plotted in Fig. 6*a–d* and given in Table 4 for the C_7–C_{10} sulfosuccinate. It can be seen from Fig. 6*a–d* that for all the sulfosuccinate surfactants studied, carbons 1, 2, 3, and 5 undergo low frequency shifts on micelle formation, whereas all other carbons undergo high frequency shifts upon the transfer of the monomer from the aqueous phase to the micellar phase. In fact, it appears that for the headgroup region, the magnitude of the shift changes is a function of the carbon chain length. For the headgroup carbons, the ^{13}C chemical-shift differences decrease as the chain length is increased, whereas for the alkyl chains, the shift changes upon micelle formation are essentially constant.

With the assumption that the shift changes upon micelle formation are due to conformational changes and (or) hydration differences only, it appears that the increase in the low frequency shifts indicates a more constrained configuration (i.e., an increase in the number of *gauche* conformers), as the carbon chain length increases. Grant and Cheney (52) have estimated that the ^{13}C chemical shift would change by a maximum of 4.8 ppm for a complete *gauche–trans* isomerization. Hence, in the case of the sulfosuccinate surfactants, the increase in the surfactant chain length decreases the area per headgroup. The packing of the two negatively charged headgroups on the micellar surface becomes more difficult. From the ^{13}C chemical-shift measurements, we propose that, on average, the 1–4 carbons in the headgroup region adopt a predominately *gauche* configuration, and that the carbons bearing the headgroups become significantly more constrained as the surfactant chain length increases.

For the alkyl chains, the $\delta_{surf,mic} - \delta_{surf,aq}$ values are observed to be essentially constant as the alkyl chain length of the surfactant increases. This is interpreted in terms of an increase in the number of *trans* conformers as the sulfosuccinate surfactants form micelles. As has been observed previously in the literature, the maximum $\delta_{surf,mic} - \delta_{surf,aq}$ values are found in the middle of the alkyl chain. This is due to the fact that the methylene groups near the end of the chain and the methyl groups are more able to bend back towards the surface of the micelle. Note that the $\delta_{surf,mic} - \delta_{surf,aq}$ values for the methyl carbons and the final few methylene groups are slightly smaller for the longer chain surfactants, which is likely due to more motional freedom in the micelle. We are currently determining the dynamics of the carbon nuclei inside the micelle via nmr ^{13}C spin – lattice relaxation time measurements. These results will be the subject of a future paper.

Conclusions

The cmc's and aggregation numbers (N_s values) for a series of two-headed surfactants, the sodium sulfosuccinates, have been determined from the nmr chemical-shift data for the appropriate nucleus. The environment of the counterion at the micellar surface has been probed using surfactant counterion chemical-shift measurements. It appears again that the addition of the second charged surfactant headgroup changes significantly the properties of the micelles formed by the two-headed surfactants, when compared to structurally related surfactants (in this case, the sodium sulfoacetates). The chemical-shift changes upon micelle formation have demonstrated that the formation of sulfosuccinate micelles is accompanied by a significant ordering of the headgroup carbons, while the alkyl chains obtain some conformational freedom upon micelle formation.

[2] B.E. Hawrylak, R. Palepu, and D.G. Marangoni. Unpublished results.

© 1998 NRC Canada

Fig. 6. Plot of the chemical-shift change upon micelle formation ($\delta_{surf,mic} - \delta_{surf,aq}$) as a function of carbon number for (*a*) C_7SS; (*b*) C_8SS; (*c*) C_9SS; and (*d*) $C_{10}SS$.

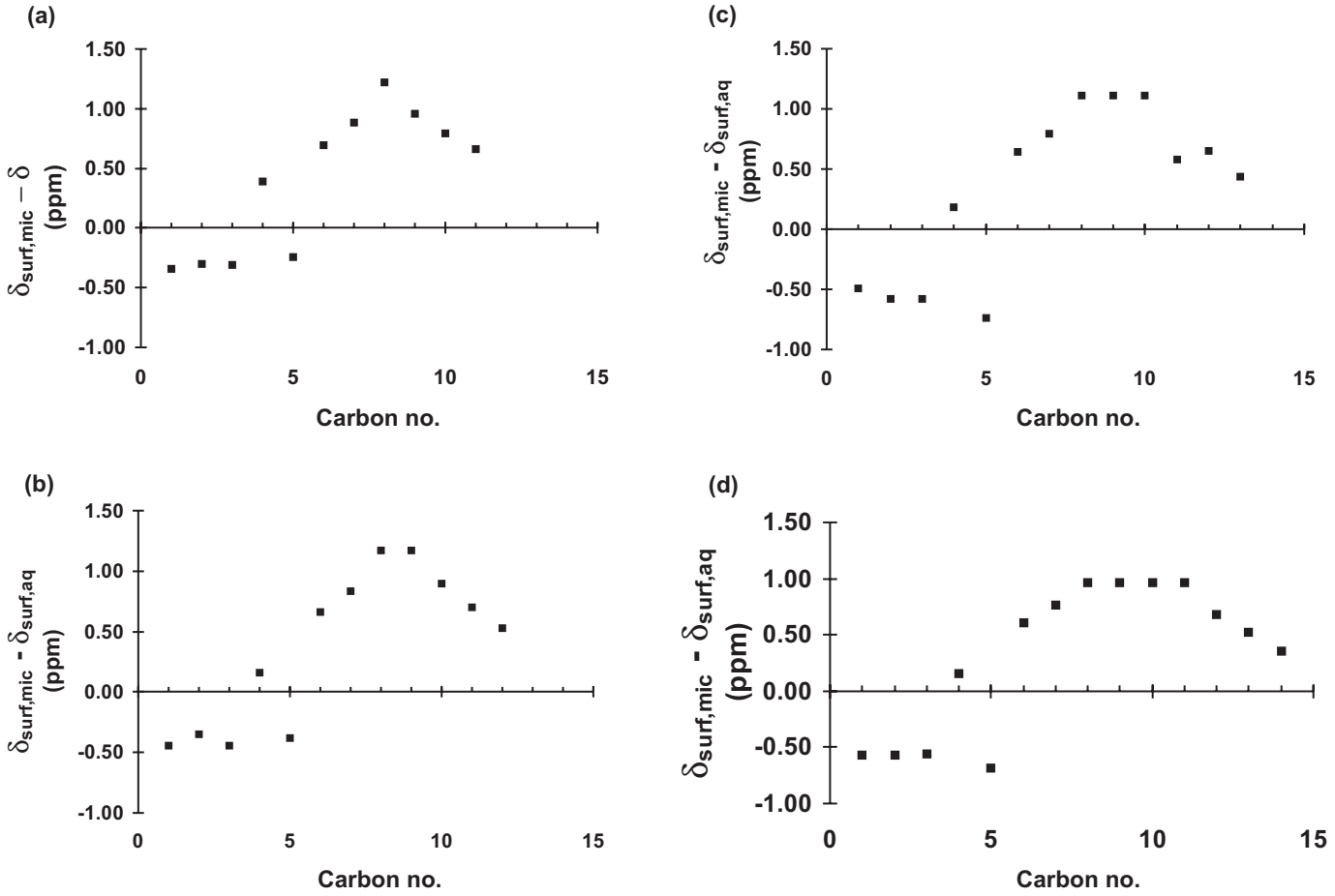

Table 4. Chemical-shift changes ($\delta_{surf,mic} - \delta_{surf,aq}$) upon micelle formation for disodium 4-alkyl-3-sulfanatosuccinate surfactants.

Carbon no.	C_7SS	C_8SS	C_9SS	$C_{10}SS$
1	–0.34	–0.44	–0.49	–0.57
2	–0.30	–0.35	–0.58	–0.57
3	–0.31	–0.44	–0.58	–0.56
4	0.39	0.16	0.18	0.16
5	–0.24	–0.38	–0.74	–0.69
6	0.69	0.66	0.64	0.61
7	0.88	0.83	0.79	0.76
8	1.22	1.17	1.11	0.96
9	0.96	1.17	1.11	0.96
10	0.79	0.90	1.11	0.96
11	0.66	0.70	0.58	0.96
12		0.53	0.65	0.68
13			0.44	0.52
14				0.36

Acknowledgments

The financial support of the Natural Sciences and Engineering Council of Canada (NSERC) (research grant, D.G.M) and the St. F.X. University Council for Research is greatly appreciated. B.E.H. acknowledges the grant of an NSERC undergraduate summer research award. A.C.M. and G.D.B. acknowledge financial support from St. F.X. University. The authors are grateful to Don Hooper and Mike Lumsden at the Atlantic Region Magnetic Resonance Centre for some of the nmr work in this paper. We are grateful to Vince Reinsborough, Don Hooper, Mike Lumsden, and Rod Wasylishen for useful discussions.

References

1. D.R. Karsa (*Editor*). Industrial applications of surfactants. The Royal Society of Chemistry, Whitestable Litho. Ltd., Kent, U.K. 1987.
2. B. Lindman and H. Wennerstrom. Top. Curr. Chem. **87**, 1 (1980).
3. G.S. Hartley. Aqueous solutions of paraffin chain salts. Hermann and Cie, Paris. 1936.
4. C. Tanford. The hydrophobic effect: formation of micelles and biological membranes. 2nd ed. John Wiley, New York. 1980.
5. S. Mazumdar. J. Phys. Chem. **94**, 5947 (1990).
6. Y. Chevalier and C Chachaty. Colloid Polym. Sci. **262**, 489 (1984).
7. B. Brycki and M. Szafran. Magn. Res. Chem. **30**, 535 (1992).

© 1998 NRC Canada

8. B.D. Perrson, T. Drakenberg, and B. Lindman. J. Phys. Chem. **83**, 3011 (1979).
9. I.D. Robb. J. Colloid Interface Sci. **37**, 521 (1971).
10. H. Gustavsson and B. Lindman. J. Am. Chem. Soc. **97**, 3923 (1975).
11. H. Gustavsson and B. Lindman. J. Am. Chem. Soc. **100**, 4647 (1978).
12. P. Stilbs. J. Colloid Interface Sci.. **87**, 385 (1982).
13. P. Stilbs. J. Colloid Interface Sci. **89**, 547 (1982).
14. J. Carlfors and P. Stilbs. J. Colloid Interface Sci. **104**, 489 (1985).
15. P. Stilbs and B. Lindman. J. Colloid Interface Sci. **99**, 290 (1984).
16. M. Jansson, P. Li, and P. Stilbs. J. Phys. Chem. **91**, 5279 (1987).
17. J. Carlfors and P. Stilbs. J. Colloid Interface Sci. **103**, 332 (1985).
18. P. Stilbs. J. Colloid Interface Sci. **94**, 463 (1983).
19. B. Lindman, K. Shinoda, M. Jonströmer, and A. Shinohara. J. Phys. Chem. **92**, 4702 (1988).
20. M. Jansson, P. Linse, and R. Rymden. J. Phys. Chem. **92**, 6689 (1988).
21. B. Balinov, P. Linse, and O. Söderman. J. Colloid Interface Sci. **182**, 539 (1996).
22. O. Söderman and L.B. Johansson. J. Colloid Interface Sci. **179**, 570 (1996).
23. Z. Gao, R.E. Wasylishen, and J.C.T. Kwak. J. Phys. Chem. **93**, 2190 (1989).
24. J.C.T. Kwak and D.G. Marangoni. Langmuir, **7**, 2083 (1991).
25. D.G. Marangoni, A.P. Rodenhiser, J.M. Thomas, and J.C.T. Kwak. ACS Symp. Series, **501**, 194 (1992).
26. Z. Gao, J.C.T. Kwak, R. Labonté, D.G. Marangoni, and R.E. Wasylishen. Colloids Surf. **45**, 269 (1990).
27. O. Söderman, G. Carlström, M. Monduzzi, and U. Olsson. Langmuir, **4,** 1039 (1988).
28. C. Chachaty, T. Ahlnas, B. Lindstrom, H. Nery, and A.M. Tistchenko. J. Colloid Interface Sci. **122**, 406 (1988).
29. C. Chachaty, J. Caniparoli, A. Faure, and A.M. Tistchenko. J. Phys. Chem. **92**, 6330 (1988).
30. O. Söderman, M. Monduzzi, A. Ceglie, and B. Lindman. J. Colloid Interface Sci. **136**, 113 (1990).
31. A. Ceglie, M. Monduzzi, and O. Söderman. J. Colloid Interface Sci. **142**, 129 (1991).
32. O. Söderman, E. Hansson, and M. Monduzzi. J. Colloid Interface Sci. **141**, 512. (1991).
33. C. Chachaty. Prog. NMR Spectrosc. **19**, 183 (1987).
34. P. Stilbs. Prog. NMR Spectrosc. **19**, 1 (1987).
35. O. Söderman and P. Stilbs. Prog. NMR Spectrosc. **26**, 445 (1994).
36. O. Söderman and U. Olsson. Curr. Opin. Colloid Interface Sci. **2**, 131 (1997).
37. D.J. Jobe and V.C. Reinsborough. Aust. J. Chem. **37**, 303 (1984).
38. P.A. Kooreman and B.F.N. Engberts. Recl. Trav. Chim. Pays-Bas, **113**, 163 (1994).
39. E.K. Comeau, E.J. Beck, J.F. Caplan, C.V. Howley, and D.G. Marangoni. Can. J. Chem. **73**, 1741 (1995).
40. K. von Berlepsch, K. Stähler, and R. Zana. Langmuir, **12**, 5033 (1996).
41. O. Söderman and P. Geuring. Colloid Polym. Sci. **265**, 76 (1987).
42. P. Wiseman, C.A. Kennedy, R. Palepu, and D.G. Marangoni. J. Solution Chem. **27**, 217 (1998).
43. R. Zana. Langmuir, **12**, 1208 (1996).
44. H.C. Evans. J. Chem. Soc. 579 (1956).
45. P. Mukerjee and K.J Mysels. Critical micelle concentrations of aqueous surfactant systems. US-NBS, No. 36, US. GPO, Washington, D.C. 1971.
46. D.J. Jobe and V.C. Reinsborough. Can. J. Chem. **62**, 280 (1984).
47. J. Lang. J. Phys. Chem. **86**, 992 (1982).
48. Z. Gao, R.E. Wasylishen, and J.C.T. Kwak. J. Colloid Interface Sci. **137**, 137 (1990).
49. T. Ahlnäs and O. Söderman. Colloids Surf. **12**, 125 (1984).
50. R.G. Griffin, L. Powers, and P.S. Pershan. Biochemistry, **17**, 2718, (1978).
51. B. Faucompré and B. Lindman. J. Phys. Chem. **91**, 383 (1987).
52. D.M. Grant and B.V. Cheney. J. Am. Chem. Soc. **89**, 5319 (1967).

© 1998 NRC Canada

Regular polyhedral molecules. P_{20} and its inclusion compounds

Lubomír Rulíšek, Zdeněk Havlas, Stanislav Heřmánek, and Jaromír Plešek

Abstract: Based upon the geometrical properties of regular polyhedrons, the possibility of the existence of certain polyhedral molecules composed of only one element is investigated. A very promising candidate — the regular dodecahedron — is selected as the convenient polyhedral structural pattern and phosphorus as the appropriate element. A series of high-level ab initio calculations is performed on the dodecahedral P_{20} molecule, including predictions of its thermodynamic and kinetic stability, natural bond orbital analysis, vibrational analysis, and inclusion of some elements into the molecular skeleton. Due to the potential stabilizing agents that may eventually form stable inclusion compounds and the estimated high kinetic stability, the question of the possible existence of P_{20} is answered in the positive.

Key words: ab initio calculations, inclusion compounds, P_{20}, phosphorus clusters, polyhedra.

Résumé : En se basant sur les propriétés géométriques de polyèdres réguliers, on a évalué la possibilité d'existence de certaines molécules polyédriques formées d'un seul élément. Comme structure polyédrique pratique, on a choisi le dodécaèdre régulier qui possède un grand potentiel et le phosphore comme élément approprié. On a effectué une série de calculs ab initio d'orbitales moléculaires à un niveau élevé sur la molécule dodécaédrique de P_{20} comprenant des prédictions relatives à ses stabilités thermodynamique et cinétique, à l'analyse de l'orbitale de la liaison naturelle, à l'analyse de vibration et à l'inclusion de quelques éléments dans le squelette moléculaire. Compte-tenu des agents stabilisant potentiels qui peuvent éventuellement former des composés d'inclusion et de sa stabilité cinétique évaluée élevée, on prévoit que l'existence du P_{20} est possible.

Mots clés : calculs ab initio, composés d'inclusion, P_{20}, agrégats de phosphore, polyèdres.

[Traduit par la Rédaction]

Introduction

The fascinating discovery of fullerenes (1) inspired us to investigate the potential existence of polyhedral E_n molecules composed of only one element. To select the most appropriate polyhedron and the most appropriate element, two main factors were considered: (*i*) Due to their high symmetry and equivalency of all vertices, edges, and faces, regular polyhedra could be considered as the favoured geometric shapes. (*ii*) The best candidate among the elements should fit the respective coordination numbers and bond angles of the geometric archetype with the least strain.

Some essential geometric parameters of polyhedral molecules are shown in Table 1.

It is apparent that, primarily, the pentagonal dodecahedron should be considered as the favoured geometric archetype. Each vertex is connected to three neighbours and all the bond angles are uniformly 108°. Such a value of bond angle is often found in compounds of the light main group elements. Moreover, the size of the internal cavity in the dodecahedron (the largest among all regular polyhedra) suggests the possibility of inclusion of some atoms or small molecules that might eventually help stabilize the E_{20} cluster.

The following preliminary and qualitative considerations led us to the selection of the best candidate among elements that might form the dodecahedral skeleton.

The "electron poor" E^{III} elements are excluded from the contest because they prefer triangular polyhedral faces as a consequence of three centre bond requirements (cf. the characteristic deltahedral faces in elemental boron, in a plethora of binary borides, and in the *closo*-$B_nH_n^{2-}$ ions). There are not enough electrons for the population of exohedral orbitals (orbitals perpendicular to the surface of the sphere circumscribed to the dodecahedron and oriented radially out) and that is why elemental boron and almost all binary borides are, instead, polymers composed of deltahedral units (2).

The "electron precise" E^{IV} elements prefer polyhedra with square, pentagonal, or hexagonal faces (3). However, the fourth electron has to either accommodate itself in an exohedral orbital or combine with the nearest neighbour to form a double bond. The latter is quite inconvenient in triangles, squares, or pentagons mainly because of the steric requirements.

Which is why fullerenes begin to be stable enough only if the number of participating carbon atoms is higher than

Received February 20, 1998.

L. Rulíšek[1] and Z. Havlas. Institute of Organic Chemistry and Biochemistry, Academy of Sciences of Czech Republic, Flemingovo nám. 2, 16610 Prague 6, Czech Republic.
S. Heřmánek and J. Plešek. Institute of Inorganic Chemistry, Academy of Sciences of Czech Republic, 250 68 Řež near Prague, Czech Republic.

[1]Author to whom correspondence may be addressed. Telephone, Fax: +420-2-20183-292. E-mail: lubos@uochb.cas.cz

 © 1998 NRC Canada

Table 1. Geometric parameters of regular polyhedral molecules expressed in multiples of the edge length *a* (covalent diameter of the vertex atom).

Polyhedron	*n*	α (°)	d_1	d_2
Tetrahedron	3	60	1.22	0.22
Octahedron	4	60	1.41	0.41
Cube	3	90	1.73	0.73
Icosahedron	5	60	1.90	0.9
Dodecahedron	3	108	2.80	1.8

Note: *n* is the number of neighbouring vertices; α is the endohedral angle between the edges; d_1 is the diameter of the circumscribed sphere; d_2 is the diameter of the inner molecular spherical cavity (distance from the centre of the polyhedron to the covalent surface of the vertex atom under the assumption that the covalent diameter of the vertex atom is equal to the edge length; then it follows that $d_2 = d_1 - 1$).

approximately 48 (14 hexagons). If the fourth electron can participate in a terminal E—X bond, this obstacle vanishes (cubane (4), dodecahedrane (5)).

The "electron rich" E^V elements seem to be very promising candidates. Their lone electron pairs might mimic terminal groups protruding radially out of the polyhedron, whereas the remaining three valence electrons might constitute three covalent single bonds connecting the neighbouring vertices. However, nitrogen with its tendency to prefer multiple bonds will be unstable in the dodecahedral vertex position. On the other hand, phosphorus might fit ideally. The same applies to its heavier homologues — As, Sb, and Bi. But these elements contain occupied orbitals of higher angular momentum (*d* and *f* shells) and may favour a different bond arrangement.

The E^{VI} and E^{VII} elements have more electrons than can be accommodated in three single bonds to their neighbours, and one exohedral orbital. They are not thought to be suitable candidates.

The aforementioned considerations led us to the computational investigation of the stability of the dodecahedral molecule P_{20} and its several inclusion compounds $Y@P_{20}$ (Y stands for an element).

There exists extensive experimental and theoretical material about the clusters of phosphorus. Only those papers pertinent to the present work will be recapitulated here. Jones and Hohl (6) systematically studied small clusters (up to P_8) and found the cuneane-like structure to be the most stable conformation of P_8. Häser et al. (7) extended their study up to P_{26}. They evaluated SCF energies corrected by MP2 contributions of 32 phosphorus clusters and suggested a possible reaction scheme for the polymerization of phosphorus. In their study they mentioned the dodecahedral P_{20} molecule and found it to be unstable with respect to P_4 decomposition. Nevertheless, the MP2 contribution decreased this instability significantly. It corroborates the significant role of correlation energy when studying anisodesmic reactions. The most stable conformations they found were oligomeric structures linked by a single covalent bond. However, their results suggested that P_{20} might be the most stable molecule from the subset of polyhedral clusters. Häser and co-workers (8) extended the above study to many other smaller clusters of phosphorus, polyphosphorus anions, and phosphanes, but the polyhedral clusters of phosphorus were not computed in these papers.

Hu et al. (9) recalculated P_{20} to P_4 and P_{20} to P_2 decompositions at the SCF and MP2 levels using a broad range of basis sets. They answered the question of possible existence in a negative way, concluding that P_{20} is not "special." However, the values of reaction energies (both SCF and MP2) exhibited a very strong basis set dependence (ranging from –165 kcal mol^{-1} at the SCF/DZ level through 23 kcal mol^{-1} calculated at the highest MP2/TZ2P level to 70 kcal mol^{-1} at the SCF/(9*s*6*p*4*d*3*f*) level). The results did not exhibit a systematic convergence.

In our work, we do not attempt to investigate all the families of phosphorus clusters. That was done in a very comprehensive way in the cited papers of Häser and his co-workers. Instead, we would like to focus attention on the possible existence of P_{20} and study this interesting molecule more thoroughly. Starting from the general chemical intuition expressed in the preliminary considerations of this introduction, we have endeavored to utilize more information than can be drawn from a single number representing reaction energy. We analyzed the electronic structure in terms of natural bonding orbitals and their population, carried out the simple thermochemical analysis, estimated the kinetic stability, and looked for "stabilizing agents."

Computational methods

All the calculations reported in this work were performed with the Gaussian 94 program suite (10). DFT calculations were carried out by using a hybrid three-parameter functional developed by Becke (11), which combines the Becke's gradient-corrected exchange functional and the Lee–Yang–Parr and Vosko–Wilk–Nusair correlation functionals (12) with part of the exact Hartree–Fock exchange energy (denoted as B3LYP). The coupled cluster method (13) with singles, doubles, and noniterative triples (CCSD(T)) with frozen core electrons has been used for the reference calculations on several model reactions. The basis sets of 6-311G (14) quality with added polarization and diffuse functions have been used in most of the calculations.

In the case of inclusion compound $Hg@P_{20}$, the Hay–Wadt effective core potential (15) was used for the mercury.

The vibrational analysis, zero point energy corrections, and thermochemical analysis were carried out at the B3LYP/6-31+G(d) (16) level. The B3LYP frequencies were scaled by 0.89 in the thermochemical analysis. We used the Natural Bond Orbital (NBO) method (17) at the HF/6-31+G(d) level.

Results and discussion

Model chemistry

To establish the applicability of the DFT method (B3LYP functional) for phosphorus clusters, we first performed a few tests with P_n molecules.

We studied two simple reactions: $2P \rightarrow P_2$ (formation of P_2) and $2P_2 \rightarrow P_4$. These reactions should provide us with a notion of the accuracy of B3LYP. Both of them are anisodesmic reactions of phosphorus atoms or compounds. The results are summarized in Table 2.

© 1998 NRC Canada

Table 2. $\Delta H°_0$ for the $2P \rightarrow P_2$ and $2P_2 \rightarrow P_4$ reactions. B3LYP/6-311+G(d) optimized geometries were used.

	$2P \rightarrow P_2$	$2P_2 \rightarrow P_4$
Method	$\Delta H°_0$ (kcal mol^{-1})	$\Delta H°_0$ (kcal mol^{-1})
B3LYP/6-311+G(d)	–108.4	–35.7
B3LYP/6-311+G(2df)	–114.6	–46.3
CCSD(T)/6-311+G(d)	–82.2	–46.2
CCSD(T)/6-311+G(2df)	–103.9	–51.6
Experimental value	–115.0 (19*b*)	–54.0 (19*b*)

The computed and experimental enthalpies are in good agreement, especially if a larger basis set is used. Excellent agreement between the computed and experimental equilibrium bond lengths has been achieved. The experimental bond lengths are 1.894 Å for P_2 (18) (calcd. 1.897 Å) and 2.21 Å for P_4 (19*a*) (calcd. 2.219 Å). We conclude that the B3LYP/6-311+G(2df)//B3LYP/6-311+G(d) method is appropriate for the quantitatively correct prediction of the stability of the P_{20} molecule. The more sophisticated and presumably more accurate methods (e.g., MP4(SDQ), CCSD(T), QCISD(T) in polarized triple zeta and higher basis sets) are beyond the present capabilities of computers.

The P_{20} molecule

We have located the minimum on the potential energy surface corresponding to the regular dodecahedral structure of the P_{20} molecule. The equilibrium bond length ($d_{P—P}$ = 2.287 Å) is elongated by 0.07 Å in comparison with the P_4 molecule. The P_{20} molecule is depicted in Fig. 1.

The absence of another minimum close to the regular dodecahedral conformation was tested for by removal of the symmetry imposed on the molecule in the previous calculation. We changed the values of several internal coordinates (0.02 Å in bond lengths and 5° in bond and torsion angles). That resulted in a distorted structure with no symmetry element. The optimization procedure resulted in the same minimum as described above.

The NBO analyses of the resulting wave functions of P_{20} and P_4 molecules verified the assumptions made in the introductory section. The molecule P_{20} can be described by single P—P covalent bonds with one lone pair protruding radially out from each vertex. The P—P bonds in P_{20} have 16% of *s* character and 84% of *p* character with *d* orbitals participating with less than 1%; the P—P bonds in P_4 have 6% of *s* and 93% of *p* character. Lone pairs on P vertices in P_{20} have 53% of *s* character and 46% of *p* character (82% *s* and 18% *p* character in P_4). The deviations in directionality of natural hybrid orbitals (from the line connecting neighbouring nuclei) are 4° in P_{20} and 24° in P_4. Therefore, the two molecules differ significantly. The bonding in P_{20} is approaching the classical model of sp^3 hybridization whereas the covalent bonds in P_4 are formed mainly by overlap of *p* orbitals of phosphorus ("banana orbitals").

To determine the relative stability of P_{20}, reaction energies and enthalpies of two reactions, $10P_2 \rightarrow P_{20}$ and $5P_4 \rightarrow P_{20}$, were calculated. The results are summarized in Table 3. With respect to the aforementioned test calculations, we estimate the error in the value of the reaction energy (38.5 kcal mol^{-1}) to be about 10%. This value qualitatively agrees with those computed by Häser et al. (7) (64 kcal mol^{-1} at the SCF/TZDP level and 20 kcal mol^{-1} at the MP2/SVP level) and Hu et al. (9) (23 kcal mol^{-1} at the MP2/TZ2P level).

Table 3. The reaction energies and standard enthalpies at 0 K (negative values indicate higher stability of the products and vice versa).

Reaction	ΔE (kcal mol^{-1})	$\Delta H°_0$ (kcal mol^{-1})
$10P_2 \rightarrow P_{20}$	–200.9	–190.3
$5P_4 \rightarrow P_{20}$	38.5	41.0

Fig. 1. P_{20} molecule in two orientations.

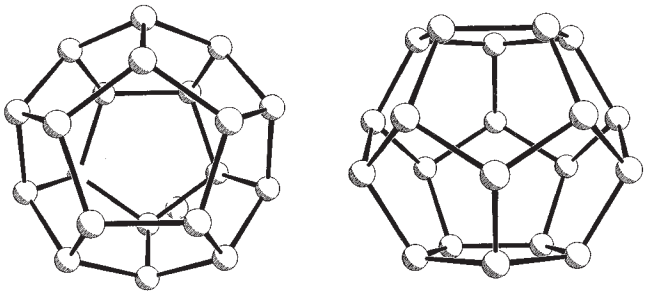

The gas phase thermodynamic stability of P_{20} is significantly higher than that of the known P_2 molecule, but lower than that of P_4 molecule. Therefore, it is theoretically possible to prepare P_{20} by increasing the temperature to above approximately 800°C to accomplish the dissociation of the most stable conformation of phosphorus (the P_4 molecule) into the P_2 species (20), and by subsequent cooling of the system under the specified conditions (e.g., presence of a substance to prevent the condensation of P_2 into P_4 molecules or some other energetically stable cluster arrangement) to obtain the P_{20} molecule. The calculation of P_{20} inclusion compounds that may assist in finding the appropriate condensation centres will be presented below.

Thermochemistry of P_{20}

Having computed the vibrational frequencies, we carried out a simple thermochemical analysis to predict the approximate conditions under which the successful synthesis of the P_{20} molecule can be expected. $5\ P_4 \rightarrow P_{20}$ was chosen as the model reaction.

It should be pointed out that the results are only qualitative, based on the assumption of ideal gas behavior of the participating molecules and upon the approximation of rigid rotor and harmonic oscillator. They confirm the expected dependence of Gibbs energy on the pressure and temperature. The introduction of entropy effects reduces the thermodynamic stability of P_{20}. We presume they may be of some importance for experimental chemists.

The results of thermochemical analysis are depicted in Fig. 2.

Kinetic stability

The second factor determining the potential existence of a given molecule is its kinetic stability. It is virtually impossible (and computationally unattainable) to explore all the possible reaction channels, i.e., to locate all the saddle points

© 1998 NRC Canada

Fig. 2. Calculated thermochemical data for the reaction: 5 $P_4 \rightarrow P_{20}$.

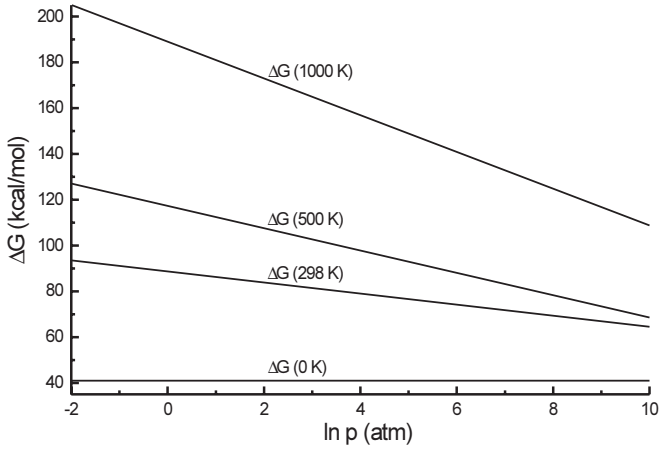

Table 4. Computed harmonic vibrational frequencies of the P_{20} molecule, their symmetry labels, absolute infrared intensities, and Raman activities.

Frequency (cm^{-1})	Symmetry	IR intensity (km mol^{-1})	Raman activity ($Å^4$ amu^{-1}) [a]
101	H_u	0	0
147	H_g	0	21.54
155	T_{2g}	0	0
190	G_u	0	0
263	A_g	0	174.35
273	G_g	0	0
293	T_{1u}	2.75	0
295	T_{2u}	0	0
316	H_g	0	4.14
348	T_{2u}	0	0
363	G_u	0	0
374	G_g	0	0
421	H_u	0	0
423	H_g	0	0.69

[a] Due to the limitations of the DFT methods within the Gaussian 94 program, the Raman scattering activities reported here were calculated at the HF/6-31+G(d) level.

encompassing the equilibrium geometry of dodecahedral P_{20}. Several attempts were made to employ the transition state optimization methods based upon following the lowest vibration modes (eigenvectors). Since neither of these was successful in locating any transition state close to the dodecahedral conformation, we chose a different approach.

The lowest saddle points usually correspond to only a moderate chemical change (conformational transition, rotation of certain group, etc.) and the saddle points corresponding to chemical reactions (breaking of a covalent bond, decomposition of a molecule, etc.) lie substantially higher.

Initially, we examined the lowest vibrational modes. They are degenerate and could be depicted as pulsing of the dodecahedral skeleton. This agrees with the above consideration, that they may correspond to certain conformational transitions. We conceived such a simple transition for the P_{20} skeleton. In their investigation of phosphorus clusters Häser et al. (7) mentioned another conformer of P_{20}, a dodecahedron with one vertex sunk in the direction of the center of the body (Fig. 3). This transition served us as the model for estimating the depth of the dodecahedral P_{20} minimum. The calculations were carried out at the B3LYP/3-21G level, with both conformers fully optimized at this level, and the transition state was located by QST2 (Synchronous Transit – Guided Quasi-Newton Method (21)) as implemented in the Gaussian 94 program. The distorted P_{20} lies energetically only 1.2 kcal mol^{-1} higher than the dodecahedral molecule. However, the energy barrier is 17 kcal mol^{-1} from the side of dodecahedral P_{20}.

Fig. 3. The conformer of P_{20} with one vertex sunk in the direction of the molecular center.

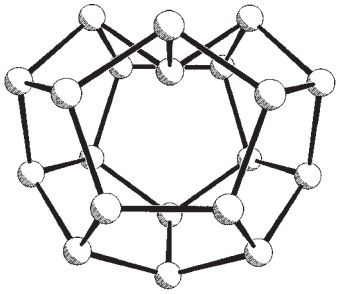

We consider it a reasonably high barrier. The more severe deformation of the P_{20} cage that must precede its decomposition (such as the disruption of a P_2 edge) must lie energetically higher. It may be concluded that P_{20} is (as far as the calculations show) a kinetically stable molecule, but we must keep in mind that the barrier as computed may not be of an accuracy comparable to the previous calculations and that the considerations are based upon the premise about the nature of the low-lying saddle points.

Vibrational analysis

The IR spectrum of the P_{20} molecule has been predicted using the computed frequencies and intensities (Table 4).

There is only one peak in the IR spectrum with a wavelength of 293 cm^{-1} and absolute intensity of 2.75 km mol^{-1} whose detection may indicate the presence of P_{20}. This peak is absent in both P_2 and P_4 molecules (the calculated frequencies with non-zero intensity are 795 and 461 cm^{-1}, respectively).

Four Raman fundamentals are allowed in the P_{20} spectrum (A_g and all three H_g vibrations).

Inclusion compounds Y@P_{20}

We have considered two classes of appropriate candidates for the condensation centers. The first group contains noble gas atoms (analogy with the known $G\cdots(H_2O)_{20}$ clusters (22)) or ions of noble gas type, such as Li^+. To the second group may belong heavy metal elements that do not form phosphides (e.g., mercury).

The subtle energy changes accompanying weak interactions of atoms with other molecules are very difficult to evaluate precisely and the results should be examined with care. That is why we have run test calculations on a smaller system for each type of interaction studied. It also helped us to estimate errors in the predictions of interaction energies

© 1998 NRC Canada

Table 5. The computed interaction energies of model systems. Negative numbers indicate stabilization of the dimer. The P_2 molecule ($d_{P—P}$ = 1.897 Å) is placed at the position equivalent to the edge in dodecahedral P_{20} and the position of the interacting atom (cation) corresponds to the centre of P_{20} (T-shape structure).

	Interaction energy (kcal mol^{-1})	
System	B3LYP/6-311+G(2df)	CCSD(T)/6-311+G(2df)
He···P_2	1.4	1.5
Ne···P_2	1.9	1.6
Ar···P_2	8.4	7
Li^+···P_2	–14.5	–14.3
Li^+···benzene[a]	–38.4	–38.3 (exp) [b]

[a] The geometry of the system was first optimized at the 6-311+G(d) level with the Li^+ ion lying in the sixfold axis of benzene, equilibrium distance from the benzene ring being 1.84 Å.
[b] Experimental value was taken as the reference (23).

of P_{20} with the atoms or cations. The results of test calculations are summarized in Table 5.

Very good agreement between DFT (B3LYP functional) and CCSD(T) methods (or experiment) was found in all cases and therefore the B3LYP functional was used for further calculations.

The atoms were placed at the center of the dodecahedral P_{20} skeleton. The geometry was optimized at the B3LYP/6-311+G(d,p) level and the energy recalculated at the B3LYP/6-311+G(2df) level. The results are summarized in Table 6.

It can be observed that the noble gas atoms are too large to fit ideally into the P_{20} cage. This is evident both from the interaction energies and equilibrium geometries. Still, they may play an important role in the earlier steps of the synthesis by acting as condensation centers and, in the latter stages, escape from the cluster.

Mercury does not appear to be a very promising inclusion element. But it should be mentioned that we did not test Hay–Wadt pseudopotentials for the Hg···P type of interaction and results may be subject to larger error than in other calculations of inclusion compounds.

On the other hand, the interaction of the Li^+ cation with the P_{20} cage is favourable (as expected for a cation–molecule complex) and the equilibrium P—P bond distance remains almost unchanged. The interaction energy is higher by 0.3 kcal mol^{-1} than in the experimentally studied complex Li^+···benzene (23), which means that the lithium monocation stabilizes P_{20} to an even greater extent. To further ascertain this point, we performed the same calculation for the interaction of Li^+ with P_4. The lithium cation was placed both inside and outside the cage. No minimum was found in the former case. The optimization of the molecular geometry led to disruption of the cage with the lithium cation escaping from the cavity inside P_4. On the other hand, the minimum was found for the system with Li^+ outside the P_4 cage. Lithium is positioned in the threefold rotation axis of P_4 (above one face of the P_4 tetrahedron). The equilibrium distance from the three vertices is 2.58 Å. The calculated interaction energy is –22.3 kcal mol^{-1}. Therefore, the stabilization of P_4 by Li^+ is lower by 16.3 kcal mol^{-1} than in the case of Li^+···P_{20}. It corroborates the hypothesis that the lithium monocation could help in the synthesis of P_{20}.

Table 6. The computed interaction energies of a series of P_{20} inclusion compounds (negative values indicate stabilization and vice versa).

System	$d_{P—P}$	Interaction energy (kcal·mol^{-1})
He···P_{20}	2.288	5.1
Ne···P_{20}	2.292	12.3
Ar···P_{20}	2.320	39.8
Hg···P_{20}[a]	2.296	60.9
Li^+···P_{20}	2.287	–38.6

[a] The Hay–Wadt effective core potential (15) with valence TZ+P basis set has been used for Hg, and the standard 6-311G(d) basis set for all electrons in phosphorus atoms.

It should be noted that all the interaction energies reported in this section represent uncorrected BSSE values. We investigated the BSSE error by the counterpoise method. It turned out to be less than 0.5 kcal·mol^{-1} in the 6-311++G(2df,2pd) basis set.

Another important inclusion compound might be P_{21}^+ with one phosphorus atom inside the dodecahedral cage. This possibility was suggested by Whetten (see ref. 3 of ref. 24), who was studying the formation of phosphorus clusters by laser-based mass spectrometric methods. Our preliminary calculation (CASSCF/3-21G) showed that the accurate evaluation of the interaction energy of P^+ with the P_{20} cage is beyond the capabilities of supercomputers as the ground state cannot be described by a single determinant. Therefore, at least the CASSCF/MP2 method with a large basis set should be used for an accurate calculation. In agreement with our study of the above-mentioned inclusion compounds, we think that the question of whether P_{21}^+ might be "special" remains open.

Conclusions

As presented, our aim is to contribute to the discussion about the existence of polyhedral molecules composed of a single element, motivated by the interest generated by the discovery of the unusual structures of fullerenes. We give a positive answer to the question of the possible existence of the dodecahedral P_{20} molecule, and endeavour to show the conditions under which its successful synthesis can be expected. We have shown the possibility of the existence of Y@P_{20} inclusion compounds (especially with Li^+), but do not dare to predict the properties of such unusual structures. They may belong to a class of high energy density molecular systems. We attempt to demonstrate the close relation between chemical intuition (molecular structural patterns as discussed in the Introduction) and high-level ab initio calculations, and give an example of the general methodology used when predicting the existence of new molecules.

References

1. W.H. Kroto, J.R. Heath, S.C. O'Brien, R.F. Curl, and R.E. Smalley. Nature, **318**, 162 (1985).
2. T. Lundstrõm. *In* Encyclopedia of inorganic chemistry. *Edited by* R.B. King. Wiley, New York. 1994. p. 327.
3. R.F. Curl and R.E. Smalley. Sci. Am. October, 54 (1991).

© 1998 NRC Canada

4. P.E. Eaton and T.W. Cole, Jr. J. Am. Chem. Soc. **86**, 3157 (1964).
5. (*a*) O. Ermer. Angew. Chem. Int. Ed. Engl. **16**, 411 (1978); (*b*) R.L. Disch and J.M. Schulman. J. Am. Chem. Soc. **112**, 3377 (1990); (*c*) R. Pinkos, J.-P. Melder, K. Weber, D. Hunkler, and H. Prinzbach. J. Am. Chem. Soc. **115**, 7173 (1993).
6. R.O. Jones and D. Hohl. J. Chem. Phys. **92**, 6710 (1990).
7. M. Häser, U. Schneider, and R. Ahlrichs. J. Am. Chem. Soc. **114**, 9551 (1992).
8. (*a*) M. Häser and O. Treutler. J. Chem. Phys. **102**, 3703 (1995); (*b*) S. Böcker and M. Häser. Z. Anorg. Allg. Chem. **621**, 258 (1995).
9. C.-H. Hu, M. Shen, and H.F. Schaefer III. Theor. Chim. Acta, **88**, 29 (1994).
10. M.J. Frisch, G.W. Trucks, H.B. Schlegel, P.M.W. Gill, B.G. Johnson, M.A. Robb, J.R. Cheeseman, T.A. Keith, G.A. Petersson, J.A. Montgomery, K. Raghavachari, M.A. Al-Laham, V.G. Zakrzewski, J.V. Ortiz, J.B. Foresman, J. Cioslowski, B.B. Stefanov, A. Nanayakkara, M. Challacombe, C.Y. Peng, P.Y. Ayala, W. Chen, M.W. Wong, J.L. Andres, E.S. Replogle, R. Gomperts, R.L. Martin, D.J. Fox, J.S. Binkley, D.J. Defrees, J. Baker, J.P. Stewart, M. Head-Gordon, C. Gonzalez, and J.A. Pople. Gaussian 94, Revision E.2. Gaussian, Inc., Pittsburgh, Pa. 1995.
11. A.D. Becke. J. Chem. Phys. **98**, 5648 (1993).
12. (*a*) A.D. Becke. Phys. Rev. A: Gen. Phys. **38**, 3098 (1988); (*b*) C. Lee, W. Yang, and R.G. Parr. Phys. Rev. B: Condens. Matter, **37**, 785 (1980); (*c*) S.H. Vosko, L. Wilk, and M. Nusair. Can. J. Phys. **58**, 1200 (1980).
13. (*a*) J. Čížek. J. Chem. Phys. **45**, 4256 (1966); (*b*) J.A. Pople, M. Head-Gordon, and K. Raghavachari. J. Chem. Phys. **87**, 5968 (1987).
14. (*a*) R. Krishnan, J.S. Binkley, R. Seeger, and J.A. Pople. J. Chem. Phys. **72**, 650 (1980); (*b*) A.D. McLean and G.S. Chandler. J. Chem. Phys. **72**, 5639 (1980).
15. P.J. Hay and W.R. Wadt. J. Chem. Phys. **82**, 270 (1985).
16. W.J. Hehre, L. Radom, P. von R. Schleyer, and J.A. Pople. Ab initio molecular orbital theory. Wiley, New York. 1986. pp. 86–87, and refs. therein.
17. (*a*) A.E. Reed, R.B. Weinstock, and F. Weinhold. J. Chem. Phys. **83**, 735 (1985); (*b*) A.E. Reed, L.A. Curtiss, and F. Weinhold. Chem. Rev. **88**, 899 (1988); (*c*) A.E. Reed and P. von R. Schleyer. J. Am. Chem. Soc. **112**, 1434 (1990).
18. K.P.H. Huber and G. Herzberg. Constants of diatomic molecules. Van Nostrand, New York. 1979.
19. R.C. West, M.J. Astle, and W.H. Beyer (*Editors*). CRC handbook of chemistry and physics. 65th ed. CRC Press, Boca Raton, Fla. 1984. (*a*) p. F-167; (*b*) p. D-78.
20. F.A. Cotton and G. Wilkinson. Advanced inorganic chemistry. 4th ed. Wiley, New York. 1980. p. 442.
21. C. Peng and H.B. Schlegel. Isr. J. Chem. **33**, 449 (1993).
22. J.C. Bailar, Jr. (*Editor*). Comprehensive inorganic chemistry. Pergamon Press, New York. 1973. p. 139.
23. R.W. Taft, F. Anvia, J.-F. Gal, S. Walsh, M. Capon, M.C. Holmes, K. Hosn, G. Oloumi, R. Vasanwala, and S. Yazdani. Pure Appl. Chem. **62**, 17 (1990).
24. C.-H. Hu, M. Shen, and H.F. Schaefer III. Theor. Chim Acta, **88**, 29 (1994), and ref. 3 therein.

© 1998 NRC Canada

^{31}P chemical shift anisotropies of trimethyl- and triphenylphosphine-substituted Group 6 metal pentacarbonyl complexes

Jordan H. Wosnick, Frederick G. Morin, and Denis F.R. Gilson

Abstract: The ^{31}P chemical shift tensor components and anisotropies of the trimethyl- and triphenylphosphine complexes of the group 6 metal pentacarbonyls, $M(CO)_5PR_3$ (M = Cr, Mo, W and R = Me, Ph), have been measured using solid-state CP-MAS ^{31}P NMR spectroscopy. For the trimethylphosphine derivatives, the chemical shift tensors have near axial symmetry and the shift tensor components are in reasonable agreement with the calculated values for the chromium and molybdenum complexes. In the triphenylphosphine complexes, the tensors are asymmetric due to the different torsion angles of the phenyl rings. The trend to higher shielding of the isotropic ^{31}P chemical shifts on descending group 6 arises from changes in the perpendicular components of the shift tensor. The one-bond coupling constants, $^1J(^{95/97}Mo–^{31}P)$, for the trimethyl- and triphenylphosphine complexes are 129 and 133 Hz, respectively.

Key words: chemical shift anisotropy, phosphines, chromium, molybdenum, tungsten.

Résumé : Faisant appel à la spectroscopie RMN «CP-MAS» à l'état solide du ^{31}P, on a mesuré les composantes du tenseur du déplacement chimique du ^{31}P et les anisotropies des complexes triméthyl- et triphénylphosphines de pentacarbonyles de métaux du groupe 6, $M(CO)_5PR_3$ (M = Cr, Mo, W et R = Me, Ph). Pour les dérivés de la triméthylphosphine, les tenseurs du déplacement chimique présentent une symétrie pratiquement axiale et les composantes du tenseur du déplacement sont en bon accord avec les valeurs calculées pour les complexes du chrome et du molybdène. Pour les dérivés de la triphénylphosphine, les tenseurs sont asymétriques à cause des différents angles de torsion des noyaux phényles. La tendance vers des blindages plus importants des déplacements chimiques isotropes du ^{31}P lorsqu'on descend dans le groupe 6 provient de changements dans les composantes perpendiculaires du tenseur du déplacement. Les constantes de couplage à travers une liaison, $^1J(^{95/97}Mo–^{31}P)$, des complexes triméthyl- et triphénylphosphines sont respectivement 129 et 133 Hz.

Mots clés : anisotropie du déplacement chimique, phosphines, chrome, molybdène, tungstène.

[Traduit par la Rédaction]

Introduction

^{31}P NMR spectroscopy has become a common tool in recent years for studying the structural and electronic properties of organometallic complexes containing phosphine ligands. Direct information about the tensor properties of the chemical shift is not available from solution spectra but can be regained from solid-state spectra under either non-spinning conditions or with magic-angle spinning, where the well-known "powder pattern" is replaced by a sharp isotropic peak surrounded by spinning side bands and the chemical shift tensor information can be recovered from the relative intensities of the spinning side-band manifolds at low spinning speeds (1). This is desirable because the components of the chemical shift tensor provide more information than do the isotropic chemical shifts.

Theoretical methods, particularly Density Functional Theory (DFT) approaches, are now capable of calculating the chemical shift tensors of molecules containing "heavy" nuclei (2), and the purpose of the present study was to determine the chemical shift tensor components for a series of phosphine-substituted group 6 metal pentacarbonyl complexes of the form $M(CO)_5PR_3$ (M = Cr, Mo, W and R = Me, Ph) and to compare these values with the results of the DFT predictions of Kaupp (3) and of Ruiz-Morales and Ziegler (4). The known trend (5) of the ^{31}P isotropic chemical shifts in the direction of increased shielding on going from chromium to tungsten was interpreted by Kaupp as arising from changes in the perpendicular components of the shift tensor. Supporting evidence for this has been reported recently for Group 6 metal pentacarbonyl complexes with the ligand 5-phenyldibenzophosphole (PhDBP) (5). Wasylishen and co-workers (6, 7) have suggested that PhDBP resembles triphenylphosphine as a ligand except that two of the phenyl groups are constrained to one plane and the ^{31}P chemical shift anisotropy reflects this difference in local symmetry. We have examined the ^{31}P chemical shift anisotropies of the triphenylphosphine complexes for

Received March 23, 1998.

J.H. Wosnick, F.G. Morin, and D.F.R. Gilson.[1] Department of Chemistry, McGill University, 801 Sherbrooke Street West, Montreal, QC H3A 2K6, Canada.

[1] Author to whom correspondence may be addressed. Telephone: (514) 398-6908. Fax: (514) 398-3797. E-mail: gilson@omc.lan.mcgill.ca

© 1998 NRC Canada

Table 1. Solid state ^{31}P chemical shift tensor components and anisotropies,[a] isotropic chemical shifts, and coupling constants for the complexes $M(CO)_5PR_3$ (M = Cr, Mo, W; R = Me, Ph). Chemical shift values are in ppm, referenced to 85% H_3PO_4, and all coupling constants are in Hz.

	δ_{iso} soln	δ_{iso} solid	δ_{11}	δ_{22}	δ_{33}	$\Delta\delta^a$	$^1J_{MP}$
$Cr(CO)_5PMe_3$	10	8	38	29	–42	–75.5	
$Cr(CO)_5PMe_3$ [b]	0.3		32	32	–63	–95	
$Cr(CO)_5PMe_3$ [c]	15.0		45.1	45.1	–45.1	–90.2	
$Mo(CO)_5PMe_3$	14	–15	13	–6	–52	–55.5	128
		–17	13	–6	–56	–59.5	129
$Mo(CO)_5PMe_3$ [b]	–22		1	1	–68	–69	
$Mo(CO)_5PMe_3$ [c]	–10.9		6.1	6.1	–45	–69	
$W(CO)_5PMe_3$	–35	–36	–31	–36	–42	–8.5	220
$W(CO)_5PMe_3$ [b]	–22		0	0	–67	–67	
$Cr(CO)_5PPh_3$	55	54	100	75	–14	–102	
$Cr(CO)_5PPh_3$ [c]	64.5		106.8	94.2	–7.4	–107.8	
$Mo(CO)_5PPh_3$	38	36	78	49	–20	–83.5	133
$Mo(CO)_5PPh_3$ [c]	50.4		85.5	71.1	–7.9	–86.2	
$W(CO)_5PPh_3$	22	19	52	22	–17	–54	236, 244[e]
$Cr(CO)_5PhDBP$ [c]		46.8	127	41	–28	–112	
$Mo(CO)_5PhDBP$ [d]		28.0	104	24	–44	–108	120
$W(CO)_5PhDBP$ [d]		7.7	69	–13	–36	–64	
$Mo(CO)_5MeDBP$ [f]		16.5	112	–23	–40	–84.5	123

[a] $\Delta\delta$ is defined as $\delta_{33} - (\delta_{11} + \delta_{22})/2$.
[b] Calulated values from ref. 3.
[c] Calculated values from ref. 4.
[d] From ref. 6.
[e] Solution value from ref. 17.
[f] From ref. 7.

comparison with the PhDBP results and the calculations of Ruiz-Morales and Ziegler (4).

Experimental

The complexes $M(CO)_5PPh_3$ (M = Cr, Mo, W) were prepared by the trimethylamine – N-oxide promoted substitution of the triphenylphosphine on the metal hexacarbonyl (8), and purified by recrystallization from a 2:1 ethanol–chloroform mixture. The trimethylphosphine complexes were prepared by displacement of the bromide ion from the tetraethylammonium bromopentacarbonylmetallate salt (9, 10) using trimethylphosphine – silver iodide adduct as the source of phosphine (11, 12). These complexes were purified by repeated sublimations or by crystallization from hexane solution at –20°C, the isolation of the compounds being complicated by their low melting points and tendency to form oils. Infrared and solution ^{31}P and ^1H nmr spectroscopy were used to confirm the identity and purity of the products by comparison with the literature spectra (5, 13, 14).

CP-MAS nmr spectra were recorded on a Chemagnetics CMX-300 spectrometer operating at 121.279 MHz, using high-power proton decoupling, contact times of 2 ms, and recycle delays of 2–180 s, depending on the complex studied. Samples were packed into 7.5 mm bullet-type zirconia rotors. Different spinning rates, ranging from 0.3 to 2.5 kHz, were used to locate isotropic peaks and the chemical shifts were referenced to 85% H_3PO_4. Line broadenings of between 0 and 25 Hz were applied to the spectra. The spectra were curve-fitted using the program Peakfit (Jandel Scientific) and the chemical shift tensor components were calculated from the spinning side-band intensities using the Herzfeld–Berger Analysis program of Eichele and Wasylishen (15).

Results and discussion

The phosphine complexes of the Group 6 metals are especially easy to study via ^{31}P NMR because, while each metal has nmr-active isotopes, none are present in a natural abundance large enough to seriously complicate the ^{31}P spectra with scalar coupling or quadrupole–dipole effects. The chemical shift tensor values, isotropic chemical shifts, and coupling constants for the six complexes studied are presented in Table 1, together with the calculated shift tensor values (3, 4) and the results reported for the PhDBP and MeDBP complexes (6, 7). The standard deviations in the δ_{ii} values, from the measurements at different spinning rates, were ±2 ppm.

The CP-MAS spectra showed only one chemical shift for all compounds except the trimethylphosphine(pentacarbonyl)molybdenum complex, where two shifts were observed separated by about 2 ppm. This difference is probably due to the presence of two crystallographically nonequivalent phosphorus atoms in the asymmetric unit cell, although the reported X-ray crystal structure (16) indicated only one molecule in the asymmetric unit. Unfortunately,

© 1998 NRC Canada

Fig. 1. ^{31}P CP-MAS spectra of the triphenylphosphine complexes of Group 6 metal pentacarbonyls. Spinning speed: 1600 Hz for all spectra. Asterisks indicate the isotropic shift position.

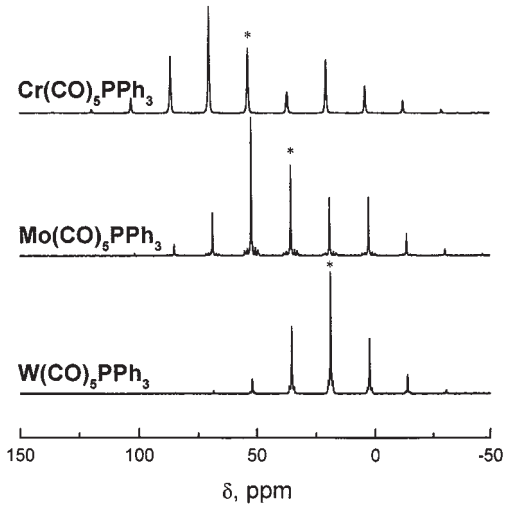

decomposition of the sample prevented the determination of the crystal structure of this polymorph.

The molybdenum and tungsten complexes showed additional splittings due to couplings from the isotopes with spin, ^{95}Mo (15.7%, I = 5/2), ^{97}Mo (9.46%, I = 5/2), and ^{183}W (14.4%, I = 1/2), but no splitting from ^{53}Cr (9.55%, I = 3/2) was observed in the spectra of either of the chromium complexes. The solid state value for ^{1}J(P–W) in the tungsten triphenylphosphine complex was slightly lower than the value in solution (17).

Couplings to quadrupolar nuclei are not always observed in solution state spectra, due to rapid relaxation, but can be observed in solid state spectra under magic-angle-spinning conditions (18). There is an additional line displacement that depends upon the residual dipole–quadrupole coupling interaction, d, given by eq. [1].

$$[1] \qquad d = -(3\chi D'/20\nu_s)(3\cos^2\beta - 1 + \eta \sin^2\beta \cos(2\alpha))$$

where $D' = (D - \Delta J/3)$, D is the dipolar coupling constant, $-(\mu_0/4\pi)\gamma_I\gamma_S h/(2\pi r^3)$, ΔJ is the anisotropy in the spin coupling, χ is the nuclear quadrupole coupling constant, and η is the asymmetry in the electric field gradient. The angles β and α are the polar and azimuthal angles relating the internuclear vector and the principal axes of the electric field gradient. The local symmetry around the metal–phosphorus bond is such that η is assumed to be zero and β and α are taken to be 0° and 90°, respectively, and eq. [1] is much simplified. The two molybdenum isotopes have very similar magnetogyric ratios and, therefore, have spin–spin coupling constants that cannot be easily distinguished, but the nuclear quadrupole moment of ^{97}Mo is much greater, 0.255×10^{-28} m^2 versus -0.022×10^{-28} m^2 for ^{95}Mo, and so, in principle, the second-order splittings can be analysed to give the quadrupole coupling constants and the anisotropy in J. The direct dipole coupling constants, calculated using a bond length of 2.508 Å (16), are –202 and –206 Hz for ^{97}Mo and ^{95}Mo, respectively. The quadrupole coupling constants of triphenylphosphine(pentacarbonyl)molybdenum have been measured (19) to be 1.972 MHz and 22.783 MHz for ^{95}Mo and ^{97}Mo, respectively, and the former is probably negative in sign (20). These values were obtained at 77 K and the room temperature quadrupole coupling constants would be lower in frequency. Thus, neglecting ΔJ and using the low-temperature χ values, the calculated second-order splittings would be –70 and 6.1 Hz for ^{97}Mo and ^{95}Mo, respectively, compared with the experimental values of –55 and 4.5 Hz. The differences could be due to the lower quadrupole coupling constants at high temperature and a finite anisotropy in the spin–spin coupling constant. The splittings in the spectra of the trimethylphosphine complex were not sufficiently well resolved for a full analysis and only the J value could be determined.

The experimentally determined chemical shift tensors for the trimethylphosphine complexes show near-axial symmetry ($\delta_{11} \approx \delta_{22}$), the deviations being attributable to solid state effects, and the values are in quite good agreement with the theoretical predictions (3) if the δ_{11} and δ_{22} values are averaged and compared with the calculated perpendicular component. The lack of agreement for the tungsten complex is not unexpected and was attributed by Kaupp to the neglect of spin-orbit contributions in the calculations (3). The agreement between the observed and calculated shift tensor components confirms the assignment of δ_{33} as lying along the bond direction in both the trimethyl- and triphenylphosphine complexes. The chemical shift tensors of the triphenylphosphine compounds deviate from axial symmetry, in contrast to free triphenylphosphine, which has an axially symmetric chemical shift tensor (21, 22). This asymmetry is attributed to the breakdown in local symmetry caused by the different torsional angles of the phenyl rings. For the chromium and molybdenum complexes, the δ_{22} component shows the largest difference between experimental and calculated values (4) but the spans and shift anisotropies, $\Delta\delta$, are in good agreement.

The influence of the metal atom on the phosphorus chemical shift anisotropy can be clearly seen in Table 1 and Fig. 1. The most noticeable trend is the marked decrease in the spans, $(\delta_{11} - \delta_{33})$, and anisotropies of the chemical shift tensors on moving from chromium to tungsten. This decrease is due almost entirely to changes in δ_{11} and δ_{22}. For example, in the trimethylphosphine complexes, where δ_{11} and δ_{22} change by nearly 70 ppm, δ_{33} varies by only 14 ppm. For the triphenylphosphine series, δ_{11} and δ_{22} decrease by about 20 ppm from Cr to Mo and by about 30 ppm from Mo to W. In contrast, δ_{33} for these complexes remains almost constant at –17 ± 3 ppm. It is this behaviour which results in the increased shielding observed for the solution chemical shift on going from chromium to tungsten. The DFT calculations of the shift tensor components for the series of trimethyl- and triphenylphosphine pentacarbonyl complexes the Group 6 metals showed good agreement with experiment, a result that should encourage further work, both experimental and theoretical.

Wasylishen and co-workers (6, 7) have suggested that the PhDBP ligand is analogous to triphenylphosphine and we are now able to compare the ^{31}P chemical shift tensor components of both ligands when bonded to the Group 6 metal carbonyls, Table 1. The changes in the δ_{ii} values are almost constant (within 5 ppm, and close to the experimental error) regardless of the metal atom; for PhDBP, the δ_{11} value is less

© 1998 NRC Canada

shielded by 23 ppm and the δ_{22} and δ_{33} values more shielded by 30 and 19 ppm, respectively, than in the triphenylphosphine complexes.

Acknowledgements

This work was supported by grants from the Natural Sciences and Engineering Research Council of Canada and from Merck-Frosst. The authors are grateful to Dr Martin Kaupp for helpful discussions and to Drs R.E. Wasylishen and K. Eichele for the HBA program.

References

1. J. Herzfeld and A.E. Berger. J. Chem. Phys. **73,** 6021 (1980).
2. M. Kaupp, V.G. Malkin, and O.L. Malkina. *In* Encyclopedia of computational chemistry. *Edited by* P. v.R. Schleyer. Wiley Interscience, New York. 1997.
3. M. Kaupp. Chem. Ber. **129,** 535 (1996).
4. Y. Ruiz-Morales and T. Ziegler. J. Phys. Chem. A, **102**, 3970 (1998).
5. S.O. Grim, D.A. Wheatland, and W.J. McFarlane. J. Am. Chem. Soc. **89,** 5573 (1967).
6. K. Eichele, R.E. Wasylishen, J.M. Kessler, L. Solujic, and J.H. Nelson. Inorg. Chem. **35**, 3904 (1996).
7. K. Eichele, R.E. Wasylishen, K. Maitra, J.H. Nelson, and J.F. Britten. Inorg. Chem. **36**, 3539 (1997).
8. T.S.A. Hor. Inorg. Chim. Acta, **143,** 3 (1988).
9. E.W. Abel, I.S. Butler, and J.G. Reid. J. Chem. Soc. 2063 (1963).
10. M.J. Wovkulich and J.D. Atwood. Organometallics, **1**, 1316 (1982).
11. J.A. Connor, E.M. Jones, and G.K. McEwen. J. Organomet. Chem. **43**, 357 (1972).
12. K.J. Lee and T.L. Brown. Inorg. Chem. **31,** 289 (1992).
13. M.F. Guns, E.G. Claeys, and G.P. van der Kelen. J. Mol. Struct. **53,** 45 (1973).
14. R. Mathieu, M. Lenzi, and R. Poilblanc. Inorg. Chem. **9,** 2030 (1970).
15. K. Eichele and R.E. Wasylishen. HBA program. Dalhousie University, Halifax, N.S.
16. M.S. Davies, R.K. Pierans, and M.J. Aroney. J. Organomet. Chem. **458**, 141 (1993); M.S. Davies, M.J. Aroney, I.E. Buys, T.W. Hambley, and J.L. Calvert. Inorg. Chem. **34**, 330 (1995).
17. R.L. Keiter and D.G. Vander Velde. J. Organomet. Chem. **258**, C34 (1983).
18. R.K. Harris and A.C. Olivieri. Prog. NMR Spectrosc. **24**, 435 (1992).
19. J.D. Blumer, C.P. Cheng, and T.L. Brown. Chem. Phys. Lett. **51**, 473 (1977).
20. K. Eichele, R.E. Wasylishen, and J.H. Nelson. J. Phys. Chem. A, **101**, 5463 (1997).
21. G.H. Penner and R.E. Wasylishen. Can. J. Chem. **67**, 1909 (1989).
22. Y. Huang, H.L. Uhm, D.F.R. Gilson, and I.S. Butler. Inorg. Chem. **36**, 435 (1997).

© 1998 NRC Canada

Ketonization of (*Z*)-2-methoxy-1,2-diphenylvinyl alcohol. Quantitative evaluation of the remarkable kinetic stability of this enol

E.A. Jefferson, A.J. Kresge, L. Matthew, and Z. Wu

Abstract: Rates of ketonization of (*Z*)-2-methoxy-1,2-diphenylvinyl alcohol were measured in aqueous perchloric acid and sodium hydroxide solutions as well as in formic acid and ammonium ion buffers, and the results were used to construct a rate profile for this reaction. These data show this substance to be a remarkably stable enol with a lifetime of 3.6 h at the bottom of its rate profile and a hydrogen ion catalytic coefficient 660 000 times less than that for the enol of acetophenone. Comparison with simple models allows partition of this rate factor into a 440-fold retardation for the β-phenyl substituent and a 1500-fold retardation for the β-methoxy substituent. A global rate of enolization of the keto isomer producing both *Z* and *E* enol isomers was also measured, and this leads to $pK_E > 5.4$ as the lower limit of the keto–enol equilibrium constant for the *Z* enol. This result could be dissected into an enol-content enhancing effect of $\delta\ pK_E = 3.2$ for the β-phenyl group and a surprising enol-content diminishing effect of $\delta\ pK_E > 0.6$ for the β-methoxy group.

Key words: enol ketonization, enol stability, keto–enol equilibrium, β-phenyl and β-methoxy substituent effects in keto–enol systems.

Résumé : Opérant en solutions aqueuses d'acide perchlorique et d'hydroxyde de sodium ainsi que dans l'acide formique et des tampons d'ion ammonium, on a mesuré les vitesses de cétonisation de l'alcool (*Z*)-2-méthoxy-1,2-diphénylvinylique et on a utilisé les résultats pour édifier un profil de vitesses de cette réaction. Ces données montrent que cette substance est un énol remarquablement stable dont le temps de vie est de 3,6 h au fond de son profil de vitesse et pour lequel le coefficient catalytique de l'ion hydrogène est 660 000 fois plus faible que dans le cas de l'énol de l'acétophénone. Une comparaison avec des modèles simples permet de diviser ce facteur de vitesse en un facteur retardant de 440 attribuable au substituant phényle en β et un facteur retardant de 1500 pour le substituant β-méthoxy. On a aussi mesuré une vitesse globale d'énolisation de l'isomère cétonique conduisant aux isomères *E* et *Z* de l'énol; elle permet d'établir à 5,4 la valeur inférieure limite du pK_E de la constante d'équilibre céto–énolique de l'énol *Z*. On peut disséquer ce résultat en un effet, $\delta\ pK_E > 0{,}6$ du groupe β-méthoxy, qui d'une façon surprenant diminue le contenu en énol.

Mots clés : cétonisation d'un énol, stabilité d'un énol, équilibre céto–énolique, effets des substituants β-phényle et β-méthoxy sur les systèmes céto–énoliques.

[Traduit par la Rédaction]

Most thermodynamically unstable enols are also unstable kinetically and cannot be isolated, let alone characterized by standard methods commonly used for stable substances. A notable exception is (*Z*)-2-methoxy-1,2-diphenylvinyl alcohol, **1**, which reverts to its more stable keto isomer, 2-methoxy-1,2-diphenylethanone, **2**, eq. [1], so slowly that its structure could even be determined by X-ray crystallography (1).

[1]

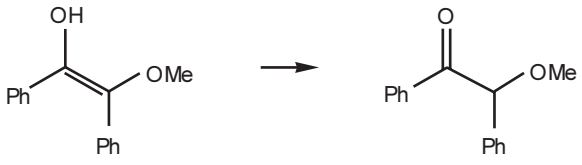

1 **2**

This enol was prepared (1) by treating 1,2-diphenyldiazoethanone, **3**, with sulfuric acid in methanol solution. Under these conditions, solvolysis of the diazo compound occurred through rapid pre-equilibrium protonation on carbonyl oxygen followed by rate-determining loss of nitrogen, eq. [2]; this generated a vinyl cation, **4**, which was captured by solvent on its less hindered side to give the methoxy enol, **1**, eq. [3].

Received May 12, 1998.

E.A. Jefferson, A.J. Kresge,[1] L. Matthew, and Z. Wu. Department of Chemistry, University of Toronto, Toronto, ON M5S 3H6, Canada.

[1]Author to whom correspondence may be addressed. Telephone: (416) 978–7259. Fax: (416) 978–7259. E-mail: akresge@chem.utoronto.ca

© 1998 NRC Canada

[2] 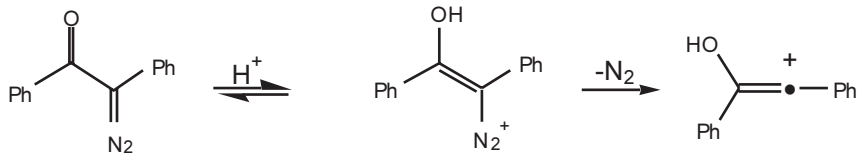

3 4

[3] 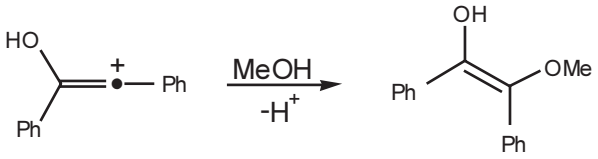

4 1

Cooling the reaction mixture caused the enol to separate in crystalline form, and this solid was then characterized by its spectra and reactions in the usual way, and its *cis*-phenyl geometry was established by X-ray diffraction.[2]

To provide a quantitative assessment of the remarkable stability of this enol we have measured rates of its ketonization in aqueous solution and have used the results to construct a reaction rate profile. We have also measured rates of enolization of the keto isomer, **2**, in order to obtain an estimate of the keto–enol equilibrium constant for this system.

Experimental section

Materials

1,2-Diphenyldiazoethanone was prepared by mercuric oxide oxidation of benzil hydrazone (3). All other materials were best available commercial grades.

Kinetics, ketonization

Rates of ketonization of (*Z*)-2-methoxy-1,2-diphenylvinyl alcohol were measured by monitoring the increase in product ketone absorbance at λ = 250 nm using a Cary 2200 spectrometer with sample compartment thermostatted at 25.0 ± 0.05°C. Reactions were initiated by adding aliquots of methanol stock solution of enol to reaction media that had come to temperature equilibrium with the spectrometer cell compartment. The enol stock solutions were made just before use by allowing 1,2-diphenyldiazoethanone to solvolyze at room temperature in methanol containing 0.1 M perchloric acid. It was found that 12 min was the optimum time for this solvolysis to take place: enol formation was nearly complete but subsequent ketonization of the enol, which was ca. 20 times slower under these conditions, had not yet occurred to any appreciable extent. Five μL aliquots of these freshly prepared enol stock solutions were then added to 3.0 mL portions of reaction media; final concentrations of enol in the solutions upon which the kinetic measurements were made were ca. 3×10^{-5} M. The enol is easily oxidized by atmospheric oxygen (1), and all solutions were therefore purged with argon. Ionic strength was maintained at 0.10 M by adding sodium perchlorate as required. The kinetic data fit the first-order rate law well, and observed first-order rate constants were obtained by least-squares fitting of an exponential function.

Kinetics, enolization

Rates of enolization of 2-methoxy-1,2-diphenylethanone were measured in aqueous sodium hydroxide solutions by using bromine to scavenge the enol as it formed. In basic solutions, bromine reacts with hydroxide ion according to eq. [4] and consequently exists as hypobromite ion; reactions were therefore followed by monitoring the absorbance of this ion at λ = 330 nm.

[4] $$Br_2 + 2HO^- \rightarrow BrO^- + H_2O + Br^-$$

Measurements were made with a Cary 2200 spectrometer whose cell compartment was thermostatted at 25.0 ± 0.05°C. In a typical experiment, 20 μL of saturated aqueous bromine solution was added to 10 mL of sodium hydroxide solution, whose ionic strength had been adjusted to 0.10 M by adding sodium bromide as required. Each of two 3.0 mL quartz cuvettes was then filled with this solution, and the absorbance of one was recorded at λ = 330 nm; this reading was later employed to calculate the hypobromite ion concentration, using ε_{330} = 300 M^{-1} cm^{-1} (4), in order to convert stoichiometric into actual sodium hydroxide concentrations according to the relationship of eq. [4]. The second cuvette was then placed in the reference compartment of the spectrometer and bromination was initiated by adding 5 μL of an acetonitrile stock solution of ketone to the first cuvette. Such double-beam operation minimized base-line drifting, which was prevalent without the use of a reference sample. Ketone concentrations in the reaction solutions were 4×10^{-4} M, and hypobromite concentrations were 1×10^{-3} M. The kinetic data conformed to the first-order rate law well, and observed first-order rate constants were obtained by least-squares fitting of an exponential function.

Results

Ketonization

Rates of ketonization of 2-methoxy-1,2-diphenylvinyl alcohol were measured in aqueous perchloric acid solutions at 10 different concentrations over the range $[HClO_4]$ = 0.001–0.1 M and in aqueous sodium hydroxide solutions at seven different concentrations over the range [NaOH] = 0.0005–0.05 M. Replicate measurements were made at each concentration. The data so obtained have been deposited and are summarized in Tables S1 and S2.[3]

[2] Sterically hindered enols for which access to the vinyl group is inhibited by bulky substituents are also remarkably stable (2).

[3] Tables S1–S4 may be purchased from: The Depository of Unpublished Data, Document Delivery, CISTI, National Research Council of Canada, Ottawa, Canada, K1A 0S2.

© 1998 NRC Canada

Fig. 1. Rate profile for the ketonization of 2-methoxy-1,2-diphenylvinyl alcohol in aqueous solution at 25°C.

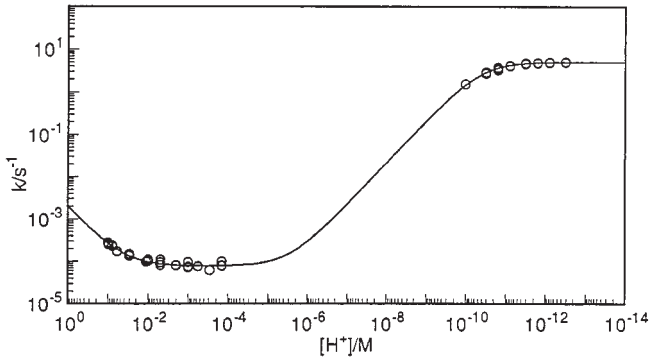

Rates of ketonization of 2-methoxy-1,2-diphenylvinyl alcohol were also measured in formic acid and ammonium ion buffers. Series of buffer solutions of constant buffer ratio and constant ionic strength (0.10 M), and therefore constant hydrogen ion concentration, but different buffer concentrations were used. Buffer concentrations were varied by a factor of five, and replicate measurements were made at each concentration. The data so obtained are summarized in Table S3 of the depository.[3]

Observed first-order rate constants measured in these buffer solutions proved to be accurately proportional to buffer concentration, and the data were therefore analyzed by least-squares fitting of eq. [5].

$$[5] \qquad k_{obs} = k_o + k_{cat}[\text{buffer}]$$

The zero-buffer-concentration intercepts, k_o, obtained in this way were then used, together with the rate constants measured in perchloric acid and sodium hydroxide solutions, to construct the rate profile shown in Fig. 1. Hydrogen ion concentrations of the buffer solutions needed for this purpose were obtained by calculation, using literature values of the buffer acid dissociation constants and activity coefficients recommended by Bates (5).

Rate profiles such as that of Fig. 1 are a characteristic feature of enol ketonization reactions (6). They reflect a reaction mechanism consisting of rate-determining protonation on β-carbon of either the enol or the enolate ion, as shown in eq. [6].

[6]

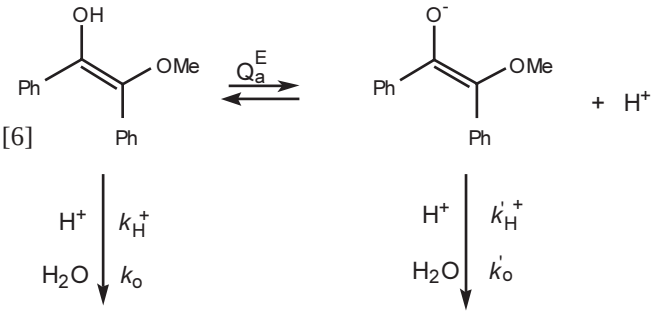

The acid-catalyzed portion at the extreme left of the profile represents carbon protonation of the enol by hydrogen ion,

Fig. 2. Relationship between hydroxide ion concentration and observed rate constants for the enolization of 2-methoxy-1,2-diphenylethanone in aqueous solution at 25°C.

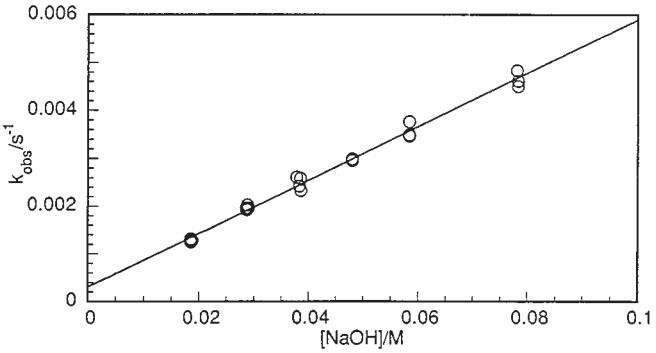

and the uncatalyzed portion adjoining that represents either protonation of enol by solvent water or ionization of enol to the much more reactive enolate ion followed by carbon protonation of that by hydrogen ion. Following this uncatalyzed region is a segment of apparent hydroxide ion catalysis produced by ionization of enol to enolate followed by carbon protonation of that by water, and saturation of this catalysis, which occurs when the position of the ionization equilibrium shifts from enol to enolate, gives the second uncatalyzed region at the very right of the profile.

The rate law that describes this reaction scheme is shown in eq. [7],

$$[7] \qquad K_{obs} = k_{H^+}[H^+] + k_{UC} + k'_o\, Q_a^E/(Q_a^E + [H^+])$$

whose symbols are defined by eq. [5] with k_{UC} = either k_o or $k'_{H^+}\, Q_a^E$. Least-squares fitting of this expression gave the following results: k_{H^+} = (1.89 ± 0.06) × 10^{-3} M^{-1} s^{-1}, k_{UC} = (7.71 ± 0.13) × 10^{-5} s^{-1}, k'_o = (4.99 ± 0.10) s^{-1}, and Q_a^E = (4.22 ± 0.34) × 10^{-11} M, pQ_a^E = 10.38 ± 0.04.[4]

Enolization

Rates of enolization of 2-methoxy-1,2-diphenylethanone were measured in aqueous sodium hydroxide solutions at six different concentrations over the range [NaOH] = 0.02–0.08 M. Replicate measurements were made at each concentration. The data so obtained are summarized in Table S4 of the depository.[3]

Observed first-order rate constants determined in these solutions proved to be accurately proportional to sodium hydroxide concentration (see Fig. 2), and linear least-squares analysis gave k_{HO^-} = (5.59 ± 0.12) × 10^{-2} as the hydroxide ion catalytic coefficient for the enolization reaction.

Discussion

Reaction identification

2-Methoxy-1,2-diphenylvinyl alcohol is a vinyl ether as well as an enol, and, in view of the fact that vinyl ethers are subject to facile acid-catalyzed hydrolysis (7), this substance might have undergone that reaction, as shown in eq. [8], rather than the intended ketonization. It is known, however, that acid-catalyzed ketonization of enols is at least an order

[4] This acidity constant is a concentration quotient applicable at ionic strength equal to 0.10 M.

© 1998 NRC Canada

[8] 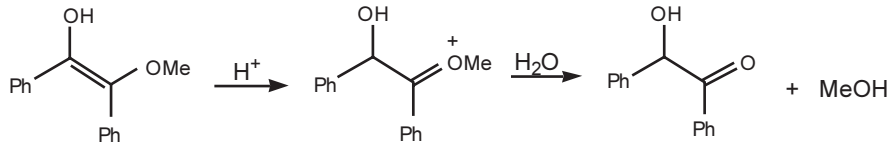

[9] 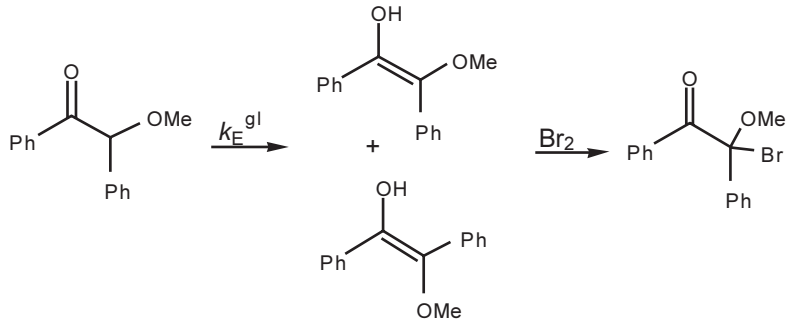

[10] 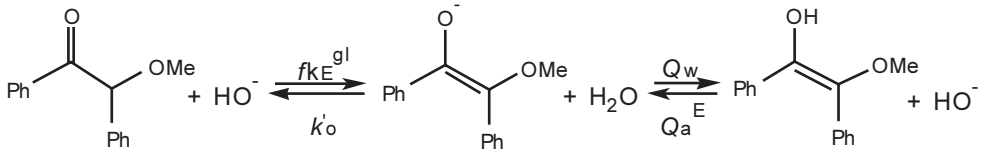

of magnitude more rapid than the hydrolysis of the corresponding methyl vinyl ethers (6). The ketonization of enols, moreover, is strongly catalyzed by bases as well as by acids, whereas the hydrolysis of vinyl ethers is catalyzed only by acids. This, plus the fact that 2-methoxy-1,2-diphenylethanone, **2**, is the only product formed (1), would appear to make it safe to conclude that the process under observation here is in fact the intended ketonization reaction.

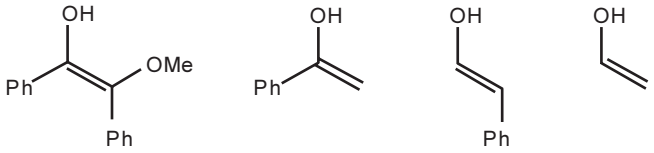

1 **5** **6** **7**

Reactivity

The lifetime of 2-methoxy-1,2-diphenylvinyl alcohol, **1**, at the bottom of its rate profile (Fig. 1) is $\tau = 3.6$ h. This contrasts sharply with the lifetime of the enol of acetophenone, **5**, in the corresponding region, $\tau = 6$ s (8), and shows that the additional β-methoxy and β-phenyl substituents in **1** have a very strong stabilizing effect.

Because the ketonization of enols at the bottom of their rate profiles can occur by either of two mechanisms (vide supra), a better assessment of the β-methoxy and β-phenyl group effects may be made using rate constants from a different region of the profile. Use of the acid-catalyzed region, moreover, allows comparison with vinyl ether hydrolysis; this is useful because acid catalysis of both ketonization and vinyl ether hydrolysis occurs by the same reaction mechanism, i.e., simple rate-determining proton transfer to the substrates's β-carbon atom. Combination of $k_{H^+} = 1.25 \times 10^3$ M^{-1} s^{-1} for acetophenone enol (9) with the presently determined value for 2-methoxy-1,2-diphenylvinyl alcohol then gives a rate factor of 660 000, which is equivalent to a difference in free energy of activation of $\delta\Delta G^{\ddagger} = 7.9$ kcal mol^{-1}.

This rate factor may be separated into effects of β-phenyl and β-methoxy by using rates of ketonization of the *trans*-enol of phenylacetaldehyde, **6**, $k_{H^+} = 7.45 \times 10^{-2}$ M^{-1} s^{-1} (10), and of vinyl alcohol, **7**, $k_{H^+} = 3.30 \times 10^1$ M^{-1} s^{-1} (11), to estimate retardation by a β-phenyl group. The result, a factor of 440, then leaves 1500 as the β-methoxy group effect. Similarly large rate retardations by β-phenyl and β-methoxy groups occur in vinyl ether hyrolysis; for example, k_{H^+} for *trans*-β-methoxystyrene (12), **8**, is 1100 times less than that for methyl vinyl ether (13), **9**, and k_{H^+} for *cis*-1,2-dimethoxyethene (14), **10**, is 13 000 times less than that for methyl vinyl ether. These retardations in rates of vinyl ether hydrolysis are believed to be the result of initial-state free-energy lowering by the well-known double-bond stabilizing effects of phenyl and methoxyl groups (15), which are partially lost in the reactions' transition states. A similar explanation can be advanced for the effect of these groups on enol ketonization reactions, and the greater velocities of the ketonizations over the vinyl ether hydrolyses, and their consequent earlier and more reactant-like transition states, can be invoked to rationalize the somewhat smaller size of the effects in ketonization than in vinyl ether hydrolysis.

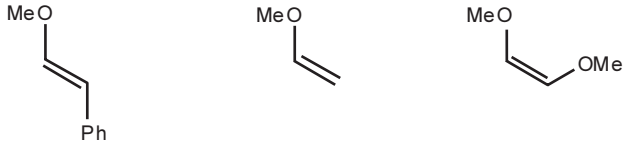

8 **9** **10**

Keto–enol equilibrium

Keto–enol equilibrium constants have traditionally been determined by the halogen titration method invented nearly

© 1998 NRC Canada

a century ago (16). This method, unfortunately, fails when enol contents are as low as is commonly the case for simple aldehydes and ketones (17), and in that situation it is useful to employ a kinetic method where the keto–enol equilibrium constant is determined as the ratio of enolization to ketonization rate constants: $K_E = k_E/k_K$.

The presently determined ketonization rate constants, of course, refer only to the *Z* enol isomer, but the enolization rate constants are global values referring to the production of both *Z* and *E* enols, as shown in eq. [9]. Simply taking the ratio of the enolization to ketonization rate constants determined here will therefore not produce a proper keto–enol equilibrium constant: the global rate constants should be separated into values for production of the individual isomers, but that cannot be done because the method of analysis used, bromination, does not distinguish between the isomers. A simple ratio of presently determined rate constants does, however, provide an upper limit to K_E for the *Z* isomer, and that is enough to produce an interesting result.

The keto–enol equilibrium involving the *Z* isomer promoted by hydroxide ion may be represented as shown in eq. [10], and the equilibrium constant for this representation is given by eq. [11].

$$[11] \qquad K_E = \frac{f k_E^{gl}}{k'_o} \frac{Q_w}{Q_a^E}$$

In the latter expression, *f* is the (unknown) fraction of the global enolization rate constant, k_E^{gl}, that refers to production of the *Z* isomer only, Q_w is the autoprotolysis constant of water, and the remaining symbols are as defined by eq. [6]. Insertion of numerical values into this expression then leads to $K_E = (f)\ (4.22 \times 10^{-6})$. Since *f* is a fraction less than one, K_E must be less than 4.22×10^{-6} with $pK_E > 5.38$ as a lower limit.

Comparison of this result with $pK_E = 7.96$ for acetophenone (18) shows that β-phenyl and β-methoxy substituents introduced together increase enol content, and since $pK_E = 5.38$ is a lower limit, the combined effect of these groups can be no greater than 7.96 – 5.38 = 2.58 p*K* units. The effect of a β-phenyl substituent introduced alone may be estimated as $\delta\Delta pK_E = 3.16$, by comparing $pK_E = 3.07$ for the *trans*-enol of phenylacetaldehyde, (10), **6**, with $pK_E = 6.23$ for acetaldehyde (11), **7**. This difference is greater than the upper limit of 2.58 p*K* units estimated above for the combined effect of β-phenyl and β-methoxy substituents, which means that the effect of β-methoxy alone must be in the opposite direction, i.e., the effect of this group must be to lower rather than to raise enol content, and its magnitude must be greater than 3.16 – 2.58 = 0.58 p*K* units.

This is a surprising result. It implies that β-methoxy substituents destabilize enols thermodynamically,[5] in contrast to the kinetic stabilization shown by their marked retarding effect on rates of enol ketonization (vide supra). It is possible, however, that the various comparisons made leading to this result are not entirely valid, inasmuch as they were made using models containing only single phenyl substituents in which steric crowding interfered little, if at all, with substituent-functional group interaction. The enol investigated, 2-methoxy-1,2-diphenylvinyl alcohol, on the other hand, is a sterically congested molecule, as shown by the fact that its phenyl groups are twisted out of the vinyl plane by some 47° (1).

Acknowledgement

We are grateful to the Natural Sciences and Engineering Research Council of Canada for financial support of this work.

References

1. J.F. McGarrity, A. Cretton, A.A. Pinkerton, D. Schwarzenbazch, and H.D. Flack. Angew. Chem. Int. Ed. Engl. **22**, 405 (1983); Angew. Chem. Suppl. 551 (1983).
2. H. Hart, Z. Rappoport, and S.E. Biali. *In* The chemistry of enols. *Edited by* Z. Rappoport. John Wiley & Sons, New York. 1990. Chap. 8.
3. C.D. Nenitzescu and E. Solomonica. Org. Synth. Coll. Vol. 2, 496 (1943).
4. J.R. Jones. Trans. Faraday Soc. **61**, 95 (1965).
5. R.G. Bates. Determination of pH theory and practice. John Wiley and Sons, New York. 1973. p. 49.
6. J.R. Keeffe and A.J. Kresge. *In* The chemistry of enols. *Edited by* Z. Rappoport. John Wiley & Sons, New York. 1990. Chap. 7.
7. A.J. Kresge. Acc. Chem. Res. **20**, 364 (1987).
8. Y. Chiang, A.J. Kresge, J.A. Santaballa, and J. Wirz. J. Am. Chem. Soc. **110**, 5506 (1988).
9. Y. Chiang, A.J. Kresge, and J. Wirz. J. Am. Chem. Soc. **106**, 6392 (1984).
10. Y. Chiang, A.J. Kresge, P.A. Walsh, and Y. Yin. J. Chem. Soc. Chem. Commun. 869 (1989).
11. Y. Chiang, M. Hojatti, J.R. Keeffe, A.J. Kresge, N.P. Schepp, and J. Wirz. J. Am. Chem. Soc. **109**, 4000 (1987).
12. Y. Chiang, A.J. Kresge, and C.I. Young. Can. J. Chem. **56**, 461 (1978).
13. A.J. Kresge, D.S. Sagatys, and H.L. Chen. J. Am. Chem. Soc. **99**, 7228 (1977).
14. A.J. Kresge and M. Leibovitch. J. Org. Chem. **55**, 5234 (1990).
15. J. Hine. Structural effects on equilibria in organic chemistry. John Wiley & Sons, New York. 1975. pp. 270–276.
16. K. Meyer. Justus Liebigs Ann. Chem. **380**, 212 (1911).
17. J.R. Keeffe, A.J. Kresge, and N.P. Schepp. J. Am. Chem. Soc. **112**, 4862 (1990).
18. J.R. Keeffe, A.J. Kresge, and J. Toullec. Can. J. Chem. **64**, 1224 (1986).

[5] It is likely that β-substituents influence the position of keto–enol equilibria largely by altering the energy of the enol rather than that of the keto isomer, because in the enol the substituent is placed directly on the functional group, whereas in the keto isomer it is insulated from the functional group by a saturated carbon atom.

© 1998 NRC Canada

Structure reassignment of the major isomer from the Diels–Alder reaction of acryloyl chloride and 4,5,6,6a-tetrahydropentalene

M. Parvez, A. Rauk, T.S. Sorensen, and F. Sun

Abstract: After hydrogenation and hydrolysis, the two adducts formed from the Diels–Alder reaction of acryloyl chloride and 4,5,6,6a-tetrahydropentalene were originally assigned 7-*exo*- and 7-*endo*-carboxylic acid structures **3** and **4**. Based on unexpected results in using these acids as starting materials for a superacid carbocation study, a reinvestigation of these structural assignments was carried out. From an extensive series of 2D NMR experiments, we conclude that **4** is correctly assigned, but that the other isomer is the 9-*endo* carboxylic acid **8**. The formation of these two isomers (out of eight possible modes of addition) can be rationalized. Finally, an X-ray study of **8** was carried out as a final proof of structure.

Key words: Diels–Alder reaction, facial selectivity, regioselectivity, X-ray structure, MO calculation.

Résumé : La réaction de Diels–Alder entre le chlorure d'acryloyle et le 4,5,6,6a-tétrahydropentalène conduit à deux adduits; on a originalement attribué les structures **3** et **4**, acides carboxyliques 7-*exo* et 7-*endo*-, aux produits obtenus après hydrogénation et hydrolyse. En se basant sur des résultats inattendus obtenus lorsque nous avons essayé d'utiliser ces acides comme produits de départ pour une étude de carbocations obtenus à l'aide de superacides, on a réexaminé les attributions de structure faites originalement. Après une série extensive d'études RMN en 2D, on en conclut que la structure **4** a été attribuée correctement, mais que l'autre isomère est plutôt l'acide carboxylique 9-*endo*, **8**. On peut rationaliser la formation de ces deux isomères (parmi les huit modes possibles d'addition). Enfin, comme preuve finale de sa structure, on a effectué une étude par diffraction des rayons X du composé **8**.

Mots clés : réaction de Diels–Alder, sélectivité faciale, régiosélectivité, structure par diffraction des rayons X, calculs d'OM.

[Traduit par la Rédaction]

Introduction

Acryloyl chloride **1** and the tetrahydropentalene **2** undergo a low temperature (–30°C) Diels–Alder (D–A) reaction in which, after hydrolysis of the acid chloride and hydrogenation of the double bond, two isomeric carboxylic acid adducts were obtained in a ratio of about 2:1 (eq. [1]) (1). Other dienophiles have also been used with **2** or related dihydropentalenes (2–5).

In the experimental procedure communicated by Holm,[2] the major and minor adducts were assigned to an *exo–endo* pair of 7-COOH epimers **3** and **4**, and then the carboxyl group was replaced with hydrogen, and a single hydrocarbon was formed from the mixture. Our interest in this tricyclic skeleton was concerned with mechanistic studies of the "adamantaneland" rearrangements (as were Holm and coworkers (1)) but we were directly studying the carbocations

[1]

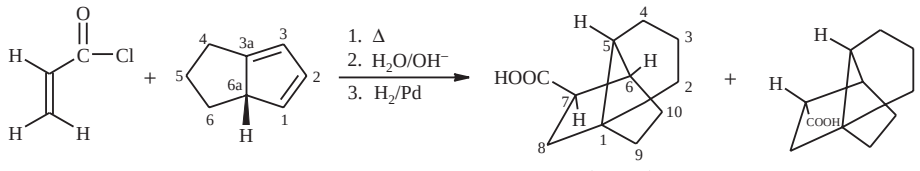

1 **2** **3** (major) **4** (minor)

Received March 9, 1998.

M. Parvez, A. Rauk, T.S. Sorensen,[1] and F. Sun. The Department of Chemistry, University of Calgary, Calgary, AB T2N 1N4, Canada.

[1]Author to whom correspondence may be addressed. Telephone: (403) 220-5361. Fax: (403) 289-9488. E-mail: sorensen@acs.ucalgary.ca

[2]K. Holm, University of Oslo, Norway. Privately communicated experimental procedure for reactions presented in ref. 1.

 © 1998 NRC Canada

involved, rather than focusing on the hydrocarbons themselves. Cation **5** was expected to be a key structure in the overall rearrangement of the tetrahydrodicyclopentadiene skeleton into adamantane. The hydride shift **6** → **5** in the already high-energy intermediate **6** was in fact a prime candidate for the "watershed" transition state on the overall potential energy surface. The generation of cation **6** under non-steady-state conditions was expected to produce only **7** as the observable species, while **5** proceeded along the pathway towards the 1-adamantyl cation (6). Our intent therefore was to prepare a suitable precursor of cation **5** to try and verify the above postulate. In this course of this work it became necessary to reassign the structure of **3**, which is the subject of this paper.

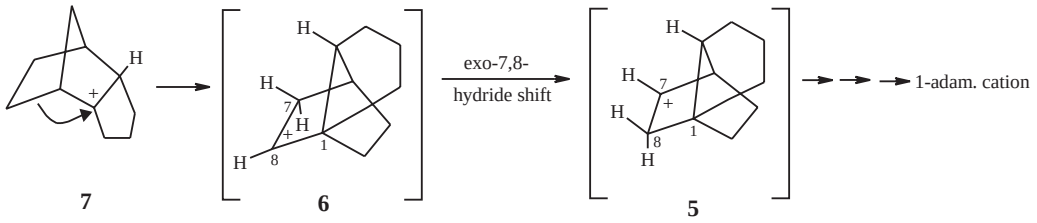

7 6 5

Results and discussion

Based on the original assignments for **3** – **4**, a modified Hunsdiecker reaction was performed on the mixture of **3** and **4**, obtaining two chlorides in approximately the same ratios as for **3** – **4**, and assignable as a C7 *exo–endo* mixture (6). When this chloride mixture was added to the superacid SbF_5/SO_2ClF, the transient cation **5** was expected to be formed and, as explained in the Introduction, this was expected to proceed toward the 1-adamantyl cation. To our surprise we obtained a mixture of two cations, which included the one expected for the forward rearrangement process. However, the major cation was **7**. This result led us to reconsider the structure assignments shown for **3** and **4**, and by implication the structures of the original Diels–Alder adducts.

From the binary acid mixture, a sample of the pure major isomer can be readily obtained by crystallization. Analysis of the minor isomer was carried out on a mixed sample enriched in this acid.

NMR analysis of the major and minor carboxylic acid isomers

At first glance the original assignment as **3** seems compatible with the d,d,d pattern for the $>C<^{COOH}_{H}$ peak (coupling to *exo* and *endo* H8 and to H6). The same proton in the minor isomer is even more complex, again consistent with an extra W coupling to *exo* H10 in the assignment **4**. Furthermore, the chemical shift of H7 in each isomer is quite consistent with expectations for the **3** – **4** structures, δ 2.74 in the major isomer, 3.26 in the minor, this ca. 0.5 ppm difference being typical for *exo* and *endo* hydrogens in a norbornyl-type skeleton, with the *endo* H at higher field.

Only when one looks in detail at the coupling interactions of the $>C<^{H}_{COOH}$ hydrogen in the major isomer does one find fatal inconsistencies with structure **3**. Three of the ten skeletal ^{13}C peaks are CH, and a HETCOR 2-D spectrum locates the three ^1H peaks, which except for $>C<^{H}_{COOH}$ are located in overlapped regions. The COSY spectrum locates the hydrogens coupling to $>C<^{H}_{COOH}$ (which are again in overlapped regions) and one can clearly deduce that a methine hydrogen is not one of these coupling hydrogens, as would be required for structure **3**.

There are eight possible Diels–Alder adducts from the reaction of **1** and **2**, and eight possible hydrogenated products. The -COOH group can be located at C7, C8, C9, or C10, and can be either *exo* or *endo* in each case. If the -COOH is located at C10, one has the same inconsistent coupling behavior as with a C7 location, i.e., expected (but not observed) coupling between H-10 and H-6. This puts the -COOH group at C8 or C9, and requires an *endo* -COOH position so that the $>C<^{H}_{COOH}$ hydrogen will have two vicinal and one W couplings. Finally, the C9 position (structure **8**) became favored because of a NOESY cross-peak between H5 and hydrogens on C7 and C8, and another NOESY interaction between H9 and a proton assigned by HETCOR and COSY spectra as one of H2 or H3.

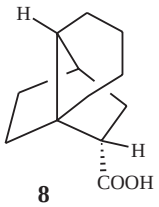

8

Analysis of the minor carboxylic acid isomer using HETCOR, COSY, HMBC, and NOESY spectra led to the conclusion that structure **4** was correct for this compound. In particular, a NOESY interaction between the $>C<^{H}_{COOH}$ hydrogen and the bridgehead H5 hydrogen placed the -COOH group in an *endo* position at C7 or C8. However, a C8 placement would lead to only three coupling interactions for the $>C<^{H}_{COOH}$ hydrogen, in conflict with the experimental spectrum.

The assignment of structure for the major isomer was subsequently verified by means of a single crystal X-ray diffraction study. Compound **8** crystallizes in a primitive tetragonal cell of space group $P4_2/n$ (no. 86). A total of 1888 unique reflections were collected and the structure was solved by direct methods (*R*-factor of 4.4%). There are eight molecules of **8** in the unit cell, arranged as four hydrogen-bonded dimers. The packing diagram is shown in Fig. 1. An ORTEP

© 1998 NRC Canada

plot of a single molecule is shown in Fig. 2. Details concerning the X-ray structure are provided as supplementary material.[3]

There have been two previous X-ray studies involving a substituted tricyclo[4.2.2.0^{1,5}] decane ring system (8, 9).

It should be mentioned that carbocation **9**, expected from a C9 chloride (via **8**), would rearrange rapidly to cation **7**, and so the mystery of how **7** was being formed in our initial experiments is now explained. Furthermore, since all of the possible Diels–Alder adducts of **1** and **2** (eight possible isomers) have the tricyclo[4.2.2.0^{1,5}] decane framework, the results of ref. 1 are easily accounted for.

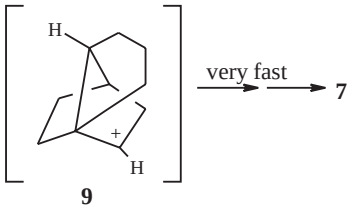

9

It is interesting to compare the contrasting diene–dienophile geometries that lead to the two D–A adducts. These are shown below:

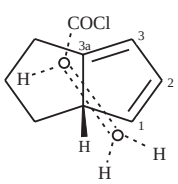

A (major)

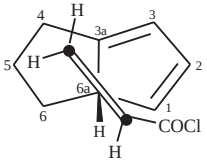

B (minor)

Molecular orbital calculations (B3LYP/6-31G*) of **2** result in a geometry where the diene part is very close to planar. However, the C3a—C4 bond is not colinear with the diene unit, leading to a somewhat curved overall geometry, with the C6a hydrogen on the convex surface.

The LUMO orbital of an acrylic dienophile is well known to have the larger coefficient on the terminal $=CH_2$ carbon, and the initial bonding interaction with the diene should be stronger at this centre (9). Experimentally, there is only a very small preference for the **A** transition state but the choice of only these two geometries (**A** and **B**) can be rationalized by noting that the C3a centre is already slightly sp^3 hybridized (4-3a-6a-1 dihedral angle of –162.6°) and to complete this rehybridization, one requires the dienophile addition geometry as shown in **B**. Conversely, dienophile addition from the concave surface of the diene could be disfavored at C3a by this same geometry. A careful examination of the HOMO p_z orbital on C3a shows that this orbital is not much affected by the ring distortion, but the concave-side lobe is very marginally smaller than the convex surface counterpart, so that both steric and orbital overlap considerations may disfavor C3a.

Fig. 1. Packing diagram for crystalline **8**. Note the existence of four hydrogen-bonded dimers in each unit cell.

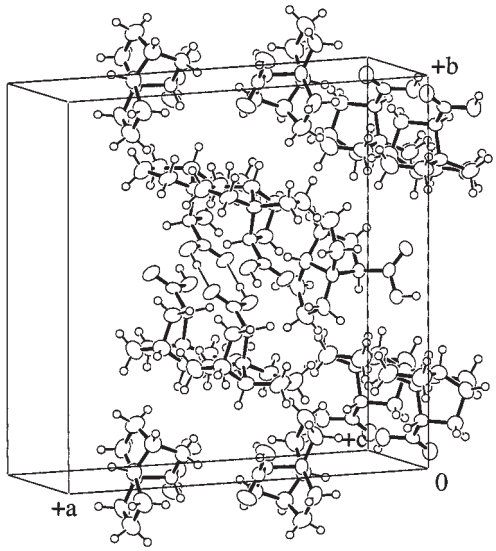

This analysis does not of course explain why one gets this almost equal bifacial attack, but given the latter, the regiochemical choices of **A** and **B** seem reasonable. A recent theoretical study by Poirier, Burnell, and co-workers (10) on the facial selectivity of D–A reactions involving 5-substituted cyclopentadienes found 20% *syn*, 80% *anti* for the 5-methylcyclopentadiene case, a compound bearing some resemblance to **2**. Using this model, transition state **A** would be equivalent to *syn* attack.

The *endo* geometry in both **A** and **B** transition states is a normal expectation, contrary to the situation that existed in the structure originally assigned for **8**, i.e., **3**.

Experimental

NMR spectra were obtained on a Bruker AM-400 spectrometer. Carbon multiplicities were determined from DEPT 135 spectra. ^1H–^{13}C correlations were obtained from normal HETCOR. Longer range correlations were made using the inverse HMBC method. Proton–proton coupled networks were determined from COSY or long-range COSY 2D spectra. NOESY 2D spectra were used to assign NOE-related protons.

The preparation of the acids **8** and **4** has been reported, as has the purification of **8** by recrystallization (1). For **8**, ^1H NMR (400 MHz, $CDCl_3$), δ: 2.74 (d,d,d, H9), 2.4–2.15 (2H, H3), 2.1–1.95 (5H, complex, H7, H5, H10, H4, H6), 1.97–1.87 (1H, H10), 1.78–1.68 (d,d,d, 1H, H7), 1.57–1.42 (3H, complex, H2, *endo*-H8, H4), 1.4–1.23 (2H, complex, H2, *exo*-H8). ^{13}C NMR (100 MHz, $CDCl_3$), δ: 182.0 (C=O),

[3] A complete set of atomic coordinates and *B*iso/*B*eq values, anisotropic displacement factors, bond lengths, bond angles, torsion angles, and complete experimental details can be purchased from: The Depository of Unpublished Data, Document Delivery, CISTI, National Research Council Canada, Ottawa, Canada K1A 0S2. Structure factor listings are no longer being deposited and may be obtained on request from the author. Tables of atomic coordinates and bond lengths and angles have also been deposited with the Cambridge Crystallographic Data Centre and can be obtained on request from: The Director, Cambridge Crystallographic Data Centre, University Chemical Laboratory, 12 Union Road, Cambridge, CB2 1EZ, U.K.

© 1998 NRC Canada

63.9 (q, C1), 63.2 (C5), 47.0 (C9), 36.8 (C7), 36.2 (C6), 30.8 (C10), 29.8 (C3), 28.2 (C4), 27.6 (C8), 20.9 (C2). The data for **4** were obtained from spectra of the **8**–**4** mixture. ^{1}H NMR (400 MHz, partial spectrum; $CDCl_3$), δ: 3.26 (1H, complex, H7), 2.42 (1H, t, H6), 1.91 (H5). ^{13}C NMR (100 MHz, $CDCl_3$), δ: 180.8 (C=O), 61.1 (C5), 58.8 (q, C1), 52.9 (C7), 41.25 (C6), 34.25, 32.0, 29.6, 28.7, 24.4 and 21.3 (all CH_2). ^{13}C assignments for the C2–C4 group in each isomer are somewhat tentative.

Computational details

The structure of dihydropentalene **2** was optimized by standard ab initio molecular orbital calculations at the B3LYP/6-31G* level of theory using the Gaussian 94 suite of programs (11) (E = –310.827 8214 hartrees).

X-ray crystallography

Data collection

A colorless needle crystal of compound **8**, $C_{11}H_{16}O_2$, having approximate dimensions of 0.25 × 0.30 × 0.50 mm was mounted on a glass fiber. All measurements were made on a Rigaku AFC6S diffractometer with graphite-monochromated Mo-Kα radiation.

Cell constants and an orientation matrix for data collection, obtained from a least-squares refinement using the setting angles of 17 carefully centered reflections in the range 24.20° < 2θ < 37.71° corresponded to a primitive tetragonal cell (Laue class: $4/m$) with dimensions a = 17.589(1) Å, c = 6.276(2) Å, V = 1941.6(7) Å^3. For Z = 8 and F.W. = 180.25, the calculated density is 1.23 g/cm^3. The systematic absences of $hk0$: $H + K \neq 2n$ and $00l$: $L \neq 2n$ uniquely determine the space group to be $P4_2/n$ (no. 86).

The data were collected at a temperature of 23 ± 1°C using the ω–2θ scan technique to a maximum 2θ value of 50.0°. ω-Scans of several intense reflections, made prior to data collection, had an average width at half-height of 0.36° with a take-off angle of 6.0°. Scans of (1.52 + 0.35 tan θ)° were made at a speed of 4.0°/min (in ω). The weak reflections ($I > 10.0\sigma(I)$) were rescanned (maximum of three rescans) and the counts were accumulated to ensure good counting statistics. Stationary background counts were recorded on each side of the reflection. The ratio of peak counting time to background counting time was 2:1. The diameter of the incident beam collimator was 0.5 mm and the crystal-to-detector distance was 400 mm.

Data reduction

Of the 2017 reflections that were collected, 1888 were unique (R_{int} = 0.045). The intensities of three representative reflections were measured after every 200 reflections. Over the course of data collection, the standards decreased by 1.4%. A linear correction factor was applied to the data to account for this phenomenon.

The linear absorption coefficient, μ, for Mo-Kα radiation is 0.078 mm^{-1}. An empirical absorption correction based on azimuthal scans of several reflections was applied; this resulted in transmission factors ranging from 0.96 to 1.00. The data were corrected for Lorentz and polarization effects. A correction for secondary extinction was applied (coefficient = 2.56519 × 10^{-7}).

Fig. 2. ORTEP plot of the X-ray structure of **8** using a crystallographic numbering scheme.

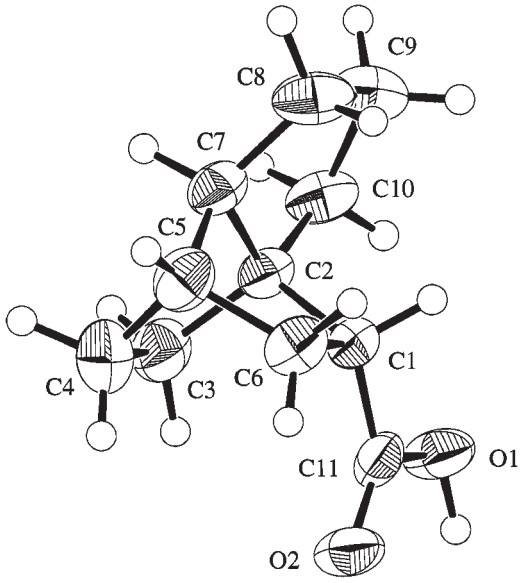

Structure solution and refinement

The structure was solved by direct methods (12) and expanded using Fourier techniques (13). The non-hydrogen atoms were refined anisotropically. The hydrogen atom coordinates were refined but their isotropic B's were held fixed. The final cycle of full-matrix least-squares refinement was based on 995 observed reflections ($I > 3.00\ \sigma\ (I)$) and 167 variable parameters and converged (largest parameter shift was 0.00 times its esd) with unweighted and weighted agreement factors of

$$R = \Sigma\ ||F_o| - |F_c||\Sigma\ |F_o| = 0.044$$

and

$$R\omega = ([\Sigma\omega(|F_o| - |F_c|)^2/\Sigma\omega F_o^2)])^{1/2} = 0.019$$

The standard deviation of an observation of unit weight was 2.91. The weighting scheme was based on counting statistics and included a factor (p = 0.001) to downweight the intense reflections. Plots of $\Sigma\omega(|F_o| - |F_c|)^2$ versus $|F_o|$, reflection order in data collection, sin θ/λ, and various classes of indices showed no unusual trends. The maximum and minimum peaks on the final difference Fourier map corresponded to 0.17 and –0.15 e$^-$/ Å^3, respectively.

Neutral atom scattering factors were taken from Cromer and Waber (14). Anomalous dispersion effects were included in Fcalc (15); the values for $\Delta f'$ and $\Delta f''$ were those of Creagh and McAuley (16). The values for the mass attenuation coefficients are those of Creagh and Hubbel (17). All calculations were performed using the teXsan crystallographic software package of the Molecular Structure Corporation (18).

Acknowledgements

Support for this research by the Natural Sciences and Engineering Research Council of Canada is gratefully acknowledged. We are indebted to K. Holm and L. Skattebøl,

© 1998 NRC Canada

University of Oslo, Norway, for a sample of the mixed acids.

References

1. P. von R. Schleyer, P. Grubmüller, W.F. Maier, O. Vostrowsky, L. Skattebøl, and K.H. Holm. Tetrahedron Lett. 921 (1980).
2. M.S. Baird and C.B. Reese. Tetrahedron Lett. 2895 (1965).
3. K. Holm and L. Skattebøl. Tetrahedron Lett. 2347 (1977).
4. F.J. Jäggi and C. Ganter. Helv. Chim. Acta, **63**, 214 (1980).
5. H. Meier, A. Pauli, and H. Kolshorn. Chem. Ber. **122**, 101 (1989).
6. R.P. Kirchen, T.S. Sorensen, and S.M. Whitworth. Can. J. Chem. **71**, 2016 (1993).
7. I.P. Sekatsis, A.A. Kemme, E.E. Liepin'sh, Ya.Ya. Bleidelis, M.P. Gavars, B.P. Raguel', and Ya.Yu. Polis. Zh. Org. Khim. **24**, 481 (1988).
8. P.A. Krasutsky, I.R. Likhotvorik, A.L. Litvyn, A.G. Yurchenko, and D. Van Engen. Tetrahedron Lett. **31**, 3973 (1990).
9. I. Fleming. Frontier orbitals and organic chemical reactions. Wiley, New York. 1976.
10. J.D. Xidos, R.A. Poirier, C.C. Pye, and D.J. Burnell. J. Org. Chem. **63**, 105 (1998).
11. M.J. Frish, G.W. Trucks, H.B. Schlegel, P.M.W. Gill, B.G. Johnson, M.A. Robb, J.R. Cheeseman, T.A. Keith, G.A. Petersson, J.A. Montgomery, K. Rachavachari, M.A. Al-Laham, V.G. Zackrewski, J.V. Ortiz, J.B. Foresman, J. Cioslowski, B.B. Stefanov, A. Nanayakkara, M. Challacombe, C.Y. Peng, P.T. Ayala, W. Chen, M.W. Wong, J.L. Andres, E.S. Replogle, R. Gomperts, R.L. Martin, D.J. Fox, J.S. Binkley, D.J. Defrees, J. Baker, J.P. Steward, M. Head-Gordon, C. Gonzales, and J.A. Pople. Gaussian 94, Revision A.1. Gaussian, Inc., Pittsburgh, Pa. 1995.
12. M.C. Burla, M. Camalli, G. Cascarano, C. Giacovazzo, G. Polidori, R. Spagna, and D. Viterbo. SIR88. J. Appl. Crystallogr. **22**, 389 (1988).
13. P.T. Beurskens, G. Admiraal, G. Beurskens, W.P. Bosman, S. Garcia-Granda, R.O. Gould, J.M.M. Smits, and C. Smykalla. The DIRDIF program system. Technical Report of the Crystallography Laboratory, University of Nijmegen, The Netherlands. 1992.
14. D.T. Cromer and J.T. Waber. International tables for X-ray crystallography. Vol. IV. The Kynoch Press, Birmingham, England. 1974. Table 2.2 A.
15. J.A. Ibers and W.C. Hamilton. Acta Crystallogr. **17**, 781 (1964).
16. D.C. Creagh and W.J. McAuley. International tables for crystallography. Vol. C. *Edited by* A.J.C. Wilson. Kluwer Academic Publishers, Boston. 1992. Table 4.2.6.8. pp. 219–222.
17. D.C. Creagh and J.H. Hubbell. International tables for crystallography. Vol. C. Edited by A.J.C. Wilson. Kluwer Academic Publishers, Boston. 1992. Table 4.2.4.3. pp. 200–206.
18. teXsan: Crystal structure analysis package. Molecular Structure Corporation, The Woodlands, Tex. 1985 and 1992.

© 1998 NRC Canada

Calculation of octanol–water partition coefficients of organic solutes from their molecular volumes

John T. Edward

Abstract: Bodor and Buchwald (8) have produced a two-parameter equation for calculating the logarithm of the partition coefficient (log *P*) of an organic solute between *n*-octanol and water. They computed the first parameter, a van der Waals volume of the of the solute molecule, using an algorithm combining analytical and numerical techniques. This parameter can be obtained more simply by addition of increments for the various atoms making up the molecule. The second parameter *N*, an integer, is obtained by summation of the integral *N* values associated with the different polar groups present in the molecule, as long as these polar groups are not too close to each other. The *N* term results in a decrease in log *P*. The *N* parameter is thought to measure the total number of H-bonds between the hydrogen of water and H-acceptor bonding sites of the various polar groups of the solute molecule. The detailed nature of the hydrogen bonds between a polar group and water can be elucidated by calculations involving *N* and $\overline{V}^0$, the partial molal volume in water of a solute molecule containing this group.

Key words: partition coefficient, molecular volume, hydrogen bonding, van der Waals volume.

Résumé : Bodor et Buchwald (8) ont proposé une équation à deux paramètres pour calculer le logarithme du coefficient de partage (log *P*) d'un soluté organique entre l'octanol et l'eau. Ils ont calculé le premier paramètre, un volume de van der Waals de la molécule de soluté, en utilisant un algorithme combinant des techniques analytiques et numériques. On peut déterminer ce paramètre d'une façon plus simple par l'addition de valeurs différentielles pour les divers atomes formant la molécule. On obtient le deuxième paramètre, *N*, un nombre entier, en faisant la somme des valeurs de *N* associées aux divers groupes polaires présents dans la molécule, à la condition que ces groupes polaires ne soient pas trop près les uns des autres. Le terme *N* provoque une diminution du log *P*. On croit que le paramètre *N* est une mesure du nombre total de liaisons hydrogènes entre l'hydrogène de l'eau et les sites de liaison pouvant accepter un H des divers groupes polaires de la molécule de soluté. On a déterminé la nature exacte des liaisons hydrogènes entre un groupe polaire et l'eau à l'aide de calculs impliquant *N* et $\overline{V}^0$, le volume molal partiel dans l'eau d'une molécule de soluté contenant ce groupe.

Mots clés : coefficient de partage, volume moléculaire, liaison hydrogène, volume de van der Waals.

[Traduit par la Rédaction]

Introduction

Hansch (1, 2) proposed that the *n*-octanol–water partition coefficient *P* of an organic solute be adopted as a quantitative measure of its lipophilic–hydrophilic character. His proposal has been generally accepted, and log *P* thus defined has found wide use in quantitative structure–activity relationships (QSAR) in pharmacology, physiology, biochemistry, toxicology and environmental sciences; a recent book (3) gives hundreds of references to papers in these different fields.

Many methods for calculating log *P* have been developed (3–7). Those most generally used start by dissecting the structural formula of a molecule into its component fragments (-CH_3, -$CONH_2$, etc.) or atoms, for which fragmental constants have been determined. The value log *P* is then obtained by summation of these fragmental constants, with correction factors for any special features (e.g., intramolecular hydrogen bonding) present in the molecule. A cumbrous array of fragmental constants and correction factors is required. Recently, Bodor and Buchwald (8) showed that for more than 700 organic compounds (including about 80 large pharmaceutically active molecules) log *P* was given with acceptable accuracy by a surprisingly simple equation:

$$\log P = 0.032 v_{BB} - 0.723N \quad [1]$$

where v_{BB} (my notation) represents the Bodor and Buchwald version of the van der Waals volume (*V* in their notation; in $Å^3$) of the individual molecule (further discussed below) and *N* is a positive integer, obtained by adding up the integers characteristic of each hydrophilic group in the molecule. Simple polar atoms or groups (-OH, -O-, -NH_2, -NH-, >N-, -CN, -NO_2, -CO-, -CO_2H, -COO-, -CH=NOH, -N=N-) have *N* = 2; -CON < and -CONH- have *N* = 4. However,

Received February 25, 1998.

J.T. Edward. Department of Chemistry, McGill University, 801 Sherbrooke St. W., Montreal, QC H3A 2K6, Canada.

[1]Author to whom correspondence may be addressed. Telephone: (514) 398–6233 (W); (514) 489–1663 (H). Fax: (514) 398–3797. E-mail: edward@omc.lan.mcgill.ca

© 1998 NRC Canada

Table 1. The van der Waals increments (in Å^3) of atoms.

Atom	Increment	Atom	Increment	Atom	Increment
>C<	5.6	F-(ar)[b]	8.9	$^-$O-	10.1
>C=	8.1	Cl-(alk)[a]	19.0	-S-	17.9
=C=	11.6	Cl-(ar)[b]	25.8	S=	20.1
-C≡	13.4	Br-(alk)[a]	26.9	>N-	7.2
H-(C)	5.5	Br-(ar)[b]	35.1	-N=	8.6
H-(N)	5.2	I-(alk)[a]	39.8	>N$^+$=	6.7
H-(O)	7.2	I-(ar)[b]	52.1	>N$^+$<	4.6
H-(S)	6.6	-O-	6.2	N≡	8.0
F-(alk)[a]	9.5	O=	11.3	>Si<	18.5

[a]Joined to alkene, alkane, or alkyne carbon.
[b] Joined to aromatic carbon.

when the polar atom or group is attached to an aromatic ring, as in Ar-OH, Ar-O-, Ar-NO_2, Ar-CN, and Ar-CO_2H, *N* equals to 1, although for Ar-NH_2, Ar-NH-, and Ar-COO- *N* remains 2; Ar-CONH- has $N = 3$, and Ar-SO_2NH_2 has $N = 4$.

Equation [1] is based on the generally accepted model of the partition process. The transfer of an organic molecule from water to the *n*-octanol layer is favoured by the greater energy required to create a cavity for the molecule in water, the more highly cohesive solvent. This energy is proportional to the size of the solute molecule, and accounts for the first term (positive) on the RHS of eq. [1]. On the other hand, the volume effect of a polar, hydrophilic group in the solute molecule will be more than compensated by its stronger hydrogen bonding to water than to *n*-octanol; this will favour transfer of the solute from *n*-octanol to the water layer, and accounts for the second term (negative) on the RHS of eq. [1]. In theory, the energy required to form a cavity in solvent should be proportional to the surface area, and not to the volume of the solute molecule, but Bodor and Buchwald found that the experimental evidence favoured (albeit only slightly) the reverse.

Calculation of molecular volumes

While eq. [1], with only two parameters, offers an apparently simple method for calculating log *P*, the calculation of the first parameter by the Bodor and Buchwald method is far from simple. In this calculation each atom is represented by a sphere centred at equilibrium position of the atomic nucleus and having a radius equal to its reported van der Waals radius (but see below). The exterior surfaces of all the spheres define the van der Waals surface of the molecule, which encloses its van der Waals volume. The van der Waals volumes and surface areas were computed with a novel algorithm developed by combining analytical and numerical techniques reported in the literature, with particular attention to the overlaps between spheres joined to a common sphere, and between spheres joined into rings. A complete program for the algorithm was developed.

In applying this program, Bodor and Buchwald adopted atomic radii r_{BB} for the common atoms (C, H, O, N) about 10% smaller than the van der Waals radii r_W adopted by Bondi (9), which since 1964 have been accepted, with small or negligible changes, by most chemists (e.g., Gavezotti (10)). Bodor and Buchwald also reduced the Bondi radii for other atoms, but by varying amounts: F, by 10%; Si, 19%; P, 3%; S, 6%; Cl, 9%; Br, 3%. The radius r_{BB} of I was increased by 4%. Furthermore, the radii r_{BB} of Cl, Br, and I attached to aromatic rings were increased over the Bondi r_W values by the following amounts: Cl, 3%; Br, 8%; I, 9%. The reasons behind these changes are discussed below.

Using these r_{BB} values and known bond lengths and angles, Bodor and Buchwald calculated v_{BB} of more than 700 molecules of which 149 are reported in Table 1 and eight in Chart 1 of their paper.

In 1964 Bondi (9; cf. also 11, 12) described a very much simpler method for obtaining the van der Waals volume v_W of a molecule, by addition of the volume increments of the constituent atoms. The increments were calculated from the bond lengths between atoms and from their van der Waals radii r_W, as estimated by a careful analysis of X-ray crystallographic data. The volume increments for a particular atom varied depending on the other atoms to which it was bonded. Thus Bondi found the increment for the ether oxygen atom -O- to vary from 5.3 to 8.6 Å^3, depending on whether the oxygen was present in a cyclic or acyclic aliphatic or an aromatic ether. In 1970 I adopted a compromise value of 6.2 Å^3 for -O- in ethers, and also in alcohols, carboxylic acids, and esters (12).[2] The same averaging procedure was applied to the Bondi increments for the other common atoms, and the 1970 values thus adopted are reproduced in Table 1, except for -H, -Cl, -Br, -I and ≡N. In the case of -H attached to C, the increment (5.5 Å^3) now given in Table 1 lies between the values reported in 1970 for -H attached to alkane, alkene, and alkyne carbon (5.7 Å^3) and to aromatic carbon (5.3 Å^3).

Increments for the common groups (-CH_3, -OH, -NH-, etc.), based on the atomic increments in Table 1, are given in Table 2. Using atomic and group increments, the calculation of v_W is simple, as illustrated in the case of benzylpenicillin in Fig. 1.

How much is lost by using the summation of the Bondi increments in place of the Bodor and Buchwald computer algorithm to find the volume of a molecule? If we compare v_{BB} and v_W of compounds containing only C, H, O, and N (111 out of 149 compounds in Table 1 of Bodor and

[2] Since in most organic molecules 80–90% of the volume is made up by contributions from C and H, the errors introduced by this averaging are not serious, particularly when the parameter sought is $r_w \equiv (3v_W/4\pi)1/3$ (cf. refs. 13–20), varying as the cube root of v_W.

© 1998 NRC Canada

Table 2. The van der Waals increments (in Å^3) of groups.

Group	Increment	Group	Increment	Group	Increment
-CH_3	22.1	-NH_2	17.6	-NO_2	28.1
-CH_2-	16.6	-NH-	12.4	-CO-O-	25.6
>CH-	11.1	-OH	13.4	-CO-OH	32.8
-C_6H_5	76.1	>C=O	19.4	-CO-NH_2	37.0
-C_6H_4-	70.6	-SO_2-	32.3	-CO-NH-	31.8

Fig. 1. Calculation of van der Waals volume v_W (in Å^3) of benzylpenicillin by addition of atomic (Table 1) or group increments (Table 2): v_W = 76.1 + 16.6 + 31.8 + 22.2 + 17.9 + 5.6 + 44.2 + 32.8 + 11.1 + 7.2 + 19.4 = 284.9 Å^3.

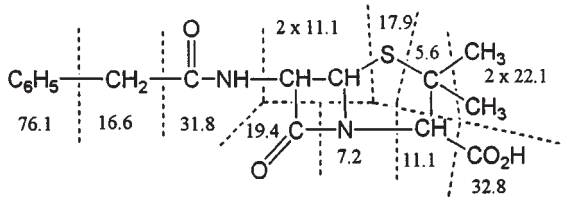

Buchwald (8)), we find that essentially nothing is lost, v_{BB} being related to v_W by the linear equation

[2] $$v_{BB} = 0.838v_w$$

with a correlation coefficient r of about 0.999. However, for the 27 other compounds in Table 1 of Bodor and Buchwald (8) containing ≡N or halogen, the correlation is poorer. This is to be expected: while Bodor and Buchwald made r_{BB} about 10% smaller than r_W for C, H, O, and N, they made it smaller or larger by varying amounts for the halogens (as discussed above) in order to bring log P calculated by eq. [1] into agreement with experiment. I have followed this policy and altered the atomic increments for -F, -Cl, -Br, -I, and ≡N from their 1970 values (12) to those now given in Table 1. With these revised increments, eq. [2] now applies to 145 out of the 149 compounds listed by Bodor and Buchwald in their Table 1 (8).[3] (The four compounds not considered, ampyzine, myleran, methopromazine, and cyanamphenicol, had structures that could not be found in the pharmacopoeias consulted, and have been ignored). The 145 compounds range from methylamine (v_{BB} 35.27 Å^3) and acetonitrile (v_{BB} 36.16 Å^3) to fluocinonide (v_{BB} 358.75 Å^3) and betamethasone-17,21-dipropionate (v_{BB} 384.97 Å^3). The excellence of the correlation is shown in Fig. 2 (slope 0.838; r = 0.99916), and further in Table 3 in which v_{BB} of eight compounds listed by Bodor and Buchwald in Chart 1 of their paper is compared with $0.838v_W$. Both measures of molecular volume prove to be essentially identical, and both equally suitable for calculating log P by eq. [1]. Accordingly, this equation may be recast as

[1*a*] $$\log P = 0.027v_w - 0.723N$$

Testing eq. [1*a*] or [3*a*] with two further data sets

Equation [1*a*] accommodates Bodor and Buchwald's data set of log P values for more than 700 compounds; we now consider how well it accommodates another data set of 187 compounds listed by Sangster (4), and a set of 37 compounds (22) containing one or another of two polar groups not listed by Bodor and Buchwald.

The 187 compounds listed by Sangster (4),[3,4] comprise a great variety of types, including 14 alkanes ranging from methane to methylcyclohexane. Bodor and Buchwald (8) showed that for alkanes eq. [1] must be expanded to

[3] $$\log P = 0.032v_{BB} - 0.723N + 0.010v_{BB}I$$

where I is a simple indicator variable, equal to 1 for alkanes and zero for other compounds. Substituting $0.838v_W$ for v_{BB} gives

[3*a*] $$\log P = 0.027v_w - 0.723N + 0.008v_wI$$

This equation with I = 1 yields values of log P in good agreement with experiment for the alkanes of Table 2S,[3] but also, surprisingly, for five perhaloalkanes in Table 4; the exception (tetrafluoromethane, no. 4) should perhaps be reinvestigated.

For the remaining 167 of the 187 compounds listed by Sangster I = 0. Using values of N given by Bodor and Buchwald's rules (except for 11 "special cases" discussed below) eq. [3*a*] gives values of log P_{calc} in good agreement with experiment. This is shown in Fig. 3, an error histogram (estimation error Δ = log P_{calc} – log P_{expt}) for the data set of 187 compounds; 52% have an error of 0.20 or less, and 98% an error of 0.80 or less, about equal to the performance of the AFC method of Meylan and Howard (23) for a data set of 8406 compounds. However, this is not a fair comparison: the data set used by Meylan and Howard is vastly greater, and the calculations were carried out by computer (no human intervention), while N for the 11 aberrant compounds in my data set were chosen to optimize agreement between experimental and calculated values of log P. Still, it shows the

[3] Table 1S giving v_W, $0.838v_W$, and v_{BB} of the 145 compounds is available as supplementary material and may be purchased from: The Depository of Unpublished Data, Document Delivery, CISTI, National Research Council of Canada, Ottawa, Canada, K1A 0S2. (Also available from this source is Table 2S, mentioned later.) The v_W values of ring compounds (e.g., benzylpenicillin in Fig. 1) were obtained by summation of increments without applying corrections for ring formation (21); these corrections resulted in a poorer correlation of v_W with v_{BB}.

[4] Table 2S, available as supplementary material,[3] lists the 187 compounds with an identifying number, formula, name, v_W, N, I, log P_{calc} by eq. [3*a*], log P_{expt}, and estimation error Δ (≡ log P_{calc} – log P_{expt}). Sangster listed 210 compounds (ref. 4, pp. 157–161); the 23 compounds omitted from consideration were amino acid zwitterions (structures contain charged groups not included in Table 2), compounds identified by trade names, not chemical names, and compounds whose structures included atoms or groups not included in Tables 1 and 2.

© 1998 NRC Canada

Fig. 2. Plot of v_{BB} (V in notation of ref. 8), calculated by Bodor and Buchwald (8) for 145 compounds, against van der Waals volume (v_W), calculated using atomic increments from Table 1; slope 0.838, correlation coefficient r = 0.99916.

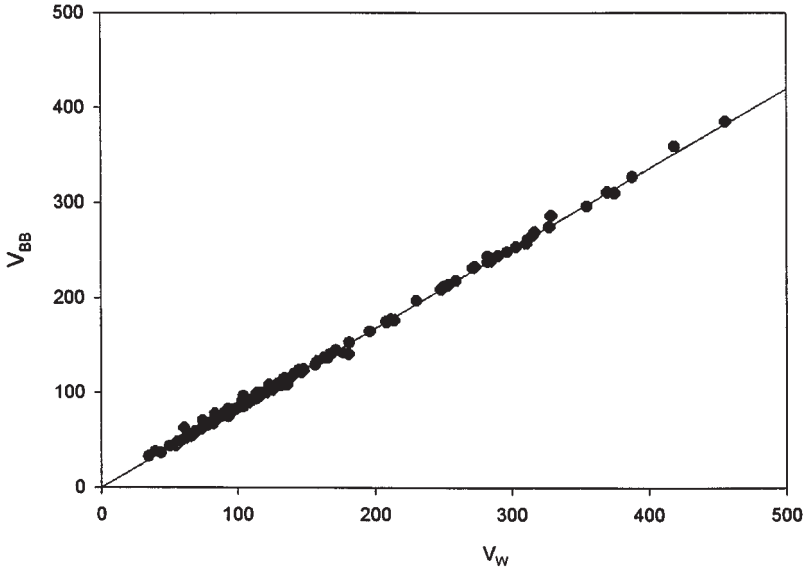

Table 3. Comparison of molecular volumes (in Å^3) calculated according to Bodor and Buchwald (8) (v_{BB}) and to Bondi–Edward (v_W), and of log P values calculated using them.

Compound	N	v_{BB}	log P_{calc} [a]	0.838v_W	log P_{calc} [b]	log P_{expt}
Tetrachloroethylene	0	76.87	2.46	77.3	2.47	2.60
Isopentyl alcohol	2	85.67	1.30	85.4	1.29	1.29
Butyldimethyl amine	2	102.77	1.85	103.8	1.87	1.70
3-Chlorobenzoic acid	1	107.16	2.71	108.3	2.75	2.68
2,4-Dinitrophenol	3	109.56	1.35	112.9	1.45	1.53
Chlorimipramine	9	255.04	5.28	258.9	5.40	5.19
Citric acid	8	122.70	–1.83	124.8	–1.78	–1.72
Sulfathiazole	7	156.23	–0.04	156.7	–0.03	0.05

[a] log P_{calc} = 0.032v_{BB} – 0.723N.
[b] log P_{calc} = 0.027v_W – 0.723N.

Table 4. Partition coefficients of perhaloalkanes.

			log P_{calc}			
No.[a]	Compound	log P_{expt} [b]	Eq. [1*a*]	Δ[c]	Eq. [3*a*][d]	Δ[c]
1	CCl_2F_2	2.16	1.69	–0.07	2.19	0.03
2	CCl_3F	2.53	1.95	–0.58	2.52	–0.01
3	CCl_4	2.83	2.20	–0.63	2.86	0.03
4	CF_4	1.18	1.18	0.00	1.53	0.35
22	$CClF_2$–$CClF_2$	2.82	2.35	–0.47	3.05	0.23
24	CCl_3–CCl_3	4.14	3.38	–0.76	4.88	0.24

[a]Number of compound as listed in Table 2S.
[b] From Sangster (4, pp. 157–158).
[c] $\Delta \equiv$ log P_{calc} – log P_{expt}.
[d] I = 1 in eq. [3*a*].

potential of eq. [3*a*] if the difficulties with N can be surmounted: it is vastly more simple than present computerized methods (cf. AFC method of Meylan and Howard, which uses 130 atom/fragment contribution values and 235 correction factors). At present it works well for compounds that contain no polar groups, one polar group, or two or more polar groups sufficiently separated from each other. This can be seen by scanning Table 2S,[3] which contains mostly simple compounds.

The larger errors shown in Fig. 3 (e.g., for hexachlorocyclopentadiene, ethylene diamine) may in fact be due to errors in reported values of log P_{expt}; these

© 1998 NRC Canada

Fig. 3. Error histogram for the 187 compounds listed by Sangster (4) showing the number N of compounds having estimation errors Δ (= log P_{calc} – log P_{expt}) in the intervals –0.99 to –0.90, ... –0.09 to 0, 0.01 to 0.10, etc.

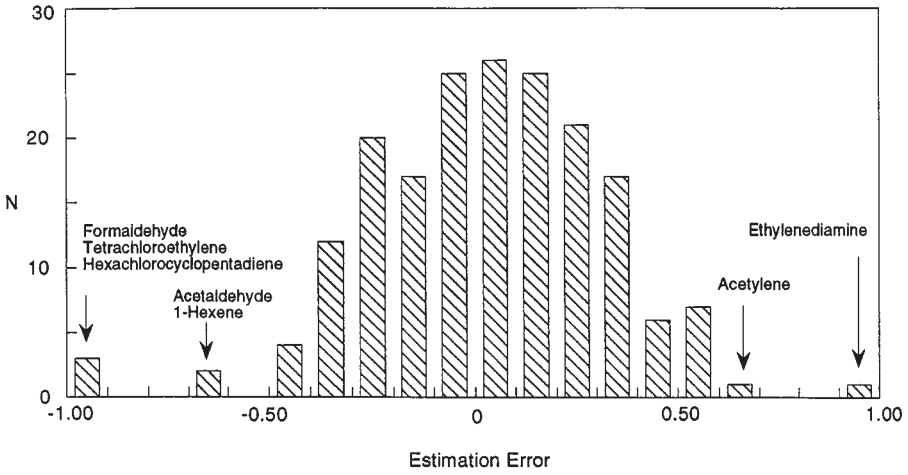

Fig. 4. General structures **1** (the 100 series), **2** (200 series), and **3** (300 series) of the iron-chelating compounds of Table 5.

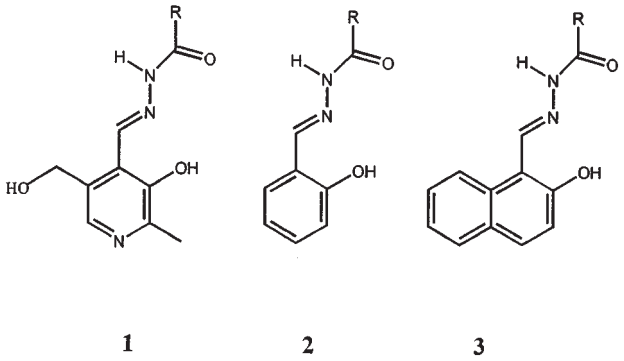

compounds should be reinvestigated. The error of –0.91 for tetrachloroethylene comes from accepting log P_{expt} = 3.40 given by Sangster (4); accepting log P_{expt} = 2.60 given by Bodor and Buchwald (8) reduces the error to –0.11.[5]

The estimation errors of –0.98 for formaldehyde and –0.63 for acetaldehyde shown in Fig. 3 are not real, log P_{calc} being based on the assumption that in water these compounds have the structures $CH_2{=}O$ and $CH_3CH{=}O$. This is almost completely false for formaldehyde (no. 12, Table 2S[3]), more than 99% of which exists in the hydrated form $CH_2(OH)_2$, and partly false for acetaldehyde (no. 38), about 55% of which exists in water in the hydrated form $CH_3CH(OH)_2$ and 45% in the unhydrated form $CH_3CH{=}O$ (24). For hydrated formaldehyde eq. [3*a*] with N = 1 (see below) gives log P_{calc} = 0.45, in good agreement (Δ = 0.10) with log P_{expt} = 0.35 (4). Accepting N = 1 for the hydrated form of acetaldehyde also, the log P_{expt} of 0.45 (4) for acetaldehyde (no. 38) is compatible with a mixture of 58% $CH_3CH(OH)_2$ and 42% $CH_3CH{=}O$, close to the proportions indicated by other properties (24) and reported above. Similarly, the log P_{expt} of 0.59 for propanal (no. 65) corresponds to a mixture of 30% $CH_3CH_2CH(OH)_2$ and 70% $CH_3CH_2CH{=}O$; the proportions in water previously reported (24) are 42:58. However, acetone (no. 64), shown to be about 99.8% in the unhydrated form in water (24), has an estimation error Δ of 0.50; a confirmation of log P_{expt} would be desirable. Furfural (no. 110) and benzaldehyde (no. 180), which undergo negligible hydration, have N = 2, like acetophenone (8), and only small errors in log P_{calc}.

The error of –0.60 for 1-hexene (Fig. 2) is reduced to +0.23 if I in eq. [3*a*] is set at 1, not zero; i.e., if 1-hexene is regarded as behaving more as an alkane than an alkene. Data for other long-chain alkenes would be interesting.

Choice of *N* values for 11 special cases

For most of the 187 compounds listed by Sangster the value of N to be used in eq. [3*a*] presented no problems. Thus for the hydroxyl group, N = 2, so that for ethanol (no. 45 in Table 2S) N = 2, for ethylene glycol (no. 47) N = 4, and for glycerol (no. 79) N = 6. In the polyhydroxy compounds each hydroxyl is separated by at least two carbon atoms from its neighbour. However, as we saw above, in order to calculate a reasonable log P for $CH_2(OH)_2$ in which the hydroxyls are separated by a single carbon atom, it was necessary to set N = 1, not 4. This is an example of the general rule: in a molecule containing several polar groups, the value of N for the molecule is the sum of the N values for the individual polar groups only if the groups are sufficiently separated from each other; otherwise the value for N of the molecule may become less than this sum (the "proximity" effect). This effect has been known for a long time (7), but is not invoked by Bodor and Buchwald for any of the 157 compounds in their paper to which they assign N values. However, it seems to show up in the N value which they assign to benzylpenicillin (Fig. 1), which contains a carboxyl group (N = 2) and two amide groups (N = 4) separated by single carbon atoms. According to simple additivity this should lead to N = 4 + 4 + 2 = 10, but Bodor and

[5] Of 187 compounds listed by Sangster in Table 2S,[3] 34 are also listed in Bodor and Buchwald's paper (8). For 31 of these compounds, log P_{expt} values reported by Sangster (4) and by Bodor and Buchwald are the same or almost the same; for only three compounds log P_{expt} values differ by more than 0.20: tetrachloroethylene (see above), ethylene glycol (–1.65 (8), –1.36 (4); 2,3-dimethylbutane (3.85 (8), 3.42 (4)).

© 1998 NRC Canada

Table 5. Experimental (log P_{expt}) and calculated (log P_{calc}) partition coefficients of compounds of the 100 series (**1**), 200 series (**2**), and 300 series (**3**).

Compound	R	log P_{expt}	N	log P_{calc}	Δ
101	Phenyl	2.23	6	2.42	0.19
102	*p*-Hydroxyphenyl	1.89	6+1	1.91	0.02
103	*p*-Methylphenyl	2.54	6	2.87	0.33
104	*p*-Nitrophenyl	1.55	6+1	2.30	0.75
105	*p*-Aminophenyl	1.19	6+2	1.30	0.11
106	*p*-*t*-Butylphenyl	3.73	6	4.21	0.48
107	*p*-Methyoxyphenyl	2.47	6+1	2.31	–0.16
108	*m*-Chlorophenyl	2.96	6	2.97	0.01
109	*m*-Fluorophenyl	2.42	6	2.51	0.09
110	*m*-Bromophenyl	3.07	6	3.21	0.14
111	4-Pyridinyl	1.14	6+2	0.84	–0.30
112	Methyl	0.65	6	0.96	0.31
113[a]	2-Pyridinyl	2.46	6	2.48	0.02
114	2-Furanyl	1.39	6	1.85	0.46
115	2-Thiophenyl	2.11	6	2.17	0.06
201	Phenyl	3.01	4	2.89	–0.12
202	*p*-Hydroxyphenyl	2.56	4+1	2.38	–0.18
203	*p*-Methylphenyl	3.39	4	3.34	–0.05
204	*p*-Nitrophenyl	3.03	4+1	2.78	–0.25
205	*p*-Aminophenyl	2.16	4+2	1.77	–0.39
206	*p*-*t*-Butylphenyl	4.73	4	4.68	–0.05
207	*p*-Methyoxyphenyl	3.34	4+1	2.78	–0.56
208	*m*-Chlorophenyl	3.83	4	3.44	–0.39
209	*m*-Fluorophenyl	3.41	4	2.98	–0.43
210	*m*-Bromophenyl	3.91	4	3.69	–0.22
211	4-Pyridinyl	2.16	4+2	1.31	–0.85
212	Methyl	1.71	4	1.43	–0.28
213[a]	2-Pyridinyl	3.24	3	2.95	–0.29
214	2-Furanyl	2.67	4	2.32	–0.35
215	2-Thiophenyl	3.03	4	2.64	–0.39
302	*p*-Hydroxyphenyl	3.95	4+1	3.55	–0.40
304	*p*-Nitrophenyl	3.58	4+1	3.95	0.37
305	*p*-Aminophenyl	3.04	4+2	2.94	–0.10
307	*p*-Methyoxyphenyl	4.06	4+1	3.95	–0.11
308	*m*-Fluorophenyl	4.06	4	4.15	0.09
312	Methyl	2.91	4	2.60	–0.31
314	2-Furanyl	3.41	4	3.49	0.08

[a]Compounds 113 and 213 have the -CH=N-NH- (N = 3) in place of the -CH=N-NHCO- (N = 4) groups of **1** and **2**.

Fig. 5. Values of molecular volume v_W, log P_{calc} from using eq. [3*a*] with N values shown, and log P_{expt} (from ref. 6), for the compounds benzalaniline **4**, benzanilide **5**, and benzaldehyde benzoylhydrazone **6**.

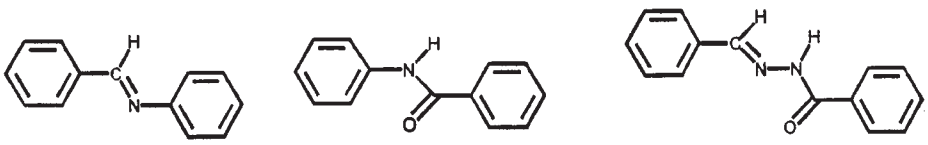

4

v_w 174.3 Å^3

log P_{calc} 1.78 (N = 4)

log P_{expt} 1.84

5

v_w 184.0 Å^3

log P_{calc} 2.62 (N =3)

log P_{expt} 2.77

6

v_w 206.2 Å^3

log P_{calc} 2.64 (N =4)

log P_{expt} 2.56

© 1998 NRC Canada

Buchwald assign to the compound $N = 8$ (without comment).

Several other examples of the proximity effect become apparent on examining Table 2S. Thus when two ether oxygen atoms ($N = 2$) are separated by at least two carbon atoms, as in 1,4-dioxane (no. 82), $N = 4$; when they are separated by one carbon atom, as in methylal (dimethoxymethane, no. 76) and 1,3-dioxalane (no. 67), N for the molecule is 3. Similarly, 1,3,5-trioxane (no. 70) has three ether oxygen atoms separated by single carbon atoms in a ring, and has $N = 3$, not 6.

Even more than proximity, juxtaposition of polar groups can reduce N. This is already apparent in the N values assigned by Bodor and Buchwald to composite polar groups. Thus -O-, -OH, and -CO- all have $N = 2$, but the composite groups -CO-O- and -CO-OH also have $N = 2$, rather than $N = 4$ expected by simple additivity. Consequently, it comes as no surprise that on the basis of their log P_{expt} values carbon dioxide O=C=O (no. 5) must have $N = 0$, urea (no. 19: H_2N-, $N = 2$, and -$CONH_2$, $N = 4$) must have $N = 5$, and theophylline (no. 183), a bicyclic compound containing one imidazole ring ($N = 2$) and a second ring containing two -CONH- groups ($N = 2 \times 4$), must have $N = 6$, not 10. At present, it is necessary (in the absence of any theory) to determine experimentally the N value for each case of juxtaposed polar groups.

Electronic or steric effects can also reduce N. Bodor and Buchwald noted that while nitrobenzene has $N = 1$, and aniline $N = 2$, *p*-nitroaniline has $N = 2$, not 3, because the electron-withdrawing effect of the nitro group reduces the N value of the amino group. The same effect may be operating progressively in the ethanolamines (nos. 51, 108, and 174 in Table 2S), as shown by their pK^{BH+} values. Monoethanolamine (no. 51; pK^{BH+} 9.98 (25)) has $N = 4$, and diethanolamine (no. 108, pK^{BH+} 8.97 (25)) has $N = 6$, as expected; triethanolamine (no. 174, pK^{BH+} 7.92 (25)) has $N = 7$, not 8. Reduced base strength and (or) steric hindrance may be responsible. *N*-Nitrosodimethylamine (no. 44) and *N*-nitrosodiethylamine (no. 97) have $N = 3$, but *N*-nitrosodipropylamine (no. 169) has $N = 2$. Steric effects may be involved here and in the case of some of the phenols which follow. Thus phenol and 2,3,4,5-tetrachlorophenol (no. 133), which has only one chlorine atom *ortho* to the hydroxyl group, have $N = 1$, but 2,3,4,6-tetrachlorophenol (no. 134) and pentachlorophenol (no. 129), which have two chlorine atoms *ortho* to the hydroxyl group, have $N = 0$. On the other hand, 2,6-dichlorophenol (no. 144, two *ortho* chlorine atoms) has $N = 1$; a buttressing effect may be missing in this molecule. Tetrachloro-4-methoxyphenol (no. 175, two chlorine atoms *ortho* to both -OH ($N = 1$) and -OCH_3 ($N = 1$)) has $N = 1$.

The N values of the 11 compounds discussed above are marked with asterisks in Table 2S[3] to show that they have been assigned on the basis of log P_{expt} values (i.e., to minimize Δ). This "fudging" reduces the overall error for the 187 compounds and narrows the spread in Fig. 3, but not by very much; the assignment of N to the other 176 compounds followed automatically from Bodor and Buchwald's rules. More experimental data for marginal compounds are required before we can discover if it is possible to extend Bodor and Buchwald's rules to accommodate them.

A second data set

The second data set for testing eq. [3*a*] consists of 37 iron-chelating compounds having the general structures **1** (the 100 series), **2** (200 series), and **3** (300 series) shown in Fig. 4; detailed structures are indicated in Table 5. These compounds all contain the composite polar group -CH=N-NHCO-, except for two (113 and 213 in Table 5), which contain instead the composite group -CH= N-NH-. The log P_{expt} values of these compounds have recently been reported (22), but Bodor and Buchwald do not give an N value for either composite group.

The experimental data under **4** in Fig. 5 require $N = 4$ for -CH=N-. Bodor and Buchwald report $N = 3$ for aromatic -NHCO-, in agreement with the log P_{expt} for **5** (Fig. 5), and in the absence of a juxtaposition effect the value of N for -CH=N-NHCO- would be 4 + 3 = 7. In fact, log P_{expt} for the compound **6** in Fig. 4 requires $N = 4$ for this grouping.

The introduction of an aromatic -OH group into an organic molecule increases N by one unit, but this is usually cancelled out when it is introduced *ortho* to a group to which it can hydrogen bond, as in *ortho*-hydroxybenzoic acid (8). Hydrogen bonding would also be expected to occur when -OH is introduced *ortho* to the >C=N- group of **6**, so that **2** would be expected to have $N = 4$. This is found to be true: compounds of the general structures **2** and **3** in which the substituent R does not have a polar group (e.g., compounds 201, 203, 206, 208, 209, 210, 212, 214, 215, 309, 310, 314 in Table 5) all have $N = 4$. When the R group contains a polar substituent (-OH in 202 and 302; -NO_2 in 204; -NH_2 in 205 and 305; pyridinyl N in 211) it should be sufficiently distant from the other polar groups to make its usual contribution to the N value of the molecule. This is what happens.

Compounds of the 100 series (Table 5) have, in addition to the polar groups found in **2** and **3** which account for $N = 4$, a -CH_2OH group ($N = 2$) and a pyridine nitrogen ($N = 2$), adding up to $N = 8$ for the simple structure (with no polar group in R). In fact, $N = 6$ is required to accommodate the experimental data for compounds 101, 102, 106, 108, 109, 110, 112, 114, and 115 in Table 5. Polar groups in R make their usual contrbutions to N of compounds 102, 104, 105, 107 and 110 in Table 5.

Compounds 113 and 213 have -CH=N-NH- in place of -CH=N-NHCO- in **1** and **2**, and R is 2-pyridinyl ($N = 2$). For these molecules the experimental data require $N = 3$ (see Table 5), a large reduction from the sum of the N values of the separate groups: CH=N- ($N = 4$), -NH- ($N = 2$), and 2-pyridinyl ($N = 2$).

If ever N can be estimated with confidence, eq. [3*a*] may prove to be one of the more accurate methods for calculating log *P*. This is shown by comparing its performance with that of the three computerized methods considered most reliable by Sangster (4), and listed in Table 6, in calculating log *P* of the 35 compounds in Table 5 (omitting the compounds 113 and 213 of different structure). A quantitative measure of performance is given by fitting calculated log *P* values to the experimental data in Table 5 according to the equation

$$[4] \qquad \log P_{calc} = a + b \log P_{expt}$$

© 1998 NRC Canada

Table 6. Comparison of four methods for calculating partition coefficients: statistical data from fitting log P_{calc} values to eq. [4] by linear regression, using experimental data (log P_{expt}) from Table 5.

Calculation method for log P_{calc}	n	a	b	r
Eq. 1[a], this paper	35	0.13	0.93	0.940
CLOGP 1.0.0 for Windows	35	–0.95	0.97	0.920
KOWWIN 1.54	37	–1.98	1.31	0.952
ACD/Log P1.0	37	–2.38	1.51	0.913

by linear regression. For a perfect correlation, $a = 0$, $b = 1$, and the correlation coefficient $r = 1.000$. The results in Table 6 show that eq. [3*a*] performs very well. A strict comparison with the results for the computerized methods would not be fair, because their parameters are based on data sets of many thousands of compounds, while the parameter N used in eq. [3*a*] was chosen to give the best possible correlation of log P_{expt} with log P_{calc} for this very limited data set of 35 compounds. Still, it shows the potential of eq. [3*a*] if the problems of estimating the parameter N can be resolved.

The value *N* and types of hydrogen bonding

Insight into the different ways in which a polar group forms H-bonds to water comes from combining information from N and from $\bar{V}^0$, the partial molal volumes of compounds containing this group.

Polar groups G: with unshared pairs of electrons such as -O-, >C=O, and >C=N- can form only one type of hydrogen bond, G:---H-OH or G:---H-OR, to the acidic hydrogen of water or *n*-octanol. We designate these as type I bonds. Polar groups -G-H containing labile hydrogen, such as -OH, -NH-, -CO_2H, and -CO-NH-, can form both type I and type II bonds, in the latter case the H of -G-H bonding to the unshared electron pairs of water and *n*-octanol: -G-H---OH_2 or -G-H---OHR.

Bodor and Buchwald (8) assert that N measures only type I bonds: *n*-octanol and water have nearly equal solvent β-strengths (26–28), and hence type II bonds by G-H to the oxygen of either *n*-octanol or water will have about equal strengths, and so will not affect the partition process. Since -O- and -N < have different numbers of unshared pairs of electrons, but both have $N = 2$, it seems plausible that they form H-bonds of different character, as shown in **7** and **8** (Fig. 6), >N- bonding a linked pair of water molecules because of its superior basicity.

Information on the total number N_H (= $N_I + N_{II}$) of hydrogen bonds formed by a polar group in water comes from $\bar{V}^0$ of organic solutes in water (21, 29–31).The value $\bar{V}^0$ is made up of the individual volume contributions $\bar{v}^0$(= $\bar{V}^0/N_a$) of N_a molecules, N_a being the Avogadro number. The contribution $\bar{v}^0$ of a single molecule can be considered to be made up of its van der Waals volume v_W plus the average void or empty volume (32) associated with it. For spherical molecules the empty volume is given by an enclosing spherical shell of thickness Δ, so that

$$[5] \qquad \bar{v}^0 = 4\pi(r_w + \Delta)^3/3$$

Fig. 6. Possible modes of H-bonding of water molecules to ether oxygen **7** and to amine nitrogen **8**.

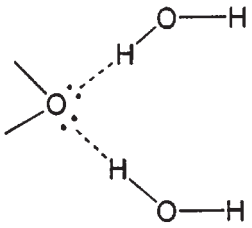

7

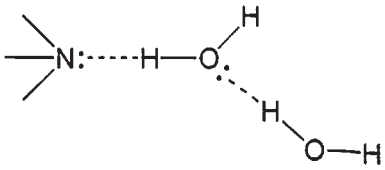

8

where $r_W = (3v_W/4\pi)^{1/3}$ and Δ = 0.57 Å for approximately spherical molecules (21, 29). For cylindrical molecules an alternative equation (also involving v_W) is required (21, 30, 33).

Equation [5] appears to be applicable to molecules that do not hydrogen bond appreciably to water. When hydrogen bonding groups G or G-H are present on the surface of the molecule, $\bar{v}^0$ is decreased according to the equation

$$[6] \qquad \bar{v}^0 = 4\pi(r_w + \Delta)^3/3 - \Sigma n_i\sigma_i$$

where n_i is the number of polar groups of type i in the molecule and σ_i is the volume decrement associated with type i (30). This equation gives fairly accurate estimates (usually to within 1–2%) of the partial molal volumes of a wide variety of compounds, ranging from methane to oligosaccharides (31). Values of σ_i determined by experiment for different polar groups are given in Table 7.

With the assumption that the formation of each hydrogen bond leads to a contraction of 1.8 Å^3 in $\bar{v}^0$ (about the estimate of Bondi (9)), the σ_i values lead to the estimates of N_H given in Table 7 (compare σ_i(expt) with σ_i(calc)). Simple arguments from structure lead to the division of N_H into numbers of H-bonds of type I (N_I) and type II (N_{II}) given in the table.

For a given group, values of N_I should correspond to Bodor and Buchwald's N. This is found to be true for the hydroxyl, primary amino, secondary amino, tertiary amino, and amide groups, but not for ketone or ester carbonyl oxygen ($N_I > N$) or for ether oxygen ($N_I = 0$, Bodor and Buchwald's $N = 2$). In the last case, n_i was assumed to be zero in order to derive the value of 0.57 Å for the fundamental parameter Δ (21); all the values of σ_i and thence N_I in Table 7 are dependent on this assumption. By assuming for ethers that $N_I = 2$ and $\sigma = 3.6$ Å^3, it is possible to recalculate Δ = 0.59 Å. This leads to larger values of σ_i for the other groups in Table 7, and to unrealistically large values of N_H.

© 1998 NRC Canada

Table 7. Hydrogen bonding of polar groups to water as calculated from σ values (ref. 29) and from Bodor and Buchwald *N* values (ref. 8).

	σ_i (eq. [8])		H-bonds			Bodor and Buchwald
Group	Expt.[a]	Calc.[b]	N_H[c]	N_{II}	N_I	N[d]
-N=	3.6	3.6	2	0	2	2
>N-H	7.2	7.2	4	2	2	2
$-NH_2$	10.8	10.8	6	4	2	2
>C=O	8.0	7.2	4	0	4	2
>C=S	0	0	0	0	0	-
-O-C(=O)-	8.0	7.2	4	0	4	2
H_2N-C(=O)-	18.8	18.0	10	6	4	4
-O-	0	0	0	0	0	2
-S-	0	0	0	0	0	0 or 1[e]
-O-H	9.8	10.8	6	4	2	2

[a] From ref. 29.
[b] Assuming $\sigma_i = 1.8\ N_H$.
[c] Chosen to make σ(calc) ~ σ(expt).
[d] From ref. 8.
[e] Bodor and Buchwald (ref. 8) report $N = 1$ for ethyl sulfide and $N = 0$ for thiophenol.

It is possible that H-bonding of pure water (the solvent for $\bar{V}^0$ studies) to ether or ketone oxygen is different from H-bonding of water saturated with *n*-octanol to these groups. Further work is needed.

Conclusions

Because of its simplicity, Bodor and Buchwald's two parameter equation has great promise. As shown in this paper, the first parameter is easily obtained from atomic increments. The second parameter (*N*) can be assigned without difficulty, following Bodor and Buchwald's rules, for compounds without a polar group, with a single polar group, or with two or more polar groups sufficiently separated from each other. However, the rules for *N* fail when two or more polar groups are too close to each other: when, for example, two ether oxygens are separated by a single carbon atom. This particular case may be due to the anomeric effect (34); other cases may involve other electronic or steric effects. Further work is required to discover whether Bodor and Buchwald's rules for *N* can be expanded to cover these special cases.

Acknowledgments

I am grateful to Professor D.F.R. Gilson for bringing ref. 8 to my attention and for counsel over many years, to Dr. J. Sangster for advice and for his invaluable book, to Professor R.B. Lennox for hospitality in his laboratory, to Dr. F.L. Chubb for drawing figures, to two anonymous referees for helpful criticism, to my son Jeremy for much help in computations and in drawing Fig. 2, and to my son Valentine for typing this paper.

References

1. C. Hansch. Acc. Chem. Res. **2**, 232 (1969).
2. C. Hansch. Quantitative structure-activity relationships in drug design. Vol. 1. *Edited by* E.J. Ariens. Academic Press, New York. 1971. p. 271
3. V. Plicka, B. Testa, and H. van der Waasterbeend (*Editors*). Lipophilicity in drug action and toxicology. VCH Publishers, New York. 1996.
4. J. Sangster. Octanol-water partition coefficients: fundamentals and physical chemistry. John Wiley and Sons, New York. 1997. pp. 157–161.
5. R.F Rekker. The hydrophobic fragmental constant: derivation and application. Elsevier, New York. 1977.
6. C. Hansch and A. Leo. Substituent constants for correlation analysis in chemistry and biology. Wiley–Interscience, New York. 1979.
7. A. Leo. Chem. Rev. **93**, 1281 (1993).
8. N. Bodor and P. Buchwald. J. Phys. Chem. **101**, 3404 (1997).
9. A. Bondi. J. Phys. Chem. **68**, 441 (1964).
10. A. Gavezotti. J. Am. Chem. Soc. **105**, 5220 (1983).
11. J.T. Edward. Chem. Ind. (London), 774 (1956).
12. J.T. Edward. J. Chem Educ. **47**, 261 (1970).
13. J.T. Edward. Sci. Proc. Roy. Dublin Soc. **27**, 273 (1956).
14. J.T. Edward. Chem. Ind. (London), 929 (1956).
15. J.T. Edward. Res. Corresp. **9**, 541 (1956).
16. J.T. Edward. Sci. Proc. Roy. Dublin Soc. **28**, 287 (1957).
17. J.T. Edward. J. Polym. Soc. **25**, 453 (1957).
18. J.T. Edward and D.W. Edward. J. Chromatogr. **20**, 563 (1965).
19. J.T. Edward. Advances in chromatography. Vol. 2. *Edited by* J.C. Giddings and R.A. Keller. M. Dekker, New York. 1966. p. 63.
20. J.T. Edward and D.W. Edward. J. Chromatogr. **24**, 125 (1966).
21. J.T. Edward, P.G. Farrell, and F. Shahidi. J. Chem. Soc. Faraday Trans. 1, **73**, 705 (1977).
22. J.T. Edward, F.L. Chubb, and J. Sangster. Can. J. Physiol. Pharmacol. **75**, 1362 (1997).
23. W.M. Meylan and P.H. Howard. J. Pharm. Sci. **84**, 83 (1995).
24. R.P. Bell. Adv. Phys. Org. Chem. **4**, 1 (1966).
25. D.D. Perrin. Dissociation constants of organic bases in aqueous solution: supplement 1972. Butterworths, London. 1972.
26. M.J. Kamlet, R.M. Doherty, M.H. Abraham, Y. Marcus, and R.W. Taft. J. Phys. Chem. **92**, 5244 (1988).
27. R.W. Taft, M. Abraham, R.M. Doherty, and M.J. Kamlet. Nature (London), **313**, 384 (1985).
28. N. El Tayer, B. Testa, and P.-A. Carrupt. J. Phys. Chem. **96**, 1455 (1992).

© 1998 NRC Canada

29. J.T. Edward and P.G. Farrell. Can. J. Chem. **53**, 2965 (1975).
30. F. Shahidi, P.G. Farrell, and J. T. Edward, J. Chem. Soc. Faraday Trans. 1, **73**, 715 (1977).
31. F. Shahidi, P.G. Farrell, and J.T. Edward. J. Solution Chem. **5**, 807 (1976).
32. A. Bondi. J. Phys. Chem. **58**, 929 (1954).
33. S. Terasawa, H. Itsuki, and S. Arakawa. J. Phys. Chem. **79**, 2345 (1975).
34. G.J. Thatcher (*Editor*). The anomeric effect and associated stereoelectronic effects, ACS Symposium Series 539. ACS, Washington, D.C. 1993.

© 1998 NRC Canada

A practical and efficient enantioselective synthesis of (2*S*)-3-(*tert*-butylsulfonyl)-2-benzylpropionic acid, a useful chiral building block for renin inhibitors

Yoshifumi Yuasa, Yoko Yuasa, and Haruki Tsuruta

Abstract: (2*S*)-3-(*tert*-Butylsulfonyl)-2-benzylpropionic acid **1**, which is used as the *N*-terminal chiral building block of renin inhibitors, is synthesized from (*Z*)-2-(*tert*-butylsulfonylmethyl)-3-phenyl-2-propenoic acid **6** by enantioselective hydrogenation using Ru–BINAP complexes in the presence of triethylamine with 84% ee. The enantioselective hydrogenation of a substrate with sulfone functionality is first reported.

Key words: hydrogenation, enantioselectivity, Ru–BINAP, oxidation, renin inhibitor.

Résumé : Faisant appel à une hydrogénation sélective catalysée par des complexes de Ru–BINAP en présence de triéthylamine, on a synthétisé l'acide (2*S*)-3-(*tert*-butylsulfonyl)-2-benzylpropionique, **1**, (ee de 84%) à partir de l'acide (*Z*)-2-(*tert*-butylsulfonylméthyl)-3-phénylprop-2-énoïque, **6**. Il s'agit du premier cas d'hydrogénation énantiosélective d'un substrat comportant une fonction sulfone.

Mots clés : hydrogénation, énantiosélectivity, Ru–BINAP, oxydation, inhibiteur de la rénine.

Introduction

(2*S*)-3-(*tert*-Butylsulfonyl)-2-benzylpropionic acid **1** (Fig. 1) has become of interest because it serves as the *N*-terminal position of many renin inhibitors (1, 2). Several preparations of **1** are known: (*i*) resolution by its diastereomeric salt with (+)-dehydroabiethylamine (2), (*ii*) enzymatic hydrolysis of the ester of racemic **1** (3), and (*iii*) synthesis from a chiral oxazoline derivative (4).

In addition, different synthetic approaches are reported for compounds related to **1** (5, 6).

On the other hand, enantioselective hydrogenation with Ru–BINAP complex catalyst is one of the most powerful tools for the synthesis of optically active compounds (for a review, see ref. 7). In particular, enantioselective hydrogenation of 3-substituted-2-propenoic acids and substituted alkylidenesuccinic acids are well known (7*a*, 8, 9). The enantioselective hydrogenation of a 2-sulfur substituted-3-naphthyl-2-propenoic acid has been reported (10, 11), however, that of 2-sulfonyl substituted propenoic acid is unknown.

We have studied the enantioselective hydrogenation of 2-sulfonyl substituted propenoic acid in order to develop a practical synthesis of **1**. We report an efficient synthesis of **1** from (*Z*)-2-(*tert*-butylsulfonylmethyl)-3-phenyl-2-propenoic acid **6** via enantioselective hydrogenation using an Ru–BINAP complex catalyst.

Received April 17, 1998.

Yoshifumi Yuasa[1] and Haruki Tsuruta. Technical Engineering Department, Fine Chemical Division, Takasago International Corporation, 1–5–1 Nishiyawata, Hiratsuka City, Kanagawa 254–0073, Japan.
Yoko Yuasa. School of Pharmacy, Tokyo University of Pharmacy and Life Science, 1432–1 Horinouchi, Hachioji, Tokyo 192–0355, Japan.

[1]Author to whom correspondence may be addressed. Telephone: 81-(0)463–21–7150. Fax: 81-(0)463–23–1655. E-mail: TIC00488@niftyserve.or.jp

Results and discussion

The starting substrates, (*Z*)-2-(*tert*-butylthiomethyl)-3-phenyl-2-propenoic acid **5** and (*Z*)-2-(*tert*-butylsulfonylmethyl)-3-phenyl-2-propenoic acid **6** were synthesized from ethyl (*Z*)-2-(chloromethyl)-3-phenyl-2-propenate **3** (12, 13). Treatment of **3** with *tert*-BuSH at room temperature for 18 h gave ethyl (*Z*)-2-(*tert*-butylthiomethyl)-3-phenyl-2-propenate **4** in 87% yield. Sulfide **4** was hydrolyzed with 1 N NaOH and a catalytic amount of benzyltriethylammonium chloride (BTEAC) at reflux (rfx) for 5 h to afford sulfide acid **5** in 88% yield. Sulfide acid **5** was oxidized with 30% H_2O_2 in the presence of a catalytic amount of Na_2WO_4 at 60°C for 3 h to provide sulfone acid **6** in 96% yield (Scheme 1).

We next investigated the enantioselective hydrogenation of sulfone acid **6** using Ru-*p*-tolyl-BINAP (*p*-tolyl-BINAP = 2,2′-bis(di-*p*-tolyl-phosphino)-1,1′-binaphtyl; see ref. 14). Sulfone acid **6** in a methanol–H_2O mixture solvent was hydrogenated using $Ru_2Cl_4[(-)$-*p*-tolyl-BINAP$]_2Et_3N$ (14) to give **1** in 84% ee (Scheme 2). Recently, Jendralla et al. (10, 11) reported the hydrogenation of the naphthyl analog of sulfide acid **5** using Ru[(–)-BINAP]$(OAc)_2$ in methanol; however, they have not reported the enantioselective hydro-

 © 1998 NRC Canada

Scheme 1. Synthesis of **5** and **6**; (*i*) conc. HCl – conc. H_2SO_4, rt, 18 h (78%); (*ii*) *t*-BuSH, K_2CO_3, CH_3CN, rt, 18 h, (87%); (*iii*) 1 N NaOH, BTEAC, rfx, 5 h, then 6 N HCl (88%); (*iv*) 30% H_2O_2, Na_2WO_4, MeOH, 60°C, 2 h (96%).

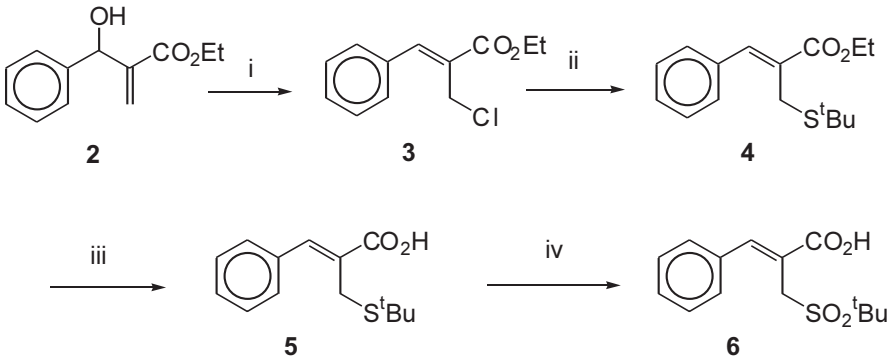

Scheme 2. Enantioselective hydrogenation of **5** and **6**; (*i*) H_2, 40 atm, Ru-*p*-tolyl-BINAP, MeOH–H_2O, as required Et_3N, 80°C, 16 h.

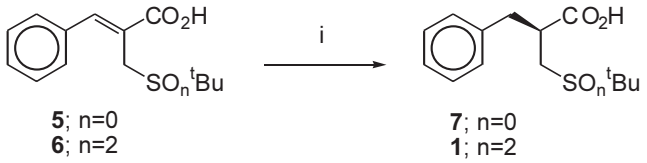

Fig. 1. (2*S*)-3-(*tert*-Butylsulfonyl)-2-benzylpropionic acid.

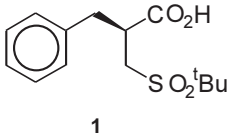

genation of sulfone acid. When sulfide acid **5** was hydrogenated using Ru_2Cl_4[(+)-*p*-tolyl-BINAP]$_2Et_3N$ as catalyst, (2*S*)-3-(*tert*-butylthio)-2-benzylpropionic acid **7** of 78% ee was produced. Enantioselectivity in the hydrogenation of sulfide **5** was lower than the reaction with sulfone **6**. The hydrogenation results using various Ru–BINAP complexes are listed in Table 1. We found that the addition of 10 wt.% H_2O to MeOH, as solvent, increased the conversion. The use of only MeOH resulted in lower conversion. The addition of a catalytic amount of triethylamine incremented the enantioselectivity of the hydrogenation to provide **1**. On the other hand, triethylamine had no effect on the enantioselectivity to provide **7**. This additional catalytic amount of triethylamine represents a new technical improvement on the hydrogenation procedure of sulfone acid. High reaction temperature (>100°C) caused decomposition of substrate. The enantiomeric purity of the target compound **1** could be enriched to 98% ee by recrystallization of its cyclohexylammonium salt.

The enantiomeric purity of **1** and **7** was determined by NMR and (or) HPLC analysis after conversion to the corresponding (*R*)-1-(1-naphthyl)ethylamides (see Experimental section). The absolute configuration of **7** was determined by oxidation to **1** under conditions similar to those previously described for the synthesis of **6** from **5**.

In conclusion, we have described a practical and efficient synthesis of a building block for renin inhibitor. (2*S*)-3-(*tert*-Butylsulfonyl)-2-benzylpropionic acid **1** was produced via an enantioselective hydrogenation of (*Z*)-2-(*tert*-butylsulfonylmethyl)-3-phenyl-2-propenoic acid **6** in an overall yield of 35% from propenate **3**.

Table 1. Enantioselective hydrogenation of **5** and **6** catalyzed by Ru–BINAP[a] product.

Run	Sub.	Cat.[b]	Conv. (%)[c]	Product	% ee[d]	config.[e]
1	**5**	(+)-A	100	**7**	78	*S*
2	**5**	(+)-A-Et_3N	100	**7**	47	*S*
3	**5**	(+)-B	99	**7**	75	*S*
4	**5**	(+)-C	82	**7**	62	*S*
5	**6**	(–)-A	18	**1**	70	*S*
6	**6**	(–)-A-Et_3N	100	**1**	84	*S*
7	**6**	(–)-B-Et_3N	100	**1**	62	*S*
8	**6**	(–)-C-Et_3N	72	**1**	64	*S*

[a]Reaction conditions: solvent, MeOH:H_2O 10:1; H_2, 40 atm, 80°C, 16 h; Et_3N, 0.003 mol%.
[b]Catalyst, 0.1 mol%; (+)-A, an empirical formula Ru_2Cl_4[(+)-*p*-tolyl-BINAP]$_2Et_3N$; (–)-A, Ru_2Cl_4[(-)-*p*-tolyl-BINAP]$_2Et_3N$; (+)-B, Ru_2Cl_4[(+)-BINAP]$_2Et_3N$; (–)-B, Ru_2Cl_4[(–)-BINAP]$_2Et_3N$; (+)-C, Ru[(+)-BINAP](OAc)$_2$; (–)-C, Ru[(-)-BINAP](OAc)$_2$,
[c]Conversion was determined by GC after converting it to the TMS ester using *N*,*O*-bis(trimethylsilyl) acetamide.
[d]Enantiomeric purity of **7** was determined by ^{1}H NMR analysis, and that of **1** was determined by HPLC after conversion to the (*R*)-1-(1-naphthyl)ethylamide, respectively.
[e]Absolute configuration of **1** was determined by the sign of the optical rotation value, and that of **7** was determined by oxidation to **1** using 30% H_2O_2.

Experimental section

All reagents and solvents were obtained from commercial sources and used without further purification. Melting points were measured using a Yanagimoto micromelting apparatus and are uncorrected. Boiling points are uncorrected. The IR spectra were recorded on a Jasco IR-810 instrument (ν in cm^{-1}). Optical rotations were measured on a Jasco DIP-4 digital polarimeter. Mass spectra (electronic impact) and high-resolution mass (HRMS) spectra were obtained using a Hitachi M-80A mass spectrometer. The ^{1}H NMR and ^{13}C NMR spectra (TMS as internal standard) were recorded on a Bruker AM-400 (400 MHz and 100 MHz). The GLC were performed using a Shimadzu GC-9A with an FID detector (column: PEG-HT (df = 0.15 μm, 0.25 mm ID × 25 m); at 100–200°C, +4.0°/min; carrier gas N_2, 1.0 kg/cm^2); HPLC were performed on a Hitachi L-6000 with a L-4000 UV as a detector (column: Inertsil ODS-2 (5 μm, 4.6 mm × 250 mm) using an eluent of CH_3CN/H_2O, 7:3 (pH 2.3; adjusted by

© 1998 NRC Canada

using H_3PO_4), and a flow rate of 0.6 mL/min with UV detection at 210 nm or 254 nm).

Ethyl (*Z*)-2-(*tert*-butylthiomethyl)-3-phenyl-2-propenate 4

To ethyl (*Z*)-2-(chloromethyl)-3-phenyl-2-propenate **3** (12, 13) (44.9 g, 0.2 mol) in acetonitrile (200 mL) were added K_2CO_3 (29 g, 0.21 mol) and *tert*-BuSH (25 mL, 0.22 mol) at room temperature. The reaction mixture was stirred at room temperature for 18 h. The insoluble solid was filtered off, and the filtrate was concentrated. To the residue, AcOEt was added, and the organic layer was separated, washed with brine, dried with $MgSO_4$, and concentrated in vacuo. The residue was distilled under reduced pressure to give **4** (48.4 g, 87% yield) as an oil; bp 142–145°C (0.5 torr); IR (neat): 1715, 1635, 1580 cm^{-1}; ^1H NMR ($CDCl_3$), δ: 1.35 (t, J = 7.1 Hz, 3H, CH_3), 1.36 (s, 9H, *t*-C_4H_9), 3.67 (s, 2H, SCH_2), 4.30 (q, J = 7.1 Hz, 2H, CH_2), 7.35–7.43 (m, 3H, Harom), 7.61–7.63 (m, 2H, Harom), 7.72 (s, 1H, CH=); ^{13}C NMR ($CDCl_3$), δ: 14.27 (CH_3), 25.92 (CH_2), 30.61 (C(**C**H_3)$_3$), 43.21 (**C**$(CH_3)_3$), 61.12 (CH_2S), 128.39 (2 X CH, Ar), 128.54 (C, Ar), 128.74 (CH, Ar), 129.63 (2 X CH, Ar), 135.09 (C=), 140.78 (CH=), 167.36 (CO); MS (EI, 70 eV), *m*/*z*: 278 (M^+, 41), 222 (45), 176 (94), 115 (100), 57 (63). HRMS calcd. for $C_{16}H_{22}O_2S$: 278.1339; found: 278.1337.

(*Z*)-2-(*tert*-Butylthiomethyl)-3-phenyl-2-propenoic acid 5

To ethyl (*Z*)-2-(*tert*-butylthiomethyl)-3-phenyl-2-propenate **4** (36.3 g, 0.13 mol) were added 1 N NaOH (240 mL) and benzyltriethylammonium chloride (BTEAC) (0.36 g). After heated to a reflux for 5 h, the reaction mixture was cooled to room temperature and adjusted to pH 2 with 6 N HCl. After extraction with AcOEt, the organic layer was washed with brine, dried with $MgSO_4$, and concentrated in vacuo to give **5** (28.6 g, 88% yield) as a white solid; mp 86–88°C; IR ($CHCl_3$): 1690, 1625, 1580 cm^{-1}; ^1H NMR ($CDCl_3$), δ: 1.39 (s, 9H, *t*-C_4H_9), 3.69 (s, 2H, SCH_2), 7.38–7.46 (m, 3H, Harom), 7.66–7.68 (m, 2H, Harom), 7.87 (s, 1H, CH=); ^{13}C NMR ($CDCl_3$), δ: 25.58 (SCH_2), 30.64 (C(**C**H_3)$_3$), 43.36 (**C**$(CH_3)_3$), 127.73 (C, Ar), 128.63 (2 X CH, Ar), 129.37 (CH, Ar), 129.90 (2 X CH, Ar), 134.22 (C=), 143.22 (CH=), 172.78 (CO); MS (EI, 70 eV), *m*/*z*: 250 (M^+, 32), 194 (65), 176 (36), 161 (61), 115 (81), 57 (100). Anal. calcd. for $C_{14}H_{18}O_2S$: C 67.17, H 7.25, S 12.81; found: C 67.20, H 7.26, S 12.89.

(*Z*)-2-(*tert*-Butylsulfonylmethyl)-3-phenyl-2-propenoic acid 6

To (*Z*)-2-(*tert*-butylthiomethyl)-3-phenyl-2-propenoic acid **5** (20 g, 80 mmol) in MeOH (250 mL), Na_2WO_4 (0.2 g, 0.6 mmol) and 2 N H_2SO_4 (10 mL) were added. The mixture was heated to 60°C and 30% H_2O_2 (40 mL) was added dropwise over a period of 1 h. The reaction mixture was stirred at 60°C for 2 h and cooled to room temperature. Ten percent aqueous $Na_2S_2O_3$ solution (100 mL) was added and concentrated in vacuo. To the residue, AcOEt was added, and the organic layer was separated, washed with brine, and dried with $MgSO_4$. The solvent was concentrated in vacuo to give a solid. The solid was recrystallized from AcOEt–*n*-hexane to give **6** (21.6 g, 96% yield) as a white solid; mp 187–188°C; IR ($CHCl_3$): 1690, 1625, 1580 cm^{-1}; ^1H NMR ($CDCl_3$), δ: 1.48 (s, 9H, *t*-C_4H_9), 4.32 (s, 2H, SO_2CH_2), 7.43–7.46 (s, 3H, Harom), 7.73–7.75 (m, 2H, Harom), 8.23 (s, 1H, PhCH=); ^{13}C NMR ($CDCl_3$), δ: 23.43 (C(**C**H_3)$_3$), 45.19 (SO_2CH_2), 60.52 (**C**$(CH_3)_3$), 119.36 (C, Ar), 128.83 (2 X CH, Ar), 129.49 (2 X CH, Ar), 130.11 (C, Ar), 133.76 (C=), 148.36 (CH=), 171.71 (CO); MS (EI, 70 eV), *m*/*z*: 282 (M^+, 3), 162 (100), 133 (27), 115 (93), 57 (100). Anal. calcd. for $C_{14}H_{18}O_4S$: C 59.55, H 6.43, S 11.35; found: C 59.59, H 6.44, S 11.30.

Hydrogenation procedure

All hydrogenations were carried out in a 100 mL stainless-steel autoclave. Under N_2, catalyst (0.028 mmol), substrate **5** or **6** (28 mmol), as required, Et_3N (6.4 μL), and the solvent MeOH–H_2O (10/1, 41.8 mL) were added. The atmosphere was then replaced with H_2 (40 atm), and the reaction mixture was stirred at 80°C for 16 h. Upon completion of the reaction, the solvent was removed under reduced pressure. The residue was dissolved in 1 N NaOH and washed twice with Et_2O. The aqueous layer was acidified with 2 N HCl and extracted with AcOEt. The extract was dried with $MgSO_4$ and concentrated in vacuo to give a crude product **7** (6.3 g, 89% yield, 78% ee by ^1H NMR) or **1** (7.41 g, 93% yield, 84% ee by HPLC). For determination of enantiomeric purity by ^1H NMR or HPLC, sulfide acid **7** and sulfone acid **1** were derivatized to the (*R*)-1-(1-naphthyl)ethylamides. To a CH_2Cl_2 solution containing crude **7** or **1** (10 mmol), (*R*)-1-(1-naphthyl)ethylamine (10 mmol), *N*,*N*′-dicyclohexylcarbodiimide (11 mmol) and 4-dimethylaminopyridine (20 mg) were added, and the mixture was stirred at room temperature for 6 h. The mixture was washed with 1 N HCl, 5% Na_2CO_3 solution, brine, and dried with $MgSO_4$. The solvent was evaporated and analyzed by ^1H NMR or HPLC. ^1H NMR (*S*,*R*)-amide of **7**, δ: 1.61 (d, J = 6.7 Hz, CH_3), 5.65 (d, J = 8 Hz, C<u>H</u>CON), 5.87(m, NC<u>H</u>CH_3); (*R*,*R*)-amide of **7**, δ: 1.36 (d, J = 6.7 Hz, CH_3), 5.44 (d, J = 8 Hz, C<u>H</u>CON), 5.76 (m, NC<u>H</u>CH_3). HPLC (t_{ret}: (*S*,*R*)-amide of **1**, 12.2 min; (*R*,*R*)-amide of **1**, 13.1 min).

(2*S*)-3-(*tert*-Butylthio)-2-benzylpropionic acid 7

To 6.3 g of crude **7**, which was previously described in the hydrogen procedure, diethyl ether – *n*-hexane mixture (1/2, 30 mL) was added, and an insoluble solid was filtered off and mother liquid was concentrated in vacuo to give 3.5 g (49% yield) of **7** as a viscous oil. The enantiomeric purity was 98% ee by ^1H NMR. $[\alpha]_D^{24}$ +7.6 (*c* 1.0, CH_2Cl_2); IR ($CHCl_3$): 1710, 1605 cm^{-1}; ^1H NMR ($CDCl_3$), δ: 1.27 (s, 9H, *t*-C_4H_9), 2.64 (dd, J = 5.7, 12.2 Hz, 1H, $PhCH_2$), 2.79 (dd, J = 7.4, 12.2 Hz, 1H, $PhCH_2$), 2.87–2.96 (m, 2H, SCH_2), 3.01–3.05 (m, 1H, $CHCO_2$), 7.20–7.29 (m, 5H, Harom); ^{13}C NMR ($CDCl_3$), δ: 29.04 (SCH_2), 30.82 (C(**C**H_3)$_3$), 37.27 ($PhCH_2$), 42.56 (**C**$(CH_3)_3$), 47.99 (CH), 126.64 (CH, Ar), 128.43 (2 X CH, Ar), 129.00 (2 X CH, Ar), 138.26 (C, Ar), 180.18 (CO); MS (EI, 70 eV), *m*/*z*: 252 (M^+, 4), 210 (11), 176 (20), 117 (30), 91 (23), 71 (7), 57 (100); HRMS calcd. for $C_{14}H_{20}O_2S$: 252.1182; found: 252.1180.

(2*S*)-3-(*tert*-Butylsulfonyl)-2-benzylpropionic acid 1

In this preparation, 7.42 g of the crude solid **1**, which was described in previous hydrogen procedure, was dissolved in 50 mL of EtOH, and then 2.78 g of cyclohexylamine was

© 1998 NRC Canada

added. The reaction mixture was cooled at 5°C, and the precipitated crystalline was filtered off and washed with 2-propanol (30 mL) to give 6.23 g of a cyclohexylamine salt of **1**. The cyclohexylamine salt was treated with 1 N HCl, and the aqueous mixture was extracted with AcOEt. After drying with $MgSO_4$, the evaporation of the solvent in vacuo gave 3.78 g (51% yield) of **1** as a white solid. The enantiomeric purity was 98% ee by HPLC (15); mp 98–99°C; lit. (4) mp 99–101°C; $[\alpha]_D^{24}$ +10.58 (*c* 1.0, CH_2Cl_2), lit. (4) $[\alpha]_D^{24}$ +10.9 (*c* 1.0, CH_2Cl_2); IR ($CHCl_3$): 1710, 1600, 1300, 1110 cm^{-1}; ^1H NMR ($CDCl_3$), δ: 1.36 (s, 9H, *t*-C_4H_9), 2.98 (dd, *J* = 3.4, 12 Hz, 1H, $CHCO_2$), 3.04 (dd, *J* = 7.1, 13.8 Hz, 1H, $PhCH_2$), 3.22 (dd, *J* = 6.1, 13.8 Hz, 1H, $PhCH_2$), 3.42 (m, 2H, SO_2CH_2), 7.23–7.33 (m, 5H, Harom); ^{13}C NMR ($CDCl_3$), δ: 23.23 (C(**C**$H_3)_3$), 37.47($PhCH_2$), 40.04 (CH), 45.52 (SO_2CH_2), 59.58 (**C**$(CH_3)_3$), 127.22 (CH, Ar), 128.79 (2 X CH, Ar), 129.24 (2 X CH, Ar), 136.75 (C, Ar), 177.22 (CO); MS (EI, 70 eV), *m*/*z*: 284 (M^+, 4), 238 (8), 164 (40), 117 (59), 91 (65), 73 (55), 57 (100). HRMS calcd. for $C_{14}H_{20}O_4S$: 284.3696; found: 284.3712.

References

1. P. Bühlmayer, A. Caselli, W. Fuhrer, R. Goshke, V H. Rasetti, H. Rüeger, J.L. Santon, L. Criscione, and J.M. Wood. J. Med. Chem. **31**, 1839 (1988).
2. H-W. Kleemann, H. Heitsch, R. Henning, W. Kramer, W. Kocher, U. Lerch, W. Linz, W.-U. Nickel, D. Ruppert, H. Urbach, R. Utz, A. Wagner, R. Weck, and F. Wiegand. J. Med. Chem. **35**, 559 (1992).
3. W. Beat and W. Wolfgang. (F. Hoffmann, La Roche und A.-G. Co.) European Patent 475255 (1990); Chem. Abstr. **117**, 24 763m (1992).
4. E.W. Holla, B. Napierski, and H-P. Rebenstock. Synlett. 333 (1994).
5. H. Mazdiyasni, D.B. Konopacki, D.A. Dickman, and T.M. Zydowsky. Tetrahedron Lett. **31**, 1569 (1990).
6. K. Tsuji, Y. Terao, and K. Achiwa. Tetrahedron Lett. **30**, 6189 (1989).
7. (*a*) K.E. Koenig. *In* Asymmetric synthesis.Vol. 5. *Edited by* J.D. Morrison. Academic Press, New York. 1985. p.71; (*b*) H. Takaya and R. Noyori. *In* Comprehensive organic synthesis. Vol. 8. *Edited by* B.M. Trost and I. Fleming. Pergamon Press, Oxford. 1991. Chap. 3.2. p. 433; (*c*) H. Takaya, T. Ohta, and R. Noyori. *In* Catalytic asymmetric synthesis. *Edited by* I. Ojima. VCH Publishers, New York. 1993; (*d*) R. Noyori. *In* Asymmetric catalysis in organic synthesis. John Wiley & Sons, Inc. New York. 1994. Chap. 2; (*e*) R. Noyori and H. Takaya. Acc. Chem. Res. **23**, 345 (1990), and refs. cited therein.
8. H. Kawano, T. Ikariya, Y. Ishii, M. Saburi, S. Yoshikawa, Y. Uchida, and H. Kumobayashi. J. Chem. Soc. Perkin Trans. 1, 1511 (1989).
9. L. Shao, S. Miyata, H. Muramatsu, H. Kawano, Y. Ishii, M. Saburi, and Y. Uchida. J. Chem. Soc. Perkin Trans. 1, 1441 (1990).
10. G. Beck, H. Jendralla, and B. Kammermeier. Tetrahedron, **50**, 4691 (1994).
11. H. Jendralla. Tetrahedron: Asymmetry, **5**, 1183 (1994).
12. A. Ameer, S.E. Drew, N.D. Emslie, P.T. Kaye, and R.L. Mann. J. Chem. Soc. Perkin Trans. 1, 2293 (1983).
13. F. Ameer, S.E. Drewes, M.S. Houston-McMillan, and P.T. Kaye. J. Chem. Soc. Perkin Trans. 1, 1143 (1985).
14. T. Ikariya, Y. Ishii, H. Kawano, T. Arai, M. Saburi, S. Yoshikawa, and S. Akutagawa. J. Chem. Soc. Chem. Commun. 922 (1985).

© 1998 NRC Canada

Observations on the stereochemistry of reduction of 2,6-dimethylcyclohexanones

Thomas E. Goodwin, Jennifer M. Meacham, and Mark E. Smith

Abstract: The reduction of *cis*-2,6-dimethylcyclohexanone with $NaBH_4$ in methanol is shown to produce predominantly the axial alcohol, an unexpected result based upon prior reports and current paradigms for similar cyclohexanone reductions. This finding prompted a careful and systematic investigation of the $NaBH_4$ and $LiAlH_4$ reductions of *cis*- and *trans*-2,6-dimethylcyclohexanones in various solvents, with additional results contrary to literature reports. Possible explanations for these discrepancies are given, an unusual solvent effect is noted, the rate of epimerization versus reduction is examined, molecular modeling results are reported, and an important caveat is offered for future stereochemical studies of this nature.

Key words: cyclic ketone reduction, stereochemistry, molecular modeling.

Résumé : On démontre que la réduction de la *cis*-2,6-diméthylcyclohexanone par le $NaBH_4$ dans le méthanol conduit d'une façon prépondérante à l'alcool axial; ce résultat est inattendu sur l'on se base sur les rapports antérieurs et sur les paradigmes actuels proposés pour les réductions de cyclohexanones semblables. Cette observation nous a amenés à réexaminer d'une façon soignée et systématique les réductions des *cis*- et *trans*-2,6-diméthylcyclohexanones par le $NaBH_4$ et le $LiAlH_4$ dans divers solvants; on a obtenu d'autres résultats sont contraires à ceux rapportés antérieurement. On présente diverses propositions pour expliquer ces différences; on note un effet de solvant inhabituel, on a examiné la vitesse d'épimérisation par rapport à la vitesse de réduction, on rapporte des résultats de modélisation moléculaire et on présente une mise en garde pour les futures études stéréochimiques de cette nature.

Mots clés : réduction de cétone cyclique, stéréochimie, modélisation moléculaire.

[Traduit par la Rédaction]

Introduction

The stereochemical course of the reduction of cyclic ketones, especially cyclohexanones, has been a topic of intense theoretical and practical interest for decades (for a convenient tabular listing of examples, see ref. 1). In general, sterically undemanding reducing agents such as $LiAlH_4$ and $NaBH_4$ are known to approach simple cyclic ketones preferentially along what is apparently the more hindered axial trajectory, thus leading to the equatorial alcohol as the major reaction product. This tendency can be reversed by using reagents or substrates that are more sterically demanding. Reduction of *cis*-2,6-dimethylcyclohexanone (**1**) can yield two diastereomeric alcohols (**2** and **3**). The *trans* isomer (**4**) provides diastereomers **5** and **6**, which are easily interconverted by a ring flip, thus yielding for all practical purposes only the more stable conformer **5**. In a seminal paper, Wigfield and Phelps (2) reported that reduction of the *cis* isomer **1** with $NaBH_4$ in 2-propanol gave a **2**:**3** alcohol ratio of 62:38. Assignment of equatorial alcohol **2** as the major product was based on relative GC retention times and analysis of 60 MHz NMR spectra. Garner (3) found that reduction of **1** with $NaBH_4$ in methanol yielded two alcohols in a ratio of 68:32; by analogy to the earlier work, the major isomer was assumed to be equatorial alcohol **2** (see Scheme 1).

When we repeated the reduction of *cis*-2,6-dimethylcyclohexanone with $NaBH_4$ in methanol, the axial alcohol **3** was clearly the major product, an unexpected result based upon prior reports and current paradigms for similar cyclohexanone reductions (see Discussion). We have carefully and systematically reexamined the $NaBH_4$ and $LiAlH_4$ reductions of *cis*- and *trans*-2,6-dimethylcyclohexanones and report herein additional results that are not entirely in accord with prior reports. Possible explanations for the discordances are given, an unusual solvent effect is noted, the rate of epimerization versus reduction is examined, molecular modeling results are reported, and an important caveat is offered for other stereochemical studies of this nature.

Received April 1, 1998.

T.E. Goodwin,[1] J.M. Meacham, and M.E. Smith.
Department of Chemistry, Hendrix College, Conway, AR 72032, U.S.A.

[1]Author to whom correspondence may be addressed. Telephone: (501) 450-1252. Fax: (501) 450-3829. E-mail: Goodwin@Hendrix.edu

Results

The reduction of a mixture of *cis*- and *trans*-2,6-dimethylcyclohexanones was performed using $LiAlH_4$ in both diethyl ether and THF, as well as with $NaBH_4$ in both methanol and 2-propanol.[2] As much as possible, reaction conditions were standardized (see Experimental). The product mixtures were directly analyzed by GC–MS before any solvent evaporation, since we experienced product loss with

 © 1998 NRC Canada

Scheme 1. Reduction products from 2,6-dimethylcyclohexanones.

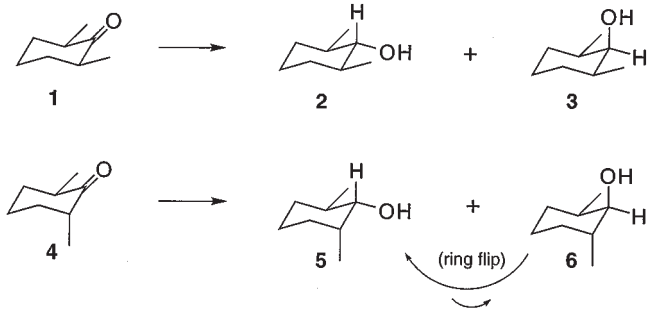

use of a rotary evaporator. Product mixtures were also analyzed by ^{1}H NMR spectroscopy. Before preparation of NMR samples, the dried product solutions were placed in a hood to allow selective solvent evaporation at the ambient temperature.

Table 1 shows the ratio of products from reduction of *cis*-2,6-dimethylcyclohexanone as determined by both GC–MS and NMR.[3] Very little stereoselectivity is evident for reduction of the *cis* ketone with the notable exception of the $NaBH_4$ reduction in methanol for which our ratios are similar to those reported by Garner (3). In contrast, however, to the earlier assumption for this reductant–solvent combination, it is clear that the axial alcohol **3** predominates over the equatorial alcohol **2** in the product mixture as shown by 300 MHz ^{1}H NMR spectral analysis and integration. Specifically, the HCOH methine hydrogen for isomer **2** appears as a triplet (J = 9.6 Hz) at δ 2.70, while that for isomer **3** appears as a broad singlet at δ 3.53, thus they are easily distinguished. The analogous hydrogen for alcohol **5** appears as a doublet of doublets (J = 7.7, 4.1 Hz) at δ 3.32).[4]

There is less consonance between our ratios for reduction of the *cis* isomer with $NaBH_4$ in 2-propanol and the 62:38 ratio reported previously (2). This reaction was run again in our laboratories under the more dilute conditions and longer reaction time used in the former work (5), to provide a **2**:**3** ratio of 49:51 as determined by GC–MS.[5] In view of the product loss in this reaction when using a rotary evaporator, it is possible that differential evaporation of isomers **2** and **3** gave rise to the apparent predominance of **2** reported by earlier workers. Support for this conclusion is evidenced in entry D of Table 1, which reports essentially no selectivity by GC–MS, but a slight excess of alcohol **2** by NMR integration after solvent evaporation, a result more in line with the prior report (2).

Table 1. Relative percent of reduction products from 2,6-dimethylcyclohexanones.

		Compound no.	
Reagent–solvent	Method	**2**:**3**	(**2** + **3**):**5**
A. LAH–THF	GC–MS	49:51	80:20
	NMR	49:51	79:21
B. LAH–Et_2O	GC–MS	53:47	80:20
	NMR	54:46	79:21
C. $NaBH_4$–MeOH	GC–MS	29:71	80:20
	NMR	33:67	79:21
D. $NaBH_4$–*i*-PrOH	GC–MS	50:50	75:25
	NMR	54:46	71:29

Our $LiAlH_4$ data disagree with a tabulated **2**:**3** ratio of 62:38 in the literature (6), although the origin of that ratio is not clear and may be a mistaken citation of the Wigfield and Phelps data (2) using $NaBH_4$ in 2-propanol.[6] Our results are, however, in line with those of Boone and Ashby (7), who observed that $LiAlH_4$ reduction of the closely related *cis*,*cis*-4-*tert*-butyl-2,6-dimethylcyclohexanone in THF gave 53% of the equatorial alcohol (axial hydride addition).

The table also lists the ratio of products (**2** + **3**) derived from reduction of *cis*-2,6-dimethylcyclohexanone to that (product **5**) from the *trans* isomer. This ratio is of interest when compared to the ratio of reactant ketones (see footnote 2). The GC–MS and ^{1}H NMR spectral analyses reveal a constant ratio for entries A, B, and C, suggesting little if any epimerization of the reactant ketones before reduction. The exception is entry D ($NaBH_4$ in 2-propanol), where the proportion of alcohol **5** in the product mixture is higher than that of ketone **4** in the reactant mix. This phenomenon has been noted previously (2*a*). This discrepancy was found to be even more pronounced in a more dilute solution of 2-propanol (see footnote 5) where a (**2** + **3**):**5** ratio of 84:16 was determined by GC–MS, although the **2**:**3** ratio was essentially unchanged relative to entry D in Table 1. The $NaBH_4$ reduction of 2,6-dimethylcyclohexanones in 2-propanol is apparently significantly slower than for the other three reductant–solvent combinations, a difference which becomes even more pronounced upon dilution. This rate decrease then allows epimerization to take place prior to reduction, giving rise to variable results.

Discussion

Boone and Ashby (7) have presented clear evidence that equatorial α-methyl substituents on a cyclohexanone ring

[2] The mixture of *cis*- and *trans*-2,6-dimethylcyclohexanones was obtained from Aldrich and was labeled as 98% pure. By GC–MS, a *cis*:*trans* ratio of 80:20 was found, remarkably close to the 81:19 ratio reported by Garner (3) in 1993. A ratio of 79:21 by integration of the ^{1}H NMR spectrum of a $CDCl_3$ solution was also observed. As the results in Table 1 and discussion in the text reveal, minor ratio discrepancies of this sort are common, and thus are at least partly related to idiosyncrasies of the two measurement techniques.

[3] The values in Table 1 represent an average of duplicate, simultaneous reactions. The NMR ratios for the two LAH–THF reactions were 51:49 and 48:52. Otherwise, agreement was excellent between duplicate runs, with differences in relative product percentages between each pair of reactions averaging 0.4 for GC–MS analysis and 0.7 for NMR analysis.

[4] A similar chemical-shift trend and coupling pattern was reported for the analogous acetates (4*a*). Coupling constants for the HCOH methine hydrogen were calculated on MMX-minimized structures using PCMODEL (Serena Software) and are in good agreement with experimental values: **2** (t, J = 10.1 Hz), **3** (t, J = 1.8 Hz), and **5** (dd, J = 10.1, 4.6 Hz). The ^{1}H NMR calculation using PCMODEL is based on a modified Karplus algorithm (4*b*). The ^{13}C NMR spectral assignments for alcohols **2**, **3**, and **5** have been reported (4*c*).

[5] The ketone mix (89 μL) and $NaBH_4$ (29 mg) were reacted in 3.2 mL of 2-propanol for 23 h.

[6] K. Houk. Personal communication.

© 1998 NRC Canada

retard axial approach of $LiAlH_4$. A simple, yet compelling steric rationalization for this trend is that with each additional equatorial α-alkyl group, a new 1,3-diaxial-type interaction exists between the incoming axial nucleophile and a C—H bond on a rotamer of the alkyl group, thus disfavoring this approach trajectory (e.g., for *cis*-2,6-dimethylcyclohexanone, four such interactions would exist: one from each axial hydrogen on carbons 3 and 5, and one from each α-methyl). When the "nonbonded" electron isodensity surface (the molecule's "electron cloud") from 3-21G(*) ab initio calculations is examined, an increasing steric bias against axial approach of a nucleophile is observed as α-substitution increases.[7]

An explanation for the usual avoidance of equatorial approach of a small nucleophile to the carbonyl carbon of an unhindered cyclic ketone invokes torsional strain with neighboring axial α-hydrogens (8). Anh (9*a*) has proposed that axial approach of the nucleophile is most favorable when the axial α-hydrogens are closer to being perpendicular to the plane of the carbonyl group (the "flattening rule"), thus maximizing the n-σ^* interaction between the unshared electron pair of the nucleophile and the antibonding orbital of each axial α-C—H bond (the "antiperiplanar effect").[8]

To examine flattening in the present case, the dihedral angle has been determined between an axial α-hydrogen and the carbonyl for cyclohexanone, 2-methylcyclohexanone, and *cis*-2,6-dimethylcyclohexanone on structures generated by geometry optimization using AM 1 semi-empirical calculations, followed by single-point 3-21G(*) ab initio calculations. The angles are 105.1°, 111.0°, and 113.1°, respectively, thus leading to a correct prediction of an increased equatorial approach of the nucleophile with α-substitution based on Anh's flattening rule.

Nucleophilic additions to carbonyl groups are often considered to result from an interaction between the HOMO of the nucleophile and the LUMO of the carbonyl group. It is of interest to note that the absolute value of the LUMO[7] for cyclohexanone, 2-methylcyclohexanone, and *cis*-2,6-dimethylcyclohexanone is greater on the face of the ring corresponding to axial approach of the nucleophile, thus suggesting preferred nucleophilic approach from that direction. As α-substitution increases, however, steric factors may become more decisive than these orbital interactions. Notably, when the 2,6-dimethylcyclohexanone mixture was reduced with the bulky reducing agent $Li(s\text{-}Bu)_3BH$ in THF, none of product **2** could be detected, thus demonstrating that axial bond formation on ketone **1** is sterically disfavored.[9]

Conclusions

For reduction of *cis*-2,6-dimethylcyclohexanone with $LiAlH_4$ in diethyl ether or THF, or with $NaBH_4$ in 2-propanol, there is apparently a very close balance between factors that hinder and (or) encourage axial and equatorial hydride addition thus leading to little stereoselectivity. With $NaBH_4$ in methanol, however, formation of the axial alcohol **3** predominates. In an earlier mechanistic study on ketone reductions with $NaBH_4$ in a protic solvent, Wigfield and Gowland (12) found a kinetic order of 1.5 with respect to 2-propanol. Therefore, solvent clearly can play a role in the $NaBH_4$ reduction mechanism. Perhaps interaction of *cis*-2,6-dimethylcyclohexanone with methanol results in a subtle conformational shift, which increases the dihedral angle between the axial α-hydrogens and the carbonyl, thus leading to increased equatorial approach of the reducing agent. Whatever the reason, the solvent-dependent stereoselectivity reported herein provides further evidence of the important role that the solvent plays in $NaBH_4$ reductions. Finally, a caveat is proffered: our experience suggests that similar studies of reduction stereochemistry should analyze isomer ratios before solvent evaporation is attempted, to avoid possible alteration of product ratios through differential rates of evaporation.

Experimental

All reductions were run in duplicate for 1 h on 89 μL (82.3 mg; 0.652 mmol) of a commercial mixture (Aldrich) of *cis*- and *trans*-2,6-dimethylcyclohexanones (see footnote 2) and an excess of the reducing agent (0.738 mmol of $LiAlH_4$ or 0.714 mmol of $NaBH_4$) with stirring in 1 mL of solvent. In all cases, the ketones were added with caution to a stirring mixture of the reducing agent in the chosen solvent at the ambient temperature (approx. 20°C). The $NaBH_4$ reductions were cautiously quenched with 3 M HCl (1 mL), diluted with saturated NaCl solution (1 mL), and extracted with diethyl ether (3 × 1 mL). The $LiAlH_4$ reactions were cautiously quenched with H_2O (two drops), aqueous NaOH solution (15%; six drops), and again with H_2O (two drops), then filtered over Celite, which was rinsed with diethyl ether (4 mL). Ether solutions were dried over anhydrous Na_2SO_4.

The GC–MS analysis was carried out using a Hewlett Packard 5890 Series II chromatograph with an HP 5971A mass selective detector. The capillary column was an HP-5 (cross-linked 5% phenyl methyl silicone) with a length of 30 m, an inner diameter of 0.25 mm, and a film thickness of 0.25 μm. Baseline separation was achieved for all three alcohol products with an initial temperature of 60°C (hold 0.5 min), followed by a 4°C/min ramp to 90°C (hold 0.5 min), then a 10°C/min ramp to 100°C. The starting ketones were not detected in any of the product mixtures. The

[7] All ab initio calculations were carried out using MacSpartan Plus from Wavefunction, Inc.

[8] Another popular and useful hypothesis proposed by Cieplak (10*a*) assumes an electron-poor transition state for nucleophilic addition to a carbonyl, thence leading to reaction preferentially antiperiplanar to the best electron-donating vicinal bond. (For a review of arguments for and against the Cieplak model, see ref. 10*b*; for a cogent commentary and new data, see ref. 10*c*.).

[9] Throughout Discussion, an assumption has been made that the reduction of the cyclic ketones proceeds via the more stable chair conformers, yet it is possible that the less populous chair conformer is reduced more rapidly (cf. ref. 11). Examination of the nonbonded electron isodensity surface from 3-21G(*) calculations for the less stable chairs of 2-methylcyclohexanone, and *cis*-2,6-dimethylcyclohexanone reveals a clear steric preference for formation of the equatorial alcohol (axial approach of the nucleophile), which upon chair flip to the more stable conformer provides the axial alcohol. This is the same major product that would be expected from reduction of the more stable ketone conformer if the reaction outcome is controlled primarily by steric factors.

© 1998 NRC Canada

^{1}H NMR spectra were obtained on a Varian Gemini 300 MHz spectrometer.

Acknowledgments

We thank Professors C. Garner (Baylor University) and K. Houk (UCLA), as well as Drs. W. Hehre and J. Nelson (both of Wavefunction, Inc.), for useful comments and advice. The early experimental assistance of E. Hurst, J. Green, and A. Guinn is appreciated. The National Science Foundation – Instrumentation Laboratory Improvement Program, Research Corporation, and The Roy and Christine Sturgis Charitable and Educational Trust are thanked for funding the purchase of an NMR spectrometer. The GC–MS instrumentation was provided by a generous grant from the Hewlett Packard Foundation.

References

1. (*a*) E.L. Eliel, S.H. Wilen, and L.N. Mander. Stereochemistry of organic compounds. Wiley–Interscience, New York. 1994. p. 886; (*b*) F.A. Carey and R.J. Sundberg. Advanced organic chemistry; part B: reactions and synthesis. 3rd ed. Plenum Press, New York. 1990. p. 243.
2. (*a*) D.C. Wigfield and D.J. Phelps. J. Am. Chem. Soc. **96**, 543 (1974); (*b*) J. Org. Chem. **41**, 2396 (1976).
3. C.M. Garner. J. Chem. Educ. **70**, A310 (1993).
4. (*a*) T. Ichikawa and T. Kato. Bull. Chem. Soc. Jpn. **41**, 123 (1968); (*b*) C.A.G. Haasnoot, F.A. A.M. de Leeuw, and C. Altona. Tetrahedron, **36**, 2783 (1980); (*c*) M.F. Grenier-Loustalot, A. Zahidi, J. Bonastre, and P. Grenier. J. Chromatogr. **150**, 429 (1978).
5. D.C. Wigfield and D.J. Phelps. Can. J. Chem. **50**, 388 (1972).
6. Y.-D. Wu and K.N. Houk. J. Am. Chem. Soc. **109**, 908 (1987).
7. J.R. Boone and E.C. Ashby. *In* Topics in stereochemistry. Vol. 11. *Edited by* N.L. Allinger and E.L. Eliel. Wiley, New York. 1979. pp. 82–85, 89–90.
8. (*a*) M. Cherest, H. Felkin, and N. Prudent. Tetrahedron Lett. 2199 (1968); (*b*) M. Cherest and H. Felkin. Tetrahedron Lett. 2205 (1968).
9. (*a*) N.T. Anh. Top. Curr. Chem. **88**, 145, (1980); (*b*) D. Mukherjee, Y-D. Wu, F.R. Fronczek, and K.N. Houk. J. Am. Chem. Soc. **110**, 3328 (1988); (*c*) Y.-D. Wu, K.N. Houk, and M.N. Paddon-Row. Angew. Chem. Int. Ed. Engl. **31**, 1019, (1992).
10. (*a*) A.S. Cieplak. J. Am. Chem. Soc. **103**, 4540 (1981); (*b*) B.W. Gung. Tetrahedron, **52**, 5263 (1996); (*c*) R.R. Fraser, N.C. Faibish, F. Kong, and K. Bednarski. J. Org. Chem. **62**, 6164 (1997).
11. D.C. Wigfield, S. Feiner, and D.J. Phelps. J. Org. Chem. **40**, 2533 (1975).
12. D.C. Wigfield and F.W. Gowland. J. Org. Chem. **42**, 1108 (1977).

© 1998 NRC Canada

Solubility of fluoranthene in organic nonelectrolyte solvents. Comparison of observed versus predicted values based upon Mobile Order theory

Carmen E. Hernández and William E. Acree, Jr.

Abstract: Experimental solubilities are reported at 25.0°C for fluoranthene dissolved in 36 different organic nonelectrolyte solvents containing ester, ether, hydroxy, chloro, methyl, and *tert*-butyl functional groups. Results of these measurements are used to test the applications and limitations of expressions derived from Mobile Order theory. For the 28 solvents for which predictions could be made, computations show that Mobile Order theory does provide fairly reasonable estimates of the saturation mole fraction solubilities. Average absolute deviation between predicted and observed values is 53%. In comparison, the average absolute deviation is 1574% when ideal solution behavior is assumed.

Key words: fluoranthene solubilities, organic nonelectrolyte solvents, solubility predictions.

Résumé : On a déterminé les solubilités expérimentales, à 25°C, du fluoranthène dissous dans 36 solvants organiques non électrolytes contenant des groupes fonctionnels ester, éther, hydroxyle, chloro, méthyle et *tert*-butyle. On a utilisé les résultats de ces mesures pour vérifier les applications et les limitations d'expressions dérivées de la théorie de l'ordre mobile. Dans le cas des 28 solvants pour lesquels il a été possible de faire des calculs, ceux-ci montrent que la théorie de l'ordre mobile conduit à des évaluations assez raisonnables des solubilités de saturation exprimées en fraction molaire. La déviation moyenne absolue entre les valeurs calculées et observées est de 53%. En comparaison, la déviation moyenne absolue est de 1574% lorsqu'on fait l'hypothèse que la solution se comporte de façon idéale.

Mots clés : solubilités du fluoranthène, solvants organiques non électrolytes, prédictions de solubilité.

[Traduit par la Rédaction]

Introduction

Solid–liquid equilibrium data for organic nonelectrolyte systems are becoming increasingly important in the petroleum industry, particularly in light of present trends towards heavier feedstocks and known carcinogenicity/mutagenicity of many of the larger polycyclic aromatic compounds. Solubility data for a number of polycyclic aromatic hydrocarbons (e.g., anthracene and pyrene) and hetero-atom polynuclear aromatics (e.g., carbazole, dibenzothiophene, and xanthene) have been published in the recent chemical literature (for listing of references see Acree (1–3)). Despite efforts by experimentalists and scientific organizations, both in terms of new experimental measurements and critically evaluated data compilations, there still exist numerous systems for which solubility data are not readily available.

To address this problem, researchers have turned to group contribution methods and semiempirical expressions to predict desired quantities. Group contribution methods have proved fairly successful in estimating solid solubility in pure and binary solvent mixtures from structural information (4–11). Practical application, however, is limited to systems for which all group interaction parameters are known. Interaction parameters can be evaluated from liquid–vapor, liquid–liquid, and solid–liquid equilibria data. It is important that the data base contain as many different functional groups as possible, preferably with adequate representation from both mono- and multi-functional solute/solvent molecules to permit evaluation of potential synergistic effects. The data base should contain sufficient experimental values near infinite dilution in the event that one wishes to determine separate interaction parameters for finite concentration and infinite dilution activity coefficient predictions.

Abraham et al. (12, 13) recently developed a general solvation equation that can be used in the correlation and understanding of physicochemical and biochemical phenomena. Physical properties that have been correlated include gas–solvent partition coefficients (as log L)

$$[1] \qquad \log L = c + rR_2 + s\pi_2^H + a\Sigma\alpha_2^H + b\Sigma\beta_2^H + d\log L^{16}$$

and water–solvent partition coefficients (as log P)

$$[2] \qquad \log P = c + rR_2 + s\pi_2^H + a\Sigma\alpha_2^H + b\Sigma\beta_2^H + vV_x$$

Received March 25, 1998.

C.E. Hernández and W.E. Acree, Jr.[1] Department of Chemistry, University of North Texas, Denton, Texas 76203-5070, U.S.A.

[1]Author to whom correspondence may be addressed. E-mail: Acree@unt.edu

© 1998 NRC Canada

where R_2 and V_x refer to the molar refraction and McGowan volume of the solute, respectively, π_2^H is the solute dipolarity/polarizability descriptor, and $\Sigma\alpha_2^H$ and $\Sigma\beta_2^H$ are measures of the hydrogen-bond acidity and hydrogen-bond basicity of the solute. For any given solvent, numerical values of the curve-fit coefficients (*c*, *r*, s, *a*, *b*, *d*, and *v*) are deduced by regressing experimental partition coefficient data in accordance with eqs. [1] and [2]. The input partition coefficients were sometimes calculated as the ratio of the solute molar solubilities in the organic solvent and water, $P = C_A^{org}/C_A^{aq}$, and as the ratio of the solute molar solubility in the organic solvent and vapor concentration, $L = C_A^{org}/C_A^{gas}$. Published papers have reported curve-fit coefficients for water (12, 13) and a few select organic solvents (13).

To increase the solubility database available for developing group contribution methods and general solvation correlations, we are in the process of measuring solubility data for polycyclic aromatic hydrocarbons (PAHs) and polycyclic aromatic nitrogen heteroatoms (PANHs). In the present communication, we report fluoranthene solubilities in 36 different organic solvents. Functional groups represented include ethers, esters, hydroxy, chloro, aromatic, and saturated hydrocarbons. Results of these measurements are used to further test the applications and limitations of predictive expressions derived from Mobile Order theory.

Materials and methods

Fluoranthene (Aldrich, 98%) was recrystallized several times from methanol. *n*-Hexane (Aldrich, 99%), *n*-heptane (Aldrich, HPLC), *n*-octane (Aldrich, 99+%, anhydrous), *n*-nonane (TCI, 99+%), *n*-decane (TCI, 99+%), *n*-hexadecane (Aldrich, 99%), cyclohexane (Aldrich, HPLC), methylcyclohexane (Aldrich, 99+%, anhydrous), cyclooctane (Aldrich, 99+%), 2,2,4-trimethylpentane (Aldrich, HPLC), *tert*-butylcyclohexane (Aldrich, 99+%), dibutyl ether (Aldrich, 99%), methyl *tert*-butyl ether (Arco, 99.9+%), butyl acetate (Aldrich, 99.7%), ethyl acetate (Aldrich, HPLC, 99.9%), 1-chlorobutane (Sigma-Aldrich, HPLC, 99.5+%), 1-chlorooctane (Aldrich, 99%), chlorocyclohexane (Aldrich, 99%), methanol (Aldrich, 99.9+%), ethanol (Aaper Alcohol and Chemical Company, absolute), 1-propanol (Aldrich, 99+%, anhydrous), 2-propanol (Aldrich, 99+%, anhydrous), 1-butanol (Aldrich HPLC, 99.8+%), 2-butanol (Aldrich, 99+%, anhydrous), 1-pentanol (Aldrich, 99+%), 2-pentanol (Acros 99+%), 1-hexanol (Alfa Aesar, 99+%), 1-heptanol (Alfa Aesar, 99+%), 2-methyl-2-butanol (Acros, 99+%), 2-methyl-1-propanol (Aldrich, 99+%, anhydrous), 3-methyl-1-butanol (Aldrich, 99+%, anhydrous), 1-octanol (Aldrich, 99+%, anhydrous), 4-methyl-2-pentanol (Acros, 99+%), 2-ethyl-1-hexanol (Aldrich, 99+%), 2-methyl-1-pentanol (Aldrich, 99%), and cyclopentanol (Aldrich, 99%) were stored over molecular sieves before use. Gas chromatographic analysis showed solvent purities to be 99.7 mol% or better.

Excess solute and solvent were placed in amber glass bottles and allowed to equilibrate in a constant temperature water bath at 25.0 ± 0.1°C for at least 3 days (often longer). Attainment of equilibrium was verified both by repetitive measurements after several additional days and by approaching equilibrium from supersaturation by preequilibrating the solutions at a higher temperature. Aliquots of saturated fluoranthene solutions were transferred through a coarse filter into a tared volumetric flask to determine the amount of sample, and were diluted quantitatively with methanol for spectrophotometric analysis at 357 nm on a Bausch and Lomb Spectronic 2000. Concentrations of the dilute solutions were determined from a Beer–Lambert law absorbance versus concentration working curve for nine standard solutions. The concentration of fluoranthene in the standard solutions varied from 6.55×10^{-5} M to 2.18×10^{-4} M. The calculated molar absorptivity of the standard solutions varied slightly over the concentration range, from $\varepsilon \approx 8260$ L mol^{-1} cm^{-1} (6.55×10^{-5} M) to $\varepsilon \approx 7915$ L mol^{-1} cm^{-1} (2.18×10^{-4} M). Experimental molar concentrations were converted to (mass/mass) solubility fractions by multiplying by the molar mass of fluoranthene, volume(s) of volumetric

Table 1. Comparison between experimental fluoranthene mole fraction

Organic solvent	$(X_A^{sat})^{exp,a}$	$(X_A^{sat})^{calc}$	% Dev [b]
n-Hexane	0.014 76	0.016 86	14.2
n-Heptane	0.018 70	0.017 97	–3.9
n-Octane	0.022 60	0.020 80	–8.0
n-Nonane	0.026 42	0.024 66	–6.7
n-Decane	0.030 15	0.025 99	–13.8
n-Hexadecane	0.050 46	0.038 00	–25.7
Cyclohexane	0.018 07	0.022 46	24.3
Methylcyclohexane	0.021 79	0.024 60	12.9
Cyclooctane	0.030 11	0.033 27	10.5
2,2,4-Trimethylpentane	0.011 62	0.012 97	11.6
tert-Butylcyclohexane	0.02482	0.034 29	38.2
Dibutyl ether	0.05177	0.1058	104.4
1-Chlorobutane	0.1133	0.1058	–6.6
1-Chlorooctane	0.1367	0.1291	–5.5
Chlorocyclohexane	0.1159	0.1540	32.9
Ethyl acetate	0.085 89	0.1991	131.8
Butyl acetate	0.1106	0.1827	65.2
Methanol	0.002 67	0.007 45	179.0
Ethanol	0.005 44	0.010 81	98.7
1-Propanol	0.006 70	0.013 23	97.5
2-Propanol	0.004 75	0.015 82	233.1
1-Butanol	0.009 96	0.016 80	68.9
2-Butanol	0.007 02	0.012 53	78.5
2-Methyl-1-propanol	0.004 95	0.009 55	92.9
1-Pentanol	0.014 46	0.017 79	23.0
1-Hexanol	0.019 86	0.016 31	–17.9
1-Heptanol	0.025 24	0.018 60	–26.3
1-Octanol	0.031 25	0.020 68	–33.8
Methyl *tert*-butyl ether	0.047 55		
2-Pentanol	0.010 21		
3-Methyl-1-butanol	0.008 62		
2-Methyl-2-butanol	0.009 70		
Cyclopentanol	0.017 72		
2-Ethyl-1-hexanol	0.017 82		
2-Methyl-1-pentanol	0.011 72		
4-Methyl-2-pentanol	0.000 948		

[a]Numerical values represent the average of between four and eight independent determinations, with the measurements being reproducible to ±1.5%.

[b]Deviations (%) = $100\,[(X_A^{sat})^{calc} - (X_A^{sat})^{exp}]\,/\,(X_A^{sat})^{exp}$.

© 1998 NRC Canada

flask(s) used, and any dilutions required to place the measured absorbances on the Beer–Lambert law absorbance versus concentration working curve, and then dividing by the mass of the saturated solution analyzed. Mole fraction solubilities were computed from (mass/mass) solubility fractions using the molar masses of the solute and solvent. Experimental fluoranthene solubilities, X_A^{sat}, in the 36 organic solvents studied are listed in Table 1. Numerical values represent the average of between four and eight independent determinations, with the measurements being reproducible to ±1.5%.

Results and discussion

Solubility data for fluoranthene are available in the chemical literature for only 2 of the 36 solvents listed in Table 1. McLaughlin and Zainal (14) previously reported the solubility of fluoranthene in cyclohexane as a function of temperature. The five temperatures studied by the authors ranged from 301.8 K to 344.2 K, and did not include 298.15 K. The mole fraction solubility at 298.15 K can be obtained by curve-fitting the experimental data to

$$[3] \qquad \ln x_A^{sat} = 60.6443 - 35{,}702/T + 4{,}896{,}935/T^2$$

a $1/T$ polynomial. Three terms were needed to accurately describe the experimental values. Using the above mathematical representation, we calculate a mole fraction solubility of x_A^{sat} = 0.018 05 at 298.15 K, which is in excellent agreement with our measured value of x_A^{sat} = 0.018 07.

Two literature values were found for the solubility of fluoranthene in 1-octanol. Pinal et al. (15) determined a molar solubility of C_A^{sat} = 0.198 at 296.15 K, whereas Miller et al. (16) measured a significantly smaller solubility of C_A^{sat} = 0.1726 at 298.15 K. Both values were determined using well-established analytical methodologies. There is no reason for us to select one value over the other. Molar solubilities can be converted to mole fractions using $V_{octanol}$ = 158.30 cm^3 mol^{-1} and $V_{fluoran}$ = 162.0 cm^3 mol^{-1} (estimated using the group contribution method of Shahidi et al. (17)), and by assuming that the excess volume of mixing is negligible. Performing this computation, mole fraction solubilities of x_A^{sat} = 0.0314 and x_A^{sat} = 0.027 34 were calculated for fluoranthene dissolved in 1-octanol, compared to our measured solubility of x_A^{sat} = 0.031 25.

The solvents listed in Table 1 include both noncomplexing alkanes and self-associating alcohols. Of the many solution models proposed in recent years, Mobile Order theory is perhaps the only one that is capable of describing solute behavior over such a wide range of solvent mixtures. The basic model (18–25) assumes that all molecular groups perpetually move, and that neighbors of a given kind of external atom in a molecule constantly change identity. All molecules of a given kind dispose of the same volume, equal to the total volume V of the liquid divided by the number N_A of molecules of the same kind, i.e., Dom A = V/N_A. The center of this domain perpetually moves. The highest mobile disorder is achieved whenever groups visit all parts of their domain without preference. Preferential contacts lead to deviations with respect to this "random" visiting. This is especially true in the case of hydrogen bonding as specific interactions result in a specific orientation of the "donor" molecule with respect to an adjacent "acceptor" molecule.

In the case of an inert crystalline solute dissolved in a self-associating solvent, Mobile Order theory expresses the volume fraction saturation solubility, ϕ_A^{sat}, as

$$[4] \qquad \ln \phi_A^{sat} = \ln a_A^{solid} - 0.5(1 - V_A/V_{solvent})\,\phi_{solvent} + 0.5 \ln [\phi_A^{sat} + \phi_{solvent}(V_A/V_{solvent})] - \phi_{solvent}^2\, V_A(\delta'_A - \delta'_{solvent})^2 (RT)^{-1} - r_{solvent}(V_A/V_{solvent})\,\phi_{solvent}$$

where the $r_{solvent}\,(V_A/V_{solvent})\,\phi_{solvent}$ term represents the contributions resulting from hydrogen-bond formation between the solvent molecules. For most of the published applications, $r_{solvent}$ was assumed to be unity for strongly associated solvents with single hydrogen-bonded chains such as monofunctional alcohols, to be two for water or diols, and to equal zero for nonassociated solvents such as saturated hydrocarbons. A more exact value for alcoholic solvents can be calculated based upon

$$[5] \qquad r_{solvent} = (K_{solvent}\,\phi_{solvent}/V_{solvent})/(1 + K_{solvent}\,\phi_{solvent}/V_{solvent})$$

with a numerical value of $K_{solvent}$ = 5000 cm^3 mol^{-1} assumed for all monofunctional alcohols.

If complexation does occur between the crystalline solute and solvent

$$[6] \qquad \ln \phi_A^{sat} = \ln a_A^{solid} - 0.5(1 - V_A/V_{solvent})\,\phi_{solvent} + 0.5 \ln [\phi_A^{sat} + \phi_{solvent}(V_A/V_{solvent})] - \phi_{solvent}^2\, V_A(\delta'_A - \delta'_{solvent})^2 (RT)^{-1} + \ln [1 + \phi_{solvent}(K_{ASolvent}/V_{solvent})]$$

then an additional term involving the solute–solvent equilibrium constant, $K_{ASolvent}$, must be introduced to describe the solubility enhancement that arises as a result of specific interactions. A slightly more complex expression applies in the case of solute complexation with a self-associating solvent. The symbols δ'_A and $\delta'_{solvent}$ denote the modified solubility parameters of the solute and solvent, respectively, V_i is the molar volume, and a_A^{solid} is the activity of the solid solute. This latter quantity is defined as the ratio of the fugacity of the solid to the fugacity of the pure hypothetical supercooled liquid. The numerical value of a_a^{solid} can be computed from

$$[7] \qquad \ln a_A^{solid} = -\Delta H_A^{fus}(T_{mp} - T)/(RTT_{mp})$$

where ΔH_A^{fus} is the solute's molar enthalpy of fusion at the normal melting point temperature, T_{mp}. Contributions from nonspecific interaction are incorporated into Mobile Order theory through the $\phi_{solvent}^2 V_A(\delta'_A - \delta'_{solvent})^2 (RT)^{-1}$ term. Ruelle et al. (21–25) have presented an impressive set of comparisons between experimental and predicted values for anthracene, naphthalene, pyrene, biphenyl, carbazole, benzil, *p*-benzoquinone, tricosane, octacosane, 10-nonadecanone, 11-heneicosanone, and 12-tricosanone solubilities in a wide range of both noncomplexing and complexing solvents to document the predictive ability of Mobile Order theory.

© 1998 NRC Canada

Table 2. Solvent and solute properties used in Mobile Order predictions.

Component (i)	$V_i/(cm^3\ mol^{-1})$	$\delta'_i/(MPa^{1/2})$ [a]
n-Hexane	131.51	14.56
n-Heptane	147.48	14.66
n-Octane	163.46	14.85
n-Nonane	179.87	15.07
n-Decane	195.88	15.14
n-Hexadecane	294.12	15.61
Cyclohexane	108.76	14.82
Methylcyclohexane	128.32	15.00
2,2,4-Trimethylpentane	166.09	14.30
Cyclooctane	134.9	15.40
tert-Butylcyclohexane	173.9	15.50
Dibutyl ether	170.3	17.45
Ethyl acetate	98.5	20.79
Butyl acetate	132.5	19.66
1-Chlorobutane	105.0	17.12
1-Chlorooctane	171.1	18.00
Chlorocyclohexane	120.3	18.45
Methanol	40.7	19.25
Ethanol	58.7	17.81
1-Propanol	75.10	17.29
2-Propanol	76.90	17.60
1-Butanol	92.00	17.16
2-Butanol	92.4	16.60
2-Methyl-1-propanol	92.8	16.14
1-Pentanol	108.6	16.85
1-Hexanol	125.2	16.40
1-Heptanol	141.9	16.39
1-Octanol	158.3	16.38
Fluoranthene [b]	162.0 [c]	20.80 [d]

[a]Tabulated values are taken from a compilation given in Ruelle et al. (21, 22, 24, 25).

[b]The numerical value of a_A^{solid} = 0.1912 was calculated from the molar enthalpy of fusion, ΔH_A^{fus} = 18,870 J mol^{-1} (26), at the normal melting point temperature of the solute, T_{mp} = 380.95 K.

[c]Numerical value of $V_{fluoran}$ = 162 cm^3 mol^{-1} was calculated using the group contribution method proposed by Shahidi et al. (17).

[d]Numerical value was calculated using the measured fluoranthene mole fraction solubilities in *n*-hexane, *n*-heptane, and *n*-octane, in accordance with eqs. [4] and [6]; with $r_{solvent}$ = 0 and (or) $K_{ASolvent}$ =0.

Predictive application of eqs. [4] and [6] is relatively straightforward. First, an average numerical value of $\delta'_{fluoran}$ = 20.80 $MPa^{1/2}$ is computed by requiring that each equation (with $r_{solvent}$ = 0 and (or) $K_{ASolvent}$ = 0) perfectly describes fluoranthene mole fraction solubility data in *n*-hexane ($\delta'_{fluoran}$ = 20.95 $MPa^{1/2}$), *n*-heptane ($\delta'_{fluoran}$ = 20.75 $MPa^{1/2}$), and *n*-octane ($\delta'_{fluoran}$ = 20.70 $MPa^{1/2}$). The numerical value of a_A^{solid} = 0.1912 is calculated using eq. [7] with ΔH_A^{fus} = 18,870 J mol^{-1} (26) and T_{mp} = 380.95 K. A numerical value of $V_{fluoran}$ = 162 cm^3 mol^{-1} was used for the molar volume of the hypothetical subcooled liquid solute.

Table 1 summarizes the predictive ability of Mobile Order theory for the 28 different organic solvents for which both fluoranthene solubility data and modified solubility parameters could be found. Solvent molar volumes and modified solubility parameters are listed in Table 2. The modified solubility parameters account for only nonspecific interactions, and in the case of the alcoholic solvents the hydrogen-bonding contributions have been removed. Numerical values of $\delta'_{solvent}$ were obtained from published compilations (21, 22, 24, 25), and were either deduced by regressing actual solubility data of solid *n*-alkanes in organic solvents in accordance with the configurational entropic model of Huyskens and Haulait-Pirson (27) or estimated using known values for similar organic solvents. Examination of the entries in Table 1 reveals that Mobile Order theory does provide fairly reasonable estimates of the solubility behavior of fluoranthene in a wide range of organic solvents. Average absolute deviation between predicted and observed values is 53%. Readers are reminded that in evaluating the applicability of Mobile Order theory one must realize that many of these particular systems are highly nonideal, and that the experimental solubility data cover over a 50-fold range in mole fraction. Had an ideal solution been assumed, then the predicted mole fraction solubility would be $X_A^{sat} = a_A^{solid}$ = 0.1912 for each solvent. The ideal solution approximation corresponds to a considerably larger average absolute deviation of 1574% between predicted and observed values.

Acknowledgements

Carmen Hernández thanks the University of North Texas and the U. S. Department of Education for support provided under the Ronald E. McNair Postbaccalaureate Achievement Program.

References

1. W.E. Acree, Jr. Polycyclic aromatic hydrocarbons in pure and binary solvents. Solubility Data Ser. **54** (1994).
2. W.E. Acree, Jr. Polycyclic aromatic hydrocarbons: binary nonaqueous systems: Part 1 (solutes A–E). Solubility Data Ser. **58** (1995).
3. W.E. Acree, Jr. Polycyclic aromatic hydrocarbons: binary nonaqueous systems: Part 2 (solutes F–Z). Solubility Data Ser. **59 (**1995).
4. W.E. Acree, Jr. Int. J. Pharm. **18**, 47 (1984).
5. U. Domanska and T. Hofman. J. Solution Chem. **14**, 531 (1985).
6. U. Domanska. Fluid Phase Equilib. **35**, 217 (1985).
7. R.S. Basu, H. Pham, and D.P. Wilson. Int. J. Pharm. **7**, 319 (1986).
8. A.B. Ochsner and T.D. Sokoloski. J. Pharm. Sci. **74**, 634 (1985).
9. R. Carta and S. Dernini. J. Chem. Eng. Data, **28**, 328 (1983).
10. W.E. Acree, Jr. and J.H. Rytting. Int. J. Pharm. **13**, 197 (1983).
11. A. Martin, P.L. Wu, A. Adjei, A. Beerbower, and J.M. Prausnitz. J. Pharm. Sci. **70**, 1260 (1981).
12. M.H. Abraham, H.S. Chadha, J.P. Dixon, and A.J. Leo. J. Phys. Org. Chem. **7**, 712 (1994).
13. M.H. Abraham, J. Andonian-Haftvan, J.P. Osei-Owasu, P. Sakellariou, J.S. Urieta, M.C. Lopez, and R. Fuchs. J. Chem. Soc. Perkin Trans. 2, 299 (1993).
14. E. McLaughlin and H.A. Zainal. J. Chem. Soc. 3854 (1960).
15. R. Pinal, P.S.C. Rao, L.S. Lee, P.V. Cline, and S.H. Yalkowsky. Environ. Sci. Technol. **24**, 639 (1990).
16. M.M. Miller, S.P. Wasik, G.-L. Huang, W.-Y. Shiu, and D. Mackay. Environ. Sci. Technol. **19**, 522 (1985).
17. F. Shahidi, P.G. Farrell, J.T. Edward, and P.J. Canonne. J. Org. Chem. **44**, 950 (1979).

© 1998 NRC Canada

18. P.L. Huyskens and G.G. Siegel. Bull. Soc. Chim. Belg. **97**, 821 (1988).
19. G.G. Siegel, P.L. Huyskens, and G. Vanderheyden. Ber. Bunsen-Ges. Phys. **94**, 549 (1990).
20. P.L. Huyskens. J. Mol. Struct. **274**, 223 (1992).
21. P. Ruelle, C. Rey-Mermet, M. Buchmann, H. Nam-Tran, U.W. Kesselring, and P.L. Huyskens. Pharm. Res. **8**, 840 (1991).
22. P. Ruelle, M. Buchmann, H. Nam-Tran, and U.W. Kesselring. Int. J. Pharm. **87**, 47 (1992).
23. P. Ruelle, M. Buchmann, and U.W. Kesselring. J. Pharm. Sci. **83**, 396 (1994).
24. P. Ruelle, E. Sarraf, and U.W. Kesselring. Int. J. Pharm. **104**, 125 (1994).
25. P. Ruelle, E. Sarraf, L. Van den Berge, K. Seghers, M. Buchmann, and U.W. Kesselring. Pharm. Acta Helv. **68**, 49 (1993).
26. F. Casellato, C. Vecchi, A. Girelli, and B. Casu. Thermochim. Acta, **6**, 361 (1973).
27. P.L. Huyskens and M.C. Haulait-Pirson. J. Mol. Liq. **31**, 135 (1985).

© 1998 NRC Canada

Formation of mixed-ligand fluoroboron cations involving C=N donors. A ^{19}F and ^{11}B NMR study

J. Stephen Hartman, Elizabeth I. Ilnicki, James A. W. Shoemaker, Wojciech R. Szerminski, and Zheng Yuan

Abstract: Mixed-donor difluoroboron and chlorofluoroboron cations $DD'BF_2^+$ and $DD'BFCl^+$ involving at least one C=N donor molecule can be formed by Cl^- displacement from the mixed boron trihalide adducts $D\cdot BF_2Cl$ and $D\cdot BFCl_2$, provided that the steric hindrance of D′ and especially D is not too great. The $DD'BF_2^+$ cations can also be formed by selective displacement of one donor molecule in certain $D_2BF_2^+$ cations, present in acetone as their PF_6^- salts, allowing isolation of the first salt of a mixed-donor difluoroboron cation, (quinuclidine)(pyridine)$BF_2^+\cdot PF_6^-$. In less favourable cases, however, either no reaction occurs or the reaction continues to give $D'_2BF_2^+$. Reactivities and ^{19}F and ^{11}B NMR parameters of mixed boron trihalide adducts and fluoroboron cations of a number of C=N donors are reported.

Key words: fluoroboron cations, mixed-ligand, fluorine-19 NMR, boron-11 NMR, oxazolines, thiazolines, C=N donors.

Résumé : À la condition que l'empêchement stérique des donneurs D′ et D ne sont pas trop important, on peut former des cations difluorobore et chlorofluorobore à donneurs mixtes $DD'BF_2^+$ et $DD'BCl^+$ impliquant au moins une molécule donneur C=N par déplacement du Cl^- à partir d'adduits mixtes trihalogénés du bore. On peut aussi former les cations $DD'BF_2^+$ par déplacement sélectif d'une molécule de donneur de certains cations $D_2BF_2^+$ présents dans l'acétone sous la forme de leurs sels de PF_6^-; cette technique a permis d'isoler le premier sel d'un cation difluorobore à donneurs mixtes, (quinuclidine)(pyridine)$BF_2^+\cdot PF_6^-$. Toutefois, dans les cas moins favorables, il n'y a pas de réaction ou celle-ci se poursuit pour donner des $D'_2BF_2^+$. On a déterminé les réactivités et les paramètres de RMN du ^{19}F et du ^{11}B d'adduits mixtes trihalogénés du bore et des cations difluorobore d'un certain nombre de donneurs C=N.

Mots clés : cations difluorobore, ligands mixtes, RMN du fluor-19, RMN du bore-11, oxazolines, thiazolines, donneurs C=N.

[Traduit par la Rédaction]

Introduction

Our studies of the formation of haloboron cations, by reaction of mixed boron trihalide adducts with nitrogen-donor Lewis bases, have shown that tertiary aliphatic amines (1, 2), pyridines (3), and amidines (4) are successively more effective in generating four-coordinate fluoroboron cations by selective displacement of the heavy halide ion from the mixed-halogen adducts. Whereas tertiary aliphatic amines only form $D_2BF_2^+$ and $DD'BF_2^+$ from $D\cdot BF_2X$ (X = Cl, Br; eq. [1]), and even then only when the amine steric hindrance is low, pyridines and amidines form $D_2BF_2^+$ and $DD'BF_2^+$

$$D\cdot BF_2X + D' \rightarrow DD'BF_2^+ + X^- \quad [1]$$

much more rapidly and also form D_2BFCl^+, D_2BFBr^+, and D_3BF^{2+} by heavy halide ion displacement from $D\cdot BFX_2$ (3, 4) (eq. [2]). These reactions allow the attacking donor D′ to be different from D, and many mixed-donor difluoroboron cations involving tertiary amines and pyridines as donors have been detected by NMR (1–3), as well as a few

$$\begin{array}{c} D\cdot BFX_2 + D' \rightarrow DD'BFX^+ + X^- \\ \downarrow \\ DD'_2BF^{2+} + X^- \end{array} \quad [2]$$

chlorofluoroboron cations (3). We here explore the formation of further mixed-ligand difluoroboron and chlorofluoroboron cations involving C=N donors according to eqs. [1] and [2], and show that these can also be prepared by ligand substitution reactions of $D_2BF_2^+$, present as its PF_6^- salt (eq. [3]).

$$D_2BF_2^+ + D' \rightarrow DD'BF_2^+ + D \quad [3]$$

To increase our range of C=N donors we have studied the formation of mixed boron trihalide adducts and fluoroboron cations of the oxazoline and thiazoline bases 2-methyl-2-oxazoline (MOZ), 2-ethyl-2-oxazoline (EOZ), 2-methyl-2-thiazoline (MTZ), and 2-(methylthio)-2-thiazoline (MTTZ). The coordination chemistry of oxazolines has recently become important in the field of enantioselective transition metal catalysis (5), and thiazolines also have an extensive

Received February 4, 1998.

J.S. Hartman,[1] E.I. Ilnicki, J.A.W. Shoemaker, W.R. Szerminski, and Z. Yuan.[2] Department of Chemistry, Brock University, St. Catharines, ON L2S 3A1.

[1]Author to whom correspondence may be addressed. Telephone: (905) 688-5550, ext. 3849. Fax: (905) 682-9020. E-mail: shartman@chemiris.labs.brocku.ca

[2]Present address: Watkins–Johnson Company, Scotts Valley, CA 95066, U.S.A.

© 1998 NRC Canada

coordination chemistry (6), but their coordination to the boron trihalides has apparently not been reported. We also report some adducts and fluoroboron cations of *N*-(*n*-propyl)dimethylketimine and *N*,*N*,*N*′,*N*′-tetramethylguanidine

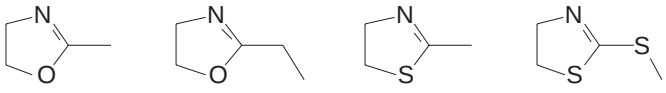

(TMG), and have investigated the formation of mixed-donor fluoroboron cations involving our new C=N donors and our previously studied (1–4) bases quinuclidine (Q; 1-azabicyclo-[2.2.2]octane), pyridine, and the amidines 1,8-diazabicyclo-[5,4,0]undec-7-ene (DBU) and 1,5-diazabicyclo[4,3,0]non-5-ene (DBN).

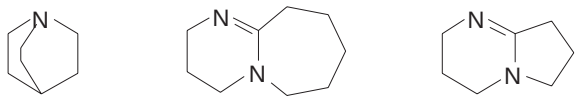

Experimental

Materials

Materials were handled with standard inert-atmosphere Schlenk line and glove bag techniques. Solvents were carefully dried: hexane with sodium wire, and $CDCl_3$ over Lindé 3 Å or 5 Å molecular sieves that had been heated in a muffle furnace at 400°C for more than 3 h and cooled over a period of 0.5 h in a vacuum desiccator. Boron trifluoride and boron trichloride were handled as described previously (4), and quinuclidine, DBU, DBN, and pyridines were obtained as described previously (3, 4). 2-Methyl-2-oxazoline (MOZ; Aldrich, 98%), 2-ethyl-2-oxazoline (EOZ; Aldrich, 99%), 2-methyl-2-thiazoline (MTZ; Aldrich, 99%), and 2-(methylthio)-2-thiazoline (MTTZ; Aldrich, 98%) were stored over Lindé 3 Å molecular sieves and used without further purification. 1,1,3,3-Tetramethylguanidine (Aldrich, 97%) was stored over Lindé 5 Å molecular sieves. *N*-(*n*-Propyl)dimethylketimine was synthesized by reacting 11.9 g of *n*-propylamine with 6.1 g of acetone over a large excess of activated Lindé 5 Å molecular sieves. The product was fractionally distilled in vacuum to give a clear oil that was stored over Lindé 3 Å molecular sieves until use.[3]

The BF_nCl_{3-n} (n = 0–3) adducts and difluoroboron cations of the various bases were prepared in $CDCl_3$ solution as for the analogous amidine complexes (4), and $DD'BF_2^+$ and $DD'BFCl^+$ cations were prepared by reacting D′ with the BF_2Cl and $BFCl_2$ adducts, respectively, of a different donor D, in $CDCl_3$ solution as in previous work (3). Optimum formation of $DD'BF_2^+$ requires optimizing the amount of $D{\cdot}BF_2Cl$ in solution (F:Cl ratio of 1:0.8), while optimum formation of $DD'BFCl^+$ requires optimizing the amount of $D{\cdot}BFCl_2$ in solution (F:Cl ratio of 1:1.2 to 1:1.5).

Reactions of $D_2BF_2^+{\cdot}PF_6^-$ salts with a second donor D′ were carried out in acetone due to the insolubility of the salts in $CDCl_3$ (2–4).

Isolation of (quinuclidine)(pyridine)difluoroboron hexafluorophosphate

In a typical ligand substitution reaction, excess solid quinuclidine was added to 33 mg of $pyr_2BF_2^+{\cdot}PF_6^-$ in 0.5 mL of acetone in a 5 mm NMR tube. On allowing this capped tube to stand in a 50°C oil bath for 1 h, the reaction went to completion with only $(Q)(pyr)BF_2^+$ being produced, as shown by ^{19}F NMR. The solvent was allowed to evaporate on standing, and the residues were washed with two portions of $CHCl_3$ to remove uncomplexed pyridine and quinuclidine. The remaining precipitate was recrystallized from 1:1 acetone/EtOH. Positive ion FAB spectrum, *m*/*z*: 623 $[\{(QpyrBF_2^+)_2PF_6^-\}^+]$, 239 $[(QpyrBF_2)^+]$ (100%), 160 $[QBF_2^+]$, and 112 $[pyrBF_2^+]$. Elemental analysis, found: C 37.56, 37.86; H 4.83, 4.73; N 7.13, 7.16; calculated: C 37.50, H 4.72, N 7.29.

Instrumentation

Most ^{19}F and ^{11}B NMR spectra were obtained on a Bruker AC-200 4.7 tesla multinuclear Fourier transform NMR spectrometer operating at 188.31 MHz (^{19}F) and 64.20 MHz (^{11}B), using 5 mm NMR tubes. The ^{19}F spectra were obtained with 16K FID's, spectral windows of up to 35 000 Hz, with between 200 and 2000 30° pulses and a relaxation delay of 1.0 s. The 90° pulse durations were 6.6 μs (^{19}F) and 17.1 μs (^{11}B). The ^{19}F chemical shifts are accurate to ±0.1 ppm and were internally referenced to C_6F_6 as a secondary standard (–162.7 ppm from $CFC1_3$), and are reported in ppm from $CFC1_3$. The ^{11}B spectra were obtained with 8K FID's and spectral windows of up to 2000 Hz. However, the narrow range of ^{11}B chemical shifts led to such severe overlap of multiplets arising from ^{11}B–^{19}F coupling, that 4.7 tesla ^{11}B spectra were not routinely obtained.

Some ^{19}F, ^{11}B, and $^{11}B\{^{19}F\}$ NMR spectra were obtained at 30°C on a Bruker DRX-500 11.7 tesla multinuclear Fourier transform NMR spectrometer (McMaster University) operating at 470.53 MHz (^{19}F) and 160.46 MHz (^{11}B) using between 40 and 128 30° pulses with 32K FID's. The 90° pulse durations were 7.5 μs (^{19}F) and 15.0 μs (^{11}B). Spectral windows of 42 016 Hz (^{19}F) and 40 000 Hz (^{11}B) were used.

Initial positive-ion fast atom bombardment mass spectra (FAB spectra) were obtained on an AEI MS-30 (Kratos Ltd., Manchester) double-beam mass spectrometer coupled to a saddle-field atom gun (Ion Tech Ltd, Teddington, U.K.), retrofitted with a Kratos FAB source in beam 1. The accelerating voltage was 4 kV. 3-Nitrobenzyl alcohol (NBA) was used as a liquid matrix. Data were collected on a DS-55 Kratos data system. A Hewlett–Packard 2631G printer was used to plot the spectra and mass-intensity data. Signals from the matrix were subtracted automatically in the computer system in most situations. The BMASROS program was utilized for interpretation of isotope patterns. More recently positive ion FAB spectra were obtained on a Concept 1S double beam mass spectrometer, with 8 kV accelerating voltage using Xe collision gas at 7.5 W power. Data were

[3] A. Fox. Unpublished research report. Brock University, St. Catharines. 1981.

© 1998 NRC Canada

Table 1. NMR parameters of $D{\cdot}BF_nCl_{3-n}$ adducts, and $D_2BF_2^+$ and D_2BFCl^+ cations formed from oxazolines and related donors.[a]

D	$D{\cdot}BF_3$	$D_2BF_2^+$	$D{\cdot}BF_2Cl$	D_2BFCl^+	$D{\cdot}BFCl_2$
		^{19}F chemical shifts			
MOZ	–149.5	–151.9	–130.7	–142.8	–122.8
EOZ	–149.1	–151.2	–130.3	–142.6	–122.5
MTZ	–147.0	–145.9	–128.2	–135.4	–118.9
MTTZ	–147.1	–145.3	–127.1	–135.1	–117.1
$(Me_2N)_2C{=}NH$	–145.8	–145.2	–129.2		–116.7
$Me_2C{=}N(n\text{-Pr})$	–145.3[b]	–141.6[b]	–127.0[b]		–115.3[b]
		^{11}B chemical shifts			
MOZ	–0.9	–0.3	0.1	3.2	4.7
MTZ	–1.1		2.1		4.7
		***J*(^{11}B–^{19}F)** (Hz)			
MOZ	11.0	25.8	37.9	49.9	63.3
EOZ	11.3	26.3	37.9	50.6	63.0
MTZ	12.7	29.8	39.5	55.5	65.1
MTTZ	13.8	30.4	40.0	53.6	65.9
$(Me_2N)_2C{=}NH$	17.5	31.5	[c]		[c]
$Me_2C{=}N(n\text{-Pr})$	15.7[b]	32.8[b]	40.0[b]		64.7[b]

[a] $CDCl_3$ solution; ^{19}F chemical shifts are in ppm to high frequency of $CFCl_3$; ^{11}B chemical shifts are in ppm to high frequency of external $Et_2O{\cdot}BF_3$.

[b] Footnote 3. Further values for $Me_2C{=}N(n\text{-Pr})$ adducts are: $D{\cdot}BF_2Br$, –120.2 ppm; *J*, 46.6 Hz; $D{\cdot}BFBr_2$, –105.2 ppm; *J* 84.3 Hz; D·BFClBr, –109.9 ppm; *J* 73.5 Hz.

[c] Not resolved.

Fig. 1. 188.31 MHz ^{19}F NMR spectrum of the $MTTZ{\cdot}BF_nCl_{3-n}$ system.

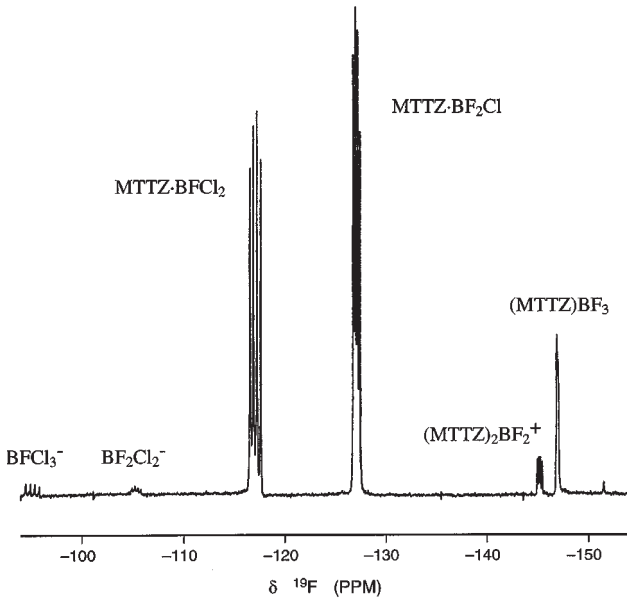

collected on a Kratos DART data system with SUN Spectrostation 10, using XMACH3 software.

Results

(*a*) BF_nCl_{3-n} adducts and fluoroboron cations of new C=N donor molecules

The BF_nCl_{3-n} adducts, and $D_2BF_2^+$ and D_2BFCl^+ cations, of the oxazoline and thiazoline bases and of further C=N donors form readily under standard conditions, (2–4, 7) and are readily detected by ^{19}F and ^{11}B NMR. Their NMR parameters (Table 1) are typical of fluoroboron cations and $D{\cdot}BF_nCl_{3-n}$ adducts (1–4, 7, 8) except that the $D_2BF_2^+$ ^{19}F signals of MOZ and EOZ occur well to low frequency (high field) of $D{\cdot}BF_3$. The ^{11}B multiplets of the BF_nCl_{3-n} adducts and $D_2BF_2^+$ cations overlap so badly at 4.7 tesla that many spectra could not be interpreted; much better ^{11}B spectra were obtained at 11.7 tesla.

The BF_nCl_{3-n} adduct system of MTTZ gives very small additional ^{19}F 1:1:1:1 quartets arising from $BFCl_3^-$ and $BF_2Cl_2^-$ (9) (Fig. 1), which along with BF_3Cl^- are formed in much larger amounts in the corresponding amidine adduct systems (4) but do not appear at all in the adduct systems of most bases. Similarly, the *N*-(*n*-propyl)dimethylketimine–BF_nCl_{3-n} system gave a ^{19}F peak arising from $BFCl_3^-$.[3] These anions apparently form by the mechanism we proposed for amidine adduct systems, involving carbene intermediates generated from the $CDCl_3$ solvent (4). Additional fluorine-containing species, apparently related to the presence of the reactive N-H proton, arise in the $TMG{\cdot}BF_nCl_{3-n}$ system; addition of excess tetramethylguanidine eliminates the ^{19}F signals of the BF_2Cl and $BFCl_2$ adducts and gives broad ^{19}F signals at –143.0 and –169.8 ppm. We have confirmed the identity of $(TMG)_2BF_2^+$ by observing its ^{11}B 1:2:1 triplet and its positive ion FAB peak at *m*/*z* 279 with the expected isotope pattern. Further studies of TMG and its adducts were not carried out because of complications introduced by the high reactivity of the N-H proton.

The D_2BFCl^+ cations of the oxazoline and thiazoline bases form more slowly than the $D_2BF_2^+$ cations, as in the analogous systems with pyridine (3) and amidine (4) donors. However, while pyridine- and amidine-system D_2BFCl^+ cations undergo further chloride ion displacement to give the

© 1998 NRC Canada

Table 2. NMR parameters of mixed-ligand difluoroboron cations.[a]

Mixed species	^{19}F chemical shift (ppm)	^{11}B chemical shift (ppm)	$J(^{11}B–^{19}F)$ (Hz)
$(DBU)(DBN)BF_2^+$	–143.8	1.0	33.0
$(DBU)(pyr)BF_2^+$	–144.1	1.9	26.0
$(DBU)(Q)BF_2^+$	–154.6	1.2	31.3
$(DBU)(MOZ)BF_2^+$	–145.3		25.9
$(DBU)(EOZ)BF_2^+$	–144.9		24.7
$(DBN)(pyr)BF_2^+$	–149.9	1.7	26.2
$(DBN)(Q)BF_2^+$	–158.6	1.5	30.8
$(DBN)(MOZ)BF_2^+$	–150.4		25.5
$(DBN)(EOZ)BF_2^+$	–149.8		24.0
$(DBN)(MTZ)BF_2^+$	–147.5		30[c]
$(pyr)(Q)BF_2^+$ [b]	–161.5		28.5
$(pyr)(MOZ)BF_2^+$	–151.8	0.8	25.8
$(pyr)(MTZ)BF_2^+$	–149.2		27.1
$(Q)(MOZ)BF_2^+$	–159.4		31.2
$(Q)(MTZ)BF_2^+$	–156.1		32.6
$(MOZ)(MTZ)BF_2^+$	–149.1		27.5
$(MOZ)(MTTZ)BF_2^+$	–147.9		28.4
$(EOZ)(MTZ)BF_2^+$	–148.5		28.2
$(EOZ)(MTTZ)BF_2^+$	–147.9		29.8
$(MTZ)(MTTZ)BF_2^+$	–145.6		30[c]

[a] $CDCl_3$ solution; ^{19}F chemical shifts are in ppm to high frequency of $CFCl_3$; ^{11}B chemical shifts are in ppm to high frequency of external $Et_2O{\cdot}BF_3$.
[b] Reference 2.
[c] Poor resolution.

D_3BF^{2+} cations under forcing conditions, a D_3BF^{2+} cation could be detected only with MOZ. In the other oxazoline and thiazoline systems, standing with excess donor at 40–50°C led only to decomposition of the already-present adducts and cations and the appearance of new ^{19}F signals without splittings due to $^{11}B–^{19}F$ coupling.

Only with MOZ as donor does a broad ^{19}F signal appear at –146.0 ppm where the D_3BF^{2+} signal was expected by analogy with the pyridine and amidine systems. This signal did not show splittings due to $^{11}B–^{19}F$ coupling on the 4.7 tesla instrument. Such splittings are not present, or if present are not well resolved, in the 4.7 tesla ^{19}F signals of confirmed D_3BF^{2+} cations, and this is attributed to slower tumbling and more efficient ^{11}B quadrupole relaxation when boron has three bulky substituents (4). Further evidence for the presence of $(MOZ)_3BF^{2+}$ comes from the 11.7 tesla ^{11}B spectrum, which includes a 1:1 doublet at 2.5 ppm with $J(^{11}B–^{19}F)$ = 51.0 Hz. The DBN system (4), which gives fluoroboron adduct and cation ^{19}F NMR parameters very similar to their MOZ-system analogs, has a well-established $(DBN)_3BF^{2+}$ cation with ^{19}F chemical shift –143.4 ppm and ^{11}B chemical shift 2.2 ppm but with no splittings due to $^{11}B–^{19}F$ coupling detectable on the 4.7 tesla NMR instrument (4). We have recently detected splittings due to $^{11}B–^{19}F$ coupling in the 11.7 tesla ^{11}B and ^{19}F spectra of this species: J = 48.6 Hz. These similarities to the NMR parameters of the species formed in the MOZ system supports the existence of the analogous $(MOZ)_3BF^{2+}$ cation.

Table 3. ^{19}F NMR parameters of mixed-ligand chlorofluoroboron cations.

Mixed species	^{19}F chemical shift (ppm)[a]	$J(^{11}B–^{19}F)$ (Hz)
$(DBU)(pyr)BFCl^+$ [b]	–128.7	50.1
$(DBN)(pyr)BFCl^+$	–133.8	[c]
$(DBN)(Q)BFCl^+$	–146.5	[c]
$(DBN)(MOZ)BFCl^+$	–137.0	[c]
$(DBN)(MTZ)BFCl^+$	–133.8	[c]
$(pyr)(MOZ)BFCl^+$	–141.5	51.5
$(pyr)(MTZ)BFCl^+$	–137.9	52.9
$(Q)(MOZ)BFCl^+$	–143.3	55.6
$(Q)(MTZ)BFCl^+$	–146.2	55.6
$(MOZ)(EOZ)BFCl^+$	–142.9	55.6
$(MOZ)(MTZ)BFCl^+$	–139.0	54.0
$(MOZ)(MTTZ)BFCl^+$	–137.4	53.6
$(EOZ)(MTZ)BFCl^+$	–137.1	54.3
$(EOZ)(MTTZ)BFCl^+$	–137.1	53.6

[a] $CDCl_3$ solution; chemical shifts are in ppm to high frequency (low field) of $CFCl_3$.
[b] ^{11}B chemical shift for $(DBU)(pyr)BFCl^+$ is 5.2 ppm from external $Et_2O{\cdot}BF_3$.
[c] Not resolved.

(*b*) Mixed-ligand fluoroboron cations from $D{\cdot}BF_2Cl$ and $D{\cdot}BFCl_2$

General

Mixed-ligand fluoroboron cations form in a manner very similar to the unmixed-ligand cations described above, but D′ for D exchange in the BF_3 adduct competes with Cl^- displacement by D′. The DD′BF_2^+ cations form readily at room temperature in $CDCl_3$ giving distinctive ^{19}F and ^{11}B NMR signals. The entire series of adducts $D{\cdot}BF_nCl_{3-n}$ (n = 0–3) is present in these solutions but as in previous work (3) the $D{\cdot}BF_2Cl$ adduct always reacts first. Following its disappearance, the $D{\cdot}BFCl_2$ adduct reacts slowly with D′ to give DD′$BFCl^+$. The NMR parameters of the difluoroboron and chlorofluoroboron cations are given in Tables 2 and 3, respectively. The ^{11}B chemical shifts show little variation in these series, and only a few were determined.

Reactions of DBU·BF_nCl_{3-n} with D′

D′ = quinuclidine: The ^{19}F NMR monitoring of the formation of $(DBU)(Q)BF_2^+$ from $DBU{\cdot}BF_2Cl$ is shown in Fig. 2. In amidine–BF_nCl_{3-n} systems all ionic and neutral adduct species and the mixed chlorofluoroborate anions are observed, the latter apparently arising from attack of the strongly basic amidines on $CDCl_3$ (4). Introduction of successive portions of quinuclidine led to rapid reaction of quinuclidine with the anions and neutral adducts. The intensity of the $DBU{\cdot}BF_2Cl$ ^{19}F resonance decreased regularly as the resonance assigned to $(DBU)(Q)BF_2^+$ (intermediate in chemical shift and coupling constant values between $(DBU)_2BF_2^+$ and $Q_2BF_2^+$) increased by similar amounts, confirming that $(DBU)(Q)BF_2^+$ forms from $DBU{\cdot}BF_2Cl$. Interestingly the reaction does not proceed further to give the well-known (1, 2) $Q_2BF_2^+$. The initially present ^{19}F signals of the mixed chlorofluoroborate anions diminished while the

© 1998 NRC Canada

Fig. 2. 188.31 MHz ^{19}F NMR monitoring of the titration of a DBU·BF_nCl_{3-n} solution in $CDCl_3$ (0.2 mmol DBU; mole ratio DBU:BF_3:BCl_3 = 2:1:1) with quinuclidine. Amount of quinuclidine (mmol) added: (*a*) 0; (*b*) 0.02; (*c*) 0.04; (*d*) 0.06; (*e*) 0.08; (*f*) 0.10.

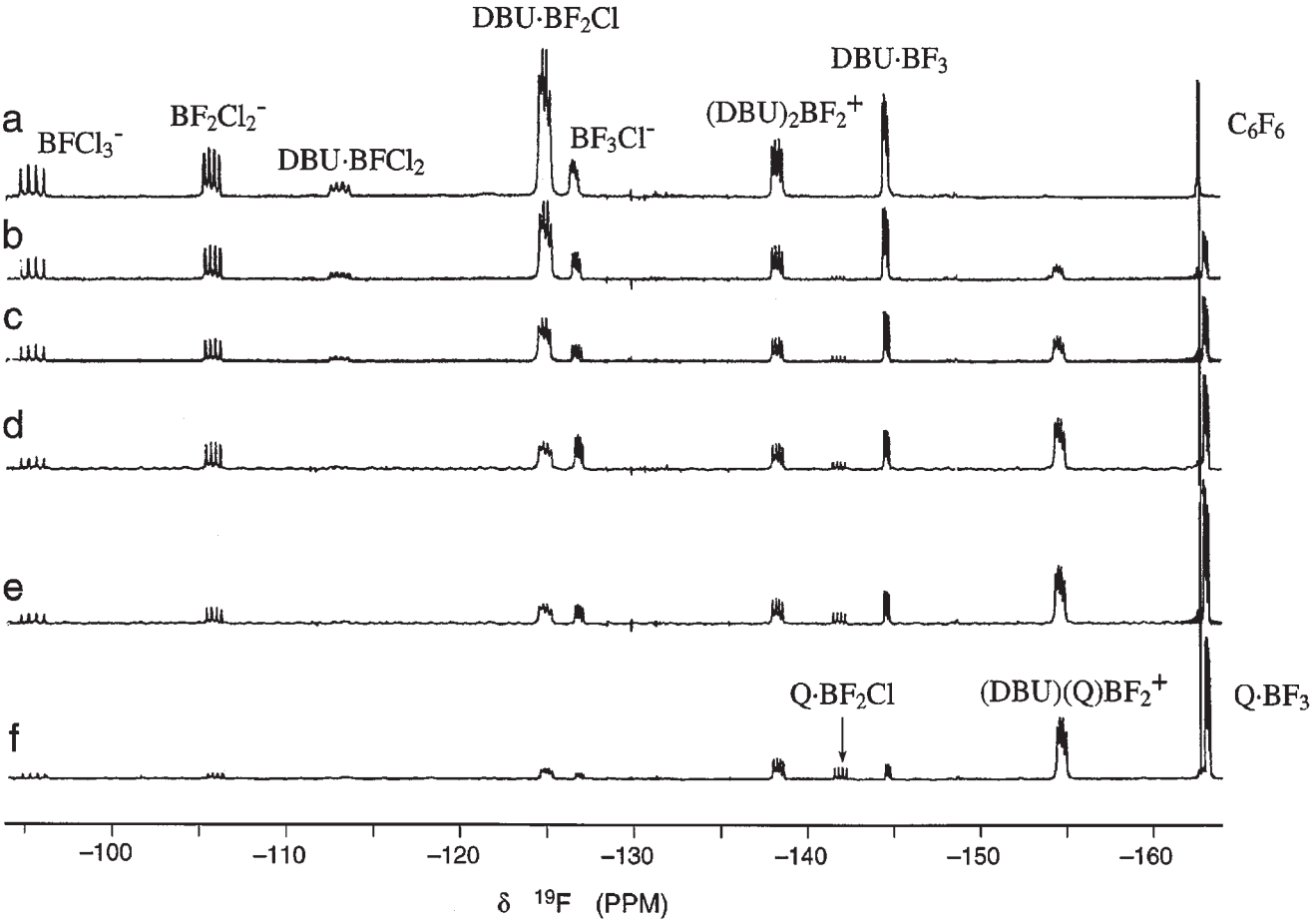

signals of the BF_3 and BF_2Cl adducts of quinuclidine increased, consistent with quinuclidine attacking these anions and driving off Cl^-. No signal appeared that would be consistent with formation of $(DBU)(Q)BFCl^+$.

D′ = DBN: The DBN readily displaces Cl^- from DBU·BF_2Cl to give $(DBU)(DBN)BF_2^+$ but $(DBU)(DBN)BFCl^+$ does not form from DBU·$BFCl_2$, nor does DBN displace DBU from its BF_3 adduct.

D′ = pyridine: Pyridine readily forms $(DBU)(pyr)BF_2^+$ from (DBU)·BF_2Cl, but $(DBU)(pyr)BFCl^+$ was observed to form from (DBU)·$BFCl_2$ only in samples in which Cl is enriched compared to F (BCl_3:BF_3 = 1.5:1 rather than 1:1). High-field ^{11}B NMR monitoring of a titration of the DBU·BF_nCl_{3-n} system with pyridine showed the formation of large amounts of pyr·BF_3 (Fig. 3 and Table 4). This no doubt forms partly by displacement of Cl^- from BF_3Cl^-, but BF_3Cl^- is a minor species so direct displacement of DBU from DBU·BF_3 must be the main source.

D′ = oxazolines: MOZ and EOZ displace Cl^- from DBU·BF_2Cl to form $(DBU)(MOZ)BF_2^+$ and $(DBU)(EOZ)BF_2^+$, but the corresponding $BFCl^+$ species do not form. Oxazolines do displace DBU from DBU·BF_3.

Reactions of DBN·BF_nCl_{3-n} with D′

The DBN·BF_nCl_{3-n} adduct system reacts similarly to the corresponding DBU·BF_nCl_{3-n} adduct system, i.e., the mixed-donor BF_2^+ and $BFCl^+$ cations form from DBN·BF_2Cl and DBN·$BFCl_2$, respectively, on reaction with quinuclidine, pyridine, oxazolines, and thiazolines. The DBN adduct system forms the mixed-donor BF_2^+ cation, but not the $BFCl^+$ cation, with DBU. DBN is displaced from its BF_3 adduct by quinuclidine, pyridine, oxazolines, and thiazolines, but not by DBU, to form D′·BF_3.

Reactions of D·BF_nCl_{3-n} (D = oxazolines and thiazolines) with D′

All of the donors studied (DBN, DBU, other oxazolines and thiazolines, pyridine, and quinuclidine) can displace Cl^- from oxazoline·BF_2Cl and thiazoline·BF_2Cl to give DD′BF_2^+, and from oxazoline·$BFCl_2$ and thiazoline·$BFCl_2$ to give DD′$BFCl^+$. The ^{19}F chemical shift of $(MOZ)(pyr)BF_2^+$ is unusual in being slightly outside the range of the corresponding unmixed-donor cations. All of these donors also displace oxazolines and thiazolines from their BF_3 adducts.

Reactions of pyr·BF_nCl_{3-n} with D′

Most of the donors studied (DBN, DBU, MTZ, and quinuclidine) give (pyr)(D′)BF_2^+ and (pyr)(D′)$BFCl^+$ species by Cl^- displacement from pyr·BF_2Cl and pyr·$BFCl_2$. Note

© 1998 NRC Canada

Fig. 3. 160.46 MHz ^{11}B NMR monitoring of the titration of a $DBU{\cdot}BF_nCl_{3-n}$ solution in $CDCl_3$ (0.2 mmol DBU; mole ratio $DBU:BF_3:BCl_3$ = 2:1:1) with pyridine. Amount of pyridine (mmol) added: (*a*) 0; (*b*) 0.02; (*c*) 0.04; (*d*) 0.06; (*e*) 0.08; (*f*) 0.10. D = DBU; D′ = pyridine.

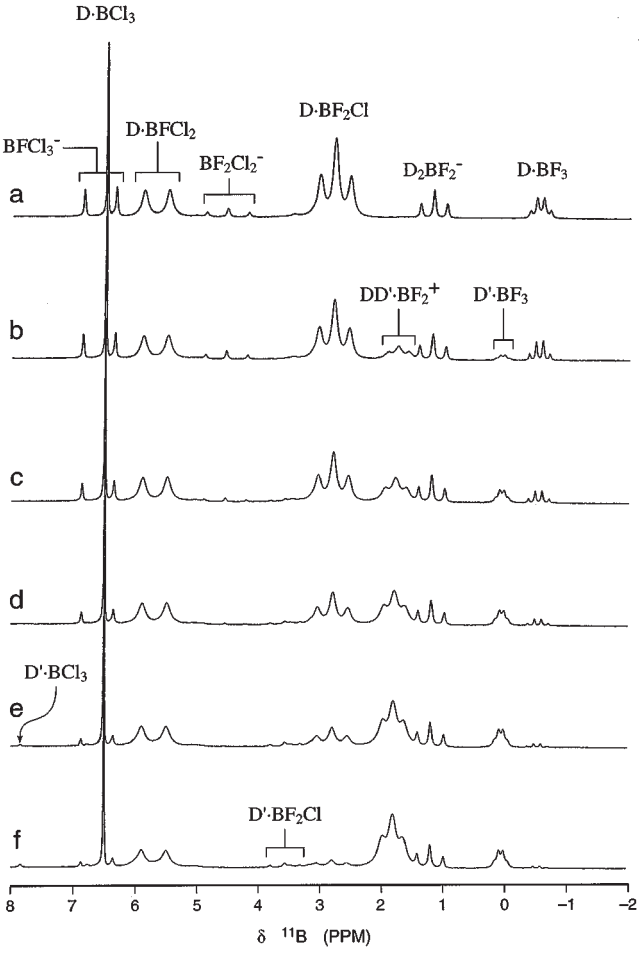

that (pyr)(Q)BF_2^+ and (pyr)(Q)$BFCl^+$ are both reported in Table 1 of ref. 2. Our early studies of the quinuclidine–pyridine system alerted us to the importance of the low steric hindrance of pyridines, compared to R_3N donors, in increasing the range of accessible fluoroboron cations (1, 2). In all of these cases, and with MOZ as donor, pyridine is displaced from its BF_3 adduct by the second donor D′. Surprisingly however, MOZ is unable to displace chloride to give (MOZ)(pyr)BF_2^+ or (MOZ)(pyr)$BFCl^+$.

Reactions of $Q{\cdot}BF_nCl_{3-n}$ with D′

No mixed difluoroboron or chlorofluoroboron cations could be formed by chloride displacement from $Q{\cdot}BF_2Cl$ or $Q{\cdot}BFCl_2$ by any of the amidine, oxazoline, thiazoline, or pyridine bases, and none of these bases are able to displace quinuclidine from its BF_3 adduct.

(*c*) $DD'BF_2^+$ formed from $D_2BF_2^+{\cdot}PF_6^-$ and D′

With many combinations of D and D′, reaction [3] either does not proceed at all or it continues past the mixed-donor cation stage to give $D'_2BF_2^+$. In the most favourable cases only one D′ substitutes, giving $DD'BF_2^+$ uncontaminated by $D_2BF_2^+$ or $D'_2BF_2^+$. Because of the insolubility of the $D_2BF_2^+{\cdot}PF_6^-$ salts in $CDCl_3$ (2–4) these reactions were carried out in acetone where the ^{19}F chemical shifts of the fluoroboron cations differ by up to 3 ppm from their values (as primarily halide salts) in $CDCl_3$.

Reactions of $pyr_2BF_2^+{\cdot}PF_6^-$

$Pyr_2BF_2^+{\cdot}PF_6^-$ (3) reacts with quinuclidine in acetone to give (Q)(pyr)BF_2^+ by ligand displacement, as shown by ^{19}F NMR (Fig. 4). The identity of the mixed-donor cation was confirmed by positive-ion FAB. It is the first mixed-ligand difluoroboron cation salt to be isolated (as its PF_6^- salt). There is no further substitution of quinuclidine to give the well-known $Q_2BF_2^+$, which would give an easily-detected ^{19}F 1:1:1:1 quartet near its $CDCl_3$ chemical shift of –161.5 ppm (1, 2).

The much stronger Lewis bases DBN, DBU, and TMG react immediately with $pyr_2BF_2^+{\cdot}PF_6^-$ in acetone and give a series of fluorine- and boron-containing products in solution, as well as some precipitate that is very air-sensitive. Figure 5, obtained after DBN addition, is a typical spectrum. The major 1:1:1:1 quartet at δ –146.6 ppm, (J = 31.5 Hz) can be assigned to $(DBN)_2BF_2^+$ (lit. –149.4 ppm, J = 31.6 Hz in $CDCl_3$ (4)); its presence was confirmed by its positive-ion FAB peak at m/z 297. The small quartet labelled J in Fig. 5 (δ –150.5 ppm, J = 27.6 Hz) probably arises from (pyr)(DBN)BF_2^+ (see Table 2), and the singlet labelled I (δ –150.2 ppm) probably arises from BF_4^-. Further species giving signals in Fig. 5[4] remain to be identified. The reactivity of the donors with $pyr_2BF_2^+$ is in the order DBN > DBU > TMG > > quinuclidine.

Reactions of $Q_2BF_2^+{\cdot}PF_6^-$

The compound $Q_2BF_2^+{\cdot}PF_6^-$ (2) does not react with any of the bases 4-methylpyridine, DBN, or TMG in acetone to give a mixed-donor cation, even on prolonged standing at 50°C.

Reactions of $(DBU)_2BF_2^+$

This cation readily undergoes complex reactions of the coordinated DBU ligand in the presence of water and alcohol, which prevented isolation of the PF_6^- salt by our usual method (4). Its reactions are the subject of a separate study (10).

(*d*) Attempted formation of mixed-donor cations from $(DBU)_3BF^{2+}{\cdot}(PF_6^-)_2$

The compound $[(DBU)_3BF^{2+}](PF_6^-)_2$ (4) is stable indefinitely in acetone at 50°C and is resistant to attack by strong organic bases at ambient temperature, but decomposes on standing for 24 h in acetone at 50°C with an excess of DBN, TMG, or quinuclidine. Although a number of new ^{19}F NMR signals appear, some of which show splittings due to ^{11}B–^{19}F coupling, we have as yet no clear evidence of formation of

[4] A, δ –135.1 ppm; B, δ –137.2 ppm; C, δ –137.8 ppm; D, δ –140.6 ppm, J = 30.8 Hz; E, δ –142.4 ppm, J = 30.4 Hz; F, δ –143.3 ppm, J = 12.8 Hz; G, δ –145.5 pm, J = 25.2 Hz; H, δ –146.2 ppm, J = ~16 Hz; K, δ –152.0 ppm.

© 1998 NRC Canada

Table 4. Changes in relative ^{11}B peak intensities of a DBU–BF_3–BCl_3 solution on titration with pyridine[a].

		Total pyridine added					
Species	Initial	0.02 mmol	0.04 mmol	0.06 mmol	0.08 mmol	0.1 mmol	After two weeks[b]
$D\cdot BF_3$	8	5	3	2	1	<1	5
$(D)_2BF_2^+$	7	7	8	8	9	9	6
$D\cdot BF_2Cl$	48	40	32	24	15	7	20
$(D)_3BF^{+2}$	1	1	1	1	1	1	<1
$BF_2Cl_2^-$	3	2	1	<1	0	0	—
$D\cdot BFCl_2$	17	17	18	18	18	17	9
$BFCl_3^-$	5	5	4	3	2	2	—
$D\cdot BCl_3$	10	11	11	11	11	11	—
$D'\cdot BF_3$	—	2	5	6	8	8	21
$DD'BF_2^+$	—	9	17	26	35	44	7
$D'\cdot BF_2Cl$	—	0	1	1	1	1	20
$D'\cdot BFCl_2$	—	0	0	0	0	<1	6
$DD'BFCl^+$	—	0	0	<1	<1	<1	—
$D'\cdot BCl_3$	—	0	0	0	<1	<1	6

[a] In $CDCl_3$; initially DBU:BF_3:BCl_3 = 0.2:0.1:0.1 mmol. Five additions of 0.02 mmol of pyridine; Bruker DRX-500 spectrometer; 160.46 MHz.
[b] On standing at 21°C.

Fig. 4. 188.31 MHz ^{19}F NMR monitoring of the formation of $(Q)(pyr)BF_2^+$ from $(pyr)_2BF_2^+\cdot PF_6^-$ and quinuclidine in acetone solution, in the presence of a fivefold molar excess of quinuclidine over $(pyr)_2BF_2^+\cdot PF_6^-$. The PF_6^- 1:1 doublet appears much farther to high frequency and is not shown. (*a*) Freshly prepared at 23°C; (*b*) after 15 min of reaction at 40°C; (*c*) plus 28 min of reaction at 50°C; (*d*) plus an additional 17 min of reaction at 50°C.

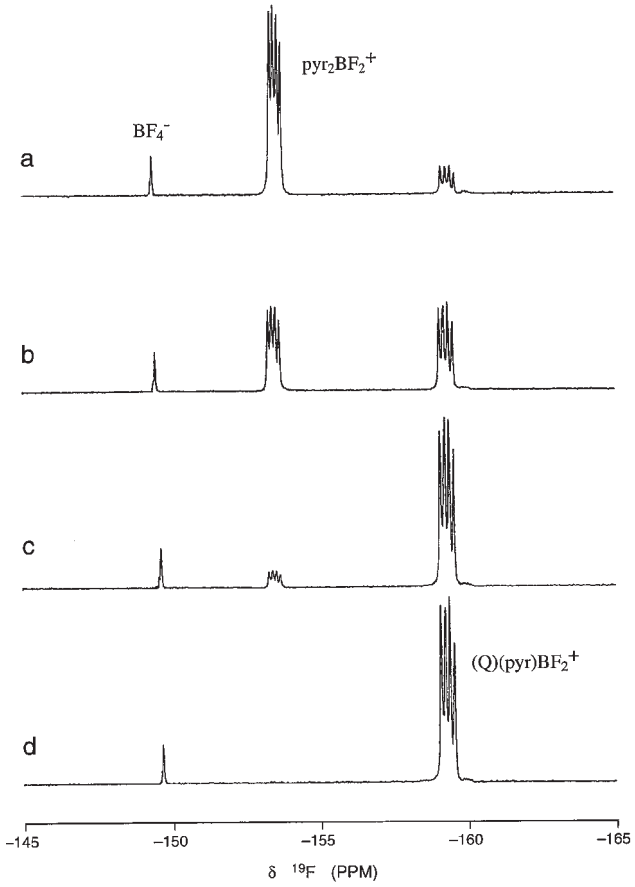

the hoped-for mixed-donor cations $(DBU)_2D'BF^{2+}$ or $(DBU)D'_2BF^{2+}$.

Discussion

Reaction of every $D\cdot BF_2Cl$ and $D\cdot BFCl_2$ adduct need not occur with every potential donor D′; thus tertiary amines R_3N generally displace Cl^- only very slowly if at all, with D′ steric hindrance the crucial factor (2). The low steric hindrance of the two-coordinate C=N nitrogen donor sites greatly facilitates reactions [1] and [2] (3, 4), and reactivity is further supplemented by the high base strength of amidines (4). The trends that appear in the present study are summarized in Table 5 and are consistent with our previous work (1–4) in demonstrating the predominant effects of D and D′ steric hindrance on reactivity in the formation of fluoroboron cations, supplemented by basicity effects.

In addition the original donor is in most cases displaced by D′ from its BF_3 adduct during the above reactions. Susceptibility to D displacement in $D\cdot BF_3$ closely parallels susceptibility to Cl^- displacement in $D\cdot BF_2Cl$ (Table 5). The displaced D then tends to displace chloride from the chlorofluoroborate anions if these are present, to form additional amounts of various already-present D-containing species. Only when both D and D′ are amidines, or when D is R_3N, does D′ displacement of D not occur in $D\cdot BF_3$ (Table 5). Similar D′ displacement in $D\cdot BF_3$ occurs regardless of whether only the $D\cdot BF_3$ adduct, or the full $D\cdot BF_nCl_{3-n}$ (n = 0–3) adduct system is present. The mixed-halogen adducts are however not susceptible to D′ displacement of D and undergo Cl^- displacement instead, while the $D\cdot BCl_3$ adducts are inert under our conditions.

Base strength certainly plays a role. (pK_b values (11, 11*b* for DBU, 11*c* for DBN) are included in Table 5.) Pyridine, MOZ, and DBU do not displace the very highly basic DBN from $D\cdot BF_3$, but DBU, DBN, and pyridine do displace the less basic MOZ. The basicity of the already-attached D is

© 1998 NRC Canada

Fig. 5. 188.31 MHz ^{19}F NMR spectrum of an acetone solution of $(pyr)_2BF_2^+ \cdot PF_6^-$ following addition of DBN.

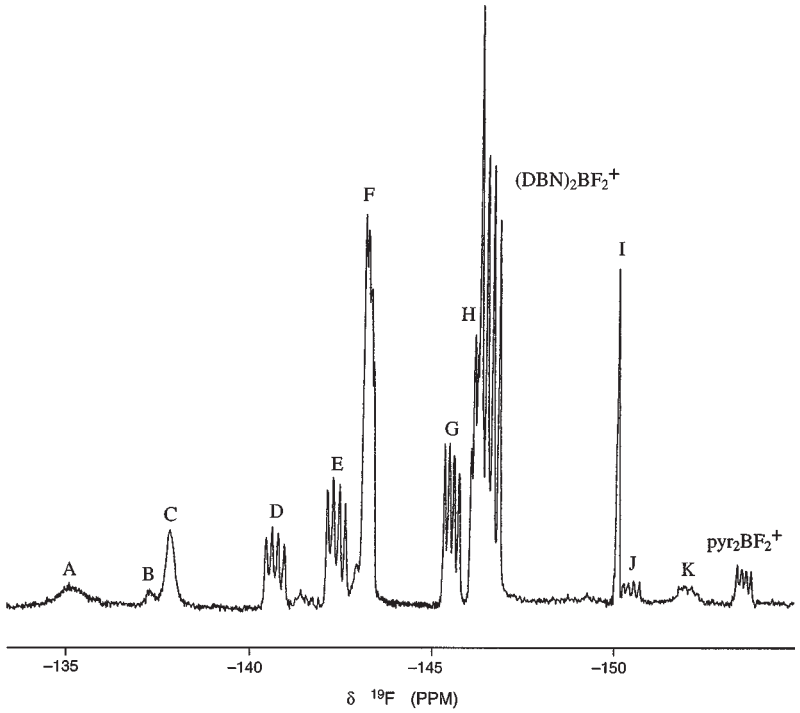

Table 5. Substitution patterns for Cl^- displacement by D′ to form $DD'BF_2^+$ from $D \cdot BF_2Cl$, and D displacement by D′ to form $D' \cdot BF_3$ from $D \cdot BF_3$.

		D′				
D	pK_b	Amidines	Pyridine	Quinuclidine	Oxazolines	Thiazolines
Amidines	0.5–1.1	[a]	Yes	Yes	Yes	Yes
Pyridine	8.8	Yes		Yes	[b]	Yes
Quinuclidine	2.9	No	No		No	No
Oxazolines	8.5	Yes	Yes	Yes	Yes	Yes
Thiazolines		Yes	Yes	Yes	Yes	Yes

[a] Forms $(DBU)(DBN)BF_2^+$ from $DBN \cdot BF_2Cl$ or $DBU \cdot BF_2Cl$, but amidines do not displace each other to form $D' \cdot BF_3$ from $D \cdot BF_3$.

[b] Does not form $(pyr)(oxazoline)BF_2^+$ from $pyr \cdot BF_2Cl$, but oxazoline does displace pyr from $pyr \cdot BF_3$ to form $oxazoline \cdot BF_3$.

not important in displacement of halide in reactions [1] and [2] (Table 5). Thus MOZ readily displaces Cl^- from adducts of the highly basic DBU to give $(DBU)(MOZ)BF_2^+$ and $(DBU)(MOZ)BFCl^+$ (but cannot displace DBU to give $(MOZ)_2BF_2^+$), just as Q readily displaces Cl^- from adducts of the much less basic pyridine. Nor does basicity have much effect on displacement of D from its BF_3 adduct by D′ (Table 5).

Formation of $DD'BFCl^+$ by Cl^- displacement from $D \cdot BFCl_2$ proceeds much less readily than the analogous formation of $DD'BF_2^+$ from $D \cdot BF_2Cl$, and is prevented by D and D′ steric effects in several cases where the analogous $DD'BF_2^+$ species do form. Thus we could not form $(DBN)(DBU)BFCl^+$ or $(DBU)(Q)BFCl^+$, and could form $(DBN)(Q)BFCl^+$ only from attack of Q on $DBN \cdot BFCl_2$ and not from attack of DBN on $Q \cdot BFCl_2$.

Displacement of D by D′ in $D_2BF_2^+ \cdot PF_6^-$, reported here for the first time, follows the same trends as displacement of Cl^- from a mixed-halogen adduct, or D from $D \cdot BF_3$. Thus the bulky quinuclidine can replace only one pyridine from $pyr_2BF_2^+ \cdot PF_6^-$, giving the first isolated mixed-donor difluoroboron cation, whereas the less bulky C=N donors tend to replace both pyridines. Similarly $(DBU)(Q)BF_2^+$, formed in $CDCl_3$ solution from $DBU \cdot BF_2Cl$ and quinuclidine, does not react further to give the well-known (1, 2) $Q_2BF_2^+$ by displacement of DBU.

In previous work we have explained reactivity trends in terms of stabilization of the S_N2 transition state by π bonding to boron from nitrogen donors that remain attached throughout the reaction (2–4). Tertiary amines such as quinuclidine cannot participate in π bonding and hence cannot stabilize the transition state, so that reactions involving Q, which remains attached to boron should occur less readily, in keeping with the observed lower reactivity when Q is already present. Reactivities are apparently determined by a complex interplay of steric effects, ligand basicity effects, and differential stabilization of the transition state by π bonding effects. Thus, in addition to the increased steric hindrance on forming $Q_2BF_2^+$, the transition state for the reaction would be less favourable because no DBU molecule

© 1998 NRC Canada

Fig. 6. Variation of ^{19}F chemical shift with *n* in several series of difluoroboron cations $D_nD'_{2-n}BF_2^+$ (*n* = 2–0).

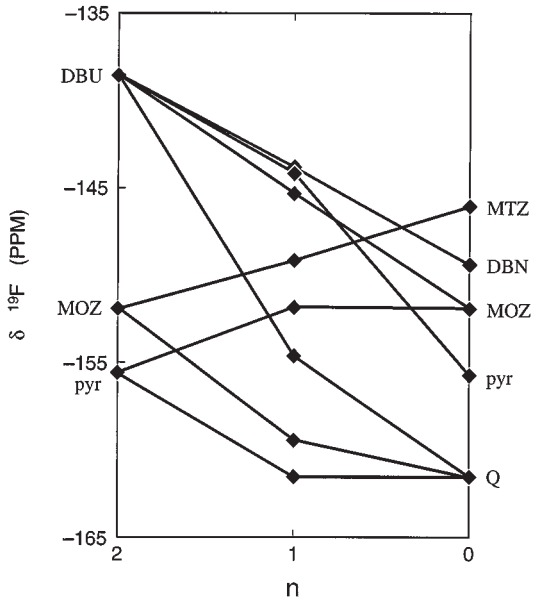

would remain to participate in π bonding. Similarly the inertness of $Q_2BF_2^+ \cdot PF_6^-$ to substitution by D′, regardless of the base strength of D′, can be attributed to the high steric hindrance imparted by the two bulky quinuclidine ligands, supplemented by a very unfavourable transition state in which neither already-attached donor molecule could participate in π bonding.

In the $D \cdot BF_nCl_{3-n}$ adduct systems with many species present and many possible redistribution reactions, chloride displacement by D′ is by far the fastest reaction. Interestingly, high-field ^{11}B NMR confirms that the total amounts of BF_3, BF_2, BF, and non-fluorinated B species do not change appreciably during chloride ion displacement in titrations of D′ into a $D \cdot BF_nCl_{3-n}$ adduct system. Table 4 shows typical results where D = DBU and D′ = pyr. Before the titration, the total amounts of BF_3, BF_2, BF, and non-fluorinated B species are present in the ratio 8:58:19:10, while after the titration, with very different species present, the ratio is unchanged within experimental error: 8:59:20:12. Prolonged standing in the capped NMR tube, however, gives a very different product distribution: the mixed-donor difluoroboron cation is no longer the major species, and the total amounts of BF_3, BF_2, BF, and non-fluorinated B species are now present in the very different ratio 26:53:15:6. (right-hand column of Table 4). The entire system appears to have moved closer to equilibrium as a number of much slower reactions proceed, which involve donor-for-fluorine and chlorine-for-fluorine exchange. It is of particular interest that the neutral adducts of both donors become predominant at the expense of the fluoroboron cations. This is reasonable on steric grounds, since the donor molecules are bulkier than the halogens, and in the adducts each boron is bonded to only one donor molecule.

However more than donor-for-fluorine and chlorine-for-fluorine rearrangement reactions must be occurring on prolonged standing. A comparison of the ratios of BF_3, BF_2, BF, and non-fluorinated B species before and after standing for two weeks, as determined from the ^{11}B peak intensity data of Table 4, indicates a 60% increase in the number of fluorines per boron for the sample as a whole. Since no precipitate formed we can exclude formation of insoluble boron–oxygen materials, which would be likely to appear if there were appreciable hydrolysis by moisture diffusing through the NMR tube cap. No new peaks in addition to those of Table 4 appeared on standing. Loss of a volatile boron species from the capped NMR tube cannot be ruled out but would be surprising in excess-donor samples. Furthermore, a sealed sample behaves similarly to a tightly capped sample except that it does not lose any $CDCl_3$ solvent by evaporation, while an uncapped sample behaves very differently, with BF_4^- becoming the predominant fluorine-containing species over the two-week period. BF_4^-, indicative of contamination by moisture, is undetectable in either the sealed or the capped sample after two weeks. We conclude that we can adequately monitor these reactions in tightly capped NMR tubes without appreciable contamination by moisture.

The mixed-donor difluoroboron cations have ^{19}F chemical shifts very close to the mean of the corresponding $D_2BF_2^+$ and $D'_2BF_2^+$ species when D and D′ are similar donors, which is how we first demonstrated the existence of $DD'BF_2^+$ ions: with (tetramethylurea)(dimethylacetamide)BF_2^+ (12), and when D and D′ were different benzoate esters (13). The pairs of donors DBU–DBN, DBU–MOZ, and MOZ–MTZ closely fit this pattern (Fig. 6). However a linear variation in chemical shift across the series need not occur when different classes of donors such as MOZ–pyridine and pyridine–quinuclidine are involved. Pyridine tends to allow the other base to determine the chemical shift of the mixed difluoroboron cation, the extreme case being MOZ–pyridine ($(MOZ)_2BF_2^+$, –151.9 ppm; $(MOZ)(pyr) \cdot BF_2^+$, –151.8 ppm; $(pyr)_2BF_2^+$, –155.6 ppm), while quinuclidine tends to influence the mixed-donor cation chemical shift towards the $Q_2BF_2^+$ value. "Pairwise interaction" NMR parameters (2, 3, 14) can be useful in calculating chemical shifts in situations in which chemical shifts vary in a non-linear fashion on successive substitution of one substituent by another.

All of the C=N donor $D \cdot BF_3$ adducts have ^{19}F chemical shifts in a narrow range, between 3,5-Me_2pyr$\cdot BF_3$ at δ –152.2 ppm and DBU$\cdot BF_3$ at δ –144.3 ppm, well to high frequency (low field) of simple tertiary-amine$\cdot BF_3$ adducts except when extreme steric hindrance is present (7). The ^{19}F shifts of adducts and cations of C=N donors, like those of R_3N donors, move to higher frequency with increasing donor steric hindrance.

Conclusions

Ligand displacement from $D_2BF_2^+$, in solution as its PF_6^- salt, can be just as selective as halide ion displacement from $D \cdot BF_2X$ in forming only the mixed-donor difluoroboron cation $DD'BF_2^+$. However, in many less favourable cases, either there is no reaction or the reaction goes further to give $D'_2BF_2^+$ and (or) additional products. The D and D′ steric hindrance, D′ base strength, and π-bonding stabilization of the transition state all apparently contribute to the large variations in reactivity, as in the displacement of Cl^- by D′ to form $DD'BF_2^+$ from $D \cdot BF_2Cl$, and $DD'BFCl^+$ from $D \cdot BFCl_2$.

© 1998 NRC Canada

D′ displacement of D from $D{\cdot}BF_3$ occurs widely, provided that the steric hindrance of D is not too high. We are exploring pyridine displacement from $pyr_2BF_2^+{\cdot}PF_6^-$ as a route to synthesis of previously inaccessible (15) chelating-donor fluoroboron cations.

Acknowledgments

We are indebted to the late Mel Farquharson for preparing $pyr_2BF_2^+{\cdot}PF_6^-$ and $(quinuclidine)_2BF_2^+{\cdot}PF_6^-$. We also thank Tim Jones for assistance with the instrumentation, Prof. Alex F. Janzen (University of Manitoba) for helpful discussions, Brian Sayer and Dr. Don Hughes (McMaster University) for assistance in using the 11.7 tesla NMR instrument, and the Natural Sciences and Engineering Research Council of Canada for financial support.

References

1. M.J. Farquharson and J.S.Hartman. J. Chem. Soc. Chem. Commun. 256 (1984).
2. M.J. Farquharson and J.S. Hartman. Can. J. Chem. **67**, 1711 (1989).
3. M.J. Farquharson and J.S. Hartman. Can. J. Chem. **74**, 1309 (1996).
4. J. S. Hartman, Z. Yuan, A. Fox, and A. Nguyen. Can. J. Chem. **74**, 2131 (1996).
5. P.G. Cozzi, C. Floriani, A. Chiesi-Villa, and C. Rizzoli. Inorg. Chem. **34**, 2921 (1995), and refs. therein.
6. E. Shuter, H.R. Hoveyda, V. Karunaratne, S. Rettig, and C. Orvig. Inorg. Chem. **35**, 368 (1996); H. Kaur and S.K. Sangal. J. Indian Chem. Soc. **71**, 621 (1994).
7. A. Fox, J.S. Hartman, and R.E. Humphries. J. Chem. Soc. Dalton Trans. 1275 (1982).
8. J.S. Hartman and J.M. Miller. Adv. Inorg. Chem. Radiochem. **21**, 147 (1978).
9. J.S. Hartman and G.J. Schrobilgen. Inorg. Chem. **11**, 940 (1972).
10. J.A.W. Shoemaker. B.Sc. thesis, Brock University, 1997.
11. (*a*) D.R. Perrin. Dissociation constants of organic bases in aqueous solutions. Butterworths, London. 1965; and Supplement, 1972; (*b*) I. Hermecz. Adv. Heterocyclic Chem. **42**, 84 (1987), Table I; (*c*) D.H.R. Barton, J.D. Elliott, and S.D. Géro. J. Chem. Soc. Perkin Trans. 1, 2085 (1982).
12. J.S. Hartman and G.J. Schrobilgen. Inorg. Chem. **13**, 874 (1974).
13. J.S. Hartman and B.D. McGarvey. Inorg. Chim. Acta, **44**, L39 (1980); J.S. Hartman, B.D. McGarvey, and C.V. Raman. Inorg. Chim. Acta, **49**, 63 (1981).
14. J.S. Hartman and J.M. Miller. Inorg. Chem. **13**, 1467 (1974); T. Vladimiroff and E.R. Malinowski. J. Chem. Phys. **46**, 1830 (1966).
15. J.S. Hartman, A.F. Janzen, and X. Ou. Paper 57, 79th Annual Canadian Chemical Conference, St. John's, Newfoundland, June 23–26, 1996.

© 1998 NRC Canada

1997 Alfred Bader Award Lecture Reactivities of arylnitrenium ions with guanine derivatives and other nucleophiles[1]

Robert A. McClelland, Timothy A. Gadosy, and Daniel Ren

Abstract: The carcinogens 4-aminobiphenyl and 2-aminofluorene are metabolized to hydroxylamine esters that undergo N-O heterolysis to produce arylnitrenium ions that react with DNA, especially at guanine residues. These nitrenium ions and a number of their derivatives have been studied by the laser flash photolysis technique, to provide direct kinetic information about the lifetimes of the electrophiles in water and their reactivities with added nucleophiles. Arylnitrenium ions $ArNH^+$ are longer-lived in water than arylcarbenium analogs $ArCH_2^+$, in some cases significantly longer-lived. The nitrenium ions do react with azide ion at the diffusion limit (providing the cation is not highly stabilized). This behaviour completely parallels that of carbenium ions. The biphenylyl- and fluorenylnitrenium ions react with guanine derivatives such as 2′-deoxyguanosine (dG) with rate constants that are close to or at the diffusion limit (2×10^9 M^{-1} s^{-1}) for the more reactive cations. Thus, in spite of cation lifetimes of the order of 100 ns to a millisecond in water, dG effectively competes with the solvent. The product is a C8 adduct, the same adduct observed with carcinogenic arylamines and DNA. With delocalized carbenium ions that have similar lifetimes, guanine derivatives compete very poorly with water. Thus, arylnitrenium ions have high dG:water selectivities; arylcarbenium ions have low selectivities. Nitrenium ions and carbenium ions do have parallel reactivities with primary alkyl amines. More reactive cations show a greater reactivity with less basic amines and the rate constants level below the diffusion limit. This can be explained by hydrogen bonding of the amine lone pair. Using the NH_2 group of the alkyl amines as a model for the C_2-NH_2 group of guanine shows why nitrenium ions show no detectable reactivity at this site. The rate constant for the nitrenium–guanine reaction that forms the C8 adduct is at least an order of magnitude greater than that of a nitrenium–NH_2 reaction. Nitrenium ions do form a guanine–NH_2 adduct in DNA, suggesting that incorporation into the polymer changes reactivity patterns. With imidazoles, nitrenium ions show reactivity trends that parallel the nitrenium–dG reaction, with rate constants levelling at the 2×10^9 limit for the more reactive cations. Imidazole itself and 1-methylimidazole are generally less reactive than dG, while 2-methylimidazole and 1,2-dimethylimidazole are very similar. A Brönsted-like plot incorporating points for dG, primary amines and imidazoles shows no correlation of nitrenium rate constants with nitrogen basicity. This is true even if only dG and imidazoles are considered. Thus a previous correlation of nitrenium reactivity with purine N7 basicity is suspect. The conclusion is that there is some feature of guanine that makes its reaction with nitrenium ions unusually fast. The reasons for this are not immediately apparent, especially since there is conflicting evidence as to the detailed nature of the mechanism of the reaction that forms the C8 adduct.

Key words: nitrenium, aryl azide, guanine, DNA, carcinogen.

Résumé : Le métabolisme des 4-aminobiphényle et 2-aminotoluène, des cancérigènes, conduit à des esters d'hydroxylamine; ceux-ci subissent une hétérolyse N-O conduisant à des ions arylnitrénium qui réagissent avec l'ADN, particulièrement avec les résidus de guanine. On a étudié ces ions nitrénium et un certain nombre de leurs dérivés à l'aide de la technique de la photolyse éclair au laser afin d'obtenir des données cinétiques directes relatives aux temps de vie des électrophiles dans l'eau et à leurs réactivités avec des nucléophiles ajoutés. Dans l'eau, les ions arylnitrénium, $ArNH^+$, ont des temps de vie plus longs que leurs analogues arylcarbénium, $ArCH_2^+$, et, dans quelques cas, les différences sont importantes. Les ions nitrénium réagissent avec l'ion azoture à une vitesse correspondant à la limite de diffusion (à la condition que le cation ne soit pas stabilisé). Ce comportement est tout à fait parallèle à celui des ions carbénium. Les ions biphénylyl- et fluorénylnitrénium réagissent avec les dérivés de la guanine, tel que la 2′-désoxyguanosine (dG); dans les cas des cations les plus réactifs, les constantes de vitesse se rapprochent ou sont égales à la limite de diffusion (2×10^9 M^{-1} s^{-1}). Donc, malgré des temps de vie de l'ordre de 100 ns à une milliseconde dans

Received June 10, 1998.

R.A. McClelland,[2] T.A. Gadosy,[3] and D. Ren. Department of Chemistry, University of Toronto, Toronto, ON M5A 3H6, Canada.

[1]This is an invited review article based on the 1997 Alfred Bader Award Lecture presented at the 80th Annual Conference of the Canadian Society for Chemistry, Windsor, Ontario, June 1–4, 1997.

[2]Author to whom correspondence may be addressed. Telephone: (416) 978-3592. Fax: (416) 978-3592.
E-mail: rmcclell@alchemy.chem.utoronto.ca
[3]Current address: Department of Chemistry and Biochemistry, Concordia University, Montreal, PQ H3G 1M8, Canada.

© 1998 NRC Canada

l'eau, la dG entre avec succès en compétition le solvant. Le produit est un adduit C8, le même adduit que celui observé lors de la réaction d'arylamines cancérigènes avec l'ADN. Avec des ions carbénium délocalisés qui ont des temps de vie semblables, les dérivés de la guanine ne compétitionnent pas bien avec l'eau. Ainsi, les ions arylnitrénium présentent des sélectivités dG:eau élevées; les ions arylcarbénium présentent de faibles sélectivités. Les réactivités des ions nitrénium et des ions carbénium vis-à-vis des alkylamines primaires sont parallèles. Les cations plus réactifs présentent une plus grande réactivité avec les amines moins basiques et les constantes de vitesse sont inférieures à la limite de diffusion. On peut probablement expliquer ce résultat par la formation d'une liaison hydrogène avec la paire d'électrons non partagée de l'azote. Utilisant le groupe NH_2 des alkylamines comme modèle du groupe C_2NH_2 de la guanine, on peut montrer pourquoi les ions nitrénium ne présentent aucune réactivité détectable à ce site. La constante de vitesse pour la réaction nitrénium–guanine conduisant à la formation de l'adduit C8 est au moins un ordre de grandeur supérieure à celle de la réaction nitrénium–NH_2. Les ions nitrénium forment un adduit guanine–NH_2 dans l'ADN; ceci suggère que l'incorporation dans un polymère provoque un changement dans les patrons réactionnels. Avec les imidazoles, les ions nitrénium présentent une tendance de réactivité qui est parallèle à celle de la réaction nitrénium–dG; pour les cations les plus réactifs, les constantes de vitesses atteignent la limite de 2×10^9. L'imidazole et le 1-méthylimidazole sont généralement moins réactifs que le dG alors que le 2-méthylimidazole et le 1,2-diméthylamidazole sont très semblables. Une courbe de type Brönsted incorporant des points pour dG, des amines primaires et des imidazoles ne permet d'observer aucune corrélation entre les constantes de vitesse des nitrénium et la basicité de l'azote. Ceci est vrai même si l'on ne considère que dG et les imidazoles. On peut donc considérer comme suspecte une corrélation proposée antérieurement pour relier la réactivité des nitrénium et la basicité du N7 de la purine. On peut conclure qu'il existe une caractéristique de la guanine qui fait que sa réaction avec les ions nitrénium est exceptionnellement rapide. Les raisons ne sont pas immédiatement apparentes, particulièrement si l'on considère qu'il existe des données contradictoires concernant la nature exacte du mécanisme de la réaction conduisant à la formation de l'adduit C8.

Mots clés : nitrénium, azidoaryle, guanine, ADN, cancérigène.

[Traduit par la Rédaction]

Scheme 1.

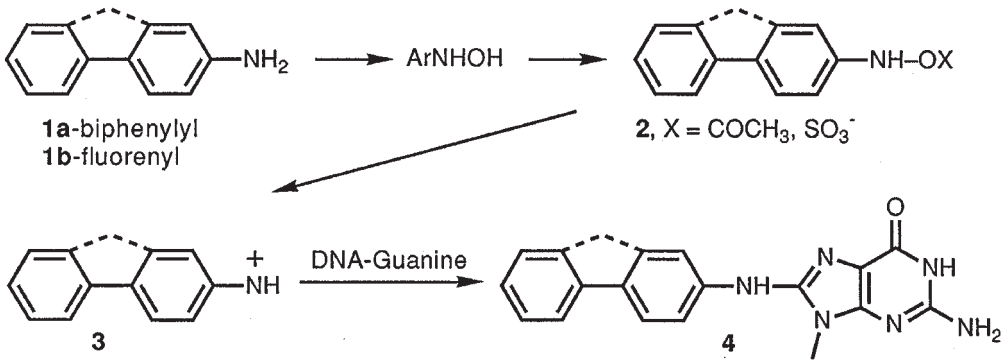

Many aromatic amines are long established carcinogens in animal models (1) and are suspect or known carcinogens in man (2). Well studied examples are 4-aminobiphenyl **1a**, a component of cigarette smoke (3–5), and 2-aminofluorene **1b**, found in diesel exhaust (6) (Scheme 1). These compounds require metabolic activation to an ultimate carcinogen, an *N*-arylhydroxylamine ester **2** (2, 7, 8). This occurs in two steps, oxidation to the hydroxylamine and then esterification with either a sulfotransferase or an acetyl transferase. There have also been indications that acetates **2** can form by N-O acetyl transfer in a hydroxamic acid (9, 10). The esters **2** are unstable in aqueous solution and undergo N-O heterolysis to an electrophilic intermediate, a nitrenium ion. This reacts with DNA to form covalent adducts (7, 8, 11–13), the most abundant being the C8 adduct **4** at guanine residues. The formation of these adducts has been correlated with the carcinogenic effects of the amines (8, 13, 14). Although there have been suggestions of the involvement of S_N2 mechanisms (15–17), there is now excellent evidence that nitrenium ions do form in aqueous solutions (18–22), and that these are the species responsible for the guanine C8 adducts (23, 24).

Arylnitrenium ions are the nitrogen analogs of arylcarbenium ions. Unlike the latter, a nitrenium ion can have either a singlet or triplet electronic configuration. While the parent NH_2^+ is a ground state triplet (25, 26), phenyl substitution stabilizes the singlet relative to the triplet, and phenylnitrenium ion is calculated to be a ground state singlet, by ~20 kcal/mol (27). Until recently, nitrenium ions had been studied experimentally as steady-state intermediates of ground state reactions, usually S_N1 solvolysis reactions. Compared to carbocations, there had been very little direct study. Examples bearing strongly stabilizing substituents had been observed in acetonitrile following electrochemical oxidation of the amine (28–30), but no arylnitrenium ion has been characterized in superacids (31, 32).

© 1998 NRC Canada

Scheme 2.

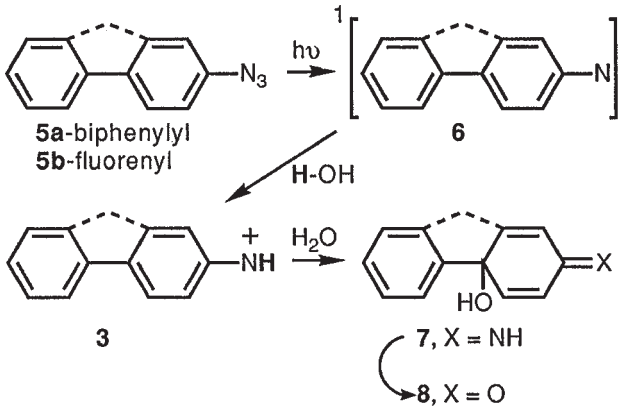

For some time now our group at the University of Toronto has been using laser flash photolysis (LFP) for the observation of carbocations in aqueous and alcoholic solvents (33). With LFP, the cation is generated photochemically by a short pulse of laser light, and is observed by fast time-resolved spectroscopic methods, in our case by UV-visible absorption spectroscopy. In addition to characterizing the cation in a solvent where it is typically found as a reactive intermediate, this approach supplies direct kinetic information about the lifetime of the cation in the solvent, and its reactions with added nucleophiles. Within the past few years, we have turned out attention to the arylnitrenium class, with a particular emphasis on the biphenylyl and fluorenyl systems. This paper summarizes our findings with these compounds. We in particular present new kinetic data on the reactions of the nitrenium ions with guanine derivatives, imidazoles, and primary amines. Also of interest is the comparison of nitrenium ions with corresponding carbenium ions.

Flash photolysis generation of 4-biphenylyl and 2-fluorenylnitrenium ions

The LFP method requires a photochemical reaction to generate the reactive intermediate of interest. As illustrated in Scheme 2, the nitrenium ions **3a** and **3b** are obtained on irradiation of the azides **5a** and **5b** in aqueous solution (34, 35). The key step is protonation of the singlet nitrene **6** by a solvent water molecule. This occurs very rapidly (35), before the unstable nitrene can undergo one of its other decay processes (36). There are several more recent examples of nitrene protonation (37–39), although in some cases the addition of strong acids is required.

The LFP studies of *N*-acetyl analogs **12** have also been performed (40), the cations being formed upon heterolytic cleavage of an N—O or N—Cl bond of precursors **9–11** (eq. [1]).

[1]

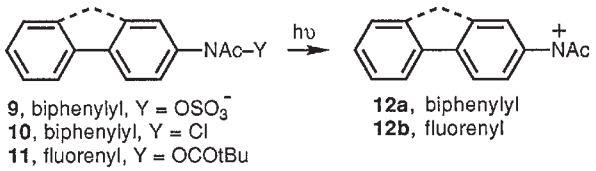

Each of these two methods has precedence in the study of carbocations by LFP. Certain carbenes can be trapped by protonation, forming secondary carbocations $R_1R_2CH^+$ (41–44). Photoheterolysis of C—Y bonds is probably the most widely used method for the study of carbocations (33) (although the actual photochemical route by which the cation eventually forms is still open to question (45–47). Photoheterolysis with neutral leaving groups has been employed by the Falvey group for the LFP investigations of nitrenium ions (48–51). The cations **13** and **14**, for example, provide nitrenium ions upon irradiation in acetonitrile.

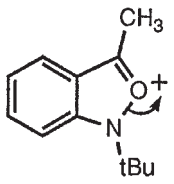

13

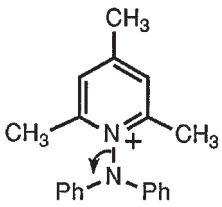

14

Characterization of nitrenium ions and trapping by azide anions

Since nitrenium ions have not been characterized under super acid conditions, the assignment of a nitrenium structure to the transients observed in LFP experiments is based on indirect methods. Nevertheless the evidence is strong. To start with, products of irradiation are exactly those expected of a nitrenium ion intermediate. As one example, irradiation of 4-azidobiphenyl **5a** in 10% acetonitrile gives a 90% yield of the ketone **8** (35), the product that results from water capture of a nitrenium ion intermediate (19). Such a compound would not form in any of the other normal reactions of a nitrene (36). Both the yield of **8**, and the intensity of the transient decrease as the acetonitrile content of the medium increases (35). This solvent dependence reflects the requirement that water trap the nitrene. The parallel behaviour indicates that the LFP transient is the precursor of the product. The quenching behaviour of the nitrenium transient is also characteristic. Oxygen, a quencher of radicals and triplet excited states, has no effect, but nucleophiles do react.

Particularly compelling evidence is supplied with azide ion as the quencher. Novak and co-workers have investigated ground state solvolysis reactions in the presence of this nucleophile (19–21), for example, employing the pivalate **15** as a precursor to the nitrenium ion **3a** (19). As azide is added, there are increasing amounts of an azide-incorporated product at the expense of products derived from solvent (e.g., **16** versus **8**). At the same time, there is no change in the rate constant for the reaction, a clear indicator of an S_N1 reaction proceeding through rate-limiting ionization. Quantitative analysis of the product ratios provides the rate constant ratio $k_{Az}:k_w$. With LFP the absolute values for these two constants are directly measured, k_w as the first-order rate constant for the decay in the solvent alone, and k_{Az} as the slope of the linear plot of k_{decay} versus $[N_3^-]$. In the cases where both have been determined, the ratio from LFP is exactly the same as the ratio from solvolysis, for example $(2.8 \pm 0.1) \times 10^3$ (LFP, ref. 35) versus (2.9 ±

© 1998 NRC Canada

Scheme 3.

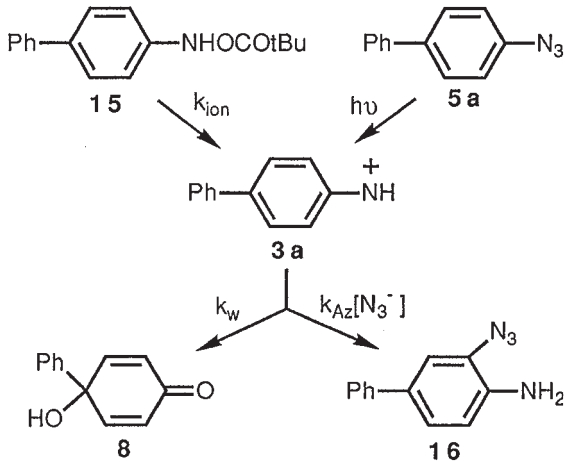

Table 1. Rate constants (20°C) for the decay of nitrenium and carbenium ions in water. Unless otherwise noted, the solvent is 0–30% acetonititrile,[a] and the rate constant is directly measured by flash photolysis.

	k_w, s^{-1}	Ref.
Nitrenium ion		
$PhNH^+$ (**17**)	4–8 × 10^{9b}	59
4-$MeOC_6H_4NH$+ (**19**)	2 × 10^6	60
2-$FlNH^+$ (**3b**)	3 × 10^4	35
1-MeImid-2-NH^{+d} (**23**)	1 × 10^1	62
Carbenium ion		
$PhCH^+$-Ph (**18**)	1 × 10^9	42
4-$MeOC_6H_4CH^+$-Ph (**20**)	2 x 10^6	54
4-$MeOC_6H_4CH_2^+$ (**21**)	2 x $10^{8b,c}$	61
2-$FlCH^+$-Ph (**22**)	2 x 10^7	40
1-MeImid-2-CH^+-Ph (**24**)	1 x 10^5	63
1-MeImid-2-CH_2^+ (**25**)	6 x 10^{7b}	64

[a]The amount of nitrile has little effect on the rate constant (refs. 35, 60).

[b]Based on clock method.

[c]50:50 2,2,2-trifluoroethanol:water.

[d]1-MeImid-2 is 1-methyl-2-imidazoyl.

0.2) × 10^3 (competition, ref. 19) for the system of Scheme 3. Such observations not only provide evidence that the transient is a nitrenium ion, but they also establish the transient as a ground state nitrenium ion, identical with one formed in a solvolysis reaction.

The azide-clock method converts selectivities measured in a ground state solvolysis into absolute rate constants, through the assumption that the azide reaction occurs at the encounter limit, so that k_{Az} = 5 × 10^9 M^{-1} s^{-1} (52, 53). The LFP provides a way of verifying this, since it supplies absolute rate constants. The situation with arylnitrenium ions and two series of carbenium ions is illustrated in Fig. 1. With the more stable ions in each series, structural changes that increase k_w also increase k_{Az}. A break is then observed, with k_{Az} being effectively constant for the more reactive cations. The limiting rate constants are of the order of magnitude associated with an encounter-controlled process, although the

Fig. 1. Variation of log k_{Az} with log k_w for carbenium and nitrenium ions showing leveling of k_{Az} for more reactive cations. Closed squares, triarylmethyl carbocations (56); open squares, diarylmethyl carbocations (56); closed circles, nitrenium ions (*a*, 4-(*N*-methyl-*N*-acetylamino)phenylnitrenium (57); *b*, 2-fluorenylnitrenium (**3b**) (35); *c*, *N*-acetyl-2-fluorenylnitrenium (**12b**) (40); *d*, 3,5-dimethyl-4-biphenylylnitrenium (58); *e*, *N*-acetyl-4-biphenylylnitrenium (**12a**) (40); others are 3′- or 4′-substituted-4-biphenylylnitrenium ions (55), e.g., *f*, 4′-methoxy; *g*, 4′-methyl; *h*, parent (**3a**); *i*, 3′-chloro). Rate constants are at 20°C, zero ionic strength, and 20% acetonitrile (nitrenium and diarylmethyl ions) or 33% acetonitrile (triarylmethyl). Units of k_{Az} are M^{-1} s^{-1}; k_w, s^{-1}. The lines drawn with each set represent the limiting rate constant, 1 × 10^{10} M^{-1} s^{-1} for the nitrenium ions, 7 × 10^9 M^{-1} s^{-1} for the diarylmethyl ions, and 5 × 10^9 M^{-1} s^{-1} for the triarylmethyl ions.

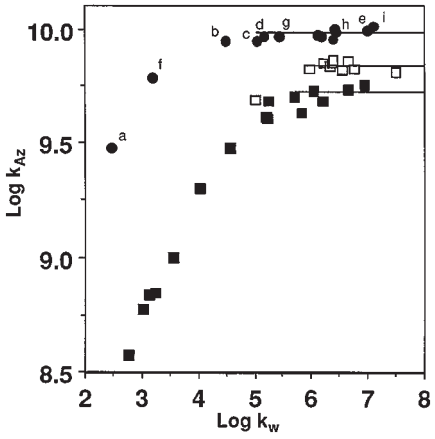

limits do depend on the type of cation. We have previously explained the difference in the carbocation series in terms of a steric effect (56), more nonproductive encounters occurring in the case of the more bulky triaryl system. The slightly higher limit with the nitrenium series would suggest that this is less sterically congested. The conclusion is that the azide-clock approach is valid for both nitrenium ions and carbenium ions, at least for more reactive cations. A second conclusion is that arylcarbenium ions and arylnitrenium ions behave in an essentially identical fashion in their reaction with azide ion. This is perhaps not surprising. The nitrenium ions react with azide ion at one of the ring carbons, that is, through a carbocation resonance contributor.

Lifetimes of nitrenium ions in water

Despite the positive charge formally sitting on a more electronegative atom, arylnitrenium ions are longer-lived than arylcarbenium analogs (Table 1). Thus the parent phenylnitrenium ion **17**, though short-lived does have a lifetime in water. There would be questions as to the existence of the parent benzyl cation (65); the diphenylmethyl cation **18**, with two stabilizing phenyl groups, has about the same lifetime as **17**. The 4-methoxyphenylnitrenium ion **19** is two orders of magnitude longer-lived than its benzyl analog **21**. In the fluorenyl system, the difference between the NH^+ and CH_2^+ ions is even greater; the carbenium ion **22** with an extra phenyl is already three orders of magnitude more reac-

© 1998 NRC Canada

tive than **3b**. With 2-imidazoyl, the difference between $ArNH^+$ and $ArCH_2^+$ (**23** versus **25**) is almost a million.

This relative kinetic stabilization of nitrenium ions is likely a reflection of their reaction with water at a ring carbon (see Schemes 2 and 3). The immediate product of hydration is therefore not aromatic. Arylcarbenium ions in general react at the external carbon, so that the product is aromatic. We would argue that this provides a driving force lowering the barrier for the carbocation hydration.

The structural representation with the positive charge on nitrogen (e.g., **26a**) is actually a minor resonance contributor. Several pieces of evidence suggest that the cation is better regarded as a delocalized cyclohexadienyl cation, comprising the resonance structures **26b**–**26d**. For example, biphenylyl derivatives $Ar\text{-}C_6H_4NH^+$ show pronounced effects of substituents in Ar, with linear free energy correlations suggesting that the interaction is more like that in a benzylic cation, e.g., as if the structure were **26c** (55). Perhaps most convincing is a recent flash photolysis study of the precursor **14** employing IR detection. The stretching frequency of the C—N bond moves towards that of an imine when the nitrenium ion Ph_2N^+ forms (66).

The importance of the carbenium ion resonance contributors is likely the reason that rate constants for simple nitrenium ions $4\text{-}XC_6H_4NH^+$ produce a highly scattered Hammett plot using the σ^+ values for X. This feature of nitrenium ion

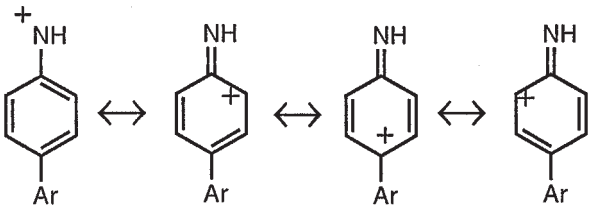

chemistry was first noted by the Novak group using k_w values obtained by the clock method (20); a more extended version of the plot is shown in Fig. 2. Lifetimes span a range of almost 13 log units from the parent $PhNH^+$ to the 4-amino derivative. There is however a very poor correlation. The data appear to separate into two families, although this is probably not real, since there is no obvious structural feature that distinguishes the two. The scatter is also quite large. The 4-methoxy derivative, for example, is four orders of magnitude more reactive than 4-NMeAc, despite the fact that 4-MeO is more stabilizing according to its σ^+ value.

Reactivity with guanine derivatives

While an ion like the 2-fluorenylnitrenium ion does have a lifetime in water, it is still a short-lived species, surviving for less than 100 μs in the solvent alone. Considering this, the guanine ring is a very effective trap. This was first seen by the Novak group in solvolysis reactions run under competition conditions (23, 24). Low concentrations of 2′-deoxyguanosine (dG) result in the formation of the C8-adduct at the expense of the water products (Scheme 4), with no change in rate constant. Selectivities k_{dG}:k_w are high

Fig. 2. Hammett plot for the hydration of arylnitrenium ions $4\text{-}XC_6H_4NH^+$. Data for H (59), 4-Me (21), and 4-Cl (21) are based on a clock method. All other rate constants are directly measured: 4-Ph (35), 2-fluorenyl (35), 4-MeO (60), 4-PhO (Ramlall and McClelland, unpublished), $4\text{-}NMeCOCH_3$ (57), 1-methyl-2-imidazoyl (62), $4\text{-}NH_2$ (monoprotonated benzoquinone bis-imine) (67). The σ^+ values for 2-fluorenyl (20) and 1-methyl-2-imidazoyl (68) are values for the entire group. The line has been drawn for the bottom six points and has a slope of +9.

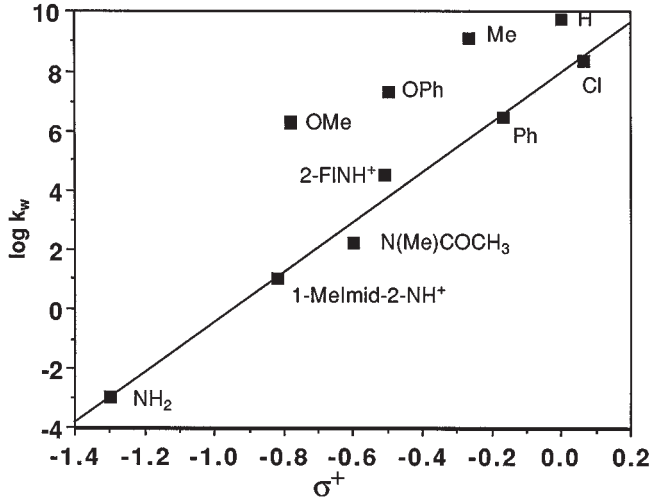

(Table 2). The dG reaction was suggested to be occurring at or near the encounter limit (24).

The nucleoside is a very effective quencher in LFP studies. Moreover, k_{dG}:k_w ratios based on the absolute rate constants are in complete agreement with Novak's competition results (Table 2). This is an important result since it conclusively establishes that these nitrenium ions do react with guanine forming the C8 adduct. As further corroboration of the photochemical system, products were analyzed following irradiation of 4-azidobiphenyl and 2-azidofluorene in an aqueous solution containing 10 mM 2′-deoxyguanosine. There is one product derived from the nucleoside, and it is the C8 adduct, as proven by isolation from scaled-up photolyses. In both cases the yield of this adduct at high concentrations of dG is 80–85%, close to the maximum yield of

Scheme 4.

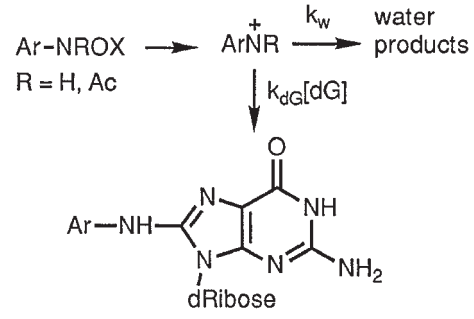

nitrenium ion (35). For the 2-fluorenyl system, the variation in yield was determined at lower concentrations, furnishing a k_{dG}:k_w ratio that is in excellent agreement with the LFP one (Table 2).

© 1998 NRC Canada

Table 2. Comparison of 2′-deoxyguanosine:water selectivities obtained by competition kinetics (product analyses) with ratios of absolute rate constants measured by laser flash photolysis.

Cation[a]	k_w, s^{-1}	k_{dG}, M^{-1} s^{-1}	LFP ratio k_{dG}:k_w, M^{-1}	Comp. kins. k_{dG}:k_w, M^{-1}
$BiPhNAc^{+b}$	$(5.9 \pm 0.2) \times 10^{6c}$	$(1.98 \pm 0.06) \times 10^9$	$(3.35 \pm 0.15) \times 10^2$	$(3.14 \pm 0.16) \times 10^{2d}$
$BiPhNH^{+b}$	$(1.8 \pm 0.1) \times 10^{6e}$	$(1.96 \pm 0.05) \times 10^9$	$(1.09 \pm 0.07) \times 10^3$	$(1.06 \pm 0.10) \times 10^{3d}$
$FlNAc^{+b}$	$(7.7 \pm 0.4) \times 10^{4c}$	$(5.6 \pm 0.1) \times 10^8$	$(7.3 \pm 0.4) \times 10^3$	$(8.0 \pm 0.6) \times 10^{3f}$
$FlNH^{+g}$	$(2.6 \pm 0.2) \times 10^4$	$(7.6 \pm 0.1) \times 10^8$	$(2.9 \pm 0.2) \times 10^4$	$(2.5 \pm 0.5) \times 10^{4h}$

[a]BiPh = 4-biphenylyl; Fl = 2-fluorenyl.

[b]20°C, 5% acetonitrile, pH 7 phosphate buffer, ionic strength = 0.5 ($NaClO_4$).

[c]Reference 35.

[d]Reference 24, determined from ground state solvolysis of sulfonatooxy (NAc) or pivalate (NH) esters in presence of 2′-deoxyguanosine.

[e]Reference 40.

[f]Reference 23, determined from ground state solvolysis of pivalate ester in presence of 2′-deoxyguanosine.

[g]20°C, 20% acetonitrile, pH 7 phosphate buffer, ionic strength = 0.1 ($NaClO_4$).

[h]From analysis of the C8 guanine adduct following irradiation of 2-azidofluorene in the presence of 2′-deoxyguanosine.

Table 3. Second-order rate constants (M^{-1} s^{-1}) for the trapping of nitrenium ions by nucleosides and nucleotides (conditions: 20°C, 20% acetonitrile, ionic strength = 0.1 ($NACLO_4$), pH 7 phosphate buffer.)

Nucleophile	4-BiPhNH+	2-FlNAc+	2-FlNH+
2′-Deoxyguanosine	2.0×10^9	4.1×10^8	7.6×10^8
Guanosine		4.3×10^8	7.2×10^8
2′-Deoxyguanosine 5′-phosphate	1.9×10^9	4.5×10^8	9.2×10^8
Guanosine 5′-phosphate	2.4×10^9	4.9×10^8	9.3×10^8
2′-Deoxyinosine		1.8×10^6	9×10^5
2′-Deoxyadenosine		3.2×10^6	

As shown in Table 3, other guanine derivatives react with rate constants very similar to dG. The nucleosides 2′-deoxyadenosine and 2′-deoxyinosine on the other hand are less effective quenchers, as has been noted by the Novak group (24).

Table 4 lists values of k_{dG} for a series of 4-biphenylylnitrenium ions, and Fig. 3 plots the dependence of log k_{dG} on log k_w. With a couple of exceptions, this figure shows a smooth curve of the same form as the azide dependencies of Fig. 1. In particular the more reactive nitrenium ions show no dependence of k_{dG} on structure, all reacting at $(2 \pm 0.2) \times 10^9$ M^{-1} s^{-1}. This can be argued to represent the diffusion limit. The value is five times smaller than the limit for azide ion with the same cations. This is the difference between a cation–neutral encounter and a cation–anion encounter. The latter pair benefits from an electrostatic attraction that increases the rate of encounter (compare $Ar_2CH^+ + N_3^-$ (54) with $Ar_2CH^+ + RNH_2$ (69)).

The two points that fall off the curve in Fig. 2 are the *N*-acetyl-2-fluorenylnitrenium ion **12b** and the 3,5-dimethyl- 4-biphenylylnitrenium ion **27**. The latter has methyl groups *ortho* to the reacting nitrogen, so that its deviation is likely due to a steric effect. The deviation with the former may indicate that *N*-acetyl derivatives do not fall on the same curve as the NH cations. (The only other *N*-acetyl derivative studied thus far, cation **12a**, is very reactive and may have reached its limit). Interestingly **12b** is less reactive towards dG than its NH analog **3b**, while the order is reversed with

Fig. 3. Variation of log k_{dG} with log k_w.

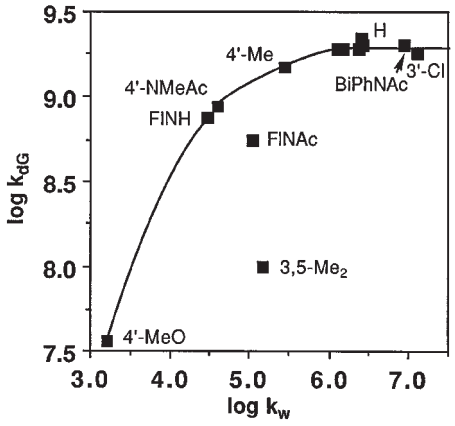

water as the nucleophile. One explanation is that with the *N*-acetylnitrenium ion, the electron withdrawing acetyl group has reduced the positive charge even more on the external nitrogen, the reacting site in the dG reaction.

In contrast to nitrenium ions, it is difficult to observe dG quenching of carbocations in LFP experiments. For example, cations **22** and **28** (70) show no change in decay rate constant in 20% acetonitrile in changing from 0 to 15 mM dG, about the maximum concentration attainable. Since an increase of 10% would be detectable, this places upper limits on k_{dG} as given in Table 5. Quenching can be observed in trifluoroethanol, where the background decay is suppressed because of the weaker solvent nucleophilicity. In TFE the cations **22** and **29** react with dG with rate constants of 10^6–10^7 M^{-1} s^{-1}. If these rate constants are applied to an aqueous solution, in 1 M dG only 22% (for **22**) and 7% (for **29**) of the products would be derived from the nucleoside.

One aspect of the comparison of nitrenium ions and carbenium ions that is important to note is that the site of reaction in guanine is different. With the 4-biphenylyl- and 2-fluorenyl nitrenium ions the only product with 2′-deoxyguanosine in water is the C8 adduct (23, 24). With carbon electrophiles on the other hand, there is no instance of reaction at C8, and the delocalized carbocations of Table 5 would be expected to react at the NH_2 group (13). It is

© 1998 NRC Canada

Table 4. Second-order rate constants (M^{-1} s^{-1}) for the trapping of nitrenium ions with 2′-deoxyguanosine, imidazole, 1-methylimidazole, 2-methylimidazole, and 1,2-dimethylimidazole (conditions: 20°C, 20% acetonitrile, ionic strength = 0.1 ($NaClO_4$)).

Cation[a]	2′-dG[b]	Imid[c]	1-MeIm[c]	2-MeIm[c]	1,2-Me_2Im[c]
3′-ClBiPhNH+	1.8×10^9	2.1×10^9	2.0×10^9	2.1×10^9	2.2×10^9
BiPhNH+	2.0×10^9	1.6×10^9	1.6×10^9	2.5×10^9	2.3×10^9
4′-ClBiPhNH+	2.2×10^9	1.7×10^9	1.9×10^9	2.7×10^9	2.2×10^9
3′-MeOBiPhNH+	1.9×10^9	1.5×10^9	1.6×10^9	2.4×10^9	2.1×10^9
4′-FBiPhNH+	1.9×10^9	1.1×10^9	1.2×10^9	2.3×10^9	2.1×10^9
3′-MeBiPhNH+	1.9×10^9	1.2×10^9	1.2×10^9	2.1×10^9	2.1×10^9
4′-MeBiPhNH+	1.5×10^9	2.6×10^8	2.9×10^8	1.7×10^9	1.9×10^9
4′-MeOBiPhNH+	3.6×10^7	8.2×10^5	7.3×10^5	7.2×10^7	3.7×10^7
3,5-Me_2BiPhNH+	1.0×10^8	4.8×10^7	2.8×10^7	1.3×10^9	5.1×10^8
FlNH+	7.6×10^8	4.7×10^7	5.7×10^7	1.2×10^9	1.1×10^9

[a]BiPh = 4-biphenylyl; Fl = 2-fluorenyl.

[b]pH 7 phosphate buffer.

[c]Determined in buffered system containing 10 parts of imidazole and 1 part imidazole perchlorate.

Table 5. Trapping of carbocations by 2′-deoxyguanosine in water (20% acetonitrile) and 2,2,2-trifluoroethanol (TFE).

Cation	k_{TFE}, s^{-1}	k_{dG}(TFE), M^{-1} s^{-1}	k_w, s^{-1}	k_{dG}(W), M^{-1} s^{-1}
9-(4-Methoxyphenyl)-9-fluorenyl (**28**)			1.7×10^5	$<10^{6a}$
9-(3-Chlorophenyl)-9-fluorenyl (**29**)	7.8×10^4	2.7×10^6	3.6×10^7	
Phenyl(2-fluorenyl)methyl (**22**)	3.1×10^4	4.3×10^6	1.5×10^7	$<10^{8a}$

[a]See text for explanation.

Table 6. Second-order rate constants (M^{-1} s^{-1}) for the trapping of nitrenium ions with primary amines (conditions: 20°C, 20% acetonitrile, ionic strength = 0.1 ($NaClO_4$)).

Cation[a]	$CH_3(CH_2)_3NH_2$	$HO(CH_2)_2NH_2$	$NC(CH_2)_2NH_2$	$CF_3CH_2NH_2$
3′-ClBiPhNH+	1.8×10^8	2.0×10^8	1.9×10^8	2.1×10^8
BiPhNH+	1.3×10^8	1.5×10^8	1.3×10^8	8.9×10^7
4′-ClBiPhNH+	1.4×10^8	1.3×10^8	1.3×10^8	9.8×10^7
3′-MeOBiPhNH+	1.3×10^8	1.5×10^8	1.2×10^8	9.5×10^7
4′-FBiPhNH+	1.0×10^8	1.3×10^8	1.1×10^8	6.5×10^7
3′-MeBiPhNH+	1.1×10^8	1.2×10^8	1.1×10^8	7.4×10^7
4′-MeBiPhNH+	6.6×10^7	6.6×10^7	5.7×10^7	2.7×10^7
4′-MeOBiPhNH+	9.2×10^6	6.8×10^6	3.7×10^6	8.7×10^5
3,5-Me_2BiPhNH+	8.1×10^7	6.1×10^7	5.7×10^7	2.5×10^7
FlNH+	6.4×10^7	4.8×10^7	3.7×10^7	1.5×10^7

[a]BiPh = 4-biphenylyl; Fl = 2-fluorenyl.

also interesting to speculate why the carbocations show such a low dG:water selectivity as compared to nitrenium ions. This is likely related to a combination of an enhanced guanine reactivity for the nitrenium ion, coupled with an unusually low water reactivity. We discussed the latter previously in comparing lifetimes of nitrenium and carbenium ions. The reactivities with imidazoles and amines to be presented in the next section point to the unusually high guanine reactivity.

Whatever the explanation, guanine monomers are capable of competing very effectively with solvent water molecules for the nitrenium ions derived from the carcinogens 2-aminofluorene and 4-aminobiphenyl. This contrasts with the situation for a fully-formed carbocation of a similar lifetime, where the competition strongly favors the solvent. In fact under conditions where the nitrenium ion is predominantly trapped by the guanine, there would be little if any guanine reaction with the carbocation.

Reactivity with imidazole derivatives and primary amines

The rate constants for four imidazoles reacting with nitrenium ions are given in Table 4. It can be seen that methyl substitution at N1 has only a minor effect, while methyl substitution at C2 has a more pronounced effect. Taking one member from each pair, plots of log k_{imid} vs. log k_w have been constructed and are shown in Fig. 4. The 2-methylimidazoles behave in a similar manner to 2′-deoxyguanosine. In particular the rate constants have become effectively constant for the more reactive ions. The limits are $(2.3 \pm 0.4) \times 10^9$ M^{-1} s^{-1} for 1-methylimidazole

© 1998 NRC Canada

Fig. 4. Variation of log k_{nuc} with log k_w. Open squares, 1,2-dimethylimidazole; closed squares, 2′-deoxyguanosine; open triangles, imidazole; closed triangles, 1-butylamine; open circles; 2-cyanoethylamine; closed circles, 2,2,2-triflouroethylamine.

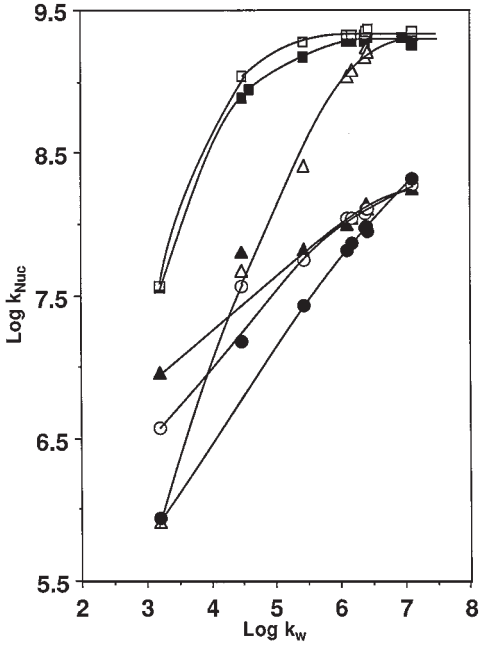

Fig. 5. Brönsted-like plots for the reactions of primary amines with nitrenium ions. Closed squares, 3′-chloro-4-biphenylylnitrenium ion; open squares, 4-biphenylylnitrenium ion; closed circles, 4′-fluoro-4-biphenylylnitrenium ion; open circles, 4′-methyl-4-biphenylylnitrenium ion; closed triangles, 2-fluorenylnitrenium ion; open triangles, 4′-methoxy-4-biphenylylnitrenium ion.

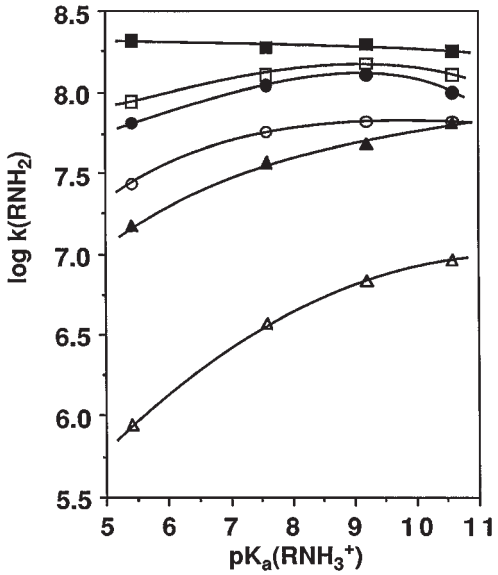

and $(2.2 \pm 0.2) \times 10^9$ M^{-1} s^{-1} for 1,2-dimethylimidazole. These numbers are very similar (if not indistinguishable considering experimental uncertainty) to the limit for 2′-deoxyguanosine. The plots for imidazole and 1-methylimidazole are also curved. However, in contrast to the 2-methylimidazoles and dG, the $\sim 2 \times 10^9$ limit is just being reached for the most reactive ion. The other nitrenium ions react below this limit, and show a dependence of rate constant on cation structure.

Data for four primary amines of varying basicity are provided in Table 6. The behaviour here is the same as previously seen for the same series of amines reacting with diarylmethyl carbocations (69). Brönsted-like plots (Fig. 5) are curved. The more reactive ions show an inversion of reactivity and basicity; i.e., 1-butylamine is less reactive than less basic analogs. Finally, as seen in Fig. 4, the limiting k_{amine} appears to fall below the 2×10^9 number associated with diffusion control. This behaviour is explained (69, 71, 72) by recognizing that the nucleophilic site is involved in a hydrogen bond with a solvent water molecule (RH_2N:----H—OH). This must be broken at some stage when the nitrogen bonds with an electrophile. For highly reactive electrophiles, breaking the hydrogen bond becomes more important than actual N–electrophile bond formation. Thus more basic amines with stronger hydrogen bonds are actually less reactive. The limiting rate constants are also less than diffusion control, since the hydrogen bond must always be broken.

If the NH_2 group of the alkyl amine is employed as a model for the C_2-NH_2 group of guanine, it is apparent from Fig. 4 why there is little reaction of the nitrenium ions at this site. Whatever the structures of amine and nitrenium ion, the dG reaction forming the C8 adduct is at least a factor of 10 faster than the amine reaction. In fact the difference is likely

Fig. 6. Failure of nitrenium ion reactivity to correlate with nitrogen basicity. Closed squares, 4-biphenylylnitrenium ion; open squares, 2-fluorenylnitrenium ion; dG, 2′-deoxyguanosine; *a*, primary amine; im, imidazole. The pK_a for dG is that for N7 protonation.

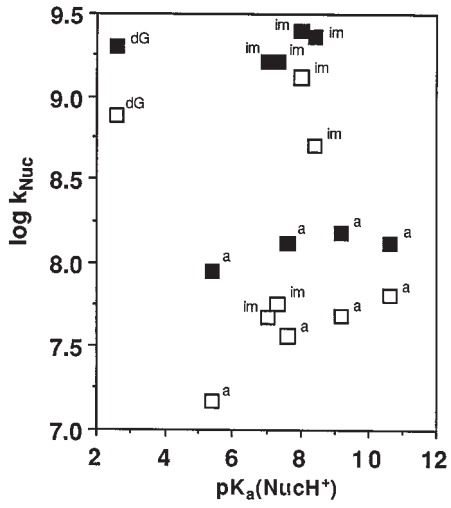

greater than this, since the NH_2 group of guanine is considerably less basic than even $CF_3CH_2NH_2$, the least basic of the alkyl amines.

It is also apparent that if 2′-deoxyguanosine and the imidazoles are included, there is absolutely no correlation of nitrogen basicity with reactivity towards nitrenium ions (Fig. 6). The imidazoles and 2′-deoxyguanosine might be considered as a series since protonation involves the same type of nitrogen, but even here there is no correlation. The

© 1998 NRC Canada

Scheme 5.

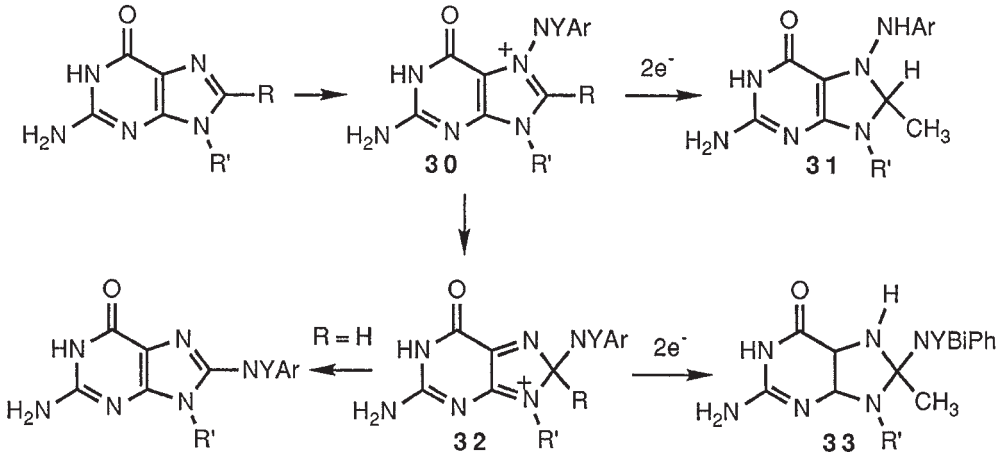

nucleoside has about the same reactivity as the 2-methylimidazoles, but is more reactive than imidazole and 1-methylimidazole, compounds that are 4–5 log units more basic. These conclusions should be regarded as preliminary since the products with the amines and imidazoles have not been determined. Such studies are in progress.

Questions regarding nitrenium-guanine chemistry

There are still several unanswered questions regarding the nitrenium–guanine reaction — why is it so fast, what is the mechanism for the formation of the C8 adduct, and are there differences between monomeric guanine and the guanine residues of DNA? With respect to the mechanism, there are conflicting reports regarding the exact details. Humphreys et al. (73) have suggested that the initial site of reaction is N7, to give intermediate **30**. This was based on experiments with an 8-methylguanine derivative and the 2-fluorenylnitrenium ion. With both NMR and MS, structures were assigned to both the unstable **30** and its reduction product **31**. The Novak group have also looked at the 8-methyl system, in their case with the biphenylylnitrenium ions **3a** and **12a**. They however assign C8 adduct structures **32** and **33** to an intermediate and its reduction product. Nevertheless they still propose that N7 is the initial site of attack, based on a correlation of reactivity with the N7 basicity. That correlation obviously breaks down if imidazoles are included, as we have just discussed. Very recent flash photolysis experiments in our group have shown that the decay of a nitrenium ion in the presence of 2′-deoxyguanosine is accompanied by the formation of an intermediate absorbing in the range 300–400 nm. Several pieces of evidence suggest that that species is the C8 adduct **32**, with R = H. In particular the decay of that intermediate exhibits a very large primary isotope effect when comparing guanine C8-H and C8-D (Scheme 5).

The situation with guanine in DNA is also an interesting one. Novak and Kennedy (74) have performed experiments that show that a double-stranded DNA hexamer containing one dG does not quench the nitrenium ion **12b**. The single-stranded form does, but on a per guanine basis, only a quarter as effectively as 2′-deoxyguanosine. Other studies have however shown an opposite behaviour, with DNA giving more adducts than monomeric guanine (see for example, ref. 75). There are also a number of reports that suggest that carbenium ions can form adducts with DNA–guanine (13, 76), despite our failure to see quenching with the monomer. As has been pointed out by Novak (24, 75), the reactivity pattern in guanine DNA is also different. Whereas the monomer studies show only the C8 adduct, with guanine in DNA there is usually a small fraction of adduct where the guanine NH_2 group has joined with one of the ring carbons of the nitrenium ion (13). Thus, the electrophile is behaving as a carbenium ion, doing typical carbenium chemistry.

Thus, there is uncertainty as to whether the results obtained with monomeric guanine derivatives can be extended to DNA. With the availability of both flash photolysis precursors and solvolytic precursors, it should be possible to examine this question in detail.

Experimental section

Precursors for the flash photolysis generation of the nitrenium and carbenium ions whose data appear in Tables 1–6 have been presented in previous publications (35, 40, 54, 55, 70). Flash photolysis experiments were conducted with 308 nm irradiation, and detection at the λ_{max} of the electrophile (35, 40, 54, 55, 70). The solutions contained 20% by volume acetonitrile in water, and the temperature was 20°C. Five to seven concentrations of the quenching nucleophile were employed, chosen such that the most concentrated solution had a rate acceleration at least a factor of ten greater than solvent alone. The exceptions to this were the 3′-chlorobiphenylylnitrenium ion and the *N*-acetyl-4-biphenylylnitrenium ion, where smaller rate accelerations were necessary because of the very fast background rate. All solutions gave excellent exponential decay traces. First-order rate constants *k*(decay) were obtained by nonlinear regression of the expression for single exponential decay. Plots of *k*(decay) versus the concentration of the quencher were excellently linear. The second-order rate constant for the quencher was determined from the slope of this line by linear regression. In general the standard deviation in this value was in the range 2–4%, except for the two more reactive ions (see above) where the errors are larger.

© 1998 NRC Canada

Acknowledgements

The continued financial support of the Natural Sciences and Engineering Research Council (NSERC) of Canada is gratefully acknowledged. TAG acknowledges NSERC for a Post-doctoral Fellowship.

References

1. J.A. Miller. Cancer Res. **30**, 559 (1970).
2. H.C. Crabtree, D. Hart, M.C. Thomas, B.H. Witham, I.G. McKenzie, and C.P. Smith. Mutat. Res. **264**, 155 (1991).
3. G. Talaska, K.L. Dooley, and F.F. Kadlubar. Carcinogenesis, **11**, 639 (1990).
4. G. Talaska, A.Z.S.S. Al-Juburi, and F.F. Kadlubar. Proc. Natl. Acad. Sci. U.S.A. **88**, 5350 (1991).
5. G. Talaska, M. Schamer, P. Skipper, S. Tannenbaum, M. Caporaso, L. Unruh, F.F. Kadlubar, H. Bartsch, C. Malaveille, and P. Vineis. Cancer Epidemiol. Biomarkers Prev. **1**, 61 (1991).
6. E.T. Wei and H.P. Shu. Am. J. Public Health, **73**, 1085 (1983).
7. F.A. Beland and F.F. Kadlubar. *In* Chemical carcinogenesis and mutagenesis. Vol. 1. *Edited by* C.S. Cooper and P.L. Grover. Springer-Verlag, Berlin. 1990. pp. 267–325.
8. F.F. Kadlubar. *In* DNA adducts, identification and biological significance. *Edited by* K. Hemminki, A. Dipple, D.E.G. Shuker, F.F. Kadlubar, D. Segerback, and H. Bartsch. IARC Publication No. 125, IARC, Lyon. 1994. pp. 199–216.
9. G. Boche, F. Bosold, and S. Schroder. Angew. Chem. Int. Ed. Engl. **27**, 973 (1988).
10. C. Meier and G. Boche. Tetrahedron Lett. **31**, 1685 (1990).
11. F.F. Kadlubar, G. Talaska, N.P. Lang, R.W. Benson, and D.W. Roberts. *In* Methods for detecting DNA damaging agents in humans: applications in cancer epidemiology and prevention. *Edited by* J. Bartsch, J. Hemminki, and I.K. O'Neill. IARC Publication No. 89, IARC, Lyon. 1988. pp. 174–199.
12. F.F. Kadlubar. *In* Xenobiotics and cancer. *Edited by* L. Ernster. Taylor and Francis, London. 1991. pp. 320–338.
13. A. Dipple. Carcinogenesis, **16**, 437 (1995).
14. E.C. Miller and J.A. Miller. Cancer, **47**, 2327 (1981).
15. M. Famulok, F. Bosold, and G. Boche. Tetrahedron Lett. **31**, 1689 (1990).
16. M. Novak, K.A. Martin, and J.L. Heinrich. J. Org. Chem. **54**, 5430 (1989).
17. J.S. Helmick, K.A. Martin, J.L. Heinrich, and M. Novak. J. Am. Chem. Soc. **113**, 3459 (1991).
18. M. Novak, M. Pelecanou, A.K. Roy, A.F. Andronico, F.M. Pourde, T.M. Olefirowicz, and T.J. Curtin. J. Am. Chem. Soc. **106**, 5623 (1984).
19. M. Novak, M.J. Kahley, E. Eiger, J.S. Helmick, and H.E. Peters. J. Am. Chem. Soc. **115**, 9453 (1993).
20. M. Novak, M.J. Kahley, J. Lin, S.A. Kennedy, and L.A. Swanegan. J. Am. Chem. Soc. **116**, 11 626 (1994).
21. M. Novak, M.J. Kahley, J. Lin, S.A. Kennedy, and T.G. James. J. Org. Chem. **60**, 8294 (1995).
22. J.C. Fishbein and R.A. McClelland. J. Am. Chem. Soc. **109**, 2824 (1987).
23. M. Novak and S.A. Kennedy. J. Am. Chem. Soc. **117**, 574 (1995).
24. S.A. Kennedy, M. Novak, and B.A. Kolb. J. Am. Chem. Soc. **119**, 7654 (1997).
25. C.J. Cramer, F.J. Dulles, J.W. Storer, and S.E. Worthington. Chem. Phys. Lett. **218**, 387 (1994).
26. S.T. Gibson, J.P. Greene, and J. Berkowitz. J. Chem. Phys. **83**, 4319 (1985).
27. C.J. Cramer, F.J. Dulles, and D.E. Falvey. J. Am. Chem. Soc. **116**, 9787 (1994).
28. U. Svanholm and V. Parker. J. Am. Chem. Soc. **96**, 1234 (1974).
29. D. Serve. J. Am. Chem. Soc. **97**, 432 (1975).
30. A. Riecker and B. Reiser. Tetrahedron Lett. **31**, 5013 (1990).
31. G.A. Olah and D.J. Donovan. J. Org. Chem. **43**, 1743 (1978).
32. G.A. Olah, G.K.S. Prakash, and M. Arvanaghi. J. Am. Chem. Soc. **102**, 6640 (1980).
33. R.A. McClelland. Tetrahedron, **52**, 6823 (1996).
34. R.A. McClelland, P.A. Davidse, and G. Hadzialic. J. Am. Chem. Soc. **117**, 4173 (1995).
35. R.A. McClelland, M.J. Kahley, P.A. Davidse, and G. Hadzialic. J. Am. Chem. Soc. **118**, 4794 (1996).
36. G.B. Schuster and M.S. Platz. Adv. Photochem. **17**, 143 (1992).
37. J. Michalak, H.B. Zhai, and M.S. Platz. J. Phys. Chem. **100**, 14 028 (1996).
38. N.P. Gritsan, T. Yuzawa, and M.S. Platz. J. Am. Chem. Soc. **119**, 5059 (1997).
39. R. Born, C. Burda, P. Senn, and J. Wirz. J. Am. Chem. Soc. **119**, 5059 (1997).
40. P.A. Davidse, M.J. Kahley, R.A. McClelland, and M. Novak. J. Am. Chem. Soc. **116**, 4513 (1994).
41. W. Kirmse, J. Kilian, and S. Steenken. J. Am. Chem. Soc. **112**, 6399 (1990).
42. J. Chateauneuf. J. Chem. Soc. Chem. Commun. 1437 (1991).
43. S.T. Belt, C. Bohne, G. Charette, S.E. Sugamori, and J.C. Scaiano. J. Am. Chem. Soc. **115**, 2200 (1993).
44. N.P. Schepp and J. Wirz. J. Am. Chem. Soc. **116**, 11 749 (1994).
45. J.W. Hilborn and J. Pincock. J. Am. Chem. Soc. **113**, 2683 (1991).
46. H.E. Zimmerman. J. Am. Chem. Soc. **117**, 8998 (1995).
47. M. Lipson, A.A. Deniz, and K.S. Peters. J. Am. Chem. Soc. **188**, 2992 (1996).
48. G.B. Anderson and D.E. Falvey. J. Am. Chem. Soc. **115**, 9870 (1993).
49. R.J. Robbins, L.L.-N. Yang, G.B. Anderson, and D.E. Falvey. J. Am. Chem. Soc. **117**, 6544 (1995).
50. R.J. Robbins, D.M. Laman, and D.E. Falvey. J. Am. Chem. Soc. **118**, 8127 (1996).
51. R.J. Moran and D.E. Falvey. J. Am. Chem. Soc. **118**, 8965 (1996).
52. J.P. Richard and W.P. Jencks. J. Am. Chem. Soc. **104**, 4689 (1982); **104**, 4691 (1982).
53. J.P. Richard, M.E. Rothenburg, and W.P. Jencks. J. Am. Chem. Soc. **106**, 1373 (1984).
54. R.A. McClelland, V.M. Kanagasabapathy, N. Banait, and S. Steenken. J. Am. Chem. Soc. **111**, 3966 (1989).
55. D. Ren and R.A. McClelland. Can. J. Chem. **76**, 78 (1998).
56. R.A. McClelland, V.M. Kanagasabapathy, N. Banait, and S. Steenken. J. Am. Chem. Soc. **113**, 1009 (1991).
57. P. Ruane, R.A. McClelland, and A. Ahmed. J. Chem. Soc. Perkin Trans. 2. In press.
58. D. Ren. Ph.D. thesis, University of Toronto. 1998.
59. J.C. Fishbein and R.A. McClelland. Can. J. Chem. **74**, 1321 (1996).
60. P. Sukhai and R.A. McClelland. J. Chem. Soc. Perkin Trans. 2, 1529 (1996).
61. J.P. Richard, T.L. Amyes, L. Bei, and V. Stubblefield. J. Am. Chem. Soc. **112**, 9513 (1990).

© 1998 NRC Canada

62. T.A. Gadosy and R.A. McClelland. J. Am. Chem. Soc. In press.
63. J.L. Bolton and R.A. McClelland. J. Am. Chem. Soc. **111**, 8172 (1989).
64. J.L. Bolton and R.A. McClelland. Can. J. Chem. **67**, 1139 (1989).
65. R.A. McClelland, C. Chan, F. Cozens, A. Modro, and S. Steenken. Angew. Chem. Int. Ed. Engl. **30**, 1337 (1991).
66. S. Srivasta, J.P. Toscano, R.J. Moran, and D.E. Falvey. J. Am. Chem. Soc. **119**, 11 552 (1998).
67. J.F. Corbett. J. Chem. Soc. (B), 213 (1969).
68. D.S. Noyce and G.T. Stowe. J. Org. Chem. **38**, 3762 (1973).
69. R.A. McClelland, V.M. Kanagasabapathy, N.S. Banait, and S. Steenken. J. Am. Chem. Soc. **114**, 1816 (1992).
70. F.L. Cozens, N. Mathivanan, R.A. McClelland, and S. Steenken. J. Chem. Soc. Perkin Trans. 2, 2083 (1992).
71. J.P. Richard. J. Chem. Soc. Chem. Commun. 1768 (1987).
72. W.P. Jencks, M.T. Haber, D. Herschlag, and K. Nazaretian. J. Am. Chem. Soc. **108**, 479 (1986).
73. W.G. Humphreys, F.F. Kadlubar, and F.P. Guengerich. Proc. Natl. Acad. Sci. U.S.A. **89**, 8278 (1992).
74. M. Novak and S. Kennedy. J. Phys. Org. Chem. **11**, 71 (1998).
75. F.F. Kadlubar, J.A. Miller, and E.C. Miller. Cancer Res. **38**, 3628 (1978).
76. L. Dasaradhi and S. Shibutani. Chem. Res. Toxicol. **10**, 189 (1997).

© 1998 NRC Canada

Diastereoselective alkoxymethylation of aromatic aldehydes with chiral lithiomethyl ethers. Synthesis of optically active monoprotected glycols

Viviana L. Ponzo and Teodoro S. Kaufman

Abstract: The synthesis of optically active α-alkoxymethyl benzyl alcohols by reaction of polysubstituted benzaldehydes with chiral α-alkoxymethyllithiums, easily obtained by transmetallation of the corresponding α-alkoxystannanes with *n*-butyllithium, is reported. Chemical yields of the transformation are good while low asymmetric induction (<1.6:1) is obtained.

Key words: diastereoselective synthesis, monoprotected glycols, chiral alkoxymethyllithiums, addition to aldehydes, optically active alcohols.

Résumé : On a réalisé la synthèse d'alcools α-alkoxyméthylbenzyliques optiquement actifs par réaction de benzaldéhydes polysubstitués avec des α-alkoxyméthyllithiens chiraux facilement obtenus par transmétallation des α-alkoxystannanes avec du butyllithium. Les rendements chimiques de la transformation sont bons et on obtient de faibles inductions asymétriques (<1,6:1).

Mots clés : synthèse diastéréosélective, glycols monoprotégés, alkoxyméthyllithiens chiraux, addition à des aldéhydes, alcools optiquement actifs.

[Traduit par la Rédaction]

The preparation of enantiomerically pure compounds is one of the most challenging problems in organic chemistry; therefore, much effort is being devoted to the development of efficient methods for the accomplishment of this objective. Among them, the enantioselective reactions of the carbonyl group involving reductions with modified boron and aluminum hydrides or nucleophilic additions of chelated organometallics have received considerable attention for a long time (for reviews, see ref. 1).

During our work on the synthesis of bioactive tetrahydroisoquinolines, we have elaborated and employed α-alkoxymethyl benzyl alcohols as key intermediates, both as racemates (2) and in their optically active form (3). We observed that, in contrast with the abundant literature on the synthesis of chiral benzylic alcohols by reduction of prochiral ketones or addition of alkylzinc derivatives to aromatic aldehydes (1), the direct enantio- and diastereoselective alkoxymethylation of the latter have been scarcely studied (4).

The extended use of this kind of compounds and the previously reported syntheses of racemic monoprotected glycols by addition of organotin derived α-alkoxymethyllithiums to aldehydes (5), prompted us to evaluate the use of our recently developed one-pot synthesis of chiral α-alkoxymethyl organostannanes (6) as an easy, convenient, and inexpensive entry to these chiral glycol monoethers.

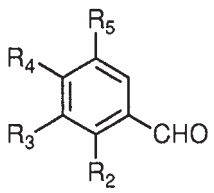

1 $R_2 = R_3 = OMe$, $R_4 = R_5 = H$
2 $R_2 = OMe$, $R_3 = R_4 = H$, $R_5 = Br$
3 $R_2 = R_5 = OMe$, $R_3 = R_4 = H$
4 $R_2 = H$, $R_3 = R_4 = R_5 = OMe$
5 $R_2 = OBn$, $R_3 = OMe$, $R_4 = R_5 = H$
6 $R_2 = R_5 = H$, $R_3 = R_4 = OMe$

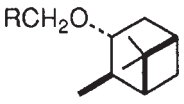

7a R= $SnBu_3$
7b R= Li

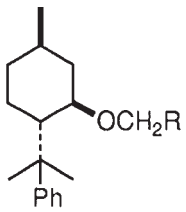

8a R= $SnBu_3$
8b R= Li

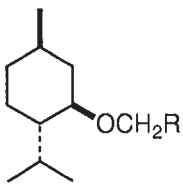

9a R= $SnBu_3$
9b R= Li

Received April 13, 1998.

V.L. Ponzo and T.S. Kaufman.[1] Instituto de Química Orgánica de Síntesis (CONICET-UNR) and Facultad de Ciencias Bioquímicas y Farmacéuticas, Universidad Nacional de Rosario, Suipacha 531, (2000) Rosario, Argentina.

[1]Author to whom correspondence may be addressed. Telephone: 54-41-804600. Fax: 54-41-370477. E-mail: tkaufman@agatha.unr.edu.ar

© 1998 NRC Canada

Table 1. Synthesis of α-alkoxymethyl benzyl alcohols by addition of α-alkoxymethyllithium derivatives to aromatic aldehydes.

Entry	Nucleophile	Aldehyde	Product	Yield (%)[b]	Diast. ratio[c]	$[\alpha]^{25}_{D}$ (*c*)[d]
1	**7b**	1	**10a–10b**	74	1.31:1	—[a]
2	**8b**	**1**	**11a**	57	1.43:1	+16.1 (0.60)
			11b			–54.0 (0.34)
3	**9b**	1	**12a**	84	1.40:1	–8.4 (0.96)
			12b			–84.3 (1.90)
4	**9b**	2	**13a**	51	1.51:1	–21.7 (0.30)
			13b			–63.1 (1.26)
5	**9b**	3	**14a**	79	1.42:1	–10.5 (1.50)
			14b			–64.8 (1.90)
6	**9b**	4	**15a**	78	1.52:1	–16.1 (0.23)
			15b			–82.5 (0.35)
7	**9b**	5	**16a**	71	1.50:1	–17.3 (0.35)
			16b			–21.8 (0.45)
8	**9b**	6	**17a–17b**	86	1.57:1	—[a]

[a]Unseparable mixture (by flash chromatography) of diastereoisomers.
[b]Isolated yield after flash chromatography (silica gel, benzene–EtOAc).
[c]More polar/less polar; determined by 200 MHz ^{1}H NMR.
[d]In $CHCl_3$.

Scheme 1.

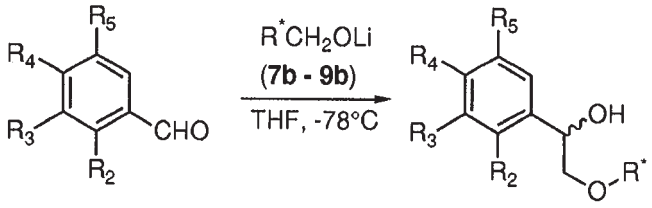

1 - 6 **10 - 17**

Herein we report the synthesis of optically active α-alkoxymethyl benzyl alcohols by reaction of aromatic aldehydes with chiral lithiomethyl ethers. For the purposes of this study, test aldehydes **1**–**6** and chiral organostannanes **7a**–**9a** derived from (+)-isopinocampheol, (–)-8-phenylmenthol, and the natural (–)-menthol, respectively, were employed.

When the aromatic aldehydes were added to THF solutions of the chiral α-alkoxymethyllithium (for examples of transmetallation of α-alkoxymethyltins and related species, see ref. 7) reagents **7b**–**9b** derived from stannanes **7a**–**9a** at –78°C, it was observed an almost immediate formation of the corresponding alkoxymethylated products (Scheme 1), very slightly contaminated with the alcohols originated in the *n*-butyllithium addition to the carbonyls (5*b*, 5*c*).

In a preliminary exploration, the nucleophiles derived from chiral stannanes **7a**–**9a** were tested against the same aldehyde, as exemplified in entries 1–3 of Table 1. Interestingly, it was observed that the products resulting from the use of **7a** could not be separated, while employing **8a** gave rise to a mixture of alcohols, the diastereoisomeric excess (de) of which was not different from that obtained when its less bulkier and less expensive congener **9a** was used; therefore the latter was selected for further experiments.

The TLC and ^{1}H NMR analysis revealed that the reactions proceeded in good yield, but with low diastereoselectivity (Table 1). Although the components of the diastereoisomeric mixture exhibited similar R_f values, careful flash chromatography of the crudes allowed the isolation of pure diastereoisomers in most of the cases, when benzene–EtOAc was employed as eluent.

The low diastereoselectivity observed can be explained taking into account the high reactivity of the α-alkoxymethyllithium intermediates, which are known to add to aldehydes at rates comparable to those of *n*-butyllithium even at low temperature (5*a*), preventing the differentiation of both prochiral faces of the electrophile (8). On the other hand, being the chiral moiety of the nucleophile far from its carbanionic centre, the proper transmission of the chiral information to the newly generated asymmetric carbon becames difficult (8*b*); this effect was also noticed by Colombo et al. (9) during their study on asymmetric induction in the α-lithioacetal and α-lithiooxazolidine series.

Noteworthy, a Lewis acid-mediated reaction of a chiral α-alkoxyorganolead compound with benzaldehyde giving a chiral glycol monoether, has been recently reported (10). Lacking the above drawbacks, this transformation demonstrated to be highly diastereoselective. In our hands, however, no reaction was observed when a mixture of stannane **9a**, and aldehyde **1** was treated with $BF_3{\cdot}Et_2O$ (2–4 equiv.) under the most different conditions (–78°C to RT and 1 h to 2 days). Presumably, this unsuccessful outcome is a consequence of the fact that tin forms stronger bonds with carbon than does lead (10*b*).

The use of an oxazaborolidine-mediated reduction of carbonyls (CBS process) was employed to obtain information about the absolute configuration of the newly formed chiral centre of the diatereoisomeric monoprotected glycols, on the basis that the mechanism of the CBS reduction with oxazaborolidine **(*S*)-18** derived from (–)-diphenylprolinol has been extensively studied (11) and shown to occur by way of a transition state assembly which allows the correct prediction of the absolute configuration of the product (12).

Thus, the mixture of **12a** and **12b** was subjected to a Swern oxidation (Scheme 2), affording ketone **19** in 91%

© 1998 NRC Canada

Scheme 2.

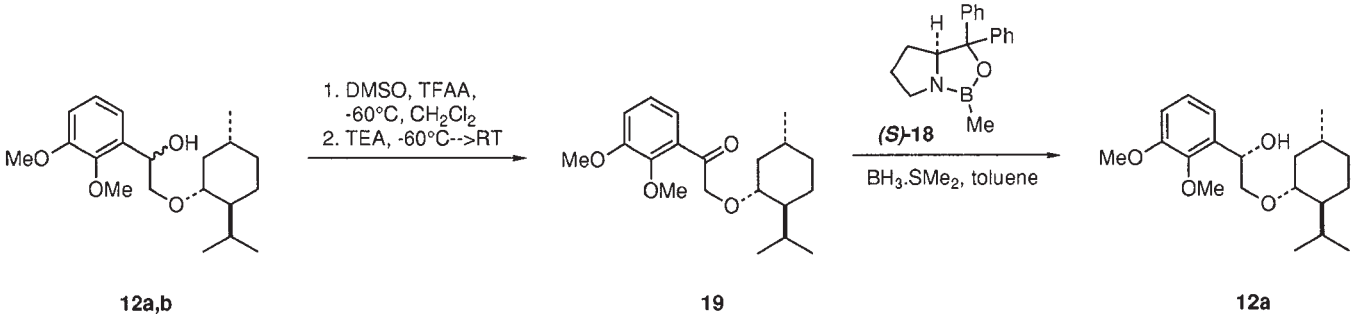

Table 2. Chromatographic behaviour, specific rotation data, and selected ^{13}C NMR resonances of α-menthyloxymethyl benzyl alcohols.

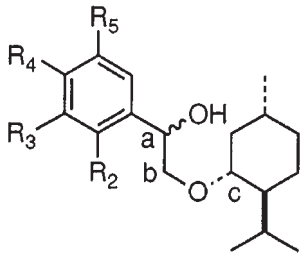

Compound	R_f	$[\alpha]^{25}_D$	δ_a	δ_b	δ_c
12a	0.69	–8.40	68.52	73.11	79.91
12b	0.65	–84.30	68.13	73.02	79.44
13a	0.74	–21.70	67.87	72.22	79.97
13b	0.64	–63.09	67.78	72.10	79.57
14a	0.72	–10.50	68.49	72.66	79.86
14b	0.66	–64.80	68.33	72.45	79.41
15a	0.62	–16.10	73.42	74.14	79.96
15b	0.57	–82.50	72.93	73.77	79.51
16a	0.60	–17.34	68.67	73.05	79.74
16b	0.58	–21.83	68.00	72.48	78.91

yield, while subsequent submission of **19** to the CBS reduction protocol (for a review about reductions in the presence of oxazaborolidines, see ref. 13) under **(*S*)-18** catalysis, furnished 97% of the less polar diastereoisomer **12a** (>98% de), to which benzylic centre was assigned the ***S*** configuration, on the basis of the reaction mechanism and literature precedents (1*b*, 13, 14).

Analysis of the ^{13}C NMR spectra of the (–)-menthyloxy derivatives **12**–**16** revealed interesting correlations between the chemical shifts of the alicyclic carbon atoms attached to oxygen of the diastereoisomers, their chromatographic behaviour and the corresponding specific rotations. As shown in Table 2, the less polar diastereoisomers exhibited higher $[\alpha]^{25}_D$ values and more deprotected oxygen-bonded alicyclic carbons than their more polar epimers. The above correlations probably indicate that the absolute configuration of the benzylic centre of all the less polar alcohols should be the same, and opposite to that of their more polar diastereoisomers.

In conclusion, the addition of chiral α-alkoxymethyllithium reagents to aromatic aldehydes as prochiral electrophiles gives good yields of optically active α-alkoxymethyl benzyl alcohols, which can be isolated in enantiomerically pure form. Asymmetric induction, however, is low.

Experimental section

Melting points were measured on an Ernst Leitz hot-stage microscope apparatus and are uncorrected. The IR spectra were taken on a Bruker IFS 25 spectrometer with solid samples as KBr pellets and liquid samples as films. The ^1H and ^{13}C NMR spectra were recorded in deuteriochloroform, on a Bruker AC-200E instrument at 200.13 and 50.33 MHz, respectively, with tetramethylsilane as the internal standard. The ^{13}C NMR resonances corresponding to two carbon atoms are designated with an asterisk. Optical rotation data were obtained employing a Jasco DIP 1000 electronic photopolarimeter. High-resolution mass spectra were obtained from UMYMFOR (Buenos Aires). Measurement of the diastereoisomeric excess of the oxazaborolidine-mediated reduction products was carried out employing a Gilson HPLC system equipped with a Chiralcel OD column, employing hexane-2-propanol (95:5) as the mobile phase at a rate of 0.5 mL/min and UV detection at 254 nm. Starting aromatic aldehydes were commercially available, and chiral α-alkoxymethyl tributyl stannanes were prepared from the corresponding chloromethyl ethers following our recently reported one-pot procedure (6). All reactions were carried out in a dry oxygen-free argon atmosphere. Reactions were monitored by thin layer chromatography on Merck's precoated silica gel 60 F_{254} TLC plates developed in benzene–EtOAc 8:2 and detected by examination under UV light, and by spraying with 2% *p*-anisaldehyde – sulfuric acid reagent in ethanol. Careful heating improved the sensitivity of the detection. All new compunds gave a single spot by TLC. The R_f values (TLC) were determined employing benzene–EtOAc 8:2 as mobile phase. Flash chromatography was carried out on Merck Kieselgel 60 (0.04–0.063 mm), packed in benzene; elution was done with mixtures of benzene–EtOAc, using gradient techniques. Compounds were preadsorbed from diethyl ether or dichloromethane solutions onto the adsorbent before column chromatography.

© 1998 NRC Canada

General procedure for the preparation of chiral α-alkoxymethyllithiums and their addition to aromatic aldehydes

A solution of *n*-butyllithium in hexanes (0.28 mL, 0.58 mmol) was added dropwise to a stirred solution of the starting chiral α-alkoxymethyl tributylstannane (0.60 mmol) in dry THF (1 mL) at –78°C. After 5 min, a solution of the aldehyde (0.5 mmol) in THF (1 mL) was incorporated to the thus formed α-alkoxymethyllithium derivative at the same temperature and stirring continued for an additional 10 min period. The reaction mixture was then quenched with saturated ammonium chloride solution (5 mL), warmed to room temperature, and extracted with EtOAc (3 × 20 mL). The combined organic extracts were dried (Na_2SO_4), concentrated in vacuo and chromatographed.

1-(2′′,3′′-Dimethoxyphenyl)-2-[(1′*S*, 2′*R*, 3′*R*, 5′*S*)-2′,6′,6′-triethylbicyclo[3.1.1]hept-3′-yloxymethyl]-ethanol (10a and 10b)

Unseparable mixture of diastereoisomers: R_f = 0.67; IR (neat): 3460, 2940, 1590, 1485, and 1290 cm^{-1}; HREIMS calcd. for $C_{20}H_{30}O_4$: 334.2144; found: 334.2155. Characteristic signals, major diastereoisomer: ^{1}H NMR, δ: 3.36 (dd, *J* = 9.9, 9.9 Hz, 1H) and 3.69 (dt, *J* = 3.2, 9.9 Hz, 1H); ^{13}C NMR, δ: 68.08, 73.53, and 79.75; minor diastereoisomer: ^{1}H NMR, δ: 3.42 (dd, *J* = 10.1, 10.1 Hz, 1H) and 3.73 (dt, *J* = 3.2, 10.1 Hz, 1H); ^{13}C NMR, δ: 67.72, 73.27, and 79.23.

1-(2′′,3′′-Dimethoxyphenyl)-2-[(1′*R*, 2′*S*, 5′*R*)-5′-methyl-2′-(1-methyl-1-phenylethyl)-cyclohexyloxy]-ethanol (11a and 11b)

*First diastereoisomer (**11a**)*: R_f = 0.64; $[\alpha]^{25}_D$ = +16.1 (*c* = 0.60, $CHCl_3$); IR (neat): 3450, 2954, 2868, 1586, 1478, 1370, 1278, 1222, 1052, 808, 752 and 702 cm^{-1}; ^{1}H NMR, δ: 0.80–1.12 (m, 3H), 0.88 (d, *J* = 6.5 Hz, 3H), 1.20–1.33 (m, 1H), 1.24 (s, 3H), 1.40 (s, 3H), 1.55–1.70 (m, 2H), 1.88–2.11 (m, 2H), 2.16 (d, *J* = 2.5 Hz, 1H), 3.06 (dd, *J* = 9.1, 9.1 Hz, 1H), 3.16 (dt, *J* = 4.1, 10.4 Hz, 1H), 3.63 (dd, *J* = 2.9, 9.1 Hz, 1H), 3.80 (s, 3H), 3.83 (s, 3H), 4.83 (ddd, *J* = 2.5, 2.9, 9.1 Hz, 1H), 6.81 (dd, *J* = 2.7, 7.9 Hz, 1H), 7.01 (dd, *J* = 7.5, 7.9 Hz, 1H), 7.02 (dd, *J* = 2.7, 7.5 Hz, 1H), and 7.08–7.40 (m, 5H); ^{13}C NMR, δ: 21.96, 26.11, 26.95, 28.01, 31.42, 34.97, 39.98, 40.65, 51.46, 55.70, 60.62, 68.60, 72.57, 80.84, 111.70, 118.92, 123.89, 124.92, 125.26,* 127.86,* 134.09, 146.11, 152.26, and 152.31; HREIMS calcd. for $C_{26}H_{36}O_4$: 412.2614; found: 412.2623.

*Second diastereoisomer (**11b**)*: R_f = 0.57; $[\alpha]^{25}_D$ = –54.0 (*c* = 0.34, $CHCl_3$); IR (neat): 3464, 2954, 2856, 1600, 1588, 1480, 1304, 1280, 1100, 1052, 752, and 702 cm^{-1}; ^{1}H NMR, δ: 0.73–1.12 (m, 3H), 0.85 (d, *J* = 6.5 Hz, 3H), 1.20–1.38 (m, 1H), 1.27 (s, 3H), 1.42 (s, 3H), 1.52–1.70 (m, 2H), 1.82–2.10 (m, 2H), 2.14 (d, *J* = 3.1 Hz, 1H), 3.17 (dt, *J* = 4.0, 10.3 Hz, 1H), 3.29 (dd, *J* = 3.4, 9.1 Hz, 1H), 3.35 (dd, *J* = 7.6, 9.1 Hz, 1H), 3.84 (s, 3H), 3.86 (s, 3H), 4.86 (ddd, *J* = 3.1, 3.4, 7.6 Hz, 1H), 6.81 (dd, *J* = 2.2, 7.5 Hz, 1H), 6.93 (dd, *J* = 2.2, 7.9 Hz, 1H), 6.98 (dd, *J* = 7.5, 7.9 Hz, 1H), and 7.10–7.40 (m, 5H); ^{13}C NMR, δ: 21.91, 25.30, 26.61, 28.17, 31.23, 34.83, 39.73, 40.20, 51.54, 55.58, 60.60, 67.73, 72.28, 80.62, 111.35, 118.65, 123.90, 124.70, 125.28,* 127.61,* 133.94, 145.72, 152.07, and 152.53; HREIMS calcd. for $C_{26}H_{36}O_4$: 412.2614; found: 412.2623.

(–)-1-(2′′,3′′-Dimethoxyphenyl)-2-[(1′*R*, 2′*S*, 5′*R*)-2′-isopropyl-5′-methylcyclohexyloxy]-ethanol (12a and 12b)

*First diastereoisomer (**12a**)*: R_f = 0.69; mp 78–79.5°C (hexane–EtOAc); $[\alpha]^{25}_D$ = –8.40 (*c* = 0.96, $CHCl_3$); IR (neat): 3418, 2930, 2870, 1581, 1478, 1280, 1110, 1086, 1052, and 752 cm^{-1}; ^{1}H NMR, δ: 0.72–1.10 (m, 3H), 0.77 (d, *J* = 7.0 Hz, 3H), 0.90 (d, *J* = 6.1 Hz, 6H), 1.20–1.45 (m, 2H), 1.58–1.71 (m, 2H), 2.03–2.31 (m, 2H), 2.93 (d, *J* = 2.5 Hz, 1H), 3.12 (dt, *J* = 3.9, 10.7 Hz, 1 H), 3.22 (dd, *J* = 8.7, 9.7 Hz, 1H), 3.83 (dd, *J* = 3.0, 9.7 Hz, 1H), 3.84 (s, 3H), 3.86 (s, 3H), 5.16 (ddd, *J* = 2.5, 3.0, 8.7 Hz, 1H), 6.85 (dd, *J* = 2.5, 7.2 Hz, 1H), 7.04 (dd, *J* = 7.2, 8.3 Hz, 1H), and 7.10 (dd, *J* = 2.5, 8.3 Hz, 1H); ^{13}C NMR, δ: 15.95, 20.82, 22.15, 23.09, 25.62, 31.36, 34.35, 40.42, 48.09, 55.59, 60.65, 68.52, 73.11, 79.91, 111.48, 118.66, 123.97, 133.86, 145.92, and 152.16; HREIMS calcd. for $C_{20}H_{32}O_4$: 336.2300; found: 336.2305.

*Second diastereoisomer (**12b**)*: R_f = 0.65; $[\alpha]^{25}_D$ = –84.3 (*c* = 1.90, $CHCl_3$); mp 53–55°C (hexane–EtOAc); IR (KBr): 3454, 2954, 2868, 1588, 1478, 1370, 1278, 1172, 1052, 1008, and 752 cm^{-1}; ^{1}H NMR, δ: 0.73–1.12 (m, 3H), 0.78 (d, *J* = 6.9 Hz, 3H), 0.91 (d, *J* = 6.8 Hz, 6H), 1.19–1.47 (m, 2H), 1.58–1.69 (m, 2H), 2.03–2.19 (m, 2H), 2.92 (d, *J* = 2.7 Hz, 1H), 3.13 (dt, *J* = 4.2, 10.5 Hz, 1H), 3.54 (dd, *J* = 9.7, 10.9 Hz, 1H), 3.57 (dd, *J* = 5.0, 10.9 Hz, 1H), 3.85 (s, 6H), 5.16 (ddd, *J* = 2.7, 5.0, 9.7 Hz, 1H), 6.80–6.90 (dd, *J* = 2.7, 6.9 Hz, 1H), 7.06 (dd, *J* = 6.9, 9.0 Hz, 1H), and 7.08 (dd, *J* = 2.7, 9.0 Hz, 1H); ^{13}C NMR, δ: 16.02, 20.81, 22.14, 23.21, 25.60, 31.41, 34.37, 40.29, 48.00, 55.58, 60.63, 68.13, 73.02, 79.44, 111.48, 118.73, 123.96, 134.04, 145.93, and 152.15; HREIMS calcd. for $C_{20}H_{32}O_4$: 336.2300; found: 336.2305.

(–)-1-(2′′-Methoxy-5′′-bromophenyl)-2-[(1′*R*, 2′*S*, 5′*R*)-2′-isopropyl-5′-methylcyclohexyloxy]-ethanol (13a and 13b)

*First diastereoisomer (**13a**)*: R_f = 0.74; $[\alpha]^{25}_D$ = –21.7 (*c* = 0.3, $CHCl_3$); IR (neat): 3452, 2954, 2868, 1596, 1488, 1370, 1248, 1172, 1092, 912, 804, and 624 cm^{-1}; ^{1}H NMR, δ: 0.70–1.12 (m, 3H), 0.73 (d, *J* = 7 Hz, 3H), 0.88 (d, *J* = 7 Hz, 3H), 0.89 (d, *J* = 6.4 Hz, 3H), 1.16–1.40 (m, 2H), 1.60–1.75 (m, 2H), 2.03–2.19 (m, 2H), 2.88 (d, *J* = 3.1, 1H), 3.10 (dt, *J* = 4.3, 10.6 Hz, 1H), 3.17 (dd, *J* = 8.2, 9.4 Hz, 1H), 3.80 (s, 3H), 3.85 (dd, *J* = 3.2, 9.4 Hz, 1H), 5.13 (ddd, *J* = 3.1, 3.2, 8.2 Hz, 1H), 6.71 (d, *J* = 8.7 Hz, 1H), 7.30 (dd, *J* = 2.5, 8.7 Hz, 1H), and 7.62 (d, *J* = 2.5 Hz, 1H); ^{13}C NMR, δ: 15.86, 20.78, 22.12, 23.12, 25.62, 31.37, 34.36, 40.46, 48.14, 55.41, 67.87, 72.22, 79.97, 111.72, 113.15, 129.85, 130.78, 130.96, and 155.13; HREIMS calcd. for $C_{19}H_{29}O_3Br$: 384.1300; found: 384.1304.

*Second diastereoisomer (**13b**)*: R_f = 0.64; $[\alpha]^{25}_D$ = –63.09 (*c* = 1.26, $CHCl_3$); IR (neat): 3450, 2954, 2868, 1594, 1488, 1370, 1248, 1172, 1092, 804, and 622 cm^{-1}; ^{1}H NMR, δ: 0.73–1.13 (m, 3H), 0.76 (d, *J* = 7 Hz, 3H), 0.90 (d, *J* = 7.3, 6H), 1.15–1.44 (m, 2H), 1.55–1.75 (m, 2H), 2.01–2.29 (m,

© 1998 NRC Canada

2H), 2.89 (d, *J* = 3.3 Hz, 1H), 3.10 (dt, *J* = 4.3, 10.5 Hz, 1H), 3.51 (dd, *J* = 8.8, 10.5 Hz, 1H), 3.54 (dd, *J* = 4.7, 10.5 Hz, 1H), 3.81 (s, 3H), 5.12 (ddd, *J* = 3.3, 4.7, 8.8 Hz, 1H), 6.72 (d, *J* = 8.7 Hz, 1H), 7.33 (dd, *J* = 2.5, 8.7 Hz, 1H), and 7.61 (d, *J* = 2.5 Hz, 1H); ^{13}C NMR, δ: 16.11, 20.84, 22.19, 23.33, 25.72, 31.49, 34.45, 40.34, 48.11, 55.49, 67.78, 72.10, 79.57, 111.85, 113.23, 130.00, 130.90, 131.09, and 155.32; HREIMS calcd. for $C_{19}H_{29}O_3Br$: 384.1300; found: 384.1304.

(–)-1-(2′′,5′′-Dimethoxyphenyl)-2-[(1′*R*, 2′*S*, 5′*R*)-2′-isopropyl-5′-methylcyclohexyloxy)]-ethanol (14a and 14b)

*First diastereoisomer (**14a**)*: R_f = 0.72; $[\alpha]^{25}_D$ = –10.5 (*c* = 1.5, $CHCl_3$); IR (neat): 3452, 2952, 2868, 1590, 1496, 1216, 1178, 1050, 804, 706, and 624 cm^{-1}; ^{1}H NMR, δ: 0.73–1.02 (m, 3H), 0.76 (d, *J* = 7.0 Hz, 3H), 0.90 (d, *J* = 7.1 Hz, 3H), 0.91 (d, *J* = 7.1 Hz, 3H), 1.20–1.46 (m, 2H), 1.60–1.71 (m, 2H), 2.06–2.29 (m, 2H), 2.92 (d, *J* = 2.8 Hz, 1H), 3.11 (dt, *J* = 4.2 Hz, 10.5 Hz, 1H), 3.20 (dd, *J* = 8.1, 9.8 Hz, 1H), 3.78 (s, 6H), 3.86 (dd, *J* = 3.0, 9.8 Hz, 1H), 5.15 (ddd, *J* = 2.8, 3.0, 8.1 Hz, 1H), 6.77 (brs, 2H), and 7.10 (brs, 1H); ^{13}C NMR, δ: 15.88, 20.84, 22.19, 23.05, 25.55, 31.38, 34.35, 40.50, 48.11, 55.62, 55.73, 68.49, 72.66, 79.86, 111.15, 112.48, 113.05, 129.61, 150.26, and 153.68; HREIMS calcd. for $C_{20}H_{32}O_4$: 336.2300; found: 336.2303.

*Second diastereoisomer (**14b**)*: R_f = 0.66; $[\alpha]^{25}_D$ = –64.8 (*c* = 1.9, $CHCl_3$); IR (neat): 3444, 2952, 2870, 1592, 1494, 1276, 1220, 1102, 1072, and 1046 cm^{-1}; ^{1}H NMR, δ: 0.71–1.05 (m, 3H), 0.77 (d, *J* = 7.0 Hz, 3H), 0.90 (d, *J* = 7.1 Hz, 3H), 0.91 (d, *J* = 7.0 Hz, 3H), 1.20–1.45 (m, 2H), 1.60–1.82 (m, 2H), 2.03–2.30 (m, 2H), 2.97 (d, *J* = 3.4 Hz, 1H), 3.11 (dt, *J* = 4.2, 10.6 Hz, 1H), 3.51 (dd, *J* = 7.7, 9.6 Hz, 1H), 3.59 (dd, *J* = 4.1, 9.6 Hz, 1H), 3.77 (s, 3H), 3.79 (s, 3H), 5.13 (ddd, *J* = 3.4, 4.1, 7.7 Hz, 1H), 6.77 (brs, 2H), and 7.09 (brs, 1H); ^{13}C NMR, δ: 16.00, 20.84, 22.19, 23.19, 25.57, 31.43, 34.39, 40.29, 48.03, 55.61, 55.74, 68.33, 72.45, 79.41, 111.19, 112.71, 113.01, 129.79, 150.36, and 153.69; HREIMS calcd. for $C_{20}H_{32}O_4$: 336.2300; found: 336.2302.

(–)-1-(3′′,4′′,5′′-Trimethoxyphenyl)-2-[(1′*R*, 2′*S*, 5′*R*)-2′-isopropyl-5′-methylcyclohexyloxy]-ethanol (15a and 15b)

*First diastereoisomer (**15a**)*: R_f = 0.62; $[\alpha]^{25}_D$ = –16.1 (*c* = 0.23, $CHCl_3$); IR (neat): 3504, 2956, 2856, 1590, 1466, 1328, 1232, 1126, 1006, 842, and 628 cm^{-1}; ^{1}H NMR, δ: 0.74–1.05 (m, 3H), 0.79 (d, *J* = 7.0 Hz, 3H), 0.92 (d, *J* = 6.8 Hz, 6H), 1.18–1.40 (m, 2H), 1.60–1.78 (m, 2H), 2.00–2.28 (m, 2H), 2.90 (d, *J* = 1.9 Hz, 1H), 3.14 (dt, *J* = 4.0, 10.4 Hz, 1H), 3.25 (dd, *J* = 9.3, 10.0 Hz, 1H), 3.79 (dd, *J* = 3.1, 10.0 Hz, 1H), 3.94 (s, 3H), 3.95 (s, 6H), 4.78 (ddd, *J* = 1.9, 3.1, 9.3 Hz, 1H), and 6.62 (s, 2H); ^{13}C NMR, δ: 16.00, 20.86, 22.18, 23.08, 25.70, 31.37, 34.32, 40.39, 48.14, 55.99,* 60.70, 73.42, 74.14, 79.96, 102.92,* 131.59, 135.93, and 153.53;* HREIMS calcd. for $C_{21}H_{34}O_5$: 366.2406; found: 366.2425.

*Second diastereoisomer (**15b**)*: R_f = 0.57; mp 66.0–66.5 °C (hexane–EtOAc); $[\alpha]^{25}_D$ = –82.5 (*c* = 0.35, $CHCl_3$); IR (KBr): 3474, 2954, 2868, 1592, 1464, 1328, 1234, 1126, 1010, and 626 cm^{-1}; ^{1}H NMR, δ: 0.72–1.10 (m, 3H), 0.77 (d, *J* = 7.0 Hz, 3H), 0.91 (d, *J* = 7.1 Hz, 3H), 0.92 (d, *J* = 7.0 Hz, 3H), 1.20–1.43 (m, 2H), 1.55–1.72 (m, 2H), 2.06–2.28 (m, 2H), 2.85 (d, *J* = 1.5 Hz, 1H), 3.12 (dt, *J* = 4.1, 10.5 Hz, 1H), 3.46 (dd, *J* = 3.5, 9.0 Hz, 1H), 3.56 (dd, *J* = 9.0, 9.1 Hz, 1 H), 3.83 (s, 3H), 3.88 (s, 6H), 4.77 (ddd, *J* = 1.5, 3.5, 9.1 Hz, 1H), and 6.62 (s, 2H); ^{13}C NMR, δ: 16.12, 20.80, 22.14, 23.22, 25.65, 31.40, 34.34, 40.25, 48.06, 55.98,* 60.66, 72.93, 73.77, 79.51, 103.08,* 136.04, 137.53, and 153.08;* HREIMS calcd. for $C_{21}H_{34}O_5$: 366.2406; found: 366.2425.

(–)-1-(2′′-Benzyloxy-3′′-methoxyphenyl)-2-[(1′*R*, 2′*S*, 5′*R*)2′-isopropyl-5′-methylcyclohexyloxy]-ethanol (16a and 16b)

*First diastereoisomer (**16a**)*: R_f = 0.60; $[\alpha]^{25}_D$ = –17.3 (*c* = 0.35, $CHCl_3$); IR (neat): 3444, 2954, 2868, 1586, 1478, 1370, 1278, 1180, 1052, 1008, 992, 752, and 698 cm^{-1}; ^{1}H NMR, δ: 0.70–1.10 (m, 3H), 0.72 (d, *J* = 7.0 Hz, 3H), 0.87 (d, *J* = 6.2 Hz, 3H), 0.88 (d, *J* = 7.2 Hz, 3H), 1.12–1.40 (m, 2H), 1.52–1.73 (m, 2H), 1.90–2.30 (m, 2H), 2.84 (d, *J* = 2.4 Hz, 1H), 3.04 (dt, *J* = 4.1, 10.5 Hz, 1H), 3.22 (dd, *J* = 9.2, 9.2 Hz, 1H), 3.77 (dd, *J* = 3.0, 9.2 Hz, 1H), 3.89 (s, 3H), 4.95 (d, *J* = 11.1 Hz, 1H), 5.13 (d, *J* = 11.1 Hz, 1H), 5.14 (ddd, *J* = 2.4, 3.0, 9.2 Hz, 1H), 6.88 (dd, *J* = 2.9, 6.8 Hz, 1H), 7.10 (dd, *J* = 6.8, 7.8 Hz, 1H), 7.12 (dd, *J* = 2.9, 7.8, 1H), and 7.30–7.50 (m, 5H); ^{13}C NMR, δ: 15.98, 20.86, 22.16, 23.09, 25.57, 31.36, 34.36, 40.65, 48.14, 55.68, 68.67, 73.05, 74.70, 79.74, 111.53, 118.76, 124.13, 127.82, 127.94,* 128.29,* 134.22, 137.58, 144.73, and 152.24; HREIMS calcd. for $C_{26}H_{36}O_4$: 412.2613; found: 412.2624.

*Second diastereoisomer (**16b**)*: R_f = 0.58; $[\alpha]^{25}_D$ = –21.8 (*c* = 0.45, $CHCl_3$); IR (neat): 3458, 2954, 2868, 1582, 1478, 1370, 1278, 1180, 1054, 990, 752, and 698 cm^{-1}; ^{1}H NMR, δ: 0.70–1.08 (m, 3H), 0.71 (d, *J* = 6.9 Hz, 3H), 0.87 (d, *J* = 6.5 Hz, 3H), 0.88 (d, *J* = 7.0 Hz, 3H), 1.10–1.40 (m, 2H), 1.52–1.72 (m, 2H), 1.93–2.30 (m, 2H), 2.75 (d, *J* = 2.4 Hz, 1H), 3.03 (dt, *J* = 4.1, 10.5 Hz, 1H), 3.44 (dd, *J* = 8.6, 9.7 Hz, 1H), 3.55 (dd, *J* = 3.4, 9.7 Hz, 1H), 3.89 (s, 3H), 4.93 (d, *J* = 11.0 Hz, 1H), 5.13 (ddd, *J* = 2.4, 3.4, 8.6 Hz, 1H), 5.15 (d, *J* = 11.0 Hz, 1H), 6.88 (dd, *J* = 3.0, 6.7 Hz, 1H), 7.11 (dd, *J* = 6.7, 8.1 Hz, 1H), 7.12 (dd, *J* = 3.0, 8.1 Hz, 1H), and 7.31–7.50 (m, 5H); ^{13}C NMR, δ: 16.05, 20.82, 22.11, 23.20, 25.60, 31.31, 34.37, 40.14, 48.00, 55.67, 68.00, 72.48, 74.73, 78.91, 111.52, 118.72, 124.15, 127.81, 127.92,* 128.28,* 134.24, 137.56, 144.71, and 152.22; HREIMS calcd. for $C_{26}H_{36}O_4$: 412.2613; found: 412.2623.

1-(3′′,4′′-Dimethoxyphenyl)-2-[(1′*R*, 2′*S*, 5′*R*)-2′-isopropyl-5′-methylcyclohexyloxy]-ethanol (17a and 17b)

Unseparable mixture of diastereoisomers: R_f = 0.62; IR (neat): 3450, 2950, 1580, 1475, 1365, and 1280 cm^{-1}; HREIMS calcd. for $C_{20}H_{32}O_4$: 336.2300; found: 336.2312. Characteristic signals, major diastereoisomer: ^{1}H NMR, δ: 3.11 (dt, *J* = 4.0, 10.5 Hz, 1H), 3.43 (dd, *J* = 9.0, 9.8 Hz, 1H), and 3.61 (dd, *J* = 3.1, 9.8 Hz, 1H); ^{13}C NMR, δ: 71.83, 73.27, 79.50; minor diastereoisomer: ^{1}H NMR, δ: 3.15 (dt, *J* = 4.0, 10.5 Hz, 1H), 3.26 (dd, *J* = 10.1, 10.1 Hz, 1H), and 3.73

© 1998 NRC Canada

(dt, J = 3.2, 10.1 Hz, 1H); ^{13}C NMR, δ: 72.28, 73.64, and 79.95.

Synthesis and oxazaborolidine-mediated reduction of 2′′,3′′-dimethoxyphenyl-[(1′*R*, 2′*S*, 5′*R*)-2′-isopropyl-5′-methylcyclohexyloxy]-ketone (19)

A CH_2Cl_2 solution of dimethyl sulfoxide (1.2 mL, 2.55 mmol) was added dropwise in 2 min to a stirred solution of trifluoroacetic anhydride (2.04 mmol) in the same solvent (1.8 mL) cooled to –60°C. Stirring continued for 7 min, when a solution containing alcohols **12a** and **12b** (172 mg, 0.51 mmol) in CH_2Cl_2 (1 mL) was incorporated dropwise. After a 20 min reaction period, triethylamine (0.43 mL, 3.1 mmol) was added and left to react for 20 min at –60°C and for 20 min at room temperature. The reaction was quenched with brine (10 mL), and the product was extracted with EtOAc (3 × 25 mL). The extracts were combined, dried over sodium sulfate, concentrated under reduced pressure, and chromatographed to furnish ketone **19** (145 mg, 91%) as an oil; R_f = 0.88; $[\alpha]^{25}_D$ = –66.2 (c = 0.61, $CHCl_3$); IR (neat): 2952, 2868, 1694, 1582, 1478, 1312, 1268, 1132, 1090, 1004, and 748 cm^{-1}; ^{1}H NMR, δ: 0.78 (d, J = 6.9 Hz, 3H), 0.80–1.11 (m, 3H), 0.89 (d, J = 7.1 Hz, 3H), 0.91 (d, J = 6.4 Hz, 3H), 1.18–1.50 (m, 2H), 1.58–1.70 (m, 2H), 2.03–2.40 (m, 2H), 3.19 (dt, J = 4.2, 10.5 Hz, 1H), 3.89 (s, 3H), 3.91 (s, 3H), 4.66 (d, J = 18.0 Hz, 1H), 4.77 (d, J = 18.0 Hz, 1H), 7.05 (dd, J = 2.3, 7.8 Hz, 1H), 7.09 (dd, J = 7.1, 7.8 Hz, 1H) and 7.26 (dd, J = 2.3, 7.1 Hz, 1H); ^{13}C NMR, δ: 16.10, 20.88, 22.17, 23.17, 25.34, 31.47, 34.35, 40.17, 48.11, 55.92, 61.24, 74.47, 80.02, 115.90, 120.92, 124.11, 131.46, 148.35, 152.70, and 199.32.

Without further treatment, a solution of ketone **19** (40 mg, 0.12 mmol) in anhydrous toluene (1.5 mL) was added at room temperature over 90 min to a stirred mixture of oxazaborolidine **(*S*)-18** (0.024 mmol) and borane – methyl sulfide (0.24 mL, 0.24 mmol) in dry toluene (1.5 mL). After the addition was completed the reaction mixture was further stirred for 15 min and quenched with MeOH (0.1 mL). Stirring continued for another 30 min, when the reaction was diluted with EtOAc (20 mL) and the organic phase washed with brine (2 × 5 mL). Drying, concentration in vacuo, and chromatography of the organic phase furnished a solid (39 mg, 97%) which melting point, $[\alpha]^{25}_D$, spectral data, as well as its chromatographic behaviour (TLC and HPLC), were in complete agreement with those recorded for **12a**. The HPLC of the crude reaction mixture indicated a diastereoisomeric excess greater than 98%.

Acknowledgements

We thank Fundación Antorchas, CONICET, and Universidad Nacional de Rosario for support of this work. V.L.P. thanks CONICET for a fellowship. Fruitful discussions with Drs. G.E. Radivoy and J.C. Podestá (UNS) are also gratefully acknowledged.

References

1. (*a*) H.C. Brown and P.V. Ramachandran. Acc. Chem. Res. **25**, 16 (1992); (*b*) V.K. Singh. Synthesis 605 (1992); (*c*) M.M. Midland. Chem. Rev. **89**, 1553 (1989); (*d*) R. Noyori and M. Kitamura. Angew. Chem. Int. Ed. Engl. **30**, 49 (1991); (*e*) K. Soai and S. Seiji. Chem. Rev. **92**, 833 (1992); (*f*) P. Knochel, S. Vettel, and C. Eisenberg. Appl. Organomet. Chem. **9**, 175 (1995).
2. (*a*) V.L. Ponzo and T.S. Kaufman. J. Chem. Soc. Perkin Trans. 1, 3131 (1997); (*b*) T.S. Kaufman. J. Chem. Soc. Perkin Trans. 1, 2497 (1996); (*c*) J. Chem. Soc. Perkin Trans. 1, 403 (1993); (*d*) Synth. Commun. **23**, 473 (1993).
3. T.S. Kaufman. Tetrahedron Lett. **37**, 5329 (1996).
4. (*a*) J. Ortiz, A. Guijarro, and M. Yus. An. Quim. Int. Ed. **93**, 44 (1997); (*b*) P. Lesimple, J.-M. Beau, and P. Sinaÿ. J. Chem. Soc. Chem. Commun. 894 (1985).
5. (*a*) W.C. Still. J. Am. Chem. Soc. **100**, 1481 (1978); (*b*) E.J. Corey and T.M. Eckrich. Tetrahedron Lett. **24**, 3163 (1983); (*c*) C. Johnson, J.R. Medich, R.L. Danheiser, K.R. Romines, H. Koyama, and S.K. Gee. Org. Synth. **71**, 140 (1992).
6. T.S. Kaufman. Synlett, 1377 (1997).
7. M. Pereyre, J.P. Quintard, and A. Rahm. Tin in organic synthesis. Butterworths, London. 1987. pp. 165–172.
8. (*a*) C. Nájera, M. Yus, and D. Seebach. Helv. Chim. Acta, **67**, 289 (1984); (*b*) A. Bachki, F. Foubelo, and M. Yus. Tetrahedron: Asymmetry, **6**, 1907 (1995).
9. L. Colombo, M. Di Giacomo, G. Brusotti, and G. Delogu. Tetrahedron Lett. **35**, 2063 (1994).
10. (*a*) J.-I. Yamada, H. Abe, and Y. Yamamoto. J. Am. Chem. Soc. **112**, 6118 (1990), and refs. cited therein; (*b*) Y. Yamamoto and J.-I. Yamada. J. Am. Chem. Soc. **109**, 4395 (1987).
11. (*a*) V. Nevalainen. Tetrahedron: Asymmetry, **2**, 63 (1991); (*b*) Tetrahedron: Asymmetry, **2**, 429 (1991); (*c*) Tetrahedron: Asymmetry, **2**, 827 (1991).
12. (*a*) E.J. Corey, M. Azimioara, and S. Sarshar. Tetrahedron Lett. **33**, 3429 (1992); (*b*) D.K. Jones, D.C. Liotta, I. Shinkai, and D.J. Mathre. J. Org. Chem. **58**, 799 (1993).
13. (*a*) E.J. Corey, R.K. Bakshi, and S. Shibata. J. Am. Chem. Soc. **109**, 5551 (1987); (*b*) S. Wallbaum and J. Martens. Tetrahedron: Asymmetry, **3**, 1475 (1992).
14. (*a*) Y. Hong, Y. Gao, X. Nie, and C.M. Zepp. Tetrahedron Lett. **35**, 5551 (1994); (*b*) A.M. Salunkhe and E.R. Burkhardt. Tetrahedron Lett. **38**, 1523 (1997); (*c*) E.J. Corey and C.J. Helal. Tetrahedron Lett. **36**, 9153 (1995); (*d*) E.J. Corey, S. Shibata, and R.K. Bakshi. J. Org. Chem. **53**, 2861 (1988).

© 1998 NRC Canada

Reaction of carbanions generated from arylmethylphosphonates with cyclic enones. Regio- and stereoselectivity of addition

Agnes M. Modro, Tom A. Modro, Malose J. Mphahlele, Wieslawa Perlikowska, André Pienaar, Marcelo Sales, and Petrus H. van Rooyen

Abstract: α-Lithiated benzylphosphonate esters, $XC_6H_4CH(Li)PO_3Et_2$, add regioselectively to cyclohex-2-enone at the carbonyl group; higher reaction temperatures lead to the reversal to the starting materials, and not to the 1,4-addition. Relative configuration of the C(1) and C_α centers in the 1,2-adducts was determined from the ^{13}C NMR spectra. For 2-methylcyclohex-2-enone the regioselectivity of the addition is decreased. The lithioderivative of diethyl 1-naphthylmethylphosphonate, $C_{10}H_7CH(Li)PO_3Et_2$, shows reverse regioselectivity yielding the 1,4-, but not the 1,2-addition product. The crystal and molecular structure of that 1,4-adduct has been determined and demonstrates that the conformation about the C(1)—C_α bond is close to that existing in solution, deduced from the value of the ^1H NMR $^3J_{HH}$ vicinal coupling constant of the H(1)-C(1)-C_α-H hydrogens. The same conformation was also confirmed as the most stable by molecular modeling.

Key words: α-lithiated arylmethylphosphonates, 1,2- vs. 1,4-addition to cyclic enones, steric effects of the cyclohex-2-enone, molecular structure and molecular modelling of the 1,4-adduct of 1-naphthylmethylphosphonate to cyclohex-2-enone.

Résumé : Les esters benzylphosphonates α-lithiés, $XC_6H_4CH(Li)PO_3Et_2$, s'additionnent régiosélectivement au groupe carbonyle de la cyclohex-2-énone; des températures plus élevées conduisent à un retour vers les produits de départ et, non pas, à une addition-1,4. On a fait appel à la RMN du ^{13}C pour déterminer les configurations relatives au niveau des centres C(1) et C_α des adduits-1,2. Avec la 2-méthylcyclohex-2-énone, la régiosélectivité de l'addition diminue. Le dérivé lithié du 1-naphtylméthylphosphonate de diéthyle, $C_{10}H_7CH(Li)PO_3Et_2$, provoque une régiosélectivité inversée conduisant au produit d'addition-1,4 et non pas 1,2. On a déterminé la structure cristalline et moléculaire de l'adduit-1,4 et elle démontre que la conformation autour de la liaison C(1)—C_α ressemble à celle qui existe en solution et qui a été déduite de la valeur de la constante de couplage $^3J_{HH}$ observée en RMN du ^1H pour les hydrogènes H(1)-C(1)-C_α-H. La modélisation moléculaire a permis de confirmer que cette même conformation est la plus stable.

Mots clés : arylméthylphosphonates α-lithiés, additions-1,2 vs. -1,4 à des énones cycliques, effets stériques de la cyclohex-2-énone, structure moléculaire et modélisation moléculaire de l'adduit-1,4 du 1-naphtylmétylphosphonate sur la cyclohex-2-énone.

[Traduit par la Rédaction]

Introduction

Nucleophilic addition to the α,β-unsaturated carbonyl compounds is one of the general methods of synthesis (1). The same can be said about the reactions of phosphorus-stabilized carbanions with electrophilic acceptors (2). In spite of this, reactions between the latter nucleophiles and enones has attracted little attention. Reference 1 does not list phosphorus-stabilized carbanions in the review of the nucleophilic reagents used in conjugate addition. There is also no mention of that reaction in ref. 2*b*, and only isolated cases are reported in ref. 2*a* (3). We have recently reported our first results on the reaction of the α-lithiated phosphonates (Wadsworth–Emmons reagents) with cyclic enones (4). It was found that the reaction outcome depends on the nature of the nucleophilic reagent ("localized," derived from an alkylphosphonate, or "delocalized," derived from an alk-2-enylphosphonate), as well as on the substitution pattern on the enone, and that the reaction can follow different mechanisms (1,2-addition, 1,4-addition, addition-elimination) with a large degree of selectivity. In this work we have extended our study on the reaction of cyclic enones with α-lithiated

Received May 12, 1998.

A.M. Modro, T.A. Modro,[1] M.J. Mphahlele, and A. Pienaar. Centre for Heteroatom Chemistry, Department of Chemistry, University of Pretoria, Pretoria 0002, South Africa.
W. Perlikowska. On leave from Center of Molecular and Macromolecular Studies, Polish Academy of Sciences, Lodz, Poland.
M. Sales and P.H. Van Rooyen. Department of Chemistry, University of Pretoria, Pretoria 0002, South Africa.

[1]Author to whom correspondence may be addressed. Telephone: 27-12-420-2512. Fax: 27-12-362-5297. E-mail: tamodro@scientia.up.ac.za

 © 1998 NRC Canada

Scheme 1.

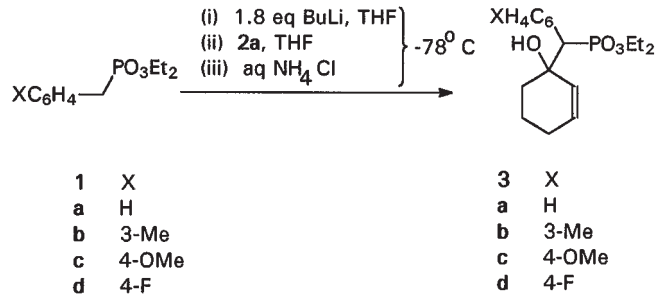

Scheme 2.

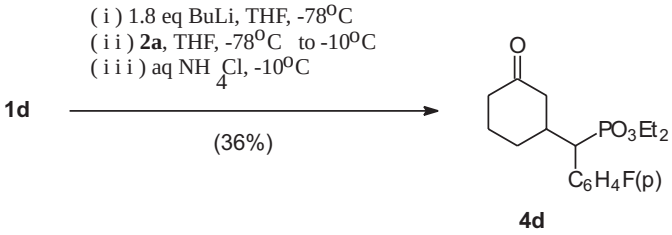

arylmethylphosphonates, and we demonstrate that the nature of the aryl group can dramatically change the regioselectivity of the addition.

Results and discussion

Petrova and co-workers studied the reactions of the carbanions derived from diethyl arylmethylphosphonates with unconjugated aldehydes and ketones (5). They concluded that the addition to the carbonyl group is reversible, which seriously reduces the yields of the olefination step and leads to the recovery of substrates upon longer reaction times. Reaction of heteroatom- (but not phosphorus-)stabilized carbanions with α,β-unsaturated carbonyl substrates has received considerable attention during the past three decades (for example, see ref. 6), and Schultz and Yee recognized that the direct addition of ester enolates to 2-cyclohexen-1-one is reversible at higher temperatures, and that the structural modifications of the nucleophile have a strong effect on the selectivity (7).

The reversibility of the 1,2-addition and steric acceleration of the reverse step was confirmed in further work on the addition of other, non-phosphorus heteroatom-stabilized carbanions with enones (for example, see ref. 8). The important conclusion on the regioselectivity was reached by Heathcock and co-workers in their extensive work on the Michael addition (9). They found that ketone enolates give 1,4-addition even at low temperatures (1,2-adducts are transient, but unstable intermediates), but for ester enolates, the 1,2-adducts can be obtained and can be rearranged to the 1,4-adducts upon warming. Thus, small differences in the nature and resultant stability of the nucleophile may have a powerful effect on the rate of the reverse of the carbonyl addition step.

Scheme 3.

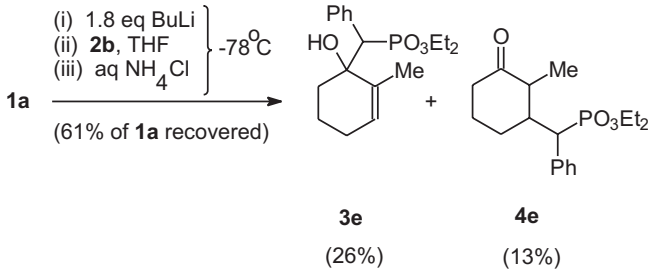

Reactions of five diethyl arylmethylphosphonates **1a**–**1e** with 2-cyclohex-1-one (**2a**) and its 2-methyl (**2b**) and 3-methyl (**2c**) derivatives were studied in this work. With **2a**, all carbanions derived from benzylphosphonic esters (**1a**–**1d**) reacted exclusively according to the 1,2-addition pattern (Scheme 1), and no reversibility was observed at –78°C. In each case two diastereomeric alcohols **3** were obtained (major and minor), which were separated by column chromatography. Attempts to change the reaction course to the conjugate addition by raising the temperature of the reaction failed, as only starting materials were recovered under those conditions. This result shows that the conjugate base of **3** is only stable at low temperature, and that upon warming it undergoes fragmentation to the starting materials, but not to the possible products of the subsequent olefination step.[2] For **1d** we were able to find an intermediate temperature at which 1,4-addition successfully competed with the carbonyl addition (Scheme 2), albeit with low yield because of the still predominant reverse reaction. It seems that at temperatures higher than –78°C the rate of the retro-1,2-addition is too fast for any of the conjugate base of **3** to accumulate in the reaction medium. Since **4d** could be prepared at –10°C, but not at room temperature, it follows that the 1,4-addition step does occur at higher temperatures, but the retro-1,4-addition step also becomes too fast to allow accumulation of the conjugate base of **4**. It also follows that at room temperature the couple: lithiated **1** + **2a** (substrates) is thermodynamically more stable than either of the Li salts of the oxyanions derived from **3** or **4**.[3] Indeed, when alcohols **3a**–**d** and ketone **4d** were treated with BuLi in THF at –78°C, and the solutions were warmed to room temperature, kept at that temperature for 24 h, and subjected to aqueous work-up, only starting materials **1a**–**d** and **2a** were recovered. It shows that the oxyanions derived from **3**, and the enolate of **4d** undergo fragmentation back to **2a** and the lithiated **1**. This result contrasts with the reported thermal stability of the adducts of sulfur-stabilized organolithium compounds with **2a** (10), shedding some light on the relative stability of the P- or S-stabilized carbanions (substrates) vs. the corresponding oxyanions (products).

With 2-methyl-2-cyclohex-1-one (**2b**) the 1,2-addition was sufficiently slowed down (and its reversal accelerated) relative to the 1,4-addition by the steric effect of the 2-Me group, so that even at –78°C the reaction showed low selectivity (Scheme 3). The observed high proportion of the start-

[2] In no case was any fragmentation of the 1,2-addition product to diethylphosphate anion and the corresponding diene observed.

[3] Spectroscopic studies suggest similar stabilization of an adjacent carbanion by the P=O and the C=O groups (2*a*). In our case additional stabilization by the Ar group seems to favor the carbanion of **1** relative to the conjugate base of a tertiary alcohol (**3**) or a simple ketone enolate (**4**).

© 1998 NRC Canada

Scheme 4.

Scheme 5.

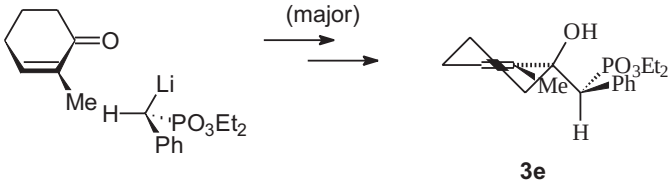

Scheme 6.

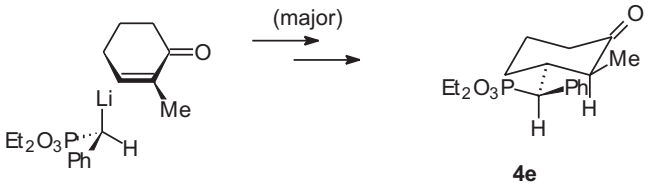

ing materials supports the conclusion on steric acceleration of the retro-addition step (for example, see ref. 8), and again indicates thermodynamic stability of the lithiated arylmethylphosphonate system relative to the corresponding oxyanions. When warmed to room temperature before the aqueous work-up, the mixture given in Scheme 3 reversed exclusively to the starting materials.

Scheme 1 shows that under "kinetic" conditions alcohols **3a**–**d** can be obtained with high yields and free of the 1,4-adducts. The diastereomeric mixtures of the 1,2-adducts were separated into individual stereoisomers, and in some cases ^{13}C NMR analysis allowed us to determine the relative configuration of the products. For example, for **3a**, **3c**, and **3d** the major stereoisomers gave rise to the ^{13}C NMR spectra from which the $^3J_{CP}$ coupling between the olefinic (C2) and the aliphatic (C6) carbons of the cyclohexene ring and the P atom could be determined as $^3J_{(C2)P}$ = 4.6, $^3J_{(C6)P}$ = 11.0 Hz for **3a** and **3c**, as well as $^3J_{(C2)P}$ = 4.4, $^3J_{(C6)P}$ = 11.3 Hz for **3d**. For **3b**, it was the minor stereoisomer that provided us with the values of $^3J_{(C2)P}$ = 10.0 and $^3J_{(C6)P}$ = 6.3 Hz. The angular dependence of the $^3J_{CP}$ values can be used to determine the configuration (and conformation) of organophosphorus compounds (11). The empirical relationship developed for the 2-phosphorylated-2-hydroxycamphane system gives the calculated values of the $^3J_{CP}$ coupling constants of 2.8 and 18.9 Hz for the *gauche* and for the *trans* orientation of the carbon and the phosphorus atoms of the C-C-C-PO_3R_2 skeleton (12). Our spectroscopic results show that alcohols **3** experience a high degree of restricted rotation about the C_α—C_1 bond and that the most populated conformation of the major stereoisomer can be represented as shown in Scheme 4, indicating spatial preference of the approach of the lithiated **1** to the enone function in **2a**. The stereochemistry of the 1,2-addition is reversed for **2b**, where the major stereoisomer of **3e** (after isolation and purification) gave rise to the $^3J_{CP}$ values of 13.2 and 5.1 Hz for C2 and C6 atoms, respectively. According to those values, the preferred conformation of the major stereoisomer of **3e** is as shown in Scheme 5; the geometry is most likely the consequence of the reluctance of the bulky PO_3Et_2 group[4] to be located in the vicinity of the 2-Me group in the transition state of the 1,2-addition.

For the 1,4-adduct **4d** we were not able to separate the product into two stereoisomers, but for the major isomer both $^3J_{CP}$ constants for both aliphatic carbons of the cyclohexanone ring (C2 and C4) could be determined as 8.2 and 9.4 Hz. It is clear that in the absence of the intramolecular hydrogen bonding between the OH and the phosphoryl group, which stabilizes the conformers in case of the 2-hydroxyalkylphosphonates **3** (14), there is a high degree of free rotation about the C_α—C_3 bond in **4d**. Finally, the 1,4-adduct **4e**, formed as a minor product in the reaction between **1a** and **2b** (Scheme 3) exists as a mixture of three streoisomers from which the major was successfully separated from the other two isomers formed in very small quantities. In contrast to **4d**, free rotation about the C_α—C_3 bond is in this case severely restricted, leading to very different values of the $^3J_{CP}$ coupling constants (14.6 and 2.2 Hz for C2 and C4, respectively). Obviously, the methyl group at C2 introduces enough steric hinderance to the PO_3Et_2 group in the condensation step to give high stereoselectivity of the reaction and is also responsible for the restriction of the free rotation (Scheme 6). Spectroscopic analysis of adducts **3** leads to a conclusion about the order of steric hinderance offered by C2 and C6 centers in the 2-cyclo-hexen-1-one system with respect to the approach of the α-PO_3Et_2 substituted carbanionic carbon to the carbonyl group during the 1,2-addition process (Schemes 4 and 5). The repulsion increases in the following order of the substitution pattern of the carbons adjacent to the carbonyl group: =C(H)- < -CH_2- < =C(Me)-.

The next carbanion studied in the addition to **2a**, derived from diethyl 1-naphthylmethylphosphonate **1e**, behaved in a unique fashion. The difference in the aromatic skeleton led to a totally different outcome of the reaction. At –78°C no reaction could be observed, and the aqueous work-up led to full recovery of substrates. The absence of the reaction (or the complete reversal of the addition) may result from either the increased steric effect of the $C_{10}H_7$ group (relative to the XC_6H_4 group) on the rate of the 1,2-addition, or from the increased resonance stabilization of the carbanion by that group that reduces its nucleophilic reactivity and disfavors the product formation. However, when the reaction mixture

[4] The steric substituent constant for the PO_3Et_2 is not available, but the $-E_S$ constant for CEt_3 substituent is 10 times larger than that of the Ph group (13).

© 1998 NRC Canada

Fig. 1. An ORTEP plot of the structure of **4f** with atomic numbering. Hydrogen atoms are not included.

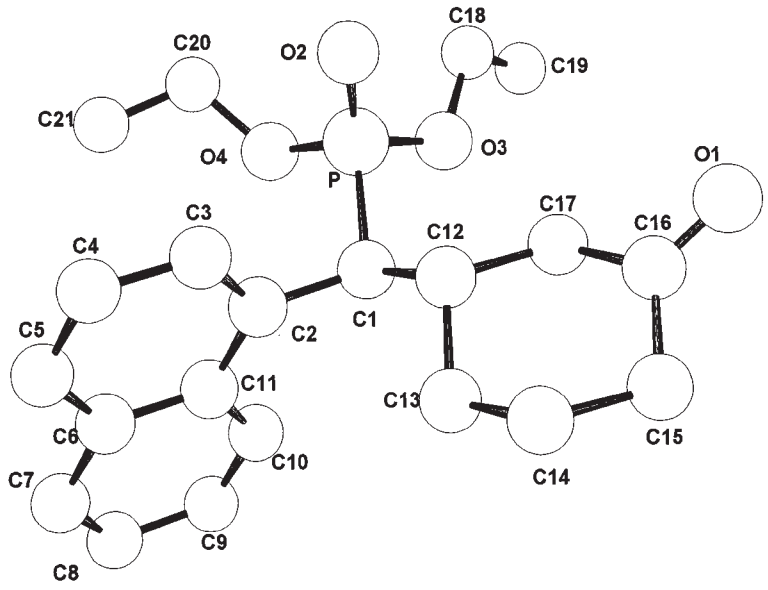

Scheme 7.

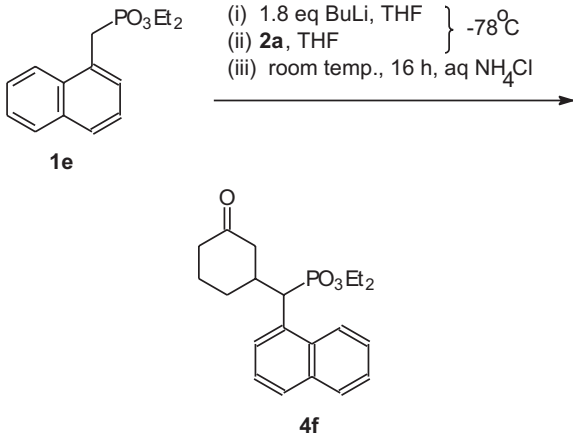

was warmed to room temperature after the addition of **2a** and left overnight, we obtained exclusively (in addition to the unreacted substrates) the product of the conjugate addition (**4f**), isolated in 55% yield (Scheme 7). As expected, **1e** failed to give any addition product with **2c**, either at –78°C or at room temperature. The 1,4-adduct **4f** was formed as a mixture of two diastereomers (ca. 1.5:1), and the major isomer was isolated in pure state by column chromatography and fractional crystallization. The $^3J_{CP}$ values for the coupling of the cyclohexanone carbon atoms C2 and C4 were found for the major isomer to be 0.64 and 10.8 Hz, respectively, indicating severe restriction of the rotation about the C_α—C_3 bond. The vicinal $^3J_{HH}$ constant involving the C_α-H and C_3-H protons was found to be 8.3 Hz, which corresponds to an average spatial orientation of those hydrogens not far from *trans* (ca. 162°). The structure of the major stereoisomer of **4f** was then determined by X-ray diffraction. The structure was solved by Patterson and direct methods (15, 16). Refinement by full-matrix least-squares methods was based on *F* (16). All non-hydrogen atoms were refined anisotropically. The hydrogen atoms were placed in idealized positions and included in the refinement with common isotropic thermal parameters that were also refined as indicated in Table 1. Atomic scattering factors were taken from the literature (17). Atomic coordinates, bond lengths and angles, anisotropic thermal parameters, and hydrogen atom coordinates have been deposited as supplementary material.[5] A perspective view of the molecule, prepared with ORTEP (18), is represented in Fig. 1, illustrating the molecular conformation and the crystallographic numbering schemes used. It can be seen that in order to minimize repulsive interactions between two bulky substituents (naphthyl and PO_3Et_2), the H atoms at C1 and C12 (C_α and C_3) are indeed oriented *trans* (the torsion angle H(1)-C(1)-C(12)-H(12) = 176.3°). The C(17)-C(12)-C(1)-P and the C(13)-C(12)-C(1)-P torsion angles were obtained from the crystal structure as 62.5 and 177.4°, respectively. Substituting those values to the Karplus equation (19) we obtained the calculated $^3J_{CP}$ values of 0.6 and 11.6 Hz, respectively. They remain in good agreement with the experimental coupling constants and suggest close correspondence of the solid-state conformation of **4f** to its preferred conformation in solution.

The correlation between the solid-state geometry and the spectroscopic (NMR) data obtained in solution prompted us to also include in the comparison the molecular dynamics (MD) method. The method known as simulated annealing was used to identify the low-energy conformations of **4f** with respect to the rotation about the C(1)—C(12) bond (20). From the plot of the potential energy (PE) vs. H(1)-C(1)-C(12)-H(12) torsion angle (Fig. 2*a*) it can be deduced

[5] Copies of material on deposit may be purchased from: The Depository of Unpublished Data, Document Delivery, CISTI, National Research Council of Canada, Ottawa, Canada, K1A 0S2. With the exception of anisotropic thermal parameters, these have also been deposited with the Cambridge Crystallographic Data Centre and can be obtained on request from: The Director, Cambridge Crystallographic Data Centre, University Chemical Laboratory, 12 Union Road, Cambridge, CB2 1EZ, U.K.

© 1998 NRC Canada

Table 1. Crystallographic data acquisition and refinement details of compound **4f**.

Empirical formula	$C_{21}H_{27}PO_4$
Molecular weight	374.42
Crystal dimension, mm	0.21 × 0.22 × 0.24
Space group	*P*2 (no. 4)
Cell dimensions:	
a, Å	8.454(2)
b, Å	10.443(2)
c, Å	11.922(2)
β, °	104.03(2)
Z	2
Volume, Å^3	1 021(1)
D(calc), g cm^{-3}	1.20
μ, cm^{-1}	1.15
Radiation (λ, Å)	MoK$_\alpha$, 0.7107
T, °C	23(1)
F(000)	378.0
Scan type (ω:2θ)	1:1
Scan range (θ°)	3 < θ < 30
Zone collected:	
h	–11, +11
k	–14, 0
l	0, +16
Max. scan speed (deg.min^{-1})	5.48
Max. scan time, s	60
Scan angle (ω + 0.34 tan θ)°	0.63
Aperture size (mm)	1.3 × 4.0
Reflections collected	2 738
Decay, %	<3.0
EAC correction factor:	
Maximum	1.000
Minimum	0.798
Average	0.887
Unique reflections used (>3σ(1))	1 952
R_{int}	0.014
Parameters refined	241
Max. positional shift/esd	0.37
Residual electron density (e Å^3):	
Maximum	0.26
Minimum	–0.23
U_{iso}(H), Å^2	0.107(4)
R	0.054
R_w	0.032

that during the simulation the barriers between all torsion angles were successfully traversed when the PE was greater than 200 kcal mol^{-1}, indicating a true Boltzmann distribution of conformers. The plot of the torsion angles H(1)-C(1)-C(12)-H(12) vs. the PE of the annealed low-energy conformers resulting from 50 cycles is given in Fig. 2*b*. Analogous plots were obtained when the conformers *b* and *c* were used as starting conformers for annealing experiments, showing that the conformers distribution is independent of the starting conformation. The conformer *a* shown in Fig. 2*b* underwent full minimalization and the resulting structure is given in Fig. 2*c*; the resemblance to the crystal structure of **4f** is evident. If the population distribution of the final annealed rotors reflects the population distribution of the rotors in solution, the calculated vicinal coupling between protons H(1) and H(12) (C_α-H and C_1-H) should agree with the experimental coupling of 8.3 Hz. The Haasnoot equation predicts that the vicinal coupling constant between these protons is a consequence of the population distribution of the rotors of **4f** defined by the H(1)-C(1)-C(12)-H(12) torsion (21). The torsion angles H(1)-C(1)-C(12)-H(12) for the fully minimized conformers *a*, *b*, and *c* were calculated as 164.2, 56.5, and –58.9°, respectively, and the populations of those conformers, calculated from their relative energies, were 60, 22, and 18%, respectively. The theoretical value of the vicinal $^3J_{HH}$ constant, obtained from the calculated fractions of the populations of the conformers and the theoretical coupling constants, is $^3J_{H(1)H(12)}$ = 9.2 Hz. The agreement with the experimental value of 8.3 Hz is reasonable, indicating that the conformational energy barriers present in the gas phase affect the population distribution of the final annealed structures to a similar degree as these barriers affect the population of the conformers in solution.

Experimental section

Solvents and commercially available reagents were purified by conventional methods before use. Reactions involving organolithium reagents were carried out in an atmosphere of dry nitrogen using flame-dried glassware. Melting points are uncorrected. For column chromatography, Merck Kieselgel 60 (0.063–0.200 mm) was used as a stationary phase. Unless otherwise stated, ethyl acetate was used as eluent. Mass spectra were recorded at an ionization potential of 70 eV. The NMR spectra were recorded as ca. 0.2 M solutions in $CDCl_3$. The ^{1}H and ^{13}C chemical shifts are given relative to the solvent ($CDCl_3$; ^{1}H: 7.24 ppm; ^{13}C: 77.0 ppm). The ^{31}P NMR chemical shifts are given relative to 85% H_3PO_4 as external standard, and ^{19}F NMR chemical shifts are given relative to $CFCl_3$ as external standard. The IR spectra were recorded as ca. 0.2 M solutions in $CHCl_3$.

Diethyl benzylphosphonate **1a** (Aldrich) was distilled before use; bp 100–101°C (0.7 mm). Diethyl arylmethylphosphonates **1b**–**1e** were prepared from triethyl phosphite, and the corresponding arylmethyl chloride or bromide according to the literature procedure for the Arbuzov reaction (22); **1b** (88%): bp 120–122°C (0.5 mm), n_D^{20} 1.4448 (lit. (23) bp 126–127°C (0.7 mm), n_D^{20} 1.4450); **1c** (83%): bp 175–180°C (0.5 mm), n_D^{20} 1.5035 (lit. (23) bp 176–178°C (0.21 mm), n_D^{20} 1.5040); **1d** (80%): bp 126–128°C (0.5 mm), n_D^{20} 1.4775 (lit. (23) bp 148–150°C (6 mm), n_D^{20} 1.478); **1e** (96%): purified by bulb-to-bulb distillation, oven temp. 220°C (0.5 mm), n_D^{20} 1.5630 (lit. (23) bp 202–205°C (0.2 mm), n_D^{25} 1.5610).

Reactions of diethyl arylmethylphosphonates 1 with cyclic enones 2. General procedure

N-Butyllithium (1.6 M solution in hexane, 1.8–2.0 mol equiv.[6]) was diluted with THF (3 mL per mmol of **1**). To this solution, cooled to –78°C, was added dropwise with stirring a solution of **1** (1 mol equiv., typically 8 mmol) in THF

[6] Any decrease in the excess of BuLi below 1.8 mol equiv. resulted in a serious decrease of the yield.

© 1998 NRC Canada

Fig. 2. (*a*) The plot of PE (kcal mol^{-1}) vs. torsion angle H(1)-C(1)-C(12)-H(12) (deg) for **4f**. (*b*) The plot of PE (kcal mol^{-1}) vs. torsion angle H(1)-C(1)-C(12)-H(12) (deg) for the low-energy conformers of **4f**. (*c*) Fully minimized structure of the conformer *a* of **4f**.

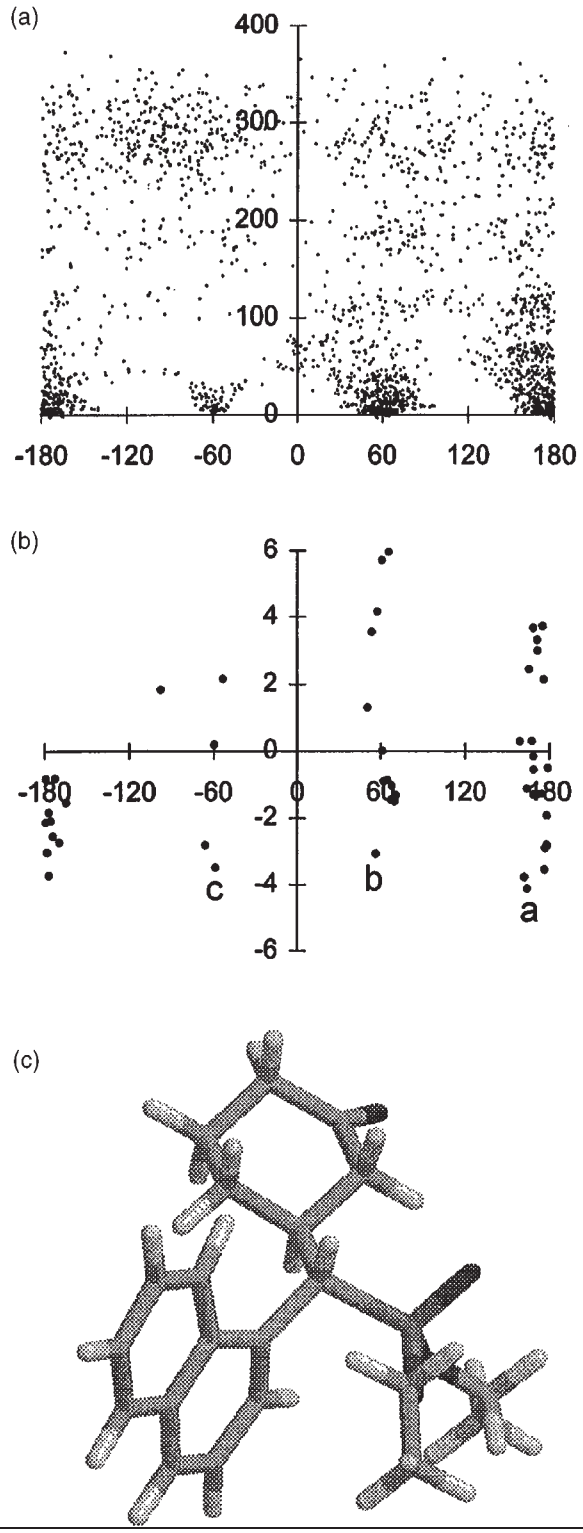

(1 mL per mmol of **1**) and the solution was stirred at that temperature for 1 h. A solution of enone **2** (1.2 mol equiv.) in THF (1 mL per mmol of **2**) was then added, and the reaction mixture was stirred at –78°C for 2 h. Saturated aq. NH_4Cl was then added at –78°C, and the solution was allowed to warm to room temperature. The mixture was extracted with ether (3 × 20 mL) after which the combined etheral layers were dried ($MgSO_4$), filtered, and evaporated under reduced pressure. The products were purified and identified as indicated for individual compounds.

In an alternative procedure, after the addition of **2** and stirring at –78°C for 2 h, the mixture was allowed to warm to a temperature indicated for individual compounds, before the aqueous work-up. Separation and purification procedure was then followed up as above. The following products **3** and **4** were prepared.[7]

*Diethyl (1-hydroxycyclohex-2-enyl)(phenyl)methylphosphonate **3a***

(All steps at –78°C.) Purified by column chromatography (99%): MS, *m*/*z*: 306 ($M^+ - H_2O$, 26%), 228 (100), 168 (55), 91 (51), 79 (7), 29 (15); IR: ν_{PO} 1231, ν_{OH} 3489. Anal. calcd. for $C_{17}H_{25}O_4P$: C 62.95, H 7.77; found: C 62.92, H 7.87. Separated by column chromatography to two isomers. Major isomer (79%), δ_H: 1.50 (2H, m), 1.61–2.00 (4H, m), 3.27 (1H, d, J_{HP} 23.7), 4.48 (1H, br s), 5.71 (1H, dt, J_{HH} 6.3, 9.8), 6.00 (1H, dd, J_{HP} 1.9, J_{HH} 10.2), 7.25 (3H, m), 7.43 (2H, m); proton-decoupled δ_C: 18.5, 24.6, 33.9 (d, J_{CP} 11.2), 53.5 (d, J_{CP} 132.4), 71.1, 127.0, 128.0, 128.1, 130.5, 132.6 (d, J_{CP} 4.6), 134.0; δ_P: 28.6. Minor isomer (20%), δ_H: 1.50 (2H, m), 1.61–2.00 (4H, m), 3.22 (1H, d, J_{HP} 22.9), 4.32 (1H, br s), 5.71 (1H, dt, J_{HH} 6.3, 9.8), 6.00 (1H, dd, J_{HP} 1.9, 10.3), 7.25 (3H, m), 7.45 (2H, m); proton-decoupled δ_C: 18.5, 24.5, 33.9 (d, J_{CP} 11.2), 54.8 (d, J_{CP} 127.9), 71.1, 127.1, 128.0, 128.1, 130.4, 132.7 (d, J_{CP} 4.6), 133.9; δ_P: 27.8.

*Diethyl (1-hydroxycyclohex-2-enyl)(3-methylphenyl)methylphosphonate **3b***

(All steps at –78°C.) Purified by column chromatography (55%): MS, *m*/*z*: 320 ($M^+ - H_2O$, 26%), 182 (9), 105 (100), 79 (13), 29 (18); IR: ν_{PO} 1209, ν_{OH} 3417. Anal. calcd. for $C_{18}H_{27}O_4P$: C 63.90, H 7.99; found: C 63.81, H 8.15. Separated by column chromatography to two isomers. Major isomer (39%), δ_H: 1.49–1.70 (4H, m), 1.83–1.99 (2H, m), 2.30 (3H, s), 3.23 (1H, d, J_{HP} 23.7), 4.51 (1H, br s), 5.70 (1H, dt, J_{HH} 3.6, 10.2), 6.00 (1H, d, J_{HH} = 10.2 Hz), 7.04 (1H, s), 7.19 (3H, m); proton-decoupled δ_C: 18.7, 21.4, 24.7, 33.0, (d, J_{CP} 11.3), 53.7 (d, J_{CP} 131.8), 70.2, 127.7 (d, J_{CP} 6.7), 128.0, 128.1, 131.2 (d, J_{CP} 7.5), 137.7 (d, J_{CP} 4.9), 141.6; δ_P: 28.7. Minor isomer (16%), δ_H: 1.49–1.66 (4H, m), 1.77–1.93 (2H, m), 2.30 (s), 3.18 (1H, d, J_{HP} 23.0), 4.50 (1H, br s), 5.62 (1H, d, J_{HH} 11.1), 5.75 (1H, m), 7.04 (1H, m), 7.19 (3H, m); proton-decoupled δ_C: 18.7, 21.4, 24.8, 36.5 (d, J_{CP} 6.3), 54.9 (d, J_{CP} 130.5), 71.1, 127.8, 127.9, 128.2, 130.2 (d, J_{CP} 10.0), 130.6, 131.3 (d, J_{CP} 4.2), 134.0, 137.6; δ_P: 28.0.

[7] All products **3** and **4** are diethyl esters of phosphonic acids. For the sake of brevity, the ^1H and ^{13}C NMR signals of the POEt ester groups are not included in the spectroscopic data of individual products. In all cases those groups gave rise to the following signals: δ_H: 1.15–1.30 (6H, t, J_{HH} 7.0–7.1), 3.95–4.15 (4H, dq, J_{HP} ca. 11, J_{HH} ca. 7); proton-decoupled δ_C: ca. 16 (d, J_{CP} ca. 5.5), ca. 62 (d, J_{CP} ca. 7). In case of diastereomeric mixtures, pairs of the corresponding signals were obtained.

© 1998 NRC Canada

*Diethyl (1-hydroxycyclohex-2-enyl)(4-methoxyphenyl)methylphosphonate **3c***

(All steps at –78°C.) Purified by column chromatography (88%): MS, *m/z*: 336 ($M^+ - H_2O$, 5%), 199 (21), 121 (100), 79 (3), 29 (8); IR: ν_{PO} 1241, ν_{OH} 3436. Anal. calcd. for $C_{18}H_{27}O_5P$: C 61.0, H 7.63; found: C 60.66, H 7.85. Separated by column chromatography to two isomers. Major isomer (69%), δ_H: 1.39–1.68 (4H, m), 1.75–1.99 (2H, m), 3.22 (1H, d, J_{HP} 23.8), 3.76 (3H, s), 4.41 (1H, br s), 5.70 (1H, dt, J_{HH} 3.7, 10.2), 5.96 (1H, dd, J_{HH} = 1.9, J_{HH} 10.2), 6.81 (2H, d, J_{HH} 8.6), 7.32 (2H, dd, J_{HH} 2.0, 8.6); proton-decoupled δ_C: 18.6, 24.7, 33.9 (d, J_{CP} 11.2), 52.8 (d, J_{CP} 132.2), 55.1, 70.3, 113.6, 126.0, 128.2, 131.6 (d, J_{CP} 6.9), 132.8 (d, J_{CP} 4.6), 158.8; δ_P: 28.9. Minor isomer (19%), δ_H: 1.49–1.66 (4H, m), 1.77–1.93 (2H, m), 3.16 (1H, d, J_{HP} 22.9), 3.78 (3H, s), 4.31 (1H, br s), 5.70 (1H, m), 5.99 (1H, d, J_{HH} 10.2), 7.04 (1H, s), 7.19 (3H, m); δ_C: 18.3, 20.4, 24.3, 33.0 (d, J_{CP} 6.1), 54.4 (d, J_{CP} 131.1), 70.7, 127.3, 127.4, 127.5, 130.0, 130.9 (d, J_{CP} 6.8), 132.6 (d, J_{CP} 4.2), 133.6 (d, J_{CP} 4.9), 137.2; δ_P: 28.0.

*Diethyl (1-hydroxycyclohex-2-enyl)(4-fluorophenyl)methylphosphonate **3d***

(All steps at –78°C.) Purified by column chromatography (98%): MS, *m/z*: 324 ($M^+ - H_2O$, 8%), 246 (76), 187 (12), 109 (100), 81 (16), 29 (16); IR: ν_{PO} 1219, ν_{OH} 3440. Anal. calcd. for $C_{17}H_{24}FO_4P$: C 59.65, H 7.02; found: C 59.40, H 7.15. Separated by column chromatography to two isomers. Major isomer (72%), δ_H: 1.43–1.52 (2H, m), 1.63–1.97 (4H, m), 2.00 (1H, br s), 3.26 (1H, d, J_{HP} 23.7), 5.72 (1H, dt, J_{HP} 3.7, 10.2), 5.99 (1H, d, J_{HH} 10.2), 6.97 (2H, dd, J_{HF} 8.6, J_{HH} 8.7), 7.40 (2H, m); proton-decoupled δ_C: 18.4, 24.5, 33.8 (d, J_{CP} 11.2), 52.7 (d, J_{CP} 132.3), 71.0, 114.8 (d, J_{CP} 21.0), 128.2, 129.8, 131.9, 132.0 (d, J_{CP} 7.7), 132.4 (d, J_{CP} 4.5), 161.9 (d, J_{CF} 247.1); δ_P: 28.2 (d, J_{PF} 3.8); δ_F: –115.5. Minor isomer (26%), δ_H: 1.51 (2H, m), 1.74–2.01 (4H, m), 3.21 (d, J_{HP} 23.0), 4.23 (1H, br s), 5.58 (1H, d, J_{HH} 10.4), 5.79 (1H, m), 6.96 (2H, dd, J_{HF} 8.6, J_{HH} 8.7 Hz), 7.40 (2H, m); proton-decoupled δ_C: 18.3, 24.4, 36.0 (d, J_{CP} 6.3), 53.7 (d, J_{CP} 132.1), 70.7, 114.7 (d, J_{CP} 21.4), 128.1, 129.8 (d, J_{CP} 9.4), 130.4, 131.9, 161.8 (d, J_{CF} 246.4); δ_P: 27.5 (d, J_{PF} 3.9); δ_F: –115.6.

*Diethyl (3-oxocyclohexyl)(4-fluorophenyl)methylphosphonate **4d***

(Aqueous work-up step after warming to –10°C). Isolated by column chromatography as a mixture of two stereoisomers (36%): MS, *m/z*: 342 (M^+, 2%), 246 (100), 204 (16), 109 (43), 81 (5), 29 (8); IR: ν_{PO} 1220, ν_{CO} 1707. Anal. calcd. for $C_{17}H_{24}FO_4P$: C 59.65, H 7.02; found: C 59.20, H 7.35. δ_H: 1.34–1.47 (1H, m), 1.86–1.92 (2H, m), 2.01–2.09 (1H, m), 2.22 (1H, m), 2.37 (2H, m), 2.56 (1H, m), 2.80 (1H, m), 3.00 (1H, d, J_{HP} 21.4), 6.91 (2H, m), 7.20 (2H, m); proton-decoupled δ_C: 24.6, 28.8 (d, J_{CP} 9.4), 39.6, 40.8, 47.1 (d, J_{CP} 8.2), 49.2 (d, J_{CP} 138.9), 115.3 (d, J_{CP} 19.0), 130.3, 131.2 (dd, J_{CP} 6.6, J_{CF} 6.7), 161.9 (dd, J_{CP} 20.5, J_{CF} 247.8), 210.3; δ_P: 27.1 (d, J_{PF} 3.3), 27.2 (d, J_{PF} 4.4); δ_F: –115.3 (major), –116.4 (minor).

*Diethyl (1-hydroxy-2-methylcyclohex-2-enyl)(phenyl)methylphosphonate **3e***

(Aqueous work-up after warming to –40°C and stirring at that temperature for 2 h.) Isolated from the reaction mixture and separated to two stereoisomers by column chromatography (hexane/AcOEt, 3:2, v/v). Major isomer (18%), δ_H: 1.59–1.71 (5H, m), 1.82–1.92 (2H, m), 2.12–2.22 (2H, m), 3.59 (1H, d, J_{HP} 25.0), 5.45 (1H, m), 7.23 (3H, m), 7.38 (2H, m); proton-decoupled δ_C: 17.9, 18.4, 24.7, 35.1 (d, J_{CP} 5.1), 52.9 (d, J_{CP} 130.6), 73.6, 126.8, 127.4, 127.5, 130.5 (d, J_{CP} 6.0), 133.6, 135.3; δ_P: 28.7; MS, *m/z*: 320 ($M^+ - H_2O$, 10%), 228 (100), 172 (66), 91 (77), 79 (8), 29 (13). Anal. calcd. for $C_{18}H_{27}O_4P$: C 63.90, H 7.99; found: C 63.55, H 8.01. Minor isomer (8%), δ_H: 1.26 (3H, s), 1.70 (3H, m), 2.01 (2H, m), 2.48 (1H, m), 3.49 (1H, d, J_{HP} 22.6), 5.41 (1H, m), 7.27 (3H, m), 7.46 (2H, m); proton-decoupled δ_C: 18.5, 18.9, 24.4, 36.3, 51.8 (d, J_{CP} 131.5), 73.6, 125.4, 127.0, 127.7, 131.2 (d, J_{CP} 8.1), 133.7, 137.8; δ_P: 27.2; MS, *m/z*: 320 ($M^+ - H_2O$, 8%), 228 (100), 172 (54), 91 (68), 79 (5), 29 (11). Anal. found: C 63.60, H 7.58.

*Diethyl (2-methyl-3-oxocyclohexyl)(phenyl)methylphosphonate **4e***

Formed together with **3e** and isolated from the reaction mixture by column chromatography (hexane/AcOEt, 3:2, v/v) as the last fraction, following the unreacted **1a** and both stereoisomers of **3e** (13%), δ_H: 1.11 (3H, d, J_{HH} 6.5), 1.46–1.55 (2H, m), 1.94–2.55 (6H, m), 3.32 (1H, d, J_{HP} 26.3), 7.28 (3H, m), 7.42 (2H, m); proton-decoupled δ_C: 11.9, 24.8, 27.2 (d, J_{CP} 2.2), 41.0, 44.9 (d, J_{CP} 139.5), 45.2, 47.0 (d, J_{CP} 14.6), 127.0, 127.9, 130.9, 132.2; δ_P: 28.6; MS, *m/z*: 338 (M^+, 3%), 228 (100), 200 (73), 172 (63), 91 (78), 79 (6), 29 (14). Anal. found: C 63.75, H 8.00.

*Diethyl (3-oxocyclohexyl)(1-naphthyl)methylphosphonate **4f***

(Aqueous work-up carried out after warming the reaction mixture to room temperature and stirring for 16 h.) Purified by bulb-to-bulb distillation, oven temp. 250°C (0.5 mm); oil, mixture of two stereoisomers (55%), δ_H: 1.29 (1H, m), 1.50 (1H, m), 1.87 (2H, m), 2.11–2.32 (3H, m), 2.68 (1H, m), 2.87 (1H, m), 3.91 (1H, dd, J_{HH} 8.2, J_{HP} 23.6), 7.49 (3H, m), 7.82 (3H, m), 8.00 (1H, d, J_{HH} 8.1); proton-decoupled δ_C: 24.6, 29.2 (d, J_{CP} 10.8), 40.9, 41.1, 43.1 (d, J_{CP} 138.3), 49.6 (d, J_{CP} 6.4), 122.7, 125.2, 125.6, 126.5, 127.0 (d, J_{CP} 6.2), 127.9 (d, J_{CP} 2.2), 129.1, 131.2 (d, J_{CP} 4.6), 132.6 (d, J_{CP} 8.5), 133.9, 210.4; δ_P: 27.56 (major),[8] 27.64 (minor); IR: ν_{PO} 1221, ν_{CO} 1707; MS, *m/z*: 374 (M^+, 16%), 278 (100), 141 (77), 81 (7), 29 (8). Anal. calcd. for $C_{21}H_{27}O_4P$: C 67.38, H 7.22; found: C 67.12, H 7.15.

Reversibility of addition

A sample of pure alcohol **3a**–**d** or ketone **4d** (typically 1–2 mmol) was dissolved in THF (1 mL per mmol of substrate), the solution was cooled to –78°C and *n*-butyllithium (1.6 M solution in hexane, 1.2 mol equiv.) was added. The

[8] According to the integrated ^{31}P NMR spectrum of **4f**, it consisted of ca. 1.5:1 mixture of diastereomers. In the ^1H and ^{13}C NMR spectra the signals of the major stereoisomer were accompanied by less intense signals derived from the minor isomer. Only the signals derived from the major isomer are given for the ^1H and ^{13}C NMR spectra.

© 1998 NRC Canada

solution was allowed to warm to room temperature, kept for 24 h, and subjected to the usual aqueous work-up. The product obtained after the evaporation of ether was examined by NMR (^{1}H and ^{13}C) spectroscopy and thin layer chromatography using authentic samples of **2a** and the corresponding phosphonate **1** as standards. Only the starting materials for the addition reactions (**1a–d**, together with **2a**), were observed.

Molecular modeling

The calculations were performed with the default values of the TRIPOS (24) (SYBYL program version 6.2 released by TRIPOS Inc.). The electrostatic point charges of the atoms were calculated with the Gasteiger–Hückel method. All minimisations were carried out using the Powell method (25) up to a gradient of 0.05 kcal mol^{-1} Å^{-1}. The default setup for simulated annealing, which applied a constant temperature algorythm based on the method of Berendsen et al. (26) and the rate for decreasing the temperature of 0.5 K fs^{-1}, was used. The thermal bath coupling constant and the integration time step were 5.0 fs and 0.5 fs, respectively. The model of **4f** was built to resemble the conformation found in the crystal structure and then minimized. The minimized structure was subjected to 50 cycles of simulated annealing using distance dependant relative permitivity and a cut-off radius of 9 Å for nonbonded interactions in vacuo. Each cycle that consisted of 12 000 fs was sampled every 50 fs.

Crystal structure determination

The major steroisomer of **4f** was isolated by dissolving the diastereomeric mixture in anhydrous ether and allowing slow evaporation of the solution.. The major stereoisomer (δ_P 27.56) separated as colourless crystals, mp 142.5°C. Crystals suitable for X-ray diffractions were obtained by dissolving the compound in a minimum volume of dichloromethane and placing the solution in a larger, closed container with anhydrous ether. Diffusion of the ether vapours to the dichloromethane solution resulted in slow formation of crystals. X-ray diffraction data were measured on an Enraf Nonius CAD4 diffractometer with MoK_α radiation (graphite monochromator, λ = 0.7107 Å) and were collected at room temperature. Accurate unit cell parameters were obtained by least-squares methods from the position of 25 carefully selected centred reflections. During data collection three reference reflections were measured periodically to check crystal stability. There was no significant crystal decay, and intensities were corrected for absorption, as well as for Lorentz and polarization effects. Crystal data and structural refinement parameters are given in Table 1.

Acknowledgment

Financial assistance from the University of Pretoria and the Foundation for Research Development is gratefully acknowledged.

References

1. P. Perlmutter. Conjugate addition reactions in organic synthesis. Pergamon Press, Oxford. 1992.
2. (*a*) B.J. Walker. *In* Organophosphorus reagents in organic synthesis. *Edited by* J.I.G. Cadogan. Academic, London. 1979. Chap. 3; (*b*) B.E. Maryanoff and A.B. Reitz. Chem. Rev. **89**, 863 (1989).
3. (*a*) C. Piechucki. Synthesis, 187 (1976); (*b*) J.R. Sundberg, P.A. Bukowick, and F.O. Holcombe. J. Org. Chem. **32**, 2938 (1967).
4. (*a*) M.J. Mphahlele and T.A. Modro. J. Org. Chem. **60**, 8236 (1995); (*b*) J. Chem. Soc. Perkin Trans. 1, 2261 (1996); (*c*) J. Chem. Soc. Perkin Trans. 2, 1455 (1996); (*d*) A. Pienaar and T.A. Modro. Heteroat. Chem. **7**, 443 (1996).
5. (*a*) J. Petrova, N.G. Vassilev, and M. Kirilov. Phosphorus Sulfur Silicon Relat. Elem. **47**, 457 (1990); (*b*) J. Petrova, S. Momchilova, and N.G. Vassilev. Phosphorus Sulfur Silicon Relat. Elem. **68**, 45 (1992); (*c*) N.G. Vassilev, J. Petrova, and M. Kirilov. Phosphorus Sulfur Silicon Relat. Elem. **85**, 49 (1993).
6. D. Seebach. Synthesis, **1**, 17 (1969).
7. A.G. Schultz and Y.K. Yee. J. Org. Chem. **41**, 4044 (1976).
8. (*a*) N.Y. Wang, S.S. Su, and L.Y. Tsai. Tetrahedron Lett. 1121 (1979); (*b*) D. Morgans and G.B. Feigelson. J. Org. Chem. **47**, 1131 (1982); (*c*) J. Bertrand, L. Gorrichon, and P. Maroni. Tetrahedron, **40**, 4127 (1984); (*d*) M. Mikolajczyk and P. Balczewski. Tetrahedron, **48**, 8697 (1992).
9. D.A. Oare and C.H. Heathcock. J. Org. Chem. **55**, 157 (1990), and preceeding papers of this series.
10. T. Cohen, W.D. Abraham, and M. Myers. J. Am. Chem. Soc. **109**, 7923 (1987).
11. S. Berger, S. Braun, and H.-O. Kalinowski. NMR Spektroskopie von Nichtmetallen. Vol. 3. Georg Thieme, Stuttgart. 1993. Chap. 3.3.3.3.
12. (*a*) G. Adividjaja, B. Meyer, and J. Thiem. Z. Naturforsch. B: Anorg. Chem. Org. Chem. **34b**, 1547 (1979); (*b*) J. Thiem and B. Meyer. Org. Magn. Reson. **11**, 50 (1978).
13. N.S. Isaacs. Physical organic chemistry. Longman, Burnt Mill. 1987. p. 298.
14. M.-P. Belciug, A.M. Modro, T.A. Modro, and P.L. Wessels. J. Phys. Org. Chem. **5**, 787 (1992), and the following papers of this series.
15. G.M. Sheldrick. SHELX86. A program for the solution of crystal structures. University of Göttingen, Göttingen. 1986.
16. G.M. Sheldrick. SHELX76. Program for crystal structure determination. University of Cambridge, Cambridge. 1976.
17. (*a*) International tables for X-ray crystallography. Vol. 4. Kynoch Press, Birmingham. 1974; (*b*) D.T. Cromer and D. Liberman. J. Chem. Phys. **4**, 1891 (1970).
18. C.K. Johnson. ORTEP. Report ORNL-3794. Oak Ridge National Laboratory, Tennessee, U.S.A. 1965.
19. H.-O. Kalinowski, S. Berger, and S. Braun. ^{13}C-NMR-Spektroskopie. Georg Thieme, Stuttgart. 1984. p. 535.
20. J.-P. Doucet and J. Weber. Computer-aided molecular design: theory and applications. Academic, San Diego. 1996. Chap. 7.
21. C.A. Haasnoot, F.A.A.M. de Leeuw, and C. Altona. Tetrahedron, **36**, 2783 (1980).
22. J. Boutagy and R. Thomas. Chem. Rev. **74**, 87 (1974).
23. R.S. Edmundson (*Editor*). Dictionary of organophosphorus compounds. Chapman and Hall, London. 1988.
24. M. Clark, R.D. Cramer, and N. Van Opdenbosch. J. Comput. Chem. **10**, 982 (1989).
25. M.J.D. Powell. Restart procedures for the conjugate gradient method. Mathematical Programming, **12**, 241 (1977).
26. H.J.C. Berendsen, J.P.M. Postman, W.F. Van Gunsteren, A. Dinola, and J.R. Haak. J. Chem. Phys. **81**, 3684 (1984).

© 1998 NRC Canada

Synthesis and comparative study of three monomeric boronates by spectroscopic methods and X-ray crystallography[1]

Herbert Höpfl, Mario Sánchez, Norberto Farfán, and Victor Barba

Abstract: Three boronates have been synthesized by reaction of tridentate azomethine ligands derived from salicylaldehyde with phenylboronic acid. The [5.4.0], [4.4.0], and [4.3.0]heterobicyclic structures obtained have been characterized by NMR spectroscopy and X-ray crystallography, whereby it could be proved that the [4.4.0]heterobicycle is the most stable one. Unexpectedly the salicylideneaminoethanol derivative does not lead to a macrocyclic structure, although molecular modeling reveals high ring strain for the monomeric product that is actually obtained.

Key words: boronates, boron complexes, tridentate azomethine ligands, phenylboronic acid, X-ray crystallography.

Résumé : On a synthétisé trois boronates par réaction de l'acide phénylboronique avec des ligands azométhines tridentates dérivés du salicylaldéhyde. On a caractérisé les structures hétérobicycliques [5.4.0], [4.4.0], et [4.3.0] par spectroscopie RMN et par diffraction des rayons X; on a ainsi pu prouver que l'hétérobicycle [4.4.0] est le plus stable. D'une manière inattendue, le dérivé salicylidèneaminoéthanol ne conduit pas à une structure macrocyclique, même si la modélisation moléculaire indique l'existence d'une forte tension de cycle pour le produit monomère qui est en fait obtenu.

Mots clés : boronates, complexes du bore, ligands azométhines tridentates, acide phénylboronique, diffraction des rayons X.

[Traduit par la Rédaction]

Introduction

During our studies of boron complexes with a coordinative N→B bond (1–10), we recently discovered the synthesis of two new macrocyclic structures that consist of a dimeric and a tetrameric boronate ring system of 20 and 10 members, respectively (**1** and **2a** in Fig. 1) (11). Both molecules are stable in the air and are obtained in high yields in one-step syntheses between the corresponding tridentate ligands and phenylboronic acid. The molecular structures of both macrocycles have been studied in detail by X-ray crystallography (11), and it could be shown that monomeric systems would be more strained due to the tetrahedral geometry at the boron atom and its small atomic radius. A detailed study of how different substituents in salicylideneaminoethanol influence the formation of monomeric or dimeric boronates with phenylboronic acid was also reported (12). Thereby, it was shown that the dimeric structure type **2** is preferred over the [4.3.0]heterobicyclic type **3** in the absence of steric effects that preclude formation of the macrocycle (Fig. 1). This is the case in compounds **3a** and **3b**, where two methyl groups on the carbon atom adjacent to the nitrogen inhibit the dimer formation (compare also to **2d**).

In search of new tridentate ligands that could be probable promoters of macrocycle formation with phenylboronic acid it was considered promising to fix the carbon–carbon bond of the 2-ethanolamine group in the ligand by a double bond using 2-aminophenol.

Received April 1, 1998.

H. Höpfl[2] and M. Sánchez. Universidad Autónoma del Estado de Morelos, Centro de Investigaciones Químicas, Av. Universidad 1001, C.P. 62210 Cuernavaca, Morelos, México. **N. Farfán[2] and V. Barba.** Departamento de Quimica, Centro de Investigación y de Estudios Avanzados del IPN, Apdo Postal 14–740, C.P. 07000 México D.F., México.

[1]Dedicated to the memory of Dr. Rigoberto García-Cantú.

[2]Authors to whom correspondence may be addressed. HH: Telephone: +52 73 29 7020. Fax: +52 73 29 7040. E-mail: hhopfl@servm.fc.uaem.mx; NF: Telephone: +52 747 3800, ext. 4031. Fax: +52 5 747 7113. E-mail: jfarfan@mvax1.red.cinvestav.mx

Experimental

Instrumentation

The NMR studies were performed with the following spectrometers: Jeol GSX 270 and Eclipse +400. Special techniques (COSY, HETCOR) were applied when necessary to assign the spectra adequately. Standards were TMS (^{1}H, ^{13}C) and $BF_3 \cdot OEt_2$ (^{11}B). Chemical shifts are stated in ppm; they are positive, when the signal is shifted to higher frequencies than the standard. The IR spectra have been recorded with a Perkin Elmer 16F-PC FT-IR spectrophotometer. Mass spectra were obtained with an HP 5989 A equipment. Melting points were determined with a Gallenkamp MFB-595 apparatus and have not been corrected.

© 1998 NRC Canada

Fig. 1. Tetrameric, dimeric, and monomeric boronates obtained with different substituents.

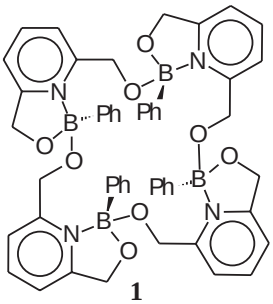

1

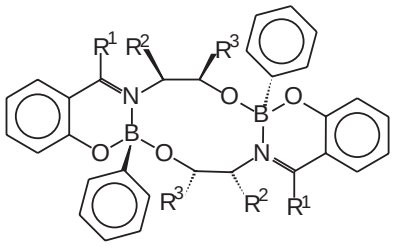

	R^1	R^2	R^3
2a	H	H	H
2b	H	H	Me
2c	H	H	Ph
2d	H	Me	Ph
2e	Me	H	H

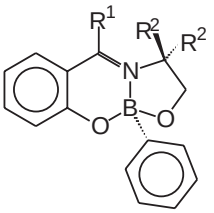

	R^1	R^2
3a	H	Me
3b	Me	Me

X-ray diffraction studies of monocrystals were determined on an Enraf–Nonius CAD4 diffractometer ($\lambda_{MoK\alpha}$ = 0.71069 Å, monochromator: graphite, T = 293 K for **5a** and **5c**, T = 193 K for **5b**, ω–2θ scan). Crystals were mounted in LINDEMAN tubes. Cell parameters were determined by least-squares refinement on diffractometer angles for 24 automatically centered reflections in the θ range of 10–11°. Crystals of compound **5a** diffracted only weakly so that reflections were only collected up to θ = 24°. Absorption correction was not necessary, corrections were made for Lorentz and polarization effects. Solution and refinement: direct methods (SHELXS-86) for structure solution and the CRYSTALS (version 9, 1994) software package for refinement and data output. Non-hydrogen atoms were refined anisotropically. Hydrogen atoms were determined by difference Fourier maps, and their positions as well as one overall isotropic thermal parameter were refined; $I > 3\sigma(I)$; ($R = \Sigma(||F_o| - |F_c||)/\Sigma|F_o|$, $R_w = [\Sigma w(|F_o| - |F_c|)^2/\Sigma wF_o^2]^{1/2}$. In all cases only independent reflections on the basis of Friedel's law have been collected and a reflection–parameter ratio >5 has been considered sufficient for the type of structural studies performed here.

Reagents

All starting materials were commercial. Solvents were used without further purification, but monocrystals were grown from spectrophotometric grade solvents.

General procedure for the preparation of ligands 4a–4c

To prepare the tridentate ligands **4a–4c**, equimolar quantities of the corresponding aminophenol or aminoalcohol and salicylaldehyde were refluxed in benzene for 30 min. The solvent and the water formed during the reaction were then removed by a Dean Stark trap to yield an oil or a solid that was washed with chloroform and used without further purification. The preparation and spectroscopic data of **4a** have already been published (13–17).

2-[[(2-Hydroxyphenyl)imino]methyl]phenol (4a)

Compound **4a** was prepared from 0.90 g (8.19 mmol) of 2-aminophenol and 1.00 g (8.19 mmol) of salicylaldehyde. The product obtained is a yellow solid (1.63 g, 7.65 mmol); mp 189–191°C; yield 93%.

2-[[(2-Hydroxyphenyl)methylene]imino]benzenemethanol (4b)

Compound **4b** was prepared from 1.00 g (8.13 mmol) of 2-aminobenzyl alcohol and 1.00 g (8.19 mmol) of salicylaldehyde. The product obtained is an orange solid (1.63 g, 7.65 mmol); mp 138–140°C; yield 76%. ^{1}H NMR (270 MHz, $CDCl_3$), δ (ppm): 4.82 (2H, AB, OCH_2), 6.91–7.51 (8H, m, aromat.), 8.57 (1H, s, H-7); ^{13}C NMR (67.8 MHz, $CDCl_3$), δ (ppm): 61.8 (OCH_2), 117.3, 118.0, 119.2 (C-3, C-5, C-6′), 118.1 (C-1), 127.1, 128.3, 128.8 (C-3′, C-4′, C-5′), 132.4, 133.4 (C-4, C-6), 134.5 (C-2′), 146.6 (C-1′), 161.0 (C-2), 163.1 (C-7). Infrared (KBr): 3260 (br, m), 2912 (m), 2862 (m), 1618 (s), 1594 (w), 1576 (m), 1570 (m), 1560 (m), 1505 (w), 1498 (w), 1432 (m), 1456 (m), 1368 (w), 1280 (m), 1230 (w), 1202 (m), 1178 (m), 1162 (w), 1150 (w), 1114 (w), 1106 (w), 1032 (s) cm^{-1}.

2-[[(2-Hydroxyphenyl)methylene]amino]benzeneethanol (4c)

Compound **4c** was prepared from 0.90 g (7.32 mmol) of 2-aminophenethyl alcohol and 0.90 g (7.32 mmol) of salicylaldehyde. The product obtained is an orange oil (1.64 g, 6.81 mmol); yield 93%. ^{1}H NMR (270 MHz, $CDCl_3$), δ (ppm): 2.95 (2H, t, J = 7 Hz, OCH_2CH_2), 3.73 (2H, t, J = 7 Hz, OCH_2), 6.83–7.30 (8H, m, aromat.), 8.42 (1H, s, H-7); ^{13}C NMR (67.8 MHz, $CDCl_3$), δ (ppm): 35.3 (OCH_2CH_2), 62.3 (OCH_2), 117.0, 117.9, 118.9 (C-3, C-5, C-6′), 119.1 (C-1), 126.8, 127.5, 130.6 (C-3′, C-4′, C-5′), 132.6 (C-2′), 132.1, 133.0 (C-4, C-6), 147.0 (C-1′), 160.9 (C-2), 162.5 (C-7). Infrared (NaCl): 3396 (br, s), 3060 (w), 3024 (w), 2932 (w), 2878 (w), 1616 (s), 1594 (m), 1570 (m), 1498 (w), 1482 (m), 1456 (w), 1404 (w), 1364 (w), 1278 (m), 1200 (w), 1178 (m), 1150 (m), 1106 (w), 1046 (w), 910 (m) cm^{-1}. EI mass spectrum (70 eV), m/z: 241 (100%, M), 222 (47%), 210 (39%), 130 (26%), 117 (35%), 91 (43%), 77 (26%), 65 (44%), 31 (25%).

General method for the preparation of compounds 5a–5c

An equimolar amount of phenylboronic acid was added to a solution of the tridentate ligand in benzene (usually about 10 mL for 2–3 mmol). The mixture was refluxed for 30 min and quantified by water and solvent separation with a Dean

© 1998 NRC Canada

Scheme 1. Synthesis of compounds **5a**–**5c**.

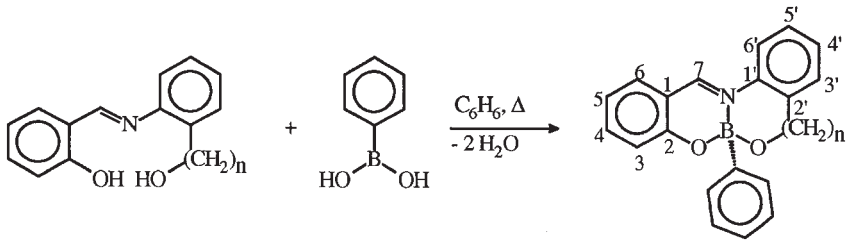

4a n = 0
4b n = 1
4c n = 2

5a n = 0
5b n = 1
5c n = 2

Stark trap. The solid obtained was collected by filtration under vacuum and washed with small amounts of benzene and hexane.

*2-Phenyldibenzo[*d,h*]-6-aza-1,3,2-dioxaboracyclonon-6-ene (**5a**)*

Compound **5a** was prepared from 0.50 g (2.34 mmol) of **4a** and 0.28 g (2.34 mmol) of phenylboronic acid. The product obtained is a yellow solid (0.61 g, 2.04 mmol) that is slightly soluble in chloroform, dichloromethane, methanol, and DMSO. Crystals suitable for X-ray diffraction were obtained, when the reaction was performed in dichloromethane at room temperature without stirring; mp 229–231°C; yield 87%. ^{1}H NMR (270 MHz, $CDCl_3$), δ (ppm): 6.90, (1H, t, J = 8 Hz, H-4′), 6.94 (1H, t, J = 8 Hz, H-5), 7.10 (1H, d, J = 8 Hz, H-6′), 7.12 (1H, t, J = 8 Hz, *p*-BC_6H_5), 7.15 (2H, m, *m*-BC_6H_5), 7.21 (1H, d, J = 8 Hz, H-3), 7.31 (2H, d, J = 7 Hz, *o*-BC_6H_5), 7.38 (3H, m, H-6, H-3′, H-5′), 7.54 (1H, t, J = 7 Hz, H-4), 8.32 (1H, s, H-7); ^{13}C NMR (67.8 MHz, $CDCl_3$), δ (ppm): 115.0 (C-3′), 115.2 (C-6′), 119.3 (C-1, C-4′), 120.3 (C-3, C-5), 127.4 (*m*-BC_6H_5), 127.8 (*p*-BC_6H_5), 131.2 (C-1′, *o*-BC_6H_5), 131.3, 132.5 (C-6, C-5′), 137.9 (C-4), 148.7 (C-7), 157.5, 158.7 (C-2, C-2′); ^{11}B NMR (86.6 MHz, $CDCl_3$), δ (ppm): 8 ($h_{1/2}$ = 120 Hz). Infrared (KBr): 3066 (w), 3040 (w), 2930 (w), 1628 (s), 1608 (m), 1576 (w), 1570 (w), 1558 (m), 1550 (m), 1540 (m), 1534 (m), 1522 (w), 1506 (w), 1472 (m), 1466 (s), 1458 (m), 1452 (w), 1436 (w), 1430 (w), 1380 (m), 1326 (m), 1314 (m), 1284 (m), 1256 (w), 1240 (w), 1226 (m), 1190 (s), 1182 (s), 1154 (s), 1122 (m), 1044 (w), 1032 (w), 1012 (s), 954 (s) cm^{-1}. EI mass spectrum (70 eV, DIP), *m*/*z*: 299 (14%, M), 222 (100%, M – C_6H_5), 193 (2%), 151 (1%), 102 (2%), 77 (26%, $C_6H_5^+$), 51 (15%), 39 (3%). Anal. calcd: C 76.30, H 4.71, N 4.68; found: C 76.31, H 4.62, N 4.63.

*2-Phenyldibenzo[*e,i*]-7-aza-1,3,2-dioxaboracyclodec-7-ene (**5b**)*

Compound **5b** was prepared from 0.50 g (2.20 mmol) of **4b** and 0.27 g (2.20 mmol) of phenylboronic acid. The product obtained is a yellow solid (0.54 g, 1.72 mmol) that is slightly soluble in benzene, chloroform, dichloromethane, methanol, ethanol, and DMSO. Crystals suitable for X-ray diffraction were obtained, when the reaction was performed in dichloromethane at room temperature without stirring; mp 224–226°C; yield 79%. ^{1}H NMR (400 MHz, $CDCl_3$), δ (ppm): 4.98 (2H, m, OCH_2), 6.84 (1H, t, J = 7 Hz, H-5), 7.03 (1H, d, J = 8 Hz, H-3), 7.13 (3H, m, *m*-BC_6H_5, *p*-BC_6H_5), 7.28 (3H, m, H-4′, *o*-BC_6H_5), 7.32 (1H, t, J = 10 Hz, H-5′), 7.36 (2H, m, H-6, H-3′), 7.47 (1H, t, J = 8 Hz, H-4), 7.62 (1H, d, J = 8 Hz, H-6′), 8.59 (1H, s, H-7); ^{13}C NMR (100.5 MHz, $CDCl_3$), δ (ppm): 63.9 (OCH_2), 118.1 (C-6′), 118.2 (C-1), 120.2 (C-5), 120.9 (C-3), 127.5 (*p*-BC_6H_5), 127.9 (C-4′), 128.2 (*m*-BC_6H_5), 128.8 (C-3′), 129.6 (C-5′), 132.1 (*o*-BC_6H_5), 132.9 (C-6), 136.5 (C-2′), 139.1 (C-1′), 139.4 (C-4), 156.7 (C-2, C-7); ^{11}B NMR (128.3 MHz, $CDCl_3$), δ (ppm): 5 ($h_{1/2}$ = 140 Hz). Infrared (KBr): 3062 (s), 3008 (s), 2928 (s), 2886 (s), 2846 (s), 2828 (s), 1624 (s), 1584 (w), 1552 (s), 1534 (w), 1474 (m), 1456 (m), 1430 (w), 1390 (w), 1376 (w), 1306 (m), 1246 (w), 1196 (s), 1176 (s), 1152 (m), 1124 (w), 1102 (m), 1048 (w), 1032 (w), 1008 (m), 960 (m), 928 (w) cm^{-1}. EI mass spectrum (70 eV, DIP), *m*/*z*: 313 (5%, M), 236 (100%, M – C_6H_5), 206 (2%), 165 (1%), 91 (4%), 77 (10%, $C_6H_5^+$), 65 (4%), 51 (6%). Anal. calcd: C 76.71, H 5.14, N 4.47; found: C 75.37, H 5.10, N 4.31.

*2-Phenyldibenzo[*f,j*]-8-aza-1,3,2-dioxaboracycloundec-8-ene (**5c**)*

Compound **5c** was prepared from 0.50 g (2.07 mmol) of **4c** and 0.25 g (2.07 mmol) of phenylboronic acid. The product obtained is a yellow solid (0.58 g, 1.77 mmol) that is slightly soluble in chloroform. Crystals suitable for X-ray diffraction were obtained, when the reaction was performed in benzene at room temperature without stirring; mp 206–208°C; yield 85%. ^{1}H NMR (400 MHz, $CDCl_3$), δ (ppm): 2.94–3.24 (2H, m, OCH_2CH_2), 4.02–4.36 (2H, m, OCH_2), 6.88 (1H, t, J = 7 Hz, H-5), 7.10 (5H, m, H-3, H-6′, *m*-BC_6H_5, *p*-BC_6H_5), 7.25 (6H, m, H-6, H-3′, H-4′, H-5′, *o*-BC_6H_5), 7.55 (1H, t, J = 8 Hz, H-4), 8.16 (1H, s, H-7); ^{13}C NMR (100.5 MHz, $CDCl_3$), δ (ppm): 35.9 (OCH_2CH_2), 59.6 (OCH_2), 117.8 (C-1), 120.0 (C-5), 120.9 (C-3), 124.4 (C-6′), 127.7 (*p*-BC_6H_5), 127.9 (*m*-BC_6H_5), 128.5 (C-4′), 129.7 (C-5′), 131.6 (C-6), 132.4 (*o*-BC_6H_5), 133.1 (C-3′), 135.4 (C-2′), 139.5 (C-4), 145.1 (C-1′), 163.2 (C-2), 164.9 (C-7); ^{11}B NMR (86.6 MHz, $CDCl_3$), δ (ppm): 6 ($h_{1/2}$ = 170 Hz). Infrared (KBr): 3020 (w), 2952 (w), 2920 (w), 2862 (w), 1622 (s), 1600 (w), 1552 (m), 1476 (m), 1454 (m), 1370 (w), 1300 (w), 1212 (m), 1196 (m), 1182 (w), 1154 (w), 1130 (m), 1098 (w), 1070 (w), 1056 (w), 1040 (w), 1030 (w), 1016 (w), 942 (m) cm^{-1}. EI mass spectrum (70 eV, DIP), *m*/*z*: 327 (3%, M), 250 (100%, M – C_6H_5), 235 (6%), 220 (13%), 165 (1%), 103 (1%), 77 (7%, $C_6H_5^+$), 51 (5%). Anal. calcd: C 76.89, H 5.52, N 4.26; found: C 76.48, H 5.67, N 4.33.

© 1998 NRC Canada

Table 1. The ^{1}H and ^{11}B NMR data (270 and 86.6 MHz) for compounds **4a**–**4c** and **5a**–**5c** in $CDCl_3$ (ppm).

Comp.	H-3	H-4	H-5	H-6	H-7	H-3′	H-4′	H-5′	H-6′	OCH_2	B-C_6H_5 *o*	B-C_6H_5 *m*	B-C_6H_5 *p*	^{11}B NMR ($h_{1/2}$ (Hz))
4a[a]		6.86–7.63			8.97		6.86–7.63			—	—	—	—	—
4b		6.91–7.51			8.57		6.91–7.51			4.82	—	—	—	—
4c[b]		6.83–7.30			8.42		6.83–7.30			3.73	—	—	—	—
5a	7.21	7.54	6.94	7.38	8.32	7.38	6.90	7.38	7.10	—	7.31	7.15	7.12	+8 (120)
5b[c]	7.03	7.47	6.84	7.36	8.59	7.36	7.28	7.32	7.62	4.98	7.28	7.13	7.13	+5 (140)
5c[c,d]	7.10	7.55	6.88	7.25	8.16	7.25	7.25	7.25	7.10	4.19	7.25	7.10	7.10	+6 (170)

[a] In DMSO-d_6.
[b] OCH_2CH_2, δ (ppm): 2.95 ppm.
[c] ^{1}H NMR: 400 MHz; ^{11}B NMR: 128.3 MHz.
[d] OCH_2CH_2, δ (ppm): 3.09.

Table 2. The ^{13}C NMR data (67.8 MHz) for compounds **4a** –**4c** and **5a** –**5c** in $CDCl_3$ (ppm).

Comp.	C-1	C-2	C-3	C-4	C-5	C-6	C-7	C-1′	C-2′	C-3′	C-4′	C-5′	C-6′	OCH_2
4a[a]	119.4	160.6	116.4[b]	132.7[c]	118.6[b]	132.2[c]	161.6	134.9	151.0	119.5[b]	119.5[b]	127.9	116.6[b]	—
4b	118.1	161.0	118.0[b]	133.4[c]	119.2[b]	132.4[c]	163.1	146.6	134.5	127.1	128.8[d]	128.3[d]	117.3[b]	61.8
4c[e]	119.1	160.9	117.9[b]	133.0[c]	118.9[b]	132.1[c]	162.5	147.0	132.6	126.8	127.5[d]	130.6[d]	117.0[b]	62.3
5a[f]	119.3	158.7[b]	120.3	137.9	120.3	131.3[c]	148.7	131.2	157.5[b]	115.0	119.3	132.5[c]	115.2	—
5b[g,h]	118.2	156.7	120.9	139.4	120.2	132.9	156.7	139.1	136.5	128.8	127.9	129.6	118.1	63.9
5c[g,i,j]	117.8	163.2	120.9	139.5	120.0	131.6	164.9	145.1	135.4	133.1	128.5	129.7	124.4	59.6

[a] In DMSO-d_6.
[b, c, d] Signals may be interchanged.
[e] OCH_2CH_2, δ (ppm): 35.3.
[f] B-C_6H_5, δ (ppm): 127.4 (*m*), 127.8 (*p*), 131.2 (*o*).
[g] 100.5 MHz.
[h] B-C_6H_5, δ (ppm): 127.5 (*p*), 128.2 (*m*), 132.1 (*o*).
[i] OCH_2CH_2, δ (ppm): 35.9.
[j] B-C_6H_5, δ (ppm): 127.7 (*p*), 127.9 (*m*), 132.4 (*o*).

Results and discussion

Although a high ring strain can be predicted from molecular modeling for the monomeric structure, the reaction between ligand **4a** and phenylboronic acid leads to compound **5a** (Scheme 1). For comparison compounds **5b** and **5c** have been synthesized, too. The formula of the three heterobicyclic compounds are proved by mass spectrometry. In all molecules the molecular ion is detected. Due to the easy loss of a phenyl radical the base peak corresponds to the $[M - C_6H_5]^+$ ion (18–21), where the boron atom is bound to two oxygens and a nitrogen atom.

The C=N stretching band in the IR spectra is shifted to higher wave numbers after the complex formation in the case of **5b** (1618 cm^{-1} for **4b** and 1624 cm^{-1} for **5b**) and **5c** (1616 cm^{-1} for **4c** and 1622 cm^{-1} for **5c**), as it has been observed already for other boron chelates (22–23), while it is shifted to lower wave numbers in the case of **5a** (1636 cm^{-1} for **4a** and 1628 cm^{-1} for **5a**).

The ^{1}H, ^{13}C, and ^{11}B NMR data of the monomeric boronates **5a–5c** and their corresponding ligands **4a–4c** are listed in Tables 1 and 2. A comparison of the ^{1}H NMR spectra shows that the azomethine hydrogen atom H-7 is shifted to higher field for **5a** and **5c** with N→B coordination (Δδ = 0.65 and 0.26 ppm), while it is not significantly displaced in **5b** (Δδ = 0.02 ppm). The resonances of the OCH_2 groups in **5b** and **5c** are detected downfield as diastereotopic signals (Δδ = 0.10 ppm and 0.34 ppm). The OCH_2CH_2 methylene hydrogens in the seven-membered heterocycle of compound **5c** are also diastereotopic (Δδ = 0.30 ppm), indicating a fixed configuration of the complex in solution.

Fig. 2. Structures of compounds **6**–**9**.

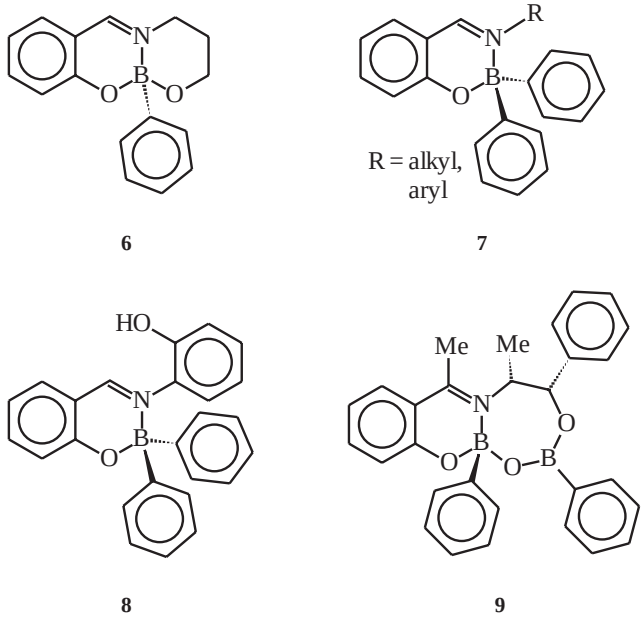

6 **7** **8** **9**

From the ^{13}C NMR spectra the most interesting observation is the extreme high field shift of the azomethine carbon atom in compound **5a** after the chelate formation (δ = 161.6 ppm ↔ δ = 148.7 ppm). The correct assignment has

© 1998 NRC Canada

Table 3. Crystallographic data for compounds **5a**–**5c**.[a]

Compound	**5a**	**5b**	**5c**
Formula	$C_{19}H_{14}BNO_2$	$C_{20}H_{16}BNO_2$	$C_{21}H_{18}BNO_2$
Crystal size, mm	0.12 × 0.39 × 0.54	0.4 × 0.4 × 0.4	0.39 × 0.45 × 0.48
fw, g mol^{-1}	299.14	313.16	327.19
Space group	*P* $2_1/c$	*P* $2_1/a$	*P* $2_1/c$
Cell parameters			
a, Å	10.038 (2)	10.485 (8)	9.0576 (6)
b, Å	18.230 (4)	11.081 (6)	13.337 (1)
c, Å	16.945 (4)	13.736 (6)	14.835 (1)
β°	95.18 (2)	100.56 (7)	106.026 (6)
V, $Å^3$	3042 (6)	1569 (2)	1722.5 (2)
Z	8	4	4
μ, mm^{-1}	0.078	0.079	0.075
$\rho_{calcd.}$ g cm^{-3}	1.29	1.33	1.26
Data collection			
Scan range, deg in ω	0.42 + 0.76 tan θ	1.09 + 1.20 tan θ	0.47 + 0.52 tan θ
Data collected	±*h*, –*k*, +*l*	±*h*, –*k*, –*l*	±*h*, +*k*, +*l*
$2\theta_{max}$, deg	48	52	56
Total reflections	5123	3370	4488
Total unique refl.	4761	3066	4152
R_{merge}	0.01	0.01	0.01
Refl. with $I > 3\sigma(I)$	2688	1448	1750
Intensity variation (σ)	<3	<3	<3
Refinement			
R	0.043	0.067	0.040
R_w	0.036	0.049	0.035
No. of variables	501	266	282
gof	2.32	4.67	2.52
Max. Δ/σ (final cycle)	0.04	0.07	0.04
$\Delta\rho_{min}$, e $Å^{-3}$	–0.23	–0.25	–0.13
$\Delta\rho_{max}$, e $Å^{-3}$	0.54	0.58	0.12
Extinction parameter	84 (11)	—	42 (7)

[a]Temperature 293 K for **5a** and **5c**, 193 K for **5b**, Enraf Nonius CAD4 diffractometer, MoK_α (λ = 0.71069) radiation, graphite monochromator, $R = \Sigma(||F_o| - |F_c||)/\Sigma|F_o|$, $R_w = [\Sigma w(|F_o| - |F_c|)^2/\Sigma wF_o^2]^{1/2}$, where $w = 1/\sigma^2$. Values given for *R*, R_w, and gof are based on those reflections with $I > 3\sigma(I)$.

been evidenced by a HETCOR experiment. This difference diminishes in compound **5b** (δ = 163.1 ppm ↔ δ = 156.7 ppm) and changes its sign in **5c** (δ = 162.5 ppm ↔ δ = 164.9 ppm). In the similar six-membered diphenylboron chelate **6** (Fig. 2) only a small high field shift could be detected (17). The downfield shift of 5–6 ppm for the C-4 carbon atom is characteristic for the formation of a boron complex and has been already reported for other boronates with a similar structure (12). It seems therefore to be a typical indicator for the N→B bond coordination in salicylideneamino chelates. The OCH_2 carbon atom in the boronates is found at lower field for **5b** (Δδ = 2.1 ppm) and at higher field for **5c** (Δδ = 2.7 ppm).

The ^{11}B NMR spectra of the boron complexes **5a–5c** specify tetracoordinated boron atoms (24). The chemical shifts indicate the weakest coordination for the [4.3.0]heterobicycle **5a** (δ = 8 ppm) and the strongest coordination for the [4.4.0]heterobicycle **5b** (δ = 5 ppm), although the difference is not very striking. The ^{11}B NMR signal for the [5.4.0]heterobicycle **5c** is detected at δ = 6 ppm.

The ^{13}C NMR spectroscopic data indicate effects in the structures of **5a–5c**, that vary the chemical shifts of the azomethine group so distinctly. To obtain more structural information an X-ray crystallographic study of the three boronates **5a–5c** was undertaken (Tables 3–6). Crystal data, atomic coordinates, anisotropic thermal parameters, bond angles and distances, and torsion angles have been deposited.[3] The molecular structures of **5a–5c** are shown in Figs. 3–5.

Table 3 shows that the asymmetric unit of **5a** contains two independent molecules.[4] The structures are not significantly different with respect to bond lengths and bond angles, but

[3] Supplementary material may be purchased from: The Depository of Unpublished Data, Document Delivery, CISTI, National Research Council of Canada, Ottawa, Canada, K1A 0S2. With the exception of anisotropic thermal parameters and torsion angles, these have also been deposited with the Cambridge Crystallographic Data Centre and can be obtained on request from: The Director, Cambridge Crystallographic Data Centre, University Chemical Laboratory, 12 Union Road, Cambridge, CB2 1EZ, U.K.

[4] The independency has been confirmed on basis of the correlation coefficients, which do not indicate a systematic correlation between the two molecules.

© 1998 NRC Canada

Fig. 3. Molecular structure of compound **5a**. The thermal ellipsoid probability level is 25%.

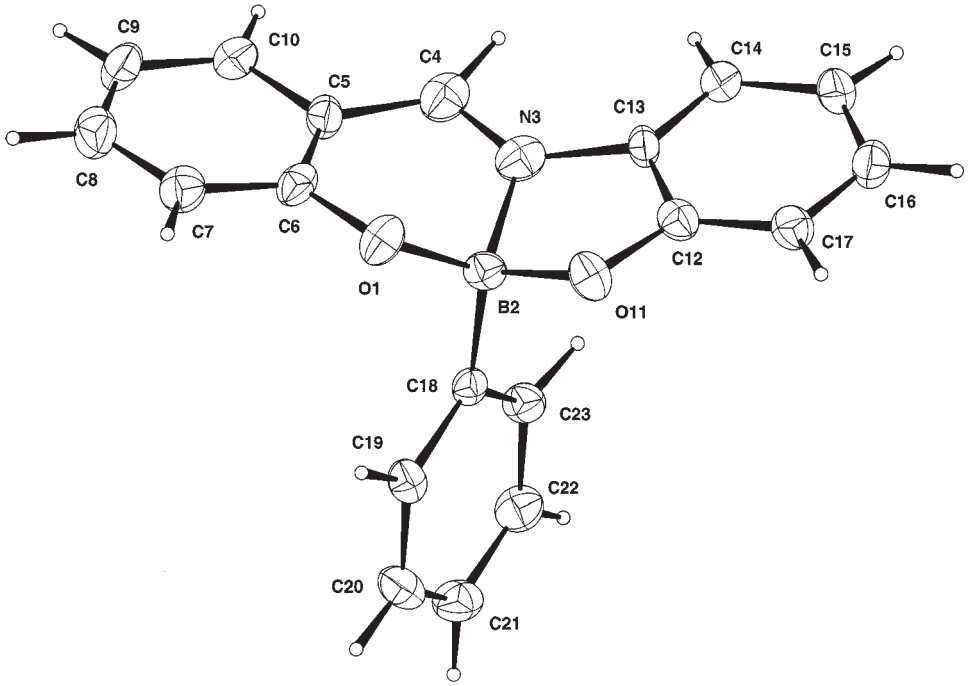

Table 4. Selected bond lengths and bond angles of compounds **5a**–**5c**.

	5a[a]	**5b**	**5c**
Bond lengths (Å)			
O(1)—B(2)	1.459 (5)	1.472 (7)	1.480 (4)
O(1)—C(6)	1.371 (4)	1.402 (6)	1.331 (3)
B(2)—N(3)	1.613 (5)	1.615 (7)	1.635 (4)
B(2)—O(11)	1.503 (5)	1.435 (6)	1.416 (3)
B(2)—C(18)	1.607 (5)	1.602 (7)	1.609 (4)
N(3)—C(4)	1.249 (4)	1.235 (6)	1.292 (3)
N(3)—C(13,14,15)	1.445 (4)	1.473 (6)	1.433 (3)
O(11)—C(12)	1.365 (4)	1.404 (7)	1.420 (4)
C(12)—C(13)	1.414 (4)	1.474 (8)	1.519 (5)
C(13)—C(14)	—	1.396 (7)	1.496 (4)
C(14)—C(15)	—	—	1.377 (4)
Bond angles (°)			
O(1)-B(2)-N(3)	108.1 (3)	109.6 (4)	103.7 (2)
O(1)-B(2)-O(11)	111.3 (3)	105.2 (4)	112.3 (2)
B(2)-N(3)-C(4)	120.5 (4)	122.3 (5)	117.9 (2)
B(2)-N(3)-C(13,14,15)	107.9 (3)	116.7 (4)	121.0 (2)
B(2)-O(1)-C(6)	114.3 (3)	119.1 (4)	117.5 (2)
B(2)-O(11)-C(12)	109.2 (3)	118.7 (5)	122.1 (3)
N(3)-B(2) -O(11)	99.1 (3)	104.7 (4)	110.4 (2)
N(3)-C(4)-C(5)	118.5 (4)	122.2 (6)	120.8 (3)
N(3)-C(13)-C(12,13,14)	105.3 (3)	114.9 (5)	117.6 (3)
C(4)-N(3)-C(13,14,15)	131.4 (4)	121.0 (5)	121.0 (2)
C(4)-C(5)-C(6)	119.4 (3)	120.0 (5)	117.8 (3)
O(11)-C(12)-C(13)	114.8 (3)	111.8 (6)	114.4 (3)
C(12)-C(13)-C(14)	—	126.4 (6)	114.1 (3)
C(13)-C(14)-C(15)	—	—	119.8 (3)

[a]There are two independent molecules in the asymmetric unit, their mean values being indicated in this table.

Table 5. Deviations from the boronate mean plane for compounds **5a**–**5c**.

	5a[b]	**5b**[c]	**5c**[d]
Mean plane[a]	Δ (Å)	Δ (Å)	Δ (Å)
C(5)	0.001/0.013	0.014	0.001
C(6)	0.011/–0.017	0.000	–0.010
C(7)	–0.015/0.007	–0.013	0.010
C(8)	0.007/0.009	0.010	0.001
C(9)	0.005/–0.013	0.005	–0.011
C(10)	–0.009/0.002	–0.017	0.010
Deviations			
O(1)	–0.018/0.017	–0.087	0.026
B(2)	0.551/–0.487	0.284	–0.585
N(3)	–0.018/0.174	0.028	0.084
C(4)	–0.165/0.286	–0.057	0.206

[a]The mean plane is calculated for C(5) to C(10) and additionally for C(55) to C(60) in the case of **5a**.
[b]Equations of the planes: $-3.99642X - 16.62096Y + 2.31592Z = -3.807$; $-8.19089X - 0.86122Y + 10.97109Z = -7.409$.
[c]Equation of the plane: $-6.53926X + 6.24804Y - 5.74052Z = -1.148$.
[d]Equation of the plane: $-5.60300X + 6.35883Y - 6.37166Z = -2.668$.
X, Y, Z are orthogonal coordinates w.r.t. axes a, b, c^*; Δ is the deviation from the mean plane.

vary in the deviation of the boron atom from the boronate mean plane (Table 5) and the orientation of the B-phenyl ring. This differences are probably due to crystal packing effects.

The N→B bond lengths are 1.613 (5) Å for **5a**, 1.615 (7) Å for **5b**, and 1.635 (4) Å for **5c** (Table 4), somewhat longer than for the monomeric structures **3b** and **7** (Figs. 1 and 2), where a value of 1.601 Å has been determined for both molecules (12).

© 1998 NRC Canada

Fig. 4. Molecular structure of compound **5b**. The thermal ellipsoid probability level is 25%.

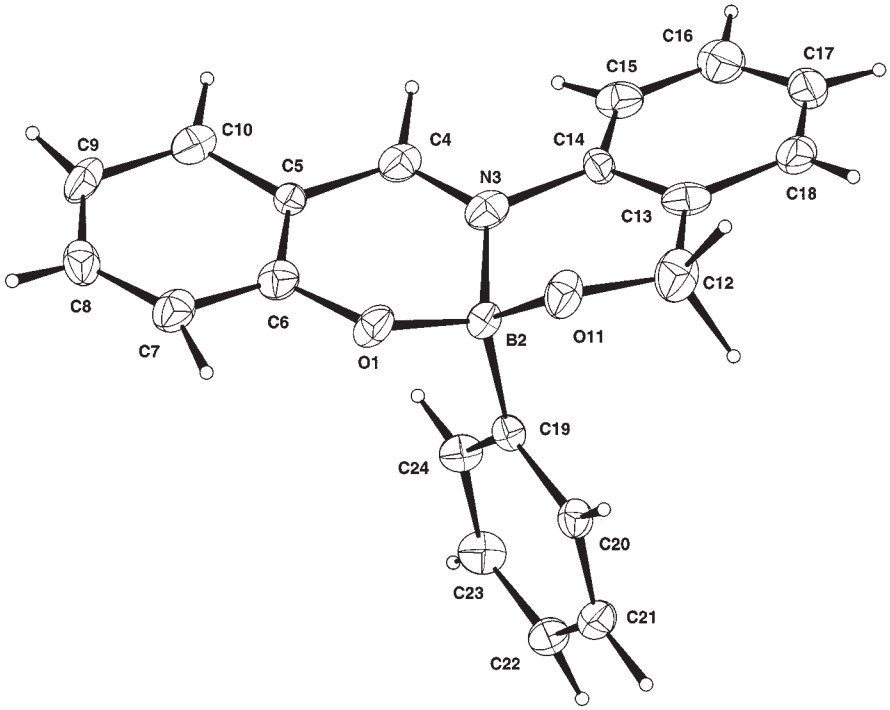

Fig. 5. Molecular structure of compound **5c**. The thermal ellipsoid probability level is 25%.

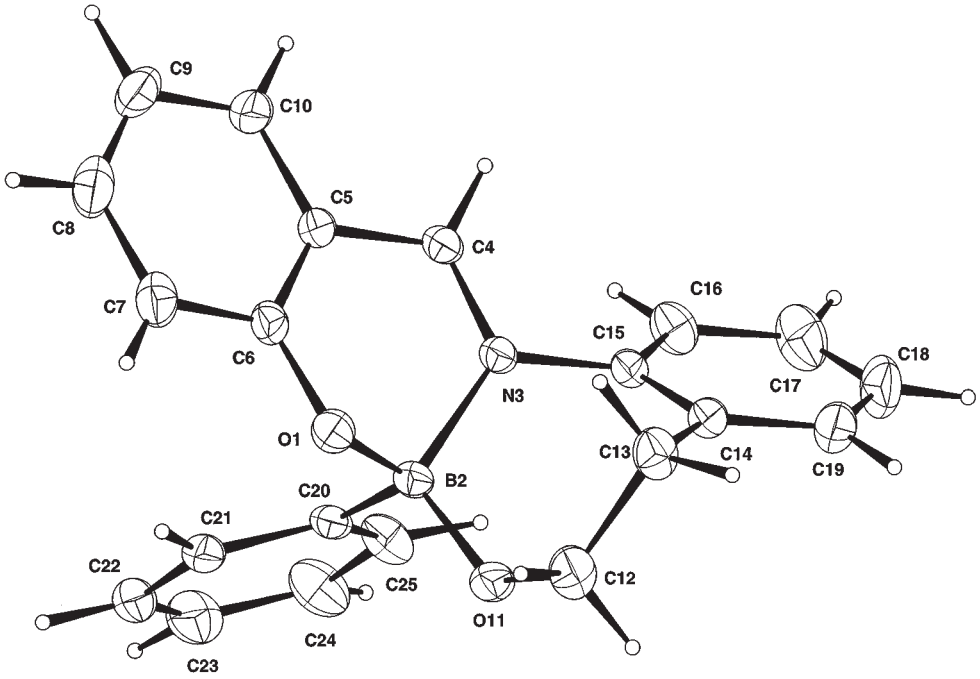

One of the interests of the crystallographic study was to investigate which one of the three heterobicycles is the most stable one. From molecular modeling it is expected that it is the [4.4.0]heterobicycle **5b**, but the N→B bond length seems to favor also the [4.3.0]heterobicycle **5a**. However, the deviation of the boron atom from the boronate mean plane (Table 5) is lowest for compound **5b** (Δ = 0.284 Å), while for **5a** and **5c** values of Δ = 0.520 and 0.585 Å are calculated. Additional evidence for the proposed relative stabilities of **5a–5c** is provided by the sum of bond lengths at the boron atom. This sum tends to be constant for a given set of bonded atoms (O_2NC) for **5a–5c**, and it has been shown that

© 1998 NRC Canada

Table 6. Selected torsion angles and sum of bond angles in the heterocycles for compounds **5a–5c**.

	5a	**5b**	**5c**
Torsion angles (°)[a]			
O(11)-B(2)-N(3)-C(13,14,15)	18.4	45.7	19.0
CPh-B(2)-N(3)-C(13,14,15)	–100.3	–79.1	–101.2
C(4)-N(3)-C(13)-C(14)	–16.2	–23.2[b]	–55.7[b]
Sum of bond angles in the heterocycles (°)			
Six-membered ring	702.0 = 6 × 117.0 (3)	713.9 = 6 × 119.0 (5)	698.7 = 6 × 116.5 (3)
Five-, six-, and seven-membered ring	536.2 = 5 × 107.2 (3)	693.2 = 6 × 115.5 (5)	819.4 = 7 × 117.1 (3)

[a]A positive rotation is counter-clockwise from atom 1 when viewed from atom 3 to atom 2.
[b]C(4)-N(3)-C(14)-C(15) in the case of **5b** and C(4)-N(3)-C(15)-C(16) in the case of **5c**.

Fig. 6. Correlation between the ^{13}C NMR chemical shift of the azomethine carbon atom and the CNCC torsion angle for compounds **5a**–**5c**.

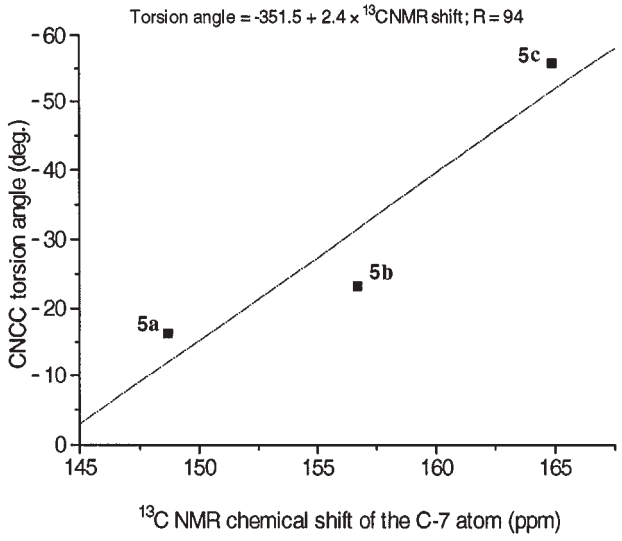

the strain at the boron center is related to the magnitude of this sum (25). The sums are 6.182, 6.124, and 6.140 Å for **5a–5c**, respectively.

The mean value of bond angles in the heterocycles (Table 6) can be added as further proof that the stability of the bicyclic boronates decreases in the following order: [4.4.0] >> [5.4.0], [4.3.0].

For **5b** mean values of 119.0(5) and 115.5(5)° for the six- and five-membered rings are calculated, while the corresponding values for **5a** are 117.0(3) and 107.2(3)° and for **5c** are 116.5(3) and 117.1(1)°. The ring strains of the three compounds are perhaps best expressed by the torsion angles summarized in Table 6. The ideal values for the O(11)-B(2)-N(3)-C(13, 14, 15) and C_{Ph}-B(2)-N(3)-C(13, 14, 15) dihedral angles are 60°, and it can be seen that both compounds **5a** and **5c** are far away from it. A zero degree value of the C(4)-N(3)-C(13)-C(14) torsion angle would correspond to a perfect π-delocalization between the two aromatic rings that are connected by the imino group. This dihedral angle is increasing from compound **5a** to **5c** (16.2 → 23.2 → 55.7°), so that the π-delocalization is strongest in **5a**, while it is practically lost in **5c** in favor of one gauche interaction less. This observation may be the explanation for the unusual high

Fig. 7. Twisted boat conformation of compound **5c**.

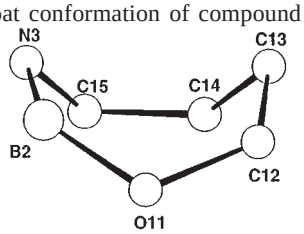

field shift of the azomethine signals in the ^{13}C NMR spectra of **5a** and **5b** and as can be seen from Fig. 6 there exists a correlation between the ^{13}C NMR shifts of C-7 and the corresponding torsion angles. It should be noted that the phenolic B(2)—O(11) bond in compound **5a** is significantly longer than the alkanolic B(2)—O(11) bond in compounds **5b** and **5c** (1.503 (5), 1.435 (6), and 1.416 (3) Å, respectively).

The N(3)—C(4) bond length is significantly shorter in **5a** and **5b** when compared to **5c** (1.249 (4), 1.235 (6), and 1.292 (3) Å, respectively). A longer bond length (1.297 (5) Å) has been reported also for the molecular structure of the diphenylboron chelate **8** (Fig. 2), where the phenol group is also twisted out of the mean plane (16).

The seven-membered heterocycle in the boronate **5c** presents a twisted boat conformation (26) with N(3) and C(13) above the plane (Fig. 7). In comparison to the [5.4.0]heterobicycle **9** (Fig. 2) with a planar B–O–B moiety the geometry is rather different (12). Nonetheless, the average values of the bond angles in the seven-membered ring are practically identical (117.1 (3) and 117.3 (3)° for **5c** and **9**, respectively). The same is true for the N→B bond lengths (1.635 (4) and 1.629 (5) Å for **5c** and **9**, respectively). But, the deviation of the boron atom from the boronate mean plane is lower in **5c** (0.585 for **5c** ↔ 0.714 Å for **9**). The resonances in the ^{11}B NMR spectra are identical for both compounds (δ = 6 ppm).

Conclusions

From the present study it can be concluded that the tridentate azomethine ligand **4a** does not lead to the formation of a macrocyclic structure, although the monomeric species **5a** is highly strained. There exist various possible explanations for this observation. From molecular modeling it can be seen that one may be the loss of coplanarity between the two aromatic systems and the imino group upon

© 1998 NRC Canada

dimer formation, and another explanation may be the introduction of additional strain in a dimeric structure due to the planarity of the 2-aminophenoxy group. It has also to be considered that **4a** is a planar ligand that favors the formation of a monomeric structure.

The comparative study of **5a–5c** has shown that in the present case the boronates with a [4.4.0] heterobicyclic structure are less strained than the corresponding [4.3.0] and [5.4.0] heterobicycles. The conjugation between the two aromatic rings and the imino group is lost, when the number of members in the second heterocyclic ring is increased. The loss of conjugation can be detected by the ^{13}C NMR chemical shifts of the carbon atoms that are in correlation with the corresponding CNCC torsion angles.

Acknowledgments

We thank Prof. Dr. H. Nöth for helpful discussions. Ing. Guillermo Uribe and Q.I. Victor Gonzalez are thanked for NMR spectra. N.F. thanks CONACYT and H.H. UAEM (Universidad Autónoma del Estado de Morelos) for financial support.

References

1. H. Höpfl, N. Farfán, D. Castillo, R. Santillan, R. Contreras, F. Martínez-Martínez, M. Galván, R. Alvarez, L. Fernández, S. Halut, and J.-C. Daran. J. Organomet. Chem. **544**, 175 (1997).
2. H. Höpfl, M. Galván, N. Farfán, and R. Santillan. J. Mol. Struct. (THEOCHEM), **427**, 1 (1998).
3. N. Farfán, D. Castillo, P. Joseph-Nathan, R. Contreras, and L.v. Szentpály. J. Chem. Soc. Perkin Trans. 2, 527 (1992).
4. N. Farfán and R. Contreras. Nouv. J. Chim. **6**, 269 (1982).
5. N. Farfán and R. Contreras. J. Chem. Soc. Perkin Trans. 2, 1787 (1988).
6. T. Mancilla, H. Höpfl, G. Bravo, and L. Carrillo. Main Group Met. Chem. **20**, 31 (1997).
7. N. Farfán and R. Contreras. Heterocycles, **23**, 2989 (1985).
8. N. Farfán, T. Mancilla, D. Castillo, G. Uribe, L. Carillo, P. Joseph-Nathan, and R. Contreras. J. Organomet. Chem. **381**, 1 (1990).
9. N. Farfán, P. Joseph-Nathan, L.M. Chiquete, and R. Contreras. J. Organomet. Chem. **348**, 149 (1988).
10. N. Farfán, D. Silva, and R. Santillan. Heteroatom Chem. **4**, 533 (1993).
11. H. Höpfl and N. Farfán. J. Organomet. Chem. **547**, 71 (1997).
12. H. Höpfl, M. Sánchez, V. Barba, N. Farfán, S. Rojas, and R. Santillan. Inorg. Chem. **37**, 1679 (1998).
13. E. Haegele. Ber. Dtsch. Chem. Ges. **25**, 2753 (1892).
14. E. Haegele. Ber. Dtsch. Chem. Ges. **26**, 394 (1893).
15. S.M. Tripathi and J.P. Tandon. J. Prakt. Chem. **320**, 685 (1978).
16. R. Allmann, E. Hohaus, and S. Olejnik. Z. Naturforsch. B: Anorg. Chem. Org. Chem. **37B**, 1450 (1982).
17. E. Hohaus. Z. Anorg. Allg. Chem. **506**, 185 (1983).
18. E. Hohaus, W. Riepe, and H.F. Gruetzmacher. Org. Mass Spectrom. **18**, 359 (1983).
19. E. Hohaus and W. Riepe. Z. Naturforsch. B: Anorg. Chem. Org. Chem. **28B**, 440 (1973).
20. E. Hohaus, K.D. Klöppel, B. Paschold, and H.R. Schulten. Z. Anorg. Allg. Chem. **493**, 41 (1982).
21. E. Hohaus and W. Riepe. Z. Naturforsch. B: Anorg. Chem. Org. Chem. **29B**, 663 (1974).
22. E. Hohaus. Monatsh. Chem. **111**, 863 (1980).
23. H.B. Singh and J.P. Tandon. J. Indian Chem. Soc. **56**, 768 (1979).
24. H. Nöth and B. Wrackmeyer. *In* NMR-basic principles and progress. Vol. 14. *Edited by* P. Diehl, E. Fluck, and R. Kosfeld. Springer Verlag, Berlin. 1978.
25. H. Amt, W. Kliegel, S.J. Rettig, and J. Trotter. Can. J. Chem. **66**, 1117 (1988).
26. D.F. Bocian, H.M. Pickett, T.C. Rounds, and H.L. Strauss. J. Am. Chem. Soc. **97**, 687 (1974).

© 1998 NRC Canada

Surface studies of nano-dimensional particle size iron–manganese spinel mixed oxides

Ellie L. Uzunova, Dimitar G. Klissurski, and Stella D. Nemska

Abstract: Monophase binary iron–manganese spinel oxides of high dispersity are prepared by thermal decomposition of carbonate precursors in the limits $0.33 \leq Fe/Mn \leq 2$, at temperatures 570–770 K. Interparticle *meso*- and macropores contribute to the surface morphology of the spinel oxides, composed from spherical-shaped particles with diameters in the range 7–12 nm. The cation distribution of manganese ferrite corresponds to $Mn_{0.85}Fe_{0.15}[Mn_{0.14}Fe_{1.86}]O_{4+\delta}$. Surface analysis by ESCA reveals high concentration of nonstoichiometric oxygen and presence of Mn(III) and Mn(IV) is indicated in the X-ray photoelectron spectra. Reduction with hydrogen proceeds in two steps and is shifted to higher temperatures with increasing the iron content.

Key words: ferrite, spinel, Fe, Mn.

Résumé : Les oxydes binaires monophases de Fe et Mn de type spinel avec une dispersion très haute sont preparés par une décomposition thermique des carbonates comme précurseurs dans les limites des rapports $0.33 \leq Fe/Mn \leq 2$ à température 570–770 K. La morphologie des oxydes est formeé, par des particules sphériques au diamètre 7–12 nm et des *meso*- et macro-pores interparticulaires. La distribution des cations correspond à la formule $Mn_{0.85}Fe_{0.15}[Mn_{0.14}Fe_{1.86}]O_{4+\delta}$. Une haute concentration d'oxygène non-stoichiométrique à la surface a été etablie par ESCA. Les spectres XPS indiquent aussi une présence de Mn(III) et Mn(IV). La réduction par l'hydrogène est effectuée en deux étapes et exige une plus haute température avec l'augmentation du contenu du fer.

Mots clés : ferrite, spinel, Fe, Mn.

Introduction

Spinel oxides, containing manganese and iron, are interesting as magnetic materials and are also acknowledged for their catalytic properties. Binary spinel oxides, containing transition metal cations in higher oxidation state, are very active combustion catalysts for CO and hydrocarbons (1–3). Catalysts in the Fischer–Tropsch synthesis are developed on the basis of different iron–manganese oxide compositions (4). For all these applications, low particle dimensions of the oxide phase is essential, and it is usually achieved by the "soft chemistry" synthesis methods in the low-temperature range of thermal decomposition and the choice of an appropriate precursor compound, containing all metal cations in a single crystalline phase (5–11). The precursor route may direct the synthesis towards particular chemical architecture (11). Nitrate salt decomposition favours higher oxidation states of the metal cations in the final product, due to the oxidative media, created during the thermolysis (5). Oxalates form mixed crystals with a number of transition metal cations and are often employed as precursors, but their thermal decomposition should be performed with care to avoid reduction (6). Transition-metal binary oxides and particularly those, containing manganese, exist in a broad range of structure types, depending on the composition and the oxidation state of the cations. Their reactivity in oxidation reactions is governed by the particular forms of adsorbed oxygen and the surface oxygen concentration. Cation-deficient oxides of high-dispersity and with Lewis-base properties are generally obtained by the thermal decomposition of basic carbonates (8, 9).

The present study reports on the structure and morphology of high-dispersity iron–manganese binary spinel oxides. The relation between surface composition, metal cation oxidation states, and oxidation reactivity is discussed.

Received January 22, 1998.

E.L. Uzunova,[1] D.G. Klissurski,[1] and S.D. Nemska. Institute of General and Inorganic Chemistry, Bulgarian Academy of Sciences, Sofia 1113, Bulgaria.

[1]Author to whom correspondence may be addressed. Telephone: +(359 2) 9793592. Fax: +(359 2) 705024. E-mail: BANCHEM@BGEARN.BITNET; inorg_ic@bgcict.acad.bg

Experimental

The iron–manganese spinel oxides were synthesised by thermal decomposition of calcite-like carbonate precursors at temperatures in the range 570–870 K. The carbonates were coprecipitated from a solution of Fe(II) and Mn(II) chlorides, taken in a desired molar ratio and total Me(II) concentration 0.6 mol/dm^3 with a sodium carbonate solution at pH 9. The iron and manganese content was determined by X-ray fluorescence analysis. The XRD analysis was performed on a diffractometer with CuK_α monochromatized radiation. Moessbauer spectra were recorded in constant acceleration mode at room temperature. The source used was a ^{57}Co/(Cr matrix), and the isomer shifts were referred to α-Fe. Full-sorption nitrogen isotherms at 77 K were re-

© 1998 NRC Canada

Table 1. Unit cell parameters and chemical composition of iron–manganese spinel oxides.

Sample code	Chemical formulae	Unit cell parameters (Å)	
MF31	$Mn_{2.25}Fe_{0.75}O_4$	a = 5.76	c = 9.35
MF21	$Mn_{2.05}Fe_{0.95}O_4$	a = 5.75	c = 9.32
MF11	$Mn_{1.51}Fe_{1.49}O_4$	a = 8.475	
MF12	$Mn_{0.99}Fe_{2.01}O_4$	a = 8.440	

Table 2. Moessbauer parameters of manganese ferrite.

Isomeric shift (mm/s)		Hyperfine magnetic field, H_{eff} (kOe)	
δ(A)	δ(B)	A	B
0.32	0.43	523	486

corded on a Omnisorp 100 equipment in a continuous flow regime. Particle dimensions were determined by transmission electron microscopy. X-ray photoelectron spectra (XPS) were registered on a ESCALAB MkII spectrometer with AlK_α radiation (1486.6 eV). Temperature-programmed reduction with hydrogen (TPR) was performed in a flow system with 5% H_2 in helium at flow rate 40 mL/min and heating rate 20 K/min.

Results and discussion

Structure and cation distribution

The samples with Fe/Mn ratios in the range $0.33 \leq Fe/Mn \leq 2$, decomposed at 670 K are with spinel structure, the first two being tetragonal (Table 1). The slight decrease of unit-cell parameters for samples with higher Fe/Mn ratio is consistent with the hypothesis of Mn(III)–Fe(III) substitution on octahedral sites. Comparison of the effective high-spin octahedral ionic radii (Mn^{3+} = 0.645 Å, Fe^{3+} = 0.645 Å) (12) does not support directly this statement; however, in iron-rich samples the cooperative effect of Jahn–Teller Mn^{3+}–$[O^{2-}]_6$ local distortions is diminished, leading to a regular cubic spinel structure and smaller unit-cell size (8, 9). At temperatures above 770 K, the spinel oxides undergo phase segregation to the individual oxides: manganese oxides (MnO and Mn_2O_3) from the manganese rich spinels and α-Fe_2O_3 from the spinels with Fe/Mn > 2. Manganese ferrite is of relatively higher thermal stability and remains as a single phase spinel up to 870 K. A stable manganese ferrite phase is obtained also at temperatures above 1300 K, while in the temperature range 870–1200 K a mixture of spinel and α-phase exist.

The Moessbauer spectra of samples, synthesised at 670 K contain a central doublet, resulting from small particle superparamagnetism. This effect may be produced also by the presence of tetrahedral site cation vacancies (8).The doublet remains even at sintering temperatures of 870 K, except in the case of manganese ferrite, where a typical sextet is registered (Fig. 1). The spectrum was computer fitted, assuming two components that are due to iron cations on tetrahedral (A) and octahedral (B) positions in the spinel structure (13). The Moessbauer parameters are presented in Table 2. The isomer shifts of the components correspond to iron(III) cations in cubic spinels, with zero quadrupole splittings. The cation distribution, deduced from the ratio of the areas of the two components and based on chemical analysis data can be written as $Mn_{0.85}Fe_{0.15}[Mn_{0.14}Fe_{1.86}]O_{4+\delta}$. This formula composition is consistent with the low affinity of Mn(II) and the preference of Mn(III) for octahedral coordination, evidenced by the value of the crystal field stabilization energy (14). The effective hyperfine magnetic field at Fe^{57} in both tetrahedral and octahedral sites is stronger, compared to the one reported by Sawatsky et al. (13) for high-temperature syntheses. We have observed a similar effect with cobalt ferrite, where the samples, synthesised at low temperature (670 K) possess higher internal magnetic field (15). This result indicates, that the presence of cation vacancies (8, 9) is rather a surface phenomenon and does not interfere with the A–A, B–B and A–B iron cation interactions.

Fig. 1. Moessbauer spectrum of manganese ferrite, synthesized at 870 K.

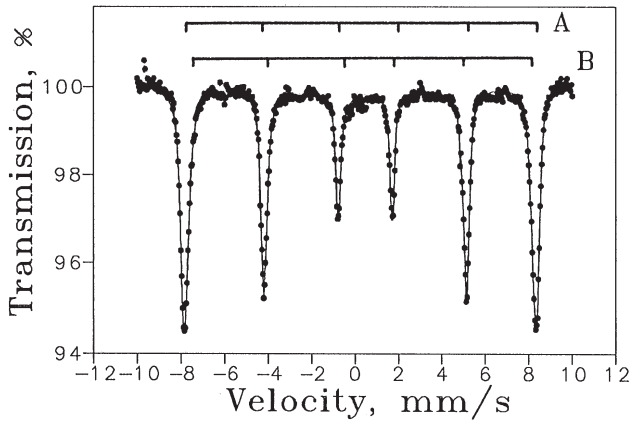

Morphology and pore distribution study

The full-sorption isotherms of all samples suggest presence of *meso*- and macropores (16). While the major contribution in pore volume for samples MF31 and MF21 comes from pores of radii 100–300 Å, the iron-rich samples contain predominantly smaller pores of radii 20–40 Å (Table 3). For all samples, the pore distribution is rather broad, and there is a significant part of macropores of radii above 250 Å. The particles are of spherical shape, and their effective diameters are within 70–120 Å, measured by TEM. Surface area increases with the Fe/Mn ratio due to both the smaller particle size of the ferrite samples and to the more developed mesopore structure.

Surface analysis

The electron binding energies are summarized in Table 4 and compared to reference measurements, reported for similar oxides. The peak position of Mn $2p_{3/2}$ is shifted towards higher binding energy, and the peak maxima correspond to a value within the range for MnO_2 and Mn_2O_3, rather than MnO (17). The Fe $2p_{3/2}$ and O1*s* peak maxima are in agreement with the values, reported earlier for ferrites (15, 17). Considerable broadening is observed for Mn $2p_{3/2}$ and Fe $2p_{3/2}$, but all peaks are symmetric in shape, Fig. 2.

© 1998 NRC Canada

Table 3. Pore size distribution and specific surface areas of Fe–Mn spinel oxides.

Sample	BET surface area (m^2/g)	Pore volume (cc/g) at radii (Å)								
		10–20	20–30	30–40	40–50	50–100	100–200	200–300	>300	Total
MF31	44	<0.01	0.01	<0.01	<0.01	<0.01	0.01	0.02	0.03	0.10
MF21	67	0.01	<0.01	<0.01	<0.01	0.03	0.13	0.08	0.06	0.33
MF11	124	0.01	0.05	0.13	0.09	0.06	0.08	0.06	0.08	0.56
MF12	135	0.03	0.09	0.08	0.04	0.05	0.06	0.04	0.04	0.43

Table 4. Electron binding energies for iron–manganese spinel oxides (eV).

Sample	Mn $2p_{3/2}$	FWHM[b]	Fe $2p_{3/2}$	FWHM[b]	O1*s*	FWHM[b]
MF31	642.0	3.8	710.5	3.9	530.2	2.2
MF21	642.8	3.9	711.3	3.8	530.6	1.9
MF11	642.5	3.8	711.4	3.7	530.4	2.0
MF12	642.7	3.8	711.0	3.9	530.3	1.8
MnO	640.9[a]					
Mn_3O_4	641.7[a]					
Mn_2O_3	641.8[a]					
MnO_2	642.4[a]					
	(643.1)[c]					

[a]Reference 17.
[b]Full width at half maximum.
[c]This study.

Fig. 2. The Mn $2p_{3/2}$, Fe $2p_{3/2}$, and O1*s* spectra of iron–manganese spinel oxides, synthesized at 670 K.

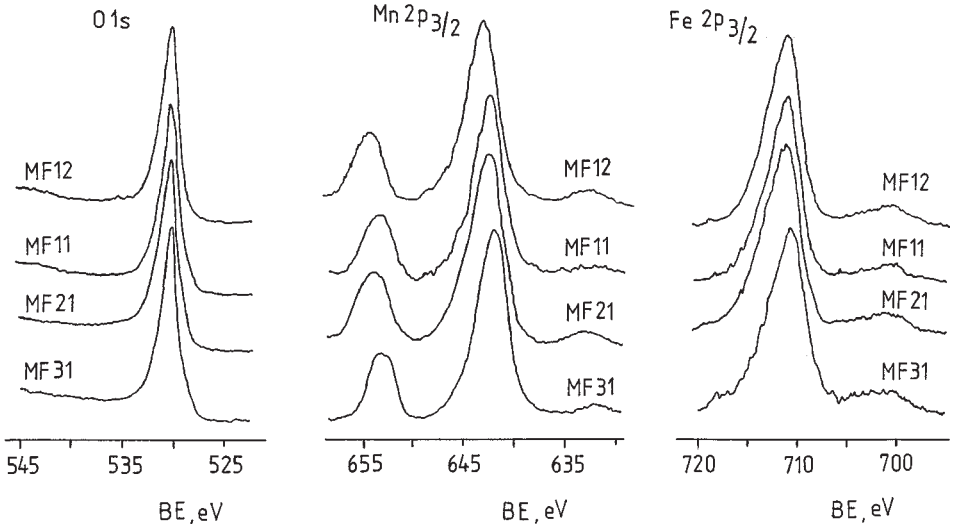

The oxygen-to-metal cation ratio on the surface slightly increases with the iron bulk concentration, Fig. 3. The non-stoichiometric surface oxygen exceeds the quantity expected for spinel oxides M_3O_4, where both divalent and trivalent cations take place in the structure; sesquioxides M_2O_3, where all cations are in the trivalent state; and even the oxygen content for $M(IV)O_2$. The very high oxygen-to-metal cation ratio on the surface, together with the shift to higher binding energies in the Mn $2p_{3/2}$ spectra can be interpreted by suggesting presence of manganese in a higher oxidation state: Mn(III) and Mn(IV). The surface cation distribution in terms of iron/manganese ratio corresponds to the bulk stoichiometry in the range $0.33 \leq Fe/Mn \leq 1$, Fig. 4. Iron-dominated compositions MF12 and MF13 possess manganese-enriched surface, suggesting that the occurrence of surface cation vacancies is mainly on behalf of the Fe(III) cations.

Temperature-programmed reduction

Two peaks are registered in the TPR spectra of iron–manganese spinel oxides, Fig. 5. The first one does not change significantly with sample composition and corresponds to reduction of nonstoichiometric surface oxygen. The second peak covers a broad temperature range and shifts to higher temperature for the iron-rich samples, $Fe/Mn \geq 1$. The trivalent cations of manganese and iron are less stable and are easily reduced to the divalent oxidation state, followed by the reduction steps Fe(II) → Fe and Mn(II) → Mn. These processes give rise to a single broad peak in the TPR pat-

© 1998 NRC Canada

Fig. 3. Oxygen to metal cation surface ratio as a function of bulk iron/manganese ratio.

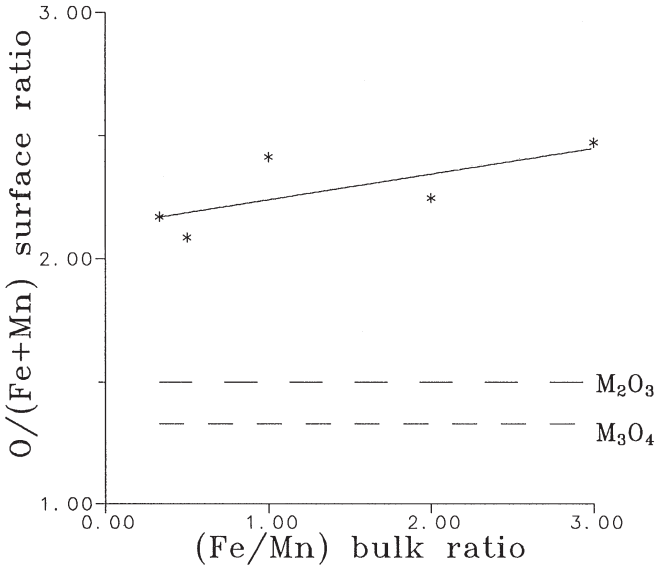

Fig. 4. Surface iron/manganese ratio as a function of the bulk one.

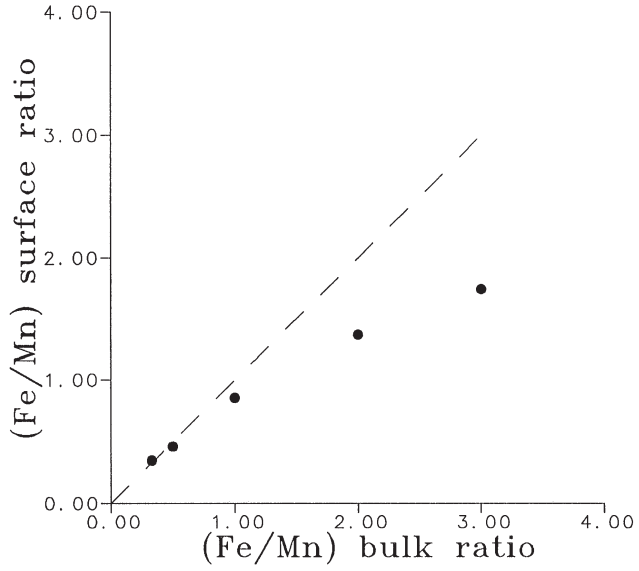

terns, and the individual steps cannot be distinguished. The resistance of manganese ferrite towards reduction is governed by two factors: the higher thermal stability of the ferrite spinel phase and the fact that reduction of divalent manganese is energetically least favoured.

Conclusions

The high-dispersity spinel iron–manganese oxides, synthesized from carbonate precursors, contain a large excess of surface oxygen, related to surface cation deficiency and presence of manganese cations in a higher oxidation state: Mn(III) and Mn(IV). Reduction with hydrogen proceeds in two steps and very high temperature is needed for the complete reduction of iron-rich compositions.

Fig. 5. Temperature programmed reduction of iron–manganese spinel oxides, synthesized at 670 K; (*a*) MF31; (*b*) MF21; (*c*) MF11; (*d*) MF12.

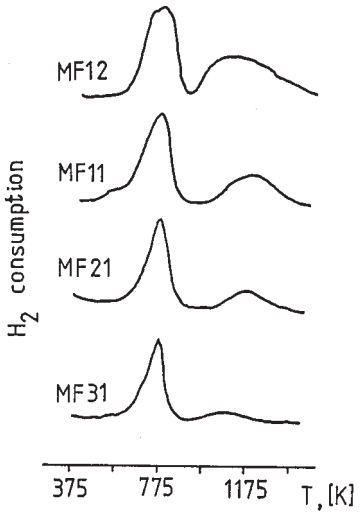

Acknowledgements

The authors thank for financial support the Bulgarian National Science Fund at the Ministry Of Science and Education under contract X-628.

References

1. G. Golodetz. Heterogeneous catalytic reactions involving molecular oxygen. *In* Studies in surface science and catalysis. Vol. 15. Elsevier, Amsterdam. 1983.
2. K. Papadatos and K.A. Shelstad. J. Catalysis, **28**, 116 (1973).
3. D.G. Klissurski, E.L. Uzunova, and K. Yankova. Appl. Catal. A: General, **95**, 103 (1993).
4. G. Maiti, R. Malessa, U. Loechner, H. Papp, and M. Baerns. Appl. Catal. **16**, 215 (1985).
5. D.G. Klissurski and E.L. Uzunova. J. Mater. Sci. **29**, 285 (1994).
6. B. Gillot, F. Jemmali, and A. Rousset. J. Solid State Chem. **50**, 138 (1983).
7. R. Rojas, E. Vila, O. Garcia-Martinez, and J. Martin de Vidales. J. Mater. Chem. **4**, 1635 (1994).
8. J. Jimenez-Mateos, W. Jones, J. Morales, and J. Tirado. J. Solid State Chem. **93**, 443 (1991).
9. E. Uzunova, I. Mitov, and D.Klissurski. J. Mater. Chem., **6,** 1035 (1996).
10. T. Baird, K. Campbell, P. Holliman, R. Hoyle, D. Stirling, and B. Williams. J. Chem. Soc. Faraday Trans. **91**, 3219 (1995).
11. F. Cavani, F. Trifiro, and A. Vaccari. Catal. Today, **11**, 173 (1991).
12. R. Shannon. Acta Crystallogr. Sect. A, **32**, 751 (1976).
13. G. Sawatzky, F. van der Woude, and A. Morrish. Phys. Rev. **187**, 747 (1969).
14. A. Wells. *In* Structural inorganic chemistry. 5th ed. Clarendon Press, Oxford. 1986. Chap. 13.
15. E. Uzunova, I. Mitov, and D. Klissurski. Bull. Chem. Soc. Jpn. **70**, 1985 (1997).
16. S. Gregg and K. Sing. *In* Adsorption, surface area and porosity. 2nd ed. Academic Press, New York. 1982.
17. G. Allen, S. Harris, J. Jutson and J. Dyke. Appl. Surf. Sci. **37**, 111 (1989).

© 1998 NRC Canada

Spectroscopic and differential scanning calorimetric studies of the phase transitions in oxanorbornane

Ralph M. Paroli, Denis F.R. Gilson, and Ian S. Butler

Abstract: Oxanorbornane (7-oxabicyclo[2.2.1]heptane, $C_6H_{10}O$) resembles other bicycloheptane-like molecules by exhibiting order–disorder transitions in the solid state. Differential scanning calorimetric studies show that five different phases may occur, with hysteresis in the transition temperatures. The vibrational spectra have been examined, and a factor group analysis of the vibrational splittings indicates that the crystal structure of the ordered phase has D_{2d} symmetry. Activation energies for molecular motions were derived from proton spin-lattice relaxation time measurements.

Key words: oxanorbornane, order–disorder, phase transitions.

Résumé : L'oxanorbornane (7-oxabicyclo[2.2.1]heptane, $C_6H_{10}O$) ressemble à d'autres molécules de type bicycloheptane qui présentent des transitions ordre–désordre dans l'état solide. Des études de calorimétrie à balayage différenciel montrent qu'il peut se produire cinq phases différentes avec une hystérèse dans les températures de transition. On a étudié les spectres de vibration et une analyse factorielle de groupe des dédoublements des vibrations indique que la structure cristalline de la phase ordonnée possède une symétrie D_{2d}. On a déterminé les énergies d'activation des mouvements moléculaires à partir de mesures de temps de relaxation spin-réseau du proton.

Mots clés : oxanorbornane, ordre–désordre, transitions de phase.

[Traduit par la Rédaction]

Introduction

The bicyclo[2.2.1]heptane series of rigid hydrocarbons is well known to have order–disorder phase transitions in the solid state (1, 2). These materials are characterized by low entropies of melting and extensive molecular motions in the disordered phase. An interesting difference between this series and other disordered materials is that the high-temperature phases tend to be hexagonal-close-packed structures instead of the more usual face-centered-cubic (3). Norbornane has a second transition, with very low entropy, from the hcp to fcc structure. Oxanorbornane (7-oxabicyclo-[2.2.1]heptane, $C_6H_{10}O$) has a similar molecular structure except that the bridging methylene group is replaced by an oxygen atom, resulting in a larger dipole moment, and the possibility that disordered phases exist for this compound seemed worth exploring.

The structures of the ordered phases at low temperature are seldom known, but information can be obtained from the splittings that occur in the vibrational spectra as a result of the change in site or factor group symmetries, and we have investigated the transitions for norbornane, norbornene, norbornadiene, and quadricyclane by examining the effects of both temperature and pressure on their vibrational spectra (4–8). We report here on the differential scanning calorimetry, the temperature dependence of the infrared and Raman spectra, and the proton spin-lattice relaxation times of oxanorbornane.

Received September 23, 1998.

R.M. Paroli, D.F.R. Gilson,[1] and I.S. Butler.[1] Department of Chemistry, McGill University, 801 Sherbrooke St. West, Montreal, PQ H3A 2K6, Canada.

[1]Authors to whom correspondence may be addressed. Telephone: (514) 398–6908. Fax: (514) 398–3797. E-mail: gilson@omc.lan.mcgill.ca; butler@omc.lan.mcgill.ca

Experimental

Oxanorbornane was obtained from Aldrich Chemical Co. and was purified by double distillation over calcium hydride. The DSC experiments were performed on a Perkin–Elmer DSC-7 calorimeter calibrated for both temperature and enthalpy scales using the melting and phase transitions of cyclohexane. Samples were scanned at 5 K min^{-1}. Infrared spectra were measured using an Analect AQS-18 spectrometer equipped with a KBr beam splitter and triglycine (TGS) detector. The temperature was varied using an evacuated cryostat cooled with liquid nitrogen and controlled with heaters attached to the liquid sample cell holder. Raman spectra were obtained using an Instruments S.A. spectrometer with a Jobin–Yvon U-1000, 1.0 m double monochromator. The 514.5 nm line of a Spectra-Physics model 164 argon-ion laser was used for excitation with a laser power of 100 mW at the sample. The sample was contained in a glass capillary tube attached with indium foil to the cold finger of a Cryodyne Model 21 Cryocooler. The resolution was 4 cm^{-1} for infrared spectra and between 1 and 3 cm^{-1} for the Raman spectra.

© 1998 NRC Canada

Fig. 1. (*a*) The DSC thermograms during repeated scanning at 20 K min^{-1}; (*b*) thermograms after cycling.

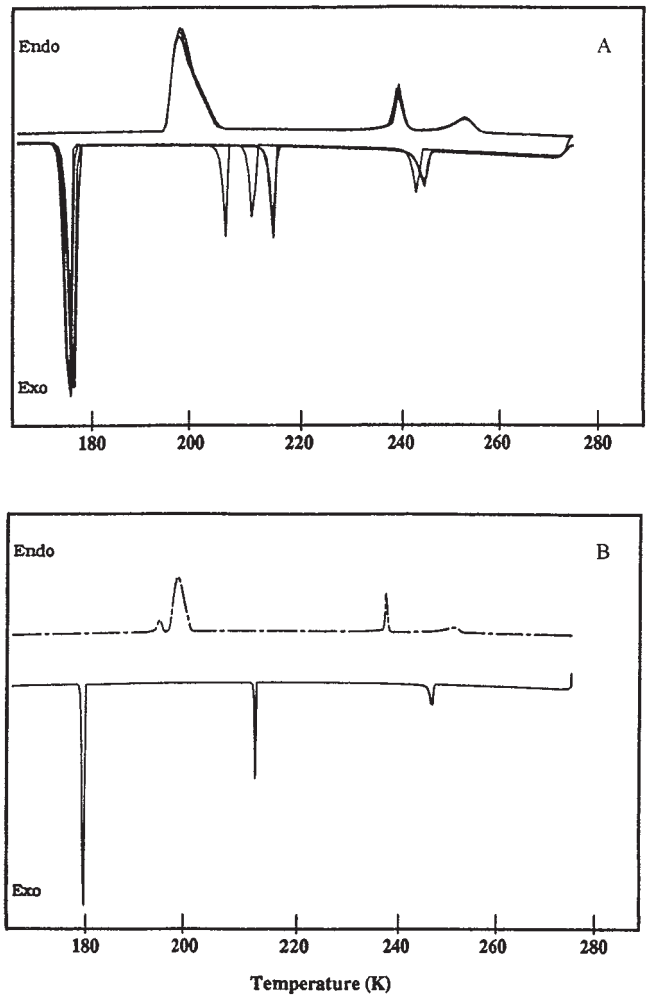

Proton spin-lattice relaxation times were measured by the inversion recovery method using a SpinLock CPS2 spectrometer at a resonance frequency of 33 MHz. Delays between measurements were at least $5T_1$. The temperature was controlled by a stream of cold nitrogen gas and measured with a copper-constantan thermocouple.

Results and discussion

DSC results

No exotherms on heating were observed, and so no glassy states were formed. On first cooling, the melting transition was observed at 244 K, followed by two other transitions at 206 and 170 K. On heating, the transition temperatures occurred at 191 and 231 K and melting at 243 K. Thus there is considerable hysteresis associated with the two solid-state transitions. The major transition was much broader on heating than on cooling. Additional DSC experiments were performed in which the sample was repeatedly scanned, Fig. 1(*a*), at a much faster rate of 20 K min^{-1}. Remarkably, the three transitions showed little change in transition temperature for the heating direction, but on cooling the higher temperature transition fluctuated for the first four cycles and then remained unchanged. A single scan, at 5 K min^{-1}, performed after the cycling procedure, showed that the lower temperature transition, which previously was rather broad, now consisted of two sharp transitions, Fig 1(*b*). Thus five possible different phases exist.

The entropies are given in Table 1, where they are compared with other members of the bicyloheptyl series. The entropy of fusion of oxanorbornane is very low, the lowest of this series of molecules, and typical of materials that melt from a disordered phase. Oxanorbornane resembles norbornane in that a low entropy transition occurred between the major transition and the melting point but the transition entropy of 4.53 J K^{-1} mol^{-1} was much higher than that of norbornane (0.3 J K^{-1} mol^{-1}), indicating that this phase might be partially ordered in oxanorbornane. The sum of the two solid-phase transitions for these two compounds is about the same but much lower than the entropies for the single transition in norbornadiene and quadricyclane. The transition in norbornylene is not directly comparable, since the symmetry of the molecule is lower. The hysteresis observed for these order–disorder transitions is attributable to lattice strain arising from the difficulty of nucleating the new crystal structure within the old. This is often associated with a large volume difference between the phases, which, in turn, can make a significant contribution to the entropy of transition (9).

Vibrational spectra

The vibrational spectra at different temperatures are shown in Figs. 2 and 3 and the frequencies listed in Table 2. The spectra of the liquid and disordered phases were very similar, and the Raman spectrum of the lattice region showed only a broadened Rayleigh line. This is the typical behaviour of disordered solid phases. In the intermediate phase, four lattice modes were observed, which confirms the DSC result that this phase is at least partly crystalline, and in the low-temperature phase there were seven lattice modes. The most pronounced changes occurred in the C–H stretching region of the Raman spectrum, where five broad peaks occurred in the disordered phase, increasing to 15 relatively sharp peaks at the first transition and then 21 sharp bands in the lowest temperature phase. Additional splittings were observed for other regions of the spectrum. For example, the peak at 888 cm^{-1} occurred as a broad singlet, which first sharpened and then split into a triplet as the temperature was decreased through the phase transitions. The peak at 938 cm^{-1} changed from a singlet at 240 K to a sharp doublet at 150 K. In the infrared spectrum, similar changes occurred for the C–H stretching modes, where four very broad bands with two shoulders at 240 K changed to 11 peaks and shoulders at 100 K. Many of the remaining peaks split into two components except for the peak at 1262 cm^{-1}, which split into four peaks on going from the intermediate to the low-temperature phase.

The point group symmetry of oxanorbornane is C_{2v}, and the representation of the 45 possible normal modes reduces to $G_{vib} = 13a_1 + 10a_2 + 12b_1 + 10b_2$. All modes are Raman active and the a_1, b_1, and b_2 modes are infrared active. There are numerous cases where the vibrations are coincident in both the infrared and Raman spectra, and therefore, the unit cell cannot be centrosymmetric. The site symmetry in the lattice must be equal or lower than the molecular symmetry, i.e., C_{2v}, C_2, C_s or C_1, and there are three different possible

© 1998 NRC Canada

Table 1. Transition temperatures and entropies of bicycloheptane series.

	Melting temperature[a]	Transition temperature[a]	ΔS^b (J K^{-1} mol^{-1})
Oxanorbornane			
First cycle		170/191	26.9
		206/231	4.5
	244		2.6
After cycling		— /189	2.9
		175/192	26.0
		213/234	5.5
	245		3.1
Norbornane[c]		129/130	31.6
		305/313	0.3
	360		12.7
Norbornylene[d]		114/127	35.8
	320		10.9
Norbornadiene[e]		175/201	41.6
	254		6.6
Quadricyclane[f]		153/180	42.5
	227		4.5

[a]In K, for the heating and cooling directions.
[b]Averaged for the heating and cooling directions.
[c]Reference 4.
[d]Reference 5.
[e]Reference 6.
[f]References 7 and 8.

Fig. 2. Raman spectra of oxanorbornane at different temperatures.

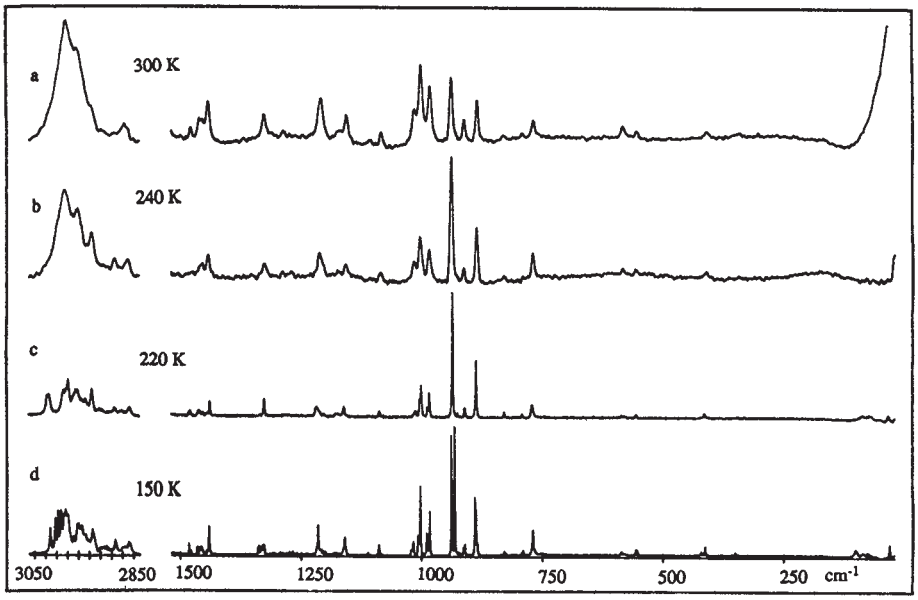

types of site and factor group combinations; (*i*) a D_2 crystal with a C_2 site or a C_{2v} crystal with either a C_2 or C_s site, (*ii*) a D_{2d} crystal with a C_s site, or (*iii*) an S_4 or C_4 crystal with a C_1 site. In the first case, some ir peaks should become doublets, and all Raman active peaks should be doublets. Since a number of Raman active peaks split into triplets, this possible crystal symmetry is unlikely. For the D_{2d} crystal, some infrared peaks should double, while Raman peaks should split into two or three peaks, and for the S_4 or C_4 crystal all the infrared peaks should double, and all Raman peaks should triple. Since seven lattice modes were observed in the Raman spectrum there are at least two molecules in the unit cell. From the observed splittings, the D_{2d} structure appears to be the most likely, i.e., a monoclinic crystal, C_s, or an orthorhombic crystal, D_2 or C_{2v}, both with two molecules per unit cell, or a tetragonal crystal, D_{2d} with $Z = 4$.

Spin-lattice relaxation time measurements

The dependence of the spin-lattice relaxation times is shown in Fig. 4. The phase transitions and the hysteresis are clearly apparent. The slopes of the ln (T_1) versus reciprocal temperature plots gave the activation energies for each re-

© 1998 NRC Canada

Table 2. Raman and infrared vibrational frequencies (cm^{-1}) of oxanorbornane.[a]

300 K (liquid)	100 K		220 K		240 K		
Raman	Raman	IR	Raman	IR	Raman	IR	Assignment
			3018w				
	3014w		3015w				
	3010m						
	3005m						
	2999m						
	2997m	2997sh		2997sh		2995sh	
	2990sh		2990sh	2990sh			
2984br,p	2987m	2985sh	2985w	2985sh	2987br		
	2980sh	2978vs	2979m	2978m,br		2977vs,br	
	2970vw		2970w,sh				
	2963w		2964w				
2960s,p	2961w	2960s	2961w		2960sh		
		2955s		2954s,br			
	2950sh	2953sh	2950br	2953sh		2951br,vw	CH str.
	2945sh		2945sh				
2940sh,p	2935m	2940s	2936s	2940s	2936s		
	2930w						
	2920w		2921vw				
		2914m		2915m,br			
	2910vw	2910sh		2911sh		2911s	
	2985w		2894w		2894w		
	2888sh						
	2880sh		2882br				
		2876m		2875sh		2871s	
2873sh,p	2870w			2869m,br	2871w		
		2867m	2868sh			2867sh	
			1490sh				
	1483w	1480vw	1482w	1479vw			
1480vw	1478vw				1479br		CH_2 str.
	1475vw		1475vw			1474vw	
	1467w	1470vw	1465sh	1470vw			
1461w	1460sh		1463vw		1462sh		
	1458w		1458vw	1458vw			
1455sh	1455vw	1456vw	1455sh				CH_2 def.
	1452vw	1450sh	1452vw			1452vw	
	1445vw		1445vw		1443vw		
1443m,p	1441m						
	1439sh		1440m		1440sh		
	1340vw						
	1338vw						
	1332w						
1328w,p	1329w	1324vw	1328w	1324vw	1329br,w	1321vw	
		1305sh				1304vw	CH_2 bend
		1303vw		1302vw			
		1270vw					
		1266vw				1265vw	
		1260vw		1262vw			
		1250vw					
	1220vw	1218vw					
	1216vw						
1210w	1210vw	1208sh	1210sh		1210sh		CH_2 bend and skeletal str.
	1205vw	1204w	1205vw	1203w	1205vw		
		1197s		1197s		1197s	

© 1998 NRC Canada

Table 2 (*continued*)**.**

300 K (liquid)	100 K		220 K		240 K		
Raman	Raman	IR	Raman	IR	Raman	IR	Assignment
	1175vw		1175br		1175br		
	1170vw						
	1165sh		1163m				COC str.
1157w	1161m				1159br		
1085m,p	1090m		1089vw		1087vw		
		1080vw		1080vw		1081vw	
	1023m						
1016m,p	1019m		1015br,w		1017br,w		CH_2 bend
			1013sh				
	1008m		1010m				
1003m,p	1004m	1001m	1003m				
	990vw	995m	990vw	996m		998m	
	987sh		986m		986m		
984m,p	983m	981w		984w	983sh	981w	skeletal str. and CH_2 bend
940vw,p	939vs		937vs		939s		
	932vs	933vs		933vs		933vs	
		930sh	930sh	931sh		932sh	
	917vw						
913m,p	913vw		912vw		914vw		
		907sh		907sh		908w	CH_2 bend
		905w					
	895w				890w		
	890w		888w	885m	888vw		
886vw	885vw	882m		882m		882m	
	831vw		830vw				
		824s		823s		824s	
		821sh		822sh		822sh	
		805w		806w		803w	
793vw			793vw				skeletal str. and bend
		787w		786w		787w	and CH_2 bend
770vw	771vw	766w	772vw	766vw	771vw	766w	
584vw			586vw		586vw		
	572vw						
556vw		551s	557vw	551s	557	550s	
	433vw						
			420sh				
411vw,p	413w		415w		413w		
	353vw						COC
			346vw				def.
	105vw						
	103vw						
	93vw						
	89vw						
	77vw		80vw				lattice modes
	75vw						
			69vw				
	31vw		32vw				
			29vw				

[a] p = polarized; s = strong; m = medium; w = weak; br = broad; sh = shoulder.

© 1998 NRC Canada

Fig. 3. Infrared spectra of oxanorbornane at different temperatures.

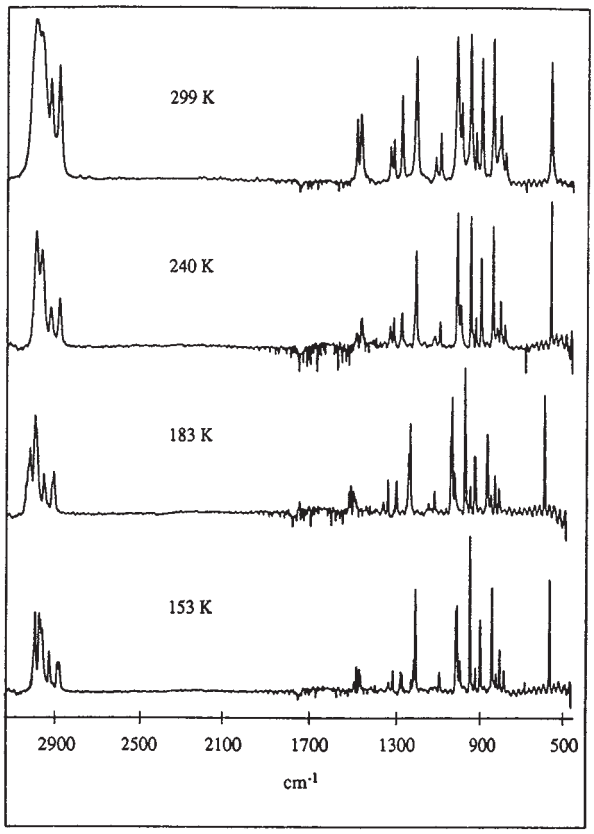

Fig. 4. Proton spin-lattice relaxation times vs. reciprocal temperature. Closed circles are for the cooling and open circles for the heating direction.

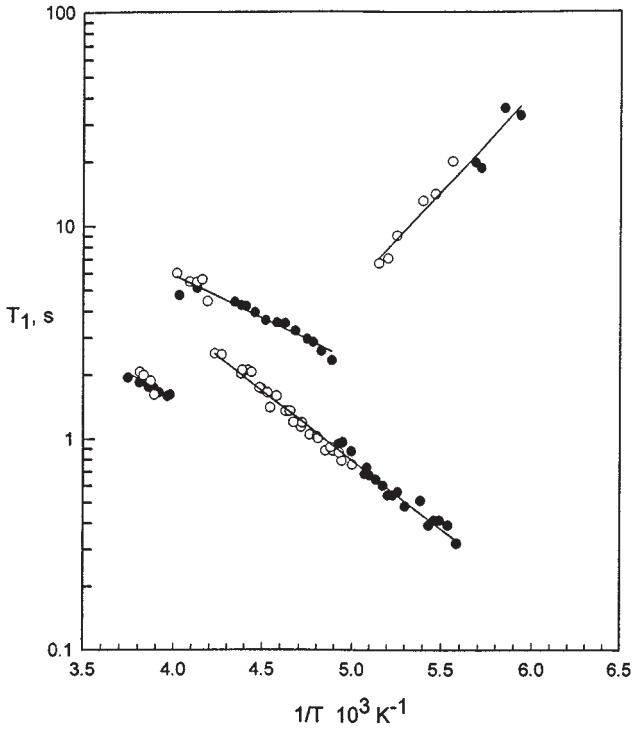

gion. In the high-temperature region, the barrier to rotation was 7.8 ± 0.5 kJ mol^{-1}, which is less than the value for the liquid phase of 9.8 ± 1.8 kJ mol^{-1}. This is unusual but has been observed previously for *t*-butyl compounds (10). In the intermediate phase the barrier was 12.5 ± 0.5 kJ mol^{-1}, rising to 17.5 ± 1.4 kJ mol^{-1} in the low-temperature phase. These energies are similar to those reported (11) for the other bicyclic compounds where, for their disordered phases, both norbornane and norbornylene showed nonlinear T_1 plots with slopes ranging from 5.4 to 8.8 kJ mol^{-1}, and 6.3 to 10.5 kJ mol^{-1}, respectively, and in norbornadiene the activation energy was 8.0 kJ mol^{-1}.

Acknowledgment

This research was supported by grants from the Natural Sciences and Engineering Research Council of Canada and FCAR (Quebec).

References

1. E.F. Westrum. *In* Molecular dynamics structure of solids. *Edited by* R.S.Carter and J.J. Rush. National Bureau of Standards, Washington. 1969. p. 459.
2. N.G. Parsonage and L.A.K. Staveley. Disorder in crystals. Clarendon, Oxford. 1978.
3. R.L. Jackson and J.H. Strange. Acta Crystallogr. Sect B: Struct. Crystallogr. Cryst. Chem.**B28**, 1645 (1972).
4. N.T. Kawai, I.S. Butler, and D.F.R. Gilson. J. Phys.Chem. **96**, 7257 (1992).
5. N.T. Kawai, I.S. Butler, and D.F.R. Gilson. J. Phys.Chem. **95**, 634 (1991).
6. N.T. Kawai, D.F.R. Gilson, and I.S. Butler. J. Phys.Chem. **94**, 5729 (1990).
7. N.T. Kawai, D.F.R. Gilson, and I.S. Butler. Mol. Cryst. Liq. Cryst. **211**, 59 (1992).
8. N.T. Kawai, D.F.R. Gilson, and I.S. Butler. J.Phys.Chem. **92**, 8556 (1991).
9. D.F.R. Gilson. J. Chem. Educ. **69**, 23 (1992).
10. S. Mooibroek, R.E. Wasylishen, J. B. Macdonald, C.I. Ratcliffe, and J.A. Ripmeester. Can. J. Chem. **66**, 734 (1988).
11. R. Folland, S.M. Ross, and J.H. Strange. Mol. Phys. **26**, 27 (1973).

© 1998 NRC Canada

The supramolecular architecture of 4-aminoacetophenone (1-(4-fluorophenyl)ethylidene)hydrazone hydrate. Double T-contacts and extremely low-density water layers in a mixed azine[1,2]

Michael Lewis, Charles L. Barnes, and Rainer Glaser

Abstract: The crystal structure of unsymmetrical azine 4-aminoacetophenone (1-(4-fluorophenyl)ethylidene)hydrazone hydrate, **1**·H_2O, was determined. Comparison to the X-ray structures of the symmetrical 4-fluoro- and 4-aminoacetophenone azines, **2** and **3**, respectively, reinforces the view of the azine bridge as a conjugation stopper. The focus of the analysis lies with the supramolecular architecture. The structure demonstrates azines as double T-contact synthons and suggests that novel L-type arene–arene contacts also might play a significant role in the supramolecular architecture. The absence of inter-water hydrogen bonding in an extremely low-density water layer is one of the surprising and unique features of the solid-state structure of the title compound. The water layers connect azine layers through a hydrogen bonded network which is described by graph set analysis.

Key words: arene–arene interaction, hydrogen bonding, graph set analysis, azine, supramolecular synthon, low density water monolayer.

Résumé : On a déterminé la structure cristalline de l'hydrate de la 4-aminacétophénone (1-(4-fluorophényl)éthylidène)hydrazone (**1**·H_2O) (dérivé asymétrique de l'azine de l'acétophénone). Une comparaison de celle-ci avec les structures cristallines des azines symétriques 4-fluoro- et 4-aminoacétophénone-azines, respectivement **2** et **3**, confirme le fait que le pont azine arrête la conjugaison. L'analyse se concentre sur l'architecture supramoléculaire. La structure démontre que les azines agissent comme synthons à doubles contacts-T et elle suggère la possibilité que de nouveaux contacts arène-arène de type-L puissent jouer un rôle significatif dans l'architecture supramoléculaire. L'absence de liaison hydrogène entre molécules d'eau dans une couche aqueuse de densité extrêmement faible est l'une des caractéristiques surprenantes et uniques de la structure à l'état solide du composé mentionné dans le titre. Les couches d'eau connectent les couches d'azines par le biais d'un réseau de liaisons hydrogènes que l'on décrit à l'aide d'une analyse d'un ensemble de graphes.

Mots clés : interaction arène–arène, liaison hydrogène, analyse d'un ensemble de graphes, azine, synthon supramoléculaire, monocouche d'eau de faible densit.

Introduction

We have been interested in the linear and nonlinear optical properties of *N*-perturbed donor–acceptor asymmetrized conjugated systems of the azine type. As a first step toward the elucidation of the underlying electronic structures and properties, we have systematically studied the crystal structures and the packing of symmetric (1, 2) and unsymmetric (3–5) acetophenone azines. These acetophenone azines have the general formula X-Ph-C(Me)=N-N=C(Me)-Ph-Y, and they are called symmetric if X = Y and unsymmetric in the case X ≠ Y(see Appendix). Our studies have resulted in the first realization of two prototypes of molecular organic materials with near-perfect dipole parallel-alignment in the pure crystal of the mixed azines 4-bromo- and 4-chloro-acetophenone (1-(4-methoxyphenyl)ethylidene)hydrazone (3, 4)[4,5].

Received May 19, 1998.

Michael Lewis, Charles L. Barnes, and Rainer Glaser.[3] Department of Chemistry, University of Missouri–Columbia, Columbia, MO 65211, U.S.A.

[1]Part 8 in the series "Stereochemistry and Stereoelectronics of Azines." For part 7, see ref. 5.
[2]Part of the projected Ph.D. dissertation of M.L.
[3]Author to whom correspondence may be addressed. Telephone: (573) 882-0331. Fax: (573) 882-2754. E-mail: chemrg@showme.missouri.edu.
[4]The piezoelectric material 4-bromo-4′-methoxyacetophenone azine has been featured as the "Molecule of the Month, December 1997" on the World Wide Web, and its crystal structure can be viewed at URL http://www.bris.ac.uk/Depts/Chemistry/MOTM/motm.htm.
[5]X-ray structures of the organic piezoelectric 4-chloro-4′-methoxyacetophenone azine. R. Glaser, M. Lewis, and C.L. Barnes. In preparation.

© 1998 NRC Canada

Scheme 1.

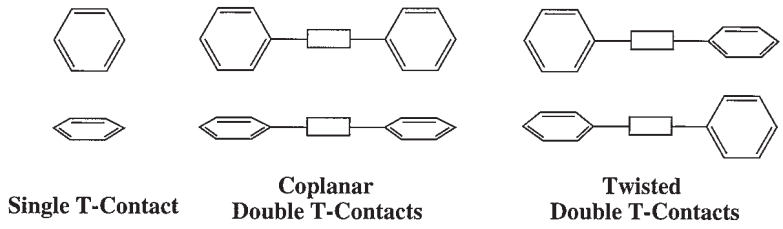

Fig. 1. ORTEP II drawing of mixed azine **1**. Major bond lengths in angstroms are F1—C5 = 1.3605(25), C2—C1 = 1.480(3), C1=N1 = 1.286(3), N1—N2 = 1.4140(23), C9—N2 = 1.293(3), C9—C10 = 1.480(3), and C13—N3 = 1.374(3).

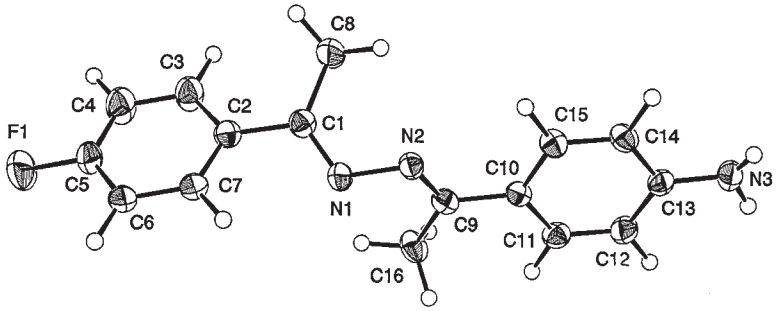

Non-centrosymmetry is a necessary requirement for all types of polar effects of crystals (6) (nonlinear optical (NLO) activity, piezo- and pyroelectric effects, and many others) but it is not a sufficient requirement. Many organic compounds crystallize in chiral space groups (7) without realizing any significant macroscopic polar effects (8, 9). The proper alignment of the polar building blocks is the pertinent issue, and the creation of large crystal polarizations remains a challenge beyond the simple quest for non-centrosymmetry. The de novo design of crystals is an undertaking of extraordinary difficulty since the lattice architecture results from the optimization of a large number of weak intermolecular interactions. These interactions are far too complex to trace and, thus, also far to complex to create by pure design. Olson (10) recently pointed out that the simplifying methods of scientific analysis can contribute to meeting this challenge when such analyses are pursued within the systems approach of engineering. Central to the systems approach is the sequential, deep and rigorous scientific analysis of a small number of prototypes. It is the goal of the prototype analysis to recognize significant intermolecular interactions. Molecular fragments capable of binding with certain other atoms or functional groups with high selectivity and high affinity are referred to as synthons (11, 12). The crystal structures of the prototypes of the ferroelectric azines show pairs of perfectly parallel aligned unsymmetrical azine molecules with two T-contact arene–arene interactions. The azine spacer is special in that its conformational flexibility (13) allows for near-orthogonality between the two benzenes in the same azine. The Ph-CR=N-N=CR-Ph system thus constitutes a "double T-contact synthon" and we believe this motif to be key to understanding the suprastructures of the prototypes. Double T-contacts occur when the arene rings of two compounds containing two arene groups each stack in such a way that two edge-to-face arene–arene contacts are realized. Scheme 1 illustrates the two possibilities for double T-contacts.

Coplanar double T-contacts result when the arene rings of each bisarene compound are (more or less) in the same plane. Thus, if the spacer between the two aromatic rings is unsaturated, there exists the possiblity of conjugation. Twisted double T-contacts require the arene rings of each bisarenes to be (more or less) orthogonal. This situation can only occur through a twisting of the spacer between the arene rings, and therefore one would not expect any conjugation between the arene rings.

As part of our studies of unsymmetric acetophenone azines we have now prepared the mixed azine 4-aminoacetophenone (1-(4-fluorophenyl)ethylidene)hydrazone (**1**, Fig. 1), and here we report the crystal structure of its hydrate,

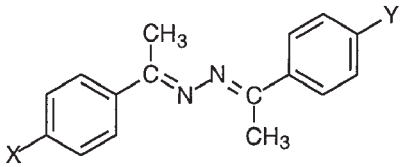

1: X=F, Y=NH_2
2: X=Y=F
3: X=Y=NH_2

1·H_2O. We have previously reported the solid-state structures of the respective symmetrical azines **2** (X = Y = F) and **3** (X = Y = NH_2) (2), and these data present the best possible reference to discuss the structural effects of asymmetrization. The structure of **1** demonstrates the importance of the double T-contact synthon. The superstructure of the title compound also is unique in two further respects. First, the supramolecular architecture of **1** features not only T-type arene–arene interactions but also exhibits highly perturbed T-contacts that can be described as L-type van-der-Waals arene–arene interactions. The other interesting feature relates to the occurrence of water layers which are exceptional in that there is no hydrogen bonding between the intra-layer water molecules.

© 1998 NRC Canada

Fig. 2. Packing of azine hydrate **1**·H_2O.

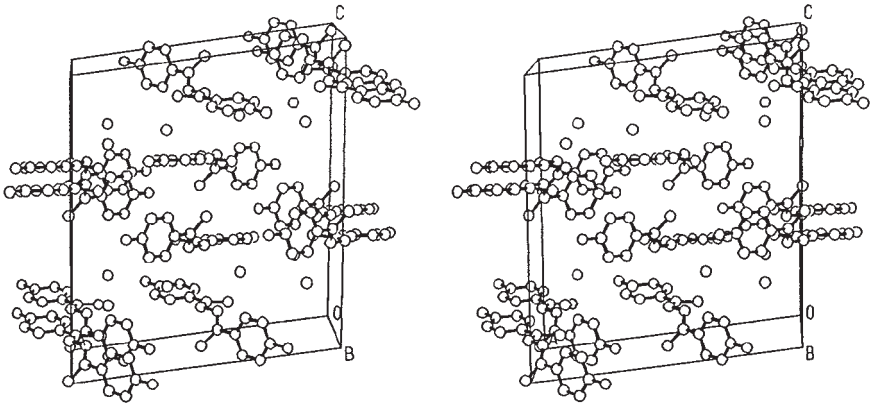

Results and discussion

Structural effects of asymmetrization and the question of π-conjugation

The ORTEP II diagram of **1** is shown in Fig. 1, and a view of the packing of **1**·H_2O is shown in Fig. 2. The crystallographic data for **1**·H_2O is presented in Tables 1–3. At first glance the title compound **1** appears to be a classical example of a donor–acceptor molecule which allows for donation of electron density from the amino-substituted phenyl ring into the fluoro-substituted phenyl ring. However, Fig. 1 reveals that mixed azine **1** is not planar, but rather the >C=N-N=C< bridge assumes a *gauche* conformation (τ = 56.4°) and the phenyl rings both are twisted more or less out of the conformation that would be best for conjugation. The amino-substituted phenyl ring is twisted only slightly by ϕ_1 = 8.4° out of the plane defined by the *ipso*-carbon and the atoms of the C9=N2 imine bond and still allows for through conjugation from the amino group to the imine functionality. Conversely, the fluoro-substituted phenyl ring is twisted by ϕ_2 = 31.2° out of the plane defined by the *ipso*-carbon and the C1=N1 imine bond, eliminating all possibilities for through-conjugation. Since the C2—C1, N1—N2, and C9—C10 bonds in **1** are almost parallel, the sum of τ, ϕ_1, and ϕ_2 provides an excellent approximation for the angle ω between the best planes through the benzene rings. Recognizing that τ and ϕ_i all serve to increase ω, this approximation gives $\omega \approx 96.0°$ and leaves the benzenes nearly orthogonal. Rather than considering the azine spacer a conjugating bridge in an extended donor–acceptor system, the azine bridge in **1** acts more like a "conjugation stopper," a term we introduced earlier to describe the electronics of asymmetric acetophenone azines. In this model the azine bridge is viewed as two oppositely oriented imine acceptors. The azine **1** should thus present itself as a system with a dipolar donor–acceptor half with an NH_2-donor and a C9=N2 imine bond acceptor, and an essentially quadrupolar half, where both the F and the C1=N1 imine bond are acceptors. Comparison with the symmetrically substituted azines **2** and **3** reinforces the view for the azine bridge as a conjugation stopper. The NH_2-half of **1** is perturbed very little as compared to the NH_2-halves for the symmetrical azine **3**. The average C_{ipso}—NH_2, C9—C10, and N2—C9 bond lengths in **3** are 1.38, 1.48, and 1.29 Å, respectively. These bond lengths are identical to the corresponding C9—C10 and N2—C9 bond lengths in **1**. The C_{ipso}—NH_2 is marginally less for **1** at 1.37 Å and a small discrepancy is to be expected since **1** crystallizes into a different H-bonded network than **3**. The same trend is present when comparing the F-half of **1** with azine **2**. The average C_{ipso}—F bond length is 1.36 Å for **2**, while the bond lengths that correspond to C2—C1, and C1—N1 are 1.48 and 1.28 Å, respectively. These bond lengths are identical to the corresponding bond lengths in **1**, except for C1—N1 which is 1.29 Å long.[6] Once again, a small variation is to be expected since **1** and **3** are in different crystal environments. Thus, the six bond lengths that would be affected most by through conjugation in fact remain almost unperturbed.

Double T-contacts in the van der Waals bonded azine layers

The crystal lattice (Fig. 2) of **1**·H_2O contains alternating layers of azines and water molecules stacked in the direction of the *c*-axis. Each azine layer is rotated by 90° from the azine layer below or above it and consists of inversion-symmetric pairs of dipole antiparallel-aligned azines with N–N *gauche* conformations (Fig. 3*a*). In the *P*/*M* nomenclature for the chirality of conformational isomers (14), the top structure of the azine pair depicted in Fig. 3*a* has *M* helicity, while the bottom structure has *P* stereochemistry. The azine pairs in Fig. 2 are characterized by two identical intermolecular arene–arene T-contacts (15, 16) that can best be described as twisted double T-contacts (Scheme 1). The near perpendicular phenyl arrangement ($\omega \approx 96.0°$) in **1** might be adopted to take full advantage of these intermolecular double T-contacts. A priori there is a choice as to which of the substituted benzenes serves as the vertex or the head of the T-contact. In the crystal structure of **1**, we find that the F-substituted benzenes always serve as the vertices. It is possible that polymorphs might exist with the opposite arrangement. The contact distance between the two phenyl rings ranges from 3.6 to over 4.1 Å (Fig. 3*b*). Alternatively, the layering of **1** along the direction of the *c*-axis can be described as involving two azine monolayers between water

[6] The estimated standard deviations (esd's) for the bond distances discussed in this section are on the order of thousandths of angstroms. Since we only cite the bond distances to hundredths of angstroms, these very small esd's strengthen our arguments.

© 1998 NRC Canada

Table 1. Crystallographic data.

Crystal data	
Source of material	$CHCl_3$
Crystal shape, colour, and size	Thin wafers, yellow, 0.15 × 0.20 × 0.45 mm
Empirical formula	$C_{16}H_{16}N_3F{\cdot}H_2O$
Formula weight	287.33
Crystal system	Monoclinic
Space group	*C*2/*c*
Unit-cell dimensions	a = 17.2988(12), b = 8.9205(6), c = 19.3557(15) α = 90.0, β = 97.5870(10), γ = 90.0
Number and θ range of reflections	4045 reflections, 10° ≤ θ ≤ 50°
Volume of unit cell	2960.7(4) Å^3
Z	8
D_{expt}	1.289 g/cm^3
D_{meas}	Density not measured
Radiation and wavelength	λ(Mo-Kα) = 0.70930 Å
Linear absorption coefficient	0.09 mm^{-1}
Temperature of measurement	293 K
Data collection	
Diffractometer	Siemens Smart CCD system
Method used to measure diffraction data	Omega scan mode
Absorption correction	Data were corrected for decay and absorption using the program SADABS based on the method of Blessing (30)
Number of reflections measured	8416
Number of independent reflections	3212
Number of observed reflections	2413
Criteria for recognizing observed reflections	$I > 2.0\sigma(I)$
Maximum value of q	$2q_{max}$ = 54.0°
Range of h, k, and l	$-22 \le h \le 21$, $0 \le k \le 11$, $0 \le l \le 24$
Refinement	
Use of F, F^2, or I	Refinement on F
R [$= \Sigma(\|\|F_o\| - \|F_c\|\|)/\Sigma\|F_o\|$]	0.053
wR {$= [\Sigma(w\|Ym - Yc\|^2)/\Sigma(wY^2m)]^{1/2}$}	0.079
Method of refining and location H atoms	Water and amino hydrogen atoms were located from a difference map, and refined with fixed isotropic thermal parameters. Ring and methyl hydrogen atoms were placed at calculated positions.
Number of parameters	202
Number of reflections used in refinement	2413
GOF {$= [\Sigma w(\|Ym\| - \|Yc\|)^2/(m - n)]^{1/2}$}	1.34
Definition of w	$w = 1/[\sigma 2(F)+0.002(F^2)]$
Maximum Δ/σ	0.004
Maximum and minimum Δρ in final difference electron density map	max = 0.260 and min = –0.220 e Å^{-3}
Source of scattering factors	*International Tables for X-ray Crystallography* (1974)
All computer programs used	NRCVAX (E.J. Gabe et al., 1989)

layers and from this vantage point the T-contacts are responsible for the cohesion between the azine monolayers. Each of these azine monolayers is completely dipole aligned but in opposite directions.

The inter-pair packing between azines in each respective layer also occurs via arene–arene interactions. These contacts are highly distorted T-contacts, and they might also be described as L-type arene–arene interactions (Fig. 3*c*). Arene–arene interactions have been studied extensively by ab initio (15, 17), Monte Carlo (18), and molecular mechanics (19) theoretical methods, using Raman (20), NMR (21), and mass selective hole-burning (22) spectroscopic techniques and also by solid-state X-ray crystallography (23). These studies produced a vast body of evidence for the significance of face-to-face and T-contacts, however there is no evidence for T-contacts perturbations that lead to L-contacts. There are many examples of perturbed T-contacts of the herringbone motif (15–17*a*) which are the result of non-orthogonal (and slipped) vertices. The L-contact exhibited in **1** is the result of a strong perturbation of the T-contact with the rings remaining perpendicular (Fig. 3*d*). Since the C_j—C_l bond is coplanar with the benzene ring shown on the

© 1998 NRC Canada

Table 2. Positional and equivalent isotropic thermal parameters, with esd's in parentheses.

	x	*y*	*z*	B_{iso}
F1	0.29633(9)	0.64047(18)	0.46105(8)	4.57(7)
O1	0.13773(9)	0.13243(17)	0.24282(9)	2.74(6)
N1	0.05454(10)	0.13509(19)	0.36419(9)	2.19(6)
N2	–0.00547(9)	0.02665(18)	0.35361(8)	2.10(7)
N3	–0.21184(12)	–0.56854(22)	0.30191(10)	2.62(8)
C1	0.05192(12)	0.22602(23)	0.41535(10)	2.25(7)
C2	0.11382(12)	0.34130(23)	0.42623(10)	2.27(8)
C3	0.13973(15)	0.3931 (3)	0.49370(12)	3.29(9)
C4	0.20119(15)	0.4946 (3)	0.50574(13)	3.71(10)
C5	0.23549(13)	0.54301(25)	0.44970(13)	3.01(9)
C6	0.21016(12)	0.49996(24)	0.38224(12)	2.55(8)
C7	0.14897(12)	0.39792(22)	0.37107(11)	2.30(8)
C8	–0.00801(15)	0.2166 (3)	0.46479(13)	3.62(10)
C9	0.01790(11)	–0.11112(22)	0.35399(10)	2.04(8)
C10	–0.04224(11)	–0.22936(22)	0.34095(9)	1.92(7)
C11	–0.02158(12)	–0.37929(24)	0.33228(11)	2.41(8)
C12	–0.07668(13)	–0.49152(23)	0.31903(11)	2.54(8)
C13	–0.15621(12)	–0.45824(22)	0.31350(10)	2.15(8)
C14	–0.17775(12)	–0.30911(23)	0.32385(11)	2.32(8)
C15	–0.12209(12)	–0.19767(22)	0.33741(11)	2.28(8)
C16	0.10195(12)	–0.1576 (3)	0.36842(12)	2.83(9)

right (containing C_k), and since the atoms C_i, C_j, and C_k lie in a plane that is almost perpendicular to the molecular planes of both phenyl rings, the angle (C_i, C_j, C_k) = 89.8° shows that the benzene planes are essentially perpendicular. It is for these reasons that we refer to this arrangement as an L-contact. As was the case for the intra-pair packing, the F-substituted phenyl rings serve as the vertices in the inter-pair arene–arene interactions. The distance between the L-packed arene rings ranges from 3.556 to 4.142 Å (Fig. 3*d*) for the edge-to-edge contacts illustrated in Fig. 3*c*. Note that the realization of the L-contacts requires a translation of neighboring azines within each monolayer along their long molecular axis such that an X-substituted benzene interacts with a Y-substituted benzene. In the absence of such a translation, the packing might benefit from face-to-face stacking of the F-substituted arenes but the amino-substituted benzenes would not be in any favorable position. It has been noted that benzene aggregates do not assume one rigid structure (24) but instead there are a variety of geometries that can be adopted (15). Thus, the formation of the L-contact should not be an entirely surprising result, as the intermolecular forces that govern arene–arene interactions are weak and could be overcome with relative ease due to a variety of competing non-covalent interactions.

Graph set analysis of the hydrogen bonding and low-density water layers

As illustrated in Fig. 2, the azine layers in **1** are held together by layers of water molecules. The positions of the water H-atoms were determined, and the water molecules do not engage in any water–water hydrogen bonding. The water molecules all are aligned such that their molecular planes are nearly parallel with the *ac*-plane, and all of the water dipole moments are nearly colinear with the crystallographic *a*-axis. Each water participates in four hydrogen bonds with

Table 3. Selected bond lengths (Å), angles (°), and selected torsion angles (°).

F1—C5	1.3605(25)	N3—C13	1.374(3)
N1—N2	1.4140(23)	C1—C2	1.480(3)
N1—C1	1.286(3)	C9—C10	1.480(3)
N2—C9	1.293(3)		
N2-N1-C1	116.32(17)	F1-C5-C6	118.30(21)
N1-N2-C9	115.23(16)	N2-C9-C10	117.65(17)
N1-C1-C2	116.72(18)	C9-C10-C11	121.10(17)
C1-C2-C3	119.87(19)	C9-C10-C15	122.03(18)
C1-C2-C7	121.64(18)	N3-C13-C12	121.44(19)
F1-C5-C4	118.65(20)	N3-C13-C14	120.58(19)
C1-N1-N2-C9	–123.6(4)	N1-N2-C9-C10	–178.1(4)
N1-C1-C2-C7	29.57(21)	N1-C1-C2-C3	–148.8(4)
N2-C9-C10-C15	–8.35(18)	N2-C9-C10-C11	172.3(4)
N2-N1-C1-C2	–179.1(4)		

four separate azines (Fig. 4). The hydrogen bonding network is best revealed via the graph set theoretical description proposed by Bernstein and Davis (25). Using their notation, the H_a- and H_b-bonds have unitary graph set notation N_1 = DD, indicating that each hydrogen bond H_a and H_b is finite. These two hydrogen bonds are formed between a water acting as a H-donor and an azine N-atom. The system of Bernstein and Davis also allows for more complex graph sets. A binary graph set describes a pattern in which only two types of hydrogen bonds are present, whereas systems with more than two hydrogen bonds can be described by complex basis sets. The hydrogen bonded pattern produced by H_a and H_b has a binary graph set of $N_2(a,b) = C_2^2(5)$ and a complex graph set of $N_2(a,b) = R_4^4(10)$ (Fig. 4*a*). We exemplify the meaning of the binary graph set for $N_2(a,b) = C_2^2(5)$. The term $N_2(a,b)$ denotes a graph set with two types of hydrogen bonds, H_a and H_b. $C_2^2(5)$ indicates a chain (C) which contains two hydrogen bond acceptors (superscript) and two hydrogen bond donors (subscript) and covers five atoms linked by either covalent or hydrogen bonds. Similarly, the complex graph set R denotes a ring pattern consisting of four donor and four acceptor sites in a 10-membered ring. The other types of hydrogen bonds H_c and H_d both involve water as the hydrogen bond acceptor and the amino groups are the hydrogen bond donors (Fig. 4*b*). The amino groups are slightly pyramidalized (sum of angles at *N* = 354.2°) and the direction of pyramidalization is such as to suggest optimization of the hydrogen-bonding interactions. The bonds H_c and H_d can be described by a unitary graph set, N_1 = DD, and a binary graph, $N_2(c,d) = C_2^1(4)$. In this case, however, there is no complex graph set that relates H_c and H_d. Finally, there also exists two complex graph sets that describe the patterns created by H_a, H_c, and H_d and by all four hydrogen bonds. The pattern produced by H_a, H_c, and H_d has the complex graph set $N_3(a,c,d) = R_4^3(14)$ and is illustrated in Fig. 4*c* by the thick broken lines. The pattern relating all four hydrogen bonds can loosely be described by the complex graph set $N_4(a,b,c,d) = R_8^7(24)$. This description does not strictly adhere to the notation of Bernstein and Davis because the pattern created by all four hydrogen bonds is not a ring. Instead, a spiro motif exists where the

© 1998 NRC Canada

Fig. 3. All distances are in angstroms. (*a*) Stereodrawing of the intra-pair azines with almost perfect double-T-contacts. The stereochemistry is such that the top and bottom azines have *M*- and *P*-helicity, respectively. (*b*) Stereodrawing of the phenyl–phenyl contact for one of the T-contacts shown in (*a*). (*c*) Inter-pair contact between azines showing an L-contact motif. (*d*) Stereodrawing emphasizing the L-contact shown in (*c*).

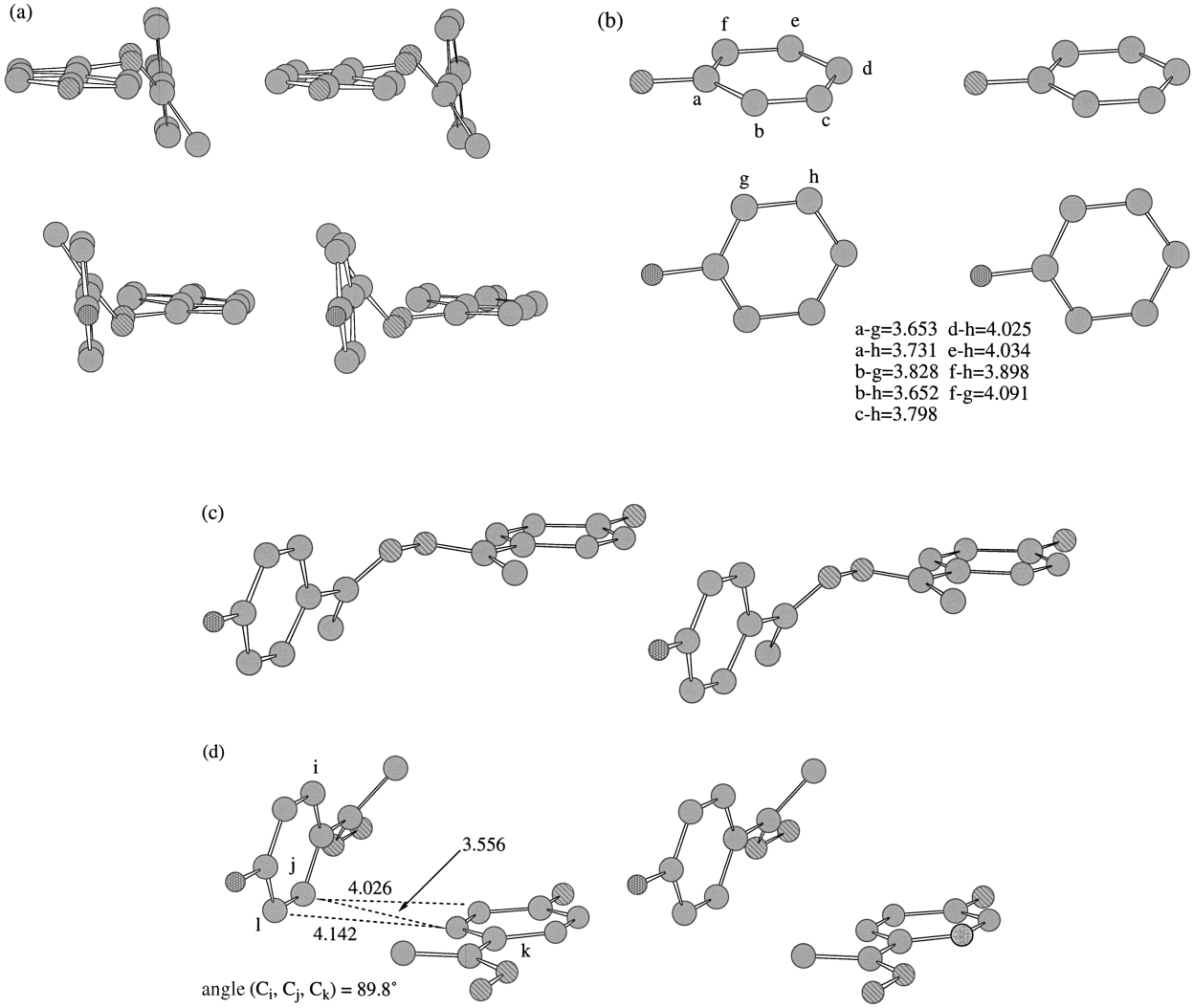

ring created by the graph set $N_3(a,c,d) = R_4^3(14)$ shares a common oxygen with the ring created by the graph set $N_2(a,b) = R_4^4(10)$ (the latter ring is shown in Fig. 4*c* by the thin broken lines). This spiral pattern of hydrogen bonds reveals the infinite two-dimensional layer which acts as the glue that holds the layers of azine pairs together. It appears that the water layer in **1** represents the least dense arrangement of water molecules in the solid state observed to date. The O—O distances of 4.81 and 5.90 Å correspond to a density of approximately one half that of ice I and II (average O—O distance of 2.79 Å (26)). This extreme low density is attributed to the absence of inter-water H-bonding. The unique arrangement of water molecules in $1\cdot H_2O$ represents a first for infinite water layers, and it is attributed to the presence of a strong H-bond acceptor in the form of the amino-N atom. The literature on hydrates shows structures of two general classes. The first family of hydrates realizes crystal lattices in which the water molecules hydrogen bond with each other (27) and the other class contains water molecules that are interspersed throughout the crystal lattice (28). Neither of these classes of hydrates show any water aggregates with cavities. It appears that the infinitely ordered water sheet of the kind demonstrated by $\mathbf{1}\cdot H_2O$ is entirely unprecedented.

Experimental

Synthesis and recrystallization

Mixed azine **1** was prepared via hydrazono-de-oxo-bisubstitution (29). Hydrazine hydrate was added to *p*-aminoacetophenone in ethanol to yield the corresponding hydrazone. Reaction of the hydrazone with *p*-fluoroacetophenone in ethanol in the presence a few drops of glacial acetic acid afforded the azine which was purified by column chromatography (hexane–ethylacetate gradient elution). Crystals of the hydrate $\mathbf{1}\cdot H_2O$ were grown by slow diffusion of hexane into a solution of **1** in chloroform.

Crystal structure determination

A single crystal X-ray analysis was performed on the hydrate ($C_{16}H_{16}N_3F\cdot H_2O$, M_r = 287.33). The compound $\mathbf{1}\cdot H_2O$

© 1998 NRC Canada

Fig. 4. All distances are in angstroms. (*a*) The water H atoms act as the hydrogen bond donors, while the azine-N atoms are the acceptors. By only considering the two unique hydrogen bonds H_a and H_b, the binary basis set $N_2(a,b) = C_2^2(5)$ is realized. The complex basis set $N_2(a,b) = R_4^4(10)$ is a result of two binary sets forming a circle. (*b*) The amino-H atoms act as hydrogen bond donors, and the water-O atoms are the acceptors. The two unique H-bonds H_c and H_d can be described by the binary basis set $N_2(c,d) = C_2^2(4)$. There is no complex basis set relating H_c and H_d. (*c*) The complex basis set $N_4(a,c,d) = R_4^4(14)$ is obtained by considering the hydrogen bonded system described by the thick broken lines. All four hydrogen bonds are related by the spiral motif created by the graph sets $N_2(a,b) = R_4^4(10)$ and $N_4(a,c,d) = R_4^4(14)$.

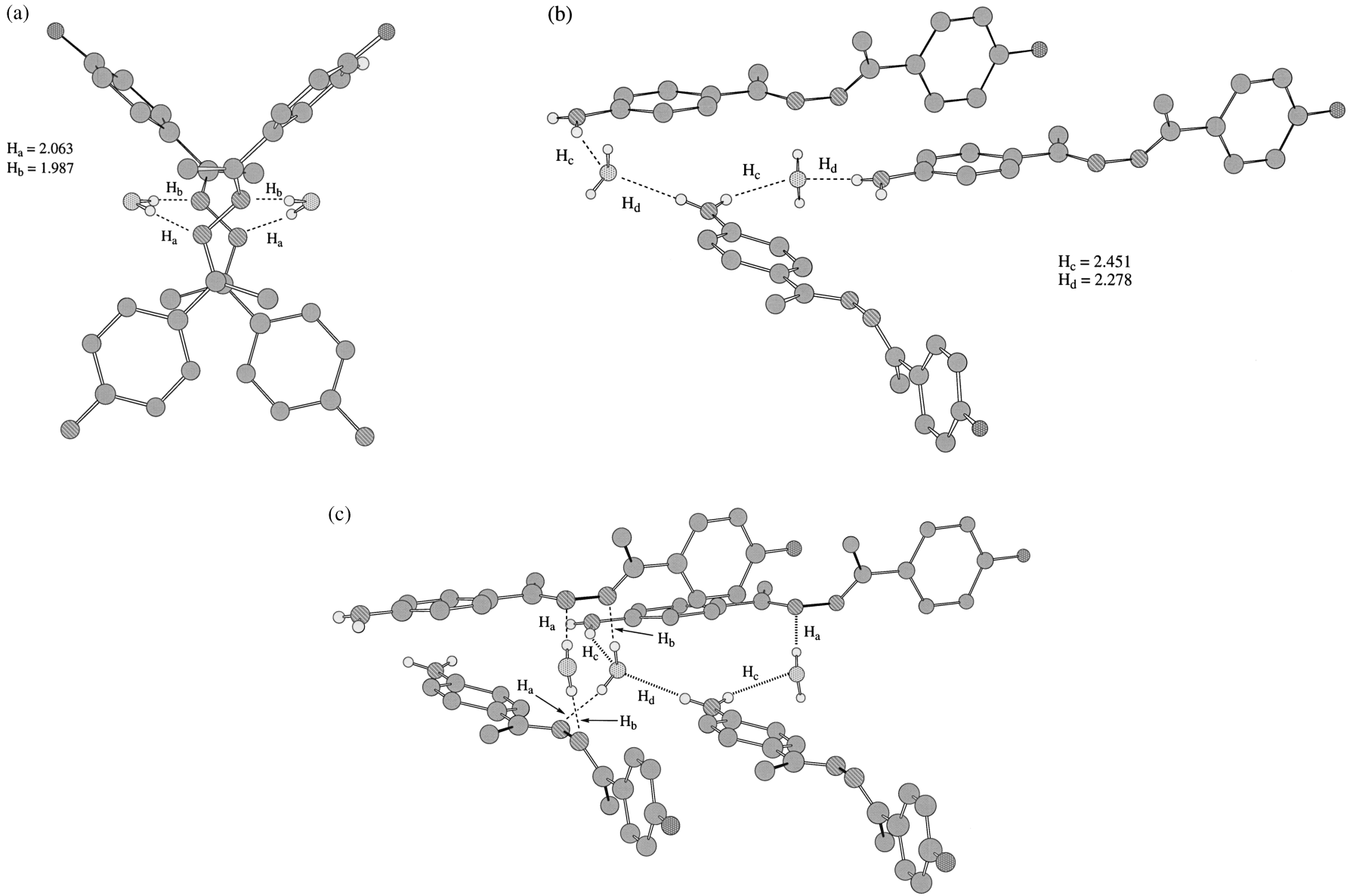

© 1998 NRC Canada

crystallizes in a monoclinic lattice (space group $C2/c$, a = 17.2988(12), b = 8.9205(6), c = 19.3557(15) Å, β = 97.5870(10)°). Final R factor = 0.053 and wR factor = 0.079 for 2413 reflections with refinement on F and 202 parameters and the GOF value was 1.34. Tables of crystal data, structure solution and refinement, atomic coordinates, bond lengths, and anisotropic thermal parameters for **1**·H_2O (12 pages print) have been deposited as supplementary material.[7]

Acknowledgments

The research was supported by a grant from the Research Board of the University of Missouri. M.L. thanks the Natural Sciences and Engineering Research Council (NSERC) of Canada for a postgraduate scholarship type A.

References

1. (*a*) G.S. Chen, M. Anthamatten, C.L. Barnes, and R. Glaser. J. Org. Chem. **59**, 4336 (1994); (*b*) Angew. Chem. Int. Ed. Engl. **33**, 1081 (1994); (*c*) R. Glaser, G.S. Chen, and C.L. Barnes. J. Org. Chem. **58**, 7446 (1993).
2. R. Glaser, G.S. Chen, M. Anthamatten, and C.L. Barnes. J. Chem. Soc. Perkin Trans. 2, 1449 (1995).
3. G.S. Chen, J.K. Wilbur, C.L. Barnes, and R. Glaser. J. Chem. Soc. Perkin Trans. 2, 2311 (1995).
4. R. Glaser and G.S. Chen. Polym. Mater. Sci. Eng. **75**, 229 (1996).
5. R. Glaser and G.S. Chen. J. Comput. Chem. **19**, 1130 (1998).
6. M.C. Petty, M.R. Bryce, and D. Bloor. Introduction to molecular electronics. Oxford University Press, New York. 1995.
7. M. Sakamoto. Chem. Eur. J. **3**, 684 (1997).
8. Molecular nonlinear optics - materials, physics, and devices. *Edited by* J. Zyss. Academic Press, New York. 1994.
9. C. Bosshard, K. Sutter, P. Prêtre, J. Hulliger, M. Flörsheimer, P. Kaatz, and P. Günter. Organic optical materials, advances in nonlinear optics, v. 1. Gordon and Breach Publishers, New York. 1995.
10. G.B. Olson. Science (Washington, D.C.) **277**, 1237 (1997).
11. G.R. Desiraju. Angew. Chem. Int. Ed. Engl. **34**, 2311 (1995).
12. A. Gavezzotti. Curr. Opin. Solid State Mater. Sci. **1**, 501 (1996).
13. J.J. Wolff. Angew. Chem. Int. Ed. Engl. **35**, 2195 (1996).
14. E.L. Eliel, S.H. Wilen, and L.N. Mander. Stereochemistry of organic compounds. John Wiley & Sons Inc., New York. 1994. p. 1120.
15. P. Hobza, H.L. Selzle, and E.W. Schlag. Chem. Rev. **94**, 1767 (1994).
16. J.H. Williams. Acc. Chem. Res. **26**, 593 (1993).
17. (*a*) C. Chipot, R. Jaffe, B. Maigret, D.A. Pearlman, and P.A. Kollman. J. Am. Chem. Soc. **118**, 11 217 (1996); (*b*) P. Hobza, H.J. Selzle, and E.W. Schlag. J. Phys. Chem. **100**, 18 790 (1996); (*c*) R.L. Jaffe and G.D. Smith. J. Chem. Phys. **105**, 2780 (1996); (*d*) P. Hobza, H.L. Selzle, and E.W. Schlag. J. Am. Chem. Soc. **116**, 3500 (1994).
18. W.L. Jorgensen and D.L. Severance. J. Am. Chem. Soc. **112**, 4768 (1990).
19. N.L. Allinger and J.-H. Lii. J. Comput. Chem. **8**, 1146 (1987).
20. (*a*) T. Ebata, I. Ishikawa, M. Ito, and S.-H. Hyodo. Laser Chem. **14**, 85 (1994); (*b*) V.A. Venturo and P.M. Felker. J. Chem. Phys. **99**, 748 (1993); (*c*) B.F. Henson, G.V. Hartland, V.A. Venturo, and P.M. Felker. J. Chem. Phys. **97**, 2189 (1992).
21. (*a*) A.S. Shetty, L. Zhang, and J.S. Moore. J. Am. Chem. Soc. **118**, 1019 (1996); (*b*) R. Laatikainen, J. Ratilainen, R. Sebastian, and H. Santa. J. Am. Chem. Soc. **117**, 11 006 (1995).
22. W. Scherzer, O. Kratzschmar, H.L. Selzle, and E.W. Schlag. Z. Naturforsch. **47A**, 1248 (1992).
23. (*a*) G.R. Desiraju and A. Gavezzotti. Acta Crystallogr. Sect. B: Struct. Sci. **45**, 473 (1989); (*b*) C.A. Hunter. Chem. Soc. Rev. 101 (1994); (*c*) F.D. Lewis, J.-S. Yang, and C.L. Stern. J. Am. Chem. Soc. **118**, 12 029 (1996).
24. (*a*) S. Sun and E.R. Bernstein. J. Phys. Chem. **100**, 13348 (1996); (*b*) P. Hobza, H.L. Selzle, and E.W. Schlag. J. Chem. Phys. **93**, 5893 (1990).
25. J. Bernstein, R.E. Davis, L. Shimoni, and N.L. Chang. Angew. Chem. Int. Ed. Eng. **34**, 1555 (1995).
26. D.W. Davidson. *In* Water: a comprehensive treatise; v.2. *Edited by* F. Franks. Plenum Press, New York. 1973. p.130.
27. (*a*) K. Toda, Y. Kameo, S. Kurita, and M. Sato. Bull. Chem. Soc. Jpn. **69**, 349 (1996); (*b*) Y. Zhang, A. Clearfield, and R.C. Haushalter. J. Solid State Chem. **117**, 157 (1995); (*c*) W.T. Harrison, L.L. Dussack, and A.J. Jacobson. J. Solid State Chem. **116**, 95 (1995); (*d*) M. Nieuwenhuyzen and C.J. Wilkins. J. Chem. Soc. Dalton Trans. 2763 (1993).
28. H. Bock, W. Seitz, M. Sievert, M. Kleine, and J.W. Bats. Liebigs Ann. 1929 (1996).
29. J. March. Advanced organic chemistry. 4th ed. John Wiley & Sons, Inc., New York. 1992. p. 904.
30. R.H. Blessing. Acta Crystallogr. Sect. A: Fundam. Crystallogr. **A51**, 33 (1995).

Appendix

Nomenclature of azines: azines are 2,3-diazabutadienes, they are characterized by the functional group >C=N-N=C<, and they formally are the products of condensation between hydrazine and two carbonyl compounds. Symmetrical or unsymmetrical (or mixed) azines are formed, respectively, if the two carbonyl compounds are the same or different. Azines have the general formula RR′C=N-N=CRR′, and they are named substitutively as an assembly of identical units using the prefix "azino-." According to functional class nomenclature, they may be named by adding the class name "azine" as a separate word after the name of the corresponding aldehyde or ketone. Hence, Me_2C=N-N=CMe_2 is called azinoacetone or, more frequently, acetone azine (see http://www.acdlabs.com/iupac/nomenclature/93/r93_469.htm). In the IUPAC nomenclature, the unsymmetrical azines RR′C=N-N=CR′′R′′′ are named as alkylidenehydrazones. Hence, Me_2C=N-N=CH_2 can be called formaldehyde (isopropylidene) hydrazone or acetone (methylidene) hydrazone.

[7] Supplementary material and the results of the crystal structure analysis may be purchased from: The Depository of Unpublished Data, Document Delivery, CISTI, National Research Council of Canada, Ottawa, Canada, K1A 0S2. With the exception of isotropic and anisotropic thermal parameters, these and the crystal structure (in CIF format) have also been deposited with the Cambridge Crystallographic Data Centre and can be obtained on request from: The Director, Cambridge Crystallographic Data Centre, University Chemical Laboratory, 12 Union Road, Cambridge, CB2 1EZ, U.K.

© 1998 NRC Canada

Synthesis and characterization of homoleptic ruthenium(II) imidazole complexes, and a carbonyl species derived by CO abstraction from DMF

Ian R. Baird, Steven J. Rettig, Brian R. James, and Kirsten A. Skov

Abstract: $[Ru(II)(L)_6]^{2+}$ complexes were synthesized from $[Ru(DMF)_6][CF_3SO_3]_3$; DMF = dimethylformamide, L = imidazole (Im), *N*-methylimidazole (NMeIm) and 5-methylimidazole (5MeIm). The 2-methylimidazole complex *trans*-$[Ru(CO)(DMF)(2MeIm)_4][CF_3SO_3]_2$ (**4**) was also synthesized via a reaction involving abstraction of CO from DMF; **4** loses CO reversibly at ambient temperature to form $[Ru(DMF)(2MeIm)_4][CF_3SO_3]_2$ (**5**), and the DMF can be removed to generate a $[Ru(CF_3SO_3)_x(2MeIm)_4][CF_3SO_3]_y$ species ($x = 2$, $y = 0$, or $x = 1 = y$), containing coordinated triflate. The complexes were characterized by elemental analysis, conductivity, UV-vis, NMR, and IR spectroscopies. The structures of $[Ru(Im)_6][CF_3SO_3]_2$ (**1**), $[Ru(NMeIm)_6][CF_3SO_3]_2$ (**2**), and $[Ru(5MeIm)_6][CF_3SO_3]_2$ (**3**) were established by X-ray crystallographic analyses. Crystals of **1**, are triclinic, $a = 7.4010(6)$, $b = 9.9846(15)$, $c = 11.275(2)$ Å, $\alpha = 113.469(5)$, $\beta = 92.419(2)$, $\gamma = 94.737(2)°$, $Z = 1$, space group $P\bar{1}$; those of **2**, are trigonal, $a = 11.558(2)$, $c = 8.109(3)$ Å, $Z = 1$, space group $P\bar{3}$; and those of **3**, are trigonal, $a = 12.6547(4)$, $c = 20.4078(12)$ Å, $Z = 3$, space group $R\bar{3}$. The structures were solved by Patterson methods and refined by full-matrix least-squares procedures to $R(F) = 0.029$, 0.034, and 0.034 ($R_w(F^2) = 0.055$, $R_w(F) = 0.031$, and $R_w(F^2) = 0.058$), respectively.

Key words: hexakis(imidazole)ruthenium(II) triflates, crystal structures, CO abstraction.

Résumé : On a synthétisé les complexes $[Ru(II)(L)_6]^{2+}$ à partir du $[Ru(DMF)_6][CF_3SO_3]_3$ dans lesquels DMF = diméthylformamide, L = imidazole (Im), *N*-méthylimidazole (NMeIm) et 5-méthylimidazole (5MeIm). On a aussi synthétisé le complexe dérivé du 2-méthylimidazole, *trans*-$[Ru(CO)(DMF)(2MeIm)_4][CF_3SO_3]_2$ (**4**), par le biais d'une réaction impliquant l'enlèvement de CO à partir du DMF; à la température ambiante, le composé **4** perd du CO d'une façon réversible pour conduire au $[Ru(DMF)(2MeIm)_4][CF_3SO_3]_2$ (**5**) et on peut enlever le DMF pour générer une espèce $[Ru(CF_3SO_3)_x(2MeIm)_4][CF_3SO_3]_y$ ($x = 2$, $y = 0$ ou $x = 1 = y$) comportant un triflate coordonné. On a caractérisé les complexes par analyse élémentaire, conductivité, spectroscopies UV-vis, IR et RMN. On a aussi déterminé les structures des composés $[Ru(Im)_6][CF_3SO_3]_2$ (**1**), $[Ru(NMeIm)_6][CF_3SO_3]_2$ (**2**), et $[Ru(5MeIm)_6][CF_3SO_3]_2$ (**3**), par diffraction des rayons X. Les cristaux du composé **1** sont tricliniques, groupe d'espace $P\bar{1}$, avec $a = 7{,}4010(6)$, $b = 9{,}9846(15)$ et $c = 11{,}275(2)$ Å, $\alpha = 113{,}469(5)$, $\beta = 92{,}419(2)$ et $\gamma = 94{,}737(2)°$ et $Z = 1$; ceux du composé **2** sont trigonaux, groupe d'espace $P\bar{3}$, avec $a = 11{,}558(2)$ et $c = 8{,}109(3)$ Å et $Z = 1$ et ceux du composé **3** sont trigonaux, groupe d'espace $R\bar{3}$, avec $a = 12{,}6547(4)$ et $c = 20{,}4078(12)$ Å et $Z = 3$. On a résolu les structures par les méthodes de Patterson et on les a affinées par la méthode des moindres carrés jusqu'à des valeurs de $R(F) = 0{,}029$, 0,034 et 0,034 et ($R_w(F^2) = 0{,}055$, $R_w(F) = 0{,}031$ et $R_w(F^2) = 0{,}058$) respectivement.

Mots clés : triflates d'hexakis(imidazole)ruthénium, structures cristallines, enlèvement de CO.

[Traduit par la Rédaction]

Introduction

Ruthenium imidazole complexes as chemotherapeutic agents show less cytotoxicity than their platinum counterparts (1, 2). These Ru complexes are of interest for their antitumor activity (3), for their ability to ligate radiosensitizing agents to DNA (4), as models for the bonding of Ru to nucleic acids (occurring most frequently on the imidazole ring of guanine (5–7)), and as a new class of compounds that, in the low nanomolar range, specifically inhibit the proliferation of human *T*-lymphocytes in vitro (2, 8). The interaction of Ru complexes with biomolecules has been studied extensively (9), and the form of the complex surviving to coordinate the biomolecules usually differs from that originally introduced into the organism. This is especially true for Ru(III) complexes which are transformed by an in vivo reduction to Ru(II), a more active species toward DNA bind-

Received May 19, 1998.

I.R. Baird, S.J. Rettig, and B.R. James.[1] Department of Chemistry, University of British Columbia, Vancouver, BC V6T 1Z1, Canada.
K.A. Skov. Advanced Therapeutics, British Columbia Cancer Research Centre, Vancouver, BC V5Z 1L3, Canada.

[1]Author to whom correspondence may be addressed. Telephone: (604) 822–4217. Fax: (604) 822–2847. E-mail: brj@chem.ubc.ca

© 1998 NRC Canada

ing, as reduction accelerates substitution reactions at the metal center (10).

Ruthenium(III) imidazole complexes such as $[ImH]_2[RuCl_5(Im)]$ (11) and *trans*-$[ImH][RuCl_4(Im)_2]$ (6, 12–14) have been synthesized and characterized, and their solution chemistry and antitumor activity thoroughly investigated. Ruthenium(II) imidazole complexes, however, are less common and, during our studies of such species, the two homoleptic species $[Ru(Im)_6]CO_3\cdot 5H_2O$ (14) and $[Ru(NMeIm)_6]Cl_2\cdot 2H_2O$ (3) were reported; X-ray structures were presented but no spectroscopic data, and indeed synthetic procedures for these complexes have not been reported, at least in the open literature. Crystals of the $(NMeIm)_6$ complex were a gift from a drug company (3), while those of the $(Im)_6$ complex grew in an NMR-tube after several weeks from a solution containing $[ImH]_2[RuCl_5(Im)]$ and excess Im (14). Several Ru(II)-imidazole species have been reported to show immunosuppression activity (15). Here we report the synthesis and structural characterization of the complexes $[RuL_6][CF_3SO_3]_2$, where L = imidazole (Im) (**1**), *N*-methylimidazole (NMeIm) (**2**), and 5-methylimidazole (5MeIm) (**3**),[2] as well as NMR, IR, and UV-vis data. The synthesis and characterization of the complex $[Ru(CO)(DMF)(2MeIm)_4][CF_3SO_3]_2$ (**4**), resulting from the decarbonylation of DMF, are also reported.

Experimental

Chemicals

Im, 2-methylimidazole (2MeIm), and 4(5)MeIm (Aldrich products) and NMeIm (from Merck) were used as received. Reagent grade DMF (Fisher) was distilled and dried over molecular sieves, and MeCN (anhydrous, Aldrich) was used as received. Other solvents were dried using the appropriate drying agent: MeOH (Mg), acetone (K_2CO_3), and CH_2Cl_2 (CaH_2). The precursor complexes $[Ru(DMF)_6][CF_3SO_3]_3$ and $[Ru(DMF)_6][CF_3SO_3]_2$ were synthesized according to literature procedures (16,17) from $RuCl_3\cdot 3H_2O$ and $Pb(CF_3SO_3)_2$ (the latter being synthesized from $PbCl_2$ and Aldrich, reagent grade CF_3SO_3H).

Physical techniques and methods

UV-vis absorption spectra were recorded on an HP 8452A diode array spectrophotometer and are given as λ_{max} (nm), [ε_{max} (M^{-1} cm^{-1})], sh = shoulder. IR spectra (as KBr pellets) were recorded on an ATI Mattson Genesis FTIR spectrophotometer (only the relatively intense bands are reported), and ^1H and $^{19}F\{^1H\}$ NMR spectra were recorded on a Bruker AC200F spectrometer. ^1H shifts are referenced to the residual proton shift of the internal deuterated solvent, and ^{19}F shifts are referenced to trifluoroacetic acid. GC analysis was done on an HP 5890A instrument using a 30 kPa He flow at 75°C with an HP-17 50% phenyl, 50% methyl, polysiloxane intermediate polarity column with a flame ionization detector and an HP 3392A Integrator. Electrochemistry was performed on 10^{-3} M solutions (MeCN) in 0.1 M TBAP (tetrabutylammonium perchlorate) on a Pine Biopotentiostat Model AFCBP1; the working and counter electrodes were Pt plates (6 mm^2) and the reference electrode was Pt wire (reduction potentials are reported vs. Ag/AgCl, the values being determined by reference to a measured ferrocene/ferrocenium couple). Conductivity measurements were made on a 10^{-3} M solution of the complex at room temperature (r.t.) using a Serfass conductance bridge model RCM15B1 (Arthur H. Thomas Co. Ltd.) connected to a 3404 cell from the Yellow Springs Instrument Co., and are reported as Λ_M (ohm^{-1} cm^2 mol^{-1}). TLC was run on precoated (0.2 mm) silica gel 60 F_{254} plates (E.M. Laboratories, Inc). Elemental analyses were performed in the UBC chemistry department by Mr. P. Borda.

Complexes

*$[Ru(Im)_6][CF_3SO_3]_2$ (**1**)*

In a 100 mL Schlenk tube $[Ru(DMF)_6][CF_3SO_3]_3$ (0.362 g, 0.367 mmol) was dissolved in MeOH (20 mL) under N_2 to yield a bright yellow solution. Finely ground Im (0.189 g, 2.78 mmol), dissolved in hot MeOH (5 mL), was then added via syringe. The reaction mixture was stirred at 70°C for 5 h over which time the solution went through orange to become dark green; however, the reaction remained incomplete according to TLC. The solution was thus stirred at 40°C for an additional 8 h. The MeOH was removed in vacuo leaving a dark green gum that contained DMF. Acetone (5 mL) was then added, followed by CH_2Cl_2 (~30 mL) which resulted in a green microcrystalline precipitate. This was collected, washed with warm CH_2Cl_2 (6 × 5 mL, to ensure removal of any excess Im) and dried in vacuo at 80°C for 2 days (yield 0.236 g, 80%). Dark green, X-ray quality crystals resulted from slow evaporation of a MeOH solution of **1**. ^1H NMR (r.t., d_6-DMSO), δ: 12.47 (s, 1H, Im-H_1), 7.23 (s, 1H, Im-H_5), 6.88 (br.s, 1H, Im-H_2), 6.22 (s, 1H, Im-H_4). ^{19}F NMR (r.t., d_6-DMSO), δ: –1.20 (s, $CF_3SO_3^-$). Anal. calcd. for $C_{20}H_{24}N_{12}F_6S_2O_6Ru$: C 29.74, H 3.00, N 20.81; found: C 29.87, H 2.87, N 20.45. UV-vis (MeOH): 218 (12 250), 288 (7590), 642 (33); for free Im, 216 (1640). Infrared (KBr), cm^{-1}: 3329, 3145, 2966, 2864, 1253, 1226(sh), 1173, 1068, 1027, 766, 636. $E°$ = 246 ± 2 mV.

*$[Ru(NMeIm)_6][CF_3SO_3]_2$ (**2**)*

In a double-neck, 25 mL flask, equipped with a reflux condenser, $[Ru(DMF)_6][CF_3SO_3]_3$ (0.088 g, 0.089 mmol) was dissolved in neat NMeIm (8 mL) under N_2 to give a bright yellow solution. The reaction mixture was stirred at 70°C. After 2 h the solution became pale green and slowly became darker with time. After 20 h, at which time the solution had become orange–brown, the mixture was immersed in an ice-bath; addition of toluene (10 mL) resulted in a creamy white precipitate, that was collected, washed with Et_2O (4 × 5 mL) and dried in vacuo at 80°C for 3 days (yield 0.0691 g, 87%). Bright yellow crystals suitable for X-ray analysis formed from slow cooling of a hot MeOH solution of **2**. ^1H NMR (r.t., d_6-DMSO), δ: 7.28 (s, 1H, Im-H_5), 7.20 (s, 1H, Im-H_2), 6.31 (s, 1H, Im-H_4), 3.68 (s, 3H, Im-*NMe*). ^{19}F NMR (r.t., d_6-DMSO), δ: –1.21 (s,$CF_3SO_3^-$).

[2] In complex **3**, the noncoordinated N-atom (with the H-atom) is defined as N(1), and the coordinated N-atom is defined as N(3); note that within the atomic labelling of Fig. 3, these N-atoms are arbitrarily labelled as N(2) and N(1), respectively.

© 1998 NRC Canada

Anal. calcd. for $C_{26}H_{36}N_{12}F_6S_2O_6Ru$: C 35.02, H 4.07, N 18.85; found: C 35.13, H 3.95, N 18.93. UV-vis (MeOH): 224 (12 080), 298 (10 200); for free NMeIm, 220 (1320). Infrared (KBr), ν cm^{-1}: 3131, 2967, 2926, 1533, 1270, 1226(sh), 1151, 1094, 1033, 637. $E°$ = 271 ± 3 mV.

*[Ru(5MeIm)$_6$][CF$_3$SO$_3$]$_2$ (**3**)*

In a 100 mL Schlenk tube $[Ru(DMF)_6][CF_3SO_3]_3$ (0.352 g, 0.357 mmol) was dissolved in MeOH (15 mL) under N_2 to give a bright yellow solution. 4(5)MeIm (0.240 g, 2.92 mmol) dissolved in hot MeOH (5 mL) was then added via syringe, when the solution became orange. After being stirred at 70°C for 4 h, the solution became dark brown–green. The MeOH was removed in vacuo leaving a dark brown gum. Acetone and CH_2Cl_2 were added (~5 mL each) to yield a brown–green solution which upon addition of Et_2O gave a yellow precipitate (yield 0.210 g, 66%). Bright yellow crystals suitable for X-ray diffraction formed from slow cooling of a hot MeOH solution of **3**. ^{1}H NMR (r.t., d_6-DMSO, for isolated crystals), δ: 12.09 (br.s, 1H, Im-H_1), 6.85 (s, 1H, Im-H_2), 6.03 (s, 1H, Im-H_4), 2.40 (s, 3H, Im-*5Me*); (for yellow precipitate) δ 12.10 (br.s, 12H, Im-H_1), 6.95 and 6.85 (overlapping singlets, 12H, Im-H_2), 6.60 (s, 1H, Im-H_5), 6.28 (s, 5H, Im-H_4), 6.03 (s, 6H, Im-H_4), 2.40 (s, 36H, Im-*5Me* + Im-*4Me* (buried)). ^{19}F NMR (r.t., d_6-DMSO), δ: –1.22 (s, C$F_3SO_3^-$). Anal. calcd. for $C_{26}H_{36}N_{12}F_6S_2O_6Ru$: C 35.02, H 4.07, N 18.85; found: C 35.07, H 4.09, N 18.77. UV-Vis (MeOH): 228 (12140), 292 (5620), 366 (sh); for free 4(5)MeIm, 220 (2715). Infrared (KBr), ν cm^{-1}: 3267, 3187, 3016, 2903, 1599, 1263, 1225(sh), 1170, 1099, 1030, 820, 637. $E°$ = 174 ± 3 mV.

N.B.: Pure complexes **1**–**3** were also synthesized from $[Ru(DMF)_6][CF_3SO_3]_2$ and the appropriate imidazole in MeOH. The reaction times were considerably shorter (2 h maximum) than those described in the above syntheses, and the yields were similar from the Ru(III) precursor.

trans-*[Ru(CO)(DMF)(2MeIm)$_4$][CF$_3$SO$_3$]$_2$ (**4**), [Ru(DMF)(2MeIm)$_4$][CF$_3$SO$_3$]$_2$ (**5**), and [Ru(CF$_3$SO$_3$)$_x$(2MeIm)$_4$][CF$_3$SO$_3$]$_y$ (x = 2, y = 0, or x = 1 = y) (**6**)*

The procedure used was identical to that used for the synthesis of **1,** but using $[Ru(DMF)_6][CF_3SO_3]_3$ (0.208 g, 0.211 mmol) and 2MeIm (0.123 g, 1.49 mmol); colour changes similar to those noted for the Im system were seen. For the work-up procedure, the MeOH volume was reduced to ~5 mL and then Et_2O (20 mL) was added slowly. The green solution became cloudy and storage at 0°C for 16 h resulted in a green crystalline solid (**4**), which was collected, washed with Et_2O (3 × 5 mL) and dried in vacuo at r.t. During pumping the green solid started to turn brown and after 4 h was a dark brown solid formulated as $[Ru(DMF)(2MeIm)_4][CF_3SO_3]_2$ (**5**). ^{1}H NMR (r.t., d_6-acetone), δ: 11.91 (br. s, 4H, Im-H_1), 8.40 (s, 1H, DMF-*H*), 6.77 (s, 4H, Im-H_5), 6.61 (s, 4H, Im-H_4), 3.22 (s, 3H, DMF-*Me*), 3.10 (s, 3H, DMF-*Me*), 2.45 (s, 12H, Im-*2Me*). ^{19}F NMR (r.t., d_6-acetone), δ: –1.21 (s, C$F_3SO_3^-$). If acetone is added to the NMR sample, a new peak appears at δ 2.14 (s, coord. $Me_2C{=}O$), slightly downfield of the free acetone peak (δ 2.04). If the brown solid was pumped on at 80°C, it turned black, being converted to $[Ru(CF_3SO_3)_x(2MeIm)_4][CF_3SO_3]_y$ (**6**). ^{1}H NMR (r.t., d_6-DMSO), δ: 12.11 (br. s, 1H, Im-H_1), 7.24 (s, 1H, Im-H_5), 7.03 (s, 1H, Im-H_4), 2.07 (s, 3H, Im-*2Me*). ^{19}F NMR (r.t., d_6-DMSO), δ: –1.21 (s, C$F_3SO_3^-$). Anal. calcd. for $C_{18}H_{24}N_8F_6S_2O_6Ru$: C 29.71, H 3.32, N 15.40; (for $C_{18}H_{24}N_8F_6S_2O_6Ru{\cdot}H_2O$ (and **6** was extremely hygroscopic): C 29.00, H 3.51, N 15.03); found: C 29.05, H 3.52, N 14.73. Infrared (KBr), ν cm^{-1}: (**4**) 3257, 3134, 2933, 2861, 2103 (C≡O), 1654 ($C{=}O_{DMF}$), 1572, 1283, 1249, 1167, 1030, 749, 638; (**5**) 3256, 3129, 2929, 2857, 1648 ($C{=}O_{DMF}$), 1572, 1284, 1248, 1167, 1030, 749, 638; (**6**) 3249, 3127, 2926, 2850, 1572, 1280, 1251, 1169, 1031, 754, 639. Conductivity of **6** (MeOH): Λ_M 115 (1 min) [1:1 electrolyte], becoming 165 after 3 h [2:1 electrolyte]. GC data: retention times for MeOH (5.26 min) and dry dimethylamine (5.06 min) match those found in the headspace of the sealed reaction vessel used for the synthesis of **4** (5.29 and 5.05 min).

*X-ray crystallographic analyses of **1**, **2**, and **3***

Crystallographic data appear in Table 1, and the respective structures are shown in Figs. 1–3. The final unit-cell parameters were obtained by least-squares on the setting angles for 5877 reflections with 2θ = 4.0–60.1° for **1**, 25 reflections with 2θ = 22.8–29.0° for **2**, and 6933 reflections with 2θ = 4.0–60.1° for **3**. The intensities of three standard reflections, measured every 200 reflections throughout the data collection for **2**, showed only small random fluctuations. The data were processed (18), corrected for Lorentz and polarization effects, and absorption (based on analysis of symmetry equivalent data for **1** and **3** and azimuthal scans for **2**).

The structures were solved by Patterson methods, all three analyses being initiated in the centrosymmetric space groups on the basis of *E*-statistics. The cation of **1** lies on a centre of symmetry, and those of **2** and **3** on points of S_6 symmetry. The triflate anion of **2** is massively disordered about the threefold axis, while that of **3** lies on a threefold axis. The triflate disorder in **2** was modeled by assigning the largest peaks in the region to partially occupied S, F, O, or C sites. Population parameters for the disordered atoms were adjusted to give roughly equivalent isotropic thermal parameters. There was some divergence in the thermal parameters when the S, F, and O sites were refined anisotropically. No attempt was made to obtain realistic triflate geometry, but care was taken to insure that the appropriate number of electrons was modeled and that the density in this region was accounted for. Geometrical parameters for the anion of **2** are very unreliable and are not given. All non-hydrogen atoms except C(5) and C(6) (the triflate carbons) for **2** were refined with anisotropic thermal parameters. Hydrogen atoms were fixed in calculated positions with C—H = 0.98 Å and $B_H = 1.2B_{\text{bonded atom}}$. A correction for secondary extinction was applied for **1** (Zachariasen type, isotropic, Gaussian), the final value of the extinction coefficient being 6.2(2) × 10^{-6}. Neutral atom scattering factors for all atoms and anomalous dispersion corrections for the non-hydrogen atoms were taken from standard tables (19). Final atomic coordinates and equivalent isotropic thermal parameters, bond lengths, and bond angles appear in Tables 2–4, respectively. Hydrogen atom parameters, anisotropic thermal parameters, torsion an-

© 1998 NRC Canada

Table 1. Crystallographic data.

Compound	**1**[a]	**2**[b]	**3**[a]
Formula	$C_{20}H_{24}F_6N_{12}O_6RuS_2$	$C_{26}H_{36}F_6N_{12}O_6RuS_2$	$C_{26}H_{36}F_6N_{12}O_6RuS_2$
fw	807.67	891.83	891.83
Crystal system	Triclinic	Trigonal	Trigonal
Space group	*P* (no. 2)	*P* (no. 147)	*R* (no. 148)
a, Å	7.4010(6)	11.558(2)	12.6547(4)
b, Å	9.9846(15)	11.558(2)	12.6547(4)
c, Å	11.275(2)	8.109(3)	20.4078(12)
α,°	113.469(5)	90	90
β,°	92.419(2)	90	90
γ,°	94.737(2)	120	120
V, Å^3	759.1(2)	938.1(4)	2830.3(2)
Z	1	1	3
ρ_{calc}, g/cm^3	1.767	1.579	1.570
F(000)	406	454	1362
μ, cm^{-1}	7.49	6.15	6.11
Crystal size, mm	0.20 × 0.30 × 0.45	0.38 × 0.45 × 0.50	0.10 × 0.20× 0.25
Transmission factors	0.87–1.00[c]	0.94–1.00	0.74–1.00[c]
Scan type	φ, ω sweeps	ω-2θ	φ, ω sweeps
Scan range, deg in ω	0.5	1.15 + 0.35 tan θ	0.5
Scan speed, deg/min	—	32 (up to 9 scans)	—
Data collected	462 frames, 40 s/frame	±*h*, +*k*, +*l*	462 frames, 75 s/frame
$2\theta_{max}$, deg	60.1	60.0	60.0
Crystal decay, %	—	5.6	—
Total reflections	7056	2078	8224
Unique reflections	3451	1830	1744
R_{merge}	0.033	0.048	0.032
No. with $I \geq 3\sigma(I)$	2883	1215	1071
No. of variables	215	135	81
$R(F)$ ($I \geq 3\sigma(I)$)	0.029	0.035	0.034
$R_w(F)$ ($I \geq 3\sigma(I)$)	0.027	0.031	0.028
$R(F^2)$ (all data)	0.050	—	0.061
$R_w(F^2)$ (all data)	0.055	—	0.058
gof	1.34	1.91	1.12
Max Δ/σ (final cycle)	0.0005	0.01	0.0001
Residual density e/Å^3	–0.79–0.84	–0.19–0.78	–1.22–1.92

[a]Temperature 180 K, Rigaku/ADSC CCD diffractometer, Mo K_α (λ = 0.71069 Å), graphite monochromator, takeoff angle 6.0°, aperture 94.0 × 94.0 mm at a distance of 39.2 mm from the crystal, $\sigma^2(F^2) = (C + B)/Lp^2$ (C = scan count, B = background count), function minimized $\Sigma w(|F_o^2| - |F_c^2|)^2$ where $w = 1/\sigma^2(F_o^2)$, $R = \Sigma||F_o^2| - |F_c^2||/\Sigma|F_o^2|$, $R_w = (\Sigma w(|F_o^2| - |F_c^2|)^2/\Sigma w|F_o^2|^2)^{1/2}$, and gof = $[\Sigma w(|F_o^2| - |F_c^2|)^2/(m - n)]^{1/2}$. All data used in the refinement.

[b]Temperature 294 K, Rigaku AFC6S diffractometer, Mo K_α radiation (λ = 0.71069 Å), graphite monochromator, takeoff angle 6.0°, aperture 6.0 × 6.0 mm at a distance of 285 mm from the crystal, stationary background counts at each end of the scan (scan/background time ratio 2:1), $\sigma^2(F^2) = [S^2(C + 4B)]/Lp^2$ (S = scan rate, C = scan count, B = normalized background count), function minimized $\Sigma w(|F_o| - |F_c|)^2$ where $w = 4F_o^2/\sigma^2(F_o^2)$, $R = \Sigma||F_o| - |F_c||/\Sigma|F_o|$, $R_w = (\Sigma w(|F_o| - |F_c|)^2/\Sigma w|F_o|^2)^{1/2}$, and gof = $[\Sigma w(|F_o| - |F_c|)^2/(m - n)]^{1/2}$. Residuals and gof based on data with $I \geq 3\sigma(I)$.

[c]Includes crystal decay, absorption, and scaling corrections.

gles, intermolecular contacts, and least squares planes are included as supplementary material.[3]

Results and discussion

Preparation and characterization of hexakisimidazole Ru(II) complexes

Availability of the starting complexes $[Ru(DMF)_6][CF_3SO_3]_x$, where x = 2 or 3 (16), provides a useful general method for access to the homoleptic hexa-coordinate Ru(II) imidazole complexes $[Ru(L)_6][CF_3SO_3]_2$ (L = Im (**1**), NMeIm (**2**), and 5MeIm (**3**)). The DMF-containing precursors provide a useful alternative to the commercially available $RuCl_3 \cdot 3H_2O$ which is of variable composition. The cations of **1** and **2** have been previously reported with X-ray structural data, but with CO_3^{2-} and $[Cl^-]_2$ as their respective anions (3, 14) and, as mentioned in Introduction, syntheses of these compounds were not reported. Further, no other characterization data were reported for $[Ru(Im)_6][CO_3] \cdot 5H_2O$, which was insoluble in common solvents (14), or $[Ru(NMeIm)_6]Cl_2 \cdot 2H_2O$

[3] Copies of material on deposit may be purchased from: The Depository of Unpublished Data, Document Delivery, CISTI, National Research Council Canada, Ottawa, Canada K1A 0S2. Tables of hydrogen atom coordinates and bond lengths and angles involving hydrogen atoms have also been deposited with the Cambridge Crystallographic Data Centre, and can be obtained on request from: The Director, Cambridge Crystallographic Data Centre, University Chemical Laboratory, 12 Union Road, Cambridge CB2 1EZ, U.K.

© 1998 NRC Canada

Fig. 1. An ORTEP view of $Ru(Im)_6^{2+}$ (**1**); 50% probability thermal ellipsoids are shown.

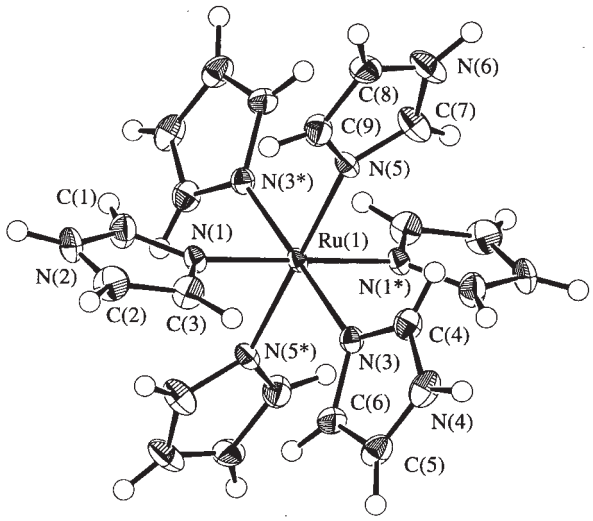

Fig. 2. An ORTEP view of $Ru(NMeIm)_6^{2+}$ (**2**); 33% probability thermal ellipsoids are shown.

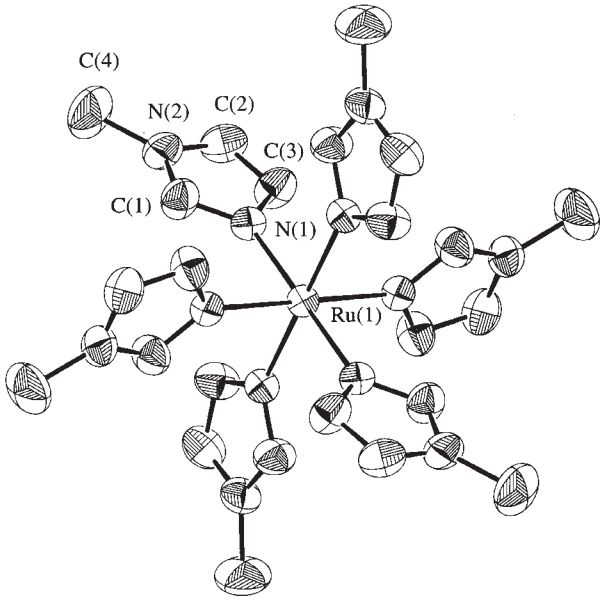

Fig. 3. An ORTEP view of $Ru(5MeIm)_6^{2+}$ (**3**); 50% probability thermal ellipsoids are shown.

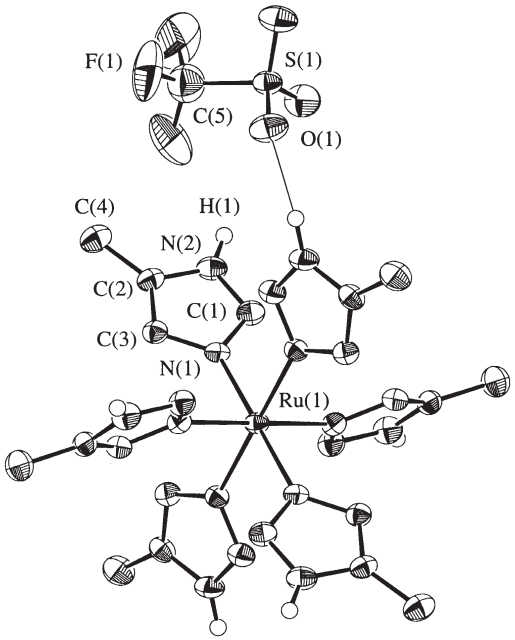

(3); CV data have been given for $[Ru(Im)_6][ClO_4]_3$ and $[Ru(NMeIm)_6][PF_6]_3$ (3).

Complexes **1**–**3**, which contain no waters of crystallization, can be obtained by simple exchange of the DMF ligands of $[Ru(DMF)_6]^{2+}$ by the imidazole. However, this Ru(II) precursor is moderately air-sensitive, and it is more convenient to use the air-stable $[Ru(DMF)_6][CF_3SO_3]_3$ precursor, although longer reaction times are needed, presumably (at least in part) because of the reduction of Ru(III) to Ru(II). There is literature precedence for both MeOH (20) and imidazoles (14, 21) acting as reductants of transition metal species, including those of Ru(III) which we have observed also in analogous nitroimidazole systems.[4] Substitution reactions at Ru(II) centres are typically faster than those at corresponding Ru(III) centres (22), and the longer Ru—O bond in $[Ru(DMF)_6]^{2+}$ vs. $[Ru(DMF)_6]^{3+}$ is consistent with such a reactivity trend (16).

Structural data on the cations within **1** and **2** have been reported previously within the structures of $[Ru(Im)_6]CO_3 \cdot 5H_2O$ (**1′**) (14) and $[Ru(NMeIm)_6]Cl_2 \cdot 2H_2O$ (**2′**) (3), respectively. The corresponding pairs of crystal structures, however, are quite different. Complex **1** crystallizes in the triclinic space group $P\bar{1}$ with the Ru atom situated on an inversion centre with the three unique Ru—N distances averaging 2.099(2) Å; crystals of **1′** are hexagonal with the Ru atom located at a point of S_6 symmetry with six equivalent Ru—N bonds of 2.102(2) Å. Complex **2** crystallizes in a trigonal space group with (like **1′**) the Ru atom at a point of S_6 symmetry and Ru—N bond lengths of 2.100(2) Å, while **2′** forms monoclinic crystals in which the Ru atom lies on a centre of symmetry (like **1**) with the three independent Ru—N distances averaging 2.106(8) Å. (Complex **3**, the $(5MeIm)_6$ species, is similar to **2** in being trigonal, with the Ru being at an S_6 site and the Ru—N length being 2.093(2) Å.) The Ru—N distances are significantly less than that reported for $Ru(NH_3)_6^{2+}$, 2.144(4) Å (23); this could result from a combination of some degree of π-backbonding from the Ru(II) to the imidazole ligands, and σ-hybridization

[4] I.R. Baird and B.R. James. To be published.

© 1998 NRC Canada

Table 2. Final atomic coordinates (fractional) and B_{eq} (10^3 Å^2).[a]

Atom	*x*	*y*	*z*	B_{eq}	Occ.
		1			
Ru(1)	0.500 00	0.500 00	0.500 00	1.235(6)	
S(1)	0.190 05(7)	0.216 25(7)	0.914 24(6)	2.120(14)	
F(1)	0.4885(2)	0.1445(2)	0.9942(2)	3.66(4)	
F(2)	0.5242(2)	0.2327(2)	0.8517(2)	4.85(5)	
F(3)	0.3976(3)	0.0135(3)	0.7969(2)	5.91(6)	
O(1)	0.1255(2)	0.2036(2)	0.7878(2)	2.91(4)	
O(2)	0.0917(2)	0.1169(2)	0.9590(2)	3.44(5)	
O(3)	0.2307(2)	0.3644(2)	1.0103(2)	3.00(4)	
N(1)	0.6451(2)	0.3574(2)	0.5536(2)	1.51(4)	
N(2)	0.8337(3)	0.2726(3)	0.6562(2)	2.58(5)	
N(3)	0.3026(2)	0.3239(2)	0.3962(2)	1.44(4)	
N(4)	0.1474(3)	0.1354(3)	0.2378(2)	2.40(5)	
N(5)	0.6399(2)	0.4505(2)	0.3323(2)	1.48(4)	
N(6)	0.7406(3)	0.4527(3)	0.1512(2)	2.74(5)	
C(1)	0.7822(3)	0.3920(3)	0.6434(3)	2.33(6)	
C(2)	0.7263(3)	0.1538(3)	0.5701(3)	2.71(6)	
C(3)	0.6097(3)	0.2068(3)	0.5069(3)	2.26(6)	
C(4)	0.2784(3)	0.2473(3)	0.2698(2)	2.07(5)	
C(5)	0.0814(3)	0.1393(3)	0.3499(3)	2.19(6)	
C(6)	0.1766(3)	0.2537(3)	0.4471(2)	1.99(5)	
C(7)	0.6319(3)	0.5123(3)	0.2471(3)	2.46(6)	
C(8)	0.8250(3)	0.3478(3)	0.1764(2)	2.31(6)	
C(9)	0.7602(3)	0.3487(3)	0.2874(2)	2.21(6)	
C(10)	0.4104(4)	0.1481(3)	0.8878(3)	2.83(6)	
		2			
Ru(1)	0.000 00	0.000 00	0.000 00	4.013(6)	1/6
S(1)	0.628(2)	0.2857(9)	0.2615(8)	10.3(3)	1/3
F(1)	0.533(2)	0.349(4)	0.083(4)	15.6(9)	0.300
F(2)	0.590(6)	0.208(4)	0.055(5)	22.0(14)	0.250
F(3)	0.686(3)	0.516(2)	0.250(6)	17.1(9)	0.250
F(4)	0.577(8)	0.373(8)	0.376(5)	19.1(18)	0.200
O(1)	0.559(2)	0.278(5)	0.162(2)	24.5(14)	1/3
O(2)	0.733(4)	0.284(6)	0.360(4)	17.7(11)	1/3
O(3)	0.504(2)	0.287(5)	0.262(5)	18.3(12)	1/3
N(1)	0.0974(2)	0.1708(2)	0.1494(2)	4.54(5)	
N(2)	0.2507(3)	0.3619(2)	0.2552(3)	6.54(7)	
C(1)	0.2197(3)	0.2707(3)	0.1352(4)	6.56(8)	
C(2)	0.1418(4)	0.3185(3)	0.3504(3)	6.87(9)	
C(3)	0.0492(3)	0.2020(3)	0.2851(4)	6.65(8)	
C(4)	0.3793(4)	0.4870(4)	0.2776(6)	11.44(13)	
C(5)	0.710(5)	0.252(5)	0.053(6)	9.4(8)	0.220
C(6)	0.6667	0.3333	0.12(2)	27.8(17)	0.110
		3			
Ru(1)	0.00000	0.00000	0.00000	1.834(7)	1/6
S(1)	–0.33333	0.33333	0.03331(7)	2.51(2)	1/3
F(1)	–0.4460(2)	0.2642(3)	–0.07733(12)	9.81(9)	
O(1)	–0.3899(2)	0.2058(2)	0.05007(11)	4.02(6)	
N(1)	0.0306(2)	0.1511(2)	–0.05623(10)	1.92(5)	
N(2)	0.0764(2)	0.3384(2)	–0.07995(12)	2.59(5)	
C(1)	0.0856(2)	0.2660(2)	–0.03460(13)	2.46(6)	
C(2)	0.0153(2)	0.2693(2)	–0.13355(13)	2.29(6)	
C(3)	–0.0115(2)	0.1539(2)	–0.11780(13)	2.13(6)	
C(4)	–0.0120(3)	0.3201(3)	–0.1920(2)	3.25(8)	
C(5)	–0.3333	0.3333	–0.0546(4)	5.41(11)	1/3

[a] $B_{eq} = (8/3)\pi^2\Sigma\Sigma(U_{ij}a_ia_j(\mathbf{a}_i\cdot\mathbf{a}_j))$.

© 1998 NRC Canada

Table 3. Bond lengths (Å) with estimated standard deviations in parentheses.

Bond	Length	Bond	Length
	1		
Ru(1)—N(1)	2.105(2)	Ru(1)—N(3)	2.095(2)
Ru(1)—N(5)	2.098(2)	S(1)—O(1)	1.437(2)
S(1)—O(2)	1.442(2)	S(1)—O(3)	1.440(2)
S(1)—C(10)	1.810(3)	F(1)—C(10)	1.325(3)
F(2)—C(10)	1.332(3)	F(3)—C(10)	1.319(3)
N(1)—C(1)	1.323(3)	N(1)—C(3)	1.378(3)
N(2)—C(1)	1.340(3)	N(2)—C(2)	1.357(4)
N(3)—C(4)	1.318(3)	N(3)—C(6)	1.396(3)
N(4)—C(4)	1.337(3)	N(4)—C(5)	1.362(3)
N(5)—C(7)	1.334(3)	N(5)—C(9)	1.364(3)
N(6)—C(7)	1.346(3)	N(6)—C(8)	1.378(3)
C(2)—C(3)	1.362(3)	C(5)—C(6)	1.344(4)
C(8)—C(9)	1.355(3)		
	2		
Ru(1)—N(1)	2.100(2)	N(1)—C(1)	1.308(3)
N(1)—C(3)	1.361(3)	N(2)—C(1)	1.345(3)
N(2)—C(2)	1.342(4)	N(2)—C(4)	1.477(4)
C(2)—C(3)	1.341(4)		
	3		
Ru(1)—N(1)	2.093(2)	S(1)—O(1)	1.442(2)
S(1)—C(5)	1.794(7)	F(1)—C(5)	1.329(3)
N(1)—C(1)	1.335(3)	N(1)—C(3)	1.372(3)
N(2)—C(1)	1.347(3)	N(2)—C(2)	1.372(3)
C(2)—C(3)	1.362(3)	C(2)—C(4)	1.476(4)

effects (a trigonal planar nitrogen has a slightly shorter bond radius than a tetrahedral nitrogen). Clarke et al. (3) have misquoted this Ru^{II}—NH_3 bond length as 2.114(4) Å, and reached a different conclusion.

The N-Ru-N angles for all of the complexes mentioned above are essentially orthogonal, and the basic geometries of the imidazoles (Im, NMeIm, 5MeIm) are very similar. Hydrogen bonding is evident between the triflate oxygens and the H-atoms of the nonbonded N-atoms of the coordinated imidazoles (e.g., in Fig. 3, N(2)...O(1) = 2.885(3) Å, with N(2)-H...O(1) = 163.5°).

The ^{1}H nmr spectra for **1**–**3** reveal sharp, well defined peaks with δ values near those of the free ligands, consistent with imidazoles bonded to a diamagnetic Ru(II) centre; in d_6-DMSO, the N-H_1 signal is readily detected. Paramagnetic shifts diagnostic of analogous Ru(III) complexes (3, 14, 24) are not seen. Free Im has signals at δ 12.02 (H_1), 7.63 (H_2), and 7.00 (H_4 and H_5, these being equivalent due to tautomerization in solution); within complex **1**, H_1 shifts downfield to δ 12.47, H_2 upfield to δ 6.88, and H_4 and H_5 split into separate resonances at 6.22 and 7.23, respectively. The proximity of the H to Ru(II), a strong π-donor, determines whether the signal will be shifted upfield (as for H_2 and H_4), or downfield (as for H_5 and H_1). The ^{1}H spectrum for **2** shows the same trend, with H_5 shifting from δ 7.08 to 7.28, and H_2 and H_4 shifting upfield from δ 7.60 and 6.92 to 7.20 and 6.31, respectively; the N-Me signal shifts slightly downfield from δ 3.61 to 3.68. The resonances of the X-ray sample of complex **3** also followed the same trend: H_1 (δ 11.89 → 12.09), H_2 (δ 7.51 → 6.85), H_4 (δ 6.69 → 6.03), and 5Me (δ 2.16 → 2.40). Of note, the ^{1}H NMR data for the initially precipitated **3** (resonances for both H_4, H_5, and H_2 (overlapping), as well as overlapping Me resonances) most likely imply the presence of a 1:1 mixture of $[Ru(5MeIm)_6]^{2+}$ and $[Ru(5MeIm)_5(4MeIm)]^{2+}$ species; X-ray results show that $[Ru(5MeIm)_6]^{2+}$ preferentially crystallizes out. Clarke et al. (3) have noted similarly formation of complexes $[Ru(NH_3)_5(5MeIm)]Cl_3$ and $[Ru(NH_3)_5(4MeIm)]Cl_3$ in a 20:1 ratio from reaction of $[Ru(NH_3)_5(H_2O)]Cl_2$ with 4(5)MeIm in air. Our results also imply that there is a preference for formation of the less sterically demanding species, $[Ru(5MeIm)_6]^{2+}$.

Complexes **1–3** in MeOH show two UV bands: the higher energy absorbances come at 218, 224, and 228 nm, respectively, slightly higher wavelengths than those of the $\pi \rightarrow \pi^*$ transitions of the free ligands, but the ε values within the complexes are an order of magnitude greater than those of the free ligands. The lower energy UV maxima in **1**–**3** have ε values of (5.6–10.2) × 10^3 M^{-1} cm^{-1} and presumably correspond to an LMCT band (25, 26). Only complex **1** (which has a crystallographic centre of symmetry) has a band in the visible region (642 nm, ε = 33) typical of a *d–d* transition which is formally Laporte forbidden for an octahedral complex; however, in the presence of unsymmetrical vibrations the centre of symmetry can be destroyed, and vibronic transitions can be observed (25). Solutions of complexes **2** and **3** (which have crystallographic S_6 symmetry) do not exhibit an absorption maximum in the visible region.

The CV data for the Ru^{III}/Ru^{II} reduction potentials for **1** ($E°$ = 246 mV vs, Ag/AgCl) and **2** ($E°$ = 271 mV) in MeCN/TBAP compare with the values of 295 and 283 mV reported by Clarke et al. (3) for the Ru(III) salts $[Ru(Im)_6][ClO_4]_3$ and $[Ru(NMeIm)_6][PF_6]_3$, respectively, in aqueous chloride media. Our $E°$ value of 174 mV for **3**, the $(5MeIm)_6$ species, shows a relative stabilization of the Ru(III) state for this system.

Reaction of $[Ru(DMF)_6][CF_3SO_3]_3$ with 2MeIm

The reaction of 2MeIm, a more sterically demanding ligand than Im, NMeIm, and 5MeIm, with $[Ru(DMF)_6][CF_3SO_3]_3$ led to the isolation of a green solid (**4**), similar in appearance to complex **1**. However, **4** is formulated as *trans*-$[Ru(CO)(DMF)(2MeIm)_4][CF_3SO_3]_2$. The CO results from the decarbonylation of DMF, and the required co-product, dimethylamine, was detected. Such decarbonylation of DMF to generate metal carbonyls is well documented (27). An example analogous to that seen here is shown in eq. [1] (porp = porphyrin dianion) (28). It has

[1] $$Ru(porp)(DMF)_2 \rightarrow Ru(porp)(CO)(DMF) + Me_2NH$$

not been possible to obtain good elemental analysis or definitive NMR data for **4** because during attempts to remove associated DMF by pumping, the CO is removed to generate the brown complex $[Ru(DMF)(2MeIm)_4][CF_3SO_3]_2$ (**5**) and, of note, **4** can be regenerated by exposing solid **5** to 1 atm CO (see Scheme 1).

Complex **4** shows υ_{CO} bands in the IR at 2103 and 1654 cm^{-1} attributed to the CO and DMF ligands, respec-

© 1998 NRC Canada

Table 4. Bond angles (deg) with estimated standard deviations in parentheses. (Symmetry operations are listed in footnotes.)

Bonds	Angle (deg)	Bonds	Angle (deg)
	1		
N(1)-Ru(1)-N(1)[a]	180.0	N(1)-Ru(1)-N(3)	89.19(7)
N(1)-Ru(1)-N(3)[a]	90.81(7)	N(1)-Ru(1)-N(5)	90.72(7)
N(1)-Ru(1)-N(5)[a]	89.28(7)	N(3)-Ru(1)-N(3)[a]	180.0
N(3)-Ru(1)-N(5)	89.48(7)	N(3)-Ru(1)-N(5)[a]	90.52(7)
N(5)-Ru(1)-N(5)[a]	180.0	O(1)-S(1)-O(2)	114.65(11)
O(1)-S(1)-O(3)	115.10(12)	O(1)-S(1)-C(10)	103.04(12)
O(2)-S(1)-O(3)	114.75(12)	O(2)-S(1)-C(10)	103.19(13)
O(3)-S(1)-C(10)	103.83(12)	Ru(1)-N(1)-C(1)	128.0(2)
Ru(1)-N(1)-C(3)	126.81(15)	C(1)-N(1)-C(3)	105.1(2)
C(1)-N(2)-C(2)	107.8(2)	Ru(1)-N(3)-C(4)	128.16(15)
Ru(1)-N(3)-C(6)	127.20(15)	C(4)-N(3)-C(6)	104.5(2)
C(4)-N(4)-C(5)	107.4(2)	Ru(1)-N(5)-C(7)	127.60(15)
Ru(1)-N(5)-C(9)	127.27(15)	C(7)-N(5)-C(9)	105.1(2)
C(7)-N(6)-C(8)	107.4(2)	N(1)-C(1)-N(2)	111.4(2)
N(2)-C(2)-C(3)	106.0(2)	N(1)-C(3)-C(2)	109.7(2)
N(3)-C(4)-N(4)	112.0(2)	N(4)-C(5)-C(6)	106.6(2)
N(3)-C(6)-C(5)	109.6(2)	N(5)-C(7)-N(6)	111.1(2)
N(6)-C(8)-C(9)	105.5(2)	N(5)-C(9)-C(8)	110.9(2)
S(1)-C(10)-F(1)	111.8(2)	S(1)-C(10)-F(2)	111.5(2)
S(1)-C(10)-F(3)	111.5(2)	F(1)-C(10)-F(2)	106.9(2)
F(1)-C(10)-F(3)	107.1(2)	F(2)-C(10)-F(3)	107.8(2)
	2		
N(1)-Ru(1)-N(1)[b]	90.05(7)	N(1)-Ru(1)-N(1)[c]	180.0
N(1)-Ru(1)-N(1)[d]	89.95(7)	Ru(1)-N(1)-C(1)	127.8(2)
Ru(1)-N(1)-C(3)	128.1(2)	C(1)-N(1)-C(3)	104.0(2)
C(1)-N(2)-C(2)	106.9(2)	C(1)-N(2)-C(4)	126.8(3)
C(2)-N(2)-C(4)	126.3(3)	N(1)-C(1)-N(2)	112.0(3)
N(2)-C(2)-C(3)	106.1(3)	N(1)-C(3)-C(2)	111.0(3)
	3		
N(1)-Ru(1)-N(1)[e]	92.81(8)	N(1)-Ru(1)-N(1)[f]	180.0
N(1)-Ru(1)-N(1)[g]	87.19(8)	O(1)-S(1)-O(1)[h]	114.56(8)
O(1)-S(1)-C(5)	103.72(10)	Ru(1)-N(1)-C(1)	124.9(2)
Ru(1)-N(1)-C(3)	129.0(2)	C(1)-N(1)-C(3)	105.8(2)
C(1)-N(2)-C(2)	109.1(2)	N(1)-C(1)-N(2)	109.8(2)
N(2)-C(2)-C(3)	104.7(2)	N(2)-C(2)-C(4)	123.1(2)
C(3)-C(2)-C(4)	132.2(3)	N(1)-C(3)-C(2)	110.6(2)
S(1)-C(5)-F(1)	110.4(3)	F(1)-C(5)-F(1)[h]	108.5(3)

[a] $1 - x, 1 - y, 1 - z$.
[b] $-y, x - y, z$.
[c] $-x, -y, -z$.
[d] $y, -x + y, z$.
[e] $-y, x - y, z$.
[f] $-x, -y, -z$.
[g] $y, -x + y, -z$.
[h] $-1 - x + y, -x, z$.

tively (for free CO and DMF, these bands appear at 2143 and 1673 cm^{-1}). More typically, υ_{CO} values for Ru(II)-N donor systems are in the range ~ 2010–1920 cm^{-1} (29, 30), and it should be recalled that the υ_{CO} value is dependent on the medium used for measurement (for example, υ_{CO} values for $[Ru(NH_3)_5CO]^{2+}$ vary from 1993 to 1923 cm^{-1} depending on the associated anion and the medium) (29). A υ_{CO} value of 2008 cm^{-1} is seen for a *trans*-Ru(porp)$(CO)_2$ species; the mutually *trans*-π-acceptor carbonyls expectedly lead to a high υ_{CO} and a relatively labile CO ligand (30). For *tcc*-$RuCl_2(CO)_2(PPh_3)_2$, the *cis*-carbonyls are each trans to the π-acceptor phosphines and υ_{CO} values of 2059 and 1995 cm^{-1} are recorded (31). The π-electron density available from the Ru(II) for back-bonding to the CO of **4** must be minimal, resulting in the remarkably high υ_{CO} value of 2103 cm^{-1}, a weak Ru—CO bond, and high lability of the CO. We did consider that the 2103 cm^{-1} band might result from "occluded" rather than coordinated CO; however, we have been

© 1998 NRC Canada

Scheme 1. Conversion of **4** → **5** → **6**, with suggested formulations (L = 2MeIm).

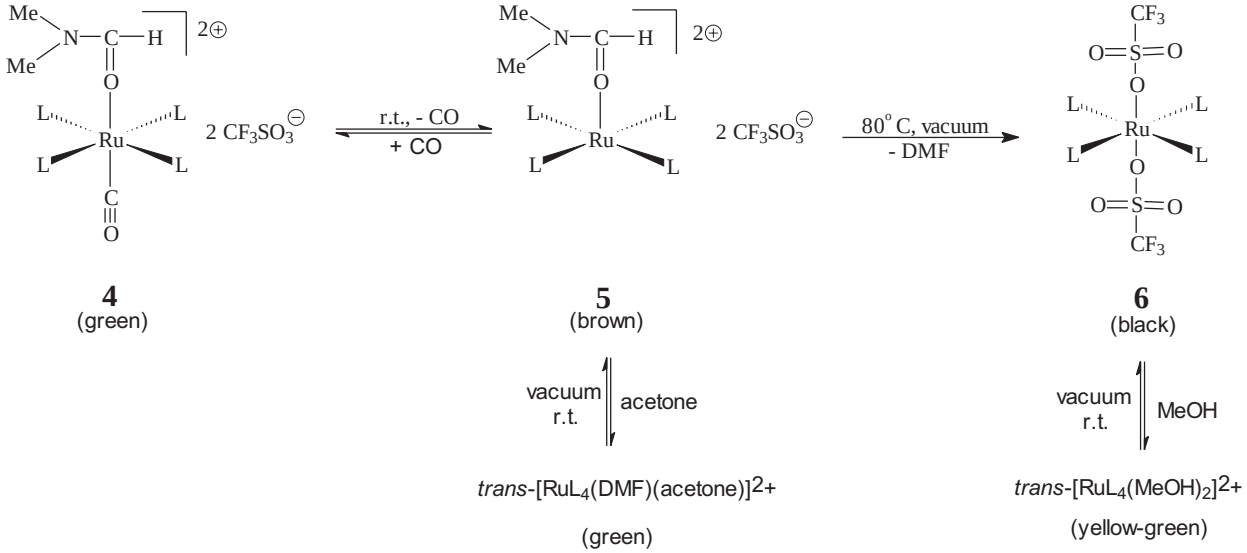

unable to find experimental evidence for this. The υ_{CO} value for the DMF in **4** is some 20 cm^{-1} below that of free DMF (υ_{CO} 1673 cm^{-1}), while that for $Ru(DMF)_6^{2+}$ is 1635 cm^{-1}. The IR spectrum of **5** is essentially identical to that of **4**, except the υ_{CO} for the CO has disappeared and υ_{CO} (DMF) has shifted to 1648 cm^{-1}, consistent with somewhat more π-back bonding available from Ru(II) to the carbonyl of DMF.

We have been unable to isolate an analytically pure sample of **5**, as its generation from **4** always leads to contamination by $[Ru(CF_3SO_3)_x(2MeIm)_4][CF_3SO_3]_y$ (**6**) (see below) which is formed from **5** by removing the coordinated DMF under vacuum (Scheme 1). Nevertheless, ^1H NMR data for samples of **5** reveal the existence of one coordinated DMF with inequivalent Me resonances at δ 3.22 and 3.10, and the formyl proton seen at δ 8.40 (these signals are downfield from those of free DMF and are comparable to those found for $[Ru(DMF)_6]^{2+}$) (16). The brown **5** reacts with acetone to give a green solution, and a singlet at δ 2.14 (downfield from that of free acetone, δ 2.04) is assigned to coordinated acetone; the acetone can be removed in vacuo to regenerate **5** (Scheme 1).

Complex **6** (Scheme 1) is obtained as an analytically pure solid; the black colour is unusual and we originally thought the complex might be $[Ru(2MeIm)_4][CF_3SO_3]_2$ containing tetrahedrally coordinated Ru. However, the NMR data and an Evan's method magnetic moment measurement (32) illustrate the diamagnetic character of **6**. On dissolution in MeOH, species **6** shows an immediate conductivity corresponding to a 1:1 electrolyte, but this increases over 3 h to a maximum Λ_M typical of a 2:1 electrolyte (33); during the conductivity measurements, the original black solution fades to a final yellow–green colouration, presumably due to *trans*-$[Ru(2MeIm)_4(MeOH)_2]^{2+}$. The data cannot distinguish between (*i*) **6** being a neutral, six-coordinate species with *trans*-triflate ligands, which on dissolution in MeOH immediately dissociates one triflate ligand, and then the second one is slowly displaced, and (*ii*) **6** being a five-coordinate species $[Ru(CF_3SO_3)(2MeIm)_4][CF_3SO_3]$ that in MeOH slowly loses the coordinated triflate. Of note, the measured υ_{SO} values for the triflate anion within $[Ru(DMF)_6][CF_3SO_3]_3$ and the $[RuL_6][CF_3SO_3]_2$ complexes **1**– **3** are seen at 1255, 1253, 1270, and 1263 cm^{-1}, respectively; in **6,** two IR bands are seen at 1280 and 1251 cm^{-1}, and such splitting could be consistent with the presence of coordinated triflate (34). Contrary to such reasoning, however, complexes **4** and **5** also show "split" bands in this region of the IR spectrum (1283 and 1249, and 1284 and 1248 cm^{-1}, respectively). Complex **5** could be reformulated as the six-coordinate species $[Ru(CF_3SO_3)(DMF)(2MeIm)_4][CF_3SO_3]$, but **4** cannot contain coordinated triflate. The measured υ_{CF3} values for **1**–**3** are seen at 1173, 1151, and 1170 cm^{-1}, while those for **4**–**6** were observed at 1167, 1167, and 1169 cm^{-1}, respectively, suggesting this IR band cannot be used as a diagnostic tool for the presence of absence of coordinated triflate. More definite evidence is needed to identify unambiguously species **4**–**6**. The incorporation of the sterically hindered 2MeIm ligand certainly enriches the chemistry of these Ru(II)-imidazole species.

Acknowledgements

This work was supported by the Natural Sciences and Engineering Research Council of Canada (operating grant to B.R.J. and a postgraduate fellowship to I.R.B.). Johnson Matthey, Ltd., and Colonial Metals Inc. kindly donated the $RuCl_3 \cdot 3H_2O$.

References

1. M.J. Clarke. Met. Ions Biol. Syst. **11**, 231 (1980).
2. B.K. Keppler (*Editor*). Metal complexes in cancer chemotherapy. VCH, Weinheim, Germany. 1993. p. 429.
3. M.J. Clarke, V.M. Bailey, P.E. Doan, C.D. Hiller, K.J. LaChance-Galang, H. Daghlian, S. Mandal, C.M. Bastos, and D. Lang. Inorg. Chem. **35**, 4896 (1996).
4. M. McNamara and M.J. Clarke. Inorg. Chim. Acta, **195**, 175 (1992).
5. M.J. Clarke and H. Taube. J. Am. Chem. Soc. **96**, 5413 (1974).
6. O.M.N. Dhubhghaill, W.R. Hagen, B.K. Keppler, K.-G. Lipponer, and P.J. Sadler. J. Chem. Soc. Dalton Trans. 3305 (1994).

© 1998 NRC Canada

7. M. Hartmann, T.J. Einhäuser, and B.K. Keppler. J. Chem. Soc. Chem. Commun. 1741 (1996).
8. T.D. Ocain, C.M. Bastos, K.A. Gordon, R.D. Granstein, J.C. Jenson, B. Jones, D.J. McAuliffe, and J.R. Newcomb. Transplant. Proc. **28**, 3032 (1998).
9. M.J. Clarke. *In* Metal complexes in cancer chemotherapy. *Edited by* B.K. Keppler. VCH, Weinheim, Germany. 1993. pp. 179–186; L. Marzilli, M. Iwamato, E. Alessio, L. Hansen, and M. Calligaris. J. Am. Chem. Soc. **116**, 815 (1994).
10. M.J. Clarke. Prog.Clin. Biochem. Med. **10**, 25 (1989).
11. B.K. Keppler, D. Wehe, H. Endres, and W. Rupp. Inorg. Chem. **26**, 844 (1987).
12. B.K. Keppler, W. Rupp, U.M. Juhl, H. Endres, R. Niebl, and W. Balzer. Inorg. Chem. **26**, 4366 (1987).
13. J. Chatlas, R. van Eldik, and B.K. Keppler. Inorg. Chim. Acta, **233**, 59 (1995).
14. C. Anderson and A.L. Beauchamp. Inorg. Chem. **34**, 6065 (1995).
15. C.M. Bastos and T.D. Ocain. U.S. Patent 5708022A (1998), through Chem. Abst. **128**, 123 807 (1998).
16. R.J. Judd, R. Cao, M. Biner, T. Armbruster, H.-B. Bürgi, A.E. Merbach, and A. Ludi. Inorg. Chem. **34**, 5080 (1995).
17. R. Cao. M.Sc. Thesis, University of Bern. 1992.
18. *d*TREK: Area Detector Software*. Version 3.13. Molecular Structure Corporation. The Woodlands, Tex., U.S.A. 1998; *teXsan: Crystal structure analysis package*. Unix version 1.8. Molecular Structure Corporation. The Woodlands, Tex., U.S.A. 1997.
19. (*a*) International tables for X-ray crystallography. Kynoch Press. Birmingham, U.K. (present distributor Kluwer Academic Publishers: Boston, Mass, U.S.A.). 1974. Vol. 4. pp. 99–102; (*b*) International tables for crystallography. Kluwer Academic Publishers. Boston, Mass., U.S.A. 1992. Vol. C. pp. 200–206.
20. P.S. Hallman, T.A. Stephenson, and G. Wilkinson. Inorg. Synth. **12**, 237 (1970).
21. D-H. Chin, A.L. Balch, and G.N. La Mar. J. Am. Chem. Soc. **102**, 1446 (1980); J.P. Collman, R.R. Gagne, T.R. Halbert, J.-C. Marchon, and C.A. Reed. J. Am. Chem. Soc. **95**, 7868 (1973).
22 R.G. Wilkins. Kinetics and mechanism of reactions of transition metal complexes. 2nd ed. VGH, New York. 1991. Chap. 4.
23. H.C. Stynes and J.A. Ibers. Inorg. Chem. **10**, 2304 (1971).
24. C. Anderson and A.L. Beauchamp. Inorg. Chim. Acta, **233**, 33 (1995).
25. J.E. Huheey, E.A. Keiter, and R.L. Keiter. Inorganic chemistry. 4th ed. Harper Collins, New York. 1993. pp.433–459.
26. R.J. Sundberg, R.F. Bryan, I.F. Taylor, Jr., and H. Taube. J. Am. Chem. Soc. **96**, 381 (1974).
27. R.M. Belani, B.R. James, D. Dolphin, and S.J. Rettig. Can. J. Chem. **66**, 2072 (1988), and refs. therein.
28. B.R. James, A.W. Addison, M. Cairns, D. Dolphin, N.P. Farrell, D.R. Paulson, and S. Walker. *In* Fundamental research in homogeneous catalysis. Vol. 3. *Edited by* M. Tsutsui. Plenum Press, New York. 1979. p. 751.
29. J. Chatt, G.J. Leigh, and N. Thankarajan. J. Organomet. Chem. **25**, C77 (1970).
30. M.J. Camenzind, B.R. James, and D. Dolphin. J. Chem. Soc. Chem. Commun. 2008 (1986).
31. F. Porta, S. Tollari, C. Bianchi, and S. Recchia. Inorg. Chim. Acta, **24**, 79 (1996).
32. D.F. Evans. J. Chem. Soc., 2003 (1959); D.H. Live and S.I. Chan. Anal. Chem. **42**, 791 (1970).
33. W.J. Geary. Coord. Chem. Rev. **7**, 81 (1971).
34. M.G. Miles, G. Doyle, R.P. Cooney, and R.S. Tobias. Spectrochim. Acta, **25A**, 1515 (1969); T. Otieno, S.J. Rettig, R.C. Thompson, and J. Trotter. Can. J. Chem. **68**, 1901 (1990).

© 1998 NRC Canada

Molecular modelling studies of a nerve growth factor receptor

Igor L. Shamovsky, Gregory M. Ross, Richard J. Riopelle, and Donald F. Weaver

Abstract: Using computer simulations, a geometry for the receptor binding site for nerve growth factor (NGF) has been proposed. Variable basis Monte Carlo simulated annealing calculations have been used to ascertain the structures of the complexes of four fully active NGF analogues with the second leucine-rich motif (LRM-2) of trkA, a putative binding site for NGF. The previously suggested bioactive conformation of the amino and carboxyl termini of NGF docks favourably with the receptor defined by the LRM-2 of trkA: only minor conformational changes take place in the NGF analogues upon docking. Extensive intermolecular van der Waals contacts arise from the geometric fit of the NGF binding domain to the LRM-2. Within this receptor environment, five distinct binding areas reveal a highly selective multiple-point NGF–trkA recognition based on hydrophobic, ionic, hydrogen bonding, and van der Waals interactions. Binding specificity is determined primarily by residues Lys^{100}, Asp^{109}, and Phe^{113} of trkA which bind to conserved NGF residues Asp^{16}, Arg^{114}, Lys^{115}, and Phe^{7}. An explicit atom-level model of the high-affinity NGF receptor is thus developed.

Key words: NGF, trkA, leucine-rich motif, protein docking, Alzheimer's disease.

Résumé : Utilisant les résultats de simulations par ordinateur, on propose une géométrie pour le site de liaison du récepteur pour le facteur de croissance des nerfs (FCN). On a utilisé des calculs de Monte Carlo à base variable pour évaluer les structures des complexes de quatre analogues actifs du FCN avec le deuxième motif riche en leucine («LRM-2») du trkA, a site de liaison putatif du FCN. La conformation bioactive proposée antérieurement pour les extrémités amino et carboxyle du FCN s'adapte favorablement au récepteur défini par le «LRM-2» du trkA: lors de la jonction, il ne se produit que de faibles changements conformationnels. Sur la base de l'ajustement géométrique du domaine de fixation du FCN au «LRM-2», il se développe d'important contacts de van der Waals intermoléculaires. Dans le cadre de l'environnement de ce récepteur, on observe que cinq portions distinctes de fixation donnent lieu à une reconnaissance FCN–trkA en plusieurs points et hautement sélective découlant d'interactions hydrophobes, ioniques, de liaisons hydrogènes et de van der Waals. La spécificité de la liaison est déterminée principalement par les résidus Lys^{100}, Asp^{109}, et Phe^{113} du trkA qui se lie aux résidus Asp^{16}, Arg^{114} et Phe^{7} préservés du FCN. On a ainsi développé un modèle explicite au niveau atomique du récepteur à grande affinité du FCN.

Mots clés : FCN, trkA, motif riche en leucine, jonction de protéines, maladie d'Alzheimer.

[Traduit par la Rédaction]

1. Introduction

Nerve growth factor (NGF), a protein involved in the pathogenesis of diverse neurological disorders, is the prototypical member of the neurotrophin family, which also includes brain-derived neurotrophic factor (BDNF), neurotrophin-3 (NT-3), and neurotrophin-4/5 (NT-4/5). Neurotrophins transduce intracellular signalling through the activation of a class of transmembrane tyrosine kinase receptor proteins (trkA, trkB, and trkC). Specificity of action of neurotrophins results from their selective interactions with members of the trk family of receptors: NGF–trkA, BDNF–trkB, NT-4/5–trkB, and NT-3–trkC, particularly when the trk's are coexpressed with the common neurotrophin receptor $p75^{NTR}$ (1–5). Explicit modelling of these receptors will be critical to the rational design of neurotrophin based drugs.

The NGF displays high and low affinity binding sites in sensory and sympathetic neurons and in pheochromocytoma PC12 cells (6–8). The coexpression of the common neurotrophin receptor $p75^{NTR}$ with trkA is required to form the high affinity binding site (9–12). Several models of the trkA–$p75^{NTR}$ interaction have been proposed to explain high

Received May 19, 1998.

I.L. Shamovsky and D.F. Weaver.[1] Departments of Chemistry and Medicine, Queen's University, Kingston, ON K7L 3N6, Canada.
G.M. Ross and R.J. Riopelle. Departments of Medicine, and Pharmacology and Toxicology, Queen's University, Kingston, ON K7L 3N6, Canada.

[1]Author to whom correspondence may be addressed. Telephone: (613) 545-6521. Fax: (613) 545-6669.
E-mail: weaver@chem.queensu.ca

© 1998 NRC Canada

affinity NGF binding (12–17). These models differ with respect to direct (conformational model) or indirect (ligand-presentation model) interaction of $p75^{NTR}$ with trkA. Direct trkA–$p75^{NTR}$ interaction is consistent with much of the existing experimental data (12, 17).

While several regions of NGF participate in the NGF–trkA interaction (3–5, 18, 19), mutation studies suggest that relatively few key residues, namely those located in the NGF amino and carboxyl termini, are required for high affinity binding (1, 19–37). The amino and carboxyl terminal regions therefore represent a "functional epitope" which contains relatively few contact residues mediating high affinity binding. The ability of a small number of residues to cause high affinity binding has previously been demonstrated and may represent a general property of protein–protein interface (38). Although a crystallographic structure of NGF has been reported (39, 40), geometry of the important amino (residues 1–11) and carboxyl (residues 112–118) termini remain unresolved. Because of high flexibility of the NGF termini, it is difficult to determine *experimentally* their bioactive conformations, particularly since transition metal cations commonly used in X-ray crystallography (39, 40) have high affinity for His residues (41) and thus may affect conformation of the NGF amino terminus. Indeed, conformational alterations within the receptor binding domains of NGF caused by transition metal cations Zn^{2+}, Cu^{2+}, and Pd^{2+} (leading to inactivation of NGF) have been described recently (42, Ross et al., submitted). A bioactive conformation of the NGF termini has been obtained *theoretically* using variable basis Monte Carlo simulated annealing (VBMC) computations (43), providing a structure compatible with experimental observations.

The location of the binding site for NGF within the trkA receptor is the subject of debate (44). Based upon published data, there is reason to believe that two trkA interactive motifs in NGF may conform to two putative NGF binding sites on the trkA protein: the "second immunoglobulin-like domain" (IgC2, residues Trp^{299}–Asn^{365}) and the "second leucine-rich motif" (LRM-2, residues Thr^{97}–Leu^{120}) (18, 37, 44–49). The LRM containing proteins represent a diverse group of molecules with different functions and cellular locations, and are known to mediate strong and selective protein–protein interactions (50–52). The amino acid sequence of a LRM is characterized by conserved hydrophobic consensus residues (45, 50–53). Typically, LRMs exist as repetitive cassettes, with an individual LRM representing a right-handed β-α hairpin unit (50–52). Recent crystallographic studies on porcine ribonuclease inhibitor indicate that the side chains of the consensus residues form the hydrophobic core of the LRM modules, thereby determining their geometric features (50).

In this study we report an explicit atom-level model of the trkA receptor site for NGF. To deduce this model, we have investigated the interaction of the bioactive conformation of the NGF amino and carboxyl termini region with the LRM-2 binding site of trkA. A series of four active NGF analogues, namely human NGF (hNGF) (23, 32), mouse NGF (mNGF) (23, 28), the 3-9 deletion of mNGF (mNGFΔ3-9) (28) and the hNGF:NT-4/5 heterodimer (35), have been docked to the LRM-2 of rat trkA. For all four NGF molecules studied, a stereochemical fit of the LRM-2 to the amino and carboxyl region was demonstrated. These results suggest that the bioactive conformation of the NGF termini represent a functional epitope which mediates high affinity binding via an interaction with the LRM-2 of trkA.

2. Methods

A sequence of three logical steps has been used to deduce a model of the interaction of NGF with its trkA receptor binding site. *Step 1*: the bioactive conformations of the amino and carboxyl termini of NGF analogues were determined; *Step 2*: the residues of the trkA protein which form a potential binding site for NGF were identified; *Step 3*: the interaction of the bioactive conformation of the NGF amino and carboxyl termini with the trkA binding site was modeled computationally. Finally, the predicted features of the NGF–trkA interaction model were validated against available experimental data. For this study, residues of the first NGF monomer are designated 1 to 118, those of the second monomer are designated 1′ to 118′; the LRM-2 residues have double-primed numbering.

2.1. Step 1: revealing the bioactive conformation of the NGF termini

The most energetically favoured conformations of the amino and carboxyl termini of NGF analogues have been obtained by VBMC computations and have been reported previously (43). Since three-dimensional structures of the termini of fully active NGF molecules were different from those of trkA-inactive analogues, these conformations were predicted to be "bioactive" for trkA-mediated activity of NGF. This implies that those geometric features, which are exclusively inherent in active NGF molecules, are anticipated to be compatible with the structure of the trkA binding site for NGF.

2.2. Step 2: selection of the LRM-2 boundaries within the trkA receptor

Since there is controversy in the literature regarding the actual boundaries of LRMs (45, 48–53), the following experimental background (Fig. 1) was used to define boundaries for this computational study. According to Schneider and colleagues (45, 53), the LRM domains of trkA begin with $Leu^{68''}$, $Leu^{93''}$, and $Leu^{117''}$, whereas those boundaries are slightly shifted in the crystallographic studies of Kobe and Deisenhofer (50). Furthermore, the boundaries of the "minimal" LRM module of trkA (designated B4 in Fig. 1), which demonstrates the same NGF binding affinity as wild type trkA, is substantially shifted towards the carboxyl terminus (48, 49) with respect to those suggested by Schneider and colleagues (45, 53). However, a comparison of active (B1 and B4) and inactive (N4) LRM domains indicates that the presence of the minimal amino acid sequence (B4) does not ensure NGF binding. Understanding those factors which maintain the essential features of the LRM geometry in segments B1 and B4, but which destroy them in N4, is of fundamental relevance to the correct assignment of the LRM boundaries.

β-Strand motifs exist in proteins only if hydrogen bonded (H-bonded) to other β-strands; otherwise their structure is unstable (51). Tandems of LRMs represent a prominent ex-

© 1998 NRC Canada

Fig. 1. The trkA leucine-rich motifs. Locations of parallel β-strands are illustrated by the shaded areas designated by symbol β. Fragments B1–B4 demonstrate NGF binding affinity, while N1–N4 do not (48, 49).

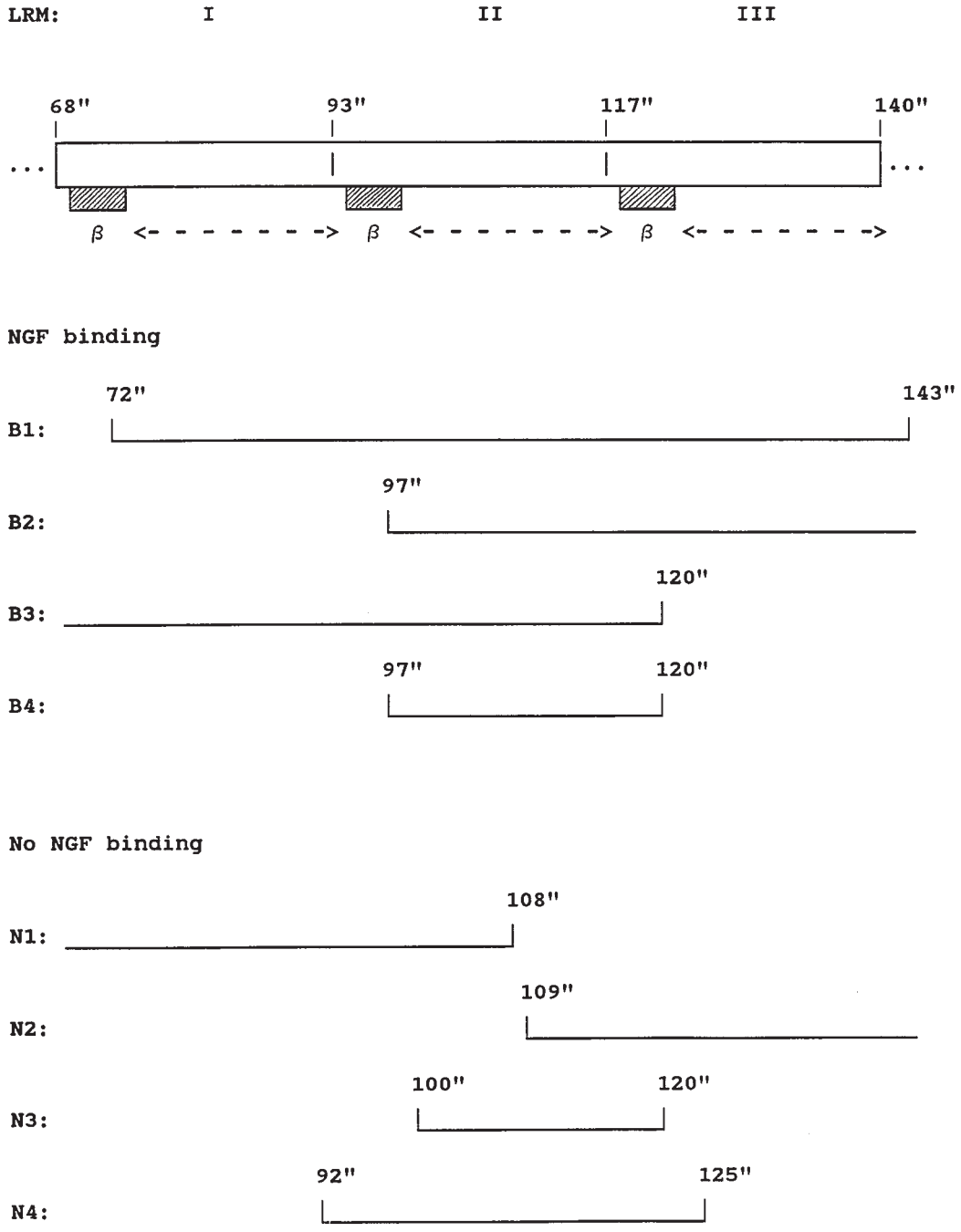

ample of H-bonded parallel β-strand motifs. The general location of the β-strand motifs in the LRM according to X-ray data is illustrated in Fig. 1; however, in a single LRM their particular geometry is destroyed (50–52). Consequently, disruption of the inter-strand H-bonding between β-strand motifs results in dramatic conformational changes, and the only way to preserve a characteristic geometry of a protein domain is to exclude those motifs. Accordingly, both boundaries of segment B4 are located in the middle of the β-strand regions of the adjacent LRMs such that this segment appears to be free of any β-strand. Nevertheless, the β-strand motif is a characteristic structural unit of LRMs, and thus it is likely that this unit is also involved in the NGF–trkA recognition process. Additionally, a short exposed β-strand motif has been detected in the bioactive conformation of the NGF termini (43). The incorporation of the β-strand regions at both sides of the B4 segment (as in N4) results in cooperative H-bonding between these β-strands and a complete loss of NGF binding, which indicates that accessibility of the β-strand motif for intermolecular contacts is essential. On the other hand, the separation of the entire LRM segment from the adjacent LRMs within the B1 molecule as a result of conformational kinking is likely to be energetically more favourable, since the entire LRM module has the internal sta-

© 1998 NRC Canada

bilizing factors. Moreover, kinking between the adjacent LRMs within the LRM tandem does not disrupt the structure of their β-strand motifs (since they remain H-bonded with their opposite sides), but makes them accessible for molecular recognition processes.

Accordingly, in the present study we used the conventional boundaries of the LRMs of trkA (45, 53), which keep the β-strand motif in the LRM, and we explicitly arranged H-bonding of this unit with the parallel β-strand motif of the NGF amino terminus (43) to preserve it from conformational reorganizations. Thus, the trkA segment between residues $Leu^{93''}$ and $Leu^{117''}$ was designated the LRM-2 of trkA.

2.3. Step 3: computational simulation of the NGF–trkA interaction

The docking interaction between the NGF termini (from Step 1) and the trkA receptor fragment (from Step 2) was simulated using a combined VBMC/CHARMM approach. VBMC is an algorithm which permits a search of conformational space (43); CHARMM is a force field which defines conformational energy (54). The goal of Step 3 was to investigate the stereochemical fit of the predicted bioactive conformation of the NGF binding determinant (43) to a putative trkA receptor binding site for NGF (48, 49) rather than to comprehensively explore the whole configurational space of the ligand–receptor complexes.

The VBMC algorithm performs conformational and orientational space searches of a complicated molecular system with the aim of finding the structure which corresponds to the global minimum on the potential energy E_{tot} surface. Periodical rotation of a basis of configurational variables in the framework of the VBMC algorithm results in directing individual Monte Carlo moves along the soft modes of a molecular system, which accelerates molecular motions and conformational transitions (43).

$$[1] \qquad E_{tot} = E_t + E_w + E_e + E_{hb} + E_{qq} + E_{hy} + E_c$$

The following potential energy terms have been considered in the framework of the united atom CHARMM force field (54; the force field parameters have been extracted from CHARMM version 23.1, Molecular Simulations Inc., San Diego, Calif.): torsional distortion E_t, van der Waals interactions E_w, electrostatic interactions E_e, and hydrogen bonding E_{hb}. Since the united atom approach is not appropriate to treat rigorously the quadrupole–quadrupole interactions of benzene rings (which are important for determining their mutual orientations in proteins (55, 56), single quadrupoles have been placed at the centers of the benzene rings of phenylalanine and tryptophan, and the energy of the quadrupole–quadrupole interactions, E_{qq}, has been calculated as suggested by Schauer and Bernstein (57). (The potential energy function of two interacting benzene molecules comprised of the E_{qq} and E_w terms has stationary points corresponding to both known electrostatically favourable "edge-to-face" and "offset stacked" orientations with the dimerization energy of 1.94 kcal/mol agreeing well with ab initio quantum mechanical calculations (58).) In addition, the conformationally dependent free energy of hydration, E_{hy}, has been calculated according to the hydration shell model including both nonspecific and specific hydration terms (59, 60). A dielectric constant equal to the interatomic separation in angstroms has been used to implicitly simulate solvation effects (61).

The E_c term represents the distance constraints which maintain the H-bonding pattern of residues Glu^{11}, His^{8}, and $Arg^{118'}$ inherent in the bioactive conformation of the NGF termini (three H-bonds; ref. 43). In addition, two intermolecular H-bonds, arising from the alignment of complementary parallel β-strand motifs of NGF and LRM-2, are also constrained and contribute to E_c. In the Monte Carlo conformational space search, E_c is defined as follows:

$$[2] \qquad E_c = 10 \times \sum_{AB} (d_{AB} - 1.8)^2$$

where d_{AB} is the distance in angstroms between selected atoms A and B which are to be H-bonded (the sum includes only five additives). The E_c term is neglected when performing final energy minimization following the VBMC simulated annealing. In addition, this term has not been utilized when studying the mNGFΔ3-9/LRM-2 complex. Since the mNGFΔ3-9 deletion mutant does not have a β-strand region (43), the geometry of its LRM-2 counterpart, namely $Leu^{93''}$-$Ile^{98''}$, has been kept fixed in the crystallographic conformation (50) during Monte Carlo simulations. The E_c term, being "soft," does not preclude conformational and orientational changes to occur during Monte Carlo simulations. This term increases rigidity of the bioactive conformation of the ligand, which allows us to utilize the knowledge obtained at Step 1 instead of explicit considerations of inactive NGF analogues in Step 3. In addition, this term keeps conformations of the β-strands of both ligand and binding site from destruction, and thereby allows us to avoid an explicit consideration of the adjacent first LRM of trkA. Furthermore, this term maintains the known orientation of the parallel β-strand motifs.

The amino acid sequences of the binding determinants of the NGF molecules under study are presented in Fig. 2. The conformational space of the NGF analogues consists of torsional angles determining geometry of the amino terminus of one monomer (residues 1–11) and the carboxyl terminus of the other (residues 112′–118′), while keeping the rest of the dimers in the experimental geometry of mNGF (39). The conformational space of the trkA LRM-2 consists of torsional angles representing fragment $Arg^{94''}$-$Leu^{117''}$. Covalent bond lengths and bond angles have been kept fixed. The geometry of each i-th residue is determined only by flexible torsional angles of the backbone (ϕ_i and ψ_i) and the side chain ($\chi_i 1$, $\chi_i 2$, ...). All torsional angles for prolines, except ψ_i have been fixed. Torsional angles describing structural motifs with planar geometries (such as peptide bonds or conjugated regions in side chains) were fixed. Likewise, the configurations of the sp^3-carbons were fixed. In addition to the conformational variables, the six orientational variables (three Euler angles and three translations along the coordinate axes) were used to describe the NGF/LRM-2 mutual orientations.

In accord with the simulated annealing approach (62–67), the molecular systems were kept at a constant temperature of 800 K for 2×10^6 Monte Carlo moves before the initiation of "cooling." The temperature was then decreased at every Monte Carlo move by a small increment such that after 2

© 1998 NRC Canada

Fig. 2. Sequences of amino and carboxyl termini of fully active NGF analogues. Regions with rigid structures are underlined.

First monomer: amino terminus

	1				5					10					15	
hNGF	S	S	S	H	P	I	F	H	R	G	E	F	S	V	C	D ...
mNGF	S	S	T	H	P	V	F	H	M	G	E	F	S	V	C	D ...
mNGFΔ3-9	-	-	-	-	-	-	-	S	S	G	E	F	S	V	C	D ...
hNGF:NT-4/5	S	S	S	H	P	I	F	H	R	G	E	F	S	V	C	D ...

Second monomer: carboxyl terminus

	75'							110'				115'					118'
hNGF	... K	H	W	N	...	C	V	C	V	L	S	R	K	A	V	R
mNGF	... K	H	W	N	...	C	V	C	V	L	S	R	K	A	T	R
mNGFΔ3-9	... K	H	W	N	...	C	V	C	V	L	S	R	K	A	T	R
hNGF:NT-4/5	... R	H	W	V	...	C	V	C	T	L	L	S	R	T	G	R

$\times 10^6$ Monte Carlo moves it reached 120 K; at this time, a local energy refinement was performed to identify the nearest stationary point on the potential energy surface. According to the VBMC algorithm, the basis of independent structural parameters was recalculated after every 7×10^4 Monte Carlo moves to direct them along the valleys of the potential energy surface, thereby accelerating conformational and orientational changes (43).

All calculations were performed on an Indigo-2 Silicon Graphics workstation and an 8-node IBM Scalable POWERparallel 2 [SP2] high performance computer.

3. Results and discussion

3.1. Conformational flexibility within receptor environment

Five independent VBMC simulations from different initial configurations were performed for each of the four molecular complexes under study. Geometries of the NGF analogues consistent with their predicted bioactive conformations (43) were the same in all of these initial configurations. The initial three-dimensional structure of the peptide backbone of the LRM-2 was the same in the independent runs being consistent with the observed geometry of the LRM domains in porcine ribonuclease inhibitor (50), whereas initial conformations of the LRM-2 amino acid side chains were random. The elimination of the distance constraints after the stationary point was reached did not result in any noticeable conformational changes within the complexes. Although independent VBMC simulations did not always converge to the same geometry for the same molecule, the final structures differed insignificantly; i.e., the conformations of the peptide backbones remained unchanged with the exception of residues 1–3 of the NGF amino terminus and the terminal residue $Leu^{117''}$ of the LRM-2. The differences between the VBMC generated structures were located in side-chain conformations of a limited number of residues, specifically Ser^{1}, $Val^{117'}$ ($Thr^{117'}$ in mNGF), $Thr^{97''}$, and $Ser^{101''}$. These residues are not involved in intermolecular or intramolecular interactions, and do not affect the overall structures of the complexes.

A grid search of the internal space of the complexes using a "water molecule" spherical probe with 1.4 Å radius (68), as incorporated into the QUANTA program (QUANTA version 4.1, Molecular Simulations Inc., San Diego, Calif.) shows that there is no internal cavity available for a solvent molecule in the hNGF/LRM-2 complex. This explains the rigidity of the complex and demonstrates the optimum stereochemical fit of the hNGF amino-carboxyl termini complex to the LRM-2.

3.2. Specific binding areas within receptor environment

Comparison of the most stable structures of the different complexes (Fig. 3) shows their striking conformational similarity. In all molecules, ligand–receptor binding is caused by similar hydrophobic, ionic, H-bonding, and van der Waals interactions. There are five distinct areas (A–E) within the NGF/LRM-2 fit: areas A and B have hydrophobic interactions, areas C and D have ionic H-bonding, and area E has the cooperative H-bonding between parallel β-strand motifs.

Area A represents the hydrophobic region at which residue $Phe^{105''}$ interacts with $Trp^{76'}$, which in turn forms hydrophobic contacts with Phe^{12} and $Leu^{112'}$. The aromatic rings of Phe^{12}, $Trp^{76'}$ and $Phe^{105''}$ are approximately perpendicular to each other, which is energetically favourable (55, 56, 58). This particular geometry would create a hole within the

© 1998 NRC Canada

Fig. 3. Predicted geometries of the free NGF binding domain (*a*; ref. 43) and the NGF/LRM-2 complexes of hNGF (*b*), mNGF (*c*), mNGFΔ3-9 (*d*), and hNGF:NT-4/5 (*e*). Only residues essential for discussion are designated. A, B, C, D, and E represent specific NGF/LRM-2 binding areas. The LRM-2 is illustrated in grey, NGF in white.

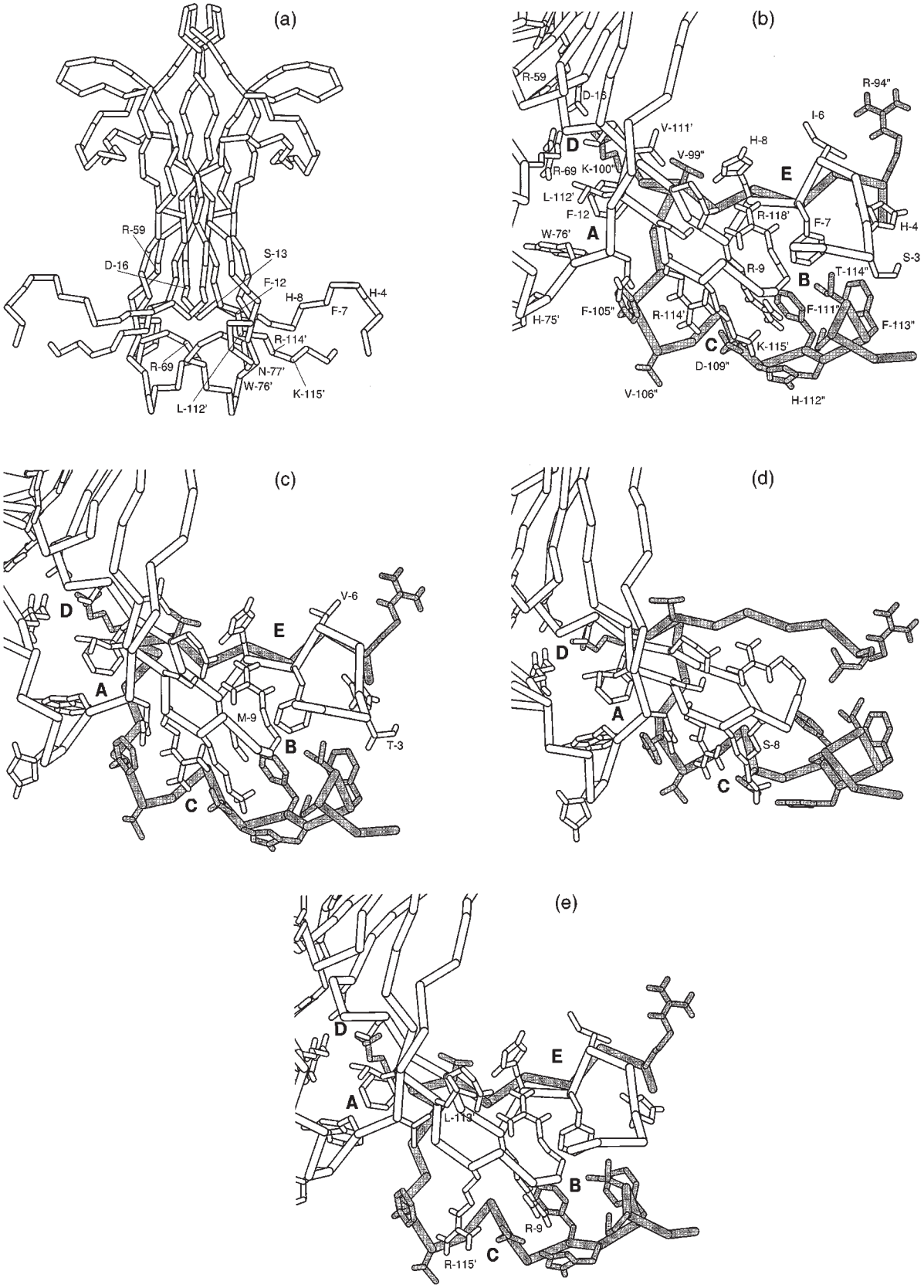

© 1998 NRC Canada

Table 1. Components of the molecular mechanical potential energy of the intermolecular NGF/LRM-2 interactions (in kcal/mol).

Term	hNGF	mNGF	mNGFΔ3-9	hNGF:NT-4/5
E_w	–61.2	–57.9	–39.3	–65.1
E_e	–96.2	–87.9	–99.0	–65.2
E_{hh}	–7.4	–5.9	–3.1	–4.6
E_{qq}	–0.3	–0.3	–0.1	–0.1
Total	–165.1	–152.0	–141.5	–135.1

complex, if it was not filled by hydrophobic residue Leu$^{112'}$. In area B, Phe^{7} of NGF is placed within the hydrophobic core of the LRM-2, created by the consensus residues (45, 50–53). Similar to the favourable orientation of the aromatic residues in area A, the aromatic rings of Phe$^{111''}$ and Phe$^{113''}$ are perpendicular to that of Phe^{7}. On the other hand, residues Phe$^{111''}$ and Phe$^{113''}$ are not perpendicular to each other; their orientation instead resembles the favourable offset stacked geometry described by Hunter and others (55, 56, 58). As in area A, a hole created by the three neighbouring favourably oriented aromatic rings is filled by the fourth residue, Thr$^{114''}$. Interactions between aromatic rings in proteins are very common and represent an important conformational driving force for folding and molecular recognition processes (56, 69). Consequently, the fact that all three phenylalanine residues of the LRM-2 find their counterparts within the NGF binding domain supports the structure of the NGF/LRM-2 complex.

In ionic binding area C, the negatively charged residue Asp$^{109''}$ exerts a central role. It is surrounded by the three positively charged amino acids His$^{112''}$, Arg$^{114'}$, and Lys$^{115'}$ in hNGF, mNGF and mNGFΔ3-9, and by His$^{112''}$, Arg$^{115'}$, and Arg^{9} in hNGF:NT-4/5. Residue His$^{112''}$ plays a secondary role: it creates the electrostatic dipole Asp$^{109''}$→His$^{112''}$ in the LRM-2, which imposes constraints to the spatial positions of the recognized positively charged residues of NGF, thereby reinforcing geometric selectivity in this area. Although the hNGF:NT-4/5 heterodimer has two substitutions in the C-area segment of the NT-4/5 carboxyl terminus, namely R114S and K115R, the geometry of the C area remains qualitatively the same, since residues Arg^{9} and Arg$^{115'}$ of hNGF:NT-4/5 functionally replace the absent Lys$^{115'}$ and Arg$^{114'}$ amino acids, respectively. Although Arg^{9} also exists in the hNGF homodimer, it is not involved in the ionic binding in this molecule, since it is separated from area C due to electrostatic repulsions. Similarly, the charged amino end of mNGFΔ3-9, which functionally replaces Arg^{9} (43), is also separated from area C. There is no place for the fourth positively charged residue in area C. Thus, in all molecules under study the two positively charged amino acids of the ligand saturate the coordination possibilities of the receptor residue Asp$^{109''}$.

Area C is partially isolated from its surrounding environment by flanking hydrophobic residues Val$^{106''}$ and Pro$^{115''}$. Similarly, the principal charged residues of NGF, namely His^{8}, Glu^{11}, and Arg$^{118'}$ (43), are located between hydrophobic residues Ile^{6} (Val^{6} in mNGF), Val$^{111'}$ (Leu$^{113'}$ in hNGF:NT-4/5), and Val$^{99''}$ within the complexes. Thus, residues Val$^{99''}$, Val$^{106''}$, and Pro$^{115''}$ of the LRM-2 participate in "compartmentalization" of the principal ionic interactions of the complexes, thereby shielding them from the destructive influence of solvation.

The organization of ionic binding area D is similar to that of area C. Positively charged residues Arg^{59} and Arg^{69} are located in the vicinity of negatively charged Asp^{16} within the NGF structure (4, 39) such that the coordination of the latter is not full. The third positively charged residue, Lys$^{100''}$, comes from the LRM-2 to complete the Asp^{16} coordination. In addition to the ionic binding, residue Lys$^{100''}$ forms a H-bond with the Ser^{13} side chain.

Area E consists of the H-bonded parallel β-strand motifs of the LRM-2 and NGF (Fig. 3*b*, *c*, and *e*), each of them consisting of three peptide bonds. The LRM-2 β-strand motif is located between the α-carbon atoms of Asn$^{95''}$ and Ile$^{98''}$ whereas the NGF β-strand is situated between the α-carbons of the sixth and ninth residues. The locations of the β-strand regions in the uncomplexed LRM (50) and NGF (43) resemble those in the complexes considered. In the complexed LRM-2, the β-strand motif is shortened by one peptide bond at the amino end to accommodate the His^{4} side chain of NGF. On the other hand, the two peptide bond β-strand of the uncomplexed NGF is lengthened by one peptide bond at its amino end in the complexes.

3.3. Ligand–receptor interaction energy

Table 1 presents the components of the intermolecular energies of the NGF–trkA complexes. Stability of the NGF/LRM-2 complexes is primarily caused by attractive electrostatic and van der Waals interactions, with intermolecular H-bonding playing a secondary role. It should be noted, however, that in the framework of the molecular mechanics approach, the H-bonding energy is partially incorporated into the electrostatic interaction energy term, so the tabulated E_{hb} values reflect only part of H-bonding energy. Accordingly, intermolecular H-bonding is more important for the NGF/LRM-2 interaction than it appears in Table 1. On the other hand, the intermolecular component of the E_{qq} term seems to be insignificant. The reason for the latter is that the aromatic moieties of Phe^{7}, Trp$^{76'}$, Phe$^{105''}$, Phe$^{111''}$, and Phe$^{113''}$ are "preorganized" for intermolecular contacts with their counterparts in the complexes in electrostatically attractive geometry in which the quadrupole–quadrupole interaction energy term is not significant. In addition, hydrophobic ligand–receptor interaction energy is presumably extremely important for the NGF/LRM-2 complexation, but rigorous quantitative evaluation is currently not possible.

Since neither electrostatic interactions nor hydrogen bonding can significantly stabilize the ligand–receptor complex in a water environment, the stability of the complex is generally caused by van der Waals and hydrophobic interactions (38). Considerable contribution of intermolecular van der Waals interaction energy E_w (Table 1) arises from the geometric complementarity of the NGF binding domain and the trkA recognition site, such that the high value of the E_w term is due to the large number of intermolecular van der Waals contacts. This complementarity is a consequence of the right-handed twists of both the NGF amino-carboxyl termini complex and the LRM-2, since this geometric feature is characteristic for each of these domains in both uncomplexed (43, 50) and complexed conformations. Thus,

© 1998 NRC Canada

Fig. 4. Detail of the LRM-2 conformation when bound to hNGF. The three groups of the β-strand backbone involved in H-bonding with parallel β-strand motif of the NGF analogues are designated by NH or CO. Hydrophobic residues are illustrated as light, polar uncharged as dark, charged as black.

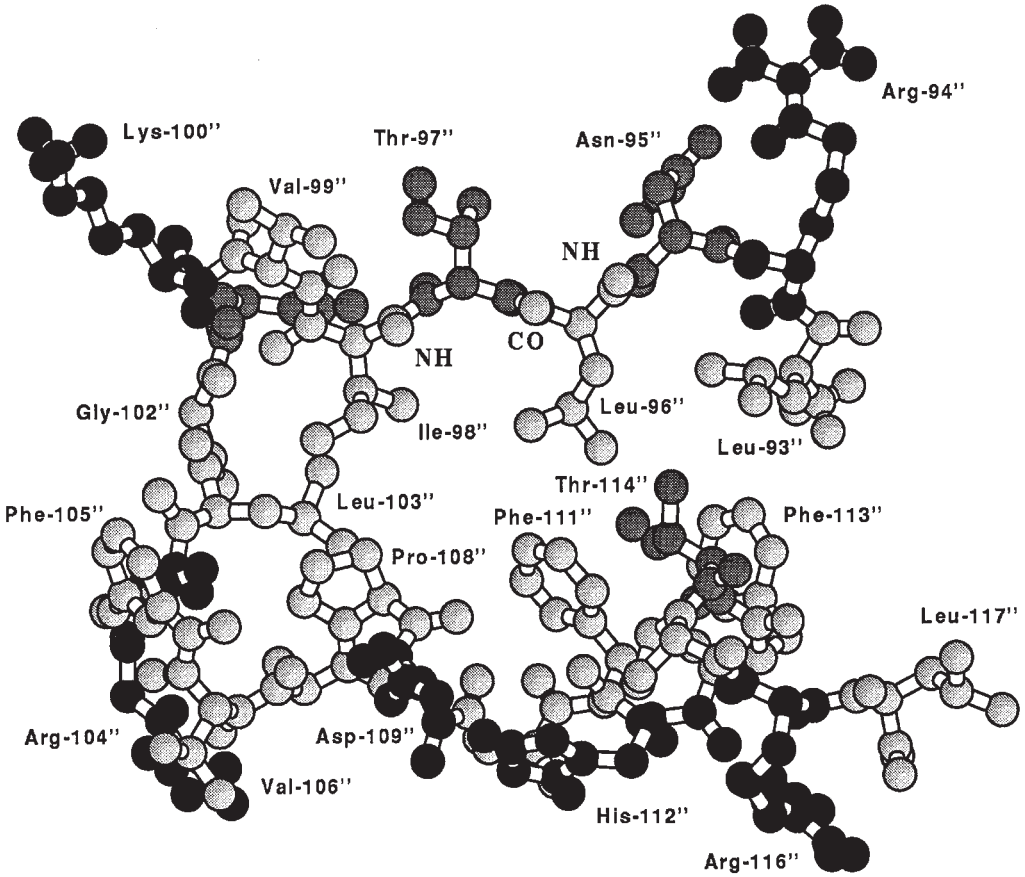

purely geometric ligand–receptor compatibility together with the distinct hydrophobic contacts play a crucial role in the NGF–trkA recognition, while attractive electrostatic interactions and H-bonding further reinforce specificity of binding, which is in agreement with generalizations made by Clackson and Wells (38).

3.4. Induced conformational changes

Conformations of the NGF amino and carboxyl termini remain almost the same after complexation with the LRM-2 (compare Fig. 3*a* with Fig. 3*b–e*). A few local conformational changes occur in the $Arg^{114'}$ and the $Lys^{115'}$ side chains, and in the backbones of residues Ser^{2} and Phe^{7}. As demonstrated previously (43), conserved charged residues $Arg^{114'}$ and $Lys^{115'}$ do not participate in principal intermolecular interactions within the NGF termini but are expected to form ionic intermolecular contacts with the trkA binding site. Indeed, these are the intermolecular ionic NGF/LRM-2 interactions in area C, which change considerably the side-chain conformations of $Arg^{114'}$ and $Lys^{115'}$ while keeping their backbone geometry intact. The LRM-2-induced conformational changes in residue Phe^{7} are caused by the intermolecular H-bonding in area E while the geometry of Ser^{2} is slightly changed to accommodate the LRM-2 residue $Thr^{114''}$. The rest of the structure of the LRM-2-complexed NGF termini retains the minimal energy conformation of the uncomplexed molecules because it is controlled by multiple intramolecular H-bonds (43). Consequently, the geometry of the NGF termini is "preorganized" for complexation with the LRM-2, and only local conformational changes, primarily in residues $Arg^{114'}$ and $Lys^{115'}$, occur upon complexation. Geometric "preorganization" of the NGF termini as a ligand for binding to a leucine-rich motif is consistent with X-ray studies of Kobe and Deisenhofer (52), who have demonstrated that ribonuclease A maintains a fixed geometry upon binding to the LRMs of ribonuclease inhibitor.

Figure 4 illustrates the isolated structure of the LRM-2 from the hNGF/LRM-2 complex. As seen, the side chains of the general consensus residues, $Leu^{93''}$, $Leu^{96''}$, $Ile^{98''}$, $Leu^{103''}$, and $Phe^{111''}$ (45, 53), form the hydrophobic core, similarly to their conformations in intact leucine-rich repeats (50). Terminal consensus residue $Leu^{117''}$ is solvent-exposed due to a boundary effect. Amino acids $Ala^{107''}$, $Pro^{108''}$, $Ala^{110''}$, and $Phe^{113''}$ are also incorporated into the LRM-2 hydrophobic core. On the other hand, residues $Val^{99''}$, $Phe^{105''}$, $Val^{106''}$, and $Pro^{115''}$ are not involved in hydrophobic interaction with the core, and seem to have their specific roles in the trkA recognition site. The most hydrophilic residues of the LRM-2, namely $Arg^{94''}$, $Lys^{100''}$, $Arg^{104''}$, $Asp^{109''}$, $His^{112''}$, and $Arg^{116''}$ are exposed from the hydrophobic core in the complexes. Amino acids $Lys^{100''}$, $Asp^{109''}$, and $His^{112''}$ participate in specific intermolecular interactions while the other three are solvent-exposed. The reasonable location of the hydrophobic and hydrophilic residues of the

© 1998 NRC Canada

Fig. 5. Principal residues of the NGF binding domain. Conserved residues of NGF molecules among all species (39) are designated by **X**, whereas those which are substituted in NGF molecules derived from different species by similar amino acids and NGF residues maintaining the bioactive conformation or interacting with specific binding areas A–E of the LRM-2 are indicated by X.

Amino terminus

	1			5						10					15	
hNGF sequence	S	S	S	H	P	I	F	H	R	G	E	F	S	V	C	D ...
Conserved in NGF	-	-	-	**X**	**X**	X	-	X	X	**X**	**X**	-	**X**	**X**	**X**	**X**
Determine structure	-	-	-	X	X	X	-	X	X	X	X	X	-	X	X	-
Interact with LRM	-	-	-	-	-	X	X	X	-	-	X	-	X	-	-	X
LRM binding sites						**E**	**B**	**E**			**E**		**D**			**D**

Carboxyl terminus

	75'					110'						115'				
hNGF sequence	... K	H	W	N	...	C	V	C	V	L	S	R	K	A	V	R
Conserved in NGF	-	**X**	**X**	**X**		**X**	**X**	**X**	**X**	X	X	X	**X**	-	-	X
Determine structure	-	X	X	X		X	X	X	X	X	X	-	-	-	-	X
Interact with LRM	-	-	X	-		-	-	-	-	-	-	X	X	-	-	-
LRM binding sites			**A**									**C**	**C**			

LRM-2 within the NGF/LRM-2 complexes with respect to water environment supports their structures.

The NGF/LRM-2 binding spans almost the whole LRM-2 domain, i.e., the residues between $Leu^{94''}$ and $Pro^{115''}$ which is comprised of three distinct regions: the β-strand, the α-helix, and the loop connecting the carboxyl terminus of the β-strand and the amino terminus of the α-helix (49–51). This is in agreement with recent crystallographic studies on the ribonuclease A – porcine ribonuclease inhibitor complex (52) in which these particular regions of leucine-rich repeats of ribonuclease inhibitor are also involved in the molecular recognition process. While the β-strand structure exists in the complexed LRM-2, the α-helix motif is destroyed by intermolecular interactions with NGF. Accordingly, the LRM-2 β-strand determines the proper orientation of the ligand with respect to the trkA recognition site but does not undergo noticeable conformational changes. Consequently, the cooperative ligand–receptor H-bonding in area E cannot directly mediate those changes in the receptor conformation which trigger receptor phosphorylation processes. Available experimental data confirm this point. First, the mNGFΔ3-9 deletion mutant, which does not have the β-strand motif (43), and consequently, cannot specifically bind area E, is as active as wild type mNGF (28). Second, the 24-residue LRM fragment $Thr^{97''}$-$Leu^{120''}$ lacking the β-strand region (50), demonstrates the same kinetics of binding to NGF as wild type trkA (48, 49).

3.5. Principal amino acids involved in NGF–trkA recognition

The amino acids of NGF which are primarily responsible for maintaining bioactive conformations (39, 43) or which directly participate in the NGF–trkA recognition are specified in Fig. 5. Almost all residues of the amino and carboxyl termini of NGF as well as the $His^{75'}$-$Asn^{77'}$ region are involved in specific intra- or intermolecular interactions. Only five amino acids of the 30-residue binding domain of NGF do not seem to be essential for either maintaining its bioactive conformation or binding to the trkA recognition site. These include Ser^{1}, Ser^{2}, Ser^{3}, $Ala^{116'}$, and $Val^{117'}$.

The observation that the important amino acids of the NGF binding domain are conserved across all species while the unnecessary five residues are variable (Fig. 5) (39) supports the particular structural features of the NGF/LRM-2 complexes. There are, however, exceptions which require explanation. In most cases principal amino acids of NGF molecules derived from different species appear to be substituted by similar residues, e.g., I6V, F7L, L112I, S113T, or R114K; in some special cases the substituent is quite different but the particular substitution is still consistent with the present model, e.g., R9M, R9L, or R118Q (39, 43); in the case of the H8N substitution (39), histidine and asparagine have the same topology with respect to H-bonding to the Glu^{11} carboxyl oxygen (43). The structure of snake NGF (sNGF) requires special consideration. Principal hydropho-

© 1998 NRC Canada

Fig. 6. Principal residues of the LRM-2 of trkA. The residues which are specific for trkA (48, 49) and critical for the present model are designated by X and **X**, respectively.

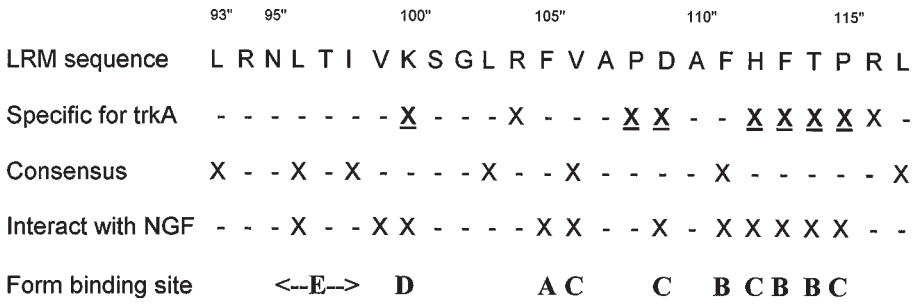

bic residues Phe[7] and Phe[12] are replaced by histidine residues in sNGF. Although these mutations could be accompanied by structural differences in snake trkA, they are consistent with the present model. According to the survey of Warme and Morgan (69), side-chain interactions of histidine with tryptophan or threonine are very common in natural proteins, which implies the existence of specific inter-residue affinities. This being the case, attractive interactions His[7]···Thr[114″] and His[12]···Trp[76′] in areas B and A, respectively, may replace corresponding hydrophobic interactions with Phe[7] and Phe[12].

The principal residues of the LRM-2 are shown in Fig. 6. The general consensus residues (45, 53) maintain the specific geometry of the LRM (50–52). The amino acids which form the distinct binding areas are involved in specific intermolecular interactions with the NGF binding domain. Since NGF does not activate the trkB receptor, those residues which are specific for the trkA receptor have been postulated to be directly involved in the NGF/LRM-2 recognition (48, 49). As seen, the LRM-2 segment has nine specific residues, seven of them directly participating in the NGF/LRM-2 recognition in the framework of the present model. Thus, Lys[100″] binds Asp[16] in area D, Pro[108″] is completely buried inside the NGF/LRM-2 complexes, residues Asp[109″], His[112″], and Pro[115″] form binding area C, and residues Phe[113″] and Thr[114″] are involved in forming area B. The other specific residues, Arg[104″] and Arg[116″], do not seem to be required for specific NGF/LRM-2 interactions. It is seen, furthermore, that binding areas A and E are not specific for the trkA recognition site, which unequivocally indicates that binding specificity of the LRM-2 is determined by Lys[100″], Asp[109″], and Phe[113″]. The fact that these particular amino acids are replaced in the trkB recognition site by residues of a different chemical nature, namely Asp[100″], Lys[109″], and Lys[113″], respectively (48, 49), which makes corresponding NGF–trkB binding absolutely impossible, supports the predicted details of the NGF/LRM-2 recognition. Principal residue Phe[105″], although being common both to trkA and trkB recognition sites (48, 49), is also important for the NGF–trkA recognition process, since oxidation of its counterpart, Trp[76], results in a complete loss of the receptor binding (70).

3.6. Explanation for structure–activity relationships

The trkA mediated activity has been evaluated for 27 point and deletion mutants of the trkA binding domain of NGF: hNGF (23, 32), mNGF (23, 28), mNGFΔ3-9 (28), (1-120)hNGF (71), (1-120)mNGF (25), (1-117)hNGF (71), and hNGF:NT-4/5 (35) retain full activity; mNGFΔ2-8, mNGFΔ61-66 (28), hNGF-R9A, hNGFΔ1-5, and hNGF-P5A (32) demonstrate intermediate potency; hNGFΔ1-9 (23–25, 28, 32, 34), mNGFΔ1-8 (22, 23), mNGFΔ1-9, mNGFΔ9-13 (36), mNGFΔ3-8, mNGFΔ3-11, mNGFΔ3-12, mNGFΔ3-13, mNGFΔ3-14, mNGFΔ9-14, mNGFΔ112-118 (28), hNGF-H4A, hNGF-H4D (32), BDNF (26), and NT-4/5 (35) are almost or completely inactive. The present model of the NGF/LRM-2 recognition enables a comprehensive explanation for the structure-activity relationships.

As demonstrated, fully active hNGF, mNGF, and hNGF:NT-4/5 fit perfectly to the five binding areas A–E of the trkA recognition site, while the mNGFΔ3-9 deletion mutant fits only to A, C, and D, without any specific binding taking place in areas B or E. Therefore, there are three common geometric features of the four fully active molecules which distinguish them from the less active analogues. *First*, conformations of the amino and carboxyl termini of these NGF analogues are "preorganized" for binding to the principal LRM-2 binding areas A, C, and D. *Second*, there is no stereochemical incompatibility in the binding areas B and E. *Third*, there is no hole inside the NGF/LRM-2 complexes.

The structures of the other three fully active NGF analogues, (1-120)hNGF, (1-120)mNGF, and (1-117)hNGF, are consistent with the above criteria. Indeed, since the NGF carboxyl end is located on the surface of the NGF/LRM-2 complexes (Fig. 3) and does not directly participate in principal intermolecular interactions, the lengthening of the NGF carboxyl terminus by the two amino acids does not explicitly affect the NGF/LRM-2 compatibility. As far as the (1-117)hNGF molecule is concerned, terminal residue Arg[118′] of NGF has been shown to form the inter-chain ionic H-bonds with Glu[11] (43), and, hence, seems to be important in maintaining the structure of the NGF bioactive conformation. On the other hand, there is the second factor stabilizing the bioactive conformation of the hNGF termini, namely inter-chain H-bonding of residue Arg[9] (43). Because of the latter binding, the above criteria are still fulfilled for (1-117)hNGF.

The deletion of the principal residue Phe[12] participating in hydrophobic interactions in area A results in a substantial loss of trkA mediated activity of the mNGFΔ3-12, mNGFΔ3-13, mNGFΔ3-14, and mNGFΔ9-14 deletion mutants (28). Likewise, the absence of the principal residues Arg[114′] and Lys[115′] essential for the ionic binding in area C is the reason for the dramatic loss of bioactivity of mNGFΔ112-118 (28). Similarly, geometric perturbations of the essential residues Arg[59] and Arg[69] in the mNGFΔ61-66 deletion mutant results in the incomplete NGF/LRM-2 com-

© 1998 NRC Canada

patibility in area D and, accordingly, a considerable loss of activity.

The specific location of the NGF ninth amino acid side chain in the "hollow" existing on the surface of the NGF rigid region has been predicted to be critical for high trkA mediated activity (43). The present study provides a detailed explanation for this prediction. Indeed, the hollow is buried inside the NGF/LRM-2 complexes, and a moiety located in this hollow fills the cavity which otherwise would exist inside the complexes and destroy the NGF/LRM-2 compatibility. Since this moiety is therefore located in the internal cavity of the complexes (Fig. 3), very severe limitations are imposed on its size. Accordingly, a short side chain does not fill this cavity; therefore, the hNGF-R9A mutant demonstrates noticeably diminished activity (32). This cavity should be filled either by a bulky amino acid side chain, such as arginine (e.g., hNGF), methionine (e.g., mNGF) or leucine (sNGF), or by the two residue peptide backbone (mNGFΔ3-9 or mNGFΔ2-8) (43). A longer amino terminus tail (e.g., in mNGFΔ3-8, mNGFΔ9-13 or mNGFΔ1-5) cannot be accommodated in the internal hole of the NGF/LRM-2 complex, and hence, interferes with binding areas B and E. In this case, most deletion or point mutations of the NGF amino terminus destroy the exposed β-strand motif Phe^7-Arg^9 and change the proper orientation of the Phe^7 side chain, thereby affecting the NGF/LRM-2 compatibility in areas B and E. Thus, incorporation of a negatively charged residue into the relatively long NGF amino terminus, as in hNGF-H4D, BDNF, NT-3, and NT-4/5, or substitution H8R, which is characteristic for BDNF and NT-4/5, has been demonstrated to cause dramatic conformational changes in the complex of the amino-carboxyl termini (43), which makes it inconsistent with the LRM-2. This is the stereochemical incompatibility of the geometry of the NGF amino terminus with binding areas B and E of the LRM-2, which is the reason for the partial or complete loss of the trkA related activity of mNGFΔ3-8, mNGFΔ1-5, hNGF-P5A, hNGF-H4A, hNGF-H4D, mNGFΔ1-8, hNGFΔ1-9, mNGFΔ1-9, mNGFΔ9-13, mNGFΔ3-11, BDNF, and NT-4/5.

As demonstrated, both NGF monomers are directly involved in specific ligand–receptor interactions, i.e., the first monomer binds areas B, D, and E, whereas the second one binds A and C. Consequently, the dimeric structure of NGF is necessary to retain high biological activity, which is consistent with experimental data (72).

In addition to the described structure–activity relationships, new data have been recently reported. The importance of residues Phe^7 (73), Leu^{112}, Arg^{114}, and Lys^{115} (74) for trkA mediated activity of NGF has been experimentally established, which is consistent with their participation in the specific NGF/LRM-2 binding in the framework of the present model.

3.7. Explanation for the NGF–trkA receptor binding kinetics

The results presented permit a plausible explanation for the kinetic properties of the NGF–trkA binding in the framework of the conformational model of the trkA–$p75^{NTR}$ interaction (11, 12). The low and high affinity binding sites of trkA are characterized by the same dissociation, but different association kinetics of NGF binding such that the latter binds NGF with a 25-fold higher rate of association k_{+1} (11). This observation invokes a hypothesis that the different NGF–trkA association kinetics might be caused by the same trkA module (48, 49), which is considerably more accessible when trkA and $p75^{NTR}$ receptors are coexpressed. In accord with this, since the LRM-2 of trkA is flanked by the adjacent LRMs in the LRM_3 cassette (45, 48, 49) and taking into account the tight packing of adjacent LRMs within LRM tandems (50–52), we would conclude that the trkA LRM-2 when not coexpressed with $p75^{NTR}$ is less accessible for direct intermolecular interactions with the NGF binding domain. On the other hand, interactions between trkA and $p75^{NTR}$ (15–17) could result in kinking between the second and the third LRMs of trkA, making the LRM-2 more accessible for NGF binding as manifest by a more rapid rate of association. This being the case, the LRM-2 with the predicted geometric features could represent one of the high affinity binding sites of trkA for NGF consistent with experimental data of Windisch and colleagues (48, 49).

4. Conclusions

The complexes of the amino and carboxyl termini of the four fully active NGF analogues with the second leucine-rich motif of trkA were obtained using variable basis Monte Carlo simulated annealing calculations. The structural features of the resulting NGF–trkA binding are supported by the following: (*i*) geometric and electronic complementarity of the binding domains of NGF and trkA without considerable conformational changes; (*ii*) appropriate environments for hydrophobic and hydrophilic residues within the complexes; (*iii*) analysis of structural variability of both binding domains; (*iv*) comprehensive explanation of currently published structure–activity relationships. Within these complexes, NGF–trkA molecular recognition is based upon multiple-point intermolecular interactions of hydrophobic, van der Waals, ionic, and hydrogen bonding origin. Extensive intermolecular van der Waals contacts arise from complementarity of the NGF binding domain and the trkA recognition site in size and shape. In addition, there are five specific binding areas within the receptor model: hydrophobic A and B, ionic C and D, and cooperative hydrogen bonding E. The NGF–trkA stereochemical compatibility in areas A, C, and D are essential for trkA receptor activation whereas areas B and E reinforce binding specificity, which makes the NGF molecule a very sophisticated key triggering the chain of biological events following receptor phosphorylation. The three-dimensional structures of the binding domains of the fully active NGF analogues are preorganized for stereochemical fit to the second leucine-rich motif of trkA. The predicted mechanism of high affinity NGF–trkA binding is consistent with the conformational model of trkA–$p75^{NTR}$ interactions (12).

Supporting information available: The full three-dimensional coordinates (in PDB format) of the complexes under study, and the optimized torsional angles of free and complexed NGF termini (Table 1S) and the complexed LRM-2 (Table 2S) are available on the WWW site: http://www.chem.queensu.ca/faculty/weaver/weaverpub.html.

© 1998 NRC Canada

Acknowledgments

This work was supported in part by operating grants from the Natural Sciences and Engineering Research Council of Canada, the University Research Incentive Fund of the Province of Ontario, the NeuroScience Network of the Networks of Centres of Excellence of the Government of Canada, and Allelix Biopharmaceuticals Inc., Mississauga, Ontario. D.F.W. acknowledges an Ontario Ministry of Health Career Scientist Award. The authors thank Dr. Tom Blundell for providing the NGF crystal solution coordinates and Dr. Magdalena Dory who identified a possible role for a specific interaction of the amino and carboxyl termini for biological activity of NGF. G.M.R. is a Queen's National Scholar.

References

1. S.O. Meakin and E.M. Shooter. Trends Neurosci. **15**, 323 (1992).
2. M. Barbacid. Oncogene, **8**, 2033 (1993).
3. M. Chao. J. Neurobiol. **25**, 1373 (1994).
4. R.A. Bradshaw, J. Murray-Rust, C.F. Ibáñez, N.Q. McDonald, R. Lapatto, and T.L. Blundell. Protein Sci. **3**, 1901 (1994).
5. C.F. Ibáñez. Trends Biotech. **13**, 217 (1995).
6. A. Sutter, R.J. Riopelle, R.M. Harris-Warrick, and E.M. Shooter. J. Biol. Chem. **254**, 5972 (1979).
7. G.E. Landreth and E.M. Shooter. Proc. Natl. Acad. Sci. U.S.A. **77**, 4751 (1980).
8. A.L. Schechter and M.A. Bothwell. Cell, **24**, 867 (1981).
9. B.L. Hempstead, D. Martin-Zanca, D.L. Kaplan, L.F. Parada, and M.V. Chao. Nature (London), **350**, 678 (1991).
10. P.A. Barker and E.M. Shooter. Neuron, **13**, 203 (1994).
11. D. Mahadeo, L. Kaplan, M.V. Chao, and B.L. Hempstead. J. Biol. Chem. **269**, 6884 (1994).
12. M.V. Chao and B.L. Hempstead. Trends Neurosci. **18**, 321 (1995).
13. M.A. Bothwell. Cell, **65**, 915 (1991).
14. M.V. Chao. Neuron, **9**, 583 (1992).
15. D.E. Wolf, C.A. McKinnon, M.-C. Daou, R.M. Stephens, D.R. Kaplan, and A.H. Ross. J. Biol. Chem. **270**, 2133 (1995).
16. A.H. Ross, M.-C. Daou, C.A. McKinnon, P.J. Condon, M.B. Lachyankar, R.M. Stephens, D.R. Kaplan, and D.E. Wolf. J. Cell Biol. **132**, 945 (1996).
17. G.M. Ross, I.L. Shamovsky, G. Lawrance, M. Solc, S.M. Dostaler, D.F. Weaver, and R.J. Riopelle. Eur. J. Neurosci. **10**, 890 (1998).
18. K. Kullander and T. Ebendal. J. Neurosci. Res. **39**, 195 (1994).
19. S.B. Woo and K.E. Neet. J. Biol. Chem. **271**, 24433 (1996).
20. J.B. Moore and E.M. Shooter. Neurobiology, **5**, 369 (1975).
21. A. Ullrich and J. Schlessinger. Cell, **61**, 203 (1990).
22. R.A.V. Taylor, J.F. Kerrigan, F.M. Longo, M. deBoisblanc, and W.C. Mobley. Soc. Neurosci. Abs. **17**, 712 (1991).
23. L.E. Burton, C.H. Schmelzer, E. Szönyi, C. Yedinak, and A. Gorrell. J. Neurochem. **5**9 1937 (1992).
24. P. Kahle, L.E. Burton, C.H. Schmelzer, and C. Hertel. J. Biol. Chem. **267**, 22 707 (1992).
25. Y. Luo and K.E. Neet. J. Biol. Chem. **267**, 12 275 (1992).
26. U. Suter, C. Angst, C.-L. Tien, C.C. Drinkwater, R.M. Lindsay, and E.M. Shooter. J. Neurosci. **12**, 306 (1992).
27. M. Benedetti, A. Levi, and M.V. Chao. Proc. Natl. Acad. Sci. U.S.A. **90**, 7859 (1993).
28. C.C. Drinkwater, P.A. Barker, U. Suter, and E.M. Shooter. J. Biol. Chem. **268**, 23 202 (1993).
29. C.F. Ibáñez, L. Ilag, J. Murray-Rust, and H. Persson. EMBO J. **12**, 2281 (1993).
30. D.O. Clary and L.F. Reichardt. Proc. Natl. Acad. Sci. U.S.A. **91**, 11 133 (1994).
31. L.L. Ilag, P. Lönnerberg, H. Persson, and C.F. Ibáñez. J. Biol. Chem. **269**, 19 941 (1994).
32. A. Shih, G.R. Laramee, C.H. Schmelzer, L.E. Burton, and J.W. Winslow. J. Biol. Chem. **269**, 27 679 (1994).
33. R. Urfer, P. Tsoulfas, D. Soppet, E. Escandón, L.F. Parada, and L.G. Presta. EMBO J. **13**, 5896 (1994).
34. G. Burton, C. Schmelzer, M. Sadic, F. Hefti, and J.J.S. Treanor. Soc. Neurosci. Abs. **21**, 1061 (1995).
35. J.J.S. Treanor, C. Schmelzer, B. Knusel, J.W. Winslow, D.L. Shelton, F. Hefti, K. Nikolics, and L.E. Burton. J. Biol. Chem. **270**, 23104 (1995).
36. S.B. Woo, D.E. Timm, and K.E. Neet. J. Biol. Chem. **270**, 6278 (1995).
37. M. Rydén and C.F. Ibáñez. J. Biol. Chem. **271**, 5623 (1996).
38. T. Clackson and J.A. Wells. Science (Washington, D.C.) **267**, 383 (1995).
39. N.Q. McDonald, R. Lapatto, J. Murray-Rust, J. Gunning, A. Wlodawer, and T.L. Blundell. Nature (London), **354**, 411 (1991).
40. B. Bax, T.L. Blundell, J. Murray-Rust, and N.Q. McDonald. Structure, **5**, 1275 (1997).
41. D.S. Gregory, A.C.R. Martin, J.C. Cheetham, and A.R. Rees. Protein Engineering, **6**, 29 (1993).
42. G.M. Ross, I.L. Shamovsky, G. Rawrance, M. Solc, S.M. Dostaler, S.L. Jimmo, D.F. Weaver, and R.J. Riopelle. Nature Med. **3**, 872 (1997).
43. I.L. Shamovsky, G.M. Ross, R.J. Riopelle, and D.F. Weaver. J. Am. Chem. Soc. **118**, 9743 (1996).
44. J.I.S. MacDonald and S.O. Meakin. Mol. Cell. Neurosci. **7**, 371 (1996).
45. R. Schneider and M. Schweiger. Oncogene, **6**, 1807 (1991).
46. P. Pérez, P.M. Coll, B.L. Hempstead, D. Martin-Zanca, and M.V. Chao. Mol. Cell. Neurosci. **6**, 97 (1995).
47. R. Urfer, P. Tsoulfas, L. O'Connell, D.L. Shelton, L.F. Parada, and L.G. Presta. EMBO J. **14**, 2795 (1995).
48. J.M. Windisch, B. Auer, R. Marksteiner, M.E. Lang, and R. Schneider. FEBS Lett. **374**, 125 (1995).
49. J.M. Windisch, R. Marksteiner, and R. Schneider. J. Biol. Chem. **270,** 28133 (1995).
50. B. Kobe and J. Deisenhofer. Nature (London), **366**, 751 (1993).
51. B. Kobe and J. Deisenhofer. Trends Biochem. Sci. **19**, 415 (1994).
52. B. Kobe and J. Deisenhofer. Nature (London), **374**, 183 (1995).
53. R. Schneider, E. Schneider-Scherzer, M. Thurnher, B. Auer, and M. Schweiger. EMBO J. **7**, 4151 (1988).
54. B.R. Brooks, R.E. Bruccoleri, B.D. Olason, D.J. States, S. Swaminathan, and M. Karplus. J. Comput. Chem. **4**, 187 (1983).
55. C.A. Hunter and J.K.M. Sanders. J. Am. Chem. Soc. **112**, 5525 (1990).
56. C.A. Hunter, J. Singh, and J.M. Thornton. J. Mol. Biol. **218**, 837 (1991).
57. M. Schauer and E.R. Bernstein. J. Chem. Phys. **82**, 3722 (1985).
58. P. Hobza, H.L. Selzle, and E.W. Schlag. J. Am. Chem. Soc. **116**, 3500 (1994).
59. A.J. Hopfinger. Conformational properties of macromolecules. Academic Press, New York and London. 1973. pp. 70–85.

© 1998 NRC Canada

60. Z.I. Hodes, G. Némethy, and H.A. Scheraga. Biopolymers, **18**, 1565 (1979).
61. S.J. Weiner, P.A. Kollman, D.A. Case, U.C. Singh, C. Ghio, G. Alagona, S. Profeta, Jr., and P. Weiner. J. Am. Chem. Soc. **106**, 765 (1984).
62. S. Kirkpatrick, C.D. Gelatt Jr, and M.P. Vecchi. Science (Washington, D.C.) **220**, 671 (1983).
63. D. Vanderbilt and S.G. Louie. J. Comput. Phys. **56**, 259 (1984).
64. A.T. Brünger. J. Mol. Biol. **203**, 803 (1988).
65. M. Nilges, G.M. Clore, and A.M. Gronenborn. FEBS Lett. **229**, 317 (1988).
66. S.R. Wilson, W. Cui, J.W. Moscowitz, and K.E. Schmidt. Tetrahedron Lett. **29**, 4373 (1988).
67. C. Wilson and S. Doniach. Proteins, **6**, 193 (1989).
68. P.K. Ponnuswamy and P. Manavalan. J. Theor. Biol. **60**, 481 (1976).
69. P.K. Warme and R.S. Morgan. J. Mol. Biol. **118**, 289 (1978).
70. R. Merrell, M.W. Pulliam, L. Randono, L.F. Boyd, R.A. Bradshaw, and L. Glaser. Proc. Natl. Acad. Sci. U.S.A. **72**, 4270 (1975).
71. C.H. Schmelzer, L.E. Burton, W.-P. Chan, E. Martin, C. Gorman, E. Canova-Davis, V.T. Ling, M.B. Sliwkowski, G. McCray, J.A. Briggs, T.H. Nguyen, and G. Polastri. J. Neurochem. **59**, 1675 (1992).
72. L.M. Maness, A.J. Kastin, J.T. Weber, W.A. Banks, B.S. Beckman, and J.E. Zadina. Neurosci. Biobehav. Rev. **18**, 143 (1994).
73. K. Kullander and T. Ebendal. Soc. Neurosci. Abs. **22**, 557 (1996).
74. A. Krüttgen, J.V. Heymach, P. Kahle, and E.M. Shooter. Soc. Neurosci. Abs. **22**, 557 (1996).

© 1998 NRC Canada

Temperature dependence of self-entanglements in protein backones near the glass-like transition

Gustavo A. Arteca and Denise I. Caughill

Abstract: Many proteins undergo a phase change whereby catalytic activity is switched on at a glass-transition temperature T^* ~ 200 K. Over T^*, large anharmonic motions dominate, most particularly on atoms coupled to the hydration layer. These changes are detectable in the positional disorder, e.g., in the Debye–Waller thermal *B*-factors. Yet, the glass transition is not detected in descriptors of backbone mean shape, e.g., the molecular size. In this work, we show that other descriptors of mean shape may be better at detecting the transition. We suggest that a property that uses the equilibrium geometry *and* the backbone connectivity can exhibit larger variations with thermal fluctuations. In particular, we contrast the effects of bond length fluctuations on the mean number of overcrossings and the radius of gyration. Using the glass transition of ribonuclease-A as a test example, we show that the change in Debye–Waller factors is also reflected in the mean overcrossing numbers computed with the backbones. The approach can be used to follow other configurational transitions and to assess the effect of various external perturbations.

Key words: Molecular shape fluctuations, isotropic temperature factors, anharmonic vibrations, glass phase transition, flexible molecular chains.

Résumé : Quelques protéines montrent une transition de phase de verre où l'activité catalytique émerge après une température T^* ~ 200 K. Au-dessus T^*, les mouvements sont principalement anharmoniques, spécialement chez les atomes couplés à la couche d'hydration. Ces changements sont détectables dans le désordre positionnel avec les facteurs de Debye–Waller. Par contre, la transition n'est pas visible avec des descripteurs de la forme moyenne, p. ex., la taille. Ici nous montrons que d'autres mesures de la forme moyenne offrent une meilleure alternative pour détecter la transition. On propose qu'une propriété qui dépend de la géométrie *et* de la connectivité de la chaîne peut varier trop avec les fluctuations thermiques. En particulier, nous étudions l'effet des fluctuations sur le rayon de gravité et les enchevêtrements. En suivant la transition chez la ribonuclease-A, on voit que le changement des facteurs de Debye–Waller est accompagné par un saut dans le nombre moyen des croissements. La méthode est applicable à l'étude d'autres transitions configurationnelles et à la mesure de l'effet des perturbations extérieures sur une protéine.

Mots clés : fluctuations de la forme moléculaire, facteurs de témperature isotrope, vibrations anharmoniques, transition de phase de verre, chaînes moléculaires flexibles.

[Traduit par la Rédaction]

Introduction

Proteins exhibit a wide scale of atomic motions (1–4). The flexibility of a protein is manifested in motions ranging from localized vibrations (with $\bar{\nu}$ ~ 2000 cm^{-1} as typical wave numbers) up to extended vibrational modes affecting the folding of entire domains (whose wave numbers are $\bar{\nu}$ < 30 cm^{-1}) (4, 5). These motions play an important role in various aspects of protein function. Large amplitude rearrangements are known to accompany the binding of some substrates or inhibitors at room temperature (6, 7). As the temperature changes, however, the range of accessible motions is greatly affected (8–14). The effect is especially strong on localized small amplitude vibrations (11–13). In this work, we deal with the characterization of the extent of these motions. In particular, we study whether the effect of temperature on the large-scale protein shape can be extracted by using *descriptors of the mean shape of the backbone*.

Classic experiments on myoglobin using Mössbauer spectroscopy (15,16) and elastic incoherent neutron scattering (11, 12) show the existence of a phase transition at T^* ~ 200 K, below which the enzymatic activity is suppressed. A similar phenomenon is found in other proteins (13, 17–19). This transition is accompanied by a shift in the amplitude of the atomic motions. At low temperature ($T < T^*$), the protein exhibits localized *harmonic* vibrations, whereas extended *anharmonic* vibrations are found at $T > T^*$. This change (sometimes referred to as "dynamical transition") is analogous to a *glass transition*. Below T^*, the structure is locked in conformationally frustrated local energy minina; over T^*,

Received August 12, 1998.

G.A. Arteca[1] and D.I. Caughill. Département de Chimie et Biochimie, Laurentian University, Ramsey Lake Road, Sudbury, ON P3E 2C6, Canada.

[1]Author to whom correspondence may be addressed. Telephone: (705) 675–1151, ext. 2117. Fax: (705) 675–4844. E-mail: Gustavo@nickel.laurentian.ca

© 1998 NRC Canada

the structure has a larger degree of conformational flexibility and a liquid-like behaviour.

This single-molecule "phase transition" can be recognized as a biphasic behaviour in descriptors of positional disorder, e.g., the isotropic (or Debye–Waller) temperature *B*-factors. (These are proportional to mean-squared displacements, $B = 8\pi^2\langle\langle(\Delta r)^2\rangle\rangle$, where $\langle\langle\ \ \rangle\rangle$ indicates an average over all nuclei.) These parameters can be evaluated experimentally (11–13) and in computer simulations (20). (For a comparison between the results derived by the two approaches, see ref. 19.) The experiments show that *B* rises rapidly when $T > T^*$ (13). Consistently, molecular dynamics simulations indicate a rapid change in the average number of conformational "jumps" among dihedral torsions (20). These jumps are virtually absent for $T < T^*$, but they increase exponentially for temperatures over T^*.

The above descriptors measure *fluctuations* about an equilibrium geometry at a given temperature. However, they provide little information as to the extent of any reorganizations in the *average three-dimensional (3D) equilibrium geometry.* Whereas it is clear that temperature effects can be extracted from dynamic information or thermal noise, detecting these transitions with standard backbone shape descriptors seems elusive (13, 20, 21). Here we address the question: *Is there an alternative 3D descriptor of average molecular folding that exhibits a change at the glass transition similar to that in the* B-*factors*?

To address this question, we must pay attention to the effect of temperature on various atomic positions. Fluctuations appear to be particularly large within the hydration layer. A biphasic behaviour is also observed in the $\langle\langle(\Delta r)^2\rangle\rangle$ values for side-chain atoms and, to a smaller extent, in main-chain atoms (13). However, the size of the protein (as measured by the backbone radius of gyration, R_G) shows typically a *smooth* marginal swelling of ca. 3% over the temperature range 100–300 K. In other words, the glass transition at $T^* \sim$ 200 K is not reflected in R_G. This is not unexpected since R_G depends only on *mean* positions, and these may be little affected by thermal fluctuations or "breathing" modes of the protein. However, there are other descriptors of mean shape that contain more information than R_G, and these can potentially exhibit larger variations near the glass transition.

In this work, we deal with the temperature effect on shape descriptors that depend on *both* atomic positions and backbone connectivity. In particular, we use a measure of "self-entanglements" in protein backbones, the *mean overcrossing number* $\overline{N}$ (or average crossing number) (22–24). Qualitatively, this descriptor can be thought as the extension to single chains of the notion of entanglements in a polymer melt. In our case, we regard a single polymer conformation (e.g., the protein backbone) as a chain immersed in a "virtual," highly viscous medium. Here, over a period of time, the chain's dynamical and structural properties will be determined by the instantaneous entanglements among its own loops. Quantitatively, $\overline{N}$ is simply the number of bond–bond intersections ("double points" or "overcrossings") in a planar projection of the polymer chain, averaged over all planes in three-space. (The symbol $\bar{a}$ indicates that the property "*a*" is averaged over all projections.) The resulting number $\overline{N}$ is a *geometrical* descriptor of global molecular shape: rod-like chains exhibit $\overline{N} = 0$, whereas $\overline{N}$ is maximized in "collapsed" (or "poor-solvent") chain configurations.

The scaling behaviour of $\overline{N}$ as a function of the monomer number has been discussed in the literature for random polymers (25–28) and proteins (25, 29). Using these results, it is possible to view $\overline{N}$ (and also the related maximum overcrossing probability) as an order parameter to compare the folding features of different polymers (30). Recently, the time-averaged values of $\overline{N}$ (computed from molecular dynamics trajectories) have been used to monitor premelting transitions in alkanes (31) and the shape stability of short helical peptides (32, 33). The results indicate that the mean overcrossing number can provide information about the onset of conformational transitions. Here, we employ $\overline{N}$ to study how thermal fluctuations affect the mean shape of protein native states.

The work is organized as follows. In the next section, we discuss some analytical properties of $\overline{N}$ for simple chains. Some of these properties suggest that $\overline{N}$ should indeed be more sensitive than R_G to thermal fluctuations or breathing modes. In a following section, we apply these ideas to the glass transition in bovine pancreatic ribonuclease-A. As far as we know, this protein is the only example in the Brookhaven Protein Data Bank (PDB) where several X-ray structures are available over an extended temperature range. The section compares the thermal behaviours of R_G and $\overline{N}$ for ribonuclease-A. We conclude with possible extensions of our method to analyze the effect of external perturbations (e.g., temperature, pH, ionic force) on proteins and their hydration layer.

Measure of self-entanglements in polymer chains with fluctuating bond lengths

The mean overcrossing number $\overline{N}$ is a geometrical descriptor of polymer shape (24). It can be defined for single polymers with arbitrary architecture (34) and also for a network of polymer chains (35). There is a great deal of interest on overcrossing numbers and related properties (e.g., the *writhe* of a curve) as descriptors of complexity in entangled polymers. Although these geometrical measures are not topological invariants, they discriminate between some polymer topologies. For example, it has recently been shown that the mean overcrossing number of the "ideal" conformation of variously knotted DNA strands correlates with diffusion velocities in gel electrophoresis (36, 37). (An ideal conformation is that of a knotted tube with maximum diameter to length ratio.) To some extent, $\overline{N}$ (or its time average, $\langle\overline{N}\rangle$) behaves as a "weak" topological invariant that can be used for knot classification (36–38). Similar correlations between knot complexity and the writhe have also been discussed in the literature (39). In our case, we deal with the extension of these descriptors to a single open polymer chain. In this case, the chain can be *thought of as "dynamically" entangled with itself*. Such a chain does not form knots, yet when studied with molecular dynamics, it behaves as if it were entangled within its own loops over a period of time.

From the computational viewpoint, $\overline{N}$ can easily be evaluated numerically (24). The simplest approach is to enclose the polymer by the smallest sphere (centred at its geometri-

© 1998 NRC Canada

cal centre) and then project the chain to randomly chosen planes tangent to the sphere. On each projected image, we compute a number of bond–bond overcrossings (N). Finally, for a linear chain with n identical monomers ("beads"), the mean overcrossing number is simply:

$$[1] \qquad \overline{N} = \lim_{m\to\infty} \sum_{N=0}^{(n-2)(n-3)/2} N\,\frac{m_N}{m}$$

where m_N is the number of projections (over a total of m) that exhibit N overcrossings. In practice, configurations show a number of overcrossings much smaller than the maximum possible (i.e., $(n-2)(n-3)/2$). In an actual calculation of $\overline{N}$, accurate results can typically be obtained with $m \sim 10^4$ random projections (24).

Note that the evaluation of $\overline{N}$ uses not only the nuclear geometry (as does R_G) but also the information on chain connectivity. It is the special arrangement and distribution of *all* bonds in space what confers a protein a particular folding feature. As such, $\overline{N}$ is a *global shape descriptor*, involving *all possible bond–bond crossings*, regardless of the internuclear distances (24). However, bonds that are far away from each other *contribute less* to the mean overcrossing number than bonds close to each other. (This is due to the fact that there will be fewer "viewing directions" that produce a crossing between bonds separated by a great distance.) As a consequence, the $\overline{N}$ descriptor takes *naturally* into account the intuitive notion that bond–bond crossings by neighbouring bonds should be "physically" more important than others. Therefore, there is no need to add a cut-off distance to "weigh" the overcrossings according to the backbone geometry. As we show in more detail below, this feature is already incorporated into the theory.

The above approach (eq. [1]) produces good numerical results but few insights on exact properties. To study the general effect of temperature on $\overline{N}$, we need an *analytical* formula. Here, we use a recently developed path-integral approach to $\overline{N}$ in order to compare the behaviour of $\overline{N}$ and R_G under thermal fluctuations.

The use of analytical descriptors of entanglement is well established in polymer theory. Path-integral representation of the Gauss linking number (40, 41) and writhe (42) have long been used to describe topological constraints on closed (linked or knotted) polymer loops (43–48). These descriptors convey the geometrical configurations of knots, links, or polymer networks by using line integrals instead of algebraic descriptors.

Using the Gauss "looping" integral (41, 42) and spherical mappings (49), one can derive a similar path-integral representation for the mean overcrossing number of *closed loops* (50–52). This approach has recently been used to study the relation between the $\overline{N}$ value and knot energies in knotted polymer rings (51–54). The same formulation can be generalized to the case of *open* chains (27, 28) and general networks,[2] instead of loops. Recently (27, 28), the path-integral representation of $\overline{N}$ has been used to explain the observed scaling behaviour with the number of monomers (25, 26). In this section, we will simply adapt some of the recent approaches (27, 50, 53) to our present objective, namely, studying the effect of bond length fluctuations on chain self-entanglements. (A more detailed analysis appears elsewhere.)[2]

Consider a *linear* (nonbranched) polymer chain, comprising a series of connected segments. These "segments" can be curved. Let n be the number of monomers, each one represented by a single (identical) bead with position vector $\mathbf{r}_i$, $i = 1, 2, ..., n$. The "segment" joining monomers i and $i+1$ will be a curve denoted by $\gamma_i (i \le n-1)$. Each of these segments can be regarded as a parametrized path over the unit interval $I = [0, 1]$:

$$[2] \qquad \gamma_i : I \to \mathcal{R}^3, \quad \gamma_i(0) = \mathbf{r}_i,\ \gamma_i(1) = \mathbf{r}_{i+1}$$

whose continuous parametric derivatives $\dot{\gamma}_i(s) = \partial\ \gamma_i(s)/\partial s$ exist for all $s \in I$, and satisfy:

$$[3] \qquad \dot{\gamma}_i(0) = \lim_{s\downarrow 0} \dot{\gamma}_i(s), \quad \dot{\gamma}_i(1) = \lim_{s\uparrow 1} \dot{\gamma}_i(s)$$

The set of all points in the segment (i.e., the image of the map γ_i) will be indicated by G_i:

$$[4] \qquad G_i = \{\gamma_i(s) \in \mathcal{R}^3, \quad s \in I\ \}$$

In the special case of straight-line segments (e.g., a polymer or protein backbone) we will use C_i instead of G_i, that is,

$$[5] \qquad C_i = \{\gamma_i(s) \in \mathcal{R}^3 : \gamma_i(s) = \mathbf{r}_i + s(\mathbf{r}_{i+1} - \mathbf{r}_i), \quad s \in I\}$$

With this notation, we can now introduce the mean number of "bond–bond" crossings associated *exclusively* with the projections where the segments G_i and G_j overcross (i.e., $\overline{N}(G_i, G_j)$). The result is given by coupled line integrals over the curves $\gamma_i(s)$ and $\gamma_j(t)$ (50, 53):

$$[6] \qquad \overline{N}(G_i, G_j) = \frac{1}{4\pi} \int_0^1 \int_0^1 \frac{|(\dot{\gamma}_i(s) \times \dot{\gamma}_j(t)) \cdot (\gamma_i(s) - \gamma_j(t))|}{\|\gamma_i(s) - \gamma_j(t)\|^3} \mathrm{d}s\ \mathrm{d}t$$

This formula describes only the overcrossings between two curves, seen as distinct "isolated" entities. When the entire polymer chain is considered, represented by the ensemble $G = \bigcup_{i=1}^{n-1} G_i$, the total mean number of overcrossings $\overline{N}(G, G)$ will involve all possible combinations of segment–segment overcrossings $\overline{N}(G_i, G_j)$, that is:

$$[7] \qquad \overline{N}(G, G) = 2\sum_{i=1}^{n-2} \sum_{j=i+1}^{n-1} \overline{N}(G_i, G_j) + \sum_{i=1}^{n-1} \overline{N}(G_i, G_i)$$

where the diagonal terms $\overline{N}(G_i, G_i)$ represent overcrossings *within* a given segment. Now, straight-line segments cannot overcross with themselves or with their connected (adjacent) neighbours. In this case, the diagonal terms in eq. [7] vanish, as well as the contributions of the form $\overline{N}(G_i, G_{i+1})$. The resulting mean number of overcrossings $\overline{N}(C, C)$ will be denoted as simply $\overline{N}_{\text{chain}}$. Using eqs. [6] and [7] we get:

[2] G.A. Arteca. Submitted.

© 1998 NRC Canada

Fig. 1. Minimal chain used for the exact computation of the mean overcrossing number. (Note that only the segments γ_1 and γ_3 can overcross. These two segments are chosen perpendicular, at a distance a, and of equal length b. The bond fluctuations Δb are indicated as thermal ellipsoids.)

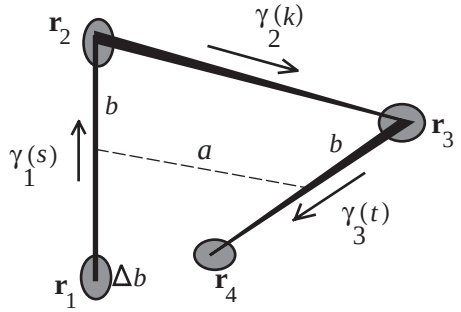

$$[8]\qquad \bar{N}_{\text{chain}} = \frac{1}{2\pi}\sum_{i=1}^{n-3}\sum_{j=i+2}^{n-1}\int_0^1\int_0^1 \frac{|(\dot{\gamma}_i(s)\times\dot{\gamma}_j(t))\cdot(\gamma_i(s)-\gamma_j(t))|}{||\gamma_i(s)-\gamma_j(t)||^3}\,\mathrm{d}s\,\mathrm{d}t$$

Equation [8] provides an analytical representation that is convenient to study the effect of thermal fluctuations on self-entanglements. To illustrate this notion, we shall apply eq. [8] to a simple "toy" chain.

Consider the simple "tetramer chain" in Fig. 1. It consists of three straight-line segments (indicated by γ_1, γ_2, γ_3). For a simpler analysis, we choose the segments γ_1 and γ_3 to be perpendicular and of equal length. These segments generate the only nonzero contributions to overcrossings, since connected straight-line segments do not overcross.

Let b be the length of each segment, and a the distance between the centres of the segments γ_1 and γ_3. The full chain is defined by the four points: $\mathbf{r}_1 = (0, 0, 0)$, $\mathbf{r}_2 = (0, 0, b)$, $\mathbf{r}_3 = (a, -b/2, b/2)$, $\mathbf{r}_4 = (a, b/2, b/2)$. Hence, the radius of gyration is given by

$$[9]\qquad R_G = \frac{1}{2}(a^2+b^2)^{1/2}$$

and it coincides with the distance from a point $\mathbf{r}_i$ to the geometrical centre of the chain. Using eq. [5], the overcrossing segments follow:

$$[10]\qquad \gamma_1(s) = \mathbf{r}_1 + s(\mathbf{r}_2 - \mathbf{r}_1) = (0,\ 0,\ sb)$$

$$[11]\qquad \gamma_3(t) = \mathbf{r}_3 + t(\mathbf{r}_4 - \mathbf{r}_3) = (a,\ b(t-1/2),\ b/2)$$

with parametric derivatives: $\dot{\gamma}_1 = (0, 0, b)$, $\dot{\gamma}_3 = (0, b, 0)$. In addition, we obtain:

$$[12]\qquad |(\dot{\gamma}_1\times\dot{\gamma}_3)\cdot(\gamma_1-\gamma_3)| = ab^2$$

$$[13]\qquad ||\gamma_1-\gamma_3||^3 = b^3[a'^2+(t-\frac{1}{2})^2+(s-\frac{1}{2})^2]^{3/2}$$

where $a' = a/b$. With these results we compute the mean overcrossing number (eq. [8]):

$$[14]\qquad \bar{N} = \bar{N}_{\text{chain}} = \frac{1}{2\pi}\int_0^1\int_0^1 \frac{|(\dot{\gamma}_1(s)\times\dot{\gamma}_3(t))\cdot(\gamma_1(s)-\gamma_3(t))|}{||\gamma_1(s)-\gamma_3(t)||^3}\,\mathrm{d}s\,\mathrm{d}t = \frac{1}{2\pi a'^2}\int_0^1\int_0^1 [1+(\frac{t-1/2}{a'})^2+(\frac{s-1/2}{a'})^2]^{-3/2}\,\mathrm{d}s\,\mathrm{d}t$$

Evaluation of the integral [14] produces a simple closed-form expression for $\bar{N}$ (55):

$$[15]\qquad \bar{N} = \frac{2}{\pi}\arctan\left(\frac{2^{1/2}}{4a'(1+2a'^2)^{1/2}}\right)$$

In principle, we expect that $\bar{N}$ may convey different shape features than a descriptor of molecular size such as R_G. We can now quantify this conjecture by using the example in Fig. 1. Firstly, note that $\bar{N}$ and R_G follow different asymptotics when the chain is squished. When $a << b$, a simple calculation from eqs. [9] and [15] gives:

$$[16]\qquad R_G/b = \frac{1}{2}+\frac{a'^2}{4}-\frac{a'^4}{16}+O(a'^6)$$

$$[17]\qquad \bar{N} = 1-\frac{2^{5/2}a'}{\pi}+\frac{a'^3}{\pi}(\frac{2^{1/2}}{3}-2^{5/2})+O(a'^5)$$

These results suggest that the effect of moving apart the segments γ_1 and γ_3 is *an order of magnitude larger* in $\bar{N}$ than in R_G. (We also note, in passing, that according to eq. [15] the mean overcrossing number *vanishes* when $a'\to\infty$. In other words, as already pointed out in the introduction, two bonds far away from each other contribute little indeed to the entanglement descriptor $\bar{N}$.)

We can now estimate the variation in shape descriptors produced by a *systematic change* in the molecular geometry (e.g., a "breathing mode" in the molecule). In Fig. 1, such a change can be represented by (*i*) a variation in the bond lengths b, or (*ii*) a change in the bond–bond distance a. Let us suppose that, for the sake of simplicity, thermal fluctuations produce an *identical* variation Δb in each of the bonds. We can regard Δb as a fluctuation that swells the entire polymer, as it is expected in a protein as temperature increases (13). This value can be estimated in terms of the Debye–Waller factors as $\Delta b^2 \approx B/8\pi^2$. This "swelling," or Δb-fluctuation, will produce fluctuations in the shape descriptors, denoted by $\Delta\bar{N}$ and ΔR_G. The effect of temperature can then be expressed in terms of the relative variations per bond fluctuation. Using eqs. [9] and [15], we obtain:

$$[18]\qquad \frac{\Delta R_G}{R_G\Delta b} = \frac{b}{(a^2+b^2)}$$

$$[19]\qquad \frac{\Delta\bar{N}}{\bar{N}\Delta b} = \frac{2^{3/2}ab}{(4a^2+b^2)(2a^2+b^2)^{1/2}}[\arctan(\frac{2^{1/2}b^2}{4a(b^2+2a^2)^{1/2}})]^{-1}$$

These two equations are compared in Fig. 2. The figure shows the relative importance of the fluctuations over a range bond length values b (measured in units of $a = 1$).

© 1998 NRC Canada

Fig. 2. Relative deviations in the molecular size and chain self-entanglement descriptors for the model "polymer" in Fig. 1. (The results given per unit of bond fluctuation Δb, over a range of possible b values. The figure shows the results corresponding to the case $a = 1$.)

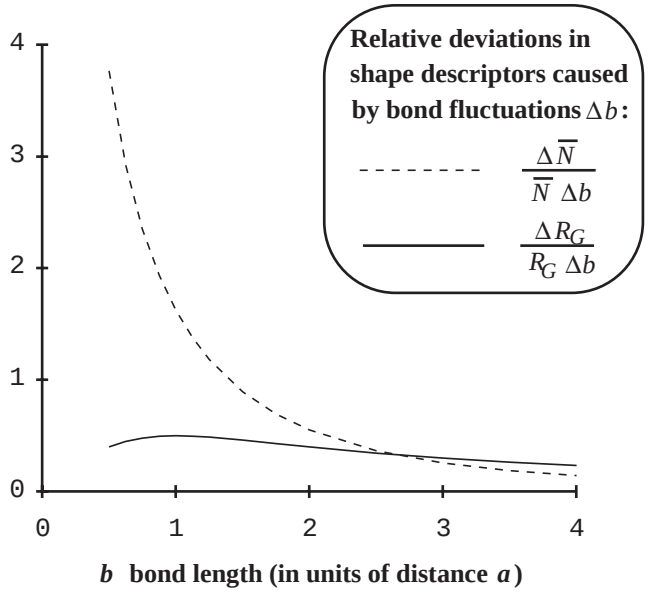

When $b > 2.5a$, a Δb-fluctuation affects the molecular size and the mean overcrossing number to the same extent. However, the effect is very different for smaller bond lengths. According to Fig. 2, we expect the effect of bond fluctuations on $\bar{N}$ to be approximately five times larger than that for R_G in compact chains, where $b \sim a$. A more conservative bound can be estimated by considering equal-length bonds in Fig. 1. (The condition $a = 1$ requires $b = 2^{1/2}$ to produce three equal length segments in Fig. 1.) Even in this case, as Fig. 2 shows, the effect of a Δb-fluctuation on $\bar{N}$ will still be more than twice that on R_G.

We arrive to a similar conclusion if the breathing mode is represented by a variation in a. Using eq. [15], a Δa-fluctuation produces the following effect in the mean overcrossing numbers:

$$[20] \quad \left|\frac{\Delta\bar{N}}{\bar{N}\Delta a}\right| = \frac{2^{3/2}b^2}{(4a^2+b^2)(2a^2+b^2)^{1/2}}\left[\arctan\left(\frac{2^{1/2}b^2}{4a(b^2+2a^2)^{1/2}}\right)\right]^{-1}$$

When this fluctuation is analyzed over a variation in bond length b, the effect is even larger than the one observed in eq. [19].

We can rationalize all these observations as follows. The radius of gyration depends only on individual nuclear positions and not on their connectivity. Therefore, a fluctuation in the position of one atom affects only slightly the contribution to R_G of all others. (The only effect is due to a small shift in the centre of mass.) The situation is very different for the mean number of overcrossings. Note that $\bar{N}$ takes into consideration the *entire* path connecting two atoms and *not* only the position of the terminal points. Moreover, the resulting overcrossings depend on relations between all pairs of paths. Consequently, a Δb- or Δa-fluctuation will affect the path lengths and their relative positions, which in turn will have an effect on how each path overcrosses all others. Clearly, the net result of a thermal fluctuation will be a strong modulation of the global overcrossing pattern throughout the polymer chain. As a result, we expect $\bar{N}$ to be always more sensitive than R_G over the whole range of nuclear motions. (It should be noted that fluctuations that leave the *mean* equilibrium geometry invariant may give rise to a large $\Delta\bar{N}$ fluctuation, while leaving the mean $\bar{N}$ value constant. On the other hand, fluctuations that *shift* the equilibrium geometry will change both $\bar{N}$ *and* $\Delta\bar{N}$. As discussed before, fluctuations in bonds far away will always have a smaller effect on the $\bar{N}$ value than fluctuations in bonds closer to each other.)

In real polymer chains, the distribution of segments is complicated and $\bar{N}$ cannot be computed in closed form by using eq. [8]. However, the overcrossing pattern of all three-segment sections should not be too different from that described by eq. [15]. We would still expect $\bar{N}$ to exhibit larger variations during thermal fluctuations when compared to R_G. In the next section, we test these ideas by studying similar effects in an actual protein.

Variation of mean overcrossing numbers during the glass transition of ribonuclease-A

The best studied examples of protein glass transitions are myoglobin (9, 10–12, 20) (a mostly α-helical protein) and ribonuclease-A (13, 19) (a primarily β-sheet protein). We shall discuss here the case of bovine pancreatic ribonuclease-A, as it is the only example in the Brookhaven PDB with a large number of available X-ray structures as a function of T.

Ribonuclease-A is a small monomeric protein ($n = 124$). Its catalytic function is to hydrolyze single-stranded RNA by binding it in a deeply buried active site. The catalytic activity and structures of this protein have been studied over a range of temperatures. Nine X-ray structures are available, with PDB codes *p*RAT ($p = 1, 2, ..., 9$), corresponding to temperatures $T = 98, 130, 160, 180, 220, 240, 260, 300, 320$ K, respectively.

The overall thermal effect on this protein is small and subtle (13). The larger changes appear at loops and α-helices, whereas the inner β-sheet core is less affected (13). Experiments (13) and computer simulations (20) indicate a mean-squared deviation of $\langle\langle(\Delta r)^2\rangle\rangle^{1/2} \approx 0.4$ Å for an *inner* residue. Considering the distances between α-carbon atoms in a protein backbone, this amounts to a bond-length fluctuation $\Delta b \approx 0.1b$.

For each of the nine structures, we have computed molecular size and self-entanglements. To monitor thermal effects with increasing resolution, we have considered two models of the chain. Firstly, we represent the chain by using only α-carbon atoms (the "C_α-skeleton"). Then, we enlarge the chain by taking into consideration all main-chain atoms (the "N-C_α-C-skeleton"). (Only fluctuations in backbone atoms can modify the value of the entanglement descriptor. As be-

© 1998 NRC Canada

Fig. 3. Variation in molecular size as a function of temperature, for two models of the protein backbone of bovine pancreatic ribonuclease-A. (The glass transition is indicated by T^*. Note that there is no clear systematic change in R_G values accompanying this transition.)

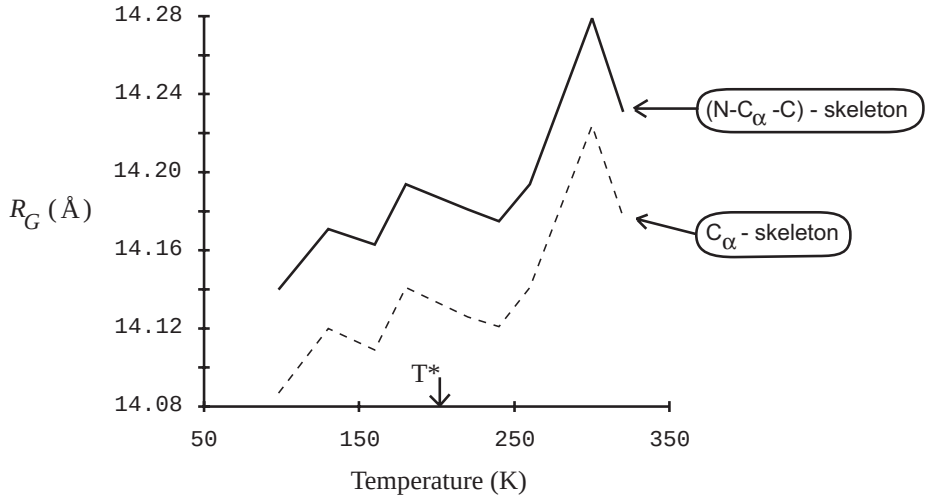

Fig. 4. Variation in chain self-entanglements as a function of temperature, for two models of the protein backbone of bovine pancreatic ribonuclease-A. (The glass transition is indicated by T^*. The boxes indicate the numerical errors in the computation of overcrossings. Note that there is a clear change in $\overline{N}$ values accompanying the transition. The extent of the transition appears to grow as the resolution of the protein backbone is increased by adding main-chain atoms.)

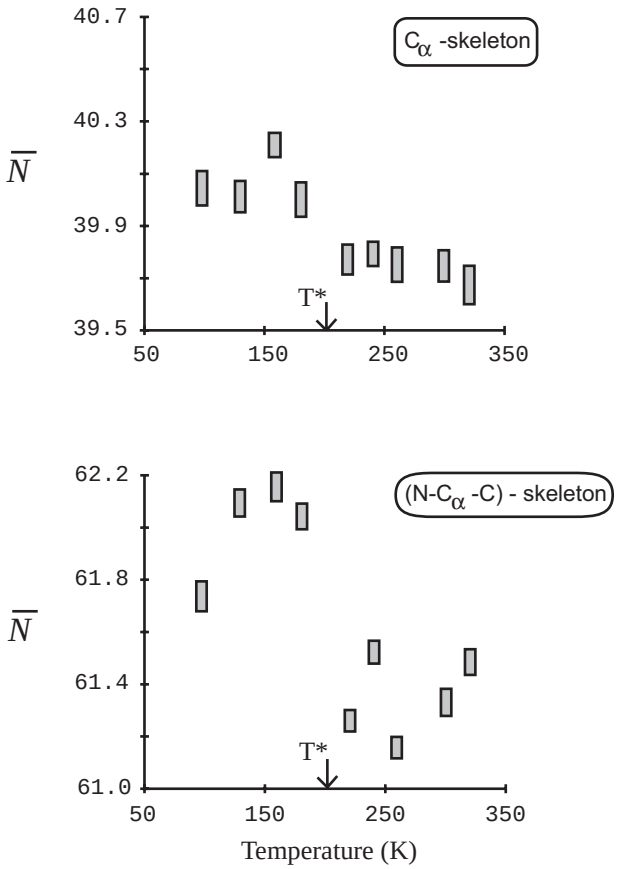

fore, fluctuations in atoms separated by large distances will affect little the global mean overcrossing number.)

For the computation of the mean overcrossing number $\overline{N}$, we follow the numerical approach indicated by eq. [1]. For each chain model, we have produced 10 independent estimations of $\overline{N}$, each one of them consisting of 5×10^5 randomized projections on the surface of a sphere enclosing the backbone (24). The final estimation is made by averaging the 10 series, with error bars expressed as standard deviations. This procedure typically generates $\overline{N}$ values with at least three significant figures.

The R_G values for each backbone model are displayed in Fig. 3. As expected, the results show that R_G does not uncover any new features as the "resolution" of the backbone increases. The overall result is a small, irregular swelling of the backbone with no particular change at the glass-transition temperature (indicated by T^*). The picture obtained is consistent with the observations in ref. 13.

These results can be contrasted with the behaviour of the mean overcrossing numbers, displayed in Fig. 4. Firstly, the $\overline{N}$ values increase markedly as more atoms are added to the backbone. For the two chain models, $\overline{N}$ shows a clear *jump* from high to low values at the glass transition temperature T^*. The *qualitative* variation in $\overline{N}$ is consistent with the behaviour of the molecular size, because larger overcrossing numbers are normally found in more compact configurations (i.e., a decrease in $\overline{N}$ indicates that the backbone becomes partially "open" as T increases). However, the *quantitative* change in $\overline{N}$ indicates two clear domains, whereby $\overline{N}$ remains relatively constant for $T > T^*$. (Of course, this conclusion is valid for temperatures *moderately* higher than T^*. We would expect other shape transitions at higher temperatures as the protein unfolds or denatures.)

In the case of the mean overcrossing number, we find evidence that a *shape transition* (31–33) in the backbone takes place at T^*. At the glass-transition, there seems to be not only a fast change in Debye–Waller B-factors but also in backbone entanglements.

The effect is small, but still noticeable, in the C_α-skeleton, which exhibits the largest "bond" distances. In contrast,

© 1998 NRC Canada

there is a remarkable shape transition when considering the N-C_α-C-skeleton. This backbone involves shorter bonds with similar lengths (i.e., the N—C_α, C_α—C, and C—N bonds), a feature that magnifies the effect of thermal fluctuations on the atomic positions. Whereas in the C_α-skeleton the jump in $\overline{N}$ values at T^* is rather marginal (only two standard deviations within the confidence of our calculations), random variations can be ruled out in the case of the N-C_α-C-skeleton.

The results for the glass-transition in ribonuclease-A are consistent with the analysis for the toy chain in the previous section. Our findings suggest that we *can* extract important information on the thermal behaviour of a macromolecule by monitoring shape features other than the molecular size. It will be important to test whether a similar behaviour is found during the glass transitions of other proteins.

Further comments and conclusions

In conclusion, we have found that transitions in the average backbone shape can be "recovered" by monitoring chain self-entanglements, even when the molecular size shows no remarkable change. The results indicate that the mean number of overcrossings $\overline{N}$ can be a more sensitive shape descriptor than R_G. By construction, $\overline{N}$ "magnifies" the effect of *thermal fluctuations on the backbone bonds*. Fluctuations in other atoms, or in backbone atoms far away from each other, have a smaller effect on $\overline{N}$.

We believe that the observation that a backbone *shape transition* may accompany the glass transition in a protein can be quite useful. Up to now, glass transitions have been monitored by using mean-squared deviations from a reference equilibrium position. However, these quantities are characterized by an error much larger than the uncertainty in the atomic positions. In fact, it is difficult to give an unambiguous interpretation to the Debye–Waller *B*-factors (8, 13). These factors depend on lattice fluctuations, protein packing in the crystal, in addition to inter- and intramolecular fluctuations. The consensus is that the thermal variation of *B*-factors during the glass transition stems mostly from *intramolecular* motions (8). However, it is hard to assess the relative importance of the other factors. In this work, we have shown that the standard analysis can be complemented by studying the chain self-entanglements. This property can be unambiguously interpreted in terms of the backbone of a single macromolecule. Therefore, a coincidence between a fast change in *B*-factors and a fast change in $\overline{N}$ would provide a stronger argument for the occurrence of an *intramolecular glass transition* (i.e., one characterized by the access to intramolecular motions of large amplitude whenever $T > T^*$).

Our analysis can be extended to the study of *all* atoms involved in the glass transition. By using the definition of overcrossings in a network (35), we can apply the present procedure to the study of fluctuations in the transient patterns of a hydrogen-bonded network. Moreover, the present technique is not restricted to the analysis of shape transitions triggered by temperature changes. In the future, we will explore whether transitions in entanglements are found when other external perturbations are applied to a protein, e.g., variations in pH, pressure, and ionic force.

Acknowledgment

G.A.A. would like to thank R. Cachau (NCI, Structural Biochemistry Lab, Frederick, Md.), L. Massa (CUNY, New York), J. Karle (Naval Research Lab, Washington, D.C.), and A. Grosberg (MIT, Cambridge, Mass.) for fruitful discussions and pointing out some useful references. The authors thank also A. Kholodenko (Clemson University, S.C.) for sending ref. 28 prior to publication and N. Grant (Sudbury) for her comments on the manuscript. This work has been supported by grants from FRUL (Laurentian University) and the Natural Sciences and Engineering Research Council of Canada (NSERC).

References

1. F.R.N. Gurd and T.M. Rothgeb. Adv. Prot. Chem. **33**, 73 (1979).
2. M. Karplus and J.A. McCammon. Annu. Rev. Biochem. **53**, 263 (1983).
3. D. Ringe and G.A. Petsko. Prog. Biophys. Mol. Biol. **45**, 197 (1985).
4. J.A. McCammon and S.C. Harvey. Dynamics of proteins and nucleic acids. Cambridge University Press, Cambridge. 1987.
5. M. Diehl, W. Doster, W. Petry, and H. Schober. Biophys. J. **73**, 2726 (1997).
6. M. Gerstein, A.M. Lesk, and C. Chothia. Biochemistry, **33**, 6739 (1994).
7. A.G. Murzin, S.E. Brenner, T. Hubbard, and C. Chothia. J. Mol. Biol. **247**, 536 (1995).
8. W.A. Gilbert, J. Kuriyan, G.A. Petsko, and D. Ringe Ponzi. *In* Structure and dynamics: nucleic acids and proteins. *Edited by* E. Clementi and R.H. Sharma. Adenine Press, New York. 1983.
9. H. Frauenfelder, H. Hartmann, M. Karplus, I.D. Kuntz, J. Kuriyan, F. Parak, G.A. Petsko, D. Ringe, R.F. Tilton, M. Connolly, and N. Max. Biochemistry, **26**, 254 (1987).
10. K. Kuczera, J. Kuriyan, and M. Karplus. J. Mol. Biol. **213**, 351 (1990).
11. B.F. Rasmussen, A.M. Stock, D. Ringe, and G.A. Petsko. Nature (London), **357**, 423 (1992).
12. W. Doster, S. Cusack, and W. Petry. Nature (London), **337**, 754 (1992).
13. R.F. Tilton, J.C. Dewan, and G.A. Petsko. Biochemistry, **31**, 2469 (1992).
14. I.V. Kurinov and R.W. Harrison. Acta Crystallogr. Sect. D: Biol. Crystallogr. **51**, 98 (1995).
15. F. Parak, E.W. Knapp, and D. Kucheida. J. Mol. Biol. **161**, 177 (1982).
16. E.R. Bauminger, S.G. Cohen, I. Nowik, S. Ofer, and J. Yariv. Proc. Nat. Acad. Sci. U.S.A. **80**, 736 (1983).
17. S. Cusack and W. Doster. Biophys. J. **58**, 243 (1990).
18. M.-C. Bellisent-Funel, J.-M. Zanotti, and S.H. Chen. Faraday Discuss. **103**, 281 (1996).
19. D. Tobias. Bull. Am. Phys. Soc. **43**, 516 (1998).
20. R.J. Loncharich and B.R. Brooks. J. Mol. Biol. **215**, 439 (1990).
21. J.E. Wampler. J. Chem. Inf. Comput. Sci. **37**, 1171 (1997).
22. G.A. Arteca and P.G. Mezey. Biopolymers, **32**, 1609 (1992).
23. E.J. Janse van Rensburg, D.W. Sumners, E. Wasserman, and S.G.Whittington. J. Phys. A: Math Gen. **25**, 6557 (1992).
24. G.A. Arteca. Biopolymers, **33**, 1829 (1993).
25. G.A. Arteca. Phys. Rev. E: Stat. Phys. Plasmas Fluids Relat. Interdiscip. Top. **49**, 2417 (1994).

© 1998 NRC Canada

26. E. Orlandini, M.C. Tesi, S.G. Whittington, D.W. Sumners, and E.J. Janse van Rensburg. J. Phys. A: Math Gen. **27**, L333 (1994).
27. A.L. Kholodenko and D.P. Rolfsen. J. Phys. A: Math Gen. **29**, 5677 (1996).
28. A.L. Kholodenko and T.A. Vilgis. Phys. Rep. **298**, 251 (1998).
29. G.A. Arteca. Phys. Rev. E: Stat. Phys. Plasmas Fluids Relat. Interdiscip. Top. **51**, 2600 (1995); **54**, 3044 (1996); **56**, 4516 (1997).
30. G.A. Arteca. Can. J. Chem. **73**, 241 (1995).
31. G.A. Arteca. Macromolecules, **29**, 7594 (1996).
32. G.A. Arteca. J. Phys. Chem. B, **101**, 4097 (1997).
33. G.A. Arteca. Biopolymers, **35**, 393 (1995).
34. G.A. Arteca. Int. J. Quantum Chem. Quantum Chem. Symp. **28**, 433 (1994).
35. G.A. Arteca. J. Comp. Chem. **15**, 633 (1994).
36. A. Stasiak, V. Katritch, J. Bednar, D. Michoud, and J. Dubochet. Nature (London), **384**, 122 (1996).
37. V. Katritch, J. Bednar, D. Michoud, R.G. Scharein, J. Dubochet, and A. Stasiak. Nature (London), **384**, 142 (1996).
38. A.Yu. Grosberg, A. Feigel, and Y. Rabin. Phys. Rev. E: Stat. Phys. Plasmas Fluids Relat. Interdiscip. Top. **54**, 6618 (1996).
39. E.J. Janse van Rensburg, E. Orlandini, D.W. Sumners, M.C. Tesi, and S.G. Whittington. J. Knot Theory Ram. **6**, 31 (1997).
40. C.F. Gauss. König. Ges. Wiss. Göttingen, **5**, 602 (1877).
41. G. Câlugâreanu. Rev. Math. Pure Appl. **4**, 5 (1959).
42. F.B. Fuller. Proc. Symp. Appl. Math. **14**, 64 (1962).
43. S.F. Edwards. Proc. R. Soc. (London), **91**, 513 (1967); J. Phys. A: Math Gen. **1**, 15 (1968).
44. M.G. Brereton and S. Shah. J. Phys. A: Math Gen. **14**, L51 (1981).
45. F.W. Wiegel. *In* Phase transitions and critical phenomena. Vol. 7. *Edited by* C. Domb and J.L. Lebowitz. Academic Press, London. 1983.
46. M. Doi and S.F. Edwards. The theory of polymer dynamics. Clarendon Press, Oxford. 1988.
47. M.G. Brereton. J. Mol. Struct. (Theochem), **336**, 191 (1995).
48. H. Kleinert. Path integrals in quantum mechanics, statistics, and polymer physics. World Scientific, Singapore. 1995.
49. B. O'Neill. Elementary differential geometry. Academic Press, Boston. 1966. p. 290.
50. V.I. Arnol'd. Sel. Math. Sov. **5**, 327 (1986).
51. M.E. Freedman and Z.-X. He. Ann. Math. **134**, 189 (1991).
52. S. Brynson, M.E. Freedman, Z.-X. He, and Z. Wang. Bull. Am. Math. Soc. (NS), **28**, 99 (1993).
53. M.H. Freedman, Z.-X. He, and Z. Wang. Ann. Math. **139**, 1 (1994).
54. V.G. Ozol'-Kalnin. Pis'ma. Zh. Eksp. Teor. Fiz. **59**, 535 (1994). (JETP Lett. **59**, 565 (1994).)
55. I.S. Gradshtein and I.M. Ryzhik. Tablitsy integralov, summ, riadov i proizvedenii. FM Publishers, Moscow. 1962.

© 1998 NRC Canada

General base-catalyzed hydrolysis and carbonyl-^{18}O exchange of *N*-(4-nitrobenzoyl)pyrrole

Laurence J. Beach, Raymond J. Batchelor, Frederick W.B. Einstein, and Andrew J. Bennet

Abstract: Base-promoted hydrolysis kinetics for *N*-(4-nitrobenzoyl)pyrrole (**1**) have been measured as a function of buffer concentration at several pH values at 25°C. In addition carbonyl-^{18}O exchange kinetics have been determined at a single pH value (9.48) as a function of 1,4-diazobicyclo[2.2.2]octane (DABCO) concentration. At zero buffer concentration the measured ratio of ^{18}O exchange to hydrolysis (k_{ex}/k_{hyd}) is approximately 0.04, and this value increases and finally levels off at about 0.23 as the DABCO concentration is increased. These observations are consistent with the buffer acting as a general-base to catalyze both the attack of water to generate an anionic tetrahedral intermediate (T_{O^-}) and the breakdown of T_{O^-} to give hydrolysis products.

Key words: amide, hydrolysis, catalysis, general-base, tetrahedral intermediate.

Résumé : Opérant à 25°C, à plusieurs valeurs de pH, on a mesuré la cinétique de l'hydrolyse catalysée par les bases du *N*-(4-nitrobenzoyl)pyrrole (**1**) en fonction de la concentration du tampon. De plus, opérant à une seule valeur de pH (9,48), on a déterminé la cinétique d'échange du ^{18}O en fonction de la concentration du 1,4-diazobicyclo[2.2.2]octane (DABCO). À une concentration nulle de tampon, le rapport des vitesses d'échange du ^{18}O et d'hydrolyse (k_{ec}/k_{hyd}) est approximativement égal à 0,04; lorsqu'on augmente la concentration du DABCO, cette valeur augmente pour atteindre une valeur limite d'environ 0,23. Ces observations sont en accord avec l'hypothèse selon laquelle le tampon agit comme une base générale qui catalyse aussi bien l'attaque de l'eau qui génère l'intermédiaire anionique tétraédrique (T_{O^-}) que la rupture de T_{O^-} qui conduit aux produits d'hydrolyse.

Mots clés : amide, hydrolyse, catalyse, basique générale, intermédiaire tétraédrique.

[Traduit par la Rédaction]

Introduction

The amide C—N bond is one of the main structural units in biological chemistry, and as such hydrolysis of this linkage has been widely studied (1). Scheme 1 shows the generally accepted mechanism for hydrolysis of amides in basic nonbuffered solutions. These hydrolysis reactions involve reversible formation of an anionic tetrahedral intermediate (T_{O^-}) followed by subsequent breakdown to generate amine and carboxylate anion.

Whether these base-promoted hydrolysis reactions exhibit a second-order domain in their pH–rate profiles depends on the basicity of the amine leaving group (2). For example, simple amides such as benzamides (3) and simple aliphatic amides (1*c*, 4) only show first-order terms in [HO^-] during hydrolysis (i.e., $k_2 >> k_3[OH^-]$). In these cases the tetrahedral intermediate T_{O^-} (Scheme 1) is sufficiently reactive to break down to products without the assistance of a second hydroxide ion. In contrast, hydroxide-catalyzed breakdown of T_{O^-} has been reported to occur during the hydrolysis of amides that contain less basic amines, for example acetanilides (5), formanilides (6), trifluoroacetanilides (7), and *N*-acyl pyrroles (8). Furthermore, during the base-promoted hydrolysis of trifluoro- and trichloroacetanilide general base-catalysis has been observed for the breakdown of T_{O^-} (9).

Menger and Donahue (8*a*) reported that the hydrolysis of *N*-(4-nitrobenzoyl)pyrrole (**1**) was catalyzed by buffers, such as 1,4-diazobicyclo[2.2.2]octane (DABCO) and trimethylamine (TMA). In contrast, Slebocka-Tilk et al. (2*c*) reported that neither hydrolysis nor ^{18}O-*carbonyl* exchange of the structurally similar amide *N*-toluoyl pyrrole (**2**) was catalyzed by added buffers.

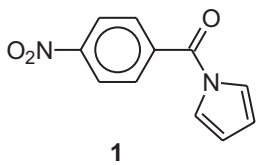

1

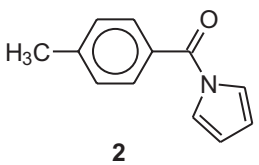

2

Menger and Donahue (8*a*) analyzed the observed effects of added buffer on the rate of hydrolysis of **1** as a buffer-assisted attack of water on the carbonyl group to generate the anionic tetrahedral intermediate T_{O^-}, i.e., general base-catalysis. However, given that the structurally similar amide **2** undergoes a hydroxide-catalyzed breakdown of T_{O^-} it is possible that the observed general base-catalyzed hydrolysis of **1** may involve catalysis of the breakdown rather than (or

Received May 22, 1998.

L.J. Beach, R.J. Batchelor, F.W.B. Einstein, and A.J. Bennet.[1] Department of Chemistry, Simon Fraser University, Burnaby, BC V5A 1S6, Canada.

[1]Author to whom correspondence may be addressed. Telephone: (604) 291-3532. Fax: (604) 291-3765. E-mail: bennet@sfu.ca

© 1998 NRC Canada

Scheme 1.

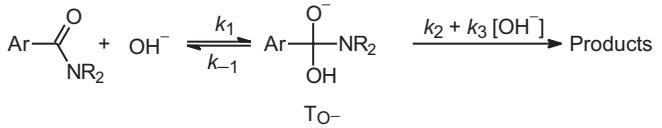

Fig. 1. Plot of k_{obs} versus [TMA] for **1**, T = 25°C, μ = 1.0 (KCl). Lines drawn through the points are the best linear fits to the data.

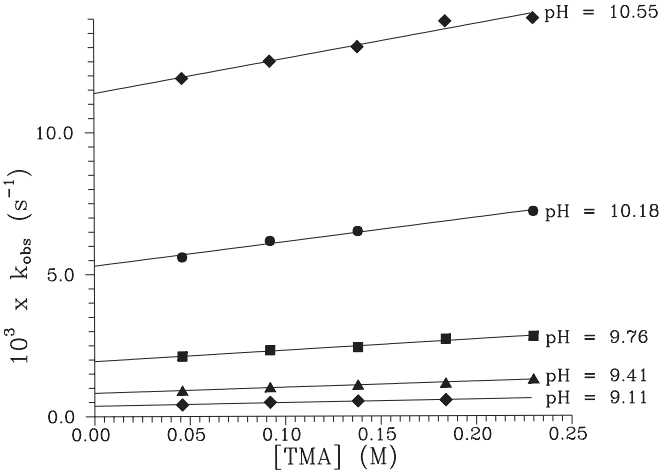

in addition to) the formation of the anionic tetrahedral intermediate.

The present report contains the details of a kinetic study on the rates of *carbonyl*-^{18}O exchange and hydrolysis for *N*-(4-nitrobenzoyl)pyrrole (**1**) as a function of buffer concentration with the aim of elucidating the mechanism of general catalysis. In addition, the measured solvent deuterium kinetic isotope effect (SDKIE) on the hydroxide-promoted rate of hydrolysis is included in this report, as is the solid state structure of *N*-(4-nitrobenzoyl)pyrrole (**1**).

Results

The experimental conditions employed in the present study to elucidate the mechanism of buffer-catalyzed hydrolysis of **1** were modified from those used by Menger and Donahue (8*a*) so that ionic strength was kept constant. Tables S1 and S2 (supplementary material)[2] list the complete rate constant data (k_{hyd}) measured for the hydrolysis of **1** at various pH values and buffer concentrations (μ = 1.0, KCl; T = 25°C). The corresponding plots of k_{hyd} versus buffer concentration are shown in Figs. 1 and 2. To determine the active component of the buffer, second-order rate constants (k_{BT}) for the TMA-catalyzed reaction were calculated using a linear fit of the data from Table S1.[3]

Figure 3 illustrates the calculated second-order rate constants (k_{BT}) versus the fraction of base (X_B) for the TMA-catalyzed hydrolysis of **1**, also included in the plot is the best linear fit to this data.

Fig. 2. Plot of k_{obs} versus [DABCO] for **1**, T = 25°C, μ = 1.0 (KCl).

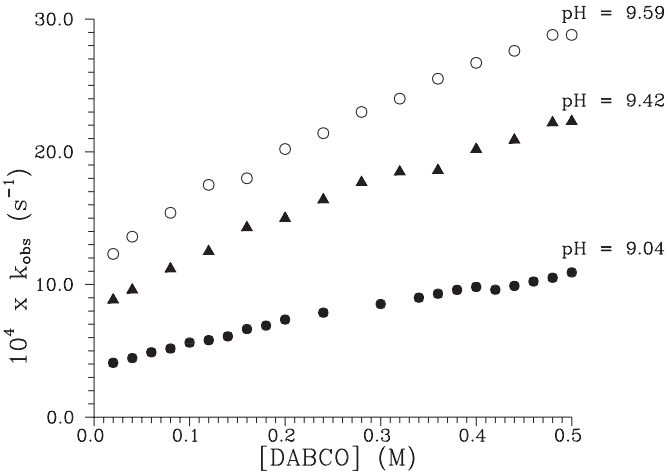

Fig. 3. Plot of k_{BT} versus fraction of base (X_B) for DABCO-catalyzed hydrolysis of **1**, T = 25°C, μ = 1.0 (KCl). Line drawn through the points is the best linear fit to the data.

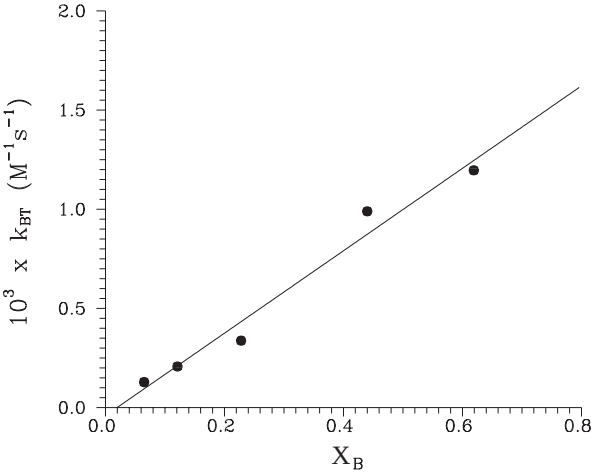

Rate constants for the hydroxide-promoted hydrolysis of **1**, at low pH values, were determined by extrapolating the measured rate constants in the presence of buffers to zero buffer concentration. The derived values (k_{calc}) are compiled in Table 1. Using the data from Table 1, for pH values <10, the calculated second-order rate constant for the hydroxide-promoted hydrolysis of **1** is 31.5 ± 2.7 M^{-1} s^{-1}.

At high pH values (12–14) the rate of hydrolysis of **1** at varying [OH^-] and [OD^-] was measured directly, and the obtained pseudo-first-order rate constants are listed in Table 2.

The second-order rate constant for hydroxide- and deuteroxide-promoted hydrolysis of **1** at high pH were calculated to be 35.2 ± 1.5 and 39.4 ± 1.4 M^{-1} s^{-1}, respectively. Thus, the SDKIE (k_{H_2O}/k_{D_2O}) for this base-promoted hydrolysis reaction is 0.89 ± 0.05 (25°C). To determine partitioning of tetrahedral intermediates formed during the hydrolysis of **1**

[2] Supplementary material may be purchased from: The Depository of Unpublished Data, Document Delivery, CISTI, National Research Council Canada, Ottawa, Canada, K1A 0S2. Tables of atomic coordinates have also been deposited with the Cambridge Crystallographic Data Centre and can be obtained on request from: The Director, Cambridge Crystallographic Data Centre, University Chemical Laboratory, 12 Union Road, Cambridge, CB2 1EZ, U.K.

[3] Only the data with [TMA] ≤ 0.138 M were used in the linear fit.

© 1998 NRC Canada

Table 1. Calculated pseudo-first-order rate constants for the hydrolysis of **1** at zero buffer concentration versus pH; T = 25°C, μ = 1.00 (KCl).[a]

Buffer	pH	$k_{calc} \times 10^4$ (s^{-1})
DABCO	9.04	3.78 ± 0.07
TMA	9.11	3.58 ± 0.03
TMA	9.41	8.20 ± 0.02
DABCO	9.42	8.24 ± 0.09
DABCO	9.59	11.4 ± 0.2
TMA	9.76	19.7 ± 0.7
TMA	10.18	51.8 ± 1.4
TMA	10.55	113.7 ± 0.6

[a]Extrapolated from the data given in Tables S1 and S2 where $[buffer]_{total} < 0.14$ M.

Table 2. Observed pseudo-first-order rate constants for the hydrolysis of **1** in the absence of added buffer versus –log [OL^-]; T = 25°C, μ = 1.00 (KCl).

–log [OH^-]	k_{hyd} (H_2O) (s^{-1})[a]	–log [OD^-]	k_{hyd} (D_2O) (s^{-1})[a]
0.31	18.2 ± 0.5	0.29	21.2 ± 0.2
0.62	8.5 ± 0.3	0.59	10.0 ± 0.5
1.01	3.38 ± 0.06	0.99	4.1 ± 0.1
1.62	0.85 ± 0.02	1.99	0.39 ± 0.02
2.01	0.33 ± 0.01		

[a]Mean value of seven or eight independent kinetic runs; quoted error = σ_{n-1}.

Fig. 4. Plot of k_{ex}/k_{hyd} versus [DABCO] for reaction of **1** at a pH value of 9.48, T = 25°C, μ = 1.0 (KCl). Line drawn through the points is the best nonlinear fit to eq. [6].

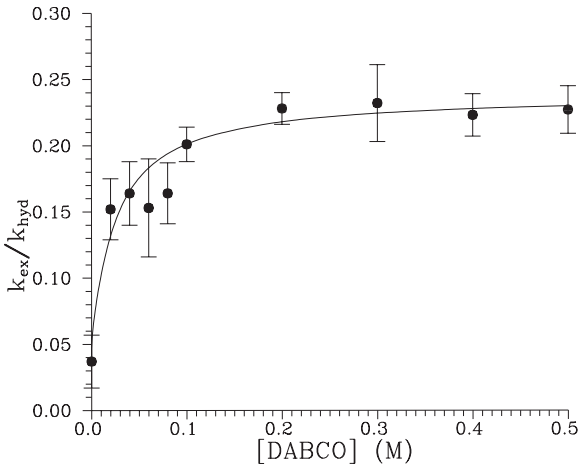

the ratio of *carbonyl*-^{18}O exchange to hydrolysis was measured as a function of buffer concentration at a single pH value. In an initial set of experiments (pH = 9.0) *carbonyl*-^{18}O labelled amide was subjected to the hydrolysis conditions for one half-time of hydrolysis. After reisolation of the labelled amide remaining and determination of the percentage of ^{18}O present estimates for the ratio k_{ex}/k_{hyd} were made using eq. [1].

$$[1] \qquad \frac{k_{ex}}{k_{hyd}} = \frac{\ln\left(^{18}O_0 / ^{18}O_t\right)}{\ln(2)}$$

Table 3. Observed pseudo-first-order rate constants for *carbonyl*-^{18}O exchange and hydrolysis of **1** in the presence of added DABCO, pH = 9.48, T = 25°C, μ = 1.00 (KCl).

DABCO (M)	$k_{ex} \times 10^4$ (s^{-1})[a]	$k_{hyd} \times 10^4$ (s^{-1})[b]	k_{ex}/k_{hyd}[c]
0.50	5.08 ± 0.41	22.4 ± 0.1	0.227 ± 0.018
0.40	4.76 ± 0.31	21.3 ± 0.6	0.223 ± 0.016
0.30	4.44 ± 0.54	19.1 ± 0.6	0.232 ± 0.029
0.20	3.65 ± 0.19	16.0 ± 0.2	0.228 ± 0.012
0.10	2.55 ± 0.15	12.7 ± 0.3	0.201 ± 0.013
0.08	1.98 ± 0.25	12.1 ± 0.8	0.164 ± 0.023
0.06	1.77 ± 0.34	11.6 ± 0.3	0.153 ± 0.037
0.04	1.75 ± 0.25	10.7 ± 0.2	0.164 ± 0.024
0.02	1.58 ± 0.23	10.4 ± 0.4	0.152 ± 0.023
0.00	0.36 ± 0.19[d]	9.7 ± 0.2[e,f]	0.037 ± 0.020[g]

[a]Exchange rate constant calculated according to ref. 10, p. 150, from the data given in Tables S4–S6.

[b]Mean value of three independent kinetic runs; quoted error = σ_{n-1}.

[c]Errors calculated according to ref. 10.

[d]Additional estimate for the pseudo-first-order rate constant k_{ex} using data from Table S6 is 0.55 ± 0.25 × 10^{-4} s^{-1}.

[e]Extrapolated value from data with [DABCO] ≤ 0.1 M.

[f]Value interpolated from the data given in Table 1 is 9.55 × 10^{-4} s^{-1}.

[g]Additional estimate using data from Table S6 is k_{ex}/k_{hyd} = 0.057 ± 0.026.

Given in Table S3 are the measured values for $^{18}O_t$ (percentage ^{18}O at time = $t_{1/2hyd}$) and the calculated rate constant ratios k_{ex}/k_{hyd}. This tabulated data suggests that the ratio k_{ex}/k_{hyd} varies as a function of buffer concentration however, the reproducibility of the measured $^{18}O_t$ values was generally worse at higher buffer concentrations, a possible consequence of the required acid quench. Therefore, it was decided to follow *carbonyl*-^{18}O exchange and hydrolysis at a higher pH value using a flow system where the rapid acid quenching of large volumes of DABCO buffers could be avoided (see experimental section).

The measured rate constants for hydrolysis, *carbonyl*-^{18}O exchange and their ratio (k_{ex}/k_{hyd}) at a pH of 9.48 using the flow system are given in Table 3 (10), and the corresponding plot of k_{ex}/k_{hyd} versus buffer concentration is shown in Fig. 4. In addition, the measured ^{16}O:^{18}O ratios for reisolated **1** are given in Tables S4, S5, and S6 (supplementary material).[2]

A single crystal diffraction study was undertaken on **1** to examine possible structural differences between **1** and **2**. Crystallographic details are summarized in Table 4. The final fractional atomic coordinates for the non-hydrogen atoms are listed in Table S7 (supplementary material).[2] The observed bond lengths and those calculated after a rigid body analysis (see experimental section) for **1** are included in Table 5, and the important bond angles are given in Table 6. Figure 5 presents an ORTEP diagram of the so obtained structure for amide **1**.

Given in Table 7 is a comparison of the C—N and C—O amide bond lengths for amides **1** and **2** (11). Also included in Table 7 are the calculated Dunitz parameters (χ_C and χ_N) for these two amides (12).

© 1998 NRC Canada

Table 4. Crystallographic data for the structure determination of **1** at 205 K.

Formula	$C_{11}H_8O_3N_2$	Crystal system	Monoclinic
fw	216.19	Space group	$P2_1/c$
a (Å)[a]	6.027(3)	ρ_c (g cm^{-3})	1.456
b (Å)	21.832(5)	λ(Mo $K_{\alpha 1}$) (Å)	0.7093
c (Å)	7.580(3)	μ(Mo K_α) (cm^{-1})	1.0
b (°)	98.63(3)	min–max 2θ (°)	4–48
V (Å^3)	986.1	Crystal dim.[b] (mm)	0.18 × 0.27 × 0.32
Z	4	Crystal dim.[c] (mm)	0.21 × 0.24 × 0.32
Temperature (K)	205	GoF[d]	2.15
R_F[e]	0.034	R_{wF}[f]	0.041

[a]Cell dimensions were determined from 22 reflections (36° ≤ 2θ ≤ 41°).

[b]First crystal: measured complete quadrant shell (±*h*, *k*, *l*; 4° ≤ 2θ ≤ 45°) and incomplete quadrant shell (±*h*, *k*, *l*; 45° ≤ 2θ ≤ 48°).

[c]Second crystal: complete quadrant shell (±*h*, *k*, *l*; 45° ≤ 2θ ≤ 48°). R_{merge} = 0.027 for ~100 reflections measured on both crystals.

[d]GoF = $[\Sigma(w(F_o - F_c)^2)/\text{degrees of freedom}]^{1/2}$.

[e]$R_F = \Sigma(||F_o| - |F_c||)/\Sigma|F_o|$ for 1142 data ($I_o \geq 2.5\sigma(I_o)$).

[f]$R_{wF} = [\Sigma(w(|F_o| - |F_c|)^2)/\Sigma(wF_o^2)]^{1/2}$ for 1142 data ($I_o \geq 2.5\sigma(I_o)$); $w = [\sigma(F_o)^2 + 0.0001F_o^2]^{-1}$.

Table 5. Selected bond distances (Å) for **1** at 205 K.

Bond	Distance	Corrected[a]	Bond	Distance	Corrected[a]
O(1)—C(10)	1.216(3)	1.22	C(4)—C(5)	1.334(4)	1.337
O(2)—N(2)	1.220(3)	1.249[b]	C(10)—C(11)	1.491(3)	1.493
O(3)—N(2)	1.214(3)	1.243[b]	C(11)—C(12)	1.389(3)	1.392
N(1)—C(2)	1.398(3)	1.402	C(11)—C(16)	1.398(3)	1.401
N(1)—C(5)	1.395(3)	1.398	C(12)—C(13)	1.380(3)	1.382
N(1)—C(10)	1.386(3)	1.388	C(13)—C(14)	1.383(3)	1.387
N(2)—C(14)	1.470(3)	1.472	C(14)—C(15)	1.371(3)	1.374
C(2)—C(3)	1.344(3)	1.346	C(15)—C(16)	1.381(3)	1.383
C(3)—C(4)	1.426(4)	1.429			

[a]Bond distances corrected for rigid-body thermal motion.

[b]Correction includes a contribution for internal libration of the NO_2 group about the N(2)—C(14) bond.

Table 6. Selected bond angles (°) for **1** at 205 K.

Bond	Angle	Bond	Angle
C(2)-N(1)-C(5)	107.15(19)	N(1)-C(10)-C(11)	119.36(18)
C(2)-N(1)-C(10)	129.33(18)	C(10)-C(11)-C(12)	117.45(19)
C(5)-N(1)-C(10)	123.51(19)	C(10)-C(11)-C(16)	122.53(19)
O(2)-N(2)-O(3)	122.95(21)	C(12)-C(11)-C(16)	119.75(20)
O(2)-N(2)-C(14)	118.35(21)	C(11)-C(12)-C(13)	120.54(21)
O(3)-N(2)-C(14)	118.70(22)	C(12)-C(13)-C(14)	118.27(21)
N(1)-C(2)-C(3)	108.39(20)	N(2)-C(14)-C(13)	118.31(21)
C(2)-C(3)-C(4)	107.70(22)	N(2)-C(14)-C(15)	119.08(21)
C(3)-C(4)-C(5)	108.05(22)	C(13)-C(14)-C(15)	122.61(21)
N(1)-C(5)-C(4)	108.71(22)	C(14)-C(15)-C(16)	118.86(21)
O(1)-C(10)-N(1)	120.26(19)	C(11)-C(16)-C(15)	119.95(21)
O(1)-C(10)-C(11)	120.38(19)		

Discussion

(*i*) Hydrolysis of 1 in the absence of buffers

The reported hydrolysis mechanism for *N*-toluoylpyrrole (**2**) includes a hydroxide-catalyzed term for breakdown of the anionic tetrahedral intermediate (T_{O^-}) to generate carboxylate and pyrrole anions (2*c*). The derived expressions of the rate constants for hydrolysis (k_{hyd}), exchange (k_{ex}), and their ratio (k_{ex}/k_{hyd}) from the mechanism shown in Scheme 1 are given by eqs. [2]–[4] where $k_2' = k_2/k_{-1}$ and $k_3' = k_3/k_{-1}$. The factor of two in eqs. [3] and [4] arises from the necessary assumption that one-half of T_{O^-} reversal to regenerate amide leads to *carbonyl*-^{18}O exchange, i.e., the two oxygen atoms in the tetrahedral intermediate are protonically equilibrated. This assumption has been shown to be valid for T_{O^-} formed during the hydrolysis of **2** (2*c*).

$$[2] \qquad k_{hyd} = \frac{k_1[OH^-](k_2' + k_3'[OH^-])}{1 + k_2' + k_3'[OH^-]}$$

© 1998 NRC Canada

Fig. 5. Molecular structure for amide **1**, 50% enclosure ellipsoids are shown.

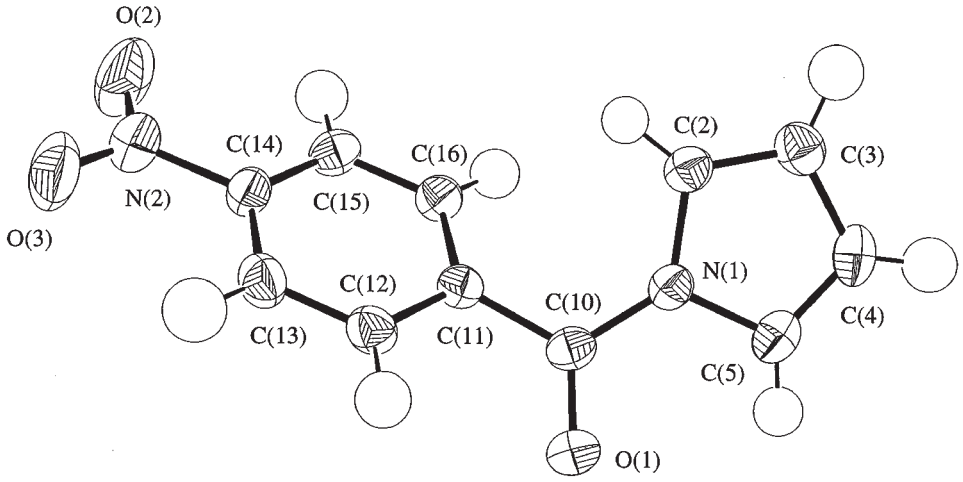

Table 7. Comparison of the structural parameters for the amides **1** and **2**.

Parameter	**1**[a]	**2**
r(C—O) (Å)	1.220	1.211
r(C—N) (Å)	1.388	1.409
χ_C (°)	1.1	0.0
χ_N (°)	1.0	10.1

[a]Bond distances corrected for rigid-body thermal motion (see Table 5).

$$[3] \qquad k_{ex} = \frac{k_1[OH^-]}{2(1 + k_2' + k_3'[OH^-])}$$

$$[4] \qquad \frac{k_{ex}}{k_{hyd}} = \frac{1}{2(k_2' + k_3'[OH^-])}$$

An indication that a similar pathway exists for the hydrolysis of **1** in the absence of buffers is shown by the difference in the calculated second-order rate constants at high and low pH values in the absence of added buffers (2*c*). In the low pH domain, $k_3'[OH^-] << k_2'$, the value for $k_{hyd}/[OH^-]$ of 31.5 ± 2.7 M^{-1} s^{-1} is equal to $k_1k_2'/(1 + k_2')$, while in the high pH domain, $k_3'[OH^-] >> k_2'$, the value for $k_{hyd}/[OH^-]$ of 35.2 ± 1.5 M^{-1} s^{-1} is equal to k_1. Using these two values an estimate of 0.12 ± 0.11 can be computed for the uncatalyzed partitioning (k_{-1}/k_2) of the anionic tetrahedral intermediate T_{O^-} between regeneration (k_{-1}) and hydrolysis (k_2) of the amide. Although, this calculated partitioning ratio contains a large associated error, a second estimate of this quantity can be made from the rate of *carbonyl*-^{18}O exchange (k_{ex}) relative to hydrolysis (k_{hyd}). Where in the absence of buffers and at a pH value of 9.48, assuming $k_3'[OH^-] << k_2'$, the measured value for k_{ex}/k_{hyd} (Table 3) of 0.037 ± 0.02 (repeat value 0.06 ± 0.03) generates an estimated value for k_{-1}/k_2 of 0.07 ± 0.04. That the observed value for k_{ex}/k_{hyd} (0.04–0.06) for the base-promoted hydrolysis of **1**, at low pH measurements, is less than that reported (k_{ex}/k_{hyd} = 0.24) for the corresponding reaction of **2** (2*c*) requires that T_{O^-} partitioning to products is favoured to a greater extent by the electron-withdrawing nitro group (**1**) than by the electron-donating methyl group (**2**). This difference corresponds to a relative reduction in the kinetic barrier (k_2) for product formation from amide **1** compared to amide **2** of approximately 3–4 kJ mol^{-1}. The anionic intermediate T_{O^-} formed during the reactions of **1** will be more stable than the corresponding intermediate formed from **2** because of the electron-withdrawing nitro group. Therefore, it can be safely assumed that the two oxygens in the intermediate (T_{O^-}) formed from **1** are protonically equilibrated and that the change in the k_{ex}/k_{hyd} ratio, in the absence of buffer, indicates a greater tendency for the unimolecular ejection of the pyrrole anion, relative to hydroxide ion, from the more stable tetrahedral intermediate. The origin of this effect could be the formation of a hydrogen bond, at the transition state for pyrrole anion ejection, between the anionic tetrahedral intermediate's O–H group and a solvating water molecule.

(*ii*) Mechanism of buffer catalysis

The intercept with the *y*-axis (X_B = 0, Fig. 3) for the second-order rate constants for buffer-catalyzed hydrolysis of **1** is, within experimental error, zero. Therefore, the basic form of the buffer is the active species for the general-catalyzed hydrolysis of **1**. Shown in Scheme 2 is the modified mechanism for hydrolysis of **1**, where the basic form of the buffer can catalyze the formation (k_{BF}) and (or) the breakdown (k_{BP}) of T_{O^-}. The principal of microscopic reversibility requires that if general base-catalysis for the formation of T_{O^-} occurs then reversal to generate starting material must also occur with general acid-catalysis.

The derived expressions of the rate constants for hydrolysis (k_{hyd}), exchange (k_{ex}), and their ratio (k_{ex}/k_{hyd}) from the mechanism shown in Scheme 2 are given by eqs. [5]–[7] where $k_{BF}' = k_{BF}/k_{-1}$, $k_{BH}' = k_{BH}/k_{-1}$, and $k_{BP}' = k_{BP}/k_{-1}$.

$$[5] \qquad k_{hyd} = \frac{(k_1[OH^-] + k_{BF}[B])(k_2' + k_{BP}'[B] + k_3'[OH^-])}{1 + k_{BH}'[BH^+] + k_2' + k_{BP}'[B] + k_3'[OH^-]}$$

$$[6] \qquad k_{ex} = \frac{(k_1[OH^-] + k_{BF}[B])(1 + k_{BH}'[BH^+])}{2(1 + k_{BH}'[BH^+] + k_2' + k_{BP}'[B] + k_3'[OH^-])}$$

$$[7] \qquad \frac{k_{ex}}{k_{hyd}} = \frac{1 + k_{BH}'[BH^+]}{2(k_2' + k_{BP}'[B] + k_3'[OH^-])}$$

© 1998 NRC Canada

Scheme 2.

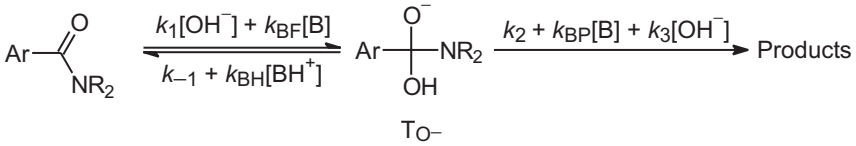

Scheme 3.

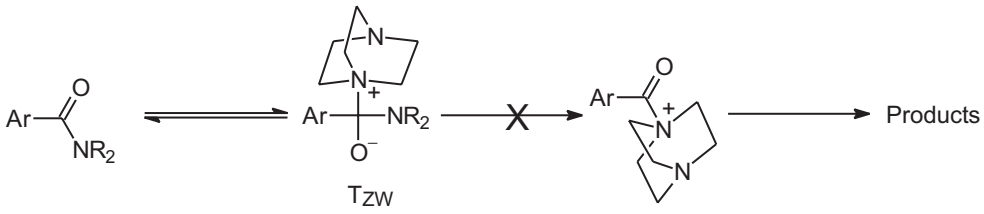

Three immediate conclusions can be drawn from the data shown in Figs. 1 and 2, and given in Table 3, namely, (*i*) the hydrolysis reactions of **1** are buffer-catalyzed; (*ii*) since $k_{ex}/k_{hyd} << 1$, at low pH and in the absence of buffer, the rate-limiting step for the hydroxide-promoted hydrolysis must be formation of T_{O^-}; and (*iii*) buffer accelerates the slow step of the hydrolysis reaction, i.e., T_{O^-} formation. However, if the buffer only catalyzed the formation of the tetrahedral intermediate ($k_{BP}' = 0$, eq. [7]) then at a constant pH value the ratio k_{ex}/k_{hyd} should increase in a linear fashion when the buffer concentration is increased. The observation that the k_{ex}/k_{hyd} ratio increases with buffer concentration and levels off at high concentration provides convincing evidence that both the attack of water on the amide to generate T_{O^-} and the breakdown of T_{O^-} to generate the hydrolysis products are catalyzed by buffer. At high buffer concentration, i.e., when $k_{BP}'[B] >> k_2' + k_3'[OH^-]$ and $k_{BH}'[BH^+] >> 1$, the derived expression for k_{ex}/k_{hyd} (eq. [7]) simplifies to eq. [8].

$$[8] \qquad \frac{k_{ex}}{k_{hyd}} = \frac{k_{BH}'[BH^+]}{2k_{BP}'[B]}$$

In DABCO buffer at a pH value of 9.48 where $(k_{ex}/k_{hyd})_{limit} \approx 0.23$ and $[B]/[BH^+] = 2.13$ substitution of these values into eq. [8] gives a ratio for k_{BH}'/k_{BP}' of approximately 1 ($0.23 \times 2 \times 2.13 = 0.98$).

Since the kinetic expression for buffer-catalyzed hydrolysis of **1** contains several variables estimation of the two parameters k_{BF} and k_{BP}' for the DABCO-catalyzed formation and breakdown of T_{O^-} were made using a constrained nonlinear least-squares fit of all the DABCO-catalyzed hydrolysis data (Tables S2 and 3) to eq. [5]. The constraints used in the nonlinear fit were as follows: $k_{BP}' = k_{BH}'$, $k_1 = 35.2\ M^{-1}\ s^{-1}$, and $k_3'[OH^-] \approx 0$. The calculated rate constants and standard errors that were derived using the program SYSTAT are $k_{BF} = 0.0066 \pm 0.0003\ M^{-1}\ s^{-1}$, $k_{BP}' = 29 \pm 6\ M^{-1}\ s^{-1}$, and $k_2' = 11.2 \pm 0.02$. Although, the complexity of eq. [5] means that these derived values are correlated the estimated value for k_2' is consistent with that obtained from the ratio of exchange to hydrolysis at zero buffer concentration (Table 3), i.e., $k_{ex}/k_{hyd} \approx 1/2k_2'$. Implicit in the above arguments is that the buffer acts as a general base rather than as a nucleophile during the catalytic reaction. If the buffer nucleophilically attacked the carbonyl carbon to generate an intermediate such as T_{ZW} then the ratio of k_{ex}/k_{hyd} should drop to zero, since no *carbonyl*-^{18}O exchange into the starting amide is possible from T_{ZW}. Therefore, if any nucleophilic attack by DABCO occurred the intermediate T_{ZW} must always revert to starting amide (Scheme 3).

From the above analysis it must be concluded that the observed DABCO-catalyzed breakdown of T_{O^-} to give hydrolysis products is an example of general base-catalysis. Consequently, the ejection of the pyrrole anion from the anionic tetrahedral intermediate must occur simultaneously with, and not subsequent to, proton removal. This conclusion is in contrast to the proposal of Menger and Donahue (8*a*).

(*iii*) Solvent deuterium kinetic isotope effect

The measured values for the SDKIE of 0.89 ± 0.05 for the hydroxide attack at the carbonyl carbon is similar to the reported value for **2** (2*c*) and is consistent with the transition state for this step involving direct attack of a partially desolvated hydroxide ion on the carbonyl carbon (2).

(*iv*) Structural comparison of amides 1 and 2

The data reported in Table 7 shows that in the solid state both amide linkages in **1** and **2** have similar structural parameters. Consequently, no information is obtained that can explain either the absence of buffer-catalysis during the hydrolysis of **2**, or the presence of this type of catalysis in the case of **1**.

Conclusions

In conclusion, replacement of the 4-methyl group in pyrrole amide **2** with a 4-nitro group (amide **1**) activates the amide linkage sufficiently that general-base-catalyzed attack of water on the carbonyl group becomes a viable mechanism. In addition, although the nitro group unquestionably increases the lifetime of the anionic tetrahedral intermediate (T_{O^-}), via inductive withdrawal, the uncatalyzed breakdown of T_{O^-} favours ejection of the pyrrole anion over hydroxide ion ($k_{ex}/k_{hyd} = 0.04–0.06$) to a greater extent than does the tetrahedral intermediate formed during the hydrolysis of **2** ($k_{ex}/k_{hyd} = 0.24$). This effect might be caused by the differences in acidity of the two respective tetrahedral intermediates. Thus, in compound **1** the electron-withdrawing nitro

© 1998 NRC Canada

group should result in the development of a stronger hydrogen bond at the transition state (k_2) for product formation.

Experimental

The following materials were purchased and used as received unless stated otherwise: pyrrole (Aldrich), 4-nitrobenzoyl chloride (Lancaster), potassium metal and thionyl chloride (Anachemia), $H_2{}^{18}O$ (Isotec, 98.5 atom % ^{18}O, lot no. DU2255), trimethylamine hydrochloride (SIGMA, TMA-HCl), deuterium oxide (Isotec, 99.9 atom % D), and potassium chloride (BDH). DABCO (1,4-diazabicyclo[2.2.2]octane; Aldrich, 98%) was recrystallized from pet ether for the ^{18}O-oxygen exchange experiments. Reagent grade tetrahydrofuran (BDH, THF) was distilled from its sodium benzophenone ketal, and reagent grade toluene (BDH) was distilled from calcium hydride. NMR spectra were acquired using a Brucker AMX400 NMR spectrophotometer operating at frequencies of 400.1 and 100.6 MHz for ^1H and ^{13}C, respectively. Mass spectra were obtained using a direct insertion probe and electron impact ionization (70 eV) on a Hewlett Packard 5985 mass spectrometer. Melting points are uncorrected.

N-(4-Nitrobenzoyl)pyrrole (1)

Under a dry nitrogen atmosphere potassium metal (0.9 g, 23.1 mmol) was added in small portions to a solution containing freshly distilled pyrrole (1.6 mL, 23.1 mmol) in anhydrous THF (20 mL). After the addition was complete the resulting solution was heated to reflux until the potassium had complete reacted. After cooling to ambient temperature anhydrous toluene (70 mL) was added followed by the dropwise addition of a solution containing 4-nitrobenzoyl chloride (4.29 g, 23.1 mmol) in anhydrous toluene (200 mL). The resulting solution was heated to reflux for 24 h, and after cooling to ambient temperature a mixture of 1:1 ice-cold water – diethyl ether (total volume 100 mL) was added. The diethyl ether layer was separated and washed with ice-cold water (50 mL). The two aqueous layers were combined and washed with diethyl ether (50 mL), after the two layers were separated the organic layers were combined and volatile materials were removed under reduced pressure. The resulting black residue was sublimed (100°C; 0.25 mTorr) onto a cold finger, and the resulting product was further purified by recrystallization from hexane:2-butanol to give an analytically pure sample of **1** (1.25 g; 25%): mp 128.5–130.0°C (lit. (8) mp 127–128°C); ir (KBr pellet), ν: 3155 (w), 3107 (w), 1692 (s), 1601 (m), 1519 (s), 1474 (s), 1409 (s), 1332 (s), 1256 (w), 1189 (w), 1112 (w), 1091 (m), 1075 (m), 1037 (w), 1012 (m), 972 (m), 884 (m), 865 (m), 844 (s), 747 (s), 730 (s) 712 (s); ^1H NMR (400 MHz; CD_3COCD_3), δ: 6.40 (2H, *app* dd), 7.29 (2H, *app* dd), 8.04 (2H, m), 8.43 (2H, m); ^{13}C NMR (100 MHz; CD_3COCD_3), δ: 166.6, 150.9, 140.0, 124.6, 122.0, 114.5; EI–MS, *m*/*z*: 216(M^+, 65), 150(100), 120(20), 104(25), 92(21), and 76(23). Anal. calcd. for $C_{11}H_8N_2O_3$: C 61.11, H 3.73, N 12.95; found: C 61.30, H 3.69, N 12.97.

N-(4-Nitro-*carbonyl*-^{18}O-benzoyl)pyrrole

To a solution of freshly distilled 4-nitrobenzoyl chloride (1.33 g, 7.2 mmol) in anhydrous THF (15 mL) was added ^{18}O-water (129 mL, 6.5 mmol) under a nitrogen atmosphere. After this solution had been stirred at ambient temperature for 24 h the volatile materials were removed under reduced pressure. To the resulting residue anhydrous toluene (15 mL) was added, followed by the dropwise addition of thionyl chloride (1.04 mL, 14.3 mmol), and the reaction mixture was heated to reflux for 18 h. After the volatile materials were removed under reduced pressure the resulting 4-nitro-*carbonyl*-^{18}O-benzoyl chloride was purified by vacuum distillation (125°C; 5 mTorr). The ^{18}O-labelled acid chloride was used to prepare *N*-(4-nitro-*carbonyl*-^{18}O-benzol)pyrrole in an analogous fashion to the preparation of unlabelled **1**. The overall yield for the synthesis of ^{18}O-labelled **1** from 4-nitrobenzoyl chloride was 21%; ir (KBr pellet), ν: 3155 (w), 3107 (w), 1692 (s), 1660 (s), 1601 (m), 1519 (s), 1474 (s), 1409 (s), 1332 (s), 1256 (w), 1189 (w), 1112 (w), 1091 (m), 1075 (m), 1037 (w), 1012 (m), 972 (m), 884 (m), 865 (m), 844 (s), 747 (s), 730 (s) 712 (s); EI–MS, *m*/*z*: 218(^{18}O-M^+, 59), 216(^{16}O-M^+, 72), 152(68), 150(100), 122(11), 120(11), 106(21), 104(30), 94(16), 92(17), and 76(44).

Hydrolysis kinetics

Hydrolysis of **1** was monitored by measuring the change in absorbance at either 240 nm (trimethylamine buffers) or 278 nm (OH^- solutions or DABCO buffers) using either a Cary-3E UV-vis spectrophotometer equipped with the Cary six cell Peltier constant temperature accessory or a DURRUM 110 stopped-flow apparatus thermostatted with a Lauda RM6 circulating water bath. The slower reactions were initiated by injection of a stock solution of **1** in DME (20–50 mL; 18.5 mM) into a equilibrated solvent mixture (3 mL; 30 min), whereas for the stopped-flow reactions an equal volume of a solution of **1** (0.4 mM) in 10^{-4} M HCl (μ = 1, KCl) was mixed with NaOH. Rate constants in deuterated solvents were measured in an analogous fashion using D_2O solutions.

Exchange kinetics

^{18}O-*Carbonyl* exchange of labelled-**1** in the presence of DABCO buffers was monitored utilizing a fluid flow system identical to that reported earlier (2*c*) except that the reaction was quenched by utilizing a pH-stat assembly consisting of Radiometer TTT80 titrator, ABU80 autoburette, a PHM82 standard pH meter, and a Broadley–James combination electrode (silver/silver chloride reference) to maintain the quenching solution at a pH of 4. The rate of ^{18}O-*carbonyl* exchange in the absence of buffer was measured using the pH-stat assembly to maintain a constant pH for a time equal to one or two times the half-time for hydrolysis of **1**. The labelled-**1** remaining in the hydrolysis medium was isolated by extracting the aqueous solution with freshly distilled CH_2Cl_2 (4 × 2 mL), and the combined organic layers were washed with a saturated $NaHCO_3$ solution (2 × 4 mL) and water (2 mL). The dichloromethane layer was dried ($MgSO_4$), filtered, and evaporated onto a small dry lint-free tissue. The tissue was inserted into a melting point tube and the ^{18}O-content of the sample was determined by mass spectroscopy. In a typical determination 20 separate scans of the M^+ and the $M^+ + 2$ ions in the mass spectrum were used to estimate the ^{18}O-content of the sample and its associated standard error. The rate constant for exchange was calculated using eq. [9] where $^{18}O_0$ is the ^{18}O-content of the start-

© 1998 NRC Canada

ing amide and $^{18}O_t$ is the ^{18}O-content of the amide reisolated from the reaction medium at time t.[4]

$$[9] \qquad k_{ex} = \frac{-\ln (^{18}O_t / ^{18}O_0)}{t}$$

Structure determination

A single colourless needle-shaped crystal of **1**, obtained from the slow evaporation of a solution of **1** in 1:1 v/v 2-butanol:hexane, was cleaved and fragments of a suitable size and shape were mounted on glass fibres using epoxy adhesive. Data were recorded at 205 K with an Enraf Nonius CAD4F diffractometer equipped with an in-house modified low-temperature attachment and using graphite monochromatized Mo K_α radiation. Two fragments of the same crystal, having comparable size and shape, were used because the first fragment became dislodged during an interruption of the cooling caused by ice build-up in the low-temperature apparatus. The same two intensity standard reflections were measured every hour of exposure time for both crystal fragments and, in either case, fluctuated by ±2.5% during the course of the measurements. No corrections for absorption were deemed necessary. Data reduction included corrections for intensity scale variations and for Lorentz and polarization effects.

The structure was solved using direct methods. All hydrogen atoms were located from an electron density difference map. All atomic coordinates, anisotropic thermal parameters for the non-hydrogen atoms and isotropic thermal parameters for the hydrogen atoms were refined.

An extinction parameter was refined (13). A weighting scheme, based on counting statistics, was used such that $\langle w(|F_o| - |F_c|)^2 \rangle$ was near constant as a function of both $|F_o|$ and sin θ/λ. Final full matrix least-squares refinement of 178 parameters for 1142 data ($I_o > 2.5\sigma(I_o)$) converged at R = 0.034 with a maximum |shift/error| of 0.001.

The programs used for data reduction, structure solution, refinement, and plot generation were from the NRCVAX crystal structure system (14). The programs suite CRYSTALS (15) was employed for analysis of structure factors and thermal parameters. Complex scattering factors for neutral atoms (16) were used in the calculation of structure factors. Computations were carried out on MicroVAX-II and 80486 computers.

Rigid body analysis (17) of the anisotropic thermal parameters of the molecule yielded R = 0.176 for the agreement between observed and calculated U_{ij} and an rms discrepancy of 0.0058 Å^2. In particular the oxygen atoms of the NO_2-group showed excess motion. Analysis of internal motion of the molecule in terms of a segmented rigid body (18) in which the NO_2 group was allowed libration about the C(14)—N(2) bond axis gave R = 0.089 and an rms discrepancy of 0.0023 Å^2.

Acknowledgements

We gratefully acknowledge financial support of this work from the Natural Sciences and Engineering Research Council of Canada and Simon Fraser University. In addition, we thank the referees of this manuscript for their insightful comments.

References

1. (*a*) W.P. Jencks. Catalysis in chemistry and enzymology. McGraw–Hill Inc., New York. 1969. p. 523; (*b*) T.H. Lowry and K.S. Richardson. Mechanism and theory in organic chemistry. 3rd ed. Harper and Row Inc., New York. 1987. p. 714; (*c*) C.J. O'Connor. Q. Rev. Chem. Soc. **24**, 553 (1970); (*d*) M.L. Bender. Chem. Rev. **60**, 53 (1960). (*e*) N. Isaacs. Physical organic chemistry. 2nd. ed. Longman Scientific and Technical and J. Wiley and Sons, New York. 1995. p. 529; (*f*) J. March. Advanced organic chemistry. 4th. ed. Wiley–Interscience, New York. 1992. p. 383; (*g*) R.S. Brown, A.J. Bennet, and H. Slebocka-Tilk. Acc. Chem. Res. **25**, 481 (1992); (*h*) A.J. Bennet and R.S. Brown. *In* Comprehensive biological catalysis. Vol. 1. *Edited by* M.L. Sinnott. Academic Press, San Diego. 1998. p. 293.
2. (*a*) H. Slebocka-Tilk, A.J. Bennet, H.J. Hogg, and R.S. Brown. J. Am. Chem. Soc. **113**, 1288 (1991); (*b*) H. Slebocka-Tilk, A.J. Bennet, R.S. Brown, J.A. Keillor, J.P. Guthrie, and A. Johdan. J. Am. Chem. Soc. **112**, 8507 (1990); (*c*) R.S. Brown, A.J. Bennet, H. Slebocka-Tilk, and A. Johdan. J. Am. Chem. Soc. **114**, 3092 (1992); (*d*) B. Yao-Liu and R.S. Brown. J. Org. Chem. **58**, 732 (1993).
3. (*a*) M.L. Bender, R.D. Ginger, and J.P. Unik. J. Am. Chem. Soc. **80**, 1044 (1958); (*b*) C.A. Bunton, B. Nayak, and C. O'Connor. J. Org. Chem. **33**, 572 (1968).
4. M. de Roo and A. Bruylants. Bull. Soc. Chim. Belg. **63**, 140 (1954).
5. S.O. Eriksson. Acta Chem. Scand. **22**, 892 (1968).
6. R.H. DeWolfe and R.C. Newcomb. J. Org. Chem. **36**, 3870 (1971).
7. (*a*) J.K. Young, S. Pazhanisamy, and R.L. Schowen. J. Org. Chem. **49**, 4148 (1984); (*b*) R.M. Pollack and T.C. Dumsha. J. Am. Chem. Soc. **95**, 4463 (1973); (*c*) S.S. Biechler and R.W. Taft, Jr. J. Am. Chem. Soc. **79**, 4927 (1957).
8. (*a*) F.M. Menger and J.A. Donahue. J. Am. Chem. Soc. **95**, 432 (1973); (*b*) A. Cipiciani, P. Linda, and G.J. Savelli. Heterocycl. Chem. **16**, 673 (1979); (*c*) A. Cipiciani, P. Linda, and G.J. Savelli. Heterocycl. Chem. **16**, 677 (1979).
9. S.O. Eriksson and C. Holst. Acta. Chem. Scand. **20**, 1892 (1966).
10. J.R. Taylor. An introduction to error analysis. University Science Books, Mill Valley. 1982. p. 57.
11. A.J. Bennet, V. Somayaji, R.S. Brown, and B.D. Santarserio. J. Am. Chem. Soc. **113**, 7563 (1991).
12. J.D. Dunitz and F.K. Winkler. Acta Crystallogr. Sect. B: Struct. Crystallogr. Cryst. Chem. **B31**, 251 (1975).
13. A.C. Larson. *In* Crystallographic computing. Munksgaard, Copenhagen. 1970. p. 293.
14. E.J. Gabe, Y. LePage, J-P. Charland, F.L. Lee, and P.S. White. J. Appl. Cryst. **22**, 384 (1989).
15. D.J. Watkin, J.R. Carruthers, and P.W. Betteridge. CRYSTALS. Chemical Crystallography Laboratory, University of Oxford, Oxford, England. 1984.
16. International Tables for X-ray Crystallography.Vol. 4. Kynoch Press, Birmingham, England. 1975. p. 99.
17. V. Shoemaker and K.N. Trueblood. Acta Crystallogr. Sect. B: Struct. Crystallogr. Cryst. Chem. **B24**, 63 (1968).
18. K.N. Trueblood. Acta Crystallogr. Sect. A: Cryst. Phys. Diffr. Theor. Gen. Crystallogr. **A34**, 950 (1978).

[4] Standard errors were calculated according to ref. 10, p. 62.

© 1998 NRC Canada

DISQUAC structure-dependent interaction parameters for mixtures containing *sec*-alkanols and benzene, toluene, or *n*-alkanones

Juan Antonio González, I. García de la Fuente, and J.C. Cobos

Abstract: Mixtures containing *sec*-alkanols and benzene, toluene, or *n*-alkanones are characterized in terms of DISQUAC by means of structure-dependent interaction parameters. The quasichemical (QUAC) interchange coefficients are independent of the size alcohol for a given organic solvent; while the dispersive (DIS) ones change with the size of the alcohol. This behaviour has been found for other many alcoholic solutions. DISQUAC represents well the thermodynamic properties of these mixtures: vapor-liquid equilibria, VLE, molar excess Gibbs energies, G^E, and molar excess enthalpies, H^E. So, the mean deviations between experimental and calculated results are about 2% for pressure, and 8% for H^E. A short comparison between DISQUAC results and those given by the Dortmund version of UNIFAC, the UNIQUAC association theory and other similar model is also presented. In the case of the Dortmund version of UNIFAC, poorer predictions are obtained for H^E, as this property is more sensitive to molecular structure. Association theories provide better results because are used as correlation equations.

Key words: thermodynamics, 2-alkanols, group contributions, interactions.

Résumé : On a caractérisé des mélanges contenant des alcanols secondaires et du benzène, du toluène ou des alcanones en termes de «DISQUAC» à l'aide de paramètres d'interaction dépendants de la structure. Pour un solvant organique donné, les coefficients d'échange quasichimique («QUAC») sont indépendants de la taille de l'alcool alors que les coefficients dispersifs («DIS») varient avec la taille de l'alcool. On a aussi observé ce comportement avec plusieurs solutions alcooliques. Les «DISQUAC» permettent de donner une bonne représentation des propriétés thermodynamiques de ces mélanges: équilibre vapeur-liquide, «VLE», énergies molaires de Gibbs en excès, G^E, et enthalpies molaires en excès, H^E. Il en résulte que les déviations moyennes entre les résultats expérimentaux et les résultats calculés sont d'environ 2% pour la pression et de 8% pour H^E. On présente aussi une courte comparaison entre les résultats «DISQUAC» et ceux donnés par la version de Dortmound d'«UNIFAC», la théorie d'association «UNIQUAC» et d'autres modèles semblables. Dans le cas de la version de Dortmound d'«UNIFAC», on obtient de moins bonnes prédictions pour le H^E parce que cette propriété dépend fortement de la structure moléculaire. Les théories d'association conduisent à de meilleurs résultats parce qu'elles sont utilisées comme équations de corrélation.

Mots clés : thermodynamiques, alcanols secondaires, contributions de groupes, interactions.

[Traduit par la Rédaction]

1. Introduction

The theoretical treatment of alcoholic solutions is a very interesting matter due to the number of factors which contribute to the values of their thermodynamic properties: (*i*) self-association of the alcohols, which seems to be more important in other than in primary alkanols (1); (*ii*) change in the extent and strength of the hydrogen bonding when the mixture is formed (2, 3); (*iii*) physical contributions; (*iv*) structural effects (4). The values of the excess properties result from balances between these contributions, and their relative importance depends on the property under consideration (2–4). So, in mixtures with *n*-alkanes, there is an increase in magnitude of H^E in the sequence: primary alkanol < secondary alkanol < tertiary alkanol; whereas the variation of G^E is produced in the inverse sequence (4, 5). In systems including water, there are miscibility gaps for those with 1-butanol, *iso*-butanol, and 2-butanol, while no miscibility gap is observed for *tert*-butanol.

Group contribution methods are a common tool to predict thermodynamic properties using a low number of interaction parameters obtained from a limited data base. However, there are weaknesess related with the solution of groups concept when a very low number of interaction parameters is fitted because then some important effects are removed, e.g., isomeric effects. These ones are taken into account in different ways, depending on the model applied. Particularly for alcohols, in the framework of the Dortmund version of UNIFAC (6) (hereafter, merely UNIFAC), the hydroxyl group in primary, secondary, and tertiary alkanols is assumed to have different geometrical parameters but identical group energy-interaction parameters (except methanol). In

Received June 22, 1998.

J.A. Gonzalez,[1] I.G. de la Fuente, and J.C. Cobos. Dpto. de Termodinámica y Física Aplicada de la Universidad de Valldolid, 47071 Valladolid, Spain.

[1]Author to whom correspondence may be addressed. Fax: +34-983-42-31-36. E-mail: jagl@wamba.cpd.uva.es

© 1998 NRC Canada

terms of DISQUAC (7, 8), the geometrical parameters of the hydroxyl group are assumed to be independent of its environment, but interaction parameters are different for 1-alkanols, *sec*-alkanols and *tert*-alkanols.

Association theories are other approach to treat alcoholic solutions. They are based on the existence in the mixture of polymeric species formed by hydrogen bonding. Actually, the model more widely applied, with excellent results, is the UNIQUAC association theory (9–13).

Under the basic assumption of structure-dependent interaction parameters (see below), we have shown that DISQUAC is a reliable method to represent thermodynamic properties, VLE, liquid–liquid (LLE), or solid–liquid equilibria, G^E, H^E, and excess heat capacities at constant pressure of alcoholic solutions. Up to now, the following classes of mixtures have been successfully characterized: 1-alkanols + *n*-alkanes (14–16), + cyclohexane (17, 18), + benzene or + toluene (19, 20), + CCl_4 (18, 21), + 1-alkanols (22, 23), + linear monocarboxylic acids (24), + propanal (25), or + *n*-alkanones (26); *tert*-alkanols (27), *sec*-alkanols (28) or cycloalkanols (29) + *n*-alkanes or cycloalkanes; and phenol + several organic solvents (30).

The purpose of the present article is to continue this previous work, extending DISQUAC to mixtures containing *sec*-alkanols and organic solvents such as benzene, toluene, or *n*-alkanones. At this end, we report the needed interaction parameters.

A short comparison between DISQUAC results and those given by UNIFAC, the UNIQUAC association model and other similar association model (see below) is also included.

2. The models

2.1. DISQUAC

2.1.1. Main features

DISQUAC is a purely physical model based on the rigid lattice theory developed by Guggenheim (31) for liquid mixtures. Some of its main features are: (*i*) the partition function is factorized into two terms, in such way that the excess functions are calculated as the sum of two contributions: a dispersive term which represents the contribution from dispersive forces, and a quasichemical term which arises from the anisotropy of the field forces created by the solution molecules; in the case of G^E, the combinatorial entropy is represented by the Flory–Huggins equation (32); (*ii*) the interaction parameters are assumed to be structure dependent; (*iii*) mixtures are studied systematically in order of increasing complexity of molecular structure and intermolecular interactions.

The fact that the coordination number, *z*, is assumed to be the same for all the contacts, is one of the more important shortcomings of DISQUAC, and can be partially removed via the hypothesis of considering structure-dependent interaction parameters. Although this means to leaving the classical concept of group contribution, it is essential for practical purposes. It leads to improved predictions, mainly in the case of branched and cyclic molecules, and for the first members of an homologous series.

2.1.2. Assessment of geometrical parameters

In the framework of DISQUAC, mixtures of *sec*-alkanols with benzene, toluene, or *n*-alkanones are regarded as possessing three types of surface: (*i*) type a, aliphatic (CH_3, CH_2, or CH in *sec*-alkanols, *n*-alkanones, or toluene); (*ii*) type h, hydroxyl (OH in *sec*-alkanols); (*iii*) type s, s = b or p, aromatic (C_6H_6 or C_6H_5 in toluene, respectively); s = k, carbonyl (CO in *n*-alkanones).

When DISQUAC is applied, the total relative molecular volumes, r_i, surfaces, q_i, and the molecular surface fractions, α_{si}, of the compounds present in the mixture are usually calculated additively on the basis of the group volumes V_G and surfaces A_G, recommended by Bondi (1968) (33). As volume and surface units, the volume V_{CH_4} and surface A_{CH_4} of methane are taken arbitrarily (32). The geometrical parameters for the groups referred to in this work are given elsewhere (28, 32, 34). They are assumed to be identical for the OH group in primary, secondary, and tertiary alkanols.

2.1.3. Equations

The equations used to calculate G^E and H^E are the same as in other applications (14). As coordination number, the reference value was chosen, that is, $z = 4$.

The temperature dependence of the interaction parameters g_{st}, h_{st}, and c_{pst} has been expressed in terms of the DIS and (or) QUAC interchange coefficients $C_{st,l}^{DIS}$ and $C_{st,l}^{QUAC}$, where s, t = a, b, k, or h, and $l = 1$ (Gibbs energy; $C_{st,l}^{DIS/QUAC} = g_{st}^{DIS/QUAC}(T_O)/RT_O$); $l = 2$ (enthalpy; $C_{st,2}^{DIS/QUAC} = h_{st}^{DIS/QUAC}(T_O)/RT_O$); and $l = 3$ (heat capacity; $C_{st,3}^{DIS/QUAC} = c_{pst}^{DIS/QUAC}(T_O)/R$); $T_O = 298.15$ K is the scaling temperature. This temperature dependence is as follows:

$$[1]\quad g_{st}^{DIS/QUAC}(T)/RT = C_{st,1}^{DIS/QUAC} + C_{st,2}^{DIS/QUAC}[(T_O/T) - 1] + C_{st,3}^{DIS/QUAC}[\ln(T_O/T) - (T_O/T) + 1]$$

where T is the system temperature. Accordingly,

$$[2]\quad h_{st}^{DIS/QUAC}(T)/RT = C_{st,2}^{DIS/QUAC}(T_O/T) - C_{st,3}^{DIS/QUAC}[(T_O/T) - 1]$$

and

$$[3]\quad C_{pst}^{DIS/QUAC}(T)/R = C_{st,3}^{DIS/QUAC}$$

2.2. Modified UNIFAC (Dortmund version)

The modified UNIFAC (6) differs from the original UNIFAC (35) by the combinatorial term and the temperature dependence of the group interaction parameters. This dependence is as follows:

$$[4]\quad \psi_{nm} = \exp\,[-(a_{nm} + b_{nm}T + c_{nm}T^2)/T]$$

The equations used to calculate G^E and H^E are obtained from the fundamental equation for the activity coefficient γ_i of component *i*:

© 1998 NRC Canada

[5] $$\ln \gamma_i = \ln \gamma_i^{COMB} + \ln \gamma_i^{RES}$$

where $\ln \gamma_i^{COMB}$ is the combinatorial term, which takes into account differences in size and shape, and $\ln \gamma_i^{RES}$ is the residual term, essentially due to energy interactions.

2.2.1. Assessment of geometrical parameters

In modified UNIFAC, alcohols are characterized by several different groups. Alkanols are represented by two main groups CH_3OH and OH; the main group CH_3OH is a group itself which characterizes methanol. The main group OH is subdivided in three subgroups, OH(p) for primary alkanols; OH(s) for secondary alkanols, and OH(t) for tertiary alkanols. Aromatic compounds are represented by two main groups ACH and $ACCH_2$, subdivided in two, ACH and AC, and three subgroups, $ACCH_3$, $ACCH_2$, and ACCH, respectively. Ketones are represented by the main group CH_2CO subdivided in two subgroups CH_3CO and CH_2CO. The subgroups have different geometrical parameters, but the subgroups within the same main group are assumed to have identical group energy-interaction parameters. The geometrical parameters, the relative van der Waals volumes and the relative van der Waals surfaces of the different subgroups are not calculated from molecular parameters like in the original UNIFAC but fit together with the interaction parameters (a_{nm}, b_{nm}, c_{nm}) to the experimental values of the thermodynamic properties considered. The geometrical and interaction parameters are taken from ref. (6) and used without modifications.

2.3. Association models

In these models, the factorization of the partition function into two terms leads to both physical and chemical contributions to the excess functions. The former can be calculated by an equation of state (EOS), e.g., the Flory EOS (36) in the ERAS model (37), or by the Scatchard–Hildebrand equation (38), NRTL (39) or UNIQUAC (40) equations in other continuous linear association models. The physical term plays an essential role when predicting LLE since the type of association normally observed is not sufficient, by itself, to produce phase separation (41). It is also important to describe H^E of ternary mixtures involving one alkanol (42). The chemical contribution is calculated assuming that the specific interactions lead to the formation of different associated species according to a well-defined set of chemical reactions of the Kretschmer and Wiebe type (43), each characterized by an equilibrium constant. The problem is to elucidate which polymeric species are present in the mixture, because the treatment and results depend on this point.

For the models considered here, the chemical contribution is similar: includes four association constants for open-chain and cyclic hydrogen-bonded groups and a solvation constant between the terminal hydroxyl group of the alcohol chain and a solvating molecule (9, 44, 45). However the physical term is different: Model I (44, 45) uses the NRTL equation and Model II (9) the UNIQUAC equation.

3. The interaction parameters

The general procedure used by us in the fitting of any interaction parameters has been described in detail elsewhere (14, 22) and will not be repeated here.

The three types of surface generate three pairs of contacts: (a, h); (a, s) and (h, s) where s = b, p, or k.

2-Propanol or 2-butanol + benzene or + toluene mixtures

These systems are characterized by three types of contact (a, h), (a, s), and (h, s) where s = b or p. The nonpolar (a, b) or (a, p) interactions are represented by DIS parameters calculated on the basis of properties of benzene or toluene + *n*-alkanes mixtures, respectively (46). In these systems, the experimental H^E values are larger than the calculated values for the higher *n*-alkanes (10 or more carbon atoms). It has been attributed to conformational and (or) short-range orientational changes when *n*-alkanes are mixed with globular molecules (Patterson's effect) (8, 46). As consequence, the interaction parameters depend on *n*, the number of carbon atoms in the *n*-alkane. However, for simplicity we have used the values corresponding to mixtures with *n*-heptane (Table 1), e.g., average values. The polar (a, h) contacts are represented by DIS and QUAC interchange coefficients (28) (Table 1). Being known the (a, b), or (a, p) and (a, h) parameters, those for the (h, s) contacts are obtained straightforward on the basis of the G^E and H^E data available (Table 2).

2-Propanol or 2-butanol + *n*-alkanones mixtures

These systems are characterized by three types of contact: (a, k), (a, h), and (h, k). The (a, k) polar interactions are represented by DIS and QUAC interchange coefficients, previously determined (47) (Table 1). Being known the (a, k) and (a, h) parameters, those for the (k, h) contacts are obtained straightforward (Table 2) using the G^E and H^E data available.

We note that, for a given solvent, the QUAC parameters are independent of the alcohol size, i.e., there is no steric effect on these parameters. This is an important result, also encountered in other many alcoholic solutions investigated in terms of DISQUAC: 1-alkanols + C_6H_6, + C_7H_8, + CCl_4, + *n*-alkanones or + propanal; cycloalkanols or phenol + alkanes. Nevertheless, some exceptions exist; e.g., in *sec*-alkanols + *n*-alkanes mixtures, the QUAC coefficients for l = 1 and l = 3 can be also kept constant, while for l = 2, one must distinguish two ensembles, depending on the situation of the OH group (2-alkanols and 3-alkanols), each characterized by different enthalpic QUAC interaction parameters (Table 1). The constancy of the QUAC parameters is probably a general characteristic of the model, very useful in absence of appropiate VLE data which can be used in the fitting of the first DIS and QUAC interchange coefficients. The latter are needed to estimate the QUAC enthalpic parameters because the quasichemical contribution to H^E depends not only on such parameters, but also on the first QUAC Gibbs energy parameters via the surface fractions and Boltzmann's factor (eqs. 40, 66, and 68 in ref. 32).

From the $C_{hk,l}^{DIS/QUAC}$ coefficients of 2-propanol or 2-butanol + *n*-alkanones, it is noted that its structure dependence is similar to that of 1-alkanols + *n*-alkanones (26). Estimation of interaction parameters for mixtures with higher *sec*-alkanols can be done easily. Such estimation is more difficult for mixtures with benzene or toluene due to the few experimental data available. It can be done assuming that only an inductive effect exists on the DIS coefficients, i.e.,

© 1998 NRC Canada

Table 1. Interchange coefficients, dispersive $C^{DIS}_{as,l}$ and quasichemical $C^{QUAC}_{as,l}$ (l = 1, Gibbs energy; l = 2, enthalpy; l = 3, heat capacity) for contacts (a, s) (type a, CH_3, CH_2, or CH in *n*-alkanes, toluene, *n*-alkanones, or *sec*-alkanols; type s = b, C_6H_6 ; type s = p, C_6H_5 in toluene; type s = k, CO in *n*-alkanones; type h, OH in *sec*-alkanols).

Solute	$C^{DIS}_{as,1}$	$C^{DIS}_{as,2}$	$C^{DIS}_{as,3}$	$C^{QUAC}_{as,1}$	$C^{QUAC}_{as,2}$	$C^{QUAC}_{as,3}$
			s = b			
Benzene[a]	0.251	0.560	–0.600	0.	0.	0.
			s = p			
Toluene[a]	0.332	0.570	–0.400	0.	0.	0.
			s = k			
2-Propanone[b]	2.90	5.05	0.	6.08	8.25	0.
2-Butanone[b]	3.25	6.16	0.	5.35	6.35	0.
≥2-Pentanone[b]	3.31	6.92	0.	5.29	5.94	0.
3-Pentanone[b]	3.60	7.27	0.	4.62	4.46	0.
≥3-Hexanone[b]	3.65	8.03	0.	4.56	4.04	0.
≥4-Heptanone[b]	3.71	8.79	0.	4.50	3.63	0.
			s = a			
2-Propanol[c]	3.00	2.50	–15.50	10.00	9.75	68.00
2-Butanol[c]	4.15	5.70	–15.50	10.00	9.75	68.00
2-Pentanol[c]	4.20	6.80	–21.50	10.00	9.75	68.00
2-Hexanol[c]	4.80	7.90	–21.50	10.00	9.75	68.00
2-Heptanol[c]	5.40	6.80	–27.50	10.00	9.75	68.00
3-Pentanol[c]	3.00	4.40	–21.50	10.00	12.75	68.00
3-Hexanol[c]	3.70	5.35	–21.50	10.00	12.75	68.00
3-Heptanol[c]	4.40	3.60	–27.50	10.00	12.75	68.00

[a]Reference 46.
[b]Reference 47.
[c]Reference 28.

increase with the size of the alcohol while the the QUAC ones remain constant (see above).

4. Results

4.1. Comparison of DISQUAC results with experiment

Tables 3–5 and Figs. 1–5 show numerical and graphical comparisons, respectively, between experimental data and DISQUAC results. For the sake of major clarity deviations in pressure, P, and in H^E defined as

$$[6] \qquad \sigma_r(P) = \{1/N \Sigma [(P_{exp} - P_{calc})/P_{exp}]^2\}^{1/2}$$

$$[7] \qquad dev(H^E) = [1/N \Sigma (H^E_{exp} - H^E_{calc})^2]^{1/2}/H^E_{exp}(x = 0.5)$$

are also included in Tables 3 and 5, respectively. In eqs. [6] and [7], N stands for the number of data points of each system. Pressures are calculated at a given temperature and at different values of the mole fraction in the liquid state (isothermal VLE of the P–x type). The mean deviations between experimental and calculated results are about 2% for pressure, 4.9% for G^E at equimolar composition, and 8% for H^E. Note the good results obtained for azeotropes coordinates. In conclusion, DISQUAC provides a good representation of VLE, G^E and H^E. Even results for H^E of the 2-propanol + 2-propanone system at the higher temperatures are still acceptable (Table 5). An improvement could be obtained by using $C^{DIS}_{hk,3}$ = –2.00 and $C^{QUAC}_{hk,3}$ = –4.00. Then, the deviations (eq. [7]) for H^E at 283.15, 323.15, 343.15, and 363.15 K are respectively: 0.093, 0.025, 0.037, and 0.039.

On the other hand, it should be remarked that preliminary calculations show that it is possible to predict thermodynamic properties, VLE and H^E, of ternary systems including 2-alkanols and two of the organic solvents considered here on the basis of binary parameters only, that is, by neglecting ternary interactions. So, for VLE at 318.15 K of the 2-propanol + cyclohexane + toluene system (48), we obtain $\sigma_r(P)$ = 0.023 (N = 23), and for H^E at 298.15 K of the 2-propanol + benzene + cyclohexane (49), we found that $\sigma_r(H^E)$, defined similarly to eq. [6], is 0.044 (N = 67). These results are similar to those obtained for other ternary alcoholic solutions previously investigated in terms of DISQUAC (22, 50, 51).

4.2. Comparison with other models

Results obtained using UNIFAC for G^E and H^E at equimolar composition are collected in Tables 3 and 5, respectively. In the case of H^E, dev(H^E) as defined by eq. [7] is also given (Table 5). The mean deviations between UNIFAC results and experimental values are 11.6% for G^E (DISQUAC: 4.6%) at equimolar composition, and 27% for H^E (DISQUAC: 8%).

The poorer results are obtained for mixtures with toluene, when the number of needed interaction parameters is maximum (up 30), as the presence of the main group $ACCH_2$ in toluene increases the number of contacts. The good predictions obtained for the 2-propanol + 2-propanone system over a rather wide range of temperature are remarkable (Table 5).

The main advantage of UNIFAC is the large available matrix of interaction parameters, which can be used for predic-

© 1998 NRC Canada

Table 2. Interchange coefficients, dispersive $C_{sh,l}^{DIS}$ and quasichemical $C_{sh,l}^{QUAC}$ (l = 1, Gibbs energy; l = 2, enthalpy; l = 3, heat capacity) for contacts (s, h) (type s = b, C_6H_6 ; type s = p, C_6H_5 in toluene; type s = k, CO in *n*-alkanones; type h, OH in *sec*-alkanols).

Alkanol	$C_{sh,1}^{DIS}$	$C_{sh,2}^{DIS}$	$C_{sh,3}^{DIS}$	$C_{sh,1}^{QUAC}$	$C_{sh,2}^{QUAC}$	$C_{sh,3}^{QUAC}$
			s = b			
2-Propanol	2.90	1.30	–10.00	8.50	12.75	32.50
2-Butanol	3.95	5.10	–10.00	8.50	12.75	32.50
2-Pentanol	4.50[a]	6.50[a]	–10.00	8.50	12.75	32.50
≥2-Hexanol	4.50[a]	7.50[a]	–10.00	8.50	12.75	32.50
3-Pentanol	3.00[a]	7.50[a]	–10.00	8.50	12.75	32.50
≥3-Hexanol	3.00[a]	8.50[a]	–10.00	8.50	12.75	32.50
			s = p			
2-Propanol	2.80	1.85	–10.00	8.50	12.75	32.50
2-Butanol	3.65	5.70[a]	–10.00	8.50	12.75	32.50
2-Pentanol	4.30[a]	5.20[a]	–10.00	8.50	12.75	32.50
≥2-Hexanol	4.30[a]	5.90[a]	–10.00	8.50	12.75	32.50
3-Pentanol	2.70[a]	6.20[a]	–10.00	8.50	12.75	32.50
≥3-Hexanol	2.70[a]	7.00[a]	–10.00	8.50	12.75	32.50
			s = k in 2-propanone			
2-Propanol	3.15	9.70	0.	1.25	3.00	0.
2-Butanol	3.15[a]	13.20	0.	1.25	3.00	0.
≥2-Pentanol	3.15[a]	16.50	0.	1.25	3.00	0.
			s = k in 2-butanone			
2-Propanol	3.15	11.20	0.	1.25	3.00	0.
2-Butanol	3.15[a]	15.75	0.	1.25	3.00	0.
≥2-Pentanol	3.15[a]	19.00[a]	0.	1.25	3.00	0.
			s = k in 2-pentanone or in 3-pentanone			
2-Propanol	3.15	13.20	0.	1.25	3.00	0.
2-Butanol	3.15[a]	16.00[a]	0.	1.25	3.00	0.
≥2-Pentanol	3.15[a]	19.00[a]	0.	1.25	3.00	0.
			s = k in ≥2-hexanone			
2-Propanol	3.15	14.50	0.	1.25	3.00	0.
2-Butanol	3.15[a]	16.00[a]	0.	1.25	3.00	0.
≥2-Pentanol	3.15[a]	19.00[a]	0.	1.25	3.00	0.

[a]Estimated value.

tion purposes. However the main groups have to be subdivided to accommodate adjacent molecular structure of the components; in this way a molecular family is represented by one or several main groups subdivided in subgroups. As consequence, the interaction parameters between two main groups are constant but some isomers can no be distinguish from each other. On the other hand, proximity effects or cyclization are not considered properly (52). In this work, results for G^E are better than for H^E as this property is more sensitive to molecular structure. For 1-alkanols + linear oxaalkanes, a similar result is encountered (53).

The regular change of the DISQUAC parameters with molecular structure allows to estimate with confidence unavailable parameters, being the calculated properties in good agreement with the measured values.

Regarding the association models considered, they provide better results than DISQUAC (Table 6), because are used as methods of correlation of binary data in such way that each mixture has its own set of adjustable parameters, two for VLE and four for H^E. So, even the same mixture at different temperatures needs different adjustable parameters to reproduce VLE and H^E. An additional complication is that many sets of association constants must be tested to represent accurately the thermodynamic data over the whole concentration range (9, 44, 45).

5. Discussion

As already mentioned, the thermodynamic properties of alcoholic solutions are the result of several contributions (1–4; see Introduction).

At a given temperature, H^E of mixtures containing alcohols and organic solvents increases in the sequence: ketones > aromatic compounds > alkanes. This behaviour is independent of the isomeric alcohol considered (linear or branched). Moreover, for a given solvent, systems with 1-alkanols present lower H^E values than those with 2-alkanols. Such results may be interpreted in terms of the effective polarity of alcohols in liquid phase. In fact, this quantity is reasonably correlated by the dimensionless ratio (54, 55):

© 1998 NRC Canada

Table 3. Molar excess Gibbs energies G^E for 2-alkanols(1) + organic solvents(2) mixtures at temperature T and equimolar composition. Comparison of experimental values (exp.) with DISQUAC calculations (DQ) using the coefficients from Tables 1 and 2, or with UNIFAC results (UNIF) obtained using the interaction parameters from ref. 6. The relative standard deviations, $\sigma_r(P)$ (eq. [6]), for pressure are also given (N is the number of data for each system).

			$\sigma_r(P)$		G^E/J mol^{-1}			
System[a]	T/K	N	Exp.[b]	Calc.	Exp.	DQ	UNIF	Ref.
2-PrOH + C_6H_6	298.15	7	0.006	0.031	1010	1057	961	57
	303.15	12	0.024	0.032	1020	1053	962	58
	318.15	12[c]	0.002	0.013	1030	1033	961	59
		14	0.004	0.015	1010			58
	323.15	15	0.005	0.019	1040	1024	958	60
	333.15	12	0.007	0.013	995	1004	950	58
		13	0.005	0.022	1020			60
	343.15	10	0.002	0.016	962	979	938	60
2-PrOH + C_7H_8	298.15	13[c]	0.018	0.018	1080	1082	966	61
	303.15	13	0.019	0.021	1060	1079	972	61
	313.15	13	0.015	0.015	1060	1069	979	61
2-BuOH + C_6H_6	298.15	8[c]	0.006	0.021	964	968	861	62
	318.15	10	0.002	0.031	865	916	848	2
	333.15	9	0.009	0.017	889	867	828	63
	343.15	10	0.002	0.039	715	830	811	63
	353.15	10	0.004	0.046	682	790	793	63
2-BuOH + C_7H_8	333.31	13[c]	0.002	0.012	866	874	849	64
	343.40	13	0.001	0.012	847	864	839	64
	353.44	12	0.002	0.012	818	795	827	64
2-PrOH + 1CO1	298.15	5	0.026	0.050	475	547	488	65
		9[c]	0.012	0.024	527			66
	328.15	14	0.007	0.032	496	435	397	67
2-PrOH + 1CO2	278.15	11	0.005	0.008	588	595	537	68
	288.15	11	0.006	0.007	558	562	511	68
	298.15	11[c]	0.003	0.006	525	528	484	68
	308.15	11	0.004	0.007	494	494	457	68
	323.15	5	0.001	0.004	433	441	417	69
		11	0.004	0.005	446			68
	328.15	9	0.003	0.030	491	424	403	70
2-BuOH + 1CO2	323.85				319	355	400	71
	359.35				210	192	295	72
	360.00				239	189	293	71

[a]The abbreviations used are the following: 2-PrOH, 2-propanol; 2-BuOH, 2-butanol; 1CO1, 2-propanone; 1CO2, 2-butanone.

[b]Obtained using an equation of the Redlich–Kister type to represent G^E.

[c]System used in the estimation of the interchange coefficients.

$$[8] \qquad \bar{\mu} = [\mu^2/4\pi\varepsilon_O\sigma^3 k_B T]^{1/2}$$

or equivalently, by virtue of the corresponding states principle by

$$[9] \qquad \bar{\mu} = [\mu^2 N_A/4\pi\varepsilon_O V_c k_B T]^{1/2}$$

where $\bar{\mu}$ is the effective dipole moment in liquid phase, μ is the dipole moment in the gas phase, ε_O the permittivity of the vacuum, σ an appropiate molecular size parameter, say the effective hard sphere diameter, N_A the Avogadro's constant, k_B the Boltzmann's constant, and V_C the critical molar volume.

It is noteworthy that, μ, of 1-alkanols in is practically the same (1.7, 1.8, and 1.8 D (56) for methanol, 1-butanol, or 1-decanol), $\bar{\mu}$ decreases with the aliphatic chain length of the alcohol (the respective values are: 0.60, 0.41, and 0.18), indicating that the alkanol–alkanol interactions in the condensed phase decrease in the sequence methanol > 1-butanol > ... 1-decanol.

For 1-propanol, 2-propanol, 1-butanol, and 2-butanol, not only the μ values are constant, 1.7, 1.7, 1.8, and 1.7 D (56), respectively, but also their $\bar{\mu}$ values have close values: 0.44, 0.44, 0.41, and 0.40, in the same order as above. This means that H^E(2-alkanols) > H^E(1-alkanols) may be well due to steric hindrance to H-bond formation, in such way that, at a given alcohol concentration, fewer hydrogen bonds would be formed in, e.g., 2-butanol (or *ter*-butanol) than in 1-butanol. This implies that more bonds are also broken in 2-alkanols than in 1-alkanols, leading to a higher value of H^E.

If the solvent is a polar compound, or a non-polar but active component, other effects come into play. Mainly, these are strong solvent-to-solvent and hydroxyl group-to-solvent interactions (2). When the solvent is a ketone, the latter produce a larger number of broken alkanol—alkanol bonds, and

© 1998 NRC Canada

Table 4. Comparison of experimental (exp.) coordinates of azeotropes: temperature (T^{az}), mole fraction (x_1^{az}), and pressure (P^{az}) for 2-alkanols(1) + organic solvents(2) mixtures with DISQUAC results (calc.) calculated using the coefficients from Tables 1 and 2.

		x_1^{az}		P^{az}/kPa		
System[a]	T^{az}/K	Exp.	Calc.	Exp.	Calc.	Ref.
2-PrOH + C_6H_6	303.15	0.239	0.248	19.377	19.447	58
	318.15	0.291	0.283	36.488	36.844	59
		0.294		37.142		58
	333.15	0.352	0.323	66.905	66.433	58
		0.354		66.138		60
	343.15	0.386	0.368	94.389	95.550	60
2-PrOH + C_7H_8	298.15	0.613	0.607	7.384	7.369	61
	313.15	0.666	0.653	16.396	16.274	61
2-BuOH + C_6H_6	298.15	0.085	0.085	13.199	13.126	62
	318.15	0.081	0.105	30.416	31.069	2
	333.15	0.133	0.132	55.130	55.132	63
	353.15	0.131	0.162	103.67	106.91	63
2-BuOH + C_7H_8	333.31	0.452	0.439	25.609	25.691	64
	353.44	0.551	0.537	57.074	56.508	64
2-PrOH + 1CO2	288.15	0.048	0.050	7.352	7.347	68
	298.15	0.070	0.083	12.124	12.142	68
	308.15	0.099	0.119	19.369	19.388	68
	323.15	0.191	0.191	36.229	36.458	68
	328.15	0.223	0.194	45.692	44.250	70

[a]For abbreviations, see Table 3.

Fig. 1. VLE for 2-alkanols(1) + toluene(2) mixtures at different temperatures. Solid lines, DISQUAC calculations; points, experimental values: ●, 2-propanol (61), 298.15 K; ■, 2-butanol (64), 333.31 K.

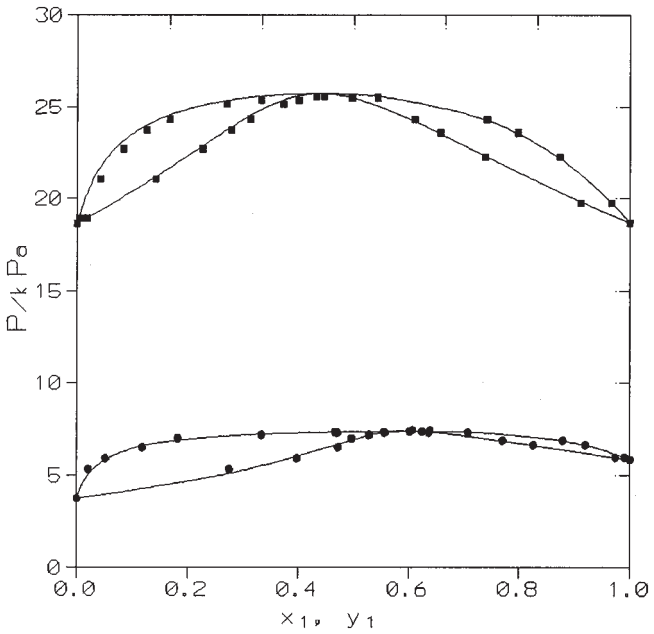

Fig. 2. H^E values for 2-propanol(1) + benzene(2) mixtures at different temperatures. Solid lines, DISQUAC calculations; points, experimental results (75): ●, 298.15 K; ■, 308.15 K; ▲, 318.15 K.

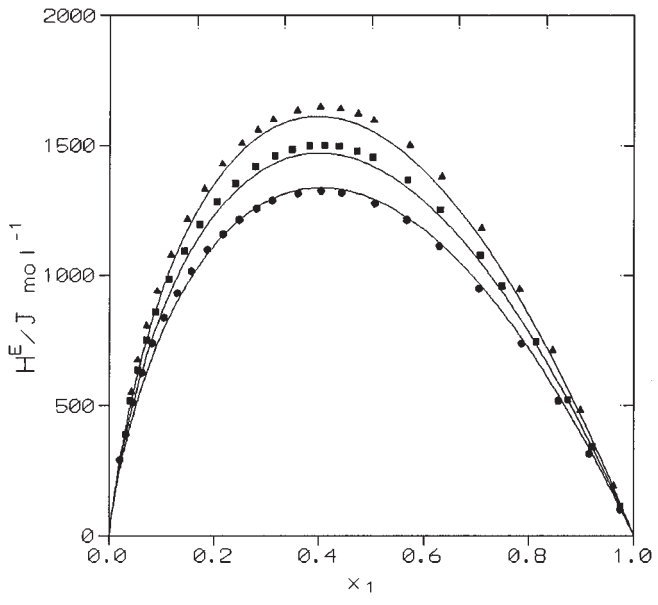

the formation of O—H---O=C bonds. Both effects decrease with the chain length of the alcohol. So, the increasing of H^E with the size of the alcohol for a given ketone is probably due to physical interactions between equal molecules.

DISQUAC describes fairly well this complex behaviour using structure-dependent interaction parameters, which follows rather simple rules. It is interesting to remark that our QUAC parameters follow the trend pointed out by Brown et al. (2) in an earlier work on alcoholic solutions. They explained the thermodynamic properties of mixtures of alcohols and *n*-alkanes by means of an idealized model in which the only exchange energies contributing to the mixture properties were the Gibbs energy, *w*, and the enthalpy, h, associated with the breaking of the hydrogen bonds. They assumed

© 1998 NRC Canada

Table 5. Molar excess enthalpies H^E for 2-alkanols(1) + organic solvents(2) mixtures at temperature T and equimolar composition. Comparison of experimental values (exp.) with DISQUAC calculations (DQ) using the coefficients from Tables 1 and 2, and with UNIFAC results (UNIF) obtained using the coefficients given in ref. 6. Deviations for H^E, dev(H^E), as defined by eq. [7], are also given (N is the number of data for each system).

			dev(H^E)			H^E/J mol^{-1}			
System[a]	T/K	N	Exp.[b]	DQ	UNIF	Exp.	DQ	UNIF	Ref.
2-PrOH + C_6H_6	298.15	10	0.003	0.020	0.23	1284	1297	827	73
		6	0.004	0.022	0.23	1280			74
		24[c]	0.001	0.021	0.21	1284			75
		17	0.017	0.020	0.24	1291			76
	308.15	10	0.002	0.026	0.23	1456	1422	962	73
		25[c]	0.001	0.027	0.21	1454			75
		17	0.001	0.013	0.21	1435			76
		14	0.001	0.120	0.22	1288			77
	318.15	10	0.010	0.064	0.26	1638	1555	960	59
		10	0.002	0.028	0.21	1604			73
		23[c]	0.001	0.028	0.20	1604			75
2-PrOH + C_7H_8	293.15	8	0.020	0.079	0.35	1040	1158	523	78
	298.15	10	0.004	0.038	0.34	1194	1224	590	73
		20	0.023	0.034	0.36	1224			78
		23[c]	0.002	0.037	0.33	1195			75
	308.15	10	0.002	0.028	0.32	1374	1368	734	73
		10	0.017	0.047	0.32	1409			78
		23[c]	0.001	0.029	0.31	1375			75
		14	0.001	0.160	0.29	1127			77
	318.15	10	0.002	0.024	0.29	1540	1525	884	73
		23[c]	0.001	0.024	0.28	1543			75
2-BuOH + C_6H_6	298.15	8	0.005	0.025	0.31	1590	1636	927	2
		18[c]	0.001	0.021	0.31	1603			79
	308.15	8	0.010	0.023	0.28	1724	1748	1053	2
	318.15	8	0.010	0.019	0.26	1860	1866	1180	2
2-PrOH + 1CO1	283.15	19	0.001	0.067[d]	0.048	1474	1634	1403	80
	298.15	9	0.0001	0.056	0.16	1711	1649	1400	81
		16	0.016	0.030	0.084	1576			82
		19[c]	0.004	0.027	0.12	1627			83
		19	0.002	0.039[d]	0.082	1552			80
	323.15	19	0.003	0.040[d]	0.11	1594	1664	1363	80
	343.15	19	0.002	0.097[d]	0.074	1468	1664	1322	80
	363.15	19	0.009	0.160[d]	0.069	1425	1646	1285	80
2-PrOH + 1CO2	298.15	21[c]	0.008	0.020	0.11	1486	1537	1280	84
		12	0.009	0.031	0.11	1474			68
	308.15	11	0.005	0.011	0.15	1542	1554	1285	84
	318.15	11	0.004	0.018	0.16	1563	1574	1287	84
2-PrOH + 1CO3	298.15	10[c]	0.002	0.016	0.16	1504	1534	1211	85
2-PrOH + 2CO2	298.15	10[c]	0.002	0.021	0.20	1465	1511	1134	85
2-BuOH + 1CO1	298.15	17[c]	0.0003	0.052	0.12	1857	1876	1576	86
2-BuOH + 1CO2	298.15	24[c]	0.002	0.037	0.17	1779	1814	1417	87

[a]For abbreviations, see Table 3.

[b]From literature or obtained using a Redlich–Kister equation to represent H^E.

[c]System used in the estimation of the interaction parameters.

[d]Data at 0.4 MPa.

that h was independent of the alcohol and that the number of broken alkanol–alkanol bonds was a function of w/k_BT. By comparing the hydroxyl group contribution to standard enthalpies of pure alcohols, they concluded that w(2-propanol) < w(1-propanol) (or w(*tert*-butanol) < w(2-butanol) < w(1-butanol)), and from here that H^E changes in the inverse sequence.

In terms of DISQUAC, we note that the first QUAC coefficients are lower for 2-alkanols than for 1-alkanols. The same occurs for the second QUAC coefficients. Probably,

© 1998 NRC Canada

Table 6. Comparison of DISQUAC results (DQ) with those obtained from the correlation of the binary data using two continuous association models that differ in the physical term: Model I uses the NRTL equation, Model II, the UNIQUAC equation (see text). *T* is the system temperature and *N* the number of data of each system (for abbreviations, see Table 3).

				Deviation[a]			
System	*T*/K	*N*	Property	I	II	DQ	Ref.
2-PrOH + C_6H_6	318.15	12[b]	P	293[c,d]	117[f,g]	390[f]/370[c]	66
	323.15	15	P	240[c,d]	145[f,g]	680[f]/600[c]	67
2-BuOH + C_6H_6	318.15	10	P	270[c,e]	153[f,g]	850[f]/770[c]	57
2-BuOH + C_7H_8	333.31	13[b]	P	190[c,e]	131[f,g]	260[f]/200[c]	71
	343.40	13	P	190[c,e]	191[f,g]	410[f]/340[c]	71
	353.44	12	P	320[c,e]	132[f,g]	580[f]/500[c]	71
2-PrOH + 1CO2	323.15	5	P	507[c,d]		120[c]	76
2-PrOH + C_6H_6	298.15	17	H^E	7[c,d]	10.5[c. g]	26[c]	51
2-PrOH + C_7H_8	298.15	10	H^E	3.6[c,d]	5.2[c,g]	46[c]	80
2-BuOH + C_6H_6	298.15	8	H^E	9.6[c,e]		35[c]	57
		18[b]			8.5[c,h]	29[c]	86
	308.15	8	H^E	10.1[c,e]		35[c]	57
	318.15	8	H^E	11.5[c,e]		32[c]	57

[a]$\Delta(M) = 1/N\ \Sigma\ |M_{exp} - M_{calc}|$ or $\sigma(M) = [1/N\ (\Sigma\ M_{exp} - M_{calc})^2]^{1/2}$ where $M = P$ or H^E. The units are, respectively, Pa or J/mol.
[b]System used in the estimation of the DISQUAC interaction parameters.
[c]Deviation = Δ.
[d]Reference 44.
[e]Reference 45.
[f]Deviation = σ.
[g]Reference 9.
[h]Reference 79.

Fig. 3. H^E values for the 2-butanol(1) + benzene(2) mixture at 298.15 K. Solid line, DISQUAC calculation; points, experimental results (79).

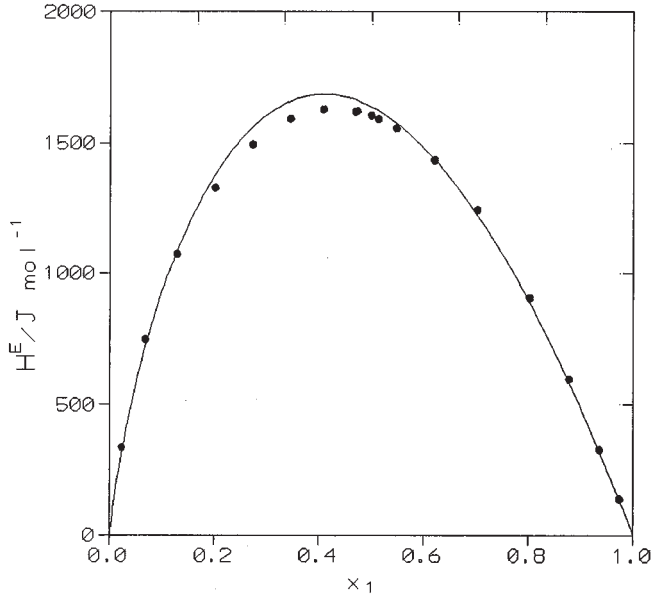

Fig. 4. H^E values for 2-alkanols(1) + 2-propanone(2) mixtures at 298.15 K. Solid lines, DISQUAC calculations; points, experimental results: ●, 2-propanol (83), ■, 2-butanol (86).

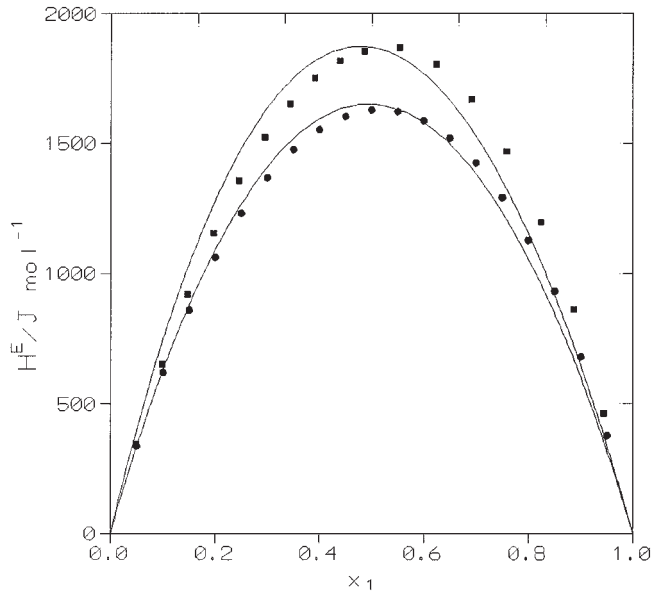

© 1998 NRC Canada

Fig. 5. H^E values of 2-alkanols(1) + 2-butanone(2) mixtures at different temperatures. Solid lines, DISQUAC calculations; points, experimental results: ■, 298.15 K and ▲, 318.15 K, 2-propanol (84); ●, 2-butanol (87), 298.15 K.

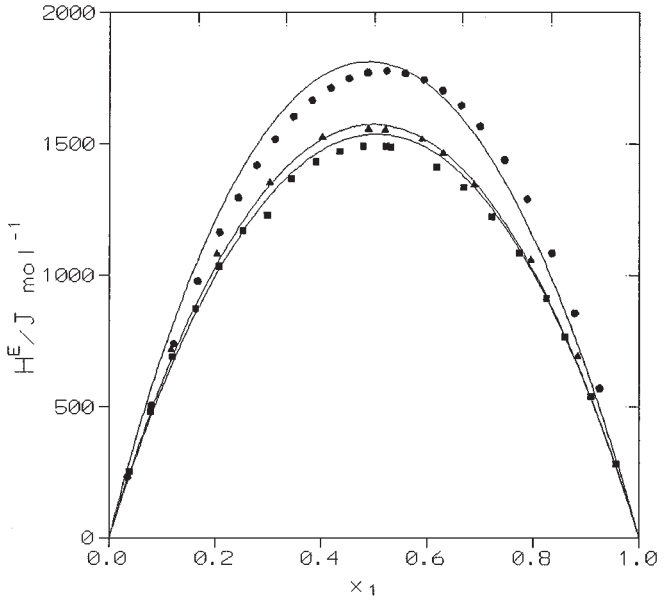

this is due to the existence of other effects, such steric hindrance, do not taken into account by Brown et al. (2).

6. Conclusions

The main conclusion is referred to the evolution of the structure-dependent interaction parameters: no steric effect is encountered in the QUAC interchange coefficients (they are independent of the compounds in the mixture for a given series), while an increasing inductive effect is observed in the DIS interchange coefficients. Using the reported interaction parameters, DISQUAC describes well a whole set of thermodynamic properties: VLE, G^E, or H^E.

Acknowledgement

This work was supported by the Consejería de Educación y Cultura de la Junta de Castilla y León (Spain), under Project VA54/98 and by the Programa Sectorial de Promoción General del Conocimiento de la S.E.U.I.yD. del M.E.C. (Spain), Project ref. PB97-0488.

References

1. J. Ortega, M.I. Paz Andrade, and E. Rodríguez. J. Chem. Eng. Data, **31**, 336 (1986).
2. I. Brown, W. Fock, and F. Smith. J. Chem. Thermodyn. **1**, 273 (1969).
3. M.I. Paz Andrade, M. García, and F. García Fente. An. Quim. **71**, 451 (1975).
4. G.C. Benson, M.K. Kumaran, C.J. Halpin, and P.J. D'Arcy. J. Chem. Thermodyn. **18**, 1007 (1986).
5. A. Kumar and S.S. Katti. Ind. J. Tech. **18**, 60 (1980).
6. J. Gmehling, J. Li, and M. Schiller. Ind. Eng. Chem. Res. **32**, 178 (1993).
7. H.V. Kehiaian. Fluid Phase Equilibria, **13**, 243 (1983).
8. H.V. Kehiaian. Pure Appl. Chem. **57**, 15 (1985).
9. I. Nagata and K. Miyamoto. Fluid Phase Equilibria, **56**, 203 (1990).
10. I. Nagata and K. Miyamoto. Thermochim. Acta, **209**, 43 (1992).
11. I. Nagata and K. Miyamoto. Thermochim. Acta, **228**, 319 (1993).
12. I. Nagata and T. Hori. Thermochim. Acta, **228**, 305 (1993).
13. I. Nagata, K. Gotoh, and K. Miyamoto. Thermochim. Acta, **249**, 89 (1995).
14. J.A. González, I. García de la Fuente, J.C. Cobos, and C. Casanova. Ber. Bunsenges. Phys. Chem. **95**, 1658 (1991).
15. J.A. González, I. García de la Fuente, J.C. Cobos, C. Casanova, and U. Domanska. Ber. Bunsenges. Phys. Chem. **98**, 955 (1994).
16. J.A. González, I. García de la Fuente, and J.C. Cobos. Ber. Bunsenges. Phys. Chem. **101**, 219 (1997).
17. J.A. González, I. García de la Fuente, J.C. Cobos, and C. Casanova. J. Solution Chem. **23**, 399 (1994).
18. U. Domanska and J.A. González. Fluid Phase Equilibria, **123**, 167 (1996).
19. J.A. González, I. García de la Fuente, J.C. Cobos, and C. Casanova. Fluid Phase Equilibria, **93**, 1 (1994).
20. U. Domanska and J.A. González. Fluid Phase Equilibria, **119**, 131 (1996).
21. J.A. González, I. García de la Fuente, J. C. Cobos, and C. Casanova. Thermochim. Acta, **237**, 261 (1994).
22. J.A. González, I. García de la Fuente, J.C. Cobos, and C. Casanova. Fluid Phase Equilibria, **78**, 61 (1992).
23. U. Domanska and J.A. González. Fluid Phase Equilibria, **129**, 139 (1997).
24. J.A. González, I. García de la Fuente, and J.C. Cobos. Fluid Phase Equilibria, **135**, 1 (1997).
25. J.A. González, I. García de la Fuente, and J.C. Cobos. J. Chem. Soc. Faraday Trans. **93**, 3773 (1997).
26. J. A. González. Can. J. Chem. **75**, 1412 (1997).
27. J.A. González, I. García de la Fuente, J.C. Cobos, and U. Domanska. Fluid Phase Equilibria, **119**, 81 (1996).
28. J.A. González, I. García de la Fuente, and J.C. Cobos. Fluid Phase Equilibria, **123**, 39 (1996).
29. J.A. González, I. García de la Fuente, and J.C. Cobos. Thermochim. Acta, **278**, 57 (1996).
30. J.A. González, I. García de la Fuente, and J.C. Cobos. Ber. Bunsenges. Phys. Chem. **100**, 1746 (1996).
31. E.A. Guggenheim. Mixtures. Oxford University Press, London. 1952.
32. H.V. Kehiaian, J.-P.E. Grolier, and G.C. Benson. J. Chim. Phys. **75**, 1031 (1978).
33. A. Bondi. Physical properties of molecular crystals, liquids and glasses. J. Wiley, New York. 1968.
34. H.V. Kehiaian, J.-P. E. Grolier, M.R. Kechavarz, and G.C. Benson. Fluid Phase Equilibria, **5**, 159 (1980).
35. A. Fredenslund, J. Gmehling, and P. Rasmussen. Vapor-liquid equilibria using UNIFAC. Elsevier, Amsterdam. 1977.
36. P.J. Flory. J. Am. Chem. Soc. **87**, 1833 (1965).
37. A. Heintz. Ber. Bunsenges. Phys. Chem. **89**, 172 (1985).
38. J.H. Hildebrand and R.L. Scott. Regular solutions. International series of chemistry. Prentice Hall, Englewood Cliffs, New Jersey. 1962.
39. H. Renon and J.M. Prausnitz. AIChE J. **14**, 135 (1968).
40. D.S. Abrams and J.M. Prausnitz. AIChE J. **21**, 116 (1975).
41. I. Prigogine and R. Defay. Chemical thermodynamics. Longmans, Green and Co., Norwich. 1964.
42. I. Nagata and Y. Kawamura. Chem. Eng. Sci. **34**, 601 (1979).

© 1998 NRC Canada

43. C.B. Kretschmer and R. Wiebe. J. Chem. Phys. **22**, 1697 (1954).
44. I. Nagata and K. Tamura. Thermochim. Acta, **87**, 129 (1985).
45. I. Nagata and K. Tamura. Thermochim. Acta, **121**, 447 (1987).
46. A. Ait-Kaci. Ph.D. Thesis. University of Lyon, France. 1982.
47. H.V. Kehiaian, S. Porcedda, B. Marongiu, L. Lepori, and E. Matteoli. Fluid Phase Equilibria, **63**, 231 (1991).
48. I. Nagata and K. Tamura. J. Chem. Eng. Data, **41**, 1355 (1996).
49. I. Nagata, K. Fujiwara, and Y. Ogasawara. J. Chem. Thermodyn. **10**, 1201 (1978).
50. J.A. González, I. García de la Fuente, J.C. Cobos, and C. Casanova. Ber. Bunsenges. Phys. Chem. **98**, 106 (1994).
51. J.A. González, I. García de la Fuente, and J.C. Cobos. Can. J. Chem. **75**, 1424 (1997).
52. J.A. González, I. García de la Fuente, and J.C. Cobos. Fluid Phase Equilibria. In press.
53. S. Delcros, J.R. Quint, J.-P.E. Grolier, and H.V. Kehiaian. Fluid Phase Equilibria, **113**, 1 (1995).
54. A.H. Roux, J.-P.E. Grolier, A. Inglese, and E. Wilhelm. Ber. Bunsenges. Phys. Chem. **88**, 986 (1984).
55. J.A. González, J.M. Fernández Martínez, I. García de la Fuente, and J.C. Cobos. Can. J. Chem. **74**, 1815 (1996).
56. R.C. Reid, J.M. Prausnitz, and B.E. Poling. The properties of gases and liquids. 4th ed. McGraw-Hill, New York. 1987.
57. A.L. Olsen and E.R. Washburn. J. Phys. Chem. **41**, 457 (1937).
58. V.V. Udovenko and T.F. Mazanko. Zh. Fiz. Khim. **41**, 1615 (1967) (cf. ref. 88).
59. I. Brown, W. Fock, and F. Smith. Austr. J. Chem. **9**, 364 (1956).
60. I. Nagata, T. Ohta, and Y. Uchiyama. J. Chem. Eng. Data, **18**, 54 (1973).
61. S.J. Ashcroft, A.D. Clayton, and R.B. Shearn. J. Chem. Eng. Data, **24**, 195 (1979).
62. V. Rodríguez, C. Lafuente, M.C. López, F.M. Royo, and J.S. Urieta. J. Chem. Thermodyn. **25**, 679 (1993).
63. H.R. Echevarría. Collect. Czech. Chem. Commun. **38**, 1295 (1973).
64. J. Lnenickova and I. Wichterle. Collect. Czech. Chem. Commun. **42**, 1907 (1977).
65. G.S. Parks and C.S. Chaffee. J. Phys. Chem. **31**, 439 (1927).
66. P.S. Puri, J. Polak, and J.A. Ruether. J. Chem. Eng. Data, **19**, 87 (1974).
67. D.C. Freshwater and K.A. Pike. J. Chem. Eng. Data, **12**, 179 (1967).
68. R. Garriga, F. Sánchez, P. Pérez, and M. Gracia. Fluid Phase Equilibria, **124**, 123 (1996).
69. V.T. Zharov, N.D. Malegina, and A.G. Morachevsky. Zh. Prikl. Khim. **38**, 2132 (1965) (cf. ref. 88).
70. I. Nagata, T. Ohta, and S. Nakagawa. J. Chem. Eng. Jap. **9**, 276 (1976).
71. S. Di Cave, A. Chianese, and A. Prantera. J. Chem. Eng. Data, **23**, 279 (1978).
72. K. Miller and H.S. Huang. J. Chem. Eng. Data, **17**, 77 (1972).
73. R.V. Mrazek and H.C. Van Ness. AICHE J. **7**, 190 (1961).
74. E.Z. Zhuravlev, N.N. Zolotarevskaya, G.I. Tupitsin, N.V. Kutuzova, and I.I. Konstantinov. Tr. Khim. Khim. Tekhnol. **41** (1967) (cf. ref. 89).
75. H.C. Van Ness and M.M. Abbott. Int. DATA Ser. Sel. Data Mixtures Ser. A, **1**, (1976).
76. I. Nagata, H. Asano, and K. Fujiwara. Fluid Phase Equilibria, **1**, 211 (1978).
77. K.C. Singh, K.C. Kalra, S. Maken, and V. Gupta. Fluid Phase Equilibria, **119**, 175 (1996).
78. V.D. Shah and H.G. Donnelly. Chem. Eng. Prog. Symp. Ser. **63**, 105 (1967) (cf. ref. 89).
79. I. Nagata and K. Tamura. Fluid Phase Equilibria, **41**, 127 (1988).
80. B. Löwen and S. Schulz. Thermochim. Acta, **262**, 69 (1995).
81. R. Thacker and J.S. Rowlinson. Trans. Faraday Soc. **50**, 1036 (1954).
82. S. Murakami, K. Amaya, and R. Fujishiro. Bull. Chem. Soc. Jpn. **37**, 1776 (1964).
83. I. Nagata. J. Chem. Thermodyn. **26**, 691 (1994).
84. I. Nagata. Int. DATA Ser. Sel. Data Mixtures Ser. A, **1**, 81 (1984).
85. T.M. Letcher and J.A. Nevines. J. Chem. Eng. Data, **40**, 995 (1995).
86. I. Nagata, K. Tamura, and H. Kataoka. J. Chem. Eng. Data, **41**, 593 (1996).
87. J.P. Chao and M. Dai. J. Chem. Thermodyn. **23**, 117 (1991).
88. J. Gmehling, U. Onken, and W. Arlt. Vapor-liquid equilibrium data collection. Vol. 1, Part 2b; J. Gmehling, U. Onken, and U. Weidlich. Vapor-liquid equilibrium data collection. Vol. 1, Part 2d. DECHEMA, Frankfurt. 1990.
89. J.J. Christensen, R.W. Hanks, and R.M. Izatt. Handbook of heats of mixing. Wiley, New York. 1982.

© 1998 NRC Canada

Synthesis of a new class of difunctional tetraphenylene crown ethers

Harry W. Gibson, Devdatt S. Nagvekar, Yadollah Delaviz, and William S. Bryant

Abstract: Three new substituted tetraphenylene crown ethers have been made. Bis(5-carbomethoxy-1,3-phenylene)-bis(*p*-phenylene)-(3*x* + 6)-crown-*x*, where *x* = 12, 16, and 20 (**11b**–**11d**) were synthesized via [1 + 1] cyclization of methyl 3,5-bis[ω-chloro(oligoethyleneoxy)]benzoates (**13b**–**3d**) with methyl 3,5-bis[ω-(*p*-hydroxyphenoxy)(oligoethyleneoxy)]benzoates (**16b**–**6d**) using K_2CO_3 as base and tetrabutylammonium iodide as a phase transfer agent in dimethylformamide (DMF). The corresponding 30-membered (*x* = 8) macrocycle **11a** could not be made by this approach; only the elimination product, 3,5-bis(vinyloxy)benzoic acid (**19**), was isolated. **16a**–**16d** were made via alkylation of *p*-benzyloxyphenol (**14**) with **13a**–**13d**, respectively, followed by hydrogenolysis with Pd/C as catalyst. No complexation of these macrocycles with dibenzylammonium ions was detected by NMR spectroscopy, but weak complexation of **11d** with a paraquat derivative was observed.

Key words: crown ethers, cyclization, macrocycles.

Résumé : On a préparé trois nouveaux éthers couronnes de type tétraphénylène substitué. On a synthétisé les bis(5-carbométhoxy-1,3-phénylène)-bis(*p*-phénylène)-(3*x* + 6)-couronnes-*x*, dans lesquelles *x* = 12, 16 et 20 (**11b**–**11d**) par le biais d'une cyclisation [1 + 1] des 3,5-bis[ω-chloro(oligoéthylèneoxy)]benzoates de méthyle (**13b**–**13d**) avec les 3,5-bis[ω-(*p*-hydroxyphénoxy)(oligoéthylèneoxy)]benzoates de méthyle (**16b**–**16d**) dans le diméthylformamide (DMF), en présence de K_2CO_3 agissant comme base et d'iodure de tétrabutylammonium agissant comme agent de transfert de phase. Utilisant cette méthode, il n'a pas été possible de préparer le macrocycle correspondant à trente chaînons (*x* = 8) (**11a**); on n'a isolé que le produit d'élimination, l'acide 3,5-bis(vinyloxy)benzoïque (**19**). On a préparé les produits **16a**–**16d** par le biais d'alkylations du *p*-benzylphénol (**14**) avec les esters **13a**–**13d**, suivies d'une hydrogénolyse avec du Pd/C comme catalyseur. Par spectroscopie RMN, on n'a pas pu détecter de complexation de ces macrocycles avec les ions dibenzylammonium; on a toutefois observé une faible complexation du composé **11d** avec un dérivé du paraquat.

Mots clés : éthers couronnes, cyclisation, macrocycles.

[Traduit par la Rédaction]

Introduction

Crown ethers are an interesting class of molecules which are known for their ability to complex with a wide variety of cations, including metal and organic species (1). We are interested in macrocyclic polyethers which are semi-flexible in nature and have the ability to undergo complexation with linear molecules to form pseudorotaxanes, rotaxanes, and polyrotaxanes (see reviews in ref. 2*a*–*f*) of various types. A number of bisphenylene crown ethers with ring sizes from 24–34 atoms have been synthesized previously in our laboratory (3–5) for these purposes (2*a*, *b*, *g*–*o*; for poly(urethane crown ether rotaxane)s see ref. 2*g*; for poly(ester crown ether rotaxane)s see refs. 2*h* and *i*; for poly(methacrylate crown ether side chain rotaxane)s see ref. 2*j*; for self-assembled supramolecular structures see refs. 2*k*–*o*).

Received March 4, 1998.

H.W. Gibson,[1] D.S. Nagvekar, Y. Delaviz, and W.S. Bryant. Department of Chemistry, Virginia Polytechnic Institute and State University, Blacksburg, VA 24061, U.S.A.

[1]Author to whom correspondence may be addressed. Telephone: (540) 231–5902. Fax: (540) 231–8517. E-mail: hwgibson@vt.edu

Larger macrocycles are also of interest for these and related applications. Bis(*p*-phenylene)-bis(*m*-phenylene)-66-crown-20 (**1b**) was isolated in 11% yield (6) as a [2 + 2] by-product from the [1 + 1] synthesis of *p*-phenylene-*m*-phenylene-33-crown-10 (**1a**) (7). Cyclization of resorcinol with tetra(ethylene glycol) ditosylate generated [1 + 1], [2 + 2], and [3 + 3] products, *m*-phenylene-16-crown-5 (**2a**), bis-*m*-phenylene-32-crown-10 (**2b**), and tris(*m*-phenylene)-48-crown-15 (**2c**) in 54, 8.4, and 1.7% yields, respectively (8). Tris(*p*-phenylene)-51-crown-15 (**3b)** and tetrakis(*p*-phenylene)-68-crown-20 (**3c**) have been reported (9) and shown to act as templates for paraquat units (**5**) in catenane syntheses and as hosts for dibenzylammonium ion (**6**), forming pseudorotaxanes with varying stoichiometries (10*a*). And recently the corresponding analogous 1,5-dioxynaphthalene family of crown ethers was expanded to include the bis-, tris-, and tetrakis- species **4a**–**4c**; these hosts were used in catenane syntheses using cyclobis(paraquat-arylene)s (10*b*). These reports have prompted us to describe our efforts with bis(5-carbomethoxy-1,3-phenylene)-bis(*p*-phenylene)-(3*x* + 6)-crown-*x* (**11a**–**11d**) systems, which began in 1990.

Our ongoing efforts led us to focus our attention on tetraphenylene macrocycles with ring sizes between 42 and 66 atoms.

© 1998 NRC Canada

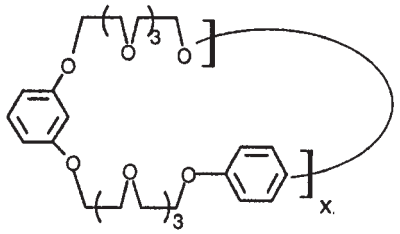

1

a) x = 1
b) x = 2

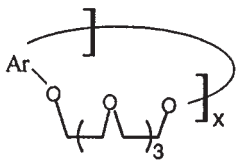

a) x = 1
b) x = 2
c) x = 3

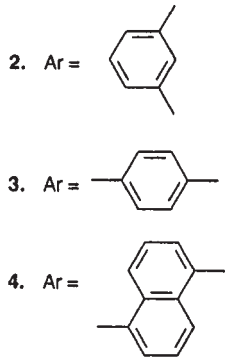

2. Ar =
3. Ar =
4. Ar =

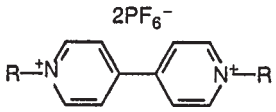

5

a. R = CH_3
b. R = CH_2CH_2OH

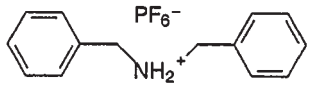

6

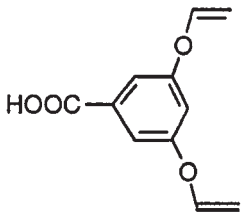

19

Results and discussion

1. The [2 + 2] cyclization approaches

Although it is well known that multistep methods are more efficient for large oligomeric macrocycles than direct [*n* + *n*] approaches (11, 12), the latter have the appeal of using simple starting materials in a one-step procedure reaction sequence. Thus, we initially attempted the synthesis of tetraphenylene crown ethers in this way.

The generic [2 + 2] route to bis(5-carbomethoxy-1,3-phenylene)-bis(*p*-phenylene)-(3*x* + 6)-crown-*x* (**11**) (Schemes 1 and 2) involves preparation of bis[ω-chloro(oligoethyleneoxy)] derivatives (**9**) of hydroquinone and their condensations with methyl 3,5-dihydroxybenzoate (**10**).

This route to bis(5-carbomethoxy-1,3-phenylene)-bis(*p*-phenylene)-30-crown-8 (**11a**) was explored via synthesis of diol **8a** and its conversion to the corresponding dichloride **9a**, both in good yields. However, from the attempted cyclization of **9a** with **10** we were unable to isolate the desired **11a**.

The larger bis(5-carbomethoxy-1,3-phenylene)-bis(*p*-phenylene)-42-crown-12 (**11b**) was approached in an analogous manner. Hydroquinone was alkylated with 2-[2′-(2′′-chloroethoxy)ethoxy]tetrahydropyran (**7b**), and the resultant THP ether was deprotected to afford *p*-bis[2-(2′-hydroxyethoxy)ethoxy]benzene (**8b**). Treatment of **8b** with thionyl chloride produced *p*-bis[2-(2′-chloroethoxy)ethoxy]benzene (**9b**). Attempts to isolate macrocycle **11b** from condensation of bisphenol **10** and **9b** were fruitless.

2. The [1 + 1] cyclization approaches

The more efficient [1 + 1] cyclization approaches to higher cyclic oligomers requires the syntheses of larger building blocks, but allows the more effective use of pseudo-high dilution (syringe pump addition) techniques (11, 12). Tetraphenylene crown ethers **11** were approached by the method depicted in Scheme 3.

*(a) Dihalide intermediates **13***

Methyl 3,5-bis(5-chloro-3-oxapentyloxy)benzoate (**13b**), methyl 3,5-bis(8-chloro-3,6-dioxaoctyloxy)benzoate (**13c**), and methyl 3,5-bis(11-chloro-3,6,9-trioxaundecyloxy)benzoate (**13d**) were each synthesized in one step by reacting large excesses of di-, tri-, and tetra-(ethylene glycol) dichlorides (**12b**–**12d**), respectively, with the disodium salt of methyl 3,5-dihydroxybenzoate (**10**) (Scheme 3), as previously reported (3, 4).

A one-pot synthesis of methyl 3,5-bis(2-chloroethoxy)benzoate (**13a**) was also attempted by reacting a suspension of the disodium salt of methyl 3,5-dihydroxybenzoate (**10**) with a large excess of dichloroethane (**12a**) in DMF. Thin layer chromatography (TLC) indicated a considerable amount of starting benzoate **10** along with the desired product **13a**, which was obtained (10%) upon Soxhlet extraction. Even at longer reaction times considerable amounts of starting material were found.

To synthesize methyl 3,5-bis(2-hydroxyethoxy)benzoate as a precursor to **13a**, the dianion of methyl 3,5-dihydroxybenzoate (**10**), generated in situ with potassium carbonate, was reacted with chloroethanol (**7a**) at 70°C for three days.

© 1998 NRC Canada

Scheme 1.

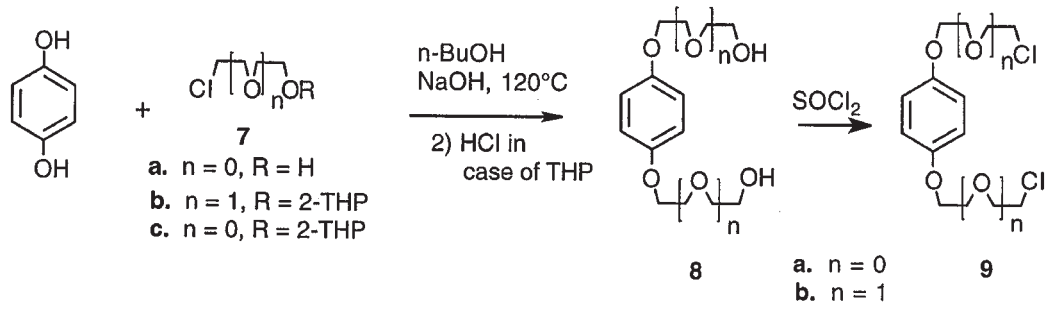

Scheme 2.

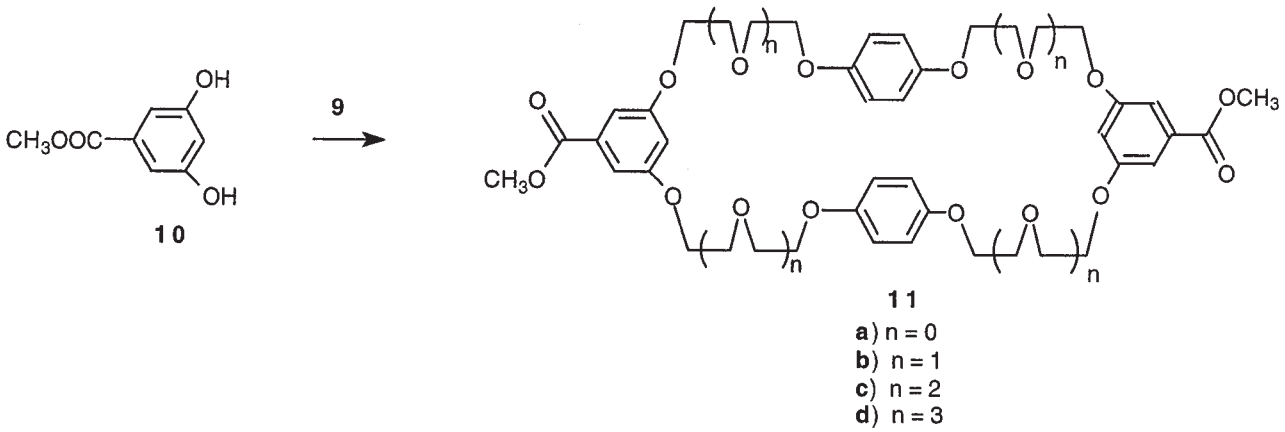

Less than a 10% yield of pure product was obtained. The use of THP protected chloroethanol (**7c**) was then examined. Treatment of methyl 3,5dihydroxybenzoate (**10**) with sodium hydride in DMF followed by reaction with **7c** gave (77%) after deprotection the desired intermediate methyl 3,5-bis(2-hydroxyethoxy)benzoate. After work-up this compound was without purification converted (88%) to the corresponding dichloride **13a** with thionyl chloride and pyridine in benzene.

*(b) Bisphenols **16***

The synthesis of the second fragment for cyclization to **11a**, methyl 3,5-bis[2-(*p*-hydroxyphenoxy)ethoxy]benzoate (**16a**), was initiated via reaction of *p*-benzyloxyphenol (**14**) with methyl 3,5-bis(2-chloroethoxy)benzoate (**13a**) using sodium hydride as base (Scheme 3), but this did not result in the formation of product **15a**. A three-step approach to **15a** was then evaluated (Scheme 4). Reaction of THP protected chloroethanol (**7c**) with *p*-benzyloxyphenol (**14**) and subsequent deprotection gave *p*-(2-hydroxyethoxy)benzyloxybenzene (**17**) in quantitative yield. The compound **17** was converted to the chloro derivative **18** with thionyl chloride and pyridine. Reaction of methyl 3,5-dihydroxybenzoate (**10**) with **18** using sodium hydride as base gave (60%) the desired product, methyl 3,5-bis[2(*p*-benzyloxyphenoxy)ethoxy]benzoate (**15a**).

Methyl 3,5-bis{[*p*-(benzyloxy)phenoxy]oligoethyleneoxybenzoates (**15b**–**15d**) were produced via reaction of *p*-benzyloxyphenol (**14**) with dichlorides **13b**–**13d** using sodium hydride as the base (Scheme 3). These intermediates were purified via flash silica gel chromatography and characterized by NMR and FAB MS.

Removal of the benzyl groups from **15a**–**15d** via hydrogenolysis with palladium on carbon as catalyst gave the desired bisphenols **16a**–**16d** in 90–99% yields (Scheme 3).

*(c) Cyclization reactions to form macrocycles **11***

Our previous cyclization studies showed that the yields were either higher (20- and 26-membered) (5) or almost identical (32-membered) (3, 4) with potassium salts, as compared to the more expensive cesium salts. Thus, we used potassium carbonate as the base in the [1 + 1] cyclization of the bisphenols **16b**–**16d** with dichlorides **13b**–**13d** in DMF at 110°C (Scheme 3). This method provided macrocycles **11b**–**11d** in 17–24% yields.

The cyclization of methyl 3,5-bis[2-(*p*-hydroxyphenoxy)ethoxy]benzoate (**16a**) with methyl 3,5-bis(2-chloroethoxy)benzoate (**13a**) under these conditions was not successful. Therefore, cyclization was attempted at 85°C using sodium hydride as base in DMF via the syringe pump technique. Sodium was used as the metal ion to match the small cavity size of 30-membered **11a**. However, we were able to isolate only (19%) 3,5-bis(vinyloxy)benzoic acid (**19**), the product of two elimination reactions.

*(d) Attempted complexation with dibenzylammonium salt **6***

Bis(*o*- and *p*-phenylene) crown ethers are known to complex strongly with secondary ammonium ions, such as dibenzylammonium hexafluorophosphate (**6**), yielding pseudorotaxanes (2*c*, *e*, *f*, 10*a*, 13) In the present work, in the ^{1}H NMR spectra of $CDCl_3$ solutions of **11b**–**11d** (individually) in the presence of solid ammonium salt **6** there were no indi-

© 1998 NRC Canada

Scheme 3.

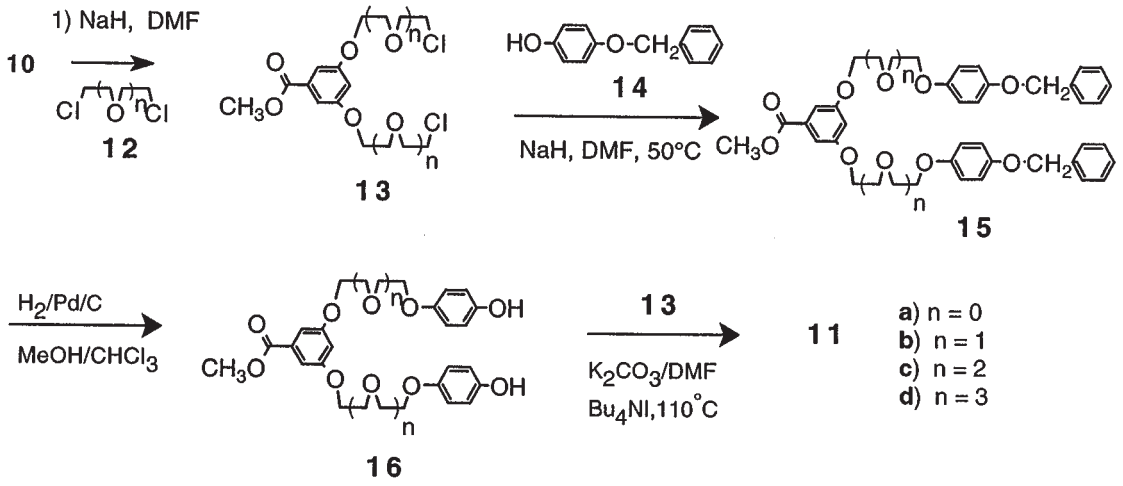

Scheme 4.

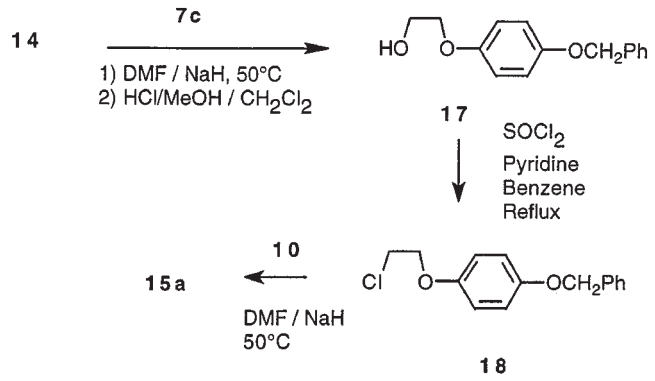

cations of complexation, i.e., no changes of chemical shifts of the proton signals; furthermore, the ammonium salt did not dissolve in $CDCl_3$ solutions of the crown ethers, a good qualitative test for complex formation.

The inclusion complexation of secondary ammonium ions such as **6** by crown ethers appears to be relatively facile based on the isolation of pseudorotaxanes of various stoichiometries for benzo and *p*-phenylene macrocycles ranging from dibenzo-24-crown-8 to tetrakis(*p*-phenylene)-68-crown-20 (**3d**) (10*a*, 13). As deduced from single crystal X-ray structures, the N-H—O bonds in these complexes involve both the phenolic and ethyleneoxy oxygen atoms, as do the benzylic C-H—O bonds, in some cases augmented by π–π interactions. However, we have found that bis(*m*-phenylene) crown ethers complex either very weakly or not at all with secondary ammonium ions (14). Bis(*m*-phenylene)-26-crown-8, in spite of its homology with dibenzo-24-crown-8, which efficiently yields a pseudorotaxane (13), does not give any indication of complexation with **6** by NMR spectroscopy. The larger bis(*m*-phenylene)-32-crown-10 (**2b**), like its 34-membered *p*-analog **3b** (13), gives [3]pseudorotaxanes with two ammmonium ions as guests, but its association constants are quite low (<10 M^{-1}) (14). X-ray analysis of the crystalline [3]pseudorotaxane **2b**:(**6**)$_2$ revealed that the structure and attractive forces are very similar to those reported for **3b**:(**6**)$_2$ (13, 14). The difference in the association constants, therefore, must be a result of poorer preorganization in the case of **2b**. In **11b**–**11d** the electron-withdrawing carbomethoxy groups on the *m*-phenylene units further decrease the tendency for the *m*-phenylene moieties to undergo complexation. However, the hydroquinol ether linkages were expected to provide suitable sites. The only explanation for the lack of complexation of secondary ammonium ions by **11b**–**11d** seems to be that the conformational properties imbued by the *m*-phenylene units are such that complexation is entropically unfavorable.

*(e) Complexation with paraquat diol **5b***

The complexation of paraquat (**5a**) with bis(*m*-phenylene)-32-crown-10 and bis(*p*-phenylene)-34-crown-10 is driven primarily by hydrogen bonding of the α-protons of the bipyridinium units with the ether oxygen atoms, but also involves donor–acceptor, π-stacking, and dipole–dipole attractions (15). It has been deduced that, because four ethyleneoxy units serve to maximize the association constants, hydrogen bonding of the central oxygen atom in the tetra(ethyleneoxy) segment is most important, but that the next nearest oxygen atom plays a role by an allosteric effect (16). X-ray crystallographic results show that both of these interactions are in force in the solid state (6, 9, 15).

Upon mixing solutions of **11d** with **5b** a pale yellow–orange color indicative of charge transfer was observed; in the ^{1}H NMR spectra shifts of the signals for the hydroquinol unit proton, the intra-annular aromatic proton of the *m*-phenylene unit and the CH_2O group adjacent to the hydroquinol unit were observed. Although we have not yet determined the stoichiometry of this complex, it is clear that some relatively weak complexation takes place. Studies with crown ethers containing *m*-phenylene linkages in comparison to their *p*-linked counterparts, e.g., **2b** vs. **3b**, and internally in catenanes derived from **1a**, have demonstrated the preference of paraquat (**5a**) complexation centered on the *p*-phenylene units (6). Thus, we hypothesize that the hydroquinol units of **11d** are the active sites, especially since we have shown that the electron-withdrawing carbomethoxy groups in bis(5-carbomethoxy-1,3-phenylene)-32-crown-10

© 1998 NRC Canada

are detrimental for complexation of paraquats.[2]

Current work is aimed at determining the stoichiometry of the complex of **11d** with **5b**, so that its association constant can be measured, and, hopefully, obtaining crystals suitable for X-ray analysis.

Experimental

Materials

Unless specified otherwise, reagent grade reactants and solvents were used as received from chemical suppliers. The compounds **5b** (17), **6** (13), **7b** (18), **7c** (19), **10** (20), **13b** (3), **13c** (3), and **13d** (4) were synthesized according to literature procedures.

Instrumentation and techniques

Melting points were taken in capillary tubes and have been corrected. The ^{1}H and ^{13}C NMR spectra were obtained at room temperature (RT) on a 400 MHz spectrometer using $CDCl_3$ as solvent with $SiMe_4$ (δ = 0) as internal standard, except as noted. The MS was carried out in house, at the Washington University Mass Spectrometry Resource and at the Nebraska Center for Mass Spectrometry using the FAB technique in 3-nitrobenzyl alcohol matrices (HR = high resolution). A syringe infusion pump was used to control the addition rates in the cyclization reactions.

p-Bis(2-hydroxyethoxy)benzene (8a)

A solution of **7c** (52.5 g, 320 mmol) in *n*-BuOH (150 mL) was added dropwise to a refluxing solution of hydroquinone (11.0 g, 101 mmol), NaOH (8.20 g, 200 mmol), sodium dithionite (40 mg), and *n*-BuOH (300 mL). The solution was refluxed for 15 h under N_2, and more NaOH (2.90 g, 72.5 mmol) was added and refluxing was continued for 15 h. The reaction mixture was cooled, filtered, and concentrated in vacuo to remove solvent and excess **7c**. The residue was dissolved in MeOH:CH_2Cl_2 (1:1 v:v, 500 mL), treated with conc. HCl (5 mL) and stirred for 4 h at RT to hydrolyze the THP ether. The solution was neutralized with $NaHCO_3$. The organic layer was dried (Na_2SO_4) and evaporated to give the crude product (17.0 g, 85%), which was recrystallized from EtOAc: mp 105–107°C; this compound is commercially available.

p-Bis[2-(2′-hydroxyethoxy)ethoxy]benzene (8b)

Application of the above procedure using **7b** on twice the scale afforded 43.6 g (76%) of colorless solid after recrystallization from EtOAc: mp 74.5–75.5°C. ^{1}H NMR, δ (ppm): 2.75 (s, 2H), 3.6–4.4 (m, 16H), 6.85 (s, 4H). Anal. calcd. for $C_{14}H_{22}O_6$: C 58.72, H 7.75; found: C 58.64, H 7.78.

p-Bis(2-chloroethoxy)benzene (9a)

The compound $SOCl_2$ (223.0 g, 1.874 mol) was added very slowly to a solution of **8a** (148.66 g, 750 mmol), pyridine (150 mL), and toluene (450 mL). The solution was refluxed for 24 h, cooled, and the precipitate was extracted with toluene (2 × 150 mL). The extract was washed with H_2O (200 mL), dried (Na_2SO_4), and evaporated to produce 149.5 g (79%) of crude product, which was recrystallized from EtOAc: mp 102–103°C, lit. (21) oil. ^{1}H NMR, δ (ppm): 3.79 (t, J = 7 Hz, 4H), 4.19 (t, J = 7 Hz, 4H), 6.87 (s, 4H). MS (EI), m/z: 238 [(M $^{37}Cl_2)^+$, 10%], 236 [(M ^{37}Cl $^{35}Cl)^+$, 67%], 234 [(M $^{35}Cl_2)^+$, 100%], 171 [(M $^{35}Cl_2$ – CH_2CH_2Cl), 90%], 109 [(M – 2(CH_2CH_2Cl)), 100%].

p-Bis[2-(2′-chloroethoxy)ethoxy]benzene (9b)

Application of the above procedure to **8b** produced (85%) crude **9b**, which was recrystallized from EtOAc: mp 62.2–64.0°C, lit. (21) oil. ^{1}H NMR, δ (ppm): 3.6–4.2 (m, 16H), 6.85 (s, 4H). MS (EI), m/z: 324 [(M ^{37}Cl $^{35}Cl)^+$, 24%], 322 [(M $^{35}Cl_2)^+$, 35%], 113 (100%). Anal. calcd. for $C_{14}H_{20}Cl_2O_4$: C 52.02, H 6.24; found: C 51.88, H 6.25.

Methyl 3,5-bis(2-hydroxyethoxy)benzoate

NaH (5.14 g, 128 mmol, 60% in mineral oil) was added to a solution of **10** (10.05 g, 59.77 mmol) in 100 mL of DMF, and the mixture was heated at 110°C for 2 h, cooled to 50°C, and **7c** (22.29 g, 135.4 mmol) was added while stirring. After 5 days the mixture was cooled to RT, filtered through Celite, and concentrated in vacuo. The resulting brown oil was extracted with MeOH:CH_2Cl_2 (70:30, 250 mL) containing 20 mL of conc. HCl. After concentration the mixture was diluted with H_2O (250 mL) and treated with satd. aq. $NaHCO_3$. After extraction with EtOAc (3 × 100 mL), the organic layer was washed with H_2O and satd. aq. NaCl. The brown oil (11.85 g, 77%) was used for the next step without further purification. ^{1}H NMR, δ (ppm): 3.89 (s, 3H), 3.96 (t, J = 4.4 Hz, 4H), 4.07 (t, J = 4.4 Hz, 4H), 6.65 (t, J = 2.2 Hz, 1H), and 7.17 (d, J = 2.2 Hz, 2H). ^{13}C NMR, δ (ppm): 52.30, 61.16, 69.48, 106.86, 107.98, 131.90, 159.56, and 166.72 (8 peaks as required).

Methyl 3,5-bis(2-chloroethoxy)benzoate (13a)

A solution of methyl 3,5-bis(2-hydroxyethoxy)benzoate (10.98 g, 42.85 mmol) in C_6H_6 (275 mL) was refluxed for 30 min using a Dean–Stark apparatus. At RT pyridine (7.0 mL, 87 mmol, 2.0 equiv.) was added along with $SOCl_2$ (6.4 mL, 88 mmol) over 1 h. After 48 h at reflux, the mixture was cooled to RT and the salt removed by decantation, washed with C_6H_6, and the organic layers were combined and then washed sequentially with H_2O, dil. HCl, and satd. aq. NaCl. Evaporation resulted in an oil; passage through a short SiO_2 column using $CHCl_3$:EtOAc (20:1) gave **13a** (11.10 g, 88%), an oil, which crystallized: mp 68.2–69.4°C. ^{1}H NMR, δ (ppm): 3.82 (t, J = 5.8 Hz, 4H), 3.90 (s, 3H), 4.25 (t, J = 5.8 Hz, 4H), 6.70 (t, J = 2.4 Hz, 1H), and 7.21 (d, J = 2.4 Hz, 2H). ^{13}C NMR, δ (ppm): 41.70, 52.26, 68.23, 107.06, 108.33, 132.20, 159.18, 166.37 (8 peaks as required). Anal. calc. for $C_{12}H_{14}Cl_2O_4$: C 49.16, H 4.81; found: C 49.48, H 4.77.

p-(2-Hydroxyethoxy)benzyloxybenzene (17)

NaH (1.84 g, 46.0 mmol, 60% in mineral oil) was added to a solution of **14** (8.02 g, 40.1 mmol) in DMF (60 mL). At 50°C, **7c** (7.45 g, 45.3 mmol) was added, and the mixture was stirred for 30 h at 50°C. After filtration, DMF was evaporated, and the oil was diluted with MeOH:CH_2Cl_2 (6:2,

[2] P.B. Balanda and H.W. Gibson. Unpublished results.

© 1998 NRC Canada

150 mL) containing conc. HCl (5 mL). After 6 h, the solvent was removed, and the mixture was diluted with H_2O. The EtOAc extract was dried (Na_2SO_4) and evaporated to give a white solid, which was recrystallized from EtOH to give **17** (10.02 g, 100%), a white solid: mp 104.2–106.0°C, lit. (22) mp 103.5–104.5. ^{1}H NMR, δ (ppm): 3.90 (m, 2H), 4.00 (t, J = 4.4 Hz, 2H), 5.00 (s, 2H), 6.86 (AB q, J = 9.2 Hz, 4H), and 7.36 (m, 5H). ^{13}C NMR, δ (ppm): 61.45, 69.80, 70.59, 115.49, 115.81, 127.40, 127.83, 128.48, 137.14, 152.88, and 153.20 (11 peaks as required).

p-(2-Chloroethoxy)benzyloxybenzene (18)

Pyridine (7.6 mL, 94 mmol) and then $SOCl_2$ (6.9 mL, 95 mmol) were added to a solution of **17** (9.53 g, 39.0 mmol) in C_6H_6 (150 mL). After 48 h at reflux, the mixture was cooled to RT, and salt was removed by decantation, washed with C_6H_6, and the organic layers were combined, washed with H_2O, dil. HCl, and satd. aq. NaCl. Evaporation gave a light yellow solid, which was recrystallized from EtOH to give **18** (8.38 g, 82%), a white solid: mp 69.7–71.2°C. ^{1}H NMR, δ (ppm): 3.75 (t, J = 5.8 Hz, 2H), 4.14 (t, J = 5.8 Hz, 2H), 4.99 (s, 2H), 6.87 (AB q, J = 9.2 Hz, 4H), and 7.37 (m, 5H). ^{13}C NMR, δ (ppm): 41.97, 68.79, 70.57, 115.83, 115.89, 127.40, 127.86, 128.49, 137.12, 152.44, and 153.46 (11 peaks as required). Anal. calc. for $C_{15}H_{15}ClO_2$: C 68.57, H 5.75; found: C 68.66, H 5.78.

Methyl 3,5-bis[2-(*p*-benzyloxyphenoxyethoxy]benzoate (15a)

Method A: NaH (316 mg, 13.2 mmol,) was added to a solution of **10** (1.02 g, 6.07 mmol) in DMF (60 mL), and the solution was stirred for 1 h at 110°C. At 65°C, **18** (3.30 g, 12.6 mmol) was added as a solid, and the mixture was stirred for 48 h. After filtration, DMF was evaporated, and the oil was subjected to column chromatography (SiO_2) with $CHCl_3$:EtOAc (20:1). The resultant oil upon trituration with hexane gave **15a**, a white solid (2.27 g, 60%): mp 79.4–81.7°C. ^{1}H NMR, δ (ppm): 3.90 (s, 3H), 4.28 (m, 8H), 5.02 (s, 4H), 6.76 (brs, 1H), 6.90 (AB q, 8H, J = 9.2 Hz, 8H), 7.25 (d, J = 2.0 Hz, 2H), and 7.37 (m, 1 OH). ^{13}C NMR, δ (ppm): 52.25, 66.95, 67.11, 70.66, 107.15, 108.22, 115.78, 115.86, 127.44, 127.87, 128.52, 132.02, 137.19, 152.878, 153.33, 159.66, and 166.69 (17 peaks as required). Anal. calc. for $C_{38}H_{36}O_8$: C 73.53, H 5.85; found: C 73.14, H 6.13.

Method B: The same except using 1.82 g (13.2 mmol) of K_2CO_3 instead of NaH at 80°C; 3.03 g (80%) of **15a**.

Methyl 3,5-bis[5-(*p*-benzyloxyphenoxy)-3-oxapentyloxy]benzoate (15b)

NaH (680 mg, 17 mmol, 60% in mineral oil) was added to a stirred solution of **14** (3.24 g, 16.2 mmol) in DMF (50 mL). After 30 min a solution of **13b** (2.95 g, 7.74 mmol) in DMF (20 mL) was added, and the mixture was stirred for 2 days at RT, filtered, and concentrated to give an oil, which was purified via flash SiO_2 chromatography using Et_2O to give 3.38 g (62%) of **15b**, a white solid, which was recrystallized from EtOAc:pet. ether (bp 39–59°C): mp 60.9–62.4°C. ^{1}H NMR, δ (ppm): 3.88 (s, 3H), 3.90 (m, 8H), 4.10 (t, J = 4.8 Hz, 4H), 4.16 (t, J = 4.8 Hz, 4H), 5.00 (s, 4H), 6.71 (t, J = 2.4 Hz, 1H), 6.87 (AB q, J = 9.2 Hz, 8H), 7.20 (d, J = 2.4 Hz, 2H), and 7.37 (m, 10H). ^{13}C NMR, δ (ppm): 52.22, 67.79, 68.13, 69.76, 70.06, 70.64, 106.93, 108.12, 115.65, 115.77, 127.46, 127.86, 128.52, 131.90, 137.25, 153.06, 153.15, 159.72, and 166.74 (19 peaks as required). MS (FAB), m/z (rel. int.): 708 [M^+, 100%], 677 [$(M - OCH_3)^+$, 76%], and 586 [$(M - OCH_3 - CH_2C_6H_5)^+$, 12%]. HRFAB, m/z, calcd. for $C_{42}H_{44}O_{10}$ [$M]^+$: 708.2934; found: 708.2955 (error 2.8 ppm).

Methyl 3,5-bis[8-(*p*-benzyloxyphenoxy)-3,6-dioxaoctyloxy]benzoate (15c)

A procedure similar to that used for **15b** was utilized to prepare **15c** (63%), which crystallized slowly to give a light yellow solid: mp 61–63°C. ^{1}H NMR, δ (ppm): 3.74 (m, 8H), 3.84 (m, 8H), 3.87 (s, 3H), 4.07 (t, J = 4.8 Hz, 4H), 4.13 (t, J = 4.8 Hz, 4H), 6.69 (s, 4H), 6.70 (t, J = 2.2 Hz, 1H), 6.86 (AB q, J = 9.2 Hz, 8H), 7.19 (d, J = 2.2 Hz, 2H), and 7.35 (m, 10H). ^{13}C NMR, δ (ppm): 52.16, 67.68, 68.00, 69.58, 69.86, 70.58, 70.79, 70.84, 106.86, 107.99, 115.71, 115.56, 127.42, 127.81, 128.48, 131.84, 137.22, 153.05, 153.08, 159.71, and 166.70 (21 peaks as required). MS (FAB), m/z (rel. int.): 819.4 [$(M + Na)^+$, 5%], 796.4 (M^+, 85%), 765.4 [$(M - OCH_3)^+$, 42%], 706.4 [$(M - COOCH_3)^+$, 8%], and 674 [$(M - OCH_3 - CH_2C_6H_5)^+$, 5%], 76 [100%]. HRFAB, m/z, calcd. for $C_{46}H_{52}O_{12}$ [$M]^+$: 796.3459; found: 796.3476 (error 2.2 ppm). Anal. calc. for $C_{46}H_{52}O_{12}$: C 69.33, H 6.58; found: C 69.48, H 6.63.

Methyl 3,5-bis[11-(*p*-benzyloxyphenoxy)-3,6,9-oxaundecyloxy]benzoate (15d)

A procedure similar to that used for **15b** was utilized to prepare **15d** (64%), an oil. ^{1}H NMR, δ (ppm): 3.70 (m, 16H), 3.82 (m, 8H), 3.87 (s, 3H), 4.06 (t, J = 4.8 Hz, 4H), 4.12 (t, J = 4.8 Hz, 4H), 4.99 (s, 4H), 6.68 (t, J = 2.4 Hz, 1H), 6.86 (AB q, J = 9.2 Hz, 8H), 7.19 (d, J = 2.4 Hz, 2H), and 7.36 (m, 10H). ^{13}C NMR (ppm): 52.19, 67.68, 67.98, 69.54, 69.80, 70.59, 70.63, 70.74, 70.79, 106.84, 107.97, 115.54, 115.71, 127.43, 127.82, 128.48, 131.82, 137.22, 153.03, 153.08, 159.70, and 166.72 (22 peaks; theory 23). MS (FAB), m/z (rel. int.): 907 [$(M + Na)^+$, 2%], 884 [M^+, 41%], 853 [$(M - OCH_3)^+$ 32%], and 762 [$(M - C_8H_{10}O)^+$, 3%], 225 (56%), 200 (100%); HRFAB, m/z, calcd. for $C_{50}H_{60}O_{14}$ [$M]^+$: 884.3983, found: 884.3982 (error 0.1 ppm).

Methyl 3,5-bis[2-(*p*-hydroxyphenoxy)ethoxy]benzoate (16a)

A solution of **15a** (1.08 g, 1.74 mmol) in $CHCl_3$:MeOH (1:1, 40 mL) containing Pd/C (100 mg) was subjected to hydrogenolysis at 60 psi for 48 h, filtered, and concentrated to give an oil, which was purified by SiO_2 column chromatography. Addition of $CHCl_3$ to the resulting oil gave **16a** (0.96 g, 90%), a white solid: mp 130.3–131.9°C. ^{1}H NMR, δ (ppm): 3.84 (s, 3H), 4.20 (m, 4H), 4.32 (m, 4H), 6.76 (AB q, J = 9.2 Hz, 8H), 6.90 (t, J = 2.2 Hz, 1H), 7.12 (d, J = 2.2 Hz, 2H), and 8.95 (s, 2H). ^{13}C NMR, δ (ppm): 52.32, 66.67, 66.98, 106.30, 107.58, 115.50, 115.74, 131.65, 151.04, 151.38, 159.61, and 165.83 (12 peaks, as required). Anal. calc. for $C_{24}H_{24}O_8 \cdot H_2O$: C 62.87, H 5.72; found: C 62.72, H 5.36.

Methyl 3,5-bis[5-(*p*-hydroxyphenoxy)-3-oxapentyloxy]benzoate (16b)

A solution of **15b** (2.58 g, 3.64 mmol) in $CHCl_3$:EtOAc (1:1, 30 mL) was subjected to hydrogenolysis (60 psi) at RT

© 1998 NRC Canada

in the presence of 10% Pd/C (150 mg) for 10 h, filtered, and concentrated in vacuo to give **16b** (1.9 g, 98%), an oil. ^{1}H NMR, δ (ppm): 3.87 (m, 11 H), 4.07 (m, 8H), 6.55 (t, *J* = 2.2 Hz, 1 H), 6.72 (s, 8H), and 7.15 (d, *J* = 2.2 Hz, 2H). ^{13}C NMR, δ (ppm): 52.33, 67.59, 68.09, 69.63, 69.98, 107.06, 108.02, 115.85, 116.07, 131.60, 150.05, 152.36, 159.53, and 167.04 (14 peaks as required). MS (FAB), *m*/*z* (rel. int.): 528 [M^+, 100%], 497 [$(M - OCH_3)^+$, 49%], and 420 ($M^+ - CH_3 - C_6H_4OH$, 16%); HRFAB, *m*/*z*, calcd. for $C_{28}H_{32}O_{10}$ $[M]^+$: 528.1995, found: 528.1981 (error 2.7 ppm).

Methyl 3,5-bis[8-(*p*-hydroxyphenoxy)-3-,6-dioxaoctyloxy]benzoate (16c)

A procedure similar to that used for **16b** was utilized to prepare **16c**, an oil (99%). ^{1}H NMR (DMSO), δ (ppm): 3.58 (m, 8H), 3.68 (t, *J* = 4.6 Hz, 4H), 3.73 (t, *J* = 4.6 Hz, 4H), 3.81 (s, 3H), 3.94 (t, *J* = 4.6 Hz, 4H), 4.12 (t, *J* = 4.6 Hz, 4H), 6.68 (AB q, *J* = 9.2 Hz, 8H), 6.80 (t, *J* = 2.2 Hz, 1 H), 7.05 (d, *J* = 2.2 Hz, 2H), and 8.89 (s, 2H). ^{13}C NMR (DMSO), δ (ppm): 52.28, 67.51, 67.60, 68.82, 69.12, 69.90, 69.95, 106.15, 107.45, 115.36, 115.69, 131.57, 151.20, 151.24, 159.69, and 165.87 (16 peaks as required). MS (FAB), *m*/*z* (rel. int.): 639 [$(M + Na)^+$, 5%], 616 [M^+, 34%], and 585 [$(M - OCH_3)^+$, 20%), 163 (100%); HRFAB, *m*/*z*, calcd. for $C_{32}H_{40}O_{12}$ $[M]^+$: 616.2520, found: 616.2511 (error 1.4 ppm).

Methyl 3,5-bis[11-(*p*-hydroxyphenoxy)-3,6,9-oxaundecyloxy]benzoate (16d)

A procedure similar to that used for **16b** was utilized to prepare **16d**, an oil (98%). ^{1}H NMR, δ (ppm): 3.69 (m, 16H), 3.79 (m, 8H), 3.87 (s, 3H), 3.96 (t, *J* = 4.8 Hz, 4H), 4.00 (t, *J* = 4.8 Hz, 4H), 6.56 (t, *J* = 2.4 Hz, 1 H), 6.65 (s, 2H), 6.69 (AB q, *J* = 9.2 Hz, 8H), 7.13 (d, *J* = 2.4 Hz, 2H). ^{13}C NMR, δ (ppm): 52.29, 67.50, 67.99, 69.57, 69.78, 70.52, 70.56, 106.644, 108.06, 115.67, 116.06, 131.62, 150.36, 152.28, 159.61, and 167.04 (16 peaks; theory 18). MS (FAB), *m*/*z* (rel. int.): 704 [$(M + Na)^+$, 8%], 391 [$(M - COOCH_3 - 2HOC_6H_4 - OCH_2CH_2)^+$, 80%], 167 (100%); HRFAB, *m*/*z*, calcd. for $C_{34}H_{48}O_{14}$ $[M + Na]^+$: 703.2941, found: 703.2952 (error 1.4 ppm).

3,5-Bis(vinyloxy)benzoic acid (19) from attempted synthesis of 11a

A solution of **13a** (814.1 mg, 2.780 mmol) and **16a** (1.16 g, 2.63 mmol) in DMF (total volume = 12 mL) was added via a syringe pump at 2.0 mL/h to a suspension of NaH (1.2 g, 30 mmol, 60% in mineral oil) in DMF (175 mL) at 110°C. After addition, the mixture was stirred at 85°C for 4 days, cooled, evaporated, treated with $CHCl_3$, and filtered. Removal of $CHCl_3$ followed by flash SiO_2 column chromatography eluting with $CHCl_3$:EtOAc (20:1) gave pure **19** (110 mg, 19%): mp 115.7–117.5°C. ^{1}H NMR, δ (ppm): 4.57 (dd, *J* = 6.0 and 2.4 Hz, 1H), 4.87 (dd, *J* = 13.6 and 2.0 Hz, 1H), 6.66 (dd, *J* = 13.6 and 2.0 Hz, 1H), 6.91 (t, *J* = 2.2 Hz, 1H), and 7.46 (d, *J* = 2.2 Hz, 2H). ^{13}C NMR, δ (ppm): 97.04, 111.42, 112.75, 131.66, 147.09, 157.86, and 170.71 (7 peaks as required). Anal. calc. for $C_{11}H_{10}O_4 \cdot 1/4\ H_2O$: C 62.70, H 5.02; found: C 62.80, H 4.93.

Bis(5-carbomethoxy-1,3-phenylene)-bis(*p*-phenylene)-42-crown-12 (11b)

A solution of **16b** (1.91 g, 3.61 mmol) and **13b** (1.38 g, 3.62 mmol) in DMF (total volume 20 mL) was added via a syringe pump at 1.5 mL/h to a suspension of K_2CO_3 (5.20 g, 37.6 mmol) and tetra(*n*-butyl)ammonium iodide (20 mg) in DMF (175 mL) at 110°C. After complete addition, the mixture was stirred vigorously at 110°C for 5 days, cooled, and evaporated. The residue was dissolved in CH_2Cl_2 and filtered. Removal of CH_2Cl_2 followed by flash column (SiO_2) chromatography eluting with Et_2O gave pure **11b** (700 mg, 23%): mp 140–142°C. ^{1}H NMR, δ (ppm): 3.89 (m, 22H), 4.08 (t, *J* = 4.6 Hz, 8H), 4.14 (t, *J* = 4.6 Hz, 8H), 6.71 (t, *J* = 2.2 Hz, 2H), 6.82 (s, 8H), and 7.19 (d, *J* = 2.2 Hz, 4H). ^{13}C NMR, δ (ppm): 52.19, 67.84, 68.16, 69.65, 69.97, 107.18, 108.09, 115.64, 131.81, 153.05, 159.70, and 166.72 (12 peaks as required). MS (FAB), *m*/*z* (rel. int.): 859.1 [$(M + Na)^+$, 14%], 836.1 (M^+, 100%), and 805.1 [$(M - OCH_3)^+$, 16%]; HRFAB, *m*/*z*, calcd. for $C_{44}H_{52}O_{16}$ [M^+]: 836.3255, found 836.3286 (error 3.6 ppm).

Bis(5-carbomethoxy-1,3-phenylene)-bis(*p*-phenylene)-54-crown-16 (11c)

A procedure similar to that used for **11b** was utilized to prepare **11c** (18%), a white solid: mp 102.9–104.3°C. ^{1}H NMR, δ (ppm): 3.73 (m, 16H), 3.83 (m, 8H), 3.89 (s, 6H), 4.05 (t, *J* = 4.8 Hz, 8H), 4.12 (t, *J* = 4.8 Hz, 8H), 6.70 (t, *J* = 2.2 Hz, 2H), 6.81 (s, 8H), and 7.18 (d, *J* = 2.2 Hz, 4H). ^{13}C NMR, δ (ppm): 52.19, 67.76, 68.07, 69.60, 69.87, 70.83, 70.91, 106.92, 108.06, 115.58, 131.84, 153.05, 159.74, and 166.72 (14 peaks as required). MS (FAB), *m*/*z* (rel. int.): 1012.9 (M^+, 100%), 981.9 [$(M - OCH_3)^+$, 15%], and 950.9 [$(M - 2OCH_3)^+$, 12%]; HRFAB, *m*/*z*, calcd. for $C_{52}H_{69}O_{20}$ $[M + H]^+$ 1013.4382; found 1013.4399 (error 1.6 ppm).

Bis(5-carbomethoxy-1,3-phenylene)-bis(*p*-phenylene)-66-crown-20 (11d)

A procedure similar to that used for **11b** was utilized to prepare **11d** (19%), a white solid: mp 77.5–79.5°C. ^{1}H NMR, δ (ppm): 3.69 (m, 32H), 3.82 (m, 16H), 3.88 (s, 6H), 4.04 (t, *J* = 4.8 Hz, 8H), 4.12 (t, *J* = 4.8 Hz, 8H), 6.69 (t, *J* = 2.2 Hz, 2H), 6.81 (s, 8H), and 7.18 (d, *J* = 2.2 Hz, 4H). ^{13}C NMR, δ (ppm): 52.17, 69.72, 68.00, 69.51, 69.77, 70.64, 70.74, 70.80, 106.86, 107.98, 115.51, 131.81, 153.01, 159.71, and 166.70 (15 peaks; theory 16). MS (FAB), *m*/*z* (rel. int.): 1211 [$(M + Na)^+$, 1%], 1188.4 (M^+, 100%), 1173.3 [$(M - CH_3)^+$, 5%], and 1157.4 [$(M - OCH_3)^+$, 16%], 1125 [$(M - 2OCH_3)^+$, 8%]; HRFAB, *m*/*z*, calcd. for $C_{60}H_{85}O_{24}$ $[M + H]^+$: 1189.5431; found 1189.5440 (error 0.8 ppm).

Conclusions

We have synthesized three new functionalized cyclic tetraphenylene polyethers, namely bis(5-carbomethoxy-1,3-phenylene)-bis(*p*-phenylene)-(3*x* + 6)crown-*x*, where *x* = 12, 16, and 20 (**11b**–**11d**) with ring sizes of 42, 54, and 66 atoms in 17–24% yields by [1 + 1] condensations of dichlorides **13b**–**13d** with the corresponding bisphenols **16b**–**16d**. These macrocycles do not complex with second-

© 1998 NRC Canada

ary ammonium ions, but in at least in one case, **11d**, do complex with paraquats such as **5b**.

Acknowledgements

We acknowledge support from the National Science Foundation (U.S.A.) (CHE-95–21738) for the work described here. Some mass spectrometry data were provided by the Nebraska Center for Mass Spectrometry, Department of Chemistry, University of Nebraska, and by the Washington University Mass Spectrometry Resource, an NIH Research Resource (grant no. P41RR0954). We thank the reviewers for their thoughtful comments, which resulted in improvements in this publication.

References

1. R.M. Izatt, K. Pawlak, T.S. Bradshaw, and R.L. Bruening. Chem. Rev. **91**, 1721 (1991).
2. (*a*) C. Gong and H.W. Gibson. Curr. Opin. Solid St. Mater. Sci, **2**, 647 (1998); (*b*) H.W. Gibson, C. Gong, S. Liu, and D.S. Nagvekar. Macromol. Symp. **128**, 89 (1998); (*c*) S.A. Nepolgodiev and J.F. Stoddart. Chem. Rev. **98**, 1959 (1998); (*d*) H.W. Gibson. *In* Large ring molecules. *Edited by* J.A. Semlyen. John Wiley & Sons, New York. 1996. pp. 191–262; (*e*) D. Philp and J.F. Stoddart. Angew. Chem. Int. Ed. Engl. **35**, 1154 (1996); (*f*) D.B. Amabilino and J.F. Stoddart. Chem. Rev. **95**, 2725 (1995); (*g*) C. Gong, C. Subramanian, Q. Ji, and H.W. Gibson. Macromolecules, **31**, 1814 (1998), and refs. therein; (*h*) C. Gong, P.B. Balanda, and H.W. Gibson. Macromolecules, **31**, 5278 (1998); (*i*) C. Gong and H.W. Gibson. Macromolecules, **30**, 8524 (1997), and refs. therein; (*j*) J. Am. Chem. Soc. **119**, 5862 (1997); (*k*) Angew. Chem. Int. Ed. Engl. **37**, 310 (1998); (*l*) Macromol. Chem. Phys. **199**, 1801 (1998); (*m*) N. Yamaguchi, D.S. Nagvekar, and H.W. Gibson. Angew. Chem. Int. Ed. Engl. **37**, 2361 (1998); (*n*) N. Yamaguchi, L.M. Hamilton, and H.W. Gibson. Angew. Chem. Int. Ed. Engl. **37** (1998). In press; (*o*) N. Yamaguchi and H.W. Gibson. Angew. Chem. Int. Ed. Engl. **38**, (1999). In press.
3. H.W. Gibson, D.S. Nagvekar, F. Wang, and W.S. Bryant. J. Org. Chem. **61**, 4798 (1997).
4. D.S. Nagvekar and H.W. Gibson. Can. J. Chem. **75**, 1375 (1997).
5. D.S. Nagvekar and H.W. Gibson. Org. Prep. Proced. Int. **29**, 234 (1997); **29**, 237 (1997).
6. D.B. Amabilino, P.-L. Anelli, P.R. Ashton, G.R. Brown, E. Cordova, L.A. Godinez, W. Hayes, A.E. Kalfer, D. Philp, A.M.Z. Slawin, N. Spencer, J.F. Stoddart, M.S. Tolley, and D.J. Williams. J. Am. Chem. Soc. **117**, 11 142 (1995).
7. D.B. Amabilino, P.R. Ashton, G.R. Brown, W. Hayes, J.F. Stoddart, and D.J. Williams. J. Chem. Soc. Chem. Commun. 2479 (1994).
8. B.J. van Keulen, R.M. Kellog, and O. Piepers. J. Chem. Soc. Chem. Commun. 285 (1979); D. B. Amabilino, P. R. Ashton and J.F. Stoddart. Supramolecular Chem. **5**, 5 (1994).
9. D.B. Amabilino, P.R. Ashton, C.L. Brown, E. Cordova, L.A. Godinez, T.T. Goodnow, A.E. Kalfer, S.P. Newton, M. Pietraskiewicz, D. Philp, F.M. Raymo, A.S. Reder, M.T. Rutland, A.M. Z. Slawin, N. Spencer, J.F. Stoddart, C. Vicent, and D.J. Williams. J. Am. Chem. Soc. **117**, 1271 (1995).
10. (*a*) P.R. Ashton, M.C.T. Fyfe, P.T. Glink, S. Menzer, J.F. Stoddart, A.J.P. White, and D.J. Williams. J. Am. Chem. Soc. **119**, 12 514 (1997); (*b*) D.B. Amabilino, P.R. Ashton, V. Balzani, S.E. Boyd, A. Credi, J.Y. Lee, S. Menzer, J.F. Stoddart, M. Venturi, and D.J. Williams. J. Am. Chem. Soc. **120**, 4295 (1998).
11. D.A. Laidler and J.F. Stoddart. *In* Crown ethers and analogs. *Edited by* S. Patai and Z. Rappoport. John Wiley & Sons, New York. 1989. pp. 1–58.
12. (*a*) B. Dietrich, P. Viout, and J.-M. Lehn. Macrocyclic chemistry. VCH Publishers, Inc., New York. 1993; (*b*) Frontiers in supramolecular organic chemistry and photochemistry. *Edited by* H.-J. Schneider and H. Durr. VCH Publishers, Inc., New York. 1991; (*c*) J.-M. Lehn. Supramolecular chemistry. VCH Publishers, Inc., New York. 1995.
13. P.R. Ashton, P.J. Campbell, E.J.T. Chrystal, P.T. Glink, S. Menzer, D. Philp, N. Spencer, J.F. Stoddart, P.A. Tasker, and D.J. Williams. Angew. Chem. Int. Ed. Engl. **34**, 1865 (1995); P.R. Ashton, A.N. Collins, M.C.T. Fyfe, P.T. Glink, S. Menzer, J.F. Stoddart, and D.J. Williams. Angew. Chem. Int. Ed. Engl. **36**, 59 (1997), and refs. therein.
14. W.S. Bryant, I.A. Guzei, A.L. Rheingold, J.S. Merola, and H.W. Gibson. J. Org. Chem. **63**, 7634 (1998).
15. B.L. Allwood, N. Spencer, H. Shahriari-Zavareh, J.F. Stoddart, and D.J. Williams. J. Chem. Soc. Chem. Commun. 1058 (1987); M. Asakawa, P.R. Ashton, R. Ballardini, V. Balzani, M. Belohradsky, M.T. Gandolfi, O. Kocian, L. Prodi, F.M. Raymo, J.F. Stoddart, and M. Venturi. J. Am. Chem. Soc. **119**, 302 (1997), and refs. therein.
16. R.E. Gillard, F.M. Raymo, and J.F. Stoddart. Chem. Eur. J. **3**, 1933 (1997).
17. Y.X. Shen, P.T. Engen, M.A.G. Berg, J.S. Merola, and H.W. Gibson. Macromolecules, **25**, 2786 (1992).
18. A. Buzas, C. Egnell, and M. Moczar. Bull. Soc. Chim. Fr. 267 (1962).
19. E.P. Kyba, R.C. Helgeson, K. Madan, G.W. Gokel, T.L. Tarnowski, S.S. Moore, and D.J. Cram. J. Am. Chem. Soc. **99**, 2564 (1977).
20. Y. Delaviz and H.W. Gibson. Macromolecules, **25**, 18 (1992).
21. R.P. Sijbesma and R.J.M. Nolte. Rec. Trav. Chim. Pays-Bas, **112**, 643 (1993).
22. S.E. Barrie, L.C. Davies, J.A. Stock, and K.R. Harrap. J. Med. Chem. **27**, 1044 (1984).

© 1998 NRC Canada

Chemical kinetics and thermodynamics of tin ionization in H_2-O_2-N_2 flames and the proton affinity of SnO

John M. Goodings and QingFeng Chen

Abstract: A small amount ($\leq 10^{-6}$ mol fraction) of tin was introduced into five, fuel-rich, H_2-O_2-N_2 flames in the temperature range 1820–2400 K at atmospheric pressure. Ions in a flame were observed by sampling the flame along its axis through a nozzle into a mass spectrometer. The major neutral tin species in these flames were SnO (>97%) and Sn (<3%). The principal tin ions observed were $SnOH^+$ and Sn^+. Thermodynamic functions for $SnOH^+$, Sn^+, SnO, and Sn were calculated by statistical mechanics using published data from ab initio calculations and spectroscopy. The $SnOH^+$ ion was formed initially by proton transfer to SnO by H_3O^+, a natural flame ion, with which it is in equilibrium. It was also produced by chemi-ionization of SnO reacting with H; $SnOH^+$ rapidly equilibrates with Sn^+. Ion ratio measurements of $SnOH^+/H_3O^+$ led to the proton affinity PA°_{298} (SnO) = 911 ± 21 kJ mol $^{-1}$ (218 ± 5 kcal mol^{-1}). A calculated equilibrium constant provided the $SnOH^+/Sn^+$ ion ratio. When electron-ion recombination of $SnOH^+$ with free electrons was made dominant by the addition of CH_4 and K, the measured recombination coefficient of $SnOH^+$ was $(0.116 \pm 0.065)T^{-(1.66\pm0.16)}$ cm^3 $molecule^{-1}$ s^{-1}; the temperature dependence is in good agreement with the $T^{-1.5}$ dependence predicted by simple theory. The rate constant for chemi-ionization could not be measured due to impurity ions from potassium and sodium, but the equilibrium constant for chemi-ionization/recombination was calculated to be 0.004 863 exp (–52 070/*T*). Assuming detailed balance and the experimental recombination coefficient, the relatively small rate constant for chemi-ionization was given by 3.27×10^{-10} exp (–48 630/*T*) cm^3 $molecule^{-1}$ s^{-1}. Finally, calculated values were obtained for the bond energy D°_0(HO—Sn^+) = 408 ± 21 kJ mol^{-1}, and the standard zero-point enthalpy of formation $\Delta_f H^\circ_0(SnOH^+)$ = 637 ± 21 kJ mol^{-1}.

Key words: flame ionization, chemi-ionization, proton affinity, mass spectrometry, tin.

Résumé : On a introduit de faibles quantités (fraction molaire $\leq 10^{-6}$) d'étain dans cinq flammes de H_2-O_2-N_2 riches en combustible, à des températures allant de 1820 à 2400 K et à la pression ambiante. On a observé les ions dans les flammes en procédant à un échantillonnage de la flamme le long de son axe à l'aide d'une canule de spectromètre de masse. L'espèce principale d'étain dans ces flammes est le SnO (>97%) accompagnée de Sn (<3%). Les ions principaux observés sont le $SnOH^+$ et le Sn^+. Faisant appel à des méthodes de mécanique statistique et utilisant des données publiées de calculs ab initio et de spectroscopie, on a calculé les fonctions thermodynamiques du $SnOH^+$, Sn^+, SnO et Sn. L'ion $SnOH^+$ se forme initialement par un transfert de proton de H_3O^+ à SnO, un ion naturel de la flamme avec lequel il est en équilibre. Il se forme aussi par chimi-ionisation du SnO réagissant avec H; le $SnOH^+$ s'équilibre rapidement avec le Sn^+. Des mesures de rapports ioniques $SnOH^+/H_3O^+$ permettent de déterminer l'affinité protonique PA°_{298}(SnO) = 911 ± 21 kJ mol^{-1} (218 ± 5 kcal mol^{-1}). On a obtenu un rapport ionique $SnOH^+$ à l'aide de la constante d'équilibre calculée. Lorsque l'addition de CH_4 et de K fait que la recombinaison électron-ion du $SnOH^+$ avec des électrons libres devient la réaction dominante, le coefficient de recombinaison mesuré du $SnOH^+$ est égal à (0,116 ± 0,065) $T^{(-1,66\pm0,16)}$ cm^3 $molécule^{-1}$ s^{-1}; la relation avec la température est en bon accord avec la dépendance $T^{-1,5}$ qui est prédite par la théorie simple. Il n'a pas été possible de mesurer la constante de vitesse de la réaction de chimi-ionisation à cause de la présence d'ions de potassium et de sodium à l'état d'impuretés; on a toutefois calculé que la constante d'équilibre chimi-ionisation/recombinaison est égale à 0,004 863 exp (–52 070/*T*). Si l'on fait l'hypothèse qu'il existe une balance détaillée et que l'on utilise le coefficient de recombinaison expérimental, on peut établir que la relativement faible constante de vitesse de la réaction de chimi-ionisation est donnée par l'équation $3,27 \times 10^{-10}$ exp (–48 630/*T*) *T* cm^3 $molécule^{-1}$ s^{-1}. Finalement, on a obtenu des valeurs calculées pour l'énergie de liaison, D°_0(HO—Sn^+) = 408 ± 21 kJ mol^{-1}, et l'enthalpie de formation au point zéro standard, $\Delta_f H^\circ_0(SnOH^+)$ = 637 ± 21 kJ mol^{-1}.

Mots clés : ionisation de flamme, chimi-ionisation, affinité protonique, spectrométrie de masse, étain.

[Traduit par la Rédaction]

Received April 2, 1998.

J.M. Goodings[1] and Q.F. Chen. Department of Chemistry, York University, 4700 Keele Street, Toronto, ON M3J 1P3, Canada.

[1]Author to whom correspondence may be addressed. Telephone: (416) 736–2100, ext. 33852. Fax: (416) 736–5936. E-mail: goodings@turing.sci.yorku.ca

 © 1998 NRC Canada

Table 1. Properties of the hydrogen–oxygen–nitrogen flames.

	Flame number				
Property	2	25	3	4	5
Equivalence ratio ϕ	1.5	1.5	1.5	1.5	1.5
$H_2/O_2/N_2$	2.74/1/2.95	3.0/1/3.5	3.18/1/4.07	3.09/1/4.74	3.12/1/5.77
Total unburnt gas flow ($cm^3\ s^{-1}$)	300	250	250	200	150
Measured flame temperature (K)	2400	2230	2080	1980	1820
Rise velocity in burnt gas ($m\ s^{-1}$)	19.8	18.6	15.6	11.4	8.4
Equilibrium burnt gas composition (mol fractions)					
H_2O	0.3460	0.3063	0.2754	0.2553	0.2249
H_2	0.1286	0.1527	0.1622	0.1390	0.1259
O_2	0.000 105 7	0.000 007 90	0.000 000 72	0.000 000 18	0.000 000 01
H	0.006 019	0.002 650	0.001 077	0.000 500 8	0.000 141 5
OH	0.003 084	0.000 795 1	0.000 213 0	0.000 088 90	0.000 017 54
O	0.000 094 69	0.000 009 35	0.000 000 99	0.000 000 23	0.000 000 01
N_2	0.5157	0.5375	0.5610	0.6052	0.6490
Percentage SnO/Sn (%)	97.1/2.9	96.9/3.1	97.0/3.0	97.6/2.4	98.1/1.9

1. Introduction

In a short note in 1969, Jensen (1) reported on the formation of tin ions when 10^{-3}–10^{-4} mol fraction of $Sn(CH_3)_4$, a rather high concentration, was introduced into a pair of H_2-O_2-N_2 flames at 2020 and 2475 K and atmospheric pressure. Using a microwave cavity resonator to measure the free electron concentration [e^-] and a mass spectrometer to sample the ions, he first showed that the $SnOH^+$ and Sn^+ ions observed were linked by a balanced (equilibrated) reaction. Further experiments indicated that the rather strongly endothermic chemi-ionization reaction of SnO with H to form $SnOH^+$ was not equilibrated in these flames. Aided by statistical thermodynamic calculations, values were obtained for the zero-point standard energy change $\Delta E_0^\circ (= \Delta H_0^\circ)$ for both reactions and the standard internal energy of formation $\Delta_f E_0^\circ(SnOH^+)$.

Very recently, Hopkinson and co-workers (2) carried out ab initio calculations of the group 14 monoxides for C, Si, Ge, and Sn to obtain their proton affinities. For tin, these were conducted at the B3LYP level of theory with wave functions optimised using density functional theory. In particular, two calculations designated A (B3LYP/DZVP) and B (B3YP/Sadlej) each provided a set of rotational and vibrational temperatures for $SnOH^+$ for statistical thermodynamic calculations. Combined with the thermodynamic data and tables for SnO from Pedley and Marshall (3) and the spectroscopic data for Sn and Sn^+ from Moore (4), this provided us with the impetus to re-examine the ionization of tin in flames.

The objectives of this study were to measure the proton affinity PA of SnO, the electron-ion recombination coefficient for $SnOH^+$ and the rate constant for chemi-ionization of SnO reacting with H using our flame-ion mass spectrometer to sample flames in the temperature range 1820–2400 K. Experimental values for PA°(SnO) by proton transfer with H_3O^+ and the recombination coefficient were obtained. For the very fast equilibrated reaction linking $SnOH^+$ and Sn^+, ion ratio measurements were falsified by cooling of the sample in the nozzle of the mass spectrometer but the equilibrium constant was calculated by statistical methods. Direct measurements of the relatively weak chemi-ionization reaction were compromised by the presence of K^+ and Na^+ impurity ions. However, values of the rate constant were obtained by calculating the equilibrium constant for chemi-ionization/recombination and multiplying it by the experimental recombination coefficient with the assumption of detailed balance.

2. Experimental

Five premixed, laminar, H_2-O_2-N_2 flames of fuel-rich composition (equivalence ratio $\phi = 1.5$) at atmospheric pressure were employed for this work spanning a temperature range 1820–2400 K. Their properties, including the calculated compositions of the equilibrium burnt gas based on the JANAF tables (5), are given in Table 1. These flames have been used extensively by Hayhurst and Kittelson who have measured their temperatures, rise velocities and free-radical compositions (6). The concentrations of free radicals overshoot their equilibrium values in the flame reaction zone and then decay downstream towards equilibrium in the burnt gas. The actual concentration is obtained using Sugden's disequilibrium parameter γ (7), defined as the ratio of the local concentration of a radical at a given position in the flame to its final equilibrium value given in Table 1; γ can achieve large values (>100) close to the reaction zone of the cooler flames before decaying downstream in the burnt gas towards unity. For fuel-rich flames where H_2O and H_2 are major product species, $\gamma_H = \gamma_{OH} \equiv \gamma$ and $\gamma_O = \gamma^2$. Plots of γ versus axial distance z are available (6) for the five fuel-rich flames listed in Table 1; thus, the radical concentrations are known at all points in the flames. These pseudo-one-dimensional (flat) flames were stabilized on a water-cooled brass burner previously described (8), consisting basically of a circular bundle of 151 stainless-steel hypodermic needle tubes. The fuel-rich flames in plug flow were cylindrical in shape with a diameter of about 12 mm.

Tin was introduced into the flames by spraying an aqueous solution of $SnCl_4 \cdot 5H_2O$ (Aldrich, 98+%) as an aerosol derived from an atomizer described previously (9) into the nitrogen supply of the premixed flame gas. This salt contained very small amounts of potassium and sodium as impurities. Spraying a 0.1 M solution introduced 9.5×10^{-7}

© 1998 NRC Canada

mol fraction of total tin into the unburnt flame gas. A small amount of a grey solid, presumably metallic tin, condensed onto the cooled sampling nozzle and mounting plate placed in front of the flame. The usual very pale blue colour of the flames developed a slightly stronger whitish luminosity with tin present. No evidence was observed for the formation of solid particles.

The five flames described in Table 1 exhibit only a low level of natural ionization. It was sometimes advantageous to add 0.25 mol% of CH_4 to the premixed flame gas to produce a high initial concentration of H_3O^+ ions stemming from the chemi-ionization of CH + O near the flame reaction zone; these ions subsequently decay downstream by electron-ion recombination. With the simultaneous addition of tin, H_3O^+ can produce tin ions by chemical ionization (CI) processes. The addition of CH_4 was small enough, however, so that the flame composition and temperature remained essentially unchanged. In other cases, it was occasionally desirable to add a small amount of KNO_3 to the tin solution sprayed by the atomizer to produce K^+ and free electrons e^- in the flame by collisional (thermal) ionization. By this means, the electron–ion recombination rate of the tin ions could be increased; there was no evidence for any direct reaction of K^+ with the tin ions. Thus, tin ionization could be enhanced early in the flame by methane and (or) suppressed later in the flame by potassium.

The burner is mounted horizontally on a motorized carriage with calibrated drive coupled to the *X*-axis of an *XY*-recorder. The flame axis *z* is accurately aligned with the sampling nozzle of the mass spectrometer. The apparatus has been described in detail previously (8) so only a brief description will be given here. Flame gas containing ions is sampled through an orifice in the tip of a conical nozzle protruding from a water-cooled sampling plate. The nozzles were fabricated by swaging a tiny electron microscope lens of Pt/Ir alloy into the tip of a 60° stainless-steel cone; orifice diameters of 0.17 and 0.20 mm were employed. Alternatively, a 60° electroformed nickel nozzle of diameter 0.20 mm exhibited less cooling of the sample in the boundary layer and was used when it was desired to minimize the formation of ion hydrates. The ions enter a first vacuum chamber maintained at 0.04 Pa (3×10^{-4} Torr), and are focused into a beam by an electrostatic lens. The beam then passes through a 3 mm orifice in the tip of a nose-cone into a second vacuum chamber pumped to a pressure below 0.003 Pa (2×10^{-5} Torr). The ions traverse a second ion lens into a quadrupole mass filter in which they have an axial ion energy of 15 eV. They are detected by a Faraday collector connected to a vibrating-reed electrometer having a grid-leak resistance of 10^{10} ohm; the ion signal is applied to the *Y*-axis of the *XY*-recorder. Thus, ion signal magnitudes quoted in the figures below as a voltage (in mV) refer to the collected ion current passing through 10^{10} ohm. By driving the flame towards the sampling nozzle, profiles may be obtained of an individual ion signal versus distance along the flame axis *z*. The zero on the *X*-axis distance scale ($z = 0$) is defined experimentally where the pressure abruptly rises when the sampling nozzle pokes through the flame reaction zone into the cooler unburnt gas upstream. The pressure is measured with an ionization gauge mounted on the second vacuum chamber.

As an alternative to individual ions, total positive ion (TPI) profiles can be measured by switching off the dc voltages to the quadrupole rods. Still with the dc voltages switched off and the spectrometer's mass dial set to a given mass number, all of the ions above that mass number are collected; e.g., TPI_{100} designates total positive ions above 100 u which includes just the tin ions whereas TPI_{12} includes all the ions (since no measureable flame ions occur below 12 u). This technique is useful in separating total tin ions from ions of low mass number such as H_3O^+, K^+, and Na^+ if present. However, the sensitivity of the mass spectrometer is different for individual ions and TPI because the former are measured at fairly high resolution whereas total ion collection amounts to zero resolution. The former sensitivity is approximately one half of the latter. Since a flame is a quasi-neutral plasma, $[TPI_{12}]$ is equal to $[e^-]$, the concentration of free electrons. It should be pointed out that no negative tin ions were detected in the FR flames.

A second method of measuring total ion signals was employed, which has a bearing on calibration procedures. With an appropriate voltage bias on the sampling plate, the total current of positive ions passing through the orifice was collected on the ion lens and nose-cone in the first vacuum chamber; it was measured with a sensitive picoammeter. This method is appealing when absolute ion concentrations must be measured because tuning errors and mass discrimination of individual ions are avoided. The total ion current was calibrated using the known rate for electron-ion recombination of H_3O^+ with e^-. With the atomizer turned off, 0.25 mol% of CH_4 was admitted. From the slope of a second-order recombination plot together with Butler and Hayhurst's rate coefficient $k = (3.6 \pm 0.5)\ T^{-2.1\pm0.7}$ cm^3 molecule^{-1} s^{-1} (10), a calibration factor was obtained for converting ion current (μA) into ion concentration (molecule cm^{-3}). The same procedure was employed with the mass spectrometer for calibrating ion signal (mV) in terms of ion concentration (molecule cm^{-3}). The calibration was routinely done for each flame when absolute ion densities were needed.

On occasion, it was noted that the ion signal slowly and steadily decreased over a period of several minutes. The worst cases occurred for the hot flames 2 and 25 when the burner was moved in close to the sampling nozzle; in these circumstances, the nozzle can become red hot. A possible explanation involves the formation of a thin layer of dielectric oxide which coats the orifice rim and subsequently acquires a positive charge which repels incoming positive ions as they approach the nozzle. Accordingly, the calibration procedure with CH_4 addition was carried out at the beginning and end of each set of tin experiments with each flame, and the results were accepted only if the calibration factor remained constant. Calibration procedures for the atomizer delivery of tin into the flame gas have been given previously (11, 12).

When the gas is sampled through the nozzle, it cools in two regions: in the thermal boundary layer surrounding the orifice and in the near-adiabatic expansion downstream of the nozzle throat. This can cause a shift of fast equilibrium reactions in the exothermic direction during sampling. In particular, ion hydrates can be enhanced with respect to the parent ion. These sampling problems have been discussed in

© 1998 NRC Canada

Table 2. Calculated parameters of the $SnOH^+$ ion (2).

Parameter	Calculation A (B3LYP/DZVP)	Calculation B (B3LYP/Sadlej)
Sn—O bond length (Å)	1.931	1.885
O—H bond length (Å)	0.973	0.969
Bond angle (degrees)	154.1	167.9
Rotational temperatures (K)	150.590 11	669.578 11
	0.409 83	0.426 47
	0.408 72	0.426 20
Vibrational temperatures (K)	339.01	120.53
	989.66	1039.94
	5427.05	5521.94

considerable detail (13–15). In general, if the relaxation time τ of an equilibrium reaction is greater than the sampling time of roughly 1 μs, it may be assumed that the reaction does not shift during sampling. In the present study, the problem arising from hydrates of the tin ions, such as $SnOH^+ \cdot H_2O$ and $Sn^+ \cdot H_2O$ which are probably not genuine flame ions, is obviated by measuring TPI_{100} such that hydrate contributions are included with the $SnOH^+$ and Sn^+ parent ion signals. At the other extreme, consider for example flame 3 in Table 1 with a rise velocity in the burnt gas of 15.6 m s^{-1}. Appreciable air entrainment is minimal for approximately the first 2.5 flame diameters downstream of the reaction zone; i.e., 30 mm, equivalent to a time of 1.9 ms. For a reaction to reach equilibrium within the time-scale of the flame, clearly τ must be small compared with 1.9 ms.

3. Statistical thermodynamic calculations

For some of the reactions involving tin, some of their properties could not be measured experimentally. Tables of thermodynamic data for many of the ancilliary species involved are listed in the JANAF tables over a wide temperature range (5); for SnO, the free-energy function $-(G_T^\circ - H_{298}^\circ)/T$ and enthalpy function $(H_T^\circ - H_{298}^\circ)$ are tabulated by Pedley and Marshall (3) up to 4000 K. Such data are not available for Sn, Sn^+, and $SnOH^+$, and it was necessary to calculate third-law absolute entropies S_T°, free energy, and enthalpy functions for some of these species by standard statistical methods. A good summary of the relevant formulae is given in the introduction to the JANAF tables (5). For the Sn neutral atom, Moore (4) lists three low-lying electronic states below 10 000 cm^{-1} with corresponding electronic temperatures θ_e (and degeneracies, g values) of 2002.5 K ($g_1 = 3$), 4931.7 K ($g_2 = 5$), and 12 392.3 K ($g_3 = 5$); for the ground state, $g_0 = 1$. For Sn^+ (4), $g_0 = 2$, and there is one low-lying state with $\theta_e = 6116.9$ K ($g_1 = 4$).

The calculation of thermodynamic functions for $SnOH^+$ was made possible by the ab initio calculations of Rodriquez et al. (2). Two of the calculations designated here as A (B3LYP/DZVP) and B (B3YP/Sadlej) each provided a set of rotational and vibrational temperatures, and also structural parameters given in Table 2. Both calculations depict $SnOH^+$ as a bent asymmetric-top molecule with one low vibrational temperature and two very low, nearly equal, rotational temperatures; conceivably, an even higher level calculation might indicate that $SnOH^+$ is linear.[2] The ground electronic state is nondegenerate, and there is no evidence of a low-lying excited state. For calculations A and B, the sum of the rotational and vibrational contributions to the thermodynamic functions had very similar magnitudes. Since there was no reason to prefer one calculation over the other, the results of the two calculations were simply averaged. Largely for reasons of conformity with the JANAF tables (5), a standard state for pressure of 0.1 MPa rather than 1 atm, designated by ° on thermodynamic quantities, was employed for the statistical calculations. Any differences, which only arise for functions involving the entropy, are small and well within the error limits.

4. Composition of neutral tin species in flames

Available spectroscopic evidence indicates that tin is present in flames only as Sn and SnO; the total concentration of tin ions is negligible in comparison. The percentage of each neutral species was found by calculating the equilibrium constant K_1 for the reaction

[1] $\quad Sn + H_2O = SnO + H_2$

The free energy function $-(G_T^\circ - H_{298}^\circ)/T$ over a wide temperature range is available for H_2O and H_2 from the JANAF tables (5) and for SnO from the tables of Pedley and Marshall (3). At any temperature T, K_1 is obtained from $\Delta G_T^\circ[1] = -RT \ln K_1$ with $\Delta G_T^\circ = \Delta H_{298}^\circ - T\Delta\{-(G_T^\circ - H_{298}^\circ)/T\}$ for reaction [1]; $\Delta H_{298}^\circ[1] = -D_{298}^\circ(SnO) + D_{298}^\circ(OH) + D_{298}^\circ(H\text{-}OH) - D_{298}^\circ(H_2) = -42.2$ kJ mol^{-1} (16) based on $D_0^\circ(SnO) = 528 \pm 13$ kJ mol^{-1} (3). A plot of $\ln K_1$ versus $1/T$ gives a very good straight line over the whole temperature range 298.15–2500 K, yielding $K_1 = 1.665 \exp(5140/T)$ from a least-squares fit; specifically over the temperature range 1820–2400 K of the five flames, $K_1 = 1.015 \exp(6064/T)$. The percentage SnO/Sn ratio for the five flames is given in Table 1; in all cases, SnO > 96.9% of the total tin present and SnOH is negligible.

5. Results and discussion

The tin atom has 10 stable isotopes (16) with mass numbers u and natural abundances (%) of 112 (0.97), 114 (0.65), 115 (0.36), 116 (14.53), 117 (7.68), 118 (24.22), 119 (8.58),120 (32.59), 122 (4.63), and 124 (5.79). With the atomizer spraying a 0.1 M aqueous solution of $SnCl_4 \cdot 5H_2O$ into flame 3, a mass spectrum measured at high resolution showing all of the tin ions present downstream at $z = 30$ mm is given in Fig. 1. With increasing mass number, these include H_3O^+, Na^+, a hydrate contribution from $H_5O_2^+$, $^{39}K^+$, $^{41}K^+$, and three groups of isotopic tin peaks above 100 u involving Sn^+, $SnOH^+$ (including a small contribution from $Sn^+ \cdot H_2O$), and $SnOH^+ \cdot H_2O$; sodium and potassium are present in the tin salt as impurities.

It is probably helpful to list all of the ionic reactions relevant to this paper in one place. These include

[2] $\quad H + H + OH \Leftrightarrow H_3O^+ + e^-$

[2] A.C. Hopkinson. Personal communication.

© 1998 NRC Canada

Fig. 1. Mass spectrum at high resolution measured at z = 30 mm downstream in flame 3 with the atomizer spraying a 0.1 M solution of $SnCl_4 \cdot 5H_2O$.

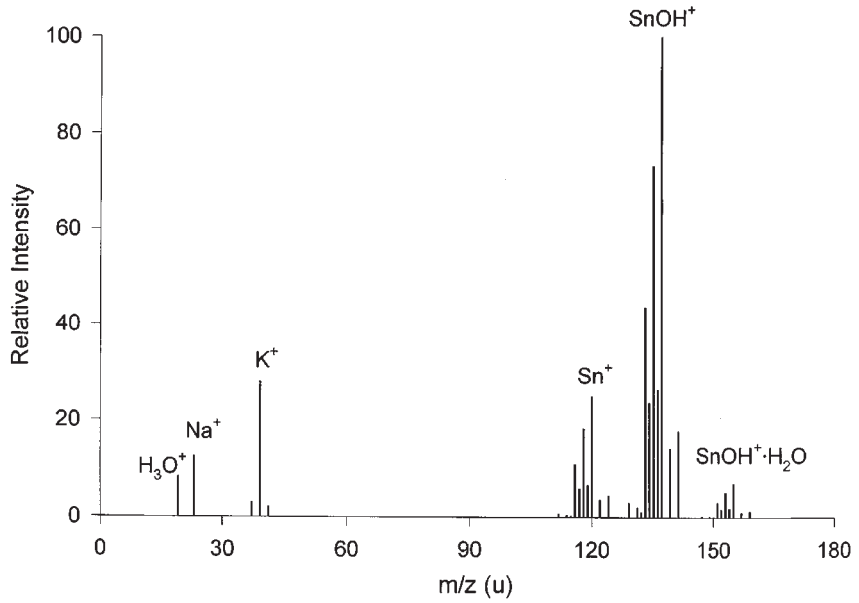

Fig. 2. Ion profiles measured at low resolution in flame 3 with the atomizer spraying a 0.1 M solution of $SnCl_4 \cdot 5H_2O$, where TPI_{12} denotes total positive ions, and TPI_{100} is total ions of tin. The flame reaction zone is located near z = 0.

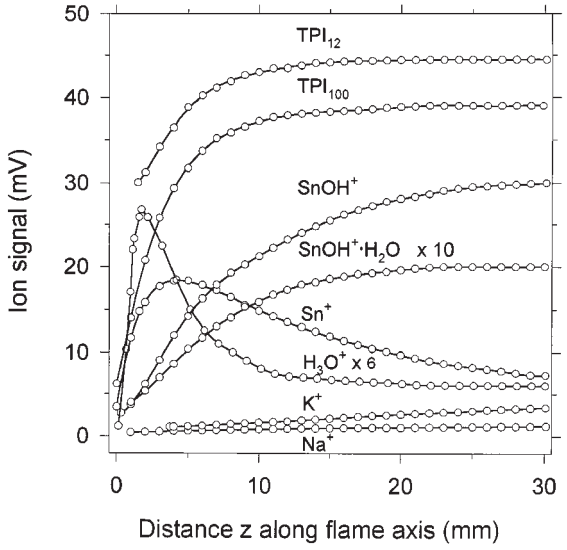

[3] $H_3O^+ + SnO = SnOH^+ + H_2O$

[4] $SnO + H \Leftrightarrow SnOH^+ + e^-$

[5] $SnOH^+ + H = Sn^+ + H_2O$

[6] $Sn^+ + e^- + M \rightarrow Sn + M$

[7] $K + M \rightarrow K^+ + e^- + M$

[8] $Na + M \rightarrow Na^+ + e^- + M$

[9] $H_3O^+ + K \Leftrightarrow K^+ + H_2O + H$

[10] $H_3O^+ + Na \Leftrightarrow Na^+ + H_2O + H$

where M is a third body. Here, the = sign refers to a fast balanced reaction at equilibrium whereas $\Leftrightarrow$ refers to a reaction proceeding in both directions which is not necessarily balanced. From this list, it is clear how the ions observed in the mass spectrum arise. The ion hydrates are not included, since they are assumed to form during sampling and are not genuine flame ions.

5.1 The $SnOH^+/H_3O^+$ equilibrium

In H_2-O_2-N_2 flames, the degree of natural ionization is measureable but small, produced by the chemi-ionization reaction [2] with a rate coefficient $k_2 = (3.3 \pm 1.6) \times 10^{-36}$ exp $(-13\,800/T)$ cm^6 molecule^{-2} s^{-1} (17) and a reverse recombination coefficient already given as $k_{-2} = (3.6 \pm 0.5)T^{-2.1\pm0.7}$ cm^3 molecule^{-1} s^{-1} (10). With the atomizer spraying distilled water (or turned off — the same signal is measured) in each of the five flames, an H_3O^+ profile is obtained (not shown; see (6)) which rises rapidly near the flame reaction zone to a constant plateau value that persists downstream; the magnitude increases with increasing flame temperature. The rapid rise reflects the γ^3-dependence of the three radical concentrations in reaction [2]. When tin is added to a flame, $SnOH^+$ is produced from H_3O^+ by the chemical ionization (CI) reaction [3] involving fast proton transfer, supplemented by the chemi-ionization reaction [4]. Atomic Sn^+ ions are also formed immediately by the fast balanced reaction [5].

Figure 2 presents profiles for the individual ions in flame 3 measured at low resolution with the atomizer spraying a 0.1 M solution of $SnCl_4 \cdot 5H_2O$. For a given tin ion, low resolution effectively blended all the tin isotopes into a single peak and yielded higher sensitivity. The total positive ions TPI_{12} and the total tin ions TPI_{100} are also shown; the difference of these two profiles is the sum of the H_3O^+, Na^+, $H_5O_2^+$, and K^+ profiles. The important point at issue is that, downstream near z = 30 mm, the $SnOH^+$ (+ hydrate) and H_3O^+ profiles are constant, indicative of equilibrium for the fast proton transfer reaction [3] between SnO and H_2O. Even

© 1998 NRC Canada

Fig. 3. Ion profiles measured at high resolution in flame 2 with the atomizer spraying a 0.01 M solution of $SnCl_4 \cdot 5H_2O$. The flame reaction zone is located near $z = 0$.

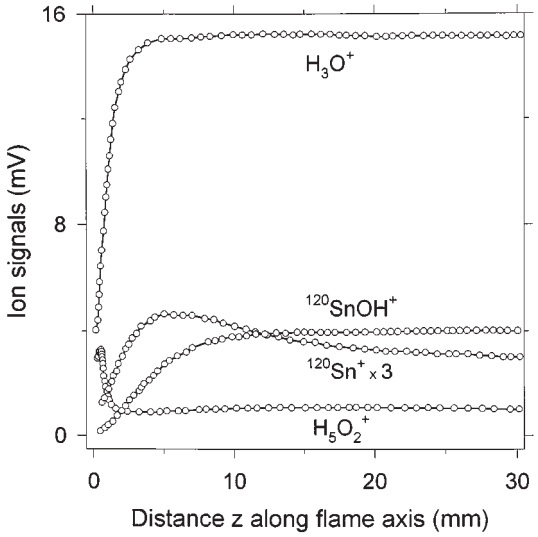

though the reaction is strongly exoergic, the large concentration ratio $[H_2O]/[SnO] \approx 3 \times 10^5$ can still bring the H_3O^+ and $SnOH^+$ ions into equilibrium in flames. Furthermore, the relaxation time $\tau_3 = 1/(k_3[SnO] + k_{-3}[H_2O])$ is of the order of 100 μs, appreciably greater than the sampling time of roughly 1 μs, such that the equilibrium reaction [3] does not shift during sampling. For this estimate, a typical value of k_3 for a proton transfer reaction of the order of 10^{-9} cm^3 $molecule^{-1}$ s^{-1} was assumed (k_3 would be somewhat higher at flame temperature than room temperature). A value for k_{-3} for the reverse reaction was estimated to be that for k_3 reduced by an exponential factor corresponding to the approximate endothermicity of the back reaction.

The objective of this aspect of the study was to measure the ion ratio $[SnOH^+]/[H_3O^+]$ to get the equilibrium constant K_3 giving $\Delta H°[3]$ from the slope of a van't Hoff plot of ln K_3 versus $1/T$ where $\Delta H°[3] = PA°(H_2O) - PA°(SnO)$, the difference of the proton affinities. There is another important feature of this method involving the measurement of K_3 in five flames spanning nearly 600 K. Suppose the two ion signals are subject to mass discrimination leading to an incorrect value of $K_3' = f \times K_3$ where f is a constant factor which is independent of temperature. The slope of the van't Hoff plot will still yield the correct value of $\Delta H°[3]$ although the intercept will be $(\Delta S°[3]/R + \ln f)$. It will be shown in the next section that reaction [5] producing Sn^+ shifts to the right during sampling such that measured values of $[SnOH^+]$ are slightly small by a nearly constant factor f which is only very weakly dependent on temperature. This is similar to the case of mass discrimination, and good values of $\Delta H°[3]$ are still obtained.

By way of contrast, the profiles in Fig. 3 were measured at high resolution in the hot flame 2 with the atomizer spraying a 0.01 M solution of $SnCl_4 \cdot 5H_2O$. Again, the $SnOH^+$ and H_3O^+ profiles are constant downstream, indicative of equilibrium. In this case, only the single biggest isotopic peak

Fig. 4. Van't Hoff plot for the equilibrium constant of the proton transfer reaction [3] involving H_3O^+ and $SnOH^+$ measured in five flames over the temperature range 1820–2400 K with the atomizer spraying aqueous solutions of $SnCl_4 \cdot 5H_2O$ of concentrations 0.1 M (open circles) and 0.01 M (closed circles).

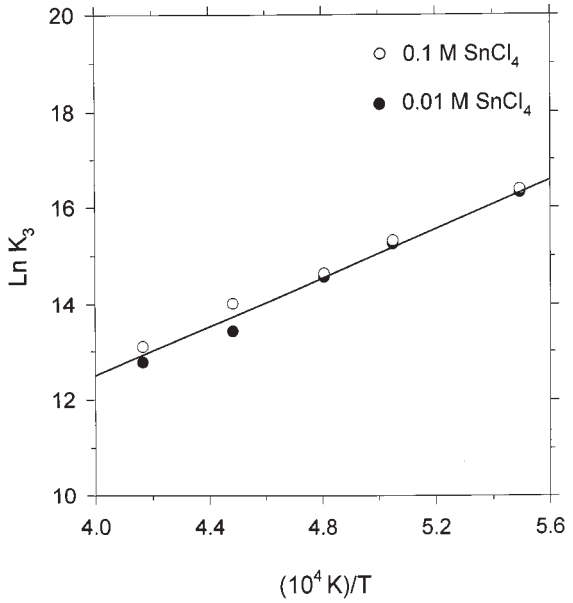

$^{120}SnOH^+$ was measured, and $[H_3O^+] > [^{120}SnOH^+]$ at the lower tin concentration. For plotting purposes, the ^{120}Sn isotopic signals were multiplied by 100/32.59 to give 100% Sn signals. Figure 4 presents a van't Hoff plot of ln K_3 versus $1/T$ for the two runs with the 0.1 and 0.01 M solutions sprayed into five flames. From the slope of the straight line fitted by least squares, $\Delta H°_{2100}[3] = -218.0 \pm 10.5$ (standard deviation) kJ mol^{-1} over the flame temperature range 1820–2400 K centred on the average temperature of 2100 K.

To obtain $PA°_{298}(SnO) = PA°_{298}(H_2O) - \Delta H°_{298}[3]$, the reaction enthalpy at 298.15 K is required, derived from $\Delta H°_{298} = \Delta H°_{2100} - \Delta (H°_{2100} - H°_{298})$ where the standard enthalpy function $(H°_{2100} - H°_{298})$ is available for H_3O^+, H_2O (5), and SnO (3) but not for $SnOH^+$. Accordingly, it was calculated by statistical methods at the average flame temperature of 2100 K. For reaction [3], the temperature correction is small; $\Delta(H°_{2100} - H°_{298}) = 1.82$ kJ mol^{-1} giving $\Delta H°_{298}[3] = -219.8 \pm 10.5$ kJ mol^{-1}. Based on the current value of $PA°_{298}(H_2O) = 691.0$ kJ mol^{-1},[3] the proton affinity of SnO has a value $PA°_{298}(SnO) = 911 \pm 21$ kJ $mol^{-1} = 218 \pm 5$ kcal mol^{-1}, in excellent agreement with the calculated value of 215.6 kcal mol^{-1} obtained by Rodriquez et al. (2).

5.2 The $SnOH^+/Sn^+$ equilibrium

The equilibration of $SnOH^+$ and Sn^+ by reaction [5] is rapid in flames. If $k_5 = 10^{-9}$ cm^3 $molecule^{-1}$ s^{-1} is assumed with k_{-5} reduced by a factor corresponding to the endothermicity of the back reaction (approximately 100 kJ mol^{-1}), the relaxation time $\tau_5 \approx 0.1$ μs. This means that the reaction will shift to the right in the exothermic direction during sampling, and measured $[SnOH^+]/[Sn^+]$ ratios will be too small.

[3] E.P. Hunter and S.G. Lias. NIST Standard Database Number 69. March 1998 release. http://webbook.nist.gov/chemistry/form-ser.html/

© 1998 NRC Canada

Fig. 5. Ion profiles measured in flame 3 with 0.25 mol% of added CH_4 and the atomizer spraying a mixed solution of 0.098 M $SnCl_4 \cdot 5H_2O$ and 0.001 M KNO_3 such that electron–ion recombination of $SnOH^+$ is the dominant process downstream; TPI_{12} denotes total positive ions and TPI_{100} is total ions of tin. The flame reaction zone is located near $z = 0$.

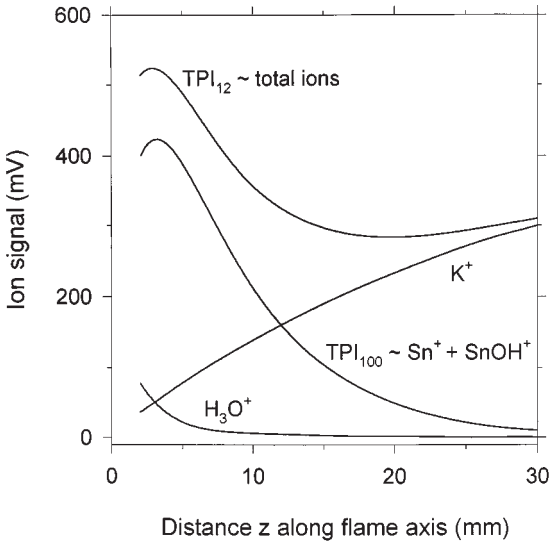

Since absolute $SnOH^+$ concentrations were needed for the recombination studies described below, it was necessary to calculate the equilibrium constant K_5 as a function of temperature. In this way, total tin ion signals [TPI_{100}] could be measured and true [$SnOH^+$] determined using K_5.

The free energy function $-(G_T^\circ - H_{298}^\circ)/T$ was calculated by statistical methods for $SnOH^+$ and Sn^+ at many temperatures up to 2500 K and combined with corresponding values from the JANAF tables (5) for H and H_2O to obtain $\Delta G_T^\circ - \Delta H_{298}^\circ$ for reaction [5]. Using all values at 298.15 K (16) and our value of $PA_{298}^\circ(SnO) = 910.8$ kJ mol^{-1}, ΔH_{298}°[5] = PA°(SnO) – IE°(H) + D°(SnO) + IE°(Sn) – D°(OH) – D°(H-OH) = –86.3 kJ mol^{-1}, giving ΔG_T° and thus K_5. A plot of ln K_5 versus $1/T$ gives a very good straight line over the range of flame temperatures 1820–2400 K with a least-squares fit represented by $K_5 = 0.077\,38 \exp(11\,450/T)$. In fact, a good straight line is obtained over the whole temperature range of 298–2500 K fitted by $K_5 = 0.1115 \exp(10\,890/T)$. The entropy change of reaction [5] was calculated to be $\Delta S_{2100}^\circ = -21.2$ and $\Delta S_{298}^\circ = -6.4$ J mol^{-1} K^{-1}. The reaction enthalpy has a value $\Delta H_{2100}^\circ = -94.8$ kJ mol^{-1} at the average flame temperature with $\Delta H_0^\circ = -84.3 \pm 20.9$ kJ mol^{-1} ($= \Delta E_0^\circ$), in reasonable agreement with the value arrived at by Jensen (1). He quotes a value ΔE_0°[5] = –100 ± 20 kJ mol^{-1} based on mass-spectrometric measurements of the [$SnOH^+$]/[Sn^+] ratio at two flame temperatures and a rough statistical calculation with vibrational temperatures estimated from those of the alkaline earth metals. His ion ratio measurements may not have been shifted appreciably by sampling cooling because, to the best of our knowledge, he was employing low-pressure flames (P = 1–10 Torr) in his mass spectrometer (18); since the relaxation time $\tau \propto 1/P$, its magnitude in his experiment may have exceeded the sampling time of approximately 1 μs.

5.3 Recombination of $SnOH^+$ with electrons

These hydrogen flames contain a small amount of H_3O^+ natural ionization formed by the chemi-ionization reaction [2], and $SnOH^+$ is formed by chemical ionization (CI) of SnO by H_3O^+ via the proton transfer reaction [3]. A further possible source of $SnOH^+$ is the chemi-ionization reaction [4]. To study the recombination reaction [–4], the objectives were to form a relatively high concentration of $SnOH^+$ rapidly near the flame reaction zone and then to assure that recombination was dominant downstream in the burnt gas. These conditions were achieved, first by adding 0.25 mol% of CH_4 to produce a superequilibrium level of H_3O^+ for CI by reaction [3]. Then, a small amount of potassium as KNO_3 was added to the atomizer solution to raise the concentration of free electrons in the flame, thereby enhancing the rate of recombination of $SnOH^+$ by reaction [–4]. Potassium atoms are chemically ionized initially by H_3O^+ to some extent by reaction [9] (19) but progressively ionize further downstream by collisional (thermal) ionization via reaction [7] (20). There is no evidence that potassium interacts with tin by any process other than its effect on recombination through [e^-]. It was necessary to adjust the relative concentrations of both $SnCl_4 \cdot 5H_2O$ and KNO_3 in the atomizer solution rather carefully so that (*i*) H_3O^+ disappears quite rapidly downstream to maximize the region in which $SnOH^+$ recombination is dominant, and (*ii*) [$SnOH^+$] falls to a value near zero at z = 30 mm downstream indicating that $SnOH^+$ ion production by the chemi-ionization reaction [4] was negligible.

Figure 5 presents profiles for flame 3 with added CH_4 and with the atomizer spraying a mixed aqueous solution of 0.098 M $SnCl_4 \cdot 5H_2O$ and 0.001 M KNO_3. At these concentrations, the profiles fulfil the conditions outlined in (*i*) and (*ii*) above. The TPI_{100} signal includes $SnOH^+$, Sn^+, and any hydrates formed during sampling. Since negative ions were not detected in these flames, the TPI_{12} profile which measures the sum of all positive ions gives [e^-] because a flame is a quasi-neutral plasma. From reaction [–4], $-d[SnOH^+]/dt = k_{-4}[SnOH^+][e^-]$ – (ion production term) with $v = dz/dt = 15.6$ m s^{-1} from Table 1. Differentiation of [TPI_{100}] gives the kinetic expression $-d[TPI_{100}]/dt = -d[SnOH^+]/dt - d[Sn^+]/dt = k_{-4}[SnOH^+][e^-] + k_6[Sn^+][e^-] - k_4[SnO][H]_{eq}\gamma$ in which the equilibrated reaction [5] does not appear. The assumptions are made that three-body recombination of atomic Sn^+ in reaction [6] is negligible compared with reaction [–4], and that the production term from reaction [4] can be ignored because of the experimental conditions set up; also, reaction [3] does not contribute downstream where [H_3O^+] ≈ 0. Since [$SnOH^+$] = $[TPI_{100}]/(1 + K_5[H]_{eq}\gamma/[H_2O])$, the kinetic expression reduces to $-v(d[TPI_{100}]/dz)(1 + K_5[H]_{eq}\gamma/[H_2O]) = k_{-4}[TPI_{100}][TPI_{12}]$. Note that the factor $(1 + K_5[H]_{eq}\gamma/[H_2O])$, which has been multiplied across to the left-hand side, is equivalent to $(1 + [Sn^+]/[SnOH^+])$; the ion ratio is small compared with unity, varying from 0.13 in flame 2 to 0.06 in flame 5.

For the final kinetic expression, Fig. 6 presents a plot for flame 3 of the left-hand side versus $[TPI_{100}][TPI_{12}]$ in the range z = 15–30 mm where [H_3O^+] ≈ 0. The slope of the plot gives the recombination coefficient $k_{-4} = 3.6 \times 10^{-7}$ cm^3 molecule^{-1} s^{-1} in this particular case. The small negative in-

© 1998 NRC Canada

Fig. 6. Plot involving the kinetic expression for $SnOH^+$ ion loss by electron–ion recombination by reaction [–4] for the range z = 15–30 mm downstream in flame 3 using the ion profiles presented in Fig. 5, where the slope yields the recombination coefficient k_{-4}.

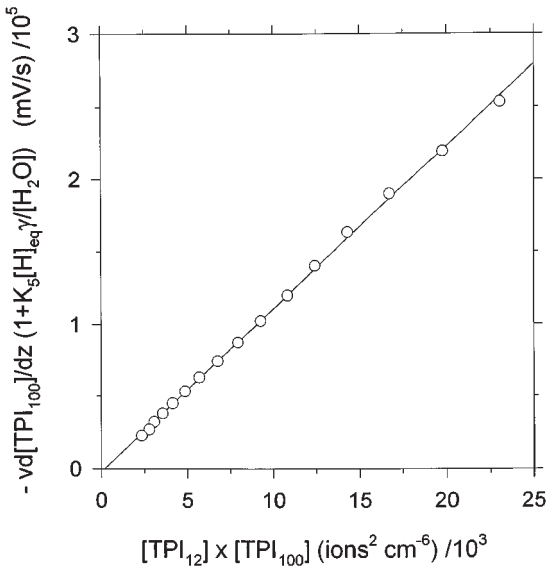

Fig. 7. Logarithmic plot of the recombination coefficient k_{-4} versus temperature T in the range 1820–2400 K. The best-fit solid line exhibits a $T^{-1.7}$ dependence, for comparison with the broken line giving the $T^{-1.5}$ dependence expected from simple theory.

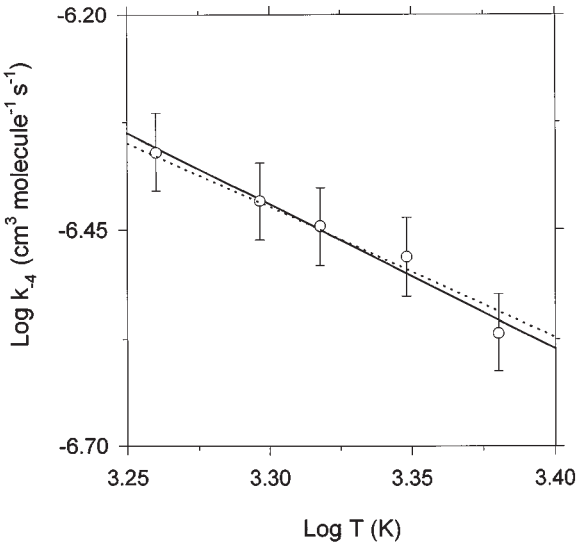

tercept shows that ion production is small and can safely be ignored. Similar profiles were measured and plots made to evaluate k_{-4} in all five flames. The results over the temperature range 1820–2400 K are given in Fig. 7 as a plot of log k_{-4} versus log T. A straight line fitted by least squares gives the temperature variation as $k_{-4} = (0.116 \pm 0.065)T^{-(1.66\pm0.16)}$ cm^3 molecule^{-1} s^{-1}. A discussion of the temperature dependence of electron-ion recombination coefficients in flames has been given by Butler and Hayhurst (10). Simple theory indicates a $T^{-1.5}$ dependence with which our value is in good agreement.

5.4 Chemi-ionization of SnO + H

Repeated attempts were made to measure the rate constant of the chemi-ionization reaction [4] directly but were frustrated by the presence of tiny amounts of potassium and sodium in the salt sample of $SnCl_4 \cdot 5H_2O$. These impurities give rise to the K^+ and Na^+ peaks visible in the mass spectrum shown in Fig. 1 which arise initially upstream by the electron transfer reactions [9] and [10] (19), and further downstream by the collisional (thermal) ionization reactions [7] and [8] (20). The initial rise of the $SnOH^+$ profile in Fig. 2 stems from proton transfer by reaction [3]. This means that the growth of the $SnOH^+$ profile in the upstream region cannot be analysed for k_4. Figure 2 also shows how the K^+ and Na^+ signals grow downstream by thermal ionization to increase [e^-]. Furthermore, k_4 cannot be readily evaluated from the constant $SnOH^+$ profile downstream near z = 30 mm because reaction [4] is not at equilibrium. The relaxation time is given by $\tau_4 = \{\ln(2e-1)\}/2(k_4 k_{-4}[SnO][[H])^{1/2}$ which has a value of the order of 10 ms for a 0.1 M solution of $SnCl_4 \cdot 5H_2O$ sprayed by the atomizer and $k_4 \approx 10^{-20}$ cm^3 molecule^{-1} s^{-1} at 2100 K (derived below); equilibrium cannot be achieved in the time of approximately 2 ms corresponding to 30 mm of flame. The same conclusion was reached by Jensen (1). A final consideration is that the rate of collisional (thermal) ionization $R_7 \approx 10^8$ ions cm^{-3} s^{-1} even for a tiny (unknown) potassium impurity concentration of 10^{-7} M in the atomizer solution (20); the rate R_4 for the chemi-ionization of tin is very comparable, and certainly not dominant. Although the experiments were not successful, these considerations seemed worthy of discussion because they indicate the complete ionization picture and may apply to other metals with small rate coefficients for chemi-ionization.

Accordingly, the equilibrium constant K_4 for reaction [4] was obtained by statistical methods, again involving the free energy function $-(G_T^\circ - H_{298}^\circ)/T$ calculated for $SnOH^+$ and available for SnO (3), H and e^- (5). At any temperature T, this gives $\Delta\{-(G_T^\circ - H_{298}^\circ)/T\} = R \ln K_4 + \Delta H_{298}^\circ/T$ with $\Delta H_{298}^\circ[4] = -PA_{298}^\circ(SnO) + IE_{298}^\circ(H) = 407.4$ kJ mol^{-1}. Over the temperature range 1820–2400 K of the five flames, a plot of ln K_4 versus $1/T$ gave a very good straight line from which $K_4 = 0.004\,868 \exp(-52\,070/T)$. Over the whole temperature range 298.15–2500 K, a similar plot gave a good straight line yielding $K_4 = 0.001\,324 \exp(-49\,710/T)$.

For reaction [4], other channels in both the forward and reverse directions are unlikely, and the assumption of detailed balance is reasonable. Using K_4 in the range of flame temperatures, the rate constant for chemi-ionization is obtained from $k_4 = k_{-4}K_4$. When combined with the experimental values of k_{-4} in the five flames, values of k_4 are obtained ranging from 5.03×10^{-19} in flame 2 at 2400 K to 8.07×10^{-22} cm^3 molecule^{-1} s^{-1} in flame 5 at 1820 K. A plot of ln k_4 versus $1/T$ is shown in Fig. 8. A good straight line fitted by least squares through the data points gives $k_4 = 3.27 \times 10^{-10} \exp(-48\,630/T)$ cm^3 molecule^{-1} s^{-1} for the temperature range 1820–2400 K. Even at flame temperatures, the values of the rate constant are small but should have been measureable experimentally were it not for the presence of potassium and sodium as impurities.

© 1998 NRC Canada

Fig. 8. Semi-logarithmic plot giving the temperature variation of the rate constant as ln k_4 versus $1/T$ for the chemi-ionization reaction [4] in the range 1820–2400 K.

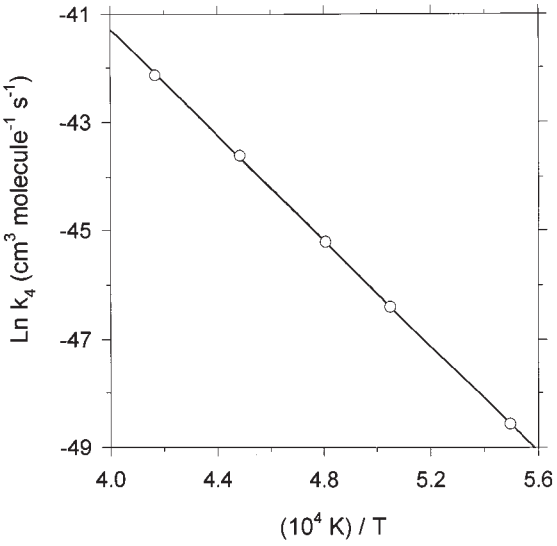

5.5 Bond energy D_0°(HO-Sn$^+$) and $\Delta_f H_0^\circ$(SnOH$^+$)

The standard Sn—O bond dissociation energy for the $SnOH^+$ ion can be found from the calculated change in the enthalpy function for the dissociation reaction

[11] $SnOH^+ \rightarrow Sn^+ + OH$

with reference to reaction [5]; i.e., $\Delta\{H_{298}^\circ - H_0^\circ\}[11] = 3.49$ kJ mol^{-1} = $\Delta H_{298}^\circ[11] - \Delta H_0^\circ[11] = \Delta H_{298}^\circ[5] + D_{298}^\circ$(H—OH) – D_0°(HO—Sn$^+$). This gives a value for the bond energy D_0°(HO—Sn$^+$) = 408 ± 21 kJ mol^{-1} (98 ± 5 kcal mol^{-1}). Finally, the standard zero-point enthalpy of formation $\Delta_f H_0^\circ(SnOH^+)$ can be obtained from $\Delta H_0^\circ[5] = -84.3$ kJ mol^{-1} with $\Delta_f H_0^\circ(Sn^+) = 1010.6$ (21), $\Delta_f H_0^\circ(H_2O) = -238.9$ and $\Delta_f H_0^\circ(H) = 216.0$ kJ mol^{-1} (5). The value is $\Delta_f H_0^\circ(SnOH^+)$ = 640 ± 21 kJ mol^{-1} (153 ± 5 kcal mol^{-1}); at room temperature, $\Delta_f H_{298}^\circ(SnOH^+)$ = 637 ± 21 kJ mol^{-1}. It is in good agreement with Jensen's value stated as the equivalent function $\Delta_f E_0^\circ(SnOH^+)$ = 655 ± 27 kJ mol^{-1} estimated nearly 30 years ago from a crude statistical model.

6. Summary and conclusions

The ionization of tin was investigated in H_2-O_2-N_2 flames in the range 1820–2400 K by mass-spectrometric sampling. The study was greatly aided by data for rotational and vibrational temperatures of the $SnOH^+$ ion from ab initio calculations (2) so that thermodynamic functions could be calculated by statistical mechanics. If total tin is present only as SnO and Sn, SnO > 97% in these fuel-rich flames. The flame conditions are such that $SnOH^+$ can be measured in equilibrium with H_3O^+, leading to the proton affinity PA°(SnO) relative to that of H_2O. The rapid equilibration of $SnOH^+$ with Sn^+ cannot be measured because it is shifted to a lower unknown temperature during sampling, but its equilibrium constant could be determined by a statistical thermodynamic calculation. This provided correct values of the $SnOH^+$ concentration for the experimental measurement of the electron-ion recombination coefficient of $SnOH^+$ as a function of temperature. Its $T^{-1.7}$ temperature dependence is close to the $T^{-1.5}$ dependence predicted by simple theory. The recombination reaction is the backward direction of the chemi-ionization reaction of SnO + H. Its relatively small rate coefficient could not be measured experimentally due to the ionization of potassium and sodium present as impurities in the tin salt. However, the equilibrium constant for chemi-ionization/recombination could be calculated by statistical methods. Assuming detailed balance, the rate coefficient for chemi-ionization as a function of temperature was obtained as the product of the experimental recombination coefficient and calculated equilibrium constant. Finally, the bond strength D_0°(HO—Sn$^+$) could be calculated, and also the standard zero-point enthalpy of formation $\Delta_f H_0^\circ(SnOH^+)$. This study combines experiment with theoretical calculations to give a fairly complete analysis of tin ionization.

Acknowledgement

The authors wish to thank Prof. Alan C. Hopkinson and members of his group for helpful discussions, and for making available to us the details of their ab initio calculations of the $SnOH^+$ ion. Support of this work by the Natural Sciences and Engineering Research Council of Canada is gratefully acknowledged.

References

1. D.E. Jensen. J. Chem. Phys. **51**, 4674 (1969).
2. C.F. Rodriquez, A. Cunje, and A.C. Hopkinson. J. Mol. Struct. (Theochem), **430**, 149 (1998).
3. J.B. Pedley and E.M. Marshall. J. Phys. Chem. Ref. Data, **12**, 967 (1983).
4. C.E. Moore. Natl. Stand. Ref. Data Ser. Natl. Bur. Stand. (U.S.) (NSRDS–NBS) 35. Vol. 3. Superintendent of Documents, U.S. Government Printing Office, Washington, D.C. Reissued 1971 (from NBS Circ. 467, 1958).
5. M.W. Chase, Jr., C.A. Davies, J.R. Downey, Jr., D.J. Frurip, R.A. McDonald, and A.N. Syverud. JANAF thermochemical tables. 3rd ed. J. Phys. Chem. Ref. Data, **14** (Suppl. 1) (1985).
6. C.J. Butler and A.N. Hayhurst. J. Chem. Soc. Faraday Trans. **93**, 1497 (1997).
7. A.N. Hayhurst and D.B. Kittelson. Proc. R. Soc. London A, **338**, 155 (1974).
8. J.M. Goodings, C.S. Hassanali, P.M. Patterson, and C. Chow. Int. J. Mass Spectrom. Ion Processes, **132**, 83 (1994).
9. J.M. Goodings, S.M. Graham, and W.J. Megaw. J. Aerosol Sci. **14**, 679 (1983).
10. C.J. Butler and A.N. Hayhurst. J. Chem. Soc. Faraday Trans. **92**, 707 (1996).
11. J.M. Goodings and P.M. Patterson. Int. J. Mass Spectrom. Ion Processes, **151**, 17 (1995).
12. S.D.T. Axford and A.N. Hayhurst. Int. J. Mass Spectrom. Ion Processes, **110**, 31 (1991).
13. A.N. Hayhurst, D.B. Kittelson, and N.R. Telford. Combust. Flame, **28**, 123 (1977).
14. A.N. Hayhurst and D.B. Kittelson. Combust. Flame, **28**, 137 (1977).
15. N.A. Burdett and A.N. Hayhurst. Combust. Flame, **34**, 119 (1979).
16. D.R. Lide (*Editor*). CRC handbook of chemistry and physics. 73rd ed. CRC Press, Boca Raton, Fla. 1992.
17. S.D.T. Axford and A.N. Hayhurst. J. Chem. Soc. Faraday Trans. **91**, 827 (1995).

© 1998 NRC Canada

18. H.F. Calcote. *In* Ion-molecule reactions. Vol. 2. *Edited by* J.L. Franklin. Plenum Press, New York. 1972. p. 673.
19. A.N. Hayhurst and N.R. Telford. Trans. Faraday Soc. **66**, 2784 (1970).
20. A.F. Ashton and A.N. Hayhurst. Combust. Flame, **21**, 69 (1973).
21. S.G. Lias, J.E. Bartmess, J.F. Liebman, J.L. Holmes, R.D. Levin, and W.G. Mallard. J. Phys. Chem. Ref. Data, **17** (Suppl. 1) (1988).

© 1998 NRC Canada

Application of [Ru((*R*)-BINAP)(MeCN)(1-3:5,6-η-C_8H_{11})](BF_4) as a catalyst precursor for enantioselective hydrogenations

Christopher J.A. Daley, Jason A. Wiles, and Steven H. Bergens

Abstract: A catalyst system employing [Ru((*R*)-BINAP)(MeCN)(1-3:5,6-η-C_8H_{11})](BF_4) as catalyst precursor was evaluated using the enantioselective hydrogenations of tiglic acid, α-acetamidocinnamic acid, itaconic acid, methyl tiglate, dimethyl itaconate, geraniol, ethyl acetoacetate, and dimethyl oxaloacetate as a series of typical substrates. Acetone and MeOH were used as model aprotic and protic solvents, respectively. The hydrogenation of substrates containing an α,β-unsaturated carboxylic acid functionality required stoichiometric quantities of NEt_3 to occur at reasonable rates in acetone solution, while in MeOH solution it did not. The enantioselectivities were typically higher in acetone than in MeOH. This catalyst system is among the more enantioselective ruthenium–BINAP type systems reported for the catalytic hydrogenation of substrates containing an α,β-unsaturated acid or ester functionality. The enantioselectivities for the hydrogenation of ketones ranged from poor (15%) to moderate (74%). 1,4-Dicarboxylate substrates with the prochiral olefin or ketone at the 2-position were all hydrogenated in good to high ee with the same enantioface selectivity both with our system and other catalysts reported in the literature. This raised the possibility that these substrates were hydrogenated through intermediates with similar structural features.

Key words: ruthenium, BINAP, enantioselective, hydrogenation, catalysis.

Résumé : Utilisant les hydrogénations énantiosélectives des acides tiglique, α-acétamidocinnamique et itaconique, du tiglate de méthyle, de l'itaconate de diméthyle, du géraniol, de l'acétoacétate d'éthyle et de l'oxaloacétate de diméthyle comme substrats typiques, on a évalué un système de catalyseur faisant appel au [Ru((*R*)-BINAP)(MeCN)(1,3,5,6-η-C_8H_{11})](BF_4) comme précurseur du catalyseur. On a utilisé l'acétone et le méthanol comme modèles de solvant respectivement aprotique et protique. Les énantiosélectivités sont généralement plus élevées dans l'acétone que dans le méthanol. Pour réaliser l'hydrogénation d'acides carboxyliques insaturés à une vitesse raisonnable dans l'acétone, il est nécessaire d'utiliser des quantités stoechiométriques de triéthylamine; ce n'est pas le cas dans le méthanol. Pour l'hydrogénation catalytique d'acides et d'esters α,β-insaturés, ce système de catalyseur se trouve parmi les systèmes de type ruthénium–BINAP les plus énantiosélectifs. Les énantiosélectivités pour l'hydrogénation des cétones vont de mauvaises (15%) à modérées (74%). Avec les substrats portant des 1,4-dicarboxylates et une oléfine ou une cétone prochirale en position 2, les hydrogénations conduisent à des ee allant de bons à élevés; notre système et les autres catalyseurs proposés antérieurement dans la littérature ont les mêmes sélectivités et ceci suggère que les hydrogénations de ces substrats se produisent par des intermédiaires possédant des caractéristiques structurales semblables.

Mots clés : ruthénium, BINAP, énantiosélectif, hydrogénation, catalyse.

[Traduit par la Rédaction]

Introduction

Asymmetric catalysis by chiral transition metal complexes is among the most successful methods to synthesize optically active organic compounds. Of the hundreds of chiral ligands reported, 2,2′-bis(diphenylphosphino)-1,1′-binaphthyl (BINAP) is one of the most successful (for recent reviews on the use of BINAP in enantioselective catalysis, see ref. 1). While rhodium–BINAP systems are highly enantioselective catalysts for the hydrogenation of certain prochiral olefins (2), ruthenium–BINAP systems hydrogenate a much wider range of prochiral olefins and ketones with high enantioselectivities (3; for earlier references see 1*d*, *f*, and refs. cited therein).

We previously reported the synthesis of [Ru((*R*)-BINAP)(MeCN)(1-3:5,6-η-C_8H_{11})](BF_4) (**I**) and its use as a catalyst precursor for several catalytic processes (4). Compound **I** reacts with H_2 in acetone, THF, or MeOH solution to generate [Ru((*R*)-BINAP)(H)$(MeCN)_n(Sol)_{3-n}$](BF_4) (**II,** Sol = acetone, THF, or MeOH; n = 0–3), which we believe is the active catalyst for the described reactions.

The catalyst system **II** is distinguished from other ruthenium–BINAP catalysts by the combination of the following three features. First, it is reasonably well-defined. Second, the active catalyst is generated in high concentrations under

Received March 23, 1998.

C.J.A. Daley, J.A. Wiles, and S.H. Bergens.[1] Department of Chemistry, University of Alberta, Edmonton, AB T6G 2G2, Canada.

[1]Author to whom correspondence may be addressed. Telephone: (403) 492-9703. Fax: (403) 492-8231. E-mail: Steve.Bergens@UAlberta.CA

© 1998 NRC Canada

mild conditions. In acetone, THF, or MeOH solution, the catalyst precursor **I** reacts under 1–2 atm of H_2 at room temperature to generate complex **II** in minutes. Third, the system has at least two readily available coordination sites (occupied by labile solvento ligands) to allow easy access by substrate molecules to the ruthenium centre. This feature is essential for the study of substrate–catalyst interactions.

We now report the use of **II** as a catalyst system for the enantioselective catalytic hydrogenation of a representative series of prochiral substrates. This work will define the utility of **II** as a catalyst system relative to the other ruthenium–BINAP catalyst systems reported in the literature, and it will explore any possible general trends in enantioselectivity by such catalysts. It is only through such trends that the general components of enantioselectivity (if they exist) by ruthenium–BINAP catalysts can be established.

Results and discussion

The nature of II

The MeCN ligand is rapidly exchanged between all the available vacant coordination sites in acetone solutions of **II** at room temperature. This exchange halts upon cooling to –80°C to give a static mixture of eight hydrides ranging from [Ru((*R*)-BINAP)(H)(acetone)$_3$](BF$_4$) to [Ru((*R*)-BINAP)(H)-(MeCN)$_3$](BF$_4$). These compounds all contain the hydride ligand in a coordination site *cis* to both phosphorus centres. This mutually *cis* disposition of the coordinated hydride and phosphorus centres presumably results from the high *trans influence* commonly observed for both of these types of ligands (5). In THF solution, the system exists mainly (~85%) as one diastereomer of the mono-MeCN complex [Ru((*R*)-(BINAP)(H)(MeCN)(THF)$_2$](BF$_4$). In MeCN solution, it exists solely as [Ru((*R*)-(BINAP)(H)(MeCN)$_3$](BF$_4$). To a first approximation, the system can be regarded as a source of the catalyst fragment "[Ru((*R*)-(BINAP)(H)]$^+$." For example, the solvento and MeCN ligands can all be displaced by arene donors to generate the corresponding [Ru((*R*)-(BINAP)(H)(η^6-arene)](BF$_4$) complexes (6).

Hydrogenations using II as catalyst

Figure 1 shows the representative substrates we hydrogenated using **I** as the catalyst precursor. Figure 1 also shows the major enantiomer of the hydrogenation products. Tables 1, 2, and 4 summarize our results.

Substrates containing an α,β-unsaturated acid or ester functionality

Hydrogenations were performed in MeOH as a model protic solvent. The hydrogenation of tiglic acid (**1a**) (Table 1, entry 1) was quantitative under mild conditions, giving 2-methylbutyric acid (**1c**) in high ee (90% (*R*)). The ee decreased to 72% (*R*) when the initial pressure of H_2 was increased from 3 to 55 atm (Table 1, entry 2). Attempts to hydrogenate methyl tiglate (**1b**) were unsuccessful under 3 atm of H_2 (Table 1, entry 3). This difference in reactivity between tiglic acid and methyl tiglate has been previously reported for another ruthenium–BINAP catalyst system (7).

We previously reported (4) that hydrogenation of (*Z*)-methyl α-acetamidocinnamate (MAC, **2b**) to *N*-acetylphenylalanine methyl ester (**2d**) in MeOH goes to completion in high ee (86% (*R*)) under mild conditions. This result is included for comparative purposes (Table 1, entry 6). Surprisingly, hydrogenation of the corresponding acid (α-acetamidocinnamic acid (**2a**)) under similar conditions proceeds much more slowly, with only 10% conversion after 94 h (Table 1, entry 4). To obtain complete conversion it was necessary to increase the pressure of H_2 to 100 atm, resulting in 46% ee (*R*) (Table 1, entry 5).

The hydrogenation of itaconic acid (**3a**) (Table 1, entry 7) proceeded smoothly under mild conditions giving methylsuccinic acid (**3c**) in 90% ee (*S*). The corresponding hydrogenation of dimethyl itaconate (**3b**) (Table 1, entry 8) under similar conditions was more successful, yielding dimethyl methylsuccinate (**3d**) in 95% ee (*S*). We note that the net enantioface selection by the catalyst for substrates **3a** and **3b** is the same as that for the structurally related substrates **2a** and **2b**.

To investigate the use of an aprotic solvent, the hydrogenations were carried out in acetone. The results of these reactions are reported in Table 2. As we previously reported (8), the hydrogenation of **2b** proceeds smoothly under mild conditions to give **2d** in higher ee (92% (*R*)) than does the hydrogenation in MeOH (86% (*R*)). This result is included for comparative purposes (Table 2, entry 6). The hydrogenation of **3b** also proceeded under mild conditions in acetone (Table 2, entry 10) to yield **3d** in similar ee to that obtained from the hydrogenation in MeOH (95% ee (*S*)). As was the case in MeOH, **1b** did not undergo hydrogenation in acetone (Table 2, entry 3). The hydrogenations of **1a**, **2a**, and **3a** were extremely slow under these conditions (4 atm H_2, 25°C, acetone), giving low to moderate conversions ranging from <10% to ~55% (Table 2, entries 1, 4, and 7, respectively). Even at 50°C and 4 atm of H_2 the hydrogenation of **3a** proceeded to a maximum of ~65% conversion (Table 2, entry 8). It is well known that addition of an equivalent of base (e.g., amines) for every acid unit in the substrate often (but not always) yields higher ee and rates for the hydrogenation of acid substrates using both ruthenium and rhodium catalyst systems (9). We examined this effect on the hydrogenations of the acids (**1a**, **2a**, and **3a**) in acetone. The hydrogenations of **1a** and **3a** (Table 2, entries 2 and 9, respectively) proceeded to completion under mild conditions in the presence of 1 equiv. of NEt_3 per acid group. Further, the ee improved from 90% (*R*) for **1a** and 90% (*S*) for **3a** in the absence of added base in MeOH to 95% ee (*R*) and 95% ee (*S*) with added base in acetone. The addition of 1 equiv. of NEt_3 did not enhance the rate of hydrogenation of **2a** (Table 2, entry 5).

Table 3 compares our results to the best results reported in the literature for other ruthenium–BINAP systems we are aware of. Apart from the hydrogenation of **2b**,[2] all the literature examples reported in Table 3 were performed in pure alcohol or binary alcohol–solvent solutions (solvent = THF or CH_2Cl_2), under mild temperatures (20–50°C), and under low to moderate pressures of H_2 (1–5 atm). The results obtained

[2] This is the only literature example we are aware of where **2b** is hydrogenated using a ruthenium–BINAP catalyst.

© 1998 NRC Canada

Fig. 1. Representative substrates and their respective hydrogenation products (major enantiomers shown) investigated using **I** as hydrogenation catalyst precursor.

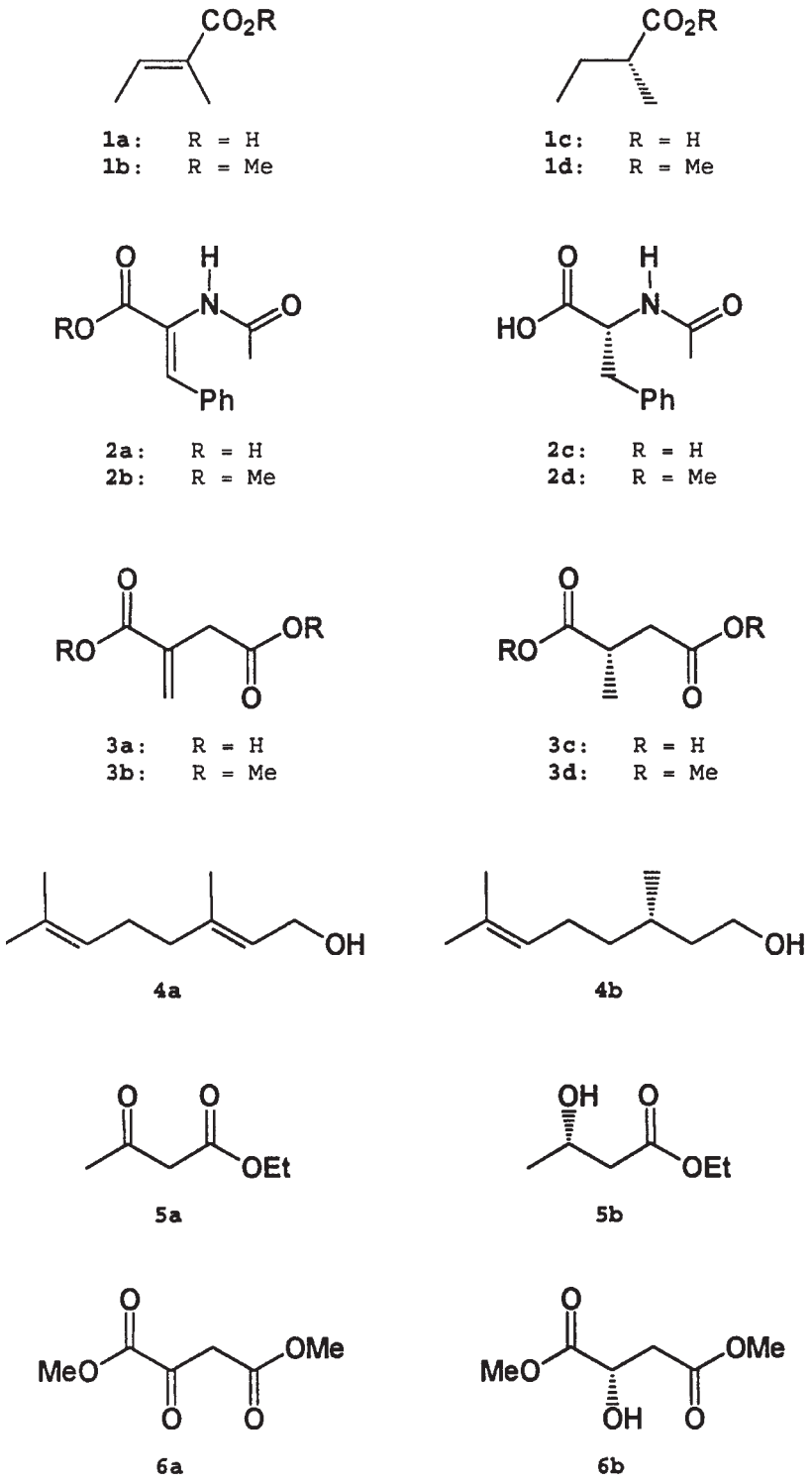

with complex **I** as the catalyst precursor show it to be among the better ruthenium–BINAP systems examined to date for the hydrogenation of these substrates.

Inspection of Table 3 shows no real trends in the absolute configuration of the major enantiomer produced by hydrogenation of tiglic acid (**1a**) using ruthenium–BINAP catalyst systems. That methyl tiglate (**1b**) does not undergo hydrogenation but tiglic acid does suggests that substrates with one ester group that are not easily supported by chelation upon coordination to ruthenium will not undergo hydrogenation. Indeed, we observed no evidence of interaction between the active catalyst species **II** and an up to 100-fold excess of

© 1998 NRC Canada

Table 1. Hydrogenation of substrates containing an α,β-unsaturated carboxylic acid or ester functionality in MeOH using **I** as catalyst precursor.[a]

Entry	Substrate	H_2 (atm)	Temp. (°C)	Time (h)	% Conv.	% ee
1	**1a**	3	25	9.5	100	90 (*R*)
2	**1a**	55	25	17.5	100	72 (*R*)
3	**1b**	3	25	18	0	—
4	**2a**	4	35	94	10	—
5	**2a**	100	40	20	100	46 (*R*)
6[b]	**2b**	4	30	30	100	86 (*R*)
7	**3a**	4	25	20	100	90 (*S*)
8	**3b**	4	25	19	100	95 (*S*)

[a] Reaction conditions: 1 mol% catalyst, [Ru] = 3.0 mM.
[b] Reaction conditions: 2 mol% catalyst, [Ru] = 2.6 mM (ref. 4).

Table 2. Hydrogenation of substrates containing an α,β-unsaturated carboxylic acid or ester functionality in acetone using **I** as catalyst precursor.[a]

Entry	Substrate	N/S[b]	H_2 (atm)	Temp. (°C)	Time (h)	% Conv.	% ee
1	**1a**	0	4	25	20	<10	—
2	**1a**	1	4	25	18	100	95 (*R*)
3	**1b**	0	4	25	20	0	—
4	**2a**	0	4	25	20.5	<10	—
5	**2a**	1	4	25	20.5	<10	—
6[c]	**2b**	0	4	30	1	100	92 (*R*)
7	**3a**	0	4	25	18.5	~55	—
8	**3a**	0	4	50	18	~65	—
9	**3a**	2	4	25	18	100	95 (*S*)
10	**3b**	0	4	25	20.5	100	95 (*S*)

[a] Reaction conditions: 1 mol% catalyst, [Ru] = 3.0 mM.
[b] *N/S* is defined as moles of NEt_3 added per mole of substrate.
[c] Reaction conditions: 2 mol% catalyst, [Ru] = 2.6 mM (ref. 6).

Table 3. Comparison of Ru((*R*)-BINAP) catalyst systems in the hydrogenation of substrates containing an α,β-unsaturated carboxylic acid or ester functionality.

	Substrates					
Catalyst system	**1a**	**2a**	**2b**	**3a**	**3b**	Reference
$[Ru(BINAP)(C_8H_{11})(MeCN)](BF_4)$	95 (*R*)	46 (*R*)	92 (*R*)	95 (*S*)	95 (*S*)	4, 8
$Ru_2Cl_4(BINAP)_2(NEt_3)$	85 (*S*)	86 (*R*)	—	90 (*S*)	68 (*S*)	10–12
$RuHCl(BINAP)_2$	79 (*R*)	80 (*R*)	—	93 (*S*)	54 (*S*)	9*a*, 11, 12
$[RuH(BINAP)_2](PF_6)$	88 (*R*)	—	—	94 (*S*)	—	9*a*
$RuCl_2(RCN)_2(BINAP)$	84 (*S*)	—	—	89 (*S*)	—	10
$[RuI_2(p\text{-cymene})]_2$ + BINAP	87 (*R*)	—	—	—	—	13
Ru(BINAP)(2-methylallyl)$_2$ + 2 HBr	—	—	85 (*R*)[a]	—	—	14
Ru(BINAP)(2-methylallyl)$_2$	90 (*R*)	—	—	—	—	15
$Ru(BINAP)(OCOCH_3)_2$	94 (*R*)	—	—	—	—	16

[a] Reaction performed under 100 atm of H_2.

methyl tiglate in acetone solution.[3] The acids and other esters studied in this report all react stoichiometrically (1:1) with **II** to generate a variety of products. The structures of these ruthenium–substrate compounds are under investigation in our laboratories.

Substrates **2a**, **2b**, **3a**, and **3b** are hydrogenated with good to excellent ee and with the same enantioface selectivity. Figure 2 shows that these substrates all contain the same basic framework, a 1,4-dicarbonyl unit with the prochiral functionality at the 2-position (**7**). That hydrogenation of **2a**, **2b**, **3a**, and **3b** all proceed with the same face selectivity for most, if not all reported ruthenium–BINAP systems (Table 3) under similar conditions, raises the possibility that they proceed through structurally related intermediates. Figure 2 illustrates one possible structure type for such a species (**8**). We suggest this structure based on the recently

[3] $[Ru((R)\text{-BINAP})(H)(MeCN)_n(acetone)_{3-n}](BF_4)$ (n = 0–3) was the only species detected by ^{31}P NMR spectroscopy.

© 1998 NRC Canada

Fig. 2. Model for a possible common intermediate structure type.

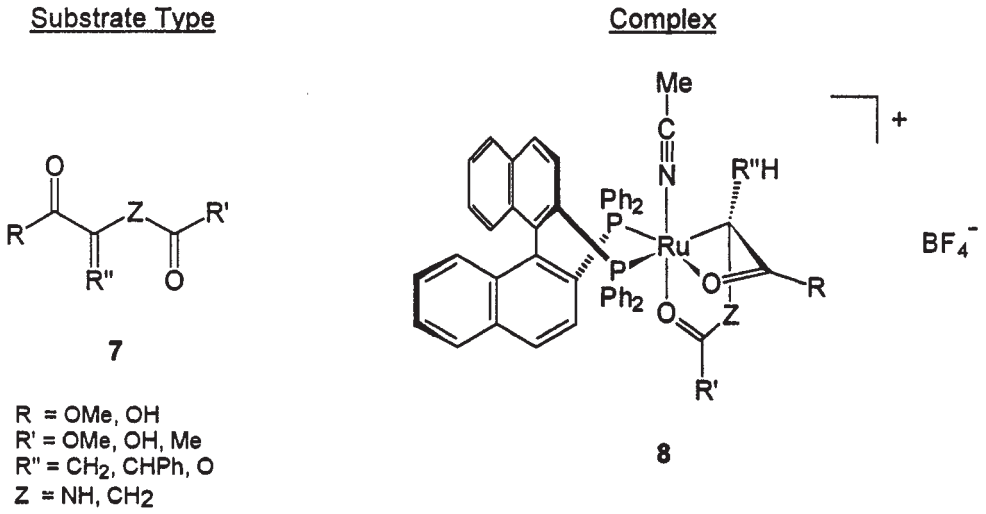

reported (6) crystallographically characterized compound we isolated from the reaction of MAC (**2b**) with **II** (Fig. 2, **8**, R = OMe, R′ = Me, R′′ = CHPh, Z = NH). If such species form with these and other related substrates, and if these species contribute to the enantioselection by the catalytic hydrogenation must be investigated by experiment.

The role of NEt_3 as promoter for the hydrogenation of tiglic acid and itaconic acid in acetone is unknown. We have found, however, that reaction of tiglic acid with **II** in acetone results in immediate protonolysis of the Ru—H bond to generate a Ru-tiglato complex (eq. [1]). Reaction of Ru—D (formed by deuteration of **I** with D_2) resulted in the formation of the Ru-tiglato complex and concomitant formation of HD. We were unable to identify the absolute configuration of the tiglato complex about the ruthenium centre. We postulate that it is the Δ configuration on the basis of the arguments previously reported for the related complex Ru((*R*)-BINAP)($O_2CCMe{=}CHMe)_2$ (17). Two possible roles of the NEt_3 as promoter for hydrogenations of unsaturated acids may therefore be to enhance the rate of carboxylate exchange on such complexes, or to prevent protonolysis of the Ru—H bond by deprotonating the acid substrate. King and others have reported that NEt_3 decomposes (perhaps via a β-hydride elimination (18)) upon reaction with $[RuCl_2(COD)]_n$ and (*R*)-BINAP, or similar bis(phosphines), from 110 to 140°C to generate $[Et_2NH_2](Ru_2Cl_5((R)\text{-}(BINAP)_2)$ (19). It seems unlikely, however, that such a process occurs under H_2 at 25°C using **II** as catalyst (Table 2, entries 2, 5, and 9). The reasons why NEt_3 is not required to promote these hydrogenations in MeOH is unknown.

Geraniol

We found that the enantioselectivity for the hydrogenation of geraniol (**4a**) using **II** as catalyst was inversely dependent on the pressure of H_2. The sense of the enantioselectivity inverted and its magnitude increased when the pressure of H_2 was increased from 1 atm (Table 4, entries 1–3). The maximum ee, 86% (*S*), was obtained at 100 atm of H_2. Noyori and co-workers (20) reported increases in ee from 70 to 98% (*S*) when the pressure of H_2 was increased from 4 to 100 atm using Ru((*R*)-BINAP)($O_2CMe)_2$ as catalyst precursor. Sowa and co-workers (21) found that the isomerization of geraniol to γ-geraniol occurs at a rate comparable to that of hydrogenation using $[Et_2NH_2](Ru_2Cl_5((S)\text{-Tol-BINAP})_2)$ (Tol-BINAP = (di-*p*-tolylphosphino)-1,1′-binaphthyl) as catalyst precursor. The enantioselectivity for the direct hydrogenation of geraniol was found to be opposite to that for the direct hydrogenation of γ-geraniol, resulting in an inversion of enantioselectivity over the course of the catalytic hydrogenation. Our results indicate that use of **II** as catalyst results in similar behaviour. We report, however, that reaction of **II** with geraniol in the absence of H_2 results in a complex mixture of olefin isomerization products, not just formation of γ-geraniol.

[1]

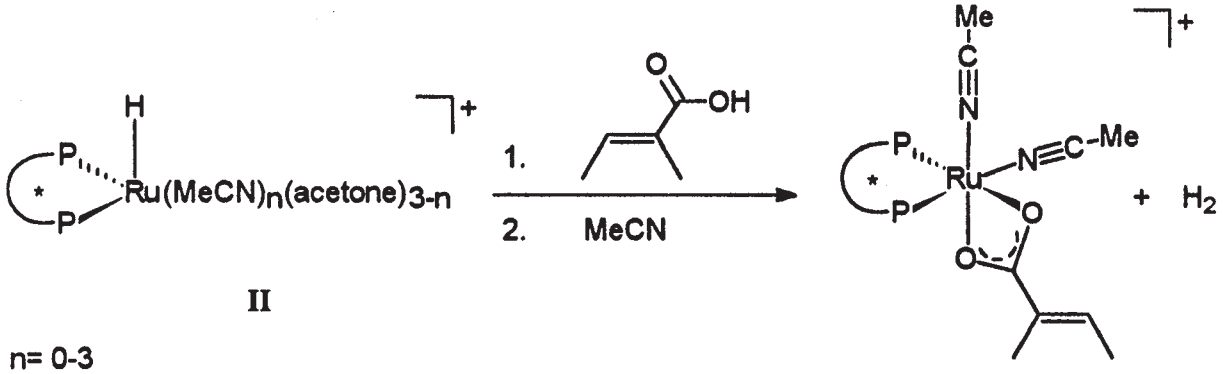

© 1998 NRC Canada

Table 4. Hydrogenation of an allylic alcohol and ketones in MeOH using **I** as catalyst precursor.[a]

Entry	Substrate	H_2 (atm)	Temp. (°C)	Time (h)	% Conv.	% ee
1	**4a**	1	25	5	100	21 (*R*)
2	**4a**	4	25	5	100	70 (*S*)
3	**4a**	100	25	0.25	100	86 (*S*)
4	**5a**	100	50	24	100	15 (*S*)
5[b]	**5a**	100	50	24	100	20 (*R*)
6[c]	**6a**	100	50	28	100	74 (*S*)

[a]Reaction conditions: 1 mol% catalyst, [Ru] = 3.0 mM.
[b]10 equiv. of LiCl added.
[c]Reaction done in acetone.

α- and β-Keto esters

The hydrogenation of ethyl acetoacetate (**5a**) to ethyl 3-hydroxybutyrate (**5b**) (Table 4, entry 4) proceeded in a quantitative fashion, but in low ee (15% (*S*)). Takaya and coworkers (22) reported that addition of 2 equiv. of HX (e.g., X = Cl, Br) to Ru((*R*)-BINAP)$(O_2CMe)_2$ followed by removal of all volatiles in vacuo gave rise to highly efficient catalysts which hydrogenate various β-keto esters with greater than 98% ee. The addition of 10 equiv. of LiCl to **I** (Table 4, entry 5) increased the ee, but only to 20% and in the opposite absolute configuration (*R*). The role of LiCl is unclear but the enantioselectivity of complex **II** remains poor compared to other reported ruthenium–BINAP systems which often yield enantiomeric excesses greater than 95% for the hydrogenation of such substrates (23).

Examining the structural framework of the model substrates for our catalyst system (Fig. 2, **7**) led to our use of dimethyl oxaloacetate (**6a**). Dimethyl oxaloacetate has similar structural characteristics to dimethyl itaconate (**3b**) where the olefinic bond is replaced by a carbonyl functionality. The hydrogenation of **6a** proceeded to completion (100 atm H_2, 50°C, acetone, Table 4, entry 6) yielding dimethyl hydroxysuccinate (**6b**) in 74% ee (*S*). Although the ee is moderate, it is a substantial increase from the hydrogenation of ethyl acetoacetate. Further, the hydrogenation product (**6b**) resulted from the same enantioface selection as those for the hydrogenations of **2b** and **3b**. These findings support the possibility that substrates with similar structural features proceed through structurally related intermediates (Fig. 2).

Conclusions

Complex **II** is among the more effective ruthenium–BINAP catalysts reported for the asymmetric hydrogenation of substrates containing an α,β-unsaturated carboxylic acid or ester functionality. Its success in the asymmetric reduction of ketones is only moderate. Prochiral substrates with the general structure **7** shown in Fig. 2 are hydrogenated with the same enantioface selection. Extrapolations of these results from mechanistic investigations of one combination of substrate, catalyst, and reaction conditions are precarious in their nature because of the large number of variables involved in such reactions. That substrates of the general structure **7** are hydrogenated with the same enantioface selection raises the possibility that a general trend may exist in these catalyst systems. Further investigations into the true significance of this apparent general trend in enantioselection by ruthenium–BINAP catalysts are underway in our laboratories.

Experimental

Materials and methods

All operations were performed under an Ar atmosphere using standard Schlenk techniques. The solvents were dried and distilled under an Ar atmosphere before use by standard methods (24). The Ar (Praxair, 99.998%) was passed through a drying train containing 3 Å molecular sieves and P_4O_{10} before use. Trace quantities of oxygen were removed from the H_2 (Praxair, 99.99%) by passage through an Alltech Oxy-Trap. All commercial reagents (Aldrich or Fluka) were recrystallized or distilled under an Ar atmosphere before use. [Ru((*R*)-BINAP)-(MeCN)(1-3:5,6-η-C_8H_{11})](BF_4) (4), (*R*)-(+)-α-methoxy-α-(trifluoromethyl)phenylacetylchloride (25), [Rh(η^4-norbornadiene)(DIPHOS)](ClO_4) (26), and dimethyl oxaloacetate (27) were prepared using established procedures.

Unless stated otherwise, all ^1H, ^{13}C, and ^{31}P NMR spectra were measured with a Bruker AM-400 spectrometer operating at 400.1 MHz, 100.6 MHz, and 161.9 MHz, respectively. ^1H and ^{13}C NMR chemical shifts are reported in ppm (δ) relative to TMS, using the solvent as an internal reference. ^{31}P NMR chemical shifts are reported in ppm (δ) relative to an 85% H_3PO_4 external reference. Mass spectra were measured using a Kratos MS50 spectrometer. Microanalyses were performed at the University of Alberta Microanalysis Laboratory. Optical rotations were measured with a Perkin–Elmer 241 polarimeter at 589 nm using 1.0 dm cells. Specific rotations, $[\alpha]_D$, are reported in degrees per decimeter at 25°C, and the concentration (*c*) is given in grams per 100 mL.

Hydrogenation procedure

A glass pressure reactor (Lab Glass) was employed for hydrogenation reactions where the pressure of H_2 was ≤ 4 atm. For reactions requiring elevated pressures, a Parr cell-disruption bomb was used. A typical hydrogenation procedure is described below.

Under an Ar atmosphere, the catalyst precursor (**I**) (0.010 mmol), substrate (1.0 mmol), and NEt_3 (1 equiv. per acid unit as required, Table 2), were introduced into the reactor. The dry, deoxygenated solvent (MeOH or acetone) was then added (3.8 mL), and the solution was stirred for 5 min. The atmosphere was then replaced by H_2, and the solution was allowed to react under the prescribed conditions (Tables 1, 2, and 4). On completion of the reaction, the sol-

© 1998 NRC Canada

vent was removed under reduced pressure, and the products were worked up as detailed below. Complete conversion and identification of the products were confirmed by CIMS and (or) ^{1}H NMR analyses.

*Tiglic acid (**1a**)*

The product residue from the hydrogenation in MeOH was dissolved in CH_2Cl_2 and passed through a Florisil plug to remove the catalyst. The solvent was then removed under reduced pressure, and the residue was converted to the corresponding diastereomeric amides of (*S*)-(–)-α-methylbenzylamine (28). The ee and absolute configuration were determined by comparison of the ^{1}H NMR spectrum of the derivatized residue to that of the corresponding amide derivatives prepared from (±)-2-methylbutyric acid and authentic (*S*)-(+)-2-methylbutyric acid, respectively.

To the acetone–NEt_3 product residue was added 10% aq. HCl (10 mL). The solution was filtered, and the filtrate extracted with Et_2O (5 × 40 mL). The combined organic layers were washed with 5% aq. HCl (3 × 8 mL), dried over $MgSO_4$, filtered, and concentrated under reduced pressure to give 2-methylbutyric acid. The ee and absolute configuration were then determined as described above. NMR data for the (*S*, *S*) diastereomer: ^{1}H (400.1 MHz, $CDCl_3$), δ: 0.84 (t, *J* = 7.4 Hz, 3H), 1.13 (d, *J* = 6.9 Hz, 3H), 1.39 (m, 1H), 1.46 (d, *J* = 6.9 Hz, 3H), 1.64 (m, 1H), 2.10 (apparent sextet, *J* = 6.9 Hz, 1H), 5.14 (apparent quintet, *J* = 7.2 Hz, 1H), 5.89 (br s, 1H), 7.15–7.40 (aromatic, 5H); NMR data for (*R*, *S*) diastereomer: ^{1}H (400.1 MHz, $CDCl_3$), δ: 0.92 (t, *J* = 7.4 Hz, 3H), 1.10 (d, *J* = 6.9 Hz, 3H), 1.38 (m, 1H, overlapped with (*S*, *S*) diastereomer), 1.47 (d, *J* = 6.9 Hz, 3H), 1.64 (m, 1H, overlapped with (*S*, *S*) diastereomer), 2.09 (apparent sextet, *J* = 6.9 Hz, 1H, overlapped with (*S*, *S*) diastereomer), 5.13 (apparent quintet, *J* = 7.2 Hz, 1H, overlapped with (*S*, *S*) diastereomer), 5.89 (br s, 1H, overlapped with (*S*, *S*) diastereomer), 7.15–7.40 (m, 5H, aromatic, overlapped with (*S*, *S*) diastereomer).

*α-Acetamidocinnamic acid (**2a**)*

The product residue was converted to the corresponding diastereomeric amides of (*S*)-(–)-α-methylbenzylamine (28). The absolute configuration of the product was determined by comparison of its optical rotation to that of the reported optical rotation of (*R*)-(–)-*N*-acetylphenylalanine (**2b**) ($[\alpha]^{27}_D$ = –40.3°, *c* = 1.0, MeOH) (29). The ee was determined by ^{1}H NMR analysis (400 MHz, $CDCl_3$) of the resulting diastereomeric amides.[4] NMR data of the diastereomeric amides: ^{1}H (400.1 MHz, $CDCl_3$), δ: 1.21 (d, *J* = 7.0 Hz, 3H; (*R*, *R*) diastereomer), 1.40 (d, *J* = 7.0 Hz, 3H; (*R*, *S*) diastereomer), 1.88 (s, 3H; (*R*, *R*) diastereomer), 1.95 (s, 3H; (*R*, *S*) diastereomer), 2.92 (m, 2H; (*R*, *S*) diastereomer), 2.97 (dd, *J* = 13.4, 8.8 Hz, 1H; (*R*, *R*) diastereomer), 3.10 (dd, *J* = 13.4, 6.1 Hz, 1H; (*R*, *R*) diastereomer), 4.70 (m, 2H), 4.91 (apparent quintet, *J* = 7.0 Hz, 1H; (*R*, *R*) diastereomer), 4.97 (apparent quintet, *J* = 7.0 Hz, 1H; (*R*, *S*) diastereomer), 6.49 (d, *J* = 7.7 Hz, 1H), 6.72 (m, 3H), 7.00–7.45 (m, 20H). N*H* signals not observed.

*Itaconic acid (**3a**)*

The product residue was converted directly to the dimethyl ester with CH_2N_2 (30), whereas the acetone–NEt_3 product was first worked up in a manner similar to that described for tiglic acid (**2a**), and then treated with CH_2N_2. The product was then dissolved in CH_2Cl_2 and passed through a Florisil plug to remove the catalyst. The solvent was removed under reduced pressure to yield dimethyl methylsuccinate. The ee and absolute configuration were then determined as described in the dimethyl itaconate (**3b**) hydrogenation work-up.

*Dimethyl itaconate (**3b**)*

The products of the MeOH and acetone reactions were treated in a similar manner. The product residue was dissolved in CH_2Cl_2 and passed through a Florisil plug to remove the catalyst. The solvent was removed under reduced pressure, yielding dimethyl methylsuccinate. The ee was spectroscopically determined (^{1}H NMR, CD_2Cl_2) upon addition of chiral lanthanide shift reagent ((+)-Eu(tfc)$_3$))[5] (31). The absolute configuration of the product was determined by comparison of its optical rotation to that of authentic (*R*)-dimethyl methylsuccinate ($[\alpha]^{25}_D$ = +4.8°, *c* = 4.0, $CHCl_3$).

*Geraniol (**4a**)*

The product residue was purified by flash distillation and reacted with (*R*)-(+)-α-methoxy-α-(trifluoromethyl)phenylacetylchloride (25). The ee was determined by ^{1}H NMR spectroscopy of the diastereomeric esters.[6] The absolute configuration of the product was determined by comparison of its rotation with the reported optical rotation of (*R*)-citronellol ($[\alpha]^{25}_D$ = +5.12°, *c* = 21.0, $CHCl_3$) (32). NMR data for the diastereomeric esters: ^{1}H (400.1 MHz, $CDCl_3$), δ: 0.90 (d, *J* = 6.3 Hz, 3H; (*R*, *S*) diastereomer), 0.91 (d, *J* = 6.3 Hz, 3H; (*R*, *R*) diastereomer), 1.19 (m, 2H), 1.33 (m, 2H), 1.51 (m, 4H), 1.59 (s, 6H), 1.68 (s, 6H), 1.74 (m, 2H), 1.95 (m, 4H), 3.50 (br s, 3H; (*R*, *S*) diastereomer), 3.56 (br s, 3H; (*R*, *R*) diastereomer), 4.37 (m, 4H), 5.06 (m, 2H), 7.35–7.70 (m, 10H, aromatic). ^{1}H NMR signals for individual diastereomers were assigned when overlap did not occur.

*Ethyl acetoacetate (**5a**)*

The product residue was purified by flash distillation and reacted with (*R*)-(+)-α-methoxy-α-(trifluoromethyl)phenylacetylchloride (25). The ee and absolute configuration were determined by comparison of the ^{1}H NMR of the derivatized residue to that of the diastereomeric Mosher's esters of (±)-3-hydroxybutyrate and authentic ethyl (*R*)-(–)-3-hydroxybutyrate, respectively. NMR data for the diastereomeric esters: ^{1}H NMR (400.1 MHz, $CDCl_3$): (*R*, *R*) diastereomer, δ: 1.23 (t, *J* = 7.1 Hz, 3H), 1.34 (d, *J* = 6.3 Hz, 3H), 2.57 (dd, *J* = 16.0, 4.7 Hz, 1H), 2.72 (dd, *J* = 16.0,

[4] The ratio of the acyl peaks at δ = 1.94 (s, CH_3, *S*) and δ = 1.78 (s, CH_3, *R*) were used to determine the ee. The ratio of these peaks was 1:1 for racemic *N*-acetyl phenylalanine.

[5] The ratio of the methoxy signals (ca. 4 ppm) were used to determine the ee. The ratio of these peaks was 1:1 for racemic dimethyl methylsuccinate.

[6] The ratio of the methyl peaks at δ = 0.91 (d, *J* = 6.4 Hz, CH_3, *R*) and δ = 0.90 (d, *J* = 6.4 Hz, CH_3, *S*) were used to determine the ee. The ratio of these peaks was 1:1 for racemic β-citronellol.

© 1998 NRC Canada

8.5 Hz, 1H), 3.49 (br s, 3H), 4.13 (qd, J = 7.1, 1.3 Hz, 2H), 5.57 (m, 1H), 7.3–7.7 (m, 5H, aromatic); (*R*, *S*) diastereomer, δ: 1.19 (t, J = 7.1 Hz, 3H), 1.43 (d, J = 6.3 Hz, 3H), 2.53 (dd, J = 16.0, 5.0 Hz, 1H), 2.68 (dd, J = 16.0, 8.3 Hz, 1H), 3.55 (br s, 3H), 4.06 (q, J = 7.1 Hz, 2H), 5.57 (m, 1H), 7.3–7.7 (m, 5H, aromatic).

*Dimethyl oxaloacetate (**6a**)*

The product residue was dissolved in CH_2Cl_2 and passed through a Florisil plug to remove the catalyst. The solvent was removed under reduced pressure, and the residue was reacted with (*R*)-(+)-α-methoxy-α-(trifluoromethyl)phenylacetylchloride (25). The ee was determined by comparison of the ^{1}H NMR spectrum of the derivatized residue to that of the Mosher's esters of (±)-dimethyl hydroxysuccinate (see achiral hydrogenation for NMR data). The absolute configuration was determined by comparison with the optical rotation of authentic (*S*)-(–)-dimethyl hydroxysuccinate ($[\alpha]^{25}_D$ = –8.85°, c = 5.2, MeOH).

Achiral hydrogenation of dimethyl oxaloacetate

A stainless-steel autoclave was charged with [Rh(η^4-norbornadiene)(DIPHOS)](ClO_4) (6.9 mg, 0.01 mmol), dimethyl oxaloacetate (160.0 mg, 1.0 mmol), and acetone (3.8 mL). The solution was stirred for 5 min, and the atmosphere was then replaced with H_2. The solution was allowed to react for 75 h at 50°C and 100 atm H_2. The product was worked up as described for the hydrogenation of dimethyl oxaloacetate with **I** as catalyst precursor and reacted with (*R*)-(+)-α-methoxy-α-(trifluoromethyl)phenylacetylchloride (25). NMR spectroscopic data: ^{1}H (300.1 MHz, $CDCl_3$): (*R*, *R*) diastereomer, δ: 2.88 (dd, J = 16.7, 8.4 Hz, 1H), 2.96 (dd, J = 16.7, 5.0 Hz, 1H), 3.60 (s, 3H), 3.63 (br s, 3H), 3.81 (s, 3H), 5.72 (dd, J = 8.4, 5.0 Hz, 1H), 7.42 (m, 3H), 7.60 (m, 2H); (*R*, *S*) diastereomer, δ: 2.92 (dd, J = 16.9, 8.9 Hz, 1H), 3.02 (dd, J = 16.9, 4.0 Hz, 1H), 3.55 (br s, 3H), 3.70 (s, 3H), 3.76 (s, 3H), 5.71 (dd, J = 8.9, 4.0 Hz, 1H), 7.42 (m, 3H), 7.60 (m, 2H).

Hydrogenation of [Ru((*R*)-BINAP)(1-3:5,6-η-C_8H_{11})(MeCN)](BF_4) (I) in acetone-d_6

Compound **I** (19.5 mg, 2.03×10^{-5} mol) was partially dissolved in acetone-d_6 (0.6 mL) in an NMR tube under an Ar atmosphere. At room temperature, the tube was flushed with H_2, pressurized (1–2 atm), and shaken until a deep orange–yellow solution was generated (~5 min). The H_2 atmosphere was replaced by Ar, and the resulting solution was analyzed by ^{1}H and ^{31}P NMR spectroscopy at –80°C. NMR spectroscopic analysis indicated a mixture of eight ruthenium-hydrido species ([Ru((*R*)-BINAP)(H)$(MeCN)_n((CD_3)_2CO)_{3-n}$]($BF_4$), where n = 0–3) and cyclooctane were present. At –80°C, D_2 (5.0 mL) was injected into the headspace of the tube. The tube was removed from the cooling bath, shaken for ~15 s, and then immediately placed in a precooled (–80°C) NMR probe. The ^{31}P NMR spectrum at –80°C remained unchanged, while the ^{1}H NMR spectrum indicated that exchange of all ruthenium-hydrido species with D_2 (to form ruthenium-deutero species) had occurred with concomitant formation of HD. NMR spectroscopic data of the hydrides (A-H): ^{1}H (400.1 MHz, $(CD_3)_2CO$, –80°C), δ: –19.87 (br, A), –19.60 (apparent t, $^2J_{H-P}$ = 30 Hz, B), –19.45 (br, C), –19.26 (apparent t, $^2J_{H-P}$ = 30 Hz, D), –13.50 (apparent t, $^2J_{H-P}$ = 25 Hz, E), –13.20 (apparent t, $^2J_{H-P}$ = 25 Hz, F), –13.15 (dd, $^2J_{H-P}$ = 28 Hz, $^2J_{H-P}$ = 24 Hz, G), –12.88 (apparent t, $^2J_{H-P}$ = 27 Hz, H), 1.65–2.35 (12 s, Ru-NCCH_3), 6.00–8.50 (aromatic); ^{31}P{^{1}H} (161.9 MHz, $(CD_3)_2CO$), δ: 59.4 (d, $^2J_{P-P}$ = 43.0 Hz, A), 60.8 (d, $^2J_{P-P}$ = 46.4 Hz, B), 63.2 (d, $^2J_{P-P}$ = 44.2 Hz, F), 63.6 (d, $^2J_{P-P}$ = 40.6 Hz, E), 66.0 (d, $^2J_{P-P}$ = 43.0 Hz, A), 68.2 (d, $^2J_{P-P}$ = 46.0 Hz, C),[7] 69.6 (d, $^2J_{P-P}$ = 40.6 Hz, E), 71.2 (d, $^2J_{P-P}$ = 49.6 Hz, D), 71.5 (d, $^2J_{P-P}$ = 42.9 Hz, G), 74.2 (d, $^2J_{P-P}$ = 47.0 Hz, H), 75.4 (d, $^2J_{P-P}$ = 42.9 Hz, G), 76.5 (d, $^2J_{P-P}$ = 46.4 Hz, B), 79.3 (d, $^2J_{P-P}$ = 49.6 Hz, D), 80.3 (d, $^2J_{P-P}$ = 44.2 Hz, F), 82.7 (d, $^2J_{P-P}$ = 47.0 Hz, H). Approximate percentages of hydrido species present: A(3), B(14), C(5), D(22), E(15), F(15), G(11), H(15). Although we were unable to assign individual structures for each hydride, we have independently prepared *fac*-[Ru((*R*)-BINAP)(H)$(MeCN)_3$](BF_4) which corresponded to hydride E.

Stoichiometric reaction of [Ru((*R*)-BINAP)(H)$(MeCN)_n(Sol)_{3-n}$](BF_4) (II, n = 0–3) with tiglic acid in acetone

A Schlenk flask was charged with **I** (40.0 mg, 4.18×10^{-5} mol), tiglic acid (4.2 mg, 4.18×10^{-5} mol), and acetone (4.0 mL) under an Ar atmosphere. At room temperature, the flask was flushed with H_2, pressurized (1–2 atm), and shaken until a deep orange–yellow solution was generated (~5 min). The H_2 atmosphere was then replaced by Ar. To this solution was added MeCN (2.6 mL, 4.98×10^{-5} mol), and the flask was shaken (~5 min) to ensure complete reaction. The solvent was removed under reduced pressure, and the remaining orange solid was washed with hexanes (3 × 5 mL). The isolated solid was stored under an Ar atmosphere at –30°C. The product readily loses MeCN in vacuo. NMR spectroscopic data of the complex: ^{1}H (400.1 MHz, $(CD_3)_2CO$), δ: 1.45 (apparent t, $CH_3CHC(CH_3)CO_2Ru$, $^4J_{H-H}$ = 1.5 Hz, $^5J_{H-H}$ = 1.2 Hz), 1.56 (dd, $CH_3CHC(CH_3).CO_2Ru$, $^3J_{H-H}$ = 7.2 Hz, $^5J_{H-H}$ = 1.2 Hz), 2.01 (s, CH_3CN), 2.03 (s, CH_3CN), 6.45 (dq, $CH_3CHC(CH_3)CO_2Ru$, $^3J_{H-H}$ = 7.2 Hz, $^4J_{H-H}$ = 1.5 Hz), 6.58–7.89 (m, 32H, BINAP). ^{31}P{^{1}H} (161.9 MHz, $(CD_3)_2CO$), δ: 52.6 (dd, $^2J_{P-P}$ = 37.5 Hz), 56.9 (d, $^2J_{P-P}$ = 37.5 Hz). ^{13}C{^{1}H} (100.6 MHz, $(CD_3)_2CO$), δ: 2.4 (CH_3CN), 4.65 (CH_3CN), 10.72 and 13.90 ($CH_3CHC(CH_3)CO_2Ru$), 123.99 (CH_3CN), 124.14 (CH_3CN), 124.42–141.45 (BINAP and $CH_3CHC(CH_3)CO_2Ru$), 185.46 ($CH_3CHC(CH_3)CO_2Ru$).

Stoichiometric reaction of [Ru((*R*)-BINAP)(D)$(MeCN)_n(Sol)_{3-n}$](BF_4) (II, n = 0–3) with tiglic acid in acetone-d_6

Compound **I** (13.5 mg, 1.41×10^{-5} mol) was partially dissolved in acetone-d_6 (~0.8 mL) in an NMR tube under an Ar atmosphere. At room temperature, the tube was flushed with D_2, pressurized (1–2 atm), and shaken until a deep orange–yellow solution was generated (~5 min). The D_2 atmosphere was replaced by Ar, and the solution was then transferred to an NMR tube containing tiglic acid (1.41 mg, 1.41×10^{-5}

[7] The corresponding ^{31}P{^{1}H} NMR signal was obscured by resonances attributed to hydrides D and G ca. 71.3 ppm.

© 1998 NRC Canada

mol) under an Ar atmosphere. To this solution was added excess CD_3CN (2.0 μL, 3.83×10^{-5} mol) via a gas-tight syringe. The solution was immediately analyzed by ^1H NMR. The product was exclusively formed with concomitant formation of HD. ^1H (400.1 MHz, $(CD_3)_2CO$), δ: 1.45 (apparent t, $CH_3CHC(CH_3)CO_2Ru$, $^4J_{H-H}$ = 1.5 Hz, $^5J_{H-H}$ = 1.1 Hz), 1.46–1.52 (br m, partially deuterated cyclooctane), 1.56 (dd, $CH_3CHC(CH_3)CO_2Ru$, $^3J_{H-H}$ = 7.2 Hz, $^5J_{H-H}$ = 1.1 Hz), 1.99 (s, CH_3CN), 3.26 (br t, HD, $^1J_{H-D}$ = 240 Hz), 6.45 (dq, $CH_3CHC(CH_3)CO_2Ru$, $^3J_{H-H}$ = 7.2 Hz, $^4J_{H-H}$ = 1.6 Hz), 6.58–7.89 (m, 32H, BINAP). $^{31}P\{^1H\}$ (161.9 MHz, $(CD_3)_2CO$), δ: 52.6 (dd, $^2J_{P-P}$ = 37.5 Hz), 56.9 (d, $^2J_{P-P}$ = 37.5 Hz).

Acknowledgments

This work was supported by the Natural Sciences and Engineering Research Council of Canada and by the University of Alberta.

References

1. (*a*) R. Noyori. Acta Chem. Scand. **50**, 380 (1996); (*b*) H. Kumobayashi. Recl. Trav. Chim. Pays-Bas, **115**, 201 (1996); (*c*) S. Akutagawa. App. Catal. A. **128**, 171 (1995); (*d*) R. Noyori. Aymmetric catalysis in organic synthesis. Wiley, New York. 1994; (*e*) Tetrahedron, **50**, 4259 (1994); (*f*) H. Takaya, T. Ohta, and R. Noyori. *In* Catalytic asymmetric synthesis. *Edited by* I. Ojima. VCH, New York, 1993; (*g*) R. Noyori. CHEMTECH, 360 (1992); (*h*) R. Noyori. Science (Washington, D.C.) **248**, 1194 (1990); (*i*) R. Noyori and H. Takaya. Acc. Chem. Res. **23**, 345 (1990).
2. (*a*) T. Ohta, H. Ikegami, T. Miyake, and H. Takaya. J. Organomet. Chem. **502**, 169 (1995); (*b*) M. Kitamura, Y. Hsiao, M. Ohta, M. Tsukamoto, T. Ohta, H. Takaya, and R. Noyori. J. Org. Chem. **59**, 297 (1994); (*c*) S. Inoue, M. Osada, K. Koyano, H. Takaya, and R. Noyori. Chem. Lett. 1007 (1985); (*d*) A. Miyashita, H. Takaya, T. Souchi, and R. Noyori. Tetrahedron, **40**, 1245 (1984); (*e*) A. Miyashita, A. Yasuda, H. Takaya, K. Toriumi, T. Ito, T. Souchi, and R. Noyori. J. Am. Chem. Soc. **102**, 7932 (1980).
3. (*a*) A.L. Monteiro, F.K. Zinn, R.F. de Souza, and J. Dupont. Tetrahedron: Asymmetry, **8**, 177 (1997); (*b*) T. Ohkuma, H. Ikehira, T. Ikariya, and R. Noyori. SYNLETT, 467 (1997); (*c*) A.S.C Chan, C.C Chen, T.K. Yang, J.H. Huang, and Y.C. Lin. Inorg. Chim. Acta, **234**, 95 (1995); (*d*) J.P. Genêt, M.C. Caño de Andrade, and V. Ratovelomanana-Vidal. Tetrahedron Lett. **36**, 2063 (1995); (*e*) T. Ohkuma, H. Ooka, S. Hashiguchi, T. Ikariya, and R. Noyori. J. Am. Chem. Soc. **117**, 2675 (1995); (*f*) M. Kitamura, M. Tokunaga, and R. Noyori. J. Am. Chem. Soc. **117**, 2931 (1995); (*g*) T. Ohta, T. Miyake, N. Seido, H. Kumobayashi, and H. Takaya. J. Org. Chem. **60**, 357 (1995); (*h*) M. Kitamura, M. Tokunaga, T. Pham, W.D. Lubell, and R. Noyori. Tetrahedron Lett. **36**, 5769 (1995); (*i*) M. Kitamura, Y. Hsiao, M. Ohta, M. Tsukamoto, T. Ohta, H. Takaya, and R. Noyori. J. Org. Chem. **59**, 297 (1994); (*j*) J.P. Genêt, C. Pinel, V. Ratovelomanana-Vidal, S. Mallart, X. Pfister, L. Bischoff, M.C. Caño de Andrade, S. Darses, C. Galopin, and J.A. Laffitte. Tetrahedron: Asymmetry, **5**, 675 (1994); (*k*) J.P. Genêt, C. Pinel, V. Ratovelomanana-Vidal, S. Mallart, X. Pfister, M.C. Caño de Andrade, and J.A. Laffitte. Tetrahedron: Asymmetry, **5**, 665 (1994); (*l*) K. Mashima, K. Kusano, N. Sato, Y. Matsumura, K. Nozaki, H. Kumobayashi, N. Sayo, Y. Hori, T. Ishizaki, S. Akutagawa, and H. Takaya. J. Org. Chem. **59**, 3064 (1994); (*m*) M. Kitamura, M. Tokunaga, and R. Noyori. J. Am. Chem. Soc. **115**, 144 (1993); (*n*) J.B. Hoke, L.S. Hollis, and E.W. Stern. J. Organomet. Chem. **455**, 193 (1993); (*o*) T. Manimaran, T.C. Wu, W.D. Kolbucar, C.H. Kolich, G.P. Stahly, F.R. Fronczek, and S.E. Watkins. Organometallics, **12**, 1467 (1993); (*p*) K. Wan and M.E. Davis. Tetrahedron: Asymmetry, **4**, 2461 (1993).
4. J.A. Wiles, C.E. Lee, R. McDonald, and S.H. Bergens. Organometallics, **15**, 3782 (1996).
5. J.P. Collman, L.S. Hegedus, J.R. Norton, and R.G. Finke. Principles and applications of organotransition metal chemistry. University Science Books, Mill Valley, Calif. 1987.
6. J.A. Wiles, S.H. Bergens, and V.G. Young. J. Am. Chem. Soc. **119**, 2940 (1997).
7. T. Ohta, H. Takaya, M. Kitamura, K. Nagai, and R. Noyori. J. Org. Chem. **52**, 3174 (1987).
8. J.A. Wiles and S.H. Bergens. Organometallics, **17**, 2228 (1998).
9. (*a*) M. Saburi, H. Takeuchi, M. Ogasawara, T. Tsukahara, Y. Ishii, T. Ikariya, T. Takahashi, and Y. Uchida. J. Organomet. Chem. **428**, 155 (1992); (*b*) T. Morimoto, M. Chiba, and K. Achiwa. Tetrahedron Lett. **29**, 4755 (1988); (*c*) I. Ojima and N. Yoda. Tetrahedron Lett. **21**, 1051 (1980); (*d*) I. Ojima, T. Kogure, and N. Yoda. Chem. Lett. 495 (1979); (*e*) K. Achiwa J. Am. Chem. Soc. **98**, 8265 (1976).
10. L. Shao, K. Takeuchi, M. Ikemoto, T. Kawai, M. Ogasawara, H. Takeuchi, H. Kawano, and M. Saburi. J. Organomet. Chem. **435**, 133 (1992).
11. H. Kawano, T. Ikariya, Y. Ishii, M. Saburi, S. Yoshikawa, Y. Uchida, and H. Kumobayashi. J. Chem. Perkin Trans. 1, 1571 (1989).
12. H. Kawano, Y. Ishii, T. Ikariya, M. Saburi, S. Yoshikawa, Y. Uchida, and H. Kumobayashi. Tetrahedron Lett. **28**, 1905 (1987).
13. N. Yamamoto, M. Murata, T. Morimoto, and K. Achiwa. Chem. Pharm. Bull. **39**, 1085 (1991).
14. R. Noyori, T. Ikeda, T. Ohkuma, M. Widhalm, M. Kitamura, H. Takaya, S. Akutagawa, N. Sayo, T. Saito, T. Taketomi, and H. Kumobayashi. J. Am. Chem. Soc. **111**, 9134 (1989).
15. J.P. Genêt, S. Mallart, C. Pinel, S. Juge, and J.A. Laffitte. Tetrahedron: Asymmetry, **2**, 43 (1991).
16. M.T. Ashby and J. Halpern. J. Am. Chem. Soc. **113**, 589 (1991).
17. M.T. Ashby, M.A. Khan, and J. Halpern. Organometallics, **10**, 2011 (1991).
18. D.E. Fogg and B.R. James. Inorg. Chem. **34**, 2557 (1995).
19. (*a*) S.A. King and L. DiMichele. *In* Catalysis of organic reactions. Vol. 62. *Edited by* M.G. Scaros and M.L. Prunier. Marcel Dekker, New York. 1995. pp. 157–166; (*b*) T. Ohta, Y. Tonomura, K. Nozaki, H. Takaya, and K. Mashima. Organometallics, **15**, 1521 (1996).
20. H. Takaya, T. Ohta, S. Inoue, M. Tokunaga, M. Kitamura, and R. Noyori. Org. Synth. **72**, 74 (1993).
21. Y. Sun, C. LeBlond, J. Wang, D.G. Blackmond, J. Laquidara, and J.R. Sowa, Jr. J. Am. Chem. Soc. **117**, 12 647 (1995).
22. K. Mashima, T. Hino, and H. Takaya. J. Chem. Soc. Dalton Trans. 2099 (1992).
23. (*a*) D.J. Ager and S.A. Laneman. Tetrahedron: Asymmetry, **8**, 3327 (1997), and refs. cited therein; (*b*) M.J. Burk, T.G.P. Harper, and C.S. Kalberg. J. Am. Chem. Soc. **117**, 4423 (1995); (*c*) J.P. Genêt, V. Ratovelomanana-Vidal, M.C. Caño de Andrade, X. Pfister, P. Guerreiro, and J.Y. Lenoir. Tetrahedron Lett. **36**, 4801 (1995).
24. M. Casey, J. Leonard, B. Lygo, and G. Procter. Advanced practical organic chemistry. Chapman & Hall, London. 1990. pp. 28–42.

© 1998 NRC Canada

25. J.A. Dale, D.L. Dull, and H.S. Mosher. J. Org. Chem. **34**, 2543 (1969).
26. R.R. Schrock and J.A. Osborn. J. Am. Chem. Soc. **93**, 2397 (1971).
27. W. Sucrow and K.P. Grosz. Syn. Commun. **9**, 603 (1979).
28. T. Shioiri, Y. Yokoyama, Y. Kasai, and S. Yamada. Tetrahedron, **32**, 2211 (1976).
29. M.D. Fryzuk and B. Bosnich. J. Am. Chem. Soc. **99**, 6262 (1977).
30. M. Casey, J. Leonard, B. Lygo, and G. Procter. Advanced practical organic chemistry. Chapman & Hall, London. 1990. pp. 70–73.
31. D. Parker. Chem. Rev. **91**, 1441 (1991).
32. H. Takaya, T. Ohta, N. Sayo, H. Kumobayashi, S. Akutagawa, S. Inoue, I. Kasahara, and R. Noyori. J. Am. Chem. Soc. **109**, 1596 (1987).

© 1998 NRC Canada

A combined QM/MM study of ligand substitution enthalpies in the $L_2Fe(CO)_3$, $RuCpL_2Cl$, and $RuCp^*L_2Cl$ systems

Luigi Cavallo, Tom K. Woo, and Tom Ziegler

Abstract: A combined density functional and molecular mechanics approach (QM/MM) has been validated in a study of the substitution reactions: (*i*) $(PH_3)_2Fe(CO)_3 + 2ER_3 \leftrightarrow (ER_3)_2Fe(CO)_3 + 2PH_3$ (ER_3 = PMe_3, PEt_3, $PMePh_2$, PPh_3, $PCyPh_2$, P^iPr_3, PBz_3, PCy_3, $AsEt_3$, $AsPh_3$); and (*ii*) $Cp'Ru(PH_3)_2Cl + 2ER_3 \leftrightarrow Cp'Ru(ER_3)_2Cl + 2PH_3$ (Cp' = C_5H_5, $C_5(CH_3)_5$; ER_3 = PMe_3, PEt_3, P^nBu_3, PMe_2Ph, $PMePh_2$, PPh_3, $AsEt_3$, $P(OMe)_3$, $P(OPh)_3$, $P(OCH_2)_3CEt$). The steric influence of the R substituents on the substitution enthalpies correlates well with experimental data. The combined QM/MM approach is also able to afford molecular structures in good accord with experimental estimates.

Key words: combined QM/MM, ligand substitutions, organometallic complexes.

Résumé : On a validé une approche combinée de densité fonctionnelle et de mécanique moléculaire (QM/MM) à l'aide d'une étude des réactions de substitution suivantes: (*i*) $(PH_3)_2Fe(CO)_3 + 2ER_3 \leftrightarrow (ER_3)_2Fe(CO)_3 + 2PH_3$ (ER_3 = PMe_3, PEt_3, $PMePh_2$, PPh_3, $PCyPh_2$, $P(iPr)_3$, PBz_3, PCy_3, $AsEt_3$, $AsPH_3$) et (*ii*) $Cp'Ru(PH_3)_2Cl + 2ER_3 \leftrightarrow Cp'Ru(ER_3)_2Cl + 2PH_3$ (Cp' = C_5H_5, $C_5(CH_3)_5$; ER_3 = PM_3, PEt_3, PBu_3, PMe_2Ph, $PMePh_2$, PPh_3, $AsEt_3$, $P(OMe)_3$, $P(OPh)_3$, $P(OCH_2)_3CEt$). Il existe une bonne corrélation entre l'influence stérique des substituants R sur les enthalpies de substitution et les données expérimentales. L'approche combinée QM/MM permet aussi d'obtenir des structures moléculaires qui sont en bon accord avec les valeurs expérimentales.

Mots clés : approche combinée de densité fonctionnelle et de mécanique moléculaire (QM/MM), substitutions de ligands, complexes organométalliques.

[Traduit par la Rédaction]

1. Introduction

Phosphine ligands play an important role in transition-metal chemistry, since their great variability in terms of steric bulk and electronic properties make it possible to fine-tune the reactivity of the metal center to which they are coordinated. The steric influence of phosphines was first studied experimentally by Tolman (1) who introduced the concept of the "cone angle" as a measure for the bulkiness of a specific ligand. Their electronic abilities as σ-donors and π-acceptors have been analyzed in a parallel series of experimental studies (2). Recently, Nolan (3–6) and co-workers have investigated how steric and electronic changes in the ER_3 ligand influence the overall reaction enthalpy of the substitution processes:

[1] $$(BDA)_2Fe(CO)_3 + 2ER_3 \leftrightarrow (ER_3)_2Fe(CO)_3 + BDA$$

[2] $$CpRu(COD)Cl + 2ER_3 \leftrightarrow CpRu(ER_3)_2Cl + COD$$

Received April 13, 1998.

T.K. Woo and T. Ziegler.[1] Department of Chemistry, University of Calgary, 2500 University Drive N.W., Calgary, AB T2N 1N4, Canada.
L. Cavallo. Dipartimento di Chimica, Università "Federico II" di Napoli, Via Mezzocannone 4, Napoli I-80134, Italy.

[1]Author to whom correspondence may be addressed. Telephone: (403) 220-5368. Fax: (403) 289-9488. E-mail: ziegler@zinc.chem.ucalgary.ca

[3] $$Cp^*Ru(COD)Cl + 2ER_3 \leftrightarrow Cp^*Ru(ER_3)_2Cl + COD$$

where BDA = PhCH=CHCOMe; COD = cyclooctadiene; Cp = η^5-C_5H_5; Cp* = η^5-C_5Me_5; ER_3 = tertiary phosphine, arsine, phosphite. Theoretical investigations to date on phosphine complexes have either focused on the steric aspects with the help of pure molecular mechanics (MM) calculations (7) or the electronic properties based on full quantum mechanical (QM) calculations (8).

In recent years attempts have been made to combine MM and QM calculations (QM/MM) in order to study chemical problems where both steric bulk and electronic effects are of importance at the same time, as in the case of the phosphine ligands. Work in this direction has been pioneered by Warshel and Karplus (9), Karplus and co-workers (10), Singh and Kollmann (11), as well as Morokuma and co-workers (12). The combined QM/MM approach has been applied to a few organometallic systems (13, 14). However, more systematic investigations are required to validate the QM/MM approach in the field of coordination chemistry. We have to this end conducted a QM/MM study of the ligand substitution reactions:

[4] $$(PH_3)_2Fe(CO)_3 + 2ER_3 \leftrightarrow (ER_3)_2Fe(CO)_3 + 2PH_3$$

where ER_3 = PMe_3, PEt_3, $PMePh_2$, PPh_3, $PCyPh_2$, P^iPr_3, PBz_3, PCy_3, $AsEt_3$, $AsPh_3$, and

© 1998 NRC Canada

[5] $CpRu(PH_3)Cl + 2ER_3 \leftrightarrow CpRu(ER_3)_2Cl + PH_3$

[6] $Cp^*Ru(PH_3)Cl + 2ER_3 \leftrightarrow Cp^*Ru(ER_3)_2Cl + PH_3$

where ER_3 = PMe_3, PEt_3, P^nBu_3, PMe_2Ph, $PMePh_2$, PPh_3, $AsEt_3$, $P(OMe)_3$, $P(OPh)_3$, $P(OCH_2)_3CEt$. We note that changes in the reaction enthalpy of the processes [4]–[6] can be compared to the corresponding differences in reactions [1]–[3] from the experimental studies of Nolan and co-workers (3–6). In the following, references to relative experimental M–ER_3 bond energies are taken from the work of Nolan and co-workers (3–6).

The PH_3 ligand has been chosen as reference in the theoretical studies due to the fact that this ligand represents the phosphine with the smallest possible steric requirements. The presence of two metal centers with different coordination geometry allows us further to study complexes where the degree of steric interaction between the ER_3 groups is quite different. Thus, the iron systems have a trigonal bipyramidal geometry with the ER_3 ligands well separated in trans-axial positions, whereas the ruthenium complexes are roughly tetrahedral with the ER_3 groups in much closer contact.

2. Computational details

All reported quantum-mechanical calculations were performed by means of the Amsterdam Density Functional (ADF) program system, developed by Baerends et al. (15, 16), and vectorized by Ravenek (17). The numerical integration scheme applied for the calculations was developed by te Velde and Baerends (18). The geometry-optimization procedure was based on the method by Versluis and Ziegler (19). The electronic configurations of the molecular systems were described by a triple-ζ basis set (20, 21) on the metal centers for the *ns*, *np*, *nd*, (*n* + 1)*s* and (*n* + 1)*p* valence shells. A double-ζ STO basis set was used for carbon (2*s*, 2*p*), hydrogen (1*s*), chlorine (3*s*, 3*p*), and phosphorus (3*s*, 3*p*), augmented with a single 3*d* polarization function, except for hydrogen where a 2*p* function was used. The inner shells on the metals, as well as carbon, oxygen, phosphorus, and chlorine, were treated within the frozen core approximation. A set of auxiliary s, *p*, *d*, *f*, and *g* STO functions (22), centered on all nuclei, was used in order to fit the molecular density and present Coulomb and exchange potentials accurately in each SCF cycle. Energy differences were calculated by augmenting the local exchange-correlation potential by Vosko et al. (23) with the nonlocal exchange of corrections of Becke (24) and the nonlocal correlation corrections of Perdew (25, 26).

The molecular mechanics force field was of the form

[7] $E_{MM} = E_{str} + E_{bend} + E_{tors} + E_{ofpl} + E_{vdw_i}$

where

[8*a*] $E_{str} = 1/2K_{str}(R - R_0)^2$

[8*b*] $E_{bend} = 1/2K_{bend}(\theta - \theta_0)^2$

[8*c*] $E_{tors} = 1/2K_{tors}(1 + \cos(n\phi - \phi_0))$

[8*d*] $E_{ofpl} = 1/2K_{ofpl}(1 - \cos(n\tau - \tau_0))$

Scheme 1.

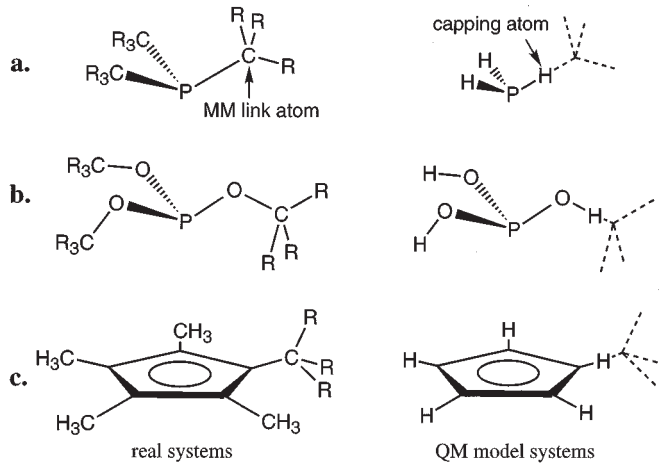

[8*e*] $E_{vdw_1} = \varepsilon_{min}[(d_{min}/d)^{12} - 2(d_{min}/d)^6]$

[8*f*] $E_{vdw_2} = D_0 \exp(\gamma(1 - d/d_0))$

For the nonbonded interactions two energy expressions have been implemented. The first, E_{vdw_1} of eq. [8*e*], employs the standard attractive–repulsive (attr–rep) 6-12 Lennard–Jones potential. The second, E_{vdw_2} of eq. [8*f*], uses an exponential expression fitted to the repulsive part of the attr–rep Lennard–Jones potential. This second approach has been adopted to eliminate spurious stabilizations from the long-range attractive part of E_{vdw_1} (7, 27), as discussed in previous applications (7, 28). The force constants were taken from the AMBER force field (29), except for the iron, ruthenium, and arsenic atoms for which we used the van der Waals parameters of the universal force field of Rappé et al. (30).

The combined QM/MM approach of Maseras and Morokuma (12) as implemented within the ADF density functional package (31) was utilized. In the combined QM/MM method, the molecular system is partitioned into QM and MM regions. Resultingly, the total molecular potential is a hybrid of a QM potential determined from an electronic structure calculation and a MM potential determined from a force-field calculation. The electronic system of the QM region is truncated with so-called "capping atoms" (11) (often hydrogen atoms), which are not part of the "real" molecular system. The capping atoms serve to allow a standard electronic structure calculation to be performed on what is termed the QM model system. Take the example illustrated in Scheme 1*a* in which a phosphine ligand, $P(CR_3)_3$, is partitioned into QM and MM regions across the three P—C bonds. Here, the electronic structure calculation would be performed on the PH_3 fragment, and a molecular mechanics potential would be used to represent the remainder of the system. In the real system, the capping atoms of the QM model system are replaced by "MM-link" atoms, which are constrained to lie along the vector of the capping atom bond.

In this study, only the bulky "R" substituents in the phosphine (PR_3), arsine (AsR_3), and phosphite ($P(OR)_3$) fragments, and the methyl groups in the Cp* groups are treated by a molecular mechanics potential. The transition-metal

© 1998 NRC Canada

Fig. 1. Optimized pure QM geometries for four conformations of the PEt_3 phosphine ligand. The corresponding geometrical parameters obtained from the QM/MM method based on the purely repulsive nonbonded energy expression E_{vdw_2} are in parentheses.

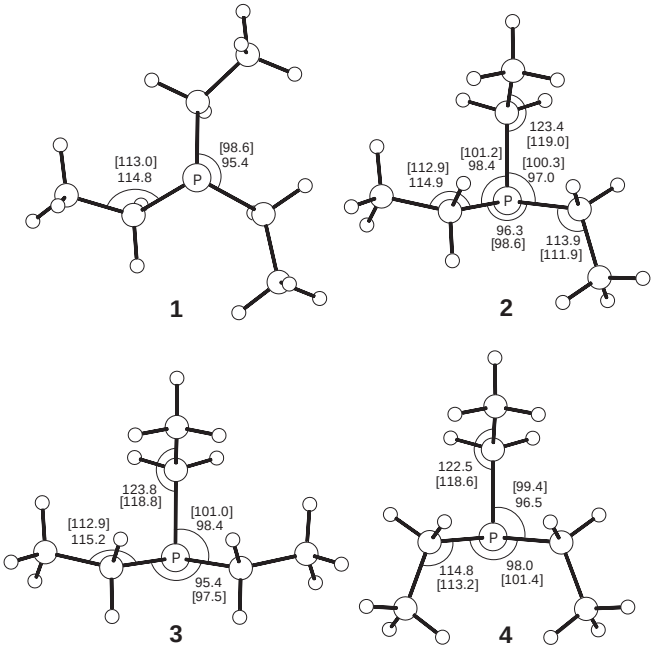

center and all other ancillary ligands are delegated to the QM region. Scheme 1 shows the real and QM model systems for the phosphines (and arsines), the phosphites, and the Cp* group that were used. The difference, ΔR, between the bond distance of the capping atom and the corresponding bond distance of the MM link atom is fixed. For sp^3 and sp^2 carbon atoms we adopted ΔR = 0.415 and 0.400 Å, respectively. This approach approximates the distances P—C (alkyl), P—C (aryl), As—C (alkyl), As—C (aryl), O—C (alkyl), O—C (aryl), and C (cyclopentadienyl)—C (methyl) to roughly 1.845, 1.830, 1.950, 1.935, 1.450, 1.435, and 1.450 Å , respectively.

The enthalpies for the substitution reactions studied by Nolan and co-workers (3–6):

[9*a*] (complex with ER_3) + BDA or COD

$$\leftrightarrow \text{(complex with BDA or COD)} + 2ER_3$$

and the substitution processes studied here:

[9*b*] (complex with ER_3) + PH_3

$$\leftrightarrow \text{(complex with } PH_3\text{)} + ER_3$$

differ only by a constant. Thus, it is possible to directly compare experimental trends from eq. [9*a*] with calculated trends from eq. [9*b*]. The reaction enthalpy for the substitution processes, eq. [9*b*], have been calculated according to the formula:

$$[10] \quad -\Delta E_{Tot} = E(\text{complex with } PH_3) + 2E(ER_3) - E(\text{complex with } ER_3) - 2E(PH_3)$$

Fig. 2. Enthalpy of ligand substitution $-\Delta E_{Tot}$ vs. Tolman cone angle for the $L_2Fe(CO)_3$ systems. The plotted $-\Delta E_{Tot}$ values are based on E_{vdw_2}. Diamonds and hollow circles represent phosphines and arsines, respectively. The ligand numbering scheme is reported in column 1 of Table 1.

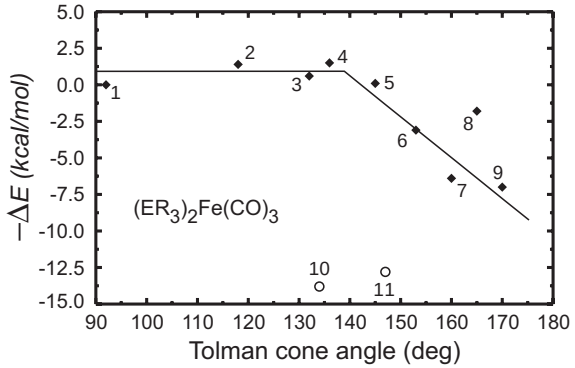

3. Results and discussion

The PEt_3 system

The first problem we have considered is the ability of the QM/MM methodology to describe properly the geometries and relative energies of different conformations for the same phosphine. We take PEt_3 as an example. We performed complete optimizations by treating PEt_3 with a pure QM method as well as the combined QM/MM approach. In the latter case the QM part of PEt_3 is represented by PH_3 whereas the ethyl groups constitute the MM component. In the QM/MM optimizations, both of the expressions for the nonbonded energy term e_{vdw_i} (i = 1, 2) of eq. [8] have been explored. The four geometries considered are reported in Fig. 1. They differ essentially in the relative orientation of the ethyl groups. Structure **1** of C_3 symmetry is the most stable independently of the computational method. Two other considered structures, **2** and **3** of C_1 and C_s symmetry, respectively, are of similar energy. According to the pure QM calculations they are 0.87 and 0.82 kcal/mol higher in energy compared to structure **1**. With the combined approach, these energy values are 1.51 and 1.52 kcal/mol, respectively, for e_{vdw_1} compared to 1.85 and 1.97 kcal/mol, respectively, in the case of e_{vdw_2}. Finally, structure **4**, was found to be 1.60 kcal/mol higher in energy than **1** according to the pure QM method, compared to 2.03 and 2.30 kcal/mol for the combined QM/MM scheme with e_{vdw_1} and e_{vdw_2}, respectively. Although the agreement is less than perfect, the relative order of stability calculated by the QM scheme is seen to be well reproduced by the QM/MM approach. We note that the steric differentiation between the conformations, as expected, is largest in the case of the purely repulsive nonbonded energy expression e_{vdw_2}.

Turning to a comparison of the optimized geometries, the main differences between QM and QM/MM structural parameters are in the C-P-C angles, which are underestimated by QM/MM. Apparently, the H–P–H force constant from the QM treatment in the QM/MM approach is too stiff to represent the electronic part of the C–P–C force constant in the PR_3 ligand and open up the C-P-C angle sufficiently. As a result, steric interaction between the different R substituents

© 1998 NRC Canada

Table 1. Calculated properties of the $L_2Fe(CO)_3$ complexes.

No.	Ligand	Cone angle (deg)	$-\Delta E_{QM}$[a] (kcal/mol)	$-\Delta E_{MM}$[a] (kcal/mol)	$-\Delta E_{Tot}$[a] (kcal/mol)	Fe—E[b] (Å)	$-\Delta E_{MM}$ (kcal/mol)	ΔE_{Tot}[c] (kcal/mol)
1	PH_3	92	0.0	0.0	0.0	2.204	0.0	0.0
2	PMe_3	118	0.7	0.7	1.4	2.209	5.8	6.5
3	PEt_3	132	0.7	–0.1	0.6	2.216	10.1	10.8
4	$PMePh_2$	136	1.3	0.2	1.5	2.216	9.7	11.0
5	PPh_3	145	2.4	–2.3	0.1	2.230	9.9	12.3
6	$PCyPh_2$	153	1.4	–4.5	–3.1	2.234	9.5	10.9
7	P^iPr_3	160	1.0	–7.4	–6.4	2.264	7.0	8.0
8	PBz_3	165	0.5	–2.3	1.8	2.227	19.7	20.2
9	PCy_3	170	0.5	–7.5	–7.0	2.270	10.4	10.9
10	$AsEt_3$	134	–14.6	0.8	–13.8	2.320	9.8	–4.8
11	$AsPh_3$	147	–12.6	–0.2	–12.8	2.324	10.6	–2.0

[a]Energies calculated during geometry optimizations with the modified purely repulsive nonbonded functional.
[b]E = P or As.
[c]The QM region is fixed with the geometry taken from the optimized structure using the purely repulsive van der Waals potential E_{vdw_2} of eq. [8*f*]. The MM region of the complex is reoptimized using the attr–rep 6-12 Lennard–Jones potential E_{vdw_1} of eq. [8*e*].

are overestimated, and the sterically determined energy differences between conformations **1**–**4** exaggerated by QM/MM compared to QM.

$L_2Fe(CO)_3$ systems

Figure 2 plots the reaction enthalpies, $-\Delta E_{Tot}$ of eq. [10], for the ligand substitution reaction [9*b*] as a function of the Tolman cone angle Θ. Increasingly negative values for $-\Delta E_{Tot}$ indicate that the substitution of ER_3 by the small PH_3 ligand becomes more and more favorable. All energy calculations were based on e_{vdw_2} of eq. [8*f*].

It is quite clear from Fig. 2 that a steric threshold angle Θ_0 is present beyond which the steric bulk of ER_3 suddenly destabilizes the M—ER_3 bond compared to the M—PH_3 linkage. This threshold angle is not yet reached for PMe_3 and PEt_3 with numerically small substitution enthalpies and cone angles equal to 118 and 132°, respectively. The presence of a steric threshold angle, and the calculated value for this angle, are in excellent agreement with the QALE treatment (quantitative analysis of ligand effects) (2, 32) performed by Stevens and Nolan (3). According to his analysis, a steric threshold of 135° is present for the $L_2Fe(CO)_3$ systems.

For bulkier ligands than PMe_3 and PEt_3 a destabilization of the M—ER_3 bond compared to PH_3 is evident. A linear fit ($y = -ax + b$) of $-\Delta E_{Tot}$ as a function of the cone angle gives a value of $a = 0.28 \pm 0.04$ kcal mol^{-1} deg^{-1}. This value is in reasonable agreement with the estimate of 0.46 kcal mol^{-1} deg^{-1} proposed by Stevens and Nolan (3) on the basis of a QALE treatment. In the linear fit, the PBz_3 phosphine was not included. As already remarked by Giering and coworkers (2) and Stevens and Nolan (3), this phosphine ligand usually proves to be a problem in such analyses (33) and is often not included.

The electronic, $-\Delta E_{QM}$, and steric, $-\Delta E_{MM}$, contributions to the total reaction enthalpy, $-\Delta E_{Tot}$, are reported in Table 1 for both e_{vdw_1} of eq. [8*e*] and e_{vdw_2} of eq. [8*f*]. We shall in the following discussions of $L_2Fe(CO)_3$, $RuCpL_2Cl$, and $RuCp^*L_2Cl$ concentrate on the results based on e_{vdw_2} and defer comments on the use of e_{vdw_1} to the end of the discussion section.

In the decomposition of $-\Delta E_{Tot}$ a negative value for $-\Delta E_{MM}$ indicates that the M—ER_3 bond has been destabilized by steric factors. Positive values in the electronic QM contribution, $-\Delta E_{QM}$, come from the fact that the H-P-H angle in the PH_3 ligand is distorted on coordination from 92 to 98°. The other phosphines already have angles close to 98° in the free state and are not distorted much further in the complex. Thus, a positive value for the QM contribution, $-\Delta E_{QM}$, stems from the fact that it takes more energy to prepare (distort) PH_3 to become as a ligand than any of the other ER_3 species.

Figure 3 plots the calculated enthalpies of reaction versus the Fe—P bond distance. A linear bond strength – bond length relationship is clearly present. For the systems with phosphines having cone angles smaller than 135°, the Fe—P bond distances are practically the same. On the other hand, for the more weakly bound and more encumbered phosphines the Fe—P bond distance increases from 2.20 up to 2.27 Å, in going from the PH_3 to the PCy_3 complex. For the correlation in Fig. 3 PBz_3 is in line with the other phosphines.

We have taken a detailed look at the deformations of the PBz_3 ligand after coordination in order to rationalize the special behavior of PBz_3 in the QALE treatment. The most noticeable change is a rotation around the C_{sp^3}—C_{s^2} bond from 107° in free PBz_3 to 92° in coordinated PBz_3. The rotation increases the contact distance between phenyl carbons and the carbon on CO from 3.1 to 3.4 Å. The deformation amounts to only 0.3 kcal/mol in the free ligand and greatly reduces the steric interaction in the complex along with the cone angle of PBz_3. It is clear that for phosphines with a flexible structure, the cone angle calculated for the uncoordinated phosphine is probably only a rough approximation to the "real" value assumed in encumbered complexes. In such cases, as suggested by several authors, use should be made of cone angles obtained from X-ray structures of the coordinates phosphine.

Figure 4 reports the optimized structure for the $Fe(PCyPh_2)_2(CO)_3$ complex with experimental values in parentheses. The overall agreement between the calculated and the experimentally observed structures is reasonably good.

© 1998 NRC Canada

Fig. 3. Enthalpy of ligand substitution vs. the average Fe—E (E = P, As) bond distance for the $L_2Fe(CO)_3$ systems. The plotted $-\Delta E_{Tot}$ values are based on E_{vdw_2}. Diamonds and hollow circles represent phosphines and arsines, respectively. The ligand numbering scheme is reported in column 1 of Table 1.

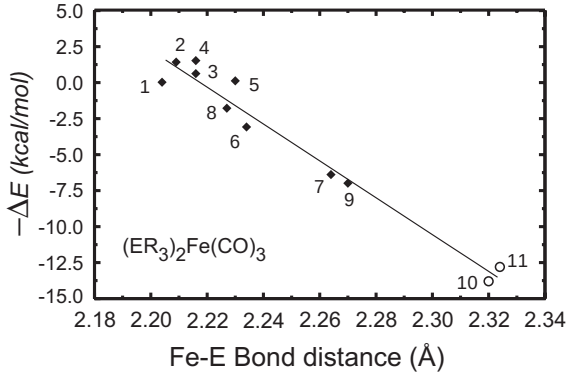

The calculated P-Fe-P angle is 178°, while the C-Fe-C angle that encloses the Cy substituents is forced by the presence of the bulky Cy rings to 128°. In the experimentally determined structure, these angles assume values of 178 and 122°, respectively.

Compared to the corresponding phosphines, the arsine ligands $AsEt_3$ and $AsPh_3$ are calculated to form bonds to iron that are weaker by 14.4 and 12.9 kcal/mol, respectively. The corresponding experimental values are 17.9 and 16.7 kcal/mol, respectively (3). For the two arsines considered, steric effects are almost insignificant. This can be explained by the larger covalent radius of the arsenic atom compared to phosporous, which keeps the R substituents further apart. This observation is reflected in the MM energy contribution due to the interaction of the arsines with the other ligands. On a per arsine basis, the MM interaction energies of the arsine with the other ligands are 0.4 and 0.7 kcal/mol in the $AsEt_3$ and $AsPh_3$ containing complexes whereas in the corresponding phosphine complexes these MM energies are 0.8 and 1.4 kcal/mol, respectively. Finally, the Fe—As bond distances in the two considered arsines are practically the same (0.004 Å longer in the $AsPh_3$ complex) whereas the Fe—P distance in the PPh_3 complex is 0.014 Å larger than in the PEt_3 system.

$RuCpL_2Cl$ systems

Table 2 displays the calculated substitution enthalpies $-\Delta E_{Tot}$ for eq. [5] decomposed into its steric, $-\Delta E_{MM}$, and electronic, $-\Delta E_{QM}$, components. The steric contribution is obtained using the purely repulsive van der Waals potential of eq. [8*f*]. Negative values indicate a destabilization compared to the PH_3 ligand. Figure 5 plots the enthalpies of ligand substitution as a function of the Tolman cone angle for the $RuCpL_2Cl$ systems. These systems have the phosphine ligands close together compared to $L_2Fe(CO)_3$, and a steric destabilization of 1.4 kcal/mol is present even for PMe_3, which is the substituted phosphine with the smallest cone angle. A linear fit of the type $y = -ax + b$ for $-\Delta E_{Tot}$ with respect to the cone angle affords a value of $a = 0.23 \pm 0.09$ in the case of the phosphine systems. This value should be compared to the corresponding estimate of $a = 0.50 \pm 0.13$ from the experimental data of Nolan and co-workers

Fig. 4. Optimized QM/MM geometry of the $Fe(PCyPh_2)_2(CO)_3$ complex based on E_{vdw_2}. Parenthetic values refer to the same geometric parameters found in the crystalline structure.

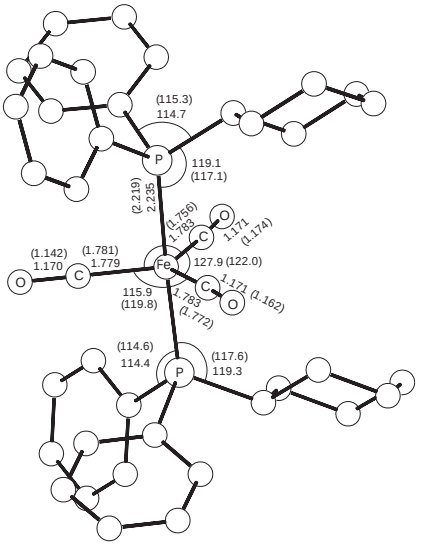

(4). Our theoretical QM/MM model takes only steric factors into account and neglects the decline in σ-donicity with the cone angles described by Nolan and co-workers (4) in their QALE analysis. That is, $-\Delta E_{MM}$ might have the right trend whereas the variation in $-\Delta E_{QM}$ is too small, since PH_3 is used to describe the electronic part for all phosphines. Thus, it is understandable that the *a* factor is underestimated by the current QM/MM approach, since a positive electronic contribution from $-\Delta E_{QM}$ is missing.

The QM/MM study of the phosphites was carried out with $P(OH)_3$ representing the QM region. We find that the coordination of $P(OCH_2)_3CEt$ and $P(OPh)_3$ are, respectively, 6.9 and 10.1 kcal/mol less favorable than the coordination of $P(OMe)_3$. These values are in a reasonable agreement with the experimental estimates of 5.9 and 7.7 kcal/mol, respectively. For $P(OPh)_3$ the weaker coordination is due to the steric bulk, $-\Delta E_{MM}$, whereas the poor coordination of $P(OCH_2)_3CEt$ with a small cone angle is electronic, $-\Delta E_{QM}$, in nature. Our analysis of the bonding orbitals suggests this is caused by the almost *trans* conformation assumed by the Ru-P-O-H torsional angles, which stabilize the σ-donor orbital and affords a poor σ-donicity of the $P(OCH_2)_3CEt$ ligand. The σ-donor orbital stabilization in the caged phosphite is due to a decrease of antibonding interactions between the O and P lone pair orbitals. It is interesting that this electronic effect, $-\Delta E_{QM}$, is represented well by the QM model ligand $P(OH)_3$ as it is forced to a *trans* conformation of the Ru-P-O-H torsional angle by the $(CH_2)_3CEt$ MM framework. A comparison between phosphites and phosphines, in particular $P(OMe)_3$ vs. PMe_3, indicates that the phosphite coordinates better by 19.7 kcal/mol. This value compares poorly with the experimental estimate of 3.4 kcal/mol. A better agreement would require PH_3 to be modeled by PMe_3 as the QM ligand. For the single arsine treated here, $AsEt_3$, the coordination is weaker by 11.3 kcal/mol compared to PEt_3. The corresponding experimental value is 15.1 kcal/mol (4).

© 1998 NRC Canada

Table 2. Calculated properties of the $RuCpL_2Cl$ complexes.

No.	Ligand	Cone angle (deg)	$-\Delta E_{QM}$[a] (kcal/mol)	$-\Delta E_{MM}$[a] (kcal/mol)	$-\Delta E_{Tot}$[a] (kcal/mol)	Fe—E[b] (Å)	$-\Delta E_{MM}$ (kcal/mol)	ΔE_{Tot}[c] (kcal/mol)
1	PH_3	92	0.0	0.0	0.0	2.304	0.0	0.0
2	PMe_3	118	–0.8	–0.6	–1.4	2.320	5.3	4.5
12	PMe_2Ph	122	–0.3	–1.2	–1.5	2.322	6.8	6.5
3	PEt_3	132	–0.8	–5.0	–5.8	2.342	5.8	5.0
13	P^nBu_3	132	–0.9	–5.3	–6.2	2.342	9.8	8.9
4	$PMePh_2$	136	0.0	–2.2	–2.2	2.325	10.6	10.6
5	PPh_3	145	–1.6	–6.6	–8.2	2.356	10.6	9.0
14	$P(OCH_2)_3CEt$	101	12.4	–1.0	11.4	2.233	1.9	14.3
15	$P(OMe)_3$	107	25.0	–6.7	18.2	2.262	0.6	25.6
16	$P(OPh)_3$	128	18.9	–10.7	8.2	2.276	7.4	26.3
10	$AsEt_3$	134	–14.3	–2.8	–17.1	2.459	7.1	7.2

[a] Energies calculated during geometry optimizations with the modified purely repulsive nonbonded functional.
[b] E = P or As.
[c] The QM region is fixed with the geometry taken from the optimized structure using the purely repulsive van der Waals potential E_{vdw_2} of eq. [8*f*]. The MM region of the complex is reoptimized using the attr–rep 6-12 Lennard–Jones potential E_{vdw_1} of eq. [8*e*].

Fig. 5. Enthalpy of ligand substitution vs. Tolman cone angle for the $RuCpL_2Cl$ systems. The plotted $-\Delta E_{Tot}$ values are based on E_{vdw_2}. Diamonds, hollow circles, and stars represent phosphines, arsines, and phosphites, respectively. The ligands numbering scheme is reported in column 1 of Table 2.

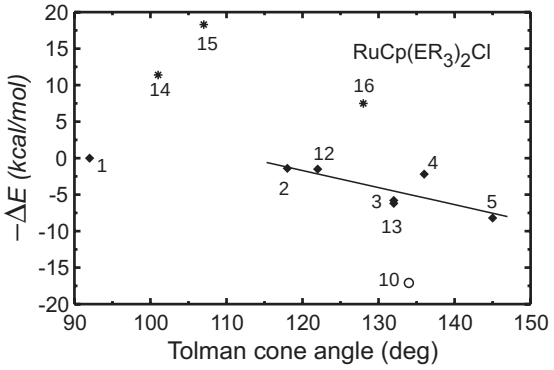

Fig. 6. Enthalpy of ligand substitution vs. the average Ru—E (E = P, As) bond distance for the $RuCpL_2Cl$ systems. The plotted $-\Delta E_{Tot}$ values are based on E_{vdw_2}. Diamonds, hollow circles, and stars represent phosphines, arsines, and phosphites, respectively. The ligands numbering scheme is reported in column 1 of Table 2.

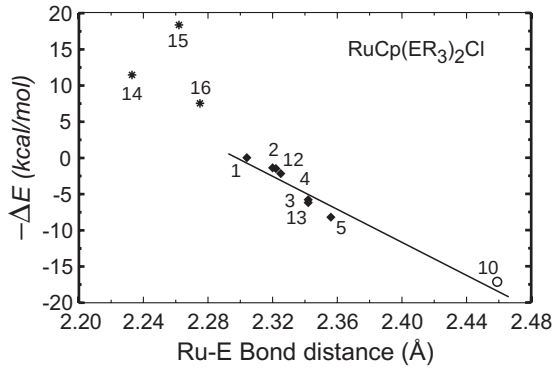

Figure 6 plots the calculated enthalpies of reaction versus the Ru—P bond distance. A linear fit, with all phosphines included, provides a slope of –112 vs. –140 kcal mol^{-1} $Å^{-1}$ determined by Nolan. Also given in the plot are the phosphites at shorter Ru—E distances and the arsine at longer Ru—E distance. As one would expect, it is not possible to extend the linear plot of the phosphines to include other types of ligands.

Figure 7 reports the optimized structure of the $RuCp(PEt_3)_2Cl$ complex. The corresponding experimental data are reported in parentheses. The overall agreement between the calculated and the experimentally observed structure is reasonably good. In particular, the steric requirements of the system open the P-Ru-P and P-Ru-Cl angles from 91° and 82° calculated for the $RuCp(PH_3)_2Cl$ complex to 96° and 88° calculated for the $RuCp(PEt_3)_2Cl$ complex. These values are to be compared with the experimental estimates of 95° and 90° obtained by Nolan in the $RuCp(PEt_3)_2Cl$ complex.

$RuCp^*L_2Cl$ systems

Figure 8 plots the enthalpies of ligand substitution as a function of the Tolman cone angle for the $RuCp^*L_2Cl$ systems based on e_{vdw_2} of eq. [8*f*]. For these species, steric effects are even more important than in the corresponding $RuCpL_2Cl$ compounds due to the bulk of Cp*. The PMe_3 complex is already destabilized by 3.6 kcal/mol with respect to the naked PH_3 complex. A linear fit, $y = -ax + b$, of $-\Delta E_{Tot}$ against the cone angle of the phosphines affords a value of $a = 0.58 \pm 0.24$. This value has to be compared with the estimate of 0.47 obtained by using the data due to Nolan and co-workers (5). Our results, as already suggested by Nolan and co-workers (5), indicate that the behavior of the permethylated ruthenium complexes is essentially determined by steric effects. The various steric, $-\Delta E_{MM}$, and electronic, $-\Delta E_{QM}$, contributions to $-\Delta E_{Tot}$ are reported in Table 3. Enthalpy data for the substitution of L by PMe_3 in $L_2Fe(CO)_3$, $RuCpL_2Cl$, and $RuCp^*L_2Cl$ are found in Table 4.

© 1998 NRC Canada

Table 3. Calculated properties of the $RuCp^*L_2Cl$ complexes.

No.	Ligand	Cone angle (deg)	$-\Delta E_{QM}$[a] (kcal/mol)	$-\Delta E_{MM}$[a] (kcal/mol)	$-\Delta E_{Tot}$[a] (kcal/mol)	Fe—E[b] (Å)	$-\Delta E_{MM}$ (kcal/mol)	ΔE_{Tot}[c] (kcal/mol)
1	PH_3	92	0.0	0.0	0.0	2.304	0.0	0.0
2	PMe_3	118	–0.6	–3.0	–3.6	2.342	4.7	4.1
12	PMe_2Ph	122	–1.2	–4.0	–5.2	2.347	7.5	6.3
3	PEt_3	132	–5.9	–11.4	–17.3	2.405	1.8	–4.1
13	P^nBu_3	132	–6.2	–11.9	–18.1	2.405	6.7	0.5
4	$PMePh_2$	136	–1.7	–6.1	–7.8	2.359	10.3	8.6
5	PPh_3	145	–6.7	–13.4	–20.1	2.405	8.4	1.7
14	$P(OCH_2)_3CEt$	101	10.0	–1.9	8.1	2.238	4.3	14.3
15	$P(OMe)_3$	107	22.3	–9.9	12.4	2.274	1.2	23.5
16	$P(OPh)_3$	128	12.3	–15.7	–3.4	2.292	8.5	20.8
10	$AsEt_3$	134	–17.6	–7.1	–24.7	2.525	5.6	–12.0

[a] Energies calculated during geometry optimizations with the modified purely repulsive nonbonded functional.
[b] E = P or As.
[c] The QM region is fixed with the geometry taken from the optimized structure using the purely repulsive van der Waals potential E_{vdw_2} of eq. [8*f*]. The MM region of the complex is reoptimized using the attr–rep 6-12 Lennard–Jones potential E_{vdw_1} of eq. [8*e*].

Fig. 7. Optimized QM/MM geometry of the $RuCp(PEt_3)_2Cl$ complex based on E_{vdw_2}. Experimental data in parentheses.

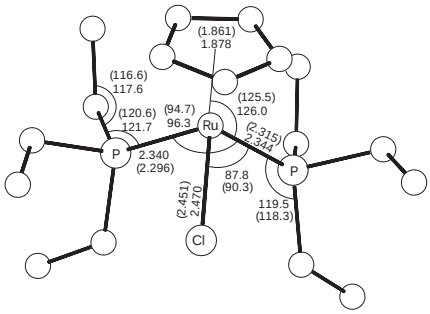

For the remaining ligand types, the phosphites are seen to bind stronger to ruthenium than the phosphines whereas $AsEt_3$ binds more weakly. Also, $P(OMe)_3$ coordinates stronger than either $P(OCH_2)_3CEt$ or $P(OPh)_3$, Fig. 3. These trends are in good agreement with experiment and were already noted (and rationalized) in the connected discussion of the $RuCpL_2Cl$ systems. Figure 9 plots the calculated enthalpies of reaction versus the Ru—E bond distances. For the phosphines we obtain a good linear bond strength – bond length relationship with a slope of –124.

Figure 10 reports the optimized structure of the $RuCp^*(P(OCH_2)_3CEt)_2Cl$ complex, with experimental numbers in parentheses. The overall agreement between the calculated and the experimentally observed structure is reasonably good. A comparison between the calculated geometries for the $RuCp^*(P(OCH_2)_3CEt)_2Cl$ and $RuCp^*(P(OMe)_3)_2Cl$ compounds indicates that for the complex with the caged phosphite the P—Ru bond distance is slightly shorter (2.238 vs. 2.274 Å). A similar trend was observed for the systems with the unsubstituted Cp ligand. Finally, in the complexes based on the caged phosphite the O-P-O angle is on average 3.5° larger than in the complexes based on the trimethyl phosphite. This value can be compared with the value of 3° found by Nolan and co-workers (6).

Fig. 8. Enthalpy of ligand substitution vs. Tolman cone angle for the $RuCp^*L_2Cl$ systems. The plotted $-\Delta E_{Tot}$ values are based on E_{vdw_2}. Diamonds, hollow circles, and stars represent phosphines, arsines, and phosphites, respectively. The ligands numbering scheme is reported in column 1 of Table 3.

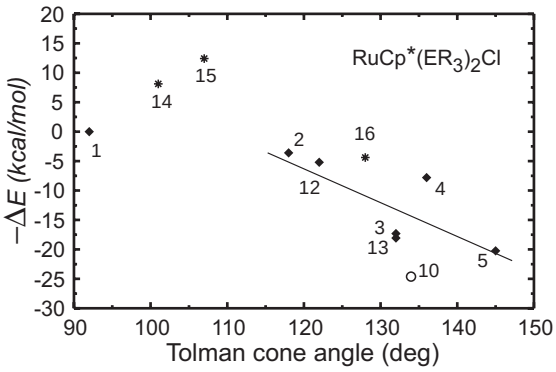

A comparison between $RuCpL_2Cl$ and $RuCp^*L_2Cl$ systems

To compare the role played by steric effects in the $RuCpL_2Cl$ and $RuCp^*L_2Cl$ systems, we calculated the enthalpies of the following reaction:

[11] $Cp^*Ru(COD)_2Cl + CpRu(ER_3)_2Cl \leftrightarrow Cp^*Ru(ER_3)_2Cl + CpRu(COD)_2Cl$

The mean value we obtained for the above reaction is 2.7 kcal/mol, which is in a reasonable agreement with the experimental value of 5.1 kcal/mol obtained from the experimental data due to Nolan and co-workers. In agreement with the experimental results, the largest values are calculated for the complexes based on PEt_3 and P^nBu_3. The theoretical values for these two ligands are 6.7 and 7.1 kcal/mol whereas the corresponding experimental estimates are 7.3 and 9.4 kcal/mol, respectively. Our results are in agreement with the hypothesis suggested by Nolan and co-workers (6) that steric effects only partially contribute to the different behavior of the Cp and Cp* systems. The comparison between the

© 1998 NRC Canada

Table 4. Calculated[a] and experimental[b] enthalpies[c] for the substitution of L by PMe_3 in $L_2Fe(CO)_3$, $RuCpL_2Cl$, and $RuCp^*L_2Cl$.

	$L_2Fe(CO)_3$		$RuCpL_2Cl$		RuC^*pL_2Cl	
Ligand L	Calc.	Expt.	Calc.	Expt.	Calc.	Expt.
PMe_3	0.0	0.0	0.0	0.0	0.0	0.0
PEt_3	–0.8	3.5	–4.4	–3.9	–13.8	–5.0
$PMePh_2$	0.1	–4.8	–0.8	–5.6	–4.2	–2.8
PMe_2Ph	—	—	–0.1	–2.5	–1.7	–0.4
PPh_3	–1.2	–12.0	–6.8	–15.5	–16.5	–14.1
$PCyPh_2$	–4.5	–11.4	—	—	—	—
P^iPr_3	–7.8	–7.3	—	—	—	—
P^nBu_3	—	—	–4.8	–3.0	–14.5	–6.2
PBz_3	–3.2	–6.1	—	—	—	—
PCy_3	–8.3	–8.2	—	—	—	—
$P(OCH_2)_3CEt$	—	—	12.8	–2.5	11.6	–0.6
$P(OMe)_3$	—	—	19.7	3.4	16.0	5.3
$P(OPh)_3$	—	—	9.6	–4.3	0.2	–1.0
$AsEt_3$	–15.2	–14.4	–15.7	–19.0	–21.1	–17.2
$AsPh_3$	–14.2	–28.7	—	—	—	—

Fig. 9. Enthalpy of ligand substitution vs. the average Ru—E (E = P, As) bond distance for the $RuCp^*L_2Cl$ systems. The plotted $-\Delta E_{Tot}$ values are based on E_{vdw_2}. Diamonds, hollow circles, and stars represent phosphines, arsines, and phosphites, respectively. The ligands numbering scheme is reported in column 1 of Table 3.

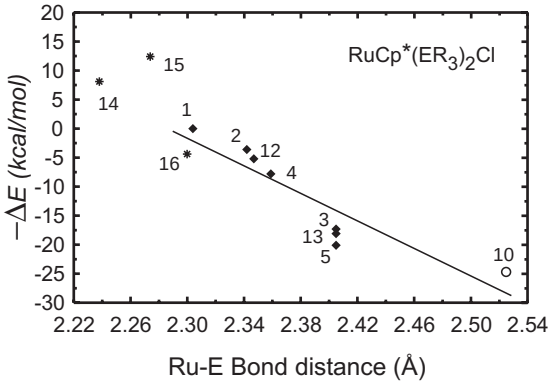

calculated and experimental geometries also supports the buildup of steric pressure in the permethylated systems. In fact, the calculated Ru–P and Ru–Cp (centroid) distances are ca. 0.063 and 0.015 Å longer in the Cp* complexes based on the PEt_3 and P^nBu_3 phosphines, with respect to the analogous complexes based on the unsubstituted Cp ring. These bond stretches have to be compared with elongations of 0.033 and 0.015 Å observed for the same distances when comparing the X-ray structures of the $CpRu(PEt_3)_2Cl$ (4) and $Cp^*Ru(P^nBu_3)_2Cl$[2] complexes. Finally, in the Cp* complexes the calculated P-Ru-Cl angles is on average 3.6° smaller than in the corresponding Cp complexes. This value can be compared with the experimentally observed reduction of 2.6° of the P-Ru-Cl angle in going from the $CpRu(PEt_3)_2Cl$ (4) to the $Cp^*Ru(PBu_3)_2Cl$ (32) complex.

Fig. 10. Optimized QM/MM geometry of the $RuCp^*(P(OCH_2)_3CEt)_2Cl$ complex based on E_{vdw_2}. Experimental values in parentheses.

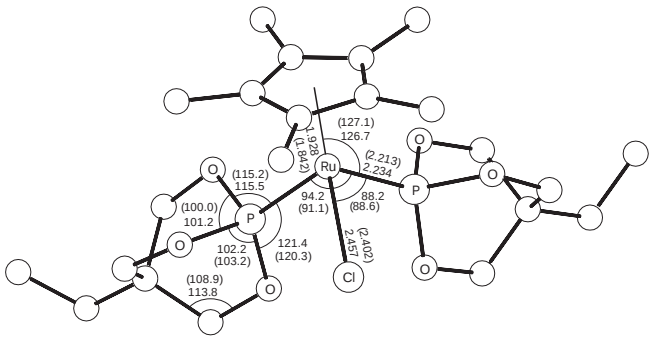

Using the standard attractive–repulsive Lennard–Jones potential

We have up to now discussed reaction enthalpies, $-\Delta E_{Tot}$, for eq. [9*b*] based on the totally repulsive nonbonding energy term E_{vdw_2} of eq. [8*f*]. Tables 1–3 also contain reaction enthalpies based on the regular attractive–repulsive Lennard–Jones potential E_{vdw_1} of eq. [8*e*]. Figure 11 plots the values of the enthalpies of ligand substitution for all the considered systems obtained using the standard attr–rep Lennard–Jones potential as a function of the cone angle. The scattered patterns obtained would prevent any linear correlation. Moreover, the plot of $-\Delta E_{Tot}$ as a function for the cone angle is qualitatively incorrect for systems such as $L_2Fe(CO)_3$ with a great number of atoms and a modest steric pressure. That is, the more stable complexes correspond to systems based on phosphines with large cone angles. This behavior is due to the long-range attractive tails of the standard 6-12 Lennard–Jones potential (7, 27, 28). For the class of reactions here considered, that is, ligands substitution reactions, the attrac-

[2] S.P. Nolan. Private communication.

© 1998 NRC Canada

Fig. 11. Enthalpy of ligand substitution vs. Tolman cone angle for the $L_2Fe(CO)_3$, $RuCpL_2Cl$, and $RuCp^*L_2Cl$ systems. The plotted $-\Delta E_{Tot}$ values are based on E_{vdw_1}. Squares, circles, and triangles represent $L_2Fe(CO)_3$, $RuCpL_2Cl$, and $RuCp^*L_2Cl$ systems, respectively.

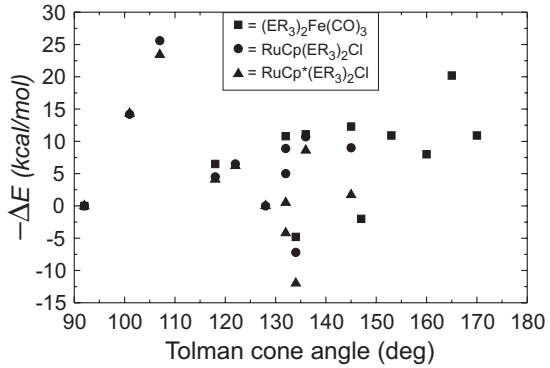

tive tails give a stabilizing contribution to the total energy that is proportional to the total number of atoms present in the molecule. However, this is a spurious effect due to the fact that our models simulate gas-phase reactions. In fact, in the presence of a solvent, these stabilizing long-range Lennard–Jones interactions occur as well with solvent molecules.

4. Concluding remarks

The combined QM/MM method has considerable potential in allowing for efficient computational modeling steric effects in coordination chemistry. However, to date, there have been only a few applications of the method to coordination compounds (13, 14). In the present investigation, we attempt to validate the approach, which so far has been lacking, by comparing theoretical results obtained by the QM/MM method with the rich source of experimental data generated by Nolan and co-workers (3–6) in their experimental studies of the substitution reactions [1]–[3].

The present QM/MM scheme is able to reproduce the gross features of the QALE analysis on the substitution reactions [1]–[3] provided by Nolan and co-workers (3–6). It can in addition provide geometrical parameters for some of the complexes involved in reactions [1]–[3] that are in good agreement with experimental structures.

Our investigation also points to a number of problems with the present QM/MM approach. First, the regular attractive–repulsive Lennard–Jones potential, E_{vdw_1} of eq. [8*e*], is inadequate for coordination compounds and provides relationships between substitution enthalpies and cone angles that are contrary to the experimental QALE analysis (3). The additive nature of the MM van der Waals potentials, leads to the large bulky ligands being bound more strongly than the smaller ligands, simply due to the sheer number of atoms associated with the larger ligands. To rectify this problem we have utilized a purely repulsive potential, E_{vdw_2} of eq. [8*f*], in accordance with previous works (7, 28). Although the purely repulsive van der Waals potential provides reasonable results, further work is required in order to generate an adequate nonbonded interaction potential.

The use of the minimal quantum mechanical units PH_3 and AsH_3 to describe the electronic properties of all phosphines and arsines, respectively, has proven to be inadequate. For phosphites, the use of $P(OH)_3$ as the quantum mechanical unit is capable of representing a broad range of phosphites. This is because the dominant electronic effect in phosphites is due to the oxygen atoms. It is evident that even for substitution reactions in which sterics are thought to dominate the substitution energies, the electronic characteristics of the ligands, which are not captured by the QM/MM method, play a substantial role. Large absolute deviations are present for some of these reactions. Thus, future work will concentrate on larger and more realistic quantum mechanical units for the various categories of ER_3 units that more effectively capture the electronic effects.

Acknowledgment

This work has been supported by the Natural Sciences and Engineering Research Council of Canada (NSERC), as well as by the donors of the Petroleum Research Fund, administered by the American Chemical Society (ACS-PRF No. 31205-AC3) and by Novacor Research and Technology Corporation (NRTC) of Calgary. L.C. thanks The University Federico II of Naples for financial support within the "Programma di Scambi Internazionali." T.K.W. wishes to thank NSERC, the Alberta Heritage Scholarship Fund, and the Izaak Walton Killam memorial foundation for graduate fellowships.

References

1. C.A. Tolman. Chem. Rev. **77**, 313 (1977).
2. A.L. Fernandez, A. Prock, and W.P. Giering. Organometallics, **13**, 2767 (1994), and refs. therein.
3. C. Li, E.D. Stevens, and S.P. Nolan. Organometallics, **14**, 3791 (1995).
4. M.E. Cucullu, L. Luo, S.P. Nolan, P.J. Fagan, N.L. Jones, and J.C. Calabrese. Organometallics, **14**, 289 (1995).
5. L. Luo, S.P. Nolan, and P.J. Fagan. Organometallics, **12**, 4305 (1995).
6. S.A. Serron, L. Luo, E.D. Stevens, S.P. Nolan, N.L. Jones, and P.J. Fagan. Organometallics, **15**, 5209 (1996).
7. (*a*) T.K. Woo and T. Ziegler. Inorg. Chem. **33**, 1857 (1994); (*b*) K.J. Lee and T.L. Brown. Inorg.Chem. **31**, 289 (1992).
8. (*a*) K. Kitaura and K. Morokuma. Int. J. Quantum Chem. **10**, 325 (1976); (*b*) T. Ziegler, V. Tschinke, and C. Ursenbach. J. Am. Chem. Soc. **109**, 4827 (1987).
9. A. Warshel and M. Karplus. J. Am. Chem. Soc. **94**, 5612 (1972).
10. M.J. Field, P.A. Bash, and M. Karplus. J. Comput. Chem. **11**, 700 (1990).
11. U.C. Singh and P.A. Kollmann. J. Comput. Chem. **7**, 718 (1986).
12. F. Maseras and K. Morokuma. J. Comput. Chem. **16**, 1170 (1995).
13. T. Matsubara, F. Maseras, N. Koga, and K. Morokuma. J. Phys. Chem. **100**, 2573 (1996).
14. L. Deng, T.K. Woo, L. Cavallo, P. Margl, and T. Ziegler. J. Am. Chem. Soc **119**, 6177 (1997).
15. E.J. Baerends, D.E. Ellis, and P. Ros. Chem. Phys. **2**, 41 (1973).
16. E.J. Baerends and P. Ros. Chem. Phys. B, 52 (1973).
17. W. Ravenek. Algorithms and applications on vector and parallel computers. Elsevier, Amsterdam, The Netherlands. 1987.

© 1998 NRC Canada

18. G. te Velde and E.J. Baerends. J. Comput. Chem. **99**, 84 (1992).
19. L. Versluis and T. Ziegler. J. Chem. Phys. **88**, 322 (1988).
20. J.G. Snijders, E.J. Baerends, and P. Vernoijs. At. Nucl. Data Tables, **26**, 483 (1982).
21. P.Vernoijs, J.G. Snijders, and E.J. Baerends. Slater type basis functions for the whole periodic system internal report (in Dutch) department of theoretical chemistry. Free University, Amsterdam, The Netherlands. 1981.
22. J. Krijn and E.J. Baerends. Fit functions in the HFS method internal report (in Dutch). Department of Theoretical Chemistry, Free University, Amsterdam, The Netherlands. 1984.
23. S.H. Vosko, L. Wilk, and M. Nusair. Can. J. Phys. **58**, 1200 (1980).
24. A. Becke. Phys. Rev. A: At. Mol Opt. Phys. **38**, 3098 (1988).
25. J.P. Perdew and A. Zunger. Phys. Rev. B: Condens. Matter, 5048 (1981).
26. J.P. Perdew. Phys. Rev. B: Condens. Matter, **33**, 8822 (1986).
27. R.R. Sauers. J. Chem. Educ. **73**, 114 (1996).
28. G. Guerra, P. Longo, L. Cavallo, P. Corradini, and L. Resconi. J. Am. Chem. Soc. **119**, 4394 (1997).
29. W.D. Cornell, P. Cieplak, C.I. Bayly, I.R. Gould, K.M. Merz, Jr., D.M. Ferguson, D.C. Spellmeyer, T. Fox, J.W. Caldwell, and P.A. Kollmann. J. Am. Chem. Soc. **117**, 5179 (1995).
30. A.K. Rappé, C.J. Casewit, K.S. Colwell, W.A. Goddard III, and W.M. Skiff. J. Am. Chem. Soc. **114**, 10 024 (1992).
31. T.K. Woo, L. Cavallo, and T. Ziegler. Theor. Chem. Acc. In press.
32. J. Bartholomew, A.L. Fernandez, B.A. Lorsbach, M.R. Wilson, A. Prock, and W.P. Giering. Organometallics, **15**, 295 (1996).
33. L.E. Manzer and C.A. Tolman. J. Am. Chem. Soc. **97**, 1955 (1975).

© 1998 NRC Canada

Color profile: Disabled
Composite Default screen

Oxidation of 2-methylpyrroles with perchlorinated iron(III) metalloporphyrin catalysts: a versatile synthesis of symmetric and asymmetric dipyrromethanes

Veranja Karunaratne and David Dolphin

Abstract: A variety of substituted 2-methylpyrroles (**3**–**8**) were oxidized using the metalloporphyrin catalysts iron(III) *meso*-tetra(2,6-dichloro-3-sulphonatophenyl)-β-octachloroporphyrin chloride **1** and iron(III) *meso*-tetra(2,6-dichlorophenyl)-β-octachloroporphyrin chloride **2** under very mild conditions. Treatment of the resulting allylic alcohols **3a**–**8a** with α-free pyrroles **9** and **10** resulted in a very efficient synthesis of the corresponding dipyrromethanes **3b**–**8b** and **3c**–**8c**. Furthermore, the above allylic alcohols when treated with furfurylamine produced the novel (2-furylmethyl)-2-pyrrolylmethylamines **3d**–**8d**.

Key words: catalytic oxidation, metalloporphyrins, pyrroles, dipyrromethanes, polyhalogenated porphyrins.

Résumé : Opérant dans des conditions très douces, on a oxydé divers 2-méthylpyrroles substitués (**3**–**8**) à l'aide de catalyseurs métalloporphyrines, le chlorure de la *méso*-tétra(2,6-dichloro-3-sulfonatophényl)-β-octachloroporphyrine fer(III), **1** et le chlorure de la *méso*-tétra(2,6-dichlorophényl)-β-octachloroporphyrine fer(III), **2**. Le traitement des alcools allyliques obtenus (**3a**–**8a**) avec les pyrroles **9** et **10** dont les positions α sont libres permet de réaliser une synthèse très efficace des dipyrrométhanes correspondants, **3b**–**8b** et **3c**–**8c**. De plus, la réaction de ces alcools allyliques avec de la furfurylamine conduit à de nouvelles (2-furfurylméthyl)-2-pyrrolylméthylamines **3d**–**8d**.

Mots clés : oxydation catalytique, métalloporphyrines, pyrroles, dipyrrométhanes, porphyrines polyhalogénées.

[Traduit par la Rédaction]

Some of the most interesting and widely studied heme proteins are cytochromes P-450 (1). Activation of dioxygen by such monooxygenase enzymes involves insertion of one of the atoms of O_2 into the organic substrate while the other is reduced to water in the presence of an electron donor. Studies to unravel the cytochrome P-450 monooxygenase activity are complicated by the protein. Since much of the oxidation chemistry occurs at the iron porphyrin, in vitro biomimetic studies have been focused on synthetic metalloporphyrins. As such, *meso*-tetraphenylporphyrins (2), which are readily synthesized, are commonly used as mimics of the natural systems.

In 1979, Groves et al. (3) first reported the cytochrome P-450 monooxygenase-like activity in a model system using iron(III) *meso*-tetraphenylporphyrin and iodosylbenzene (PhIO) as a co-oxidant. Several other metalloporphyrins were also shown to catalyze both alkene epoxidations (4) and hydroxylation of unactivated hydrocarbons (1, 5) mimicking the natural system. However, the utility of these catalysts in organic synthesis has been limited. While the first-generation

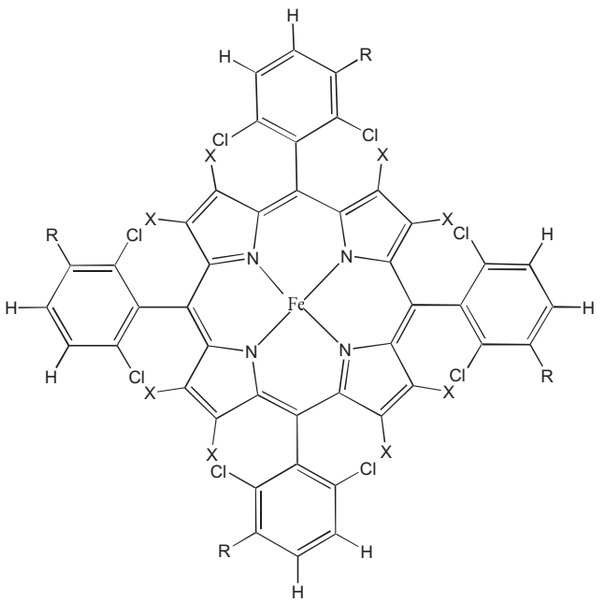

1 R = SO_3H X = Cl
2 R = H X = Cl
2a R = H X = Br

Received February 27, 1998.

V. Karunaratne and D. Dolphin.[1] Department of Chemistry, University of British Columbia, 2036 Main Mall, Vancouver, BC V6T 1Z1, Canada.

[1]Author to whom correspondence may be addressed.
Telephone: (604) 822-4571. Fax: (604) 822-9678.
E-mail: david@dolphin.chem.ubc.ca

© 1998 NRC Canada

Can. J. Chem. Downloaded from www.nrcresearchpress.com by China University of Science and Technology on 09/05/12
For personal use only.

I:\cjc\cjc76\cjc-10\OctCHEM-D.vp
Wednesday, January 06, 1999 10:03:51 AM

Color profile: Disabled
Composite Default screen

Scheme 1.

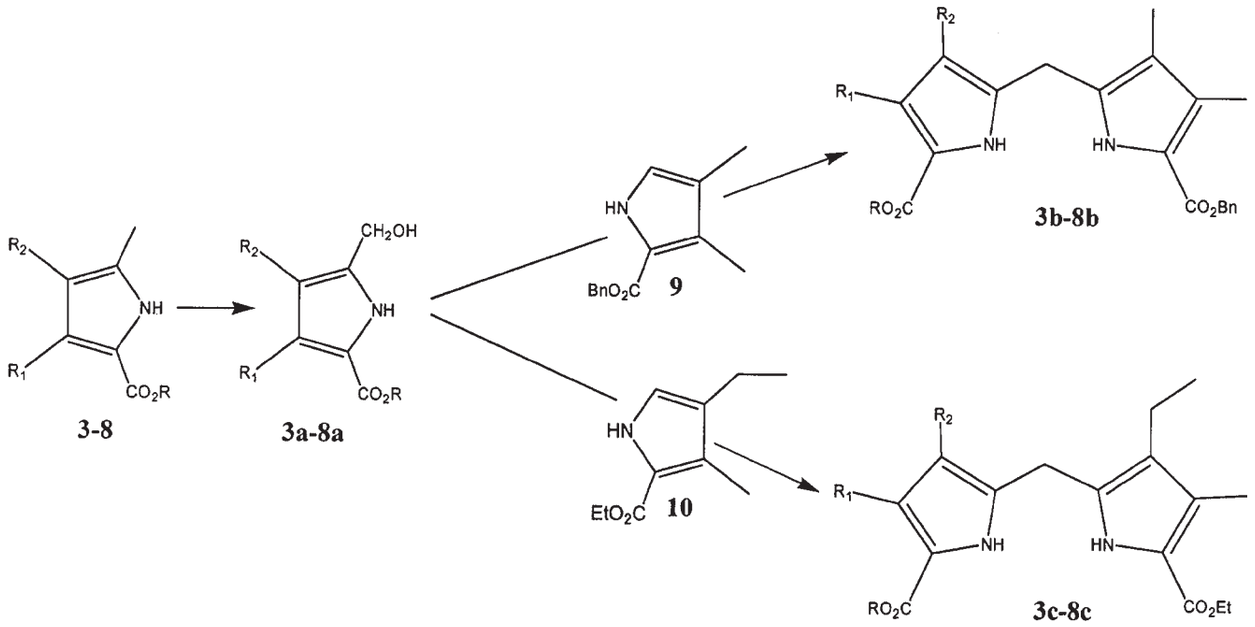

3	R = Bn	R_1 = Me	R_2 = Et
4	R = Bn	R_1 = Me	$R_2 = (CH_2)CO_2CH_3$
5	R = Bn	R_1 = Me	$R_2 = (CH_2)_7CH_3$
6	R = Et	R_1 = Me	R_2 = Et
7	R = Et	R_1 = Et	R_2 = Et
8	R = Et	R_1 = Me	R_2 = ME

catalysts qualitatively exhibited cytochrome P-450 reactions, their catalytic activity was rapidly lost by destruction of the metalloporphyrin. Firstly, these catalysts were improved by introduction of halogens at the *ortho*-positions of the phenyl groups (6). Halogenation imparts steric protection and electronic activation of the metalloporphyrin. Secondly, further halogenation of the β-positions has given the full benefit of such a dual effect, producing more robust catalysts with additional resistance to oxidative catalyst destruction (7). For example, Mansuy and Battioni (8) have shown that when iron(III) *meso*-tetra(2,6-dichlorophenyl)-β-octachloroporphyrin chloride (**2**) ($ClFeTPPCl_8\beta Cl_8$) and the corresponding β-octabromo substituted porphyrin catalyst, iron(III) *meso*-tetra(2,6-dichlorophenyl)-β-octabromoporphyrin chloride (**2a**) ($ClFeTPPBr_8\beta Br_8$), were used in the hydroxylation of heptane the total yield of heptanols produced was increased. Furthermore, the polyhalometalloporphyrin catalysts showed greater chemoselectivity for alkane hydroxylation over alkene epoxidation. Such perhalogenated metalloporphyrins can be rendered water soluble by sulphonation of the *meta*-positions of the phenyl ring (9). All of the available evidence from model studies suggest the $O{=}Fe^{IV}Por^{+\cdot}$ (porphyrin π-cation radical) (9) formulation for the oxidizing intermediate, although the exact nature of this high-valent oxo-metal complex will depend on both the metalloporphyrin and the co-oxidant.

In continuation of our efforts in the area of polyhaloporphyrin catalysts (10), we report herein a straightforward and efficient oxidation of substituted 2-methylpyrroles (for a preliminary account of the work described see ref. 11) using both iron(III) *meso*-tetra(2,6-dichloro-3-sulphonatophenyl)-β-octachloroporphyrin chloride (**1**) ($ClFeTPPCl_8S_4\beta Cl_8$) and iron(III) *meso*-tetra(2,6-dichlorophenyl)-β-octachloroporphyrin chloride (**2**) ($ClFeTPPCl_8\beta Cl_8$).

Specifically, when a cold (0°C) solution of 2-methylpyrrole (**3**, 0.2 mmol) in 3 mL of $HCl–CH_3CN$ (1:1 v/v) containing a catalytic amount of the catalyst **1** (0.0009 mmol) in the presence of PhIO (1 equiv.) was allowed to react for 10 min, the crude allylic alcohol **3a** was obtained (Scheme 1). The ^1H NMR spectrum of crude **3a** was clean with no trace of starting material and showed a singlet (2H) at δ 4.58 corresponding to the allylic methylene group. The ^1H NMR and the high resolution mass spectra of **3a** were in full accord with the assigned structure. Purification of this compound was not attempted due to its known instability. Furthermore, its IR spectrum exhibited an absorption at 3300 cm^{-1} due to the allylic alcohol moiety while the low-resolution mass spectrum gave a peak at m/z 225 ($M^+ - H_2O$). Importantly, compound **3a** underwent coupling to the α-free pyrrole, 2-benzyloxycarbonyl-3,4-dimethylpyrrole (**9**) under very mild

© 1998 NRC Canada

Can. J. Chem. Downloaded from www.nrcresearchpress.com by China University of Science and Technology on 09/05/12
For personal use only.

I:\cjc\cjc76\cjc-10\OctCHEM-D.vp
Wednesday, January 06, 1999 10:03:58 AM

Color profile: Disabled
Composite Default screen

Scheme 2.

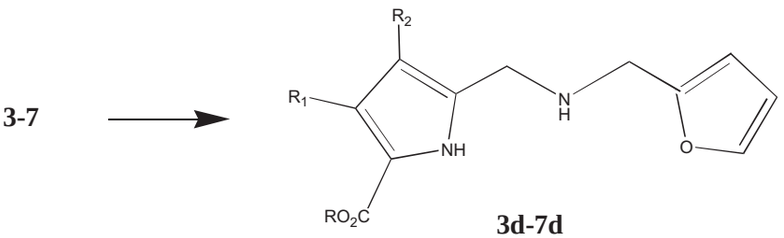

3d-7d

conditions (CH_2Cl_2, rt) to provide the dipyrromethane **3b** in 42% yield (from **3**). In a similar fashion pyrroles **4**–**8** were oxidized and coupled as before to provide the dipyrromethanes **4b**–**8b**. In a control experiment, a solution (HCl–CH_3CN, 1:1 v/v) of pyrrole **3** was treated with PhIO in the absence of the catalyst **1**, and the resulting crude mixture was treated with 2-benzyloxycarbonyl-3,4-dimethylpyrrole. The yield of the dipyrromethane **3b** isolated varied between 5–15%. Upon further investigation of the effect of PhIO alone on several other 2-methylpyrroles, it became evident that the yields of the dipyrromethanes produced were without exception substantially lower than in the presence of the catalyst. Interestingly, the HCl–CH_3CN combination was found to be crucial for the effective oxidation of the substrates. For example, the oxidation in the H_2O–CH_3CN medium was very sluggish, clearly indicating the necessity of an acidic medium for the success of the reaction.

Next, we turned our attention to the utilization of catalyst **2** in the same oxidation reaction. More explicitly, when a TFA–CH_2Cl_2 (1:9) solution of pyrrole **3** (0.194 mmol) was treated with the catalyst **2** (0.0015 mmol) and PhIO (1 equiv.), oxidation of the 2-methyl group occurred within 5 min. As was the case with the catalyst **1**, an acidic medium was also found to be necessary for clean and effective oxidation with the catalyst **2**. Neither *p*-toluenesulphonic acid nor acetic acid were suitable for this purpose, presumably due to the acids themselves undergoing oxidation along with the substrates. However, trifluoroacetic acid proved to be an excellent reagent. Thus, addition of 2-benzyloxycarbonyl-3,4-dimethylpyrrole (**9**) into the same reaction mixture resulted in an in situ coupling to provide (after neutralization of the mixture with $NaHCO_3$ followed by chromatography) the corresponding dipyrromethane **3b** in 62% yield. In a different run, when 2-ethoxycarbonyl-4-ethyl-3-methylpyrrole (**10**) was added to the reaction mixture obtained after the initial oxidation, the dipyrromethane **3c** was obtained in 60% yield. In a similar fashion, the dipyrromethanes **4c**–**8c** were prepared from pyrroles **4**–**8**. Thus, by using the appropriate monopyrrole unit it is possible to synthesize 1,9-dioxycarbonyldipyrromethanes with either symmetric (**8b**, **3c**, **6c**) or asymmetric (**3b**–**7b**, **4c**, **5c**, **7c**, **8c**) substitution patterns. To the best of our knowledge, this is the first report of a one-pot synthesis of dipyrromethanes starting from the corresponding monopyrrole units. Catalyst **1**, due its insolubility in organic solvents, is not suitable for use under these conditions. On the other hand, when the same one-pot procedure was attempted with catalyst **1** in aqueous acidic medium (HCl–CH_3CN), the reaction was less clean, and the yields of the dipyrromethanes obtained were substantially lower than with catalyst **2**.

In contrast to $Pb(OAc)_4$ which is the only other reliable oxidant of 2-methylpyrroles, the ease of oxidation with both catalysts **1** and **2** stands out as a clear advantage. Furthermore, the sequence of $Pb(OAc)_4$ oxidation(HOAc, Ac_2O, 80°C, 24h) followed by dipyrromethane formation (conc. HCl, reflux) employs considerably harsher conditions and longer reaction times and leads only to symmetric dipyrromethanes. To assess the coupling ability of 2-acetoxypyrroles with an α-free pyrrole under our reaction conditions, 2-acetoxymethyl-5-benzyloxycarbonyl-3-ethyl-4-methylpyrrole was treated overnight at room temperature with 2-benzyloxycarbonyl-3,5-dimethylpyrrole in CH_2Cl_2. The ^1H NMR spectrum of the crude reaction mixture indicated only 15% conversion to the dipyrromethane **4b**. On the other hand, direct generation of allylic alcohols by our method allows ready manipulation of pyrrole units with diverse substitution patterns and facile generation of synthetically and biosynthetically important dipyrromethane units.

As a further example of the applicability of our oxidation protocol, the reaction of allylic alcohols (**3a**–**7a**) with furfurylamine was examined. Thus, when a solution of compound **3a** in CH_2Cl_2 was allowed to react with an excess of furfurylamine, the novel (2-furylmethyl)-2-pyrrolylmethylamine (**3d**) was obtained in 36% yield (from **3**). Similarly, the furan derivatives **4d**–**7d** were prepared from their corresponding allylic alcohols (Scheme 2).

Aromatic macrocyclic molecules capable of absorbing in the far red or near infrared region are now finding applications in biomedical research, specifically as photosensitizers for use in photodynamic therapy (PDT) of hyperproliferative diseases such as cancer and psoriasis (12, 13). Substituted dipyrromethanes which are functionalized with 1,9-diester groups are precursors in the preparation of the corresponding 1,9-dicyanodipyrromethanes (14). These dicyano compounds have been successfully employed in the synthesis of porphocyanins, a new class of expanded porphyrins (15, 16). These compounds due to their long wavelength absorptions in the visible-near infrared region, and their ability to make singlet oxygen makes them potential candidates for PDT. Thus, the methodology described above provides access to a large library of symmetrical and unsymmetrical 1,9-diacyldipyrromethanes as key intermediates in the synthesis of porphocyanins and other polypyrrolic macrocyclic systems.

Experimental

Proton nuclear magnetic resonance (^1H NMR) spectra were obtained from samples dissolved in $CDCl_3$ on a Bruker AC-200 (200 MHz) or a Bruker WH-400 (400 MHz). Low- and high-resolution electron impact (EI) mass spectra were

© 1998 NRC Canada

Can. J. Chem. Downloaded from www.nrcresearchpress.com by China University of Science and Technology on 09/05/12
For personal use only.

I:\cjc\cjc76\cjc-10\OctCHEM-D.vp
Wednesday, January 06, 1999 10:04:00 AM

Color profile: Disabled
Composite Default screen

recorded on a Kratos/AEI MS-902 spectrometer. Microanalyses was carried out using a Carlo Erba Elemental Analyzer 1106. Flash chromatography was performed on silica gel 60 (70–230 mesh supplied by E. Merck Co.). All chemical and solvents were reagent grade.

Oxidation of 2-methylpyrroles with PhIO/ClFeTPPCl$_8$S$_4$βCl$_8$ (1). General procedure A

To a cold (0°C) solution of the pyrrole in CH_3CN – 3 N HCl (1:1, v/v, 2.5 mL/mmol) was added the catalyst **1** (0.0009 mmol) in one portion. To the resulting light yellow–brown solution was added PhIO (1 equiv.) in one portion. After stirring the resulting mixture (all of the PhIO dissolves rapidly) at 0°C for 10 min, CH_2Cl_2 (10 mL/mmol) was added followed by water (5 mL/mmol). The layers were separated, and the organic layer was dried ($MgSO_4$) and evaporated to provide the corresponding allylic alcohol as a yellow oily substance which was used immediately in the next step.

Coupling of 2-benzyloxycarbonyl-3,4-dimethyl pyrrole with the allylic alcohols 3a–8a. General procedure B

To a solution of the allylic alcohol obtained in the above reaction in CH_2Cl_2 (2 mL/mmol) was added 2-benzyloxycarbonyl-3,4-dimethylpyrrole (**9**) or 2-ethoxycarbonyl-4-ethyl-3-methylpyrrole (**10**) (1.5 equiv.) The resulting mixture was stirred at rt for 3 h. The solvent was evaporated, and the resulting yellow oil was subjected to column chromatography on silica gel to afford the pure dipyrromethane.

Preparation of 2(furylmethyl)-2-pyrrolylmethylamines 3c–7c. General procedure C

To a solution of the crude allylic alcohol (obtained in the general procedure A) in CH_2Cl_2 (3 mL/mmol) was added furfurylamine (3 mmol) in one portion. The resultant solution was stirred at rt for 6 h. Evaporation of the solvent afforded the crude product as a yellow oil. Flash chromatography of the crude material on silica gel afforded the pure 2(furylmethyl)-2-pyrrolylmethylamines.

Oxidation of 2-methylpyrroles with PhIO/ClFeTPPCl$_8$βCl$_8$ (2). One-pot synthesis of dipyrromethanes. General procedure D

To a cold (0°C) solution of the pyrrole in CH_2Cl_2–TFA (9:1, v/v, 1.5 mL/mmol) containing the catalyst **2** (0.0009 mmol) was added PhIO (1 equiv.) in one portion. After ~5 min (when all the solids had dissolved) was added the appropriate α-free pyrrole (1.5 equiv.). The slightly reddish-orange solution obtained was stirred at 0°C for 1.5 h. Water (5 mL/mmol) was added and the layers were separated. The organic phase was washed with saturated $NaHCO_3$ until the aqueous phase was basic to litmus. The organic layer was separated, dried ($MgSO_4$), and evaporated to afford the crude dipyrromethane as a yellow oil. The crude material was separated by flash chromatography on silica gel to afford the pure dipyrromethane.

Allylic alcohol 3a

The pyrrole **3** (0.05 g, 0.193 mmol) was converted into the allylic alcohol **3a** according to the general procedure A, by treatment with PhIO (0.042 g, 0.193 mmol) and the catalyst **1** (0.0015 g, 0.0009 mmol). The crude material isolated exhibited ^{1}H NMR (200 MHz), δ: 1.10 (t, 3H, J = 7.5 Hz), 2.30 (s, 3H), 2.44 (q, 2H, J = 7.5 Hz), 4.58 (s, 2H), 5.30 (s, 2H), 7.20–7.41 (m, 5H), 9.00 (br s, 1H); LREIMS (m/z): 255 (M^+ – 18).

2-[(5-Benzyloxycarbonyl-3,4-dimethylpyrrole-2-yl)methyl]-5′-benzyloxycarbonyl-3′-ethyl-4′-methylpyrrole (3b)

The crude material obtained from the above reaction was treated with the pyrrole (general procedure B) to provide the crude dipyrromethane **3a**. This material was flash chromatographed on silica gel (1 g, CH_2Cl_2) to provide the pure compound (0.039 g, 42% from pyrrole **3**) as a pale white solid which exhibited ^{1}H NMR (400 MHz), δ: 1.04 (t, 3H, J = 8 Hz), 1.95 (s, 3H), 2.24 (s, 3H), 2.29 (s, 3H), 2.40 (q, 2H, J = 8 Hz), 3.80 (s, 2H), 5.25 (s, 4H), 7.23–7.45 (m, 10H), 8.95, 8.97 (pair of overlapping s, 1H each). Exact mass calcd. for $C_{30}H_{32}O_4N_2$: 484.2362; found: 484.2359.

Allylic alcohol 4a

This material was prepared according to the general procedure A, by treatment of the pyrrole **4** (0.05 g, 0.158 mmol) with PhIO (0.34 g, 0.158 mmol) and the catalyst **1** (0.0015 g, 0.0009 mmol). The crude substance **4a** obtained showed ^{1}H NMR (200 MHz), δ: 2.29 (s, 3H), 2.50 (t, 2H, J = 6 Hz), 2.78 (t, 2H, J = 6 Hz), 3.68 (s, 3H), 4.63 (s, 2H), 5.30 (s, 2H), 7.22–7.43 (m, 5H), 8.98 (br s, 1H); LRFABMS (m/z): 314 ($M^+ - H_2O + H$).

2-[(5-Benzyloxycarbonyl-3,4-dimethylpyrrole-2-yl)methyl]-5′-benzyloxycarbonyl-3′(carbomethoxyeth-2-yl)-4′-methylpyrrole 4b

The crude material obtained from the above reaction was treated with 2-benzyloxycarbonyl-3,4-dimethylpyrrole (**9**) (general procedure B) to provide the crude dipyrromethane **4b**. This material was flash chromatographed on silica gel (1 g, CH_2Cl_2/EtOAc, 95:5) to provide the pure compound (0.033 g, 38% from pyrrole **5**) as a white solid ; ^{1}H NMR (400 MHz), δ: 2.00 (s, 3H), 2.25 (s, 3H), 2.27 (s, 3H), 2.45 (t, 2H, J = 7.5 Hz), 2.72 (t, 2H, J = 7.5 Hz), 3.57 (s, 3H), 3.90 (s, 2H), 5.25 (s, 2H), 5.27 (s, 2H), 7.27–7.40 (m, 10H), 8.55 (s, 1H), 9.08 (s, 1H). Exact mass calcd. for $C_{32}H_{34}O_6N_2$: 542.2417; found: 542.2427.

Allylic alcohol 5a

This compound was obtained according to the procedure A, by treatment of the pyrrole **5** (0.05 g, 0.146 mmol) with PhIO (0.032 g, 0.146 mmol) and the catalyst **1** (0.0015 g, 0.0009 mmol). The crude material exhibited ^{1}H NMR (200 MHz), δ: 0.89 (br t, 3H, J = ~7 Hz), 1.40–1.50 (m, 10H), 2.30 (s, 3H), 2.40 (t, 2H, J = 8 Hz), 4.50 (s, 2H), 5.30 (s, 2H), 7.20–7.50 (m, 5H), 9.30 (br s, 1H); LREIMS (m/e): 339 (M^+ – 18).

2-[(5-Benzyloxycarbonyl-3,4-dimethylpyrrole-2-yl)methyl]-5′-benzyloxycarbonyl-3′-octyl-4′-methylpyrrole (5b)

The crude material obtained from the above reaction was treated with 2-benzyloxycarbonyl-3,4-dimethylpyrrole (**9**) (general procedure B) to provide the crude dipyrromethane

© 1998 NRC Canada

Can. J. Chem. Downloaded from www.nrcresearchpress.com by China University of Science and Technology on 09/05/12
For personal use only.

I:\cjc\cjc76\cjc-10\OctCHEM-D.vp
Wednesday, January 06, 1999 10:04:02 AM

Color profile: Disabled
Composite Default screen

5b. This material was flash chromatographed on silica gel (1 g, CH_2Cl_2) to provide the pure compound (0.033 g, 40% from pyrrole **5**) as a white solid; ^{1}H NMR (400 MHz), δ: 0.87 (t, 3H, *J* = 8 Hz), 1.10–1.40 (m, 10H), 1.93 (s, 3H), 2.25 (s, 3H), 2.27 (s, 3H), 2.33 (t, 2H, *J* = 8 Hz), 3.30 (s, 2H), 5.25 (s, 4H), 7.25–7.40 (m, 10H), 8.25, 8.28 (pair of overlapping s, 1H each). Exact mass calcd. for $C_{36}H_{44}O_4N_2$: 568.3300; found: 568.3309.

Allylic alcohol 6a

The pyrrole **6** (0.05 g, 0.256 mmol) was treated with PhIO (0.056 g, 0.256 mmol) and the catalyst **1** (0.0015 g, 0.0009 mmol), according to the general procedure A, to yield the crude compound; ^{1}H NMR (200 MHz), δ: 1.00 (t, 3H, *J* = 8 Hz), 1.22 (t, 3H, *J* = 8 Hz), 2.00 (s, 3H), 2.40 (q, 2H, *J* = 8 Hz), 4.22 (q, 2H, *J* = 8 Hz), 4.45 (s, 2H), 8.80 (br s, 1H); LREIMS (*m*/*e*): 193 (M^+ – 18).

2-[(5-Benzyloxycarbonyl-3,4-dimethylpyrrole-2-yl)methyl]-5′-ethoxycarbonyl-3′-ethyl-4′-methylpyrrole (6b)

The crude material obtained from the above reaction was treated with 2-benzyloxycarbonyl-3,4-dimethylpyrrole (**9**) (general procedure B) to provide the crude dipyrromethane **6b**. This material was flash chromatographed on silica gel (1 g, CH_2Cl_2/EtOAc, 95:5) to provide the pure compound (0.035 g, 32% from pyrrole **6**) as a white solid; ^{1}H NMR (400 MHz), δ: 1.01 (t, 3H, *J* = 8 Hz), 1.29 (t, 3H, *J* = 8 Hz), 1.95 (s, 3H), 2.24 (s, 3H), 2.26 (s, 3H), 2.40 (q, 2H, *J* = 8 Hz), 3.32 (s, 2H), 4.22 (q, 2H, *J* = 8 Hz), 5.24 (s, 2H), 7.24–7.34 (m, 5H), 9.15, 9.17 (pair of overlapping s, 1H each). Exact mass calcd. for $C_{25}H_{30}O_4N_2$: 422.2205; found: 422.2206. Anal. calcd. for $C_{25}H_{30}O_4N_2$: C 71.11, H 7.15, N 6.63; found: C 71.15, H 7.19, N 6.59.

Allylic alcohol 7a

This material was prepared according to the general procedure A, by treatment of the pyrrole **7** (0.05 g, 0.239 mmol) with PhIO (0.052 g, 0.239 mmol) and the catalyst **1** (0.0015 g, 0.0009 mmol). The crude material obtained showed ^{1}H NMR (200 MHz), δ: 1.00–1.20 (two overlapped q, 6H, *J* = 8 Hz each), 1.32 (t, 3H, *J* = 8 Hz), 2.41 (q, 2H, *J* = 8 Hz), 2.68 (q, 2H, *J* = 8 Hz), 4.25 (q, 2H, *J* = 8 Hz), 4.60 (s, 2H), 9.00 (br s, 1H); LREIMS (*m*/*e*): 207 (M^+ – 18).

2-[(5-Benzyloxycarbonyl-3,4-dimethylpyrrole-2-yl)methyl]-5′-ethoxycarbonyl-3′,4′-diethylpyrrole (7b)

The crude material obtained from the above reaction was treated with 2-benzyloxycarbonyl-3,4-dimethylpyrrole (**9**) (general procedure B) to provide the crude dipyrromethane **7b**. This material was flash chromatographed on silica gel (1 g, CH_2Cl_2/EtOAc, 95:5) to provide the pure compound (0.036 g, 35% from pyrrole **7**) as a white solid; ^{1}H NMR (400 MHz), δ: 1.05 (t, 3H, *J* = 8 Hz), 1.14 (t, 3H, *J* = 8 Hz), 1.29 (t, 3H, *J* = 7.5 Hz), 1.95 (s, 3H), 2.25 (s, 3H), 2.41 (q, 2H, *J* = 8 Hz), 2.71 (q, 2H, *J* = 8 Hz), 3.34 (s, 2H), 4.25 (q, 2H, *J* = 7.5 Hz), 5.26 (s, 2H), 7.27–7.38 (m, 5H), 8.78 (br s, 2H). Exact mass calcd. for $C_{26}H_{32}O_4N_2$: 436.2362; found: 436.2371.

Allylic alcohol 8a

This substance was prepared according to the procedure A, by treatment of the pyrrole (0.05 g, 0.276 mmol) with PhIO (0.06 g, 0.276 mmol) and the catalyst **1** (0.0015 g, 0.0009 mmol). The crude material obtained exhibited ^{1}H NMR (200 MHz), δ: 1.25 (t, 3H, *J* = 8 Hz), 2.20 (s, 3H), 2.22 (s, 3H), 4.24 (q, 2H, *J* = 8 Hz), 4.40 (s, 2H), 8.83 (br s, 1H); LREIMS (*m*/*e*): 179 (M^+ – 18).

2-[(5-Benzyloxycarbonyl-3,4-dimethylpyrrole-2-yl)methyl]-5′-ethoxycarbonyl-3′,4′-dimethylpyrrole (8b)

The crude material obtained from the above reaction was treated with the pyrrole (general procedure B) to provide the crude dipyrromethane **8b**. This material was flash chromatographed on silica gel (1 g, CH_2Cl_2/EtOAc, 95:5) to provide the pure compound (0.029 g, 25% from pyrrole **8**) as a white solid; ^{1}H NMR (400 MHz) δ: 1.31 (t, 3H, *J* = 8 Hz), 1.92 (s, 3H), 1.94 (s, 3H), 2.22 (s, 3H), 2.25 (s, 3H), 3.32 (s, 2H), 4.25 (q, 2H, *J* = 8 Hz), 5.25 (s, 2H), 7.30–7.41 (m, 5H), 8.65 (br s, 2H). Exact mass calcd. for $C_{24}H_{28}O_4N_2$: 408.2449; found: 408.2049. Anal. calcd. for $C_{24}H_{28}O_4N_2$: C 70.60, H 6.91, N 6.86; found: C 70.66, H 6.95, N 6.84.

2-(Furylmethyl)-2(5-benzyloxycarbonyl-3-ethyl-4-methyl)pyrrolylmethylamine (3d)

The pyrrole **3** (0.05 g, 0.194 mmol) was transformed into compound **3d** by treatment with furfurylamine (0.05 g, 0.582 mmol) (general procedure C). The crude product was purified by flash chromatography on silica gel (1 g, CH_2Cl_2) and yielded the pure compound (0.025 g, 36% from pyrrole **3**) as a colorless oil; ^{1}H NMR (400 MHz) δ: 1.02 (t, 3H, *J* = 7.5 Hz), 2.29 (s, 3H), 2.36 (q, 2H, *J* = 7.5 Hz), 3.71 (s, 2H), 3.75 (s, 2H), 5.30 (s, 2H), 6.15 (d, 1H, *J* = ~2 Hz), 6.31 (d, 1H, *J* = ~2 Hz), 7.30–7.45 (m, 6H), 9.07 (br s, 1H). Exact mass calcd. for $C_{21}H_{24}O_3N_2$: 352.1786; found: 352.1795.

2-(Furylmethyl)-2[5-benzyloxycarbonyl-3(carbomethoxyeth-2-yl)]4-methyl)pyrroloylmethylamine (4d)

The pyrrole **4** (0.05 g, 0.158 mmol) was transformed into compound **4d** by treatment with furfurylamine (0.045 g, 0.474 mmol) (general procedure C). The crude product, purified by flash chromatography on silica gel (1 g, CH_2Cl_2), yielded the pure compound (0.21 g, 32% from pyrrole **4**) as a colorless oil; ^{1}H NMR (400 MHz), δ: 2.44 (s, 3H), 2.58 (t, 2H, *J* = 6.5 Hz), 2.85 (t, 2H, *J* = 6.5 Hz), 3.79 (s, 3H), 3.89 (s, 2H), 3.91 (s, 2H), 5.45 (s, 2H), 6.33 (d, 1H, *J* = ~2 Hz), 6.74 (d, 1H, *J* = ~2 Hz), 7.46–7.60 (m, 6H), 9.30 (br s, 1H). Exact mass calcd. for $C_{22}H_{26}O_5N_2$: 410.1841; found: 410.1839. Anal. calcd. for $C_{23}H_{26}O_5N_2$: C 67.34, H 6.38, N 6.82; found: C 67.38, H 6.41, N 6.79.

2-(Furylmethyl)-2-(5-benzyloxycarbonyl-4-methyl-3-octyl) pyrrolylmethylamine (5d)

The pyrrole **5** (0.05 g, 0.146 mmol) was transformed into compound **5d** by treatment with furfurylamine (0.042 g, 0.438 mmol) (general procedure C). The crude product, purified by flash chromatography on silica gel (1 g, CH_2Cl_2), yielded the pure compound (0.019 g, 30%) as a colorless oil; ^{1}H NMR (400 MHz), δ: 0.79 (t, 3H, *J* = 7 Hz), 1.10–1.32 (m, 12H), 2.19 (s, 3H), 2.25 (t, 2H, *J* = 7 Hz), 3.63 (s, 2H),

© 1998 NRC Canada

Can. J. Chem. Downloaded from www.nrcresearchpress.com by China University of Science and Technology on 09/05/12
For personal use only.

I:\cjc\cjc76\cjc-10\OctCHEM-D.vp
Wednesday, January 06, 1999 10:04:04 AM

Color profile: Disabled
Composite Default screen

3.68 (s, 2H), 5.21 (s, 2H), 6.09 (d, 1H, J = ~2 Hz), 6.23 (d, 1H, J = ~2 Hz), 7.23–7.36 (m, 6H), 9.00 (br s, 1H). Exact mass calcd. for $C_{27}H_{36}O_3N_2$: 436.2725; found: 436.2717.

2-(Furylmethyl)-2-(5-ethoxycarbonyl-3-ethyl-4-methyl) pyrrolylmethylamine (6d)

The pyrrole **6** (0.05 g, 0.256 mmol) was transformed into compound **6d** by treatment with furfurylamine (0.074 g, 0.768 mmol) (general procedure C). The crude product purified by flash chromatography on silica gel (1 g, CH_2Cl_2) yielded the pure compound (0.021 g, 28%) as a colorless oil; ^{1}H NMR (400 MHz) δ: 1.03 (t, 3H, J = 7 Hz), 1.35 (t, 3H, J = 7.5 Hz), 2.28 (s, 3H), 2.37 (q, 2H, J = 7 Hz), 3.22 (s, 2H), 3.28 (s, 2H), 4.29 (q, 2H, J = 7.5 Hz), 6.18 (d, 1H, J = ~2 Hz), 6.34 (d, 1H, J = ~2, Hz), 7.39 (d, 1H, J = 1 Hz), 8.96 (br s, 1H). Exact mass calcd. for $C_{16}H_{22}O_3N_2$: 290.1630; found: 290.1659.

2-(Furylmethyl)-2-(5-ethoxycarbonyl-3,4-diethyl) pyrrolylmethylamine (7d)

The pyrrole **7** (0.05 g, 0.239 mmol) was transformed into compound **7d** by treatment with furfurylamine (0.069 g, 0.717 mmol) (general procedure C). The crude product was purified by flash chromatography on silica gel (1 g, CH_2Cl_2) and yielded the pure compound (0.023 g, 32%) as a colorless oil; ^{1}H NMR (400 MHz), δ: 1.21 (t, 3H, J = 7 Hz), 1.33 (t, 3H, J = 8 Hz), 1.53 (t, 3H, J = 7.5 Hz), 2.55 (q, 2H, J = 7 Hz), 2.90 (q, 2H, J = 8 Hz), 3.91 (s, 2H), 3.95 (s, 2H), 3.47 (q, 2H, J = 7.5 Hz), 6.37 (d, 1H, J = ~2 Hz), 6.51 (d, 1H, J = 2. Hz), 7.58 (d, 1H, J = 1 Hz), 9.21 (br s, 1H). Exact mass calcd. for $C_{17}H_{24}O_3N_2$: 304.1768; found: 304.1786. Anal. calcd. for $C_{17}H_{24}O_3N_2$: C 67.12, H 7.94, N 9.20; found: C 67.15, H 7.98, N 8.89.

2-[(5′-Ethoxycarbonyl-3′-ethyl-4′-methylpyrrole-2-yl)methyl-5-benzyloxycarbonyl-3-ethyl-4-methylpyrrole (3c)

The pyrrole **3** (0.05 g, 0.194 mmol) was converted into the dipyrromethane **3c** according to the general D by treatment with PhIO (0.42 g, 1 equiv.), the catalyst **2** (0.002 g, 0.0015 mmol), and 2-ethoxycarbonyl-4-ethyl-3-methyl-pyrrole (**10**). Flash chromatography of the crude material on silica gel (1 g, CH_2Cl_2/EtOAc 95:5) provided the dipyrromethane (0.05 g, 60%) as a pale white solid; ^{1}H NMR (400 MHz), δ: 1.02 (pair of overlapping t, 3H each, J = ~7 Hz each), 1.27 (t, 3H, J = 7.5 Hz), 2.25 (s, 3H), 2.26 (partially buried q, 2H, J = ~7 Hz), 2.28 (s, 3H), 2.41 (q, 2H, J = 7 Hz), 3.84 (s, 2H), 4.20 (q, 2H, J = 7.5 Hz), 5.20 (s, 2H), 7.24–7.35 (m, 5H), 8.98, 9.00 (pair of overlapping s, 1H each). Exact mass calcd. for $C_{26}H_{32}O_4N_2$: 436.2362; found: 436.2378.

2-[(5-Benzyloxycarbonyl-3(carbomethoxyeth-2-yl)-4-methylpyrrole-2-yl)methyl]-5′-ethoxycarbonyl-3′-ethyl-4′-methylpyrrole (4c)

The pyrrole **4** (0.05 g, 0.158 mmol) was converted into the dipyrromethane **4c** according to the general procedure D by treatment with PhIO (0.34 g, 1 equiv.), catalyst **2** (0.002 g, 0.0015 mmol), and 2-ethoxycarbonyl-4-ethyl-3-methyl-pyrrole (**10**). Flash chromatography of the crude material on silica gel (1 g, CH_2Cl_2/EtOAc 90:10) provided the dipyrromethane (0.038 g, 48%) as a white solid; ^{1}H NMR (400 MHz), δ: 1.05 (t, 3H, J = 7 Hz), 1.30 (t, 3H, J = 7.5 Hz), 2.27 (s, 6H), 2.43 (partially buried t, 2H, J = 6.5 Hz), 2.46 (overlapping q, 2H, J = 7 Hz), 2.23 (q, 2H, J = 6.5), 3.67 (s, 3H), 3.91 (s, 2H), 4.25 (q, 2H, J = 7.5 Hz), 5.24 (s, 2H), 7.28–7.39 (m, 5H), 8.68 (br s, 1H), 9.08 (br s, 1H). Exact mass calcd. for $C_{28}H_{34}O_6N_2$: 294.5929; found: 494.5932. Anal. calcd. for $C_{28}H_{34}O_6N_2$: C 67.99, H 6.92, N 5.66; found: C 68.02, H 6.96, N 5.61.

2-[(5-Benzyloxycarbonyl-4-methyl-3-octylylpyrrole-2-yl)methyl]-5′-ethoxycarbonyl-3′-ethyl-4′-methylpyrrole (5c)

The pyrrole **5** (0.05 g, 0.146 mmol) was converted into the dipyrromethane **5c** according to the general procedure D by treatment with PhIO (0.032 g, 1 equiv.), the catalyst **2** (0.002 g, 0.0015 mmol) and 2-ethoxycarbonyl-4-ethyl-3-methyl-pyrrole (**10**). Flash chromatography of the crude material on silica gel (1 g, CH_2Cl_2/EtOAc 95:5) provided the dipyrromethane (0.042 g, 55%) as a white solid; ^{1}H NMR (400 MHz), δ: 0.88 (t, 3H, J = 6.5 Hz), 1.03 (t, 3H, J = 7.5 Hz), 1.20–1.36 (m, 17H), 2.25 (s, 6H), 2.37 (t, 2H, J = 6.5 Hz), 3.83 (s, 2H), 4.24 (q, 2H, J = 7.5 Hz), 5.25 (s, 2H), 7.28–7.40 (m, 5H), 8.74, 8.80 (pair of overlapping s, 1H each). Exact mass calcd. for $C_{32}H_{44}O_4N_2$: 520.3300; found: 520.3304.

2-[(5-Ethoxycarbonyl-3-ethyl-4-methylpyrrole-2-yl)methyl]-5′-ethoxycarbonyl-3′-ethyl-4′-methylpyrrole (6c)

The pyrrole **6** (0.05 g, 0.256 mmol) was converted into the dipyrromethane **6c** according to the general procedure D by treatment with PhIO (0.056 g, 1 equiv.), the catalyst **1** (0.002 g, 0.0015 mmol) 3-ethoxycarbonyl-3-ethyl-4-methyl-pyrrole (**10**). Flash chromatography of the crude material on silica gel (1 g, CH_2Cl_2/EtOAc 95:5) provided the dipyrromethane (0.042 g, 44%) as a white solid; ^{1}H NMR (400 MHz), δ: 1.04 (t, 6H, J = 8 Hz), 1.32 (t, 6H, J = 8 Hz), 2.28 (s, 6H), 2.41 (q, 4H, J = 8 Hz), 3.86 (s, 2H), 4.27 (q, 4H, J = 8 Hz), 8.61 (br s, 2H). Exact mass calcd. for $C_{21}H_{30}O_4N_2$: 374.4842; found: 374.4851. Anal. calcd. for $C_{21}H_{30}O_4N_2$: C 67.35, H 8.07; N 7.47; found: C 67.38, H 8.09, N 7.42.

2-[(5-Ethoxycarbonyl-3,4-diethylpyrrole-2-yl)methyl]-5′-ethoxycarbonyl-3′-ethyl-4′-methylpyrrole (7c)

The pyrrole **7** (0.05 g, 0.293 mmol) was converted into the dipyrromethane **7c** according to the general procedure D by treatment with PhIO (0.052 g, 1 equiv.), the catalyst **1** (0.002 g, 0.0015 mmol), and 2-ethoxycarbonyl-4-ethyl-3-methyl-pyrrole (**10**). Flash chromatography of the crude material on silica gel (1 g, CH_2Cl_2/EtOAc 95:5) provided the dipyrromethane (0.048 g, 52%) as a white solid; ^{1}H NMR (400 MHz), δ: 1.02, 1.05 (pair of overlapping t, 3H, J = ~7 Hz each), 1.15 (t, 3H, J = 7.5 Hz), 1.30 (t, 6H, J = 8 Hz), 2.25 (s, 3H), 2.38–2.47 (m, 4H), 2.70 (q, 2H, J = 7.5 Hz), 3.78 (s, 2H), 4.24 (q, 4H, J = 8 Hz), 8.90 (br s, 2H). Exact mass calcd. for $C_{22}H_{32}O_4N_2$: 388.2362; found: 388.2359.

2-[(5-Ethoxycarbonyl-3,4-dimethylpyrrole-2-yl)methyl]-5′-ethoxycarbonyl-3′-ethyl-4′-methylpyrrole (8c)

The pyrrole **8** (0.05 g, 0.276 mmol) was converted into the dipyrromethane **8c** according to the general procedure D by treatment with PhIO (0.060 g, 1 equiv.), the catalyst **1**

© 1998 NRC Canada

Can. J. Chem. Downloaded from www.nrcresearchpress.com by China University of Science and Technology on 09/05/12
For personal use only.

I:\cjc\cjc76\cjc-10\OctCHEM-D.vp
Wednesday, January 06, 1999 10:04:07 AM

Color profile: Disabled
Composite Default screen

(0.002 g, 0.0015 mmol) 2-ethoxycarbonyl-4-ethyl-3-methylpyrrole (**10**). Flash chromatography of the crude material on silica gel (1 g, CH_2Cl_2/EtOAc 95:5) provided the dipyrromethane (0.039 g, 39%) as a white solid; ^{1}H NMR (400 MHz), δ: 1,05 (t, 3H, *J* = 7.5 Hz), 1.28 (br t, 6H, *J* = ~8 Hz), 1.96 (s, 3H), 2.23 (s, 3H), 2.27 (s, 3H), 2.40 (q, 2H, *J* = 7.5 Hz), 3.87 (s, 2H), 4.22 (br q, 4H, *J* = ~8 Hz), 9.11,9.15 (pair of overlapping s, 1H each). Exact mass calcd. for $C_{20}H_{28}O_4N_2$: 360.2049; found: 360.2053. Anal. calcd. for $C_{20}H_{28}O_4N_2$: C 66.68, H 7.83, 7.77; found: C 66.71, H 7.88, N 7.72.

2-[(5-Benzyloxycarbonyl-3,4-dimethylpyrrole-2-yl)methyl]-5′-benzyloxycarbonyl-3′-ethyl-4′-methylpyrrole (3b)

This material was prepared from the pyrrole **3** (0.05 g, 0.193 mmol) according to the general procedure D. Pure **3b** (0.058 g, 55%) obtained after flash chromatography on silica gel (1 g, CH_2Cl_2) was identical in all respects to that prepared via the general procedure B.

2-[(5-Benzyloxycarbonyl-3,4-dimethylpyrrole-2-yl)methyl]-5′-benzyloxycarbonyl-3′(carbomethoxyeth-2-yl)-4′-methylpyrrole (4b)

This material was prepared from the pyrrole **4** (0.05 g, 0.158 mmol) according to the general procedure D. Pure **4b** (0.047 g, 62%) obtained after flash chromatography on silica gel (1 g, CH_2Cl_2/EtOAc, 95:5) was identical in all respects to that prepared via the general procedure B.

2-[(5-Benzyloxycarbonyl-3,4-dimethylpyrrole-2-yl)methyl]-5′-benzyloxycarbonyl-3′-octyl-4′-methylpyrrole (5b)

This material was prepared from the pyrrole **5** (0.05 g, 0.146 mmol) according to the general procedure D. Pure **5b** (0.042 g, 62%) obtained after flash chromatography on silica gel (1 g, CH_2Cl_2) was identical in all respects to that prepared via the general procedure B.

2-[(5-Benzyloxycarbonyl-3,4-dimethylpyrrole-2-yl)methyl]-5′-Ethoxycarbonyl-3′-ethyl-4′-methylpyrrole (6b)

This material was prepared from the pyrrole **6** (0.05 g, 0.256 mmol) according to the general procedure D. Pure **6b** (0.062 g, 57%) obtained after flash chromatography on silica gel (1 g, CH_2Cl_2/EtOAc, 95:5) was identical in all respects to that prepared via the general procedure B.

2-[(5-Benzyloxycarbonyl-3,4-dimethylpyrrole-2-yl)methyl]-5′-ethoxycarbonyl-3′,4′-diethylpyrrole (7b)

This material was prepared from the pyrrole **7** (0.05 g, 0.239 mmol) according to the general procedure D. Pure **7b** (0.046 g, 44%) obtained after flash chromatography on silica gel (1 g, CH_2Cl_2/EtOAc, 95:5) was identical in all respects to that prepared via the general procedure B.

2-[(5-Benzyloxycarbonyl-3,4-dimethylpyrrole-2-yl)methyl]-5′-ethoxycarbonyl-3′,4′-dimethylpyrrole (8b)

This material was prepared from the pyrrole **8** (0.05 g, 0.276 mmol) according to the general procedure D. Pure **8b** (0.053 g, 47%) obtained after flash chromatography on silica gel (1 g, CH_2Cl_2/EtOAc, 95:5) was identical in all respects to that prepared via the general procedure B.

Acknowledgments

This work was supported by the Natural Sciences and Engineering Research Council of Canada.

References

1. P.R. Ortiz de Montellano (*Editor*). Cytochrome P-450: structure, mechanism and biochemistry. 2nd ed. Plenum Press, New York. 1995.
2. J.S. Lindsey, I.C. Schreimann, H.C. Hsu, D.C. Keanney, and A.M. Marguerettuz. J. Am. Chem. Soc. **52**, 827 (1987).
3. J.T. Groves, T.E. Nemo, and R.S. Myers. J. Am. Chem. Soc. **101**, 1032 (1979).
4. H. Minoun. J. Mol. Catal. **7**, 1 (1980); R.A. Sheldon. J. Mol. Catal. **7**, 107 (1980); K.B. Sharpless and T.R. Verhoeven. Aldrichim. Acta, **12**, 63 (1979); R.A. Sheldon and J.K. Kochi. Metal catalyzed oxidations of organic compounds. Academic Press, New York. 1981; K.A. Jorgensen. Chem. Rev. **89**, 431 (1989).
5. C.K. Chang and F. Ebina. J. Chem. Soc. Chem. Commun. 778 (1981).
6. P.S. Traylor, D. Dolphin, and T.G. Traylor. J. Chem. Soc. Chem. Commun. 279 (1984).
7. T.P. Wijesekara, A. Matsumoto, and D. Dolphin. Angew. Chem. Int. Ed. Engl. **29**, 1028 (1990); T.G. Traylor and S. Tsuchia. Inorg. Chem. **26**, 1338 (1987).
8. D. Mansuy and P. Battioni. *In* Metalloporphyrins in catalytic oxidations. *Edited by* R.A. Sheldon. Marcel Dekker, New York. 1994. pp. 99–132.
9. T. Nakano, T.P. Wijesekera, D. Dolphin, T.K. Maion, T.K. Kirk, and R.L. Farrel. U.S. Patent No. 4892241. 1989; L. Barloy, J.P. Lallier, P. Battioni, D. Mansuy, Y. Piffard, M. Tournoux, J.B. Valim, and W. Jones. New J. Chem. **61**, 71 (1992).
10. D. Dolphin, T.G. Traylor, and L.Y. Xie. Acc. Chem. Res. 251 (1997).
11. V. Karunaratne and D. Dolphin, J. Chem. Soc. Chem. Commun. 2105 (1995).
12. R. Bonnet. Chem. Soc. Rev. 19 (1995).
13. (*a*) E. Sternberg, C. Bruckner, and D. Dolphin. Tet. Rep. **54**, 4151 (1998); (*b*) E. Sternberg and D. Dolphin. Curr. Med. Chem. **3**, 293 (1996).
14. R.W. Boyle, V. Karunaratne, A. Jasat, and E.K. Mar. Synlett. **11**, 939 (1994).
15. D. Dolphin, S.J. Rettig, H. Tang, T. Wijesekara, and L.Y. Xie. J. Am. Chem. Soc. **115**, 9301 (1993).
16. L.Y. Xie, R.W. Boyle, and D. Dolphin. J. Am. Chem. Soc. **118**, 4853 (1996).

© 1998 NRC Canada

Can. J. Chem. Downloaded from www.nrcresearchpress.com by China University of Science and Technology on 09/05/12
For personal use only.

I:\cjc\cjc76\cjc-10\OctCHEM-D.vp
Wednesday, January 06, 1999 10:04:08 AM

The absolute kinetics for radical addition and electronic energy transfer to [1.1.1]propellane

P.F. McGarry and J.C. Scaiano

Abstract: Free radicals react more readily with [1.1.1]propellane, **1**, than with styrene. For example $Et_3Si\cdot$ reacts with **1** and styrene with rate constants of 6×10^8 M^{-1} s^{-1} and 2×10^8 M^{-1} s^{-1}, respectively. Fluorenone, phenanthrene, triphenylene, benzophenone, and pyrene transfer electronic energy to **1** with rate constants well below the diffusion-controlled limit. For example, triplet benzophenone is quenched by **1** with a bimolecular rate constant of 9.9×10^6 M^{-1} s^{-1}. A linear dependence of the log of the quenching rate constants, log k_q, upon the excited-state energy of the donors is found.

Key words: propellane, laser flash photolysis, free radicals, triplet states.

Résumé : Les radicaux libres réagissent plus facilement avec le [1.1.1]propellane, **1**, qu'avec le styrène. Par exemple, les constantes de vitesse de réaction du $Et_3Si\cdot$ avec **1** et avec le styrène sont respectivement de 6×10^8 M^{-1} s^{-1} et 2×10^8 M^{-1} s^{-1}. Le transfert d'énergie électronique de la fluorénone, du phénanthrène, du triphénylène, de la benzophénone et du pyrène vers **1** se fait à des constantes de vitesse de beaucoup inférieure à la limite contrôlée par la diffusion. Par exemple, le triplet de la benzophénone est désactivé par **1** avec une constante bimoléculaire de $9{,}9 \times 10^6$ M^{-1} s^{-1}. On a observé qu'il existe une relation linéaire entre le logarithme des constantes de vitesse de désactivation, log k_q, et l'énergie de l'état excité des donneurs.

Mots clés : propellane, photolyse laser éclair, radicaux libres, états triplets.

[Traduit par la Rédaction]

Introduction

Since Von Baeyer's works in the 1880's the effect of angle strain upon molecular reactivity has been of interest to organic chemists (1). In this respect [1.1.1]propellane is abnormally stable despite a high strain energy content in the molecule (2). The accepted rationalization used to explain the experimentally observed stability is that the lowest energy pathway to reactivity, breakage of the central bond, releases little strain energy (3, 4). Work on the free-radical reactions of [1.1.1]propellane, **1**, by a number of groups has been reviewed by Wiberg et al. (5, 6). Three general rules regarding the free-radical reactions of [1.1.1]propellane can be distilled from these summaries and some more recent contributions (7):

(*i*) Free radicals react with **1** solely by addition reactions in which the central bridgehead–bridgehead bond is cleaved via an S_H2 mechanism (excepting perhaps one instance reported by Zefirov et al. (8) for addition of chlorine atoms).

(*ii*) The new nonplanar carbon-centered radical is an unusually reactive species which exhibits nucleophilic character.

Received May 29, 1998.

P.F. McGarry[1] and J.C. Scaiano.[2] Department of Chemistry, University of Ottawa, 10 Marie Curie, Ottawa, ON K1N 6N5, Canada.

[1]Present address: Paprican, 570 St. John's Blvd., Claire, PQ H9R 3J9, Canada.
[2]Author to whom correspondence may be addressed. Telephone 613-562-5896. Fax: (613) 562-5633.

(*iii*) The resulting bicyclo[1.1.1]pent-1-yl radicals do not rearrange except in the cases of excited states or carbenes (9).

Despite definitive works probing the qualitative reactivity of **1** (4, 10–12), measurements of the absolute rate constants for the radical reactions of **1** have been mostly absent from the literature (13). A few values of absolute rate constants for carbene additions to **1** have been published (9, 14). We report here on our nanosecond laser flash photolysis measurements of the absolute rate constants for the free-radical addition reactions of **1** shown in Scheme 1.

Whereas the mechanisms of free-radical reactions of **1** are well established the electronic excited states of **1** and the chemistry ensuing from them are not. The lowest triplet and singlet excited-state energies and geometries of **1** have been the subject of theoretical studies (15–21). Only recently, however, have experimental values have been reported (22). In light of the continuing interest in the abnormal properties of **1** we undertook the study of electronic energy transfer to [1.1.1]propellane. Thus we report our findings concerning the rate constants and mechanisms for electronic energy transfer to **1** and on possible mechanisms for electronic relaxation of excited **1**.

Experimental section

Materials

The solvents used were of the highest quality commercially available and were generally used as received. In some cases, however, it was found that best results for flash photolysis studies were obtained when the solvents were purified just prior to use. These special cases are described be-

© 1998 NRC Canada

Scheme 1.

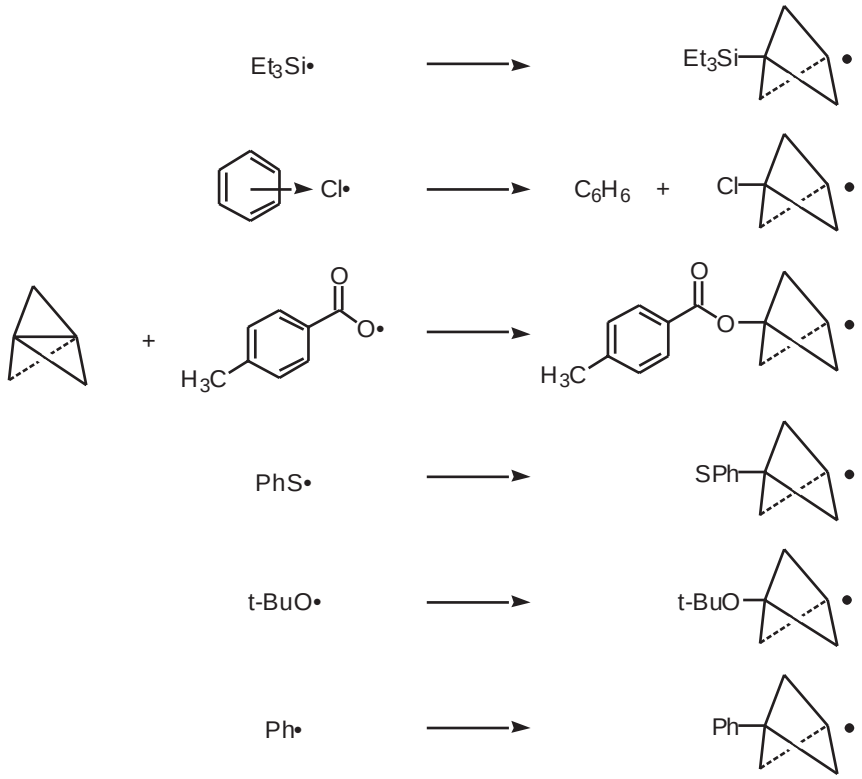

low. Di-*tert*-butylperoxide was passed over alumina just prior to use to remove traces of hydroperoxide. Benzene was washed with dilute sulfuric acid (10%) and water. It was dried with $MgSO_4$ and distilled from calcium hydride.

Synthesis of [1.1.1]propellane

The method of Szeimies and co-workers (23) was used. The dilute mixture of propellane in ether obtained from this synthesis was tediously purified by preparative gas chromatography (vide infra). Thus we modified the method by reducing the solvent volume by one half prior to reaction (many attempts to exchange the methyllithium solvent from ether to a less volatile one such as triglyme resulted in a dismal yield of propellane) thus affording a propellane–ether solution of twice the propellane concentration and reducing the prep GC time by half. Pure, neat [1.1.1]propellane polymerizes spontaneously at room temperature (24). It is essential for kinetic measurements of propellane reactivity that solutions of **1** contain no reactive impurities. Thus for most experiments the outlet gas mixture from the prep GC was fed through gas-tight tubing equipped with a three-way valve. Ether and methyl bromide were passed through to a –78°C trap and discarded. Propellane was diverted through to a needle submerged in the inert solvent of choice at –15 to –20°C to trap the propellane more efficiently and to reduce the likelihood of polymerization. Solutions up to 2.0 M in **1** could be prepared in this way. The concentrations were checked using ^{1}H NMR.

Apparatus

Laser photolysis experiments were carried out using either a Lumonics EX 530 XeCl excimer laser (λ = 308 nm, 6–8 ns pulse duration, <20 mJ/pulse) or a Molectron UV-24 nitrogen laser (λ = 337 nm, 8 ns pulse duration, <10 mJ/pulse). Further details of the laser flash photolysis instrument have been published previously (25, 26).

Fluorescence spectra were recorded with a Perkin–Elmer LS5 spectrofluorimeter equipped with a PE data station. Fluorescence lifetimes were recorded with a PRA single photon counting instrument.

Results

Free-radical reactions

t-*Butoxyl radical addition*

A 1:1 benzene/di-*tert*-butyl peroxide mixture (v/v) was irradiated with a pulse from a nitrogen laser (λ = 337 nm). Neither the *tert*-butoxyl radical nor the adduct radical formed by reaction of *t*-butoxyl with **1** have appreciable absorptions in the region of the UV-vis spectrum available to us (300–800 nm). Thus we employed diphenylmethanol as a kinetic probe (27). The ketyl radical produced by reaction of this substrate with *t*-butoxyl radicals (the same as that produced in the photoreduction of benzophenone) has a characteristic absorption at λ = 535 nm. The proposed mechanism for this system is summarized by the following equations:

© 1998 NRC Canada

[1] t-BuOO(t-Bu) ⟶ 2 t-BuO•

[2] -BuO• t ⟶ First order decay

[3] t-BuO• + Ph_2CHOH ⟶ t-BuOH + $Ph_2\dot{C}OH$

[4] t-BuO• + 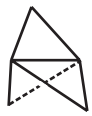 ⟶ 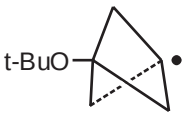

1

Fig. 1. Plot according to eq. [5] for [Ph_2CHOH] = 69 mM. *Insert:* Transient absorption trace showing the buildup of ketyl signal at 535 nm for 85 mM [1.1.1]propellane.

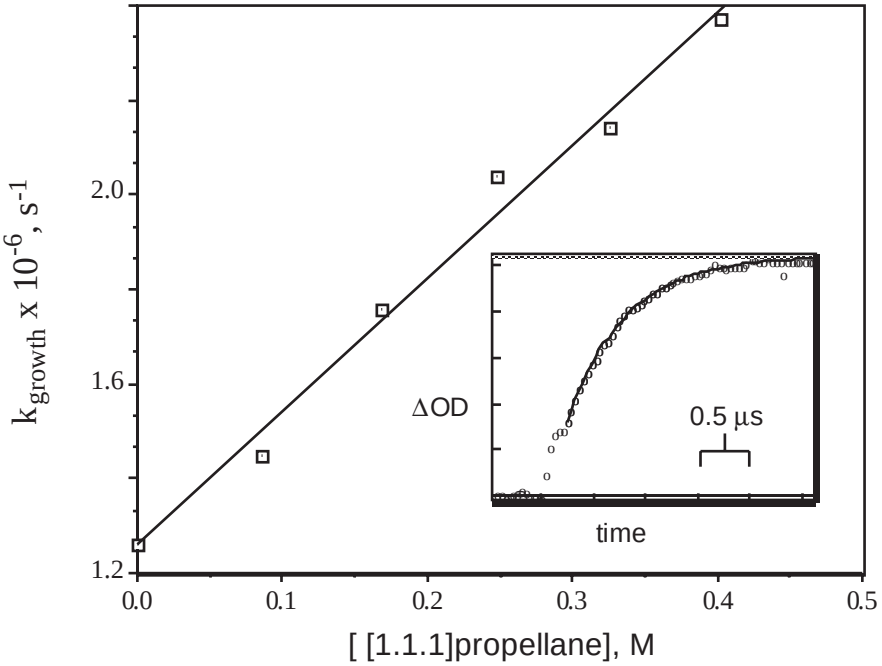

The buildup of the ketyl radical signal at 535 nm according to eq. [3] follows clean first-order kinetics (see insert in Fig. 1); a monoexponential fit of the signal growth leads to k_{growth}, which is related to the rate constants of interest according to:

[5] $k_{growth} = k_2 + k_3[Ph_2CHOH] + k_4[propellane]$

Thus, a plot of k_{growth} against the concentration of [1.1.1]propellane at constant diphenylmethanol concentration yields from the slope the value of k_4. The plot of Fig. 1 leads to $k_4 = (2.8 \pm 0.3) \times 10^6$ M^{-1} s^{-1}. This is a remarkably fast reaction for *t*-butoxyl radical addition to unsaturated systems (28, 29).

The kinetic probe technique cannot be used to determine the mechanism of reaction (30). For the mechanistic details we turned to precedence in the literature (4, 31) and to our own product studies. For instance it has been shown (4) that *t*-butyl hypochlorite gives addition products with **1** which are consistent with a free-radical S_H2 addition to the central bond in **1** by *t*-butoxyl radical:

[6] t-BuOCl ⟶ 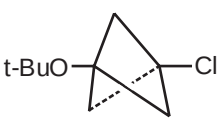

1

© 1998 NRC Canada

That *t*-butoxyl radicals add to the central bond in **1** rather than abstract a hydrogen atom from one of the methylene groups is also consistent with observations by Maillard and Walton (31) who studied the ESR spectrum of the bicyclo[1.1.1]pent-1-yl radical. Cyclopropane is often used as the solvent for such studies because its C—H bonds are relatively impervious to radical abstraction reactions. It was found, however, when cyclopropane was used as solvent for **2** in the presence of *t*-butoxyl radical the main species observed was the cyclopropyl radical. When no solvent was employed H-abstraction preferentially gave the cyclopent-1-yl, **3**, and no cyclopent-2-yl radical (reactions [7] and [8]):

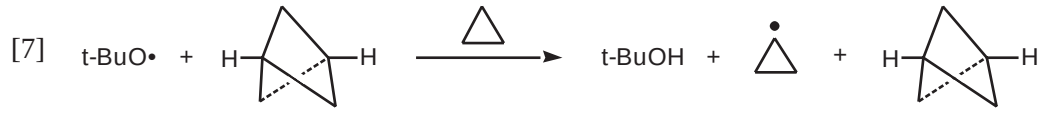

2

(reaction only with cyclopropane solvent)

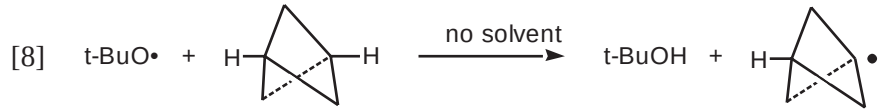

3

The results of Maillard and Walton (31) clearly demonstrate that the methylene hydrogens of the bicyclopentane ring system are extraordinarily unreactive towards H-atom abstraction.

Despite the compelling evidence in favour of S_H2 addition by *t*-butoxyl to **1** given above we carried out product studies of our own because under the conditions of laser flash photolysis of the peroxide in the presence of **1** there was no possibility for a chain reaction. Thus mixtures of **1** in 1:1 benzene/cyclohexane (v/v) were exposed to either thermal or photochemical sources of *t*-butoxyl radical (di-*t*-butyl hyponitrite or di-*t*-butyl peroxide, respectively). In both cases the solutions became opaque shortly after initiation of the reactions due to the precipitation of flocculant white material. The cyclohexane cosolvent was used in the hope that the adduct radical formed by addition of *t*-butoxyl radical to **1** could be trapped if it abstracted hydrogen from this solvent. Following removal of the insolubles, GC–MS of the supernatant reaction mixture indicated several products which incorporated both *t*-butoxyl and [1.1.1]bicyclopentane substructures as determined from the MS fragmentation patterns (vide infra). Unfortunately the nature of the *t*-butoxyl extension of the oligomers of **1** can be expected to result in facile fragmentation of the molecular ion. Indeed for all peaks observed in the GC trace no molecular ion peaks could be found in the corresponding GC–MS analysis.

Several features of the fragmentation pattern are worth noting. No molecular ion peak is observed. Differences in *m*/*e* between important peaks frequently correspond to the mass of propellane moiety (66). The propellane plus hydrogen peak of *m*/*e* = 67 is relatively important (the intermediacy of a bridgehead bicyclo[1.1.1]pentane carbocation has been reported in the reaction of electrophiles with [1.1.1]propellane) (32). Thus we concluded (14) that addition of *t*-butoxyl initiates polymerization of **1** resulting in oligomers which are similar to those already characterized by Michl et al. (33, 34).

Addition of thiophenoxyl radical

Thiophenoxyl radicals, which have a characteristic absorption with λ_{max} at 440 nm (35), were readily generated by laser irradiation (308 nm) of diphenyl disulfide. Experiments in deaerated cyclohexane showed that the radicals decayed by second-order kinetics, presumably to regenerate the starting material (Fig. 2). When [1.1.1]propellane was added, little or no effect on the rate of thiophenoxyl radical decay was observed, despite the fact that Wiberg et al. (4) have clearly shown that the disulfide adds across the central bond to give **4**, reaction [9].

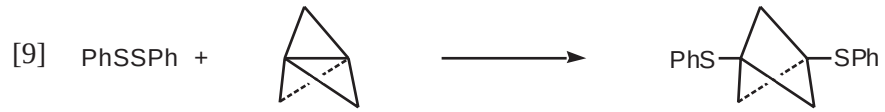

4

This situation is not uncommon for resonance stabilized radicals and reflects the fact that additions of PhS· are frequently reversible. Ito and Matsuda (35) have demonstrated that oxygen can be employed to trap carbon-centered radicals produced by reaction of thiophenoxy radicals with styrenes (vide infra) and that under these conditions it is possible to prevent the back reaction. In our case we observe that in the presence of air or oxygen [1.1.1]propellane does quench thiophenoxy radicals and that under these conditions the thiophenoxy radicals decay by pseudo-first-order kinetics; however, the bimolecular rate constant, k_{exptl}, obtained from a plot of k_{decay} vs. the propellane concentration (Fig. 3) is a function of the oxygen concentration (e.g., $(6.4 \pm 0.6) \times 10^6$ M^{-1} s^{-1} under air), suggesting that oxygen trapping is not quantitative. Reactions [10]–[13] show the mechanism proposed and is similar to that for thiophenoxyl addition to alkenes.

Oxygen is known to scavenge quite readily carbon-centered radicals, with rate constants that normally exceed 10^9 M^{-1} s^{-1} in fluid solution (31). In this system oxygen inhibits the regeneration of PhS·, which we suggest occurs via back reaction [12]. In principle, the regeneration of PhS· could have two different origins: (*a*) reaction [12] may be reversible, as already indi-

© 1998 NRC Canada

Fig. 2. Transient decay trace of phenylthiyl radical in cyclohexane at room temperature monitored at 440 nm.

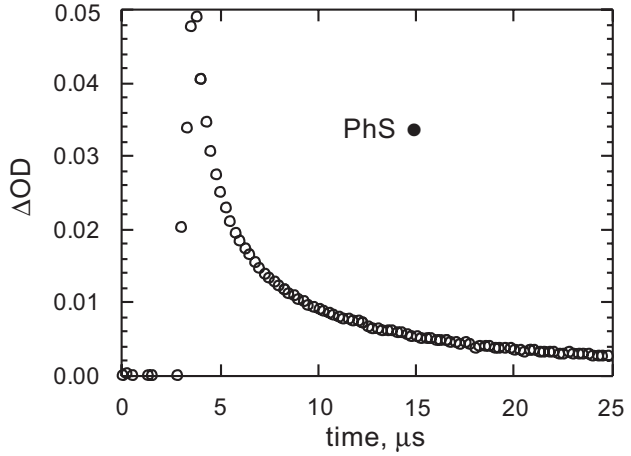

Fig. 3. Plot of the observed decay rate constant for phenylthiyl radical against [1.1.1]propellane concentration under aerated conditions in cyclohexane at room temperature.

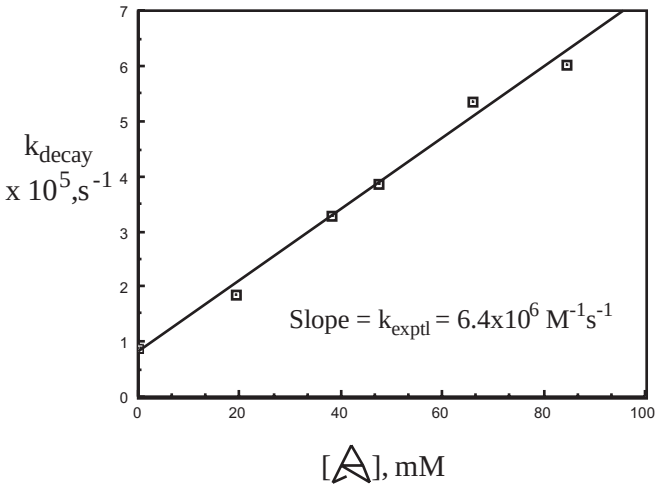

[10] PhSSPh $\xrightarrow{h\nu}$ 2 PhS•

[11] 2 PhS• ⟶ PhSSPh

[12] PhS• + 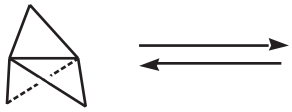 ⇌ 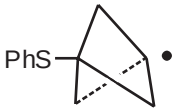

[13] 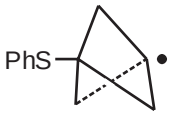 + O_2 ⟶

5

cated (by analogy with the case of olefins) (36, 37), or (*b*) radical **5** may react with the disulfide to yield another PhS· radical. The kinetic analysis that follows is independent of which mechanism is followed for the regeneration of PhS·. We believe that (*a*) is the correct explanation (vide infra). The values of k_{exptl} can be related with the rate constants of interest according to eq. [14]; the derivation of this expression can be found in the literature (13, 35).

$$[14] \quad \frac{1}{k_{apparent}} = \frac{1}{k_{12}} + \frac{k_{-12}}{k_{12}k_{13}[O_2]}$$

Thus, if the oxygen concentration is sufficiently high, the value of $k_{apparent}$ corresponds directly to k_{12}. Unfortunately, in our case saturation with oxygen in cyclohexane was not sufficient to meet this criterion. In our studies of $1/k_{apparent}$ vs. the reciprocal oxygen concentration, the intercepts of plots according to eq. [14] were always too small to allow a meaningful determination of anything other than an upper limit of 5×10^{-8} Ms. This establishes a lower limit of 2×10^7 M^{-1} s^{-1} for k_{12} in cyclohexane. However, in the case of Freon-113 as a solvent (where the oxygen solubility is much higher than in cyclohexane) (38),we were able to obtain significantly better data. Weighted least-squares analysis according to eq. [14] (Fig. 4) gives an intercept which, in spite of the large error, is significantly different from zero and leads to a k_{12} value of $(6.2 \pm 2.0) \times 10^7$ M^{-1} s^{-1}. Combining this with the slope leads to $k_{13}/k_{-12} \approx 59$ M^{-1}. Further, examination of reported absolute rate constants for radical reactions with oxygen suggest that the value of k_{13} should be in the neighborhood of 4×10^9 M^{-1} s^{-1} (31); combining this estimate with the slope from eq. [14] we estimate $k_{-12} \approx 6.8 \times 10^7$ s^{-1} in Freon-113. This is a remarkably fast rate, and may suggest that the addition of PhS· to propellane is thermoneutral, or slightly exothermic. Wiberg and Waddell (39) noted that the adduct of [1.1.1]propellane and PhSSPh can revert back to [1.1.1]propellane by reaction with diaryl lithium radical anion. Related examples of central bond formation via radical reactions have recently been reported (40).

© 1998 NRC Canada

Fig. 4. Plot according to eq. [14] for the reaction of PhS· with [1.1.1]propellane. The error bars are based on the dispersion of the data obtained for the decay of PhS· as a function of [**1**] for each oxygen concentration.

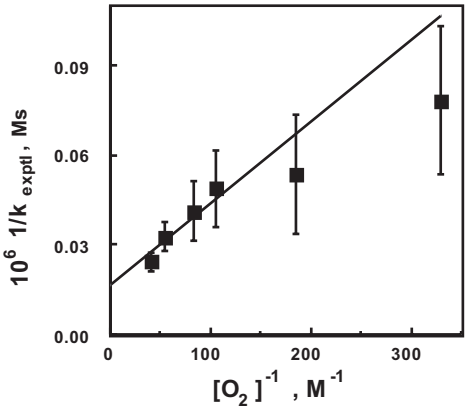

We wished to show independently that the composite thiyl-propellane radical, **5**, does dissociate to yield thiyl radical and propellane. Thus 1-(thiophenoxy)bicyclo-[1.1.1]pentane, **6** (reaction [15]), in 33% di-*tert*-butyl peroxide in benzene (v/v) solution was irradiated with an excimer laser pulse (λ = 308 nm). No growth of phenylthiyl radical at 440 nm was observed. Addition of varying amounts of **6** had no effect on the *t*-butoxyl radical lifetime (investigated using the benzhydrol kinetic probe) which indicated the inability of *t*-butoxyl to abstract the bridgehead hydrogen from **6** as shown in eq. [15].

[15] t-BuO• + PhS—H ⟶ no reaction

6

We also investigated the reactivity of **6** towards benzophenone triplet. Thiyl radical was observed at 440 nm. It must have arisen from energy transfer from benzophenone triplet to **6** rather than H-abstraction, since the absorption expected at 535 nm (indicating the presence of benzophenone ketyl radical) was absent. The fact that the bridgehead hydrogen of **6** is not easily abstracted is not unexpected, since crystal structures of the oligomers of **1** indicate that the corresponding C—C bond is short (1.48 Å) (34) and thus strong.

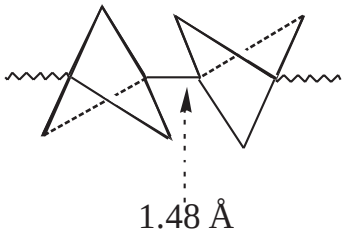

We also measured a rate constant for the addition of thiophenoxy radical to styrene to be 2.2×10^7 M^{-1} s^{-1}, in excellent agreement with the reported value of 2.0×10^7 M^{-1} s^{-1} (35). That phenylthiyl addition to propellane is faster than addition to styrene attests to the high reactivity of inverted structures at carbon towards addition reactions.

Triethylsilyl radical addition

Silyl radicals have been the subject of several extensive flash photolysis studies (41, 42). One convenient method for generation of silyl radicals is borrowed from successful studies of the triethylsilyl radicals by ESR spectroscopy (41, 43). This involves the photodecomposition of di-*tert*-butyl peroxide in the presence of triethylsilane. In this way a sufficient concentration of silyl radical can be obtained such that their further reactions may be studied.

[16] $t\text{-BuO}\cdot + Et_3SiH \rightarrow t\text{-BuOH} + Et_3Si\cdot$

The concentration of triethylsilane used is about 3.0 M. This concentration combined with the rate constant for hydrogen abstraction from triethylsilane by *t*-butoxyl radical of 6×10^6 M^{-1} s^{-1} gives an estimated lifetime for the grow-in of silyl radicals to be ≈53 ns (44). On the other hand, at the highest concentration of **1** employed, 2.3 mM, <<1% of the *t*-butoxyl radicals are trapped by propellane.

© 1998 NRC Canada

Fig. 5. Transient absorption trace showing the buildup of the adduct radical, **23**, at 380 nm, for 1.4 mM [1.1.1]propellane and 0.4 mM benzil. *Insert*: Plot according to eq. [20] for the reaction of $Et_3Si\cdot$ with [1.1.1]propellane with [benzil] = 0.4 mM. The slope yields a rate constant for addition of (6.0 ± 0.7) × 10^8 M^{-1} s^{-1}.

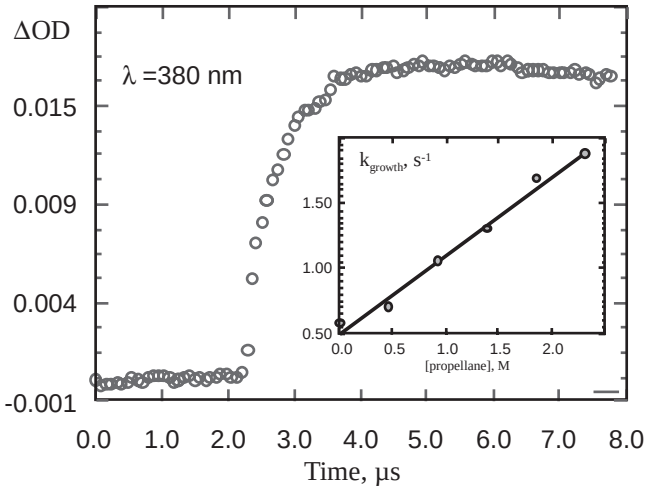

The triethylsilyl–propellane adduct radical **8**, does not show any significant absorptions above λ > 300 nm, and triethylsilyl radical itself absorbs only weakly below 340 nm (44, 45). Therefore we resorted to the use of benzil to probe the kinetics of the reaction between trethylsilyl radical and [1.1.1]propellane, **1** (41). This probe method takes advantage of the well known addition of silyl radicals to the oxygen of a carbonyl group (43) to give the carbon-centered adduct radical, **7**, as summarized in eq. [18]. The silyl radicals were generated by laser photolysis of di-*tert*-butyl peroxide at 337 nm in 1:1 triethylsilane/di-*tert*-butyl peroxide mixture (v/v). The generation of silyl radicals under these conditions was quite fast (vide supra), and in the presence of 0.4 mM benzil led to the grow-in of a strong absorption centered at ~380 nm, corresponding to the adduct radical **7** (eq. [18]). Reactions [17]–[19] show the mechanism proposed for reaction of triethylsilyl radical with **1**.

[17] $Et_3Si\bullet$ ⟶ First order decay

[18] $Et_3Si\bullet$ + 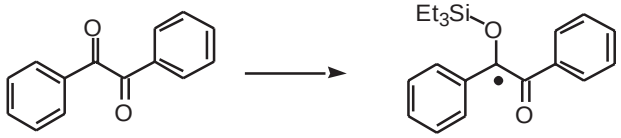 →

7

[19] $Et_3Si\bullet$ + 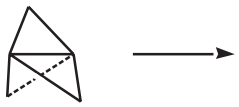 →

8

The signal monitored at 380 nm exhibits smooth monoexponential growth kinetics; a first-order fit of the data leads to k_{growth}. By analogy with eq. [5], the rate constant of reaction of triethylsilyl radical with the substrate of interest is related to k_{growth}, for the triethylsilyl–benzil adduct by the following equation.

[20] $k_{growth} = k_{17} + k_{18}[\text{benzil}] + k_{19}[\text{propellane}]$

When the concentration of benzil is held constant a plot of k_{growth} vs. [**1**] yields a straight-line plot whose slope is equated to k_{19}, the rate constant for reaction of triethylsilyl radical with **1**.

Figure 5 shows a plot of k_{growth} vs. [propellane]. The slope of the best line fit to the data represents the rate constant for addition of the triethylsilyl radical to **1** and was found to be k_{19} = (6.0 ± 0.7) × 10^8 M^{-1} s^{-1}. The rate constant for addition of triethylsilyl radical to [1.1.1]propellane compares favorably to that for addition to styrene (2 × 10^8 M^{-1} s^{-1}) and is much faster than the rate constant for addition to 1-hexene (5 × 10^6 M^{-1} s^{-1}) (46). That **1** is more reactive than styrene with triethylsilyl radical probably reflects the localized charge density at the bridgehead carbons in **1** and the electrophilic nature of $Et_3Si\cdot$ (4, 46).

The mechanism of addition of triethylsilyl radical is clearly established by Wiberg et al. (5) as being one of S_H2 attack at one of the bridgehead sites of **1** to cleave the central bond (reaction [19]), ultimately leading to **8**. In his study Wiberg also

© 1998 NRC Canada

noted that the triethylsilane–propellane adduct **10** was formed.

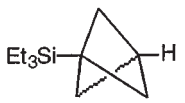

9

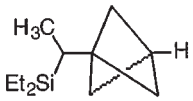

10

11

This clearly implicates radical **11** as an important species in their free-radical chain process. This radical plays no role in our kinetic studies (43, 44), given that the probe (benzil) is not expected to react significantly with it.

Benzene – chlorine atom π-complex reaction

Absolute rate constants for reaction of "free" chlorine atoms have been measured using laser flash photolysis (47–49). The techniques used are not practical for measuring a rate constant for the reaction between Cl· and **1** because they frequently employ Cl_2 as the chlorine atom precursor with which [1.1.1]propellane reacts spontaneously. One alternative is to investigate the rate of reaction of the chlorine atom – benzene π-complex (50). This species (51–53) has been extensively and thoroughly characterized by laser flash photolysis (47). Of five methods for generating the chlorine atom by flash photolysis only photolysis (47) of α-chloroacetophenone is suitable for study with **1**, since reaction between this chlorine atom precursor and **1** is unlikely.

Presumably the photolysis of α-chloroacetophenone in benzene produces the triplet state of this molecule which has, as the principal route of decay, β-cleavage to give a chlorine atom. The lifetime of the triplet and thus the growth of the benzene π-Cl· complex was estimated to be about 50 ns (47). The proposed mechanism is shown in eqs. [21] and [22].

[21] 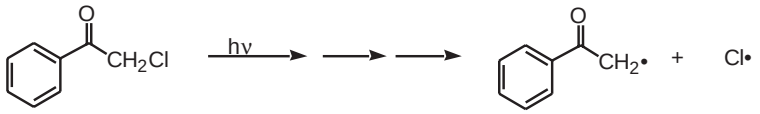

[22] 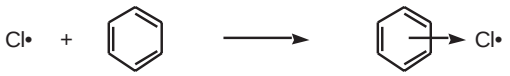

π-complex

This source of chlorine atom – benzene π-complex is limited by the lifetime of the precursor excited states (47, 54). Because the production of benzene-Cl· is limited by the lifetime of the triplet precursor the production of the complex is not quite "instantaneous." Thus in our investigations we were limited to conditions where the lifetime of the complex is greater than 200 ns.

Laser excitation (λ = 337 nm) of α-chloroacetophenone in benzene gave a strong absorption at 490 nm in deoxygenated benzene at 293 K. Upon addition of small amounts of [1.1.1]propellane the kinetics of decay changed from predominantly second order to predominantly first order. To help reduce error due to second-order radical–radical interactions the nitrogen laser beam was attenuated to 40% of its full power by use of a neutral density filter. The clean monoexponential decay traces were fit to first-order kinetics to yield k_{decay} of the complex in the presence of various concentrations of **1**. The rate constant for addition of π-complexed chlorine atom to **1** was then determined by plotting k_{decay} against the propellane concentration according to eq. [23].

$$[23] \quad k_{decay} = \tau^{-1} + k_{24}[\text{propellane}]$$

where τ^{-1} is the rate constant for decay of the complex by any first- or pseudo-first-order processes in the absence of **1**, and k_{24} is the rate constant for addition of π-Cl· to **1** according to eq. [24].

[24]

The rate constant for addition of the benzene – chlorine atom π-complex to [1.1.1]propellane, k_{24} is obtained from the slope of the line to be $(3.1 \pm 0.5) \times 10^9$ M^{-1} s^{-1}. This rate constant is close to the diffusion-controlled limit and indicates an exothermic reaction. It implies that the complex is reacting directly with **1** and is not just the source of free chlorine atom in equilibrium with the complex. The rate of addition of "free" chlorine atoms with **1** must be diffusion-controlled as these radicals are more reactive than the complexed ones (51).

© 1998 NRC Canada

The products of the reaction of halogen atoms with [1.1.1]propellane has been unambiguously established by Zefirov et al. (8). The principal mode of addition is S_H2 displacement of the central bond at one of the bridgehead carbons to ultimately give the 1,3-disubstituted bicyclo[1.1.1]pentane in a radical chain reaction as summarized in reactions [25] to [27].

[25] $Cl_2 \xrightarrow{h\nu} 2\ Cl\bullet$

[26] $Cl\bullet$ + $\longrightarrow C_6H_6$ + 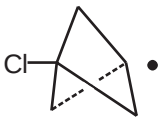

[27] 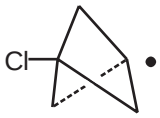 + Cl_2 $\longrightarrow$ 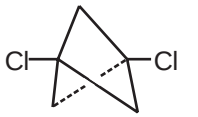 + $Cl\bullet$

Addition of p-*methoxybenzoyloxyl*

Benzoyloxyl radicals have been studied by laser photolysis techniques (42, 55) and by time resolved ESR spectroscopy (56, 57). While these radicals are known to undergo facile decarboxylation, by use of time resolved techniques it was possible to investigate other reactions which competed with their unimolecular decomposition. Equations [28]–[32] show the proposed mechanism for the photolysis of a bis(aroyloxyl) peroxide in the presence of [1.1.1]propellane.

[28] 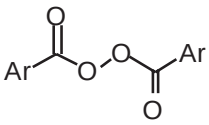 $\xrightarrow{h\nu}$ 2 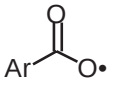

[29] 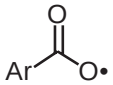 $\longrightarrow$ Ar• + CO_2

[30] 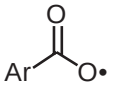 + RH $\longrightarrow$ $ArCO_2H$ + R• (or addition)

[31] 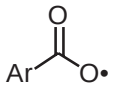 + 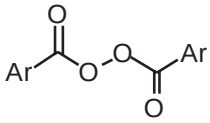 $\longrightarrow$ Products

[32] 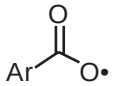 + $\longrightarrow$ 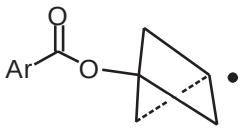

Thus aryloxyl radicals may decarboxylate, react with the solvent, with the peroxide precursor, or some added substrate possibly by hydrogen atom abstraction or by addition. We chose to study the reaction of *p*-methoxybenzoyloxy radical with **1**, since this is the longest lived of the known aroyloxyl radicals (55, 58). It undergoes decarboxylation in CCl_4, slowly giving it a lifetime of about 2 μs and decarboxylates even slower ($\tau > 50$ μms) in acetonitrile. The decreased rate for decarboxylation is attributed to a stabilization of the *p*-methoxybenzoyloxy radical by this solvent (42).

The decay of *p*-methoxybenzoyloxy radical was monitored at 720 nm, at room temperature (20°C) in aerated acetonitrile. It exhibited a ~5 μs lifetime showing first-order decay kinetics, following laser excitation (308 nm) of bis-(4-methoxybenzoyloxyl) peroxide. Since no radical scavengers were present, and the radical does not react with this solvent or oxygen, the principal mode of decay was taken to be reaction with the peroxide precursor whose concentration was ≈10 mM (42). Upon addition of [1.1.1]propellane to the system the observed rate of decay of the radical increased. Thus the rate constant for addition of the benzoyloxyl radical to **1**, k_{32}, is related to the experimentally observed decay rate constant, k_{decay}, according to eq. [33].

© 1998 NRC Canada

Table 1. Summary of room-temperature-solution rate constants for addition of various radicals to [1.1.1]propellane and comparison to styrene rate constants where applicable.

Radical	Propellane (M^{-1} s^{-1})	Styrene (M^{-1} s^{-1})	Ratio *P*/*S*
t-Butoxy	2.8×10^6	0.91×10^6	3.0
Thiophenoxy	6.2×10^7	2.2×10^7	2.8
Triethylsilyl	6.0×10^8	2.0×10^8	3.0
Benzene – chlorine atom π-complex	3.1×10^9	—	—
p-Methoxybenzoyloxyl	1.0×10^7	5.5×10^6	1.8

Table 2. Rate constants for electronic energy transfer to [1.1.1]propellane.

Sensitizer	Excited state	Energy (kcal mol^{-1})[a]	$k_q/10^6$ (M^{-1} s^{-1})	Solvent
Triphenylene	$^3(\pi,\pi^*)$	67	6.8	Benzene
Benzophenone	$^3(n,\pi^*)$	69	9.9	Benzene
Benzophenone	$^3(n,\pi^*)$	69	7.6	Acetonitrile
Phenanthrene	$^3(\pi,\pi^*)$	62	0.92	Benzene
Fluorenone	$^3(\pi,\pi^*)$	53	0.063	Benzene
Pyrene	$^1(\pi,\pi^*)$	77	140	Benzene

[a]Values from ref. 61.

[33] $$k_{decay} = k_0 + k_{32}[\text{propellane}]$$

where k_0 incorporates all pseudo-first- or first-order modes of decay that are independent of the propellane concentration, such as reactions [29]–[31]. This yields a rate constant for addition of *p*-methoxybenzoyloxyl to [1.1.1]propellane of $(1.0 \pm 0.1) \times 10^7$ M^{-1} s^{-1}.

Thus, *p*-methoxybenzoyloxy radicals are about as reactive as *t*-butoxyl radicals in hydrogen atom abstractions but far more reactive in additions to multiple bonds. This was of interest, since in reaction with [1.1.1]propellane we could expect a faster addition rate across the central bond than that for *t*-butoxy. As expected we measured a larger rate constant of addition then that for *t*-butoxyl radical addition to **1**. How does this compare to *p*-methoxybenzoyloxy addition to styrene? It is slower than the rate measured by Chateauneuf et al. (70) (5.5×10^7 M^{-1} s^{-1}) but their measurement was carried out using CCl_4 as the solvent. Since they noted a consistent reduction in rates on changing solvent from CCl_4 to acetonitrile we can assume that the rate constants for addition of *p*-methoxybenzoyloxyl to styrene and to **1** are roughly equal. The rate constants for radical substitution of **1** are summarized in Table 1.

Interaction of [1.1.1]propellane with excited molecules

Triplet excited states and [1.1.1]propellane

The rate constants for the deactivation of the first triplet states of benzophenone, triphenylene, phenanthrene, and fluorenone by [1.1.1]propellane have been measured. The method for determining the rate constants was almost identical for each of the four triplet donors. Thus a detailed description of the experiment for benzophenone which is provided below is representative for all the measurements.

An oxygen-free solution of benzophenone in benzene (5 mM) was excited with the pulses of a nitrogen laser (337.1 nm, ~8 ns, <10 mJ/pulse). The transient absorption of benzophenone triplet may be monitored in the 500–600 nm region. We chose to monitor this triplet at 600 nm in order to avoid contributions from possible ketyl radical absorption at 540 nm (59). The triplet lifetime, τ_o, in benzene in the absence of **1** was usually 2–3 μs. Longer lifetimes could undoubtedly be obtained by exhaustive purification of the solvent, but this would not give an improvement in our results and could even introduce errors due to triplet–triplet annihilation processes.

The rate constant for quenching of benzophenone triplet by propellane may be related to the observed rate constant, k_{obs}, obtained by monoexponential fitting of the experimental decay, by the following expression, eq. [34].

[34] $$k_{obs} = \frac{1}{\tau_o} + k_q[\text{propellane}]$$

Thus, a plot of the observed rate constant against the concentration of **1** lead to a straight line whose slope represents the bimolecular rate constant of interest. This plot is shown in Fig. 6, and from the slope the value of k_q has been determined to be $(9.9 \pm 1.1) \times 10^6$ M^{-1} s^{-1}. Similar experiments for triplet triphenylene, triplet fluorenone, and triplet phenanthrene were analyzed in the same manner to yield the rate constants summarized in Table 2.

© 1998 NRC Canada

Fig. 6. Plot of k_{obs} vs. [**1**] for the benzophenone–propellane system. The slope yields a bimolecular rate constant of (9.9 ± 1.1) × 10^6 M^{-1} s^{-1}. *Insert*: Decay trace for benzophenone triplet monitored at 600 nm. The concentration of **1** is 0.39 M in benzene at 21°C.

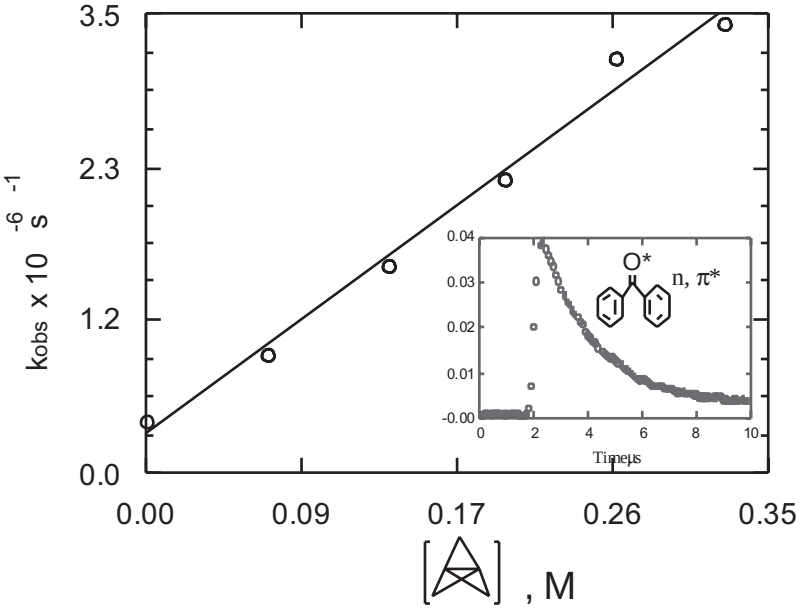

Pyrene fluorescence quenching by [1.1.1]propellane

The rate constant for quenching of pyrene fluorescence by **1** was measured via Stern–Volmer analysis (60). The proposed mechanism following excitation of pyrene to its excited singlet state and deactivation by **1**, as shown below (Py = pyrene).

[35] $Py^* \xrightarrow{k_e} Py + h\nu$

[36] $Py^* \xrightarrow{k_d} Py$

[37] $Py^* +$ $\xrightarrow{k_q} Py +$

The Stern–Volmer equation relates the relative fluorescence efficiency to the rate constant for fluorescence quenching by **1** as shown in eq. [38].

$$[38] \quad \frac{\Phi_e^o}{\Phi_e} = 1 + k_q \tau_{Py}[\text{propellane}]$$

where τ_{Py} is the lifetime of the pyrene singlet state in the absence of quenchers. Thus, a plot of the ratio of the efficiencies, $\Phi_e°/\Phi_e$, of pyrene in the presence and absence of **1** versus the concentration of **1** yields a straight line whose slope is equated to $k_q\tau_{Py}$ with an intercept of 1. The fluorescence lifetime of pyrene under the experimental conditions was measured by single photon counting to be 382 ns, in good agreement with the literature value (61). Combining τ_{Py} with the value of the Stern–Volmer slope lead to k_q = (1.42 ± 0.13) × 10^8 M^{-1} s^{-1}.

Product and steady-state photolysis studies for excited-state quenching

Analysis of the samples used in the kinetic studies by GC and GC–MS showed no new products corresponding to 1:1 adducts of **1** and pyrene, benzophenone, triphenylene, phenanthrene, or fluorenone. In the benzophenone–propellane system polymerization was evident. In acetonitrile a cloudy white precipitate was formed, and when benzene was used as solvent a sharp increase in viscosity followed irradiation, indicative of polymer formation. Several lower molecular weight products (m/e < 182, i.e., less than the molecular weight of benzophenone) were detected. These corresponded to propellane dimerization and addition to solvent (acetonitrile). Except for the dimer of **1** (**13**) they were not considered important, as they also arose in the absence of irradiation. The order of magnitude measurements for the quantum yield for propellane dimer production and sensitizer consumption were measured using steady-state photolysis and valerophenone as an actinometer in a few cases (62). The results are summarized in Table 3.

© 1998 NRC Canada

Table 3. Quantum yields for the dimerization of **1**.

Sensitizer	Φ consumption	Φ dimerization
Benzophenone	0.130	0.072
Triphenylene	0.003	0.062

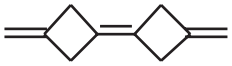

13

Table 4. Comparison of *t*-butoxyl addition rate constants.

Hydrocarbon	k (M^{-1} s^{-1})
Cyclopentene	0.64×10^{6a}
Cyclopentadiene	4.06×10^{6a}
Norbornene	1.00×10^{6a}
Norbornadiene	3.22×10^{6a}
Styrene	9.1×10^{5b}
[1.1.1]Propellane	2.80×10^{6}

[a]The rate constants have been taken from ref. 29 and converted from composite (addition + abstraction) rate constants to addition rate constants by employing the measured *t*-butanol quantum yields which were used as a measure of H-abstraction. These rate constants have been calculated for reactions occurring at 293 K by using the reported activation parameters in order that they match the temperature at which the rate constant for addition to propellane was measured.

[b]Rate constant taken from ref. 70 was measured in CCl_4 as solvent at 21°C.

Discussion

Free-radical addition rate constants

We have compared, whenever possible, our measured rates of radical reactions with **1** to rates of additions of the same radicals with olefins (styrene in particular) which have been measured with a similar methodology. We feel this is more useful than comparison with rates of addition to other inverted geometries at carbon because (*i*) there is only one other example at present (63) and (*ii*) most chemists already have an appreciation for the reactivity of carbon–carbon π-bonds. In fact S_H2 reactions at carbon centers are so uncommon (64) that one has no choice but to compare them with the next closest option, addition to C—C double bonds. Thus it is felt that the radical addition reactions to olefins in general and to styrene in particular supply the ruler by which we can measure the reactivity of the inverted geometry in [1.1.1]propellane. Our discussion begins with the relative reactivity of propellane with respect to *t*-butoxyl radical addition to it and to several mono- and dienes and subsequently several rate constants involving radical additions to styrene.

Of the radical additions studied *t*-butoxyl is the one for which the most information is available regarding its reactivity with a number of olefins (29). For example, when given a choice between addition or of H-atom abstraction on the same hydrocarbon the latter is clearly preferred, especially in the cases where olefins bear allylic hydrogens. In the case of **1** addition is the only mode of attack. This indicates that the methylene hydrogens in **1** are unreactive towards H atom abstraction (vide infra). Some rates for addition of *t*-butoxyl to unsaturated systems are reproduced in Table 4 for comparison to the measured rate of addition to [1.1.1]propellane. One will note that Table 4 shows that the rate of addition of *t*-butoxyl to **1** is fast and intermediate between the rate constants for addition to mono- and dienes.

[1.1.1]Propellane may be compared most consistently with styrene, however, when considering it as a reactive substrate, since there are addition rate constants available for styrene for most of the radicals studied here. The rate constants are summarized in Table 1. For all but one case **1** reacts more rapidly with a given radical than does styrene. The exception is for the *p*-methoxybenzoyloxyl radical. It is instructive to note, however, that the two reported rate constants for this radical were measured in different solvents (acetonitrile for **1** and carbon tetrachloride for styrene). A consistent reduction in rate of reaction has been demonstrated for most additions of *p*-methoxybenzoyloxyl radical in acetonitrile compared with CCl_4 due to a strong stabilizing effect by the former solvent compared to the latter. The overall conclusion is that the central carbon–carbon single bond of [1.1.1]propellane is more reactive towards radical addition reactions than most hydrocarbons containing double bonds. A result which underlines the unique properties of the inverted structure within **1**.

Discussion of the interaction of electronic excited states with [1.1.1]propellane

The quenching of the triplet states of fluorenone, phenanthrene, triphenylene, and benzophenone by **1** must occur by the electron exchange mechanism. Several mechanisms can be proposed for this interaction. In the case of all the triplets a two-step exchange mechanism via radical ion pair intermediates is unlikely, since there was no enhancement in the quenching rate constant when acetonitrile, a more polar solvent, was employed. For the π,π* triplet states, fluorenone, phenanthrene, and triphenylene, the covalent bonding mechanism at the bridgehead is probably not operational, since biradical intermediates were not observed for these systems. To observe the biradical intermediate, a high concentration of propellane is employed which rapidly and quantitatively quenches all triplet states present. Possible biradical intermediates, such as that illustrated below for benzophenone (**14**), if generated rapidly in good yields, should be easily detectable by their unique UV-vis absorption spectra. The new intermediate should exhibit growth kinetics coincident with the decay kinetics of the precursor triplet state. A successful example of this experiment is the observation of the propellane – triplet diphenylcarbene adduct biradical (14). For the excited states described here, all such experiments yielded no detectable transient signals and thus biradical intermediates are unlikely. Thus triplet–triplet energy transfer to give triplet **1** by the concerted electron exchange mechanism is likely for π,π* triplet quenching by [1.1.1]propellane.

© 1998 NRC Canada

Fig. 7. Qualitative illustration of the transitions involved in triplet excitation transfer to **1**. Note that we have assumed a bound triplet state, but with a significantly longer C—C distance. The triplet is likely to have a more shallow surface.

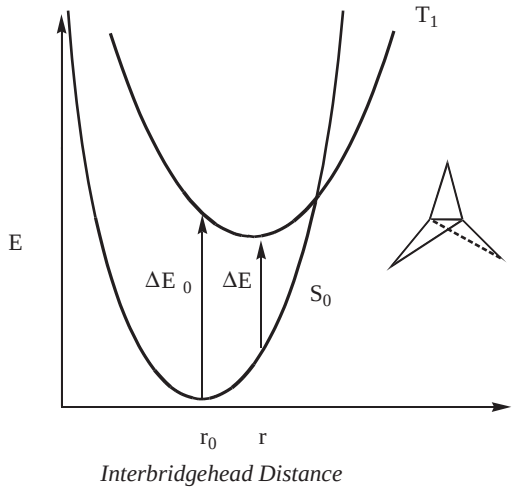

Fig. 8. Dependence of log (k_q) in benzene on the excited-state energy of the sensitizer. The slope of the best line is 0.14 mol/kcal.

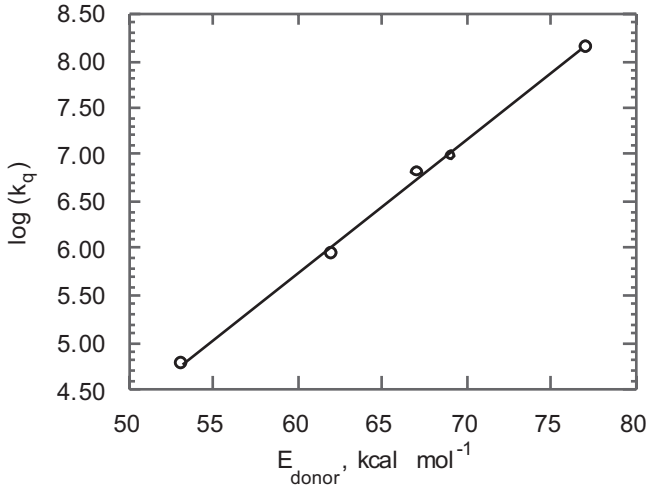

Discerning the operating mechanism by which triplet benzophenone is quenched by **1** is not as easy as in the π,π* case. Since the triplet *n*,π* state of benzophenone is radical-like, one might expect it to behave similarly to the *t*-butoxyl radical and add across the central bond of **1** to form biradical **14**. At short triplet lifetimes, corresponding to high quenching concentrations of **1**, no new transients such as **14** could be detected in our laser flash photolysis experiments. No 1:1 benzophenone/propellane adduct was detectable in product studies. Thus the possibility that the quenching of benzophenone triplet by **1** occurs by concerted electron exchange rather than the covalent bonding mechanism must be considered. There is, however, evidence of polymerization of **1** possibly initiated by benzophenone.

The benzophenone system differs in that polymerization of propellane is detectable, much greater than for the other triplet π,π* systems, and that the sensitizer is partially consumed. The benzophenone system is similar to the others in that most en-

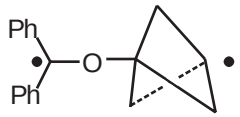

14

counters between benzophenone triplet and **1** generate ground-state benzophenone, as evidenced by the modest quantum efficiency of consumption of benzophenone in steady-state product studies. One possible mechanism which can explain these observations is that triplet benzophenone covalently bonds to **1** to form the biradical **14**, but the reaction is reversible and yields benzophenone unchanged in 9 cases out of 10. The tenth would, presumably, yield polymeric material by further reaction of **14** with propellane monomers.

The quenching rate constants for all the sensitizers are smaller than that expected for a diffusion-controlled process. This may reflect a large Frank–Condon S_0–T_1 or S_0–S_1 energy gap from the zero vibrational level in S_0. In fact the energies of the vertical transitions have been measured recently by low energy electron impact excitation (22). The estimates for the vertical energy gaps from S_0 to S_1 and from S_0 to T_1 are 167 and 108 kcal/mol, respectively. The difference between the electronic energies of the donor states which are quenched by **1** and the energy reported for the vertical transition must lie in the steepness of the excited-state surface at the ground-state interbridgehead distance as shown in Fig. 7. For example one may see that the vertical transition energy required to reach T_1 at r_0 on Fig. 7 is much greater than that at *r*. This results in energy transfer requiring an activation energy. This is illustrated by the approximately linear relationship which is found between the logarithm of k_q and the energy of the electronic energy donor (see Fig. 8). This type of behavior has been observed before (65–68), particularly for singlet and triplet energy transfer to molecules containing dissociative S_1 or T_1 states as in the case for di-*tert*-butylperoxide (67, 68).

In the case of [1.1.1]propellane the S_1 and T_1 states should be dissociative due to rupture of the weak central bond (15, 16). The bridgehead carbons cannot separate completely, however, since three bridging methylene groups between the bridgehead carbons hold them together. Thus the lowest excited states of propellane should have Morse-like potential energy curves. The correlation of log (k_q) with E_{donor} for energy transfer to **1** may be explained in the same way as for peroxides because the equilibrium bridghead–bridgehead distance in the excited state is larger than in the ground state (the difference in r_0 for S_0 and r_0 for S_1 is about 0.2 Å) (69).

© 1998 NRC Canada

Scheme 2.

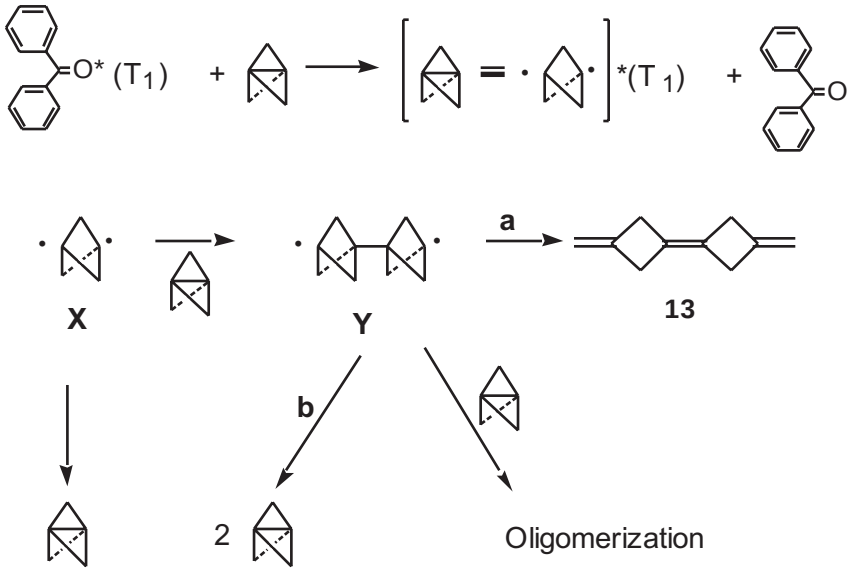

From the plot of log (k_q) vs. E_{donor} (Fig. 8) we can draw a number of conclusions about the mechanism of energy transfer to [1.1.1]propellane. First, the principal factor which controls the rate of energy transfer to **1** is the excited-state energy of the donor and not the type (π,π^* or n,π^*) nor the multiplicity (S_1 or T_1). This implies that either the mechanism of electronic excited-state quenching by **1** is the same for all the electronic energy donors studied or that the rate of quenching is independent of the energy transfer mechanism. Secondly, the value of the slope from Fig. 8 (0.14 mol/kcal) is larger than that observed for energy transfer to di-*tert*-butyl peroxide (0.072 mol/kcal) (67) but smaller than that for triplet energy transfer to bound excited states (0.733 mol/kcal) (65). If the slope of an upper potential curve is inherently steeper when the state is more bound, then the excited state of propellane might be considered as intermediate in nature between the two extremes of dissociative and bound excited states.

Thus the results obtained for excited-state quenching by [1.1.1]propellane can be explained by a mechanism where thermally excited propellane molecules (ones that have greater bridghead–bridgehead bond lengths than the equilibrium value) are responsible for quenching excited states whose energies are less than the vertical energy gap of equilibrium S_0 T_1 or S_1 transition in propellane.

Bis(1,1′-methylenecyclobutylidene): the dimer of [1.1.1]propellane

From the apparent quantum yield of dimer production at 350 nm in benzene under sensitized conditions (energy transfer from either benzophenone or triphenylene, see Table 3) it is obvious that if dimer is a result of [1.1.1]propellane excited state that it is an inefficient process. Most propellane excited states must revert to propellane ground state with only a small fraction forming dimer. The existence of excited states of propellane, however, have not been proven by our studies but are merely implied. Thus any mechanism described by us where the dimer of propellane arises from excited singlet or triplet propellane must be considered entirely speculative.

Nevertheless, the dimer of **1** is formed in substantially enhanced yields under conditions of triplet–triplet sensitization. It has been shown from a number of theoretical studies that the lowest excited triplet state of **1** is the biradical formed by dissociation of the central bond in **1**. Thus, we tentatively suggest that the propellane dimer **13** is formed by the mechanism of Scheme 2.

Conclusion

Several radical addition reactions of [1.1.1]propellane are studied and the absolute bimolecular rate constants for the reactions are measured and compared to those for unsaturated hydrocarbons and, in particular, styrene. The rate constants range from $<1 \times 10^5$ to 3.1×10^9 M^{-1} s^{-1} (benzyl and benzene – chlorine atom π-complex radicals, respectively). In most cases the central single carbon–carbon bond reacts more readily with radicals than the carbon–carbon double bond of styrene. Thus a remarkable reactivity towards S_H2 radical additions, unparalleled in any carbon–carbon single bonds of more "normal" hydrocarbons, is displayed by the inverted geometry of the central bond in [1.1.1]propellane.

Acknowledgments

Thanks are due to the Natural Sciences and Engineering Research Council of Canada for support of J.C.S. and P.F.M. This work was partially carried out at the National Research Council Laboratories in Ottawa; the support received during this stage of the work is acknowledged.

© 1998 NRC Canada

References

1. A.v. Baeyer. Ber. Dtsch. Chem. Ges. **18**, 2269 (1885).
2. K.B. Wiberg, W.P. Dailey, F.H. Walker, S.T. Waddell, L.S. Crocker, and M. Newton. J. Am. Chem. Soc. **107**, 7247 (1985).
3. K.B. Wiberg, and F.H. Walker. J. Am. Chem. Soc. **104**, 5239 (1982).
4. K.B. Wiberg, S.T. Waddell, and K. Laidig. Tetrahedron Lett. **27**, 1553 (1986).
5. K.B. Wiberg, S.T. Waddell, and R.E. Rosenberg. J. Am. Chem. Soc. **112**, 2184 (1990).
6. K.B. Wiberg. Chem. Rev. **89**, 975 (1989).
7. E.W. Della, P.E. Pigou, C.H. Scheisser, and D.K. Taylor. J. Org. Chem. **56**, 4659 (1991).
8. N.S. Zefirov, L.S. Surmina, N.K. Sadovaya, and A.S. Koz'min. Izv. Akad. Nauk. SSSR Ser. Khim. 2871 (1987).
9. P.F. McGarry and J.C. Scaiano. Tetrahedron Lett. **34**, 1243 (1993).
10. P. Kaszynski, N.D. McMurdie, and J. Michl. J. Org. Chem. **56**, 307 (1991).
11. K.P. Dockery and W.G. Bentrude. J. Am. Chem. Soc. **119**, 1388 (1997).
12. K.P. Dockery and W.G. Bentrude. J. Am. Chem. Soc. **116**, 10 332 (1994).
13. P.F. McGarry, L.J. Johnston, and J.C. Scaiano. J. Org. Chem. **54**, 6133 (1989).
14. P.F. McGarry, L.J. Johnston, and J.C. Scaiano. J. Am. Chem. Soc. **111**, 3750 (1989).
15. M.D. Newton and J.M. Schulman. J. Am. Chem. Soc. **94**, 773 (1972).
16. W.D. Stohrer and R. Hoffmann. J. Am. Chem. Soc. **94**, 779 (1972).
17. K.B. Wiberg. J. Am. Chem. Soc. **105**, 1227 (1983).
18. N.D. Epiotis. J. Am. Chem. Soc. **106**, 3170 (1984).
19. J.E. Jackson and L.C. Allen. J. Am. Chem. Soc. **106**, 591 (1984).
20. D. Feller and E.R. Davidson. J. Am. Chem. Soc. **109**, 4133 (1987).
21. T. Ushio, T. Kato, K. Ye, and A. Imamura. Tetrahedron, **45**, 7743 (1989).
22. O. Schafer, M. Allan, G. Szeimies, and M. Sanktjohanser. J. Am. Chem. Soc. **114**, 8180 (1992).
23. K. Semmler, G. Szeimies, and J. Belzner. J. Am. Chem. Soc. **107**, 6410 (1985).
24. H. Bothe and A.-D. Schlüter. Chem. Ber. **124**, 587 (1991).
25. J.C. Scaiano. J. Am. Chem. Soc. **102**, 7747 (1980).
26. J.C. Scaiano, M. Tanner, and D. Weir. J. Am. Chem. Soc. **107**, 4396 (1985).
27. H. Paul, R.D. Small, Jr., and J.C. Scaiano. J. Am. Chem. Soc. **100**, 4520 (1978).
28. M.V. Encinas and J.C. Scaiano. J. Am. Chem. Soc. **103**, 6393 (1981).
29. P.C. Wong, D. Griller, and J.C. Scaiano. J. Am. Chem. Soc. **104**, 5106 (1982).
30. J.C. Scaiano. Kinetic studies of alkoxyl radicals. *In* Oxygen radicals in biology and medicine. *Edited by* Simic, Taylor, Ward, and von Sonntag. Plenum, New York. 1989. p. 59.
31. B. Maillard and J.C. Walton. J. Chem. Soc. Chem. Commun. 900 (1983).
32. K.B. Wiberg and N. McMurdie. J. Am. Chem. Soc. **113**, 8995 (1991).
33. P. Kaszynski, A.C. Friedli, and J. Michl. Mol. Cryst. Liq. Cryst. Lett. **6**, 27 (1988).
34. J. Michl, P. Kaszynski, A.C. Friedli, G.S. Murthy, H.-C. Yang, R.E. Robinson, N.D. McMurdie, and T. Kim. Putting strain to work: from [1.1.1]propellanes to tinkertoys. NATO advanced research workshop on strain and its implications in organic chemistry. 1988.
35. O. Ito and M. Matsuda. J. Am. Chem. Soc. **101**, 5732 (1979).
36. C. Walling and W. Helmreich. J. Am. Chem. Soc. **81**, 1144 (1959).
37. O. Ito and M. Matsuda. J. Am. Chem. Soc. **101**, 1815 (1979).
38. R. Battino. Solubility data series: oxygen and ozone. Pergamon Press, Oxford. 1981.
39. K.B. Wiberg and S.T. Waddell. Tetrahedron Lett. **29**, 289 (1988).
40. W. Adcock, G.T. Binmore, A.R. Krstic, J.C. Walton, and J. Wilkie. J. Am. Chem. Soc. **117**, 2758 (1995).
41. C. Chatgilialoglu, K.U. Ingold, and J.C. Scaiano. J. Am. Chem. Soc. **104**, 5119 (1982).
42. C. Chatgilialoglu, K.U. Ingold, and J.C. Scaiano. J. Org. Chem. **52**, 938 (1987).
43. A. Hudson and R.A. Jackson. Chem. Commun. 1323 (1969).
44. C. Chatgilialoglu, J.C. Scaiano, and K.U. Ingold. Organometallics, **1**, 466 (1982).
45. C. Chatgilialoglu, K.U. Ingold, J.C. Scaiano, and H. Woynar. J. Am. Chem. Soc. **103**, 3231 (1981).
46. C. Chatgilialoglu, K.U. Ingold, and J.C. Scaiano. J. Am. Chem. Soc. **105**, 3292 (1983).
47. N.J. Bunce, K.U. Ingold, J.P. Landers, J. Lusztyk, and J.C. Scaiano. J. Am. Chem. Soc. **107**, 5464 (1985).
48. R. Breslow, M. Brandl, J. Hunger, N. Turro, K. Cassidy, K. Krogh-Jesperson, and J.D. Westbrook. J. Am. Chem. Soc. **109**, 7204 (1987).
49. Z.B. Alfassi, S. Mosseri, and P. Neta. J. Phys. Chem. **93**, 1380 (1989).
50. K.D. Raner, J. Lusztyk, and K.U. Ingold. J. Am. Chem. Soc. **111**, 3652 (1989).
51. G.A. Russell. J. Am. Chem. Soc. **80**, 4997 (1958).
52. J. Walton. J. Chem. Soc. Perkin Trans. 2, 1989 (1988).
53. P.S. Skell, H.N. Baxter, and C.K. Taylor. J. Am. Chem. Soc. **105**, 120 (1983).
54. W.G. McGimpsey and J.C. Scaiano. Can. J. Chem. **66**, 1474 (1988).
55. J. Chateauneuf, J. Lusztyk, and K.U. Ingold. J. Am. Chem. Soc. **110**, 2886 (1988).
56. S. Yamauchi, N. Hirota, S. Takahara, H. Sakuragi, and K. Tokumaru. J. Am. Chem. Soc. **107**, 5021 (1985).
57. S. Yamauchi, N. Hirota, S. Takahara, H. Misawa, K. Sawabe, H. Sakuragi, and K. Tokumaru. J. Am. Chem. Soc. **111**, 4402 (1989).
58. J. Chateauneuf, J. Lusztyk, and K.U. Ingold. J. Am. Chem. Soc. **110**, 2877 (1988).
59. J.C. Scaiano, E.B. Abuin, and L.C. Stewart. J. Am. Chem. Soc. **104**, 5673 (1982).
60. N.J. Turro. Modern molecular photochemistry. Benjamin/Cummings Publishing Co., Menlo Park. 1978.
61. S.L. Murov. Handbook of photochemistry. Marcel Decker, New York. 1973.
62. P.J. Wagner, P.A. Kelso, A.E. Kemppainen, J.M. McGrath, H.N. Schott, and R.G. Zepp. J. Am. Chem. Soc. **94**, 7506 (1972).
63. M. Anpo, C. Chatgilialoglu, and K.U. Ingold. J. Org. Chem. **48**, 4104 (1983).
64. K.U. Ingold and B.P. Roberts. Free-radical substitution reactions. Wiley–Interscience, New York. 1971.
65. K. Sandros. Acta Chem. Scand. **18**, 2355 (1964).
66. W.L. Wallace, R.P. Van Duyne, and F.D. Lewis. J. Am. Chem. Soc. **98**, 5319 (1975).

© 1998 NRC Canada

67. J.C. Scaiano and G.G. Wubbels. J. Am. Chem. Soc. **103**, 640 (1981).
68. M.V. Encinas and E.A. Lissi. J. Photochem. **20**, 153 (1982).
69. K.B. Wiberg. Acc. Chem. Res. **17**, 379 (1984).
70. J. Chateauneuf, J. Lusztyk, and K.U. Ingold. J. Am. Chem. Soc. **109**, 897 (1987).

© 1998 NRC Canada

Uniaxial deformation of nylon-6 and nylon-11: changes in orientation and crystal phase

Sonia Moffatt, Abdellah Ajji, Bernard Lotz, and Josée Brisson

Abstract: The effect of uniaxial drawing on orientation of the crystalline fraction of two polymers forming hydrogen bonds, nylon-6 and nylon-11, has been investigated using X-ray diffraction. These two polymers have similar crystal phases, although their hydrogen bond density differs. For both polymers, the deformation occurs in two steps, the first being a plastic deformation of the α-phase spherulites. This leads to two populations of crystals, one with the chain axis oriented parallel to the draw direction, the second with the *a* axis (hydrogen bond direction) aligned along the draw direction. In the second step, the *a*-axis aligned population gradually tilts, leading to a uniaxial orientation of the samples with chain axis aligned along the draw direction. For nylon-11, the onset of this step corresponds to the emergence of crystals of the γ phase, which rapidly becomes the major phase. It reaches a higher orientation than the α phase, and stems from crystallization upon tension of the polymer. For nylon-6, although the γ phase also appears during drawing, at the maximum draw ratio only a small fraction is present. This difference is attributed to the relative stability of the two phases, which is different for nylon-6 than for nylon-11.

Key words: orientation, X-ray diffraction, nylon, hydrogen bonds.

Résumé : L'effet d'un étirement uniaxial sur l'orientation des cristaux de deux polymères formant des liaisons hydrogène, soit le nylon-6 et le nylon-11, a été étudié par diffraction des rayons X. Ces deux polymères possèdent des phases cristallines semblables, bien que la densité de liaisons hydrogène diffère. Pour les deux polymères, la déformation se produit en deux étapes, la première étant une déformation plastique des sphérolites de la forme α. Ceci conduit à l'existence de deux populations de cristaux, un orientée avec l'axe de chaîne parallèle à la direction d'étirement, l'autre avec l'axe *a* (direction des liaisons hydrogène) parallèle à cette même direction. Dans le second stade, il y a bascul des cristaux ayant l'axe *a* orienté avec l'axe d'étirement, résultant en une orientation uniaxe où l'axe de chaîne est orienté avec la direction d'étirement. Pour le nylon-11, ce stade correspond à l'apparition de la phase γ, qui devient rapidement majoritaire. Celle-ci est plus orientée que la phase α, et son apparition est attribuée principalement à la cristallisation sous tension du polymère. Pour le nylon-6, la phase γ apparaît aussi en cours d'étirement, mais elle reste minoritaire. Cette différence est attribuée à la stabilité relative de ces deux phases, qui est différente pour le nylon-6 et pour le nylon-11.

Mots clés : orientation, diffraction des rayons X, nylon, liaisons hydrogène.

Introduction

Polymers have become some of the most widely used materials in industry. They were first used as cheap substitution materials for more noble substances, but they are now firmly entrenched in high-technology applications. One way of modifying the properties of these materials is via orientation. The polymer chains, when submitted to an external force or when in a liquid-crystalline state, will change directions. The final morphology can be characterized in terms of orientation of the chain axis along the draw direction(s). Classical orientation techniques, such as drawing or compression, lead to limited orientation as compared to the theoretical maximum values. Specific techniques such as gel (1) and liquid-crystalline spinning (2), ram extrusion (3), and solid-state roll-drawing (4) from the melt–gel or rubbery state have been developed to overcome such limitations. These lead to ultra-high orientation in polymers that have Young moduli close to theoretical values along the direction of the chain axis (close to that of steel for polyethylene).

Even when the orientation is more moderate, mechanical properties become anisotropic. Orientation is detrimental in the case of injection-moulded parts where preferred orientation in one direction leads to weaknesses in other directions. Orientation is, however, desirable in fibres and films, and post-extrusion drawing in one or many directions is standard procedure to achieve optimal properties for these samples. Film blowing is also used to produce biaxial orientation,

Received February 2, 1998.

S. Moffatt and J. Brisson.[1] Department of chemistry and CERSIM (Centre de recherche en sciences et ingénierie des macromolécules), Faculté des sciences et de génie, Université Laval, Québec, QC G1K 7P4, Canada.
A. Ajji. Industrial Materials Institute, National Research Council Canada, 75 Boul. de Mortagne, Boucherville, QC J4B 6Y4, Canada.
B. Lotz. Institut Charles Sadron, 6, rue Boussingault, 67083 Strasbourg. France.

[1]Author to whom correspondence may be addressed: Telephone: (418) 656-3536. Fax: (418) 656-7916. E-mail: josee.brisson@chm.ulaval.ca

© 1998 NRC Canada

which leads to superior mechanical properties. Other properties, such as gas permeability, impact strength, barrier, shrinkage, optical properties, and so forth, can also be modified when inducing orientation in a polymer sample.

Previous work by some members of our group has focussed on the effect of hydrogen bonds on orientation of amorphous polymers (5, 6). In the present work, hydrogen-bond-forming semicrystalline polymers will be studied. The orientation of semicrystalline polymers is governed mainly by crystal fracture and transformation mechanisms, leading to a fibrillar structure (7).

The two polymers chosen for this study, nylon-6 and nylon-11, are both commercial polyamides that differ by the length of their aliphatic segment, and therefore by the density of hydrogen bonds vs. van der Waals interactions. This has a profound influence on various properties of the polymer, in particular the melting temperature and water absorption, which are lower for the polymer having the lowest density of hydrogen bonds, nylon-11. What influence this may have on orientation at relatively low deformation rates is unknown, and will be the focus of this article.

Structurally, these polymers adopt similar crystal packings, the so-called α and γ phases being the most documented, although many variations have been reported. Nylon-6 has been studied throughly in this respect, and reviews of the various crystal forms proposed are available in the literature (8, 9). The α phase is characterized by an all-*trans* fully extended conformation of the chains. This crystal structure was first resolved for nylon-6 by Holmes, Bunn and Smith (10). Aélion proposed the first crystal structure for nylon-11 (11), but many alternate structures were proposed later (12, 13), and no clear consensus exists as to which better describes the actual experimental data.

The γ phase can be obtained by treatment of nylon-6 with KI–I_2 (14), by annealing (15) or by melt spinning at very high speeds (16). This structure is a twisted or pleated-chain conformation, which exhibits a repeat distance shorter than that of the all-*trans* α phase. The aliphatic segment itself is in an all-*trans* conformation, the twist being located between the amide group and the aliphatic segment. This conformational change was confirmed by the frequency shift of the amide V vibration (17, 18).

In the case of nylon-11, it has been shown that converting the α form into the γ form was possible at elevated temperatures or pressures (19) or by chemical treatment (20). At 95°C and 1 atm (= 101.3 kPa), the γ form was observed, whereas at room temperature and pressure, it is the α form that is usually obtained.

It is well known that changes in crystallinity and crystal structure are liable to occur during deformation of a crystalline sample. In the case of PBT (21), this change has been shown to be reversible, the β phase being obtained only as long as an extensional force is applied on the fibers. Upon removal of this force, the structure reverts to the more stable α phase. In other cases, such as PET, crystallization is induced during deformation.

In the present study, the evolution of orientation of various diffraction planes of nylon-6 and nylon-11 will be followed with respect to crystal phases present and draw ratio. Because of the industrial importance of nylon-6, countless papers dealing with almost every aspect of this polymer have been published. Orientation is no exception, and will not be reviewed fully here. The reader is referred to the review by Perkings and Porter (22) on solid-state deformation, by Peterlin (23) on drawing and extrusion of semicrystalline polymers, and on more recent work on nylon-6 by Galeski, Argon, and Cohen (24) for a brief overview of the orientation studies published in the literature concerning nylon-6. Nylon-11 has, however, been studied very little in these respects. It must therefore be stressed that although the behavior of nylon-6 has already been studied throughly by previous authors, it is reported here, processed under the same conditions as nylon-11, as a comparison point to nylon-11 and to highlight differences related to changes in the hydrogen bond content. This will allow a better understanding of the characteristics of these hydrogen-bond-forming polymers.

Experimental

Polymers used in this study

Nylon-6 used for this study was Zytel Z11 NC010 from Du Pont (melting temperature T_m = 220°C, glass transition temperature T_g = 50°C). For nylon-11, Elf Atochem Besno was used (T_m = 180°C, T_g = 46°C). The polymer granules were first dried under vacuum at 95°C during 24 h. Films were prepared using a Carver press at T = 230°C for nylon-6 and 200°C for nylon-11, which was followed by a slow cooling in order to relax the compression-induced orientation and to allow optimal crystallization of the polymer. Film dimensions prior to stretching were 10 mm in width, 65 mm in length, and 0.5 mm in thickness.

These films were stretched at a constant speed of 5 mm/min on an Instron machine. Stretching temperature was 80°C for both nylons. Samples were air-quenched after stretching, to limit orientation relaxation immediately after cessation of deformation.

An amorphous sample of nylon-6 was obtained by rapid cooling of a pressed sample. The diffraction spectrum was registered immediately in the case of this sample, in order to avoid any recrystallization.

Electron diffraction

Samples for electron diffraction were obtained by epitaxial crystallization on benzoic acid, hydroxyquinone, and polytetrafluoroethylene following the technique described in ref. 25. The substrate was placed on a glass slide, the polymer deposited in the form of solutions in trifluoroacetic acid, and a second glass slide deposited over the polymer. Samples were heated above melt temperature and cooled slowly. A few samples were subjected to annealing at 150°C followed by slow cooling. Samples were deposited on carbon-coated electron diffraction grids and observed under low-dose conditions on a Philips CM12 transmission electron microscope functioning at 120 kV, resulting in a wavelength of approximately 0.03 Å for the electron beam.

X-ray diffraction

X-ray diffraction of the stretched polymers was performed using a Rigaku RU200 B rotating anode generator functioning at 55 kV and 190 mA with copper Kα Ni-filtered radiation and equipped with a scintillation counter. The θ–2θ geometry was used for both 2θ scans and for orientation

© 1998 NRC Canada

scans, θ being the diffraction or Bragg angle and 2θ the angle between the diffracted beam and the direct beam. For orientation scans, the sample and detector were fixed at the θ–2θ geometry corresponding to a given diffraction plane, and the sample was slowly rotated about the normal to its surface from χ = 0°(equator position) to χ = 90° (meridian position). The χ value thus experimentally obtained corresponds to the angle between the normal to the lattice plane considered and the machine direction.

Calculation of the orientation function $\langle P_n \rangle$

The orientation function $\langle P_n(\cos\chi)\rangle$ was calculated using various diffraction planes by fitting the observed azimuthal intensity of a given diffraction plane to a Legendre polynomial series $P_n \cos\chi$. In all cases, the value is reported for the orientation of a given diffraction plane with respect to the draw or machine direction. The observed coefficients are first calculated for a given reflection using the following equation:

$$[1] \qquad \langle P_n(\cos\chi)\rangle_{obs} = \frac{\int_0^{180} I(\chi)\, P_n(\cos\chi)\, \sin(\chi)\, d\chi}{\int_0^{180} I(\chi)\, \sin(\chi)\, d\chi}$$

$I(\chi)$ is corrected for background scattering prior to calculation of $\langle P_n(\cos\chi)\rangle_{obs}$ by determining the baseline by linear interpolation of the intensity on the θ–2θ scan before and after the maximum of the peak under consideration.

When samples exhibit uniaxial symmetry, it is customary to report the orientation of the chain axis with respect to the draw direction. When the peak used for the calculation in a uniaxially oriented sample is centered at the meridian (which corresponds to an azimuthal value of 90°), the $\langle P_n(\cos\chi)\rangle_{obs}$ values correspond directly to the orientation functions along the chain axis, $\langle P_n(\cos\chi)\rangle_{chain}$. If this is not the case, the following relationship first proposed by Lovell and Mitchell (26) can be used to derive $\langle P_n(\cos\chi)\rangle_{chain}$ values for uniaxially oriented samples:

$$[2] \qquad \langle P_n(\cos\chi)\rangle_{chain} = \frac{(-1)^n\, 2^{2n}\, (n!)^2\, \langle P_n(\cos\chi)\rangle_{obs}}{(2n)!}$$

The $\langle P_n(\cos\chi)\rangle_{chain}$ values are used to compare orientation of different systems and will be abbreviated $\langle P_n\rangle$. Although X-ray diffraction gives access to the whole range of $\langle P_n\rangle$ values (values for $\langle P_2\rangle$ to $\langle P_{32}\rangle$ have been reported for polyethylene), for samples that do not exhibit ultra-high orientation, the use of the second moment of the orientation function $\langle P_2\rangle$ is sufficient, and will be the only orientation factor reported in this study. This value corresponds to Herman's orientation factor. $\langle P_2\rangle$ values range from 1.0 for a perfect orientation of the chain axis along the draw direction to –0.5 for a perfect orientation with chain axis perpendicular to the draw direction, while an isotropic sample yields a value of zero.

Fig. 1. X-ray diffraction scans of nylon-6: (*a*) unoriented sample; (*b*) oriented sample (λ = 3.0), equatorial scan (χ = 0°); (*c*) oriented sample (λ = 3.0), meridional scan (χ = 90°); (*d*) unoriented amorphous sample.

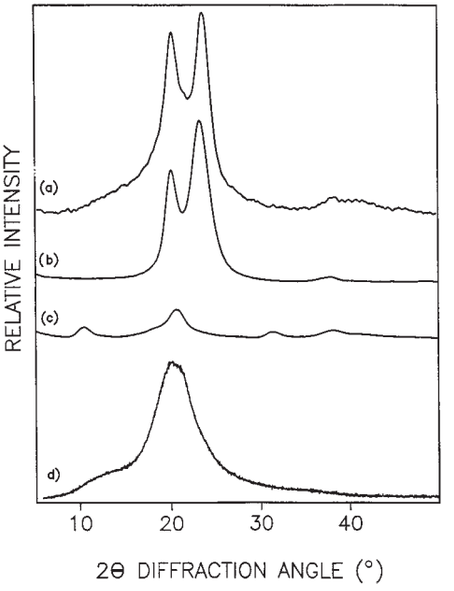

Results and discussion

Choice of conditions for deformation and orientation measurements

Draw conditions influence markedly the final morphology and orientation of the samples. A single draw temperature was chosen for both polymers in this study (80°C, which is 30°C above T_g for nylon-6 and 34°C above T_g for nylon-11). When comparing the orientation of amorphous polymers, it is customary to report the deformation temperature with respect to T_g. The choice of a unique draw temperature, in this case, was prompted by the desire to avoid necking, which would preclude studies at low deformation. For the same reason, a slow deformation speed, 5 mm/min, was chosen. This value is the same as was used in a previous study by Peterlin (28). In all cases, the samples studied did not exhibit any detectable necking.

As reported in previous work on nylon-6 (29) and on other semicrystalline polymers (30), at low deformation ratios there is a certain degree of biaxiality in the deformation process in spite of the fact that the force is applied uniaxially. This disappears at higher deformation ratios, where true uniaxial symmetry becomes apparent This has been linked to a morphology-related deformation mechanism in semicrystalline polymers (30). It was therefore decided to follow the orientation of reflections pertaining to different axes of the unit cell. It was also necessary to verify which crystal form was present in both the initial nonoriented samples and in the final oriented samples since, as mentioned in the introduction, both nylon-6 and nylon-11 can exhibit polymorphism.

As can be seen from Fig. 1, for nylon-6, no change in the diffraction spectra (other than changes in relative intensity)

© 1998 NRC Canada

Fig. 2. X-ray diffraction scans of nylon-11: (*a*) unoriented sample; (*b*) oriented sample (λ = 3.0), equatorial scan (χ = 0°); (*c*) oriented sample (λ = 3.0), meridional scan (χ = 90°).

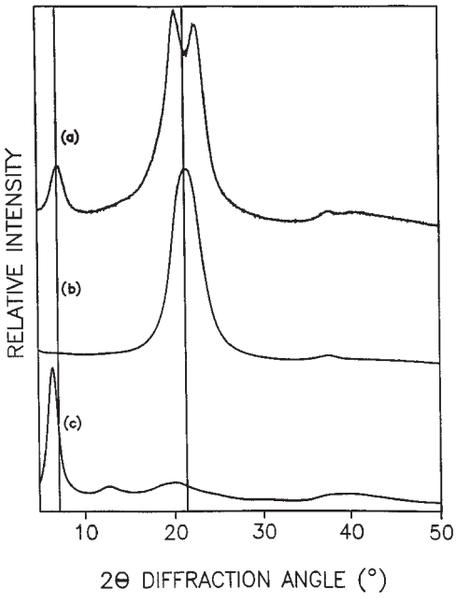

was seen between the unoriented sample and the sample with a draw ratio λ of 3.0. The presence of two intense peaks on the equator (spectrum taken at χ = 0°) at 20.3° (*d* spacing = 4.37 Å) and 23.4° (*d* spacing = 3.80 Å) is a clear indication that the α form dominates. The γ form, when present, yields a single intense peak at an intermediate position of 21.5° (*d* spacing = 4.13 Å) on the equator, as well as a medium-intensity peak on the meridian, at a position of 10.6° (*d* spacing = 8.35 Å). To ascertain whether this crystal phase is present or not, the latter peak is the most useful. A weak peak can be observed at this position on the meridional scan (spectrum taken at χ = 90°), indicating that a small amount of the γ form has indeed appeared during stretching. Changes from the α to the γ form have been reported previously, for instance in the study by Stepaniak, Garton, Carlsson, and Wiles (31) on extrusion combined with in-line drawing. This phase can, however, be detected only at relatively high draw ratio (from λ = 3.0 and higher), and only in small quantity, which makes the characterization of its orientation difficult. It has therefore not been studied in the present work.

The unit cell proposed by Holmes, Bunn, and Smith was used for indexation of the diffraction peaks of the nylon-6 α form (monoclinic, *a* = 9.56 Å, *b* = 17.24 Å (chain axis), *c* = 8.01 Å, β = 67.5°). The peak positioned at 20.3°, which is assigned to the 200 plane of the α form, is almost perfectly superimposed with the amorphous phase scattering halo, which would definitely cause an important underestimation of the orientation function. It was, however, used to follow qualitatively the evolution of orientation for the *a* axis of the unit cell, which is parallel to the direction of the hydrogen bonds. The peak at 2θ = 23.4° is due mostly to the 002 plane of the α phase, although the 202 plane also contributes to a much smaller extent to its intensity (32). It is the most intense peak of the spectra and is only slightly superimposed with that of the amorphous halo. It was therefore used to ascertain the relative orientation of the *c* axis. This crystallographic axis is roughly perpendicular to the hydrogen-bonded sheets of molecules. Finally, the 0 14 0 peak, positioned at 2θ = 77.4° (*d* spacing = 1.23 Å), will be used to follow the orientation changes along the chain or *b* axis. Although it has a relatively low intensity and is situated at a high 2θ position, at which broadening due to crystal defects and crystal size is often quite important, it offers the advantage of being characteristic of the α phase and of not being superimposed with peaks of the amorphous halo.

In the case of nylon-11, as can be seen from Fig. 2, it soon became evident that the orientation behaviour would be less straightforward, but also more interesting to study. The sample showed two intense peaks at 2θ = 20.5° and 23.5° prior to orientation, characteristic of the α phase, as expected. Upon orientation, only one intense peak remained on the equatorial scan (χ = 0°), at an intermediate angle of 21.5° (*d* spacing = 4.13 Å), which is typical of the γ phase. At the same time, the small peak observed at 7.0° (*d* spacing = 12.63 Å) for the unoriented sample is gradually superseded by a medium-intensity peak at 6.3° (*d* spacing = 14.0 Å) on the meridian spectrum (χ = 90°). At the end of the stretching procedure, the γ phase clearly forms the major phase in the samples. It is striking that under the same processing conditions, the γ form is much more favoured for nylon-11 than for nylon-6, which may be related to the relative stability afforded to the γ phase by van der Waals interactions for longer aliphatic segments. Newman, Sham, and Pae (19) showed that, for nylon-11, a reversible phase transition occurs from the α to the γ phase at 95°C, a temperature only slightly above that used for drawing in the present work (80°C). Under drawing conditions, the transition temperature may become lower, which would explain the predominance of the γ form in our samples. The transition, in this case, may not have been reversible because of the quenching procedure used to limit relaxation.

Since it was evident that the γ crystal phase becomes predominant upon orientation, it was imperative to follow the orientation of this phase for nylon-11. Positions for the maximum intensity of various diffraction planes of each of the two phases were selected. It was impossible to choose a position where no superimposition was present because of the intrinsic width of the diffraction peaks for polymers, of the presence of a large amorphous halo centred around 20°, and because of the proximity of most peaks in the diffraction spectra. For the α phase, peaks centred at 7.0°, 20.5°, and 23.5° were selected, which correspond to the 001 (chain axis), 120 (direction of hydrogen bonds), and 020 + 220 (which should correspond, by analogy to nylon-6, to the direction perpendicular to the hydrogen bonds) diffraction planes in the unit cell proposed by Hasegawa, Kimoto, Chatani, Tadokoro, and Sekiguchi (33) (triclinic, *a* = 9.5 Å, *b* = 10.0 Å, *c* = 15.0 Å, α = 60°, β = 90°, γ = 67°). This unit cell gave the best fit with our experimental data, especially in the case of the 7.0° diffraction peak. For the γ phase, the unit cell selected to represent the data is that proposed by Kawagushi, Ikawa, Fujiwara, Tabuchi, and Monobe (34) (*a* = 9.48 Å, *b* = 29.4 Å, *c* = 4.51Å, β = 118.5°). The peaks centred at 6.3° and 21.5°, corresponding to the 020 (chain axis) and 200 diffraction planes (attributed to the direction

© 1998 NRC Canada

of hydrogen bonds by analogy to nylon-6), were used for estimation of the orientation.

Qualitative description of the orientation changes upon deformation

Using the 2θ peak positions selected in the previous section, orientation scans were measured and are grouped according to direction in the unit cell. Figure 3 contains spectra related to chain axis orientation, Fig. 4 to orientation perpendicular to the hydrogen bond direction, and Fig. 5 to orientation parallel to the hydrogen bonds. In all of these spectra, it must be emphasized that the baseline does not correspond to the position at which the minimum intensity occurs: baseline is considerably lower for low-draw ratio samples, corresponding to the fact that, at the low orientation achieved in these samples, a small number of crystals segregate to a preferred orientation, the rest remaining dispersed along all azimuthal angles. Peak areas are therefore insufficient to quantitatively compare the orientation, and spectra are only reported to compare the deformation behaviour at low orientation.

As can be seen in Fig. 3, for nylon-6 and both phases of nylon-11, the chain axis orientation evolves in a constant fashion, with the appearance of a maximum in intensity at χ = 90°, as expected. At very low orientation (λ = 1.25), one can barely distinguish two maxima centred at 60° and 120° for the nylon-6 and 70° and 110° for the nylon-11 α forms. The γ form differs, the orientation always being along the chain axis and χ remaining, within experimental error, centred at 90°. This indicates that, as previously reported for nylon-6 by Galeski, Argon and Cohen (29), for the α phase of both nylon-6 and nylon-11, at the beginning of stretching, orientation does not occur only along the chain direction. For nylon-11, the small fraction of γ phase at λ = 1.25 and the low intensity of this peak do not allow us, with any certainty, to draw conclusions on the deformation mechanism from the data presented here.

The peaks corresponding to the orientation perpendicular to the hydrogen bonds are presented in Fig. 4. Orientation evolves in a continuous and very comparable fashion for nylon-6 and both forms of nylon-11. Orientation is easier to detect on the λ = 1.25 spectra than in the case of the chain axis, an indication that orientation is stronger in this direction, giving rise to a broad peak centred around 25° and 155°. As the stretching proceeds further, this maximum shifts towards the final position of 0° and 180° for this peak maximum.

Orientation scans parallel to the hydrogen bonds are reported in Fig. 5. The information is unavailable for the nylon-11 γ form, since no peaks with sufficient intensity have been isolated in this case. Nylon-6 and nylon-11 (α form) behave similarly, albeit in a completely different manner than that depicted for the planes perpendicular to the hydrogen bonds. Orientation first proceeds along χ = 90° at low draw ratio with an intensity similar to that of the direction perpendicular to the hydrogen bonds and, again, much larger than that along the chain axis direction. As the draw ratio is increased, a second population appears centred around 0° for nylon-6 and 30° for nylon-11. The population of crystals with planes parallel to the draw direction decreases as orientation proceeds, whereas the reverse is true for the second

Fig. 3. Chain axis orientation scans: (*a*) nylon-6, (0 14 0) diffraction plane (2θ = 77.4°); (*b*) nylon-11, α phase, (0 0 1) diffraction plane (2θ = 7.0°); (*c*) nylon-11, γ phase, (0 2 0) diffraction plane (2θ = 6.3°).

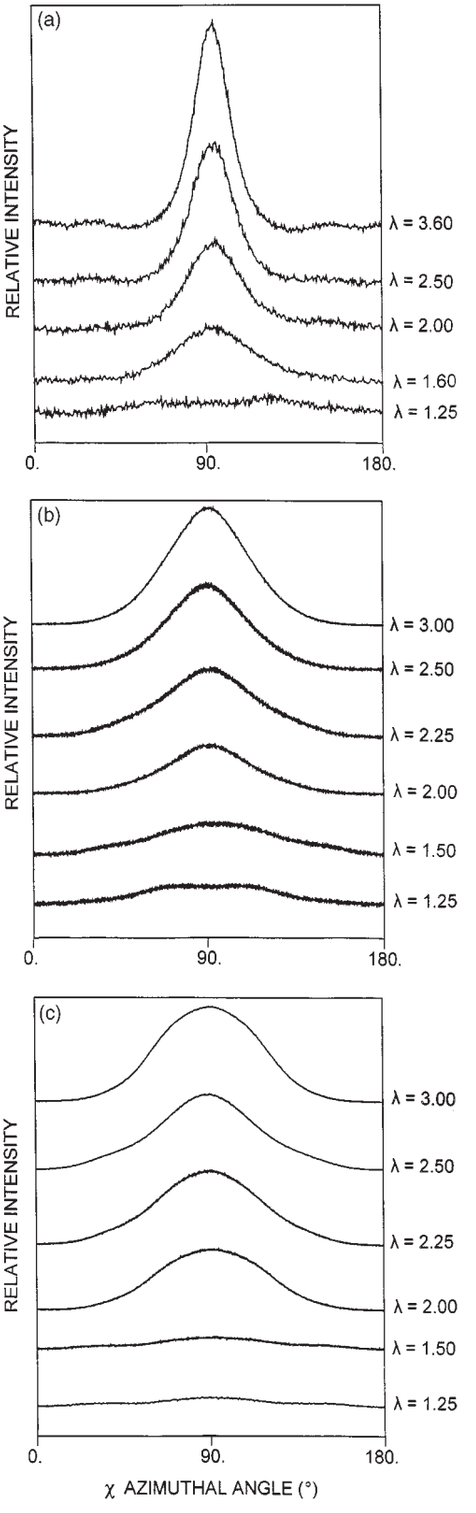

© 1998 NRC Canada

Fig. 4. Orientation scans of planes perpendicular to hydrogen bonds: (*a*) nylon-6, (0 0 2) diffraction plane (2θ = 23.5°); (*b*) nylon-11, α phase, (0 2 0) + (2 2 0) diffraction planes (2θ = 23.5°); (*c*) nylon-11, γ phase, (2 0 0) diffraction plane (2θ = 21.5°).

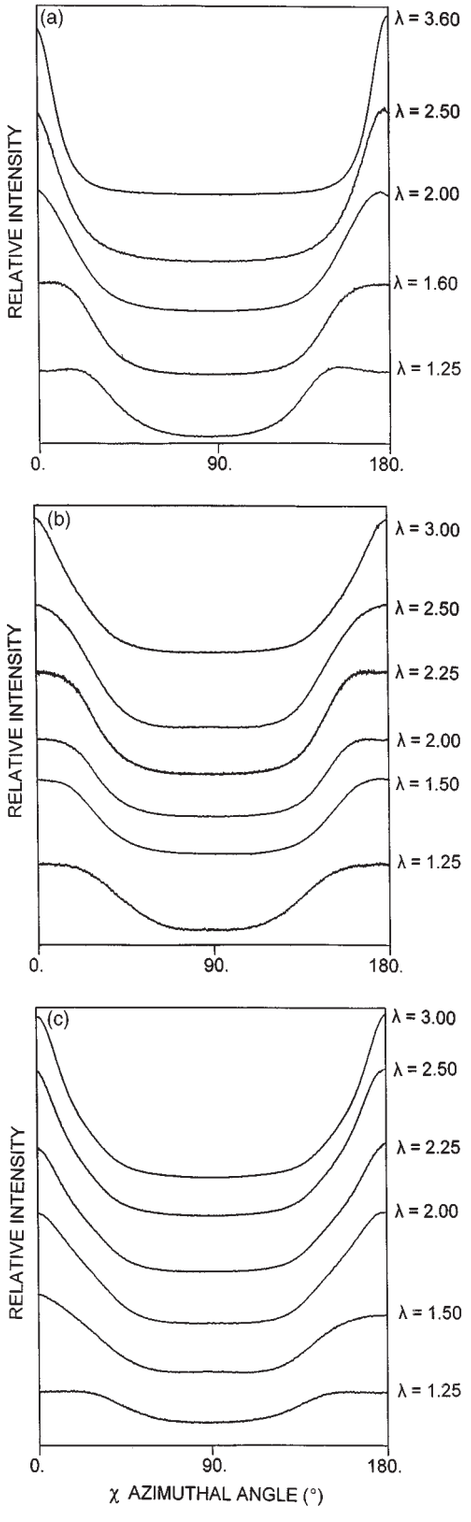

Fig. 5. Orientation scans of planes parallel to the hydrogen bonds: (*a*) nylon-6, (2 0 0) diffraction plane (2θ = 20.1°); (*b*) nylon-11, α phase, (1 2 0) diffraction plane (2θ = 20.3°).

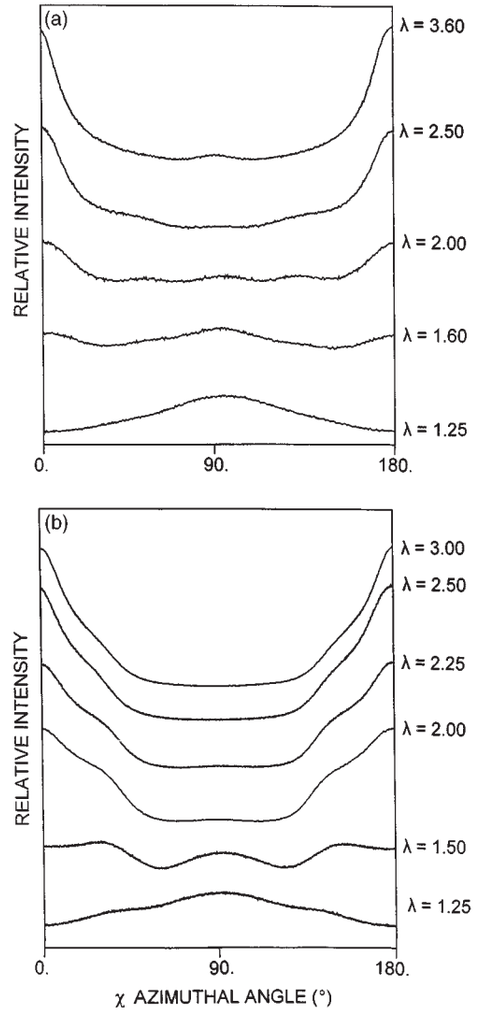

population whose planes are perpendicular to the draw direction. In the case of nylon-11, a third population appears near λ = 2, centred at χ = 0°, and supersedes the two previous ones. At maximum draw ratio, for nylon-6, there remains only a small peak at χ = 90°, but it is unclear whether this is due to a separate diffraction peak or to residual crystals in the first population. For nylon-11, on the other hand, no peak remains at χ = 0°, but a strong shoulder is seen at χ = 25°.This shoulder is attributed to the 210 reflection, and, accordingly, will alter the value obtained for $\langle P_2 \rangle$ unless it is removed prior to calculations. Therefore, this peak position has not been used for quantitative evaluation of the orientation function.

A full description of the deformation mechanism at low deformation would require acquisition of pole figures (which have already been reported in the case of nylon-6 by Galeski, Argon, and Cohen (29)), and is not the aim of this article. Furthermore, at low deformation, the orientation mechanism strongly depends on the initial morphology of the samples (35), the complexitiy of which has been fully

© 1998 NRC Canada

Fig. 6. Evolution of orientation with draw ratio λ (filled symbol = chain axis, open symbol = perpendicular to hydrogen bonds): (*a*) nylon-6; (*b*) nylon-11, α phase; (*c*) nylon-11, γ-phase.

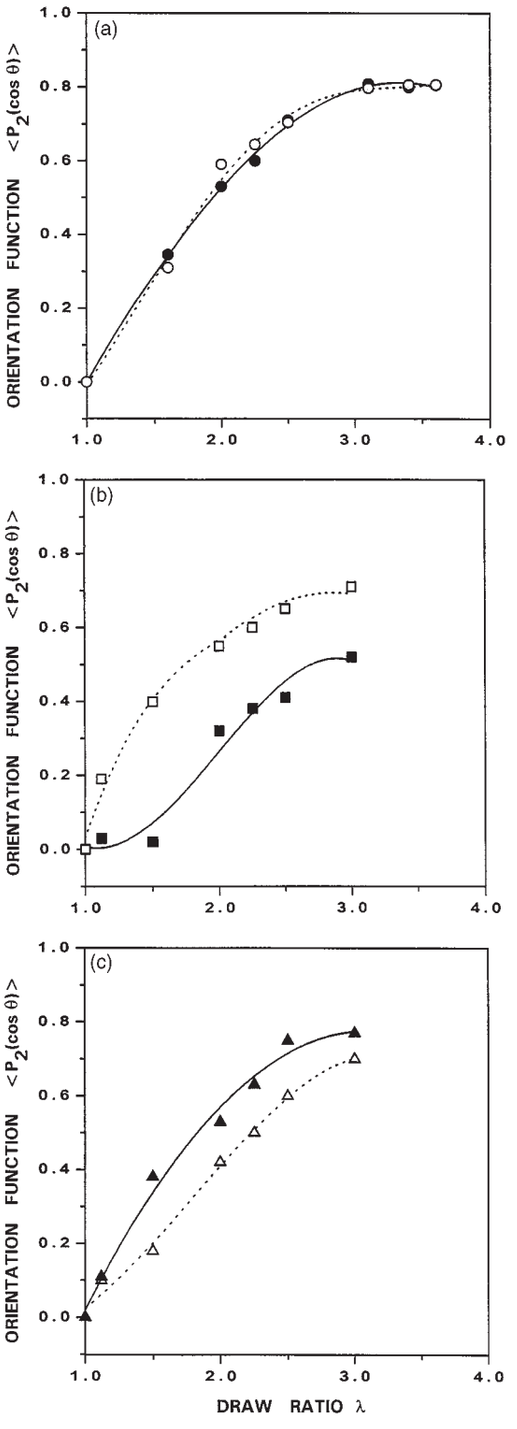

demonstrated (36). Nevertheless, one of the main observations stemming from this work, and one that was possible because the drawing and measurement conditions are the same for both polymers, is the striking similarity in behaviour of the α phase of both nylon-6 and nylon-11, as can be seen in Figs. 3–5. It is also interesting to note that, at low deformation, the axis parallel to the hydrogen bonds and, to a much smaller extent, the chain axis show a tendency to align along the machine or draw direction. The direction perpendicular to the hydrogen bonds remains resolutely perpendicular to the draw direction throughout the drawing process. The fact that the two long axes of the crystallites, the directions parallel and perpendicular to the hydrogen bonds, are those that yield the highest orientation function, points to a deformation mechanism in which the hydrogen-bonded platelets act as the structural rigid unit. These deform along the draw direction, leading to a morphology reminiscent of the cross-β texture observed for fibrous proteins (37). Spherulite deformation modes have been discussed in detail by Samuels (30), and have been shown for polypropylene to yield, through intraspherulite rearrangements, two crystal populations. Similar rearrangements could explain the chain axis orientation and the appearance of peaks off the equatorial and meridian in the first deformation stage.

At higher deformation, crystals deform or tilt and the hydrogen bond direction aligns along the equatorial, the chain axis becoming more and more oriented in the stretching direction, yielding a typical uniaxial orientation. This behaviour corresponds well with the orientation model proposed by Peterlin (38). The first step is a plastic deformation of spherulites, which occurs for nylon-6 below λ = 2 according to this author (28). In the second step, the lamellae stacks are destroyed and unravel to form microfibrils, with the chain axis orienting in the draw direction. In the case of the polymers studied here, the first step would correspond to the initial stage where both the chain axis and the hydrogen bond direction orient along the draw direction.

The present data concerning the appearance of the γ phase confirm a previous pole figure study of nylon-6 by Galeski, Argon, and Cohen (29). However, the morphology they report is much closer to uniaxial than that observed here. This may be due to the higher draw ratio of the samples they have studied (λ = 2.16), which lies, for nylon-6 (28), near the limit for the first step of the mechanism proposed by Peterlin. Differences in initial morphology of the samples may also cause discrepancies between their observations and the present work.

For the γ form of nylon-11, it is not possible to draw conclusions about the exact mechanism of deformation at low draw ratio, due to the uncertainty of the assignment of the 21.3° peak and to the low intensity of the peak used to follow chain axis orientation.

Quantitative description of the orientation changes upon deformation

Using the various diffraction scans studied, the orientation function $\langle P_2 \rangle$ was evaluated quantitatively. Two peaks can be used to quantify the orientation for nylon-6: the 0 14 0 peak and the 002 peak. The 200 peak is superimposed with the amorphous phase in such a way that all attempts to use this peak quantitatively failed. Results for these two peaks appear in Fig. 6*a* and yield, within experimental error, the same $\langle P_2 \rangle$ values. The maximum $\langle P_2 \rangle$ value achieved, 0.81, is relatively low for a crystalline phase, and considerably lower than those reported for nylon-6 in the literature, which are closer to the ideal value of 1.0. For example, Sakaoku,

© 1998 NRC Canada

Fig. 7. Comparison between orientation changes and draw ratio λ for nylon-6 and nylon-11 (○, nylon-6, perpendicular to hydrogen bonds; □, nylon-11, α phase, perpendicular to hydrogen bonds, ▲, nylon-11, γ phase, chain axis).

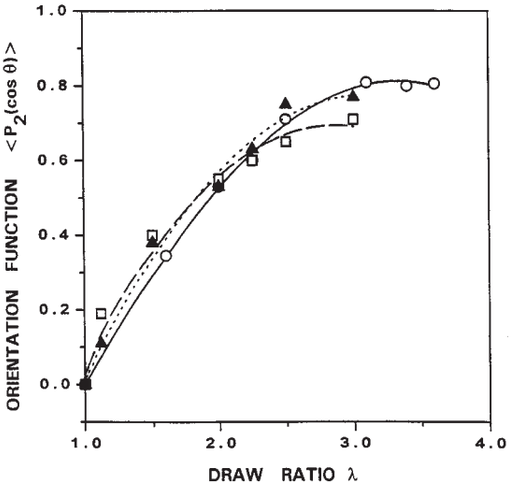

Fig. 8. Changes in the relative intensity of the α-phase diffraction plane and of the γ-phase diffraction plane upon deformation for nylon-11 (■, α form, ▲, γ form).

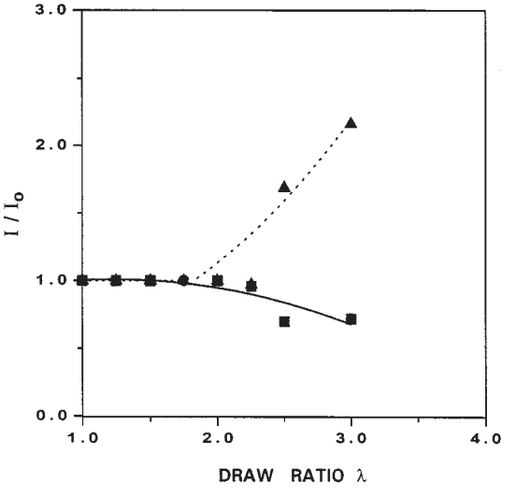

Morosoff, and Peterlin (39) report a value of 0.97 for λ = 5. The lower value we obtain is proposed to stem from differences in the processing conditions, and in particular to the fact that no annealing was performed in the present work after drawing.

Orientation functions for nylon-11 are reported in Figs. 6*b* (α phase) and 6*c* (γ phase). In these cases, considerable variations result from the use of different diffraction peaks for the same phase. For the α phase, orientation reaches a maximum value of 0.73 for the second moment of the orientation function $\langle P_2 \rangle$ when measured using the 020 peak at 23.4°, whereas a much lower value of 0.52 is obtained when calculating, using the diffraction peak on the meridian. It is proposed that this lower value is due to a slight shift of the ideal position of the peaks at 7.0° with respect to the azimuthal angle. Although the experimental value is positioned at 90°, calculations using previously proposed unit cells yield an azimuthal angle of 75°. The use of a wrong χ angle causes an underestimation of the orientation function, which could be corrected using the equation of Mitchell and Lovell. Therefore, correct $\langle P_2 \rangle$ values should be obtained using the 23.4° reflection.

For the γ phase, the reverse is observed. The maximum value of 0.77 is obtained when using the 6.3° meridional diffraction peak. In this case, this is attributed to an important overlap with the amorphous phase at approximately 21.4°, leading to a lower calculated value of 0.70. Since it is well known that the amorphous phase is less oriented than its crystalline counterpart, this superimposition leads to an underestimation of the actual orientation of the crystalline phase. For this phase, the correct $\langle P_2 \rangle$ values are therefore obtained using the 6.3° reflection.

A comparison of the orientation functions obtained for nylon-6 (23.4° peak), nylon-11 α phase (23.4° peak), and nylon-11 γ phase (6.3° peak) is shown in Fig. 7. As can be seen, although the maximum draw ratio is lower for nylon-11 than for nylon-6, the maximum orientation is comparable, being slightly lower (0.73 vs. 0.77) for the nylon-11 α phase. At low orientation, the α phase of nylon-6 shows a tendency to orient more rapidly than both nylon-11 and the nylon-11 γ form, although this may simply be related to differences in orientation mechanism at the stretching onset.

It is interesting to note that, for nylon-11, a higher orientation is achieved for the γ phase than the α phase. To determine the significance of this observation in terms of deformation mechanism, it is necessary to determine whether the γ phase observed comes only from the crystalline transformation from the α to the γ phase, or whether it can also be attributed to recrystallization of amorphous domains.

Evaluation of the crystal phase change upon orientation

During orientation, the relative proportion of amorphous, crystalline α, and crystalline γ phases also varies, as was observed qualitatively in Fig. 2. Because of severe overlaps, it is difficult to precisely quantify these changes. This is particularly true of the region between 20° and 24°, where peaks stemming from the amorphous phase and the crystalline α and γ phases overlap extensively. Although it is possible to conduct a deconvolution, it was preferred in the present work to rely on the less overlapped region between 6° and 8°, which is amenable to semiquantitative evaluation. The values obtained are fraught with intrinsic error, as differences in width and therefore perfection or size of crystals between the two crystal forms are not taken into account. A further limitation is that the total intensity of the peak is assumed proportional to that of a single χ angle position, which would be true only if no change in crystal size or perfection occurred during drawing, a factor that has not been evaluated quantitatively in the present work. These approximations are expected to have only a small impact on the actual values in this case, since the starting material is crystalline, and since changes in peak width were not observed for this spectral region, as can be verified in Fig. 2. The intensity I of the 020 and 001 peaks was integrated along the χ angle at a fixed 2θ angle (6.3° and 7°, respectively) and compared to the intensity measured for an unoriented sample I_o. The I/I_o ratio is reported with respect to the draw

© 1998 NRC Canada

Fig. 9. Electron diffraction pattern of nylon-11, α-phase, epitaxially grown on benzoic acid.

ratio in Fig. 8, and measures the relative increase in intensity of each peak. As can be seen, the proportion of α and γ phases does not vary, within experimental error, until a draw ratio of 2.25 is reached. Once this value is passed, however, the intensity of the γ phase clearly increases, reaching a value of 2.2 at λ = 3. The fraction of γ phase present has therefore more than doubled. Meanwhile, this ratio decreases only slightly for the α phase, going down to a value of 0.7. Although the relative intensity of the γ-phase peak is intrinsically larger than that of the α-phase peak, as seen in Fig. 2, crystallization of the α phase is still not sufficient to explain such a large increase in γ phase. It is therefore proposed that the appearance of the γ phase is due in large part to conversion of amorphous or interfacial domains in this new crystalline form, whereas a certain amount of α phase is also converted during deformation to the γ phase.

Epitaxial crystallization was performed on various substrates for nylon-11, using a crystallization temperature close to that used for drawing, in an attempt to obtain more information on the unit cell of nylon-11 for both the α and the γ phases. A typical photograph of diffraction patterns obtained in this way is presented in Fig. 9. Only few diffraction spots are present on the equator, which excludes a fiber-type orientation. Only the 6th and 12th strata appear with good intensity, and meridian or quasi-meridian reflections appear at 1.13 Å, a distance characteristic of a projection of the carbon–carbon bond distance upon the chain axis. Tilting of the samples results in the appearance of equator diffraction spots with *d*-spacings of 4.40 and 3.73 Å. These observations are consistent with a superimposition of two distinct orientations of the α phase. In the first, the hydrogen-bonded sheets are parallel to the substrate, giving rise to a typical *hk*0 diffraction pattern similar to that observed for polyglycine (40) (*c* being taken as the chain axis). Additional reflections are observed and were attributed, again by comparison with polyglycine, to crystals tilted by 90° from this orientation. This is typical of two *hk*0-twinned unit cells, one growing on the crystal surface of the epitaxic substrate, the second growing on the edges of the crystal substrate, the "*a*" direction being common to the two and acting as the growth direction for crystals.

Various attempts were made to obtain the γ phase, including annealing at various temperatures from 80 to 170°C, followed by rapid quenching. In all cases, only the α phase was observed in the final samples. This again confirms that, whether the γ phase emerges because of temperature-driven phase transition or not, drawing is essential to its stabilization in melt-processed samples and to its consequent observation at room temperature. This does not exclude the possibility that draw temperatures play a role in the relative proportions of the α and γ phases.

Most γ-phase crystals are proposed to stem from draw-induced crystallization. Since, as mentioned previously, the γ phase is more oriented than the α phase, it is concluded that, in this case, stress-induced crystallization yields a higher orientation than deformation of existing crystals. This is in agreement with observations made on nylon-6 by McKerron (41).

Conclusions

Comparison of two hydrogen-bond forming polymers, nylon-6 and nylon-11, which differ mainly by the length of the aliphatic segment and by the relative density of hydrogen bonds, shows that these factors have little effect on the deformation mode in the first deformation stage (up to approximately λ = 2). Orientation proceeds in a remarkably similar fashion. Deformation mechanisms strongly depend on the initial morphology of the sample and deformation conditions. In terms of morphology, for the two polymers studied, this study shows the importance of the initial crystal phase, in terms of chain packing and organization of hydrogen-bonded sheets.

Maximum orientation is also similar, although a slightly smaller maximum draw ratio was achieved for nylon-11. The main difference in the behaviour of these polymers upon orientation lies in the relative amount of the γ phase that appears during crystallization. The onset of crystallization appears clearly around λ = 2 for nylon-11, therefore at the end of the first plastic deformation stage and at the onset of crystal unravelling to form the microfibrillar morphology. The γ phase soon supersedes the initial α phase for nylon-11, partly by the occurrence of stress-induced crystallization. The initial α phase decreases, indicating that some of the γ crystals are obtained by a solid-state phase transition at the draw temperature. In the case of nylon-6, as previously

© 1998 NRC Canada

reported in the literature (29), only a small fraction of the γ phase appears at higher draw ratios. These differences in crystallization are attributed to the relative stability of each phase and are believed to be related to the hydrogen and van der Waals interaction energies, which are different for the two polymers.

Acknowledgements

This work was made possible through the financial contribution of the Natural Sciences and Engineering Research Council of Canada (NSERCC) and the Fonds pour la formation des chercheurs et l'aide à la recherche (FCAR) of the government of Québec. The authors would also like to thank Annette Thierry for her help in technical aspects of sample preparation for electron microscopy.

References

1. P. Smith and P.J. Lemstra. J. Mater Sci. **15**, 505 (1980).
2. D. Tanner, J.A. Fitzgerald, and B.R. Philips. Angew. Chem. Int. Ed. Engl. **28**, 649 (1989).
3. N. Legros, A. Ajji, and M.M Dumoulin. Polym. Eng. Sci. **37**, 1845 (1997).
4. A.E. Zachariades. US Patent 4,820,466, April 11 1989.
5. D. Li and J. Brisson. Polymer, **35**, 2078 (1994).
6. D. Li and J. Brisson. Macromolecules, **26**, 8425 (1997).
7. A.J. Owen. *In* Development in oriented polymers. Vol. 2. *Edited by* I.M. Ward. Elsevier, Applied Science, London. 1987. p. 237.
8. L.G Roldan and H.S. Kautman. J. Polym. Sci. Part B: Polym. Lett. **1**, 603 (1963).
9. J.P. Parker and P.H. Lindenmeyer. J. Appl. Polym. Sci. **21**, 821 (1977).
10. D.R Holmes, C.W. Bunn, and D.J. Smith. J. Polym. Sci. **17**, 159 (1955).
11. M.R. Aélion. Ann. Chim. (Paris), **3**, 5 (1948).
12. W.P. Slichter. J. Polym. Sci. **36**, 259 (1959).
13. M. Genas. Angew. Chem. **74**, 535 (1962).
14. H. Arimoto, M. Ishibashi, M. Hirai, and Y. Chatani. J. Polym. Sci. Part A: Gen. Pa**p. 3**, 317 (1965).
15. K.H. Illers, H. Haberkorn, and P. Simak. Makromol.Chem. **158**, 285 (1972).
16. A. Ziabicki and K. Kedzkrska. J. Appl. Polym. Sci. **2**, 14 (1959).
17. H. Arimoto. J. Polym. Sci. Part A: Gen. Pap. **2**, 2283 (1964).
18. I. Sandeman and A. Keller. J. Polym. Sci. **19**, 401 (1956).
19. B.A. Newman, T.P. Sham, and K.D. Pae. J. Appl. Phys. **48**, 4092 (1977).
20. T. Sasaki. J. Polym. Sci. Polym. Lett. Ed. **3**, 557 (1965)
21. R. Jakeways, I.M. Ward, M.A. Wilding, I.H. Hall, I.J. Desborough, and M.G: Pass. J. Polym. Sci. Polym. Phys. Ed. **13**, 799 (1975).
22. W.G. Perkins and R.S. Porter. J. Mater. Sci. **12**, 2355 (1977).
23. A. Peterlin. Colloid Polym. Sci. **265**, 357 (1987).
24. A. Galeski, A.S. Argon, and R.E. Cohen. Macromolecules, **24**, 3953 (1991).
25. J.-C. Wittmann and B. Lotz. Polymer, **30**, 27 (1989).
26. R. Lovell and G.R. Mitchell. Acta Crystallogr. Sect. A: Cryst. Phys. Diffr. Theor. Gen. Crystallogr. **A37**, 135 (1981).
27. C.-P. Lafrance, M. Pézolet, and R.E. Prud'homme. Polymer, **24**, 4948 (1991).
28. A. Peterlin. Polym. Eng. Sci. **1**7, 183 (1977).
29. A. Galeski, A.S. Argon, and R.E. Cohen. Macromolecules, **24**, 3945 (1991).
30. R.J. Samuels. J. Polym. Sci. Part C: Polym. Sym**p. 20**, 253 (1967).
31. R.F. Stepaniak, A. Garton, D.J. Carlsson, and D.M. Wiles. J. Polym. Sci. Polym. Phys. Ed. **17**, 987 (1979).
32. N.S. Murthy and H. Minor. Polym. Commun. **32**, 297 (1991).
33. R.K. Hasegawa, K. Kimoto, Y.Chatani, H. Tadokoro, and H. Sekiguchi. Discuss. Meet. Soc. Polym. Sci. Jpn.., Tokyo, 1974. Preprints p. 713.
34. A. Kawagushi, T. Ikawa, Y. Fujiwara, M. Tabuchi, and K. Monobe. J. Macromol. Sci. Phys. **B20**, 1 (1981).
35. A. Galeski, A.S. Argon, and R.E. Cohen. Macromolecules, **21**, 2761 (1988).
36. A. Galeski, A.S. Argon, and R.E. Cohen. Macromol. Chem. **188**, 1195 (1987).
37. A.J. Geddes, K.D. Parker, E.D.T. Atkins, and E. Beighton. J. Mol. Biol. **32**, 343 (1968).
38. A. Peterlin. Colloid Polym. Sci. **253**, 809 (1975).
39. K. Sakaoku, N. Morosoff, and A. Peterlin. J. Polym. Sci. Polym. Phys Ed. **11**, 31 (1973).
40. B. Lotz. J. Mol.Biol. **87**, 169 (1974).
41. D.H. McKerron. Polym. Commun. **26**, 130 (1985).

© 1998 NRC Canada

Phase behaviour of model stratum corneum lipid mixtures: an infrared spectroscopy investigation

Michel Lafleur

Abstract: The stratum corneum, the top layer of the epidermis, is the material that constitutes the membrane enveloping our body. The lipids that are present are responsible for the permeability properties of the skin and, as a consequence, are essential to maintain the hydration of the internal components and to protect our body from external agents. In the present work, the mixing and the structural properties of model mixtures formed by the main lipids of the stratum corneum have been examined by infrared spectroscopy. The model is formed by an equimolar mixture of ceramides (type III), cholesterol, and perdeuterated palmitic acid. Binary mixtures as well as mixtures for which the ceramides were substituted by sphingomyelin, a ceramide precursor, have also been studied. The results indicate that the stratum corneum model mixture exhibits a rich polymorphism, ranging from crystalline domains with heterogeneous lipid composition and orthorhombic chain packing, to a fluid and homogeneous phase. To obtain this particular behaviour, the three components are essential and the specific role of each species is discussed. In addition, the results reveal that the homogeneous lipid distribution observed for temperatures higher than 70°C can be maintained at low temperatures, leading to the formation of a metastable phase. Several weeks are needed to obtain the thermodynamically stable phase if the sample is incubated at 5°C. However, it is rapidly induced by annealing the sample at 40°C.

Key words: stratum corneum, lipid, infrared spectroscopy, ceramide.

Résumé : Le stratum corneum, la couche supérieure de l'épiderme, est le matériau constituant la membrane enveloppant notre corps. Les lipides qu'on y retrouve sont responsables des propriétés de perméabilité de la peau et, en conséquence, sont nécessaires au maintien de l'hydratation des composantes internes et à la protection du corps contre les agents externes. Dans le présent travail, les propriétés de mélange et structurales de mélanges modèles constitués des principaux lipides du stratum corneum ont été examinées par spectroscopie infrarouge. Le modèle utilisé est constitué d'un mélange équimolaire de céramides (de type III), de cholestérol et d'acide palmitique perdeutéré. Des mélanges binaires ainsi que des mélanges pour lesquels les céramides sont replacés par la sphingomyéline, un précurseur des céramides, ont été aussi étudiés. Les résultats montrent que le mélange modèle du stratum corneum montre un riche polymorphisme, allant de domaines cristallins hétérogènes du point de vue de leur composition en lipide et où les chaînes possèdent un empilement orthorhombique, à une phase fluide homogène. Pour obtenir ce comportement, les trois composantes sont essentielles et le rôle spécifique de chaque espèce est discuté. De plus, les résultats révèlent que la distribution homogène des lipides obtenue à des températures supérieures à 70°C peut être maintenue à basses températures, conduisant à la formation d'une phase métastable. Plusieurs semaines sont nécessaires pour obtenir la phase thermodynamiquement stable si l'échantillon est maintenu à 5°C. Cependant, celle-ci est rapidement induite par un recuit à 40°C.

Mots clés : stratum corneum, lipide, spectroscopie infrarouge, céramide.

Introduction

The stratum corneum (SC),[2] the top layer of the epidermis, is a material with vital functions since it constitutes the envelope around our body (a membrane of about 20 000 cm^2 for an adult) that tightly controls exchanges with the external world (1–4). It is of particular importance in the case of water, contributing to the preservation of adequate hydration of the internal components, and as protection from the toxins of the external world. The selective permeability of this

Received February 2, 1998.

M. Lafleur.[1] Department of Chemistry, C.P. 6128, Succ. Centre Ville, Université de Montréal, Montréal, QC H3C 3J7, Canada.

[1]Fax: (514) 343-7586. E-mail: lafleur@ere.umontreal.ca

[2]Abbreviations used in this paper: CER, ceramide III; chol, cholesterol; ^{13}C-PA, palmitic acid bearing a ^{13}C-labelled carboxylic group; DBPC, dibehenoylphosphatidylcholine; δ_{CH_2}, CH_2 scissoring; δ_{CD_2}, CD_2 scissoring; EDTA, ethylenediaminetetraacetic acid; IR, infrared; Mes, 2-[morpholino]ethanesulfonic acid; NMR, nuclear magnetic resonance; ν_{C-H}s, symmetric C–H stretching of the methylene groups; ν_{C-D}s, symmetric C–D stretching of the methylene groups; ν_{C-D}a, antisymmetric C–D stretching of the methylene groups; $\nu_{C=O}$, C=O stretching; PA, palmitic acid; PA-d_{31}, perdeuterated palmitic acid; SC, stratum corneum; SPM, sphingomyelin; T_m, gel-to-liquid crystalline phase transition temperature.

© 1998 NRC Canada

biomaterial also represents a permanent challenge in the development of transdermal drug delivery. These physiological functions of the SC make it the main constituent of the *skin barrier*. The SC is formed by the stacking of dead skin cells filled with fibrous proteins and called corneocytes, embedded within a lipid matrix (5, 6). The unique permeability properties of SC have been intimately related to its lipidic portion (2, 7, 8). The organization of the SC has been depicted by the brick (the corneocytes) and mortar (the lipids) model. However, it is now established that the lipidic portion is not an "isotropic mortar" but presents defined structures. To understand the molecular basis of the properties of this material, considerable effort has been devoted to determining the organization of the SC lipids. A significant proportion of the lipids has been found to exist in crystalline domains with an orthorhombic and hexagonal packing (9–12). It has been proposed that these domains would have a crucial impact on the SC permeability (13). The SC lipids undergo a transition from an ordered to a disordered phase between 60 and 80°C (4, 8, 14–16). This transition has considerable impact on the permeability properties: the permeability of the disordered phase is generally greater than that of the ordered one (4, 7, 8) (e.g., a 1000-fold increase for the hydrocortisone permeability is observed upon heating the SC above its transition). Therefore, a lipidic organization appears to be crucial for the permeability properties of the SC.

The lipid composition of SC is peculiar. It essentially comprises a mixture of ceramides (CER), cholesterol (chol) and some derivatives, and free fatty acids (5, 17–19). The ceramides are *N*-acyl-sphingosine, the acyl chain being linked to the head group by an amide group. In vivo, they are partly derived from the sphingomyelin (SPM), which exists in the deeper layers of the skin and which is hydrolysed by a sphingomyelinase during the migration towards the surface (20). The enzymatic cleavage of the phosphorylcholine group, replaced by a hydroxyl, leads to a lipid with a relatively small head group. The free fatty acids constitute about 20% of the lipid composition. They are mainly saturated, ranging from 14 to 20 carbon atoms in length, C_{16} and C_{18} being the most abundant (5, 18).

Because the lipid composition of the SC is complex, model systems have often been used to investigate the molecular details of lipid behaviour. Several studies have used model mixtures that include ceramide, cholesterol, and fatty acid, the three main components of SC (21–26). The ceramide that has often been used is ceramide III extracted from bovine brain because of its similarity to SC ceramides and its commercial availability. Stearic (octadecanoic) and nervonic (15-tetracosenoic) acyl chains are the most abundant in these derived ceramides (26). Despite the simplification, the model reproduces several features of the SC. A transition from an ordered to a disordered lipid phase has been observed in the model mixtures (21–25); as well, the presence of crystalline or solid regions has been reported. In an equimolar mixture of CER–chol – palmitic acid (PA), it has been shown that a large proportion of the cholesterol and the fatty acids exists in a solid form below 40°C (23, 24). Recently it was found, in a similar mixture, that PA and ceramide independently form crystalline domains (25).

In the present paper, the mixing properties of ceramide with cholesterol and PA were investigated, and the conditions for which lipid crystallization occurs were examined. The behaviour of binary mixtures was also investigated to gain a deeper understanding of the role played by the different components in the ternary mixture. The thermotropism of the investigated mixtures was compared with that of equivalent systems for which CER had been replaced by SPM; this latter lipid displays a simpler behaviour, as will be discussed, and the comparison highlights the importance of the sphingolipid head group in the SC structure. Infrared (IR) spectroscopy is a powerful technique for investigating the structure of such systems because several vibrations give rise to bands that constitute local probes of the organization. This technique has already been used to characterize the phase transitions of the SC (4, 7–8, 14, 18, 27) and of related model systems (22, 25). These transitions were detected by the shift of the methylene stretching bands since their positions are sensitive to the conformational order of the lipid acyl chains (25, 28). In the present work, the C–H and the C–D stretching modes were used to characterize independently the behaviour of the sphingolipid and the deuterated fatty acid, respectively, in SC models. IR spectroscopy also provides valuable tools for investigating crystalline phase formation. The intermolecular vibrational coupling in a crystal can give rise to a factor group splitting of certain bands. This phenomenon has been observed, at the acyl chain level, for the scissoring (29, 30) and the rocking (25, 31) modes of the methylenes. A recent study has taken advantage of these spectral features to identify the formation of orthorhombic structures in an SC model mixture (25). Recently, a similar splitting was proposed for the Amide I band of the ceramide (32). The Amide I band as well as the C=O stretching ($\nu_{C=O}$) of the carboxylic group of the fatty acid were also examined as IR probes to investigate the interface. Preliminary results were obtained in a buffer made with H_2O (33). However, in the present work, D_2O-based buffer was used to avoid the overlap of the H_2O deformation band at 1640 cm^{-1} with the lipid bands in this region.

Material and methods

Sphingomyelin from bovine brain, derived ceramide III, and cholesterol were purchased from Sigma Chemical Co (St. Louis, Mo., U.S.A.). The ceramide was prepared from the SPM, using phospholipase C. Therefore the two lipids are different at the head-group level but the acyl chain composition is the same. The perdeuterated palmitic acid (PA-d_{31}) was obtained from the deuteration of palmitic acid (Sigma) according to a procedure described elsewhere (34). The deuterated acid was recrystallized in hexanes. Palmitic acid bearing a ^{13}C-labelled carboxylic group (^{13}C-PA) was purchased from CDN Isotopes (Pointe-Claire, Québec).

To obtain lipid mixtures, a stock solution of each lipid was prepared in a benzene/MeOH 92/8 (v/v) mixture. Aliquots of these solutions were mixed together to provide the desired composition. The organic solutions were then freeze-dried. The solid lipids were hydrated with a 100 mM Mes buffer, containing 100 mM NaCl, 5 mM EDTA, in D_2O, at pH 5.2 (corresponding to a pD of 5.6 (35)); this pH is in the range of the recognized physiological pH of the SC layer (36, 37). The final lipid concentration was about 20 (w/v)% for the samples containing SPM. For the samples

© 1998 NRC Canada

Fig. 1. Thermotropism of (*A*) CER–PA-d_{31}–chol and (*B*) SPM–PA-d_{31}–chol equimolar mixtures as probed by the shift of the (■) ν_{C-H}s and (●) ν_{C-D}s bands. The relative position and amplitude of the two *y* axes were determined to obtain the overlap of the transition of SPM and PA-d_{31} in the binary mixture (see Fig. 6) and the same scales were kept for this figure. The empty symbols represent the positions of the bands when the samples were quenched from high temperature down to 11°C.

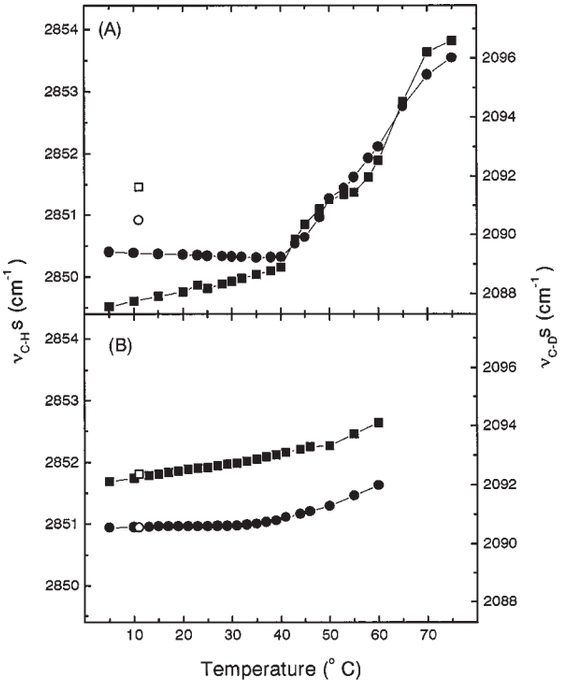

containing ceramides, a large excess of buffer was used during the incubation (≈3 (w/v)% in lipid). The samples were incubated for three 10 min periods at 80°C for the mixtures containing CER or at 70°C for the mixtures containing SPM. Between incubation periods, the samples were cooled down to room temperature. The samples containing ceramides were finally incubated at 40°C for 15 min, prior to recording the spectra; the importance of this step in the incubation procedure is discussed below. During the incubations, the samples were periodically vortexed. Other incubation procedures were used and they are explicitly described in the text.

An aliquot of the sample was transferred between two CaF_2 windows, and the sample thickness was controlled by a 5 μm thick Teflon ring. The cell was mounted in a brass sample holder whose temperature is regulated by thermopumps. The infrared spectra were recorded on a FTS-25 Bio-Rad spectrometer equipped with a water-cooled globar source and a medium-band mercury – cadmium telluride detector. For each spectrum, 100 scans with a resolution of 2 cm^{-1} were coadded, and were Fourier transformed using a triangular apodization function. The spectra were recorded as a function of increasing temperature. Subsequently a spectrum was measured at 11°C to examine the reversibility of the transition; it took about 10 min to cool the sample from 75 to 11°C. The contribution of the O–D stretching band at 2500 cm^{-1} has been corrected for in the C–H and C–D stretching regions by subtracting a least-squares-fitted polynomial simulating the edge of the water band. The band positions reported in this paper correspond to the centers of gravity of the top 5% of the bands.

Results

The thermotropism of the model SC lipid mixture (CER–PA-d_{31}–chol in equimolar proportion) as well as the analogous mixture in which ceramide was replaced by SPM is presented in Fig. 1. The thermal evolution of the sphingolipid was probed by the symmetric C–H stretching of the lipid methylene groups (ν_{C-H}s) (the contribution of cholesterol in this region is considered to be constant) whereas the band assigned to the symmetric C–D stretching of the methylene groups (ν_{C-D}s) is associated with PA-d_{31}. The behaviour of the SPM–PA-d_{31}–chol mixture is relatively simple. Both the ν_{C-H}s and ν_{C-D}s frequencies show a progressive increase upon heating. Pure SPM undergoes a gel-to-liquid crystalline phase transition at a temperature (T_m) of 35°C (38, 39). For the ν_{C-H}s band, the values obtained below the T_m of the pure SPM are higher than those observed for pure SPM (2851 cm^{-1}) whereas they are smaller than those of the pure SPM for temperatures higher than the T_m of pure SPM (2853.2 cm^{-1}). These spectral features indicate that cholesterol disorders the lipid gel phase whereas it orders the liquid crystalline phase.

The thermotropism of the CER–PA-d_{31}–chol mixture is drastically different. First of all, a significant increase in frequency is observed as a function of increasing temperature for both the ν_{C-H}s and ν_{C-D}s band positions. In the case of the ν_{C-H}s band, the frequency has a value lower than 2850 cm^{-1} at low temperature, a value typical of a very ordered phase (ref. 25, for example). It increases by about 1.5 cm^{-1} between 40 and 50°C. Between 55 and 70°C, there is a second increase, by about 2 cm^{-1}, the frequency reaching the values observed for a lipid in the fluid phase (Fig. 6 of this work, and refs. 25 and 28, for example). This behaviour contrasts with that of the pure ceramide, which remains very ordered over this temperature range (32). The variation of the position of the ν_{C-D}s band as a function of temperature is also reported. The value between 5 and 40°C is constant and indicative of an ordered phase. Between 40 and 60°C, the band shifts continuously up to 2096 cm^{-1}; an inflection is observed around 55°C. The ν_{C-D}s profile is somewhat different than that derived from the asymmetric C–D methylene stretching (ν_{C-D}a) (data not shown). The ν_{C-D}a band experiences an abrupt shift by 3 cm^{-1} during the first transition (between 40 and 47°C) to reach about 2196 cm^{-1} and increases by less than 1 cm^{-1} between 50 and 70°C. This illustrates that the ν_{C-D}a and the ν_{C-D}s bands are not sensitive, to the same extent, to certain molecular changes. The variation of ν_{C-D}s displays a thermal profile similar to that reported by the first moment of the ^{2}H NMR spectrum of an equivalent mixture (23). As seen on the curves, the transition is not readily reversible since the positions of both ν_{C-H}s and ν_{C-D}s bands are shifted when quenching the sample at 11°C (open symbols) towards frequencies higher than those observed at the beginning of the experiment (i.e., after incubation at 40°C).

© 1998 NRC Canada

Fig. 2. Infrared spectra in the Amide I′ and $\nu_{C=O}$ (1800–1550 cm^{-1}), the δ_{CH_2} (1525–1400 cm^{-1}), and the δ_{CD_2} (1100–1070 cm^{-1}) regions for (*A*) CER–PA-d_{31}–chol and (*B*) SPM–PA-d_{31}–chol equimolar mixtures. The temperatures are indicated on the left side.

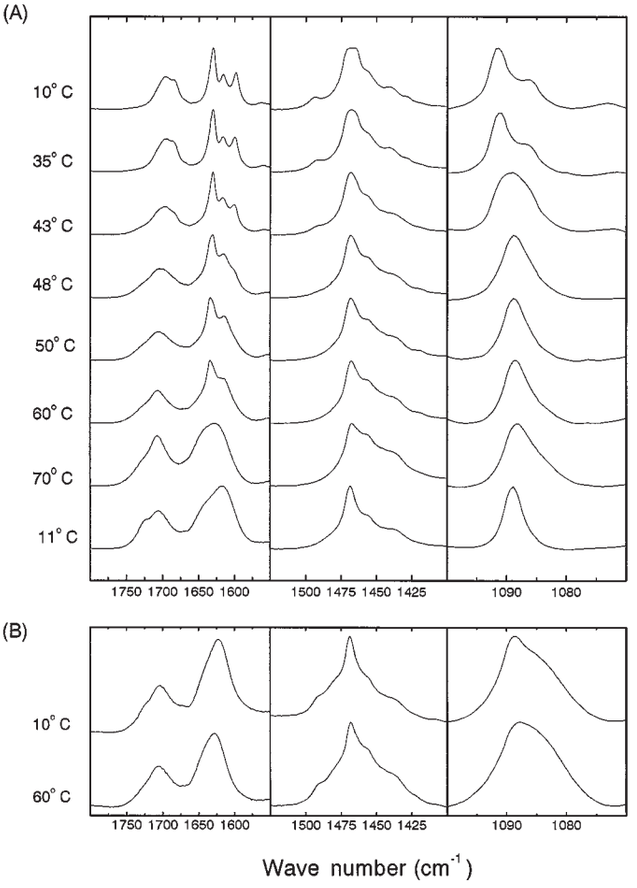

The Amide I′, the CH_2, and CD_2 scissoring (δ_{CH_2} and δ_{CD_2}) regions have also been examined (Fig. 2). The prime (′) of the Amide I′ band indicates that the amide bond is deuterated as a consequence of the use of a D_2O-based buffer. The H–D exchange of the amide protons is indicated by the absence of the Amide II band, which would appear around 1550 cm^{-1} for the hydrogenated amide bond whereas it is shifted to 1450 cm^{-1} upon deuteration. In the 1800–1550 cm^{-1} region, two broad features are observed for the SPM–PA-d_{31}–chol mixture. The Amide I′ appears at about 1623 and 1627 cm^{-1} at 10 and 60°C, respectively, similar to its position for pure SPM (data not shown). It is lower than 1651 cm^{-1}, the value measured for the non-hydrogen-bonded SPM amide in $CHCl_3$ (data not shown). It is concluded that the SPM carbonyls participate in hydrogen bonding but there is no formation of crystalline structure as inferred from the broadness of the band. The second feature shows two components at 1724 and 1702 cm^{-1}, assigned to the carbonyl stretching ($\nu_{C=O}$) of the carboxylic group of the fatty acid (40), indicating that the fatty acid exists in the protonated form at pH = 5.2. The frequency values are lower than that measured for the non-hydrogen-bonded C=O in a dilute solution of PA-d_{31} in $CHCl_3$, appearing at 1745 cm^{-1} (data not shown). It can be concluded that both SPM and PA-d_{31} participate in hydrogen bonding in this mixture. Between 1525 and 1400 cm^{-1}, the main component (1468 cm^{-1}) corresponds to the acyl chain δ_{CH_2} band (29, 30). This region is cluttered with the contribution of the Amide II′ band but the maximum of the δ_{CH_2} band is well defined and its position is indicative of a hexagonal chain packing or a fluid phase (29, 30). In the region between 1100 and 1170 cm^{-1}, the CD_2 scissoring (δ_{CD_2}) band is a single component at about 1088 cm^{-1}, superimposed on the antisymmetric PO_4^- band at about 1085 cm^{-1} (28). There is no important spectral change in these areas between 10 and 60°C.

The CER–PA-d_{31}–chol mixture shows a different profile in these regions. At 10°C, three components are observed, at 1630, 1615, and 1597 $cm^{-1,}$ for the Amide I′ band; these three frequencies are significantly lower than that for the non-hydrogen-bonded amide carbonyl (1652 cm^{-1}). The first two peaks are similar to those observed in the pure ceramide spectra (32). It is proposed that the low-frequency component be attributed to a strongly hydrogen-bonded amide carbonyl, as will be discussed later. The band associated with the $\nu_{C=O}$ of the palmitic acid shows at least two components, at 1694 and 1683 cm^{-1}. These values are close to that measured for solid PA-d_{31} in a KBr pellet where a peak at 1698 cm^{-1} is observed (data not shown), suggesting that the carbonyls participate in hydrogen bonding comparable to those in the solid fatty acid. At 10°C, the δ_{CH_2} band is broad

© 1998 NRC Canada

Fig. 3. Variations of selected spectral features as a function of temperature for the CER–PA-d_{31}–chol equimolar mixture. (*A*) Variation of the intensity at (▲) 1600, (◆) 1683, and (▼) 1726 cm^{-1}. (*B*) Position of the maximum of Amide I′ component at about 1630 cm^{-1}: for $T > 60°C$, a single broad component is observed at about 1620 cm^{-1}. (*C*) Splitting of the δ_{CH_2} band. (*D*) Splitting of the δ_{CD_2} band.

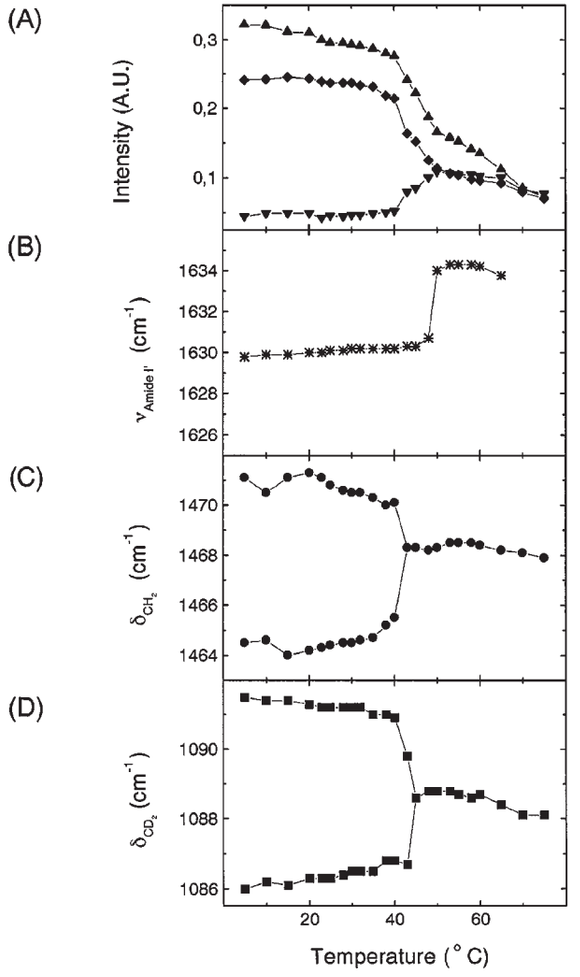

and Fourier self-deconvolution reveals two components at 1471 and 1464 cm^{-1}, a splitting similar to that observed for pure ceramide (32). This splitting is indicative of molecules packed in an orthorhombic subcell (29, 30). The δ_{CD_2} band is also split and the two components appear at 1091 and 1086 cm^{-1}, in agreement with previous results (25). This splitting has also been associated with the formation of domains with orthorhombic chain packing (41, 42). At 35°C, the three regions are similar to those recorded at 10°C. Upon increasing temperature, several spectral features change (Figs. 2 and 3). At about 43°C, the CH_2 and CD_2 scissoring band splittings collapse and a single component is obtained at 1468 and 1089 cm^{-1} for the CH_2 and CD_2 scissoring bands, respectively. Between 55 and 70°C, this latter band shifts slightly to 1088 cm^{-1}. In parallel, the components of the $\nu_{C=O}$ band of the palmitic acid are upshifted to 1726 and 1707 cm^{-1} between 40 and 50°C. This shift is due to a transition involving two defined species as indicated by two isosbestic points observed when the spectra are stacked. Therefore, it is concluded that the fatty acid undergoes a transition from a state in which the chains are highly ordered and the head groups participate in strong intermolecular H-bonding to a structure in which the chains are more disordered and which involves weaker intermolecular hydrogen bonds between the head groups or with water molecules, similar to those formed by PA-d_{31} mixed with SPM. This thermally induced change is concomitant with changes in the Amide I′ region. First, there is the disappearance of the component at 1597 cm^{-1}. Second, the other two components shift from 1630 and 1616 cm^{-1} at 40°C to 1634 and 1615 cm^{-1} at 50°C. When the temperature is increased above 70°C, a broad and asymmetric feature with a maximum around 1620 cm^{-1} is observed in the Amide I′ region. It must be added that the three regions investigated indicate, according to the position of the methylene stretching bands, that the thermally induced transition is not readily reversible: when quenched at 11°C, the Amide I′ band remains broad, and the CH_2 and CD_2 scissoring regions do not show the initial splittings.

To confirm the band assignment in the $\nu_{C=O}$ region, particularly that of the component at 1597 cm^{-1}, spectra were obtained from a ternary mixture prepared using ^{13}C-PA (Fig. 4). The Amide I′ region shows the three components at 1630, 1614, and 1597 cm^{-1}, as previously observed for the mixture prepared with the deuterated acid (Fig. 2). Conversely, the band associated with the carboxylic acid is shifted to 1650 cm^{-1}, as expected from the isotopic effect and in agreement with a previous report (43). These results reinforce the proposition that the component at 1597 cm^{-1} be attributed to the Amide group. Upon heating, changes similar to those observed with the mixture prepared with the deuterated fatty acid are obtained. Between 40 and 50°C, there is the disappearance of the 1597 cm^{-1} component, and the shift of the most intense Amide I′ component from 1630 to 1634 cm^{-1}, as well as that of the $\nu_{C=O}$ of the carboxylic acid towards higher frequencies (from 1651 to 1665 cm^{-1} in the case of ^{13}C-PA). Above 65°C, a broad feature is observed, the bands from the ceramide amide and the acid carboxylic group no longer being resolved. As already shown, the temperature-induced transition is not readily reversible.

The literature reports that low-temperature incubation is necessary to obtain the solid phase (24). To estimate the kinetics of the formation of the solid phases in fully hydrated samples and to identify the sequence of appearance of the spectral features associated with these, samples that had been incubated at 75°C for three 10 min periods were quenched at 5°C and spectra were acquired as function of time (Fig. 5*A*). The appearance of the spectral features associated with solid phases can be roughly divided into two categories. First, the appearance of the $\nu_{C=O}$ bands of PA-d_{31} at 1694 and 1683 cm^{-1}, the splitting of the Amide I′ band giving rise to the two components at 1630 and 1615 cm^{-1}, as well as the splitting of the δ_{CD_2} band are observable after 9 days of incubation at 5°C and evolve up to 50 days of incubation. The second category includes the splitting of the δ_{CH_2} band and the appearance of the 1597 cm^{-1} component, which require more than 90 days of incubation at 5°C to become apparent. Figure 5*B* shows the same type of experiment but this time

© 1998 NRC Canada

Fig. 4. Infrared spectra in the Amide I′ and $\nu_{C=O}$ (1800–1550 cm^{-1}) region for CER–^{13}C-PA–chol equimolar mixtures. The temperatures are indicated on the left side.

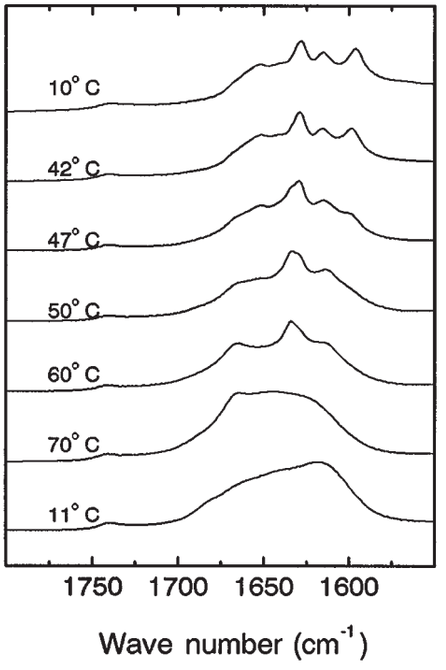

the incubation temperature is 40°C. In this case, all the features of the solid domains are already observed after 10 min. It is concluded that heating the sample leads to an annealing during which the ordering occurs.

To obtain more insight into the role of the different constituents in our model system, binary mixtures of PA-d_{31} with ceramide or SPM were prepared. The addition of palmitic acid to SPM and to ceramide has a different effect on their thermotropism. In the case of sphingomyelin (Fig. 6*B*), the gel-to-liquid crystalline transition of SPM, as probed by the ν_{C-H}s frequency, is shifted towards higher temperatures; the abrupt change in frequency is observed at about 60°C for the SPM–PA-d_{31} mixture. A similar shift is observed for the ν_{C-D}s mode at the same temperature. The results show that the disordering of the two lipid species occurs in a concomitant manner, indicating that SPM and PA-d_{31} form a homogeneous mixture. The incorporation of the fatty acid in the SPM bilayers leads to an increase in the T_m of SPM, going from about 35°C for the pure lipid (38, 39) to 60°C for the equimolar mixture with palmitic acid. A SPM–PA-$d_3$1 2:1 mixture (in mol) exhibits a T_m of about 50°C (33), indicating a progressive shift of the gel-to-liquid crystalline phase transition.

The behaviour of the CER–PA-d_{31} mixture is different (Fig. 6*A*). The ν_{C-D}s region indicates that the fatty acid is ordered at low temperature and experiences a very cooperative transition towards a disordered phase at about 52°C. The thermal changes associated with ceramide, as reported by the ν_{C-H}s mode, are different. At low temperatures, the ceramide exists in a very ordered form. Around 55°C, there is a small shift of the ν_{C-H}s frequency by about 0.5 cm^{-1} towards higher values. At 68°C, the shift becomes more abrupt, and the ν_{C-H}s frequency reaches 2853 cm^{-1} at 75°C, a value close to those measured for a disordered phase. The other regions investigated also reveal the presence of a transition (Figs. 7 and 8). At low temperature (T < 52°C), the spectral regions indicate that this binary lipid mixture forms solid domains. The $\nu_{C=O}$ band components of PA-d_{31} are observed at 1694 and 1683 cm^{-1}, the Amide I′ shows two components at 1635 and 1614 cm^{-1}, and the scissoring bands show a splitting at 1465 and 1471 cm^{-1} for the δ_{CH_2} mode and at 1086 and 1091 cm^{-1} for the δ_{CD_2} mode. The two components in the Amide I′ regions are present over the whole temperature range investigated (10–75°C). It is noted that the low-frequency component at 1598 cm^{-1} is not observed for this mixture. Conversely, the two components of the δ_{CH_2} band merge at about 50°C. Those of the δ_{CD_2} band merge at 53°C, simultaneously with the main transition observed from the ν_{C-D}s band position. During this transition, the $\nu_{C=O}$ bands of the acid also shift toward high frequencies, to 1726 and 1707 cm^{-1}. It is inferred from these results that the acid undergoes a transition at 54°C, from an ordered phase with the characteristics of a solid to a disordered phase, whereas ceramide remains ordered up to 65°C. If the sample is heated at 90°C outside the cell (this temperature is practically inaccessible with the setup used in these experiments), the spectra at temperatures below 40°C consist of broad bands in the Amide I′, δ_{CH_2}, and δ_{CD_2} regions (data not shown). In this case, the frequencies of the ν_{C-H} and ν_{C-D} bands are also significantly higher than those reported in Fig. 6.

Discussion

It is established that the chemical transformation of SPM into ceramide leads to drastic changes in their polymorphism. The particular ceramide head group provides a high stability of the lipid packing as illustrated by the formation of an orthorhombic chain packing and an ordered to a fluid phase transition at about 80°C (32). In contrast, SPM undergoes a gel-to-liquid crystalline phase transition at about 35°C (38, 39). In the present work, it is shown that the different head-group structure of the ceramide and the SPM has a drastic impact on the organization of the binary and ternary mixtures. In the case of SPM mixed in equimolar proportion with cholesterol and palmitic acid, the gel-to-liquid crystalline transition of SPM is no longer observed, as inferred from progressive changes in the methylene stretching band positions. The abolition of gel-to-liquid crystalline transition is also observed in the SPM–chol equimolar mixture (data not shown). This abolition was previously observed for similar binary mixtures (38, 44). For the ternary mixture, cholesterol induces an increase of chain order in the gel phase whereas it leads to a decrease of order in the fluid phase, similar to the behavior of SPM–chol mixtures (38). This behaviour, also observed for various phosphatidylcholines and phosphatidylethanolamine in the presence of cholesterol (28, 45–47), is likely associated with the formation of a liquid-ordered phase in which the lipid diffusion is similar to that observed in a fluid phase but the lipid acyl chains are ordered. The abolition of the gel-to-liquid crystalline phase transition suggests that a considerable proportion of cholesterol is present in the lipid bilayers. The ν_{C-D}s frequency

© 1998 NRC Canada

Fig. 5. Infrared spectra in the Amide I′ and $\nu_{C=O}$ (1800–1550 cm^{-1}), the δ_{CH_2} (1525–1400 cm^{-1}), and the δ_{CD_2} (1100–1070 cm^{-1}) regions for CER–PA-d_{31}–chol equimolar mixture incubated at (*A*) 5°C and (*B*) 40°C, after three 10 min periods of incubation at 70°C. The time was set to 0 at the end of the high-temperature incubation.

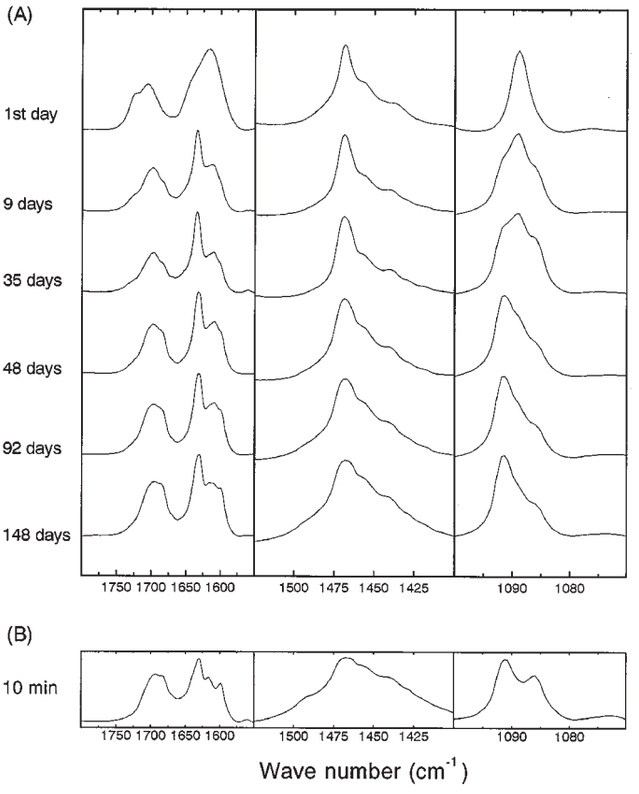

variation as a function of temperature also displays a monotonic increase, indicating that the palmitic acid is inserted in the liquid-ordered matrix. This conclusion is in agreement with previous ^2H NMR results (23) showing that PA-d_{31} in a similar ternary mixture displays a spectrum typical of a liquid-ordered phase. Our results show that SPM is also involved in the liquid-ordered phase in the ternary mixture, suggesting that this mixture is homogeneous.

If SPM is replaced by ceramide in the ternary mixture, a completely different behaviour is observed. At low temperatures (between 5 and 40°C), several spectral features indicate the formation of a highly ordered structure. Both the CH_2 and the CD_2 scissoring modes indicate that the ceramide and the fatty acid exist in an orthorhombic subcell. Because the observed splittings are due to short-range interchain couplings and occur only if the vibrations of the adjacent groups have a similar frequency (i.e., the vibrational coupling between hydrogenated and deuterated chains is negligible), their presence in mixtures containing chains of both types is an indication of lipid demixing (41, 42). In the SC model lipid mixture, the splittings of the methylene scissoring bands are similar to those observed in the pure lipids (ceramide and PA-d_{31}), suggesting extensive lipid demixing. The splitting of the δ_{CH_2} band ($\Delta\nu$ = 6.5 cm^{-1}) is smaller than that measured for long-chain phosphatidylcholine at 0°C (e.g., $\Delta\nu$ = 12 cm^{-1} for dibehenoylphosphatidylcholine (DBPC), (C_{22})) (30), but this difference is likely associated with the chain heterogeneity of the ceramide sample. The formation of orthorhombic crystalline domains was previously reported for a similar mixture, based on the analysis of the δ_{CD_2} and the CH_2 rocking modes (25). The present work provides additional spectral indications of the very ordered structure. The carboxylic $\nu_{C=O}$ band indicates that the carbonyl is involved in strong hydrogen bonding, comparable to the crystalline fatty acid. The presence of this band also confirms that the palmitic acid in this ternary mixture exists in the protonated form. The amide I′ region is also indicative of high order since the two components corresponding to pure ceramide are observed. The presence of solid PA-d_{31} has been also reported for a ternary mixture with the same lipid composition, in ^2H NMR studies (23, 24).

The crystalline domains undergo a transition towards a disordered phase upon heating. It was reported (25) that PA and ceramide experience separate conformational disordering of the chains, centered at 50 and 67°C, respectively. In the present system, a different thermal evolution is observed for the CER–PA-d_{31}–chol mixture since both ceramide and fatty acid are involved in both transitions. The transition at around 40–50°C is related to the solid–fluid transition of PA (23, 25), confirmed by the collapse of the δ_{CD_2} band splitting and the shift of the $\nu_{C=O}$ band. In the present work, it is shown that the ceramide is involved in this transition. First, the ceramide population associated with the low-frequency component of the Amide I′ region of the ternary mixture (made up with PA-d_{31} or ^{13}C-PA) vanishes during the transition associated with the PA-d_{31} crystalline domains. Its

© 1998 NRC Canada

Fig. 6. Thermotropism of (*A*) CER–PA-d_{31} and (*B*) SPM–PA-d_{31} equimolar mixtures as probed by the shift of the (■) ν_{C-H}s and (●) ν_{C-D}s bands. The empty symbols represent the position of the band when the samples were quenched from high temperature down to 11°C.

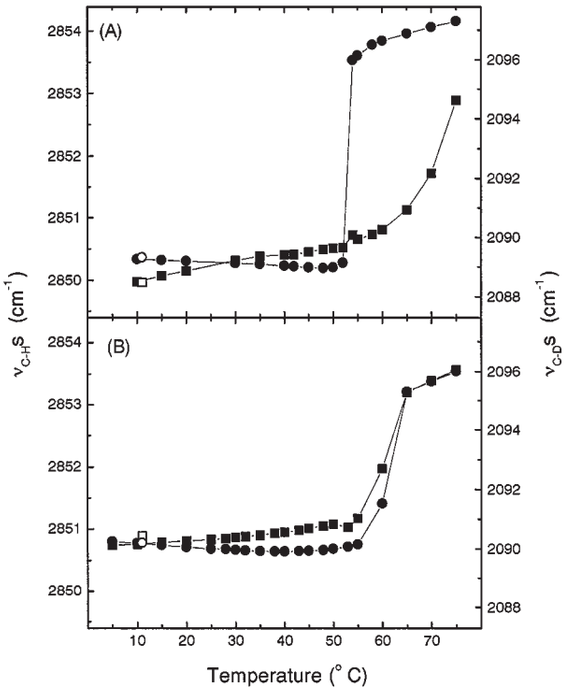

position suggests that the carbonyl is involved in very strong hydrogen bonding or that the amide bond has an unusual conformation. This ceramide fraction likely involves interactions with both PA and cholesterol since the band is absent from the spectra of the pure ceramide or the binary mixtures of ceramide with PA-d_{31} or with cholesterol (data not shown). Second, the positions of the two other Amide I′ components are shifted between 40 and 50°C. Third, this phase transition of PA-d_{31} occurs at a relatively low temperature and implies interactions with the other components. PA-d_{31} by itself is insoluble in aqueous media and has a melting temperature of 59°C. When the fatty acid is in equimolar mixture with only ceramide or only cholesterol, the transition probed by the ν_{C-D} shift occurs at about 53–54°C (data not shown). The presence of both ceramide and cholesterol is necessary to observe the transition at around 45°C, suggesting that a certain proportion of ceramide and cholesterol is involved in this transition. Fourth, the participation of ceramide in the PA-d_{31} domain transition is also supported by the concurrent occurrence of the ν_{C-H}s frequency shift. The participation of ceramide is in agreement with a previous NMR study (48) where the transition at about 40°C in a CER–PA-d_{31}–chol equimolar mixture was detected as a variation of the second moments of both the ^{2}H NMR (associated with the deuterated acid) and the ^{1}H NMR (whose variations are associated with the ceramide) signals. It is proposed that a limited proportion of ceramide participates in the transition since most of the ceramide appears to remain ordered, as illustrated by the presence of the two components of the Amide I′ band at 1634 and 1615 cm^{-1}. At this point, it is not possible to determine whether the ceramides participating in the transition are present in the PA crystalline phase, the fluid phase, or in both. It may be tempting to suggest that the low-frequency component of the Amide I′ is associated with ceramide strongly H-bonded to crystalline PA. However, it is clear that if some ceramide is present in the crystalline PA, it is in limited amount since the δ_{CD_2} splitting is not significantly affected (only about 10% of hydrogenated species can be introduced into a *n*-$C_{36}D_{74}$ matrix without significantly affecting the δ_{CD_2} splitting (41)). It is also proposed that this transition corresponds to the introduction of cholesterol into the fluid PA matrix (25). This is supported by the shift of the ν_{C-D}s band to an intermediate value close to that measured in the SPM–PA-d_{31}–chol mixture, and is also in good agreement with previous ^{2}H NMR studies (23, 48) in which PA-d_{31}, under similar conditions, led to a spectrum of a fluid but ordered phase.

The second transition, occurring between 55 and 70°C, is associated with the transition of the ordered ceramide domains towards a disordered phase (25) as supported by the increase of the ν_{C-H}s frequency to a value typical of a disordered chain, and by the disappearance of the narrow Amide I′ components. The present work highlights the participation of the fatty acid in this transition. First, the shift of the ν_{C-D}s band indicates further disordering of the fatty acid. Second, fluid spectral features related to the ceramide are not observed for the pure spingolipid, or for CER–PA-d_{31} or CER–chol mixtures at temperatures below 75°C. This finding is also supported by the drastic profile change in the ^{2}H NMR spectrum of PA-d_{31} in the equivalent ternary mixture, going from a fluid powder pattern to an isotropic line (23). This transition was also detected as a variation of the second moments of both the ^{2}H NMR (associated with the deuterated acid) and the ^{1}H NMR (whose variations are associated with the ceramide) signals (48). It is proposed that this second transition corresponds to the formation of a homogeneous fluid mixture by the three components, giving rise to a liquid-like phase.

It is concluded from ref. 25 and this work that, at low temperatures, there is an extensive or complete phase separation leading to the formation of crystalline domains with orthorhombic chain packing. The homogenization of the ternary mixture and the formation of a fluid phase at high temperatures are also proposed. It appears that the participation of the lipidic species in the transitions between these two states may vary and this phenomenon can have several origins. A recent study on SC lipids in monolayers (26) provides a possible explanation. It has been proposed that, in a monolayer, the mixture of ceramides (also ceramides III from Sigma), cholesterol, and free palmitic acid form domains. The short-chain ceramides (such as those bearing a C_{16} chain) mix with cholesterol and PA whereas the long-chain ceramides (such as those bearing a C_{24} chain) form domains on their own. The different chain composition of the ceramides can be at the origin of the difference between the results obtained by Moore et al. (25) and in this work, and the effect of acyl chain length on the mixing properties should therefore be carefully examined. The influence of other factors such as pH or incubation protocol should also be taken into consideration.

© 1998 NRC Canada

Fig. 7. Infrared spectra in the Amide I′ and $\nu_{C=O}$ (1800–1550 cm^{-1}), the δ_{CH_2} (1525–1400 cm^{-1}), and the δ_{CD_2} (1100–1070 cm^{-1}) regions for the CER–PA-d_{31} equimolar mixture. The temperatures are indicated on the left side.

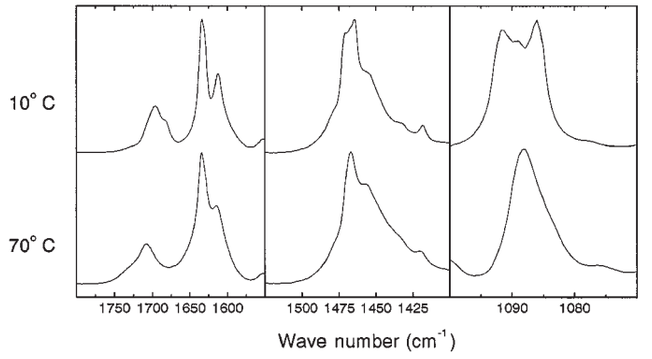

Fig. 8. Variations of selected spectral features as a function of temperature for the CER–PA-d_{31}–chol equimolar mixture. (*A*) Variation of the intensity at (◆) 1683 and (▼) 1726 cm^{-1}. (*B*) Position of the maximum of Amide I′ component at about 1630 cm^{-1}. (*C*) Splitting of the δ_{CH_2} band. (*D*) Splitting of the δ_{CD_2} band.

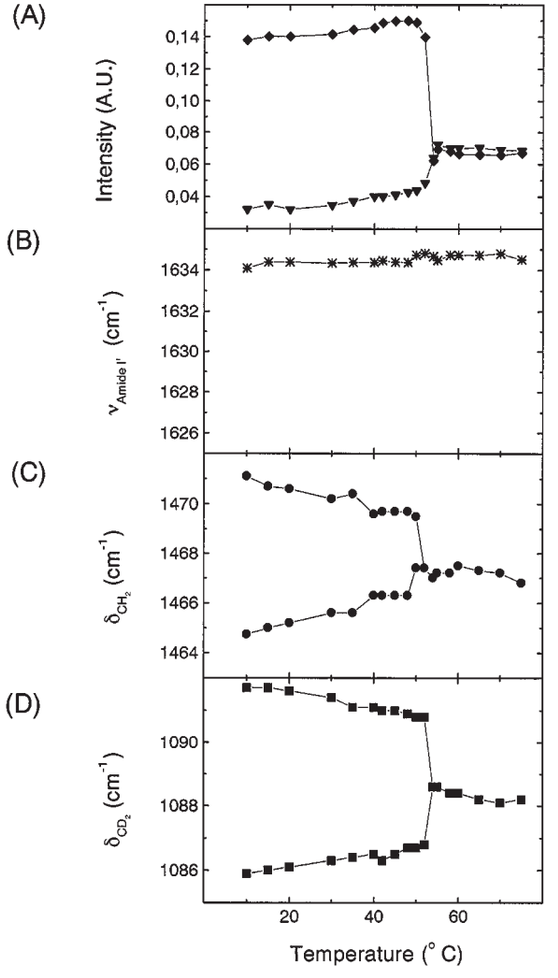

The present study shows that the homogenous distribution of ceramide, cholesterol, and PA-d_{31} obtained above 65°C can be quenched at lower temperatures. If the homogenous sample at high temperature is rapidly cooled to 10°C, the lipids form an ordered phase but no crystalline structures. This is illustrated by the ν_{C-H}s and ν_{C-D}s frequencies, which decrease upon cooling but not down to the values obtained when solid domains exist in the mixture. In addition, there is no sign of splitting for the scissoring CH_2 and CD_2 modes or for the Amide I′ band. The $\nu_{C=O}$ band shows also that the hydrogen bonds are not as strong as in the crystalline domains. Actually, all the regions investigated are very similar to those obtained for the homogeneous SPM–PA-d_{31}–chol mixture, suggesting that the homogeneous distribution obtained at high temperatures can be quenched in a metastable state and that the slow diffusion or molecular reorientation rate of the lipids at low temperatures prevents the rapid formation of the crystalline domains. Such a time-dependent phenomenon is a parameter that should be examined during the lipid migration through the SC. The results also indicate that the kinetics of the crystallization and the segregation are strongly temperature dependent. The thermodynamically stable state, where lipid demixing and crystallization have occurred, can be easily obtained by annealing at 40°C whereas it takes several weeks when the incubation is done at 5°C. The identification of this behaviour is critical to studying the mixtures in a reproducible and thermodynamically stable macroorganization.

It is interesting to examine the influence of palmitic acid on the sphingolipid polymorphism, in order to highlight the role of the components in the ternary mixture. In the case of the SPM–PA-d_{31} mixture, a gel-to-liquid phase transition that involves both lipids is observed at about 60°C, suggesting the formation of a homogeneous phase. The transition is shifted towards a higher temperature than that observed for pure SPM. This phenomenon is rationalized by the small polar head-group size of the fatty acid, leading to a tighter lipid packing and therefore a higher temperature for the gel-to-liquid phase transition. Similar behaviour was also observed when saturated fatty acids were introduced into phosphatidylcholine (43, 49, 50).

The CER–PA-d_{31} mixture has again different lipid mixing properties. At temperatures below 55°C, both lipids exist in separate crystalline domains with orthorhombic chain packing. This is inferred from the low ν_{C-H}s and ν_{C-D}s band

© 1998 NRC Canada

frequencies, the splitting of the methylene scissoring modes, and the narrow components of the Amide I′ band. Conversely to the ternary mixture that includes cholesterol, the ceramide and the fatty acid undergo a transition at a different temperature: the PA molecules experience the transition towards a fluid phase at 53°C, whereas the disordering of the ceramide acyl chains occurs above 65°C. The transition of PA-d_{31} is in agreement with a previous ^{2}H NMR study on a similar mixture (23) showing that PA-d_{31} exists in a solid form below 50°C and forms a phase that gives rise to an isotropic line at higher temperature. The present study reveals that the participation of the ceramide in this transition is very limited and that the lipid demixing is practically complete in the binary mixture. The comparison between this behaviour and that observed for the ternary mixture suggests that cholesterol plays a crucial role in the mixing properties of the SC lipids. The temperature at which there is the formation of a homogeneous mixture supports this proposition. The homogeneous mixing is observed at a lower temperature in the presence of the sterol (for $T > 70$°C) than in absence of the sterol (not determined precisely but for $T > 75$°C). The sterol appears to favour the mixing of the PA-d_{31} and the ceramide. Cholesterol was previously shown to act as a homogenizing agent in some lipid mixtures with limited miscibility (51, 52).

In the present work, the importance of the head group in the mixing properties of the SC lipids is highlighted. While the SPM forms a homogeneous liquid ordered mixture with cholesterol and the fatty acid, the CER–PA-d_{31}–chol mixture exhibits a rich polymorphism. The particular thermotropism of the CER–PA-d_{31}–chol mixture requires the three components. The ceramide, because of the strong intermolecular interactions, provides a stable crystalline structure. This structure is a direct consequence of the enzymatic cleavage of the SPM head group since the SPM appears incapable of forming crystalline phases in an aqueous environment. PA-d_{31} acts as an enhancer of fluid structures since the PA-d_{31} crystalline domains are the first to undergo a transition toward a fluid phase, and because the fatty acid reduces the temperature at which ceramide becomes fluid. Finally, cholesterol promotes the lipid mixing. As a consequence, this composite biomaterial displays a unique polymorphic behaviour that includes different structures, going from lipid demixing and the formation of orthorhombic crystalline domains at low temperatures, to a homogeneous fluid phase at high temperatures. The structural information is very much in agreement with the suggestion that the SC is organized as a domain mosaic model (13). It is found here that the domain mosaic can be modulated by temperature or, more physiologically relevant, by lipid composition or time, if the metastable state is involved.

Despite the simplicity of the model used in the present study, the behaviour reported for the SC lipid model mixture shows striking similarities to that of the real SC. In the case of mouse (9, 11) and human (12) SC, an orthorhombic lateral packing is observed at low temperatures. Between 40 and 45°C, this packing disappears, leading to the formation of a hexagonal packing and, at 80°C, the lipids show only a fluid structure. In addition, a splitting of the δ_{CH_2} band observed on porcine SC (16) suggests the formation of orthorhombic domains. The thermotropic features that are common to the SC and the model mixture may have similar molecular origin, and the present work suggests details of the lipid organization and the conditions under which such structures may be obtained.

Acknowledgments

This work was supported by the Natural Sciences and Engineering Research Council of Canada (NSERC) and the Fonds pour la formation de chercheurs et l'aide à la recherche (FCAR).

References

1. I.H. Blank. J. Invest. Dermatol. **45**, 249 (1965).
2. T.M. Sweeney, and D.T. Downing. J. Invest. Dermatol. **55**, 135 (1970).
3. P.W. Wertz and D.T. Downing. Drugs Pharm. Sci. **35**, 1 (1989).
4. R.O. Potts and M.L. Francoeur. Proc. Natl. Acad. Sci. U.S.A. **87**, 3871 (1990).
5. P.M. Elias. J. Invest. Dermatol. **80**, 44s (1983).
6. N.Y. Schurer and P.M. Elias. Adv. Lipid Res. **24**, 27 (1991).
7. K. Knutson, R.O. Potts, D.B. Guzek, G.M. Golden, J.E. McKie, W.J. Lambert, and W.I. Higuchi. J. Controlled Release, **2**, 67 (1985).
8. G.M. Golden, D.B. Guzek, A.H. Kennedy, J.E. McKie, and R.O. Potts. Biochemistry, **26**, 2382 (1987).
9. J.A. Bouwstra, G.S. Gooris, J.A. van der Spek, S. Lavrijsen, and W. Bras. Biochim. Biophys. Acta, **1212**, 183 (1994).
10. J.A. Bouwstra. Colloids Surf. A: **123**–**124**, 403 (1997).
11. S.H. White, D. Mirejovsky, and G.I. King. Biochemistry, **27**, 3725 (1988).
12. J.A. Bouwstra, G.S. Gooris, M.A. Salomons-de Vries, J.A. van der Spek, and W. Bras. Int. J. Pharm. **84**, 205 (1992).
13. B. Forslind. Acta Derm.-Venereol. **74**, 1 (1994).
14. G.M. Golden, D.B. Guzek, R.R. Harris, J.E. McKie, and R.O. Potts. J. Invest. Dermatol. **86**, 255 (1986).
15. R.O. Potts. Drugs Pharm. Sci. **35**, 23 (1989).
16. B. Ongpipattanakul, M.L. Francoeur, and R.O. Potts. Biochim. Biophys. Acta, **1190**, 115 (1994).
17. H.J. Yardley and R. Summerly. Pharmacol. Ther. **13**, 357 (1981).
18. M.A. Lampe, A.L. Burlingame, J. Whitney, M.L. Williams, B.E. Brown, E. Roitman, and P.M. Elias. J. Lipid Res. **24**, 120 (1983).
19. P.W. Wertz, D.C. Swartzendruber, W. Abraham, K.C. Madison, and D.T. Downing. Arch. Dermatol. **123**, 1381 (1987).
20. R.K. Freinkel and T.N. Traczyk. J. Invest. Dermatol. **85**, 295 (1985).
21. W. Abraham and D.T. Downing. Biochim. Biophys. Acta, **1068**, 189 (1991).
22. R. Lieckfeldt, J. Villalain, J.C. Gomez-Fernandez, and G. Lee. Biochim. Biophys. Acta, **1151**, 182 (1993).
23. N. Kitson, J. Thewalt, M. Lafleur, and M. Bloom. Biochemistry, **33**, 6707 (1994).
24. D.B. Fenske, J.L. Thewalt, M. Bloom, and N. Kitson. Biophys. J. **67**, 1562 (1994).
25. D.J. Moore, M.E. Rerek, and R. Mendelsohn. Biochem. Biophys. Res. Commun. **231**, 797 (1997).
26. E. ten Grotenhuis, R.A. Demel, M. Ponec, D.R. Boer, J.C. van Miltenburg, and J.A. Bouwstra. Biophys. J. **71**, 1389 (1996).
27. S.-Y. Lin, R.-C. Liang, and T.-C. Lin. J. Chinese Chem. Soc. **41**, 425 (1994).
28. J. Umemura, D.G. Cameron, and H.H. Mantsch. Biochim. Biophys. Acta, **602**, 32, 1980.

© 1998 NRC Canada

29. D.G. Cameron, H.L. Casal, E.F. Gudgin, and H.H. Mantsch. Biochim. Biophys. Acta, **596**, 463 (1980).
30. D.G. Cameron, E.F. Gudgin, and H.H. Mantsch. Biochemistry, **20**, 4496 (1981).
31. R.G. Snyder. J. Chem. Phys. **71**, 3229 (1979).
32. D.J. Moore, M.E. Rerek, and R. Mendelsohn. J. Phys. Chem. **101**, 8933 (1997).
33. D. Bonenfant. M.Sc. Thesis, Université de Montréal. 1996.
34. C.Y.Y. Hsiao, C.A. Ottaway, and D.B. Wetlaufer. Lipids, **9**, 913 (1974).
35. P.K. Glasoe and F.A. Long. J. Phys. Chem. **64**, 188 (1960).
36. D. Wilhelm, P. Elsner, and H.I. Maibach. Acta Derm.-Venereol. **71**, 123 (1991).
37. H. Öhman and A. Vahlquist. Acta Dermato-Venereol. (Stockh) **74**, 375 (1994).
38. E. Oldfield and D. Chapman. FEBS Lett. **21**, 303 (1972)
39. Y. Barenholz and T.E. Thompson. Biochim. Biophys. Acta, **604**, 129 (1980).
40. N.B. Colthup, L.H. Daly, and S.E. Wiberley. Introduction to infrared and Raman spectrosocopy. Academic Press, New York. 1975.
41. R.G. Snyder, M.C. Goh, V.J.P. Srivatsavoy, H.L. Strauss, and D.L. Dorset. J. Phys. Chem. **96**, 10008 (1992).
42. R.G. Snyder, H.L. Strauss, and D.A. Cates. J. Phys. Chem. **99**, 8432 (1995).
43. J. Villalaín and J.C. Gómez-Fernández. Chem. Phys. Lipids, **62**, 19 (1992).
44. P.R. Maulik and G.G. Shipley. Biophys. J. **70**, 2256 (1996).
45. C. Paré and M. Lafleur. Biophys. J. **74**, 899 (1998).
46. M.R. Vist and J.H. Davis. Biochemistry, **29**, 451 (1990).
47. J.L. Thewalt and M. Bloom. Biophys. J. **63**, 1176 (1992).
48. J. Thewalt, N. Kitson, C. Araujo, A. MacKay, and M. Bloom. Biochim. Biophys. Res. Commun. **188**, 1247 (1992).
49. S. Mabrey and J.M. Sturtevant. Biochim. Biophys. Acta, **486**, 444 (1977).
50. R.D. Koynova, B.G. Tenchov, P.J. Quinn, and P. Laggner. Chem. Phys. Lipids, **48**, 205 (1988).
51. J.R. Silvius. Biochemistry, **31**, 3398 (1992).
52. J.R. Silvius, D. del Giudice, and M. Lafleur. Biochemistry, **35**, 15198 (1996).

© 1998 NRC Canada

^{2}H NMR studies of dipalmitoylphosphatidylcholine and dipalmitoylphosphatidylcholine–cholesterol bilayers at high pressure

Boyan B. Bonev and Michael R. Morrow

Abstract: Wideline deuterium nuclear magnetic resonance was used to investigate the phase behaviour of bilayer dispersions of chain-perdeuterated dipalmitoylphosphatidylcholine (DPPC-d_{62}) and DPPC-d_{62} containing 28.5 mol% cholesterol for temperatures between 0°C and 90°C and pressures from ambient to 270 MPa. Spectra were obtained over a range of temperature at ambient pressure, 100 MPa, and 210 MPa and over a range of pressure at fixed temperatures of 0°C and 45°C (40°C for the sample containing cholesterol). The combination of complementary isobaric and isothermal scans produced observations that suggest two possible refinements to previously reported DPPC-d_{62} pressure–temperature phase diagrams. In contrast to DPPC-d_{62}, which displays at least three transitions as temperature is lowered from 90°C to 0°C at a fixed pressure of 210 MPa, the sample containing 28.5 mol% cholesterol displayed a continuous change from fluid to ordered over a wide temperature range for 210 MPa and below. These observations suggest that pressure does not induce any substantial repositioning of cholesterol in the bilayer over the range of conditions studied and that cholesterol reduces the sensitivity of bilayer properties to pressure.

Key words: deuterium nuclear magnetic resonance, model membrane, high pressure, cholesterol, phase transition.

Résumé : Opérant à des températures allant de 0° à 90°C et à des pressions allant de la pression ambiante à 270 MPa et faisant appel à la résonance magnétique nucléaire du deutérium à bande large, on a étudié comportement de phase de dispersions en bicouches de chaînes perdeutérées de dipalmitoylphosphatidylcholine (DPPC-d_{62}) et de DPPC-d_{62} contenant 28,5 mol% de cholestérol. Les spectres ont été obtenus à diverses températures à la pression ambiante, à 100 MPa et à 210 MPa et à diverses pressions à des températures fixes de 0° et de 45°C (40°C pour l'échantillon contenant du cholestérol). La combinaison de balayages complémentaires isobares et isothermes a permis d'obtenir des observations supplémentaires qui suggèrent deux raffinements possibles pour les diagrammes de phase pression–température rapportés antérieurement pour le DPPC-d_{62}. Par opposition avec le DPPC-d_{62} qui présente au moins trois transitions lorsqu'on abaisse la température de 90° à 0°C, à pression fixe de 210 MPa, l'échantillon contenant 28,5 mol% de cholestérol présente un changement continue de fluide à ordonné sur une gamme importante de température à des pressions allant jusqu'à 210 MPa. Ces observations suggèrent que, dans le domaine des conditions étudiées, la pression n'induit pas de repositionnement important du cholestérol dans la bicouche et que le cholestérol réduit la sensibilité des propriétés de la bicouche à la pression.

Mots clés : résonance magnétique nucléaire du deutérium, membrane modèle, pression élevée, cholestérol, transition de phase.

[Traduit par la Rédaction]

Introduction

Natural membranes consist of lipid bilayers, which typically comprise a complex mixture of phospholipids, glycolipids, and sterols, along with embedded or surface-associated proteins. The lipid bilayer acts as the structural base for the membrane and defines the physical environment in which membrane proteins function. Lipid bilayers are also remarkable examples of self-assembling soft material with a rich array of physical properties that are largely determined by interactions between bilayer components. The dynamic and anisotropic aspects of the bilayer mechanical properties in a natural membrane exert a substantial influence on processes that occur at and in the membrane. Studying lipid bilayers can yield information about the relationship between structure and function in natural membranes and, at the same time, provide insights into the range of properties accessible in self-assembled soft materials.

Cholesterol is an important component of animal cell membranes. Because it can significantly modify bilayer physical properties such as acyl chain orientational order,

Received January 5, 1998.

B.B. Bonev and M.R. Morrow.[1] Department of Physics and Physical Oceanography, Memorial University of Newfoundland, St. John's, NF A1B 3X7, Canada.

[1]Author to whom correspondence may be addressed. Telephone: (709) 737-4361. Fax: (709) 737-8739. E-mail: myke@kelvin.physics.mun.ca

© 1998 NRC Canada

model membranes containing cholesterol have been studied extensively. Effects of cholesterol on membrane properties have been reviewed by Presti (1) and Yeagle (2). Magnetic resonance experiments indicate that cholesterol in a liquid crystalline bilayer increases the orientational order of the lipid acyl chains without substantially restricting the translational diffusion or the axially symmetric nature of acyl chain segmental reorientation in the liquid crystalline phase (3–10). Cholesterol, in effect, thickens a liquid crystalline bilayer and increases the packing density of lipid acyl chains in the plane of the bilayer in a way that has been referred to as a condensing effect (4).

A number of studies have focussed on the temperature–composition phase diagram of phospholipid bilayers containing cholesterol. Some of these studies have used deuterium spectral differences to obtain the end points of tie lines in two-phase coexistence regions where the spectra obtained from chain-perdeuterated lipid samples are superpositions of characteristic gel and liquid crystalline phase spectra with proportions determined by the lever rule (9, 11, 12). Studies based on this approach have tended to yield phospholipid–cholesterol phase diagrams displaying a eutectic point. At low cholesterol concentration, the low-temperature phase, which is essentially the phospholipid gel phase, is often referred to as the *solid-ordered (so)* phase. Above the phospholipid main transition temperature, for low cholesterol concentration, the bilayer is in a liquid crystalline phase that, on phospholipid–cholesterol phase diagrams, is often labelled as the *liquid-disordered (ld)* phase. Most phospholipid–cholesterol phase diagrams obtained in this way display a region of *so–ld* two-phase coexistence in a narrow temperature range close to the pure phospholipid main transition temperature. This region of two-phase coexistence ends at a eutectic point between 5 mol% cholesterol and 10 mol% cholesterol. For cholesterol concentrations above about 20 mol%, the bilayers are generally found in a phase that displays a high degree of acyl chain orientational order along with fast, axially symmetric, chain segment reorientation. This phase, often referred to as the *liquid-ordered (lo)* phase, extends over a wide temperature range. Its properties have been examined in detail by Reinl et al. (13) using a range of physical techniques. At intermediate cholesterol concentrations, the *so* and *lo* phases coexist at low temperature and the *ld* and *lo* phases coexist at higher temperature. These two-phase coexistence regions in the binary phase diagram are separated by a three-phase coexistence line close to the pure phospholipid main transition temperature. It should be noted that aspects of this phase diagram, such as the existence of a eutectic point, are still debated (14, 15).

Hydrostatic pressure also affects a number of bilayer properties. Comparing the response of bilayer properties to the application of pressure with the response to other perturbations can provide general insights into bilayer properties at ambient pressure. Early studies of the effect of pressure on bilayer phase behaviour, compressibility, and chain order made use of volumetric measurements (16, 17), calorimetry (18), neutron scattering (19–21), and vibrational spectroscopy (22–25). More recently, NMR has been used to examine the effect of pressure on bilayer properties including phase behaviour (26–30) and headgroup orientation (31, 32). One reason that pressure is a particularly interesting variable for bilayer studies is that the response of a phospholipid bilayer to the application of pressure, like its response to temperature, is anisotropic. In the liquid crystalline phase, the application of pressure increases bilayer thickness and reduces area per lipid (20, 21).

The present study is focussed on the effect of hydrostatic pressure on dipalmitoylphosphatidylcholine (DPPC) bilayers and DPPC bilayers containing 28.5 mol% cholesterol. As pressure is increased isothermally, DPPC bilayers pass through a series of ordered phases (23, 25) including one that is reported to be a chain-interdigitated phase (19, 21, 25). Recently, Jonas and co-workers have studied the pressure–temperature phase diagram of DPPC bilayers using ^{2}H NMR spectroscopy, on bilayers of chain-perdeuterated DPPC (27) and selectively labelled DPPC (33), and ^{31}P NMR spectroscopy (31). They estimated the location of phase boundaries in the pressure–temperature diagram by examining spectra obtained while scanning pressure at a number of fixed temperatures. While DPPC-d_{62} results reported in the present study are primarily intended to provide a context in which to discuss the behaviour of bilayers containing cholesterol, they do provide some additional insights into the DPPC-d_{62} pressure–temperature diagram. The DPPC-d_{62} results presented here were obtained while scanning temperature under isobaric conditions of ambient pressure, 100 MPa, and 210 MPa as well as while scanning pressure under isothermal conditions. As such, they complement previous explorations of this pressure–temperature diagram. Spectra of DPPC-d_{62} bilayers containing 28.5 mol% cholesterol have been obtained under similar conditions. At ambient pressure, DPPC-d_{62} bilayers with this cholesterol concentration are in the *lo* phase over a wide temperature range straddling the pure lipid transition temperature. The responses to pressure of DPPC-d_{62} bilayers with and without cholesterol present are compared. One issue of particular interest in this study is whether there is any evidence of a pressure-induced change in the location of cholesterol molecules in the bilayer. Cholesterol-containing bilayers have previously been studied at high pressure using neutron scattering (20) and Fourier transform infrared spectroscopy (34, 35).

Methods and materials

DPPC-d_{62} was synthesized by acylation of glycerophosphocholine (Sigma, St. Louis, Mo.) with chain-perdeuterated palmitic anhydride using the method of Gupta et al. (36). Perdeuterated palmitic acid was prepared by the method of Hsiao et al. (37). The final product was purified on a 1.5 m Sephadex LH-20 liquid chromatography column (Pharmacia Biotech, Baie d'Urfe, Que.) and eluted with 100% ethanol, which was redistilled before use. Using thin-layer chromatography, the product was found to migrate as a single spot.

Samples of 28.5 mol% cholesterol in DPPC-d_{62} were prepared by mixing the two components in chloroform solution and then removing the solvent under dry nitrogen flow after which the mixture was vacuum-dried for approximately 5 h. Both DPPC-d_{62} and DPPC-d_{62}–cholesterol samples were hydrated in excess 0.1 M phosphate buffer (pH 7.2). The buffer to lipid ratio was about 2:1 by weight. Suspensions of multilamellar vesicles were prepared by stirring thoroughly with a

© 1998 NRC Canada

fine glass rod. The suspended samples were transferred to thin-walled polyethylene tubes, which then were heat-sealed.

Deuterium NMR was carried out in a 3.5 T superconducting solenoid (Nalorac Cryogenics, Martinez, Calif.) using a probe capable of operating at applied hydrostatic pressures up to 2.7 kbar and temperatures ranging from –20°C to 80°C (38). The coil and the tube containing the sample are both contained within a beryllium–copper cell that was pressurized with hydraulic oil (AW ISO grade 32). Pressure in the cell was measured using a Bourdon tube pressure gauge, which was calibrated using a dead-weight gauge. To maintain isobaric conditions while varying sample temperature, the pressure cell in the NMR probe was connected to a temperature-controlled external vessel of approximately twice the volume.

Spectra were obtained using a quadrupole echo sequence (39) with $\pi/2$ pulses of between 2.35 and 2.55 μs and a pulse separation of 35 μs. For each spectrum, between 8000 and 72 000 transients were averaged. Free induction decays were digitized at 2 μs per point in the liquid crystalline phase and 1 μs per point in the gel and ordered phases. Oversampling (40) by a factor of two was used to obtain effective digitizer dwell times of 4 μs and 2 μs in the liquid crystalline and ordered phases, respectively.

The weighted mean splitting of the ^{2}H NMR spectrum can be obtained by calculating the first spectral moment over half of the spectrum using (41)

$$M_1 = \frac{\int_0^\infty \omega f(\omega) d\omega}{\int_0^\infty f(\omega) d\omega}$$

where $f(\omega)$ is the spectrum. For a chain-perdeuterated lipid in the liquid crystalline phase, M_1 is proportional to the average, over all deuterons on the chain, of the orientational order parameter,

$$S_{CD} = \frac{1}{2} + \left\langle 3\cos^2 \theta_{CD} - 1 \right\rangle$$

where θ_{CD} is the instantaneous angle between a given carbon–deuterium bond and the axis of rotational symmetry of the molecules.

Results and discussion

By varying the pressure at fixed temperature, Driscoll et al. (27) used ^{2}H NMR to partially locate boundaries between ordered phases in the pressure–temperature phase diagram of DPPC-d_{62}. Complementary phase diagram information can be obtained from similar experiments in which temperature is scanned with the hydrostatic pressure fixed. Figure 1 shows the ^{2}H NMR spectra of DPPC-d_{62} for a series of temperatures at ambient pressure, 100 MPa, and 210 MPa. Above the transition, the spectra at ambient pressure and 100 MPa are superpositions of Pake doublets characteristic of axially symmetric reorientation. Below the transition, the spectra reflect slower axially asymmetric motions characteristic of the gel phase. It is difficult to distinguish the L_β and P_β' phases using ^{2}H NMR and we do not distinguish those phases here. Selected ordered-phase spectra obtained at 210 MPa are shown in Fig. 1*c*. The temperature dependence of the first spectral moment, M_1, at ambient pressure, 100 MPa, and 210 MPa is shown in Fig. 2.

As can be seen from the spectra of Fig. 1, the main transitions at ambient pressure and at 100 MPa are from the liquid crystalline phase to the normal gel phase. While the temperature dependence of M_1 at 210 MPa shows a similar jump at the main transition, it is clear from the spectra of Fig. 1*c* that the ordered phase just below the transition is not the gel phase seen at ambient pressure. This is consistent with the phase diagram presented by Driscoll et al. (27) who show the liquid crystal to gel transition being replaced by a liquid crystal to interdigitated gel transition near 200 MPa and 80°C. Interdigitation has been reported under similar conditions by workers using a variety of techniques including neutron diffraction (19, 21), Fourier-transform infrared spectroscopy (24, 25), and deuterium NMR on specifically labelled lipid (33).

The isobaric series of spectra shown in Fig. 1*c* provide some insight into the location of boundaries between ordered phases at 210 MPa. The shape of the spectrum evolves continuously from 81°C to 38°C. Between 38°C and 36°C there is a subtle but distinct change in the spectrum, which begins to display a shoulder near ±40 kHz in addition to the shoulder near ±20 kHz. In Fig. 2, this transition can also be seen as a slight break in M_1 versus T results for 210 MPa. The phase below this transition is identified as GIII on the basis of a comparison with results of Driscoll et al. (27) that show a DPPC-d_{62} spectrum displaying similar shoulders situated within this region of the pressure–temperature phase diagram. Peng et al. (33) display ^{2}H NMR spectra of selectively chain-deuterated DPPC in several ordered phases at high pressure. In the GIII phase, deuterons at the C13 position give rise to a prominent doublet with peaks at about ±40 kHz. If deuterons on neighbouring carbons display similar spectra, their superposition could account for the shoulders that seem to be characteristic of the DPPC-d_{62} GIII spectrum.

Structures of the ordered phases, including GII and GIII, have been described by Wong et al. (25). In both GII and GIII, chains are extended and tilted with respect to the bilayer normal. While the degree of interchain ordering is higher in GIII than in GII, neither phase is entirely static on the NMR time scale. As discussed below, the GII phase can be identified with one of the ordered bilayer phases observable at ambient pressure. The current measurements at 210 MPa do not display a region of GII around 40°C but the selective label studies of Peng et al. (33) suggest that the distinction between GII and GIII is most apparent in the spectra of deuterons near the methyl end of the acyl chain. The GII and GIII phases may thus be difficult to distinguish with perdeuterated samples.

While the phase existing between 38°C and 26°C corresponds to the GIII phase described by Jonas and co-workers (27, 33), the width of this region seems to be substantially smaller than indicated in their phase diagram. At 24°C and below, the major component of the spectrum is axially symmetric with a splitting corresponding to the full quadrupole interaction. The central component, due to the methyl deuterons, is narrowed by rotation about the symmetry axis of

© 1998 NRC Canada

Fig. 1. ^{2}H NMR spectra of DPPC-d_{62} at selected temperatures for (*a*) ambient pressure, (*b*) 100 MPa, and (*c*) 210 MPa.

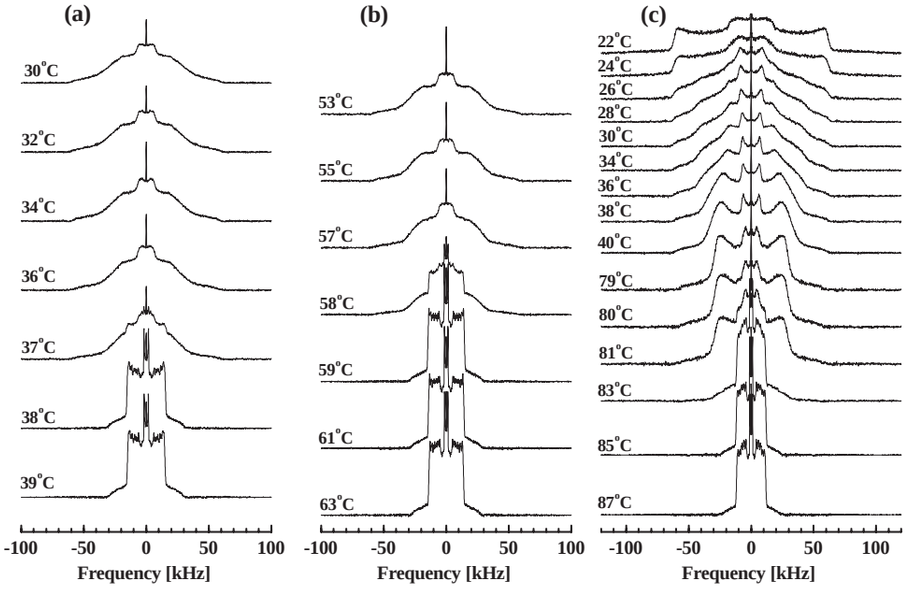

Fig. 2. Temperature dependence of first spectral moments (M_1) for ^{2}H NMR spectra of DPPC-d_{62} at ambient pressure (●), 100 MPa (◆), and 210 MPa (▲).

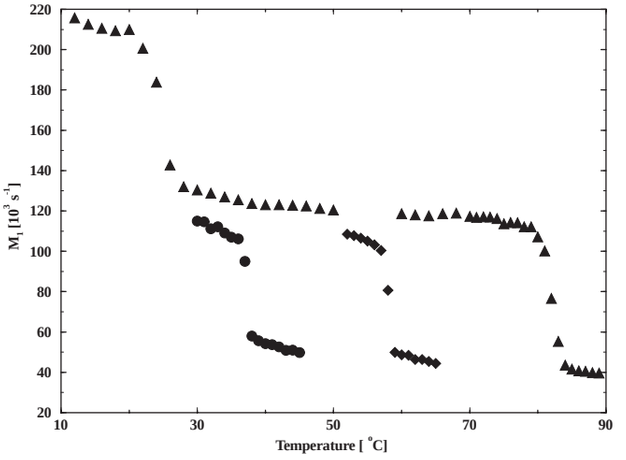

the methyl group. This phase, in which the chains appear to be rigid, has been labelled phase X by Driscoll et al. (27).

One interesting question that requires comment is the relationship between the ordered phases identified at high pressure and the subgel or L_C phase that has been reported for a variety of phospholipid systems at ambient pressure and high pressure (29, 42–45). In some cases, formation of this phase requires incubation of the sample at a temperature that is low enough for the ordered phase to be stable but high enough that molecular rearrangement into the more ordered phase is not frozen out. For some unsaturated lipids (45) or saturated lipids at elevated pressure (29), this temperature range can be limited to a few degrees.

The formation of the subgel phase of DPPC-d_{62} near 0°C is barely discernable in the temperature dependence of ambient pressure first and second spectral moments presented by Davis (46). Results obtained with different effective cooling

Fig. 3. ^{2}H NMR spectra of DPPC-d_{62} at selected pressures and temperatures representing phases encountered in these experiments: (*a*) L_α at 40°C, ambient pressure; (*b*) P_β' (GI) at 32°C, ambient pressure; (*c*) L_C (subgel) at 0°C, ambient pressure; (*d*) GIII at 0°C, 100 MPa; (*e*) Gi (interdigitated gel) at 50°C, 270 MPa; (*f*) *X* at 0°C, 270 MPa.

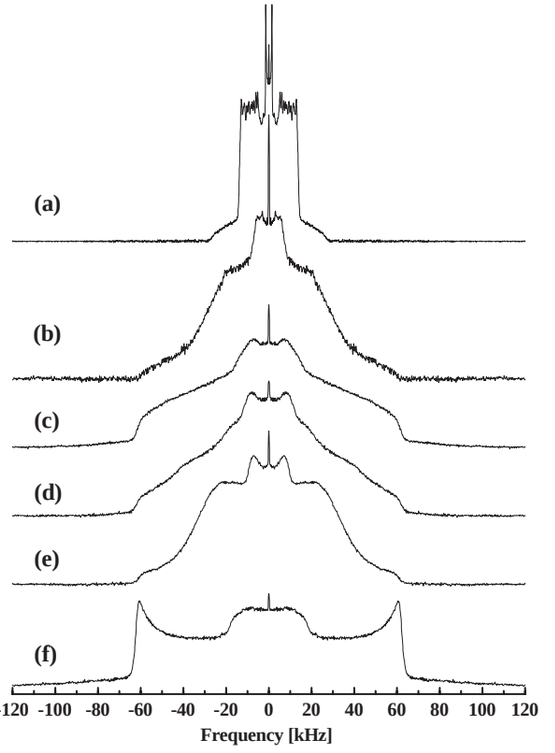

rates have sometimes fortuitously displayed a clearer transition near 0°C (47). Given that there is a transition from a gel phase to a more ordered phase near 0°C at ambient pressure,

© 1998 NRC Canada

Fig. 4. ^{2}H NMR spectra of DPPC-d_{62} at selected pressures for (*a*) 0°C and (*b*) 45°C.

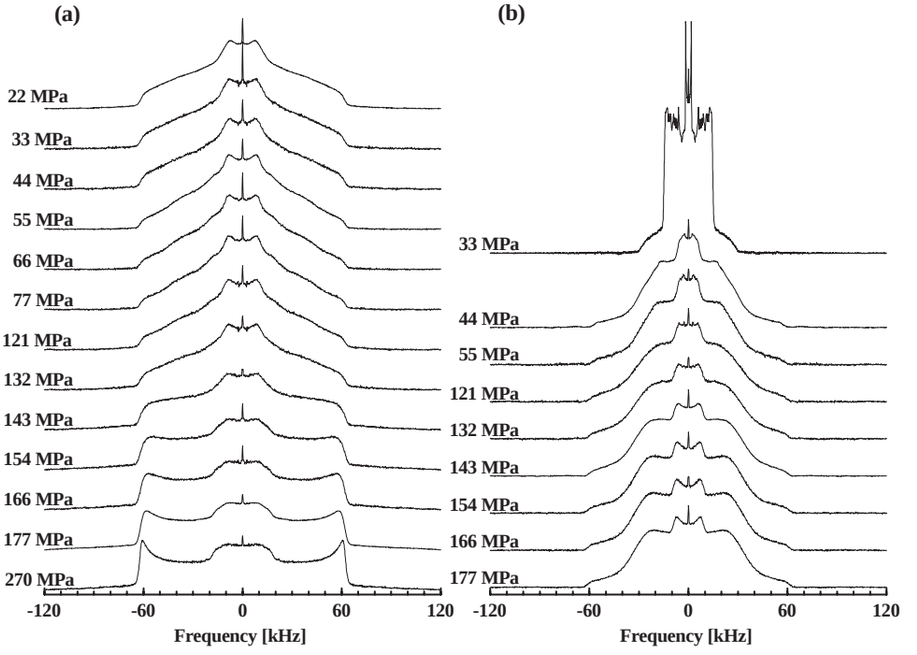

Fig. 5. Pressure dependence of first spectral moments (M_1) for ^{2}H NMR spectra of DPPC-d_{62} at 0°C.

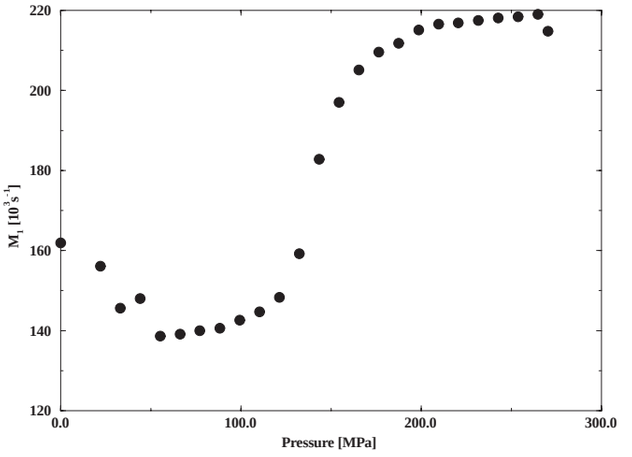

the low-pressure, low-temperature region of the phase diagram presented by Driscoll et al. (27) is presumably incomplete since the GII to GIII and GIII to X boundaries both extrapolate to ambient pressure at temperatures below 0°C. Wong et al. (25) have pointed out, however, that pressure can hinder the molecular reorientations required to bring about the transition into or out of the subgel phase and make the phase transformation effectively unobservable.

Because the subgel phase falls outside of the naming convention used by Driscoll et al. (27), it is helpful to make note of Luzatti's naming convention (48) in which the liquid crystalline phase is L_α, the tilted gel phase just below the transition is P_β', the gel phase below the pretransition is L_β, and the subgel phase is L_C. Figure 3 shows representative spectra for these ambient pressure phases plus the phases observed at high pressure. The L_β and P_β' spectra are similar except for some rounding of the shoulders in the former phase. The difference between the L_C and GIII spectra near the transition is subtle but distinct and it is clear that these phases can be distinguished by ^{2}H NMR if conditions permit formation of the subgel phase.

Figure 4 shows spectra for series of decreasing pressures at 0°C and 45°C. At 45°C, the change in spectral shape from the interdigitated phase to the GI (or P_β') phase seems to occur between 121 and 55 MPa. At 0°C, the spectra evolve from the rigid lattice spectrum characteristic of the *X* phase to spectra characteristic of the GIII phase between 270 and 143 MPa. The spectra for 121–55 MPa are characteristic of the GIII phase. The spectra are characteristic of the L_C phase for 44 MPa and below. It is interesting to note that the spectra at 22 and 132 MPa are strikingly similar, which reinforces the point that the difference between the L_C and GIII phases is subtle. The pressure dependence of M_1 for 0°C, shown in Fig. 5, confirms the existence of three pressure ranges in which the spectra appear to display distinct behaviours. These transition pressures are close to those indicated in the phase diagram of Driscoll et al. (27) but the lowest pressure phase is L_C rather than GII (or L_β). This implies a nearly vertical boundary, in the pressure–temperature diagram, between the L_C and GII (or L_β) phases. To be consistent with the results presented by Driscoll et al. (27), this boundary must presumably terminate at a L_C–GII–GIII triple point in the neighbourhood of 50 MPa and at a temperature slightly above 0°C.

Except for the two points noted above, the present observations are consistent with the DPPC-d_{62} pressure–temperature phase diagram presented by Driscoll et al. (27). At ambient pressure, the accessible phases are the liquid crystalline phase, L_α, the gel phases, P_β' and L_β, and the subgel phase, L_C. At 210 MPa, the phases observed are the liquid

© 1998 NRC Canada

Fig. 6. ^{2}H NMR spectra of DPPC-d_{62} plus 28.5 mol% cholesterol at selected temperatures for (*a*) ambient pressure, (*b*) 100 MPa, and (*c*) 210 MPa.

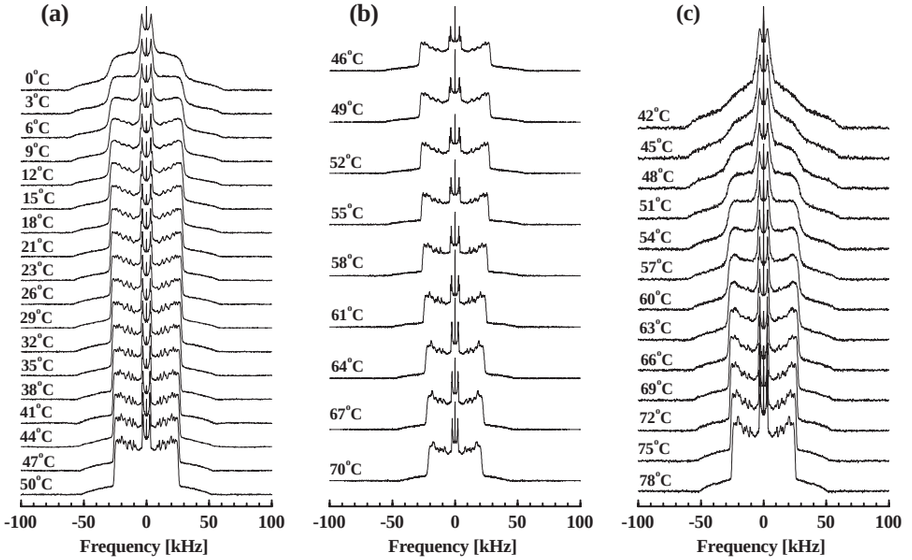

crystalline phase, the interdigitated gel phase, the GIII phase, and the nearly rigid lattice *X* phase. Knowledge of this phase diagram provides a background from which to consider the effect of pressure on the interaction of cholesterol with DPPC and, in particular, to address the question of whether pressure alters the location of cholesterol within the bilayer.

For concentrations above 25 mol% cholesterol in DPPC, at ambient pressure, the bilayer is in the liquid-ordered (*lo*) phase (13). Within this region of the temperature–composition phase diagram, the bilayer changes continuously from a relatively ordered lipid phase at low temperature to a more fluid phase at higher temperature with no crossings of phase boundaries (9). Similar results have been observed for other cholesterol–phospholipid systems (11, 12) although it must be noted that other phase diagrams have been proposed (14, 15). Figure 6 shows ^{2}H NMR spectra of DPPC-d_{62} containing 28.5 mol% cholesterol for a series of temperatures at ambient pressure, 100 MPa, and 210 MPa. At 50°C, the ambient pressure spectrum is a superposition of Pake doublets, characteristic of fast axially symmetric motion, but with significantly larger splittings than would be seen in the liquid crystalline phase of the pure lipid. The larger splittings reflect the ordering effect of cholesterol on the lipid acyl chains. At 0°C, the ambient pressure spectrum is broader and no longer characteristic of fast axially symmetric reorientation. Between these two temperatures, however, the evolution of spectral shape is continuous and there is no change that can be identified as a phase transition. The spectra retain the sharp features characteristic of a fluid phase down to at least 20° below the transition temperature of pure DPPC-d_{62}. Figures 6*b* and 6*c* show spectra obtained from the same sample for a series of temperatures at 100 MPa and a series of temperatures at 210 MPa. At both 100 and 210 MPa, the spectra again display large splittings but remain characteristic of a fluid phase to well below the DPPC-d_{62} transition temperature at that pressure. For 210 MPa, the collection of spectra was continued to nearly 40° below the DPPC-d_{62} transition temperature at that pressure. While the spectra evolved into a shape that increasingly departed from that characteristic of fast axially symmetric reorientation, there was again no clear transition. Figure 7 shows spectra of the cholesterol-containing sample for a series of pressures at 40°C. Continuous evolution of the spectrum through a range of spectral shape is again observed. While the spectra around 40°C and 210 MPa display some resemblance to gel phase spectra that are characteristic of slow, axially asymmetric, reorientation, the prominence of the central doublet suggests that enough motion persists for there to be a significant variation of quadrupole echo decay time along the chain. Similarly distorted spectra have been observed in mixtures of unsaturated lipid and cholesterol, which also order continuously with decreasing temperature (45).

Figure 8 shows the temperature dependence of M_1 for DPPC-d_{62} and DPPC-d_{62} containing 28.5 mol% cholesterol at ambient pressure, 100 MPa, and 210 MPa. Except for a pressure-induced shift in temperature, the behaviour of M_1 is similar for all three cases. This is particularly interesting at 210 MPa where the transition in the pure DPPC-d_{62} system is from the liquid crystalline phase to an interdigitated phase. There was no evidence in these results of the formation of an interdigitated phase in the cholesterol-containing sample. Indeed, the behaviour of the cholesterol-containing sample at high pressure appears to be analogous to that observed in the liquid-ordered (*lo*) phase at ambient pressure. In essence, cholesterol modifies the response of the bilayer phase behaviour to applied pressure. For all three pressures, the spectrum of the cholesterol-containing sample was characteristic of a fluid phase at the temperature corresponding to the pure lipid transition for that pressure. The first moments of these spectra, however, were close to those observed in the ambient-pressure gel phase of DPPC-d_{62}. Bearing in mind that increased chain order generally corresponds to increased bilayer thickness, this observation suggests that, for a given

© 1998 NRC Canada

Fig. 7. ^{2}H NMR spectra of DPPC-d_{62} plus 28.5 mol% cholesterol at selected pressures for 40°C.

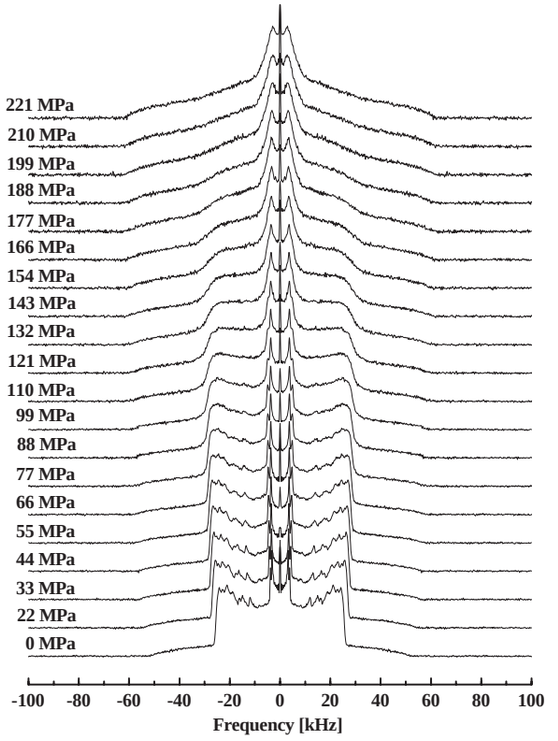

temperature, the presence of cholesterol may substantially diminish the effect of pressure on the thickness of fluid bilayers. Reis et al. (35) have drawn a similar conclusion from Fourier transform infrared studies of internal chain motions in DPPC–cholesterol bilayers at high pressure. The observation that the temperature dependence of M_1 does not change with increased pressure, aside from an overall shift, is indirect evidence that pressure does not substantially alter the interaction of cholesterol with the bilayer and thus that the location of cholesterol within the bilayer is not changed by the application of pressure despite the anisotropic response of the bilayer to applied pressure.

Conclusions

The pressure and temperature dependences of ^{2}H NMR spectra reported here are consistent with the DPPC-d_{62} phase diagram reported by Driscoll et al. (27) with the exceptions of the position of the boundary between the GIII and *X* phases and the presence of the L_C phase at low pressure and temperature. Near 200 MPa, DPPC-d_{62} passes through a variety of phases including the liquid crystalline phase, an interdigitated phase, the GIII phase, and the *X* phase as temperature is lowered from 80 to 0°C. Under the same conditions, the sample containing 28.5 mol% cholesterol changes continuously from fluid to ordered without passing through this series of phases. The behaviour at high pressure thus appears to be analogous with that observed at ambient pressure where DPPC bilayers containing this concentration of cholesterol remain in the liquid-ordered (*lo*) phase over a wide temperature range. The presence of cholesterol also reduces

Fig. 8. Temperature dependence of first spectral moments (M_1) for ^{2}H NMR spectra of DPPC-d_{62} (solid symbols) and DPPC-d_{62} plus 28.5 mol% cholesterol (open symbols) at ambient pressure (circle), 100 MPa (diamond) and 210 MPa (triangles). Inverted and upright open triangles represent two separate runs on the same sample.

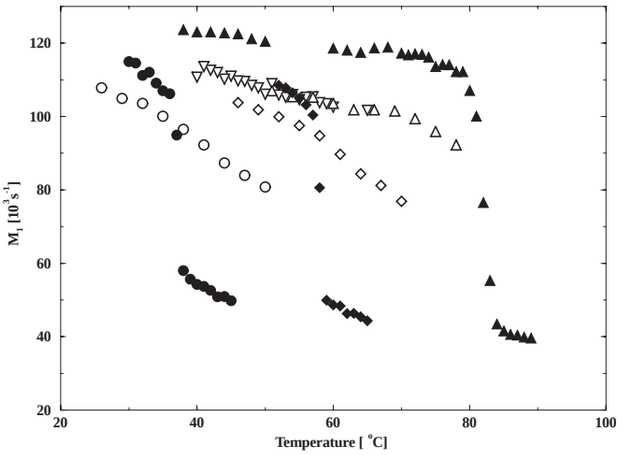

the sensitivity of bilayer thickness to pressure. These observations provide an example of how the response of bilayer properties to pressure can be substantially altered by addition of a second amphiphilic component. This point is particularly interesting in light of the complexity of natural membranes that have evolved under the influence of various stresses.

Acknowledgements

This work was supported by the Natural Sciences and Engineering Research Council of Canada (NSERC). The authors are grateful to Mr. William Kieley for his contributions to the construction of the high-pressure NMR probe.

References

1. F.T. Presti. *In* Membrane fluidity in biology. Vol. 3. *Edited by* R.C. Aloia and J.M. Boggs. Academic Press, New York. 1985. pp. 97–146.
2. P.L. Yeagle. Biochim. Biophys. Acta, **822**, 267 (1985).
3. H.U. Gally, A. Seelig, and J. Seelig. Hoppe-Seyler's Z. Physiol. Chem. **357**, 1447 (1976).
4. G.W. Stockton and I.C.P. Smith. Chem. Phys. Lipids, **17**, 251 (1976).
5. R.A. Haberkorn, R.G. Griffin, M.D. Meadows, and E. Oldfield. J. Am. Chem. Soc. **99**, 7353 (1977).
6. R. Jacobs and E. Oldfield. Biochemistry, **18**, 3280 (1979).
7. E.J. Dufourc, E.J. Parish, S. Chitrakorn, and I.C.P. Smith. Biochemistry, **23**, 6062 (1984).
8. M.B. Sankaram and T.E. Thompson. Biochemistry, **29**, 10676 (1990).
9. M.R. Vist and J.H. Davis. Biochemistry, **29**, 451 (1990).
10. J.H. Davis. *In* Cholesterol in membrane models. *Edited by* L. Finegold. CRC Press, Boca Raton, Fla. 1993. pp. 67–135.
11. J.L. Thewalt and M. Bloom. Biophys. J. **63**, 1176 (1992).
12. F.M. Linseisen, J.L. Thewalt, M. Bloom, and T.M. Bayerl. Chem. Phys. Lipids, **65**, 141 (1993).

© 1998 NRC Canada

13. H. Reinl, T. Brumm, and T.M. Bayerl. Biophys. J. **61**, 1025 (1992).
14. T.-H. Huang, C.W.B. Lee, S.K. Das Gupta, A. Blum, and R.G. Griffin. Biochemistry, **32**, 13277 (1993).
15. T.P.W. McMullen and R.N. McElhaney. Biochim. Biophys. Acta, **1234**, 90 (1995).
16. N.-I. Liu and R.L. Kay. Biochemistry, **16**, 3484 (1977).
17. R.E. Tosh and P.J. Collings. Biochim. Biophys. Acta, **859**, 10 (1986).
18. S. Utoh and T. Takemura. Jpn. J. Appl. Phys. **24**, 356 (1985).
19. L.F. Braganza and D.L. Worcester. Biochemistry, **25**, 2591 (1986).
20. L.F. Braganza and D.L. Worcester. Biochemistry, **25**, 7484 (1986).
21. R. Winter and W.-C. Pilgrim. Ber. Bunsen-Ges. Phys. Chem. **93**, 708 (1989).
22. P.T.T. Wong and H.H. Mantsch. Biochemistry, **24**, 4091 (1985).
23. P.T.T. Wong and H.H. Mantsch. J. Chem. Phys. **83**, 3268 (1985).
24. D.J. Siminovitch, P.T.T. Wong, and H.H. Mantsch. Biochim. Biophys. Acta, **900**, 163 (1987).
25. P.T.T. Wong, D.J. Siminovitch, and H.H. Mantsch. Biochim. Biophys. Acta, **947**, 139 (1988).
26. J. Jonas, C.-L. Xie, A. Jonas, P.J. Grandinetti, D. Campbell, and D. Driscoll. Proc. Natl. Acad. Sci. U.S.A. **85**, 4115 (1988).
27. D.A. Driscoll, J. Jonas, and A. Jonas. Chem. Phys. Lipids, **58**, 97 (1991).
28. D.A. Driscoll, S. Samarasinghe, S. Adamy, J. Jonas, and A. Jonas. Biochemistry, **30**, 3322 (1991).
29. B. Bonev and M.R. Morrow. Biophys. J. **70**, 2727 (1996).
30. B.B. Bonev and M.R. Morrow. Phys. Rev. E: Stat. Phys. Plasmas Fluids Relat. Interdiscip. Top. **55**, 5825 (1997).
31. X. Peng and J. Jonas. Biochemistry, **31**, 6383 (1992).
32. B.B. Bonev and M.R. Morrow. Biophys. J. **69**, 518 (1995).
33. X. Peng, A. Jonas, and J. Jonas. Biophys. J. **68**, 1137 (1995).
34. M. Auger, H.C. Jarrell, I.C.P. Smith, D.J. Siminovitch, H.H. Mantsch, and P.T.T. Wong. Biochemistry, **27**, 6086 (1988).
35. O. Reis, R. Winter, and T.W. Zerda. Biochim. Biophys. Acta, **1279**, 5 (1996).
36. C.M. Gupta, R. Radhakrishnan, and H.G. Khorana. Proc. Natl. Acad. Sci. U.S.A. **74**, 4315 (1977).
37. C.Y.Y. Hsiao, C.A. Ottaway, and D.B. Wetlaufer. Lipids, **9**, 913 (1974).
38. B.B. Bonev and M.R. Morrow. Rev. Sci. Instrum. **68**, 1827 (1997).
39. J.H. Davis, K.R. Jeffrey, M. Bloom, M.I. Valic, and T.P. Higgs. Chem. Phys. Lett. **42**, 390 (1976).
40. R.S. Prosser, J.H. Davis, F.W. Dahlquist, and M.A. Lindorfer. Biochemistry, **30**, 4687 (1991).
41. J.H. Davis. Biochim. Biophys. Acta, **737**, 117 (1983).
42. S.C. Chen, J.M. Sturtevant, and B.J. Gaffney. Proc. Natl. Acad. Sci. U.S.A. **77**, 5060 (1980).
43. M.J. Ruocco and G.G. Shipley. Biochim. Biophys. Acta, **684**, 59 (1982).
44. L. Finegold and M.A. Singer. Biochim. Biophys. Acta, **855**, 417 (1986).
45. M.R. Morrow, P.J. Davis, C.S. Jackman, and K.M.W. Keough. Biophys. J. **71**, 3207 (1996).
46. J.H. Davis. Biophys. J. **27**, 339, (1979).
47. M.R. Morrow, J.P. Whitehead, and D. Lu. Biophys. J. **63**, 18 (1992).
48. V. Luzzatti. *In* Biological membranes. Vol. 1. *Edited by* D. Chapman. Academic Press, London. 1968. pp. 71–123.

© 1998 NRC Canada

Evidence for room temperature mesomorphism in a mixed-valent diruthenium(II,III) quintapalmitoleate polymer

Jennifer F. Caplan, Christopher A. Murphy, Susan Swansburg, Robert P. Lemieux, T. Stanley Cameron, and Manuel A.S. Aquino

Abstract: The synthesis of $Ru_2(\mu\text{-}O_2CR)_4(\mu'\text{-}O_2CR)$ **(1)**, R = $\text{-}CH_2(CH_2)_6CH{=}{=}CH(CH_2)_5CH_3$, has been achieved and characterization using elemental analysis and FTIR and UV–Vis spectroscopies undertaken. Strong evidence for a hexagonal discotic mesophase has been found using differential scanning calorimetry, variable-temperature polarizing optical microscopy, and X-ray powder diffraction. A solid to liquid crystal transition was found upon heating at 128°C and the mesophase is found to persist to room temperature upon cooling from 150°C. This is the first report of room temperature mesomorphism in a mixed-valent metallomesogen.

Key words: ruthenium carboxylate, liquid crystal, metallomesogen, mixed valence, polymer.

Résumé : On a effectué la synthèse du complexe $Ru_2(\mu\text{-}O_2CR)_4(\mu'\text{-}O_2CR)$ (**1**) [R = $\text{-}CH_2(CH_2)_6CH{=}CH(CH_2)_5CH_3$] et on l'a caractérisé par analyse élémentaire et par spectroscopies IR par TF et UV–Vis. Faisant appel à la calorimétrie à balayage différentiel, à la microscopie optique polarisante à température variable et à la diffraction des rayons X, on a obtenu de fortes indications suggérant l'existence d'une mésophase discotique hexagonale. Par chauffage à 128°C, on a établi la présence d'une transition de solide à cristal liquide et on a observé que, lors de son refroidissement de 150°C à la température ambiante, la mésophase persiste. Il s'agirait du premier cas de mésomorphie à température ambiante pour un métallomésogène à valence mixte.

Mots clés : carboxylate de ruthénium, cristal liquide, métallomésogène, valence mixte, polymère.

[Traduit par la Rédaction]

Introduction

The synthesis of transition metal containing liquid crystals (metallomesogens) is one of the fastest growing areas of inorganic materials science, and stresses the importance of coordination chemistry in inorganic materials design (1). In contrast to their organic cousins, few metallomesogens display liquid crystalline behaviour at room temperature. Metallomesogens derived from homovalent dinuclear metal carboxylates, $M_2(\mu\text{-}O_2CR)_4L_2$ (M = Cr, Mo, W, Rh, Ru, and Cu), have proven to be some of the most interesting systems (2–5). These compounds offer much flexibility in that the metal and R (often a long-chain alkyl group) can be varied to elicit desired electronic, magnetic, and (or) mesogenic properties.

Received January 27, 1998.

J.F. Caplan, C.A. Murphy, and M.A.S. Aquino.[1] Department of Chemistry, St. Francis Xavier University, P.O. Box 5000, Antigonish, NS B2G 2W5, Canada.
S. Swansburg and R.P. Lemieux. Department of Chemistry, Queen's University, Kingston, ON K7L 3N6, Canada.
T.S. Cameron. Department of Chemistry, Dalhousie University, Halifax, NS B3H 4J3, Canada.

[1]Author to whom correspondence may be addressed. Telephone: (902) 867-5336. Fax: (902) 867-2414. E-mail: maquino@stfx.ca

Ruthenium carboxylates are the only examples in which both homovalent Ru_2(II,II) and mixed-valent Ru_2(II,III) systems have been studied (2*a*, 4*b*, 5, 6). The homovalent $Ru_2(\mu\text{-}O_2CR)_4$ systems, despite their inherent air sensitivity, have received more attention. Their structure consists of chains of dimer units linked by intermolecular Ru···O bonds (Fig. 1*a*). Mesophases are observed with linear, saturated R = $n\text{-}C_4H_9$ chains that have a transition temperature of 151°C. These values drop as the chain length increases, and plateau at ~ 100°C for R = $n\text{-}C_8H_{17}$ to $n\text{-}C_{19}H_{39}$ chains (5*b*). A later study found that by introducing branching or unsaturation into the side-chain R groups a drop in the transition temperature could be achieved. In the 11-undecenoic acid derivative of Ru_2(II,II) the transition was found to drop to 53°C, compared to 103°C in the saturated linear analogue (2*a*). The mixed-valent diruthenium carboxylates are of great interest because of their significantly greater air stability and their unique magnetic and electronic properties. (Each dimer has three unpaired electrons due to an accidental degeneracy of the π^* and δ^* orbitals) (7). The $Ru_2(\mu\text{-}O_2CR)_4(\mu'\text{-}O_2CR)$ complexes (where R = $n\text{-}C_8H_{17}$ and $n\text{-}C_{11}H_{23}$) were the first reported examples of mixed-valent metallomesogens (6). Both derivatives displayed a transition temperature of 149°C (with ΔH = 15 and 66 kJ mol^{-1}, respectively). They contain five bridging linear-chain carboxylic acids, four *intra*dimer and one *inter*dimer (see Fig. 1*b*).

We wish to report here the first example of a mixed-valent metallomesogen, $Ru_2(\mu\text{-}O_2CR)_4(\mu'\text{-}O_2CR)$ **(1)**, incorporating

 © 1998 NRC Canada

Fig. 1. Proposed structure of (*a*) homovalent $Ru_2(\mu\text{-}O_2CR)_4$ chains and (*b*) mixed-valent $Ru_2(\mu\text{-}O_2CR)_4(\mu'\text{-}O_2CR)$ chains.

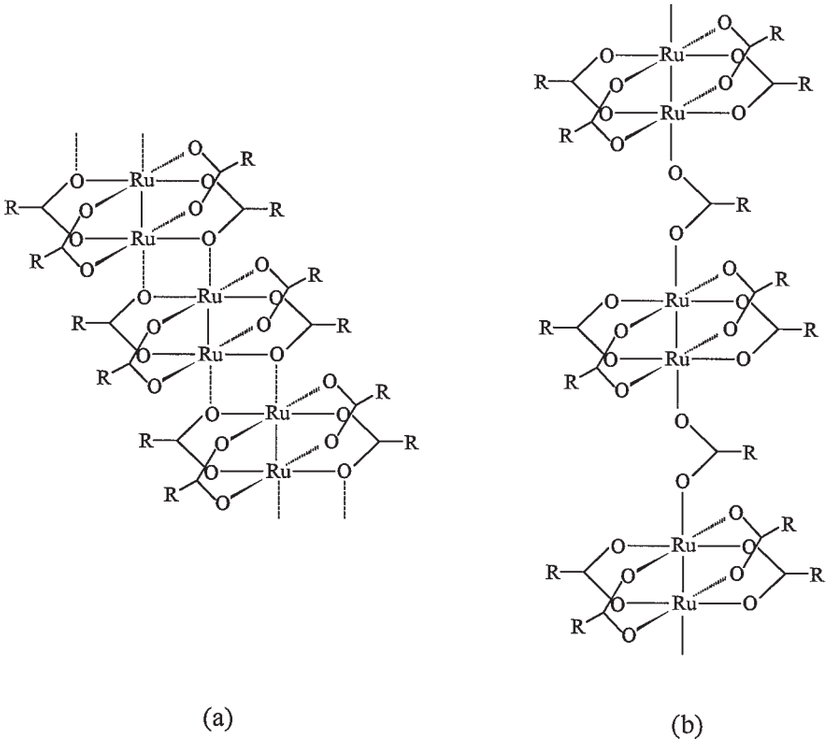

an unsaturated side chain derived from palmitoleic acid (*cis*-9-hexadecenoic acid), i.e., R = $-CH_2(CH_2)_6CH{=}CH(CH_2)_5CH_3$, that displays liquid crystal behaviour at room temperature.

The synthesis of **1** was carried out in aqueous solution using a carboxylate exchange reaction (2*a*) in which the bridging acetates of $[Ru_2(\mu\text{-}O_2CCH_3)_4(H_2O)_2]^+$ (generated in situ by prior dechlorination of $Ru_2(\mu\text{-}O_2CCH_3)_4Cl$ with Ag_2SO_4) are replaced by palmitoleic acid by vigorous stirring at room temperature for 1 week.

$$[1]\quad Ru_2(\mu\text{-}O_2CCH_3)_4Cl + Ag^+ + 2\,H_2O \rightarrow [Ru_2(\mu\text{-}O_2CCH_3)_4(H_2O)_2]^+ + AgCl$$

$$[2]\quad [Ru_2(\mu\text{-}O_2CCH_3)_4(H_2O)_2]^+ + 5RCOO^- \rightarrow Ru_2(\mu\text{-}O_2CR)_4(\mu'\text{-}O_2CR) + 2H_2O + 4CH_3COO^-$$

Subsequent extraction of the resulting dark brown oil with heptane and precipitation with cold acetone gave the product **(1)** in 22% yield. (Anal. calcd. for $C_{80}H_{145}O_{10}Ru_2$: C 65.40, H 9.95, Ru 13.76; found: C 65.04, H 9.85, Ru 13.89.) The product is insoluble in most solvents but slightly soluble in dichloromethane, dichloroethane, and longer chain hydrocarbons such as heptane.

Elemental analysis (C, H, and Ru) is consistent with five carboxylates per diruthenium unit. The infrared spectrum shows strong bands at 2925 and 2850 cm^{-1} due to C–H stretching. $\nu_{sym}(OCO)$ and $\nu_{asym}(OCO)$ at 1416 and 1455 cm^{-1}, respectively, are characteristic of the four intradimer bridging carboxylates (8), a strong band at 1524 cm^{-1} being diagnostic of the $\nu_{asym}(OCO)$ for the interdimer bridging carboxylate (9). The total absence of a band at ~1720 cm^{-1} indicates that there is no free acid present. A UV–visible spectrum in dichloromethane shows the characteristic $\pi^*(Ru_2) \leftarrow \pi(RuO, Ru_2)$ transition at 429 nm (ε = 2270 M^{-1} cm^{-1}). Typically these bands lie around 425 nm (7) with molar absorptivities in the range 500–800 M^{-1} cm^{-1} for non-polymeric species. The extinction coefficient is higher, possibly due to the polymeric nature of the complex. It has been found that π interactions with *inter*dimer bridging ligands cause the $\pi^*(Ru_2)$ orbital to have more ligand character therefore making the $\pi^*(Ru_2) \leftarrow \pi(RuO, Ru_2)$ transition less forbidden (10). In addition, preliminary gel permeation chromatography (GPC) measurements in dichloroethane indicate an average $M_w = 2 \times 10^5$.

The stoichiometry revealed by the elemental analysis, the presence of the distinct *inter*dimer carboxylate stretch in the infrared spectra and the absence of any free acid carbonyl, the higher than usual molar absorptivities in the electronic spectra, and the limited solubility of this complex, together with the GPC results, lead us to postulate a polymeric structure (Fig. 1*b*).

Using differential scanning calorimetry (DSC), variable-temperature polarizing optical microscopy, and X-ray powder diffraction, we have been able to provide strong evidence that compound **1** exhibits room-temperature liquid-crystalline behaviour.

Heating and cooling cycles were performed and, upon heating, the compound displays an endotherm with a transition temperature of 128°C (ΔH = 9.6 kJ mol^{-1}) corresponding to a solid-to-liquid crystal transition. However, upon subsequent cooling from 160°C no peaks are observed down to room temperature. A second cycle yields a flat line for

© 1998 NRC Canada

Fig. 2. Optical texture of the mesophase for **1** obtained upon cooling from 150°C. Top: 100°C, bottom: 50°C.

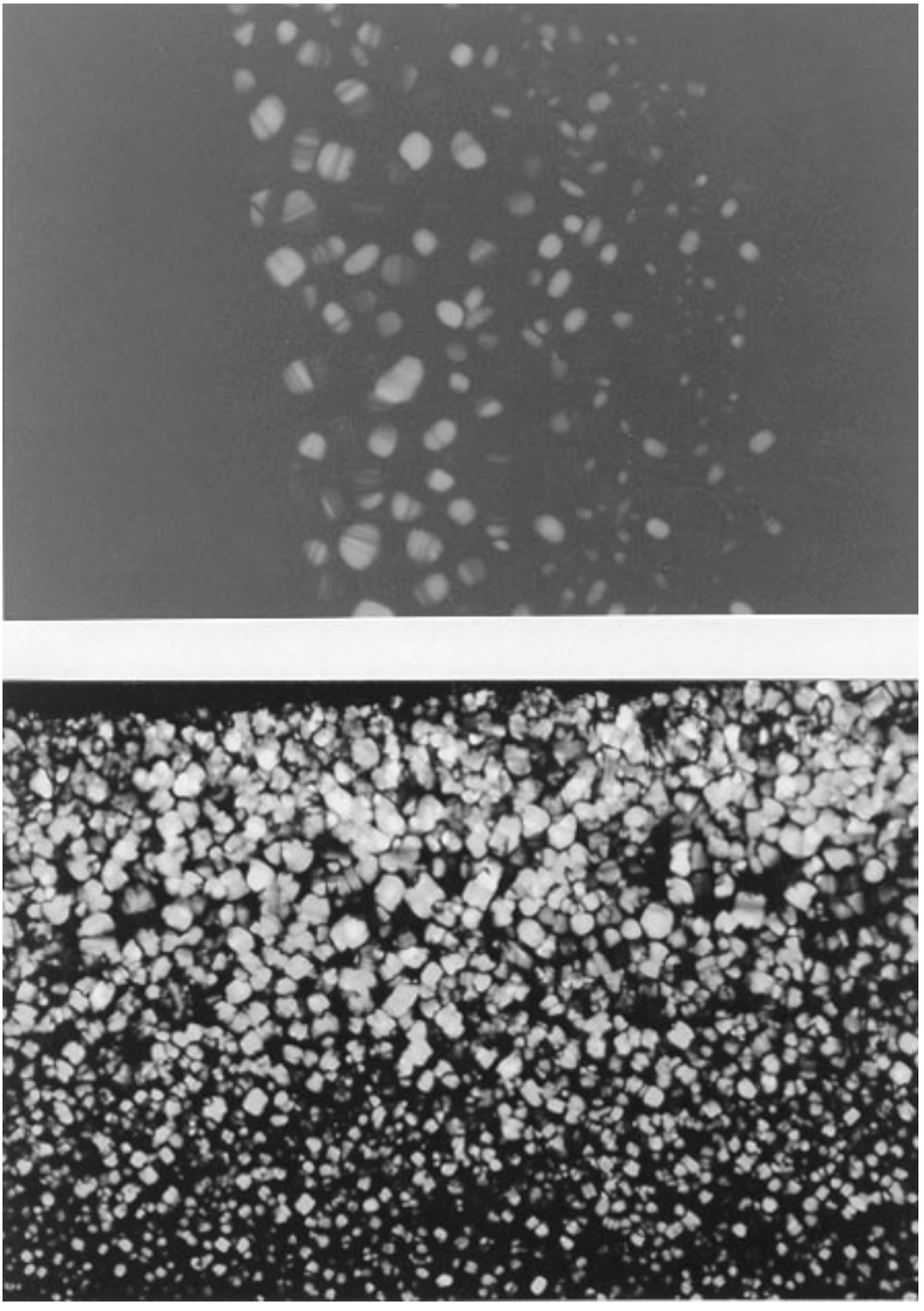

both heating and cooling. Scans to higher temperatures reveal decomposition at >300°C. There is no evidence of clearing to an isotropic liquid. The transition temperature is 20°C less than those observed by Cukiernik et al. (6) for the mixed-valent, $Ru_2(\mu\text{-}O_2C\text{-}n\text{-}C_8H_{17})_4(\mu'\text{-}O_2C\text{-}n\text{-}C_8H_{17})$, and $Ru_2(\mu\text{-}O_2C\text{-}n\text{-}C_{11}H_{23})_4(\mu'\text{-}O_2C\text{-}n\text{-}C_{11}H_{23})$ species with saturated side chains but even more dramatic is the substantial drop in the ΔH value. It has generally been observed for the

© 1998 NRC Canada

homovalent Ru_2(II,II) complexes with the saturated side chains that ΔH increases with increasing length of the side chain (although the dependence is by no means linear) from 20 kJ mol^{-1} in $Ru_2(\mu\text{-}O_2C\text{-}n\text{-}C_4H_9)_4$ to 155 kJ mol^{-1} in $Ru_2(\mu\text{-}O_2C\text{-}n\text{-}C_{19}H_{39})_4$ (5*b*). Introduction of unsaturation and branching does serve to lower the ΔH values over the saturated analogues. $Ru_2(\mu\text{-}O_2C(CH_2)_8CH{=}CH_2)_4$ has ΔH = 32 kJ mol^{-1} versus 78 kJ mol^{-1} for the saturated derivative (2*a*). In our case the value of 9.6 kJ mol^{-1} is significantly smaller than the value for any of the Ru_2(II,II) complexes of comparable chain length and, more importantly, less than the 15 kJ mol^{-1} reported for the mixed-valent $Ru_2(\mu\text{-}O_2C\text{-}n\text{-}C_8H_{17})_4$ (μ'-O_2C-*n*-C_8H_{17}), which has only half the side-chain length!

Polarizing optical microscopy reveals a liquid crystal phase for **1** at slightly above 100°C upon cooling the sample from 150°C. As shown in Figs. 2*a* and 2*b*, cooling results in the appearance of small fan-like domains from a homeotropic domain, which merge on further cooling into a mosaic texture that persists to room temperature. The texture is consistent with a monotropic columnar hexagonal discotic phase, D_H, (11), which has been observed for other metal carboxylate mesogens. The absence of any visible birefringence upon heating is due to the fact that uniaxial phases such as hexagonal discotics tend to form large homeotropic domains with the column axis perpendicular to the glass.

The X-ray diffraction pattern obtained for **1** at room temperature before heating shows a broad peak at 4.4 Å, most likely due to the stacking period of the binuclear ruthenium core along the column axis (5*b*). After heating the sample past the transition temperature to 140°C, a series of sharp peaks appear with *d*-spacings of 6.8, 7.8, 10.3, and 11.6 Å, in addition to the broad peak at 4.4 Å. These peaks persist virtually unshifted when subsequent scans are taken upon cooling to 60°C and room temperature. Scans taken 24 h later at room temperature on the same sample still show evidence of these same peaks although their intensities have diminished. This behaviour parallels nicely the DSC and optical microscopy measurements and the new peaks are assigned to the appearance of the mesophase. Due to instrument limitations, the intercolumnar *d*-spacing (assuming a columnar structure) in the liquid-crystal phase, which would be predicted to lie higher than 17.6 Å (the *d*-spacing limit corresponding to $2\theta = 5°$) is not seen (5*b*, 6) and no direct ratio comparisons could be made to the peaks that do appear. However, the reciprocal spacings of the peaks that are observed are very close to the $3^{1/2} : 4^{1/2} : 7^{1/2} : 9^{1/2}$ ratio predicted for an hexagonal discotic phase (4*a*, 5*b*).

It is probably not appropriate to compare our mixed-valent system with the homovalent Ru_2(II,II) complexes; the structures are different (compare Figs. 1*a* and 1*b*), but it is clear that even a small degree of unsaturation lowers the transition temperature somewhat and ΔH substantially. When unsaturation is present, particularly near the middle of the side chain, the packing of these chains will be less efficient since there is less flexibility and the result is a less stable crystalline phase. It will require less energy and lower temperatures to undergo the transition to the mesophase. Despite the still relatively high transition temperature, persistence of a mesophase to room temperature for a mixed-valent system is, as far as we know, unprecedented. Since this occurs after only one heating cycle it may be due to a supercooling effect. The material eventually (2–3 days) reproduces the original IR and DSC measurements albeit with some decomposition. Supercooling has been seen in *homovalent* Cu_2(II,II) tetraoleates and tetracitronellates (2*a*). Further insight into this interesting effect will hopefully be gained by increasing the degree of unsaturation as well as by studying the effect of branching in the side chain in a series of analogous compounds. Studies in this direction are currently underway.

Acknowledgements

M.A.S.A. wishes to acknowledge the financial support of the Natural Sciences and Engineering Research Council of Canada (NSERC) and St. Francis Xavier University's Council for Research (UCR). J.F.C. wishes to thank Professor Mary-Anne White and Shane Harnish for assistance with some of the early DSC measurements.

References

1. (*a*) J.L. Serrano (*Editor*). Metallomesogens: synthesis, properties and applications. VCH Publishers, Weinheim. 1996; (*b*) P. Espinet, M.A. Esteruelas, L.A. Oro, J.L. Serrano, and E. Sola. Coord. Chem. Rev. **117**, 215 (1992); (*c*) L. Oriol and J.L. Serrano. Adv. Mater. **7**, 348 (1995); (*d*) A.M. Giroud-Godquin and P.M. Maitlis. Angew. Chem. Int. Ed. Engl. **30**, 375 (1991); (*e*) D.W. Bruce. J. Chem. Soc. Dalton Trans. 2983 (1993).
2. Cu: (*a*) P. Maldivi, L. Bonnet, A.M. Giroud-Godquin, M. Ibn-Elhaj, D. Guillon, and A. Skoulios. Adv. Mater. **5**, 909 (1993); (*b*) G.S. Attard and P.R. Cullum. Liq. Cryst. **8**, 299 (1990); (*c*) H. Abied, D. Guillon, A. Skoulios, P. Weber, A.M. Giroud-Godquin, and J.C. Marchon. Liq. Cryst. **2**, 269 (1987); (*d*) M.H. Chisholm, M.R. Mackley, R.T.J. Marshall, and E.F. Pulilina. Chem. Mater. **7**, 1938 (1995); (*e*) G.S. Attard and R.H. Templer. J. Mater. Chem. **3**, 207 (1993).
3. Rh: (*a*) M. Bardet, P. Maldivi, A.M. Giroud-Godquin, and J.C. Marchon. Langmuir, **11**, 2306 (1995); (*b*) J. Barbera, M. Esteruelas, A.M. Levelut, L.A. Oro, J.L. Serrano, and E. Sola. Inorg. Chem. **31**, 732 (1992).
4. Cr, Mo, W: (*a*) D.V. Baxter, R.H. Cayton, M.H. Chisholm, J.C. Huffman, E.F. Pulilina, S.L. Tagg, J.L.Wesemann, J.W. Zwanzinger, and F.D. Darrington. J. Am. Chem. Soc. **116**, 4551 (1994); (*b*) R.H. Cayton, M.H. Chisholm, and F.D. Darrington. Angew. Chem. Int. Ed. Engl. **29**, 1481 (1990).
5. Ru_2(II,II): (*a*) P. Maldivi, A.M. Giroud-Godquin, J.C. Marchon, D. Guillon, and A. Skoulios. Chem. Phys. Lett. **157**, 552 (1989); (*b*) L. Bonnet, F.D. Cukiernik, P. Maldivi, A.M. Giroud-Godquin, J.C. Marchon, M. Ibn-Elhaj, D. Guillon, and A. Skoulios. Chem. Mater. **6**, 31 (1994).
6. Ru_2(II,III): F.D. Cukiernik, P. Maldivi, A.M. Giroud-Godquin, J.C. Marchon, M. Ibn-Elhaj, D. Guillon, and A. Skoulios. Liq. Cryst. **9**, 903 (1991).
7. F.A. Cotton and R.A. Walton. Multiple bonds between metal atoms. 2nd ed. Clarendon Press, Oxford. 1993.
8. K. Nakamoto. Infrared and Raman spectra of inorganic and coordination compounds, 4th ed. John Wiley and Sons, New York. 1986.
9. M. Spohn, J. Strahle, and W. Hiller. Z. Naturforsch. B: Anorg. Chem. Org. Chem. **41B**, 541 (1986).
10. J.L. Wesemann and M.H. Chisholm. Inorg. Chem. **36**, 3258 (1997).
11. C. Destrade, P. Foucher, H. Gasparoux, N.H. Tinh, A.M. Levelut, and J. Malthete. Mol. Cryst. Liq. Cryst. **106**, 121 (1984).

© 1998 NRC Canada

Synthesis and properties of a sterically encumbered poly(thienylene vinylene): poly[*E*-1,2-(4,4′-dihexyl-2,2′-dithienyl)ethylene]

Jimmy Lowe, Carl Bartels, and Steven Holdcroft

Abstract : Electrically conducting poly[*E*-1,2-(4,4′-dihexyl-2,2′-dithienyl)ethylene] was synthesized and structurally characterized by UV–visible, ^{1}H NMR, and FTIR spectroscopy. The head-to-head arrangement of the alkylthiophene dyads directly affects the UV–visible, photoluminescence, and electroluminescence maxima of the polymer. The conductivity of the doped polymer was measured to be ~2 S cm^{-1} and the stability of the oxidized polymer possessing various dopants was compared. UV–visible irradiation of PDHDTE rendered the films insoluble and photolithography was used to produce micron-size images. FTIR was used to monitor the photoproducts during photolysis of PDHDTE. Mechanisms of photooxidation were proposed, based on the photoproducts observed.

Key words: polythiophene derivative, head-to-head dyad, photolithography, photooxidation, electroluminescence.

Résumé : On a synthétisé le poly[*E*-1,2-(4,4′-dihexyl-2,2′-dithiényl)éthylène] qui conduit l'électricité et on a caractérisé sa structure par spectroscopies UV–visible, IR à TF et RMN du ^{1}H. L'arrangement tête-à-tête des diades alkylthiophènes affecte directement les maxima du polymère dans les spectres UV–visible, la photoluminescence et l'électroluminescence. On a mesuré que la conductivité du polymère dopé est approximativement égale à 2 S cm^{-1} et on a comparé la stabilité du polymère oxydé comportant divers dopants. L'irradiation UV–visible du PDHDTE rend les films insolubles et on a fait appel à la photolithographie pour produire des images de la taille du micron. On a utilisé l'IR à TF pour détecter les photoproduits obtenus par photolyse de PDHDTE. On propose des mécanismes de photooxydation qui tiennent compte des photoproduits observés.

Mots clés : dérivé polythiophène, diade tête-à-tête, photolithographie, photooxydation, électroluminescence.

[Traduit par la Rédaction]

Introduction

The growing interest in conjugated polymers for applications in devices such as light-emitting diodes (LEDs), electrical conductors, and electrochromic displays has led to the design of many new materials. Much work has recently been devoted to the synthesis of polymers containing vinylene linkages, e.g., poly(phenylene vinylene) (PPV) and poly(thienylene vinylene) (PTV), because regioregular copolymers can be made with new or enhanced properties (1–3). Unsubstituted PPV and PTV polymers are insoluble, infusible, and therefore difficult to process. To overcome these difficulties they are often prepared via a soluble precursor polymer. More recently, this problem has been overcome by the attachment of flexible side chains on the polymeric backbone, which confers solubility on the polymer.

An alternative route to PTV and its derivatives has been achieved through organometallic chemistry (4–6). These polymers contain repeat thienylenevinylene or (2,2′-dithienyl-5,5′-vinylene) units and are soluble due to the presence of alkyl or alkoxy substituents. For example, Catellani et al. have synthesized regioregular poly[*E*-1,2-(3,3′-dialkyl-2,2′-dithienyl)ethylenes] (Fig. 1) where the repeat unit is thienylene–vinylene–thienylene (TVT) in which 3-alkylated thiophene dyads are linked via a tail-to-tail (TT) configuration (5). These materials display low band gaps, ~1.7 eV, and are transparent in the doped state. Poly(3,4-dibutoxythiophenevinylene) and poly[bis(3,4-dibutoxythienylene)vinylene] have been synthesized using nickel-catalyzed Grignard coupling reactions with *trans*-1,2-dichloroethene (6). The polymers were reported to possess absorption maxima of 607 and 527 nm, respectively, and conductivities in the range of 0.03 –1 S cm^{-1} using ferric chloride as a dopant.

Previous work in our group has shown that the quantum yield of photoluminescence in poly(3-alkylthiophenes) films increases with both the alkyl chain length and the head-to-head (HH) content (7, 8). We were therefore interested to learn what effect the regioregularity had on the properties of alkylated PTVs. This paper reports the synthesis and properties of poly[*E*-1,2-(4,4′-dihexyl-2,2′-dithienyl)ethylene] (PDHDTE) (Fig. 1) in which the thiophene dyads are linked via a HH configuration. The polymer, made by oxidative coupling of the oligomer, is soluble in common organic solvents due to the presence of the side chains. Our research group has an ongoing interest in the photochemistry and photolithography of conjugated materials. We therefore describe preliminary work on the photolithography of this material and discuss

Received December 9, 1997.

J. Lowe, C. Bartels, and S. Holdcroft.[1] Department of Chemistry, Simon Fraser University, Burnaby, BC V5A 1S6, Canada.

[1]Author to whom correspondence may be addressed. Telephone: (604) 291-3345. Fax: (604) 291-3765. E-mail: steveh@bohr.chem.sfu.ca

© 1998 NRC Canada

Fig. 1. Structure of poly[*E*-1,2-(3,3′-dialkyl-2,2′-dithienyl)-ethylene] (top) and poly[*E*-1,2-(4,4′-dialkyl-2,2′-dithienyl)ethylenes] (bottom). R = alkyl.

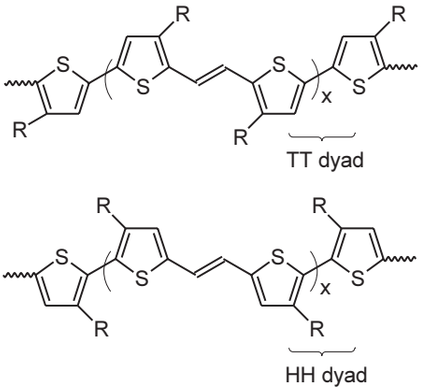

mechanisms of its photooxidation. The conductivity and half-life of PDHDTE possessing various dopants were measured.

Experimental section

Chemicals

A hexane solution of *n*-butyllithium (2.5 M), magnesium bromide diethyl etherate ($MgBr_2 \cdot Et_2O$), *trans*-1,2-dichloroethene (Aldrich), 1,3-bis(diphenylphosphino)propane nickel(II) chloride ($NiCl_2$dppp, Stern Chemicals), and $FeCl_3$ (BDH) were used as received. $CHCl_3$ (BDH) and diethyl ether (Anachemia) were dried over Na and freshly distilled under N_2 before use. 3-Hexylthiophene was synthesized according to the procedure outlined by Kumada and co-workers (9).

Synthesis of *E*-1,2-(4,4′-dihexyl-2,2′-dithienyl)ethylene (DHDTE) (Scheme 1)

This procedure was adopted from Blohm et al. (6). A 250 mL round-bottom flask fitted with a nitrogen inlet and a condenser was charged with 3-hexylthiophene (3.355 g, 19.93 mmol). Freshly distilled ether (90 mL) was added, followed by the addition of 2.5 M *n*-butyllithium in hexanes (7.97 mL, 19.93 mmol) at 0°C. After stirring for 40 min, crushed $MgBr_2 \cdot Et_2O$ was added to the yellow solution and the mixture was stirred for 2 h. *trans*-1,2-Dichloroethene was injected by syringe (0.78 mL, 9.96 mmol) into the suspension at 0°C. Upon addition of the catalyst, $NiCl_2$dppp, the mixture turned orange in colour. The suspension was gently refluxed for 24 h. The reaction mixture was worked up by extraction with diethyl ether and washed with saturated NH_4Cl solution and saturated NaCl solution. The organic layer was dried over anhydrous $MgSO_4$ and concentrated to yield yellow crystals. The crystals were recrystallized from hexanes, collected by suction filtration, and washed with ice-cold heptane. The yield of the recrystallized product was 25%; mp 68–69°C. FTIR (KBr) cm^{-1}: 3075, 3013, 2955, 2921, 2849, 1545, 1466, 1372, 1272, 1200, 1177, 1139, 937, 853, 831, 746, 720, 662. UV–vis ($CHCl_3$), λ_{max}: 350 nm. 1H NMR (400 MHz, $CDCl_3$), δ: 6.95 (2H, -CH=*CH*-), 6.86 (2H, ring, H-5), 6.75 (2H, ring, H-3), 2.54 (4H, t, J = 8 Hz, α-CH_2-ring), 1.51 (4H, dt, J = 8 Hz, β-CH_2-), 1.28 (12H, m, -$(CH_2)_3$-), 0.89 (6H, t, J = 8 Hz, -CH_3). Anal. calcd. for $C_{22}H_{32}S_2$: C 73.33, H 8.89; found: C 73.12, H 9.10.

Synthesis of poly[*E*-1,2-(4,4′-dihexyl-2,2′-dithienyl)ethylene] (PDHDTE)

A round-bottom flask was charged with anhydrous $FeCl_3$ (1.011 g, 6.32 mmol) in $CHCl_3$ (25 mL) and cooled in an ice bath. *E*-1,2-(4,4′-Dihexylthienyl)ethylene (0.5021 g, 1.39 mmol) was dissolved in $CHCl_3$ (10 mL) and added dropwise to the stirred mixture. The addition of the monomer formed a dark purple colour and an hour later a dark blue precipitate was observed. After 4 h, the polymer was precipitated in methanol (75 mL) and stirred overnight. The precipitate was collected and washed with triethylamine followed by acidified methanol. The orange precipitate was extracted via Soxhlet with methanol and pumped dry. Yield: 73%. FTIR (KBr) cm^{-1}: 3075, 3016, 2954, 2925, 2854, 1684, 1652, 1559, 1541, 1457, 1377, 934, 833, 722. UV–vis ($CHCl_3$), λ_{max}: 422 nm. ^{1}H NMR (400 MHz, $CDCl_3$), δ: 6.94 (2H, -*CH*=*CH*-), 6.90 (2H, ring, H-3), 2.51 (4H, br, α-CH_2-ring), 1.54 (4H, br, β-CH_2-), 1.28 (12H, m, -$(CH_2)_3$-), 0.89 (6H, t, J = 8 Hz, -CH_3).

Characterization

^{1}H NMR spectra were recorded on a 400 MHz Bruker AMX400 in $CDCl_3$. Molecular weight distribution curves of polymers were determined by gel permeation chromatography (GPC) using 10^5, 10^4, 10^3 Å μ-Styragel columns at 25°C. Polymers were eluted with tetrahydrofuran (BDH, HPLC grade) and detected using a UV–visible spectrophotometer (Spectra-Physics, model SP8000) and a refractive index detector (Waters, model R400). Data were acquired, stored, and analyzed using an IBM personal computer and custom-written software. Polystyrene (PS) standards (Polymer Labs. Inc.) of molecular weights ranging from 233 000 to 750 Da were used for calibrating GPC columns for hydrodynamic volume versus elution volume. The PS calibration curve was converted to a poly(3-hexylthiophene) (P3HT) based calibration using the following Mark–Houwink constants: for P3HT, $K = 2.28 \times 10^{-3}$ cm^3/g and $a = 0.96$; for PS, $K = 1.29 \times 10^{-2}$ cm^3/g and $a = 0.713$ (10, 11). Infrared spectra were recorded on a Bomem Michelson FTIR (120 series) spectrometer. UV–visible absorption spectra were recorded on a Perkin–Elmer Lambda 3A UV–vis spectrophotometer at 25°C.

For measurements of conductivity, chloroform solutions of polymer were spin-cast on to glass slides. The polymers were oxidized to their electronically conductive form by submersion of the polymer/substrate into an anhydrous 0.1 M solution of gold trichloride in acetonitrile, ferric chloride in nitromethane, or exposed to I_2 vapour. Electronic conductivities were measured using the four-point probe technique.

Photolysis and photolithography

Polymer films were spin-cast from chloroform solution on glass slides. The optical density of the films at λ_{max} was 0.5–0.8. The illumination source was a 200 W high-pressure mercury lamp (Illumination Industries Ltd.). The wavelength of incident light was >300 nm due to the presence of a 300 nm cutoff filter and the light was focused to a diameter of 3 cm. Thin films of PDHDTE were solvent evaporated

© 1998 NRC Canada

Scheme 1. Synthesis of poly[*E*-1,2-(4,4′-dihexyl-2,2′-dithienyl)ethylene]. *Conditions:* i. 0°C, *n*-BuLi; ii. $MgBr_2 \cdot Et_2O$; iii. *trans* ClCH=HCCl, $NiCl_2$(dppp); iv. 4 equiv. $FeCl_3$, $CHCl_3$.

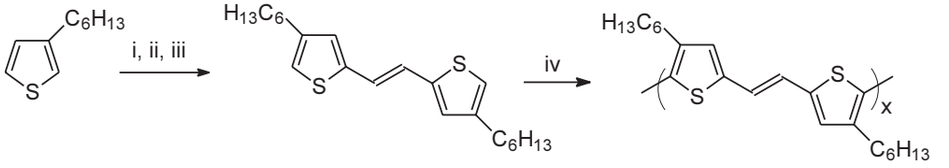

onto KBr disks and the FTIR recorded before and during irradiation for various time intervals. To obtain photoimages, polymers were spin-cast onto glass or silicon. The films were irradiated for 3 min through a photomask and an image was obtained upon dissolution of the unexposed polymer in chloroform. All experiments were performed using front-face irradiation of films in ambient air at 25°C.

Electroluminescence of PDHDTE

Steady state luminescence and electroluminescence were measured on an LS-100 spectrofluorometer (Photon Technology International Inc.). For construction of the light-emitting diode (LED), indium tin oxide coated glass slides (ITO) were used as the hole injecting contact. A solution of PDHDTE was used to spin-coat a film of thickness 125 nm. Aluminum (99.999%, Aldrich) was deposited on top of the polymer by vapour deposition to act as the electron-injecting contact.

Results and discussion

The oligomer synthesized possesses a thienylene–vinylene–thienylene (TVT) sequence with the hexyl chains in the 4-position of the thiophene rings. Addition of *n*-butyllithium at 0°C to 3-hexylthiophene favourably lithiates the 5-position due to the presence of the large alkyl group in the 3-position (12). Grignard formation occurs upon addition of $MgBr_2 \cdot Et_2O$. Two equivalents of the Grignard reagent are coupled to *trans*-1,2-dichloroethene using $NiCl_2$(dppp) catalyst. Polymers prepared from *E*-1,2-(3,3′-disubsituted-2,2′-dithienyl) ethylenes have previously been synthesized by chemical polymerization with $FeCl_3$ with retention of the vinyl double bond (4–6). Poly[*E*-1,2-(4,4′-dihexyl-2,2′-dithienyl)ethylene] (PDHDTE) prepared in this work is expected to have the thienyl groups coupled in a head-to-head (HH) dyad and this is confirmed spectroscopically (see below).

Spectroscopic analysis

The polymer is soluble in organic solvents such as chloroform and tetrahydrofuran due to the presence of the pendent hexyl side chains. The number average molecular weight of the polymer was 2500 and the molecular weight distribution was 2.3. M_n is similar to values determined by Toyoshima et al. for poly[*E*-1,2-(dihexyl-2,2′-dithienyl)ethylene] prepared under similar reaction conditions (13).

The infrared spectrum of PDHDTE shows absorptions that are characteristic of alkyl-substituted polydithienylethylenes. The peak assignments were based on FTIR data of similar TVT oligomers and polymers (5, 14). The *trans* geometry of the vinylic double bond is detected by the out-of-plane bending of the C—H bond at 934 cm^{-1} and its C–H stretch at 3016 cm^{-1}. The band at 1457 cm^{-1} is due to the stretching mode of the thiophene ring, which overlaps with the CH_2 and CH_3 deformations. Also, the peak at 833 cm^{-1} is due to the thiophene ring C–H out-of-plane bend.

^{1}H NMR provided more structural information on the oligomer and polymer. The α-protons of thiophene in DHDTE are observed at 6.86 ppm but are not present in the spectrum of the polymer, indicating a predominantly α–α′ coupling of the oligomer. Two signals in the aromatic region of the polymer correspond to the thienyl ring and vinylene protons. Integration of the aromatic signals is equivalent to the integrated signal obtained for the α-methylene of PDHDTE. A peak is observed at 2.51 ppm for the α-methylene. This is taken as evidence for HH linkages in chemically polymerized PDHDTE and is consistent with the spectrum of poly(3,3′-dihexyl-2,2′-bithiophene) where only one α-methylene signal was observed at 2.51 ppm (15). Poly[*E*-1,2-(3,3′-dialkyl-2,2′-dithienyl)ethylene] also gives one α-methylene signal, at 2.66 ppm, showing that this isomer has a different chemical shift than PDHDTE (5). Collectively, the ^{1}H NMR spectra indicate that an HH configuration of hexylthiophene dyads is obtained in the repeating unit (TVT sequence) of the polymer.

UV–visible spectra of solutions and films of PDHDTE exhibit broad maxima due to the π–π* absorption transition. The solutions are yellow and exhibit a λ_{max} of 422 nm. λ_{max} for films is 426 nm, which indicates that a significant degree of twist exists between thiophene–thiophene linkages in the solid state; that is, there is very little difference in coplanarity of the polymer chains for polymers in solution and in the solid state. This twisting is attributed to the HH dyad linkage associated with the hexylthiophene units. PDHDTE is blue-shifted in the solid state by 153 nm compared to the analogous polymer, poly[*E*-1,2-(3,3′-dioctyl-2,2′-dithienyl)-ethylene] (PDODTE, λ_{max} = 577 nm), which is reported to contain tail-to-tail (TT) octylthiophene dyad couplings (5). Furthermore, PDODTE displays a relatively large red shift of 32 nm between $CHCl_3$ solutions and films. It is interesting to note that poly(3,3′-dihexyl-2,2′-bithiophene) exhibits an absorption maximum that is blue-shifted by 112 nm compared to poly(3-hexylthiophene) containing 100% HT links (i.e., 398 vs. 510 nm for films) (15, 16). The presence of the vinylene group along the polymer backbone provides a 24 nm red shift in λ_{max} when compared with poly(3,3′-dihexyl-2,2′-bithiophene) solutions, presumably because it facilitates π-conjugation. Table 1 shows a comparison of photoluminescence maxima for derivatives of polythiophene and poly(dithienyl ethylene) found in the literature.

Conductivity

To obtain comparative results for the conductivity and relative stabilities of the polymer, we used thin spin-coated films that possessed an average thickness of 75 nm. The

© 1998 NRC Canada

Table 1. Comparison of visible absorption data for derivatives of polythiophene and poly(thienylene vinylene).

Polymer	λ_{max}, soln, (nm)	λ_{max}, film, (nm)	PL, film, (nm)	Ref.
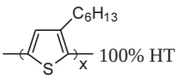 100% HT	442[a]	510[a]	717[b]	(*a*) 16; (*b*) 17
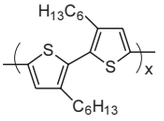	398[a]	398[a]	533[b]	(*a*) 15; (*b*) 18
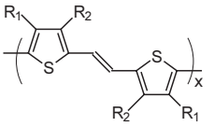				
$R_1 = R_2 = H$	Insoluble	496		19
$R_1 = H$; $R_2 = C_8H_{17}$	545	577		5
$R_1 = C_6H_{13}$; $R_2 = H$	422	426	576	This work

conductivity of doped PDHDTE was measured by the four-point probe technique. The doped films were exposed to ambient light at 25°C. Films doped with $AuCl_3$ and $FeCl_3$ were bluish-gray in colour while films doped with I_2 vapour were golden brown. Doping the polymer with $AuCl_3$ decreases the absorption intensity at 426 nm and new maxima form at 910 nm and 1560 nm, indicating the formation of polaronic and bipolaronic charge carriers. Similar spectra were obtained for films doped with $FeCl_3$ and I_2. The measured conductivities (0.1–2 S cm^{-1}) are of the same magnitude as literature values for alkyl-substituted (5, 13) and alkoxy-substituted (3, 6) poly[*E*-1,2-(2,2′-dithienyl)ethylene]'s. This indicates that the HH thiophene dyad does not adversely affect the conductivity when compared to polymers possessing TVT sequences coupled via the TT configuration.

The stability of doped films in ambient atmosphere was monitored in the presence and absence of light. A plot of log (σ/σ_o) versus time confirms that PDHDTE is very sensitive to the combined effects of light and air. Exposed films that were doped with $AuCl_3$ ($t_{1/2}$ = 35 h) provide a greater stability than $FeCl_3$ ($t_{1/2}$ = 4 h) and I_2 doped films ($t_{1/2}$ = 0.2 h). For films stored in the dark, the respective half-lifetimes for $AuCl_3$ and $FeCl_3$ were 75 and 28 h. For comparison, $t_{1/2}$ values determined for $FeCl_3$-doped and $AuCl_3$-doped poly(3-hexylthiophene) were 8 h and several months, respectively (20). It is important to stress that thin films of conjugated polymers dedope much more rapidly than thicker films. Therefore, thicker films were substantially more stable in the oxidized state.

Photochemistry and photolithography

PTV and its derivatives are being investigated as potential materials for electrooptical and optoelectronic devices. It is therefore useful to examine the stability of these films upon exposure to light. With a better understanding of the photodegradation of these materials, their stability and performance can perhaps be improved. The photoproducts of PDHDTE films exposed to UV–visible irradiation in ambient atmosphere were examined by FTIR. Figure 2 shows the FTIR of the polymer film before and after photolysis with polychromatic light (>300 nm) for various times. The spectra show the growth of peaks in the regions of 3400–3080, 1717–1650, and 1300–1090 cm^{-1}. Previous work has shown that residual Fe salts from the chemical polymerization reaction generate free radicals upon exposure to light (21, 22). Consequently, these radicals abstract H-atoms from the α-methylene of the alkyl thiophene, which in the presence of O_2 leads to the formation of -OOH and -OH (3600–3080 cm^{-1}) (23, 24). The polymer-bound radicals have also been postulated to undergo various other reactions: by reacting with another α-methylene of a neighbouring polymer chain, C-O-C linkages (1230 cm^{-1}) are formed leading to crosslinking and insolubilization of the polymer; the radical can undergo β-scission to yield an aldehyde (1717 cm^{-1}) or abstract a H atom to yield a secondary hydroxyl group (3400 cm^{-1}). Thiophene oligomers and polymers have also been shown to be $^1O_2$ photosensitizers (25–29). Photogenerated $^1O_2$ is known to react via a 1,4-Diels–Alder addition to thiophene, producing carbonyl groups (1710 cm^{-1}) and sulfines (1230 cm^{-1}). These reactions destroy the conjugation along the polymer and thus films are photobleached during irradiation. The growth of FTIR peaks is consistent with the photochemistry of both poly(3-hexylthiophene) in solution and in the solid state (21, 22). This suggests that the degradation and crosslinking mechanism of PDHDTE has similarities to that found for poly(3-alkylthiophenes).

During irradiation the FTIR also shows a simultaneous decrease in the peaks at 3016 and 934 cm^{-1}, and an increase in the peaks at ~2927 cm^{-1}. These regions are assigned to the vinyl C–H stretch, the out-of-plane bending of the *trans* vinyl group, and the aliphatic C–H stretching, respectively. Apparently singlet oxygen not only targets thiophenes but

© 1998 NRC Canada

Fig. 2. FTIR of PDHDTE (——) and after photolysis for 30 min (- - -). Arrows show the growth and decrease of various peaks. Film thickness ~100 nm.

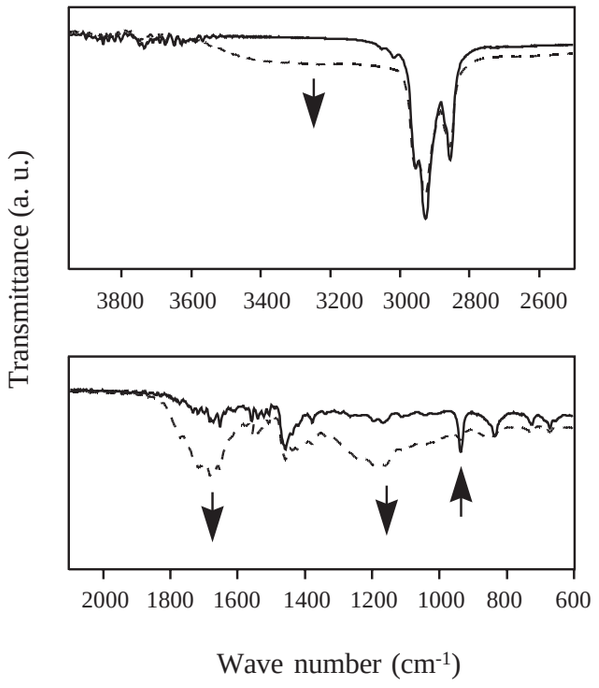

the vinylene backbone is also susceptible to attack. This confirms a previous report in which $^1O_2$ is shown to be the reactive intermediate in the photodegradation of poly(2,5-(bis(cholestanoxy)-1,4-phenylene vinylene) (BCHA-PPV) (30). BCHA-PPV irradiated in dry air results in the formation of ester and aldehyde species (30, 31). IR reflection absorption spectra of BCHA-PPV films show a decrease of the *trans* vinyl C–H wagging at 975 cm^{-1} and the concurrent growth of a C=O peak at 1723 cm^{-1} (31). A mechanism was proposed that claimed the initial point of photooxidation was the 1,2-cycloaddition of singlet oxygen to a vinylene unit, resulting in the formation of a biradical (30, 31). This would account for the decrease of the *trans* vinyl peak of PDHDTE following irradiation as observed in the present study.

In the construction of conjugated polymer devices it is desirable to find techniques to deposit the material with well-defined structure and architecture. Several studies have been reported in which photolithography is employed to achieve patterned images of alkyl- (22, 32), methacryloyl- (33), and water-soluble (34) polythiophenes. Irradiation of PDHDTE renders the films insoluble in organic solvents, showing that such polymers can be photochemically imaged. Using conventional photolithography, we were able to obtain patterned images of the polymer. The spin-cast film (125 nm thick) was irradiated for 3 min through a mask and developed in $CHCl_3$ to produce images with resolution of 15 μm for the smallest image (Fig. 3). The images appeared yellow under the microscope, indicating that π-conjugation is not visibly destroyed by the cross-linking processes under the low irradiation doses employed for imaging.

Photoluminescence and electroluminescence of PDHDTE

An ITO anode/PDHDTE (195 nm)/Al electroluminescence device was constructed. Figure 4 shows the normalized photoluminescence (PL) and electroluminescence (EL) spectra of the device. The respective λ_{max} were 576 nm (2.15 eV), using a excitation wavelength of 426 nm and ~610 nm (2.03 eV) for the LED. The colour output of the LED was observed to be green-blue. The photoluminescence and electroluminescence spectra are similar although the EL is slightly red-shifted. Inganas and co-workers observed green electroluminescence from poly(3-cyclohexylthiophene) based LEDs (35). The absorbance and PL spectra are similar in wavelength to those of the polymer investigated in this study. In the case of poly(3-cyclohexylthiophene), steric hindrance resulting from the cyclohexyl side chain forces the main chain out of coplanarity. This results in the blue shift of the absorption and emission spectra compared to polythiophene polymers in which steric hindrance is absent. This effect of sterically encumbering poly(thienylene vinylene) polymers is therefore also demonstrated in PDHDTE by the incorporation of HH dyads.

Conclusions

Poly[*E*-1,2-(4,4′-dihexyl-2,2′-dithienyl)ethylene] (PDHDTE) has been prepared in which the hexylthiophene dyads are configured in a head-to-head (HH) arrangement. Interestingly, the conductivity of this polymer is of the same magnitude as that of poly[*E*-1,2-(3,3′-dialkyl-2,2′-dithienyl)ethylene], which consists of tail-to-tail (TT) thiophene dyads. The differences between these two polymer isomers are clearly indicated by their ^1H NMR and UV–visible spectra. The steric interaction of the HH thiophene dyads results in similar absorption spectra for the polymer in solution and in the solid state, whereas the TT isomer, poly[*E*-1,2-(3,3′-dialkyl-2,2′-dithienyl)ethylene] (5), displays a 32 nm difference in λ_{max} between polymer solutions and polymer films. Upon irradiation, PDHDTE films become insoluble due to photo-cross-linking. FTIR identifies the formation of OH, C-O-C, and OOH functional groups due to the reaction of oxygen with the polymer. The mechanisms of photooxidation and photo-cross-linking are similar to those observed for poly(3-alkylthiophenes) with the addition that the vinylic functionality also participates in photodegradation. Photo-cross-linking enables these materials to be imaged photolithographically. Images of micron (μm) resolution were achieved for which π-conjugation of the polymer was retained. A LED device based on this polymer gives emission of blue-green light. This is of higher energy than regioregular poly(3-alkylthiophenes) incorporating linear side chains, due to the twisted nature of the PDHDTE polymer chains, and results from the incorporation of sterically encumbered HH thiophene dyads.

Acknowledgments

This research was supported by the Natural Sciences and Engineering Research Council of Canada. We thank Mr. M. Bilany and Mr. S. Wilson for the use of the vapour deposition apparatus.

© 1998 NRC Canada

Fig. 3. Patterned image of PDHDTE film. Photograph shows a segment of the interdigitized pattern. Film thickness: 125 nm.

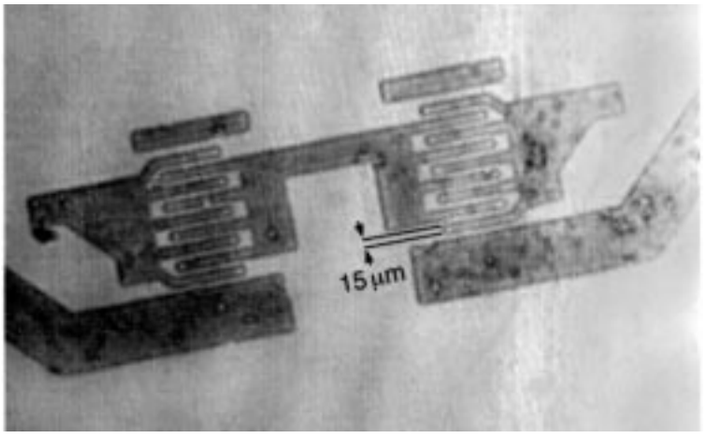

Fig. 4. Photoluminescence and electroluminescence spectra of PDHDTE.

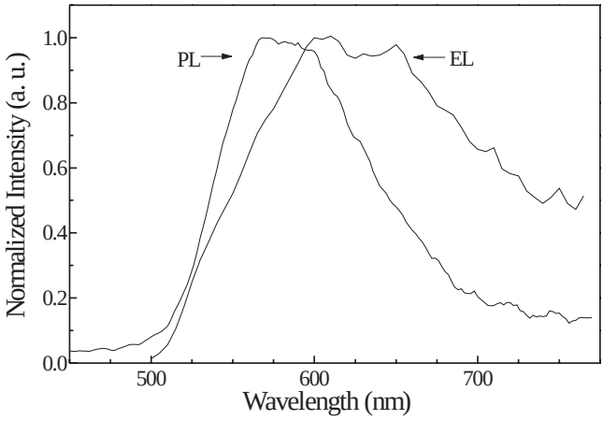

References

1. A.J. Brasset, N.F. Colaneri, D.D.C. Bradley, R.A. Lawrence, R.H. Friend, H. Murata, S. Tokito, T. Tsutsui, and S. Saito. Phys. Rev. B: Condens. Matter, **41**, 10586 (1990).
2. D.D.C. Bradley. J. Phys. D: Appl. Phys. **20**, 1389 (1987).
3. K.-Y. Jen, M. Maxfield, L.W. Shackelette, and R. Elsembaumer. J. Chem. Soc. Chem. Commun. 309 (1987).
4. K.-Y. Jen, H. Eckhardt, T.R. Jow, W. Shackelette, and R. Elsembaumer. J. Chem. Soc. Chem. Commun. 215 (1988).
5. M. Catellani, S. Luzzati, A. Musco, and F. Speroni. Synth. Met. **62**, 223 (1994).
6. M.L. Blohm, J.E. Pickett, and P.C. Van Dort. Macromolecules, **26**, 2704 (1993).
7. B. Xu and S. Holdcroft. Macromolecules, **26**, 4457 (1993).
8. B. Xu, J. Lowe, and S. Holdcroft. Thin Solid Films, **243**, 638 (1994).
9. K. Tamao, S. Kodama, J. Nakajima, and M. Kumada. Tetrahedron, **38**, 3347 (1982).
10. S. Holdcroft. J. Polym. Sci. Part B: Polym. Phys. **29**, 1585 (1991).
11. L.H. Tung and J.C. Moore. *In* Fractionation of synthetic polymers. *Edited by* L.H. Tung. Marcel Dekker Inc., New York. 1977.
12. S. Gronowitz, B. Cederlund, and A. Hornfeldt. Chem. Scr. **5**, 217 (1974).
13. R. Toyoshima, K. Akagi, and H. Shirakawa. Synth. Met. **84**, 431 (1997).
14. J.Y. Mevellec, J.P. Buisson, S. Lefrant, H. Eckhard, and K.-Y. Jen. Synth. Met. **35**, 209 (1990).
15. R.M. Souto Maior, K. Hinkelmann, H. Eckert, and F. Wudl. Macromolecules, **23**, 1268 (1990).
16. R.D. McCullough, R.D. Lowe, M. Jayaraman, and D.L. Anderson. J. Org. Chem. **58**, 904 (1993).
17. F. Chen, P.G. Mehta, L. Takiff, and R.D. McCullough. J. Mater. Chem. **6**, 1763 (1996).
18. R.E. Gill, G.G. Malliaras, J. Wildeman, and G. Hadziioannou. Adv. Mater. **6**, 132 (1994).
19. M. Martinez, J.R. Reynolds, S. Basak, D.A. Black, D.S. Marynick, and M.J. Pomerantz. Polym. Sci. Part B: Polym. Phys. **26**, 911 (1988)
20. M.S.A. Abdou and S. Holdcroft. Chem. Mater. **6**, 962 (1994).
21. M.S.A. Abdou and S. Holdcroft. Macromolecules, **26**, 2954 (1993).
22. M.S.A. Abdou and S. Holdcroft. Can. J. Chem. **73**, 1893 (1995).
23. B. Ranby and J.F. Rabek (*Editors*). Singlet oxygen, reactions with organic compounds and polymers. John Wiley & Sons, U.K. 1978.
24. L.S. Silbert. *In* Organic peroxides. *Vol. 2. Edited by* D. Swern. Interscience, New York. 1971. pp. 683–697.
25. C. Evans and J.C. Scaiano. J. Am. Chem. Soc. **112**, 269 (1990).
26. D. McLachlan, T. Arnason, and J. Lam. Photochem. Photobiol. **39**, 177 (1984).
27. C. Evans, D. Weir, J.C. Scaiano, A. MacEachern, J.T. Arnason, P. Moran, B. Hollebone, L.C. Leitch, and B.J.R. Philogene. Photochem. Photobiol. **44**, 441 (1986).
28. J.P. Reyftmann, J. Kagan, R. Santos, and P. Moliere. Photochem. Photobiol. **41**, 1 (1985).
29. C. Kutsche, J. Targove, and P. Haaland. J. Appl. Phys. **73**, 2602 (1993).
30. R.D. Surlock, B. Wang, P.R. Ogilby, J.R. Sheats, and R.L. Clough. J. Am. Chem. Soc. **117**, 10194 (1995).
31. B.H. Cumpston and K.F. Jensen. Synth. Met. **73**, 195 (1995).
32. M.S.A. Abdou, G.A. Diaz-Guiada, M.I. Arroyo, and S. Holdcroft. Chem. Mater. **3**, 1003 (1991).
33. J. Lowe and S. Holdcroft. Macromolecules, **28**, 4608 (1995).
34. M.I. Arroyo-Villan, G.A. Diaz-Quijada, M.S.A. Abdou, and S. Holdcroft. Macromolecules, **28**, 975 (1995).
35. M. Berggren, G. Gustafsson, O. Inganas, M.R. Anderson, O. Wennerstrom, and T. Hjertberg. Adv. Mater. **6**, 488 (1994).

© 1998 NRC Canada

Surface functionalization of cadmium sulfide quantum-confined nanoclusters. 4. Formation and reactivity of an aniline surface quantum dot[1]

Jonathan G.C. Veinot, Josie Galloro, Linda Pugliese, Valerie Bell, Robert Pestrin, and William J. Pietro

Abstract: The preparation, characterization, properties, and reactivity of a novel quantum-confined CdS nanocluster containing a chemically active aniline surface are described, along with three general methods for the covalent attachment of a wide scope of molecular moieties to the cluster surface. The formation of facile covalent linkages via DCC mediated amidization, secondary amine formation, and thiourea condensation is discussed and, as the introduction of surface functionality is crucial for the eventual realization of molecular electronic devices fabricated from such nanoclusters, several derivatized nanoclusters bearing interesting chromophoric, fluorescent, electroactive, and chiroptical tethered species are described. All three derivatization techniques occur under very mild conditions that have been demonstrated not to disturb the integrity of the nanocluster core.

Key words: quantum dot, nanocluster, semiconductor, surface-functionalized, nanostructured.

Résumé : On décrit la préparation, la caractérisation, les propriétés et la réactivité d'un nouveau nanoagrégat de CdS, confiné d'un point de vue quantique et contenant une surface d'aniline chimiquement active; on décrit aussi trois méthodes générales pour attacher d'une façon covalente un grand nombre de parties de molécules à la surface de l'agrégat. On discute de la formation facile de liaisons covalentes par le biais d'une amidisation facilitée par le DCC, la formation d'amine secondaire et la condensation de la thiourée et, comme l'introduction d'une fonctionnalité à la surface est cruciale à la réalisation de dispositifs électroniques moléculaires à partir de tels nanoagrégats, on décrit plusieurs dérivés de nanoagrégats portant des espèces chromophores, fluorescentes, électroactives et chiroptiques. Les trois techniques de transformations en dérivés peuvent être réalisées dans des conditions très douces et il a été démontré qu'elles ne provoquent pas de modifications à l'intégrité du noyau du nanoagrégat.

Mots clés : point quantique, nanoagrégat, semiconducteur, surface fonctionnalisée, nanostructuré.

[Traduit par la Rédaction]

Introduction

Much recent intensive research has focused on the formation of particles of metallic or semiconducting materials having nanometer dimensionality (for recent reviews, see ref. 1). These interesting systems, commonly referred to as quantum-confined nanoclusters or quantum dots, exhibit electronic and optical properties significantly different from their bulk counterparts. Such differences arise from the confinement of conduction electrons within regions smaller than the Bohr radius of the material's exciton (2). The so-called quantum confinement effect may give rise to the fabrication of electronic devices possessing properties heretofore unheard of in conventional semiconductor electronics, such as dynamically tunable light-emitting diodes, unusual nonlinear optical materials, and coulomb blockade devices such as single-electron diodes and transistors.[3] The realization of such devices may well occur via covalent or coordinative coupling to the surface of chemically activated nanoclusters. Thus, the creation of a few surface-functionalized semiconductor nanocrystallites has recently been reported, along with the use of the surface functionalities to assemble macromolecular aggregates of discrete semiconductor nanoclusters (4). We have previously reported the synthesis and physical and chemical properties of a variety of cadmium sulfide quantum-confined nanoclusters bearing chemically active

Received January 27, 1998.

J.G.C. Veinot, J. Galloro, L. Pugliese, V. Bell, R. Pestrin, and W.J. Pietro.[2] Department of Chemistry, York University, 4700 Keele Street, Toronto, ON M3J 1P3, Canada.

[1]For part 3 in this series see ref. 5*c*.

[2]Author to whom correspondence may be addressed. Telephone: (416) 736-5246. Fax: (416) 736-5936. E-mail: pietro@yorku.ca

[3]Single-electron phenomena have recently been experimentally demonstrated in quantum dots and in quantum sheet – nanowire junctions, see ref. 3. Also, M. Moskovits, personal communication, 1997.

© 1998 NRC Canada

surfaces. We have also demonstrated that these surface-activated nanoclusters can participate in a number of subsequent reactions capable of coupling a wide range of interesting optical, chromophoric, luminescent, and electroactive species to the surface without disrupting the integrity of the nanocluster core (5). We now report the formation of a cadmium sulfide quantum dot having a chemically active aniline surface, and describe three methods for covalently coupling a wide scope of molecular moieties to the nanocluster surface.

Experimental section

Chemicals

Reagent grade acetonitrile and dimethylformamide (DMF) were dried over 4 Å molecular sieves and filtered prior to use. Methanol and acetic acid were obtained reagent grade from Caledon Laboratories and used without further purification. Water was first deionized by passage through a Sybron–Barnstead D8902 mixed-bed ion-exchange column and then freed from organic impurities using a Sybron–Barnstead D8204 activated charcoal filter. All deuterated solvents used for ^{1}H NMR spectroscopy were purchased in sealed ampules from Cambridge Isotope Laboratories (Andover, Mass.) and used immediately upon opening the ampule. Cadmium acetate (Aldrich reagent grade) was recrystallized once from glacial acetic acid and dried at 100°C in vacuo. Sodium sulfide nonahydrate, dicyclohexylcarbodiimide (DCC), benzyl chloroformate, and ferrocene carboxylic acid were purchased reagent grade from Aldrich and used without further purification. Fluorescein (Aldrich) was obtained as the sodium salt and converted to the acid form with 1 M HCl. Erythrosin B isothiocyanate (Aldrich, 99%) was recrystallized from acetone prior to use. 4-Mercaptoaniline (Aldrich reagent grade) was purified by sublimation at 60°C and 100 mTorr (1 Torr = 133.3 Pa), and stored under dry N_2 at temperatures below 18°C. *l*-Histidine was purchased from BDH and purified by successive free-base – acid precipitation cycles, then recrystallized as the hydrochloride from absolute ethanol. 8-Hydroxyquinoline (Aldrich) was recrystallized from methanol. Chlorotriphenylmethane was purchased 98% from Aldrich and purified by precipitation from benzene (containing 0.1% v/v acetyl chloride) upon addition of petroleum ether.

Preparation of aniline surface CdS quantum dots ($QDNH_2$, 1)

The preparation of the aniline surface CdS nanoclusters ($QDNH_2$) followed a modification of a known kinetic trapping technique (5, 6). All procedures were carried out under subdued light and under N_2, and all solutions were thoroughly N_2 deoxygenated. A solution containing 2.53 g (11 mmol) of $Na_2S{\cdot}9H_2O$ and 4.96 g (40 mmol) of 4-mercaptoaniline in 125 mL of a 1:1:2 (v/v/v) CH_3OH–CH_3CN–H_2O solvent mixture was added with rapid stirring to a solution of 5.00 g (22 mmol) of cadmium acetate in the same solvent mixture, producing an immediate bright yellow precipitate. The reaction mixture was stirred at room temperature for 1 h, then concentrated at room temperature under reduced pressure to two thirds of its volume using a rotary evaporator. The precipitate was isolated by centrifugation, washed with water, and resuspended by sonication in DMF. Bulk solid particulate was removed from the DMF suspension by centrifugation at 4400 × *g* in a Baxter Biofuge 17R refrigerated centrifuge, and the quantum dots were subsequently precipitated by doubling the volume of the DMF suspension with water. The quantum dots were further purified by repeated sequential sonication–centrifugation cycles in water, methanol, acetone, and diethyl ether until no aromatic signal could be detected in the ^{1}H NMR of the concentrated washings. The yellowish white solid was then dried for 18 h at 85°C in high vacuum (~10^{-4} Torr), pulverized, then dried for an additional 18 h at 85°C in high vacuum in a drying pistol (charged with solid KOH), and stored in a vacuum desiccator in darkness for no longer than 3 days before use. Yield: 2.49 g.

5-Chloromethyl-8-hydroxyquinoline

8-Hydroxyquinoline was 5-chloromethylated via a modification of a literature procedure (7). A solution containing 50.6 g (0.35 mol) of 8-hydroxyquinoline, 125 mL of 37% aqueous formaldehyde, and 125 mL of concentrated hydrochloric acid was bubbled with anhydrous HCl for 6 h and allowed to stand overnight. The bright yellow precipitate was washed repeatedly with diethyl ether and dried in vacuo at 65ºC over KOH in a drying pistol. Yield: 42.0 g (62%), mp 280–283ºC. ^{1}H NMR (400 MHz, DMSO-d_6) δ (ppm): 5.32 (s, 2H, -CH_2Cl), 7.52 (d, 1H, $|J_{H-H}|$ = 8 Hz, C7-H), 7.86 (d, 1H, $|J_{H-H}|$ = 8 Hz, C6-H), 8.08 (m, 1H, C3-H), 9.11 (d, 1H, $|J_{H-H}|$ = 5 Hz, C4-H), 9.21 (d, 1H, $|J_{H-H}|$ = 8 Hz, C2-H).

N-*Carbobenzoxy*-l-*histidine hydrochloride*

l-Histidine was N-protected using a modification of the method of Patchornik et al. (8). Benzyl chloroformate (17 mL, 0.12 mol) was added in 1 mL portions to a cooled, stirring solution of 10.5 g of *l*-histidine hydrochloride (55 mmol) in 50 mL of 2 M NaOH. After each addition the mixture was allowed to stir for 5 min, after which time the solution was readjusted to pH 9 with 2 M NaOH. Following the last addition the reaction mixture was allowed to stir for 20 min and the pH was adjusted to 2.4 using 6 M HCl. The resulting precipitate was recrystallized from methanol and dried in vacuo for 3 h. Yield: 11.4 g (45%), mp 127–130°C (lit. (8) mp ~107°C); $[\alpha]_D^{20}$ +15.3º (DSMO); ^{1}H NMR (D_2O) δ (ppm): 2.89 (m, 1H, α-CH), 3.23 (m, 2H, Im-CH_2-), 3.93 (br, 1H, ImN-H), 4.20 (br, 1H, amide NH), 4.92 (m, 2H, ϕ-CH_2-OC(O)-), 7.07 (s, 1H, ImC4-H), 7.22 (m, 5H, arom), 8.31 (d, 1H, ImC2-H).

Amidization of $QDNH_2$ via DCC mediated coupling of carboxylic acids (method 1)

All amidization reactions of **1** followed the same procedure; the formation of the acetamide (QDNHAc, **2a**) will be described as a representative example. All procedures were carried out under dry N_2 in subdued light. **1** (1.63 g) was suspended in 15 mL of dry, deoxygenated DMF, sonicated, and centrifuged to yield a clear, non-opalescent suspension. A solution of 0.64 mL (11.3 mmol) of glacial acetic acid and 2.3 g of DCC (11.1 mmol) in 20 mL of dry deoxygenated DMF was stirred at room temperature for 20 min, then added to the $QDNH_2$ suspension. This reaction mixture was stirred for 24 h. The white precipitate of dicyclohexylurea

© 1998 NRC Canada

Fig. 1. 400 MHz ^{1}H NMR spectrum of the underivatized $QDNH_2$ CdS nanocluster, **1**, in DMF-d_7. * indicates DMF residual signals and ‡ indicates water.

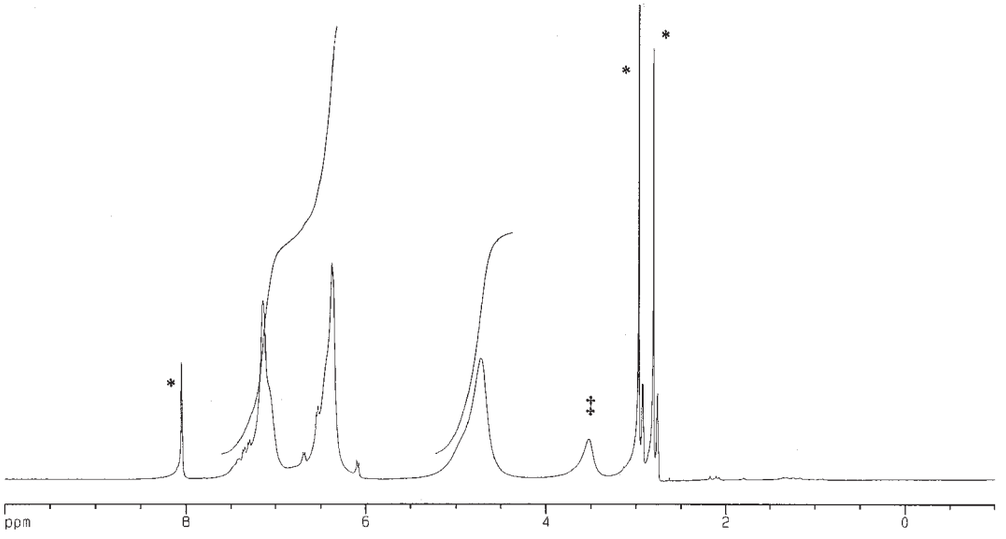

was removed by filtration and 35 mL of water was added to the filtrate. The resulting yellowish white precipitate was washed by repeated sonication–centrifugation cycles using water, acetonitrile, acetone, and finally diethyl ether. The solid was dried for 12 h at 85°C under high vacuum (~10^{-4} Torr). Yield: 1.27 g.

Coupling via secondary amine formation (method 2)

All procedures were carried out under dry N_2 in subdued light. **1** (0.5 g) was suspended in 25 mL of dry DMF, sonicated, and centrifuged to produce a clear, non-opalescent suspension. 5-Chloromethyl-8-hydroxyquinoline (0.67 g) was added to the suspension and stirred at room temperature to dissolve. Triethylamine (0.5 mL) was then added and the reaction mixture was stirred for 1 h. The reaction was quenched with water and the resulting yellow precipitate was collected and washed by repeated sonication–centrifugation cycles with, sequentially, water, ethanol, and acetone until no aromatic signal could be detected in the ^{1}H NMR of the concentrated washings, then dried overnight at 85°C in high vacuum. Yield: 0.32 g.

Coupling via thiourea formation (method 3)

The general procedure for modification of the $QDNH_2$ surface via thiourea formation is a modification of the method of Castro et al. (9); the phenylurea derivatization will be described as a representative example. All procedures were carried out under dry N_2 in subdued light. **1** (0.3 g) was suspended in 100 mL of dry, deoxygenated DMF, sonicated, and centrifuged to yield a clear, non-opalescent suspension. Phenyl isothiocyanate (34 mL) was added with rapid stirring, and the reaction mixture was stirred for 12 h at room temperature. The reaction mixture was added to 200 mL of water and the yellow precipitate was separated by centrifugation. The solid was washed by repeated sonication–centrifugation cycles using water, acetonitrile, acetone, and diethyl ether until no aromatic signal could be detected in the ^{1}H NMR of the concentrated washings, then dried in high vacuum (~10^{-4} Torr) at 85°C for 24 h. Yield: 0.22 g.

Spectroscopy

Infrared spectra were recorded as KBr (Aldrich FT-IR grade KBr) pellets with a Mattson 3000 Fourier transform infrared spectrometer. ^{1}H NMR spectra were obtained on a Brucker ARX 400 MHz Fourier transform nuclear magnetic resonance spectrometer using DMSO-d_6 or DMF-d_7 as solvent. Electronic spectroscopy on $QDNH_2$ and all of its amides was performed in DMF in 1 cm quartz cuvettes using a Hewlett–Packard 8452 diode array spectrophotometer. Optical rotation measurements were carried out on a Perkin–Elmer 241 polarimeter in a 10.002 cm quartz cell using 1 s integration time. Fluorescence measurements were made in 1 cm quartz cuvettes using a Shimadzu RF-551 spectrofluorometric detector driven by PC-551 software.

Electron microscopy

Transmission electron microscopy (TEM) was performed using a Philips EM-301 transmission electron microscope. Nanocluster samples for TEM analysis were prepared by applying a few drops of a freshly sonicated and centrifuged DMF suspension of the nanocluster (2.5 mg of nanocluster to 3 mL of solvent) onto J. B. EM Services (Pointe Claire, Dorval, Que.) JBS-183 300 mesh carbon-coated copper grids (cleaned in acetone, then chloroform, then acetone, and air-dried). The solvent was absorbed through the grid by a layer of filter paper, leaving aggregates as well as individual nanoclusters adhering to the grid wires. The grids were then air-dried at room temperature. Size calibration was performed using a precision silicon grid of 21 600 lines per cm.

Results and discussion

Cadmium sulfide nanoclusters prepared via the kinetic trapping method afford a convenient starting point for the eventual fabrication of nanocluster-based molecular electronic

© 1998 NRC Canada

Fig. 2. Infrared absorption spectrum of the $QDNH_2$ CdS nanocluster, **1**, in KBr (*a*) before and (*b*) after amidization with DCC activated acetic acid.

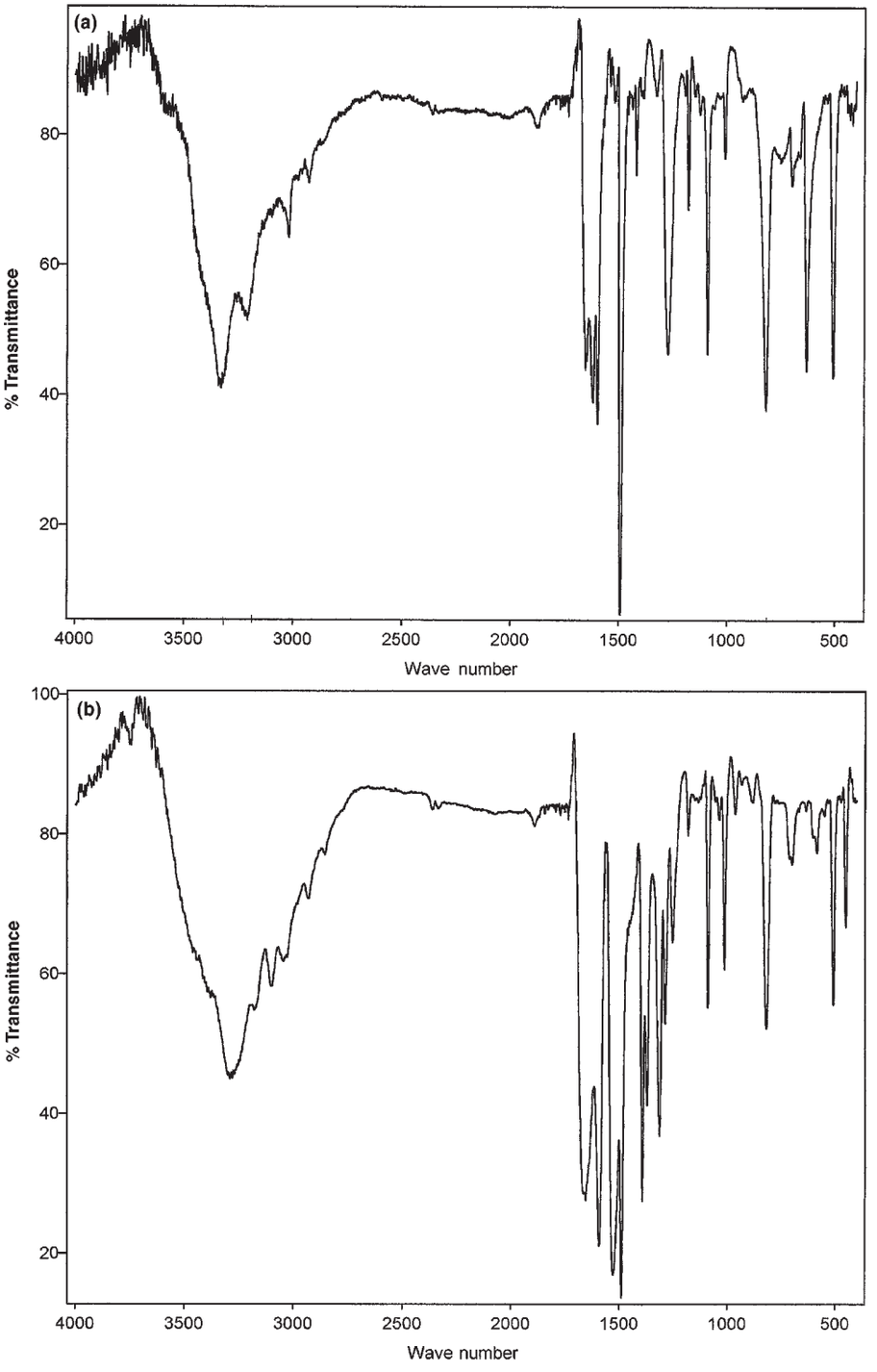

devices. Not only does the surface organic layer prevent coalescence into bulk (6), but also provides a platform for linking chemically active functionalites (5). The covalent attachment of molecular moieties such as chromophores, luminophores, redox centers, or quantum wires to the surface of semiconductor nanoclusters is a likely necessary step towards the realization of quantum dot based molecular electronic or optoelectronic devices. However, once a chemically active functional group has been introduced on the surface of a II–VI semiconductor nanocluster, the problem of lability of the cluster core towards a variety of common organic reaction conditions (acidic, basic, oxidizing, reducing, nucleophilic,

© 1998 NRC Canada

Scheme 1.

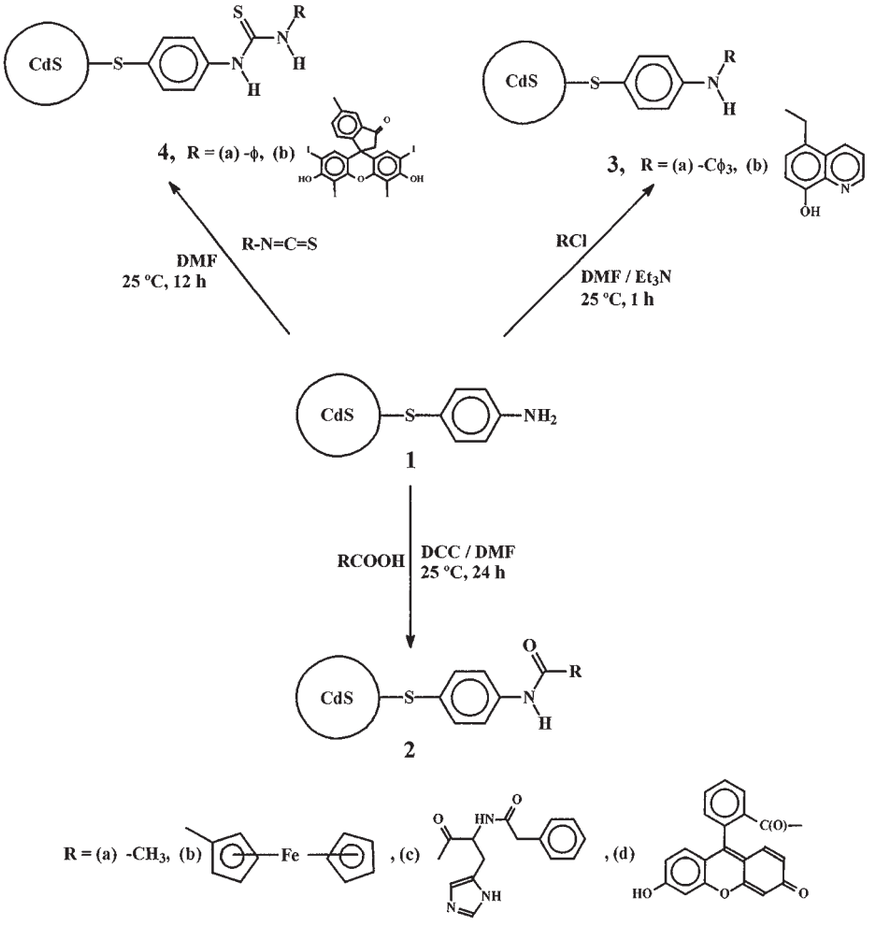

or electrophilic) can still pose a major obstacle towards the attachment of other molecular species via the surface functionality. Moreover, electrophilic reagents intended for the functionality may instead attack the thiol sulfur. For example, aniline surface CdS nanoclusters would certainly not survive the conditions employed in conventional amidization reactions, i.e., from acids, acid anhydrides, or acyl chlorides.

The introduction of an aniline surface to CdS quantum dots ($QDNH_2$, **1**) has been accomplished here by the precipitation of CdS in the presence of 4-mercaptoaniline, in an analogous fashion to the formation of phenolic surface CdS nanoclusters (5*c*). The ^1H NMR spectrum of **1**, presented in Fig. 1, is clearly indicative of binding to the cluster through sulfur. The characteristic ϕ-SH singlet at δ 3.79 ppm of 4-mercaptoaniline is completely absent in the cluster, while the ϕ-NH_2 and aromatic proton resonances remain intact and integrate to exactly 1:2, respectively. As is generally observed with thiophenolate-capped nanoclusters, all ^1H NMR signals appear homogeneously broadened, and, as has been previously observed with phenolic surface CdS nanoclusters (5*c*), the aromatic and ϕ-NH_2 signals are superimposed with structure, indicative of ring and amino protons in multiple environments. The infrared spectrum of **1** (Fig. 2*a*) shows the expected strong benzene ring C=C vibration at 1484 cm^{-1} as well as weak overtone and combination bands between 1700 and 1900 cm^{-1} and a sharp C–H out-of-plane wag at 816 cm^{-1} characteristic of 1,4-disubstitution. The strong N–H stretching absorption is quite broad, ranging from about 2600 to 3600 cm^{-1}, and splits at its peak into two bands corresponding to the NH_2 symmetric (3184 cm^{-1}) and antisymmetric (3316 cm^{-1}) motions. The broadness of this band is again indicative of the amino group existing on the surface in multiple environments. Superimposed on the N–H band is a sharp ring C–H stretch at 3020 cm^{-1}.

Our strategies for coupling molecular moieties to the quantum dot surface are summarized in Scheme 1. Methods, starting reagents, reaction conditions, and percent conversion data for $QDNH_2$ and all derivatives are presented in Table 1. All CdS nanoclusters prepared in this contribution form transparent, non-opalescent suspensions in DMF and DMSO that do not settle and cannot be centrifuged at conventional speeds, but exhibit pronounced Tyndall effects under the direct illumination of a He–Ne laser. In most cases, ^1H NMR spectra reveal residual -NH_2, along with -C(O)NH-, -NH-C(S)-NH-, or -NHR signals, enabling percent conversions to be calculated. Where separate amine vs. amide proton signals were not discernable (as in the case of the fluorescein derivative, **2d**), integration of aliphatic proton signals from the tethered group were used to obtain conversion ratios. ^1H NMR data for **1** and all derivatives appear in

© 1998 NRC Canada

Table 1. Methods, starting reagents, reaction conditions, and percent conversions for formation and derivatization of $QDNH_2$ nanoclusters.

Compd.	Starting reagent	Method	Reaction time (h)	Comments	% conv.
1	4-Mercaptoaniline	Kinetic trapping	1	Chemically active amino surface	—
2a	CH_3COOH	1	24		100
2b	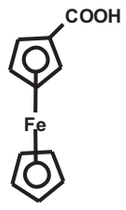	1	16		22
2c	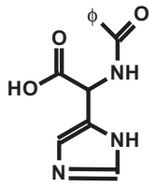	1	18	Optically active nanocluster $[a]_D^{20}$ –106.8° (DMSO)	52
2d	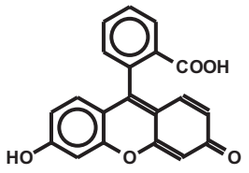	1	16	Pink nanocluster no observed fluorescence	12
3a	ϕ_3C-Cl	2	1		46
3b	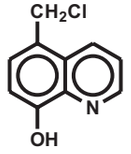	2	1	Surface contains small amount of deprotonated anion or Cd complex Nanocluster avidly coordinates metals	77
4a	ϕNCS	3	12		37
4b	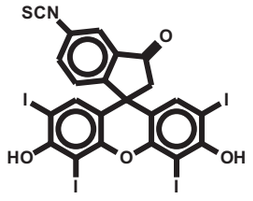	3	12	Red fluorescent nanocluster	4

Table 2. Coupling via amide linkages involves the action of a DCC activated acid on the $QDNH_2$ amino group. Equimolar quantities of acid and DCC are first allowed to react in DMF, then added to a DMF suspension of **1**. The reaction proceeds smoothly over 24 h with near quantitative amidization for low molecular weight acids (i.e., acetyl) but typically amidizing less than 50% of the surface amino groups in the case of sterically bulkier moieties, as determined by ^{1}H NMR integration ratios. By-product cyclohexylurea precipitates as a crystalline solid that can be removed from the nanocluster suspension by conventional filtration or low-field centrifugation. ^{1}H NMR spectra for the amide derivatives of **1** are straightforward, appearing as a superposition of the tethered group and thiophenolate sig-

© 1998 NRC Canada

Table 2. 400 MHz ^{1}H NMR data for aniline-functionalized CdS nanoclusters and derivatives.

Cluster	Solvent	δ (ppm)
1	DMF-d_7	4.72 (br s, 2H, -NH_2), 6.37–6.69 (br m, 2H, ring C2-H), 7.14–7.36 (br m, 2H, ring C3-H)
2a	DMSO-d_6	2.0 (br s, 3H, -CH_3), 7.25 (br m, 4H, arom), 9.70 (br s, 1H, -C(O)NHϕ)
2b	DMSO-d_6	4.18–4.97 (br m, cp-H), 6.28–7.30 (br m, arom), 9.60 (weak, structured, -C(O)NHϕ)
2c	DMSO-d_6	2.85–3.17 (br m, α-C-CH_2), 4.36 (br m, α-CH), 4.99 (br s, -CH_2ϕ), 6.27–7.61 (br m, arom), 9.75 (br, s, -C(O)NHϕ)
2d	DMF-d_7	6.07–7.29 (br m, fluorescein and ring arom), 4.63 (vbr s, resid -NH_2)
3a	DMSO-d_6	6.17–7.32 (br m, ϕ_3C- and ring arom), 4.61–4.71 (vbr s, resid -NH_2)
3b	DMSO-d_6	4.30 (br s, -CH_2-), 4.51 (br s, resid -NH_2), 5.22 (br s,-NHR), 6.45–7.10 (br m, ring arom), 7.59 (br m, quin C3-H), 8.54–8.56 (br m, quin C6-H), 8.78 (br s, quin C4-H), 12.5 (vbr s, -OH—N)
4a	DMSO-d_6	4.77 (vbr s, resid -NH_2), 6.13–7.50 (br m, arom), 9.56 (br, structured, -NH-C(S)-NH-)
4b	DMF-d_7	4.77 (vbr, structured, resid -NH_2), 5.62–7.30 (br m, arom)

Table 3. FT IR data of $QDNH_2$ and derivatized CdS nanoclusters as KBr pellets.

Cluster	Wave numbers (cm^{-1})
1	3300, 3200 (s, br, N–H str), 3020 (w, arom C-H), 1880 (w, 1,4-disub overtone pattern), 1617, 1596 (m-s, shrp, NH_2 deform), 1490 (vs, shrp, NH bend), 1088, 1009 (m, shrp, ϕ-S), 817 (m, shrp, ϕ-H out-of-plane)
2a	3280 (s, br, N–H asym str), 3178 (m, br, N–H sym str), 3100, 3040 (m, br, arom C-H), 2930 (m), 2852 (m, br, aliph C–H str), 1889 (w, 1,4-disub overtone pattern), 1760 (w), 1661 (s, shrp, amide I C=O), 1590 (s, shrp, amide II C=O), 1251 (w, shrp, -C(O)NH- combination), 1089, 1012 (m, shrp, ϕ-S) 819 (m, srhp, ϕ-H out-of-plane), 508 (s)
2b	3340 (m, br, N–H asym str), 3209 (m, br, N–H sym str), 3085 (m, br, cp C–H str), 1618 (m), 1595 (m, shrp, resid NH_2 deform) 1490 (vs, shrp, arom), 1510 (w, shldr, cp C-H deform), 817 (m, shrp, ϕ-H out-of-plane), 632 (s), 508 (s)
2c	3332 (m, br, N–H str), 3023 (m, br, arom C–H str), 2937 (m, br, aliph C–H str), 1878 (w, 1,4-disub overtone pattern), 1707 (m, shrp, amide I C=O), 1594 (s, shrp, amide II C=O), 1270 (w, shrp, C–N str), 1087, 1014 (m, shrp, ϕ-S), 817 (m, shrp, ϕ-H out-of-plane), 696 (w), 628 (m), 507 (m)
2d	3335, 3215 (m, br, N–H str), 3050 (m, arom C–H str), 2928 (m), 2854 (s, shrp, conj C-H), 1880 (w, 1,4-disub overtone pattern), 1653 (s, shrp, amide I C=O), 1579 (s, shrp, amide II C=O), 1329 (w, shrp, C–N str), 1088 (m), 1011 (m, shrp, ϕ-S)
3a	3412, 3324 (m, br, 2° N–H str) 3014 (w, arom, C–H str), 1865 (w, 1,4-disub overtone pattern), 1484 (s, N–H bend), 1269 (m, shrp, C–N str), 1083 (m), 1005 (m, shrp, ϕ-S), 811 (m, shrp, ϕ-H out-of-plane), 697 (s), 625 (s), 507 (s)
3b	3350 (m, br, 2° N–H str), 3023 (m, shrp, arom C–H str), 2923, 2851 (w, shrp, aliph C–H str), 1592 (s, N–H scis), 1457 (s, shrp, N–H bend), 818 (s, shrp, ϕ-H out-of-plane), 780 (s), 634 (w), 603 (w), 504 (m)
4a	3136 (m, br, N–H str), 2951 (m, br, conj C–H str), 1530 (m), 1486 (s, shrp, C=S str), 1265 (w, shrp C-N), 1080 (m, shrp, -NH-C(S)- comb), 1012 (w, shrp), 924–690 (many w-m bands)
4b	3144 (m, br, N–H str), 2944 (m, br, conj C–H str), 1591 (m), 1533 (m), 1484 (s, shrp, C=S str), 1083 (m, shrp, -NH-C(S)- comb), 926–691 (many w-m bands)

nals. Most characteristic, however, is the appearance of a -C(O)NHϕ resonance at ca. δ 9.6–9.8 ppm, located significantly downfield from the underivatized ϕ-NH_2 protons (ca. δ 4.6–4.8 ppm). Infrared absorption peak assignments for $QDNH_2$ and its amide derivatives are collected in Table 3. The infrared spectra for all amide-linked CdS quantum dots exhibit the characteristic amide I carbonyl and amide II C–N stretching vibrations at ca. 1660 and 1590 cm^{-1}, respectively, as illustrated by the spectrum of a representative amidized surface in Fig. 2*b*. These systems also show a sharp characteristic absorption at ca. 1250 cm^{-1}, indicative of a *trans* -NH-CO- amide linkage. The broad N–H stretching band is also present between 2800 and 3800 cm^{-1}. In the case of the acetamide quantum dot, this band exhibits one peak at 3290 cm^{-1} instead of the split two-peak pattern (characteristic of -NH_2), providing further evidence of quantitative conversion in this case. The absorption bands and overtones indicative of 1,4-disubstituted phenyl also remain discernable. The scope of the reaction is quite wide; Table 1 summarizes some of the CdS nanoclusters prepared by this method. Of particular interest is **2c**, which bears a chiral surface induced by amide linkages to N-protected *l*-histidine. These clusters are optically active with a specific rotation significantly higher than the pure untethered enantiomer

© 1998 NRC Canada

Fig. 3. Optical absorption stpectum of a 10^{-4} M $QDNH_2$ nanocluster suspension in DMF (1 cm path length) (*a*) before and (*b*) after amidization with DCC activated ferrocene carboxylic acid.

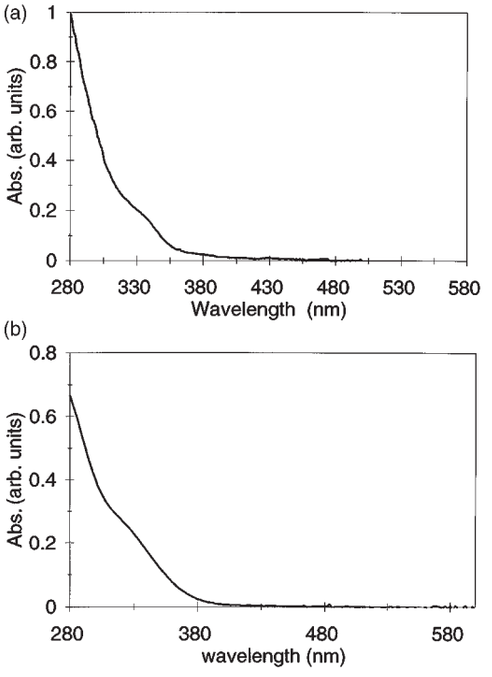

($[\alpha]_D^{20}$ –106.8° for the cluster vs. $[\alpha]_D^{20}$ +15.3° for the protected *l*-histidine). Studies are presently underway in our laboratories to determine the extent to which the surface chirality of this species and other amino acid functionalized quantum dots affects the optical and possibly electronic properties of the semiconductor core.

Another useful class of reagents for extending the functionality of the aniline surface quantum dot are the isothiocyanates, RNCS, which couple molecular moieties to the nanocluster via thiourea linkages, also shown in Scheme 1. The reaction conditions are gentle, proceeding in DMF suspension at room temperature for ca. 12 h. ^{1}H NMR analysis indicates again that surface conversion is not complete and, for sterically large groups, the percent conversion is quite small (4% for erythrosin B isothiocyanate), as summarized in Table 1. Nevertheless, the reagents do not appear to disrupt the integrity of the nanocluster in any detectable manner. The IR spectrum for the phenylthiourea derivative, **4a**, exhibits a strong, sharp absorption at 1534 cm^{-1} and a broad, structured band between 1182 and 1305 cm^{-1}, both characteristic of a thiourea linkage. In addition, the N–H stretching region has considerably broadened, as expected of a mixture of -NH_2 and thioamide -NH- groups. The ring C=C and ϕ-S bands appear nearly unchanged relative to their $QDNH_2$ counterparts. Table 3 summarizes the IR peak assignments for thiourea linked nanoclusters.

The aniline N-protons are also active towards direct substitution (Scheme 1). Hence, treatment of a sonicated DMF suspension of $QDNH_2$ with 5-chloromethyl-8-hydroxyquinoline in the presence of triethylamine resulted in 77% conversion of the aniline amino groups to the corresponding *N*-methyl-8-hydroxyquinoline derivative. Both the protons α to the quinoline nitrogen and on the 4-carbon in the same ring are clearly visible in the ^{1}H NMR spectrum at δ 8.8 and 8.5 ppm, respectively (this is an area of the NMR spectrum distinct from the thiophenolate aromatic region). These protons appear shifted somewhat upfield from their counterparts in unbound 5-chloromethyl-8-hydroxyquinoline (δ 9.2 and 9.1 ppm, respectively). A very broad -OH proton signal is also observed for the cluster at ca. δ 12.5 ppm; its significant downfield location is indicative of intramolecular hydrogen bonding with the quinoline nitrogen. Although the resonances are broad, the aromatic region between δ 6.2 and 7.6 ppm is sufficiently structured to enable the three remaining quinoline ring protons to be distinguished from the four thiophenolate ring protons. The integration ratio of the entire aromatic region between δ 6.2 and 7.6 ppm and the two signals between δ 8.5 and 8.8 ppm is close to 4:1, as expected. These data are collected in Table 2. The methylene proton signal appears at δ 4.3 ppm in the cluster, shifted upfield from the corresponding chemical shift of 5.3 ppm in the unbound 5-chloromethyl-8-hydroxyquinoline. Accordingly, an upfield shift of approximately 0.8 ppm for the methylene protons is expected upon substitution of a chlorine with an amino nitrogen. Both primary and secondary amine protons (at δ 4.5 and 5.2 ppm, respectively) are observed with an integration ratio of 0.59, indicating that 77% of the surface amino groups have been substituted. Similar treatment of $QDNH_2$ with chlorotriphenylmethane resulted in conversion of 46% of the aniline amino groups to the corresponding *N*-triphenylmethyl derivative.

The electronic absorption spectra of **1** and all derivatives prepared in this contribution are typical of thiolate-capped CdS quantum-confined nanloclusters (6), with the onset of band-to-band absorption at ca. 380 nm (Fig. 3*a*), affording a bandgap energy of 3.27 eV. The difference of 0.74 eV between the bandgap of the $QDNH_2$ nanocluster and that of bulk CdS (E_g = 2.53 eV) arises from carrier quantum-confinement effects and can be used to estimate a diameter of

Table 4. UV–visible absorption, calculated (ref. 10), and measured (TEM) nanocluster diameters.

Cluster	λ [a] (nm)	Diam. calcd. [b] (Å)	Diam. meas. [c] (Å)
1	360	22	27 ± 8
2a	390	24	24 ± 7
2b	375	23	29 ± 9
2c	370	22	28 ± 8
2d	400	26	27 ± 7
	450 [d]		
3a	364	22	28 ± 7
3b	386	24	26 ± 7
	410 [e]		
4a	375	23	27 ± 8
4b	375	23	27 ± 8
	542 [f]		

[a]CdS band-to-band absorption unless otherwise noted.
[b]Tight-binding band theory.
[c]Transmission electron microscopy. 7 Å represents the resolution limit of the microscope.
[d]Fluorescein π–π^* absorption.
[e]8-Hydroxyquinoline π–π^* absorption.
[f]Erythrosin B π–π^* absorption.

© 1998 NRC Canada

Fig. 4. Fluorescence spectrum for the 5-methylene-8-hydroxyquinoline derivatized $QDNH_2$ CdS nanocluster, **3b**, in DMF. $\lambda_{ex.}$ = 325 nm.

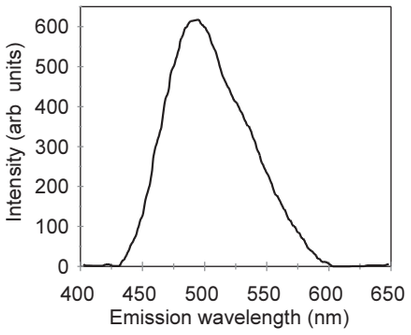

approximately 21 Å for the $QDNH_2$ cluster, in accordance with tight-binding band analysis (10). Upon derivatization using any of the methods described herein the cluster diameters do not change significantly, nor do the CdS core excitonic absorption wavelengths (see Fig. 3*b*), providing further indication that the core integrity is not disrupted. These diameters are in good agreement with the unfunctionalized diameters and a variety of other functionalized CdS nanoclusters prepared under similar conditions (ca. 20–30 Å) (4–6). Tight-binding band calculated diameters for the $QDNH_2$ derivatives are collected in Table 4. The electronic absorption spectrum for **3b** shows, in addition to the CdS excitonic band, an absorption due to 8-hydroxyquinoline. Interestingly, however, this band, assigned in the free compound as π–π* (11), is significantly red-shifted with respect to free 8-hydroxyquinoline (λ_{max} = 314 nm). Moreover, the intensity of the π–π* absorption in free 8-hydroxyquinoline is far too weak to give rise to the moderately intense band in the derivatized nanocluster. Upon deprotonation of the phenolic group, however, the 8-hydroxyquinoline π–π* band is known to red-shift to 400 nm and dramatically increase in intensity (11), and is reassigned as *n*–π* (12). Our ^1H NMR and FT IR data, however, indicate intact -OH. We therefore conclude that a small fraction of the tethered moiety exists in a deprotonated or, perhaps more likely, cadmium-complexed form. This is confirmed by the fluorescence spectrum of **3b,** which exhibits a strong broad emission centered at 495 nm (Fig. 4), consistent with previously measured emission wavelengths for the free anion (13) as well as a number of M^{2+} and M^{3+} 8-hydroxyquinoline complexes (11, 14). Investigations concerning the coordination chemistry and photophysical properties of **3c** are currently underway in our laboratories.

Transmission electron microscopy (TEM) of **1** and all derivatives studied in this work demonstrates that the nanoclusters tend to agglomerate into larger spheroids of various sizes embedded in fields of individual nanoclusters, behavior that we have observed in our previous studies concerning phenolic surface CdS quantum dots (5*c*). Histogram analyses (see Figs. 5 and 6 for a typical TEM picture and histogram, respectively) indicate that all systems are fairly monodisperse in diameter, as presented in Table 4, and agree well with nanocluster diameters calculated from tight-binding band treatment of the optical absorption data. TEM confirms

Fig. 5. Computer-enhanced transmission electron micrograph of the fluorescene derivatized $QDNH_2$ CdS nanocluster, **2d**. Magnification: ×370 000 (1 cm = 27 nm).

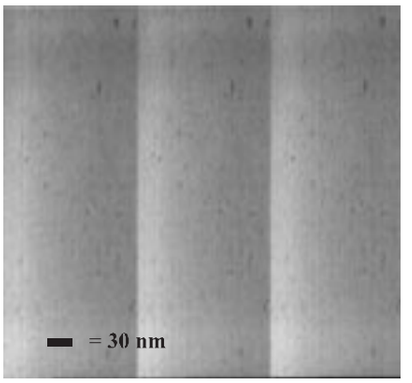

Fig. 6. Diameter distribution histogram for the fluorescene derivatized $QDNH_2$ CdS nanocluster, **2d**.

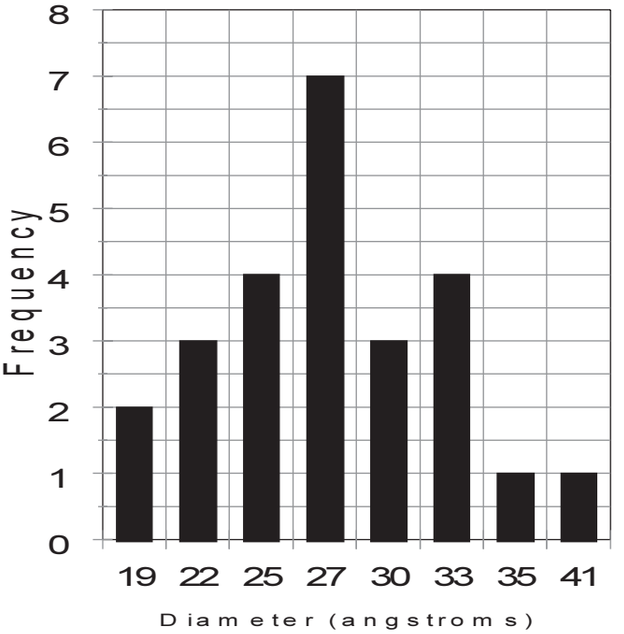

that derivatization of the aniline surface affects neither the size nor size distribution of the nanoclusters, further evidence that the CdS core integrity is not disrupted.

Conclusions

The realization of novel molecular electronic or optoelectronic devices fabricated from semiconductor quantum-confined nanoclusters, or quantum dots, will necessarily involve the formation of covalent linkages to the cluster surfaces. We have been investigating the chemical activation of the surfaces of cadmium sulfide quantum dots with such purpose in mind, and have previously demonstrated that the introduction of pyridyl (5*a*, 5*b*) and hydroxy (5*c*) functional groups enables CdS nanoclusters to participate in a wide scope of surface-extending reactions, resulting in a variety of interesting new materials. We demonstrate here that CdS

© 1998 NRC Canada

nanoclusters bearing an aniline surface can provide a wide range of new quantum dots, including nanoclusters with unusual fluorescent and chiroptical properties. We present three types of surface-extending reactions that can be employed to conveniently tether interesting molecular moieties to the nanocluster surface without disrupting the integrity of the CdS core.

Acknowledgment

The authors wish to thank Professor A.B.P. Lever, Leah Veinot, Robert Metcalfe, and Dr. Abdiaziz Farah for their helpful suggestions and input, and Karen Rethoret for assistance with the electron microscopy. We also acknowledge the financial support of the Natural Sciences and Engineering Research Council of Canada (NSERC).

References

1.(*a*) A.P. Alivisatos. J. Phys. Chem. **100**, 13266 (1996); (*b*) H. Weller. Angew. Chem. Int. Ed. Engl. **32**, 41 (1993); (*c*) G. Schmid. Chem. Rev. **92**, 1709 (1992); (*d*) M.L. Steigerwald and L.E. Brus. Acc. Chem. Res. **23**, 183 (1990); (*e*) A. Henglein. Chem. Rev. **89**, 1861 (1989).

2. (*a*) U. Merkt and Ch. Sikorski. Semicond. Sci. Technol. **5**, 182 (1990); (*b*) T.A. Fulton. Nature, **346**, 408 (1988); (*c*) B. Zorman, M.V. Ramakrishna, and R.A. Friesner. J. Phys. Chem. **99**, 7649 (1995).
3. (*a*) D.L. Klein, R. Roth, A.K.L. Lim, A.P. Alivisatos, and P.L. McEven. Nature, **389**, 699 (1997); (*b*) M. Moskovits and J.M. Xu. U.S. Patent US 5,581,091, 1996.
4. (*a*) T. Torimoto, K. Maeda, J. Maenaka, and H. Yoneyama. J. Phys. Chem. **98**, 13658 (1994); (*b*) Y. Nosaka, N. Ohta, T. Fukuyama, and N. Fujii. J. Colloid Interface Sci. **155**, 23 (1993); (*c*) T. Torimoto, H. Uchida, T. Sakata, H. Mori, and H. Yoneyama. J. Am. Chem. Soc. **115**, 1874 (1993); (*d*) J.M. Stipkala, F.N. Castellano, T.A. Heimer, C.A. Kelly, K.J.T. Livi, and G.J. Meyer. Chem. Mater. **9**, 2341 (1997); (*e*) T. Gacoin, L. Malier, and J.-P. Boilot. Chem. Mater. **9**, 1502 (1997); (*f*) T. Løver, W. Henderson, G.A. Bowmaker, J.M. Seakins, and R.P. Cooney. Chem. Mater. **9**, 1878 (1997).
5. (*a*) H. Noglik and W.J. Pietro. Chem. Mater. **6**, 1593 (1994); (*b*) Chem. Mater. **7**, 1333 (1995); (*c*) J.G.C. Veinot, M. Ginzburg, and W.J. Pietro. Chem. Mater. **9**, 2117 (1997).
6. N. Herron, Y. Wang, and H. Eckert. J. Am. Chem. Soc. **112**, 1322 (1990).
7. M. Kolobielski. J. Heterocycl. Chem. **3**, 275 (1966).
8. A. Patchornik, A. Berger, and E. Katchalski. J. Am. Chem. Soc. **79**, 6416 (1957).
9. E.A. Castro, R.B. Moodie, and P.J. Sansom. J. Chem. Soc. Perkin Trans. 2, 737 (1985).
10. (*a*) Y. Wang and N. Herron. Phys. Rev. **42**, 7253 (1990); (*b*) J. Phys. Chem. **95**, 525 (1991); (*c*) T. Vossmeyer, L. Katsikas, M. Giersig, I.G. Popovic, K. Diesner, A. Chemskkine, A. Eychmüller, and H. Weller. J. Phys. Chem. **98**, 7665 (1994); (*d*) H. Weller, H.M. Schmidt, U. Koch, A. Fojtik, S. Baral, A. Henglein, W. Kunath, K. Weiss, and E. Dieman. Chem. Phys. Lett. **124**, 557 (1986).
11. R. Ballardini, G. Varani, M.T. Indelli, and Scandola. Inorg. Chem. **25**, 3858 (1986).
12. M. Kasha and H.R. Rawls. Photochem. Photobiol. **7**, 561 (1968).
13. (*a*) D.C. Bhatnagar and L.S. Forster. Spectrochim. Acta, **21**, 1803 (1965); (*b*) F.E. Lytle, D.F. Storey, and M.E. Juricich. Spectrochim. Acta, Part A: **29A**, 1357 (1973).
14. (*a*) W.E. Ohnesorge and A. Capotosto, Jr. J. Inorg. Nucl. Chem. **24**, 829 (1962); (*b*) W.E. Ohnesorge. J. Inorg. Nucl. Chem. **29**, 485 (1967); (*c*) E.A. Bozhevol'nov and G.V. Serebryakove. Opt. Spectrosc. (Engl. Transl.), **13**, 216 (1962); (*d*) A.V. Karyakin, T.S. Sorokina, L.I. Anikina, and M.G. Ezernitskaya. Dokl. Akad. Nauk SSSR, **241**, 617 (1978).

© 1998 NRC Canada

Phonon dispersion and defect energies for rubidium chloride, bromide, iodide, and sulphide

Patrick W.M. Jacobs and Marcia L. Vernon

Abstract: New crystal potentials have been developed for rubidium chloride, bromide, iodide, and sulphide, and also strontium chloride, by first calculating the pair-interactions in the electron-gas approximation and then refitting the potential parameters to available crystal properties. These potentials were then further tested by calculating the phonon dispersion in these materials along principal symmetry directions, with generally good agreement with experiment (except for rubidium sulphide for which no experimental neutron scattering data are available). The potentials were then used in the HADES computer code to calculate the energies of formation and migration of point defects in these materials. Our calculations indicate that several transport mechanisms may be important in the Rb halides and this has been verified in the case of RbCl by a recent very detailed analysis of the ionic conductivity of pure and doped RbCl.

Key words: rubidium halides, defect energies, ionic transport, phonon dispersion, strontium chloride, rubidium sulphide.

Résumé : On a développé de nouveaux potentiels cristallins pour les chlorure, bromure, iodure et sulfure de rubidium ainsi que pour le chlorure de strontium en calculant les interactions de paires à l'aide de l'approximation gaz-électron et en les affinant ensuite les paramètres de potentiel avec les propriétés cristallines disponibles. On a alors revérifié ces potentiels en calculant la dispersion phonique dans ces matériaux le long des principales directions de symétrie; il y a généralement un bon accord entre ces valeurs et les données expérimentales (excepté dans le cas du sulfure de rubidium pour lequel il n'existe aucune donnée expérimentale de dispersion des neutrons). On a ensuite utilisé les potentiels dans le code « HADES » d'ordinateur pour calculer les énergies de formation et de migration des défauts ponctuels dans ces matériaux. Nos calculs indiquent que plusieurs mécanismes de transport peuvent jouer un rôle important dans les halogénures de Rb et cette hypothèse a été vérifiée dans le cas du RbCl grâce à l'analyse détaillée de la conductivité ionique du RbCl, pur et dopé, rapportée récemment.

Mots clés : halogénures de rubidium, énergies de défauts, transport ionique, dispersion phonique, chlorure de strontium, sulfure de rubidium.

[Traduit par la Rédaction]

Introduction

There have been several previous calculations of defect energies for the rubidium halides RbCl, RbBr, RbI (1–6) but because of differing crystal potentials and the conditions under which the calculations were carried out, there are considerable variations in the results. For example the calculated energy to form a Schottky defect (that is, a vacant site on each of the cation and anion sub-lattices) varies from 2.16 to 2.52 eV (1–6) for RbCl, while the calculated activation energy for the migration of cation vacancies in RbCl varies from 0.63 to 0.80 eV (2–5). Similar variations exist for the calculated anion vacancy migration energy in RbCl and for calculated defect energies for RbBr and RbI. This paper reports a new study of defect properties of RbCl, RbBr, and RbI, and also of Rb_2S for which no previous calculations have been published. Particular attention has been paid to the development of new crystal potentials and the agreement between calculated perfect-crystal properties and experimental data, including phonon dispersion. A necessary feature of this work was the development of a new interatomic pair-potential for the Cl^-–Cl^- interaction, and so we took advantage of this to recalculate the phonon dispersion and defect properties of $SrCl_2$, which had been the subject of a previous investigation in this laboratory (7). Sr^{2+}–Rb^+ and S^{2-}–Cl^- potentials were also calculated in order to investigate the properties of doped RbCl. The availability of recent ionic conductivity measurements for pure and doped RbCl from this laboratory meant that a particularly careful comparison with experiment could be made for this material.

Received November 25, 1997.

P.W.M. Jacobs[1] and M.L. Vernon.[2] Department of Chemistry, The University of Western Ontario, London, ON N6A 5B7, Canada.

[1]Author to whom correspondence may be addressed. Telephone: (519) 661-3933. Fax: (519) 661-3022. E-mail: pjacobs@uwo.ca

[2]Present address: National Optics Institute, Sainte-Foy, QC G1P 4N8, Canada.

The calculations

The method of calculation adopted was that based on the two-region strategy of Mott and Littleton (8) as implemented in the computer codes HADES (9) and CASCADE (10). The theoretical basis of the Mott–Littleton method has been described in the literature (11, 12) and the results obtained for various classes of compounds have been assessed (12–14). It is therefore only necessary to state the region

© 1998 NRC Canada

sizes and to discuss the crystal potentials employed. In our calculations the inner region consisted of approximately 100 ions. (It is essential that the inner region contain complete symmetry classes and therefore the precise number of ions in region I may vary slightly with defect symmetry.) The adjacent region IIa, which separates region I from the outer region IIb (which in the Mott–Littleton method is treated as a dielectric continuum), consisted of 1000–1500 ions. These region sizes are sufficient to ensure adequate convergence of the defect energies. As is invariably so in applying this method, the calculations were done with constant lattice parameter and since no calculations were done at elevated pressures, the results are indistinguishable from defect energies at constant volume. The errors involved in comparing such constant-volume energies with experimental enthalpies determined at constant pressure at elevated temperatures can be expected to be no more than about 2% (12, 15).

Any defect-energy simulation of an ionic crystal involves the calculation of the self-consistent energy of interaction between the ions in their fully relaxed positions. At long range this interaction is dominated by Coulombic forces but, as ionic separations decrease, dispersion forces become significant. These forces arise from the interaction of mutually induced multipoles, the strongest being the dipole–dipole interaction $\phi^{DD}(r)$. At even closer separations the ionic charge densities overlap and a strong closed-shell repulsion results. This overlap repulsion energy $\phi^{R}(r)$ is commonly described by a Born–Mayer exponential term. If many-body effects and angle-dependent forces are neglected, which is a reasonable approximation for alkali halide crystals (12), the short-range interaction can be described by the pair-potential

$$[1] \qquad \phi^{SR}(r) = \phi^{R}(r) + \phi^{DD}(r) = A_{ij} \exp\left(-\frac{r}{\rho_{ij}}\right) + \phi^{DD}(r)$$

where A_{ij} is the repulsive parameter and ρ_{ij} the hardness parameter (for ions of species i and j). Traditionally, ϕ^{DD} has been represented by $-C_{ij}r^{-6}$ and the resulting potential [1] is then called a Buckingham potential. A_{ij} and ρ_{ij} must be found either by fitting crystal properties (12, 16) or determined by calculation. Because of the difficulties involved in doing a quantum-mechanical calculation of the short-range energy in a realistic crystal environment (17, 18), the method of choice (12) has frequently been some variant of what have come to be called "electron-gas calculations" (19, 20). These involve the HFSCF calculation of single-ion charge densities (ρ_i, ρ_j), followed by a calculation of the interaction energy between a pair of ions of species i and j in the Thomas–Fermi–Dirac approximation in which the kinetic and exchange contributions are taken to be those of a uniform free-electron gas of density $\rho = \rho_i + \rho_j$. One worries about the accuracy of this *conserved density approximation* (12) and that is why it is best to test the results of electron-gas calculations by calculating known properties of perfect crystals and modifying the hardness and repulsive parameters where necessary to obtain the best possible fit to the lattice constant and elastic constants, and this has been done in this work. Estimates of C may be obtained from the Slater–Kirkwood formula (18, 21, 22) and refined by fitting.

Nearly all calculations of defect energies use the shell model to simulate the polarizability of an ion and the shell-model charges Y_i, Y_j, and the force constants K_i, K_j are adjusted to fit the relative permittivities ϵ_s, ϵ_∞, anion polarizability, and the zone-centre frequency of the transverse optic mode. Some hints on fitting procedures are given in ref. 12. Generally, we prefer to reserve the calculation of the phonon dispersion in the principal symmetry directions in the Brillouin zone as a final test of the crystal potential.

Table 1. Potential parameters for RbCl, RbBr, and RbI.

Interaction	A_{ij}/eV	ρ_{ij}/Å	C_{ij}/eV Å^6	r_m/Å
RbCl				
Cl^-–Cl^-	596.54	0.380	170.06	4.0
Rb^+–Cl^-	2 050.94	0.348	108.87	4.1
Rb^+–Rb^+	4 959.53	0.286	68.31	3.8
RbBr				
Br^-–Br^-	1 445.89	0.361	127.59	4.3
Rb^+–Br^-	5 800.44	0.319	85.00	4.5
Rb^+–Rb^+	5 020.49	0.285	70.02	3.8
RbI				
I^-–I^-	1 833.12	0.369	115.53	4.9
Rb^+–I^-	29 540.18	0.287	27.00	5.6
Rb^+–Rb^+	5 080.49	0.285	70.02	3.8

Our potentials differ from those commonly employed in one significant respect, namely, the insertion of a damping coefficient $\chi(r)$ so that

$$[2] \qquad \phi^{DD}(r) = -\chi(r)\, C_{ij}/r^6$$

where (23, 24)

$$[3] \qquad \chi(r) = \exp[-((1.28\, r_m/r) - 1)^2]; \quad r < 1.28\, r_m$$
$$\chi(r) = 1; \quad r \geq 1.28\, r_m$$

r_m being the ionic separation at the potential minimum. The inclusion of $\chi(r)$ reduces the undamped energies in the charge-overlap region. r_m is a scaling factor and the number 1.28 comes from extensive tests using experimental data (23).

Theoretical formulae for damping coefficients have been given by Pyper (17) but, in our experience (24), eq. [3] is a simple but effective method of removing the unphysical net attraction in the Buckingham potential at small r. For some impurity potentials, fitting is not possible because of lack of data and in these instances the calculated electron-gas potentials were employed without further refinement.

Results

Crystal potentials

Pair-potentials for the three rubidium halides are given in Table 1 and shell-model parameters in Table 2. Calculated perfect-crystal properties are compared with experimental values in Table 3. In these calculations the lattice constants a_o were taken to be the experimental values at 0 K. Any deviation from the minimum in the calculated cohesive energy as a function of a_o would then appear as a bulk lattice strain. In all our calculations the calculated bulk lattice strains were extremely small (about 0.0001). This is equivalent to saying that the structure and lattice constant are fitted almost exactly. The experimental cohesive energy u_c elastic constants

© 1998 NRC Canada

Table 2. Shell model parameters for RbCl, RbBr, and RbI.

Ion	Y/eV	K/eV Å^{-2}
Cl^-	–2.485	29.5
Rb^+ (in RbCl)	5.000	171.0
Br^-	–3.205	34.7
Rb^+ (in RbBr)	5.000	175.0
I^-	–4.087	36.9
Rb^+ (in RbI)	5.000	185.0

and relative permittivities are the 0 K values but the experimental frequencies of the longitudinal (LO) and transverse (TO) optic modes come from experimental measurements at 80 K. There were insufficient experimental data to extrapolate these quantities to 0 K. The overall agreement with experiment is very good for this type of work. Since we are using pair-potentials and every ion is at a centre of cubic symmetry, our calculated values of the elastic constants c_{12} and c_{44} satisfy the Cauchy relation $c_{12} = c_{44}$. The modest failure of this relation for experimental values of the elastic constants indicates small contributions from many-body interactions. These are clearly much smaller than in the silver halides, for example (25), and we believe that the contributions from many-body forces will have only a relatively small effect on the calculated defect energies (compare ref. 16). Calculated phonon dispersion curves are compared with experiment in Figs. 1–3. Agreement for acoustic modes is uniformly excellent. For RbI the agreement between calculated and experimental optic modes is also excellent. For RbBr the calculated TO mode lies slightly below the experimental data, while from RbCl the calculated TO and LO modes are both somewhat low. This is a result of the relatively poor fitting of the zone-centre transverse optic mode frequency ω_{TO}, coupled with the excellent fitting of the high- and low-frequency permittivities, which will inevitably drag the LO mode down as well. The fitting of crystal potentials is always a compromise between various considerations. Here we adopted as an article of faith the principle that the shell parameters for Rb^+ should be, as far as practicable, transferable between the three halides, with only minor variations permitted in the spring-constant K to allow for the different crystal environments. The same principle was applied to the Rb^+–Rb^+ Buckingham potential and the success of these two assumptions may be seen in Tables 2 and 3. We feel that this principle is basically sound, though the constraints that it implies in practice may have been a little too severe, with some minor repercussions in the RbCl potential. In assessing the phonon dispersion curves, it is important to recall that only one point, the ω_{TO} frequency at Γ, is used in fitting the rock-salt structured rubidium halides. Although ω_{LO} appears in the tables because it helps to give an idea of the quality of the fitting achieved to the experimental data, it is not an independent point because of the Lydane–Sachs–Teller relation and the fact that the static and high-frequency permittivities are also fitted properties. In the fluorite-structured Rb_2S and $SrCl_2$ the Raman frequency is an independent parameter and it is therefore included in the fitting. So the calculated phonon dispersion curves involve only one (or two) fitted points and the rather good overall agreement with experiment in Figs. 1–3 and 5 should be seen in that light.

Table 3. Experimental and calculated crystal properties of RbCl, RbBr, and RbI.

Property	Calculated	Experimental
RbCl		
a_0/Å		3.259[a]
u_c/eV	–7.02	–6.91[b]
$c_{11}/10^{10}$ N m^{-2}	3.94	4.30[c]
$c_{44}/10^{10}$ N m^{-2}	0.61	0.49[c]
$c_{12}/10^{10}$ N m^{-2}	0.61	0.65[c]
ϵ_s	4.53	4.53[d]
ϵ_∞	2.21	2.20
ω_{LO}/THz	5.00	5.17
ω_{TO}/THz	3.34	3.72
RbBr		
a_0/Å		3.410[a]
u_c/eV	–6.71	–6.62[b]
$c_{11}/10^{10}$ N m^{-2}	3.69	3.86[c]
$c_{44}/10^{10}$ N m^{-2}	0.54	0.41[c]
$c_{12}/10^{10}$ N m^{-2}	0.54	0.47[c]
ϵ_s	4.51	4.51[d]
ϵ_∞	2.36	2.36
ω_{LO}/THz	3.79	3.88
ω_{TO}/THz	2.70	2.81
RbI		
a_0/Å		3.628[a]
u_c/eV	–6.29	–6.28[b]
$c_{11}/10^{10}$ N m^{-2}	3.34	3.21[c]
$c_{44}/10^{10}$ N m^{-2}	0.43	0.20[c]
$c_{12}/10^{10}$ N m^{-2}	0.43	0.36[c]
ϵ_s	4.55	4.55[d]
ϵ_∞	2.61	2.61
ω_{LO}/THz	3.26	3.15
ω_{TO}/THz	2.47	2.41

[a]Reference 38.
[b]Reference 39.
[c]Reference 40.
[d]Reference 41.
[e]Reference 42.

The alkali chalcogenides have not been investigated as thoroughly as the alkali halides. In fact the only available crystal data for Rb_2S are the lattice constant, cohesive energy, and refractive index n, from which the high-frequency permittivity may be calculated using the relation $\epsilon_\infty = n^2$. Potential parameters for Rb_2S are given in Table 4 and calculated and available experimental values of crystal properties are in Table 5. Potential parameters for $SrCl_2$ are given in Table 6 and the comparison of calculated and experimental properties in Table 7. The difference between this and the previous work on $SrCl_2$ (7) is that the hardness parameter ρ_{ij} and van der Waals coefficient C_{ij} for the Cl^-–Cl^- interaction were fixed at the values found for RbCl and only the Cl^-–Cl^- repulsive parameter and the Sr^{2+}–Cl^- and Sr^{2+}–Sr^{2+} parameters were allowed to vary during fitting. The overall agreement with experiment in Table 7 shows some improvement over previous work, although the difficulty in fitting the elastic constants c_{12} and c_{44} has not been resolved completely.

© 1998 NRC Canada

Fig. 1. Calculated phonon dispersion for RbCl compared with experiment (∇) (26).

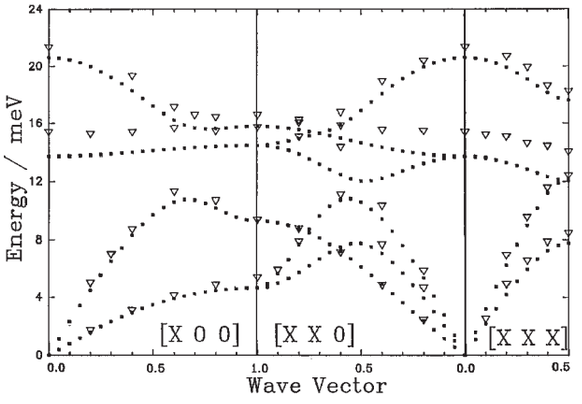

Fig. 2. Calculated phonon dispersion for RbBr compared with experiment (∇) (27).

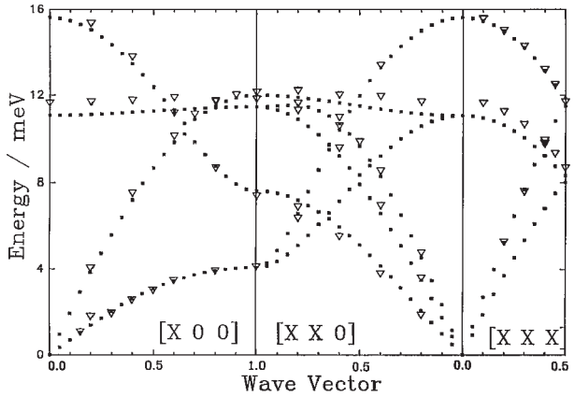

The calculated phonon dispersion for Rb_2S and $SrCl_2$ is shown in Figs. 4 and 5. There are no experimental data for Rb_2S but the general form of the dispersion curves (for example, the very flat Raman branch along ΓX) resembles that of other fluorite-structured ionic crystals, such as Na_2S, for which there are experimental data (7), $SrCl_2$ (Fig. 5), and Li_2O (30). The remarkable feature of these crystals is the minimum in the LO mode and the corresponding maximum in the transverse Raman (TR) mode, which occur at the same q-point, [q_1 q_1 0] with q_1 about 0.66. This behaviour is very marked in Na_2S and Li_2O (7, 26). In $SrCl_2$ the LO minimum appears in the calculated curves and there is a strong hint of a Raman peak in the experimental data that, however, is not reproduced in our calculations. In Rb_2S the TR and LO modes meet at this point (q_1 = 0.65), strongly suggesting that the same type of cooperative dynamical motion that exists in Li_2O (30) might be operative also in the formation of Rb^+ interstitials in Rb_2S. In Rb_2S the TO and TR modes are well separated at Γ but in $SrCl_2$ they are much closer and in Na_2S they are almost degenerate, no doubt a consequence of differing atomic masses and crystal potentials.

Two additional potentials Sr^{2+} – Rb^+ and S^{2-} – Cl^- were needed for defect calculations on doped crystals and these were calculated by fitting results of electron-gas calculations to the Born–Mayer repulsion. No fitting to crystal properties is possible in these cases. The results of these calculations

Fig. 3. Calculated phonon dispersion for RbI compared with experiment (∇) (28).

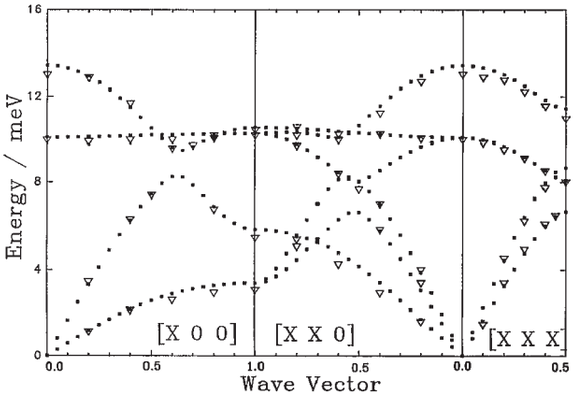

Table 4. Potential parameters for Rb_2S.

Interaction	A_{ij} /eV	ρ_{ij} /Å	C_{ij} /eV Å^6	r_m/Å
S^{2-}–S^{2-}	73.38	0.627	0.00	—
Rb^+–S^{2-}	1419.00	0.397	194.48	4.9
Rb^+–Rb^+	4793.04	0.289	54.96	4.1
Ion	**Y/eV**		**K/eV Å^{-2}**	
S^{2-}	–3.7		28.5	
Rb^+	5.0		128.35	

are given in Table 8. Shell-model parameters for the individual impurity ions S^{2-} and Sr^{2+} were taken to be the same as in the pure crystals Rb_2S and $SrCl_2$ (Tables 4, 6).

Defect energies

In this work defect formation energies are calculated using the convention that the final state of an ion removed from the lattice to form a vacancy is at rest at infinity and similarly the initial state of an ion that ends up in an interstitial site is the ion at rest at infinity. Consequently the energy required to form a Frenkel defect (u_F) is the sum of vacancy and interstitial formation energies for ions from the appropriate sub-lattice, indicated by subscripts c for cation and a for anion. The energy to form a Schottky defect (u_S) is the sum of cation and anion vacancy formation energies required to make up the stoichiometric unit (MX, M_2X, or MX_2) minus the cohesive energy of the crystal. The vacancy migration energy is the energy required for an ion to jump from a nearest neighbour (nn) sub-lattice site into the vacancy (v) along a direct path. Interstitials in the rock-salt structure can jump into a nn interstitial site by one of three mechanisms: along a direct path (id), by a collinear interstitialcy mechanism (ic), or by a non-collinear interstitialcy mechanism (inc). In the fluorite structure only the inc mechanism is possible. Migration energies are indicated in the tables by the symbol Δu with appropriate subscripts to show the sub-lattice (c or a), the defect (v or i), and the interstitial mechanism. The vacancy pair-formation energy (u_p) is the energy to form a pair of vacancies on nn sites from two isolated vacancies in the crystal, and Δu_{cp}, Δu_{ap} are the energies required for a nn cation or anion to hop into a vacancy pair.

© 1998 NRC Canada

Table 5. Calculated and experimental crystal properties of Rb_2S.

Property	Calculated	Experimental
a_0/Å		3.835[a]
u_c/eV	–19.35	–19.55[b]
$c_{11}/10^{10}$ N m^{-2}	3.79	
$c_{44}/10^{10}$ N m^{-2}	0.42	
$c_{12}/10^{10}$ N m^{-2}	1.44	
ϵ_s	7.90	
ϵ_∞	3.14	3.13[c]
$\tilde{\nu}_{LO}$/cm^{-1}	215	
$\tilde{\nu}_R$/cm^{-1}	125	
$\tilde{\nu}_{TO}$/cm^{-1}	81	

[a]Reference 43.
[b]Reference 44.
[c]Reference 45.

Table 6. Potential parameters for $SrCl_2$.

Interaction	A_{ij} /eV	ρ_{ij} /Å	C_{ij} /eV Å^6	r_m/Å
Cl^-–Cl^-	715.54	0.380	0.380	3.7
Sr^{2+}–Cl^-	4655.00	0.313	0.0	—
Sr^{2+}–Sr^{2+}	9949.10	0.245	0.0	—
Ion	Y/eV		K/eV Å^{-2}	
Cl^-	–2.15		112.5	
Sr^{2+}	9.6		198.5	

Table 7. Calculated and experimental crystal properties of $SrCl_2$.

Property	Calculated	Experimental[a]
a_0/Å		3.49
u_c/eV	–21.48	–21.40
$c_{11}/10^{10}$ N m^{-2}	7.55	7.55
$c_{44}/10^{10}$ N m^{-2}	1.73	1.03
$c_{12}/10^{10}$ N m^{-2}	2.24	1.72
ϵ_s	6.94	6.94
ϵ_∞	2.74	2.70
$\tilde{\nu}_{LO}$/cm^{-1}	230	248
$\tilde{\nu}_R$/cm^{-1}	172	188
$\tilde{\nu}_{TO}$/cm^{-1}	145	155

[a]Reference 46.

Table 8. Additional pair potentials for doped RbCl.

Interaction	A_{ij} /eV	ρ_{ij} /Å	C_{ij} /eV Å^6	r_m/Å
Sr^{2+}–Rb^+	16398.1	0.241	0.0	—
S^{2-}–Cl^-	277.00	0.444	0.0	—

Association energies u_1, u_2 are the energy to form nn or next nn (nnn) complexes between a divalent impurity ion and a vacancy on the same sub-lattice (Fig. 6). The various possible jumps of a vacancy in a complex are designated w_1, w_2, w_3, and w_4 and these are defined in Fig. 6. Corresponding migration energies are designated Δu_1 through Δu_4.

The contribution of a particular defect species to ionic transport in a material can be assessed from its Arrhenius energy designated by E, with a superscript showing the defect type (S or F or p) and a subscript that indicates the migration mechanism. Thus, for example,

Fig. 4. Calculated phonon dispersion for Rb_2S.

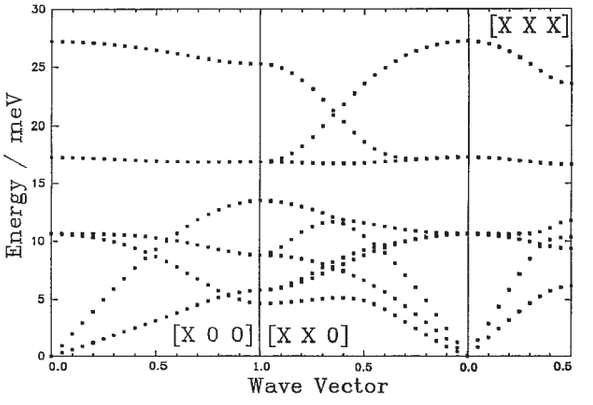

Fig. 5. Calculated phonon dispersion for $SrCl_2$ compared with experiment (∇) (29).

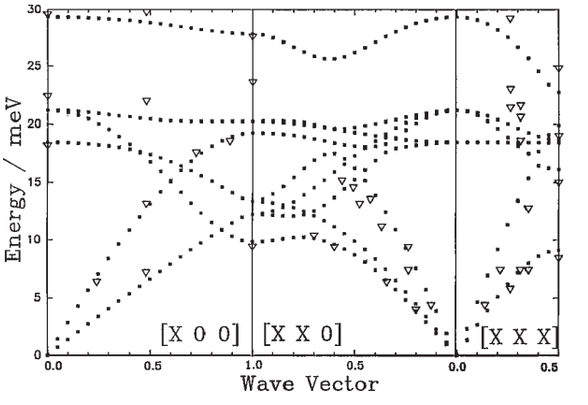

$$[4]\quad E^{F}_{cv} = (u_{Fc}/2) + \Delta u_{cv}\ ;\ E^{F}_{cic} = (u_{Fc}/2) + \Delta u_{cic}$$
$$E^{S}_{av} = (u_S/2) + \Delta u_{av}\ ;\ E^{p}_{ap} = u_S + u_p + \Delta u_{ap}$$

Calculated defect energies for RbCl, RbBr, and RbI are given in Table 9, using the symbols already defined in the text. We have already remarked that the results of previous calculations (1–6) are spread over quite wide ranges because of the various potentials and calculation parameters employed. Even when the same models and potentials were employed discrepancies arise; for example, the calculations of Rowell and Sangster (5) were intended to supplement those of Uppal et al. (3) but the calculated energies in the two sets differ by up to 0.2 eV, which the former authors attribute to a difference in the short-range potential cutoff used. We standardized this parameter at 1.5 × the nn distance a_o so that first and second neighbours were always included in the short-range contribution (16).

Table 10 shows the binding energies for nn and nnn complexes in RbCl and also the vacancy jump energies. These are important parameters in discussions of diffusion and dielectric loss in doped crystals (31). Atom transport in doped crystals depends on the five jump frequencies w_1, w_2, w_3, w_4, and w_0, which is that of a free vacancy. These jump frequencies involve the corresponding entropies as well, and these

© 1998 NRC Canada

Fig. 6. RbCl:Sr^{2+} nn and nnn complexes and vacancy jumps in these complexes.

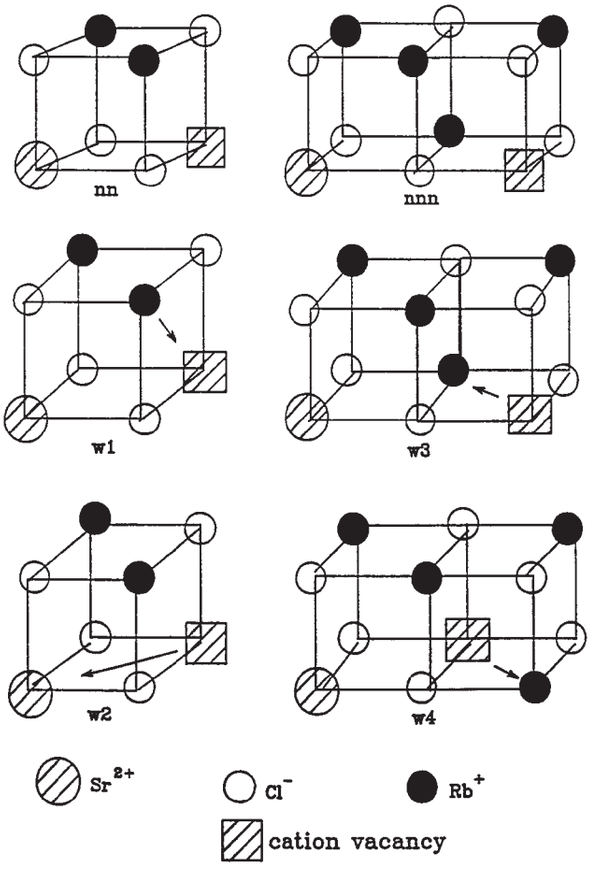

elusive quantities are much more difficult to calculate than defect energies (32). However, in divalent-cation doped crystals the calculated migration energies Δu_1, Δu_3, Δu_4 are often quite similar to Δu_{cv}, while Δu_2 is very different (13). Hence the five-frequency model can often be approximated by a two-frequency model. From the results in Table 10 this appears to be a reasonable first approximation for RbCl:Sr^{2+} but not for RbCl:S^{2-}. The binding energies of nn and nnn complexes in RbCl:Sr^{2+} are similar, which is quite often the case (13) except when the substitutional ion is larger than the host-lattice ion it replaces, when the nn complex becomes more favoured. These ion-size effects are apparent in the results for RbCl:S^{2-}. Calculated defect energies for Rb_2S are given in Table 11. Since there are no other calculated or experimental values to compare with these, we include the corresponding values for Na_2S from ref. 7. The trends are similar, with quantitative differences probably due to the greater ion polarizability of Rb^+. One can safely predict cation interstitial disorder in Rb_2S with vacancy motion along ⟨100⟩ predominating but with some contribution from interstitials.

The best test of theoretical calculations of defect energies is with experiment. We have recently published (33) a thorough analysis of the ionic conductivity of pure and doped crystals of RbCl. Ionic transport data are usually represented as plots of log σT vs. T^{-1} or log D vs. T^{-1} (σ = ionic conductivity, D = diffusivity) and consequently the gradients of these plots, when multiplied by 2.3026 k_B, are called Arrhenius energies. Arrhenius energies for RbCl, RbBr, and RbI (calculated from equations like [4]) are given in Table 11. This contains important information about transport mechanisms. We can expect both cv and av to contribute significantly to ionic transport in all three of the Rb halides, with the majority of these vacancies coming from Schottky rather than Frenkel defects. We must also expect substantial contributions from interstitials resulting from cation and anion Frenkel defects. Vacancy pairs will also contribute significantly to diffusion, though anion diffusion will be dominated by anion interstitials from Frenkel defects and anion vacancies from Schottky defects. Cation interstitials can be expected to dominate cation diffusion with smaller contributions form cation vacancies and pairs. These expectations may undergo some modifications in practice because the rate of transport depends on defect Gibbs energies rather than just enthalpies. Nevertheless defect energy calculations are a very useful guide in the analysis of transport data (33–35). It is the multiplicity of transport mechanisms in alkali halides that makes ionic conductivity data on pure crystals so difficult to analyze without additional data on σ for doped crystals and (or) diffusion. The above predicitions were substantially verified for RbCl and especially by the predictions of diffusion coefficients from defect parameters that resulted from analysis of conductivity data (see Fig. 11 of ref. 33).

Table 9. Calculated defect energies in eV at 0 K for RbCl, RbBr, and RbI.

Defect	RbCl	RbBr	RbI
u_S	2.52	2.365	2.139
Δu_{cv}	0.661	0.684	0.706
Δu_{av}	0.667	0.699	0.723
u_{Fc}	3.457	3.290	3.062
u_{Fa}	3.480	3.542	3.439
Δu_{cid}	0.264	0.303	0.335
Δu_{cic}	0.208	0.249	0.291
Δu_{cinc}	0.252	0.287	0.314
Δu_{aid}	0.241	0.265	0.330
Δu_{aic}	0.188	0.194	0.237
Δu_{ainc}	0.226	0.258	0.325
u_{vp}	–0.940	–0.908	–0.851
Δu_{cp}	0.795	0.806	0.803
Δu_{ap}	0.808	0.800	0.765

Table 10. Binding energies and vacancy jump energies, in eV, for RbCl:Sr^{2+} and RbCl:S^{2-} complexes

Defect	RbCl:Sr^{2+}	RbCl:S^{2-}
u_1	–0.596	–0.650
u_2	–0.583	–0.515
Δu_1	0.642	0.712
Δu_2	1.250	0.937
Δu_3	0.624	0.634
Δu_4	0.637	0.770

© 1998 NRC Canada

Table 11. Arrhenius energies in eV for RbCl, RbBr, and RbI.

Energy	RbCl	RbBr	RbI
E_{cv}^{S}	1.92	1.87	1.78
E_{cv}^{F}	2.39	2.33	2.34
E_{av}^{S}	1.93	1.88	1.79
E_{av}^{F}	2.41	2.47	2.44
E_{ci}^{F}	1.94	1.89	1.82
E_{ai}^{F}	1.93	1.92	1.96
E_{c}^{p}	2.38	2.42	2.47
E_{a}^{p}	2.39	2.41	2.43

Table 12 shows a comparison of values of defect enthalpies determined from ionic conductivity of RbCl with the calculated defect energies. The agreement is very close for cation parameters and somewhat less so for anion parameters. This is not too suprising because of the limited solubility of S^{2-} (and other divalent anions) in RbCl. The calculations for impurities also involve pair-potentials that could not be checked independently.

The ionic conductivity of RbBr and the diffusion of Rb^+ in RbBr have been measured by Downing and Friauf (36). They found Arrhenius energies of 2.01 and 1.99 eV for diffusion of Rb and Br and a value of 2.017 eV from conductivity. Since they considered only cation and anion vacancies and vacancy pairs, the implication is that the migration enthalpies for cv and av are very similar. However, an Arrhenius plot of conductivity data showed signficant curvature that our results (Table 11) indicate to be due to contributions from interstitials. Conductivity measurements on divalent cation- and anion-doped crystals are needed to permit a detailed analysis of the transport data for RbBr.

The ionic conductivity of pure RbI and RbI:Sr^{2+} has been measured by Chandra and Rolfe (37) and their Schottky defect formation enthalpy of 2.1 eV agrees well with our calculated energy. Unfortunately the conductivity of divalent anion-doped RbI could not be measured due to the low solubility of $RbCO_3$ in RbI, and consequently anion parameters could not be determined accurately. As for RbBr and RbCl, our calculations show that multiple transport mechanisms can be expected. Interstitials and vacancy pairs certainly should be considered in all three Rb halides.

Conclusions

The generally good agreement with experiment when such comparisons are possible supports the reliability of the pair potentials and defect energies reported in this paper. Such calculations make an invaluable contribution to our understanding of transport processes in ionic materials. They distinguish between possible transport mechanisms and are a useful guide in the analysis of transport data. Specifically, these results were indispensable in the analysis of ionic conductivity data for RbCl. They also suggest the models that should be used in the analysis of transport data for RbBr and RbI when further experimental data become available. The support received for these potentials indicates that the relatively straightforward hybrid method employed (namely, electron-gas calculations, supplemented by fitting of potential parameters to crystal data) is a reliable and useful method. The use of some form of dispersion damping in the charge overlap region is recommended both in potential fitting and in defect calculations. These calculations also provide further support (12, 13) for the reliablity of the Mott–Littleton method and of the HADES code.

Table 12. Defect enthalpies determined from ionic conductivity measurements on RbCl in the temperature range 520–960 K (29). Values quoted are the means from the computer-analysis of nine runs on pure RbCl, RbCl:Sr^{2+}, and RbCl:S^{2-}. Subscripts have the same meaning as in Tables 9 and 10. Frenkel defect formation enthalpies and interstitial migration enthalpies were held constant during nonlinear least-squares fitting of the data, so although their values do not provide an independent check on the calculations one can at least say that the calculated values are consistent with experiment. h_{1c} and h_{1a} are the nn association enthalpies determined from three runs each on RbCl:Sr^{2+} and RbCl:S^{2-}. Corresponding defect energies are reproduced from Tables 9 and 10 to facilitate comparison.

	Experimental (33) defect enthalpy/eV		Calculated defect energy/eV
h_s	2.520	u_s	2.52
Δh_{cv}	0.661	Δu_{cv}	0.66
Δh_{av}	0.720	Δu_{av}	0.67
h_{1c}	–0.592	u_1	–0.60
h_{1a}	–0.878	u_1	–0.65

A serious effort was made to see if a single set of Rb^+ shell parameters and Rb^+–Rb^+ Buckingham parameters could be established. However, it was found impossible to achieve this kind of accuracy in fitting properties without including some substance-dependent effects. As Table 1 shows, when Y for Rb^+ was held fixed, the variation in K was $\leq \pm 5\%$, while for the Buckingham parameters: ϱ /Å = 0.2853 ± 0.2%, A /eV = 5020.17 ± 1.2%, C /eV Å^6 = 69.45 ± 1.6%. These seem to be the limits to which a single transferable set can be developed for the Rb halides. Until such time as the calculation of ab initio potentials becomes a routine procedure, the present hybrid method can be recommended as a useful and relatively straightforward procedure.

Acknowledgement

Financial support by the Natural Sciences and Engineering Council of Canada (NSERC) through a research grant to P.W.M. Jacobs is gratefully acknowledged.

References

1. I.M. Boswarva and J.H. Simpson. Can. J. Phys. **51**, 1923 (1973).
2. J. Corish, B.M.C. Parker, and P.W.M. Jacobs. Can. J. Chem. **54**, 3839 (1976).
3. M.K. Uppal, C.N.R. Rao, and M.J.L. Sangster. J. Phys. C: Solid State Phys. **14**, 2909 (1981).
4. C.R.A. Catlow, J. Corish, K.M. Diller, P.W.M. Jacobs, and M.J. Norgett. J. Phys. C: Solid State Phys. **12**, 451 (1979).
5. D.K. Rowell and M.J.L. Sangster. J. Phys. C: Solid State Phys. **14**, 2909 (1981).
6. S.P. Sanyal, N. Agnihotri, and R.K. Singh. Philos. Mag. A: **57**, 661 (1988).
7. I.E. Hooton and P.W.M. Jacobs. Radiat. Eff. Defects Solids, **115**, 224 (1990).

© 1998 NRC Canada

8. N.F. Mott and M.J. Littleton. Trans. Faraday Soc. **34**, 485 (1938).
9. M.J. Norgett. Tech. Report R765, AERE, Harwell. 1974.
10. M. Leslie. Daresbury Laboratory Report DL/SCI/TM3IT. 1982.
11. C.R.A. Catlow and W.C. Mackrodt. Lect. Notes Phys. **166,** 3 (1982).
12. P.W.M. Jacobs. *In* Diffusion in materials. *Edited by* A.L. Laskar, J.L. Bocquet, G. Brébec, and C. Monty. Kluwer, Dordrecht. 1990. pp. 203–250.
13. P.W.M. Jacobs. J. Chem. Soc. Faraday Trans. 2, **85**, 415 (1989).
14. J.H. Harding. Rep. Prog. Phys. **53**. 1403 (1990).
15. J.H. Harding. Physica B (Amsterdam), **131**, 13 (1985).
16. C.R.A. Catlow, K.M. Diller, and M.J. Norgett. J. Phys. C: Solid State Phys. **10**, 1395 (1977).
17. N.C. Pyper. Philos. Trans. R. Soc. London Ser. A: **320**, 107 (1986).
18. P.W. Fowler and P.A. Madden. J. Phys. Chem. **89**, 258 (1985).
19. R.G. Gordon and Y.S. Kim. J. Chem. Phys. **56**, 3122 (1972).
20. P.T. Wedepohl. J. Phys. C: Solid State Phys. **10**, 1855, 1865 (1977).
21. J.C. Slater and J.G. Kirkwood. Phys. Rev. **37**, 682 (1931).
22. P.W. Fowler and N.C. Pyper. Proc. R. Soc. London Ser. A: **398**, 377 (1985).
23. R. Ahlrichs, R. Penco, and G. Scoles. Chem. Phys. **19**, 119 (1977).
24. P.W.M. Jacobs and M.L. Vernon. J. Chem. Soc. Faraday Trans. 2, **86**, 1233 (1990).
25. R.C. Baetzold, C.R.A. Catlow, J. Corish, F.M. Healy, P.W.M. Jacobs, M. Leslie, and Y.T. Tan. J. Phys. Chem. Solids, **50**, 791 (1989).
26. G. Raunio and S. Rolandson. J. Phys. C: Solid State Phys. **3**, 1013 (1970).
27. G. Raunio and S. Rolandson. J. Phys. C: Solid State Phys. **4**, 958 (1971).
28. G. Raunio and S. Rolandson. Phys. Status Solidi, **40**, 749 (1970).
29. A. Sadoc, F. Moussa, and G. Pepy. J. Phys. Chem. Solids, **37**, 197 (1976).
30. J.L. Gavartin, C.R.A. Catlow, A.L. Shluger, P.W.M. Jacobs, and Z.A. Rycerz. Radiat. Eff. Defects Solids, **134**, 104 (1995).
31. A.R. Allnatt and A.B. Lidiard. Atomic transport in solids. Cambridge University Press, Cambridge, U.K. 1993.
32. P.W.M. Jacobs. J. Chem. Soc. Faraday Trans. 2, **86**, 1197 (1990).
33. P.W.M. Jacobs and M.L. Vernon. J. Phys. Chem. Solids, **58**, 1007 (1997).
34. L. Acuna and P.W.M. Jacobs. J. Phys. Chem. Solids, **41**, 595 (1980).
35. I.E. Hooton and P.W.M. Jacobs. Can. J. Chem. **66**, 830 (1988).
36. H.L. Downing and R.J. Friauf. Phys. Rev. B: Solid State, **12**, 5981 (1975).
37. S. Chandra and J. Rolfe. Can. J. Phys. **51**, 236 (1973).
38. P.B. Ghate. Phys. Rev. A: **139**, 1666 (1965).
39. M.P. Tosi. Solid State Phys. **16**, 1 (1964).
40. J.T. Lewis, A. Lehoczky, and C.V. Briscoe. Phys. Rev. **161**, 877 (1967).
41. R.P. Lowndes and D.H. Martin. Proc. R. Soc. London Ser. A: **308**, 473 (1969).
42. R.P. Lowndes and D.H. Martin. Proc. R. Soc. London Ser. A: **316**, 351 (1970).
43 R.W.G. Wyckoff. Crystal structures. Interscience. Vol. 1. New York. 1963.
44. V.K. Jain and J. Shankar. Phys. Status Solidi B: **114**, 271 (1982).
45. E.W. Pearson, M.D. Jackson, and R.G. Gordon. J. Phys. Chem. **88**, 119 (1984).
46. D.H. Kuhner, H.V. Lauer, and W.E. Bron. Phys. Rev. B: Solid State, **5**, 4112 (1972).

© 1998 NRC Canada

Computer simulation of time correlation functions and matter transport coefficients for a model order–disorder alloy

Ziqiang Qin, Alan R. Allnatt, and E. Loftus Allnatt

Abstract: The time correlation functions associated with the Onsager phenomenological coefficients for isothermal matter transport have been calculated by Monte Carlo simulation for a binary system (A,B) at the equiatomic composition according to the Kikuchi–Sato model of an order–disorder alloy with vacancy transport mechanism. The diagonal (AA) time correlation functions are positive, decay monotonically to zero, and exhibit a long time tail where they vary as t^{-n} where t is time; the exponent n varies weakly with temperature at high temperatures and more rapidly as the temperature is lowered through the order–disorder transition temperature. In the region of short-range order the off-diagonal (AB) time correlation function is negative but otherwise shows similar behaviour to the diagonal one, although as the transition temperature is approached n varies more rapidly. At the transition temperature and below, the off-diagonal time correlation function increases from an initial negative value to a maximum where it is positive and then, at later times, decreases to zero. The implications of these observations for approximate theoretical calculations of the phenomenological coefficients are briefly indicated.

Key words: diffusion, non-equilibrium phenomena, statistical mechanics, transport properties.

Résumé : On a calculé les fonctions de corrélation de temps associées aux coefficients phénoménologiques d'Onsager pour le transport isotherme de la matière en utilisant une simulation de Monte Carlo pour un système binaire (A,B) à composition équiatomique, dans le modèle de Kikuchi–Sato d'un alliage en ordre–désordre et suivant le mécanisme de transports des lacunes. Les fonctions de corrélation de temps diagonales (AA) sont positives, elles donnent une décroissance monotone vers zéro et elles présentent une longue traitée en fonction du temps qui varie selon la fonction t^{-n} dans laquelle t est le temps; à température élevée, l'exposant n varie faiblement avec la température et il varie plus rapidement lorsqu'on abaisse la température et qu'elle croise la température de transition ordre–désordre. Dans la région d'ordre à courte distance, la fonction de corrélation de temps hors diagonale (AB) est négative, mais elle présente autrement un comportement similaire à celui de la diagonale même si, lorsqu'on approche la température de transition, elle varie plus rapidement. Jusqu'à la température de transition, la fonction de corrélation de temps hors diagonale augmente en passant d'une valeur initiale négative jusqu'à un maximum qui est positif avant de redescendre avec le temps jusqu'à zéro. On indique brièvement les implications de ces observations pour les calculs théoriques approximatifs des coefficients phénoménologiques.

Mots clés : diffusion, phénomène de non équilibre, mécanique statistique, propriétés de transport

[Traduit par la Rédaction]

1. Introduction

The transport of matter through solids underlies a great range of the phenomena of concern in materials science and in solid state physics and chemistry. In this context linear non-equilibrium thermodynamics provides an economical unifying theoretical framework (1) that has been increasingly adopted (2, 3); at its heart is the symmetric matrix of phenomenological coefficients, L_{ij}. For an isothermal system L_{ij} denotes the coefficient of proportionality between the flux of atoms of species i and the thermodynamic force acting on species j. Measured matter transport properties can all be expressed as functions of the L coefficients. It is important to recognize that in many practical cases, such as the annealing of radiation damage, the demixing of materials in externally maintained chemical potential gradients and even for simpler properties such as the intrinsic diffusion coefficients, both the diagonal and off-diagonal elements of the L matrix are significant (2, 3). Furthermore, the L coefficients for the major chemical components, with which we are concerned in this paper, cannot necessarily be expressed in terms of the more easily measured tracer diffusion coefficients of these components, although there is evidence that approximate relationships may hold in some circumstances (3, 4). These considerations, coupled with the difficulty of measuring the individual L coefficients experimentally, mean that it is invaluable to have statistical mechanical theories of these

Received January 23, 1998.

Z. Qin, A.R. Allnatt,[1] and E.L. Allnatt. Department of Chemistry, University of Western Ontario, London, ON N6A 5B7, Canada.

[1]Author to whom correspondence may be addressed. Telephone: (519) 679-2111, ext. 6316. Fax: (519) 661-3022. E-mail: aallnatt@julian.uwo.ca

© 1998 NRC Canada

coefficients for molecular models whose parameters are energies of interaction between atoms and between the various lattice defects, as well as the jump frequencies of atomic jumps between lattice sites in various local environments. For dilute alloys there are well-established and routine methods (3) for such calculations of the L coefficients for the main vacancy and interstitial migration mechanisms of atom transport but for concentrated alloys and highly defective systems this is far from being the case. The present paper is concerned with the L coefficients for a model of concentrated alloys with matter transport by a small concentration of vacancies.

The interacting lattice gas model with nearest-neighbour interactions between atoms (the Ising model (5)) has provided the basis for much of our understanding of the equilibrium properties of concentrated alloys. To describe matter transport this model must be supplemented with a consistent recipe for the jump frequencies; that due to Kikuchi and Sato (6) has been almost universally used and is the only one considered in this paper. The Kikuchi (7) path probability method has been used to calculate approximate expressions for the L coefficients of this model and later applications of this method have been reviewed (8). Apart from a recent work (27) described below, there appear to be no other kinetic theories of the non-tracer L coefficients of the Kikuchi–Sato model with which this paper is concerned, although there are interesting adaptations (9) of ideas, from the Manning theory (10) of the random alloy model to calculations of the tracer diffusion coefficients. (In the random alloy model all configurations have the same energy and each atom–vacancy exchange frequency depends only on the species of the jumping atom and is independent of the species of nearby atoms.) In principle, the L coefficients of the major chemical components could therefore be calculated by coupling these tracer diffusion coefficient expressions (9) with the approximate relationships (4) already referred to, but we shall not investigate this alternative route here.

In recent years Monte Carlo simulation results have been obtained for the L coefficients of the Kikuchi–Sato model of binary alloys with a very small vacancy content, mainly for the order–disorder case (11) but also for the strictly regular solution case (12). There are also results for the important extension of the order–disorder model to a wide range of vacancy concentrations (13). All these simulations are based on an exact linear response formula for the L coefficients written in a form that is a generalization of the familiar Einstein expression for tracer diffusion coefficients (3, 14). Two recent approaches have emphasized the utility of carrying out simulations on alloy models, which, unlike the Einstein method, provide additional kinetic data that can be associated with particular analytical approaches, thus providing additional tests and insights for approximate analytical theories. In one method (15), based on a decomposition of the Einstein type of formula and closely related to random walk methods that are well established for analyses of dilute alloys, attention is focused on averages of certain "collective" cosines of the angle between successive atom jumps. The method has so far been applied to the random alloy model. In this paper we concentrate on the second method, which simulates time correlation functions from which the L coefficients can be found by an integration over time. It has the advantage that, for analytical work, one can draw on adaptations of the Mori memory function formalism (16) for time correlation functions, which has proved so useful in the theory of the transport coefficients of fluids (17). A widely used method in the latter field has been to construct approximations to the time correlation functions from a knowledge of their lowest order moments (essentially, the coefficients of the Taylor expansion in powers of time of the time correlation functions). We have applied a scheme of this kind to the L coefficients of the random alloy and a two-sublattice generalization of that model (18). Recently we extended such calculations to the Kikuchi–Sato model of a simple cubic binary alloy with short-range order and a low vacancy content (27). The complexity of the moment calculations restricted these new results to an approximation for the time correlation functions that is expected to be good only at short times. In the present paper we summarize some features of new Monte Carlo simulations for such a system at the equiatomic composition as a function of temperature. These allow us to characterize the longer time behaviour of the time correlation functions and define more closely the structure needed for further development of the theory. Although we are primarily concerned with the region of short-range order covered by the recent theory, these simulations overlap the high-temperature end of the region with long-range order.

2. Model and simulation method

The model adopted is the same as that described and used in simulations by Murch and co-workers (11, 19) for order–disorder alloys. It is a rigid lattice model of a simple cubic alloy with nearest neighbour interaction energies E_{AA}, E_{BB}, and E_{AB} between atomic components A and B. These energies enter the partition function through the parameter

$$E = E_{AA} + E_{BB} - 2E_{AB} \quad [1]$$

For $E > 0$ there is a phase with long-range order at low temperatures. It exists within a boundary symmetric about the equiatomic composition, at which the transition temperature is given by $E/kT_c = 0.887$.

An atom can migrate by exchanging with a nearest neighbour vacancy. It is assumed that the vacancies are single and at such low concentration that they affect the bulk thermodynamic properties negligibly. The Kikuchi–Sato expression for the exchange frequency of an A atom with a nearest neighbour vacancy is

$$w_A^\alpha = \nu_A \exp(-U_A/kT) \exp([z_A^\alpha E_{AA} + z_B^\alpha E_{AB}]/kT) \quad [2]$$

and there is a similar expression for B. Here ν_A, the attempt frequency, and U_A, the energy of the jumping atom at the saddle point, are both taken as independent of the configuration α of the surroundings. The energy in the second exponential is that of the jumping atom before its jump, and z_A^α and z_B^α are the numbers of A and of B atoms, respectively, that are nearest neighbors to the jumping A atom before its jump. Following the practice in the earlier simulations on the order–disorder model (11) we shall set the quantities ν_i and $\exp(-U_i/kT)$ equal to unity in the simulation.

© 1998 NRC Canada

The linear response expression (3) for a phenomenological coefficient L_{ij} is the sum of a so-called uncorrelated part, $L_{ij}^{(0)}$, which is the value calculated neglecting correlations between successive molecular states and a term, $L_{ij}^{(1)}$, which contains such correlations and can be expressed in terms of a time correlation function. For the vacancy mechanism the off-diagonal ($i \neq j$) uncorrelated parts are zero. It has become conventional (3) to express theoretical results for the correlated parts in terms of correlation functions $f_{ij}^{(j)}$ defined as

$$[3] \qquad f_{ij}^{(j)} = \frac{L_{ij}}{L_{jj}^{(0)}}$$

where we drop the superscript j when $i = j$. The order of subscripts in $f_{ij}^{(j)}$ is immaterial because of the Onsager relation $L_{ij} = L_{ji}$. Using the linear response expression for the L coefficients this definition yields (20), for a simple cubic lattice, the equation

$$[4] \qquad f_{ij}^{(j)} = \delta_{ij} - \frac{2}{r_j}\int_0^\infty C_{ij}(t)\,\mathrm{d}t$$

Here δ_{ij} is a Kroenecker delta, r_j is the mean number of j atom jumps per unit time, and $C_{ij}(t)$ is a time correlation function which can be expressed as

$$[5] \qquad C_{ij}(t) = \left\langle \boldsymbol{V}_i(t) \cdot \boldsymbol{V}_j(0) \right\rangle$$

where the angular brackets denote an equilibrium average. For a given configuration of atoms at time t the quantity $\boldsymbol{V}_i(t)$ is the jump frequency multiplied by a unit vector in the direction moved by the jumping atom added up for all possible i atom jumps that can occur in that configuration. $\boldsymbol{V}_i$ is a stochastic analogue of the collective velocity of the i atoms. The matrix of the time correlation functions is symmetric, $C_{ij}(t) = C_{ji}(t)$. The uncorrelated part $L_{jj}^{(0)}$ is proportional to the mean jump rate r_j calculated in the simulations (20); these quantities will not be discussed here since they pose a problem in equilibrium statistical mechanics that is relatively straightforward. Our interest in this paper is mainly in the structure of the time correlation functions, i.e., in the truly kinetic (non-equilibrium) part of the problem. It should be noted that despite the naming of the $f_{ij}^{(j)}$ as correlation functions it is $f_{ij}^{(j)} - \delta_{ij}$ which is a measure of the size of the correlation effects.

Calculations were made for a 20 × 20 × 20 simple cubic lattice with periodic boundary conditions. As in earlier simulations for this model (11, 19), an equilibrium system was first generated by conducting a grand canonical ensemble Monte Carlo simulation exactly as described in ref. 19*a* using a fully ordered initial state without vacancies. After 8×10^6 states a vacancy was introduced by removing a randomly chosen atom and the kinetic simulation was started. The latter followed the method already described for the random alloy (20) and for a random model with two sublattices (21). With the system in a known configuration at time t, the waiting time in that state was calculated and the next jump of the vacancy was selected by the procedure described in more detail by Reed and Ehrlich (22). This required calculating the exchange frequencies of the vacancy for the six possible jumps out of its current site and then forming the sum w_T of these frequencies. The waiting time t_W in the current state was then set equal to $-(\ln R)/w_T$, where R is a random number in the interval from 0 to 1 and the actual jump to be made was selected in accord with the relative probabilities of the six possible jumps using a further random number. The next configuration was then set up by moving the vacancy to the selected nearest neighbour site and the time counter was increased from t to $t + t_W$. A long sequence of configurations was generated in this way and the velocity vectors $\boldsymbol{V}_A$ and $\boldsymbol{V}_B$ were determined at equally spaced intervals Δt of time. The time correlation functions $C_{ij}(t)$ were calculated from the average of the scalar product of the appropriate velocity vectors each measured at an interval apart of time t. The correlation functions $f_{ij}^{(j)}$ were calculated by time integration of the time correlation functions using Simpson's rule. Runs were made until significant changes in the results of interest were no longer apparent. This required 40 to 60 million vacancy jumps (although longer runs were sometimes made) and took several hours on a Cray J90se computer.

Fig. 1. The f correlation functions (f_{AA} and $f_{AB}^{(A)}$) (as functions of E/kT: (●) present Monte Carlo simulation points; (— × —) simulation points by Einstein method (11) with a smooth line added; (– – –) Mori-type theory (27); (-----) path probability theory (23).

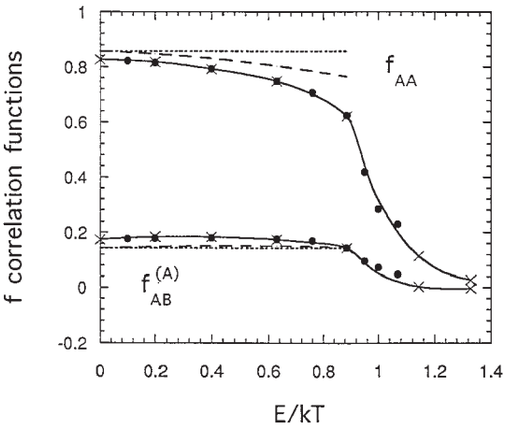

Results in this paper all refer to the equiatomic concentration with $E_{AA} = E_{BB}$. The zero of energy was chosen as $E_{AA} = 0$ for convenience. At the chosen composition one expects that $f_{AA} = f_{BB}$, and $f_{AB}^{(A)} = f_{AB}^{(B)}$; this was verified to high accuracy in all the simulations.

3. Results and discussion

Our results for the correlation functions f_{AA} and $f_{AB}^{(A)}$ as functions of E/kT are shown in Fig. 1 for five temperatures in the "high temperature" region above T_c and also at T_c and three lower temperatures. Points calculated by Murch and co-workers (11) by the Einstein method, plus the exact theoretical values at $E/kT = 0$, are also shown with a smooth curve drawn between them. Agreement is excellent in the high-temperature region but there are small discrepancies below T_c where slow convergence can be a problem in both methods.

© 1998 NRC Canada

Fig. 2. Logarithm of the normalized time correlation function N_{ij} as a function of the reduced time t: (——) interpolated line through Monte Carlo simulation points taken at intervals in t of 0.014 in (*a*) and 0.03 in *(b)*; (-----) Mori-type theory for N_{AA} (27); (— - —) Mori-type theory for N_{AB}. (*a*) N_{AA} for E/kT = 0.2; (*b*) N_{AA} and N_{AB} for E/kT = 0.76.

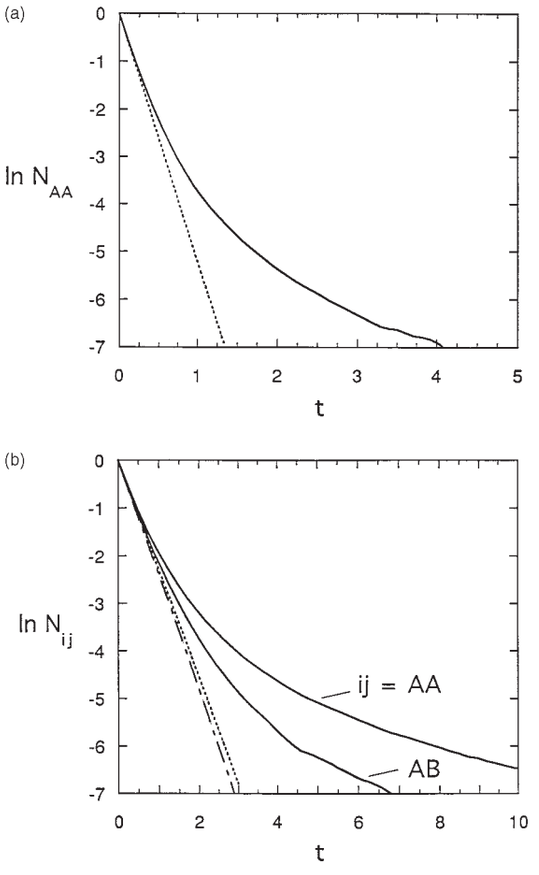

The results in Fig. 1 also show that the predictions from our recent theory based on the Mori formalism for the system with short-range order underestimate the correlation effects but are a useful guide to the correct results. For f_{AA} our predictions are slightly more successful than those that are shown from the path probability method (23), but for $f_{AB}^{(A)}$ there is little difference. References to later versions of the path probability method than the version employed in ref. 23 can be found in the review (8) cited earlier, but these have not so far been applied in detail to the model of interest here.

Our theory uses approximate expressions for the two lowest order moments of each of the time correlation functions and a truncation of the Mori continued fractions for the time correlation functions. It is expected to supply a correct short-time approximation to the time correlation functions. This is verified at all the temperatures by plots of ln N_{ij} versus t, where we employ the normalized time correlation function defined by

$$[6] \qquad N_{ij}(t) = C_{ij}(t)/C_{ij}(0)$$

Fig. 3. Log–log plots of normalized time correlation functions N_{ij} as functions of reduced time t at three values of E/kT: (○) Monte Carlo simulation points for $-6 < \ln N_{ij} < -3$; (——) linear least- squares fit. For the two N_{AA} plots all the points shown are fitted but for N_{AB} only $-6 < \ln N_{AB} < -4$ is used.

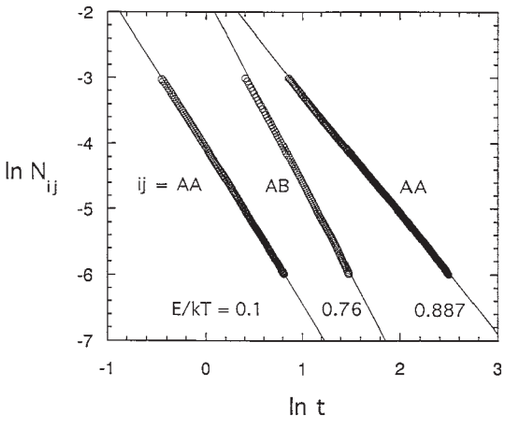

Examples are shown in Fig. 2 for temperatures towards the high- and low-temperature ends of the short-range order region. In the former case (E/kT = 0.2) $N_{AA}(t)$ and $N_{AB}(t)$ would be almost indistinguishable on the plot shown in Fig. 2(*a*) but for the latter case (E/kT = 0.76) the two functions are, as shown in Fig. 2(*b*), appreciably different. We should note that $C_{ij}(0)$ is always positive for ij = AA and always negative for ij = AB, and that the difference between $C_{AA}(t)$ and $C_{BB}(t)$ in the simulation results is negligible. The reduced time t in the figures is a dimensionless quantitity that is the actual time in units of $(\nu_i \exp(-U_i/kT))^{-1}$. (As noted earlier, $\nu_i \exp(-U_i/kT)$ has been set equal to 1 for i = A, B.)

Since the discrepancy between the theory and simulations is at long times we turn to the characterization of the long-time behaviour of the simulated time correlation functions. Examination of plots of ln N_{AA} versus ln t shows a linear relation at the largest times. Noise in the plots is greater the larger the value of t and can be decreased only by longer simulation runs. It was concluded that for the data presented here no values of $N_{AA}(t)$ smaller than 0.002 should be considered in any numerical analysis. With this limitation one finds that the linear regions extend over about the last three decades in t; examples are shown in Fig. 3 at the highest temperature simulated (E/kT = 0.1) and at the transition temperature (E/kT = 0.887). We find from least-squares fitting that $N_{AA}(t)$ varies as $t^{-n_{AA}}$ where, in the high-temperature region, n_{AA} decreases with increasing E/kT, as shown in Fig. 4. This figure includes a theoretical value of n_{AA} = 2.5 at E/kT = 0, which is consistent with the simulation data. The origin of this theoretical result is as follows.

At the high-temperature limit (E/kT = 0) the model is equivalent to the random alloy model at the equiatomic composition for two components with equal jump frequencies. It was shown earlier (20), both theoretically and in simulation, that the normalized time correlation function for the latter system is the same as that for a tracer atom migrating in a pure crystal with the host atom and tracer atom jump frequencies equal; an analysis of the asymptotic form of the

© 1998 NRC Canada

Fig. 4. The exponents n_{ij} for the power law tails of the time correlation functions as functions of E/kT: (●) for n_{AA}, (×) for n_{AB}; lines have been added to guide the eye. Values are determined from plots in Fig. 3 plus similar plots for other values of E/kT. For $E/kT = 0.887$, n_{AB} refers to the approach to the minimum where $N_{AB}(t) > 0$ and not to the tail at longer times where $N_{AB}(t) < 0$, see Fig. 5.

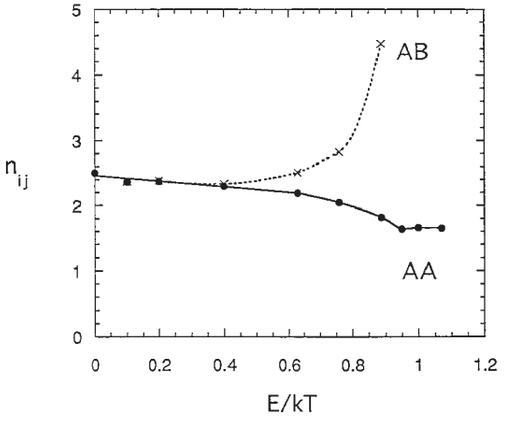

theoretical expression for this time correlation function (24) shows that the tail decays as t^{-n} with $n = 2.5$. The same result is also obtained (25) from an analysis of the tracer system based on an adaptation of mode coupling ideas, more usually formulated for Hamiltonian models (17*b*), to the domain of hopping models. The compatibility of the trend of our simulated results at finite temperatures with this limiting theoretical value therefore suggests that the tail behaviour we have found lies within the region accessible to mode coupling methods, although we know of no such analysis for the model studied here.

Referring again to Fig. 4 we note that n_{AA} drops more rapidly with decreasing temperature in the neighbourhood of T_c than at higher temperatures. It falls to 1.86 at the transition temperature, $E/kT_c = 0.887$. At the three temperatures below the transition that we have studied it is in the range 1.65–1.68.

At the highest temperature studied ($E/kT = 0.1$) $N_{AB}(t)$ is essentially indistinguishable from $N_{AA}(t)$ but as the temperature is lowered N_{AB} is found to decay as a function of time more rapidly than N_{AA} and, as shown in Fig. 3, the linear portion of the log–log plot for $N_{AB}(t)$ shrinks to about two decades in t at $E/kT = 0.76$. As shown in Fig. 4, n_{AB} (from fits of $N_{AB}(t)$ to $t^{-n_{AB}}$) is therefore equal to n_{AA} at the highest temperature simulated, but at $E/kT = 0.63$ and lower temperatures the two quantities diverge in value as the transition temperature is approached, with n_{AB} increasing as T is decreased (in contrast to n_{AA}). Whereas $N_{AA}(t)$ at all temperatures and $N_{AB}(t)$ at temperatures above T_c both decrease monotonically to zero, we find that at T_c and lower temperatures $N_{AB}(t)$ decreases to a minimum where it is negative and then, at later times, increases to zero. As shown in Fig. 5, in the limited range studied here the well depth increases as T is decreased. The long-time tail at the temperatures below T_c, where $N_{AB}(t)$ is negative at the longest times, is large enough to be quite significant in calculating $f_{AB}^{(A)}$. Unfortunately, the noise level is too large to determine

Fig. 5. Normalized time correlation functions N_{AB} as functions of reduced time t in the region of the minimum in N_{AB} at the transition temperature and below for values of E/kT as marked. Interpolated curves are shown because of the high density of sample points used.

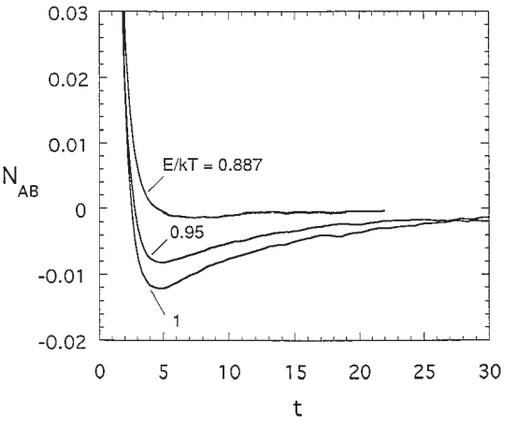

whether the tail of N_{AB} accurately obeys a power law decay to zero in this region. (We should remark that the AB time correlation function decreases in magnitude compared with the AA time correlation function as T is lowered. The ratio $-C_{AB}(0)/C_{AA}(0)$ decreases from 0.99 at $E/kT = 0$ to 0.54 at T_c, and decreases from 0.37 to 0.28 as T is lowered from $E/kT = 0.95$ to $E/kT = 1.07$. In practice, the length of simulation used here is quite adequate to allow characterization of the tail of C_{AA} but not of C_{AB} at the transition temperature and below.)

4. Concluding remarks

The simulation results described show that the time correlation functions associated with the phenomenological coefficients for the Kikuchi–Sato model of a binary alloy with a low vacancy content show a slow decay at long times. As already indicated, a possible route to understanding the change with temperature of the time dependence of this decay is through mode coupling methods that have so far been worked out only for tracer mixtures (25). In addition, an improved approach to the theory of approximate analytical formulae for the L coefficients may be made through the inclusion of mode coupling ideas in the calculation of time correlation functions and their associated memory functions within the framework of the projection operator formalism; in effect, one can seek to build on our recent theory, which employs just low-order moments within this framework. Earlier examples of such procedures in the theory of transport in fluids (17*b*, 26) provide indications of the techniques possible in this context. As a preliminary, we have recently investigated, in the context of the Mori (16) type of theory, the use of projection operator methods for time correlation functions that, as here, are based on a discrete master equation (3) rather than the Liouville equation description employed for fluids (Qin and Allnatt, in preparation).

A second striking feature of the simulation results is the occurrence of a sign reversal at intermediate times in the off-diagonal time correlation function but not in the diagonal

© 1998 NRC Canada

one when there is long-range order. We hesitate to attempt a quick physical interpretation of this result, in part because it is not clear to us whether it is connected with the occurrence of cycles of vacancy jumps recently found to be significant in recent simulations (26) of two models of ordered alloys.

Acknowledgement

Financial support by the Natural Sciences and Engineering Research Council of Canada is gratefully acknowledged.

References

1. R.E. Howard and A.B. Lidiard. Rep. Prog. Phys. **27**, 161 (1964).
2. J. Philibert. Atom movements — diffusion and matter transport in solids. Les Éditions de Physique, Les Ulis, France. 1991.
3. A.R. Allnatt and A.B. Lidiard. Atomic transport in solids. Cambridge University Press, Cambridge. 1993.
4. A.B. Lidiard, G.E. Murch, Z. Qin, and L. Zhang. Philos. Mag. A: **62**, 595 (1990).
5. T.L. Hill. Statistical mechanics. McGraw–Hill, New York. 1956.
6. (*a*) R. Kikuchi and H. Sato. J. Chem. Phys. **51**, 161 (1969); (*b*) J. Chem. Phys. **53**, 2702 (1970); (*c*) J. Chem. Phys. **57**, 4962 (1972).
7. R. Kikuchi. Prog. Theor. Phys. Suppl. **35**, 1 (1966).
8. S.A. Akbar. J. Mater. Sci. **27**, 3125 (1992).
9. (*a*) H. Bakker. Philos. Mag. A: **40**, 525 (1979); (*b*) N.A. Stolwijk. Phys. Status Solidi B: **105**, 223 (1981).
10. J.R. Manning. Phys. Rev. B: Solid State, **4**, 1111 (1971).
11. (*a*) L. Zhang, W.A. Oates, and G.E. Murch Philos. Mag. A: **58**, 937 (1988); (*b*) Philos. Mag. B: **60**, 277 (1988); (*c*) Z. Qin and G.E. Murch. Philos. Mag. A: **67**, 757 (1993).
12. A.R. Allnatt and E. L. Allnatt. Philos. Mag. A: **64**, 341 (1991).
13. (*a*) L. Zhang and G.E. Murch. Solid State Ionics, **47**, 125 (1991); (*b*) Z. Qin and G.E. Murch. Philos. Mag. A: **71**, 323 (1995).
14. A.R. Allnatt. J. Phys. C: Solid State Phys. **15**, 5605 (1982).
15. (*a*) Z. Qin and G.E. Murch. Philos. Mag. A: **66**, 957 (1992); (*b*) Philos. Mag. A: **70**, 481 (1994); (*c*) I.V. Belova and G.E. Murch. Philos. Mag. A: **72**, 871 (1996).
16. H. Mori. Prog. Theor. Phys. **34**, 399 (1965).
17 (*a*) J.P. Boon and S. Yip. Molecular hydrodynamics. McGraw–Hill, New York. 1980; (*b*) J.P. Hansen and I.R. McDonald. Theory of simple liquids. 2nd ed. Academic Press, New York. 1986.
18. (*a*) Z. Qin and A.R. Allnatt. Philos. Mag. A: **71**, 975 (1995); (*b*) Philos. Mag. A: **76**, 615 (1997).
19. (*a*) G.E. Murch. Philos. Mag. A: **45**, 941 (1982); (*b*) Philos. Mag. A" **46**, 565 (1982); (*c*) Philos. Mag. A: **46**, 575 (1982).
20. Z. Qin, A.R. Allnatt, and E.L. Allnatt. Philos. Mag. A: **71**, 291 (1995).
21. A.R. Allnatt and E.L. Allnatt. Philos. Mag. Lett. **64**, 393 (1991).
22. D.A. Reed and G. Ehrlich. Surf. Sci. **105**, 819 (1981).
23. C.C. Wang and S.A. Akbar. J. Phys. D: Appl. Phys. **28**, 120 (1995).
24. (*a*) H. van Beijeren and K.W. Kehr. J. Phys. C: Solid State, **19**, 1319 (1986); (*b*) Z. Qin and A.R. Allnatt. Philos. Mag. A: **70**, 677 (1994).
25. H. van Beijeren. J. Stat. Phys. **35**, 399 (1984).
26. (*a*) I.V. Belova, M.E. Ivory, and G.E. Murch. Philos. Mag. A: **72**, 871 (1995); (*b*) M. Athènes, P. Bellon, and G. Martin. Philos. Mag. A: **76**, 565 (1997).
27. Z. Qin, A.R. Allnatt, and E.L. Allnatt. J. Phys. Condens. Matter, **10**, 5295 (1998).

© 1998 NRC Canada

Composite poly(*p*-phenylenevinylene)–Nafion thin films

Troy A.E. Loss, Cerrie W. Rogers, and Michael O. Wolf

Abstract: Composite thin films of poly(*p*-phenylenevinylene) and the polyelectrolyte Nafion have been prepared by the polymerization of 1,1′-[(*p*-phenylene)bis(methylene)bis[tetrahydrothiophenium] dichloride electrostatically bound to Nafion. The composite films are strongly fluorescent. The absorption and photoluminescence spectra of the films have been measured and are similar to those of poly(*p*-phenylenevinylene). X-ray microanalysis and weight gain experiments performed on the films suggest that the dicationic monomer occupies less than 15% of the cation exchanging sites in the Nafion, leaving sites available for binding of additional small cations.

Key words: thin films, conducting polymers, poly(*p*-phenylenevinylene), polyelectrolyte, photoluminescence.

Résumé : Des films composites minces de poly(*p*-phénylènevinylène) et de polyélectrolyte Nafion ont été préparés par polymérisation de dichlorure de 1,1′-[(*p*-phénylène)bis(méthylène)-bis(tétrahydrothiophénium)] électrostatiquement lié au Nafion. Ces films composites fluorescent fortement. Leur spectres d'absorbance et de photoluminescence ont été mesurés et sont comparable à ceux du poly(*p*-phénylvinylène). Le taux d'occupation des sites par les dications monomères est de moins de 15%, mesuré par microanalyses rayons X et gain de poids. Il reste de nombreux sites disponibles capable d'accepter de petits cations.

Mots clés : films minces, polymères conducteurs, poly(*p*-phénylènevinylène), polyélectrolyte, photoluminescence.

Introduction

In the past several years, the efforts of many materials scientists have been focused on developing highly luminescent, conducting polymers for use in polymer-based light-emitting diodes (LEDs). LEDs are devices that emit light when electrons and holes injected into a layer of emissive material recombine and release energy. Emissive polymers open the door to low-cost, flexible, large-area colour displays because of their enhanced processibility and structural variety (1). Polymer LEDs were first prepared by Friend and co-workers in 1990 using poly(*p*-phenylenevinylene) (PPV) **1** sandwiched between indium tin oxide and Al electrodes (2). One method of synthesizing PPV is by polymerization of 1,1′-[(*p*-phenylene)bis(methylene)-bis[tetrahydrothiophenium] dichloride **2** (3).

Much work has been devoted to improving the overall efficiency of polymer LEDs (4). Chemical modifications of the PPV framework have led to both easier polymer processing and tuning of the colour of the emitted light (5). Since the mobility of charge carriers (electrons and holes) is critical to the functioning of polymer LEDs, conducting polymers have been coupled with other materials in order to develop systems that exhibit high charge mobility. Progress has been made using multicomponent systems, typically multilayer devices that incorporate hole-injecting and electron-injecting layers, as well as a variety of electrode-polymer combinations (5).

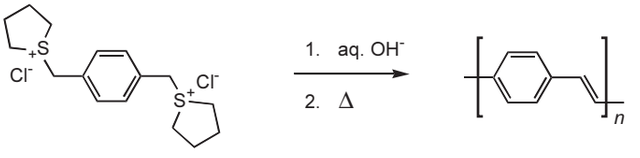

2 **1**

Composites of polyelectrolytes and conducting polymers have been the subject of much interest recently (6–12). Polyelectrolytes, such as poly(styrenesulfonate) and Nafion,[2] function as ion exchange polymers through which charged species can readily migrate. They are therefore ideal hosts for conducting polymers such as polythiophene, polypyrrole, and polyaniline because these heterocyclic polymers are readily electropolymerized, a process that requires mobile charges. By first embedding the appropriate monomer into the polyelectrolyte, this electropolymerization can be carried out in situ. The properties of the resulting composite materials are often different from those of the pure conducting polymer. Although the conductivity of such composites has been extensively studied (6–12), there are only a few studies of

Received February 2, 1998.

T.A.E. Loss, C.W. Rogers, and M.O. Wolf.[1] Department of Chemistry, The University of British Columbia, Vancouver, BC V6T 1Z1, Canada.

[1]Author to whom correspondence may be addressed. Telephone: (604) 822-1702. Fax: (604) 822-2847. E-mail: mwolf@chem.ubc.ca

[2]Registered trademark of E.I. duPont de Nemours & Co., Inc., for its perfluorosulfonic acid polymer products.

© 1998 NRC Canada

Fig. 1. Schematic representation of preparation of the PPV–Nafion composite material. PPV monomer and developing polymer are shown on the surface of the Nafion film for simplicity. Sulfonate groups represent the Nafion side-chain ionophores.

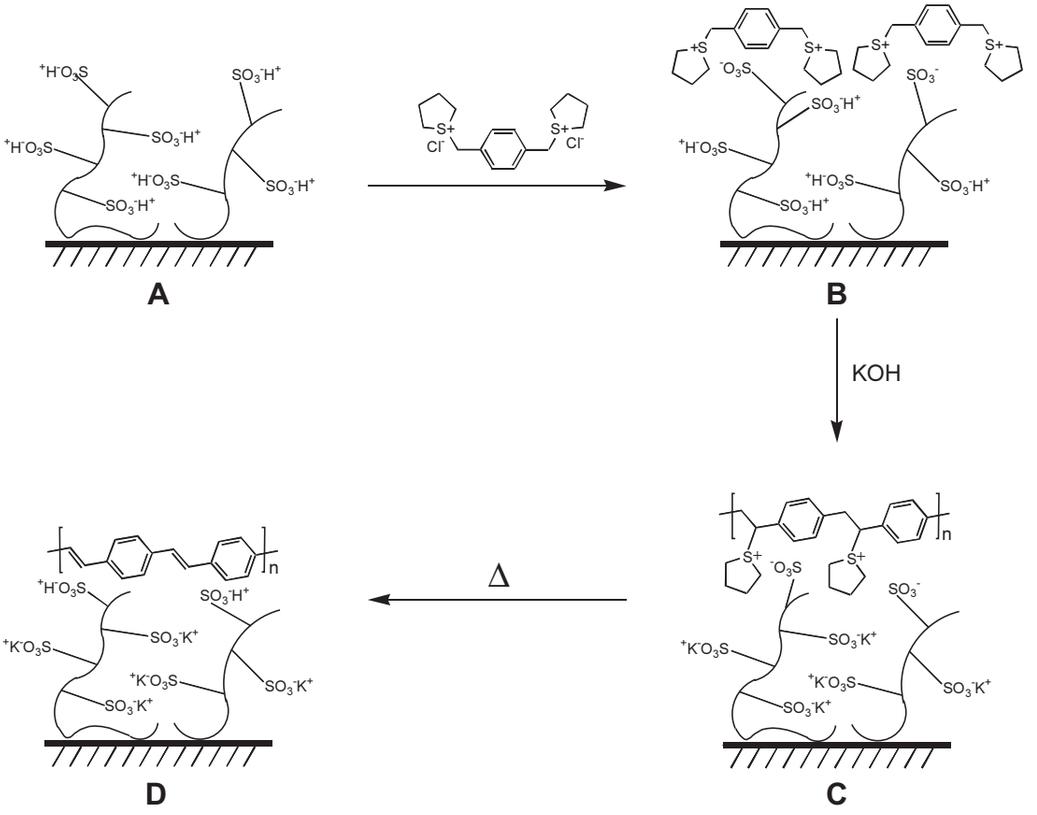

the electroluminesence of composite materials containing conducting polymers and polyelectrolytes (13–21).

LEDs in which the emitting layer is a composite of PPV and a polyelectrolyte have been shown to perform efficiently because the device functions as a solid state electrochemical cell (13–21). We are developing polymer LEDs based on composite materials formed by polymerizing PPV within a polyelectrolyte matrix. In this paper, we describe the preparation and properties of such composites of PPV and the polyelectrolyte Nafion. Our approach is novel in that the dicationic PPV monomer is exchanged into a Nafion film, followed by in situ chemical polymerization of the PPV. Figure 1 schematically illustrates the sequence of steps used to prepare the PPV–Nafion composite material.

Results and discussion

Film preparation

Nafion **3** is a perfluorinated polymer containing sulfonated side chains (22) that is used as an ion-exchange matrix (23). Cations are strongly absorbed by Nafion films, and composite cation–polyelectrolyte materials have been used in a variety of applications. High-quality Nafion films can readily be prepared by evaporating solutions of the polymer onto a surface. Such films adhere to glass surfaces; however, we find that Nafion films cast on glass peel easily upon immersion into aqueous solutions, even for short immersion times.

Since the PPV monomer **2** polymerizes in aqueous base, it was necessary to find a surface treatment that would prevent peeling of the Nafion film in base solutions. This was accomplished by pretreating the glass surface overnight with neat 3-aminopropyltriethoxysilane. Organosilanes are well known to behave as adhesion promoters for polymers on glass surfaces (24, 25). Nafion films cast onto such pretreated surfaces are more durable in base than those cast onto untreated surfaces; however, extended immersion in base still causes peeling of the films. Adhesion of the Nafion is likely enhanced by the aminosilane treatment because of protonation of the surface amino groups by the free-acid form of Nafion, resulting in electrostatic binding of the Nafion to the surface. In neutral aqueous solutions, such films on aminosilanized glass are stable; however, in basic solution, deprotonation of the surface ammonium groups results in eventual cleavage due to removal of the electrostatic stabilization.

The monomer **2** is incorporated into the Nafion matrix by immersion of prepared films in a dilute aqueous solution of **2** for 10 min (Fig. 1B). Subsequent immersion into a solution of the highly coloured tris(2,2′-bipyridyl)ruthenium(II) dication ($Ru(bpy)_3^{2+}$) does not result in any colour change in the film, suggesting that most of the binding sites in the film that are available to large cations are occupied by **2.** In comparison, immersion of a pristine Nafion film in a solution of

© 1998 NRC Canada

$Ru(bpy)_3^{2+}$ results in a rapid colour change from colourless to deep orange.

Weight gain experiments to determine monomer loading show that monomer **2** occupies a small fraction of the total available ion exchange sites in the Nafion film.[3] Based on the ion exchange capacity of Nafion (equiv. wt. 1100), occupation of all sites by **2** would result in mass increase of 16%,

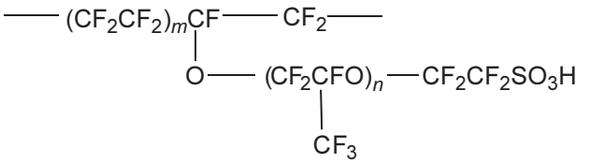

3

assuming one monomer per two sulfonate groups. However, the observed mass increase is negligible, which corresponds to occupation of fewer than 15% of the sites by **2**.

The Nafion films treated with **2** are polymerized by immersion in 1 M KOH for 2 min (Fig. 1C). Extended immersion in base results in peeling of the films, and even with the surface pretreatment it has not been possible to obtain completely uniform, well-bonded films. After base treatment, the films are heated to promote the thermal elimination of tetrahydrothiophene that produces the conjugated PPV structure (Fig. 1D). During heating, the films become yellow and fluoresce strongly under UV light (366 nm). Visually, the films are smooth and uniformly coloured.

Absorption and photoluminescence spectra

The absorption and photoluminescence spectra of the PPV–Nafion composite at 25°C are shown in Fig. 2*a*. The absorption spectrum is nearly identical to that observed for PPV prepared by thermal treatment of base-polymerized **2** (Fig. 2*b*), the absorption maximum falling in the visible region at approximately 390 nm. The similarity of the two absorption spectra suggests that the conjugation length in the two materials is comparable.

The PPV–Nafion films are highly fluorescent, emitting in the green region as do PPV films. The photoluminescence spectrum of the composite has one band (λ_{max} = 510 nm) with a small low-energy shoulder. The spectrum of the composite is, however, significantly different from that observed for PPV (Fig. 2*b*), in which two well-defined bands are observed (A: λ_{max} = 510 nm; B: λ_{max} = 540 nm) plus a low-energy shoulder. These bands are due to coupling of the electronic transitions to vibrational modes; band A corresponds to the 0–0 transition, band B corresponds to the 0–1 transition. Resolved vibrational structure is typically observed for samples with a high degree of intrachain order (26), and the relative intensities of the transitions vary with temperature (26). In the spectrum of the composite film, the vibrational structure is not resolved, which suggests that the constrained environment of the Nafion host gives rise to PPV that is more disordered than conventional PPV.

It is conceivable that limited polymerization may have occurred within the Nafion matrix, yielding oligomeric PPV. PPV oligomers exhibit blue-shifted emission but retain the same spectral shape as long-chain PPV, with the energy of oligomer emission converging to that of the polymer for chains containing over six monomer units (27). Based on the observed emission spectrum of the composite film (Fig. 2*a*), if limited polymerization has occurred, the oligomers must be over six monomer units long. This is consistent with the absorption spectrum as noted above.

Fig. 2. Absorption (---) and photoluminesence (——) spectra of (*a*) a PPV–Nafion composite film and (*b*) a PPV film. Photoluminescence spectra were obtained using excitation at 420 nm.

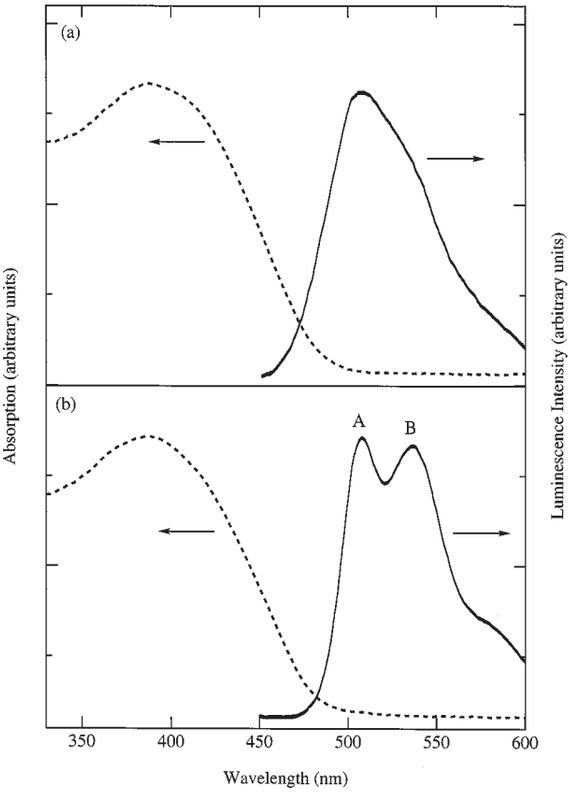

X-ray microanalysis

The films were characterized by energy-dispersive X-ray microanalysis (EDX) in order to determine elemental content. We analyzed samples corresponding to the four stages of film preparation as depicted in Fig. 1A–D. The data indicate that all samples contain approximately the same percentage of sulfur, consistent with only a small percentage of the available ion exchange sites being occupied by **2** (vide supra). Interestingly, the composite films contain a significant amount of potassium (~20%) after base treatment (Fig. 1C). The potassium is not removed by rinsing with water and is therefore presumed to be electrostatically bound to the Nafion. Thus, the large fraction of sites inaccessible to **2** may be occupied by K^+ ions. This is likely due to the large differences in size and shape between **2** (effective radius ~ 10 Å) and K^+ (1.37 Å) (28).

[3] Number of ion exchange sites calculated as follows: 1000 × (equiv. wt.)$^{-1}$ = mequiv./g Nafion.

© 1998 NRC Canada

Recent investigations of Nafion film microstructure (29–32) have shown that the films consist of hydrophilic pores containing clusters of $-SO_3^-$ groups dispersed in a hydrophobic fluorocarbon matrix. These ionic clusters range from 30 to 100 Å in diameter. Monomer **2** is sufficiently large that it may be difficult to exchange it into the smaller hydrophilic clusters in the Nafion film, leaving the smaller pores to exchange K^+ ions upon base treatment of the film. Also, the rodlike monomer molecules may "plug" the smaller pores if their orientation is correct; this would prevent further incorporation of monomer (32). The variation in pore size and the "plugging effect" may account for the low monomer loading observed. The clustered nature of the ionophores in Nafion may also influence the morphology of the PPV that is produced within this matrix, perhaps inducing decreased conformational order as is suggested by the fluorescence spectrum of the PPV–Nafion composite.

Conclusions

The PPV–Nafion composite has several properties that suggest it will be an interesting material for use in LED devices. The absorption and fluorescence spectra indicate that PPV is formed, although it appears to be more disordered than conventionally prepared PPV. The incorporation of K^+ ions into the composite indicates that binding additional small cations is possible. These sites may be useful for binding additional lumophores. Further investigations into the properties of the composite are underway.

Experimental section

Materials

Nafion (free acid form, 5 wt.% solution in a mixture of lower aliphatic alcohols) and 3-aminopropyltriethoxysilane (98%) were used as received from Aldrich. Tris(2,2′-bipyridyl)ruthenium(II) chloride trihydrate (>98%) was used as received from Strem Chemical. 1,1′-[(*p*-Phenylene)bis(methylene)bis(tetrahydrothiophenium)] dichloride was prepared as described in the literature (3).

Film preparation

Glass surfaces were cleaned by sonicating for 10 min in soapy water, rinsing with distilled water, sonicating 10 min each in methanol and acetone, and air-drying. The clean surfaces were then immersed overnight in neat 3-aminopropyltriethoxysilane, rinsed with acetone, and dried in air. Nafion films were cast onto the treated surfaces and the solvent was allowed to evaporate completely. To incorporate monomer, Nafion films were immersed in 3 mM aqueous **2** for 10 min, rinsed with distilled water, and air-dried. Polymerization was carried out in the Nafion matrix by immersing prepared films in 1 M KOH for 1–2 min, followed by rinsing with distilled water. The PPV-precursor polymer within the resulting polyelectrolyte composite was thermally converted to PPV by heating to >250°C with a heat gun until the film became visibly yellow-green. Reference PPV films were prepared similarly from dilute methanolic solutions of base-polymerized **2** cast directly onto clean glass surfaces.

Film characterization

UV–vis absorption and fluorescence spectra of the films were measured on a UNICAM UV2 UV–vis spectrometer and a Perkin–Elmer LS-5B photoluminescence spectrometer, respectively. EDX microanalysis was carried out using a Hitachi S-2300 scanning electron microscope coupled with a Kevex 8000 (with quantum window) microanalyzer system. Weight gain upon monomer incorporation was determined by weighing dry Nafion films before and after treatment with aqueous monomer **2**.

Acknowledgements

We would like to thank Dr. L. Burtnick for the use of the photoluminescence spectrometer and Mary Major (Dept. of Metals and Materials Engineering, UBC) for assistance with the EDX measurements. We are grateful to the Natural Sciences and Engineering Research Council of Canada (NSERC) for funding in the form of a research grant to M.O.W. and a postgraduate fellowship to C.W.R.

References

1. P.E. Burrows, G. Gu, Z. Shen, S.R. Forrest, and M.E. Thompson. IEEE Trans. Electron Devices, **44**, 1188 (1997).
2. J.H. Burroughes, D.D.C. Bradley, A.R. Brown, R.N. Marks, K. Mackay, R.H. Friend, P.L. Burns, and A.B. Holmes. Nature, **347**, 539 (1990).
3. R.W. Lenz, C.-C. Han, J.S. Smith, and F.E. Karasz. J. Polym. Sci. Part A: Polym. Chem. **26**, 3241 (1988).
4. I.D. Parker. J. Appl. Phys. **75**, 1656 (1994).
5. A. Kraft, A.C. Grimsdale, and A.B. Holmes. Angew. Chem. Int. Ed. Engl. **37**, 402 (1998).
6. F.F. Fan and A.J. Bard. J. Electrochem. Soc. **133**, 301 (1986).
7. Y. Fu and R.A. Weiss. Synth. Met. **84**, 129 (1997).
8. Y. Fu and R.A. Weiss. Synth. Met. **84**, 103 (1997).
9. M.C. de Jesus, R.A. Weiss, and Y. Chen. J. Polym. Sci. Part B: Polym. Phys. **35**, 347 (1997).
10. T.F. Otero and V. Olazabal. Electrochim. Acta, **41**, 213 (1996).
11. (*a*) C. Barthet and M. Guglielmi. Electrochim. Acta, **41**, 2791 (1996); (*b*) B. Sixou, J.P. Travers, C. Barthet, and M. Guglielmi. Phys. Rev. B: Condens. Matter, **56**, 4608 (1997).
12. H. Yoneyama, T. Hirai, S. Kuwabata, and O. Ikeda. Chem. Lett. 1243 (1986).
13. G. Yu, Q. Pei, and A.J. Heeger. Appl. Phys. Lett. **70**, 934 (1997).
14. G. Yu, Y. Yang, Y. Cao, Q. Pei, C. Zhang, and A.J. Heeger. Chem. Phys. Lett. **259**, 465 (1996).
15. J. Tian, C.-C. Wu, M.E. Thompson, J.C. Sturm, R.A. Register, M.J. Marsella, and T.M. Swager. Adv. Mater. **7**, 395 (1995).
16. Q. Pei, Y. Yang, G. Yu, Y. Cao, and A.J. Heeger. Synth. Met. **85**, 1229 (1997).
17. Q. Pei, G. Yu, C. Zhang, Y. Yang, and A.J. Heeger. Science, **269**, 1086 (1995).
18. O. Onitsuka, A.C. Fou, M. Ferreira, B.R. Hsieh, and M.F. Rubner. J. Appl. Phys. **70**, 4067 (1996).
19. H. Hong, D. Davidov, Y. Avny, H. Chayet, E.Z. Faraggi, and R. Neumann. Adv. Mater. **7**, 846 (1995).
20. M. Onoda and K. Yoshino. Jpn. J. Appl. Phys. **34**, L260 (1995).
21. M. Ferreira, O. Onitsuka, A.C. Fou, B. Hsieh, and M.F. Rubner. Mat. Res. Soc. Symp. Proc. **413**, 49 (1996).
22. W. Grot. Chem.-Ing.-Tech. **50**, 299 (1978).
23. I. Rubinstein and A.J. Bard. J. Am. Chem. Soc. **102**, 6642 (1980).

© 1998 NRC Canada

24. I. Haller. J. Am. Chem. Soc. **100**, 8050 (1978).
25. W.D. Bascom. J. Colloid Interface Sci. **24**, 789 (1968).
26. K. Pichler, D.A. Halliday, D.D.C. Bradley, R.H. Friend, P.L. Burn, and A.B. Holmes. Synth. Met. **55–57**, 230 (1993).
27. S.C. Graham, D.D.C. Bradley, R.H. Friend, and C. Spangler. Synth. Met. **41–43**, 1227 (1991).
28. R.C. Weast (*Editor*). CRC Handbook of chemistry and physics. 64th ed. CRC Press, Inc., Boca Raton, Fla. 1983–1984.
29. T.D. Gierke, G.E. Munn, and F.C. Wilson. J. Polym. Sci. Part B: Polym. Phys. **19**, 1687 (1981).
30. M. Fujimura, T. Hashimoto, and H. Kawai. Macromolecules, **15**, 136 (1982).
31. Z. Porat, J.R. Fryer, M. Huxham, and I. Rubinstein. J. Phys. Chem. **99**, 4667 (1995).
32. G. Xie and T. Okada. J. Chem. Soc. Faraday Trans. **92**, 663 (1996).

© 1998 NRC Canada

The adsorption of bis(hexafluoroacetylacetonato)zinc(II) on Si(111)-7×7

J. Hugh Horton, Johann Rasmusson, Joseph G. Shapter, and Peter R. Norton

Abstract: The adsorption of the organometallic compounds bis(hexafluoroacetylacetonato)zinc(II) ($Zn(hfac)_2$) and bis(hexafluoroacetylacetonato)nickel(II) ($Ni(hfac)_2$) on the surface of Si(111)-7×7 were studied by a combination of scanning tunnelling microscopy (STM) and X-ray photoelectron spectroscopy (XPS). These compounds are analogues of the compound bis(hexafluoroacetylacetonato)copper(II), which is an important precursor for the chemical vapour deposition of copper that we have previously studied. Both XPS and STM results indicate that the $Zn(hfac)_2$ is adsorbed intact on the surface, and remains intact on the surface at temperatures up to 300 K. The XPS shows a transition from a physisorbed state to a chemisorbed state at temperatures between 160 and 300 K. At higher temperatures $Zn(hfac)_2$ decomposed to form Zn and fluorocarbon fragments. The metal component diffused into the substrate. The $Ni(hfac)_2$ complex could not be successfully adsorbed on the Si surface: it was shown that this was due to decomposition of the molecule in the vapour phase, probably due to the higher temperatures needed to evaporate this relatively involatile compound.

Key words: scanning tunnelling microscopy, chemical vapour deposition, zinc, copper.

Résumé : Faisant appel à une combinaison de microscopie tunnel à balayage (« STM ») et de spectroscopie photoélectronique par rayons X (SPX), on a étudié l'adsorption des composés bis(hexafluoroacétylacétonato)zinc(II) ($Zn(hfac)_2$) et bis(hexafluoroacétylacétonato)nickel(II) ($Ni(hfac)_2$) sur la surface de Si(111)-7×7. Ces composés sont analogues au composé bis(hexafluoroacétylacétonato)cuivre(II) qui est un précurseur important pour la déposition chimique de vapeurs de cuivre que nous avons étudié antérieurement. Les résultats tant de SPX que de STM indiquent que le $Zn(hfac)_2$ est absorbé d'une façon intacte sur la surface et qu'il reste dans cet état sur la surface à des températures allant jusqu'à 300K. Les données de SPX montrent que, à des températures entre 160 et 300 K, il se produit une transition d'un état physisorbé à un état chimisorbé. Aux températures plus élevées, le $Zn(hfac)_2$ se décompose pour former du Zn et des fragments fluorocarbonés. Le composant métallique diffuse dans le substrat. Il n'a pas été possible d'adsorber correctement le complexe de $Ni(hfac)_2$ sur la surface Si : il a été démontré que cette situation résulte d'une décomposition de la molécule en phase vapeur qui est probablement due aux températures plus élevées nécessaires pour évaporer ce composé qui est relativement peu volatil.

Mots clés : microscopie tunnel à balayage, déposition chimique de vapeurs, zinc, cuivre.

[Traduit par la Rédaction]

Introduction

Organometallic chemical vapour deposition (OMCVD) from chemical precursors containing the hexafluoroacetylacetonato ligand, $[CF_3COCHCOCF_3]^-$, or $hfac^-$, has attracted considerable interest of late (1). The most widely studied of these compounds contain copper, and include such compounds as $Cu(hfac)_2$ and Cu(hfac)X where X can be a number of neutral ligands including cyclooctadiene or vinyltrimethylsilane. These copper compounds have shown considerable promise in the OMCVD of copper for use in microelectronics applications (2). This is because Cu is a potentially good interconnect metal due to its high conductivity and resistance to electromigration. OMCVD is also promising because deposition also takes place at relatively low temperatures (200–300°C) under low-vacuum conditions. Cu OMCVD from these compounds is also selective: that is, it will nucleate and grow films preferentially on some surfaces (3).

To understand the initial nucleation of copper during the OMCVD process we recently undertook a study of the deposition of $Cu(hfac)_2$ on the surface of Si(111)-7×7 (4). The initial deposition was examined using a combination of scanning tunnelling microscopy (STM), X-ray and ultraviolet photoelectron spectroscopy (XPS, UPS), and Rutherford backscattering (RBS). It was found that $Cu(hfac)_2$ decomposed on the surface even at temperatures of about 160 K to

Received December 23, 1997.

J.H. Horton.[1] Department of Chemistry, Queen's University, Kingston, ON K7L 3N6, Canada.
J. Rasmusson and P.R. Norton. Department of Chemistry, University of Western Ontario, London, ON N6A 5B7, Canada.
J.G. Shapter. Department of Chemistry, Flinders University, GPO Box 2100, Adelaide 5001, Australia.

[1]Author to whom correspondence may be addressed. Telephone: (613) 545-2379. Fax: (613) 545-6669. E-mail: hortonj@chem.queensu.ca

© 1998 NRC Canada

Table 1. Binding energies, kinetic energies, and Auger parameters of Zn and F photoelectron spectra observed for the adsorption of $Zn(hfac)_2$ on Si(111)-7×7.

	Temperature		
Transition	160 K	300 K	600 K
Zn $2p_{3/2}$ B.E.	1 024.2	1 023.6	1 022.5
Zn $L_3M_{4.5}M_{4.5}$ K.E.	984.6	987.4	Not observed
Zn α	2 009.3	2 011.8	Not observed
F 1*s* B.E.	689.5	688.9	687.4
F $KL_{2.3}L_{2.3}$	651.9	652.2	653.3
F α	1 341.4	1 341.1	1 340.7

form metallic Cu and free $hfac^-$ ligand. STM and RBS investigations at 300 K showed that the Cu nucleated as small clusters of about 10 atoms on the surface and, furthermore, that the cluster size was invariant with Cu coverage, at least over the range studied, which was from a Cu to Si surface atom ratio (Cu/Si) of ~0.001 to ~0.2–0.3. This remarkable effect is not understood, but we suggested that it could be related to a change in reactivity of existing clusters on the surface towards the addition of Cu atoms once the cluster contained 8–10 atoms; this could be due to a "magic number" effect, in which addition of Cu atoms costs energy. Alternatively, the clusters might be terminated with hfac ligands at this critical cluster size and hence become unreactive, although why this should occur at 8–10 atoms is not clear, unless the cluster reactivity decreases as it becomes "three-dimensional"; i.e., second and third layer growth occurs. Certainly the STM images and the measured average cluster size were consistent with a pyramid of Cu atoms with three layers.

We therefore decided to examine the reactivity of similar organometallic compounds on Si(111)-7×7, in order to discover whether other metals showed behaviour analogous to copper on the surface. A number of $M(hfac)_2$ compounds are commercially available, including those in which M = Pt, Ni, and Zn. We have examined the latter two, $Ni(hfac)_2$ and $Zn(hfac)_2$, adsorbed on Si(111)-7×7, by means of both XPS and STM.

Experimental

These experiments were conducted using two UHV chambers. Each chamber had a base pressure $<1 \times 10^{-10}$ Torr (1 Torr = 133.3 Pa) and has been described in detail previously (4–6). Samples were prepared in both the STM and the XPS chambers. The 0.5 cm × 1.7 cm, 0.3 Ω cm Si samples (Virginia Semiconductors) are prepared by outgassing at 600°C for at least 6 h followed by repeated flashing to ~1100°C. In the case of the STM, the microscope was used to check the surface after this preparation. An excellent 7×7 reconstruction is observed with fewer than 1% defects. LEED was used to compare the extent and quality of the reconstruction in each chamber.

The CVD precursor was dosed using two home-built dosers designed for dosing solids into the vacuum environment (7). The two dosers (one on the STM chamber and the other on the XPS chamber) are similar in design in that they both have heatable, differentially pumped reservoirs for the solid precursors and allow a directed flow of the precursor to the sample. Both dosers were mounted on linear transfers that allowed them to be moved close to the samples during dosing, and hence, even for very low vapour pressure precursors, a reasonable flux of adsorbate reaches the surface. All coverages were controlled via the *apparent* exposure, that is, by measuring the rise in background pressure during gas dosing, which was between 5×10^{-10} and 2×10^{-9} Torr. This provides a reproducible method of controlling the organometallic precursor dose.

All the organometallic compounds used here were obtained commercially and used without subsequent purification. $Zn(hfac)_2$ (Aldrich, 98%) was deposited by heating the doser reservoir to 35°C, while attempts to deposit $Ni(hfac)_2$ (Aldrich, 98%) were run with the reservoir temperature at up to 150°C. In both cases the compounds were pumped for 24 h at a pressure of 1×10^{-7} Torr to remove any residual water in the sample. In the case of $Zn(hfac)_2$, contamination by residual $Cu(hfac)_2$ in the doser from previous experiments proved to be a problem. This difficulty was solved by differentially pumping the empty doser at 150°C for several hours before adding the $Zn(hfac)_2$.

Results

In Figs. 1*a*–1*c* we show constant current STM images of a Si(111)-7×7 surface that has been exposed to 0.02 L of $Zn(hfac)_2$ at 300 K. The images are each 40 nm × 40 nm in size and are taken at tip bias voltages of –1.5, –0.5, and +1.5 V, respectively. Several points are immediately apparent. First, the surface consists of a standard Si(111)-7×7 pattern overlaid with small irregular patches some 1–3 nm across. As the tip bias voltage is changed the underlying Si substrate pattern changes in the manner expected for clean Si(111)-7×7 (8). The small irregular patches, however, appear in bright contrast with respect to the substrate in Figs. 1*a* and 1*c* (–1.5 and +1.5 V) but appear in dark contrast at a bias voltage of –0.5 V.

Zn $2p_{3/2}$ XPS and $L_3M_{4,5}M_{4,5}$ X-ray induced Auger spectra (XAES) are presented in Figs. 2*a* and 2*b*, respectively. In this case, the spectra were initially taken of 0.02 L of $Zn(hfac)_2$ adsorbed on the Si(111)-7×7 substrate held at a temperature of 140 K. The substrate was subsequently allowed to warm to 300 K (i.e., room temperature) for the second set of spectra and a third set were then taken after annealing the substrate to 600 K. Other than a decrease in intensity, there is little change in peak shape among the three sets of spectra. However, in both cases a drift to lower binding energy (higher kinetic energy) can be observed. This is summarized in Table 1, which also contains values for the Auger parameter, α, where α is defined as

$$\alpha = \text{B.E.} + \text{K.E.(Auger)}$$

where B.E. is the binding energy of the photoelectron, and K.E. is the kinetic energy of the main Auger peak. The signal intensity of the Zn Auger transition was quite weak, and thus a peak position and Auger parameter for the 600 K annealed sample could not be obtained.

Figure 3 shows the C 1*s* XP spectrum for $Zn(hfac)_2$ deposited on the Si(111)-7×7 surface. The spectra were taken

© 1998 NRC Canada

Fig. 1. STM images of 0.02 Langmuir $Zn(hfac)_2$ adsorbed on Si(111)-7×7 at 300 K. All images are 40 nm × 40 nm. The tunnelling current was 0.2 nA and the tip bias voltages were (*a*) –1.5 V, (*b*) –0.5 V, and (*c*) +1.5 V.

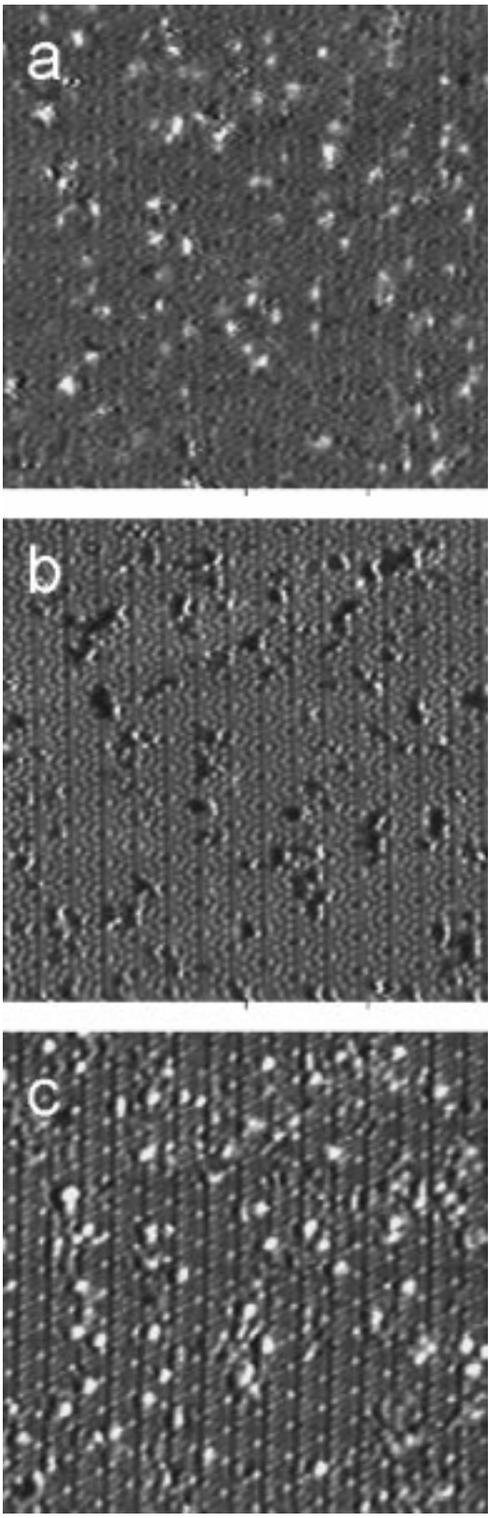

Fig. 2. (*a*) Zn $2p_{3/2}$ XPS spectra and (*b*) Zn $L_3M_{4,5}M_{4,5}$ X-ray excited Auger spectra of 0.02 Langmuir $Zn(hfac)_2$ molecule adsorbed on Si(111)-7×7 at various temperatures. The exciting radiation was Al Kα (1486.6 eV).

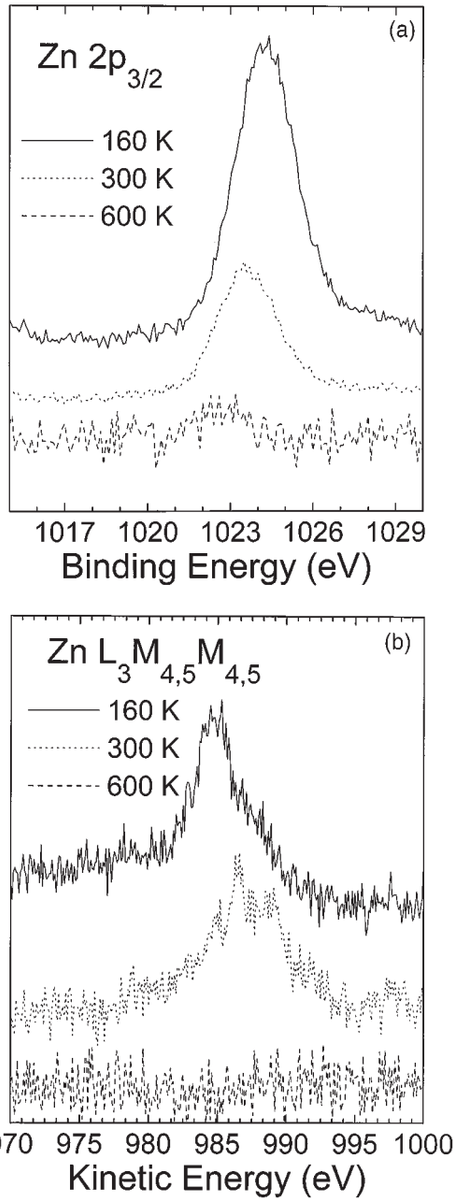

under identical conditions to those described for the Zn data. In the 140 K spectrum three peaks can be seen at binding energies of 283.8, 288.0, and 292.8 eV. A similar spectrum is observed at 300 K, although the 283.8 eV peak has grown in intensity relative to the other two. At 600 K, only the 283.8 eV peak remains: it has grown considerably in intensity compared with those for the spectra taken at lower temperatures.

We also acquired the F 1*s* and F Auger spectra under the same conditions as those above. Chemical shift and Auger parameter data for these peaks are also included in Table 1.

© 1998 NRC Canada

Fig. 3. C 1*s* XPS spectra of 0.02 Langmuir $Zn(hfac)_2$ molecule adsorbed on Si(111)-7×7 at various temperatures. The exciting radiation was Al Kα (1486.6 eV).

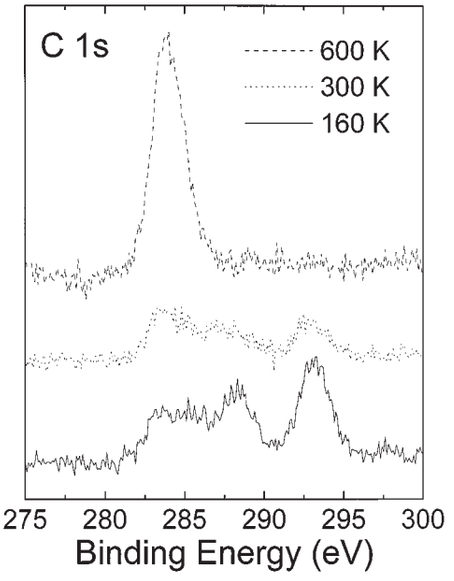

Attempts were also made to use XPS to analyse the adsorption of $Ni(hfac)_2$ on a Si(111)-7×7 surface. In this case, O, F, and C 1*s* XPS spectra indicated the presence of intact hfac ligand on the surface, but no Ni signals were observed. No Ni deposition was observed even when the doser reservoir temperature was increased to 150°C.

Discussion

One important difference between $Cu(hfac)_2$ and the two compounds examined here is the higher vapour pressure associated with the Cu compound. In our previous work, $Cu(hfac)_2$ could be introduced into the UHV system without any heating of the doser reservoir. This is not surprising since at room temperature the vapour pressure of $Cu(hfac)_2$ is ~30 mTorr (9). While the vapour pressure of $Zn(hfac)_2$ does not appear to have been measured, it has a melting point of 155°C, which is somewhat higher than that of $Cu(hfac)_2$ at 130°C. It is thus not surprising that it required a heated sample reservoir in order to deposit $Zn(hfac)_2$ on the Si surface. $Ni(hfac)_2$ has a melting point of 213°C, considerably higher than either of the Zn or Cu compounds. When attempts were made to deposit $Ni(hfac)_2$ on the surface, C, O, and F XPS signals, which had magnitudes similar to those obtained when $Zn(hfac)_2$ was deposited on the surface, were obtained. Since the Ni $2p_{3/2}$ X-ray absorption cross section is not greatly different from that for Zn $2p_{3/2}$ (10), it seems likely that very little Ni was present on the surface, certainly less than 0.1 monolayer. While we cannot rule out the presence of trace amounts of Ni on the surface, these results suggest that the higher temperatures required to evaporate the $Ni(hfac)_2$ led to the decomposition of the molecule before it reached the surface. The most likely reaction would be similar to that obtained in a CVD process

$$Ni(hfac)_2 + H_2, H_2O \rightarrow hfacH + Ni, NiO$$

where hfacH is the protonated $hfac^-$ ligand, and residual water and (or) hydrogen in the gas doser act as reducing agents, resulting in the deposition of Ni or NiO on the walls of the gas doser. Another path would involve the heterogeneous decomposition on the walls of the doser, perhaps even catalyzed by Ni first deposited by a homogenous process.

Since it did not prove possible to adsorb significant amounts of $Ni(hfac)_2$ on the Si surface, further (and more difficult) STM experiments were not attempted with this compound. However, XPS shows that it is indeed possible to adsorb $Zn(hfac)_2$ on the surface. The STM images shown in Fig. 1 demonstrate that there is only one type of feature associated with the adsorption of $Zn(hfac)_2$. The appearance of the feature is sensitive to tip bias voltage: at $|V_{tip}| > 0.5$ V the $Zn(hfac)_2$ feature is bright, while for $|V_{tip}| \leq 0.5$ V the features are dark. This is in considerable contrast to the case of $Cu(hfac)_2$ where we found two distinct features present on the surface upon adsorption of the organometallic complex. In that case, areas of bright contrast were associated with clusters of Cu atoms, while regions of dark contrast were found to correspond to hfac ligand adsorbed on the surface. Since we know that the hfac ligand gives rise to dark areas at tip biases of –1.5 V (4), the images demonstrate that there is no free hfac ligand on the surface when $Zn(hfac)_2$ is adsorbed at 300 K. Thus, the $Zn(hfac)_2$ molecule must remain intact upon adsorption at this temperature. A $Zn(hfac)_2$ molecule has dimensions of about 0.65 × 1.0 nm, while the features observed in the STM images are rather larger than this (1–3 nm) and also irregular in shape. This suggests that what we are observing is small clusters of anywhere from one to four $Zn(hfac)_2$ molecules adsorbed on the surface.

The Zn XPS spectra tend to support the hypothesis of intact $Zn(hfac)_2$ molecules adsorbed on the surface. In Fig. 2 and Table 1 we have an overview of the Zn chemical shifts and Auger parameters under various conditions. Unlike some other first-row transition elements, Zn XPS spectra generally do not contain any strong satellites due to shake-up or shake-off transitions and, more importantly, the chemical shift is reasonably insensitive to chemical environment. This is because the chemical shift, $\Delta\zeta$, is a function of both the core hole binding energy shift, $\Delta\varepsilon$, and extra-atomic relaxation energy ΔR^{ea} (i.e., polarizability of the environment of the X-ray excited atom) (11). These two effects are often opposed to one another, resulting in little or no net chemical shift in the XPS peak. However, it has been shown that the Auger parameter, defined above, is a sensitive measure of the extra-atomic relaxation effect (11). If both the XPS and XAES transitions used involve core electrons only, it can be shown that $\Delta\alpha = 2\Delta R^{ea}$. In the case of the Zn Auger parameters measured here and generally quoted in the literature this relationship does not strictly hold, since the most intense Auger transition, and hence most widely measured, $L_3M_{4,5}M_{4,5}$, involves valence band electrons. Nonetheless, since the Auger parameter is defined by taking the *difference* in energy of two peak positions, any instrumental calibration errors of the binding or kinetic energies tend to cancel out and Auger parameters obtained from different laboratories can be compared with considerable confidence.

We first consider the XP and XAE spectra acquired at sample temperatures of 160 K and 300 K. The Zn Auger parameter at 160 K is 2009.3 eV. This is quite similar to that

© 1998 NRC Canada

measured for ZnO of 2009.8 eV (12), suggesting that the Zn atom is in a similar environment in the two compounds. Since in the $Zn(hfac)_2$ molecule Zn is coordinated through four Zn—O bonds, this indicates that at 160 K, at least, the molecule lies intact on the surface. Upon warming the sample to 300 K, several changes are noted in the Zn spectra. First, the 2*p* binding energy decreases while the Auger kinetic energy is increased. The Auger parameter shifts to 2011.8 eV. At the same time, the Zn peak intensity falls to about one-half its initial value. This decrease in Zn signal intensity could have two explanations. At 300 K, Zn has either diffused into the bulk of the substrate, or a physisorbed overlayer of $Zn(hfac)_2$ has been desorbed from the surface. Since the former possibility requires the $Zn(hfac)_2$ to have decomposed at this temperature and this is not borne out in the STM results, the desorption model is more appropriate. The fact that only half of the Zn intensity is lost suggests a very thin overlayer in which XPS can detect molecules in all layers. Second, the observation that the Auger parameter for Zn at 160 K is consistent with *all* the Zn being present in the complex suggests that the molecules in the first layer (next to the Si) and in the second (physisorbed) layer, are very similar. Upon warming to 300 K, the Auger parameter shifts by +2.5 eV to 2011.8 eV. This value is intermediate to those observed for ZnO, 2009.8 eV, and for metallic Zn, 2013.8 eV (13). These observations together suggest that two phenomena occur upon warming from 160 to 300 K: desorption of physically adsorbed precursor and reaction of the remainder to form a new chemisorbed state. The Auger parameter measured at 300 K indicates that Zn does not appear to exist in the metallic state on the surface; the change in is more probably associated with a shift to a more polarizable environment with the $Zn(hfac)_2$ bound directly to Si substrate. When coupled with the STM results, this indicates that, in contrast to the case of $Cu(hfac)_2$, the Zn analogue does not form metal clusters on the surface.

The C 1*s* spectra presented in Fig. 3 also tend to support the above conclusions. The spectra taken at 160 K and 300 K are both consistent with those previously obtained for intact hfac ligand, both adsorbed directly on the surface and bound to a metal centre in $Cu(hfac)_2$. The peaks at 292.8, 288.0, and 283.8 eV correspond to C in CF_3, C=O, and C-H sites in the ligand, respectively. At 300 K the spectral intensity has decreased compared to that at 160 K, again demonstrating partial desorption of the $Zn(hfac)_2$ complex. By 600 K, C XPS indicates that the hfac ligand has completely decomposed on the surface, as the single, much more intense peak at 283.8 eV is typical of graphitic carbon on the surface. The increase in signal intensity suggests that some background carbon contamination has occurred by this point in the experiment. At the same time, the Zn 2*p* intensity has also decreased, suggesting that the zinc released during the process has probably diffused into the bulk, similar to the behaviour of Cu at these temperatures.

Finally, in the F 1*s* spectra, we note trends similar to those above. As the substrate annealing temperature is increased, the signal intensity decreases, particularly between 160 and 300 K, demonstrating desorption from the surface. At the same time there is a downward shift in the F 1*s* binding energy, consistent with chemisorption of $Zn(hfac)_2$ to the electron-donating substrate at higher temperatures. The small shift in F Auger parameter is more difficult to interpret, especially as few data seem available in the literature, but it is not inconsistent with a shift to a more polarizable environment at higher temperatures.

Conclusions

We have examined the adsorption of $Zn(hfac)_2$ on the Si(111)-7×7 surface by means of XPS and STM. The behaviour of this organometallic molecule differs considerably from that shown by its copper analogue, $Cu(hfac)_2$. Examination of the C and Zn XPS chemical shift and Auger parameter data indicates that molecules adsorbed at 160 K remain intact, and are physisorbed on the surface. In further contrast to $Cu(hfac)_2$, the zinc organometallic complex remains intact on the surface upon adsorption at 300 K or on warming from 160 to 300 K. This warming is accompanied by desorption of about half of the physisorbed complex, but the Zn Auger parameter shift at this temperature indicates a change in the bonding of the remaining $Zn(hfac)_2$ to the surface, while the C and F 1*s* XPS data indicate that the molecule remains intact. STM indicates that direct chemisorption in clusters of one to four molecules occurs at 300 K. There was no evidence either for the formation of metallic Zn clusters similar to those observed during $Cu(hfac)_2$ adsorption on the surface, or for the formation of clusters of hfac ligand.

Acknowledgements

J.H.H. acknowledges financial support by a Natural Sciences and Engineering Research Council of Canada (NSERC) Postdoctoral Fellowship and we gratefully acknowledge the financial support of NSERC.

References

1. M.J. Hampden-Smith and T.T. Kodas. Polyhedron, **14**, 699 (1995).
2. E. Kondoh, Y. Kawano, N. Takeyasu, and T. Ohta. J. Electrochem. Soc. **141**, 3494 (1994).
3. L.H. Dubois and B.R. Zegarski. J. Electrochem. Soc. **139**, 3295 (1992).
4. J.H. Horton, J.G. Shapter, T. Cheng, W.N. Lennard, and P.R. Norton. Surf. Sci. **375**, 171 (1997).
5. X.R. Qin and P.R. Norton. Phys. Rev. B: Condens. Matter, **53**, 11100 (1996).
6. T.D. Pope, K. Griffiths, and P.R. Norton. Surf. Sci. **306**, 294 (1994).
7. S. Serghini-Monim, L.L. Coatsworth, K. Griffiths, P.R. Norton, and R.J. Puddephatt. Rev. Sci. Instrum. **67**, 3672 (1996).
8. H.N. Waltenburg and J.T. Yates, Jr. Chem Rev. **95**, 1589 (1995).
9. D. Kim, R.H. Wentorf, and W.N. Gill. J. Electrochem. Soc. **140**, 3267 (1993).
10. D. Briggs and M.P. Seah. *In* Practical surface analysis. Vol. 1: Auger and X-ray photoelectron spectroscopy. John Wiley & Sons Ltd., Chichester, England. 1990.
11. C.D. Wagner. Faraday Discuss. Chem. Soc. **60**, 291 (1975).
12. S.W. Gaarenstroom and N. Winograd. J. Chem. Phys. **67**, 3500 (1977).
13. C.D. Wagner, W.M. Riggs, L.E. Davis, J.F. Moulder, and G.E. Muilenberg. *In* Handbook of X-ray photoelectron spectroscopy. Perkin–Elmer Corporation, Physical Electronics Division, Eden Prarie, Minnesota. 1979.

© 1998 NRC Canada

Three-dimensional H-bonded supramolecular complexes. Synthesis and crystal structures of $[Mn(\mu\text{-bpe})(H_2O)_4](ClO_4)_2\cdot 4(bpe)\cdot 2H_2O$ and $[M(\mu\text{-bpe})(bpe)_2(H_2O)_2](ClO_4)_2\cdot bpe\cdot H_2O$, where M = Zn, Ni and bpe = 1,2-bis(4-pyridyl)ethane

Fernande D. Rochon, Marius Andruh, and Robert Melanson

Abstract: The reaction of Mn(II), Zn(II), and Ni(II) perchlorate with 1,2-bis(4-pyridyl)ethane (*bpe*) was studied and the products were characterized by IR spectroscopy and X-ray diffraction methods. The zinc and nickel compounds are isomorphous with a metal–*bpe* molar ratio of 1:4, while the manganese compound is quite different with a Mn–*bpe* ratio of 1:5. $[Mn(\mu\text{-bpe})(H_2O)_4](ClO_4)_2\cdot 4(bpe)\cdot 2H_2O$ (**1**) is monoclinic, *C*2/*c*, with a = 30.141(7), b = 13.993(4), c = 19.765(4) Å, β = 129.41(1)°, and R = 0.059. The Mn atom is located on an inversion centre and forms an infinite chain with the bridged *bpe* ligand. The four other *bpe* molecules are hydrogen-bonded to the aqua ligands and form an extensive H-bonded interpenetrating 3D network. The bonds Mn—N = 2.316(3) Å and Mn—OH_2 = 2.148(4) and 2.178(3) Å. $[Zn(\mu\text{-bpe})(bpe)_2(H_2O)_2](ClO_4)_2\cdot bpe\cdot H_2O$ (**2**) crystallized in the $P2_1/c$ space group, with a = 14.609(4), b = 21.164(5), c = 16.482(5) Å, β = 114.69(2)°, and R = 0.058. For $[Ni(\mu\text{-bpe})(bpe)_2(H_2O)_2](ClO_4)_2\cdot bpe\cdot H_2O$ (**3**), a = 14.511(6), b = 21.216(7), c = 16.467(7) Å, β = 114.76(3)°, and R = 0.065. The aqua ligands are located *trans* to each other. The bridged *bpe* ligands form an infinite chain with the metal atoms. Two other terminal *bpe* ligands are coordinated to the metal in *trans* positions to each other. These ligands form H-bonds with the aqua ligands of other chains resulting in an H-bonded 3D network. The Zn—N distances vary from 2.151(3) to 2.185(4) Å while the Ni—N bonds are between 2.098(10) and 2.126(11) Å. The bonds Zn—OH_2 = 2.125(4), 2.161(4) Å and Ni—OH_2 = 2.077(11), 2.110(11) Å.

Key words: crystal structure, manganese complex, zinc complex, nickel complex, 1,2-bis(4-pyridyl)ethane.

Résumé : La réaction des perchlorates de Mn(II), Zn(II) et Ni(II) avec 1,2-bis(4-pyridyl)ethane (*bpe*) a été étudiée et les produits ont été caractérisés par spectroscopie IR et par diffraction des rayons- X. Les composés du zinc et du nickel sont isomorphes et la proportion metal–*bpe* est 1 : 4, tandis que le composé de manganèse est différent avec une proportion molaire métal–*bpe* de 1 : 5. $[Mn(\mu\text{-bpe})(H_2O)_4](ClO_4)_2\cdot 4(bpe)\cdot 2H_2O$ (**1**) est monoclinique, *C*2/*c* avec a = 30,141(7), b = 13,993(4), c = 19,765(4) Å, β = 129,41(1)° et R = 0,059. L'atome de Mn est situé sur un centre d'inversion et forme une chaîne infinie avec les ligands *bpe* pontés. Les quatre autres molécules *bpe* sont liées par ponts-hydrogène aux ligands aqua et forment un réseau étendu entrecroisé tridimensionnel. Les distances Mn—N = 2,316(3) Å et Mn—OH_2 = 2,148(4) et 2,178(3) Å. $[Zn(\mu\text{-bpe})(bpe)_2(H_2O)_2](ClO_4)_2\cdot bpe\cdot H_2O$ (**2**) cristallise dans le système monoclinique $P2_1/c$, avec a = 14,609(4), b = 21,164(5), c = 16,482(5) Å, β = 114,69(2)° et R = 0,058. Pour $[Ni(\mu\text{-bpe})(bpe)_2(H_2O)_2](ClO_4)_2\cdot bpe\cdot H_2O$ (**3**), a = 14,511(6), b = 21,216(7), c = 16,467(7) Å, β = 114,76(3)° et R = 0,065. Les ligands aqua sont localisés en position *trans*. Les ligands pontants *bpe* forment une chaîne infinie avec les atomes métalliques. Deux autres ligands *bpe* terminaux situés en position *trans* sont coordinés au métal. Ces derniers sont liés par des ponts-hydrogène avec les ligands aqua d'autres chaînes, formant un réseau tri-dimensionnel. Les distances Zn—N varient de 2,151(3) à 2,185(4) Å, et les liens Ni—N sont entre 2,098(10) et 2,126(11) Å. Les liaisons Zn—OH_2 = 2,125(4), 2,161(4) Å et Ni—OH_2 = 2,077(11), 2,110(11) Å.

Mots clés : structure cristalline, complexe de manganèse, complexe de zinc, complexe de nickel, 1,2-bis(4-pyridyl)éthane.

Received January 23, 1998.

F.D. Rochon,[1] M. Andruh, and R. Melanson. Department of Chemistry, Université du Québec à Montréal, C.P. 8888, Succ. Centre-ville, Montreal, QC H3C 3P8, Canada.

[1]Author to whom correspondence may be addressed. Telephone: (514) 987-3000, ext. 4896#. Fax: (514) 987-4054. E-mail: rochon.fernande@uqam.ca

Introduction

In recent years, considerable progress has been achieved in the field of crystal engineering. Several remarkable compounds illustrating predictions of the crystal structures have recently been reported (1–5). However, the design of crystalline materials with specific functions and properties still remains a target difficult to attain. The well-planned design of

 © 1998 NRC Canada

Table 1. Crystal data.

Crystal	**1**	**2**	**3**
Compound	$C_{60}H_{72}Cl_2MnN_{10}O_{14}$	$C_{48}H_{54}Cl_2ZnN_8O_{11}$	$C_{48}H_{54}Cl_2NiN_8O_{11}$
Mol. wt.	1283.1	1055.3	1048.6
Crystalline system	Monoclinic	Monoclinic	Monoclinic
Space group	$C2/c$	$P2_1/c$	$P2_1/c$
a (Å)	30.141(7)	14.609(4)	14.511(6)
b (Å)	13.993(4)	21.164(5)	21.216(7)
c (Å)	19.765(4)	16.482(5)	16.467(7)
β (°)	129.410(10)	114.69(2)	114.76(3)
Volume (Å^3)	6440(3)	4630(2)	4633(3)
Z	4	4	4
F(000)	2692	2200	2192
ρ_{calcd} (Mg m^{-3})	1.323	1.514	1.503
μ(MoKα) (mm^{-1})	0.358	0.718	0.607
No. of parameters	511	600	600
Weighting scheme w^{-1}	$\sigma^2(F)+0.0007F^2$	$\sigma^2(F)+0.0007F^2$	$\sigma^2(F)+0.0007F^2$
$R = \Sigma \lvert F_o - F_c \rvert / \Sigma \lvert F_o \rvert$	0.0590	0.0579	0.0654
$R_w = [\Sigma w(\lvert F_o - F_c \rvert)^2 / \Sigma w\lvert F_o \rvert)]^{1/2}$	0.0605	0.0570	0.0601
Goodness-of-fit	1.44	1.34	1.32

organic or inorganic crystals is possible only by understanding the interplay of the noncovalent interactions, as well as their role in the self-assembly process. At this stage, new examples of structurally characterized compounds are needed and the subsequent retrospective analysis of these will further inform researchers about the factors governing the interactions at the supramolecular level.

A key point in this field is the search for versatile building blocks, able to generate materials with extended structures. e*xo*-Bidentate ligands, such as pyrazine and 4,4′-bipyridine, are classical building blocks for the design of coordination compounds with extended structures. A 1:1 ligand-to-metal molar ratio usually leads to either linear or zigzag chains (6–9). In a few cases, interesting tetranuclear complexes forming molecular boxes have been synthesized from *cis*-dichloro complexes of Pd(II) or Pt(II) with 4,4′-bipyridine (10, 11). A change in the stoichiometry, namely, an increase in the ligand-to-metal molar ratio, led to the formation of elegant 2D and 3D solid-state architectures. Diamondlike or interpenetrating diamondlike networks (12–14), square grid sheets (15, 16) or interpenetrating square grid sheets (17), honeycomb (13) or fully interlocked honeycomb networks (13, 18), and 2D waferlike polymers (19) have been recently synthesized by the self assembly of different metal ions with pyrazine or 4,4′-bipyridine. Several novel supramolecular architectures have been reported using a rigid, rodlike building block, namely, *trans*-1,2-bis(4-pyridyl)ethylene (20), or a conformationally flexible bridging ligand such as *N*,*N*′-*p*-phenylene-dimethylene-bis(pyridine-4-one) (21, 22).

In addition to the clever choice of the building blocks, the synthetic strategies leading to one-, two-, or three-dimensional arrays are usually based on the ingenious use of directional hydrogen bonds, π–π stacking interactions, and metal coordination. These factors are very efficient organizing forces in the self-assembly process (23–29). The coordination algorithm of the metal atoms plays a crucial role in the type of long-range order that will be formed.

To test the ability of another 4-pyridyl-containing building block to generate extended structures, we have studied the reaction of some transition metal(II) compounds with the flexible, potentially bridging, ligand 1,2-bis(4-pyridyl)ethane (*bpe*). A few compounds with this ligand have been reported (30, 31). Because of the different conformations exhibited by this type of ligand, as well as its capability of forming hydrogen bonds, it was anticipated that the products would present interesting and outstanding structural features. We report in this paper the synthesis and characterization of some H-bonded supramolecular complexes of Mn(II), Zn(II), and Ni(II). The synthetic approach is based on a metal-to-ligand starting molar ratio of 1:4.

Experimental

The chemicals were purchased from Aldrich and were used as received. The IR spectra (KBr pellets) were measured on a Perkin–Elmer 783 spectrophotometer.

Synthesis

The three compounds were prepared following the same general procedure. An ethanolic solution (5 mL) containing 2 mmol of 1,2-bis(4-pyridyl)ethane (*bpe*) was added with stirring to an aqueous solution (15 mL) containing the manganese(II), zinc(II), or nickel(II) perchlorate (0.5 mmol). The slow evaporation of the resulting mixtures obtained from the reactions of the Mn(II) and Ni(II) compounds produced highly crystalline materials, while the Zn(II) compound precipitated immediately as a white microcrystalline powder. Single crystals of the Zn(II) product were obtained by recrystallization from a water–acetonitrile 1:2 mixture. ***Caution!*** No problems were encountered during the preparation of the perchlorate derivatives described above. However, suitable care and precautions must be taken when handling potentially explosive compounds.

[Mn(μ-*bpe*)$(H_2O)_4$]$(ClO_4)_2$·4(*bpe*)·2H_2O (**1**): Yield: 58%, white-yellowish crystals. IR data (cm^{-1}): 3600w, 3540w, 3040m, 2830m, 1610s, 1560m, 1505w, 1420m, 1220w, 1090vs, 1010m, 825m, 810m, 620m, 550m, 530w, 500w.

© 1998 NRC Canada

Fig. 1. Labelled diagram of $[Mn(\mu\text{-}bpe)(H_2O)_4](ClO_4)_2\cdot 4(bpe)\cdot 2H_2O$ (**1**).

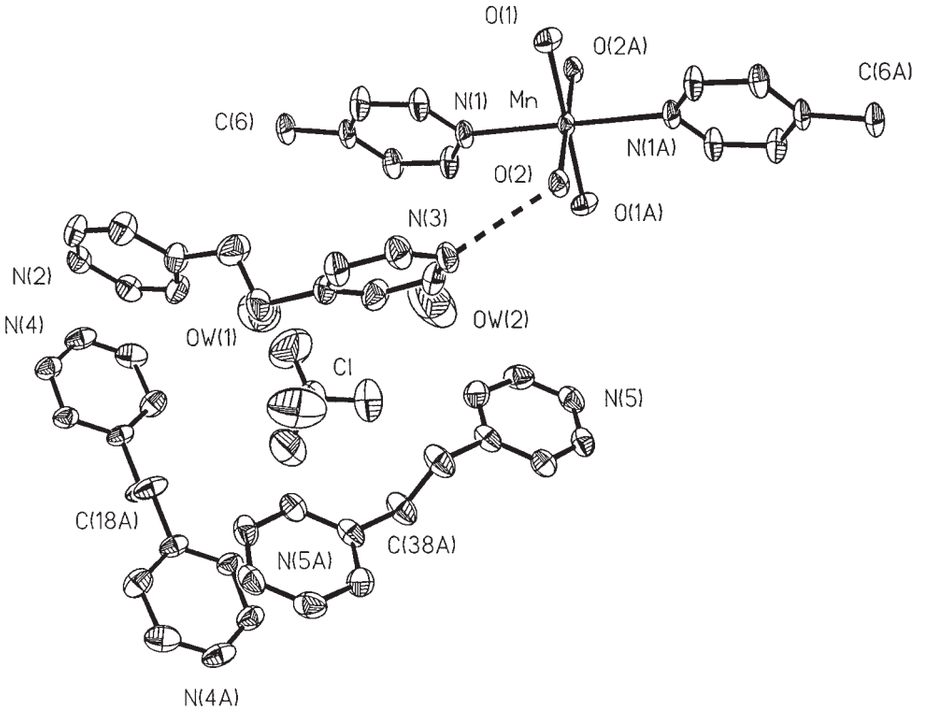

$[Zn(\mu\text{-}bpe)(bpe)_2(H_2O)_2](ClO_4)_2\cdot bpe\cdot H_2O$ (**2**): Yield: 64%, white crystals. IR data (cm^{-1}): 3400m, 3040m, 2860m, 1640s, 1620s, 1600s, 1560m, 1500w, 1460w, 1430m, 1220w, 1100vs, 1020m, 980m, 830s, 810m, 625s, 550s.

$[Ni(\mu\text{-}bpe)(bpe)_2(H_2O)_2](ClO_4)_2\cdot bpe\cdot H_2O$ (**3**): Yield: 77%, light blue crystals. IR data (cm^{-1}): 3300m, 3060m, 2970m, 1640s, 1620s, 1560m, 1500w, 1430m, 1230w, 1100vs, 1020m, 1000m, 930w, 880w, 830s, 810m, 620s, 550s.

X-ray structure determination and refinement

The crystals were selected after examination for homogeneity under a polarizing microscope. The data collections were made at room temperature on a Siemens P4 diffractometer with graphite-monochromatized MoKα radiation (λ = 0.71073 Å). The XSCANS program was used for the data collection. The unit cell parameters were obtained by least-squares refinement of the angles 2θ (16°–30°), ω, and χ for about 30 well-centered reflections. The coordinates of the heavy atoms were determined from direct methods and the positions of all the other non-hydrogen atoms were found by the usual Fourier methods. The O atoms in the perchlorate ions in **1** were found to be disordered on three positions (occupation factors of component a: 0.54, b: 0.33, and c: 0.13). The refinement of the structures was done by full-matrix least-squares analysis. The H atoms, except those of the water molecules and a few methylene H atoms in *bpe*, which were located and refined, were fixed at their calculated positions (riding model). The H atoms on OW1 in crystal **1** could not be located. The calculations were done on a SHELXTL system.[2] The scattering factors and other pertinent crystallographic information were taken from the *International tables for X-ray crystallography* (32). The crystal data are summarized in Table 1. The experimental details of the crystallographic studies and the coordinates of the atoms are available as supplementary material.[3]

Results and discussion

The three coordination compounds, $[Mn(\mu\text{-}bpe)(H_2O)_4](ClO_4)_2\cdot 4(bpe)\cdot 2H_2O$(1), $[Zn(\mu\text{-}bpe)(bpe)_2(H_2O)_2]$ $(ClO_4)_2\cdot bpe\cdot H_2O$ (**2**), and $[Ni(\mu\text{-}bpe)(bpe)_2(H_2O)_2](ClO_4)_2\cdot bpe\cdot H_2O$ (**3**), were prepared by simply mixing an aqueous solution of the metal(II) perchlorate with an ethanolic solution of the *bpe* ligand in a metal(II):*bpe* molar ratio of 1:4. The starting molar ratio was recovered in crystals **2** and **3**, whereas in the case of manganese, the product that crystallized had a molar ratio of 1:5. The supramolecular order on the nanometer scale in the crystalline state of these compounds is created by the interplay of metal coordination, hydrogen bonding, and π–π interactions as described below.

The first compounds that we prepared and characterized were the manganese(II) (**1**) and the zinc(II) (**2**) derivatives.

[2] SHELXTL PLUS (PC version, 1990-1993). Siemens Analytical Instruments Inc. Madison, Wis., U.S.A.

[3] The following tables and figures have been deposited: experimental details of the crystallographic studies (S1), positional parameters (S2), anisotropic thermal factors (S3), bond distances and angles (S4), and H-atom coordinates (S5), and may be purchased from: The Depository of Unpublished Data, Document Delivery, CISTI, National Research Council Canada, Ottawa, Canada K1A 0S2. Tables S2, S4, and S5 have also been deposited with the Cambridge Crystallographic Data Centre and can be obtained on request from The Director, Cambridge Crystallographic Data Centre, University Chemical Laboratory, 12 Union Road, Cambridge, CB2 1EZ, U.K. Tables of structure factors are no longer being deposited and are available on request from the author.

© 1998 NRC Canada

Table 2. Selected bond lengths (Å) and angles (°).
(*a*) [Mn(μ-*bpe*)(H_2O)](ClO_4)$_2$·4(*bpe*)·2H_2O (**1**).

Mn—O(1)	2.148(4)	Mn—O(2)	2.178(3)
Mn—N(1)	2.316(3)	N—C (avg. bonded)	1.326(8)
N—C (avg. nonbonded)	1.318(8)	O(1)—H (avg.)	0.805(25)
O(2)—H (avg.)	0.764(20)	Ow(2)—H	1.189(31)
O(1)-Mn-O(2)	90.7(1)	O(1)-Mn-N(1)	90.2(1)
O(1)-Mn-O(2)′	89.3(1)	O(1)-Mn-N(1)′	89.8(1)
O(2) - Mn - N(1)	93.0(1)	O(2) - Mn - N(1)′	87.0(1)
Mn-N(1)-C(1)	120.5(4)	Mn-N(1)-C(5)	122.8(3)
C(1)-N(1)-C(5) (bonded)	116.2(4)	C-N-C (avg. nonbonded)	116.1(4)
N(1)-C-C (avg. bonded)	123.9(6)	N-C-C (avg. nonbonded)	123.8(6)
C(2)-C(3)-C(4) (*para* bonded)	117.0(4)	C-C-C (*para* avg. nonbonded)	116.8(5)
C-C-C (*meta* avg. bonded)	119.5(7)	C-C-C (*meta* avg. nonbonded)	119.8(6)
C-C-CH_2 (avg. bonded)	121.5(6)	C-C-CH_2 (avg. nonbonded)	121.6(5)
C(3)-CH_2-CH_2 (bonded)	114.1(7)	C-CH_2-CH_2 (avg. nonbonded)	113.0(6)

(*b*) [M(μ-*bpe*)(*bpe*)$_2$(H_2O)$_2$](ClO_4)$_2$·*bpe*·H_2O (M = Zn (**2**), Ni (**3**)).

	2 (Zn)	**3** (Ni)		**2** (Zn)	**3** (Ni)
M—O(1)	2.125(4)	2.077(11)	Cl—O (avg.)	1.366(9)	1.38(2)
M—O(2)	2.161(4)	2.110(11)	N—C (avg.)	1.333(7)	1.33(2)
M—N(1)	2.151(3)	2.098(10)	C—C (aromatic, avg.)	1.379(8)	138(2)
M—N(2)	2.156(3)	2.112(9)	C—C (nonaromatic, avg.)	1.510(9)	1.51(2)
M—N(3)	2.185(4)	2.126(11)	O—H (avg.)	0.74(2)	0.75(5)
M—N(4)	2.174(4)	2.127(11)			
O(1)-M-O(2)	175.5(1)	176.1(3)	N(3)-M-O(2)	89.7(2)	90.1(5)
N(1)-M-O(1)	89.1(2)	89.6(4)	N(4)-M-O(1)	89.8(2)	88.6(4)
N(1)-M-O(2)	86.5(2)	86.6(4)	N(4)-M-O(2)	90.0(2)	91.4(4)
N(1)-M-N(2)	177.3(2)	177.4(5)	M-N-C (avg.)	121.0(3)	120.7(9)
N(1)-M-N(3)	89.8(1)	89.3(4)	C-N-C (avg.)	116.3(5)	116.8(13)
N(1)-M-N(4)	93.0(1)	93.4(4)	N-C-C (avg.)	123.5(5)	122.9(14)
N(2)-M-O(1)	93.6(2)	92.9(4)	C-C-C (aromatic, *para* avg.)	117.2(5)	116.4(14)
N(2)-M-O(2)	90.8(2)	91.0(4)	C-C-C (aromatic, *meta* avg.)	119.6(6)	120.1(14)
N(2)-M-N(3)	89.6(1)	90.0(4)	C-C-CH_2 (avg.)	121.4(5)	121.8(14)
N(2)-M-N(4)	87.5(1)	87.4(4)	C-CH_2-CH_2 (avg.)	111.5(5)	112.2(13)
N(3)-M-N(4)	177.1(1)	177.0(4)	M-O-H (avg.)	119(2)	120(4)
N(3)-M-O(1)	89.8(2)	90.0(5)			

The two compounds have different stoichiometries, although the starting metal:ligand molar ratio was the same, 1:4. In both compounds the metal ions exhibit pseudo-octahedral geometries and only one *bpe* molecule acts as a genuine bridging ligand, forming infinite linear chains. The very different and unpredictible packing patterns for crystals **1** and **2** prompted us to pursue the investigation. Since the geometry around the metals in the two compounds is essentially octahedral and since both compounds have been obtained under the same conditions, the following question was raised: which structure will select, under the same conditions, another metal ion with a marked preference for octahedral stereochemistry, for instance, nickel(II)? Consequently, we have studied a similar reaction with nickel perchlorate and characterized its product (**3**). The crystallographic results have shown that **3** is isomorphous with the zinc derivative (**2**).

The structural investigation of [Mn(μ-*bpe*)(H_2O)$_4$] (ClO_4)$_2$ ·4(*bpe*)·2H_2O (**1**) has shown that the manganese atoms are bridged by one *bpe* molecule, resulting in infinite chains parallel to the *b* axis. The manganese atom is located on an inversion center and is hexacoordinated by two nitrogen atoms arising from two bridging *bpe* molecules, disposed *trans* to each other, and by four aqua ligands. The local symmetry of the manganese(II) atoms is therefore approximately D_{4h}. The labelling scheme is shown in Fig. 1. Selected bond distances and angles are collected in Table 2. The Mn—N distances (2.316(3) Å) are slightly longer than those found in polymeric Mn(II)-4,4′-bipyridine systems (e.g., 2.265 Å (7), 2.278 Å (8)). The metal–aqua bonds Mn—O(1) and Mn—O(2) are 2.148(4) and 2.178(3) Å, respectively. The distance between the manganese atoms within the chain corresponds to the *b* axis, 13.993(4) Å.

The other four *bpe* molecules are not coordinated to the metal atoms, but they are involved in an interesting extensive hydrogen-bonding system. Each aqua ligand is hydrogen-bonded to two nitrogen atoms arising from the organic molecules. There are intra- and inter-chain hydrogen bonds, which present the most intriguing feature of the crystal structure of this compound. Two *trans* aqua ligands (O(2)) from one manganese atom are "bridged" through intra-chain

© 1998 NRC Canada

Fig. 2. Infinite triple chain parallel to the *b* axis in crystal **1**.

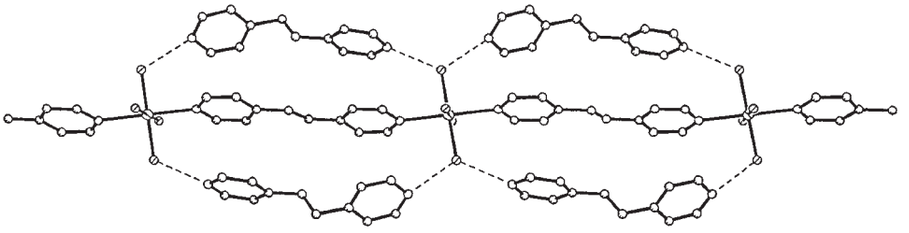

Fig. 3. Diagram of the packing in crystal **1** (*b* axis horizontal, *a* axis vertical). The ClO_4^- ions and the free H_2O molecules have been omitted. The *bpe* molecules and ligands are shown as straight lines between the two N atoms.

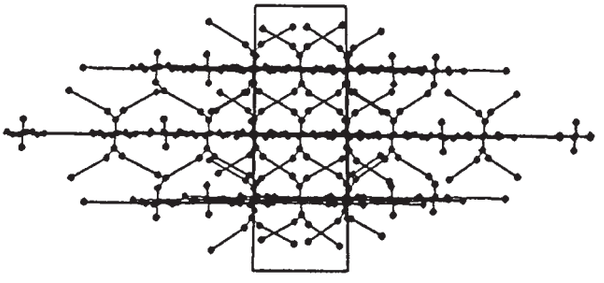

hydrogen bonds, by two *bpe* molecules, to the equivalent aqua ligands on the next manganese atom along the chain. The O(2)···N(2) and O(2)···N(3) distances are 2.828 and 2.811 Å, respectively. The angles are Mn—O(2)···N(2) = 123.2° and Mn—O(2)···N(3) = 116.2°. These two *bpe* molecules together with the main *bpe*-bridged manganese(II) chain form infinite triple chains running along the crystallographic *b* axis (Fig. 2). The angle around the H-bonded aqua ligand N(2)···O(2)···N(3) is 118.1°.

The other two aqua ligands (O(1)) are then inter-chain hydrogen-bonded, via the fourth and fifth *bpe* molecules (containing N(4) and N(5), respectively), resulting in two equivalent interpenetrating infinite 2D chicken-wire sheets (Fig. 3). The O(1)···N(4) and O(1)···N(5) distances are 2.771 and 2.737 Å, respectively. The angles are Mn—O(1)···N(4) = 119.8° and Mn— O(1)···N(5) = 118.2°, while the angle around the H-bonded aqua ligand N(4)···O(1)···N(5) is 121.8°. According to the classification of such networks (33), compound **1** belongs approximately to class II-*h*, where the interpenetration of 2D infinite nets of hexagonal (*h*) meshes occurs in (approximately) mutually perpendicular directions, forming a 3D network. The hexagonal meshes have two short and four long edges: the short ones (4.297 Å) represent the O(1)—Mn—O(1′) distance, while each of the four long edges (14.650 and 14.755 Å) is formed by one *bpe* molecule that is hydrogen-bonded to two aqua ligands (O(1) belonging to two different Mn—μ-*bpe*–Mn—μ-*bpe* chains. A layer is made up of edge-sharing hexagons, with O(1) at each corner, and a manganese(II) atom in the centre of the short edges. The separation between the parallel layers is about 12.6 Å. The stacking of these layers generates large hexagonal channels perpendicular to the *b* axis. The center of each channel is occupied by a Mn—μ-*bpe*–Mn—μ-*bpe* chain belonging to the other equivalent 2D chicken-wire sheet. The dihedral angle between the two interlocking sheets was calculated approximately as 52°. Another example of meshed honeycomb hydrogen-bonded 2D networks is the solid-state structure of 1,3,5-benzenetricarboxylic acid (34).

The bond distances and angles in the bonded and nonbonded *bpe* ligands are identical as shown in Table 2. It is interesting to note that the angles in the pyridine rings are not all identical. The C-N-C angles are significantly smaller (avg. 116.2(4)°) than the *ortho* N-C-C angles (avg. 123.9(6)°). The average *meta* C-C-C angle is 119.7(7)°, while the average *para* angle is smaller, 116.9(5)°.

The O atoms of the perchlorate ions are disordered on three positions. The compound crystallized with two molecules of water located in the lattice on twofold axes. These molecules are extensively hydrogen-bonded to the perchlorate ions. The Ow···O (perchlorate) distances vary between 2.706 and 2.925 Å.

The main differences between compounds **1** and $[Zn(\mu\text{-}bpe)(bpe)_2(H_2O)_2](ClO_4)_2\cdot bpe\cdot H_2O$ (**2**) arise from their stoichiometry and from the coordination spheres of Mn(II) (MnN_2O_4) and Zn(II) (ZnN_4O_2). As already mentioned, the nickel derivative, **3**, is isomorphous with compound **2**. Three *bpe* molecules are directly coordinated to the Zn(II) or the Ni(II) atoms. Again, only one *bpe* ligand is bridged between the metallic centres forming a chain parallel to the *a* direction. The distance between the metal atoms in the chain is 13.494 Å for **2** and 13.406 Å for **3**. The other two *bpe* ligands act as terminal ligands and are located in *trans* positions to each other. The metal centres exhibit a pseudo-octahedral geometry (Fig. 4). Selected bond distances and angles are collected in Table 2. As expected, the Zn—N distances (avg. 2.167(4) Å) are shorter than those found in compound **1**, and slightly longer than the ones reported for Zn(II)-4,4′-bipy complexes (15, 17). The Ni—N bonds are even shorter and vary between 2.098(10) and 2.127(11) Å. The bond distances M—N(1) and M—N(2) (avg. 2.154(3) Å for Zn and 2.105(10) Å for Ni) located in the M—μ-*bpe*—Mn chain seem slightly shorter (≈0.025 Å) than the M— N(3) and M—N(4) bonds (avg. 2.180(4) Å for Zn and 2.127(11) Å for Ni) of the terminal ligands. The difference is significant for the Zn complex, but not for the Ni compound because of the high esd's obtained for crystal **3**. The Zn—O bond distances are 2.125(4) and 2.161(4) Å, while the Ni —O bonds are also shorter, 2.077(11) and 2.110(11) Å.

The bridged (N(1)——N(2)) and one terminal *bpe* (N(3)——N(5)) ligands in crystals **2** and **3** exhibit, as in compound **1**, the more stable *antiperiplanar* conformation. Interestingly, the second terminal *bpe* ligand (N(4)——N(6)) is frozen into the *gauche* conformation. The latter conforma-

© 1998 NRC Canada

Fig. 4. Diagram of $[Zn(\mu\text{-}bpe)(bpe)_2(H_2O)_2](ClO_4)_2 \cdot bpe \cdot H_2O$ (**2**) The ClO_4^- ions and the molecule of H_2O are not shown for clarity. (The same diagram can be applied for **3**).

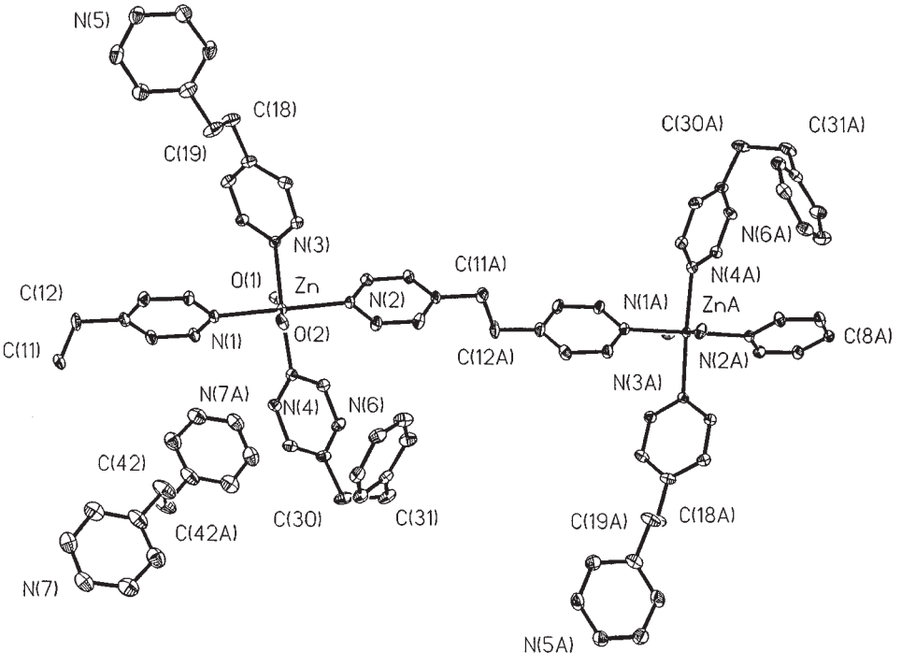

Fig. 5. Packing in $[Zn(\mu\text{-}bpe)(bpe)_2(H_2O)_2](ClO_4)_2 \cdot bpe \cdot H_2O$ (**2**) (*b* axis horizontal, *a* axis vertical). The *bpe* ligands are shown as straight lines between the two N atoms. The perchlorate ions and the unbonded *bpe* and H_2O molecules are not shown.

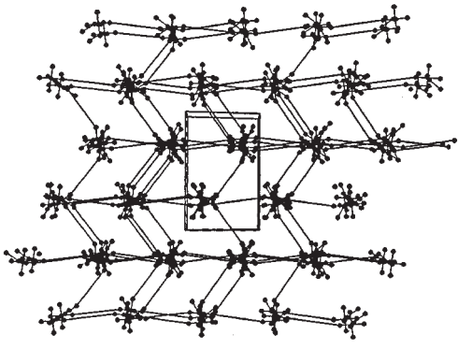

tion is chiral and seems to influence very strongly the directional properties of the inter-chain hydrogen-bonding system. The different stoichiometry, the presence of two terminal *bpe* molecules, and the *gauche* conformation of one of them generate a hydrogen-bonding network pattern, which is very different from the one observed in crystal **1**. In compounds **2** and **3**, the centre of the bridging *bpe* ligand is located on an inversion center. Consequently, the *gauche pbe* ligands have alternate chiralities along the infinite chain. Each *gauche bpe* molecule of one chain is hydrogen-bonded (through N(6)) to the aqua ligand (O(1)) from the metal atoms of a second chain located at a distance of $c/2$ Å. The distances are O(1)···N(6) = 2.757 Å and 2.772 Å and the angles M—O(1)···N(6) = 125.5° and 126.1° for Zn and Ni, respectively. The second chain is further connected in the same way to a third chain in the *c* direction, and so on, resulting in infinite layers parallel to the *ac* plane. Due to this particular conformation of the terminal *bpe* ligand, the distance between the metal atoms of two different chains, H-bonded through the *gauche bpe* molecules, is much shorter (8.321 Å for **2** and 8.320 Å for **3**) than the distance between the metal atoms within a chain. *Gauche bpe* molecules have also been observed in a few Co(II) (31) and Cd(II) (30) compounds.

Each layer is then connected on both sides to the adjacent layers in the *b* direction, through hydrogen bonds established between the *antiperiplanar bpe* terminal ligand from one layer and one aqua ligand from another layer and vice versa with distances O(2)···N(5) = 2.776 and 2.778 Å and with angles M—O(2)···N(5) = 126.8° and 127.5° for Zn and Ni, respectively. The H-bonded sheets that are parallel to the *ac* plane can be observed in Fig. 5. The metal–metal distance M—N(3)——N(5)···H_2O(2)—M is the largest, 14.991 and 14.921 Å for **2** and **3**, respectively. An H-bonded three-dimensional network results, with large channels occupied by the water molecules, the perchlorate anions, as well as by the fourth nonbonded *bpe* molecule. The latter is hydrogen-bonded to the water molecule with N(7)···Ow = 2.747 Å for **2** and 2.703 Å for **3**. The water molecule is further hydrogen-bonded to the perchlorate ions with Ow···O(7) = 2.884 Å for **2** and 2.968 Å for **3**. The aqua ligands are also hydrogen-bonded to the water molecule with O(1)···Ow = 2.813 and 2.807 Å and angles M—O(1)···Ow = 126.0° and 128.1° for **2** and **3**, respectively. The second aqua ligand is also hydrogen-bonded to the water molecule with O(2)···Ow distances = 2.733 and 2.734 Å and angles M—O(2)···Ow = 129.8° and 131.0° for **2** and **3,** respectively. This water molecule acts as a hydrogen-bond donor to the free *bpe* molecule (N(7)) and the perchlorate ions with an angle O(7)···Ow···N(7) = 120.4° and 119.6° for**2** and **3**, respec-

© 1998 NRC Canada

tively, and as a hydrogen-bond acceptor towards the two aqua ligands.

Interestingly, the M—O(1) bond distances, where the aqua ligand is H-bonded to the *gauche bpe* ligand seems slightly shorter (by ≈0.035 Å) than the M—O(2) bonds. The latter aqua ligand is H-bonded to the *antiperiplanar bpe* terminal ligand.

The minor differences between compounds **2** and **3** arise from the slightly smaller ionic radius of nickel(II) (d^8 configuration with the paired electrons in the low energy t_{2g} orbitals) in comparison with zinc(II) (d^{10}) (Table 2). The crystallographic results are much better for the Zn compound. The standard deviations obtained on the Ni compound are quite high, since all the crystals were small. Therefore, the number of observed reflections (1988) was rather low for the number of parameters varied (600).

Stacking of the aromatic rings seems also to play a stabilizing role in the crystal packing, especially between the chains, which are H-bonded by the *gauche bpe* ligands. This type of π–π interaction seems quite general in this type of crystals and is an important factor in the synthetic strategies leading to the synthesis of specifically designed supramolecular materials.

Magnetic measurements of compound **3** were made, but the results were not reproducible. This was attributed to anisotropy. The sample is a light fluffy powder and was probably moving as the measurements were being taken. Compacting the powder would stop the realignment but usually a preferred orientation is obtained. Therefore, the magnetic measurements of an anisotropic compound are difficult to interpret, since it is not possible to know what is really being measured.

The structures reported in this paper illustrate the ability of a flexible ligand such as 1,2-bis(4-pyridyl)ethane to generate novel supramolecular complexes through simultaneous metal coordination, hydrogen-bond interactions, and π–π stacking. It is difficult, at this stage, to rationalize our results to other species. However, the three examples described here, as well as the isomorphism of compounds **2** and **3,** have shown that this class of materials could be extended with other new metal compounds. Further work in this area is in progress.

Acknowledgment

The authors are grateful to the Natural Sciences and Engineering Research Council of Canada for financial support.

References

1. G.R. Desiraju. Crystal engineering. The design of organic solids. Elsevier, Amsterdam. 1989.
2. M.C. Etter. Acc. Chem. Res. **23**, 120 (1990).
3. D. Shekhar Reddy, Y.E. Ovchinnikov, O.V. Shishkin, Y.T. Struchkov, and G.R. Desiraju. J. Am. Chem. Soc. **118**, 4085 (1996).
4. J.C. MacDonald and G.M. Whitesides. Chem. Rev. **94**, 2383 (1994).
5. C.B. Aakeröy and K.R. Seddon. Chem. Soc. Rev. 397 (1993).
6. S.A. Bajue, F.B. Bramwell, M.A. Charles, F. Cervantes-Lee, and K. Pannell. Inorg. Chim. Acta, **197**, 83 (1992), and refs. therein.
7. M. Andruh, H.W. Roesky, M. Noltemeyer, and H.G. Schmidt. Z. Naturforsch. B: Chem. Sci. **49**, 31 (1994).
8. M.X. Li, G.Y. Xie, and Y.D. Gu. Polyhedron, **14**, 1235 (1995).
9. A.S. Batsanov, M.J. Begley, P. Hubberstey, and J. Stroud. J. Chem. Soc. Dalton Trans. 1947 (1996).
10. M. Fujita, J. Yazaki, and K. Ogura. J. Am. Chem. Soc. **112**, 5645 (1990).
11. P.J. Stang and D.H. Cao. J. Am. Chem. Soc. **116**, 4981 (1994).
12. L. Carlucci, G. Ciani, D.M. Proserpio, and A. Sironi. J. Chem. Soc. Chem. Commun. 2755 (1994).
13. L.R. MacGillivray, S. Subramanian, and M.J. Zaworotko. J. Chem. Soc, Chem. Commun. 1325 (1994).
14. T. Kuroda-Sowa, M. Yamamoto, M. Munakata, M. Seto, and M. Maekawa. Chem. Lett. 349 (1996).
15. S. Subramanian and M.J. Zaworotko. J. Angew. Chem. Int. Ed. Engl. **34**, 2127 (1995).
16. M. Fujita, Y.J. Kwon, S. Washizu, and K. Ogura. J. Am. Chem. Soc. **116**, 1151 (1994).
17. R.W. Gable,B.F. Hoskins, and R. Robson. J. Chem. Soc. Chem. Commun. 1677 (1990).
18. O.M. Yaghi and G. Li. Angew. Chem. Int. Ed. Engl. **34**, 207 (1995).
19. L. Carlucci, G. Ciani, D.M. Proserpio, and A. Sironi. Angew. Chem. Int. Ed. Engl. **34**, 1895 (1995).
20. J.A. Real, E. Andrés, M.C. Munoz, M. Julve, T. Granier, A. Bousseksou, and F. Varet. Science, **268**, 265 (1995).
21. D.M.L. Goodgame, S. Menzer, A.M. Smith, and D.J. Williams. Angew. Chem. Int. Ed. Engl. **34**, 574 (1995).
22. D.M.L. Goodgame, S. Menzer, A.M. Smith, and D.J. Williams. J. Chem. Soc. Chem. Commun. 1975 (1995).
23. J.M. Lehn. Science, **260**, 1762 (1993).
24. D.S. Lawrence, T. Jiang, and M. Levett. Chem. Rev. **95**, 2229 (1995).
25. D.B. Amabilino and J.F. Stoddart. Chem. Rev. **95**, 2725 (1995).
26. A.D. Burrows, C.W. Chan, M.B. Chowdhry, J.E. McGrady, and D.M.P. Mingos. Chem. Soc. Rev. 329 (1995).
27. M.J. Zaworotko. Chem. Soc. Rev. 283 (1994).
28. M. Munakata, L.P. Wu, T. Kuroda-Sowa, and M. Maekawa. J. Am. Chem. Soc. **118**, 3117 (1996).
29. S. Subramanian and M.J. Zaworotko. Coord. Chem. Rev. **137**, 357 (1994).
30. M. Fujita, Y.J. Kwon, M. Miyazama, and K. Ogura. J. Chem. Soc. Chem. Commun. 2127 (1996).
31. T.L. Henniger, D.C. MacQuarrie, P. Losier, R.D. Rodgers, and M.J. Zaworotko. Angew. Chem. Int. Ed. Engl. **36**, 9, 972 (1997).
32. International tables for X-ray crystallography. Vol IV. Kynoch Press, Birmingham, U.K. 1974. pp. 55, 99, and 149.
33. L. Carlucci, G. Ciani, D.M. Proserpio, and A. Sironi. Angew. Chem. Int. Ed. Engl. **35**, 1088 (1996).
34. D.J. Duchamp and R.E. Marsh. Acta Crystallogr. Sect. B: Struct. Sci. **B25**, 5 (1969).

© 1998 NRC Canada

Optical and electrical properties of fluorene-based π-conjugated polymers

Maxime Ranger and Mario Leclerc

Abstract: Electroactive and photoactive copolymers derived from fluorenes have been prepared from palladium-catalyzed Suzuki couplings. For instance, poly((4,4′-biphenylene)-2,7-(9,9-dioctylfluorene)) and poly((2,5-thienylene)-2,7-(9,9-dioctylfluorene)) exhibit strong emission in the blue region (406 nm, ϕ_{fl} = 0.72) and in the green region (496 nm, ϕ_{fl} = 0.49), respectively. These fluorene-based π-conjugated polymers also show reversible electroactivity upon reduction and oxidation. The good electrical transport of both *p*-type and *n*-type charge carriers combined with excellent luminescent properties should lead to the development of efficient light-emitting devices.

Key words: polyfluorenes, Suzuki couplings, luminescence, electrochromism, *n* and *p* doping.

Résumé : Une série de copolymères électroactifs et photoactifs possèdant des unités fluorène a été préparée par couplages de type Suzuki (catalyse au palladium). Parmi ces polymères, le poly((4,4′-biphenylene)-2,7-(9,9-dioctylfluorene)) et le poly((2,5-thienylene)-2,7-(9,9-dioctylfluorene)) montrent, par exemple, des propriétés intéressantes de fluorescence dans la région du bleu (406 nm, ϕ_{fl} = 0.72) et dans la région du vert (496 nm, ϕ_{fl} = 0.49), respectivement. Ces polymères π-conjugués dérivés du fluorène montrent également une électroactivité réversible en réduction et en oxydation. Ce bon transport de porteurs de charge de types *p* et *n* combiné aux excellentes propriétés de luminescence devrait permettre le développement de diodes électroluminescentes efficaces.

Mots clés : polyfluorenes, couplages de type Suzuki, luminescence, électrochromisme, dopage *n* et *p*.

Introduction

Conjugated polymers (poly(phenylene vinylene)s, polythiophenes, polyphenylenes, polyfluorenes, etc.) show unusual and interesting properties for the development of different electrical and (or) optical devices such as lightweight batteries, electrochromic display devices, light- emitting diodes, optical switches, etc. (1–19). Among these properties, electroluminescent polymers have recently attracted great attention due to their possible utilization in flat display devices (1–6). In particular, there is presently great interest in developing efficient and stable blue-light- emitting materials to get access to the three primary colors. Along these lines, several authors, such as Pei and Yang (14) and Yoshino and co-workers (15, 16), have reported blue- light-emitting diodes using polyfluorene derivatives. Moreover, Reynolds and co-workers (17) recently reported the utilization of polyfluorene derivatives in electrochromic display devices while some polyfluorene derivatives have also shown interesting liquid crystalline (18) and lasing properties (19). From all these results, it is then clear that polyfluorenes are particularly promising for various optical applications.

Received January 29, 1998.

M. Ranger and M. Leclerc[1]. Départements de chimie, Université de Montréal et Université Laval, Centre de recherche de science et génie en macromolécules, Cité universitaire, QC G1K 7P4, Canada.

[1]Author to whom correspondence may be addressed. Telephone: (418) 656-3452. Fax: (418) 656-7916. E-mail: mario.leclerc@chm.ulaval.ca

On the other hand, light-emitting diodes need also a good and balanced transport of both injected electrons and holes to permit an efficient recombination of these electrical charges in the luminescent chromophores (1–6, 14–16). In this regard, it has been shown that copolymers containing alternating donor and acceptor (push–pull structure) π-conjugated units exhibit reduced band gaps and, by this fact, allow both n-*type* (reduced) and p-*type* (oxidized) electrical transport (20). Therefore, on the basis of these recent results, the development of well-defined alternating copolymers derived from fluorenes should lead to tunable electrochromic, electrochemical, and photophysical properties and should combine, in principle, in one material the required optical and electrical properties for the development of efficient light-emitting diodes. For all these reasons, we report here the preparation, from Suzuki couplings (11, 21–24), of alternating conjugated copolymers, namely, poly((1,4-phenylene)-2,7-(9, 9-dioctylfluorene)) (**PPF**),poly((4,4′-biphenylene)-2,7-(9,9-dioctylfluorene)) (**PBPF**), poly-((2,5-thienylene)-2,7-(9,9-dioctylfluorene)) (**PTF**), and poly((2,2′-bithienylene)-2,7-(9,9-dioctylfluorene)) (**PBTF**) (see Chart 1). Their electrical, electrochemical, and optical properties have been characterized and show promising features for various electrooptical applications.

Experimental part

Material

Fluorene, 2,5-dibromothiophene, 1,4-dibromobenzene, 2,2′-bithiophene, and 4,4′-dibromo-1,1′-biphenyl were obtained from the Aldrich Co. Tetrakis(triphenylphosphine)-palla-

© 1998 NRC Canada

Chart 1.

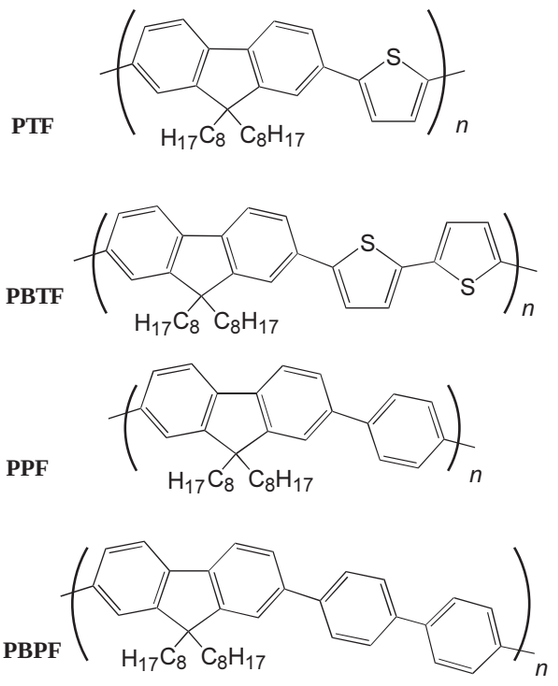

dium(0) was synthesized following a procedure reported in the literature (25). Acetonitrile (Aldrich) was dried on CaH_2 under inert atmosphere (Ar) during 24 h. Tetraethylammonium tetrafluoroborate ($TEABF_4$, Aldrich) was recrystallized in a 60/40 mixture of methanol/water and dried at 100°C under reduced pressure (1 Torr (= 133.3 Pa)).

Instrumentation

^1H and ^{13}C NMR spectra were recorded on a Bruker AMX300 or AMX400 apparatus in deuterated chloroform solutions at 298 K. Number-average (M_n) and weight-average (M_w) molecular weights were determined by size exclusion chromatography (SEC) with an HPLC Waters 510 pump using a Waters 410 differential refractometer. The calibration was made with a series of monodispersed polystyrene standards in THF (HPLC grade, Aldrich) at 308 K.

Fluorescence measurements were carried out with a Spex Fluorolog 1681 spectrometer. For fluorescence analysis in solution, the polymer concentration was about 10^{-6} M (on the basis of one repeat unit), giving absorbances always less than 0.06 to avoid any inner filter effect. The quantum yields of fluorescence were determined in argon-saturated solutions at 298 K in chloroform against 9,10-diphenylanthracene (Aldrich) in cyclohexane (ϕ_F = 0.90) (26) or 3″,4‴-didecyl-2,2′;5′,2″;5″,2‴;5‴,2⁗;5⁗,2⁗′-sexithiophene in $CHCl_3$ (ϕ_F = 0.24) (27), as standards. For fluorescence analysis in the solid state, the polymer was applied on a quartz plate and was disposed at 45° of the incident beam. All corrected fluorescence excitation spectra were found to be equivalent to their respective absorption spectra. UV–visible absorption spectra were recorded on a Hewlett–Packard diode-array spectrophotometer (model 8452A).

All electrochemical analyses were done with a Solartron and an EG&G Princeton Applied Research model 273 potentiostat/galvanostat. Electrochemical experiments were carried out in 1 M $TEABF_4$ – acetonitrile solution, under inert and anhydrous atmosphere. The working electrode was a platinum disc with a diameter of 0.8 cm and platinum sheet (1.4 cm^2) was used as counter electrode. The reference electrode was Ag/AgNO3 0.0998 M in acetonitrile (0.287 V vs. SCE). The deposition of polymers on the electrode was done by the evaporation of a dilute chloroform solution.

In situ electrical conductivities were obtained with a platinum two-band microelectrode (a separation of 60 mm between the bands) according to a procedure described elsewhere (28). Determination of the electrical conductivity was carried out by the two-probe technique with this two-band microelectrode. Spectroelectrochemical analyses were carried out with an indium tin oxide (ITO) coated glass electrode as working electrode, platinum counter electrode (sheet) and a silver wire as quasi-reference electrode in 0.1 M $TEABF_4$ – MeCN (0.30 V vs. Ag/Ag^+).

Synthesis

*9,9-Dioctylfluorene (**1**) (ref. 29)*

To a solution of 16.96 g (102.2 mmol) of fluorene (Aldrich) in THF (210 mL) at –78°C was added, dropwise, 85.84 mL (214.6 mmol) of *n*-butyllithium (2.5 M in hexane, Aldrich). The mixture was stirred at –78°C for 45 min and 45.40 g (235.06 mmol) of octyl bromide (Aldrich) in THF (40 mL) was added dropwise to the mixture. The solution was allowed to warm to room temperature and was stirred for 3 h. The mixture was poured into water and extracted with ether. The organic extracts were washed with brine and dried over magnesium sulfate. The solvent was removed under reduced pressure. Excess of octyl bromide was removed by distillation (44°C/0.3 Torr) to give 39.50 g of 9,9-dioctylfluorene (99%). (R_f: 0.87, silica TLC in hexane). Pale-brown powder; mp 34–37°C. ^1H NMR (300 MHz, $CDCl_3$) δ (ppm): 7.82 (dd, 2H, *J* = 4.3 Hz), 7.42 (m, 6H), 2.12 (m, 4H, *J* = 3.8 Hz), 1.35–1.24 (m, 20H), 0.96 (t, 6H, *J* = 7.1 Hz), 0.79 (m, 4H, *J* = 3.8 Hz). ^{13}C NMR (75 MHz, $CDCl_3$) δ (ppm): 150.63, 141.15, 126.98, 126.70, 122.78, 119.64, 55.01, 40.46, 31.84, 30.11, 29.26, 29.05, 23.77, 22.64, 14.09. HRMS calcd. for $C_{29}H_{42:}$ 390.651; found: 390.598.

*2,7-Dibromo-9,9-dioctylfluorene (**2**) (ref. 30)*

To a solution of 9,9-dioctylfluorene (**1**) (18.01 g, 46.10 mmol) in $CHCl_3$ (70 mL) at 0°C were added 115.2 mg (0.706 mmol) of ferric chloride and 4.97 mL (96.62 mmol) of bromine. It is important that the reaction proceeds in the dark to avoid any bromination of the aliphatic part of the molecule. The solution was warmed to room temperature and was stirred for 3 h. The resulting slurry was poured into water and washed with sodium thiosulfate until the red color disappeared. The aqueous layer was extracted with $CHCl_3$ (×2), and the combined organic layers were dried over magnesium sulfate to afford 25.28 g (99%) of the title product as a pale-brown solid. (R_f: 0.85, silica TLC in hexane); mp 44–47°C. ^1H NMR (300 MHz, $CDCl_3$) δ (ppm): 7.53 (d, 2H, *J* = 7.7 Hz), 7.46 (d, 2H, *J* = 1.8 Hz), 7.44 (d, 2H, *J* = 1.1 Hz), 1.91 (m, 4H, *J* = 3.7 Hz), 1.26–1.05 (m, 20H), 0.83 (t, 6H, *J* = 3.6 Hz), 0.58 (m, 4H, *J* = 3.5 Hz). ^{13}C NMR

© 1998 NRC Canada

Scheme 1.

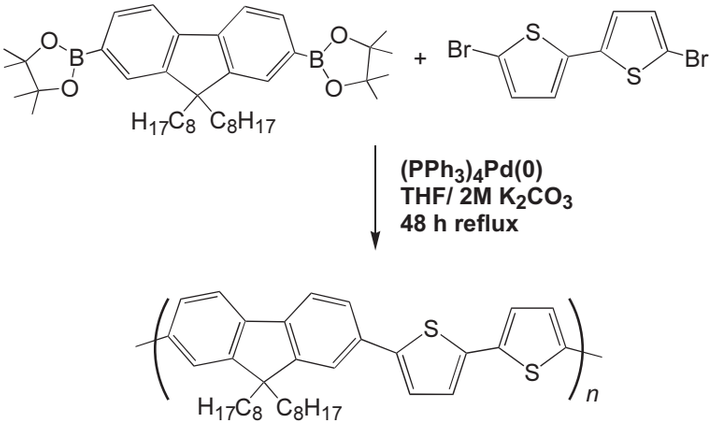

(75 MHz, $CDCl_3$) δ (ppm): 152.44, 138.94, 130.04, 126.07, 121.38, 120.96, 55.56, 40.02, 31.63, 29.78, 29.04, 29.01, 23.51, 22.47, 13.94. HRMS calcd. for $C_{29}H_{40}{}^{79}Br_2$: 546.150; found: 546.149.

2,7-Dibromofluorene ***(3)*** *(ref. 30)*

Same procedure as for 2,7-dibromo-9,9-dioctylfluorene (**2**). Yield 97%. Recrystallization was made from a THF–ethanol mixture to yield pale-yellow crystals; mp 159–161°C (lit. (22) mp 160–161°C). ^{1}H NMR (300 MHz, $CDCl_3$) δ (ppm): 7.67 (2H, d, *J* = 1 Hz), 7.61 (2H, d, *J* = 8 Hz), 7.51 (2H, dd, *J* = 8 Hz), 3.87 (2H, s). ^{13}C NMR (75 MHz, $CDCl_3$) δ (ppm): 144.65, 139.55, 130.01, 128.16, 121.04, 120.82, 36.43. HRMS calcd. for $C_{13}H_8{}^{79}Br_2$: 321.898; found: 321.899.

2,7-Bis(4,4,5,5-tetramethyl-1,3,2-dioxaborolan-2-yl)-9,9-dioctylfluorene ***(4)*** *(refs. 29, 31)*

To a solution of 2,7-dibromo-9,9-dioctylfluorene (**2**, 5.00 g, 9.1 mmol) in THF (70 mL) at –78°C was added, by syringe, 7.64 mL (19.11 mmol) of *n*-butyllithium (2.5 M in hexanes, Aldrich). The mixture was stirred at –78°C, warmed to 0°C for 15 min, and cooled again at –78°C for 15 min. 2-Isopropoxy-4,4,5,5-tetramethyl-1,3,2-dioxaborolane (4.00 g, 21.5 mmol, Aldrich) was added rapidly to the solution, warmed to room temperature, and stirred for 24 h. The mixture was poured into water and extracted with ether. The organic extracts were washed with brine and dried over magnesium sulfate. The solvent was removed by rotary evaporation, and the residue was purified by column chromatography (silica gel, 7% ethyl acetate in hexane, R_f: 0.20) to provide 3.80 g (65%) of the title product as a pale-yellow solid. ^{1}H NMR (300 MHz, $CDCl_3$) δ (ppm): 7.84 (d, 2H, *J* = 7.6 Hz), 7.78 (s, 2H), 7.75 (d, 2H, *J* = 7.6 Hz), 2.03 (m, 4H, *J* = 3.4 Hz), 1.43 (s, 24H), 1.26–1.04 (m, 20H), 0.83 (t, 6H, *J* = 6.6 Hz), 0.58 (m, 4H). ^{13}C NMR (75 MHz, $CDCl_3$) δ (ppm): 150.31, 143.78, 133.54, 128.77, 119.23, 83.54, 55.03, 39.36, 31.65, 29.79, 29.05, 29.00, 24.80, 23.44, 22.45, 13.94. HRMS calcd. for $C_{41}H_{64}O_4{}^{11}B_2$: 642.499; found: 642.497.

2,2′-Dibromo-5,5′-bithiophene ***(5)***

Synthesized by the method reported in literature (32, 33).

Polymerization

Carefully purified dibromo derivatives (1.00 equiv.), 2,7-bis(4,4,5,5-tetramethyl-1,3,2-dioxaborolan-2-yl)-9,9-dioctylfluorene (1.00 equiv.), and $(PPh_3)_4Pd(0)$ (0.5–1.5 mol%) were dissolved in a mixture of THF ([monomer] = 0.4 M) and aqueous 2 M K_2CO_3 (1:1.5 THF). The solution was first put under argon atmosphere and was refluxed with vigorous stirring for 48 h. The whole mixture was then poured into methanol (150 mL). The precipitated material was recovered by filtration with a Büchner funnel and washed with a dilute HCl solution. The solid material was washed for 24 h in a Soxhlet apparatus using acetone to remove oligomers and catalyst residues. The resulting polymers were soluble in THF and $CHCl_3$. Yields ~86–95%.

Poly((1,4-phenylene)-2,7-(9,9-dioctylfluorene)) ***PPF***:
^{1}H NMR (400 MHz, $CDCl_3$) δ (ppm): 7.85 (4H), 7.65–7.5 (6H), 2.1 (4H), 1.15 (24H), 0.85(6H).

Poly((4,4′-biphenylene)-2,7-(9,9-dioctylfluorene)) ***PBPF***:

^{1}H NMR (300 MHz, $CDCl_3$) δ (ppm): 7.81 (8H), 7.67 (6H), 2.96 (4H), 1.58 (2H), 1.12 (22H), 0.83 (6H).

Poly((2,5-thienylene)-2,7-(9,9-dioctylfluorene)) ***PTF***:
^{1}H NMR (300 MHz, $CDCl_3$) δ (ppm): 7.54 (4H), 7.32 (4H), 1.96 (4H), 1.01 (24H), 0.71 (6H).

Poly((2,2′-bithienylene)-2,7-(9,9-dioctylfluorene)) ***PBTF***:
^{1}H NMR (300 MHz, $CDCl_3$) δ (ppm): 7.56 (6H), 7.17 (4H), 1.92 (4H), 1.47 (2H), 0.99 (18H), 0.73 (6H), 0.59 (4H).

Results and discussion

Synthesis and characterization of polymers

As illustrated in Scheme 1, palladium-catalyzed Suzuki couplings have allowed the easy preparation of well-defined alternating conjugated polyfluorene derivatives. The utilization of 2,7-bis(4,4,5,5-tetramethyl-1,3,2-dioxaboron-2-yl)-9 ,9-dioctylfluorene simplified the purification of this monomeric precursor combined with a protective effect (1,1,2,2-tetramethylethylene glycol) of the boronic acid moieties. During the polymerization, the presence of such protective groups as ethylene glycol did not affect the yield of the couplings (34), because a hydroxylation deprotection reaction is also

© 1998 NRC Canada

Table 1. Polymerization yield, number-average (M_n) and weight-average (M_w) molecular weights of the copolymers.

Polymer	Yield, %	M_n	M_w	M_w/M_n
PPF	91	12 000	22 000	1.8
PBPF	92	15 000	33 000	2.2
PTF	90	10 000	26 000	2.6
PBTF	86	11 000	21 000	1.9

Table 2. Optical properties of polyfluorene derivatives.

Polymers	λ_{exc} (nm)[a]	λ_{em} (nm)[a]	ϕ_{fl}[a]	λ_{abs} (nm)[b]	λ_{em} (nm)[b]
PPF	362	407	0.87	364	442; 513
PBPF	363	406	0.72	365	443
PTF	431	496	0.49	438	531
PBTF	427	488	0.30	427	599

[a]Evaluated in chloroform solution.
[b]Evaluated in the solid state on a quartz plate; λ_{exc}: excitation wavelength; λ_{em}: emission wavelength; λ_{abs}: absorption wavelength; ϕ_{fl}: fluorescence quantum yield.

taking place during the polymerization process. Tetrahydrofuran (THF) was used to increase the solubility of the growing polymeric chains. Indeed, **PPF** has a higher molecular weight (M_n: 12000) when prepared in a polymerization mixture of THF–water than our first attempt (M_n: 4600) performed in a toluene–water mixture (22). All polymers are completely soluble in $CHCl_3$ and THF. Most polymers exhibit a relatively high molecular weight with a polydispersity index (M_w/M_n) around 2 (Table 1). These polydispersity indexes are consistent with a polycondensation reaction.

UV–visible and fluorescence measurements

In all cases, excitation spectra were found to be similar to the corresponding absorption spectra. Moreover, the absorption spectra for solutions and cast films were almost identical, indicating little structural rearrangement in the condensed phase (19). These optical properties of the fluorene-based π-conjugated polymers are presented in Table 2. By incorporating thiophene units in the polymer, the backbone conformation should be more planar since the energy barrier for the *thienyl–phenyl* rotation is lower than for the *phenyl–phenyl* rotation (35, 36). This can partially explain the fact that the absorption maxima of **PPF** and **PBPF** are blue-shifted by about 65 nm compared to **PBTF** and **PTF**. Furthermore, all these copolymers are strongly luminescent in chloroform solution. Not surprisingly, **PTF** and **PBTF** show lower quantum yield of fluorescence than **PPF** and **PBPF**, the sulfur atom being well known to quench the excited state by the heavy-atom effect. All Stokes shifts are lower than 2800 cm^{-1} (in solution), which can be related to the rigidity of the fluorene moiety that contributes to a fast emission with very similar molecular geometries in both the ground and the excited states. In the solid state, the emission maxima of **PPF** and **PBPF** are red-shifted by about 40 nm compared to those obtained in solution (Figs. 1*a* and 1*b*). These results could be explained by a more delocalized excited state in the condensed phase while **PPF** even shows an additional emission maximum around 510 nm possibly associated with the formation of an excimer (14, 19, 37, 38). The emission in solution and in the solid state of **PPF** and **PBPF** shows a vibronic structure associated with coupling of a C=C vibration mode (around 1500–1600 cm^{-1}).

Fig. 1. Fluorescence spectra (—-) in the solid state, excitation spectra (·····), and fluorescence spectra (——) in chloroform solution for (*a*) **PPF**; (*b*) **PBPF**; (*c*) **PTF**; (*d*) **PBTF**.

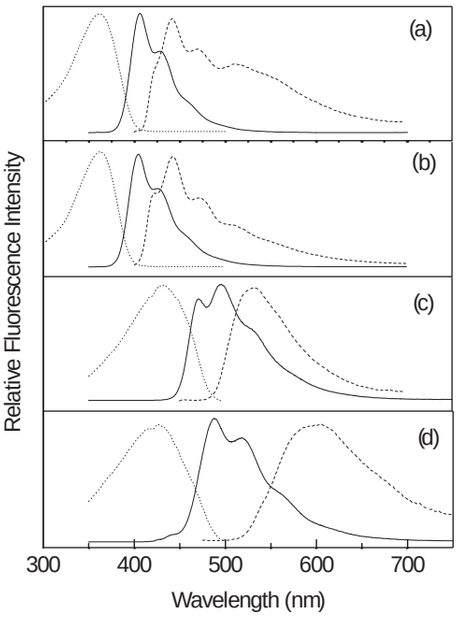

The emission spectra of **PTF** and **PBTF** exhibit a similar vibronic structure in solution. However, in contrast to **PPF**, **PBPF**, and **PTF** (Figs. 1*a*–1*c*), the emission spectrum of **PBTF** in the solid state is remarkably different from that observed in solution (Fig. 1*d*). From these preliminary results, it is supposed that an excimer is also formed in **PBTF** in the solid state but it is clear that further measurements will be necessary to get a clear understanding of the photophysical processes involved in these polymeric materials. Nevertheless, it is already evident that it is possible to modulate the maximum emission wavelength by incorporating different aromatic units in a fluorene-based conjugated polymer while keeping relatively high fluorescence quantum yields.

Electrochemical measurements

As shown in Figs. 2 and 3 (and summarized in Table 3), all copolymers also exhibit some electroactivity upon reduction and oxidation. This is not the case for most homopolymers derived from fluorenes or thiophenes. By alternating thiophene (or phenylene) and fluorene moieties, the reduction potential of the resulting copolymers appears around –2.7 V vs. Ag/Ag^+. It is now well established that the alternation of aromatic units with different electronic properties (push–pull structure) leads to conjugated polymers with lower band gaps and accessible *p*- and *n*-doping reactions (20, 39). Although all cyclic voltammograms seem to indicate a low reversibility of the redox processes, most of the electrochemical charges are slowly recovered in the backward processes (see Table 3), indicating some kinetic

© 1998 NRC Canada

Fig. 2. Cyclic voltammogram of **PPF** (—-) and **PBPF** (——), film on Pt disc, 0.8 cm diameter. Scanning rate: 50 mV s^{-1}.

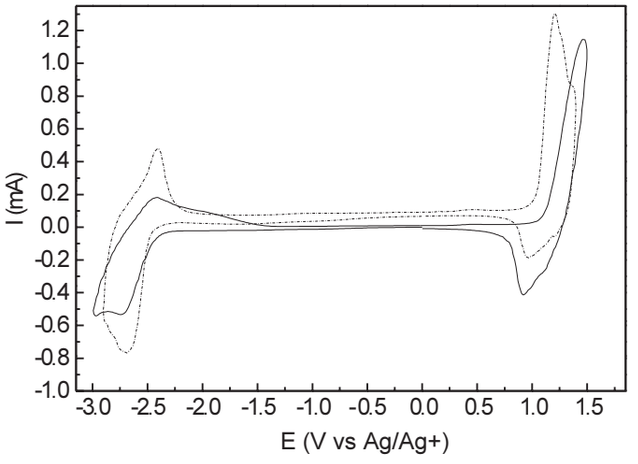

Fig. 3. Cyclic voltammogram of **PBTF** (—-) and **PTF** (——), film on Pt disc, 0.8 cm diameter. Scanning rate: 50 mV s^{-1}.

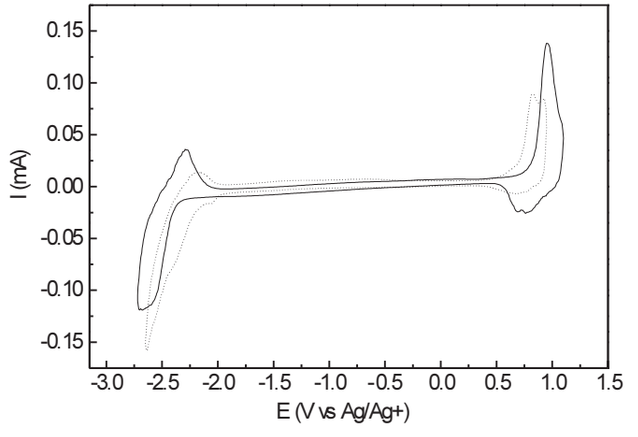

problems in ejecting the counterions inserted during the oxidation or reduction of these copolymers. It is also worth noting that the oxidation potential decreases with the presence of thiophene or bithiophene units (compared to phenyl or biphenyl moieties) in the copolymers, whereas the reduction potential remains almost constant for these four different copolymers. These latter results could indicate that the energy of the LUMO level is almost the same in all these copolymers and would be mainly driven by the nature of the fluorene units. In contrast, the energy of the HOMO level would be more sensitive to the presence of thiophene units.

Interestingly, in situ conductivity measurements have revealed similar electrical conductivities for both reduced and oxidized forms (Fig. 4). The thickness of the films cast onto the microelectrode was difficult to measure with great precision but electrical conductivities up to 10^{-4} S cm^{-1} have been calculated for these polymers in the doped state. These values are in agreement with previous results reported for polyfluorene derivatives (17). The relatively low conductivity levels of these conjugated polymers could be related to important interchain distances caused by the presence of two alkyl side chains (neccessary to keep the solubility of the co-

Table 3. Oxidation and reduction potential of copolymers with the percentage of loss charge after 30 cycles.[a] Scannning rate: 50 mV s^{-1}, electrolyte: 1 M $TEABF_4$ – MeCN (V vs. Ag/Ag^+).

Polymers	E_{ox} (V)	E_{red} (V)	$\%Q_{loss}$
PPF	1.47	–2.73	6.2
PBPF	1.21	–2.69	3.6
PTF	0.97	–2.69	7.2
PBTF	0.82	–2.63	10.1

[a] E_{ox}: oxidation potential; E_{red}: reduction potential; Q_{loss}: charge loss after 30 cycles.

Fig. 4. In situ current of copolymers versus applied potential. Average thickness of film: 100 mm. Residual current between –2.0 V and 0.4 V (I < 150 nA).

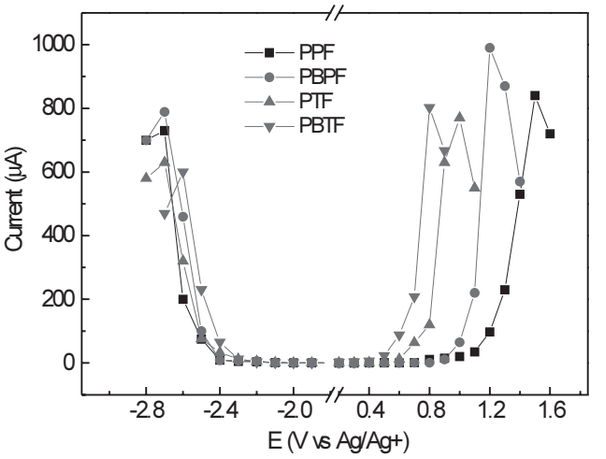

polymers) onto the fluorene unit (40). Higher electrical conductivities are expected with the incorporation of a double bond at the 9-position bearing two flexible alkyl chains; such new monomers are being currently developed in our laboratory. Nevertheless, the present combination of luminescence properties with a good and comparable electrical transport for both positive and negative charge carriers should be particularly useful for the development of efficient light-emitting diodes (41).

Spectroelectrochemical measurements

These polymers not only possess interesting fluorescence and electrochemical properties but also show reversible electrochromism upon reduction and oxidation. By synthesizing a series of copolymers as presented in this paper, it is possible to modulate the absorption maximum from 364 to 660 nm in the solid state. For instance, upon oxidation, **PTF** exhibits a new absorption band around 660 nm while the intensity of the 438 nm band (related to the neutral form) decreases (Fig 5). This new absorption band is related to the formation of positive charge carriers, probably dications (bipolarons) in the present case. **PTF** absorbs in practically the same region in its reduced form (formation of dianions). In Fig. 6, the oxidation of **PPF** shows the appearance of a band at 530 nm and the beginning of another band in the near-infrared (NIR) range. In Fig. 7, the absorption maximum of the reduced form of **PBPF** shifts to 485 nm and a

© 1998 NRC Canada

Fig. 5. Spectroelectrochemical analysis in the solid state of **PTF** in the oxidized form, performed in 0.1 M $TEABF_4$ in MeCN at various electrochemical potentials (V vs. Ag wire).

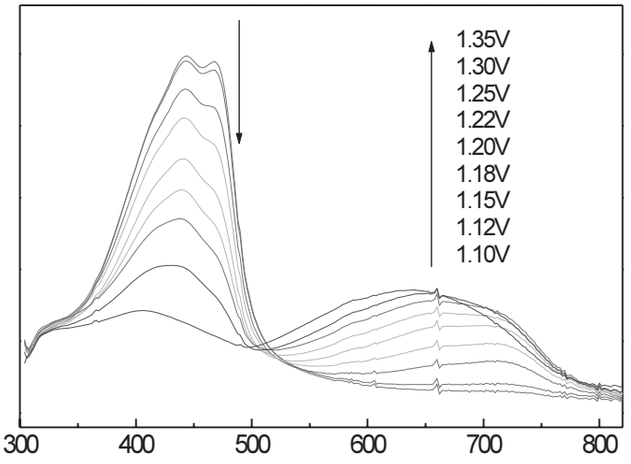

Fig. 6. Spectroelectrochemical analysis in the solid state of **PPF** in the oxidized form, performed in 0.1 M $TEABF_4$ in MeCN at various electrochemical potentials (V vs. Ag wire).

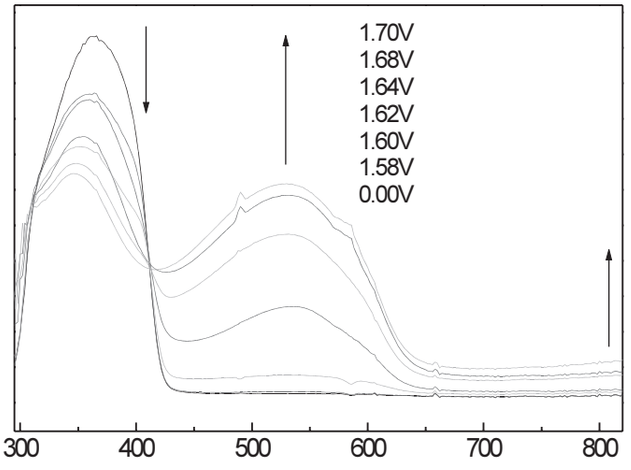

new band appears at the beginning of NIR range. **PBTF** shows similar electrochromic properties, which are consistent with those previously reported by Reynolds and co-workers (17) for oxidized **PBTF**. However, in our study, a vibronic structure is presumably associated with a well-defined structure. **PBTF** synthetized by electrochemical polymerization (17) could have some defects causing by irregular couplings.

Conclusions

The incorporation of alternating thiophene or phenyl moieties in fluorene-based π-conjugated polymers has permitted the preparation of processable, tunable, electroactive, and photoactive materials. **PPF** and **PBPF** exhibit emissive properties in the blue area, an important feature for the development of full-color flat display devices. With an electrical conductivity around 10^{-4} S cm^{-1}, the combination of a good electrical transport for both *n*- and *p*-type charge carriers and a high fluorescence quantum yield for these copolymers may lead to the development of well-defined and efficient light-emitting devices, electrochromic display devices, and electrochemical cells. All these electrooptical devices should be fabricated and tested in the near future.

Fig. 7. Spectroelectrochemical analysis in the solid state of **PBPF** in the reduced form, performed in 0.1 M $TEABF_4$ in MeCN at various electrochemical potentials (V vs. Ag wire).

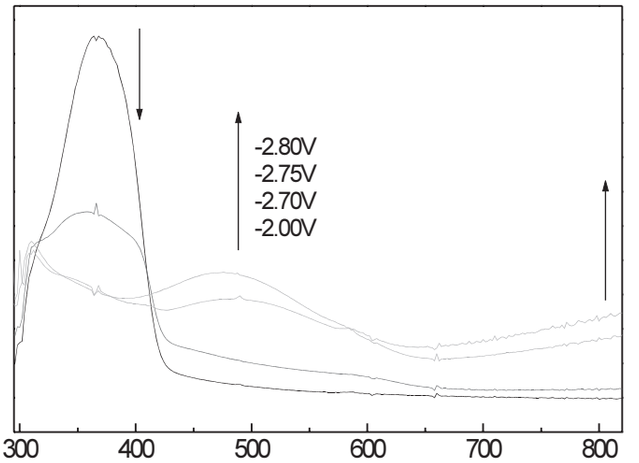

Acknowledgements

This work was supported by grants from the Natural Sciences and Engineering Research Council of Canada (NSERC). We thank Dr. M. Belletête and Prof. G. Durocher for their assistance during the fluorescence measurements. We are also grateful to Prof. M. Armand and Dr. J.Y. Bergeron for their help in the SEC experiments and to Prof. D. Belanger (Université du Québec à Montréal) for his assistance in the electrochemical measurements. M. Ranger is also grateful to NSERC for a scholarship during his Ph.D. studies.

References

1. J.H. Burroughes, D.D.C. Bradley, A.R. Brown, R.N. Marks, K. Mackay, R.H. Friend, P.L. Burns, and A.B. Holmes. Nature, **347**, 539 (1990).
2. D. Braun and A.J. Heeger. Appl. Phys. Lett. **58**, 1982 (1991); Q. Pei, Y. Yang, G. Yu, C. Zhang, and A.J. Heeger. J. Am. Chem. Soc. **118**, 3922 (1996).
3. P.L. Burns, A.B. Holmes, A. Kraft, D.D.C. Bradley, A.R. Brown, R.H. Friend, and R.W. Gywer. Nature, **356**, 47 (1992); Q. Pei, G. Yu, C. Zhang, Y. Yang, and A.J. Heeger. Science, **269**, 1086 (1995).
4. G. Gustafsson, Y. Cao, G.M. Treacy, F. Klavetter, C. Colaneri, and A.J. Heeger. Nature, **357**, 477 (1992).
5. J.S. Miller. Adv. Mater. **5**, 671 (1993).
6. M.G. Kanatzidis. Chem. Eng. News, **68**, 8 (1990); **68**, 36 (1990).
7. M. Sato, S. Tanaka, and K. Keariyama. J. Chem. Soc. Chem. Commun. 873 (1986).
8. R.L. Elsenbaumer, K.Y. Jen, and R. Oboodi. Synth. Met. **15**, 169 (1986).

© 1998 NRC Canada

9. A.O. Patil, Y. Ikenoue, F. Wudl, and A.J. Heeger. J. Am. Chem. Soc. **109**, 1858 (1987).
10. M. Leclerc and K. Faïd. Adv. Mater. **9**, 1087 (1997).
11. M. Rehahn, A.D. Schlüter, G. Wegner, and W.J. Feast. Polymer, **30**, 1054 (1989).
12. M. Ueda, T. Hayakama, O. Haba, H. Kawagushi, and J. Inoue. Macromolecules, **30**, 7069 (1997).
13. B.S. Kang, D.H. Kim, S.M. Lim, J. Kim, M.-L. Seo, K.-M. Bark, S.C. Shin, and K. Nahm. Macromolecules, **30**, 7196 (1997).
14. Q. Pei and Y. Yang. J. Am. Chem. Soc. **118**, 7416 (1996).
15. M. Fukuda, M. Sawada, and K. Yoshino. Jpn. J. Appl. Phys. **28**, L1433 (1989).
16. M. Fukuda, M. Sawada, and K. Yoshino. J. Polym. Sci.: Part A, Polym. Chem. **31**, 2465 (1993); Y. Ohmori, M. Uchida, K. Muro, and K. Yoshino. Jpn. J. of Appl. Phys. **30**, L1941 (1991).
17. F. Larmat, J.R. Reynolds, B.A. Reinhardt, L.L. Brott, and S.J. Clarson. J. Polym. Sci.:Part A, Polym. Chem. **35**, 3627 (1997).
18. M. Grell, D.D.C. Bradley, M. Inbasekaran, and E.P. Woo. Adv. Mater. **9**, 798 (1997).
19. X. Long, A. Malinowski, D.D.C. Bradley, M. Inbasekaran, and E.P. Woo. Chem. Phys. Lett. **272**, 6 (1997).
20. Y. Yamamoto, Z.-h. Zhou, K. Takaki, M. Shimura, K. Kizu, T. Maruyama, Y. Nakamura, T. Fukuda, B.-L. Lee, N. Ooba, S. Tomaru, T. Kurihara, T. Kaino, K. Kubota, and S. Sasaki. J. Am. Chem. Soc. **118**, 10389, (1997).
21. J.M. Kauffman, P.T. Litak, J.A. Novinski, C.J. Kelley, A. Ghiorghis, and Y. Qin. J. Fluoresc. **5**, 295 (1995).
22. M. Ranger, D. Rondeau, and M. Leclerc. Macromolecules, **30**, 7686 (1997).
23. H. Witteler, G. Lieser, G. Wegner, and M. Schulze. Makromol. Chem. Rapid Commun. **14**, 471 (1993).
24. T. Vahlenkamp and G. Wegner. Macromol. Chem. Phys. **195**, 1933 (1994).
25. D.R. Coulson. Inorg. Synth. **13**, 121 (1972).
26. M. Belletête, L. Mazerolle, N. Desrosiers, M. Leclerc, and G. Durocher. Macromolecules, **28**, 8587 (1995).
27. N. DiCesare, M. Belletete, A. Donat-Bouillud, M. Leclerc, and G. Durocher. Macromolecules. Submitted.
28. G. D'Aprano, M. Leclerc, and G. Zotti. J. Electroanal. Chem. **351**, 145 (1993).
29. M. Ranger and M. Leclerc J. Chem. Soc. Chem. Commun. 1571 (1997).
30. R. Wu, J.S. Schumm, D.L. Pearson, and J.M. Tour J. Org. Chem. **61**, 6906 (1996).
31. J.P. Parakka, J.A. Jeevarajan, A.S. Jeevarajan, L.D. Kispert, and M.P. Cava. Adv. Mater. **8**, 54 (1996).
32. G. Barbarella, A. Bongini, and M. Zambianchi. Macromolecules, **27**, 3039 (1994).
33. Y. Wei, Y. Yang, and J.-M. Yeh. Chem. Mater., **8**, 2659 (1996).
34. C. Kowitz and G. Wegner. Tetrahedron, **53**, 15553 (1997); F.E. Goodson and B.M. Novak. Macromolecules, **30**, 6047 (1997).
35. A. Karpfen, C.H. Choi, and M. Kertesz. J. Phys. Chem. **101**, 7426 (1997).
36. B.S. Kang, D.H. Kim, S.M. Lim, J. Kim, M.-L. Seo, K.-M. Bark, S.C. Shin, and K. Nahm. Macromolecules, **30**, 7196 (1997).
37. U. Lemmer, S. Heun, R.F. Mahrt, U. Scherf, M. Hopmeier, U. Siegner, E.O. Göbel, K. Müllen, and H. Bässler. Chem. Phys. Lett. **240**, 373 (1995).
38. M. Aguiar, B. Hu, F.E. Karasz, and L. Akcelrud. Macromolecules, **29**¸ 3161 (1996).
39. M. Pomerantz. *In* Handbook of conducting polymers. 2nd ed. *Edited by* T. Skotheim, R.L. Elsenbaumer, and J.R. Reynolds. Marcel Dekker, New York. 1997. pp. 277–309.
40. M. Leclerc, M. Ranger, and F. Bélanger-Gariépy. Acta Crystallogr. Sect. C: Cryst. Struct. Commun. **C54**, 799 (1998).
41. F. Demanze, J. Cornil, F. Garnier, G. Horowitz, P. Valat, A. Yassar, R. Lazzaroni, and J.L. Brédas. J. Phys. Chem. B, **101**, 4553 (1997), and refs. therein.

© 1998 NRC Canada

A simple method for the generation of negative pressure in liquids

William D. Machin

Abstract: A new technique for the generation of negative pressure in liquids is described, based on the pressure difference that exists across a curved liquid–vapour interface. Menisci in pores having very small radii may induce large negative pressures, or tensions, within the liquid phase. The magnitude of this tension is readily controlled through the pressure of the external vapour phase. Liquid butane when contained in hollow capsules, or Bertholet tubes, with walls formed from Vycor porous glass (pore radius ca. 5 nm) has developed negative pressures as large as –4 MPa for brief periods and lesser tensions for much longer times. This tension approaches the theoretical limit (ca. –6 MPa) calculated from the Laplace equation. Maximum possible tensions based on the theory of homogenous nucleation and on spinodal decomposition are much larger and, in principle, may be reached by reducing the pore size. Our unsuccessful attempts to do so are described.

Key words: Bertholet tube, liquid, negative pressure, nucleation.

Résumé : On décrit une nouvelle technique permettant de générer une pression négative dans des liquides; elle est basée sur la différence de pression qui existe à travers une interface liquide–vapeur courbe. Les ménisques des pores possédant de très faibles rayons peuvent induire de grandes pressions négatives (ou tensions) dans la phase liquide. L'amplitude de cette tension est rapidement contrôlée par la pression de la phase vapeur externe. Lorsqu'on enferme du butane liquide dans des capsules creuses (ou des tubes de Bertholet) dont les parois sont faites de verre poreux, de type Vycor (avec des rayons de pores d'environ 5 nm), il développe des pressions négatives allant jusqu'à –4 MPa pour de faibles périodes et des tensions plus faibles pour des temps beaucoup plus longs. Cette tension s'approche de la limite théorique (environ –6 MPa) calculée d'après l'équation de Laplace. Les tensions maximales possibles sur la base de la théorie de nucléation homogène et sur une décomposition spinodale sont beaucoup plus importantes et, en principe, on peut les atteindre en réduisant la taille des pores. On décrit nos efforts infructueux de la faire.

Mots clés : tube de Bertholet, liquide, pression négative, nucléation.

[Traduit par la Rédaction]

Introduction

While a variety of methods have been used to generate negative pressures in liquids (1), the Bertholet method is most often used to generate static negative pressures. This method employs a sealed container of fixed volume completely filled with liquid at a given temperature and then slowly cooled. Since the thermal expansivity of the liquid is much larger than that of the container the pressure within the liquid decreases rapidly with temperature. Ohde et al. (2), using a metal Bertholet tube, reported negative pressures as great as –20 MPa for several organic liquids while Henderson and Speedy (3) obtained similar tensions with water in a glass tube. More recently Zheng et al. (4), using an inclusion synthesis technique whereby microscopic volumes of water are trapped in fissures within various crystals, obtained tensions of ca. –140 MPa, close to the homogenous nucleation limit of liquid water. Our interest in liquids at negative pressure stems from our work on capillary-condensed liquids. For example, we have found that the equation of state proposed by Speedy (5) provides an excellent description of water at negative pressures, when condensed in a microporous silica gel (6). From a theoretical point of view, however, it is better to study macroscopic volumes of liquid.

Tensions observed in macroscopic Bertholet tubes are usually much less than those predicted from theoretical considerations. As Ohde et al. (7) have pointed out, this may be due to the presence in the system of potential nuclei such as minute or nascent air bubbles, surface impurities that foster heterogenous (surface) nucleation, or microscopic crevices holding minute amounts of trapped air. Some of these contaminants originate with the method of filling the apparatus, where the tube is almost completely filled with liquid, then sealed. The small bubble of air is removed by warming the tube and as the liquid expands to fill the entire tube the air dissolves in the liquid. Subsequent cooling induces negative pressure in the liquid along a given isochore if vapour phase (bubble) nucleation is absent. To obtain data for different isochores it is necessary to reopen the tube and change the amount of liquid. This is not only inconvenient and time consuming but also provides opportunity for further contamination of the liquid. In this work we describe a Bertholet

Received January 21, 1998.

W.D. Machin.[1] Department of Chemistry, Memorial University of Newfoundland, St. John's, NF A1B 3X7, Canada.

[1]Telephone: (709) 737-8763. Fax: (709) 737-3702.

© 1998 NRC Canada

Fig. 1. Bertholet tube. Stippled region corresponds to Vycor porous glass tubing (ca. 5 mm diameter) and the sealed ends are essentially nonporous silica.

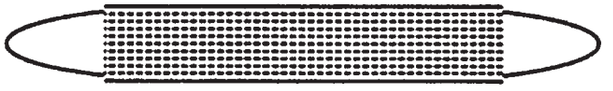

tube that avoids many of these problems and we present some results for liquid butane. The method is based on the development of a large pressure difference across a highly curved liquid–vapour interface and is similar, in principle, to the method developed by Marinho (8) to study capillary suction in soils.

Experimental

The cell, shown in Fig. 1, is a section of Vycor porous glass tubing (ca. 5 mm diameter) sealed at both ends. While the ends are nonporous vitreous silica, the walls of the tube contain many submicroscopic pores (diameter 2–6 nm) that pass through the cell walls (9). The cell is mounted in an apparatus (Fig. 2) where it can be baked out under vacuum. Butane, stored in the reservoir, is degassed by several freeze–thaw cycles, then condensed around the cell at ice temperature so that the cell is completely covered. The liquid slowly flows through the pores until the cell is filled. This may take several days but the process may be accelerated if condensed butane extends into warmer ambient temperatures as shown in Fig. 2 (inset A). Cells that fill rapidly are usually defective. Once the cell is filled, excess butane, external to the cell, is slowly (without boiling) returned to the reservoir. After all the external liquid has evaporated (Fig. 1, inset B) further removal of vapour reduces the pressure in the vapour phase, P_{vap}, below the saturation vapour pressure of butane, P^{o}_{vap}. This causes the formation of hemispherical menisci within the pores in the cell walls. The capillary pressure difference, ΔP_c, across the curved liquid–vapour interface is given by the Laplace equation,

$$[1] \qquad \Delta P_c = P_{vap} - P_{liq} = 2\gamma/r$$

where γ is the surface tension of the liquid, P_{liq} is the pressure within the liquid, and r is the radius of curvature of the meniscus. If r is very small P_{liq} may be negative. It is readily shown (10) that

$$[2] \qquad \Delta P_c = -(RT/V_{liq}) \ln (P_{vap}/P^{o}_{vap})$$

where V_{liq} is the liquid molar volume. For our present purposes only a small error is introduced if the liquid is assumed to be incompressible, but at large negative pressures, close to the spinodal limit, this assumption will not be valid (6). When the relative pressure, P_{vap}/P^{o}_{vap}, is less than unity and the cell remains filled with (metastable) liquid, P_{liq} is readily calculated. Further removal of vapour results in the evaporation of some of the liquid through the porous cell walls and an increase in ΔP, i.e., P_{liq} becomes more negative. This process can be continued until a bubble forms within the liquid, at which point the liquid evaporates and the vapour phase pressure rapidly increases to the saturation vapour pressure. Two runs are shown as examples in Fig. 3.

Fig. 2. Apparatus for filling and testing Bertholet tubes (schematic). S is a 2 L storage bulb and F is a freeze-out for degassing the butane. V are stainless steel bellows-seal valves and M is a similar metering valve. The pressure sensor (MKS Baratron) reads to 1000 Torr (1 Torr = 133.3 Pa) with an accuracy of at least 0.1%. Inset A shows an expanded view of a partially filled tube submerged in liquid butane while inset B shows the tube filled with the external excess butane removed.

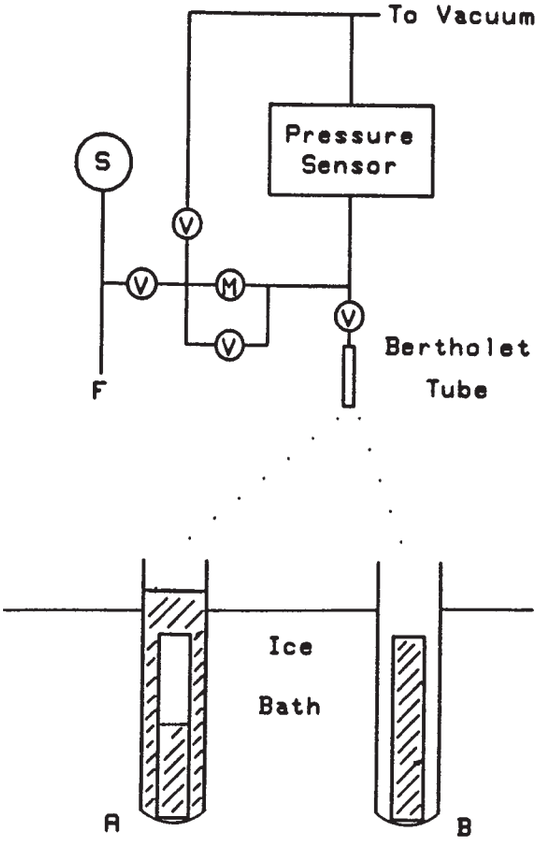

Discussion

There are four possible mechanisms for the formation of a bubble within the liquid: (*i*) heterogenous nucleation at the inner surface of the cell; (*ii*) homogenous nucleation within the liquid; (*iii*) spinodal failure of the liquid, and (*iv*) penetration of the external vapour phase through the porous cell wall. The latter will occur when the radius of curvature of the liquid–vapour interface (eq. [1]) becomes less than the radius of at least one pore connecting the internal liquid phase with the external vapour phase, i.e., when $r < r_p - t$, where r_p is the pore radius and t is the thickness of the adsorbed layer on the pore walls (10). The pressure at which homogenous nucleation occurs is calculated from the equation given by Fisher (11),

$$[3] \qquad \Delta P_{hn} = [16\pi\gamma^3/3kT \ln (nkT/h)]^{1/2}$$

where k and h are the Boltzmann and Planck constants and n is the number of molecules in the liquid. Spinodal

© 1998 NRC Canada

Fig. 3. Example runs. Curve A (circles): at t < ca. 1000 s a small amount of liquid remains outside the Bertholet tube. This establishes the baseline saturation pressure P^{o}_{vap}. Between 1000 and 2000 s all of the excess liquid and some of the residual vapour is slowly removed to establish a tension of ca. –1.8 MPa within the liquid ($P_{vap} < P^{o}_{vap}$, see eq. [2]). Nucleation occurs at ca. 7000 s. Curve B (crosses): as for curve A but after 3000 s a plateau is established at ca. –2.7 MPa. Continued slow removal of vapour after 6000 s leads to nucleation at ca. –4 MPa. The maximum possible tension, imposed by the pore size in the Bertholet tube, is estimated to be –5.9 MPa (see text).

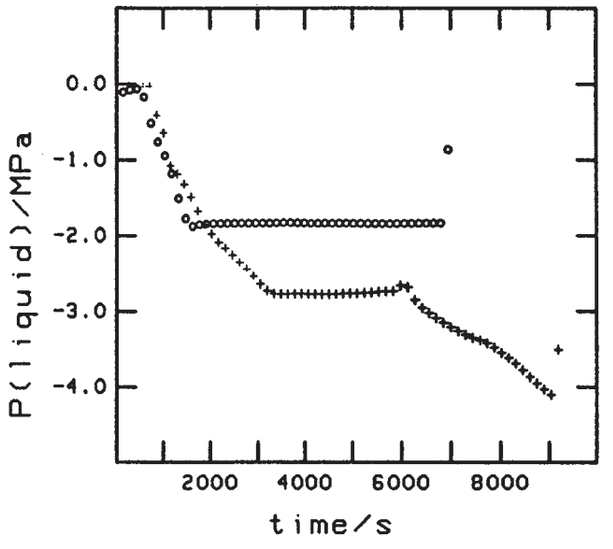

decomposition occurs when the negative pressure is sufficiently large that the liquid passes from a metastable to an unstable state. The pressure, ΔP_{sp}, at which this occurs can be estimated from the hard-sphere equation of state with an attractive van der Waals tail as given by Ben-Amotz and Herschbach (12). In general $\Delta P_{sp} > \Delta P_{hn}$, i.e., homogenous nucleation will occur before spinodal decomposition (4), but the relative magnitude of ΔP_{hn} and ΔP_{c} (eq. [1]) will depend on the radius of the pores in the cell walls. Heterogenous nucleation occurs at relatively small negative pressures when the liquid does not completely wet the walls of the tube (13). For butane at the ice point $\Delta P_{sp} \cong 20$ MPa, $\Delta P_{hn} = 13.6$ MPa, and, for pores of radius 5.0 nm (14), $\Delta P_{c} = 5.9$ MPa.

Typical behaviour of the liquid at negative pressure is shown in Fig. 3. Curve A in this figure is characteristic of several runs at constant negative pressure. Metastable liquid can persist for long periods (up to 2×10^4 s) but eventually bubble formation occurs. A light blow or tap on the external supporting tube (Fig. 2) may be sufficient to initiate nucleation. When the external vapour pressure is slowly decreased (curve B) the liquid fails at ca. –4 MPa, which is comparable to the pressure limit imposed by the pore size ($\Delta P_{c} \cong 5.9$ MPa).

This method offers an advantage over other types of Bertholet tubes in that the tube can be filled with degassed, microfiltered liquid in a closed system. For volatile liquids it also has the major advantage that P_{liq} can be controlled through the external pressure, P_{vap} (eq. [2]), and that P_{liq} can be changed isothermally. In principle, with tubes having sufficiently small pore radii, it should also be possible to distinguish between homogenous nucleation and spinodal decomposition. The latter should be accompanied by divergence of the isothermal compressibility as the spinodal limit is approached. This would be noted as a marked diminution in the liquid density, observed as a decrease in the overall mass of the liquid in the tube.

Unfortunately, these tubes are difficult to make and, in some respects, are relatively fragile. For example, they cannot be abruptly immersed in liquids, especially those having high surface tension such as water. They often fail in use, tending to form a ring crack near the boundary between the nonporous (fused) end and the main porous (unfused) wall of the tube. In an attempt to circumvent this problem several tubes were sealed with epoxy resin but this material appeared to serve as a nucleating surface and only insignificant negative pressures could be developed. In an attempt to decrease the pore size and hence extend the range of ΔP_{c}, other tubes were immersed in a water–TMOS (tetramethyl orthosilicate) solution but all cracked after short exposure to the solution. Vapour phase adsorption of water on the pore walls, followed by vapour phase adsorption – reaction with TMOS proved similarly unsuccessful. In principle, this type of Bertholet tube offers significant advantages over other types, especially for volatile liquids. However, the tubes are difficult to make and have a short lifetime.

Acknowledgements

Mr. G. Lewis carried out many of the runs, such as those shown in Fig. 3, and Professor P.D. Golding provided useful discussion. This work was supported by the Natural Sciences and Engineering Research Council of Canada. The author thanks one of the referees for pointing out ref. 8.

References

1. D.H. Trevena. Comtemp. Phys. **8**, 185 (1967).
2. Y. Ohde, H. Watanabe, K. Hiro, K. Motoshita, and Y. Tanzawa. J. Phys. D: Appl. Phys. **26**, 1188 (1993).
3. S.J. Henderson and R.J. Speedy. J. Phys. E: Sci. Instrum. **13**, 778 (1980).
4. Q. Zheng, D.J. Durben, G.H. Wolf, and C.A. Angell. Science, **254**, 829 (1991).
5. R.J. Speedy. J. Chem. Phys. **86**, 982 (1982).
6. W.D. Machin and J.T. Stuckless. J. Chem. Soc. Faraday Trans. 1, **81**, 597 (1985).
7. Y. Ohde, M. Ikemizu, H. Okamoto, W. Hosokawa, and T. Ando. J. Phys. D: Appl. Phys. **21**, 1540 (1988).
8. F.A.M. Marinho. Ph.D. Thesis, Imperial College of Science and Technology, London. 1994.
9. M.E. Nordberg. J. Am. Ceram. Soc. **27**, 299 (1944).
10. S.J. Gregg and K.S.W. Sing. *In* Adsorption, surface area and porosity. Academic Press, London. 1982. pp. 154–160.
11. J.C. Fisher. J. Appl. Phys. **19**, 1062 (1948).
12. D. Ben-Amotz and D.R. Herschbach. J. Phys. Chem. **94**, 1038 (1990).
13. J.L. Green, D.J. Durben, G.H. Wolf, and C.A. Angell. Science, **249**, 649 (1990).
14. W.D. Machin. Langmuir, **10**, 1235 (1994).

© 1998 NRC Canada

An ab initio and neutron diffraction study of ammonium chloride

A. Alavi, R.M. Lynden-Bell, P.A. Willis, I.P. Swainson, and R.J.C. Brown

Abstract: Ab initio density functional calculations have been carried out on the ordered phase of ammonium chloride and the results compared with experimental data. Powder neutron diffraction measurements have been carried out on $^{14}ND_4Cl$ and $^{15}ND_4Cl$ at a temperature of 5 K; the lattice parameter is 3.8224(4) Å and the N—D bond length is 1.0318(8) Å. Calculated structural and spectroscopic quantities agree well with the results of the neutron diffraction refinements, and with measured spectroscopic data. The calculated barrier to reorientation of the ammonium ion about the fourfold axis is 29 kJ mol^{-1}, and the calculated compressibility is 3.78×10^{-11} Pa^{-1}. The octopole moment of the ammonium ion in the crystal has been estimated from the calculated electron density, and is about 10–20% greater than for the free ion. The octopole moment does not vary appreciably with the orientation of the ammonium ion in the lattice. There is no evidence of any covalent interaction between the ammonium and chloride ions.

Key words: ammonium chloride, density functional theory, neutron diffraction, ab initio calculations.

Résumé : On a effectué des calculs ab initio de densité fonctionnelle sur la phase ordonnée du chlorure d'ammonium et on a comparé les résultats avec les données expérimentales. On a effectué des mesures de diffraction de neutrons par des poudres de $^{14}ND_4Cl$ et $^{15}ND_4Cl$ à 5 K; le paramètre de réseau est égal à 3,8224(4) Å et la longueur de la liaison N—D est égale à 1,0318(8) Å. Les valeurs structurales et spectroscopiques calculées sont en bon accord avec les résultats de l'affinement de la diffusion de neutrons et les données spectroscopiques mesurées. La barrière calculée pour la réorientation de l'ion ammonium autour de l'axe quaternaire est de 29 kJ mol^{-1} et la compressibilité calculée est de $3,78 \times 10)^{11}$ $Pa)^{1}$. On a évalué le moment octapolaire de l'ion ammonium dans le cristal à partir de la densité électronique calculée et elle est environ de 10 à 20% plus élevée que celle de l'ion libre. Le moment octapolaire ne varie pas beaucoup avec l'orientation de l'ion ammonium dans le réseau. On n'a relevé aucune indication de présence d'interactions covalentes entre les ions ammonium et chlorure.

Mots clés : chlorure d'ammonium, théorie fonctionnelle, diffraction de neutrons, calculs ab initio.

[Traduit par la Rédaction]

Introduction

The ammonium ion is singly charged, small, and approximately spherical. It forms ionic crystals, which have many similarities to those of the alkali metals. However, because it has additional orientational degrees of freedom, these crystals have a range of structures and phase transitions that have no counterparts in the salts of the alkali metals. The ammonium ion is also a potential hydrogen bond donor, but the extent to which this occurs in halide crystals has been a matter of discussion. In this work we combine an accurate determination of the crystal structure of the low-temperature ordered phase of ammonium chloride with an ab initio quantum calculation of the electronic energy and density in this structure.

At room temperature ammonium chloride (NH_4Cl) forms an ionic crystal in which there is orientational disorder of the ammonium ions. The discovery of the order–disorder phase transition in 1922 (1) was followed by extensive spectroscopic, thermodynamic, and other studies (2). At temperatures below 457.6 K ammonium chloride crystallizes in the CsCl structure. In the ordered phase below 242.5 K the space group is $P\bar{4}3m$ and the ammonium ions are aligned parallel to each other with bonds along four of the [111] directions. At temperatures between 242.5 and 457.6 K the space group is $Pm3m$ and the crystal is orientationally disordered with equal populations of the two possible orientations. In the deuterated salt ND_4Cl, the order–disorder phase transition takes place at 249.7 K. The order–disorder phase transition is first order at atmospheric pressure, but becomes second order at a tricritical point at a pressure of approximately 100 MPa. The structures of these two phases have been established by neutron diffraction (3, 4).

Many of the interesting spectroscopic and thermodynamic properties of ammonium chloride are related to motion of the ammonium ion. The potential energy surface for the ammonium ion has been discussed by many authors (5–11), usually on the basis of either an electrostatic or atom–atom

Received January 20, 1998.

A. Alavi and R.M. Lynden-Bell. School of Mathematics and Physics, The Queen's University, Belfast BT7 1NN, U.K.
I.P. Swainson. Neutron Program for Materials Research, Steacie Institute for Molecular Sciences, National Research Council, Chalk River, ON K0J 1J0, Canada.
R.J.C. Brown[1] and P. Willis[2]. Department of Chemistry, Queen's University, Kingston, ON K7L 3N6, Canada.

[1]Author to whom correspondence may be addressed. Telephone: (613) 545-2652. Fax: (613) 545-6669. E-mail: brownrjc@chem.queensu.ca
[2]Present address: Chemistry Department, Cornell University, Ithaca, NY 14853, U.S.A.

© 1998 NRC Canada

potential expressed in terms of a symmetry-adapted expansion of the potential function. In some cases an empirical potential function is fitted to such measured data as librational frequencies. Smith has recently reviewed potential functions for ammonium ions in crystalline salts (12).

Classical molecular dynamics calculations based on these potential functions have been carried out by several groups and used to study the ammonium ion dynamics and the nature of the phase transition in solid NH_4Cl (13–15) and in $(NH_4Cl)_n$ clusters (16).

In recent years there has been a great increase in the availability of ab initio methods suitable for solid state problems. The innovation that has been particularly appropriate for the solid state is the use of density functional theory, with modern density functionals that have been used successfully for semiconductor, metallic, and ionic systems (see, for example, the website http://gserv1.dl.ac.uk/TCSC/HCM/PSIK/main.html). The main results of such calculations are the energy and electron density as functions of nuclear positions. These can be used to obtain a better understanding of the electron distribution and hence of the bonding in the material under study. In this work we use such a calculation to study the low-temperature ordered phase of ammonium chloride. The results of the calculation are compared with the structural parameters of ammonium chloride at low temperature determined by neutron diffraction. Our interest in this substance is informed by our earlier attempts to model orientationally disordered phases containing molecular ions (17). We address the question of how far the ammonium ion can be described as a distinct molecule interacting weakly with the other ions, or whether there is a high degree of covalency. How much hydrogen bonding is present and how much does the electronic structure change as the ammonium ions are rotated relative to the chloride lattice? How adequate is a classical model with fixed charges on atomic sites? While answering these questions we also obtain values for the bond length, lattice parameter, compressibility, and vibrational frequencies for the model.

The structure of the paper is as follows. The following two sections report the methods used for the ab initio calculations and the neutron diffraction experiment. Then the results of the calulations are compared with the structural properties determined experimentally and with published spectroscopic data. Finally, the electronic structure of the ammonium ion in this crystal is discussed and compared with the results of other calculations.

Ab initio calculations — method

The method we use is Alavi's FEMD method (18–20) in which the free energy functional of Mermin (21) is minimized. In fact, as the gap between the highest occupied and lowest unoccupied orbitals is large, the use of this method rather than a more standard total energy method such as Car–Parrinello (22) or other density functional total energy methods is immaterial. We used the local density approximation with gradient corrections (23, 24). The electronic orbitals were expanded in plane-wave basis set up to a cutoff of 73.2 Ry, corresponding to approximately 16 500 plane waves. We used the pseudopotential method to obviate the need to explicitly include core electrons. Troullier–Martins pseudopotentials (25) in the Kleinman–Bylander form (26) using *s* and *d* non-locality for Cl and N were employed. The pseudopotentials were generated using core radii of 1.4 a.u. for the valence states of both N and Cl. The above cutoff was sufficient to give well-converged results. Calculations were done on a single unit cell of NH_4Cl with periodic boundary conditions. Given this unit cell, we found it essential to construct the density from orbitals that sample adequately the Brillouin zone. For this purpose we used a $4 \times 4 \times 4$ Monkhorst–Pack k-point mesh. Using fewer k points gave rise to large errors, including for example a 30% error in the lattice spacing. For the calculation of the compressibility the number of plane waves was fixed at 16 494, to eliminate the discontinuities that arise from changes in the number of the plane waves as the cell dimensions are varied.

Calculations were performed with a number of lattice parameters and a number of N—H bond lengths to find the energy minimum. These results also gave the compressibility and the N–H symmetrical stretching frequency. The transverse optical frequency was calculated by displacing the chloride ions from their lattice positions and calculating the corresponding force constant. The energy was then mapped out by keeping the lattice parameter and bond length constant and rotating the ammonium ions around (in turn) twofold and threefold ion symmetry axes. Electron distributions were compared in the extremes of these orientations. Following Klein et al. (13), we shall refer to the orientation with the ion rotated by 45° about one of its C_2 (or S_4) symmetry axes as the D_{2d} orientation and the orientation with the ion rotated by 60° about an N—H bond or C_3 symmetry axis as the C_{3v} orientation.

Neutron diffraction — methods

Structural data for ammonium chloride were determined by powder neutron diffraction measurements on ND_4Cl and on $^{15}ND_4Cl$. The objective of using two samples with different nitrogen isotopes was to test the validity of the N—H bond length and the torsional thermal parameters by independent refinement of data for two samples with identical moments of inertia for the ammonium ion, but different neutron scattering properties. Powdered $^{14}ND_4Cl$ (99.3% D) and $^{15}ND_4Cl$ (99.2% D, 99% ^{15}N) supplied by Isotech Inc. (Miamisburg, Ohio) were examined at five temperatures from 5 K to ambient temperature. The materials were checked initially by X-ray diffraction and were used as supplied. The powder samples were contained in vanadium tubes of 5 mm inside diameter and wall thickness 0.18 mm, which were filled with helium exchange gas. The samples were rotated about one axis throughout data collection to improve averaging over crystallite orientation.

The experiment was done on the C2 Dualspec high-resolution powder diffractometer at the NRU reactor at Chalk River, and data were collected from 5° to 120° with a step size of 0.025°. The monochromator was Si (531) and the take-off angle was $2\theta = 110.05°$. The neutron wavelength of 1.50443(3) Å was calibrated using a separate Si powder standard. Sample temperature was controlled by a helium cryostat, with separate thermocouples for the measurement and control of temperature. Structure refinement was carried out using the GSAS Rietveld refinement code (27). Rigid

© 1998 NRC Canada

Fig. 1. Neutron diffraction intensity profiles and calculated fits for ammonium chloride at 5 K. (*a*) $^{14}ND_4Cl$; (*b*) $^{15}ND_4Cl$. In each case the upper part of the diagram shows the observed and calculated profiles, and the lower part of the diagram shows the difference between observed and calculated profiles.

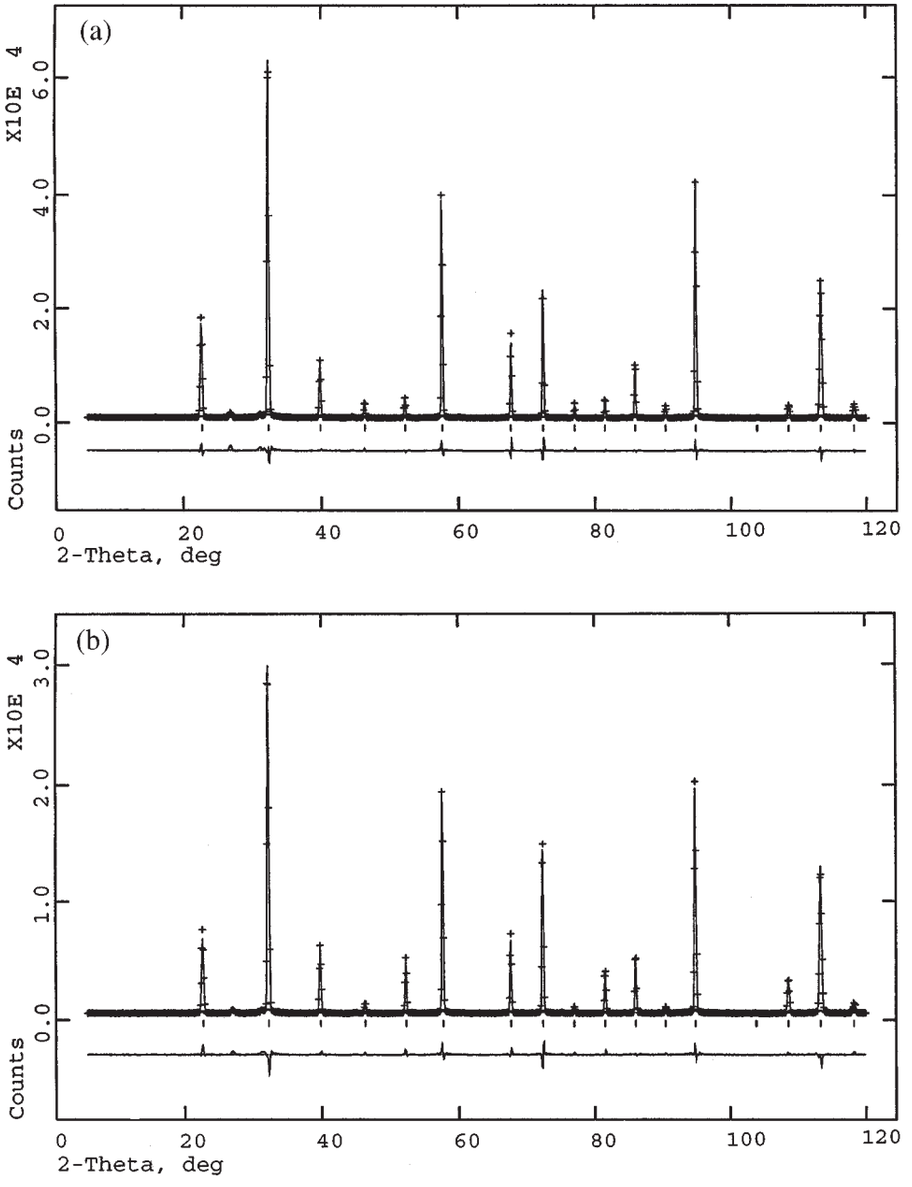

body constraints were used to define the ammonium ion as a regular tetrahedron, and the thermal parameters for the ammonium ion were expressed in the TLS format. The profiles were corrected for absorption before refinement with an overall absorption factor for the unit cell. Figure 1 shows the observed and calculated powder patterns for the two sets of data.

Neutron diffraction — results

The results of the refinements are summarized in Table 1. The unit cell parameters of the two samples do not agree as well as might be expected based on the indicated statistical precision. This effect has been noted before for independent experiments (28), and is thought to be due to nonreproducibility in the sample position. The average value for the cell parameter is 3.8224(4) Å. The bond lengths for the ammonium ion derived from the two samples agree satisfactorily and the average bond length is 1.0318(8) Å. This bond length is longer than that found in ND_4ReO_4 at 20 K, 1.025(1) Å (29), but shorter than the bond lengths in NH_4F at 77 K, which are 1.035(8) Å and 1.045(6) Å (30). The thermal parameters for the ammonium ion agree well between the two samples, and indicate an r.m.s. torsional amplitude of 6.6°.

Ab initio calculations — results

The results of the calculations are summarized in Table 2. In comparing the calculated structural parameters with the

© 1998 NRC Canada

Table 1. Structural and thermal parameters for ND_4Cl at 5 K determined by neutron diffraction. T and L are the thermal parameters for the ammonium ion expressed in TLS notation; U is the thermal parameter for the chloride ion.

T/K	Sample	a/Å	r(N—D) / Å	$T \times 100$/Å^2	L/deg^2	$U \times 100$/Å^2	R_{wp}
5.08(2)	$^{14}ND_4Cl$	3.82278(4)	1.0323(8)	0.48(1)	44.9(5)	0.22(2)	0.0752
4.88(5)	$^{15}ND_4Cl$	3.82193(4)	1.0314(7)	0.48(1)	42.1(5)	0.13(2)	0.0654

Table 2. Comparison of calculated and observed properties.

Quantity	Calculated	Experimental and reference
Lattice parameter	3.891 Å	3.8224(4) Å [a]
N—H bond length	1.0323 Å	1.0318(8) Å [a]
Symmetric stretching frequency	3133 ± 20 cm^{-1}	3048 cm^{-1} (31)
Librational frequency	437 ± 2 cm^{-1}	389 cm^{-1} (31)
Transverse optical frequency	167 ± 8 cm^{-1}	186 cm^{-1} (31)
Longitudinal optical frequency	242 ± 12 cm^{-1}	277 cm^{-1} (31)
Compressibility	3.78 × 10^{-11} Pa^{-1}	3.73 × 10^{-11} Pa^{-1} (37)
Rotational barrier	29 kJ mol^{-1} [b]	27.2 kJ mol^{-1} (38–41)

[a] This work.

[b] The calculated barrier is for simultaneous rotation of all ammonium ions (see text).

neutron diffraction results, it should be kept in mind that the calculations refer to the protonated salt, NH_4Cl, but do not include any averaging over vibrational motion; the neutron diffraction results refer to the actual deuterated salt ND_4Cl including zero point motion and residual thermal motion at a temperature of 5 K. The calculated vibrational frequencies in the table refer to NH_4Cl.

The calculated lattice parameter and equilibrium bond length are in reasonable agreement with experiment. It was found that the calculated lattice parameter was sensitive to the number of k-points included in the calculations and to the cutoff. The lattice parameter is about 2% larger than the measured value, but the N—H bond length is in good agreement with the neutron diffraction results.

The vibrational spectra of both protonated and deuterated ammonium chloride were reported by Schumaker and Garland (31). The dispersion curves of the external modes have been determined in a neutron scattering study of ND_4Cl by Teh and Brockhouse (32, 33). The calculated and experimental spectroscopic results listed in Table 2 all pertain to the zone centre vibrational modes in which the displacement in every unit cell is identical. The calculated symmetrical stretching frequency of the ammonium ion is larger than the measured frequency by about 3%. In the calculation all three translational optic modes (in which the chloride and ammonium ions move in opposite directions) are degenerate. This frequency gives the predicted transverse optic mode frequency; the longitudinal optic mode has a higher frequency due to the interaction of the local oscillating dipole moment with the electric field. The calculated transverse optical frequency agrees satisfactorily with experiment; the longitudinal optical frequency was calculated from the calculated transverse optical frequency using the ratio of dielectric constants at low and high frequencies, namely $\varepsilon_s/\varepsilon_\infty = 2.17$, and the Lyddane–Sachs–Teller relation (34, 35), following Teh and Brockhouse (32).

The compressibility was calculated by fitting a parabola to the calculated total energy as a function of lattice parameter, and comparing with the strain energy for a cubic crystal (36). The estimated experimental value is based upon the ultrasonic measurements of Garland and Renard (37). Their measured values of the isentropic elastic constants c_{11} and $C' = (c_{11} - c_{12})/2$ as a function of temperature were extrapolated to absolute zero, at which temperature the difference between the isentropic and isothermal elastic constants is zero. The estimated experimental compressibility was then calculated from the formula $\kappa^{-1} = c_{11} - 4C'/3$ (36). The agreement between the calculated and experimental values is very good.

Figure 2 shows the variation of energy with rotation of the ammonium ion in the ordered phase. In these calculations all the ammonium ions in the crystal are rotated in phase about either a C_3 symmetry axis (dotted line, period 120°) or an S_4 symmetry axis (full line, period 90°). The curvature around the T_d orientation is identical for both displacements as the librations of the ammonium ion at the G point are all degenerate. As the energy curves are very close to sinusoidal, it follows that the lowest barrier is for the rotation with the smallest angular period. At the barrier for rotation about an S_4 axis the ions are in the D_{2d} orientation; the bonds are still equivalent but the bond angles need no longer be equal. At the barrier for rotation about a C_3 axis, the bonds are no longer even equivalent. In our calculations the internal geometry of the ion is fixed at the equilibrium tetrahedral geometry. If this restriction were relaxed one would expect a slight lowering of the barriers. The calculated barriers are 29 kJ mol^{-1} for simultaneous rotation of all molecules about parallel S_4 axes and 35.5 kJ mol^{-1} for rotation about parallel C_3 axes; rotation about the S_4 axis is preferred.

Experimental values for the barrier to rotation are based primarily upon NMR determinations of the activation energy for rotation from relaxation time measurements (38–40) and quasi-elastic neutron scattering (41). Mandema and Trappeniers (38) give the activation energy in the ordered phase as 21.2 kJ mol^{-1}, while Woessner and Snowden (39) and Sharp and Pintar (40) both give 19.7 kJ mol^{-1}. Töpler et al. give the activation energy for reorientation about the S_4 axis as 20.4 kJ mol^{-1} (41). The average of these values, 20.2

© 1998 NRC Canada

Fig. 2. Energy as function of angle of rotation of the ammonium ions about their S_4 axes (solid line) and their C_3 axes (dotted line). The barriers to rotation are 29 kJ mol^{-1} for the S_4 rotation and 35.5 kJ mol^{-1} for the C_3 rotation.

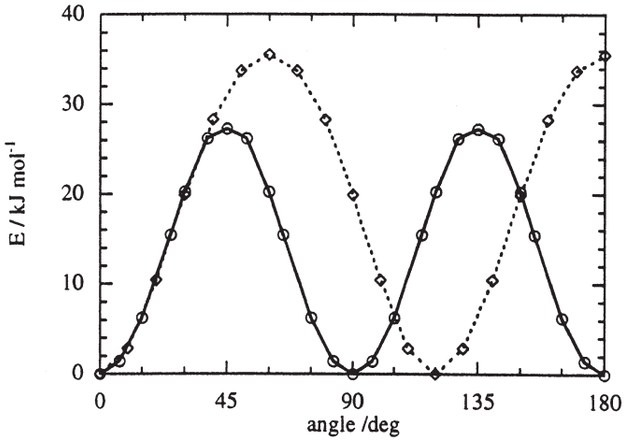

kJ mol^{-1}, has been used in the following. The barrier height is the sum of the activation energy and the zero point energy for the triply degenerate librational mode with an experimental frequency of 389 cm^{-1} (Table 2). The result is 27.2 kJ mol^{-1}, which agrees well with the calculation, and confirms the earlier conclusion (9, 15) that reorientation takes place about the S_4 rather than the C_3 axis of the ammonium ion. The main difference between the calculated and experimental barrier height is probably due to the fact that the calculated result is for the simultaneous rotation of every ammonium ion in the crystal while the experimental result is for the reorientation of a single ion.

We conclude that the ab initio calculations give results that agree with the experimental quantities within about 5% or better for most quantities.

Electronic structure of the ions

Figure 3 shows electron density contours with the ammonium ion in its most stable T_d orientation. The electron density has been computed in a (110) plane through the lattice, containing two N—H bonds (long bold lines) in each ammonium ion, and the adjacent chloride ions to which they point. The shorter bold lines are the projections of the out-of-plane N—H bonds, while the chloride ions are at the centres of circles. Figure 4 shows electron density contours in the (110) plane with the ammonium ion in the C_{3v} orientation. The plane of the diagram contains chloride ions and two N—H bonds. One of the two in-plane N—H bonds lies along the N—H···Cl axis about which the 60° rotation has taken place, and the other in-plane N—H bond points between chloride ions. Figure 5 shows electron density contours in the (100) plane through the nitrogen atom with the ammonium ion in the D_{2d} orientation. In this orientation none of the N—H bonds point at a chloride ion.

In each of these figures the contours are plotted at logarithmic intervals so that low-lying contours are at very low values of the electron density. Note that the use of a pseudopotential gives a distorted electron density near the Cl and N cores. Comparing these three plots we see that the contours

Fig. 3. Contour plot of the electron density in ammonium chloride with the cation in the most stable (T_d) orientation. The plot shows the electron density in a (110) plane passing through the nitrogen atoms. This plane contains two N—H bonds (long bold lines) that point at chloride ions (circles). The two shorter bold lines show the other N—H bonds projected onto this plane.

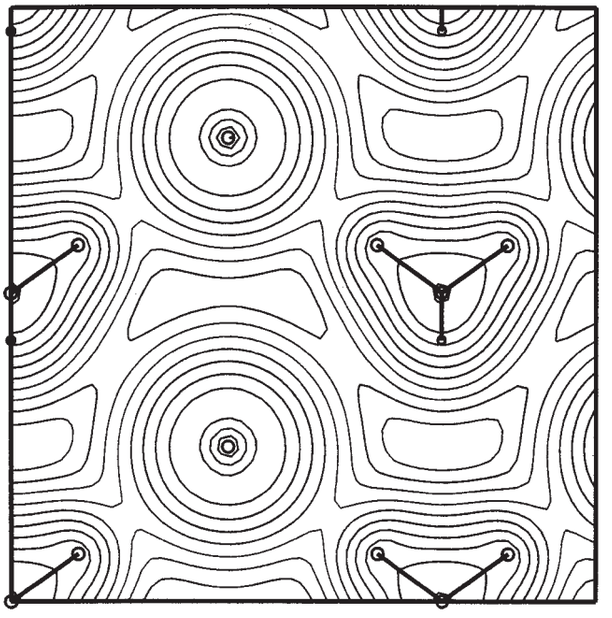

near both the chloride ions and the ammonium ions are very similar in all configurations. It is only for electron densities of 0.03 electrons per cubic bohr and lower that we see any differences between the configurations. This is consistent with the idea that the molecules and ions remain distinct with little or no covalent interactions. There is also little evidence for induced moments in the ions. The chloride ion, for example, remains spherical rather than being distorted. The concentric equally spaced circles around these atoms show that the electron density falls off exponentially and that there is little distortion of the electron density by the ammonium ion.

The minimum electron density along the N—H···Cl vector in both the lowest energy T_d orientation (Fig. 3) and in the C_{3v} orientation (Fig. 4) is about 0.026 electrons per cubic bohr, which is about twice as high as the minimum electron density (0.011 electrons per cubic bohr) along the N···Cl direction when the ammonium ion is in the D_{2d} orientation (Fig. 5) and there is no hydrogen atom close to a chloride ion. This may be interpreted as being due to the overlap of the tails of the molecular electron distributions, which gives a repulsive contribution, or may be a sign of very weak covalency, which would give part of the attractive force and contribute to the formation of a weak hydrogen bond. In density functional theory, the local energy contains a repulsive part that increases as the electron density increases, and an electrostatic part, which contains the stabilization due to the mutual attraction of the nuclei and the electrons, and it is not possible to distinguish between these possibilities.

© 1998 NRC Canada

Fig. 4. Contour plot of the electron density in ammonium chloride with the cation rotated by 60° about an N—H bond into the C_{3v} orientation. The plot shows the same (110) plane as in Fig. 3. There are two N—H bonds per cation in this plane; only one N—H bond points at a chloride ion, and the other lies midway between two chloride ions.

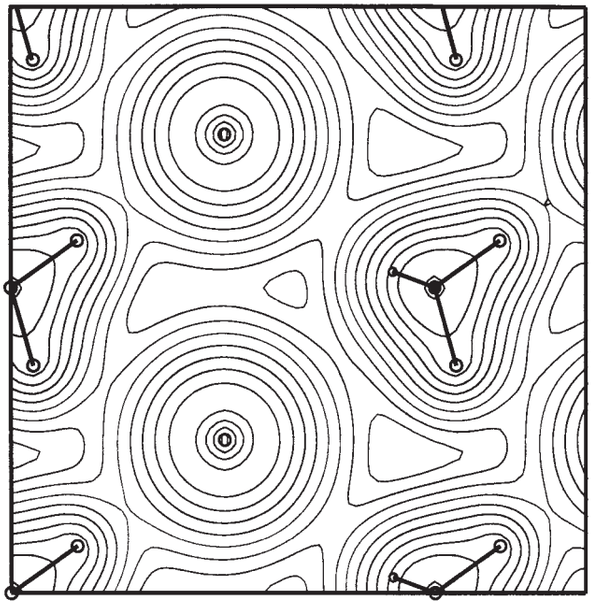

Fig. 5. Contour plot of the electron density in ammonium chloride with the cation rotated by 90° about an S_4 axis into the D_{2d} orientation. The plot shows a (100) plane passing through the nitrogen atom containing two N—H bonds; all the N—H bonds lie midway between chloride ions, all of which lie outside this plane.

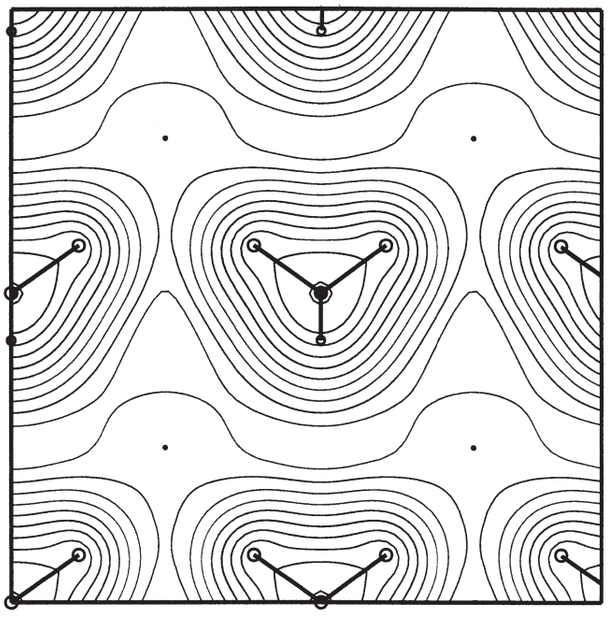

Electrical properties of the ammonium ion

In classical simulations of ammonium salts (13–17) it has been usual to model the ammonium ion by a tetrahedron with interaction sites on the nuclei. A very important parameter for the simulation is the value of the partial charge on each site, and Table 3 lists some of the charge distributions that have been used in previous work. The unit of electrical charge is the magnitude of the electronic charge.

The lowest multipole moment of a tetrahedral ion is the octopole moment. In molecule- based coordinates with the C_2 axes parallel to the Cartesian axes there is only one non-zero component, namely the *xyz* component

$$\Omega_{xyz} = 2.5\int xyz\rho(x, y, z)\mathrm{d}s\ \mathrm{d}y\ \mathrm{d}z$$

where the integral is taken over the molecule with the N atom at the origin, and includes the nuclear charges. In a model with partial charges of $+q_H$ on the protons the octopole moment is $10/(3(3)^{1/2})q_H r^3$ where r is the bond length. Brown and Lynden-Bell (16) chose the hydrogen charge q_H to fit the octopole moment calculated by Fowler et al. (43). Once q_H is fixed, the higher multipole moments of the model ion are completely determined.

We have attempted to evaluate the octopole moment of the ammonium ion in its surroundings from our ab initio calculations. The octopole moment is difficult to calculate accurately because the integral is heavily weighted towards large values of *r.* Furthermore, it is difficult to define the outer limit of a molecule in a crystal because the electron density is continuous. To estimate the octopole moment we evaluated the integral over a sphere centred on the nitrogen atom containing exactly eight electrons. The radius of this sphere is 1.8 Å and corresponds closely to the saddle point between the hydrogen and chlorine atoms shown in Fig. 3. Adding the positive contribution from the four protons to the value of the octopole integral over this sphere gives an octopole moment Ω = 8.0 atomic units. This is higher than the value of 6.48 a.u. calculated for a free ammonium ion by Fowler et al. (43). If the octopole were modelled by placing a charge on each hydrogen atom site with a net cation charge of +1, then one would need an effective charge q_H = +0.56 rather than +0.469.

An alternative method is to calculate the dipole moment of each of the eight octants and to take the differences between octants containing bonds and empty octants. As this calculation weights the positions by distance rather than by the cube of the distance, it may be more accurate. Applying this method we obtain an estimate of the octopole of 7.4 a.u., which corresponds to a charge of +0.52 on each proton.

The calculation of octopole moment was repeated in all three orientations of the ammonium ion (T_d, C_{3v}, and D_{2d}). The striking result of these calculations is that the variation found between the three orientations is only about 1%. This shows that the molecular ion is not significantly polarized during reorientation. It is probable that the increase in the octopole in the crystal compared to the free ion, which results from the lowering of the magnitude of the electronic contribution, is due to the compression of the electron density in the outer parts of the ion.

© 1998 NRC Canada

Table 3.

Total charge on cation	Hydrogen charge	References
+1	+0.194	10, 42
+1	+0.35	13, 15
+0.8	+0.5	14
+1	+0.469	16

Discussion and conclusions

In this study we have performed accurate ab initio calculations on the ordered phase of ammonium chloride, and neutron diffraction measurements of the structural parameters of the same material. The results of the calculation have also been compared with experimental data for spectroscopic and thermodynamic quantities. Calculation and experiment agree well in spite of various approximations inherent in ab initio methods. From the calculations we conclude that the electron distribution in the ammonium ion does not vary significantly with orientation and that the electrostatic intermolecular forces should be described by an octopole moment that is 10–20% greater than for the free ion. We recommend a value for the octopole moment of about 7.4 a.u., which corresponds to $q = +0.52$ on each hydrogen atom and $q = -1.08$ on the nitrogen atom. We find no evidence of any covalent interaction between the ammonium and the chloride ions, which is consistent with previous speculation about participation of ammonium ions in hydrogen bonding (44).

Acknowledgement

This work was supported by the Natural Sciences and Engineering Research Council of Canada (NSERC) and by the Engineering and Physical Sciences Research Council (EPSRC) (U.K.) (grants GR/K20651 and GR/L08427).

References

1. F. Simon. Ann. Phys. **68**, 241 (1922).
2. N.G. Parsonage and L.A.K. Staveley. Disorder in crystals. Clarendon Press, Oxford. 1978.
3. H.A. Levy and S.W. Peterson. Phys. Rev. **86**, 766 (1952).
4. W.B. Yelon and D.E. Cox. Solid State Commun. **11**, 1011 (1972).
5. T. Nagamiya. Proc. Phys. Math. Soc. Jpn. **24**, 137 (1942).
6. H.S. Gutowsky, G.E. Pake, and R. Bersohn. J. Chem. Phys. **22**, 643 (1954).
7. H.F. King and D.F. Hornig. J. Chem. Phys. **44**, 4520 (1966).
8. C.W. Garland and B.B. Weiner. J. Chem. Phys. **53**, 1609 (1970).
9. A. Hüller and J.W. Kane. J. Chem. Phys. **61**, 3599 (1974).
10. D. Smith. J. Chem. Phys. **82**, 5133 (1985).
11. D. Smith. Chem. Phys. Lett. **145**, 371 (1988).
12. D. Smith. Chem. Rev. **94**, 1567 (1994).
13. M.L. Klein, I.R. McDonald, and Y. Ozaki. J. Chem. Phys. **79**, 5579 (1983).
14. S.L. Chaplot and Rao. Phys. Rev. B: Condens. Matter, **33**, 4327 (1986).
15. R.W. Gerling and A. Hüller. J. Chem. Phys. **78**, 446 (1983).
16. A. Matro, D.L. Freeman, and R.Q. Topper. J. Chem. Phys. **104**, 8690 (1996).
17. R.J.C. Brown and R.M. Lynden-Bell. J. Phys.: Condens. Matter, **6**, 9903 (1994).
18. P.L. Silvestralli, A. Alavi, M. Parrinello, and D. Frenkel. Phys. Rev. Lett. **77**, 3149 (1996).
19. A. Alavi. Proc. Conf. on Monte Carlo and Molecular Dynamics of Condensed Matter Systems. SIF, Bologna, Italy. 1996. *Edited by* K. Binder and G. Ciccotti (SIF, Bologna). Vol. 49. p. 651.
20. A. Alavi, J. Kohanoff, M. Parinello, and D. Frenkel. Phys. Rev. Lett. **73**, 2599 (1994)).
21. N.D. Mermin. Phys. Rev. **137**, A1441 (1965).
22. R. Car and M. Parrinello. Phys. Rev. Lett. **55**, 2471 (1985).
23. A.D. Becke. Phys. Rev. A: At. Mol. Opt. Phys. **38**, 3098 (1988).
24. C. Lee, W. Yang, and R.G. Parr. Phys. Rev. B: Condens. Matter, **37**, 785 (1988).
25. N. Troullier and J.L. Martins. Phys. Rev. B: Condens. Matter, **43**, 1993 (1991).
26. L. Kleinman and D.M. Bylander. Phys. Rev. Lett. **48**, 1425 (1982).
27. A.C. Larson and R.B. Von Dreele. Los Alamos National Laboratory Report No. LA-UR-86–748 (1987).
28. B.M. Powell, R.J.C. Brown, A.M.C. Harnden, and J.K. Reid. Acta Crystallogr. Sect. B: Struct. Sci. **B49**, 463 (1993).
29. I.P. Swainson and R.J.C. Brown. Acta Crystallogr. Sect. B: Struct. Sci. **B53**, 76 (1997).
30. H.W.W. Adrian and D. Feil. Acta Crystallogr. Sect. A: Found. Crystallogr. **A25**, 438 (1969).
31. N.E. Schumaker and C.W. Garland. J. Chem. Phys. **53**, 392 (1970).
32. H.C. Teh and B.N. Brockhouse. Phys.Rev.B: Solid State, **B3**, 2733 (1971).
33. H.C. Teh and B.N. Brockhouse. Phys. Rev. B: Solid State, **B8**, 3928 (1973).
34. W. Cochran. Z. Kristallogr. **112**, 30 (1959).
35. W. Cochran and R.A. Cowley. J. Phys. Chem. Solids, **28**, 799 (1967).
36. J.F. Nye. Physical properties of crystals. Oxford University Press, Oxford. 1985.
37. C.W. Garland and R. Renard. J. Chem. Phys. **44**, 1130 (1966).
38. W. Mandema and N.J. Trappeniers. Physica, **76**, 102 (1974).
39. D.E. Woessner and B.S. Snowden. J. Phys. Chem. **71**, 952 (1967).
40. A.R. Sharp and M.M. Pintar. Chem. Phys. **15**, 431 (1976).
41. J. Töpler, D.R. Richter, and T. Springer. J. Chem. Phys. **69**, 3170 (1978).
42. A.L. Goodliffe, H.D.B. Jenkins, S.V. Martin, and T.C. Waddington. Mol. Phys. **21**, 761 (1971).
43. P.W. Fowler, H.M. Kelly, and R.J.C. Brown. Chem. Phys. Lett. **216**, 200 (1993).
44. R.J.C. Brown. J. Mol. Struct. **345**, 77 (1995).

© 1998 NRC Canada

Ternary cobalt germanium pnictides $CoGe_xPn_{1-x}$ (*Pn* = P, As, Sb) and the structure of Co_3Ge_2Sb, an intermetallic compound with stuffed Sb_2 pairs

Allison M. Mills, Robert Lam, and Arthur Mar

Abstract: The ternary cobalt germanium pnictide systems $CoGe_xPn_{1-x}$ (*Pn* = P, As, Sb; $0 < x < 1$) were investigated. The ternary phosphides $CoGe_xP_{1-x}$ and arsenides $CoGe_xAs_{1-x}$ adopt the MnP structure (*Pnma*) in the range $0 < x < 0.8$, with Ge and *Pn* (*Pn* = P, As) disordering over the anion sites. Reactions in the antimonide system $CoGe_xSb_{1-x}$ result in a mixture of ternary phases, one with the NiAs structure ($P6_3/mmc$) in which Ge and Sb disorder over the anion sites, and another that is a new intermetallic compound, Co_3Ge_2Sb. Single-crystal X-ray diffraction reveals that Co_3Ge_2Sb crystallizes in the hexagonal space group $P6/mmm$ with $a = 8.9128(13)$ Å, $c = 7.6312(8)$ Å, and $Z = 6$ ($T = 22$°C). The structure of Co_3Ge_2Sb comprises alternating kagomé nets of Co atoms and 6^3 nets of Ge atoms, with Sb_2 pairs stuffed along the centres of the concentric hexagons of these nets. Co_3Ge_2Sb may be regarded as an intermediate structure that is distorted from the limiting CoSn and $CaCu_5$ structures.

Key words: cobalt, germanium, antimony, pnictide, crystal structure.

Résumé : On a étudié les systèmes ternaires de pnictures de germanium et de cobalt, $CoGe_xPn_{1-x}$ (*Pn* = P, As, Sb; $0 < x < 1$). Dans la plage de valeurs $0 < x < 0{,}8$, les phosphorures $CoGe_xP_{1-x}$ et les arséniures $CoGe_xAs_{1-x}$ ternaires adoptent la structure MnP (*Pnma*) alors que le Ge et le *Pn* (*Pn* = P, As) se répartissent dans le désordre sur les sites anioniques. Les réactions dans le système antimoniure $CoGe_xSb_{1-x}$ provoquent un mélange des phases ternaires; une possède une structure NiAs ($P6_3/mmc$) dans laquelle le Ge et le Sb se répartissent dans le désordre sur les sites anioniques et une autre correspond à un nouveau composé intermétallique, Co_3Ge_2Sb. La diffraction des rayons X par un cristal unique de Co_3Ge_2Sb révèle qu'il cristallise dans le groupe d'espace $P6/mmm$ avec $a = 8{,}9128(13)$ et $c = 7{,}6312(8)$ Å et $Z = 6$ ($T = 22$°C). La structure de Co_3Ge_2Sb comporte des réseaux «kagomé» alternants d'atomes de Co et des réseaux 6^3 d'atomes de Ge avec des paires de Sb_2 insérés le long des centres des hexagones concentriques de ces réseaux. On peut considérer le Co_3Ge_2Sb comme une structure intermédiaire qui est déformée par rapport aux structures limites du CoSn et du $CaCu_5$.

Mots clés : cobalt, germanium, antimoine, pnicture, structure cristalline.

[Traduit par la Rédaction]

Introduction

Ternary pnictides have long merited investigation because they exhibit a wide array of useful electrical and magnetic properties. Most of these studies have focused on mixed-metal systems, in which the effect of differing proportions of transition metals on these properties has been measured. For instance, mixed-metal monopnictides $M_xM'_{1-x}Pn$ (*M*, *M′* = first-row transition metals; *Pn* = P, As, Sb; $0 < x < 1$) (1–8) have been prepared with an aim towards modifying the unusual magnetic properties found in such binaries as FeP (9) or CoAs (10), and to understand the effect of electron count on the transitions between the MnP or NiAs structures that these binaries typically adopt (11–13). However, given that the parent NiAs structure is prevalent not only in transition-metal pnictides, but also in chalcogenides and germanides, it is surprising that relatively little has been done in mixed-anion systems. Investigations in the cobalt-containing Co/Si/P (1), Co/B/P (1), Co/As/Sb (6), Co/Sn/As (14), and Co/Sn/Sb (14) systems have been reported. We present here structural studies on the cobalt germanium pnictides, $CoGe_xPn_{1-x}$ (*Pn* = P, As, Sb; $0 < x < 1$) and the regions of their phase stability. In addition, we describe the structure of a new intermetallic compound, Co_3Ge_2Sb, and draw attention to the close relationship between this structure and those of CoSn and $CaCu_5$. Reasons are suggested for the adoption of different structures for these cobalt germanium phosphides and arsenides on the one hand, and for the antimonides on the other.

Experimental section

Synthesis

Reagents used were the elemental powders: Co, 99.8% (Cerac); Ge, 99.999% (Cerac); P, 99.995% (Cerac); As, 99.99%

Received January 30, 1998.

A.M. Mills, R. Lam, and A. Mar.[1] Department of Chemistry, University of Alberta, Edmonton, AB T6G 2G2, Canada.

[1]Author to whom correspondence may be addressed. Telephone: (403) 492-5592. Fax: (403) 492-8231. E-mail: amar@gpu.srv.ualberta.ca

© 1998 NRC Canada

Table 1. Crystallographic data for Co_3Ge_2Sb.

Formula Co_3Ge_2Sb	*P6/mmm* (No. 191)
fw 437.43	T = 22°C
a = 8.9128(13) Å [a]	λ= 0.71073 Å
c = 7.6312(8) Å [a]	ρ_{calc} = 8.302 g cm^{-3}
V = 524.99(12) Å^3	μ = 377.9 cm^{-1}
Z = 6	$R(F)$ for $F_o^2 > 2\sigma(F_o^2)$ [b] = 0.039
	$R_w(F_o^2)$ [c] = 0.094

[a]Obtained from a refinement constrained so that α = β = 90° and γ = 120°.
[b]$R(F) = \Sigma ||F_o| - |F_c|| / \Sigma |F_o|$.
[c]$R_w(F_o^2) = [\Sigma [w(F_o^2 - F_c^2)^2] / \Sigma wF_o^4]^{1/2}$; $w^{-1} = [\sigma^2(F_o^2) + (0.0275p)^2 + 6.7810p]$ where $p = [\max(F_o^2,0) + 2F_c^2]/3$.

(Alfa-Aesar); Sb, 99.995% (Aldrich). Reactions were generally carried out on a 0.250–0.500 g scale in evacuated fused-silica tubes (8 cm length, 10 mm i.d.). Elemental compositions were determined by EDX (energy-dispersive X-ray) analysis on a Hitachi F2700 scanning electron microscope. X-ray powder patterns were obtained on an Enraf–Nonius FR552 Guinier camera (Cu$K\alpha_1$ radiation; Si standard).

Co_3Ge_2Sb was originally identified in a reaction of Co, Ge, and Sb in a 1:1:3 ratio, heated at 570°C for 1 day and then at 950°C for 4 days, cooled to 500°C over 4 days, and finally cooled to 20°C over 12 h. The product consisted of a shiny grey regulus, which was crushed to reveal short hexagonal prismatic crystals within. Anal. (mol%): Co 50(2), Ge, 37(2), Sb 13(1) (average of 4 analyses). One of these crystals was subsequently selected for the structure determination. Although this synthesis is reproducible, it is not ideal as the products contain significant amounts of impurities, including $CoSb_3$ and Sb.

Phase-pure samples of Co_3Ge_2Sb are difficult to prepare. While Co_3Ge_2Sb can be obtained by arc-melting a pellet of the elements combined in the stoichiometric ratio, the resulting product is contaminated with binary impurities, suggesting that this phase is incongruently melting. Moreover, stoichiometric reactions performed at increasingly higher temperatures (from 500° to 900°C) show that a greater proportion of the product (~15% at 900°C) consists of a ternary phase with the NiAs structure, in addition to the major phase, Co_3Ge_2Sb. At lower temperatures (< 600°C), other unidentified impurities appear. The phase transition from the Co_3Ge_2Sb structure (*P6/mmm*) to the NiAs structure (*P6$_3$/mmc*) (which is usually characterized as a high-temperature phase) is thus a sluggish one. For the purposes of physical property measurements, pure samples of Co_3Ge_2Sb can be obtained by manually separating these crystals on the basis of their different habits. Reaction at 900/800°C with the addition of a few grains of I_2 as a mineralizer affords masses of short, shiny, hexagonal prismatic crystals of the Co_3Ge_2Sb phase, which are easily distinguished from the longer, dull, acicular crystals of the NiAs phase.

To investigate the regions of phase stability in the Co*Pn*–CoGe (*Pn* = P, As, Sb) quasibinary systems, the series of reactions with the loading stoichiometry $CoGe_xPn_{1-x}$ ($0 < x < 1$) were prepared at 700°C. X-ray powder patterns were analyzed with the FilmScan and Jade 3.0 software packages (15). The cell parameters were refined with the use of the program POLSQ (16), and are listed in Tables S1 and S2.[2] The observed and calculated interplanar distances of Co_3Ge_2Sb, as well as the intensities determined with the program LAZY-PULVERIX (17), are listed in Table S3.[2]

We attempted to prepare substitutional analogues of Co_3Ge_2Sb (replacing Co by other transition metals, and Ge and Sb by congeneric elements), but so far without success. Substitutional studies in the P and As systems indicate that Fe can replace Co, but with a more limited range of phase stability.

Structure determination of Co_3Ge_2Sb

Weissenberg photographs reveal hexagonal Laue symmetry *6/mmm*; in particular, upper-level photographs clearly display sixfold rotational symmetry, ruling out trigonal space groups. Moreover, long-exposure photographs show weak but observable intensities for reflections with odd *l*, establishing the presence of superstructure along *c*. Final cell parameters were determined from a least-squares analysis of the setting angles of 24 reflections in the range 20° ≤ 2θ(Mo$K\alpha$) ≤ 30° centred on an Enraf–Nonius CAD4 diffractometer. Intensity data were collected at 22°C with the θ–2θ scan technique in the range 2° ≤ 2θ(Mo$K\alpha$) ≤ 70°. Crystal data and further details of the data collection are given in Tables 1 and S4.[2]

Calculations were carried out with the use of the SHELXTL (Version 5.0) package (18). Conventional atomic scattering factors and anomalous dispersion corrections were used (19). Intensity data were reduced and averaged, and face-indexed Gaussian-type absorption corrections were applied in XPREP. The centrosymmetric space group *P6/mmm* was chosen on the basis of intensity statistics and the successful structure solution. The higher symmetry space group *P6$_3$/mmc*, which would lead to an undistorted structure, was definitively ruled out because of widespread violations of the systematic extinction (*hh*2*hl*, *l* = 2*n* + 1) required for a *c*-glide plane. Out of 384 such data, 176 had $I > 3\sigma(I)$, and the

[2] Tables S1–S6 (comprising cell parameters, X-ray powder diffraction data, crystallographic data, anisotropic displacement parameters, and selected interatomic distances and angles) are available as supplementary material, which may be purchased from: The Depository of Unpublished Data, Document Delivery, CISTI, National Research Council Canada, Ottawa, Canada K1A 0S2. With the exception of the anisotropic displacement parameters, these tables have also been deposited with the Cambridge Crystallographic Data Centre, and can be obtained on request from: The Director, Cambridge Crystallographic Data Centre, University Chemical Laboratory, 12 Union Road, Cambridge, CB2 1EZ, U.K.

© 1998 NRC Canada

Table 2. Positional and equivalent isotropic displacement parameters for Co_3Ge_2Sb.

Atom	Wyckoff position	*x*	*y*	*z*	U_{eq} (Å^2) [a]
Co(1)	12o	0.16701(8)	0.3340(2)	0.24288(10)	0.0050(2)
Co(2)	6i	1/2	0	0.2638(2)	0.0050(3)
Ge(1)	6k	0.31623(11)	0	1/2	0.0051(2)
Ge(2)	6j	0.34759(13)	0	0	0.0054(2)
Sb(1) [b]	4h	1/3	2/3	0.31106(13)	0.0058(2)
Sb(2)	2e	0	0	0.1853(2)	0.0052(2)

[a] U_{eq} is defined as one-third of the trace of the orthogonalized U_{ij} tensor.
[b] Partial occupancy of 92(1)%.

Table 3. Selected interatomic distances (Å) in Co_3Ge_2Sb.

Co(1)—Ge(2)	2.4178(7) (×2)	Ge(1)—Co(1)	2.4197(7) (×4)
Co(1)—Ge(1)	2.4197(7) (×2)	Ge(1)—Co(2)	2.4357(11) (×2)
Co(1)—Co(2)	2.5752(7) (×2)	Ge(1)—Ge(1)	2.8185(11) (×2)
Co(1)—Co(1)	2.5782(13) (×2)	Ge(2)—Co(1)	2.4178(7) (×4)
Co(1)—Sb(2)	2.6153(13)	Ge(2)—Co(2)	2.4283(12) (×2)
Co(1)—Sb(1)	2.6198(13)	Ge(2)—Ge(2)	2.717(2)
Co(2)—Ge(2)	2.4283(12) (×2)	Sb(1)—Co(2)	2.5981(4) (×3)
Co(2)—Ge(1)	2.4357(11) (×2)	Sb(1)—Co(1)	2.6198(13) (×3)
Co(2)—Co(1)	2.5752(7) (×4)	Sb(1)—Sb(1)	2.884(2)
Co(2)—Sb(1)	2.5981(4) (×2)	Sb(2)—Co(1)	2.6153(13) (×6)
		Sb(2)—Sb(2)	2.829(2)

peak profiles of some of these reflections were individually scanned to confirm their presence. The initial positions of all atoms were found by direct methods, and the structure was then refined by least-squares methods. The displacement parameter for Sb(1) was somewhat higher than the others, and as nonstoichiometry is a common feature of solid state compounds, refinements were performed in which the occupancies of successive atoms were allowed to vary. These refinements resulted in essentially 100% occupancy for all atoms except for Sb(1), which is partially occupied at 92(1)% and whose displacement parameter is now similar to the others. For simplicity, we retain the formulation "Co_3Ge_2Sb" in referring to this structure. The atomic positions were standardized with the program STRUCTURE TIDY (20). The final cycle of least-squares refinement on F_o^2 of 27 variables (including anisotropic displacement parameters and an isotropic extinction parameter) and 513 averaged reflections (including those having $F_o^2 < 0$) converged to residuals of $R_w(F_o^2)$ of 0.094 and $R(F)$ (for $F_o^2 > 2\sigma(F_o^2)$) of 0.039. The final difference electron density map shows no features with a height greater than 2% that of an Sb atom. Final values of the positional and displacement parameters are given in Table 2, anisotropic displacement parameters in Table S5, interatomic distances in Table 3, and angles in Table S6.[2] Final structure amplitudes are available from A.M.

Results and discussion

Description of the Co_3Ge_2Sb structure

A view of the structure of Co_3Ge_2Sb perpendicular to the *bc* plane is shown in Fig. 1. Although bonding interactions extend in all three dimensions, it is convenient to describe this intermetallic structure as a stacking of nets along the *c* axis, alternating in composition from Co to Ge, as shown in Fig. 2. Then, Sb_2 pairs are viewed as being stuffed into the open sites within the structure. At $z \approx$ ¼ and ¾, the Co(1) and Co(2) atoms form a ruffled 3636 (kagomé) net (Fig. 2*b*). At z = ½, the Ge(1) atoms form a 6^3 net, distorted to present six-membered Ge_6 rings (Fig. 2*a*). At z = 0, the Ge(2) atoms form a similar 6^3 net, but they segregate into short and long Ge–Ge pairwise interactions (Fig. 2*c*). If the kagomé nets are denoted by α and the 6^3 nets by **a**, Co_3Ge_2Sb is described as a four-layer structure, **aαaα**, in which a superstructure of the simpler α**a** stacking arises because of the slightly different arrangement of Ge atoms in the **a** nets. Slight displacement of the Sb atoms above or below the centres of each hexagon in the Co kagomé nets results in Sb_2 pairs that are twice as dense in the Ge(1) layer as in the Ge(2) layer.

The coordination around each atom may be examined. The Co(1) and Co(2) atoms reside in similar coordination environments with CN10. Each Co atom has four other Co neighbours at 2.5752(7)–2.5782(13) Å and two Sb neighbours at 2.5981(4)–2.6198(13) Å in the same plane, and four Ge neighbours at 2.4178(7)–2.4357(11) Å above or below the plane. These correspond to reasonable bonding distances, as may be compared to the Co—Co distances in elemental *hcp*-Co (2.497–2.507 Å) (21) or CoGe (2.47(2)–2.57(2) Å) (22), the Co—Sb distances in CoSb (2.59 Å) (23) or $CoSb_3$ (2.5287(3) Å) (24), and the Co—Ge distances in CoGe (2.38(2)–2.58(1) Å) (22), respectively. The Ge(1) and Ge(2) atoms are each coordinated in a trigonal prismatic fashion by triangles of Co atoms above and below. There is further coordination to neighbouring Ge atoms within the same plane. The Ge(1) atoms clustered into six-membered rings contain Ge–Ge interactions at 2.8185(11) Å; the inter-ring Ge—Ge distances of 3.276(2) Å are too long to be significant. The Ge(2) atoms are paired at a short distance of 2.717(2) Å, with longer distances occurring at 3.098(2) Å. These distances are longer than the full Ge—Ge bonds in the isolated

© 1998 NRC Canada

Fig. 1. View of Co_3Ge_2Sb perpendicular to the *bc* plane, showing the stacking of the nets. The small open circles are Co atoms, the partly-shaded circles are Ge atoms, and the filled circles are Sb atoms.

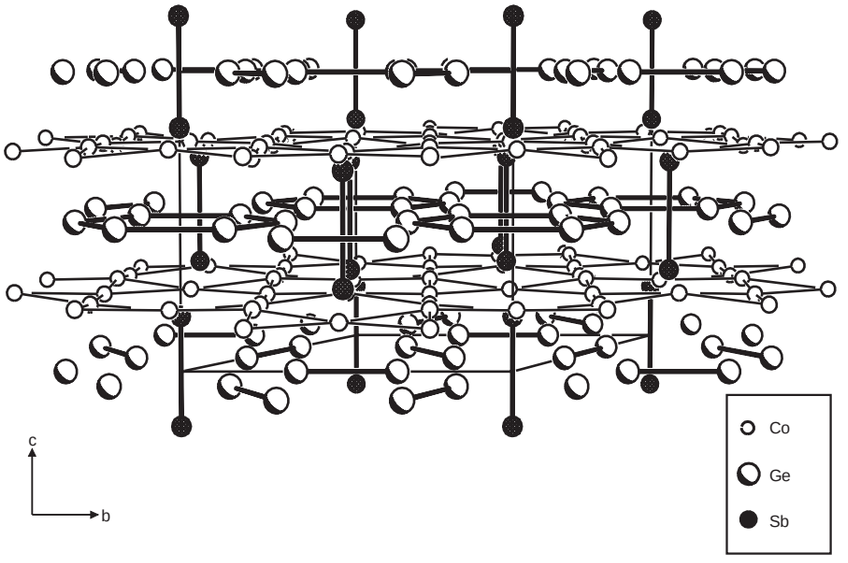

Ge_6 units found in Ge_6Ph_{12} (~2.46 Å) (25) and $Ba_{10}Ge_7O_3$ (2.475 Å) (26). However, longer Ge–Ge interactions indicative of weak bonding can also be found in CoGe (2.77(2) Å is the shortest such distance) and the Zintl ion Ge_9^{3-} (2.494(7)–3.324(8) Å) (27). If Pauling's bond-order relation ($D_n = D_1 - 0.71 \log n$) is applied and a single Ge—Ge bond is assumed to be 2.44 Å (28), a Ge–Ge distance of ~2.8 Å corresponds to a bond order of 0.31. Lastly, the Sb(1) and Sb(2) atoms are each arranged in Sb_2 pairs (2.829(2)–2.884(2) Å) in addition to being coordinated to a hexagon of Co atoms. These Sb–Sb distances indicate strong interactions, when compared to those found in elemental α-Sb (2.908 Å) (21) or in the Sb_4 squares in $CoSb_3$ (2.8540(6)–2.9760(6) Å) (24).

It is useful to search for structural relationships between Co_3Ge_2Sb and other known intermetallic structure types. While Co_3Ge_2Sb can be described as a distortion of the CoSn structure, it also serves as an intermediate structure that draws attention to the close relationship between the rare CoSn structure type (29) (with only 11 known examples (30)) and the much more prevalent $CaCu_5$ structure type (31) (with well over 200 examples (30)). As shown in Fig. 3, the CoSn, Co_3Ge_2Sb, and $CaCu_5$ structures are composed of alternating 3636 and 6^3 nets. They differ in the placement of the remaining large atom that must fit into the structure. In CoSn, the Sn(1) atoms reside at the centres of large hexagons within the 3636 Co nets (Fig. 3*a*). In $CaCu_5$, the Ca atoms reside at the centres of large hexagons within the 6^3 Cu(1) nets (Fig. 3*c*). Compared to Sn(1) atoms in CoSn, the Sb atoms in Co_3Ge_2Sb are displaced ~0.5 Å above or below the centres of the hexagons of the 3636 Co nets (Fig. 3*b*). Alternatively, Co_3Ge_2Sb can be viewed as a variant of the $CaCu_5$ structure, if some of the Ca atoms are replaced by Sb_2 *pairs*, leaving other Ca atoms to be replaced by vacancies. In both viewpoints, the resulting skewers of short–long Sb–Sb distances, which are aligned along the axes of concentric hexagons, are ordered in such a fashion so as to double the *c* parameter and triple the area $\vec{a} \cdot \vec{b}$.

Phase stability in $CoGe_xSb_{1-x}$

Reactions at 700°C with loading stoichiometries $CoGe_xSb_{1-x}$ ($0 < x < 1$) result in a mixture of ternary compounds, the dominant phase with the new Co_3Ge_2Sb-structure ($P6/mmm$) and a minor phase with the simpler NiAs-structure ($P6_3/mmc$). Crystals of the latter phase obtained as a side product in the preparation of Co_3Ge_2Sb crystals were confirmed by EDX measurements to contain all three elements, and the cell parameters from Weissenberg analysis are consistent with the NiAs structure. The powder pattern of this component matches with the NiAs structure in which Ge and Sb are presumed to be disordered over the anion sites. The cell parameters of these two phases, which will be referred to as the Co_3Ge_2Sb and NiAs phases, are plotted as a function of *x* in Fig. 4. Although the compositions cannot be directly related to the loading stoichiometries because the products are not single phase, some useful conclusions can still be drawn from these data.

The cell parameters of the Co_3Ge_2Sb phase (Fig. 4*a*) vary as *x* is decreased from 0.9 to 0.7, at which point limiting values are reached as suggested by the plateaus below $x = 0.7$. This implies that "$CoGe_{0.7}Sb_{0.3}$" represents a limiting composition, which is consistent with that determined from the crystal structure, "Co_3Ge_2Sb." There is also evidence from the single-crystal data that the Co_3Ge_2Sb structure is subject to Sb deficiencies. If the reaction conditions do not supply sufficient Sb (e.g., at $x = 0.9$), the cell volume is smaller because of these vacancies. As more Sb becomes available, the contraction in *c* suggests that bonding is strengthened along the axes of the Sb_2 pairs, while the expansion in *a* suggests that the structure is spread apart within the Co and Ge nets.

The variation in the cell parameters of the minor NiAs phase is more difficult to interpret. Presumably this phase adopts whatever composition remains after the Co_3Ge_2Sb phase is accounted for. Starting with the binary CoSb, which adopts the NiAs structure, replacement of Sb with the smaller Ge atom should result in a reduction of cell volume. As Fig. 4*b* shows, while an abrupt decrease in cell vol-

© 1998 NRC Canada

Fig. 2. View down the *c* axis of Co_3Ge_2Sb showing the composition of the individual nets at (*a*) *z* = ½, (*b*) *z* = ¼, ¾, and (*c*) *z* = 0. The unit cell is outlined.

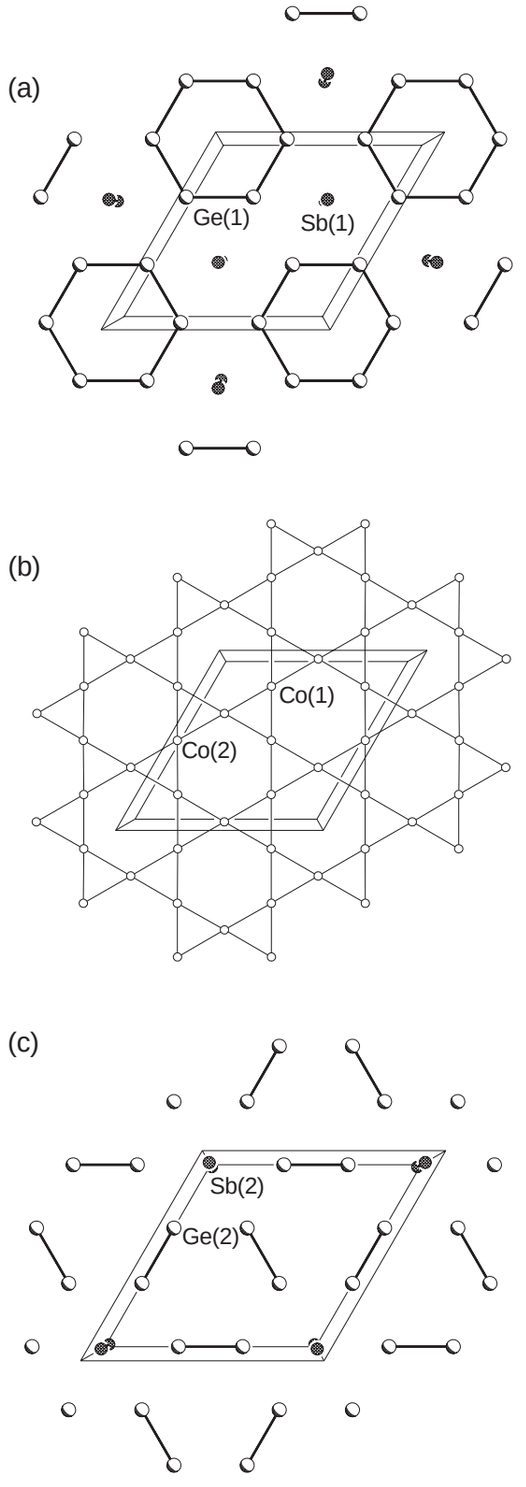

Fig. 3. Comparison of the closely related (*a*) CoSn, (*b*) Co_3Ge_2Sb, and (*c*) $CaCu_5$ structures, all in space group *P6/mmm*. The views are perpendicular to the (110) plane of the CoSn and $CaCu_5$ unit cells, and perpendicular to the (010) plane of the larger Co_3Ge_2Sb unit cell.

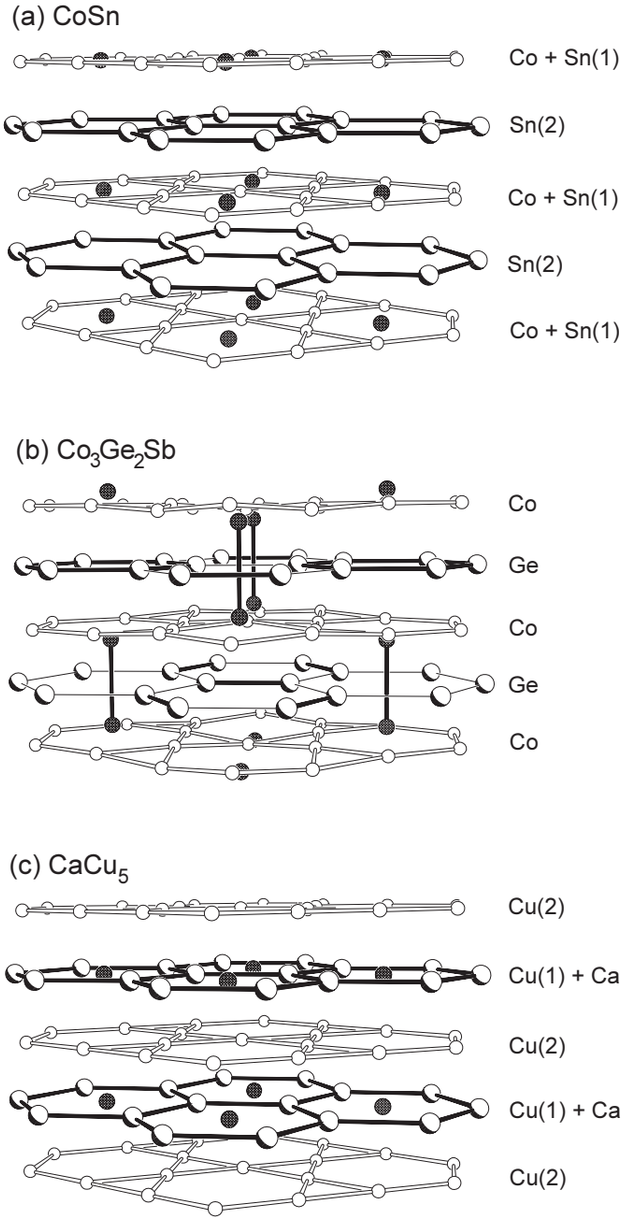

ume does occur initially as *x* is increased, the competition between the formation of the NiAs and Co_3Ge_2Sb phases complicates the interpretation until *x* reaches 0.6–0.7. Beyond this point, there is an excess of Ge that can now enter into the NiAs structure and disorders over the anion sites to cause a more pronounced cell volume contraction.

$CoGe_xP_{1-x}$ and $CoGe_xAs_{1-x}$

Reactions at 700°C with loading stoichiometries in the range $0 < x < 0.8$ result in a single phase whose powder pattern is consistent with the orthorhombic MnP structure

© 1998 NRC Canada

Fig. 4. Plots of cell parameters of phases with (*a*) the Co_3Ge_2Sb structure ($P6/mmm$) and (*b*) the NiAs structure ($P6_3/mmc$) obtained as products from reactions Co + *x* Ge + (1–*x*) Sb ($0 < x < 1$). The values of *x* merely indicate the loading stoichiometry in the reactions and cannot be directly related to the composition of these phases.

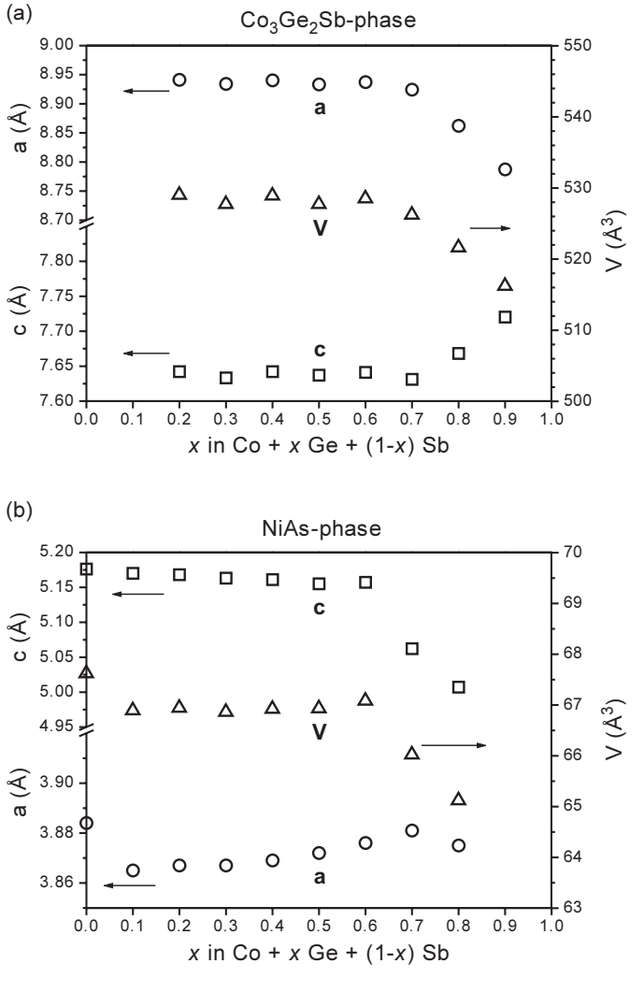

(*Pnma*) in which the germanium and pnicogen atoms are disordered over the anion sites. The cell parameters are plotted as a function of *x* in Fig. 5. The MnP structure is a distortion of the NiAs structure, in which zigzag chains of metal atoms are aligned along the *a* direction, and similar chains of nonmetal atoms are aligned along the *b* direction (1). (The *c* direction is a less useful indicator because both types of zigzag chains have components along it.) Figure 5*a* shows that the cell volume in $CoGe_xP_{1-x}$ increases monotonically as more of the larger Ge atoms are substituted for the P atoms in CoP. This occurs in conjunction with an initial weakening of both the metal–metal bonds and anion–anion bonds, up to $x = 0.4$, at which point the anion–anion bonds actually strengthen. In contrast, the variation in cell parameters in $CoGe_xAs_{1-x}$ is generally less pronounced given the more similar size of Ge and As atoms. Figure 5*b*

Fig. 5. Plots of cell parameters of ternary (*a*) $CoGe_xP_{1-x}$ and (*b*) $CoGe_xAs_{1-x}$ phases with the MnP structure (*Pnma*) obtained from reactions Co + *x* Ge + (1–*x*) *Pn* ($0 < x < 1$). The products are single-phase, so the loading stoichiometry can be directly related to their composition.

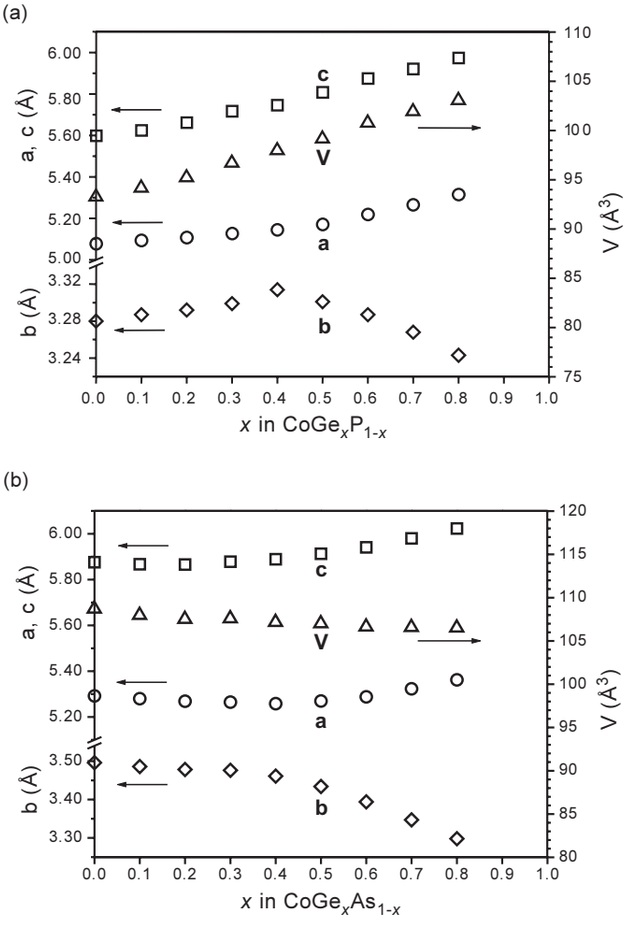

shows that the cell volume in $CoGe_xAs_{1-x}$ decreases slightly as more Ge is substituted for As in CoAs. This contraction is dominated by the strengthening of the anion–anion bonds along the *b* direction, at the expense of metal–metal bonding along the *a* direction. These variations are probably controlled to a greater extent by size and orbital differences than by electron count.

Bonding

Several models have been developed to account for structural variations in the transition metal monopnictides M*Pn* (or mixed-metal solid solutions thereof), which commonly take on the related NiAs, MnP, or NiP structures (1, 3, 11–13, 32, 33). Partial substitution of the pnicogen *Pn* with another nonmetal introduces changes that are more drastic than would be possible in the mixed-metal systems, so it is of interest to see if the same bonding models are applicable.

In the most general case, Mooser–Pearson plots show regions of phase stability as a function of the average principal quantum number of the valence shell, $\bar{n}$, and the difference in electronegativities of cation and anion, $\Delta\chi$ (32, 33). The

© 1998 NRC Canada

binary pnictides CoP ($\bar{n}$ = 3.5, $\Delta\chi$ = 0.4), CoAs ($\bar{n}$ = 4.0, $\Delta\chi$ = 0.3), and CoSb ($\bar{n}$ = 4.5, $\Delta\chi$ = 0.1) segregate clearly into the MnP region for the first two and the NiAs region for the last. Substitution of Ge for P or As has as its main effect a reduction in the average electronegativity difference, $\Delta\chi$, placing all members of the $CoGe_xP_{1-x}$ and $CoGe_xAs_{1-x}$ ($0 < x < 0.8$) series still within the MnP region. In contrast, substitution of Ge for Sb reduces $\bar{n}$ in the $CoGe_xSb_{1-x}$ system, which straddles the boundary between the MnP and NiAs structural regions. With its high symmetry and high coordination for all atoms (nondirectional bonding), the NiAs structure is typically adopted by many intermetallic compounds such as CoSb where the electronegativity difference is low. Rather than undergoing a simple distortion of the NiAs structure to form the MnP structure, with its zigzag chains of metal–metal and nonmetal–nonmetal bonds, the $CoGe_xSb_{1-x}$ system responds instead by going to a different structure, that of Co_3Ge_2Sb, in which anion *pairs* (Sb–Sb and Ge–Ge) form.

Alternatively, it has been noted that the transition between the NiAs, MnP, and NiP structures correlates with electron count, the MnP structure being stable in the range from 10 or 11 to 14 valence electrons per formula unit (3, 13). All members of the $CoGe_xP_{1-x}$ and $CoGe_xAs_{1-x}$ ($0 < x < 0.8$) systems fall within this range (13.2–14 e^-), consistent with their adopting the MnP structure. For the antimonides, this rule no longer applies (binary metal antimonides invariably adopt the NiAs structure (13, 32)), probably because the lower electronegativity differences make them less prone to the distortions that accompany the formation of the MnP structure. One would predict, therefore, that $FeGe_xP_{1-x}$ and $FeGe_xAs_{1-x}$ (12–13 e^-) should adopt the MnP structure, while $NiGe_xP_{1-x}$ and $NiGe_xAs_{1-x}$ (14–15 e^-) will not, and we have evidence for both. Equally, "Fe_3Ge_2Sb" is a compound worth targeting.

On a firmer basis, band structure calculations show that the occupation of metal–metal bonding levels favours the MnP structure at precisely the electron counts mentioned above (13), and this should apply to $CoGe_xP_{1-x}$ and $CoGe_xAs_{1-x}$ as well. However, Co_3Ge_2Sb presents an unrelated structure, and a calculation comparing the CoSn and Co_3Ge_2Sb is a more natural one to perform that may provide insight into the different kinds of distortion that occur here. Although size effects introduced by substitution of the larger Sb atom cannot be discounted, the displacement of Sb atoms to form pairs indicates that Sb—Sb bonding is an important component of the stability of this structure. Finally, given that kagomé nets in Co_3Ge_2Sb are a feature that has been associated with magnetically frustrated spin systems (34, 35), we anticipate interesting magnetic properties for this compound.

Acknowledgments

This work was supported by the Natural Sciences and Engineering Research Council of Canada and the University of Alberta. We are grateful to Dr. Robert McDonald (Faculty Service Officer, Structure Determination Laboratory) for the data collection.

References

1. S. Rundqvist. Acta Chem. Scand. **16**, 287 (1962).
2. K. Selte, L. Birkeland, and A. Kjekshus. Acta Chem. Scand. Ser. A: **32**, 731 (1978).
3. H. Fjellvåg and A. Kjekshus. Acta Chem. Scand. Ser. A: **40**, 8 (1986).
4. K. Selte, A. Kjekshus, S. Aaby, and A.F. Andresen. Acta Chem. Scand. Ser. A: **29**, 810 (1975).
5. K. Selte, A. Kjekshus, G. Valde, and A.F. Andresen. Acta Chem. Scand. Ser. A: **30**, 468 (1976).
6. H. Fjellvåg, K. Selte, and F.E. Stave. Acta Chem. Scand. Ser. A: **38**, 687 (1984).
7. H. Fjellvåg, A. Kjekshus, A.F. Andresen, and A. Zieba. J. Magn. Magn. Mater. **73**, 318 (1988).
8. V. Seshu Bai and K.V.S. Rama Rao. J. Phys. F: Met. Phys. **13**, 695 (1983).
9. G.P. Felcher, F.A. Smith, D. Bellavance, and A. Wold. Phys. Rev. B: Solid State, **3**, 3046 (1971).
10. K. Selte and A. Kjekshus. Acta Chem. Scand. **25**, 3277 (1971).
11. H.F. Franzen, C. Haas, and F. Jellinek. Phys. Rev. B: Solid State, **10**, 1248 (1974).
12. K. Selte and A. Kjekshus. Acta Chem. Scand. **27**, 3195 (1973).
13. W. Tremel, R. Hoffmann, and J. Silvestre. J. Am. Chem. Soc. **108**, 5174 (1986).
14. H. Fjellvåg and A. Kjekshus. Acta Chem. Scand. Ser. A: **40**, 23 (1986).
15. FilmScan and Jade 3.0. Materials Data Inc., Livermore, Calif. 1996.
16. POLSQ: Program for least-squares unit cell refinement. Modified by D. Cahen and D. Keszler. Northwestern University, Evanston, Ill. 1983.
17. K. Yvon, W. Jeitschko, and E. Parthé. J. Appl. Crystallogr. **10**, 73 (1977).
18. G.M. Sheldrick. SHELXTL Version 5.0. Siemens Analytical X-ray Instruments, Inc., Madison, Wis. 1994.
19. International tables for X-ray crystallography, Vol. C. *Edited by* A.J.C. Wilson. Kluwer, Dordrecht. 1992.
20. L.M. Gelato and E. Parthé. J. Appl. Crystallogr. **20**, 139 (1987).
21. J. Donohue. The structures of the elements. Wiley, New York. 1974.
22. S. Bahn and K. Schubert. Z. Metallkd. **51**, 327 (1960).
23. A. Kjekshus and K.P. Walseth. Acta Chem. Scand. **23**, 2621 (1969).
24. Th. Schmidt, G. Kliche, and H.D. Lutz. Acta Crystallogr. Sect. C: Cryst. Struct. Commun. **C43**, 1678 (1987).
25. M. Dräger and L. Ross. Z. Anorg. Allg. Chem. **476**, 95 (1981).
26. H.G. von Schnering, U. Bolle, J. Curda, K. Peters, W. Carillo-Cabrera, M. Somer, M. Schultheiss, and U. Wedig. Angew. Chem. Int. Ed. Engl. **35**, 984 (1996).
27. T.F. Fässler and M. Hunziker. Inorg. Chem. **33**, 5380 (1994).
28. L. Pauling. The nature of the chemical bond. 3rd ed. Cornell University Press, Ithaca, N.Y. 1960.
29. O. Nial. Z. Anorg. Allg. Chem. **238**, 287 (1938).
30. P. Villars and L.D. Calvert. Pearson's handbook of crystallographic data for intermetallic phases. 2nd ed. ASM International, Materials Park, Ohio. 1991.
31. W. Haucke. Z. Anorg. Allg. Chem. **244**, 17 (1940).
32. W.B. Pearson. The crystal chemistry and physics of metals and alloys. Wiley–Interscience, New York. 1972.
33. E. Mooser and W.B. Pearson. Acta Crystallogr. **12**, 1015 (1959).
34. X. Obradors, A. Labarta, A. Isalgué, J. Tejada, and M. Pernet. Solid State Commun. **65**, 189 (1988).
35. A.P. Ramirez, G.P. Espinosa, and A.S. Cooper. Phys. Rev. Lett. **64**, 2070 (1990).

© 1998 NRC Canada

Engineering of magnetic properties using ultrathin metallic structures prepared by Molecular Beam Epitaxy

B. Heinrich, M. Kowalewski, and J.F. Cochran

Abstract: The interface magnetic energy in fcc Cu/Co/Cu(001) and Pd/Co/Pd(001) and the interlayer exchange coupling in bcc Fe/Cu/Fe(001) will be discussed and compared to recent theoretical models. The effect of interface magnetostriction and interface magnetic anisotropy will be described using a model proposed by Victora and MacClaren. The Victora–MacLaren theory of magnetic anisotropies is based on a generalized Néel pair interaction model that allows one to express the total interface energy in terms of the interface anisotropy and interface magnetoelastic contributions. It will be argued that the change in the sign of the interface anisotropy K_s as a result of replacing Cu atoms by Pd atoms is caused primarily by the enhanced role of the spin-orbit interaction in the Co–Pd pair interaction and in the tendency of Pd to acquire a significant magnetic moment in the proximity of ferromagnetic atoms. It will be shown that the interface lattice separations play an important role and the balance between these two magnetoelastic terms determines the total magnetoelastic contribution to the interface energy. The magnetoelastic interface contributions to K_s are +0.08 ergs/cm^2 and +0.17 ergs/cm^2 for the fcc Cu/Co/Cu(001) and Pd/Co/Pd(001) structures, respectively. The interlayer exchange coupling has been investigated in bcc trilayer structures Fe/Cu/X_cCu_{1-c}/Cu/Fe where X_cCu_{1-c} represents an alloyed atomic layer with X = Fe, Cr, Ag. The purpose of these studies was to determine the effect of foreign atoms inside a nonmagnetic spacer on the direct interlayer exchange coupling between the outside Fe layers mediated by the valence electrons of the Cu spacer. The experimental results will be compared with recent first principles calculations using the Layer Korringa–Kohn–Rostoker (LKKR) method. It will be shown that the local electron potential of the foreign atoms affects the spin transport across the spacer and is chiefly responsible for the observed behavior of the interlayer exchange coupling in Fe/Cu/X_cCu_{1-c}/Cu/Fe. The interlayer exchange coupling depends very strongly on the magnetic state of the foreign atoms within the spacer. For foreign atoms with no long-range ferromagnetic order the exchange coupling is mainly affected by the 3*d* valence band electrons. Foreign atoms that are isoelectronic with the spacer atoms modify the strength of the exchange coupling only due to lattice relaxations that are associated with their atomic size.

Key words: ultrathin metallic magnetic films, magnetic anisotropy, exchange interaction, Molecular Beam Epitaxy.

Résumé : On discute de l'énergie magnétique interfaciale dans le Cu/Co/Cu(001) et le Pd/Co/Pd(001) ainsi que le couplage d'échange intercouche dans le Fe/Cu(Fe(001) et on les compare aux valeurs obtenues à l'aide de modèles théoriques récents. On décrit l'effet de la magnétostriction interfaciale et de l'anisotropie magnétique interfaciale à l'aide d'un modèle proposé par Victora et MacClaren. La théorie des anisotropies magnétiques de Victora–MacClaren est basée sur un modèle généralisée de l'interaction de paires de Néel qui permet d'exprimer l'énergie interfaciale totale en termes de l'anisotropie interfaciale et de contributions magnétolastiques interfaciales. On suggère que le changement de signe de l'anisotropie d'interface K_s, qui accompagne le remplacement d'atomes de Cu par des atomes de Pd, est provoqué principalement par une augmentation du rôle de l'interaction spin-orbite dans l'interaction de la paire Co–Pd et par la tendance du Pd d'acquérir un moment magnétique significatif lorsqu'ils sont à proximité d'atomes ferromagnétiques. On démontre que les séparations dans l'interface du réseau jouent un rôle important et que la balance entre ces deux termes magnétolastiques détermine la contribution magnétolastique totale à l'énergie interfaciale. Les contributions magnétolastiques interfaciales à la valeur K_s sont de +0,08 ergs/cm^2 et +0,17 ergs/cm^2 respectivement pour les structures de Cu/Co/Cu(001) et Pd/Co/Pd(001). On a étudié le couplage d'échange intercouche dans les structures à trois couches Fe/Cu/X_cCu_{1-c} /Cu/Fe dans lesquelles X_cCu_{1-c} correspond à une couche atomique d'alliage avec X = Fe, Cr et Ag. Le but de ces études était de déterminer l'effet d'atomes étrangers dans un espaceur non magnétique sur couplage d'échange intercouche direct entre des couches de Fe extérieures facilité par les électrons de valence du Cu intercalé. On compare les résultats expérimentaux avec des calculs récents basés sur des principes fondamentaux en utilisant la méthode de la couche de Korringa–Kohn–Rostoker (LKKR). On

Received February 3, 1998.

B. Heinrich,[1] M. Kowalewski, and J.F. Cochran. Physics Department, Simon Fraser University, Burnaby, BC V5A 1S6, Canada.

[1]Author to whom correspondence may be addressed. Telephone: (604) 291-4402. Fax: (604) 291-3592.
E-mail: bheinric@sfu.ca

© 1998 NRC Canada

démontre que le potentiel de l'électron local des atomes étrangers affecte le transport de spin à travers l'atome intercalé et qu'il est le principal responsable du comportement observé pour le couplage d'échange intercouche dans le $Fe/Cu/X_cCu_{1-c}/Cu/Fe$. Le couplage d'échange intercouche dépend très fortement de l'état magnétique des atomes étrangers présents dans l'espaceur. Pour des atomes étrangers ne possédant pas d'ordre ferromagnétique à longue distance, le couplage s'effectue principalement par les électrons de la bande de valence 3*d*. Les atomes étrangers qui sont isoélectroniques avec les atomes intercalés ne modifient la force du couplage d'échange que par des relaxations du réseau associées à leur taille atomique.

Mots clés : films magnétiques métalliques ultraminces, anisotropie magnétique, interaction d'échange, épitaxie du faisceau moléculaire.

[Traduit par la Rédaction]

Introduction

Ultrathin magnetic metallic films have been intensely investigated and have resulted in a wide range of exciting studies that are attractive to scientists working on basic aspects of low dimensional systems and to materials scientists interested in nanostructures and nanostructure devices. The applied aspects of magnetic metallic ultrathin structures have been pursued in parallel and have provided needed inspiration and excitement. The success of this field has been based on the ability to create new structures in which the interfaces play a crucial role. In-plane lattice matching of an epitaxial layer to the substrate template allows one, for the correct growth conditions, to create atomic structures having very sharp interfaces. The magnetic properties of interface atoms are often very different from those in the bulk. Ultrathin films behave like giant magnetic molecules characterized by novel magnetic properties: these novel magnetic properties depend upon the presence of a large fraction of interface atoms. Three major phenomena have strongly affected progress in the development of new magnetic materials based on ultrathin metallic structures: (*a*) interface magnetic anisotropies; (*b*) interlayer exchange coupling; and (*c*) magneto-electron transport. The ability to admix interface and bulk magnetic properties allows one to engineer new materials whose properties are different from standard magnetic materials. The individual magnetic atoms are replaced by ultrathin films that act as giant magnetic molecules having unique magnetic properties, and the magnetic exchange coupling between layers can be controlled by nonmagnetic interlayers separating the ultrathin magnetic films. The magnetic interface and strain energies can be used to control the overall magnetic anisotropies, allowing one to obtain magnetic moments of the ultrathin films oriented either parallel or perpendicular to the film surface. For example, metallic ferromagnetic iron films separated by suitable thicknesses of copper spacer layers can be used to produce an intrinsic antiferromagnet in which the magnetizations of successive iron layers are oriented antiparallel. One can go even further. Multilayers can be grown in which ferromagnetic thin films are separated by nonmagnetic spacer layers. By adjusting the thicknesses of the spacer layers, and by controlling the widths of the interface atomic terraces, one can adjust the angle between the magnetizations on adjacent magnetic films (giant magnetic molecules) to lie at any angle between 0° and 180°. Using atomic engineering one is able to create materials that do not have any equivalents occurring in natural form. Truly new magnetic materials can be manufactured that do not exist in nature and that can only be grown by these artificial means. Magnetoresistance (GMR) in spin valves, and tunneling magnetoresistance (TMR) have provided enormous opportunities in the development of a new generation of magnetic technologies that are based on nanoscale systems. The GMR and spin-valve effects have very quickly found their place in device applications, magnetic sensors, and spin-valve magnetic read and write memories (MRAM). Spin-polarized FET and hybrid ferromagnet–semiconductor nonvolatile gates have become a part of very active applied research programs and provide a solid basis for the future generation of nonvolatile magnetoelectronics.

The future success of this field will depend very strongly on our ability to improve our understanding of underlying physical concepts and on our capability to control the quality of interfaces. In this article we will describe our recent studies of the role of atomic interfaces on fundamental magnetic properties, interface magnetic energies, and exchange coupling.

Interface magnetic energy

Epitaxial structures are most often affected by lattice strains. The in-plane lattice spacing of the template is usually somewhat larger than that of the epitaxial overlayer grown on it. Typical examples are fcc Cu/Co/Cu(001) and Pd/Co/Pd(001) structures. Metastable fcc Co(001) structures have been grown on bulk Cu(001) substrates. LEED and Thermal-Energy Atomic Scattering studies by de Miguel et al. (1) have shown that for the first 10 ML the fcc Co structures grown on Cu(001) substrates are characterized by a $p(1\times1)$ symmetry with the cobalt lattice expanded in the plane of the surface. Detailed LEED investigations in combination with dynamical scattering calculations revealed a change in the average tetragonal distortion for films 3 ML and thinner (2). The vertical lattice compression in films more than 5 ML thick is more or less constant, and amounts to ~3%, corresponding to a ratio $c/a = 0.96$. A homogeneous and constant strain due to the lattice mismatch between Co(001) and Cu(001) is expected for samples between 5 and 10 ML, $e_{xx} = e_{yy} = e_{\|} = +0.019$ and a vertical contraction $e_{zz} = e_{\perp} = -0.025$. The measured strains in fcc Pd/Co/(001) structures having a Co thickness less than 10 ML are even bigger, $e_{\|} = +0.08$, $e_{\perp} = -0.096$ (3, 4) based on an unstrained fcc Co cubic primitive cell 3.545 Å on a side. We have used a coordinate system in which the *z*-axis is directed along the film normal.

© 1998 NRC Canada

The contribution to the volume anisotropy energy due to magnetoelastic energy can be estimated for a tetragonally distorted cubic crystal by means of the expression quoted by Chikazumi (5):

$$[1] \qquad E_{me} = B_1[e_{xx}(\alpha_1^2 - 1/3) + e_{yy}(\alpha_2^2 - 1/3) + e_{zz}(\alpha_3^2 - 1/3)]$$

where the e_{ii} are strain components and α_1, α_2, α_3 are direction cosines of the magnetization vector. But if $e_{xx} = e_{yy}$, and using $\alpha_1^2 + \alpha_2^2 = 1 - \alpha_3^2$, this expression can be written in the form (neglecting terms independent of magnetization direction)

$$[2] \qquad E_{me} = B_1(e_{zz} - e_{xx}) \cos^2(\vartheta)$$

where

$$[3] \qquad B_1 = -(3/2)\, \lambda_{100}(C_{11} - C_{12})$$

λ_{100} is the usual magnetostrictive coefficient for a cubic magnetic material (5), and ϑ is the angle of the saturation magnetization with respect to the surface normal.

The strains quoted by Navas et al. (2) for fcc Co grown on Cu(001) are a lateral expansion of 1.9% in the plane, corresponding to a ratio $e_{xx} / e_{zz} = -0.76$. The value of this ratio can be estimated from $e_{xx} / e_{zz} = (n_{100} - 1)/(2n_{100})$, where n_{100} is Poisson's ratio. Poisson's ratio is given by $n_{100} = C_{12}/(C_{11} + C_{12})$, where C_{11}, C_{12} are elastic constants. For fcc Co these constants are $C_{11} = 2.42 \times 10^{12}$ ergs/cm^3 and $C_{12} = 1.60 \times 10^{12}$ ergs/cm^3 (6) corresponding to $n_{100} = 0.40$. This value for Poisson's ratio gives $e_{xx} / e_{zz} = -0.75$, in good agreement with the observed ratio of in-plane strain to vertical strain. This agreement emphasizes the fact that linear magnetoelastic theory can be profitably applied to ultrathin structures that exhibit large lattice distortions. We have used the observed strains, along with the observed room temperature uniaxial anisotropy constant, $K_u = -10.8 \times 10^6$ ergs/cm^3 (7), to estimate the magnetostrictive constant, λ_{100}, for fcc Co from eqs.[2] and [3]: the negative sign for K_u corresponds to an easy plane. One obtains $B_1 = -2.45 \times 10^8$ ergs/cm^3 and $\lambda_{100} = 2 \times 10^{-4}$. The magnetostrictive constant deduced from measurements on fcc Co rich Co/Pd alloys is $\lambda_{100} = 1.3 \times 10^{-4}$ (8). The value of the magnetostrictive constant that is required to explain the observed bulk uniaxial anisotropy for Co(001) grown on Cu(001) is approximately 50% larger than that suggested by the alloy data.

Victora and MacClaren (9, 10) have shown that the interface energies in fcc lattices can be very well represented by a nearest neighbour pair Néel interaction model (11). The difference between their model and the original Néel idea of pair interactions (11) is that the pair interaction between magnetic and nonmagnetic atoms is included as an independent parameter. For simplicity, they also neglect any dependence of the pair interaction parameters L_{f-f}, L_{f-n} on the nearest neighbour distance. The effective pair interaction between magnetic moments can be determined by comparing the Néel uniaxial strain anisotropy with that obtained from electronic structure calculations for the interface orientation(001). The pair interaction between magnetic and nonmagnetic atoms can be obtained by fitting the Néel–Victora expression to the fcc(001) interface energy obtained using a first principles electronic structure calculation. This approach was applied to Pd/Co superlattices (9, 10) and yielded 0.67, 0.61, and 0.56 ergs/cm^2 (energies per one interface) for the [111], [011], and [001] oriented interfaces, in agreement with the experimental results obtained by Engel et al. (4). The calculations made using an unstrained structure having an (001) interface resulted in 0.4 ergs/cm^2, showing that the strain makes an important contribution to the strength of the interface energies.

It is interesting to compare the pair interaction coefficients for the Cu/Co/Cu(001) and Pd/Co/Pd(001) structures. The pair interaction can be described by simple uniaxial terms

$$[4] \qquad -L_{f-f} \cos^2(\theta),\ -L_{f-n} \cos^2(\theta)$$

where L_{f-f} and L_{f-n} describe the pair interaction coefficient between ferromagnetic–ferromagnetic atom pairs and ferromagnetic–nonferromagnetic atom pairs, and θ is the angle between the local magnetic moments and the bond direction. For the (001) orientation the uniaxial bulk anisotropy energy is given by (10)

$$[5] \qquad E_V = -[L_{f-f}(6\alpha_{f-f}^2 - 3)/V_{atom}] \cdot \cos^2(\vartheta)$$

and the surface anisotropy energy is given by

$$[6] \qquad E_S = -([2L_{f-n}(3\alpha_{f-n}^2 - 1) - L_{f-f}(3\alpha_{f-f}^2 - 1)]/S_{atom}) \cdot \cos^2(\vartheta)$$

where α_{f-f} and α_{f-n} are the cosines of the angles between the lines joining nearest neighbours and the normal to the surface, the *z*-direction. V_{atom} is the atomic volume and S_{atom} is the surface area per atom at the interface.

The above expressions for magnetic anisotropies use a minimum number of free parameters: only the two pair interaction energies L_{f-f}, L_{f-n}. Structural information is contained in the two parameters α_{f-f} and α_{f-n}. The structural information is usually obtained from X-ray diffraction studies. The use of only two structural parameters represents the simplest possible case of a constant lattice strain independent of the sample thickness. The Co/Cu(001) and Co/Pd(001) structures satisfy this requirement over the thickness range from 5 to 10 ML, and therefore one is able to calculate in a simple manner the contributions to the interface and bulk magnetic energies. The measured lattice strains give $\alpha_{f-f} = 0.691$ and $\alpha_{f-f} = 0.642$ for the Cu/Co/Cu(001) ($e_{\parallel} = +0.019$, $e_{\perp} = -0.025$ (2)) and Pd/Co/Pd(001) ($e_{\parallel} = +0.08$, $e_{\perp} = -0.096$ (3, 4)) structures, respectively. The measured values of the bulk anisotropies, K_u(Co/Cu) = -10.8×10^6 ergs/cm^3 (7), and K_u(Co/Pd) = -3.2×10^7 ergs/cm^3 (4) together with eq. [5] allow one to calculate the pair interaction coefficients. For an unstrained fcc Co lattice parameter of 3.545 Å the results are $L_{f-f} = 9.00 \times 10^{-16}$ ergs for Cu/Co/Cu(001), and $L_{f-f} = 7.12 \times 10^{-16}$ ergs for Pd/Co/Pd(001). These pair interaction coefficients are positive, which implies that the spin-orbit interaction in Co systems prefers to orient the magnetic moments along the nearest neighbour bond direction. The strength of the pair interaction is 20% stronger for the Co–Co pair bond in the Co/Cu system than for the Co–Co pair bond in the Co/Pd system. The difference in the Co–Co pair interaction parameter for the Co/Cu and the Co/Pd systems is a clear

© 1998 NRC Canada

indication that the Victora–MacLaren model is oversimplified. Probably one should take into account the dependence of the pair interaction strength on the nearest neighbour (nn) distance (11). In a strained lattice the in-plane and out-of-plane nn distances are different. For example, in the case of Co/Cu the in-plane nn distance is 2.554 Å, whereas the out-of-plane nn distance is 2.500 Å. The equivalent distances for Co/Pd are 2.708 and 2.497 Å. The original Néel theory would ascribe a different pair interaction parameter, L_{f-f}, to in-plane and out-of-plane nearest neighbours. This would, of course, complicate the model by the introduction of a new parameter, namely, dL_{f-f}/dr.

In the limit of small strains one can write

$$[7] \qquad \alpha^2_{f-f} = (1/2)[1 + e^f_\perp - e^f_\parallel]$$

Substitution of eq. [7] into eq. [5] leads to an expression similar in form to eq. [2] with $B_1 = -3L_{f-f} / V_{atom}$. Using the above values of L_{f-f} leads to B_1(Co/Cu) = -2.40×10^8 ergs/cm^3 and B_1(Co/Pd) = -1.82×10^8 ergs/cm^3. Substituting these values for B_1 into eq. [3], and using the elastic parameters for Co, $C_{11} = 2.42 \times 10^{12}$ ergs/cm^3, $C_{12} = 1.6 \times 10^{12}$ ergs/cm^3, leads to $\lambda_{100} = 2.0 \times 10^{-4}$ for the Cu/Co/Cu(001) system and $\lambda_{100} = 1.5 \times 10^{-4}$ for the Pd/Co/Pd(001) system. These values are reasonably close to the experimentally measured value, $\lambda_{100} = 1.3 \times 10^{-4}$, for fcc Co rich Co–Pd alloys (8). It is noteworthy that the λ_{100} value calculated for the Co/Pd system is closer to the experimental value $\lambda_{100} = 1.3 \times 10^{-4}$ than that calculated for the Co/Cu system even though the tetragonal distortion for the Co/Pd system ($c/a = 0.837$) is larger than that for the Co/Cu system ($c/a = 0.957$). It is likely that the introduction of the Néel parameter dL_{f-f}/dr would produce a larger correction to λ_{100} for Co/Pd than to λ_{100} for Co/Cu because the difference between out-of-plane and in-plane nn distances is greater for Co/Pd than for Co/Cu. This correction would therefore be in the wrong direction to bring the calculated values for λ_{100} into agreement with experiment. One must conclude that the pair interaction parameter L_{f-f} must be a more complex function of the electronic band structure than a simple dependence on the inter-atomic separation.

Schick et al. (12) proposed that in eq. [3] the elastic constant parameter $C_{11} - C_{12}$ should be replaced by C_{11}, because the lateral spacing of the Cu(001) lattice is clamped by the Cu spacer. However, in this case one would get values of λ_{100} considerably smaller than that determined from Co rich alloys. Probably the Cu clamping is not completely rigid and the small variations in the lateral lattice spacing required by magnetostriction are permitted.

The strength of L_{f-n} can be estimated using eq. [6]. One should point out that the surface anisotropy at the fcc (001) interface is non-zero even for $L_{f-n} = 0$. In fact, since $(3\alpha^2_{f-f} - 1)$ is positive in general, formula [6] shows that the contribution of the L_{f-f} (>0) parameter to the interface anisotropy energy is positive (leading to an easy magnetic plane, $K_s < 0$). It is the strength of the parameter L_{f-n} that decides the sign of the overall surface anisotropy. In most cases the parameter α_{f-n} is not known because one does not have available an experimental measurement of the separation between the interface magnetic and nonmagnetic layers. However, one can proceed by making the reasonable assumption that the interface spacing is given by the average of the unstrained lattice spacings of the two adjacent metals. For example, in the case of the Fe(001)/Pd system the spacing between the interface Fe and Pd layers has been measured and the result is 1.77 ± 0.1 Å (13). The layer spacings for unstrained Fe(001) and Pd(001) films are 1.433 and 1.945 Å. These give an average spacing of 1.69 Å, a value in substantial agreement with the measured interface spacing. Applying this idea to the Co/Cu system, for which the (001) interlayer spacings in the unstrained metals are 1.773 Å for fcc Co and 1.808 Å for Cu, one obtains an interface spacing 1.790 Å. The in-plane lattice spacing for the strained Co is 3.612 Å and the area per atom is $S_{atom} = 6.52 \times 10^{-16}$ cm^2. A little applied geometry gives the result $\alpha_{f-n} = 0.704$. The uniaxial interface anisotropy energy for the Co(001)/Cu system is $E_s = 0.26 \cos^2(\vartheta)$ (7) at room temperature: a comparison of this expression with eq. [6], using L_{f-f}(Co–Cu) = 9.00×10^{-16} ergs, $\alpha_{f-f} = 0.691$, and the values for α_{f-n} and S_{atom} given above, results in L_{f-n}(Co–Cu) = 2.26×10^{-16}. A similar calculation yields L_{f-n}(Co–Pd) = 6.92×10^{-16} ergs for the Co/Pd system where we have used $K_s = +0.63$ ergs/cm^2, L_{f-f}(Co–Pd) = 7.12×10^{-16} ergs, $\alpha_{f-f} = 0.642$, and 1.773 Å for the unstrained Co layer spacing and 1.945 Å for the unstrained Pd layer spacing. The latter spacings result in an average of 1.859 Å, and when this is used together with a Co in-plane strained lattice spacing of 3.829 Å one finds $\alpha_{f-n} = 0.697$. A significantly higher value of the parameter L_{f-n}(Co–Pd) compared to that of L_{f-n}(Co–Cu) is reasonable because the spin-orbit interaction in Pd is much stronger than that in Cu, and the induced magnetic moments on the Pd interface atoms are expected to be much larger than those in Cu. Therefore the observed change in the sign of the interface anisotropy as a result of replacing Cu atoms by Pd atoms is caused primarily by the enhanced role of the spin-orbit interaction in the Co–Pd interaction and in the tendency of Pd to acquire a significant magnetic moment in the proximity of ferromagnetic atoms.

The splitting of the interface energy into surface magnetic anisotropy and surface magnetoelastic contributions was introduced by O'Handley and co-workers (14). They split the interface energy into two terms; the first term represented a true interface magnetic anisotropy, and the second term was proportional to the lattice strains and therefore could be labeled an interface magnetoelastic energy. Their argument was based on the original Néel model in which only the L_{f-f} and the α_{f-f} parameters were considered. The Néel model contains only one magnetic parameter, and therefore it yields interface magnetic anisotropy and bulk magnetoelastic contributions that are related. In this respect the model used by Victora and MacLaren is more flexible because it admits of interface anisotropy and bulk magnetoelastic contributions that are independent. The expressions [5] and [6] include all the physics that is required to describe the measured anisotropies.

The expression used by MacLaren and Victora for the interface energy can be split into two parts: one part belongs to the unstrained lattice and the other part is proportional to the interface lattice strains. For this purpose it is convenient to define

$$[8] \qquad e^n_\perp - e^n_\parallel = 2\alpha^2_{f-n} - 1$$

© 1998 NRC Canada

Inserting eqs. [7] and [8] into eq. [6] and using the definition $E_s = -K_s \cos^2(\vartheta)$, one finds

$$[9] \qquad K_s = \left(\frac{\left(L_{f\text{-}n} - \frac{L_{f\text{-}f}}{2} \right)}{S_{atom}} \right) + \left(\frac{3L_{f\text{-}n}(e_{\perp}^{n} - e_{\parallel}^{n})}{S_{atom}} \right) - \left(\frac{3L_{f\text{-}f}(e_{\perp}^{f} - e_{\parallel}^{f})}{2S_{atom}} \right)$$

where $e_{\perp}^{f}$, $e_{\parallel}^{f}$ represent the vertical and in-plane strains for the interior layers of the Co film, and $e_{\perp}^{n}$ and $e_{\parallel}^{n}$ are the strains associated with the positions of the interface nonmagnetic atoms. The first term in eq. [9] represents an intrinsic contribution to the interface magnetic anisotropy. The last two terms represent magnetoelastic contributions to the interface anisotropy. The third term is the surface magnetoelastic term introduced by the O'Handley group. As was shown above, the parameter L_{f-f} can be determined from the volume anisotropy, and the measured surface anisotropy can be used to determine the parameter L_{f-n}. Using the values L_{f-f}(Co–Cu) = 9.00×10^{-16} ergs and L_{f-n}(Co–Cu) = 2.26×10^{-16} ergs, the interface anisotropy parameter for Co/Cu is calculated to be –0.34 ergs/cm^2. The second term in eq. [9] makes a negative contribution of –0.009 ergs/cm^2. The last term in eq. [9] results in an interface magnetoelastic contribution of +0.091 ergs/cm^2, resulting in an overall interface magnetoelastic contribution of +0.08 ergs/cm^2. This means that the measured interface anisotropy, –0.26 ergs/cm^2, underestimates the intrinsic value of the interface crystalline anisotropy. The surface magnetoelastic contribution favours a magnetization directed along the specimen normal. The first principles calculations (12) predicted a magnetoelastic interface contribution of +0.56 ergs/cm^2.

A similar analysis can be carried out for the Pd/Co/Pd(001) system using L_{f-f}(Co–Pd) = 7.12×10^{-16} ergs and L_{f-n}(Co–Pd) = 6.92×10^{-16} ergs. The magnetoelastic interface contributions to K_s are 0.26 and –0.08 ergs/cm^2 for the Co–Co and Co–Pd strains, respectively. The resulting total interface magnetoelastic interface contribution is +0.17 ergs/cm^2. The interface magnetoelastic energy in Pd/Co/Pd(001) prefers to orient the magnetization along the surface normal, just as it does in Cu/Co/Cu(001). The total interface magnetocrystalline surface energy parameter for Pd/Co/Pd(001) is +0.46 ergs/cm^2, which is somewhat smaller than the total measured value K_s = +0.63 ergs/cm^2.

Summary

The Victora–MacLaren model allows one to express the total interface energy in terms of interface anisotropy and interface magnetoelastic contributions. The interpretation of Co(001) ultrathin film data using Cu and Pd as growth templates shows that the Victora–MacClaren model is more complete than that based on a simple Néel model. The observed change in the sign of the interface anisotropy K_s as a result of replacing Cu atoms by Pd atoms is caused primarily by the enhanced role of the spin-orbit interaction in the Co–Pd pair interaction and in the tendency of Pd to acquire a significant magnetic moment in the proximity of ferromagnetic atoms.

The interface magnetoelastic energy does not depend only on the Co interplanar spacing. The interface lattice separations play an important role and the balance between these two magnetoelastic terms determines the total magnetoelastic contribution to the interface energy. The magnetoelastic interface contributions to K_s are +0.08 ergs/cm^2 and +0.17 ergs/cm^2 for fcc Cu/Co/Cu(001) and Pd/Co/Pd(001) structures, respectively.

Studies of interlayer exchange coupling in Fe/Ce/Fe ultrathin heterostructures

Our group has extensively studied the exchange coupling in structures consisting of two ferromagnetic iron Fe(001) layers separated by a non-ferromagnetic spacer (15–23). Such trilayer structures are the simplest systems exhibiting interlayer exchange coupling between the two ferromagnetic layers. In particular, detailed studies of the thickness dependence of the interlayer exchange coupling were performed for a pure bcc Cu(001) spacer (15, 17). Recently, we have been investigating the effect on the direct coupling between two ferromagnetic iron layers of placing foreign atoms in the copper spacer layer. The idea behind these studies is to investigate the effect of heterogeneous spacers on the exchange coupling mediated by the valence Cu electrons. The following heterostructures have been studied:

(*i*) 5.7 Fe / 5 Cu / 1 Fe_cCu_{1-c} / 5 Cu / 10 Fe
(*ii*) 5.7 Fe / 5 Cu / 1 Cr_cCu_{1-c} / 5 Cu / 10 Fe
(*iii*) 8.7 Fe / 5 Cu / 1 Ag_cCu_{1-c} / 5 Cu / 16 Fe

where X_cCu_{1-c} indicates one atomic layer (AL) of Cu atoms alloyed with foreign atoms X (Fe, ^{57}Fe, Cr, or Ag) of concentration *c*. The spacer between Fe layers is 11 AL thick in series (*i*)–(*iii*). The total thickness of the spacer was chosen such that the exchange coupling has the strongest value for pure Cu (11 AL) and is relatively insensitive to small thickness variations (15, 17).

Growth and structure

The structures were grown on single-crystal Ag(001) substrates at room temperature using Molecular Beam Epitaxy (MBE). Each structure was covered by a 20 AL thick protective layer of Au(001) before exposing it to ambient conditions. The quality of growths was monitored by observing Reflection High Energy Electron Diffraction (RHEED) patterns and RHEED intensity oscillations of the specular spot at the first anti-Bragg condition. All deposited layers were terminated at the RHEED intensity maxima, see Fig. 1. The RHEED oscillation intensities of copper were not significantly affected by the deposition of the alloyed X_c Cu_{1-c} layers, see Fig. 1, which leads us to believe that the alloyed layer followed the quasi layer-by-layer growth mode of the Cu spacer (15, 17, 24). Trilayer bcc Fe/Cu/Fe(001) structures were one of the first systems in which a long-wavelength oscillation of the exchange coupling as a function of the spacer thickness was clearly established (15), see Fig. 2. The short-wavelength oscillations (~2 ML) are not visible in Fig. 2 due to the roughness at the Fe–Cu and Cu–Fe interfaces (all elements were grown at room temperature). The growth of 5 or more AL of bcc Fe(001) on a Ag(001) substrate at room temperature yielded an average

© 1998 NRC Canada

Fig. 1. RHEED intensity oscillations of the specular spot at the first anti-Bragg condition during the growth of the Cu spacer for sample 5.7Fe/5Cu/1$Cr_{0.45}Cu_{0.55}$/5Cu/10Fe. The arrow points to the growth of the alloyed layer. Note that the growth was terminated at the RHEED intensity maximum.

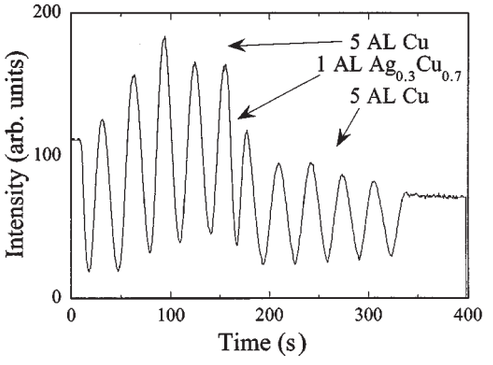

Fig. 2. Thickness dependence of the total exchange coupling, J_1–$2J_2$, through a pure Cu spacer. The Cu spacer thickness is measured in atomic layers (AL).

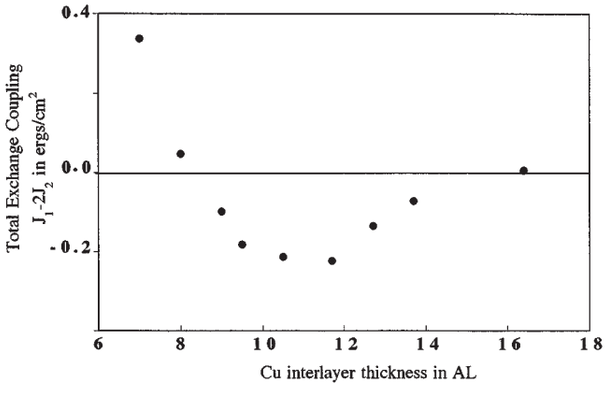

atomic terrace separation of approximately 50–60 Å (13, 17, 24). The terrace width can be increased by raising the substrate temperature during the growth of the last few atomic layers of Fe (17). In that case the short- wavelength oscillations start to be visible. However, the lack of short-wavelength oscillations was used to our advantage. We have tried to isolate the effect of placing different types of foreign atoms X within the Cu spacer. In samples having large atomic terraces, small changes in the growth conditions resulted in large variations of exchange coupling, making the systematic studies of heterogeneous spacers very difficult. It was important to eliminate unpredictable variations in the strength of the exchange coupling, and therefore all growths were performed at room temperature where the presence of short-wavelength oscillations was averaged out and the long-wavelength coupling was found to be very reproducible. The total spacer thickness of 11 AL provided a maximum antiferromagnetic coupling so that the interlayer exchange coupling was found to be relatively insensitive to small variations of spacer thickness (~0.2 ML), see Fig. 2.

The magnetic properties were measured using Ferromagnetic Resonance (FMR) (25), Magneto-Optical Kerr Effect (MOKE), and Brillouin Light Scattering (BLS) (26). The FMR measurements were carried out at temperatures of 77, 195, 273, and 373 K. BLS studies were performed at room temperature.

We found that the exchange coupling between ferromagnetic layers can be described by bilinear, J_1, and biquadratic, J_2, terms:

$$[10] \quad E = -J_1 \cos(\Theta) + J_2 \cos^2(\Theta)$$

where Θ is the angle between the magnetic moments of the two Fe layers, Fe_I and Fe_{II}. The biquadratic term is attributed to the interface roughness (16, 17, 27). The results of FMR, BLS, and MOKE at room temperature are in good agreement; the maximum variation in the strength of the exchange coupling was found to be within 20%. The FMR results are shown in Fig. 2. The magnetic anisotropies of the iron layers Fe_I and Fe_{II} were determined from the FMR absorption peak of each single Fe layer grown separately. The single and trilayer samples were grown on the same substrate using a shutter and appropriate rotations of the sample holder. Values of the total exchange coupling $J_{tot} = J_1 - 2J_2$ were obtained from the absorption FMR peak fields corresponding to acoustic and optical FMR modes, see refs. 15 and 25 for details. From the field dependence of the magnetic excitation frequencies measured by BLS, see Fig. 3, and the field positions in MOKE at which the Fe films are in the saturated and antiparallel states, see Fig. 4, values of bilinear, J_1, and biquadratic, J_2, exchange couplings were determined. The detailed analysis of MOKE and BLS measurements can be found in refs. 16, 17, and 26.

In Fig. 5 each graph shows the strength of J_{tot} as a function of concentration at four different temperatures for series (*i*)–(*iii*). Each temperature shows a similar pattern. As the concentration of the foreign atoms increases, the antiferromagnetic coupling is reduced from that of the reference, pure 11 AL Cu spacer. At lower concentrations (below 60%) Ag, Cr, and Fe atoms seem to affect the coupling in a similar manner. However, as the concentration of Ag and Cr atoms is increased the antiferromagnetic exchange coupling reaches a plateau, while in the case of Fe atoms the coupling becomes ferromagnetic (FM, $J_{tot} > 0$).

The 3*d* unfilled shells of Fe and Cr atoms can provide long-range magnetic order. In higher concentrations the magnetic moments of Fe atoms are most likely affected by some degree of ferromagnetic ordering. Since this ordering introduces a "quasi ferromagnetic layer" inside the Cu spacer, one expects an appreciable change in the exchange coupling. The magnetic behaviour of metallic Cr is different from that of Fe. The magnetic moments in metallic Cr are stabilized by the presence of a short-wavelength antiferromagnetic spin density wave in Cr (28). The Néel temperature of Cr in our samples is well below the temperature range of our measurements (29). Therefore the magnetic moments in Cr are oriented completely randomly and their direction rapidly fluctuates in time; they behave like "loose spins." Slonczewski showed (30) that loose spins can, in principle, introduce an additional exchange coupling that is absent in simple spacers having no magnetic moments. Loose spins get partly magnetized by the exchange field from the surrounding Fe layers and that in turn results in an additional energy, which depends on the orientation of the magnetic

© 1998 NRC Canada

Fig. 3. BLS peak frequencies as a function of applied magnetic field for the sample 5.7Fe/5Cu/$Cr_{0.45}Cu_{0.55}$/5Cu/10Fe. The integers represent the numbers of atomic layers. The upper and lower branches correspond to the acoustic and optical precessional modes. The solid lines represent theoretical fits using J_1 = –0.074 ergs/cm^2 and J_2 = 0.015 ergs/cm^2; $4\pi M_{eff}$ = 4.20 kOe, 13.55 kOe; $2K_1/M_s$ = 0.12 kOe, 0.30 kOe for the Fe layers 5.7 and 10 AL thick, respectively. The upper cusp corresponds to the field H_1 at which the magnetic moments start to turn away from the applied field; the lower cusp corresponds to the field H_2 at which the magnetic moments orient antiparallel.

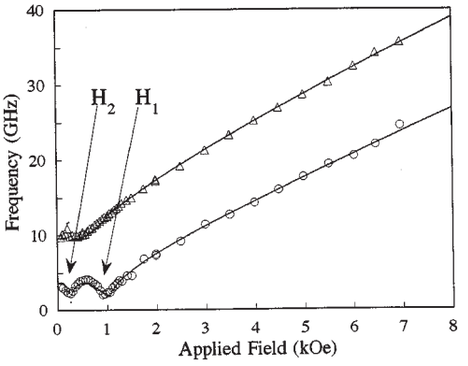

Fig. 4. The magnetization curve for the sample 8.7Fe/5Cu/$Ag_{0.30}Cu_{0.70}$/5Cu/16Fe obtained from MOKE measurements. The values J_1 = –0.172 ergs/cm^2 and J_2 = 0.015 ergs/cm^2 were obtained by fitting the positions of the critical fields H_1 (saturation state) and H_2 (antiparallel state) using $4\pi M_{eff}$ = 7.50 kOe, 16.55 kOe; $2K_1/M_s$ = 0.26 kOe, 0.40 kOe for the Fe layers 8.7 and 16 AL thick, respectively. Notice that as the field increases there is a well-defined jump at H_2 where the magnetic moments in both Fe layers start to deviate from their antiparallel orientation. This jump indicates an excellent homogeneity of the bilinear exchange coupling for this sample. The lack of a well-defined jump at H_1 is due to the presence of biquadratic exchange coupling.

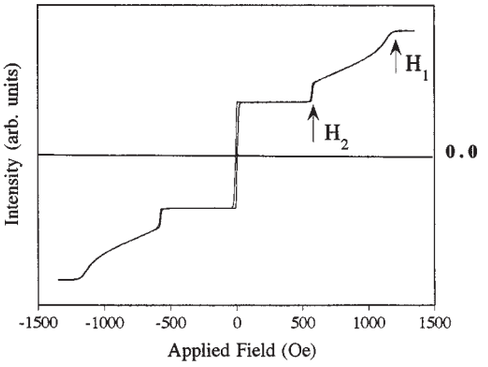

moments of the Fe layers and therefore contributes to the exchange coupling. The exchange coupling due to loose spins scales proportionally with paramagnetic susceptibility, which is inversely dependent on temperature, $1/T$. Mössbauer spectra show that the Fe foreign atoms in the low concentration limit behave definitely as loose spins (31), and yet the measured concentration and temperature dependence of the exchange coupling in series Ag_cCu_{1-c} and Cr_cCu_{1-c}, and Fe_cCu_{1-c} ($c < 0.6$), see Fig. 5, does not show any appreciably different behaviour. The difference is apparent only in a more pronounced decrease of the coupling with an increasing concentration of foreign atoms. The behavior of Ag atoms is different from that of Fe and Cr atoms. The Ag atoms are characterized by an *sp* valence band similar to that of Cu, while the Cr and Fe atoms are different from Cu and Ag due to their 3*d* valence electrons. The 3*d* unfilled states in Cr and Fe atoms perturb the electronic potential of the Cu spacer more strongly than the *sp* valence states of Ag atoms. The more pronounced decrease in the exchange coupling in the Cr_cCu_{1-c} and in the Fe_cCu_{1-c} series compared to that of the Ag_cCu_{1-c} series is most likely due to a stronger electronic perturbation of the Cu spacer for the Cr_cCu_{1-c} and the Fe_cCu_{1-c} series. In our view the contribution of loose spins to the interlayer exchange coupling as envisioned by the Slonczewski model is not observed in our samples. This conclusion is further enforced by calculations employing the loose spin model and using a reasonable estimate of the exchange coupling between the loose spins and the surrounding Fe layers. The estimate of the exchange coupling between loose spin and the surrounding Fe layers was obtained using the measured exchange coupling between Fe layers as a function of the Cu spacer thickness. The results of these calculations show that the contribution of loose spins leads to a small ferromagnetic coupling that increases with decreasing temperature as 1/T. $J_{ls}(300)$ = 0.01 and $J_{ls}(77)$ = 0.04 ergs/cm^2. These values are significantly smaller than those obtained from the FMR, MOKE, and BLS measurements. Consequently, it is the local electron potential of the foreign atoms that affects the spin transport across the spacer and is chiefly responsible for the observed behavior of the interlayer exchange coupling.

The change of the coupling from AF to FM at higher concentrations of Fe atoms is related to the magnetic state of the Fe atoms in the Cu spacer. In the sample 5.7Fe/5Cu/1^{57}Fe/5Cu/20Au, the Mössbauer studies showed a narrow Mössbauer doublet peak indicating that ^{57}Fe is in a paramagnetic state (31). However, the Mössbauer spectra in the sample 5.7Fe/5Cu/1^{57}Fe/5Cu/10Fe/20Au, with two iron layers Fe_I and Fe_{II}, showed that the foreign ^{57}Fe atoms were subjected to a non-zero hyperfine field. In this sample the Fe atoms in the alloyed layer were partially ferromagnetically ordered (31), and that ordering resulted in a ferromagnetic interlayer coupling. A relatively narrow Mössbauer doublet observed in the sample 5.7Fe/5Cu/$1^{57}Fe_{0.5}Cu_{0.5}$/5Cu/10 Fe indicated that no magnetic ordering was present, and therefore for Fe concentrations less than 60% the samples behaved like the ones that contained Cr atoms, see Fig. 5.

The MOKE and BLS room temperature measurements of bilinear and biquadratic exchange coupling showed that the decrease of the total coupling with an increasing concentration of foreign atoms is mainly due to the decrease of J_1. Furthermore, the measurement of bilinear coupling, J_1, and biquadratic coupling, J_2, by MOKE showed that the ratio J_1/J_2 was temperature independent as was observed in samples having pure Cu spacers (32).

Comparison with first principles calculations

Recently we performed first principles calculations of the interlayer exchange coupling for some of the above struc-

© 1998 NRC Canada

Fig. 5. The total exchange coupling, J_{tot}, obtained from FMR measurements as a function of the foreign atom concentration for four different temperatures: (*a*) 77 K, (*b*) 195 K, (*c*) 273 K, and (*d*) 373 K. The symbol (○) indicates samples from the series (*i*) 5.7Fe/5Cu/Fe_cCu_{1-c}/5Cu/10Fe; the symbol (◇) indicates samples from the series (*ii*) 5.7Fe/5Cu/Cr_cCu_{1-c}/5Cu/10Fe; and the symbol (□) indicates samples from the series (*iii*) 8.7Fe/5Cu/Ag_cCu_{1-c}/5Cu/16Fe. The solid lines are cubic spline fits to help guide the eye.

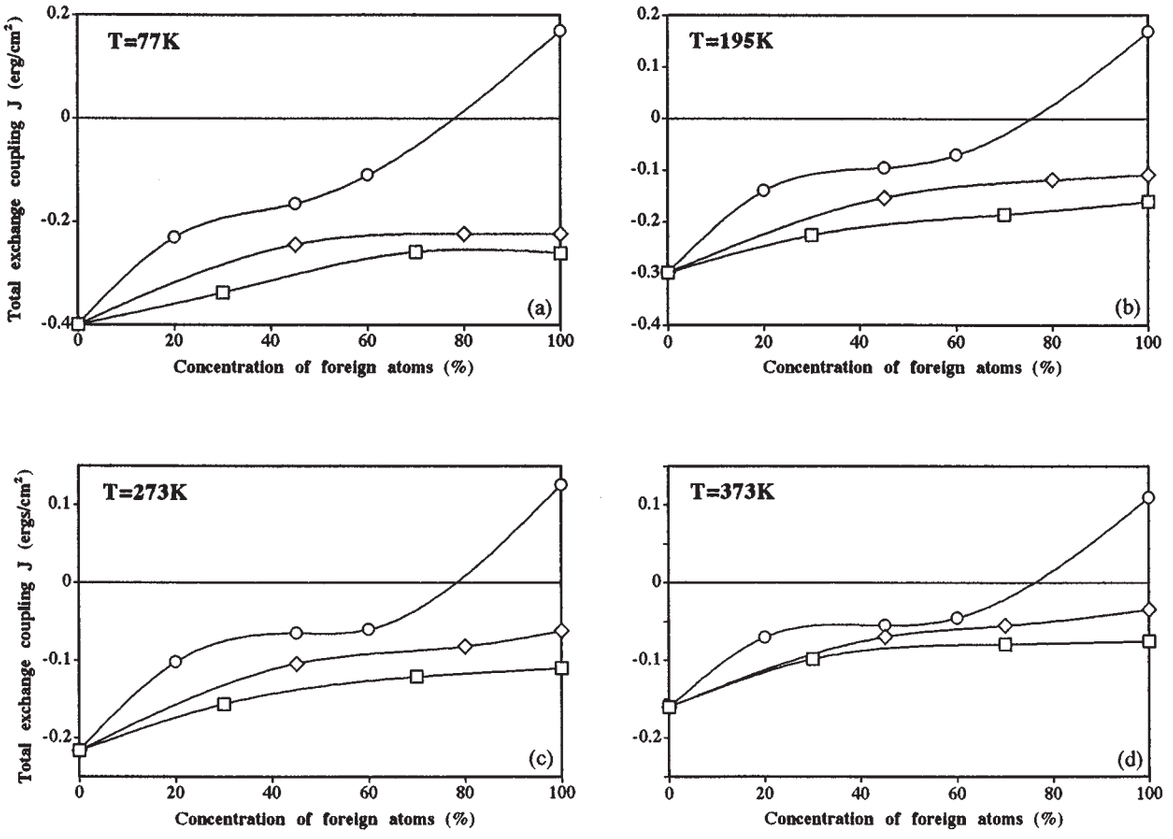

tures, to determine the theoretical trends in the exchange coupling due to replacing the central Cu atomic layer by an atomic layer of foreign atoms X. The first principles calculations were performed using the Layer Korringa–Kohn–Rostoker (LKKR) method. This work was carried out in cooperation with T.C. Schultess and W.H. Butler at the Oak Ridge National Laboratory using their LKKR computer codes (33). The theoretical thickness dependence of the exchange coupling between two semi-infinite Fe layers was calculated for pure Cu spacer thicknesses in the range of 1–16 AL. The effect of the foreign atoms X on the exchange coupling was investigated using a structure having a 9 AL Cu spacer as a reference sample.

Homogeneous spacer trilayers: bcc Fe/Cu/Fe(001)

The interlayer exchange coupling calculated as a function of the copper spacer thickness is shown in Fig. 6. The results were fit using two cosine functions of different amplitudes and a common $1/d^2$ thickness dependence:

$$[11] \quad \{A_1 \cos[(2\pi d/\lambda_1) - \phi_{10}] + A_2 \cos[(2\pi d/\lambda_2) - \phi_{20}]\}/d^2$$

where d is the thickness of the spacer in atomic layers (AL), A_i, ϕ_{i0}, and λ_i are the amplitude, phase, and period of oscillations (in AL), respectively, for the short- (i = 1) and the long- (i = 2) range oscillations. We used spacer thicknesses d >5 AL for which the above asymptotic formula is likely to be accurate (34). The values λ_1 = 2.1 ± 0.2 AL and λ_2 = 10.0 ± 1.0 AL found from the fit to eq. [11] are in good agreement with those predicted by Bruno for a pure bcc Cu(001) spacer using extremal spanning vectors along G–X, G, and M lines in the Fermi surface (35).

To include realistic variations of the spacer thickness due to interface roughness we simulated the interfacial roughness by averaging the coupling over several adjacent spacer thicknesses. It is reasonable to take the final thickness of the copper spacer to contain approximately 50% of the nominal thickness with some of the spacer being thinner and some thicker (17, 24). Therefore, we calculated the moving average of the earlier calculated points for a roughness confined to the three topmost layers, see Fig. 7. Comparison of the calculated results in Fig. 7 with the experimental points, Fig. 2, shows striking similarities in the behaviour of the coupling. However, there are also notable differences. The crossover from ferromagnetic to antiferromagnetic coupling occurs at ~6.5 AL in the theoretical calculation and at ~8 AL in the experimental data. Moreover, the maximum antiferromagnetic coupling in the theoretical calculation occurs at ~9 AL whereas in the experiment it occurs at ~10–11 AL. The 1–2 atomic layer shift between theory and experi-

© 1998 NRC Canada

Fig. 6. Interlayer exchange coupling plotted as a function of Cu spacer thickness for atomically smooth interfaces. Our theoretically calculated points are fitted with the sum of two cosine functions of different amplitude and a common $1/d^2$ thickness dependence to determine the short- and long-period oscillations, see eq. [11] in the text. The short-period wavelength was found to be 2.1 ± 0.2 AL; the long-period wavelength was found to be 10.0 ± 1.0 AL.

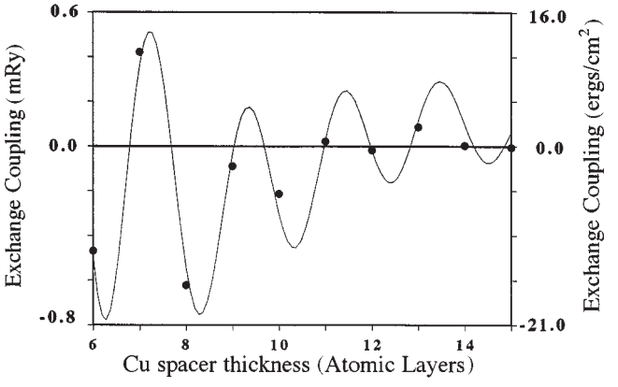

ment in both features is not surprising and can be attributed partly to the interface roughness and partly to the fact that LKKR calculations do not predict exact values for the oscillatory periods of the exchange coupling. It is also very likely that around each Fe–Cu interface up to one AL of Cu is effectively ferromagnetic and removed from the pure Cu spacer. A significant decrease in the measured coupling from that obtained from first principles calculations strongly suggests that mixed Fe–Cu interfaces also profoundly affect the strength of the coupling. Similar behaviour was observed in Fe/Cr/Fe(001) systems where interface alloying strongly reduces the strength of the interlayer coupling (22, 23).

Heterogeneous spacers: bcc Fe/Cu(4)X(1)Cu(4)/Fe(001)

The structure with pure 9 AL copper spacer was chosen as the reference sample to simplify this set of calculations. Atomically abrupt interfaces were used at both Fe–Cu and Cu–Fe interfaces as well as at the interfaces of the single foreign atomic layer X with the surrounding copper matrix. Foreign atoms of Fe, Cr, and Ag were used. Table 1 lists all the calculated values of the exchange coupling and magnetic moments of the relevant foreign atoms in the central spacer. The value of the exchange coupling for the pure 9 AL copper spacer is listed as the first entry in Table 1 for comparison. First, Fe, Cr, and Ag were placed in the unrelaxed Cu lattice and the exchange couplings calculated, see entries 2, 3, and 4, respectively, in Table 1. For Fe and Cr atoms each volume per atom in the lattice structures (and Wigner–Seitz radius) is nearly the same as that for Cu. However, the lattice constant of Ag is about 10% larger; therefore, the Cu lattice was allowed to relax in order to accommodate the Ag atoms. Silver atoms were assumed to maintain the in-plane lattice spacing of bcc Cu(001) and only the lattice spacing between the two Cu atomic layers next to silver was expanded to accommodate the correct volume per silver atom. The result of this calculation is shown as entry 5 in Table 1. The final (sixth) entry in Table 1 is the calculation of the exchange coupling for one atomic layer of Fe having fully disordered moments. The magnetic disorder was modeled by a disordered alloy consisting of equal amounts of Fe that have moments pointing in the + and – z directions, respectively. The disorder was treated within the coherent potential approximation (CPA).

Fig. 7. The calculated interlayer exchange coupling as a function of the Cu spacer thickness for simulated rough interfaces. The exchange coupling values in this graph were obtained by calculating a moving average of the couplings for pure Cu spacers having ideally smooth interfaces, Fig. 6. The interfacial roughness was simulated by averaging over values of the exchange coupling, J(N), for three adjacent pure Cu spacer thicknesses: $J_N = 0.25\ J(N-1) + 0.5J(N) + 0.25J(N+1)$, where J_N is the interlayer exchange coupling across a Cu spacer having simulated rough interfaces. The line through the points is a cubic spline fit to guide the eye. Notice that the short period oscillations are suppressed.

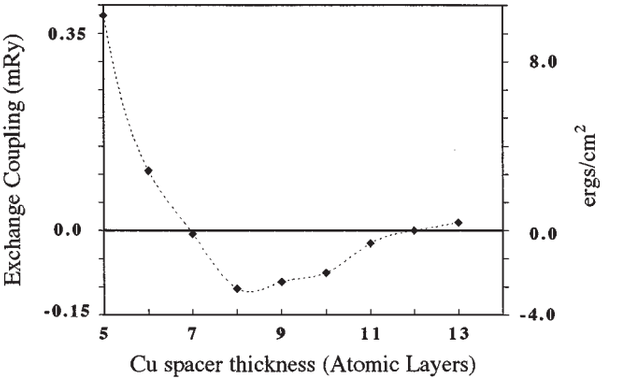

The results listed in Table 1 show that the foreign Fe atomic layer in the ordered magnetic state with the strongest average moment per atom affects the coupling the most. The magnetically ordered Cr atomic layer has an intermediate effect with a magnetic moment per atom an order of magnitude smaller, and Ag has the least effect with approximately zero magnetic moment per atom. The experimental Mössbauer studies of the Fe/Cu(5)/Fe(1)/Cu(5)/Fe sample indicated that the full atomic layer of Fe within the copper spacer is partially magnetically ordered (21, 31). Furthermore, similar studies of an Fe/Cu(5)/Fe(0.5)Cu(0.5)/Cu(5)/Fe sample showed that an atomic layer with 50% Fe and 50% Cu at the center of the copper spacer is magnetically disordered (21, 31). The first sample exhibited a strong ferromagnetic coupling whereas the second sample maintained antiferromagnetic coupling, similar to the homogeneous Cu spacer, but having approximately half the coupling strength. The theoretical calculation for the fully ordered and disordered Fe foreign layer, entries 2 and 6 in Table 1, confirm that the magnetic ordering of foreign atoms is the most significant factor affecting the sign and strength of the exchange coupling. A fully ordered Fe layer changes the coupling from AF to FM, similar to the behaviour observed for the partially ordered Fe atomic layer in the experiment. Additionally, the magnetically disordered model calculation for an iron atomic layer at the center of the spacer yields an antiferromagnetic coupling that is approximately half the value of the coupling across the pure Cu spacer; just this behaviour was observed experimentally for the magnetically

© 1998 NRC Canada

Table 1. Summary of results for heterogeneous Cu spacer. The interlayer exchange coupling and the magnetic moment per foreign atom for the heterogeneous spacer where the central atomic Cu layer was replaced by the atomic layer of foreign atoms of Fe, Cr, and Ag. The average magnetic moment per atom in the fully disordered Fe is zero.

Foreign atom	Exchange coupling (ergs/cm^2)	Magnetic moment (Bohr magnetons)
1. Pure Cu	–4.8	–0.004
2. Fully ordered Fe	32	2.55
3. Cr	13	0.25
4. Unrelaxed Ag	–4.6	–0.002
5. Relaxed Ag	1.9	–0.002
6. Fully disordered Fe	–2.1	±2.55

disordered iron layer, Fig. 5. These results indicate that the interlayer exchange coupling depends very strongly on the magnetic state of the atoms within the spacer. Obviously atoms within the spacer possessing some degree of magnetic ordering scatter the majority and minority valence electrons within the copper spacer in a manner that is different from that of disordered spins and this affects not only the value but also the sign of the exchange coupling. Following the Stiles (34) and Bruno (35) theories of interlayer exchange coupling, the spin asymmetry of the reflection coefficients for majority and minority spins in the quantum well of the spacer is the major variable in determining the sign and the magnitude of the coupling across homogeneous spacers. It is not surprising that placing magnetically ordered layers of atoms within the homogeneous spacer introduces further potential barriers for up and down spins of the valence electrons, thus affecting the spin reflection asymmetry and possibly even changing the sign of the coupling.

A less significant but nevertheless very visible effect on the coupling is the change of the width of the quantum well of the spacer when the lattice relaxations are included in the case of Ag, see entries 4 and 5 of Table 1. In the case of a Ag layer in an unrelaxed Cu lattice (entry 4 in Table 1) the exchange coupling was essentially the same as for pure Cu. This result is not particularly surprising since the valence band of Ag is similar to that of Cu. However, when the Cu spacer was allowed to relax around the plane of Ag atoms (entry 5 in Table 1) the coupling changed to weakly ferromagnetic. The mechanism by which the coupling is affected is now related to a change in the width of the quantum well that the Cu valence electrons are traversing.

The experimental results did not show a crossover to FM coupling for either Cr or for Ag foreign atoms deposited in the center of the Cu spacer. One has to keep in mind that the above first principles calculations were carried out for an ideal structure and for one foreign atomic layer. In these structures one should expect short-wavelength oscillations. One calculated point is certainly not enough to obtain the overall behaviour of the exchange coupling. However, one can argue that a smaller absolute value of the coupling in the Cu/Ag/Cu spacer than that in a pure Cu spacer indicates that the foreign Ag atoms weaken the overall coupling. This is in agreement with our observations. The antiferromagnetic coupling is much stronger in the Cu/Cr/Cu spacer than in Cu/Ag/Cu. However, the first principles calculations predict that the Cr atomic layer should be fully ferromagnetically ordered at $T = 0$ K. In our temperature range even a full Cr atomic layer possesses no long-range order, and therefore one should expect behaviour nearly like that of paramagnetic Fe. Indeed, the exchange coupling in the Cr_cCu_{1-c} series decreases in a manner similar to, but less than, that observed in the Fe_cCu_{1-c} series at a low concentration of Fe. The larger decrease in the coupling for the Fe_cCu_{1-c} series compared to that for the Cr_cCu_{1-c} series is due to the fact that the Cr atomic moment is smaller than the Fe atomic moment.

Summary

The strength of the exchange coupling through nonferromagnetic spacers can be controlled by the insertion of foreign atoms. The local electron potential of the foreign atoms affects the spin transport across the spacer and is chiefly responsible for the observed behaviour of the interlayer exchange coupling. The interlayer exchange coupling depends very strongly on the magnetic state of the foreign atoms within the spacer. Atoms within the spacer possessing some degree of magnetic ordering scatter the Cu majority valence electrons differently from the Cu minority valence electrons and this affects not only the value but also the sign of the exchange coupling. For foreign atoms having no long-range ferromagnetic order, the exchange coupling is mainly affected by the presence of 3*d* valence band electrons. However, the strength of this 3*d* band effect is significantly weaker than the effect of a long-range ferromagnetic order. Foreign atoms that have an atomic structure similar to that of the spacer atoms modify the strength of the exchange coupling only because of changes in the local atomic volume. Foreign atoms having the same atomic size as the spacer atoms do not affect the coupling.

Acknowledgments

The authors would like to thank the National Research Council of Canada for financial support. The authors would also like to express their thanks to Drs. P. Schurer, T.C. Schultess, and W.H. Butler for their contributions to our collaborative studies.

References

1. J.J. de Miguel, A. Cebollada, J.M. Gallego, R. Miranda, C.M. Schneider, P. Schuster, and J. Kirschner. J. Magn. Magn. Mater. **93**, 1 (1991).
2. E. Navas, P. Schuster, C.M. Schneider, J. Kirschner, A. Cebollada, R. Miranda, J. Cerdá, and P. de Andrés. J. Magn. Magn. Mater. **121**, 65 (1993).
3. B.N. Engel, M.H. Wiedmann, R.A. van Leeuwen, C.M. Falco, L. Wu, N. Nakayama, and T. Shinjo. Appl. Surf. Sci. **60–61**, 776 (1992).
4. B.N. Engel, C.D. England, R.A. van Leeuwen, M.H. Wiedmann, and C.M. Falco. J. Appl. Phys. **70**, 5873 (1991); Phys. Rev. Lett. **67**, 1910(1991).
5. S. Chikazumi. *In* Physics of magnetism. Robert E. Krieger Publishing Company, Malabar, Fla. 1986. pp. 167–176.
6. K.H. Hellwege and A.H. Hellwege. Elastic, piezoelectric, pyroelectric, piezooptic, electrooptic constants, and nonlinear

© 1998 NRC Canada

dielectric susceptibilities of crystals. Landolt–Börnstein, New Ser. Group 3. Vol. 18. Springer-Verlag, Berlin. 1984.
7. M. Kowalewski, C.M. Schneider, and B. Heinrich. Phys. Rev. B: Condens. Matter, **47**, 8748 (1993).
8. H. Fujiwara, H. Kadomatsu, and T. Tokunaga. J. Magn. Magn. Mater. **31–34**, 809 (1983).
9. R.H. Victora and J.M. MacLaren. J. Appl. Phys. **73**, 6415 (1993).
10. R.H. Victora and J.M. MacLaren. Phys. Rev. B: Condens. Matter, **47**, 11583 (1993).
11. L. Néel. J. Phys. Radium, **15**, 225 (1954).
12. A.B. Shick, D.L. Novikov, and A.J. Freeman. J. Appl. Phys. **83**, 7258 (1998).
13. E.E. Fullerton, D. Stoeffler, K. Ounadjela, B. Heinrich, Z. Celinski, and J.A.C. Bland. Phys. Rev. B: Condens. Matter, **51**, 6364 (1995).
14. O. Song, C.A. Ballentine, and R.C. O'Handley. Appl. Phys. Lett. **64**, 2593 (1994); G. Bochi, O. Song, and R.C. O'Handley. Phys. Rev. B: Condens. Matter, **50**, 2043 (1994).
15. B. Heinrich and J.F. Cochran. Adv. Phys. **42**, 523 (1993).
16. B. Heinrich, J.F. Cochran, M. Kowalewski, J. Kirschner, Z. Celinski, and A.S. Arrott. Phys. Rev. B: Condens. Matter, **44**, 9348 (1991).
17. B. Heinrich, Z. Celinski, J.F. Cochran, A.S. Arrott, K. Myrtle, and S.T. Purcell. Phys. Rev. B: Condens. Matter, **47**, 5077 (1993).
18. Z. Celinski and B. Heinrich. J. Magn. Magn. Mater. **99**, l55 (1990).
19. B. Heinrich, Z. Celinski, L.X. Liao, M. From, and J.F. Cochran. J. Appl. Phys. **75**, 6187 (1994).
20. B. Heinrich, M. From, J.F. Cochran, M. Kowalewski, D. Atlan, and K. Myrtle. J. Magn. Magn. Mater. **140–144**, 545 (1995).
21. M. Kowalewski, B. Heinrich, J.F. Cochran, and P. Schurer. J. Appl. Phys. **81**, 3904 (1997).
22. B. Heinrich, J.F. Cochran, D. Venus, K. Totland, D. Atlan, S. Govorkov, and K. Myrtle. J. Appl. Phys. **79**, 4518 (1996).
23. B. Heinrich, J.F. Cochran, and T. Monchesky. J. Appl. Phys. **81**, 4350 (1997).
24. P. Schurer, Z. Celinski, and B. Heinrich. Phys. Rev. B: Condens. Matter, **51**, 2506 (1995).
25. B. Heinrich. *In* Ultrathin magnetic structures II. *Edited by* B. Heinrich and J.A.C. Bland. Springer-Verlag, Berlin. 1994. pp.
26. J.F. Cochran. *In* Ultrathin magnetic structures II. *Edited by* B. Heinrich and J.A.C. Bland. Springer-Verlag, Berlin. 1994. pp. 222.
27. J.C. Slonczewski. Phys. Rev. Lett. **67**, 3172 (1991).
28. D. Stoeffler and F. Gautier. NATO Adv. Study Inst. Ser. B: **309**, 411 (1992).
29. E.E. Fullerton, K.T. Riggs, C.H. Sowers, and S.D. Bader. Phys. Rev. Lett. **75**, 330 (1995).
30. J.C. Slonczewski. Phys. Rev. Lett. **67**, 3127 (1993).
31. M. Kowalewski, B. Heinrich, K. Totland, J.F. Cochran, S. Govorkov, D. Atlan, K. Myrtle, and P. Schurer. Mater. Res. Soc. Symp. Proc. **384**, 171 (1995).
32. Z. Celinski, B. Heinrich, and J.F. Cochran. J. Magn. Magn. Mater. **145**, L1 (1995).
33. M. Kowalewski, B. Heinrich, T.C. Schultess, and W.H. Butler. IEEE Trans. Magn. **34**, 1225 (1998).
34. M.D. Stiles. Phys. Rev. B: Condens. Matter, **48**, 7238 (1993).
35. P. Bruno. Phys. Rev. B: Condens. Matter, **52**, 411 (1995).

© 1998 NRC Canada

Fundamentals of oxygen delignification. Part II. Functional group formation/elimination in residual kraft lignin

Faraj Asgari and Dimitris S. Argyropoulos

Abstract: The complex interaction of softwood residual kraft lignin with oxygen at elevated temperatures, pressures, and pH's was investigated by isolating and systematically oxidizing the lignin, as a function of time and temperature. The isolation of the oxidized lignin was carried out using a multistep procedure developed specifically to recover all species. Detailed quantitative ^{31}P NMR measurements provided, for the first time, three-dimensional plots describing the formation and (or) elimination of the various functional groups. Oxidative demethoxylation reactions were found to induce the formation of catechols, which are, most likely, reactive intermediates of the oxidation. The rate of carboxylic acid formation and guaiacyl phenol elimination was found to follow two distinct phases: a rapid initial phase followed by a slower phase. More specifically, the rate of carboxylic acid group formation was found to dramatically increase as the reaction temperature increased, analogous to the profiles obtained for the elimination of guaiacyl phenolic units. At reaction temperatures typical of conventional commercial oxygen delignification installations (80–100°C), only minor oxidation was found to occur within the lignin. At these temperatures, increasing the reaction time did not significantly aid the formation of carboxylic acid groups on lignin despite the idealized two-phase homogeneous conditions. The technological ramifications of these data imply that a three-phase oxygen delignification system, operating at temperatures below 100°C, causes only minor oxidative changes to the structure of the lignin in the fibre. It was also possible to isolate the effect of alkali and temperature on the structure of residual kraft lignin through experiments in which pressurized oxygen was replaced by nitrogen. These data revealed a concealed set of alkali-induced condensation and fragmentation reactions.

Key words: bleaching, catechols, carboxylic acids, delignification, guaiacyl, kinetics, oxygen, phenols, phosphorus, nuclear magnetic resonance (nmr), residual kraft lignin.

Résumé : En procédant à son isolement et son oxydation systématique en fonction du temps et de la pression, on a étudié l'interaction complexe de la lignine kraft résiduelle de bois mou avec l'oxygène à des températures, pressions et pH élevés. On a réalisé l'isolation de la lignine oxydée en appliquant une méthode en plusieurs étapes développées spécifiquement pour récupérer toutes les espèces. Des mesures quantitatives détaillées de RMN du ^{31}P ont permis d'obtenir pour la première fois des courbes tridimensionnelles décrivant la formation et (ou) l'élimination de divers groupes fonctionnels. On a trouvé que les réactions de déméthoxylation oxydante induisent la formation de catéchols qui sont vraisemblablement des intermédiaires réactifs dans l'oxydation. On a trouvé que la vitesse de formation de l'acide carboxylique et d'élimination de guaïacol phénolique suit deux phases distinctes : une phase initiale rapide suivie d'une phase plus lente. D'une façon plus spécifique, on a trouvé que la vitesse de formation d'acide carboxylique augmente d'une façon dramatique lorsqu'on élève la température; on a obtenu des profils analogues pour l'élimination des unités guaiacyles phénoliques. À des températures réactionnelles semblables à celles utilisées dans les installations commerciales conventionnelles de délignification par l'oxygène (80-100°C), on observe peu d'oxydation de la lignine. À ces températures, une augmentation du temps de réaction n'aide pas d'une façon significative à la formation d'acides carboxyliques sur la lignine malgré les conditions homogènes en deux phases idéalisées. Les ramifications technologiques de ces données impliquent qu'un système de délignification à l'oxygène en trois phases, à des températures inférieures à 100°C, ne provoque que des changements oxydants mineurs de la lignine de la fibre. Il a aussi été possible d'isoler l'effet des métaux alcalins et de la température sur la structure de la lignine kraft résiduelle en procédant à des expériences dans lesquelles l'oxygène sous pression est remplacé par de l'azote. Ces données révèlent certaines conditions induisent des réactions de condensation et de fragmentation.

Mots clés : blanchiment, catéchols, acides carboxyliques, délignification, guaiacyle, cinétique, oxygène, phénols, phosphore, résonance magnétique nucléaire, lignine kraft résiduelle.

[Traduit par la Rédaction]

Received June 16, 1998.

F. Asgari and D.S. Argyropoulos.[1] PAPRICAN and Department of Chemistry, McGill University, Pulp & Paper Research Centre, 3420 University Street, Montreal, QC H3A 2A7, Canada.

[1]Author to whom correspondence may be addressed. Telephone: (514) 398-6178. Fax: (514) 398-8254.
E-mail: dimitria@shared1.lan.mcgill.ca

© 1998 NRC Canada

Introduction

Regulatory pressures, motivated by concerns regarding the toxicity of pulp and paper mill effluents containing chlorinated organic matter, have driven this industry to consider and (or) implement new delignification and bleaching technologies. In this context, the use of oxygen delignification is becoming of paramount global importance. The environmental, technical, and economic benefits of oxygen delignification include lower chemical requirements in the subsequent bleaching sequence, higher brightnesses with an equivalent amount of chemicals, lower amounts of rejects, and lower water consumption due to the greater recycling potential of oxygen stage effluent (1, 2). However, an oxygen delignification stage allows for limited delignification (3, 4). Beyond approximately 50% delignification, severe cellulose depolymerization takes place, causing deterioration of pulp viscosity and strength characteristics. This lack of selectivity is the main drawback of oxygen delignification (5).

The fundamental interactions of oxygen in aqueous alkali with various lignin model compounds have been the subject of various structural and kinetic enquiries (6–12). However, it should be noted that the conclusions of such studies cannot fully describe the events that occur when oxygen interacts with lignin macromolecules. The polymeric and cross-linked nature of lignin induces physical constraints that make it significantly less reactive toward oxygen than model compounds (12). It is likely that the multitude of branching and cross-linking variations that occur within lignin may cause significant accessibility variations of reactive moieties toward even the same functional groups.

Moreover, during oxygen delignification, molecular oxygen can be transformed into a variety of species possessing different reactivities, with different lignin functional groups adding to the complexity of the process. In actual fact, the stepwise reduction of molecular oxygen can proceed via either four one-electron transfer steps or two two-electron transfer steps (Scheme 1) (9). In the course of these transformations some extremely reactive species are formed, including hydroperoxy radicals, hydroxy radicals, and hydrogen peroxide (13).

Scheme 1. The stepwise reduction of molecular oxygen (biradical) via four one-electron transfer steps and two two-electron transfer steps (9).

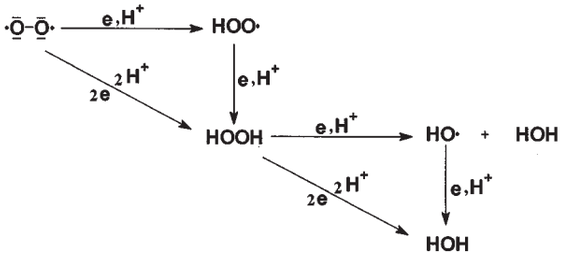

The reactions in Scheme 2, between the species produced during the stepwise reduction of oxygen depicted in Scheme 1, are also possible, both in the presence and in the absence of metal ions (14).

Scheme 2. The reactions that may occur between the species produced during the stepwise reduction of biradical oxygen in the presence and absence of metal ions (14).

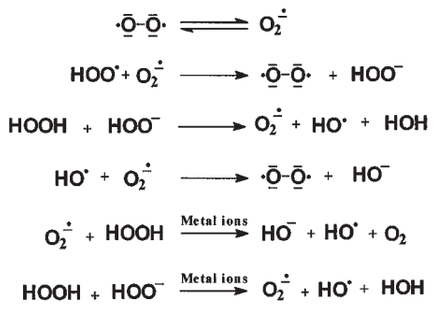

The chemistry depicted in Schemes 1 and 2 clearly indicates that hydrogen peroxide is inevitably present under conditions of oxygen delignification. Therefore, both oxygen and hydrogen peroxide may cooperatively participate in defining the delignification chemistry of such systems. Gierer has classified hydroxyl radicals and the oxygen biradical as electrophilic species, while hydroperoxide anions and superoxide anion radicals are classified as nucleophilic species (14, 15). Consequently, the electrophiles will react with the centres of high electron density in lignin, while the nucleophiles will react with the centres of low electron density as shown in Scheme 3.

Scheme 3. The centres of high and low electron densities on the C_9 unit of lignin. These are the respective sites for attack by electrophiles or nucleophiles.

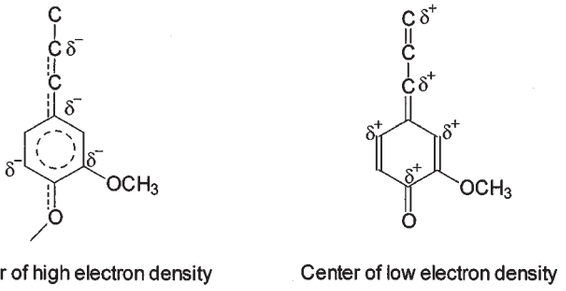

Numerous studies have also demonstrated that the phenolic units of lignin are amongst the most significant reaction sites for oxygen delignification (11). The primary interaction of alkali with these structures yields anions that are candidate structures for attack by oxygen and its multitude of coexisting species (16).

In an effort to provide an additional perspective on the complex interaction of kraft lignin with oxygen in alkaline media at elevated temperatures and pressures, we isolated residual softwood kraft lignin and systematically oxidized it as a function of time and temperature. This was carried out to bridge the existing knowledge gap between model compounds and actual residual kraft lignin. Detailed quantitative ^{31}P NMR measurements on the oxidized lignins provided, for the first time, the actual kinetics of formation and (or) elimination of guaiacyl phenols, carboxylic acids, catecholic phenols, and aliphatic alcohols present in residual kraft lignin.

© 1998 NRC Canada

Scheme 4. Schematic representation of the recovery method developed to quantitatively isolate lignin and its fragments after oxidation with oxygen at elevated temperatures and pH's.

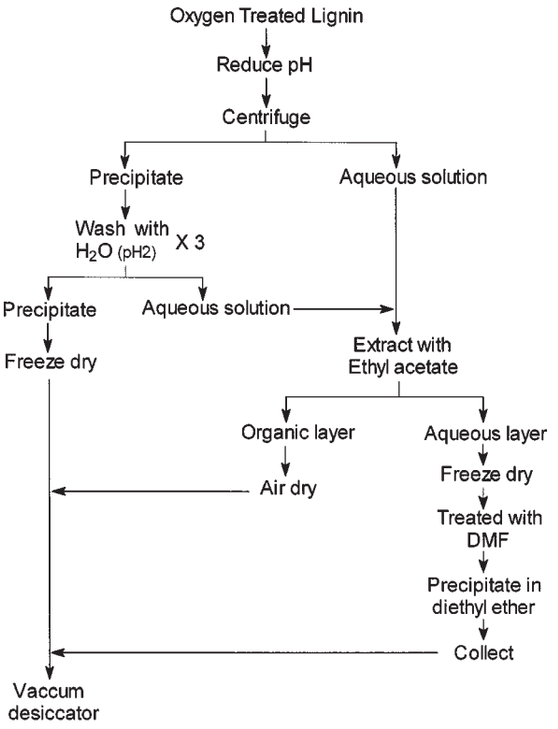

Experimental

Isolation of residual kraft lignin

A black spruce (*Picea mariana*) kraft pulp (kappa number 30.9) was freed from metal ions by stirring the pulp in a DTPA solution (60°C, 1 h) and, after a washing step, the pulp was treated in an acid solution (H_2SO_4 at pH 3, room temperature, 2 h), followed by thorough washing with deionized water. The residual lignin was then isolated from the pulp in several batches by using a slightly modified acidolysis procedure described elsewhere (17). The residual lignin samples were thoroughly homogenized to ensure sample uniformity. The yield of the isolation procedure varied between 35 and 45% while its purity was confirmed by UV and Klasson lignin content measurements.

Oxidation of residual kraft lignin

The residual kraft lignin was oxidized with pressurized oxygen under alkaline conditions at 80, 95, 110, 125, and 140°C for 20, 40, 60, and 80 min using a 1 L Parr reactor. To avoid metal ion contamination, all interior parts of the reactor (including cooling coils and sampling ports) were coated with Teflon. A customized glass liner was used as the actual reaction flask. The following parameters were applied to all oxidations described in this work: 560 mg of residual kraft lignin was mixed with 400 mL of deionized, distilled water. Sodium hydroxide (280 mg, which is equivalent to 2.3 wt.% based on pulp (κ no. 30.9)) was then added, causing solubilization of the lignin. The pH prior to the onset of the reaction was between 11.5 and 11.6. Prior to placing the lignin sample in the reactor, the whole system was heated to 80°C. After sealing the system, the reactor was rapidly heated to the desired temperature. It was then purged with oxygen several times prior to being subjected to a constant oxygen pressure (100 psig or 0.68 MPa) that was maintained for the duration of the oxidation.

To isolate the effect of alkalinity in the absence of oxygen, a series of samples was reacted at 140°C using 0.68 MPa of nitrogen pressure under the same conditions described above.

Quantitative recovery of oxidized and fragmented lignins

After the treatment, the sampling valve of the Parr reactor was opened and an aliquot of lignin solution was cooled to room temperature by passing it through an efficiently cooled reflux condenser. The pH of the sample was then immediately adjusted to 2, which caused the remaining polymeric fraction of the lignin to precipitate out. The precipitated lignin was then recovered by centrifugation, washed with deionized distilled water whose pH had been adjusted to 2, freeze-dried, and stored in a desiccator (see Scheme 4).

The above washings were all combined with the initial filtrate, which contained lower molecular weight lignin fractions combined with hydrophilic lignin fragments. At this point the molecules soluble in organic solvents were extracted with ethyl acetate until the organic layer was no longer coloured. The ethyl acetate extract was allowed to dry in air and stored in a desiccator.

Consequently, the remaining aqueous portion of the sample was enriched in oxidized lignin fragments. The volume of this fraction was first reduced in a rotary evaporator (set at 35–40°C) and it was freeze-dried. The collected solids were then treated with dry dimethylformamide, DMF, filtered to remove inorganic salts, and the filtrate was added dropwise in an excess of diethyl ether (400 mL), allowing the precipitation of the hydrophilic fragments and washing out excess DMF. Finally, the collected lignin fractions were combined, mixed thoroughly, and stored in a vacuum desiccator prior to ^{31}P NMR analyses.

^{31}P NMR analyses of oxidized lignins

Quantitative ^{31}P NMR analyses were carried out on the starting and the oxidized lignins using published procedures (18–20). Since oxidized lignins were found to be of limited solubility in pyridine–$CDCl_3$, a new solvent system for the acquisition of these spectra was used in this effort. Approximately 40 mg of our lignin sample was dissolved in 500 μL of deuterated DMF. A mixture of pyridine/$CDCl_3$ (300 mL, 1.6/1 v/v) was then added and the samples were phosphitylated with 100 mL of 2-chloro-4,4,5,5-tetramethyl-1,3,2-dioxaphospholane, synthesized according to published procedures (21, 22). Solutions of 100 mL of cyclohexanol (1.1 mg) and chromium acetylacetonate (0.55 mg) in 10 mL of pyridine/$CDCl_3$ (1.6/1 v/v) were also added to serve as the internal standard and relaxation reagent, respectively.

The ^{31}P NMR spectra were acquired on a Varian XL-300 MHz spectrometer (operating at 121.5 MHz). The chemical shifts reported are relative to the reaction product of water with the phosphitylation reagent, which has been reported to give a sharp signal at 132.2 ppm (20, 23). For each spectrum 128

© 1998 NRC Canada

Table 1. The amounts of the various hydroxyl groups present within the starting and the oxidized residual kraft lignins, determined by quantitative ^{31}P NMR.

Temperature of oxidation (°C)	Time of oxidation (min)	Carboxylic acids (mmol/g)	Guaiacyl phenols (mmol/g)	Catecholic phenols (mmol/g)	Aliphatic alcohols (mmol/g)
80	20	0.48	0.52	0.18	1.97
	40	0.5	0.45	0.14	1.91
	60	0.51	0.43	0.16	1.78
	80	0.54	0.39	0.14	1.8
95	20	0.41	0.57	0.19	2.07
	40	0.47	0.49	0.25	2.13
	60	0.57	0.37	0.16	1.78
	80	0.56	0.34	0.26	1.76
110	20	0.63	0.37	0.16	1.72
	40	0.71	0.26	0.15	1.65
	60	0.73	0.19	0.13	1.68
	80	0.92	0.19	0.18	1.48
125	20	0.62	0.38	0.24	1.74
	40	1.14	0.25	0.22	1.71
	60	1.16	0.24	0.22	1.89
	80	1.21	0.21	0.21	1.81
140	20	0.98	0.21	0.27	1.33
	40	1.1	0.2	0.18	1.42
	60	1.4	0.15	0.23	1.23
	80	1.5	0.11	0.17	1.13
Control lignin		0.26	0.57	0.2	2.01

Fig. 1. Typical quantitative ^{31}P NMR spectra, signal assignment, and integration ranges applied during the course of this work. The phosphitylation reagent employed was 2-chloro-4,4,5,5-tetramethyl-1,3,2-dioxaphospholane (19, 20).

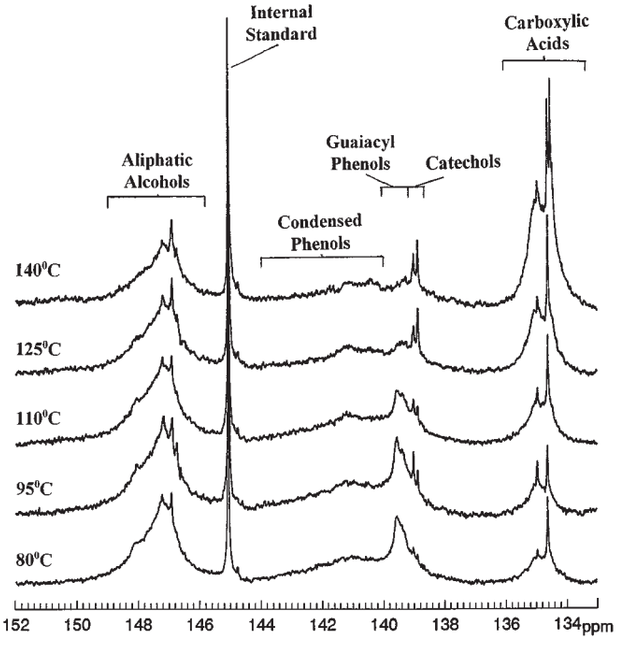

transients were acquired with a delay time of 25 s between acquisitions.

Results and discussion

The oxidation of residual kraft lignin under high pressure and alkalinity is known to partially degrade the lignin with concomitant formation of functional groups such as quinones and carboxylic acids (24), significantly altering its solubility. Since the primary objective of this work was to identify and quantify these structural changes under conditions of an oxygen delignification stage, extensive efforts were made to quantitatively isolate the lignin after the reaction.This ensured that most of the highly oxidized and low molecular weight fragments were included in the quantitative ^{31}P NMR analyses that followed. To accomplish this, a multistep procedure was developed (Scheme 4) to recover all of the species possessing different solubility characteristics in different solvents.The application of this scheme provided recovery yields between 75–95%.

Careful optimization work showed that the oxidized lignins could be divided into three distinct fractions. One fraction could easily be precipitated out of aqueous alkali by decreasing its pH to 2. More hydrophilic fractions were then recovered by extracting aqueous lignin solutions with ethyl acetate. Finally, highly oxidized lignin macromolecules and fragments were isolated by selectively dissolving them with dimethylformamide (DMF), separating them from inorganic salts. It should be noted that no attempt was made to recover

© 1998 NRC Canada

Scheme 5. The major reactions involving phenolic units and free radical species during oxygen delignification (9–16).

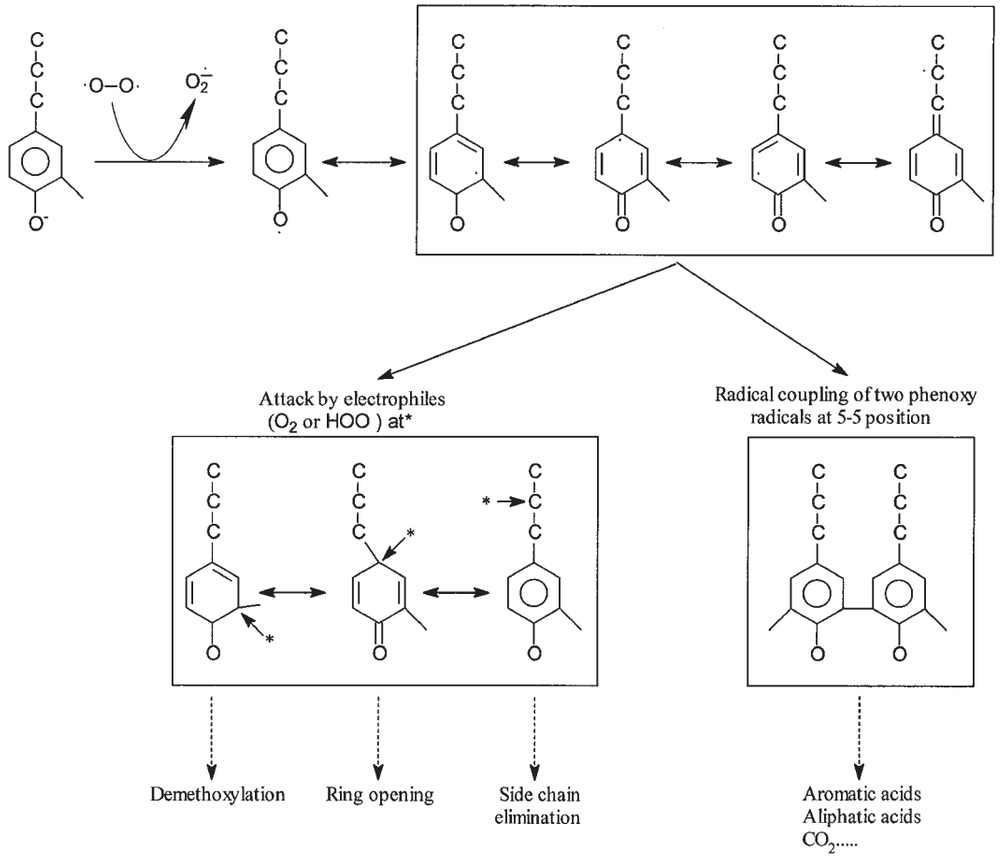

and quantify volatile by-products such as CO, CO_2, and methanol.

A series of typical quantitative ^{31}P NMR spectra of softwood residual kraft lignins obtained after phosphitylation with 2-chloro-4,4,5,5-tetramethyl-1,3,2-dioxaphospholane is displayed in Fig. 1. The integration ranges and signal assignment were similar to those reported by Sun and Argyropoulos (23, 25) based on previous model compound (20) and lignin studies (19). Therefore, the foundations of the following discussion belong in the quantitative ^{31}P NMR data of Table 1, which summarizes the amounts of the various hydroxyl groups present within the starting and oxidized residual kraft lignins.

The reactivity of guaiacyl phenolic units with oxygen

Molecular oxygen, in alkaline media at elevated temperatures, has been considered to behave as a biradical species (9, 13). Therefore, the first step in the oxidative degradation of phenolic units is thought to be the abstraction of an electron from the phenolate anion by biradical oxygen, giving the corresponding phenoxy and superoxide anion radicals (9). At the same time, the protonation of reduced oxygen gives rise to hydroperoxy radicals, which are known to behave as stronger oxidants than molecular oxygen (13), reacting faster with lignin units. As such, phenoxy radicals are attacked by hydroperoxy radicals at the centres of high electron densities as shown in Scheme 3. The reaction products are known to be the relatively unstable cyclohexadienone hydroperoxide intermediates (14–16), leading to demethoxylation, ring-opening, and side-chain elimination reactions (Schemes 5 and 6). In fact, such species have been detected, isolated, and quantified as photochemical transformation products of commercial antioxidants (26–28). The demethylation and ring-opening reactions give rise to catechols and various mono and dicarboxylic acids, such as maleic and muconic acids (Scheme 6), while the side-chain elimination reactions cause the formation of other organic acids and *para*-quinones, thus depolymerizing lignin. The outcome of all these reactions is the actual elimination of guaiacyl phenolic units.

In an attempt to shed more light in this complex series of events, the profiles of guaiacyl phenolic group elimination during the oxidation of residual kraft lignin were determined and are plotted as a function of temperature and time in Fig. 2.

It is apparent that the rate of guaiacyl phenolic unit elimination increases as the oxidation intensifies. The reaction temperature, rather than the reaction time, seems to be of primary significance in causing the elimination of these units. The rate of guaiacyl unit elimination is considerably slower at 80 and 95°C than at 110, 125, or 140°C. Furthermore, the degradation of guaiacyl units at temperatures above 100°C seems to proceed in two distinct phases: an initial rapid decrease of the guaiacyl units is observed within 20–40 min, followed by a significantly slower regime. Similarly, Lai et al. (29) claimed that 10% of these uncondensed phenolic

© 1998 NRC Canada

Scheme 6. Reactions proposed to occur under oxygen delignification conditions involving phenolic moieties and superoxide anion radicals via dioxetane intermediates (14).

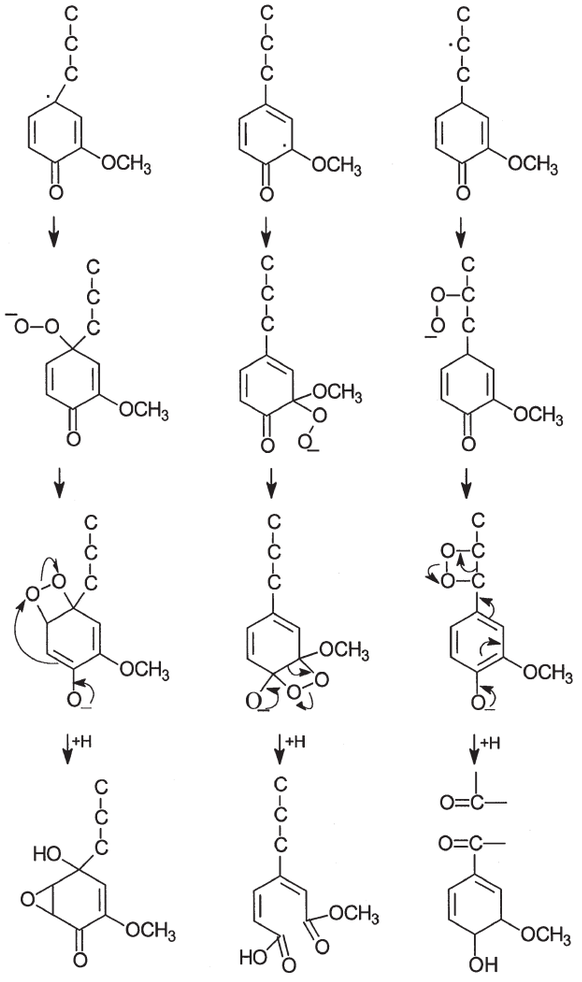

units are eliminated rapidly during oxygen delignification at 100°C and 90 psi oxygen pressure (1 psi = 6.9 kPa), followed by a slow phase during which their concentrations remain relatively constant. Such behaviour is reminiscent of the kappa number reduction profiles usually encountered during oxygen delignification of kraft pulps. Physical constraints such as a diffusion-controlled reaction whose rate depends on the rate of transport of reagents from one phase to another could be responsible for stalling the reactivity in the slow phase (30). However, the data of Fig. 2 represent the oxidative elimination of guaiacyl phenolic units from within residual kraft lignin under homogeneous oxygen delignification conditions, making it likely that guaiacyl phenolic units may exist within residual kraft lignin whose reactivity toward oxidative reactions is different. Branching and cross-linking variations that occur within lignin may be responsible for the observed reactivity and (or) accessibility variations.

Fig. 2. Three-dimensional plots depicting the oxidative elimination of guaiacyl phenolic units from within residual kraft lignin under homogeneous oxygen delignification conditions.

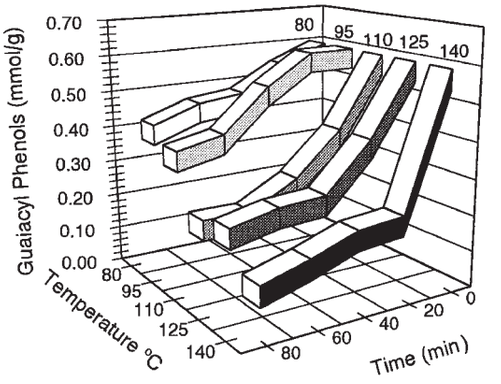

Fig. 3. Three-dimensional plots depicting the buildup of carboxylic acids within residual kraft lignin as a function of time and temperature under homogeneous oxygen delignification conditions.

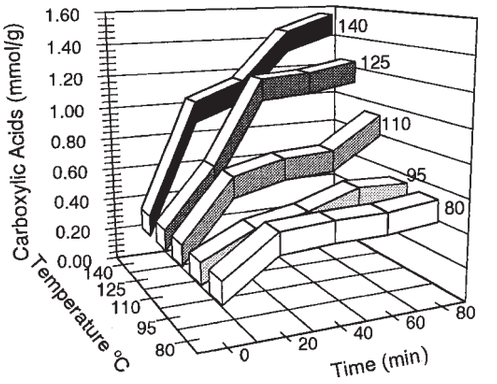

Formation of carboxylic acids within residual kraft lignin

The presence of carboxylic acid groups on the lignin macromolecule is considered to promote lignin solubilization in alkaline media during oxygen delignification (10, 23) or other bleaching stages (25). Lignin oxidation reactions may induce the formation of carboxylic acids via a number of pathways either as monomeric fragments or functional groups attached at the end of side chains of the lignin macromolecules (12, 31, 32). The most significant pathway involves side-chain elimination and ring-opening reactions in phenolic centres. Side-chain elimination reactions would form vanillin-like structures (which degrade further) while ring-opening reactions lead to moieties resembling muconic acid moieties (16). Another pathway may involve an electrophilic attack at lignin centres of high electron density, causing the formation of a four- membered cyclic peroxide intermediate termed dioxetane (14, 16, 24); (Scheme 6). This reactive species rearranges to induce efficient cleavage of C—C bonds. It should be noted that after the initial electrophilic attack, the molecule may also be attacked by external nucleophiles, but according to Gierer (14) these are only minor reactions.

© 1998 NRC Canada

Scheme 7. Possible reactions, operating on phenolic units, that may account for the formation and subsequent elimination of catechols, during the oxidation of residual kraft lignin at elevated temperatures and alkalinities.

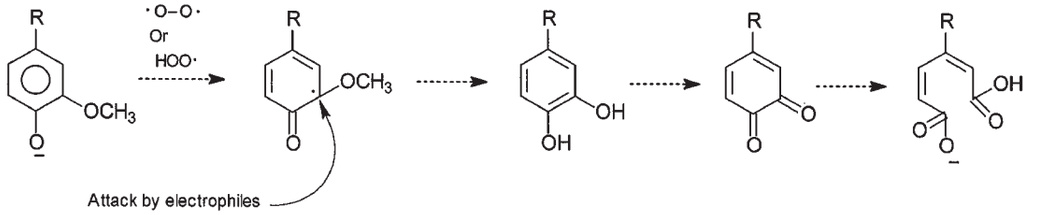

Fig. 4. Three-dimensional plots depicting the pH profiles of the medium as a function of time and temperature during the oxidation of residual kraft lignin, under homogeneous oxygen delignification conditions.

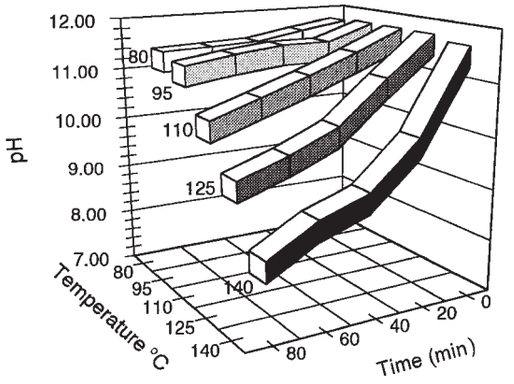

Figure 3, displaying the three-dimensional plots for the buildup of carboxylic acids within residual kraft lignin as a function of time and temperature, is very revealing. For all temperatures studied, two regimes can be distinguished describing the rate of carboxylic acid group formation: an initial rapid phase that dominates the process for the first 20 min (at all temperatures), followed by a slower one. At temperatures between 125 and 140°C, the rate of carboxylic acid group formation within the first 20 min of the process is very high. For example, the concentration of these groups after 20 min of reaction reaches and exceeds 1.0 mmol/g; while at 80–95°C, 80 min of reaction caused only a minor enrichment of the lignin structure in carboxylic acid groups (less than 0.5 mmol/g).

The rate of carboxylic acid group formation seems to dramatically increase as the reaction temperature increases, analogous to the profiles obtained for the elimination of guaiacyl phenolic units. It is interesting to observe that only minor oxidation occurs within the residual kraft lignin at reaction temperatures typical of conventional commercial oxygen delignification installations (80–100°C).

At these temperatures, increasing the reaction time does not seem to significantly aid the formation of carboxylic acid groups. Higher temperatures, however, cause the concentration of carboxylic acid groups to steadily increase as a function of treatment time. In general, the efficiency of oxidation of residual kraft lignin significantly increases above 100°C even though these experiments were conducted under idealized two-phase homogeneous conditions. The data imply that a three-phase oxygen delignification system operating at temperatures below 100°C causes only minor oxidative changes on the structure of the lignin on the fibre.

The effect of oxidation on the pH of the medium

Since pH is known to seriously affect the efficiency of an oxygen delignification stage, it was deemed appropriate to examine the dependence of pH as a function of temperature and time during the oxidation of residual kraft lignin. The amount of sodium hydroxide used in the present sequence of experiments was similar to that used during a commercial softwood oxygen delignification installation (2.3% based on oven dry fibre, see Experimental).

The data of Fig. 4 show the contribution of the oxidized groups in residual kraft lignin toward lowering the pH of the aqueous medium during oxygen delignification conditions. In a manner analogous to the formation of carboxylic acid groups (Fig. 3), the pH of the medium is practically unaffected at temperatures below 100°C. This could be significant information when one considers the design of oxygen delignification operations at temperatures above 100°C. For such a case, one should make provisions so that enough alkali is present in the medium to compensate for the greater pH losses that the oxidation of lignin will cause above 100°C. A benchmark observation guiding such a design could be that at 110°C and after 80 min of reaction, the pH of the medium was found to be slightly below 10. The trend of decreasing pH in an alkaline oxidative extraction was observed previously when the temperature was raised from 70 to 110°C, with some benefits observed by increasing the alkali charge (33).

Another interesting feature of the data of Fig. 4 is the fact that the pH profiles show two- phase reactions only at temperatures of 125 and 140°C, in contrast to the data of Fig. 3 (see relevant discussion). At lower temperatures the pH decrease is smooth throughout the examined time range.

Oxidative demethoxylation reactions

Model compound studies have shown that demethoxylation reactions may occur under oxygen delignification conditions (13). However, there has been no direct quantitative evidence for the occurrence of such reactions in residual kraft lignin during oxygen delignification. Despite the fact that the exact mechanism of demethoxylation is not known, Kratzl et al. (13) have assumed that a phenoxy radical may react with oxygen or hydroperoxy radicals, yielding cyclohexadienone hydroperoxides (Scheme 7). For these species, after demethoxylation, rearrangement and ring rearomatization yield catechols that are easily oxidized to *ortho* quinones and then to a muconic acid type of structures (13).

© 1998 NRC Canada

Fig. 5. Three-dimensional plots depicting the profile of catechol formation as a function of time and temperature during the oxidation of residual kraft lignin under homogeneous oxygen delignification conditions.

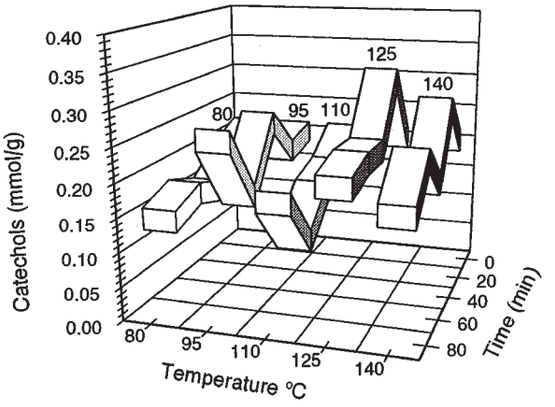

Fig. 6. A comparison of carboxylic acid group formation on residual kraft lignin in the presence and absence of oxygen at 140°C.

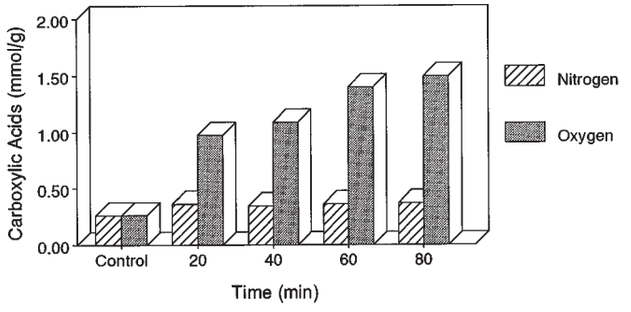

The quantitative ^{31}P NMR spectra of Fig. 1 show the characteristic signals of catechols in the region 138.6–139.1 ppm (19, 20, 23). Apparently, catechols form during the oxidation of residual kraft lignin, since these signals are not as obvious in the spectrum of the starting material (Fig. 1). Since this novel methodology allows the detection and quantification of catechols in a lignin sample, it was used to quantify them as a function of time and temperature (Fig. 5).

One can observe some minor but irregular variations in the abundance of catechols within oxidized residual kraft lignin as a function of time and temperature (Fig. 5). In general, their concentration can be considered relatively constant over the whole temperature range examined, implying that catechols are involved in the oxidation process as intermediates.Their participation in an oxygen delignification has been suggested by Gellerstedt and Lindfors (30) and Renard et al. (31, 32). It is likely that while there is a supply of guaiacyl units in the system, these intermediates would form and then be oxidized in a continuous fashion. In addition to the catechols acting as important intermediates in the oxidation process, they also increase the hydrophilicity of the lignin, augmenting its solubility in alkaline media.

Fig. 7. A comparison of condensed phenolic units on residual kraft lignin in the presence and absence of oxygen at 140°C.

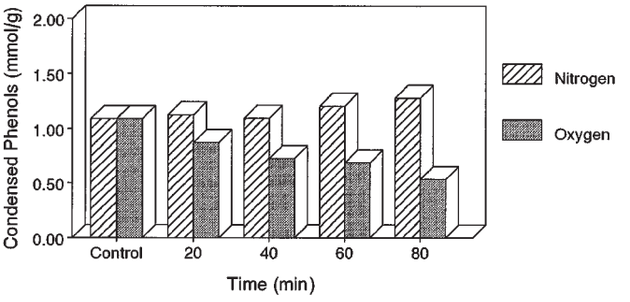

The effect of alkali and temperature on the reaction pathways

During this effort we attempted to isolate the effect of alkali and temperature on the structure of residual kraft lignin by substituting pressurized oxygen with nitrogen, in otherwise identical conditions to those described so far. To emphasize the overall effects, this study was conducted at 140°C and the functional group distribution changes induced on the residual kraft lignin were compared to those in Figs. 2 and 4 obtained at 140°C.

The dramatic effect of oxygen toward inducing the formation of carboxylic acid groups within residual kraft lignin, under oxygen delignification conditions, is shown in Fig. 6. In the absence of oxygen, temperature (140°C) and alkali alone do not induce the formation of carboxylic acids in residual kraft lignin. For comparison purposes under the same conditions and in the presence of oxygen, an approximate 450% increase in carboxylic acid content was measured.

Phenolic structures that are substituted at the C5 position may be termed condensed phenols. The fate of such units, under both an oxidative and an inert atmosphere, at 140°C, is shown in Fig. 7. It appears that at 140°C the amount of condensed phenolic units decreased over 50% via oxidative degradation reactions. However, in the absence of oxygen, the condensed phenolic units increased by about 17%. It is therefore likely that this increase describes alkaline condensation reactions taking place within residual kraft lignin under the examined conditions. At elevated alkalinities and temperatures, phenoxy anions (33) may attack the α position of other C9 units and consequently, after rearrangement, new C_α–C_5 units may form, see Scheme 8 (34, 35).

In addition, any residual β-O4 units present in residual kraft lignin, albeit in minor amounts (36), may rearrange and cause the formation of minor amounts of formaldehyde. These species may then methylolate the C5 position of phenolic units, eventually creating new diphenyl methane structures (Scheme 8).The data of Fig. 7, therefore, reveal a concealed set of condensation reactions.

Figure 8 displays the changes in the actual amounts of guaiacyl phenolic units under inert and oxidative conditions. In the presence of oxygen, the amount of guaiacyl phenolic units decreases but in the absence of oxygen, the amount of guaiacyl phenolic units increased somewhat. The rationale that may be offered to explain these data is that under the examined conditions, the small amounts of β-O4 bonds that have been documented to remain on residual kraft lignin

© 1998 NRC Canada

Scheme 8. Alkaline condensation reactions that may operate on phenolic units of residual kraft lignin (34).

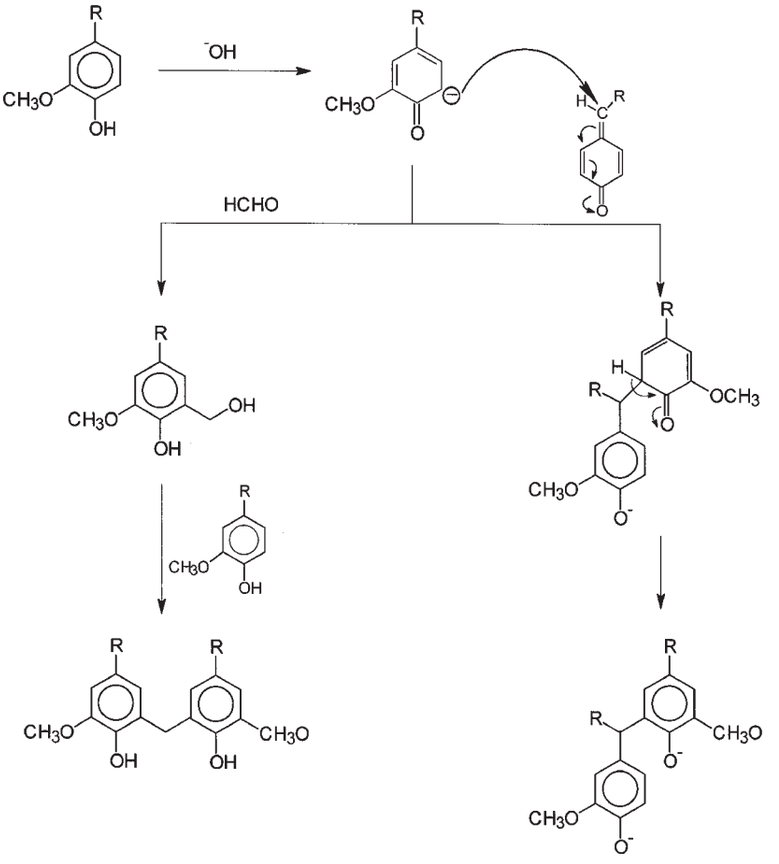

Fig. 8. A comparison of the fate of guaiacyl phenolic units present on residual kraft lignin in the presence and absence of oxygen at 140°C.

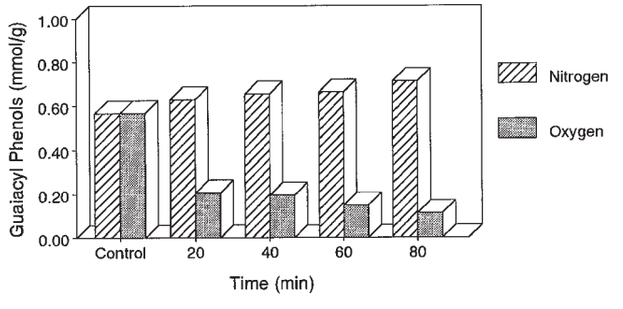

may cleave (36), and will inevitably cause the formation of new guaiacyl phenolic units.

Concluding remarks

During oxygen delignification the guaiacyl phenolic units of softwood residual kraft lignin eliminate with the concomitant formation of carboxylic acids. The rates for the elimination of phenols and the formation of acids were found to significantly increase when the reaction temperature was above 100°C. The concentration of catechols was found to be relatively constant over the whole temperature range examined, implying that catechols are involved in the oxidation process as intermediates.

In general, reaction temperatures varying between 80 and 100°C caused only minor functional group changes on softwood residual kraft lignin. The reactivity of this kraft lignin substantially increased at temperatures above 110°C. Therefore considerable oxidative delignification should be obtained at elevated temperatures. The challenge remains, however, for developing strategies that may prevent the unwanted deterioration of pulp quality.

Acknowledgements

The authors would like to thank Ms. B. Van Lierop and Mr. Y. Sun for their input while reviewing the manuscript. The constructive criticism of Dr. Sten Ljunggren of the Swedish Pulp and Paper Research Institute is also gratefully acknowledged. This research was supported by the Goverment of Canada in the form of a Strategic Grant and by the Air Products & Chemicals Corporation.

References

1. T.J. McDonough. TAPPI, **69**(6), 46 (1986).
2. V. Masura. Cellul. Chem. Technol. **27**, 201 (1993).
3. L. Olm and A. Teder. TAPPI, **62**(12), 43 (1979).
4. D. Lachenal and C. DeChoudens. Cellul. Chem. Technol. **20**, 553 (1986).

© 1998 NRC Canada

5. C.L. Hsu and J.S. Hsieh. TAPPI, **70**(12), 197 (1987).
6. S. Ljunggren. Nord. Pulp Paper Res. J. **1**, 38, (1990).
7. S. Ljunggren and E. Johansson. Nord. Pulp Paper Res. J. **5**(3), 148 (1990).
8. S. Ljunggren. J. Pulp Paper Sci. **12**(2), 54 (1986).
9. K. Kratzl, J. Gratzl, and P. Claus. Adv. Chem. Ser. **59**, 157 (1966).
10. G. Gellerstedt, K. Gustafsson, and E.-L. Lindfors. Nord. Pulp Paper Res. J. **1**(3), 14 (1986).
11. E. Johansson and S. Ljunggren. J. Wood Chem. Technol. **14**(4), 507 (1994).
12. S. Ljunggren, G. Gellerstedt, and M. Petterson. 6th Int. Symp. Wood and Pulping Chem. **1**, 229 (1991).
13. K. Kratzl, P. Claus, W. Lonsky, and J. Gratzl. J. Wood Sci. Technol. **8**, 35 (1974).
14. J. Gierer. Int. Symp. Wood and Pulp Chemistry, Paris. 1987. p. 279.
15. J. Gierer. Proc. Proc. Int. Symp. Wood and Pulping Chemistry CTAPI, Beijing. 1993. p. 303.
16. J. Gierer and F. Imsgard. Sven. Papperstidn. **16**, 510 (1977).
17. Z. Jiang and D. S. Argyropoulos. J. Pulp Pap. Sci. **20**(7), J183 (1994).
18. D.S. Argyropoulos. J. Wood Chem. Technol. **14**, 45 (1994).
19. A. Granata and D.S. Argyropoulos. J. Agric. Food Chem. **43**, 1538 (l995).
20. Z.-H. Jiang, D.S. Argyropoulos, and A. Granata. Magn. Reson. Chem. **33**, 375 (1995).
21. A. Zwierzak. Can. J. Chem. **45**, 2501 (1967).
22. H.J. Lucas, F.W. Mitchell, Jr., and C.N. Scully. J. Am. Chem. Soc. **72**, 4591 (1950).
23. Y. Sun and D.S. Argyropoulos. J. Pulp Paper Sci. **21**(6), J185 (1995).
24. H.-M. Chang and J. Gratzl. Proc. Int. Symp. Chemistry of Delignification with Oxygen, Ozone, and Peroxides: Ring Cleavage Reaction of Lignin Models with Oxygen and Alkali. 1986. p. 151.
25. Y. Sun and D.S. Argyropoulos. Holzforschung, **50**(2),175 (1996).
26. T. Matsuura, K. Omura, and R. Nakashima. Bull. Chem. Soc. Jpn. **38**, 1398 (1965).
27. L. Taimr and J. Pospisil. Makromol. Chem. **39**, 189 (1974); **39**, 619 (1974).
28. R.G. Lichtenthaler and F. J. Ranfelt. **148**, 553 (1978).
29. Y.-Z. Lai, M. Funaoka, and H.-T. Chen. Holzforschung, **48**(4), 355 (1994).
30. G. Gellerstedt and E. -L. Lindfors. Tappi J. **70**, 119 (1987).
31. J.J. Renard, D.M. Mackie, and H.I. Bolker. Pap. Puu, **57**(11), 1 (1975).
32. J.J. Renard, D.M. Mackie, H.I. Bolker, and D.W. Clayton. Cellul. Chem. Technol. **9**, 341 (1975).
33. W.I. Taylor and A.R. Battersby. *In* Oxidative coupling of phenols. Chap. 1: Phenol coupling. Marcel Dekker, Inc., New York. 1967.
34. J. Marton. Reactions in alkaline pulping. *In* Lignins: occurrence, formation, structure, and reactions. John Wiley and Sons, Inc., New York. 1971. pp. 639–694.
35. J. Gierer. Wood Sci. Technol. **14**, 241 (1980).
36. M. Kleen, B. Hortling, and T. Tamminen. 4th Eur. Workshop on Lignocellulosics and Pulp, Stresa, Italy, Sept. 8–11, 1996. pp. 44–50.

© 1998 NRC Canada

Second-harmonic generation studies of chiral organic salts

Bozena Borecka-Bednarz, Alan V. Bree, Brian O. Patrick, John R. Scheffer, and James Trotter

Abstract: Second-harmonic generation in the solid state is restricted to materials that crystallize in non-centrosymmetric space groups. Unfortunately, the vast majority of solids crystallize in centrosymmetric space groups and are therefore SHG-inactive. The requirement for solid-state asymmetry is addressed in a new series of organic salts. The acid *p*-nitrophenylglycine, SHG-inactive due to its centrosymmetric ($P\bar{1}$) packing, was coupled to six optically pure amines to form salts and (or) complexes that, by virtue of their chiral counterion, crystallized in non-centrosymmetric space groups. The 1064 nm output from a Nd:YAG laser produced 532 nm second-harmonic generation from each of the six salts, with three of the salts producing second-harmonic intensities at least an order of magnitude greater than that of our standard, urea. X-ray crystallographic analysis was carried out on five of the six salts, and an attempt was made to rationalize the second-harmonic intensity of each of these five salts based on the orientation of its molecular charge-transfer axis in the unit cell and on its chromophore density.

Key words: second-harmonic generation, nonlinear optics, chiral organic salts, crystal structures.

Résumé : La génération de secondes harmoniques dans l'état solide est possible seulement pour les matériaux qui cristallisent dans des groupes spatiaux non-centrosymétriques. Malheureusement, la grande majorité des solides cristallisent dans un des groupes spatiaux centrosymétriques et sont, par conséquent, inactifs en ce qui concerne la génération de secondes harmoniques. Cette condition sur l'asymétrie cristalline est adressé dans une nouvelle serie de sels organiques. L'acide *p*-nitrophénylglycinique, inactive pour la génération de secondes harmoniques dû à sa cristallisation centrosymétrique ($P\bar{1}$), fut combineé avec six amines optiquement actives pour former des sels et (ou) des complèxes qui, dû à leurs contre-ions chiraux, cristallisent dans un des groupes spatiaux non-centrosymétriques. Soumis à un rayonnement lumineux de 1064 nm produit par un laser Nd:YAG (grenat d'yttrium et d'aluminium), chacun des six sels a géneré une seconde harmonique de 532 nm. Trois de ces sels ont produit des secondes harmoniques ayant des intensités d'au moins une ordre de grandeur supérieures à celle produite par notre étalon, l'urée. Cinq des six sels ont été soumis à une analyse cristallographique aux rayons X. Une tentative fut effectueé pour modeliser l'intensité de la seconde harmonique produite par chacun des cinq sels en se basant sur l'orientation de l'axe de transfert de charge dans la maille élémentaire, et sur la densité chromophorique de chacun d'entre eux.

Mots clés : génération de seconde harmonique, sels organiques chiraux, optique non-linéaire, structures cristallines.

Introduction

Over the course of the last 15 years extensive development of organic nonlinear optical (NLO) materials has led to compounds potentially suitable for application in optical telecommunication and data storage devices (1–5). Much of this research has been directed toward materials that produce second-harmonic generation (SHG), the frequency doubling of laser light. Organic materials possess several attractive properties that invite further study: they often have molecular hyperpolarizabilities (β, γ) significantly larger than inorganics that fall within the same transparency range (6, 7), while the ease with which molecules can be "designed" for efficient SHG by established synthetic methodologies is an exciting advantage for organic materials. Molecules with large hyperpolarizabilities, like *p*-nitroaniline (**PNA**), tend to contain strong electron-accepting and electron-donating groups bridged by a π-conjugated system. Several molecules bearing this type of one-dimensional charge-transfer chromophore have produced crystals that are excellent materials for SHG (8–10). Materials scientists, however, are still presented with the challenge of inducing non-centrosymmetric packing of these materials if they are to have non-zero macroscopic susceptibilities and exhibit second-order NLO properties (11, 12). Since approximately 75% of all organic materials crystallize in centrosymmetric space groups (13, 14), significant effort has been invested in developing techniques designed to force a polar alignment of chromophores, such as the various poled-polymer (15) and self-assembly techniques (16, 17). There is, however, a theoretical limit to the conversion of the molecular nonlinearity of these one-dimensional systems into crystalline nonlinearity for the SHG process. Factors such as space group and chromophore orientation

Received January 28, 1998.

B. Borecka-Bednarz, A.V. Bree, B.O. Patrick,[1] J.R. Scheffer, and J. Trotter. Department of Chemistry,University of British Columbia,2036 Main Mall,Vancouver, BC V6T 1Z1, Canada.

[1]Author to whom correspondence may be addressed. Telephone: (604) 822-4865. Fax: (604) 822-2847. E-mail: brian@xray1.chem.ubc.ca

© 1998 NRC Canada

Fig. 1. *p*-Nitrophenylglycine **(1)** and the molecular axis system describing the orientation of the charge-transfer axis.

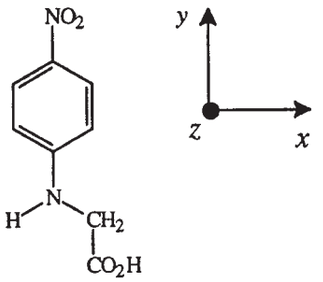

1

limit the contribution to the crystalline nonlinearity to a maximum of 38% for phase-matched SHG (18, 19).

One approach to achieving bulk asymmetry has been to introduce a resolved chiral centre in the crystal of interest. This approach is well illustrated in the case of *p*-nitrophenyl-L-prolinol (**NPP**) (8) and *N*-(5-nitropyridyl)-2-L-prolinol (**PNP**) (20), each of which is a D-π-A system like **PNA**, forced to crystallize in a non-centrosymmetric space group due to the optical purity of the material. It has been suggested that highly polar materials such as **PNA** are biased towards centrosymmetric packing, in part due to the dipolar forces that encourage neighboring molecules to pack in an anti-parallel manner. While there is some debate over what role the magnitude of the dipole moment plays in influencing molecular orientation in the crystal (21), the presence of a resolved stereogenic centre in an SHG chromophore can only ensure non-centrosymmetry. Chirality itself does little to diminish these dipolar forces. Some authors have suggested that the Coulombic interactions found in salts could overcome the dipolar forces that may be favoring the anti-parallel packing commonly found in covalent compounds of this type, by shielding adjacent dipoles from one another (2). One means of inducing an asymmetric packing arrangement that could prove advantageous for SHG materials is the *chiral ionic auxiliary* approach (22–26). In this approach an achiral acid or amine is coupled to an optically pure amine or acid to produce a salt that, by virtue of its optical purity, must crystallize in a non-centrosymmetric space group. Extended to the production of SHG materials, coupling an SHG chromophore containing acid to an optically pure amine (or a chromophore containing amine to an optically pure acid) produces a salt that, in the solid state, must reside in an asymmetric environment. As such, the chiral ionic auxiliary approach has the added advantage of employing a counterion potentially capable of separating the SHG chromophores, in addition to inducing non-centrosymmetry by virtue of its optical purity.

This paper reports the measured SHG efficiency and X-ray structural determination of a series of salts prepared using the chiral ionic auxiliary approach. Compound **1 (***p*-nitrophenylglycine), an achiral acid containing the **PNA** chromophore (Fig. 1) was synthesized. Although originally SHG-inactive, coupling of the acid to a series of optically pure amines activated the second-order NLO properties of the chromophore. The SHG intensity of each salt was measured relative to a urea standard using the Kurtz and Perry powder method (27). The theoretical macroscopic second-order susceptibilities were then estimated using an oriented gas model derived by Zyss and Oudar (18, 19), and the relative SHG intensities were rationalized on the basis of these susceptibilities.

General experimental

Reagents and general procedures

All chemicals were obtained as reagent grade materials and were used as supplied by either Aldrich, BDH, Fischer Scientific, or Sigma. Melting points (mp) were determined on a DSC 910S differential scanning calorimeter connected to the Thermal Analyst 2000 system (TA Instruments). Melting point ranges are reported as the peak of the melting endotherm. Infrared spectra (IR) were recorded from KBr pellets on a Perkin–Elmer 1710 Fourier transform infrared spectrometer. Absorption bands characteristic of amines, carboxylic acids, carboxylates, and esters are listed in reciprocal centimeters (cm^{-1}). The abbreviations used in describing the relative strength of the absorption bands are as follows: s = strong, m = medium, w = weak. Low- resolution electron impact mass spectra (EIMS) were obtained using a Kratos MS 50 mass spectrometer with 70 eV electron bombardment. Liquid secondary-ion mass spectra (LSIMS), both positive and negative, were obtained for all salts using an AEI MS 9 mass spectrometer. Each of these procedures was performed by the mass spectrometry laboratory of the University of British Columbia Chemistry Department. The mass to charge ratio (m/e) followed by the relative abundance in parentheses is given for the most abundant fragments in each spectrum. Proton nuclear magnetic resonance (^{1}H NMR) spectra were recorded on a Brüker AC-200 (200 MHz) or a Brüker WH-400 (400 MHz) spectrometer in either $CDCl_3$, CD_3OD, or acetone-d_6. Chemical shifts (δ) are given in parts per million (ppm) with the multiplicity and the number of protons in parentheses following the position. The abbreviations used in describing the signal multiplicity are as follows: s = singlet, d = doublet, t = triplet, q = quartet, m = multiplet. UV–vis spectra were recorded on a Perkin-Elmer Lambda 4B UV/VIS spectrophotometer using a 1 cm quartz cell. HPLC grade (BDH) solvent was used without further purification. Wavelengths (λ) in nanometers (nm) are reported and the extinction coefficients (ε, M^{-1} cm^{-1}) are given in parentheses. Carbon, hydrogen, and nitrogen elemental analyses were performed by Mr. P. Borda of the microanalysis lab in the University of British Columbia Chemistry Department. A Hewlett Packard 5890A gas chromatograph fitted with a flame ionization detector, a Hewlett Packard 3392 A integrator, and a 15 m × 0.25 mm DB1 column (J & W Scientific Inc.) with helium as a gas carrier was employed for gas–liquid chromatographic analysis.

Syntheses

Synthesis of N-p-*nitrophenylglycine (1)*

Following the procedure of Lantz and Obellianne (28), 2.80 g of *p*-fluoronitrobenzene (19.8 mmol, Aldrich) was dissolved in 20 mL of ethanol. The hydrochloride salt of glycine methyl ester (2.77 g, 22.0 mmol, Sigma) and 3.99 g of $NaHCO_3$ (47.4 mmol, Aldrich) were added to a 100 mL

© 1998 NRC Canada

round-bottomed flask. The fluoronitrobenzene solution was added to the round-bottomed flask, as well as 20 mL of H_2O and several boiling chips. The flask was then equipped with a reflux condenser and the mixture was refluxed overnight, after which the now orange solution was acidified with 5 mL of 1 M HCl, causing the immediate precipitation of a yellow solid. The crude product was allowed to settle and was then vacuum filtered, dried in air, and recrystallized from methanol to afford yellow prisms (2.15 g, 11.0 mmol, 55% yield); mp > 230°C (dec.) (229°C, ref. 28); IR (KBr disc), ν (cm^{-1}): 3363 (s, N–H *str*), 1736 (s, C=O *str*), 1289 (C–O *str* / O–H *def*); UV–Vis (EtOH), λ_{max} : 363 nm (ε = 16 400 M^{-1} cm^{-1}); ^{1}H NMR (acetone-d_6, 200 MHz), δ: 2.9 (br s, 1H), 4.1 (d, 2H, *J* = 3 Hz), 6.6 (br s, 1H), 6.8 (d, 2H, *J* = 9 Hz), 8.1 (d, *J* = 9 Hz, 2H) ppm; EIMS, *m/e* (relative intensity): 196 (M, 25.7), 151 (100), 150 (67.7), 149 (34.3), 138 (28.7), 120 (54.0). Anal. calcd. for **1**, $C_8H_8N_2O_4$: C 48.98, H 4.11, N 14.28; found: C 48.75, H 4.19, N 14.50.

*Synthesis of the (1*S*, 2*S*)-(+)-pseudoephedrine salt of **1**: **1.eph***

Acid **1** (81.8 mg, 0.417 mmol) was dissolved in 150 mL of diethyl ether. The amine (1*S*, 2*S*)-(+)-pseudoephedrine (67.8 mg, 0.410 mmol, Sigma) was dissolved in 20 mL of diethyl ether and added to the solution of **1**. A light yellow precipitate formed immediately. The solution was stirred for 0.5 h, then gravity filtered and dried in air. The crude product was recovered (120.0 mg, 0.332 mmol, 81% yield) and recrystallized from ethanol; mp 178.2°C; IR (KBr disc), ν (cm^{-1}): 3377 (s, N–H *str*) 1605 (s, C–O *str*); ^{1}H NMR (CD_3OD, 400 MHz), δ: 1.09 (d, 3H, *J* = 7 Hz), 2.74 (s, 3H), 3.50 (m, 1H), 3.82 (s, 2H), 4.65 (d, 1H, *J* = 9 Hz), 6.59 (d, 2H, *J* = 9 Hz), 7.42 (m, 5H), 8.06 (d, 2H, *J* = 9 Hz) ppm; –LSIMS, *m/e* (relative intensity): 391(2 × (M^- +1), 20), 195 (M^-, 100), 179 (6.7). +LSIMS, *m/e* (relative intensity): 166 (M^+, 100), 148 (29). Anal. calcd. for **1.eph**, $C_{18}H_{23}N_3O_5$: C 59.82, H 6.41, N 11.63; found: C 59.51, H 6.48, N 11.66.

Synthesis of the S*-(–)-proline* tert*-butyl ester salt of **1**: **1.pro-but***

Acid **1** (52.1 mg, 0.266 mmol) was dissolved in 200 mL of diethyl ether with stirring. Once the solid was completely dissolved, 50 mL *S*-(–)-proline *tert*-butyl ester (50 mg, 0.292 mmol, Sigma) was added to the ether solution and stirred. The solution was concentrated to approximately 25 mL by rotary evaporation and was left to stand, stoppered, overnight. A yellow precipitate was gravity filtered, dried in air, then recrystallized from an acetone–hexane mixture (72.3 mg, 0.197 mmol, 74% yield); mp 122.3°C; IR (KBr disc), ν (cm^{-1}): 3289 (s, N–H *str*), 1726 (s, C=O *str*), 1602 (s, C–O *str*); ^{1}H NMR (CD_3OD, 400 MHz), δ: 1.5 (s, 9H), 2.0–2.4 (m, 4H), 3.35 (m, 3H), 3.78 (s, 2H), 6.61 (d, 2H, *J* = 9 Hz), 8.08 (d, 2H, *J* = 9 Hz) ppm; –LSIMS, *m/e* (relative intensity): 195 (100, M^-; +LSIMS, *m/e* (relative intensity): 172 (M^+, 91), 116 (100). Anal. calcd. for **1.pro-but**, $C_{17}H_{25}N_3O_6$: C 55.58, H 6.86, N 11.44; found: C 55.83, H 6.99, N 11.62.

Synthesis of the S*-(–)-prolinol salt of **1**: **1.pro-ol***

Acid **1** (97.6 mg, 0.498 mmol) was dissolved in 10 mL of acetone. Once the solid was completely dissolved, 50 mL of *S*-(–)-prolinol (50 mg, 0.495 mmol, Aldrich) was added to the acetone solution. This solution was stirred briefly, then concentrated to approximately 5 mL. Approximately 20 mL of diethyl ether was added to the acetone solution, immediately producing a bright yellow precipitate. The crude product was gravity filtered and dried in air, then recrystallized from a 1:1 acetone–ethanol mixture (125 mg, 0.420 mmol, 85% yield); mp 166.2°C; IR (KBr disc), ν (cm^{-1}): 3300 (s, N–H *str*), 1612 (s, C–O *str*); ^{1}H NMR (acetone-d_6, 200 MHz), δ: 1.5–2.0 (m, 4H), 2.5 (m, 1H), 3.1 (t, 2H, *J* = 9 Hz), 3.6 (m, 5H), 6.7 (d, 2H, *J* = 9 Hz), 7.1 (t, 1H, *J* = 7 Hz), 8.0 (d, 2H, *J* = 9 Hz) ppm; –LSIMS, *m/e* (relative intensity): 391 (2 × (M^- + 1), 10), 195 (M^-, 100), 179 (7.5); +LSIMS, *m/e* (relative intensity): 102 (M^+, 100). Anal. calcd. for **1.pro-ol**, $C_{13}H_{19}N_3O_5$: C 52.52, H 6.44, N 14.13; found: C 52.23, H 6.32, N 13.96.

Synthesis of the S*-(–)-prolinamide salt of **1**: **1.pro-amide***

Acid **1** (47.0 mg, 0.240 mmol) was dissolved in 125 mL of diethyl ether with stirring. The amine *S*-(–)-prolinamide (29.4 mg, 0.258 mmol, Aldrich) was added to the ether solution, immediately producing a bright yellow precipitate. The solution was stirred for 0.5 h, then gravity filtered and dried in air. The crude product (59.0 mg, 0.190 mmol, 79% yield) was recrystallized from an acetone–hexane mixture; mp 172.3°C; IR (KBr disc), ν (cm^{-1}): 3285 (s, N–H *str*), 1687 (s, C=O *str*/N–H *def*), 1600 (s, C–O *str*); ^{1}H NMR (CD_3OD, 400 MHz), δ: 2.0–2.5 (m, 4H), 3.39 (m, 3H), 3.83 (s, 2H), 6.61 (d, 2H, *J* = 9 Hz), 8.08 (d, 2H, *J* = 9 Hz) ppm; –LSIMS, *m/e* (relative intensity): 391 (2 × (M^- + 1), 17), 195 (M^-, 100), 179 (6.7); +LSIMS, *m/e* (relative intensity): 115 (M^+, 100), 70 (22). Anal. calcd. for **1.pro-amide**, $C_{13}H_{18}N_4O_5$: C 50.32, H 5.85, N 18.06; found: C 50.16, H 5.65, N 18.06.

Synthesis of the S*-(–)-proline methyl ester complex of **1**: **1.pro-meth***

The hydrochloride salt of *S*-(–)-proline methyl ester (54.4 mg, 0.329 mmol, Sigma) and 13.2 mg of NaOH (0.330 mmol, BDH) were dissolved in approximately 10 mL of ethanol, producing a cloudy precipitate (NaCl). The solution was centrifuged for 30 min, then added to a flask containing 66.2 mg of **1** (0.337 mmol) dissolved in approximately 150 mL of diethyl ether. The resultant bright yellow solution was rotary evaporated to near dryness, producing a yellow oil. Approximately 10 mL of acetone was added to the flask, then hexane was added until the solution became faintly cloudy. Over the course of several hours a light yellow solid precipitated along the walls of the flask. The crude product was recrystallized from ethanol (27.3 mg, 0.026 mmol, 15.5% yield); mp: two overlapping endotherms, the first peaking at 132.2°C, the second peaking at 138.2°C; IR (KBr disc), ν (cm^{-1}): 3377 (s, N–H *str*), 1746 (s, C=O *str*), 1607 (s, C–O *str*); ^{1}H NMR (D_2O, 400 MHz), δ: 2.0–2.5 (m, 4H), 3.4(m, 3H), 3.83 (s, 4H), 3.85 (s, 3H), 6.61 (d, 4H, *J* = 9 Hz), 8.09 (d, 4H, *J* = 9 Hz) ppm; –LSIMS, *m/e* (relative intensity): 391 (2 × (M^- + 1), 38), 195 (M^-, 100), 179 (5.6); +LSIMS, *m/e* (relative intensity): 130 (M^+, 100), 70 (24). Anal. calcd. for **1.pro-meth**, $C_{22}H_{27}N_5O_{10}$: C 50.67, H 5.22, N 13.43; found: C 50.63, H 5.17, N 13.42.

Synthesis of the S*-(–)-proline benzyl ester salt of **1**: **1.pro-benz***

The hydrochloride salt of *S*-(–)-proline benzyl ester (120.9 mg, 0.500 mmol, Sigma) and 32.4 mg of crushed KOH (0.579 mmol, Aldrich) were dissolved in 30 mL of ethanol, producing a

© 1998 NRC Canada

Fig. 2. Chemical structures considered in the CSD search for **PNA** analogs.

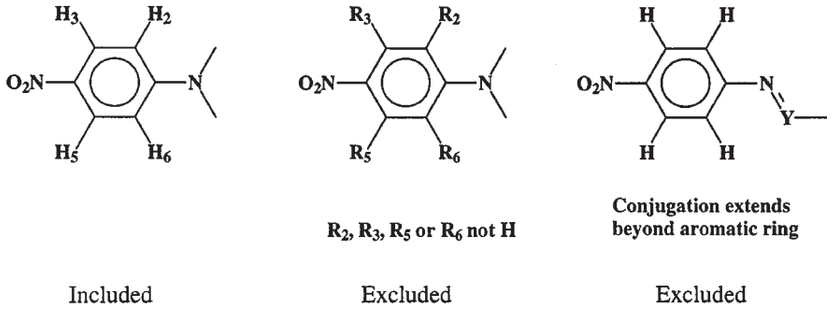

white solid precipitate (KCl). The solution was centrifuged for 10 min, after which the liquid was decanted and added to a solution of acid **1** (95.9 mg, 0.489 mmol) in 20 mL of ethanol. The resultant solution was rotary evaporated to dryness, leaving a bright yellow precipitate that was dried under vacuum. The crude product (180.6 mg, 0.450 mmol, 92% yield) was recrystallized from methanol; mp 130.5°C; IR (KBr disc), ν (cm^{-1}): 3277 (s, N–H *str*), 1732 (s, C=O *str*), 1603 (s, C–O *str*); ^{1}H NMR (CD_3OD, 400 MHz), δ: 2.0–2.5 (m, 4H), 3.4 (m, 2H), 3.83 (s, 2H), 4.5 (t, 1H, J = 9 Hz), 5.30 (m, 2H), 6.61 (d, 2H, J = 9 Hz), 7.45 (s, 5H), 8.08 (d, 2H, J = 9 Hz) ppm; –LSIMS, m/e (relative intensity): 391 (2 × (M^- + 1), 50), 195 (M^-, 100); +LSIMS, m/e (relative intensity): 206 (M^+, 100), 91 (51), 70 (24). Anal. calcd. for **1.pro-benz**, $C_{20}H_{23}N_3O_6$: C 59.84, H 5.78, N 10.47; found: C 59.60, H 5.85, N 10.54.

SHG measurements

Measurements were made using the Kurtz and Perry powder method (27). Approximately 50 mg of material were loaded into the sample cell, which was formed between two Pyrex 25 × 75 × 1 mm microscope slides (Canlab). Two strips of masking tape with a 2 cm diameter hole cut through the centre were placed 3 cm from the end of one of the slides. The circular window was filled with a thin layer of sample (~0.3 mm thick). The second microscope slide was clipped onto the first, sandwiching the sample between the slides.

The 1064 nm fundamental output from a Q-switched Nd:YAG laser (Quanta Ray) was divided by a beam splitter, where one portion of the light was directed onto a reference cell containing urea. The resultant second-harmonic signal (532 nm) was passed through a sharp-cut filter (Corning 527) designed to eliminate any stray visible light from the laser flash pump, and several neutral density filters (Wratten, 0.30 + 0.70) designed to attenuate the second-harmonic signal, before being focused onto a photomultiplier tube (RCA IP28). The second portion of the fundamental beam was directed onto a second cell containing the sample to be measured. Any second harmonic produced was passed through a series of neutral density filters (Wratten, 1.0 + 0.7), then focused into a monochromator (Beckman DU spectrophotometer, model 2400) in order to discriminate between SHG light and any stray visible light and IR light. Monochromatic 532 nm light was then directed onto a second photomultiplier (RCA IP28) for measurement. In order to measure the SHG efficiency of a given material accurately, urea was first placed in both the sample and reference cells and the relative SHG intensities were measured. The relative amounts of light directed onto the two photomultiplier tubes by the same material were then used to normalize subsequent measurements of relative intensities between a given material and urea. To gauge the accuracy of our experimental setup, the relative efficiency of **NPP** was measured. Large crystals of **NPP** and urea were crushed to a powder and passed through sieves in order to isolate the desired range of particle size. Using particles within the 125–149 μm diameter range for both urea and **NPP**, the relative SHG efficiency of 53 ± 5 for **NPP** was close to the relative efficiency of 60 previously reported (8). The SHG efficiencies of the acids, amines, and salts were first measured in the form of unsized powders. Single crystals, large enough to be crushed into a wide range of particle sizes (i.e., from ~250 μm to less than 125 μm in diameter), were grown (if possible), of any material displaying significant SHG intensity (approximately that of urea). These were then crushed and isolated on the basis of their particle size. SHG measurements were made over a series of particle size ranges in order to test for phase matchability. The SHG intensities quoted hereafter represent the measurements made with particles in the 125–149 μm diameter range.

Survey of the Cambridge Structural Database

As with all organic materials, the likelihood of a **PNA**-type molecule crystallizing in a non-centrosymmetric space group should be relatively small. While non-centrosymmetry is a prerequisite for SHG, it is insufficient by itself to ensure a strong SHG response. It is possible, for example, for chiral materials to adopt highly symmetric orientations within the crystal, and yet lack any formal centre of inversion. Materials crystallizing with their charge-transfer axes in an anti-parallel alignment adopt an orientation that is highly unfavorable for SHG. A survey of the Cambridge Structural Database (CSD) was undertaken in order to examine the packing trends of materials that are structurally similar to **PNA**. The survey was limited to materials that are unsubstituted at the 2, 3, 5, and 6 positions around the benzene ring, and whose conjugation does not extend beyond the amine nitrogen, as shown in Fig. 2.

The results of the survey, summarized in Table 1, found 119 molecules fitting the above criteria, 30 of which (25.2%) crystallized in non-centrosymmetric space groups. A further analysis of the packing geometries of the non-centrosymmetric structures was carried out by calculating the angle between the charge-transfer axes of the various symmetry-related molecules in each unit cell. Any two molecules with their charge-transfer axes separated by 175° or

© 1998 NRC Canada

Table 1. Packing trends of **PNA** analogs.[a]

Total	119		
Centrosymmetric	89		
		Achiral	Chiral
Non-centrosymmetric	30	16	14
Anti-parallel	9	2	7
Potential SHG compounds	21	14	7

[a]Results compiled from the Cambridge Structural Database (1996).

more were considered to be in an anti-parallel alignment. Of these molecules, 9 were found to be oriented in this way, leaving 21 (17.6%) as potential molecules for SHG. Of the 30 non-centrosymmetric structures found, 14 were composed of optically pure molecules and were thus forced to crystallize without a centre of inversion. Even with the addition of optical activity, half of these molecules (7) crystallized with an anti-parallel alignment of their molecular charge-transfer axes.

X-ray crystallographic analyses

General

Single crystals suitable for X-ray crystallographic analyses were grown and the structures of the materials determined for all but **1.pro-benz**. No solvent system was found in which **1.pro-benz** would recrystallize in any form other than a fine powder. Crystallographic data for **1, 1.eph, 1.pro-but, 1.pro-ol, 1.pro-amide**, and **1.pro-meth** appear in Table 2. The final unit cell parameters were obtained by least squares on the setting angles for 25 reflections with 2θ = 75.4°–99.9° for **1**, 2θ = 75.2°–98.8° for **1.eph**, 2θ = 55.3°–89.9° for **1.pro-but**, 2θ = 46.3°–72.1° for **1.pro-ol**, 2θ = 41.0°–67.8° for **1.pro-amide**, and 2θ = 51.3°–93.6° for **1.pro-meth**. The intensities of three standard reflections, measured every 200 reflections throughout the data collection, decayed linearly by 1.3% for **1.pro-but** and by 1.7% for **1.pro-meth**. All other crystals exhibited decay of less than 1%.

The data were processed, and corrected for Lorentz and polarization effects, decay, and absorption (based on three azimuthal scans). The structures were solved by direct methods, the coordinates of the non-hydrogen atoms being defined from an *E*-map or from subsequent difference Fourier syntheses and refined with anisotropic thermal parameters, with the exception of the disordered *p*-nitrophenylglycinate anion of **1.eph** (see subsequent discussion). Hydrogen atoms were located either from a difference map and refined isotropically or they were fixed in calculated positions with C—H = 0.98 Å and $B_H = 1.2\ B_{\text{bonded atom}}$. Neutral atom scattering factors for all atoms and anomalous dispersion corrections for non-hydrogen atoms were taken from the *International tables for X-ray crystallography* (29, 30). Final atomic coordinates and equivalent isotropic thermal parameters for all refined atoms are given in Table 3, and a summary of bond lengths and bond angles appears in Tables 4 and 5, respectively. Tables of unrefined hydrogen atom parameters, anisotropic thermal parameters, torsion angles, full bond lengths and bond angles, intermolecular contacts, and least-squares planes are available as supplementary material.[2]

Fig. 3. Crystal packing of **1**, viewed down the *b*-axis.

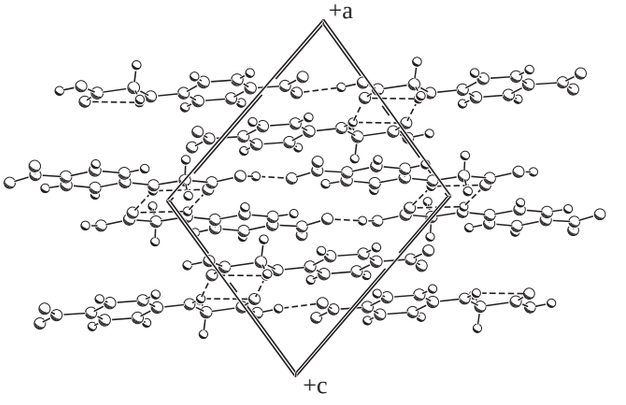

Fig. 4. ORTEP packing diagram of **1.eph** (50% probability ellipsoids). Only the major disordered fragment is shown. Hydrogens have been removed for clarity.

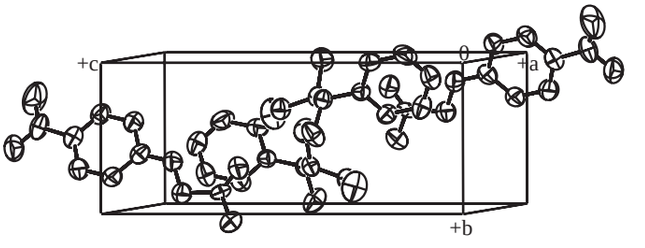

p-*Nitrophenylglycine (1)*

The SHG-inactive parent acid **(1)** crystallizes in centrosymmetric space group $P\bar{1}$. The packing of **1**, shown in Fig. 3, consists of two molecules per asymmetric unit. The carboxylic acid proton of each molecule is linked via intermolecular O—H···O hydrogen bonds to the NO_2 oxygens directly behind it. A second set of hydrogen bonds, in this case intermolecular N—H···O bonds, links each molecule to its symmetry-related neighbor, forming an infinite chain of oppositely oriented dimer pairs.

*Salt **1.eph***

The crystal packing of **1.eph** is shown in Fig. 4. The *p*-nitrophenylglycinate moiety is disordered such that it adopts two separate orientations, with the minor fragment related to the major fragment by rotating it about its charge-transfer axis by 180°. The directions of the charge-transfer axes of the major and minor fragments are then offset by approximately 16°. The orientations of both fragments are shown in Fig. 5. All of the atoms in the mi-

[2] Supplementary material may be purchased from: The Depository of Unpublished Data, Document Delivery, CISTI, National Research Council Canada, Ottawa, Canada K1A 0S2. Tables of hydrogen atom parameters, bond lengths, and bond angles have also been deposited with the Cambridge Crystallographic Data Centre, and can be obtained on request from: The Director, Cambridge Crystallographic Data Centre, University Chemical Laboratory, 12 Union Road, Cambridge, CB2 1EZ, U.K.

© 1998 NRC Canada

Table 2. Crystallographic data. [a]

Compound	**1**	**1.eph**	**1.pro-but**	**1.pro-ol**	**1.pro-amide**	**1.pro-meth**
Formula	$C_8H_8N_2O_4$	$C_{18}H_{23}N_3O_5$	$C_{17}H_{25}N_3O_6$	$C_{13}H_{19}N_3O_5$	$C_{13}H_{18}N_4O_5$	$C_{22}H_{27}N_5O_{10}$
fw	196.16	361.40	367.40	297.31	310.31	521.48
Crystal system	Triclinic	Monoclinic	Monoclinic	Orthorhombic	Monoclinic	Orthorhombic
Space group	$P\bar{1}$	$P2_1$	$P2_1$	$P2_12_12$	$P2_1$	$P2_12_12_1$
a, Å	9.687(1)	11.646(1)	5.4759(5)	13.280(3)	16.653(2)	14.595(1)
b, Å	10.089(1)	5.7799(8)	28.160(3)	26.182(3)	4.869(1)	24.152(2)
c, Å	9.328(1)	13.846 (1)	6.0041(7)	8.464(6)	17.585(2)	7.103(2)
α (°)	107.00(1)	90	90	90	90	90
β (°)	100.67(1)	99.121(6)	94.116(8)	90	99.17(1)	90
γ (°)	97.07(1)	90	90	90	90	90
V, Å^3	841.3(2)	920.2(2)	923.5(2)	2942(2)	1407.6(4)	2503.9(5)
Z	4	2	2	8	4	4
ρ_{calcd}, g/cm^3	1.55	1.30	1.32	1.34	1.46	1.38
F(000)	408	384	392	1264	656	1096
μ (Cu K_α), cm^{-1}	10.90	7.6	8.0	8.3	9.7	9.5
Crystal size, mm	0.18 × 0.20 × 0.25	0.07 × 0.20 × 0.50	0.25 × 0.20 × 0.10	0.15 × 0.15 × 0.20	0.45 × 0.18 × 0.10	0.25 × 0.20 × 0.40
Transmission factors	0.91–1.00	0.87–1.00	0.95–1.00	0.97–1.00	0.94–1.00	0.94–1.00
Scan type	ω-2θ	ω-2θ	ω-2θ	ω-2θ	ω-2θ	ω-2θ
Scan range,° in ω	1.10 + 0.20 tan θ	1.00 + 0.20 tan θ	1.00 + 0.20 tan θ	0.94 + 0.20 tan θ	0.94 + 0.20 tan θ	1.05 + 0.20 tan θ
Scan speed,°/min	32	16	16	8.0	8.0	32
Data collected	$+h, \pm k, \pm l$	$+h, +k, \pm l$	$+h, +k, \pm l$	$+h, +k, +l$	$+h, +k, \pm l$	$+h, +k, +l$
$2\theta_{max.}$,°	155.2	155.4	155.3	155.2	155.3	155.2
Crystal decay	Negligible	Negligible	1.3%	Negligible	Negligible	1.7%
Total reflections	3641	2179	2167	3575	3279	2972
Total unique reflections	3434	2083	1969	3575	3173	2972
R_{merge}	0.025	0.021	0.017		0.022	
Reflections with $I \geq 3\sigma(I)$	2148	1788	1672	2240	2151	2094
No. of variables	318	330	255	408	456	351
R	0.040	0.042	0.037	0.043	0.042	0.042
R_w	0.044	0.053	0.039	0.041	0.052	0.041
Goodness of fit (gof)	2.33	3.62	2.68	2.74	2.45	2.83
Max. Δ/σ (final cycle)	0.00	0.10	0.02	0.02	0.02	0.02
Residual density *e*/Å^3	–0.18 to +0.20	–0.14 to + 0.15	–0.14 to + 0.16	–0.16 to +0.14	–0.17 to 0.17	–0.21 to +0.21

[a]Temperature 294 K, Rigaku AFC6S diffractometer, Cu *K*α radiation (λ =1.54178 Å), graphite monochromator, takeoff angle 6.0°, aperture 6.0 × 6.0 mm at a distance of 285 mm from the crystal, stationary background counts at each end of the scan (scan:background time ratio 2:1), $\sigma^2(F^2) = [S^2(C + 4B)]/Lp^2$ (*S* = scan rate, *C* = scan count, *B* = normalized background count), function minimized $\Sigma w(|F_o| - |F_c|)^2$ where $w = 1/\sigma^2(F_o)$, $R = \Sigma||F_o| - |F_c||/\Sigma|F_o|$, $R_w = (\Sigma w(|F_o| - |F_c|)^2/\Sigma w|F_o|^2)^{1/2}$, and gof = $[\Sigma w(|F_o| - |F_c|)^2/(m - n)]^{1/2}$. Values given for *R*, R_w, and gof are based on those reflections with $I \geq 3\ \sigma(I)$.

© 1998 NRC Canada

Table 3. Final atomic coordinates (fractional) and *B*(eq) (10^3 Å^2).[a]

Atom	*x*	*y*	*z*	*B*(eq)	Occ.
1					
O(1)	0.2127(2)	0.5890(2)	–0.0957(2)	4.90(5)	
O(2)	0.2743(2)	0.7924(2)	–0.1211(2)	4.98(5)	
O(3)	1.0432(2)	0.8976(2)	0.6153(2)	4.12(5)	
O(4)	1.0136(2)	0.6958(2)	0.6696(2)	4.36(5)	
O(5)	0.3768(2)	0.5942(2)	0.5855(3)	6.22(6)	
O(6)	0.5111(2)	0.7945(2)	0.6290(2)	4.94(5)	
O(7)	–0.1646(2)	0.8950(2)	–0.1019(2)	4.69(5)	
O(8)	–0.3134(2)	0.6876(2)	–0.1789(2)	4.35(5)	
N(1)	0.7977(2)	0.8108(2)	0.3925(3)	3.53(5)	
N(2)	0.2972(2)	0.7010(2)	–0.0590(3)	3.60(5)	
N(3)	0.0159(2)	0.8165(2)	0.1074(3)	3.53(5)	
N(4)	0.4001(2)	0.7056(2)	0.5595(3)	3.82(6)	
C(1)	0.6736(3)	0.7836(3)	0.2848(3)	2.93(5)	
C(2)	0.5747(3)	0.6578(3)	0.2446(3)	3.01(6)	
C(3)	0.4514(3)	0.6302(3)	0.1316(3)	3.06(6)	
C(4)	0.4249(3)	0.7285(3)	0.0591(3)	3.16(6)	
C(5)	0.5206(3)	0.8547(3)	0.0990(4)	3.96(7)	
C(6)	0.6434(3)	0.8819(3)	0.2103(3)	3.80(7)	
C(7)	0.8343(3)	0.7186(3)	0.4790(4)	3.30(6)	
C(8)	0.9759(3)	0.7839(3)	0.5943(3)	3.19(6)	
C(9)	0.1074(2)	0.7886(3)	0.2188(3)	2.76(5)	
C(10)	0.0850(3)	0.6595(3)	0.2465(3)	3.08(6)	
C(11)	0.1797(3)	0.6327(3)	0.3592(3)	3.13(6)	
C(12)	0.2991(3)	0.7355(3)	0.4459(3)	2.97(6)	
C(13)	0.3217(3)	0.8646(3)	0.4220(3)	3.40(6)	
C(14)	0.2281(3)	0.8915(3)	0.3106(3)	3.32(6)	
C(15)	–0.1083(3)	0.7157(3)	0.0085(4)	3.25(6)	
C(16)	–0.1961(3)	0.7790(3)	–0.0948(3)	3.29(6)	
H(1)	0.592(2)	0.591(2)	0.294(3)	2.2(5)	
H(2)	0.389(3)	0.549(3)	0.105(3)	5.0(8)	
H(3)	0.495(3)	0.920(3)	0.049(3)	3.8(6)	
H(4)	0.707(3)	0.966(3)	0.240(3)	5.6(8)	
H(5)	0.853(3)	0.889(3)	0.417(3)	3.2(6)	
H(6)	0.842(3)	0.633(3)	0.418(3)	4.8(8)	
H(7)	0.767(3)	0.709(3)	0.539(3)	3.1(6)	
H(8)	1.102(4)	0.739(4)	0.734(4)	8(1)	
H(9)	0.001(3)	0.589(3)	0.186(3)	3.3(6)	
H(10)	0.159(3)	0.548(3)	0.374(3)	5.2(8)	
H(11)	0.405(3)	0.932(3)	0.489(3)	3.5(6)	
H(12)	0.248(3)	0.977(3)	0.290(3)	4.8(7)	
H(13)	0.033(3)	0.895(3)	0.093(3)	3.5(7)	
H(14)	–0.081(3)	0.639(3)	–0.053(3)	3.2(6)	
H(15)	–0.164(3)	0.688(3)	0.068(3)	3.9(7)	
H(16)	–0.368(3)	0.729(3)	–0.235(3)	5.1(8)	
1.eph					
O(1)	0.6030(5)	0.0917	–0.3098(4)	6.6(1)	0.75
O(1*)	0.530(2)	–0.350(4)	–0.230(2)	8.5(6)	0.25
O(2)	0.5305(9)	–0.233(2)	–0.2651(7)	10.3(3)	0.75
O(2*)	0.562(2)	–0.038(4)	–0.309(2)	8.0(5)	0.25
O(3)	0.7783(4)	0.211(1)	0.3407(3)	6.26(9)	0.75
O(3*)	0.783(1)	0.611(3)	0.253(1)	9.2(4)	0.25
O(4)	0.8483(3)	0.562(1)	0.3322(2)	5.21(8)	0.75
O(4*)	0.8127(9)	0.329(4)	0.3743(9)	7.9(4)	0.25
O(5)	0.9326(2)	0.977(1)	0.5745(2)	6.07(6)	
N(1)	0.7179(4)	0.172(1)	0.1486(3)	5.2(1)	0.75
N(1*)	0.7403(9)	0.311(2)	0.1093(8)	4.7(3)	0.25
N(2)	0.5803(5)	–0.048(2)	–0.2441(4)	5.2(1)	0.75
N(2*)	0.558(2)	–0.164(5)	–0.243(2)	6.0(6)	0.25
N(3)	0.7485(2)	0.822(1)	0.4525(2)	4.50(6)	
C(1)	0.6850(4)	0.124(1)	0.0529(3)	4.37(10)	0.75
C(1*)	0.696(2)	0.194(5)	0.030(1)	11.289	0.25
C(2)	0.7067(4)	0.275(1)	–0.0203(4)	4.9(1)	0.75
C(2*)	0.647(2)	–0.026(5)	0.031(1)	11.289	0.25
C(3)	0.6727(4)	0.225(1)	–0.1186(4)	5.1(1)	0.75
C(3*)	0.599(2)	–0.131(3)	–0.057(2)	11.289	0.25
C(4)	0.6136(5)	0.019(1)	–0.1442(4)	4.4(1)	0.75
C(4*)	0.602(2)	–0.017(5)	–0.146(1)	11.289	0.25
C(5)	0.5904(6)	–0.133(1)	–0.0727(4)	4.9(1)	0.75
C(5*)	0.652(2)	0.202(5)	–0.146(1)	11.289	0.25
C(6)	0.6239(5)	–0.082(1)	0.0242(3)	5.0(1)	0.75
C(6*)	0.699(2)	0.308(3)	–0.058(2)	11.289	0.25
C(7)	0.7768(4)	0.377(1)	0.1845(3)	4.9(1)	0.75
C(7*)	0.743(1)	0.220(3)	0.207(1)	5.3(4)	0.25
C(8)	0.798(1)	0.368(2)	0.2950(7)	3.9(2)	0.75
C(8*)	0.795(3)	0.442(6)	0.290(3)	5.8(7)	0.25
C(9)	0.9182(2)	0.697(1)	0.7043(2)	3.71(5)	
C(10)	0.8817(2)	0.848(1)	0.7693(2)	4.40(6)	
C(11)	0.8984(3)	0.799(1)	0.8686(2)	5.21(8)	
C(12)	0.9536(3)	0.599(1)	0.9027(2)	5.52(8)	
C(13)	0.9920(3)	0.449(1)	0.8393(3)	5.95(8)	
C(14)	0.9742(3)	0.496(1)	0.7392(2)	5.07(7)	
C(15)	0.8961(2)	0.748(1)	0.5955(2)	4.06(6)	
C(16)	0.7676(2)	0.737(1)	0.5560(2)	4.00(6)	
C(17)	0.7188(3)	0.498(1)	0.5624(3)	6.43(9)	
C(18)	0.6255(3)	0.863(1)	0.4103(3)	7.5(1)	
H(5)	0.702(4)	0.09(1)	0.201(4)	5(1)	
H(14)	0.991(4)	0.98(1)	0.587(3)	10(1)	
H(19)	0.783(3)	0.702(8)	0.419(3)	5.7(9)	
H(20)	0.784(2)	0.941(6)	0.447(2)	3.1(6)	
1.pro-but					
O(1)	0.0840(4)	0.6158	0.2968(5)	8.45(7)	
O(2)	0.1700(5)	0.6447(1)	0.6244(4)	9.75(8)	
O(3)	1.0791(3)	0.4380(1)	1.1467(2)	4.28(3)	
O(4)	0.7539(3)	0.43862(9)	0.9054(2)	3.93(3)	
O(5)	0.1666(3)	0.3212(1)	1.0380(3)	6.06(4)	
O(6)	0.4539(2)	0.26792(9)	0.9564(2)	3.65(3)	
N(1)	0.9884(3)	0.4897(1)	0.5932(3)	4.10(4)	
N(2)	0.2054(5)	0.6165(1)	0.4743(5)	6.75(6)	
N(3)	0.5168(3)	0.3864(1)	1.1846(3)	3.05(3)	
C(1)	0.7979(4)	0.5208(1)	0.5701(3)	3.51(4)	
C(2)	0.6606(4)	0.5239(1)	0.3654(3)	4.10(4)	
C(3)	0.4665(4)	0.5546(1)	0.3342(4)	4.46(5)	
C(4)	0.4109(4)	0.5838(1)	0.5094(4)	4.60(5)	
C(5)	0.5442(5)	0.5821(1)	0.7109(4)	5.04(5)	
C(6)	0.7351(5)	0.5509(1)	0.7442(4)	4.42(5)	
C(7)	1.1159(4)	0.4776(1)	0.8027(4)	4.20(5)	
C(8)	0.9707(4)	0.4487(1)	0.9644(3)	3.21(4)	
C(9)	0.5893(3)	0.3366(1)	1.1356(3)	2.87(3)	
C(10)	0.6918(4)	0.3163(1)	1.3579(3)	4.25(5)	
C(11)	0.565(2)	0.3509(3)	1.526(1)	4.8(1)	0.29
C(11*)	0.7750(6)	0.3585(1)	1.4947(4)	3.96(6)	0.71
C(12)	0.5727(4)	0.3950(1)	1.4283(3)	4.24(4)	

Table 3 (*continued*).

© 1998 NRC Canada

Table 3 (*continued*).

Atom	*x*	*y*	*z*	*B*(eq)	Occ.
C(13)	0.3754(3)	0.3082(1)	1.0358(3)	3.26(4)	
C(14)	0.2835(3)	0.2286(1)	0.8785(3)	3.48(4)	
C(15)	0.1028(4)	0.2466(1)	0.6945(4)	4.93(5)	
C(16)	0.4565(4)	0.1927(1)	0.7906(5)	6.08(7)	
C(17)	0.1594(5)	0.2101(1)	1.0739(4)	5.32(6)	
H(5)	1.019(4)	0.4723(8)	0.473(4)	4.5(5)	
H(8)	0.617(5)	0.409(1)	1.064(5)	7.8(7)	
H(9)	0.363(5)	0.3932(8)	1.135(4)	5.4(6)	
1.pro-ol					
O(1)	–0.2463(3)	0.5213(2)	0.4290(6)	9.1(2)	
O(2)	–0.1206(3)	0.4908(1)	0.5589(6)	8.2(1)	
O(3)	–0.0799(3)	0.7803(1)	0.5426(4)	5.1(1)	
O(4)	–0.2095(3)	0.8282(1)	0.6062(5)	5.7(1)	
O(5)	–0.0357(3)	0.7928(2)	0.1141(6)	8.3(1)	
O(6)	0.2541(3)	0.9828(2)	1.0776(6)	8.4(2)	
O(7)	0.1203(3)	1.0112(1)	0.9645(6)	8.0(1)	
O(8)	0.0877(3)	0.7261(1)	0.9520(4)	4.76(9)	
O(9)	0.2093(3)	0.6732(1)	0.8895(4)	4.80(9)	
O(10)	0.0532(4)	0.7142(2)	1.3798(6)	9.1(1)	
N(1)	–0.1129(3)	0.7161(2)	0.8039(6)	4.5(1)	
N(2)	–0.1770(4)	0.5259(2)	0.5232(7)	6.0(1)	
N(3)	–0.1432(3)	0.8644(1)	0.2970(6)	3.67(9)	
N(4)	0.1237(3)	0.7892(1)	0.6937(6)	4.3(1)	
N(5)	0.1802(4)	0.9766(2)	0.9926(6)	5.8(1)	
N(6)	0.1499(3)	0.6377(2)	1.1836(6)	4.2(1)	
C(1)	–0.1293(3)	0.6711(2)	0.7324(6)	3.8(1)	
C(2)	–0.2114(4)	0.6622(2)	0.6309(7)	4.4(1)	
C(3)	–0.2252(4)	0.6151(2)	0.5639(6)	4.9(1)	
C(4)	–0.1605(4)	0.5756(2)	0.5962(7)	4.4(1)	
C(5)	–0.0780(4)	0.5824(2)	0.6954(7)	4.5(1)	
C(6)	–0.0635(3)	0.6295(2)	0.7600(6)	4.1(1)	
C(7)	–0.1718(4)	0.7616(2)	0.7803(6)	4.4(1)	
C(8)	–0.1508(4)	0.7913(2)	0.6307(7)	3.9(1)	
C(9)	–0.0496(3)	0.8769(2)	0.2066(6)	4.1(1)	
C(10)	–0.0070(4)	0.9219(2)	0.2971(9)	6.4(2)	
C(11)	–0.0905(5)	0.9444(2)	0.3908(8)	6.9(2)	
C(12)	–0.1828(4)	0.9146(2)	0.3514(7)	5.4(1)	
C(13)	0.0177(3)	0.8313(2)	0.1944(6)	5.2(1)	
C(14)	0.1381(4)	0.8333(2)	0.7734(6)	3.9(1)	
C(15)	0.2219(4)	0.8425(2)	0.8697(7)	4.6(1)	
C(16)	0.2352(3)	0.8892(2)	0.9411(6)	4.5(1)	
C(17)	0.1656(4)	0.9275(2)	0.9187(7)	4.5(1)	
C(18)	0.0824(4)	0.9188(2)	0.8262(8)	4.6(1)	
C(19)	0.0672(4)	0.8726(2)	0.7552(6)	4.3(1)	
C(20)	0.1837(4)	0.7434(2)	0.7166(6)	4.3(1)	
C(21)	0.1582(3)	0.7126(2)	0.8640(7)	3.6(1)	
C(22)	0.0401(4)	0.6374(2)	1.2268(6)	4.6(1)	
C(23)	0.0127(4)	0.5811(2)	1.2258(9)	7.5(2)	
C(24)	0.0916(5)	0.5552(2)	1.1293(9)	7.0(2)	
C(25)	0.1828(4)	0.5837(2)	1.1678(8)	5.6(1)	
C(26)	0.0229(4)	0.6632(2)	1.3825(8)	7.0(2)	
H(5)	–0.065(2)	0.722(1)	0.851(5)	1.8(9)	
H(8)	–0.127(4)	0.840(2)	0.389(7)	7(1)	
H(9)	–0.179(3)	0.848(1)	0.222(5)	3(1)	
H(19)	0.004(3)	0.770(2)	0.084(6)	6(1)	
H(24)	0.067(4)	0.789(2)	0.608(8)	9(1)	
H(27)	0.169(4)	0.653(2)	1.074(7)	8(1)	

Table 3 (*continued*).

Atom	*x*	*y*	*z*	*B*(eq)	Occ.
H(28)	0.197(4)	0.654(2)	1.254(6)	5(1)	
1.pro-amide					
O(1)	–0.3287(1)	–0.115(2)	0.3202(2)	6.49(8)	
O(2)	–0.3491(2)	–0.075(2)	0.4375(2)	7.31(9)	
O(3)	0.0707(1)	0.480(2)	0.3952(1)	3.17(5)	
O(4)	0.0794(1)	0.791(2)	0.3055(1)	3.58(5)	
O(5)	0.1996(2)	0.540(2)	0.1615(2)	5.55(6)	
O(6)	0.8332(1)	0.838(2)	0.1823(2)	6.18(8)	
O(7)	0.8593(2)	0.778(2)	0.0679(2)	6.78(9)	
O(8)	0.4311(1)	0.254(2)	0.1028(2)	4.87(7)	
O(9)	0.4339(2)	–0.018(2)	0.2033(1)	4.77(6)	
O(10)	0.2971(1)	0.753(2)	0.3381(1)	4.68(6)	
N(1)	–0.0624(1)	0.758(2)	0.4426(1)	2.77(6)	
N(2)	–0.3117(2)	–0.013(2)	0.3846(2)	4.38(7)	
N(3)	0.0757(2)	0.273(2)	0.2252(1)	2.89(6)	
N(4)	0.2603(2)	0.132(2)	0.1488(2)	4.30(7)	
N(5)	0.5659(2)	–0.030(2)	0.0583(2)	3.80(7)	
N(6)	0.8197(2)	0.730(2)	0.1190(2)	4.62(7)	
N(7)	0.4210(2)	0.477(2)	0.2787(2)	3.50(6)	
N(8)	0.2359(2)	0.347(2)	0.3564(2)	3.58(6)	
C(1)	–0.1232(2)	0.571(2)	0.4269(2)	2.64(6)	
C(2)	–0.1423(2)	0.440(2)	0.3552(2)	2.97(6)	
C(3)	–0.2030(2)	0.248(2)	0.3421(2)	3.11(7)	
C(4)	–0.2471(2)	0.185(2)	0.4000(2)	3.28(6)	
C(5)	–0.2304(2)	0.312(2)	0.4712(2)	3.37(6)	
C(6)	–0.1691(2)	0.499(2)	0.4847(2)	3.23(7)	
C(7)	–0.0195(2)	0.870(2)	0.3841(2)	2.73(6)	
C(8)	0.0480(2)	0.696(2)	0.3609(2)	2.48(6)	
C(9)	0.1250(2)	0.131(2)	0.1721(2)	3.65(7)	
C(10)	0.0648(5)	0.075(3)	0.1016(4)	5.1(1)	0.70
C(10*)	0.069(1)	0.206(7)	0.0860(9)	11.1(7)	0.30
C(11)	–0.0011(3)	0.283(2)	0.0995(2)	6.1(1)	
C(12)	–0.0084(2)	0.319(2)	0.1823(2)	4.54(8)	
C(13)	0.1994(2)	0.293(2)	0.1619(2)	3.27(6)	
C(14)	0.6270(2)	0.154(2)	0.0744(2)	3.19(7)	
C(15)	0.6441(2)	0.290(2)	0.1455(2)	3.34(7)	
C(16)	0.7056(2)	0.477(2)	0.1594(2)	3.61(7)	
C(17)	0.7536(2)	0.532(2)	0.1035(2)	3.51(7)	
C(18)	0.7392(2)	0.398(2)	0.0335(2)	4.42(8)	
C(19)	0.6776(2)	0.211(2)	0.0186(2)	4.09(8)	
C(20)	0.5219(2)	–0.134(2)	0.1171(2)	3.53(8)	
C(21)	0.4574(2)	0.053(2)	0.1418(2)	3.44(7)	
C(22)	0.3732(2)	0.343(2)	0.3332(2)	3.76(7)	
C(23)	0.4323(2)	0.320(2)	0.4072(2)	7.8(1)	
C(24)	0.4946(7)	0.481(3)	0.4036(6)	6.3(2)	0.50
C(24*)	0.5162(6)	0.352(3)	0.3867(6)	5.3(2)	0.50
C(25)	0.5078(2)	0.502(2)	0.3175(2)	5.7(1)	
C(26)	0.2969(2)	0.505(2)	0.3418(2)	3.13(6)	
H(5)	–0.063(2)	0.83(1)	0.488(2)	6.2(9)	
H(8)	0.101(2)	0.47(1)	0.251(2)	7(1)	
H(9)	0.074(3)	0.16(1)	0.276(3)	11(1)	
H(17)	0.259(2)	–0.080(9)	0.148(2)	5.2(9)	
H(18)	0.304(2)	0.217(9)	0.139(2)	6(1)	
H(23)	0.558(2)	–0.106(8)	0.016(2)	3.4(7)	
H(26)	0.419(2)	0.363(9)	0.231(2)	4.5(7)	
H(27)	0.403(2)	0.66(1)	0.255(2)	5.8(9)	
H(35)	0.247(2)	0.166(8)	0.356(2)	3.2(7)	

© 1998 NRC Canada

Table 3 (*concluded*).

Atom	*x*	*y*	*z*	*B*(eq)	Occ.
H(36)	0.187(2)	0.42(1)	0.368(2)	7(1)	
1.pro-meth					
O(1)	1.4594(2)	–0.1569(1)	0.5960(6)	8.2(1)	
O(2)	1.4355(2)	–0.2331(1)	0.4488(7)	8.1(1)	
O(3)	0.8503(2)	–0.1439(1)	0.5227(6)	6.97(9)	
O(4)	0.8474(2)	–0.0595(1)	0.6498(5)	5.23(7)	
O(5)	0.0677(2)	0.0416(1)	0.4823(6)	8.1(1)	
O(6)	0.0918(2)	0.1172(1)	0.6331(6)	7.6(1)	
O(7)	0.6621(2)	0.0164(1)	0.6843(5)	5.55(8)	
O(8)	0.6810(2)	–0.0634(1)	0.5360(4)	4.92(7)	
O(9)	0.6109(2)	0.1403(1)	0.5620(6)	7.7(1)	
O(10)	0.6474(2)	0.2291(1)	0.5907(6)	7.6(1)	
N(1)	1.0311(2)	–0.1542(1)	0.5659(6)	4.60(8)	
N(2)	1.4077(2)	–0.1916(1)	0.5279(7)	5.7(1)	
N(3)	0.4937(2)	0.0308(1)	0.5715(6)	4.19(8)	
N(4)	0.1194(2)	0.0750(2)	0.5566(6)	5.4(1)	
N(5)	0.7774(2)	0.1043(1)	0.6846(5)	4.61(8)	
C(1)	1.1227(2)	–0.1641(1)	0.5633(6)	3.75(8)	
C(2)	1.1572(2)	–0.2134(1)	0.4871(6)	4.21(9)	
C(3)	1.2497(3)	–0.2225(1)	0.4742(7)	4.5(1)	
C(4)	1.3092(2)	–0.1827(1)	0.5425(7)	4.22(9)	
C(5)	1.2781(3)	–0.1344(2)	0.6222(6)	4.30(9)	
C(6)	1.1849(2)	–0.1246(1)	0.6306(6)	4.12(9)	
C(7)	0.9895(2)	–0.1037(2)	0.6278(6)	4.6(1)	
C(8)	0.8883(3)	–0.1045(2)	0.5952(7)	4.7(1)	
C(9)	0.4026(2)	0.0412(1)	0.5621(6)	3.55(8)	
C(10)	0.3684(2)	0.0919(1)	0.6323(6)	4.10(9)	
C(11)	0.2767(3)	0.1028(1)	0.6279(6)	4.4(1)	
C(12)	0.2165(2)	0.0643(1)	0.5528(6)	4.02(9)	
C(13)	0.2480(3)	0.0150(1)	0.4803(6)	4.05(9)	
C(14)	0.3406(2)	0.0035(1)	0.4836(6)	3.85(9)	
C(15)	0.5362(2)	–0.0203(2)	0.5161(7)	4.45(9)	
C(16)	0.6348(2)	–0.0211(2)	0.5846(6)	4.08(9)	
C(17)	0.7606(3)	0.1651(2)	0.6707(7)	5.2(1)	
C(18)	0.8356(4)	0.1853(2)	0.541(1)	10.4(2)	
C(19)	0.8632(4)	0.1401(2)	0.4309(9)	9.8(2)	
C(20)	0.8461(3)	0.0888(2)	0.5376(8)	6.5(1)	
C(21)	0.6647(3)	0.1753(2)	0.6021(7)	5.3(1)	
C(22)	0.5548(4)	0.2444(2)	0.527(1)	9.2(2)	
H(5)	0.998(2)	–0.181(1)	0.535(5)	3.5(8)	
H(8)	0.771(4)	–0.057(2)	0.60(1)	14(1)	
H(13)	0.532(2)	0.053(1)	0.634(6)	5(1)	
H(23)	0.718(3)	0.083(2)	0.673(8)	8(1)	

[a] $B_{eq} = (8/3)\pi^2\Sigma\Sigma(U_{ij}a_i^*a_j^*(\mathbf{a}_i\mathbf{a}_j))$.

nor fragment were eventually found from large peaks on the difference maps. This fragment, however, was severely distorted, particularly the aromatic ring, therefore the ring was modeled as a rigid body with idealized positions and bond lengths of 1.39 Å. The relative populations of the major and minor fragments were refined to 0.75 and 0.25, respectively. There is no evidence of disorder in the pseudoephedrinium moiety.

*Salt **1.pro-but***

The crystal packing of **1.pro-but**, shown in Fig. 6, consists of alternating layers of cations and anions stacked one upon the other along the *b*-axis of the unit cell. Each layer of

Table 4. Selected bond lengths (Å) with estimated standard deviations in parentheses.

Bond	Length	Bond	Length
1			
O(1)—N(2)	1.227(3)	C(1)—C(2)	1.400(3)
O(2)—N(2)	1.246(3)	C(1)—C(6)	1.397(4)
O(3)—C(8)	1.191(3)	C(2)—C(3)	1.376(3)
O(4)—C(8)	1.329(3)	C(3)—C(4)	1.378(4)
O(5)—N(4)	1.221(3)	C(4)—C(5)	1.387(3)
O(6)—N(4)	1.243(3)	C(5)—C(6)	1.365(4)
O(7)—C(16)	1.196(3)	C(7)—C(8)	1.513(3)
O(8)—C(16)	1.321(3)	C(9)—C(10)	1.399(3)
N(1)—C(1)	1.356(3)	C(9)—C(14)	1.410(3)
N(1)—C(7)	1.434(3)	C(10)—C(11)	1.375(3)
N(2)—C(4)	1.433(3)	C(11)—C(12)	1.391(3)
N(3)—C(9)	1.355(3)	C(12)—C(13)	1.383(4)
N(3)—C(15)	1.439(3)	C(13)—C(14)	1.361(3)
N(4)—C(12)	1.431(3)	C(15)—C(16)	1.500(4)
1.eph			
O(1)—N(2)	1.275(9)	C(7)—C(8)	1.51(1)
O(2)—N(2)	1.23(2)	C(9)—C(15)	1.516(4)
O(3)—C(8)	1.15(1)	O(1*)—N(2*)	1.15(4)
O(4)—C(8)	1.33(1)	O(2*)—N(2*)	1.18(4)
O(5)—C(15)	1.430(9)	O(3*)—C(8*)	1.11(4)
N(1)—C(1)	1.348(6)	O(4*)—C(8*)	1.32(5)
N(1)—C(7)	1.42(1)	N(1*)—C(7*)	1.45(2)
N(2)—C(4)	1.428(8)	C(7*)—C(8*)	1.76(4)
1.pro-but			
O(3)—C(8)	1.244(4)	N(1)—C(7)	1.435(5)
O(4)—C(8)	1.247(4)	N(2)—C(4)	1.457(5)
O(5)—C(13)	1.201(4)	C(10)—C(11)	1.496(6)
O(6)—C(13)	1.314(3)	C(11)—C(12)	1.542(6)
O(6)—C(14)	1.500(4)	C(10)—C(11*)	1.60(1)
N(1)—C(1)	1.362(4)	C(11*)—C(12)	1.37(1)
1.pro-ol			
O(3)—C(8)	1.235(6)	N(1)—C(1)	1.344(6)
O(4)—C(8)	1.259(5)	N(1)—C(7)	1.439(5)
O(5)—C(13)	1.407(6)	N(2)—C(4)	1.458(7)
O(8)—C(21)	1.247(5)	N(4)—C(14)	1.352(6)
O(9)—C(21)	1.253(5)	N(4)—C(20)	1.453(5)
O(10)—C(26)	1.394(6)	N(5)—C(17)	1.443(6)
1.pro-amide			
O(3)—C(8)	1.241(6)	N(5)—C(20)	1.449(6)
O(4)—C(8)	1.265(5)	N(6)—C(17)	1.455(7)
O(5)—C(13)	1.201(6)	N(8)—C(26)	1.332(6)
O(8)—C(21)	1.238(7)	C(9)—C(10)	1.49(1)
O(9)—C(21)	1.255(6)	C(10)—C(11)	1.49(1)
O(10)—C(26)	1.209(6)	C(9)—C(10*)	1.69(3)
N(1)—C(1)	1.356(6)	C(10*)—C(11)	1.28(4)
N(1)—C(7)	1.448(5)	C(23)—C(24)	1.50(2)
N(2)—C(4)	1.437(7)	C(24)—C(25)	1.41(2)
N(4)—C(13)	1.331(6)	C(23)—C(24*)	1.31(2)
N(5)—C(14)	1.354(7)	C(24*)—C(25)	1.57(2)
1.pro-meth			
O(3)—C(8)	1.218(5)	N(1)—C(1)	1.359(4)
O(4)—C(8)	1.299(4)	N(1)—C(7)	1.432(5)
O(7)—C(16)	1.217(4)	N(2)—C(4)	1.456(5)
O(8)—C(16)	1.272(4)	N(3)—C(9)	1.355(4)
O(9)—C(21)	1.188(5)	N(3)—C(15)	1.436(5)
O(10)—C(21)	1.326(5)	N(4)—C(12)	1.441(4)
O(10)—C(22)	1.472(6)		

© 1998 NRC Canada

Table 5. Selected bond angles (°) with estimated standard deviations in parentheses.

Bonds	Angle	Bonds	Angle
1			
C(1)-N(1)-C(7)	123.3(2)	N(1)-C(7)-C(8)	109.7(2)
O(1)-N(2)-O(2)	121.6(2)	O(3)-C(8)-O(4)	125.0(2)
O(1)-N(2)-C(4)	119.6(2)	O(3)-C(8)-C(7)	125.1(2)
O(2)-N(2)-C(4)	118.8(2)	O(4)-C(8)-C(7)	109.9(2)
C(9)-N(3)-C(15)	122.7(2)	N(3)-C(9)-C(10)	121.6(2)
O(5)-N(4)-O(6)	121.5(2)	N(3)-C(9)-C(14)	119.8(2)
O(5)-N(4)-C(12)	119.9(2)	C(10)-C(9)-C(14)	118.6(2)
O(6)-N(4)-C(12)	118.6(2)	C(9)-C(10)-C(11)	120.8(2)
N(1)-C(1)-C(2)	121.5(2)	C(10)-C(11)-C(12)	119.3(2)
N(1)-C(1)-C(6)	119.7(2)	N(4)-C(12)-C(11)	119.2(2)
C(2)-C(1)-C(6)	118.7(2)	N(4)-C(12)-C(13)	120.0(2)
C(1)-C(2)-C(3)	120.6(2)	C(11)-C(12)-C(13)	120.8(2)
C(2)-C(3)-C(4)	119.4(2)	C(12)-C(13)-C(14)	120.1(2)
N(2)-C(4)-C(3)	120.0(2)	C(9)-C(14)-C(13)	120.5(2)
N(2)-C(4)-C(5)	119.3(2)	N(3)-C(15)-C(16)	111.1(2)
C(3)-C(4)-C(5)	120.8(2)	O(7)-C(16)-O(8)	124.5(2)
C(4)-C(5)-C(6)	119.9(3)	O(7)-C(16)-C(15)	125.3(2)
C(1)-C(6)-C(5)	120.5(3)	O(8)-C(16)-C(15)	110.3(2)
1.eph			
C(1)-N(1)-C(7)	124.2(6)	C(1*)-N(1*)-C(7*)	124(4)
O(1)-N(2)-O(2)	121.7(7)	O(1*)-N(2*)-O(2*)	139(3)
C(16)-N(3)-C(18)	114.7(3)	O(5)-C(15)-C(9)	112.0(4)
O(3)-C(8)-O(4)	124.5(8)	O(3*)-C(8*)-O(4*)	147(4)
1.pro-but			
C(13)-O(6)-C(14)	122.5(2)	C(10)-C(11)-C(12)	101.6(3)
C(1)-N(1)-C(7)	124.3(3)	C(10)-C(11*)-C(12)	104.7(8)
O(1)-N(2)-O(2)	123.3(4)	N(3)-C(12)-C(11)	103.8(3)
C(9)-N(3)-C(12)	107.9(2)	N(3)-C(12)-C(11*)	105.1(6)
O(3)-C(8)-O(4)	125.4(3)	O(5)-C(13)-O(6)	127.1(3)
C(9)-C(10)-C(11)	105.2(3)	O(5)-C(13)-C(9)	123.2(3)
C(9)-C(10)-C(11*)	100.1(5)	O(6)-C(13)-C(9)	109.7(2)
1.pro-ol			
C(1)-N(1)-C(7)	125.2(5)	C(22)-N(6)-C(25)	107.7(4)
O(1)-N(2)-O(2)	123.2(6)	O(3)-C(8)-O(4)	123.4(5)
C(9)-N(3)-C(12)	104.9(4)	O(5)-C(13)-C(9)	107.7(4)
C(14)-N(4)-C(20)	124.2(4)	O(8)-C(21)-O(9)	122.5(5)
O(6)-N(5)-O(7)	122.2(6)	O(10)-C(26)-C(22)	111.9(5)
1.pro-amide			
C(1)-N(1)-C(7)	123.0(4)	C(10*)-C(11)-C(12)	116(1)
O(1)-N(2)-O(2)	121.7(5)	O(5)-C(13)-N(4)	125.8(6)
C(9)-N(3)-C(12)	108.3(4)	O(5)-C(13)-C(9)	121.9(5)
C(14)-N(5)-C(20)	122.0(5)	N(4)-C(13)-C(9)	112.2(5)
O(6)-N(6)-O(7)	123.2(5)	O(8)-C(21)-O(9)	124.3(5)
C(22)-N(7)-C(25)	108.6(4)	C(22)-C(23)-C(24)	106.8(7)
O(3)-C(8)-O(4)	123.6(4)	C(22)-C(23)-C(24*)	109.1(9)
N(3)-C(9)-C(10)	103.9(6)	C(23)-C(24)-C(25)	107(1)
N(3)-C(9)-C(10*)	100(1)	C(23)-C(24*)-C(25)	109(1)
C(10)-C(9)-C(13)	117.1(5)	N(7)-C(25)-C(24)	107.8(8)
C(10*)-C(9)-C(13)	97(1)	N(7)-C(25)-C(24*)	99.1(8)
C(9)-C(10)-C(11)	106.8(8)	O(10)-C(26)-N(8)	126.6(5)
C(9)-C(10*)-C(11)	107(2)	O(10)-C(26)-C(22)	120.1(5)
C(10)-C(11)-C(12)	103.2(6)	N(8)-C(26)-C(22)	113.2(4)
1.pro-meth			
C(21)-O(10)-C(22)	116.1(4)	O(3)-C(8)-O(4)	124.8(4)
C(1)-N(1)-C(7)	124.9(3)	O(7)-C(16)-O(8)	125.5(4)
O(1)-N(2)-O(2)	122.6(4)	O(9)-C(21)-O(10)	123.8(5)
C(9)-N(3)-C(15)	124.8(3)	O(9)-C(21)-C(17)	125.3(4)
O(5)-N(4)-O(6)	122.6(4)	O(10)-C(21)-C(17)	111.0(4)
C(17)-N(5)-C(20)	108.1(4)		

Fig. 5. Orientations of the disordered *p*-nitrophenylglycinate anion in **1.eph**. The major fragment, with labeled atoms, makes an angle of θ_{maj} = 76.7° to the *b*-axis, while the minor fragment, unlabeled, makes an angle of θ_{min} = 61.0° to the same axis.

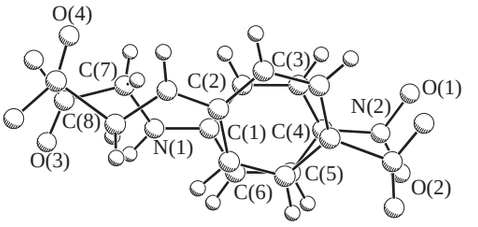

Fig. 6. ORTEP packing diagram of **1.pro-but** (50% probability ellipsoids).

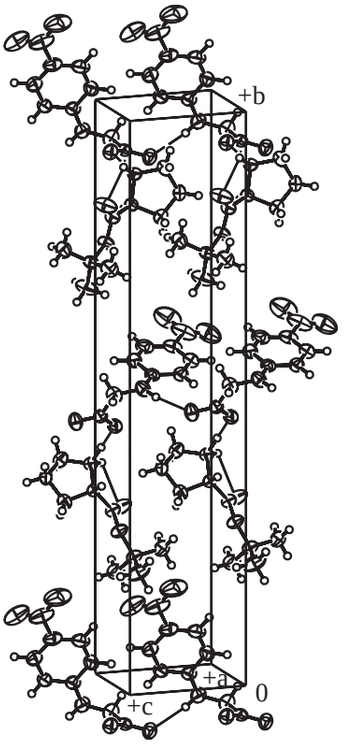

anions is an infinite chain formed by intermolecular N—H···O hydrogen-bonds between glycinate functionalities on adjacent anions. The proline *tert*-butyl ester cations comprising the cation layer are linked to each other, while the proline NH's are linked to the anion layer above, also via N—H···O hydrogen-bonds. The only disorder is found in the proline ring, which is found to adopt both of the "envelope" conformations.

*Salts **1.pro-ol** and **1.pro-amide***

Each salt packs with two formula units in the asymmetric unit, with their two *p*-nitrophenylglycinate moieties related by pseudo centres of inversion (Figs. 7 and 8). In the case of **1.pro-ol**, both *p*-nitrophenylglycinate units are linked by a pair of N—H···O hydrogen bonds between the glycine NH and carboxylate O to form a dimer. In the case of **1.pro-amide**, each prolinamide cation is bound via N—H···O hydrogen bonds to both *p*-nitrophenylglycinate

© 1998 NRC Canada

Fig. 7. ORTEP diagram of **1.pro-ol** (50% probability ellipsoids).

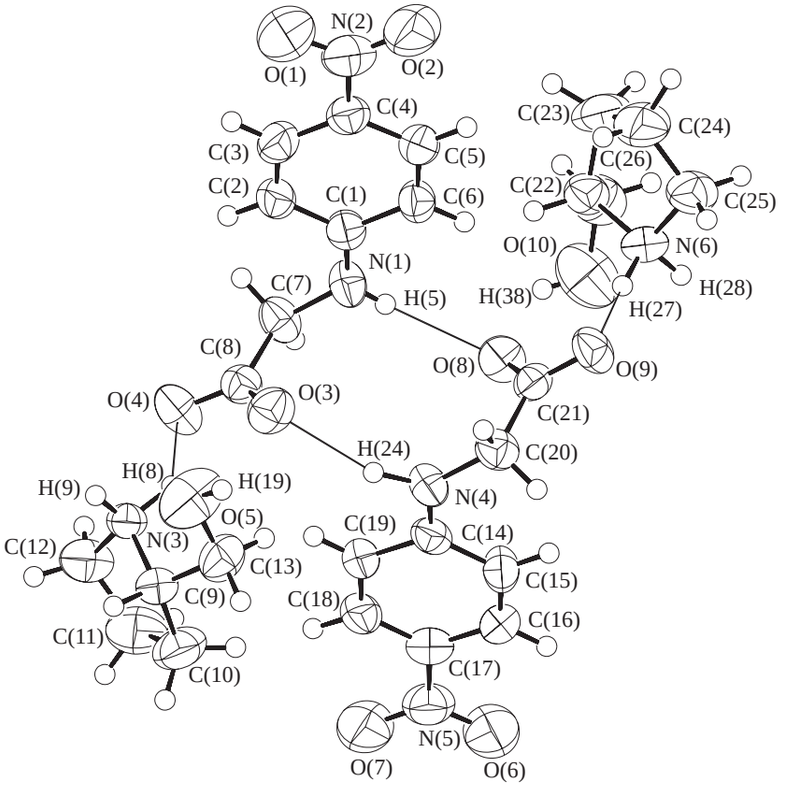

Fig. 8. ORTEP diagram of **1.pro-amide** (50% probability ellipsoids).

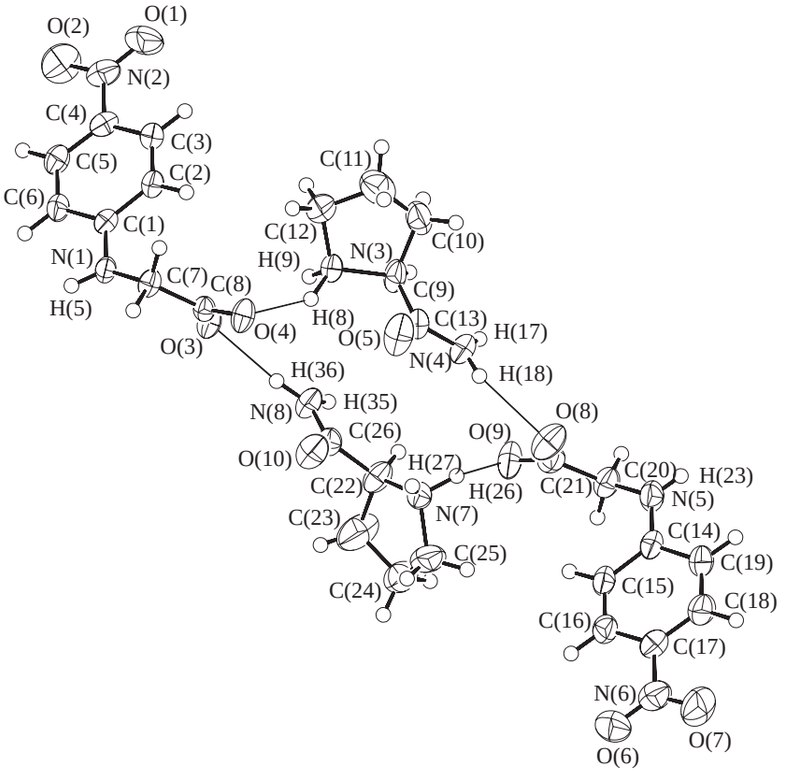

© 1998 NRC Canada

Fig. 9. ORTEP diagram of **1.pro-meth** (50% probability ellipsoids).

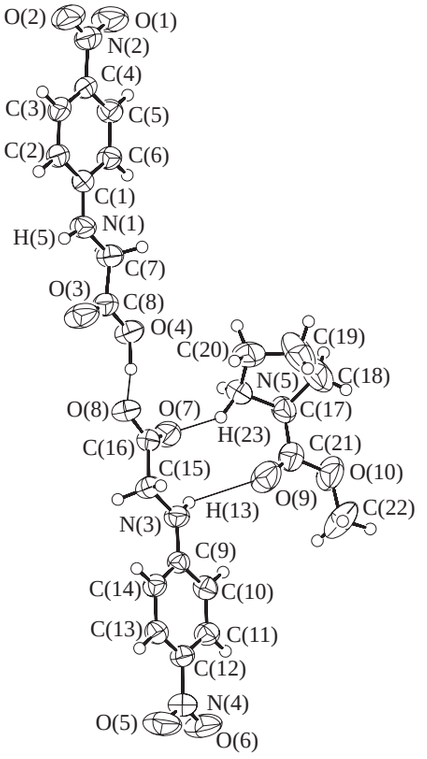

anions in the asymmetric unit, forming a dimer, while an intermolecular N—H···O hydrogen bond linking neighboring *p*-nitrophenylglycinate anions forms an infinite chain of dimers that propagate through the crystal diagonally between the *a*- and *c*-axes.

Table 6. SHG results for **1**, **NPP**, and all six salts containing the **1** chromophore.

Acid/salt			SHG vs. urea
1		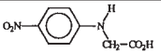	0
NPP		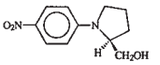	53 ± 5
1.eph	**1** +	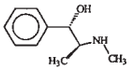	18 ± 2
1.pro-but	**1** +	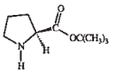	13 ± 2
1.pro-benz	**1** +	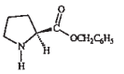	11 ± 2
1.pro-ol	**1** +		0.010 ± 0.004
1.pro-amide	**1** +	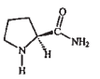	0.012 ± 0.008
1.pro-meth	**1** +	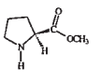	0.022 ± 0.005

*Complex **1.pro-meth***

The **1.pro-meth** complex crystallizes with the two *p*-nitrophenylglycinate moieties oriented in an anti-parallel manner (Fig. 9). While there is no pseudo centre of inversion between the chromophores, the two charge-transfer axes are separated by almost 180°. The two *p*-nitrophenylglycine moieties share one proton via a strong N—H···O hydrogen bond between their respective carboxylate groups so that the two charge-transfer axes are anti-parallel to one another. The position of the shared proton was refined and the difference in O—H distances (1.18 Å vs. 1.39 Å) suggests that the proton is more strongly held to one oxygen than to the other. The proline ring is linked to the deprotonated carboxyl group via a strong N—H···O hydrogen bond.

Results and discussion

Macroscopic quadratic susceptibilities

Excluding the salt **1.pro-benz**, for which there is no structural information, all other salts in the series crystallize in point groups 2 or 222. According to Zyss and Oudar (18, 19), the relationship between the macroscopic quadratic susceptibility, d_{IJK}, and the molecular second-order hyperpolarizability, β_{ijk}, is given by

$$[1] \qquad d_{IJK} = N f_I^{2\omega} f_J^{\omega} f_K^{\omega} \frac{1}{n} \sum_{s=1}^{n} \sum_{ijk} \cos\ (I, i(\mathrm{s}))\ \cos\ (J, j(\mathrm{s}))\ \cos\ (K, k(\mathrm{s}))\beta_{ijk}(\mathrm{s})$$

$$[2] \qquad d_{IJK} = N f_I^{2\omega} f_J^{\omega} f_K^{\omega} b_{IJK}$$

where N is the chromophore density; f is a local-field factor used to correct for mutual polarization from neighboring molecules; n is the number of symmetry-related molecules in the unit cell (indexed by s); i, j, and k describe the direction of polarization of all the interacting electric fields in the three orthogonal directions of the molecular frame of reference, x, y and z; I, J, and K describe the direction of polarization of the interacting fields in the three orthogonal directions of the crystal frame of

© 1998 NRC Canada

Fig. 10. Axis systems used to define the molecular (*xyz*) reference frame with respect to the crystal (XYZ) reference frame for point groups (*a*) 2 and (*b*) 222.

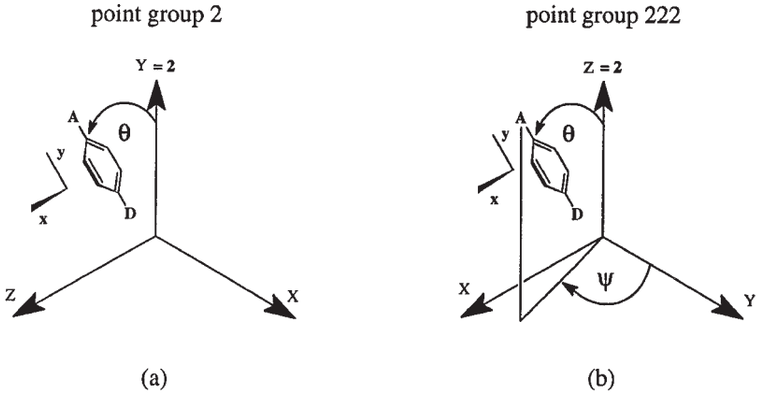

Fig. 11. UV–visible absorption spectra of **1, NPP**, and **PNA** in EtOH.

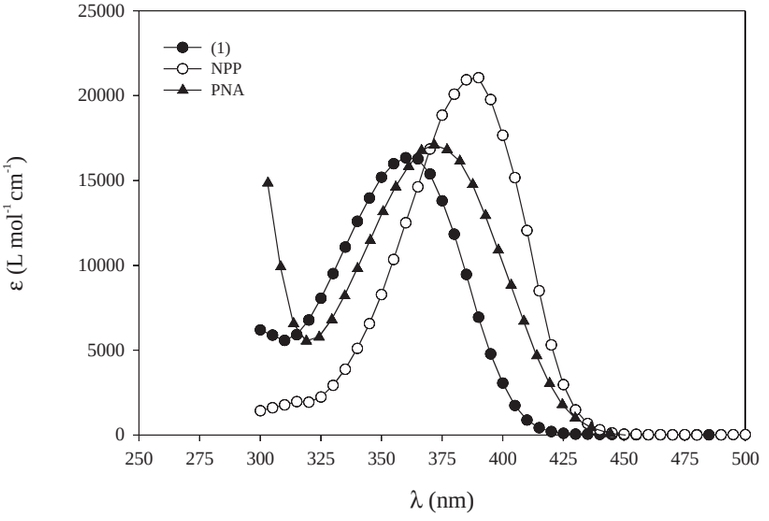

reference, *X*, *Y*, and *Z*; the cosine terms represent the rotation of the molecular reference frame from (*i*,*j*,*k*) onto the crystal reference frame (*I*,*J*,*K*); b_{IJK} in eq. [2] represents the crystalline nonlinearity per molecule. This last term can be calculated from the molecular orientations in the cell, derived from the structural data. Evaluation of the various d_{IJK} susceptibility elements requires some estimate of the local-field factors, usually taken in the Lorentz form:

$$[3] \qquad f^{\omega} = \left(\frac{n_{\omega}^2 + 2}{3} \right)$$

Assuming a one-dimensional *b* tensor (20, 31, 32) oriented in the *y*-direction defined in Fig. 1 (as is conventionally done when discussing **PNA**-type materials whose polarizability lies predominantly along the molecular charge-transfer axis) and Kleinman symmetry (33), eq. [1] reduces to

$$[4] \qquad d_{YZZ} = N f_Y^{2\omega} f_Z^{\omega} f_Z^{\omega} (\cos\theta \sin^2\theta) \beta_{yyy} \text{ [point group 2]}$$

and

$$[5] \qquad d_{XYZ} = N f_X^{2\omega} f_Y^{\omega} f_Z^{\omega} (\cos\psi \sin\psi \cos\theta \sin^2\theta) \beta_{yyy} \text{ [point group 222]}$$

where angles θ and ψ are defined as shown in Fig. 10.

SHG intensities

The measured SHG intensities of each of the six salts and of **NPP** are found in Table 6. Studies calculating and measuring the molecular hyperpolarizability of **PNA** and its derivatives have consistently shown that those with tertiary amines, such as

© 1998 NRC Canada

Table 7. Space group, chromophore density (N), and orientational parameters (θ, ψ) for **NPP** and the six salts made from **1**.

Acid/salt	Space group	N ($\times 10^{-3}$ / Å^3)	θ (°) [a]	ψ (°)
1	$P\bar{1}$	4.75	n/a [b]	n/a
NPP	$P2_1$	3.68	58.7	n/a
1.eph	$P2_1$	2.17	76.7, 61.0	n/a
1.pro-but	$P2_1$	2.17	50.3	n/a
1.pro-benz	Undetermined	—	—	—
1.pro-ol	$P2_12_12$	2.72	64.8, –117.1	80.2, –98.8
1.pro-amide	$P2_1$	2.84	47.6, –131.5	n/a
1.pro-meth	$P2_12_12_1$	3.20	–92.7, 88.9	170.7, –11.1

[a]Entries with more than one angle correspond to structures with more than one chromophore per asymmetric unit or with a disordered chromophore.
[b]n/a: not applicable.

NPP, possess molecular hyperpolarizabilities roughly comparable to or only marginally greater than **PNA** and its secondary amine derivatives, such as **1** (34–36). As a result, factors such as chromophore density and orientation should have a far greater influence on the observed SHG intensities of these salts than should their molecular hyperpolarizability, when compared with **NPP**. Assuming roughly equivalent local-field factor terms, an assumption that is consistent with their similar absorption characteristics (Fig. 11), the calculated ratio of SHG intensities between **NPP** and the salts in this study can therefore be given (9, 37) by

$$[6] \qquad \frac{I^{2\omega}(1)}{I^{2\omega}(2)} = \left(\frac{d_{IJK}(1)}{d_{IJK}(2)}\right)^2 = \left(\frac{N^{(1)}b_{IJK}^{(1)}}{N^{(2)}b_{IJK}^{(2)}}\right)^2$$

where d_{IJK} (and b_{IJK}) refers to the predominant d (and b) tensor for phase-matched SHG, d_{YZZ} for materials crystallizing in point group 2, and d_{XYZ} for those in point group 222. Included in Table 7 are the pertinent data derived for each salt whose X-ray crystal structure was determined.

*Salt **1.eph***

Although its SHG intensity is considerably weaker than that of **NPP, s**alt **1.eph** produces the greatest SHG intensity of the six salts in the series. The reduced chromophore density and unfavorable chromophore orientation, relative to **NPP**, acts to limit its phase-matching d_{YZZ} component, and consequently its SHG efficiency. The effective b_{YZZ} element for the disordered structure, taking into account the relative populations of each fragment, is

$$[7] \qquad b_{YZZ}\ (\mathbf{1.eph}) = (0.75 \cos\theta_{maj} \sin^2\theta_{maj} + 0.25 \cos\theta_{min} \sin^2\theta_{min})\ \beta_{yyy}(\mathbf{1.eph}) = 0.256\ \beta_{yyy}(\mathbf{1.eph})$$

The chromophore orientation of **NPP** leads to a near-maximized phase-matching element of: $b_{YZZ}(\mathbf{NPP}) = 0.379\beta_{yyy}(\mathbf{NPP})$.

Taking into account the different chromophore densities of the two materials and assuming roughly equivalent local-field factor correction terms, the ratio of SHG intensities between **1.eph** and **NPP** was estimated as

$$[8] \qquad \frac{I^{2\omega}(\mathbf{1.eph})}{I^{2\omega}(\mathbf{NPP})}(\text{estimated}) = \left(\frac{d_{YZZ}(\mathbf{1.eph})}{d_{YZZ}(\mathbf{NPP})}\right)^2 = 0.16$$

In fact, the measured ratio appears to be approximately twice the estimated ratio.

$$[9] \qquad \frac{I^{2\omega}(\mathbf{1.eph})}{I^{2\omega}(\mathbf{NPP})}(\text{measured}) = 0.34 \pm 0.07$$

Barring the unlikely contribution to the overall molecular hyperpolarizability from the pseudoephedrinium counterion (35), the surprisingly high SHG intensity of **1.eph** relative to **NPP** may be the result of the assumptions made regarding equivalent local-field factor correction terms. These terms are intended to account for any contribution to the polarization of the chromophores from their immediate surroundings (i.e., neighboring molecules), and are assumed to be consistent throughout the crystal. The considerable fraction of disordered chromophores (25%) may have an additional influence on the refractive indices of the salt. Without direct measurement of the refractive indices for both wavelengths in question, the extent to which the disorder contributes to the increased SHG response of **1.eph** is unclear.

*Salt **1.pro-but***

The SHG-chromophore in **1.pro-but** is almost ideally oriented for phase-matched SHG. Crystallizing in space group $P2_1$, with $\theta = 50.1°$, the phase-matching element b_{YZZ} is $0.378\,\beta_{yyy}$. The decreased SHG intensity, with respect to **NPP**, appears to be the result of the significantly lower chromophore density of **1.pro-but** (2.17×10^{-3} Å^{-3} vs. 3.68×10^{-3} Å^{-3} for **NPP**), leading to an estimated SHG intensity ratio of

© 1998 NRC Canada

Fig. 12. Change in SHG intensity with particle size for **NPP**, **1.eph**, and **1.pro-but**.

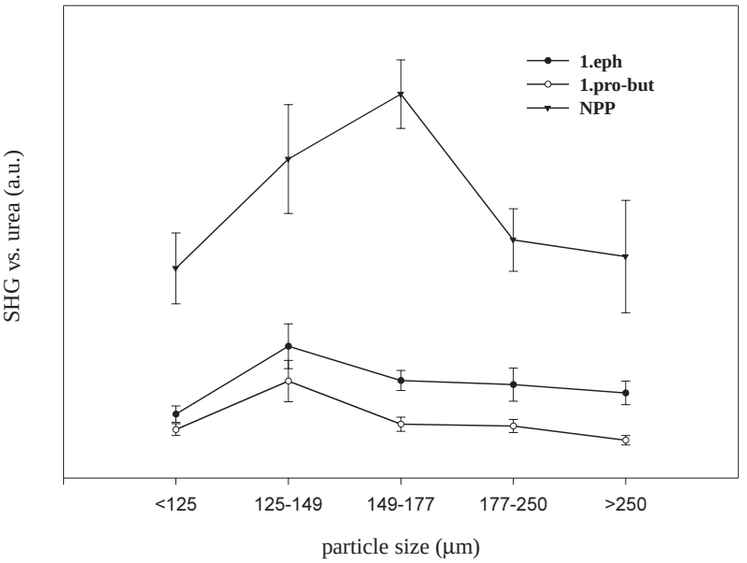

$$[10]\quad \frac{I^{2\omega}(\textbf{1. pro - but})}{I^{2\omega}(\textbf{NPP})}(\text{estimated}) = \left(\frac{d_{YZZ}(\textbf{1. pro - but})}{d_{YZZ}(\textbf{NPP})}\right)^2 = 0.34$$

The observed ratio of SHG intensities is

$$[11]\quad \frac{I^{2\omega}(\textbf{1. pro - but})}{I^{2\omega}(\textbf{NPP})}(\text{measured}) = 0.25 \pm 0.05$$

*Salts **1.pro-ol** and **1.pro-amide***

Both **1.pro-ol** and **1.pro-amide** produce small but measurable amounts of SHG. The packing of each material consists of two formula units per asymmetric unit, with the two *p*-nitrophenylglycinate moieties related by a pseudo centre of inversion. In the case of **1.pro-ol**, neither chromophore in the asymmetric unit appears to be oriented to maximize its crystalline nonlinearity for materials in point group 222. In addition, the contribution from each chromophore leads to the near-complete cancellation of the overall b_{XYZ} element. This anti-parallel alignment of the two chromophores in the asymmetric unit leads to a powder SHG intensity several orders of magnitude lower than the standard, urea:

$$[12]\quad \begin{aligned} &b_{XYZ}(1) = 0.058\beta_{yyy},\ \ b_{XYZ}(2) = -0.055\beta_{yyy} \\ &b_{XYZ}(\text{tot}) = b_{XYZ}(1) + b_{XYZ}(2) = 0.003\beta_{yyy}\quad (\textbf{1. pro - ol}) \end{aligned}$$

The situation is slightly different in the case of **1.pro-amide**. Individually, each *p*-nitrophenylglycinate moiety in the asymmetric unit is favorably oriented for SHG, according to the $P2_1$ space group in which the salt crystallizes. However, addition of the two b_{YZZ} tensor elements (with $\theta(1) = 47.6°$ and $\theta(2) = -131.5°$), leads to their nearly complete cancellation, and subsequently to its weak powder SHG intensity relative to urea:

$$[13]\quad \begin{aligned} &b_{YZZ}(1) = 0.368\beta_{yyy},\quad b_{YZZ}(2) = -0.372\beta_{yyy} \\ &b_{YZZ}(\text{tot}) = b_{YZZ}(1) + b_{YZZ}(2) = -0.004\beta_{yyy}\quad (\textbf{1. pro - amide}) \end{aligned}$$

*Complex **1.pro-meth***

According to the space group in which the complex crystallizes, $P2_12_12_1$, neither of the two chromophores is favorably oriented for SHG. Addition of the two b_{XYZ} tensors gives

$$[14]\quad \begin{aligned} &b_{YXZ}(1) = 0.004\beta_{yyy},\quad b_{XYZ}(2) = -0.008\beta_{yyy} \\ &b_{XYZ}(\text{tot}) = b_{XYZ}(1) + b_{XYZ}(2) = -0.004\beta_{yyy} \end{aligned}$$

© 1998 NRC Canada

Phase-matching results

Where possible, salts displaying significant SHG activity (i.e., SHG(salt) ≥ SHG(urea)) were tested for phase matchability. Phase-matchable materials can be distinguished from non phase-matchable materials by their different behavior with increasing particle size (27, 38), with the SHG intensity of phase-matchable materials increasing to a maximum with increasing particle size before leveling off to a relatively constant intensity. In the case of **1.pro-benz**, recrystallization produced only a microcrystalline powder, therefore no test for phase matchability was carried out. The phase-matching analysis of both **1.eph** and **1.pro-but** reveals a maximum SHG intensity in the 125–149 μm range before decreasing slightly with larger particle sizes and leveling off to a constant intensity (Fig. 12). These results would appear to indicate that both are phase matchable. The behavior of **NPP**, a known phase-matchable material (39), was similar to the behavior displayed by the two salts when subjected to the same analysis. The decrease in SHG intensity for larger particle sizes is likely due to a decrease in the amount of material exposed to the incident radiation. The larger sized particles are likely to occupy the volume in the sample cell less efficiently than smaller particles, producing voids containing no sample. In addition, crystal morphology may limit the number of orientations a particle may adopt in the sample cell, possibly excluding the orientations best suited for phase matching.

Discussion

It would appear from the preceding results that the coupling of chiral ionic auxiliaries to SHG chromophores not only ensures non-centrosymmetric packing, but also significantly enhances the potential for packing that leads to large SHG efficiencies compared to achiral compounds and nonionic systems. Of the six salts prepared from the otherwise SHG-inactive parent acid **(1)**, three displayed significant SHG activity on coupling with the chiral auxiliary. While no structural information is as yet available for **1.pro-benz** (SHG vs. urea ~ 11) it seems reasonable to surmise, based on the magnitude of its SHG response, that addition of the proline benzyl ester has allowed the *p*-nitrophenylglycinate chromophore to align in a favorable orientation for SHG. Examination of all the SHG results reveals, however, that none of the salts, even those with favorably oriented chromophores, approach the SHG efficiency of **NPP**, as a result of the reduced chromophore densities associated with the salts. This is as expected since the chiral counterion is responsible only for inducing an acentric packing environment, and should have a negligible contribution to the hyperpolarizability of the salt.

Also of note is the seemingly conflicting relationship between chromophore density and SHG activity. In the case of salts with significant SHG activity (whose crystal structures were determined) both chromophore densities were ~2.2 × 10^{-3} Å^{-3}, whereas the three salts or complexes and parent acid that showed little or no SHG activity (**1.pro-ol**, **1.pro-amide**, **1.pro-meth,** and **1)** had chromophore densities of 2.7 × 10^{-3} Å^{-3} or greater. The three most strongly SHG-active salts contained the three bulkiest counterions. These bulky counterions may be more adept at separating the polar chromophores, thus diminishing the electrostatic attraction that may lead to anti-parallel packing. This, however, limits the maximum possible SHG efficiency by "diluting" the chromophore density.

Acknowledgments

We thank the Natural Sciences and Engineering Research Council of Canada and the Petroleum Research Fund, administered by the American Chemical Society, for financial support.

References

1. J.F. Nicoud and R.J. Twieg. *In* Nonlinear optical properties of organic molecules and crystals. Vol. 1. *Edited by* D.S. Chemla and J. Zyss. Academic Press, Inc., Orlando, Fla. 1987. p. 227.
2. G.R. Meredith. *In* Nonlinear optical properties of organic and polymeric materials. *Edited by* D.J. Williams. ACS Symp. Ser. **233**, Washington, D.C. 1983. p. 27.
3. J. Messier, F. Kajar, P. Prasad, and D. Ulrich. Nonlinear optical effects in organic polymers. Kluwer Academic Publishers, Dordrecht. 1989.
4. H.S. Nalwa, T. Watanabe, and S. Miyata. *In* Progress in photochemistry and photophysics. Vol. 5. *Edited by* J.F. Rabek. CRC Press, Boca Raton, Fla. 1990. p. 103.
5. P.N. Prasad and D.J. Williams. Introduction to nonlinear optical effects in molecules and polymers. John Wiley and Sons, Inc., New York. 1991.
6. C.T. Chen, Y.C. Wu, and R.K. Li. Chin. Phys. Lett. **2**, 389 (1985).
7. D.A. Eaton. *In* Materials for nonlinear optics: chemical perspectives. *Edited by* S.R. Marder, J.E. Sohn, and G.A. Stucky. ACS Symp. Ser. **455**, Washington, DC. 1991. p. 128.
8. J. Zyss, J.F. Nicoud, and M. Coquillay. J. Chem. Phys. **81**, 4160 (1984).
9. M. Barzoukas, D. Josse, P. Fremaux, J. Zyss, J.F. Nicoud, and J.O. Morley. J. Opt. Soc. Am. B: **4**, 977 (1987).
10. J.F. Lipscomb, A.F. Garito, and R.S. Narang. J. Chem. Phys. **75**, 1509 (1981).
11. J.F. Ward. Rev. Mod. Phys. **37**, 1 (1965).
12. N. Bloembergen. *In* Nonlinear optics. W.A. Benjamin Inc., Reading, Mass. 1965.
13. A.D. Mighell and J.R. Rodgers. Acta Crystallogr. Sect. A: Cryst. Phys. Diffr. Theor. Gen. Crystallogr. **B36**, 321 (1980).
14. A.D. Mighell, V.L. Himes, and J.R. Rodgers. Acta Crystallogr. Sect. A: Found. Crystallogr. **B39**, 737 (1983).
15. D.M. Burland, R.D. Miller, and C.A. Walsh. Chem. Rev. **94**, 31 (1994).
16. W. Lin, S. Yitzchaik, A. Malik, M.K. Durbin, A.G. Richter, G.K. Wong, P. Dutta, and T.J. Marks. Angew. Chem. Int. Ed. Engl. **34**, 1497 (1995).
17. D. Li, M.A. Ratner, T.J. Marks, C.H. Zhang, J. Yang, and G.K. Wong. J. Am. Chem. Soc. **112**, 7389 (1990).
18. J.L. Oudar and J. Zyss. Phys. Rev. A: At. Mol. Opt. Phys. **26**, 2016 (1982).
19. J. Zyss and J.L. Oudar. Phys. Rev. A: At. Mol. Opt. Phys. **26**, 2028 (1982).
20. C.W. Dirk, R.J. Tweig, and G. Wagniere. J. Am. Chem. Soc. **108**, 5387 (1986).
21. J.K. Whitesell, R.E. Davis, L.L. Saunders, R.J. Wilson, and J.P. Feagins. J. Am. Chem. Soc. **113**, 3267 (1991).

© 1998 NRC Canada

22. A.D. Gudmundsdottir and J.R. Scheffer. Tetrahedron Lett. **31**, 6807 (1990).
23. A.D. Gudmundsdottir and J.R. Scheffer. Photochem. Photobiol. **54**, 535 (1991).
24. R. Jones, J.R. Scheffer, J. Trotter, and J. Yang. Tetrahedron Lett. **33**, 5481 (1992).
25. A.D. Gudmundsdottir, W. Li, J.R. Scheffer, S. Rettig, and J. Trotter. Mol. Cryst. Liq. Cryst. **240**, 81 (1994).
26. A.D. Gudmundsdottir, J.R. Scheffer, and J. Trotter. Tetrahedron Lett. **35**, 1397 (1994).
27. S.K. Kurtz and T.T. Perry. J. Appl. Phys. **39**, 3798 (1968).
28. R. Lantz and P. Obellianne. Bull. Soc. Chim. Fr. 311 (1955).
29. D.T. Cromer and J.T. Waber. *In* International tables for X-ray crystallography. The Kynoch Press, Birmingham, England. 1974.
30. D.C. Creagh and W.J. McAuley. *In* International tables for crystallography. Vol. C. *Edited by* A.J.C. Wilson. Kluwer Academic Publishers, Boston. 1992. p. 219.
31. D. Li, T.J. Marks, and M.A. Ratner. Chem. Phys. Lett. **131**, 370 (1986).
32. D. Li, T.J. Marks, and M.A. Ratner. J. Phys.Chem. **96**, 4325 (1992).
33. D.A. Kleinman. Phys. Rev. **128**, 1761 (1962).
34. C.M. Whitaker, E.V. Patterson, K.L. Kott, and R.J. McMahon. J. Am. Chem. Soc. **118**, 9966 (1996).
35. L. Cheng, W. Tam, S.H. Stevenson, G.R. Meredith, G. Rikken, and S.R. Marder. J. Phys. Chem. **95**, 10631 (1991).
36. P.C. Leung, J. Stevens, R.E. Harelstad, M.S. Spiering, D.J. Gerbi, C.V. Francis, J.E. Trend, G.V.D. Tiers, G.T. Boyd, D.A. Ender, and R.C. Williams. Proc. – SPIE Int. Soc. Opt. Eng. **1147**, 48 (1989).
37. C. Serbutoviez, J.-F. Nicoud, J. Fischer, I. Ledoux, and J. Zyss. Chem. Mater. **6**, 1358 (1994).
38. S.P. Velsko. *In* Materials for nonlinear optics: chemical perspectives. *Edited by* S.R. Marder, J.E. Sohn, and G.D. Stucky. American Chemical Society, Washington, D.C. 1991.
39. I. Ledoux, C. Lepers, A. Perigaud, J. Badan, and J. Zyss. Opt. Commun. **80**, 149 (1990).

© 1998 NRC Canada

Characterization of macroscopic disorder in a porous glass with NMR microimaging and scanning electron microscopy

Luc Tremblay, Serge Lacelle, and Charles G. Fry

Abstract: A study of the intensity fluctuations in one-dimensional NMR microimaging profiles of imbibed porous Pyrex glass filters is presented. An approach to characterize some aspects of the macroscopic randomness from the NMR microimaging profiles of this porous medium is developed. Statistical properties, such as the arithmetic and geometric means, of the distributions of peak separations between the intensity fluctuations are shown to reveal information about the pore size and the pore-to-pore distances in porous media. The intensity–intensity correlation functions of the one-dimensional NMR profiles display an interplay, as a function of length scale, among the dimensions of the porous network and its embedding space, and their respective dimensions in the projections. Corroboration of these NMR results are achieved with similar analysis of SEM two-dimensional images and their corresponding one-dimensional projections obtained with the same porous Pyrex glass. The approach developed to characterize the macroscopic randomness in these porous glass filters should prove generic for the study of other random materials.

Key words: NMR imaging, scanning electron microscopy, porous media, disorder, statistical characterization.

Résumé : On a réalisé une étude des fluctuations d'intensité des profils de microimagerie RMN unidimensionnelle de filtres de verre Pyrex poreux imbibés. On a développé une approche dans le but de caractériser un certain nombre d'aspects du caractère macroscopique aléatoire des profils de microimagerie RMN de ce milieu poreux. On a démontré que des propriétés statistiques, comme les moyennes arithmétiques et géométriques des distributions des séparations des pics entre les fluctuations d'intensité, fournissent de l'information relative à la taille des pores ainsi que sur les distances entre les pores du milieu poreux. Les fonctions de corrélation des profils de RMN unidimensionnelle présentent une interrelation des dimensions du réseau poreux, de la taille de son incrustation ainsi que de leurs dimensions relatives en projections en fonction de la longueur de l'échelle. On a corroboré ces résultats de la RMN à l'aide d'analyses similaires d'images bidimensionnelles microscopie électronique à balayage et des projections unidimensionnelles correspondantes obtenues avec le même verre Pyrex poreux. L'approche développée pour caractériser le caractère macroscopique aléatoire de ces filtres de verre poreux devrait s'avérer assez générale pour permettre l'étude d'autres matériaux aléatoires.

Mots clés : microimagerie RMN; microscopie électronique à balayage; milieu poreux; désordre; caractéristique statistique.

[Traduit par la Rédaction]

1. Introduction

A unifying theme in materials science is the relationship between microstructures and macroscopic properties of materials (1). This interplay of length scales involves a hierarchy of structures, starting from atoms and molecules to phase configurations, which are controlled through processing to yield engineered materials and products. Disorder, which appears as an integral part at all structural levels of materials, ranges from point defects, dislocation lines, grain boundaries, domain shapes, and crystal facets (2–5). The performance of materials depends to various degrees on both structures and their disorder. It is thus surprising that only in the last two decades or so has the study of disordered materials become respectable in the sense of not being denigrated, or viewing disorder solely as perturbations in ordered systems. In this paper, we characterize some aspects of the structural disorder of a macroscopically homogeneous (in a statistical sense) porous glass with nuclear magnetic resonance (NMR) microimaging and scanning electron microscopy (SEM).

Early efforts to characterize disordered materials with NMR have focused on the microscopic structural level by monitoring the dispersion of chemical environments with chemical shift measurements and local mobilities through relaxation studies. Spin-diffusion NMR methodologies have been developed and refined to probe certain aspects of domain

Received February 3, 1998.

L. Tremblay and S. Lacelle.[1] Département de chimie, Université de Sherbrooke, Sherbrooke, QC J1K 2R1, Canada. **C.G. Fry.**[2] Research Laboratories, McDonnell Douglas Corporation, St. Louis, MO 63166, U.S.A.

[1]Author to whom correspondence may be addressed. Telephone: (819) 821-7823. Fax: (819) 821-8017. E-mail: slacelle@courrier.usherb.ca

[2]Present address: Department of Chemistry, University of Wisconsin, Madison, WI 53706, U.S.A.

© 1998 NRC Canada

Fig. 1. Profiles of ^{1}H nuclear spin densities (intensities in arbitrary units) of the critical binary mixture, aniline–cyclohexane, in porous Pyrex glass along the gravitational (z) direction (abscissa in kHz) at t = 0 s and t = 2750 s after a thermal quench below the upper consolute solution temperature of the bulk mixture (T_c = 30°C). The bottom of the samples is in the positive frequencies; the residual binary fluid between the porous glass and the NMR tube is seen at that position.

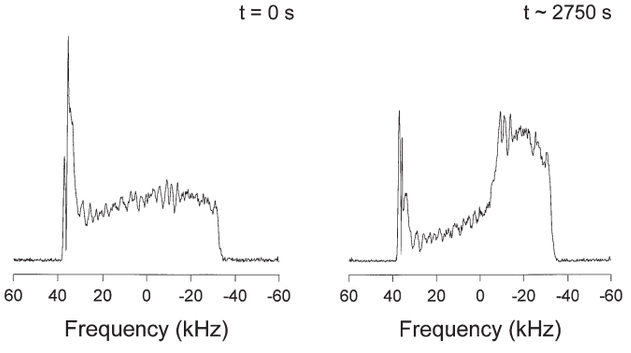

structural disorder over ranges extending from 1 nm up to several hundred nanometers. In materials with macroscopic disorder, such as certain porous media, self-diffusion (6) and relaxation (7) NMR measurements and NMR microimaging (8) have contributed to the elucidation of structural features on length scales above tens of micrometers (μm).

For several years now, we have studied the phase separation of critical binary liquid mixtures in porous media (9, 10). To understand the role of confinement and disorder in the phase separation processes, two relevant length scales need to be examined in this problem: the correlation length of the critical composition fluctuations, ξ, and the "typical" length scale of the disorder, e.g., the average pore size L or any other moment of the pore size distribution. When $\xi > L$, the phase separation is strongly affected, as compared to the situation in the bulk (9). In the late stages of the phase separation processes, when $\xi < L$, another length scale, the so-called capillary length (arising from the competition between surface tension and gravitational stresses of interfaces between domains of different compositions and densities), becomes important when its size reaches L (10).

To probe this latter regime of phase separation in a confined space, we have measured time-dependent one-dimensional NMR microimaging profiles of the critical aniline–cyclohexane mixture in a porous Pyrex glass with $L \approx 160$ μm and $\xi \approx 50$ Å (10). Figure 1 displays the profiles of the ^{1}H nuclear spin densities of the critical binary mixture, as a function of position along the gravitational direction (z-direction) in a porous glass sample (1.5 cm in length), at t = 0 and at $t \sim 2750$ s after a thermal quench below the upper consolute solution temperature of the bulk mixture (T_c = 30°C). These results clearly indicate that phase separation has indeed occurred, and demonstrate the presence of a widespread "interface" between the two liquid phases of different densities in the porous Pyrex glass at $t \sim 2750$ s. However, some other remarkable features of such profiles are the intensity fluctuations arising from the disorder in the glass. These intensity fluctuations appear noticeably different in character from thermal noise in the NMR signal (see the signal on either side of the glass sample in Fig. 1). The specific question we address in the present work is the following: what information can be inferred about the disorder in the porous glass from such intensity fluctuations in one-dimensional NMR microimaging profiles? The interpretation of the NMR results will be compared with information gathered from analysis of SEM images of the porous glass.

In NMR imaging, as in other forms of tomography, projection profiles are extensively used to reconstruct higher dimensional images (8). Obviously, different efforts and resources are required and expended in order to obtain and analyze images of different dimensions. Advantages and disadvantages of imaging approaches are dictated by a host of factors that affect both signal-to-noise and resolution considerations (8). For example, in our time-dependent studies of binary liquid phase separation in porous Pyrex glass (10), NMR microimaging of one-dimensional projections proved to be the most convenient method at our disposal because of the time constraint imposed by the phenomenon. It is well known (11, 12) that the projection of a D-dimensional object, embedded in a d-dimensional space, onto a subspace of dimension d_s unveils some information with new perspectives. A case in point, the dimensionality of the projection D_p, is identical to d_s if $D \geq d_s$, or is equal to D if $D < d_s$. Visualization of chemical and physical processes from different perspectives appears to help to better appreciate, probe, and understand simple and complex phenomena (13). As the development of computer software and hardware evolves, it is expected that applications in the field of visualization and imaging, including projections in different dimensions, will become more common and will be used more proficiently in the study of complex disordered phenomena. It is in this sense that we present our modest contribution, to reveal and extract some features of the disorder in porous Pyrex glass, relevant to the phase separation processes of the critical binary mixture aniline–cyclohexane, from one-dimensional NMR profilometry and corroborated by SEM image analysis.

2. Experimental section

Cylindrical samples of porous Pyrex glass filters (8.97 mm in diameter and 15 mm in length) were obtained from Ace Glass Inc. (14). These filters are commercially produced by sintering small glass cylinders (see digitized SEM image, Fig. 4 in Results and discussion, Sect. 3B). The chemical composition of the glass is 81% SiO_2, 12% B_2O_3, 4.5% Na_2O, and 2.5% Al_2O (14). The cut-off particle size filtered by this porous glass is 160 ± 15 μm as determined by Ace Glass (14), by measuring the pressure necessary to force the first air bubbles through the glass when submerged in a liquid with a known surface tension. The porosity of 18% was established by analysis of SEM and optical microscopy images, and by gravimetric and NMR methods (10). The glass filters were cleaned by soaking in a large excess of deionized water for at least 24 h, followed by further soaking in ethanol for a similar duration, and finally dried in an oven at about 130°C under vacuum for at least 24 h. Prior to experiments, an extra 3 h drying period at 130°C under vacuum was allowed. Following a cooling-off period, the

© 1998 NRC Canada

Fig. 2. Profiles of ^{1}H nuclear spin densities (intensities in arbitrary units) of cyclohexane in the porous Pyrex glass sample along the gravitational (z) direction (abscissa in kHz) and perpendicular to the gravitational directional direction (y). The cylindrical porous glass sample is 15 mm in length and 8.97 mm in diameter with its long axis oriented parallel to the z-direction. In the z-profile, the bottom of the sample is in the positive frequencies. The signal of the residual cyclohexane between the porous glass and the bottom of the NMR tube has been truncated to better observe the intensity fluctuations in the z-profile.

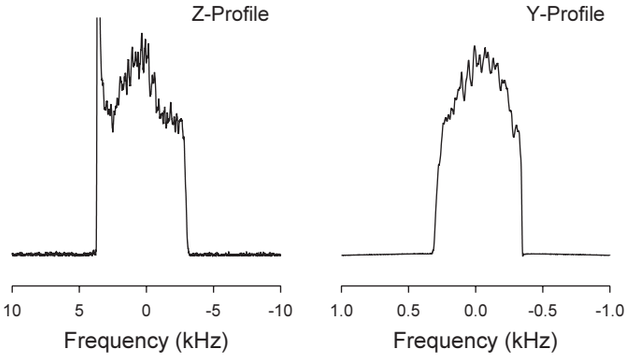

porous filters were subsequently inserted in flat-bottom 10 mm high-precision NMR tubes from Wilmad Inc. Spectroscopic grade cyclohexane, acquired from Sigma Chemical Company, was poured in excess over the glass. Air bubbles were then pumped out of the porous glass, and the excess cyclohexane was removed from the top of the samples.

Scanning electron microscopy (SEM) was performed with a JEOL JSM-840A instrument. To obtain SEM images, the porous glass was first injected and impregnated with a Buehler Epo-Kwick epoxy resin for 6 h. This step was necessary to reinforce the structure of the porous glass so that it could withstand the following sample preparation. After a drying period of at least 12 h, the sample was sliced in several cross sections with a diamond saw. The surface of each of these sections was polished, then covered with a 150 Å layer of Au–Pd mixture by cathodic sputtering. SEM images of these samples were obtained with a secondary electron method and with a scattered electron method at a working distance of 39 mm with a 15 kV acceleration voltage. The results were captured with a Nikkon camera on black and white TMAX 100 ASA film. These SEM images were digitized with a Hewlett–Packard ScanJet scanner with a resolution of 300 dpi; as a result, each surface pixel represents an area of 21 × 21 μm^2.

NMR experiments were performed on a Bruker MSL-300 spectrometer equipped with a microimaging unit and operating at a frequency of 300 MHz for ^{1}H. The sample temperature in the probe was controlled to ± 0.5 K with the temperature control unit supplied with the instrument. The acquisition parameters for all experiments were optimized to yield a maximum signal-to-noise ratio with a single scan. Imaging profiles in one dimension were obtained with a spin echo rf pulse sequence (8), with a typical 90° pulse width of 26 μs. Magnetic field gradient pulses were applied along the selected direction during the delay between the 90° and 180° rf pulses of the spin echo, and after the 180° pulse during the acquisition. Following the π pulse, the ensuing free induction decays (FIDs) were digitized at a rate of 250 kHz with 2048 points, providing a digital resolution of 122 Hz per point in the Fourier transformed spectra. The magnetic field gradients were 0.11 T m^{-1}, which produced a spatial resolution of 26 μm per point in the one-dimensional images along the z-direction.

The chemical composition of the glass filters and traces of residual impurities were ascertained with X-ray fluorescence using an energy dispersive Kevex 0700/8000 spectrometer. Radiation produced within the X-ray tube, by accelerating electrons with a 5 kV potential on a rhodium target in the vacuum, allowed the direct measurement of fluorescence of Na, Al, and Si. The excitation of impurities was accomplished with the secondary fluorescent source of a germanium target nominally irradiated with the X-ray tube operating at 15 kV; subsequent detection of the fluorescence identified Fe, Ni, and Cu impurities that could potentially affect the NMR results through paramagnetic relaxation as discussed in Sect. 3E.

3. Results and discussion

3A. NMR microimaging one-dimensional projection profiles

^{1}H NMR microimaging projection profiles of cyclohexane in the porous Pyrex glass parallel (z-direction along the length of the cylindrical sample) and perpendicular (y-direction) to the gravitational field (Fig. 2) clearly reveal intensity fluctuations due to the glass disorder. As the spatial resolution of these images is 26 μm per pixel, the signal intensities yield the relative number of ^{1}H nuclear spins at different positions and projected from the three-dimensional sample along a particular direction selected by the magnetic field gradients. Sample geometry and the finite radiofrequency excitation profile across the sample dictate part of the overall signal features (8, 10).

Our analysis of these NMR intensity fluctuations will proceed along two complementary avenues. First, we examine the distribution of peak separation in the NMR one-dimensional profiles. These results are compared to distributions obtained from one-dimensional projections of scanning electron microscopy images of two-dimensional slices of the porous Pyrex glass and superpositions of such SEM images. A two-dimensional chord analysis (15) of the SEM images was also performed, and the statistical characteristics of pore size distribution obtained from this analysis is contrasted to the NMR microimaging and SEM projection results. Second, from the NMR intensity profiles, intensity correlation functions are measured as a function of distance, and compared to those calculated from the distributions of one-dimensional projections of SEM images.

Figure 3 shows a histogram of the frequency of peak separations obtained from the one-dimensional profile of ^{1}H nuclear spin densities of cyclohexane in the porous Pyrex glass sample along the gravitational (z) direction from the NMR spectrum in Fig. 2. The peak separations between nearest-neighbor local intensity maxima, or peak-to-peak distances, were measured with the program Grams/32 version 4.02 from Galactic Industries Corporation. The binning of peak

© 1998 NRC Canada

Fig. 3. Histogram (frequency of occurrence) of peak separations obtained from the one-dimensional profiles of ^{1}H nuclear spin densities of cyclohexane in the porous Pyrex glass sample along the gravitational (z) direction from Fig. 2.

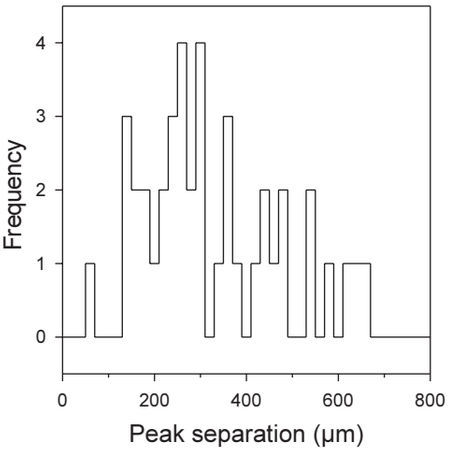

separations, in increments of 20 μm, corresponds approximately to the spatial resolution in the NMR microimaging experiments (26 μm) and in the projections of the digitized SEM images (21 μm). An asymmetry in the distribution appears evident in Fig. 3. In such a situation, it is often expected that the first moment, or arithmetic mean, of the distribution will be different than the most probable value, or the mode (16). A statistical measure that more accurately reflects the most probable value is the geometric mean of the distribution, defined here as $\exp\{\langle \ln(\text{peak separation})\rangle\}$, where $\langle\ \rangle$ indicates the average. The arithmetic mean of the peak separation distribution in Fig. 3 is 318 μm, and the geometric mean is 283 μm (see Table 1).

What do the arithmetic and geometric means of the distribution of peak separations in the NMR microimaging one-dimensional projections of the imbibed porous glass filters represent? The peak intensities are proportional to the number of cyclohexane ^{1}H, while the glass is "NMR-transparent" due to the lack of hydrogens in its structure. Thus, it would appear plausible that the peak separation should be sensitive to the pore size, which gives the intensities of the peaks due to the presence of cyclohexane, and to the glass region between pores, which gives the "troughs" between peaks. As these one-dimensional projections arise from a three-dimensional sample, it would be expected that the intensities and the separations of the peaks would correspond to statistical features characteristic of the three-dimensional sample. Note that no algorithm exists that could reconstruct, in a unique fashion, the three-dimensional object from a single one-dimensional projection. Hence we suggest that the peak separation in the one-dimensional NMR projections represent the pore-to-pore distance in a statistical sense. The arithmetic and geometric means of the distribution of peak separations would thus correspond to the typical pore-to-pore distance in the porous media. For wide distributions, the geometric mean would be expected to better represent the typical pore-to-pore distance.

This plausibility argument is further supported with the following mean-field approach or effective-medium treatment of the disorder in a three-dimensional porous glass. Let R be the typical pore radius. Then, for spherical pores, the typical pore volume is $(4\pi/3)\ R^3$. If the pores are homogeneously embedded, as in a cubic lattice, then for a region of space containing a single pore and the glass, the pore volume is given as $f\cdot(\langle \text{ppd}\rangle)$, where f is the porosity, and $\langle \text{ppd}\rangle$ is the average pore-to-pore distance. Equating these two typical pore volumes yields

$$\langle \text{ppd}\rangle = \left(\frac{4\pi}{3f}\right)^{1/3} R$$

For the porous Pyrex glass filters, R = 80 ± 7.5 μm (14), while f = 0.18 (10), which gives $\langle \text{ppd}\rangle$ = 210–250 μm. The most probable value of the distribution of peak separation in Fig. 3, as estimated by the geometric mean, is 283 μm, in close agreement with the predicted mean-field values.

Table 1. Geometric and arithmetic means of distributions.

Distribution	Geometric mean/μm	Arithmetic mean/μm
1-D NMR z-profile: peak separation	283	318
1-D SEM (coarse): peak separation	285	341
1-D SEM (fine): peak separation	134	178
1-D SEM superposition: peak separation	190	203
Pore chord analysis: chord length	157	227

In random systems, statistical properties of distributions are the most we can expect to measure and (or) calculate. These statistical properties are characteristic of the ensemble and do not necessarily describe the individual members of the ensemble. Our interpretation of the peak separations observed in the intensity fluctuations of the one-dimensional NMR profiles in Figs. 1 and 2 conforms to this generic outlook of disordered systems.

3B. SEM one-dimensional projection profiles

To corroborate this interpretation of the intensity fluctuations in the one-dimensional NMR profiles, scanning electron microscopy images of cross sections of the porous Pyrex glass were produced and analyzed to reveal analogous information. A digitized SEM image of a representative cross section of the porous Pyrex glass is displayed in Fig. 4. The white regions correspond to pore spaces, while the black regions depict the glass. The circle symbolizes the NMR tube. The analysis of such an image and its projection unveils rich information concerning the disorder. For example, the determination of the porosity from this image is particularly crucial, as efforts to understand mechanisms of late-stage phase separation of binary mixtures in such a confined environment (10) depend on the presence/absence of continuum percolation, or percolation path of the pore space (the volume percolation threshold is 16% in three dimensions).

Projections of the two-dimensional SEM images were obtained and the peak separation distributions inferred from

© 1998 NRC Canada

Fig. 4. Digitized SEM image of the porous glass cross section; the white regions correspond to the pore space, while the black regions represent the glass. The circle depicts the circumference of the NMR tube.

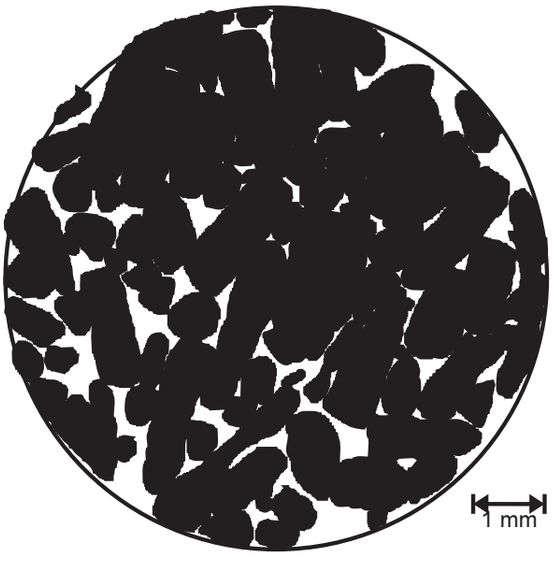

these profiles were used for direct comparison with the NMR statistical features. The projection and analysis procedure is presented in Fig. 5. The one-dimensional projection of the pore space and the porous glass is obtained by counting the respective pixels in the digitized image that contribute at a particular position along the projection. The spatial resolution of the resulting profiles is 21 μm. The intensities in the profiles therefore correspond to pore densities in the projections, and would be identical to the expected NMR signal observed in the same one-dimensional projection of the same cross section. It is noteworthy to observe the "edge effects" arising from the projection of the two-dimensional cross section "sample" in the one-dimensional profiles of the pores and glass (see right side of Fig. 5). Such effects are a simple consequence of the fact that in the one-dimensional projections, more material, i.e., glass and pores, contributes to the middle of the projections than at the edges.

A resulting one-dimensional SEM profile from such a procedure is shown in Fig. 6. This profile appears more "ragged" than the one-dimensional NMR profiles in Figs. 1 and 2 due to the small number of pixels that contribute to the SEM projection. For example, in the NMR profile along the *z*-direction, each pixel intensity would arise from the sum of all pore space pixels in a two-dimensional SEM cross section. To take into account this effect, we have used two procedures in the peak separation measurements: (*i*) direct measurements of peak separations, and (*ii*) smoothing of the SEM profile by using a running average of the intensities by 3-pixel increments followed by peak separation measurements. The first method yields "fine" resolution, while the coarse-graining procedure gives "coarse" resolution. The corresponding distributions of peak separation are displayed in Fig. 7, with fine (*A*) and coarse (*B*) resolution, while their arithmetic and geometric means are indicated in Table 1. The statistical properties of the peak separation distribution measured with the coarse resolution appear in good qualitative agreement with the NMR results. The fine resolution yields a preponderance of peak separations below 200 μm, which reduces considerably the arithmetic and geometric means.

An alternative to the heuristic smoothing method applied above consists of superposing several one-dimensional SEM profiles, each obtained by rotating a two-dimensional SEM image before the projection operation. Physically, such a procedure is closer in spirit to the projection of images of slices from *x*–*y* planes onto the *z*-axis to produce one-dimensional NMR density profiles. Figure 8 illustrates the distribution of peak separations observed by superposing the projections obtained from a single two-dimensional SEM image projected along 10 different directions; the SEM image of Fig. 4 was rotated by 18°, projected to produce one-dimensional profiles of pores, and this operation was repeated 10 times. Interestingly, the statistical properties of these superposed one-dimensional SEM profiles appear intermediate between the results of the "fine" and "coarse" method used above.

3C. SEM pore chord analysis

A chord analysis of two-dimensional SEM images of three different cross sections as in Fig. 4 was performed in order to further characterize the pore size distribution of the porous Pyrex glass filters. The arithmetic and geometric means of the pore size distributions thereby obtained were then used to calculate the average peak-to-peak distances in the NMR and SEM one-dimensional profiles with our mean-field argument of Sect. 3A.

In this method, several bundles of parallel straight lines of equal length are generated and uniformly distributed along different random directions. The histogram of the number of each intersection length inside the pores represents the pore chord distribution. In situations where pore structures can be represented by a random distribution of polydispersed spheres, the pore chord distribution can then be used to evaluate the pore size distribution (15). However, the pore network in the porous Pyrex glass appears complex, and a mathematical relationship between the distributions is certainly model dependent. A similar situation has been encountered with Vycor porous glass, which has a pore network similar in morphology to the porous Pyrex glass filters (17). Very good agreement was observed between the most probable value of the pore size obtained from the chord analysis and the average pore size measured by N_2 adsorption in Vycor porous glass. Hence we believe that the pore chord distribution should capture and represent to a good approximation some essential features of the three-dimensional structure of the pore network in the Pyrex glass filters without the need to make any assumptions about the geometry of the pores.

The pore chord distribution, obtained from the digitized two-dimensional SEM cross sections, is presented on linear and logarithmic length scales in Fig. 9. Nine different realizations of bundles of lines on the three different digitized SEM images were used to generate the distribution in Fig. 9. The large "error bars" on the small values of chord lengths arise from the digital resolution of 21 μm per pixel in the images. The geometric mean of the chord distribution is

© 1998 NRC Canada

Fig. 5. Schematic of the procedure to produce a one-dimensional projection profile of the pore density from SEM images by counting pore pixels that contribute at different positions along the projection (left side), and the resulting density profile of pores, glass, and their sum (right side). The spatial resolution of the projection is 21 μm.

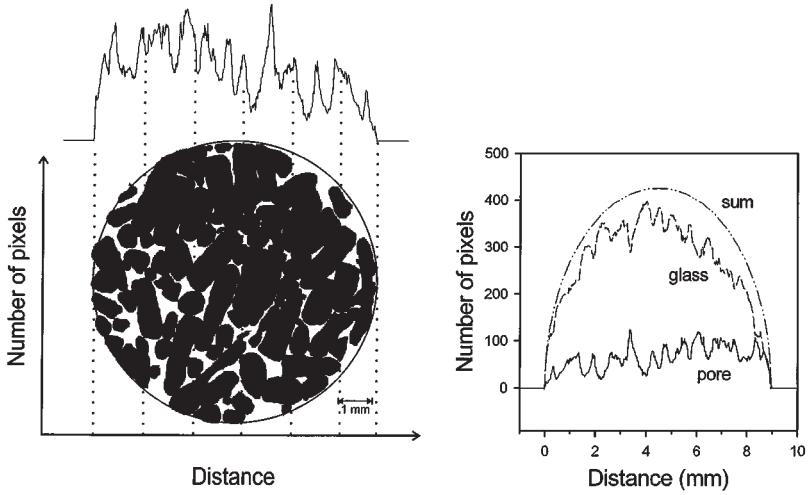

Fig. 6. One-dimensional SEM projection profile of pore density (number of pixels), obtained from Fig. 5, as a function of spatial position (mm). The spatial resolution is 21 μm.

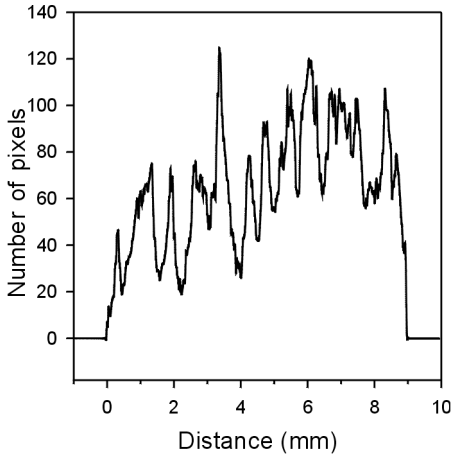

157 μm, while the arithmetic mean is 227 μm (see Table 1). The geometric mean of the chord distribution corresponds very closely to the typical pore size of 160 ± 15 μm, as observed by Ace Glass Inc. with pressure measurements (14). Thus, from these statistical features of the pore chord distribution and our mean-field model of disorder, the peak-to-peak separation in the NMR and SEM one-dimensional projection profiles would give values from 224 μm (obtained from the geometric mean) to 323 μm (obtained from the arithmetic mean). These values are in close agreement with the NMR data, and also agree with the SEM data, although in this latter case the choice of which situation is representative of the NMR microimaging results is more difficult to assess.

3D. NMR and SEM intensity correlation functions of one-dimensional projection profiles

Up to this point, we have focused exclusively on the peak separations, associated with the intensity fluctuations, in the one-dimensional NMR and SEM projection profiles of pore densities in the porous Pyrex glass. In this section, we examine the correlation of the intensity fluctuations in the same profiles. The intensity–intensity correlation function, $C(r)$, is defined as

$$[1] \qquad C(r) = \sum_{i=1}^{N} \frac{h(i)h(i+r)}{N-r} \Big/ \sum_{i=1}^{N} \frac{h(i)h(i)}{N}$$

where i is the pixel position along the projection, and $h(i)$ is the intensity at the ith pixel corresponding to the pore density at the location i in the projection. The factor $N - r$ in the numerator is necessary to normalize the contributions of $i \times (i + r)$ spatial correlations due to their different numbers along the one-dimensional projections. For example, there are $N - 1$ nearest-neighbor correlations, while there is only a single $r = N$ correlation among the two most extreme pixels in the projections.

Figure 10 displays this intensity correlation function for the NMR and SEM one-dimensional projection profiles. The same basic generic features characterize the correlation functions of these different profiles; at short distances, $C(r)$ appears to be independent of r, and then decreases rather abruptly at long r due to finite size effects. Note that the range of length scales in the SEM cross sections, or transverse images, and the longitudinal NMR profile are slightly different. However, such a difference is not significant since the statistical properties of the distributions of peak separation and the intensity–intensity correlation functions are identical for longitudinal (the analysis presented in this paper) and transverse (the analysis not presented in this paper) NMR profiles of Fig. 2. Hence the disorder in the porous Pyrex glass filters is isotropic. Furthermore, as the correlation function is normalized as explained above, one could use a reduced length scale, i.e., $0 \le r/r_{max} \le 1$; then both SEM and NMR intensity correlation functions would appear similar with identical reduced length scales. Absolute length scales were used instead in Fig. 10 simply as a matter of taste in order to stay closer and better appreciate the raw $C(r)$ data.

© 1998 NRC Canada

Fig. 7. Histograms (frequency of occurrence) of peak separations (μm) obtained from the one-dimensional SEM projection profile of pore density in Fig. 6 measured with "fine" resolution (*A*) and "coarse" resolution (*B*).

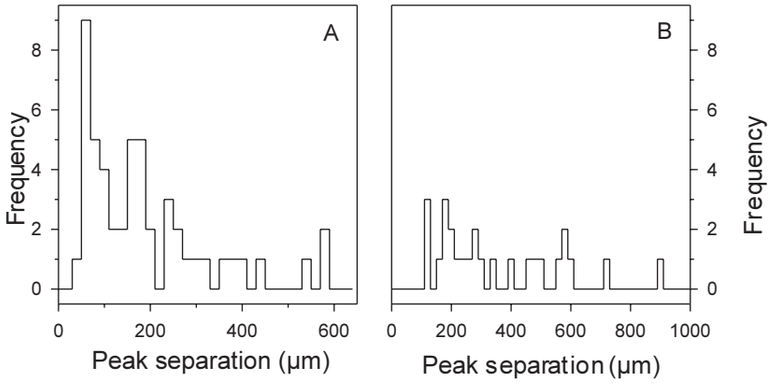

Fig. 8. Histogram (frequency of occurrence) of peak separations (μm) obtained from the superposition of 10 one-dimensional SEM projection profiles of pore space density, each produced from the two-dimensional SEM image in Fig. 4 rotated at 10 different angles (and separated by 18° increments) in the same plane.

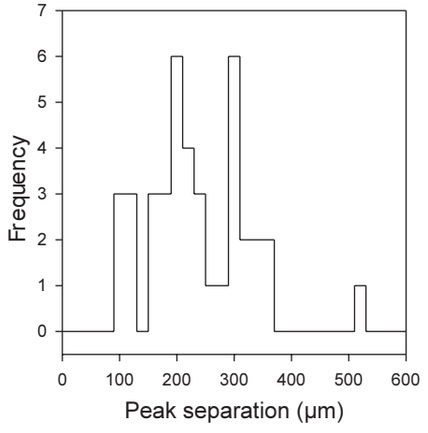

Two issues are needed to understand the behavior of $C(r)$. First, the intensities observed in the NMR and SEM one-dimensional projection profiles correspond to the number of pores that contribute at a pixel position. Hence the intensities in the projections also represent the density of pores, and $C(r)$ is thus a density–density correlation function that varies with the spatial separation along the projections. Second, for a D-dimensional object embedded in a d-dimensional space, the density–density correlation function (and also the mass–mass correlation function) scales as r^{D-d} (11, 12). As discussed in the introduction, for a projection of a D-dimensional object in a d_s subspace, the dimension of the projected object D_p depends on the relationship between D and d_s. For one-dimensional projections $d_s = 1$. If $D > d_s$, then $D_p = d_s$. The density–density correlation function of the D_p-dimensional object in the d_s-subspace, which scales as $r^{D_p - d_s}$, should therefore be independent of r when $D > d_s$. Such is the case in the present situation, and one concludes that the one-dimensional NMR and SEM projections appear to be statistically homogeneous.

3E. Influence of paramagnetic impurities on the NMR one-dimensional projection profiles

The presence of paramagnetic impurities in the glass could impose limitations, even distortions, on the statistical properties of the one-dimensional NMR microimaging profiles. With X-ray fluorescence, traces of impurities, some of which exhibit paramagnetic oxidation states, were measured in the porous Pyrex glass filters; these include Fe (208 ppm), Ni (68 ppm), and Cu (13 ppm). Due to the cleaning procedure of the glass (see Sect. 2), it is reasonable to assume that these impurities are fixed in the glass. Here, we only consider the dipolar interactions between the paramagnetic impurities and the solvent nuclei (18, 19). Since hydrogen is absent in the glass, the effects of indirect magnetization transfer to the paramagnetic impurities through spin diffusion can be safely neglected.

Static dipolar interactions between the paramagnetic forms of these impurities and the magnetic moments of solvent nuclei at the surface of the glass induce shifts of the resonance frequency of the solvent nuclei. For example, with the combination of spin and orbital moments, the effective magnetic moment of Fe(III), $\mu_{eff} \approx 6$ Bohr magneton (20), produces a local field, $H_{loc} \sim \mu_{eff} / r^3$, of roughly 56 G at 10 Å from the Fe(III) centers. This static field yields a 238 kHz frequency shift of these surface ^{1}H nuclei. Thus, a layer of tens of Å of immobilized solvent nuclei on the porous glass would not be detected due to this frequency shift. Nevertheless, such an effect would also be totally irrelevant in our experiments in view of the lower limit of spatial resolution, i.e., 26 μm, imposed by the NMR imaging experimental protocol.

However, the thermal fluctuations of dipolar interactions between the paramagnetic forms of these impurities in the glass and the solvent magnetic moments can lead to a macroscopic layer of molecules on the porous glass that relaxes rapidly, i.e., more quickly than their NMR signals can be detected. To estimate the thickness and volume of such a layer in the porous glass, we will consider a worst-case scenario in our experiments.

First, we assume that the impurities detected by X-ray fluorescence are all in their paramagnetic oxidation states, and all are found solely in the first two atomic layers of the glass. Hence, by diffusion, the solvent molecules in the neighborhood of the impurities are relaxed by the thermally

© 1998 NRC Canada

Fig. 9. Pore chord distribution on linear (left side) and logarithmic length (right side) scales. The solid line corresponds to a lognormal distribution, the solid points represent the average number of chords, and the "error bars " represent the interval between the minimum and maximum number of chords of a certain length observed in nine independent realizations of chord analysis. The statistical characteristics, arithmetic mean (AVG), median (MED), and the most probable value (MPV) of the lognormal distribution are indicated on the plot with the logarithmic scale.

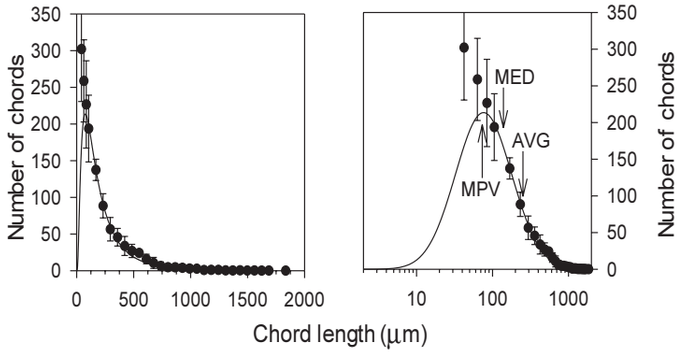

Fig. 10. Intensity correlation function, $C(r)$, versus the length scale (mm). (*A*) One-dimensional SEM projection profile of pore density from Fig. 6. (*B*) One-dimensional SEM projection profile from the superposition of 10 one-dimensional SEM projection profiles of pore space density, each produced from the two-dimensional SEM image in Fig. 4 rotated at 10 different angles (and separated by 18° increments) in the same plane. (*C*) One-dimensional NMR projection profile of pore space density from Fig. 2*A*.

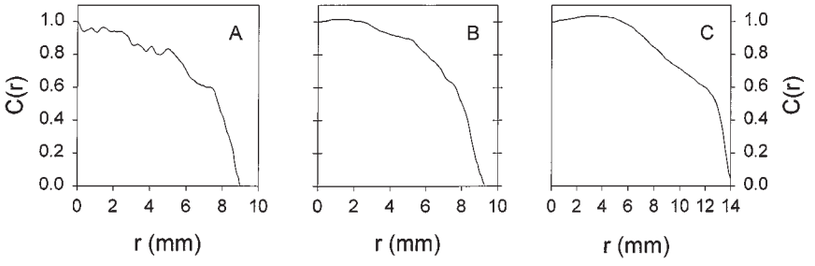

induced fluctuations of the direct dipolar interactions. In such a diffusion-limited situation, de Gennes (16) has shown that the thickness layer is given by $2(Dt/\pi)^{1/2}$, where D is here the self-diffusion of the solvent molecules, and t is the time scale of the experiment. At room temperature, $D = 1.45 \times 10^{-5}$ cm^2/s for bulk cyclohexane (21), and in our experiments the longest relevant time is 25 ms. Hence, a layer thickness of 7 μm of solvent molecules would be "transparent." Such a layer would still be much smaller than the lower limits of spatial resolution in the NMR imaging profiles.

The volume fraction of this layer over the pore volume is given by $2(Dt/\pi)^{1/2} A_v$, where A_v is the surface per unit pore volume (18). Due to the rather large pore structures of the porous Pyrex glass filters, our attempts to measure A_v with nitrogen adsorption isotherms were unsuccessful. Instead, the surface-to-volume ratio of the pores was determined from the SEM digitized image (see Fig. 4) by measuring the length of interface to surface ratio of the pores in the two-dimensional SEM cross sections. Using the arguments of dimensional properties of the projections as discussed at the end of Sect. 3D, this ratio corresponds to the surface/volume pore ratio if the dimension of the pore surface equals 2, i.e., if the surface is not fractal. Such measurements produce $A_v = 110$ cm^2/cm^3, which implies that 7.5% of pore solvent would not be detectable.

With a more realistic scenario, i.e., uniform distribution of the impurities in the glass, and considering that only a fraction of the impurities are in the paramagnetic oxidation states, we estimate that the undetectable layer thickness and volume fraction of relaxed solvent molecules in the pores would be at least one order of magnitude smaller than those calculated in the worst-case scenario presented above. Thus, the effects of paramagnetic impurities in our one-dimensional NMR microimaging profiles are well within experimental uncertainty, and should not significantly affect our results.

4. Summary

In this work, we have characterized some aspects of the macroscopic disorder in porous Pyrex glass filters with one-dimensional NMR microimaging projection profiles. It was argued and demonstrated that the intensity fluctuations in these profiles (see Figs. 1 and 2) can reveal some useful statistical information concerning the randomness in porous media. In particular, the statistical properties, such as the arithmetic and geometric means, of the distribution of peak separations between intensity fluctuations, carry information concerning the pore sizes and the pore-to-pore distances. The intensity–intensity correlation functions in the one-dimensional projections were shown to display an interplay, as a function of length scale, of the dimensions D of the porous network, d the embedding space, $d_s = 1$ for the embedding dimension of the projection, and d_p the dimension of the projected porous network. As such, *the statistical analy-*

© 1998 NRC Canada

sis of the distribution of peak separations and the intensity–intensity correlation functions represent the most information that can be extracted from intensity fluctuations in the one-dimensional NMR projection profiles of porous media. These observations were corroborated with similar analysis of the one-dimensional SEM projections obtained from the two-dimensional SEM images, and pore chord distributions derived from these same images. The approach developed in this work should prove useful and generic in studies of materials with macroscopic randomness and where only one-dimensional NMR microimaging profiles can be reliably measured.

Acknowledgments

We would like to thank Dr. F. Cau for useful discussions in the early parts of these studies, Dr. F. Gitzhofer and P. Magny for their help with the SEM, and Dr. R. Zamojska for her assistance with the X-ray fluorescence measurements. This work was supported by the Natural Sciences and Engineering Research Council of Canada (NSERC) and the McDonnell Douglas Independent Research and Development Program. L.T. is grateful to the Fonds pour la formation de chercheurs et l'aide à la recherche (FCAR) of Québec for scholarships, and for the hospitality of the McDonnell Douglas Corporation Research Laboratories.

References

1. W.W. Mullins. MRS Bull. **21**, 20, (1996).
2. J.M. Ziman. Models of disorder. Cambridge University Press, London. 1979.
3. R. Zallen. The physics of amorphous solids. J. Wiley & Sons, New York. 1983.
4. N.E. Cusak. The physics of structurally disordered matter: an introduction. Adam Higer, Bristol. 1987.
5. M.H. Cohen and C. Lin. *In* Macroscopic properties of disordered media. *Edited by* R. Burridge, S. Childress, and G. Paparricolaon. Lect. Notes Phys. **154**, 74 (1982).
6. K.S. Mendelson. Phys. Rev. B: Condens. Matter, **47**, 1081 (1993).
7. P.T. Callaghan, A. Coy, D. MacGowan, K.J. Packer, and F.O. Zelaya. Nature, **351**, 467 (1991).
8. P.T. Callaghan. Principles of nuclear magnetic resonance microscopy. Clarendon Press, Oxford. 1991.
9. S. Lacelle, L. Tremblay, Y. Bussière, F. Cau, and C.G. Fry. Phys. Rev. Lett. **74**, 5228 (1995).
10. L.Tremblay. Ph.D. Thesis, Université de Sherbrooke, 1997.
11. P. Meakin. Fractals, scaling, and growth far from equilibrium. Cambridge University Press, New York. 1998. p. 84.
12. D.A. Weitz and J.S. Huang. *In* Kinetics of aggregation and gelation. *Edited by* F. Family and D.P. Landau. North Holland, Amsterdam. 1984. pp. 19–28.
13. F. Frankel and G.M. Whitesides. On the surface of things: images of the extraordinary in science. Chronicle Books, San Francisco. 1997.
14. Ace Glass Catalog, Ace Glass Inc., Vineland, New Jersey. 1992. p. 166.
15. F.A.L. Dullien. Porous media: fluid transport and pore structure. Academic Press, London. 1979. Chap. 3.
16. S. Lacelle and L. Tremblay. J. Chem. Phys. **98**, 3642 (1993).
17. P. Levitz, G. Ehret, S.K. Sinha, and J.M. Drake. J. Chem. Phys. **95**, 6151 (1991).
18. P.G. de Gennes. C. R. Acad. Sci. (Paris), **295**, 1061 (1982).
19. A. Abragam. Principles of nuclear magnetism. Oxford Univ. Press, Oxford. 1961. pp. 378–389.
20. R.S. Drago. Physical methods in chemistry. W.B. Saunders, Philadelphia. 1977. Chap. 10.
21. J.N. Sherwood. J. Phys. Chem. **85**, 102 (1985).

© 1998 NRC Canada

Orientation in stretched polymer-dispersed liquid crystals

Julien Brazeau, Yanick Chénard, and Yue Zhao

Abstract: The orientation behavior of liquid crystal molecules in stretched films of polymer-dispersed liquid crystals (PDLC) was investigated by means of infrared dichroism. The liquid crystal used is 4′-octyl-4-biphenyl-carbonitrile (8CN); the polymer matrices are semicrystalline poly(ε-caprolactone) (PCL) and an amorphous miscible blend of PCL with poly(vinyl chloride) (PVC). 8CN was found to have a limit of solubility below 5 wt.% in PCL. We show that an uniaxial stretching can effectively induce a macroscopic orientation of 8CN, and that this orientation can be preserved in the films after removal of the extensional force at room temperature, where 8CN is in its liquid crystalline phase. The molecular orientation is obtained even by stretching PDLC films with 8CN in the liquid state. These results suggest that an elongated polymer cavity in stretched PDLC imposes LC director fields with respect to the long axes of the droplets, which are aligned parallel to the strain direction. The experiments also reveal that the orientation of 8CN is higher in stretched PDLC with a semicrystalline matrix (PCL) than with an amorphous matrix (the PCL–PVC blend), and that the sizes of the LC droplets also have a slight effect on the induced orientation. This work represents a first step in the exploration of new electrooptical effects of PDLC through the presence of a uniform orientation of the liquid crystal molecules and modifications of the polymer cavity at the electrical field-off state.

Key words: polymer-dispersed liquid crystals, molecular orientation, infrared dichroism, electrooptical materials.

Résumé : Faisant appel au dichroïsme infrarouge, on a étudié le comportement orientationnel de molécules de cristaux liquides dans des films étirés de cristaux liquides dispersés dans un polymère (CLDP). Le cristal liquide utilisé est le 4′-octyl-4-biphénylcarbonitrile (8CN); les matrices de polymère comprennent poly(ε-caprolactone) (PCL) semicristalline et un mélange amorphe miscible de PCL et de chlorure de polyvinyle (PVC). On a trouvé que la limite de solubilité du 8CN dans le PCL est inférieure à 5% en poids. On a montré qu'une extension uniaxiale permet d'induire efficacement une orientation macroscopique du 8CN et que, à la température ambiante où le 8CN existe dans sa phase cristalline liquide, cette orientation est maintenue dans les films même après l'élimination de la force d'extension. On peut même obtenir une orientation moléculaire par extension de films de CLDP comportant du 8CN à l'état liquide. Ces résultats suggèrent qu'une cavité allongée présente dans le CLDP étiré impose des champs directeurs CL par rapport aux grands axes des gouttelettes et que ceux-ci sont parallèles à la direction d'élongation. Les expériences révèlent aussi que l'orientation du 8CN est plus importante dans le CLDP avec une matrice semicristalline de PCL que dans une matrice amorphe (mélange de PCL–PVC) et que la taille des gouttelettes de CL a aussi un léger effet sur l'orientation induite. Ce travail correspond à une première étape dans l'exploration de nouveaux effets électrooptiques des CLPD provoqués par la présence d'une orientation uniforme des molécules du cristal liquide et par des modifications de la cavité du polymère en absence d'un champ électrique.

Mots clés : cristaux liquides dispersés dans un polymère, orientation moléculaire, dichroïsme infrarouge, matériaux électrooptiques.

[Traduit par la Rédaction]

Introduction

Polymer-dispersed liquid crystals (PDLC) possess attractive electrooptic properties. Intensive research has been carried out since the mid-eighties in order to explore their applications, which include light shutter, display, and various photonic and optoelectronic devices (1, 2). Generally, a PDLC film contains a nematic liquid crystal that is phase separated from a polymer matrix, in the form of spherical droplets. Figure 1 sketches the basic operating principle of PDLC. The LC molecules inside the droplets can adopt different configurations (director fields) depending mainly on their interface-anchoring and elastic properties. The bipolar configuration illustrated in Fig. 1 is most often observed where the nematic director fields develop along an axis. Because of the random alignment of those droplets axes, the effective refractive index of the droplets, n_{eff}, is the mean value given by $(n_e + n_o)/2$, where n_e and n_o are the extraordinary and ordinary refractive indices associated with the long axis of the LC molecules and the other two perpendicular directions, respectively. Choosing appropriate LC and polymers, it is possible to have $n_e \approx 1.7$, $n_o \approx 1.5$, and n_p, the refractive index of the polymer matrix, also close to 1.5. Un-

Received January 16, 1998.

J. Brazeau, Y. Chénard, and Y. Zhao.[1] Département de chimie, Université de Sherbrooke, Sherbrooke, QC J1K 2R1, Canada.

[1]Author to whom correspondence may be addressed. Telephone: (819) 821-7090. Fax: (819) 821-8017. E-mail: yzhao@courrier.usherb.ca

© 1998 NRC Canada

Fig. 1. Sketch of the operating principle of PDLC: (*a*) normal mode, and (*b*) stretched film.

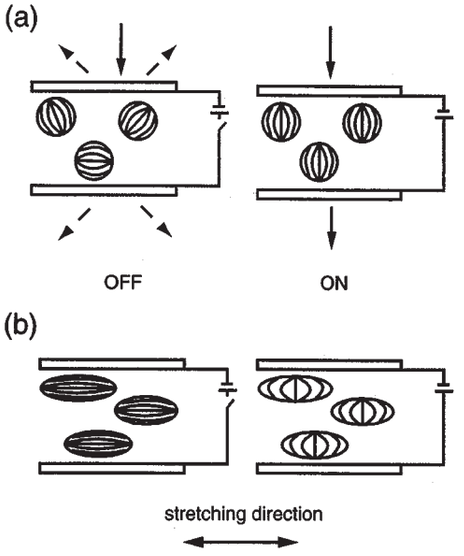

der these conditions, n_{eff} of the LC droplets differs from n_p. When such a PDLC film is sandwiched between two transparent and conductive substrates, the system strongly scatters the incident light because of the mismatch between n_{eff} and n_p; the film appears opaque. When an electric field is applied through the film, LC molecules inside the droplets can be aligned along the field direction (the film thickness direction); the incident light now experiences n_o, which equals n_p. As a result of the matching refractive indices, the PDLC film becomes transparent. This reversible change of the film transparency under the voltage-off and voltage-on state is the basis for most applications of PDLC. The phase separation is, among other things, a key step in the fabrication of a PDLC. Generally, it can be induced by solvent evaporation, thermal effect, and polymerization from an initially homogeneous mixture of LC with polymer or polymer precursor or monomer (1–3).

A number of parameters, such as LC concentration and droplet sizes, influence the electrooptical properties of PDLC. The polymer cavity, determined by the shape of the LC droplets, is also known to play a major role (1, 2). The polymer cavity influences the anchoring of the LC molecules at the interface and, hence, the director field configuration inside the droplets. At the voltage-on state, those LC molecules anchored to the interface also behave differently from the molecules more distant from the interface. Despite the tremendous effort already dedicated to studying PDLC, it was noticed that very few studies considered stretched or sheared PDLC (1, 4), showing little interest in characterizing and relating molecular orientation of LC to the electrooptical properties. This has motivated us to undertake investigations on PDLC. Our basic idea is to introduce changes in the orientation of the LC molecules and the polymer cavity at the electrical field-off state and to study the possible new electrooptical effects.

The changes expected by stretching a PDLC film containing bipolar spherical droplets are also sketched in Fig. 1, displaying elongated LC domains and a uniform LC molecular orientation along the stretching direction. Even in this simple case, new electrooptical effects may show up. For instance, an incident light polarized parallel to the stretching (orientation) direction should see n_e at the voltage-off state and n_o at the voltage-on state. If the conditions as described above are fulfilled, the contrast of the film between opaque and transparent, which is a continuing research subject, could be improved since the refractive index mismatch at the voltage-off state is $(n_e - n_p)$, which is greater than $(n_{eff} - n_p)$ in the normal case. The approach is complementary to the existing techniques for PDLC, but it can lead to discoveries of new electrooptical effects. The possibilities exist because LC molecular orientation can be altered by different mechanical fields such as uniaxial stretching, biaxial stretching, and compression, causing different modifications of the polymer cavities. There is also the possibility of tuning the refractive indices in a specific system through the polymer matrix orientation.

To explore such an approach, some fundamental questions must be answered: can a uniform orientation of LC molecules be effectively achieved by stretching a PDLC film? and, more importantly, can the stretching-induced orientation be preserved in the deformed film once the extensional force is removed? Generally, a macroscopic orientation of LC molecules induced by an external stimulus is not thermodynamically stable, and the system tends to recover its initial state after the stimulus is removed. In the case where a liquid crystalline polymer (LCP) is dispersed in a conventional polymer matrix, the answers are yes (5). But the two systems are different in that the orientation of the mesogenic groups of LCP is frozen when the polymer is cooled below its glass transition temperature T_g. This feature obviously is not a characteristic of PDLC. In this paper, we report our very first experiments aimed at answering the above questions.

Experimental

The liquid crystal used to prepare PDLC was 4′-octyl-4-biphenyl-carbonitrile (8CN), purchased from Aldrich. It has a crystal-to-liquid-crystal transition at 24°C and a nematic-to- isotropic transition (clearing temperature) at 40°C. The choice of an appropriate polymer matrix is important, and there are several limitations. First, good PDLC films are necessary in order to perform mechanical stretching, meaning that the LC concentration generally can not exceed 40 wt.%. If the LC solubility limit in a particular polymer is substantial, that polymer cannot be used as matrix. This is known to be the case for many polymers that can solubilize LC molecules up to an LC concentration of about 30 wt.%. When we started this work, we used 30 wt.% of 8CN in several matrices including a polystyrene–poly(vinyl methyl ether) blend, a styrene–butadiene–styrene tri-block copolymer, and a couple of polyacrylates; none of those systems worked because of a high 8CN solubility in these polymers (only a few 8CN phase-separated and the rest acting as plasticizer). In other words, it is necessary to use a polymer in which 8CN has a low solubility. Secondly, on the basis of our previous studies on LCP (5), to obtain a uniform orientation it is more effective to stretch samples in their liquid

© 1998 NRC Canada

Fig. 2. DSC heating curves of 8CN and the PCL–8CN 70:30 blend.

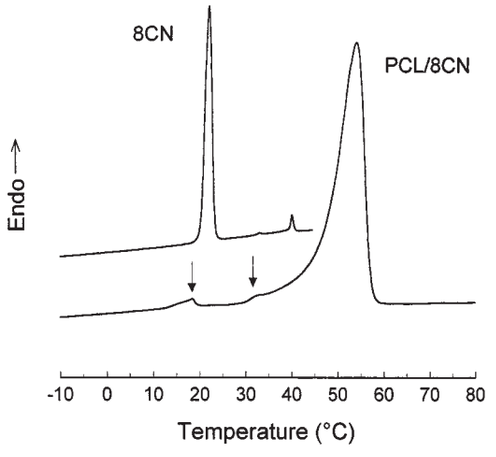

crystalline phases. This means that the polymer matrix used for PDLC should be stretchable at temperatures below the clearing temperature of 8CN.

The matrix used in this study was poly(ε-caprolactone) (PCL), which is a semicrystalline polymer. The solubility limit of 8CN in PCL was found to be very low, probably because of the polymer crystallization. As amorphous PCL, located in the interlamellar region, has a low T_g of about –60°C, films of PCL can easily be cold-drawn at room temperature or stretched at temperatures below the crystal melting point at about 55°C. A miscible and amorphous PCL blend containing 45 wt.% of poly(vinyl chloride) (PVC) was also utilized in order to investigate the polymer matrix effects. The stretching and orientation measurements were performed on PDLC samples containing 10 and 30% of 8CN. Typically, a homogeneous solution of 8CN and the polymer was prepared using THF as solvent; then the solution-cast films were dried under vacuum at room temperature for 3 days. The film thickness was about 20–30 μm. The phase separation in the dried PDLC films is induced by solvent evaporation. Heating these PDLC films to the isotropic state, at 70°C, the mixture becomes homogeneous, but a subsequent cooling again leads to the phase-separated system, the phase separation being induced by thermal effects. The samples of PCL and PVC were also purchased from Aldrich ($M_w \approx 65\,000$ for PCL and $M_w \approx 161\,000$ for PVC).

Uniaxial stretching of the PDLC films was carried out on a laboratory-made apparatus at a rate of about 20 mm/min. In the case of PCL–8CN, the orientation of 8CN was measured on films released from the stretching machine ("relaxed films"); the deformation of the semicrystalline matrix is plastic and permanent. For stretching at temperatures above ambient, the films were cooled, under strain, to room temperature for 20 min before being removed from the stretching machine. In the case of (PCL–PVC 55:45)–8CN, the amorphous matrix has a low T_g of about –40°C; the orientation measurements were performed on films under strain in order to avoid film shrinkage.

Orientation of 8CN averaged over all molecules can be characterized by the orientation function defined as $F = (3\langle\cos^2\Theta\rangle - 1)/2$, where Θ is the angle between the long molecular axis of 8CN and the stretching direction. The value of this orientation function varies between –0.5 and unity. $F = 1$ indicates a perfect orientation parallel to the stretching direction, while $F = -0.5$ corresponds to a perfect perpendicular orientation. In PDLC, if the LC droplets are randomly aligned, the director fields of the LC molecules are randomly distributed in space; the lack of a macroscopic orientation leads to $F = 0$. Of course, F also equals zero if the LC is heated to the isotropic liquid state. In this study, infrared dichroism was used to determine the molecular orientation of 8CN in the stretched PDLC films. Using the characteristic C≡N band near 2230 cm^{-1}, the orientation function of 8CN is calculated (5) from $F = (A_\parallel / A_\perp - 1) / (A_\parallel / A_\perp + 2)$, where $A_\parallel$ and $A_\perp$ are the absorbances of the 2230 cm^{-1} band with the infrared beam polarized parallel and perpendicular to the film stretching direction, respectively. Infrared spectra of 4 cm^{-1} resolution were recorded on a Bomem MB-102 FTIR spectrometer using a wire-grid infrared polarizer placed between the sample and the DTGS detector; 50 interferograms were averaged for each spectrum. A Perkin–Elmer DSC-7 differential scanning calorimetor and a Leitz DMR-P polarizing microscope were also used for the characterizations of PDLC.

Results and discussion

For the PCL–8CN blends, the LC droplets cannot be observed with the polarizing microscope because of the rapid crystallization of PCL, giving rise to a birefringent matrix that overlaps the birefringent LC droplets. However, the phase separation is confirmed by the DSC measurements. Figure 2 shows the heating curves of pure 8CN and the PCL–8CN 70:30 blend. The large endotherm centered at 52°C for the blend is due to the PCL crystal melting; two small endothermic peaks, indicated by arrows, are noted at about 18 and 32°C and correspond to the two transitions of pure 8CN at 21 and 40°C. Such a depression of transition temperatures as well as a decrease in transition enthalpies in PDLC are a common feature, understandably resulting from interfacial interactions between the LC and the polymer matrix. For the present PDLC system, what is important is that 8CN is in its liquid crystalline phase at room temperature (about 22°C), which is necessary for LC molecular orientation under cold-drawing of the film and for any LC reorientation at the voltage-on state.

The PDLC films were stretched to various draw ratios λ, which is defined as ratio of the film length after stretching over the film length before stretching; the orientation of 8CN was measured as a function of film extension. Figure 3 presents the results obtained with samples containing 10 and 30% of 8CN by plotting the orientation function of 8CN versus the draw ratio. It is clear that a macroscopic orientation of 8CN, parallel to the strain direction, develops in the stretched films. The orientation increases continuously with the film extension up to $\lambda = 4$–5. This behavior is somewhat different from blends containing an LCP (5), whose orientation generally attains a plateau level at $\lambda = 2$–3. On the other hand, the orientation level of 8CN is similar in the two blends. This is indicative of a very low solubility of 8CN in PCL. As mentioned earlier, solubilized LC molecules act as a diluent in the polymer matrix and do not orient upon

© 1998 NRC Canada

Fig. 3. Orientation function of 8CN vs. draw ratio for PDLC films of PCL–8CN 70:30 and PCL–8CN 90:10.

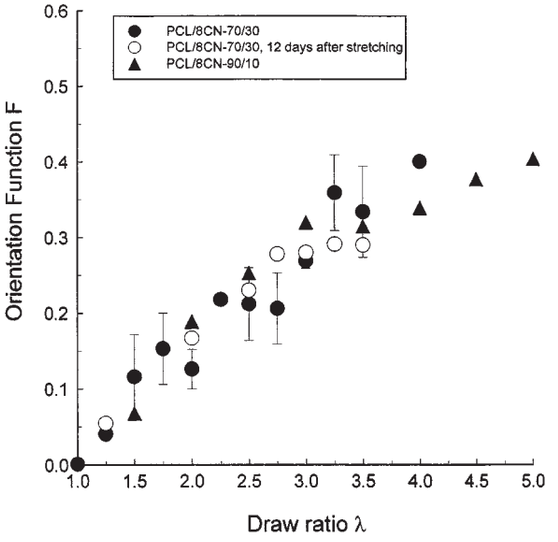

Fig. 4. Orientation function of 8CN vs. stretching temperature for PDLC films of PCL–8CN 70:30 and PCL–8CN 90:10.

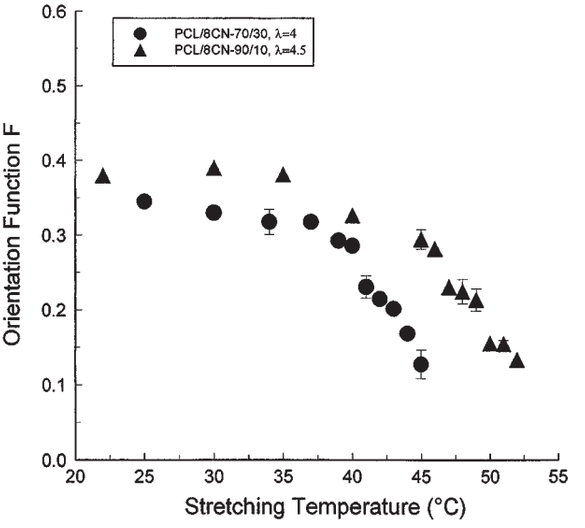

stretching. Even if the solubility limit for PCL–8CN is, for example, ca. 5%, its orientation function averaged over all molecules should be much lower in the PCL–8CN 90:10 blend than in the PCL–8CN 70:30 blend. We have made DSC measurements that confirmed this low 8CN solubility. It was found that T_g of the amorphous PCL at about –60°C, for pure PCL, is almost unchanged in blends containing 5, 10, and 30% of 8CN, indicating that the solubility limit is below 5%.

Also shown in Fig. 3 are the data obtained with the same films of the PCL–8CN 70:30 blend 12 days after stretching. During that period of time, the films were left at room temperature and allowed to relax without any constraints. No significant film shrinkage was observed and, as can be seen, the orientation of 8CN remains unchanged. The results indicate that, under the plastic deformation of PCL, the orientation of 8CN can be conserved in the stretched films after the removal of the mechanical stress. This observation is important since such a permanent LC orientation at room temperature is the basis of the approach outlined in the Introduction. At this point we can only suggest that an elongated LC droplet, and hence an elongated polymer cavity, may be responsible for retaining the LC orientation.

The influence of the stretching temperature on the LC orientation was investigated. Figure 4 shows the orientation function of 8CN versus stretching temperature. The samples containing 10% of 8CN were stretched to $\lambda = 4.5$, while those containing 30% of 8CN were stretched to $\lambda = 4$. In both cases, up to about 40°C the stretching temperature has little effect on the orientation of 8CN, but when the stretching temperature is raised further, the orientation level decreases rapidly. Considering the fact that the clearing temperature of 8CN in the blends with PCL is about 32°C (Fig. 2), the results seem to indicate that, even with 8CN in its liquid state, stretching the PDLC film can result in a uniform orientation of 8CN. Again, this feature is different from what is known for the blends containing an LCP (5), where the orientation of the mesogenic groups generally drops to zero when the stretching is performed with LCP in the isotropic state. These results are consistent with the observation of a stable 8CN orientation in relaxed films, suggesting that an elongated polymer cavity in the stretched films may be the dominant factor imposing the director fields of LC inside the droplets. The following mechanism is conceivable: Above the clearing temperature, 8CN is a liquid inside the droplets before and after the stretching, but the stretching transforms the droplets from spherical to elongated shapes; once 8CN enters into the nematic phase during the film cooling to room temperature, the polymer cavity leads to director fields aligned along the long axes of the droplets, as sketched in Fig. 1. Because of the parallel alignment of LC molecules at the interface, the symmetry axes of the elongated bipolar droplets should lie along the stretching direction in order to minimize the curvature of the director fields and the associated elastic free energy. On the other hand, if there is no coalescence of the LC droplets after the stretching, the transformation from spherical to elongated shape means an increased surface-to-volume ratio and, thus, a more important anchoring effect at the interface on the LC director fields. The severely lowered orientation of 8CN at stretching temperatures above 40°C is probably due to an enhanced miscibility between 8CN and PCL as the temperature is close to the PCL melting point. Finally, the orientation difference for the two blends is attributed to different draw ratios.

Blends of PCL with PVC are known to be miscible (6). The crystallization of PCL is slowed down by the presence of PVC because of the miscibility; having 45% of PVC in the blend, the crystallization of PCL starts about 3 h after the cooling from the liquid state. In this study, we have also investigated the orientation of 8CN dispersed in the amorphous PCL–PVC 55:45 blend. The advantages of having an amorphous matrix are (*i*) the polarizing microscope can be used to observe the LC droplets in the PDLC, and (*ii*) the LC orientation behavior can be compared to that of PDLC having the semicrystalline PCL matrix. Only one concentration of 8CN, namely 30%, was used to prepare this PDLC.

© 1998 NRC Canada

Fig. 5. Polarized photomicrographs of a PDLC film containing 30% of 8CN in the amorphous PCL–PVC 55:45 blend matrix: (*a*) 30 min and (*b*) 45 min after cooling to room temperature; (*c*) 45 min after cooling, stretched to $\lambda = 3$. Magnification: 250×.

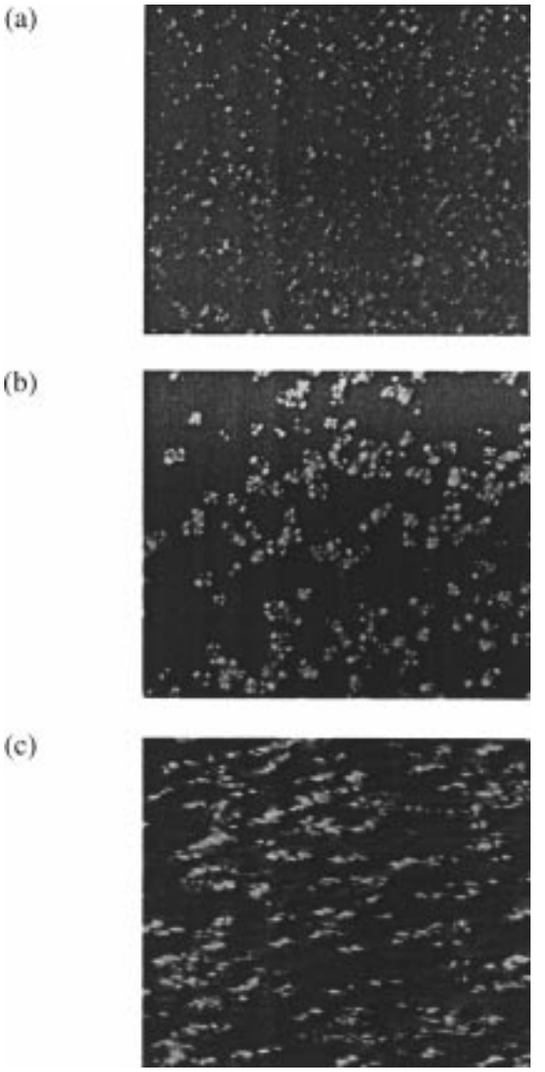

Figure 5 shows some polarized photomicrographs of this PDLC system. Two of them (5*a* and 5*b*) were taken 30 and 45 min after the film was allowed to cool from 70°C to ambient (it took several min for the sample to reach room temperature), and the third one (5*c*) was taken on the film, 45 min after the cooling, stretched to $\lambda = 3$. It is seen that the sizes of the birefringent spherical droplets in the non-stretched film grow with time. Also, the microphotographs confirm that the stretching transforms the shape of the LC droplets, and thus the polymer cavity, from spherical to elongated. The long axes of the elongated domains are aligned along the strain direction. These morphological changes in stretched PDLC films were expected, but could not be observed with the PCL–8CN films as explained above.

The orientation of 8CN in PDLC with the amorphous matrix was determined for samples stretched under different

Fig. 6. Orientation function of 8CN vs. draw ratio for PDLC films of (PCL–PVC)–8CN containing 30% of 8CN, films being stretched immediately (triangle) and 1 h (circle) after cooling to room temperature.

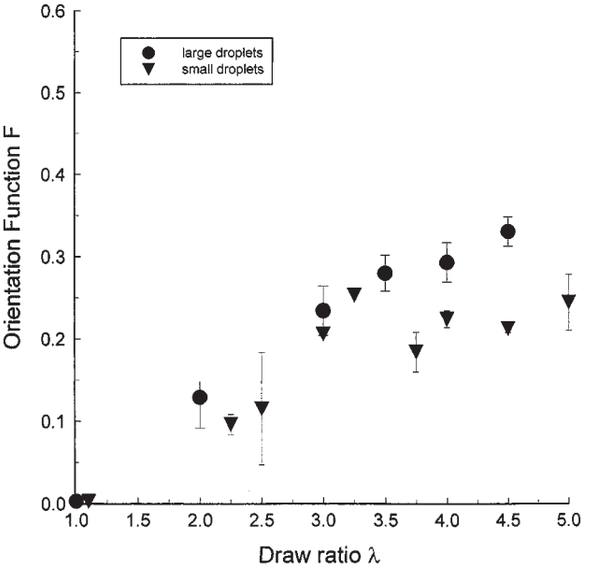

conditions. One series of the films was stretched immediately after cooling from the isotropic state, and the other films were stretched 1 h after cooling. The results are shown in Fig. 6. Several observations can be made. First, comparing the orientation of 8CN with that in the semicrystalline PCL (Fig. 3), it appears that the orientation is lower in this amorphous matrix. This apparently suggests certain effects of the matrix on the LC orientation. Secondly, the orientation in the films stretched immediately following cooling is lower than that in the films subjected to the stretching 1 h afterwards. This result seems to indicate an effect of the LC droplet size on the stretching-induced orientation; large LC droplets formed after longer times at room temperature (Fig. 5) favor the induction of a macroscopic orientation. Actually, in samples immediately after cooling, the droplets of 8CN are so small that they cannot be detected by optical microscopy (the birefringent spots were detectable 20—25 min after cooling). However, for the reasons pointed out earlier concerning the LC solubility, the results in Fig. 6 can also be explained by an increasing phase separation with time between 8CN and the matrix. As the phase separation develops, more and more molecules of 8CN are inside the droplets and contribute to the average stretching-induced orientation, which is also accompanied by a growth in size of the LC droplets.

As explained in the Introduction, this work was not aimed at studying new electrooptical effects of this particular PDLC system of PCL–8CN. Nevertheless, we have checked the reorientation of 8CN in some stretched samples having an elongated polymer cavity and a macroscopic molecular orientation. In all cases, the reorientation was observed at the electrical field-on state. When a stretched film was sandwiched between two glass plates coated with a transparent electrode of indium-tin-oxide (ITO) and placed between crossed polarizers, a decrease in the transmitted light inten-

© 1998 NRC Canada

sity occurred once the voltage was turned on, indicating the reorientation of 8CN molecules along the electrical field direction (the test voltages were 40–100 V with a 1000 Hz a.c. signal).

Conclusions

Uniaxially stretching PDLC films of PCL–8CN and (PCL–PVC 55:45)–8CN can effectively induce a macroscopic orientation of 8CN molecules parallel to the strain direction. Because of the low solubility limit of 8CN in PCL (less than 5 wt.%), the stretching-induced 8CN orientation is similar in PDLC films containing 10 and 30% of 8CN. The orientation can even be obtained by stretching PDLC at temperatures above the clearing point of 8CN. This observation suggests that elongated droplets and polymer cavity, resulting from the stretching, impose the director fields with respect to the long axes of the droplets, which are aligned parallel to the strain direction. This feature is different from orientation of liquid crystalline polymers, for which cooperative effects, characteristic of liquid crystalline phases, are important in the orientation process. For the same reason as given in connection with the elongated polymer cavity, it was found that at room temperature, where 8CN is in its liquid crystalline phase, the stretching-induced orientation of 8CN is stable in deformed PCL–8CN films after the removal of the mechanical stress. The results of this study represent a first step and the basis of an approach that explores possible new electro-optical effects of PDLC systems having a macroscopic orientation of LC molecules and modified polymer cavity at the electrical field-off state.

Acknowledgments

We thank Ms. Mireille Vézina for her assistance in some experiments. We are also grateful to the Natural Sciences and Engineering Research Council of Canada and the Fonds pour la Formation de Chercheurs et l'Aide à la Recherche of Québec for their financial support for this work.

References

1. P.S. Drzaic. Liquid crystal dispersions. World Scientific, London. 1995.
2. G.P. Crawford and S. Zumer (*Editors*). Liquid crystals in complex geometries. Taylor & Francis, London. 1996.
3. L. Bouteiller and P. Le Barny. Liq. Cryst. **21**, 157 (1996).
4. O.A. Aphonin, Y.V. Panina, A.B. Pravdin, and D.A. Yakovlev. Liq. Cryst. **15**, 395 (1993).
5. H. Lei and Y. Zhao. Polymer, **35**, 104 (1994).
6. F.B. Khambatta, F. Warner, T. Russell, and R.S. Stein. J. Polym. Sci. Polym. Phys. Ed. **14**, 1391 (1976).

© 1998 NRC Canada

Irradiance and temperature dependence of photoinduced orientation in two azobenzene-based polymers

Dennis Hore, Almeria Natansohn, and Paul Rochon

Abstract: This paper concerns itself with photoinduced anisotropy in two azobenzene-functionalized polymers. A simple physical model of the process that considers only three possible states of azo chromophores is proposed. This model predicts an equilibrium level of anisotropy that depends on the pump irradiance and temperature. Each of these influences is examined in turn, with experimental illustrations from the two polymers poly[4-[2-(methacryloxy)-ethyl-ethyl]azobenzene] (pMEA) and poly[4′-[[2-(methacryloxy)ethyl]-ethyl]amino-4-nitroazobenzene] (pDR1M).

Key words: azobenzene polymers, photoinduced orientation, irradiance, temperature.

Résumé : Dans ce travail, on traite de l'anisotropie photoinduite dans deux polymères d'azobenzènes fonctionnalisés. On propose un modèle physique simple qui ne prend en considération que trois états possibles des chromophores azo. Ce modèle permet de prédire un niveau d'équilibre d'anisotropie qui dépend de l'irradiance de la pompe et de la température. On a examiné l'influence de ces divers facteurs à tour de rôle, en donnant des illustrations expérimentales à l'aide des deux polymères suivants : poly[4-[2-(méthacryloxy)éthyl]azobenzène] (pMEA) et poly[4'-[[2-(méthacryloxy)éthyl]éthyl]amino-4-nitroazobenzène] (pDR1M).

Mots clés : polymère de l'azobenzène, orientation photoinduite, irradiance, température.

[Traduit par la Rédaction]

Introduction

The linking of observable macroscopic properties to molecular-scale mechanisms remains one of the fundamental challenges and enticements of materials science. These properties are often geared toward engineering and technology applications and so are zealously sought. The study of the photoinduced orientation of azobenzene-based polymers represents just such an endeavour.

Anisotropy may be photoinduced in thin films of amorphous polymers containing azobenzene moieties in their side chains. This anisotropy exists well below the glass transition temperature (T_g) in an area as small as a beam can be focussed, exhibits long-range stability, and has high contrast with isotropic regions of the material. These properties make such polymers possible candidates for technologies such as reversible optical storage and waveguides.

Although the details of the orientation mechanism and underlying processes are yet to be agreed upon, a simple physical picture may be proposed. An isotropic distribution of chromophores (as present in an amorphous film) is subject to a linearly polarized pump and individual species are promoted to the lowest energy π^* excited state. One of the relaxation processes from π^* is conversion to the other geometric isomer. Since the *trans* ground state lies lower in energy than that of the *cis* isomer, any *cis* species created revert to *trans* via a thermal and (or) a photochemical route. Therefore in the presence of the pump, many *trans* $\rightarrow$ *cis* $\rightarrow$ *trans* isomerization cycles occur, resulting in orientation of the side chains. This motion may continue until the chromophores find themselves in a position where their dipole moments (along the long axis of the molecule) lie perpendicular to the polarization plane of the pump. Since there can be no further absorption in this orientation, isomerization, and therefore the accompanying side-chain motion, stops and the chromophores become "locked." Although steric interactions prohibit the complete orientation of all chromophores, at equilibrium there is a net alignment perpendicular to the pump. This anisotropy manifests itself as a measurable difference in refractive index, or birefringence.

In this study a simple model of photoinduced orientation is presented. The effect of irradiance and temperature on the order parameter is shown for two polymers whose structural units are depicted in Fig. 1. Poly[4′-[[2-(methacryloxy)ethyl]-ethyl]amino-4-nitroazobenzene] (pDR1M) belongs to the pseudo-stilbene spectral class according to Rau's classification scheme (1) since the energy ordering of the (n, π^*) and (π, π^*) states is reversed. For this polymer the bands are practically overlapping, resulting in both *trans* $\rightarrow$ *cis* and *cis* $\rightarrow$ *trans* photoisomerizations at the same excitation wavelength. Poly[4-[2-(methacryloxy)-ethyl]azobenzene] (pMEA) belongs to the azobenzene spectral class (1) with a low-intensity (n, π^*) band in the visible and a high-intensity (π, π^*) band in the UV. This results in an efficient *cis* $\rightarrow$ *trans* back-

Received February 25, 1998.

D. Hore and A. Natansohn.[1] Department of Chemistry, Queen's University, Kingston, ON K7L 3N6, Canada.
P. Rochon. Department of Physics, Royal Military College, Kingston, ON K7K 5L0, Canada.

[1]Author to whom correspondence may be addressed. Telephone: (613) 545-2008. Fax: (613) 545-6669. E-mail: natansoh@chem.queensu.ca

© 1998 NRC Canada

Fig. 1. The structural units of pMEA (top) and pDR1M (bottom).

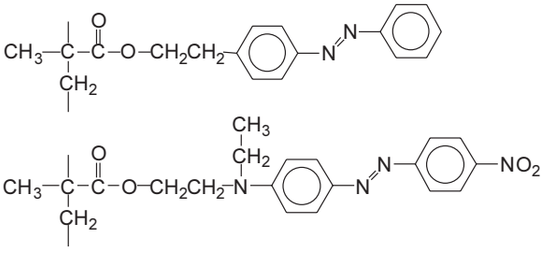

isomerization at 488 nm while the *trans* → *cis* process experiences only the tail of the absorption band.

Model

An elementary model of photoisomerization is based upon the phenomenological mechanism proposed by Sekkat and Dumont (2). There are four dominant processes that contribute to the orientation. These are (*i*) photochemical *trans* → *cis* isomerization, (*ii*) photochemical *cis* → *trans* back-isomerization, (*iii*) thermal *cis* → *trans* back-isomerization, and (*iv*) angular redistribution among species. It is assumed that only the *trans* species may contribute to the observed order parameter on account of its elongated rodlike shape. To make things even simpler, all possible angles at which the side groups can lie are reduced to two: parallel or perpendicular to the pump. As a consequence of the highly delocalized π-electron density of the azo chromophores, the probability that a species will absorb the pump radiation is proportional to $\cos^2\theta$, where θ is the angle between the electronic dipole moment and the polarization vector of the pump. Considering our two orientations, this implies complete absorption for parallel species while perpendicular groups are oblivious to the pump. An identical solution for the *photostationary* order parameter is obtained with and without the photochemical back-isomerization. Therefore, for the primary purpose of representing this equilibrium, only the thermal back-isomerization will be included in the model, keeping in mind that both occur in the actual experimental system. With these considerations in mind, three populations have to be monitored: *cis* (*C*), *trans* parallel to the pump ($T_{\|}$), and *trans* perpendicular to the pump ($T_{\perp}$). The pump I^* creates *cis* species that thermally relax back to *trans* with a reciprocal lifetime of γ. The *trans* species may flip back and forth between parallel and perpendicular orientations with a diffusion constant Γ.

The model is implemented by means of three coupled differential equations that govern the change in each population with time.

$$[1] \qquad \frac{dT_{\|}}{dt} = -I^*T_{\|} + \frac{1}{2}\gamma C - \Gamma T_{\|} + \Gamma T_{\perp}$$

In the first equation, the $T_{\|}$ population is being diminished by the pump and by rotation to the perpendicular direction, increased by *cis* → *trans* thermal relaxation and rotational diffusion from the perpendicular towards the parallel position. The thermal *cis* → *trans* process is here assumed to equally populate $T_{\|}$ and $T_{\perp}$.

Fig. 2. An energy level diagram for the three-state model of photoinduced reorientation. Here promotion to π* is shown only for the photochemical *trans* → *cis* isomerization. The *cis* species thermally relax to *trans*, and redistribution among *trans* species is also allowed to occur.

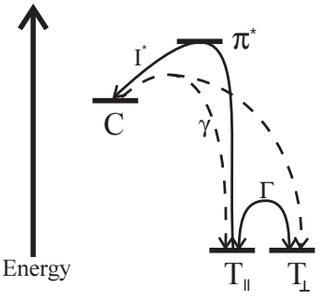

$$[2] \qquad \frac{dT_{\perp}}{dt} = +\frac{1}{2}\gamma C + \Gamma T_{\|} - \Gamma T_{\perp}$$

In the second equation, the number of $T_{\perp}$ chromophores is increased by thermal back-isomerization and is also susceptible to rotational diffusion.

$$[3] \qquad \frac{dC}{dt} = +I^*T_{\|} - \gamma C$$

In the last equation, the *cis* species is increased in number by pumping from *trans* and suffers losses to the thermal back-isomerization. An energy level diagram for such a system is shown in Fig. 2.

Experimental

The synthesis of pMEA (3) and pDR1M (4) has been described in previous publications. The polymers were spin-cast from THF onto glass substrates and then held at their glass transition temperatures (120°C for pDR1M and 80°C for pMEA) for 1 h. This served to adhere the matrix onto the substrate, drive out solvent, and remove any anisotropy that may have been induced by spin-coating. Film thickness was measured using a Sloan Dektak II profilometer. Before beginning any of the experiments, it was necessary to choose films of an appropriate maturity to obtain reproducible rates and saturation levels, and there has been a similar report of such an age requirement in the literature (5). Consistent results were achieved with films left for 2–4 weeks at room temperature following preparation.

A schematic of the optical bench is given in Fig. 3. In the detection circuit a diode laser operating near 690 nm was incident onto a linear polarizer at 45°. The beam then passed through a focussing lens, the sample, and a crossed polarizer before reaching the detector, a photomultiplier tube. The square root of the signal from the detector is proportional to the phase lag suffered by the probe through a birefringent sample. Refractive index difference ($\Delta n = n_{\|} - n_{\perp}$) was then calculated using

$$[4] \qquad \Delta n = \frac{\sqrt{I}\,\Delta\varphi}{\sqrt{I_{\mathrm{ref}}}\,kd}$$

© 1998 NRC Canada

Fig. 3. A schematic of the optical bench used to induce and measure birefringence.

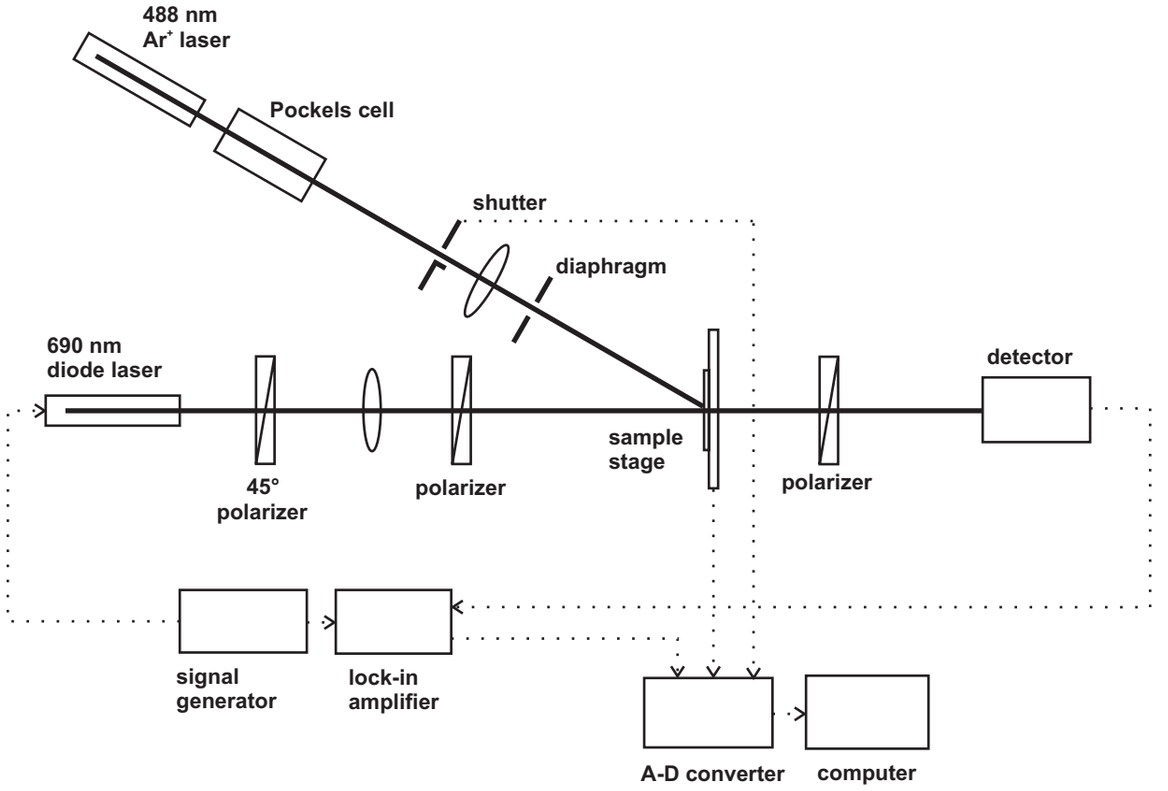

where I is the signal from the amplifier, $\Delta\varphi$ is the phase lag at reference, d is the sample thickness, $k = 2\pi / \lambda$ is the wave vector, and I_{ref} is the reference signal used in the calibration. From this, the order parameter S was obtained using

$$[5] \qquad \langle S \rangle = \frac{\Delta n}{3n_{band}}$$

where n_{band} refers to the effective isotropic index of refraction of the chromophores alone. Since the birefringence is likely the result of an anisotropic distribution of azo side groups, a measure of their orientation should include the contribution to the refractive index of just those groups. This was obtained from the (π, π^*) and (n, π^*) absorption bands using a Kramers–Kronig relation

$$[6] \qquad n_{band}(\lambda) = \int_{band} \frac{\alpha(\lambda')}{1-(\lambda'/\lambda)^2} d\lambda'$$

where $\alpha(\lambda)$ is the absorption coefficent. For pDR1M this gave a photostationary order parameter of –0.13, in agreement with that obtained by dichroic infrared (6) and transient absorption spectroscopy (7).

The 488 nm line of an Ar^+ laser was used as an excitation source, intersecting the probe beam at the sample surface. A Pockels cell was used to vary the laser polarization between linear and circular. A typical experimental protocol involved irradiating the sample for 200 s while collecting data at a rate of 1 point/s for the first 10 s, followed by 10 points/s for the remaining time. An Instec temperature controller and heating stage were used to maintain temperatures accurate to within ±0.1°C.

Results and discussion

Model predictions

When a simulation of photo-orientation based on the above model is run, the macroscopic order parameter S reaches a saturation value, as is observed experimentally (Fig. 4). It is possible to derive an analytical expression for this saturation value by solving the linear system (eqs. [1]– [3]) with the steady-state approximation, giving

$$[7] \qquad \langle S \rangle = \frac{T_{\parallel} - T_{\perp}}{T_{\parallel} + 2T_{\perp}} = -\frac{I^*}{6\Gamma + 2I^*}$$

Although the model assumes the orientation to be two-dimensional (in the plane of the film), the order parameter must approximate a three-dimensional system to be compared with the experimental value given by eq. [5]. For the calculation of S, the total *trans* population occupies three states. Here an additional $T_{\perp}$ exists (chromophores oriented normal to the film surface and hence also perpendicular to the pump) that is, for simplicity, assumed to have the same population as the original in-plane $T_{\perp}$. The result is nearly identical to that obtained by Labarthet and Sourisseau (7) in their implementation of the model of Sekkat and Dumont (2) obtained with a more complete theory where all angular distributions are taken into account.

© 1998 NRC Canada

Fig. 4. The photostationary order parameter attained by an experimental system (pDR1M) and by simulation with the model.

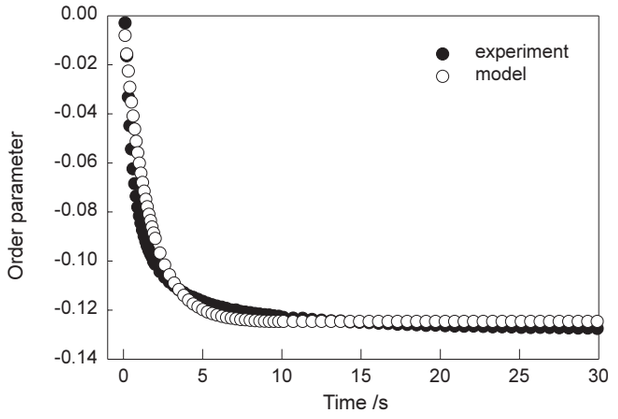

The model predicts a photostationary order parameter that is independent of the reciprocal *cis* lifetime γ. The only influences that remain are the pumping rate I^* and the *trans* diffusion constant Γ. It is possible to obtain an estimate of the pumping rate based on the *trans* $\rightarrow$ *cis* quantum efficiency Φ and experimentally measurable *trans* absorption cross section σ.

$$[8] \qquad I^* = I_{\text{pump}}\Phi\sigma$$

The likelihood of photon absorption leading to isomerization is directly related to the free volume available for such a configurational change, and so the quantum efficiency is sensitive to the polymer matrix. It has been shown to vary by more than four orders of magnitude from solution values of 0.25 (1) to 0.11 for doped systems (8) to 7.4×10^{-6} in Langmuir–Blodgett films (9). Our modelling suggests a quantum efficiency in the range 5×10^{-3} to 5×10^{-2}, which is low but reasonable, considering the inevitable crowding in a fully chromophore-loaded functionalized system. The absorption cross section was estimated based on the absorbance, film thickness, and chromophore density. Such a calculation gives a value of $\sigma = 1.3 \times 10^{-18}$ cm^2 for pMEA and $\sigma = 1.2 \times 10^{-16}$ cm^2 for pDR1M. The other parameter of interest here, the *trans* diffusion constant Γ, will be discussed along with the temperature results.

Effect of pump irradiance

It is of primary interest to compare the experimental results of the effect of pump irradiance on the photostationary order parameter with those predicted by eq. [7]. For pump irradiances in the range 13–60 mW/cm^2, the order parameter remained constant at –0.13 for pDR1M and increased in absolute value for pMEA (Fig. 5) in qualitative agreement with eq. [7]. This variation for pMEA, however, was slight (less than 5%) so the dependence is weak. Still, the adherence of pMEA to, and disagreement of pDR1M with, the predicted irradiance behaviour suggests that dipolar interactions in pDR1M may be the cause of the observed differences. This idea will be discussed further in the following section. Below 10 mW/cm^2, the absolute saturation level decreases with irradiance for both polymers. Unfortunately, the long time required to reach equilibrium at such low

Fig. 5. The variation in photostationary order parameter with pump irradiance for pMEA.

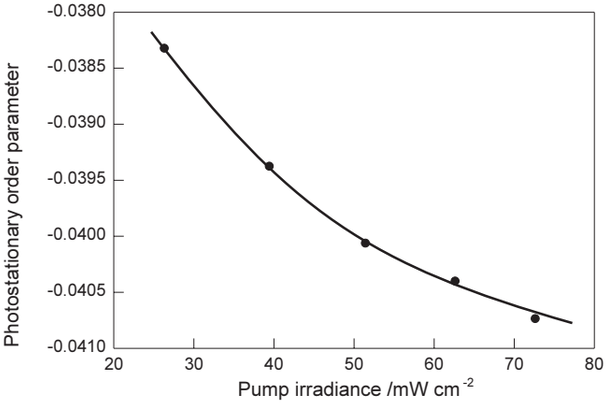

pump irradiances (ca. 4 h at 5 mW/cm^2) makes a quantitative investigation of the relationship impractical by these methods. A similar study on the same chromophore as contained in pDR1M (Disperse Red 1) doped into a poly(methyl methacrylate) matrix revealed changes in the attainable orientation when pumping below 100 mW/cm^2 (7). This larger saturation order parameter is to be expected for a doped system, due to a much lower chromophore density.

The normalized order parameter (S_n) vs. time curves at each irradiance were fitted to the biexponential equation

$$[9] \qquad S_n = A\,[1 - \exp(-k_a t)] + B\,[1 - \exp(-k_b t)]$$

where A and B represent the amplitudes of the two exponentials, k_a and k_b the rate constants. The fitting indicates that for both polymers k_a and k_b increase with increasing irradiance. This is shown for pMEA in Fig. 6 and for pDR1M in Fig. 7. The amplitude A of the term describing the fast process increases as well, slightly faster for pMEA than for pDR1M at lower irradiances (Fig. 8). Song et al. carried out similar studies on an azobenzene-functionalized polymer (5) over the same range of pump irradiances. Although there are slight differences in the fitting procedure, their results showed no change in rate constant for different pump irradiances. Their data also show that the amplitude of the exponential describing the fast process increases linearly with pump irradiance. The three values of irradiance used in that study are indicated with arrows in Fig. 8, illustrating that this region may appear to be linear for our samples as well. Measurements at lower irradiances, however, reveal that the contribution of the fast process decreases sharply in favour of the slower one.

Effect of temperature

For both pMEA and pDR1M, the photostationary order parameter increases monotonically as a function of temperature, approaching zero as the systems restore their isotropic distribution of chromophores around T_g (Fig. 9). Here the influence and temperature dependence of the *trans* rotational diffusion constant may be seen. At higher temperatures there is more redistribution and a greater tendency towards isotropy. When Γ becomes very large, eq. [7] predicts that the order parameter S tends towards zero. Examining the other limit, as $\Gamma \rightarrow 0$, $S \rightarrow -0.5$, the maximum order achievable in

© 1998 NRC Canada

Fig. 6. (*a*) Fast process rate constant k_a vs. irradiance and (*b*) slow process rate constant k_b vs. irradiance for pMEA.

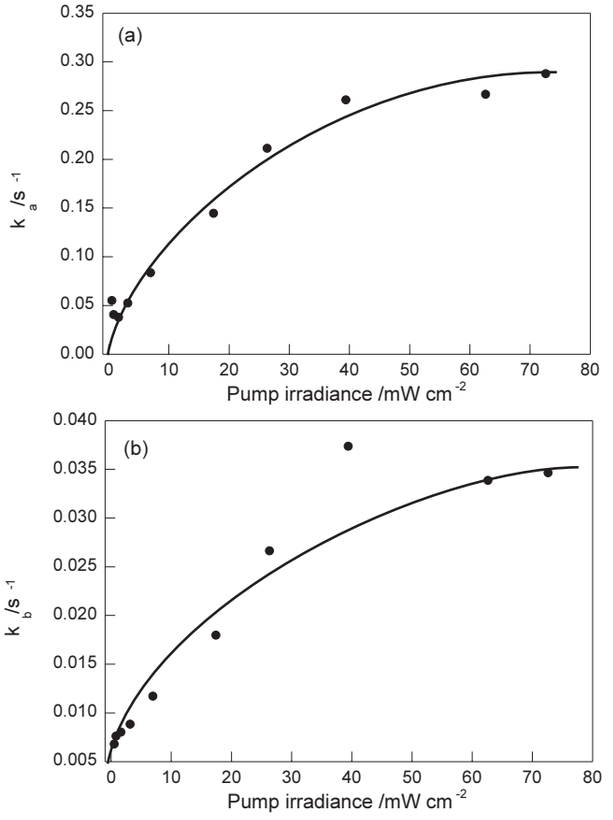

Fig. 7. (*a*) Fast process rate constant k_a vs. irradiance and (*b*) slow process rate constant k_b vs. irradiance for pDR1M.

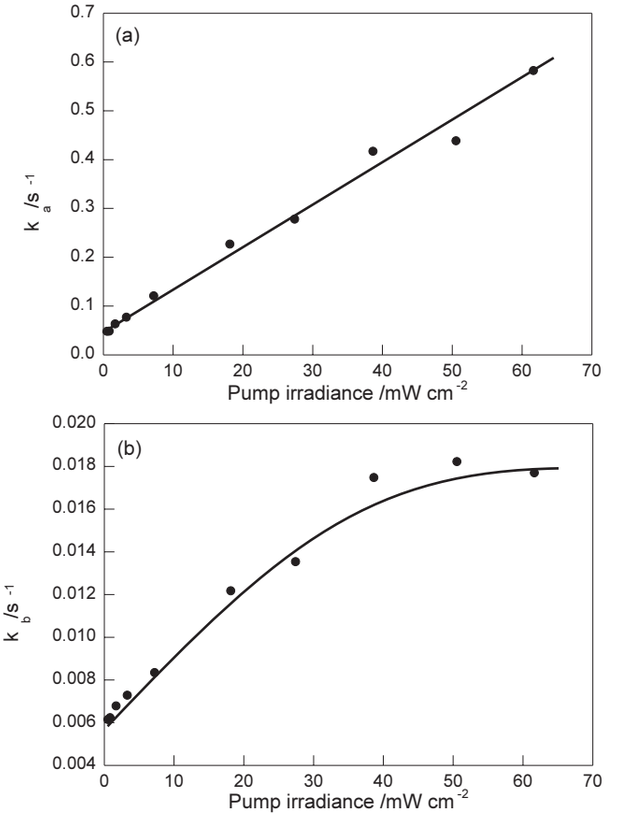

theory. That this may never be fullfilled is largely the result of steric factors. The magnitude of Γ is, however, not as closely related to the absolute temperature as it is to the glass transition temperature, for it is above T_g that polymers find the maximum free volume available to redistribute their pendant chromophores. This suggests a comparison on the basis of a reduced temperature, such as $T - T_g$ (Fig. 10). Although the manner in which both polymers lose their ability to maintain ordered chromophores appears markedly different in Fig. 9 (linear in the case of pMEA, sigmoidal for pDR1M), Fig. 10 shows that for a temperature region in which both systems may be compared (55° below to 5° above their respective T_g) the behaviour is remarkably similar.

A surprising result came from fitting the normalized order parameter curves to the biexponential described by eq. [9]. For both polymers, the variation in rate constant (k_b) with temperature showed no trend for the slow process, the data being completely scattered. The rate constant (k_a) for the fast process, however, increased with increasing temperature for pMEA and decreased for pDR1M (Fig. 11). This behaviour is in contrast to the rate constant dependence on irradiance discussed in the previous section where rates for both polymers increase with increasing pump irradiance. A possible explanation might involve the larger dipole moment of the donor–acceptor substituted pDR1M (10). Large dipole–dipole interactions have been shown to give rise to cooperative effects (11) where neighbouring groups participate in orientation in an effort to minimize the electronic repulsion in energetically unfavourable chromophore alignment.

These results are best considered with the two competing processes involved in mind. On the one hand there is alignment due to the polarization of the laser; on the other there is a tendency towards disorder and restoration of the equilibrium isotropy. Larger pump irradiances would favour the orientation process and have very little effect on thermal randomization, as was demonstrated experimentally. Increasing the temperature, however, would increase the rates of both processes due to an enhanced mobility accompanying an increasing free volume. The interplay between the two processes at higher temperatures is likely sensitive to dipolar interactions, resulting in a rate constant that decreases on heating for pDR1M. Since such electronic interactions are much weaker in pMEA, the resulting behaviour is different. A separate study to verify this hypothesis, analyzing copolymers and blends with different orientations of the dipoles, is in progress.

Summary and conclusions

The photoinduced reorientation of azobenzene-based polymers is a complex phenomenon, especially in the case of functionalized polymers, since there are many possible interactions between the chromophores and the matrix. The simple model presented here accounts for experimentally observed order parameters using optical pumping and

© 1998 NRC Canada

Fig. 8. Amplitude of the fast process vs. irradiance for pMEA and pDR1M.

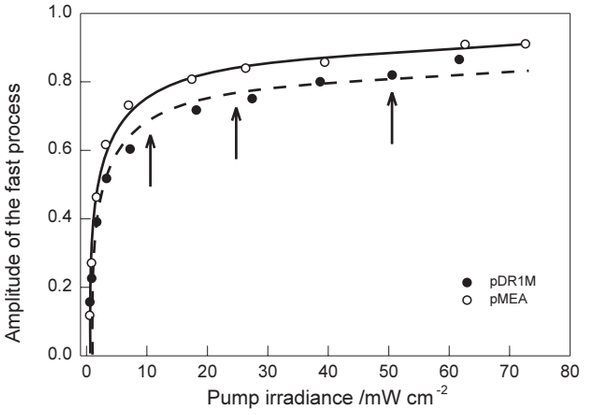

Fig. 9. The variation in photostationary order parameter for pMEA and pDR1M with increasing temperature.

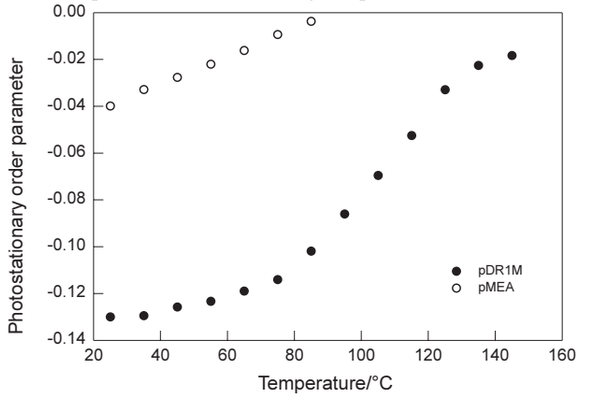

thermal redistribution. It has been used to arrive at an expression for the photostationary order parameter in terms of the pumping rate and the *trans* rotational diffusion constant. The predicted irradiance dependence of the orientation process has been qualitatively verified for pMEA, while pDR1M appears to be less dependent on the pump intensity. The rotational diffusion constant is a function of temperature and causes the photostationary order parameter to decrease at higher temperatures. For the polymer pDR1M, strong dipole–dipole interactions may be responsible for an orientation rate constant that decreases at higher temperatures. All of the experimental evidence suggests that the model of photoinduced orientation is only sufficient to describe a system such as pMEA where the lack of strong dipolar interactions allows the chromophores to be aligned independently, similar to the situation in a doped system with low chromophore density. For a system such as pDR1M, electronic effects such as dipole–dipole interactions will have to be taken into account.

Acknowledgments

We thank the Office of Naval Research U.S.A., the Natural Sciences and Engineering Council of Canada (NSERC), and the Department of National Defence Canada for funding.

Fig. 10. Photostationary order parameter plotted against the difference between experimental temperature and sample T_g, shown for a range over which both polymers may be compared.

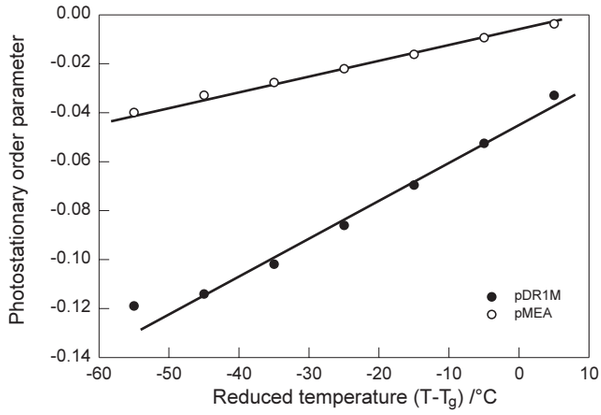

Fig. 11. The temperature behaviour of the rate constant describing the fast process (k_a) for pMEA and pDR1M.

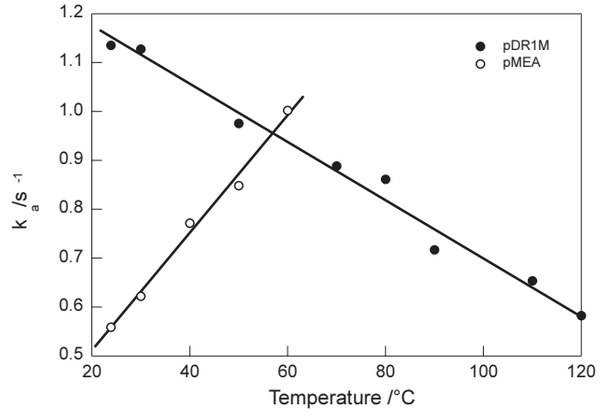

References

1. H. Rau. *In* Photochemistry and photophysics. Vol. 2. *Edited by* J.F. Rabek. CRC Press, Inc., Boca Raton, Fla. 1990. p. 119.
2. Z. Sekkat and M. Dumont. Synth. Met. **54**, 373 (1993).
3. A. Natansohn, P. Rochon, M.-S. Ho, and C. Barrett. Macromolecules, **28**, 4179 (1995).
4. M.-S. Ho, A. Natansohn, and P. Rochon. Macromolecules, **28**, 6124 (1995).
5. O.-K. Song, C.H. Wang, and M.A. Pauley. Macromolecules, **30**, 6913 (1997).
6. A. Natansohn, P. Rochon, M. Pézolet, P. Audet, D. Brown, and S. To. Macromolecules, **27**, 2580 (1994).
7. F.L. Labarthet and C. Sourisseau. New J. Chem. **21**, 879 (1997).
8. Z. Sekkat and W. Knoll. J. Opt. Soc. Am. B: **12**, 1855 (1995).
9. M. Schönhoff, M. Mertesdorf, and M. Lösche. J. Phys. Chem. **100**, 7558 (1996).
10. D. Brown, A. Natansohn, and P. Rochon. Macromolecules, **28**, 6116 (1995).
11. A. Natansohn, P. Rochon, X. Meng, C. Barrett, T. Buffeteau, S. Bonenfant, and M. Pézolet. Macromolecules, **31**, 1155 (1998).

© 1998 NRC Canada

The self-assembly of a layered material: metal–alkanethiolate bilayers

F. Bensebaa, T.H. Ellis, E. Kruus, R. Voicu, and Y. Zhou

Abstract: Layered materials composed of metal–alkanethiolate units have been synthesized and characterized. The self-assembly occurs at the interface between a metal-ion-containing aqueous phase and an alkanethiol-containing organic phase. Key features of the structure have been determined from X-ray diffraction and infrared spectroscopy measurements. The highly ordered bilayers are characterized by tilted, all-*trans* alkyl chains. A new model for the in-plane structure has been presented, which is based on a hexagonal arrangement of metal atoms in the central plane.

Key words: self-assembly, alkanethiolates, layered materials, vibrational spectroscopy.

Résumé : On a synthétisé et caractérisé des matériaux en couches formés d'unités alcanethiolate de métal. L'autoassemblage se produit à l'interface entre une phase aqueuse contenant l'ion métallique et une phase organique contenant l'alcanethiol. On a déterminé les caractéristiques principales de la structure par diffraction des rayons X et par spectroscopie infrarouge. Les bicouches bien ordonnées sont caractérisées par des chaînes alkyles inclinées, complètement *trans*. On propose un nouveau modèle pour la structure dans le plan; elle est basée sur un arrangement hexagonal des atomes métalliques dans le plan central.

Mots clés : autoassemblage, matériaux en couche, spectroscopie de vibration.

[Traduit par la Rédaction]

Introduction

Alkanethiols ($HS(CH_2)_nCH_3$) are known to react and adsorb onto the clean surfaces of coinage metals, and to self-assemble into highly ordered monolayers (1, 2). These self-assembled monolayers (SAMs) provide a means of creating well-defined surface structures whose properties can be manipulated through substitutions to the initial alkanethiol molecules (3). A wide range of surface analysis techniques has been applied to the study of alkanethiolate SAMs, yielding a wealth of information.

Less well known than SAMs are layered materials composed of metal–alkanethiolate units (4–6). These are also materials that self-assemble in solution, forming a multibilayer structure that is illustrated in Fig. 1. Such materials can be viewed as SAMs having an infinite surface-to-volume ratio. As such, we have undertaken to study these materials as model systems for SAMs. Because it is a bulk material, this greatly expands the range of measurement techniques available.

The goal of the present work is to describe the synthesis of these materials and the methods used to characterize their structure. Our preparation methods are a modification of those used for the preparation of short-chain silver–alkanthiolates (6), and we now have prepared copper–thiolate materials as well. Particular emphasis will be given to infrared spectroscopy measurements, where new information is revealed as a result of the enhanced signal from the bulk material.

Received February 9, 1998.

Y. Zhou and E. Kruus.[1] Département de chimie, Université du Québec à Montréal, Montréal, QC H3C 3P8, Canada. **F. Bensebaa,**[2] **R. Voicu, and T.H. Ellis.**[3] Département de chimie, Université de Montréal, Montréal, QC H3C 3J7, Canada.

[1]Author to whom correspondence may be addressed. Telephone: (514) 987-3000, ext 8230. Fax: (514) 987-4054. E-mail: kruus.erik@uqam.ca

[2]Present address: Institute for Chemical Process and Environment Technology, National Research Council of Canada, Ottawa, ON K1A 0R6, Canada.

[3]Author to whom correspondence may be addressed. Telephone: (514) 343-6910. Fax: (514) 343-7586. E-mail: ellis@chimie.umontreal.ca

Experimental section

The alkanethiols were purchased from Aldrich and used without further purification. All other reagents were acquired from general sources and used as received. Elemental analysis was performed on a Fisons Instruments model EA1108 analyser, and neutron activation analysis used the SLOWPOKE reactor at École Polytechnique de Montréal. The X-ray diffractometer is a Siemens D5000, using Co Kα radiation. Infrared spectra were recorded on a Bomem MB 100 FTIR spectrometer in transmission mode using a DTGS detector. Several drops of the metal–alkanethiolate material suspended in toluene were dropcast onto a NaCl disk and dried in air. Typically, 20 scans were co-added, and the resolution was 1 cm^{-1}.

Results and discussion

The self-assembly process

The chemistry of the preparation procedure is elegant in its simplicity. The metal begins in the aqueous phase, in the

 © 1998 NRC Canada

Fig. 1. Cross-sectional view of the layered structure. Metal atoms: shaded circles; sulfur atoms: open circles; alkyl chains: rounded rectangles.

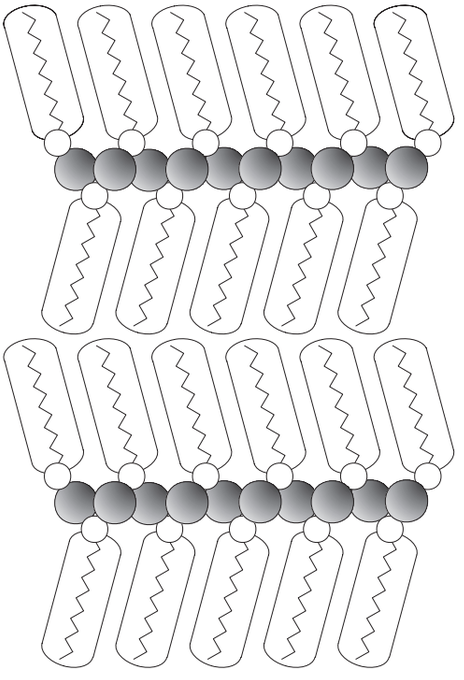

form of silver nitrate or cupric nitrate. The alkanethiol is dissolved in an organic solvent (toluene). When the two immiscible phases are brought into contact the metal–alkanethiolate material appears near the interface as a solid suspension in the organic phase. The reaction can take several hours to complete, and can be accelerated by mixing.

The reaction to form the silver–alkanethiolate material can be written as follows:

$$AgNO_3(aq) + HS(CH_2)_nCH_3(org) \Rightarrow HNO_3(aq) + AgS(CH_2)_nCH_3(org)$$

(The product will be abbreviated as AgSC(n + 1)). The exchange between the proton from the alkanethiol and the silver ion is confirmed by an analysis of the aqueous phase after the completion of the reaction: the pH of this phase is greatly diminished and no silver can be detected via precipitation with Cl^-.

The two phases are then separated, the organic phase is washed several times with water, and the suspension is collected by centrifuging. The resulting powder is washed several times with toluene and centrifuged again to purify. Analyses by elemental and neutron activation analysis (Table 1) confirm that the stoichiometry is exactly 1:1 (metal-to-alkanethiolate).

The following is an example of the synthetic conditions of AgSC12: 0.2 mL $HS(CH_2)_{11}CH_3$ (~0.84 mmol) in 15 mL toluene was added to 0.10 g $AgNO_3$ (~0.59 mmol) in 30 mL H_2O with stirring. After 1 h, the aqueous phase is clear and the measured pH is 1.5. The precipitate in the organic phase was washed three times with 50 mL H_2O, then three times with 50 mL toluene, then vacuum dried.

Table 1. Measured and calculated composition (%) of AgC12 and CuC12.

	C	H	S	Metal
Silver	46.7[a]	8.2[a]	10.4[a]	36[b]
	46.6[c]	8.1[c]	10.4[c]	34.9[c]
Copper	54.4[a]	9.7[a]	12.4[a]	—
	54.4[c]	9.5[c]	12.1[c]	24.0[c]

[a]Elemental analysis measurements, ±0.2%.
[b]Neutron activation measurement, ±2%.
[c]Calulated based on a 1:1 stoichiometry.

In the case of the copper–thiolate material, the reaction is slightly more complex. Since the starting material is in the Cu(II) oxidation state, it must be reduced during the reaction. Elemental analysis (Table 1) proves that the final product has a 1:1 metal-to-thiolate stoichiometry. Our copper–thiolate material is probably similar to a precipitate that was synthesized as part of a study of multilayer films on copper (7), although the structure of that material was not determined. In that work it was suggested that copper may be reduced when two thiols react to form a disulfide. It is also possible that nitrate groups can be oxidized and liberated as gaseous products during the reaction. The overall reaction tends to be slower for copper, compared to silver, perhaps because of this extra complexity.

Both silver and copper thiolate materials have been synthesized using a variety of chain lengths. The resulting AgSC7–AgSC18 powders are pale yellow in colour. Shorter chains routinely produce bright yellow powders. Natan and co-workers have made an extensive study of butane thiolate (6), and found that powders of either colour can be produced by varying the synthesis conditions. They have labeled these materials *trans* and *gauche*, since the bright yellow *gauche* material has been found to contain *gauche* conformational defects in the alkyl chain. It was previously demonstrated that the yellow colour correlates to a trigonal sulfur-to-metal coordination, in contrast to a digonal coordination for white compounds (8). Finally, our copper material has a pale green colour (CuSC8, CuSC12, and CuSC18 have been studied to date).

Both silver and copper materials often have the form of small, flat sheets (flakes). The largest size flakes are seen in the copper material, sometimes being several millimeters long and wide. It has also been observed that both materials can turn black, either as a result of heating or aging. Curiously, no significant change in composition or structure has been detected that correlates to this alteration.

The structure

Powder X-ray diffraction (XRD) measurements of both the Ag and Cu materials are dominated by lines that can be indexed to the interlayer spacing of the two-dimensional layered structure illustrated in Fig, 1, as shown in Fig. 2. It is worth noting that there is a complete absence of lines corresponding to the bulk (three-dimensional) metal structure. We have observed the latter in measurements of thiolate-capped metal nanoparticles, which were also produced using chemical synthesis (9, 10). Clearly, the procedures used in the present work result in a very different material.

© 1998 NRC Canada

Fig. 2. XRD patterns of the CuSC12 and AgSC12 layered materials. Lines indexed to the interlayer spacing (0*k*0) are labeled. The line assigned to the in-plane structure is indicated by an asterisk.

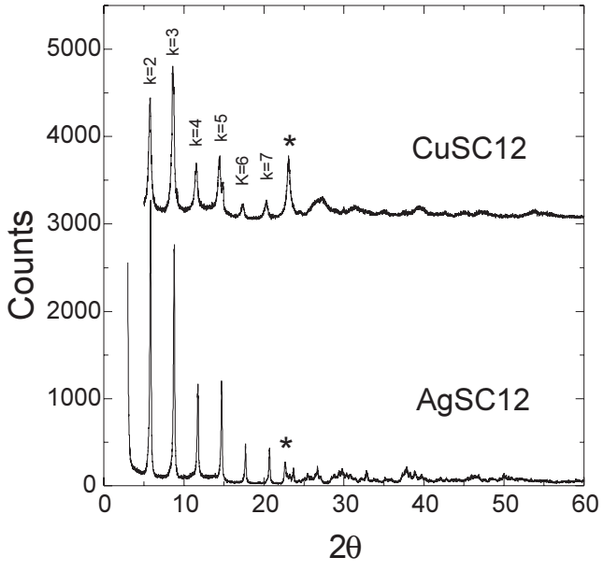

The interlayer spacings of the Ag and Cu materials determined in this way are 35.0 ± 0.2 Å and 35.6 ± 0.2 Å, respectively. These distances are not consistent with the smaller copper radius, which could make the central layer smaller. Figure 1 indicates that the alkyl chains can be tilted with respect to the direction normal to the central plane of metal atoms. It is therefore likely that the two materials have a different chain tilt angle. A preliminary analysis of the data, for all measured chain lengths, indicates that the tilt angles with respect to the surface normal are 12 ± 3° and 10 ± 3° for Ag and Cu, respectively. It is not possible at present to determine whether the tilted chains adopt the herringbone structure shown in Fig. 1, or some other combination of positive and negative tilt angles.

The tilt angle of the silver layered materials compares well to the value of 13 ± 2° obtained by Laibinis et al. (2) for alkanethiolate SAMs on silver surfaces. Their angles were determined from a detailed modeling of the infrared spectra. For comparison, it is generally accepted that alkanethiolate SAMs on gold surfaces are more tilted, with values ranging from 26° to 34°, as determined by IR (2) and XRD (11) measurements. It is often speculated that tilting is driven by the optimization of van der Waals interactions between alkyl chains, due to the mismatch between the metal surface lattice and the close-packed spacing in bulk alkanes. However, it is worth noting that both Ag(111) and Au(111) have virtually identical lattice constants. While SAMs on Au(111) form a commensurate v3 × v3 structure, it is now known that SAMs on Ag(111) are in fact incommensurate with the underlying silver lattice (12–14). The measured overlayer lattice constant is 4.4–4.8 Å, as compared to 5.0 Å on Au(111). This would explain the smaller tilt angle observed for SAMs on Ag(111). Further, the driving forces for this incommensurate structure of these SAMs is undoubtedly related to the assembly mechanism of the layered material.

Fig. 3. Top view of the central plane. Metal atoms: shaded circles; sulfur atoms: open circles; alkyl chains: not shown. The row-to-row spacing is shown.

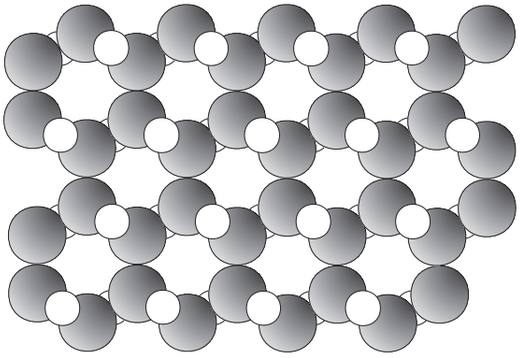

We can now add to this discussion the tilt angle of ~11° determined for the copper layered material. Since copper is significantly smaller than both silver and gold, it is logical to expect that the alkyl chains would be packed closer together, and there would be less of a tendency to tilt. Other factors will certainly play a role as well, such as the inherent metal–sulfur–carbon bond angle, and fine details of the alkyl chain packing.

Previous studies of silver layered materials were not able to determine the in-plane structure from XRD measurements (4, 6). A new proposal for the in-plane structure is shown in Fig. 3. It features a plane of metal atoms that adopt a hexagonal structure. By placing sulfur atoms in the digonal (twofold bridging) sites shown, they template a close-packed arrangement of the attached alkyl chains (which are not shown in this view). This is the main feature that separates this model from previous models (4, 6). A close examination of Fig. 3 shows that digonal bonded sulfur atoms appear both above and below the plane, which results in the formation of long rows composed of covalently bonded metal–sulfur units. These rows run horizontally in the drawing. The digonal bonding of the S atoms is confirmed by the pale yellow colour of the Ag material (8). Other structural features remain to be determined, such as the possible buckling of metal atoms in the central plane.

We have observed a number of XRD lines, both sharp and broad, that do not shift when the chain length is varied. They probably originate from the in-plane structure. For example, there is sharp peak at 4.55 ± 0.03 Å and 4.47 ± 0.04 Å for the Ag and Cu materials, respectively (see Fig. 2). This is much less than the difference in the size of the metal atoms (Ag is 13% larger than Cu), and indicates that chain packing plays a significant role in determining the in-plane lattice distances. The slightly smaller size of the Cu lattice is also consistent with the observed smaller tilt angle.

Vibrational spectroscopy

Previous studies of alkyl chain systems have shown that many spectral features are highly sensitive to the chain conformational order. Figure 4 shows transmission IR spectra of the AgSC12 and CuSC12 materials. It is first evident that there are a large number of sharp, well-resolved peaks. This is different from IR measurements on monolayers,

© 1998 NRC Canada

Fig. 4. Transmission FTIR spectra of the CuSC12 and AgSC12 layered materials. Peak positions and assignments are given in Table 2.

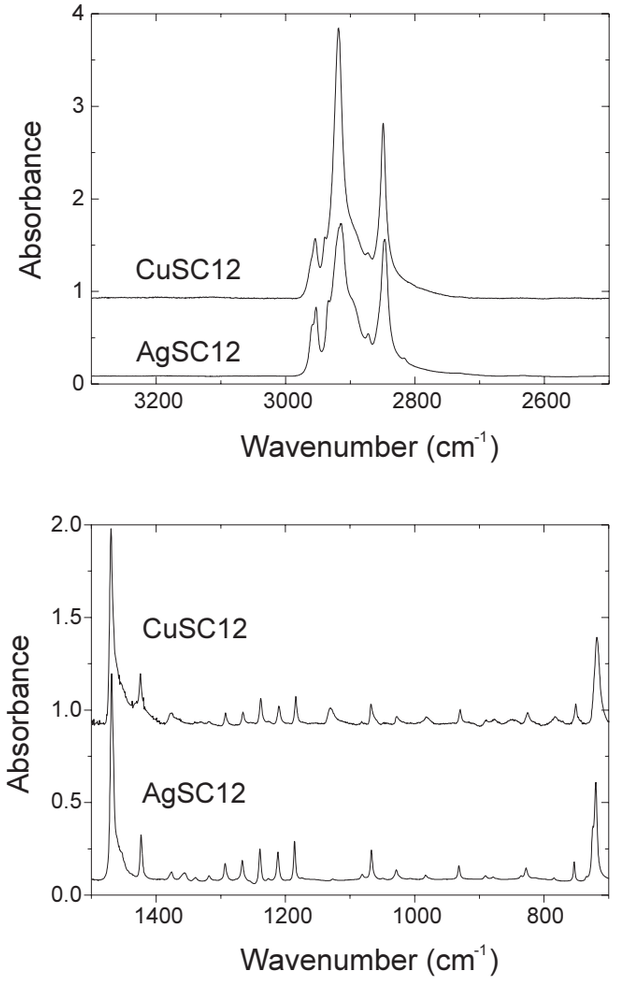

Table 2. Peak positions (in cm^{-1}) and assignments for AgSC12 and CuSC12 layered materials. The nomenclature conforms to refs. 2 and 21.

Assignment	AgSC12		CuSC12	
r_a^-	2958	sh	2960	sh
r_b^-	2953	s	2954	s
FR	2934	m	2939	m
d^-	2916	vs	2918	vs
FR	2895	sh	2890	sh
r^+	2872	m	2873	m
d^+	2847	vs	2849	vs
δ	1469	vs	1470	vs
δ_s	1423	s	1424	s
U	1377	m	1376	m
	1356	m		
W_7	1339	w		
W_6	1318	w	1319	vw
W_5	1293	s	1293	s
W_4	1267	s	1266	s
W_3	1240	s	1238	s
W_2	1212	s	1210	s
W_1	1186	s	1184	s
R_2	1127	vw	1130	s
R_3	1081	w	1082	vw
R_n	1067	s	1068	s
P_{11}	1028	m	1028	m
P_{10}	983	w	981	w
P_9	932	m	930	m
β	891	w	890	w
P_8	879	vw	877	w
P_7	828	m	825	m
P_6	784	vw	783	w
P_5	753	s	751	s
P_4	734	w		
P_3	724	sh		
P_1	720	vs	718	vs

where signal levels are too low to permit detailed observation of the low-wavenumber region (2, 15). The spectra are also more detailed than those reported for thiolate capped nanoparticles (9, 10).

The degree of order can be better quantified by a detailed analysis of the peaks, whose positions are summarized in Table 2. The CH_2 stretching peaks, which can be measured with sensitivity in all alkyl chain systems, are known to shift to lower frequency with increasing conformational order. In general, antisymmetric (d^-) peaks at 2918–2920 cm^{-1} and below are typical of ordered solid systems, where all-*trans* chain conformations predominate. In liquid (disordered) systems, the peaks tend to be above 2920 cm^{-1}, indicating large percentages of *gauche* conformational defects in the chains (16–18). As seen in Table 2, the layered materials are clearly characterized by all-*trans* chain conformations. For all the chain lengths studied, values of 2915–2917 cm^{-1} and 2917–2920 cm^{-1} have been found for Ag and Cu, respectively. By comparison, well-ordered monolayers (2) on gold surfaces and thiolate-capped gold nanoparticles (9, 10) are typically characterized by d^- peak values of 2918–2920 cm^{-1}. (In all cases, the higher wavenumbers are systematically observed to occur with shorter chain lengths.) It can therefore be concluded that the layered materials are the most highly ordered (in terms of chain conformational order) of all the thiolate self-assembled systems. This is probably because in other systems the metal lattice is constrained by sub-surface metal atoms, whereas there will be more flexibility in the single layer of metal atoms in the layered materials, producing less strain in the alkyl chain structure.

A preliminary temperature-dependent study indicates that this order remains right up to the disordering transition, at about 402 K for AgSC12 and 416 K for CuSC12. This would be in contrast to temperature-dependent studies of SAMs on gold (12, 19, 20) and thiolate-capped gold nanoparticles (10), where a more continuous shift as a function of temperature is observed. Perhaps more importantly, the disordering of those systems occurred at a much lower temperature (at or below 350 K).

A second measure of order is the observation of peaks that belong to the wagging (W_x) and rocking–twisting progressions (P_x), located in the 1180–1350 cm^{-1} and 715–1030 cm^{-1} ranges, respectively. These progressions result from the coupling

© 1998 NRC Canada

of *n* identical methylene oscillators (21). They have been observed in the spectra of solid alkanes (21) and lipid bilayers (18), and they were previously used as order parameters (18). They have not been previously observed for thiolate monolayers, but they were observed, less well resolved, with thiolate-capped nanoparticles (9). Because the peaks are so clearly resolved in the present case, it has been possible to assign each indivdual peak. As seen in Table 2, both silver and copper layered materials have virtually identical peak values, indicating a similar chain conformation in both cases. Clearly, the different tilt angles do not affect the chain conformation. Once again, preliminary temperature-dependent studies indicate that a high degree of order remains right up to the phase transition that occurs above 400 K.

The peak that is labeled as δ_s in Table 2 is assigned as the CH_2 bending mode arising from the carbon atom that is bonded to S, and it is observed between 1421 and 1425 cm^{-1}. This was previously suggested by Murray and co-workers (9) based on measurements of thiolate-capped gold nanoparticles, where it is observed at 1414–1423 cm^{-1}. There is no obvious correlation to the nature of the metal atom, the tilt of the chain, or the length of the chain.

Because the spectra are composed of well-resolved peaks on a flat background, it is possible to comment on the absence of small peaks that are known to be associated with conformational defects. It has been established that peaks at 1338 cm^{-1}, 1368/1308 cm^{-1}, and 1344 cm^{-1} can be assigned to double *gauche*, internal kink, and end-*gauche* defects, respectively (22). These peaks are systematically absent from spectra of layered materials, for all chain lengths, both Ag and Cu. In contrast, some end-*gauche* defects were observed on thiolate-capped nanoparticles, where domain sizes are much smaller, and where there may be less end-to-end packing.

Information about conformational defects can also be obtained from C–C stretching peaks. In solid alkanes, these peaks form the progression labeled as R_x. The evolution of these peaks as a function of the chain length of these peaks is less systematic than the W_x and P_x series, but we have tentatively assigned three peaks in both AgSC12 and CuSC12 to this series. A detailed Raman study of this region exists for solid alkanethiols and thiolate monolayers (23). In the case of the former, three peaks are systematically observed at values close to those shown in Table 1, and all three are assigned to the *trans* conformation. One issue yet to be resolved is the fact that the peak at 1068 cm^{-1} is consistently the most intense peak in this series, and it is not clear why. Secondly, the peak at 1131 cm^{-1} is anomalously intense in the CuSC12 material, compared to all others. It is perhaps worth noting that the CuSC12 material is slightly less conformationally ordered than the AgSC12 material, as judged by peak positions and shapes.

Taking all of the above observations together, it is clear that the self-assembly process of the layered materials allows the alkyl chains to adopt an all-*trans* configuration. This will allow for the full optimization of the attractive interactions between the chains. Further, the organization of the thiolate groups appears to create a stabilization of the entire structure. In addition to the preliminary temperature-dependent studies, it should be mentioned that the short-chain materials that have been synthesized are also highly ordered. For example, the AgSC7 material has a d^- wavenumber at 2917 cm^{-1}, and 12 peaks assigned to progressions are clearly resolved. At room temperature, bulk alkanes and lipid bilayers of similar chain length are disordered. A similar stabilization of the alkyl chains occurs in other thiolate systems. Although some authors have suggested that short-chain systems are disordered at room temperature, there are now clear indications that it is indeed possible to have ordered thiolate monolayers and thiolate-capped nanoparticles with very short chains (9, 24). Combined with results from the layered materials, one can now say that self-assembled alkanethiolate systems have an inherent stabilization, with the layered materials being the most stable.

Conclusions

Layered materials composed of silver and copper thiolates have been synthesized and analyzed. They form a highly ordered bilayer structure, characterized by tilted, all-*trans* alkyl chains. A new model for the in-plane structure has been presented that is based on a hexagonal arrangement of metal atoms in the central plane. These systems lend themselves to detailed analysis by a large number of techniques, which makes them an excellent model system for other metal–thiolate materials.

Acknowledgments

We wish to thank the Natural Sciences and Engineering Research Council of Canada and the Group de recherche en physique et technologie des couches minces (GCM) for financial support.

References

1. R.G. Nuzzo and D.L. Allara. J. Am. Chem. Soc. **105**, 4481 (1983).
2. P.E. Laibinis, G.M. Whitesides, D.L. Allara, Y.-T. Tao, A.N. Parikh, and R.G. Nuzzo. J. Am. Chem. Soc. **113**, 7152 (1991).
3. A. Ulman. Chem. Rev. **96**, 1533 (1996).
4. I.G. Dance, K.J. Fisher, R.M. Herath Banda, and M.L. Scudder. Inorg. Chem. **30**, 183 (1991).
5. M.J. Baena, P. Espinet, M.C. Lequerica, and A.M. Levelut. J. Am. Chem. Soc. **114**, 4182 (1992).
6. H.G. Fijolek, J.R. Grohal, J.L. Sample, and M.J. Natan. Inorg. Chem. **36**, 622 (1997).
7. H. Kellor, P. Simak, W. Schrepp, and J. Dembowski. Thin Solid Films, **244**, 799 (1994).
8. I.G. Dance, L.J. Fitzpatrick, A.D. Rae, and M.L. Scudder. Inorg. Chem. **22**, 3785 (1983).
9. M.J. Hosterler, J.J. Stokes, and R.W. Murray. Langmuir, **12**, 3604 (1996).
10. A. Badia, S. Singh, L. Demers, L. Cuccia, R.G. Brown, and R.B. Lennox. Chem. Eur. J. **2**, 359 (1996).
11. P. Fenter, P. Eisenberger, P. Burrows, S.R. Forrest, and K.S. Liang. Physica B (Amsterdam): **221**, 145 (1996).
12. P. Fenter, P. Eisenberger, N. Camillone III, S. Bernasek, G. Scoles, T.A. Ramanarayanan, and K.S. Liang. Langmuir, **7**, 2013 (1991).
13. R. Heinz and J.P. Rabe. Langmuir, **11**, 506 (1995).
14. A. Dhirani, M.A. Hines, A.J. Fisher, O. Ismail, and P. Guyot-Sionnest. Langmuir, **11**, 2609 (1995).
15. R.G. Nuzzo, E.M. Korenic, and L.H. Dubois. J. Chem. Phys. **93**, 767 (1990).

© 1998 NRC Canada

16. R.G. Snyder, H.L. Strauss, and C.A. Elliger. J. Phys. Chem. **86**, 5145 (1982).
17. D.G. Cameron, H.L. Casal, and H.H. Mantsch. Biochemistry, **19**, 3665 (1980).
18. L. Senak, D. Moore, and R. Mendelsohn. J. Phys. Chem. **96**, 2749 (1992).
19. L.H. Dubois, B. Zegarski, and R.G. Nuzzo. J. Electron Spectrosc. Relat. Phenom. **54/55**, 1143 (1990).
20. F. Bensebaa, T.H. Ellis, A. Badia, and R.B. Lennox. J. Vac. Sci. Technol. A: **13**, 1331 (1995).
21. R.G. Snyder and J.H. Schachtschneider. Spectrochim. Acta, **19**, 85 (1963).
22. R.G. Snyder. J. Chem. Phys. **47**, 1316 (1967).
23. M.A. Bryant and J.E. Pemberton. J. Am. Chem. Soc. **113**, 8284 (1991).
24. K.D. Truong and P.A. Rowntree. J. Phys. Chem. **100**, 19917 (1996).

© 1998 NRC Canada

A solid state ^{31}P NMR study of the synthesis of phosphorus sulfides from PCl_3 and H_2S in microporous materials[1]

Garry S. H. Lee, Christopher I. Ratcliffe, and John A. Ripmeester

Abstract: The interaction and reaction of PCl_3 and PCl_3–H_2S mixtures with the microporous materials Silicalite, ALPO-5, NaY, NaX, and NaA have been investigated, with the intention of producing phosphorus sulfide clusters in the pores. A rich chemistry was observed and monitored by solid state ^{31}P NMR. The presence of P_4S_3, α-P_4S_5, β-P_4S_6, and P_4S_7 inside the NaY α-cages was demonstrated, as well as a new species that is possibly a third geometric isomer of P_4S_4 with C_{3v} symmetry. ^{129}Xe NMR showed the exclusion of Xe from the micropores by the phosphorus sulfides. Sulfides lower than P_4S_7 are small enough that they undergo rapid pseudo-isotropic reorientation inside the NaY α-cage.

Key words: phosphorus sulfides, intrazeolitic cluster synthesis.

Résumé : On a étudié l'interaction et la réaction du PCl_3 et de mélanges de PCl_3–H_2S avec de materiaux microporeux, comme Silicalite, ALPO-5, NaY, NaX et NaA, dans le but de produire des agrégats de sulfures phosphoreux dans les pores. On a observé une chimie intéressante qui a été observée par RMN du ^{31}P à l'état solide. Dans les cages-α de NaY, on a mis en évidence la présence de P_4S_3, α-P_4S_5, β-P_4S_6 et P_4S_7 ainsi qu'une nouvelle espèce qui pourrait être un troisième isomère géométrique du P_4S_4 de symétrie C_{3v}. La RMN du ^{129}Xe montre qu'il y a exclusion du Xe des micropores par les sulfures phosphoreux. Les sulfures de formules inférieures à P_4S_7 sont suffisamment petits pour subir une réorientation pseudoisotropique à l'intérieur de la cage-α de NaY.

Mots clés : sulfures phosphoreux, synthèse d'agrégat intrazéolitique.

[Traduit par la Rédaction]

Introduction

The chemistry of the phosphorus–sulfur system is well known, having been extensively studied by crystallographic methods, NMR spectroscopy, and vibrational spectroscopy. A large number of molecules, all based on expansions of the P_4 tetrahedron of elemental white phosphorus, is now established and includes P_4S_n (n = 3–10) (1, 2). In mixtures of phosphorus and sulfur that contain between 0 and 25 at.% P, glassy materials are formed (3–5). These glasses are particularly attractive to the material sciences due to their optical and electrical properties, particularly their infrared transmitting properties (6).

The renewed interest in the study of phosphorus sulfides is based on the recent developments in solid state NMR allowing increased spectroscopic resolution of both ordered crystalline compounds and disordered systems such as the glasses (7). This permits the identification of chemical environments via chemical shift ranges and provides valuable information on the short-range order of these potentially useful materials. Currently there is also much interest in nano-clusters with properties much modified from those in the bulk material, and also for nonlinear optical and semiconductor properties. To this end zeolites and other microporous solids are being used as minireactors and templates to grow size-restricted clusters and to produce periodic arrays of clusters or nano-wires (8, 9).

With this in mind and also with a longer term interest in studying clusters and unusual entrapped species, we attempted to synthesize phosphorus–sulfur compounds within the cavities of zeolites and other microporous materials, and used ^{31}P NMR to characterize the species involved. ^{31}P NMR is perhaps the most useful tool for studying phosphorus species within zeolites, since many other techniques are hampered to some extent by the nature of the system, e.g., Raman spectroscopy suffers from problems with fluorescence, IR has problems with strong overlapping vibrational modes of the lattice, X-ray diffraction has problems with disorder, EXAFS is not so useful where numerous sites are involved. Here we describe the results of exploratory experiments on PCl_3 in microporous materials and its reactions with H_2S, focussing particularly on the behaviour with NaY zeolite.

Received February 19, 1998.

G.S.H. Lee,[2] C.I. Ratcliffe,[3] and J.A. Ripmeester. Steacie Institute for Molecular Sciences, National Research Council of Canada, Ottawa, ON K1A 0R6, Canada.

[1]Published as NRCC No. 40997.
[2]Present address: Department of Chemistry, University of Technology, Sydney, Australia.
[3]Author to whom correspondence may be addressed. Telephone: (613) 991-1240. Fax: (613) 998-7833. E-mail: cir@ned1.sims.nrc.ca

Experimental

Silicalite (UOP), zeolites NaY (LZY-52, Linde), NaX (13X, Linde), NaA (Linde 4A), and aluminophosphate ALPO-5 (a gift of S. Zones, Chevron) were dehydrated

© 1998 NRC Canada

Fig. 1. ^{31}P NMR of PCl_3 in Silicalite. (*a*) Static spectrum showing chemical shift anisotropy powder pattern for PCl_3. The signal in the vicinity of 3 ppm is probably $POCl_3$ and other P/O/Cl species. (*b*) MAS spectrum of a sample with twice the loading of PCl_3, ν_r = 2.0 kHz.

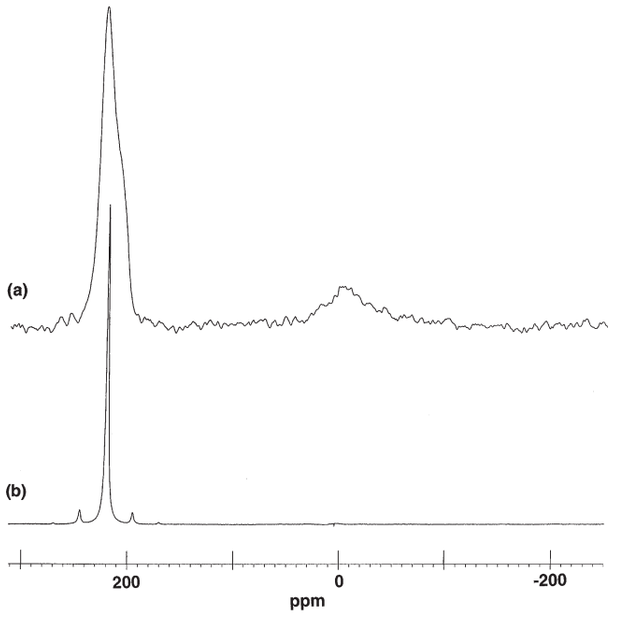

under vacuum, at progressively higher temperatures up to 450°C. All the preparative steps were carried out on a vacuum line and great care was taken to exclude all water. Measured quantities of degassed PCl_3 (liquid) were then condensed into these materials from a side arm and sealed in 5 mm o.d. tubes, allowing $4PCl_3$ per α-cage for X, Y, and A. The reactions with H_2S were carried out "in situ" after first condensing (at liquid nitrogen temperature) a known quantity of the gas onto samples of the microporous materials with PCl_3 already adsorbed (reactant ratio range used: PCl_3:H_2S = 4:3–4:10). These samples, in 5 mm o.d. tubes, were then sealed and annealed at various temperatures from 76 to 164°C. One sample was sealed after admitting a small amount of xenon gas. Solid state NMR spectra were recorded on a Bruker MSL 200 spectrometer operating at 80.962 MHz for ^{31}P and 55.321 MHz for ^{129}Xe, using a Chemagnetics magic angle spinning (MAS) pencil probe, both static and with spinning rates of 1.9–4.5 kHz. The glass sample tubes were inserted into the zirconia pencil rotors and held in place by Teflon spacer rings. Spectra were acquired using single pulses (90° pulse length 2.8–3.0 μs) with quadrature phase cycling. Positions of isotropic shifts were determined, when necessary, from MAS spectra obtained at different spinning rates. ^{31}P spectra were referenced to 85% H_3PO_4 and typically required 80 scans with recycle times of up to 100 s. The ^{129}Xe spectra were referenced to Xe gas at zero pressure.

Results and discussion

With the exception of a short note on ^{129}Xe, all the following discussion focusses on ^{31}P NMR results (Figs. 1–6, 8), which show a rich chemistry for phosphorus compounds inside zeolites. Most reactions seem to produce several products and it is a major problem to identify all of the species present. It is convenient to describe results first for the simpler systems with only PCl_3 and then with the addition of H_2S.

Fig. 2. ^{31}P NMR MAS spectrum of PCl_3 with NaY, ν_r = 4.5 kHz. Residual molecular PCl_3 shows at 220 ppm. Stars indicate spinning side bands of the line tentatively assigned to framework-attached $SiOPCl_2$.

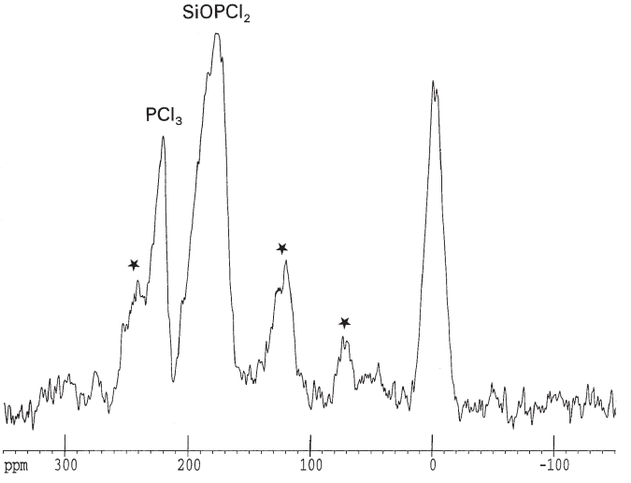

(a) PCl_3 with microporous materials

PCl_3 is a liquid (mp –93.6°C) with a ^{31}P NMR chemical shift of 219 ppm (10). When introduced into Silicalite the spectra, Fig. 1, clearly show that the PCl_3 remains intact. However, the line indicates only a single type of PCl_3, with a small chemical shift anisotropy: δ_{iso} = 220 ± 0.4, $\delta_{11,22}$ = 227.8 ± 1.0, δ_{33} = 204.3 ± 1.0, axially symmetric within error, and there is no trace of any sharp liquid line. This anisotropy can only mean that the molecule is adsorbed in the Silicalite channels or on the surface. At the loading levels used there is not enough surface area to accommodate all the PCl_3 and consequently one must conclude that the signal most likely arises from molecules in the channels. Similar behaviour was observed with ALPO-5, which has one-dimensional channels.

With activated NaY and NaX the spectra initially show mainly the PCl_3 resonance, but with time this is very much reduced, Fig. 2, and is replaced by rather broad MAS lines with several spinning side bands that indicate considerable anisotropy. The isotropic shifts, which are at about 180–183 ppm for NaY and 153–156 ppm for NaX, can possibly be assigned to Si-O-PCl_2 and (Si-O-)$_2$PCl species (10, 11); the former were recently observed at 184 ppm in studies of PCl_3 reacting with a silica surface (10), and the latter suggested assignment of a line at 156 ppm observed by Bogatyrev et al. (11), though, ideally, further substantiation of these assignments is desirable. The presence of these chemically attached species would imply the production of NaCl (and perhaps a little HCl by reaction with any residual OH groups on the framework). Unfortunately the spectra are not good enough to determine the chemical shift anisotropies.

© 1998 NRC Canada

Fig. 3. ^{31}P NMR spectra of NaY with PCl_3–H_2S in a 4:3 ratio after heating to 76°C. (*a*) Static; (*b*) MAS, ν_r = 3.05 kHz; (*c*) 10× expansion of (*b*).

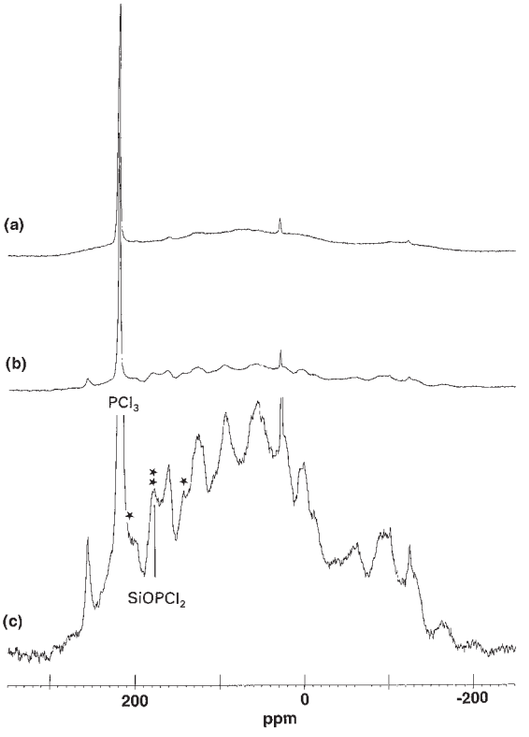

Fig. 4. ^{31}P NMR spectra of NaY with PCl_3–H_2S in a 4:3 ratio after heating to 100°C. (*a*) MAS, ν_r = 2.0 kHz; (*b*) MAS, ν_r = 2.9 kHz, 5 days after (*a*). Isotropic peaks of identified species are indicated by ○, P_4S_3; ◇, α-P_4S_5; □, β-P_4S_6.

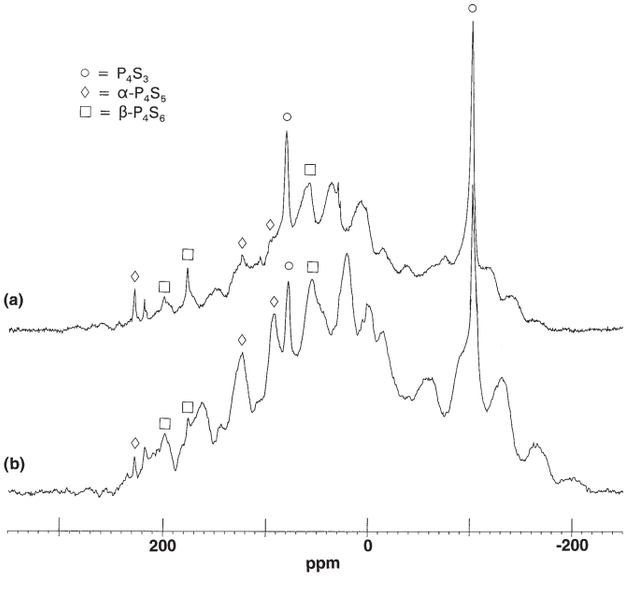

These materials also show a line in the 1.8–4.6 ppm range, which is weak in Silicalite (Fig. 1) and stronger in NaY (Fig. 2). One possible source of tis line could be $POCl_3$, a

Fig. 5. ^{31}P NMR spectra of NaY with PCl_3–H_2S in a 4:5 ratio after heating to 100°C. (*a*) Static; (*b*) MAS, ν_r = 1.95 kHz; (*c*) MAS, ν_r = 3.02 kHz, 18 days after (*a*, *b*). In (*c*) the spectrum of P_4S_7 predominates and P_4S_3 lines are much reduced. Isotropic peaks of identified species are indicated by ○, P_4S_3; ◇, α-P_4S_5; □, β-P_4S_6. The two P_4S_7 lines are indicated by × = P_3,P_4; ● = P_2,P_1. Double symbols indicate the isotropic shift.

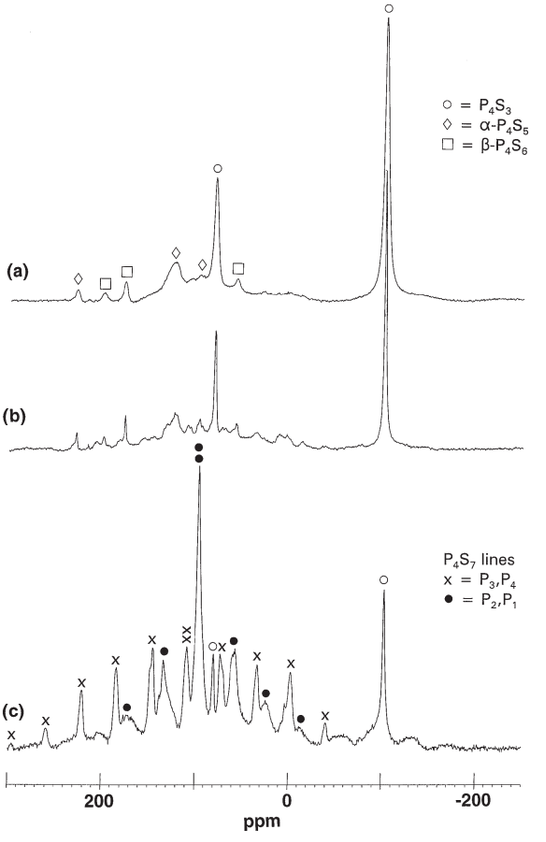

common impurity in PCl_3 (less than 1%), which in the liquid state has a shift of 3 ppm (10). However, the intensity of the line in the NaY spectrum cannot be explained by $POCl_3$ alone, and a more likely alternative with a shift in the same range would be some other P/O/Cl or phosphorus oxy compound produced by reaction of the PCl_3 with any residual -OH groups or defect sites in the framework.

(b) PCl_3 and H_2S within microporous materials

The main phosphorus species observed in the cases of Silicalite (with a $4PCl_3$:$3H_2S$ ratio, annealed at 76°C) and ALPO-5 (with a $4PCl_3$:$5H_2S$ ratio, annealed at 80°C) was absorbed but unreacted PCl_3. In the case of Silicalite when annealed at 170°C, the main signal was still PCl_3 but several other small signals appeared, at 3.6 and 85 ppm (broad), and 48 and 55 ppm (sharp), which we have not been able to assign with any certainty.

In the reactions combining PCl_3 and H_2S (in ratios of 4:3, 4:5, and 4:10) with NaY we observe that in samples heated only to 76°C (Fig. 3), PCl_3 remains prominent in the spectra, and there is a trace of the Si-O-PCl_2 species and a strong unidentified broad signal or signals underlying the whole

© 1998 NRC Canada

Fig. 6. ^{31}P NMR spectra of NaY with PCl_3–H_2S in a 4:10 ratio after heating to 164°C. (*a*) Static; (*b*) MAS, ν_r = 2.95 kHz. Isotropic peaks of identified species are indicated by ○, P_4S_3; ◇, α-P_4S_5; □, β-P_4S_6; ■, new species.

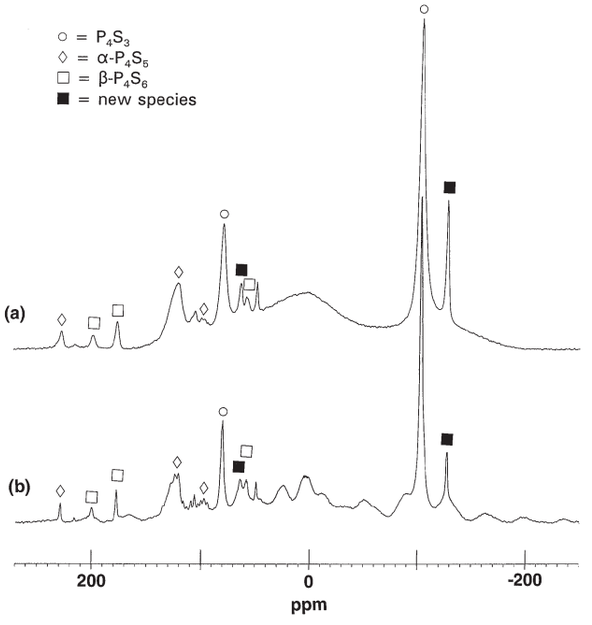

spectrum. Heating to 100°C or higher, however, initiates a complex series of reactions, and the spectra show virtually no PCl_3 and numerous new species (Figs. 4–6), which turn out to be phosphorus sulfides, as anticipated, Fig. 7. Assignments were made by comparison with known chemical shift ranges from numerous previous studies of phosphorus sulfides in solution, the melt, and the solid state, summarized in Table 1. In the early stages a major identifiable component is P_4S_3, with smaller quantities of α-P_4S_5 and β-P_4S_6. Again there are other unidentified species, which in some of the preparations have considerable intensity and large chemical shift anisotropies. The $4PCl_3$:$5H_2S$ preparation was monitored for some time after heating, and the lines of P_4S_3 were observed to diminish while those of P_4S_7 grew, Fig. 5*c*. The structures of the phosphorus sulfides identified are shown in Fig. 7.

A preparation of $4PCl_3$:$3H_2S$ with NaX zeolite showed none of the sharp phosphorus sulfide lines observed for the NaY samples. The MAS spectra showed a very broad, intense spectrum centred around 108 ppm with rather broad spinning side bands superimposed, and several sharp lines between 30 and –12 ppm, with the strongest at 2 ppm. The broader features could conceivably be phosphorus sulfides and the sharp features P/O/Cl species. The different behaviour of NaX compared to NaY is noteworthy, but any discussion of this is necessarily speculative due to the lack of any firm assignments in the NaX spectra. The higher cation content of NaX, however, means that there is also a higher Al content in the framework, and as a consequence of this there will likely be more defects where different reactions with PCl_3–H_2S and their products could occur.

A reaction with NaA with a $4PCl_3$:$7H_2S$ ratio, annealed at 80°C, was carried out with the notion that the much smaller window into the NaA large cage would prevent access even to PCl_3. The spectrum showed principally P_4S_7, again with many spinning side bands, with some P_4S_3, represented by two single lines, Fig. 8*c*. This was one of the cleanest spectra with only a trace of any other species (a broad line with several spinning side bands).

Fig. 7. Molecular structures of P_4S_3, α-P_4S_5, β-P_4S_6, and P_4S_7 (small atoms represent P).

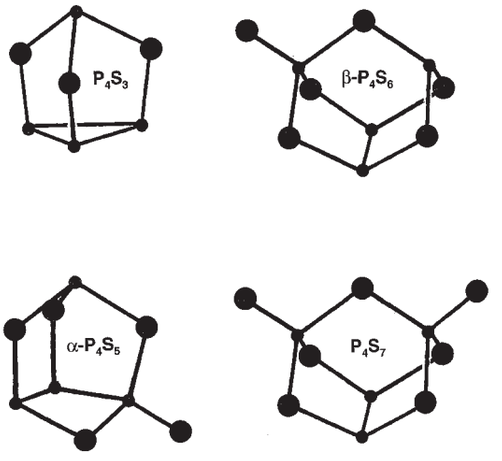

We now proceed to a detailed discussion of the evidence for the phosphorus sulfide assignments, and whether these molecules are located inside or outside the zeolites:

P_4S_3

P_4S_3 is a globular cage molecule (Fig. 7) consisting of a triangle of three basal P_b atoms each linked via an S atom to a single apical P_a atom. The two sharp lines, which are seen in many of the current spectra at 82 ± 2 and –101 ± 2 ppm in a roughly 1:3 intensity ratio, may be assigned confidently to P_a and P_b, respectively. The low-frequency resonance is a unique characteristic of P_4S_3 that distinguishes it from the other phosphorus sulfides. There have been numerous previous studies of P_4S_3 in solution (12) and the solid state(13–18). In various solvents the P_a shift is in the range 62–79 ppm and the P_b shift is from –100 to –135 ppm (12), whereas the most recent studies of the solid give shifts of 91.0/84.5 and –87.5 ppm for the room temperature β-phase (13). (Note, in the solid, P_a appears as two lines due to crystallographically inequivalent molecules.) Clearly there is considerable variation depending on the environment, and our results fall well in the middle of the respective shift ranges.

What is most striking about the P_4S_3 resonances seen in the spectra with NaY zeolite is that the lines are isotropic, since they display no spinning side bands under MAS and remain quite sharp and featureless when static. On its own this isotropic behaviour might be taken as evidence for P_4S_3 being inside the α-cages: Within the Y zeolite α-cage a single P_4S_3 molecule would have considerable rotational freedom, and since the cage has elements of T_d symmetry the dynamic averaging of the chemical shift tensor (arising from pseudo-isotropic reorientation of the molecule) would produce an isotropic line. This is in marked contrast to the room temperature crystalline β-phase, which shows rather large chemical shift anisotropies of several hundred ppm (13).

© 1998 NRC Canada

Table 1. Ranges of reported ^{31}P NMR isotropic shifts for phosphorus sulfides compared with observed lines for the same in NaY.[a]

Compound	Equivalent P atoms [b]	Shift ranges (ppm)	Shifts in NaY (ppm) [c]	Refs.
P_4S_3	1	62–91	81.9 ± 1	12–18
	3	(–87)–(–135)	–101 ± 2	
α-P_4S_4	4	201.9		26
β-P_4S_4	2	205–207.5		2, 26
	1	174.7–185.8		
	1	85.7–97		
α-P_4S_5	1	231.7–237.4	229.6 ± 1	2, 13, 22
	1,1	111.4–139.8	123.8 ± 6	
	1	89.6–120.2	98 ± 3	
β-P_4S_5	2	129.8–142.3		2, 27
	2	80.1–87.2		
α-P_4S_6	1	132.3–133.5		2
	1	114.9–115.8		
	1,1	54.9–65.7		
β-P_4S_6	1	198.9–206.7	200 ± 1	2
	2	178.2–184.8	178.2 ± 1	
	1	55.7–61.0	59.6 ± 1	
P_4S_7	2	109.5–113	110.4 ± 0.5	2, 13–15, 22, 23
	2	81.9–98	97.7 ± 0.5	
P_4S_8	2	135.4		28
	2	13.4		
P_4S_9	1	57.9–67.5		13, 15, 25
	3	57.8–63.6		
P_4S_{10}	4	49.7–60.1		13, 15 25

[a]Shift ranges from reported values in solution, melt, and solid phases. α's and β's in this instance refer to different molecular structural isomers (not different crystal phases).

[b]Distinct P atoms in isolated molecule.

[c]This work.

Similar anisotropies were also obtained from studies of P_4S_3 dissolved in a nematic phase (19). However, there is a second plausible explanation: Crystalline P_4S_3 is known to have a plastic phase (16, 18, 20, 21), where the molecule sits on specific lattice sites but reorients rapidly and thus gives rise to an isotropic NMR spectrum. Although the room temperature β-phase transforms to the plastic α-phase at 313.7 K, the α-phase can be supercooled to a lower limit of 259 K (20). However, it does not always have to be cooled this far down to transform back to the β-phase; for example in a T_1 study the material supercooled by about 35 degrees (21), though in a MAS study the supercooled state was only observed for a few minutes before it reconverted to the β-phase at ambient temperatures (18). Since the preparation of our zeolite / phosphorus sulfides all involved heating to 100°C or more, it is possible that the isotropic lines are from α-crystalline P_4S_3 outside the zeolite. Furthermore, resonances for the α-phase have been reported at 72 and –113 ppm (16) and, more recently, at 80.1 and –104.0 ppm (18). The latter result is very close to our results for NaY. To distinguish between these two possibilities, two of the NaY reaction samples ($4PCl_3$:$5H_2S$ and $4PCl_3$:$10H_2S$) and the NaA reaction sample were cooled to 77 K for 10 min and then allowed to warm back to room temperature; the isotropic lines were unchanged, thus demonstrating unequivocally the presence of P_4S_3 inside these zeolites.

α-P_4S_5 and β-P_4S_6

The static NMR spectra also show series of weak, sharp lines with no chemical shift anisotropy, which we assign to α-P_4S_5 and β-P_4S_6 in the zeolite α-cage, see Figs. 4–6 and Table 1. The identification of three lines for β-P_4S_6 is reasonably certain; the lines are in the correct shift regions (Table 1) and in the correct intensity ratio of 1:2:1 (2). The assignment of α-P_4S_5 must rely mainly on the unique high-frequency shift at 230 ppm (2, 13, 22), as the other expected resonances are partly obscured by other lines. Plastic (rotator) phases for α-P_4S_5 and β-P_4S_6 have not been reported and indeed, since both have a pendant S atom that makes these molecules much less globular than P_4S_3 (see Fig. 7), one would not expect them to have plastic phases. Consequently, the argument for these two products being inside the α-cages and undergoing rapid pseudo-isotropic reorientation is strong.

P_4S_7

The major product in the preparation of both NaY with $4PCl_3$:$5H_2S$, Fig. 8*a*, and NaA with $4PCl_3$:$7H_2S$, Fig. 8*c*, was P_4S_7, but this product is in two quite different states. The experiment with NaA produced crystalline α-P_4S_7, which has four resolved peaks at 82, 96, 111.5, and 113 ppm (13, 23), whereas the spectrum of NaY/P_4S_7 is definitely not that of the crystalline α-form and the isotropic shifts at 110.4

© 1998 NRC Canada

Fig. 8. ^{31}P NMR MAS spectrum of P_4S_7. (*a*) NaY/PCl_3/H_2S preparation, ν_r = 3.02 kHz; (*b*) α-crystalline preparation (no zeolite), ν_r = 4.09 kHz; (*c*) NaA/PCl_3/H_2S preparation, ν_r = 4.03 kHz. (*a*) and (*c*) both show isotropic P_4S_3 lines and traces of broader underlying resonances. (Note that spectrum (*a*) is the same as in Fig. 5*c*). × = P_3,P_4; ● = P_2; ◆ = P_1. In (*a*) P_1, P_2 overlap. Double symbols indicate the isotropic shift.

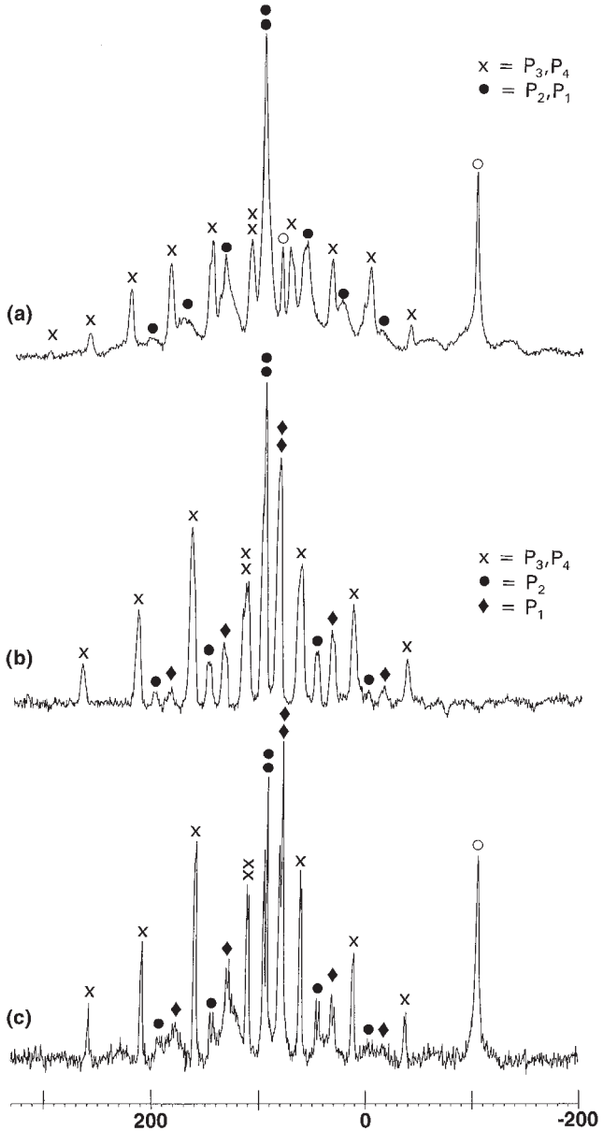

and 97.7 ppm are very similar to those observed for the amorphous form (measured by Bjorholm at 109.5 and 98 ppm (23)). In both spectra the lines show sizeable anisotropies. The molecular point group symmetry of the free P_4S_7 molecule is C_{2v}. There are two distinct pairs of equivalent P atoms and hence one expects two ^{31}P NMR resonances for the C_{2v} molecule (aside from any *J* couplings). In the solid α-phase of P_4S_7, however, the molecule is distorted because of a moderately strong and asymmetric interaction between two P atoms on one molecule and an S atom of another molecule, which makes all four P atoms inequivalent. This well-defined intermolecular interaction does not occur in the amorphous solid, which shows only two resonances, at shifts similar to those in the melt and solution. Likewise for a molecule isolated in the α-cage of NaY, only two resonances would be expected.

Table 2. ^{31}P NMR isotropic shift and principal components of the apparent [a] chemical shift tensors obtained from MAS spectra for P_4S_7 in NaY compared with crystalline α-P_4S_7.

Atom	δ_{iso}	δ_{11}	δ_{22}	δ_{33}
$P_{3,4}$ [b]	109.4	254	109	–36
$P_{1,2}$ [b]	97.8	158	92	44
P_4 [c]	113	271	124	–55
P_3 [c]	111.6	275	131	–72
P_2 [c]	96	187	85	20
		170	78	36
P_1 [c]	82	172	84	–6
		163	69	10

[a]The reader should note that these are not true chemical shift tensors, since direct and indirect coupling tensors are also involved (see ref. 13). In particular, the dipolar coupling between the directly bonded P atoms will be substantial.

[b]Data for P_4S_7 in NaY (this work).

[c]Data for crystalline α-P_4S_7 (13). The double entries for P_2 and P_1 correspond to *J*-split components.

Once again we are left with a choice between two equally plausible assignments for the NaY preparation: the amorphous solid outside the zeolite or isolated molecules inside the cages. Moreover, if the P_4S_7 molecule is inside the cages, this time it cannot be undergoing rapid reorientations because the chemical shift anisotropy is not averaged. The principal components of the chemical shift anisotropies for both resonances of NaY–P_4S_7 were determined by spinning side-band analysis at various spinning speeds using the Herzfeld–Berger method (24), which is incorporated in the Bruker software, see Table 2. From the table we note that our results, which clearly would not be expected to be the same as for crystalline α-P_4S_7 determined previously (13), nevertheless show anisotropies of similar span and skew. This rules out any question of dynamic averaging.

There are two main arguments that favour the existence of single molecules of P_4S_7 inside the cages of NaY: (*a*) There is the circumstantial evidence of the precursors being inside the cages, and several of the smaller sulfides also being formed there. (*b*) The amorphous form of P_4S_7 has only been formed previously by quenching the melt rapidly to 77 K (23), conditions quite remote from our preparation where the PCl_3 was sublimed into the zeolite and H_2S gas was added separately before annealing at 100°C.

P_4S_9 and P_4S_{10}

Since P_4S_7 appears to be static it is highly unlikely that we would see dynamic P_4S_9 and P_4S_{10}, which enables us to exclude making any assignment of sharp lines in the 50–60 ppm region to these species. Although their isotropic shifts fall in this region the static molecules have large chemical shift anisotropies (13, 15, 25).

© 1998 NRC Canada

A new P_4S_4 species in NaY ?

The $4PCl_3$:$10H_2S$ NaY preparation heated to 163°C shows three sharp lines in the static spectrum, at –126.3, 49, and 64 ppm, which do not appear for any of the other samples. Furthermore, when this material was reexamined after considerable aging, the P_4S_3 lines and the 49 ppm line had diminished considerably, and the lines due to α-P_4S_5 and β-P_4S_6 had disappeared completely, leaving a broad background centred around zero shift and more prominent lines at –126.3 and 64 ppm. The latter two lines occur in a roughly 3:1 ratio and appear to be associated with one species. The –126.3 ppm shift is very unusual, and does not appear to have been observed in the solid state before. The unique –101 ppm shift seen for P_4S_3 arises from its ring of three P atoms, so we suspect that the –126.3 ppm line may also be due to a P_3 ring, perhaps of a P_4S_3 derivative with a pendant S on the unique P atom. In this case the shift of 64 ppm for the unique P is in the region expected for $S_3P{=}S$ units. Such a P_4S_4 molecule would be a new geometric isomer with C_{3V} symmetry, and it would still have room to undergo pseudo-isotropic reorientation inside the α-cage. Why this new isomer would form in preference to the α or β forms is debatable, but it is likely influenced by the zeolite framework. A P_4S_3 molecule protonated on the unique P, $P_4S_3H^+$, is another possibility, though this has not been reported before and the S_3PH^+ unit would not be expected to have a 64 ppm shift. A chloro derivative seems much less likely since H_2S is in excess, and in fact it can be excluded, since we have observed the same two resonances in a preparation involving elemental P with H_2S in NaY annealed at 420°C (work to be reported later). One final possibility is that these resonances are from P_4S_3 in a second distinct kind of environment, though it is difficult to envisage where this might be.

^{129}Xe NMR results

The characteristic chemical shift of ^{129}Xe in pure NaY samples arises from exchange of the Xe between the zeolite cavities and the gas phase. The observed shift is a population weighted average of the shifts in the two types of situation (a high-frequency shift inside, and a low-frequency shift outside). The shifts for similar amounts of Xe in pure NaY and in an NaY with $4PCl_3$:$3H_2S$ reaction sample were 87.6 and 16.1 ppm, respectively. The much smaller shift of the Xe in the reaction sample indicates that the Xe is effectively excluded from the zeolite, implying that the cages are occupied by the phosphorus compounds. The 16.1 ppm shift, compared to that of the isolated Xe atom, indicates that the Xe is under significant pressure, the shift being caused by collisions with Xe atoms, the HCl reaction product, and any residual H_2S.

Molecular dimensions

An important consideration regarding the encapsulation of the phosphorus sulfide molecules is whether they can fit inside the zeolite cage and, if so, whether they have room to rotate. All the dimensions in the following discussion take into account the van der Waals radii of the atoms (O = 1.4, P = 1.9, S = 1.85, and Cl = 1.8 Å (29)).

NaY: The diameter of the Y zeolite α-cage, without taking into account Na^+ cations, is 11.0 Å and the diameter of the 12-ring window is 7.4 Å (30, 31).

NaA: The diameter of the A zeolite α-cage is 11.4 Å, and the diameter of the 8-ring window is only 4.1 Å (31, 32), excluding the Na^+ ions.

P_4S_3: The dimensions of P_4S_3 show a maximum diameter of 7.5 Å, and the largest diameter perpendicular to the 3-fold axis is 7.24 Å (calculated from available structural data (20, 33)). Inside the large cages of both NaY and NaA it will have considerable room. This molecule should therefore be able to go easily through the 12-ring window of NaY, but it should not be able to get through the 8-ring window of NaA zeolite.

α-P_4S_5: This is slightly smaller than β-P_4S_6 with a largest dimension of 9.3 Å (calculated from the crystal structure (34)).

β-P_4S_6: This is basically a P_4S_7 with one pendant S removed, so we have calculated its size based on the structural information for P_4S_7 (see below). Its largest dimension is 9.4 Å, and from the NMR it would appear that this is still small enough to allow rapid reorientation in the NaY cage.

P_4S_7: The smallest dimension of P_4S_7 (calculated from the crystal structure information (34–36)) is 7.7 Å and the largest is 10.2 Å.

One molecule of P_4S_7 can therefore fit inside the cage without too much trouble, but it would be difficult to get through the window. This has several implications: (*a*) The particular interactions that distort the molecules in the α-phase should not be present. (*b*) If it is inside the cage the molecule must have formed in situ from smaller precursors. (*c*) Once formed inside, the molecules will remain trapped. When the presence of Na^+ ions is also considered together with the long dimension of the molecule it is highly likely that the P_4S_7 will experience considerable hindrance to rotation, and hence the chemical shift anisotropy will not display the effects of dynamic averaging.

P_4S_9 and P_4S_{10}: Isolated P_4S_{10} is a tetrahedral molecule. The largest dimension (between two pendant S atoms) is 10.24 Å, but if the molecule were rotating pseudo-isotropically its effective diameter would be 11.71 Å (calculated from the structural data (34, 35)). P_4S_9 is structurally similar to P_4S_{10} but with one pendant S removed, hence its largest dimensions are virtually identical.

PCl_3: PCl_3 is a pyramidal molecule with dimensions (*a*) along a P—Cl bond of 5.74 Å, (*b*) along a Cl—-Cl edge of 6.73 Å, and (*c*) for the pyramid height of 4.65 Å (calculated from microwave structural data (37)). It should therefore have easy access to the NaY α-cage, and a tetrahedral cluster of four PCl_3 will just fit inside the cage. PCl_3 should not, however, be able to get through the window of the α-cage of NaA.

Other components of the spectra

We will emphasize again that the picture is incomplete as there are signals that we have been unable to assign, in particular, the broad background of signals with large chemical shift anisotropies. The MAS lines of these signals are themselves broad, whereas most crystalline materials would be expected to show sharp MAS lines. The broadening could be due to intermediate rate dynamics but a much more likely

© 1998 NRC Canada

explanation is that it is due to a distribution of species and (or) a distribution of environments for the same species.

We may be seeing impure and mixed P–S species outside the zeolite, and any species attached to the framework (inside or on the external surface) would also give broad lines with anisotropies.

Chemistry

The chemical complexity of these systems must now be quite apparent, so beyond a few obvious points our comments regarding reactions must necessarily be speculative:

1. A basic assumption is that any -SH will react with P–Cl bonds, provided the two are able to access each other, so if PCl_3 is in excess all the -SH will be depleted and there may be P/S/Cl species present, and, vice versa, in reactions where H_2S is in excess, any PCl species will disappear and there may be P/S/H species produced. The HCl by-product could itself influence further reactions.

2. We observed P_4S_3 at the early stages after heating to 100°C or more, and that this is depleted as P_4S_7 forms, suggesting a building of S onto the P_4S_3 framework.

3. It was surprising to find P_4S_3 inside NaA (demonstrated by the persistence of isotropic lines after cooling to 77 K). Since P_4S_3 cannot get through the window of NaA it must be constructed inside the cage, and yet PCl_3 is also too large to get through the window. This suggests some smaller precursor must first form at the zeolite surface and migrate into the cages, say, perhaps PCl_2^+.

4. An interesting feature of these experiments is that the zeolites seem to have a catalytic effect, enhancing the formation of the phosphorus sulfides. The thiosolvolysis reaction of PCl_3 in liquid H_2S is known to produce some P_4S_7 as part of a mixture after 60–70 h (38), while PCl_3 and H_2S in the presence of base react to give P_4S_3, among other products (1, 39). We found, however, that a yellowish white solid produced after 4 days of reaction between PCl_3 and H_2S in the absence of zeolite still showed mainly PCl_3 signals in the ^{31}P NMR (over 90% of the "observable" phosphorus), and no P_4S_7 was detected in this solid even after 3 months. The ionic nature of NaY and NaA and their microporosity probably play important roles in orchestrating the chemistry.

Conclusions

We have clear evidence for the formation of phosphorus sulfides inside the micropores; however, the chemistry is rather complicated. Moreover, with the numerous different products present, the goal of producing a regular array of identical molecules using the zeolite framework has not been realized. However, the results point the way: Perhaps this might be achievable by starting with pure P_4S_3 instead of PCl_3.

Acknowledgment

The authors would like to thank J. Bennett for expert technical assistance with the NMR instrumentation, and S. Zones for the kind donation of the ALPO-5.

References

1. D.E.C. Corbridge. Phosphorus. An outline of its chemistry, biochemistry and technology. 4th ed. Studies in inorganic chemistry 10, Elsevier, New York. 1990.
2. T. Bjorholm and H.J. Jakobsen. J. Am. Chem. Soc. **113**, 27 (1991).
3. F. Heyder and D. Linke. Z. Chem. **13**, 480 (1973).
4. Y. Monteil and H. Vincent. Z. Anorg. Allg. Chem. **428**, 259 (1977).
5. R. Blachnik and A. Hoppe. J. Non-Cryst. Solids, **34**, 191 (1979).
6. P.C. Taylor. MRS Bull. **12**, 36 (1987).
7. M. Tullius, D. Lathrop, and H. Eckert. J. Phys. Chem. **94**, 2145 (1990).
8. G.D. Stucky and J.E. MacDougall. Science, **247**, 669 (1990).
9. G.A. Ozin, A. Kuperman, and A. Stein. Angew. Chem. Int. Ed. Engl., **28**, 359 (1989).
10. B.A. Morrow, S.J. Lang, and I.D. Gay. Langmuir, **10**, 756 (1994).
11. V.M. Bogatyrev, V.V. Brei, and A.A. Chuiko. Theor. Expt. Chem. (Engl. Transl.), **24**, 603 (1988).
12. G. Heckmann and E. Fluck. Z. Naturforsch. **26B**, 982 (1971).
13. R.K. Harris, P.J. Wilkes, P.T. Wood, and J.D. Woollins. J. Chem. Soc. Dalton Trans. 809 (1989).
14. C.Brevard and M.Demarcq. Chem. Phys. Lett. **82**, 167 (1981).
15. H. Eckert, C.S. Liang, and G.D. Stucky. J. Phys. Chem. **93**, 452 (1989).
16. E.R. Andrew, W.S. Hinshaw, and A.Jasinski. Chem. Phys. Lett. **24**, 399 (1974).
17. M.G. Gibby, A. Pines, W.-K. Rhim, and J.S. Waugh. J. Chem. Phys. **56**, 991 (1972).
18. T. Bjorholm and H.J. Jakobsen. J. Magn. Reson. **84**, 204 (1989).
19. N. Zumbulyadis and B.P. Dailey. Chem. Phys. Lett. **26**, 273 (1974).
20. T. Chattopadhyay, E. Gmelin, and H.G. Von Schnering. J. Phys. Chem. Solids, **43**, 925 (1982).
21. E.R. Andrew, W.S. Hinshaw, M.G. Hutchins, and A. Jasinski. Chem. Phys. Lett. **27**, 96 (1974).
22. R. Thamm, G. Heckmann, and E. Fluck. Phosphorus Sulfur, **11**, 273 (1981).
23. T. Bjorholm. Chem. Phys. Lett. **143**, 259 (1988).
24. J. Herzfeld and A.E. Berger. J. Chem. Phys. **73**, 6021 (1980).
25. E.R. Andrew, W. Vennart, G. Bonnard, R.M. Croiset, M.C. Demarcq, and E. Mathieu. Chem. Phys. Lett. **43**, 317 (1976).
26. A.M. Griffin, P.C. Minshall, and G.M. Sheldrick. J. Chem. Soc. Chem. Commun. 809 (1976).
27. A.M. Griffin and G.M. Sheldrick. Acta Crystallogr. Sect. B: Struct. Crystallogr. Cryst. Chem. **B31**, 2738 (1975).
28. J.-J. Barieux and M.C. Demarcq. J. Chem. Soc. Chem. Commun. 176 (1982).
29. F.A. Cotton and G. Wilkinson. Advanced inorganic chemistry. 3rd ed. Interscience, New York. 1972. p. 120.
30. G.R. Eulenberger, D.P. Shoemaker, and J.G. Keil. J. Phys. Chem. **71**, 1812 (1967).
31. W.M. Meier and D.H. Olson. Atlas of zeolite structure types. 3rd ed. Butterworth–Heinemann, London. 1992.
32. J.J. Pluth and J.V.Smith. J. Am. Chem. Soc. **102**, 4704 (1980).
33. Y.C. Leung, J. Wazer, S. Van Houten, A. Vos, G.A. Wiegers, and E.H. Wiebenga. Acta Crystallogr. **10**, 574 (1957).
34. A. Vos, R. Olthof, F. van Bolhuis, and R. Botterweg. Acta Crystallogr. **19**, 864 (1965).
35. A. Vos and E.H. Wiebenga. Acta Crystallogr. **8**, 217 (1955).
36. D.T. Dixon, F.W.B. Einstein, and B.R. Penfold. Acta Crystallogr. **18**, 221 (1965).
37. P. Kisliuk and C.H. Townes. J. Chem. Phys. **18**, 1109 (1950).
38. A.R. Pitochelli and L.F. Audrieth. J. Am. Chem. Soc. **81**, 4458 (1959).
39. E. Fluck and B. Neumuller. Z. Anorg. Allg. Chem. **534**, 27 (1986).

© 1998 NRC Canada

Adhesion to dentin: studies of surface chemical reactions towards the goal of improved bonding

M. Di Renzo, F. El Feninat, B. Jiménez-Esquivel, S. Poulin, M. Yavari, J. Xu, T.H. Ellis, E. Kruus, E. Sacher, and I. Stangel

Abstract: Human dentin consists of protein and mineral phases in the form of a collagen network reinforced with apatite. The bonding of materials to dentin, an important goal of dental materials research, can be achieved by the reaction of adhesion promoters with either of these phases. Our group is concerned with such bonding, and has used surface-sensitive instrumentation to elucidate the nature of a variety of surface treatments of dentin. Here, we discuss some of our findings, with particular emphasis on the kinetics of surface demineralization and deproteination, the reaction of formaldehyde with collagen, and the reaction of organophosphate with dentin apatite. The ramifications of our findings will be examined.

Key words: dentin, adhesion, vibrational spectroscopy, atomic force microscopy.

Résumé : La dentine humaine est composée de phases protéiniques et minérales formées d'un réseau de collagène renforcé par de l'apatite. Pour obtenir une liaison entre des matériaux et la dentine, un objectif important de la recherche des matériaux dentaires, on peut faire appel à la réaction de promoteurs d'adhésion avec l'une ou l'autre de ces phases. Notre groupe s'intéresse particulièrement à cette liaison et fait appel à une instrumentation sensible aux surfaces pour élucider la nature d'une variété de traitements de surface de la dentine. Dans ce travail, on discute de nos observations, en mettant l'accent sur la cinétique de la déminéralisation et de la déprotéination de la surface, la réaction du formaldéhyde avec le collagène et sur la réaction des organophosphates avec l'apatite de la dentine. On examine les ramifications de nos observations.

Mots clés : dentine, adhésion, spectroscopie de vibration, microscopie des forces atomiques.

[Traduit par la Rédaction]

Introduction

Dentin is the inner bulk structure of teeth. Human dentin is composed of about 69% (w/w) dentin apatite (i.e., a form of hydroxyapatite that contains a number of impurities, particularly carbonate), 18% proteins (90% type I collagen, the rest consisting mainly of phosphoproteins bonded to the collagen surface), and the remainder, water. The dentin is permeated by tubules 1–3 mm in diameter, which contain elongated cell bodies radiating from the dental pulp. Figure 1 shows an atomic force microscopy (AFM) view of a dentin surface, cut parallel to the occlusal plane (top surface) of the tooth and polished using an adapted metallurgical polishing protocol. A review of the composition and structure of dentin is found in ref. 1.

One of the goals of dental materials research is to develop adhesives capable of producing durable high-strength bonds to dentin. The successful adhesive retention of materials to teeth would result in minimal and less invasive operative procedures, the quality of interfaces between materials and mineralized tissues would be improved, and the cost of providing restorative care would be reduced in many cases. In contrast, dental amalgam, which does not adhere to dentin, requires the use of complex geometric designs to mechanically lock it into tooth structure. This results in the removal of otherwise healthy tissue, which unnecessarily weakens tooth structure and leads to eventual complications.

Although several polymeric dentin restorative materials are presently being used, existing materials have been shown to be less effective than amalgam in the long term (2). To improve on their durability, it is important to understand the basis of their interaction with dentin. While various theories of dentin bonding have been proposed, most rely on the extensive microscopic analysis of the resin–dentin interface. Thus, morphological, rather than molecular, information is elucidated and such theories do not generally consider chemical adhesion at the dentin–restorative interface (3).

Chemical adhesion may, in fact, occur with either phase of dentin (4, 5). Bonding to apatite may occur through complexation to the calcium ion, to the phosphate group, or by reaction with the hydroxyl group. The chemical bonding

Received February 23, 1998.

M. Di Renzo, F. El Feninat, and T.H. Ellis.[1] Département de chimie, Université de Montréal, Montréal, QC H3C 3J7, Canada.
S. Poulin and E. Sacher. Département de génie physique, École Polytechnique, Montréal, QC H3C 3A7, Canada.
J. Xu, M. Yavari, and I. Stangel. Faculty of Dentistry, McGill University, Montreal, QC H3A 1A4, Canada.
B. Jiménez-Esquivel and E. Kruus. Département de chimie, Université du Québec à Montréal, Montréal, QC H3C 3P8, Canada.

[1]Author to whom correspondence may be addressed. Telephone: (514) 343-6910. Fax: (514) 343-7586. E-mail: ellis@chimie.umontreal.ca

© 1998 NRC Canada

Fig. 1. AFM image of the surface of polished dentin, showing exposed tubules. The final polishing step of 0.05 μm alumina powder.

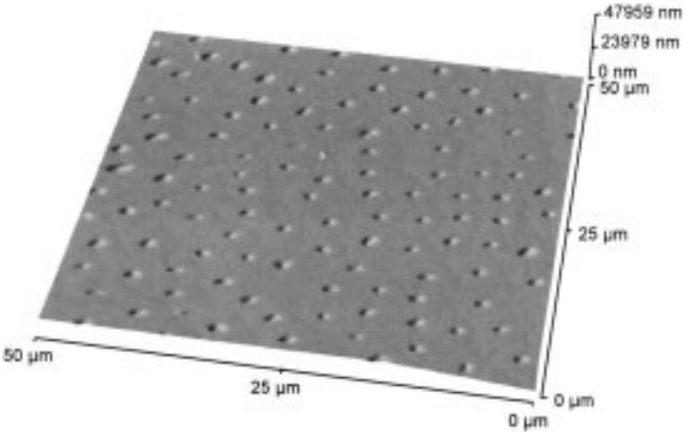

to collagen is a largely unexplored area. Reaction to the protein could occur through any exposed reactive group, provided that its concentration is high enough to give good bonding. An obvious candidate to be explored is free carboxyl, whose frequency of occurrence in collagen is about 1 in 13 residues (6). Although collagen is the predominant protein in collagen, the exact composition of the exposed surface would depend, to some extent, on whether or not phosphophoryns (the main form of phosphoproteins) are removed by pretreatments, since the relative concentrations of reactive groups on the protein surface differ significantly from phosphophoryn to collagen. Acid treatment has been found to remove at least some phosphoproteins (7).

From the onset of our studies, almost a decade ago, it was evident that two factors would be crucial for achieving a molecular-level understanding of adhesion to dentin. The first was the ability to produce conditioned, reproducible surfaces and the second, the use of highly surface-sensitive instruments and techniques capable of giving information on chemical structure at this surface. Here, we use the results of a broad range of measurements toward the goal of developing a comprehensive picture of the conditioning of the dentin surface and adhesion promotion to its components.

Experimental section

Samples for most studies were obtained from freshly extracted human molars. A diamond saw was used to prepare wafers, ~1.5 mm thick, having surfaces parallel to the occlusal plane of the tooth. The study with formaldehyde was conducted using freshly extracted bovine molars, as there was an insufficient supply of human teeth at the time of the experiment. Bovine dentin is often used a model for human dentin, due to the similarities between the two materials.

The acid etching of dentin apatite, by citric, hydrochloric, maleic, and phosphoric acids, was carried out in the pH range of 0.7–1.4. Calcium loss was detected by atomic absorption at 422.7 nm, with the output of the detector sampled by a computer interface at 0.5 s intervals. The exposed surface area of each sample was 12 mm^2, and the volume of acid solution was 100 mL.

Photoacoustic infrared spectra (PA-FTIRS) of surfaces were obtained on a Mattson RS-1 FTIR spectrometer, using an MTEC 300 photoacoustic cell. This cell measures the gas pressure change, in an enclosed volume, due to the adsorption and dissipation of infrared energy, and is, therefore, directly applicable to opaque samples. An advantage of this technique is that the major part of the signal comes from the first thermal diffusion length of the substrate, which can be shortened by increasing the modulation frequency, which, in this case, is determined by the speed of the interferometer mirror.

AFM topographic images were obtained using a TopoMetrix model 2010 Discoverer microscope (Santa Clara, Calif.). Cantilevers with nominal spring constants of 0.047 N/m and silicon carbide Supertips having radii of 10 nm were used. After storage in water, samples were imaged under ambient conditions. Excess water was removed by gentle blotting with absorbent paper.

The adhesive joint strength was measured by bonding polymer-matrix composites to both polished and acid-etched dentin using the adhesion promoters to be evaluated. After 24 h storage in water, assemblies were placed in specially designed grips in an Instron electromechanical testing device (model 4465), and tested to failure in shear, at a cross-head speed of 2 mm/min. Peak loads at failure were normalized to the surface area of the joint.

Results and discussion

Chemical conditioning of dentin

The etching kinetics of dentin apatite, irrespective of the acid used, were found to follow diffusion-controlled kinetics:

$$[1] \qquad [Ca^{2+}] = Kt^{1/2}$$

where K is a proportionality constant. As such, measurements of the amount of dissolved calcium as a function of the square root of time were found to be linear, except for a brief induction period, as seen in Fig. 2.

The rate of etching can be evaluated either by the value of K, or by measuring the total amount of calcium removed over a fixed period of time. For the latter, a period of 2 min was chosen, to reduce errors arising from the finite time required to introduce and remove the sample from the solution. We had already determined that diffusion-controlled

© 1998 NRC Canada

Fig. 2. Atomic absorption measurement of the Ca^{2+} concentration in solution, plotted as a function of the square root of acid exposure time, for HCl at pH = 1.2.

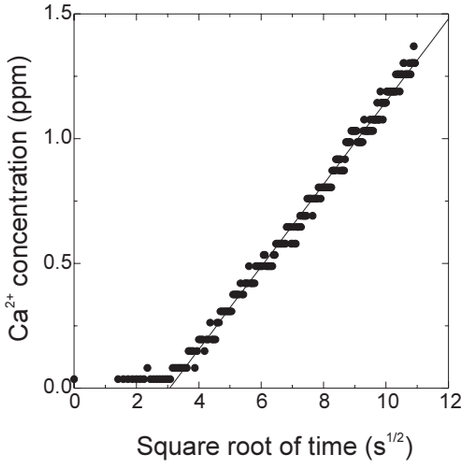

Fig. 3. PA-FTIR spectra of human dentin surfaces: (*a*) as cut; (*b*) acid etched (maleic acid, pH = 1, 2 min); (*c*) NaOCl treated (12% aqueus solution, 48 h); (*d*) acid etched as in (*b*), followed by NaOCl treatment (2 min).

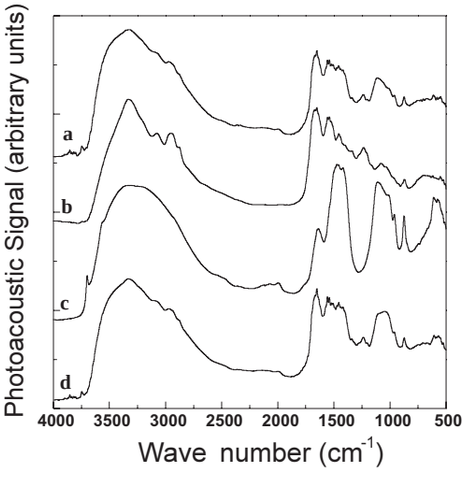

kinetics are valid for times ranging from a few seconds to several minutes. Using this procedure, a quantitative comparison was made between the rates of etching of the four different acids. For each acid, the acid concentration was adjusted until the desired pH value was obtained. By comparing different acids having the same pH values the role of the acid anions is highlighted.

The results at pH = 1.0 are shown in Table 1. Each acid should be compared to hydrochloric acid, whose anion (Cl^-) has the lowest tendency to form precipitates with calcium ions. Citric acid had the lowest etching rate, and its anion is the most likely to produce precipitates (calcium citrate tetrahydrate). The effect is the establishment of an equilibrium between the rates of etching and precipitate formation at the interface. The formation of precipitates limits access of the etchant to the surface, resulting in an etching rate lower than that which would have occurred in the absence of precipitation. Maleic and phosphoric acids had intermediate etching

Table 1. Acid etching rates at pH = 1.0.

Acid	Total calcium etched after 2 min (ppm)
Citric	0.14 ± 0.16
Phosphoric	0.74 ± 0.06
Maleic	0.91 ± 0.14
Hydrochloric	1.31 ± 0.16

rates at this pH. Additional information about acid etching was gained through a study of each acid as a function of proton concentration (8). The important conclusion from all of these studies is that, in addition to pH, acid anions play a consequential role in determining etching rates.

Our previous work on the photoacoustic IR contributions of the components of dentin demonstrated that each component contributed additively to the overall spectrum (9). A typical spectrum of human dentin is shown in Fig. 3*a*. In order to assign individual features, we also show spectra of demineralized (acid etched) and of deproteinated (NaOCl treated) dentin (Figs. 3*b* and 3*c*, respectively). A summary of peak assignments is given in Table 2. Acids preferentially remove dentin apatite, and NaOCl preferentially removes collagen. The spectrum of demineralized dentin is very similar to that of pure type I collagen (such as bovine tendon collagen). The spectrum of deproteinated dentin compares favorably to that of pure hydroxyapatite, with the exception of intense carbonate peaks in dentin apatite, these being inherent to biological apatites. The large non-hydrogen bonded O–H stretching peak from interfacial water at 3698 cm^{-1} indicates a very high surface-to-volume ratio in NaOCl-treated dentin.

PA-FTIRS probes, at most, the outer 10 μm of the surface. It was found that a 2 min acid treatment at pH = 1 was sufficient to completely demineralize the probed region, the only exception being citric acid. This slower etching by citric acid was predicted by the atomic absorption experiment.

The deproteination of dentin with NaOCl was found to differ from demineralization in a number of ways. The latter is known to be homogeneous: a demineralized zone of fairly uniform thickness is observed in TEM images of acid-etched dentin (10, 11). We have found that deproteination with NaOCl is a slower and more heterogeneous process: some collagen is observed to remain in the surface region even after the deproteination has, on average, penetrated deep into the sample. This is due to the fact that the morphology of dentin is playing a key role, and the encapsulation of collagen by apatite limits the deproteination process. On the other hand, surface collagen (i.e., collagen on the surface exposed by demineralization) was found to be removed rapidly, returning the surface to the composition of bulk dentin. This is illustrated in Fig. 3*d*, where a surface was etched for 2 min (see Fig. 3*b*) and then treated with NaOCl for 2 min, which completely removes all traces of exposed collagen. In contrast, a 2 min treatment of unetched dentin has no detectable result.

In addition to spectroscopic measurements, it is always beneficial to correlate chemical and structural information. Our group has been one of first to apply the high resolution of AFM to the study of dentin surfaces (12–14). It had already been established that the ultrastructure of collagen,

© 1998 NRC Canada

Table 2. Vibrational assignments.

	Wave number (cm^{-1})	Assignment
Collagen	3330	Amide A (NH stretch)
	3078	Amide B
	2954, 2879	CH_2 stretch
	1655	Amide I (CO stretch)
	1455	CH_2 bend
	1535	Amide II (NH bend + CN stretch)
	1235	Amide III (CN stretch + NH bend)
Dentin apatite	3572	OH stretch
	1472, 1415	CO in carbonate
	1110, 963	PO in phosphate
	873	CO in carbonate
	611, 568	PO in phosphate
Water	3698	OH stretch (not H-bonded)
	3600–2800 (broad)	OH stretch (H-bonded)
	1636	H_2O bend (scissor)

Fig. 4. AFM image of the surface of acid-etched dentin, following storage in water for an extended period. Intact collagen fibers show 67 nm periodic banding perpendicular to the long axis of the fiber.

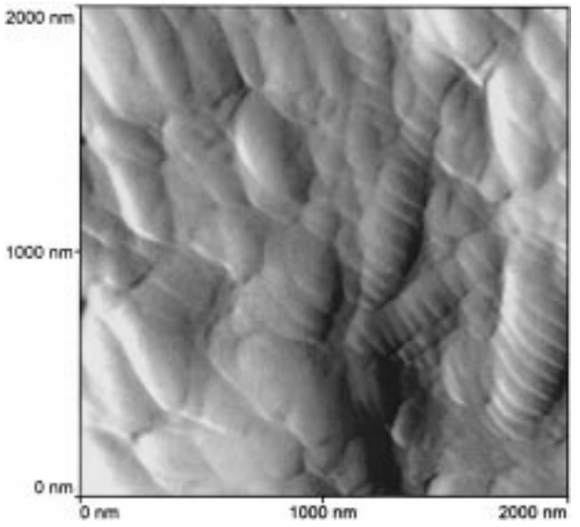

such as the characteristic 67 nm periodic banding, can be observed on isolated fibers using AFM (15, 16). It is more challenging to observe this level of structure in situ, on the surface dentin. Figure 4 shows the surface of demineralized dentin; fibers with periodic banding can be clearly seen. Two factors have been found to be crucial for this observation. First, the sample must be stored for hours to days in water after acid etching, in order to renature any denaturation induced by the acids. Second, the sample cannot be allowed to become too dry, which can lead to the permanent loss of structure. These results are of interest because any damage to the collagen layer can inhibit the penetration of resins into the demineralized zone. It will be important to find ways to renature collagen on a more practical time scale, or to reduce the degree of denaturation during demineralization.

Adhesion to the components of dentin

Surfaces prepared according to these techniques were used to study site-specific chemical reactions to the individual phases of dentin. In the case of demineralized dentin, there are a number of chemical reactions with collagen side groups that could potentially be used for the purpose of adhesion. For example, it is common practice to treat collagen with glutaraldehyde, a known fixative, prior to performing structural studies with electron microscopies. It is thought that glutaraldehyde forms chemical cross-links between collagen fibers. The reaction between amine side groups and an aldehyde would occur via the formation of a Schiff's base. To test for such reactions, demineralized bovine dentin was treated with formaldehyde, and PA-FTIRS spectra before and after treatment are shown in Fig. 5. Proof of the reaction is the appearance of a new peak at 1205 cm^{-1}, assigned to a secondary amine. The ability to observe the formation of this bond is enhanced by the fact that the peak appears in a region of the spectrum that is relatively uncongested. Although formaldehyde itself is not necessarily useful as an adhesion promoter, these results point the way to the development of adhesives that can react with collagen in a similar fashion.

An example of bonding to apatite concerns the use of alkyl phosphates (17); phosphates are capable of reacting with hydroxyl groups, even those of surface P-OH groups. In our studies, we have used derivatives of dipentaerithritol, $DP(OH)_6$, which has six reactive hydroxyl groups. Further reaction with acrylic acid gives dipentaerithritol pentaacrylate, $DP(A)_5(OH)$, having one remaining reactive hydroxyl group. This group may further react with phosphoric acid to give dipentaerithritriol pentaacrylate monophosphate, $DP(A)_5(H_2PO_4)$, a component of some commercial dental restoratives (see Scheme 1). This phosphate is capable of bonding to the hydroxyl groups of apatite (17); in doing so, it introduces to the surface strongly anchored acryloxy groups capable of further reaction with the chemically similar methacryloxy groups in the restorative resin.

In a similar fashion, $DP(A)_5(OH)$ is capable of providing hydroxyl groups for reaction with phosphate groups in apatite, and it is no surprise that this material, too, bonds to the

© 1998 NRC Canada

Fig. 5. PA-FTIR spectra of acid-etched bovine dentin (middle trace) after treatment with formaldehyde (top trace). The difference spectrum is also shown (bottom trace).

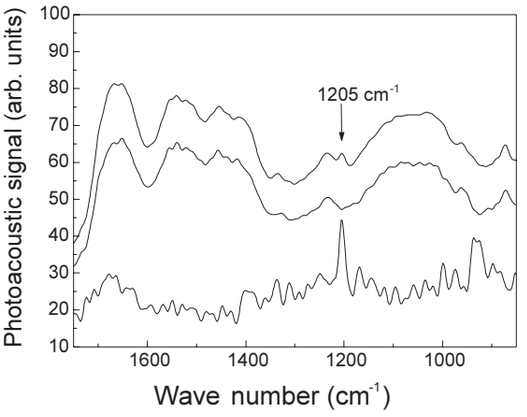

Table 3. Shear bond strengths at resin-dentin interface.

	Shear bond strength (MPa)	
Adhesive	Smeared surface	Acid etched surface
None	0.74 ± 0.56	—
$DP(A)_5(OH)$	4.2 ± 1.2	7.4 ± 2.5
$DP(A)_5(H_2PO_4)$	23.7 ± 4.3	28.0 ± 1.3

dentin surface. Similarly, phosphate can also react with groups (e.g., hydroxyl) in the exposed collagen and hydroxyl groups can react with collagenous carboxylate and partially phosphorylated serine (1) groups, creating a situation where extents of reaction are controlled by surface preparation, all potentially capable of giving strong bonds to the restorative.

The formation of such bonds can be extremely difficult to demonstrate spectroscopically, because similar bonds already exist in high concentration. Secondary evidence may sometimes be used to *infer* the existence of such bonds. Here, too, problems exist, as one may see by a consideration of bond strengths: because $DP(A)_5(OH)$ and $DP(A)_5(H_2PO_4)$ are each capable of bonding to either apatite or collagen, bond strength increases are expected in all cases.

In this regard, we consider the results of a shear bond evaluation, a technique previously described (14), which was carried out to gauge the efficiencies of $DP(A)_5(OH)$ and $DP(A)_5(H_2PO_4)$. Although it is well known that such tests are limited in their ability to simulate conditions in the oral environment, they are particularly useful for the purpose of screening candidate adhesives. As seen in Table 3, both molecules are shown to enhance resin bonding to dentin, although the $DP(A)_5(H_2PO_4)$ is by far the better. Table 3 also clearly indicates that, for this type of adhesive, the condition of the surface can be less important than the presence of the phosphate group in the adhesive. Two surface conditions were studied, one being polished (600 grit, which simulates a smear layer), and the other being acid etched (maleic acid, pH = 1.2, 30 s). Although many adhesives are thought to require a demineralized surface in order to establish a "hybrid zone" (3), this is clearly less important for the present system. Certainly, a complete understanding of bonding to dentin in only possible when both micromechanical and chemical bonding are be taken into account.

Scheme 1. Dipentaerithritriol pentaacrylate monophosphate, $DP(A)_5(H_2PO_4)$.

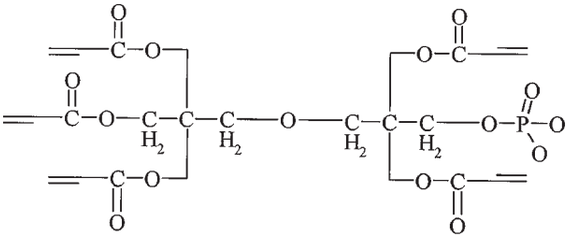

Conclusions and ramifications

Site-specific reactions are capable of occurring between either of the solid components of dentin and properly chosen reactants. Such reactions may form the basis of adhesion promotion to the dentin when other sites on the reactants are chosen for reaction with the (meth)acrylic groups of the resin. Adhesion promoters, having sufficiently high adhesive strength and sufficient durability in an oral environment, may potentially reduce the trauma involved in dental restorations because they eliminate the necessity of removing large amounts of tissue in order to introduce the geometrical designs necessary to fix non-adhering dental restoratives. Both spectroscopic and bond strength measurements can be valuable in providing a molecular level understanding of adhesion to dentin.

Acknowledgments

We wish to thank the Natural Sciences and Engineering Research Council of Canada and the Group de recherche en physique et technologie des couches minces (GCM) for financial support.

References

1. W.T. Butler. *In* Dentin and dentinogenesis. Vol II. *Edited by* A. Linde. CRC Press, Boca Raton, Fla. 1984.
2. A. Jokstad, I.A. Mjor, and V. Qvist. Acta Odontol. Scand. **54**, 234 (1994).
3. N. Nakabayashi. J. Jpn. Dent. Mater. **1**, 78 (1982).
4. M. Di Renzo, T.H. Ellis, E. Sacher, and I. Stangel. Prog. Surf. Sci. **50**, 407 (1995).
5. D.H. Pashley, B. Ciucchi, H. Sano, R.M. Carvaalho, and C.A. Russell. Arch. Oral. Biol. **40**, 1109 (1995).
6. J.E. Eastoe. *In* Chemistry of collagen. *Edited by* G.N. Ramachandran. Academic Press, London. 1967. p. 29.
7. I. Stangel, S.H. Dickens, and J.M. Antonucci. J. Dent. Res. **75** (special issue), 614 (1995).
8. M. Di Renzo, T.H. Ellis, E. Sacher and I. Stangel. Arch. Oral. Biol. Submitted.
9. I. Stangel, E. Ostro, A. Domingue, E. Sacher, and L. Bertrand. Proc. Int. Conf. Polymer–Solid Interfaces. *Edited by* J.J. Pireaux, P. Bertrand, and J.L. Brédas. Institute of Physics, Bristol. 1992. p. 157.
10. B. Van Meerbeek, A. Dhem, M. Goret-Nicaise, M. Braem, P, Lambrechts, and G. Vanherle. J. Dent. Res. **72**, 495 (1993).

© 1998 NRC Canada

11. A.J. Gwinnett, F.R. Tay, K.M. Pang, and S.H.Y. Wei. Am. J. Dent. **9**, 140 (1996).
12. G.W. Marshall, Jr., M. Blooch, R.J. Tench, J.H. Kinney, and S.J. Marshall. Dent. Mater. **9**, 265 (1993).
13. C. Cassinelli and M. Morra. J. Biomed. Mat. Res. **28**, 1427 (1994).
14. I. Stangel, C. Young, E. Sacher, and S. Hanley. J. Adhes. **47**, 133 (1994).
15. E.A.G. Chernoff and D.A. Chernoff. J. Vac. Sci. Technol. A: **10**, 596 (1992).
16. M. Raspanti, A. Alissandrini, P. Gobbi, and A. Ruggeri. Microsc. Res. Tech. **35**, 87 (1996).
17. H. Tanaka, A. Yasukawa, K. Kandori, and T. Ishikawa. Langmuir, **13**, 821 (1997), and refs. therein.

© 1998 NRC Canada

FTIR analysis of the phase content in low-density polyethylene

P. Bernazzani, V.T. Bich, H. Phuong-Nguyen, A. Haine, C. Chapados, Lê H. Dao, and G. Delmas

Abstract: The phase content of a low-density polyethylene was studied by analysis of the CH_2 rocking vibrations in non-oriented films prepared from the press (P-films) or from solution (S-films). Spectral simulations of the transmission spectra give the mass fractions of the orthorhombic phase α_{ortho} and of two noncrystalline phases (monoclinic-like and amorphous). The values of α_{ortho} (IR) are compared to α_{ortho} (*i*) where (*i*) stands for the X-ray diffraction, density, and DSC techniques. New results are obtained concerning the orthorhombic order and the change of phase content with aging. A two-phase analysis is justified for non-aged films containing a small amount of the monoclinic-like phase. The values of α_{ortho} (IR) are larger than α_{ortho} (*i*), the difference ranging between 0.12 and 0.43. The difference is a measure of the short-range order. α_{ortho} (IR) can reach 0.73 for the S-films. The stability of the short-range order phase is investigated. The sample is also analyzed using the trace of slow calorimetry. The difference between α_{ortho} by DSC and by slow calorimetry is a measure of strainable order. During aging, the variation in the phase content is large for the noncrystalline phases (in content and frequency) and small for the orthorhombic. The increase of the monoclinic-like phase during aging suggests that it is a precursor of the more stable orthorhombic organization. The quantification of two noncrystalline phases on fresh and aged films clarifies some ambiguity found in the literature about the monoclinic-like phase and the localization of bands in the rocking region for sample characterization. Analysis of other regions of the spectrum is needed to confirm the present results.

Key words: low-density PE, phase content, FTIR, network phase, slow calorimetry.

Résumé : On a étudié le contenu de la phase d'un polyéthylène de faible densité en faisant une analyse des vibrations de rotation des CH_2 dans les films non orientés préparés à l'aide d'une presse (films-P) ou d'une solution (films-S). Des simulations spectrales des spectres de transmission fournissent les fractions molaires de la phase orthorhombique, α_{ortho}, et des deux phases non cristallines (de type monoclinique et amorphe). On a comparé les valeurs α_{ortho} (IR) aux valeurs α_{ortho} (*i*) pour lesquelles (*i*) correspond à diffraction des rayons X, densité et analyse calorimétrique différentielle (ACD). On a obtenu de nouveaux résultats relatifs à l'ordre orthorhombique et le changement dans le contenu de la phase avec le vieillissement. Il est justifié d'utiliser une analyse en deux phases avec les films qui n'ont pas vieilli et qui contiennent de faibles quantités de phase de type monoclinique. Les valeurs de α_{ortho} (IR) sont plus élevées que les valeurs α_{ortho} (*i*); les différences varient entre 0,12 et 0,43. La différence est une mesure de l'ordre à faible distance. La valeur de α_{ortho} (IR) peut atteindre 0,73 pour les films-S. On a examiné la stabilité de phase d'ordre à faible distance. On a aussi étudié l'échantillon à partir d'un tracé de calorimétrie lente. La différence entre l'α_{ortho} obtenu par ACD et la calorimétrie lente est une mesure de l'ordre contraignable. Au cours du vieillissement, la variation du contenu de la phase est important pour les phases non cristallines (tant en contenu qu'en fréquence) et il est faible pour l'orthorhombique. L'augmentation de la phase de type monoclinique au cours du vieillissement suggère qu'elle est un précurseur de l'organisation orthorhombique plus stable. La quantification des deux phases non cristallines dans les films frais et vieillis clarifie des ambiguïtés retrouvées dans la littérature concernant la phase de type monoclinique et la localisation des bandes dans la région de vibration pour la caractérisation des échantillons. L'analyse d'autres régions du spectre est nécessaire pour confirmer les résultats actuels.

Mots clés : PE de faible densité, contenu de la phase, «FTIR», phase réseau, calorimétrie lente.

[Traduit par la Rédaction]

Received February 9, 1998.

P. Bernazzani, V.T. Bich,[1] H. Phuong-Nguyen, A. Haine, and G. Delmas.[2] Chemistry Department, University of Quebec in Montreal, CP 8888, Succ. A, Montreal, QC H3C 3P8, Canada.
C. Chapados. Chemistry and Biophysics Department, University of Quebec in Trois-Rivières, Trois-Rivières, QC G9A 5H7, Canada.
Lê H. Dao. Institut National pour la recherche scientifique – Energy and Materials, CP 1020, Varennes, QC J3X 1S2, Canada.

[1]Present address: Institut des matériaux scientifiques, Centre national des sciences naturelles et de la technologie, Hanoi, Vietnam.
[2]Author to whom correspondence may be addressed. Telephone: (514) 987-3000, ext. 8238#. Fax: (514) 987-4054. E-mail: delmas-patterson.genevieve@uqam.ca

 © 1998 NRC Canada

Fig. 1. (*A*) Melting trace of the as-received sample at a low scanning rate (1K/h). See Table 2 for the values of ΔH. (*B*) Base line of the calorimeter under the same conditions.

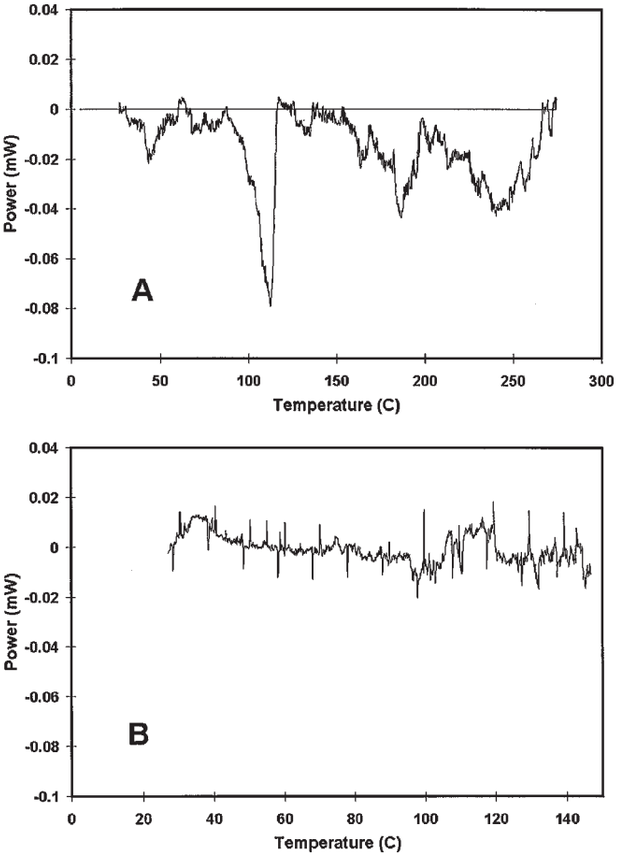

Introduction

In the two-phase model of semicrystalline polymers, the fraction of the long-range order phase is obtained by X-ray scattering or calorimetry and the other phase is assumed to be liquid-like. In polyethylene (PE), the presence of a third phase with mobility and order intermediate to that of the crystalline and amorphous phases has been suggested by a variety of techniques. The name and the characteristics of this third phase depend on the type of crystal growth (bulk, solution, or fiber crystals) and also on the technique used to analyze it. The chains of the third phase may be entangled chains inside the crystallites or connecting them. In consequence, this phase is heterogeneous with a range of order and tension determined by the polymerization conditions and the sample history. In NMR (1) and Raman (2–4) studies, the third phase in PE has been called interlamellar, interfacial, or interzonal, in reference to its links to the crystalline and amorphous phases. The presence of more than two phases in a semicrystalline polymer is supported by analysis of the melt. In this state, two relaxation times (5) were found by ^{13}C NMR. Bremner and Rudin (6) identified three phases by the same technique. A heterogeneous melt suggests that the solid melts in a complex mode and incompletely. From measurements such as birefringence, electron microscopy, or small-angle neutron scattering it is clear that, at the end of the endotherm of melting, a sizable amount of ordered domains remains in the melt for a long period of time. The order in the melt decreases by shear and recovers by annealing (7). The presence of a nonmeltable order is consistent with the presence of at least three phases in semicrystalline samples.

In recent studies, we have analyzed the noncrystalline phases in polyolefins (8–15). Using a sensitive calorimeter, the heat flow in the melt was analyzed. It was found that disordering of the melt can be followed if a very slow heating rate (*T*-ramp) is used. The usual fast *T*-ramp creates strain in the sample and prevents melting. The slow-melting phase has been called the network phase because the physical junctions in the network prevent normal expansion in the *T*-ramp and induce strain in the ordered regions. Another name for the network phase is the short-range order phase since the ordered CH_2 sequences are usually too short to give sharp peaks in the X-ray diffraction pattern. With samples having a large concentration of entanglements and junctions such as chemically cross-linked PE, non-orthorhombic X-ray diffraction patterns have been found in the melt.

Phase content by IR analysis

After having identified short-range order in a variety of polyolefins by slow calorimetry, we were interested in finding it by FTIR (16, 17). The advantage of the IR technique compared to calorimetry is being able to analyze the sample as it is at room temperature (RT). The inconvenience is that the vibrations of those CH_2 groups with different conformations overlap, a situation that requires spectral simulation.On the other hand, less superposition occurs in slow calorimetry because the strain generated by the expansion leads to the separation of the regions with different tension, i.e., between the different phases. An example of the range of melting typical of a semicrystalline polymer is given in Fig. 1*A*. Another drawback of transmission FTIR is the preparation of the film itself (press or solution), which brings modifications difficult to control in the morphology of the sample to be analyzed.

The elucidation of the molecular structure of PE by IR has been the subject of many articles (18–27). The assignment of the *trans–trans* and *gauche* conformations has led to the identification of ordered and less ordered regions. The ordered regions in the orthorhombic modification give a doublet in the rocking (730–720 cm^{-1}) and bending regions (1500–1400 cm^{-1}) due to the interaction between two chains in the unit cell. By analyzing the spectra of liquid, linear, and cyclic alkanes and of molten PE, information on the less ordered regions of a semicrystalline polymer has been obtained (21). The amorphous regions have been associated with peaks at 725, 720, 1078, and 1300–1368 cm^{-1}. To help resolve the active debate of the 1970's, concerning how a chain folds on itself to reenter the lamella, the conformations of the folds have been analyzed extensively, mainly on solution-grown crystals with different crystal habits. Mixtures of PE and deuterated polyethylene gave information on two- and three-dimensional order between the chains (18–20).

The characterization of the deformed crystals has also been studied extensively (18–20, 23–27). The bands associ-

© 1998 NRC Canada

Table 1. Characteristics of the as-received sample.

Sample	d g/cm^3	M_w [a] $\times 10^{-3}$	M_w/M_n [b]	[η] [c] dL/g	CH_3/ 1000 C	MI g/10 min	α_{ortho} [d] d	X-ray	DSC
UC8	0.9132	260	2	1.80	30	0.08	0.418	0.437	0.38

[a] Polymer extruded and aged.
[b] Using the Lower Critical Solution Temperature (LCST) technique.
[c] In decalin at 130°C.
[d] Crystallinity obtained by standard methods from the three different techniques. The value of α_{ortho} (IR) has not been obtained by transmission for the as-received material. The microtome technique has been discarded because of risk of phase modification.

ated with a monoclinic-like organization have been studied on fibers and modified samples where the orthorhombic crystals had been deformed by shaking or drawing. A singlet at 715–718 cm^{-1} appears and eventually replaces the doublet in these samples (19, 20, 26). This band can also be detected in solution-grown crystals and on annealed melt-crystallized samples by spectral subtraction. It could be detected in samples where the X-ray scattering spectra could not detect the monoclinic organization (19). In an analysis of the rocking region of linear PE, the term monoclinic-like was proposed (26). It was to take account of the fact that some samples could present monoclinic IR bands without monoclinic X-ray diffraction peaks. The range of frequency at which the monoclinic-like peak appears in the present work is another reason for using this term in the description made below of the phase content. If reference is made of large absorbance at 716–717 cm^{-1} on a drawn sample, the term monoclinic is suitable.

Evaluation of crystallinity

Analysis of the bands in the bending region was used early on to relate the X-ray or density crystallinity to the IR spectra of semicrystalline samples (22). Wedgewood and Seferis (23) analyzed the absorbance of crystalline and noncrystalline bands of well-characterized films. They found good correlation between the absorbance of the bands mentioned above and the crystallinity by density. Quantitative measurements of crystalline and noncrystalline phase orientation were also obtained. Using multiple internal reflection spectroscopy, the ratio of the absorbances of the 730 and 720 cm^{-1} bands was recently determined (25) in the characterization of the amorphous content of a commercial film and its heterogeneity as a function of penetration depth.

Several papers have remarked upon the objective difficulty of comparing the crystallinity of semicrystalline PE by different techniques. In spite of the knowledge that the vibrations are sensitive to near neighbors, i.e., to short-range order as well as long-range order, efforts were made to match the crystallinity obtained by IR and by X-ray or density measurements. The information on short-range order as seen by FTIR should complement well the short-range order as seen by slow calorimetry.

In the present work, we report the evaluation of the phase content of a low-density PE. The spectacular improvement in IR techniques during the last 10–15 years (FTIR and software), which permits calculating integrated absorbance rather than the maximum absorbance, leads to quantitative and reproducible results. During the investigation that we have been pursuing for several years on a variety of linear PE samples with different histories, we have developed confidence in the validity of the method (16, 17). The results on low-density PE seem suited to be published first since the more difficult phases to characterize, the noncrystalline phases, are the main constituents of the overall material. The first results on films made with the press showed that the fraction of orthorhombic order by IR was higher than that obtained by the other techniques. It was then decided to prepare more ordered films from solution to evaluate the limit of orthorhombic crystallinity of the sample.

To evaluate the phase content, two regions of the spectra have been analyzed, namely, those corresponding to the wagging and and to the rocking vibrations of the CH_2 groups. However, only the results for the rocking modes will be given here because the peaks of absorbance were simpler and the spectral simulation was straightforward in this region.

Experimental

Sample

Low-density PE (Union Carbide) polymerized using the high-pressure process was received already extruded and stored at RT for several years. Table 1 lists the characteristics of the sample. The columns, respectively, give the density, M_w, M_w/M_n, the intrinsic viscosity in decalin, [η], at 130°C, the number of methyls per 1000 C atoms, and the melt index. The last three columns show the values of α_{ortho} calculated by standard methods using X-ray diffraction, density, and heats of fusion from DSC measurements. In the text below, the fraction of crystallinity by FTIR will be designated as an orthorhombic crystallinity, α_{ortho} (IR). The term α_{ortho} (i) is the value obtained with the other techniques. Note that α_{ortho} (DSC) is considered as orthorhombic and comparable to the others even if it may include some non-orthorhombic order. The molecular weight distribution has been obtained by the Lower Critical Solution Temperature (LCST) technique (28).

Wide-angle X-ray scattering

Diffraction diagrams were recorded using Inel X-ray equipment operating at 40 kV and 30 mA. CuK_α1 radiation (λ = 0.15405 nm) was selected using a quartz monochromator. The values of α_{ortho} (X-ray) were determined from the ratio of the sum of the areas of all the crystalline peaks to the area of the large amorphous halo in the diffractogram.

Density measurements

The density of a liquid solution of trichlorobenzene and toluene in which the solids (film or small pellet) were equilibrated was obtained using an Anton Paar quartz densitome-

© 1998 NRC Canada

ter. The quantity α_{ortho} (d) was calculated from the density, d, using eq. [1]

$$[1] \qquad 1/d = \alpha_{ortho}/1.008 + (1 - \alpha_{ortho})/0.856$$

where 1.008 g/cm^3 is the density of the orthorhombic crystal and 0.856 g/cm^3 is the density of a fully amorphous CH_2 chain.

Calorimetry

Two significantly different calorimeters where used. In the standard DSC, a Perkin Elmer DSC7, 2–5 mg of the sample was placed in an aluminum cupola under nitrogen flow. A heating ramp of 20 K/min was used. In a special calorimeter, a C80 from Setaram (Lyon, France), 20–35 mg of the polymer was placed over 1 cm^3 Hg, in a glass tube sealed under nitrogen. The heating ramp here was extremely slow (1 K/h). The Setaram calorimeter is a very stable calorimeter that was used previously (9–12).

The absence of oxidative degradation in the slow heating was checked, as reported in previous publications. Furthermore, the high-T endotherms are seen as exotherms in slow cooling of the melt. Successive runs on the same samples confirm the findings of the first melting (9).

FTIR

A Bomem MB-series spectrometer was used in transmission mode at a resolution of 1 cm^{-1} with 25 scans.

Methods

Film preparation

Thin transparent films must be prepared for transmission measurements. Two methods were used, as reported in Table 3: (*a*) by pressing the pellets for 5 min at 130°C in a Carver press under air and a pressure of 21 metric tons (IV), and quenching, and (*b*) from solution. The 1% solution in xylene was prepared at 50°C and quenched at RT. The solvent was left to evaporate at either room temperature or 70°C. The films can be used as such (I) or pressed at different temperatures, namely, 90°C (II) and 130°C (III). The difference in phase content between the films evaporated at RT and 70°C being small, the results given have been averaged for these two treatments. The procedure was not aimed at the growth of single crystals so quenching at RT was used rather than isothermal crystallization. Probably the slower crystallization rate of this low-density PE explains the lack of sensitivity of the content of long- and short-range order in this sample to the exact conditions of crystallization. It is possible also that the two parameters that are different in these two treatments, namely, the temperature of growth of the crystals and the temperature of evaporation of the solvent, compensate each other in the final amount of total orthorhombic order. We have indications that IR measurements cannot distinguish between short- and long-range order but refined X-ray measurements should be made to confirm this observation.

The term S-films is used in the text only for films prepared without press (I) and the term P-films for the films prepared without solvent (IV). Treatments II and III give results intermediate between I and IV as will be detailed in the text. The spectrum of an unaged film corresponds to that of a film whose residence time at room temperature is less than 3 days after its preparation.

Spectral simulations

The spectra were base-line corrected and the absorbance zero was put at 800 cm^{-1}. Spectral simulations of the 775–675 cm^{-1} regions in the IR spectra were then performed using the software BGRAMS/386 by Galactic industries. The simulations were performed using a Gauss + Lorenz band shape with a band width at half-height of 3.5 cm^{-1} for the orthorhombic peaks (730 and 720 cm^{-1}), 10–16 cm^{-1} for the single-chain band or amorphous region (725 cm^{-1}), and 15–19 cm^{-1} for the monoclinic-like peak (717 cm^{-1}). The abbreviation FWHM (full width at half maximum) is sometimes used. When Fourier self-deconvolution was used, the location of the peaks was found to be quite constant for the orthorhombic phase. On the other hand, the frequency of the noncrystalline phase was changing with the history of the film, i.e., the sample morphology. When three phases were introduced, the frequency of the amorphous phase was found to be constant. However, the frequency of the monoclinic-like phase was found to change with the treatment. The physical reason, we think, is the following: in a sample under stress during the IR measurements, a band is found at 715–717 cm^{-1}. The samples prepared at the press or in solution do not retain for long the tension associated with preparation, so the 717 cm^{-1} disappears to be replaced by another band described in the literature as a noncrystalline band (24). In the present work, this band is associated with the network phase. The area of the orthorhombic doublet is found easily without repeating the simulation. On the other hand, the decomposition of the non-orthorhombic phases into the amorphous and the monoclinic-like phases was more difficult until it became clear that the frequency of the monoclinic-like band was varying with the sample treatment. Details on the decomposition are given in the section on *Justification* (Sect. C, Part II, of Results and discussion).

The phase fractions were calculated from the simulated spectra using eq. [2]. The integrated absorbance of each band was ratioed against the total area of the 775–675 cm^{-1} region. The integrated absorbance of the two peaks at 730 and 720 cm^{-1}, both representing the orthorhombic fraction, were summed.

$$[2] \qquad \alpha_{,phase,(I)} = \text{Integrated area}_{phase(I)} / \text{Integrated areas}_{all\ the\ phase}$$

Extinction coefficients

The calculation of the fraction of each phase from the area of the peaks is suitable if the extinction coefficients of the different phases are the same. The extinction coefficient ε is obtained by plotting the integrated absorbance of the entire rocking region versus the film thickness for films with the same history. The value of ε has been obtained for linear and branched PE films of different densities. When the thickness is expressed in microns (μm), ε varies between 0.34 and 0.42 for $0.4 < \alpha_c (d) < 0.8$. When the value of ε is corrected by the density, the ratio ε/d is found to increase from 0.37 to 0.43 (17).This result indicates that the crystalline phase has a higher extinction coefficient than the noncrystalline phases. No correction was introduced in eq. [2] to take this

© 1998 NRC Canada

Fig. 2. Variation of the integrated absorbance in the rocking region as a function of sample thickness for P-films.

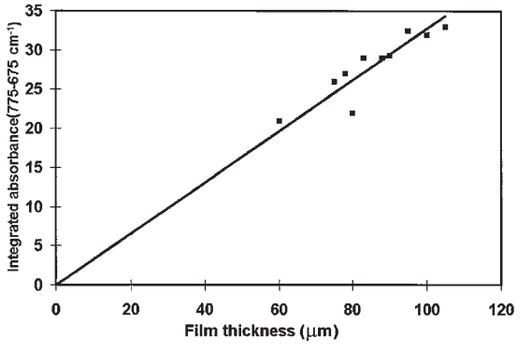

difference into account, first, because raw data are useful for other laboratories to reproduce and also because further analysis was needed to make an adequate correction. The use of the simple eq. [2] will lead to an overestimate of α_{ortho} (IR). In the rocking region, the integrated absorbance is linear with the film thickness for thicknesses up to about 100 μm. Figure 2 is such a plot for the S-films.

Results and discussion

1. Phase content by slow calorimetry

Before presenting the FTIR results, the melting trace of this sample using a very slow ramp will be given. As reported in previous work (8–12), slow calorimetry reveals endotherms not observed by fast DSC. The semi-ordered phase can melt when strain during the *T*-ramp is reduced. The rate of heating does not alter significantly the melting of the ordered chains that are not linked by entanglements. Slow calorimetry, on the other hand, allows the chains in a physical network to move during the *T*-ramp and avoids the level of strain that arrests melting in the usual rapid *T*-ramp. Figure 1*A* is an example of a melting trace of the as-received sample. The first two rows of Table 2 give the values of the enthalpies and the interval of *T* used for integration. The trace has been divided into three parts: the main sharp peak corresponds to the melting of long-range order, the medium size endotherm at low temperature is associated with crystals within the regions of the physical network that melt at low *T* because they have few entanglements. The integrated heat flow between 30 and 125°C is 142 J/g, i.e., about 60 J/g higher than in DSC. The next large endotherms have maxima at 180 and 250°C. They correspond to the melting of order within an entanglement-rich network. The total enthalpy of disordering the chains between 30 and 280°C is

$$[3] \qquad \Delta H_{total} = \Delta H_{DSC} + \Delta H_{disor.network}$$

ΔH_{DSC} is the enthalpy measured in the fast *T*-ramp. The value of ΔH_{total} is now about 400 J/g, i.e., larger than ΔH_o (293 J/g), the heat of fusion of perfect orthorhombic crystals. Discussion of this value is not suitable in the present paper on FTIR. It suffices to say here that the value of ΔH_o, obtained by different methods, corresponds to the change in enthalpy between 70°C and 145°C only. In the present technique, the change of enthalpy is followed over a larger *T*-interval and accounts for changes in enthalpy of the melt above T_m. The third and fourth rows of Table 2 give the analysis of a trace obtained at a more rapid rate of heating (12 K/h). The smaller value of ΔH_{total} is an indication that the strained network is not completely melted. Figure 1*B* is the signal for the calorimeter without the sample under the same conditions.

2. Phase content by FTIR

This part has five sections. In parts A and B the phases of fresh films (A1 and A2) and of aged films (B1 and B2) are analyzed. In part C, the justification of a three-phase decomposition is given. In part D, we compare the information on a sample provided by FTIR and by the standard techniques of analysis and, in part E, an attempt is made to relate the meltable order of a sample as given by the slow melting trace presented in Fig. 1*A* with the phase composition found by FTIR.

A. Un-aged films

A1. The orthorhombic phases: Figure 3*A* shows the IR spectra of an S-film aged at RT for less than 3 days. The spectral simulation results in four bands. The two narrow bands correspond to the well-known orthorhombic organization. The two wide bands of lower absorbance correspond to the amorphous and monoclinic-like phases. In Fig. 3*A*, the fraction of the orthorhombic phase, α_{ortho}, is 0.642, the monoclinic-like phase, α_{mono}, is 0.100, and the amorphous phase, α_{amor}, is 0.258.

Table 3 gives the values of α_{ortho} by the different techniques, for the films prepared with different histories (I–IV). The first row lists data for a short aging (3 days or less) and the second and third for longer aging times (4 and 11 months). Analyses made on some films after 17 months did not differ significantly from those at 11 months so they have not been reported. The data for α_{ortho} in these tables are averages of several films (4–7) for slightly different preparations (where the parameters were the initial concentration and the temperature of evaporation of the solvent).

The values obtained by density measurements and calorimetry for the P-samples are similar to those of the as-received sample (Table 1). As expected, the value of α_{ortho} (IR) is higher for the S-films than for the P-films. The films made using solvent and press have, after aging, values of α_{ortho} (IR) near those of the S- and P-films, respectively. The overall result is that α_{ortho} (IR) – α_{ortho} (*i*) is positive, the difference increasing with α_{ortho}. Each value of α_{ortho} (IR) – α_{ortho} (*i*) will be commented on separately.

Difference between crystallinity determined by IR and X-rays. The difference for the non-aged films is large, but larger for the S-films (0.30) than for the P-films (0.11). As the X-ray diffraction measures solely the long-range order, the origin of the difference resides in the short-range order:

$$[4] \qquad \alpha_{ortho}(\text{IR}) = \alpha_{ortho}(\text{long-range order}) + \alpha_{ortho}(\text{short-range order})$$

Obviously, there is a continuum of order in the sample but the simple separation into two types of order in eq. [4] corresponds to the limit in size, which gives a sharp X-ray diffraction pattern.

© 1998 NRC Canada

Table 2. Analysis of two traces in slow calorimetry.

ν (K/h)	Mass (mg)	T_m (°C)	ΔH_{DSC} long-range order (J/g)	$\Delta H_{dis.net}$ low strain (J/g)	$\Delta H_{dis.net}$ high strain (J/g)	ΔH total (J/g)
1	29.56	112.8	100 (87–120°C)	40 (30–87°C)	240 (120–273°C)	380
12	37.24	113.1	100 (87–127°C)	10 (48–87°C)	40 (127–237°C)	150

Fig. 3. (*A*) Spectrum in the rocking region of an S-film showing the three phases. 1: Orthorhombic; 2: monoclinic-like; 3: amorphous. (*B*) Same film as in *A* after a 4 month aging period showing an increase in the monoclinic-like phase.

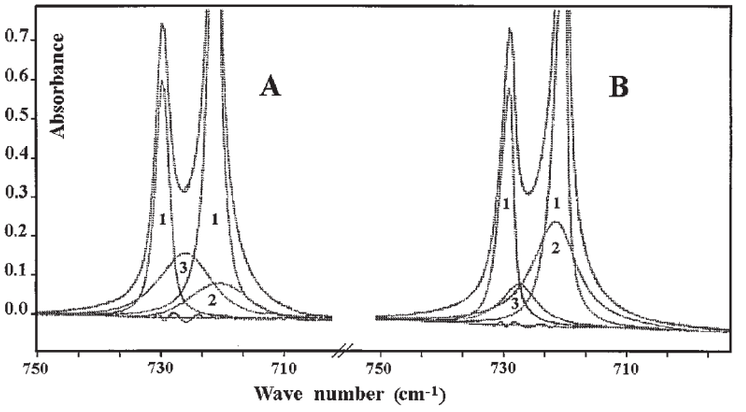

[5] α_{ortho}(short-range order)

$$= \alpha_{ortho}(\text{IR}) - \alpha_{ortho}(\text{X-ray})$$

Difference between crystallinity determined by IR and DSC.[3] The value of α_{ortho} (DSC), obtained by dividing ΔH by 293 J/g is 0.32 ± 0.04 for all the samples. The figures for the different treatments and the effect of aging for the P-films and S-films have not been reported in detail because the trends are not clear. The value of α_{ortho} (DSC) is lower than that of α_{ortho} (IR) because the latter contains some order that cannot melt because it is subject to strain ("strainable") in the *T*-ramp.

[6] $$\alpha_{ortho}(\text{strainable order}) = \alpha_{ortho}(\text{IR}) - \alpha_{ortho}(\text{DSC})$$

In the low *T*-ramp of Fig. 1*A*, 140 J/g is absorbed at low *T*, i.e., below 120°C (instead of 85 J/g in DSC). The meltable order, under these special conditions, has increased from 0.32 to 0.48 but remains lower than α_{ortho} (IR).

Difference between crystallinity determined by IR and density. The difference varies as α_{ortho} (IR) since α_{ortho} (*d*) varies little. It is smaller (0.17) for the non-aged S- and P-films. After aging, the similarity of the values of α_{ortho} (*d*) and α_{ortho} (X-ray) permits evaluation of α_{ortho} (short-range order) from the density:

[7] $$\alpha_{ortho}(\text{short-range order}) = \alpha_{ortho}(\text{IR}) - \alpha_{ortho}(d)$$

An illustration of the difference between α_{ortho} (IR) and α_{ortho} (*d*) for the different treatments is given in Fig. 4 where α_{ortho} (*d*) and α_{ortho} (IR) are plotted as abscissa and ordinate. If the two estimates of α_{ortho} were the same, the data would be on the line $x = y$. The difference between the bar and the x–y line is seen to vary with the treatment (0.16–0.25). The range of α_{ortho} (IR) is seen to be very narrow for the P-films (IV) and wide for the other treatments (I–III). The range of α_{ortho} (*d*) is narrow. This implies that movements of the chains that modify short-range order can be carried out without changing the overall density. A trace similar to Fig. 4 could have been done using the values of α_{ortho} (X-ray) for the abscissa but with a lower precision than α_{ortho} (*d*).

Solvent and vapor stability. To verify that the solvent in which the densities were taken was inert towards the low-density PE analyzed, the values of d, α_{ortho} (X-ray), and α_{ortho} (IR) were obtained after immersion in the usual solvent mixture used for density and in another mixture (ethanol–water). They were found to be the same. On the other hand, α_{ortho} (IR) can be made to increase by leaving the films to be swollen in the vapor of a solvent. After 3 days in the vapors of CCl_4 at 40°C the value of α_{ortho} (IR) increased to 0.72 for the S-films and to 0.60 for the P-films.

Order of the skin of the film. Some X-ray data have been recorded in a Siemens D-5000 reflection diffractometer the beam of which, in the actual settings, goes at a depth of a few dozen Å across the sample surface. For the P-films and the aged S-films, α_{ortho} (X-ray) has the same value as for the transmission measurements. However, for the non-aged S-films the diffractogram is diffuse and the value of value of α_{ortho} (X-ray), is found to be around 0.1. This suggests that the first few layers of the surface seen by the beam have little long-range order. The time for recovery of the usual spectra has not been measured. A similar difference has been found on thin films of amylose (Hylon VII) made from solution whose crystallinity was also measured with the two X-ray techniques.

Resistance of the orthorhombic phase to mechanical deformation. When the films made in solution are pressed at

[3] DSC measurements in this lab.

© 1998 NRC Canada

Table 3. Values of α_{ortho} (IR), α_{ortho} (*d*), and α_{ortho} (X-ray) for treatments I–IV as a function of aging time.

Aging (months)		Sample preparation: I, solution [a] no press	II, solution [a] pressed at 90°C	III, solution [a] pressed at 130°C	IV pressed at 130°C
<0.1	α_{ortho} (IR)	0.64	0.60	0.54	0.58
4	α_{ortho} (IR)	0.59	0.51	0.46	
11	α_{ortho} (IR)	0.67	0.67	0.57	0.56
<0.1	α_{ortho} (*d*)	0.48	0.47	0.38	0.38
4	α_{ortho} (*d*)	0.50	0.47	0.40	0.40
11	α_{ortho} (*d*)	0.49	0.46	0.39	0.39
<0.1	α_{ortho} (X-ray)	0.34	—	—	0.45
4	α_{ortho} (X-ray)	—	—	—	0.45
11	α_{ortho} (X-ray)	0.50	—	0.43	0.48

[a] In xylene (1%).

Note: The values above are averages of 4–7 films for each treatment. The range of data for the same treatment is the same: α_{ortho} (*d*): 0.001–0.01, with the lower values for aged samples. α_{ortho} (IR): 0.01–0.04 with the lower values also for aged samples. α_{ortho} (X-ray) : 0.04.

90°C they do not melt completely but deformation occurs, possibly as a consequence of a temperature gradient between the surface and the interior. As a result, the value of α_{ortho} (IR) is diminished from 0.64 to 0.60 (II in Table 3) with an increase in the amorphous and monoclinic-like phases. It is interesting to note that the density is not changed with the deformation. With time, these films recover almost to the values of the S-films. The films made in solution and pressed at 130°C have no memory of the preparation in solution, with one exception. This is the diminution of α_{mono} (IR) aged 4 months that seems to be a feature of all the films made in solution (I–III) as illustrated in Fig. 5.

A2. The non-orthorhombic phases: Table 4 gives the fractions of the non-orthorhombic phases for the films whose orthorhombic content is given in Table 3. The first two rows, labeled "two-phase decomposition," give the results of decomposition. The very small amount of monoclinic-like phase observed (0.05) implies that it can be considered a two-phase system. This occurs only for non-aged films. In the next rows one sees that the non-aged S-films have little monoclinic-like content. This will be discussed further in the following section describing the effect of aging. The data of Tables 3 and 4 have been plotted in Figs. 4 and 5. Further details on the two- and three-phase decomposition are given below under the title *Justification*.

B. Films aged or in the process of aging

According to practice and thermodynamic theory, aging at room temperature enables the lowest free energy phase, the crystalline phase, to grow within the limits imposed by the kinetics of chain reorganization in the solid state. The usual techniques of crystallinity evaluation should show an increase in crystallinity during aging. When more refined probes, such as small angle X-ray scattering (SAXS) or Raman spectroscopy (30), are used one notes that aging is a complex phenomenon that involves exchange of the CH_2 segments between the phases, widening of the distribution of the lamellar thickness, and sometimes a displacement of T_m away from the high temperature (31). In consequence, one cannot expect that aging will take place only in the orthorhombic phase, with short-range order becoming more long range with increase in aging time. The data from

Fig. 4. Correlation between α_{ortho} (IR) and α_{ortho} (*d*) for treatments I–IV. The higher values within the same treatment are for aged samples.

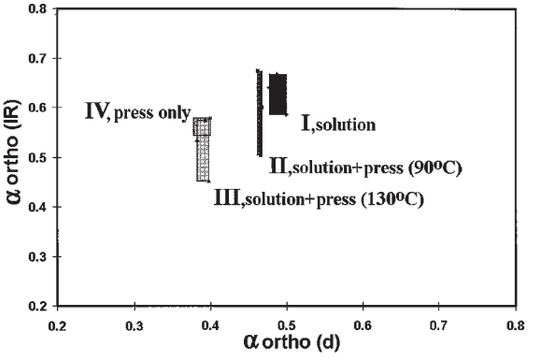

Figs. 5 and 6 below, show that changes in the three phases occur with time.

B1. The orthorhombic phase: The change of α_{ortho} (IR) with time is reported in Table 3 and also in Fig. 5. The ordinate of the bottom trace follows the variation of α_{ortho} (IR) with time for the different treatments. It is informative to note that α_{ortho} (IR) diminishes by 0.06–0.1 in the first months of aging, before increasing. This can be understood by the analysis made above where part of α_{ortho} (IR) does not belong to the stable long-range order but is part of the short-range orthorhombic order associated with the network phase. The movements in these chains is subordinated to those in the non-orthorhombic phases.

Table 3 shows that the change of α_{ortho} (*d*) with aging is small and difficult to interpret since a two-phase model has been used to calculate it. It is somewhat surprising that α_{ortho} (*d*) does not increase more. Linear PE, on the other hand, when submitted to a long gradual *T*-ramp up to a few degrees below T_m, reaches a value of α_{ortho} (*d*) = 0.92 (31).The authors succeeded in proving, in several year-long experiments, that regular PE could reach the same equilibrium state as high-pressure crystallized PE. Probably the low value of α_{ortho} (*d*) in the present sample that may be due to the branches could be increased by specific annealing at

© 1998 NRC Canada

Fig. 5. Phase composition of films as a function of aging for I–IV. The lower and upper regions represent the orthorhombic phase and the amorphous phase, respectively. The region in between is the monoclinic-like phase. The scale for the orthorhombic values starts at 0.4, not at 0. The dotted lines in IV represent extrapolation from incomplete data.

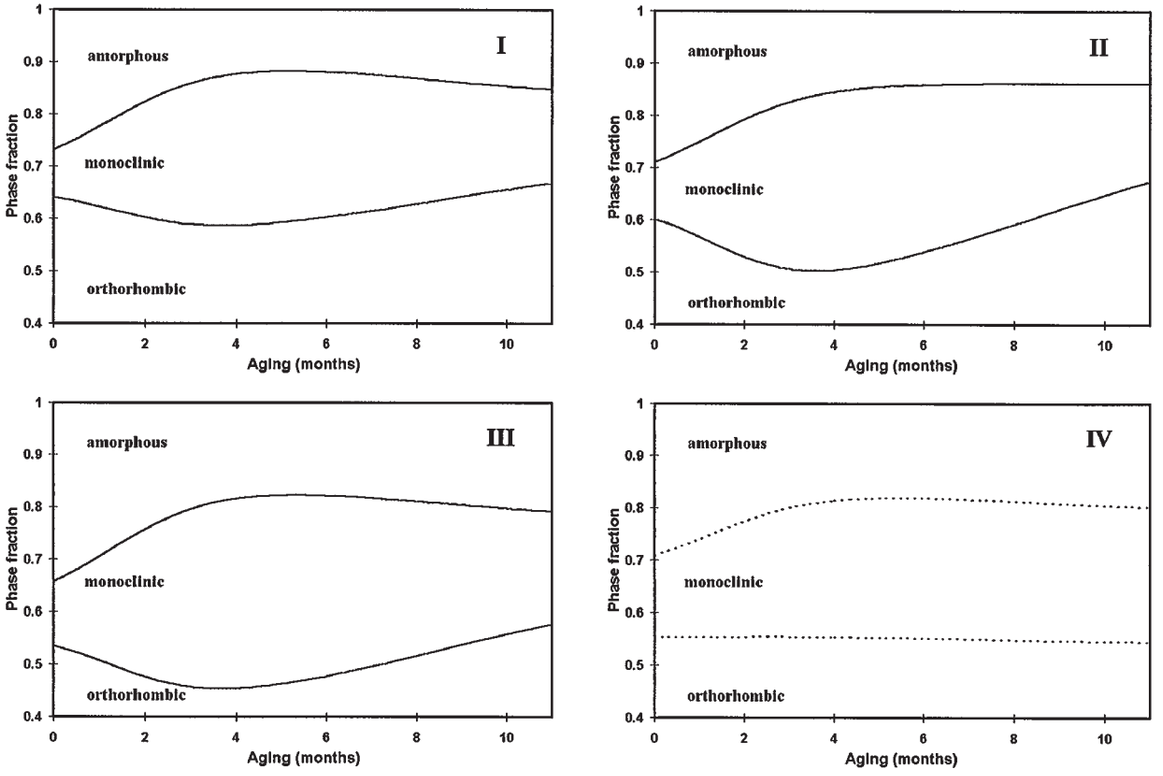

Table 4. Values of α_{mono} (IR), α_{amor} (IR) for treatments I–IV as a function aging time.

		Sample preparation			
		I, solution [a] no press	II, solution [a] pressed at 90°C	III, solution [a] pressed at 130°C	IV pressed at 130°C
Two-phase decomposition [b]					
	α_{mono}	<0.05	0.05	0.04	0.05
	α_{amor}	0.31	0.35	0.40	0.42
Three-phase decomposition					
Aging (months)					
<0.1	α_{mono}	0.09	0.11	0.12	0.16
<0.1	α_{amor}	0.27	0.29	0.34	0.26
4	α_{mono}	0.29	0.34	0.36	
4	α_{amor}	0.12	0.15	0.18	
11	α_{mono}	0.18	0.19	0.22	0.26
11	α_{amor}	0.15	0.14	0.21	0.18

[a] In xylene (1%).
[b] The two- and three-phase decompositions are similar when α_{mono} is less than 0.05, see Table 6. The ranges of data are the same as in Table 3.

higher temperature. The "long annealing" experiment showed also that no change in molecular weight occurs in well-purged samples as a consequence of the high-*T* treatment.

Correction of α_{ortho} *(d) in low-density PE*. The values of α_{ortho} (*d*) in the tables have been calculated with the data of eq. [1]. Recent X-ray scattering studies of linear low-density PE give higher cell dimensions and lower values of *d*(orthorhombic), namely, 0.9679 and 0.9820 g cm^{-3} (32, 33) for samples having, respectively, 20 and 22.7 methyls per 1000 C atoms. If an intermediate value of *d* is used, for instance, 0.975 instead of 1.008 g cm^{-3}, the α_{ortho} (*d*) values found from eq. [1] are higher than those given in Table 3. As an example, α_{ortho} (*d*) for the films formed from solution becomes 0.60, not too different from the value obtained by

© 1998 NRC Canada

Fig.6. Phase content variation of an S-film during an aging period of 150 days.

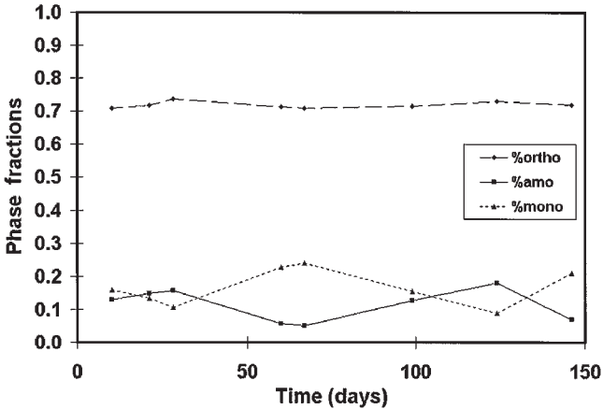

IR (0.64). The present X-ray measurements have not been analyzed with sufficient detail to spot an eventual difference in the peak position of the S- and P-films.

The results of DSC will not be commented upon since, as said above, we were not able to see a trend in α_{ortho} (DSC) with time. After long aging, α_{ortho} (X-ray) reaches about 0.50 for the S- and P-films and the difference between them, found before aging (0.1), disappears.

B2. The non-orthorhombic phases and the overall composition: The spectrum of the S-film shown in Fig. 3*A* is given in Fig. 3*B* after it has been aged for 4 months. The monoclinic-like phase (curve 2) increases for this sample from 0.10 to 0.28 while the amorphous phase (curve 3) diminishes from 0.26 to 0.12. This suggests that the monoclinic-like organization is a necessary step for increasing long-range order. This has been reported qualitatively in the literature (18–20).

One can visualize the change in phase composition with time in Fig. 5 (I–IV) for the four treatments. The lower and upper regions represent the orthorhombic phase and the amorphous phase, respectively, while the region in between is the monoclinic-like phase. The scale for the orthorhombic values starts at 0.4 and not at 0.

As seen in the graphs (I–III) (for after 4 months), the concentration of the monoclinic-like phase increases significantly with time, reaching 0.29–0.36 at an aging time of 4 months for the S-films. After 11 months, the concentrations of the two noncrystalline phases are similar, the monoclinic-like phase being reduced to about the amount of the amorphous phase. For the P-films (with the trace shown as a dotted line because they were not analyzed after a 4 month aging), α_{mono} is still high after an 11 month aging time, an indication of incomplete aging in the non-orthorhombic phases. This interesting feature may be related to the state of the melt: more thoroughly disordered by the solvent than by the fusion under the press. We intend to obtain the spectra of the sample crystallized from the melt that has been subjected to the slow *T*-ramp in the calorimeter. It is likely that slow melting has the same effect as the solvent for increasing chain mobility in the sample after recrystallization. It is noteworthy that the non-orthorhombic phases retain a memory of the solvent history (III) even after pressing and long aging at RT. The increase of α_{mono} with time has been observed in many samples of PE with different densities.

The change of phase content with time for one sample is demonstrated in Fig. 6. Eight spectra of the same film were analyzed over a period of 150 days. For that sample, the orthothombic content (top line) fluctuates little with time (0.04 at maximum) with a small decrease at around 2 months of aging that follows the initial increase. The monoclinic-like fraction (bottom line) is seen to increase by more than a factor of 3 over the same period, the amorphous content varying in a complementary way. The fact that a maximum in α_{mono} (IR) occurs after 2 months while it occurred after 4 months for the films made and averaged in Table 3 may come from small differences in the film preparation.

Movements of methylene chains in the solid state. It was stated above that α_{ortho} (IR) could diminish during aging due to the mobility of some of the chains in this phase, since they do not belong to long-range order. Other information suggests chain mobility at RT: It was discovered quite late in the history of orthorhombic morphology, perhaps because it was counterintuitive, that chains packed in long-range order can move. The heat capacity of solid linear PE between RT and T_m has been found higher (34) than the value calculated, using a two-phase model, from its crystallinity and the known vibrations of the methylene groups in the two phases. Through modelization (34), this feature was explained by recognizing that the ordered chains in the orthorhombic crystals rotate with a high frequency, a freedom of movement unexpected for chains so close to each other. One can expect that the non-orthorhombic phases will be even more mobile, at least in the regions distant from the knots. In consequence, the change with time of the relative amounts of the phases as seen by FTIR is not unexpected. The diminution of the α_{ortho} (IR) in the first months of aging comes, in our opinion, mostly from changes in the short-range order as explained above. However, it is likely that some unfolding of the chains also takes place in the long-range order, to permit the growth of thicker lamellae.

Assuming that aging corresponds to a slow annealing, insight into aging can be obtained through studies of the change of morphology during annealing. Different techniques have been used to follow annealing, each viewing a different size or different order in the sample. One of these techniques, which measures the straight-chain lengths in PE by Raman spectroscopy, may give information relevant to the present analysis (30). The study reveals unexpected and drastic changes in straight-chain length distribution as a result of annealing. Since the frequency ν of the longitudinal acoustic mode (LAM) is related by a simple equation to L, the straight-chain length, the distribution of frequency of the LAM band permits calculation of the distribution of straight-chain lengths in the sample. Snyder et al. find that the band half-width increases from 100 to 300 Å upon annealing. They observe also that the shape of the band does not change regularly with time. Since some annealing temperatures for the LAM experiments were low (90°C), i.e., well above the value of T_m, the physical phenomena underlying the movements of the chains in the crystalline phase as seen by LAM and FTIR are likely to be similar. Again, the varia-

© 1998 NRC Canada

Fig. 7. Correlation between the peak position of the monoclinic-like phase and its amount in the samples. The points for $\alpha_{mono} > 0.30$ correspond to films with only two phases, the abscissa being for α_{amor} instead of α_{mono}.

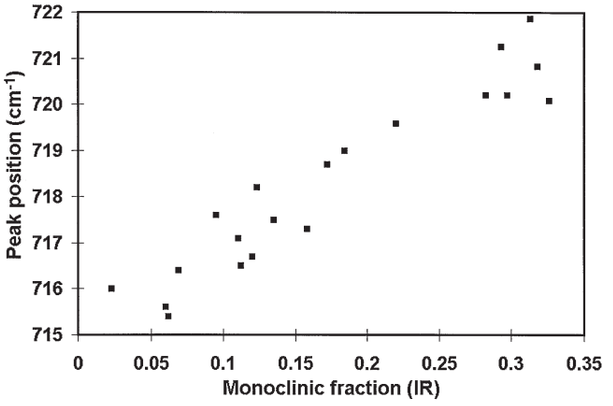

tion observed, by Raman spectroscopy, in the high-density phase during aging permits us to accept that the large variations that we observe in the lower density phases by FTIR have a physical significance.

Change of frequency of the characteristic bands. The description of the phase change given in Fig. 5 is incomplete since the frequency of the noncrystalline phases changes with time. It has been observed that the frequency shift of the monoclinic-like phase is related to its concentration in the sample. Figure 7 is a plot of the frequency of the monoclinic-like phase as a function of α_{mono} (IR). The lower frequency is found in freshly prepared samples and highly deformed material but the amount of this phase is different for these two histories. The regular shift of the frequency with α_{mono} (IR) seems to indicate that the deformed phase, which is not abundant after the preparation, is replaced by a phase with specific characteristics, not closely linked with the monoclinic structure that may have existed in the fresh film. This result clarifies some ambiguity in the literature in which the monoclinic-like band had to be associated with monoclinic reflections in the X-ray pattern (18–20, 26). The points at the upper right of the graph correspond to films in which the monoclinic-like and the amorphous phases are a single phase. The frequency of the amorphous band at 725 cm^{-1} is also shifted when α_{amor} (IR) diminishes. The chains in the monoclinic phase are thought to belong to the physical network described to explain the slow calorimetry results. Phase separation between the network chains and the free chains, which favors better interactions within the same phase, may be at the origin of the shift during aging.

The frequencies of the orthorhombic bands after decomposition have not been found to change with treatment. The distance between the two peaks, 10.6 ± 0.2 cm^{-1}, is very similar to that found (10.5) for linear PE (18). The bandwidths were not found to be wider than for linear PE.

C. Justification of the decomposition of the aged films with a three-phase model

Tables 5 and 6 give, for an S-film and a P-film, details of the decomposition using either a two- or three- phase model. The corresponding spectra are given in Figs. 8 and 9. The columns give, successively, the type of simulation and the aging status of the films, the phase content, the frequencies of the bands, their width at mid-height, their shape, and the χ^2 values. The number χ^2 corresponds to the difference between the experimental and calculated absorbances over the whole band. The rows (*A*) and (*B*) are for the unaged films and (*C*) and (*D*) for the aged films. The data for a two- and three-phase decomposition of the unaged film given in (*A*) and (*B*) present the following features: (*i*) the orthorhombic phase content is the same in (*A*) and (*B*), i.e., it does not depend on the number of phases; (*ii*) neither the frequency of the amorphous band nor its shape (completely Gaussian) varies when the decomposition introduces a small amount of monoclinic-like phase (<0.05). The data in (*C*) for an aged film give a different picture: the frequency and amount of the orthorhombic phase are still independent of the number of phases but the characteristics of the amorphous phase are different. The value of ν is shifted to 720.8 cm^{-1}, the band width has increased by 3 cm^{-1} (13.7 to 16.9), and the band shape is changed from 100% to 60% Gaussian. With a three-phase simulation (*D*), the characteristics of the amorphous phase (frequency, width, and shape) are restored to the values obtained with the two-phase model (*A*). Note that the frequency of the monoclinic-like phase has increased between *C* and *D* as reported in Fig. 8. The same results are obtained in Table 6 on the S-film.

We believe that the information obtained through spectral simulation for samples with different histories as well as the consistency found between the results justify the usefulness of studying the decomposition at this stage. To our knowledge, a single technique, Raman spectroscopy, has led to the definition of four phases for linear PE (2). The conditions of the experiment (geometry of the film, temperature of crystallization, time of aging), different from the present ones, do not permit comparison of the phase content of this in-depth investigation with the present one. Combination of IR and Raman data for the same sample should permit verification of the present results. We are also planning to explore other regions of the IR spectra that could confirm the change of the relative amount of the non-orthorhombic phases with sample history.

D. Information on the sample given by the phase content obtained by FTIR

Long-range order: When precise information on a sample having undergone a specific history is required, IR by transmission with its unavoidable stage of film preparation (press or solution/crystallization) may not be the best method because the film preparation may obscure the exact properties of the sample. To overcome this problem, reflectance techniques such as internal or attenuated reflectance have been used. An advantage of these techniques is, for instance, ability to probe into the sample at different depths and reveal heterogeneity or orientation of the material (24). However, these techniques are more delicate to operate than transmission IR as they require excellent physical contact between the crystal and the sample, a requirement that is sometimes difficult to address without changing the history of the sample. If the overall crystallinity of a sample is needed (i.e., the long-range order), measurement of the density, of the X-ray

© 1998 NRC Canada

Table 5. Justification of the three-phase model for an aged P-film: Characteristics of a spectrum simulation with a two- and three-phase decomposition.

	Sample P-film	Fraction	Position (cm^{-1})	FWHM (cm^{-1})	Shape (%Lorentz)	χ^2
	Unaged	0.60(α_{ortho})	730.1	3.56	85	
Fig. 8*A*	Two phase		719.4	4.14	100	10^{-5}
	Simulation	0.40(α_{amor})	725.4 [a]	13.73 [b]	0 [c]	
	Unaged	0.58(α_{ortho})	730.3	3.56	85	
Fig. 8*B*	Three phase		719.0	4.14	100	10^{-5}
	Simulation	0.37(α_{amor})	725.2	13.73	0	
		0.05(α_{mono})	716.4	16.85	38	
	Aged	0.51(α_{ortho})	730.5	3.50	78	
Fig. 8*C*	Two phase		719.6	3.33	82	0.80
	Simulation	0.49(α_{amor})	720.8 [a]	16.89 [b]	40 [c]	
	Aged	0.57(α_{ortho})	730.3	3.54	84	
Fig. 8*D*	Three phase		719.4	3.55	100	10^{-2}
	Simulation	0.17(α_{amor})	725.3 [d]	13.49 [e]	0 [f]	
		0.26(α_{mono})	718.2	17.46	53	

Aging has three effects on the characteristics of the amorphous phase, as follows:
[a]A displacement of the frequency.
[b]An increase in band width.
[c]A change in band shape.
These effects are reduced by the introduction of a third monoclinic-like phase. The data with the superscripts *d, e, f* are similar to those with the superscripts *a, b, c*.

Table 6. Justification of the three-phase model for an aged S-film: Characteritics of a spectrum simulation with a two- and three-phase decomposition.

	Sample S-film	Fraction	Position (cm^{-1})	FWHM (cm^{-1})	Shape (%Lorentz)	χ^2
	Unaged	0.65(α_{ortho})	730.1	3.65	80	
Fig. 9*A*	Two phase		719.6	3.54	100	10^{-5}
	Simulation	0.35(α_{amor})	724.0 [a]	14.00 [b]	0 [c]	
	Unaged	0.64(α_{ortho})	730.2	3.65	80	
Fig. 9*B*	Three phase		719.5	3.54	100	10^{-5}
	Simulation	0.32(α_{amor})	723.4	14.00	0	
		0.04(α_{mono})	716.6	16.00	43	
	Aged	0.58(α_{ortho})	730.2	3.61	78	
Fig. 9*C*	Two phase		719.3	3.48	94	0.37
	Simulation	0.42(α_{amor})	719.7[a]	17.79[b]	37[c]	
	Aged	0.68(α_{ortho})	730.3	3.54	80	
Fig. 9*D*	Three phase		719.6	3.56	100	10^{-8}
	Simulation	0.11(α_{amor})	724.8 [d]	14.05 [e]	0 [f]	
		0.21(α_{mono})	718.0	17.46	60	

Aging has three effects on the characteristics of the amorphous phase, as follows:
[a]A displacement of the frequency.
[b]An increase in band width.
[c]A change in band shape.
These effects are reduced by the introduction of a third monoclinic-like phase. The data with the superscripts *d, e, f* are similar to those with the superscripts *a, b, c*.

pattern, or of the heat of fusion of annealed films is, in most cases, capable of giving a good picture of the sample morphology. Data in Table 3 indicate, however, that the density is not too sensitive to sample history. The measurement of density does give other information, since it can reveal unambiguously heterogeneity in large samples crystallized with an unwanted temperature gradient (e.g., insulating material for cables).

In spite of the changes of morphology induced by film preparation, measurement of the phase content by FTIR gives sound information. Analysis of the phase content of linear PE (16, 17) gives α_{ortho} = 0.84 and 0.81 for the S- and P-films. These values are, as expected, higher than for branched PE. Furthermore, in films stabilized by their history, a controlled melting under the press does not erase the film history. Samples of linear PE have been cooled at 3 K/h to record, for instance, the different crystallization endotherms and analyze the monoclinic-like morphology induced by slow cooling. The material had to be pressed for IR measurements but it retained, in this process, a high

© 1998 NRC Canada

Fig. 8. Spectrum in the rocking region of a P-film with a two-phase decomposition (*A*, *C*) and a three-phase decomposition (*B*, *D*). The spectra *A*, *B* are for non-aged films and the spectra *C*, *D* are after a 4 month aging period at RT. The dotted vertical line shows the frequency of the maximum of the amorphous phase in the two- and three-phase decompositions.

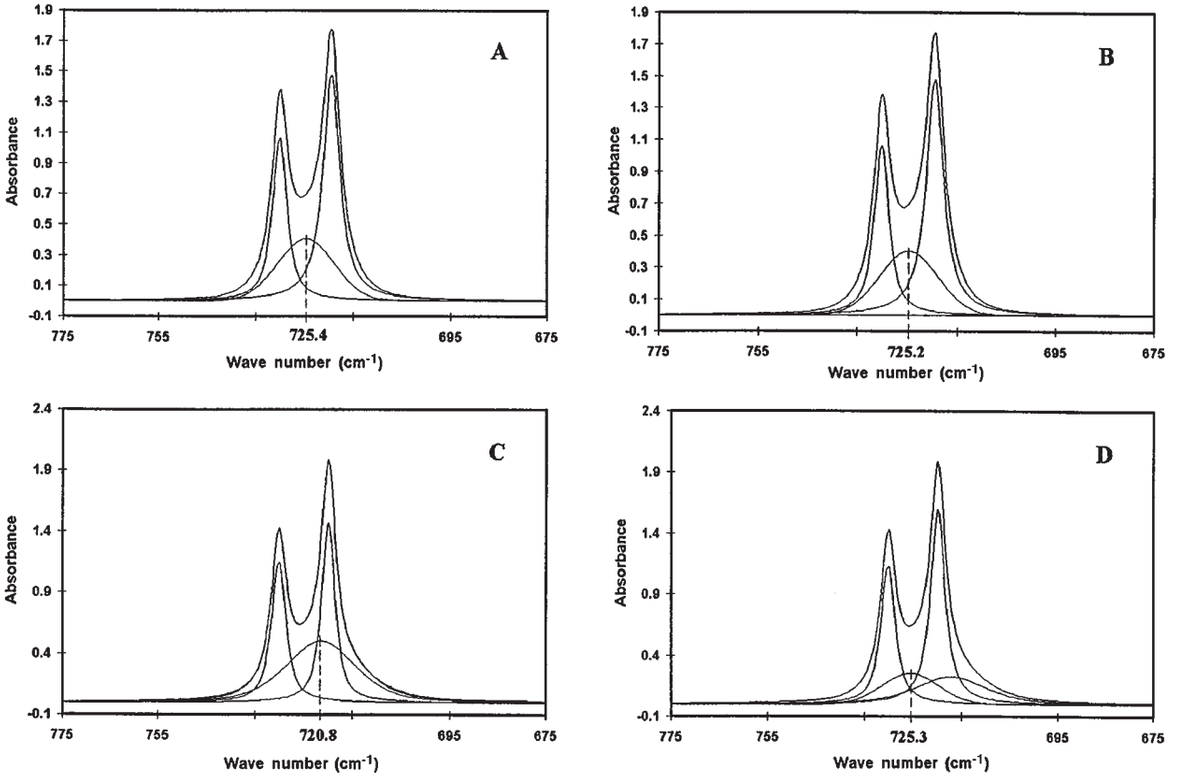

amount (0.25) of monoclinic-like material. The evaluation of short-range order from spectral simulations and measurement of its density or X-ray diagram (eq. [4]) represents unique information drawn from FTIR.

The non orthorhombic phases: The knowledge of the complexity of the non-orthorhombic phase obtained by our group or others (5–7) permits integration of information in the literature related to FTIR analysis and to other polymer techniques. Studies of the rocking bands made, for instance, to evaluate the sample crystallinity locate two amorphous bands at 720 and 725 cm^{-1} (25, 26). But no quantitative treatment has been done using both bands. The merit of the present study is to have detached the monoclinic-like band of that observed in deformed samples and show that it exists in most samples and allows us to characterize a distinct noncrystalline phase. This is an important result, which was made possible through the previous phase content analysis by slow calorimetry.

The variation of the non-orthorhombic phases with preparation and aging is unique information that the usual techniques measuring long-range order cannot give. The data given in Figs. 5 and 8 show large amplitude in the phase content variations with a periodicity that must depend on many parameters. The equilibrium phase content of an S-film (0.70, 0.15, 0.15 for the orthorhombic, monoclinic-like, and amorphous) is useful information to obtain. It may be related not only to the methyl content of the sample but also to the catalyst used for the polymerization.

The network phase: If the query does not concern the final crystallization but rather the morphology of the polymer itself, the IR spectra can give important information concerning the amount of network phase and its localization in the different phases. Entanglements must be distributed in all the samples but their concentration is expected to be higher in the noncrystalline phase. It was interesting to discover that half of α_{ortho} (IR) of the S-film (data obtained from α_{ortho} (IR) – α_{ortho} (DSC) did not melt in a fast *T*-ramp. This points to the fact that a fraction of short-range order is subject to strain due to its inclusion in a network. In a non-strained situation, the network content of the non-orthorhombic phases is difficult to evaluate quantitatively. An indication of the presence of the network phase in the monoclinic-like phase is that its shape and peak position change the most under strong deformation. Further work continues on the characterization of the network phase by FTIR.

E. The sum of all meltable order

We undertook this analysis to evaluate the phases that could correspond to those disordered in the trace of Fig. 1. To account for large value of ΔH (Table 1), we searched for indications of phases that could be disordered and give the endotherms found at high temperature. With the reasonable assumptions that the orthorhombic and monoclinic-like fractions can be disordered in the *T*-ramp, the sum of these two phases is about 0.8 for the P-films. The as-received sample whose melting trace is given in Fig. 1 has a morphology

© 1998 NRC Canada

Fig. 9. Spectra in the rocking region of an S-film with a two-phase decomposition (*A*, *C*) and a three-phase decomposition (*B*, *D*). The spectra *A*, *B* are for non-aged films and the spectra *C*, *D* are after a 4 month aging period at RT. The dotted vertical line shows the frequency of the maximum of the amorphous phase in the two- and three-phase decompositions.

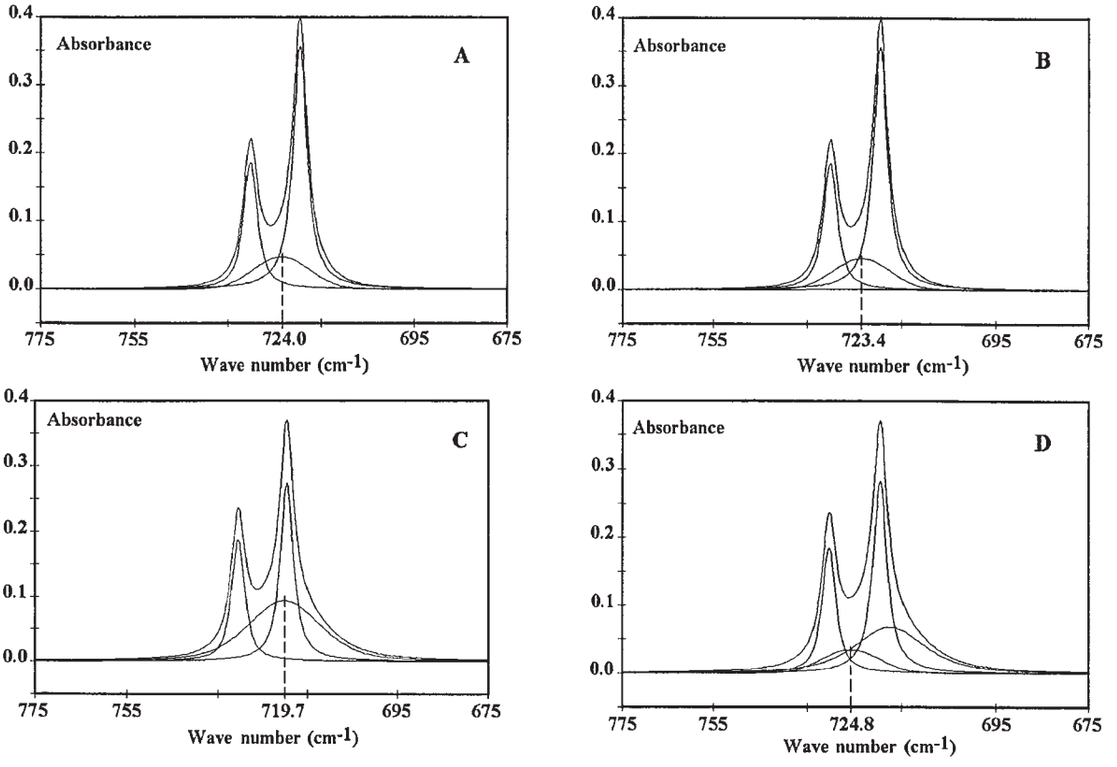

similar to aged P-films. From the value of ΔH, all the phases appear to be meltable in a low *T*-ramp. The question to be asked now concerns the possibility of finding the complement (0.2) of meltable order in the third phase, i.e., the amorphous phase. It seems that the answer is positive. It has been reported in the literature that in melt-crystallized samples some of the chains fold in the 200 plane rather than the 110 plane common to single crystals (18–20). These chains are too far apart to experience field splitting so they absorb as a singlet at 725 cm^{-1} instead of the usual doublet. Due to their high fraction of *trans–trans* conformations, they have been called *trans*-planar chains (24). The *trans*-planar chains are more numerous in a low-density PE or in a deformed sample (24) than in a high-density PE. If this assumption is exact, the supplement of order needed to make consistent the slow calorimetry and FTIR analyses would be contained in the amorphous phase whose *trans*-planar chains would become disordered when the temperature is raised.

Conclusions

This investigation of the rocking regions of low-density PE has permitted the detection of three phases in films made in solution or in pressed films associated, respectively, with the orthorhombic, monoclinic-like, and amorphous morphologies. The quantitative measurement of two noncrystalline phases in non-strained samples is a new and probably general finding for semicrystalline polymers. The orthorhombic content of aged films formed in solution can reach 0.67 while the value is 0.5 by X-ray and density measurements. FTIR constitutes an unique way of detecting short-range order orthorhombic (0.2) in this highly branched PE. The fraction of meltable order by DSC is low (0.32) due to the easily strainable entangled regions. The phase with short-range order and the monoclinic-like phase are associated with the network fraction whose melting can occur under melting conditions that diminish the strain (slow calorimetry).

During aging, the concentration of the three phases changes. The monoclinic-like structure increases in size and its frequency is displaced during aging, changes associated with phase separation of free and entangled chains. The monoclinic-like phase seems to be an intermediate step to increased crystallinity. IR analysis confirms the findings of slow calorimetry but it uses a quicker and more widely available technique. The present report is not, however, definitive. We are currently analyzing other regions of the spectrum to confirm or complete the information given on this low-density PE.

Acknowledgements

The financial support of the National Research Council of Canada is gratefully acknowledged. We would also like to thank Dr. Patricia Le Bail (Institut National de Recherche Agronomique, Nantes) for the X-ray measurements.

© 1998 NRC Canada

References

1. R. Kitamura, F. Horii, and K. Murayama. Macromolecules, **19**, 636 (1986).
2. R. Matter, W. Stille, and G.R. Strobl. J. Polym. Sci. Polym. Phys. Ed. **31**, 99 (1993).
3. G.R. Strobl and W. Hagedorn. J. Polym. Sci. Polym. Phys. Ed. **16**, 1181 (1978).
4. M. Glotin and L. Mandelkern. Colloid Polymer Sci. **260**, 182 (1982).
5. P.-G. de Gennes. Macromolecules, **17**, 703 (1984).
6. T. Bremner and A. Rudin. J. Polym. Sci. Polym. Phys. Ed. **30**, 1247 (1992).
7. M. van Prooyen, T. Bremner, and A. Rudin. Report of the Institute for Polymer Research, University of Waterloo. 1992.
8. G. Delmas. J. Polymer Sci. Polym. Phys. Ed. **31**, 2011 (1993).
9. H. Phuong-Nguyen and G. Delmas. Macromolecules, **25**, 408 (1992).
10. H. Phuong-Nguyen and G. Delmas. Macromolecules, **25**, 414 (1992).
11. H. Phuong-Nguyen, G. Charlet, and G. Delmas. J. Therm. Anal. **46**, 809 (1996).
12. H. Phuong-Nguyen and G. Delmas. Collect. Czech. Chem. Commun. **60**, 1905 (1995).
13. F.G. Morin, G. Delmas, and D.F R. Gilson. Macromolecules, **28**, 3248 (1995).
14. P. Bernazzani and G. Delmas. J. Therm. Anal. **49**, 449 (1997).
15. X. Zhang, H. Phuong-Nguyen, P. Bernazzani, I. Lapes, and G. Delmas. Can. J. Chem. **75**, 1354 (1997).
16. P. Bernazzani. M. Sc. Thesis, University of Quebec in Montreal (1995).
17. A. Haine. M. Sc. Thesis, University of Quebec in Montreal (1996).
18. M.I. Bank and S. Krimm. J. Polym. Sci. Part A: **27**, 1809 (1969).
19. S. Krimm. Adv. Polym. Sci. **2**, 51 (1960).
20. K. Yoshikaru and S. Krimm. J. Macromol. Sci. Phys. **B4**, 461 (1970).
21. M. Maroncelli, S.P. Qi, H.L. Strauss, and R.G. Snyder. J. Am. Chem. Soc. **104**, 6237 (1982).
22. T. Okada and L. Mandelkern. J. Polym. Sci. Part A: **25,** 239 (1967).
23. A.R. Wedgewood and J.C. Seferis. IUPAC publication. *Edited by* J.C. Seferis and P.S. Theocaris.1983.
24. E. Agosti, G. Zerbi, and I. Ward. Polymer, **34**, 4219 (1993).
25. G. Zerbi, G. Gallino, N. del Fanti, and L. Baini. Polymer, **30**, 2324 (1989).
26. P.C. Painter, J. Havens, W.W. Hart, and J.L. Koenig. J. Polym. Sci. Polym. Phys. Ed. 1237 (1977).
27. H.W.Siesler. Infrared Phys. **24**, 239, (1984).
28. T. Bohossian and G. Delmas. J. Appl. Polym. Sci. **46**, 411 (1992).
29. E.W. Fischer, H. Giddar, and G.F. Schmidt. J. Polym. Sci. Part B: Polym. Lett. **5**, 619 (1967).
30. R.G. Snyder, J.R. Scherer, D.H. Reneker, and J.P. Colson. Polymer, **23**, 1286 (1982).
31. D.A. Blackadder and G.J. Poidevin. Polymer, **19**, 483 (1978).
32. A. Marigo, R. Zannetti, and F. Milani. Eur. Polym. J. **33**, 595 (1997).
33. A. Marigo, G. Cingano, C. Marega, R. Zannetti, G. Ferrara, and G. Paganetto. Macromol. Chem. Phys. **196,** 2537 (1995).
34. B. Wunderlich. Thermal analysis. Academic Press, Toronto. 1990.

© 1998 NRC Canada

Electrochemical study of the pore structure of sandstone and similar media

Jan C. Myland, Keith B. Oldham, Jörg Schiewe, and Alicia L. Taylor

Abstract: Three methods are discussed by which the internal geometry of a porous insulator may be investigated electrochemically. By adopting a simple model, the pore geometry is characterized by two parameters: the tortuosity and the porosity. In each method, a cylindrical sample of the porous medium is soaked with an aqueous electrolyte solution and its lower face is brought into contact with a mercury pool electrode. The other electrode is also a mercury pool, but in the first technique it is remote, whereas in the second and third methods it floods the upper surface of the cylindrical sample. The first technique employs a d.c. potential step, whereby the concentration of a probe ion is depleted at the lower electrode. The attempt of diffusion to replenish this surface concentration leads to a faradaic current whose time dependence is analyzed to provide estimates of the tortuosity and porosity parameters. The second method measures the frequency-dependent cell impedance. The pore structure parameters are estimated from the equivalent circuit of the cell. No faradaic process is involved in the third method, which measures the frequency-dependent conductance of the cell as a means of characterizing the pore structure. These methods are applied successfully to sandstone and fritted glass samples.

Key words: porous media, Fourier-transform methods, impedance.

Résumé : On discute de trois méthodes permettant d'étudier électrochimiquement la géométrie interne d'un isolant poreux. En adoptant un modèle simple, on caractérise la géométrie des pores à l'aide de deux paramètres, l'un de tortuosité et l'autre de porosité. Dans chaque méthode, on imbibe un échantillon cylindrique du milieu poreux à l'aide d'une solution électrolytique aqueuse et on place sa face inférieure en contact avec un réservoir de mercure servant d'électrode. L'autre électrode comporte aussi un réservoir de mercure; dans la première méthode elle est éloignée alors que, dans les deux autres techniques, elle recouvre la surface supérieure de l'échantillon cylindrique. La première technique fait appel à un régulateur de potentiel cd pendant que la concentration d'un ion sonde s'épuise à l'électrode inférieure. Les tentatives de diffusion pour régénérer la concentration de cette surface donnent lieu à un courant faradaïque dont on analyse la dépendance en fonction du temps pour obtenir des évaluations des paramètres de tortuosité et de porosité. La deuxième méthode mesure l'impédance de la cellule qui dépend de la fréquence. On évalue les paramètres de structures des pores à partir du circuit équivalent de la cellule. Il n'y a pas de procédé faradaïque d'impliquer dans la troisième méthode qui implique une mesure la conductance dépendante de la fréquence de la cellule comme moyen de caractériser la structure des pores. On a appliqué ces méthodes avec succès à des échantillons de grès et de verre fritté.

Mots clés : milieu poreux, méthodes par transformation de Fourier, impédance.

[Traduit par la Rédaction]

Introduction

Many techniques are available for studying the pore structure of a porous medium (1–3). Common methods involve forcing fluids such as air, water, or mercury through, or into, the pores. Our approach is to fill the pores with an aqueous solution containing some *probe ion* and then initiate the transport of that ion across the medium. By analyzing the rate at which the ion passes through the material, and its time or frequency dependence, we can obtain structural information about the pores.

Some of our earlier work (4–6) was successful in characterizing the properties of thin sheets of porous materials of interest as filtration media or battery separators. The present study is aimed at characterizing porous minerals. This article will discuss the theory of three methods and report experimental results obtained with sandstone and fritted glass samples. The probe ion used in much of our work is

Received February 23, 1998.

J.C. Myland, K.B. Oldham,[1] J. Schiewe,[2] and A.L. Taylor. Department of Chemistry, Trent University, Peterborough, ON K9J 7B8, Canada.

[1]Author to whom correspondence may be addressed. Telephone: (705) 748-1336. Fax: (705) 748-1625. E-mail: Koldham@TrentU.CA

[2]Present address: Abteilung Chemie, Institut für Mikrotechnik Mainz GmbH, Carl-Zeiss-Strasse 18–20, D-55129 Mainz-Hechtsheim, Germany.

© 1998 NRC Canada

Fig. 1. Uniform tortuosity model of porous media.

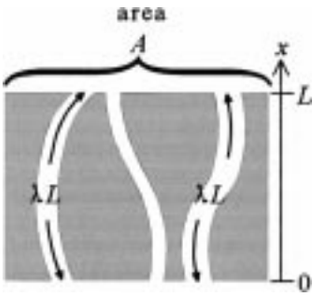

Fig. 2. Apparatus used for the progressive method.

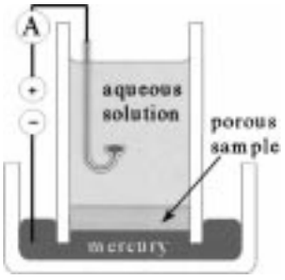

the mercurous ion $Hg_2^{2+}(aq)$, dissolved in a mildly acidic[3] aqueous solution of high electrical conductivity.[4] The advantage of this particular probe ion is that it can be removed electrochemically from solution, via the reaction

$$[1] \qquad Hg_2^{2+}(aq) + 2e^- \rightarrow 2Hg(\ell)$$

and deposited onto mercury, which, being a liquid, can be forced into close contact with the surface of the porous matrix. Some experiments used an alternative probe ion, tetraiodomercury(II), $HgI_4^{2-}(aq)$, for which the reaction is

$$[2] \qquad HgI_4^{2-}(aq) + 2e^- \rightarrow Hg(\ell) + 4I^-(aq)$$

In experiments that employed migratory transport, all the ions present, mostly $K^+(aq)$ and $NO_3^-(aq)$, served as probes.

Three different electrochemical approaches have been employed. All these techniques, however, rely on similar physical principles. A cylindrically shaped sample of the porous medium is soaked with an aqueous electrolyte solution, containing probe ions. It is the journeying of these ions through the pores that is monitored to provide information on the characteristics (tortuosity, porosity) of the medium. In none of these techniques does the solution itself flow through the porous medium.

Model of the pore structure

The media of concern here are treated as solid rigid structures permeated by voids but without ion-exchange or other physicochemical properties. The void spaces may be interconnected pores, dead-end pores, or isolated voids. Our model involves only the pores that allow transport across the medium. For these, we adopt a "uniform tortuosity model" (4, 7), shown in Fig. 1. We assume that the pores are a collection of cylindrical tubules, all of the same length λL, where L is the thickness of the material and λ its tortuosity, and all of uniform, though not necessarily the same, cross-sectional area. We recognise that this is a simplistic model of the pore structure and have investigated models that incorporate other features, but we have found that this simple picture captures the essence of the media that we have studied.

Another characteristic of a porous material is its porosity, θ. This is the fraction of the total sample volume contributed by the pores. This parameter can be measured gravimetrically by comparing the mass, m_{dry}, of a dry cylindrical sample with that, m_{soaked}, of the same sample soaked with a liquid of known density ρ

$$[3] \qquad \theta = \frac{\text{void volume}}{\text{total volume}} = \frac{m_{soaked} - m_{dry}}{AL\rho}$$

According to the uniform tortuosity model, the total effective cross-sectional area of the pores is given by $A\theta/\lambda$. However, this is probably a poor estimate of the solution–mercury interfacial area when mercury is brought into contact with a soaked sample of porous medium. Indeed, our experiments suggest that this interfacial area is closer to the total area A.

Progressive method

In this technique, a disc of the porous material to be studied is mounted as shown in Fig. 2. The lower face of the sample sits on a mercury pool. Contact between the porous matrix and the mercury is maintained by a "head" on the mercury pool. The pores of the sample are filled with an aqueous solution of the probe ion, at concentration c^b, and a bulk supply of this solution contacts the upper face of the porous sample. Dipping into the solution is a J-tube electrode containing a small mercury pool. Anaerobic conditions were maintained in the solution during the experiment by gentle bubbling with argon. This also creates a mild stirring action that maintains a uniform bulk probe-ion concentration in the upper solution compartment. The experiment is started by the sudden imposition of an electrical potential difference, typically 190 mV, between the two mercury pools, that below the porous material being negative. The effect is to totally remove, via reaction [1] or [2], probe ions from the surface of the lower pool. Diffusion from the pores then occurs in an attempt to replenish the removed ions. At the anodic mercury pool, the reverse reaction occurs. The net result is a diffusive flow of probe ions through the porous medium. The rate at which these ions pass through the sample can conveniently be measured as a faradaic electric current. This current, initially declining but eventually settling down to a constant value, has three distinct time regimes — the early or transient current, the approach-to-steady-state current, and the final or steady-state current. These three regimes provide complementary data that, when combined

[3] To prevent hydrolysis.
[4] To ensure that transport by migration is minimized and diffusion is the dominant transport mode.

© 1998 NRC Canada

with the physical properties of the medium, can be used to characterize the pore structure.

When the potential step is applied, a concentration imbalance results that engenders motion of the probe ion. Since the experiment has been designed so that diffusion is the only operative mode of ion transport, the motion of the ion is assumed to be governed by Fick's second law for planar diffusion (8):

$$[4] \qquad \frac{\partial c}{\partial t} = -\frac{\partial}{\partial x}\left\{-D\frac{\partial c}{\partial x}\right\} = D\frac{\partial^2 c}{\partial x^2}$$

where D is the diffusivity (diffusion coefficient) of the probe ion, and c, its local concentration at position x and time t. The spatial variable x has its origin at the mercury – porous medium interface and t is measured from the instant the potential is stepped. Under the experimental conditions we have imposed and in terms of our model, Fick's second law must be solved subject to the initial condition:

$$[5] \qquad c = c^{\mathrm{b}} \text{ for } 0 < x < \lambda L, \quad t = 0$$

and the boundary conditions:

$$[6] \qquad c = 0 \text{ for } x = 0, \quad t > 0$$

and

$$[7] \qquad c = c^{\mathrm{b}} \text{ for } x = \lambda L, \quad t \geq 0$$

This third condition is maintained by gentle stirring of the solution above the porous sample, ensuring that the concentration at the end of the pores equals the original bulk value.

Subject to these conditions, Fick's second law can be solved to yield either of the following two expressions (4):

$$[8] \qquad c = c^b\left[1 - \sum_{k=0}^{\infty}\mathrm{erfc}\left\{\frac{k\lambda L + x/2}{\sqrt{Dt}}\right\} + \sum_{k=1}^{\infty}\mathrm{erfc}\left\{\frac{k\lambda L - x/2}{\sqrt{Dt}}\right\}\right]$$

where erfc{} is the error function complement (9) and

$$[9] \qquad c = c^b\left[\frac{x}{\lambda L} - \frac{2}{\pi}\sum_{k=1}^{\infty}\left\{\frac{(-)^k}{k}\right\}\sin\left\{\frac{k\pi(\lambda L - x)}{\lambda L}\right\} \times \exp\left\{\frac{-k^2\pi^2 Dt}{\lambda^2 L^2}\right\}\right]$$

Though they appear very different, these two equations describe the same dependence of concentration on time and distance but each has distinct advantages.

Fick's first law (8)

$$[10] \qquad j = -D\frac{\partial c}{\partial x}$$

relates the flux density j of a species (a measure of the amount of the species crossing unit area in unit time) to its concentration gradient. The negative sign denotes that diffusion occurs down the concentration gradient. By differentiating eqs. [8] and [9] and substituting the resulting expressions for $\partial c/\partial x$ into eq. [10] we get

$$[11] \qquad j = -c^b\sqrt{\frac{D}{\pi t}}\left[\sum_{k=0}^{\infty}\exp\left\{\frac{-(k\lambda L + x/2)^2}{Dt}\right\} + \sum_{k=1}^{\infty}\exp\left\{\frac{-(k\lambda L - x/2)^2}{Dt}\right\}\right]$$

and

$$[12] \qquad j = -c^b\frac{D}{\lambda L}\left[1 + 2\sum_{k=1}^{\infty}(-)^k\cos\left\{\frac{k\pi(\lambda L - x)}{\lambda L}\right\}\exp\left\{\frac{-k^2\pi^2 Dt}{\lambda^2 L^2}\right\}\right]$$

These expressions can be used in Faraday's law (8)

$$[13] \qquad I = nF\frac{A\theta}{\lambda}j^{\mathrm{s}}$$

which links the flux j^{s} of ions across the electrode surface (i.e., at $x = 0$) to the faradaic current, I. n is the number of electrons involved in the electrochemical reaction, 2 in this case, and F is Faraday's constant (96 485 C mol^{-1}). Setting $x = 0$ in eqs. [11] and [12] and substituting for j^{s} in eq. [13] gives

$$[14] \qquad I = -\frac{nFA\theta c^b\sqrt{D}}{\lambda\sqrt{\pi t}}\left[1 + 2\sum_{k=1}^{\infty}\exp\left\{\frac{-k^2\lambda^2 L}{Dt}\right\}\right]$$

or equivalently

$$[15] \qquad I = -\frac{nFA\theta c^b D}{\lambda^2 L}\left[1 + 2\sum_{k=1}^{\infty}\exp\left\{\frac{-k^2\pi^2 Dt}{\lambda^2 L^2}\right\}\right]$$

The significance of the negative sign is that we follow the IUPAC convention of treating current as negative if it arises from a reduction at the working electrode (8). Expressions [14] and [15] yield identical current values; however, eq. [14] is more useful at short times while eq. [15] is better at long times. Notice that both these equations show the proportionality of the current I to the *overall* effective cross-sectional area of the pores, $A\theta/\lambda$. What this implies is that our method does not provide information about individual pore sizes, just their average tortuosity and total area.

Immediately following the imposition of the potential step (i.e., at very small t), eq. [14] can be well approximated by

$$[16] \qquad I_0 \approx -\frac{nFA\theta c^{\mathrm{b}}}{\lambda}\sqrt{\frac{D}{\pi t}}$$

where the subscript "0" denotes initial behaviour. This equation is, as would be expected, equivalent to the Cottrell expression (10), which describes the current at a planar electrode under conditions of planar (or "linear") diffusion. Using eq. [16] we can predict that a graph of $It^{1/2}$ versus time will be horizontal during the initial stage of an experiment. This horizontal segment corresponds to

$$[17] \qquad (I\sqrt{t})_0 \approx -\frac{nFA\theta c^{\mathrm{b}}}{\lambda}\sqrt{\frac{D}{\pi}}$$

© 1998 NRC Canada

Fig. 3. Current versus time during the application of the progressive method to a sandstone sample.

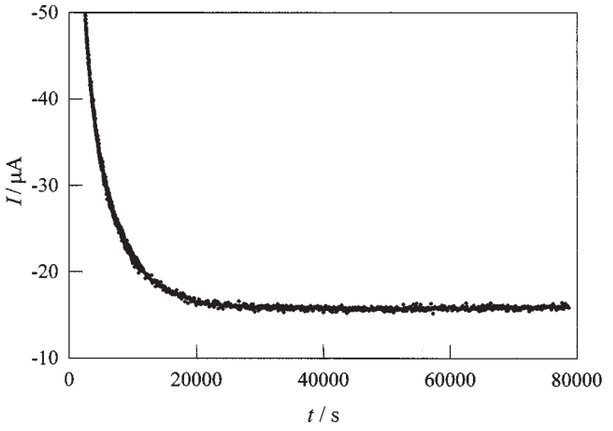

At somewhat longer times we retain the first exponential term in the summation in eq. [14] and treat the higher order terms as negligible. This gives

$$[18] \quad (I\sqrt{t}) \approx (I\sqrt{t})_0\left[1 + 2\exp\left\{\frac{-\lambda^2 L^2}{Dt}\right\}\right]$$

after some rearrangement and incorporation of eq. [17]. Equation [18] can be rewritten as

$$[19] \quad \ln\left\{\frac{2(I\sqrt{t})_0}{(I\sqrt{t}) - (I\sqrt{t})_0}\right\} \approx \frac{\lambda^2 L^2}{D}\frac{1}{t}$$

Thus a plot of $\ln\{2(It^{1/2})_0/[(It^{1/2}) - (It^{1/2})_0]\}$ versus $1/t$, at short times, should be a straight line through the origin. The slope of this line, abbreviated G_1, can be used to determine the tortuosity. As eq. [19] shows, the model predicts that this slope should equal $\lambda^2 L^2/D$ and, since the two parameters L and D are known, the tortuosity λ is easily calculated.

At longer times, eq. [15] is more useful than eq. [14]. At very long times, all the exponential terms in this equation are negligible and we can write:

$$[20] \quad I_{ss} = -\frac{nFA\theta c^b D}{\lambda^2 L}$$

where the "ss" subscript denotes that this is the final, steady-state, current. At slightly shorter times, in the approach to steady state, we treat the second and higher order exponential terms as negligible and then

$$[21] \quad I \approx I_{ss}\left[1 + 2\exp\left\{\frac{-\pi^2 Dt}{\lambda^2 L^2}\right\}\right]$$

Rearrangement gives

$$[22] \quad \ln\left\{\frac{2I_{ss}}{I - I_{ss}}\right\} \approx \frac{\pi^2 D}{\lambda^2 L^2}t$$

from which we see that, at long times, a plot of $\ln\{2I_{ss}/(I - I_{ss})\}$ versus t should give a straight line. Tortuosity can be calculated from the slope of this line, denoted by G_2, since the model predicts that G_2 equals $\pi^2 D/\lambda^2 L^2$.

Fig. 4. "Short time" analysis of the current during a progressive experiment. Circled data points were used in the linear regression that yielded the straight line.

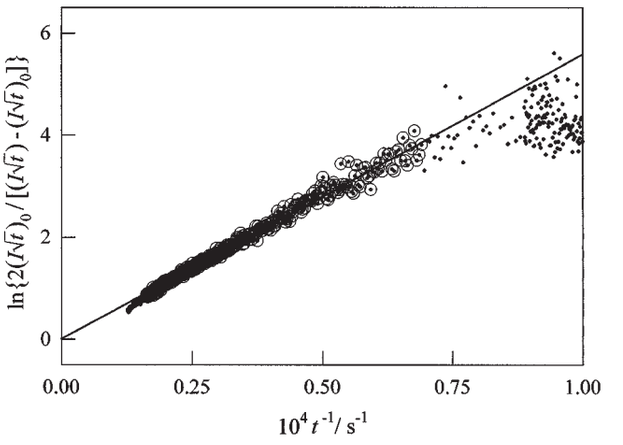

Yet another method of determining the tortuosity utilizes eqs. [17] and [20] combined as

$$[23] \quad \lambda = \frac{\sqrt{\pi D}}{L}\frac{(I\sqrt{t})_0}{I_{ss}}$$

The same two equations may also be combined into

$$[24] \quad \theta = \frac{\pi}{nAFc^b L}\frac{(I\sqrt{t})_0^2}{I_{ss}}$$

to provide a method of estimating the porosity of the sample.

Though we have carried out scores of such experiments on a variety of porous media, we shall report only an experiment with a sandstone disc of length L = 4.25 mm and area A = 1314 mm^2. The aqueous electrolyte solution was 2.00 M KNO_3, 10.0 mM HNO_3, 5.00 mM $Hg_2(NO_3)_2$, deoxygenated with argon and degassed prior to use. The results are shown in Figs. 3–5.

Figure 3 shows the current decline, which approaches a constant value of –15.75 μA after about 1 h. Figure 4 shows a graph of $\ln\{2(It^{1/2})_0/[(It^{1/2}) - (It^{1/2})_0]\}$ versus $1/t$, using a value of $(It^{1/2})_0$ equal to –2100 A s$^{1/2}$. The line shown has a slope of 5.58×10^4 s, from which we find a tortuosity of

[25] λ = 1.73 from eq. [19]

by using a measured value (6), $D = 9.7 \times 10^{-10}$ m^2 s^{-1}. Similarly, Fig. 5 shows a graph of $\ln\{2I_{ss}/(I - I_{ss})\}$ versus t, and from the slope, 1.75×10^{-4} s^{-1}, we calculate

[26] λ = 1.74 from eq. [22]

A third value of the tortuosity, namely,

[27] λ = 1.73 from eq. [23]

was calculated directly from the $(It^{1/2})_0$ and I_{ss} values. The agreement is gratifying. Less satisfactory, however, is the agreement between the porosity value

[28] θ = 0.163 from eq. [24]

compared with the value

© 1998 NRC Canada

Fig. 5. "Long time" analysis of the current during a progressive experiment. Circled data points were used in the linear regression that yielded the straight line.

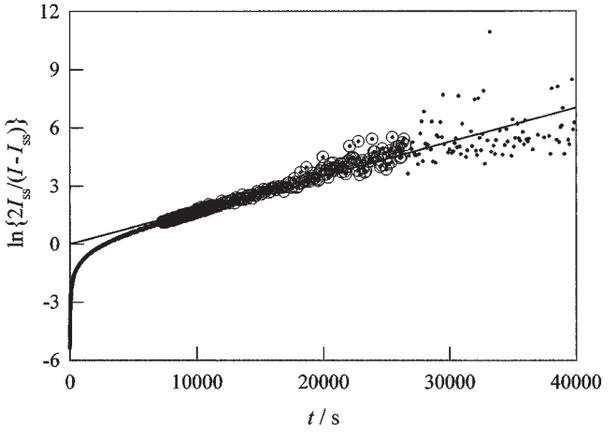

Fig. 6. Comparison of experimental data (points) with the prediction (line) of eq. [14], using $It^{½}$ = 2100 μA s^{½} and λ = 1.73, showing the inadequacy of the model at short times.

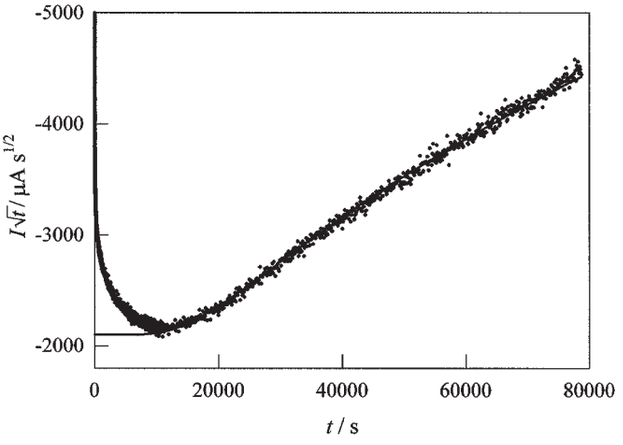

[29] θ = 0.239 by gravimetry from eq. [3]

This disagreement might have been expected from the fact that our model ignores cross-channels, which add void space but do not contribute to the current path. Note that the gravimetrically determined porosity is close to the value 0.260, appropriate to close-packed spheres (11), as might be expected for a mineral such as sandstone, composed of compacted grains.

One aspect of our experimental results that does *not* match the theory is illustrated in Fig. 6. According to the discussion surrounding eq. [17], the product $It^{½}$ should be initially constant as indicated by the line in the figure. Evidently an enhanced current flows during the first 10 000 s of electrolysis.

It is not difficult to find an explanation of this behaviour. The theory assumes that the pore structure is homogeneous right up to the junction of the mercury – porous medium, and that the area of contact between the mercury electrode and solution is the same $A\theta/\lambda$ as in the interior of the medium. There are two effects that could be imagined to augment this area and thereby lead to an elevated initial current. Firstly, one might well imagine that the pores would flare as they approach the surface. Secondly, it is not unreasonable to picture the mercury–solution interface as curved. Figure 7 is a diagram illustrating both effects.

To look further into this effect was one of the motivating reasons for evolving the second method.

Impedance method

This technique uses a disc of the porous medium sandwiched between two mercury pool electrodes. The disc was presoaked with a solution similar to that used in the progressive method, and containing the Hg_2^{2+}(aq) probe ion at a concentration of 5.00 mM, and other electrolytes. A Fourier-transform electrochemical instrument (FTEI) (12) was used to apply an alternating electrical potential between the pools and monitor the resulting current.

The signal applied by the FTEI consists of 36 superimposed sinusoidal waves, of frequencies in the 20 Hz – 30 kHz range. The amplitude of each component is in the submillivolt range and the phase angle relationships are carefully chosen so that the net voltage amplitude never exceeds 5.0 mV. The instrument has the facility to apply a simultaneous d.c. potential, and this feature was used in some experiments that are not reported here.

The program controlling the FTEI used the fast Fourier-transform algorithm to measure the real and imaginary parts of the 36 components of the current. These data are accessed as values of the real and imaginary parts, Z' and Z'' respectively, of the impedance.

The presence of an ample concentration of probe ion ensures that, provided frequencies above about 2 kHz are discounted, the a.c. current can be carried across the mercury–solution interface solely by the faradaic pathway

[30] $2Hg(\ell) \rightleftharpoons Hg_2^{2+}(aq) + 2e^-$

On the other hand, *all* the ions present will participate in carrying the a.c. current through the body of the porous medium. The equivalent circuit will therefore consist of a resistor representing the porous medium and Warburg impedances representing each electrode interface

The Warburg impedance is adequate to represent the faradaic pathway because the Hg_2^{2+}–Hg electron transfer is known to be very fast (13).

Established theory (14) predicts that the real and imaginary impedances associated with each Warburg element are

[31] $$Z_w' = -Z_w'' = \frac{RT}{8F^2ac^b\sqrt{\pi Df}}$$

where f is the frequency of the a.c. component, a is the area of the mercury exposed to solution, and other symbols have been defined previously. The resistance of the solution in the pores contributes only to the real component of the imped-

© 1998 NRC Canada

Fig. 7. Possible "flared" geometry of pore exit, with partial mercury intrusion.

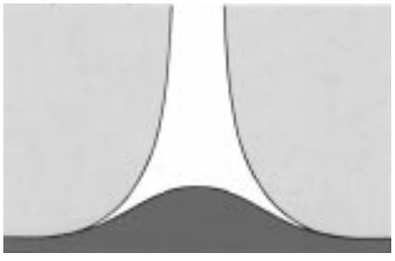

ance and its contribution, according to the uniform tortuosity model is

$$[32] \quad Z_R' = \frac{\lambda^2 L}{\kappa\theta A}; \qquad Z_R'' = 0$$

where κ is the conductivity of the solution.

Experiments were carried out on a small glass frit of dimension L = 2.5 mm, A = 50.3 mm^{2,} and with a measured gravimetric porosity of 0.18. The solution conductivity was measured in a separate experiment and found to be 16.8 S m^{-1}.

Figure 8 shows experimental plots of Z' and Z'' versus $1/f^{1/2}$. These data are the averages of eight experiments. The first plot should obey the relationship

$$[33] \quad Z' = Z_R' + 2Z_W' = \frac{\lambda^2 L}{\kappa\theta A} + \frac{RT}{4F^2 a c^b \sqrt{\pi D f}}$$

and was analyzed to derive

[34] λ = 1.26

from the intercept and

[35] a = 38.5 mm^2

from the slope.

For the imaginary plot, we expect

$$[36] \quad Z'' = 2Z_W'' = \frac{-RT}{4F^2 a c^b \sqrt{\pi D f}}$$

and analysis of the lower curve in Fig. 8 leads to

[37] a = 33.7 mm^2

in fair agreement with result [35].

These a values, representing the area of the mercury–solution interface, are seen to be smaller than the overall geometric area A = 50.3 mm^2 but larger than the total pore cross-sectional area of $A\theta/\lambda$ = 7.1 mm^2. This is as expected for the configuration hypothesized in Fig. 7.

Migration method

The experimental arrangement for this technique is very similar to that for the impedance method. The major distinction is the absence of any deliberately added electroactive species. Instead, the aqueous soaking solution consisted of 10 mM HNO_3, 2.00 M KNO_3 of conductivity 15.8 S m^{-1}. The FTEI instrument was used again to measure the impedance by the same procedure described earlier. This time, however, the impedance was analyzed via the circuit

Fig. 8. Real and imaginary components of the impedance measured for a glass frit by the impedance method. Circled data ($f \leq$ 1.6 kHz) were included in the regression to fit eqs. [33] and [36].

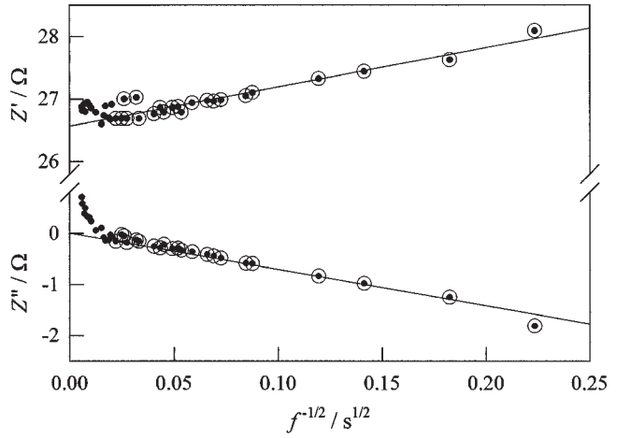

in which the capacitors represent the double layer at the mercury–solution interface.

The theoretical real and imaginary components predicted by this equivalent circuit have the impedances

$$[38] \quad Z' = Z_R' = \frac{\lambda^2 L}{\kappa\theta A}$$

and

$$[39] \quad Z'' = 2Z_C'' = \frac{-1}{\pi\gamma a f}$$

where γ is the specific capacitance (F m^{-2}) of the interface.

To permit comparison with previous data, we used the same glass frit that was the subject of study by the impedance method. This time, however, the high-frequency end of the range (f >1600 Hz) of the FTEI was appropriate to use, thus avoiding any faradaic contribution resulting from adventitious electroactive impurities.

Figure 9 shows graphs of Z' and Z'' from the averages of four distinct experiments. Analysis of the upper plot in terms of eqs. [38] and [39] leads to the result

[40] λ = 1.27

which agrees well with the value 1.26 reported in eq. [34] from the impedance method. Analysis of the slope of the lower line in Fig. 9 via eq. [39] leads to a value of γ = 20.5 μF cm^{-2} when combined with the average a = 36.1 mm^2 from results [35] and [36]. This γ value is consistent with literature values (15) of specific capacitances at mercury – aqueous solution interfaces.

© 1998 NRC Canada

Fig. 9. Real and imaginary components of the impedance measured for the glass frit by the migration method. Circled data (f > 1.6 kHz) were included in the regression to fit eqs. [38] and [39].

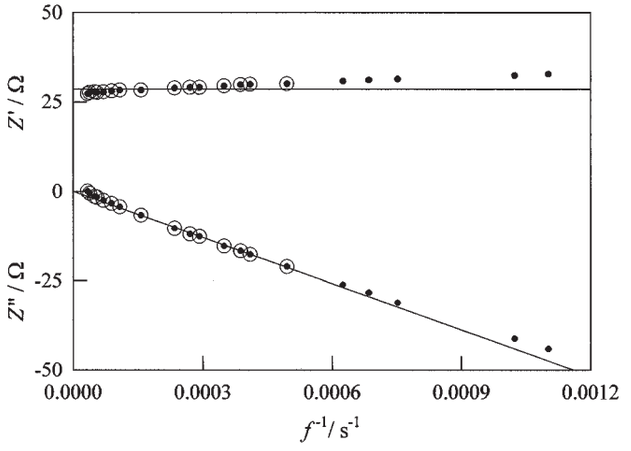

Summary

Three electrochemical methods of investigating porous media have been described and the results of experiments on two media have been reported. The uniform-tortuosity model is adequate to explain the behaviour of the interior of the media, but the model must be modified to represent the surface structure.

Acknowledgements

The financial support of Imperial Oil and the Natural Sciences and Engineering Research Council of Canada is acknowledged with gratitude.

References

1. N.McN. Alford and A.A. Rahman. J. Mater. Sci. **16**, 3105 (1981).
2. M.D. Hurlimann, T.M. Deswiet, and P.N. Sen. J. Non-Cryst. Solids, **182**, 198 (1995).
3. L.F. Gladden. Chem. Eng. J. (Lausanne), Biochem. Eng. J. **56**, 149 (1995).
4. L.E. Topol and K.B. Oldham. J. Phys. Chem. **71**, 3007 (1967).
5. L.E. Topol and K.B. Oldham. J. Phys. Chem. **73**, 1455 (1969).
6. K.B. Oldham. Electrochemical investigation of porous media. Report to the Canadian Defence Research Board. 1975.
7. R.K. Sharma and D.L. Cresswell. Ind. Eng. Chem. Res. **30**, 1428 (1991).
8. K.B. Oldham and J.C. Myland. Fundamentals of electrochemical science. Academic Press, San Diego. 1994.
9. J. Spanier and K.B. Oldham. An atlas of functions. Hemisphere, Washington, and Springer, Berlin. 1987. Chap. 40.
10. Z. Galus. Fundamentals of electrochemical analysis. Ellis Horwood Ltd., Chichester. 1976. p. 25.
11. P.W. Atkins. Physical chemistry. 2nd ed. W.H. Freeman and Co., San Francisco. 1982. p. 748.
12. J. Hazi, D.M. Elton, W.A. Czerwinski, J. Schiewe, V.A. Vicente-Beckett, and A.M. Bond. J. Electroanal. Chem. **437**, 1 (1997).
13. J. Imai and P. Delahay. J. Phys. Chem. **66**, 1108 (1962).
14. M. Sluyters-Rehbach and J.H. Sluyters. *In* Electroanalytical chemistry. Vol. 4. *Edited by* A.J. Bard. Marcel Dekker, Inc., New York. 1970.
15. P. Delahay. Double layer and electrode kinetics. Interscience, New York. 1965. Chap. 3.

© 1998 NRC Canada

Origins of thermodynamic stability of urea:alkane inclusion compounds

Mary Anne White

Abstract: Using existing thermodynamic data, the thermodynamic stabilities of urea inclusion compounds with three different alkane guests (decane, dodecane, and hexadecane) have been determined. In all cases the inclusion compounds are found to be thermodynamically stable with respect to their component species up to their melting points. From the present analysis, the solid–solid phase transitions are found to play only a minor role in stabilization, and the thermodynamic stability is found to be predominantly enthalpically driven. At a given temperature, the stability increases in the order urea:decane < urea:dodecane < urea:hexadecane. The present analysis shows that above the melting point of the guest species the inclusion compounds become much less stable because of the competition of the liquid guest. This destabilization eventually leads to incongruent melting.

Key words: urea inclusion compounds, thermodynamic stability.

Résumé : À partir des données thermodynamiques existantes, on a déterminé les stabilités thermodynamiques des composés d'inclusion de l'urée impliquant trois alcanes différents comme molécule-hôte (décane, dodécane et hexadécane). Dans tous les cas, on a trouvé que les composés d'inclusion sont thermodynamiquement stables par rapport à leurs composants et ce jusqu'à leur point de fusion. Cette analyse révèle que les transitions de phase solide–solide jouent un faible rôle dans la stabilisation et que l'enthalpie contribue de façon prédominante à la stabilité thermodynamique. À une température donnée, la stabilité augmente dans l'ordre suivant : urée : décane < urée : dodécane < urée : hexadécane. Cette analyse révèle qu'au-dessus du point de fusion de la molécule-hôte, les composés d'inclusion deviennent moins stables en raison de la compétition de la molécule-hôte à l'état liquide. Cette déstabilisation conduit éventuellement à une fusion anormale.

Mots clés : composés d'inclusion de l'urée, stabilité thermodynamique.

[Traduit par la Rédaction]

Introduction

Inclusion compounds — materials in which one component forms a host lattice in which other components reside — are an important family of materials. They can range from clays to zeolites, clathrates to channel compounds. The confined environments provided by the host lattice can modify both chemical and physical properties of the guest species. An extensive review of inclusion compounds has been published recently (1).

One of the most studied host compounds is urea. It forms inclusion compounds with a hexagonal lattice in which guest molecules, e.g., linear hydrocarbons beyond a chain length of about six carbons (2), reside in parallel channels that have a diameter of ca. 5.5 Å. The walls of the channels are composed of urea molecules hydrogen bonded to each other. The *c*-axis periodicity of an alkane guest usually is incommensurate with that of the urea host (i.e., the guest–host repeat distance ratio is not a small-denominator rational number) and the main guest–host interaction arises from weak van der Waals forces (for a review, see ref. 3). However, some urea inclusion compounds, such as those with $(\alpha + 1),(\omega - 1)$-alkanedione guests, can form structures in which the guest and host are commensurate (see, for example, ref. 4). Most urea inclusion compounds undergo low-temperature solid–solid phase transitions involving both a change in symmetry of the host structure and a change in dynamics of the guest molecules (for a recent review, see ref. 5). The structure of pure urea is different from that of the inclusion compounds; it is tetragonal with close packing of the urea molecules (6).

World production of urea is about 10^8 ton/year, mostly for fertilizers using the tetragonal form of urea (7). However, urea inclusion compounds (UIC) also have their uses. The petroleum refining industry uses urea inclusion compounds in the separation of hydrocarbons by extractive crystallization for the production of aviation jet fuels (7). Urea is also used in dewaxing lubricant oils in the petroleum refining industry by formation of urea:alkane inclusion compounds; in a subsequent step the inclusion compound is broken down by dissolution in water, allowing recovery of the urea (7). Urea inclusion compounds are especially useful because of their selective inclusion: the chain length of the guest in the urea inclusion compound that is formed depends on the temperature in extractive crystallization (7), and petroleum feedstocks passed through fixed beds of urea take up high molecular weight *n*-alkanes in preference to lower molecular weight *n*-alkanes (8). Urea inclusion compounds also can

Received January 29, 1998.

M.A. White.[1] Department of Chemistry, Dalhousie University, Halifax, NS B3H 4J3, Canada.

[1]Telephone: (902) 494-3894. Fax: (902) 494-1310. E-mail: Mary.Anne.White@Dal.CA

© 1998 NRC Canada

separate linear from branched hydrocarbons. Petroleum product purities above 99% can be obtained by separations using urea inclusion (9), and hydrocarbon separation with urea inclusion compounds remains an important processing method at present (10). Such separations must rely, at least in part, on different thermodynamic stabilities of urea inclusion compounds with different guests.

On heating, most urea inclusion compounds with hydrocarbon guests melt incongruently (11) as follows:

[1] urea·*m* guest (s) → *m* guest (l) + urea (s)

→ *m* guest (l) + urea (l)

where the second step takes place at the melting point of pure urea, T = 406 K (11); urea and its liquid guest are immiscible in this example, as is often the case for hydrocarbon guests.

Why some inclusion compounds melt congruently and others melt incongruently has been the subject of an earlier investigation (12). We have recently extended those studies to the melting behaviour of urea:hexadecane compared with hexadecane included in a similar host lattice, perhydrotriphenylene, abbreviated PHTP (13). Whereas urea:hexadecane melts incongruently to give solid urea and liquid hexadecane, PHTP:hexadecane melts congruently, i.e., giving liquid directly. Through examination of Gibbs energies, determined from adiabatic calorimetry, we concluded that both inclusion compounds are thermodynamically stable with respect to their components, and melting behaviour is dictated by the stability of the host lattice at the melting point (13).

The origins of thermodynamic stability of binary compounds relative to their components are of considerable interest, especially for urea inclusion compounds, given the relevance to petroleum separations. In the present study, we consider the thermodynamic stabilities as a function of temperature for urea inclusion compounds relative to their components for three different guests, viz. decane, dodecane, and hexadecane. All form incommensurate urea inclusion compounds, i.e., the guest and host *c*-axis repeat distances are not related by whole number ratios (14). These particular guests were chosen because the vapour pressures are low enough that only solid and liquid phases need be considered. Furthermore, all required experimental thermodynamic data were available. Through calculation of the thermodynamics of association of these urea inclusion compounds, we have looked at stability as a function of temperature from T = 0 K to the melting point, and separated out enthalpic and entropic contributions to the stability.

The purpose of this investigation was to address the following questions: How does the type of hydrocarbon guest influence the stability of urea inclusion compounds? How do enthalpic and entropic terms contribute to thermodynamic stability of urea inclusion compounds? What role do solid–solid phase transitions play in stabilizing urea inclusion compounds? Why do very short-chain hydrocarbon guests not form urea inclusion compounds? Could some urea inclusion compounds be expected to melt above the melting point of urea?

Methods and results

The thermodynamic stability of a urea inclusion compound can be considered in terms of association of the host and guest to form the inclusion compound:

[2] urea + *m* guest → urea·*m* guest (s)

where the inclusion compound is designated as urea·*m* guest, and *m* is the guest-to-urea mole ratio. From differential scanning calorimetry (11, 13), the values of *m* for urea:decane, urea:dodecane, and urea:hexadecane are 0.120, 0.103, and 0.081, respectively. The enthalpy, entropy, and Gibbs energy changes corresponding to association (eq. [2]) are designated here as $\Delta_{as}H$, $\Delta_{as}S$, and $\Delta_{as}G$.

To assess the thermodynamics of the association process, thermodynamic data for each compound are required. Using T = 0 K as the reference point, $H(T)$ for each compound, defined as

$$[3] \qquad H(T) \equiv H(T) - H(T = 0\ \mathrm{K}) = \int_{T=0}^{T} C\ \mathrm{d}T$$

and $S(T)$ for each compound, defined as

$$[4] \qquad S(T) \equiv S(T) - S(T = 0\ \mathrm{K}) = \int_{T=0}^{T} C\ \mathrm{d}\ln T$$

have been determined from experimental heat capacity data for urea (15), the urea:alkane inclusion compounds (16), and the alkanes (17). $G(T)$, also referenced to T = 0 K, for each compound was determined from

$$[5] \qquad G(T) \equiv G(T) - G(T = 0\ \mathrm{K}) = H - TS$$

The association changes are defined as

$$[6] \qquad \Delta_{as}H = H(\mathrm{UIC}) - H(\mathrm{urea}) - mH(\mathrm{guest}) + \Delta_{as}H(T = 0\ \mathrm{K})$$

$$[7] \qquad \Delta_{as}S = S(\mathrm{UIC}) - S(\mathrm{urea}) - mS(\mathrm{guest})$$

and

$$[8] \qquad \Delta_{as}G = G(\mathrm{UIC}) - mG(\mathrm{guest}) + \Delta_{as}G(T = 0\ \mathrm{K})$$

where, at T = 0 K, S(urea) = S(guest) = S(UIC) = 0 (i.e., residual entropy is assumed to be zero) and $\Delta_{as}G(T = 0\ \mathrm{K}) = \Delta_{as}H(T = 0\ \mathrm{K})$. The latter has been assessed through the thermodynamic cycle shown in Fig. 1, using literature data for heat capacities of the hydrocarbons (17), urea (15), and the urea inclusion compounds (16), and melting enthalpies of urea (11, 13), the alkanes (17), and the urea inclusion compounds (11, 13). The cycle involves a determination of the difference between two large numbers, which leads to considerable uncertainty in the result, and the calculated values for $\Delta_{as}H(T = 0\ \mathrm{K})$ for urea:decane, urea:dodecane, and urea:hexadecane are indistinguishable at –1500 J (mol urea)$^{-1}$, with an estimated uncertainty of ±1000 J (mol urea)$^{-1}$. (This uncertainty may be overestimated by about a factor of two: the present results for $\Delta_{as}H$ at 25°C for urea:decane and urea:hexadecane are 5.1 and 5.7 kJ (mol urea)$^{-1}$, respectively, which compare well with direct calorimetric determinations (18), 4.6 and 5.1 kJ (mol urea)$^{-1}$, respectively.)

© 1998 NRC Canada

Fig. 1. The thermodynamic cycle used to determine $\Delta_{as}H$ (T = 0 K) = $\Delta_{as}G(T = 0$ K) for urea:decane, urea:dodecane, and urea:hexadecane. T_m, T_u, and T_g designate, respectively, the melting points of the inclusion compound, urea, and the guest. $\Delta_{fus}H$ is the enthalpy change on melting of the inclusion compound (total enthalpy change over two steps), urea, or the guest, depending on the process shown. Literature data were used for the heat capacity of the inclusion compound (16), urea (15), and the hydrocarbon guest (17), and for the enthalpies of fusion of the inclusion compound (11, 13), urea (11, 13), and the hydrocarbon guest (17).

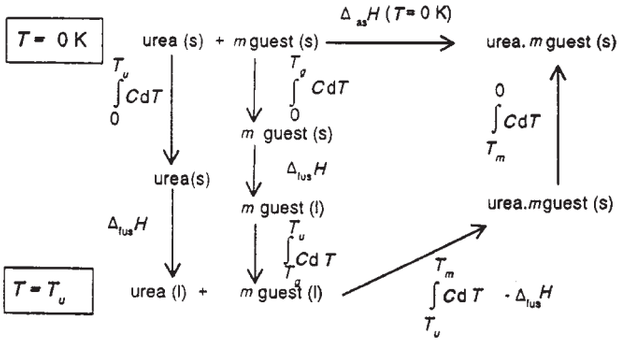

$\Delta_{as}G$ and its components, $\Delta_{as}H$ and $-T\,\Delta_{as}S$, have been calculated as functions of temperature for each of the urea inclusion compounds; the results are shown in Figs. 2, 3, and 4, for urea:decane, urea:dodecane, and urea:hexadecane, respectively.

Discussion

All three urea inclusion compounds are found to be stable with respect to their components ($\Delta_{as}G < 0$ in Figs. 2, 3, and 4) from T = 0 K up to their melting points. The formation of urea:alkane inclusion complexes is known from calorimetric experiments to be exothermic (9), and this is confirmed here ($\Delta_{as}H < 0$). From the contributions to $\Delta_{as}G$, the stability is mostly a result of enthalpic interactions ($\Delta_{as}H < 0$); entropic interactions are mostly destabilizing ($-T\Delta_{as}S \geq 0$). Urea is polar and the guests are nonpolar, so there is a tendency to think of the guest–host interactions as being unfavourable in the formation of urea:alkane inclusion compounds, but the sign of $\Delta_{as}H$ indicates otherwise. Unfortunately, analysis of bulk thermodynamic data does not delineate specific interactions, and the present results do not test the theoretical finding that interaction between adjacent alkane guest molecules in urea channels is repulsive (19).

Each of the urea inclusion compounds investigated here has at least one solid–solid transformation: at 110.9 K for urea:decane, 123.2 K for urea:dodecane, and 135.3 and 151.8 K for urea:hexadecane (16). The solid–solid transitions slightly stabilize the inclusion compound further (most for urea:decane; least for urea:hexadecane) but the effect is minor and noticeable only as a slight decrease in ($d\Delta_{as}G/dT$).

The major feature common to Figs. 2, 3, and 4 is the marked decrease in stability of the inclusion compound beyond the melting point of the guest species, 243.5 K for decane, 263.6 K for dodecane, and 291.3 K for hexadecane (17). In each case the analysis shows that destabilization of

Fig. 2. Thermodynamic changes for association of urea:decane, as shown in eq. [2] with m = 0.120. $\Delta_{as}G = \Delta_{as}H - T\Delta_{as}S$. Urea:decane has a solid–solid transition at 110.9 K (16), and melts incongruently at 355 K (11). Decane melts at 243.5 K (17).

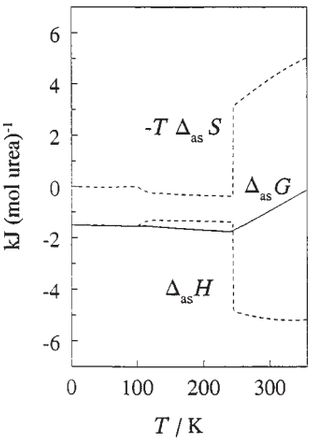

Fig. 3. Thermodynamic changes for association of urea:dodecane, as shown in eq. [2] with m = 0.103. $\Delta_{as}G = \Delta_{as}H - T\Delta_{as}S$. Urea:dodecane has a solid–solid transition at 123.2 K (16), and melts incongruently at 364 K (11). Dodecane melts at 263.6 K (17).

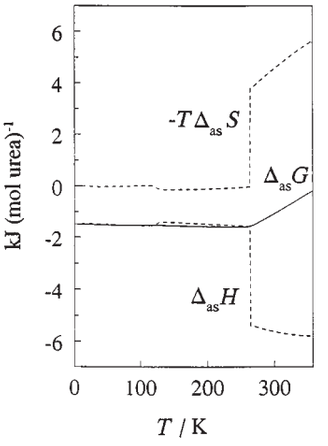

the urea inclusion compound can be considered to be driven by the high entropy of the guest species in its competing liquid phase. Ultimately it leads to $\Delta_{as}G = 0$ at the incongruent melting point of the urea inclusion compound: 355 K for urea:decane, 364 K for urea:dodecane, and 384 K for urea:hexadecane (11, 13). As these temperatures are below the melting point of pure urea (406 K), all three melt incongruently.

In the separation of alkanes on a urea bed, the capacity has been found to decrease as the temperature increases, and this was attributed to weakened interactions between the guest and the urea molecules at elevated temperatures (8). However, we can see from Figs. 2–4 that enthalpy favours UIC formation as the temperature is increased; it is the competing entropy of the liquid guest that makes the UIC less stable as the temperature is increased.

© 1998 NRC Canada

Fig. 4. Thermodynamic changes for association of urea:hexadecane, as shown in eq. [2] with $m = 0.081$. $\Delta_{as}G = \Delta_{as}H - T\Delta_{as}S$. Urea:hexadecane has solid–solid transitions at 135.3 and 151.8 K (16), and melts incongruently at 384 K (13). Hexadecane melts at 291.3 K (17).

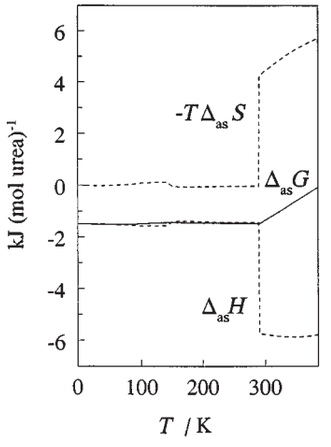

Figures 2, 3, and 4 also indicate the trend to increased stability of urea inclusion compounds with longer alkane guests, as observed experimentally (8). For example, at T = 300 K, the values of $\Delta_{as}G$ for urea:decane, urea:dodecane, and urea:hexadecane are –0.95 kJ (mol urea)$^{-1}$, –1.06 kJ (mol urea)$^{-1}$ and –1.34 kJ (mol urea)$^{-1}$, respectively.

The main determinant in stability from one urea:alkane inclusion compound to another would appear to be the melting point of the guest (assuming that the vapour pressure plays a negligible role). Below that temperature $\Delta_{as}G$ is almost independent of guest, but above the melting point of the guest the UIC becomes dramatically destabilized with respect to its components. The correlation between stability and alkane melting point would also explain instability of urea:alkanes with very short hydrocarbon chains: their low melting points could lead to $\Delta_{as}G > 0$ at room temperature. We have recently found that urea inclusion compounds can be destabilized by photochemical means; when photoactive guests lead to fragmentation products that are too small to stabilize the inclusion compound structure, the close-packed tetragonal form of urea results (20).

The present results provide benchmarks for future theoretical investigations of stability and intermolecular forces in urea:alkane inclusion compounds. The same approach could be used to investigate other urea inclusion compounds, if experimental data were available. For example, for a given carbon chain length of guest species, the stability of urea inclusion compounds has been shown to increase in the order alkane < alcohol < amine < acid (21). It would be interesting to extend the present studies to other guests, especially to delineate the importance of commensurability of guest and host along the *c*-axis and the role of guest–host interaction in stability of urea inclusion compounds.

Acknowledgements

The author is grateful to K.C. Smith for useful comments. This work was supported by the Natural Sciences and Engineering Research Council of Canada and the Killam Trusts.

References

1. J.L. Atwood, J.E.D. Davies, D.D. MacNicol, and F. Vögtle (*Editors*). Comprehensive supramolecular chemistry, Pergamon, Oxford. 1996.
2. W.J. Zimmerschied, R.A. Dinerstein, A.W. Weitkamp, and R.F. Marschner. Ind. Eng. Chem. **42**, 1300 (1950).
3. M.D. Hollingsworth and K.D.M. Harris. *In* Comprehensive supramolecular chemistry. Vol. 6. Solid state supramolecular chemistry: crystal engineering. *Edited by* D.D. MacNicol, F. Toda, and R. Bishop. Pergamon, Oxford. 1996. pp. 177–237, and references cited therein.
4. M.D. Hollingsworth, M.E. Brown, A.C. Hillier, B.D. Santarsiero, and J.D. Chaney. Science, **273**, 1355 (1996).
5. K.D.M. Harris. Chem. Soc. Rev. **26**, 279 (1997).
6. S.B. Hendricks. J. Am. Chem. Soc. **50**, 2455 (1928).
7. I. Mavrovic and A.R. Shirley, Jr. *In* Kirk–Othmer encyclopedia of chemical technology. Vol. 23. 3rd ed. John Wiley & Sons, New York. 1978. pp. 548–575.
8. R.S. Al-Ameeri, F. Owaysi, and M. Hassan. Ind. Eng. Chem. Res. **30**, 202 (1991).
9. L.C. Fetterly. *In* Non-stoichiometric compounds. *Edited by* L. Mandelcorn. Academic Press, New York. 1964. pp. 491–567.
10. I. Mavrovic. Hydrocarbon Process. **77**, 137 (1998).
11. H.G. McAdie. Can. J. Chem. **40**, 2195 (1962).
12. M.A. White and R.T. Perry. Chem. Mater. **6**, 603 (1994).
13. M.A. White and R.S. Harnish. Chem. Mater. **10**, 833 (1998).
14. I.J. Shannon, K.D.M. Harris, A.J.O. Rennie, and M.B. Webster. J. Chem. Soc. Faraday Trans. **89**, 2023 (1993).
15. O. Andersson, T. Matsuo, H. Suga, and P. Ferloni. Int. J. Thermophys. **14**, 149 (1993).
16. R.C. Pemberton and N.G. Parsonage. Trans. Faraday Soc. **61**, 2112 (1965).
17. H.L. Finke, M.E. Gross, G. Waddington, and H.M. Huffman. J. Am. Chem. Soc. **76**, 333 (1954).
18. W. Schlenk, Jr. Justus Liebigs Ann. Chem. **565**, 204 (1949).
19. A.J.O. Rennie and K.D.M. Harris. J. Chem. Phys. **96**, 7117 (1992).
20. K.C. Smith, J.A. Pincook, and M.A. White. Chem. Mater. **10**, 3626 (1998).
21. H.G. McAdie. Can. J. Chem. **41**, 2114 (1963).

© 1998 NRC Canada

Characterization of deacetylated chitosan and chitosan molecular weight review

Jonathan Z. Knaul, Mohammad R. Kasaai, V. Tam Bui, and Katherine A.M. Creber

Abstract: Starting from a chitosan sample with a degree of deacetylation of 71%, three separate sample sets were generated by successive deacetylation and reacetylation processes. The degree of deacetylation of samples was determined by UV spectrometry supported by thermogravimetric analysis. The molecular weight of chitosan samples was determined in a solvent system of 0.25 M CH_3COOH/0.25 M CH_3COONa, using viscometry and gel permeation chromatography (GPC) with a TSK-gel column. The first set of samples had a similar degree of deacetylation (DDA) but differing molecular weights. The second set of samples had a similar molecular weight but differing degrees of deacetylation. The Mark–Houwink–Sakurada constants used for the determination of viscosity average molecular weight and the universal calibration of the GPC system were $K = 1.40 \times 10^{-4}$ dL/g and $a = 0.83$. Results showed that molecular weights determined from both techniques are in good accord only at lower degrees of deacetylation. This may be attributed to the fact that the chemical structure of chitosan samples could have been largely altered with increasing or decreasing degree of deacetylation. Nevertheless, the trend with which the molecular weights vary with the deacetylation time is consistent over a limited DDA range. A literature review of molecular weight analysis of chitosan is included.

Key words: chitosan, degree of deacetylation, gel permeation chromatography, molecular weight, viscometry.

Résumé : Utilisant comme produit de départ un échantillon de chitosane avec un degré de désacétylation de 71%, on a préparé trois ensembles différents d'échantillon par des processus successifs de désacétylation et de réacétylation. On a déterminé le degré de désacétylation des échantillons par spectrométrie UV associée à des analyses thermogravimétriques. On a déterminé le poids moléculaire des échantillons de chitosane par viscosimétrie et par chromatographie par perméation de gel (CPG) avec une colonne de gel de TSK, dans un système de solvant à 0,25 M CH_3COOH/0,25 M CH_3COONa. Le premier ensemble d'échantillons présentait un degré de désacétylation (DDA) semblable, mais des poids moléculaires différents. Le deuxième ensemble d'échantillons présentait des poids moléculaires semblables, mais des degrés de désacétylation différents. Les constantes de Mark–Houwink–Sakurada utilisées pour la détermination des poids moléculaires moyens par viscosité et pour la calibration universelle du système de CPG sont les suivantes : $K = 1{,}40 \times 10^{-4}$ dL/mg et $a = 0{,}83$. Les résultats montrent que les poids moléculaires déterminés par les deux techniques ne sont en bon accord qu'aux faibles degrés de désacétylation. On peut attribuer cette observation au fait que la structure chimique des échantillons de chitosane peut avoir été fortement modifiée par une augmentation ou une diminution du degré de désacétylation. Malgré tout, la tendance avec laquelle les poids moléculaires varient avec le temps de désacétylation est consistent pour un degré limité de «DDA». On a inclus une revue de la littérature relative à l'analyse des poids moléculaires des chitosanes.

Mots clés : chitosane, degré de désacétylation, chromatographie par perméation de gel, poids moléculaire, viscosimétrie.

Introduction

Chitin, a (1–4)-linked 2-acetamido-2-deoxy-β-D-glucan, is a natural polysaccharide that occurs mainly in invertebrates, fungi, and yeasts. It is the second most abundant natural polymer after cellulose (1). Chitosan, a (1–4)-linked 2-amino-2-deoxy-β-D-glucan, is the N-deacetylated derivative of chitin, although 100% N-deacetylation is almost never achieved. It is generally accepted that this biopolymer is referred to as "chitosan" if chitin is N-deacetylated to such a degree that it becomes completely soluble in dilute aqueous acidic systems (1–5% by volume aqueous acetic

Received February 25, 1998.

J.Z. Knaul, V.T. Bui,[1] and K.A.M. Creber. Department of Chemistry and Chemical Engineering, Royal Military College of Canada/College Militaire Royal du Canada, P.O. Box 17 000, Stn Forces, Kingston, ON K7K 7B4, Canada.
M.R. Kasaai. Department of Food Science and Nutrition, Faculty of Agriculture, Pavillon Comtois, Laval University, Ste-Foy, QC G1K 7P4, Canada.

[1]Author to whom correspondence may be addressed. Telephone: (613) 541-6000. Fax: (613) 542-9489. E-mail: bui-v@rmc.ca

© 1998 NRC Canada

Fig. 1. Segments of cellulose, chitin, and chitosan polymers.

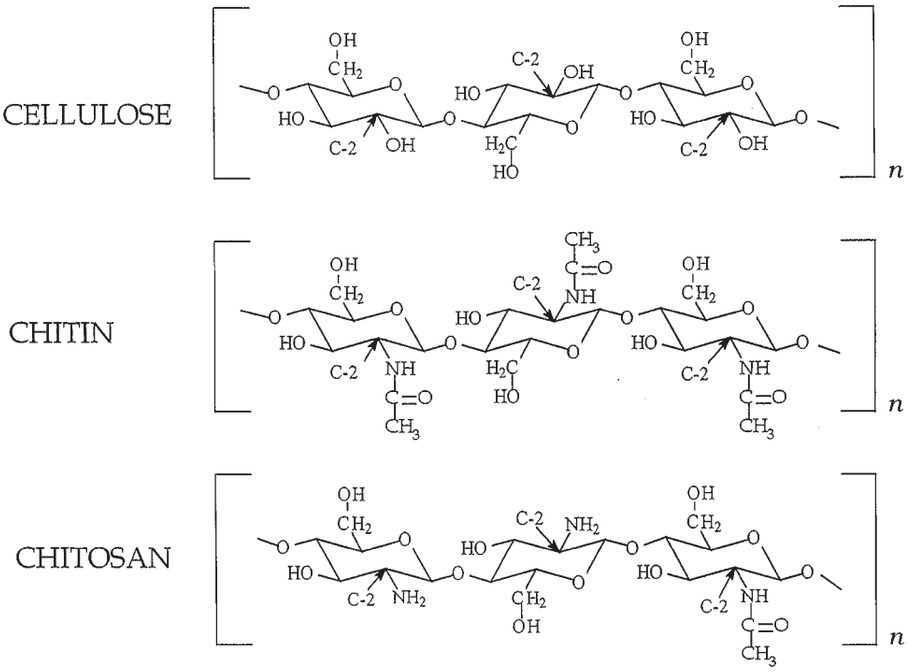

acid would be considered a dilute acidic medium). Structural examples of chitin, chitosan, and the structurally similar biopolymer cellulose can be found in Fig. 1. Chitosan is well known as a nontoxic and degradable polymer. It is used widely in the medical industry in products ranging from burn dressings to drug delivery capsules.

Chitosan samples can be characterized for several parameters including degree of deacetylation (DDA), turbidity, solubility, ash content, glass transition temperature, average molecular weight, and molecular weight distribution. It is known that viscometry and gel permeation chromatography (GPC) are the two most commonly used secondary methods for determining the molecular weight of polymers. They are virtually related to each other through the use of the Mark–Houwink–Sarakuda constants in both techniques (2, 3), and the reliability of these constants for a given polymer–solvent system determines the applicability of these secondary methods. As will be shown in the following section, the use of these techniques is not always straightforward, especially in the case of chitosan because of its complex hydrodynamic behaviour, which greatly depends upon its degree of deacetylation and the solvent system used.

In this study, one chitosan sample with a DDA of 71% was deacetylated and then reacetylated, providing two series of samples with either varying DDA or varying molecular weight, and one series with constant DDA and molecular weight. The samples were then characterized for the degree of deacetylation by UV spectrometry supported by thermogravimetric analysis, and for the molecular weights by viscometry and gel permeation chromatography (GPC) using a commonly used solvent system, 0.25 M CH_3COOH/0.25 M CH_3COONa. The main objective of this work is first to determine to what extent the viscometric and GPC data, based on available values of the Mark–Houwink–Sarakuda constants for the selected solvent system and for limited ranges of DDA and molecular weight, could yield reliable molecular weights of the above sets of chitosan samples, and secondly, to determine the effects of the deacetylation and reacetylation conditions, such as the reaction time and amounts of reactants used, on the properties of the chitosan samples obtained.

Literature review

Viscometric studies on chitosan

The intrinsic viscosity, [η], of a polymer solution, including nonelectrolytic and electrolytic polymers, is related to the viscosity average molecular weight, M_v, of the polymer through the Mark–Houwink–Sakurada equation (2, 3):

$$[1] \qquad [\eta] = K M_v^a$$

where K and a are constants depending on the polymer and the solvent system used, as well as the temperature. Their values are determined experimentally by evaluating the intrinsic viscosities of solutions of polymers for which the molecular weight has been determined by an independent method. Several authors have reported the K and a values for chitosan of varying DDA, in various solvent systems. Table 1 summarizes data for M_v and related the constants K and a, for different solvent systems and molecular weight ranges of chitosan. The most commonly used solvent systems are buffer solutions formed with acetic acid/sodium acetate at various concentrations. A significant result was reported by Rinauldo et al. (10): for a narrow molecular weight range, K and a were found to be nearly unchanged for three samples of DDA of 98, 88.5, and 79%, respectively. Normally, these constants have been found to vary significantly when the DDA range of 69–100% is studied over a large molecular weight range (9).

© 1998 NRC Canada

Table 1. Published Mark–Houwink–Sakurada constants for chitosan.

Solvent	T (°C)	% DDA	K (mL/g)	a	Method	M_v range ($\times 10^4$)	Ref. (year)
0.2 M CH_3COOH/ 0.1 M NaCl/ 0.4 M Urea			8.93×10^{-2}	0.71	SD	1.38	4 (1974)
0.1 M CH_3COOH/ 0.2 M NaCl	25	Derived chitosan	3.04×10^{-5}	1.26	Absorbance		5 (1982)
0.17 M CH_3COOH/ 0.47 M NaCl	25	90–100	1.115	0.147	SD	1.5–0.16	6 (1980)
2% CH_3COOH/ 0.2 M CH_3COOH + dichloroacetic acid	25	82–88	1.38×10^{-2}	0.85	SD	1.5–0.16	7 (1985)
0.33 M CH_3COOH/ 0.3 M NaCI	21	80–82	3.41×10^{-3}	1.02	Diffusion SD	5.2–13.3	8 (1986)
0.1 M CH_3COOH/ 0.2 M NaCl	25	≈80	1.81×10^{-3}	0.93		63–0.48	5, 9 (1988)
0.2 M CH_3COOH/ 0.1 M CH_3COONa	30	69 84 91 100	0.104×10^{-3} 1.424×10^{-3} 6.589×10^{-3} 16.80×10^{-3}	1.12 0.96 0.88 0.81	LS	25.1–1.94 1.94	9 (1991)
0.3 M CH_3COOH/ 0.2 M CH_3COONa	25	98 88.5 79	0.082 0.076 0.074	0.76 0.76 0.76	GPC/MALL LS/LALLS	20.3–29.0	10 (1993)
0.02 M CH_3COOH/ 0.1 M CH_3COONa and chitosan chloride	20	100 85 40	Log $K_{0.1}$ = –0.427 – $3.821F_A$	$a_{0.1}$ = 0.6169 + $0.759F_A$	OM	1.5–31.0	11 (1993)
0.2 M CH_3COOH/ 0.2 M CH_3COONa	25	42 89		1.14 0.521	SD		12 (1993)
1% CH_3COOH	30		0.0474	0.723	LS	20.46–65.74	13 (1993)
0.5 M CH_3COOH/ 0.5 M CH_3COONa	25	69.8	0.119	0.59	GPC/LS	274–11.5	14 (1993)
0.3 M CH_3COOH/ 0.2 M CH_3COONa	25		Plots but no values provided		SEC[3], LS		15 (1993)

Gel permeation chromatography (GPC) studies on chitosan

The first study using a GPC system (16) was reported in 1976, using a long column packed with glass beads, and 2% aqueous acetic acid as the mobile phase. A strong absorbance peak was observed at 254 nm, which would appear to be an unusual result, as chitosan is known to absorb between 200 and 204 nm (17). The chitosan sample studied was found to have an M_n of 9.36×10^5 and an M_w of 2.05×10^6. The GPC system was calibrated based on dextran standards, but a universal calibration was not done. In a later study (18) by the same authors, it was assumed that the difference in solution behavior between chitosan and the dextran standards was negligible given their similarity in molecular structure.

The molecular weight of chitosan samples varying in degree of deacetylation between 78 and 99% was analyzed using an in-line GPC/LALLS method (19), using a solvent system of 0.2 M acetic acid/0.l M sodium acetate at 30°C. The molecular weights were found to be between 8.5×10^5 and 4.9×10^5. These values decreased with a rise in treatment temperature and with an increase in degree of deacetylation. This is in accordance with results obtained using an off-line laser light scattering method (20). Nine chitosan samples of different sources and varying molecular weights were analysed using a GPC/MALLS system (21) with dextran standards for the calibration. A dissimilarity between the hydrodynamic behaviour of dextran standards and chitosan samples was suggested as the probable cause of the overestimation of the molecular weights of chitosan samples.

In a recent study (22) using a size exclusion chromatography (SEC) system with different solvents ranging from a 0.3 M acetic acid solution to a 0.3 M acetic acid/0.2 M sodium acetate buffer, polystyrene standards were used for the calibration of the SEC system. A universal calibration was not mentioned.

© 1998 NRC Canada

Table 2. Deacetylated and reacetylated chitosan sample information.

Sample code	% DDA (±3.4%)	% Water + impurities (±1.5%)	Deacetylation/reacetylation conditions
P59a	70.8	15.4	As received from NovaChem Ltd.
Deacetylated samples:			
P59b9	87.3	12.5	P59a, 1 h, 50% $NaOH_{(aq)}$, 100°C, N_2
P59c9i	94.5	4.8	P59b9, 1 h, 50% $NaOH_{(aq)}$, 100°C, air
P59c9ii	94.9	5.9	P59b9, 2 h
P59c9iii	95.0	6.2	P59b9, 3 h,
P59c9iv	95.1	5.9	P59b9, 4 h
P59c9v	95.3	5.1	P59b9, 5 h
P59c9vi	95.3	5.3	P59b9, 5.4 h
P59c9vii	95.3	3.8	Same conditions as for P59c9ii
P59c9viii	95.1	3.2	
P59c9ix	95.4	3.0	
P59d9i	96	3	P59c9ix, 0.5 h, 50% $NaOH_{(aq)}$, 100°C, air
Reacetylated samples:			
B	90.1	4.3	P59d9i with 0.1004 g acetic anhydride
C	87.7	4.0	P59d9i withO.1236 g acetic anhydride
D	87.8	3.6	P59d9i withO.1445 g acetic anhydride
E	79.2	5.9	P59d9i withO.2845 g acetic anhydride
F	64.3	12.6	P59d9i with 0.5202 g acetic anhydride

Finally, four chitosan samples with degrees of deacetylation (23) varying between 91 and 92% were characterized using a GPC system with a series of TSK-gel columns and a mobile phase consisting of 0.3 M acetic acid/0.l M ammonium acetate buffer. This study showed that a more accurate analysis of the molecular weight distribution of chitosan samples can be made through GPC by application of the polydispersity index and the statistical skewing factor "*g*." This factor is a statistical measure of skewness of the chromatographic peaks. When $g = 0$, the peak of the sample is symmetrical. When $g > 0$, the peak has a long tail at high elution volumes and thus is skewed toward low molecular weights. When $g < 0$, the peak is skewed toward higher molecular weights. Thus *g* gives an indication of whether the polymer contains more high or low molecular weight chains. However, the chromatographic peaks are, in effect, influenced by both molecular separation and by axial dispersion as well as adsorption effects. Thus, for example, a skewed peak can result from adsorption.

The above GPC work can be summarized in the following manner. Buffer solutions of acetic acid are suitable for the mobile phase, dextran standards are commonly used for the calibration of the GPC columns, and the dissimilarity in hydrodynamic behaviour between chitosans and calibration standards should be taken into account. However, a large difficulty frequently encountered in the calibration of GPC systems arises from the fact that the hydrodynamic behaviour of chitosan in a given solvent system, indirectly represented by the Mark–Houwink–Sakurada constants, varies with its degree of deacetylation as well as with its molecular weight range.

Experimental

Materials

One chitosan sample with a degree of deacetylation of 71%, lot no. P59a, was obtained in the form of flake from Novachem Limited of Dartmouth, Nova Scotia, Canada. This is a shrimp-based product from the Gulf of St. Lawrence. The viscosity of a solution of 1% chitosan (by weight) in 1% (by volume) aqueous acetic acid was provided as 740 cP. The following chemicals were all obtained and used as reagent grade from Sigma–Aldrich Canada Ltd: sodium hydroxide, acetic acid, acetic anhydride, methanol, and sodium acetate. Chemicals used in the GPC experimentation were HPLC grade.

One set of six samples having similar degrees of deacetylation but differing molecular weights, and another set of six samples with differing degrees of deacetylation, but similar molecular weights, were prepared from the original chitosan sample according to the following deacetylation and reacetylation processes. In addition, three samples of the same DDA and molecular weight were also prepared.

Deacetylation and fragmentation

Chitosan identification codes and the particulars of deacetylation are noted in Table 2. Deacetylations were carried out by heating solutions of chitosans in aqueous NaOH solution, 50% by weight, at 100°C, for the times noted in Table 2, under a nitrogen atmosphere. The reaction product was subsequently washed in distilled water until reaching a neutral pH, and then dried in an oven at 50°C for 16 h. In the first experiment, the original chitosan, code P59a, was deacetylated for 1 h; the reaction product was code-named P59b9. All subsequent deacetylation reactions were conducted under air in order to aid in the breakup of chitosan molecules. After washing and drying, this sample, P59b9, was further reacted over the course of 6 h and one sample was removed every hour, yielding a set of chitosan samples with similar degrees of deacetylation but decreasing molecular weight. The products from this experiment were code-named P59c9(i–vi). In a second experiment, three separate samples of P59b9 were further deacetylated for 2 h under the same conditions in order to arrive at three samples with similar DDA values and molecular weights. Their code names are P59c9(vii–ix). The final DDA values, also listed in Table 2, were determined by UV spectrometry, following a reported method (17).

© 1998 NRC Canada

Reacetylation

To obtain a series of chitosan samples with similar molecular weights but varied degrees of deacetylation, a method previously described (24) was followed. The experiment used a sample of P59c9(ix) and further deacetylated it for 30 min. After washing and drying the product, it was code named P59d9(I). Five samples (2 g) of P59d9(i) were each placed into a flask containing 100 mL distilled water and stirred for 1 h before adding 100 mL of 2% aqueous acetic acid, then continuously stirred for one more hour. Methanol (200 mL) was added to each flask and stirred for a further 10 min. The final addition to each solution included 100 mL of methanol containing acetic anhydride, ranging in amount from 6.86×10^{-4} mol for sample B to 5.10×10^{-3} mol for sample F.

The solutions were then stirred for a further 16.5 h at room temperature. At the end of this period, methanolic ammonia was added to each solution in order to precipitate the chitosan. The precipitants were recovered and washed with distilled water using a sintered glass funnel under vacuum. The solids were finally dried in a convection oven at 50°C for 72 h.

Characterization

Thermogravimetric analysis

The water content of the chitosan samples, listed in Table 2, was determined using a Texas Instruments 2050 TGA thermogravimetric analyser. The sample was heated from room temperature to 300°C at 10°C per min under nitrogen. The loss in weight of a chitosan sample up to 180°C was taken to be the result of evaporation of water and volatile impurities.

Viscometry measurements

The viscosities of the chitosan samples were measured in a solvent of 0.25 M CH_3COOH/ 0.25 M CH_3COONa at 24.95 ± 0.05°C using an Ubbelohde capillary viscometer, model Cannon no. 100 E482, which yielded an average flow time of 62.29 s for the solvent system. The uncertainty in flow time was ±0.5 s, with at least three measurements for each solution. Six dilutions with the solvent were used for each chitosan sample. The flow time data were used to calculate the relative viscosity, the reduced viscosity, and then the intrinsic viscosity, [η] (by a linear regression of the reduced viscosity versus concentration). The overall error in the intrinsic viscosity, resulting mainly from the flow time and concentration uncertainties, and the temperature fluctuation, was estimated as being ±0.6 dL/g, which led to a maximum error of ±5% in the values of viscometric average molecular weight. The correlation coefficients were better than 0.950 for all chitosan samples.

Gel permeation chromatography (GPC)

GPC was carried out using the same instrumentation and method as previously described by Kasaai et al. (25). The solvent used was the same as that used in the viscosity measurements. The GPC system incorporated a Hewlett–Packard 1050 series pump. The flow rate was maintained at 0.40 mL/min under a pressure of 1.041 ± 0.021 MPa with zero attenuation. The system also included an HP 1050 series autoinjector and an HP 1047A refractive index detector. The column used was a TSK-gel GMPWXL column provided by Phenomenex with dimensions of 300 mm × 7.8 mm. The temperature of the column was maintained at 35°C. The standards used to calibrate the column were pullulan. All data provided by the GPC system were collected and analysed using the Hewlett–Packard ChemStation software package, B.02.06, 1994.

Results and discussion

Degree of deacetylation and thermogravimetric analysis

Table 2 summarizes all relevant information concerning the deacetylated and reacetylated chitosan samples obtained from the original sample, P59a. Knowledge of the water content as well as traces of volatile impurities in the chitosan samples was essential since these amounts would affect, first, the determination of their degree of deacetylation, DDA, presented in Table 2 (using data from UV spectrometry), and, secondly, the calculation of the concentration C in viscosity measurements. A typical thermogravimetric analysis (TGA) curve for chitosan samples shows a significant weight loss up to about 150°C followed by a plateau until about 250°C, and then a marked decrease in the weight of sample. It is believed that beyond 180°C all sample weight loss should be due to the thermal degradation of short and long molecular chains of chitosan. Repeated TGA runs on the same chitosan samples showed an uncertainty in water and impurities content of about 1.5%. This was the largest contributing factor to the error in the DDA determination, which was estimated as being ±3.4%. This error refers to the maximum single standard deviation after several DDA determinations performed on the same chitosan sample. The TGA results for the temperature range up to 180°C are in good agreement with those obtained by weighing chitosan samples before and after being placed in an oven at 50°C for 24 h. This TGA method for determining the water and volatile impurities content has also been successfully used by Qin (26) for the same purpose.

The deacetylation of the original chitosan sample, P59a, for 1 h in a nitrogen atmosphere increased the DDA from 70.8 to 87.3% and then up to 94.5% with one more hour of deacetylation in air. For further deacetylation times, the DDA remained nearly constant at about 95.0% while the molecular weight of samples decreased only slightly; this is shown in Table 3 and will be discussed later. It is hard to draw firm conclusions about the oxidative effect caused by oxygen in air on the deacetylation of chitosan, but it is clear that longer reaction times contribute to the chain degradation, or possibly to some branching formation of chitosan polymer molecules. Values of DDA for the reacetylation series, B–F, showed an appreciable decrease in DDA with increasing amount of acetic anhydride, which confirms the success of the reacetylation method used.

Intrinsic viscosity, [η], and viscosity average molecular weight, M_v

Reduced viscosity values for typical chitosan samples are plotted in Fig. 2 as a function of concentration. The linearity of all traces is attributed to the presence of a suitable amount of sodium acetate in the acetic acid solution. Without this salt, one would expect to observe a large depend-

© 1998 NRC Canada

Table 3. Average molecular weight values for chitosan samples.

Sample code	% DDA (±3.4%)	[η] (dL g^{-1})	$M_v \times 10^{-3}$ (±5%)	$M_n \times 10^{-3}$	$M_w \times 10^{-3}$	M_w/M_n
P59a	70.8	12.03	881	855	1619	1.89
P59b9	87.3	11.22	809	427	842	1.97
P59c9i	94.5	10.22	724	119	302	1.52
P59c9ii	94.9	9.84	691	223	333	1.49
P59c9iii	95.0	9.60	671	200	310	1.55
P59c9iv	95.1	9.75	684	221	318	1.44
P59c9v	95.3	9.40	654	183	269	1.47
P59c9vi	95.3	9.2	637	184	265	1.44
P59c9vii	95.3	9.93	699	208	307	1.48
P59c9viii	95.1	9.79	687	233	341	1.46
P59c9ix	95.4	9.77	685	223	319	1.43
P59d9i	96	9.00	621	179	252	1.41
B	90.1	8.58	586	247	457	1.85
C	87.7	8.57	585	260	502	1.93
D	87.8	8.51	580	297	608	2.05
E	79.2	7.90	531	270	550	2.04
F	64.3	7.52	500	335	699	2.09

Fig. 2. Reduced viscosity versus concentration for some chitosan samples.

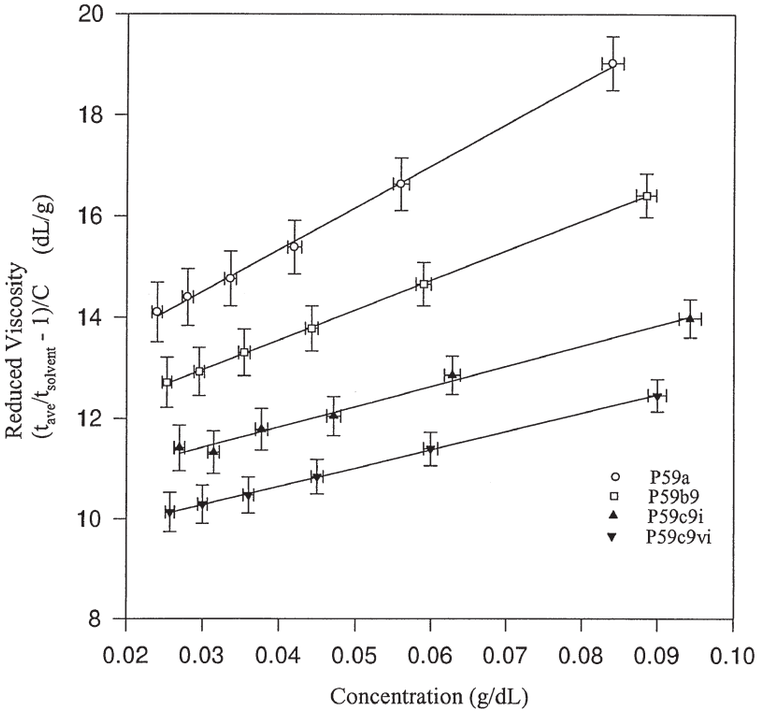

ence of the reduced viscosity on the concentration, most importantly in the low concentration range. This is typical for a polyelectrolyte whose molecular chains become extended as they progressively lose their charge due to the escape of some counterions from the polymer backbones, leaving the latter oppositely charged. The effect of an extended polymer molecule on the viscosity of the solution is greater than that of a random polymer chain. Consequently, if the polyelectrolyte solutions contain a sufficiently large amount of simple electrolyte, such as sodium chloride or sodium acetate, their reduced viscosity is expected to change linearly with concentration similar to that of an uncharged polymer solution.

The intrinsic viscosity values, [η], and the limited value of reduced viscosity at $C = 0$, are presented in Table 3. These values allowed the calculation of the viscosity average molecular weight, M_v, also reported in Table 3, according to the following equation:

$$[\eta] = 1.40 \times 10^{-4} M_v^{0.83} \quad [2]$$

© 1998 NRC Canada

This equation for the solvent system of 0.25 M acetic acid/0.25 M sodium acetate has been developed by Kasaai et al. (25), using combined viscometry–GPC methods performed on relatively monodisperse chitosan samples, with pullulan standards used for the calibration of the GPC system where the discrepancy between the hydrodynamic behaviour of chitosan and pullulan standards was taken into account by a universal calibration method. The value of $a = 0$ means that chitosan molecules behave like random polymer chains in the given solvent system. This is supported by the results of other authors (7, 9, 10), Table 1, for similar solvent systems. As an approximation, the hydrodynamic behaviour of chitosan in the given solvent system is assumed to be nearly the same within a limited DDA range (e.g., between 71 and 95%). It is thus found that the intrinsic viscosity and then M_v largely decrease with increasing DDA, up to 2 h of reaction time, and then only slightly diminish with further reaction times. Chain scission might have occurred during the deacetylation process, and this may, to a certain degree "outweigh," but not occlude, the effect of coil expansion due to electrostatic repulsion, which closely depends on the DDA of samples. The above results do not agree with those reported by Roberts and co-workers (5, 24), where an opposite trend was observed (e.g., the intrinsic viscosity and molecular weight increased with increasing DDA). This trend was attributed (5, 24) to the fact that the cationic effect of the positively charged amine groups on the chitosan backbone plays a greater role in coil expansion than do the acetyl groups present on a more highly acetylated chitosan solution. However, the reported trend has been observed with the use of a 0.1 M acetic acid/0.2 M sodium chloride solvent system (5), which did not have the same buffer effect as the acetic acid/sodium acetate solvent systems. Consequently, it is suggested in this study that, as a result of their suitable buffer effect, the acetic acid/sodium acetate solvent systems could well minimize the difference in electrolytic effects of amine groups and acetyl groups. This, at least for a limited DDA range, leads to a lesser dependence of K and a on DDA. Furthermore, it has been proposed (9) that, with increasing DDA, chitosan chain stiffness decreases due to a decreased presence of hydrogen bonds between the monomer units of the chitin chain. In the more acetylated chitosan chain, two types of intramolecular H-bonds are available to restrict coiling of the chains: first, between the CH_2OH group and the O atom of the acetyl group of two neighbouring repeat units and, secondly, between the OH group and the β-deoxy of two neighbouring segments. Thus, by increasing the DDA, the former type of H-bonds will be reduced, leading to an increase in the coiling of chitosan chains. This H-bond effect may be a significant factor contributing to the dependence of K and a constants on the DDA of chitosan. Regarding the reacetylated sample series, the B–F samples, their intrinsic viscosity and molecular weight show only a slight decrease as the DDA greatly decreases from 96.0 to 64.3%. This may result from combined effects of, first, a possible chain scission following the reacetylation process and, secondly, changes in the conformation of chitosan chains due to differences in their electrostatic repulsion, H-bonds, and branching extent, over a large DDA range. Finally, the almost unchanged values of the intrinsic viscosity and M_v of the samples from P59c9vii to P59c9ix may lend support to the reproducibility of the deacetylation process used as well as the reliability of the DDA determination and the viscosity measurements.

Fig. 3. Size exclusion chromatograrns of initial chitosan (*A*) P59a, and three deacetylated samples: (B) P59b9, (C) P59c9i, (D) P59c9vi, respectively.

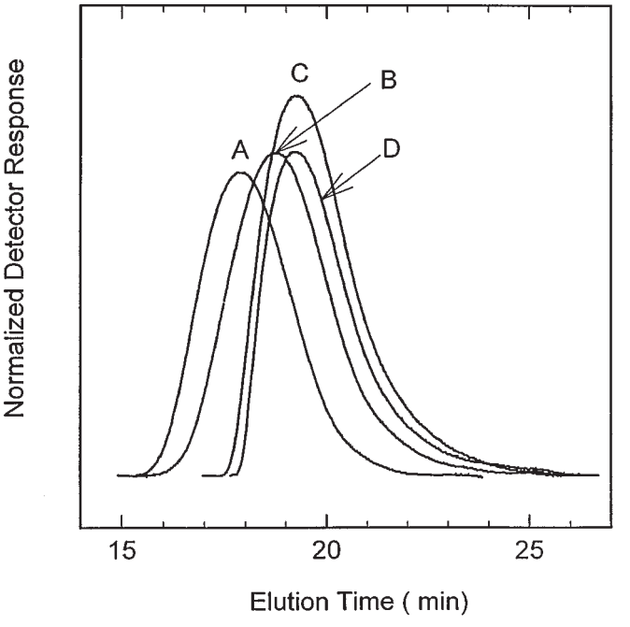

Gel permeation chromatography

The typical GPC chromatograms of some samples are presented in Fig. 3, from which the number and weight average molecular weights, M_n, M_w, and the polydispersity index were deduced, and are listed in Table 3. The original chitosan sample P59a has a relatively narrow molecular weight distribution with a polydispersity index of 1.89 and, interestingly, all deacetylated samples have even narrower molecular weight distributions with a polydispersity index of as low as 1.41. This likely resulted from the washing operation performed on deacetylated samples where relatively short chitosan chains could have been advantageously drained out. In most cases, except for samples P59a and P59b9, M_w and M_n are smaller than M_v obtained from viscosity measurements. This is typical of most polymers when applying a statistical analysis of the molecular weight distribution (25). On the other hand, results for the reacetylated samples, B–F, do not exhibit this trend, e.g., M_w becomes larger than M_v when the DDA of the samples decreases. This is likely due to the uncertainty in the use of the K and a values for the calibration of the GPC system over such a large DDA range within which the differences in the molecular conformation of chitosan such as discussed above should become overwhelming. In addition, there may be another cause, such as a greater tendency for the samples, with increasing DDA, to adhere to the column bed, thus resulting in longer elution times. Column bed – sample interaction is typically associated with an electrostatic attraction. The buffer effect of the solvent used would have suitably attenuated this interaction within a small DDA range but not completely eliminated it

© 1998 NRC Canada

over such a large DDA range. Furthermore, due to the branching conformation of chitosan (27)[2], neither the secondary viscometry nor the GPC methods used can provide accurate values of molecular weights compared to an absolute method (for example, off-line laser light scattering). Regarding the series P59c9, it was expected at the beginning that with increasing deacetylation time chitosan would reach a plateau in its DDA (27), while the molecular weight would lower significantly. This is not the case since the molecular weights change just slightly, and it is shown that 6 h of deacetylation caused virtually no reduction in molecular weight.

Conclusions

In this study, starting from one mother chitosan sample, three series of deacetylated and reacetylated samples were successfully produced: one with similar DDA values of 95% but molecular weight varying slightly from 724 000 to 637 000, another with DDA values decreasing from 90% to 61% and molecular weight varying only slightly from 586 000 to 500 000, and the last one with both DDA and molecular weight constant. The DDA of samples was determined using UV spectrometry with the help of thermogravimetric analysis, which provided the water and volatile impurities content of the samples. The reduced viscosity as well as molecular weights of samples were determined by viscometry and GPC methods using the solvent system of 0.25 M acetic acid/0.25 M sodium acetate and pullulan standards for the universal calibration of the GPC system. The difficulty with which accurate values of molecular weights could be deduced from the above methods is related to the dependence of the constants K and a, for a given solvent system, on the DDA and molecular weight ranges of the chitosan samples. Nevertheless, the results obtained did show consistent trends in variation of the intrinsic viscosity and molecular weights with the deacetylation time and with the amount of acetic anhydride used in the reacetylation process. It remains unclear whether there may be a possible oxidative effect on the deacetylation performance caused by oxygen in the air.

References

1. F. Shahidi. Canadian Chemical News. **47**(8), 25 (1995).
2. P.J. Flory. Principles of polymer chemistry. Cornell University Press, Ithaca, N.Y. 1953.
3. P.J. Flory. J. Am. Chem. Soc. **65**, 372 (1943).
4. V.F. Lee. University Microfilms (Ann Arbor) 74/29446 (1974).
5. G.A.F. Roberts and J.G. Domszy. Int. J. Biol. Macromol. **4**, 374 (1982).
6. L.A. Berkovich, G.I. Timofeyera, M.P. Tsyurupa, and V.A. Davankov. Vysokomol. Soedin. Ser. A. **22**, 1834 (1980).
7. A.I. Gamzazade, V.M. Slimak, A.M. Skljar, E.V. Stykova, S.S.A. Pavlova, and S.V. Rogozin. Acta Polym. **8**, 420 (1985).
8. N.V. Pogodina, G.M. Pavlov, S.V. Bushin, A.B. Mel'nikov, et al. Polym. Sci. USSR, **28**, 251 (1986).
9. W. Wang, B. Shuqin, L. Shuqing, and W. Qin. Int. J. Biol. Macromol. **13**, 281 (1991).
10. M. Rinaudo, M. Milas, and P.L. Dung. Int. J. Biol. Macromol., **15**, 281 (1993).
11. M.W. Anthonsen, K.M. Varum, and O. Smidsrod. Carbohydr. Polym. **22**, 193 (1993).
12. N. Errington, S.E. Harding, K.M. Varum, and L. Illum. Int. J. Biol. Macromol. **15**, 113 (1993).
13. D.G. Rao. J. Food Sci. Technol. **30**, 66 (l993).
14. G.A.F. Roberts. Chitin chemistry. Macmillian Press, London. 1992. p. 64.
15. G.A.F. Roberts and W. Wang. Adv. Chitin Sci. **1**, 279 (1996).
16. A.C.M. Wu and W.A. Bough. J. Chromatogr. **128**, 87 (1976).
17. R.A.A. Muzzarelli, C. Jeuniaux, and G.W. Gooday. Chitin in nature and technology. Plenum, New York. 1986. p. 385.
18. A.C.M. Wu. Methods Enzymol. **161**, 447 (1988).
19. M. Miya, R. Iwamoto, S. Yoshikawa, and S. Mima. Kobunshi Ronbunshu, **43**, 83 (1986).
20. R.A.A. Muzzarelli, C. Lough, and M. Emanuelli. Carbohydr. Res. **164**, 433 (1987).
21. R.G. Beri, J. Walker, E.T. Reese, and J.E. Rollings. Carbohydr. Res. **238**, 11 (1993).
22. I. Hall, D. Gillespie, K. Hammons, and J. Li. Adv. Chitin Sci. **1**, 361 (1996).
23. A. Denuziere, N. Yagoubi, A. Baillet, and D. Ferrier. S.T.P. Pharma. Sci. **5**, 481 (1995).
24. G.G. Maghami and G.A.F. Roberts. Makromol. Chem. **189**, 195 (1988).
25. M.R. Kasaai, J.A. Arul, and G. Charlet. Proc. 7th Int. Conf. on Chitin and Chitosan. Lyon, France. 1997. p. 421.
26. Y. Qin. The production of fibres from chitosan. Ph.D. Thesis 12085, University of Leeds, England. 1991. p. 70.
27. C. Yomota, T. Miyazaki, and S. Okada. Colloid Polym. Sci. **271**, 76 (1993).

List of abbreviations

DDA:	degree of deacetylation
GPC:	gel permeation chromatography
HPLC:	high-performance liquid chromatography
LS:	light scattering
LALLS:	low-angle laser light scattering
MALLS:	multiple angle laser light scattering
OM:	osmometry
SD:	sedimentation and diffusion
SEC[3]:	size exclusion chromatography with three detectors (refractive index, in-line viscosity, and light scattering)
VIS:	viscometry

[2] Dr. W.S. Wong. Viscotek Corporation, Houston, Texas. Private communication, January, 1998.

© 1998 NRC Canada

Gold nanoclusters reductively deposited on porous silicon: morphology and electronic structures

I. Coulthard, S. Degen, Y.-J. Zhu, and T.K. Sham

Abstract: Utilizing porous silicon as a reducing agent and a substrate, gold complex ions $[AuCl_4]^-$ were reduced from aqueous solution to produce nanoparticles of gold upon the surface of porous silicon. Scanning electron microscopy (SEM) was utilized to study the morphology of the porous silicon layers and the deposits of gold nanoparticles. It is found that preparation conditions have a profound effect on the morphology of the deposits, especially on porous silicon prepared from a p-type wafer. The gold nanoparticles, varying from micrometric aggregates of clusters of the order of 10 nm, to a distribution of nearly spherical clusters of the order of 10 nm, to strings of ~10 nm were observed and compared to bulk gold metal using X-ray diffraction (XRD), X-ray photoelectron spectroscopy (XPS), and X-ray absorption spectroscopy (XAS). These techniques confirm and complement the SEM findings. The potential for this reductive deposition technique is noted.

Key words: gold nanostructures, reductive deposition, porous silicon, morphology, X-ray spectroscopy.

Résumé : Utilisant de la silice poreuse comme agent de réduction et comme substrat, on a réduit des ions complexe d'or, $[AuCl_4]^-$, présents en solutions aqueuses et on a obtenu des nanoparticules d'or sur la surface de la silice poreuse. On a utilisé la microscopie électronique à balayage (MEB) pour étudier la morphologie de couches de silice poreuse et des dépôts de nanoparticules d'or. On a trouvé que les conditions de préparation ont un effet important sur la morphologie des dépôts, particulièrement sur la silice poreuse préparée à partir de plaquettes de type p. On a observé des nanoparticules d'or dont la taille varie de celle d'agrégats micrométriques de l'ordre de 10 nm, à celle d'agrégats pratiquement sphériques de l'ordre de 10 nm, à celle de chaînes d'environ 10 nm et on les a comparées à de l'or métallique à l'aide de la diffraction des rayons X (DRX), de la spectroscopie photoélectronique des rayons X (SPX) et de la spectroscopie d'absorption des rayons X (SAX). Ces techniques confirment et servent de complément aux observations faites par MEB. On note le potentiel de cette technique de dépôt par réduction.

Mots clés : nanostructures d'or, dépôt par réduction, silice poreuse, morphologie, spectroscopie des rayons X.

[Traduit par la Rédaction]

Introduction

Porous silicon (PS) is formed during the electrochemical etching of a silicon wafer in an HF solution (1). On the micro scale, the resultant porous silicon layer is a series of vertical micron-sized channels generated by current focussing during the etching process (2). At the nano scale, however, the layer is more akin to a sponge-like network of silicon containing many pillars, wires, and nodules with nanometre scale (3). The surface of freshly prepared porous silicon is passivated by hydrogen. Oxidation takes place when PS is exposed to the ambient atmosphere. Henceforth we use "ambient" to denote ambient atmosphere conditions; e.g., ambient porous silicon means porous silicon exposed to ambient air, etc. Thus the vast internal surface of a typical porous silicon sample is covered with a thin layer of silicon oxide.

An explosion of interest in porous silicon was generated when Canham (4) reported intense room temperature luminescence, from porous silicon, in the visible spectral region. This behaviour is completely unlike bulk crystalline silicon, an indirect band-gap material with a band gap of 1.1 eV. Bulk crystalline Si luminesces only very weakly in the IR region. The most widely accepted theory for the origin of the luminescence in PS is that the nano dimensions of the silicon features in porous silicon create a quantum size effect that widens the band-gap energy into the visible and relaxes the effect of momentum selection rules upon the luminescence (5, 6). Many papers on porous silicon have been published, including studies of the suitability of this material for

Received February 2, 1998.

I. Coulthard, S. Degen, Y.-J. Zhu,[1] and T.K. Sham.[2] Department of Chemistry, The University of Western Ontario, London, ON N6A 5B7, Canada.

[1]On leave from Department of Chemistry, University of Science and Technology of China.
[2]Author to whom correspondence may be addressed. Telephone: (519) 679-2111, ext. 6341. Fax: (519) 661-302.
E-mail: Sham@uwo.ca

© 1998 NRC Canada

optoelectronic devices (7), of the insulating layer in silicon in insulator (SOI) technology (8), of the preparation of stress-free silicon nitride/oxynitride films (9), and as a chemical (10) sensor.

Although porous silicon research has received enormous attention (11), one important property, its ability to act as a modest reducing agent (12, 13), is relatively unexplored. Porous silicon can effectively reduce from solution any system with a positive half-reduction potential with respect to hydrogen (13, 14). That is, PS acts like a hydrogen electrode. It is immediately apparent that noble metals with a positive reduction potential would be ideally suited for this process. If the result of the reduction is a solid element, then porous silicon will act as both a reducing agent and a substrate for the deposition of the solid material. In solutions of noble metal ions, the ions are reduced to atoms that will diffuse to form metal clusters or aggregates onto the vast internal surface of the porous silicon (15, 16). The objective of this work is to investigate the effect of the preparation conditions upon the morphology of Au clusters on porous silicon. Based on previous studies (Pd, Ag, Pt, Au, Cu, etc. on PS) (13–16), we expect that Au nanoparticles with various dimensions will form under controlled conditions and these nano systems will generally exhibit electronic properties different from those of the bulk materials (17–19). Thus this study will have interesting implications for the fabrication of nanostructures in electronic and chemical materials applications such as interconnects and catalysis, respectively. In the latter, small particle size and increased surface area are beneficial (20).

In this report, we concentrate our study upon the reduction of $[AuCl_4]^-$ from an aqueous solution by porous silicon. This results in the deposition of Au onto the surface of porous silicon. The effects of the preparation conditions of the porous silicon, and of the conditions of deposition, upon the morphology of the Au deposits were studied. Emphasis is placed on the systematics of Au deposition on p-type based porous silicon. The structure and electronic properties of the Au deposits on porous silicon were examined with X-Ray powder Diffraction (XRD), X-ray Photoelectron Spectroscopy (XPS), and X-ray Absorption Near-Edge Structure (XANES). We will also report the effect of Au deposition on the luminescence property of porous silicon using a synchrotron light induced luminescence technique, sometimes known as XEOL (X-ray Excited Optical Luminescence) (21, 22).

Experimental

Porous silicon samples were prepared as described earlier (13) using a single electrochemical cell configuration with the silicon wafer acting as the anode and a Pt foil as the counter electrode. Both p-type (B doped) and n-type (As doped) Si (100) wafers with resistivity in the range of 1–10 Ω cm were utilized to produce porous silicon. A 1:1 mixture of 48 wt.% HF and absolute ethanol was used as the cell electrolyte. Anodization time was typically 20 min with a current density of 1–500 mA/cm^2. For p-type samples, etching is the dominant process (23) at a current density below 100 mA/cm^2 whereas for n-type samples the current density requirement is much higher (>100 mA/cm^2). The porous silicon thus prepared was left attached to the silicon substrate as a thin layer with thickness typically of 10–100 μm. The porous silicon layers, though passivated in HF by hydrogen, readily oxidize when expose to air. Samples could be *refreshed* with HF to remove the surface oxide layer.

Au was reductively deposited onto the porous silicon using aqueous solutions of $Na[AuCl_4]$. The deposition took place either by immersion of the porous silicon sample into a $Na[AuCl_4]$ solution or by the placement of a surface tension bubble of the solution on the top of the porous silicon layer. Solution concentration of $[AuCl_4]^-$ (pH = 3) was varied from 1×10^{-3} M to 1×10^{-4} M and the deposition time was varied from 15 s to 5 min. It is interesting to note that a 1 mL portion of a 1×10^{-4} M solution contains ~6×10^{16} Au atoms, which amounts to ~60 monolayers/cm^2. It was observed that oxidation in ambient air inhibited the reductive deposition, which would only take place effectively when a freshly prepared sample or an HF "refreshed" sample was utilized. During the deposition, evolution of bubbles of hydrogen is evident. Although the details of the mechanism are not clearly understood, it is known that Au is reduced from Au(III) to Au(0) and the surface hydrides of PS are oxidized to H_2 gas, leaving behind some surface Si dangling bonds that will be immediately oxidized upon exposure to the ambient atmosphere.

The morphology of the substrate and the Au deposits was investigated with a Hitachi S-4500 field emission scanning electron microscope at Surface Science Western (SSW). A voltage of 10 kV was used in the measurement. We have also carried out X-ray studies on several selected samples. X-ray powder diffraction patterns were recorded with a Rigaku Gieger Plex X-ray diffractometer using a Cu Kα source. X-ray photoelectron spectroscopy was carried out at SSW using an SSX-100 small spot spectrometer that is equipped with a monochromatic Al Kα source and a channel plate detector. X-ray absorption experiments in the soft X-ray range (Si K-edge and Au $M_{3,2}$-edge) were carried out at the Canadian Synchrotron Radiation Facility (CSRF), which is located at the Synchrotron Radiation Center, University of Wisconsin–Madison. Au $L_{3,2}$-edge measurements were made at the X11A beamline of the National Synchrotron Light Source at Brookhaven National Laboratory. Synchrotron light induced optical luminescence measurements were carried out at the Mark II grasshopper beamline at CSRF using a J-Y H10 monochromator and a Hamamatsu R943–02 PMT (photomultiplier tube).

Preparation, morphology, and structure of Au deposits on porous silicon

The chemistry of the process is clearly a redox reaction in which the surface of porous silicon is a reducing agent and the $[AuCl_4]^-$ ion is the oxidizing agent. Although the mechanism of the process is still not clearly understood, it is conceivable that the first step must be the diffusion of the complex ion to the surface, followed by adsorption and reductive detachment of the chloride ion. After that, nucleation takes place and the observed morphology results. The last step is perhaps the most complex one because it depends on the surface condition of the substrate and its history. The evolution of hydrogen gas suggests that the surface hydrides are involved in the process. This is also supported by the

© 1998 NRC Canada

Fig 1. SEM images of two typical porous silicon samples. (*a*) Normal image, p-type (B doped) Si (100) wafer, 50 mA/cm^2, 20 min; (*b*) profile image, same sample as (*a*); (*c*) normal image, n-type (As doped) Si (100), 300 mA/cm^2, 20 min; (*d*) profile image, same sample as (*c*).

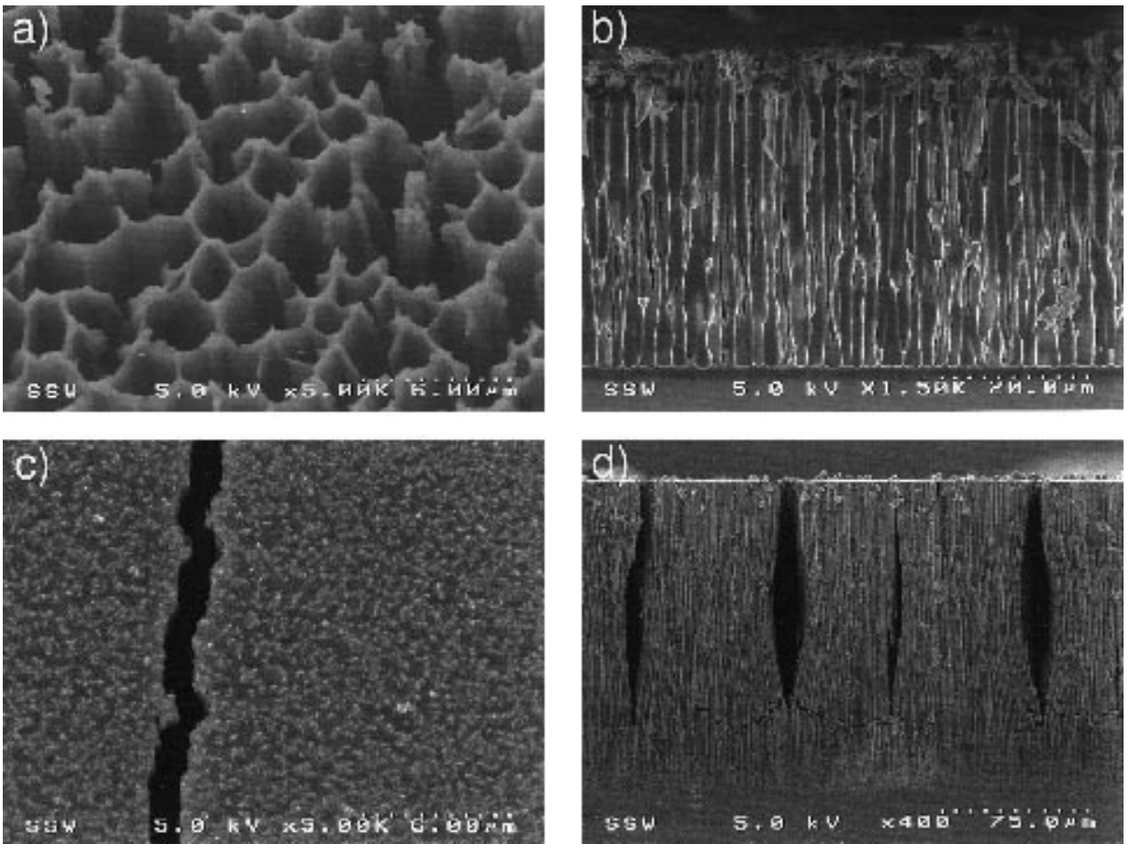

fact that Au deposition on an oxidized PS was negligible.[3] In addition, the amount of Au deposited depends on the $[AuCl_4]^-$ concentration and deposition time.[4] The process is complicated by the gas bubbles trapped inside the microchannels. In several runs we used an ultrasonic bath to minimize the effect of trapped bubbles by agitation. This process further alters the morphology of the Au aggregates. Some examples will be given. However, in this report, we remain focussed on results obtained under typical conditions. More details concerning the mechanism must await further kinetics studies and will be reported elsewhere.

Figure 1 shows the SEM micrographs, which reveal the morphology of two types of porous silicon layers. Figures 1*a* and 1*b* are SEM images (normal and cross sectional) of a sample generated using a p-type Si(100) wafer with a current density of 50 mA/cm^2 for 20 min. Figures 1*c* and 1*d* are SEM images of a sample using an n-type wafer with a current density of 300 mA/cm^2 for 20 min. These images clearly show the effect that the choice of wafer and preparation conditions can have upon the resulting morphology of the porous silicon layer. The current density utilized to generate the n-type sample is much higher due to the nature of the doping (23). Nevertheless, this difference in current density has had an effect upon the thickness and the porosity of the porous silicon layers. The images clearly show a film thickness of ~30 μm and ~120 μm for the p-type and n-type samples, respectively. In general, higher current densities produce thicker layers. For the p-type samples, there is a linear relationship between current density and thickness up to 100 mA/cm^2. The thickness for the 20 mA/cm^2 film on p-type PS that we used extensively as the substrate for Au deposition is ~10 μm. In these images, the micron-sized channels in the n-type sample appear more uniform and straight than in the p-type sample with the exception of the areas in the n-type where the thickness of the sample has caused significant stress effects as evidenced by the sample fractures deep in the layer (24).

The normal SEM images also reveal significant information. Both samples show micron-sized vertical channels; however, there is a distinct difference in channel porosity. The p-type sample shows a network of channel walls with occasional incidence of channel coalescence. Although, due to poor contrast, the n-type samples show no clearly visible channel walls as seen in the p-type PS, the dark areas are the channel

[3] This is supported by positron and X-ray fluorescence results, unpublished.
[4] Supported by preliminary kinetics data on similar systems where we correlated the Au $M_{3,2}$-edge jump with deposition time and concentration.

© 1998 NRC Canada

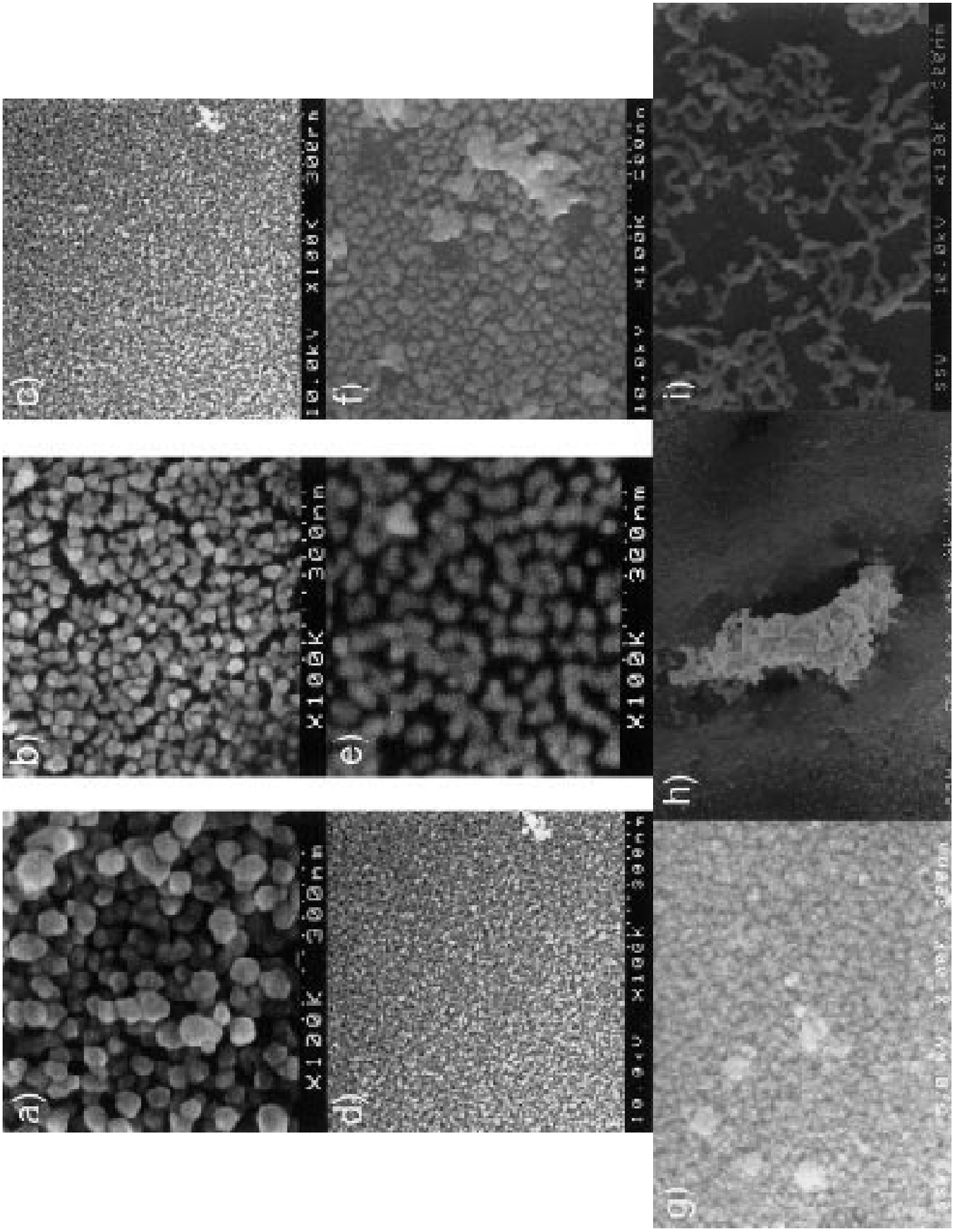

© 1998 NRC Canada

Fig. 2. SEM images of Au reductively deposited onto different porous silicon samples. (*a*)–(*c*): Au (1×10^{-3} M solution) deposited onto p-type PS (20 mA/cm^2, 20 min) with deposition time of 5 min, 1 min, and 15 s, respectively; (*d*) same as (*c*); (*e*) and (*f*): Au (4.3×10^{-5} M solution, 5 min) deposited onto p-type PS with intermittent and continuous ultrasonic agitation, respectively; (*g*) Au deposited onto n-type PS; (*h*): Au (1×10^{-4} M, 5 min, on freshly prepared p-PS); (*i*) Au (1×10^{-4} M, 1 min on freshly prepared p-PS).

openings and they are on average significantly smaller than those of the p-type PS. Thus the microchannels on n-type PS have a higher density than those of the p-type PS. It appears that increased current density has increased the porosity (hence a larger internal surface area) of the n-type sample relative to the p-type PS. This is also borne out in the reactivity of the surface towards the reduction of $[AuCl_4]^-$ ions (see below).

Figure 2 shows the SEM images of a number of porous silicon samples upon which Au has been reductively deposited. Figures 2*a*–2*c* are Au on p-type PS samples prepared with different deposition conditions (1×10^{-4} M $[AuCl_4]^-$ for 5 min, 1 min, and 15 s, respectively). They clearly show the systematics of the cluster-size dependence on deposition time. In this series of depositions, the same PS substrate and current density (20 mA/cm^2) were used. It is apparent that the 5 min deposition (Fig. 2*a*) results in clusters in the range of 30–40 nm uniformly distributed on the surface. Reducing the deposition time to 1 min yields smaller clusters (10–20 nm, Fig. 2*b*) while 15 s deposition results in very small clusters that appear as white dots. Cross-sectional SEM shows that the metal deposits generally do not penetrate the entire PS layer (25). For Au, 1–2 μm is the typical thickness. The lack of penetration depth relative to the thickness of the PS may be due to trapped gas bubbles that inhibit the diffusion of the liquid into the PS sponge. Figures 2*d*–2*f* compare the images of Au/p-type PS under three conditions: (*i*) without ultrasonic agitation, (*ii*) with intermittent agitation, and (*iii*) with constant agitation. Figure 2*d* is the same as Fig. 2*c* while Figs. 2*e* and 2*f* correspond to samples prepared with a 4.3×10^{-4} M $[AuCl]_4^-$ solution for a deposition time of 5 min. We can see that samples with agitation treatment exhibit still different patterns from those without agitation. This procedure usually increases the deposition depth into the PS layer. On the n-type samples (Fig. 2*g*), nanometre-sized clusters of gold are generally formed (bright dots and patches). These clusters seem to form nominally anywhere upon the surface of the sample and soon coalesce to form a thin but uniform layer of gold across the entire surface. This behaviour is in contrast to the p-type porous silicon where the morphology of Au deposits is much more variable depending on the preparation conditions (Figs. 2*a*–2*c*). The morphology of the deposited Au also varies somewhat depending on whether a freshly prepared or a refreshed sample is used, and upon the history of the specimen. In one example, Fig. 2*h*, the deposits of gold from freshly prepared PS are concentrated near the pores where there is a larger number of high-energy sites; smaller clusters coalesce to form a very large cluster on the order of micrometres. Grains of a size of the order of 10 nm are clearly seen. In another example, a very curious network of nanoscale strings of gold is formed on a freshly prepared PS (Fig. 2*i*).

The difference between the morphology of Au on n-type and p-type based PS seems to be related to the nature of the doping, the porosity, and the effect these have on the reductive deposition, which requires the presence of surface hydrides. The reduction is facilitated by higher porosity, which yields a larger internal surface and negative carriers in n-type PS. The p-type PS must rely more upon surface defects and other high-energy sites such as dangling bonds for initial Au nucleation, and thus many p-type samples show preferential deposition of the gold near the pores. The difference among Au/p-type PS samples is also related to the porosity of the substrate and the time of deposition. Freshly prepared samples that receive little exposure to ambient conditions tend to deposit gold preferentially near the pores as in Fig. 2*h*. Samples that are "refreshed" with HF just before deposition, on the other hand, tend to produce a more uniform distribution of Au clusters, as observed in Figs. 2*a*–2*c*.

The structure of these clusters revealed in SEM can be confirmed with X-ray powder diffraction measurements, which show diffraction patterns characteristic of fcc Au. Figure 3 shows the broadening in the Au (111) diffraction peaks as the Au cluster size decreases (Fig. 2*a* to Fig. 2*b*). The width of the diffraction line *B* can be related to the crystalline size of the cluster according to the Scherrer equation (26):

$$[1] \qquad \tau = \frac{K\lambda}{\beta_\tau \cos\theta}$$

where *K* is the shape factor and usually has a value of 0.9, λ is the wavelength of the X-rays, β_τ is given by $(B^2 - b^2)^{1/2}$ in radian units where *B* is the width at half-maximum of the observed diffraction peak (2θ) of the small crystalline clusters, *b* is the width of Au to which the contribution is mainly that of the X-ray photon width and the Darwin width of the crystal plane, and θ is the Bragg angle.

Using the values from Fig. 3 (β_τ of 1.396×10^{-2} rad and 8.56×10^{-3} rad, respectively, for the 1 min and 5 min samples), we estimated an average crystallite size of ~10 nm and ~17 nm for the Au clusters corresponding to Figs. 2*a* and 2*b*, respectively, in semiquantitative agreement with the SEM observation. These values are slightly smaller than seen in the SEM and obviously have large uncertainties since the width arises from a distribution of cluster sizes. They nevertheless represent an average of various cluster sizes. A small shift to higher 2θ value is also observed at 38.2° and 38.4° for the 5 min and 1 min samples, respectively, relative to 38.09° for Au powder. This observation indicates that the volume of the unit cell of Au in the clusters shrinks slightly (by ~1% and 1.4%, respectively) relative to bulk Au (a = 4.0786 Å). This slight compression of the Au lattice is of some interest in connection with the electronic structure of these clusters and will be discussed below.

Electronic structure from X-ray spectroscopy

The electronic structure of the Au deposits was studied by XPS, which probes the core level (4*f*) binding energies and the valence band structure of the clusters, and with Au $L_{3,2}$-

© 1998 NRC Canada

Fig. 3. XRD diffraction pattern, Au (111), for Au/PS (Figs. 2*a* and 2*b*) vs. Au.

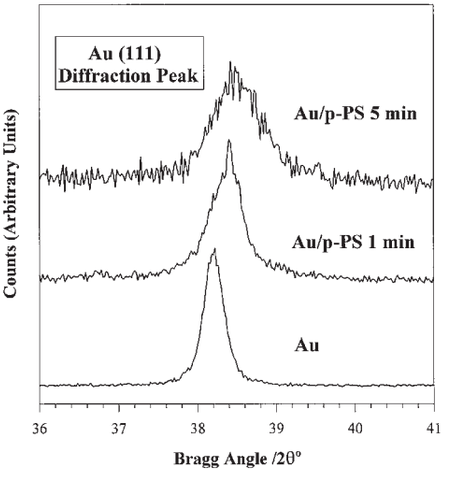

Fig. 4. Typical XPS for Au/p-PS and Au; upper panel, Au 4*f*; lower panel, Au valence band.

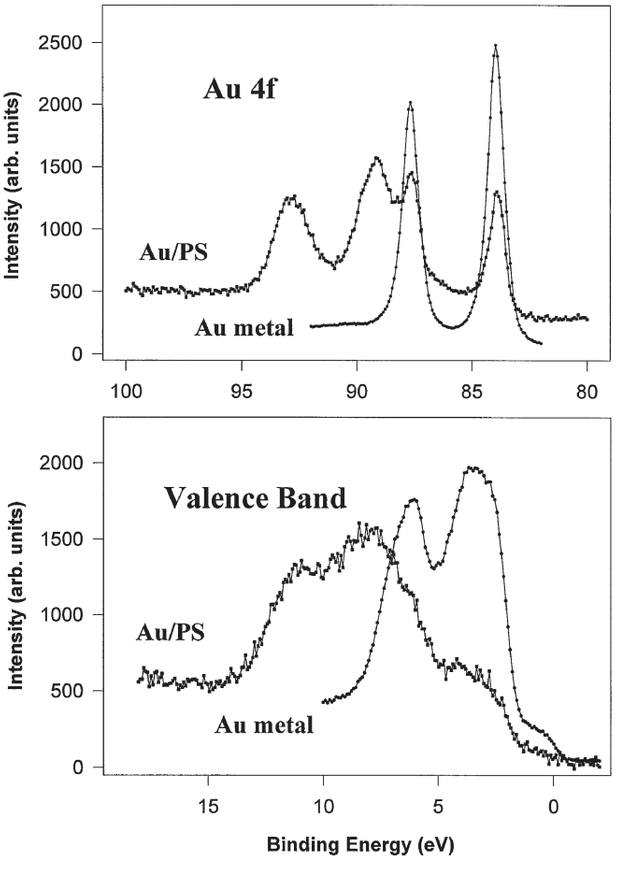

and $M_{3,2}$-edge XANES (X-ray Absorption Near Edge Structures), which probe the unoccupied densities of state of *d* character above the Fermi level. The Au 4*f* levels together with the valence band spectra can be used to identify the presence of small Au clusters. It has been shown that Au

Fig. 5. Au 4*f* for Au/p-PS, Au/n-PS, and Au metal. Charging in the spectrum for Au/p-PS has been compensated with a flood gun and the peak maximum is aligned to that of the Au metal.

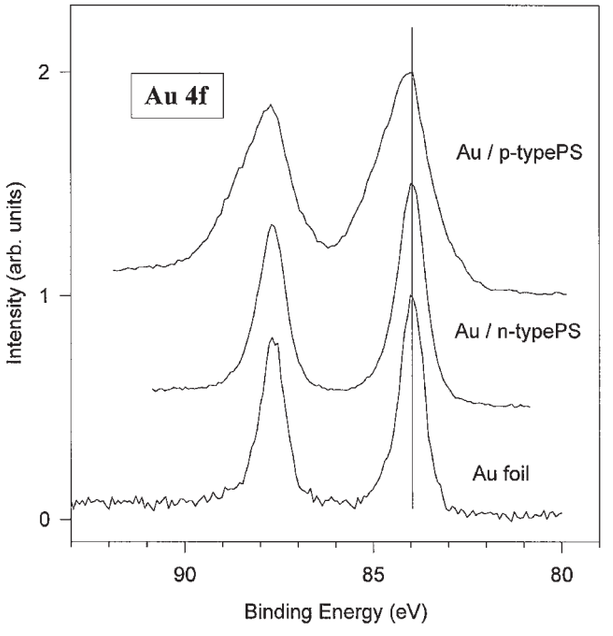

clusters of ~10 nm and smaller exhibit a progressive positive 4*f* core level shift relative to that of Au in the bulk (18, 19, 27). This is due to a combination of changes in electron distribution (rehybridization), an initial state effect, and final state screening. The Au 4*f* core level shift ΔBE between Au cluster and Au metal (bulk) can be expressed as

$$[2] \qquad \Delta BE = -\Delta\epsilon_1 - \Delta\phi$$

where the initial state contribution to the binding energy, $-\Delta\epsilon_i$, is due to the difference in the one-electron energy of the 4*f* level (ϵ is a negative value) and is due primarily to the change in electronic configuration (rehybridization involving 5*d* and conduction electrons of 6*s* and 6*p* character) (28) and

$$[3] \qquad \Delta\epsilon_i = \Delta n_d F(5d,4f) + \Delta n_c F(\text{cond},4f) + \Delta S_f$$

The Δn terms in eq. [3] are changes in 5*d* and conduction electron (primarily 6*s*) counts between Au in Au cluster and in Au metal. The *F* terms are the Coulombic integral where F_d is significantly larger than F_c (28). Thus a *d* charge loss (decrease in *d* count) would contribute to a positive binding energy shift. The ΔS_f term is the difference in final state screening, which is negligible for metallic systems and becomes increasingly important as the cluster becomes smaller (18). A poorly screened atomic site would contribute to a positive binding energy shift. Finally, the $\Delta\phi$ term is the difference in work function between bulk Au and Au cluster and ϕ is not well known for a small cluster. It also depends on the surface conditions of the cluster. It has been reported that for Au clusters of less than 150 atoms, the final state screening becomes important. That is, the cluster becomes less metallic (18). The latter can account for the fact that the observed Au 4*f* shift is often larger than would be expected based on initial effect alone for pure Au. The Au 5*d* band is also informative. The Au *d* band normally exhibits a quasi

© 1998 NRC Canada

Fig. 6. Au 4*f* XPS of the strings (Fig. 2*i*), the 1 min deposition (Fig. 2*b*), and Au metal. The strings spectrum has been shifted by ~5 eV to offset charging.

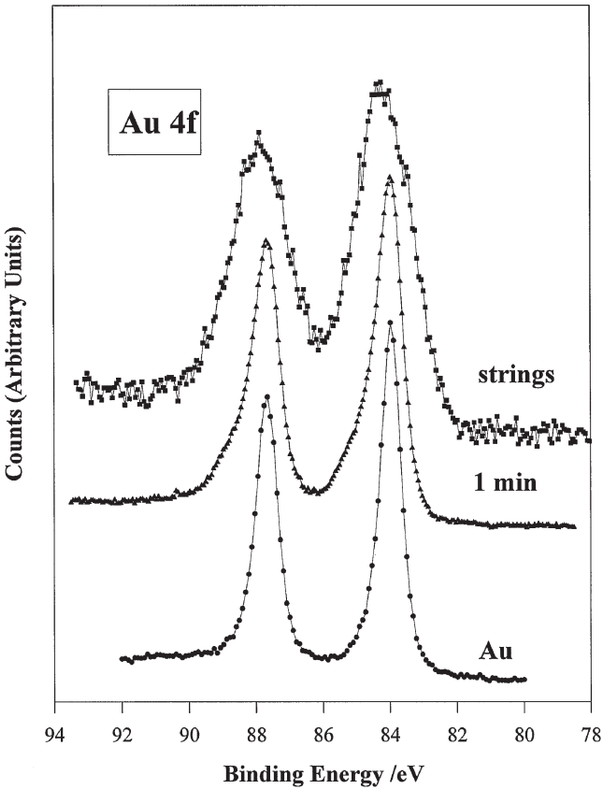

Fig. 7. Au valence band spectra for selected samples (Figs. 2*a*, 2*b*, and 2*i*) and Au metal.

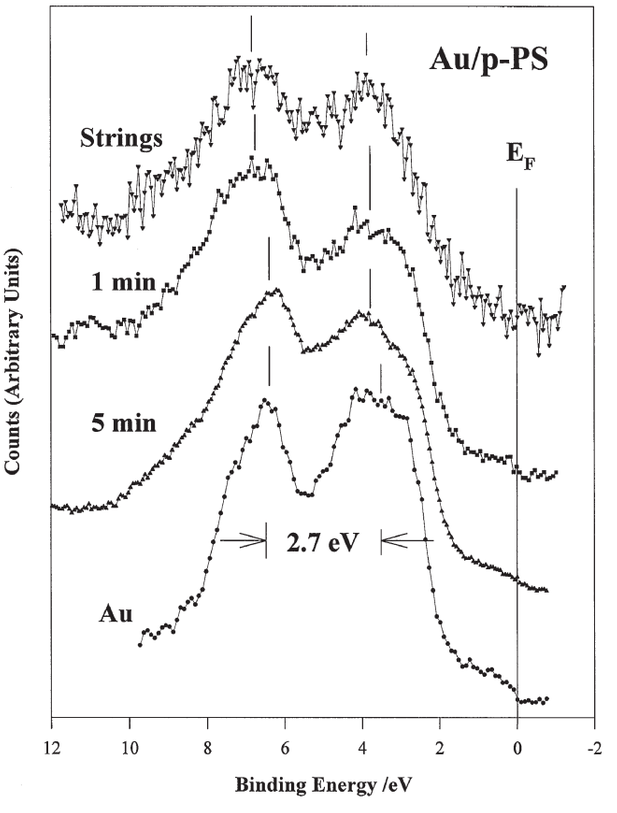

$d_{5/2}$ and $d_{3/2}$ doublet with a separation of ~2.7 eV as the result of strong spin-orbit and *d–d* interaction. This separation is considerably greater than the spin-orbit interaction, ~1.5 eV, of atomic Au. Phenomenologically, the *d* band doublet separation Δ can be expressed as the sum of contributions from the atomic spin-orbit interaction $\Delta_{s.o.}$ and a band formation term Δ_e where the latter is related to the degree of *d–d* interaction (number of like nearest neighbours: the higher the coordination number the larger the interaction) (28):

$$[4] \qquad \Delta = [\Delta_{s.o.}{}^2 + \Delta_e{}^2]^{1/2}$$

When the crystalline cluster becomes small, the number of surface atoms increases. For example, in a spherical Au cluster with a 17 nm diameter, the surface atoms constitute ~8% of the total atoms. The effect is a reduction in the coordination number of the Au atoms on average and a reduction in the doublet separation in the valence band.

Figure 4 shows the Au 4*f* core level and valence band of Au on a typical freshly prepared p-type PS substrate (Fig. 2*h*) relative to Au metal. It is interesting to note that two sets of Au 4*f* doublets appear, one at the same binding energy as that of Au metal (83.97 and 87.68 eV) and the other at several electronvolts higher binding energy. It turns out that the higher binding energy doublets are due to charging, indicating that a significant fraction of the nanocrystallites, most likely those of smaller sizes, are either becoming nonmetallic or are in poor electrical contact with the substrate. When a low-energy e-flood gun was used during XPS measurement, the charging peaks coalesce towards the higher binding energy side of the main Au peak (Fig. 5). This observation suggests that they can be attributed to smaller Au clusters since it is well known that the Au 4*f* binding energy increases as the crystallite size decreases (18, 19, 27). The Au valence band shows a similar behaviour where the *d* bands for the smaller clusters are shifted to higher binding energy. The observation of two sets of Au 4*f* peaks is common for Au on p-type PS depending on the preparation conditions (Au 4*f* for Fig. 2*a* exhibits a similar pattern). However, the higher binding energy doublet can be the sole component for samples at shorter deposition time (15 s) or with unusual dimensions (Fig. 2*i*). It is clear that the normal Au 4*f* peaks arise from the large aggregates near the micron pores where high densities of active sites (hydrides) are available for the redox reaction. The higher binding energy 4*f* peaks in Fig. 4 are attributed to the smaller clusters dispersed throughout the PS network in the near surface region. These results are in good accord with the SEM and XRD measurements.

Figure 5 shows a comparison of the Au 4*f* XPS for Au/p-type PS, Au/n-type PS, and Au metal. The effect of charging for Au/p-type PS (Fig. 4) has been removed with a low-energy electron flood gun. The high binding energy doublet seen in Fig. 4 now becomes a shoulder on the higher binding energy side of the main peaks. The broadening and the

© 1998 NRC Canada

Fig. 8. Au $L_{3,2}$-edge XANES for Au/p-PS, Au/n-PS, and Au metal.

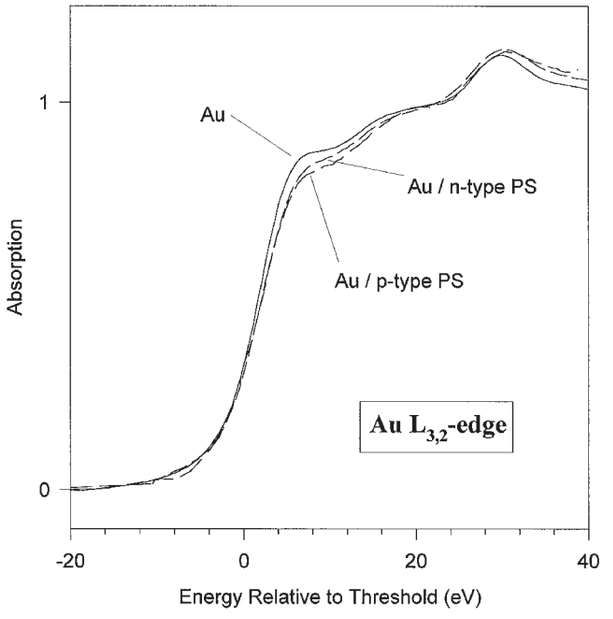

Fig. 9. Optical luminescence from ambient PS and Au deposited PS. The excitation energy of 100 eV corresponds to energy just above the PS Si $L_{3,2}$ threshold but below that of SiO_2.

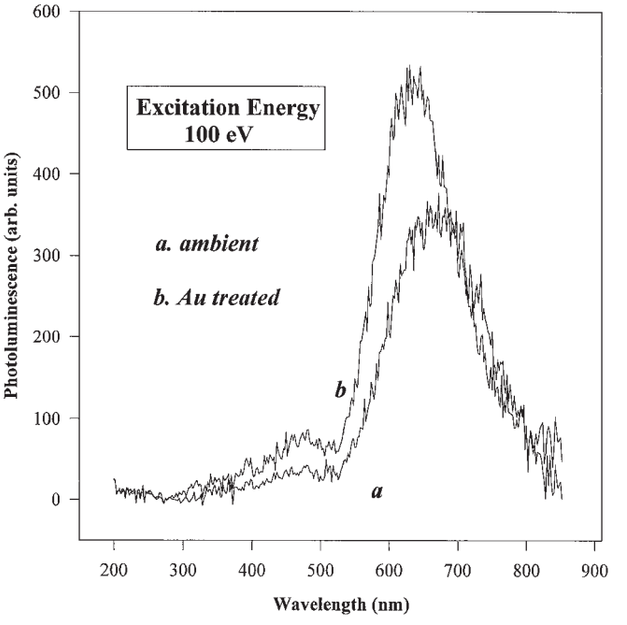

asymmetry of the peak confirms the presence of small clusters. It is interesting to note that although the effect of charging is quite common among samples of Au/p-type PS, it is hardly observed for Au/n-type PS where Au apparently wets the surface better. This is probably because Au on n-type PS tends to form more uniform films and the Au deposits are in good electrical contact with the substrate, as seen from the SEM results. This property is related to the electron-rich dopant, which possibly lowers the surface energy, and to the significantly smaller pore size and higher porosity (denser active sites) of the n-type based PS.

A comparison of the Au 4*f* linewidth is given in Fig. 6 for the 1 min deposition (Fig. 2*b*) and the strings (Fig. 2*i*) together with that of Au metal. The spectrum for the Au strings has been shifted by ~5 eV (charging) so that it aligns with that of Au metal. It is interesting to note that the Au 4*f* spectrum for the strings shows no sign of the normal Au 4*f* for large aggregates/clusters, indicating that no large clusters are formed on this surface and the Au strings are not in good electric contact with the substrate. The broadening/splitting of the Au 4*f* peaks in Au strings is due to differential charging and to a distribution of clusters with various sizes including those not readily revealed by the SEM. It is conceivable that some of the small deposits are sitting on top of an oxide layer formed after deposition and exposure to ambient air. This results in poor electrical contact. The broadening and asymmetry on the higher binding energy site of the Au 4*f* peaks of the 1 min sample again is characteristic of the presence of small clusters as described earlier (18, 19, 28).

The valence band spectra of several representative samples are shown in Fig. 7. All exhibit the characteristic Au 5*d* band. It should be noted that the Au 5*d* is the dominant signal because its photoemission cross section is significantly larger than the valence band of Si and the technique is surface sensitive. Several interesting features can be seen as the dimension of the Au deposits shrinks. First, the sharp rise of the top of the *d* band (~2 eV) in Au becomes much less steep in Au/PS as the coverage (deposition time) decreases. This behaviour is due to a reduction in coordination number and is typical of smaller cluster size as observed previously (18, 19). Second, the centre of gravity of the *d* band shifts to higher binding energy and associated with it is a slight broadening in the overall width. Since Au has the maximum coordination number of 12 in the metal and the *d*-band width is determined by the number of like nearest neighbours, it is impossible to have a Au *d* band of a cluster wider than that of the Au metal; we attribute this broadening to the overlapping of a distribution of clusters of different size, some of which exhibit a larger final state screening term, hence a higher binding energy shift of its centre of gravity despite a reduction in the doublet separation in an individual cluster (eq. [4]). The contribution of small-dimension Au deposits is also borne out in the shift of the quasi-$d_{3/2,5/2}$ peaks to higher binding energy, as previously observed (18, 19), and a negative surface atom core-level shift in Au.

The electronic structures of these Au deposits have also been investigated by X-ray Absorption Near Edge Structures (XANES). This technique measures the absorption coefficient above an absorption edge of an element in a chemical environment and permits the probing of the unoccupied densities of states just above the absorption edge. In the case of Au, the Au $L_{3,2}$-edge ($2p_{3/2,1/2}$) and $M_{3,2}$-edge ($3p_{3/2,1/2}$) are ideally suited for this investigation because we can probe the unoccupied *d* states above the Fermi level via dipole transition selection rules (29, 30). Although the *d* band in Au is nominally full, it has been shown that *d* and non-*d* (*sp*) rehybridization pushes some *d* character to above the Fermi level and the rehybridization of *d* and non-*d* electrons in Au

© 1998 NRC Canada

Fig. 10. Si L-edge absorption spectrum recorded in the total electron yield mode for the PS oxidized in air before and after Au deposition of which the luminescence spectra are shown in Fig. 9 together with an HF refreshed sample. Only surface oxide was detected for the ambient PS and Au/p-PS samples. After the surface oxide was removed with HF, the PS Si $L_{3,2}$-edge spectrum emerges.

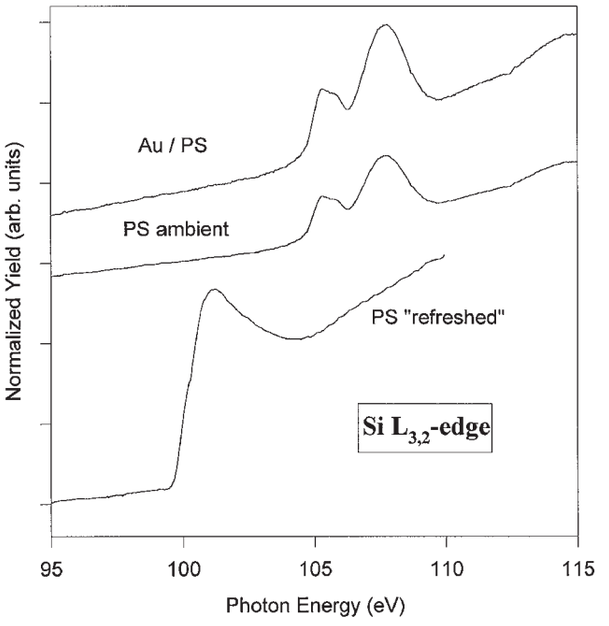

has a significant and measurable effect in XPS and XANES on alloy formation (30, 31). In general, the first peak at the L_3 absorption edge is related to the unoccupied densities of *d* states associated with the absorbing atom in the materials of interest. A difference in intensity (area under the peak) reflects the change in densities of unoccupied *d* states above the Fermi level. All the resonance features above the threshold are characteristic of the extended local structure (several shells) of the absorbing atom. It has been shown with multiple scattering calculations that 5–6 shells of atoms are required for the cluster to reproduce a XANES spectrum similar to those of bulk metal (31). Thus XANES is a complimentary tool to XPS for the characterization of the structure and bonding of the specimen.

Figure 8 shows the Au $L_{3,2}$ XANES of representative Au/p-type PS and Au/n-type PS. Similar data have also been obtained at the $M_{3,2}$-edge (16). It is important to note that charging is not a problem in XANES measurements, therefore it will not induce any energy shift. From Fig. 8, we see that the Au metal spectrum exhibits a three-peak pattern within the first 40 eV above the threshold. These features are characteristic of transition and noble metals with an fcc structure except for the first peak for which the intensity varies dramatically depending on the number of *d* holes associated with the metal (30). It is evident from the spectra that Au deposits on PS have an fcc structure and generally exhibit a small but noticeable decrease in the intensity of the first peak above the edge (sometimes known as a whiteline). This indicates that, on average, small Au deposits (isolated clusters and aggregates alike) gain *d* charge (lose *d* hole count via rehybridization) relative to Au metal. This observation indicates that for small Au clusters supported on porous silicon, the *d–d* interaction is even stronger than in bulk metal. This would favour $s \rightarrow d$ rehybridization, reducing the *d* hole count. This observation is consistent with the slightly compressed lattice constant of the clusters on average as observed in XRD (Fig. 3).

We now explore further the implication of the *d* charge gain in Au clusters by considering a cluster as an intermediate between atoms and bulk metal. In transition metals in general, the electronic configuration in an atomic state is usually ns^2, $(n-1)d^m$ where *n* varies from 4 to 6 and *m* is the number of *d* electrons, which is nominally 9 for Au (31, 32). However, metals tend to adopt a configuration of ns^1, $(n-1)d^{m+1}$ or $6s^1$, $5d^{10}$ for Au. In addition, *s–d* rehybridization pushes a small amount of *d* character above the Fermi level yielding $ns^{1+\delta}$, $(n-1)d^{10-\delta}$ where δ is of the order of ~0.1 e. Thus one expects that as atoms assemble to become a cluster and then a bulk metal, the *d* configuration for Au clusters would be somewhere between d^9 and $d^{10-\delta}$. This notion, though in line with a higher binding energy Au 4*f* shift for the Au clusters due to the reduction of *d* count (*d* electrons screen the core better than the itinerant conduction electrons), does not take into account structural and surface effects and does not fit the observed XAS. Thus it is plausible that the XPS observation of higher binding energy shift for the Au clusters may be due largely to a final state effect complicated by a modified structure, surface effects, and charging. Besides, it is known that the surface atoms in Au metal exhibit a 4*f* shift to lower binding energy relative to that of the bulk (33). It appears then that although it is still useful to associate the XPS high binding energy shoulder with small Au clusters (~10 nm and smaller), as reported previously for Au clusters on graphite (18) and on pyrite (27), more work must be done on Au clusters to reveal the true origin of the shift in XPS and the behaviour of the whiteline in XAS.

The effect of Au deposition on the luminescence of porous silicon

Figure 9 shows the luminescence property of an ambient PS sample (p-type, 20 mA/cm^2, 20 min) before and after Au deposition. The Au deposit was made with 1 min deposition with $[AuCl_4]^-$, at a concentration of 1×10^{-3} M immediately after the PS was refreshed with HF. The sample was then stored in an atmospheric environment. It is obvious from Fig. 9 that Au deposition on PS enhances the luminescence intensity with the peak shifted slightly to the blue. In fact we notice visually that, in general, the luminescence becomes more uniform after reductive Au deposition. Note that the excitation energy is 100 eV, which corresponds to an energy just above the Si $L_{3,2}$ threshold. Thus absorption at this energy will enhance the luminescence from unoxidized porous silicon (see Fig. 10). The low-energy (longer wavelength) peak is due to luminescence from the "bulk" while the luminescence in the green (short wavelength) is from the Si – Si oxide surface/interface. These issues will be discussed elsewhere. The difference in the characteristics for the luminescence before and after Au deposition is likely due to subsequent oxidation of PS in the ambient and that the Au

© 1998 NRC Canada

aggregates are good light scatterers. Since Au deposition under these conditions is at least micrometres deep, the little Au mirrors will provide a more uniform luminescence. We have XAS evidence to suggest that Au deposition on p-type PS does not inhibit the oxidation of PS; in fact it facilitates the process. Figure 10 shows the Si L-edge of an ambient PS, a refreshed PS immediately after HF treatment, and the Au-deposited PS after being stored in air. In a total electron detection mode, the ambient and Au/PS samples show only SiO_2 signals, which are more intense for the Au/PS sample. The PS underneath cannot be revealed because of short electron escape depth for low-energy electrons. When the oxide is removed by HF, the spectrum of PS emerges. The oxidation of PS after Au deposition will result in smaller Si nodules and pillars, hence a blue shift in the luminescence.

Summary and conclusion

We have reported the preparation and characterization of a number of Au deposits on porous silicon. By varying the conditions in the reductive deposition technique, we have been able to prepare a variety of Au aggregates of the order of 10^2 nm and 10 nm dimensions on PS. This technique can be extended to study other metals. SEM and X-ray techniques reveal the morphology, structure, and electronic properties of these nanostructures. We show that both the chemistry and the nature of the substrate contribute to the morphology of the cluster. In turn, the ability to make clusters or aggregates of various dimensions will provide a useful testing ground for a study of the electronic property–structure relationship for materials of unusually small dimensions.

Acknowledgements

Research at the University of Western Ontario is supported by the Natural Sciences and Engineering Research Council of Canada (NSERC) and an ADF grant (UWO). The Synchrotron Radiation Center and National Synchrotron Light Source are supported by the U.S. National Science Foundation, under grant no. DMR9212658, and the Office of Basic Energy Sciences, U.S. Department of Energy, under contract no. DE-AC02-76CH00016, respectively.

References

1. D.R. Turner. J. Electrochem. Soc. **105**, 402 (1958).
2. H. Föll. Appl. Phys. A: Solids Surf. **53**, 8 (1991).
3. V. Lehmann and U. Gösele. Adv. Mater. **4**, 114 (1992).
4. L.T. Canham. Appl. Phys. Lett. **57**, 1046 (1990).
5. V. Lehmann and U. Gösele. Appl. Phys. Lett. **58**, 857 (1991).
6. T.K. Sham, D.-T. Jiang, I. Coulthardt, J.W. Lorimer, S.P. Frigo, X.H. Feng, K.H. Tan, D.C. Houghton, B. Bryskiewicz, and R.A. Rosenberg. Nature, **363**, 331 (1993).
7. F. Namavar, H.P. Maruska, and N.M. Kalkhoran. Appl. Phys. Lett. **60**, 2514 (1992).
8. G. Bomchil, A. Halimaoui, and R. Herino. Appl. Surf. Sci. **41/42**, 604 (1989).
9. S.S. Tsao, T.R. Gulianger, M.J. Kelly, H.J. Stein, J.C. Barbour, and J.A. Knapp. J. Appl. Phys. **67**, 3842 (1990).
10. R.C. Anderson, R.S. Muller, and C.W. Tobias. Sens. Actuators, A: **A21–A23**, 835 (1990).
11. P.M. Fauchet, C.C. Tsai, L.T. Canham, I. Shimizu, and Y. Aoyagi (*Editors*). Microcrystalline semiconductors: materials science and devices. Mater. Res. Soc. Symp. Proc. **233** (1993).
12. I. Coulthard, D.-T. Jiang, J.W. Lorimer, and T.K. Sham. Langmuir, **9**, 3441 (1993).
13. T.K. Sham, I. Coulthard, J.W. Lorimer, A. Hiraya, and M. Watanabe. Chem. Mater. **6,** 2085 (1994).
14. D. Andsager, J. Hilliard, and M.H. Nayfeh. Appl. Phys. Lett. **64**, 114 (1994).
15. I. Coulthard and T.K. Sham. Mater. Res. Soc. Symp Proc. **452**, 547 (1997).
16. I. Coulthard, A. Bzowski, T.K. Sham, S.M. Heald, and M. Kuhn. J. Phys. Colloq. Suppl. **C2**, 1133 (1997).
17. H. Gleiter. Prog. Mater. Sci. **33**, 223 (1989).
18. S.B. DiCenzo, S.D. Berry, and E.H. Hartford, Jr. Phys. Rev. B: Condens. Matter, **38,** 8465 (1988).
19. O. Cordes and Harsdorff. Appl. Surf. Sci. **33/34**, 153 (1988).
20. J.H. Sinfelt. Bimetallic catalysts. John Wiley and Son, New York. 1983.
21. J. Goulon, P. Tola, M. Lemonnier, and J. Dexpert-Ghys. Chem. Phys. **78**, 347 (1983).
22. T.K. Sham, D.-T. Jiang, I. Coulhardt, J.W. Lorimer, S.P. Frigo, X.H. Feng, K.H. Tan, D.C. Houghton, B. Bryskiewicz, and R.A. Rosenberg. Synchrotron Radiat. News, **7**, 32 (1994).
23. R.L. Smith, and S.D. Collins. J. Appl. Phys. **71**, R1 (1992).
24. L.A. Jones. Ph.D. Thesis, University of Guelph. 1996.
25. I. Coulthard and T.K. Sham. Appl. Surf. Sci. **126**, 287 (1998).
26. R. Jenkins and R.L. Snyder. Introduction to X-ray powder diffractometry. John Wiley and Sons, Inc. 1996.
27. J. Mycroft, G.M. Bancroft, N.S. McIntyre, and J.W. Lorimer. Geochim. Cosmochim. Acta, **59**, 3351 (1995).
28. A. Bzowski, T.K. Sham, M. Werneirt, and R.E. Watson. Phys. Rev. B: Condens. Matter, **51**, 9979 (1995).
29. T.K. Sham, S.J. Naftel, and I. Coulthard. J. Appl. Phys. **79**, 7134 (1996).
30. M. Kuhn and T.K. Sham. Phys. Rev. B: Condens. Matter, **49**, 1647 (1994).
31. R.E. Watson and M.L. Perlman. Structure Bonding, **24**, 83 (1975).
32. W. Drube, R. Treusch, T.K Sham, A. Bzowski, and A.V. Soldatov. Phys. Rev. B: Condens. Matter. **58**, 6871 (1998).
33. P.H. Citrin, G.K. Wertheim, and Y. Baer. Phys. Rev. Lett. **41**, 1425 (1978).

© 1998 NRC Canada

Photoinduced structural relaxation and densification in sol-gel-derived nanocomposite thin films: implications for integrated optics device fabrication

Kalaichelvi Saravanamuttu, Xin Min Du, S. Iraj Najafi, and Mark P. Andrews

Abstract: The solution sol-gel method is used to produce thin films of photosensitive hybrid organic–inorganic glass on silicon. Glasses consisted of photoinitiator, methacryloxypropyltrimethoxysilane, methacrylic acid, and zirconium oxide. Clear, low optical loss films are obtained, indicating nanophase homogeneity in the samples. The nanocomposite films are shown to be suitable for fabricating optical components such as ridge wave guides and Bragg diffraction gratings. The increase in the refractive index of the glass relative to the surrounding material during photolithographic processing is identified as a key material parameter in device fabrication. Accordingly, electronic and vibrational spectroscopy are used to provide insight into the structural changes that occur when glasses are irradiated with continuous narrow band 4.9 eV and pulsed 6.4 eV light. Arguments are advanced, linking the changes in refractive index to collateral densification leading to volume compaction of the silicate network during organic free-radical polymerization. This was shown by following the time evolution of relevant IR absorption bands. Free silanol and unreacted methoxysilane are consumed in the process. Matrix densification is indicated by shifts to low wave number in the transverse optical phonon mode associated with decreasing Si-O-Si bond angles of the antisymmetric stretching vibration (compression). Growth in the Si-O-Si framework is observed through increased intensity in this IR absorption. Similar behaviour is observed for films irradiated with 6.4 eV light from an excimer laser. A phase mask in combination with pulsed 6.4 eV light is used to inscribe a 1.5 mm, high-reflectivity polarization-independent Bragg grating into a ridge wave guide. The high reflectivity is thought to arise from a periodic modulation of the volume compaction of the matrix. Overall, the organic component of the glass confers unique properties on the material that allow it to be densified even with 4.9 eV light. By comparison, sol-gel silica with no organic component must be densified at nearly twice the photon energy.

Key words: sol-gel, wave guide, Bragg grating, photochemistry, densification, refractive index, photolithography.

Résumé : On a fait appel à la méthode de solution sol-gel pour produire des films minces de verres hybrides organiques–inorganiques sur silice photosensibles. Les verres sont formés d'un photoinitiateur, de méthacryloxypropyltriméthoxysilane, d'acide méthacrylique et d'oxyde de zirconium. On obtient des films clairs donnant de faibles pertes optiques qui indiquent l'homogénéité de la nanophase des échantillons. On a démontré que les films nanocomposites sont appropriés pour la fabrication de composantes optiques, telles que des guides à moulure et des réseaux de diffraction de Bragg. On a mis en évidence que l'augmentation de l'indice de réfraction du verre par rapport à celle du matériel avoisinant au cours du processus de photolithographie correspond au paramètre matériel clé pour la fabrication de l'appareil. En conséquence, on a utilisé les spectroscopies électronique et vibrationnelle pour obtenir des données relatives aux changements de structure qui se produisent lorsqu'on irradie des verres avec une bande de lumière étroite continue de 4,9 eV et pulsée de 6,4 eV. On apporte des arguments permettant de relier les changements d'indices de réfraction avec la densification collatérale conduisant à une compaction du réseau de silicate au cours de la polymérisation organique par radicaux libres. On a fait cette démonstration en suivant l'évolution, en fonction du temps, des bandes appropriées d'absorption IR. Le silanol libre et le méthoxysilane qui n'a pas réagi sont consommés dans ce processus. La densification de la matrice est mise en évidence par des déplacements vers les faibles nombres d'onde dans le mode de phonon optique transversal associé avec une diminution des angles de liaison Si-O-Si de la vibration d'élongation antisymétrique (compression). On observe une croissance du réseau Si-O-Si par le biais d'une augmentation de l'intensité de cette absorption IR. On a observé un comportement similaire avec les films

Received February 11, 1998.

K. Saravanamuttu and M.P. Andrews.[1] Department of Chemistry, McGill University, 801 Sherbrooke St. West, Montreal, PQ H3A 2K6, Canada.
X.M. Du and S.I. Najafi. Department of Electrical Engineering, École Polytechnique de Montréal, PQ H3C 3A7, Canada.

[1]Author to whom correspondence may be addressed. Telephone: (514) 398-4459. Fax: (514) 398-3797.
E-mail: andrews@omc.lan.mcgill.ca

© 1998 NRC Canada

irradiés avec une lumière de 6,4 eV provenant d'un laser excimère. On fait appel à un masque de phase en combinaison avec la lumière pulsée de 6,4 eV pour inscrire, dans un guide d'onde à moulure, un réseau de diffraction de Bragg de 1,5 mm, de réflectivité élevée et indépendant de la polarisation. On croit que la réflectivité élevée provient d'une modulation périodique de la compaction du volume de la matrice. Dans l'ensemble, la composante organique du verre confère des propriétés uniques au matériel qui lui permettent de se densifier, même avec de la lumière de 4,9 eV. Par comparaison, il est nécessaire d'utiliser une énergie photonique double pour densifier la silice sol-gel ne comportant pas de composante organique.

Mots clés : gel-sol, guide d'onde, réseau de diffraction de Bragg, photochimie, densification, indice de réfraction, photolithographie.

[Traduit par la Rédaction]

Introduction

Photonics is concerned with optical input–output processes mediated primarily by light, rather than electrons. The chemistry of photonic materials is concerned among other things with articulating the molecular point of view on how matter acquires its suite of functional optical properties. In photonics, these properties include spatial confinement of the electromagnetic field, birefringence, photorefraction, nonlocal effects, Kerr and cascaded nonlinear responses. In turn, these properties are of significant technological and scientific interest (1, 2), which is incentive to understand how to control bulk optical properties at the molecular level. The properties of micro-optical components like silica glass wave guides and Bragg gratings are manifestations of their ramifying molecular networks. The refractive index of silica-based glasses plays a key role in defining the boundary conditions for light propagation in integrated optics components, devices, and circuits (2–7). Accordingly, the refractive index emerges as a fundamental device performance material parameter. In this regard, network relaxations that lead to densification of glass are important because the local microstructural rearrangements are often accompanied by increases in the refractive index that can be useful for fabricating optical devices. Douay et al. (8) have cogently argued this point.

Inorganic glasses can be densified not only by thermal sintering, but also by irradiation with electron beams (9–15), neutrons (16–18), ions (19), X-rays (11), γ-rays (11–16), or ultra-violet (UV) light (12, 20–23). UV-induced densification has also been studied for its relevance to optical damage in silicate glasses (20), where it has been observed that two-photon events induce elastic and inelastic densification of the structural framework. While most studies have focused on glasses derived from more or less traditional methods of high-temperature processing, a low-temperature route to glasses is attracting adherents (24). It is well known that inorganic glasses can be prepared near room temperature by solution sol-gel processing. This method can produce very pure materials by acid- or base-catalyzed hydrolysis and polycondensation of main-group and transition-metal alkoxides. A high-temperature postconsolidation step is usually required to collapse the pore structure of the gel-phase material. Reductions in porosity (internal surface area) in this case are driven by gradients in curvature. Viscous flow, surface diffusion, and evaporation–condensation usually conjoin to reduce the surface area that leads to densification in thin films (25).

High-temperature densification is a drawback if the glass must be deposited onto substrates that would be damaged above 500°C. Some effort has therefore gone into identifying methods to lower the postprocess densification temperature so that gel films might be deposited onto more fragile substrates like organic polymers, or semiconductor integrated circuits. To some extent, densification at lower temperatures can be achieved by photons having energies greater than the band gap of the oxide (though this approach is problematic for photosensitive semiconductors and organic compounds). For example, Imai et al. (22) examined the structural changes induced when sol-gel-derived silica was exposed to 9–18 eV vacuum UV (VUV) radiation. Compaction and dehydration of SiO_2 occurred to an extent similar to what was observed when gel films were sintered at 1000°C. The authors suggested that bond cleavage–formation pathways, and light-enhanced polycondensation steps were responsible for consumption of silanol Si-OH species leading to densification of the sol-gel glass (22). The findings of Imai et al. are significant for the present study. In the research described below we propose a different mechanism based on UV-light-initiated free-radical polymerization of an acrylate monomer and collateral work densification in a hybrid organic–inorganic silica glass.

In general, sol-gel processing of silica glass has been far less attractive as a route to integrated optics structures because high-temperature consolidation also carries the disadvantage of compressive interfacial stresses that cause cracking and optical-device failure. More significant perhaps is the fact that high-temperature glass integrated optics is excluded from the opportunities created by organic chemistry; and this means the exciting advances in organic small molecule and polymer optical nonlinearities. A hybrid sol-gel glass, with an appetite for both organic and inorganic phases, can rationalize the attractive features of both material regimes.

As an alternative to high-temperature gel-phase densification, we have been exploring organically modified low-temperature sol-gel glass fabrics to prepare micro-optical components and devices, including wave guides (1, 26), directional couplers (27, 28), beam splitters, and high-reflectivity Bragg gratings on ridge wave guides (2, 3, 7, 29, 30). The introduction of organic character into the silicate network offers exciting potential for the new materials field of hybrid glasses for photonics (2). This potential has been discussed elsewhere by the authors (2, 3). Our materials belong to the category of glasses, variously known as "ormocers," "ormosils," "ceramers," "polycerams," or simply hybrid sol-gel glasses (HSGGs) (31, 32). These are usu-

© 1998 NRC Canada

ally formed by acid- or base-catalyzed reactions of mixtures of organosiloxanes with tetrafunctional silicon alkoxides. The covalently bonded organic group does not normally undergo hydrolysis, and so imparts organic character to the composite. The properties of HSGGs can therefore be varied at the molecular level between those of the parent organic polymer, and those of the homogeneous inorganic glass. This is accomplished by introducing the organic component as a pendant, bridging, or polymerizable group. The latter can be polymerized sequentially or simultaneously with polycondensation of the inorganic component to provide a mutually interpenetrating network. A principal advantage of a hybrid glass is that it admits elaborate molecular-level control over macroscopic expressions of physical and chemical properties that are important for photonic devices. This gives the device designer an attractive generic silica-based medium (i.e., refractive index matched to optical fibre) that allows rapid prototyping of devices and assessment of material reliability. On the other hand, complex permutations of compositional and processing variables demand that researchers understand molecular ultrastructure and correlations with intended optical and physical properties. To this end, we have undertaken a series of spectroscopic studies to formulate a picture of how changes in the organic and inorganic network of one particular HSGG can be used to advantage to design and fabricate functional photonic devices. The ability of the HSGG material to accommodate industry standard photolithographic techniques was considered at the outset to be essential to our device agenda. Methacryloxypropyltrimethoxysilane (MAPTMS) and methacrylic acid were therefore selected as the photopolymerizable components in our glasses. Choice of the trifunctional R-$Si(OCH_3)_3$ is significant for the present work because R-group substitution at silicon reduces glass network connectivity and mechanical stiffness. Reduction in the mechanical stiffness of the network promotes capillary stress-induced collapse of the gel network during drying. This is reflected in enhanced relaxation rates and lower densification temperatures for the glasses. Choice of the vinyl ester functionality was also motivated by the large literature that has accumulated on acrylate photochemistry and photolithographic applications (33).

For acrylate hybrid glasses, UV light intervenes at the molecular level to modify the structure of the overall network, hence the refractive index, in ways that are not trivially related to radical polymerization of the organic monomer component alone. Increases in the refractive index appear to be linked both to volume compaction due to organic chain growth, and to the simultaneous onset of local relaxations and chemical condensation of siloxy species in the metastable silica network. The following is an account of our understanding of these events to date.

Experimental

Preparation of sol-gel-derived Zr HSGG

A hybrid organosilicate glass was prepared from 10:4:4 molar ratios of methacryloxypropyltrimethoxysilane:zirconium(IV)-*n*-propoxide ($Zr(OC_3H_7)_4$):methacrylic acid (MAA). Zirconium was selected as a second network former in our materials to increase mechanical stability and raise the refractive index of the composite sufficiently for waveguiding. Its careful hydrolysis in the presence of methacrylic acid is required to ensure that ZrO_2 particle diameters do not exceed 40 nm (34) and that the ZrO_2 phase is dispersed homogeneously. Methacrylic acid is therefore added to the system to regulate the hydrolysis of the zirconium alkoxide by complexation. Finally, the hydrolysis and condensation of the Zr/MAA complex is carried out in the presence of prehydrolyzed MAPTMS to avoid undesired precipitation of ZrO_2.

Accordingly, partial hydrolysis and polycondensation of MAPTMS was initiated with 0.75 equiv. of acidified H_2O (HCl, 0.05 M). Hydrolyzed zirconium propoxide was dispersed as the oxide into the host glass by addition as the MAA:$Zr(OC_3H_7)_4$ (1:1 molar ratio) complex. Hydrolysis and condensation of the remaining silicon alkoxide functionalities and the zirconium propoxide were resumed with the remaining equivalent of H_2O. A photoinitiator (1-hydroxycyclohexyl-1-phenylketone, IRGACURE-184, CIBA Geigy) was then added to the solution. The free-flowing sol was finally passed through a 0.2 μm filter before storage in the dark.

Instrumentation

A Headway photoresist spinner (EC101D & PM101D series) was used for depositing thin films. Low-energy photolyses were conducted with a mercury–xenon arc lamp having a maximum output at 4.9 eV. A 193 nm ArF excimer laser (model AQX-150, MPB Technologies) gave 60 mJ/cm^2 pulses (12–15 ns pulse width) at a repetition rate of 30 Hz for the higher energy photolysis studies. A deep UV, narrow band light illumination system and mask aligner (500 W mercury–xenon arc lamp, Oriel 87000 series, 14 W cm^{-2}) were used for photolithography. Bragg gratings were produced from the 193 nm output of the ArF laser. The gratings were written through a phase mask to give maximum reflectivity at 1.55 μm. Infrared spectra were acquired over a range of 400–5000 cm^{-1} with a Bruker IFS-48 Fourier transform infrared spectrometer. A Hewlett Packard 8452A diode array spectrophotometer was used to collect electronic absorption spectra over the range from 200 to 800 nm. GRAMS/32 software (version 4.01A, Galactic Industries, Salem, NH) was used for spectral data processing.

Preparation of films for electronic absorption spectroscopy

Thick films (5 μm) were cast onto fused silica plates (25 cm^2) by spin-coating at 3000 rpm for 40 s. Samples were dried at room temperature before being exposed to UV irradiation (2.5–5.0 eV) at a distance of 25 cm from the exit aperture of the light source. Irradiation times ranged from 0 to 60 min.

Preparation of thin films for Fourier transform infrared (FT-IR) spectroscopy

A homogeneous 5 μm film was spin-coated onto double-polished Si wafers (NOVA Electronic Materials, Texas). The film was dried at 100°C for 30 min. The wafer was then cleaved into 2 × 1 cm pieces before being irradiated. Three series of samples were prepared to cover various combinations of photon energy and irradiation times. These were as

© 1998 NRC Canada

follows: (*i*) 2.5–5.0 eV irradiation over a period of 0–60 min; (*ii*) 6.4 eV irradiation over a period of 15–300 s; (*iii*) 0.5 min of 2.5–5.0 eV irradiation followed by 6.4 eV irradiation over a period of 0–180 s. The 6.4 eV light was provided by the pulsed ArF laser having a fluence of 60 mJ/cm^2 at a 30 Hz repetition rate.

Ridge wave guide fabrication

Silicon wafer substrates with a thermally grown 2 μm thick SiO_2 layer were acquired from Nova Electronic Materials, Inc., Texas. Wafers were soaked consecutively in warm trichloroethylene, acetone, and isopropanol. They were then cleaned with distilled H_2O in an ultrasonic bath and dried under flowing N_2.

A 5 μm film of sol was spin-coated at 3000 rpm for 40 s on a 2 × 1 cm wafer fragment. The film was then dried in air at 100°C for 30 min to prevent the contact photomask from adhering to the gel film. A fused silica substrate photomask (QPS Technologies, Dorval, Que.) inscribed with an array of wave-guide openings was placed in direct contact with the film surface. The film was irradiated with 4.9 eV light from a distance of 25 cm. This corresponds to an intensity of 14 W cm^{-2}. Photolithographic elaboration of the ridge wave guides was completed by a wet-etching process described in detail elsewhere (30). In brief, the irradiated film was immersed in isopropanol to dissolve the unexposed gel regions of the film. The ridge wave guide was then heated at 120°C for 2 h.

Fabrication of Bragg gratings

Bragg gratings of high reflectivity at 1.55 μm were photoinscribed in ridge wave guides by phase-mask processing (29). A phase mask is a binary three-dimensional quartz grating that is produced by reactive ion etching. The etch depth is optimized such that upon illumination from a UV source, light is diffracted equally into the plus/minus first orders, while energy deposited from the zero and higher orders is minimized. Interference from the diffracted first-order beams produces a near-field fringe pattern. The phase mask was provided by QPS Technologies (Dorval, Que.). The mask defined a period size (Λ) of 1055 nm, where the zero-order energy was suppressed to less than 1% for the 193 nm ArF laser line used to write the grating. The ridge wave guide was placed in direct contact with the phase mask and was aligned such that the wave-guide long axis was normal to the grooves of the mask surface relief grating. Samples were irradiated at distance of 90 cm from the exit port of the raw ArF excimer laser beam.

Results and discussion

Effects of 4. 9 eV radiation

Control experiments showed that the refractive index of the hybrid glass increased very slowly when photoinitiator was absent. The CIBA Irgacure-184 photoinitiator used in this work is in fact 1-hydroxycyclohexyl-1-phenylketone. When excited to its triplet state, the molecule undergoes α-cleavage to produce benzoyl and 1-hydroxycyclohexyl radicals. The benzoyl radical is primarily responsible for initiating polymerization of the methacryloxypropyl and methacrylic acid groups. Phan (35) has provided evidence that the 1-hydroxycyclohexyl radical also initiates acrylate chain growth.

Fig. 1. UV-vis absorption spectra of sol-gel-derived films irradiated with 4.9 eV UV light at 0, 5, 15, 30, and 60 min.

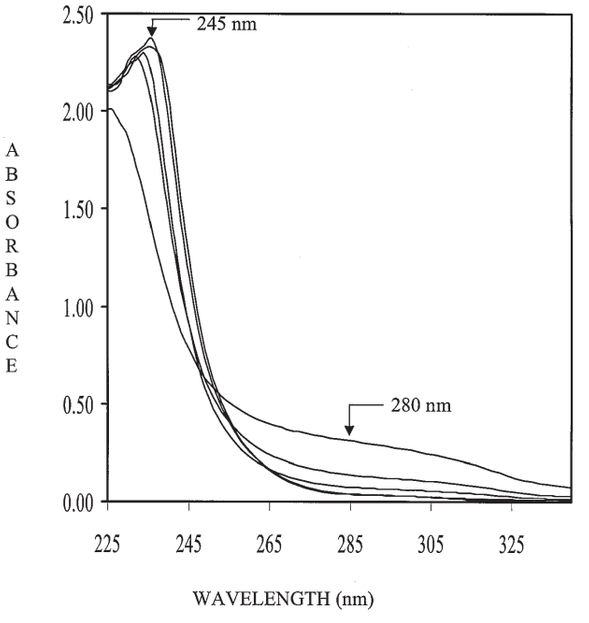

Electronic absorption spectroscopy of hybrid glass films

Figure 1 records the outcome of sequential irradiation of thin hybrid gel films over a period of 60 min. The spectral features are dominated by those belonging to the MAPTMS moiety, despite the presence of MAA and Zr(IV)propoxide in the starting materials. This was confirmed in separate experiments which showed that Zr(IV)propoxide is fully hydrolysed and that MAA is complexed with the resulting ZrO_2 (strong infrared absorption at 1550 cm^{-1}). The final products of the reaction between MAA and Zr(IV) contribute a weak absorption centred at 271 nm.

The spectrum of the film acquired prior to photolysis exhibits a prominent band peaking near 240 nm. In Mulliken notation, this transition is formally V ← N, and originates in the $\pi \rightarrow \pi^*$ excitation of the conjugated ester carbonyl of MAPTMS (36, 37). In the gel-phase host, this band is blue-shifted from its peak maximum of 282 nm for the MAPTMS molecule dissolved in dry isopropanol. A second high-energy $\pi \rightarrow \pi^*$ transition is observed at 214 nm. It too is blue-shifted from its position at 242 nm in MAPTMS–isopropanol. The localized $n \rightarrow \pi^*$ transition (i.e., Mulliken Q ← N) of the carbonyl substituent conjugated with the olefin occurs near 310 nm, but it is of very low intensity and is not visible on this scale. The $n \rightarrow \pi^*$ transition undergoes a hypsochromic shift of about 10 nm in the gel matrix relative to MAPTMS in isopropanol. The shift of the band to higher energy in the thin film suggests that the guest carbonyl is located in a more polar (hydrogen-bonding) environment, most likely containing water and silanol. In fact, this kind of behaviour for carbonyl compounds in activated silica has been noted elsewhere (38). The well known blue-shift in the $n \rightarrow \pi^*$ absorption band is the result of cooperative electro-

© 1998 NRC Canada

Fig. 2. FT-IR spectrum of an organically modified sol-gel thin film prior to photolysis (top) and after 25 min of photolysis (bottom).

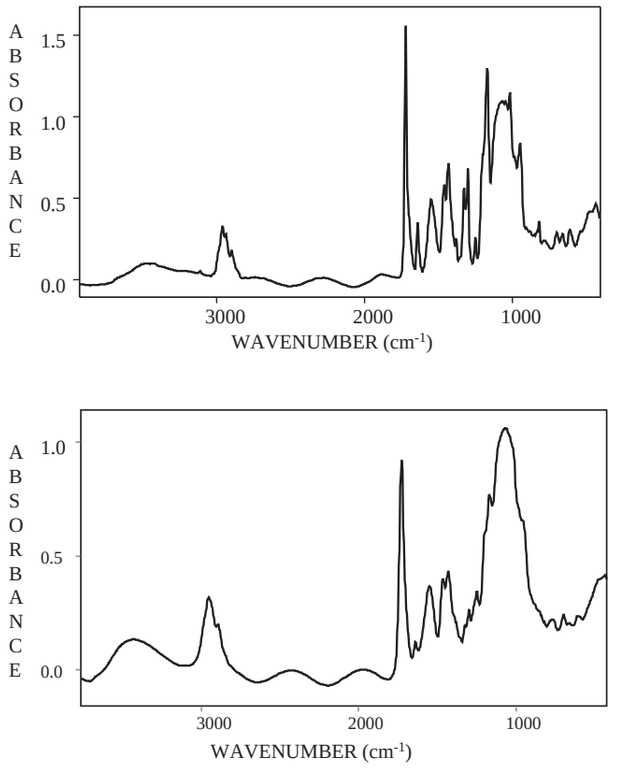

static and hydrogen-bonding interactions with the solute propyl ester carbonyl group (39). Hydrogen bonding to the carbonyl expresses itself in infrared absorption by a shoulder at 1700 cm^{-1} adjacent to the 1722 cm^{-1} band belonging to the carbonyl stretching mode. This spectral feature is discussed later.

As the irradiation proceeded, the 240 nm band was gradually depleted, revealing an underlying absorption maximizing at 225 nm. Simultaneously, significant intensity developed at approximately 280 nm. The 280 nm band is too intense to be associated solely with the $n \rightarrow \pi^*$ transition of the carbonyl group of polymerized acrylate. Photolysis of polymer side-chain ester groups is widely documented (33), and it is well known that polyacrylates undergo main-chain and side-chain scission reactions, so that the 280 nm absorption probably contains contributions from ketone and aldehyde species, as noted elsewhere (40, 41). Further evidence of the polymerization process is presented in the following section.

Infrared spectroscopy

Photoinitiated polymerization of hybrid glass films

Infrared spectra of the gel film at various stages of photolysis are gathered in Figs. 2–5. Band assignments (42–47) are collected in Table 1. Figure 2 (bottom) emphasizes that 25 min of UV radiation causes significant changes in the vibrational spectrum, primarily in the transverse optical phonon ν_{as}(Si-O-Si) region centred at 1060 cm^{-1}. Overall, there is a substantial increase in intensity of the band. This

Fig. 3. FT-IR spectra of thin films irradiated with 4.9 eV UV light at 0, 0.5, 2, 5, 10, 15, 20, 25, 30, 35, 45, and 60 min where (*A*) ν(C=O) at 1718 cm^{-1}; (*B*) ν(C=O—H) at 1720 cm^{-1}; and (*C*) ν(C=C) at 1638 cm^{-1}.

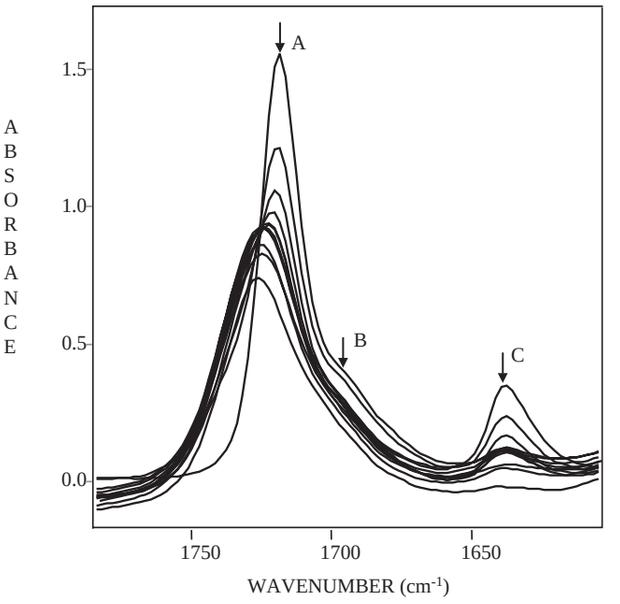

Fig. 4. Changes in the IR spectral features of thin-film hybrid glass with increasing time of 4.9 eV irradiation where (*A*) -CH_3 rock of Si-OCH_3 at 1168 cm^{-1}; (*B*) and (*C*) *trans* (oop) CH wag and CH_2 wag of $=CH_2$ at 1012 and 980 cm^{-1}; (*D*) ν(Si-OH) at 944 cm^{-1}; (*E*) ν(Si-O-C) at 816 cm^{-1}. Time of irradiation (min): 0, 0.5, 2, 5, 10, 15, 20, 25, 30, 35, 45, 60.

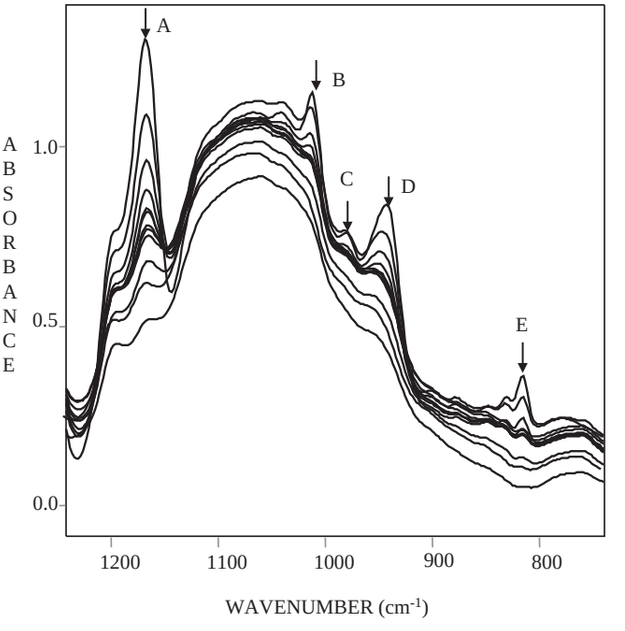

will be shown later to be linked to silanol and silicon alkoxide polycondensation reactions enhanced by "photosintering" of the matrix as the acrylate substituents attached

© 1998 NRC Canada

Table 1. Vibrational frequency assignments for organically modified, sol-gel-derived thin films.

Wave number (cm^{-1})	Assignment
	A. Methacryloxypropyl group
980	CH_2 wag of $=CH_2$
1012	*trans* (oop) C-H wag of $=CH_2$
1296	-CH bending in vinyl
1638	ν(C=C)
1720	ν(C=O) of hydrogen-bonded carbonyl group
1722	ν(C=O)
2890	$\nu_s(CH_3)$
2930	ν_s(CH) of terminal methylene in $=CH_2$
3100	$\nu_{as}(CH_2)$ of terminal methylene
	B. Silicate and zirconia network
430	δ_{as}(Si-O-Si)
760	ν_s(Si-O-Si)
1060	ν_{as}(Si-O-Si)
1546	ν(C=O) of zirconium – methacrylic acid complex
	C. Methoxy and silanol groups
472	δ_{as}(Si-O-C) of two or more -OCH_3 groups attached to Si
816	ν_s(Si-O-C) stretch
944	ν(Si-OH)
1168	-CH_3 rock of Si-OCH_3
2844	$\nu_s(CH_3)$ of Si-OCH_3
2960	ν_{as}(CH) of Si-OCH_3
3436	ν(OH) broad low band H-bonded molecular H_2O
3648	ν(OH) of hydrogen-bonded internal Si-OH

Fig. 5. Diminishing intensities of (*A*) $\nu_{as}(CH_2)$ of $=CH_2$ at 3100 cm^{-1}; (*B*) ν_{as}(CH) of Si-OCH_3 at 2960 cm^{-1}; (*C*) ν_s(CH) of $=CH_2$ at 2930 cm^{-1}; (*D*) $\nu_s(CH_3)$ of Si-OCH_3 at 2844 cm^{-1} at increasing periods of UV (4.9 eV) irradiation. Time of irradiation (min): 0, 0.5, 2, 5, 10, 15, 20, 25, 30, 35, 45, 60.

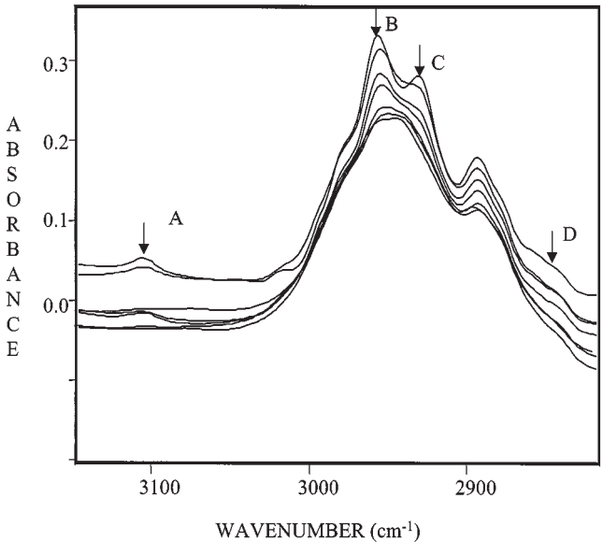

to silicon polymerize. The gross features of the spectrum are indistinguishable from those of poly(methylmethacrylate) in sol-gel-derived silica hosts (48). Additional changes in the spectra are evident in the loss of $\nu_{C=C}$ intensity at 1638 cm^{-1}, and a dimunition in contributions from the -CH_3 rocking mode (1168 cm^{-1}) of ≡Si-OCH_3.

Polymerization of the olefinic components was followed by monitoring the loss of intensity of appropriate bands in the mid-infrared region (Figs. 3–5). We focus in Fig. 3 on the vinyl group, ν(C=C) mode at 1638 cm^{-1}, the CH_2 wag, and *trans* (out-of-plane (oop)) C-H wag at 1012 and 980 cm^{-1}, respectively, and higher energy modes belonging to C-H symmetric (2930 cm^{-1}) and antisymmetric (3100 cm^{-1}) stretches. Consumption of the ν(C=C) 1638 cm^{-1} band (peak C, Fig. 3) is accompanied by a shift of the carbonyl ν(C=O) stretching mode from 1718 cm^{-1} (peak A in Fig. 3) to higher energy at 1724 cm^{-1}. The shift is typical for an ester carbonyl that is no longer conjugated with a vinyl substituent. Polymerization is indicated, since the two events are related through the isosbestic point. The shoulder at position B (1700 cm^{-1}) in Fig. 3 is evidence of hydrogen-bonded interactions between the carbonyl group and the host matrix (49–51).

The relative intensity of the acrylate ν(C=O) 1718 cm^{-1} and ν(C=C) 1638 cm^{-1} bands is plotted as a function of irradiation time in Fig. 6. Both curves show the same qualitative trends, with polymerization being most rapid within the first 10 min of irradiation. As described below, this time span coincides with the largest changes in the refractive index of the glass. This period of conversion would seem to involve acrylate groups that are sufficiently close to each other, since mass

© 1998 NRC Canada

Fig. 6. Intensity of ν(C=O) and ν(C=C) at 1718 cm^{-1} and 1638 cm^{-1}, respectively, vs. time of irradiation.

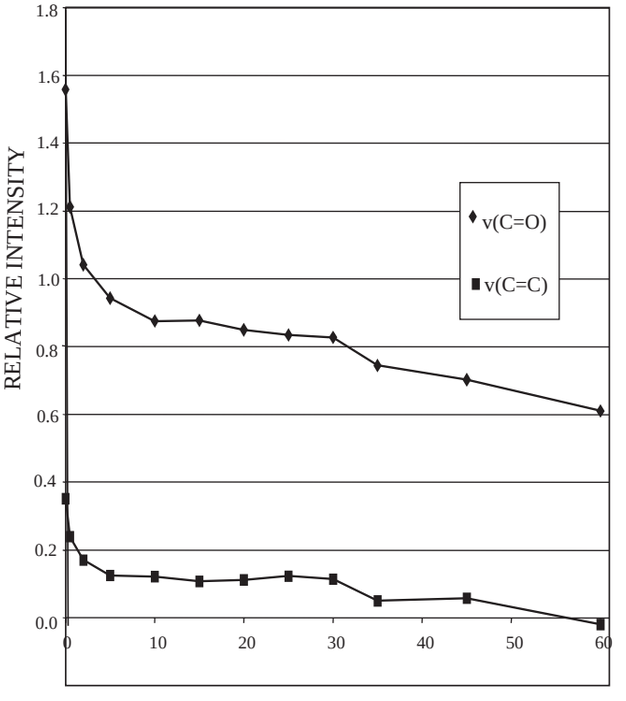

transport in the glassy host must surely be suppressed. After 10 min, the curves for these modes flatten out; there is no longer much change in the intensity of ν(C=O) and ν(C=C) bands beyond 20 min of irradiation. This effect is clearly kinetic in origin, since there can be little or no monomer diffusion in the highly crosslinked organosilicate film.

Figure 3 also indicates that additional photochemistry occurs at the longer irradiation times. This is indicated by the loss of the isosbestic point, the diminishing intensities of both the ν(C=O) and ν(C=C) bands, as well as a definite shift in the peak position of the ν(C=O) towards higher energy.

Structural changes related to increases in refractive indices

In previous publications (52, 53), we showed that low loss hybrid sol-gel glass channel wave guides for use in the key 1.55 μm telecommunications window could be deposited by UV photoinscription. Indeed, we have recently carried out an in-depth investigation of the effects of UV-light exposure on the evolution of the refractive index of hybrid glass wave guides (53, 54). This work included a systematic study of the effects of UV light on the increase in the refractive index, *n*, of MAPTMS/MAA/ZrO_2 film wave guides. For slab wave guides, increases in the refractive index were significant, as large as $\Delta n = 0.006$. The greatest increases occurred within the first 10 min of irradiation. This time frame matches the early stage of rapid consumption of the vinyl groups traced by IR spectroscopy, as described above. There were no significant changes in the refractive index of films beyond 30 min of irradiation. This observation corresponds to the flat region of the curves in Fig. 6.

Our spectroscopic evidence suggests that the changes in *n* are coupled to microstructural transformations in the glass. Close examination of Figs. 3–5 reveals features of the matrix that indicate that the photoinduced radical polymerization indeed causes a cascade of chemical reactions and structural relaxations in the matrix. Observe in the figures that there is a significant amount of residual Si-OH and alkoxy (Si-OCH_3) groups present within the film prior to photolysis. The carriers of this information are indicated in section C of Table 1. Band assignments are given in the figure captions and marked by letters on the corresponding spectra. Hydrogen bonding between the acrylate carbonyl and acidic silanol groups is indicated in Fig. 3 by the shoulder located at approximately 1700 cm^{-1}, at slightly lower energy with respect to the major ν(C=O) peak (55). Hydrogen bonding between silanol and the carbonyl oxygen of PMMA is well established (55), and it has been argued elsewhere that such interactions may be essential to control phase separation to give transparent organosilicate composites that are homogeneous on a nanometer scale (nanocomposites) (55, 56). Figure 3 shows that these hydrogen-bonded interactions are disrupted when samples containing MAPTMS are irradiated with 4.9 eV photons. Moreover, as the monomer polymerizes, the silicate network is simultaneously elaborated through further hydrolysis and polycondensation; both silanol and methoxide are lost, and there is growth in the numbers of Si-O-Si linkages, as expressed in the Si-O-Si 1063 cm^{-1} band (see also Fig. 2, bottom). These events are indicated in Fig. 4 by reductions in intensity of Si-OCH_3 and Si-OH group bands located at positions A (CH_3 rock of Si-OCH_3, 1638 cm^{-1}), D (ν(Si-OH) 944 cm^{-1}), and E (ν(Si-O-C) at 816 cm^{-1}). The decrease in absorption of the 944 cm^{-1} peak of silanol indicates loss of hydroxyl groups upon irradiation; however, the effect cannot be due to excitation of the Si-OH hydroxyl because this requires 8 eV photons (22).

Figure 5 documents the condensation of ≡Si-OCH_3 by loss of methanol. This is evidenced through loss of intensity in the $\nu_s(CH_3)$ mode of Si-OCH_3 at 2844 cm^{-1} and its asymmetric mode partner $\nu_{as}(CH_3)$ at 2960 cm^{-1}. The tell-tale band for the methanol product was detected through its Raman vibration at ~1100 cm^{-1} (mixed ν_a(C-O) + δ(COH)). This datum was obtained by launching 514.5 nm TE polarized laser light into the slab wave guide of the hybrid glass supported in a custom-built precision integrated optics spectrometer equipped with a fast imaging spectrograph and charge coupled device detector (57). The spectral data were acquired in real-time while the film was irradiated with UV light. This strategy allowed us to capture the spectrum of the methanol before the molecule diffused out of the film. Detailed results of the Raman experiments will be reported in a forthcoming publication.[2]

From the above account, we can speculate on the origin of the increase in the refractive index of this type of hybrid glass. The film is clearly metastable with respect to further polycondensation of the silicate network, and polymerization

[2] K. Saravanamuttu and M.P. Andrews. Manuscript in preparation.

© 1998 NRC Canada

Fig. 7. Changes in the ν(C=O) and ν(C=C) bands in thin-film hybrid glass upon ArF (6.4 eV) laser irradiation. Time of irradiation (30 Hz @ 20 mJ/cm^2): 15, 20, 60, 300 s.

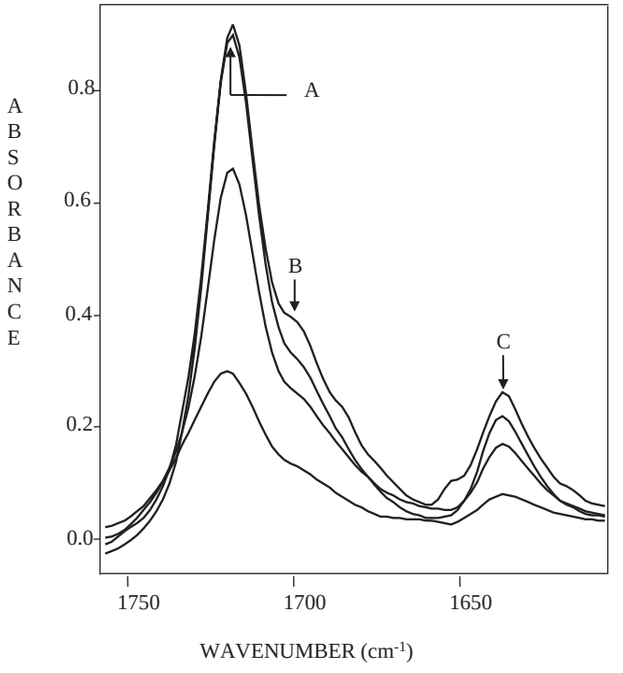

Fig. 8. Changes in the spectral features of thin films upon 6.4 eV irradiation. The line is a guide to the shifting of ν_{as}(Si-O-Si) from 1090 to 1048 cm^{-1}. The arrows mark the spectrum prior to photolysis.

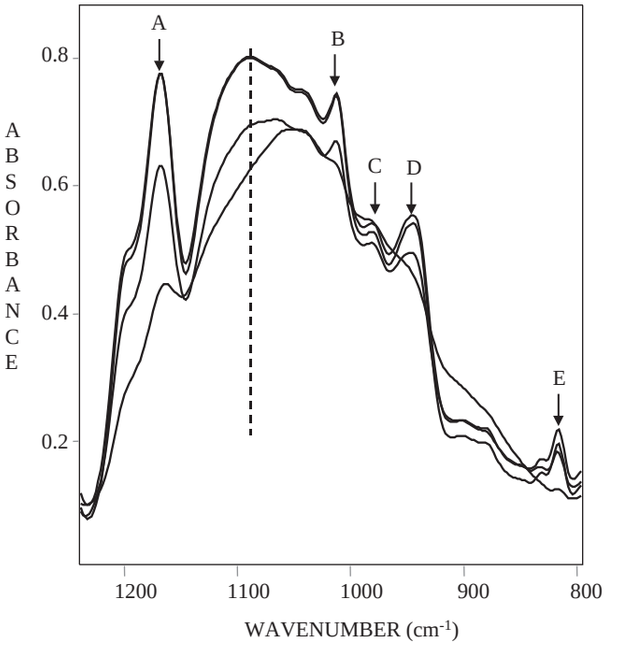

of the inorganic framework continues in concert with radical polymerization of the acrylate moieties. We suggest that a form of "photoinduced sintering" takes place in the thin film. In this view, volume compaction is initiated by molecular rearrangements associated with vinyl substituent free-radical formation, propagation and cross-linking. The latter is a standard way of increasing both the density and refractive index of polymer materials, where density and refractive index are linearly correlated (58). Network contraction during polymerization of the acrylate is caused by conversion of nonbonded distances between monomers to shorter bonding distances in polymers (59).

Volume compaction as a result of densification in this manner shows up in the Si-O-Si bond angle as an important local structural variable. In our case, UV irradiation leads to densification of hybrid glass films that is accompanied by a loss of hydroxyl groups in a manner that superficially resembles high-temperature annealing. A notable difference is that heat treatment of silica at 1000°C shifts the position of the SiO_2 ω_4-transverse optical phonon mode (60) to 1080 cm^{-1} (61). In our films this mode is peaked at 1060 cm^{-1}, with a slight shift to lower wave number after photolysis. The position of this stretching mode depends primarily on the average Si-O-Si bond angle, $\theta_{Si\text{-}O\text{-}Si}$. The decrease in energy of the peak position in our case is caused by a decrease in $\theta_{Si\text{-}O\text{-}Si}$. This band is also broadened by a distribution in the Si-O-Si angles. A shift in the IR band to lower frequency has been noted for silica films thermally grown on silicon (62). The shift to lower energy in the vibrational peak corresponded to increasing biaxial compressive stress in the thin film. In fact, increases in fictive temperature, hydrostatic pressure, or compressive stress, all cause $\theta_{Si\text{-}O\text{-}Si}$ to decrease, and the peak maximum of the TO mode to shift to lower wave number (63). We conclude that the 1060 cm^{-1} peak position for the TO phonon mode in the HSGG film also indicates an increase in density of the matrix.

In closing this section, we point out that the photoinduced densification process we have observed in the hybrid glass films is achieved at considerably lower energy than what is required to densify sol-gel-derived silica (64, 65). In the latter case, a high-energy photon (>8 eV) is involved in direct electronic excitation either of Si-OH and (or) to the conduction band of SiO_2. Bond rupture to create defects, and reassembly in the course of nonradiative decay of self-trapped excitons, could then lead to permanent atomic displacements consistent with network restructuring in SiO_2, densification, and an increase in refractive index. In contrast, the principal role of the photon in the *hybrid* glass is to decompose the photoinitiator, which in turn generates vinyl monomer free radicals. We surmise that the polymerization step precipitates the chemical and skeletal changes in the glass that are responsible for the increase in the refractive index.

Effect of 6.4 eV ArF excimer laser radiation

Bragg gratings are key building blocks of integrated optic devices (66). They are used in distributed feedback lasers, in optical-fibre amplifiers for gain flattening, and in wavelength division multiplexing. Bragg gratings can be used as mirrors to transmit light in free-space or wave guide interconnects between optical planes of photonic integrated circuits, and they have significant potential as sensing elements. Glass optical-fibre Bragg gratings have seen explosive development since the discovery (67) that periodic refractive index modulations can be written by the mutual

© 1998 NRC Canada

Fig. 9. Scanning electron micrograph of a hybrid sol-gel glass ridge wave guide produced by 4.9 eV (UV) photolithography, followed by wet-etching with isopropanol at room temperature.

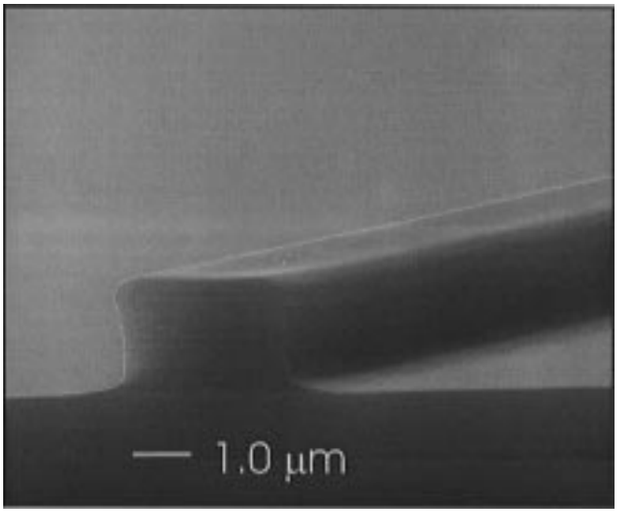

Fig. 10. Scanning electron micrograph of Bragg grating on hybrid sol-gel glass ridge wave guide. The grating is 6 μm wide by 1.5 mm long. Grating was produced by pulsed 193 nm (ArF) irradiation through a phase mask in 60 s.

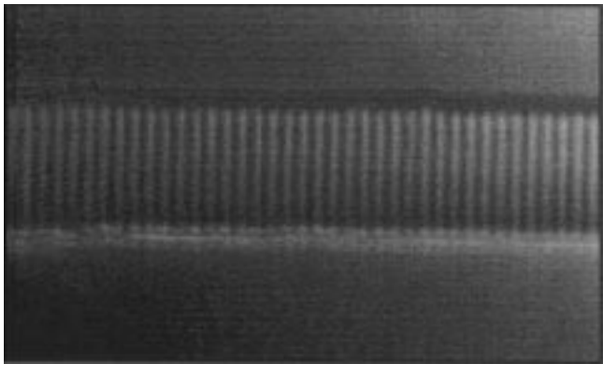

interference of counter-propagating laser beams, or by optical phase-mask technologies. It is the UV response of optical fibre that has stimulated so much recent activity into the research and technology of the photoresponse of glass (8, 68–72). The origin of the isotropic index changes in optical fibers is not still not fully understood, but it is clear that several light-activated mechanisms are involved (8, 73–77), and light-induced densification figures prominently among them (8, 78). Unfortunately, the UV-induced refractive index change in glass fibre is too small to be of practical use for making "photonic chips" the optical analogs of microelectronic integrated circuits. Among other things, this is because fibre gratings must typically be ≥1.5 cm to achieve 100% reflectivity. Recently, we reported a breakthrough in Bragg grating technology by depositing a 1.5 mm structure in a hybrid glass ridge wave guide. The grating is a factor of 10 smaller than state-of-the-art fibre gratings, and achieves

Fig. 11. Measure and calculated reflection spectra of a ridge wave guide with 6.4 eV light imprinted grating (cf. Fig. 10) for (*a*) TE and (*b*) TM modes. (Figure reproduced from ref. 54 by permission of The Society of Photo-Optical Instrumentation Engineers.)

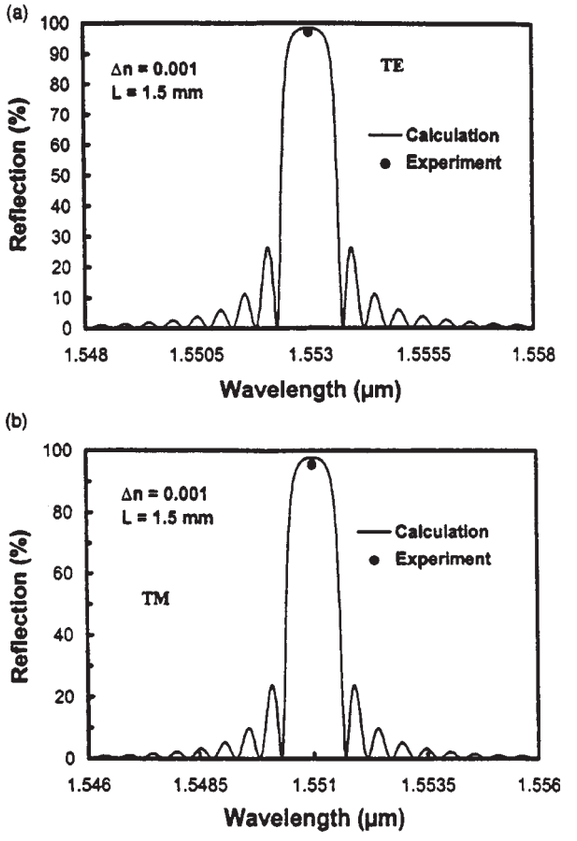

nearly 100% reflectivity, independent of polarization. Given the importance of the Bragg grating as a micro-optical element, we chose to compare the effects of 4.9 eV irradiation with those of 6.4 eV irradiation from the ArF laser.

We observed that pulsed 6.4 eV light polymerized the acrylate component of the hybrid glass within a few seconds. Changes in the electronic absorption spectra (not shown) were indistinguishable from those caused by 4.9 eV photons, except that the changes occurred in a matter of seconds. Polymerization is confirmed in Fig. 7 by the infrared spectra acquired from the thin films exposed to 6.4 eV light for various times. There is loss of ν(C=C) intensity at 1638 cm^{-1}, while the ν(C=O) mode shifts from 1718 to 1720 cm^{-1} as conjugation with the vinyl group is relieved. The accompanying silica network polycondensation reactions are also recorded in the diminishing intensities of the Si-OCH_3 and Si-OH bands (see Fig. 8). Note that the film was not exposed to 4.9 eV light at any stage of this experiment. Figure 8 shows that the ν_{as}(Si-O-Si) stretch shifts from 1090 to 1048 cm^{-1} and broadens. By comparison, only a small shift was recorded for films irradiated with the lower energy UV lamp alone. In all other respects, the spectra show the same trends elicited by radiation from the 4.9 eV

© 1998 NRC Canada

Fig. 12. FT-IR spectra showing the effects of 0.5 min of 2.5–5.0 eV irradiation followed by 6.4 eV exposure. Spectra going down are (*a*) nonirradiated; (*b–g*) 0.5 min of 2.5–5.0 eV irradiated samples exposed to 6.4 eV irradiation for 0, 5, 10, 45, 60, and 180 s.

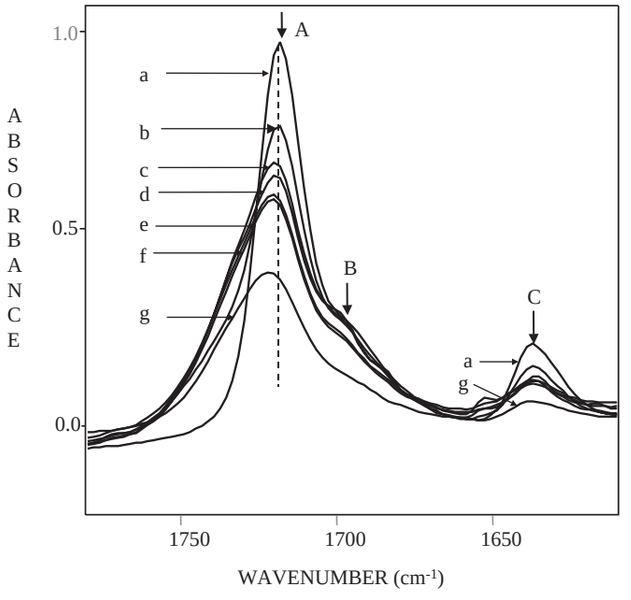

Fig. 13. FT-IR spectra showing the effects of 0.5 min of 2.5–5.0 eV irradiation followed by 6.4eV exposure. Spectra going down are (*a*) nonirradiated; (*b–g*) 0.5 min of 2.5–5.0 eV irradiated samples exposed to 6.4 eV irradiation for 0, 5, 10, 45, 60, and 180 s.

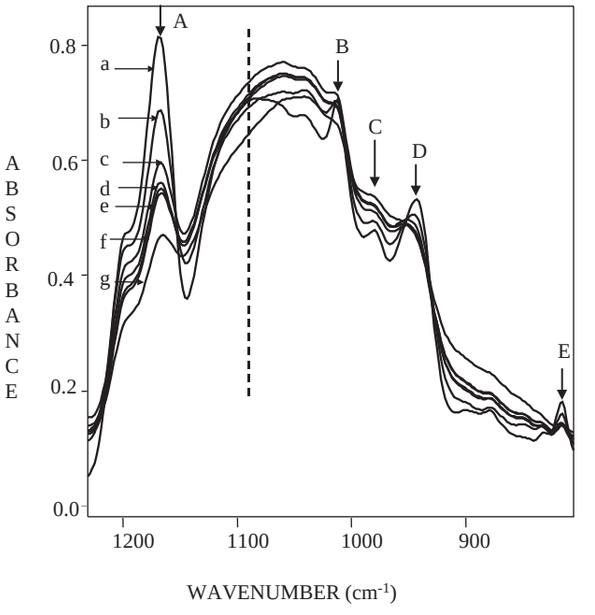

light source. This implies that matrix densification is triggered by the ArF laser as well.

Role of photosensitivity in Bragg grating fabrication

The fabrication of ridge wave guides equipped with Bragg gratings is a multistep process that includes two different UV-radiation interventions. The wave guide is first defined as a channel by narrow band 4.9 eV UV illumination through a photomask. A propanol wet-etch step is then used to remove hybrid glass from regions of the silicon wafer not exposed to the light source. Smooth-walled rectangular prism ridge wave guides exhibiting low 0.1 dB/cm loss at 1.55 μm are produced by limiting the UV exposure time to 30 s. A scanning electron micrograph of a typical ridge wave guide is shown in Fig. 9. A Bragg grating was inscribed as a volume element by generating a plus/minus first-order 6.4 eV interference pattern in the target ridge wave guide by excimer laser illumination through a precision phase mask. The 193 nm light from an ArF laser was used to deposit the grating in the wave guide in 60 s. A scanning electron micrograph of a grating is shown in Fig. 10. The structure is 6 μm wide × 2.5 μm high and has a step refractive-index profile at 1.55 μm of 0.0585. The wave guide and grating were evaluated with an Er-doped fibre laser by measuring the reflectivity of light coupled to the fundamental mode. A polarization splitter separated the TE and TM states. The TE mode gave a reflection peak at 1.553 μm and a reflectivity of 97%. At 1.551 μm, the TM mode showed 95% reflectivity. Vectoral coupled mode theory (54) was used to simulate the reflectivity of the grating for TE and TM polarization states. Figure 11 illustrates that the theoretical and experimental values for the TE (98.4%) and TM (97%) modes agree at the peak maxima. Elsewhere (79), we have obtained agreement between the measured and predicted values over the entire wavelength range.

Because the ridge wave guide/Bragg grating construction is made with two different UV energies, we chose to simulate the procedure by irradiating a hybrid glass film on thermal oxide-on-silicon substrates under the same conditions used to make the Bragg device. The response of the hybrid glass to this radiation sequence was then monitored by infrared spectroscopy. Spectra of thin gel films exposed to 0.5 min of 4.9 eV radiation, followed by periods of 6.4 eV radiation were acquired (Figs. 12 and 13).

Spectrum (*b*) in Fig. 12 was acquired after 30 s of UV radiation from the 4.9 eV source. The film was not exposed to radiation from the excimer laser. The curve reveals, as expected, that the initial phase of irradiation to define the channel guide through the photomask stimulates radical polymerization in the matrix. Spectra (*c–g*) record the outcome of successive treatments with the ArF laser. Polymerization is indicated by the gradual loss of intensity in the 1638 cm^{-1} ν(C=C) band (position C). Clearly, the conversion of vinyl substituents occurs much more rapidly (within 3 min) under the 6.4 eV source. Comparison of Figs. 3, 7, and 12 shows that the ν(C=O) stretch near 1722 cm^{-1} undergoes the same qualitative shift to higher wave number, regardless of the photon energy or sequence of irradiation. There is no clear isosbestic point in either of Figs. 7 or 12. This suggests that 6.4 eV photons open up additional photochemical channels in the hybrid glass. Indeed, the same results are obtained when the 1-hydroxycyclohexyl-1-phenylketone photoinitiator is omitted from the glass composition. By comparing Figs. 4 and 13 (*c–g*) we confirm that polymerization of the methacryloxypropyl groups at 193 nm

© 1998 NRC Canada

elicits the same kind of activity from the silicon network: there is simultaneous polycondensation of residual silanol and alkoxy groups. These events are indicated in Fig. 13 by reductions in intensity of Si-OCH_3 and Si-OH group bands (labeled A through E) in the same manner as discussed above for ~5 eV radiation.

The TE–TM polarization insensitivity of the Bragg grating, and the very high reflectivity of the diffraction element, prove that the refractive index modulation in the ridge wave guide is a volume grating in which the refractive index is periodically modulated. Scanning electron microscopy reveals that there is also a small surface corrugation on top of the ridge guide. This is certainly evident in the optical micrograph in Fig. 10 as well. The surface texture on the wave guide might be caused by laser ablation; but we have observed elsewhere (52) that direct photoinscription of channel wave guides in hybrid glass films caused material to swell out of the plane of the film. Atomic force microscopy (79) revealed topographical relief features on the order of 40 nm. Interestingly, there is evidence (80) that swelling is somewhat suppressed when a wave guide is photoinscribed through an photoinert sol-gel overlayer into a photosensitive underlayer. Shrinkage based on oligomer cross-linking in photocurable polymer systems is well understood (81). In contrast, expansion of our photolysed sol-gel films in a direction roughly normal to the film surface is unusual when considered in a simple picture of constrained densification (82). In this view, when a densified region of glass flanked by undensified glass is allowed to relax, the densified region develops tensile stress. This tensile zone will be bounded by compressive stress in the undensified region. Densification should be greatest nearest the surface of the glass where there is least constraint, with the result that the bounding glass should pull outward on the densified glass, and a depression should appear where the sample has been irradiated through the mask. This is contrary to what we observe. On the other hand, swelling in photopolymer films has been used to define relief features (83). In this case, diffusion of monomer to the illuminated region accounts for the creation of microrelief structures due to swelling normal to the surface of the film. It is difficult to argue that mass transport in our films occurs on the scale observed in photopolymer systems. Nevertheless, given the photoinduced structural reorganization of the gel matrix, we cannot eliminate the possibility that swelling may be linked to larger scale motions of monomer whose movements show up in surface microrelief.

It is tempting to attribute the refractive index modulation in the grating to densification of the hybrid glass, although additional experiments must be performed at 6.4 eV to evaluate this notion. The mechanism of Bragg grating formation in our samples is a subject for further inquiry. The change in the refractive index of an isotropic substance undergoing densification can be associated with a change in the number of oscillators per unit volume, anisotropy in the Lorentz–Lorenz polarization under stress, and variations in atomic polarizibilities with interatomic distance. Through compaction, a fractional increase in the refractive index may be viewed as the product of reorganization of existing bond structure coupled with bond formation. This is what we have argued in this paper. But there can also be contributions to the refractive index through the products of bond scission and defect formation. Schenker (20) has reported that two 6.4 eV photons densify fused silica. He concludes, nevertheless, that there is no compelling evidence that bond rupture or defect formation is associated with densification. Although defect formation is possible in our hybrid glass composites, we believe that, should they exist, their contributions to the refractive index are small compared with the collateral densification that we observe. Future studies in this laboratory will clarify the role that 193 nm light plays in the evolution of our high-reflectivity gratings.

Conclusions

New insight was provided into how integrated optics devices like ridge wave guides and Bragg gratings are inscribed by photolithography in acrylate-rich hybrid sol-gel silica glass films on silicon substrates. Arguments were advanced linking the changes in the refractive index of the composites to chemical transformations and structural relaxation leading to densification. Electronic absorption spectroscopy indicated that the acrylate species underwent polymerization when irradiated with 4.9 eV photons. Prolonged irradiation appeared to lead to secondary photochemistry that may involve polymer chain scission. Infrared spectroscopy confirmed that photoinitiated polymerization occurs in the glass. Scrutiny of the time evolution of the IR absorption bands indicated that free-radical polymerization was accompanied by additional simultaneous polycondensation in the silica matrix. Free silanol and unreacted methoxysilane were consumed in the process. Matrix densification was indicated by shifts in the transverse optical phonon mode associated with decreases in the Si-O-Si bond angle of the antisymmetric stretching vibration. Substantial growth in the Si-O-Si framework was observed through increased intensity in this IR absorption. Similar behaviour was observed for films irradiated with 6.4 eV light from an excimer laser. A phase mask in combination with pulsed 6.4 eV light was used to write a 1.5 mm, polarization-independent high-reflectivity Bragg grating into a ridge wave guide. The high reflectivity was rationalized by postulating a periodic modulation of the volume compaction of the matrix. Overall, the organic component of the glass conferred unique properties on the material that allowed it to be densified even with 4.9 eV light. By comparison, sol-gel silica with no organic component must be densified at nearly twice the photon energy.

Acknowledgments

We gratefully acknowledge support for this research through research grants from the Natural Sciences and Engineering Research Council of Canada and the National Research Council of Canada. We thank Jean-Francois Nadeau (QPS Technologies) for instruction in the operation of the ArF laser.

References

1. M.C. Goopta (*Editor*). Handbook of photonics. CRC Press, Boca Raton, Florida. 1996.

© 1998 NRC Canada

2. M.P. Andrews and S.I. Najafi (*Editors*). Sol-gel and polymer photonic devices. Critical reviews of optical science and technology. Vol. CR68. SPIE Opt. Eng. Press, Bellingham, Wash. 1997.
3. M.P. Andrews and S.I. Najafi. *In* Sol-gel and polymer photonic devices. Critical reviews of optical science and technology. Vol. CR68. *Edited by* M.P. Andrews and S.I. Najafi. SPIE Opt. Eng. Press, Bellingham, Wash. 1997. pp. 253–285.
4. M.P. Andrews. Proc. SPIE Int. Soc. Opt. Eng. **2997**, 48 (1997).
5. S.I. Najafi. Introduction to glass integrated optics. Artech House, Boston. 1992.
6. R.R.A. Syms, W. Huang, and V.M. Schneider. Electron. Lett. **32**, 1233 (1996).
7. P. Coudray, J. Chisham, M.P. Andrews, and S.I. Najafi. Opt. Eng. **36**, 1234 (1997).
8. M. Douay, W.X. Xie, T. Taunay, P. Bernage, P. Niay, P. Cordier, B. Poumellec, L. Dong, J.F. Bayon, H. Poignant, and E. Delevaque. J. Lightwave Tech. **15**, 1329 (1997).
9. (*a*) W. Primak and R. Kampwirth. J. Appl. Phys. **39**, 5651 (1968); (*b*) J. Appl. Phys. **39**, 6010 (1968).
10. P.L. Higby, E.J. Friebele, C.M. Shaw, M. Rajaram, E.K. Graham, D.L. Kinser, and E.G. Wolf. J. Am. Ceram. Soc. **71**, 796 (1988).
11. E.J. Friebele and P.L. Higby. *In* Laser induced damage in optical materials, 1987, NIST Spec. Publ. 756. *Edited by* H.H. Bennett, A.H. Guenther, D. Milam, B.E. Newman, and M.J. Soileau. NIST, Boulder, Colo. 1988. p. 89.
12. M. Rajaram, T. Tsai, and E.J. Friebele. Adv. Cer. Mater. **3**, 598 (1988).
13. C.I. Merzbacher, E.J. Friebele, J.A. Ruller, and P. Matic. Proc. SPIE Int. Soc. Opt. Eng. **1533**, 222 (1991).
14. T.A. Dellin, D.A. Tichenor, and E.H. Barsis. J. Appl. Phys. **48**, 1131 (1977).
15. C.B. Norris and E.P. EerNisse. J. Appl. Phys. **45**, 3876 (1974).
16. J.S. Lukesh. Phys. Rev. **97**, 345 (1955).
17. W. Primak. Phys. Rev. **110**, 1240 (1958).
18. J.B. Bates, R.W. Hendricks, and L.B. Schaffer. J. Chem. Phys. **61**, 4163 (1974).
19. J.L. Brebner, L.B. Allard, M. Verhaegen, M. Essed, J. Albert, P. Simpson, and A. Knights. Proc. SPIE Int. Soc. Opt. Eng. **2998**, 122 (1997).
20. R.E. Schenker and W.G. Oldham. J. Appl. Phys. **82**, 1065 (1997).
21. D.C. Allan, C. Smith, N.F. Borelli, and T.P. Seward III. Opt. Lett. **21**, 1960 (1996).
22. H. Imai, K. Awazu, M. Yasumori, H. Onuki, and H. Hirashima. J. Sol-Gel. Sci. Technol. **8**, 365 (1997).
23. D.C. Allan, C. Smith, N.F. Borelli, and T.P. Seward III. Opt. Lett. **21**, 1960 (1996).
24. (*a*) C.J. Brinker and G.W. Scherer. Sol-gel science. Academic Press, New York. 1990; (*b*) *In* Chemistry, spectroscopy and applications of sol-gel glasses. *Edited by* R.R. Reisfeld and C.K. Jørgenson. Springer-Verlag, Berlin. 1992; (*c*) L.C. Klein. Ann. Rev. Mater. Sci. **23**, 437 (1993).
25. G.W. Scherer. J. Sol-Gel Sci. Technol. **8**, 353 (1997).
26. P. Coudray, J. Chisham, M.P. Andrews, A. Malek-Tabrizi, C.-Y. Li, and S.I. Najafi. Opt. Commun. **128**, 19 (1996).
27. C.-Y. Li, J. Chisham, M.P. Andrews, S.I. Najafi, J.D. Mackenzie, and N. Peyghambarian. Electron. Lett. **31**, 271 (1995).
28. P. Coudray, J. Chisham, M.P. Andrews, and S.I. Najafi. Opt. Eng. **36**, 1234 (1997).
29. M.A. Fardad, T. Touam, P. Meshkinfam, R. Sara, X. M. Du, M.P. Andrews, and S.I. Najafi. Electron. Lett. **33**, 1069 (1997).
30. M.A. Fardad, M.P. Andrews, G. Milova, A. Malek-Tabrizi, and I. Najafi. Appl. Opt. **37**, 2429 (1998).
31. M.P. Andrews and S.I. Najafi. Proc. SPIE Int. Soc. Opt. Eng. **2998**, 293 (1997).
32. (*a*) B. Novak. Adv. Mater. **5**, 422 (1993); (*b*) P. Judenstein and C Sanchez. J. Mater. Chem. **6**, 511 (1996); (*c*) U. Schubert, N. Husing, and A. Lorenz. Chem. Mater. **7**, 2010 (1995).
33. J.F. Rabek. Mechanisms of photophysical processes and photochemical reactions in polymers. Wiley, New York. 1987.
34. H. Krug, F. Tiefensee, P.W. Oliviera, and H. Schmidt. Proc. SPIE Int. Soc. Opt. Eng. **1758**, 448 (1992).
35. X.T.P. Phan. J. Radiat. Curing, **13**, 18 (1986).
36. C.N.R. Rao. Ultra-violet and visible spectroscopy, chemical applications. 3rd ed. Butterworths, London. 1974. pp. 42–47.
37. J.G. Calvert and J.N. Pitts. Photochemistry. Wiley, New York. 1966. pp. 247–268.
38. P.A. Leermakers and H.T. Thomas. J. Am. Chem. Soc. **87**, 1621 (1965).
39. M. Ito, K. Inuzuka, and S. Imanishi. J. Am. Chem. Soc. **82**, 1317 (1960).
40. T. Mitsuoka, A. Torikai, and K. Fuenki. J. Appl. Polym. Sci. **47**, 1027 (1993).
41. P.M.Fritz, Q.Q. Zhu, and W. Schnabel. Eur. Poly. J. **30**, 1335 (1994).
42. D.L. Ou and A.B. Seddon. J. Non-Cryst. Solids. **210**, 187 (1997).
43. R.T. Conley. Espectroscopia infraroja. Alhambra, Madrid. 1979. pp. 187–194.
44. A.L. Smith. Spectrochim. Acta, **16**, 87 (1960).
45. A.L. Smith. Analysis of silicones. Wiley, New York. 1974. pp. 257–281.
46. B. Stuart. Modern infrared spectroscopy. *Edited by* D.J. Ando. Wiley, New York. 1996.
47. K. Nakamoto. Infrared and raman spectra of inorganic and coordination compounds. 4th ed. Wiley, New York. 1986.
48. M. In, C. Gerardin, J. Lambard, and C. Sanchez. J. Sol-Gel Sci. Technol. **5**, 101 (1995).
49. X. Li and T.A. King. J. Non-Cryst. Solids, **204**, 235 (1996).
50. C.N.R. Rao. Chemical applications of infrared spectroscopy. Academic Press, New York. 1963. p. 24.
51. B.K. Coltrain, C.J.T. Landry, J.M. O'Reilly, A.M. Chamberlain, G.A. Rakes, J.S. Sedita, L.W. Kelts, M.R. Landry, and V.K. Long. Chem. Mater. **5**, 1445 (1993).
52. P. Coudray, J. Chisam, M.P. Andrews, and S.I. Najafi. Opt. Eng. **36,** 1234 (1997).
53. (*a*) T. Touam, G. Milova, Z. Saddiki, M.A. Fardad, M.P. Andrews, J. Chrostowski, and S.I. Najafi. Thin Solid Films, **203**, 307 (1997); (*b*) T. Touam, G. Milova, Z. Saddiki, M.A. Fardad, M.P. Andrews, and S.I. Najafi. Proc. SPIE Int. Soc. Opt. Eng. **2997**, 79 (1997).
54. X.M. Du, T. Touam, L. Degachi, J.L. Guilbault, M.P. Andrews, and S.I. Najafi. Opt. Eng. **37**, 91 (1998).
55. C.J.T. Landry, B.K. Coltrain, J.A. Wesson, J.L. Lippert, and N. Zumbulyadis. Polymer, **33**, 1496 (1992).
56. N.K. Raman, M.T. Anderson, and C.J. Brinker. Chem. Mater. **8**, 1682 (1996).
57. J. Baldwin, N. Schuhler, I.S. Butler, and M.P. Andrews. Langmuir, **12**, 6389 (1996).
58. H.M. Cohen and R. Roy. Phys. Chem. Glasses, **6**, 149 (1965).
59. J.G. Kloosterboer, G.M.M. van de Hei, R.G. Gossink, and G.C.M. Dortant. Polymer Commun. **25**, 322, (1984).
60. F.L. Galeener. Phys. Rev. B: Condens. Matter, **19**, 4292 (1979).
61. R.M. Almeida, T.A. Guiton, and C.G. Patano. J. Non-Cryst. Solids, **121**, 193 (1990).
62. G. Lucovsky, J.T. Fitch, E. Kobeda, and E.A. Irene. *In* The physics and chemistry of the SiO_2 and Si-SiO_2 interface. *Edited by* C.R. Helms and B.E. Deal. Plenum Press, New York. 1988. p. 139.

© 1998 NRC Canada

63. A. Agarwal and M. Tomozawa. J. Non-Cryst. Solids, **209**, 166 (1997).
64. H. Imai, H. Hiroshima, K. Awazu, and H. Onuki. J. Ceram. Soc. Jpn. **102**, 1092 (1994).
65. H.Himai, H. Hirashima, K. Awazu, and H. Onuki. Proc. SPIE. Int. Soc. Opt. Eng. **2288**, 71 (1994).
66. T. Tamir. Guided-wave optoelectronics. Springer-Verlag, Heidelberg, Germany. 1988.
67. K.O. Hill, Y. Fujii, D.J. Johnson, and B.S. Kawasaki. Appl. Phys. Lett. **32**, 647 (1978).
68. G. Meltz, W.W. Morey, and W.H. Glenn. Opt. Lett. **14**, 823 (1989).
69. D.P. Hand and P. St. J. Russell. 17th Int. Conf. Integrated Optics Optical Commun. IOOC '89. Paper 21C3–4. Kobe, Japan. 1989.
70. J.-L Archambault, L. Reekie, and P. St. J. Russell. Electron. Lett. **26**, 453 (1993).
71. P. Simon, H. Gerhardt, and S. Szatmari. Opt. Lett. **14**, 1207 (1989).
72. T. Tomie, I. Okuda, and M. Yano. Appl. Phys. Lett. **55**, 325 (1989).
73. P. St. J Russell, L.J. Poyntz-Right, and D.P. Hand. Proc. SPIE Int. Soc. Opt. Eng. **1373**, 126 (1990).
74. Photosensitivity and quadratic nonlinearity in glass waveguides: fundamentals and applications. Technical digest. Vol. 22. Optical Society of America, Washington, D.C. 1995.
75. (*a*) K.O. Hill, B. Malo, F. Bilodeau, and D.C. Johnson. Ann. Rev. Mater. Sci. **23**, 125 (1993); (*b*) M.G. Sceats, G.R. Atkins, and S.B. Poole. Ann. Rev. Mater. Sci. **38**, 123 (1993).
76. D.P. Hand and P. St. J. Russell. Opt. Lett. **15**, 102 (1990).
77. D. Wong, S.B. Poole, and M.G. Sceats. Opt. Lett. **17**, 1773 (1992).
78. J.P. Bernardin and N.H. Lawandy. Opt. Commun. **79**, 194 (1990).
79. T. Touam, X.M. Du, M.A. Fardad, M.P. Andrews, and S.I. Najafi. Opt. Eng. **37**, 1136 (1998).
80. P. Coudray, Y. Moreau, P. Etienne, and J. Porque. *In* Sol-gel and polymer photonic devices. Critical reviews in optical science and technology. Vol. CR68. *Edited by* M.P. Andrews and S.I. Najafi. SPIE, Bellingham, Wash. 1997. pp. 286–303.
81. P. Karrer, S. Corbel, J.C. Andre, and D. Lougnot. J Polym. Sci. A: Polym. Chem. **30**, 2715 (1992).
82. N.F. Borelli, C. Smith, D.C. Allen, and T.P. Seward III. J. Opt. Soc. Am. **14**, 1606 (1997).
83. V. Krongauz. *In* Processes in photoreactive polymers. *Edited by* V. Krongauz and A. Trifunac. Chapman and Hall, New York. 1994. pp. 185–259.

© 1998 NRC Canada

Vibrational spectra and structure of tris(8-hydroxyquinoline)aluminum(III)

Mathew D. Halls and Ricardo Aroca

Abstract: The vibrational spectra of one of the most commonly used light-emitting materials for organic electroluminescence (EL) devices, tris(8-hydroxyquinoline)aluminum (Alq_3), is presented. The geometry and normal modes of *fac*-Alq_3 isomer in the ground state have been computed for the first time using ab initio methods (HF/6-31G*) to aid in discussion of normal-mode assignment. Normal inelastic scattering excited at 633 nm and low-temperature FT-Raman in addition to the infrared spectra of this material are reported. The vibrational characterization of thin solid films of the material was attempted using transmission and reflection–absorption FT-IR spectroscopy (RAIRS) on smooth silver films.

Key words: tris(8-hydroxyquinoline)aluminum, Alq_3, ab initio, assignments, infrared, Raman, thin films.

Résumé : On a déterminé le spectre de vibration du tris(8-hydroxyquinoléine)aluminium (Alq_3), l'un des produits les plus couramment utilisés comme émetteur de lumière dans des appareils d'électroluminescence (EL) organique. Utilisant des méthodes ab initio (HF/6-31G*) comme aide dans la discussion de l'attribution du mode normal, on a calculé pour la première fois la géométrie et les modes normaux de l'isomère *fac*-Alq_3 dans son état fondamental. En plus de son spectre infrarouge, on a aussi observé une diffusion inélastique normale excitée à 633 nm ainsi que le spectre Raman « FT » à basse température de ce produit. On a tenté de faire une caractérisation vibrationnelle de films solides minces de ce produit en faisant appel à la spectroscopie de transmission et de réflexion infrarouge FT (« RAIRS ») de films d'argent lisses.

Mots clés : tris(8-hydroxyquinoléine)aluminium, Alq_3, attributions ab initio, infrarouge, Raman, films minces.

[Traduit par la Rédaction]

Introduction

The properties of a class of organic materials, polymers, and metal complexes are being intensively investigated in relation to light-emitting diodes. Organic electroluminescent (EL) devices are light-emitting diodes in which the active components consist entirely of organic materials (1–3). Organic EL devices are one of the most promising next generation flat panel display systems. In the fabrication of these devices organic materials are incorporated as vacuum-deposited thin solid films. The research and development of the EL devices requires in situ characterization of the organic material in order to understand aging and other variables related to device performance. One of the objectives of the current work is to provide the reference vibrational spectra as well as the interpretation of the thin solid film spectra for these materials. One of the key materials, commonly used in quinolate organic heterojunction light emitting devices, is the electron-transporting aluminum complex tris(8-hydroxyquinoline)aluminum (Alq_3) (2, 3). The present report discusses structural and vibrational properties of Alq_3. Aided by ab initio computations, the interpretation of normal modes observed in FT-Raman spectra, at room and liquid nitrogen temperatures, and in the infrared spectra of Alq_3 in KBr matrices and thin solid films is given. The photophysics and exciton dynamics in thin solid films of Alq_3 have been recently studied (4, 5). The electronic spectroscopy of Alq_3 films has also been reported by Hopkins et al. (6). Ultraviolet photoemission spectroscopy and semiempirical molecular orbital calculations have been used to investigate the electronic structure of Alq_3 (7). Methods for the fabrication of Alq_3 films have also been discussed in the literature (8). However, the complete vibrational analysis of Alq_3 has not been reported and there are no ab initio calculations published on this molecular system. There are reports on certain aspects of the vibrational spectra of Alq_3. The infrared spectrum in the 600–250 cm^{-1} region (9) was studied to identify the isomers of Alq_3: three infrared bands at 466, 455, and 444 cm^{-1} were associated with the C_{2v} isomer, while bands at 418 and 402 cm^{-1} were assigned to the C_{3v} isomer. The SERS (Surface Enhanced Raman Spectra) of Alq_3 films on silver is the only report on the Raman spectrum of Alq_3.[2]

Received March 12, 1998.

M.D. Halls. Department of Chemistry, Wayne State University, Detroit, MI 88202, U.S.A.
R. Aroca.[1] Materials and Surface Science Group, Department of Chemistry and Biochemistry, University of Windsor, Windsor, ON N9E 3P4, Canada.

[1]Author to whom correspondence may be addressed. Telephone: (519) 253–4232, ext. 3591, 3528.
E-mail: G57@server.uwindsor.ca

[2]N.S. Ferris and J.E. Littman. Private communication.

© 1998 NRC Canada

The interpretation of vibrational spectra collected for large molecules can be difficult due to the high density of states resulting in spectral complexity and congestion, particularly in the spectral region below 1600 cm^{-1}. In recent years, in order to complement experimental data and assist in the assignment of vibrational spectra, it has become standard to perform ab initio computations at the Hartree–Fock (HF) level to obtain normal frequencies, atomic displacement representations, and spectral intensities. The present-day application of electronic structure methods to predict vibrational properties for reasonably large molecular systems (50–100 atoms) is due to both the availability of analytic HF second derivatives since the 1980s (10) and the dramatic progress in computer technology.

Caution should be exercised when comparing calculations for molecules in gas phase and experimental data obtained for molecules in solid phase. There are several factors that could lead to considerable differences between computed and observed spectra. The computed frequencies are for the ab initio harmonic potential and the spectral intensities are computed in the double harmonic approximation (11). Also the dipole-moment derivatives and polarizability derivatives are those for the isolated molecular system. In the solid there may be a change in the shape and intensity of the vibrational bands, and each nondegenerate vibrational energy level of the free molecule in a crystal splits into as many components as there are molecules in primitive unit cell (Davydov splitting) (12). Finally, both external vibrations and internal vibrations may be observed experimentally. The comparison between the unperturbed (calculated) and the perturbed molecule is approximately valid as long as the molecular identity is retained in the solid phase.

Experimental

A sample of the purified material was provided by Dr. J. Duff of the Xerox Research Centre of Canada. The main reference in the infrared spectra is the transmission spectrum of the isotropically dispersed Alq_3 in KBr. Infrared spectra were recorded in the region of 400–4000 cm^{-1} on the Bomem DA3 FT-IR spectrometer with 1 cm^{-1} resolution. The reflection absorption infrared spectra were recorded on an in-house modified Bomem 110-E equipped with a Judson midrange (650 cm^{-1}) 1 × 1 mm MCT detector. The substrate holder consisted of a flat aluminum heating element, which was thermally controlled by a 100 V variastat. The temperature of the substrate was monitored using a thermocouple. Annealing of the sample during the RAIRS measurements was performed in situ on the heating plate.

The FT-Raman spectrum of Alq_3 was recorded with a Bruker RFS100. A Nd:YAG laser (1064 nm with 60 mW at sample location) was used as the excitation source, and the spectra were collected with a 2 cm^{-1} resolution at liquid nitrogen temperature. The Raman spectra were also recorded at room temperature with 2 cm^{-1} resolution using the 633 nm laser line in a Renishaw System 2000.

Computational

Calculations were carried out at the MNDO (13) and Hartree–Fock levels of theory. Hartree–Fock calculations were performed using the standard split-valence basis set augmented with a single set of polarization functions on heavy atoms (6-31G*) (14). Computations consisted of geometry optimization followed by a subsequent harmonic frequency calculation at the same level of theory. The calculations were carried out using Gaussian 94 RevD.3 (15) running on a Cray J90 computer, requesting two processors and 381 MB of dynamic memory with total running time of 3.6 days.

Experience using HF/6-31G* to predict ground-state molecular properties is quite extensive. It is well known that ab initio computed frequencies are typically larger than the observed fundamentals. This overestimation is due to the neglect of electron correlation, basis-set truncation, and neglect of anharmonicity (16). To compensate overestimation, various scaling strategies are employed to bring the computed harmonic frequencies into better agreement with observed fundamentals (17). In the present work the simplest strategy is employed, that of homogeneous frequency scaling, using the empirical scaling factor (0.8953) determined by Scott and Radom (18). The vibrational assignments reported in this work were made using a combination of atomic displacement vector analysis, visual interpretation of normal modes, intensity pattern, and frequency matching as well as using previously reported assignments of related molecules.

Fig. 1. Computed geometric parameters for the 8-hydroxyquinoline aluminum unit at the HF/6-31G* level. Bond lengths are in boldface, interatomic angles are in regular face. The predicted quinoline ring geometry is planar.

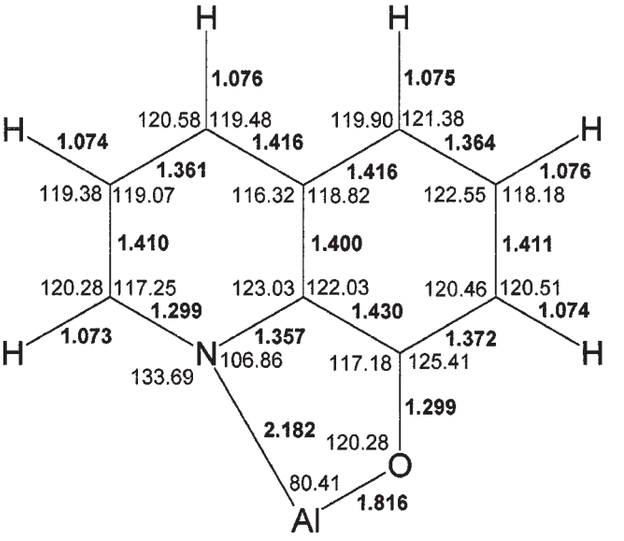

Results and discussion

Molecular structure

The geometry of Alq_3 was calculated without symmetry constraints (C_1). Subsequent frequency calculations verified these results to be true energy minima, yielding only positive harmonic frequencies. A preliminary geometry optimization was performed using the semiempirical method MNDO for comparison with the higher level of theory. Structural parameters are shown in Fig. 1. Good agreement was found between the predicted geometries of MNDO and HF/6-31G*. Both methods predict a planar geometry for the

© 1998 NRC Canada

Fig. 2. Computed Mulliken atomic charges for the the 8-hydroxyquinoline aluminum unit at the HF/6-31G* level. Overall predicted dipole moment is 9.369 Debye.

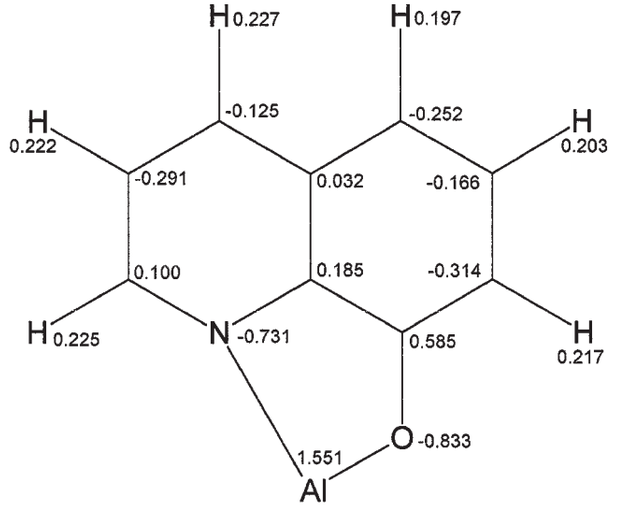

quinolate ligand with negligible deviations. The oxine ligands make improper torsion angles of 13.48° and 16.22° with each other, measured with respect to the central C—C bond at the MNDO and HF levels. N-Al-N and O-Al-O bond angles are predicted to be 88.15° and 101.50°, respectively, at the MNDO level and 87.76° and 100.69° at the HF/6-31G* level.

To the best of our knowledge a detailed analysis of the crystal structure of Alq_3 has not been reported to date. In thin films Alq_3 is believed to form amorphous, monomeric films (6, 8). Several reports have been published of the crystal and molecular structures of other metalo-quinolates. Comparison between the HF/6-31G* Alq_3 geometry and reported experimental structures for Cuq_2 (19) and Znq_2 (20) show that the geometry of the quinolate ligand is largely insensitive to metal substitutions. It is reported that in both Mq_2 complexes the ligand was planar within experimental error, with the quinolate geometry having identical dimensions, although the metal centres have different electronic configurations (20). The calculations reported here support this trend of quinolate geometry conservation with Alq_3.

Frontier orbitals and charge

Atomic charges are important in considering infrared intensities, molecular packing in crystals, and are useful in molecular dynamics simulations. The most popular scheme for partitioning atomic charges is the Mulliken scheme. The Mulliken charges are shown in Fig. 2. The overall permanent dipole moment computed at the HF/6-31G* level is 9.369 Debye for the *fac*-Alq_3 isomer.

The computed highest occupied and lowest unoccupied molecular orbital energies are presented in Table 1. Frontier orbital energies for electroluminescent materials, such as Alq_3, are important in determining operating voltages and efficiency of thin film devices, since they determine barriers to carrier injection as well as emission characteristics. Numerous reports of experimental determinations of the ionization potential and frontier orbital energies by UPS and optical spectroscopies have appeared in the literature (6, 7, 21). These reports are in agreement in assigning a HOMO energy of 6.65 eV, and an ionization potential of 5.93 eV. The Hartree–Fock calculations in this work predicted a HOMO energy of 7.34 eV in good agreement with the experimental data. Analysis of the electronic structure obtained from high-level quantum chemical calculations for organic EL materials is needed to elucidate structure–property relationships and to rationalize the mobility of carriers over the molecular structure. The detailed electronic structure of Alq_3 in its neutral and ionic state will be described elsewhere.[3]

Table 1. Calculated energies of some of the highest occupied and lowest unoccupied molecular orbitals of Alq_3.

	HF/6-31G*	
	(Hartrees)	(eV)
	0.226	6.141
	0.197	5.366
	0.197	5.366
	0.19	5.179
	0.125	3.396
	0.125	3.396
	0.113	3.085
	0.081	2.191
	0.076	2.08
LUMO	0.076	2.08
HOMO	–0.27	–7.34
	–0.271	–7.363
	–0.271	–7.363
	–0.328	–8.938
	–0.328	–8.938
	–0.332	–9.027
	–0.398	–10.837
	–0.398	–10.837
	–0.405	–11.029
	–0.431	–11.733
	–0.431	–11.733

Vibrational spectra

Low frequency and M-L vibrations

The calculated Raman spectrum at HF/6-31G* level of theory is presented in Fig. 3 and can be compared with the FT-Raman spectrum of the solid at liquid nitrogen temperature. There is generally good agreement for the relative intensities of different group frequencies. The strongest Raman bands are in the 1300–1600 cm^{-1} region and correspond to the ring-stretching vibrations. The low wave number region recorded at liquid nitrogen and room temperatures is illustrated in the inset in Fig. 3. Three strong bands are observed in the low-temperature Raman spectrum at 71, 98, and 120 cm^{-1}. Two weaker bands are seen at 154 and 167 cm^{-1}. The lowest observed vibrational mode for 8-hydroxyquinoline is at 162 cm^{-1} (22) and an ab initio at HF/6-31G* level of theory gives the lowest calculated wave

[3] M.D. Halls, R. Aroca, and H.B. Schlegel. To be published.

© 1998 NRC Canada

Fig. 3. Calculated Raman spectrum and FT-Raman spectrum of Alq_3. Inset contains the low spectral region recorded at two different temperatures.

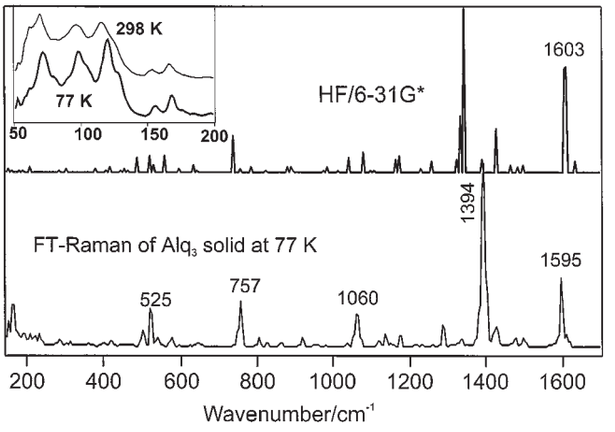

number at 165 cm^{-1}. Therefore, the bands at 154 and 167 cm^{-1} are confidently assigned to ring-wagging modes of the 8-hydroxyquinoline ligands. A far-infrared spectrum recorded with the Bruker (model 113) vacuum bench FT-IR instrument gives two bands with wave numbers in the low region at 123 and 111 cm^{-1}. The FT-Raman at room temperature shows a broad band with a maximum at 117 cm^{-1} and a shoulder at 124 cm^{-1}. The calculated spectra predicts two bands at 117 cm^{-1}. It seems reasonable to assign the low-temperature band at 120 cm^{-1} to the Al–oxine deformation + Al–N stretching. The infrared band at 111 cm^{-1} is assigned to the Al–oxine deformation. The Raman band at 98 cm^{-1} in the low-temperature spectrum (broad-band centre at 97 cm^{-1} in the room-temperature spectrum) is also assigned to an Al–oxine deformation mode. Less definitive is the assignment of the lowest observed Raman band at 71 cm^{-1} (69 cm^{-1} at room temperature with a shoulder at 61 cm^{-1}). The shoulder is not observed at low temperature, and only the sharp peak at 71 cm^{-1} is seen as shown in Fig. 3. Therefore, the apparent shift could be due to less overlapping of the two bands, or to the fact that this particular mode could be an external vibration. We assumed that this band corresponds to an internal vibration.

The calculated infrared spectrum and the reflection–absorption infrared spectrum (RAIRS) of a thin solid film of Alq_3 are given in Fig. 4. It can be seen that there is good agreement between the general patterns of relative intensities. For completeness, a comparison between the FT-IR spectrum of the reference, Alq_3 dispersed in KBr, and the Raman spectrum of the powder are shown in Fig. 5. A discussion of the vibrational spectra of the ligand and references to some metallo-quinolates can be found in the report of Marchon et al. (22). Correlations of metal–oxygen vibrations in quinolate transition-metal complexes (Mn^{2+}, Co^{2+}, Ni^{2+}, Cu^{2+}, Zn^{2+}, Cr^{2+}, Cr^{3+}, Fe^{3+}) have been collected and discussed by Shabaka et al. (23). The metal–oxygen vibration is observed with a strong relative infrared intensity in the spectral region from 487 cm^{-1} (Mn^{2+}) to 522 cm^{-1} for the Cr^{3+} complex. Similarly, the M–N stretching vibration in the complexes has been found in the 392–417 cm^{-1} infrared region. The AlO diatomic frequency is observed at 979 cm^{-1}, and the complex Al-O is expected at a lower value. The

Fig. 4. Calculated infrared spectrum and RAIRS spectrum of the Alq_3 thin solid film.

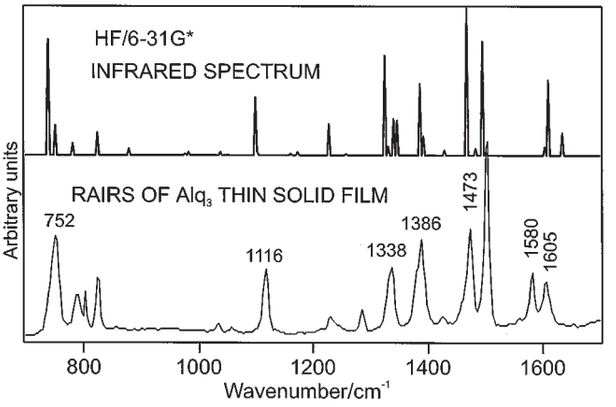

Fig. 5. Raman spectrum of Alq_3 solid powder and infrared spectrum of Alq_3 dispersed in a KBr pellet.

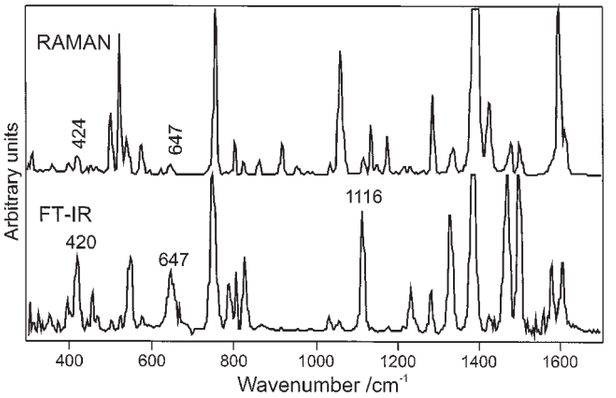

scaled ab initio vibrational frequencies, spectral intensities, observed wave numbers, and vibrational assignments are given in Table 2. The first column has been included to indicate the accidental degeneracy (deg.) found due to characteristic frequencies of the quinoline moities. Characteristic wave numbers to be used in materials characterization applications appear in **bold** in Table 2. The units quoted for experimental integrated intensities are various. However, the unit recommended (SI) is km mol^{-1}. The calculated infrared intensities are given in km mol^{-1}. The common unit "dark" (cm $mmol^{-1}$) divided by 100 gives the intensity in km mol^{-1}. A very strong absorption band is on the order of 1000 km mol^{-1} (for example, the band at 1464 cm^{-1} has an intensity of 962 km mol^{-1}). A weak absorption band is in the order of 0.1 km mol^{-1}. The scattering coefficients are commonly given in $cm^4\ g^{-1}$ ($N \times 10^{-32}$). The calculated values are given in $Å^4$ amu^{-1} and the numerical values are identical. For instance, the scattering coefficients for the ν_1 (in CH_4) is 223 $\times 10^{-32} \times N$ ($cm^4\ g^{-1}$) = 223 $Å^4$ amu^{-1}.

Wave numbers of the oxine ligand

The $Al(C_9H_6NO)_3$ complex has 150 normal modes, and in order to discuss the vibrational spectrum, the quinolinato chelating-agent vibrations and the metal–oxygen vibrations are discussed separately. The chelating agent 8-quinolinol,

© 1998 NRC Canada

Table 2. HF/6-31G* scaled normal mode frequencies, spectral intensities, experimental wave numbers, and proposed assignments of Alq_3.

				Observed		
Deg.	Scaled (cm^{-1})	IR intensity (km/mol)	Raman ($Å^4$/amu)	IR (cm^{-1})	Raman (cm^{-1})	Interpretation
3	3057	41	412	3067	3068	C–H stretch
3	3040	39	627	3049	3052	C–H stretch
3	3038	55	296	3035		C–H stretch
3	3025	115	615	3012		C–H stretch
3	3018	6	165		3010	C–H stretch
3	3006	28	209	3005	3008	C–H stretch
3	1629	99	31			Ring stretching
3	1607	314	162	**1605**	1609	Ring stretching
3	1603	36	183	**1580**	**1595**	Ring stretching
1	1500	17	2	1539		Ring stretching
2	1494	238	5	**1500**	1507	Ring stretching
1	1478	28	6		1478	Ring stretching
2	1464	962	11	**1473**	1471	Ring stretching
3	1425	22	96	1425	1424	Ring stretching + CH bend
1	1390	80	19		**1394**	Ring stretching + CH bend
2	1384	303	11	**1386**		CH bend + ring stretching
1	1343	151	476		1335	Ring str. + CO str. + CH bend
2	1337	157	195	**1338**		Ring str + CO str. + CH bend
1	1329	41	85	1328		CH bend + ring str
2	1323	416	18	1310		CH bend
3	1257	19	27	1282	1285	CH bend
1	1229	0	4	1245	1245	CN stretch + CH bend
2	1223	133	4	1230	1230	CN stretch + CH bend
3	1168	16	24	1174	1173	CH bend
3	1159	9	20	1135	1133	CH bend
1	1100	19	2	**1116**	1117	C–O stretch + CH bend
2	1096	243	3			CH bend
3	1077	1	29	1055	**1060**	CH bend
3	1037	20	32	1033	1036	CH bend
3	1007	1	1	1000	1001	CH wag
3	986	2	7	988		CH wag
3	981	22	2	981	981	Ring deformation
1	977	2	1	966		CH wag
2	974	5	1		950	CH wag
1	893	0	2		918	Ring def. + AlN str
2	889	3	7	898		Ring def.+ AlN str
3	880	28	7	862	862	CH wag
3	822	153	1	**825**	825	CH wag
3	783	50	9	806	804	Ring deformation
3	781	50	6	**789**		CH wag
3	753	123	5	**752**		CH wag
3	741	480	55		**757**	Ring breathing
3	643	136	3	656	656	CH wag
2	636	99	8	648	647	AlO str. + ring def.
1	632	50	11		625	AlO str. + AlN str. + ring def.
3	595	2	6		596	CH torsion
3	561	16	23	577	577	Ring def. + AlOC bend
2	533	191	11	545	548, 541, 534	AlO str. + AlN str. + ring def.
1	519	7	24	525	**525**	Ring def. + AlO str
1	491	2	7	504	504	Ring deformation
2	488	15	23	471	470	Ring deformation
3	467	3	0			Ring deformation
2	456	33	4	458	456	CH torsion

© 1998 NRC Canada

Table 2. (*concluded*)

Deg.	Scaled (cm^{-1})	IR intensity (km/mol)	Raman ($Å^4$/amu)	Observed IR (cm^{-1})	Observed Raman (cm^{-1})	Interpretation
1	447	0	1	447	445	CH torsion
2	415	97	7	420	428	Ring deformation
1	405	25	1	405	404	Ring def. + AlO str
2	378	125	4		364	Ring def. + AlOC bend
1	305	22	6	315	314	AlN str. + CCO bend
3	284	4	3		294, 288, 282	Ring torsion
1	220	1	0		239	Ring torsion
2	211	9	6	224	227, 211	Oxine wag
1	190	6	1	197	197	Oxine wag
2	181	22	1	191	186	Ring torsion
1	164	0	1		**168**	"Butterfly" mode
2	152	3	4		156	Oxine wag
1	122	0	1		127	C–O–Al bend
2	117	6	5	123	120	Al–oxine def. + AlN str
1	53	1	14	111	104	Al–oxine def.
2	45	1	7		98	Al–oxine def.
1	38	1	3		80	Al–oxine def.
2	21	1	12		71	Al–oxine def.

also known as 8-hydroxyquinoline or oxine (Ox) forms stable complexes with many metal cations (22).

The six C–H stretching vibrations (18 internal modes) are observed in the infrared and Raman spectra forming a broad band produced by the overlapping of several components. The wave numbers reported in Table 2 correspond to the centre of the components obtained by fitting using Voigt profiles.

The oxine C–H out-of-plane bending modes are observed (22) with strong relative intensity at 742, 781, and 818 cm^{-1}. Similarly, there are three strong infrared bands in Alq_3 at 752, 789, and 825 cm^{-1}, in good agreement with the calculated spectrum, that are assigned to the C–H out-of-plane modes of the oxine moiety. The computations confirm the commonly observed fact that the C–H out-of-plane modes are strong only in the infrared spectrum. These frequencies are seen in Table 2 with an accidental degeneracy of 3, confirming their assignment as a characteristic frequency of oxine in Alq_3. The ring-breathing vibration of oxine is observed at 710 cm^{-1} with a strong Raman intensity. The calculated value for Alq_3 is 741 cm^{-1}, carrying large infrared and Raman intensities. The only strong Raman band in that region is seen at 757 cm^{-1} and is thereby assigned to the breathing mode of the oxine moiety.

Characteristic ring-stretching modes (shown in boldface in Table 2) are observed in reasonably good agreement with calculated values. The strongest Raman band in the Alq_3 spectrum is observed at 1394 cm^{-1}, in contrast to the oxine Raman spectrum (22) where three strong bands are present in this region at 1351, 1378, and 1435 cm^{-1}.

Vibrational wave numbers observed in the spectral region below 700 cm^{-1} correspond to modes that are highly coupled and their assignment is generic. The description given is from the computed spectrum. For practical applications the spectral region given in Fig. 3 is clearly the most appropriate, and the vibrational assignments for the observed wave numbers are reliable. It should be pointed out that from the low-temperature Raman spectra we could not extract conclusive information about external modes. At low temperature, band narrowing is observed; but the expected shift for external wave numbers is not evident in the observed wave numbers. The far-infrared spectrum at room temperature was also recorded, and the observed wave numbers are listed in Table 2.

Fig. 6. Reflection–absorption infrared spectra of an Alq_3 thin solid film formed by vacuum deposition onto smooth silver showing the effect of annealing.

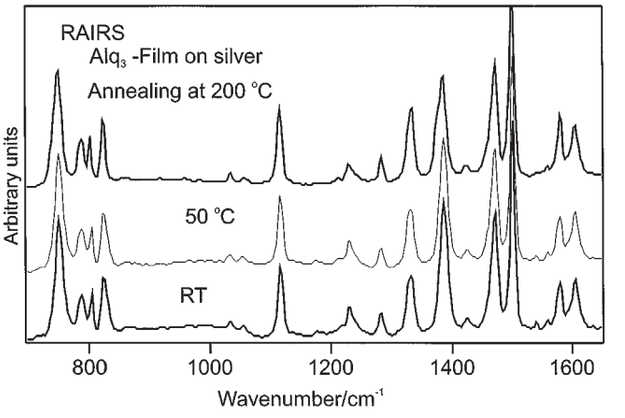

Thin solid films

Thin solid films of 200 nm mass thickness of Alq_3 were prepared by vacuum evaporation onto KBr and smooth silver substrates. The transmission and RAIRS were recorded and compared with that of the KBr pellet (Fig. 5). All of the infrared spectra were identical. It is concluded that thin films of Alq_3 are completely amorphous. Usui et al. (8) found the same results for Alq_3 films formed using an ionization-

© 1998 NRC Canada

assisted deposition method. It is also important to establish the effect of temperature on film structure. The Alq_3 film on silver was annealed from room temperature to 200°C and monitored by collecting the RAIRS spectrum at intermediate temperatures. Figure 6 reproduces three spectra taken at room temperature, 50°C and 200°C. The spectral analysis indicates that there is no change in the film structure, and the absorbance values confirm the preservation of the integrity of the film within this range of temperature.

Conclusions

The Raman spectra of tris(8-hydroxyquinoline)aluminum recorded at room and liquid nitrogen temperatures complemented with FT-IR spectra are interpreted with the aid of a high-level ab initio calculation. The fundamental vibrational modes most suitable for materials characterization are established. Thin solid films of the Alq_3 material deposited by vacuum evaporation are amorphous and remain unchanged under thermal annealing up to 200°C.

Acknowledgements

We are thankful to Janice Hellman from Bruker Canada for her assistance in the FT-Raman experiments and Natural Sciences and Engineering Research Council of Canada (NSERC) for financial support. We would also like to thank Prof. H.B. Schlegel, Wayne State University, and the Pittsburgh Supercomputing Centre for computer time.

References

1. R.F. Service. Science (Washington, D.C.) **267,** 1262 (1995).
2. J. Kido, M. Kimura, K. Nagai. Science (Washington, D.C.) **267**, 1332 (1995).
3. C.W. Tang and S.A. VanSlyke. Appl. Phys. Lett. **51**, 913 (1987).
4. I. Sokolik, A.D. Walser, R. Priestley, C.W. Tang, and R. Dorsinville. Synth. Met. **84**, 921 (1997).
5. J. Kalinowski, G. Giro, P. DiMarco, N. Camaioni, and V. Fattori. Chem. Phys. Lett. **265**, 607 (1997).
6. T.A. Hopkins, K. Meerholz, S. Shaheen, M.L. Anderson, A. Schmidt, B. Kippelen, A.B. Padias, H.K. Hall, N. Peyghambarian, and N.R. Armstrong. Chem. Mater. **8**, 344 (1996).
7. H. Ishi, D. Yoshimura, K. Sugiyama, S. Narioka, Y. Hamatani, I. Kawamoto, T. Miyazaki, Y. Ouchi, and K. Seki. Synth. Metals, **85**, 1389 (1997).
8. H. Usui, H. Kameda, and K. Tanaka. Thin Solid Films, **288**, 229 (1996).
9. R. Larsson and O. Eskilsson. Acta Chem. Scand. **22**, 1067 (1968).
10. J.A. Pople, K. Raghavachari, H.B. Schlegel, and J.S. Binkley. Int. J. Quantum Chem. Quantum Chem. Symp. **13**, 225 (1979).
11. P. Pulay. *In* Modern electronic structure theory. Vol. 2. *Edited by* D. Yarkony. World Scientific Pub Co., New Jersey. 1995. p. 1191; J. Overend. *In* Infrared spectroscopy and molecular structure. *Edited by* M. Davies. Elsevier Scientific Publishing Co., Amsterdam. 1963. p. 345.
12. G.N. Zhizin and A.F. Goncharov. *In* Vibrational spectra and structure. Vol. 13. *Edited by* R. Durig. Elsevier Scientific Publishing Co., Amsterdam. 1984. p. 223.
13. M.J.S. Dewar and W. Thiel. J. Am. Chem. Soc. **99**, 4899 (1977).
14. P.C. Hariharan and J.A. Pople. Theor. Chim. Acta, **28**, 213 (1973).
15. M.J. Frisch, G.W. Trucks, H.B. Schlegel, P.M. Gill, B.G. Johnson, M.A. Robb, J.R. Cheeseman, T. Keith, G.A. Petersson, J.A. Montgomery, K. Raghavachari, M.A. Al-Laham, V.G. Zakrzewski, J.V. Ortiz, J.B. Foresman, J. Cioslowski, B.B. Stefanov, A. Nanayakkara, M. Challacombe, C.Y. Peng, P.Y. Ayala, W. Chen, M.W. Wong, J.L. Andres, E.S. Replogle, R. Gomperts, R.L. Martin, D.J. Fox, J.S. Binkley, D.J. Defrees, J. Baker, J.P. Stewart, M. Head-Gordon, C. Gonzalez, and J.A. Pople. Gaussian 94, Revision D.3. Gaussian, Inc., Pittsburgh, Pa. 1995.
16. J.A. Pople, H.B. Schlegel, R. Krishnan, D.J. Defrees, J.S. Binkley, M.J. Frisch, R.A. Whiteside, R.F. Hout, and W.J. Hehre. Int. J. Quantum Chem. Quantum Chem. Symp. **15**, 269 (1981).
17. Y.N. Panchenko. Russ. Chem. Bull. **45**(4), 753 (1996).
18. A.P. Scott and L. Radom. J. Phys. Chem. **100**, 16 502 (1996).
19. G.L. Palenik. Acta. Cryst. **17**, 687 (1964).
20. G.L. Palenik. Acta. Cryst. **17**, 696 (1964).
21. A. Schmidt, M.L. Anderson, and N.R. Armstrong. J. Appl. Phys. **78**, 5619 (1995).
22. B. Marchon, L. Bokobza, and G. Cote. Spectrochim. Acta, **42A**, 537 (1986).
23. A.A. Shabaka, M. Fadly, M.A. ElGhandoor, and F.M. Abdel-Kerim. J. Mat. Sci. **25**, 2193 (1990).

© 1998 NRC Canada

Initial stages of cobalt-disilicide formation in mesotaxy

G.R. Carlow and M. Zinke-Allmang

Abstract: We present results on the formation of buried silicide layers at ion implantation doses in the range of 1–60% of the critical dose for formation of a uniform layer. We emphasize observations for the low-dose range of 1–5% where the precipitate density is quite dilute. The Co redistribution during post-implant annealing is measured using Rutherford backscattering techniques and secondary ion mass spectrometry. Experimental observations during post-implantation annealing at 1000°C involves (*i*) a contraction of the Co depth profile for all doses, (*ii*) shifting of the peak of the profile towards the bulk, and (*iii*) formation of a secondary Co peak near the surface. The secondary peak is only present in samples implanted to greater than 3% of the critical dose. The interpretation of the shift of the main peak and the occurrence of the secondary peak requires a model exceeding the standard ripening model used previously to describe mesotaxy. We suggest that more recent ripening-based concepts allow for a full description of these observations with a minimum of parameters, particularly not requiring interaction with the complex defect profiles formed initially during implantation. Essential for this model is a proper inclusion of precipitate–precipitate interactions and the role of diffusion screening.

Key words: silicide, Co implantation, mesotaxy, precipitate, ripening, screening.

Résumé : On a examiné l'effet, sur la formation de couche uniforme, de la formation de couches de siliciure enfouies à des implantations ioniques allant de 1 à 60% de la dose critique. On a particulièrement examiné les effets aux faibles doses allant de 1 à 5% alors que la densité du précipité est relativement diluée. On a utilisé la spectrométrie de masse des ions secondaires et des techniques de rétrodiffraction de Rutherford pour mesurer la redistribution du Co au cours de la recuisson suivant l'implantation. Les observations expérimentales faites au cours de la recuisson à 1000°C suivant l'implantation mettent en évidence: (*i*) une contraction du pic de profondeur du Co pour toutes les doses; (*ii*) un déplacement du maximum du profil vers la masse et (*iii*) la formation d'un pic secondaire près de la surface. Le pic secondaire n'est présent que dans les échantillons pour lesquels l'implantation est supérieure à 3% de la dose critique. L'interprétation du déplacement du pic principal et de la présence du pic secondaire nécessite l'utilisation d'un modèle plus important que le modèle de maturation utilisé antérieurement pour décrire la mésotaxie. On suggère l'utilisation du modèle de maturation proposé plus récemment qui est basé sur des concepts qui permettent une description complète de ces observations avec un minimum de paramètres qui ne nécessitent en particulier pas d'interaction avec les profils de défaut du complexe qui se forme initialement au cours de l'implantation. Pour ce modèle, il est essentiel d'inclure des interactions précipité–précipité correctes ainsi que le rôle d'effet d'écran de la diffusion.

Mots clés : siliciure, implantation de Co, mésotaxie, précipité, maturation, effet d'écran.

[Traduit par la Rédaction]

1. Introduction

Cobalt disilicide is one of the more promising metal silicides for use in the microelectronics industry due to its low resistivity, good thermal stability, and its good lattice match with silicon. A technique extensively studied for the formation of buried silicides in silicon is ion beam synthesis (IBS). IBS of silicides, termed "mesotaxy" (1), has been successful in achieving both high-quality buried silicide layers and silicon overlayers, although annealing temperatures above 1000°C are required, and such high temperatures are not compatible with existing Si processing in the microelectronics industry.

The standard mesotaxy process for $CoSi_2$ formation includes Co implantation into Si at about 350–400°C and results in a nominally Gaussian Co depth profile. During this step silicide precipitates nucleate in the Si matrix. The elevated temperature is beneficial, as it preserves the crystalline quality of the Si overlayer (2). Post-implantation annealing, requiring temperatures of typically 1000°C or greater, causes the Co depth profile to "collapse" from Gaussian to rectangular while forming a stoichiometric, crystalline, buried

Received January 15, 1998.

G.R. Carlow and M. Zinke-Allmang.[1] Department of Physics and Astronomy, The University of Western Ontario, London, ON N6A 3K7, Canada.

[1]Author to whom correspondence may be addressed. Telephone: (519) 661-3986. Fax: (519) 661-2033.
E-mail: mzinke@uwo.ca

© 1998 NRC Canada

$CoSi_2$ layer with commensurate interfaces to bulk silicon and capping layer. To achieve a continuous buried layer, a minimum implantation concentration of about 18% Co (i.e., a local stoichiometry of $Co_{0.18}Si$) is required at the peak of the as-implanted profile (3), and this requires a minimum, or critical implantation dose. This critical dose determines the thickness of the final buried layer. Just below the critical dose, pinholes result in an otherwise continuous layer while far below the critical dose, isolated $CoSi_2$ precipitates result (4).

The mesotaxy technique has been developed, following closely advances in the SIMOX technology. In SIMOX a buried insulating oxide layer is formed through IBS with an oxygen beam (5–8). Similarities of both techniques allow for better control of defect formation in the silicon matrix during mesotaxy (5) and provide a wide range of modelling efforts which can be adapted to cobalt IBS (9, 10). Of interest are particularly nonuniform structural developments, such as secondary peaks in the oxygen distribution (6). These have been associated with defect profiles in the earlier literature. However, the SIMOX layer is not crystalline, and thus strain and defect issues in both techniques may influence the morphological evolution differently.

Due to the complexity of the mesotaxial process, a complete description of the film formation process is still lacking. Reiss and Heinig (9) noted that at least five overlapping stages need to be addressed: (*i*) formation of supersaturation during implantation, (*ii*) nucleation through chemical compound formation of the implanted species and substrate atoms, (*iii*) precipitate growth at the expense of the supersaturation (possibly concurrent with continuous implantation), (*iv*) post-implantation growth of precipitates through Ostwald ripening, and (*v*) coalescence and percolation. These processes correspond to the basic stages of phase separation on surfaces for mass nonconserved systems (*i, ii, iii,* and *v*) and mass conserved systems (*iii* and *iv*) (11).

Several theoretical studies identified the ripening stage as most crucial in film formation (9, 10, 12). However, correlating the results of these studies with existing experimental data is not possible, since no single mechanism such as ripening occurs in isolation during mesotaxial formation of buried layers. The first objective of this study is to provide such experimental data. In the first section of this paper, a detailed study at dilute precipitate densities identifies specific features of the clustering process any model must reproduce.

In the second part a theoretical formulation is discussed. Starting with the well-known Ostwald ripening theory by Lifshitz and Slyozov (13, 14) a model is developed which is in agreement with the experimental data. We compare this model with computer simulations by Reiss and Heinig (9, 10) and a study by Trinkaus and Mantl (12). We show that a minimum model requires the inclusion of finite volume fraction effects of the precipitate phase (15, 16) and the screening length concept limiting dissolution of neighboring structures as proposed by Beenakker and Ross (17).

2. Ripening experiments during mesotaxy

A few experimental studies of the film formation stages of mesotaxy have been carried out by Co implantation to less than the critical dose (4, 18–20), where precipitate–precipitate distances remain sufficiently large so coalescence and percolation of precipitates do not dominate. At 10% of the critical dose (i.e., 1.8% Co peak concentration), collapse of the Co profile still occurs leading to isolated $CoSi_2$ precipitates. Concurrently the Co peak shifts toward the bulk region of the substrate with a possible smaller Co peak near the Si surface. The shifting of the main peak has not been reported for substrates implanted to the critical dose. In experiments where damage is intentionally introduced within the Co implant profile (by following the Co implant with low-temperature Si implantation) the collapse of the Co profile is centered around the damaged region (19). In has been suggested that the gettering of Co by defects is responsible for the shift of the peak towards the bulk where the end-of-range (EOR) damage caused by implantation is located. The small Co peak near the surface has received no attention.

In our study, *n*-type Si(100) wafers were implanted with 400 keV Co^+ to total doses of 15.0, 1.3, 1.0, 0.7, 0.55, and 0.30×10^{16} Co atoms/cm^2. The critical dose at 400 keV is about $2.4 \times 10^{17}/cm^2$ (3, 21), thus the implant doses represent approximately 60, 5, 4, 3, 2, and 1% of the critical dose, respectively. The samples were held at a temperature of 375°C and oriented 7° off the <100> axis during implantation to minimize channeling effects.[2] Post-implant annealing was done by rapid thermal processing in dry, flowing N_2. Samples were analyzed using Rutherford Backscattering Spectroscopy (RBS), using 3 MeV He^{++} with a backscattering angle of 170°, and Secondary Ion Mass Spectroscopy (SIMS).

Figure 1 shows the Co portion of a RBS spectrum for a sample implanted to 5% of the critical dose. The abscissa is labeled both by backscattering energy (bottom) and depth into the sample (top). Included are the Co profiles for the as-implanted sample and samples post-implant annealed at 1000°C for 1, 10, and 30 min. The as-implanted sample has a peak at a depth of about 280 nm and a full width at half maximum (FWHM) of about 270 nm. After annealing for 1 min (Fig. 1*a*), even at a lower Co dose than in earlier studies (19, 20), the Co profile narrows to a width of about 110 nm and increases in height by a factor of about 1.9 as compared to the as-implanted profile. In addition to this narrowing, the peak height position shifts about 100 nm towards the bulk, and a secondary "peak," or shoulder, forms near the surface at a depth of about 100 nm. Note that this peak does not rise above the as-implanted level. The shift of the main peak towards the bulk of the crystal is consistent with other studies (19, 20). Annealing for 10 and 30 min at 1000°C (Figs. 1*b* and *c*) results in a further small shift of the main peak towards the bulk and a slight broadening of the main peak, but very little change to the secondary peak.

The dose dependence of the Co depth profile for 1000°C annealing for 10 min is shown in Figs. 2*a–d* for the 5, 4, 3, and 1% doses, respectively. For comparison, the as-implanted profiles for each dose are shown. After annealing, the main peak for each dose narrows to about 110–150 nm and shifts about 100 nm towards the bulk, and the height of the main peak is about 1.7–2.0 times the as-implanted peak height. Note, in particular, that the secondary peak is not

[2] G. Amsel. Université de Paris, France. Private communication.

© 1998 NRC Canada

Fig. 1. Co portion of RBS spectra for a sample implanted to 5% of the critical dose. The spectra are plotted for the backscattering yield as a function of backscattering energy. Also shown is the equivalent depth using the stopping power of 25 eV/Å. (*a*) The as-implanted profile and the profile after annealing at 1000°C for 1 min. (*b*) The profiles after post-implant annealing at 1000°C for 1 and 10 min. (*c*) The profiles after post-implant annealing at 1000°C for 10 and 30 min. During annealing the main peak narrows and shifts towards the bulk.

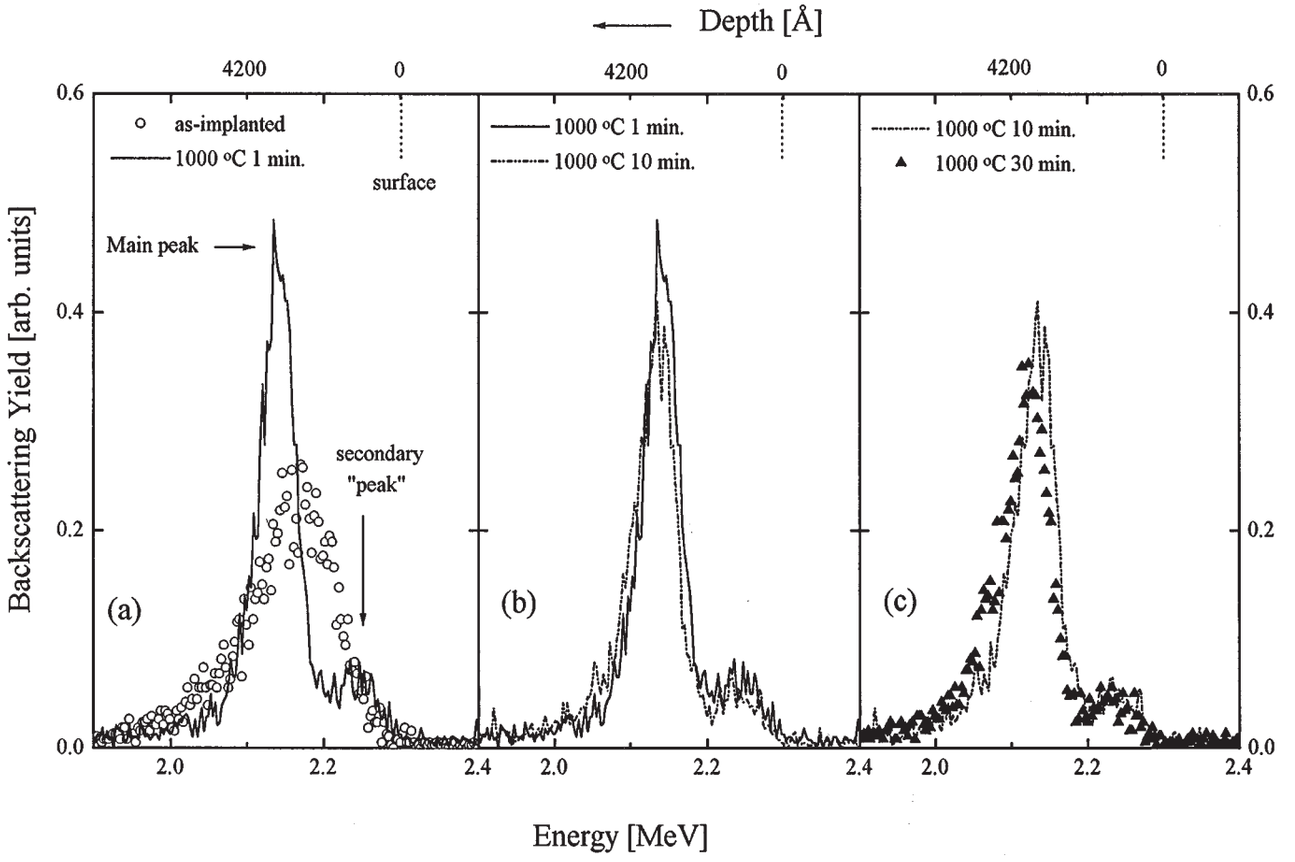

visible for doses less than 3% of the critical dose. Due to the low RBS signal levels at these doses, this fact was verified using SIMS depth profiling. Figures 2*e* and *f* show the SIMS profiles for the 5 and 1% doses, respectively. These profiles are consistent with the profiles obtained by ion scattering (Figs. 2*a* and *d*).

Figure 3 shows the evolution of the Co profile during annealing at 1000°C for implantation to 60% of the critical dose. A shift of the main peak towards the bulk is not observed in agreement with studies at the critical dose (1, 2). However, the evolution of the profile is not symmetric about the as-implanted profile. Material accumulating in the main peak has predominantly come from the surface region of the as-implanted profile and the formation of a secondary peak, or tail, near the surface is evident after annealing for 1 min. This tail is not present after annealing for 10 min.

The details of the Co redistribution at 1000°C annealing are summarized in Table 1. Included for each dose are the main peak position relative to the surface, the main peak width (FWHM), the main peak height relative to the as-implanted peak height, and the secondary peak height. The profile for the higher dose samples tend to narrow and reach the maximum main peak height quicker than the lower dose samples. Also, once the main peak has narrowed, it subsequently tends to broaden and decrease in height with further annealing. During this broadening, the total amount of Co in the main and secondary peaks remained constant; indicating that no significant amounts of Co were diffusing away from these features deeper into the bulk of the crystal.

A secondary peak does occur in the lower dose samples, but is only detectable when annealing at lower temperatures. Figure 4*a* shows the profile for a 1% dose sample annealed at 850°C for 20 s; conditions for which a secondary peak is visible. This peak however, occurs at a depth of about 170 nm from the surface and is nearer the main peak as compared to the higher dose samples (such as the 5% dose shown in Fig. 1). Further annealing at 900°C for 20 s results in the decomposition of this peak (Fig. 4*b*).

Thus, we have established for Co depth profile redistribution during annealing for the doses in the range 1–5% of the critical dose: (*i*) the main peak initially increases in height by about a factor of 1.7–2.0 and narrows from about 270 nm to a minimum of about 110 nm. Once the main peak has reached its maximum height and corresponding minimum width, further annealing results in the main peak broadening and decreasing in height (see Table 1); (*ii*) the main peak shifts about 100 nm toward the bulk for samples; (*iii*) with 1000°C annealing the secondary peak near the surface does

© 1998 NRC Canada

Fig. 2. Co depth profiles for different doses after implantation (○) and after post-implant annealing at 1000°C for 10 min (—). (*a*)–(*d*) The profiles from RBS for the 5, 4, 3, and 1% implant doses, respectively. The yield axes have different scales for the different doses. Note that the secondary peak is not present for doses less than 3% of the critical dose. The main peak is similar for the different doses. (*e*) and (*f*) The profiles from SIMS for the 5 and 1% doses, respectively. These profiles are similar to those obtained with RBS ((*a*) and (*d*)).

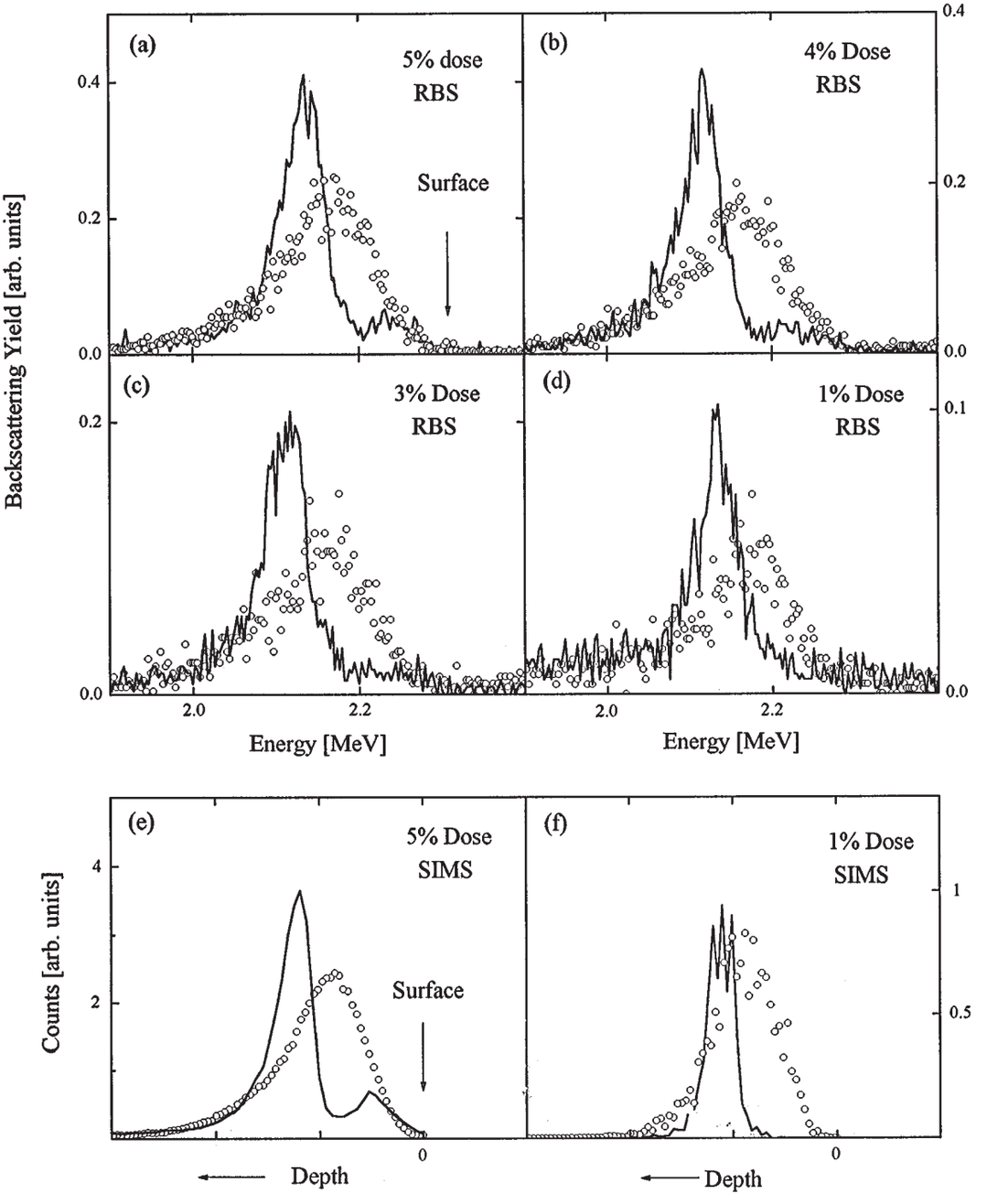

not occur in samples implanted to less than 2–3% of the critical dose. With lower temperature annealing (850°C), this secondary peak occurs in the lower dose samples (1% of the critical dose), and anneals out quickly (within 20 s) at 900°C.

At 60% of the critical dose, no shift of the main peak towards the bulk is detected. However, the evolution of the main peak is asymmetric about the as-implanted profile, and a secondary peak is present after annealing for 1 min at 1000°C. Note that for the evolution of the 60% dose, the

© 1998 NRC Canada

Fig. 3. Co portion of RBS spectra for a sample implanted to 60% of the critical dose. (*a*) The as-implanted profile and the profile obtained after annealing at 1000°C for 1 min. (*b*) The profiles after post-implant annealing at 1000°C for 1 and 10 min. At this relatively high dose, a secondary peak still forms near the surface, and the evolution of the Co profile is not symmetric about the as-implanted profile.

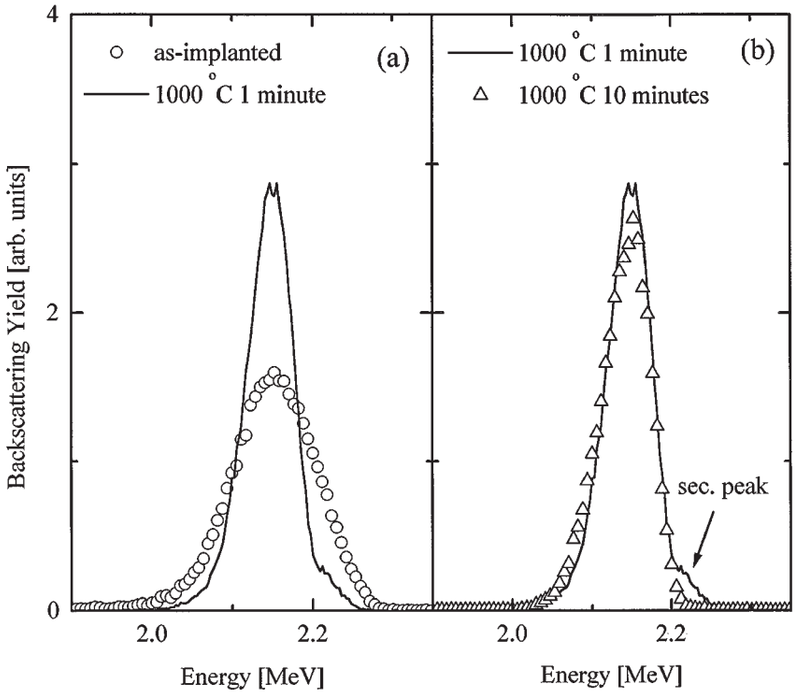

secondary peak is the last feature to disappear in the profile at 1000°C annealing temperatures.

3. Model for role of ripening during mesotaxial growth

In this section we try to develop a minimum model (model with the least parameters) which is consistent with the experimental observations in this and previous studies. Since defect profiles generated during ion implantation are highly complex, including little understood depth profiles of mono-vacancies, interstitials, and various defect conglomerates, a simple model cannot evolve if these features have to be taken into account. Therefore, the first three models discussed in section 3.1 are based on the assumption that implantation-caused defects anneal much faster at 1000°C than the observed morphological structures form and change. This assumption can be justified with observations of defect annealing after silicon self-implantation, where annealing to significantly lower temperatures is sufficient to fully recrystallize the substrate (22). In SIMOX studies, threading dislocations remain the only detectable defect structure after the annealing step (5), with typical densities of 10^5 per cm^2 and as low as 10^3 per cm^2 (23). Displacement damage did also not play a significant role in metal atom diffusion during ion implantation of cobalt and nickel at various energies (12). This assumption and a model including defect interaction are discussed more carefully in section 3.2.

3.1. Early stage mesotaxy models in a perfect matrix

In this section we present three models. The first model is based on the generally accepted mean-field analysis of Ostwald ripening by Lifshitz and Slyozov (LSW theory, refs. 13 and 14); the second model extends the LSW model to include precipitate–precipitate interactions for finite volume fractions, based on simulations by Enomoto et al. (15) and Voorhees and Glicksman (16). In the last model the diffusional screening is properly included to account for the inhomogeneous character of the system. We follow the approach proposed for open thermodynamic systems by Beenakker and Ross (17). Only the last model is not in conflict with the experimental observations.

Model 1: Mean-field Ostwald ripening model at zero volume fraction

The LSW theory is an analytical model for an infinite system. Since the model is independent of the relative precipitate positions, it does not include precipitate–precipitate interactions which have been shown to alter the evolution of the morphology at volume fractions as low as 0.1% (24). Thus, the LSW theory is only exact for zero volume fraction of the minority phase. It predicts a power law for precipitate growth with a growth rate independent of the size of the precipitate (11). Since the LSW theory predicts that all precipitates grow at the same rate, an initial profile should maintain its shape unless size variations of precipitates during nucleation or early stage growth (preceding late stage Ostwald ripening) exceed statistical size fluctuations. Standard nucleation theory (25) does not allow such an assumption, as

© 1998 NRC Canada

Table 1. Summary of the Co depth profiles obtained by RBS. Shown are the implant dose, the post-implant anneal time at 1000°C, the depth of the main Co peak, the width of the main Co peak, the main peak height, and the secondary peak height.

Implant dose ($\times 10^{16}$ ions/cm^2)	Anneal time at 1000°C (min)	Main peak depth (nm)	Main peak width (nm)	Main peak height (arb. units)	Secondary peak height (arb. units)
15.0	0	280	250	1.00	—
	1	280	130	1.80	0.11
	10	280	140	1.63	—
1.3	0	270	270	1.00	—
	1	340	110	1.92	0.27
	10	340	140	1.64	0.20
	30	370	150	1.40	0.19
1.0	0	280	270	1.00	—
	1	360	120	2.02	0.21
	10	380	110	1.82	0.15
	30	370	140	1.61	0.15
0.7	0	280	290	1.00	—
	1	360	120	2.02	—
	10	390	120	1.69	—
	30	380	150	1.86	—
0.5	0	290	280	1.00	—
	1	350	220	1.42	—
	10	390	150	1.52	—
	30	390	130	1.71	—
0.3	0	250	230	1.00	—
	1	300	210	1.32	—
	10	350	120	1.87	—
	30	350	110	1.81	—

Fig. 4. Co portion of RBS spectra for a sample implanted to 1% of the critical dose. (*a*) As- implanted and post-implant annealing at 850°C for 20 s. (*b*) As-implanted and post-implant annealed at 850°C for 20 s and 900°C for 20 s. The secondary peak, seen for higher doses at 1000°C annealing, forms at these lower temperatures, but decomposes quickly.

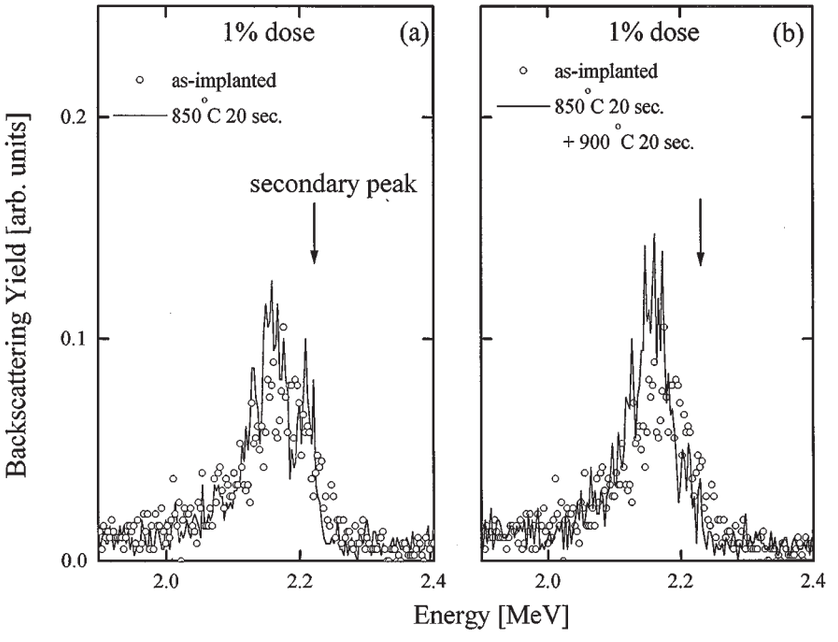

© 1998 NRC Canada

supersaturation levels are usually associated with variable nucleation densities and not with significant differences in the nucleus size. Early stage growth is not sufficiently investigated to make firm predictions, however, the highly local character of growth during that stage should more likely enhance statistical fluctuations as resulting from the nucleation stage rather than develop long-range size gradients (11). Thus a model based on the LSW theory does not predict a contraction of the Co depth profile. The mean field nature of this theory does further not allow for spatial inhomogeneities of the precipitate phase.

In the computer simulations by Reiss and Heinig (9, 10), growth rates of all precipitates are assumed equal and the initial size distribution is assumed uniform. Consequently, no contraction of the initial, spherical distribution of matter is observed. Trinkaus and Mantl (12) developed their model with a mean-field, zero volume fraction assumption. To achieve profile contraction, an initially nonuniform precipitate size profile is postulated.

Model 2: Ostwald ripening model with finite volume fraction

Several authors have proposed extensions of the LSW theory to include finite volume fractions of the precipitate phase (15, 16). They predict consistently that the rate of precipitate growth and the width of the precipitate size distribution increase with increasing volume fraction (24). Both of these predictions have been experimentally observed for cluster growth on surfaces for volume fractions as low as 0.1% and are associated with diffusive cluster–cluster interactions (26).

The finite volume fraction model can explain two fundamental experimental features, the significant contraction of the Co profile during ripening and the subsequent slight spreading: after implantation, the largest cobalt concentration in the peak region leads to the highest nucleation density and thus the highest volume fraction of the minority silicide phase. Likewise, the tails of the implantation profile contains a smaller volume fraction. Subsequent ripening leads to accelerated precipitate growth in the initial implantation peak region, i.e., larger precipitates are present during the late stages of the phase separation in the central region. The competition for monomers between the central section of the peak and the tail regions is decided by the Gibbs–Thomson effect (27), i.e., the capillarity effect that small precipitates have a larger chemical potential than large precipitates. The large central precipitates grow at the expense of the small precipitates in the peripheries. Material is therefore transported towards the central region and contraction of the Co profile occurs. In addition to the contraction, some spreading of the profile should occur as small precipitates in the periphery decompose and also transport material towards the bulk and surface regions. This spreading is only observed late in the annealing process (Table 1).

In the study by Trinkaus and Mantl (12), this effect has been obtained with assigning an arbitrary excess size to precipitates in the peak region. However, the collapse of the precipitate distribution is a much weaker effect in their model, as the relative size difference of precipitates does not change during ripening, leading to a fast decreasing monomer gradient toward the peak center. The collapse may even not proceed sufficiently far to reach the coalescence regime in their model if realistic fluctuations of the monomer concentration are included as the variation in supersaturation with precipitate size is a very small effect (11). The current model allows the precipitates in the denser peak region continuously to grow faster than precipitates elsewhere, thus maintaining a sufficient monomer gradient toward the peak region.

Model 3: Ostwald ripening model with finite volume fraction and screening

Model 2 does not explain several of the experimental observations, e.g., the asymmetric evolution of the profile which includes the shift of the main peak towards the bulk and the occurrence of the secondary peak near the surface. To develop the model further, the spatial inhomogeneity of the mass distribution after implantation has to be integrated. In a complete fashion, this would require adopting the actual depth profile after implantation. However, this would not only lead to a complex multiparameter system, but also confine the model to a particular system. Instead, we test a simplified model with three distinguished regions, a surface region with lower cobalt-disilicide precipitate density, the peak region with high precipitate density, and the silicon bulk free of precipitates. Focussing on the two regions near the surface first, we can use the thermodynamic open two-zone ripening model introduced by Beenakker and Ross (17). Their model is based on open mass exchange between a half-space reservoir of low monomer concentration and a region in late stage Ostwald ripening. It has been predicted and experimentally confirmed for cluster growth on surfaces (28) that the precipitates nearest to the reservoir interface screen the influence of the reservoir from the remainder of the ripening system. The reservoir then only effects the ripening system up to a characteristic screening length which is of the order of the mean precipitate spacing.

For bulk systems, this has been confirmed in computer simulations by Reiss and Heinig (9, 10). Their model involves however unrealistic assumptions preventing the prediction of the observed morphology. They assume a stable, uniform monomer concentration across a finite area. Wave-like zones of clusters, separated by a distance related to the screening length, emerge. However, fluctuations in the monomer concentration or precipitate distribution have major impact on computer simulations, as the ripening model is inherently instable against such variations as noted by Karpov (29).

The morphological evolution in model 3 allows for the decomposition of precipitates within the screening length but gives rise to a secondary peak or shoulder near the surface region when the screening length remains shorter than the peak–surface distance during the annealing. Since the screening length is larger at any given time interval for a system with larger precipitate–precipitate spacing, a lower Co implantation dose leads to dilute precipitates which can be dissolved, while a higher dose leads to a denser precipitate zone which is protected. The depleted zone should then be wider for the lower doses. This is consistent with the observation that the secondary peak completely dissolves faster for lower dose implantation. For doses less than 3% of the

© 1998 NRC Canada

critical dose, the screening length therefore extends all the way to the surface after 10 min annealing at 1000°C.

This model for the low-dose regime does not include processes such as precipitate coalescence or percolation, which occur when the spatial density of precipitates is much larger. However, at high doses, small precipitate densities should still be present in the periphery of the profile. Thus the same screening effect as in the low-dose regime should occur. This is illustrated for the 60% dose sample where similarities to the low-dose regime include an asymmetric evolution of the Co depth profile and the formation of a secondary peak near the surface region. Note that the secondary peak decomposes more quickly than in the 5% dose regime. This is associated with coalescence, percolation, and strain-induced effects that occur at the higher doses.

We note further that after post-implantation annealing at doses between 1% and 60% of the critical dose two features are identical to annealing at the critical dose. First, the peak Co concentration increases by a factor of about 1.7–2.0. This ratio is very similar to the ratio of 1.86, i.e., 33:18, that occurs at the critical dose. Secondly, the Co depth profile contracts to a minimum width of about 110 nm. This value is also very similar to the final silicide layer thickness of about 100 nm that forms at the critical dose. These similarities suggest that the same mechanisms are responsible, limiting the layer thickness at both the doses used here and the critical dose. This eliminates percolation and coalescence of precipitates as dominant mechanisms since these processes only occur at high doses, emphasizing that ripening plays a major role during mesotaxy as proposed previously.

Model 3 has one major weakness. The significant shift of the peak during annealing cannot be explained very straightforward. Without further assumptions, such a shift requires an asymmetry of the initial profile. This may be provided by the surface, which distincts the current model from SIMOX processes. Given the very shallow character of the concentration gradients within the two regions near the surface (surface peak and main peak area) and the experimentally observed minimal loss of monomers to the third region (bulk), to first order a mass redistribution toward the center of the two regions near the surface may be expected. However, this does not quantitatively agree with the experimental data.

3.2. Early stage mesotaxy model in a defective matrix

Model 3 can be extended to a defective matrix. This would strengthen the argument for the shift of the main peak toward the bulk during annealing without interfering with the arguments for the secondary peak formation in the previous section. Usually, the stopping process of implanted ions near normal incidence leads to defect structures at somewhat greater depth than the projected range of the implanted ion. This is due to a forward momentum the implanted ion carries when it interacts with nuclei of the host atoms near the EOR. If we allow for a damage zone at slightly greater depth during annealing, cobalt diffusion could be slowed down and cobalt trapping may be enhanced at this depth. This would lead to an increase of cobalt in that region. When the defects are fully decorated with cobalt, effectively larger precipitates would have emerged which would ripen more effectively than precipitates at other depths as discussed in the previous section.

Still, model 3 should not be extended to this scenario unless necessary, since the broad range of defects with variable dynamics leads to a quite complex description. Such a model would depend on many materials parameters, thus limiting the applicability of the concept. Further experimental analysis should first establish a link between the shift of the peak and other system parameters, such as the initial depth distribution and the actual monomer concentration profile.

4. Conclusions

Co was implanted into Si(100) to doses 1–60% of the critical dose required for continuous silicide layer formation. The Co depth redistribution during post implant annealing at 1000°C results in the following: (*i*) a shift of the position of the Co peak concentration towards the bulk region; (*ii*) during this shift, the Co profile narrows to a width which is typical of the width that a continuous, buried silicide layer resumes for critical dose implantation; and (*iii*) the formation of a secondary peak near the surface.

The secondary peak and the contraction can only be described with a ripening model which includes interactions between silicide precipitates (finite volume fraction effects) and diffusive screening against precipitate dissolution. Precipitate screening is the mechanism responsible for the persistence of the secondary peak at higher implant doses, i.e., a hindrance for the formation of sharp $CoSi_2$/Co-free Si interfaces toward the sample surface.

Acknowledgments

We thank J. Hendricks and S. Brawn for operation of the Tandem accelerator used for Co implantation and RBS analysis. This work was supported by the Natural Sciences and Engineering Research Council of Canada.

References

1. A.E. White, K.T. Short, R.C. Dynes, J.P. Garno, and J.M. Gibson. Appl. Phys. Lett. **50**, 95 (1987); A.E. White, K.T. Short, Y.-F. Hsieh, and R. Hull. Mater. Sci. Eng. B, **B12**, 107 (1992).
2. K. Radermacher, S. Mantl, K. Kohlhof, and W. Jäger. J. Appl. Phys. **68**, 3001 (1990).
3. A.E. White, K.T. Short, R.C. Dynes, J.M. Gibson, and R. Hull. Mater. Res. Soc. Symp. Proc. **100**, 3 (1988); Y.-F. Hsieh, R. Hull, A.E. White, and K.T. Short. Appl. Phys. Lett. **58**, 122 (1991); R. Hull, A.E. White, K.T. Short, and J.M. Bonar. J. Appl. Phys. **68**, 1629 (1990).
4. P.F.P. Fichtner, W. Jäger, K. Radermacher, and S. Mantl. Nucl. Instr. Meth. B, **59/60**, 632 (1991).
5. M.A. Guerra. Solid State Technol. **33** (no. 11), 75 (1990).
6. P.L.F. Hemment, K.J. Reeson, J.A. Kilner, R.J. Chater, C. Marsh, G.R. Booker, G.K. Celler, and J. Stoemenos. Vacuum, **36**, 877 (1986).
7. K.J. Reeson. Nucl. Instr. Meth. **B19/20**, 269 (1987).
8. A.H. van Ommen. Nucl. Instr. Meth. **B39**, 194 (1989).
9. S. Reiss and K.-H. Heinig. Nucl. Instr. Meth. **B102**, 256 (1995).

© 1998 NRC Canada

10. S. Reiss and K.-H. Heinig. Nucl. Instr. Meth. **B84**, 229 (1994); **B112**, 223 (1996).
11. M. Zinke-Allmang, L.C. Feldman, and M.H. Grabow. Surf. Sci. Repts. **16**, 377 (1992).
12. H. Trinkaus and S. Mantl. Nucl. Instr. Meth. **B80/81**, 862 (1993).
13. I.M. Lifshitz and V.V. Slyozov. Sov. Phys. JETP, **35**, 331 (1959).
14. C. Wagner. Z. Elektrochem. **65**, 581 (1961).
15. Y. Enomoto, M. Tokuyama, and K. Kawasaki. Acta Met. **34**, 2119 (1986).
16. P.W. Voorhees and M.E. Glicksman. Acta Met. **32**, 2013 (1984).
17. C.W.J. Beenakker and J. Ross. J. Chem. Phys. **83**, 4710 (1985).
18. R. Jebasinski, S. Mantl, K. Radermacher, P. Fichtner, W. Jäger, and C. Buchal. Mat. Res. Soc. Symp. Proc. **201**, 411 (1991).
19. A. Witzmann, S. Schippel, A. Zentgraf, and P.I. Gajduk. J. Appl. Phys. **73**, 7250 (1993).
20. S. Schippel and A. Witzmann. Mat. Res. Soc. Symp. Proc. **316**, 789 (1994).
21. S. Mantl. Mat. Sci. Rep. **8**, 1 (1992), and refs. therein.
22. R.D. Goldberg, T.W. Simpson, I.V. Mitchell, P.J. Simpson, M. Prikryl, and G.C. Weatherly. Nucl. Instr. Meth. **B106**, 216 (1995).
23. T.F. Cheek and D. Chen. Mat. Res. Soc. Symp. Proc. **107**, 53 (1988); T.R. Guilinger, M.J. Kelly, J.W. Medernach, S.S. Tsao, J.O. Stevenson, and H.D.T. Jones. IEEE SOS/SOI Tech. Conf. 1989. p. 93.
24. R. Barel, Y. Mai, G.R. Carlow, and M. Zinke-Allmang. Appl. Surf. Sci. **104/105**, 669 (1996), and refs. therein.
25. J.A. Venables. Surf. Sci. **299/300**, 798 (1993).
26. G.R. Carlow and M. Zinke-Allmang. Surf. Sci. **328**, 311 (1995).
27. J.W. Gibbs. Trans. Connect. Acad. **3**, 108 (1876); W. Thomson. Phil. Mag. **43**, 448 (1871).
28. G.R. Carlow and M. Zinke-Allmang. Can. J. Phys. **72**, 812 (1994).
29. V.G. Karpov. Phys. Rev. Lett. **74**, 3185 (1995).

© 1998 NRC Canada

Charge-transfer phenomena in holographic recording material: dichromated poly(acrylic acid)

Christine Pizzocaro, Roger A. Lessard, and Michèle Bolte

Abstract: Dichromated poly(acrylic acid) (DCPAA) has been used as real time holographic recording material. We report here the photochemical behavior of DCPAA when irradiated under conditions representative of those used for hologram recording. Under UV–vis spectroscopy a photoredox process ($Cr^{VI} \rightarrow Cr^{III}$) was observed whose efficiency depends on the presence of dimethylformamide (DMF) used as an electron donor. ESR spectroscopy upon irradiation permits detection of the formation of Cr(V) of photochemical origin. We also identified chromium(V) of thermal origin (in the dark), organic macroradicals, and chromium(III). The formation of CO_2 and carboxylate ions was clearly shown by IR spectroscopy. The photoreaction is assumed to go through an acido–basic reaction between dichromate in the excited state and poly(acrylic acid). The resulting unstable chromium polyacrylate undergoes a redox process that gives rise to chromium(V) and a macroradical R-COO$^{\bullet}$ from which CO_2 is formed. The presence of DMF (10% by volume) makes the overall reaction faster by a factor of approximately 3.5–4. The similar shape of the curves giving chromium(V) formation as a function of irradiation time and the curves giving the diffraction efficiencies of the hologram recorded in DCPAA as a function of exposure energy, with and without DMF, strongly argues in favor of a direct involvement of chromium(V) in the quality of the resulting hologram.

Key words: holography, dichromated poly(acrylic acid), dimethylformamide, chromium.

Résumé : L'acide polyacrylique bichromaté (DCPAA) est utilisé comme matériau d'enregistrement holographique en temps réel. Nous décrivons le comportement photochimique de DCPAA sous irradiation dans des conditions représentatives de l'enregistrement holographique. Un processus de photooxydoréduction est observé; son efficacité dépend de la présence de diméthylformamide (DMF) utilisé comme donneur d'électron. Par spectroscopie RPE, nous avons pu détecter la formation de chrome(V) d'origine photochimique. Nous avons aussi identifié du chrome(V) d'origine thermique (à l'obscurité), des macroradicaux organiques et du chrome(III). La formation de CO_2 et de groupements carboxylates a été établie par spectroscopie infra-rouge. La photoréaction mettrait en jeu une réaction acide–base entre le bichromate à l'état excité et l'acide polyacrylique. Le polyacrylate de chrome résultant est instable, il subit un processus redox qui donne naissance au chrome(V) et au macroradical R-COO$^{\bullet}$ à partir duquel CO_2 est formé. La présence de DMF (10% en volume) multiplie la vitesse de la réaction par un facteur 3,5–4. La similitude des courbes donnant la formation de chrome(V) en fonction du temps d'irradiation et des courbes donnant l'efficacité de diffraction de l'hologramme enregistré dans DCPAA en fonction de l'énergie d'exposition avec et sans DMF est en faveur de l'implication du chrome(V) dans la qualité de l'hologramme.

Mots clés : holographie, l'acide polyacrylique bichromaté, diméthylformamide, chrome.

Introduction

Oxidation by chromates has been used for both preparative and analytical purposes for a long time (1–5). The reaction can be accelerated by light (6) and the process is the one involved in photosensitive dichromated materials used in holography: recording a hologram involves the illumination of the material by a pattern created by the interference of two laser beams, the object and the reference beams.

The chemical process implies the photoinduced polymerization or cross-linking of organic macromolecules such as poly(methylmethacrylate) or gelatin (7). Dichromated material such as dichromated gelatin has been used for phase holograms (8) and dyed gelatin plates (9) with electron donors (10) have been developped to form the phase gratings involving chemical development after recording the holograms.

More recently, dichromated polymer materials such as dichromated poly(vinyl alcohol) (DCPVA) and dichromated poly(acrylic acid) (DCPAA) have been employed to realize various applications in holography and, more precisely, in real time holographic recording (11). Our interest in exploiting these systems led us to the necessity of investigating the

Received January 28, 1998.

C. Pizzocaro and M. Bolte.[1] Unité Mixte de Recherche à Centre national de la recherche scientifique, 6505, Clermont-Ferrand, 63177 Aubière Cedex, France.
R.A. Lessard. Centre d'Optique Photonique et Laser, Québec, QC G1K 7P4, Canada.

[1]Author to whom correspondence may be addressed. Telephone: 33 4 73 40 71 71. Fax: 33 4 73 40 77 00. E-mail: boltem@cicsun.univbp-clermont.fr

© 1998 NRC Canada

primary photoprocess occurring upon irradiation of the polymer films at room temperature. It is known that the formation of holograms with dichromated photosensitive materials involves a reduction process giving rise to chromium(III) from the starting chromium(VI) species. Our earlier work on DCPVA permitted us to establish that the first step in such a system is electron transfer from the organic polymeric material to the cationic center, giving rise to chromium(V) and an organic macroradical (12).

In this paper, we report the primary photoprocess taking place in dichromated poly(acrylic acid) with or without dimethylformamide (DMF) used as an electron donor in order to enhance the reduction phenomenon. This work was focused on the photosensitive materials used to record holograms, which implied that the experiments be performed with DCPAA films. The work is to be correlated with our previous results concerning the quality of holograms obtained with such systems: the presence of DMF makes the diffraction efficiency of the resulting hologram higher by a factor of three (13).

To better understand the mechanism of hologram formation, three complementary techniques have been employed: (*i*) UV–visible spectroscopy to measure the quantum yield of chromium(III) formation; (*ii*) FTIR spectroscopy to monitor chromium(VI) disappearance and photoproducts formation; and (*iii*) real time electron spin resonance (ESR) technique employed to detect the intermediate paramagnetic species, sometimes unstable, formed upon irradiation.

Experimental

Materials

Ammonium dichromate $(NH_4)_2Cr_2O_7$ was of commercial origin (Fluka Purum) used without further purification. Dimethylformamide (DMF) was purchased from Aldrich (spectrometric grade). Poly(acrylic acid) (PAA) was in aqueous solution (Aldrich), 35% in water, M_w = 250 000). All the starting solutions were prepared in water purified by a Millipore Milli-Q system.

Fabrication of DCPAA films

DCPAA films were prepared by the gravity settling method. After dissolving 0.1 g of ammonium dichromate in 1 mL of water or of a water–DMF mixture, 4 mL of PAA (25%) were added and well stirred to obtain a homogeneous solution ([Cr(VI)] = 0.16 mol L^{-1}); 0.5 mL of this solution was poured onto a levelled cleaned glass substrate (2.5 × 7.5 cm^2). This was allowed to dry in a dark chamber under normal laboratory conditions for 24 h and orange-yellow clear transparent films with a thickness of 45–55 μm were obtained. The films were irradiated and analysed by UV–visible spectrometry directly on the substrate or peeled from the substrate for IR spectroscopy and finely ground for ESR experiments. Some IR experiments were performed on KBr plates.

Apparatus and procedures

A high-pressure mercury lamp with a Bausch and Lomb grating monochromator was used for irradiations at 365 nm. The light intensity was measured by ferrioxalate actinometry (14) ($I_0 \approx 2 \times 10^{15}$ photons s^{-1} cm^{-2}).

UV–visible spectra were recorded on a CARY 3 double-beam spectrophotometer. ESR spectra were recorded on a Brucker ER 200 D spectrometer at 9.30 GHz with a modulation field of 100 Hz. A Xe–Hg Hanovia lamp was used for irradiation in the ESR spectrometer cavity. When necessary, the emission was filtered at λ > 345 nm. IR spectra were recorded on a Nicolet 20SXC FT-IR spectrometer. The holographic recording was performed as previously described (13).

Results

Evolution in the dark

The DCPAA films were allowed to stand in the dark (in the absence of light at room temperature): in the absence of DMF, there was no evolution of the UV–visible spectrum of the film even after several days. In the presence of a high concentration of DMF, a darkening was observed, likely due to the formation of chromium(III) by a dark redox process. The presence of chromium(III) under these conditions was established by ESR and UV–visible spectroscopy.

The influence of DMF was also detected by measuring the formation of chromium(V) in a DCPAA film as a function of DMF concentration before irradiation. The presence of DMF made the formation of chromium(V) of thermal origin strongly decrease; a factor of 7 was observed with 10% of DMF (Table 1).

Table 1. Intensity of chromium(V) signal of thermal origin (arbitrary unit) versus DMF concentration.

DMF (vol.%)	0	2	5	10
Chromium(V) signal (arbitrary units)	20	15	13	3

Photochemical evolution

UV–visible evolution

The UV–visible spectrum of DCPAA film is represented in Fig. 1. The maximum at 350 nm and the plateau at 440 nm are characteristic of chromium(VI) as dichromate in acidic medium in film or in solution (12). Poly(acrylic acid) does not absorb significantly at a wavelength >300 nm. Upon irradiation at 365 nm, the absorbance at 350 and 440 nm decreased and the original yellow colour disappeared. For prolonged irradiations the film turned light blue: two absorption bands at 420 and 575 nm reflecting chromium(III) formation appeared. The presence of an isosbestic point at 520 nm illustrates the transformation of chromium(VI) into chromium(III). The quantum yield of chromium(III) formation was calculated from the initial slope of the curve giving the optical density at 575 nm where only chromium(III) absorbs in a significant way as a function of irradiation time.

Prior to this calculation, the molar extinction coefficients ε of the starting chromium(VI) and of the final chromium(III) in a DCPAA film have to be determined. By coating a known surface of substrate by a known amount of the mixture DCPAA, it was possible to measure ε for chromium(VI): at 350 nm it is equal to 1100 L mol^{-1} cm^{-1}. It is worth noting that the value is different from the value obtained for an aqueous solution of either DCPAA or pure dichromate in acidic medium (ε = 1600 L mol^{-1} cm^{-1}). The ε value of chromium(III) in the film was obtained by irradi-

© 1998 NRC Canada

Fig. 1. Spectral evolution of a DCPAA film upon irradiation at 365 nm.

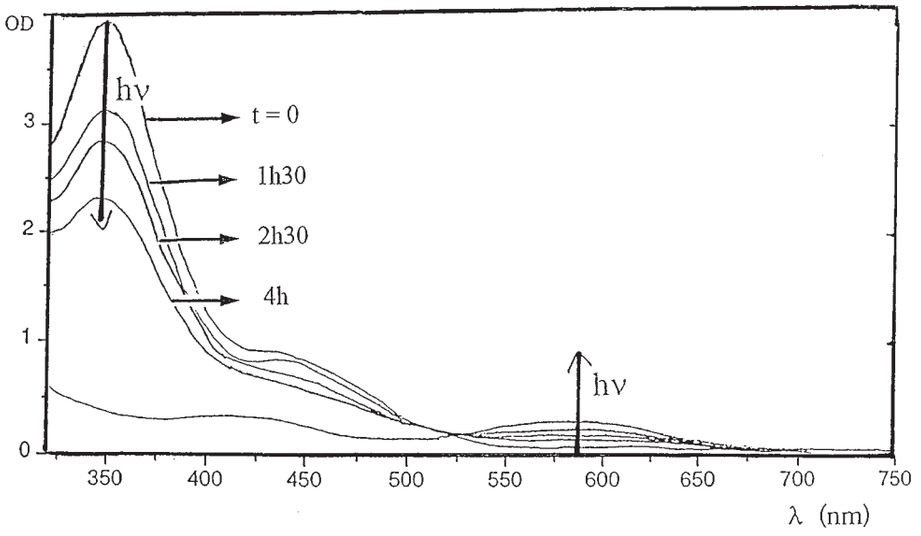

Fig. 2. Influence of DMF concentration on the formation of chromium(III) in a DCPAA film: (*a*) OD evolution (575 nm) upon irradiation (-■- 0%, -●- 5%, -▲- 10 vol.% DMF); (*b*) quantum yield evolution versus DMF percentage.

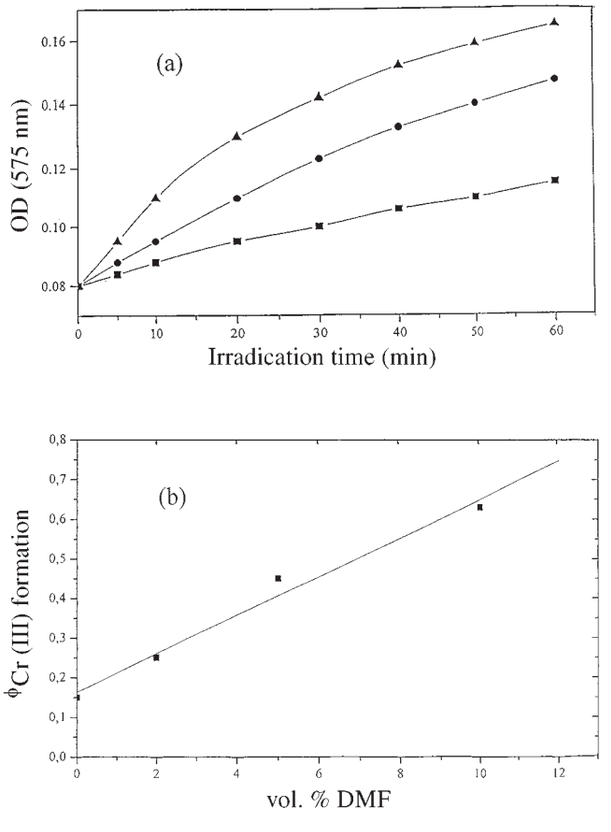

ating such a coated substrate up to complete reduction of chromium(VI) into chromium(III). A value of 45 L mol^{-1} cm^{-1} at λ = 575 nm was determined for the resulting chromium(III). These values are valid whatever the percentage of DMF in the range 0–10%. The presence of DMF does not affect the spectral evolution of a DCPAA film in the domain of wavelengths longer than 320 nm.

Table 2. Quantum yield of chromium(III) formation versus DMF concentration.

DMF (in vol.%)	0	2	5	10
$\Phi_{365\ nm}$ (Cr^{III} formation)	0.15	0.25	0.45	0.63

The experiments were performed at different concentrations of DMF (Fig. 2). We can observe a fast increase in the absorbance at 575 nm; then a plateau is reached. We observed a strong influence of the DMF on the photoreaction: the higher the concentration, the faster the formation of chromium(III) (Fig. 2*a*).

The error in the determination of the quantum yield Φ was roughly ±5% for triplicate measurements. It is noteworthy that the presence of DMF enhances the rate of the photochemical formation of chromium(III) by a factor of about 4 (Table 2).

IR analysis

In Fig. 3 is represented the FTIR spectrum of a DCPAA film upon irradiation at 365 nm. In the range 1100–700 cm^{-1} (Fig. 3*a*) the only evolution is the disappearance of the chromium(VI) bands at 903 and 950 cm^{-1} (ν CrO_3).

In the range 2500–1400 cm^{-1} (Fig. 3*b*) we can see the formation of two bands: the first one at 2338 cm^{-1} is characteristic of CO_2 coming from a decarboxylation of the polymer. The second one, at 1550 cm^{-1}, corresponds to the formation of carboxylate groups COO^-.

The presence of 5% by volume of DMF in a film enhances the rate of chromium(VI) disappearance and CO_2 and COO^- group formation by a factor of about 3.3.

ESR experiments

By performing ESR experiments upon irradiation on DCPAA films, we were able to detect the presence of two different signals (Fig. 4): according to previous studies in similar systems, they were both attributed to chromium(V) but from different origins (6, 12): (*i*) chromium(V) of ther-

© 1998 NRC Canada

Fig. 3. FTIR spectrum of a DCPAA film (with 5 vol.% DMF) upon irradiation at 365 nm.

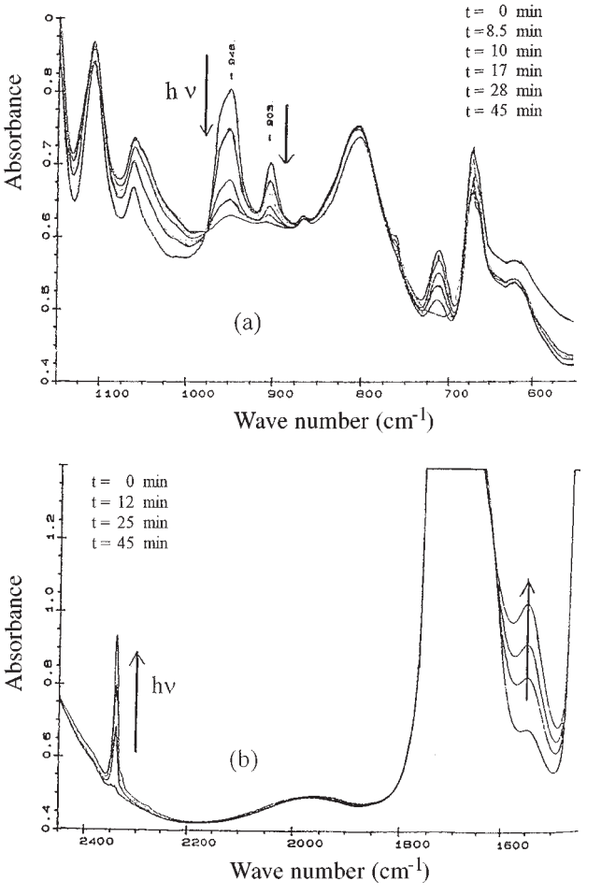

mal origin (I), and (*ii*) chromium(V) of photochemical origin (II), which increased, went through a maximum, then disappeared (Fig. 4*a*), leading to the final weak and broad chromium(III) signal observed for prolonged irradiations.

Chromium(V) formed upon irradiation was thermally unstable and disappeared, giving back the original (dark) signal (Fig. 4*b*). In the presence of DMF (10% by volume) the intensity of the signal reached a higher maximum value and the rate of chromium(V) formation is multiplied by a factor of about 30 (Fig. 5). The maximum of the chromium(V) signal intensity was reached for a longer irradiation time (25 min) in the absence of DMF.

The disappearance of chromium(V) formed upon irradiation was also followed in the dark: (*i*) in the absence of DMF, the decrease was very slow, which made a kinetic treatment of the evolution impossible; (*ii*) in the presence of DMF, a good linear relationship ($R_{corr} > 0.999$) was obtained when plotting 1/(height of the signal) as a function of irradiation time (Fig. 6).

This dependence reveals a bimolecular process of disappearance according to

[1] $2\ Cr(V) \rightarrow Cr(VI) + Cr(IV)$

The formation of a macroradical was evidenced by ESR spectroscopy upon irradiation. When PAA was directly irradiated ($\lambda > 250$ nm), a signal corresponding to an organic radical with a binomial distribution 1 4 6 4 1 was observed

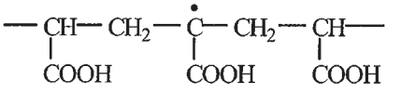

(A)

(Fig. 7). This signal was also present upon irradiation of DCPAA ($\lambda > 345$ nm) but was very weak and partly obscured by the chromium(V) signal. The signal can be attributed to the macroradical (**A**) and results from the coupling of the radical with the two sets of two hydrogens on the carbons in the α position.

The high stability of the radical that makes the direct observation possible is because of its position on a tertiary carbon. This is the first time that such a stable organic signal has been reported in a dichromated polymeric system.

Discussion

Active species of chromium

In our system, chromium(VI) is the only absorbing species. In acidic aqueous solution it exists either as $HCrO_4^-$ or $Cr_2O_7^{2-}$ (15).

$$HCrO_4^- \rightleftharpoons CrO_4^{2-} + H^+ \qquad pK = 6.49$$

$$2HCrO_4^- \rightleftharpoons Cr_2O_7^{2-} + H_2O \qquad K_d = 48\ mol^{-1}\ L$$

© 1998 NRC Canada

Fig. 4. ESR signal of chromium(V) in a DCPAA film: (*a*) upon irradiation (λ > 345 nm); (*b*) thermal decay (after irradiation).

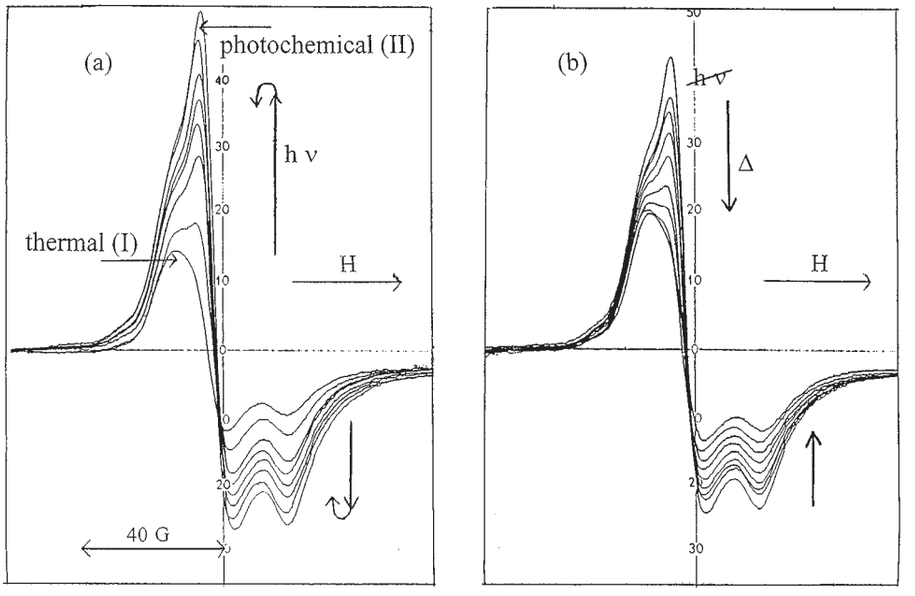

Fig. 5. Chromium(V) formation upon irradiation of DCPAA films (ESR signal intensity) (λ > 345 nm) without (-●-) DMF and with 10 vol.% DMF (-■-).

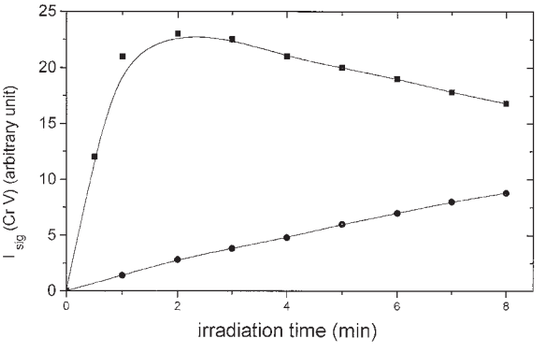

Fig. 6. Chromium(V) ESR signal evolution: (*a*) upon irradiation (λ > 345 nm); (*b*) thermal decay (after irradiation). Insert: 1/height of chromium(V) ESR signal after stopping the irradiation.

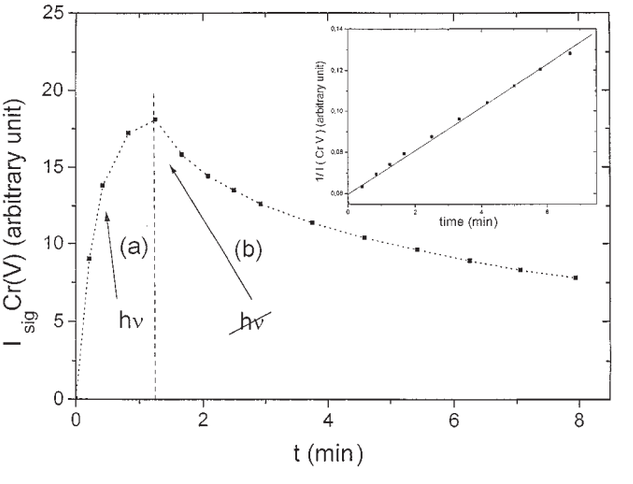

From these equations, it is possible to calculate the concentration of each species according to the concentration of dichromate in the solution (Table 3).

It is difficult to extrapolate the results obtained in solution to the films. In the films prepared from a solution 0.16 mol L^{-1} in chromium(VI), the dimer was supposed to be the predominant species, even though the monomer could be present. Because of this uncertainty, chromium(VI) will be noted Cr(VI) in the reaction mechanism without specifying the species.

Photochemical process in DCPAA

There were no detectable changes in a DCPAA film with respect to the sum of PAA and chromium(VI) spectra: there was no reaction between the two constituents. This was further confirmed by the FTIR spectrum of a DCPAA film.

Upon irradiation, the only chromium(III) formation was observed by UV–visible spectrophotometry, whereas the formation of CO_2 and carboxylate groups was established by FTIR spectrophotometry.

Such a result had already been found when studying the photochemical behaviour of the chromium(VI)–acrylic system (16). Inasmuch as there is no reaction between PAA and chromium(VI) in the ground state, this implies a quenching reaction between chromium(VI) in the excited state and PAA, leading to the formation of a chromium polyacrylate. From ESR spectroscopy measurements, it is possible to propose that a redox process by electron transfer then occurs, giving rise to Cr(V) and a macroradical that undergoes a very fast decarboxylation. Cr(V), an unstable species, is then reduced into the final chromium(III).

© 1998 NRC Canada

Fig. 7. ESR signal of PAA macroradical formed upon irradiation ($\lambda > 250$ nm).

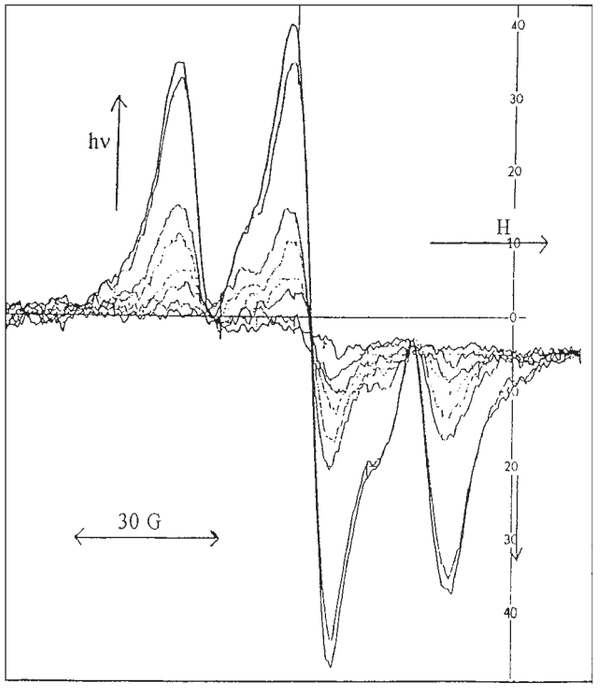

Table 3. Calculated percentage of $Cr_2O_7^{2-}$ in aqueous solution for three chromium(VI) concentrations.

Cr(VI) mol L^{-1}	% Cr(VI) as $Cr_2O_7^{2-}$
10^{-3}	10
10^{-2}	37.5
10^{-1}	72.5

This process, involving the formation of a chromium(VI) salt by a quenching reaction between chromium(VI) in the excited state and a carboxylic acid, has already been established in the photochemical behavior of chromium(VI) – acrylic acid (16).

The redox process can also occur by hydrogen abstraction, giving rise to the stable tertiary macroradical observed by ESR spectroscopy.

The two processes are present but the second reaction seems to be a minor route. The macroradicals evolve either by mutual annihilation and (or) by a reaction with chromium(VI), which is known to be a very efficient termination agent in polymerization processes (17):

[3] $R^{\bullet} + R^{\bullet} \rightarrow$ polymer

The following mechanism can be put forward:

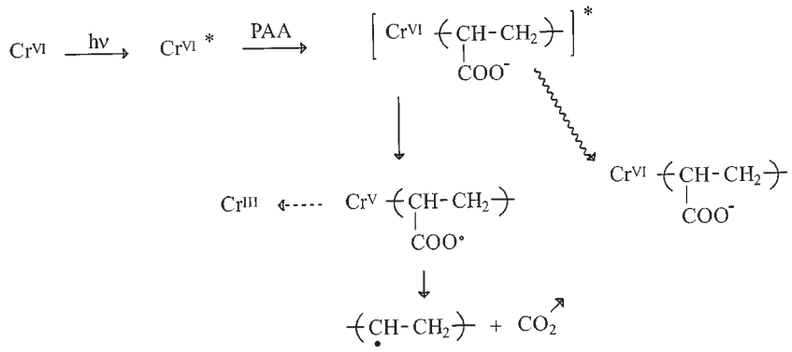

Effect of DMF on the photochemical behaviour

It is worth noting that there is no photoreduction of chromium(VI) in the presence of only DMF: the presence of poly(acrylic acid) appears to be necessary for the reduction of chromium(VI) to take place. The presence of DMF strongly increases the formation of chromium(V) upon irradiation, which requires the involvement of DMF in the first step of the reaction. This result, together with the linear relationship between the quantum yield of chromium(III) formation and the concentration of DMF, suggests a quenching reaction between chromium(VI) in the excited state and DMF. We checked that this increase was not due to a "diluting" effect of DMF in the film. A similar result was obtained when irradiating an aqueous solution of DCPAA with and without DMF.

The fact that the photoproducts are identical and that the only effect of DMF is the increase of the reaction rate reflects the formation of an analogous intermediate in the presence and in the absence of DMF. In addition, the factor of acceleration measured by FTIR is roughly identical for the chromium(VI) disappearance and photoproduct formation (R-COO$^{\bullet}$ and CO_2).

Thus we infer a mechanism similar to that described for DCPAA alone, in which DMF, through the eventual formation of a complex with chromium(VI) either in the ground state or in the excited state, enhances the basic character of chromium(VI), making easier the reaction with poly(acrylic acid) and the formation of chromium polyacrylate. Actually, when increasing the percentage of DMF in a chromium(VI) water–DMF solution it appeared that a complex exists in the

© 1998 NRC Canada

Fig. 8. UV spectra of ammonium dichromate solution in water–DMF mixtures: vol.% DMF: (1) 0%; (2) 10%; (3) 50% (4) 100%.

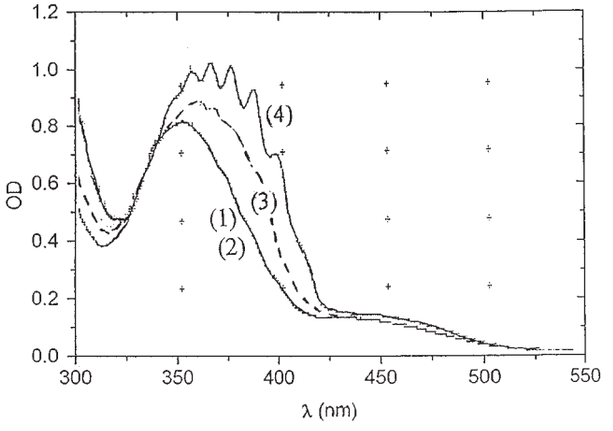

Fig. 9. Diffraction efficiency with DMF (2.2 mol L^{-1}) and without DMF as a function of exposure energy.

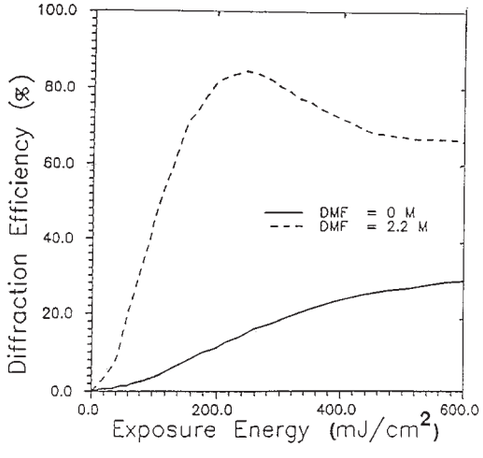

ground state provided the percentage of DMF is high enough (Fig. 8). The formation of the complex is not detectable with 10% DMF, which is the maximum used in this work.

As far as holography is concerned, we report in Fig. 9 the curves of diffraction efficiency as a function of exposure and the DMF effect; they closely resemble the curves of chromium(V) formation. It seems that the optimization of the quality of a hologram recorded in DCPAA requires the optimization of chromium(V) formation. It addresses the question of the extension of this conclusion to other dichromated systems. The work is in progress.

References

1. J. Eder. J. Prakt. Chem. **14**, 294 (1879).
2. F. Westheimer. Chem. Rev. **45**, 419 (1949).
3. K. Wiberg and H. Schäfer. J. Am. Chem. Soc. **91**, 927 (1969).
4. M. Rahman and J. Rouk. J. Am. Chem. Soc **93**, 5455 (1971).
5. C. Palopoli, S. Signorella, and L. Sala. New J. Chem. **21**, 343 (1997).
6. M. Bolte, B. Robert, and J. Lemaire. Can. J. Chem. **64**, 1864 (1986).
7. W. Tomlinson and E. Chandros. Adv. Photochem. **12**, 201 (1980).
8. (*a*) T. Schankoff. Appl. Opt. **7**, 2101 (1968); (*b*) B. Chang. Opt. Eng. **19**, 642 (1980).
9. C. Solano and R. Lessard. Appl. Opt. **24**, 1776 (1985).
10. R. Changkakoti, S. Babu, and S. Pappu. Appl. Opt. **27**, 324 (1988).
11. G. Manivannan and R. Lessard. Trends Polym. Sci. (Cambridge, U.K.),**2**, 282 (1994).
12. G. Manivannan, R. Changkakoti, R. Lessard, G. Mailhot, and M. Bolte. J. Phys. Chem. **97**, 7228 (1993).
13. R. Lessard, G. Manivannan, and R. Changkakoti. Proc. SPIE — Int. Soc. Opt. Eng. **2429**, 2 (1994).
14. J.G. Calvert and J.M. Pitts. Photochemistry. John Wiley and Sons, New York. 1966. p. 783.
15. G. Linge and A. Jones. Aust. J. Chem. **21**, 2189 (1968); J. Tong and E. King. J. Am. Chem. Soc. **75**, 6180 (1953).
16. T. Galcera, X. Jouan, and M. Bolte. J. Photochem. Photobiol. A: **45**, 249 (1988).
17. P. Fageol and M. Bolte. Makromol. Chem. **190**, 367 (1989).

© 1998 NRC Canada

Three-dimensional magnetic resonance imaging of rigid polymeric materials using single-point ramped imaging with T_1 enhancement (SPRITE)

Christopher B. Kennedy, Bruce J. Balcom, and Igor V. Mastikhin

Abstract: A new MRI method, recently employed in porous-media studies, is introduced for the imaging of rigid polymeric materials. The method, Single-Point Ramped Imaging with T_1 Enhancement (SPRITE), is designed to spatially encode short lifetime, T_2*, signals characteristic of rigid materials. We investigate the advantages of the SPRITE technique over conventional imaging methods by comparing a 2D SPRITE image of four common polymers to a 2D spin-echo image of the same substances. We demonstrate the general applicability of SPRITE by imaging two commercial products, a stop-valve made of chlorinated polyvinyl chloride and a solid-core, multilayer golf ball, both containing synthetic materials with effective ^{1}H spin–spin relaxation times, T_2*, well under 300 μs. Three-dimensional images of millimeter resolution reveal internal physical differentiation and chemical inhomogeneities that cannot be observed using conventional MRI methods. We also consider the incorporation of active spoiler gradients in SPRITE for visualization of samples with long spin–spin relaxation times, T_2.

Key words: MRI, NMR, SPI, SPRITE, polymers, imaging.

Résumé : Une nouvelle méthode d'imagerie par résonnance magnétique (IRM), employée récemment dans les études des milieux poreux, est introduite pour obtenir l'image tridimensionnelle de polymères solides. La méthode : amplification du temps de relaxation T_1 d'image tridimensionnelle à une seule ligne de fuite (SPRITE), est désignée pour encoder la distribution spatiale des temps de vie courts T_2*, des signaux caractéristiques des matériaux rigides. Nous avons étudié les avantages de la technique SPRITE par rapport aux méthodes conventionnelles d'imagerie, en comparant les images 2D de la technique SPRITE de quatre polymères courants à l'image obtenue par écho de spin de ces mêmes substances. Nous démontrons la généralisation de cette technique en réalisant l'imagerie par résonnance magnétique de deux produits commerciaux : une valve d'arrêt faite de chlorure de polyvinyle chloré et un noyau solide, une balle de golf multicouches, ces deux produits contiennent des matériaux synthétiques ayant des temps de relaxation spin–spin du ^{1}H, T_2* bien en dessous de 300 μs. Les images 3D avec une résolution spatiale de l'ordre du millimètre révèlent une différenciation physique interne et des hétérogénéités chimiques qui ne peuvent être observées par les méthodes conventionnelles de la IRM. Nous envisageons d'incorporer un dispositif actif de gradient de champ dans la technique de SPRITE pour représenter des échantillons ayant un temps long de relaxation spin–spin T_2.

Mots clés : IRM, RMN SPI, SPRITE, polymères, imagerie.

[Traduit par la Rédaction]

1. Introduction

As the demand for high-performance polymers increases, so does the need for an analytical method which can provide information on the physical and chemical parameters of a species of interest (1). Despite the outstanding success of solid-state NMR (2–6) in determining polymer structure and dynamics, the methods do not permit spatial localization. This is, however, vital if one considers a real polymeric material which will be macroscopically heterogeneous, for example, due to processing, weathering, and aging. Spatial resolution requires MRI where an NMR signal is spatially encoded, usually with an applied magnetic-field gradient. Chemical and physical molecular parameters, as well as larger scale sample features such as strain, can be exploited in MRI to correlate localized inhomogeneities to material properties (7). These correlations may give information on the state of the material under investigation, such as the degree to which its molecules are oriented or its cross-link density, or they may be used as a diagnostic to observe changes in matter, such as physical aging or chain scission (7).

While the opportunities and the applications of MRI have been identified, its use in polymer and material science has been hampered by the short T_2 and T_2* values characteristic of

Received March 4, 1998.

C.B. Kennedy, B.J. Balcom,[1] and I.V. Mastikhin. MRI Centre, Department of Physics, P.O. Box 4400, University of New Brunswick, Fredericton, NB E3B 5A3, Canada.

[1]Author to whom correspondence may be addressed. Telephone: (506) 453-4723. Fax: (506) 453-4581. E-mail: bjb@unb.ca

© 1998 NRC Canada

rigid materials (8). At present, practical MRI of polymeric materials is limited to elastomers with relaxation times which are an order of magnitude longer than more rigid solids (9).

Many new MRI pulse sequences and imaging methods have been developed in an effort to overcome the interactions specific to solids. These include imaging with the use of oscillating field gradients (10), stray field imaging (STRAFI) (11), magic echo imaging (12, 13), magic angle spinning (MAS) imaging (14, 15) and single-point imaging (SPI) (16–18). While each method has been used successfully to image solid and solid-like materials, each also has major limitations ranging from prolonged gradient switching times and loss of signal, to restrictions on sample size and the number of dimensions that can be spatially encoded. To quote Bernhard Blümich "most solid-state MRI sequences introduced to date have been demonstrated on phantoms chosen to fit the method" (1).

In this paper we demonstrate the advantages of the SPRITE technique (19) over traditional MRI methods for the imaging of ^{1}H in rigid polymer materials. The imaging method has previously been applied to the study of porous materials, including concrete (20–23). In these materials the T_1 is typically <10 ms, however, in this contribution we introduce an important extension to long T_1 materials (>100 ms). The capacity of SPRITE to encode signal from species with a T_2* less than 100 μs, and its flexible contrast parameters, are revealed in a comparison between a 2D SPRITE image and a 2D spin-echo image of a phantom consisting of *cis*-polybutadiene, polyvinyl chloride, polyethylene, and plexiglass. We do not wish to demonstrate the method with "samples chosen to suit the method," therefore we have imaged two commercial, multicomponent polymeric samples to illustrate the general utility of the SPRITE method. These samples are a plastic stop-valve and a three-piece, solid-core, multilayer golf ball. Both contain short T_2* components and are difficult or impossible to image with other MRI methods. We also investigate the origin and effect of echoes on SPRITE images and discuss the mechanisms which play a role in their elimination.

2. Methods

The basic SPRITE method was developed by Balcom et al. (19) in 1996. It is a pure phase encode imaging modality based on the original single-point-imaging (SPI) sequence developed by Emid and Creyghton (16). Unlike the SPI sequence, the magnetic field gradients in the SPRITE sequence are not switched on/off for each acquisition. Instead, the primary phase encode gradient is ramped in equally spaced discrete steps. Figure 1 shows a 3D SPRITE sequence where G_z is the primary phase encode gradient and G_x and G_y are the secondary and tertiary phase encode gradients, respectively. A broad-band RF pulse with flip angle α, is applied at each step of the primary phase encode gradient. Uniform excitation of all spins requires a pulse bandwidth (1/pulse length) greater than the maximum spectral width (G_{max} × sample length). A single complex point on the free induction decay (FID) is sampled after a constant encoding time, t_p, following each α pulse. The ramped gradient greatly reduces imaging times, minimizes gradient vibration, and enables the introduction of quantitative T_1 contrast into images

Fig. 1. Schematic of a 3D SPRITE sequence. The primary phase encode gradient, $\boldsymbol{G}_z$, is stepped with the application of a RF pulse and the acquisition of a single point at each gradient level. The signal is encoded for time t_p after the pulse. The repetition time is TR. The figure shows only 16 steps, however 64 or 128 are usually applied.

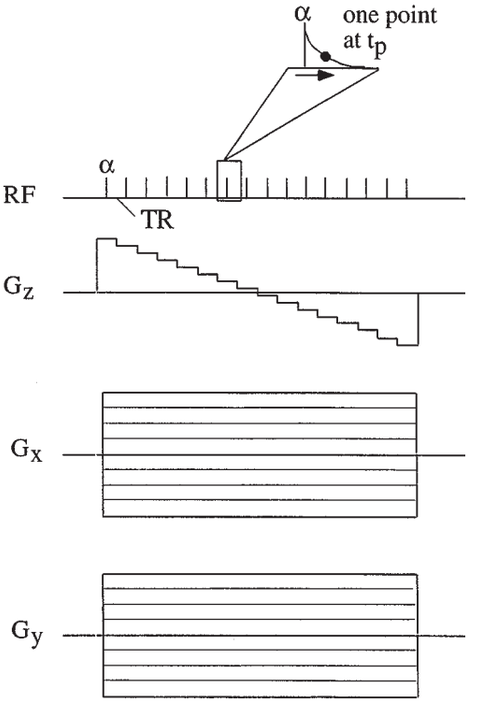

(19). Unlike traditional frequency encoding methods, SPRITE images are free from distortions due to the inhomogeneity of the main magnetic field, B_0, susceptibility variations, and chemical shift.

In the following paragraphs, we outline pertinent ideas on position encoding in one dimension, *Z*. The extension to *X* and *Y* follows logically. Position is encoded in reciprocal space or *k* space as a function of the stepped phase gradient $\boldsymbol{G}_z$, where $\boldsymbol{k}_z = (1/2\pi)\gamma \boldsymbol{G}_z t_p$. The signal detected as a function of $\boldsymbol{k}_z$, $S(\boldsymbol{k}_z)$, is the sum of all signal from the sample, encoded for time t_p which incorporates relaxation weighted proton densities $\rho(\boldsymbol{z})$,

$$[1] \qquad S(\boldsymbol{k}_z) = \int_{-\infty}^{+\infty} \exp\left[-t_p/T_2^*(\boldsymbol{z})\right]\rho(\boldsymbol{z}) \exp\left[i2\pi \boldsymbol{k}_z \boldsymbol{z}\right] d\boldsymbol{z}$$

where

$$[2] \qquad \rho(\boldsymbol{z}) = R(\boldsymbol{z})\rho_0(\boldsymbol{z})$$

The variable $\rho_0(\boldsymbol{z})$ is the true proton density. A Fourier transform relationship exists between $S(\boldsymbol{k}_z)$ and $\rho(\boldsymbol{z})$, eq. [1], and a relaxation weighted image can be obtained through application of the inverse Fourier transform to the experimental $(\boldsymbol{k}_z)$ data. Our ideas on relaxation and contrast in SPRITE are more extensively outlined in Prado et al. (24) and Beyea et al. (25).

© 1998 NRC Canada

In this work we consider the relaxation weighting, $R(\boldsymbol{z})$, for the longitudinal steady-state limiting case, which results from a train of equally spaced α pulses. The expression for $R(\boldsymbol{z})$, is therefore,

$$[3] \qquad R(\boldsymbol{z}) = \left\{ \sum_{i=1}^{n} A_i \left[\frac{1 - \exp\left[-\mathrm{TR}/T_{1i}(\boldsymbol{z})\right]}{1 - \cos(\alpha) \exp\left[-\mathrm{TR}/T_{1i}(\boldsymbol{z})\right]} \right] \right\} \sin(\alpha)$$

where TR is the repetition time, constant for each step in the SPRITE ramp, α is the RF pulse flip angle, and A_i is the weighting attributed to T_{1i}. The term in square brackets is the familiar expression for steady-state longitudinal magnetization. The overall image intensity is determined by the amplitude of the *k*-space origin points. Given the pulse sequence of Fig. 1, the longitudinal steady state is usually well established before the $\boldsymbol{k_z}$ origin is acquired.

In eqs. [1] and [3] we assume a single exponential T_2* for each isochromat as well as independent T_{1i} populations. These assumptions are not universally true, however, they are reasonable approximations for this work. The selection of sequence parameters for a particular sample greatly influences the observed image. In the limit of a short t_p and a long TR and (or) small α, a true proton density, $\rho_0(\boldsymbol{z})$, image will result.

The relationship, embodied in eqs. [1]–[3], between image intensity, relaxation times, and SPRITE timing parameters, shows that to properly understand image intensity and image contrast, knowledge of the bulk relaxation times is highly advantageous.

3. Experimental

The SPRITE technique and all other MRI measurements were implemented on a Nalorac (Martinez, Calif.) 2.35 Tesla 32 cm i.d. horizontal bore superconducting magnet. The gradient set used for the spoiled SPRITE and chlorinated polyvinyl chloride (CPVC) stop-valve images was a water cooled 20 cm i.d. self-shielded gradient set (maximum gradient 10 G cm^{-1}). The gradient set used for the golf-ball images and the SPRITE–spin-echo comparison experiment was a 7.5 cm i.d. water-cooled microimaging gradient set (maximum gradient 25 G cm^{-1}). Both gradient sets were driven by Techron (Elkhart, Ind.) 7780 amplifiers except for the SPRITE–spin-echo comparison, where Techron 8710 amplifiers were used. The RF probe used for the CPVC stop-valve experiments was a commercial quadrature bird cage (Morris Instruments, Ottawa), while the RF probe used for the golf-ball image, SPRITE resolution, SPRITE spoiling, and SPRITE–spin-echo experiments was a homebuilt 32-strut bird-cage coil. Each probe had a typical 90° pulse length of 30 μs. Both RF probes were driven by a 2 MW AMT (Brea, Calif.) 3445 RF amplifier. All experiments were performed with a Tecmag (Houston, TX) Libra S-16 console at ambient temperature. Pulse programming and some image reconstruction was undertaken with MacNMR 5.4 software (Tecmag, Houston, Tex.). Most image reconstruction and display employed IDL 5.0 (Research Systems, Boulder, Colo.).

Bulk T_1 and T_2* measurements were performed on all samples. All T_1 measurements were made using basic inversion recovery methods with exponential fitting. The T_2* values were determined from the line width of the Lorentzian fit of the Fourier transform of the FID. All the polymer materials, except for the O-ring in the stop-valve and the plexiglass sample, demonstrated multiexponential T_1 relaxation parameters. The T_2* values of most polymer materials were also multiexponential, however, their short lifetimes made accurate assessments difficult and, therefore, only one approximate value for T_2* was considered for each sample.

The SPRITE–spin-echo phantom was assembled from a *cis*-polybutadiene disc cut from the core of a multilayer golf ball. The polyvinyl chloride, polyethylene, and plexiglass discs were sliced from long rods, obtained in bulk from an industrial plastics manufacturer. The CPVC stop-valve was purchased in a local hardware store, as were the multilayer golf balls.

The spin-echo sequence, SPRITE–spin-echo comparison, had an echo time, TE, of 1.28 ms, an acquisition time of 800 μs, a dwell time of 12.5 μs, and a spectral width of ±40 kHz. The phase encode gradient was applied for 435 μs, *X* axis, with a maximum strength of 1.9 G cm^{-1}. It was stepped in 64 equal intervals to –1.9 G cm^{-1}. The field of view, *X* direction, (FOV$_x$) was 7.3 cm. The read gradient, *Z* axis, was 1.9 G cm^{-1} yielding a FOV$_z$ of 7.4 cm. Thirty-two signal averages were performed for each 64-point echo acquisition, giving a total imaging time of 35 min.

The SPRITE sequence, SPRITE–spin-echo comparison, 64 × 64 points, had an α pulse of 8°, a t_p of 50 μs, and a TR of 2.2 ms. The primary phase encode gradient, *Z* axis, had a maximum value of 15.6 G cm^{-1} while the secondary phase encode gradient, *X* axis, had a maximum value of 15.9 G cm^{-1}. The field of view was therefore 7.4 × 7.4 cm. The SPRITE acquisition, total time 15 min, was signal-averaged 64 times to ensure that the low signal intensity from the plexiglass (T_2* = 38 μs) could be distinguished from background noise.

The SPRITE resolution experiments, 64 × 64 points, employed an 8° α pulse, a 2 ms TR, and a t_p of 100 μs. Four signal averages, quadrature phase cycling, were acquired. The gradients, G_x and G_y, had maximum values of 12 G cm^{-1}, which gave a 5.6 × 5.6 cm FOV in the *X* and *Y* directions with a nominal pixel resolution of 0.9 mm.

The CPVC stop-valve was imaged, 64^3 points, with an α pulse of 14°, a t_p of 100 μs, and a TR of 2.5 ms. Four signal averages were acquired, quadrature phase cycling, with a 1 s delay at the end of each cycle of the primary phase encode gradient. The overall imaging time was approximately 5.5 h. The primary phase encode gradient, *X* axis, had a maximum value of 5.2 G cm^{-1}. The FOV$_x$ was therefore 14.5 cm. The secondary and tertiary phase encode gradients, *Y* and *Z* axes, had maximum values of 4.0 and 7.1 G cm^{-1}, yielding a FOV$_y$ of 18.6 cm and a FOV$_z$ of 10.2 cm.

The multilayer golf ball was imaged, 64^3 points, with a 14° α pulse, a 50 μs t_p, and a 5 ms TR. Eight scans, quadrature phase cycling, were performed with a delay at the end of each primary phase encode gradient cycle of 0.5 s. The total imaging time was approximately 7.5 h. The gradients were set at maximum values of G_x 23.9 G cm^{-1}, G_y 21.5 G cm^{-1}, and G_z 23.9 G cm^{-1}. This produced a FOV$_x$ of 6.3 cm, a FOV$_y$ of 7.0 cm, and a FOV$_z$ of 6.3 cm.

The SPRITE spoiling experiment, 64 points, employed an α pulse of 8°, a t_p of 400 μs, and a TR of 2.8 ms. Four signal averages, quadrature phase cycling, were acquired. The G_x

© 1998 NRC Canada

Table 1. The T_1 and T_2* relaxation values for samples used in Figs. 2*a* and *b*.

	T_{1i} (ms)[a]	A_i[b]	T_2* (μs)
cis-Polybutadiene	225	0.87	290
	10	0.13	
Polyvinyl chloride	230	0.70	442
	64	0.30	
Polyethylene	307	0.55	98
	9	0.45	
Plexiglass	284	1.00	38

[a]Samples listed with two T_{1i} values were fit to a double exponential.

[b]Each weighting, A_i, is associated with its adjacent counterpart in the adjacent T_{1i} column.

gradient had a maximum value of 3.5 G cm^{-1}, giving a one-dimensional FOV$_x$ of 7.6 cm. The maximum spoiling gradient, *Z* axis, was 0.9 G cm^{-1}.

4. Results and discussion

Comparison of spin-echo and SPRITE imaging methods

To illustrate the advantages of the SPRITE technique for polymer imaging we performed a simple phantom experiment with two dimensional SPRITE and spin-echo imaging methods. The spin-echo sequence is the simplest and most commonly used pulse sequence in MRI (26). It is a T_2 based imaging method which requires the formation of a spin-echo generated by a 90° excitation pulse and a 180° refocusing pulse. The time between the 90° pulse and the peak of the echo is the echo time, TE. The echo is acquired in the presence of a pulsed magnetic field gradient known as the read gradient. A series of spin-echo acquisitions, performed with a variable amplitude pulsed phase encode gradient, results in a 2D map of *k* space which can then be Fourier transformed to give an image.

The polymer phantom was a composite cylinder composed of four stacked polymer discs (2.5 cm diam. × 1.2 cm ht.). The four discs were polyethylene, plexiglass, polyvinyl chloride and *cis*-polybutadiene. Individual discs were separated by 0.3 cm teflon spacers. Bulk T_1 and T_2* relaxation times were measured for each disc individually, Table 1.

The two-dimensional, 64 × 64, SPRITE, and spin-echo phantom images are reproduced in Fig. 2. No image processing was performed, other than Fourier reconstruction of the raw *k*-space data. The grey scale images are displayed with identical windowing, the maximum intensity (white) in each image corresponding to the peak image intensity. In each image the polymer discs, rectangular projection in two dimensions, are arranged left to right: polyethylene, plexiglass, polyvinyl chloride, and *cis*-polybutadiene. The polyethylene and plexiglass phantoms are not apparent in the spin-echo image due to their short T_2 relaxation times which will attenuate the observable transverse magnetization by more than 10 and 20 exponential time constants, respectively, during the 1.28 ms echo time. Very low intensity, poor *S*/*N*, polyethylene, and plexiglass images are in fact apparent if one lowers the display window. These low-intensity images are, however, only apparent due to minor, long T_2, signal components present in each polymer.

Fig. 2. Comparison of (*a*) spin-echo and (*b*) SPRITE acquisitions on a phantom consisting of, left to right: polyethylene, plexiglass, polyvinyl chloride, and *cis*-polybutadiene. The spin-echo image has noticeable image artifacts. The short T_2* polymer components, polyethylene and plexiglass, are not detected in the spin-echo image. The image contrast and *S*/*N* differs in the spin-echo and SPRITE images.

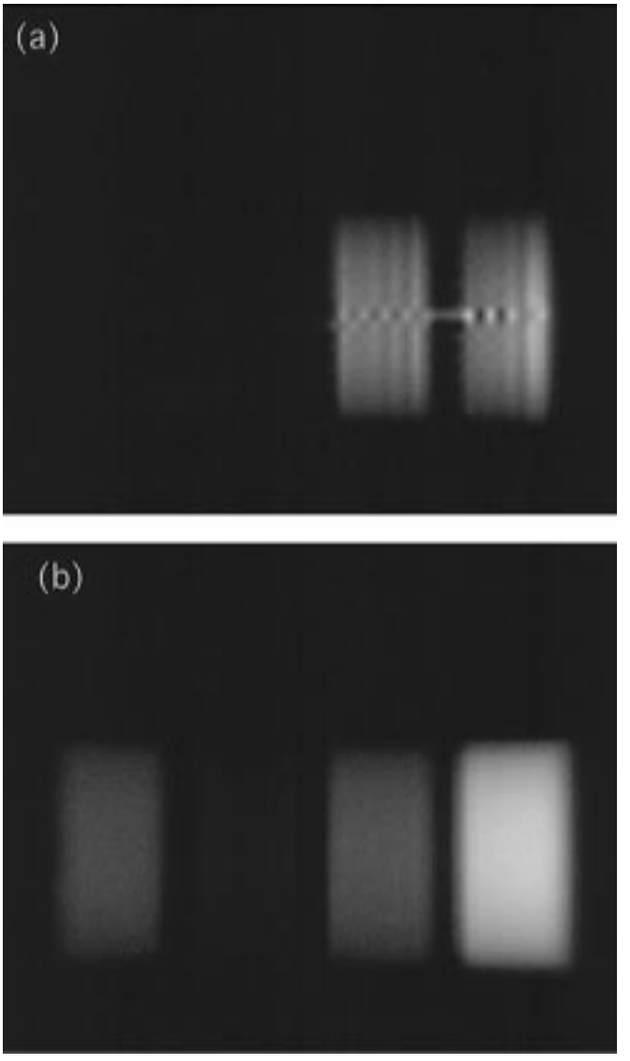

Although intuitively appealing it is not possible to greatly reduce the echo time to regain lost signal. A typical gradient rise time, in a reasonable size gradient set is on the order of 200 μs, and a stable gradient is required as one digitizes the echo signal. Switched magnetic field gradients, before and after the 180° pulse, are required because the RF pulses must be applied in the absence of a field gradient. Since, in addition, a finite acquisition time (800 μs in this case) is required to symmetrically sample the echo, an echo time much longer than many polymer T_2 relaxation times is difficult to avoid. The *S*/*N* ratio of the polyvinyl chloride and *cis*-polybutadiene was 150 and 160, respectively, as determined from the experimental images. The *S*/*N* determination

© 1998 NRC Canada

was greatly hindered by the obvious image artifacts in the spin-echo image.

The most striking feature of Fig. 2*a*, the spin-echo image, is the zipper artifact transverse to each polymer in the image and the ripple artifact parallel to the edge of the discs. A zipper artifact in the direction of the read gradient, horizontal direction in the image, is well known to result from a residual FID generated by an imperfect 180° refocusing pulse (27). The residual FID was clearly present in the experimental *k*-space data. One of the most common methods of eliminating the residual FID artifact is to spoil transverse magnetization immediately after the 180° pulse with a set of matched spoiler sandwiching the 180° pulse (27). This solution is not possible in the present circumstances because it would have required increasing the echo time still further to accommodate switching the spoil gradient on and off twice. The ripple artifact is an unusual manifestation of a truncation artifact (27). It occurs in this instance because the transverse magnetization is rapidly changing, because of the short T_2, during the acquisition window. Very fast signal digitization would be necessary to remove this truncation artifact. Note that no such artifact is apparent in the vertical, phase encode, direction of Fig. 2*a*.

The SPRITE image, Fig. 2*b*, of the same phantom is artifact free. The nearly identical field of view and an equivalent 64 × 64 data matrix, means that *k* space has been equivalently sampled by each method, yet the SPRITE technique is clearly more robust. It has also clearly visualized the polyethylene polymer (*S*/*N* of 31) in addition to the polyvinyl chloride (*S*/*N* of 40) and *cis*-polybutadiene discs (*S*/*N* of 180). The plexiglass disc is barely visible with the default display windowing in the grey scale image, Fig. 2*b*, due to its low signal (*S*/*N* of 7).

The SPRITE image has minimal artifacts and is clearly able to visualize shorter lifetime signals because of the unique manner with which it encodes transverse magnetization. In the SPRITE sequence pulse application and signal acquisition are performed in the presence of a stable gradient (Fig. 1). This permits a greatly reduced time between signal excitation and detection which permits encoding of much shorter lifetime signals. The acquired points in SPRITE *k* space are consistently encoded at a constant t_p of 50 μs, allowing for the signal contribution from polyethylene and plexiglass to be sampled before complete dephasing occurs. We therefore observe polyethylene and plexiglass in the SPRITE image (Fig. 2*b*) despite their short signal lifetimes in the transverse plane.

Figure 2*b* also shows that *cis*-polybutadiene is visualized with better *S*/*N* than in the spin-echo image, and the image contrast between the *cis*-polybutadiene and polyvinyl chloride has radically changed. They appeared to have near identical image intensities, zero contrast, in the spin-echo image.

The T_1 and T_2* values for rigid polymer materials are typically multiexponential with the longer T_1 values ranging from 300 to 400 ms and the shortest T_2* values falling under 100 μs. Equation [3] shows that TR and α experimental parameters will manipulate the signal intensity through T_1 effects without influencing the T_2* decay contribution to the observed signal in eq. [1]. The significant difference between polymer T_1 and T_2* values thereby leads to great flexibility in SPRITE contrast. From eq. [1] we see that the observed signal in a SPRITE experiment maybe dominated by T_2* dephasing. In Fig. 2*b* the two polymers with the shortest T_2* values have the lowest image intensity.

Fig. 3. (*a*) Two-dimensional SPRITE 64^2 image of a resolution phantom composed of a cross-linked *cis*-polybutadiene polymer with holes and slots of various dimensions. No image processing, other than Fourier reconstruction, was performed to maintain a pixel size on the order of the 1 mm holes. The dimensions of the smaller holes located on the edge of the sample are 2 mm (top), 1.5 mm (left), 1.25 mm (bottom), and 1 mm (right). (*b*) Schematic of the phantom with the slots and the central hole position and dimensions indicated.

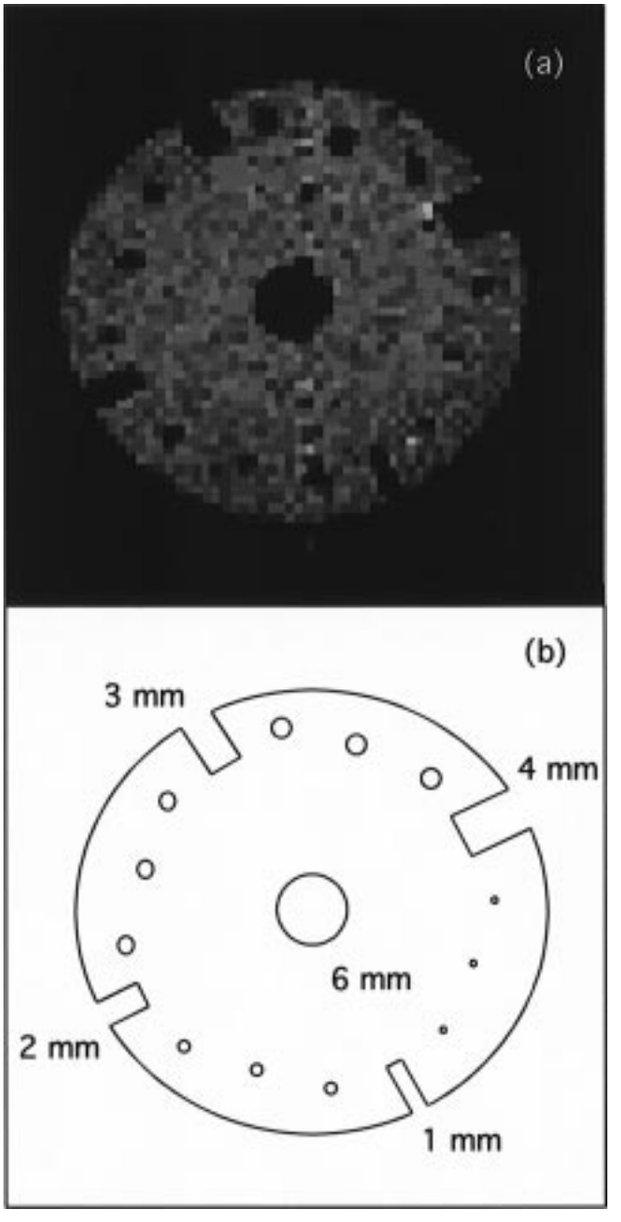

The T_1 image contrast is governed by the *R* term of eq. [2] which may be calculated from eq. [3]. The T_1 contrast in a SPRITE image depends on the sample T_1, its weighting, A_i, the repetition time, TR, and the RF flip angle, α. The short

© 1998 NRC Canada

Fig. 4. (*a*) Photograph of CPVC stop-valve. (*b*) Photograph of the components of the valve including the shaft, O-ring, screws, and washer.

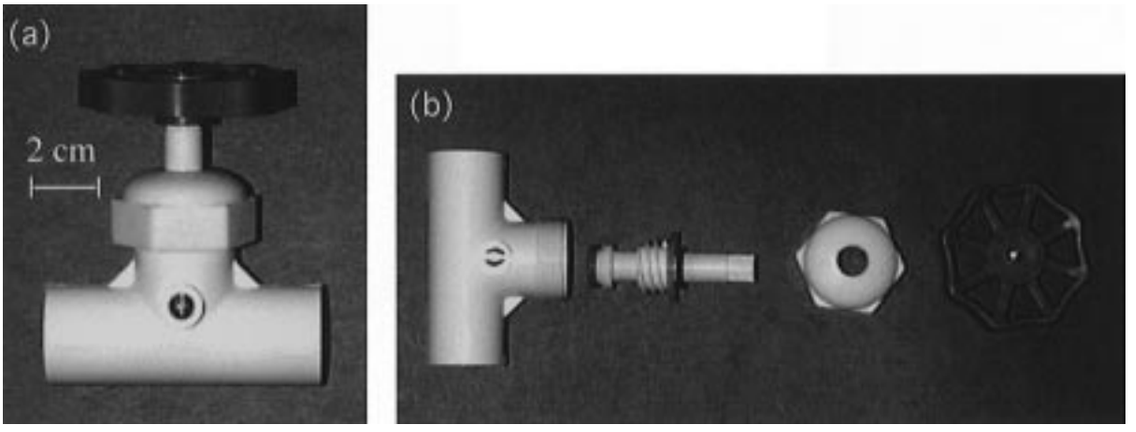

Table 2. The T_1 and T_2* relaxation values for the CPVC stop-valve and the solid-core, multilayer golf ball.

	T_{1i} (ms)[a]	A_i[b]	T_2* (μs)
CPVC stop-valve			
O-ring	213	1.00	308
T-joint and shaft	163	0.85	68
	22	0.15	
Valve handle	221	0.69	32
	33	0.31	
Washer	118	0.85	360
	7	0.15	
Solid-core, multilayer golf ball			
Soft Surlyn cover	210	0.76	87
	83	0.24	
Hard Surlyn second layer	372	0.79	58
	14	0.21	
Cross-linked *cis*-polybutadiene core[c]	221	0.85	336
	10	0.15	

[a]Components listed with two T_{1i} values were fit to a double exponential.

[b]Each weighting, A_i, is associated with its adjacent counterpart in the adjacent T_{1i} column.

[c]This sample is different from the polybutadiene sample of Table 1.

T_1 component (45% of the total) of polyethylene contributes significantly to the final image intensity when a short TR, typical of SPRITE, is employed. No T_1 effects are observed in the spin-echo image because a delay of $5 \times T_1$ is maintained after each echo acquisition, allowing for full recovery of the longitudinal magnetization. It would be possible to introduce T_1 contrast in the spin-echo image, further reducing the observable signal, by implementing a repetition time which is less than $5 \times T_1$. The image in Fig. 2*a* is a purely T_2 weighted image where the relative intensity of PVC is increased in comparison to the SPRITE image. The partial saturation of longitudinal magnetization, eq. [3], diminishes the PVC signal in the SPRITE acquisition. We have proposed alternate *k*-space sampling strategies, such as centric sampling, which will change the T_1 contrast observed through the *R* parameter (28).

Gravina and Cory (17) have demonstrated that single-point methods provide better sensitivity than analogous spin-echo experiments when the sample T_2 is less than the gradient switching time. It is thus no surprise that the polyethylene and plexiglass polymers (T_2* of 98 and 38 μs) are more readily observed with the SPRITE technique. Although the SPRITE and SPI class of imaging methods suffer from low efficiency, due to the fact that only one *k*-space point is sampled for each RF excitation, they do have a clear advantage in detecting otherwise invisible short T_2* signals.

Experimental sensitivity in the SPRITE experiment, without degradation of resolution, has a complicated dependence on the sample and the sequence parameters. It is currently an active area of investigation.

SPRITE resolution

In principle pure phase encode methods, such as SPRITE, are always capable of higher resolution than frequency encode methods such as the spin-echo (17). In this relatively low resolution work, we demonstrate the millimeter resolution capabilities of SPRITE. Figure 3 is a 2D image of a *cis*-polybutadiene phantom, with holes and slots of various dimensions drilled and cut into its edges and inner surface. The hole diameters range from 6 mm at the centre to 2, 1.5,

© 1998 NRC Canada

Fig. 5. Three-dimensional SPRITE 64^3 image of a CPVC stop-valve, externally rendered using IDL. The field of view was 15 × 19 × 10 cm^3. The encoding time was 100 μs and the TR was 2 ms. Total imaging time was 5.5 h. The long acquisition time ensured the gradient amplifiers did not overheat.

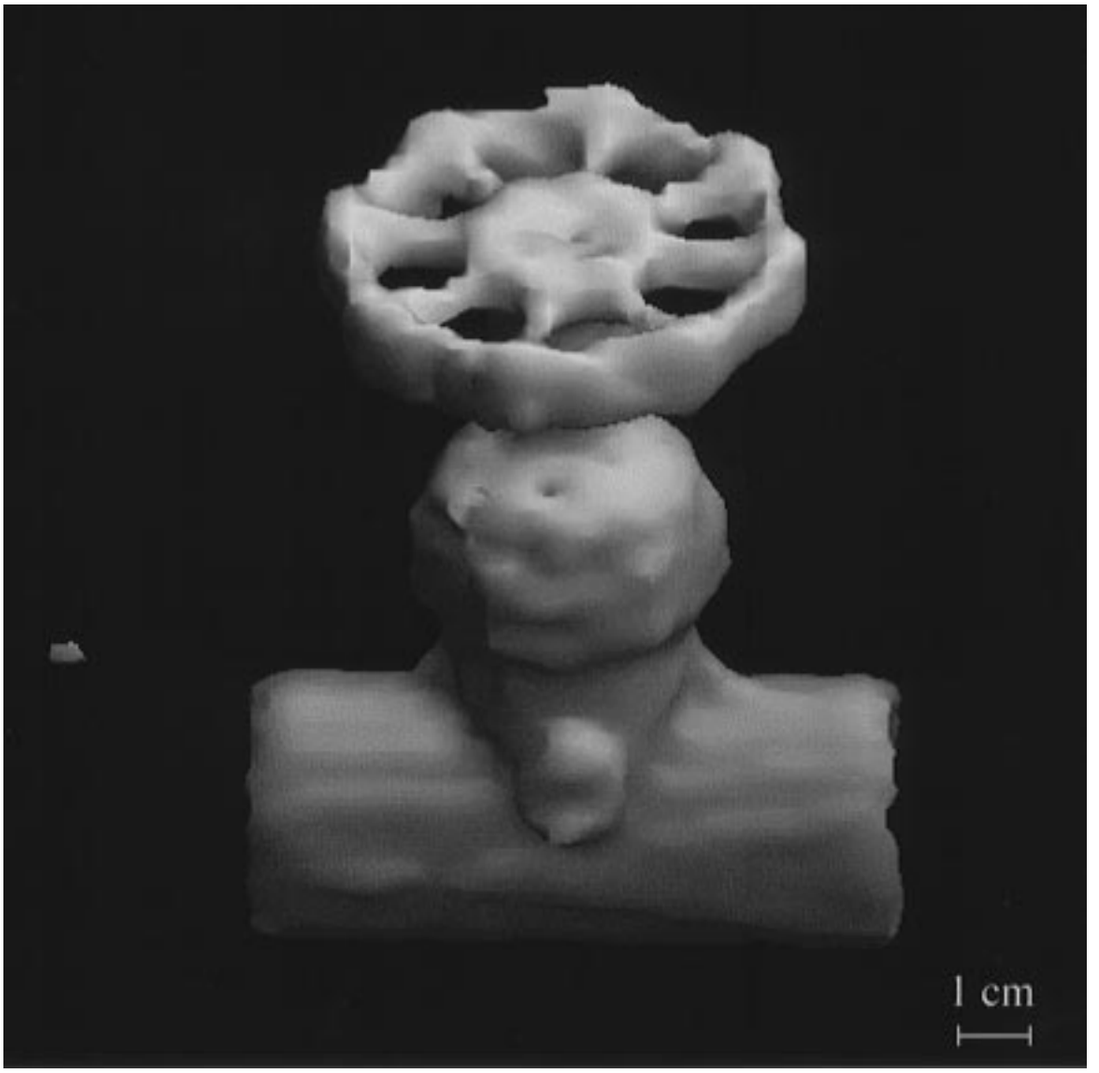

1.25, and 1 mm near the outer edges of the phantom. The slots cut into the edge of the phantom are 4, 3, 2, and 1 mm wide. Examination of Fig. 3 shows that under these conditions, as expected, the small 1 mm holes are discernible but not well resolved.

The protons in a solid sample experience large dipolar interactions which result in rapid dephasing of the FID (a short T_2 and T_2*) and very broad spectral line widths. This poses a major problem to conventional imaging methods, such as the spin-echo, which employ frequency encode gradients where the sample line width is the resolution limit. To remove the line width restriction on resolution, individual pixel widths (spectral width/number of points) must be larger than the sample line width. Large amplitude magnetic field gradients with attendant large spectral widths across the sample and very short dwell times (15) are therefore typically required. If, as frequently occurs, this condition cannot be achieved the result is edge degradation and blurring in the reconstructed image.

Blurring was not observed in Fig. 2*a* because both *cis*-polybutadiene and polyvinyl chloride had line widths smaller then the pixel width, while the plexiglass and polyethylene had large line widths but minimal image intensity.

Resolution in the SPRITE experiment is not limited by the sample line width. It is limited by the strength of the phase encode gradients and the encoding time, t_p, employed (17). The pixel resolution for SPRITE, Δx, also known as the sampling point spread function, is given by eq. [4] (17, 28).

$$[4] \qquad \Delta x = \frac{\mathrm{FOV}_x}{N} = \frac{1.2\pi}{\gamma G_{x,\max} t_p}$$

where γ is the gyromagnetic ratio and $G_{x,\max}$ is the maximum gradient strength. Based on eq. [4] we see that the resolution

© 1998 NRC Canada

Fig. 6. Selected gray scale image of a 2D slice from the 3D data set of Fig. 5. Internal structure of the stop-valve is well defined. Signal from the CPVC is less than that of the O-ring because of saturation effects and T_2* differences.

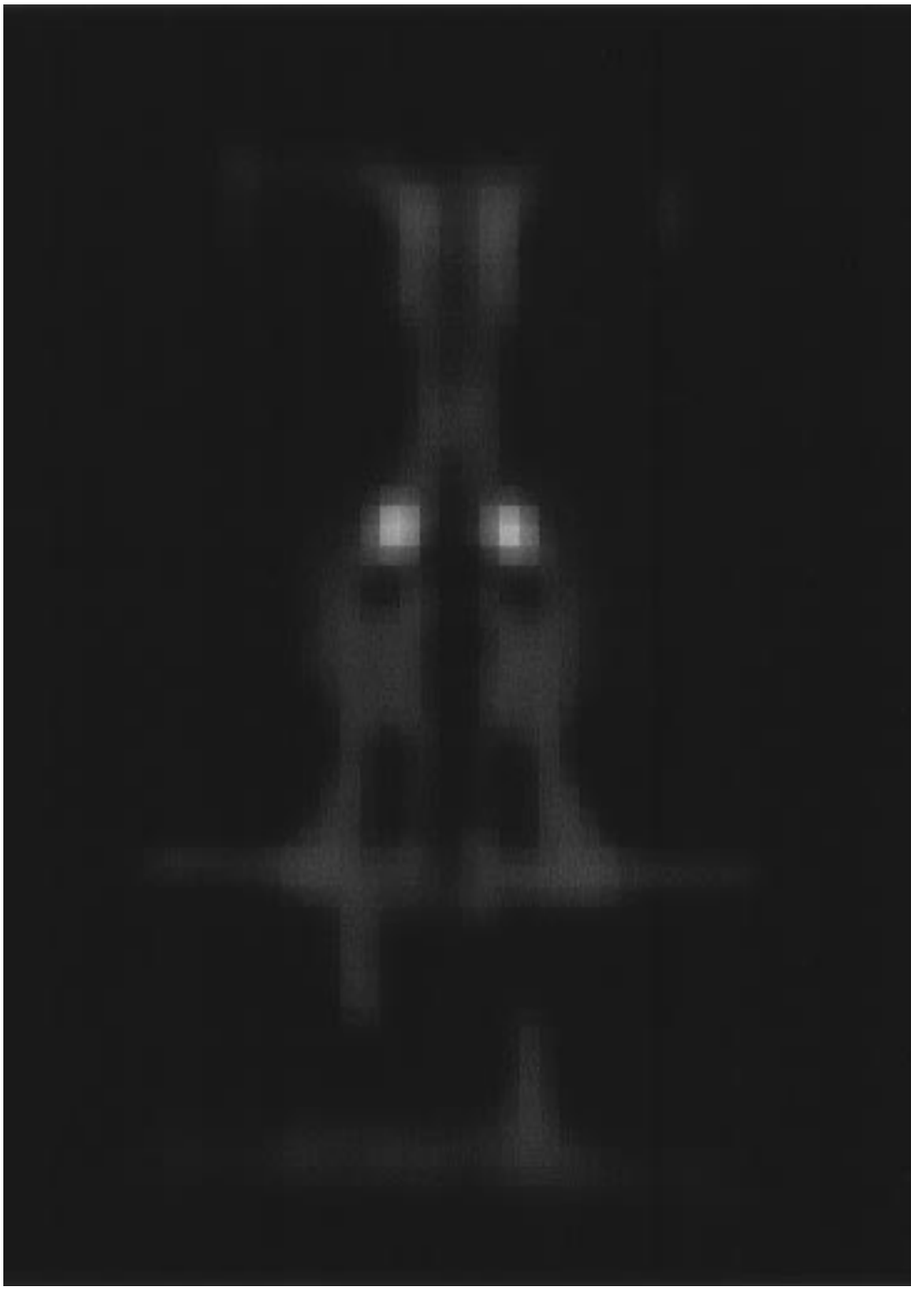

in Fig. 3 can be greatly improved by increasing $G_{x,max}$ and acquiring more *k*-space points, *N*. This would, however, require more extensive signal averaging to achieve an adequate *S*/*N*.

Chlorinated polyvinyl chloride (CPVC) stop-valve

To explore the utility of the SPRITE method for imaging real polymeric materials we imaged in 3D a CPVC stop-valve. The valve consisted of a valve handle and T-joint, a threaded shaft, polymeric washer, and two elastomeric O-rings (Fig. 4). Bulk T_1 and T_2* measurements of the disassembled pieces, Fig. 4*b*, revealed that the longest T_1 and the shortest T_2* of the stop-valve were 221 ms and 32 μs, respectively, both resulting from signal detected from the CPVC handle (Table 2).

Given knowledge of the relaxation times of the sample a rational choice of the 3D SPRITE imaging parameters was possible. The image displayed in Fig. 5 required an overall imaging time of approximately 5 h 30 min for the entire 3D data set. The main reason for this excessively long acquisi-

© 1998 NRC Canada

Fig. 7. Photograph of the multilayer golf ball in a variety of physical states and orientations. No voids were observed after the ball was physically cut (bottom left).

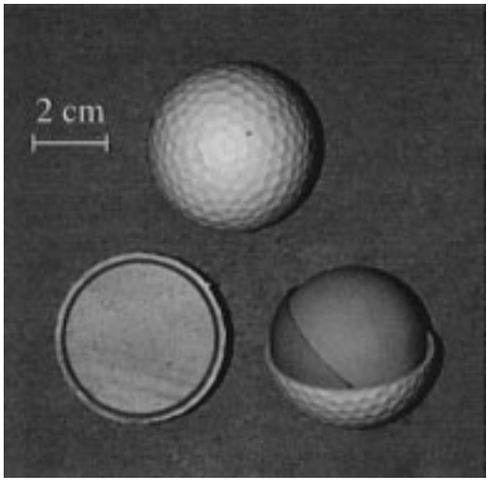

tion time is a conservative delay inserted in the pulse sequence at the end of each cycle of the primary phase encode gradient (Fig. 1). It is present to ensure that the gradient amplifiers do not overheat. Improved gradient amplifiers have reduced this restriction and should decrease the imaging time for an equivalent experiment to a more agreeable 15 min.

The 64^3 image of Fig. 5, clearly shows the ability of SPRITE to encode signal from short T_2* polymers. With a nominal pixel resolution of 2.3 mm in the *x* direction and 1.6 mm in the *z* direction, the structure of the handle and the T-joint are clearly defined. Also, note in Fig. 4 the presence of two brass screws located in the T-joint and the valve handle. While the presence of the metallic screws will distort the B_0 homogeneity, no geometrical distortions are observed in Fig. 5 because the SPRITE experiment is a pure phase encode method (17). Distortions of the main field homogeneity within a pixel decrease in the local T_2*, which may decrease the observable signal.

A two-dimensional slice taken from the 3D image data set, Fig. 6, reveals the internal structure of the stop-valve. Voids along the internal axis of the shaft and inside the T-joint are defined as well as the divisions in the pipe. Perhaps the most interesting feature of this image is the contrast observed between the O-ring and the bulk CPVC structure. Assuming a constant proton density, allowing for T_1 partial saturation effects, and estimated T_2* differences (Table 2), we predicted a factor of two difference in image intensity. The experimentally observed difference is a factor 2.4. The contrast between the two regions is primarily due to the T_2* difference.

It is clear, based on these results, that SPRITE can observe short T_2* materials such as the valve handle (Table 2 and Fig. 5), distinguish polymer materials based on image contrast, and achieve adequate resolution to observe physical differentiation within the sample (Fig. 6).

Solid-core multilayer golf ball

Our second realistic polymer test sample was a solid-core multilayer golf ball. Once more, bulk relaxation times were measured on the individual golf-ball components (Table 2). The golf ball had three distinct layers: a soft Surlyn™ cover (type 1855), a hard Surlyn™ second layer (type 1605), and an injection moulded *cis*-polybutadiene core (Fig. 7). Surlyn™, a DuPont product, is described in the patent literature as a polymeric material composed of an ionomer resin. The constituents of this resin include ethylene acid copolymers whose acid functionalities are neutralized by zinc (Zn) or sodium (Na) ions.

The initial objective of this 3D SPRITE imaging experiment was to image the outer Surlyn™ cover and discriminate it from its inner layers. Figure 8 is a 64^3 image of an intact golf ball. The raised areas on the Surlyn™ cover are signal from glue which was used to position the ball in the RF probe. The dimples on the outer cover are apparent. The internal structure is clearly revealed in a 2D slice removed from the original 3D data set shown in Fig. 9. In this 64^2 gray scale image the deviations between cover, layer, and core are clearly defined. Figure 9, also, reveals a series of signal voids in the core of the golf ball. These voids are not physical spaces in the ball, as determined by physical sectioning, but are representations of areas where the NMR signal has decayed more rapidly relative to its surroundings, probably because of a localized T_2* decrease. We hypothesize that these localized discontinuities result from an inhomogeneous distribution of additives in the golf-ball core.

It is evident that while the sensitivity and resolution of SPRITE allow each golf-ball component to be distinguished, a second, and perhaps more important, SPRITE feature is revealed. Localized chemical differences are manifest as local relaxation time differences which, as discussed above, may be manipulated to produce image contrast (Fig. 9). While the nature of the voids in the ball are not the subject of this work, it is clear that SPRITE has great potential for the noninvasive detection and investigation of a variety of polymer manufacturing defects and inhomogeneities.

5. SPRITE spoiling

Balcom et al. (19) have observed artifacts with the SPRITE sequence from samples with spin–spin relaxation times, T_2, greater than TR. We believe that this is due to the introduction of unwanted spin and stimulated echoes during data acquisition.

In most cases SPRITE imaging of rigid polymeric materials will not require a consideration of spin-echo artifacts. The short T_2 values of these materials allow for dephasing to occur naturally and rapidly before any subsequent RF excitation pulses. One can envision, however, a variety of MRI experiments where the observation of a rigid polymer material, in the presence of a long T_2 species, is necessary, and the elimination of spin-echoes due to multiple RF pulses becomes a concern. Examples of such experimental conditions would include the presence of liquid monomers in a partially formed polymer or fluid penetration into a solid polymer.

We can discriminate between three mechanisms which would prevent unwanted echoes in a SPRITE experiment. These are an increased repetition time, TR, the passive spoiling of signal due to the primary phase encode gradient, $\boldsymbol{G_z}$, and the active spoiling of signal resulting from administered spoiling gradients, $\boldsymbol{G_{spoil}}$. We will examine each mechanism in turn.

© 1998 NRC Canada

Fig. 8. Three-dimensional SPRITE 64^3 image of a multilayer golf ball externally rendered using IDL. The field of view was 6 × 6 × 7 cm^3. The encoding time, t_p, was 50 μs and the TR was 5 ms. The dimpled Surlyn cover with a T_2* of approximately 87 μs is observed. Total imaging time was 7.5 h.

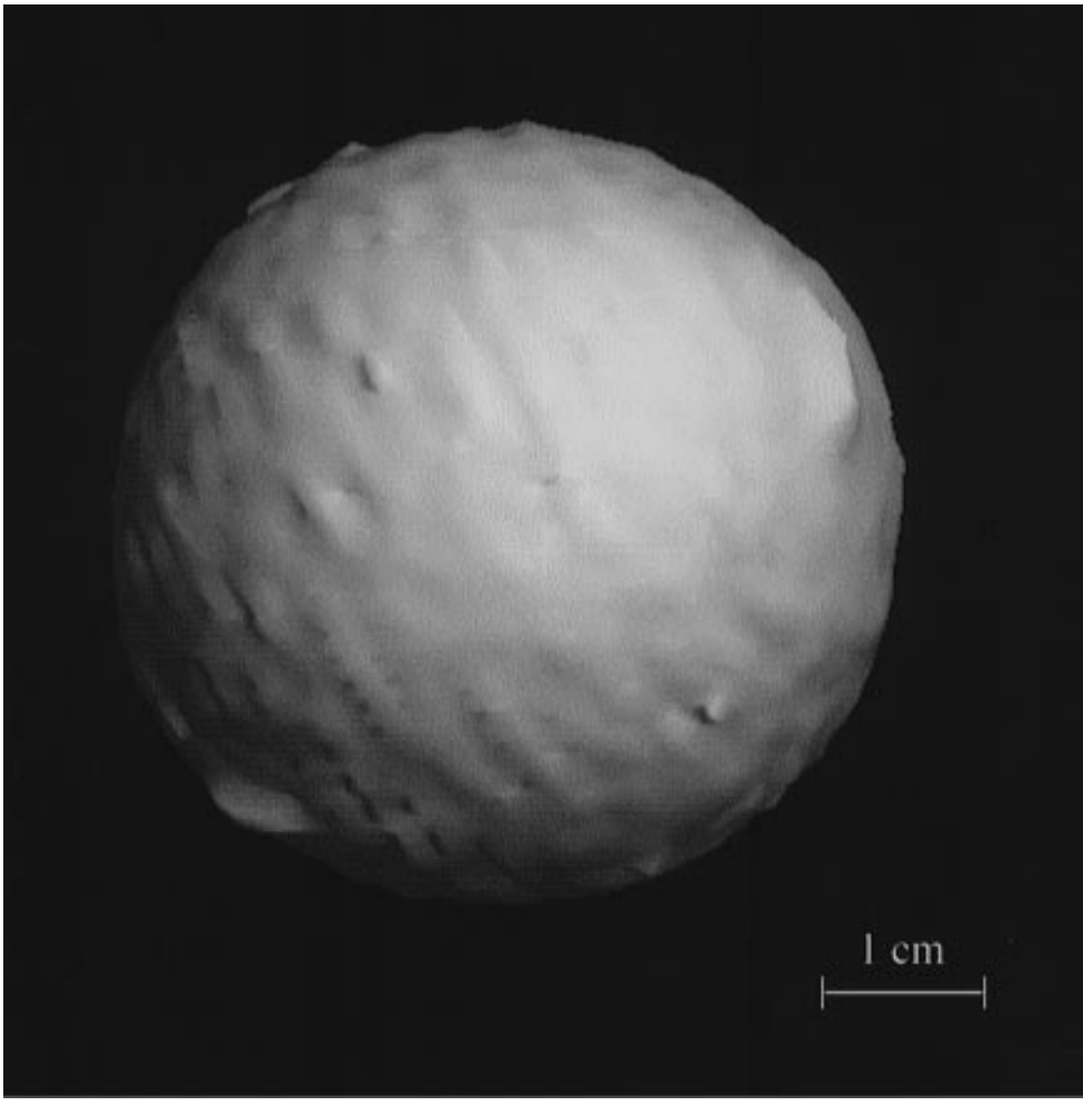

Investigating dephasing effects and echo formation in the SPRITE sequence requires consideration of the amount of transverse magnetization present immediately prior to the succeeding excitation pulse at time TR (Fig. 1). We rewrite eq. [1], substituting for $\boldsymbol{k_z}$ and exchanging t_p with TR to consider the transverse magnetization at time TR following an excitation pulse,

$$[5] \qquad M_{xy} \propto S(\boldsymbol{k_z}) = \int_{-\infty}^{+\infty} \exp[-\mathrm{TR}/T_2^*]\rho(\boldsymbol{z}) \exp[i\gamma \boldsymbol{G_z z}(\mathrm{TR})]\, \mathrm{d}\boldsymbol{z}$$

Spin and stimulated echoes are possible when T_2 = TR and multiple RF pulses manipulate coherent magnetization (29). Therefore one very simple and obvious method of eliminating echo artifacts is to increase TR. As TR is increased the effectiveness of the natural dephasing process is increased, which is observed as a decrease in the term, exp [–TR/T_2*] in eq. [5], and a concomitant decrease in M_{xy}. Although we discuss signal dephasing in terms of T_2* decay, our concern is primarily with T_2, the time constant which is the major culprit in echo formation. While the increase of TR is a natural solution to the elimination of echo artifacts in SPRITE, constraints must be placed on its duration to achieve adequate imaging times and to not exceed the duty cycle restrictions of the gradient coils (19) or gradient amplifiers. Therefore, as the limits of TR are reached alternative methods of ensuring signal dephasing must be considered.

If we examine eq. [5] we see that the signal from the previous pulse/encode period is really a normal FID with a weighting exp [$i\gamma \boldsymbol{G_z z}$(TR)] whose value is governed by $\boldsymbol{G_z}$. In Fig. 1, we see that for each step in the primary phase encode gradient, $\boldsymbol{G_z}$ is applied for a period TR before being

© 1998 NRC Canada

Fig. 9. Selected 2D gray scale image slice from the 3D image data set of Fig. 8. The three layers of the ball are well defined. Inhomogeneities in the core of the ball are observed.

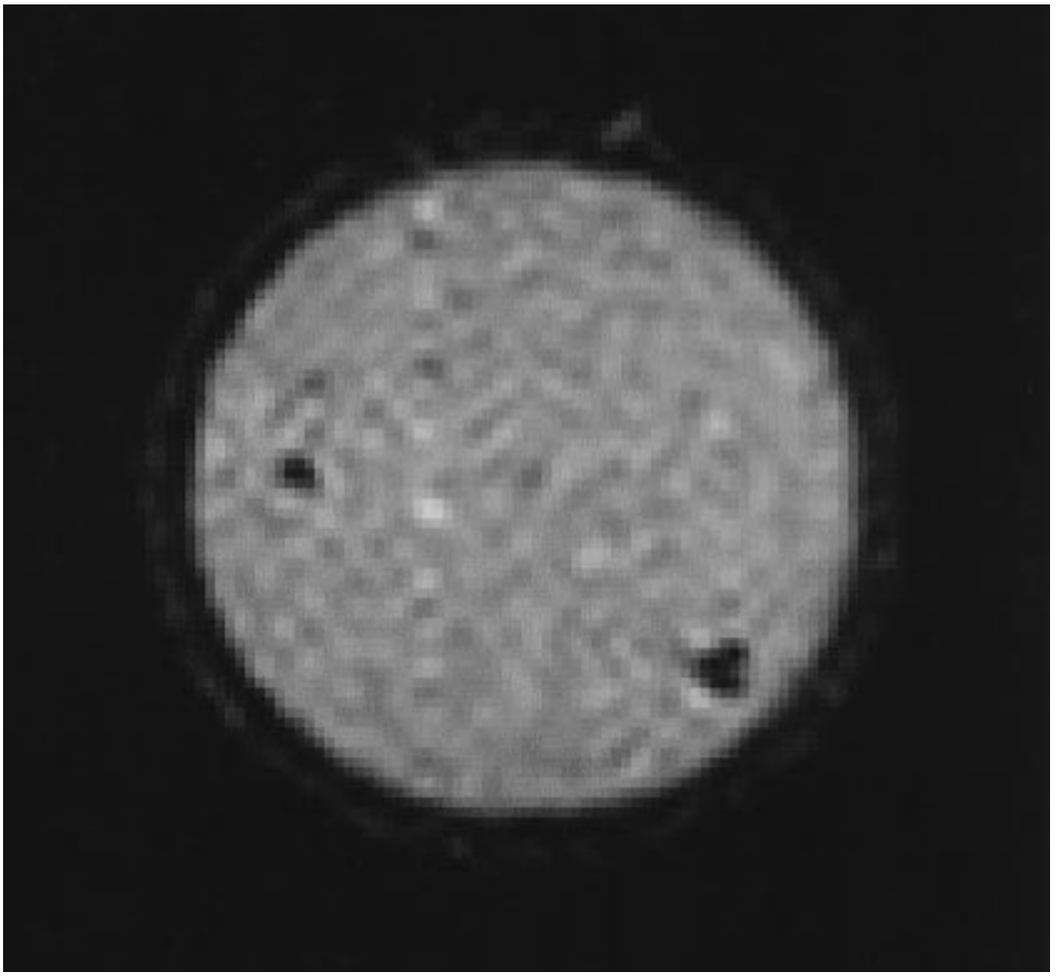

stepped to a lower gradient level. This continuous change in gradient area is a passive dephasing condition that effectively spoils transverse magnetization. Therefore, when a large $\boldsymbol{G_z}$ is applied for the observed point at time t_p, it is evident that even if the natural dephasing process of the sample fails to eliminate M_{xy}, the passive spoiling of $\boldsymbol{G_z}$ will, as shown in eq. [5]. An exception to this condition does occur, however, at the *k*-space origin where $\boldsymbol{G_z}$ is low and echo formation can prevail.

To overcome the problems at the *k*-space origin, a rapidly switched spoiling gradient, $\boldsymbol{G_{spoil}}$, can be introduced into the SPRITE sequence (Fig. 10). Pseudo-random amplitude spoiler gradients can be applied at steps in the SPRITE sequence where little or no dephasing is otherwise achieved (i.e., where $\boldsymbol{G_z}$ is small). This SPRITE modification is very similar to spoiling in the Fast Low-Angle Shot (FLASH) imaging method (30, 31). In both sequences spoiling gradients of fixed duration but random amplitude are applied after each acquisition to actively dephase transverse magnetization before the succeeding α pulse (32). In both SPRITE and FLASH sequences we use and exploit the steady-state longitudinal magnetization but wish to remove all transverse magnetization from pulse to pulse.

This implementation of random area spoiler gradients differs greatly from the original use of spoiler gradients in spin-echo sequences such as RARE (33). As discussed earlier, this spoiling scheme will remove image artifacts which may result from transverse magnetization generated by imperfect 180° refocusing pulses (27, 33). The dephasing effects of the spoiling pulse must be balanced, however, by a matched gradient pulse prior to the 180° refocusing pulse to avoid attenuating transverse magnetization which will contribute to echo formation.

One can systematically consider the integration of passive and active spoiling in terms of an equation. An integral similar to eq. [5] could be developed to demonstrate the effects of active spoiling, where $\boldsymbol{G_z}$ is substituted for $\boldsymbol{G_{spoil}}$ and TR is replaced with the spoiling gradient application time, t_{spoil}. Alternatively, and more simply, complete signal dephasing will occur when

$$[6] \qquad \gamma \boldsymbol{G_i} \boldsymbol{L_i} t >> 2\pi$$

For spoiling in the SPRITE sequence to be effective in preventing echo formation, the product of the gradient $\boldsymbol{G_i}$, its duration, *t*, and the sample length, L, in the *i* direction, must

© 1998 NRC Canada

Fig. 10. Schematic of 3 pulses from a 1D SPRITE sequence with spoiler gradients. The gradients are applied with pseudo-random amplitudes in the central regions of *k* space to ensure complete dephasing of transverse magnetization. TR is the gradient step length and also the time between RF pulses.

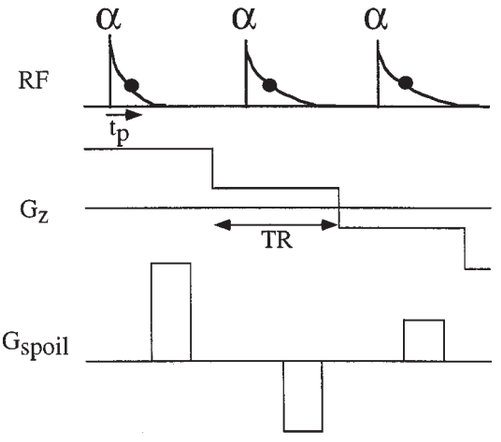

completely disperse transverse magnetization. In addition this dispersal must occur rapidly and dominate the natural dephasing processes of the sample. This condition is achieved at the extremes of *k* space where $i = z$ and t = TR and at the center of *k* space where i = spoil and $t = t_{spoil}$. Equation [6] is essentially the spoiling condition originally proposed by Hennig (34).

To illustrate the necessity of spoiling in SPRITE we have performed a simple phantom study with a uniform object where T_2^* = TR. A spin-echo artifact is observed in a 1D, 64-point SPRITE acquisition performed on a homogeneous manganese (Mn) doped 1% (wt./vol.) agarose phantom (3 cm diam. × 4 cm) (Fig. 11*a*). The T_1 and T_2^* of the phantom were determined using bulk measurements to be 87 and 2.7 ms, respectively. During the application of the SPRITE sequence the ramped phase encode gradients are at their minimum during the central *k*-space acquisitions with a zero crossing occurring at point 1. Figure 11*a* shows a signal offset in the central points of *k* space for the experiment without active spoiling.

We now consider the origin of this signal offset and show that it is due to echo formation. The evolution of transverse magnetization for the central *k*-space points in the absence of strong gradients can be considered through the application of vector product operators. We proceed with a consideration of the behaviour of one isochromat (small region of sample of a particular frequency), recognizing the fact that the sample as a whole evolves as the summation of multiple isochromats. After an interval α-TR-α-TR, it can be shown that an echo of normalized magnitude 1/2 sin α(cos α + 1) will form at point 1 in the transverse plane on the *y* axis of the rotating frame, assuming a $-x$ phase α pulse is applied. The timings of the SPRITE sequence reveal that the echo will have peaked at the exact time of application of the succeeding α pulse. Therefore, signal dephasing for time t_p from the echo peak will be mixed with the FID point sampled at point 1 leading to the observed offset (Fig. 11*b*). Also, the slight offset observed at point 0 in *k* space can be explained by some signal from the leading edge of the echo

Fig. 11. SPRITE 1D acquisition of a manganese-doped gel phantom where $T_2^* \approx$ TR, demonstrating the adverse effects of spin-echoes on *k*-space sampling and the benefits of spoiler gradients; (*a*) *k* space of signal data, real channel, with spoiling (—) and without spoiling (○); (*b*) Mn phantom profile with artifact; and (*c*) spoiled Mn phantom profile, artifact removed.

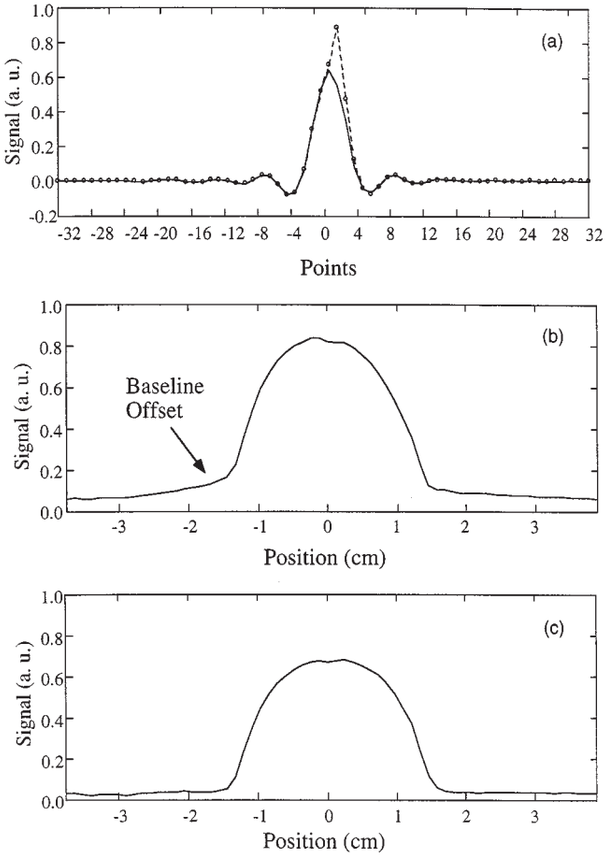

mixing with the FID signal sampled at point 0 or by an echo formed earlier in point –1.

The corruption of the image in going from reciprocal space (*k*-space) to real space can be explained using the linearity property of the Fourier transform. The addition of two functions in one domain is equivalent to the addition of the Fourier transforms of these two functions in the reciprocal domain (35). The signal offset in reciprocal space, point 1 in Fig. 11*a*, can be approximated by an impulse added to a noncorrupted, "ideal" *k*-space data set. Taking the respective FT of these two functions and moving to the spatial domain, one can see that Fig.11*b* is composed of a very low frequency wave (essentially DC) being added to a noncorrupted, ideal profile. The result of the addition is an MRI effect quite analogous to a DC offset which is frequently observed in phase-sensitive NMR experiments (36). In the later instance the DC offset in the time domain manifests itself as a spike at zero frequency in the frequency domain.

Having identified the artifact origin in Figs. 11*a* and *b* we introduced spoiling gradients into our experiment to ensure transverse magnetization is eliminated prior to successive α pulses. The spoiling gradients were applied during the nine central *k*-space acquisitions of the primary phase encode

© 1998 NRC Canada

gradient. The spoil gradients consisted of rapidly switched magnetic fields of pseudo-random amplitude on an axis perpendicular to the primary phase encode gradient. The maximum amplitude used for the spoil gradients was arbitrarily set at 1/10 the maximum level. The gradient strength could have been increased for the experiment but because 1/10 the maximum satisfied the condition put forth in eq. [6] and was experimentally successful, it was deemed unnecessary. It should be noted as well that too strong a gradient level may lead to excessive gradient vibration and noise. The gradient vibration from each set of nine spoil gradients of restricted amplitude introduces a useful audio cue to monitor the advancement of the SPRITE experiment which is otherwise silent.

The reciprocal space data from the spoiled SPRITE acquisition is shown in Fig. 11*a* as a solid line. A great improvement in the symmetry of the function relative to the nonspoiled acquisition is observed. A comparison of the spoiled profile to the nonspoiled, corrupted profile reveals a flat baseline with no DC offset (Fig. 11*c*). Thus the application of rapidly switched, low amplitude, randomized spoil gradients can be used to remove artifacts which may prevail in systems where the T_2 = TR.

6. Conclusion

SPRITE can successfully produce quantitative 2D and 3D images of polymeric materials of both variable chemical and physical composition with T_2* values <100 μs. High-resolution images of two off-the-shelf samples, a solid-core, multilayer golf ball and a CPVC stop-valve, show the flexibility and the versatility of the technique. Images of each sample reveal different levels of contrast which can be correlated to nonmolecular parameters such as $\rho_0(\boldsymbol{x})$ or molecular physical parameters such as T_2*.

The visualization of long T_2 signals in the presence of short T_2* species without echo artifacts is possible through the implementation of spoiling gradients in the SPRITE sequence.

The SPRITE sequence is rapidly developing. Improvements in hardware and software permit increased signal-to-noise and decreased imaging times. Additional contrast through NMR relaxation times such as T_1, T_2, T_2 solid echo and $T_{1\rho}$ is possible and is under active investigation. These and other developments will be the subject of subsequent publications.

Acknowledgments

We thank the Natural Sciences and Engineering Research Council of Canada (NSERC) for operating and equipment grants (B.J.B.) and Robin Armstrong for establishing the UNB MRI Research Centre. We wish to thank Albert Cross for his work with IDL, Pablo Prado, Derrick Green, and Steven Beyea for their guidance, patience, and advice, and Rod MacGregor for answering numerous questions (C.B.K.). I.V.M. thanks NATO for a Postdoctoral Science Fellowship.

References

1. B. Blümich, P. Blümler, E. Günther, J. Jansen, G. Schauss, and H.W. Spiess. *In* Magnetic resonance microscopy. *Edited by* B. Blümich and W. Kuhn. VCH, Weinheim. 1992. pp. 167–185.
2. K. Schmidt-Rohr and H.W. Spiess. *In* Multidimensional solid-state NMR and polymers. Academic Press, London. 1994. Chap. 1.
3. H. Oschkinat, T. Mueller, and T. Dieckmann. Angew. Chem. Int. Ed. Engl. **33**, 277 (1994).
4. E.R. Andrew. Philos. Trans. R. Soc. London, **505**, A299 (1981).
5. K. Eichele, R.E. Wasylishen, J.S. Grossert, and A.C. Olivieri. J. Phys. Chem. **99**, 10 110 (1995).
6. K. Eichele and R.E. Wasylishen. Inorg. Chem. **33**, 2766 (1994).
7. B. Blümich. Concepts Magn. Res. **10**, 19 (1998).
8. A. Abragam. The principles of nuclear magnetism. Oxford, London. 1983. Chap. 4.
9. P. Jezzard, J.J. Attard, T.A. Carpenter, and L.D. Hall. Prog. NMR Spec. **23**, 1 (1991).
10. S.P. Cottrell, M.R. Halse, and J.H. Strange. Meas. Sci. Technol. **1**, 624 (1990).
11. S. Black, D.M. Lane, P.J. MacDonald, D.J. Hannant, M. Mulheron, G. Hunter, and M.R. Jones. J. Mater. Sci. Lett. **14**, 1175 (1995).
12. S. Hafner, D.E. Demco, and R. Kimmich. Solid State NMR, **6**, 275 (1996).
13. F. Weigand, S. Hafner, and H.W. Spiess. J. Magn. Reson. Ser. A, **120**, 201 (1996).
14. W.S. Veeman. *In* Magnetic resonance microscopy. *Edited by* B. Blümich and W. Kuhn. VCH, Weinheim. 1992. pp. 29–47.
15. P.T. Callaghan. Principles of nuclear magnetic resonance microscopy. Clarendon Press, Oxford. 1995. Chap. 5.
16. S. Emid and J.H.N. Creyghton. Physica B (Amsterdam), **128**, 81 (1985).
17. S. Gravina and D.G. Cory. J. Magn. Reson. Ser. B, **104**, 53 (1994).
18. D.E. Axelson, A. Kantzas, and T. Eads. Can. J. Appl. Spec. **40**, 16 (1995).
19. B.J. Balcom, R.P. MacGregor, S.D. Beyea, D.P. Green, R.L. Armstrong, and T.W. Bremner. J. Magn. Reson. Ser. A, **123**, 131 (1996).
20. P.J. Prado, B.J. Balcom, S.D. Beyea, R.L. Armstrong, and T.W. Bremner. Solid State NMR. **10**, 1 (1997).
21. S.D. Beyea, B.J. Balcom, T.W. Bremner, P.J. Prado, D.P. Green, R.L. Armstrong, and P.E. Grattan-Bellew. Cem. Conc. Res. **28**, 453 (1998).
22. P.J. Prado, B.J. Balcom, S.D. Beyea, T.W. Bremner, R.L. Armstrong, and P.E. Grattan-Bellew. Cem. Conc. Res. **28**, 261 (1998).
23. F.R. Rack, B.J. Balcom, R.P. MacGregor, and R.L. Armstrong. J. Paleolimnology. **19**, 255 (1998).
24. P.J. Prado, B.J. Balcom, S.D. Beyea, T.W. Bremner, R.L. Armstrong, R. Pishe, and P.E. Grattan-Bellew. J. Phys D: Appl. Phys. **31**, 2040 (1998).
25. S.D. Beyea, B.J. Balcom, P.J. Prado, A.R. Cross, C.B. Kennedy, R.L. Armstrong, and T.W. Bremner. J. Magn. Reson. **135**, 156 (1998).
26. M.A. Brown and R.C. Semelka. *In* MRI basic principles and applications. Wiley–Liss, New York. 1995. pp. 45–65.
27. R.M. Henkelman and M.J. Bronskill. Rev. Magn. Reson. Med. **2**, 1 (1987).
28. I.V. Mastikhin, B.J. Balcom, P.J. Prado, and C.B. Kennedy. J. Magn. Reson. **136** (1999). In press.
29. E.L. Hahn. Phys. Rev. **89**, 580 (1950).
30. H.Z. Wang and S.J. Riederer. Magn. Reson. Med. **15**, 175 (1990).
31. J. Frahm, W. Hanicke, and K.-D. Mernoldt. J. Magn. Reson. **72**, 307 (1987).
32. J. Hennig. Concepts Magn. Res. **3**, 179 (1991).
33. J. Hennig, A. Nauerth and H. Friedburg. Magn. Reson. Med. **3**, 823 (1987).
34. J. Hennig. J. Magn. Reson. **78**, 397 (1988).
35. R.N. Bracewell. The Fourier transform and its applications. McGraw–Hill, New York. 1986. Chap. 6.
36. D. Hoult. Prog. NMR Spec. **12**, 41 (1978).

© 1998 NRC Canada

Molecular self-assembly of rigid-rod alkynyl chromophores on inorganic oxide surfaces

Chi Ming Yam, Adam Dickie, Aramice Malkhasian, Ashok K. Kakkar, and M.A. Whitehead

Abstract: The hydrolysis of surface-bound basic tin-amide moieties with acidic protons of alkynyl chromophores leads to molecular self-assembly of a variety of rigid-rod alkynes on inorganic oxide surfaces such as glass, quartz, and single crystal silicon. Characterization of these newly developed thin films was achieved by contact-angle goniometry, FTIR–ATR, ellipsometry, and X-ray photoelectron spectroscopy, which indicate that these thin films are densely packed. Comparative molecular mechanics modeling studies on unbound and chemisorbed -Sn-C≡C-H monomer, dimer, trimer, and a 12 × 12 (144 molecule) model substrate, suggest that surface anchoring of Sn-alkynyl units is essential for highly ordered thin-film structures that can effect topochemical polymerization. Preliminary MO calculations on a 4 × 4 model show conjugated molecular orbitals through the system.

Key words: molecular self-assembly, rigid-rod alkynes, acid–base hydrolysis, tin-alkynyl thin films, molecular mechanics modeling studies, topochemical polymerization, molecular orbitals.

Résumé : L'hydrolyse de portions basiques d'amides d'étain liées à une surface à l'aide de protons acides de chromophores alcynyles conduit à la formation d'autoassemblages moléculaires de divers alcynes en forme de tiges rigides sur des surfaces d'oxydes inorganiques comme le verre, le quartz et des cristaux uniques de silice. On a caractérisé les films minces ainsi formés par goniométrie de l'angle de contact, «FTIR–ATR», ellipsométrie et spectroscopie photoélectronique des rayons X et les données indiquent que ces films minces sont entassés d'une façon dense. Des études comparatives de mécanique moléculaire du monomère -Sn-C≡C-H non lié et chimisorbé, du dimère, du trimère et d'un substrat modèle 12 × 12 (144 molécules) suggèrent que l'ancrage en surface des unités alcynyles d'étain est essentiel pour que les structures fortement ordonnées des films minces puissent donner lieu à une polymérisation topochimique. Des calculs préliminaires d'OM sur un modèle 4 × 4 montrent la présence d'orbitales moléculaires conjuguées à travers tout le système.

Mots clés : autoassemblage moléculaire, alcynes en forme de tiges rigides, hydrolyse acide–base, films minces d'alcynyles d'étain, études de modélisation moléculaire par mécanique moléculaire, polymérisation topochimique, orbitales moléculaires.

[Traduit par la Rédaction]

1. Introduction

Molecular self-assembly is an important and valuable technique for the construction of highly ordered interfaces which offer great potential for a variety of technological applications (1). Self-assembled monolayers (SAMs) based on long-chain alkanes can be prepared using chemisorbed processes involving trichlorosilanes on inorganic oxides, thiols on gold, and carboxylic acids on silver surfaces (2). These "first generation" thin films have been widely characterized and shown to form highly uniform and ordered systems (3). There have been a number of attempts to introduce other useful moieties into the alkanes while retaining the basic long-chain structure that leads to self-organization via van der Waals forces of attraction (4). However, investigations of the organic microstructures with extensive conjugation in the backbone which will involve purely intermolecular π–π interactions for molecular self-assembly, have just begun (5, 6). These "second-generation" SAMs offer tremendous opportunities for building thin-film devices by molecular design. We have recently developed a simple acid–base hydrolytic approach to the functionalization of inorganic oxide surfaces (6). Using this synthetic approach, a variety of thin-film structures including highly conjugated rigid-rod alkynes can be assembled on glass, quartz, and single crystal Si. We report herein our recent results on the self-organization of alkynyl chromophores on inorganic oxide surfaces including a preliminary theoretical evaluation of the behavior of conjugated organic molecules with respect to each other on interfaces. The PM3 calculations on a 4 × 4

Received February 19, 1998.

C.M. Yam, A. Dickie, A. Malkhasian, A.K. Kakkar,[1] and M.A. Whitehead.[1] Department of Chemistry, McGill University, 801 Sherbrooke St. West, Montreal, PQ H3A 2K6, Canada.

[1]Authors to whom correspondence may be addressed: AKK: Telephone: (514) 398-6912. Fax: (514) 398-3797. E-mail: ashok_kakkar@maclan.mcgill.ca; MAW: Telephone: (514) 398-6239. Fax: (514) 398-3797. E-mail: tony@maw.chem.mcgill.ca

© 1998 NRC Canada

tin-acetylene chemisorbed on silica surface show clearly the possibility of topochemical polymerization of the acetylene moieties. This 4 × 4 model is developed from initial studies by molecular mechanics and PM3 calculations of the isolated monomer, dimer, and trimer of tin-acetylene, these chemisorbed on a 12-membered silica ring, a model 12 × 12 tin-acetylene unit calculated using molecular mechanics, and a 12 × 12 tin-acetylene bonded to a 12 × 12 silica surface calculated by molecular mechanics. The 4 × 4 molecular orbitals relate to the monomer, dimer, and trimer molecular orbitals on a 12-membered silica ring. The conjugated molecular orbitals in the 4 × 4 unit presage a fully conjugated conducting band in a real system.

2. Experimental section

Materials

Phenylacetylene and 1,9-decadiyne were purchased from Aldrich and used as received. The other alkynes employed in this study were conveniently prepared using literature procedures (7). $Sn(NEt_2)_4$ was prepared from $SnCl_4$ and $LiNEt_2$ (8*c*). Toluene was distilled over sodium. The substrates were placed in a plastic carousel fitted with a magnetic stir-bar at the bottom. Thin-film depositions were performed under nitrogen in a self-assembly apparatus similar in design to a Schlenk flask but with a flat bottom.

Sample preparation and monolayer self-assembly

The glass, quartz, or Si wafers were first cleaned (*i*) by soaking in soap solution and sonocating for 1 h; (*ii*) repeated washings with deionized water; (*iii*) treatment with a solution mixture containing 70% conc. H_2SO_4 and 30% H_2O_2 (piranha solution) at 100°C for 1 h. Caution: Piranha solution is highly explosive, and care should be taken while using this mixture; (*iv*) repeated washings with deionized water; and (*v*) finally heating in oven at 150°C for 5 min and vacuum drying for 5 min to remove physisorbed water. The surface functionalization involved a two-step process of (*i*) reaction with 1% solution by volume of $Sn(NEt_2)_4$ in toluene for 18 h; followed by (*ii*) treatment with the organic chromophore in dry toluene at 80°C for 18 h.

Contact-angle measurements

The static contact angles were measured with a Rame–Hart NRL 100 goniometer using water and hexadecane as probe liquids. On average, six drops of equal volume were measured on different areas of the substrate for each sample, and the values reported are the mean values.

Fourier transform infrared spectroscopy in the attenuated total reflection mode (FTIR–ATR)

The thin films were grown on the <100> surfaces of the single side polished silicon wafers. A KRS crystal was sandwiched between the reflective faces of two silicon wafers (1.2 × 4.0 cm), and the angle of incident light was set at 45°. All spectra were run for 4000 scans at a resolution of 4 cm^{-1}, using a Bruker IFS-48 spectrometer. Spectrum of a clean silicon wafer was measured as a background correction.

Ellipsometry measurement

A Gaertner Scientific ellipsometer operating with a 633 nm He-Ne laser (λ = 6328 Å) was employed. The angle of incidence was 70°, and the compensator was set at 45°. All reported values are the average of at least six measurements taken at different locations on the sample. The thicknesses were calculated by comparing data from the same substrate before and after functionalization, and using a value of 1.46 for the refractive index.

X-ray photoelectron spectroscopy (XPS)

The XPS spectra were obtained by using a INRS 220i XL spectrometer with monochromatized AlK_α radiation source at 10^{-9} Torr pressure.

All modelling and semi-empirical calculations were performed using HyperChem™ Release 3 for Windows and Cerius 2 version 3.0/MOPAC 6. The molecular mechanics force field was MM+, and geometry optimizations were carried out using the Polak–Ribiere conjugate gradient set to terminate at an RMS gradient of 0.1 kcal/Å mol.

3. Results and discussion

3.1. Acid–base hydrolysis: in solution

The chemistry of aminostannanes, which can be conveniently prepared by the reaction of the corresponding chloride and $LiNR_2$ (8), with organic compounds containing acidic protons, is well established. For example, the compound, $(CH_3)_3Sn\text{-}NR_2$ (R = CH_3, C_2H_5), reacts with R′OH, R′SH, R′COOH (R′ = alkyl or aryl group), and alkynes (e.g., $H\text{-}C{\equiv}C\text{-}C_6H_5$) via acid–base hydrolysis to give $(CH_3)_3Sn\text{-}OR'$, $\text{-}SR'$, $\text{-}OOCR'$, and $\text{-}C{\equiv}C\text{-}C_6H_5$, respectively, in quantitative yields (eq. [1]) (8). Similarly, the reaction of 2 equiv. of $(CH_3)_3Sn\text{-}NR_2$ with $H\text{-}C{\equiv}C\text{-}R\text{-}C{\equiv}C\text{-}H$ (R = *p*-C_6H_4, *p*-C_6H_4-C_6H_4, *p*-$C_{14}H_8$, $\text{-}C{\equiv}C\text{-}C_6H_4\text{-}C{\equiv}C\text{-}$, and $(CH_2)_6$), yields the corresponding trimethyltin substituted alkynes with the elimination of diethylamine.

Evolution of this chemical methodology on inorganic oxide surfaces can lead to thin-film assemblies of molecules containing desired chemical frameworks.

3.2. On surfaces

The surfaces of inorganic oxides such as silica, glass, and quartz are acidic in nature, and contain surface hydroxyl groups (9, 10). Thus, the acid–base hydrolytic chemistry described above can be easily applied to these surfaces to give a versatile chemisorption method for a variety of organic microstructures. A general surface modification strategy is shown below in Scheme 1, which involves the chemical processes described in detail in the experimental section, and depicts a cartoon representation of the various steps involved in the thin-film construction process.

The evolution of thin-film structures was routinely monitored by surface wettability measurements, FT–IR, ellipso-

[1] $$(CH_3)_3Sn\text{-}Cl + NR_2Li \xrightarrow{-\,LiCl} (CH_3)_3Sn\text{-}NR_2 \xrightarrow[E = O, S, COO, \text{-}C{\equiv}C\text{-}]{REH} (CH_3)_3Sn\text{-}ER + NR_2H$$

© 1998 NRC Canada

Scheme 1.

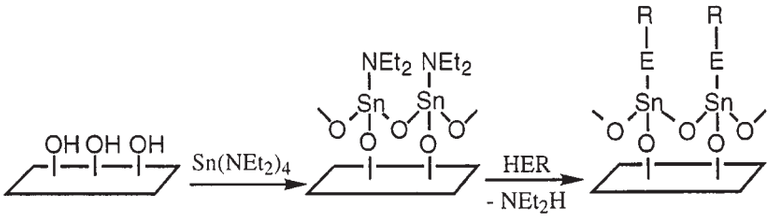

Table 1. Contact-angle, thickness, and XPS data for the thin films prepared from the rigid-rod alkynes on inorganic oxide surfaces.

Alkyne	Contact angle H_2O (HD)[a]	Calculated thickness (Å)	Thickness by ellipsometry (Å)	XPS data (eV) C(1*s*), O(1*s*), Si(2*p*), Sn($3d_3$, $3d_5$)
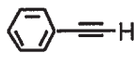	86 (15)	11	10	284.9, 532.4, 103.9, 495.5, 487.1
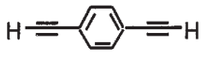	85 (15)	13	12	284.9, 533.1, 104.0, 496.0, 487.6
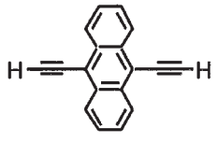	85 (15)	13	13	285.0, 533.2, 103.7, 496.1, 487.7
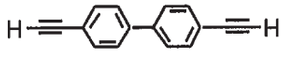	88 (20)	18	17	285.0, 533.2, 103.6, 496.1, 487.7
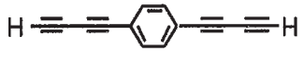	88 (18)	18	17	284.9, 532.6, 103.4, 495.1, 486.7
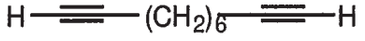	85 (15)	18	17	284.9, 533.0, 103.5, 495.4, 487.5

[a]HD = hexadecane.

Fig. 1. Sn-acetylene monomer, $(HO)_3Sn\text{-}C{\equiv}C\text{-}H$, showing the PM3-optimized structure and the molecular orbital on C≡C, the HOMO isolated from the rest of the molecule.

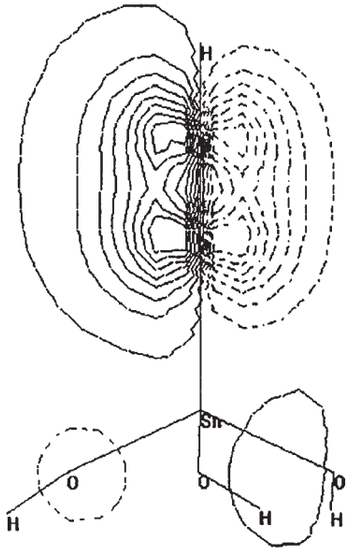

Fig. 2. Sn-acetylene dimer, $\{O\text{-}[(HO)_2Sn\text{-}C{\equiv}C\text{-}H]_2\}$, showing the PM3-optimized structure and the molecular orbitals on the C≡C HOMO orthogonal to the remaining molecular orbitals.

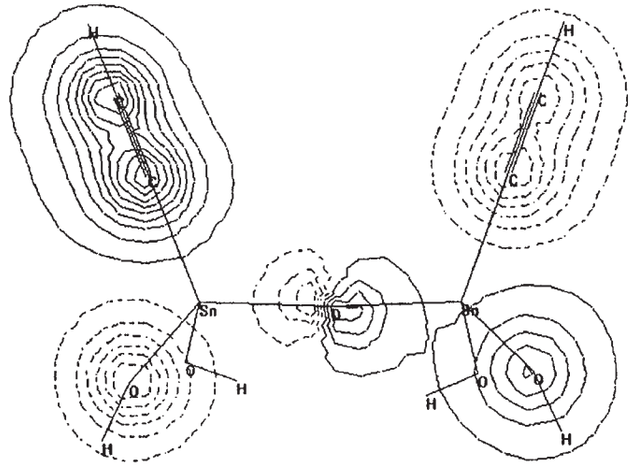

© 1998 NRC Canada

Fig. 3. Sn-acetylene trimer, {(HO)(C≡C-H)Sn-[O-(HO)$_2$Sn-C≡C-H]$_2$}, showing the PM3-optimized structure and the orthogonal HOMO C≡C molecular orbitals.

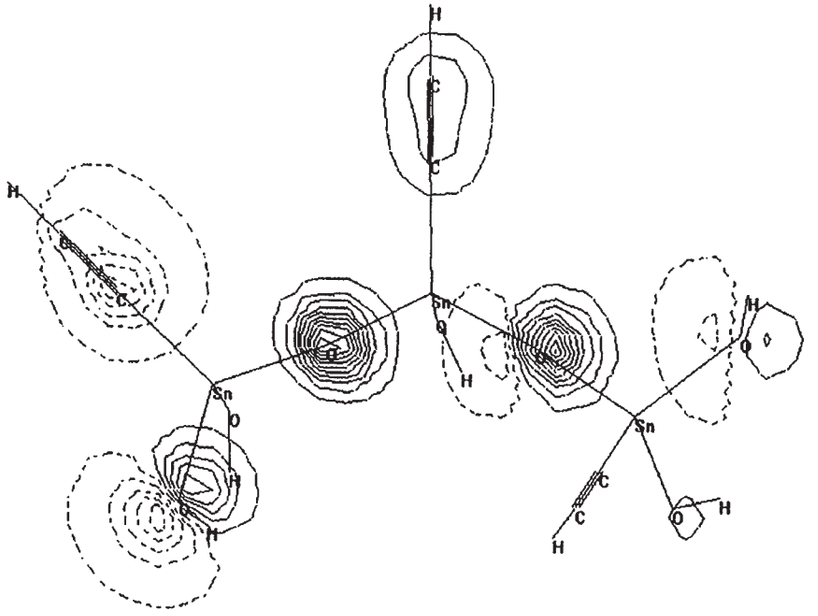

Table 2. Geometries and energies, (HO)$_3$Sn-C≡C-H monomer.

(*a*) Geometries			
	MM	MNDO	PM3
d(C≡C) (Å)	1.20	1.20	1.20
C-Sn-O angle (°)	110	111	112
(*b*) Energies (kcal/mol)			
	MM	MNDO	PM3
Binding energy	0.40	–849.692	–907.491
Bond energy	8.04×10^{-5}		
Angle energy	3.49×10^{-4}		
Dihedral energy	1.00		
van der Waals energy	–0.60		
Stretch–bend energy	1.06×10^{-5}		
Electrostatic energy	0		
Total energy		–31 625.911	–29 080.33
Isolated atomic energy		–30 776.219	–28 172.84
Electronic energy		87 784.369	–85 341.585
Core–core interaction		56 158.458	56 261.255
Heat of formation		–48.627	–106.426

metry, X-ray photoelectron spectroscopy, etc., and the pertinent data is presented in Table 1. Surface wettability measurements have been widely used to approximate the hydrophobicity and to estimate chromophore density in thin-film assemblies (1–3). Contact-angle goniometry measures the angle that the drop of a liquid makes on a surface, and is dependent on the relative hydrophobicity or hydrophilicity of the thin-film surface and the liquid. For example, a clean and unfunctionalized glass surface produces a contact angle of ~18° with water. When a nonpolar liquid such as hexadecane is deposited onto a hydrophilic surface such as unfunctionalized glass slide, an increase in the forces of repulsion at the solid–liquid interface results in a higher contact angle (~85°). Conversely, when hexadecane is deposited onto an organic monolayer, an increase in the forces of attraction results in the lowering of the contact angle.

Fig. 4. C^1_a to C^2_b separation in tin-alkyne molecules.

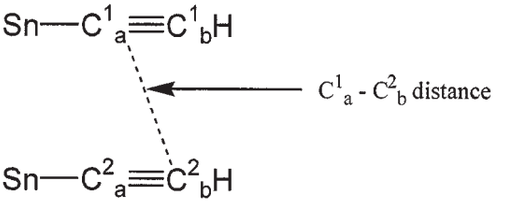

© 1998 NRC Canada

Table 3. Geometries and energies, $\{O\text{-}[(HO)_2Sn\text{-}C\equiv C\text{-}H]_2\}$ dimer.

(*a*) Geometries			
	MM	MNDO	PM3
d(C≡C) (Å)	1.21	1.20	1.20
C-Sn-O angle (°)	110	112 ± 2	112 ± 2
C^1_a —C^2_b distance (Å)	3.66 ± 0.03	4.53 ± 0.02	5.72 ± 0.01
(*b*) Energies (kcal/mol)			
	MM	MNDO	PM3
Binding energy	–1.83	–1474.306	–1608.103
Bond energy	1.19×10^{-3}		
Angle energy	0.11		
Dihedral energy	0.07		
van der Waals energy	–1.93		
Stretch–bend energy	1.53×10^{-3}		
Electrostatic energy	–0.08		
Total energy		–55 147.239	–50 678.314
Isolated atomic energy		–53 672.932	–49 070.210
Electronic energy		–204 172.693	–197 114.858
Core–core interaction		149 025.454	146 436.544
Heat of formation		–35.939	–169.736

Fig. 5. Different conformers of the trimer, $\{(HO)(C\equiv C\text{-}H)Sn\text{-}[O\text{-}(HO)_2Sn\text{-}C\equiv C\text{-}H]_2\}$, from the PM3 calculations.

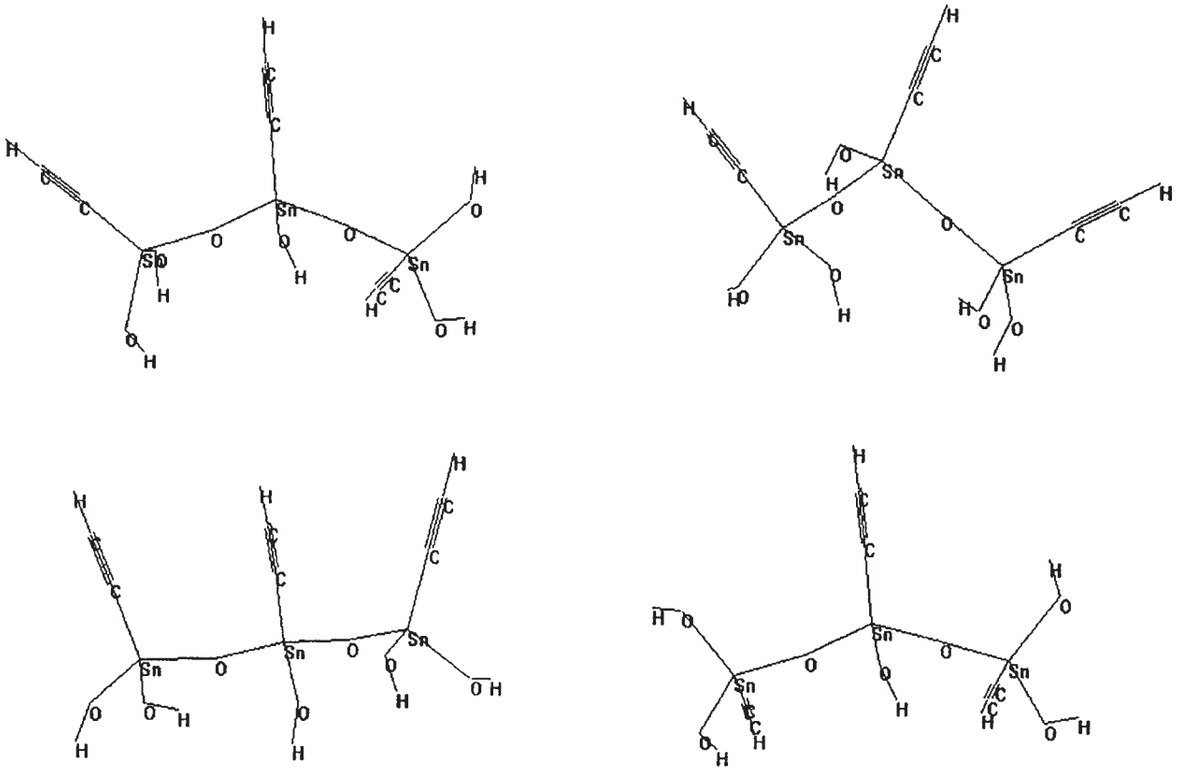

For long-chain alkanes deposited on the inorganic oxide or gold surfaces, contact angles of ~110° with water and 35–40° with hexadecane have been observed (2). The wetting nature of alkynyl surfaces is expected to be different than long-chain alkane self-assembled thin films, and may depend on a number of factors. The latter are currently under investigation in our laboratory. Table 1 summarizes static contact-angle data obtained from thin films of a variety of rigid-rod alkynes employed in the present study. These values that are comparable to those obtained from thio-alkynyl thin films on Au (11, 12) suggest that these thin films are densely packed.

Fourier transform infrared spectroscopy in the attenuated total reflection mode (FTIR–ATR) has been extensively used

© 1998 NRC Canada

Table 4. Geometries and energies, {(HO)(C≡C-H)Sn-[O-(HO)$_2$Sn-C≡C-H]$_2$} trimer **1**.

(*a*) Geometries			
	MM	MNDO	PM3
d(C≡C) (Å)	1.21	1.20	1.20
C^1_a—C^2_h distance (Å)	3.69 ± 0.02 6.7 ± 0.3	4.41 ± 0.02 6.7 ± 0.1	5.61 ± 0.01 6.84 ± 0.04
C-Sn-O angle (°)	110 ± 1	112 (±2)	112 (±1)
(*b*) Energies (kcal/mol)			
	MM	MNDO	PM3
Binding energy	–4.02	–2098.409	–2308.330
Bond energy	2.10×10^{-3}		
Angle energy	0.17		
Dihedral energy	0.11		
van der Waals energy	–3.95		
Stretch–bend energy	1.91×10^{-3}		
Electrostatic energy	–0.357		
Total energy		–78 668.055	–72 275.912
Isolated atomic energy		–76 569.646	–69 967.581
Electronic energy		–350 650.607	–337 805.361
Core–core interaction		271 982.552	265 529.450
Heat of formation		–22.740	–232.661

Fig. 6. A 12 × 12 model layer of Sn-C≡C-H molecules without surface attachments calculated by molecular mechanics.

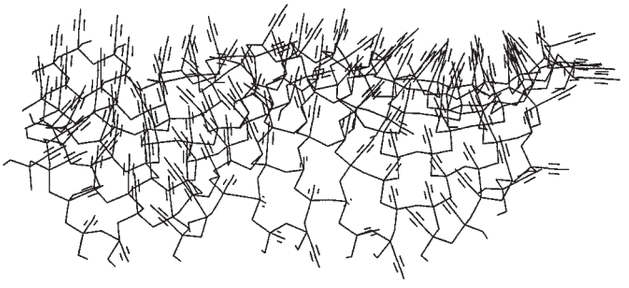

Table 5. MM energy, 12 × 12 (Sn-R)$_{144}$ monolayer, kcal/mol.

Binding energy	2225.85
Bond energy	4.38
Angle energy	2420.63
Dihedral energy	244.43
van der Waals energy	–444.16
Stretch–bend energy	1.26
Electrostatic energy	–0.69

in the characterization of thin-film structures (2). This sensitive surface technique confirms the chemical identity of the newly developed thin film. The spectra of the thin films containing alkynyl chromophores typically displayed peaks at 2097, 3260, 3033, and 1498 (br) cm^{-1}, which can be assigned to acetylene and phenyl groups of the rigid-rod structure. These values are similar to those obtained from alkynylthiols chemisorbed on Au (11).

Ellipsometry is a commonly employed technique to measure thicknesses of the molecularly self-assembled thin films (13). A detailed evaluation of this technique has been discussed elsewhere (2, 14). However, to calculate thickness of an interface one compares data from the same substrate before and after functionalization, and an assumption is made for the refractive index of the organic phase. For long-chain alkanes, a typical value of the refractive index employed for calculating thicknesses is 1.45 (13). For self-assembled alkynyl thin films reported in this study, we used a similar value (1.46). The data obtained from the functionalized silicon wafers is shown in Table 1. Calculation of the theoretical thicknesses was based on typical values of bond lengths between elements projected on the surface. There is a good agreement between calculated and experimental thicknesses of the alkynyl thin-film assemblies, and it suggests a close-packed arrangement of the rigid-rod alkynyl chromophores.

X-ray photoelectron spectroscopy is a well-known technique to determine the surface composition of the anchored species in the molecularly self-assembled thin films (2). We employed this technique for the analytical evaluation of the various alkynyl thin films on glass, and the data is presented in Table 1 that confirms the composition of the thin-film structures. A slight increase in binding energies was observed for Si 2*p*, Sn $3d_{3/2}$, and Sn $3d_{5/2}$. This increase in binding energies of the elements in chemisorbed thin films is consistent with the values expected for Si of SiO_2 and Sn of SnO_2.

4. Theoretical evaluation of alkynyl thin-film assemblies

4.1. Unbound molecules

A detailed understanding of the interactions between alkynyl molecules, and the role of the substrate in molecular self-assembly, is essential in building densely packed thin-film materials. Alkynyl moieties in supramolecular structures can be polymerized topochemically to give one-dimensional conductors and third-order nonlinear optical materials (2). An essential requirement for surface polymerization is the orientation of the alkynyl chromophores on the surface.

© 1998 NRC Canada

Fig. 7. Geometry-optimized Sn-C≡C-H monomer on a 12-membered ring SiO_2 by PM3 calculations showing that the C≡C molecular orbital now involves the surrounding Sn and H atoms (–30.714 69 eV).

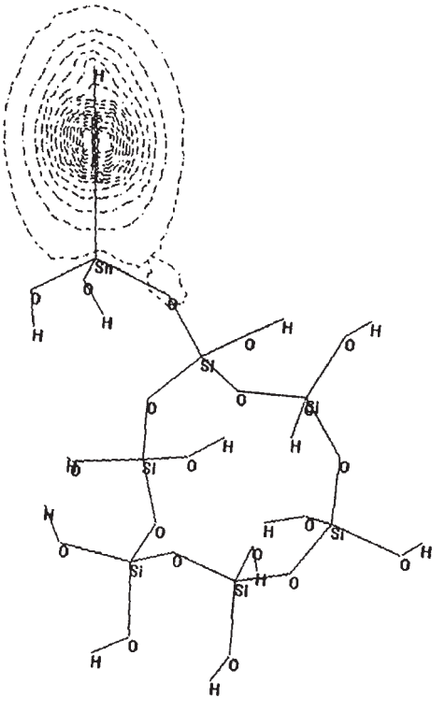

Therefore, to get an understanding of molecular self-assembly of rigid-rod alkynes on solid substrates molecular modelling and semiempirical calculations were used. For simplicity, the Sn-C≡C-H molecule was studied which can be elaborated and provides a basis for other conjugated structures.

Molecular modelling (MM) and the MNDO and PM3 semi-empirical molecular orbital theories were first applied to the unbound tin-alkynyl molecules, the monomer (Fig. 1), dimer (Fig. 2), trimer (Fig. 3), and finally a 12 × 12 (144 molecule) structure which approximates the structure of the tin alkynyl film when surface bound to silica. The results are presented in Tables 2–4. The molecular mechanics reference binding energy of this molecule is 0.399 kcal/mol relative to the free atoms. The main contributions to the MM binding energy are the dihedral (0.998 kcal/mol) and the van der Waals (–0.599 kcal/mol) attractive forces. The C≡C bond distance is 1.20 Å, and the C-Sn-O bond angle 110°. Dimerization of the molecule, $\{O\text{-}[(HO)_2Sn\text{-}C{\equiv}C\text{-}H]_2\}$ (Fig. 2, Table 3*a* and *b*) did not change the geometry. The binding energy decreased to –1.828 kcal/mol, mainly because of the MM van der Waals attractive energy (–1.926 kcal/mol). Note the large separation (3.6 Å) between $C^1{}_a$ of the first molecule and $C^2{}_b$ of the second (Fig. 4). Topochemical polymerization on the surface requires bonding between these two carbon atoms to give a conjugated structure. Any attempt to bond this dimer results in a stable MM molecule with a 4.7 Å double bond length! The trimer, $\{(HO)(C{\equiv}C\text{-}H)Sn\text{-}[O\text{-}(HO)_2Sn\text{-}C{\equiv}C\text{-}H]_2\}$ (Fig. 3) has four equally stable conformations (Fig. 5) and is a flexible molecule. These conformations display changes in geometry from the monomer as well as the dimer (Table 4*a* and *b*). The molecules display strong MM van der Waals attractions ranging from –3.423 to –4.323 kcal/mol, and the MM binding energies for different conformers vary from –4.017 to –3.340 kcal/mol.

The MNDO and PM3 MO theories parallel molecular modelling, giving almost identical geometric structures, but show that the C≡C HOMO orbital is localized on the bond and energetically separated from the remaining molecular orbital which bonds the tin to the hydroxyls (Figs. 1–3). Therefore, it appears to be available for conjugation. The

Table 6. Geometries and energies, $(HO)_2Sn\text{-}C{\equiv}C\text{-}H$ monomer on SiO_2 ring.

(*a*) Geometries		
	MM	PM3
d(C≡C) (Å)	1.21	1.20
C-Sn-O angle (°)	109	110 ± 3
(*b*) Energies (kcal/mol)		
	MM	PM3
Binding energy	–12.44	–4673.414
Bond energy	0.51	
Angle energy	4.17	
Dihedral energy	1.86	
van der Waals energy	–13.47	
Stretch–bend energy	–1.00	
Electrostatic energy	–4.51	
Total energy		–158 673.342
Isolated atomic energy		–153 999.928
Electronic energy		–1 132 144.298
Core–core interaction		973 470.955
Heat of formation		–1688.486

Table 7. Geometries and energies, $\{O\text{-}[(HO)_2Sn\text{-}C{\equiv}C\text{-}H]_2\}$ dimer on SiO_2 ring.

(*a*) Geometries		
	MM	PM3
d(C≡C) (Å)	1.21 ± 0.01	1.20
$C^1{}_a$—$C^2{}_b$ distance (Å)	7.32 ± 0.01	5.84 ± 0.02
C-Sn-O angle (°)	108 ± 1	111 ± 2
(*b*) Energies (kcal/mol)		
	MM	PM3
Binding energy	–7.53	–5153.539
Bond energy	0.45	
Angle energy	6.77	
Dihedral energy	5.76	
van der Waals energy	–14.94	
Stretch–bend energy	–0.78	
Electrostatic energy	–4.79	
Total energy		–172 775.370
Isolated atomic energy		–167 621.830
Electronic energy		–1 310 513.541
Core–core interaction		1 137 738.171
Heat of formation		–1695.072

© 1998 NRC Canada

Fig. 8. Geometry-optimized Sn-C≡C-H dimer on a 12-membered ring SiO_2 by PM3 calculations showing that the molecular orbitals are on both C≡C and involved Sn and H (–30.661 52 and –30.634 11 eV).

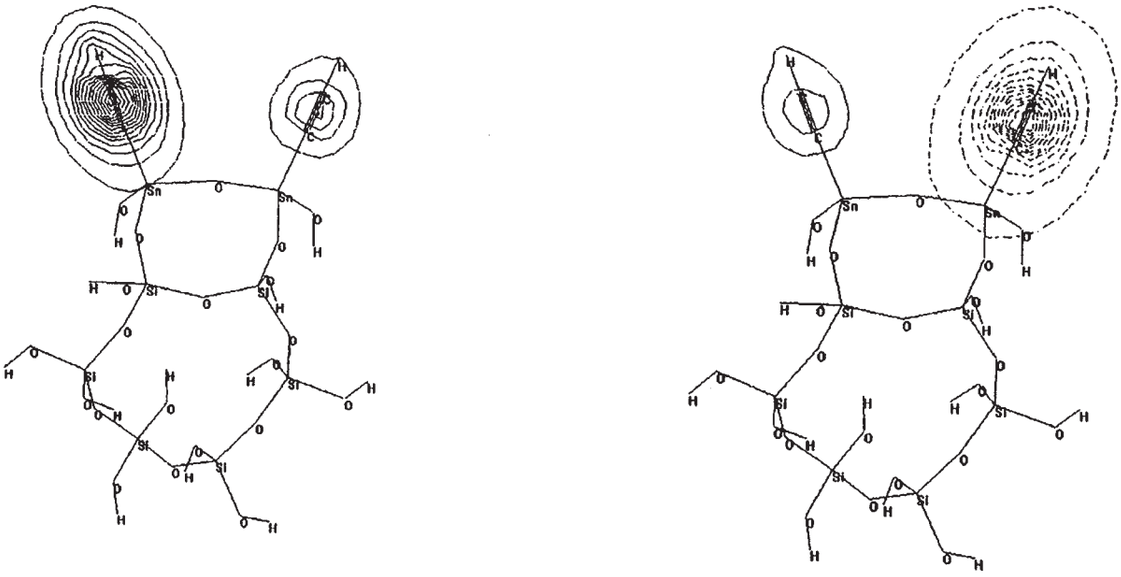

Table 8. Geometries and energies, (C≡C-H)Sn-[O-(HO)Sn-C≡C-H]$_2$} trimer on SiO_2 ring.

(*a*) Geometries		
	MM	PM3
d(C≡C) (Å)	1.21	1.20
C^1_a—C^2_b distance (Å)	7.67 ± 0.01 6.7 ± 0.3	7.32 ± 0.01 7.20 ± 0.02
C-Sn-O angle (°)	109 ± 1	112 ± 3
(*b*) Energies (kcal/mol)		
	MM	PM3
Binding energy	–6.51	–5635.381
Bond energy	0.56	
Angle energy	6.44	
Dihedral energy	7.03	
van der Waals energy	–15.53	
Stretch–bend energy	–0.94	
Electrostatic energy	–4.07	
Total energy		–186 879.113
Isolated atomic energy		–181 243.732
Electronic energy		–1 494 325.723
Core–core interaction		1 307 446.610
Heat of formation		–1703.375

reliability of modelling for geometric structure predictions justified approximating the formation of a Sn-C≡C-H thin film on a surface and the role of surface in molecular self-assembly by modelling a 12 × 12 layer of Sn-C≡C-H molecules with and without surface attachments (Fig. 6). For the unattached system, the MM binding energy increased dramatically to 2225.848 kcal/mol (Table 5), and the C^1_a-C^2_b chain separation covered a range of values with the attractive van der Waals energy of –444.157 kcal/mol, decreasing in importance compared to the MM bond angle bending energy of 2420.63 kcal/mol. Even by ignoring edge effects which relate to tipping of molecules near the edges away from each other, and considering a 6 × 6 spread of molecules in the centre of the monolayer as typical of the extended structure, no discernible order was observed. This suggests that binding of the alkynyl chromophore to a surface must play a significant role in molecular self-assembly of alkynes.

4.2. Surface-bound molecules: role of silica substrate

The geometry-optimized Sn-C≡C-H monomer on a 12-membered SiO_2 ring is shown in Fig. 7, and the data is given in Table 6*a* and *b*. Compared to the free monomer, the binding energy decreased to –12.442 kcal/mol with the main contribution coming from the attractive MM van der Waals energy (–13.474 kcal/mol). The C≡C bond length and the

© 1998 NRC Canada

Fig. 9. Geometry-optimized Sn-C≡C-H trimer on a 12-membered ring SiO_2 by PM3 calculations showing that the three molecular orbitals are on all three C≡C and involved Sn and H (–30.683 11, –30.653 10, and –30.630 27 eV); one MO is not visible in this plane.

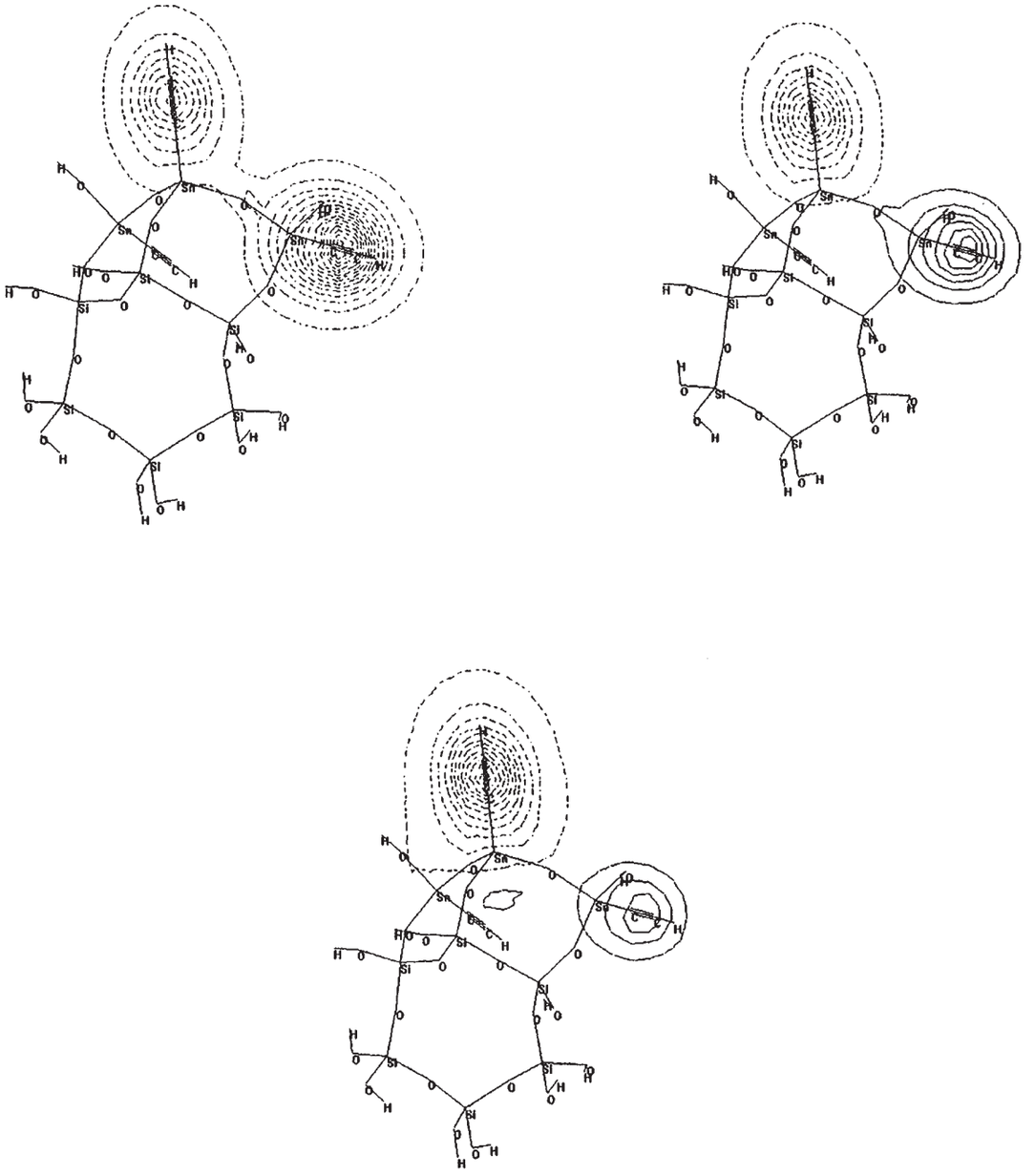

C-Sn-O bond angle are similar to the unbound monomer. The construction of a dimer on a 12-membered SiO_2 ring (Fig. 8) leads to interesting changes compared to the unattached dimer (Fig. 2), notably the separation between the two molecules. It has a MM van der Waals attractive energy of –14.939 kcal/mol (Table 7*b*) which indicates a possible strong π–π attraction compared to the unbound dimer (van der Waals attractive energy = –1.926 kcal/mol, Table 2*b*). The C^1_a—C^2_b chain separation increases to 7.32 Å (Table 7*a*) from 3.66 Å in the free dimer. Although, the MM binding energy decreases to –7.531 kcal/mol and the C-Sn-O bond angles remain relatively constant, the two molecules move away from each other. The addition of another molecule of Sn-C≡C-H to the silica ring leads to the trimer (Fig. 9), the MM binding energy decreases to –6.509 kcal/mol, and an increase in the π–π interaction leads to a MM van der Waals attractive energy of –15.528 kcal/mol (Table 8*b*). The alkyne-to-alkyne separation (C^1_a—C^2_b chain distance) is in the range of 6.7–7.7 Å, and the C-Sn-O angles (Table 8*a*) are the same as in the unattached trimer. Thus the alkyne molecules are bonded to the silica and through the silica to each other. By locking tin-alkynes into a fixed geometric position on a model representation of a silica surface, interactions between acetylene molecules are expected to

© 1998 NRC Canada

Table 9. MM energies and MM geometries, 12 × 12 $(Sn\text{-}R)_{144}$ monolayer on $(SiO_2)_{144}$ substrate.

(*a*) Energies (kcal/mol)

Binding energy	12574.26
Bond energy	493.45
Angle energy	5248.02
Dihedral energy	548.39
van der Waals energy	–6155.87
Stretch–bend energy	127.71
Electrostatic energy	0.83

(*b*) C-Sn-O angles (°)[a]

	Column					
Row	4	5	6	7	8	9
4	53	47	54	51	50	49
5	53	55	53	52	50	47
6	50	47	46	57	50	48
7	50	43	57	51	51	53
8	55	51	50	54	52	49
9	58	46	55	54	52	44

(*c*) C^1_a—C^2_b distance (Å)

Row	Column 7
4	3.51
5	3.09
6	3.58
7	3.06
8	3.40
9	3.30

[a]Note: Surface geometries in later tables are supplied for column 7 only; data from this region provides an effective representation of the surface variations within the studied 6 × 6 area.

lead to an ordered self-assembled thin film. The MO for the single tin-alkyne on a 12-membered SiO_2 ring shows the C≡C molecular orbital covering the H and tin. It is not localized on the C≡C bond as in the free molecules. Note that the binding energies in the MM results follow the same trend as the true MO binding energies. This MO (Fig. 7) is energetically separate from all other molecular orbitals at –30.714 69 eV. When the dimer (Fig. 8) and trimer (Fig. 9) on the 12-membered SiO_2 ring are considered, the molecular orbitals are at –30.661 52, –30.634 11, –30.683 11, –30.653 10, and –30.630 27 eV.

A monolayer of Sn-C≡C-H on a 12 × 12 SiO_2 model substrate composed of interconnected 12-membered rings (Fig. 10) was calculated by molecular mechanics. The surface of SiO_2 units was frozen and held rigid, and only the $(Sn\text{-}R)_{144}$ monolayer was examined directly with molecular modelling. The 12 × 12 monolayer model substrate shows a highly ordered structure. The tipping of molecules away from the surface near edges is due to the edge effect. The latter should be ignored, since these molecules are not surrounded by a sufficient number of other molecules to experience all the necessary molecular interactions. Therefore the isolated middle 6 × 6 molecule will be discussed as free of edge effects. The binding energy of 12 574.26 kcal/mol (Table 9*a*) is mainly the MM van der Waals attractive energy (–6155.87 kcal/mol). The average of the bond angles of the

Fig. 10. A monolayer of Sn-C≡C-H on a 12 × 12 SiO_2 model substrate prepared from interconnected 12-membered rings calculated by molecular modeling.

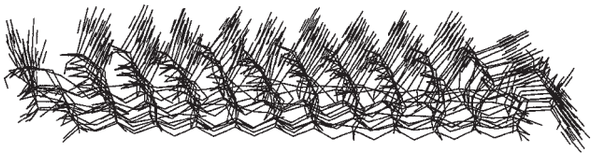

Fig. 11. Topochemical polymerization: A [=C=C=C=C=] representation of the polymer on the 12 × 12 monolayer calculated by molecular modeling.

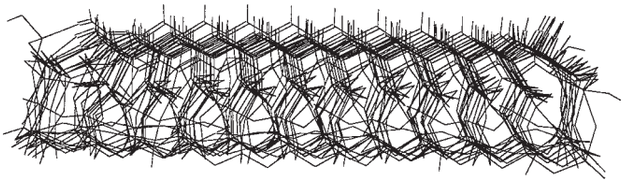

Fig. 12. The localized PM3 molecular orbital on one of the C≡C in a frozen 4 × 4 section of the 12 × 12 molecular modelling result (Fig. 10) with a different silica base to simplify the calculations. The tin-alkynyls are geometry optimized on this frozen base. This clearly shows the C≡C to be an isolated molecular orbital to the rest of the molecule and silica base. The angle is 45 ± 9° and the bond length is 1.20 Å.

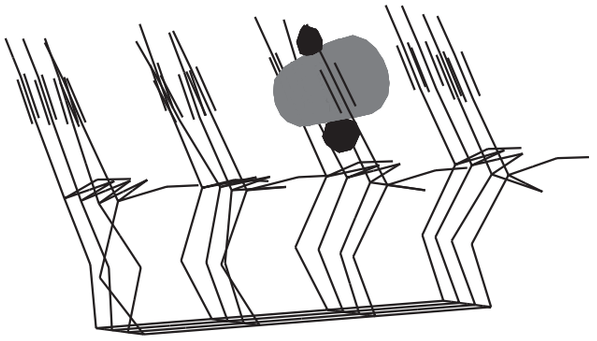

alkynyl groups is 51 ± 3° (Table 9*b*). The small variations observed reflect the underlying surface of the model SiO_2 substrate because the angles are measured against an artificial horizontal plane for convenience. The C^1_a—C^2_b chain separation decreases to 3.4 Å (Table 9*c*), suggesting that conjugation is possible, leading to surface polymerization. The MM predictions can be accepted because as shown above they parallel the MO calculations of bond lengths and angles.

Topochemical polymerization was modelled by replacing the acetylene bonds on the 12 × 12 monolayer with a $[\text{-}C_a{}^1{=}C_b{}^2\text{-}C_a{}^1{=}C_b{}^2\text{-}]$ representation of the polymer (Fig. 11) where the conjugation is easily seen at the top of the figure. Once again, only the interior 6 × 6 structure was selected for analysis. The MM binding energy increased to 49841.105 kcal/mol. The conjugated C=C and C—C bonds have identical lengths (1.50 ± 0.01 Å, Table 10*a* and *b*), suggesting a highly conjugated system, which is supported by finding the first example of a repulsive MM van der Waals

© 1998 NRC Canada

Table 10. MM energies and column 7 MM geometries, polymerized 12 × 12 $(Sn\text{-}R)_{144}$ monolayer on $(SiO_2)_{144}$ substrate.

(*a*) Energies (kcal/mol)

Binding energy	49 841.11
Bond energy	12 412.50
Angle energy	23 818.70
Dihedral energy	605.52
van der Waals energy	13 668.50
Stretch–bend energy	–665.62
Electrostatic energy	1.50

(*b*) Column 7 MM geometries

Row	C=C-Sn angles (°)	*d*(C=C) (Å)	*d*(C—C) (Å)
4	77	1.51	1.52
5	83	1.52	1.52
6	73	1.51	1.51
7	73	1.51	1.51
8	78	1.51	1.52
9	76	1.51	1.51

Table 11. PM3 energies for 4 × 4 $(Sn\text{-}R)_{16}$ monolayers on model Si surface (kcal/mol).

	Nonpolymerized surface	Polymerized surface
Total energy	–395 304.059	–393 941.591
Electronic energy	–6 761 962.550	–6 941 496.378
Core–core repulsion	6 366 658.502	6 547 554.786
Heat of formation	79.985	1438.777

Fig. 13. Delocalized C=C molecular orbital on a 4 × 4 central section, calculated by PM3 with 4 × 4 geometry-optimized orbitals. Bond lengths are 1.20 Å, showing that orbital conjugation may be possible.

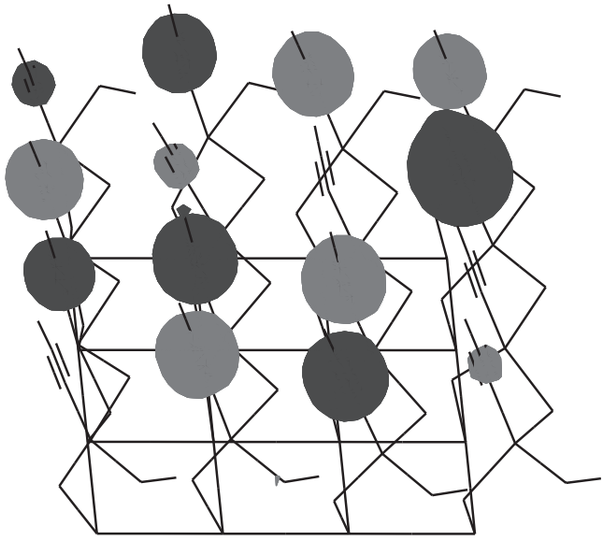

energy of +13.668 kcal/mol, when the bond angles average around 75 ± 3°. Consequently polymerization can only occur when the alkyne molecules are surface adsorbed.

Fig. 14. The localized PM3 molecular orbital on one of the conjugated C=C in a frozen 4 × 4 section. The tin-alkynyls joined from C^1_a to C^2_b were then optimized by the PM3 method to give the conjugated structure. The angle is 35 ± 6° and the bond length is 1.6 ± 0.1 Å.

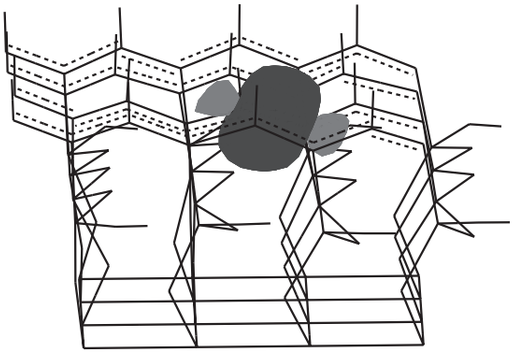

Because the SiO_2 surface anchors the tin-acetylenes, it was represented by a model silica square surface (Fig. 12). This simplified MO calculation sufficiently to allow results to be obtained in a day or two per calculation. Preliminary PM3 calculations were performed on the centre 4 × 4 of the 12 × 12 molecule. The localized molecular orbitals (LMO) (Fig. 12) were found to be on the C≡C as in the free monomer (Fig. 7), small surface-bound tin-alkyne quite different from and clearly separated from all other molecular orbitals in the molecule. It is therefore free to bond when the C≡C are close enough top to tail C_a^1-C_b^2 (Fig. 4). The angles change from the MM calculations, because of the changed model surface to 45 ± 9°, and the C_a^1—C_b^2 distance reduces to 3.2 ± 0.2 Å. Bonding the C_a^1-C_b^2 head to tail in this 4 × 4 model gave delocalized MO (Fig. 13) between levels 37 and 48 at –33.256 23 to –26.175 55 eV and energetically separate as a band from the MO covering the tin and model SiO_2 surface. The preliminary localized molecular orbital (LMO) of this system is shown in Fig. 14, and it shows clearly that

© 1998 NRC Canada

Fig. 15. Delocalized C=C-C=C to give C=C=C=C conjugation on a 4 × 4 section. PM3 geometry-optimized orbitals. Bond lengths are 1.6 ± 0.1 Å, showing that topochemical polymerization has occurred. The MO of energies (*a*) –30.642 18 eV (MO 40) and (*b*) –29.813 73 (MO 42) shown as typical of the wide range of MO in this band which is energetically separated from all other MO on the structure.

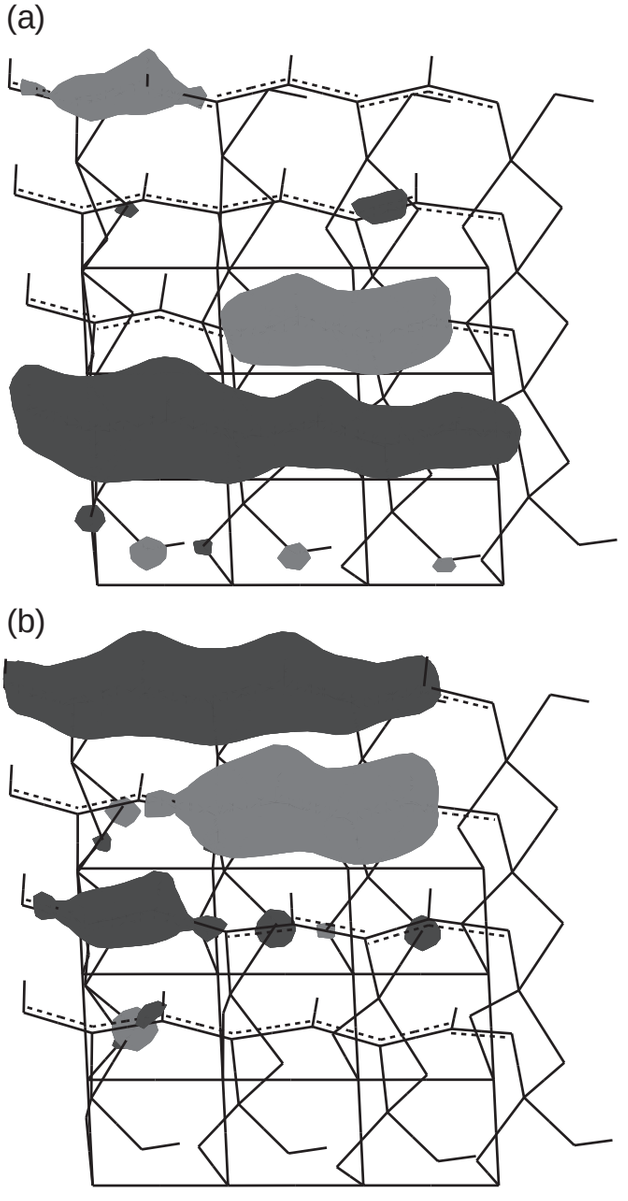

the C≡C LMO has rotated to become a C=C conjugative molecular orbital with the 178 ± 1° C≡C-H angle becoming 110 + 3° as the carbon rehybridizes from Cdidiππ (di = digonal, *sp* hybridization) to Ctrtrtrπ (tr = trigonal, sp^2 hybridization). The C-C-C angle is 138 ± 3°. The C≡C bond length of 1.20 Å becomes a conjugated C=C=C bond length of 1.6 ± 0.1 Å. The separation of the conjugated rows is 3.5 ± 0.1 Å compared to 3.3 ± 0.2 Å in the C≡C case. Thus, there is no hydrogen replacement, just rehybridization at the carbon to approximately trtrtrπ, with angles 138 ± 3°, 110 ± 3°, 112 ± 3° at all the carbons. A detailed study of the MO calculations will be published when the analysis is complete.[2] The bond lengths and bond angles essentially reflect the molecular modelling results on which the initial ideas were based.

Figure 14 and Table 11, show clearly how the C≡C level of the isolated molecule becomes the band of isolated molecular orbitals for a mere 4 × 4 silica adhered tin-acetylene structure and the change in contributions to the energy upon conjugation. These can then conjugate to give linear molecular orbitals parallel to each other. If these were extended to a true structure, this band of levels would become a conducting band similar to metal structures. The various molecular orbitals in Figs. 14 and 15 merging into a continuous band along each row of C=C=C atoms. In the real system they would generate a set of conjugated molecular orbitals, as suggested by the molecular modelling of the 12 × 12 system. The change in bond length from the C≡C (1.2 Å) and the row separation of 3.2 Å to the conjugated repetitive C=C—C=C length of 1.6 Å and the row separation of 3.5 ± 0.1 Å require a greater tilt in the angle from 45 ± 9° to 35 ± 6°. The angle change along the conjugated chain from the C≡C-H (178 ± 1°) to C=C-H of 110 + 1° show rehybridization at the carbon atoms from Cdidiππ to Ctrtrtrπ. There is no hydrogen abstraction, just rehybridization to supply three sigma and one delocalized π conjugated orbital.

Conclusions

Simple acid–base hydrolysis of surface-bound tin-amides with a variety of alkynes is a versatile approach for constructing thin films containing rigid-rod alkynes. The π–π interactions in the molecules can lead to highly ordered and densely packed thin-film structures. These results, reflected by molecular mechanics modelling studies of Sn-acetylene chromophores on a model substrate, suggest that for the formation of a highly ordered system, chemical bonding of Sn to the silica surface is essential. The C_a^1–C_b^2 interchain distance in these chemisorbed thin films is optimal for surface polymerization, leading to a highly conjugated structure. Preliminary MO calculations on a model 4 × 4 surface adhered tin-acetylene give evidence to conjugated orbitals between –32.089 11 eV and –18.865 85 eV and typical conjugated bond lengths around 1.6 ± 0.1 Å with carbon trigonal π-bonded with 138 ± 3° and two 111 ± 3° angles. This band of levels is completely separate from all other eigenvalues.

Acknowledgment

We would like to thank the Natural Sciences and Engineering Research Council of Canada (NSERC) for financial support.

[2] A. Dickie, M.A. Whitehead, and A.K. Kakkar. To be published.

© 1998 NRC Canada

References

1. A. Ulman. Adv. Mater. **2**, 573 (1990).
2. (*a*) A. Ulman. An introduction to ultrathin films from Langmuir–Blodgett to self-assembly. Academic Press, New York. 1991; (*b*) Y-T. Tao. J. Am. Chem. Soc. **115**, 4350 (1993); (*c*) M.D. Porter, T.B. Bright, D.L. Allara, and C.E.D. Chidsey. J. Am. Chem. Soc. **109**, 3559 (1987).
3. (*a*) R.J. Jackman, J.L. Wilbur, and G.M. Whitesides. Science (Washington, D.C.) **269**, 664 (1995); (*b*) L.H. Dubois and R.G. Nuzzo. Ann. Rev. Phys. Chem. **43**, 437 (1992); (*c*) C.E.D. Chidsey. Science (Washington, D.C.) **251**, 919 (1991).
4. Y-T. Tao, M-T. Lee, and S-C. Chang. J. Am. Chem. Soc. **115**, 9547 (1993).
5. (*a*) R.W. Zehner and L.R. Sita. Langmuir, **13**, 2973 (1997); (*b*) J.M. Tour, L-R. Jones II, D.L. Pearson, J.J.S. Lumba, T.P. Burgin, G.M. Whitesides, D.L. Allara, A.N. Parikh, and S.V. Atre. J. Am. Chem. Soc. **117**, 9529 (1995).
6. C.M. Yam and A.K. Kakkar. J. Chem. Soc. Chem. Commun. 907 (1995).
7. (*a*) J. Lewis, M.S. Khan, A.K. Kakkar, B.F.G. Johnson, T.B. Marder, H.B. Fyfe, F. Wittmann, R.H. Friend, and A.E. Dray. J. Organomet. Chem. **425**, 165 (1992); (*b*) J. Jiang, E. Kobayashi, and S. Aoshima. Polym. J. **22**, 274 (1990); (*c*) S. Takahashi, Y. Kuroyama, K. Sonogashira, and N. Hagihara. Synth. Commun. 627 (1980).
8. (*a*) K. Jones and M.F. Lappert. *In* Organotin compounds. Vol. 2. *Edited by* A.K. Sawyer. Marcell Dekker, Inc., New York. 1977; (*b*) K. Jones and M.F. Lappert. J. Organomet. Chem. **3**, 295 (1965); (*c*) I.M. Thomas. Can. J. Chem. **39**, 1386 (1961).
9. R.K. Iler. The chemistry of silica. John Wiley & Sons, New York. 1979.
10. F. Pintchovski, J.B. Pricew, P.J. Tobin, J. Peavy, and K. Kobold. J. Electrochem. Soc. **126**, 1428 (1979).
11. A-A. Dhirani, R.W. Zehner, R.P. Hsung, P. Guyot-Sionnest, and L.R. Sita. J. Am. Chem. Soc. **118**, 3319 (1996).
12. (*a*) E. Sabatini, J. Cohen-Boulakia, M. Bruening, and I. Rubinstein. Langmuir, **9**, 2974 (1993); (*b*) H.W. Fox, E.F. Hare, and W.A. Zisman. J. Colloid Sci. **8**, 194 (1953).
13. S.R. Wasserman, G.M. Whitesides, I.M. Tidswell, B.M. Ocko, P.S. Pershan, and J.D. Axe. J. Am. Chem. Soc. **111**, 5852 (1989).
14. R.M.A. Azzam and N.M. Bashara. *In* Ellipsometry and polarized light. North-Holland Publishing Company, Amsterdam. 1977.

© 1998 NRC Canada

Dissolution behavior in water of a model hydrophobic alkali-swellable emulsion (HASE) polymer with $C_{20}H_{41}$ groups

Kazunaga Horiuchi, Yahya Rharbi, Ahmad Yekta, Mitchell A. Winnik, Richard D. Jenkins, and David R. Bassett

Abstract: The dissolution behavior of a hydrophobic alkali-swellable emulsion (HASE) in water was examined by dynamic light scattering and pyrene fluorescence probe experiments. The HASE polymer was obtained by the copolymerization of ethyl acrylate (EA), methacrylic acid (MAA), and a macromonomer containing a $C_{20}H_{41}$ group separated from the polymer backbone by 32 ethylene oxide units. The behavior of the copolymer was followed as a function of the neutralization degree α = [NaOH]/[COOH] of the MAA component. Particles swell with increasing α until α = 0.4 after which polymer dissolution begins. At low α, pyrene, added as a probe to the solution, dissolves in the EA–MAA copolymer phase; whereas at high α, pyrene is largely localized in $C_{20}H_{41}$ micelles. Pyrene fluorescence measurements show that the striking viscosity increase of the solution with increasing α correlates with polymer dissolution and intermolecular network formation.

Key words: associative polymer, hydrophobic substituents, polymeric micelles.

Résumé : Faisant appel à la diffusion dynamique de la lumière et à des expériences de sondes à fluorescence du pyrène, on a étudié le comportement d'une émulsion hydrophobe gonflable par les alcalis (« HASE ») lors de sa dissolution dans l'eau. On a obtenu le polymère HASE par copolymérisation de l'acrylate d'éthyle (« EA »), de l'acide méthacrylique (« MAA ») et d'un macromonomère contenant un groupe $C_{20}H_{41}$ séparé du squelette du polymère par 32 unités d'oxydes d'éthylènes. On a suivi le comportement du copolymère en fonction du degré de neutralisation, α = [NaOH]/[COOH], de la portion MAA. Les particules se gonflent avec une augmentation d'α jusqu'à α = 0,4; après la dissolution du polymère commence. À de faibles valeurs d'α, le pyrène — ajouté comme sonde à la solution — se dissout dans la phase de copolymère « EA–MAA »; toutefois, à des valeurs d'α élevées, le pyrène se localise principalement dans les micelles de $C_{20}H_{41}$. Des mesures de fluorescence du pyrène montrent la corrélation qui existe entre l'augmentation étonnante de la viscosité de la solution associée à une augmentation d'α et la dissolution du polymère et la formation d'un réseau intermoléculaire.

Mots clés : polymère associatif, substituants hydrophobes, micelles polymériques.

[Traduit par la Rédaction]

Introduction

Hydrophobically modified water-soluble polymers (1, 4) are being used in a wide range of commercial applications, particularly in paints and paper coatings. In paints, these polymers are used as thickeners ("associative thickeners" (AT)) increasing the viscosity of the formulation to prevent pigment settling during storage, and to impart an appropriate viscosity profile when the system is subjected to shear. Solutions of these polymers exhibit unusual and often very complicated rheological behavior. The type of behavior one obtains depends sensitively upon the polymer structure and the nature and location of the hydrophobic substituents.

For water-borne coatings, good performance requires the formulation to possess a viscosity low enough at high shear rates to achieve uniform coverage of the substrate, but at the same time high enough to produce a good film thickness. At low shear rates, the viscosity must be significantly higher to

Received March 12, 1998.

K. Horiuchi,[1] Y. Rharbi, A. Yekta,[2] and M.A. Winnik.[3] Department of Chemistry, University of Toronto, Toronto, ON M5S 3H6, Canada.
R.D. Jenkins. Technical Center, Union Carbide Asia Pacific Inc., 16 Science Park Drive, No. 04–01/02 The Pasteur, 118227 Singapore.
D.R. Bassett. Union Carbide Corporation, UCAR Emulsion Systems, Research and Development, 410 Gregson Drive, Cary, NC 27511, U.S.A.

[1]Permanent address: Fuji-Xerox Co. Ltd., 1600 Takematsu, Minamiashigara-shi, Kanagawa 250–01, Japan.
[2]Present Address: Imaging Research Inc., 500 Glenridge Ave., St. Catherines, ON L2S 3A1, Canada.
[3]Author to whom correspondence may be addressed. Telephone: (416) 978–6495. Fax: (416) 978–0541. E-mail: mwinnik@chem.utoronto.ca

© 1998 NRC Canada

Fig. 1. Chemical structure of the model $C_{20}E_{32}$ HASE polymer, 28RDJY72–6. The name $C_{20}E_{32}$ denotes copolymer in which the associative macromonomer unit contains a $C_{20}H_{41}$ hydrophobe is attached to the polymer backbone via a linker containing 32 units of ethylene oxide. The monomer molar ratio is $X/Y/Z$ = 49.06/50.04/0.90.

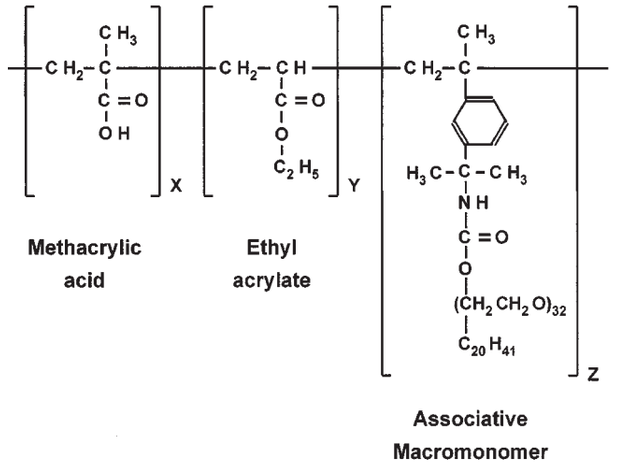

prevent the paint from running, but still low enough to exhibit good flow-out and leveling on the surface. These seemingly mutually exclusive demands require the dispersion to exhibit time-dependent rheological properties specific to each particular type of application in which the viscosity changes in a controlled way with shear rate. To achieve this kind of performance, we need a much deeper understanding of the structures formed by associating polymers in aqueous solution and the response of these structures to shear and extensional stress.

One class of polymers about which our knowledge is particularly limited is the hydrophobic modified alkali-swellable emulsion (HASE) polymers (2, 3). These are long-chain acrylic polymers, typically copolymers of ethyl acrylate and methacrylic acid, containing hydrophobic pendant groups. These polymers are prepared by emulsion polymerization at low pH where they form a polyelectrolyte with hydrophobic substituents. An increase of pH results in ionization of the acid groups, leading to polymer solubility in water. The thickening efficiency in HASE polymers is achieved both by the associative mechanism as well as by expansion of the macromolecule backbone. The chain expansion has two components, the first due to particle-to-coil expansion upon dissolution, and the second due to electrostatic repulsion between the neutralized carboxylic groups. These materials are not difficult to prepare and have a striking advantage to formulate for high concentration, typically 2 wt.% for the AT applications. The dispersions in the latex formed at low pH have water-like viscosity, and raising the pH beyond 7 leads to a very large increase in viscosity and to other interesting rheological properties of the system.

These polymers, however, are significantly more complex and difficult to understand than linear water-soluble associating polymers with hydrophobic end groups. While it is fair to say that a decade ago our knowledge of all associating polymers in water was very poor, there have been over the intervening years many interesting experiments carried out on the linear associative polymers. We start to have an understanding of the origin in at least some of the globally more important properties for these telechelic polymers (4). The systems we understand best are poly(ethylene oxide) polymers with hydrophobic end groups, including the ethoxylate urethane-coupled HEUR polymers (5).

In the present paper, we examine the dissolution step of a model HASE polymer. This polymer is one of several model polymers prepared by Jenkins at Union Carbide. One of the distinguishing features of these polymer structures is that the hydrophobic substituents are separated from the polymer backbone by a polyethylene glycol (PEG) spacer chain. Recently Tirtaatmadja et al. (6, 7) and English et al. (8) reported rheological measurements on some of these polymers and discussed the striking rheological behavior observed under shear, especially strong shear, where the polymer network is imagined to be broken or rearranged. The long-term goal of our experiments is to provide a molecular-level understanding of the association mechanism in these polymers, and its connection to bulk solution rheological properties.

Materials and methods

Materials

The polymer examined in the present work is $C_{20}E_{32}$ (28RDJY72–6), shown in Fig. 1, with molar ratios *x*:*y*:*z* of 49.06:50.04:0.90. Full details of the synthesis and characterization of this and similar HASE polymers have been reported by Jenkins et al. (3*b*). In short, a macromonomer was prepared first by ethoxylation to 32 mol of the C_{20} alcohol, followed by reaction with α,α-dimethyl meta-isopropenyl benzyl isocyanate (TMI). This macromonomer was introduced into a conventional seeded semicontinuous emulsion polymerization under monomer starved conditions with appropriate amounts of methacrylic acid and ethyl acrylate. In this work, we designate this polymer $C_{20}E_{32}$. According to the structure and composition of the polymer, it contains 2.12×10^{-2} g $C_{20}H_{41}$ groups per g polymer (7.53×10^{-6} mol/g polymer).

The latex emulsion was dialyzed against 3.0 L of deionized water for more than 2 weeks with a cellulose membrane, formulated to cut off from M_w 12 000 to 14 000 (Fisher Scientific). A series of different polymer concentrations was prepared by dilution of the dialyzed HASE solution with deionized water. Salt was added to give an ionic strength of 1.0 mM NaCl for viscosity and fluorescence measurements. To minimize concentration changes of the polymer solution, 1.0 M NaOH was used to neutralize the polymer.

Titration

In the titration of the HASE solution, 15 mL was placed in a 25 mL beaker equipped with magnet stirring. For forward and backward titration processes, 1.0 M NaOH and 1.0 M HCl were used, respectively. Potentiometric and conductometric signals were recorded 5 min after each dosage, using a Cole–Palmer no. 5985–80 portable pH meter and a Fisher Scientific model no. 09–326–2 portable conductivity meter.

© 1998 NRC Canada

Fig. 2. Potentiometric and conductometric titration of $C_{20}E_{32}$ for C_{pol} = 1.6 g/L and C_{pol} = 0.8 g/L, plotted as a function of degree of neutralization α = [NaOH]/[COOH].

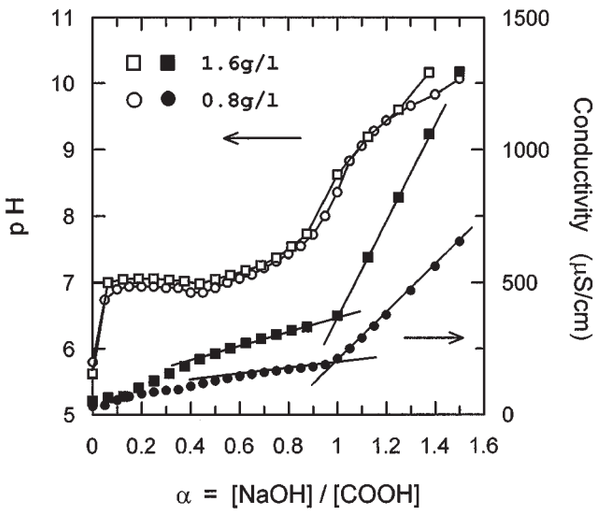

Viscosity measurement

Relative viscosities (η/η_0) were measured using a Ubbelohde suspended-level viscometer, keeping the temperature at 25 ± 0.1°C in a temperature-controlled bath.

Dynamic light scattering measurement

Light scattering measurements were carried out on a dilute polymer solution, 0.16 g/L, to reduce multiple scattering from the latex. A series of the different neutralizations were made by adding 0.1 M NaOH with a 10 mL microsyringe. The 514.5 nm line from an Argon-ion laser (Excel 3000) was used as the excitation source, and the signal was processed in a digital correlator (Brookhaven BI-2030AT) with 136 channels. The temperature was fixed at 22.0 ± 0.1°C in a thermally stabilized container filled with a refractive-index matching liquid (toluene). The large variation of scattered intensity during the titration was compensated by adjusting the laser power without changing the pinhole and signal discriminator.

The intensity autocorrelation functions $g_2(t)$ obtained from the DLS measurements were analyzed in terms of a continuous distribution of relaxation times:

$$[1] \qquad g_1(t) = \int_0^\infty A(\tau) \exp(-t/\tau) d\tau$$

Here $g_1(t)$ is the normalized electric field autocorrelation function related to $g_2(t)$ via the so-called Siegert relation (9*a*). The REPES routine was used to obtain $A(\tau)$ without assuming a specific shape (9*b*). For converting the averaged relaxation time to a hydrodynamic radius, the Stokes–Einstein relationship for small, dilute, and noninteracting spheres was used, with η_{water} = 0.97 cP at 22°C.

Pyrene solubilization

Pyrene (Aldrich) was purified by recrystallization and twice-repeated sublimation. For pyrene solubilization into HASE solutions, a dilute acetone solution containing a known amount of pyrene was placed in a flask, and then the acetone was evaporated completely under a gentle flow of nitrogen. To equilibrate the pyrene in the HASE solution, the mixture was stirred at room temperature for 1 week. Subsequent centrifugation of the solution at 15 000 rpm for 60 min caused the insoluble pyrene crystals to sediment without affecting the dispersion or solution stability.

UV absorbance measurements

The UV absorbance of the HASE solution was measured in 10 mm quartz cuvettes using a Perkin–Elmer Lambda 6 dual-beam spectrometer. Solution turbidity was monitored at 360 nm, where there is no detectable absorption by the HASE polymer. The pyrene concentration was monitored at the strongest absorption peak at 339 nm, with a correction for the background absorption (turbidity) of the polymer.

Steady-state fluorescence measurements

A SPEX Fluorolog 2, with double-grating monochromators for both the excitation and emission, was used to observe steady-state fluorescence spectra in a right-angle geometry. The intensity ratio of the first peak to the third peak of each emission spectrum (I_1/I_3) was determined from peak heights. The excimer-to-monomer ratios (I_E/I_M) were calculated from the area integrations of the emission spectrum, from 360 to 400 nm for $I_{M,}$ and from 450 to 550 nm for I_E.

Dynamic fluorescence measurements and fluorescence-decay analysis

Fluorescence-decay profiles were measured by the single photon timing technique, using a 50 kHz D_2 lamp. The wavelengths of the excitation and emission monochromators were fixed at 339 and 371.5 nm, respectively, and a long-pass was used to prevent scattered 339 nm light from reaching the detector.

Pyrene-decay curves were fitted to the Poisson-quenching micelle model expressed by the equation (10–12):

$$[2] \qquad I(t) = I(0) \exp\{-\frac{t}{\tau} - \langle n \rangle [1 - \exp(-k\,t)]\}$$

In this equation, there are four fitting parameters, the initial intensity $I(0)$, the unquenched lifetime τ, the mean number of pyrenes per micelle $\langle n \rangle$, and the first-order rate constant k for quenching (excimer formation) in a micelle.

Results and discussions

Potentiometric and conductometric titration of $C_{20}E_{32}$ polymer solution

The titration behavior of polymer $C_{20}E_{32}$, purified by extensive dialysis, is shown for two concentrations in Fig. 2. In this figure, the relationships are plotted as a function of degree of neutralization α along the *x*-axis, where α = [NaOH]/[COOH], and the bulk concentration of COOH groups was calculated from the methacrylic acid composition of the polymer. The sharp increase in pH at small α may be due to neutralization of a small amount of $-SO_3H$ groups introduced from the initiator during the polymer synthesis. For the two concentrations examined here, C_{pol} =

© 1998 NRC Canada

Fig. 3. Optical density at 360 nm and relative viscosity (η/η_0) of $C_{20}E_{32}$ polymer for C_{pol} = 1.6 g/L, plotted as a function of the degree of neutralization α = [NaOH]/[COOH].

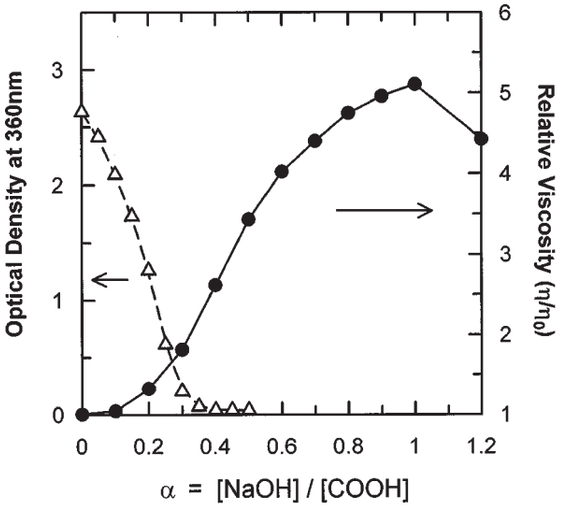

Fig. 4. Concentration dependence of the solution viscosity of $C_{20}E_{32}$ HASE polymer at α = 0.4 and at α = 1.0.

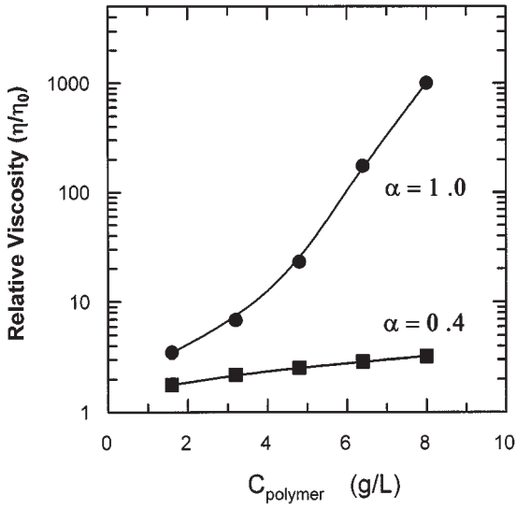

1.6 g/L and C_{pol} = 0.8 g/L, the two conductivity curves exhibit a clear inflection at approximately α = 1.0. The two potentiometric curves overlap. It could be concluded that there is no concentration dependence of α.

Note that the pH is independent of α up to about 0.4 and then begins to increase. These results serve as a reminder that because of the buffer capacity of the polymer, α provides a much better description of the state of the system than the measured pH. These potentiometric and conductometric features show good agreement with the previous results reported by Muroi et al. (13) for the titration of nonassociative alkali-swellable emulsion polymers containing copolymerized carboxylic acid. He assigned the inflection point in the conductometric titration as the point of complete neutralization of the copolymerized MAA, which is located at α = 1.0 in our HASE system.

Fig. 5. Hydrodynamic radius R_H of $C_{20}E_{32}$ HASE latex in C_{poly} = 0.16 g/L, determined by dynamic light scattering, plotted as a function of the degree of neutralization α = [NaOH]/[COOH].

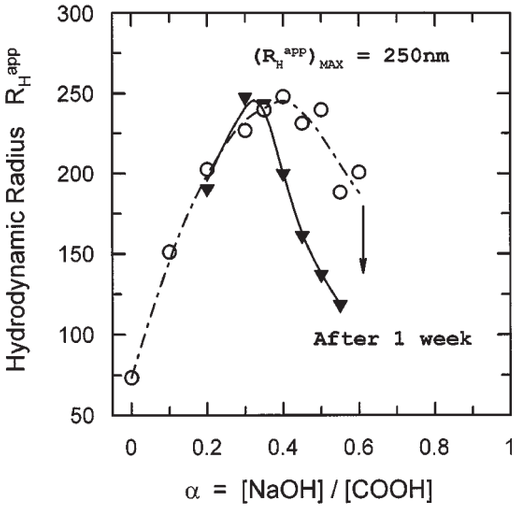

Turbidity and thickening behavior in $C_{20}E_{32}$ polymer solution

As base is added to the system, the solutions become less turbid and more viscous. We quantify these results in Fig. 3, where, for a solution of $C_{20}E_{32}$ at C_{pol} = 1.6 g/L, we plot both the relative viscosity and the optical density of the solution at 360 nm vs. the degree of neutralization of the system. At this concentration, a drastic decrease in the optical density from α = 0 to 0.4 is accompanied by a remarkable increase in the solution viscosity. In other alkali-swellable systems (13*e*), optical clarity often requires higher values of α. In our system, solution viscosity reaches the maximum value α = 1.0 where the polymer is completely neutralized, and drops at α > 1.0 due to the increase of ionic strength in the solution.

The degree of neutralization has a much bigger effect at high polymer concentration on the solution viscosity, as seen in Fig. 4. At α = 0.4, the increase of polymer solution viscosity with increasing polymer concentration is relatively small. At α = 1.0, the solution exhibits a large viscosity increase. The viscosity at α = 1.0 is more than 300 times as large as the viscosity at α = 0.4 for C_{poly} = 8 g/L. Both swelling of the polymer dimensions and formation of networks with hydrophobic junctions contribute to the solution viscosity at α = 1.0.

Hydrodynamic radius (dynamic light scattering)

Some deeper insights into the origin of the viscosity changes are possible through dynamic light scattering measurements on these solutions at much lower polymer concentrations, where the behavior of individual particles can be characterized. Our results are presented in Fig. 5 for a solution at C_{poly} = 0.16 g/L. The initial latex is characterized by a hydrodynamic radius of 75 nm. The water content in a latex particle with fully protonated acid groups is roughly 30 wt.%, determined from separate experiments to check water adsorption into the dried latex film. As base is added to the

© 1998 NRC Canada

Fig. 6. Pyrene solubilization in $C_{20}E_{32}$ and C_1E_{35} HASE polymer solutions at $\alpha = 0.4$ and $\alpha = 1.0$, determined by UV absorbance measurements at 338 nm. C_1E_{35} refers to a HASE polymer with a structure analogous to that of the polymer shown in Fig. 1 in which a methyl group replaces the $C_{20}H_{41}$ group.

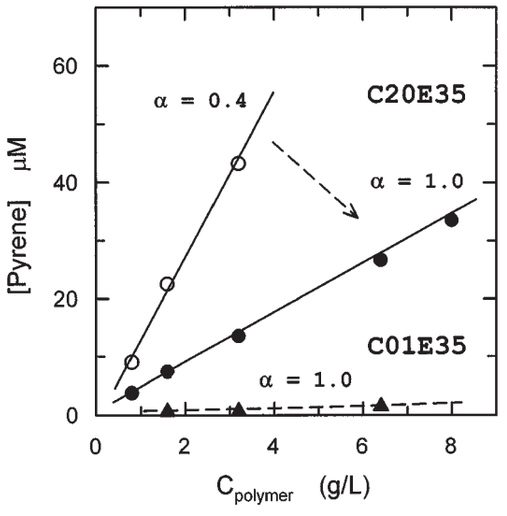

system, swelling of the particle occurs on the time scale of minutes. The particles double in radius at $\alpha = 0.1$ and reach a maximum radius of 250 nm at $\alpha = 0.35$–0.4. At higher degrees of neutralization, the particle size decreases, as the polymer begins to dissolve into the water phase. There is a time-dependence to the swelling and dissolution process at $\alpha > 0.3$, which is particularly pronounced at $\alpha > 0.4$.

If the system is rapidly taken to $\alpha = 0.6$, there is a large drop in signal on the time scale of minutes associated with dissolution of the latex into individual polymer molecules. At lower values of α, the particles have a much slower response, and addition of base leads to relatively small changes in the hydrodynamic radius R_H. Over time, the changes become more pronounced. One can see that for $0.4 < \alpha < 0.6$, a drop in R_H occurs when the samples are aged for 1 week. It is also noteworthy that there is no obvious angular dependence in the two series of measurements, consistent with swollen particles maintaining their spherical shape.

In calculating the data presented in Fig. 5, we used the viscosity of water to calculate hydrodynamic radius from the relaxation times in the DLS experiments. We should, in principle, consider viscosity changes in the series of samples as a function of neutralization, especially for $\alpha > 0.4$ where intermolecular networks start to form. However these are very dilute solution, and changes in bulk solution viscosity are very small. Below $\alpha = 0.4$, on the other hand, we can safely state that the estimated radii are not too far from the true radii, because there are only swollen particles, well separated from each other at $C_{poly} = 0.16$ g/L.

Solubilization of pyrene in HASE solutions

Pyrene has a solubility in water of 7×10^{-7} M at 22°C (5, 11). Water-soluble polymers with hydrophobic domains can bind or solubilize additional pyrene molecules, increasing the total solubility of pyrene in the system. To calculate the amount of pyrene dissolved in the system, one must first determine the extinction coefficients of pyrene in the polymer phase. The extinction coefficient for pyrene at 338 nm decreases from 3.7×10^4 M^{-1} cm^{-1} at $\alpha = 0.4$ to 3.2×10^4 M^{-1} cm^{-1} for $\alpha \geq 1.0$. When the limiting solubilities of pyrene are plotted vs. polymer concentration, Fig. 6, straight lines are obtained, but we note that much more pyrene is solubilized by the system at $\alpha = 0.4$ than at $\alpha = 1.0$. The polymer is fully neutralized at $\alpha = 1.0$ and is likely to exist in a highly swollen state. We anticipate that the dominant hydrophobic domains under these conditions are formed by the C_{20} hydrophobes. Under these conditions where the polymer is saturated with pyrene, there are approximately 0.05 molecules of pyrene per C_{20} hydrophobe. In terms of the liquid drop model we calculate a partition coefficient $K_v = [Py_w]/[Py_{C20}] = 2.0 \times 10^5$, where $[Py_w]$ denotes the molar concentration of pyrene in water phase and $[Py_{C20}]$ denotes the molar concentration of pyrene in the hydrocarbon phase. At $\alpha = 0.4$, approximately 60% of the MAA groups are protonated. The protonated MAA–EA copolymer is a modestly hydrophobic polymer, insoluble in water, but capable of solubilizing pyrene molecules. The difference in the behavior of the system at full and partial neutralization is that at $\alpha = 0.4$, the system contains MAA–EA domains which can solubilize additional pyrenes.

To examine whether the fully neutralized MAA–EA polymer can also solubilize pyrene, we examined pyrene solubilization in a model polymer C_1E_{35}, which has the same backbone as $C_{20}E_{32}$ polymer, containing 35 mol of ethylene oxide units with a CH_3 end group instead of $C_{20}H_{41}$. Data for this polymer are also plotted in Fig. 6. There is a small amount of pyrene solubilized in the C_1E_{35} solution at $\alpha = 1.0$. By assuming the same solubility for pyrene in the polymer backbone of $C_{20}E_{32}$, we can calculate a difference of more than 20 times for the pyrene concentration between the C_{20} hydrophobic domains and the polymer backbone. This result allows us to consider that the dominant contribution to the fluorescence spectra comes from pyrenes localized in the C_{20} hydrophobic domains.

Steady-state pyrene fluorescence in $C_{20}E_{32}$ polymer solution

Fluorescence emission spectra of pyrene (6×10^{-6} mol/L) in the presence of polymer ($C_{pol} = 1.6$ g/L) at different degrees of neutralization are plotted in Fig. 7(*a*). Pyrene, below the solubilization limit for the fully neutralized polymer, was added to the initial emulsion to prevent precipitation during the neutralization. These spectra have been normalized to the intensity of the (0,0) band (I_1) at 371.5 nm. The most obvious features of the spectra are the absence of excimer band at $\alpha < 0.4$ and the increase of the excimer band at 475 nm for $\alpha \geq 0.4$.

In a complex system like this, it is important to distinguish between static excimers formed from pyrenes, which are associated prior to absorption of light, and dynamic excimers formed through diffusion after pyrene molecules are excited. In the former case, one can expect the excitation spectrum monitored at the excimer emission at 475 nm to be significantly red-shifted compared to that of the monomer emission at 371.5 nm. In Fig. 7(*b*), we see that both excitation spectra are identical, consistent with excimers formed in a dynamic process after excitation of nonassociated pyrenes.

© 1998 NRC Canada

Fig. 7. (*a*) Fluorescence spectra of pyrene (6×10^{-6} M) in the presence of the $C_{20}E_{32}$ polymer for C_{pol} = 1.6 g/L at different degrees of neutralization. (*b*) Comparison of the excitation spectra of excimer emission monitored at 475 nm and monomer emission monitored at 371.5 nm.

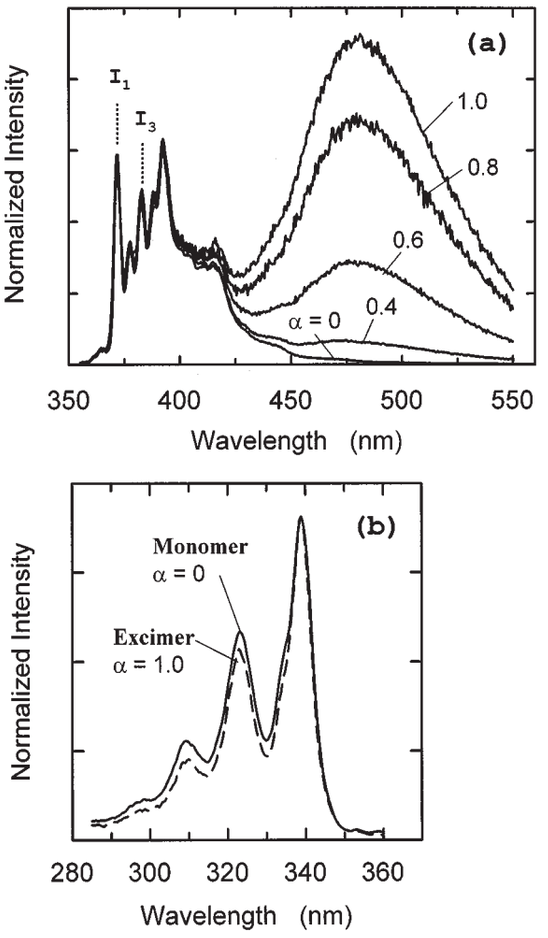

Fig. 8. (*a*) The intensity ratio I_1/I_3 of the I_3 band to the I_1 band (cf. Fig. 7) and the excimer-to-monomer intensity ratio I_E/I_M plotted as a function of degree of neutralization of the polymer. (*b*) I_1/I_3 and I_E/I_M in reacidification of the polymer solution by adding HCl.

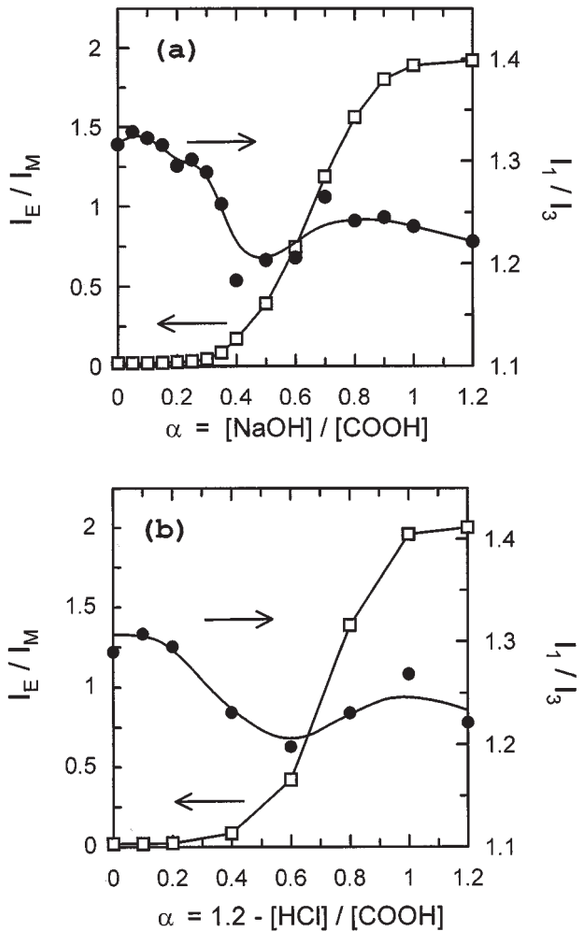

From these results, one can expect that dissolved pyrene is dispersed molecularly in the system, and that the extent of excimer formation reflects the density and mobility of pyrene in local hydrophobic domains.

There are also changes in the intensity ratio I_1/I_3 at different values in α, where I_1 and I_3 are defined in Fig. 7(*a*). The I_1/I_3 ratio is sensitive to the local environment of the pyrene in the system. Values of I_1/I_3 and of the excimer-to-monomer intensity ratio I_E/I_M, calculated from the spectra in Fig. 7(*a*), are plotted in Fig. 8(*a*). The excimer intensity is close to zero for all samples of $\alpha < 0.3$ and increases sharply between $\alpha = 0.5$ and 0.9. The I_E/I_M ratio levels off for $\alpha \geq 1.0$.

Values of I_1/I_3 are close to 1.32 at low degrees of neutralization. They decrease sharply as base is added to the system, pass through a minimum, and then level off at a value of 1.22–1.23 for $\alpha \geq 1.0$. I_1/I_3 values of 1.2 are typical for pyrene solubilized in hydrophobic micelles in water. While the values near 1.32 found at $\alpha < 0.2$ are not as large as that (1.7) of pyrene in water (14), they do indicate that the pyrenes are on average located in a more polar environment than in a hydrocarbon domain. This information, coupled with the absence of excimer emission and the increased solubility of pyrene in the system, strongly suggests that the pyrenes are simply dissolved in the EA–MAA copolymer latex at low degrees of neutralization or at low pH.

Reacidification of the polymer, by adding HCl to the system, reprotonates the polymer. This process does not reform the original latex, but it allows us to examine the effect of reprotonation. The results are plotted in Fig. 8(*b*). Except for the small shift to the acidic side, which might be explained by the increase of salt concentration resulting from acid–base reaction, both I_1/I_3 and I_E/I_M shows good correspondence to the behavior observed in the neutralization of the latex. The small minimum observed in the I_1/I_3 ratio in the region near $\alpha = 0.5$ was surprisingly reproduced in the reprotonation. We do not have a unique explanation for this effect, but it must point to a deep-seated rearrangement of the system.

While pyrene fluorescence shows good reproducibility in the cycle of base-then-acid treatment, the fully protonated polymer at the end of reacidification forms smaller particles

© 1998 NRC Canada

Fig. 9. Comparison of the I_1/I_3 behavior for $C_{20}E_{32}$ at different polymer concentrations: C_{pol} = 3.2 g/L, C_{pol} = 1.6 g/L, and C_{pol} = 0.8 g/L.

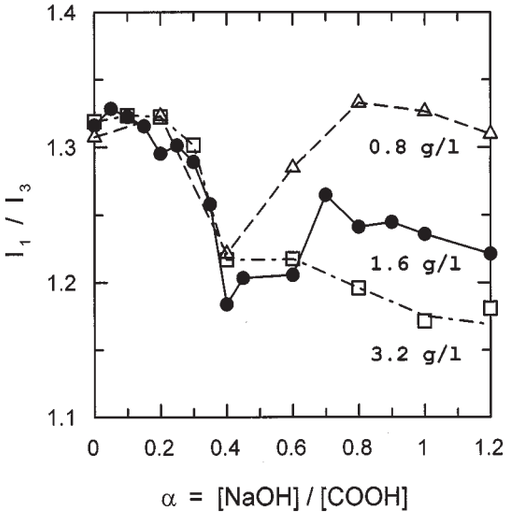

Fig. 10. Polymer concentration dependence of I_E/I_M and I_1/I_3 at α = 0.38 (*a*), at α = 1.0 (*b*).

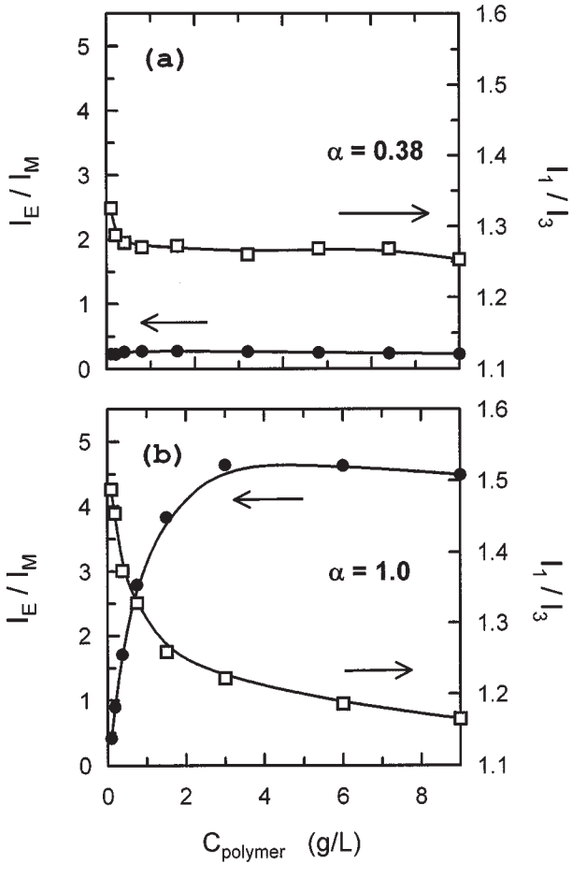

than the original latex, and the solution shows less turbidity. These results parallel those reported by Muroi (13*a*), and indicate that the polymer, once neutralized and dissolved, does not reform the initial particle, but microscopically reforms the hydrophobic domains of the EA–MAA polymer as detected by the dissolved pyrene.

Fig. 11. Comparison of the excitation spectra of the excimer emission monitored at 475 nm and monomer emission monitored at 371.5 nm for different $C_{20}E_{32}$ polymer concentrations: C_{pol} = 0.8 g/L and C_{pol} = 8.0 g/L. The broken line indicates the excitation spectrum for pyrene in water.

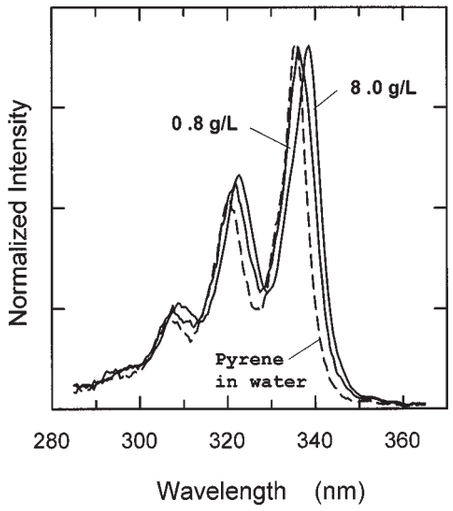

The complexity of the system is indicated by the influence of polymer concentration on I_1/I_3, plotted in Fig. 9, where the ratio of pyrene-to-polymer was kept constant. The I_1/I_3 values are constant at a low degree of neutralization (α < 0.2) but show a sharp decrease from α = 0.2 to 0.4 for all the concentrations. In contrast, there is considerable concentration dependence above α = 0.7, which seems to commence at α = 0.4. Our explanation for these results is that at α > 0.4, neutralization of the polymer is accompanied by a change in the partition of pyrene between the polymer and the water phase.

To obtain further information about the concentration dependence, we examined the ratio I_1/I_3 and I_E/I_M at α = 0.38 and 1.0 for a series of polymer concentrations. These results are plotted in Figs. 10(*a*) and (*b*). These experiments were carried out by preparing polymer samples of C_{pol} = 9 g/L at α = 0.4 and α = 1.0, saturated with pyrene, and examining the spectra after successive dilutions with water. Thus the ratio of pyrene-to-polymer in these experiments is kept constant. In Fig. 10(*a*) at α = 0.38, I_E/I_M values are very small and quite constant, and I_1/I_3 values are almost constant around 1.25 except at very low concentrations, below C_{pol} = 0.2 g/L. At almost all polymer concentrations, pyrene remains dissolved in the polymer phase. In Fig. 10(*b*) at α = 1.0, I_E/I_M values are very high and constant at concentrations above C_{pol} = 3 g/L. Over the same concentration range, there is a small decrease in I_1/I_3 values. The surprise occurs at lower polymer concentrations, where I_E/I_M drops sharply and approaches zero, and I_1/I_3 rises sharply to a value approaching 1.5. These results indicate that as the system is diluted, a greater fraction of the pyrene is found in the aqueous phase, where it contributes only to the monomer emission in the I_E/I_M values and to a large increase I_1/I_3 in

© 1998 NRC Canada

Fig. 12. Fluorescence decay profiles of pyrene (6×10^{-6} M) in the presence of $C_{20}E_{32}$ polymer for C_{pol} = 1.6 g/L at different degrees of neutralization.

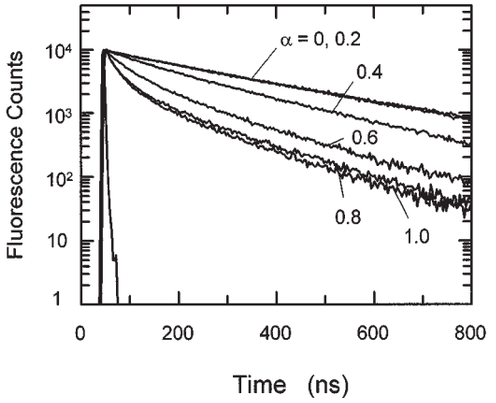

the ratios. From the data in Fig. 6 we calculate that at C_{pol} = 1.6 g/L, ca. 10% of the pyrene is in the water phase, and at C_{pol} = 0.8 g/L about 25% of the pyrene is in the water phase. To confirm this explanation, we checked the excitation spectra associated with monomer, plotted in Fig. 11. Excitation spectra associated with excimer does not change in the polymer dilution process as described in Fig. 7(*b*). However, the excitation spectra associated with monomer shows a definite blue-shift with the longest wavelength absorption maximum shifting from 339 nm at C_{pol} = 8 g/L to 337 nm at C_{pol} = 0.8 g/L.

Dynamic pyrene fluorescence in $C_{20}E_{32}$ polymer solution

In Fig. 12, we show a series of fluorescence decay profiles for pyrene at 6×10^{-6} M in a $C_{20}E_{32}$ solution of C_{pol} = 1.6 g/L. At α = 0 the decay is almost a single exponential and does not change significantly as base is added to the system until α reaches 0.4. Further neutralization leads to more rapid decays, consistent with confinement of pyrenes into smaller compartments. To get further insights into the behavior of the system, we have fitted these decays with the Poisson quenching model, eq. [2] (see above), commonly used to determine micelle aggregation numbers (6–8). As applied here, this model has four fitting parameters: the initial intensity, the unquenched pyrene lifetime τ, the rate constant *k* for excimer formation within a micelle, and the mean number of pyrene per micelle <*n*>. Equation (2) is a powerful fitting function, and it is not surprising that we get good fits to each decay curve with the four variable parameters (plus a term to correct for light scattering). The best values found for the fitting parameters are plotted in Figs. 13(*a*) and (*b*).

One sees first that *k* and <*n*> increase and τ decreases as α increases, and all the values settle above α = 0.8. The <*n*> values seem to follow the I_E/I_M values in Fig. 8(*a*). While almost all the polymer-bound pyrenes are located in a micellar phase comprised of the C_{20} hydrophobes at α = 1.0, considerable amounts of pyrenes are located in other hydrophobic domains below α = 1.0, which contain both EA and protonated MAA units. The decrease of <*n*> and I_E/I_M with

Fig. 13. (*a*) The apparent mean number <*n*> of pyrenes per micelle plotted as a function of the degree of neutralization α = [NaOH]/[COOH]. (*b*) The corresponding values of the unquenched pyrene lifetime τ and the rate constant *k* for excimer formation in a micelle obtained by fitting the fluorescence decay curves in Fig. 12 to the Poisson quenching model, eq. [2].

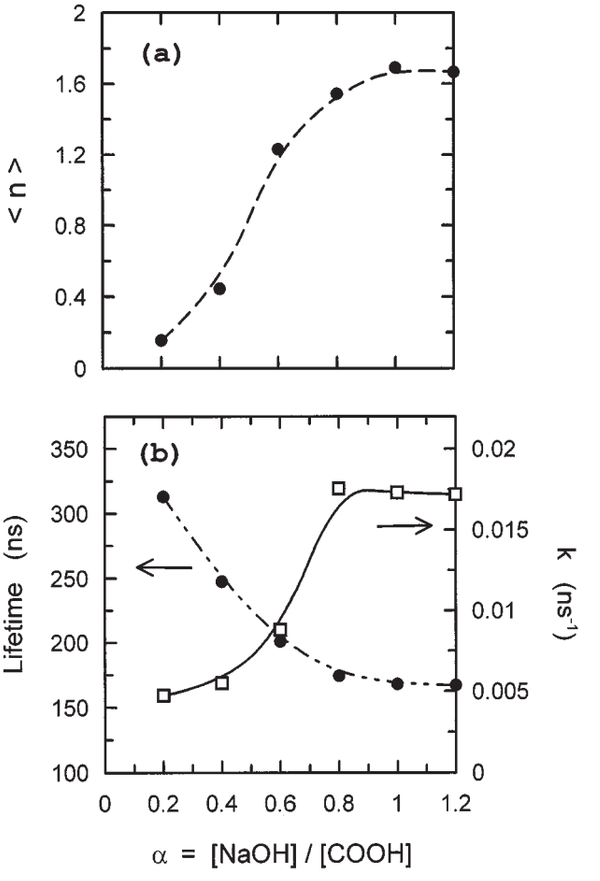

decrease of α is related to the dilution of pyrene into these domains, which becomes more extensive when a larger fraction of the MAA units are protonated. These explanations are consistent with the behavior of the τ values, which reflect the polarity change of hydrophobic domains. When we estimate an apparent micelle aggregation numbers from the value of <*n*> at α = 1.0, we find a value smaller than 20 C_{20} hydrophobes per micelle. We now know that this number is significantly smaller than the true aggregation number. For example, the results in Fig. 10(*b*) and Fig. 11 indicate that not all the pyrenes are in a micelle-forming environment and some pyrenes in water emit considerable amounts of fluorescence for C_{pol} = 1.6 g/L. To obtain reliable numbers, one should repeat these experiments at higher polymer concentrations, above C_{pol} = 4 g/L, to increase the fraction of pyrene in the micelles relative to that in water. Even these experiments yield complicated data. (The apparent aggregation number depends on the probe concentration and varies from 20 to 60 (15).) Further results about the determination of aggregation numbers in this system will be described in a future report.

© 1998 NRC Canada

Fig. 14. A summary of our view of the response of the $C_{20}E_{32}$ polymer latex to an increasing extent of neutralization in water.

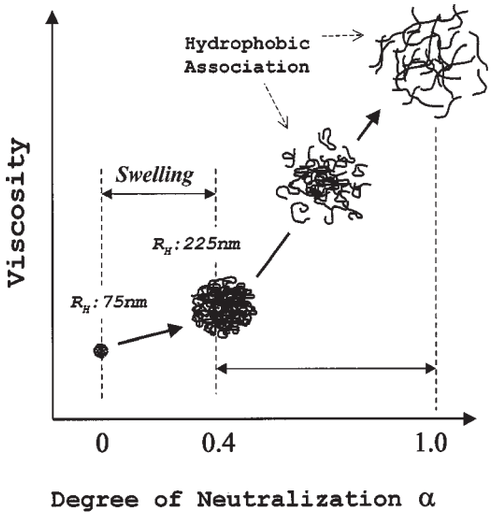

Summary

The dissolution behavior of a HASE polymer $C_{20}E_{32}$ has been examined. The results are summarized in Fig. 14. The titration behavior of this HASE polymer indicates that α = [NaOH]/[COOH] provides the best description of the degree of neutralization of the polymer MAA. The HASE particle of R_H = 75 nm at α = 0 swells gradually with neutralization by base, and the maximum swollen condition R_H = 225 nm appears at α = 0.4, as observed by dynamic light scattering. Above α = 0.4, the swollen particles disintegrate. The polymer molecules dissolve in the water phase and form hydrophobic associations, which leads to a very viscous solution. In fluorescence probe measurements, pyrene monitors the growth of the association through both I_E/I_M and I_1/I_3. At low α, the pyrene partitions into the EA–MAA copolymer, whereas at high α it is located in micelle-like domains formed by the $C_{20}H_{41}$ groups. Pyrene fluorescence decay measurements provide semi-quantitative information about the rate of excimer formation in the system.

Acknowledgments

This research owes much to thoughtful and helpful support by Mr. K. Nishikawa and Drs. K. Schillén and C. Chassenieux. The authors would like to thank Drs. K.C. Tam and V. Tirtaatmadja at Nanyang University, Singapore, for useful discussions. The authors thank Fuji–Xerox Co. Ltd. Japan, the Natural Sciences and Engineering Research Council of Canada (NSERC), and the Singapore/Ontario Collaborative Research for their support of this research.

References

1. (*a*) J.E. Glass (*Editor*). Water soluble polymers. ACS Adv. Chem. Ser. 213, Washington, D.C. 1986; (*b*) Polymers in aqueous media. ACS Adv. Chem. Ser. 223,Washington, D.C. 1989; (*c*) Hydrophobic polymers: performance with environmental acceptance. ACS Adv. Chem. Ser. 248, Washington, D.C. 1996; (*d*) D.N. Schulz and J.E. Glass (*Editors*). Polymers as rheology modifiers. ACS Sym. Ser. 462, Washington, D.C. 1991.
2. (*a*) R.D. Jenkins. Ph.D. thesis. Lehigh University, Bethlehem, Pa. 1990; (*b*) R.E. Jenkins, C.A. Silebi, and M.S. El-Aasser. Polym. Mat. Sci. Eng. **61**, 629 (1989).
3. (*a*) S. Nishida, M.S. El-Aasser, A. Klein, and J.W. Vanderhoff. *In* Emulsion polymers and emulsion polymerization. *Edited by* D.R. Bassett and A.E. Hamielec. ACS Symp. Ser. 165, Washington, D.C. 1981. pp. 291–314; (*b*) R.D. Jenkins, L.M. DeLong, and D.R. Bassett. *In* Hydrophobic polymers. *Edited by* J.E. Glass. ACS Sym. Ser. 462, Washington, D.C. 1996. pp. 425; (*c*) G.D. Shay, F.K. Kravitz, and P.V. Brizgys. *In* Polymers as rheology modifiers. *Edited by* D.N. Schulz and J.E. Glass. ACS Sym. Ser. 462, Washington, D.C. 1989. pp. 121–141; (*d*) G.D. Shay. *In* Polymers in aqueous media. *Edited by* J.E. Glass. ACS Adv. Chem. Ser. 223, Washington, D.C. 1987. pp. 457–494.
4. M.A. Winnik and A. Yekta. Current opinion in colloid and interface sci. **2**, 424 (1997).
5. (*a*) A. Yekta, J. Duhamel, P. Brochard, H. Adiwidjaja, and M.A. Winnik. Macromolecules, **26**, 1829 (1993); (*b*) A. Yekta, B. Xu, J. Duhamel, H. Adiwidjaja, and M.A. Winnik. Macromolecules, **28**, 956 (1995).
6. V. Tirtaatmadja, K.C. Tam, and R.D. Jenkins. Macromolecules, **30**, 1426 (1997).
7. V. Tirtaatmadja, K.C. Tam, and R.D. Jenkins. Macromolecules, **30**, 3271 (1997).
8. R.J. English, H.G. Gulati, R.D. Jenkins, and S.A. Khan. J. Rheology, **41**, 427 (1997).
9. (*a*) B. Berne and R. Pecora (*Editor*s). Dynamic light scattering. Wiley, New York. 1976; (*b*) P. Stepanek. *In* Dynamic light scattering. *Edited by* W. Brown. Oxford University Press, Oxford. 1993. Chap. 4.
10. (*a*) P.P. Infelta. Chem. Phys. Lett. **61**, 88 (1979); (*b*) A. Yekta, M. Aikawa, and J. Turro. Chem. Phys. Lett. **63**, 543 (1979).
11. R. Zana. *In* Surfactant solutions, new methods of investigation. *Edited by* R. Zana. Marcel Dekker Inc., New York. 1997. pp. 241–294.
12. E. Kumacheva, Y. Rharbi, M.A. Winnik, L. Guo, K.C. Tam, and R.D. Jenkins. Langmuir, **13**, 182 (1996).
13. (*a*) S. Muroi. J. Appl. Polym. Sci. **10**, 713 (1966); (*b*) S. Muroi, K. Hosoi, and T. Ishikawa. J. Appl. Polym. Sci. **11**, 1963 (1967); (*c*) L.F. Guziak and W.N. Maclay. J. Appl. Polym. Sci. **7**, 2258 (1963); (*d*) C.J. Verbrugge. J. Appl. Polym. Sci. **14**, 911 (1970); (*e*) C.J. Verbrugge. J. Appl. Polym. Sci. **14**, 897 (1970); (*f*) J.S. Yudelson and R.E. Mack. J. Polym. Sci. Part A: Gen. Pap. **2**, 4683 (1964).
14. (*a*) D.C. Dong and M.A. Winnik. Can. J. Chem. **62**, 2560 (1984); (*b*) K. Kalyanasundaram and J.K. Thomas. J. Am. Chem. Soc. **99**, 2039 (1977).
15. K. Horiuchi, Y. Rharbi, A. Yekta, and M.A. Winnik. Langmuir (1999). In press.

© 1998 NRC Canada

Reaction of ketoximes with aliphatic aldehydes and diphenylborinic acid. Crystal and molecular structure of a diphenylboron chelate derived from the pivaldehyde adduct to cyclohexanone oxime[1]

Wolfgang Kliegel, Ulf Riebe, Steven J. Rettig, and James Trotter

Abstract: Various ketoximes have been reacted with aliphatic aldehydes in the presence of oxybis(diphenylborane) in order to assess the influence of increasingly bulky residues on the nature of the products. Crystals of 5-*tert*-butyl-2-cyclohexylidene-3,3-diphenyl-1,4-dioxa-2-azonia-3-boratacyclopentane, **4***c*, are monoclinic, a = 14.0647(9), b = 11.416(1), c = 14.756(1) Å, β = 115.696(4)°, Z = 4, space group $P2_1/c$. The structure was solved by direct methods and refined by full-matrix least-squares procedures to R = 0.038 (R_w = 0.038) for 2511 reflections with $I \geq 3\sigma(I)$. A bulky substituent at the aldehyde favors α-hydroxyalkylation at the oxime oxygen atom and subsequently leads to the formation of BOCON diphenylboron chelates, whereas formaldehyde reacts by *N*-alkylation of the oximes, resulting in COBON diphenylboron chelates.

Key words: ketoximes, organoboron compounds, crystal structure.

Résumé : Afin d'évaluer l'influence de résidus de plus en plus volumineux sur la nature des produits, on a fait réagir diverses cétoximes avec des aldéhydes aliphatiques en présence d'oxybis(diphénylborane). Les cristaux du 5-*tert*-butyl-2-cyclohexylidène-3,3-diphényl-1,4-dioxa-2-azonia-3-boratacyclopentane, **4***c*, sont monocliniques, groupe d'espace $P2_1$/c, avec a = 14,0647(9), b = 11,416(1) et c = 14,756(1)Å, β = 115,696(4)° et Z = 4. On a résolu la structure par des méthodes directes et on l'a affinée par la méthode des moindres carrés (matrice complète) jusqu'à des valeurs de R = 0,038 et R_w = 0,038 pour 2511 réflexions avec $I \geq 3\sigma(I)$. La présence d'un substituant volumineux dans l'aldéhyde favorise l'α-hydroxyalkylation de l'atome d'oxygène de l'oxime et conduit éventuellement à la formation de chélates diphénylbores, BOCON; par ailleurs, le formaldéhyde réagit par *N*-alkylation des oximes conduisant à la formation de chélates diphénylbores COBON.

Mots clés : cétoximes, composés organiques du bore, structure cristalline.

[Traduit par la Rédaction]

Introduction

We have previously shown that the addition of formaldehyde to ketoximes, **1**, in the presence of diphenylborinic acid (anhydride) gives five-membered boron chelates, **2** (R^3 = H) (1), Scheme 1. The heterocyclic 1,3-betaine structure was established by an X-ray crystallographic analysis of the acetone oxime derivative **2***a*, thus demonstrating the preferred *N*-alkylation of the ambident nucleophilic ketoxime by formaldehyde with subsequent trapping of the labile primary adduct as a "chelate" of the Ph_2B^+ cation. It could be assumed that higher aliphatic aldehydes would give homologous chelates **2** (R^3 = alkyl) under the same conditions. However, an *O*-alkylation of the ketoxime by the aliphatic aldehyde with subsequent formation of the isomeric boron chelate **4** had to be considered, especially since this type of compound had been formed applying trichloroacetaldehyde as a strong electrophilic carbonyl compound in the synthesis of the ketoxime derivatives **4** (R^3 = CCl_3) (1). Here we report the results of the experiments carried out with various ketoximes and aliphatic aldehydes, focusing on the influence of increasingly bulky residues.

Received June 15, 1998.

W. Kliegel and U. Riebe. Institut für Pharmazeutische Chemie der Technischen Universität Braunschweig, Beethovenstrasse 55, 38106 Braunschweig, Germany.
S.J. Rettig and J. Trotter.[2] Department of Chemistry, University of British Columbia, 2036 Main Mall, Vancouver, BC V6T 1Z1, Canada.

[1]Structural studies of organoboron compounds LXIX. Previous paper in this series: ref. 13.
[2]Author to whom correspondence may be addressed. Telephone: (604) 822-4865. Fax: (604) 822-2847. E-mail: jtrt@xray4.chem.ubc.ca

© 1998 NRC Canada

Scheme 1.

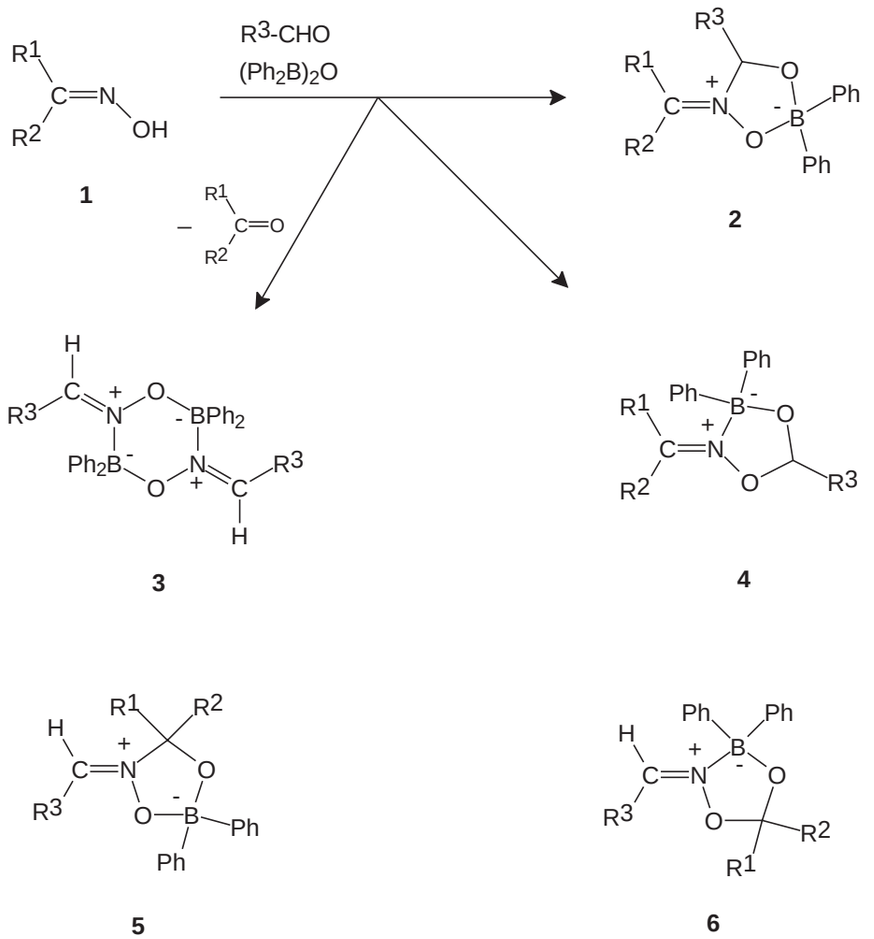

	R^1	R^2	R^3		R^1	R^2	R^3
1*a*	Me	Me		**2***e*	Ph	Ph	H
1*b*	—$(CH_2)_4$—			**2***f*	—(C_9H_{14})—		H
1*c*	—$(CH_2)_5$—			**2***g*	*i*-Pr	*i*-Pr	H
1*d*	Ph	Me		**3***a*			H
1*e*	Ph	Ph		**3***b*			Et
1*f*	—(C_9H_{14})—			**3***c*			*i*-Pr
1*g*	*i*-Pr	*i*-Pr		**4***a*	Me	Me	*t*-Bu
2*a*	Me	Me	H	**4***b*	—$(CH_2)_4$—		*t*-Bu
2*b*	—$(CH_2)_4$—		H	**4***c*	—$(CH_2)_5$—		*t*-Bu
2*c*	—$(CH_2)_5$—		H	**4***d*	—$(CH_2)_5$—		i-Pr
2*d*	Ph	Me	H				

Experimental

General procedures

All preparations and reactions were carried out under normal conditions, without protective gas atmosphere. Commercial solvents and reagents were used as supplied. Oxybis(diphenylborane) was prepared according to literature methods (2). Melting points were measured on a Linström SPA-1 apparatus and are uncorrected. Elemental analyses: (C, H, N) Carlo Erba Elemental Analyzer 1106; (B) oxidative disintegration (Schöninger) and potentiometric titration. Infrared spectra: Phillips PU 9800 FT-IR spectrometer, V 3.00 and Mattson Genesis Series FTIR Rev. I (ATI Unicam). ^{1}H nmr: Varian EM 390. ^{11}B nmr: Bruker AC 200. Mass spectra: Finnigan MAT 8430.

4-(1-Phenylethylidene)-2,2-diphenyl-1,3-dioxa-4-azonia-2-boratacyclopentane, 2*d*

Acetophenone oxime (0.83 g, 5.0 mmol), oxybis(diphenylborane) (0.87 g, 2.5 mmol), and formaldehyde (1 mL 35% aqueous solution) are reacted as described in the literature for compounds **2***a–c* (1). Yield: 1.20 g (73%) of color-

© 1998 NRC Canada

Fig. 1. Stereoview of **4***c*; 33% probability thermal ellipsoids are shown for the non-hydrogen atoms.

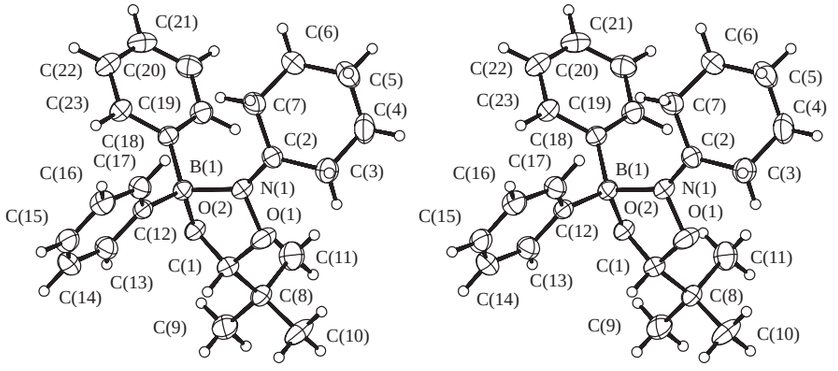

less crystals; mp 137–138°C (from ethanol). Infrared (KBr, cm^{-1}): 1610, 1590 (C=N, C=C); ^1H nmr (90 MHz, $CDCl_3$–TMS), δ (ppm): 2.66 (s, CH_3), 5.45 (s, N-CH_2-O), 7.10–7.80 (m, 15 aromatic H); ^{11}B nmr (64 MHz, $CDCl_3$–Et_2OBF_3), δ (ppm): 13.0 ($W_{1/2}$ = 240 Hz) and 46.6 ($W_{1/2}$ = 300 Hz); ratio of peak areas: 10:1. Mass spectrum (EI, 70 eV, 100°C): *m*/*z* (%) = 299 (26) [$M^+ - CH_2O$], 284 (55) [$M^+ - CH_2O - CH_3$], 242 (24), 222 (21) [$M^+ - CH_2O - C_6H_5$], 181 (24) [Ph_2BO], 165 (77) [Ph_2B], 135 (14), 118 (74), 77 (100). Anal. calcd. for $C_{23}H_{26}BNO_2$: C 76.62, H 6.12, B 3.28, N 4.25; found: C 76.50, H 6.12, B 3.29, N 4.26. The product gives a blue-colored solution in ethanol upon addition of diphenylcarbazone, indicating the presence of the chelated diphenylborenium (Ph_2B^+) ion (3).

4-Diphenylmethylene-2,2-diphenyl-1,3-dioxa-4-azonia-2-boratacyclopentane, 2*e*

Benzophenone oxime (0.99 g, 5.0 mmol) is reacted with oxybis(diphenylborane) (0.87 g, 2.5 mmol) and formaldehyde (1 mL 35% aqueous solution) as described for **2***d*. Yield: 1.46 g (75%) of colorless crystals; mp 138–139°C (from ethanol). Infrared (KBr, cm^{-1}): 1605, 1593 (C=N, C=C); ^1H nmr (90 MHz, $CDCl_3$–TMS), δ (ppm): 5.36 (s, N-CH_2-O), 7.06–8.13 (m, 20 aromatic H); ^{11}B nmr (64 MHz, $CDCl_3$–Et_2OBF_3), δ (ppm): 13.8 ($W_{1/2}$ = 360 Hz) and 46.6 ($W_{1/2}$ = 300 Hz); ratio of peak areas: 25:1. Anal. calcd. for $C_{26}H_{22}BNO_2$: C 79.81, H 5.67, B 2.76, N 3.58; found: C 79.68, H 5.62, B 2.77, N 3.66. **2***e* gives a blue-color reaction with diphenylcarbazone as described for **2***d*.

4-Adamantylidene-2,2-diphenyl-1,3-dioxa-4-azonia-2-boratacyclopentane, 2*f*

Adamantanone oxime (0.83 g, 5.0 mmol) is reacted with oxybis(diphenylborane) (0.87 g, 2.5 mmol) and formaldehyde (1 mL 35% aqueous solution) as described for **2***d*. Yield: 1.31 g (73%) of colorless crystals; mp 157–159°C (from ethanol). Infrared (KBr, cm^{-1}): 1660 (C=N); ^1H nmr (90 MHz, $CDCl_3$–TMS), δ (ppm): 1.50–2.23 (m, 12 aliphatic H), 2.60 and 3.80 (m_c and m_c, 2 N=C-CH), 5.40 (s, N-CH_2-O), 7.06–7.66 (m, 10 aromatic H); ^{11}B nmr (64 MHz, $CDCl_3$–Et_2OBF_3), δ (ppm): 11.8 ($W_{1/2}$ = 260 Hz). Anal. calcd. for $C_{22}H_{26}BNO_2$: C 76.89, H 7.29, B 3.01, N 3.90; found: C 76.16, H 7.22, B 3.03, N 3.83. **2***f* gives a blue-color reaction with diphenylcarbazone as described for **2***d*.

2,5-Dimethylene-3,3,6,6-tetraphenyl-1,4-dioxa-2,5-diazonia-3,6-diboratacyclohexane, 3*a*

Method A

Formaldehyde oxime trimer hydrochloride (0.57 g, 3.3 mmol) in 10 mL of absolute ethanol is mixed with 3.3 mL of 1 N KOH solution. The precipitating KCl is filtered off, and a solution of oxybis(diphenylborane) (1.74 g, 5.0 mmol) in 10 mL of ethanol is added to the reaction mixture. After 1 min of refluxing the crystalline deposit is filtered off and washed with a small amount of cooled ethanol. Yield: 0.73 g (70%) of colorless crystals (poor solubility in methanol, ethanol, benzene, $CHCl_3$, DMSO); mp 209–210°C (decomp.); lit. (4)[3] mp 209°C (from ethyl acetate). Infrared (KBr, cm^{-1}): 1640 (C=N), 1600 (C=C); identical to the infrared spectrum of the compound prepared from dimeric *E*-(aminoxy)-diphenylborane (5) and formaldehyde by condensation (4)[3]. Mass spectrum (EI, 70 eV, 150°C): *m*/*z* (%) = 209 (48) [1/2 M^+], 181 (34) [Ph_2BO], 165 (64) [Ph_2B], 105 (71) [PhBOH], 77 (100) [C_6H_5], 51 (49) [C_4H_3]. **3***a* gives a blue-color reaction with diphenylcarbazone as described for **2***d*.

Method B

Diisopropylketone oxime[4] (0.56 g, 5.0 mmol) is reacted with oxybis(diphenylborane) (0.87 g, 2.5 mmol) and formaldehyde (1 mL 35% aqueous solution) as described for **2***d*. Yield: 0.73 g (74%) of colorless crystals; mp 209°C. Infrared (KBr): identical to **3***a*.

5-*tert*-Butyl-2-isopropylidene-3,3-diphenyl-1,4-dioxa-2-azonia-3-boratacyclopentane, 4*a*

Acetone oxime (0.37 g, 5.0 mmol), oxybis(diphenylborane) (0.87 g, 2.5 mmol), and pivalaldehyde (0.43 g, 5.0 mmol) are dissolved in 5 mL of ethanol and heated briefly. If no spontaneous crystallization commences upon cooling, the solvent is removed in vacuo, and the residue taken up in chloroform. Crystallization is then induced by the addition of petroleum ether. Yield: 0.37 g (23%) of colorless crystals; mp 101–102°C (from ethanol). Infrared

[3] W. Kliegel and D. Nanninga. Unpublished results.
[4] 2,4-Dimethyl-3-pentanone oxime.

© 1998 NRC Canada

Table 1. ^{11}B nmr shift values (δ (Et_2OBF_3), ppm) for **2** and **4**.

2*a*	12.7[a]	**4** (R^3 = CCl_3)	8.7–9.5[a]
2*b*	12.7[a]	**4***a*	8.7
2*c*	12.1[a]	**4***b*	8.2
2*d*	13.0	**4***c*	8.8
2*e*	13.8	**4***d*	8.4
2*f*	11.8		

[a] From ref. 1.

(KBr, cm^{-1}): 1665 (C=N); ^{1}H nmr (90 MHz, $CDCl_3$–TMS), δ (ppm): 1.07 (s, $(CH_3)_3C$), 1.80 and 2.20 (s and s, $(CH_3)_2C$=N), 5.10 (s, 65% of 1H, O-CH-O), 7.20–7.60 (m, 10 aromatic H), 9.47 (s, 35% of 1H, CH—O); ^{11}B nmr (64 MHz, $CDCl_3$–Et_2OBF_3), δ (ppm): 8.7 ($W_{1/2}$ = 280 Hz). Anal. calcd. for $C_{20}H_{26}BNO_2$: C 74.32, H 8.11, B 3.34, N 4.33; found: C 73.50, H 7.70, B 3.72, N 3.96. **4***a* gives a blue-color reaction with diphenylcarbazone as described for **2***d*. (See Fig. 1 for stereoview of **4***c*.)

5-*tert*-Butyl-2-cyclopentylidene-3,3-diphenyl-1,4-dioxa-2-azonia-3-boratacyclopentane, 4*b*

Cyclopentanone oxime (0.50 g, 5.0 mmol), oxybis(diphenylborane) (0.87 g, 2.5 mmol), and pivalaldehyde (0.43 g, 5.0 mmol) are reacted as described above for **4***a*. Yield: 0.83 g (48%) of colorless crystals; mp 183–185°C (from ethanol). Infrared (KBr, cm^{-1}): 1688 (C=N); ^{1}H nmr (90 MHz, $CDCl_3$–TMS), δ (ppm): 1.10 (s, $(CH_3)_3C$), 1.43–3.00 (m, -$(CH_2)_4$-), 5.20 (s, 60% of 1H, O-CH-O), 7.17–7.60 (m, 10 aromatic H), 9.50 (s, 40% of 1H, CH=O); ^{11}B nmr (64 MHz, $CDCl_3$–Et_2OBF_3), δ (ppm): 8.2 ($W_{1/2}$ = 320 Hz). Anal. calcd. for $C_{22}H_{28}BNO_2$: C 75.65, H 8.08, B 3.10, N 4.01; found: C 75.76, H 7.99, B 3.20, N 3.93. **4***b* gives a blue-color reaction with diphenylcarbazone as described for **2***d*.

5-*tert*-Butyl-2-cyclohexylidene-3,3-diphenyl-1,4-dioxa-2-azonia-3-boratacyclopentane, 4*c*

Cyclohexanone oxime (0.57 g, 5.0 mmol), oxybis(diphenylborane) (0.87 g, 2.5 mmol), and pivalaldehyde (0.43 g, 5.0 mmol) are reacted as described above for **4***a*. Yield: 1.14 g (63%) of colorless crystals; mp 148–149°C (from ethanol). Infrared (KBr, cm^{-1}): 1665 (C=N); ^{1}H nmr (90 MHz, $CDCl_3$–TMS), δ (ppm): 1.10 (s, $(CH_3)_3C$), 1.25–2.90 (m, -$(CH_2)_5$-), 5.10 (s, 50% of 1H, O-CH-O), 7.14–7.66 (m, 10 aromatic H), 9.50 (s, 50% of 1H, CH=O); ^{11}B nmr (64 MHz, $CDCl_3$–Et_2OBF_3), δ (ppm): 8.8 ($W_{1/2}$ = 340 Hz). Anal. calcd. for $C_{23}H_{30}BNO_2$: C 76.04, H 8.32, B 2.98, N 3.86; found: C 75.69, H 8.33, B 3.01, N 3.67. **4***c* gives a blue-color reaction with diphenylcarbazone as described for **2***d*. (See Fig. 1 for stereoview of **4***c*.)

Crystals suitable for X-ray analysis were obtained by very slow crystallization from $CHCl_3$ – petroleum ether using the liquid diffusion method (6).

2-Cyclohexylidene-5-isopropyl-3,3-diphenyl-1,4-dioxa-2-azonia-3-boratacyclopentane, 4*d*

Cyclohexanone oxime (0.57 g, 5.0 mmol), oxybis(diphenylborane) (0.87 g, 2.5 mmol), and isobutyraldehyde (0.36 g, 5.0 mmol) are reacted as described above for **4***a*. Yield: 1.02 g (58%) of colorless crystals; mp 164–165°C (from ethanol). Infrared (KBr, cm^{-1}): 1655 (C=N); ^{1}H nmr (90 MHz, $CDCl_3$–TMS), δ (ppm): 1.07 and 1.15 (d and d, J = 4 Hz, $(CH_3)_2C$), 1.30–2.90 (m, -$(CH_2)_5$-, C-CH-C), 5.27 (d, J = 4 Hz, O-CH-O), 7.17–7.53 (m, 10 aromatic H), 9.50 (s, 50% of 1H, CH=O); ^{11}B nmr (64 MHz, $CDCl_3$–Et_2OBF_3), δ (ppm): 8.4 ($W_{1/2}$ = 340 Hz). Anal. calcd. for $C_{22}H_{28}BNO_2$: C 75.65, H 8.08, B 3.10, N 4.01; found: C 75.45, H 8.30, B 3.08, N 3.89. **4***d* gives a blue-color reaction with diphenylcarbazone as described for **2***d*.

The ^{11}B nmr chemical shifts for compounds **2** and **4** are summarized in Table 1.

Table 2. Crystallographic data.[a]

Compound	**4***c*
Formula	$C_{23}H_{30}BNO_2$
fw	363.31
Crystal system	Monoclinic
Space group	$P2_1/c$ (no. 14)
a, Å	14.0647(9)
b, Å	11.416(1)
c, Å	14.756(1)
β,°	115.696(4)
V, Å^3	2135.1(4)
Z	4
ρ_{calcd}, g/cm^3	1.130
$F(000)$	784
μ(Cu K_α), cm^{-1}	5.14
Crystal size, mm	0.08 × 0.25 × 0.25
Transmission factors	0.87–1.00
Scan type	ω-2θ
Scan range, deg in w	0.79 + 0.20 tan θ
Scan speed, deg/min	16 (up to 9 scans)
Data collected	$+h$, $+k$, $\pm l$
$2\theta_{max}$, deg	155
Crystal decay, %	Negligible
Total reflections	4754
Total unique reflections	4566
R_{merge}	0.027
Reflections with $I \geq 3\sigma(I)$	2511
No. of variables	245
R	0.038
R_w	0.038
gof	2.18
Max Δ/σ (final cycle)	0.002
Residual density e/Å^3	–0.12–0.13

[a] Temperature 294 K, Rigaku AFC6S diffractometer, Cu K_α radiation (λ = 1.54178 Å), graphite monochromator, takeoff angle 6.0°, aperture 6.0 × 6.0 mm at a distance of 285 mm from the crystal, stationary background counts at each end of the scan (scan/background time ratio 2:1), $\sigma^2(F^2) = [S^2(C + 4B)]/Lp^2$ (S = scan rate, C = scan count, B = normalized background count), function minimized $\Sigma w(|F_o| - |F_c|)^2$ where $w = 4F_o^2/\sigma^2(F_o^2)$, $R = \Sigma||F_o| - |F_c||/\Sigma|F_o|$, $R_w = (\Sigma w(|F_o| - |F_c|)^2/\Sigma w|F_o|^2)^{1/2}$, and gof = $[\Sigma w(|F_o| - |F_c|)^2/(m - n)]^{1/2}$. Values given for R, R_w, and gof are based on those reflections with$I \geq 3\sigma(I)$.

X-ray crystallographic analysis of 4*c*

Crystallographic data appear in Table 2. The final unit-cell parameters were obtained by least-squares on the setting angles for 25 reflections with 2θ = 45.4–80.4°. The intensities of three standard reflections, measured every 200 reflections throughout the data collection, showed only small random

© 1998 NRC Canada

Table 3. Final atomic coordinates (fractional) and B_{eq} (10^3 Å^2).[a]

Atom	*x*	*y*	*z*	B_{eq}
O(1)	0.4138(1)	0.1698(1)	0.4104(1)	5.35(4)
O(2)	0.35776(9)	0.1134(1)	0.24663(9)	3.83(3)
N(1)	0.3085(1)	0.2046(1)	0.3603(1)	3.82(4)
C(1)	0.4376(1)	0.0959(2)	0.3414(2)	4.21(5)
C(2)	0.2804(2)	0.2831(2)	0.4059(1)	3.92(5)
C(3)	0.3549(2)	0.3377(2)	0.5025(2)	5.53(6)
C(4)	0.3479(2)	0.4708(2)	0.4937(2)	7.32(8)
C(5)	0.2357(2)	0.5135(2)	0.4574(2)	7.39(8)
C(6)	0.1664(2)	0.4592(2)	0.3564(2)	6.10(7)
C(7)	0.1699(2)	0.3260(2)	0.3617(2)	4.67(5)
C(8)	0.5459(2)	0.1302(2)	0.3519(2)	4.32(5)
C(9)	0.5743(2)	0.0512(2)	0.2826(2)	6.82(7)
C(10)	0.6270(2)	0.1157(3)	0.4614(2)	7.29(7)
C(11)	0.5435(2)	0.2581(2)	0.3182(2)	6.83(7)
C(12)	0.2107(1)	0.0087(2)	0.2759(1)	3.57(4)
C(13)	0.2331(2)	–0.0978(2)	0.2440(2)	4.88(6)
C(14)	0.1900(2)	–0.2025(2)	0.2561(2)	5.59(6)
C(15)	0.1220(2)	–0.2030(2)	0.3010(2)	5.39(6)
C(16)	0.0982(2)	–0.1002(2)	0.3329(2)	5.16(6)
C(17)	0.1423(2)	0.0039(2)	0.3209(2)	4.42(5)
C(18)	0.1766(1)	0.2041(2)	0.1613(1)	3.64(4)
C(19)	0.2035(2)	0.3140(2)	0.1391(2)	4.56(5)
C(20)	0.1360(2)	0.3797(2)	0.0583(2)	5.25(6)
C(21)	0.0383(2)	0.3363(2)	–0.0045(2)	5.49(6)
C(22)	0.0089(2)	0.2280(2)	0.0139(2)	5.26(6)
C(23)	0.0768(2)	0.1633(2)	0.0956(2)	4.31(5)
B(1)	0.2573(2)	0.1282(2)	0.2542(2)	3.61(5)

[a] $B_{eq} = (8/3)\pi^2\Sigma\Sigma(U_{ij}a_i a_j(\mathbf{a}_i\mathbf{a}_j))$.

fluctuations. The data were processed,[5] corrected for Lorentz and polarization effects, and absorption (based on azimuthal scans).

The structure was solved by direct methods, the coordinates of the non-hydrogen atoms being determined from *E*-maps or from subsequent difference Fourier syntheses. All non-hydrogen atoms were refined with anisotropic thermal parameters. Hydrogen atoms were fixed in calculated positions with C—H = 0.98 Å and $B_H = 1.2B_{bonded\ atom}$. A correction for secondary extinction was applied (Zachariasen type, isotropic, Gaussian), the final value of the extinction coefficient being 1.18(2) × 10^{-5}. Neutral atom scattering factors for all atoms and anomalous dispersion corrections for the non-hydrogen atoms were taken from the *International Tables for X-Ray Crystallography* (7). Final atomic coordinates and equivalent isotropic thermal parameters, bond lengths, bond angles, and intra-annular torsion angles appear in Tables 3–6, respectively. Hydrogen atom parameters, anisotropic thermal parameters, torsion angles, intermolecular contacts, and least squares planes are included as supplementary material.[6]

Table 4. Bond lengths (Å) with estimated standard deviations in parentheses.

Bond	Length	Bond	Length
O(1)—N(1)	1.396(2)	O(1)—C(1)	1.468(2)
O(2)—C(1)	1.376(2)	O(2)—B(1)	1.474(2)
N(1)—C(2)	1.281(2)	N(1)—B(1)	1.659(3)
C(1)—C(8)	1.515(3)	C(2)—C(3)	1.490(3)
C(2)—C(7)	1.484(3)	C(3)—C(4)	1.526(3)
C(4)—C(5)	1.510(4)	C(5)—C(6)	1.515(3)
C(6)—C(7)	1.522(3)	C(8)—C(9)	1.540(3)
C(8)—C(10)	1.529(3)	C(8)—C(11)	1.539(3)
C(12)—C(13)	1.389(3)	C(12)—C(17)	1.387(3)
C(12)—B(1)	1.604(3)	C(13)—C(14)	1.388(3)
C(14)—C(15)	1.379(3)	C(15)—C(16)	1.360(3)
C(16)—C(17)	1.387(3)	C(18)—C(19)	1.389(3)
C(18)—C(23)	1.396(3)	C(18)—B(1)	1.604(3)
C(19)—C(20)	1.380(3)	C(20)—C(21)	1.375(3)
C(21)—C(22)	1.367(3)	C(22)—C(23)	1.383(3)

Table 5. Bond angles (deg) with estimated standard deviations in parentheses.

Bonds	Angle	Bonds	Angle
N(1)-O(1)-C(1)	107.8(1)	C(1)-O(2)-B(1)	109.0(1)
O(1)-N(1)-C(2)	114.8(2)	O(1)-N(1)-B(1)	106.0(1)
C(2)-N(1)-B(1)	139.2(2)	O(1)-C(1)-O(2)	106.9(1)
O(1)-C(1)-C(8)	107.6(2)	O(2)-C(1)-C(8)	114.1(2)
N(1)-C(2)-C(3)	123.1(2)	N(1)-C(2)-C(7)	120.1(2)
C(3)-C(2)-C(7)	116.8(2)	C(2)-C(3)-C(4)	110.0(2)
C(3)-C(4)-C(5)	111.7(2)	C(4)-C(5)-C(6)	110.1(2)
C(5)-C(6)-C(7)	111.5(2)	C(2)-C(7)-C(6)	110.9(2)
C(1)-C(8)-C(9)	108.6(2)	C(1)-C(8)-C(10)	109.7(2)
C(1)-C(8)-C(11)	109.4(2)	C(9)-C(8)-C(10)	110.4(2)
C(9)-C(8)-C(11)	108.4(2)	C(10)-C(8)-C(11)	110.2(2)
C(13)-C(12)-C(17)	115.7(2)	C(13)-C(12)-B(1)	120.3(2)
C(17)-C(12)-B(1)	123.9(2)	C(12)-C(13)-C(14)	122.3(2)
C(13)-C(14)-C(15)	119.9(2)	C(14)-C(15)-C(16)	119.3(2)
C(15)-C(16)-C(17)	120.3(2)	C(12)-C(17)-C(16)	122.5(2)
C(19)-C(18)-C(23)	115.6(2)	C(19)-C(18)-B(1)	121.7(2)
C(23)-C(18)-B(1)	122.6(2)	C(18)-C(19)-C(20)	122.6(2)
C(19)-C(20)-C(21)	119.9(2)	C(20)-C(21)-C(22)	119.5(2)
C(21)-C(22)-C(23)	120.2(2)	C(18)-C(23)-C(22)	122.2(2)
O(2)-B(1)-N(1)	95.4(1)	O(2)-B(1)-C(12)	113.9(2)
O(2)-B(1)-C(18)	110.1(2)	N(1)-B(1)-C(12)	107.8(2)
N(1)-B(1)-C(18)	112.3(2)	C(12)-B(1)-C(18)	115.5(2)

Results and discussion

Reacting the oximes of acetophenone (**1***d*), benzophenone (**1***e*), or adamantone (**1***f*) with formaldehyde and diphenylborinic acid anhydride gave crystalline diphenylboron chelates, **2***d–f*, having spectroscopic characteristics similar to

[5] teXsan: Crystal structure analysis package. Unix version 1.7. Molecular Structure Corporation. The Woodlands, Tex. 1995.

[6] Copies of material on deposit may be purchased from: The Depository of Unpublished Data, Document Delivery, CISTI, National Research Council Canada, Ottawa, Canada, K1A 0S2. Tables of hydrogen atom coordinates and bond lengths and angles involving hydrogen atoms have also been deposited with the Cambridge Crystallographic Data Centre and can be obtained on request from: The Director, Cambridge Crystallographic Data Centre, University Chemical Laboratory, 12 Union Road, Cambridge, CB2 1EZ, U.K.

© 1998 NRC Canada

Table 6. Intra-annular torsion angles (deg) with standard deviations in parentheses.

Atoms	Value (deg)	Atoms	Value (deg)
C(7)-C(2)-C(3)-C(4)	–50.2(3)	C(1)-O(1)-N(1)-B(1)	8.7(2)
C(2)-C(3)-C(4)-C(5)	53.1(3)	O(1)-N(1)-B(1)-O(2)	–27.3(2)
C(3)-C(4)-C(5)-C(6)	–58.1(3)	N(1)-B(1)-O(2)-C(1)	37.9(2)
C(4)-C(5)-C(6)-C(7)	57.3(3)	B(1)-O(2)-C(1)-O(1)	–36.5(2)
C(5)-C(6)-C(7)-C(2)	–52.2(3)	O(2)-C(1)-O(1)-N(1)	15.4(2)
C(6)-C(7)-C(2)-C(3)	50.0(3)		

those observed for the diphenylboron chelates **2***a–c*. The latter had been reported (1) as a result of the same reaction using less bulky oximes (**1***a–c*). The ^{11}B nmr chemical shifts for the tetracoordinated boron nuclei of **2***d–f* between δ (Et_2OBF_3) 11.8 and 13.8 ppm[7] are similar to the values ranging from 12.1 to 12.8 ppm observed for **2***a–c* (1). The bulkier diisopropylketoxime[4] **1***g*, however, did not give the expected chelate **2***g* upon addition of formaldehyde and diphenylborinic acid, but produced instead a diphenylborinate of formaldoxime having a cyclodimeric structure **3***a*. The structure **3** has been established for several diarylborinates of aliphatic and aromatic aldoximes (11). Relatively stable dimers of type **3** are also formed by borinates of cyclic ketoximes. Noncyclic ketoxime derivatives like the acetonoxime diphenylborinate are easily converted under slight thermal stress into another type of cyclic boron compound which has been described with full structural characterization (12). In the presence of a less bulky aldehyde the bulkier ketoxime borinates (monomer or dimer) tend to exchange the carbonyl component resulting in the aldoxime derivatives **3**. A very bulky aldehyde, however, might not exchange with the ketone component of a ketoxime, as shown by the reaction with pivaldehyde. So far, no specific experiments have been carried out to investigate the extent or the equilibria of these exchange reactions. In the case of **1***g* the bulky substitution might favor the exchange of the carbonyl component in the oxime leading to the formaldoxime derivative **3***a* rather than the more sterically hindered **2***g*.

Similar "reoximations" were also observed during the reaction of the less bulky ketoximes **1***a–c* with propanal as the aldehyde component and diphenylborinic acid. In all cases the known (11) BONBON cyclodimer **3***b* was isolated. Using isobutyraldehyde in the same reaction system, **1***a* and **1***b* also gave the BONBON type cyclic dimer **3***c*. The use of cyclohexanone oxime (**1***c*) resulted in the formation of a diphenylboron chelate containing the isobutyraldehyde component, as did all three of the ketoximes **1***a–c* with pivaldehyde and diphenylborinic acid. The ^{11}B nmr signals of these diphenylboron chelates, however, have chemical shift values of about 8.5 ppm (see Table 1), distinctly different from those near 13 ppm reported for the diphenylboron chelates of type **2** (1). The similarity of these ^{11}B nmr shift values to those ranging from 8.7 to 9.5 ppm found for boron chelates formed by the trichloroacetaldehyde adducts of ketoximes (**4**, $R^3 = CCl_3$) suggests a BOCON ring system of type **4** for the pival- and isobutyraldehyde derivatives **4***a–d*, rather than a COBON chelate ring system of type **2**. Infrared and ^{1}H nmr spectra are not sufficient to discriminate between the isomeric structural types **2** and **4**. The other isomeric structures **5** and **6** containing COBON and BOCON heterocycles, respectively, in which the aldehyde and ketone functions have changed places, can be excluded on the basis of an acetalic methine proton signal (O-CH-O or O-CH-N) near δ = 5 ppm in the ^{1}H nmr spectra.[8] Compounds **5** or **6** would display an azomethine proton signal (N=CH) near 7 ppm, as observed in the ^{1}H nmr spectra of type **3** compounds (11). To verify the assumption of a BOCON ring of type **4**, containing an *O,O*-acetal function, an X-ray crystallographic analysis of **4***c* (which gave suitable crystals) was performed.

The X-ray analysis unambiguously establishes the molecular structure of **4***c*. It appears that a bulky substituent at the aldehyde (R^3-CH=O) favors the α-hydroxyalkylation at the oxime oxygen atom and subsequently leads to the formation of the diphenylboron chelates of type **4**, whereas formaldehyde (R^3 = H) reacts by *N*-alkylation of the oximes, resulting in the diphenylboron chelates of type **2** (1). Compounds **4***a–d* represent further examples of boron chelates forming a BOCON heterocycle, in addition to the previously reported trichloroacetaldehyde derivatives **4** ($R^3 = CCl_3$) (1). The controlling factor in the formation of **4***a–d* is obviously a steric effect rather than the strong electrophilicity that had been assumed to be the reason for the *O,O*-acetal formation in the case of the trichloroacetaldehyde derivatives **4** ($R^3 = CCl_3$) (1). In view of the current findings, it is likely that the bulkiness of the trichloromethyl group is the primary factor in the formation of **4** ($R^3 = CCl_3$).

The five-membered BOCON ring of **4***c* has a distorted O(2)-envelope conformation (Table 6). The B(1)-N(1)-O(1)-C(1) moiety (torsion angle = 8.7(2)°) is planar to within 0.017(1) Å, with O(2) displaced by 0.133(1) Å from the the BNOC mean plane. The moiety consisting of the ring atoms N(1), B(1), and O(1) along with the carbonyl (sp^2) carbon

[7] The weak side signals at 46.6 ppm in the spectra of **2***d* and **2***e* indicate the presence of a small quantity of a Ph_2B-O-R moiety (for examples see ref. 8), probably arising from partial ring opening at the weak oxime oxygen O—B coordinative bond and thus forming a trivalent (sp^2)-boron species. The stability of the acetophenone and benzophenone oxime derivatives **2***d* and **2***e* appears to be reduced relative to that of the adamantanonoxime derivative **2***f* and the other aliphatic ketoxime derivatives **2***a–c* (1) because of a decreased nucleophilicity of the (oxime) *N*-oxide ligand. A comparable phenomenon, additional side signals near 47 ppm, has been observed in the ^{11}B nmr spectra of similar boron chelates with reduced chelate stability (9, 10).

[8] Partial solvolysis can be seen in the ^{1}H nmr spectra of **4***a–c*, possibly a result of the very bulky aldehyde component. The acetal (O-CH-O) group is retained to an extent of 50–65% in the $CDCl_3$ solution of the ^{1}H nmr experiment, in accordance with the appearance of 50–35% of a free carbonyl (CH=O) group.

© 1998 NRC Canada

atom C(2) is planar to within 0.005(2) Å. The boron atom has a slightly distorted tetrahedral coordination geometry, bond angles at B(1) ranging from 95.4(1)° within the five-membered heterocycle (O(1)-B(1)-O(2)) to 115.5(2)° between the the *B*-phenyl groups (C(12)-B(1)-C(18)). The B—C(phenyl) distances are identical at 1.604(3) Å. The dimensions of the cyclohexanone oxime moiety in **4***c* are very similar to those of the acetone oxime moiety in **4** ($R^1 = R^2$ = Me, $R^3 = CCl_3$): C=N/N-O = 1.281(2)/1.396(2) Å for **4***c*, 1.278(3)/1.401(2) Å for **4** (1). The acetalic C—O bonds in the pivaldehyde derivative **4***c* are somewhat longer than the corresponding acetalic C—O bonds in the trichloroacetaldehyde derivative **4** ($R^3 = CCl_3$) (1): C(1)—O(1)/C(1)—O(2) = 1.468(2)/1.376(2) Å for **4***c*, 1.450(2)/1.357(2) Å for **4** ($R^1 = R^2$ = Me, $R^3 = CCl_3$) (1). This difference in the acetalic C—O bond lengths may be due to the lower electrophilicity of the pivaldehyde component in **4***c* relative to the trichloroacetaldehyde component of **4**. Consistent with the longer acetal C—O bonds in **4***c*, the O-C-O angle of 106.9(1)° is slightly compressed compared to the corresponding value of 109.1(2)° in the trichloroacetaldehyde derivative (1). The coordinative N→B bond in **4***c* (1.659(3) Å) is nearly 0.03 Å longer than that in **4** ($R^1 = R^2$ = Me, $R^3 = CCl_3$) (1.631(3) Å) (1) which indicates the weakened Lewis acid character of the diphenylborinate moiety in **4***c* compared to that for the trichloroacetaldehyde derivative. The overall geometry of the BOCON rings in **4***c* and **4** ($R^1 = R^2$ = Me, $R^3 = CCl_3$) is very similar.

The packing of **4***c* is dominated by van der Waals forces, all nonbonded intermolecular contacts between non-hydrogen atoms being greater than 3.6 Å. There is one relatively strong intramolecular C-H···O interaction that may influence the orientation of the cyclohexyl moiety: C(3)-H(3)···O(1), H···O = 2.23 Å, C···O = 2.680(3) Å, C-H···O = 107°.

Acknowledgments

We thank the Natural Sciences and Engineering Research Council of Canada and the Fonds der Chemischen Industrie, Frankfurt am Main, for financial support. We are grateful to the spectroscopy laboratory of the Chemische Institute der Technischen Universität, Braunschweig, for running the ^{11}B nmr and mass spectra.

References

1. W. Kliegel, U. Riebe, S.J. Rettig, and J. Trotter. Can. J. Chem. **73**, 835 (1995).
2. (*a*) R. Neu. Chem. Ber. **87**, 802 (1954); (*b*) G.N. Chremos. H. Weidmann, and H.K. Zimmerman. J. Org. Chem. **26**, 1683 (1961).
3. (*a*) R. Neu. Z. Anal. Chem. **176**, 334 (1960); (*b*) B. Friese and F. Umland. Anal. Chim. Acta, **96**, 303 (1978).
4. D. Nanninga. Dissertation. Braunschweig. 1980.
5. H.J. Roth and B. Miller. Arch. Pharm. Ber. Dtsch. Pharm. Ges. **297**, 744 (1964).
6. P.G. Jones. Chem. Br. **17**, 222 (1981).
7. (*a*) International tables for X-Ray crystallography. Kynoch Press, Birmingham, U.K. (present distributor Kluwer Academic Publishers: Boston, Mass.). 1974. Vol. 4. pp. 99–102; (*b*) International tables for crystallography. Kluwer Academic Publishers, Boston, Mass. 1992. Vol. C. p. 200–206.
8. (*a*) H. Nöth and B. Wrackmeyer. Nuclear magnetic resonance spectroscopy of boron compounds. Springer, Berlin. 1978; (*b*) R. Köster (*Editor*). Houben-Weyl: Organobor-Verbindungen III. Vol. 13/3c. Thieme, Stuttgart. 1984.
9. W. Kliegel, J. Metge, S.J. Rettig, and J. Trotter. Can. J. Chem. **75**, 1830 (1997).
10. W. Kliegel, J. Metge, S.J. Rettig, and J. Trotter. Can. J. Chem. **76**, 389 (1998).
11. W. Kliegel, D. Nanninga, U. Riebe, S.J. Rettig, and J. Trotter. Can. J. Chem. **72**, 1735 (1994).
12. W. Kliegel, D. Nanninga, S.J. Rettig, and J. Trotter. Can. J. Chem. **61**, 2329 (1983).
13. W. Kliegel, J. Metge, S.J. Rettig, and J. Trotter. Can. J. Chem. **76**, 1082 (1998).

© 1998 NRC Canada

SIMS studies of the effect of H at interfaces formed by oxidized zirconium

K. Shimizu, B.J. Flinn, P.C. Wong, and K.A.R. Mitchell

Abstract: Secondary ion mass spectrometry (SIMS) has been used to guide the search for an oxidation procedure that can produce a thin and relatively sharp oxide layer on macroscopic zirconium. A new preparation based on dip coating in H_2O_2 solution is indicated to be suitable for this purpose. SIMS further indicates that the oxide interface, for such a prepared sample, shows substantial degradation when it is heated in H_2 gas at 300°C. The presence of H appears to facilitate O migration into the metallic region, an observation that supplements those made previously on oxidized thin-film samples of zirconium prepared by deposition under ultrahigh-vacuum conditions.

Key words: secondary ion mass spectrometry, interfacial reactivity, oxidized zirconium.

Résumé : On a fait appel à la spectrométrie de masse des ions secondaires (SMIS) pour orienter la recherche d'une méthode d'oxydation pouvant conduire à une couche mince et relativement nette d'oxyde sur du zirconium macroscopique. Une nouvelle préparation fondée sur un revêtement par immersion dans une solution de H_2O_2 semble appropriée pour cet usage. La SMIS indique de plus que l'interface d'oxyde d'un échantillon préparé de cette manière subit une dégradation importante lorsqu'on le chauffe en présence de H_2 à l'état gazeux, à 300°C. La présence d'H semble faciliter la migration de l'O dans la région métallique; cette observation corrobore celles faites antérieurement avec des échantillons de films minces oxydés de zirconium préparés par dépôt dans des conditions de vide extrêmement élevé.

Mots clés : spectrométrie de masse d'ions secondaires, réactivité interfaciale, zirconium oxydé.

[Traduit par la Rédaction]

Introduction

The development of improved understanding of the interfacial stability of oxide on zirconium and its alloys, particularly in the presence of hydrogen, provides an interesting scientific challenge, but this is also one with high relevance to nuclear reactor technology (1). For example, knowledge is still extremely limited in relation to the mechanisms of H/D ingress through passivating oxide layers on CANDU reactor pressure tubes (Zr – 2.5 wt.% Nb), even though there is a considerable economic cost when metallic embrittlement results. A useful mechanistic description for real pressure-tube material has not yet been obtained but, in order to help establish basic principles for the chemical processes involved, we have been studying some model situations that highlight particular parts of the whole. Our previous work in this area emphasized studies of the stability and reactivity of thin metallic oxide layers (e.g., ~20 Å thick) deposited under well-controlled ultrahigh-vacuum (UHV) conditions onto gold, a relatively inert substrate (2, 3). This approach has permitted direct examination of the underlying interface with X-ray photoelectron spectroscopy (XPS), and has yielded insight into the nature and stability of the oxide–metal interfaces in the presence of hydrogen in an environment made slightly oxidizing by the trace presence of H_2O. For the case of deposited zirconium, the interface region may be expressed as $ZrO_2/ZrO_x/Zr/Au$, where ZrO_x indicates an O-deficient region between the stable bulk oxide ZrO_2 and Zr metal (4). The UHV studies show that the behaviour of ZrO_2/ZrO_x can be sensitively affected by the presence of hydrogen; indeed, observations were made of the interfacial compositions being systematically changed with temperature and exposure to H_2 and hydrogen plasmas (5).

Further study of the effect of H ingress on the Zr oxide – metal interface in real CANDU pressure-tube material, formed under working conditions, is generally hindered by the interface being sufficiently far below the surface that it is no longer accessible by such conventional non-destructive techniques as XPS or Auger electron spectroscopy. In principle, that interface is accessible by deeper probing techniques, such as depth profiling in secondary ion mass spectrometry (SIMS) (6) or with the use of high-energy beams, as for example in nuclear reaction analysis or Rutherford backscattering (7). Studies that have focussed on the depth profiling of H have generally not given much consideration to how the Zr oxide – metal interfacial region is affected by the H ingress, but the UHV studies indicate that the interfacial stoichiometry may change with the presence of hydrogen, apparently as a result of this atom facilitating O migration into the metallic region (4, 5). These effects may have relevance to stability of such materials in technological application, and therefore

Received August 25, 1998.

K. Shimizu, B.J. Flinn, P.C. Wong, and K.A.R. Mitchell.[1]
Department of Chemistry, University of British Columbia, 2036 Main Mall, Vancouver, BC V6T 1Z1, Canada.

[1]Author to whom correspondence may be addressed. Telephone: (604) 822-3266. Fax: (604) 822-2847. E-mail: karm@chem.ubc.ca

© 1998 NRC Canada

Table 1. Sample treatments used in this work.

Designation	Preparation treatment
A1	Zr sample etched, washed, and dried (see text)
A2	A1 dip-coated in 30% H_2O_2 solution for 0.5 h
A3	A1 heated in air (200°C) for 0.5 h
A4	A1 exposed to cold O_2 plasma for 0.5 h
A5	A1 exposed to air plasma for 0.5 h
B1	A1
B2	A1 heated in N_2 (300°C) for 2 h
B3	A1 heated in H_2 (300°C) for 2 h
C1	A1 dip-coated in 30% H_2O_2 solution for 12.5 h with stirring
C2	C1 heated in N_2 (300°C) for 2 h
C3	C1 heated in H_2 (300°C) for 2 h

it appears important to be able to study them under reasonably realistic (i.e., non-UHV) conditions.

Study of chemical effects at the oxide-to-metal boundary depends fundamentally on an ability to have an accurate positioning of the interface. A complication for real industrial materials is that these interfaces are not likely to be (atomically) smooth, but the point of the work reported here was to characterize oxide-to-zirconium interfaces, prepared by different methods, with the view of searching for a procedure that allows the formation of a relatively smooth (perhaps better expressed as "less rough") interfacial region. The presence of such an interface should greatly facilitate observations of its changes as a result of H ingress, as well as help separate the changes that occur from physical variables (e.g., temperature) that also influence the H ingress.

The present work uses SIMS to probe various preparations of thin oxide layers on zirconium foil, and their subsequent changes on exposure to reactive gases including hydrogen. This study is part of a broader program whose objective is to test whether the types of H effects seen in very thin film UHV-deposited samples of zirconium (4, 5) can also be observed for oxide on bulk samples.

Experimental

SIMS characterizations were performed with a VG MM12-12S quadrupole spectrometer using a duoplasmatron source (gas 90% Ar, 10% O_2) operated at 10 kV with a current density of 12.5 μA cm^{-2} (the O_2 is filtered out before reaching the sample). The zirconium samples were cut into a suitable form (area 0.5 cm^2, thickness 0.5 mm) from polycrystalline Zr foil (99.99% pure, AESAR Chemicals), and were etched for 45 s in a solution of concentrated HF, concentrated HNO_3, and H_2O (vol. ratio 5:45:50); this was followed by a water rinse (~3 s) and drying at room temperature in a covered petri dish. This approach both limits the presence of native oxide on the surface and ensures an essentially common starting point for all samples. Subsequent treatments are listed in Table 1. Figure 1 illustrates the isolated reactor (Physical Electronics model 04-800) attached to a sample transfer vessel, which was used for the preparation of samples B2, B3, C2, and C3. This device enabled samples to be heated in a gas flow at slightly over 1 atm (101.3 kPa), followed by pump-down to around 10^{-7} Torr (1 Torr = 133.3 Pa) and transfer to the SIMS facility without atmospheric exposure. Other samples (A4 and A5) were treated by oxygen and air (cold) plasmas in a side chamber on our XPS facility as described previously (in both cases the flowing gas pressure was held at about 0.2 Torr) (4). After preparation and pump-down, these samples were also taken in the transfer vessel to the SIMS without exposure to the regular atmosphere.

Fig. 1. Schematic view of reactor/transfer device in which samples can be heated (to 600°C) in presence of gas (to ~1 atm) followed by pump-down (to ~10^{-7} Torr) and transfer to the SIMS facility without atmospheric exposure.

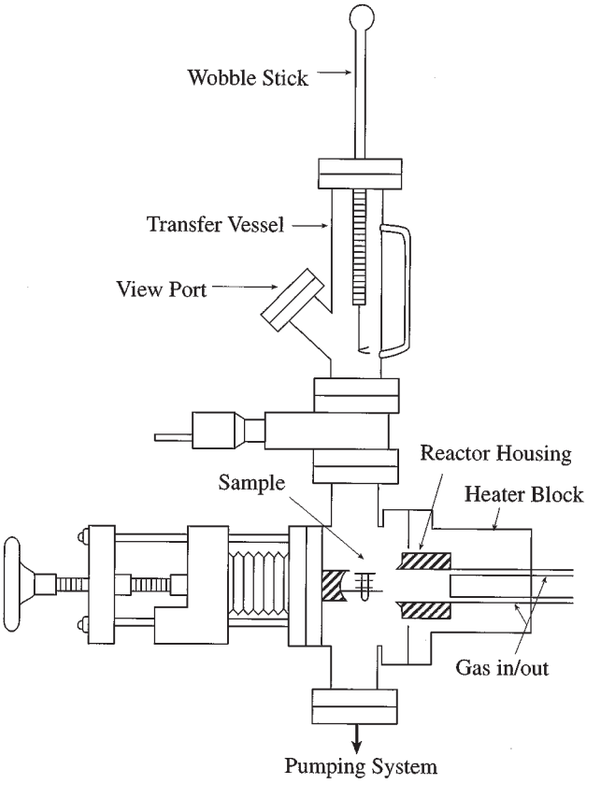

Results and discussion

The first comparison is made for the different preparation procedures investigated for forming the initial oxide layer (Table 1). Following Hultquist et al. (8), the oxide is characterized with SIMS by following the ZrO^+ count rate as a function of sputtering time (the initial rise reflects the effect of the inevitable contamination layer on the top of the sample). The ZrO^+ count rate directly gives insight into the distribution of O bonded to Zr below the surface. Figure 2 shows significant differences between the different preparation procedures. The etched-only sample (A1) has the thinnest oxide layer; all samples can be interpreted as having a common outermost layer that corresponds to the ZrO_2 composition. In each case this oxide is separated from the pure metal (where the ZrO^+ counts are negligible) by a transition region, which is taken to correspond to the non-stoichiometric ZrO_x-type regions identified in X-ray photoelectron spectra from samples of oxidized zirconium. It

© 1998 NRC Canada

Fig. 2. ZrO^+ depth profiles measured from oxide-covered zirconium samples prepared by five different procedures defined in Table 1: A1 (acid-etched), A2 (dip-coated in H_2O_2), A3 (heated to 200°C in air), A4 (exposed to cold O_2 plasma), and A5 (exposed to cold air plasma).

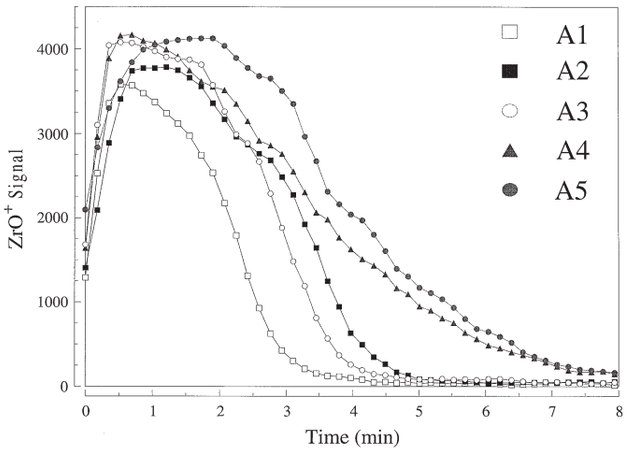

Fig. 3. ZrO^+ depth profiles measured (*a*) from three samples that do not receive an H_2O_2 treatment: B1 (acid-etched), B2 (heated in N_2), B3 (heated in H_2); and (*b*) from three samples whose preparation starts with the H_2O_2 treatment: C1, C2 (heated in N_2), C3 (heated in H_2).

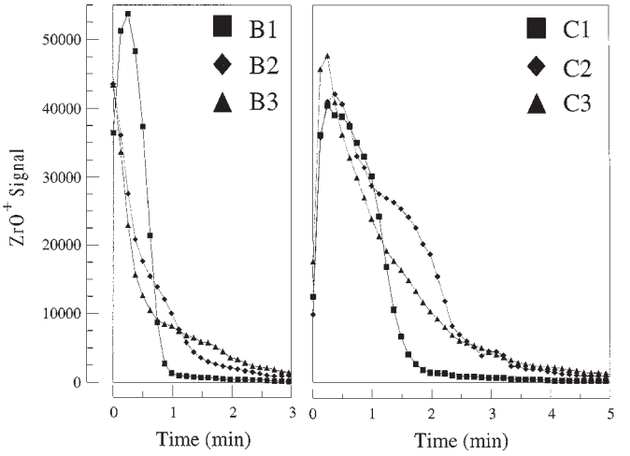

is clear that the air and O_2 plasma treatments give broader transition regions than those formed by heating in air at 200°C or by treating with 30% H_2O_2 at room temperature. The latter is indicated to give significant ZrO_2 with a relatively sharp interface region to the metal. Such features can make this approach to oxide formation particularly helpful for assessing degradation by hydrogen, and it is therefore used for some further samples tested here. Incidentally all curves in Fig. 2, except for A1, show irregularities as the depth profiling proceeds; it is believed that these are real effects that depend on the ZrO^+ ion yield increasing as the probing beam intersects grain boundaries at which oxide may be preferentially formed.

Figure 3 compares ZrO^+ depth profiles for two sets of samples that have received parallel treatments (B1 to B3 and C1 to C3 in Table 1). Samples in the B series all start with acid etching of the zirconium foil, whereas those for the C series are subsequently treated in H_2O_2. The depth profiles for both B1 (etched) and C1 (etched, followed by H_2O_2 treatment) show steep downward slopes, indicative of a similar interface region, although C1 has the thicker oxide film. When these samples are heated in H_2, to form samples B3 and C3, both interfacial regions are seriously degraded, and less negative slopes are apparent in Fig. 3; these effects result from the oxide barrier migrating toward the bulk (4, 5). However, there are two contributing factors here: (*i*) the direct effect of hydrogen, and (*ii*) the effect of the heating. To help separate these two factors, samples B2 and C2 were treated exactly similarly to B3 and C3, respectively, except that the heating was done in N_2 instead of H_2. It is clear that the O migration still occurs with the heating in N_2, consistent with sufficient thermal energy being available to surmount the activation barrier to diffusion, but in each case the migration is less than that indicated for the equivalent heating in H_2. All trends shown in Fig. 3 have been checked by working with independent samples; quite generally the effect of heating in H_2 leads to the surface oxide being more degraded, with O migrating further into the Zr sample than is the case with heating in N_2.

Concluding remarks

The observations with SIMS reported in this paper reinforce those made earlier with XPS, from atomically thin films of oxidized Zr, which showed that exposure to hydrogen can modify the oxide–metal interface, apparently by facilitating O migration into the metallic region (4, 5). This broadening to bulk samples should enable the more fundamental research to be extended to materials related to those used in engineering practice. It is well known that, at the operating temperature of the CANDU reactor (300°C), O moves readily into zirconium metal (9). Therefore, in this context, thick oxide films formed by autoclaving offer only limited possibilities for probing their interfacial chemistries using the established techniques of electron spectroscopy. However, this work has introduced a new approach to forming model oxide layers at room temperature, specifically by dipping Zr samples in H_2O_2 solution. It is anticipated that these films, by being reasonably sharp and thin, will have useful applications for designing new experiments that can help to improve our knowledge of chemical reactivity, mechanism, and passivation at their interfaces. Extensions to actual pressure-tube alloys are also planned.

Acknowledgements

We are grateful for the support provided for this research by the CANDU Owners Group (through the Atomic Energy of Canada Ltd.) and by the Natural Sciences and Engineering Research Council of Canada. We thank the referees for some helpful comments.

References

1. R.L. Tapping. J. Nucl. Mater. **107**, 151 (1982); R.L. Tapping and T.S. Gendron. A survey of in-reactor data relevant to the

© 1998 NRC Canada

corrosion and hydriding of zirconium alloys in annulus gas environments. Report RPC-101/COG-88-136 for Atomic Energy of Canada Ltd., December 1988; C.S. Zhang, B.J. Flinn, and P.R. Norton. Surf. Sci. **264**, 1 (1992).
2. J.R. Lou, U. Hess, and K.A.R. Mitchell. Appl. Surf. Sci. **62**, 175 (1992); Y.M. Wang, Y.S. Li, P.C. Wong, and K.A.R. Mitchell. Appl. Surf. Sci. **72**, 237 (1993).
3. Y.S. Li, K.C. Wong, P.C. Wong, and K.A.R. Mitchell. Appl. Surf. Sci. **103**, 389 (1996); K.C. Wong, P.C. Wong, Y.S. Li, and K.A.R. Mitchell. Surf. Rev. Lett. **4**, 33 (1997).
4. P.C. Wong, Y.S. Li, M.Y. Zhou, and K.A.R. Mitchell. Appl. Surf. Sci. **89**, 255 (1995).
5. Y.S. Li, P.C. Wong, and K.A.R. Mitchell. Appl. Surf. Sci. **89**, 263 (1995).
6. N.S. McIntyre, R.D. Davidson, C.G. Weisener, B.D. Warr, and M.B. Elmoselhi. Surf. Interface Anal. **17**, 757 (1991).
7. T. Laursen, J.R. Leslie, and R.L. Tapping. J. Nucl. Mater. **182**, 158 (1991).
8. G. Hultquist, G.K. Chuah, and K.L. Tan. Corros. Sci. **31**, 149 (1990).
9. P.C. Wong and K.A.R. Mitchell. Can. J. Phys. **65**, 464 (1987); C.S. Zhang, B.J. Flinn, I.V. Mitchell, and P.R. Norton. Surf. Sci. **245**, 373 (1991).

© 1998 NRC Canada

Coordination complexes derived from 3,6-di(2-pyridyl)-1,4-dihydro-1,2,4,5-tetrazine (DPDHT). Synthesis and molecular structure of [(DPT)($GaMe_2$)$_2$]

Peter N. Preston, Steven J. Rettig, Alan Storr, and James Trotter

Abstract: The facile reaction of 3,6-di(2-pyridyl)-1,4-dihydro-1,2,4,5-tetrazine (DPDHT) (**1**) with trimethylgallium has resulted in the formation of the purple crystalline product, [(DPT)($GaMe_2$)$_2$] (**2**), via methane elimination. Crystals of [(DPT)($GaMe_2$)$_2$] are orthorhombic, *Pbca*, a = 15.380(2), b = 21.642(4), c = 11.355(2) Å, Z = 8. The structure was solved by heavy-atom Patterson methods and refined by full-matrix least-squares procedures to R = 0.035 for 1570 reflections with $I \geq 3\sigma(I)$ (R_w = 0.063 for all 4342 reflections). The [(DPT)($GaMe_2$)$_2$] molecule is roughly planar (apart from the four methyl groups), in contrast to the folded structure of the DPDHT molecule; molecular dimensions are normal.

Key words: methylgallium, crystal structure, dipyridyldihydrotetrazine.

Résumé : La réaction facile de la 3,6-di(2-pyridyl)-1,4-dihydro-1,2,4,5-tétrazine (DPDHT) (**1**) avec le triméthylgallium conduit à la formation du produit cristalline violet, [(DTP)($GaMe_2$)$_2$] (**2**) avec élimination de méthane. Les cristaux de [(DTP)($GaMe_2$)$_2$] sont orthorhombiques, groupe d'espace *Pbca*, avec a = 15,380(2), b = 21,642(4) et c = 11,355(2) Å, Z = 8. On a résolu la structure par la méthode des atomes lourds de Patterson et on l'a affinée par la méthode des moindres carrés jusqu'à une valeur de R = 0,035 pour 1570 réflexions avec $I \geq 3\sigma(I)$ (R_w = 0,063 pour l'ensemble des 4342 réflexions). La molécule de [(DTP)($GaMe_2$)$_2$] est pratiquement plane (à l'exception des quatre groupes méthyles) et cette situation est en opposition à celle observée dans la molécule de DPDHT qui comporte une structure repliée; les dimensions moléculaires sont normales.

Mots clés : méthylgallium, structure cristalline, dipyridyldihydrotétrazine.

[Traduit par la Rédaction]

Introduction

We have described a number of polymeric transition metal complexes with pyrazolate (1–4) and, most recently, with imidazolate (5) ligands. The relative positions of pyrrole-type and pyridine-type nitrogen atoms in the ligand are crucial in determining the dimensionality of the ensuing polymer. Thus a three-dimensional polymetallic iron-containing imidazolate complex has proven particularly interesting, exhibiting canted spin antiferromagnetic coupling along chains of tetrahedrally coordinated iron centers with concomitant molecular magnet properties at low temperatures. We are presently extending our studies using more complex heterocycles and have included for study 3,6-di(2-pyridyl)-1,4-dihydro-1,2,4,5-tetrazine, DPDHT (**1**), deprotonation of which yields a symmetrical tetradentate ligand, DPT^{2-}, hitherto unused in coordination chemistry. In this report we illustrate the use of DPDHT in its reaction with trimethylgallium.

Received August 18, 1998.

P.N. Preston.[1] Department of Chemistry, Heriot–Watt University, Riccarton, Edinburgh EH14 4AS, U.K.
S.J. Rettig, A. Storr,[1] **and J. Trotter.** Department of Chemistry, University of British Columbia, 2036 Main Mall, Vancouver, BC V6T 1Z1, Canada.

[1]Authors to whom correspondence may be addressed: PNP: Telephone: 44-131-449-511. Fax: 44-131-451-3180. E-mail: p.n.preston@hw.ac.uk; AS: Telephone: (604) 822-3962. Fax: (604) 822-2847. E-mail: storr@chem.ubc.ca

Experimental

Materials were handled in a conventional high-vacuum line or in a glove box under an atmosphere of oxygen-free dry dinitrogen. All solvents were dried and distilled before use. Gas volumes are at STP. Trimethylgallium was prepared, as previously described, from gallium and dimethylmercury (6). The DPDHT ligand–precursor was synthesized by a literature method (7).

Preparation of DPT·2$GaMe_2$

The orange ligand–precursor DPDHT, (**1**), (0.307 g; 1.3 mmol) was transferred to a 250 mL round-bottomed flask fitted with a break-seal side-arm. Xylene solvent (~60 mL) was added to give a pale orange solution. The reaction flask was then cooled to –196° and evacuated. Me_3Ga (0.296 g; 2.6 mmol) was vacuum-transferred into the reaction vessel which was then flame-sealed. On warming to

© 1998 NRC Canada

Table 1. ^{1}H NMR assignments[a] for DPDHT ligand (**1**) and complex [(DPT)($GaMe_2$)$_2$] (**2**).

	Chemical shifts[b]				Coupling constants[c]					
	$H^{3'}$	$H^{4'}$	$H^{5'}$	$H^{6'}$	$J_{3',4'}$	$J_{3',5'}$	$J_{3',6'}$	$J_{4',5'}$	$J_{4',6'}$	$J_{5',6'}$
Ligand **1**[d]	8.04	7.78	7.38	8.58	8.0	1.1	1.1	7.6	1.7	4.9
Complex **2**[e]	7.88	6.66	6.20	7.20	8	1.0	1.1	7.7	1.4	1.5
Chemical shift diff.	0.16	1.12	1.18	1.38						

[a]Assignments for the complex (**2**) are made on the basis of decoupling experiments and the magnitude of coupling constants relative to those in the ligand (**1**).

[b]Quoted in ppm with respect to tetramethylsilane.

[c]Quoted Hz.

[d]Measured at 400 MHz in CD_2Cl_2 solvent at 25°C; the NH resonance appeared at δ 8.53.

[e]Measured at 400 MHz in C_6D_6 solvent at 25°C.

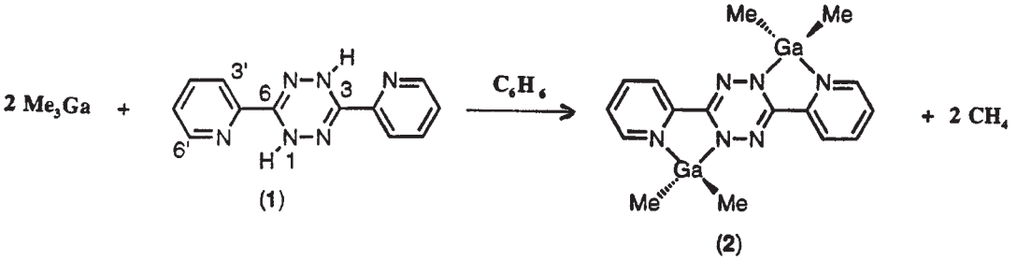

room temperature the orange solution gradually darkened through amber, golden-brown, dark brown, to deep purple. On standing overnight at room temperature the solution deposited dark purple crystals of the product [DPT·2$GaMe_2$] (**2**) in quantitative yield. The reaction flask was again cooled to –196° and the volume of methane evolved during the reaction measured using a Toepler pump (calcd. 57.8 mL; found 57.6 mL). The purple crystals were isolated in the glove box. The purple crystals were stable under a dinitrogen atmosphere but quickly turned yellow–orange on exposure to air. The infrared spectrum showed characteristic (8) Ga-C stretching frequencies ν_{asym} 590 cm^{-1} and ν_{sym} 535 cm^{-1} and was devoid of the N-H stretching frequencies observed at 3299 and 3344 cm^{-1} in the spectrum of the ligand–precursor DPDHT. The ^{1}H NMR spectrum of the complex in C_6D_6 solution showed one signal for the $GaMe_2$ groups at δ 0.20. The signals due to the protons of the pyridyl fragments of the ligand precursor, DPDHT, and the product, [DPT·2$GaMe_2$], are summarized in Table 1 and discussed below. The mass spectrum (EI) of the purple crystals displayed the expected three-line pattern for the molecular ion (M^+) and a stronger signal cluster for the M-2Me^+ ion. Anal. calcd. for [DPT·2$GaMe_2$]: C 44.1, H 4.6, N 19.3; found: C 44.4, H 4.7, N 19.2%.

X-ray crystallographic analysis

Crystallographic data appear in Table 2. The final unit-cell parameters were obtained by least-squares on the setting angles for 25 reflections with 2θ = 20.3–25.2°. The intensities of three standard reflections, measured every 200 reflections throughout the data collection, decayed by 7.4%. The data were processed, corrected for Lorentz and polarization effects, and absorption (based on azimuthal scans).

The structure was solved by heavy-atom, Patterson methods. All non-hydrogen atoms were refined with anisotropic thermal parameters. Hydrogen atoms were fixed in calculated positions with C—H = 0.98 Å and $B_H = 1.2B_{bonded\ atom}$. No secondary extinction correction was required. Neutral atom scattering factors for all atoms and anomalous dispersion corrections for the non-hydrogen atoms were taken from the *International Tables for X-Ray Crystallography* (9). Final atomic coordinates and equivalent isotropic thermal parameters, bond lengths and angles appear in Tables 3–5, respectively. Hydrogen atom parameters, anisotropic thermal parameters, torsion angles, intermolecular contacts, and least-squares planes are included as supplementary material.[2]

Results and discussion

The reaction of group 13 trialkyls with ligands containing acidic hydrogen yields adducts which readily eliminate alkanes to produce coordinatively unsaturated intermediates (10). Coordinative saturation is usually achieved by cyclization, the degree of association being determined by a balance between steric effects, valency angle strain and entropy factors (8, 10, 11). The methane elimination reactions of trimethylgallium with pyrazoles to yield dimeric products containing central six-membered Ga_2N_4 rings are well documented (12–14). The reaction of Me_3Ga with 2-methylimidazole, on the other hand, results in the formation of tetrameric species, a consequence of the steric demands of the azolate moiety (15).

[2]Supplementary material may be purchased from: The Depository of Unpublished Data, Document Delivery, CISTI, National Research Council Canada, Ottawa, Canada, K1A 0S2. Tables of bond lengths and angles have also been deposited with the Cambridge Crystallographic Data Centre and can be obtained on request from: The Director, Cambridge Crystallographic Data Centre, University Chemical Laboratory, 12 Union Road, Cambridge, CB2 1EZ, U.K.

© 1998 NRC Canada

Table 2. Crystallographic data.[a]

Formula	$C_{16}H_{20}Ga_2N_6$
Formula weight	435.81
Crystal color, habit	Dark, prism
Crystal dimensions, mm	0.28 × 0.40 × 0.48
Crystal system	Orthorhombic
Space group	*Pbca*
a, Å	15.380(4)
b, Å	21.642(4)
c, Å	11.355(2)
V, Å^3	3780(1)
Z	8
ρ_{calc}, g/cm^3	1.532
F(000)	1760
μ(MoK_α), cm^{-1}	28.6
Transmission factors	0.92–1.00
Scan type	ω-2θ
Scan range, deg in ω	1.10 + 0.35 tan θ
Scan speed, deg/min	16 (up to 9 scans)
Data collected	$+h$, $+k$, $+l$
$2\theta_{max}$, deg	55
Crystal decay	7.4%
Total reflections	4852
Total unique reflections	4342
R_{merge}	0.04
Reflections $I > 3\sigma(I)$	1570
No. of variables	217
R (*F*, 1570 refelctions)	0.035
R_w (F^2, 4342 reflections)	0.063
gof	1.16
Max Δ/σ (final cycle)	0.0003
Residual density, e/Å^3	–2.47 to +1.27 (near Ga)

[a]Temperature 294 K, Rigaku AFC6S diffractometer, MoK_α radiation (λ = 0.71069 Å), graphite monochromator, takeoff angle 6.0°, aperture 6.0 × 6.0 mm at a distance of 285 mm from the crystal, stationary background counts at each end of the scan (scan/background time ratio 2:1), $\sigma^2(F^2) = [S^2(C + 4B)]/Lp^2$ (S = scan rate, C = scan count, B = normalized background count), function minimized $\Sigma w(|F_g| - |F_c|)^2$ where $w = 4F_o^2/\sigma^2(F_o^2)$, $R = \Sigma||F_o| - |F_c||/\Sigma|F_o|$, $R_w = (\Sigma w(|F_o| - |F_c|)^2/\Sigma w(|F_o|^2)^{1/2}$, and gof = $[\Sigma w(|F_o| - |F_c|)^2/(m - n)]^{1/2}$.

Table 3. Atomic coordinates and B_{eq} (10^3 Å^2).[a]

Atom	*x*	*y*	*z*	B_{eq}
Ga(1)	0.05675(3)	0.19977(2)	0.16226(4)	4.418(11)
Ga(2)	0.26458(3)	0.06009(2)	0.58552(4)	5.098(13)
N(1)	0.1134(2)	0.1547(2)	0.2862(3)	5.50(11)
N(2)	0.0684(2)	0.12807(14)	0.3830(3)	3.88(9)
N(3)	0.2065(2)	0.0935(2)	0.4496(3)	6.69(12)
N(4)	0.2500(2)	0.11847(13)	0.3518(3)	3.64(8)
N(5)	0.1386(2)	0.04063(14)	0.6289(3)	4.40(9)
N(6)	0.1836(2)	0.20379(14)	0.1029(3)	3.69(8)
C(1)	0.1189(3)	0.0997(2)	0.4553(3)	3.60(11)
C(2)	0.2005(3)	0.1464(2)	0.2781(3)	3.25(11)
C(3)	0.0802(3)	0.0681(2)	0.5575(4)	3.68(11)
C(4)	–0.0079(3)	0.0633(2)	0.5786(4)	4.76(12)
C(5)	–0.0362(3)	0.0290(2)	0.6735(5)	5.74(14)
C(6)	0.0234(4)	0.0007(2)	0.7442(5)	6.5(2)
C(7)	0.1106(3)	0.0073(2)	0.7231(4)	5.81(15)
C(8)	0.2398(3)	0.1748(2)	0.1741(3)	3.21(10)
C(9)	0.3268(3)	0.1723(2)	0.1483(4)	4.24(12)
C(10)	0.3577(3)	0.2013(2)	0.0489(4)	4.91(13)
C(11)	0.3001(3)	0.2311(2)	–0.0241(4)	5.44(14)
C(12)	0.2140(3)	0.2317(2)	0.0049(4)	4.79(13)
C(13)	0.0251(3)	0.2827(2)	0.2118(4)	6.99(15)
C(14)	–0.0109(3)	0.1500(2)	0.0520(4)	5.98(14)
C(15)	0.3242(3)	-0.0174(2)	0.5547(4)	6.77(15)
C(16)	0.2972(3)	0.1246(2)	0.6970(4)	8.1(2)

[a]$B_{eq} = (8/3)\pi^2\Sigma\Sigma(U_{ij}a_ia_j(\mathbf{a}_i\mathbf{a}_j))$.

Table 4. Bond lengths (Å), with estimated standard deviations in parentheses.

Bond	Length	Bond	Length
Ga(1)—N(1)	1.921(3)	Ga(1)—N(6)	2.066(3)
Ga(1)—C(13)	1.943(4)	Ga(1)—C(14)	1.952(4)
Ga(2)—N(3)	1.924(3)	Ga(2)—N(5)	2.042(3)
Ga(2)—C(15)	1.944(5)	Ga(2)—C(16)	1.951(5)
N(1)—N(2)	1.421(4)	N(1)—C(2)	1.355(4)
N(2)—C(1)	1.286(4)	N(3)—N(4)	1.405(4)
N(3)—C(1)	1.355(4)	N(4)—C(2)	1.282(4)
N(5)—C(3)	1.348(4)	N(5)—C(7)	1.360(5)
N(6)—C(8)	1.339(4)	N(6)—C(12)	1.349(4)
C(1)—C(3)	1.473(5)	C(2)—C(8)	1.463(5)
C(3)—C(4)	1.380(5)	C(4)—C(5)	1.378(5)
C(5)—C(6)	1.363(6)	C(6)—C(7)	1.371(6)
C(8)—C(9)	1.370(5)	C(9)—C(10)	1.376(5)
C(10)—C(11)	1.374(5)	C(11)—C(12)	1.365(5)

In the present study the reaction of Me_3Ga with DPDHT has been investigated to gain insights into the potential of this heterocyclic system to act as a ligand precursor in the preparation of polymeric transition metal compounds. The chemistry of DPDHT has received little attention (16). A useful aspect of its reactivity with regard to coordination chemistry, however, is sequential oxidation and alkyne dipolar cyclcoaddition which leads to substituted bis(pyridyl) pyridazines, of value as ligating heteroarenes (17). In the present study the initial adduct formation between trimethylgallium and DPDHT, probably via the lone pair on the pyridyl nitrogen atoms, places the trialkyl moieties in proximity of the N-H groups of the dihydrotetrazine ring. Facile methane elimination, at or even below room temperature, leads to the formation of the five-membered heterocyclic, GaN_2C_2, rings observed in the purple crystalline product.

The ^{1}H NMR spectrum of the ligand has been previously reported but without definitive assignments (18). In this work, long range N-H correlation experiments provided assignments of 300 (pyrimide-N), 275 (N-1), and 259 ppm (N-2), with definitive assignment of H-6′ at 8.58 ppm. (See Table 1.)

The magnitudes of coupling constants are in accord with those anticipated for substituted pyridines, a notable feature of which is the relatively low value of $J_{5'6'}$ (= 4.9 Hz) involving coupling to the proton on the carbon adjacent to the pyridine nitrogen (19). Assignments of chemical shifts in the ^{1}H NMR spectrum of the complex (**2**) were made on the basis of decoupling experiments and on the relative magnitudes of coupling constants in respect to (**1**). Complexation of the ligand causes shifts to high field for all the ring protons, but particularly (>1 ppm) for H-4′, H-5′, and H-6′. The

© 1998 NRC Canada

Table 5. Bond angles (deg), with estimated standard deviations in parentheses.

Bond	Angle	Bond	Angle
N(1)-Ga(1)-N(6)	80.33(13)	N(1)-Ga(1)-C(13)	111.7(2)
N(1)-Ga(1)-C(14)	115.6(2)	N(6)-Ga(1)-C(13)	107.0(2)
N(6)-Ga(1)-C(14)	108.51(15)	C(13)-Ga(1)-C(14)	124.2(2)
N(3)-Ga(2)-N(5)	80.24(13)	N(3)-Ga(2)-C(15)	113.5(2)
N(3)-Ga(2)-C(16)	111.7(2)	N(5)-Ga(2)-C(15)	108.2(2)
N(5)-Ga(2)-C(16)	103.6(2)	C(15)-Ga(2)-C(16)	127.8(2)
Ga(1)-N(1)-N(2)	123.5(3)	Ga(1)-N(1)-C(2)	117.8(3)
N(2)-N(1)-C(2)	118.7(3)	N(1)-N(2)-C(1)	113.1(3)
Ga(2)-N(3)-N(4)	123.9(3)	Ga(2)-N(3)-C(1)	117.4(3)
N(4)-N(3)-C(1)	118.2(3)	N(3)-N(4)-C(2)	114.5(3)
Ga(2)-N(5)-C(3)	113.3(3)	Ga(2)-N(5)-C(7)	126.8(3)
C(3)-N(5)-C(7)	119.7(4)	Ga(1)-N(6)-C(8)	113.1(3)
Ga(1)-N(6)-C(12)	127.9(3)	C(8)-N(6)-C(12)	118.9(3)
N(2)-C(1)-N(3)	128.2(4)	N(2)-C(1)-C(3)	118.7(4)
N(3)-C(1)-C(3)	113.1(4)	N(1)-C(2)-N(4)	127.2(4)
N(1)-C(2)-C(8)	114.1(3)	N(4)-C(2)-C(8)	118.7(4)
N(5)-C(3)-C(1)	114.2(4)	N(5)-C(3)-C(4)	121.1(4)
C(1)-C(3)-C(4)	124.7(4)	C(3)-C(4)-C(5)	119.1(4)
C(4)-C(5)-C(6)	119.3(4)	C(5)-C(6)-C(7)	120.5(5)
N(5)-C(7)-C(6)	120.2(5)	N(6)-C(8)-C(2)	114.7(4)
N(6)-C(8)-C(9)	121.4(4)	C(2)-C(8)-C(9)	124.0(4)
C(8)-C(9)-C(10)	119.5(4)	C(9)-C(10)-C(11)	119.2(4)
C(10)-C(11)-C(12)	118.9(4)	N(6)-C(12)-C(11)	122.1(4)

Fig. 1. View of the [(DPT)($GaMe_2$)$_2$] molecule; 33% probability thermal ellipsoids are shown for the non-hydrogen atoms.

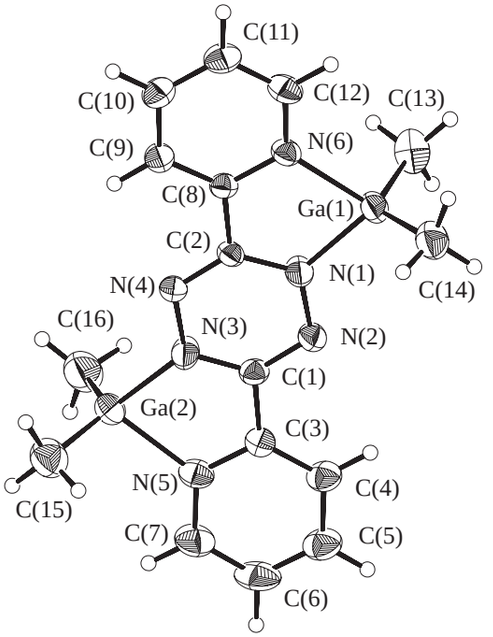

disparity in electronic influence of the gallium moieties on chemical shifts of H-3′ vs. H-4′, 5′ and 6′ is curious, and warrants further theoretical studies of complex (**2**) and related compounds.

The X-ray analysis unambiguously establishes the molecular structure of [(DPT)($GaMe_2$)$_2$] (Fig. 1). The DPT^{2-} ligand exhibits statistically significant deviations from exact planarity, but is roughly planar (maximum displacement from mean plane = 0.192(5) Å for C(6); maximum angle between planes of the various rings = 7.0°). This is in contrast to the parent DPDHT molecule, which is folded with a boat-shaped tetrazine ring, in both the triclinic (20) and orthorhombic (21) forms. The torsion angles in the tetrazine ring of the DPDHT molecule are as high as 44°, while the corresponding angles in the DPT^{2-} ligand have a maximum of 3.0(6)°. The Ga atoms both lie 0.24 Å above the mean plane of the ligand.

Bond lengths and angles (Tables 4 and 5) are close to expected values. In particular, the C(1)—N(2) and C(2)—N(4) bond distances of the tetrazine ring (1.286(4) and 1.282(4) Å) correspond to double bonds. The Ga—N(pyridine) bonds (2.066(3) and 2.042(3) Å) are significantly longer than the Ga—N(tetrazine) bonds (1.921(3) and 1.924(3) Å); this situation has analogy in the molecular structure of Ga{2-[$NCH_2C_6H_5$]NC_5H_4}$_2$Me (cf. 2.216(3), 2.236(3) Å for Ga—N(pyridine) bonds, and 1.933(3) Å for Ga—N(amine) bonds), although it should be noted that the gallium in the latter compound is pentacoordinate (22).

The crystal packing is dominated by van der Waals forces, the shortest intermolecular contact between non-hydrogen atoms being a C···C distance of 3.28(1) Å.

Conclusions

3,6-Di(2-pyridyl)-1,4-dihydro-1,2,4,5-tetrazine (**1**) reacts readily with trimethylgallium to provide the novel pentacyclic heteroaromatic complex (**2**) in quantitative yield. Studies by X-ray crystallography and NMR spectroscopy suggest considerable bond localization in the tetrazine ring,

© 1998 NRC Canada

and marked electronic influence of the gallium moieties on chemical shift values of the pyridine protons.

A key feature to note from the work is that the known DPDHT is easily synthesized (7) in multigram quantities from commercially available materials; applications of the ligand for use in the synthesis of coordination polymers can be envisaged.

Acknowledgements

We thank Dr. A.S.F. Boyd for assistance with the NMR spectroscopy, Mr. P. Borda for elemental analysis, and the Natural Sciences and Engineering Research Council of Canada for financial support.

References

1. S. J. Rettig, A. Storr, D.A. Summers, R.C. Thompson, and J. Trotter. Can. J. Chem. **75**, 949 (1997).
2. M.K. Ehlert, S.J. Rettig, A. Storr, R.C. Thompson, and J. Trotter. (*a*) Can. J. Chem. **67**, 1970 (1989); (*b*) Can. J. Chem. **69**, 432 (1991); (*c*) Can. J. Chem. **70**, 2161 (1992); (*d*) Can. J. Chem. **71**, 1425 (1993).
3. M.K. Ehlert, A. Storr, and R.C. Thompson. (*a*) Can. J. Chem. **70**, 1121 (1992); (*b*) Can. J. Chem. **71**, 1412 (1993).
4. M.K. Ehlert, A. Storr, D.A. Summers, and R.C. Thompson. Can. J. Chem. **75**, 491 (1997).
5. S.J. Rettig, A. Storr, D.A. Summers, R.C. Thompson, and J. Trotter. J. Am. Chem. Soc. **119**, 8675 (1997).
6. A. Storr and B.S. Thomas. Can. J. Chem. **48**, 3667 (1970).
7. J.F. Geldhard and F. Lyons. J. Org. Chem. **30**, 318 (1965).
8. A. Storr and B.S. Thomas. J. Chem. Soc. A, 3850 (1971).
9. (*a*) International tables for X-ray crystallography. Kynoch Press, Birmingham, U.K. (present distributor Kluwer Academic Publishers, Boston, Mass.). 1974. Vol. 4. pp. 99–102; (*b*) International tables for crystallography. Kluwer Academic Publishers, Boston, Mass. 1992. Vol. C. pp. 200–206.
10. G.E. Coates and K. Wade. Organometallic compounds: vol. 1, the main group elements. 3rd ed. Methuen, London. 1967. Chap. 3.
11. M.F. Lappert, M.K. Majumdar, and B.P. Tilley. J. Chem. Soc. A, 1590 (1966).
12. A. Arduini and A. Storr. J. Chem. Soc. Dalton Trans. 503 (1974).
13. D.F. Rendle, A. Storr, and J. Trotter. (*a*) Can. J. Chem. **53**, 2390 (1975); (*b*) Can. J. Chem. **53**, 2944 (1975).
14. L.K. Peterson and K.I. The. Can. J. Chem. **57**, 2520 (1979).
15. K.R. Breakell, D.F. Rendle, A. Storr, and J. Trotter. J. Chem. Soc. Dalton Trans. 1584 (1975).
16. W.J. Wang and C.C. Chen. Synth. Met. **27**, B219 (1988).
17. C.M. Asselin, G.C. Fraser, H.K. Hall, W.E. Lindsell, A.B. Padias, and P.N. Preston. J. Chem. Soc. Dalton Trans. 3765 (1997).
18. R.A. Bowie, M.D. Gardiner, D.G. Neilson, K.M. Watson, S. Mahmood, and V. Ridd. J. Chem. Soc. Perkin Trans. 1, 2395 (1972).
19. A.R. Katritzky. Handbook of heterocyclic compounds. Pergamon Press Ltd., Oxford. 1985. p. 33.
20. M.R. Caira, R.G.F. Giles, L.R. Nassimberi, G.M. Sheldrick, and R.G. Hazell. Acta Crystallogr. Sect. B: Struct. Crystallogr. Cryst. Chem. **B32**, 1467 (1976).
21. L.S. Liou, P.S. Chen, C.H. Sun, and J.C. Wang. Acta Crystallogr. Sect. C: Cryst. Struct. Commun. **C52**, 1841 (1996).
22. Y. Zhou and D.S. Richeson. Organometallics, **14**, 3558 (1995).

© 1998 NRC Canada

Peroxidations initiated by lignin model compounds: investigating the role of singlet oxygen in photo-yellowing

L. Ross C. Barclay, Jennifer K. Grandy, Heather D. MacKinnon, Heather C. Nichol, and Melinda R. Vinqvist

Abstract: 3,5-Di-*tert*-butyl-*ortho*-quinone, **6**, and 1-(3,4-dimethoxyphenyl–2-(2-methoxyphenoxy)-1-propanone, **7**, models for oxidized lignin and for lignin, were used as sensitizers of photo-oxidation. Product studies by HPLC from oxidation of methyl linoleate in solution sensitized by **6** or **7**, and in sodium dodecyl sulfate (SDS) sensitized by **6**, showed a product distribution of six hydroperoxides, the four conjugated 9- and 13-hydroperoxides of the geometrical isomers: *trans*-10, *cis*-12 (**2**), *cis*-9, *trans*-11 (**3**), *trans*-10, *trans*-12 (**4**), and *trans*-9, *trans*-11 (**5**)-octadecadienoates plus two nonconjugated hydroperoxides. The higher *cis*/*trans* to *trans*/*trans* (ct/tt) of geometrical isomers (**2** + **3**//**4** + **5**) compared to ct/tt from known thermal free-radical peroxidations (Type 1) indicate that singlet oxygen (Type 2) oxidation occurs in reactions sensitized by **6** or **7**. Kinetic studies by oxygen uptake are reported on oxidations of hydrocarbons 1-phenyl-2-methylpropene, **8**, and *trans*-stilbene, **9**, sensitized by the quinone, **6**, or by a dye, Rose Bengal. Quenching studies imply singlet oxygen reactions. Milled wood lignin undergoes self-initiated photo-oxidation in water, and oxygen uptake was quenched by sodium azide. Cellobiose, a cellulose model, undergoes sensitized photo-oxidation using model quinone, **6**, in a mixture of *tert*-butyl alcohol and water or using the sensitizers benzophenone or the lignin model, **7**, delivered on a solid support, silica gel, and these oxidations were quenched with sodium azide. These results implicate singlet oxygen in the photo-yellowing of high lignin content wood pulps.

Key words: lignin models, *ortho*-quinone, photo-oxidation, singlet oxygen, lignin, cellobiose.

Résumé : La 3,5-di-*tert*-butyl-*ortho*-quinone, **6**, et la 1-(3,4-diméthoxyphényl-2-(2-méthoxyphénoxy)propan-1-one, **7**, des modèles de lignine oxydée et de lignine, ont été utilisées comme sensibilisateurs de photooxydation. On a effectué l'oxydation du linoléate de méthyle, en solution sensibilisée par les produits **6** ou **7** et dans du dodécylsufate de sodium (DSS) sensibilisé par le produit **6**; la nature des produits, établie par CLHP, montre la présence de six hydroperoxydes: les quatre isomères géométriques des 9- et 13-hydroperoxydes conjugués (*trans*-10, *cis*-12 (**2**), *cis*-9, *trans*-11 (**3**), *trans*-10, *trans*-12 (**4**) et *trans*-9, *trans*-11 (**5**)-octadiénoates) en plus de deux hydroperoxydes qui ne sont pas conjugués. Le rapport plus élevé d'isomères géométriques *cis*/*trans* comparé aux isomères *trans*/*trans* (ct/tt) (**2** + **3**//**4** + **5**) observé dans ce cas par comparaison à ce qui est observé pour les peroxydations radicalaires thermiques (Type 1) indique que, dans les réactions sensibilisées par les produits **6** et **7**, il se produit une oxydation par de l'oxygène singulet (Type 2). On a aussi effectué des études cinétiques, basées sur l'absorption d'oxygène, sur les oxydations des hydrocarbures suivants: 1-phényl-2-méthylpropène, **8**, et *trans*-stilbène, **9**, sensibilisées par la quinone **6** ou par un colorant, le Rose Bengale. Des études de désactivations suggèrent que les réactions impliquent de l'oxygène singulet. La lignine de bois broyé subit une photooxydation autoinitiée dans l'eau et l'absorption d'oxygène est arrêtée par l'azoture de sodium. Le cellobiose, un modèle pour la cellulose, mis en solution dans un mélange d'alcool *tert*-butylique et d'eau, subit une photooxydation sensibilisée lorsqu'on utilise le modèle de la quinone, **6**, ou lorsqu'on utilise comme sensibilisateurs de la benzophénone ou le modèle de la lignine, **7**, livré sur un support solide, le gel de silice; ces oxydations sont arrêtées par l'azoture de sodium. Ces résultats impliquent l'oxygène à l'état de singulet dans le photojaunissement des pulpes de bois contenant des quantités importantes de lignine.

Mots clés : modèles de la lignine, *ortho*-quinone, photooxydation, oxygène singulet, lignine, cellobiose.

[Traduit par la Rédaction]

Received August 18, 1998.

L.R.C. Barclay,[1] J.K. Grandy, H.D. MacKinnon, H.C. Nichol, and M.R. Vinqvist. Department of Chemistry, Mount Allison University, Sackville, NB E4L 1G8, Canada.

[1]Author to whom correspondence may be addressed. Telephone: (506) 364–2369. Fax: (506) 364–2313. E-mail: rbarclay@mta.ca

Introduction

The oxidative photo-yellowing of lignin-rich pulps and derived papers is a significant factor in limiting the full potential of mechanical pulps in Canada. Consequently the possible role of active oxygen species, such as singlet oxygen, in photo-yellowing is an important issue both from the economical and fundamental standpoint. The first excited state of molecular oxygen, $^1\Delta_g$ ($^1O_2$), has been recognized

© 1998 NRC Canada

Fig. 1. Structural formulas.

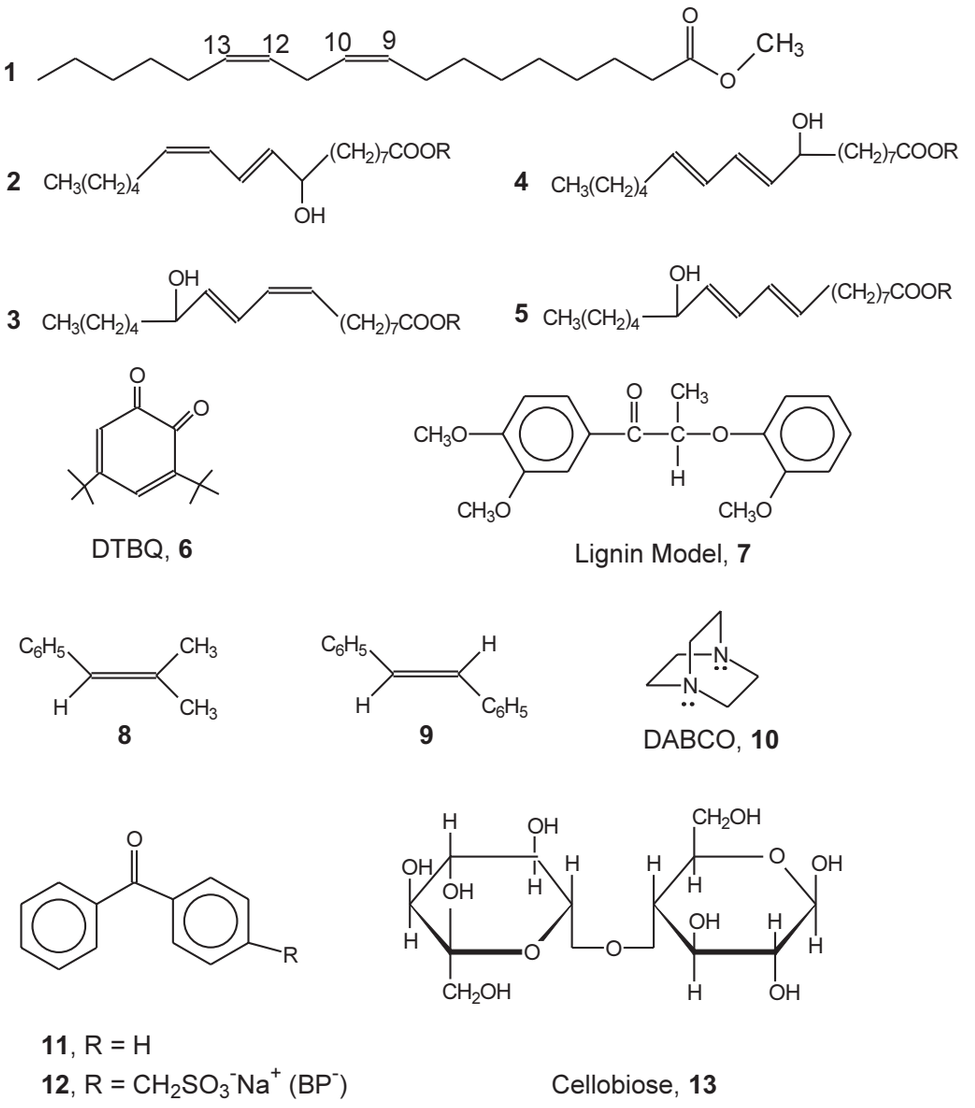

for at least six decades (1) as an important intermediate in the oxidation of a wide variety of organic substrates, and it has been the subject of many reviews (2–8), including the possible role of singlet oxygen in the oxidation of lignin (9) and its light-induced yellowing (10). Research on the possible role of singlet oxygen in photo-yellowing of pulps and papers has concentrated on the reaction of singlet oxygen *separately generated*, usually by dye-sensitization, with lignin model compounds (11–16), lignin (17), high-yield pulps (e.g., high lignin content) (12, 13, 18–20), cellobiose (21), and cellulose (22, 23).

The purpose of this current investigation is to determine if lignin model compounds, on photo-excitation in the presence of oxygen, produce singlet oxygen, and if this singlet oxygen reacts readily with organic substrates in various media and with cellobiose, a model cellulose compound. (See Fig. 1 for structural formulas.) To establish a relationship between these processes the following strategy was used. (*a*) An unsaturated lipid (methyl linoleate, 18:2) was selected as a marker for singlet oxygen, since its oxidation products are known to distinguish between classical free-radical peroxidation (Type 1 mechanism) versus that involving singlet oxygen (Type 2 mechanism) (22–27). (*b*) Comparisons were made between the product distributions resulting from dye-sensitized oxidation (e.g., singlet oxygen) of linoleate versus those from oxidation sensitized by a typical lignin model ketone, and from sensitization with a lignin model oxidation product (e.g., a quinone). Product analyses from thermal, azo-initiated, free-radical peroxidation of linoleate were compared with the above results. (*c*) Kinetic experiments employing oxygen uptake and quenching studies were conducted in solution and in aqueous heterogeneous phases. The heterogeneous systems included sodium dodecyl sulfate (SDS) micelles, and a solid support (silica

© 1998 NRC Canada

Scheme 1.

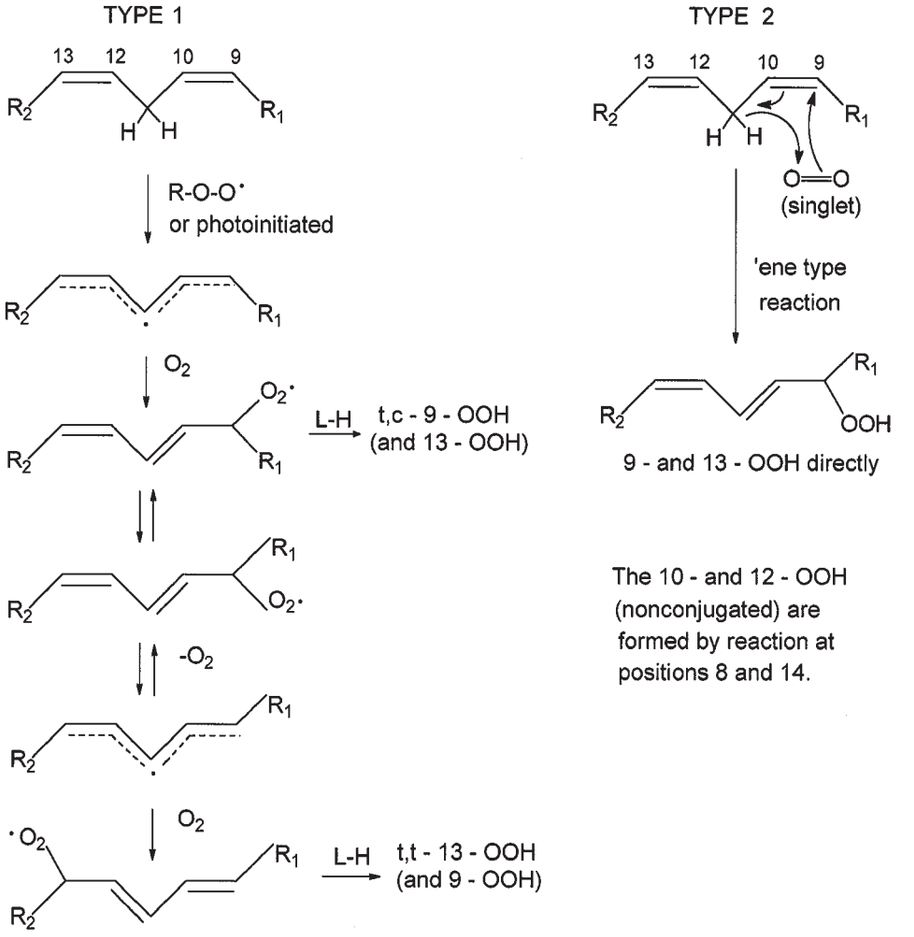

gel) containing sensitizer with the substrate (cellobiose) in the aqueous phase, to mimic a natural system.

Results

1. Peroxidation of linoleate: singlet oxygen versus free-radical oxidation

(a) Oxidations in homogeneous solution: dye-sensitized compared to thermal and photo-initiated autoxidation

Lipid peroxidation is a very useful method to distinguish between pathways involving singlet oxygen (Type 2) and free-radical autoxidation (Type 1). We used the well-known different products from peroxidation of linoleate (18:2) as an aid in distinguishing between these two types. The Type 1 reaction on linoleate normally yields a mixture of four regio-geometrical isomers: the conjugated diene 9- and 13-hydroperoxides, two having the *cis*, *trans* configuration (kinetic products) and two with the *trans*, *trans* configuration (thermodynamic products). The detailed mechanism for this Type 1 reaction has been reviewed by Porter (28) and the factors controlling the relative amounts of the isomers, e.g., the *cis*, *trans* to *trans*, *trans* ratio, such as the hydrogen atom donating ability of the system, are now well known (29). This reaction, which is initiated by hydrogen atom abstraction, proceeds through initial carbon and peroxyl radicals, and a brief outline is given in Scheme 1. In contrast the Type 2 reaction does not involve radical intermediates but proceeds directly to the hydroperoxides via a cyclic (ene) mechanism as outlined in Scheme 1. In this reaction the "kinetically controlled" 9- and 13- *cis*, *trans* hydroperoxides are accompanied by nonconjugated isomers, the hydroperoxides at positions 10 and 12 (24–27). The greater concentration observed for the 9- and 13- isomers has been attributed to internal cyclization of the initial 10 and 12 hydroperoxides (26).

We conducted some initial studies of linoleate peroxidation under conditions where the products of the different reactions give the expected typical patterns; namely, (*i*) thermal azo-initiated oxidation by 2,2-azo-bis(2,4-dimethylvaleronitrile) ADVN, (*ii*) photo-initiated oxidation by benzophenone, and (*iii*) dye-sensitized oxidation employing methylene blue. The HPLC traces of the products from typical reactions of reaction types (*i*) and (*iii*) are illustrated in Fig. 2. Both the thermal reaction initiated by peroxyl radicals derived from ADVN and the photo-initiated one employing benzophenone (type (*ii*) reaction on 5.6×10^{-2} M methyl linoleate, 1.43×10^{-6} M benzophenone initiated in octane by a Hg arc lamp gave an HPLC trace, not shown, comparable to the one shown for type (*i*) in Fig. 2*A*) gave

© 1998 NRC Canada

Fig. 2. HPLC profiles of methyl linoleate oxidation product separations at 234 nm. Peaks **3**, **5**, **2**, **4** are the 13 c,t, 13 t,t, 9 c,t, and 9 t,t products, respectively. (See Fig. 1.) (*A*) Thermally initiated oxidation of 8.6×10^{-2} M methyl linoleate using 2.0×10^{-2} M ADVN, in octane. Sample is 7.7% oxidized with a ct/tt product ratio of 0.18. Average ct/tt = 0.18 ± 0.00. (*B*) Photochemically initiated oxidation of 22.4×10^{-2} M methyl linoleate using 5.35×10^{-4} M methylene blue, irradiated using a 1000 W tungsten lamp in *tert*-butanol. Sample is 10.0% oxidized with a ct/tt product ratio of 33.3. Average ct/tt = 35.2 ± 1.5.

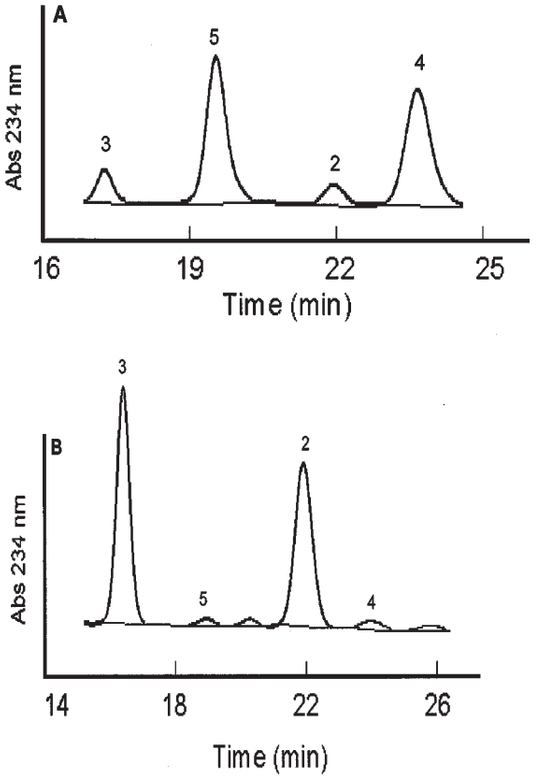

Fig. 3. HPLC profiles of methyl linoleate oxidation product separations at 234 nm. Peaks **3**, **5**, **2**, **4** are the 13 c,t, 13 t,t, 9 c,t, and 9 t,t products, respectively. (See Fig. 1.) (*A*) Photochemically initiated oxidation of 5.0×10^{-2} M methyl linoleate using 1.80×10^{-3} M **6**, irradiated using a commercial slide projector in *tert*-butanol. Sample is 6.21% oxidized with a ct/tt product ratio of 31.3. Average ct/tt = 36.2 ± 4.9. (*B*) Photochemically initiated oxidation of 22.4×10^{-2} M methyl linoleate using 9.21×10^{-4} M lignin model compound, **7**, irradiated using a 1000 W tungsten lamp in *tert*-butanol. Sample is 3.00% oxidized with a ct/tt product ratio of 7.4. Average ct/tt = 7.45 ± 0.39.

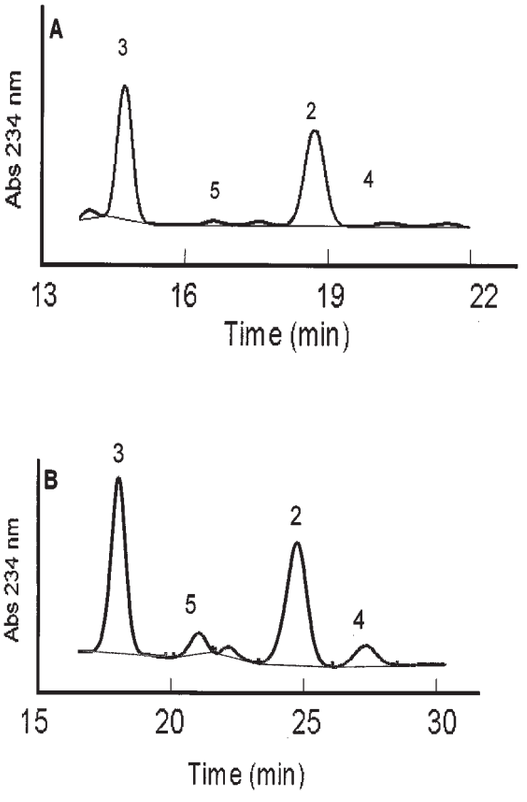

the four known (28, 29) oxidation products (e.g., **2**–**5**) and with *cis*, *trans* to *trans*, *trans* (ct/tt) ratios in the range 0.18–0.24, consistent with the free-radical (Type 1) mechanism (Scheme 1). In contrast the dye-sensitized oxidation gave a product profile of six isomers typical of the singlet oxygen reaction, where the 13- and 9-*cis*, *trans* isomers (kinetic products) are dominant and the ct/tt ratio is raised to 35. The HPLC peaks labeled **3**, **5**, **2**, and **4** in their order of elution for these four isomers (Fig. 1) were identified by comparison with thermal products using comparative HPLC traces. The additional two HPLC peaks are assigned to the nonconjugated isomers which have lower absorptivities (30).

(b) Oxidations sensitized by lignin model compounds in solution

Two model compounds were selected as potential initiators of lipid oxidation. 3,5-Di-*tert*-butylquinone (DTBQ, **6**) was used to model the oxidation products of lignin, since *ortho* quinones are known to be the major structures formed in photo-yellowing (31–33), and redox reactions of *ortho* quinones and catechols appear to be significant in the yellowing pathways (34–37). 1-(3,4-Dimethoxyphenyl)-2-(2-methoxyphenoxy)-1-propanone (**7**) was selected to model the lignin structure. Considerable information is available on the photochemistry of this and related systems (38–44), and its electronic absorption spectrum extends into the near ultraviolet range (λ_{max} 310 nm, ε = 10 000). While milled wood lignin contains carbonyl chromophores (45), we are aware of the limitations involved in the extrapolation of results using models as **6** and **7** to the more complex structure in native lignin.

First it was of interest to find that the HPLC product profiles (not shown) obtained from photo-initiation of methyl linoleate (4.3×10^{-2} to 5.0×10^{-2} M in *tert*-butanol) sensitized by the quinone, **6** (1.80×10^{-3} to 1.90×10^{-3} M), were similar whether using a simple visible projector lamp or a high intensity (1000 W) light source, although the actual ct/tt ratios varied (27 and 13, respectively). The HPLC analyses from oxidations of methyl linoleate, sensitized by **6** and

© 1998 NRC Canada

Table 1. Photosensitized and quenched peroxidation of linoleate.[a]

No.	Methyl linoleate	Solvent	Sensitizer	$-d[O_2]/dt$	Quencher and $-d[O_2]/dt$	
	($M \times 10^2$)		($M \times 10^4$)	($M\ s^{-1} \times 10^6$)	Dabco ($M \times 10^3$)	($M\ s^{-1} \times 10^6$)
1	2.2	*t*-BuOH	MB,[b] 5.4	7.3	9.9	0.78
2	2.6	Octane	**6**, 3.1	4.4	2.2	1.34
3	5	*t*-BuOH	**6**, 1.8[c]	0.79	5.6	0.37
4	2	*t*-BuOH	**6**, 3.0[c]	0.21	4.7	0.06
5	27	*t*-BuOH	**7**, 9.2[d]	0.41	7.3	0.13
	(mol $\times 10^6$)		(mol $\times 10^6$)	($M\ s^{-1} \times 10^6$[e])	NaN_3 (mol $\times 10^5$)	($M\ s^{-1} \times 10^6$)
6	12	0.5 M SDS	MB, 0.93	69.3	1.7	41.3
7	60.4	0.5 M SDS	**6**, 10.7	41.4	—	—
8	DLPC bilayers 44.6	0.1 M buffer, pH 7.0	MB, 1.55	31.8	29	12.9

[a]Numbers 1, 4, and 5 were irradiated with a 1000 W tungsten lamp, 2 and 3 with a commercial slide projector, and 6–8 with a 200 W Hg vapor lamp.

[b]MB, methylene blue.

[c]Analysis for sensitizer **6** by UV at 386 nm on aliquots during the run showed that 75% remained in expt. no. 3 and 68% in no. 4, near the end of the two runs. In the absence of substrate (projector lamp) 82% of **6** remained after 2 h irradiation.

[d]Analysis for sensitizer **7** by HPLC (retention time 33 min), along with products **2**–**5**, showed that **7** was recovered unreacted after 2 h irradiation when ct/tt = 8.4; **7** did exhibit decay on extended reaction.

[e]Rates were calculated assuming that the reactions occurred within the hydrophobic phase of the micelles or the bilayers. In nos. 6–8, amounts are given in mol due to the heterogeneous system.

Fig. 4. Plots to determine kinetic order with respect to light for the photochemically initiated oxidation of methyl linoleate in homogeneous solution. (*A*) Experiment initated with 6.17×10^{-4} M **7** oxidizing 4.27×10^{-2} M methyl linoleate in *tert*-butanol at 37°C, irradiated with a 200 W Hg arc lamp. Kinetic order = 0.91, $R^2 = 0.94$. (*B*) Experiment initiated with 1.827×10^{-3} M **6** oxidizing 4.35×10^{-2} M methyl linoleate in *tert*-butanol at 37°C, irradiated using a commercial slide projector. Kinetic order = 1.02, $R^2 = 0.99$.

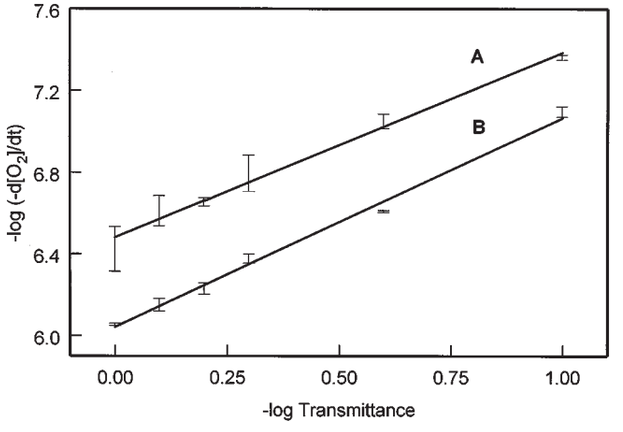

7, are shown in Figs. 3*A* and *B*. The profile of products when employing **6** and a projector lamp (Fig. 3*A*) showed the pattern of six products typical of oxidation by singlet oxygen (compare Fig. 2*B*), and the ct/tt ratio increased to 36. Oxidation of linoleate to 3% conversion sensitized by **7** was observed by using a more intense 1000 W visible lamp. At this point in the oxidation, the ct/tt ratio was 7.5 (see Fig. 3*B*). The kinetic order in oxygen uptake with light intensity was determined for reactions initiated by **6** and **7**, as illustrated in Fig. 4. Both reactions showed linear plots, and the order was unity for **6** and approximately unity (0.91 ± 0.07) for initiation by **7**. Some quenching experiments were carried out for both reactions under these conditions using a singlet oxygen quencher, Dabco, and the results are shown in Table 1, nos. 2–5.

(c) Oxidations in heterogeneous systems: aqueous micelles and phospholipid bilayers

We conducted experiments employing sodium dodecyl sulfate (SDS) micelles and dilinoleoyl-phosphatidylcholine (DLPC) bilayers, expected to mimic the more complex solid–aqueous system of natural material such as lignin or wood pulp. Earlier reviews appeared on some singlet oxygen oxidations in these media (46–48), and interest in singlet oxygen oxidations in these systems continues (30, 49). For comparative purposes, we first carried out experiments in these systems using dye-sensitized oxidations. Methylene blue sensitized oxidation of methyl linoleate in SDS micelles yielded products typical of singlet oxygen oxidation (Fig. 5*A*, ct/tt = 6.7) with kinetic order in light intensity of 1.05, as did reaction sensitized by the natural dye, hematoporphyrin (not shown), with kinetic order in light intensity of 0.98. Methylene blue, 1.55 μm, sensitized oxidation of linoleate in DLPC bilayers, 44.6 μm, using a Hg arc lamp, also gave products typical of singlet oxygen oxidation with ct/tt ratio = 29 (not shown). The quinone, **6**, was an effective sensitizer for the oxidation of methyl linoleate in SDS micelles. The HPLC product analysis showed products typical of singlet oxygen oxidation of linoleate in this system (see Fig. 5*B*, ct/tt = 9.1). The results of typical quenching experiments for sensitized oxidation in SDS micelles and DLPC bilayers employing sodium azide quencher are given in Table 1, nos. 6–8. While sodium azide is a convenient quencher of singlet oxygen to use in aqueous systems, its effect can be quite ambiguous due in part to its possible quenching of the sensitizer (50) at high concentrations, and there is even some evidence that sodium azide can produce reactive peroxyl radicals (51). Therefore it was considered prudent in our experiments to use relatively small concentra-

© 1998 NRC Canada

Table 2. Photo-oxidations[a] of hydrocarbons, sensitized by the quinone, **6**, and by rose bengal, RB.

No.	Hydrocarbon[b] (M)	Solvent	Sensitizer (M × 10^4)	$-d[O_2]/dt$ (M s^{-1} × 10^6)	Dabco and $-d[O_2]/dt$ (M × 10^3)	(M s^{-1} × 10^6)
1(*a*)	**8**, 0.324[c]	*t*-BuOH	RB, 3.62	55.8	5.29	24.8
1(*b*)	**8**, 0.166	*t*-BuOH	RB, 3.38	50.1	14.9	10.5
2	**8**, 0.166	*t*-BuOH	**6**, 6.94[d]	46	4.47	19.3
3	**9**, 0.824	C_6H_5Cl	RB, 4.50	2.27	0.79	0.66
4	**9**, 0.780	C_6H_5Cl	**6**, 8.70	0.38	4.74	0.1

[a]Numbers 1 and 2 used a commercial slide projector; 3 and 4 a 1000 W Oriel tungsten lamp.

[b]**8** and **9** refer to 1-phenyl-2-methyl-1-propene and *trans*-stilbene, respectively.

[c]Analyses for the formation of hydroperoxides during the run showed that their formation paralleled the consumption of hydrocarbon **8**; at the end of the run the yield of hydroperoxides reached 1.56 ± 0.11 mmol, while the loss of **8** was 1.52 ± 0.31 mmol (see Experimental).

[d]Analysis for **6** by UV at 386 nm showed that 73% remained by the end of the experiment.

Fig. 5. HPLC profiles of methyl linoleate oxidation product separations at 234 nm. Peaks **3**, **5**, **2**, **4** are the 13 c,t, 13 t,t, 9 c,t, and 9 t,t products, respectively. (See Fig. 1.) (*A*) Photochemically initiated oxidation of 6.6 × 10^{-5} mol methyl linoleate using 9.30 × 10^{-7} mol methylene blue, irradiated using a 200 W Hg arc lamp in 2.32 mL 0.16 M SDS. Sample is 10.0% oxidized with a ct/tt product ratio of 6.68. Average ct/tt = 6.65 ± 0.03. (*B*) Photochemically initiated oxidation of 6.04 × 10^{-5} mol methyl linoleate using 1.06 × 10^{-5} mol **6**, irradiated using a 1000 W tungsten lamp in 2.02 mL 0.5 M SDS. Sample is 10.0% oxidized with a ct/tt product ratio of 9.36. Average ct/tt = 9.09 ± 0.27.

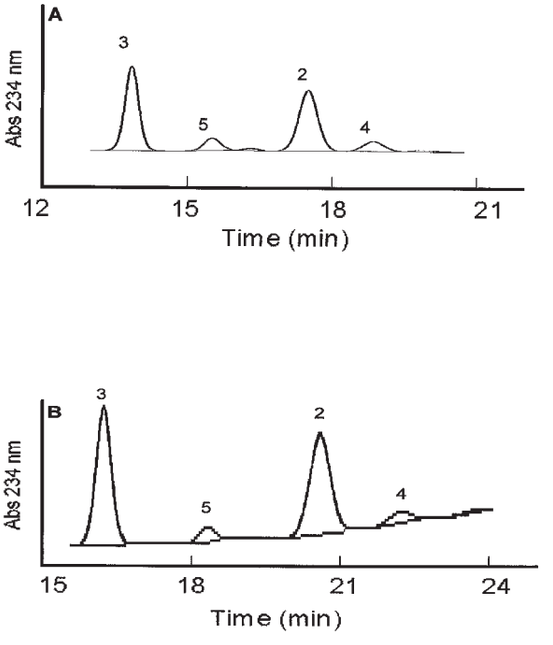

Fig. 6. Plot to determine kinetic order with respect to light intensity for the photochemically initiated oxidation of hydrocarbons in homogeneous solution. (*A*) Experiment initiated with 1.73 × 10^{-3} M **6** oxidizing 0.205 M 1-phenyl-2-methylpropene in *t*-BuOH at 30°C, irradiated using a commercial slide projector. Kinetic order = 0.99, R^2 = 0.99. (*B*) Experiment initated with 4.5 × 10^{-4} M Rose Bengal oxidizing 0.824 M *trans*-stilbene in chlorobenzene at 37°C, irradiated using a 1000 W tungsten lamp. Kinetic order = 1.23, R^2 = 0.99. (*C*) Experiment initiated with 8.7 × 10^{-4} M **6** oxidizing 0.78 M *trans*-stilbene in chlorobenzene at 37°C, irradiated using a 1000 W tungsten lamp. Kinetic order = 1.21, R^2 = 0.95.

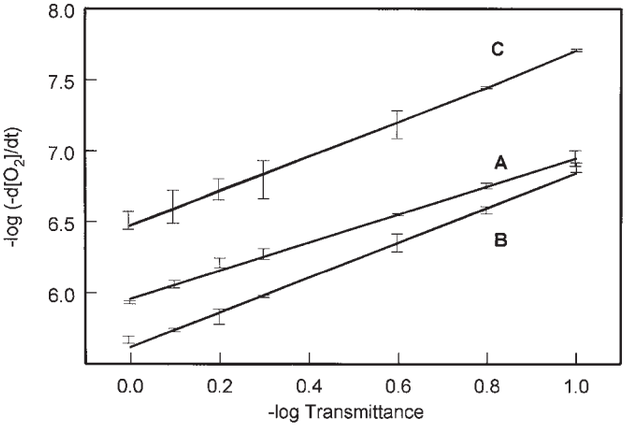

tions of sodium azide or carry out a "quenching profile" using successive additions of this quencher, vide infra.

2. Oxidations of hydrocarbons. Sensitization by the quinone, 6, compared to that by a dye

Lignin possesses a very complex structure which contains a variety of organic functional groups attached to frameworks that include aromatic rings, and alkene connecting links among others (45). Stilbene derivatives are important structures that are formed during mechanical processing of pulp (52). In addition, stilbenes are well known to be reactive with singlet oxygen (53–57). We therefore selected two simple unsaturated hydrocarbons, 1-phenyl-2-methylpropene (**8**) and *trans*-stilbene (**9**), as substrates to test the possible effect that the lignin model quinone (**6**) might have when used as a sensitizer in their oxidation. In these experiments, oxidations initiated by the known singlet oxygen sensitizer, Rose Bengal (53), were also carried out for comparison purposes. Kinetics of oxygen uptake and quenching were used to compare the effects of the model quinone, **6**, and the dye on the photo-oxidation of these hydrocarbons. Results of these experiments are summarized in Table 2. They show that the model quinone as well as the dye initiate oxidation

© 1998 NRC Canada

Table 3. Photo-oxidations[a] of lignin[b] and cellobiose.

No.	Lignin	Solvent	Sensitizer	$-d[O_2]/dt$	NaN_3 and $-d[O_2]/dt$	
	(mg)[c]		($M \times 10^3$)	(mol $s^{-1} \times 10^9$)	(mol $\times 10^5$)	(mol $s^{-1} \times 10^9$)
1	62	H_2O	—	1.09	3.26	0.37
2	63	0.5 M SDS	—	0.11	0.1	0.02
	Cellobiose (M)		($M \times 10^3$)	($M\ s^{-1} \times 10^8$)	($M \times 10^3$)	($M\ s^{-1} \times 10^8$)
3	0.15	H_2O	RB, 0.30	1.39	2.32	0.44
4	0.26	H_2O	**12**, 1.28	35	1.77	5.22
5	0.3	Si–H_2O[d]	**11**	15.86	2.95	8.34
6	0.29	Si–H_2O[d]	**7**	2.03	2.42	1.36
7	0.15	*t*-BuOH–H_2O[e]	**6**, 1.80	2.93	2.31	—[f]

[a]Number 1 used a UV Oriel lamp; 2 a 1000 W Oriel tungsten lamp; 3 and 7 a commercial slide projector; 4, 5, and 6 a 200 W Hg vapour lamp.

[b]Lignin refers to lignin from milled unbleached softwood. It is insoluble in water and SDS and was suspended as particles via sonication in these media.

[c]The molecular weight of lignin is unknown, thus it is reported as mass.

[d]The sensitizer, 0.0114 mmol of **11**, 0.0104 mmol of **7**, was coated onto silica gel and added to the reaction cell (see Experimental).

[e]The alcohol to water ratio was 1:1.

[f]Oxygen uptake could not be detected.

Fig. 7. Profile of oxygen consumption by irradiated milled wood lignin suspended in heterogeneous solution. Explanation of symbols: *a*, irradiation of sample; *b*, lamp turned off; *c*, sample irradiated again with the singlet oxygen quencher NaN_3 present. (*A*) Irradiation of 62.6 mg lignin suspended in 2.0 mL 0.5 M SDS using a 1000 W tungsten lamp. Sample was quenched with 9.6×10^{-7} mol NaN_3. (*B*) Irradiation of 62.0 mg lignin suspended in 2.0 mL water using an Hg arc lamp. Sample was quenched with 3.26×10^{-5} mol NaN_3.

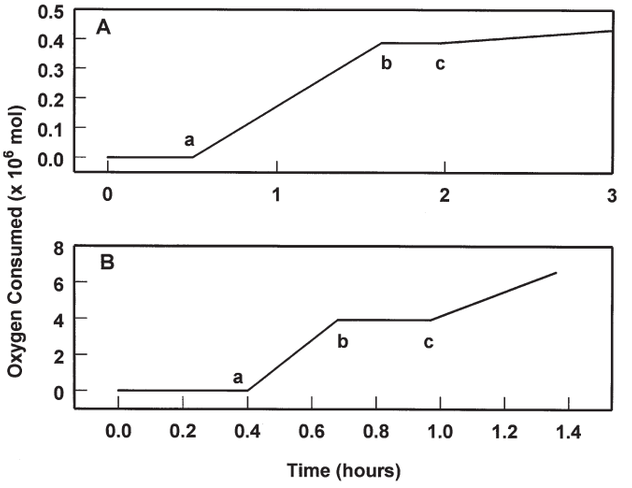

Fig. 8. Plot to determine kinetic order with respect to light intensity for the photochemically initiated oxidation of cellobiose in water at 37°C, irradiated using a 200 W Hg arc lamp. (*A*) Oxidation of 0.26 M cellobiose initiated with 1.3×10^{-6} M benzophenone derivative, **12**. Kinetic order = 1.00, $R^2 = 0.98$. (*B*) Oxidation of 0.30 M cellobiose initiated with 1.14×10^{-5} mol benzophenone coevaporated onto 200 mg silica gel. Kinetic order = 1.08, $R^2 = 0.99$.

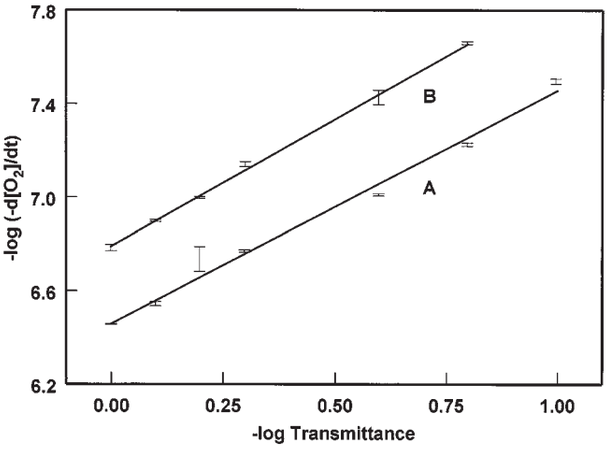

of the hydrocarbon **8** in *tert*-butyl alcohol and **9** in chlorobenzene, and that for either system the oxygen uptake is reduced with the singlet oxygen quencher, Dabco. In addition, some experiments were conducted to determine the kinetic order in oxygen uptake with light intensity. For example, Fig. 6*A* illustrates the result for the oxidation of **8** initiated by the quinone **6.** This shows a linear plot and a kinetic order of unity. Linear plots for the order in light intensity were observed for oxidation of *trans*-stilbene initiated by Rose Bengal and by **6** as shown in Fig. 6*B* and *C*. The kinetic orders in oxygen uptake were somewhat higher in these reactions at around 1.2.

3. Applications to the oxidation of lignin and cellobiose

(a) Self-initiated oxidation and quenching of lignin

Our sensitive oxygen uptake method proved to be applicable to measure the oxidation of lignin. A small sample dispersed in SDS micelles gave measurable oxygen uptake on irradiation with a visible source, and sodium azide was an effective quencher under these conditions, as shown in Fig. 7*A*. Irradiation using an ultraviolet source (pyrex filter) of a lignin sample dispersed in water gave a much more rapid rate of oxidation as shown in Fig. 7*B*, along with a

© 1998 NRC Canada

Fig. 9. Effect of increasing concentrations of NaN_3 on the rate of **12** (1.3×10^{-6} M) initiated oxidation of 0.255 M cellobiose in water at 37°C, irradiated using a 200 W Hg arc lamp.

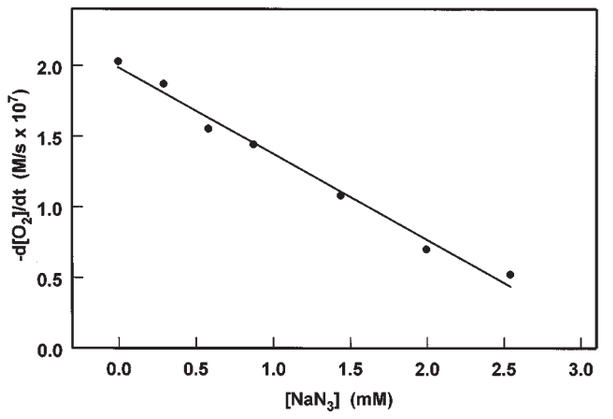

typical partial quenching with sodium azide. Analyses for hydroperoxide buildup were carried out on aliquots taken during the experiment. The results indicate that approximately 1/4 to 1/3 of the oxygen consumed resulted in lignin hydroperoxides.

(b) Oxidation of cellobiose sensitized from solution, SDS micelles, and from a solid support

Cellulose and model compounds have long been known to be susceptible to ultraviolet light (58), and singlet oxygen reacts readily with these systems (21–23). Therefore it was of interest to conduct some experiments on the sensitized oxidation of cellobiose. For these studies we used various model systems, including initiation from the same aqueous phase employing the water-soluble benzophenone derivative, **12**, initiation from a micellar phase using the quinone, **6**, in SDS micelles and from benzophenone or the lignin model, **7**, adsorbed on a solid support, silica gel. Such solid supports have attracted considerable interest (59, 60) and should better reflect the situation in the heterogeneous lignocellulose systems. Some typical oxidation experiments on cellobiose sensitized by **6**, **7**, **12**, benzophenone, or Rose Bengal are given in Table 3. Oxygen uptake was observed in all systems on irradiation, and the rates were reduced with small amounts of sodium azide. In addition the kinetic orders in oxygen uptake were unity, determined for initiation by **12** and by benzophenone, as shown in Fig. 8*A* and *B*. A profile for the sodium azide quenching of oxidation initiated by **12** gave the linear relationship shown in Fig. 9.

Discussion

The possible role of singlet oxygen in the photo-yellowing of high-yield pulps is characterized by considerable controversy and uncertainty. Typical previous reports provide a variety of conclusions which differ remarkably; for example, singlet oxygen is stated to be "... the main actor of the discoloration process... formed by energy transfer from photoexcited lignin" (20); or "... singlet oxygen treatment had little or no effect on the brightness of the bleached TMP" (13); or "... singlet oxygen... exerts a significant *bleaching* effect on pulp sheets" (19). It is emphasized again that the significant competition which determines whether Type 1 (free radical) or Type 2 (singlet oxygen) predominates is between the selected substrate and oxygen for the excited sensitizer (5). So whether Type 1 or Type 2 predominates (or both occur) will depend on the sensitizer selected, the substrate (e.g., its H-atom donating ability) and experimental conditions such as the nature of the light source.

The linoleate lipid is a very useful substrate (marker) to test the possible role of singlet oxygen in photo-oxidation in the current research because (*i*) on the one hand, it is an effective H-atom donor so that a triplet sensitizer can readily abstract a H-atom from the substrate to permit Type 1 autoxidation over Type 2, such as with benzophenone sensitized oxidation of linoleate (61), yet (*ii*) on the other hand the products of singlet oxygen oxidation of linoleate clearly differ for this pathway compared to the Type 1 pathway (vide supra), so that product studies can serve as a test for the dominant pathway. The results of our current studies on sensitized peroxidation of linoleate are representative of a wide variety of experimental conditions so that the two pathways might be in competition.

In all cases for sensitized peroxidation of linoleate, the qualitative pattern of the HPLC analyses of oxidation products, and their high ct/tt product ratios compared to those obtained during thermal oxidation, indicate the involvement of singlet oxygen as a major pathway (see Figs. 2, 3, and 5). It is especially significant to note that this is the case for reactions sensitized by the "model" quinone, **6** (Figs. 3*A* and 5*B*), and the lignin model, **7** (Fig. 3*B*). On the other hand, the ct/tt ratios for reactions sensitized by **6** or **7** were seen to vary considerably *even for reactions under what appears to be similar conditions*. For example, this ratio for initiation employing the quinone, **6**, and a 750 W projector lamp (ct/tt = 27) is quite different from that when using a 1000 W high-intensity tungsten lamp (ct/tt = 13). In addition, the ct/tt ratio for reactions sensitized by the lignin model, **7**, are rather low (ct/tt = 7.5) compared to dye sensitized reactions or quinone sensitized reactions. We do not have a quantitative explanation for these variations but suggest that these differences reflect a competition between Type 1 and Type 2 pathways. Such a competition has been reported before in the case of the products from dye-sensitized peroxidation of linolenic ester (62). Furthermore the quinone, **6**, has been observed to abstract H from reactive donors (35), so a competition between Type 1 and Type 2 pathways may well occur with minor changes in experimental conditions. Reactions sensitized by **6** or **7** are further complicated by their consumption during experiments which were lengthy in order to obtain significant conversion of substrate (see Tables 1 and 2, footnotes *c* and *d*). Kinetic measurements of oxygen uptake were carried out during comparatively short irradiation times when conversion of **6** or **7** is small. These results contrast with earlier ones using benzophenone in photo-oxidation (Type 1), where the benzophenone was completely regenerated (61).

Quantitative kinetic studies of oxygen consumption using the sensitive pressure transducer system provide important evidence on the pathways of the peroxidation of linoleate and of the hydrocarbons **8** and **9** under various conditions. Oxygen uptake was measured by this system for these oxidations initiated by the model compounds **6** and **7** as well as

© 1998 NRC Canada

by the dyes used. Known singlet oxygen quenchers Dabco and sodium azide caused significant reductions in the rates of oxygen uptake in these experiments, as shown in Tables 1 and 2. Furthermore, we found that injections of efficient antioxidants such as 2,2,5,7,8-pentamethylhydroxychroman (PMHC) during sensitized oxidations of **8** and of linoleate in solution, or injections of 2,5,7,8-tetramethyl-6-hydroxychroman-2-carboxylate (Trolox) during oxidation of linoleate in SDS micelles, did not cause inhibition of oxidation typical of their peroxyl trapping action (e.g., did *not* produce an induction period) (61), in contrast to the earlier results for benzophenone photo-oxidation of linoleate in SDS, and had only a slight effect on the rate of oxidation. Hydroxychromans of the vitamin E class are known to act as singlet oxygen quenchers (63–66), but the observed reductions in oxidation of a substrate are quite different from the characteristic well-defined induction periods observed for Type 1 oxidations in the presence of antioxidants (61). We conclude that our sensitized reactions proceeded mainly or entirely via Type 2 pathways. The kinetic order in oxygen uptake provided a useful test of this conclusion. Photoinitiated Type 1 reactions as well as thermal-initiated ones are known to follow the classical rate law for autoxidations where the oxidation is half order in the rate of free-radical chain initiation (R_i). This was shown to be the case for benzophenone initiated oxidation of linoleate (61) where the R_i was changed by varying the light intensity through the use of filters. In contrast, the kinetic order in light intensity for reactions initiated by the quinone, **6**, or by the lignin model, **7**, in the present study were approximately unity for oxidation of methyl linoleate (Fig. 4) or for oxidation of hydrocarbon **8**. We cannot make a complete analysis from this limited kinetic data because the concentrations of substrates were not systematically varied; nevertheless, these limited results suggest a simple first-order dependence on the steady-state concentration of singlet oxygen which is expected to vary directly with light input.

Our results from photo-oxidations sensitized by the model quinone, **6**, and the lignin model, **7**, provide a very useful background for experiments on the more relevant systems containing lignin and cellobiose. The light-induced self-initiated oxidation of lignin in aqueous mixtures most certainly occurs by a singlet oxygen pathway, according to the oxygen uptake and quenching studies with sodium azide (Fig. 7). The free-radical pathway for oxidation of lignin under these conditions is not significant, since we find that the antioxidant Trolox causes only a slight reduction in oxygen uptake, and no definite "inhibition period" was observed. Excited chromophoric groups in the lignin structure must be acting to sensitize these self-initiated, singlet oxygen oxidations. We acknowledge that this is an oversimplification of a very complex system like lignin. Lignin hydroperoxides build up during the self-sensitized peroxidation, and presumably other, more complex, products form, since only 1/4 to 1/3 of the oxygen uptake is accounted for by hydroperoxide formation. We are not aware of previous use of *ortho* quinones as sensitizers in photo-oxidation. However even the simple diketene, biacetyl, when used as a model for oxidized lignin, is reported to photo-oxidize an azo dye by two "oxidizing species"; singlet oxygen and an adduct of ground-state molecular oxygen and triplet biacetyl (67). Similar conclusions were made earlier for the sensitized photo-oxidation of alkenes by benzil and biacetyl (68).

In recent years, comparatively little attention has been centered on the question of oxidation of the cellulose component of high-yield pulps. Therefore we carried out some initial studies using the readily available water-soluble model compound cellobiose. Results from studies in solution show that the water-soluble dye Rose Bengal, the benzophenone derivative **12**, and in particular the quinone, **6** (in *tert*-butanol–water), sensitize the oxidation of cellobiose (Table 3). The rates are reduced in the presence of sodium azide, indicating a singlet oxygen component to the oxidation. The oxidations sensitized using benzophenone and especially the lignin model, **7**, carried on silica gel as a solid support are of particular interest, since this heterogeneous system provides a model of the more complex situation in high-lignin pulps. While these data are somewhat preliminary, the oxidation rates and sodium azide quenching results suggest that these reactions involve singlet oxygen attack on the cellobiose structure.

Overall our results leave no doubt that singlet oxygen is indeed the main active oxygen which participates in photo-oxidations initiated by model compounds such as an *ortho* quinone (e.g., **6**) or a lignin model ketone, **7**, in homogeneous solution or in mixed phases. The initial results on lignin and cellobiose indicate that the singlet oxygen pathway must be considered when designing strategies, such as employment of quenchers and (or) sunscreens, to inhibit photo-yellowing of high lignin content pulps.

Experimental

Materials and preparations

The solvents used were of HPLC grade and were distilled before use. Phosphate buffer (pH 7.0) for use in preparation of micelles or lipid bilayers was prepared from 0.05 M each of Na_2HPO_4 and NaH_2PO_4 in distilled, deionized water containing 1×10^{-4} M EDTA. Immediately before use the buffer was passed through a Chelex-100 column (Bio-Rad 50–100 mesh) to remove traces of heavy metal ions. Electrophoresis pure sodium dodecyl sulfate (SDS) was purchased from Bio-Rad Laboratories. Dilinoleoylphosphatidylcholine (DLPC) was obtained in sealed vials from Avanti Polar Lipids and stored at –25°C. The procedure for preparation of DLPC bilayers is described elsewhere (69). Methyl linoleate was obtained from Nu-Chek-Prep in sealed vials and stored at –25°C. 3,5-Di-*tert*-butyl-*o*-quinone, **6**, was prepared by oxidation of 3,5-di-*tert*-butylcatechol (Aldrich) with lead oxide as described (70) and recrystallized from hexane in dark red needles, mp 117–119°C (lit. mp 113–114°C (70)). 1-(3,4-Dimethoxyphenyl)-2-(2-methoxyphenoxy)-1-propanone (**7**) was synthesized as described (71) and recrystallized from methanol as colorless crystals, mp 118–120°C (lit. mp 117–120°C (71)). Mass spectroscopic analysis (GC/MS) of **7** gave the theoretical parent mass at m/e = 256 and the expected ^1H and ^{13}C NMR spectra. 1-Phenyl-2-methylpropene (**8**) was obtained from Aldrich. Larger quantities were prepared by dehydration of 2-methyl-1-phenyl-2-propanol (Aldrich) in boiling xylene containing a catalytic amount of *para*-toluenesulfonic acid. The product was separated from solvent by fractional distillation. Analysis by GC/MS showed it

© 1998 NRC Canada

to be 94% of the conjugated isomer, **8**. This was confirmed ^{1}H and ^{13}C NMR in comparison with commercial **8**. 2,2-Azo-bis(2,4-dimethylvaleronitrile) (ADVN) was obtained from Polysciences, Inc. *trans*-Stilbene, 1,4-diazabicyclo-[2.2.2]octane (Dabco), benzophenone, *p*-methoxyacetophenone, heptadecane, Trolox, and cellobiose were obtained from Aldrich. *p*-(Methyl sodium sulphonate)-benzophenone (**12**) was a gift from J.C. Scaiano, University of Ottawa. Pentamethylhydroxychroman (PMHC) was synthesized as described (72). Preparations of sensitizers on silica gel were carried out by dissolving known amounts of sensitizer (**6**, **7**, or benzophenone) in methylene chloride containing a known weight of silica gel, Merck silica gel 60, 230–400 mesh. The solvent was removed under reduced pressure. The resulting solid support normally contained 1% by weight of the sensitizer. Milled wood lignin from unbleached softwood was supplied by PAPRICAN, Pointe Claire, Quebec.

Peroxidation procedures

Peroxidations and quenching studies of oxygen uptake were carried out at 30° or 37°C under oxygen at 760 Torr (1 Torr = 133.3 Pa) in a sensitive dual-channel calibrated pressure transducer system that is described elsewhere (73, 74). In the kinetic studies, each sample containing substrate, sensitizer, and solvent in a nominal 2 mL total volume was shaken under oxygen in a calibrated pyrex cell on the pressure transducer until a steady baseline was established on a recorder. Then the sample was irradiated and the oxygen uptake recorded. The light was then blocked while a known amount of quencher or antioxidant was added using a gas-tight micro syringe with an extended teflon needle. The sample was shaken again until a baseline was re-established, the light turned on again and the new oxygen uptake rate measured. This procedure is illustrated in a typical way for the oxidation and quenching of lignin in Fig. 7. The effect of light intensity was carried out by inserting a series of six neutral density filters supported on a filter wheel and measuring oxygen consumption for at least three measurements randomly positioned for each filter. Three different light sources were used. For initiations by broad-band visible light, a quartz tungsten–halogen lamp (Oriel no. 6315, 1000 W) with a photo-feedback attachment was used to ensure constant light intensity and for comparison purposes a simple commercial 750 W tungsten projector lamp was also used. Irradiations in the near UV were carried out with a mercury–xenon arc lamp (Oriel no. 6291, 200 W). In the latter case, the light intensity was monitored by sampling the light with a fibre optics cable leading to a phototube.

Analyses

Studies on product formation from methyl linoleate oxidation were conducted by HPLC. Samples of known volume were removed from an experiment at controlled intervals, and the product hydroperoxides were reduced to alcohols using an excess of triphenylphosphine (TPP) in hexane. For experiments in organic solvents, the solvent volume was reduced using a stream of argon and the sample prepared in a small volume (500 mL) of hexane. For experiments in aqueous media, TPP in methanol was used to reduce the hydroperoxides, and the product alcohols were extracted from the aqueous mixture using 2–1 mL aliquots of hexane, which were combined then condensed to 500 mL using a stream of argon. Two HPLC systems were used to determine the ct/tt product profiles: (*i*) a Varian system – Varian 9012 pump, Varian 9050 variable wavelength detector and Varian 9100 autosampler for sample introduction, with the Varian Star Chromatography workstation v.4.5 for processing results, or (*ii*) an HP system – HP1050 pump and variable wavelength detector with a manual injector and HP3365 Chemstation for processing results. Columns used were either an Apex Si 10 μ column (Jones Chromatography, 25 cm) or a Lichrosorb Si 100 10μ column (Brownlee, 25 cm). Samples were eluted with a mixture of 99.2% hexane, 0.4% isopropyl alcohol, and 0.4% acetone with a flow rate of 1 mL/min and monitored at 234 nm. Deviations of peak retention time (Figs. 2–4, 6) are due to the differences in the columns, and peak identity was confirmed by comparison of product profiles obtained from the photochemically initiated runs with product profiles from thermally initiated experiments. At least three injections were made for each sample. Some experiments used *p*-methoxy-acetophenone as an internal standard to quantify the amount of hydroperoxides being formed. Peaks eluted in the following order: *p*-methoxyacetophenone, **3**, **5**, **2**, **4**. Unconjugated products from the Type 2 pathway eluted just after **5** and after **4**. Using the same column and solvent conditions it was possible to monitor the loss of the sensitizer, **7**, which eluted after the four product alcohols, at 33 min (not shown).

Changes in concentration of the sensitizer, **6**, were monitored using a Shimadzu UV-1201 equipped with a Spectrum program pack, v.5. Samples were taken from experiments before and during irradiation and prepared to a known volume for analyses. The molar absorptivity for **6**, $\varepsilon = 2346$ at 386 nm, was calculated using a sample of **6** of known concentration.

Quantitative measurements of the formation of hydroperoxides during an experiment were made by reducing the hydroperoxides to alcohols using TPP and measuring the resultant amount of triphenylphosphine oxide (TPPO) generated, compared to an internal standard, heptadecane. Analyses were made on a Varian 3700 GC using a Durabond DB-1 fused silica megabore capillary column (1 μm film thickness, 15 m × 0.32 mm) with a flame ionization detector. The carrier gas, He, had a flow rate of 30 cm^3/min. Using a temperature program (initial temperature 130°C (held 6 min) increased 10°C/min to 220°C (held 8 min)) with fixed injector and detector temperatures of 200 and 220°C, respectively, the products separated as follows: heptadecane, 10.6 min; TPP, 15 min; TPPO, 20 min.

Mass spectra were obtained on a HP5988A GC/MS instrument using an HP5890 series 2 gas chromatograph. ^{1}H and ^{13}C NMR were measured in $CDCl_3$ (TMS internal standard) on a JEOL JNM GSX 270 FT NMR.

Acknowledgments

This research was supported by grants from the Natural Sciences and Engineering Research Council of Canada and the Mechanical and Chemimechanical Wood-Pulps Network, part of Canada's Network of Centres of Excellence, which we gratefully acknowledge. H.C. Nichol received an under-

© 1998 NRC Canada

graduate summer research scholarship from Mt. Allison University.

References

1. H. Kautsky. Trans. Faraday Soc. **35**, 216 (1939).
2. D.R. Kearns. Chem. Rev. **71**, 395 (1971).
3. C.S. Foote. Acc. Chem. Res. **1**, 104 (1968).
4. N.I. Krinsky. *In* Oxygen radicals in chemistry and biology. Walter de Gruyter and Co., Berlin. 1984. pp. 453–464.
5. C.S. Foote. *In* Free radicals in biology. Vol 2. *Edited by* W.A. Pryor. Academic Press, New York. 1980. pp. 85–133.
6. Singlet oxygen reactions with organic compounds and polymers. *Edited by* B. Ranby and J.F. Rabek. J. Wiley and Sons, Ltd., Chichester. 1978.
7. Singlet oxygen. *Edited by* H.H. Wasserman and R.W. Murray. Academic Press, New York. 1979.
8. R.C. Straight and J.D. Spikes. *In* Singlet O_2, vol. IV: polymers and biomolecules. *Edited by* A.A. Frimer. CRC Press, Inc, Boca Raton, Florida. 1985. pp. 91–143.
9. G. Gellerstedt, K. Kringstad, and E.L. Lindfors. *In* Singlet oxygen reactions with organic compounds and polymers. *Edited by* B. Ranby and J.F. Rabek. J. Wiley and Sons, Ltd., Chichester. 1978. pp. 303–310.
10. G. Brunow, I. Forsskahl, A.C. Gronlund, G. Lindstrom, and K. Nyberg. *In* Singlet oxygen reactions with organic compounds and polymers. *Edited by* B. Ranby and J.F. Rabek. J. Wiley and Sons, Ltd., Chichester. 1978. pp. 311–315.
11. C. Crestini and M. D'Auria. Tetrahedron, **53**, 7877 (1997).
12. K. Fischer, M. Beyer, and H. Koch. Holzforschung, **49**, 203 (1995).
13. H. Takagi, I. Forsskahl, H. Derakyla, S. Omori, and C.W. Dence. Holzforschung, **44**, 217 (1990).
14. S. Omori, H. Takagi, R.C. Francis, and C.W. Dence. Holzforschung, **46**, 47 (1992).
15. H. Tylli and C. Olkkonen. J. Photochem. Photobiol. A, **49**, 397 (1989).
16. I. Forsskahl. J. Photochem. **27**, 363 (1984).
17. M.G. Neumann and A.E.H. Machado. J. Photochem. Photobiol. B, **3**, 473 (1989).
18. J. Szabo, M. Fiserova, and M. Kosik. Cellul. Chem. Technol. **28**, 183 (1994).
19. I. Forsskahl, C. Olkkonen, and H. Tylli. J. Photochem. Photobiol. A, **43**, 337 (1988).
20. M. Beyer, Ch. Bäurich, and K. Fischer. Das Papier, **49**, 8 (1995).
21. B. Garston. J. Soc. Dye Chem. **100**, 376 (1984).
22. J. Griffiths and C. Hawkins. Polymer, **17**, 1113 (1976).
23. B. Garston. J. Soc. Dye Chem. **96**, 535 (1980).
24. M.J. Thomas and W.A. Pryor. Lipids, **15**, 544 (1980).
25. J. Terao and S. Matsushita. J. Am. Oil Chem. Soc. **54**, 234 (1977).
26. E.N. Frankel, W.E. Neff, E. Selke, and D. Weisleder. Lipids, **17**, 11 (1982).
27. H.W.-S. Chan and G. Levett. Lipids, **12**, 99 (1977).
28. N.A. Porter. Acc. Chem. Res. **19**, 262 (1986).
29. N.A. Porter and D.G. Wujek. J. Am. Chem. Soc. **106**, 2626 (1984).
30. L.R.C. Barclay, E. Crowe, and C.D. Edwards. Lipids, **32**, 297 (1997).
31. J.A. Schmidt and C. Heitner. J. Wood Chem. Technol. **15**, 223 (1995).
32. D.S. Argyropoulos, C. Heitner, and F.G. Morin. Holzforschung, **46**, 211 (1992).
33. S.E. Lebo, W.F.W. Lonsky, T.J. McDonough, P.J. Meduecz, and D.R. Dimmel. J. Pulp Pap. Sci. **16**, J139 (1990).
34. S.V. Jovanovic, K. Konya, and J.C. Scaiano. Can. J. Chem. **73**, 1803 (1995).
35. F. Xi and L.R.C. Barclay. Can. J. Chem. **76**, 171 (1998).
36. J. Abbot. Res. Chem. Intermed. **21**, 535 (1995).
37. I.A. Shkrob, M.C. Depew, and J.K.S. Wan. Res. Chem. Intermed. **17**, 271 (1992).
38. L.R.C. Barclay, G.R. Cromwell, and J.W. Hilborn. Can. J. Chem. **72**, 35 (1994).
39. L. Hurrel, L.J. Johnston, N. Mathivanan, and D. Wong. Can. J. Chem. **71**, 1340 (1993).
40. D. Shukla, N.P. Schepp, N. Mathivanan, and L.J. Johnston. Can. J. Chem. **75**, 1820 (1997).
41. J.K.S. Wan, I.A. Shkrob, and M.C. Depew. *In* Photochemistry of lignocellulosic materials. ACS symposium series no. 531. 1993. Chap. 7. pp. 99–110.
42. J.C. Scaiano, J.C. Netto-Ferreira, and V. Wintgens. J. Photochem. Photobiol. A, **59**, 265 (1991).
43. J.A. Schmidt, A.B. Berinstain, F. DeRege, C. Heitner, L.J. Johnston, and J.C. Scaiano. Can. J. Chem. **69**, 104 (1991).
44. W.U. Palm and H. Dreeskamp. J. Photochem. Photobiol. A, **52**, 439 (1990).
45. H.F.J. Wenzl. The chemical technology of wood. Academic Press, New York. 1970. Chap. 3, pp. 92–156.
46. Y. Usui. *In* Singlet oxygen reactions with organic compounds and polymers. *Edited by* B. Ranby and J.F. Rabek. J. Wiley & Sons, Ltd., Chichester. 1978. Chap. 20. pp. 203–210.
47. B.A. Lindig and M.A.J. Rodgers. Photochem. Photobiol. **31**, 617 (1980).
48. K. Ogino, H. Uchiyama, and M. Abe. *In* Mixed surfactant systems. *Edited by* K. Ogino and M. Abe. Marcel Dekker, New York. 1992. Chap. 6. pp. 189–216.
49. W.C. Eisenberg, J. Anand, S. Wang, and R.J. Stevensen. Photochem. Photobiol. **56**, 441 (1992).
50. D. Bellus. *In* Singlet oxygen reactions with organic compounds and polymers. *Edited by* B. Ranby and J.F. Rabek. J. Wiley & Sons, Ltd., Chichester. 1978. Chap. 9. pp. 61–109.
51. C.D. Edwards. M.Sc. thesis. Mount Allison University, Sackville, N.B. 1996.
52. D.F. Wong, G. Leary, and G. Arct. Res. Chem. Intermed. **21**, 329 (1995).
53. C. Salemi-Delvaux, B. Luccioni-Houze, G. Baillet, G. Giusti, and R. Guglielmetti. Tetrahedron Lett. **37**, 5127 (1996).
54. K. Gollnick and S. Held. J. Photochem. Photobiol. B, **5**, 65 (1990).
55. B.-M. Kwon, C.S. Foote, and S.I. Khan. J. Org. Chem. **54**, 3378 (1989).
56. R.S. Davidson, G.M. Ismall, and D.M. Lewis. J. Soc. Dyers Col. **103**, 261 (1987).
57. K. Gollnick and A. Schnatterer. Photochem. Photobiol. **43**, 365 (1986).
58. A. Beelik and J.K. Hamilton. J. Org. Chem. **26**, 5074 (1961).
59. S. Kazanis, A. Azarani, and L.J. Johnston. J. Phys. Chem. **95**, 4430 (1991).
60. I.K. Lednev, N. Mathivanan, and L.J. Johnston. J. Phys. Chem. **98**, 11 444 (1994).
61. L.R.C. Barclay, K.A. Baskin, S.J. Locke, and T.D. Schaefer. Can. J. Chem. **65**, 2529 (1987).
62. J.N. Chacon, J. McLeavie, and R.S. Sinclair. Photochem. Photobiol. **47**, 647 (1985).
63. K. Fukuzawa, K. Matsuura, A. Tokumura, A. Suzuki, and J. Terao. Free Radical Biol. Med. **22**, 923 (1997).
64. S. Nonell, L. Moncayo, F. Trull, F. Amat-Guerri, E.A. Lissi, A.T. Soltermann, S. Criado, and N.A. Garcia. J. Photochem. Photobiol. B, **29**, 157 (1995).
65. K. Mukai, K. Daifuku, K. Okabe, T. Tanigaki, and K. Inoue. J. Org. Chem. **56**, 4188 (1991).

© 1998 NRC Canada

66. R.L. Clough, B.G. Yee, and C.S. Foote. J. Am. Chem. Soc. **101**, 683 (1979).
67. J.G. Neevel, M. Peereboom, and B. van der Groof. J. Soc. Dye Chem. **109**, 116 (1993).
68. N. Shimizu and P.D. Bartlett. J. Am. Chem. Soc. **98**, 4193 (1976).
69. L.R.C. Barclay and M.R. Vinqvist. Free Radical Biol. Med. **16**, 779 (1994).
70. W. Flaig, T. Ploetz, and H. Biergans. Ann. Chem. **597**, 196 (1955).
71. V.L. Pardini, C.Z. Smith, J.H.P. Utley, R.R. Vargas and H. Viertler. J. Org. Chem. **56**, 7305 (1991).
72. L.I. Smith, H.E. Ungnade, H.H. Hoehn, and S. Wawzonek. J. Org. Chem. **4**, 311 (1939).
73. D.D.M. Wayner and G.W. Burton. *In* Handbook of free radicals and antioxidants in biomedicine. Vol. 3. CRC Press, Boca Raton, Fla. 1989. pp. 223–232.
74. L.R.C. Barclay, K.A. Baskin, K.A. Dakin, S.J. Locke, and M.R. Vinqvist. Can. J. Chem. **68**, 2258 (1990).

© 1998 NRC Canada

Cleavage of neutral alkenes and alkene radical cations; hybrid Hartree–Fock/density functional theory results

Leif A. Eriksson, C. Magnus Jansson, Donald R. Arnold, and Russell J. Boyd

Abstract: The cleavage reactions of the 1-butene and 4,4-dimethyl-1-pentene molecules and their cations, to form neutral and charged hydrocarbon products, are investigated using hybrid Hartree–Fock/density functional theory. In comparison with previous theoretical results (Du et al.), the density functional cleavage and ionization energies, including zero-point vibrational energy, lie in better agreement with experimental and thermochemical data. Assuming vertical ionization processes the mean absolute deviation (MAD) compared with experiment is 3.4 kcal/mol for the reaction sequences studied. Using adiabatic ionization processes instead gives a MAD of 5.2 kcal/mol. The largest deviation from experiment occurs for the cleavage reactions of the neutral parent molecules, where the difference between theory and experiment is up to 12.8 kcal/mol. In addition to reaction energies we also report optimized ground-state structures, and for the radicals studied, isotropic hyperfine coupling constants that are compared to experimental data. It is found that the experimental hyperfine properties of the 1-butene cation can be explained by rotational averaging caused by the flat potential surface for rotation about the C2—C3 bond.

Key words: density functional theory (DFT), alkenes, radical cations, bond cleavage, isotropic hyperfine coupling constants.

Résumé : Faisant appel à la théorie de densité fonctionnelle hybride de Hartree–Fock, on a étudié les réactions de clivage des molécules de but-1-ène et de 4,4-diméthylpent-1-ène et de leurs cations conduisant à la formation d'hydrocarbures neutres et chargés. Par comparaison avec les résultats théoriques publiés antérieurement (Du et al.), la densité fonctionnelle de clivage et les énergies d'ionisation, y compris l'énergie vibrationnelle au point zéro, sont en meilleur accord avec les données expérimentales et thermochimiques. En faisant l'hypothèse que les processus d'ionisation sont verticaux, on a déterminé que la déviation absolue moyenne (DAM) comparée à la valeur expérimentale est égale à 3,4 kcal/mol pour les séquences de réaction étudiées. Si l'on utilise plutôt des processus d'ionisation adiabatique, la valeur de DAM obtenue est égale à 5,2 kcal/mol. Les réactions de clivage des molécules parentes neutres donnent les plus grandes déviations entre les valeurs calculées et expérimentales; la différence atteint 12,8 kcal/mol. En plus des énergies de réaction, on a aussi calculé les structures optimisées des états fondamentaux et, pour les radicaux étudiés, on a aussi comparé les constantes de couplage hyperfin isotrope avec les données expérimentales. On a trouvé que les propriétés hyperfines expérimentales du cation but-1-ène peuvent être expliquées par une pondération rotationnelle moyenne provoquée par une surface de potentiel plane pour la rotation autour de la liaison C2—C3.

Mots clés : théorie de la densité fonctionnelle (DFT), alcènes, cations radicaux, clivage de liaison, constantes de couplage hyperfin isotrope.

[Traduit par la Rédaction]

1. Introduction

During the last few years, the new generation of methods based on density functional theory (DFT) has attracted much attention in the quantum chemical community. Today, we can find successful applications in practically every area of theoretical chemistry, traditionally focused by conventional ab initio theory. At the same time, much effort is being devoted to the development of new functional forms, fitting procedures, and hybrid methods between DFT and, e.g., ab initio theory, molecular mechanics, or molecular dynamics simulations (1–4). Of particular interest for the present work is the performance of gradient-corrected and hybrid Hartree–Fock/density functional theory (HF-DFT) methods for chemical reactivity and properties of unsaturated hydrocarbons, and the effects of photoionization of such systems.

The applicability of DFT for radical hyperfine properties is also of interest, and it has been shown (footnotes 2 and 3,

Received June 17, 1998.

L.A. Eriksson[1] and C.M. Jansson. Department of Physics, University of Stockholm, Box 6730, S-113 85 Stockholm, Sweden.
D.R. Arnold and R.J. Boyd. Department of Chemistry, Dalhousie University, Halifax, NS B3H 4J3, Canada.

[1]Author to whom correspondence may be addressed. Telephone: 46-18-4713264. Fax: 46-18-502402. E-mail: leifaxel@kvac.uu.se
[2]V.G. Malkin, O.L. Malkina, L.A. Eriksson, and D.R. Salahub. In ref. 3.
[3]V. Barone. In ref. 4.

 © 1998 NRC Canada

ref. 5) that the two functionals overall performing the best — often in very close agreement with highly advanced correlated ab initio methods — are the gradient-corrected DFT functional "PWP86" (6, 7) and the "B3LYP" hybrid functional (8–11), frequently reproducing experimental isotropic hyperfine coupling constants (HFCC) to 85–90% of experimental values. The density functional theories for geometric structures and radical properties of pure hydrocarbons have previously been thoroughly investigated in our laboratory (12–14). More recent applications of DFT for chemical reactivity and photoionization problems involve, e.g., the work by Wong and Radom (15) on a number of prototypical radical addition reactions, and a study of the radical cations of, e.g., silacyclobutane cations (16).

The compounds and reactions focused on in the present work serve as model systems for larger compounds and proposed reactions of interest in synthetic organic chemistry (17, 18), and where there is sufficient previous experimental and theoretical data available to enable a good evaluation of the present methods. For a more detailed survey on the more complex parent systems, we refer to ref. 17.

2. Theoretical details

All geometries, energies, and hyperfine parameters reported in the present work are computed using hybrid Hartree–Fock gradient-corrected density functional theory, as implemented in the Gaussian 94 program (19). We throughout use the B3LYP functional, i.e., Becke's three-parameter hybrid functional (8), consisting of Hartree–Fock exchange, Slater local exchange (20), Becke (B88) nonlocal exchange (10), with the Vosko–Wilk–Nusair local correlation (21), and the Lee–Yang–Parr (LYP) gradient-corrected correlation functional (11). The B3LYP functional has been previously shown to yield highly accurate geometries and hyperfine properties (footnotes 2 and 3, ref. 5). The orbital basis sets used are 6-31G(d,p) for geometry optimization and zero-point vibrational energies (ZPVE) and 6-311G(2df,p) (22) for energies and hyperfine coupling constants (HFCC). Important indirect information about the geometry and the localization of the unpaired electron in radical species can be obtained via the electron spin resonance (ESR) techniques. If the calculated HFCCs match the experimental ones, and the system does not undergo vibrational or rotational motion, one may assume the experimental and calculated structures to match. For a doublet radical the isotropic HFCC (the "Fermi contact term") of a nucleus N is obtained through the relation:

$$A_{\mathrm{iso}}^{\mathrm{N}} = \frac{8\pi}{3} C \sum_{\mu\nu} \mathrm{P}_{\mu,\nu}^{\alpha-\beta} \left\langle \phi_\mu(\vec{r}_{\mathrm{k,N}}) | \delta(\vec{r}_{\mathrm{k,N}}) | \phi_\nu(\vec{r}_{\mathrm{k,N}}) \right\rangle$$

where the constant $C = g\beta g_{\mathrm{N}}\beta_{\mathrm{N}}$, $\mathbf{P}^{\alpha-\beta}$ is the spin-density matrix, and the Dirac delta function ensures the overlap integrals to be evaluated at the position of the nucleus only. For a more detailed description of the calculation of hyperfine parameters, the reader is referred to footnote 2 and refs. 23 and 24.

3. Results

(a) Optimized geometries

The two net reactions investigated are

$$H_2C{=}CHCH_2CH_3 \rightarrow CH_2CHCH_2\cdot + CH_3^+ + e^-$$

and

$$H_2C{=}CHCH_2C(CH_3)_3 \rightarrow CH_2CHCH_2^+ + C(CH_3)_3\cdot + e^-$$

Each reaction sequence can proceed through two different pathways: an initial ionization of the neutral reactant, followed by cleavage and electron transfer, or by initial cleavage of the neutral species into two radical moieties, followed by ionization of one of them, and subsequent electron transfer. The B3LYP optimized geometries of the various reactants, intermediates, and products are shown in Figs. 1–3.

In the cleavage reaction of 1-butene, the fragmentation products are the allyl radical cation and the methyl radical cation, Figs. 3*a–d*, whereas for the 4,4-dimethyl-1-pentene system, the products of the cleavage reactions are instead the allyl and *t*-butyl radicals cations, Figs. 3*a, b, e, f*.

1-Butene conformers

For the neutral nonplanar 1-butene the highest occupied molecular orbital (HOMO) is localized to the π-bond, i.e., the C1 and C2 p_z orbitals perpendicular to the C1-C2-C3 plane. When 1-butene is ionized the HOMO (now the singly occupied molecular orbital, SOMO) changes localization to the antibonding σ*-orbital between C3 and C4, whereby the π-bond interaction between C1 and C2 is much reduced. Thus the length of the C1=C2 bond increases to above 1.40 Å, and attains a value close to that associated with a bond order of "1.5," observed in, e.g., the benzene molecule. Also the C3—C4 distance lengthens from 1.54 to 1.61.

Interestingly enough, also the local geometry of the β-carbon (C3) is strongly affected by the ionization. As seen in Figs. 1*a* and *b*, the C2—C3 bond length is markedly shortened after ionization, from 1.50 to 1.45, and the C2-C3-C4 bond angle now more resembles that of an sp^2 hybridized carbon. Furthermore the H-C3-H angle decreases by roughly 5°. All other C—H bond lengths and H-C-C bond angles remain more or less unaltered by the ionization process. The B3LYP optimized geometry of the 1-butene cation closely resembles those from previous MP2 and DFT optimizations (12, 25); the largest difference in C—C bond length between B3LYP and MP2 is 0.005 Å, and the mean deviation is 0.002 Å.

For the 1-butene radical cation three different stationary points were found, two planar (*eclipsed* and *anti*) and one nonplanar (*skewed*). The energy differences between the three forms are within 0.9 kcal/mol, with the skewed 1-butene conformer being lowest in energy. The frequency calculations showed one negative frequency for the *anti* conformer but none for the eclipsed and skewed forms. Hence, at the B3LYP level, the *anti* conformer is a transition state, not a local minimum, corresponding to out-of-plane motion connecting the two mirror images of the skewed conformer. However, after adding the ZPVE the *anti* conformer becomes the lowest in energy of the three, and the skewed con-

© 1998 NRC Canada

Fig. 1. The optimized geometries of the skewed 1-butene (energy = –157.274 70 Hartree) (*a*) and its radical cation (*b*), eclipsed 1-butene (*c*) and its radical cation (*d*), and the *anti* 1-butene (*e*) and its radical cation (*f*). All calculations are performed using the gradient corrections and basis sets described in the text.

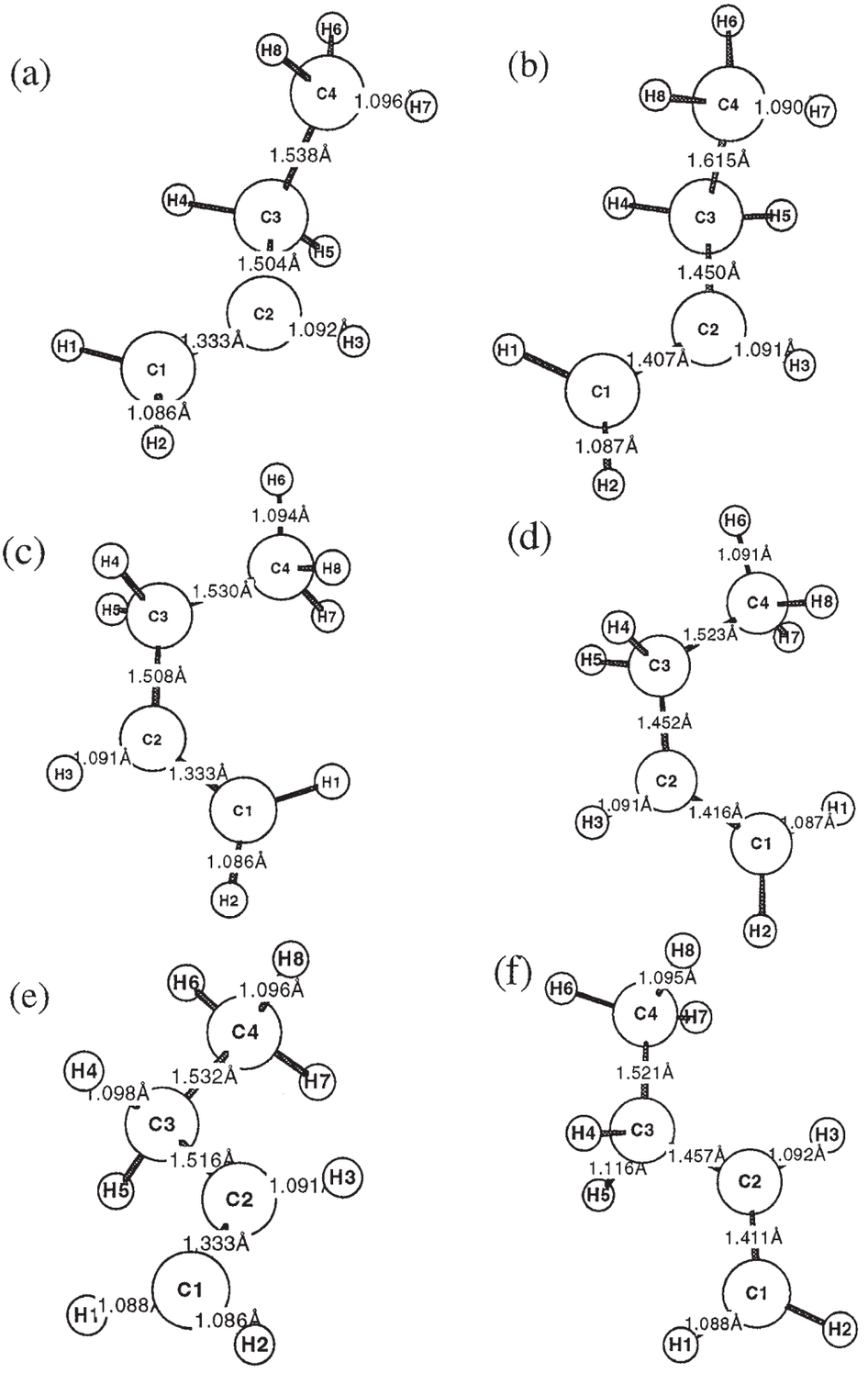

former the highest. The ZPVE-corrected energies are now in a range of 0.5 kcal/mol. For the neutral 1-butene the three conformers are within 2 kcal/mol of each other without ZPVE, and 1.7 kcal/mol with ZPVE included. Since the en-

© 1998 NRC Canada

Fig. 2. The optimized geometries of the 4,4-dimethyl-1-pentene (energy = –275.250 57 Hartree) (*a*) and its radical cation (*b*). All calculations are performed using the gradient corrections and basis sets described in the text.

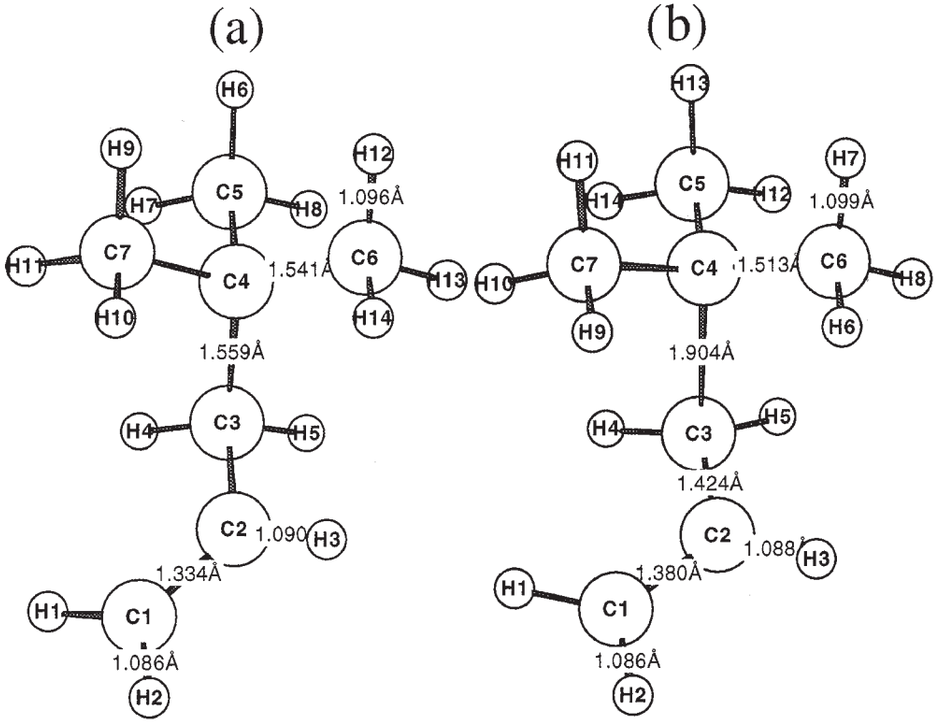

ergy differences are so small we may expect substantial rotation to occur in the 1-butene both for the neutral and the cationic species. The present results are in close accord with previous MP2//UHF calculations that yielded a 1 kcal/mol energy difference between the eclipsed and anti conformer (17).

The differences in C—C bond lengths in the C1–C3 part of the three neutral conformers of 1-butene are at most 0.012 Å, and for the corresponding ions 0.009 Å. The C1-C2-C3 angle varies 1.4° among the different neutral conformers, and 2.5° among the ionic ones. The difference in methyl–allyl bond length is 0.008 Å among the neutral conformers and 0.094 Å between the ionic forms.

4,4-Dimethyl-1-pentene

When 4,4-dimethyl-1-pentene is ionized the allyl–*t*-butyl bond length increases from 1.56 to 1.90 Å, the C=C2 bond lengthens from 1.33 to 1.38 Å, the C2—C3 bond shortens from 1.51 to 1.42 Å, and the C1=C2-C3 angle decreases from 125° to 123° (Figs. 2*a* and *b*). This indicates the same type of orbital interactions for this compound as those observed for 1-butene. For computational reasons we only examined the skewed form of 4,4-dimethyl-1-pentene. The out-of-plane angle (dihedral C4-C3-C2-C1) is for this system 117.1° (neutral) and 99.8° (cation), compared with 119.9° (neutral) and 98.5° (cation) for the skewed form of 1-butene. These dihedral angles compare well with earlier findings at HF and MP2 levels (12, 17, 25).

t-*Butyl and methyl*

The *t*-butyl radical is found to be pyramidal at the present level of calculations, Fig. 3*e*, as in previous UHF and CIS calculations (26, 27). The top angle (the angle between the C—H or C—C bond and its projection in the nodal plane of the p_z orbital of the central carbon atom) is found to be 6.2°. Upon ionization, the electron is removed from the central carbon p_z orbital perpendicular to the molecular plane. The planar conformation is thereby stabilized as the possibility of gaining energy by means of a partial sp^3 type hybridization of the central carbon atom (yielding a pyramidal structure) is diminished. In the *t*-butyl cation, which is planar at the present level of calculation, all bond lengths are reduced somewhat as a result of the ionization, Fig. 3*f*, whereas for CH_3^+ we instead note an increase in the C—H bond lengths, Figs. 3*c* and *d*. The C—H bond distance for the methyl radical is in satisfactory agreement with experiment (1.082 vs. 1.079 Å). The equilibrium geometries of most of these molecules have previously been thoroughly investigated by theory as well as experiment. For both the *t*-butyl (27, 28) and methyl radicals, the potential energy surfaces are known to be very flat with respect to pyramidal motions, and it has been shown that the vibrational motion affects the hyperfine properties of the central carbon significantly (14, 27, 29–33).

Allyl

For the allyl radical, DFT calculations have previously been shown to yield too short C—C bond lengths relative to experiment (14). This is true also for the present calculations, although a minor improvement is noted. The main effect of the ionization is a decreased C1-C2-C3 bond angle (125° to 119°), whereas the C—C bond lengths are unaltered (cf. Figs. 3*a* and *b*). Minor modifications are also noted in the C—H bond lengths.

© 1998 NRC Canada

Fig. 3. The optimized structures of the fragmentation products of 1-butene and 4,4-dimethyl-1-pentene. The allyl radical (*a*) and its cation (*b*), the methyl radical (*c*) and its cation (*d*), and the *t*-butyl radical (*e*) and its cation (*f*). All calculations are performed using the gradient corrections and basis sets described in the text.

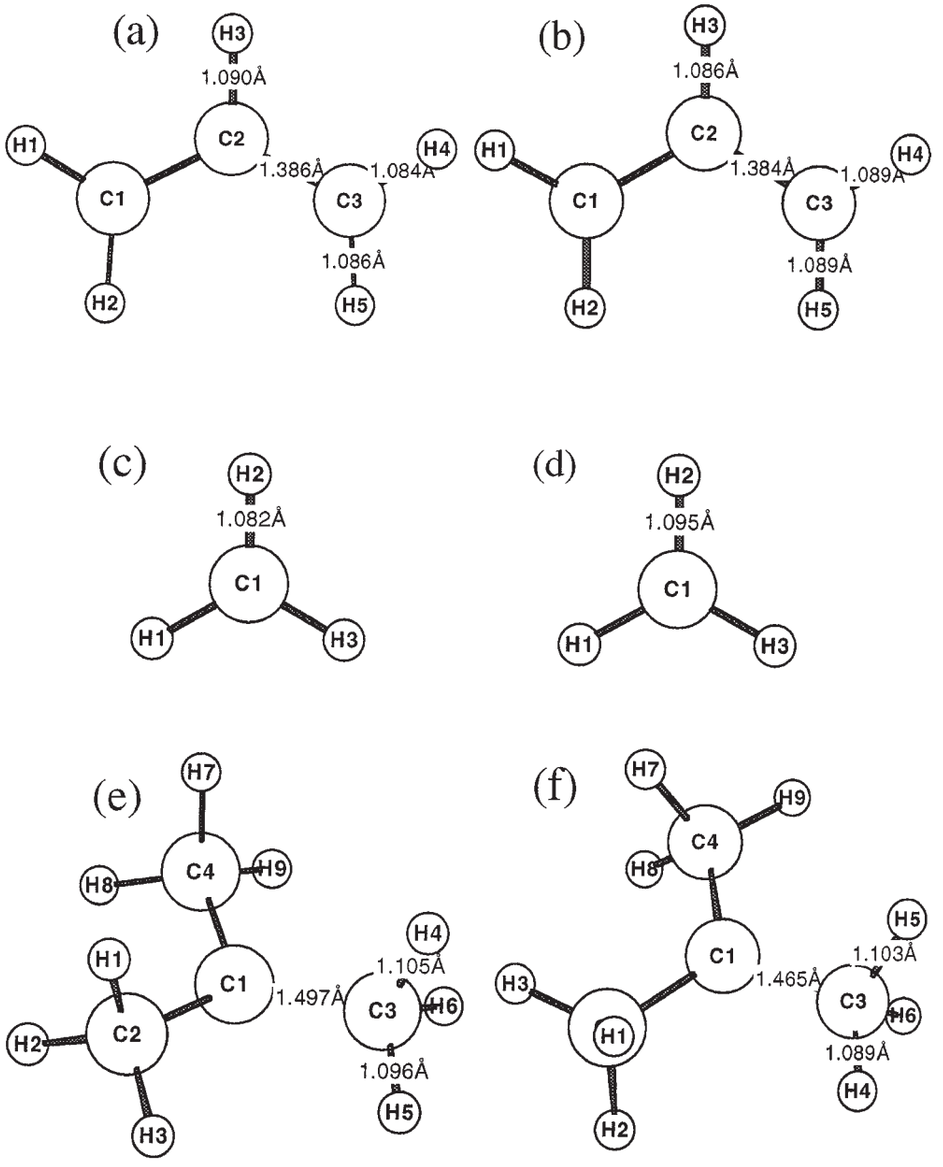

(b) Energetics

We show in Figs. 4 and 5 the energetics of the different ionization-, cleavage-, and electron-transfer reactions investigated in the present work. In Fig. 4 the reactions starting from the 1-butene molecule are displayed, and in Fig. 5 the corresponding reaction sequences for the 4,4-dimethyl-1-pentene system are presented. All energies are obtained from B3LYP/6-311G(2df,p) calculations using the corresponding B3LYP/6-31G(d,p) optimized geometries. Since the ZPVE is only well defined if the molecule is at a stationary point on its potential surface, the ZPVE correction is omitted from the energies involving the vertical ionization.

1-Butene

Following the two pathways of the 1-butene radical system (Fig. 4), we first of all note a very good overall agreement between the present DFT calculated energies and experimental data. We also note that the energetics predicted from the present DFT calculations are in far better agreement with experiment than the previous MP2//UHF data (17), with a mean absolute deviation of 3.0 kcal/mol vs. 19.7 kcal/mol (including adiabatic ionization process and without ZPVE). The main discrepancies occur for the reactions involving the neutral 1-butene. The ground state of the cation appears to be some 4.3 kcal/mol too low in energy

© 1998 NRC Canada

Fig. 4. Schematic representation of the energetics of the cleavage reactions of 1-butene. All energies (kcal/mol) have been calculated at B3LYP/6-311G(2df,p)//B3LYP/6-31G(d,p) level with ZPVE correction, except for the vertical ionization energy (see text). Experimental data (34), where available, are given in parentheses.

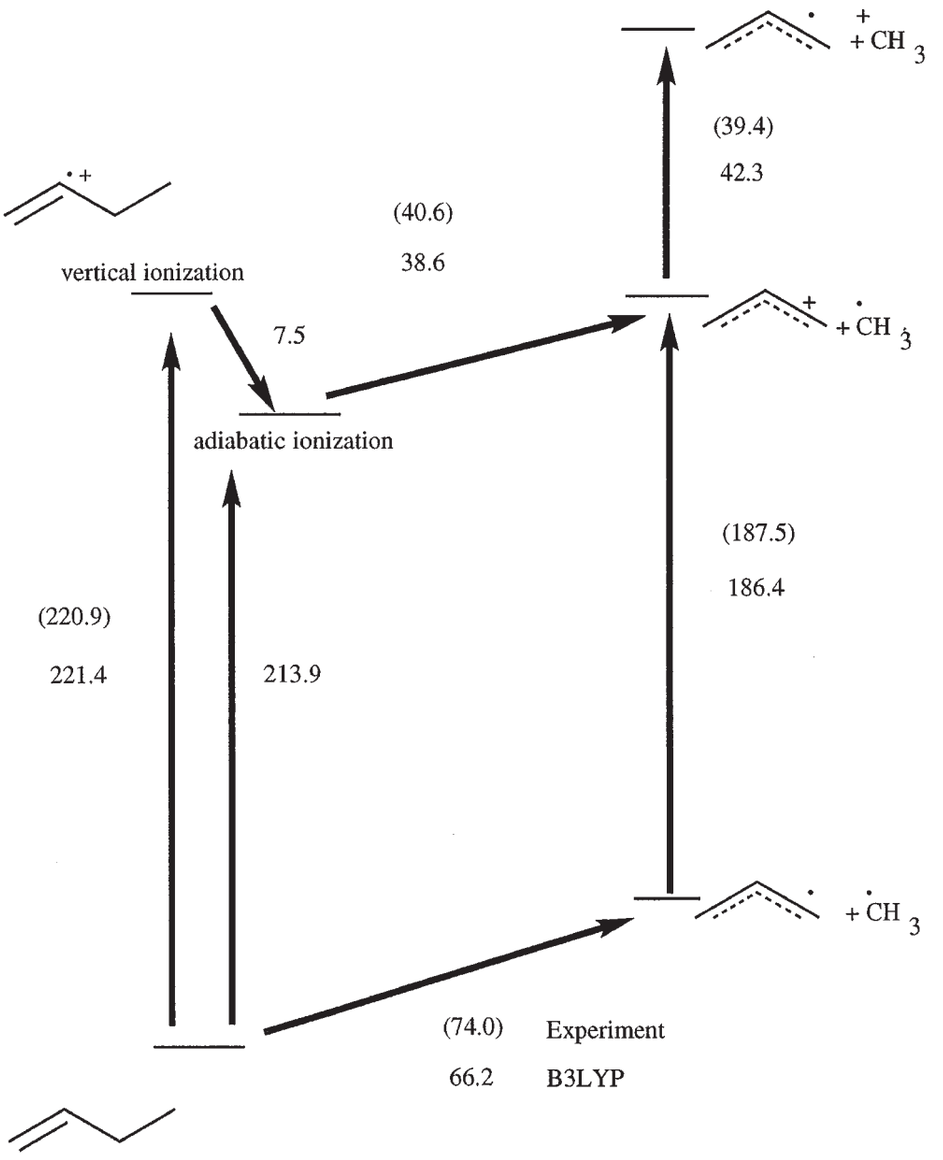

relative to the other reactants and products involved. The differences compared to experiment are reduced considerably if we assume vertical ionization of the neutral molecule, Table 1. For 1-butene, the vertical ionization will raise the relative position of $C_4H_8^+$ by 7.5 kcal/mol, whereby the energy difference between calculated and experimental data for this ionization process is reduced from 7.0 to 0.5 kcal/mol. As noted above, the different rotational conformers of 1-butene and 1-butene cation lie very close in energy. It is hence unlikely that the deviation is caused by different rotational structures for the neutral and cationic species. For the electron transfer process between the allyl cation – methyl radical and the allyl radical – methyl cation, there is a difference between theory and experiment of 2.9 kcal/mol.

As a comparison between the MP2 and B3LYP methods we also calculated the energies for the 1-butene reaction sequence at the HF and MP2/6-311G(2df,p) levels using the same B3LYP/6-31G(d,p) optimized geometries. This gives a MAD of 21 kcal/mol at HF and 8–10 kcal/mol at MP2 level, respectively (cf. Table 1), i.e., in worse agreement with experiment.

4,4-Dimethyl-1-pentene

For the second set of reactions, starting with the 4,4-dimethyl-1-pentene molecule, the agreement is again found to be most satisfactory. For this sequence the steps involving the ionization and electron transfer of the cleavage products allyl and *t*-butyl agree very well with experiment. We also

© 1998 NRC Canada

Fig. 5. Schematic representation of the energetics of the cleavage reactions of 4,4-dimethyl-1-pentene. All energies (kcal/mol) have been calculated at B3LYP/6-311G(2df,p)//B3LYP/6-31G(d,p) level with ZPVE correction, except for the vertical ionization energy (see text). Experimental data (34), where available, are given in parentheses.

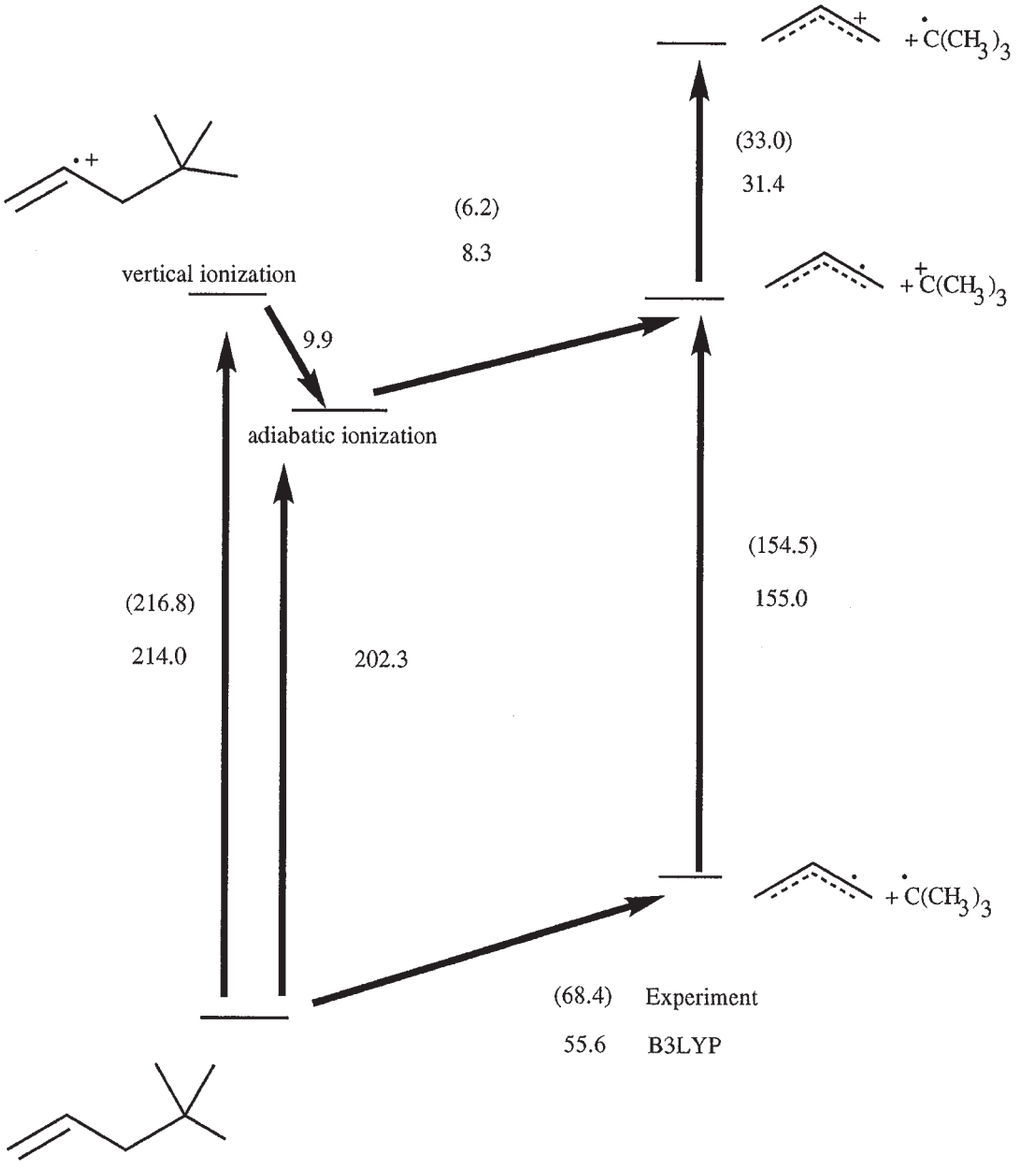

Table 1. Mean absolute deviation from experiment for the full processes investigated.

Method[a]	1-Butene	4,4-Dimethyl-1-pentene	Average
B3LYP,[b] ZPVE, vertical	2.86	3.96	3.41
B3LYP,[b] no ZPVE, vertical	1.94	4.00	2.97
B3LYP,[b] ZPVE, adiabatic	4.16	6.30	5.23
B3LYP,[b] no ZPVE, adiabatic	2.96	5.98	4.47
HF[c]/MP2[d], no ZPVE, vertical	20.6/9.5		
HF[c]/MP2[d], no ZPVE, adiabatic	21.2/8.2		

[a]Indicates if ZPVE is included or not, and if ionization process from neutral parent molecule is vertical or adiabatic.
[b]B3LYP/6-311G(2df,p)//B3LYP/6-31G(d,p).
[c]HF/6-311G(2df,p)//B3LYP/6-31G(d,p).
[d]MP2/6-311G(2df,p)//B3LYP/6-31G(d,p).

© 1998 NRC Canada

Table 2. Isotropic hyperfine parameters (in Gauss) of the different radicals investigated in the present work (see Figs. 1–3).

(*a*) $\cdot H_2C{=}CHCH_2CH_3^+$

	B3LYP				
Atom	Skew	*anti*	Eclipsed	CISD	Expt.
C1	12.2	12.2	12.6		
C2	0.9	1.4	1.5		
C3	–4.0	–5.0	–5.0		
C4	11.7	–1.4	–0.8		
H1-H2	–10.4	–12.9	–13.5	–12.6, –12.3	(–)9.8, (–)16.6
H3	–3.3	–6.7	–6.3	–3.1	(–)6.4
H4-H5 (2)	4.5	59.3	51.7	19.8, 27.8	39.0
H6-H8 (3)	7~9	5.1	2.1	0	"0"
Ref.		This work		25	32
ΔE (kcal/mol)	0	0.87	0.64		
ΔE + ZPVE	0	–0.49	–0.38		

(*b*) $\cdot H_2C{=}CHCH_2CH_3^+$

Atom	Rotationally averaged	Expt.
C1	12.3	
C2	1.2	
C3	–4.5	
C4	5.3	
H1-H2	–11.8	(–)9.8, (–)16.6
H3	–4.9	(–)6.4
H4-H5 (2)	30.0	39.0
H6-H8 (3)	5.8	"0"
Ref.	This work	(32)

(*c*) $\cdot H_2C{=}CHCH_2C(CH_3)_3^+$

Atom	B3LYP
C1	11.3
C2	–5.7
C3	2.1
C4	2.2
C5-C7 (3)	–1.5
H1-H2	–9.8
H3	0.0
H4-H5 (2)	5.3
H6-H14 (9)	7.7
Ref.	This work

(*d*) $\cdot CH_2\text{-}CH\text{-}CH_2$

Atom	B3LYP	CIS[a]	Expt.
C2	–16.0	–23.7/–19.2	(–)17.2
C1, C3 (2)	17.5	21.8/17.3	21.9
H2	4.3	5.5/2.0	4.2
H3, H5	–14.4	–20.5/–14.5	(–)14.8
H4, H6	–13.6	–19.7/–13.7	(–)13.9
Ref.	This work	(35)	(35*a*, *b*)

(*e*) $\cdot C(CH_3)_3$

Atom	B3LYP	CIS	Expt.
C1	41.7	32.6/49.9	38/46
C2-C4 (3)	9.6	–14.9/ –11.6	(–)12.3
H1-H9 (9)	21.1	18.0/16.4	22.7
Ref.	This work	Plan/pyr., (27)	(31, 32)

(*f*) $\cdot CH_3$

Atom	B3LYP	B3LYP-MD	CIS	CISD	Expt.[b]
C1	27.6	26.5	30.4	16.3	27
H1-H3 (3)	–20.89	–23.0	–29.8	–26.3	(–)23.0
Ref.	This work	4K (33)	Vib. avg., (29)	(36)	(35)

[a]CIS(MCSCF)/CIS(RHF).

[b]Vibrational effect removed.

note the interesting fact that the energetic order between the allyl cation + *t*-butyl radical vs. allyl radical + *t*-butyl cation is reversed relative to that in Fig. 4 (allyl and methyl systems), as has also been observed experimentally (34).

The theoretical predictions, DFT as well as ab initio (17), deviate the most for the neutral 4,4-dimethyl-1-pentene system. With the present gradient-corrected DFT method, the deviation in adiabatic ionization energy towards the experimental data is 14.5 kcal/mol for the neutral molecule, including ZPVE. If we use the vertical ionization of 4,4-dimethyl-1-pentene instead of the energy for the optimized radical cations the deviation from experiment decreases from 14.5 to 2.8 kcal/mol. For the cleavage process of the neutral molecule the deviation from experiment is 12.8 kcal/mol, including ZPVE, and we have been unable to find the reason for this high deviation.

(c) Hyperfine parameters

The computation of hyperfine data has been one of many successful applications of gradient-corrected density func-

© 1998 NRC Canada

tional theory during recent years, with results often in close agreement with experimental data and highly accurate MRCI calculations (footnotes 2 and 3, ref. 5). The isotropic HFCC data of the presently studied cationic 4,4-methyl-1-pentene and 1-butene radical systems, and the neutral methyl, allyl, and *t*-butyl radicals, are listed in Table 2. For the 1-butene cation, Table 2*a*, previous CISD calculations on UHF, MP2, and semiempirical MNDO optimized geometries (25) have indicated that the radical is twisted about the weakened double bond. Geometry optimization calculations at the BP/DZP level (12) as well as the present calculations however indicate that the C=C-C (allyl) framework is planar (the C1 and C2 hydrogens remain in the plane of the C1-C2-C3 carbons). Furthermore, since the rotational barrier about the terminal C3—C4 bond, and also the middle C2—C3 bond are both very minor (17, 25), one may assume that the HFCC should be rotationally averaged with respect to C2–C3 and C3–C4 rotations. The data shown in the table are the static data (except for the rotational averaging of the terminal methyl groups), and are hence numerically larger than when averaging over a full 360° rotational motion. We note the very good agreement between the present data and that from CISD calculations on the 21° H1-C1-C2-C3 twisted structure (25). The too large H4 and H5 couplings in the present work can be ascribed to the neglect of rotational averaging. As seen from Table 2*a* the HFCC at, in particular, these positions vary markedly between the three conformers studied. Assuming a rotationally averaged set (eclipsed–skewed–*anti*–skewed), the agreement becomes much improved for all atoms, Table 2*b*. The need for rotationally averaged data also explains the poor agreement for H4-H5 also obtained at the CISD level, Table 2*a*.

For the allyl radical, the agreement between the B3LYP calculations and experiment is most satisfactory, Table 2*d*. For the two previous CIS studies (35), it seems that the one where the orbitals are obtained from preliminary MCSCF calculations render less satisfactory results relative to the more "simple" CIS(RHF) study.

For both the methyl and the *t*-butyl radical, there has been much discussion among theoreticians and experimentalists, as to the planarity/nonplanarity of the systems (for a brief summary of this, see ref. 33). The most recent conclusion in this matter, based on a collective matrix isolation ESR and theoretical picture, is that the methyl group is planar, whereas *t*-butyl carries a slight pyramidal angle as outlined above.

For methyl, previous calculations on both planar structures and those where a 5° nonplanarity is introduced (cf. Table 2*f*.) as well as coupled DFT – molecular dynamics simulations (33) indicate that the main changes occur on the central carbon. The potential surface is, however, extremely flat with respect to out-of-plane motion, and hence a vibrationally averaged HFCC is observed experimentally, rather than one arising from a static geometry (29). The effects of vibrational averaging on the HFCCs of methyl and deuterated methyl has recently been demonstrated in a hybrid B3LYP-MD simulation of CH_3 in rare gas matrices at 4 and 85 K (33). Within the static framework, i.e., subtracting the effects of vibration from the experimental data, the overall agreement seems better at the DFT level than when using the various single reference ab initio methods, Tables 2*d* and *e*.

4. Conclusions

In the present work, we have investigated the suitability of hybrid HF gradient-corrected density functional theory to predict geometries, energetics, and hyperfine properties of two sets of alkene cleavage reactions. The emphasis has been on the relative energies involved, which are found to be in close agreement with experimental data. Mean absolute deviation from experiment for the two reaction sequences studied is 3.4 kcal/mol, Table 1, which is a marked improvement over the 19.7 kcal/mol (17) for the previous study of the same process. At the MP2/6-311G(2df,p) level (this work) the mean absolute deviation for the process starting from 1-butene are considerably larger than at the corresponding B3LYP level (9.5 vs. 1.9 kcal/mol) In addition, the B3LYP/6-311G(2df,p) calculations yield HFCC in very good agreement with experimental data. The HFCCs together with calculated energies for the three 1-butene cation conformers indicate that the molecule undergoes significant rotational motion about the C2—C3 bond, leading to a rotationally averaged structure.

Acknowledgments

This work was supported by the Swedish Natural Science Research Council (NFR) and the Natural Sciences and Engineering Research Council of Canada (NSERC).

References

1. J. Labanowski and J. Andzelm. (*Editors*). Density functional methods in chemistry. Springer-Verlag, New York. 1991.
2. P. Politzer and J.M. Seminario (*Editors*). Theoretical and computational chemistry. Vol. 2. Modern density functional theory - a tool for chemistry. Elsevier, Amsterdam. 1995.
3. D.P. Chong (*Editor*). Recent advances in density functional theory, part 1. World Scientific, Singapore. 1995.
4. M. Springborg (*Editor*). Density functional methods: applications in chemistry and materials science. Wiley, New York. 1997.
5. L.A. Eriksson. Mol. Phys. **91**, 827 (1997).
6. J.P. Perdew and Y. Wang. Phys. Rev. **B33**, 8800 (1986).
7. J.P. Perdew. Phys. Rev. **B33**, 8822 (1986); **B34**, 7406 (1986).
8. A.D. Becke. J. Chem. Phys. **98**, 1372 (1993).
9. P.J. Stephens, F.J. Devlin, C.F. Chablowski, and M.J. Frisch. J. Phys. Chem. **98**, 11 623 (1994).
10. A.D. Becke. Phys. Rev. **A38**, 3098 (1988).
11. C. Lee, W. Yang, and R.G. Parr. Phys. Rev. **B37**, 785 (1988).
12. L.A. Eriksson, S. Lunell, and R.J. Boyd. J. Am. Chem. Soc. **115**, 6896 (1993); N. Salhi-Benachenhou, L.A. Eriksson, and S. Lunell. Acta Chem. Scand. **51**, 636 (1997).
13. L.A. Eriksson, V.G. Malkin, O.L. Malkina, and D.R. Salahub. J. Chem. Phys. **99**, 9756 (1993); L.A. Eriksson, O.L. Malkina, V.G. Malkin, and D.R. Salahub. J. Chem. Phys. **94**, 100 (1994).
14. L.A. Eriksson, V.G. Malkin, O.L. Malkina, and D.R. Salahub. Int. J. Quantum Chem. **52**, 879 (1994).
15. M.W. Wong and L. Radom. J. Phys. Chem. **99**, 8582 (1995).
16. T. Fängström, S. Lunell, B. Engels, L.A. Eriksson, M. Shiotani, and K. Komaguchi. J. Chem. Phys. **107**, 297 (1997).
17. X. Du, D.R. Arnold, R.J. Boyd, and Z. Shi. Can J. Chem. **69**, 1365 (1991).
18. A.L. Perrott, H.J.P. de Lijser, and D.R. Arnold. Can. J. Phys. **75**, 384 (1997).

© 1998 NRC Canada

19. M.J. Frisch, G.W. Trucks, H.B. Schlegel, P.M.W. Gill, B.G. Johnson, M.A. Robb, J.R. Cheeseman, T. Keith, G.A. Petersson, J.A. Montgomery, K. Raghavachari, M.A. Al-Laham, V.G. Zakrzewski, J.V. Ortiz, J.B. Foresman, J. Cioslowski, B.B. Stefanov, A. Nanayakkara, M. Challacombe, C.Y. Peng, P.Y. Ayala, W. Chen, M.W. Wong, J.L. Andres, E.S. Replogle, R. Gomperts, R.L. Martin, D.J. Fox, J.S. Binkley, D.J. Defrees, J. Baker, J.P. Stewart, M. Head-Gordon, C. Gonzalez, and J.A. Pople. Gaussian 94, Revision B.2. Gaussian, Inc., Pittsburgh, Pa. 1995.
20. J.C. Slater. Quantum theory of molecules and solids. McGraw–Hill, New York. 1974.
21. S.H. Vosko, L. Wilk, and M. Nusair. Can. J. Phys. **58**, 1200 (1980).
22. R. Krishnan, J.S. Binkley, R. Seeger, and J.A. Pople. J. Chem. Phys. **72**, 650 (1980); **80**, 3265 (1984).
23. W. Meyer. J. Chem. Phys. **51**, 5149 (1969).
24. W. Weltner, Jr. Magnetic atoms and molecules. Van Nostrand, New York. 1983.
25. S. Lunell, L.A. Eriksson, and M.-B. Huang. J. Mol. Struc. (Theochem), **230**, 263 (1991).
26. I. Carmichael. J. Phys. Chem. **89**, 4727 (1985).
27. R.E. Overill. J. Comput. Chem. **12**, 231 (1991).
28. A.L.L. East. J. Chem. Phys. 3914 (1997).
29. D.M. Chipman. J. Chem. Phys. **78**, 3112 (1983).
30. I. Carmichael. J. Phys. Chem. **89**, 4727 (1985).
31. D.E. Wood and R.F. Sprecher. J. Am. Chem. Soc. **94**, 6241 (1972); Mol. Phys. **26**, 1311 (1973), and refs. therein.
32. A. Abu-Raqabah and M.C.R. Symons. Chem. Phys. Lett. **183**, 171 (1991), and refs. therein.
33. L.A. Eriksson and A. Laaksonen. Recent Res. Dev. Phys. Chem. **2**, 369 (1998).
34. H.M. Rosenstock, K. Draxl, B.W. Steiner, and J.T. Herron. J. Phys. Chem. Ref. Data Suppl. **6**, 1 (1977); F.P. Lossing. Can. J. Chem. **50**, 3973 (1972); D.P. Wang, L.C. Lee, and S.K. Srivastava. Chem. Phys. Lett. **152**, 513 (1988); J.L. Holmes and F.P. Lossing. Int. J. Mass. Spectrom. Ion Processes, **58**, 113 (1984); D. Griller, J.M. Kanobus-Kaminska, and A. Maccoll. J. Mol. Struc. (Theochem), **40**, 125 (1988); P. Masclet, D. Grosjean, and G. Mouvier. J. Electron Spectrosc. Relat. Phenom. **2**, 225 (1973); W. Tsang. J. Am. Chem. Soc. **107**, 2872 (1985).
35. (*a*) H.J. McManus, R.W. Fessenden, and D.M. Chipman. J. Phys. Chem. **92**, 3778 (1988); R.W. Fessenden and R.H. Schuler. J. Chem. Phys. **39**, 2147 (1963); T. Nanako, K. Morihashi, and O. Kikuchi. Bull. Chem. Soc. Jpn. **65**, 603 (1992).
36. D. Feller and E.R. Davidson. J. Chem. Phys. **80**, 1006 (1984).

© 1998 NRC Canada

Spectroscopic studies of triphenyltin azide and of its adducts with *O*- and *N*-donor ligands; the crystal and molecular structures of triphenyltin azide and of azido(hexamethylphosphoramide)triphenyltin(IV)[1]

Ivor Wharf, Ryszard Wojtowski, Carol Bowes, Anne-Marie Lebuis, and Mario Onyszchuk

Abstract: Complete far-IR and Raman data (<400 cm^{-1}) are reported for triphenyltin azide (**1**) as well as for adducts $Ph_3SnN_3 \cdot L$ (L = hexamethylphosphoramide (HMPA), triphenylphosphine oxide, pyridine-*N*-oxide, 4-picoline-*N*-oxide, or pyridine). The small changes in $\nu(Sn\text{-}N_3)$ noted on going from (**1**) to the adducts, as well as solid-state ^{119}Sn nmr data, indicate that (**1**), like the adducts, has five-coordinate tin atoms. X-ray analysis shows that (**1**) crystallizes with two different chains of five-coordinate Ph_3Sn units joined by 1,3-azide bridges. In one unit, the geometry around tin is similar to that found for the monomeric HMPA adduct (**2**), which has *trans*-axial HMPA and azide ligands. The other unit in (**1**) has nonplanar -SnC_3- groups connected by less symmetric 1,3-azide bridges and thus resembles the structure of isoelectronic triphenyltin isocyanate.

Key words: triphenyltin azide, *O*- and *N*-donor adducts, far-IR/Raman, crystal structures.

Résumé : On a enregistré les spectres Raman et IR-lointain complets (<400 cm^{-1}) de l'azoture de triphénylétain (**1**) et de ses adduits $Ph_3SnN_3 \cdot L$ (L = hexaméthylphosphoramide (HMPA), oxyde de triphénylphosphine, *N*-oxyde de pyridine, *N*-oxyde de 4-picoline ou pyridine). Les faibles changements dans les $\nu(Sn\text{-}N_3)$ observés en passant du produit **1** à ses adduits, ainsi que les données de RMN à l'état solide du ^{119}Sn, indiquent que le composé **1**, comme ses adduits, comporte des atomes d'étain pentacoordinés. Une analyse par diffraction des rayons X montre que le composé **1** cristallise avec deux chaînes différentes d'unités Ph_3Sn pentacoordinées liées par des ponts azotures-1,3. Dans l'une des unités, la géométrie autour de l'étain est semblable à celle que l'on retrouve dans l'adduit monomère du HMPA, **2**, qui comporte des ligands HMPA et azoture *trans*-axiaux. L'autre unité du composé **1** comporte des groupes -SnC_3- non planaires reliés par des ponts azotures-1,3 moins symétriques qui ressemblent donc à la structure de l'isothiocyanate de triphénylétain isoélectronique.

Mots clés : azoture de triphénylétain, adduits *O*- et *N*-donneurs, IR-lointain/Raman, structures cristallines.

[Traduit par la Rédaction]

Introduction

Triaryltin halides (Ar_3SnX, X = Cl, Br) are monomeric with four-coordinate tin (**A**) (1–6) but they form stable five-coordinate adducts ($Ar_3SnX \cdot Y$), which when X = Y have exact trigonal-bipyramidal geometry at tin with aryl groups occupying the equatorial positions (**C**) (7, 8), and almost this geometry when Y is the donor atom of a strong ligand such as a sulfoxide (9) or Ph_3PO (10, 11).

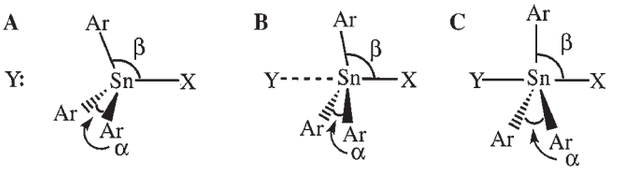

However, (**A**) and (**C**) represent extremes of a $YSnC_3X$ structural continuum (12, 13), and if Y is a weaker donor atom than X, intermediate geometries (**B**) will occur where Y is less strongly coordinated than X, and the SnC_3 moiety is nonplanar (14). With an ambidentate chalcocyanate unit anion (-X = -NCZ; Z = O, S, Se) further possibilities arise. Thus while monomeric Ar_3SnNCS (**A**) have been identified (15) and stable five-coordinate adducts ($Ar_3SnNCZ \cdot L$) (**C**) are well known (15, 16), less hindered Ph_3SnNCS is poly-

Received March 24, 1998.

I. Wharf,[2] R. Wojtowski, C. Bowes, A.-M. Lebuis, and M. Onyszchuk. Department of Chemistry, McGill University, 801, Sherbrooke St. W., Montreal, PQ H3A 2K6, Canada.

[1]Presented in part at the Royal Society of Chemistry 1997 Autumn Meeting, Aberdeen, Scotland, U.K., September 2–5, 1997.

[2]Author to whom correspondence may be addressed. Telephone: (514) 398-6931. Fax: (514) 398-3797. E-mail: wharf@omc.lan.mcgill.ca

© 1998 NRC Canada

Table 1. Synthesis and characterization details for triphenyltin azide adducts, $Ph_3SnN_3 \cdot L$.

Ligand (**L**[a]) (g)	Solvent (mL)	Yield (%)	mp (°C)	%C[b]	%H[b]	%N[b]	$\nu_{as}(N_3)$ (cm^{-1})	$\nu(X=O)$ (cm^{-1})
HMPA (1.0)	Toluene (5.0)	99	107 (105–106)[c]	—	—	—	2057	1189
Ph_3PO (1.0)	Toluene (25)	99	148	64.20 (64.40)	4.41 (4.50)	6.17 (6.25)	2062	1149
pyO (0.75)	Toluene (35)	60	121	56.89 (56.71)	4.20 (4.13)	11.46 (11.50)	2063, 2055	1217
4-picO (0.35)	Toluene (20)	86	139	57.19 (57.51)	4.33 (4.42)	10.99 (11.17)	2064	1204
py (10.0)	Hexane (70)	83	112	59.03 (58.63)	4.08 (4.27)	11.96 (11.89)	2060	1590 [8*a*][d] 1567 [8*b*][d] 1414 [14][d]

[a]HMPA = hexamethylphosphoramide; pyO = pyridine-*N*-oxide; 4-pico = 4-picoline-*N*-oxide; py = pyridine.
[b]Calculated values in parentheses.
[c]Reference 24.
[d]Pyridine ring modes (27).

meric with a planar -SnC_3- moiety (**D**) (15, 17). In contrast, triphenyltin isocyanate has a less strongly bridged structure (**E**) (18) with a nonplanar geometry at tin.

While tin Mössbauer and NMR spectra may be used to

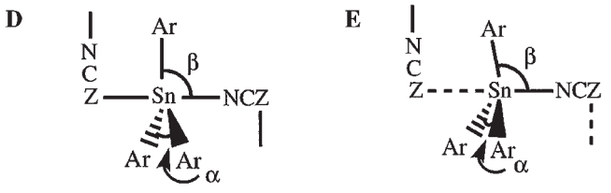

ascertain the degree of coordination at tin in Ar_3Sn systems, the change in ν(Sn-X) when Ph_3SnX is converted to its five-coordinate (1/1) adduct also depends on the coordination at tin in the given Ph_3SnX (16). Thus if X = Cl or Br, ν(Sn-X) decreases by ~25 or ~35%, respectively, indicative of the change from structure (**A**) to (**C**). For Ph_3SnNCS, with the same geometry at tin (**D**) as in the adducts (**C**), no change in ν(Sn-NCS) occurs on adduct formation, but with Ph_3SnNCO, the decrease by ~10% in ν(Sn-NCO) on adduct formation was considered consistent with its asymmetric five-coordinate geometry at tin (**E**) (16, 18).

Triphenyltin azide, isoelectronic with the isocyanate, was proposed on the basis of powder X-ray diffraction results (19) to be isomorphous with Ph_3SiN_3, later determined to be molecular with four-coordinate silicon (20). In contrast Mössbauer data for Ph_3SnN_3 (21) were considered more consistent with five-coordinate tin and a trigonal bipyramidal structure, as found also for the anions $Ph_3SnN_3X^-$ (X = N_3, NCS) (22) and the adduct $Ph_3SnN_3 \cdot Ph_3SnOH$ (23). Thus the question remains whether the Ph_3SnN_3 structure resembles that of Ph_3SnNCO (**E**) or that the *symmetric* azide ion forms symmetric 1,3-bridges, giving rise to a planar environment at tin (**D**). Since triphenyltin azide forms many adducts with neutral *O*- and *N*-donor ligands (24, 25), we have now extended our earlier far-infrared (far-IR) and Raman spectral studies (16) to Ph_3SnN_3 and its adducts, in order to shed more light on the structure of triphenyltin azide.

Experimental

All experimental procedures including microanalyses, and Raman (powder) and infrared (Nujol mull) spectral measurements were as described earlier (16), as were also solution tin-119 nmr studies (26). Solid-state tin-119 CPMAS nmr spectra were obtained on a Chemagnetics CMX-300 operating at 111.7 MHz. The sample was contained in a 7.5 mm rotor and spun at 3–4 kHz. The contact time and recycle delay were 3 ms and 240 s, respectively. Typically 200–300 transients were acquired. Sidebands were suppressed using a six-pulse TOSS pulse sequence. Chemical shifts were referenced to external $Sn(CH_3)_4$.

Preparations

*(a) Triphenyltin azide (**M**)*

Previously dried sodium azide (10.4 g, 0.160 mol) was added to a solution of triphenyltin chloride (30.8 g, 0.080 mol) in acetone (600 mL) and the mixture stirred, first with refluxing for 3 h, and then at room temperature for 16 h. Evaporation of the filtrate under vacuum to dryness yielded the crude *product*, which gave fine needles when recrystallized from hexane (900 mL); yield 84%; mp 113–5°C (lit. 115°C (19)); $\nu_{as}(N_3)$, IR: 2097m, 2077s, 2064s cm^{-1}.

(b) Triphenyltin azide adducts

The ligand **L** and **M** (1.00 g) were dissolved in the given solvent by heating or stirring and the clear solution then left overnight at room temperature or in the refrigerator to yield crystals of the *adduct*, $Ph_3SnN_3 \cdot L$. The adduct with HMPA was also prepared by reacting $Ph_3SnCl \cdot HMPA$ with sodium azide in acetone (24). Adding ether to the concentrated acetone solution at 0°C gave the crystals used for X-ray analysis. Complete synthesis and characterisation details are given in Table 1.

X-ray structure determinations

Crystal parameters together with data collection and structure solution details are given in Table 2. For triphenyltin azide (**1**), a crystal was selected from the bulk sample and examined using a diffractometer equipped with a CCD detector and a rotating anode source. One complete hemisphere of data was collected to better than 0.8 Å resolution; the decay correction was done by remeasuring the first 50 frames at the end of data collection, which was 99.6% complete. For the HMPA adduct (**2**) a crystal was cut from a large parallelepiped and crystal data determined from 21 reflections. Three standard reflections measured after every 250, served for decay correction (~1.2%), and absorption correction was applied (NRCVAX (28)).

© 1998 NRC Canada

Table 2. Crystal parameters, data collection, and structure refinement information.

	$(C_6H_5)_3SnN_3$ (**1**)	$(C_6H_5)_3SnN_3$·HMPA (**2**)
Formula	$C_{18}H_{15}N_3Sn$	$C_{24}H_{33}N_6OPSn$
Formula mass (M_r)	392.02	571.22
Crystal system	Orthorhombic	Triclinic
Space group	*Pbca*	$P\bar{1}$
Cell constants		
a, Å	17.5884(2)	10.291(5)
b, Å	12.4406(1)	10.701(7)
c, Å	31.1137(3)	14.587(7)
α, deg	90	111.33(4)
β, deg	90	90.70(4)
γ, deg	90	112.57(4)
V, Å^3	6808.00(10)	1360.0(13)
Z	16	2
Z′	2	1
D_{calc}, Mg/m^3	1.530	1.395
Crystal size, mm	0.55 × 0.12 × 0.08	0.49 × 0.42 × 0.40
T, K	300(2)	293(2)
Diffractometer	Siemens SMART P4 (CCD detector)	Rigaku AFC6S
Scan method	ω scans	ω/2θ scans
μ, mm^{-1}	1.501	1.025
Radiation (λ), Å	MoKα$_1$ (0.710 73)	MoKα$_1$ (0.709 30)
θ_{min}, θ_{max}, deg	1.31, 26.41	2.15, 26.00
h, *k*, *l* ranges	0 → +21, 0 → +15 0 → +38	–12 → +12, –13 → +13 –18 → +18
F(000)	3104	584
No. refl. measured	54 768	10 729
No. independent refl.	6958	5365
R_{int}	0.028	0.037
No. obs. refl. ($I \geq 2\sigma(I)$)	5703	3762
No. of parameters	398	299
Absorption type	Multi-scan	ψ-scan
Transmission range	0.75–0.87	0.60–0.78
R_1 obs. (total)[a]	0.029 (0.042)	0.054 (0.088)
wR_2 obs. (total)[b]	0.055 (0.061)[d]	0.114 (0.126)[e]
S (on F^2)[c]	1.179	1.030
Max shift/σ ratio	–0.008	0.009

[a] $R_1 = \Sigma(||F_o| - |F_c||)/\Sigma(|F_o|)$.
[b] $wR_2 = [\Sigma[w(F_o^2 - F_c^2)^2]/\Sigma[w(F_o)^2]]^{1/2}$.
[c] $S = [\Sigma[w(F_o^2 - F_c^2)^2]/(\text{no. of reflns.} - \text{no. of params.})]^{1/2}$.
[d] $w^{-1} = \sigma^2(F_o^2) + (0.0150P)^2 + 5.9138P$ where $P = (F_o^2 + 2F_c^2)/3$.
[e] $w^1 = \sigma^2(F_o^2) + (0.0611P)^2 + 0.4299P$ where $P = (F_o^2 + 2F_c^2)/3$.

Structures were solved by the Patterson method (**1**) or direct methods (**2**) (SHELXS-86)[3] and difference Fourier syntheses (SHELXL-93)[4]; all non-hydrogen atoms were anisotropic with H-atoms isotropic and calculated at idealized positions using a riding model ((**1**) *d*(C—H) 0.93 Å; (**2**) *d*(C—H) 0.93–0.96 Å); for phenyl hydrogens, U_{iso} for each H was set at 20% greater than U_{iso} for its adjacent carbon atom, while methyl U_{iso}(H) values were at 1.50 × U_{iso}(C). One phenyl ring in each structure ((**1**), ring (5); (**2**), ring (2)) exhibited considerable thermal motion which could not be effectively represented by a two-position disorder model. Neutral atom scattering factors were from the *International Tables for X-Ray Crystallography* (29). Tables ((**1**) S1–S6, (**2**) S7–S12) of atomic coordinates, anisotropic thermal parameters, full bond lengths and angles (including torsion angles), and least-squares planes data, as well as stereoviews of the unit cells, are on deposit.[5]

Results

Tables 3 and 4 list vibrational data in the skeletal region for triphenyltin azide and its (1/1) adducts with pyridine and

[3] G.M. Sheldrick. SHELXS-86 programme for the solution of crystal structures. University of Göttingen, Germany. 1986.
[4] G.M. Sheldrick. SHELXL-93 programme for structure analysis. University of Göttingen, Germany. 1993.
[5] Supplementary material may be purchased from: The Depository of Unpublished Data, Document Delivery, CISTI, National Research Council Canada, Ottawa, Canada, K1A 0S2. With the exception of torsion angles, thermal parameters, and least-squares planes, these have also been deposited with the Cambridge Crystallographic Data Centre and can be obtained on request from: The Director, Cambridge Crystallographic Data Centre, University Chemical Laboratory, 12 Union Road, Cambridge, CB2 1EZ, U.K.

© 1998 NRC Canada

Table 3. Skeletal frequencies (400–100 cm^{-1}) for Ph_3SnN_3 (**a**) and Ph_3SnN_3·py (**b**).

(**a**)		(**b**)		
IR	Raman	IR	Raman	Assignment[a]
394sh	393vw	399vw	—	(w)
349s	346m	324vs	321sm	ν(Sn-N_3)
321sm	319wbr			
283vs		279vs	277vw	ν_{As}($SnPh_3$) (t)
278vs	278vw			
	238w			
229sh	231w	230s	228w	(u)
220s	216sh			
	212vs		212vs	ν_s($SnPh_3$) (t′)
207brsh			209sh	δ(Sn-N_3)
195sm	197sm	203sm	200sm	
181vw				
151sh			161m	(x)
144w				
136w		132sh		
158s	153sm			ν(Sn···N_β)
		153mbr	150s	ν(Sn-N_{py})
127wm		122m		δ(Sn···N_β)
120m		108wm		+δ(Sn-N_{py})

[a]Whiffen's notation (30) for phenyl ring modes.

various *O*-donor ligands, with the assignments following the patterns established earlier (16) for their pseudohalide analogues. For the adducts $\nu(Sn—N_3)_{ave}$ = 322 cm^{-1} but two values, (**a**) 320 and (**b**) 348 cm^{-1}, were assigned for Ph_3SnN_3. Thus adduct formation causes effectively no change in (**a**) but an ~8% decrease in (**b**). This would suggest that for Ph_3SnN_3 there are at least two different five-coordinate -(Ph_3)Sn- environments in the solid state, one planar (**D**) similar to the adducts, the other resembling Ph_3SnNCO (**E**) with unequal axial Sn—N bonds.

The solid state tin-119 nmr spectrum shows two absorptions of almost equal intensity, at –128.25 and –204.5 ppm. Comparison with data for Ph_3SnN_3 in various coordinating solvents (Table 5) would suggest that one tin in the solid azide is in an environment resembling that found for Ph_3SnN_3 in acetone, a weak donor solvent, while the other tin is more like that found for Ph_3SnN_3 in the stronger donor solvent DMSO, or the adduct Ph_3SnN_3·HMPA.

Selected geometric parameters for the two independent Ph_3SnN_3 moieties, (**a**) and (**b**), in the asymmetric unit of (**1**) (Fig. 1(*a*)) listed in Table 6(*a*), clearly show the two different five-coordinate tin environments in triphenyltin azide. In (**a**) the environment around the tin with an almost *syn*-diazide grouping, (torsion angle N(2)-N(1)-N(3′)-N(2′) = 38.6(6)°) resembles one of those recently reported (32) for some bis(azido)triphenylstannate anions, with the azide ligands acting as quasi-symmetric bridges (Fig. 2 (**a**)). In (**b**), the azide ligands are in an almost *anti*-conformation, (torsion angle N(5)-N(4)-N(6′)-N(5′) = –170.7(3)°) and provide

Table 4. Skeletal frequencies (350–100 cm^{-1}) for Ph_3SnN_3·L.

(*a*) L = HMPA[a]		(*b*) L = Ph_3PO[b]		
IR	Raman	IR	Raman	Assignment[c]
324s	323sh	330sm	326sm	ν(Sn-N_3)
318s	315w			
276vs	276w	275vs	275wvbr	ν_{as}($SnPh_3$) (t)
		255w	257m	δ(PPh_3) (u)
			245sh	
237vs	237vw	234s	231w	ν(Sn-O)
				+ δ($SnPh_3$) (u)
219sh		218w	215vs	
213sh	214vssp	209vw	208vs	ν_s($SnPh_3$) (t′)
	207sm		(208vs)	
199s		197m	197sm	δ(Sn-N_3)
		182sh	182w	
164w	160brsh	152w	155m	δ($SnPh_3$) (x)
148m	144sm	141w	134sh	
124w		126w		
(*c*) L = pyO[d]		(*d*) L = 4-picO		
IR	Raman	IR	Raman	Assignment[c]
325s		318vs	314sm	ν(Sn-N_3)
				+ ν(Sn-O)
301s				
275vs		281vs		ν_{As}($SnPh_3$) (t)
		273vs	271w	
		254vw	249w	
237vs		234vs		δ($SnPh_3$) (u)
				+ γ(N-O)
223m		224m	223sm	
210m			208sh	
			204vs	ν_s($SnPh_3$) (t′)
		202s		
197sm		196s		δ(Sn-N_3)
166sm		154m	151sm	δ($SnPh_3$) (x)
				+ τ(N-O)
149m				
144m		137sh		
127w		127m		δ(Sn-O)
		116w		

[a]Internal HMPA modes at ~350 and ~250 cm^{-1} omitted.
[b]δ(*P*=O) (cm^{-1}) at (IR) 313sm, (Raman) 316wm.
[c]Whiffen's notation (30) for phenyl ring modes.
[d]Raman spectrum not measured.

asymmetric bridges between tin atoms, giving an environment (Fig. 2 (**b**)) similar to that found in Ph_3SnNCO (18). These two polymeric units then pack as alternate parallel chains running through the unit cell (Fig. 3).

Selected geometric parameters for the HMPA adduct are given in Table 6(*b*). The conformation around tin (Fig. 1(*b*)) shows the effects of the bent tin-azide moiety and the ligand on the dihedral angles between the phenyl rings and the SnC_3 unit, viz., (1) 60.3(2), (2) 22.4(3), (3) 88.0(2)°. Thus

© 1998 NRC Canada

Table 5. Solution NMR data[a] for Ph_3SnN_3 and Ph_3SnN_3·HMPA.

	Ph_3SnN_3				Ph_3SnN_3·HMPA
Solvent	$CDCl_3$	C_6D_6	$(CD_3)_2CO$	$(CD_3)_2SO$	$CDCl_3$
$\delta(^{119}Sn)$, ppm[b]	–86.2	–85.6	–154.2	–252.3 (–235.7)[c]	–238.3
$^1J(^{119}Sn\text{-}^{13}C)$, Hz	620.6	584.2	709.6	819.0	808.8

[a]Concentration, 0.5 M; ref. external $(CH_3)_4Sn$.
[b]Literature (31) (0.05 M): $CHCl_3$, –88.1 ppm; $(CH_3)_2CO$, –161.0 ppm.
[c]Peaks assigned to the Ph_3Sn-N_3 atom are widened by characteristic unresolved splitting, presumably due to ^{119}Sn-^{14}N coupling. This narrow, less intense absorbance is assigned to the species $Ph_3Sn[(CD_3)_2SO]_2^+$ formed by ionization of Ph_3SnN_3.

Fig. 1. (*a*) ORTEP view (40% probability) of the two independent N_3-$SnPh_3$-N_3' moieties, (**a**) and (**b**), in compound **1**, showing the differing relative orientations of the two azide groups. (*b*) ORTEP view (30% probability) of the Ph_3SnN_3·HMPA molecule.

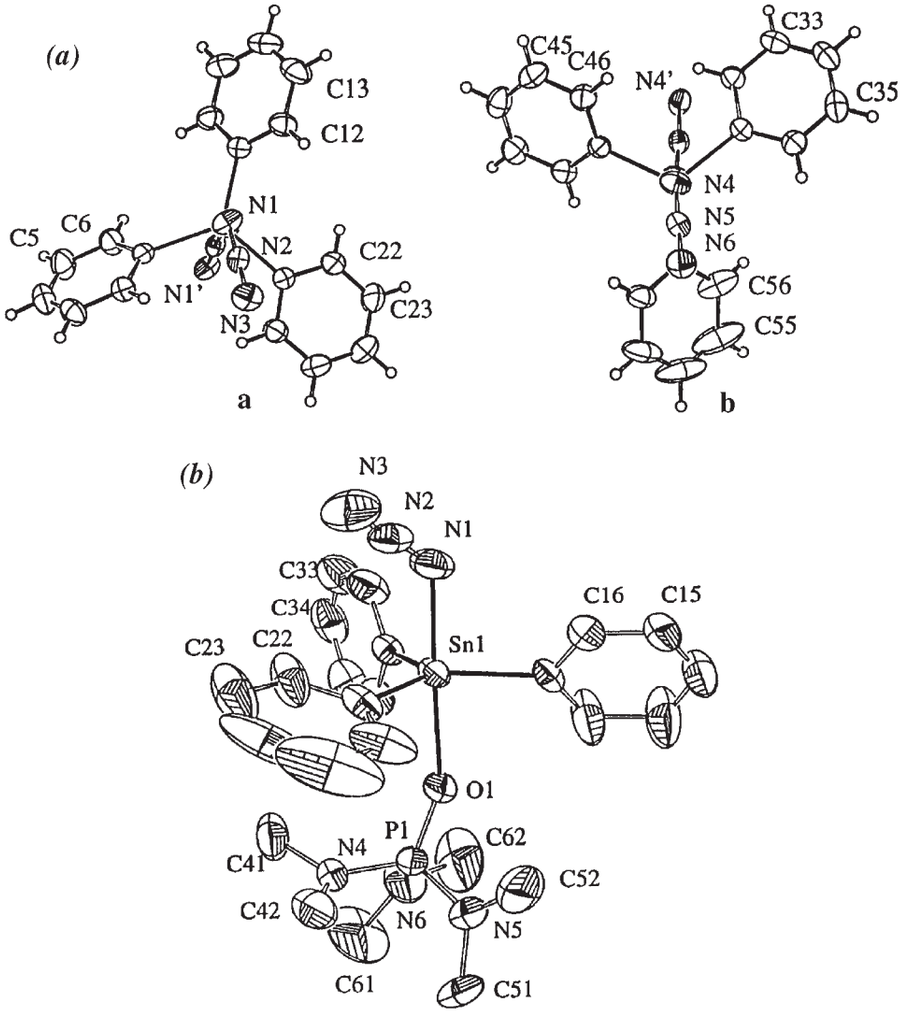

ring (2), with thermal motion, is sandwiched by the azide group and one $(CH_3)_2N$ group of the ligand, but ring (3) is almost in line with the N-Sn-O axis, a motif noted earlier in other X-Ph_3Sn-Y systems (32). For the parent azide, dihedral angles between the phenyl rings and the SnC_3 unit for both (**a**), (0) 58.0(1), (1) 40.6(1), (2) 15.2(1)°, and (**b**), (3) 22.7(1), (4) 37.4(1), (5) 39.2(1)° indicate highly distorted propellor geometries in both cases.

Discussion

Data describing the two tin environments in (**1**) together with those for selected model systems for comparison are given in Table 7(*a*). One approach used to study the transition from four-coordinate R_3Sn-X (**A**) to *sym*-five-coordinate Y-R_3Sn-X with equivalent axial Sn—X and Sn—Y

© 1998 NRC Canada

Table 6. Selected geometric parameters (distances, Å; angles, °).

(*a*) Triphenyltin azide			
Sn(1)—N(1)	2.210(3)	Sn(2)—N(4)	2.162(3)
Sn(1)—N(3)[a]	2.565(3)	Sn(2)—N(6)[b]	2.861(3)
Sn(1)—C(01)	2.125(3)	Sn(2)—C(31)	2.115(3)
Sn(1)—C(11)	2.114(3)	Sn(2)—C(41)	2.120(3)
Sn(1)—C(21)	2.120(3)	Sn(2)—C(51)	2.113(3)
N(1)—N(2)	1.187(4)	N(4)—N(5)	1.200(4)
N(2)—N(3)	1.151(4)	N(5)—N(6)	1.143(4)
N(1)-Sn(1)-N(3)[a]	174.10(11)	N(4)-Sn(2)-N(6)[b]	178.49(9)
N(2)-N(1)-Sn(1)	122.2(2)	N(5)-N(4)-Sn(2)	122.2(2)
N(2)-N(3)-Sn(1)[c]	144.6(3)	N(5)-N(4)-Sn(2)[d]	122.8(2)
C(01)-Sn(1)-C(11)	121.63(11)	C(31)-Sn(2)-C(41)	114.20(11)
C(01)-Sn(1)-C(21)	116.74(11)	C(31)-Sn(2)-C(51)	123.36(12)
C(11)-Sn(1)-C(21)	119.17(11)	C(41)-Sn(2)-C(51)	115.97(12)
C(01)-Sn(1)-N(1)	97.64(11)	C(31)-Sn(2)-N(4)	96.55(11)
C(11)-Sn(1)-N(1)	93.41(11)	C(41)-Sn(2)-N(4)	100.15(11)
C(21)-Sn(1)-N(1)	94.65(10)	C(51)-Sn(2)-N(4)	98.93(11)
C(01)-Sn(1)-N(3)[a]	88.23(11)	C(31)-Sn(2)-N(6)[b]	82.16(10)
C(11)-Sn(1)-N(3)[a]	82.89(10)	C(41)-Sn(2)-N(6)[b]	79.72(10)
C(21)-Sn(1)-N(3)[a]	83.23(10)	C(51)-Sn(2)-N(6)[b]	82.45(10)
(*b*) Azido(hexamethylphosphoramide)triphenyltin(IV)			
Sn(1)—C(11)	2.127(5)	Sn(1)—C(21)	2.107(6)
Sn(1)—C(31)	2.145(6)	Sn(1)—N(1)	2.217(6)
Sn(1)—O(1)	2.304(4)	P(1)—O(1)	1.487(4)
N(1)—N(2)	1.174(8)	N(2)—N(3)	1.137(8)
N(1)-Sn(1)-O(1)	176.4(2)	N(2)-N(1)-Sn(1)	126.0(5)
C(11)-Sn(1)-C(21)	121.9(2)	C(11)-Sn(2)-C(31)	120.1(2)
C(21)-Sn(1)-C(31)	117.7(2)	C(11)-Sn(1)-N(1)	91.0(2)
C(21)-Sn(1)-N(1)	90.5(2)	C(31)-Sn(1)-N(1)	93.6(2)
C(11)-Sn(1)-O(1)	86.5(2)	C(21)-Sn(1)-O(1)	88.6(2)
C(31)-Sn(1)-O(1)	89.9(2)	P(1)-O(1)-Sn(1)	152.1(2)

[a] $\bar{x}$, $y - 1/2$, $-z + 1/2$.
[b] $-x + 1/2$, $y - 1/2$, z.
[c] $\bar{x}$, $y + 1/2$, $-z + 1/2$.
[d] $-x + 1/2$, $y + 1/2$, z.

bonds (**C**) has been to note the changes, Δd(SnX) and Δd(SnY) observed during this transition as well as the variations in the average angles $C\hat{S}nX$ and $C\hat{S}nY$ (12, 13). Thus in Table 7(*a*) there is a gradual decrease in the primary *d*(Sn—N) value in going from (**C**) $[Ph_3Sn(NCS)_2]^-$ to (**A**) $(t\text{-}C_4H_9)_3SnN_3$. However, $(CH_3)_3SnN_3$ with geometry (**C**) at tin attained by using 1,1-azide bridges (34), has *d*(Sn—N) greater than found in the model system used, $[Ph_3Sn(NCS)_2]^-$. To avoid the ambiguities involved in using axial bond-length changes, the transition from structure type (**A**) to (**C**) or (**D**) may be followed instead in terms of the changes in the angles around the tin atom, $\alpha = C\hat{S}nC_{(ave)}$ and $\beta = C\hat{S}nX_{(ave)}$ (12, 16). Thus exact trigonal-bipyramidal geometry at tin, (**C**) or (**D**), requires that $\alpha = 120°$ and $\beta = 90°$. Consideration of various Ar_3SnX (X = Cl, Br) structures (1–6) gives $\alpha = 113°$ and $\beta = 105°$ as characteristic of a monomeric four-coordinate structure (**A**). Using these criteria (Table 7(*a*)), the tin environment in unit (**a**) of Ph_3SnN_3 is like that found in $Ph_3SnNCO \cdot pyO$ rather than the HMPA adduct of (**1**) or the anion $Ph_3Sn(N_3)_2^-$. For unit (**b**) of (**1**), the structure resembles that of Ph_3SnNCO (**E**), where the tin geometry is between those of the two extreme structure types (**A**) and (**D**). Unfortunately the example for a four-coordinate R_3SnN_3, $(t\text{-}C_4H_9)_3SnN_3$ (35), has larger α and smaller β values than those specified by the model given above, presumably because of repulsions between bulky *t*-butyl groups. A "typical" monomeric R_3SnN_3 thus remains to be characterized.

The azide groups in the triorganotin azide systems listed in Table 7(*a*), show bond-length changes (Table 7(*b*)) that also correlate with the transition from structure type (**A**) to (**C**) or (**D**). The azide ion itself is symmetric (35) but covalently bound azide may be considered as a hybrid of two main resonance forms **P** and **Q**

$$\mathbf{P} \quad M\text{-}N_\alpha{=}\overset{+}{N}_\beta{=}\overset{-}{N}_\gamma \leftrightarrow M\text{-}\overset{-}{N}_\alpha\text{-}\overset{+}{N}_\beta \equiv N_\gamma \quad \mathbf{Q}$$

with the contribution of **Q** causing the azide moiety to become asymmetric (38). Thus $R = d(N_\alpha—N_\beta)/d(N_\beta{=}N_\gamma) = 1.00$ for the azide ion but for covalent HN_3, $R = 1.10$. How-

© 1998 NRC Canada

Fig. 2. Views of polymer chain fragments (**a**) and (**b**) showing the 1,3-azide bridges.

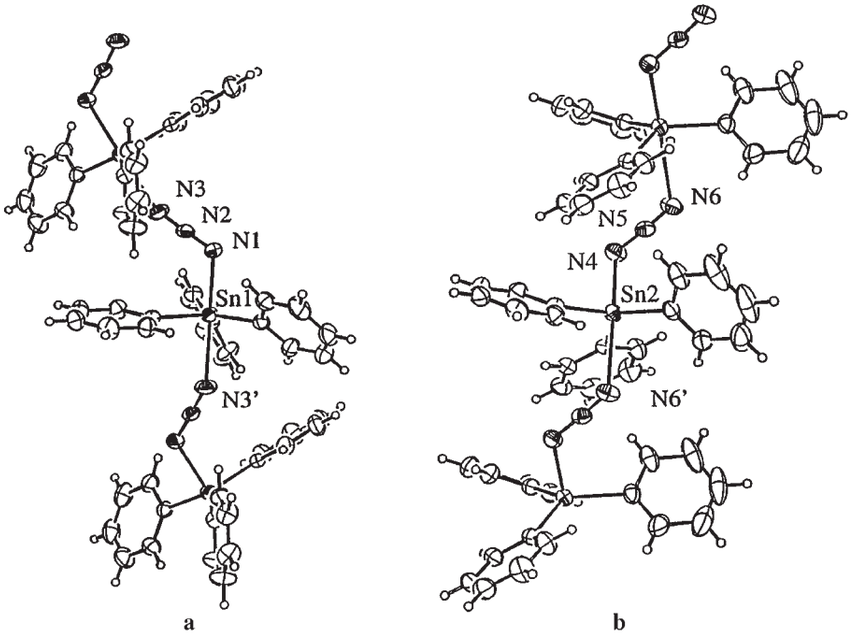

Table 7. Comparative geometries[a] for various triorganotin azides and other related systems.

(*a*) The N—R_3Sn--Y unit

System	*d*(Sn—N) (Å)	*d*(Sn--Y[b]) (Å)	$\wedge$ $CSnC_{av}$ (°) (α)	$\wedge$ $NSnC_{av}$ (°) (β)	Structure type[c]
$[Ph_3Sn(NCS)_2]^-$[d]	2.268	2.268	120	90	(**C**)
$[Ph_3Sn(N_3)_2]^-$[e]	2.23	2.37	120	92	(**C**)
Ph_3SnN_3·HMPA	2.217	2.304	120	92	(**C**)
Ph_3SnNCO·pyO[f]	2.169	2.355	119	$94._5$	(**C**)
Ph_3SnN_3 (**a**)	2.210	2.565	119	95	(**D**)
Ph_3SnN_3 (**b**)	2.162	2.861	118	$98._5$	(**E**)
Ph_3SnNCO[g]	2.122	2.807	118	98	(**E**)
$(CH_3)_3SnN_3$[h]	2.386	2.386	120	90	(**C**)
$(t\text{-}C_4H_9)_3SnN_3$[i]	2.101	—	117	$101._5$	(**A**)

(*b*) The azide group

System	*d*(N_α—N_β) (Å)	*d*(N_β—Nγ) (Å)	*d*(N_α—N_β)/*d*(N_β—N_γ) (*R*)
$(N_3)^-$[j]	1.17	1.17	1.00
HN_3[k]	1.243	1.134	1.10
$(t\text{-}C_4H_9)_3SnN_3$[h]	1.188	1.122	1.06
$[Ph_3Sn(N_3)_2]^-$[e]	1.16	1.15	1.01
Ph_3SnN_3·HMPA	1.174	1.137	1.03
Ph_3SnN_3 (**a**)	1.187	1.151	1.03
Ph_3SnN_3 (**b**)	1.200	1.143	1.05
$(CH_3)_3SnN_3$[i]	1.22	1.14_5	1.06_5

[a]Average data are given to only three significant figures, as are values of *R*.
[b]Y = N or O.
[c]See text.
[d]Reference 33.
[e]Average values; ref. 32.
[f]Reference 16.
[g]Reference 18.
[h]Reference 34.
[i]Reference 35.
[j]Average of data for MN_3, M = K, Rb, Cs, and Tl; ref. 36.
[k]Reference 37.

© 1998 NRC Canada

Fig. 3. Partial view of a double unit cell of triphenyltin azide showing polymer chains (**a**) and (**b**).

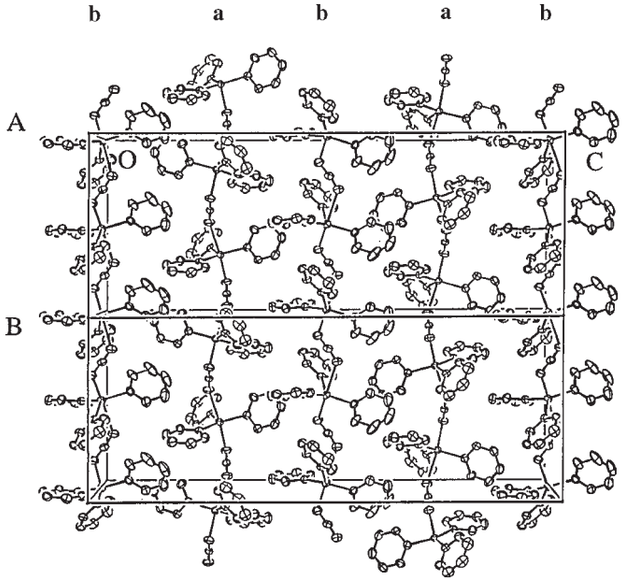

ever, R is <1.10 for $(t\text{-}C_4H_9)_3SnN_3$ and closer to 1 for the monomeric five-coordinate systems given in Table 7(*b*). This is consistent with the partial ionic character of the Sn—N_3 bond, which increases where this bond is in the axial position in a trigonal bipyramidal structure. Trends in R values also correlate with the bridging mode of the azide moiety. Thus for Ph_3SnN_3, as the geometry at tin becomes more symmetric, i.e., (**b**) and then (**a**), the 1,3-azide bridge becomes more symmetric, showing an increase in the contribution of form **P**. In contrast, the configuration of a 1,1-bridging azide, corresponding to a greater contribution of form **Q**, should resemble that found in a terminal azide by being asymmetric, and we see that the R value for polymeric $(CH_3)_3SnN_3$ is almost the same as that for its monomeric *t*-butyl analogue.

Conclusions

Our spectroscopic (far-IR/Raman and tin-119 nmr) data confirm that triphenyltin azide has five-coordinate tin in Ph_3Sn units, in agreement with earlier Mössbauer results (21). X-ray analysis shows that there are, in fact, two different five-coordinate tin environments, formed using 1,3-azide bridges, giving rise to two different $(Ph_3SnN_3)_n$ polymer chains. One has almost planar Ph_3Sn units, while the other has a geometry similar to that found for Ph_3SnNCO (18). Thus triphenyltin azide would appear to form part of a structural continuum from molecular Ph_3SiN_3 (20) to polymeric Ph_3PbN_3 (19). A reinvestigation of this series is clearly needed.

Of equal interest is the contrast between the 1,3-azide bridges in Ph_3SnN_3 and the symmetric environment around each tin found in $(CH_3)_3SnN_3$, where 1,1-azide bridges occupy the axial positions (34) and which may be due to both crystal packing and (or) electronic factors. However knowledge of a much larger number of structures of polymeric R_3SnN_3 is required before any further generalizations can be made.

Acknowledgements

The financial assistance of the Fonds FCAR (Programmes ACC, Actions spontanées) of the Government of Quebec is most gratefully acknowledged. The authorities of Dawson College, Montreal, are thanked for granting release (IW) time during which part of this research was carried out, as are Drs. Françoise Sauriol and Fred Morin of McGill University for solution and solid-state tin-119 nmr data, respectively.

References

1. H. Preut and F. Huber. Acta Crystallogr. B**35**, 745 (1979).
2. J.S. Tse, F.L. Lee, and E.J. Gabe. Acta Crystallogr. C**42**, 1876 (1986).
3. H. Reuter and H. Puff. J. Organomet. Chem. **362**, 53 (1989).
4. I. Wharf and M.G. Simard. Acta Crystallogr. C**47**, 639 (1991).
5. I. Wharf and A.-M. Lebuis. Acta Crystallogr. C**52**, 3025 (1996).
6. I. Wharf and M.G. Simard. J. Organomet. Chem. **532**, 1 (1997).
7. I. Wharf and M.G. Simard. Acta Crystallogr. C**47**, 1065 (1991).
8. S.W. Ng. Acta Crystallogr. C**51**, 1124 (1995).
9. C.A.L. Filgueiras, P.R. Holland, B.F.G. Johnson, and P.R. Raithby. Acta Crystallogr. B**38**, 2684 (1982).
10. S.W. Ng and V.G. Kumar Das. Acta Crystallogr. C**48**, 1839 (1991).
11. S.W. Ng. Acta Crystallogr. C**51**, 2563 (1995).
12. D. Britton and J.D. Dunitz. J. Am. Chem. Soc. **103**, 2971 (1981).
13. H.-B. Bürgi and V. Shklover. *In* Structure correlation. Vol. 1. *Edited by* H.-B. Bürgi and J.D. Dunitz. VCH, Weinheim. 1994. pp. 307–309.
14. I. Wharf, A.-M. Lebuis, and H. Lamparski. Acta Crystallogr. C**52**, 2477 (1996).
15. I. Wharf and M.G. Simard. Inorg. Chim. Acta, **282**, 30 (1998).
16. I. Wharf, L. Piehler, B.M. Sailofsky, M. Onyszchuk, and M.G. Simard. Can. J. Chem. **65**, 639 (1987), and refs. therein.
17. A.M. Domingos and G.M. Sheldrick. J. Organomet. Chem. **67**, 257 (1974).
18. T.N. Tarkhova, E.V. Chuprunov, M.A. Simonov, and N.V. Belov. Sov. Phys.-Cryst. **22**, 571 (1977).
19. J.S. Thayer and R. West. Inorg. Chem. **3**, 406 (1964), and refs. therein.
20. E.R. Corey, V. Cody, M.D. Glick, and L.J. Radonovich. J. Inorg. Nucl. Chem. **35**, 1714 (1973).
21. R.H. Herber, H.A. Stöckler, and W.T. Reichle. J. Chem. Phys. **42**, 2447 (1965).
22. R. Barbieri, N. Bertazzi, C. Tomarchio, and R. Herber. J. Organomet. Chem. **84**, 39 (1975).
23. G. Alonzo, N. Bertazzi, F. DiBianca, and G.C. Stucco. Atti Accad. Sci. Lett. Arti Palermo, Parte 1, **33**, 77 (1973); Chem. Abs. **83**, 68 624a.
24. K.A. Elegbede and R.A.N. McLean. J. Organomet. Chem. **69**, 405 (1974).
25. T.N. Srivastava, P.C. Srivastava, and S.K. Srivastava. Synth. Reac. Inorg. Met.-Org. Chem. **12**, 533 (1982).
26. I. Wharf. Inorg. Chim. Acta, **159**, 41 (1989).
27. C.H. Kline, Jr. and J. Turkevich. J. Chem. Phys. **12**, 300 (1944).
28. E.J. Gabe, Y. LePage, J.P. Charland, F.L. Lee, and P.S. White. J. Appl. Crystallogr. **22**, 384 (1989).

© 1998 NRC Canada

29. International tables for crystallography. Vol. C. Tables 4.2.6. Kluwer Academic Publishers, Boston, Mass. 1992.
30. D.H. Whiffen. J. Chem. Soc. 1350 (1956).
31. P.A.W. Dean and J.J. Vittal. Can. J. Chem. **66**, 2443 (1988).
32. I. Wharf, R. Wojtowski, M. Onyszchuk, and M.G. Simard. Acta Crystallogr. C**53**, 1791 (1997), and refs. therein.
33. P.J. Cox and J.L. Wardell. Acta Crystallogr. C**52**, 317 (1996).
34. R. Allman, R. Hohlfeld, A. Waskowska, and J. Lorberth. J. Organomet. Chem. **192**, 353 (1980).
35. D. Hänssgen, M. Jansen, C. Leben, and T. Oster. J. Organomet. Chem. **494**, 223 (1995).
36. U. Müller. Z. Anorg. Allg. Chem. **392**, 159 (1972).
37. B.P. Winnewisser. J. Mol. Spectrosc. **82**, 220 (1982).
38. U. Müller. Struct. Bonding (Berlin), **14**, 141 (1973).

© 1998 NRC Canada

Mixed anion effect in sodium thiocyanate + sodium thiosulfate + water systems

G. Kalita, N.N. Dass, and S. Mahiuddin

Abstract: Densities and viscosities of $R[x\text{NaSCN} + (1 - x)\text{Na}_2\text{S}_2\text{O}_3] + (1 - R)\text{H}_2\text{O}$ systems with R = 0.05, 0.10, 0.14, and 0.18 were measured as functions of mole fraction, x (= 0.0–1.0), and temperature ($293.15 \leq T/\text{K} \leq 323.15$). A significant mixed anion effect has been observed within the temperature range of the study. The normalized viscosity isotherms were found to detect the mixed anion effect ~1.2 to 3.7 times more than the simple viscosity isotherms. The progressive replacement of $S_2O_3^{2-}$ ions by SCN^- ions causes the systems to be less structured and $S_2O_3^{2-}$ ions polarized Na^+ ions more towards themselves than towards the SCN^- ions. Both these effects govern the variation of the viscosity with mole fraction, x. The mixed anion effect was found to vanish at around R = 0.0106.

Key words: mixed anion effect, sodium thiocyanate, sodium thiosulfate, viscosity.

Résumé : Opérant à des températures allant de 293,15 à 323,15 K et à des fractions molaires, x, allant de 0,0 à 1,0, on a mesuré les densités et les viscosités de systèmes $R[x\text{NaSCN} + (1 - x)\text{Na}_2\text{S}_2\text{O}_3] + (1 - R)\text{H}_2\text{O}$ dans lesquels R = 0,05, 0,10, 0,14 et 0,18. Dans le domaine de températures de l'étude, on a observé un effet significatif d'anion mixte. On a trouvé que les isothermes normalisées de viscosité permettent de détecter l'effet d'anion mixte d'environ 1,2 à 3,7 fois plus facilement que les isothermes de viscosité simples. Le remplacement progressif des ions $S_2O_3^{2-}$ par des ions SCN^- rend les systèmes moins structurés et fait que les ions Na^+ polarisés par les ions $S_2O_3^{2-}$ se déplacent vers ceux-ci plutôt que vers les ions SCN^-. Ces deux effets orientent la variation de la viscosité en fonction de la fraction molaire, x. On a trouvé que l'effet d'anion mixte disparaît aux environs de R = 0,0106.

Mots clés : effet d'anion mixte, thiocyanate de sodium, thiosulfate de sodium, viscosité.

[Traduit par la Rédaction]

Introduction

A pronounced deviation (either positive or negative) from linearity has been observed in the conductivity and viscosity isotherms in ternary melt or glass systems when one of the alkali ions is progressively replaced by another alkali ion in a glass or melt medium (1–6). This phenomenon is referred to as the mixed alkali effect. A similar deviation in the electrical conductivity isotherm has been reported in the mixed alkaline earth and alkali – alkaline earth systems (7). Recently, Chandra and Chandra (8) and Choi and Kim (9) have reported negative and(or) positive deviations in the electrical conductivity isotherms for systems such as $[x\text{MA} + (1 - x)\text{MA}'] + \text{PEO}$, where M is the alkali metal, A and A′ are the different anions, and PEO stands for poly(ethylene) oxide, and they suggested the deviation in the conductivity was due to the mixed anion effect. It seems that the mixed alkali or mixed anion effects are not then restricted to only the alkali ions or the anions, but are a particular example of the general phenomenon of the mixed ion or the dissimilar pair of ions effect.

To study more about the effect of anion pairs on the deviation in the transport property (viscosity and conductivity) isotherms, we report the viscosities of $R[x\text{NaSCN} + (1 - x)\text{Na}_2\text{S}_2\text{O}_3] + (1 - R)\text{H}_2\text{O}$ systems, with R = 0.05, 0.10, 0.14, and 0.18, as functions of temperature and mole fraction, x.

Experimental section

Sodium thiocyanate (Loba, 99%) was recrystallized from conductivity water and dried over P_2O_5. Sodium thiosulfate pentahydrate (E. Merck, 99.5%) was recrystallized from conductivity water, and the anhydrous sodium thiosulfate was prepared as per the reported procedure (10) and was stored in a vacuum desiccator over P_2O_5.

Densities (ρ) and viscosities (η) of $0.05[x\text{NaSCN} + (1 - x)\text{Na}_2\text{S}_2\text{O}_3] + 0.95\ \text{H}_2\text{O}$, $0.1[x\text{NaSCN} + (1 - x)\text{Na}_2\text{S}_2\text{O}_3] + 0.9\text{H}_2\text{O}$, $0.14[x\text{NaSCN} + (1 - x)\text{Na}_2\text{S}_2\text{O}_3] + 0.86\text{H}_2\text{O}$, and $0.18[x\text{NaSCN} + (1 - x)\text{Na}_2\text{S}_2\text{O}_3] + 0.82\ \text{H}_2\text{O}$ systems were measured as functions of mole fraction, x (= 0.0–1.0), and temperature ($293.15 \leq T/\text{K} \leq 323.15$). The uncertainties in densities and viscosities were found to be ±0.01% and ±0.4%, respectively. Measurement techniques were the same as described elsewhere (11). A Schott Geräte thermostat type CT-1450 was used to maintain the temperature of the study to ±0.02 K.

Received January 30, 1998.

G. Kalita and S. Mahiuddin.[1] Material Science Division, Regional Research Laboratory, Jorhat-785006, Assam, India.
N.N. Dass. Department of Chemistry, Dibrugarh University, Dibrugarh-786004, Assam, India.

[1]Author to whom correspondence may be addressed. Fax: 0091-0376-321-158.

© 1998 NRC Canada

Table 1. Least-squares fitted values of the parameters of the density equation $\rho = a - b(T - 273.15)$ for $R[x\text{NaSCN} + (1 - x)Na_2S_2O_3] + (1 - R)H_2O$ systems.

x	a/kg m^{-3}	b/kg m^{-3} K^{-1}	Std. dev. in ρ
$0.05[x\text{NaSCN} + (1 - x)Na_2S_2O_3] + 0.95H_2O$			
0	1302.7 ± 0.3	0.669 ± 0.006	0.2
0.2	1266.9 ± 0.4	0.661 ± 0.008	0.2
0.4	1229.8 ± 0.5	0.644 ± 0.012	0.2
0.6	1193.8 ± 0.6	0.662 ± 0.014	0.2
0.8	1153.4 ± 0.2	0.593 ± 0.005	0.1
1.0	1117.5 ± 0.5	0.679 ± 0.012	0.1
$0.1[x\text{NaSCN} + (1 - x)Na_2S_2O_3] + 0.9H_2O$			
0	1469.8 ± 0.9	0.727 ± 0.021	0.3
0.2	1423.6 ± 0.8	0.757 ± 0.018	0.2
0.4	1381.0 ± 0.5	0.769 ± 0.014	0.2
0.6	1323.1 ± 0.8	0.773 ± 0.019	0.2
0.8	1266.3 ± 0.4	0.793 ± 0.011	0.2
1.0	1204.8 ± 0.4	0.773 ± 0.010	0.2
$0.14[x\text{NaSCN} + (1 - x)Na_2S_2O_3] + 0.86H_2O$			
0	1626.1 ± 0.6	0.757 ± 0.016	0.2
0.2	1560.8 ± 0.5	0.793 ± 0.010	0.2
0.4	1494.6 ± 0.3	0.815 ± 0.006	0.1
0.6	1421.6 ± 0.5	0.836 ± 0.010	0.2
0.8	1345.4 ± 0.5	0.827 ± 0.012	0.2
1.0	1261.8 ± 0.5	0.805 ± 0.012	0.2
$0.18[x\text{NaSCN} + (1 - x)Na_2S_2O_3] + 0.82H_2O$			
0	1655.0 ± 0.6	0.705 ± 0.014	0.1
0.2	1605.5 ± 0.1	0.796 ± 0.028	0.3
0.4	1536.3 ± 0.9	0.825 ± 0.022	0.3
0.6	1467.1 ± 0.4	0.825 ± 0.010	0.2
0.8	1391.3 ± 0.5	0.835 ± 0.012	0.2
1.0	1310.3 ± 0.4	0.827 ± 0.010	0.2

Results and discussion

The measured densities (ρ) for $0.05[x\text{NaSCN} + (1 - x)Na_2S_2O_3] + 0.95\ H_2O$, $0.1[x\text{NaSCN} + (1 - x)Na_2S_2O_3] + 0.9H_2O$, $0.14[x\text{NaSCN} + (1 - x)\ Na_2S_2O_3] + 0.86H_2O$, and $0.18[x\text{NaSCN} + (1 - x)Na_2S_2O_3] + 0.82H_2O$ systems are found to be a linear function of temperature and are presented in Table 1.

Viscosity values for the above systems are presented in Table 2. To examine the mixed anion effect in the present systems, the dependence of the concentration, x, on the viscosity at different temperatures has been depicted in Fig. 1. It is interesting to note that a pronounced negative deviation (~6–47% depending on the temperature) from the linearity of η vs. x plots (Fig. 1) has been observed. Such a deviation may be attributed to the onset of the mixed anion effect, which decreases from ~47% to 10% at 298.15 K (Fig. 1) as the mole fraction of water, $(1 - R)$, increases.

Dietzel (7) has suggested that the larger the difference between the cation field strength, ΔF ($\Delta F = \Delta (z/a^2)$, where z is the valency of the cation and a is the cation–anion distance in 10^{-10} m), the more pronounced is the mixed alkali effect. For example, in ternary systems containing Na^+–K^+, with $\Delta F = 0.04$ (7) either in ionic or molecular liquid medium, the deviation in viscosity and(or) conductivity isotherm was reported as ~4% (5, 6, 12). The ternary system, $0.45[x\text{LiNO}_3 + (1 - x)\text{KNO}_3] + 0.55\text{Ca}(\text{NO}_3)_2 \cdot 4.09H_2O$ with $\Delta F(Li^+–K^+) = 0.10–0.14$ (7), exhibits ~12.5% deviation in the electrical conductivity isotherm (4). A similar cation field strength difference criterion may be applied in the present system. Even though the present system contains a similar cation and different anions, cation–anion distances for Na^+–SCN^- and Na^+–$S_2O_3^{2-}$ are different, resulting in different cation field strengths, F. The crystal ionic radius for the $S_2O_3^{2-}$ ion is not available, to the best of our knowledge, and, considering that the $S_2O_3^{2-}$ ion is analogous to the SO_4^{2-} ion and the reported ionic radii of Na^+, SCN^-, and SO_4^{2-} ions (13), the difference between the cation field strength was found to be ~0.024 and would cause only ~2.4% deviation in the viscosity isotherm. In fact, we observed ~6–47% deviation in the viscosity isotherms (Fig. 1). On the other hand, the system $0.25[x\text{KSCN} + (1 - x)\text{NaSCN}] + 0.75CH_3CONH_2$ (14) showed ~27–55% deviation in the viscosity isotherms even though $\Delta F(Na^+–K^+)$ is 0.04. It seems that the field strength criterion may not be a universal parameter, particularly in liquid media with nonrigid structure, for explaining the mixed anion effect although the present system is a particular example of mixed ion systems. Therefore, the onset of the mixed anion effect in the present system may be of different origin.

The viscosities (η) of all the systems were fitted to the Vogel–Tammann–Fulcher equation of the following form:

© 1998 NRC Canada

Table 2. Values of viscosities for $R[x\text{NaSCN} + (1 - x)\ Na_2S_2O_3] + (1 - R)H_2O$ systems.

T/K	η/mPa s	*T*/K	η/mPa s	*T*/K	η/mPa s
$0.05[x\text{NaSCN} + (1 - x)Na_2S_2O_3] + 0.95H_2O$					
x = 0.0		***x* = 0.2**		***x* = 0.4**	
293.15	3.207	293.15	2.643	293.15	2.185
298.15	2.782	298.15	2.306	298.15	1.926
303.15	2.438	303.15	2.042	303.15	1.712
308.15	2.158	308.15	1.819	308.05	1.535
313.05	1.926	313.15	1.633	313.15	1.385
318.05	1.733	318.15	1.476	318.15	1.259
323.15	1.568	323.15	1.343	323.15	1.151
***x* = 0.6**		***x* = 0.8**		***x* = 1.0**	
293.15	1.804	293.15	1.508	293.15	1.260
298.15	1.601	298.15	1.347	298.15	1.130
303.15	1.430	303.15	1.211	303.15	1.020
308.15	1.290	308.15	1.096	308.15	0.9294
313.15	1.168	313.15	0.9980	313.15	0.8496
318.15	1.066	318.15	0.9146	318.15	0.7833
323.15	0.9837	323.15	0.8454	323.15	0.7191
$0.1[x\text{NaSCN} + (1 - x)Na_2S_2O_3] + 0.9H_2O$					
***x* = 0.0**		***x* = 0.2**		***x* = 0.4**	
298.15	8.359	298.15	6.073	298.15	4.654
303.15	7.008	303.15	5.156	303.15	3.990
307.85	5.982	307.85	4.466	307.85	3.509
313.15	5.092	313.15	3.842	313.15	3.047
317.85	4.465	317.85	3.404	317.85	2.714
323.15	3.869	323.15	2.984	323.15	2.403
***x* = 0.6**		***x* = 0.8**		***x* = 1.0**	
298.15	3.256	298.15	2.344	298.15	1.669
303.15	2.843	303.15	2.076	303.15	1.498
307.95	2.521	307.85	1.864	307.85	1.361
313.15	2.227	313.15	1.668	313.15	1.231
317.85	2.008	317.85	1.519	317.85	1.133
323.15	1.800	323.15	1.376	323.15	1.037
$0.14[x\text{NaSCN} + (1 - x)Na_2S_2O_3] + 0.86H_2O$					
***x* = 0.0**		***x* = 0.2**		***x* = 0.4**	
293.15	40.87	293.15	23.42	293.15	13.67
298.15	30.84	298.15	18.28	298.15	11.01
303.15	23.88	303.15	14.60	303.15	9.068
308.15	18.98	308.15	11.92	308.15	7.587
313.15	15.39	313.15	9.890	313.15	6.430
318.15	12.73	318.15	8.344	318.15	5.535
323.15	10.69	323.15	7.132	323.15	4.822
***x* = 0.6**		***x* = 0.8**		***x* = 1.0**	
293.15	7.941	293.15	4.731	293.15	2.804
298.15	6.608	298.15	4.049	298.15	2.462
303.15	5.587	303.15	3.507	303.15	2.182
308.15	4.792	308.15	3.073	308.15	1.949
313.15	4.153	313.15	2.711	313.15	1.756
318.15	3.643	318.15	2.421	318.15	1.592
323.15	3.221	323.15	2.176	323.15	1.452
$0.18[x\text{NaSCN} + (1 - x)Na_2S_2O_3] + 0.82H_2O$					
***x* = 0.0**		***x* = 0.2**		***x* = 0.4**	
298.15	44.45	298.15	29.62	298.15	16.99
303.15	33.86	303.15	23.14	303.15	13.70
308.15	26.47	308.15	18.47	307.95	11.33
313.15	21.17	313.15	15.06	313.15	9.381
317.85	17.48	317.85	12.61	317.85	8.013

© 1998 NRC Canada

Table 2. (*concluded*).

T/K	η/mPa s	*T*/K	η/mPa s	*T*/K	η/mPa s
323.15	14.32	323.15	10.50	323.15	6.824
***x* = 0.6**		***x* = 0.8**		***x* = 1.0**	
298.15	10.47	298.15	6.168	298.15	3.756
303.15	8.676	303.15	5.250	303.15	3.273
308.15	7.295	307.85	4.561	307.85	2.902
313.15	6.228	313.15	3.953	313.15	2.559
317.85	5.416	317.85	3.498	317.85	2.314
323.15	4.686	323.15	3.086	323.15	2.072

Table 3. Least-squares fitted values of the parameters of eq [1] for $R[x\text{NaSCN} + (1 - x)Na_2S_2O_3] + (1 - R)H_2O$ systems.

x	T_0/K	*A*/mPa s	*B*/K	Std. dev. in ln η
$0.05[x\text{NaSCN} + (1 - x)Na_2S_2O_3] + 0.95H_2O$				
0.0	170.4	0.0834	448.0	0.001
0.2	164.3	0.0736	461.3	0.001
0.4	157.1	0.0628	482.9	0.001
0.6	152.8	0.0570	484.6	0.002
0.8	146.2	0.0490	503.4	0.002
1.0	139.7	0.0416	523.4	0.002
$0.1[x\text{NaSCN} + (1 - x)Na_2S_2O_3] + 0.9H_2O$				
0	175.4	0.0881	558.8	0.003
0.2	171.8	0.0822	543.6	0.001
0.4	169.2	0.0795	524.9	0.002
0.6	166.4	0.0794	489.3	0.001
0.8	162.6	0.0766	463.8	0.001
1.0	159.6	0.0741	431.5	0.001
$0.14[x\text{NaSCN} + (1 - x)Na_2S_2O_3] + 0.86H_2O$				
0.0	199.2	0.1597	520.8	0.002
0.2	192.0	0.1293	525.7	0.002
0.4	187.0	0.1204	502.0	0.002
0.6	179.8	0.1067	488.4	0.001
0.8	175.4	0.1030	450.6	0.001
1.0	164.5	0.0864	447.7	0.001
$0.18[x\text{NaSCN} + (1 - x)Na_2S_2O_3] + 0.82H_2O$				
0	204.2	0.2030	506.3	0.002
0.2	198.5	0.1678	515.5	0.001
0.4	192.8	0.1450	501.9	0.001
0.6	186.2	0.1283	492.8	0.001
0.8	181.5	0.1219	457.7	0.001
1.0	175.8	0.1127	429.1	0.001

$$[1] \qquad \eta = A \exp[B/(T - T_0)]$$

to explain the temperature dependence of the viscosity. In eq. [1] *A* and *B* are the adjustable parameters and T_0 is the ideal glass transition temperature. The T_0 values obtained by the iteration method for the systems showed an irregular trend in the variation of T_0 with composition. This is expected because, in the temperature ranges of the study, the viscosity data in the present system vary only by factors of ~1.8 to 2.0, ~1.6 to 2.2, ~1.9 to 3.8, and ~1.8 to 3.1 for $R[x\text{NaSCN} + (1 - x)Na_2S_2O_3] + (1 - R)H_2O$ systems with R = 0.05, 0.10, 0.14, and 0.18, respectively, and the computed T_0 values may not be precise. In such a situation, an alternative method suggested by Moynihan et al. (15) was adopted to estimate the T_0 values for the present systems.

The least-squares fitted values of the *A*, *B*, and T_0 parameters are listed in Table 3 and the variation of T_0 with *x* for both systems has been illustrated in Fig. 2. For x = 0.0 and 1.0 the systems represent binary systems with composition $NaSCN{\cdot}19H_2O$ (2.92 mol kg^{-1}), $Na_2S_2O_3{\cdot}19H_2O$ (2.92 mol kg^{-1}), $NaSCN{\cdot}9H_2O$ (6.168 mol kg^{-1}), $Na_2S_2O_3{\cdot}9H_2O$ (6.168 mol kg^{-1}), $NaSCN{\cdot}6.14H_2O$ (9.04 mol kg^{-1}), $Na_2S_2O_3{\cdot}6.14H_2O$ (9.04 mol kg^{-1}), $NaSCN{\cdot}4.56H_2O$ (12.18 mol kg^{-1}), and $Na_2S_2O_3{\cdot}4.56H_2O$ (12.18 mol kg^{-1}), respectively. The computed T_0 values of these binary systems are in good agreement with the reported T_0 values (16, 17) at the

© 1998 NRC Canada

Fig. 1. Variation of viscosity with mole fraction, *x*, for (*a*) 0.05[*x*NaSCN + (1 – *x*)$Na_2S_2O_3$] + 0.95H_2O, (*b*) 0.1[*x*NaSCN + (1 – *x*)$Na_2S_2O_3$] + 0.9H_2O, (*c*) 0.14[*x*NaSCN + (1 – *x*)$Na_2S_2O_3$] + 0.86H_2O, and (*d*) 0.18[*x*NaSCN + (1 – *x*)$Na_2S_2O_3$] + 0.82H_2O systems at (○) –298.15 K, (□) –313.15 K, and (△) –323.15 K. The symbols are the observed and the solid curves are the theoretical (calculated from the polynomial equation up to the second degree) values, respectively.

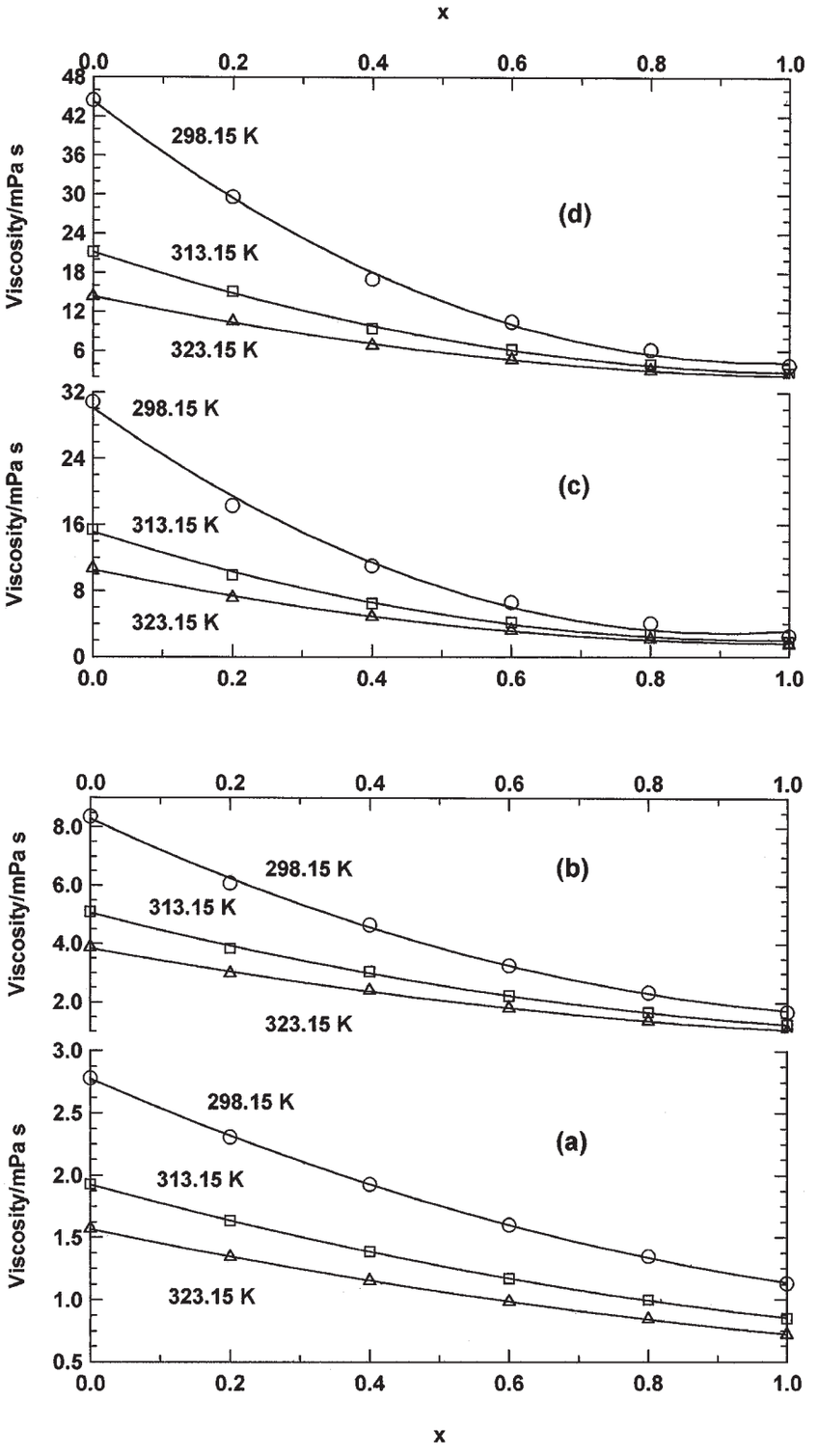

© 1998 NRC Canada

Fig. 2. Plots of T_0 versus x for (○) –0.05[xNaSCN + (1 – x)$Na_2S_2O_3$] + 0.95H_2O, (□) –0.1[xNaSCN + (1 – x)$Na_2S_2O_3$] + 0.9H_2O, (△) –0.14[xNaSCN + (1 – x)$Na_2S_2O_3$] + 0.86H_2O, and (◇) –0.18[xNaSCN + (1 – x)$Na_2S_2O_3$] + 0.82 H_2O systems. The symbols and the solid lines are observed and calculated (from the linear equation), respectively.

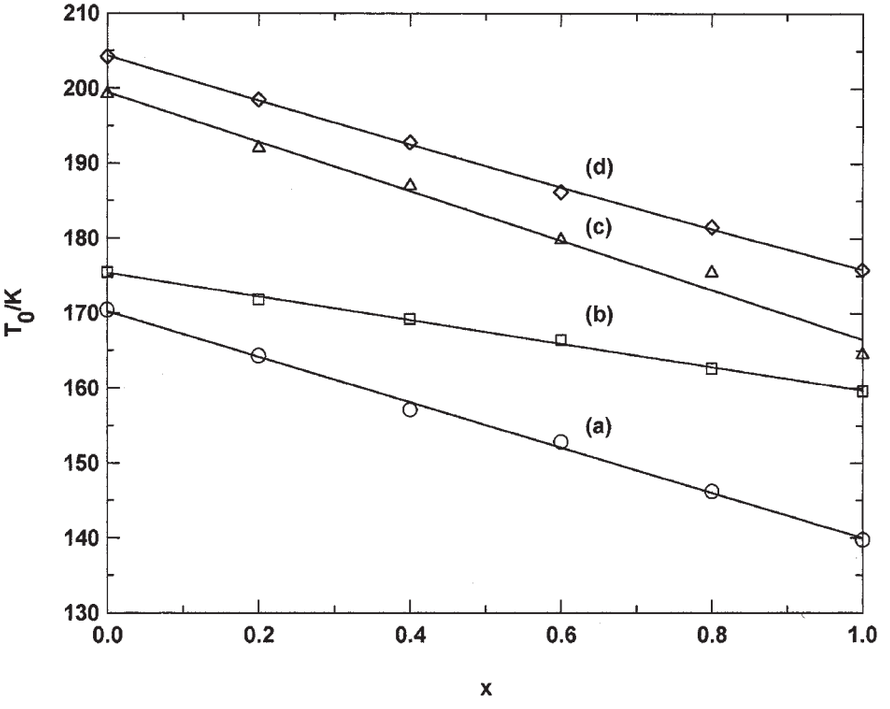

corresponding composition and justify our data fitting. T_0 vs. x plots (Fig. 2) do not exhibit any mixed anion effect, unlike the case in other mixed alkali systems (18, 19).

Although the viscosity isotherms exhibit a significant mixed alkali and mixed anion effects, normalized viscosity isotherms (4) are also used to detect the mixed alkali effect. We have plotted the normalized viscosity, $F_\eta = (\eta_{x=0.0} - \eta)/(\eta_{x=0.0} - \eta_{x=1.0})$ where $\eta_{x=0.0}$ and $\eta_{x=1.0}$ are the viscosities at x = 0.0 and x = 1.0, respectively, and η is the viscosity of solution, versus mole fraction, x, in Fig. 3 at different temperatures. From Fig. 3 we note that very significant mixed anion effects with ~22–54% deviation from linearity have been observed and the normalized viscosity isotherms are ~1.2 to 3.7 times more accessible to the mixed anion effect than the simple viscosity isotherms (Fig. 1) irrespective of ΔF values.

Numerous theories have been proposed for explaining the onset of the mixed alkali effect, particularly for the system where rigid structure prevails (2). For a nonrigid system, as in the present study, an anion polarization model (20, 21) has been applied to explain the mixed alkali effect. The existence of the mixed anion effect in the present systems may be of different origin.

Earlier we reported that there are ~25 and 19 molecules of water in the primary hydration shell of sodium thiosulfate (22) and sodium thiocyanate (23) at 2.5 and 3.0 mol kg^{-1}, respectively. The system 0.05[xNaSCN + (1 – x)$Na_2S_2O_3$] + 0.95H_2O at x = 0.0 and 1.0 represents binary systems with composition $Na_2S_2O_3 \cdot 19H_2O$ (2.92 mol kg^{-1}) and $NaSCN \cdot 19H_2O$ (2.92 mol kg^{-1}), respectively. At 2.92 mol kg^{-1} there are ~24 and 19 molecules of water in the primary hydration shell of sodium thiosulfate (22) and sodium thiocyanate (23), respectively. The primary hydration shell for the $Na_2S_2O_3 \cdot 19H_2O$ system at x = 0.0 is deficient in one water molecule and becomes more structured, resulting in higher viscosity (Fig. 1) than the $NaSCN \cdot 19H_2O$, which may be due to the formation of the solvent shared ion-pair.[2] As the $S_2O_3^{2-}$ ions are progressively replaced by the SCN^- ions the system becomes less structured, resulting in lower viscosity at x = 1.0 (Fig. 1). On the other hand, $S_2O_3^{2-}$ ions polarize Na^+ ions more towards themselves than towards the SCN^- ions since the $S_2O_3^{2-}$ ion, as discussed in the preceding section, has a larger ionic radius than the SCN^- ion. Both these effects contribute towards the net deviation in the viscosity isotherms (Fig. 1). A similar inference may also be drawn for the R[xNaSCN + (1 – x)$Na_2S_2O_3$] + (1 – R)H_2O systems with R = 0.10, 0.14, and 0.18. Finally, we have plotted the percentage deviation in the viscosity isotherm obtained from Fig. 1 at x = 0.5 versus R, at 298.15 and 323.15 K, in Fig. 4. From Fig. 4 it is apparent that at R = 0.0106 the system does not exhibit any mixed anion effect within the temperature range of the study, and the higher the R value, the larger is the deviation in the viscosity isotherms (Figs. 1 and 3), which is also one of the criteria (18) for detecting the mixed ion effect.

[2] Reference 13, p. 221.

© 1998 NRC Canada

Fig. 3. Plots of normalized viscosity versus x for (*a*) $0.05[x\text{NaSCN} + (1 - x)Na_2S_2O_3] + 0.95H_2O$, (*b*) $0.1[x\text{NaSCN} + (1 - x)Na_2S_2O_3] + 0.9H_2O$, (*c*) $0.14[x\text{NaSCN} + (1 - x)Na_2S_2O_3] + 0.86H_2O$, and (*d*) $0.18[x\text{NaSCN} + (1 - x)Na_2S_2O_3] + 0.82H_2O$. The symbols and solid curves are observed and calculated (from the polynomial equation up to the second degree) values, respectively, and the broken lines are an additive property.

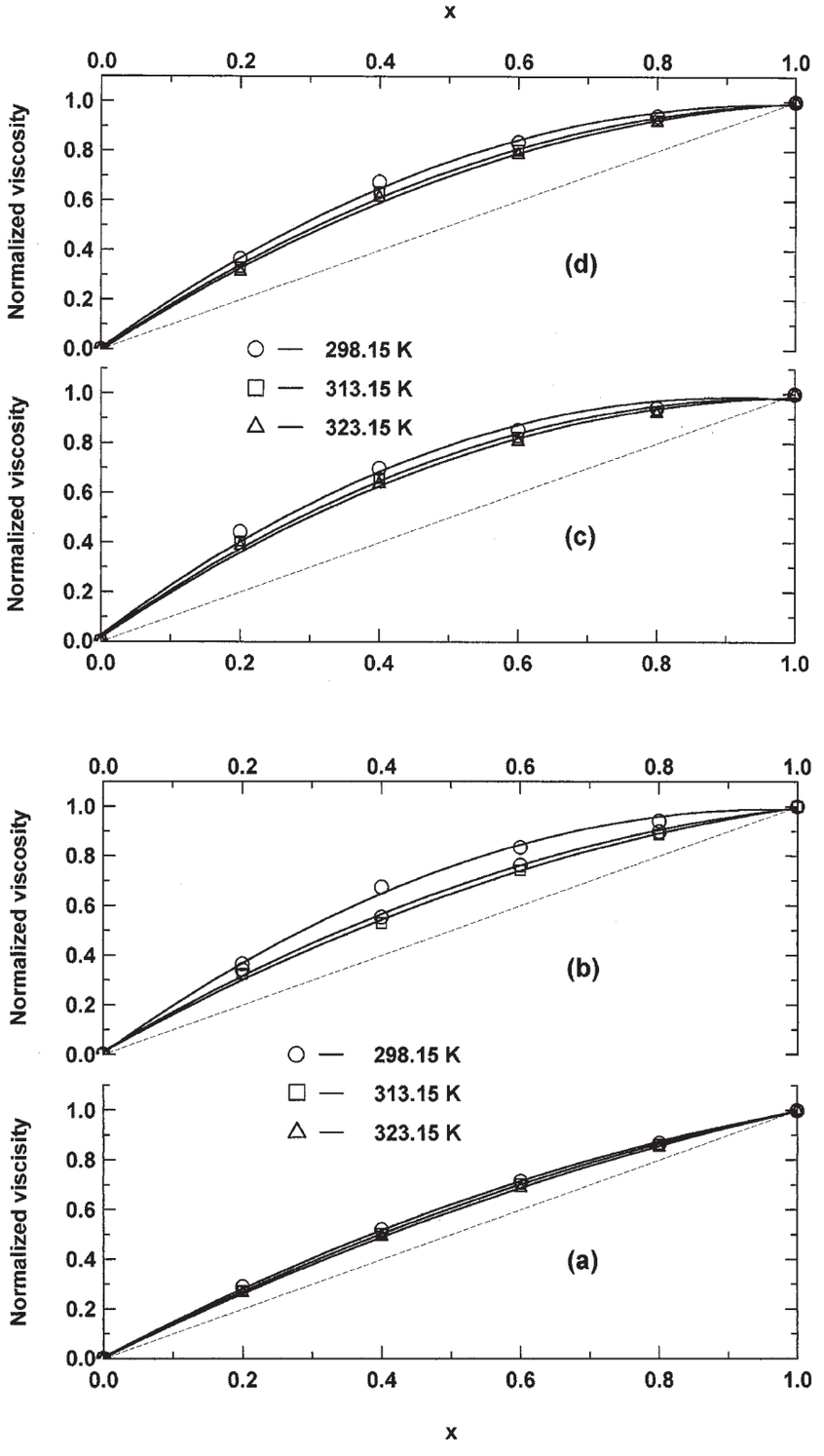

© 1998 NRC Canada

Fig. 4. Plots of percentage of deviation in viscosity isotherms versus composition, *R* at (○) –298.15 K and (□) –323.15 K.

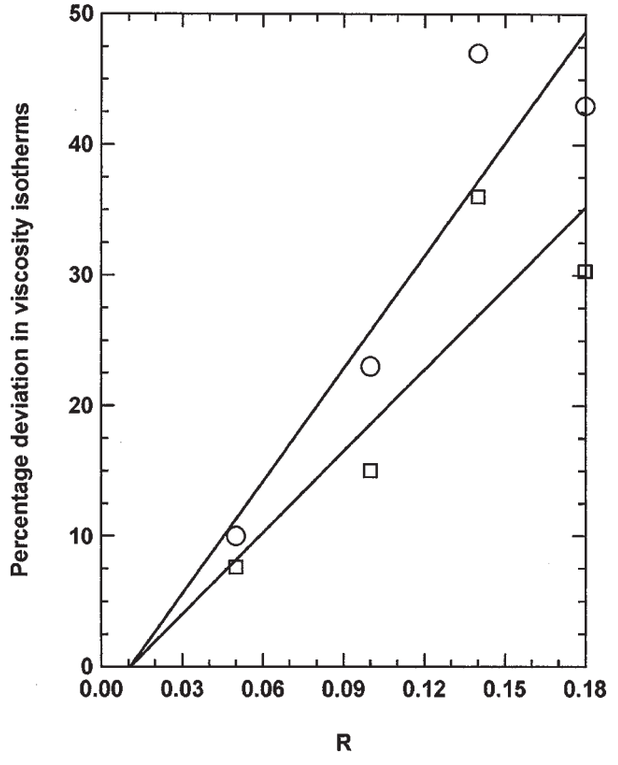

Acknowledgments

The authors thank the Director of the laboratory and the Head, Material Science Division, for encouragement and interest in this work. One of us (G.K.) is indebted to the Principal, J. B. College, Jorhat, India, for allowing him to pursue this work.

References

1. J.O. Isard. J. Non-Cryst. Solids, **1**, 295 (1969).
2. D.E. Day. J. Non-Cryst. Solids, **21**, 343 (1976).
3. C.T. Moynihan. J. Electrochem. Soc. **126**, 2144 (1979).
4. A.J. Easteal. Aust. J. Chem. **34**, 1853 (1981).
5. P. Sangma, S. Mahiuddin, and K. Ismail. J. Phys. Chem. **88**, 2378 (1984).
6. S. Mahiuddin. Can. J. Chem. **72**, 2286 (1994).
7. A.H. Dietzel. Phys. Chem. Glasses, **24**, 172 (1983), and refs. therein.
8. A. Chandra and S. Chandra. J. Phys. D: Appl. Phys. **27**, 2171 (1994).
9. B.-K. Choi and Y.-W. Kim. Mater. Res. Soc. Symp. Proc. **369**, 535 (1995).
10. A.A. Woolf. Anal. Chem. **54**, 2134 (1982).
11. G. Kalita, N. Rohman, and S. Mahiuddin. J. Chem. Eng. Data, **42**, 943 (1997).
12. S.S. Islam and K. Ismail. J. Chem. Eng. Data, **35**, 348 (1990).
13. Y. Marcus. Ion solvation. John Wiley & Sons Ltd., Chichester. 1985. pp. 46–47.
14. S. Mahiuddin. Can J. Chem. **74**, 760 (1996).
15. C.T. Moynihan, C.R. Smalley, C.A. Angell, and E.J. Sare. J. Phys. Chem. **73**, 2287 (1969).
16. R.L. Gupta and K. Ismail. J. Chem. Eng. Data, **36**, 142 (1991).
17. S. Mahiuddin and K. Ismail. Fluid Phase Equilib. **123**, 231 (1996).
18. G. Kalita, N. Rohman, and S. Mahiuddin. Aust. J. Chem. **51**, 201 (1998).
19. J. Easteal and M.C. Emson. J. Phys. Chem. **84**, 3330 (1980).
20. C.T. Moynihan and R.W. Laity. J. Phys. Chem. **68**, 3312 (1964).
21. C.T. Moynihan. *In* Ionic interactions. Vol. 1. *Edited by* S. Petrucci. Academic Press, New York. 1971. p. 261.
22. N. Rohman and S. Mahiuddin. J. Chem. Soc. Faraday Trans. **93**, 2053 (1997).
23. N. Rohman, S. Mahiuddin, and N.N. Dass. J. Chem. Eng. Data. In press.

© 1998 NRC Canada

Crystal structures of highly stabilized ylides: methyl(3-methoxy,2-methoxycarbonylbenzoyl)triphenylphosphoranylideneacetate and methyl(2-methoxycarbonyl,6-nitrobenzoyl)triphenylphosphoranylideneacetate and the salt methyl(triphenylphosphoranylidene)acetate tetrafluoroborate

Fernande D. Rochon, Robert Melanson, and Margaret M. Kayser

Abstract: At lower temperatures stabilized ylides react with unsymmetrically substituted phthalic anhydrides to give two acyclic adducts. When the reactions are allowed to proceed at higher temperature enol lactones are formed. Identification of the acyclic intermediates was necessary to understand the mechanism of these Wittig reactions. The transient species trapped in the reaction with trimethyloxonium tetrafluoroborate were unambiguously identified by crystallographic methods. The crystal structures of the tetrafluoroborate salt of methyl(triphenylphosphoranylidene)-acetate (**8**), methyl(3-methoxy,2-methoxycarbonylbenzoyl)triphenylphosphoranylideneacetate (**6**β), and methyl(2-methoxycarbonyl,6-nitrobenzoyl)triphenylphosphoranylideneacetate (**7**α) were studied by X-ray diffraction. The ionic salt (**8**) is monoclinic, $P2_1/c$, a = 12.640(5), b = 13.945(9), c = 14.825(6) Å, β = 125.32(3)°, Z = 4, and R = 0.065 ($F > 5.4\ \sigma(F)$). Crystal **6**β is monoclinic, $P2_1/c$, a = 16.391(16), b = 9.029(6), c = 19.835(19) Å, β = 116.60(6)°, Z = 4, and R = 0.070 ($F > 4.6\ \sigma(F)$), while crystal **7**α is also monoclinic, $P2_1/c$, a = 9.513(5), b = 9.361(3), c = 30.908(13) Å, β = 98.42(3)°, Z = 4, and R = 0.057 ($F > 5\sigma(F)$). In the BF_4^- salt (**12**), the four P—C distances are equal (1.791(5)–1.801(7) Å) with identical tetrahedral angles. For the two triphenylphosphoranylideneacetate compounds, the fourth P—C(1) bond is shorter (1.762(6)–1.734(5) Å) than the three P—C(Ph) bonds (avg. 1.809(5) Å). The angles C(1)-P-C(Ph) are also larger (avg. 112.9(2)° for **6**β and 111.9(2)° for **7**α) than the C(Ph)-P-C(Ph) angles (avg. 105.8(2)° for **6**β and 106.9(2)° for **7**α). These values suggest a multiple nature for the P—C(1) bond. In the nitro derivative, the nitro and the ester groups are disordered equally in positions 2 and 6.

Key words: Wittig reactions, cyclic anhydrides, stabilized ylide, phosphoranylidenes, crystal structures.

Résumé : À de faibles températures, les ylures stabilisés réagissent avec des anhydrides phtaliques substitués de façon non symétrique pour donner deux adduits acycliques. Lorsqu'on laisse les réactions se produire à des températures plus élevées, il se forme des lactones énoliques. Il a été nécessaire d'identifier les intermédiaires acycliques pour comprendre le mécanisme de ces réactions. Les espèces transitoires piégées dans la réaction du tétrafluoroborate de triméthyloxonium ont été identifiées sans ambiguïté par des méthodes cristallographiques. Faisant appel à la diffraction des rayons X, on a déterminé les structures cristallines des tétrafluoroborates de (triphényphosphoranylidène)acétate de méthyle (**8**), (3-méthoxy-2-méthoxycarbonylbenzoyl)triphénylphosphoranylidènediacétate de méthyle (**6**β) et (2-méthoxy-6-nitrobenzoyl)triphénylphosphoranylidèneacétate de méthyle (**7**α). Le sel ionique **8** est monoclinique, groupe d'espace $P2_1/c$, avec a = 12,640(5), b = 13,945(9) et c = 14,825(6) Å, β = 125,32(3)°, Z = 4 et R = 0,065 ($F > 5{,}4\ \sigma(F)$). Les cristaux de **6**β sont monocliniques, groupe d'espace $P2_1/c$, avec a = 16,391(16), b = 9,029(6) et c = 19,835(19) Å, β = 116,60(6)°, Z = 4 et R = 0,070 ($F > 4{,}6\ \sigma(F)$) alors que les cristaux de **7**α sont aussi monocliniques, groupe d'espace $P2_1/c$, avec a = 9,513(5), b = 9,361(3) et c = 30,908(13) Å, β = 98,42(3)°, Z = 4 et R = 0,057 ($F > 5\ \sigma(F)$). Dans le tétrafluoroborate **12**, les quatre distances P—C sont égales (1,791(5) à 1,801(7) Å) et les angles tétraédriques sont identiques. Pour les deux composés triphénylphosphoranylidèneacétate, la quatrième liaison P—C(1)

Received November 11, 1997.[1]

F.D. Rochon and R. Melanson. Département de chimie, Université du Québec à Montréal, C. P. 8888, Succ. A, Montréal, QC H3C 3P8, Canada.
M.M. Kayser.[2] Department of Chemistry, University of New Brunswick, Saint John, NB E2L 4L5, Canada.

[1]Revision received September 8, 1998.
[2]Author to whom correspondence may be addressed.

 © 1998 NRC Canada

est plus courte (1,762(6) à 1,734(5) Å) que les trois liaisons P—C(Ph) (moyenne de 1,809(5) Å). Les angles C(1)-P-C(Ph) sont aussi plus grands (moyenne de 112,9(2)° pour le composé **6**β et de 111,9(2)° pour le composé **7**α) que les angles C(Ph)-P-C(Ph) (moyenne de 105,8(2)° pour le composé **6**β et de 106,9(2)° pour le composé **7**α). Ces valeurs suggèrent que la liaison P—C(1) adopte des natures multiples. Dans le dérivé nitré, les groupes nitro et ester des positions 2 et 6 sont également désordonnés.

Mots clés : réactions de Wittig, anhydrides cycliques, ylure stabilisé, phosphoranylidènes, structures cristallines.

[Traduit par la Rédaction]

Introduction

The reactions of stabilized ylides with cyclic anhydrides lead to the formation of synthetically and biologically important enol-lactones (1). The condensation of phthalic anhydride with carbonyl-stabilized ylides was first studied by Chopard et al. (2), who discovered that the product enol-lactones showed a surprisingly high stereoselectivity in favor of *E* geometry (Scheme 1). Although an acyclic transition state with the COX group of the ylide in a plane parallel to the phenyl ring of phthalic anhydride (structure **2**) was proposed to account for the observed results, the mechanism of these reactions was not systematically investigated until recently (3–7). The experimental data accumulated over the years showed that the condensations with succinic and maleic anhydrides also give *E* enol-lactones as major products (8), suggesting that π-stacking was not a necessary element in the stereochemical control. Also, acyclic keto phosphoranes, such as **1**, were detected during these condensations (2, 8–10), and were generally assumed to be the intermediate species on the reaction pathway leading to enol-lactones.

Systematic investigation by ^{1}H and ^{31}P NMR and trapping

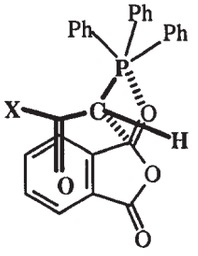

2

experiments showed that low-temperature condensations of phthalic, maleic, and succinic anhydrides with methyl (triphenylphosphoranylidene)acetate, **3**, give acyclic keto phosphoranes as the initial product and that these reactions are reversible. Subsequent studies of the condensations with unsymmetrically substituted cyclic anhydrides provided further insights into the mechanism of these reactions. One of the problems that surfaced during these studies was a failure to predict regioselectivity of the product enol-lactones on the basis of steric and electronic effects of the substituents (3–5). This was particularly evident in reactions with 3-methoxy and 3-nitrophthalic anhydrides, where experimental findings did not correspond to the regioselectivity projections based on electronic or steric effects (3). Furthermore, low-temperature NMR-monitored reactions indicated that the ratios of regioisomeric acyclic keto phosphoranes observed during the reactions were quite different from the ratios of regioisomeric enol lactones produced at the end (Schemes 2 and 3). Positive identification of the acyclic intermediates became necessary in order to trace the mechanistic path of these transformations.

Experimental

General procedure

An ylide (0.5 mmol) dissolved in $CDCl_3$ (0.5 mL) and cooled to –40°C was added to a cooled (–40°C) suspension of an anhydride (0.5 mmol) in $CDCl_3$ (0.5 mL) in an NMR tube. The mixture was shaken and the spectrum was recorded after a few minutes of equilibration at this temperature. The temperature was slowly raised while the reaction mixture was continuously monitored by ^{31}P NMR. When the maximum accumulation of the acyclic products was reached (generally at –20° to –10°C), the reaction mixture was rapidly divided, at –20°C, into two equal portions. One half was allowed to proceed to completion at higher temperature (still followed by NMR), the other half was treated with trimethyloxonium tetrafluoroborate (0.25 mmol) in $CDCl_3$ (0.5 mL), agitated for 30 min at 0°C, and analyzed by NMR. The products were isolated and purified chromatographically as described previously (3, 7). The chromatographically purified samples were crystallized from ethanol. Finally, crystals suitable for X-ray diffraction were recrystallized from methanol (crystals **8** and **6**β) or from a methanol – diethyl ether mixture (crystal **7**α).

Crystallographic measurements and structure determination

The crystals were selected after examination for homogeneity under a polarizing microscope. The unit cell parameters were obtained by least-squares refinement of the angles 2θ (11°–25°), ω, and χ for about 30 well-centered reflections on a Siemens P4 diffractometer using graphite-monochromatized MoKα radiation. The P3 program was used for the three crystals. The data collections were made at room temperature by the 2θ–θ scan technique. Crystal data and other information are summarized in Table 1. Corrections were made for Lorentz and polarization effects.

The structures were solved using direct methods.[3] Other non-H atoms were located by structure factors and Fourier-map calculations. The refinement of the structures was done using full-matrix least-squares calculations minimizing

[3] SHELXTL PLUS (PC version 1990–96). Siemens Analytical Instruments Inc., Madison, Wis., U.S.A.

© 1998 NRC Canada

Scheme 1.

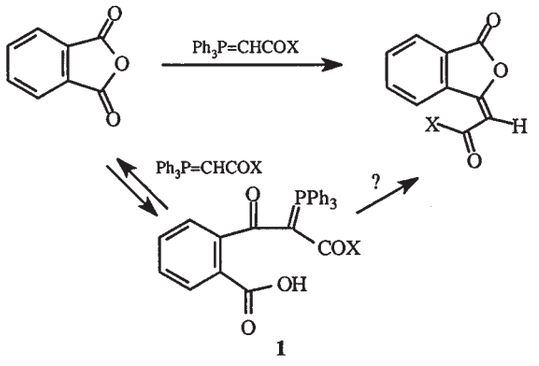

1

$\Sigma\, w(|F_o| - |F_c|)^2$. The H atoms were fixed at their calculated positions with U_{eq} = 0.08 Å^2. The nitro and ester groups in crystal **7**α were found to be equally disordered in the two *ortho* positions. The refinement of the scale factor, coordinates, and anisotropic temperature factors of all atoms converged to R = 0.070 and R_w = 0.065 for **6**β, R = 0.057 and R_w = 0.049 for **7**α, and R = 0.065 and R_w = 0.069 for **8**. The residual peaks were less than 0.98 e/Å^3. The calculations were done on a Siemens SHELXTL system[3] and the crystallographic data were taken from the *International Tables for X-ray Crystallography* (11). The coordinates and the equivalent isotropic displacement parameters are shown in Table 2.

Results and discussion

In an initial effort to identify the acyclic adducts, they were trapped with diazomethane at 5°C (3-methoxy) and 15°C (3-nitro) (7). The structures were assigned on the basis of ^{13}C spectra of the isolated compounds. The assignments were tentative, since only one isomer in each pair, **6**α and β and **7**α and β, was obtained as a pure compound and the carbonyl and quarternary C signals were weak. The C–P couplings could not be unequivocally ascertained. We were not convinced that our provisionary assignment of structures was correct. In a modified series of experiments, the low temperature (–20° → –5°) reaction of ylide **3** with 3-methoxy- or 3-nitrophthalic anhydride was followed by NMR until a maximum accumulation of acyclic intermediates was reached (–5°C). At that point, one half of the reaction was allowed to proceed at higher temperature to give enol lactones, while the other half was treated with trimethyloxonium tetrafluoroborate $(CH_3)_3O^+BF_4^-$, to trap the acyclic acids as their methyl esters (Scheme 2). The trapped esters were separated by chromatography and crystallized. The *minor* regioisomer from the reaction with 3-methoxyphthalic anhydride and the *major* regioisomer from the reaction with 3-nitrophthalic anhydride were subjected to X-ray crystallographic analyses for structure determination. These compounds were identified as **6**β and **7**α, respectively. The crystal structures of the two compounds are described below.

In addition, a small quantity of another crystalline compound was isolated from the trapping experiment with 3-nitrophthalic anhydride. It was identified by crystallography as $Ph_3PCH_2COOCH_3^+BF_4^-$, **8**, the tetrafluoroborate salt of the conjugate acid of the original ylide. Its crystal structure was also determined by X-ray diffraction and the results are described below. The formation of **8** confirms that a reaction of the cyclic anhydride with a stabilized ylide is indeed an equilibrium, and that ylide **3** molecules, present at equilibrium, pick up protons from the acidic intermediates to give cationic species $Ph_3P^+CH_2COOCH_3$, which form a crystalline salt on treatment with trimethyloxonium tetrafluoroborate as shown in Scheme 4.

The advantage of having the crystal structure determinations became evident when it turned out that the initial assignment of the structure of the *major* adduct in the reaction of 3-nitrophthalic anhydride with ylide **3** was incorrect. A positive identification of the acyclic adducts leads to better understanding of the mechanism involved and allows better predictability for these reactions. The higher proportion of adducts **4**α and **5**α suggests that intrinsic electron-donating and electron-withdrawing effects of 3-methoxy and 3-nitro groups are less important than their ability to form stabilizing complexes with ylide **3**, similar to that illustrated in **2**. The particularly high stability of acyclic compound **5**α may be due to strong internal complexation between highly electron-rich oxygen of the 3-nitro substituent and the neighboring phosphorus of the ylide, as illustrated in **9**.

Labelled diagrams of the three crystals are shown in Figs. 1–3. The bond distances and angles are shown in Table 3. The crystal structure of the ionic salt

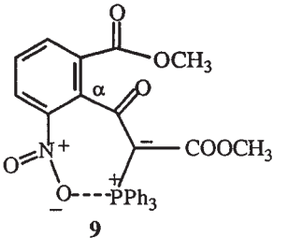

9

$PPh_3CH_2COOCH_3^+$ BF_4^- (**8**) is quite different from the other two structures. The four bonds around the P atom are of equal distances, with the three P—Ph bonds varying from 1.790(5) to 1.793(4) Å while the fourth bond is 1.801(7) Å. All the angles around the P atom are very similar with average angles C(3)-P-C(Ph) = 109.2(2)° and C(Ph)-P-C(Ph) = 109.7(2)°. The other bond distances and angles are normal. The B—F distances in the anions vary between 1.329(7) and 1.353(7) Å, while the average angle is 109.5(6)°.

In crystal **6**β, the ester group is located at the 2-position (*ortho*), while the methoxy group is in the 3-position (*meta*). The conformation of the molecule is such as to reduce the steric hindrance between the two large ester groups, which are located far from one another. In crystal **7**α, the ester and nitro groups on the phenyl ring are both located in *ortho* positions and the two groups are equally disordered on the two positions. For this reason, the bond distances in the two disordered groups are not precise. The ester group on C(1) is approximately in the center between the ester and nitro groups on the phenyl ring.

For crystals **6**β and **7**α, the P—C(phenyl) distances are normal and vary from 1.802(4) to 1.821(6) Å (**6**β), and 1.801(5) to 1.815(4) Å (**7**α), while the fourth bond P—C(1) is shorter, 1.762(6) Å (**6**β) and 1.734(5) Å (**7**α). These results are close to those obtained for similar crystal structures

© 1998 NRC Canada

Scheme 2.

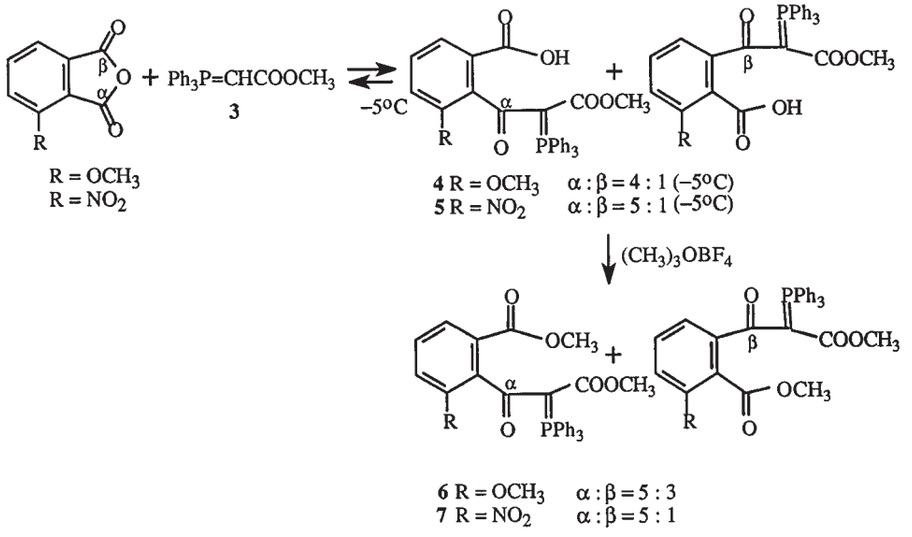

Scheme 3.

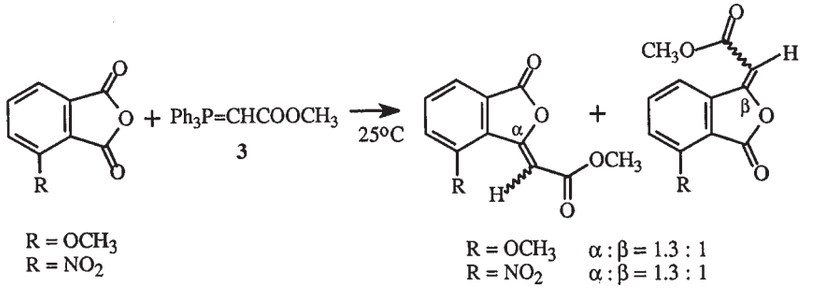

Table 1. Crystal data and experimental details of the X-ray diffraction studies.

	8	**6β**	**7α**
Crystal compound	$C_{21}H_{20}BF_4O_2P$	$C_{31}H_{27}O_6P$	$C_{30}H_{24}O_7NP$
M_w	422.1	526.5	541.5
Line system	Monoclinic	Monoclinic	Monoclinic
Space group	$P2_1/c$	$P2_1/c$	$P2_1/c$
a (Å)	12.640(5)	16.391(16)	9.513(5)
b (Å)	13.945(9)	9.029(6)	9.361(3)
c (Å)	14.825(6)	19.835(19)	30.908(13)
β (°)	125.32(3)	116.60(6)	98.42(3)
Volume (Å^3)	2132(2)	2425(4)	2723(2)
Z	4	4	4
F(000)	872	1104	1128
ρ_{calcd} (Mg m^{-3})	1.315	1.332	1.321
μ(MoKα) (mm^{-1})	0.177	0.149	0.149
2θ max (°)	50.0	55.0	50.0
No. of measured reflections	3930	6277	5115
No. of unique refl. (R_{int})	3754 (0.015)	6071 (0.067)	4806 (0.039)
No. of ind. obsd. reflections	2286 ($F > 5.4\sigma(F)$)	2669($F > 4.6\sigma(F)$)	2015($F > 5\sigma(F)$)
R	0.065	0.070	0.057
R_w	0.069	0.065	0.049

© 1998 NRC Canada

Table 2. Atomic coordinates (10^4) and equivalent isotropic displacement parameters (Å^2 × 10^3) U_{eq} = (1/3) $\sum_i \sum_j U_{ij} a_i^* a_j^* \mathbf{a}_i . \mathbf{a}_j$.

	x	*y*	*z*	U_{eq}
$PPh_3CH_2COOCH_3^+$ BF_4^- (**8**)				
P	1943(1)	1399(1)	9315(1)	38(1)
O(1)	4324(3)	2684(3)	8837(3)	74(2)
O(2)	2234(3)	2945(3)	8069(3)	70(2)
C(1)	4435(6)	3626(6)	8430(7)	128(6)
C(2)	3181(5)	2467(4)	8623(4)	48(3)
C(3)	3271(5)	1550(3)	9193(4)	46(2)
C(11)	1802(4)	2438(3)	9947(3)	41(2)
C(12)	2903(5)	2956(3)	10713(4)	50(3)
C(13)	2808(6)	3736(4)	11239(4)	59(3)
C(14)	1623(6)	4001(4)	10997(4)	61(4)
C(15)	527(6)	3482(4)	10250(4)	58(3)
C(16)	602(5)	2707(3)	9715(4)	50(3)
C(21)	468(4)	1160(3)	7988(4)	41(2)
C(22)	187(5)	204(3)	7623(4)	51(3)
C(23)	–921(5)	5(4)	6590(4)	61(3)
C(24)	–1754(5)	714(5)	5939(4)	66(3)
C(25)	–1488(5)	1654(4)	6290(4)	64(3)
C(26)	–379(5)	1890(4)	7314(4)	55(3)
C(31)	2315(4)	386(3)	10194(4)	43(2)
C(32)	1754(5)	320(4)	10772(4)	60(3)
C(33)	2013(6)	–453(4)	11439(5)	74(4)
C(34)	2803(6)	–1171(4)	11536(5)	74(4)
C(35)	3351(6)	–1115(4)	10966(5)	76(4)
C(36)	3128(5)	–341(4)	10301(5)	61(3)
B	3297(6)	6266(4)	2792(5)	53(3)
F(1)	4135(4)	6969(3)	3370(3)	141(3)
F(2)	3770(4)	5413(3)	3311(4)	116(3)
F(3)	2954(5)	6261(3)	1747(3)	127(3)
F(3)	2198(5)	64184)	2696(5)	159(4)
$PPh_3C(COOCH_3)COPh(COOCH_3)(OCH_3)$ (**6**β)				
P	2331(1)	5285(2)	1722(1)	27(1)
O(1)	3434(2)	6175(4)	1070(2)	37(1)
O(2)	3685(3)	8022(4)	–318(3)	65(1)
O(3)	2266(3)	7296(4)	–635(2)	56(1)
O(4)	1260(3)	3586(5)	–349(2)	70(1)
O(5)	942(3)	3158(5)	603(2)	62(1)
O(6)	3910(3)	5834(4)	–1243(2)	55(1)
C(1)	2202(3)	4621(5)	845(2)	30(1)
C(2)	2909(3)	5192(5)	680(3)	31(1)
C(3)	1455(3)	3784(5)	307(3)	37(1)
C(4)	105(4)	2454(7)	97(4)	78(1)
C(5)	1988(5)	8824(6)	–732(4)	78(1)
C(6)	3156(4)	7054(6)	–415(3)	43(1)
C(7)	4310(4)	5254(7)	–1698(3)	71(1)
C(11)	3134(3)	4493(5)	92(3)	30(1)
C(12)	3344(3)	5441(5)	–370(3)	34(1)
C(13)	3740(3)	4826(5)	–806(4)	38(1)
C(14)	3911(3)	3342(6)	–779(4)	43(1)
C(15)	3690(4)	2406(6)	–336(3)	45(1)
C(16)	3296(3)	3004(6)	98(3)	43(1)
C(21)	3472(3)	4897(5)	2433(3)	30(1)
C(22)	3945(3)	3691(5)	2342(3)	40(1)
C(23)	4816(4)	3373(6)	2899(3)	52(1)
C(24)	5198(4)	4218(7)	3521(3)	63(1)

Table 2 (*concluded*).

	x	*y*	*z*	U_{eq}
C(25)	4729(4)	5425(7)	3623(3)	64(1)
C(26)	3874(4)	5752(6)	3078(3)	48(1)
C(31)	2098(3)	7239(5)	1728(3)	30(1)
C(32)	1941(3)	7857(6)	2307(3)	45(1)
C(33)	1766(4)	9354(6)	2306(3)	54(1)
C(34)	1727(4)	10250(6)	1738(3)	57(1)
C(35)	1876(4)	9652(6)	1161(3)	53(1)
C(36)	2063(3)	8161(5)	1154(3)	39(1)
C(41)	1585(3)	4441(5)	2072(3)	30(1)
C(42)	1941(4)	3558(5)	2713(3)	37(1)
C(43)	1363(4)	2981(6)	2995(3)	49(1)
C(44)	459(4)	3279(6)	2643(4)	63(1)
C(45)	98(4)	4152(7)	2013(4)	67(1)
C(46)	649(3)	4778(6)	1726(3)	50(1)
$PPh_3C(COOCH_3)COPh(COOCH_3)(NO_2)$ (**7**α)				
P	3629(1)	9865(1)	3378(1)	40(1)
O(1)	1545(3)	7508(3)	3557(1)	58(1)
O(2)	2157(6)	4947(5)	4603(2)	176(1)
O(3)	3447(4)	6655(4)	4433(1)	92(1)
O(4)	2882(3)	10369(4)	4571(1)	76(1)
O(5)	4751(3)	10796(3)	4228(1)	59(1)
O(6)	–113(4)	10534(5)	3602(2)	103(1)
O(7)	–1066(5)	11560(5)	4136(2)	160(1)
N	–443(5)	10507(5)	3955(2)	99(1)
C(1)	2910(4)	9482(4)	3848(2)	40(1)
C(2)	1839(5)	8429(5)	3841(2)	48(1)
C(3)	3447(5)	10231(5)	4250(2)	53(1)
C(4)	5334(5)	11732(5)	4577(2)	82(1)
C(5A) (occ. 0.5)	4696(9)	5758(9)	4499(4)	138(1)
C(5B) (occ. 0.5)	–1339(9)	12953(9)	3995(5)	150(1)
C(6)	2297(6)	6180(5)	4516(2)	76(1)
C(11)	933(5)	8367(5)	4215(2)	52(1)
C(12)	–161(5)	9293(5)	4264(2)	63(1)
C(13)	–1026(5)	9100(6)	4585(2)	91(1)
C(14)	–832(6)	7978(6)	4858(2)	103(1)
C(15)	234(6)	7024(6)	4820(2)	93(1)
C(16)	1131(6)	7225(5)	4508(2)	68(1)
C(21)	3905(4)	11772(5)	3361(2)	43(1)
C(22)	5133(5)	12387(5)	3249(2)	63(1)
C(23)	5305(6)	13846(5)	3257(2)	85(1)
C(24)	4256(5)	14725(5)	3363(2)	82(1)
C(25)	3033(5)	14144(5)	3475(2)	72(1)
C(26)	2851(5)	12674(5)	3479(2)	53(1)
C(31)	2449(4)	9392(4)	2883(2)	39(1)
C(32)	1413(4)	10314(5)	2693(2)	51(1)
C(33)	535(5)	9949(6)	2313(2)	65(1)
C(34)	691(5)	8671(5)	2119(2)	63(1)
C(35)	1699(5)	7699(5)	2304(2)	60(1)
C(36)	2580(4)	8064(5)	2686(2)	49(1)
C(41)	5289(4)	8991(5)	3333(2)	52(1)
C(42)	5954(5)	8198(5)	3678(2)	72(1)
C(43)	7228(6)	7508(6)	3642(2)	107(1)
C(44)	7823(6)	7622(7)	3274(3)	133(1)
C(45)	7163(6)	8385(6)	2923(3)	117(1)
C(46)	5892(5)	9071(6)	2945(2)	77(1)

© 1998 NRC Canada

Scheme 4.

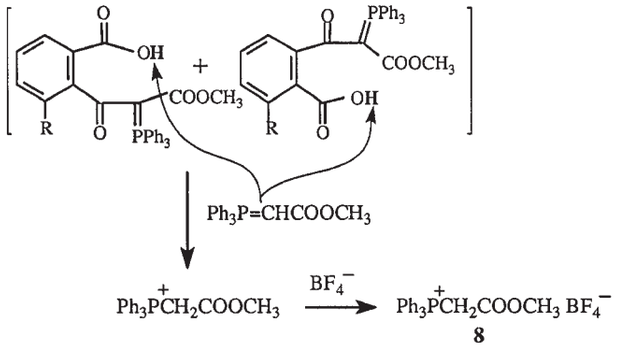

Fig. 1. Labelled diagram of the cation in the ionic salt $PPh_3CH_2COOCH_3^+$ BF_4^- (**8**).

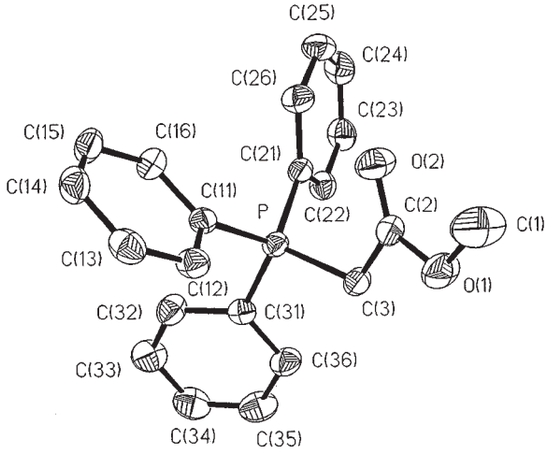

(12, 13), where the shorter distances were attributed to the multiple nature of the P—C bond. These authors have assigned the phosphorane structure in both solution and the solid state rather than the phosphonium salt. Other structures (14) have been reported showing similar results. For $Ph_3P{:}CH_2$, the P—CH_2 bond distances are much shorter, 1.662(8) and 1.659(8) Å (15).

The angles around the P atom in the two crystals are close to the tetrahedral value. The angles C(1)-P-C(Ph) are larger (avg. 112.9(2)° for **6**β and 111.9(2)° for **7**α) than the C(Ph)-P-C(Ph) values (avg. 105.8(2)° for **6**β and 106.9(2)° for **7**α), which is in agreement with the hypothesis of multiple bonding for the bond P—C(1). In crystal **6**β, the angle P-C(1)-C(2)O is much smaller (110.6(3)°) than the P-(1)-C(3)O(OCH_3) angle (126.9(5)°). The difference is significant and the values are similar to those reported by Abell et al. (12) and by Rochon et al. (13) For crystal **7**α, the two angles P-C(1)-C(2)O and P-C(1)-C(3)O(OCH_3) appear similar (120.2(3)°, 119.0(3)°). because of the disorder of the nitro and ester groups on the phenyl ring.

In crystals for **6**β and **7**α, the angle C(2)-C(1)-C(3) is 122.1(5)° and 120.8(4)°, respectively. The average value of the three angles around C(1) is consistent with an sp^2 hybridization. The two C—C bonds (C(2)—C(1) and (C(1)—C(3)) are also shorter than single bonds (1.432(8),

Fig. 2. Labelled diagram of $PPh_3C(COOCH_3)COPh(COOCH_3)(OCH_3)$ (**6**β).

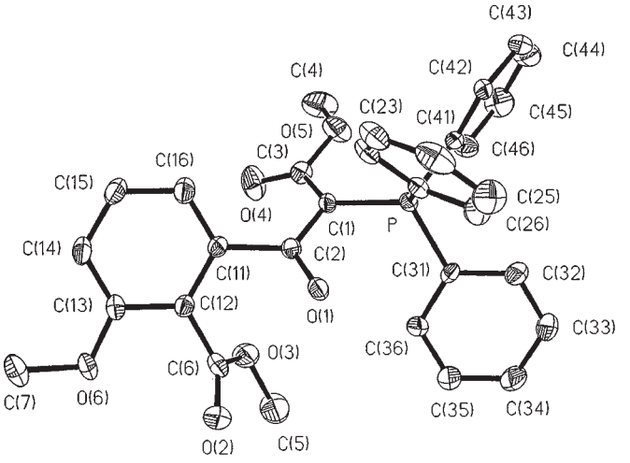

Fig. 3. Labelled diagram of $PPh_3C(COOCH_3)COPh(COOCH_3)(NO_2)$ (**7**α). (The nitro and the $COOCH_3$ groups are equally disordered in the two *ortho* positions. Only one component is shown in the drawing.)

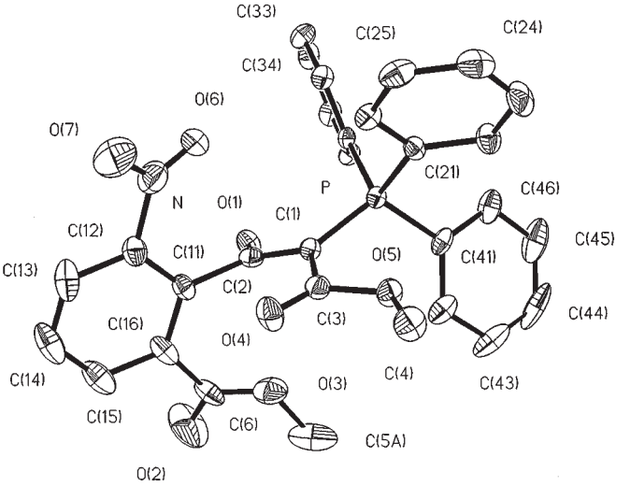

1.428(6) Å for **6**β and 1.415(6), 1.452(7) Å for **7**α), indicating that the double bond character is extended on the three bonds around C(1). The carbonyl bond C(2)—O(1) (1.237(5) Å (**6**β) and 1.234(6) Å (**7**α)) is also slightly longer than a normal double bond.

The torsion angles for crystals **6**β and **7**α have been calculated and are shown in Table 3. For crystal **6**β, the methoxy group on C(13) is in the same plane as the phenyl ring. The deviations of O(6) and C(7) from the best plane calculated through the phenyl ring are –0.034 and –0.039 Å. This planarity might extend the aromaticity of the phenyl ring. The four atoms P, C(1), C(2), and C(3) are planar. The mean deviation from the best plane calculated through the four atoms is 0.0212 Å. The dihedral angle between this plane and the phenyl ring (C(11) to C(16)) is 116.2°. For crystal **7**α, the acetyl and nitro groups located in *ortho* positions are not in the same plane as the phenyl ring. Again, the four atoms

© 1998 NRC Canada

Table 3. Selected bond distances (Å) and angles (°).

	$PPh_3CH_2COOCH_3^+$ BF_4^- (**8**)		
P—C(3)	1.801(7)	P—C(11)	1.791(5)
P—C(21)	1.793(4)	P—C(31)	1.790(5)
O(1)—C(1)	1.487(10)	O(1)—C(2)	1.322(8)
O(2)—C(2)	1.189(6)	C(2)—C(3)	1.501(7)
B—F(1)	1.329(7)	B—F(2)	1.353(7)
B—F(3)	1.347(9)	B—F(4)	1.329(11)
C(3)-P-C(11)	109.8(2)	C(3)-P-C(21)	110.5(3)
C(11)-P-C(21)	111.7(2)	C(3)-P-C(31)	107.3(2)
C(11)-P-C(31)	108.7(3)	C(21)-P-C(31)	108.7(2)
C(1)-O(1)-C(2)	116.8(4)	O(1)-C(2)-O(2)	124.2(5)
O(1)-C(2)-C(3)	110.1(4)	O(2)-C(2)-C(3)	125.7(6)
P-C(3)-C(2)	112.7(4)	P-C(11)-C(12)	119.6(4)
P-C(11)-C(16)	120.7(3)	P-C(21)-C(22)	118.0(3)
P-C(21)-C(26)	122.1(3)	P-C(31)-C(32)	119.1(4)
P-C(31)-C(36)	121.7(5)	F(1)-B-F(2)	110.9(4)
F(1)-B-F(3)	110.5(7)	F(2)-B-F(3)	113.1(6)
F(1)-B-F(4)	110.3(6)	F(2)-B-F(4)	107.0(7)
F(3)-B-F(4)	104.9(5)		
	(**6**β)	(**7**α)	
P—C(1)	1.762(6)	1.734(5)	
P—C(21)	1.802(4)	1.807(4)	
P—C(31)	1.806(5)	1.815(4)	
P—C(41)	1.821(6)	1.801(5)	
O(1)—C(2)	1.237(5)	1.234(6)	
O(2)—C(6)	1.184(7)	1.197(7)	
O(3)—C(5)	1.438(7)	1.445(9) (C(5A))	
O(3)—C(6)	1.341(8)	1.242(7)	
O(4)—C(3)	1.206(7)	1.200(7)	
O(5)—C(3)	1.346(8)	1.359(6)	
O(5)—C(4)	1.435(7)	1.436(6)	
O(6)—C(7)	1.431(10)		
O(6)—C(13)	1.368(7)		
C(1)—C(2)	1.432(8)	1.415(6)	
C(1)—C(3)	1.428(6)	1.452(7)	
C(2)—C(11)	1.510(8)	1.539(7)	
C(6)—C(12)	1.483(7)		
O(6)—N	1.178(8)		
O(7)—N	1.316(8)		
O(7)—C(5B)	1.387(10)		
N—C(12)	1.485(8)		
C(1)-P-C(21)	109.2(3)	107.7(2)	
C(1)-P-C(31)	114.0(2)	112.7(2)	
C(21)-P-C(31)	109.5(2)	107.0(2)	
C(1)-P-C(41)	115.5(2)	115.4(2)	
C(21)-P-C(41)	105.0(2)	108.4(2)	
C(31)-P-C(41)	103.0(3)	105.4(2)	
C(5)-O(3)-C(6)	115.6(5)	119.6(5) (C(5A))	
C(3)-O(5)- C(4)	118.0(5)	117.0(4)	
C(7)-O(6)-C(13)	115.9(4)		
P-C(1)-C(2)	110.6(3)	120.2(3)	
P-C(1)-C(3)	126.9(5)	119.0(3)	
C(2)-C(1)-C(3)	122.1(5)	120.8(4)	
O(1)-C(2)-C(1)	121.4(5)	125.8(5)	
O(1)-C(2)-C(11)	116.2(5)	114.5(4)	
C(1)-C(2)-C(11)	121.9(4)	119.7(4)	
O(4)-C(3)-O(5)	119.5(4)	121.5(4)	

© 1998 NRC Canada

Table 3 (*concluded*).

O(4)-C(3)-C(1)	127.5(6)	127.8(4)
O(5)-C(3)-C(1)	113.0(5)	110.7(4)
O(2)-C(6)-O(3)	122.9(5)	121.5(6)
O(2)-C(6)-C(12)	126.7(6)	
O(3)-C(6)-C(12)	110.2(5)	
C(2)-C(11)-C(12)	117.7(4)	125.0(4)
C(2)-C(11)-C(16)	121.1(5)	118.6(4)
C(12)-C(11)-C(16)	120.1(6)	116.2(5)
C(6)-C(12)-C(11)	122.2(5)	
C(6)-C(12)-C(13)	119.4(5)	
O(6)-C(13)-C(12)	114.1(4)	
O(6)-C(13)-C(14)	125.5(6)	
P-C(21)-C(22)	119.6(3)	123.1(4)
P-C(21)-C(26)	120.9(4)	118.5(3)
P-C(31)-C(32)	120.8(4)	121.5(3)
P-C(31)-C(36)	120.7(4)	120.0(3)
P-C(41)-C(42)	120.7(3)	119.7(4)
P-C(41)-C(46)	119.7(4)	120.8(4)
N-O(7)-C(5B)		130.3(8)
O(6)-N-O(7)		125.1(6)
O(6)-N-C(12)		124.4(5)
O(7)-N-C(12)-		110.4(6)
O(2)-C(6)-C(16)		122.3(6)
O(3)-C(6)-C(16)		116.2(5)
N-C(12)-C(11)		118.5(5)
N-C(12)-C(13)		119.3(5)
C(6)-C(16)-C(11)		123.2(5)
C(6)-C(16)-C(15)		115.8(5)
C(4)-O(5)-C(3)-C(1)	172.0(5)	171.7(4)
P-C(1)-C(2)-O(1)	–9.4(5)	16.6(6)
P-C(1)-C(2)-C(11)	162.2(3)	–163.9(3)
P-C(1)-C(3)-O(4)	163.2(5)	160.7(4)
C(3)-C(1)-C(2)-C(11)	–24.8(6)	17.7(6)
C(2)-C(1)-C(3)-O(4)	–8.7(8)	–20.9(7)
C(2)-C(1)-C(3)-O(5)	170.5(4)	158.8(4)
O(1)-C(2)-C(11)-C(16)	120.8(5)	69.8(5)
C(1)-C(2)-C(11)-C(12)	140.7(4)	76.1(6)
C(4)-O(5)-C(3)-O(4)	–8.8(7)	–8.6(6)
C(3)-C(1)-C(2)-O(1)	163.6(4)	–161.7(4)
P-C(1)-C(3)-O(5)	–17.7(6)	–19.6(5)
O(1)-C(2)-C(11)-C(12)	–47.3(5)	–104.3(5)
C(1)-C(2)-C(11)-C(16)	–51.3(6)	–109.7(5)
C(2)-C(11)-C(12)-C(13)	166.7(4)	173.8(5)
C(5)-O(3)-C(6)-O(2)	–1.3(9)	C(5A)-O(3)-C(6)-O(2) –8.6(10)
C(5)-O(3)-C(6)-C(12)	–177.4(5)	C(5A)-O(3)-C(6)-C(16) 170.5(7)
O(2)-C(6)-C(12)-C(11)	126.2(7)	O(2)-C(6)-C(16)-C(11) –145.4(6)
O(2)-C(6)-C(12)-C(13)	–54.3(7)	O(2)-C(6)-C(16)-C(15) 35.7(8)
O(3)-C(6)-C(12)-C(13)	121.6(5)	O(3)-C(6)-C(16)-C(15) –143.4(5)
C(2)-C(11)-C(12)-C(6)	–13.7(6)	C(2)-C(11)-C(12)-N –4.3(7)
O(3)-C(6)-C(12)-C(11)	–57.9(6)	O(3)-C(6)-C(16)-C(11) 35.5(8)
C(7)-O(6)-C(13)-C(12)	–179.8(4)	
C(7)-O(6)-C(13)-C(14)	–0.7(6)	

P, C(1), C(2), and C(3) are planar with an average deviation of 0.004 Å. The dihedral angle between this plane and the phenyl ring (C(11) to C(16)) is 97.0°.

The packing diagrams of the molecules in the crystals were made. No hydrogen bond is expected in these compounds. Therefore, the molecules in crystals **6**β and **7**α are

© 1998 NRC Canada

held together only by van der Waals forces. In the ionic salt $PPh_3CH_2COOCH_3^+$ BF_4^- (**8**), the structure is further stabilized by normal electrostatic forces.

The unambiguous identification of trapped keto phosphoranes confirmed that the regioselectivity of the initial formation of these transient products differs significantly from the regioselectivity of enol lactones, as shown in Schemes 2 and 3. The crystallographic structure determination of the major keto phosphorane trapped in the reaction with 3-nitrophthalic anhydride demonstrated that previous tentative identification of that species was incorrect (7). The results of the crystallographic identification of the intermediate products favor a mechanism in which a lower energy reversible formation of acyclic adducts is affected mainly by attractive interactions between the phosphorus atom of the ylide and oxygen-rich substituents in the 3-position, while a higher energy "Wittig olefination" leading to enol-lactones is more sensitive to steric impact of these substituents. It is clear, however, that a more highly organized transition state, in which π-stacking and stabilizing complexations must play an important role, defies predictions based on the consideration of simple electronic and steric effects.

Supplementary material

The following tables have been deposited: crystal data and experimental details of the X-ray diffraction studies (S1), anisotropic thermal factors (S2), bond distances and angles (S3), and H coordinates (S4), and may be purchased from: The Depository of Unpublished Data, Document Delivery, CISTI, National Research Council Canada, Ottawa, Canada K1A 0S2. With the exception of the anisotropic thermal factors, the same tables have also been deposited with the Cambridge Crystallographic Data Centre, and can be obtained on request from The Director, Cambridge Crystallographic Data Centre, University Chemical Laboratory, 12 Union Road, Cambridge, CB2 1EZ, U.K. Structure factor tables (S5) and the packing diagrams can be obtained from the authors.

Acknowledgment

The authors are grateful to the Natural Sciences and Engineering Research Council of Canada for financial support.

References

1. G. Pattenden. Fortschr. Chem. Org. Naturst. **35**, 133 (1978); S.B. Daniels and J.A. Katzenellenbogen. Biochemistry, **25**, 1436 (1986); R.W. Spencer, T.F. Tam, E. Thomas, V.J. Robinson, and A.J. Kranz. J. Am. Chem. Soc. **108**, 5589 (1986); D.J. Beak, S.B. Daniels, P.E. Reed, and J.A. Katzenellenbogen. J.Org. Chem. **54**, 3963 (1989); W. Dei and J.A. Katzenellenbogen. J. Org. Chem. **56**, 6893 (1991); S. Ma and X. Lu. J. Org. Chem. **58**, 1245 (1992).
2. P.A. Chopard, R.F. Hudson, and R.J.G. Searle. Tetrahedron Lett. 2357 (1965).
3. L. Breau and M.M. Kayser. Can. J. Chem. **67**, 569 (1989).
4. M.M. Kayser and L. Breau. Can. J. Chem. **67**, 1401 (1989).
5. M.M. Kayser and L. Breau. Tetrahedron Lett. **29**, 6203 (1988).
6. M.M. Kayser, K.L. Hatt, and D.L. Hooper. Can. J. Chem. **70**, 1985 (1992).
7. M.M. Kayser, K.L. Hatt, H. Yu, and D.L. Hooper. Can. J. Chem. **71**, 1010 (1993).
8. C.F. Ingham, R.A. Massy-Westropp, G.D. Reynolds, and W.D. Thorpe. Aust. J. Chem. **28**, 2499 (1975).
9. A.D. Abell and R.A. Massy-Westropp. Aust. J. Chem. **35**, 2077 (1982).
10. L. Breau. M. Sc. Thesis, Mount Allison University, Sackville, N. B. (1986).
11. International tables for X-ray crystallography. Vol. 12V. Kynoch Press, Birmingham. 1974.
12. A.D. Abell, B.M. Clark, and W.T. Robinson. Aust. J. Chem. **41**, 1243 (1988).
13. F.D. Rochon, R. Melanson, and M.M Kayser. Acta Crystallog. Sect. C: Cryst. Struct. Commun. **C50**, 1165 (1994).
14. A.F. Cameron, F.D. Duncanson, A.A. Freer, V.W. Armstrong and R. Ramage. J. Chem Soc. Perkin Trans. 1030 (1975).
15. J.C. Bart. J. Chem. Soc. B, 350 (1969).

© 1998 NRC Canada

Synthesis and structural characterization of (2′-hydroxyacetophenoneazine)mono(diphenylboron) chelate

Herbert Höpfl and Norberto Farfán

Abstract: Boron chelates obtained from salicylaldehyde and 2′-hydroxyacetophenone azines are colored compounds with potential applications in analytical chemistry. Up to now these complexes have not been studied by X-ray crystallography, although two structures with a six- or a seven-membered chelate ring are possible. This contribution presents the X-ray analysis of 2′-hydroxyacetophenone azine and its corresponding new mono(diphenylboron) chelate with a six-membered boron heterocyclic ring. With these data structural changes of the ligand on chelate formation and structural differences in comparison to salicylaldehyde azomethine boron chelates are discussed.

Key words: boron complex, borinate, azine, azomethine.

Résumé : Les chélates de bore obtenus à partir des salicylaldéhyde-azine et 2′-hydroxyacétophénone-azine sont des composés colorés qui peuvent avoir des applications en chimie analytique. Même si ces chélates peuvent prendre deux structures cycliques, l'une à six et l'autre à sept chaînons, ces complexes n'ont pas été étudiés par diffraction des rayons-X jusqu'à maintenant. Dans ce travail, on présente les résultats d'une analyse par rayons X de la 2′-hydroxyacétophénone-azine et de son nouveau mono(diphénylbore)chélate comportant un hétérocycle du bore à six chaînons. Sur la base de ces données, on discute des changements de structure du ligand qui se produisent lors de la formation du chélate ainsi que des différences de structure par comparaison avec celles des chélates du bore avec l'azométhine du salicylaldéhyde.

Mots clés : complexe du bore, borinate, azine, azométhine.

[Traduit par la Rédaction]

Introduction

Boron chelates of salicylaldehyde and 2′-hydroxyacetophenone azomethines (**1**) were synthesized for the first time in 1965 (1) and 1973 (2), respectively, followed by extensive spectroscopic studies of a series of derivatives in order to analyze the influence of different substituents at the imino functional group and the boron atom (Fig. 1) on the formation and stability of these compounds (3–8). The particular interest in the formation and the properties of these chelates is related to their analytical application in the separation and identification of primary alkylamines by high-performance liquid chromatography (9). Thereby, the boron chelates can be prepared in a one-step synthesis from salicylaldehyde or 2′-hydroxyacetophenone, the primary amine, and diphenylborinic acid.

Due to their color-deepening effect on chelate formation, boron complexes obtained from salicylaldehyde and 2′-hydroxyacetophenone azines (2–6, 8) as well as 2,2′-dihydroxyazobenzenes (10) could be important for the quantitative determination of chelate components. These compounds are also of interest from a structural viewpoint, because there exist four different possibilities of chelate formation, as it is illustrated by the example of 2′-hydroxyacetophenone azine (Scheme 1).

Compounds **3** and **4** are spectroscopically not clearly discernible isomers with a six- and seven-membered boron heterocyclic ring, respectively. Further reaction products with distinctly different compositions could be compound **5**, the corresponding bischelate of compound **3**, or compound **6** obtained by elimination of a benzene molecule, as it has been already observed for other diphenylboron complexes (9). Up to now it is known that compounds **5** and **6** are not formed in this reaction, even when 2 equiv. of the diphenylborinic acid are used. Between the monochelates **3** and **4** the most probable structure is **3** (3), although the formation of a seven-membered heterocycle cannot be completely excluded, since seven-membered rings are formed in the case of

Received April 1, 1998.

H. Höpfl.[1] Universidad Autónoma del Estado de Morelos, Centro de Investigaciones Químicas, Av. Universidad 1001, C.P. 62210 Cuernavaca, Morelos, Mexico.
N. Farfán.[1] Departamento de Quimica, Centro de Investigación y de Estudios Avanzados del IPN, Apdo Postal 14–740, C.P. 07000 Mexico D.F., Mexico.

[1]Authors to whom correspondence may be addressed: HH: Telephone: +52 73 29 7020. Fax: +52 73 29 7040.
E-mail: hhopfl@servm.fc.uaem.mx; NF: Telephone: +52 5 747 3800, ext. 4031. Fax: +52 5 747 7113.
E-mail: jfarfan@mail.red.cinvestav.mx

© 1998 NRC Canada

Scheme 1. Different possibilities of chelate formation between 2′-hydroxyacetophenone azine and diphenylborinic acid.

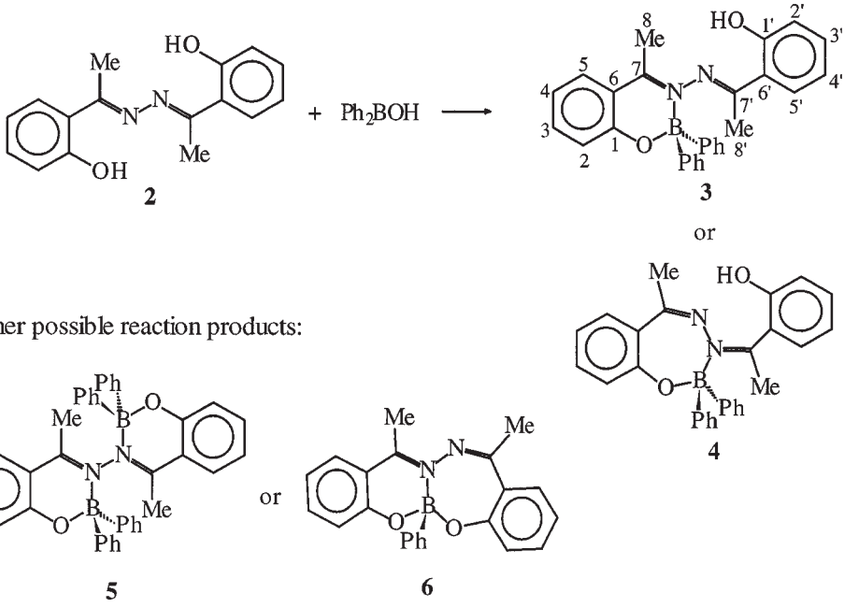

Fig. 1. Boron complexes with salicyladehyde and 2′-hydroxyacetophenone azomethines.

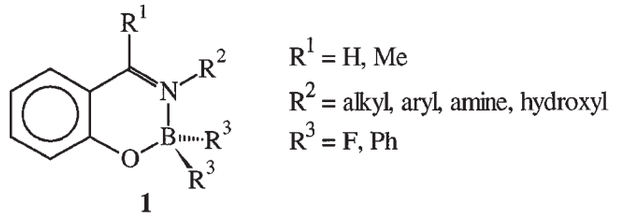

salicylaldehyde nitrones (11). It should be noted that the ^{1}H, ^{13}C, and ^{11}B NMR spectra alone do not allow an unambiguous prediction of the structure type.

Therefore, an X-ray crystallographic study was undertaken to decide between the two structures **3** and **4**. The molecular structure of the ligand was also examined, because there is some recent interest in the stereochemistry and stereoelectronics of acetophenone azines (12).

Experimental

Instrumentation

NMR studies were performed with the following spectrometers: Jeol GSX 270 and Bruker Avance 300. Standards were TMS (^{1}H, ^{13}C) and $BF_3 \cdot OEt_2$ (^{11}B). Chemical shifts are stated in ppm; they are positive, when the signal is shifted to higher frequencies than the standard.

IR spectra have been recorded with a Perkin Elmer 16F-PC FT-IR spectrophotometer. Mass spectra were obtained with an HP 5989 A equipment.

Melting points were determined with a Gallenkamp MFB-595 apparatus and have not been corrected. Elemental microanalyses were performed by Oneida Research Service., Whitesboro, N.Y.

*X-ray crystallographic study of **2** and **3***

The crystallographic studies of **2** and **3** were performed on an Enraf–Nonius CAD4 diffractometer (λ_{MoK_α} = 0.710 69 Å, monochromator: graphite, T = 293 K, ω-2θ scan). Cell parameters were determined by least-squares refinement on diffractometer angles for 24 automatically centered reflections. Absorption correction was not necessary, corrections were made for Lorentz and polarization effects. Solution and refinement: direct methods (SHELXS-86) for structure solution and the CRYSTALS (version 9, 1994) software package for refinement and data output. $I > 3\sigma(I)$. $R = \Sigma(||F_o| - |F_c||)/\Sigma|F_o|$, $R_w = [\Sigma w(|F_o| - |F_c|)^2/\Sigma w F_o^2]^{1/2}$. Non-hydrogen atoms were refined anisotropically and a reflections:parameter ratio >5 was considered sufficient for the studies performed in here. Hydrogen atoms have been found by difference Fourier maps, and their coordinates as well as one overall isotropic thermal parameter were refined.

Reagents

All starting materials were commercially available. Solvents were used without further purification, but monocrystals were grown from spectrophotometric grade solvents.

*2′-Hydroxyacetophenone azine (**2**)*

Compound **2** was prepared as described in the literature for salicylaldehyde azine (2, 8). A yellow solid is obtained. Crystals suitable for X-ray crystallography were obtained from THF/hexane; mp 197–199°C. Yield: 90%. Infrared (KBr): 3446 (br, w), 2918 (w), 2850 (w), 1624 (m), 1606 (s), 1590 (s), 1560 (s), 1506 (w), 1494 (m), 1438 (m), 1364 (m), 1300 (s), 1252 (m), 1160 (m) cm^{-1}. ^{1}H (300 MHz, DMSO-d_6), δ (ppm): 2.54 (3H, s, H-8), 6.96 (1H, dd, H-4), 6.98 (1H, d, H-2), 7.41 (1H, dd, H-3), 7.78 (1H, d, H-5), 12.95 (1H, s, OH); ^{13}C (75.5 MHz, $CDCl_3$), δ (ppm): 15.8 (C-8), 118.1 (C-2), 119.9 (C-4), 120.2 (C-6), 130.6 (C-5), 133.6 (C-3), 160.4 (C-1), 169.0 (C-7). EI mass spectrometry (70 eV, DIP), *m*/*z*: 268 (100%, M^+), 253 (67%), 134 (31%),

© 1998 NRC Canada

Table 1. Crystallographic data for compounds **2** and **3**.

	2[a]	**3**[a]
Compound		
Formula	$C_{16}H_{16}N_2O_2$	$C_{28}H_{25}BN_2O_2$
Crystal size, mm	0.42 × 0.48 × 0.50	0.4 × 0.4 × 0.6
fw, g mol^{-1}	268.31	432.33
Space group	$P\ 2_12_12_1$	$P\ 2_1/c$
Cell parameters		
a, Å	6.3399 (7)	10.761 (1)
b, Å	13.5567 (12)	15.876 (1)
c, Å	15.9931 (17)	13.651 (1)
β°	90	96.721 (6)
V, Å^3	1374.6 (2)	2316.1 (3)
Z	4	4
μ, mm^{-1}	0.081	0.072
ρ_{calcd}, g cm^{-3}	1.30	1.24
Data collection		
Scan range, deg in ω	1.03 + 0.71 tan θ	0.41 + 0.51 tan θ
Data collected	$-h, -k, \pm l$	$\pm h, +k, -l$
2θ max, deg	50	56
Total reflections	2765	5996
Total unique refl.	2137	5549
R_{merge}	0.02	0.03
Refl. with $I > 3\sigma(I)$	1386	2911
Intensity variation (σ)	<3	<3
Refinement		
R	0.043	0.039
R_w	0.042	0.032
No. of variables	231	375
gof	1.66	2.09
Max. Δ/σ (final cycle)	0.08	0.07
$\Delta\rho_{min}$, e Å^{-3}	–0.18	–0.12
$\Delta\rho_{max}$, e Å^{-3}	0.20	0.17
Extinction parameter	80(11)	535(15)

[a]Temperature 293 K, Enraf Nonius CAD4 diffractometer, MoK_α (λ = 0.710 69 Å) radiation, graphite monochromator, ($R = \Sigma(||F_o| - |F_c||)/\Sigma|F_o|$, $R_w = [\Sigma w(|F_o| - |F_c|)^2/\Sigma wF_o^2]^{1/2}$, where $w = 1/\sigma^2$. Values given for R, R_w, and gof are based on those reflections with $I > 3\sigma(I)$.

120 (16%), 91 (33%), 65 (33%), 42 (26%). Elemental analysis: calcd.: C 71.64, H 5.97, N 10.45; found: C 70.93, H 5.64, N 10.27.

*(2′-Hydroxyacetophenoneazine)mono(diphenylboron) chelate (**3**)*

Compound **3** was prepared in dichloromethane at a temperature range of –20 to 0°C from 0.050 g (0.186 mmol) of 2′-hydroxyacetophenone azine **2** and diphenylborinic acid prepared from 0.042 g (0.186 mmol) of 2-aminoethyldiphenylborinate (13). After slow evaporation of the solvent a yellow solid (0.062 g, 0.144 mmol) separated that was further purified with hexane. Crystals suitable for X-ray crystallography were obtained from THF/hexane; mp 207–209°C. Yield: 77%. Infrared (KBr): 3452 (br, w), 3068 (w), 3042 (w), 1606 (s), 1568 (m), 1550 (s), 1480 (m), 1452 (s), 1432 (m), 1368 (m), 1350 (m), 1322 (m), 1306 (m), 1278 (m), 1248 (m), 1184 (m), 1148 (m), 1086 (w), 1030 (w), 1000 (m) cm^{-1}. ^{1}H (270 MHz, DMSO-d_6), δ (ppm): 1.68 (3H, s, H-8), 2.49 (3H, s, H-8′), 6.81–7.08 (4H, m, H-2, H-2′, H-4, H-4′), 7.10 (6H, m, *m*-BC_6H_5, *m*′-BC_6H_5, *p*-BC_6H_5, *p*′-B-C_6H_5), 7.27 (1H, dd, H-5), 7.36 (1H, m, H-3′), 7.37 (4H, m, *o*-BC_6H_5, *o*′-BC_6H_5), 7.48 (1H, t, H-3), 7.74 (1H, dd, H-5′), 11.05 (1H, OH); ^{13}C (67.8 MHz, DMSO-d_6), δ (ppm): 15.1 (C-8′), 18.1 (C-8), 116.8, 118.8, 118.9, 119.7 (C-2, C-2′, C-4, C-4′), 117.9 (C-6), 120.0 (C-6′), 125.6, 126.0 (*p*-BC_6H_5, *p*′-BC_6H_5), 126.0, 126.8 (*m*-BC_6H_5, *m*′-BC_6H_5), 129.3, 129.5 (C-5, C-5′), 131.5, 133.6 (*o*-BC_6H_5, *o*′-BC_6H_5), 132.7 (C-3′), 135.9 (C-3), 145.6, 149.0 (*i*-BC_6H_5, *i*′-BC_6H_5), 157.6 (C-1), 159.7 (C-1′), 161.8 (C-7), 172.9 (C-7′); ^{11}B (86.6 MHz, DMSO-d_6), δ (ppm): +7 ($h_{1/2}$ = 2400 Hz). EI mass spectrometry (70 eV, DIP), *m*/*z*: 432 (2%, M^+), 355 (100%), 298 (2%), 277 (44%), 222 (17%), 134 (29%), 78 (11%). Elemental analysis: calcd.: C 77.70, H 5.78, N 6.48; found: C 77.22, H 5.54, N 6.56.

Table 2. Fractional atomic coordinates for compound **2**.

Atom	*x*/*a*	*y*/*b*	*z*/*c*	*U* (equiv.)
O(1)	0.3170(7)	0.4361(3)	0.4731(2)	0.0738
O(51)	–0.3442(6)	0.5235(3)	0.7603(2)	0.0640
N(10)	0.0849(7)	0.4831(3)	0.5959(3)	0.0492
N(60)	–0.0938(7)	0.4685(3)	0.6459(2)	0.0484
C(2)	0.435(1)	0.5153(4)	0.4935(3)	0.0591
C(3)	0.3891(8)	0.5752(4)	0.5631(3)	0.0466
C(4)	0.5247(9)	0.6546(4)	0.5797(4)	0.0537
C(5)	0.6995(9)	0.6719(5)	0.5295(4)	0.0637
C(6)	0.741(1)	0.6137(6)	0.4632(4)	0.0719
C(7)	0.612(1)	0.5352(5)	0.4443(4)	0.0721
C(8)	0.2006(8)	0.5589(4)	0.6157(3)	0.0455
C(9)	0.154(1)	0.6284(5)	0.6843(5)	0.0676
C(52)	–0.4536(8)	0.4402(4)	0.7424(3)	0.0506
C(53)	–0.3928(8)	0.3745(4)	0.6798(3)	0.0476
C(54)	–0.5184(9)	0.2908(4)	0.6666(4)	0.0623
C(55)	–0.702(1)	0.2755(5)	0.7136(5)	0.0723
C(56)	–0.756(1)	0.3424(5)	0.7751(4)	0.0689
C(57)	–0.6361(9)	0.4233(5)	0.7908(4)	0.0615
C(58)	–0.2023(8)	0.3911(4)	0.6286(3)	0.0495
C(59)	–0.146(1)	0.3204(6)	0.5606(6)	0.0795

Results and discussion

The X-ray analysis (Table 1) establishes the six-membered chelate structure **3** and is thus consistent with the peak of *m*/*z* = 134 (29%) in the mass spectrum that corresponds to the C_8H_8NO fragment. Compound **3** is the first boron complex with a salicylaldehyde or 2′-hydroxyacetophenone azine characterized by X-ray crystallography. The final coordinates, selected bond lengths, and selected bond angles for compounds **2** and **3** are summarized in Tables 2–5. The molecular structures of **2** and **3** can be seen from Figs. 2 and 3. Crystal data, atomic coordinates, bond angles, interatomic distances, torsion angles, and anisotropic thermal parameters have been deposited as supplementary material.[2]

[2] Copies of material on deposit may be purchased from: The Depository of Unpublished Data, Document Delivery, CISTI, National Research Council Canada, Ottawa, Canada, K1A 0S2. With the exception of torsion angles and anisotropic thermal parameters these have also been deposited with the Cambridge Crystallographic Data Centre and can be obtained on request from: The Director, Cambridge Crystallographic Data Centre, University Chemical Laboratory, 12 Union Road, Cambridge, CB2 1EZ, U.K.

© 1998 NRC Canada

Table 3. Fractional atomic coordinates for compound **3**.

Atom	*x*/*a*	*y*/*b*	*z*/*c*	*U* (equiv.)
O(1)	0.3152(1)	0.633 52(9)	0.023 69(9)	0.0449
O(17)	0.1192(2)	0.5200(1)	–0.3840(1)	0.0654
B(2)	0.2759(2)	0.6361(1)	–0.0836(2)	0.0400
N(3)	0.2393(1)	0.5372(1)	–0.1109(1)	0.0383
N(12)	0.2358(1)	0.5128(1)	–0.2103(1)	0.0411
C(4)	0.1939(2)	0.4856(1)	–0.0500(1)	0.0399
C(5)	0.1515(3)	0.3992(2)	–0.0826(2)	0.0534
C(6)	0.1862(2)	0.5147(1)	0.0501(1)	0.0397
C(7)	0.1243(2)	0.4682(1)	0.1172(2)	0.0498
C(8)	0.1216(2)	0.4960(2)	0.2123(2)	0.0559
C(9)	0.1802(2)	0.5707(2)	0.2428(2)	0.0533
C(10)	0.2436(2)	0.6165(1)	0.1793(2)	0.0492
C(11)	0.2471(2)	0.5894(1)	0.0825(1)	0.0412
C(13)	0.3356(2)	0.4817(1)	–0.2404(1)	0.0423
C(14)	0.4528(2)	0.4635(2)	–0.1742(2)	0.0563
C(15)	0.3284(2)	0.4633(1)	–0.3464(1)	0.0454
C(16)	0.2227(2)	0.4836(1)	–0.4130(2)	0.0527
C(18)	0.2193(3)	0.4654(2)	–0.5129(2)	0.0674
C(19)	0.3198(3)	0.4277(2)	–0.5471(2)	0.0754
C(20)	0.4248(3)	0.4070(2)	–0.4842(2)	0.0787
C(21)	0.4289(3)	0.4243(2)	–0.3847(2)	0.0653
C(22)	0.1513(2)	0.6924(1)	–0.1096(2)	0.0432
C(23)	0.0750(2)	0.6900(1)	–0.1992(2)	0.0507
C(24)	–0.0303(2)	0.7404(2)	–0.2192(2)	0.0606
C(25)	–0.0619(2)	0.7956(2)	–0.1490(2)	0.0660
C(26)	0.0112(3)	0.8013(2)	–0.0607(2)	0.0703
C(27)	0.1164(2)	0.7504(2)	–0.0410(2)	0.0612
C(28)	0.3934(2)	0.6646(1)	–0.1390(1)	0.0409
C(29)	0.3837(2)	0.6810(1)	–0.2397(2)	0.0491
C(30)	0.4855(2)	0.7053(2)	–0.2868(2)	0.0583
C(31)	0.6005(2)	0.7143(2)	–0.2331(2)	0.0654
C(32)	0.6142(2)	0.6999(2)	–0.1336(2)	0.0679
C(33)	0.5118(2)	0.6755(2)	–0.0871(2)	0.0566

Table 4. Selected bond lengths and bond angles of compound **2**.

Bond lengths (Å)			
O(1)—C(2)	1.347 (7)	O(51)—C(52)	1.355 (6)
N(10)—C(8)	1.302 (6)	N(60)—C(58)	1.285 (6)
C(2)—C(3)	1.407 (7)	C(52)—C(53)	1.395 (7)
C(3)—C(8)	1.478 (6)	C(53)—C(58)	1.477 (7)
C(8)—C(9)	1.477 (7)	C(58)—C(59)	1.493 (8)
N(10)—N(60)	1.401 (5)		
Bond angles (°)			
N(10)-C(8)-C(3)	115.8 (4)	N(60)-C(58)-C(53)	116.3 (5)
N(10)-C(8)-C(9)	124.8 (5)	N(60)-C(58)-C(59)	123.6 (5)
C(8)-N(10)-N(60)	115.4 (4)	C(58)-N(60)-N(10)	115.1 (4)
C(3)-C(8)-C(9)	119.4 (5)	C(53)-C(58)-C(59)	120.1 (5)
O(1)-C(2)-C(3)	122.6 (5)	O(51)-C(52)-C(53)	122.8 (5)
C(2)-C(3)-C(8)	121.9 (5)	C(52)-C(53)-C(58)	121.8 (5)

The crystal structure of the 2′-hydroxyacetophenone azine **2** consists of discrete molecules with intramolecular hydrogen bonds O-H···N (1.579 Å, 141.5° for H(11)···N(10) and 1.862 Å, 155.8° for H(511)···N(60)) and an (*E*,*E*)-*trans* conformation. The value of the C=N-N=C torsion angle is 177.0° and is different in comparison to other *para*-substituted (H, F, Cl, Br, OH, etc.) acetophenone azines with values between 124.7 and 148.0° (12, 14).

The crystal structure of **3** consists of discrete molecules with a strong intramolecular hydrogen bond at the nonchelated site of the molecule (O-H···N = 1.627 Å and 149.1°). The (*E*,*E*)-*trans* conformation is lost upon chelate formation due to a steric interaction between one of the BC_6H_5 groups and the C(14) methyl group. The C=N-N=C torsion angle changes from 177.0 to 99.1°, whilst the N—N bond length remains rather constant (1.401 (5) Å for **2** and 1.408 (2) Å for **3**). The mean N—N bond length of other *para*-acetophenone azines is 1.395 (3) Å (12).

In Table 6 some interesting bond lengths of **2** and **3** are summarized and compared to the corresponding data of the salicylaldehyde azomethine boron chelates **8** (15) and **9** (7) (Fig. 4). There are significant differences in the N→B, the B—O, the C(6)—C(7)[3], and the C=N bonds, specially between the boron complexes **3** and **8**. Compound **8** shows the shortest N→B bond with a value of 1.602 (3) Å, while the N→B bonds of **3** and **9** are significantly longer, 1.651 (3) and 1.634 (6) Å, respectively. The B—O bond lengths of **8** and **9** with values of 1.513 (2) and 1.522 (6) Å are significantly longer than in **3** with only 1.477 (2) Å. The structural differences between **3**, **8**, and **9** could be explained with a compromise between the mesomeric forms I and II (Scheme 2) (16). The mean value for a single B—O bond in different 2-aminoethyl diphenylborinates is 1.477 (2) Å (17), while a coordinative O→B bond should be in the range of 1.561 (5) to 1.595 (3) Å (18–21). Although these resonance structures fit well for the differences in the N→B and B—O bond lengths in the case of **3** (I is preferred) and **8** (II is preferred), no such correlation can be found for structure **9**. There is a small, but significant difference in the C(6)—C(7)[3] and C=N bond lengths of the three molecules, however the change is not conclusive in the case of the imine bond. Instead of being shorter in compound **3** it is longer than in compound **8**. Also, the C—O and C(1)—C(6)[3] bonds are not significantly different for the three structures. Therefore, it may be more reasonable not to consider this mesomeric scheme and to state instead that a longer N→B bond results in a shorter B—O bond, and vice versa, in order to compensate the electron deficiency of the boron atom. An explanation for the longer N→B bond in the azine chelate **3** could be the presence of the second nitrogen atom that is more electronegative than a carbon atom and attracts electron density from the trivalent nitrogen atom. The competition for electron density of the two atoms should also be the reason why a bischelate with two electron-withdrawing diphenylboryl groups cannot be obtained (2).

If the bond lengths of ligand **2** are compared to the ones of chelates **3**, **8**, and **9**, there is only one striking difference and that is the C(6)—C(7)[3] bond. The mean value for five para-substituted acetophenone azines is 1.480 (4) Å (1.478 (6) Å for **2**), while the mean value of structures **3**, **8**, and **9** is 1.441 (4) Å, indicating that there exists some delocalization between the imine group and the aromatic ring on chelate formation.

[3] The numbering used here corresponds to the one shown in Schemes 1 and 2.

© 1998 NRC Canada

Table 5. Selected bond lengths, bond angles, and torsion angles of compound **3**.

Bond lengths (Å)			
O(1)—B(2)	1.477 (2)	B(2)—N(3)	1.651 (3)
O(1)—C(11)	1.345 (2)	B(2)—C(22)	1.616 (3)
B(2)—C(28)	1.612 (3)	N(3)—C(4)	1.302 (2)
N(3)—N(12)	1.408 (2)	C(4)—C(6)	1.454 (3)
C(6)—C(11)	1.402 (3)	N(12)—C(13)	1.292 (2)
C(13)—C(15)	1.470 (3)	C(15)—C(16)	1.408 (3)
C(16)—O(17)	1.355 (2)		
Bond angles (°)			
O(1)-B(2)-N(3)	103.3 (2)	O(1)-B(2)-C(22)	111.6 (2)
O(1)-C(11)-C(6)	121.3 (2)	O(1)-B(2)-C(28)	108.9 (2)
B(2)-N(3)-N(12)	117.3 (1)	B(2)-N(3)-C(4)	123.5 (2)
N(3)-B(2)-C(22)	107.8 (2)	N(3)-B(2)-C(28)	109.9 (2)
N(3)-N(12)-C(13)	118.8 (2)	N(3)-C(4)-C(6)	117.8 (2)
C(4)-C(6)-C(11)	119.3 (2)	N(12)-C(13)-C(15)	116.1 (2)
C(13)-C(15)-C(16)	122.4 (2)	C(15)-C(16)-O(17)	122.6 (2)
Torsion angles (°)[a]			
O(1)-B(2)-N(3)-C(4)	31.5	O(1)-C(11)-C(6)-C(4)	–1.7
B(2)-O(1)-C(11)-C(6)	34.1	B(2)-N(3)-C(4)-C(6)	–5.9
N(3)-C(4)-C(6)-C(11)	–11.4	N(3)-B(2)-O(1)-C(11)	–44.2
C(4)-N(3)-N(12)-C(13)	–99.1		

[a]A positive rotation is counterclockwise from atom 1, when viewed from atom 3 to atom 2.

Table 6. Comparison of interesting bond lengths (Å) of compounds **2**, **3**, **8**, and **9**.

Compound	N—B	B—O	C—O	C(1)—C(6)[a]	C(6)—C(7)[a]	C=N
2	—	—	1.351 (7)	1.401 (7)	1.478 (7)	1.293 (6)
3	1.651 (3)	1.477 (2)	1.345 (2)	1.402 (3)	1.454 (3)	1.302 (2)
			1.355 (3)[b]	1.408 (3)[b]	1.470 (3)[b]	1.292 (2)[b]
8[c]	1.602 (3)	1.513 (2)	1.352 (2)	1.405 (2)	1.436 (2)	1.279 (2)
9	1.634 (6)	1.522 (6)	1.344 (6)	1.393 (6)	1.432 (6)	1.297 (6)

[a]The numbering used here corresponds to the one shown in Schemes 1 and 2.

[b]Second, unchelated molecule moiety.

[c]Mean values for the two independent molecules in the asymmetric unit of the crystal lattice.

Fig. 2. Molecular structure of the 2′-hydroxyacetophenone azine **2**. The thermal ellipsoid probability level is 25%.

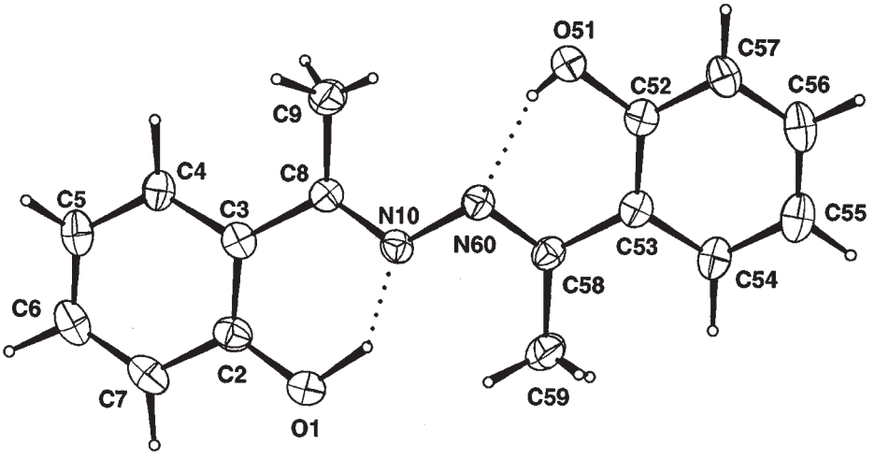

© 1998 NRC Canada

Fig. 3. Molecular structure of the (2′-hydroxyacetophenoneazine)mono(diphenylboron) chelate **3**. The thermal ellipsoid probability level is 25%.

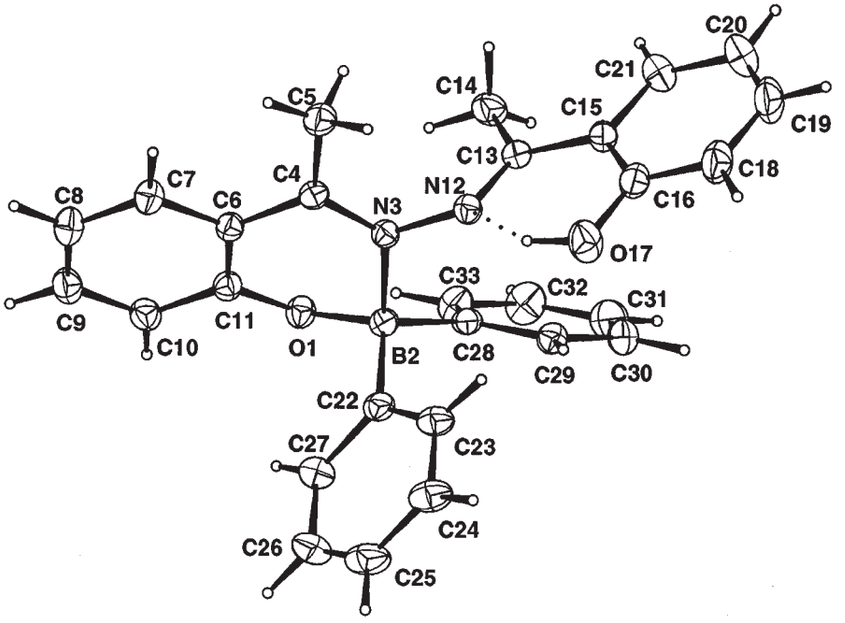

Fig. 4. Boron chelates **8** and **9**.

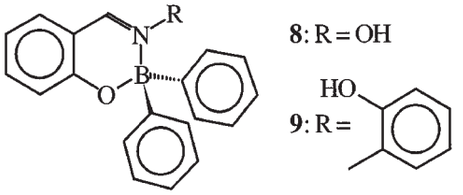

Scheme 2. Mesomeric forms of salicylaldehyde and 2′-hydroxyacetophenone diphenylboron chelates.

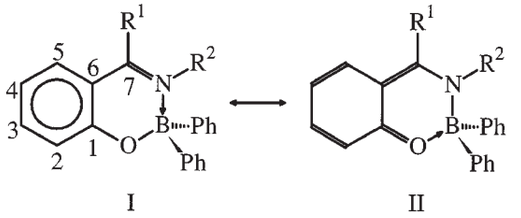

The mean values of the bond angles in the six-membered heterocycles of the three boron complexes are 117.5 (2) for **3**, 118.3 (1) for **8**, and 116.8 (2) for **9**. Smaller values indicate a higher ring strain (22). This is confirmed by the deviation of the boron and oxygen atoms from the borinate mean plane. The deviation of the boron atom is highest for **9**, 0.691 Å, whilst **3** and **8** present similar values, 0.481 and 0.427 Å, respectively. The deviations of the oxygen atom are 0.026 Å for **9**, 0.083 Å for **8**, and –0.144 Å for **3**. Therefore, the C_3BNO chelate rings are significantly nonplanar and may be described as either boron-envelopes (**8**, **9**) or half-chairs with boron and oxygen atoms displaced in opposite directions from the approximate plane (**3**).

Acknowledgements

The authors thank Prof. R. Santillan for critical reading of the manuscript. N.F. thanks CONACYT and H.H. thanks UAEM (Universidad Autónoma del Estado de Morelos) for financial support.

References

1. F. Umland and C. Schleyerbach. Angew. Chem. Int. Ed. Engl. **4**, 426 (1965).
2. F. Umland, E. Hohaus, and K. Brodtke. Chem. Ber. **106**, 2427 (1973).
3. E. Hohaus. Monatshefte für Chem. **111**, 863 (1980).
4. E. Hohaus. Z. Anorg. Allg. Chem. **484**, 41 (1982).
5. E. Hohaus, and W. Riepe. Z. Naturforsch. **29b**, 663 (1974).
6. E. Hohaus, K.D. Klöppel, B. Paschold, and H.-R. Schulten. Z. Anorg. Allg. Chem. **493**, 41 (1982).
7. R. Allmann, E. Hohaus, and S. Olejnik. Z. Naturforsch. **37b**, 1450 (1982).
8. E. Hohaus. Z. Anorg. Allg. Chem. **506**, 185 (1983).
9. K.E. Claas and E. Hohaus. Fresenius Z. Anal. Chem. **322**, 343 (1985).
10. E. Hohaus and K. Wessendorf. Z. Naturforsch. **35b**, 319 (1980).
11. W. Kliegel and D. Nanninga. J. Organomet. Chem. **243**, 373 (1983).
12. G.S. Chen, M. Anthamatten, C.L. Barnes, and R. Glaser. J. Org. Chem. **59**, 4336 (1994).
13. G.N. Chremos, H. Weidmann, and H.K. Zimmerman, J. Org. Chem. **26**, 1683 (1961).
14. M.C. García-Mina, M. Arrese, M. Martinez-Ripoll, S. García-Blanco, and J.L. Serrano. Acta Cryst. **B38**, 2726 (1982).
15. W. Kliegel, S.J. Rettig, and J. Trotter. Can. J. Chem. **62**, 1363 (1984).
16. O.E. Kompan, N.G. Furmanova, Y.T. Struchkov, L.M. Sitkina, V.A. Bren, and V.I. Minkin. Zh. Strukt. Khim. **21**, 90 (1980); Chem. Abstr. **93**, 204 721r (1980).
17. S.J. Rettig and J. Trotter. Can. J. Chem. **54**, 3130 (1976), and refs. therein.

© 1998 NRC Canada

18. S.J. Rettig and J. Trotter. Can. J. Chem. **54**, 1168 (1976).
19. W.R. Cullen, S.J. Rettig, J. Trotter, and E.B. Wickenheiser. Can. J. Chem. **66**, 2007 (1988).
20. C. Orvig, S.J. Rettig, and J. Trotter. Can. J. Chem. **65**, 590 (1987).
21. C. Orvig, S.J. Rettig, J. Trotter, and Z. Zhang. Can. J. Chem. **68**, 1803 (1990).
22. H. Höpfl, M. Sánchez, V.Barba, N.Farfán, S. Rojas, and R. Santillan. Inorg. Chem. **37**, 1679 (1998).

© 1998 NRC Canada

Temperature dependence of the excess volumes of binary mixtures containing cyclohexane + some higher *n*-alkanes

Mohamed M. El-Banna and Mervette M. El-Batouti

Abstract: Excess molar volumes, V^E, for three binary liquid mixtures of cyclohexane + *n*-dodecane, *n*-tetradecane, and *n*-hexadecane were determined from density measurements at seven different temperatures in the range from 283.15 to 313.15 K and atmospheric pressure, over the entire range of mole fractions. The V^E values were derived and the results show a regular negative pattern of behaviour for each of the three sets of the binary system. For cyclohexane, the magnitude of V^E increases with the alkane chain length. The Prigogine–Flory–Patterson theory was applied to analyze the experimental behaviour by calculating three different contributions to V^E, i.e., interactional, free volume, and internal pressure. The theory gives a representation of the main feature of the systems studied by using a fitted parameter to describe the behaviour throughout the composition range.

Key words: excess molar volumes, binary mixtures, cyclohexane, *n*-dodecane, *n*-tetradecane, *n*-hexadecane, Prigogine–Flory–Patterson theory.

Résumé : Faisant appel à la mesure de densités à sept températures allant de 283,15 à 313,15 K, à la pression atmosphérique et à des fractions molaires couvrant l'ensemble des concentrations, on a déterminé les volumes molaires en excès, V^E, pour les mélanges liquides binaires du cyclohexane avec le dodécane, le tétradécane et l'hexadécane. Les valeurs de V^E ont été obtenues et chacun des trois ensembles de système binaire présente un patron de comportement régulièrement négatif. Pour le cyclohexane, l'amplitude de V^E augmente avec la longueur de la chaîne de l'alcane. On a appliqué la théorie de Prigogine–Flory–Patterson pour analyser le comportement expérimental; à cette fin, on a calculé trois contributions différentes à la valeur de V^E, soit celle des interactions, du volume libre et de la pression interne. Si l'on utilise un paramètre ajusté pour décrire le comportement sur l'ensemble des concentrations, la théorie donne une représentation de la principale caractéristique des systèmes étudiés.

Mots clés : volumes molaires en excès, mélanges binaires, cyclohexane, dodécane, tétradécane, hexadécane, théorie de Prigogine–Flory–Patterson.

[Traduit par la Rédaction]

Introduction

Excess thermodynamic properties of hydrocarbon-containing mixtures are currently attracting considerable interest from the viewpoint of providing information on the variation of such properties with increasing number of carbon atoms in long-chain hydrocarbons (1–8). A comparative study of the thermodynamic properties and molecular interactions based on group contribution methods in *n*-alkane mixtures has been carried out (9, 10). This study suggested a decrease of the molecular order in pure *n*-alkanes when mixed with other solvents. As a contribution to an extensive study on thermodynamic and physical properties for the pure *n*-alkane mixtures, the excess molar volumes, V^E, of binary mixtures of cyclohexane with higher *n*-alkanes (12, 14, and 16 carbon atoms) *n*-dodecane, *n*-tetradecane, and *n*-hexadecane were calculated from the experimental densities over the whole composition range at seven different temperatures in the range from 283.15 to 313.15 K and at atmospheric pressure.

The Prigogine–Flory–Patterson (PFP) theory (11) was used to calculate V^E and to derive the three different contributions considered in the theory. The results were used to calculate the different coefficients describing the variation of the V^E with isobaric change of temperature.

Prigogine–Flory–Patterson theory

The PFP theory has been described (11, 12), and can be expressed as the calculation of V^E as the sum of three contributions: the interactional contribution, which is proportional to the χ_{12} parameter; the free volume contribution, which arises from the dependence of the reduced volume on the reduced temperature as a result of the difference between the degrees of expansion of the two components; and the contribution that depends on the difference in both internal pressures and reduced volumes of the components.

The expression of V^E in terms of the three contributions is

Received February 24, 1998.

M.M. El-Banna.[1] Chemistry Department, Faculty of Education, El-Shatby, 21526, Alexandria University, Egypt.
M.M. El-Batouti. Chemistry Department, Faculty of Science, El-Shatby, 21526, Alexandria University, Egypt.

[1]Author to whom correspondence may be addressed. Fax: 203 542-1526. E-mail: pcs@dataxprs.com.eg

© 1998 NRC Canada

Table 1. Experimental densities (ρ) of pure components at different temperatures.

		ρ /g cm $^{-3}$	
Liquid	Temp. (K)	Expt.	Lit. (ref.)
Cyclohexane	283.15	0.787 75	0.787 78 (16)
	288.15	0.783 20	0.783 17 (16)
	293.15	0.778 85	
	298.15	0.773 95	0.773 90 (17)
	303.15	0.769 15	0.769 28 (18)
	308.15	0.764 38	0.764 38 (16)
	313.15	0.760 35	
n-Dodecane	283.15	0.763 57	
	288.15	0.748 02	
	293.15	0.748 80	0.748 83 (19)
	298.15	0.745 45	0.745 40 (2)
	303.15	0.741 68	
	308.15	0.737 99	
	313.15	0.734 02	
n-Tetradecane	283.15	0.769 54	
	288.15	0.766 25	
	293.15	0.762 80	0.762 78 (19)
	298.15	0.759 65	0.759 71 (20)
	303.15	0.756 15	
	308.15	0.752 54	
	313.15	0.748 63	0.748 70 (19)
n-Hexadecane	283.15	0.777 19	
	288.15	0.774 35	
	293.15	0.773 60	0.773 62 (19)
	298.15	0.770 94	0.770 89 (20)
	303.15	0.765 78	
	308.15	0.762 88	
	313.15	0.759 76	0.759 78 (19)

$$[1]\quad V^{E}_{\text{interactional}}/(x_1V_1^* + x_2V_2^*) = [(\bar{v}^{1/3} - 1)\bar{v}^{2/3}\psi_1\theta_2\chi_{12}] / [(4/3)\bar{v}^{-1/3} - 1]\bar{v}$$

$$[2]\quad V^{E}_{\text{free volume}}/(x_1V_1^* + x_2V_2^*) = [(\bar{v}_1 - \bar{v}_2)^2\{(14/9)\bar{v}^{-1/3} - 1\}]\psi_1\psi_2/[(4/3)\bar{v}^{-1/3} - 1]\bar{v}$$

$$[3]\quad V^{E}_{p^*\ \text{effect}}/(x_1V_1^* + x_2V_2^*) = [(\bar{v}_1 - \bar{v}_2)\cdot(p_1^* - p_2^*)]\psi_1\psi_2/(p_1^*\psi_2 - p_2^*\psi_1)$$

The reduction parameters of the pure components (i = 1 and 2) or solutions are obtained through the relationships of the Flory model (13). Thus, the thermal expansion coefficient α_i, is used to calculate the reduced volume $\bar{v}_i$

$$[4]\quad \bar{v}_i = [1 + (\alpha_i\, T)/3(1 + \alpha_i\, T)]^3$$

and the parameters ρ_i^* are derived from experimental data of the thermal pressure coefficient γ_i:

$$[5]\quad \rho_i^* = T\gamma_i v_i^2$$

The reduced volume for the mixture $\bar{v}_i$ is obtained from the reduced equation of state given by Flory et al. (13) using the following relation for $\bar{T}$:

$$[6]\quad \bar{T} = (\psi_1\bar{T}_1 + \psi_2\bar{T}_2) / [1 - \psi_1\theta_2(\chi_{12}/p_1^*)]$$

where the contact energy fraction is obtained as

$$[7]\quad \psi_1 = (1 - \psi_2) = \phi_1 p_1^*/(\phi_1 p_1^* + \phi_2 p_2^*)$$

and the hard core volume fraction ϕ_i is defined as (14)

$$[8]\quad \phi_1 = (1 - \phi_2) = x_1V_1^*/(x_1V_1^* + x_2V_2)$$

where the volume reduction parameters V_i^* are derived from experimental molar volume values V_m, and reduced volume data $\bar{v}_i$, with the relation $V_i^* = V_m / \bar{v}_i$.

The surface or site fraction θ_i, calculated in eq. [1], is expressed as

$$[9]\quad \theta_1 = (1 - \theta_2) = \phi_1/[\phi_1 + \phi_2(s_2/s_1)]$$

where s_i is the molecular surface. The ratio s_1 / s_2 has been approximated (14) by

$$[10]\quad s_1/s_2 = (V_2^* / V_1^*)^{1/3}$$

where V_i^* is the hard core volume.

In the Flory theory of nonpolar molexules, χ_{12} is an adjustable mixing parameter and it was calculated from the experimental V^E data. χ_{12} is supposed to be a constant parameter independent of temperature.

Experimental

The pure cyclohexane and higher *n*-alkanes used in this work were obtained from Aldrich, reported purity >99.5 mol%, and were used without further purification other than storing over molecular sieve to remove any possible traces of moisture.

Density (ρ) measurements of the pure components and binary mixtures, over the complete composition range, were carried out using a Kyoto electronic vibrating tube densimeter (model DA 110) with a temperature sensor keeping the temperature within ± 0.005 K. The apparatus was calibrated several times with the well-known density values of deionized doubly distilled and degassed water, benzene, and dry air at atmospheric pressure.

The mixtures were prepared by syringe, inserting a weighed amount (Mettler A 160 range balance 0.01 mg) of the pure liquids into stoppered bottles to prevent preferential evaporation. This process was repeated four times for each measurement. The experimental technique has previously been described (15). The precision of the densities was ± 0.001 g cm^{-3} and of the mole fraction ± 0.005 mol%.

Densities of the pure liquids at the temperatures of interest in this work, together with some values from the literature, are given in Table 1.

Results and discussion

The experimental density measurements at the temperatures studied for the binary systems, at several known composition values, were used to derive the corresponding V^E values from the following equation:

$$[11]\quad V^E/\text{cm}^3\ \text{mol}^{-1} = x_1\, M_1\, (\rho_m^{-1} - \rho_1^{-1}) + x_2 M_2(\rho_m^{-1} - \rho_2^{-1})$$

where x_i, ρ_i, and M_i are the mole fraction, density, and relative molar mass of the pure components, with i = 1 for the

© 1998 NRC Canada

Table 2. Experimental density (ρ) values and standard deviation *s* for the binary mixtures of (*x*)cyclohexane + (1 – *x*)*n*-alkanes.

T =	283.15	288.13	293.15	298.13	303.15	308.15	313.15
x	ρ (g cm^{-3})						
	(*x*)Cyclohexane + (1 – *x*)*n*-dodecane						
0.015 83	0.763 92	0.748 43	0.749 17	0.745 79	0.742 01	0.738 29	0.734 32
0.019 21	0.764 49	0.749 01	0.749 71	0.746 26	0.742 37	0.738 46	0.734 52
0.049 80	0.765 58	0.750 06	0.750 58	0.747 04	0.743 11	0.738 99	0.735 09
0.082 72	0.766 85	0.751 31	0.751 24	0.747 89	0.743 59	0.739 65	0.735 65
0.105 16	0.767 51	0.752 07	0.751 93	0.748 50	0.744 21	0.740 13	0.736 05
0.149 42	0.768 81	0.753 59	0.753 30	0.749 71	0.745 29	0.741 06	0.736 89
0.204 13	0.770 41	0.755 47	0.755 00	0.751 22	0.746 85	0.742 12	0.738 03
0.268 15	0.772 25	0.757 69	0.756 99	0.753 00	0.748 32	0.743 53	0.739 46
0.299 01	0.773 13	0.758 76	0.757 96	0.753 87	0.749 32	0.744 31	0.740 21
0.443 01	0.777 12	0.763 84	0.762 48	0.755 19	0.750 46	0.745 70	0.741 33
0.346 21	0.774 46	0.760 41	0.759 44	0.756 59	0.751 90	0.747 09	0.742 52
0.395 42	0.775 82	0.762 15	0.760 98	0.757 95	0.753 35	0.748 57	0.743 77
0.500 32	0.778 65	0.765 88	0.764 29	0.759 61	0.754 99	0.750 15	0.745 34
0.552 14	0.779 99	0.767 75	0.765 93	0.761 12	0.756 51	0.751 65	0.746 66
0.613 40	0.781 53	0.769 98	0.767 88	0.762 92	0.758 05	0.753 32	0.748 23
0.667 29	0.782 85	0.771 98	0.769 61	0.764 55	0.759 57	0.754 68	0.749 65
0.713 56	0.783 90	0.773 66	0.771 07	0.765 93	0.760 59	0.755 65	0.750 86
0.772 13	0.785 19	0.775 85	0.772 94	0.767 73	0.762 30	0.756 67	0.752 20
0.832 01	0.785 91	0.777 19	0.773 88	0.768 18	0.764 73	0.758 25	0.753 92
0.897 14	0.786 75	0.779 33	0.775 88	0.770 66	0.765 20	0.760 41	0.756 19
0.951 05	0.787 50	0.781 27	0.777 28	0.772 23	0.767 27	0.762 46	0.758 06
s	0.000 24	0.000 35	0.000 29	0.000 52	0.000 34	0.000 25	0.000 38
	(*x*)Cyclohexane + (1 – *x*)*n*-tetradecane						
0.014 89	0.769 81	0.766 52	0.763 04	0.759 87	0.756 34	0.752 72	0.748 79
0.019 75	0.769 90	0.766 60	0.763 12	0.759 93	0.756 41	0.752 78	0.748 85
0.054 21	0.770 75	0.767 22	0.763 67	0.760 42	0.756 86	0.753 19	0.749 24
0.079 93	0.771 39	0.767 67	0.764 08	0.760 79	0.757 20	0.753 49	0.749 53
0.108 56	0.771 90	0.768 18	0.764 54	0.761 20	0.757 58	0.753 84	0.749 85
0.153 42	0.772 71	0.768 98	0.765 26	0.761 84	0.758 17	0.754 37	0.750 36
0.210 05	0.773 71	0.769 98	0.766 17	0.762 64	0.758 91	0.755 05	0.751 00
0.258 90	0.774 54	0.770 84	0.766 96	0.763 34	0.759 55	0.755 63	0.751 56
0.288 76	0.775 15	0.771 37	0.767 44	0.763 77	0.759 94	0.755 98	0.751 90
0.356 03	0.776 36	0.772 54	0.768 52	0.764 73	0.760 83	0.756 78	0.752 67
0.405 87	0.777 03	0.773 41	0.769 32	0.765 44	0.761 48	0.757 37	0.753 24
0.453 14	0.778 39	0.774 23	0.770 08	0.766 11	0.762 09	0.757 94	0.753 78
0.511 22	0.779 51	0.775 23	0.771 01	0.766 94	0.762 85	0.758 63	0.754 46
0.564 53	0.780 54	0.776 15	0.771 86	0.767 70	0.763 55	0.759 26	0.755 08
0.605 57	0.781 33	0.776 85	0.772 52	0.768 29	0.764 08	0.759 74	0.755 56
0.660 51	0.782 46	0.777 77	0.774 30	0.769 07	0.764 79	0.760 39	0.756 20
0.722 43	0.783 62	0.778 80	0.774 40	0.769 96	0.765 60	0.761 12	0.756 94
0.766 38	0.784 32	0.779 53	0.775 10	0.770 59	0.766 16	0.761 64	0.757 46
0.829 57	0.785 55	0.780 56	0.776 12	0.771 50	0.766 98	0.762 39	0.758 23
0.888 54	0.786 06	0.781 49	0.777 06	0.772 34	0.767 73	0.763 08	0.758 95
0.966 32	0.788 17	0.782 69	0.778 31	0.776 46	0.768 72	0.763 98	0.759 92
s	0.000 41	0.00055	0.00039	0.00031	0.00029	0.00036	0.00041
	(*x*)Cyclohexane + (1 – *x*)*n*-hexadecane						
0.015 07	0.777 35	0.774 48	0.773 68	0.770 98	0.765 82	0.762 90	0.759 76
0.019 46	0.777 40	0.774 52	0.773 70	0.771 00	0.765 83	0.762 91	0.759 77
0.066 33	0.777 88	0.774 92	0.773 94	0.771 16	0.765 97	0.762 98	0.759 79
0.087 15	0.778 10	0.775 09	0.774 04	0.771 23	0.766 03	0.763 01	0.759 81
0.112 64	0.778 37	0.775 31	0.774 17	0.771 34	0.766 10	0.763 05	0.759 82
0.168 39	0.778 95	0.775 79	0.774 46	0.771 50	0.766 27	0.763 13	0.759 85
0.200 53	0.779 28	0.776 06	0.774 62	0.771 59	0.766 36	0.763 18	0.759 87
0.245 17	0.779 75	0.776 45	0.774 85	0.771 72	0.766 49	0.763 25	0.759 90

© 1998 NRC Canada

Table 2 *(concluded)*.

T =	283.15	288.13	293.15	298.13	303.15	308.15	313.15
x				ρ (g cm^{-3})			
0.275 42	0.780 06	0.776 71	0.775 00	0.771 84	0.766 59	0.763 29	0.759 92
0.351 24	0.780 85	0.777 36	0.775 39	0.772 06	0.766 82	0.763 41	0.759 96
0.400 77	0.781 37	0.771 79	0.775 65	0.772 23	0.766 97	0.763 48	0.759 99
0.469 72	0.782 10	0.778 39	0.776 00	0.772 45	0.767 19	0.763 58	0.760 03
0.512 25	0.782 54	0.778 76	0.776 22	0.772 57	0.767 32	0.763 65	0.760 06
0.570 21	0.783 15	0.779 27	0.776 52	0.772 74	0.767 51	0.763 73	0.760 09
0.611 46	0.783 59	0.779 63	0.776 74	0.772 86	0.767 65	0.763 80	0.760 12
0.668 80	0.784 19	0.780 14	0.777 04	0.773 02	0.767 84	0.763 88	0.760 15
0.733 20	0.784 87	0.780 72	0.777 38	0.773 24	0.768 07	0.763 98	0.760 19
0.771 05	0.785 28	0.781 06	0.777 59	0.773 31	0.768 21	0.764 03	0.760 21
0.836 34	0.785 98	0.781 66	0.777 94	0.773 49	0.768 46	0.764 13	0.760 25
0.899 55	0.786 66	0.782 24	0.778 29	0.773 67	0.768 71	0.764 23	0.760 29
0.966 27	0.787 38	0.782 88	0.778 66	0.773 90	0.769 00	0.764 33	0.760 33
s	0.000 47	0.00050	0.00039	0.00035	0.00033	0.00029	0.00031

Fig. 1. Excess molar volumes vs. mole fraction of cyclohexane for (x)cyclohexane + (1 – x)n-dodecane at: 283.15 (- · -), 288.15 (– - –), 293.15 (◇), 298.15 (□), 303.15 (△), 308.15 (×), and 313.15 K (*).

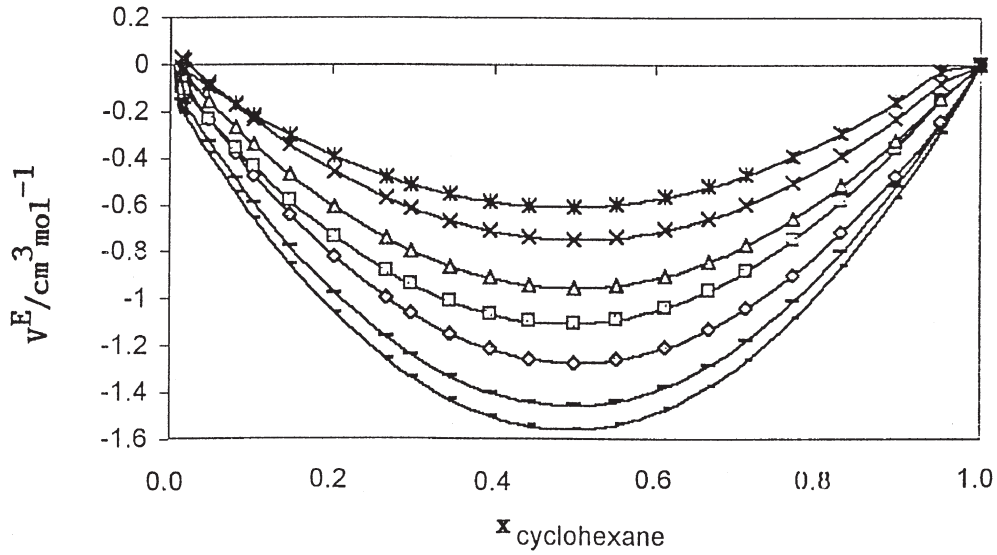

cyclohexane and i = 2 for the n-alkane, and ρ_m is the density of the mixture at a given composition.

The experimental density values and the standard deviation s of each system are listed in Table 2. The derived V^E values, as a function of composition, for the three binary systems are shown in Figs. 1, 2, and 3.

The V^E values of the binary mixtures were fitted as a function of the mole fraction and temperature to a polynomial of the form:

$$[12] \quad V^E / \text{cm}^3\ \text{mol}^{-1} = x(1-x) \sum_{i=1}^{3} \sum_{j=1}^{3} B_{ij}\,(2x-1)^{i-1}\,(T-T_0)^{j-1}$$

where T is the temperature and T_0 is the reference temperature (T_0 = 278.15 K).

The coefficients B_{ij} and standard deviation s, are listed in Table 3. The V^E values for the systems (x)cyclohexane + (1 – x)n-alkane are negative; they become more negative when the temperature decreases, and are almost symmetrical with the minimum lying always near x = 0.5. The range of maximum V^E values is between –1.533 and –0.647 (Fig. 1); –1.030 and –0.555 (Fig. 2); and –0.605 and –0.035 cm^3 mol^{-1} (Fig. 3).

It was found that $V^E(x = 0.5)$ increases with increasing temperature for the same system, and increases with the n-alkane chain length in the sequence: n-hexadecane > n-tetradecane > n-dodecane. According to the above order, negative deviations occur when dispersion forces are preponderant (21).

Table 4 contains the characteristic parameters for the pure components used for the application of PFP theory. The values of the interaction parameter χ_{12} for each binary system using experimental equimolar V^E values are given in Table 5 together with equimolar values for each of the three sets of binaries at 298.15 K. It is observed that χ_{12} and the corresponding interactional contribution term are always positive

© 1998 NRC Canada

Fig. 2. Excess molar volumes vs. mole fraction of cyclohexane for (*x*)cyclohexane + (1 – *x*)*n*-tetradecane at : 283.15 (- · -), 288.15 (– - –), 293.15 (◇), 298.15 (□), 303.15 (△), 308.15 (×), and 313.15 (*).

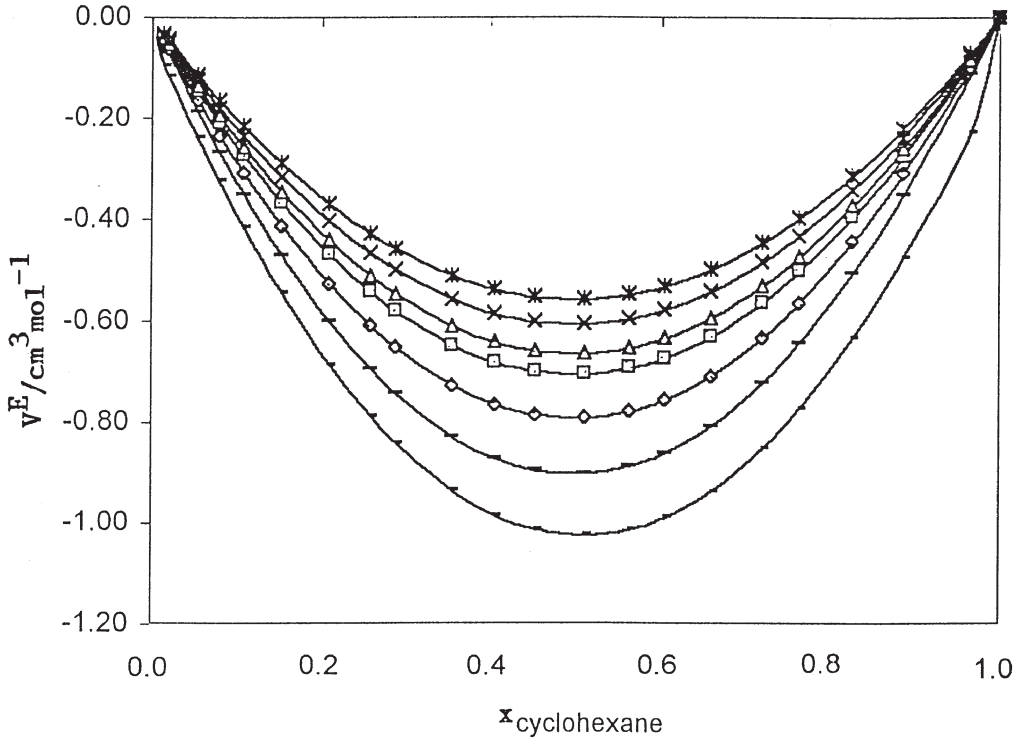

Fig. 3. Excess molar volumes vs. mole fraction of cyclohexane for (*x*)cyclohexane + (1 – *x*)*n*-hexadecane at: 283.15 (◇), 288.15 (□), 293.15 (△), 298.15 (×), 303.15 (*), 308.15 (○), and 313.15 (+).

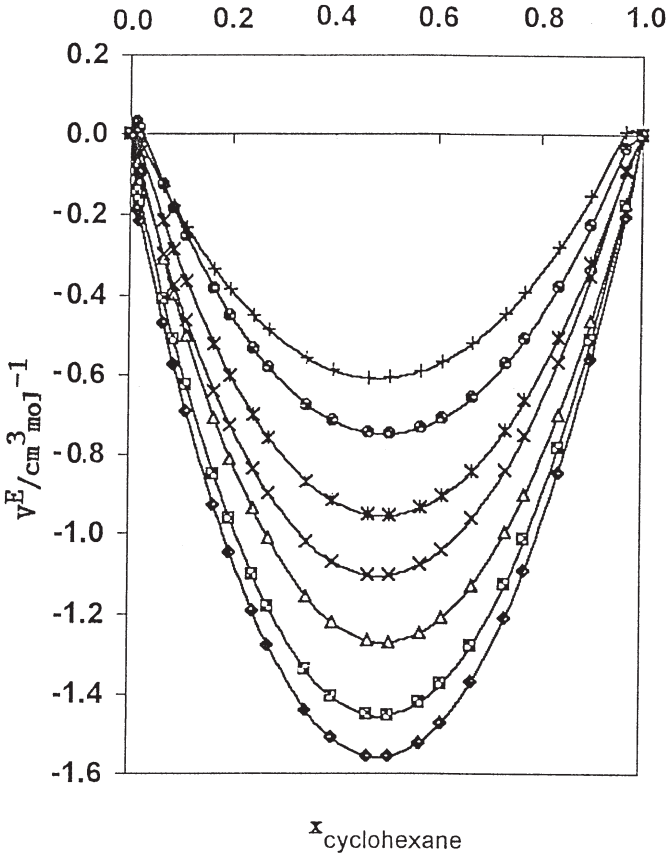

Table 3. Coefficients B_{ij} for eq. [12] and standard deviation s.

	Cyclohexane +		
Parameter	*n*-Dodecane	*n*-Tetradecane	*n*-Hexadecane
B_{11}	–0.849 526	–0.916 300	–0.498 366
*B*12	0.140 954	0.130 652	0.132 286
B_{13}	–0.000 335	0.002 007	–0.001 832
B_{21}	–0.331385	–0.396 331	–0.580 040
B_{22}	–0.065312	–0.207 478	0.198 863
B_{23}	0.003 065	0.007 010	–0.002 284
*B*31	0.198 642	0.543 340	–0.517 235
B_{32}	0.065 128	0.364 071	–0.347 998
B_{33}	–0.002 662	–0.011 009	0.006 046
s	0.0173	0.0070	0.0115

and large for the systems. This is reasonable considering the weak unlike interactional forces that are characteristic between nonpolar molecules. The free volume contribution is negative for the binary mixtures owing to the difference in free volume, or thermal expansion coefficient, eq. [4], between the corresponding cyclohexane and *n*-alkane studied. Also the contribution is larger in magnitude than the free energy term. This suggests that the repulsion forces have a predominant effect (2, 22).

© 1998 NRC Canada

Table 4. Parameters for the pure components at different temperatures.

T / K	$\bar{v}$/ cm^3 mol^{-1}	$\alpha \cdot 10^3$ / K^{-1}	γ / J mol^{-1}	p^* / MPa	$\bar{T}$ / K
		Cyclohexane			
283.15	1.2678	1.1580	0.2461	112.00	0.0600
288.15	1.2752	1.1767	0.2393	112.11	0.0610
293.15	1.2832	1.1986	0.2320	111.94	0.0622
298.15	1.2904	1.2160	0.2256	112.14	0.0631
303.15	1.2984	1.2377	0.2193	112.07	0.0642
308.15	1.3065	1.2597	0.2129	111.99	0.0653
313.15	1.3100	1.2597	0.2099	112.82	0.0657
		***n*-Dodecane**			
283.15	1.2080	0.8556	0.1470	60.73	0.0505
288.15	1.2315	0.9041	0.1322	57.79	0.0540
293.15	1.2319	0.9398	0.1314	58.26	0.5045
298.15	1.2374	0.9500	0.1270	58.29	0.5054
303.15	1.2437	0.9643	0.1242	58.22	0.0564
308.15	1.2500	0.9782	0.1210	58.25	0.0573
313.15	1.2567	0.9937	0.1174	58.08	0.0584
		***n*-Tetradecane**			
283.15	1.2105	0.8671	0.1257	52.14	0.0510
288.15	1.2157	0.8778	0.1227	52.24	0.0518
293.15	1.2212	0.8888	0.1193	52.14	0.0528
298.15	1.2263	0.8980	0.1165	52.24	0.0536
303.15	1.2320	0.9089	0.1135	52.24	0.0545
308.15	1.2379	0.9217	0.1106	52.24	0.0545
313.15	1.2443	0.9363	0.1074	52.05	0.0554
		***n*-Hexadecane**			
283.15	1.2076	0.8486	0.1126	46.48	0.0505
288.15	1.2120	0.8508	0.1102	46.65	0.0512
293.15	1.2132	0.8528	0.1096	47.28	0.0514
298.15	1.2174	0.8559	0.1064	47.44	0.0521
303.15	1.2256	0.8794	0.1031	46.97	0.0535
308.15	1.2363	0.8863	0.1009	47.05	0.0543
313.15	1.2353	0.8954	0.0986	47.11	0.0551

Table 5. Calculated contributions in V^E (x = 0.5), from PFP theory for (x)cyclohexane + (1 – x)n-alkane at 298.15 K.

		Contributions V^E / cm^3 mol^{-1}			V^E / cm^3 mol^{-1}	
Cyclohexane +	χ_{12} / J cm^{-3}	Interactional	Free volume	p*	Theor.	Expt.
n-Dodecane	15.144	0.294	–0.144	1.105	–1.083	–1.100
n-Tetradecane	19.633	0.392	–0.236	1.722	–0.695	–0.702
n-Hexadecane	24.353	0.499	–0.331	2.322	–0.191	–0.202

It can be concluded that PFP theory is capable of reproducing the main features of the experimental V^E results by using fitted binary interaction parameters.

References

1. T.M. Aminabhavi,V.B. Patil, and M.I. Aralaguppi. J. Chem. Eng. Data, **41**, 526 (1996).
2. R. Eustaquio-Rincon and A. Trejo. J. Chem. Soc. Faraday Trans. **90,** 113 (1994).
3. M.I. Aralaguppi, T.M. Aminabhavi, R.H. Balundgi, and S.S. Joshi. J. Phys. Chem. **95**, 5299 (1991).
4. M. Pintos, R. Bravo, and A. Amigo. J. Chem. Thermodyn. **25**, 337 (1993).
5. Y. Tanaka, H. Hosokawa, H. Kubota, and T. Makita. Int. J. Thermophys. **12,** 245 (1991).
6. A. Arimoto, H. Ogawa, and S. Murakami. Thermochim. Acta, **163**, 191 (1990).
7. A.M. Awwad and M.A. Salman. Fluid Phase Equilib. **25**, 195 (1986).
8. S.N.Bhattacharya, M. Costas, D. Patterson, and H.V. Tra. Fluid Phase Equilib. **20,** 27 (1985).
9. H.V. Kehiaian and B. Marongiu. Fluid Phase Equilib. **40**, 23 (1988).
10. H.V. Kehiaian. Pure Appl. Chem. **78**, 15 (1985).
11. H.T. Van and D. Patterson. J. Solution Chem. **11**, 793 (1982).
12. D. Patterson and G. Delmas. Discuss. Faraday Soc. **49**, 98 (1970).

© 1998 NRC Canada

13. P.J. Flory, R.A. Orwoll, and A. Vrij. J. Am. Chem. Soc. **86**, 3507 (1964).
14. A. Abe and P.J. Flory. J. Am. Chem. Soc. **87**, 1838 (1965).
15. J. Ortega, M.I. Paz-Andrade, E. Rodriguez-Nunez, and L. Romani. Aust. J. Chem. **38,** 1435 (1985).
16. J. Peleteiro, C.A. Tovar, J.L. Legido, and L. Romani. Can. J. Chem. **72**, 454 (1994).
17. K.N. Marsh. TRC data bases for chemistry and engineering — TRC thermodynamic tables. Texas A & M University. College Station, Tex. 1994.
18. B. Riedl and G. Delmas. Can. J. Chem. **61**, 1876 (1983).
19. G. Hahn and P. Svejda. J. Chem. Eng. Data, **41**, 619 (1996).
20. M. Witek, A. Golden, T. Hofman, and U. Domanska. J. Chem. Eng. Data, **42**, 60 (1997).
21. P.R. Sekar, R. Venkateswarlu, and K.S. Reddy. Can. J. Chem. **68**, 363 (1990).
22. R. Bravo, M. Pintos, and A. Amigo. Can. J. Chem. **73**, 375 (1995).

© 1998 NRC Canada

Spectroelectrochemical study of the nucleophilic substitution of diacyl disulfides by 2-nitrophenyl thiolate ions in *N*,*N*-dimethylacetamide

A. Ahrika, M. Anouti, J.E. Robert, and J.L. Paris

Abstract: *S*-Aryl thiol esters RC(O)SAr and ArS_2^- ions are the end products resulting from the reactions between bis(2-nitrophenyl) disulfide Ar_2S_2 and thiocarboxylate ions $RC(O)S^-$ (R = Me, Ph) at 20°C. The apparent SNAr process in fact occurs in two steps as shown by UV–vis absorption spectrophotometry coupled with voltammetry: (*i*) formation of diacyl disulfides $[RC(O)]_2S_2$ and ArS^- ions by redox exchange; (*ii*) subsequent nucleophilic substitution of 2-nitrophenyl thiolate ions at the carbonyl carbon of diacyl disulfides.

Key words: diacyl disulfides, 2-nitrophenyldisulfide ions, *N*,*N*-dimethylacetamide, nucleophilic substitution, spectroelectrochemistry.

Résumé : Les *S*-aryl thiol esters RC(O)SAr et les ions aryldisulfures ArS_2^- sont les produits issus des réactions mises en oeuvre entre le bis (2-nitrophényl) disulfure Ar_2S_2 et les ions thiocarboxylates $RC(O)S^-$ (R = Me, Ph) à 20°C. Le processus étudié par spectrophotométrie d'absorption UV–visible couplée à la voltammétrie, est apparemment de type SNAr; il s'effectue en fait en deux étapes : (*i*) formation des diacyl disulfures $[RC(O)]_2S_2$ et des ions ArS^- par échange redox; (*ii*) substitution nucléophile ultérieure des ions 2-nitrophényl thiolates sur le groupement carbonyle des diacyl disulfures.

Mots clés : diacyl disulfures, ions 2-nitrophényldisulfures, *N*,*N*-diméthylacétamide, substitution nucléophile, spectroélectrochimie.

Introduction

Previous studies have demonstrated that electrogenerated polysulfide ions S_6^{2-} ($\rightleftharpoons S_3^{\bullet -}$) add nucleophilically to carbonyl carbons in *N*,*N*-dimethylacetamide (DMA) (1, 2), a dipolar aprotic medium. For substrates with sufficiently good leaving groups (acyl chlorides (1) and thioanhydrides (2)) evidence for two steps was obtained:

[1] $RC(O)X + S_6^{2-} \rightarrow RC(O)S^- + 5/2S_2 + X^-$

[2] $RC(O)S^- + 1/2S_2 + RC(O)X \rightarrow [RC(O)]_2S_2 + X^-$

Stable diacyl disulfides further react with S_6^{2-} ions in excess with conversion [3] into thiocarboxylate ions (1):

[3] $[RC(O)]_2S_2 + S_6^{2-} \rightarrow 2RC(O)S^- + 3S_2$

Reaction [3] can occur either as an oxidation–reduction process or as a nucleophilic substitution of $[RC(O)]_2S_2$ by the polysulfide anion. To distinguish between these two alternatives, products of reactions of diacyldisulfides $[RC(O)]_2S_2$ (for R = Me, Ph) with 2-nitrophenylthiolate ions were identified and stoichiometry found. These reactions were followed at 20°C by voltammetry coupled with UV–vis absorption spectrophotometry.

Received May 29, 1998.

A. Ahrika, M. Anouti, J.E. Robert, and J.L. Paris.[1]
Laboratoire de physicochimie des interfaces et des milieux réactionnels, UFR Sciences et Techniques, Parc de Grandmont, 37200 Tours, France.

[1]Author to whom correspondence may be addressed. Fax: 0033247366960. E-mail: paris@univ-tours.fr

Experimental

Materials

N,*N*-Dimethylacetamide, bis(2-nitrophenyl) disulfide, acyl chlorides, and thioacids (R = Me, Ph) were obtained from Aldrich. Dibenzoyl sulfide was previously synthesized (3) by reaction of thiobenzoate ions with benzoyl chloride. Distilled DMA was stored on molecular sieves (4 Å) after addition of the supporting electrolyte, tetraethylammonium perchlorate (Fluka, 0.1 mol dm^{-3}). Acyl chlorides and thioacids were distilled just before use.

Preparation of diacyl disulfides $[PhC(O)]_2S_2$ and $[CH_3C(O)]_2S_2$

Dibenzoyl disulfide was obtained by exhaustive electrooxidation of $PhC(O)S^-$ ions, which were themselves electrogenerated by reduction of thiobenzoic acid in DMA. The reaction medium (120 cm^3) was treated as already described (1, 3). Dibenzoyl disulfide was recrystallized from 1,2-dichloroethane. Thiobenzoic acid: 1.71 g (12.4 mmol). Dibenzoyl disulfide: 1.12 g (66%), mp 135–136°C (lit. (4)

© 1998 NRC Canada

mp 136–136.5°C); δ_H: 7.53–7.75 (6H, m) and 8.13 (4H, d, *J* 7.4); direct introduction mode *m/z*: 274 (M^+, 4%), 105 (50), 77 (100), and 51 (25). Diacetyl disulfide was prepared according to Robert et al. (1), by reaction of S_4^{2-} ions on acetyl chloride in excess (overall eq. [4]):

[4] $2CH_3C(O)Cl + S_4^{2-} \rightarrow [CH_3C(O)]_2S_2 + S_2 + 2Cl^-$

S_4^{2-} ions were chemically generated (5) in DMA by heating a solution (200 cm^3) of Li_2S (Alfa, 2.32 g, 50 mmol) with a stoichiometric quantity of sulfur (4.81 g, 150 mmol S) at 50°C for 30 min. The green polysulfide ions were progressively added with acetyl chloride dissolved in 40 cm^3 of DMA up to decoloration (95 mmol $CH_3C(O)Cl$). After extraction of the crude product (1), traces of sulfur were carefully eliminated by column chromatography on silical gel (three successive times, hexane as eluent for sulfur, then hexane – diethyl ether, 70:30). Products: 3.15 g (≈42%); from GC–MS, diacetyl disulfide ((~94%) and diacetyl sulfide (~6%). Diacetyl disulfide: δ_H: 2.54 (6H, s); *m/z:* 150 (M^+, < 2%) and 43 (100). Diacetyl sulfide: δ_H: 2.52 (6H, s); *m/z:* 118 (M^+, <2%) and 43 (100).

Equipment

The solutions were transferred from the thermostatted (20 ± 0.5°C) electrolysis vessel (usable volume of 50 cm^3) to the spectrophotometric cell (1 mm pathlength) by means of PTFE tubing in a nitrogen-flushed arrangement (6), according to the flow apparatus described by Billon et al. (7). Voltammograms at a rotating gold-disc electrode (diameter = 2 mm, w = 1000 rev min^{-1}) were recorded by using a EGG-PAR 273 A potentiostat; in that case the N_2 stream was directed above the solution. The electrolyses of bis(2-nitrophenyl) disulfide (Ar_2S_2) and of $[RC(O)]_2S_2$ species leading, respectively, to ArS^- and $RC(O)S^-$ ions (c_i < 5.0 × 10^{-3} mol dm^{-3}) were carried out at a large gold grid electrode. The counter electrode was always a platinum foil, the anodic compartment being separated from the solution by a no. 4 glass frit. All potentials referred to the $Ag/AgCl_{(s)}$, KCl saturated in DMA–$N(Et)_4ClO_4$ 0.1 mol dm^{-3} electrode. Absorption spectra were obtained with a Kontron Uvikon 930 spectrophotometer. All the reactions described below were fast enough to give stable absorbances (±0.002) within 12 s after the addition of reagents, which corresponds to the dead-time of transfer and homogenization. The synthesized diacyl disulfides were analysed by ^1H (200.132 MHz) NMR spectroscopy (Bruker AC 200 spectrometer, $CDCl_3$ as solvent, *J* values in Hz) and GC–MS spectrometry (Hewlett–Packard 5989 A, EI 70 eV).

Results

Characteristics of $[RC(O)]_2S_2$/$RC(O)S_x^-$ and $(2\text{-}NO_2C_6H_4S)_2$/$2\text{-}NO_2C_6H_4S_x^-$ (x = 1, 2) species

$[RC(O)]_2S_2$/$RC(O)S_x^-$ (R = Me, Ph, x = 1, 2) and $(2\text{-}NO_2C_6H_4S)_2$/$2\text{-}NO_2C_6H_4S_x^-$ (x = 1, 2) systems will be implicated in all the processes described below. At first, their known spectroelectrochemical characteristics are reported. 2-Nitrophenyl thiolate ions (noted ArS^-) and thiocarboxylate ions $RC(O)S^-$ (R = Me, Ph) were generated by electrolysis of bis(2-nitrophenyl) disulfide (8) and of thiocarboxylic acids (3) at a controlled potential (–0.9 and –1.4 V, respectively) on the plateau of their reduction waves (eqs. [5f] and [6]):

[5] $Ar_2S_2 + 2e^- \underset{b}{\overset{f}{\rightleftharpoons}} 2ArS^-$

[6] $RC(O)SH + e^- \rightarrow RC(O)S^- + 1/2H_2$

The reduction wave of Ar_2S_2 and the oxidation waves for ArS^- and $RC(O)S^-$ ions had limiting currents, which checked the criteria of convective diffusion.

During the oxidation of $RC(O)S^-$ ions ([overall eq. [7]), the acyl thioradicals $RC(O)S^\bullet$ dimerize into diacyl disulfides without any decomposition (9):

[7] $2RC(O)S^- - 2e^- \rightarrow [RC(O)]_2S_2$

Characteristics (λ_i, ε_i, $E_{1/2}$) of Ar_2S_2, and those of $[RC(O)]_2S_2$, ArS^-, and $RC(O)S^-$ species that were previously obtained in the course of electrooxidations [5b] (8, 10) and [7] (3) are summarized in Table 1. The redox processes are highly irreversible, as shown by the reduction (R) potentials of disulfides compared with the oxidation (O) potentials of anionic species.

We reported earlier that $2\text{-}NO_2C_6H_4S^-$ and $CH_3C(O)S^-$ ions (noted RS^- in eqs. [8] and [9]) partly react with S_2 molecules (3, 8, 10) in equilibrium [10] with cyclic S_8 (6); the affinity of RS^- ions for sulfur is analogous to that of a number of "S-nucleophiles" (11) such as CN^-, SO_3^{2-}, Ar_3P...

[8] $2RS^- + S_2 \underset{b}{\overset{f}{\rightleftharpoons}} 2RS_2^-$

[9] $K_1 = [RS_2^-]^2\,[RS^-]^{-2}\,[S_2]^{-1}$

[10] $S_8 \rightleftharpoons 4S_2$

[11] $K_2\ (297\ K) = [S_2]^4\,[S_8]^{-1} = 10^{-7}\ mol^3\ dm^{-9}$

From the values of constants K_1 (10) (Table 1) and dissociation constant K_2 (6), the formation of RS_2^- ions attains 70% with R = $2\text{-}NO_2C_6H_4$ and 19% for R = $CH_3C(O)$ at initial conditions $[RS^-] = 8[S_8]_0 = 3 \times 10^{-3}$ mol dm^{-3}. In the presence of traces of sulfur the anodic wave of RS^- ions totally shifts over towards more cathodic potentials because of the electrocatalytic process [8f] + [12] already described (R = Ar (8), $CH_3C(O)$ (3)):

[12] $2RS_2^- - 2e^- \rightarrow RS_2R + S_2$

This phenomenon implies the fast formation [8f] of RS_2^- ions, followed by their electrooxidation [12] at a greater rate than that of RS^-, with recovery of sulfur.

Reactivity of $2\text{-}NO_2C_6H_4S^-$ ions with diacetyl disulfide

Figures 1 and 2 show the dependence of UV–vis spectra and voltammograms on the progressive addition of a concentrated solution of bis(2-nitrophenyl) disulfide (v_{max} = 4.5 cm^3) to an initial solution (40 cm^3) $[CH_3C(O)S^-]_0 = 2.25 \times 10^{-3}$ mol dm^{-3} at successive ratios y = $[Ar_2S_2]_{ad.}/[CH_3C(O)S^-]_0$. The fast formation of ArS_2^- ions is detected by the growths of its maximum absorptions at 681 and 362 nm up to y = 1 (Fig. 1, curves 2–6). ArS_2^- ions

© 1998 NRC Canada

Table 1. Electrochemical and spectrophotometric characteristics of disulfides RS_2R (R = 2-$NO_2C_6H_4$, $CH_3C(O)$, PhC(O)), RS^- and RS_2^- ions in dimethylacetamide. $E_{1/2}$ at a rotating gold-disc electrode vs. ref. Ag/AgCl, KCl sat. in DMA/ $N(Et)_4ClO_4$ 0.1 mol dm^{-3}.

	RS_2R			RS^-			RS_2^-			
R	$E_{1/2}$(R)/V	λ_{max}/nm	$\varepsilon^a{}_{max}$	$E_{1/2}$(O)/V	λ_{max}	$\varepsilon^a{}_{max}$	$E_{1/2}$(O)[c]	λ_{max}	$\varepsilon^a{}_{max}$	K_1 [e]
2-$NO_2C_6H_4$ [b]	-0.72	360	7.5	+0.52	502	1.86	+0.10	681	5.2	1.1×10^4
		261	12.0		302	>20.0		362	7.0	
$CH_3C(O)$	–1.19	265	3.0	+0.30	262	8.0	+0.12	336	4.8	48
								467	0.80	
PhC(O)	–1.15	267	20.0	+0.75	310	5.1	+0.38 [d]	—	—	—

[a] $\varepsilon/10^3$ dm^3 mol^{-1} cm^{-1}.

[b] At 502 nm, ε (2-NO_2PhS_2) = 350 dm^3 mol^{-1} cm^{-1}.

[c] $E_{1/2}$(O) for initial conditions $[RS^-]_0 = 8[S_8]_0$.

[d] The formation of $PhCOS_2^-$, in the diffusion layer only, gives rise to a kinetic oxidation wave (3).

[e] K_1 (293 K)/mol^{-1} dm^3.

Fig. 1. Dependence of UV–vis spectra on the addition of bis(2-nitrophenyl) disulfide to a solution $[CH_3C(O)S^-]_0 = 2.25 \times 10^{-3}$ mol dm^{-3} at ratio $y = [Ar_2S_2]_{ad.}/[CH_3C(O)S^-]_0$ = 0 (1); 0.15 (2); 0.33 (3); 0.52 (4); 0.70 (5); 0.98 (6); 1.32 (7). Thickness of the cell = 0.1 cm; scan rate 1000 nm min^{-1}.

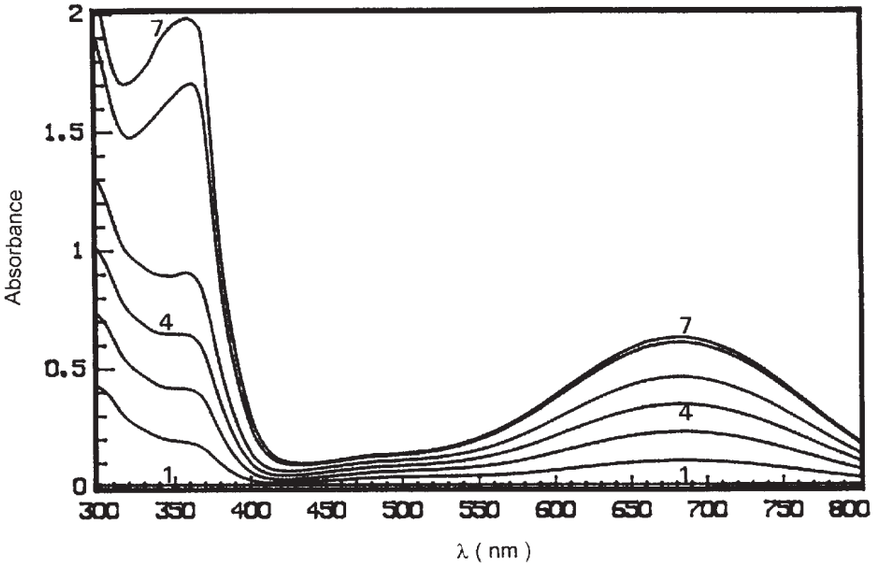

partly dissociate into ArS^- ions (eq. (8b)) (λ_{max1} = 502 nm, λ_{max2} = 302 nm); their respective concentrations deducted from molar absorbances (Table 1) remain in a proportion close to $[ArS_2^-]/[ArS^-]$ = 70/30. The stoichiometry

$$z = \sum_{x=1,2} [ArS_x^-]/[Ar_2S_2]_{ad.} \approx 1/1$$

is in agreement with eq. [13]:

[13] $RC(O)S^- + Ar_2S_2 \rightarrow RC(O)SAr + ArS_2^-$

The cathodic wave, which increases with *y* (Fig. 2, curves 2–6) at the same time as $[ArS_x^-]$, has the characteristics of that of $CH_3C(O)SAr$, which was obtained in the course of reaction [14] going to completion ($E_{1/2}$(R) = –0.75 V, *i*(R)/*C* = 22.5 μA $mmol^{-1}$ dm^3):

[14] $ArS^- + CH_3C(O)Cl \rightarrow CH_3C(O)SAr + Cl^-$

At the end of reaction [14] the only absorption of the *S*-aryl thiol ester gives λ_{max1} [$CH_3C(O)SAr$] = 352 nm, ε_{max1} = 1200 dm^3 mol^{-1} cm^{-1}; λ_{max2} = 260 nm, ε_{max2} = 4900 dm^3 mol^{-1} cm^{-1}.

From the first addition of Ar_2S_2 (curve 2), the anodic wave of $CH_3C(O)S^-$ ($E_{1/2}$ (O) = +0.30 V) shifts to the lower oxidation potentials of ArS_2^- ($E_{1/2}$ (O) = +0.10 V) and $CH_3C(O)S_2^-$ ($E_{1/2}$ (O) = +0.12 V) ions (catalytic process described above). For *y* greater than 1 (curve 7), Ar_2S_2 in excess entails both increases of the absorbance at 360 nm (ε_{360} (Ar_2S_2) = +7.500 dm^3 mol^{-1} cm^{-1}) and of the reduction current ($E_{1/2}$ (R, Ar_2S_2) = –0.72 V). Worth noting is that eq. [13] appears to be the unlikely aromatic substitution of thiocarboxylate ions on disulfide Ar-S_2Ar. It could, instead,

© 1998 NRC Canada

Fig. 2. Changes in voltammograms during the reaction of bis(2-nitrophenyl) disulfide with $CH_3C(O)S^-$ ions. Same conditions as for Fig. 1. Scan rate: 10 mV s^{-1}.

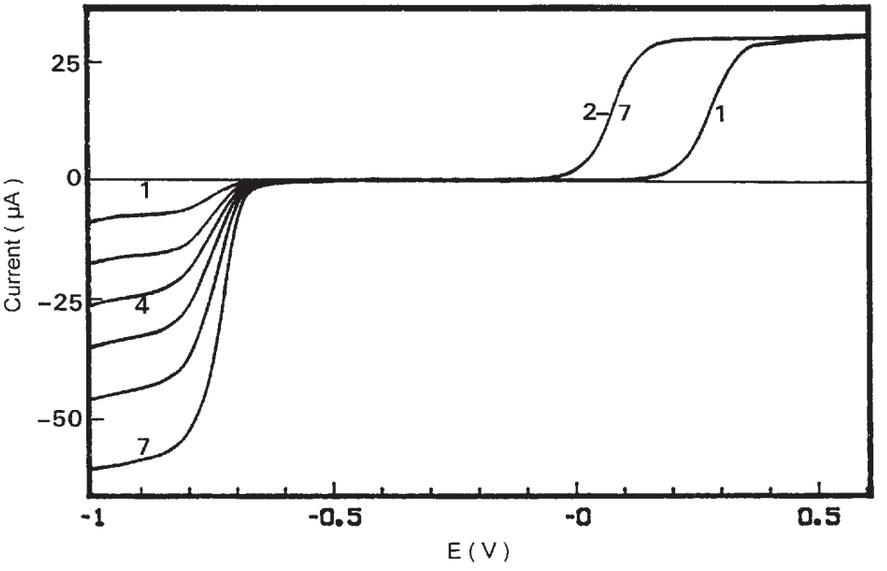

be initiated by the redox exchange reaction [15], with a subsequent substitution of ArS^- ions on diacyl disulfide:

[15] $2RC(O)\ S^- + Ar_2S_2 \rightarrow [CH_3C(O)]_2S_2 + 2ArS^-$

Equation [15] can also be viewed as the overall balance of "thiolate"–disulfide interchanges [16] and [17], which have been studied extensively (11):

[16] $RC(O)\ S^- + ArSSAr \rightarrow RC(O)SSAr + ArS^-$

[17] $RC(O)\ S^- + RC(O)SSAr \rightarrow [RC(O)]_2S_2 + ArS^-$

To check this assumption, diacetyl disulfide was added to a solution of 2-nitrophenyl thiolate ions $[ArS^-]_0 = 4.91 \times 10^{-3}$ mol dm^{-3} ($y = [(RCOS)_2]_{ad.}/[ArS^-]_0$), which is illustrated by the changes of spectra and voltammograms of Figs. 3*a*, 3*b*, and 4. For $0 < y < 0.5$ (Fig. 3*a*, curves 2–9) the absorption of ArS^- ions (λ_{max1} = 502 nm, λ_{max2} = 302 nm) decreases in favor of that of ArS_2^- ions (λ_{max1} = 681 nm, λ_{max2} = 362 nm) with the occurrence of three isosbestic points at λ_{is1} = 562 nm, λ_{is2} = 403 nm, and λ_{is3} = 337 nm. The consumption of ArS_x^- ions, $([ArS_x^-]_y = [ArS^-]_0 - \sum_x [ArS_x^-]_y$, agrees with eq. [18]:

[18] $2ArS^- + [RC(O)]_2S_2 \rightarrow RC(O)SAr + ArS_2^- + RC(O)S^-$

$CH_3C(O)S_2^-$ ions, which are displaced by substitution of ArS^- at the carbonyl carbon of the substrate, greatly dissociate (eq. [8b], R = $CH_3C(O)$) with a favoured formation of ArS_2^- ions (eq. [8f], R = Ar). The reduction wave of $CH_3C(O)SAr$ ($E_{1/2}$ (R) = –0.75 V) increases ($0 < y \leq 0.5$, Fig. 4, curves 2–9) with a limiting intensity in accordance with the stoichiometry $1[CH_3C(O)]_2S_2 \rightarrow 1CH_3C(O)SAr$; as soon as diacetyl disulfide is added, the anodic current of ArS^- ions (curve 1, $E_{1/2}(O)$ = +0.52 V), shifts to the lower oxidation potentials of ArS_2^- and $CH_3C(O)S_2^-$ ions (curves 2–14, $E_{1/2}(O) \sim$ +0.10 V).

ArS_2^- ions are known as better nucleophilic species than the corresponding thiolates: their reactivities compared in DMA (Ar = 2-$NO_2C_6H_4$, k_2/k_1 ratio of SN_2 or SNAr reaction rates) are $k_2/k_1 \sim 10$ towards alkyl halides (12), 18 with 2-fluoro nitrobenzene (13), and 27 with 1,2-dinitrobenzene (14). Because of this enhanced reactivity due to an "α-effect" between the unshared electron pairs on the sulfur atoms (15), the competing formations of $CH_3C(O)SAr$ (eq. [18]) and $CH_3C(O)S_2Ar$ (eq. [19]) should be observed in the course of overall reactions ArS^- + $[CH_3C(O)]_2S_2$:

[19] $ArS_2^- + [RC(O)]_2S_2 \rightarrow RC(O)S_2Ar + RC(O)S_2^-$

This is not the case, because reaction [18] is practically quantitative for $0 < y < 0.5$. Moreover, with further additions of diacetyl disulfide ($1.60 > y > 0.5$) the consumption of ArS_x^- ions (Fig. 3*b*, curves 10–14, decreases of A_{681} and A_{502}) is only observed to a low extent: as an example, $\Delta[ArS_x^-]_y / [(RCOS)_2]_{ad.} = 0.58$ for $y = 1.20$ (curve 13). This unexpected poor affinity of ArS_2^- ions for $[RC(O)]_2S_2$ can be explained by the limited redox reaction [20b] between $CH_3C(O)S_2Ar$ and $CH_3C(O)S^-$ ions in excess, since the latter are better reducing agents than ArS^- (eq. [15]):

[20] $ArS_2^- + [CH_3C(O)]_2S_2 \underset{b}{\overset{f}{\rightleftharpoons}} CH_3C(O)S_2Ar + CH_3C(O)S^- + 1/2S_2$

We previously discussed (16, 17) processes analogous to [20]: when 1,2- or 1,4-dinitrobenzenes were added to RS_2^- ions (R = 4-$CH_3C_6H_4$, 4-FC_6H_4, $C_6H_5CH_2$) evidence for two steps was found: (*i*) initial nucleophilic substitution (eq. [21]) similar to eq. [20f]:

[21] $NO_2C_6H_4NO_2 + RS_2^- \rightarrow NO_2C_6H_4S_2R + NO_2^-$

(*ii*) displacement of $NO_2C_6H_4S_2^-$ ions by redox exchange [22] similar to eq. [20b]:

[22] $NO_2C_6H_4S_2R + RS_2^- \rightarrow NO_2C_6H_4S_2^- + R_2S_2$

© 1998 NRC Canada

Fig. 3. (*a*) Dependence of UV–vis spectra on the addition of diacetyl disulfide to a solution $[2\text{-}NO_2PhS^-]_0 = 4.91 \times 10^{-3}$ mol dm^{-3} at ratio $y = [(CH_3COS)_2]_{ad.}/[ArS^-]_0 = 0$ (1); 0.058 (2); 0.116 (3); 0.172 (4); 0.23 (5); 0.29 (6); 0.34 (7); 0.40 (8); 0.46 (9). (*b*) $y = 0.52$ (10); 0.63 (11); 0.82 (12); 1.20 (13); 1.60 (14).

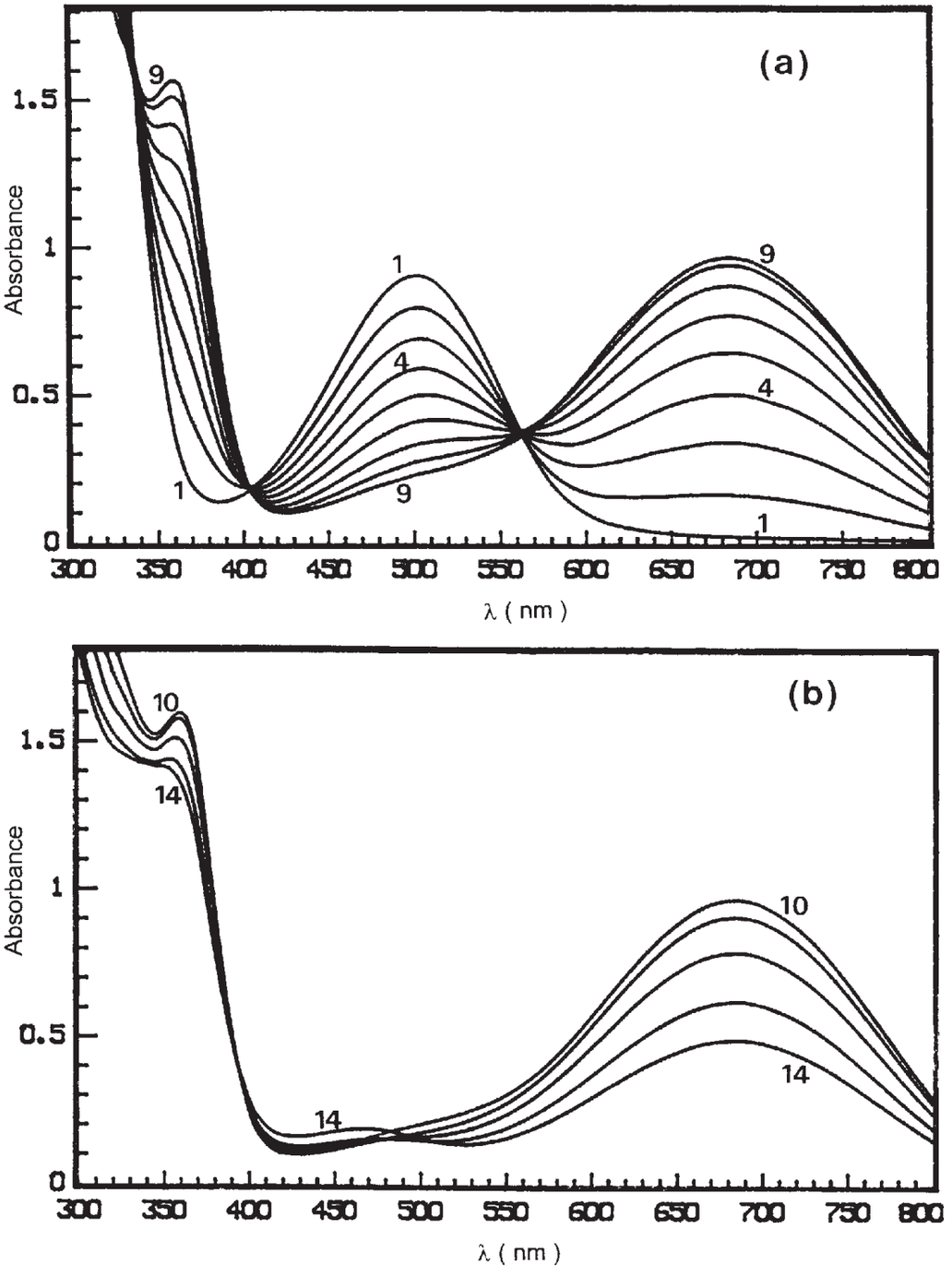

The partial generations of acyl aryl disulfide and sulfur from reaction [20f] ($y > 0.5$) are evidenced by their respective bielectronic reduction waves (Fig. 4, curves 11–13, $CH_3C(O)S_2Ar$: $E_{1/2} \approx -0.73$ V; S_8: $E_{1/2} = -0.40$ V, $S_8 + 2e^- \rightarrow S_8^{2-}$ (6)); $CH_3C(O)S_2Ar$ probably absorbs at $\lambda_{max} \approx$ 360 nm with the same characteristics (Table 1) as Ar_2S_2 ($\varepsilon_{360} = 7500$ dm^3 mol^{-1} cm^{-1}) and ArS_2^- ($\varepsilon_{362} = 7000$ dm^3 mol^{-1} cm^{-1}) since A_{360} remains constant for $y > 0.5$; $[CH_3C(O)]_2S_2$ in excess entails the growth of its cathodic current ($E_{1/2}(R) = -1.19$ V) whereas $CH_3C(O)S_2^-$ ions are detected at the greater y values (Fig. 3*b*, curves 13 and 14) by their maximal absorbance ($\lambda_{max} = 467$ nm).

© 1998 NRC Canada

Fig. 4. Changes in voltammograms during the reaction of diacetyl disulfide with 2-nitrophenyl-thiolate ions. Same conditions as for Fig. 3.

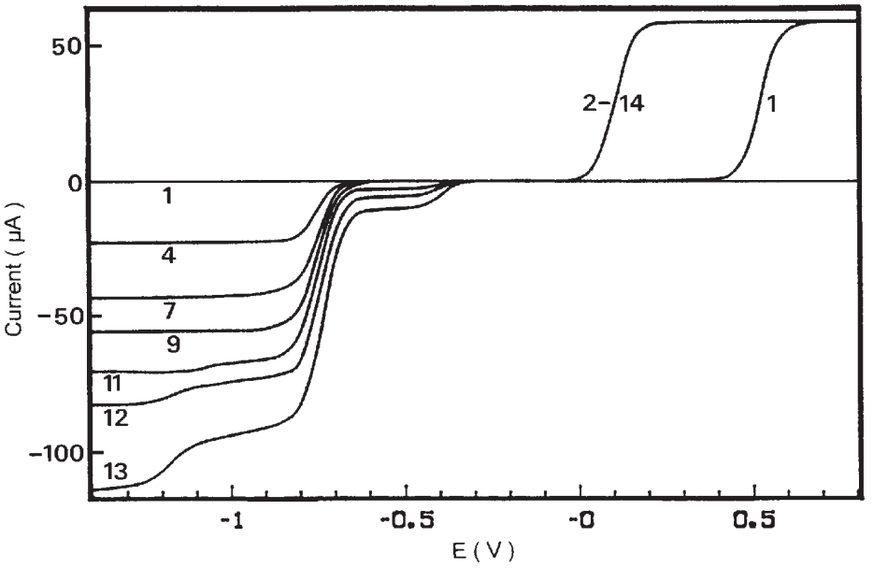

Fig. 5. Changes in voltammograms during the reaction between benzoyl chloride and a solution $[2\text{-}NO_2C_6H_4S^-]_0 = 8[S_8]_0 = 3.45 \times 10^{-3}$ mol dm^{-3}. $y = [PhC(O)Cl]_{ad.}/[ArS^-]_0 = 0$ (1); 0.11 (2); 0.33 (3); 0.56 (4); 0.78 (5); 0.98 (6).

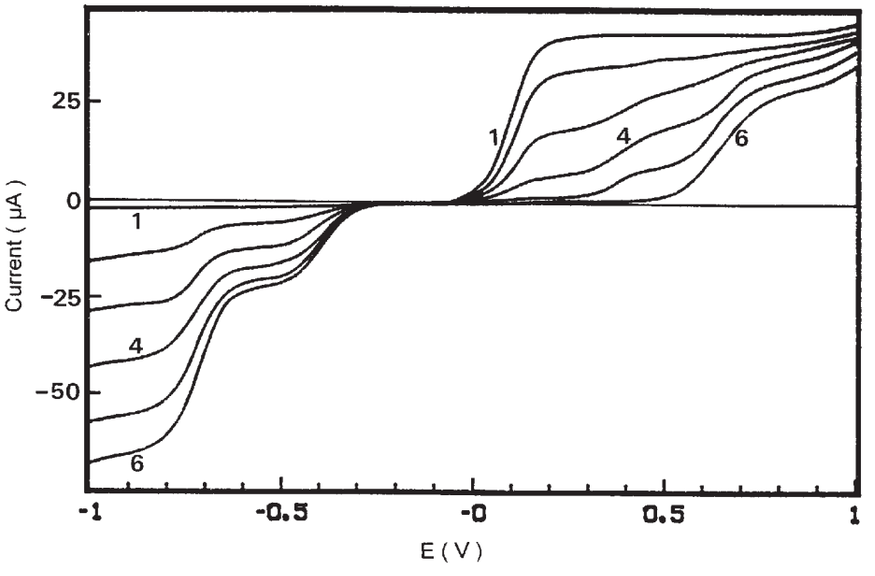

Reactivity of $NO_2C_6H_4S^-$ ions with dibenzoyl disulfide

The addition of bis(2-nitrophenyl) disulfide (Ar_2S_2) to a solution $[PhC(O)S^-]_0 = 3.0 \times 10^{-3}$ mol dm^{-3} gives the only detection of ArS_2^- and ArS^- ions on spectra (increase of A_{681}, A_{362}, and A_{502}) in a proportion $[ArS_2^-]/[ArS^-]$ 70/30 as shown with $CH_3C(O)S^-$ ions (Fig. 1). However, the overall balance, eq. [13], develops here to a moderate extent such as:

$$0.50 < \sum_{x=1,2} [ArS_x^-]/[Ar_2S_2]_{ad.} < 0.28$$

$$\text{for } 0 < [Ar_2S_2]_{ad.}/\ [PhC(O)S^-]_0 \leq 1.07$$

It can be assumed that the E^o standard potential of $[PhC(O)]_2S_2$ is a little more negative than that of Ar_2S_2; the redox initial exchange [15] is then unfavourable in spite of a fast chemical follow-up reaction analogous to eq. [18]. The addition of dibenzoyl disulfide to 2-nitrophenyl thiolate ions ($[ArS^-]_0 = 3.53 \times 10^{-3}$ mol dm^{-3}) entails changes of spectra and voltammograms similar to the diacetyl disulfide reaction. However, contrary to the reaction of $[CH_3C(O)]_2S_2$, the consumption of ArS_x^- (x = 1, 2) ions, $\Delta[ArS_x^-]_y/[(PhCOS)_2]$, remains at the greater constant value, 1.55 ± 0.05 for $0 < y = [(PhCOS)_2]_{ad.}/[ArS^-]_0 < 0.5$, and ArS_2^- ions (A_{681}, A_{362}) are here generated in solution in a lower proportion.

© 1998 NRC Canada

Table 2. Consumption of 2-$NO_2C_6H_4S_x^-$ (x = 1, 2) ions during the addition of benzoyl chloride to a solution $[ArS^-]_0 = 8[S_8]_0 = 3.45 \times 10^{-3}$ mol dm^{-3}.

$[PHC(O)Cl]_{ad.}/[ArS^-]_0$	0.11	0.22	0.33	0.44	0.56	0.67	0.78	0.89	0.98
$\Delta[ArS_x^-]/[PhC(O)Cl]_{ad.}$	1.87	1.82	1.74	1.63	1.51	1.36	1.23	1.11	1.02

The nucleophilic substitution of ArS_x^- ions on $[RC(O)]_2S_2$ giving $RC(O)S_xAr$ (x = 1, 2) is probably easier with R = Ph than with R = CH_3, but unlike R = CH_3 (see before), ArS_x^- ions could reduce $PhC(O)S_2Ar$ in agreement with $E^o((PhCOS)_2) < E^o(Ar_2S_2)$. This assumption was verified by the addition of benzoyl chloride to ArS_2^- ions coming from an initial solution $[ArS^-]_0 = 8[S_8]_0 = 3.45 \times 10^{-3}$ mol dm^{-3}, with $y = [PhC(O)Cl]_{ad.}/[ArS_x^-]_0$. Equations [23], [24], and [25] with the overall balance, eq. [26], explain the changes in spectra and voltammograms (Fig. 5):

[23] $PhC(O)Cl + ArS_2^- \rightarrow PhC(O)S_2Ar + Cl^-$

[24] $PhC(O)S_2Ar + ArS_2^- \rightarrow Ar_2S_2 + 1/2S_2 + PhC(O)S^-$

[25] $PhC(O)S^- + PhC(O)Cl \rightarrow [PhC(O)]_2S + Cl^-$

[26] $2PhC(O)Cl + 2ArS_2^- \rightarrow Ar_2S_2 + [PhC(O)]_2S + 1/2S_2 + 2Cl^-$

The variations $\Delta[ArS_x^-]/[PhC(O)Cl]_{ad.}$ as a function of y are reported in Table 2. At the lower y values ($y \leq 0.5$, curves 2, 3), ArS_2^- ions in excess preferentially react with PhC(O)Cl in a proportion close to 2/1 according to eqs. [23] + [24], similar to eqs. [21] + [22], with the appearance of sulfur ($E_{1/2}$ (R) = – 0.40V), Ar_2S_2 ($E_{1/2}$ (R) = –0.72 V), and $PhC(O)S^-$ ions ($E_{1/2}$ (O) = +0.38 V). Then concurrent substitutions of $PhC(O)S^-$ and ArS_2^- occur. At the stoichiometry 1/1 of eq. [26] (curve 6), the wave of Cl^- ions is the only anodic one ($E_{1/2} \approx$ + 0.65V, $3Cl^- \rightarrow Cl_3^- + 2e^-$), with an intensity close to that calculated after calibration with a solution of $N(CH_3)_4$ Cl; the UV spectrum and the two cathodic waves are the same as those obtained when diaryl disulfide, dibenzoyl sulfide, and sulfur are mixed at concentrations $[Ar_2S_2] = [(PhCO)_2S] = 8\ [S_8] = [ArS^-]_0/2 = 1.72 \times 10^{-3}$ mol dm^{-3} (S_8: i (–0.60 V) ≈ 23 μA; Ar_2S_2, $(PhCO)_2S$: i (–1.10 V) ≈ 70 μA, $A_{360} \approx 1.20$). So $A = f(\lambda)$ and $i = f(E)$ recordings in the course of the reaction of ArS^- ions with $[PhC(O)]_2S_2$ ($0 < y < 0.5$) are consistent with the two competing processes [27] and [28] (= [19] + [24]), which yield close concentrations of PhC(O)SAr and Ar_2S_2 species from $\Delta[ArS_x^-]_y/[(PhCOS)_2]_{ad.} = 1.55$:

[27] $2ArS^- + [PhC(O)]_2S_2 \rightarrow PhC(O)SAr + ArS_2^- + PhC(O)S^-$

[28] $2ArS_2^- + [PhC(O)]_2S_2 \rightarrow Ar_2S_2 + 2PhC(O)S^- + S_2$

Equation [28] is equivalent to the reduction of diacyl disulfide by ArS_x^- ions. ArS_2^- concentration (A_{681}) increases up to $y = 0.5$, then decreases ($0.5 \leq y \leq 1.2$) as shown with the addition of PhC(O)Cl, with release of sulfur (appearance of the reduction wave of S_8, $E_{1/2}$ (R) = –0.40 V, $i(R)/C = 30$ μA mol^{-1}), giving a limiting current in agreement with the stoichiometry of eq. [28].

Discussion

From our results, the close standard potentials of disulfides can be qualitatively classified as $E^o(Ar_2S_2) \geq E^o[(PhCOS)_2] > E^o[(CH_3COS)_2]$. However ArS_x^- ions (Ar = 2-$NO_2C_6H_4$) preferentially react with $RC(O)S_2C(O)R$ (R = CH_3, Ph) by nucleophilic substitution at the carbonyl carbon rather than by redox process (R = Ph), which would imply the cleavage of the S—S bond.

Stable polysulfide ions S_8^{2-}, S_6^{2-} ($\rightleftharpoons S_3^{\bullet -}$), S_4^{2-} can be obtained by chemical or electrochemical reduction of sulfur in dipolar aprotic media (DMA, DMF, DMSO, CH_3CN...) (6, 18). These species, which reduce "activated" diaryl disulfides Ar_2S_2 (e.g., Ar = $NO_2C_6H_4$) (8) into ArS^- ions ($E^o(S_8) < E^o(Ar_2S_2)$), entail the formation of thiocarboxylate ions from diacyl disulfides (1, 3). Similarly, $RC(O)O^-$ ions are generated from diacyl peroxides in the presence of superoxide ions (eq. [29]) (19):

[29] $[RC(O)]_2O_2 + 2O_2^{\bullet -} \rightarrow 2RC(O)O^- + 2O_2$

Both reactions [3] and [29] were encountered in the course of substitutions of acyl chlorides (1, 19*a*, 19*c*), anhydrides (2, 19*a*, 19*f*), and esters (19*b*, 19*d*, 19*g*) by S_6^{2-} or $O_2^{\bullet -}$ ions in excess. The occurrence of reaction [29] by either electron transfer ("redox," eq. [30]) or by nucleophilic displacement (eq. [31]), followed by superoxide reduction of the acyloxy or acylperoxy radicals, was thoroughly discussed (19*f*) without a convincing conclusion.

[30] $RC(O)OOC(O)R + O_2^{\bullet -} \rightarrow RC(O)O^{\bullet} + RC(O)O^- + O_2$

[31] $RC(O)OOC(O)R + O_2^{\bullet -} \rightarrow RC(O)OO^{\bullet} + RC(O)OO^-$

We conclude that overall processes [3] and [29] should proceed largely via initial nucleophilic steps, as this accommodates all of our experimental observations on the reactivity of 2-nitrophenyl thiolate ions towards diacyl disulfides.

Acknowledgements

The authors thank Dr P. Dubois (Service d'Analyse Chimique du Vivant – Tours) for recordings of NMR and mass spectra.

References

1. J. Robert, M. Anouti, M. Abarbri, and J. Paris. J. Chem. Soc. Perkin Trans. 2, 1759 (1997).
2. J. Robert, M. Anouti, and J. Paris. New J. Chem. **22**, 53 (1998).
3. J. Robert, M. Anouti, and J. Paris. J. Chem. Soc. Perkin Trans. 2, 473 (1997).
4. C. Christophersen and P. Carlsen. Tetrahedron, **32**, 745 (1976).
5. (*a*) M. Delamar and J.C. Marchon. J. Electroanal. Chem. **63**, 351 (1975); (*b*) F. Seel, H.J. Güttler, G. Simon, and A. Wieckowski. Pure Appl. Chem. **49**, 45 (1977).
6. G. Bosser and J. Paris. New J. Chem. **19**, 391 (1995).

© 1998 NRC Canada

7. J.P. Billon, G. Cauquis, and J. Combrisson. J. Chim. Phys. 374 (1964).
8. M. Benaïchouche, G. Bosser, J. Paris, J. Auger, and V. Plichon. J. Chem. Soc. Perkin Trans. 2, 31 (1990).
9. (*a*) B. Svenmark. Organic electrochemistry. *Edited by* M.M. Baizer and H. Lund. Marcel Dekker, New York and Basel. 1993. pp. 523–524; (*b*) Y. Hirabayashi and T. Mazume. Bull. Chem. Soc. Jpn. **39**, 1971 (1966).
10. G. Bosser, M. Anouti, and J. Paris. J. Chem. Soc. Perkin Trans. 2, 1993 (1996).
11. S. Oae. Organic sulfur chemistry: structure and mechanism, CRC Press, Boca Raton, Fla. 1991. pp. 123–129, and refs. cited therein.
12. M. Benaïchouche, G. Bosser, J. Paris, and V. Plichon. J. Chem. Soc. Perkin Trans. 2, 1421 (1990).
13. M. Benaïchouche, G. Bosser, J. Paris, and V. Plichon. J. Chem. Soc. Perkin Trans. 2, 817 (1991).
14. G. Bosser, M. Benaïchouche, R. Coudert, and J. Paris. New J. Chem. **18**, 511 (1994).
15. J.E. Dixon and T.C. Bruice. J. Am. Chem. Soc. **94**, 2052 (1972), and refs. cited therein.
16. J. Robert, M. Anouti, G. Bosser, J.-L. Parrain, and J. Paris. J. Chem. Soc. Perkin Trans. 2, 1639 (1995).
17. J. Robert, M. Anouti, and J. Paris. New J. Chem. **21**, 1187 (1997).
18. F. Gaillard and E. Levillain. J. Electroanal. Chem. **398**, 77 (1995).
19. (*a*) A. Le Berre and Y. Berguer. Bull. Soc. Chim. Fr. **7**, 2368 (1966); (*b*) J. San Filippo, Jr., L.J. Romano, C.I. Chern, and J.S. Valentine. J. Org. Chem. **41**, 586 (1976); (*c*) R.A. Johnson. Tetrahedron Lett. **5**, 331 (1976); (*d*) F. Magno and G. Bontempelli. J. Electroanal. Chem. **68**, 337 (1976); (*e*) M.T. Gibian, D.T. Sawyer, T. Ungermann, R. Tangpoonpholvivat, and M.M. Morrison. J. Am. Chem. Soc. **101**, 640 (1979); (*f*) J.P. Stanley. J. Org. Chem. **45**, 1413 (1980); (*g*) A.R. Forrester and V. Purushotam. J. Chem. Soc. Perkin Trans. 1, 945 (1987).

© 1998 NRC Canada

Valorisation chimique du méthane par plasmas micro-ondes

N. Kopytko et F. Baronnet

Résumé : Opérant à des pressions allant de 4 à 28 torr, dans un réacteur tubulaire placé dans une cavité de Moreau parallépipédique, on a étudié la conversion du méthane dans un plasma à microondes direct. Le but principal de ce travail était de déterminer la nature des produits obtenus par conversion du méthane, particulièrement les hydrocarbures en C_2. On a analysé les produits de la réaction par chromatographie en phase gazeuse. On a étudié l'influence de divers paramètres réactionnels (temps de résidence, écoulement, pression, puissance...). Les résultats expérimentaux montrent que l'on peut obtenir des rendements substantiels d'hydrocarbures en C_2. On compare nos résultats expérimentaux avec ceux obtenus à l'aide de procédés différents, particulièrement le couplage oxydant et le couplage thermique ainsi que ceux obtenus par d'autres auteurs utilisant des techniques de microondes.

Mots clés : méthane, plasma micro-ondes, cavité Moreau, réactions chimiques.

Abstract: The conversion of methane in a direct microwave plasma was investigated at pressures ranging from 4 to 28 Torr in a tubular flow reactor located in a parallelepipedic Moreau cavity. The main purpose of this work was the determination of the products obtained by methane conversion, especially C_2 hydrocarbons. The reaction products were analysed by gas phase chromatography. The influence of various reaction parameters (residence time, flow, pressure, power…) was studied. The experimental results showed that substantial yields in C_2 hydrocarbons could be obtained. Our experimental results are compared to those obtained by other processes, especially oxidative coupling and thermal coupling, and also to those obtained by other authors using microwave techniques.

Key words: methane, microwave plasma, Moreau cavity, chemical reactions.

[Traduit par la Rédaction]

Introduction

En raison de la relative abondance des réserves de gaz naturel dont le méthane est le principal constituant ainsi que des difficultés et du coût liés au transport du gaz naturel, les procédés de conversion du méthane en hydrocarbures supérieurs ont fait l'objet de très nombreux travaux. Le passage par le gaz de synthèse présentant des inconvénients, dont l'endothermicité importante de l'étape de vaporéformage correspondant à une perte énergétique de l'ordre de 25 %, un effort considérable de recherche en vue d'une conversion directe du méthane, en particulier en hydrocarbures supérieurs, a été fait depuis une quinzaine d'années. Parmi les procédés étudiés, la réaction de couplage oxydant du méthane découverte en 1982 par Keller et Bhasin (1) est apparue comme une des voies les plus prometteuses. Cependant, il est apparu que, quels que soient le type de catalyseur et les conditions opératoires utilisées, le rendement en hydrocarbures supérieurs, notés C_{2+}, restait inférieur à 25 % (2) ce qui, compte tenu des recyclages en résultant, limitait sérieusement les possibilités de ce procédé. Des travaux sur cette réaction ont été conduits au laboratoire (3, 4).

La réaction dite de couplage thermique du méthane qui consiste à le faire réagir vers 1200°C en présence d'hydrogène pour limiter la formation de coke a également été étudiée au laboratoire (5, 6) mais il est certain que les niveaux thermiques nécessaires sont un inconvénient et nécessitent en particulier de réaliser le réacteur en matériaux résistant à ces températures.

Il est clair que les difficultés liées à ces différents procédés proviennent essentiellement de la relative «inertie» chimique de la molécule de méthane, plus précisément de la liaison C—H dont l'énergie de dissociation est de 104 kcal/mol; difficulté supplémentaire, les produits (éthane, éthylène, par exemple) sont moins stables que le réactif de départ dans les conditions où s'effectue la réaction, que ce soit à 1200°C (couplage thermique) ou à 800°C en présence d'oxygène (couplage oxydant).

Ceci montre donc les limites de l'amorçage thermique des réactions de conversion du méthane, puisque si de hautes températures sont nécessaires en raison de l'inertie chimique de la molécule de méthane, elles conduisent en contrepartie à la dégradation des produits formés et à des réactions secondaires indésirables; il semble donc incompatible d'obtenir en même temps une activation suffisante et une sélectivité élevée.

Une autre méthode qui pourrait éviter ces difficultés est l'activation du méthane par des plasmas micro-ondes. Il y a

Reçu le 29 avril 1998.

N. Kopytko et F. Baronnet.[1] Département de chimie physique des réactions, UMR n° 7630 du Centre national de la recherche scientifique, Institut national polytechnique de Lorraine, École nationale supérieure des industries chimiques, 1, rue Grandville, BP 451, F-54001 Nancy Cedex, France.

1.Auteur à qui adresser toute correspondance.
Tél. : 33.(0)3.83.17.50.06. Téléc : 33.(0)3.83.37.81.20.
Mél : dcpr@ensic.u-nancy.fr

© 1998 CNRC Canada

de toute évidence de nombreux radicaux libres dans un plasma, ce qui permet d'obtenir une activation directe tout en restant à des températures peu élevées. Nous avions fait une première tentative dans ce sens en utilisant des décharges radiofréquences (7) mais nous avions été limités très rapidement dans la gamme des pressions utilisables. Ceci nous a conduits à nous intéresser aux plasmas micro-ondes; dans ce travail, nous avons travaillé en plasma direct contrairement à d'autres auteurs qui avaient eu recours aux plasmas différés, c'est-à-dire à la réalisation d'un plasma d'air ou d'azote avec injection de méthane dans la zone post-décharge (8). Nous comparerons les deux méthodes dans ce mémoire.

Montage expérimental

Comme nous l'avons mentionné dans ce qui précède, nous avons choisi d'exciter directement le méthane par plasma micro-ondes (plasma direct). Nous évitons ainsi les problèmes dus à l'utilisation d'un gaz plasmagène, en particulier la formation de produits indésirables.

La figure 1 donne un schéma général du montage; nous pouvons considérer qu'il se compose de trois parties successives. (*i*) Le réactif (méthane pur) est introduit dans l'installation à l'aide de RDM (régulateurs de débit massique) qui permettent à la fois la mesure du débit gazeux et son réglage à une consigne donnée (fig. 1*a*). (*ii*) Le méthane passe ensuite dans le réacteur constitué d'un tube de quartz de 20 mm de diamètre qui se trouve placé dans une cavité micro-ondes de type Moreau couplée à un magnétron par l'intermédiaire d'un guide d'ondes. L'appareillage micro-ondes est schématisé dans la figure 1*b*. (*iii*) La dernière partie du montage est constituée de la station de prélèvement des échantillons qui sont ensuite analysés par chromatographie en phase gazeuse. La figure 1*c* donne une vue plus précise de cette partie de l'installation et permet de comprendre le procédé de prélèvement : en cours d'expérience les deux vannes notées A sont ouvertes, la vanne B est fermée, le flux gazeux passe donc entre les deux vannes A. Les ampoules de prélèvement, dans lesquelles le vide a été fait au préalable, sont isolées à l'aide d'un robinet. Au moment de la prise d'échantillon les vannes sont commutées, ce qui permet d'isoler les gaz à prélever sans provoquer d'augmentation brutale de la pression dans le réacteur. Le robinet menant aux ampoules de prélèvement est ensuite ouvert.

La pression dans l'installation est réglée à l'aide d'une vanne pointeau, et une pompe à palettes placée en sortie de montage permet l'évacuation des gaz. Des capteurs de pression de type Barocell et MKS sont placés en plusieurs points de l'installation, avant et après le réacteur, ce qui a permis de vérifier que le plasma entraînait une très faible perte de charge, et au niveau de la prise d'échantillon. Enfin, un piège de laine de silice placé en sortie du réacteur permet de retenir les goudrons formés et d'éviter ainsi les problèmes d'encrassement en aval.

L'ensemble du matériel utilisé pour la production du plasma nous a été fourni par la SAIREM. Cette installation se compose d'un magnétron de Thomson CSF alimenté par un générateur haute tension de type GMP 12 KTS dont la puissance peut varier de façon continue entre 0 et 1200 W.

Fig. 1. Schéma du montage : (*a*) réacteur et périphériques; (*b*) appareillage micro-ondes; (*c*) système de prélèvement par détente dans les ampoules.

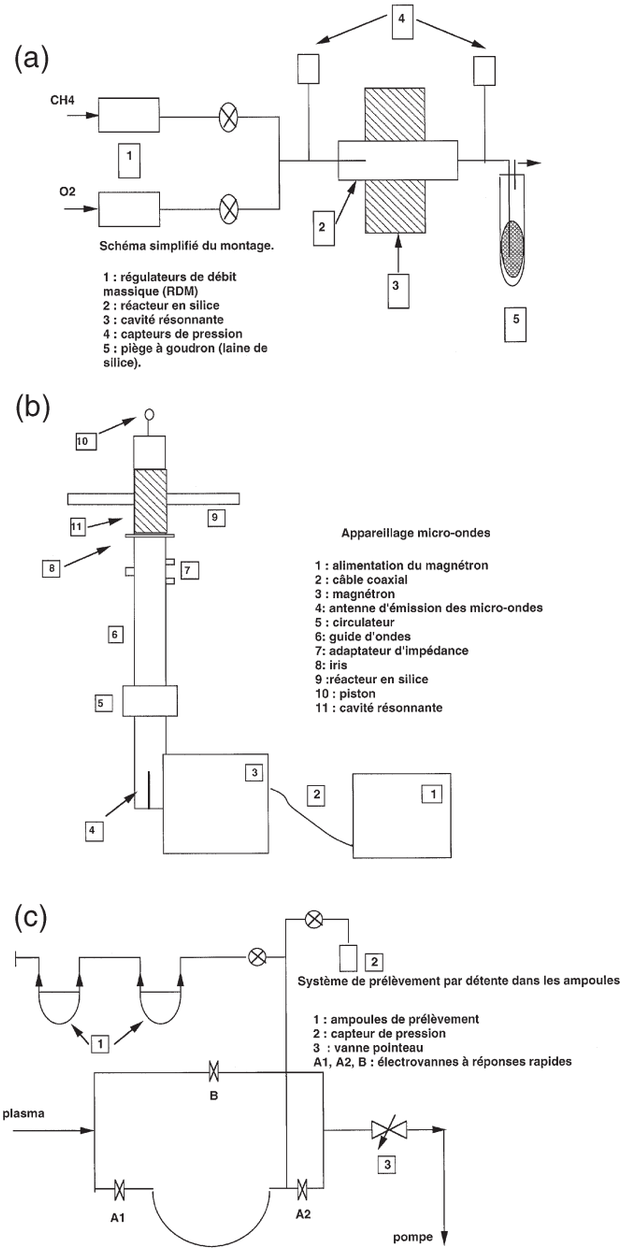

Le magnétron joue le rôle d'un oscillateur micro-ondes ayant une fréquence de sortie n = 2450 MHz et transmet

© 1998 CNRC Canada

Fig. 2. Schéma de la cavité Moreau.

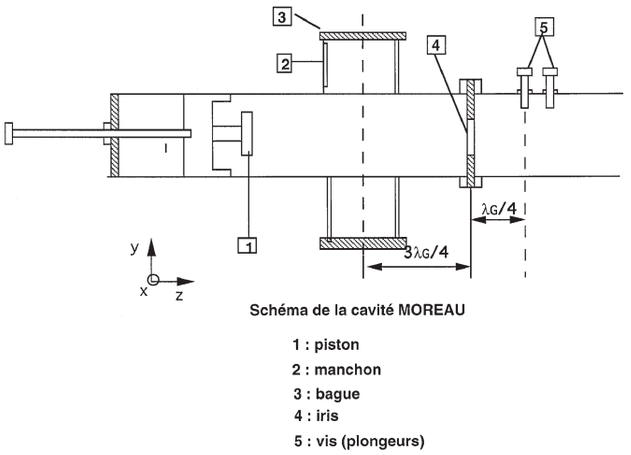

l'énergie le long du guide d'ondes au moyen d'une antenne d'émission.

Un wattmètre monté sur le générateur permet de connaître à tout moment la puissance incidente P_i et la puissance réfléchie P_r. La différence $P_i - P_r$ permet de connaître approximativement la puissance transmise au plasma (étant donné qu'une certaine quantité de cette puissance transmise est en fait dissipée sous forme de chaleur dans le tube à décharge).

Un circulateur refroidi à l'eau protège l'antenne des retours d'énergie micro-ondes qui peuvent se produire en cas de désadaptation.

Les ondes propagées le long du guide entrent dans une cavité résonnante parallélépipédique de type Moreau, schématisée sur la figure 2 (9). Cette cavité est limitée en amont du réacteur par un iris au travers duquel est transmise l'énergie et en aval par un piston mobile qui doit se trouver réglé de manière à ce que la longueur de la cavité corresponde à un nombre entier de demi-longueurs d'onde et permette ainsi l'instauration d'un système d'ondes résonnantes.

Le mode de résonance est un mode transverse électrique noté TE_{mnp}. Les trois indices *m*, *n* et *p* sont relatifs au nombre de demi-longueurs d'ondes établis lors de la résonance dans chacune des trois directions *xyz* repérées sur la figure 2. Le mode de résonance choisi est tel que l'axe du réacteur corresponde à un ventre des ondes électriques. Notre installation fonctionne avec un mode TE104.

Avec un tel réglage, l'oscillation du champ électrique est maximale au niveau du passage du réacteur à l'intérieur de la cavité. Elle permet de mettre en mouvement les quelques électrons libres déjà présents dans le méthane. Pour être pleinement efficace cette oscillation doit avoir lieu dans l'axe du réacteur de façon à minimiser les pertes aux parois. Dans ces conditions, les électrons accélérés rentrent en collision avec les molécules de méthane pour former soit des ions si leur énergie est suffisante, soit des espèces neutres excitées. Les électrons libérés lors de la formation d'ions vont à leur tour entrer en collision avec d'autres molécules, ce qui va entraîner une réaction en chaîne pour finalement aboutir à la création d'un plasma.

Lors de nos travaux nous nous sommes surtout attachés à l'aspect chimique du problème : dosage des produits formés, mesure de la consommation des réactifs. Il s'agissait principalement d'une recherche exploratoire destinée à déterminer l'intérêt des procédés «plasma froid» appliqués au méthane, ce qui a nécessité une mise au point relativement longue, au détriment de bilans-matière détaillés.

Résultats obtenus

Le maintien du plasma s'étant avéré relativement difficile, en particulier à cause de problèmes d'encrassement, nous avons, dans un premier temps, essayé de déterminer quelles étaient les conditions d'obtention d'un plasma stable, en fonction des principaux paramètres qui nous étaient accessibles. Nous avons ensuite plus précisément étudié l'influence sur les résultats du temps de passage, de la puissance incidente, du débit et de la pression de méthane.

Conditions d'obtention d'un plasma stable

Pour plusieurs débits, nous avons déterminé, en fonction de la pression, les puissances incidentes minimales et maximales admissibles pour obtenir un plasma stable pendant une durée de 15 min.

Il est certain que les résultats obtenus seraient modifiés en choisissant une durée plus longue de stabilité exigible pour le plasma. Mais l'intérêt présenté par ce travail est avant tout d'avoir une vue d'ensemble de l'importance d'une variation des différents paramètres.

Dans ces conditions nous avons étudié successivement les débits suivants : 15, 30, 60, 120, 160 et 240 mL/min.

Le réacteur était nettoyé à l'aide d'un plasma d'oxygène après chaque expérience. Les conditions de nettoyage ont été fixées aux normes suivantes : P_i = 300 W, P = 9 torr (1 torr = 133,3 Pa), durée 2 min. Les démontages qui ont été effectués de temps à autre ont permis de vérifier que ce nettoyage était suffisant, même dans des conditions d'encrassement important.

L'ensemble des courbes obtenues a été rassemblé sur la figure 3 où nous avons représenté, pour différents débits de méthane, les puissances incidentes minimales et maximales en fonction de la pression. Nous obtenons une forme générale «en cloche» : l'amplitude entre puissance minimale et puissance maximale diminue quand la pression augmente. D'autre part, nous remarquons qu'une augmentation du débit permet d'accéder à des domaines de pression plus importants. La pression maximale passe ainsi de 17 torr pour 15 mL/min à 28 torr pour 240 mL/min. Toutefois, il semble que le domaine de pression admissible plafonne à environ 28 torr : nous n'observons plus d'évolution notable entre 120 et 240 mL/min. Nous pouvons supposer par conséquent que 28 torr constituent une limite pour ce type de montage expérimental (guide d'onde adapté à une cavité parallélépipédique de type Moreau, réacteur de 2 cm de diamètre).

Influence du temps de passage

Le temps de passage des gaz dans le réacteur est donné par la relation

$$[1] \qquad \tau = V/QE$$

© 1998 CNRC Canada

Fig. 3. Recherche des limites de stabilité du plasma : puissances incidentes minimales et maximales admissibles en fonction des conditions de débit et de pression de méthane dans le réacteur.

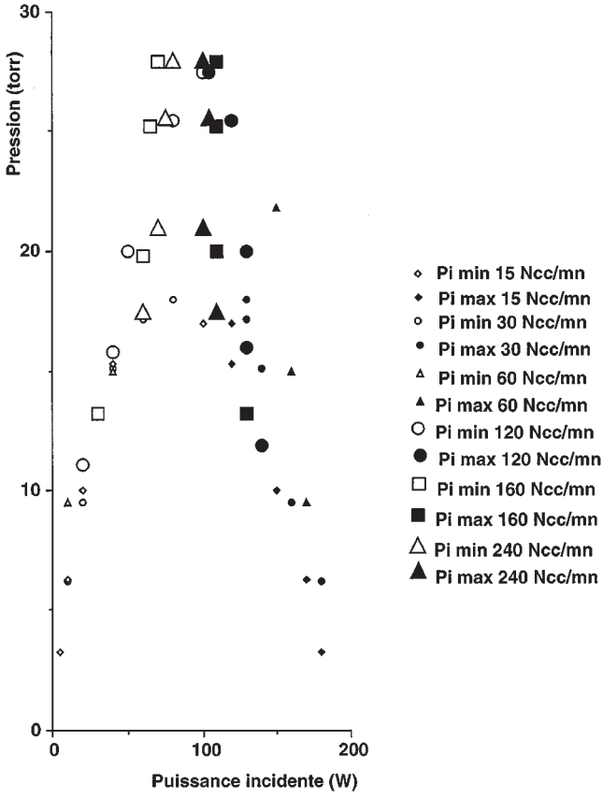

avec *V,* volume du réacteur, ici pris arbitrairement comme la portion du tube en quartz passant à l'intérieur du guide d'ondes. Cette définition présente le défaut de ne guère tenir compte de la «réalité plasma», dans la mesure où la zone lumineuse n'est pas toujours la même en fonction des conditions de manipulation. Elle permet au moins d'avoir une base de calcul pour étudier ce paramètre «temps de passage». QE est le débit volumique du méthane à l'entrée du réacteur, pris à la pression d'entrée des gaz.

Nous nous sommes placés à une pression de 20 torr (pression mesurée sans plasma à l'entrée du réacteur), et avec une puissance incidente fixe de 80 W. Dans ces conditions nous avons pu faire varier le débit de méthane entre 40 et 150 NmL/min, ce qui correspondait à des temps de passage allant de 0,15 s à 0,60 s. (NmL signifie mL mesuré à 273 K, 1 atm.)

Les résultats obtenus en faisant varier le temps de passage des gaz dans le réacteur plasma sont rassemblés sur les courbes des figures 4 (pour la conversion et le rendement global en hydrocarbures en C_2) et 5 (pour les rendements respectifs en acétylène, éthylène et éthane).

La conversion du méthane croît en fonction du temps de passage de manière quasi-linéaire à partir d'une valeur de l'ordre de 0,15 s. Il n'a pas été possible de faire des points à de très faibles temps de passage, mais l'allure de la courbe laisse supposer qu'on a un «démarrage» très rapide de la réaction, ce qui semble compatible avec ce qu'on sait des milieux plasmas (milieux à forte réactivité).

Fig. 4. Conversion du méthane et rendement en hydrocarbures en C_2 en fonction du temps de passage. P = 20 torr; P_i = 80 W.

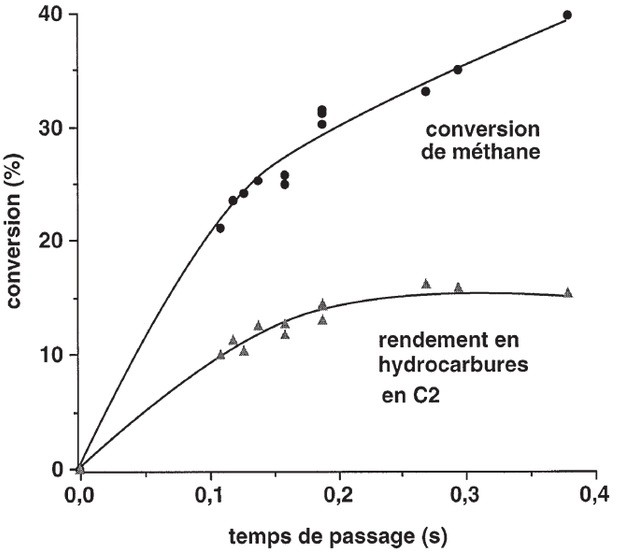

Fig. 5. Rendement en éthane, éthylène et acétylène en fonction du temps de passage. P = 20 torr; P_i = 80 W.

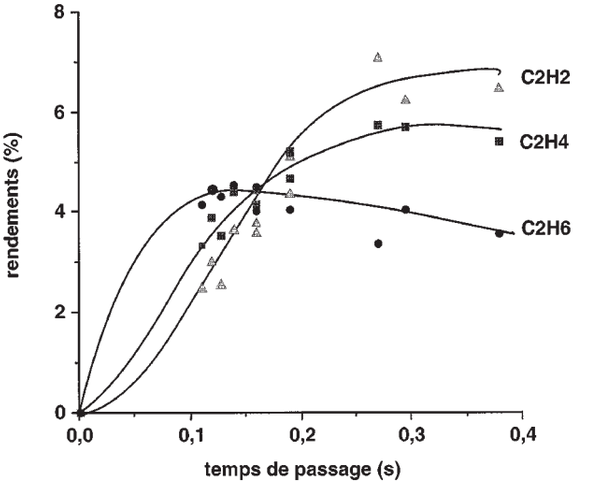

Le rendement global en hydrocarbures C_2 croît également de façon quasi-linéaire jusqu'à environ 0,2 s, puis il semble atteindre une sorte de palier. La conservation en carbone et en hydrogène est d'autant meilleure que le temps de passage est plus court. Cette évolution s'explique par la formation accrue de produits lourds (goudrons) quand le temps de passage augmente.

La figure 5 qui donne en fonction du temps de passage les rendements respectifs en acétylène, éthylène et éthane permet de voir que l'éthane est le produit majoritaire pour de faibles temps de passage, et que l'éthylène et l'acétylène deviennent ensuite prédominants. Les valeurs des pentes à l'origine paraissent a priori trop fortes pour affirmer que l'éthylène et l'acétylène sont des produits secondaires. Mais il est difficile de trancher car nous n'avons pas pu obtenir des temps de passage inférieurs à 0,1 s.

© 1998 CNRC Canada

Fig. 6. Rendement en éthane, éthylène et acétylène en fonction de la puissance incidente. P = 9,5 torr; débit = 60 mL/min.

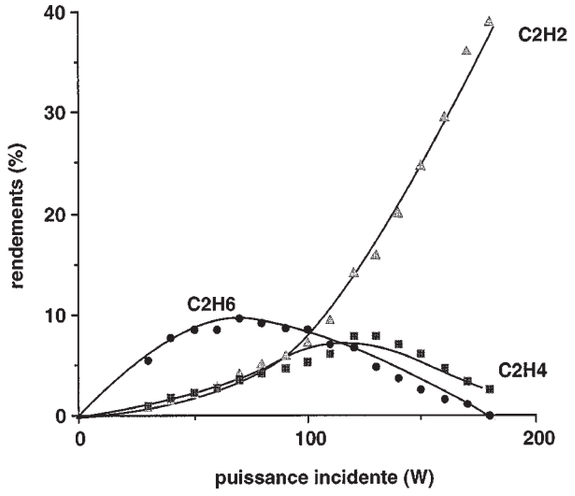

Fig. 7. Bilan en carbone : conversion du méthane, rendement en hydrogène et en acétylène en fonction de la puissance incidente. P = 9,5 torr; débit = 60 mL/min.

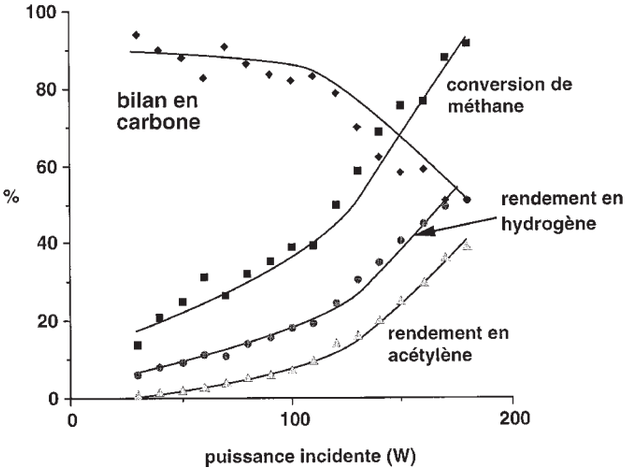

Les rendements obtenus en hydrocarbures C_2 sont de l'ordre de 14 % pour des temps de passage allant de 0,3 à 0,5 s.

Parallèlement, quelques mesures ont été faites concernant la formation d'hydrocarbures en C_3 ou en C_4. Nous avons ainsi pu constater la présence de propène, d'allène et de propyne, ainsi que des traces d'hydrocarbures en C_4. Les meilleurs rendements en hydrocarbures en C_3 (3,65 % au total) ont été obtenus dans des conditions expérimentales assez douces (P_i = 80 W, t = 0,045 s, D = 100 NmL/min). Nous pouvons supposer que dans des conditions plus dures les hydrocarbures en C_3 qui se forment sont très vite eux-mêmes polymérisés en goudrons sur les parois et n'apparaissent donc pas dans les bilans. La formation dans ce cas de figure de quantités importantes d'acétylène corrobore cette hypothèse (dans la mesure où l'acétylène peut être considéré comme un précurseur d'aromatiques).

Influence de la puissance incidente

Pour mener cette étude nous nous sommes placés dans des conditions expérimentales telles que l'amplitude de puissance accessible soit maximale. La pression choisie était de 9,5 torr et le débit de 60 NmL/min, ce qui nous permettait de faire varier la puissance incidente entre 30 et 180 W.

La figure 6 montre en fonction de la puissance incidente les rendements en hydrocarbures en C_2.

Quand nous rassemblons sur un même graphique (fig. 7) les variations de la conversion de méthane, du rendement en acétylène et en hydrogène et du bilan en élément carbone en fonction de la puissance incidente, il apparaît une variation très nette dans la pente des différentes courbes pour une puissance incidente d'environ 110 W. À partir de cette valeur nous pouvons remarquer un accroissement de la vitesse de conversion du méthane, en même temps qu'une augmentation plus rapide des quantités d'acétylène et d'hydrogène formés. Tout le méthane converti ne se transforme pas en hydrocarbures légers, ce qui explique la diminution plus rapide du pourcentage de l'élément carbone retrouvé dans le bilan de matière.

Nous pouvons en déduire que cette valeur de puissance incidente correspond, dans les conditions expérimentales choisies, à l'apparition des réactions de «troisième stade» selon Back et Back (10), c'est-à-dire à la formation de l'acétylène et des produits formés par polymérisation des hydrocarbures en C_2.

Le bilan en hydrogène est toujours meilleur que celui en carbone. Ceci est en accord avec le fait que le dépôt de goudrons formé sur les parois est beaucoup plus riche en carbone qu'en hydrogène.

Les rendements obtenus en C_2 sont très intéressants par rapport à ceux obtenus par les méthodes classiques. Nous obtenons à forte puissance plus de 40 % de rendement global en C_2, avec cette réserve qu'il y a une forte proportion d'acétylène alors qu'il serait sans doute préférable, pour une utilisation industrielle en aval, d'obtenir de l'éthylène.

Notons toutefois que ces résultats sont obtenus à relativement faible pression (9,5 torr). À titre d'exemple nous avons tracé pour chacun des hydrocarbures en C_2 les rendements en fonction de la puissance incidente pour des pressions successives de 9,5, 15,1, et 20 torr (figs. 8 à 10). Nous pouvons voir que pour C_2H_6 et C_2H_4 les rendements obtenus diminuent avec la pression, alors que le rendement en C_2H_2 est indépendant de ce paramètre, au moins dans le domaine étudié.

Les figures 9 et 10 montrent également de façon assez claire que les optima de rendements correspondent à des puissances incidentes plus élevées pour C_2H_4 que pour C_2H_6. En ce qui concerne C_2H_2 (fig. 8), l'optimum de rendement, s'il existe, n'est même pas atteint dans le cadre de nos conditions expérimentales. Ce glissement vers les fortes puissances des optima de rendement pourrait accréditer l'hypothèse d'un schéma de déshydrogénations successives du type de celui de Back et Back.

Influence de la pression et du débit de méthane

Nous nous sommes placés à une puissance incidente constante et nous avons étudié, pour 5 débits compris entre 15 et 240 NmL/min, les résultats obtenus en faisant varier la pression dans le réacteur. Le réglage de la pression s'effectuait à

© 1998 CNRC Canada

Fig. 8. Rendement en acétylène en fonction de la puissance incidente pour des pressions de 9,5, 15,1 et 20 torr; débit = 60 mL/min.

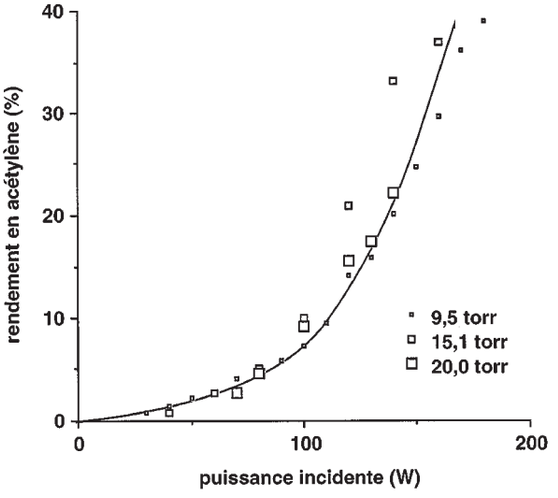

Fig. 9. Rendement en éthylène en fonction de la puissance incidente pour des pressions de 9,5, 15,1 et 20 torr; débit = 60 mL/min.

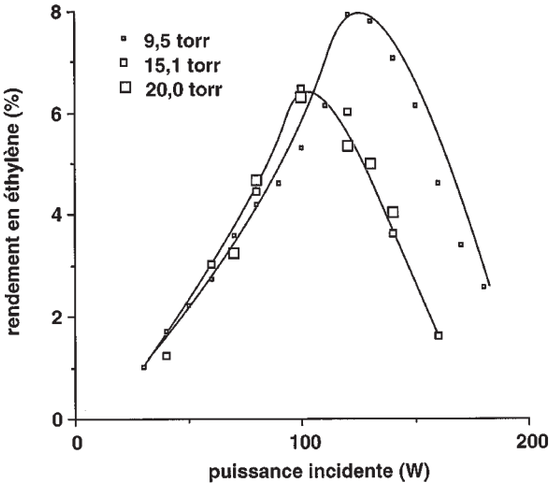

Fig. 10. Rendement en éthane en fonction de la puissance incidente pour des pressions de 9,5, 15,1 et 20 torr; débit = 60 mL/min.

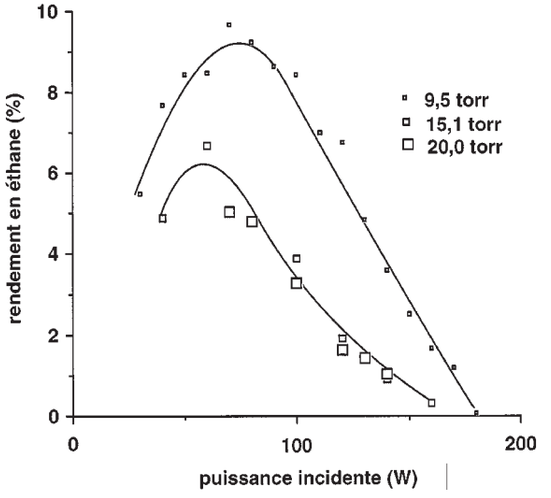

Fig. 11. Rendement en acétylène en fonction de la pression pour différents débits P_i = 80 W.

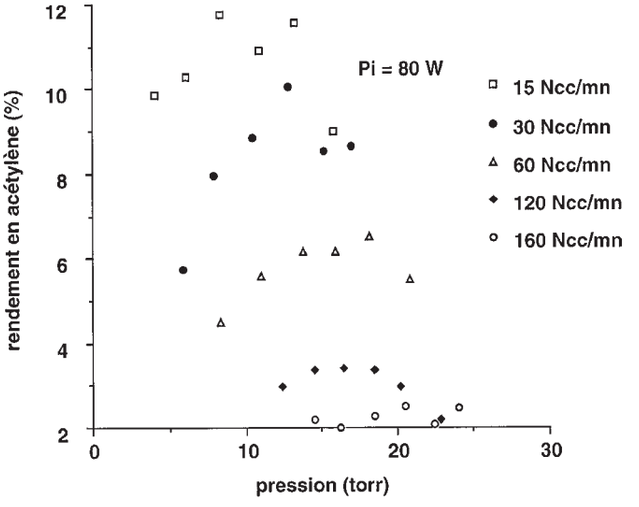

l'aide des vannes situées en aval de la section de prélèvement.

Compte tenu des résultats donnés figure 3, nous avons choisi P_i = 80 W. Cette valeur de la puissance incidente est en effet celle qui nous permettait d'étudier la plus grande amplitude de pression pour chacun des débits.

Nous avons ensuite calculé à diverses pressions les rendements obtenus pour les différents hydrocarbures en C_2 : C_2H_2 (fig. 11), C_2H_4 (fig. 12) et C_2H_6 (fig. 13).

Lorsque le débit augmente et à pression constante, les rendements en C_2H_2 et en C_2H_4 diminuent, ce qui correspond bien à l'effet produit à la fois par une diminution du temps de passage (voir la figure 5) de la puissance incidente (voir la figure 6), à condition dans ce dernier cas de se trouver pour C_2H_4 avant l'optimum de rendement. Le rendement en C_2H_6 augmente par contre légèrement. D'après les figures 5 et 6, cela veut dire que nous nous trouvons alors dans la partie descendante de la courbe, à droite de l'optimum de rendement en éthane.

Si nous nous plaçons désormais à un débit fixé, les rendements de C_2H_2 et de C_2H_4 présentent un maximum en fonction de la pression. La décroissance des rendements obtenus quand la pression augmente s'explique aisément dans la mesure où la puissance disponible restant constante, ceci correspond à une baisse de la quantité d'énergie disponible par molécule, donc à un moindre avancement de la réaction. D'autre part, la réduction du libre parcours moyen des électrons les rend moins énergétiques, ce qui contribue à réduire la constante de vitesse pour les collisions inélastiques qui sont à l'origine de la formation des radicaux libres. Il est plus délicat d'expliquer pourquoi dans un premier temps une augmentation de la pression dans le réacteur provoque une

© 1998 CNRC Canada

Fig. 12. Rendement en éthylène en fonction de la pression pour différents débits P_i = 80 W.

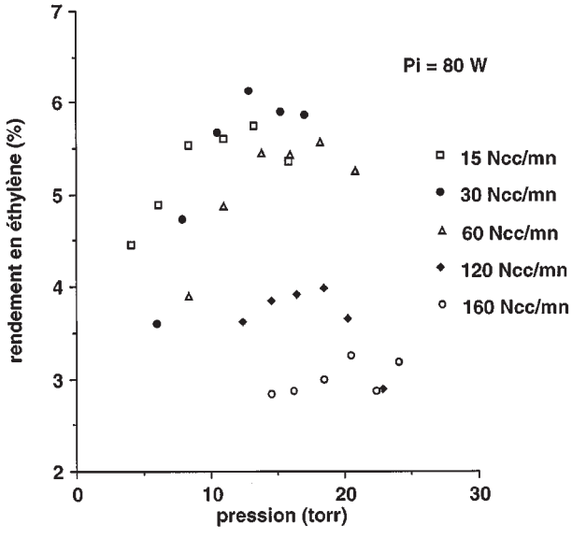

Fig. 13. Rendement en éthane en fonction de la pression pour différents débits P_i = 80 W.

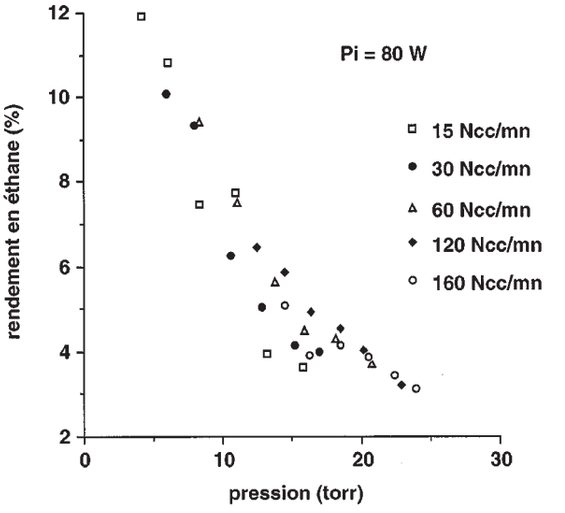

amélioration des rendements en C_2H_2 et en C_2H_4. Nous pouvons toutefois supposer que les réactions de déshydrogénation se produisent à beaucoup plus faible température et donc hors de la zone plasma. L'augmentation de la pression augmente le temps de passage et la concentration des radicaux libres dans la partie du réacteur chauffée par conduction, et donc favorise dans un premier temps la formation d'acétylène et d'éthylène. L'existence de deux effets contraires explique l'allure «en cloche» obtenue pour les tracés des rendements.

Pour les forts débits l'évolution de la pression semble être de moins en moins déterminante dans le cas de C_2H_2 et de C_2H_4. Si nous nous rapportons aux courbes donnant le rendement en fonction de la puissance incidente (fig. 6), nous constatons que pour de faibles puissances incidentes — ce qui correspond à de forts débits — la pente de la courbe obtenue est faible, ce qui est cohérent avec notre observation.

D'autre part, une augmentation de la pression pour un débit fixé se traduit par une décroissance continue du rendement en C_2H_6. L'absence d'optimum peut s'expliquer de la façon suivante : l'augmentation de la pression se traduit, comme nous l'avons déjà vu, premièrement par une diminution du libre parcours moyen des électrons et donc par une diminution de la conversion de méthane, deuxièmement par une augmentation du temps de passage des molécules dans le réacteur, défavorable à la formation d'éthane. Ainsi pouvons-nous expliquer que d'après la figure 13 le rendement en éthane soit d'autant plus élevé que la pression dans le réacteur est faible.

Interprétation mécanistique sommaire

De nombreux travaux ont déjà été réalisés concernant les mécanismes réactionnels du méthane en milieu plasma. Nous pouvons très brièvement résumer la situation en disant que la réaction du méthane en milieu plasma obéit vraisemblablement à (*i*) un mécanisme ionique en l'absence d'hydrogène (les conditions favorables se retrouvant soit au tout début de la réaction dans le cas d'un plasma de méthane pur, soit avec une forte dilution d'argon, gaz porteur de charge qui offre en plus l'avantage de favoriser ce type de réaction); (*ii*) un mécanisme radicalaire dès que la concentration d'hydrogène devient suffisamment élevée, c'est-à-dire à partir d'un certain avancement de la réaction pour un plasma de méthane pur ou dès le début dans le cas d'un plasma méthane–hydrogène (travaux de Okeke et Stori (11)).

Les travaux d'Hiraoka, Aoyama et Morise (12) qui ont été, à notre connaissance, parmi les premiers auteurs à établir un mécanisme complet concernant la réaction du méthane en milieu plasma, favorisent également l'hypothèse d'un mécanisme radicalaire. Ces auteurs ont ajouté à un plasma radio-fréquence de méthane pur successivement de l'iode (piège à radicaux) et de l'ammoniac (piège à ions). Les résultats obtenus montrent que le rendement en éthane décroît rapidement quand la quantité d'iode ajoutée dans le plasma de méthane augmente. Les rendements en éthylène et en acétylène sont par contre à peu près insensibles à l'ajout d'iode, mais les précurseurs de ces hydrocarbures sont considérés être moins sensibles à l'iode. Par contre, aucun des trois hydrocarbures éthane, éthylène ou acétylène n'est sensible à un ajout d'ammoniac, ce qui semble indiquer que le mécanisme de transformation du méthane dans un plasma froid est principalement de nature radicalaire.

Le mécanisme proposé par ces auteurs possède les caractéristiques suivantes : (*i*) les quatre radicaux formés à partir du méthane (CH_3, CH_2, CH, C) sont pris en compte, mais le radical CH_3 est considéré comme très minoritaire (13); (*ii*) nous avons toujours des déshydrogénations successives, mais elles s'opèrent ici directement à partir des radicaux libres et non de leurs produits de recombinaison, contrairement à ce qui a été établi dans le cadre du mécanisme de Back et Back.

[2] $$CH_3 \rightarrow CH_2 \rightarrow CH \rightarrow C$$

(*iii*) Les hydrocarbures en C_2 se forment ensuite par réaction des radicaux libres avec le méthane de départ. Ce sont donc

© 1998 CNRC Canada

tous des produits primaires de la réaction, au sens cinétique du terme.

Le mécanisme proposé par Hiraoka et al. pour la formation des hydrocarbures en C_2 est schématisé ci-dessous. Il est important de préciser qu'il s'agit là d'un mécanisme simplifié ne pouvant donner lieu qu'à une première approche mécanistique. Les mécanismes réels sont sûrement beaucoup plus complexes.

Initiation

Les travaux de Mahan et Mandal (14) suggèrent que CH_2 et H_2 sont les principaux produits obtenus lors de la décomposition du méthane par irradiation. Ceux de Magee (15) permettent de penser que le méthane excité se décompose en ($CH_2 + H_2$) dans 85 % des cas et en ($CH_3 + H$) dans 15 % seulement.

[3] $CH_4 = CH_3 + H$ (15%)

[4] $CH_4 = CH_2 + H_2$ (85%)

Formation de l'éthane

[5] $^1CH_2 + CH_4 = (C_2H_6)^* = 2\ CH_3$

$k = 1{,}9 \times 10^{-12}$ cm^3 molécule^{-1} s^{-1} (Laufer)

Telle qu'elle est écrite dans ce mécanisme, la formation d'une molécule d'éthane nécessite sa stabilisation par collision avec une troisième molécule. La formation d'éthane devrait donc être favorisée quand la pression d'expérience augmente, or la figure 13, que nous avons déjà commentée, montre que c'est le contraire qui se produit. Il est possible que plusieurs influences contraires s'exercent : il se forme certes davantage de molécules d'éthane grâce aux meilleures possibilités de stabilisation collisionnelle, mais des conditions plus dures règnent dans le plasma (une pression plus élevée entraîne une température plus forte, en même temps qu'un temps de passage plus long des molécules dans la zone réactive). Dans ces conditions les molécules d'éthane ont tendance à se déshydrogéner très rapidement suivant les processus classiques de Back et Back (10).

Formation de l'éthylène

[6] $CH + CH_4 = (C_2H_5)^* = C_2H_4 + H$

$= C_2H_5$

$k = 5\times10^{-11}(\exp 200/T)\text{cm}^3\,\text{molécule}^{-1}\text{s}^{-1}$(Warnatz))

Formation de l'acétylène

[7] $C + CH_4 = (C_2H_4)^* = C_2H_2 + H_2$

Qualitativement, ce mécanisme peut rendre compte de l'apparition successive des hydrocarbures en C_2 quand la puissance incidente augmente. Il permet également de justifier les paliers observés en fonction du temps de passage pour les différents rendements.

(*i*) Lorsque les conditions expérimentales (pression, puissance incidente) sont fixées, l'approximation de l'état quasi-stationnaire (AEQS), qui constitue la base des calculs de cinétique chimique, permet d'affirmer que la concentration des différentes espèces activées reste constante. Chacun des hydrocarbures en C_2 étant formé séparément par réaction d'un radical sur une molécule de méthane, nous pouvons alors comprendre la relative stabilité observée pour l'éthane, l'éthylène et l'acétylène en fonction du temps de passage (fig. 5) dans la mesure où ces molécules apparaissent et disparaissent de façon indépendante.

(*ii*) D'autre part, une augmentation de la puissance incidente se traduit par un déplacement vers la formation des radicaux les plus déshydrogénés, eux-mêmes à l'origine de la formation d'éthylène puis d'acétylène. Le mécanisme d'Hiraoka et al. permet donc également d'expliquer l'allure des courbes obtenues en fonction de P_i (fig. 6).

Il convient de noter, comme suggéré par un des rapporteurs, que le mécanisme d'Hiraoka et al. ne prend pas en compte des réactions classiques conduisant également à la formation d'hydrocarbures en C_2.

[8] $CH_3 + CH = C_2H_6$

$k = 3{,}98 \times 10^{-11}$ cm^3 molécule^{-1} s^{-1} (Baulch)

[9] $CH_3 + {}^3CH_2 = C_2H_4 + H$

$k = 7 \times 10^{-11}$ cm^3 molécule^{-1} s^{-1} (Laufer)

[10] $^3CH_2 + {}^3CH_2 = C_2H_2 + H_2$

$k = 5{,}3 \times 10^{-11}$ cm^3 molécule^{-1} s^{-1} (Laufer)

Les données partielles dont on peut disposer (cf. valeurs données ci-dessus) suggèrent que les réactions [8], [9] et [10] ont des constantes de vitesse comparables à celles des réactions [5], [6] et [7] proposées par Hiraoka et al. On tient compte pour écrire la réaction [5] du fait que dans un plasma CH_2 se trouve excité électroniquement et donc sous la forme $^1CH_2$.

Les réactions proposées par Hiraoka doivent donc être largement prépondérantes dans la mesure où la concentration en CH_4 est très supérieure dans tous les cas à celle en radicaux CH_x (puisqu'il s'agit d'un plasma froid).

Étude des ajouts

Nous nous sommes ici intéressés aux résultats obtenus en ajoutant au méthane des quantités plus ou moins importantes d'hydrogène, d'oxygène ou de dioxyde de carbone.

Les travaux déjà réalisés au laboratoire sur le couplage thermique du méthane (5) avaient montré que la dilution par l'hydrogène permettait d'accroître le rendement d'hydrocarbures en C_2 et de diminuer la formation de coke. Nous avons pu vérifier que la même influence se retrouvait en milieu plasma, et de façon d'autant plus nette que la puissance incidente était élevée. Toutefois à forte dilution nous avons observé que les rendements en hydrocarbures en C_2 diminuaient à cause de la moindre puissance micro-ondes disponible par mole de méthane.

L'ajout de faibles quantités d'oxygène dans le plasma n'a pas par contre permis de mettre en évidence un effet accélérateur important comme cela avait été le cas pour la pyrolyse d'alcanes en C_2–C_4 (16).

Les résultats les plus intéressants ont été obtenus avec des ajouts de dioxyde de carbone. Pour un mélange équimolaire CH_4–CO_2 nous avons observé à la fois une augmentation de

© 1998 CNRC Canada

la conversion du méthane et du rendement en hydrocarbures en C_2, d'autant plus marquée que la puissance incidente était élevée (avec P_i = 160 W et DCH$_4$ = 100 Ncc/min, le rendement global en hydrocarbures en C_2 était égal à 34 % avec du méthane pur et 41 % avec un mélange équimolaire CH_4–CO_2). Il est à noter que l'effet positif de ces ajouts pourrait présenter un intérêt du point de vue de l'environnement dans la mesure où les fortes quantités de dioxyde de carbone dégagées, en particulier par les combustions au niveau industriel, posent de façon de plus en plus aiguë le problème de l'effet de serre.

Discussion — comparaison avec les résultats d'autres auteurs

Dans la présente étude, les produits pris en compte dans les analyses ont été le méthane, les hydrocarbures en C_2 et l'hydrogène (avec dans certains cas particuliers la recherche d'hydrocarbures en C_3 et en C_4, qui se sont révélés être formés en faibles quantités).

Les bilans obtenus dans le cas du plasma de méthane pur pour les éléments carbone et hydrogène s'avèrent satisfaisants lorsque les conditions d'excitation du méthane sont relativement douces (faible puissance micro-ondes incidente, donc conversion limitée). Il apparaît bien que les hydrocarbures en C_2 et l'hydrogène sont les produits formés de façon majoritaire dans ces conditions expérimentales.

Par contre, pour des conditions d'excitation plus sévères, c'est-à-dire avec des conversions plus élevées, les bilans de matière deviennent de moins en moins bons, en particulier en ce qui concerne l'élément carbone. Parallèlement nous observons un accroissement de la vitesse d'encrassement du réacteur et du piège en silice par des produits solides riches en carbone (goudrons et coke).

Ces produits se forment principalement par polymérisation de l'acétylène soit en chaînes carbonées beaucoup plus longues, soit en noyaux aromatiques.

En fait, nous avons dû nous contenter d'un bilan simplifié, compte tenu de la complexité d'une analyse complète de l'ensemble des produits, y compris les difficultés liées au piégeage de certaines fractions lourdes. De plus, il faudrait inclure dans ces bilans les dépôts de carbone sur les parois du réacteur, ce qui impliquerait leur transformation en CO_2 et le dosage correspondant.

Compte tenu du caractère exploratoire de ce travail, il nous a paru prioritaire de mettre au point le montage expérimental et surtout de fixer les conditions de formation d'un plasma stable. Un autre objectif essentiel était de réaliser une étude paramétrique aussi complète que possible de manière à déterminer les conditions expérimentales permettant d'obtenir des rendements intéressants en hydrocarbures en C_2.

Il est certain également qu'une analyse plus poussée du mécanisme réactionnel serait intéressante, en particulier au niveau de l'identification des processus élémentaires et de la nature des intermédiaires réactifs. De ce point de vue, l'utilisation de méthodes spectroscopiques adaptées pourrait être un moyen intéressant d'identification de ces espèces. La connaissance suffisamment précise d'un mécanisme réactionnel est un des moyens d'amélioration d'un procédé car elle permet d'agir sur les processus importants. C'est par exemple une des approches qui a été développée dans le cas du couplage oxydant du méthane.

Un autre point que nous n'avons pas abordé dans cette étude compte tenu de l'approche plus «chimique» que nous avons retenue est la comparaison de l'efficacité de différentes cavités et c'est effectivement un aspect qui pourrait être abordé avec profit.

Au cours de cette étude, nous avons eu connaissance de travaux voisins sur la dimérisation du méthane par plasmas micro-ondes : (*i*) les travaux d'Oumghar et coll. sur l'activation du méthane à l'aide d'un plasma différé d'air ou d'azote (8, 17); (*ii*) ceux d'Huang et Suib sur la dimérisation du méthane par un plasma direct (18, 19); (*iii*) ceux de Rusanov sur la production d'hydrogène par pyrolyse de gaz naturel dans un réacteur plasma micro-ondes (20).

Travaux d'Oumghar et al. (8, 17)

Le travail effectué par A. Oumghar et al. était basé sur l'excitation du méthane à l'aide d'un plasma différé d'air ou d'azote. Le système de création du plasma est très voisin de celui que nous avons employé (applicateur micro-ondes avec cavité résonnante parallélépipédique). Toutefois la méthode d'excitation du méthane n'est pas la même.

Dans notre montage le méthane était introduit à l'entrée du réacteur pour former un plasma et nous pouvions considérer que la zone réactionnelle était constituée par la portion du tube à décharge située à l'intérieur de la cavité micro-ondes. Le domaine de puissance incidente était limité à environ 180 W dans le meilleur des cas pour éviter le cokage du réacteur et la pression de méthane pouvait varier entre 5 et 25 torr.

Dans le montage par plasma différé le méthane est introduit dans la post-décharge d'un plasma d'azote ou d'air. Le problème du cokage est éliminé car les gaz plasmagènes utilisés ne créent pas d'encrassement. La puissance plasma utilisée peut donc être beaucoup plus élevée (de l'ordre de 400 à 800 W). C'est du reste nécessaire dans la mesure où le méthane n'est excité que de manière indirecte. Les conditions de la réaction sont de toute façon beaucoup plus douces et aucune formation de produits lourds n'est observée.

Chacune des deux installations possède donc ses paramètres propres. Dans le cas du plasma différé il est possible d'étudier l'influence sur les résultats de la distance d'introduction du méthane par rapport au guide d'ondes; par contre il devient impossible de déterminer de façon exacte la zone de réaction et donc de calculer un temps de passage.

Il serait assez fastidieux de faire ici une comparaison détaillée en faisant varier les différents paramètres communs (débit de méthane, pression dans la zone réactionnelle et puissance absorbée par le gaz).

Nous pouvons toutefois retenir que l'injection de méthane en post-décharge d'un plasma d'azote conduit à des résultats voisins de ceux obtenus avec notre montage, tout en nécessitant des puissances micro-ondes fortement supérieures. Pour des pressions de l'ordre de 10 torr dans les deux cas, on obtient avec un plasma direct (P_i = 80 W) environ 20 % de rendement en hydrocarbures en C_2 pour une conversion de 40 % du méthane de départ, et en post-décharge d'un plasma d'azote (P_i = 800 W), 14 % de rendement pour une conversion de 29 %. Dans les deux cas les sélectivités obtenues en hydrocarbures en C_2 sont de l'ordre de 50 %.

© 1998 CNRC Canada

Par contre, l'injection de méthane en post-décharge d'un plasma d'air conduit à des conversions beaucoup plus fortes (de 60 à 80 %). Mais la sélectivité obtenue en hydrocarbures en C_2 est dans ce cas beaucoup plus faible (entre 16 et 34 %) car il se forme des quantités importantes de CO. Ceci nous conduit à penser que l'utilisation d'un plasma d'air pour exciter le méthane paraît être mieux adaptée à la fabrication de gaz de synthèse $CO + H_2$ et pourrait trouver des applications telles que le réformage embarqué de gaz naturel pour l'alimentation de piles à combustibles.

Il est intéressant également de considérer que la conversion de méthane varie de façon beaucoup plus nette avec la puissance absorbée dans le cas d'un plasma direct. Nous pouvons supposer que dans le cas d'un plasma différé les pertes augmentent beaucoup plus rapidement.

Travaux de Huang et Suib (18, 19)

Ces travaux se rapprochent beaucoup des nôtres puisqu'il s'agit d'une étude en plasma direct avec une puissance de 100 W à une fréquence fixe de 2,45 GHz, les pressions de méthane étant de l'ordre de 10 à 100 torr. Deux types de cavités ont été essayés : le type Beenakker (21) et le type Evenson (22). Il a été observé, en accord avec nos résultats, que le type la conversion du méthane dépend de la pression, de la puissance et du débit.

Un certain nombre d'observations se rapprochent des nôtres, y compris sur l'aspect visuel du plasma; des problèmes de cokage ont également été observés.

Cependant, les auteurs n'ont pas séparé l'éthylène de l'acétylène et il n'est donc pas possible de confirmer les observations faites sur la répartition des produits.

Des sélectivités en C_2 de l'ordre de 35 % pour des conversions de l'ordre de 25 % ont été atteintes. Les résultats obtenus suggèrent aussi aux auteurs que l'éthane serait le produit primaire et que les autres espèces en C_2 seraient de nature secondaire, alors que d'après le mécanisme de Hiraoka, Aoyama et Morise, les trois hydrocarbures en C_2 seraient de nature primaire, parce que formés par réaction entre une molécule de méthane et un radical.

Les résultats obtenus par ces auteurs suggèrent que la cavité Beenakker est la plus efficace. Des conversions de l'ordre de 90 % ont été atteintes alors que, dans notre cas (cf. fig. 4), nous nous sommes bornés à 40 % avec des rendements de l'ordre de 15 % en C_2. Huang et Suib ont atteint des sélectivités en C_2 pouvant atteindre 50 %, avec une sélectivité maximale pour une conversion du méthane de l'ordre de 20 %.

Travaux de Rusanov (20)

Ces travaux menés à l'institut Kurchatov concernent un procédé de production d'hydrogène par pyrolyse de gaz naturel dans un réacteur plasma. Un montage pilote fonctionne à ce jour sur le site et les auteurs affirment que ce procédé serait très économe en énergie (0,3 kWh (1 kWh = 3,6 MJ) par m^3 d'hydrogène), mais il se pose le problème de l'utilisation du noir de carbone ainsi formé.

Conclusion

Les résultats et comparaisons précédents montrent que le méthane peut être converti en hydrocarbures en C_2 en plasmas micro-ondes avec des rendements intéressants, comparables avec ceux obtenus par d'autres procédés. Il faut également souligner qu'à ce stade de nos recherches, nous n'avons pas cherché à optimiser la conception de la cavité résonnante. Le caractère exploratoire de notre travail a fait que nous avons surtout voulu déterminer les possibilités et les limites de l'activation par plasma froid micro-ondes.

En fait, les problèmes qui restent posés à ce stade paraissent relever de deux domaines : fondamental et appliqué.

Sur le plan fondamental, il apparaît clairement qu'il serait utile de mieux connaître le mécanisme réactionnel, en particulier la nature et l'état des espèces actives propageant la réaction, ainsi que les interactions électrons-matière. Si dans un plasma à pression réduite, la température du gaz est inférieure à celle des électrons en raison de l'état hors équilibre, il serait intéressant d'avoir une meilleure connaissance de ces paramètres. Les aspects énergétiques présenteraient également de l'intérêt.

Sur le plan appliqué, il paraît utile de comparer ce procédé aux deux procédés de conversion directe du méthane qui ont déjà été mentionnés dans l'introduction : le couplage oxydant et le couplage thermique. Comme nous l'avons rappelé, le principal inconvénient du couplage oxydant est son rendement limité à 25 % environ par passage; compte tenu des séparations et recyclages nécessaires, ce rendement est insuffisant pour permettre l'industrialisation du procédé. Il faut noter également que la formation parallèle de CO_2 est aussi un inconvénient sérieux.

Quant au couplage thermique, ses principaux inconvénients sont le niveau des températures nécessaires (1200°C) d'où des problèmes de tenue des matériaux et l'utilisation d'un ballast d'hydrogène. Par ailleurs, il se forme également du coke et de nombreux produits indésirables, dont des fractions relativement lourdes, précurseurs des suies et des dépôts carbonés.

Si l'on se reporte aux résultats obtenus dans la présente étude, l'excitation du méthane en plasma froid a permis d'obtenir des rendements atteignant 40 % d'hydrocarbures en C_2. Toutefois, les quantités de goudrons et de coke qui se forment simultanément constituent un inconvénient proche de celui mentionné pour le couplage thermique. L'acétylène qui, dans les deux cas, est un produit prépondérant de la réaction présente moins d'intérêt industriel que l'éthylène.

Il faut surtout revenir sur le problème de la pression d'expérience. Alors que dans les procédés de couplage thermique ou oxydant la réaction a lieu à pression atmosphérique (dilution par l'hydrogène dans le premier cas, par l'azote dans le second), la pression totale de méthane dans le plasma ne peut guère dépasser quelques dizaines de torr, condition sine qua non pour limiter le phénomène de cokage.

Signalons toutefois que ceci ne constitue pas un obstacle rédhibitoire, et que certains procédés industriels fonctionnent déjà sous pression réduite. Nous pouvons citer par exemple la distillation sous vide utilisée pour séparer les fractions lourdes dans les installations de raffinage.

Malgré ces limitations et réserves, la réaction de dimérisation du méthane par plasmas micro-ondes mérite d'être étudiée et développée, tant d'un point de vue fondamental que d'un point de vue plus appliqué. Les potentialités de la technique sont réelles et on peut envisager d'autres applica-

© 1998 CNRC Canada

tions. Les travaux de l'Institut Kurchatov paraissent à cet égard intéressants, d'autant qu'ils ont été étendus au traitement de l'hydrogène sulfuré (pilote de la raffinerie d'Orenburg dans l'Oural). De plus ces procédés sont facilement interruptibles et constituent un moyen intéressant d'utilisation de l'énergie électrique dans des procédés chimiques.

Remerciements

Ce travail a été financé par Electricité de France, Direction des Etudes et des Recherches. Les auteurs remercient Monsieur Joseph Chapelle, Professeur à l'Université d'Orléans (UMR 6606 CNRS) pour ses conseils et des discussions intéressantes et fructueuses.

Bibliographie

1. G.E. Keller et M.M. Bhasin. J. Catal. **73**, 9 (1982).
2. J.G. McCarty, A.B. McEwen et M.A. Quinlan. Communication à l'International Gas Research Conference, Tokyo, Japan. 6–9 novembre 1989.
3. P. Barbe. Thèse de Doctorat INPL, Nancy (1993).
4. N. Gueritey. Thèse de Doctorat INPL, Nancy (1996).
5. C. Gueret. Thèse de Doctorat INPL, Nancy (1993).
6. F. Billaud, C. Gueret, F. Baronnet et J. Weill. Ind. Eng. Chem. Res. **31**, 2748 (1992).
7. H. Tokoto. Thèse de Doctorat INPL, Nancy (1990).
8. A. Oumghar, J.C. Legrand, N. Diamy, A.M. Turillon et R.I. Ben-Aïm. J. Phys. III, **4**, 99 (1994).
9. G. Moreau, O. Dessaux et P. Goudmand. J. Phys. E: Sci. Instrum. **6**, 11 (1983).
10. M.H. Back et R.A. Back. Pyrolysis: theory and industrial practice. Academic Press, New York. 1982. pp. 1–24.
11. L. Okeke et H. Stori. Plasma Chem. Plasma Process. **11**, 489 (1991).
12. K. Hiraoka, K. Aoyama et K. Morise. Can. J. Chem. **63**, 2899 (1985).
13. R. Avni, U. Carmi, I. Rosenthal et A. Inspektor. 6th Int. Symp. on Plasma Chemistry, Montreal, Canada. 24–28 juillet 1983.
14. B.H. Mahan et R. Mandal. J. Chem. Phys, **37**, 207 (1962).
15. E.M. Magee. J. Chem.Phys. **39**, 855 (1963).
16. R. Martin, M. Niclause et G. Scacchi. ACS Symp. Ser. **32**, 37 (1976).
17. A. Oumghar. Thèse de Doctorat, Université Pierre et Marie Curie, Paris (1992).
18. J. Huang et S.L. Suib. J. Phys. Chem. **97**, 9403 (1993).
19. J. Huang et S.L. Suib. Res. Chem. Intermed. **20**, 133 (1994).
20. V.D. Rusanov. Concept of zero emission vehicle based on hydrogen and nontraditional ways of large scale hydrogen production. Séminaire Franco-Russe Inter-Académie des Sciences. Paris, 25–26 sept 1996.
21. C.I.M. Beenakker. Spectrochim. Acta, **31B**, 483 (1976).
22. F.C. Fehsenfeld, K.M. Evenson et H.P. Broida. Rev. Sci. Instrum. **36**, 294 (1965).

© 1998 CNRC Canada

Synthèse critique de la caractérisation électrochimique de zéolithes et d'aluminophosphates chimiquement modifiés

Lionel Roué, Emmanuel Briot et Fethi Bedioui

Résumé : L'électrochimie a montré sa capacité à nous renseigner sur le comportement rédox des zéolithes et tamis moleculaires chimiquement modifiés. Cependant, la caractérisation par voltampérométrie cyclique de ces nouveaux matériaux souffre de certaines zones d'ombre telle que l'influence de l'électrolyte support, du solvant, du mode de fixation de l'espèce électroactive et de son encombrement sur la réponse électrochimique. Aussi, avant d'entreprendre la caractérisation électrochimique de ces matériaux, il est indispensable d'analyser le processus électrochimique afin de mieux comprendre les phénomènes de compensation de charge et de transfert électronique. À cet effet, nous analyserons dans cette revue le comportement électrochimique de complexes et d'espèces électroactives se différenciant essentiellement par leur mode d'incorporation et de fixation dans le systeme microporeux des zeolithes et de certains tamis moléculaires. Bien que la nature du processus électrochimique demeure un peu confuse, il semble que les divergences d'opinion proviennent principalement du fait que les matériaux utilisés par les différentes équipes s'intéressant à ce sujet ne sont pas équivalents.

Mots clés : électrochimie, voltampérométrie cyclique, électrode modifiée, zéolithe, complexe rédox, encapsulation, tamis moléculaire, aluminophosphate.

Abstract: Zeolites that have been chemically modified by incorporating transition metal complexes in their porous network and molecular sieves chemically modified by incorporating transition metal in their framework have led to numerous applications of which the most widespread is undoubtfully catalysis. However, the catalytic activity of these inorganic compounds is still not well understood and there is a lack of evidence concerning the encapsulation efficiency of complexes within the zeolites and the location of transition metals inside the framework of molecular sieves. Numerous studies have shown that zeolite encapsulation has an influence on the redox behaviour of these complexes, such as in preventing aggregation or the dimerization process. Moreover, analysis of the electrochemical process at this type of modified electrode demonstrates solvant and electrolyte effects on the electroactivity of the encapsulated complexes. However, these different studies highlighted the unsatisfactory electrochemical accessibility of intrazeolitic or framework species. Thus, we undertake here a discussion of the different strategies reported in the literature aimed at promoting the electroactivity of these molecular materials.

Key words: electrochemistry, cyclic voltammetry, modified electrode, zeolite, redox complex, encapsulation, molecular sieve, aluminophosphate.

I. Introduction

I. 1. Généralités sur les zéolithes

Les zéolithes appartiennent à la grande famille des aluminosilicates dont font également partie les argiles. Elles sont constituées d'une structure cristalline rigide comprenant des canaux et des cavités de tailles variables. Du point de vue de la systématique, le terme de « zéolithe » ne s'applique qu'aux aluminosilicates microporeux non modifiés. En accord avec ce qui est couramment pratiqué dans la littérature, nous utiliserons le terme de « zéolithe » pour tous les aluminosilicates dont nous parlerons, qu'ils soient modifiés ou non. Nous réserverons l'utilisation du terme de « tamis moléculaire » à tous les matériaux apparentés aux zéolithes (en particulier

Reçu le 7 novembre 1997.[1]

L. Roué,[2] E. Briot[3] et F. Bedioui.[4] Laboratoire d'électrochimie et de chimie analytique (U.M.R. n° 7575 du Centre national de la recherche scientifique), École nationale supérieure de chimie de Paris, 11 rue Pierre et Marie Curie, 75231 Paris Cedex 05, France.

1.Révision reçue le 26 juin 1998.
2.Adresse actuelle: Institut national de la recherche scientifique — Énergie et materiaux, 1650, Bd Lionel Boulet, case postale 1020, Varennes, QC J3X 1S2, Canada.
3.Adresse actuelle: Laboratoire des systèmes interfaciaux à l'échelle nanométrique, T54–55 case 196, 4 Place Jussieu, 75252 Paris cedex 05, France.
4.Auteur à qui adresser toute correspondance. Téléc : 33 147 27 67 50. Mél : bedioui@ext.jussieu.fr

© 1998 CNRC Canada

les aluminophosphates), dont la composition chimique est différente de celle des zéolithes. Dans le groupe de matériaux constitué par les zéolithes et les tamis moléculaires, on dénombre actuellement 40 zéolithes naturelles et environ 200 matériaux synthétiques (1–3).

La charpente des zéolithes est constituée d'un enchaînement de tétraèdres de SiO_4 et AlO_4 reliés entre eux par des sommets oxygène. Le degré formel d'oxydation des ions aluminium est de trois et leur coordinence est de quatre, ce qui implique que les tétraèdres de AlO_4 sont porteurs d'une charge négative. Pour satisfaire au principe d'électroneutralité, ces charges négatives sont compensées par des cations mobiles généralement alcalins ou alcalino-terreux. La présence de ces cations extra-réseaux confère naturellement des propriétés d'échangeur de cations à la zéolithe. La formule générale d'une zéolithe peut s'écrire de la manière suivante : $M^+{}_m\,[(AlO_2)_m(SiO_2)_n] \cdot x\,H_2O$. Dans cette formule, M^+ représente le cation extra-réseau compensateur de charge et x le nombre de molécules d'eau qui est une fonction du volume poreux de la zéolithe et de son hydrophilie. La partie entre crochet représente à proprement dit la charpente de la zéolithe. La nature du cation compensateur de charge, le rapport Si/Al, la taille des cristaux et la structure de la zéolithe sont les paramètres principaux dont dépend la stabilité de ces matériaux.

La zéolithe NaY compte parmi les plus utilisées, tant dans l'industrie que dans le cadre d'études théoriques à l'échelle du laboratoire. Sa popularité s'explique principalement par le fait que cette zéolithe a été l'une des premières à être synthétisée, et les nombreuses études qui ont été produites sur cette zéolithe ont permis d'avoir une bonne connaissance de ses propriétés physico-chimiques et de sa réactivité. De plus, les dimensions de la zéolithe NaY et notamment les diamètres d'entrée et interne de sa supercage s'accordent assez bien avec un certain nombre de complexes dont nous parlerons un peu plus loin dans ce chapitre. La figure 1 présente la structure de la zéolithe faujasite (et des zéolithes synthétiques apparentées X et Y) ainsi que quelques-unes de ses caractéristiques physico-chimiques. C'est ce matériau qui est généralement utilisé pour y incorporer des complexes de métaux de transition.

L'agencement de cette structure, comme celui de toutes les zéolithes, se fait à partir d'unités secondaires constituées d'un assemblage de polyèdres. Dans le cas de la faujasite, ces unités de base sont des cubooctaèdres (ou cage sodalite ou encore β-cage) qui sont reliés par l'intermédiaire de prismes hexagonaux. L'agencement de ces structures de base délimite un espace intérieur que l'on nomme supercage (ou α-cage) d'un diamètre interne de 13 Å et d'un diamètre d'ouverture de 7,4 Å. La maille élémentaire (ou cellule unitaire) de la zéolithe faujasite est cubique. Elle est constituée de 8 supercages et a pour formule à l'état hydraté : $Na_{56}[(AlO_2)_{56}(SiO_2)_{136}] \cdot 250\ H_2O$.

La figure 1 montre également la répartition des sites anioniques au sein de la cavité zéolithique. Certains sont localisés dans les prismes hexagonaux (SI) et d'autres au niveau des cages sodalites (SU, SI′, SII et SII′) et de la supercage (SII*, SIII, SIV et SV). Ces sites anioniques représentent bien sûr les positions privilégiées qu'occupent les cations compensateurs de charge. Cependant, l'occupation de ces sites varie en fonction de la nature du cation compensateur de charge (charge, taille), de la température et de l'état d'hydratation de la zéolithe. Les molécules polaires de petite taille telle que l'eau peuvent en effet venir se positionner à proximité de ces sites anioniques.

I. 2. Généralités sur les aluminophosphates

Historiquement, il semble que ce soit l'utilisation d'agents structurants organiques lors de la synthèse des zéolithes qui ait permis d'envisager la synthèse de tamis moléculaires dont la nature chimique et l'organisation structurale sont différentes des zéolithes classiques. L'un des groupes les plus importants de ces tamis moléculaires est sans aucun doute celui des aluminophosphates dont on dénombre une trentaine de structures différentes. C'est en 1982 que Wilson et al. (4) ont synthétisé pour la première fois un aluminophosphate microporeux et cristallin. Depuis lors, la famille des aluminophosphates (AlPO) s'est considérablement agrandie avec la synthèse de silicoaluminophosphates (notés SAPO (5)) et de métalloaluminophosphates (notés MeAPO (6)). Dans la famille des MeAPO, le métal qui substitue Al(III) ou P(V) selon les cas peut être le cobalt, le fer, le magnésium, le manganèse, le zinc, l'arsenic, le gallium, le bore, le beryllium, le germanium, le vanadium, le chrome, le lithium ou le titane, et cette liste n'est bien sûr pas exhaustive.

D'une manière similaire à ce qui existe pour les aluminosilicates, la structure des aluminophosphates est constituée de tétraèdres de AlO_4 et de PO_4 reliés entre eux par des sommets oxygène. La particularité de ces structures provient de l'exacte parité qui existe entre les ions Al(III) et les ions P(V) du réseau des AlPO. Il en résulte que la charpente de ces tamis moléculaires est neutre. De plus, les liaisons P—O—P et Al—O—Al n'existent pas dans ces matériaux. La structure des AlPO peut être appréhendée en considérant que tous les matériaux peuvent être obtenus à partir d'une construction mettant en relation des réseaux bidimensionnels (2-D), c'est à dire situés dans un plan. Ces réseaux sont bien sûr constitués de tétraèdres TO_4 dans lequel l'atome T représente indistinctement l'aluminium ou le phosphore, mais la représentation dans le plan impose de ne considérer que trois connexions.

La figure 2 représente la structure hexagonale à laquelle appartient le tamis moléculaire AlPO-5. Les atomes d'aluminium ou de phosphore se situent au niveau des sommets et les atomes d'oxygène relient entre eux ces sommets. Par soucis de clarté, les atomes d'oxygène ne sont pas représentés sur cette figure. La classification des aluminophosphates est encore plus complexe que celle des zéolithes car elle dépend de la coordinence des atomes d'aluminium. Nous ne détaillerons pas cette partie et nous retiendrons simplement que la structure AlPO-5 possède des atomes d'aluminium tétracoordonnés. Ces structures sont thermiquement très stables et peuvent résister à des températures allant jusqu'à 1000°C. La parité entre les atomes d'aluminium et de phosphore dans la structure d'AlPO-5 implique que la charpente de ce tamis est globalement neutre et qu'il ne possède donc pas de propriété d'échangeur d'ions. Les aluminophosphates possèdent donc quelques propriétés intéressantes mais ce sont les modifications apportées à ces structures qui sont à l'origine de l'engouement des chercheurs pour ces matériaux.

© 1998 CNRC Canada

Fig. 1. Structure et caractéristiques physico-chimiques de la faujasite.

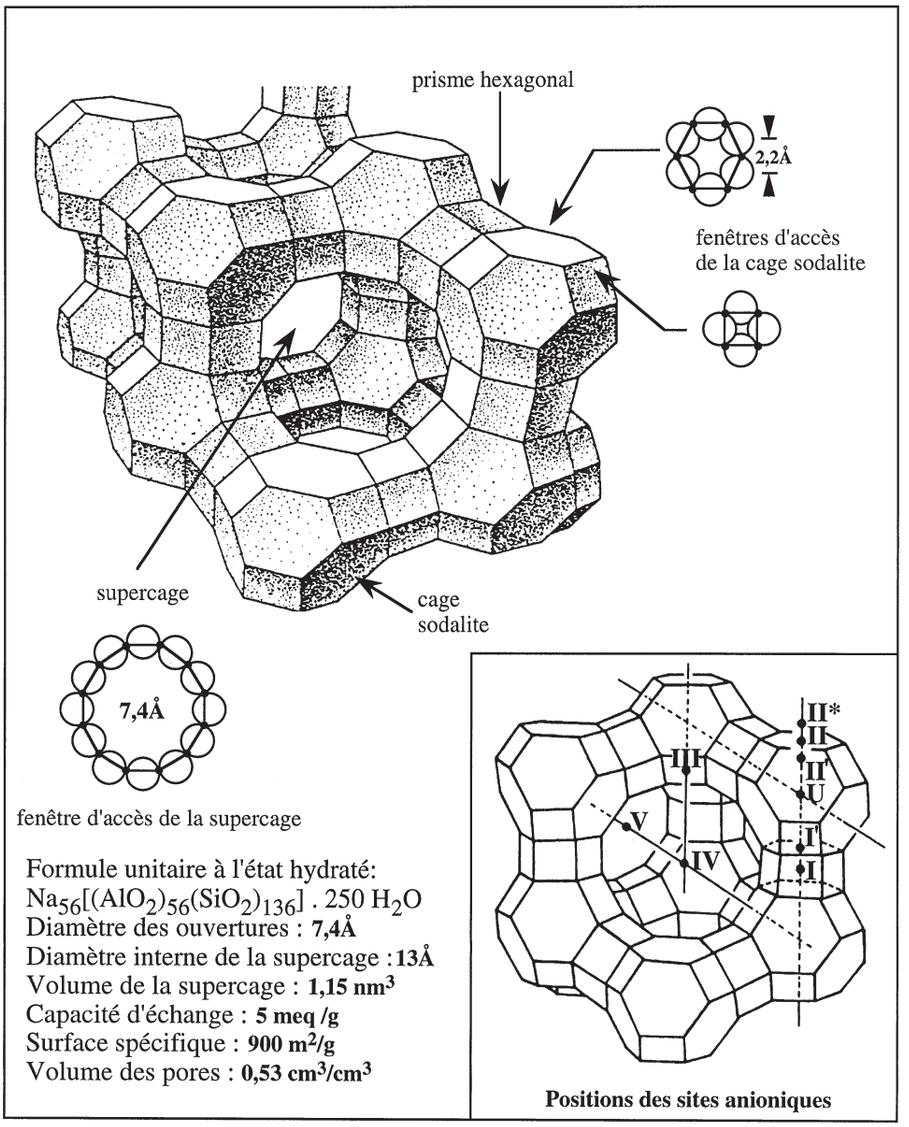

II. Modification chimique des zéolithes et des aluminophosphates

Malgré l'importante variété des zéolithes et des tamis moléculaires qu'il est possible de synthétiser, il arrive parfois que les caractéristiques physico-chimiques du matériau final ne correspondent pas exactement avec l'application envisagée. Pour remédier à cela, il est alors possible d'effectuer un certain nombre de modifications de ces matériaux qui peuvent intervenir pendant la synthèse ou après celle-ci.

II. 1. Modifications des zéolithes

Les modifications de la porosité, de l'acidité et de la charpente des zéolithes ont déjà été largement décrites dans la littérature (3). Notre propos s'orientera donc plus précisément vers la modification des zéolithes par incorporation de complexes de métaux de transition dans leur système poreux. En effet, dans le contexte de la catalyse, de nombreux efforts ont été fournis pour immobiliser des catalyseurs agissant habituellement en phase homogène sur des supports solides comme la silice, l'alumine ou les polymères (7, 8). Dans des conditions idéales, de tels catalyseurs hybrides combinent les avantages de la catalyse homogène (conditions douces, réactivité spécifique, etc.) et de la catalyse hétérogène tout en minimisant leurs désavantages respectifs (9). Cependant, ces catalyseurs n'ont pas toujours permis d'aboutir aux résultats escomptés, principalement à cause de leur manque de sélectivité. L'idée d'incorporer ces complexes au sein des cavités zéolithiques est donc apparue comme une solution à ce défaut de sélectivité.

Dès lors, de nombreuses équipes se sont intéressées à la modification des zéolithes par incorporation de diverses espèces telles que des cations métalliques (Ag^+, Cu^{2+}, Fe^{3+}, etc.), des clusters (Pt_5, $Pd_{10}Fe_3$, CdSe, etc.), des molécules

© 1998 CNRC Canada

Fig. 2. Représentation de la structure hexagonale de AlPO-5. Diamètre interne des canaux : 7,4 Å. Formule d'une cellule unitaire : $Al_{12}P_{12}O_{48} \cdot qH_2O$.

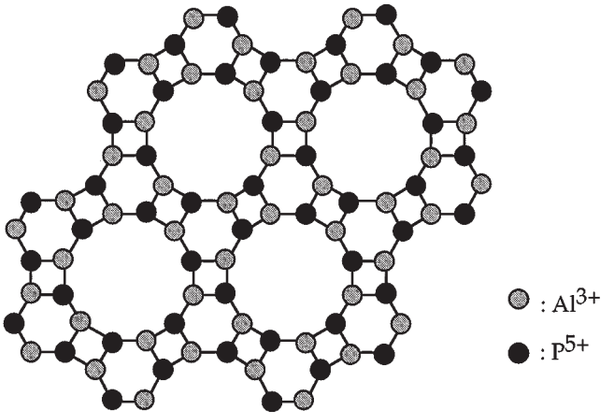

organiques (polypyrrole, méthylviologène, etc.) et des complexes organométalliques (métallocènes, métallophtalocyanines, etc.) (9–12).

Les méthodes d'incorporation des espèces au sein de la zéolithe dépendent principalement de la taille de la molécule à incorporer et de sa flexibilité. Les molécules de taille inférieure au diamètre d'ouverture des pores de la zéolithe sont incorporées par simple échange d'ions (lorsque celles-ci sont sous forme ionique) ou par adsorption en phase liquide ou gazeuse dans le cas d'espèces neutres ou lorsque la zéolithe ou le tamis moléculaire n'est pas échangeur de cation.

L'incorporation de composés dont la taille est supérieure au diamètre des ouvertures des pores de la zéolithe nécessite une méthodologie d'incorporation plus complexe que dans la cas de l'incorporation de petites molécules. Cette méthode d'incorporation est appelée « encapsulation » (néologisme inspiré de la langue anglo-saxonne et qui signifie fixation irréversible d'un complexe au sein de la cavité zéolithique). Elle a pour principe la synthèse in situ du complexe à l'intérieure des cavités de la zéolithe pour former des complexes « ship-in-a-bottle » (13). Zakharov et al. (14–17) ont été les premiers à encapsuler un complexe à base de phtalocyanine dans la zéolithe NaY en 1977. Depuis lors, de nombreuses équipes ont étudié l'encapsulation et la réactivité des complexes à base de phtalocyanines (notés Pc) et de bases de Schiff telles que le Salen (Salen = *N*,*N*′-bis(salicylaldéhyde) éthylènediimine). Les références 11 et 12 contiennent toutes les publications qui se rapportent à ce sujet et la figure 3 présente les différentes stratégies d'encapsulation. Les méthodes d'encapsulation, fonction du complexe à incorporer, peuvent être classées selon trois catégories : (*i*) la méthode dite du « ligand flexible » ; (*ii*) la méthode avec synthèse in situ du ligand; (*iii*) la synthèse de la zéolithe autour du complexe.

La méthode dite du « ligand flexible » consiste à introduire, à l'état fondu, un ligand (flexible) capable de diffuser dans le réseau poreux de la zéolithe et d'accéder aux cavités zéolithiques. Le ligand se complexe aux cations métalliques préalablement échangés avec les cations compensateurs de charge de la zéolithe. La complexation a lieu lorsque l'espace est suffisant, c'est à dire dans les grandes cavités et

Fig. 3. Les différentes stratégies d'encapsulation de complexes de métaux de transition tels que phtalocyanine (Pc) et base de Schiff (Salen = *N*,*N*′-bis(salicylaldéhyde) éthylènediimine).

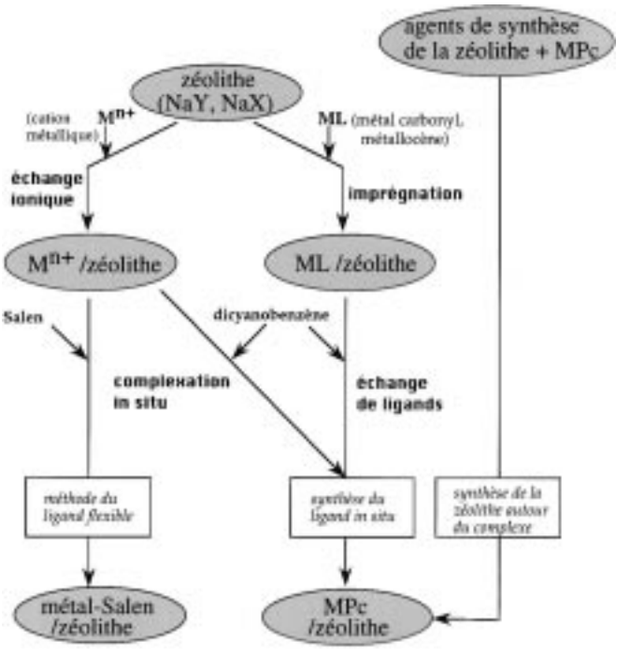

à la surface de la zéolithe. Dans la mesure où les complexes formés sont de taille supérieure au diamètre des fenêtres de ces cavités, ils sont incapables d'en sortir et se retrouvent prisonniers de la structure. Cette approche est particulièrement bien adaptée à l'encapsulation de complexes métal–Salen dans la zéolithe Y, le ligand Salen offrant la flexibilité requise. Ainsi, après coordination du métal, on obtient un complexe rigide d'une dizaine d'angström emprisonné dans des supercages d'un diamètre interne de 13 Å et dont les ouvertures ont un diamètre voisin de 7–8 Å.

La méthode avec synthèse in situ du ligand dérive de la précédente. Elle est appliquée lorsque le ligand, trop volumineux ou pas suffisamment flexible, ne peut pas pénétrer directement dans la supercage de la zéolithe. La synthèse du ligand est, dans ce cas, effectuée in situ. Cette procédure est caractéristique de l'encapsulation des métallophtalocyanines dans les zéolithes X et Y : 4 dicyanobenzènes diffusent dans la structure hôte pour se condenser autour d'un ion métallique et former le macrocycle tétradentate trop large pour sortir. La première étape, c'est à dire l'incorporation du métal au sein de la zéolithe, peut se faire soit par un simple échange ionique, soit via l'adsorption d'un métallocène ou d'un complexe métalcarbonyl. Cette étape est suivie de l'élimination des ligands (respectivement H_2O, cyclopentadiène, CO) par chauffage sous atmosphère inerte. La seconde étape consiste à additionner le dicyanobenzène à une température supérieure à sa température de fusion (140°C), l'ensemble étant agité plusieurs heures. Le dicyanobenzène diffuse dans le réseau poreux de la zéolithe pour se complexer au métal présent dans les supercages.

La méthode de synthèse de la zéolithe autour du complexe est la méthode d'encapsulation la plus récente (12). La synthèse du réseau cristallin de la zéolithe est réalisée autour du

© 1998 CNRC Canada

Fig. 4. Mécanismes de substitution isomorphe pour les structures de type AlPO-5.

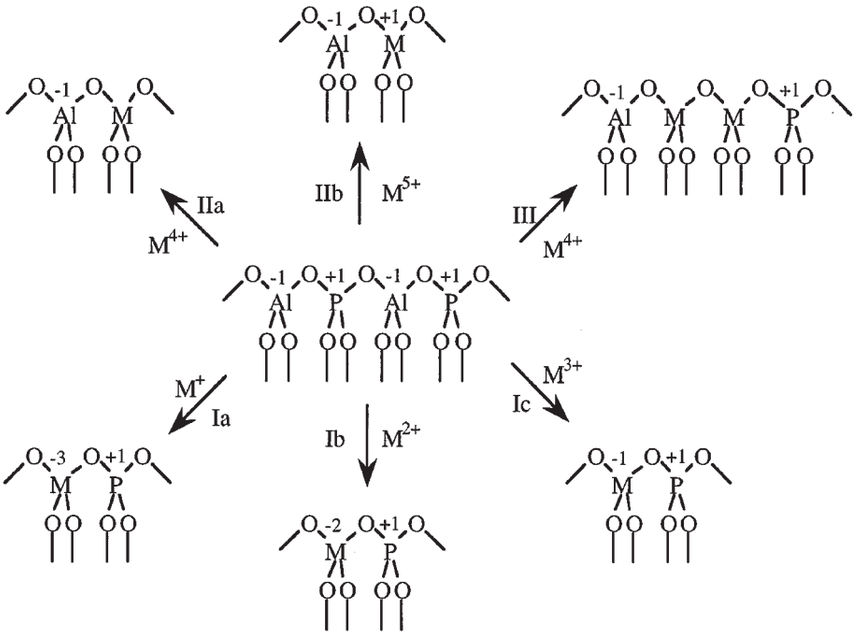

complexe qui préexiste à l'état dissout dans la solution de germination. L'élaboration de cette « nouvelle » méthode d'encapsulation a été motivée par les limitations et désavantages des deux méthodes précédentes. En effet, cette méthode permet d'obtenir des complexes intra-zéolithiques parfaitement définis sans contamination du système poreux de la zéolithe par des ligands libres, par le métal non complexé ou par des oxydes métalliques. Les contraintes de taille complexe/zéolithe sont en outre moins restrictives, l'encapsulation n'étant pas limitée par des problèmes diffusionnels. Cependant, des modifications des paramètres de maille de la zéolithe paraissent inévitables. L'absence de résultats publiés sur la cristallinité de la zéolithe ne permet pas d'infirmer cette opinion. C'est également la méthode idéale pour l'encapsulation de complexes volumineux comme les métallophtalocyanines subtituées (cas des perfluorophtalocyanines de cobalt et de cuivre, incorporées dans la zéolithe X). Cependant, le complexe à encapsuler doit être suffisamment stable pour supporter les conditions opératoires de la synthèse. C'est le cas des métallophtalocyanines.

Il est important de préciser ici que quelque soit la procédure d'encapsulation choisie, il est extrêmement important de procéder à un rinçage extensif de la zéolithe modifiée afin de garantir l'absence totale de complexes formés à l'exterieur des supercages (c'est à dire à la surface de la zéolithe).

II. 2. Modifications des aluminophosphates

D'une manière similaire à ce qui a été dit dans le cas des zéolithes classiques, les tamis moléculaires peuvent subir plusieurs types de modifications pendant ou après la synthèse, entraînant des changements au niveau de leurs propriétés physico-chimiques. Nous discuterons essentiellement des modifications chimiques de ces matériaux par incorporation de cations métalliques au sein même de leur réseau, et précisément dans le cas des aluminophosphates.

Par définition, une substitution isomorphe correspond au remplacement d'un élément d'un réseau cristallin par un autre élément possédant un rayon ionique et une coordinence proche de l'élément substitué. Cette substitution est effectuée pendant la synthèse. Dans le cas des aluminophosphates, plusieurs sortes de substitutions isomorphes sont possibles. La complexité du processus provient de la présence de deux atomes différents dans le réseau et de la diversité des états de coordination possibles des atomes d'aluminium. L'aluminium et le phosphore sont en effet tous les deux susceptibles d'être substitués. Ainsi, les éléments qui se substituent à l'aluminium dans les aluminophosphates peuvent adopter la coordinence IV, V ou VI.

Les mécanismes de substitution isomorphe sont au nombre de trois et sont classés en fonction de l'atome substitué. La figure 4 résume ces trois types de mécanismes. Le mécanisme I concerne la substitution des atomes d'aluminium, le mécanisme II celle des atomes de phosphore et le mécanisme III traduit la substitution de paires adjacentes d'atomes d'aluminium et de phosphore (18, 19) et ne concerne que la substitution par le silicium. Dans le cas des aluminophosphates, c'est le degré d'oxydation formel de l'ion substituant plutôt que son rayon ionique qui détermine s'il substitue l'aluminium ou le phosphore. Les mécanismes I et II peuvent être détaillés selon la valence de l'élément introduit : monovalents (Ia), divalents (Ib), trivalents (Ic), tétravalents (IIa) et pentavalents (IIb). Aucun autre mécanisme n'est décrit dans la littérature pour la substitution des atomes d'aluminium et de phosphore dans les AlPO, car ils pourraient conduire à l'obtention d'une charpente chargée positivement ou au contraire à une densité de charge négative trop importante. Ainsi, de nombreux cations métalliques ont pu être incorporés dans la structure des AlPO et il n'existe pas

© 1998 CNRC Canada

moins de 18 éléments dont l'incorporation au sein de la structure AlPO a pu être mise en évidence : Li(I), Co(II), Fe(II), Mg(II), Mn(II), Zn(II), Be(II), Ni(II), Sn(II), B(III), Ga(III), Fe(III), Cr(III), Si(IV), Ge(IV), Ti(IV), As(V) et V(V) (18).

III. Caractérisation des zéolithes et des aluminophosphates chimiquement modifiés

Après avoir effectué la synthèse d'une zéolithe et l'encapsulation d'un complexe et avant d'envisager son utilisation, il convient de se poser plusieurs questions concernant les caractéristiques physico-chimiques du matériau :

la structure du minéral est-elle préservée après l'encapsulation?

a-t-on formé le complexe souhaité?

quelle est la répartition des complexes au sein du matériau, est-elle homogène?

existe-t-il des complexes à la surface de la zéolithe? etc.

D'une manière similaire, plusieurs questions doivent être posées après la synthèse et la modification d'un tamis moléculaire :

quelle est la structure du matériau obtenu?

quels sont la coordinence, l'état d'oxydation et la position des atomes incorporés au tamis moléculaire?

la présence des éléments substitués à l'intérieur du réseau du tamis engendre-t-elle des évolutions de la structure ou de la cristallinité du matériau?

Cette liste de questions n'est pas exhaustive et elle montre combien la tâche semble ardue pour parvenir à une connaissance approfondie du matériau. Elles peuvent être résumées par deux questions fondamentales : comment prouver l'encapsulation et comment prouver l'incorporation d'un cation métallique dans la structure d'un tamis ? Répondre à ces questions est souvent délicat et nécessite la conjonction de différentes techniques d'analyses. Le choix des techniques applicables à ce type de matériaux moléculaires est vaste : analyses chimiques élémentaires, analyses de surface, microscopie électronique à haute résolution, diffraction RX, spectroscopie infrarouge à tranformée de Fourier, spectroscopie UV–visible, résonnance paramagnétique électronique, spectroscopie Mössbauer, analyses thermiques, analyses d'adsorption, modélisation et électrochimie. À ce titre, on peut citer l'étude remarquable de Paez-Mozo et al. (20), consacrée à la pthalocyanine de cobalt encapsulée dans la zéolithe Y et rassemblant l'essentiel des techniques citées ci-dessus appliquées aux différentes étapes de la synthèse (sauf l'électrochimie). À caractère plus général, la mise au point de Balkus et Gabrielov (12) mettant à jour les différentes méthodes de caractérisation de complexes intra-zéolithiques est également intéressante.

IV. Caractérisation électrochimique des zéolithes et des aluminophosphates chimiquement modifiés

L'électrochimie peut être appliquée à la caractérisation des zéolithes et aluminophosphates chimiquement modifiés. Par rapport aux autres méthodes de caractérisation, elle a l'avantage d'être économique et rapide. En outre, l'électrochimie est particulièrement intéressante parce qu'elle intervient sur le comportement rédox des entités introduites dans le système microporeux de ces matériaux. Or les propriétés rédox de ces matériaux sont directement responsables de leur activité catalytique. Ainsi, par une technique électrochimique simple comme la voltampérométrie cyclique, on peut obtenir des informations essentielles sur leur activité rédox. Même de faibles perturbations d'ordre structural sont perceptibles par des déplacements de potentiels rédox.

Parallèlement à la caractérisation de ces matériaux, l'électrochimie appliquée aux zéolithes et aluminophosphates s'est considérablement développée durant ces dix dernières années. Il est vrai que la zéolithe offre un potentiel attractif dans le domaine des électrodes modifiées. Ses propriétés de tamis moléculaire, d'échangeur de cations, de catalyseur et de structure hôte ouvrent un large champ d'investigation aux électrochimistes. L'idée directrice est de tranférer les propriétés de la zéolithe à l'électrode (pour des soucis de simplification du texte, nous utiliserons dorénavant le terme générique « zéolithe » pour designer l'ensemble des matériaux étudiés, sauf exception mentionnée dans le texte). On peut ainsi, grâce aux propriétés de sélectivité et de préconcentration de la zéolithe, obtenir des détecteurs électrochimiques performants (21–30). On peut citer comme exemple le cas de la détection ampérométrique de glucose (27) ou de dopamine, méthylviologène, Ag^+ et Cu^{2+} (29) avec une électrode à pâte de carbone contenant la zéolithe Y et la glucose oxydase ou les zéolithes A, X et Y, respectivement. La possibilité d'incorporer dans la zéolithe des espèces électroactives a conduit à la conception de matériaux moléculaires élaborés dont l'application la plus élégante est l'étude de transferts électroniques orientés (31–33). Dans le domaine de l'électrocatalyse, l'électrode composite à base de zéolithe témoigne également d'un potentiel indéniable (34–38), comme cela a été montré dans le cas de la réduction sélective de bromure de benzyle, par rapport au bromure de triphénylméthyle, par le complexe zéro valent du nickel bis-bipyridine encapsulé dans la zéolithe Y (34). L'électrochimie peut également être un moyen d'étudier des processus fondamentaux inhérents aux zéolithes telles que les cinétiques d'échange d'ions ou la diffusion intra-zéolithique d'espèces réactives (39–42). En bref, les exemples ne manquent pas pour démontrer l'intérêt de coupler zéolithe et électrochimie.

La construction d'une électrode modifiée est la première étape dans une étude électrochimique appliquée aux zéolithes. Plusieurs méthodes de modification des électrodes existent et sont reportées dans la littérature. Elles seront répertoriées ici de manière exhaustive avant d'aborder ensuite les concepts fondamentaux de l'électrochimie des zéolithes, c'est à dire les phénomènes de diffusion et de transfert électronique.

IV. 1. Fabrication de l'électrode

Le caractère isolant des zéolithes rend particulièrement délicat leur étude en électrochimie. De ce fait, le problème majeur lors de l'élaboration d'une électrode composite à base de zéolithe est d'obtenir un contact physique étroit entre le collecteur de courant et la zéolithe. La méthode la

© 1998 CNRC Canada

Fig. 5. Schéma d'une électrode du type « électrode à pâte de carbone », adapté de la reférence 46.

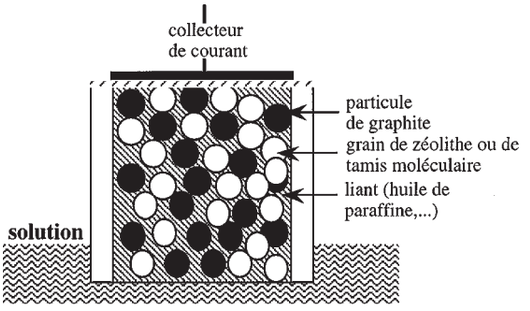

plus simple et la plus usuelle consiste à former une électrode en mélangeant intimement de la poudre de carbone et la zéolithe ou à fixer une couche de zéolithe à la surface d'une électrode. La multiplication des études électrochimiques portant sur les zéolithes depuis la fin des années 1980 a favorisé le développement de nouvelles techniques de fabrication. Ces différentes techniques ont fait l'objet de plusieurs mises au point (30, 43–46) d'où il est important de noter que chaque équipe de recherche a sa méthode de préparation. Ceci a le désavantage de rendre difficile la comparaison des travaux de chacun.

IV. 1. 1. Electrode à pâte de carbone

C'est une des méthodes les plus simples pour fabriquer une électrode composite à base de zéolithe. Un liant, le plus souvent de l'huile de silicone ou de paraffine, est additionné à un mélange poudre de graphite–zéolithe (contenant de 10 à 50 % de zéolithe). La pâte obtenue est incorporée dans un système à électrode à pâte de carbone conventionnel (fig. 5). Le principal avantage de ce type d'électrode est que la surface de l'électrode est facilement renouvelable par une simple élimination de la pâte contiguë à la solution. Ces électrodes présentent une bonne stabilité et les résultats obtenus sont en général reproductibles. L'inconvénient de ces électrodes est qu'elles nécessitent un liant. Ce liant engendre une chute ohmique non-négligeable surtout en milieu organique où l'utilisation de cette électrode est à proscrire (aussi à cause de la dissolution éventuelle de ce liant dans le solvant organique utilisé). De plus, la diffusion du liant de l'intérieur vers l'extérieur de l'électrode conduit à une accumulation du liant à la surface de l'électrode qui est susceptible d'altérer la réponse électrochimique (39). Par ailleurs, on peut estimer que les phénomènes observés sont principalement surfaciques (interface solution–électrode) car la diffusion au sein de l'électrode est limitée par sa compacité et par la présence du liant. La quantité de zéolithe impliquée est en conséquence faible (47). Cependant, cette remarque doit être nuancée. D'après l'étude de El Murr et al. (48) concernant le comportement rédox du Cu^{II} incorporé dans la mordenite, la quantité de cuivre réduit à l'électrode est supérieure de 600 fois (à 200 mV/s) à 2200 fois (à 10 mV/s) à la quantité de cuivre incorporé dans la première monocouche de zéolithe située à l'interface électrode–solution. En outre, Walcarius et al. (39) ont déterminé par chronocoulométrie l'épaisseur de l'électrode impliquée lors de la réduction du méthylviologène à 11 μm après 50 s d'expérience et à 84 μm après 1 h. La diffusion du méthylviologène dans l'électrode est par ailleurs limitée par l'état d'hydratation très partiel de celle-ci.

Shaw et Creasy (22) ont élaboré une électrode basée sur le principe de l'électrode à pâte de carbone mais avec un polymère comme agent liant. Ce polymère est formé à partir d'un mélange de styrène et de divinylbenzène; la polymérisation est initiée par le 2,2′-azobis(2-méthylpropionitrile). Ils obtiennent une électrode composite résistante. La surface est renouvelable par un simple polissage comme avec une électrode en carbone vitreux. Cette électrode montre une électroactivité vis à vis de la réduction de l'oxygène supérieure à celle obtenue avec l'électrode à pâte de carbone malgré une quantité de zéolithe huit fois moindre. La matrice polymérique gênerait moins que l'huile de silicone l'accès de la zéolithe aux espèces en solution. Toujours selon Shaw et Creasy (22), cette électrode est plus facile à utiliser, plus reproductible et le temps de réponse est plus rapide comparé à l'électrode du type pâte de carbone. L'amélioration de la reproductibilité est attribuée à une dispersion plus intime de la zéolithe avec le carbone mais aussi à une meilleur rigidité de l'électrode. La diminution du temps de réponse peut s'expliquer par des phénomènes observés purement surfaciques du fait d'une électrode faiblement poreuse vis à vis de la solution électrolytique.

IV. 1. 2. Electrode pressée

Également très simple à fabriquer, l'électrode du type électrode pressée peut être préparée avec ou sans poudre de graphite. Elle est pressée à 2 à 3 tonnes (1 t = 1000 kg) sous la forme d'une pastille. La comparaison des spectres RX avant et après pressage permet de s'assurer qu'il n' y a pas d'amorphisation notable des cristaux de la zéolithe et que la structure de celle-ci est bien preservée aprés l'action mécanique qui lui a été impartie. En l'absence de graphite, elle est utilisée entre autres comme électrode de batterie (49), comme membrane pour l'élaboration d'électrodes sélectives (50–52) ou bien encore comme électrolyte solide à haute température (53–55) sans que le problème posé par la probable existence de chute ohmique induite par l'absence de conducteur électronique ne soit pour autant clairement discuté. Préparée à partir d'un mélange zéolithe – poudre de graphite (1/1) pressé sur une grille d'acier inoxydable, ce type d'électrode a été utilisé pour la première fois par Pereira-Ramos et al. (56, 57) pour l'étude du comportement rédox de l'argent incorporé dans la mordenite. Les densités de courant mesurées sont importantes (jusqu'à 10 $mA/cm^{2)}$ et 75 % environ des ions Ag^+ initialement présents dans la zéolithe sont réductibles par coulométrie intentiostatique. C'est également le type d'électrode utilisé au laboratoire (34, 58–75). Son élaboration est simple : 30 mg de zéolithe sont mélangés à 30 mg de poudre de graphite, l'ensemble est pressé sous 2,5 $tonnes/cm^2$ sur une grille de platine ou d'or pendant 2–3 min (fig. 6). On obtient une pastille d'environ 12 mm de diamètre et 0,5–1 mm d'épaisseur, sa surface géométrique totale est estimée à 2 cm^2. L'avantage fondamental de cette électrode par rapport à ses concurrentes est qu'elle ne nécessite pas de liant. Les interactions solution–zéolithe ne sont donc pas modifiées par la présence d'un polymère, d'huile de silicone ou autres. Son utilisation en milieu organique est possible car sa tenue mécanique ne risque pas d'être altérée suite à la dissolution éventuelle du liant. Cependant, une dé-

© 1998 CNRC Canada

Fig. 6. Schéma d'une électrode du type « électrode pressée », adapté de la référence 46.

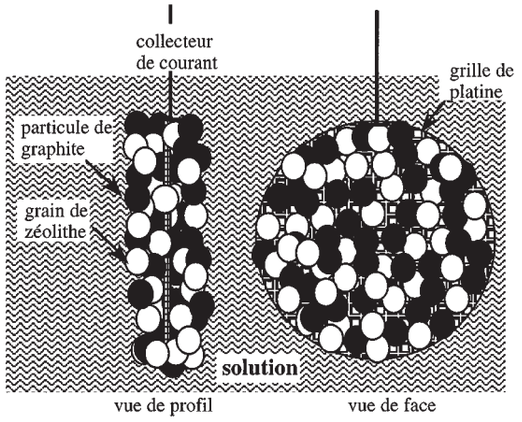

sagrégation partielle de l'électrode au cours de sa manipulation est inévitable car l'absence de liant la rend friable. De ce fait, la quantité de zéolithe à l'électrode varie d'une expérience à l'autre. Il en résulte une reproductibilité sur les intensités de courant mesurées modeste (estimée à environ ± 20 %). Néanmoins, la quantité de zéolithe impliquée dans le processus électrochimique est plus importante par rapport aux autres types d'électrodes et les densités de courant (mesurées pour un même système rédox) sont en général supérieures. On estime que l'électrolyte pénètre dans l'intégralité de l'électrode. La zone électroactive n'est donc pas limitée à la surface de l'électrode; la totalité de sa masse intervient dans la réaction électrochimique.

IV. 1. 3. Dépot d'une suspension (zéolithe + polymère)

C'est certainement le type d'électrode le plus usuel dans l'étude électrochimique des zéolithes. Une suspension de zéolithe et le polymère dissout sont déposés à la surface d'une électrode, généralement de carbone. Après évaporation du solvant, le polymère recouvre la zéolithe et la maintient à la surface de l'électrode. Le polymère universellement choisi, depuis sa première utilisation par De Vismes et al. (58), est le polystyrène et ce grâce à sa grande solubilité dans les solvants organiques tels que le dichlorométhane et le chloroforme, ce qui permet une excellente mise en oeuvre de la procédure de fabrication de l'électrode, et grâce aussi à sa porosité importante. L'inconvénient de cette électrode est la faible cohésion du dépôt. Shaw et al. (21) ont montré par microscopie électronique à balayage que le polystyrène manifeste une bonne adhérence à l'électrode mais médiocre à la surface des particules de zéolithe. Cette électrode est par conséquent mécaniquement fragile. Son utilisation dans des conditions hydrodynamiques n'est pas envisageable (contrairement à l'électrode à pâte de carbone). De plus, on observe rarement une équivalence d'un dépôt à l'autre d'où une faible reproductibilité des résultats. Shaw et al. (21) ont aussi observé une reproductibilité de ±14 %. Sauf exception (40, 76), ce type d'électrode est exclusivement exploité en milieu aqueux car on observe, dans les solvants organiques, une dissolution progressive du polymère. L'intérêt de cette électrode est qu'elle engendre des voltammogrammes bien définis du fait d'un dépot de faible épaisseur et de faible surface qui minimise les problèmes de diffusion, au sein du corps de l'électrode modifiée, et de courant capacitif. Cependant, l'électroactivité du système parait susceptible d'être faussée par une accumulation d'espèces électroactives sortantes de la zéolithe et qui se trouveraient confinées dans le film polymère ou par une entrée de l'électrolyte dans la zéolithe qui soit entravée par la présence du polymère à la surface de celle-ci.

Fig. 7. Schéma d'une électrode du type « électrode monocouche », adapté de la référence 46.

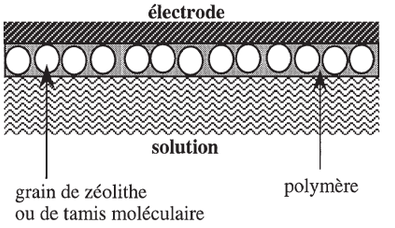

Le dépôt peut être aussi généré par électrodéposition comme l'ont démontré Rolison et coll. (25, 77). La zéolithe est mise en suspension dans une solution contenant un oxydant (par exemple, le 1,4-dinitrobenzène). Un dépôt à l'électrode se forme par la réduction répétée de l'oxydant qui s'adsorbe à la surface de l'électrode conjointement à la zéolithe. L'apport de matière est entretenu par la rotation de l'électrode. Le phénomène d'adsorption n'est observable qu'en présence de la zéolithe. Aucune explication n'a pour l'instant été donnée mais la forte nature anionique de la zéolithe doit sans doute affecter la réduction de l'oxydant. En présence de pyrrole et de zéolithe, un dépôt zéolithe–polypyrrole est formé à la surface de l'électrode par oxydation du pyrrole. Le dépôt peut être amélioré en oxydant une goutte de la solution déposée à la surface de l'électrode. La zéolithe pénètre par gravitation dans le polypyrrole naissant (25). À noter qu'il existe quelques exemples d'incorporation dans une zéolithe de polymères conducteurs tels le polypyrrole, le polyaniline, le polythiophène (78–81). Cependant, leur utilisation dans l'élaboration d'une électrode composite à base de zéolithe n'a pas pour l'instant été envisagée. Il est vrai que leur présence a le défaut d'encombrer le réseau de la zéolithe et les rares mesures de conductivité effectuées ne sont pas probantes. Aucune indication n'a été reportée dans la littérature quant à une éventuelle amélioration de la tenue mécanique de l'électrode lorsque le dépôt du film de polymère est réalisé par électrodéposition.

IV. 1. 4. Electrode type « monocouche »

La figure 7 représente une électrode type « monocouche » développée par Calzaferri et coll. (82–85). Cette électrode est en fait une évolution de l'électrode « polystyrène ». Sa fabrication consiste en un dépôt d'une suspension de zéolithe ou de tamis moléculaire suivi du dépôt de polymère qui est en général le polystyrène. D'après les travaux de Calzaferri et coll. (82–85), il est possible de réaliser un dépôt homogène d'une monocouche de zéolithe sur la surface de l'électrode. De plus, la maîtrise de la qualité du dépôt leur permet d'atteindre de bons niveaux de reproductibilité (quelques pour cent). La faible épaisseur de l'électrode (qui correspond à la taille des cristaux de zéolithe étudiés) permet de minimiser le courant capacitif et de simplifier les phénomè-

© 1998 CNRC Canada

Fig. 8. Stratégie d'élaboration d'un système trimoléculaire à partir d'une électrode fonctionnalisée.

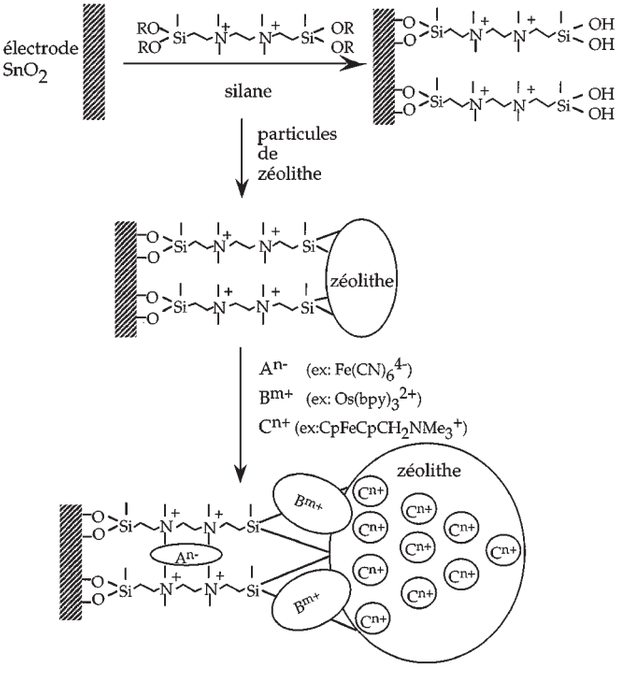

nes de diffusion. La bonne tenue mécanique de l'électrode permet d'effectuer des études en voltampérométrie hydrodynamique mais la présence du polystyrène proscrit son utilisation dans les solvants organiques dans lesquels ce polymère est soluble. Le principal problème de cette électrode est qu'elle met en jeu de faibles quantités d'espèces électroactives lorsque le matériau étudié contient lui-même peu d'espèces électroactives.

IV. 1. 5. Electrode fonctionnalisée

Li et al. (33) ont élaboré une électrode de conception originale : un silane bifonctionnalisé est lié par une extrémité à la surface d'une électrode SnO_2 via des liaisons Sn—O—Si et par l'autre extrémité à la zéolithe Y via des liaisons Si—O—Si. Ils obtiennent un dépôt d'une monocouche de particules de zéolithe à la surface de l'électrode. Ce film est mécaniquement stable et peut fixer divers cations et anions électroactifs (fig. 8). Ainsi, il est possible de construire des « systèmes trimoléculaires» : un anion peut se lier aux sites cationiques du silane et deux cations de taille différente peuvent se fixer à la zéolithe (l'un à l'intérieur de la zéolithe, l'autre à sa surface).

IV. 1. 6. Electrode dispersée

Les surfaces des électrodes précédemment décrites sont insuffisantes pour des applications en électrosynthèse. Une solution, élaborée par Rolison et al. (37), consiste à utiliser la zéolithe à l'état dispersé et de considérer chaque particule comme une ultramicroélectrode. Pour cela, des clusters de platine sont incorporés dans et sur la zéolithe. La suspension de zéolithe modifiée est placée entre deux électrodes cylindriques de platine et un champ électrique (0–300 V/cm) est appliqué. Les électrolyses de l'eau et du mélange eau–benzène (8 : 20, v/v), en l'absence d'ajout de sel support, effectuées en présence des ultramicroélectrodes de platine supportées sur la zéolithe donnent des courants de 10 à 1000 fois supérieurs à ceux mesurés en l'absence de platine. La mise en suspension d'une zéolithe modifiée par adsorption d'une porphyrine de manganèse est une méthode qui a été également utilisée au laboratoire pour l'électrocatalyse d'oxydation de di-*tert*-butyl phénol par l'oxygène moléculaire (86). Récemment, Bessel et Rolison (87, 88) ont utilisé ce type de suspension pour l'analyse électrochimique de complexes encapsulés dans la zéolithe Y, ainsi que pour leur application en electroacatalyse préparative (cas de la carboxylation du chlorure de benzyle catalysée par le complexe CoSalen encapsulé dans la zéolithe Y).

En résumé, l'électrode idéale est une électrode suffisamment conductrice, mécaniquement stable et facile à préparer. Cette électrode n'existe pas encore. Des améliorations dans la conception d'électrodes composites à base de zéolithe doivent donc être accomplies. En fait, chaque type d'électrode décrit précédemment a ses avantages et ses inconvénients. Et selon leurs caractéristiques, elles seront mieux appropriées à une application donnée. Le tableau 1 résume les caractéristiques fondamentales de chaque type d'électrode.

IV. 2. Techniques électrochimiques

La voltampérométrie cyclique est la technique de prédilection pour étudier l'électrochimie des zéolithes. Cette suprématie se justifie avant tout par la simplicité de la méthode et son caractère usuel. C'est généralement la première technique utilisée par un électrochimiste lors de l'étude d'un nouveau système rédox. La voltampérométrie cyclique est une méthode puissante car non seulement elle permet de caractériser un système rédox mais elle rend également compte des mécanismes réactionnels mis en jeu. De plus, des paramètres cinétiques essentiels tels que les coefficients de diffusion au sein de la zéolithe peuvent être déterminés. Plus rarement utilisées, la chronoampérométrie (42, 53, 56, 58, 89), la chronopotentiométrie (54, 56, 90) et la spéctroscopie d'impédance électrochimique (45) sont généralement couplées à la voltampérométrie cyclique et s'appliquent essentiellement à une étude cinétique des phénomènes de diffusion au sein de la zéolithe. Lors d'études très spécifiques, d'autres techniques peuvent être employées. À titre d'exemple, on peut citer l'étude de la sélectivité cationique d'une membrane zéolithique par mesure de la f.é.m. de la cellule électrochimique (50–52).

IV. 3. Description des processus électrochimiques

La présence de la zéolithe à l'électrode introduit de nouvelles variables qui modifient les mécanismes électrochimiques conventionnels. Le transfert électronique entre l'électrode et l'espèce électroactive incorporée dans le système poreux de la zéolithe est de fait une opération complexe. De nombreuses mises au point récentes présentent cette complexité de manière assez détaillée (30, 43–46, 66, 87, 91, 92) et nous n'examinerons ici que les étapes-clé de la procédure d'analyse électrochimique des différentes zéolithes chimiquement modifiées recencées dans la littérature.

© 1998 CNRC Canada

Tableau 1. Avantages et inconvénients des différents types d'électrodes modifiées à base de zéolithe.

Type d'électrode	Avantages	Inconvénients	Application type
Électrode à pâte de carbone	Fabrication simple Surface renouvelable Bonne stabilité Mesures reproductibles	Nécessité d'un liant Inutilisable en milieu organique Diffusion limitée	Électroanalyse (détection)
Électrode pressée	Fabrication simple	Fragile	Électrochimie de complexes encapsulés
	Totalité de l'électrode impliquée Pas de liant Utilisable en milieu organique	Reproductibilité faible	
Dépôt à l'électrode	Courant capacitif faible	Fragile (sauf monocouche)	Étude de transferts électroniques
	Voltammogrammes bien définis	Reproductibilité faible (sauf monocouche) Peu utilisable en milieu organique Interférence possible avec le polymère	Photoélectrochimie
Électrode fonctionnalisée	Bonne stabilité	Construction complexe	Étude de systèmes trimoléculaires
Électrode dispersée	Densité de courant levée Aucune contrainte mécanique exercée sur la zéolithe		Électrosynthèse

Shaw et al. (21) proposent deux mécanismes pour décrire les processus électrochimiques à une électrode modifiée par une matrice solide poreuse contenant une espèce électroactive (zéolithe, tamis moléculaire) :

$$[1] \quad E_{(z)}^{m+} + mC_{(s)}^{+} \Leftrightarrow E_{(s)}^{m+} + mC_{(z)} + E_{(s)}^{m+} + ne^{-} \Leftrightarrow E_{(s)}^{(m-n)+}$$

$$[2] \quad E_{(z)}^{m+} + ne^{-} + nC_{(s)}^{+} \Leftrightarrow E_{(z)}^{(m-n)+} + nC_{(z)}^{+}$$

E^{m+} représente l'espèce électroactive, C^{+} le cation de l'électrolyte et les indices (z) et (s) respectivement la zéolithe et la solution.

Le mécanisme [1] ne concerne que les espèces électroactives mobiles, pouvant diffuser librement dans la structure des zéolithes ou des tamis moléculaires. Il est constitué d'une première étape qui est un échange ionique entre le cation de l'électrolyte support et l'espèce électroactive présente dans la zéolithe. Lors de la seconde étape, l'espèce électroactive subit un transfert de charge à l'extérieur de la zéolithe. Ce mécanisme est dit *extra-zéolithique*.

Le mécanisme [2] s'effectue en une seule étape dans laquelle il y a à la fois un transfert d'électrons faisant intervenir l'espèce électroactive située à l'intérieur de la zéolithe et une diffusion du cation de l'électrolyte vers l'intérieur du système poreux de la zéolithe afin de compenser la charge créée par la réaction de réduction (ou une diffusion du cation mobile compensateur de charge de la charpente zéolithique vers l'extérieur du système poreux de la zéolithe afin de compenser la charge créée par la réaction d'oxydation). Ce second mécanisme, dit *intra-zéolithique*, concerne plus particulièrement les espèces fixées irréversiblement dans la structure du matériau telles que les complexes encapsulés dans les zéolithes ou encore les cations métalliques incorporés aux réseaux des tamis moléculaires. Cependant, comme nous le verrons dans la discussion ci-après, certains auteurs pensent pouvoir attribuer à un mécanisme intra-zéolithique l'activité électrochimique observée pour de petits cations pouvant diffuser librement dans le système poreux de la zéolithe.

IV. 3. 1. Processus rédox extra-zéolithique

À ce jour, la majorité des travaux sur l'électrochimie des zéolithes implique un processus rédox extra-zéolithique. Le transfert électronique a lieu à l'extérieur de la zéolithe. Il n'est par conséquent applicable qu'aux espèces électroactives capables de diffuser hors de la zéolithe. Son mécanisme a été étudié et mis en évidence dans le cas d'espèces électroactives incorporées dans la zéolithe par simple échange ionique : Ag^{+} (54) incorporé dans la mordénite; MV^{2+} (méthylviologène) (39, 40, 76), $Ru(NH_3)_6^{3+}$ (21, 91), Cu^{2+} (21), Co^{2+} et Ag^{+} (41, 42, 59, 66, 68, 92–94) incorporés dans la zéolithe Y.

Le transfert électronique s'effectue de façon classique à la surface de la zéolithe. Il est rapide par rapport aux autres phénomènes intervenant dans le mécanisme rédox extra-zéolithique. Il ne contrôle donc pas le processus électrochimique. Aussi notre attention se focalisera sur la première étape du mécanisme extrazéolitique, c'est à dire l'échange ionique entre l'espèce électroactive intra-zéolithique et le cation de l'électrolyte support. C'est l'étape limitante du processus rédox. Les phénomènes de diffusion (diffusion de l'espèce électroactive et diffusion de l'électrolyte) ont une influence majeure sur l'électroactivité du système. Plusieurs paramètres interviennent sur les phénomènes de diffusion : la configuration de l'électrode, la structure de la zéolithe, le solvant, la température, la taille des espèces mobiles, la na-

© 1998 CNRC Canada

Fig. 9. Représentation des différents phénomènes diffusionnels inhérents à un processus rédox extra-zéolithique.

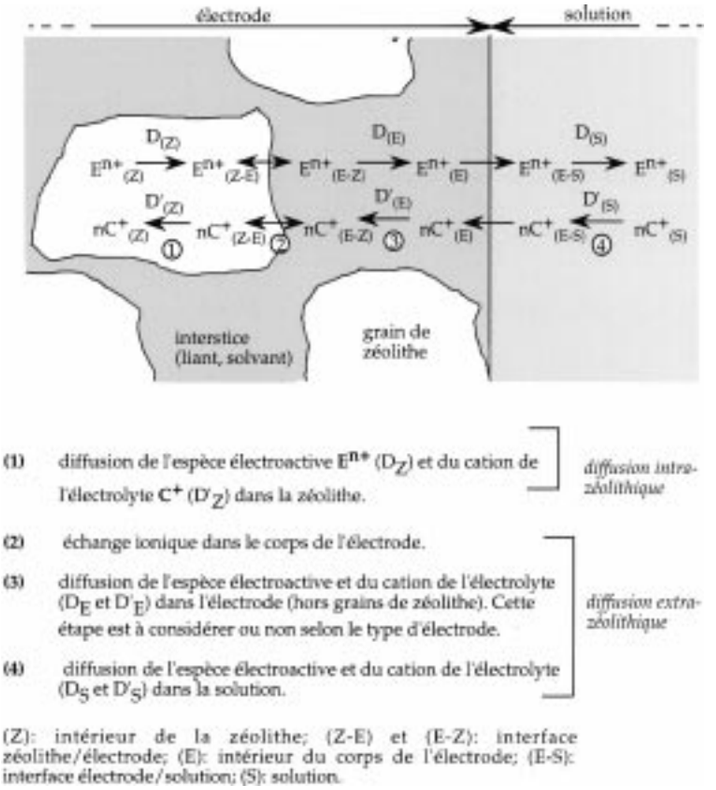

ture des intéractions entre les espèces mobiles et la zéolithe. La multiplicité des paramètres fait apparaître la complexité du processus. L'échange ionique pris dans sa globalité peut être subdivisé en trois processus (fig. 9) : (*i*) *diffusion intra-zéolithique* : diffusion de l'espèce électroactive et du cation de l'électrolyte dans le système poreux de la zéolithe; (*ii*) *échange ionique*; (*iii*) *diffusion extra-zéolithique* : diffusion de l'espèce électroactive et du cation de l'électrolyte dans le corps de l'électrode (hors zéolithe) et diffusion de l'espèce électroactive et du cation de l'électrolyte dans la solution.

Ces trois processus sont fortement interdépendants, il n'est donc pas aisé de les traiter séparément. Il est par exemple difficile de savoir si la taille des espèces cationiques interviendra plus particulièrement sur l'échange ionique ou sur les phénomènes de diffusion. Ou encore, lorsqu'on mesure un coefficient de diffusion, il n'est pas possible de différencier sa composante intra-zéolithique de sa composante extra-zéolithique. Toutefois, on tentera ci-après de mettre en avant les différents paramètres susceptibles d'influer sur ces différents processus.

IV. 3. 1. 1. Diffusion extra-zéolithique : (a) Diffusion dans la solution. La diffusion de l'espèce électroactive et du cation de l'électrolyte dans la solution est rapide par rapport à leur diffusion dans la zéolithe et dans l'électrode. Dès immersion de l'électrode dans la solution d'électrolyte, on observe un passage en solution de l'espèce électroactive (21, 76). Elle diffuse dans la solution en s'éloignant de l'électrode et ne participe pas au processus électrochimique. Une faible quantité est cependant susceptible d'être au contact de l'électrode et d'engendrer un courant faradique. Mais sa dilution dans la solution d'électrolyte rend ce courant insignifiant par rapport au courant engendré par l'espèce intra-zéolithique.

Afin de minimiser la perte de matière électroactive due à son passage en solution, il est profitable d'effectuer la mesure électrochimique immédiatement après contact de l'électrode avec la solution. Durant l'expérience, la perte d'espèce électroactive est inévitable. En voltampérométrie cyclique, cette perte se traduit par une décroissance, cycle après cycle, des intensités de pics (39, 66).

(*b*) *Diffusion dans l'électrode.* L'électrode à base de zéolithe est un système complexe constitué de grains de zéolithe et, selon les cas de particules de graphite, de polymère, d'huile de paraffine, etc. Ce milieu est plus ou moins poreux et doit laisser un espace suffisant pour permettre la diffusion de la solution d'électrolyte et des espèces issues de la zéolithe. On entendra par diffusion dans l'électrode les phénomènes diffusionnels propres à l'électrode mais ne concernant pas la diffusion intra-zéolithique. Selon le type d'électrode utilisé, les phénomènes de diffusion dans l'électrode sont considérés ou non. Li et Calzaferri (84) — qui utilisent une électrode modifiée par un dépôt d'une monocouche de grains de zéolithe — ne prennent pas en compte la diffusion des espèces dans l'électrode. Dans ce cas, le processus d'échange ionique est contrôlé par la diffusion des espèces dans la zéolithe. Toutefois, le polymère nécessaire à la cohésion des électrodes préparées à partir d'un dépôt est susceptible d'entraver la diffusion des espèces dans l'électrode et leur entrée dans le système poreux de la zéolithe. En effet, la

© 1998 CNRC Canada

porosité partielle du polymère, son agrégation à la surface des grains de zéolithe et son caractère hydrophobe sont des facteurs qui ne facilitent pas les phénomènes de diffusion. À ce type d'électrode, aucune étude n'a cependant montré une diffusion des espèces limitée par leur diffusion dans l'électrode. En revanche, à une électrode à pâte de carbone, Walcarius et al. (39, 40) ont montré que la diffusion des espèces dans l'électrode doit être considérée. Ils ont déterminé un coefficient de diffusion du cation méthylviologène dans l'électrode (8×10^{-11} cm^2 s^{-1}) inférieur à celui mesuré dans la zéolithe (2×10^{-8} cm^2 s^{-1}). Ce résultat est surprenant car il témoignerait de contraintes diffusionnelles beaucoup plus importantes dans le corps de l'électrode que dans la zéolithe. Le processus d'échange ionique serait donc limité par la diffusion des espèces dans l'électrode et non dans la zéolithe. La diffusion dans l'électrode peut être améliorée par son hydratation préalable. Ainsi, le coefficient de diffusion du méthylviologène dans l'électrode est multiplié par quatre lorsque celle-ci est immergée 12 h dans de l'eau hautement purifiée (39). À noter également l'importance de la vitesse de balayage et du temps d'immersion de l'électrode qui modulent l'épaisseur de l'électrode impliquée dans le phénomène de diffusion. À 1 V/s, le phénomène observé est essentiellement surfacique et dans ce cas, la diffusion des espèces dans l'électrode ne doit pas être considérée (40). En bref, si la structure de la zéolithe est toujours prise en compte lors des processus de diffusion inhérents au processus rédox, la porosité, la compacité et la mouillabilité de l'électrode sont des critères souvent sous-estimés malgré leur implication dans le phénomène observé.

IV. 3. 1. 2. L'échange ionique : L'échange ionique est ici considéré à l'équilibre. La constante d'équilibre thermodynamique de l'échange ionique entre l'espèce électroactive intra-zéolithique ($E_{(Z)}^{m+}$) et le cation monovalent de l'électrolyte support (C^+) est définie par :

$$E_{(Z)}^{m+} + mC_{(s)}^{+} \overset{K}{\Leftrightarrow} E_{(s)}^{m+} + mC_{(z)}^{+}$$

$$K = \frac{(aC_{(z)})^m \times (aE_{(s)}^{m+})}{(aC_{(s)}^{+}) \times (aE_{(z)}^{m+})}$$

L'équilibre s'établit en fonction de l'activité de chaque espèce en solution et dans la zéolithe, c'est à dire en fonction de leur concentration et de leur coefficient d'activité dans leur milieu respectif.

Au départ de l'expérience, la concentration de l'espèce électroactive dans la solution d'électrolyte est nulle, elle est par contre importante dans la zéolithe (appliquée à la zéolithe Y, la concentration est estimée à 1 M en considérant que la zéolithe contient une entité électroactive par supercage). On a donc un gradiant de concentration élevée, entre l'intérieur et l'extérieur de la zéolithe. Le passage en solution de l'espèce intra-zéolithique est en conséquence fortement favorisé. L'équilibre d'échange ionique s'établit rapidement. Ainsi, si des particules de zéolithe contenant du méthylviologène sont mises en suspension dans une solution aqueuse de NaCl 0,05 M, l'équilibre est atteint en moins d'une seconde (40).

Cependant, l'équilibre ne s'établit pas simplement en fonction de la concentration des cations dans la zéolithe et dans la solution, il faut également tenir compte de la différence d'affinité vis à vis de la zéolithe entre les deux cations. C'est à dire qu'une fois l'équilibre atteint, les deux cations ne seront pas partagés de façon identique entre la zéolithe et la solution, l'un d'eux sera en plus forte proportion que l'autre dans la zéolithe. Pour une zéolithe donnée, cette sélectivité dépend principalement de la taille et de la charge des espèces concernées mais aussi du solvant qui influe sur leur volume molaire et sur les intéractions ioniques cation–zéolithe. L'utilisation d'un cation de l'électrolyte support de grande taille peut défavoriser l'échange ionique jusqu'à l'interdire si le cation est de taille supérieure aux pores de la zéolithe. Ainsi selon Gemborys et Shaw (76), l'utilisation de l'ion tétrabutylammonium (TBA^+) ne permet pas l'échange ionique et la faible électroactivité observée a pour seule origine les espèces fixées à la surface de la zéolithe. À noter que la capacité du tétrabutylammonium à pénétrer dans le réseau poreux de la zéolithe Y est un sujet de controverse. En effet, selon les travaux effectués au laboratoire (60, 61) et ceux de Baker et al. (24, 41, 42), le cation tétrabutylammonium parait être capable de pénétrer dans la zéolithe Y. En revanche, Walcarius et al. (39) et Gemborys et Shaw (76) considérent sa pénétration dans la zéolithe Y comme incertaine. Ces résultats contradictoires témoignent du flou qui existe encore sur l'action du cation de l'électrolyte. Il est important de noter que le cation et les fenêtres d'accès de la supercage ne doivent pas être considérés comme totalement rigides, ils sont doués d'une certaine flexibilité. Ainsi, selon Barrer (95), une espèce d'un diamètre cinétique de 10 Å peut pénétrer au sein de la zéolithe Y dont le diamètre des ouvertures n'est pourtant que de 7,4 Å. En conséquence, selon ce principe, le cation tétrabutylammonium d'un diamètre cinétique compris entre 8,1 et 9 Å et dont la flexibilité est reconnue peut logiquement pénétrer au sein de la zéolithe Y. D'autre part, la pénétration du cation de l'électrolyte peut être favorisée par un déplacement de l'équilibre d'échange grâce à un effet de complexation avec l'anion de l'électrolyte. Par exemple, les courants observés lors de l'étude de l'ion Co^{2+} incorporé dans la zéolithe Y avec comme électrolyte support le cation tétrabutylammonium et l'anion I^- ou SCN^- sont supérieurs à ceux observés avec l'anion BF_4^-, l'échange ionique étant accentué par une complexation des ions cobalt avec les ions I^- et SCN^- (41). Enfin, si la taille du cation est inférieure au diamètre des pores de la zéolithe mais nécessite une perte partielle de sa sphère de solvatation lors de l'échange ionique, l'énergie de désolvatation peut être élevée et dans ce cas la réaction d'échange est énergétiquement défavorable (cas du cation Li^+ vis à vis de la zéolithe analcime (41)). Lors de la réaction d'échange, il est donc important de considérer non pas le cation seul mais le couple cation–solvant.

IV. 3. 1. 3. Diffusion intra-zéolithique : Pour être électroactive, l'espèce intra-zéolithique mais aussi le cation de l'électrolyte doivent diffuser dans le réseau poreux de la zéolithe. Pour la grande majorité des auteurs, la diffusion intra-zéolithique est considérée comme l'étape limitante du processus rédox extra-zéolithique. Par chronoampérométrie, Pereira-Ramos et al. (56) ont montré que l'électrodépôt

© 1998 CNRC Canada

Fig. 10. Mécanisme électrochimique mis en jeu lors de la réduction des ions Ag^+ fixés dans la zéolithe $Ag_nNa_{(56-n)}Y$ avec $n < 5,9$ (d'après reférence 94). *pc* : petits canaux; *gc* **:** grands canaux; *s* **:** solution; *ies* **:** interface électrode–solution.

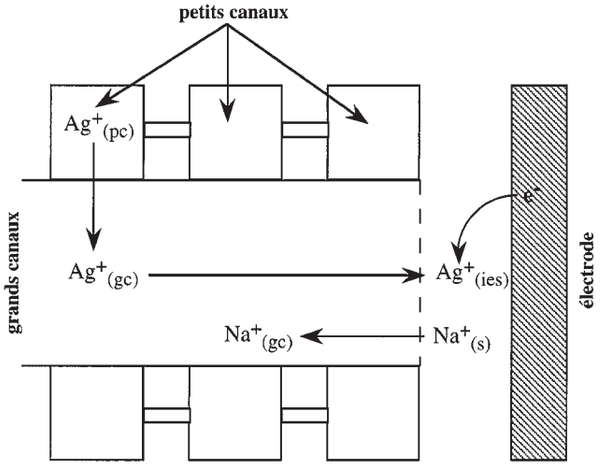

d'argent dans une zéolithe est contrôlé par la diffusion intra-zéolithique. Leurs résultats sont confirmés par les travaux de Baker et al. (42) qui ont par ailleurs montré la dépendance de la température sur les coefficients de diffusion. Par voltampérométrie cyclique, Shaw et Creasy (22), El Murr et al. (48) et Walcarius et al. (39) ont mesuré, avec différentes espèces électroactives, des intensités de pics proportionnelles à la racine carrée de la vitesse de balayage. Walcarius et al. (40) ont également montré que l'évolution du courant de réduction de l'ion méthylviologène incorporé dans la zéolite Y est similaire à l'évolution de la concentration en méthylviologène d'une solution contenant une suspension de zéolithe chargée en méthylviologène.

Plusieurs facteurs ont une influence sur les phénomènes de diffusion dans la zéolithe : la structure de la zéolithe bien sûr, mais aussi la taille des espèces concernées par le processus électrochimique ainsi que leur état de solvatation.

Selon la structure de la zéolithe, la diffusion des espèces impliquées dans le processus rédox sera plus ou moins facilitée. Par exemple, l'électroactivité du cuivre incorporé dans la zéolithe Y est 3,3 fois supérieure à celle du cuivre incorporé dans la zéolithe A (la zéolithe Y contenant cependant 1,6 fois plus de cuivre). Ce résultat peut être interprété par une plus grande mobilité des ions Cu^{2+} dans la zéolithe Y (21).

La taille du cation de l'électrolyte a également une incidence sur la réponse électrochimique observée. Toujours appliqué au cas du cuivre incorporé dans la zéolithe Y, le remplacement du cation Li^+ (rayon de l'ion hydraté = 5 Å) par un cation de taille inférieure tel Cs^+ (rayon de l'ion hydraté = 2,5 Å) a pour conséquence d'augmenter d'un facteur 2 l'intensité de pic correspondant à la réduction du cuivre (21). Plusieurs études ont montré une corrélation entre les intensités de pics et la taille du cation de l'électrolyte (21, 39, 41, 76, 84). En règle générale, l'électroactivité de l'espèce intra-zéolithique s'accroît avec la diminution de la taille du cation de l'électrolyte et avec l'augmentation du diamètre des pores de la zéolithe. En d'autres termes, lors d'un processus rédox extra-zéolithique, plus l'espèce électroactive et le cation de l'électrolyte sont mobiles au sein de la zéolithe, plus l'échange ionique est rapide et efficace, et plus la quantité d'espèces électroactives au contact de l'électrode est importante.

Les intéractions électrostatiques peuvent également avoir une incidence non négligeable sur la mobilité des cations dans la zéolithe (surtout dans les larges pores). Aussi, la charge de la charpente zéolithique et les propriétés diélectriques du solvant sont supposées jouer un grand rôle dans le contrôle des vitesses de diffusion intra-zéolithique. Ainsi, le caractère hydrophile de la zéolithe ralentit fortement la diffusion des cations solvatés par des solvants non-aqueux et la conductivité ionique de la zéolithe dépendra de son degré d'hydratation. Senaratne et Baker (23) ont ainsi étudié en milieu organique l'effet de trace d'eau sur l'électrochimie de l'argent incorporé dans la zéolithe A déshydratée. Ils ont obtenu une limite de détection de l'eau dans le diméthylformamide d'environ 20 ppb.

Dernièrement, Baker et al. (42, 94) ont montré la complexité des phénomènes de diffusion intra-zéolithique lors du processus rédox. Appliqué au cas de l'argent incorporé dans la zéolithe Y, ils montrent l'influence notable de la position initiale des ions Ag^+ dans le réseau poreux de la zéolithe (fonction de la quantité d'argent incorporé dans la zéolithe) sur les phénomènes de diffusion donc indirectement sur la réponse électrochimique observée. Une première distinction est faite entre les ions mobiles et les ions fixés aux sites anioniques de la charpente zéolithique. Une seconde distinction est établie entre les ions présents dans les supercages et ceux présents dans les cages sodalites et prismes hexagonaux. De fait, la diffusion intra-zéolithique doit être considérée en plusieurs étapes. Par voltampérométrie cyclique et chronoampérométrie, Baker et al. ont montré que le mécanisme de transfert de charge nécessite un échange ionique entre l'argent intra-zéolithique et le cation de l'électrolyte. Quand les supercages sont occupées par les ions Ag^+, la réaction électrochimique est contrôlée par la diffusion intra-zéolithique. En revanche, lorsque les ions Ag^+ sont exclusivement présents dans les cages sodalites et les prismes hexagonaux (c'est à dire quand la zéolithe contient peu d'argent), le processus rédox est contrôlé par la réaction d'échange intra-zéolithique (échange entre les cations de l'électrolyte présents dans les supercages et les cations Ag^+ présents dans les cages sodalites et prismes hexagonaux). La figure 10 représente le mécanisme proposé par les auteurs (94).

L'étude approfondie du comportement électrochimique du cation Cu^{2+} incorporé dans la zéolithe Y établie par Li et Calzaferri (84) a également mis en évidence l'importance des phénomènes de diffusion intra-zéolithique lors du processus rédox. Cette étude montre que plusieurs paramètres influent sur l'électroactivité du cuivre : la position de l'espèce électroactive dans la zéolithe, l'épaisseur du dépôt de zéolithe à l'électrode, la nature du cation et de l'anion de l'électrolyte support. L'étude de l'influence de la taille du cation de l'électrolyte a permis, entre autres, de démontrer que le processus rédox est limité par la diffusion intra-zéolithique du cation de l'électrolyte et non pas par la migration de l'espèce électroactive vers la surface de la zéolithe. Par ailleurs, ils estiment qu'une migration du cuivre, sous forme Cu^+ ou Cu(0), vers l'intérieur de la zéolithe

© 1998 CNRC Canada

après la réduction de Cu^{2+} à la surface de la zéolithe est possible. Une certaine ambiguïté apparaît concernant le site du transfert électronique. L'étude de l'influence de l'anion de l'électrolyte sur la réponse électrochimique montre que la réduction du cuivre ne se fait pas au sein de la zéolithe mais à l'interface zéolithe–électrode–solution. Cependant, doit-on considérer que le transfert électronique se produit exclusivement à la surface des grains de zéolithe ou bien peut-il avoir lieu dans les supercages présentes à la périphérie des grains de zéolithe? Et s'il a lieu dans les supercages, peut-on encore considérer que la réaction électrochimique s'établit selon un processus rédox extra-zéolithique. Cette ambiguïté montre qu'il est difficile de fixer une frontière bien définie entre une réaction électrochimique s'opérant selon un mécanisme rédox extra-zéolithique et celle qui s'établit selon un mécanisme rédox intra-zéolithique. Aussi, dans le cas d'espèces électroactives incorporées dans la zéolithe par un simple échange ionique, il semblerait que la mise en place d'un processus rédox extra-zéolithique n'interdise pas totalement un processus rédox intra-zéolithique. À ce titre, les travaux récents de Calzaferri et coll. (85), concernant l'étude électrochimique de l'ion Ag^+ incorporé dans la zéolithe A, démontrent que la réduction de l'argent s'effectue non seulement à la surface de la zéolithe mais aussi dans le réseau poreux de la zéolithe. À noter cependant que leur analyse n'est pas en accord avec celle de Baker et coll. (41, 92, 93) — appliquée à l'étude électrochimique de Ag^+ incorporé dans les zéolithes Y et A — qui considèrent que la réduction de l'argent ne peut se faire au sein de la zéolithe. Cependant, ils n'excluent pas une réduction de l'argent dans les supercages présentes à la surface des grains de zéolithe, supercages surfaciques qu'ils estiment représentatives de l'ensemble des supercages du réseau poreux du matériau zéolithique (93).

D'autres ions (Hg(II), Cd(II), Fe(II), etc.) dont la taille est inférieure à celle des canaux des zéolithes ont été étudiés par électrochimie mais peu de précisions ont été apportées sur le mécanisme électrochimique susceptible d'intervenir (27, 28, 89, 96, 97). Walcarius et Lamberts (98) ont étudié le comportement électrochimique des ions $Ru(NH_3)_6^{3+}$ fixés dans la zéolithe NaY en utilisant une électrode à pâte de carbone. Le système Ru(III)/Ru(II) est caractérisé par un unique couple de pics lors de l'étude du complexe $Ru(NH_3)_6^{3+}$ en solution, tandis que l'étude du même complexe fixé dans la zéolithe NaY fait apparaître un pic d'oxydation et deux pics de réduction. La représentation de l'intensité des pics de réduction n'est pas une fonction de la racine carré de la vitesse de balayage. En conséquence, les auteurs ont attribué les deux pics de réduction aux complexes $Ru(NH_3)_6^{3+}$ situés dans deux environnements différents. Afin de déterminer précisément le mécanisme mis en jeu, ils ont utilisé dans un premier temps un cation de l'électrolyte reconnu comme pouvant être exclu, du fait de sa taille, des canaux de la zéolithe Y : le cation TBA^+. Les résultats montrent clairement que le premier pic de réduction (situé au potentiel le plus positif) disparaît lors de l'utilisation de TBA^+ et les auteurs expliquent ce phénomène en considérant que ce pic est associé à un mécanisme électrochimique extra-zéolithique. En effet, la réaction de transfert de charge est dans le cas du mécanisme [1] précédée par l'échange ionique entre le cation de l'électrolyte et l'espèce électroactive. Si l'échange ionique n'a pas lieu, l'ensemble de la réaction électrochimique est bloqué. En revanche, le second pic de réduction (situé au potentiel le plus négatif) ne semble pas influencé par la nature du cation de l'électrolyte support, ce qui peut dans certains cas s'accorder avec un mécanisme électrochimique de type intra-zéolithique. D'après ces auteurs, même si le cation TBA^+ doit être considéré comme pouvant être exclu des canaux de la zéolithe Y, l'existence d'une force motrice telle que la création d'une charge négative dans le réseau de la zéolithe est en mesure de provoquer la diffusion de TBA^+ vers l'intérieur de la zéolithe. Cela permet également d'expliquer pourquoi le second pic de réduction se situe à environ 0,5 V du premier pic vers les potentiels négatifs. En effet, la surtension observée peut être due aux interactions entre le complexe et la zéolithe mais elle représente aussi l'énergie qu'il faut mettre en jeu pour imposer la pénétration du cation TBA^+ dans la zéolithe. Walcarius et Lamberts (98) ont également proposé une autre explication en ce qui concerne le second pic de réduction. Il est possible que l'électrode constituée de carbone graphite, d'huile minérale, de zéolithe et de l'espèce électroactive provoque des surtensions d'électrode suffisamment importantes pour expliquer la présence du second pic de réduction.

La majorité des travaux précédemment cités vont dans le sens d'une électroactivité s'établissant selon le processus rédox extra-zéolithique suggéré par Shaw et al. (21). Malgré la complexité du système due à l'intervention de nombreux paramètres, il en ressort que les phénomènes de diffusion intra-zéolithique ont une incidence majeure sur la réponse électrochimique observée. En règle générale, lorsque l'espèce électroactive est incorporée dans la zéolithe par un simple échange d'ions, la réaction électrochimique s'établit selon un mécanisme extra-zéolithique. Cependant, dans certains cas — l'exemple type est celui de l'argent — une réduction intra-zéolithique de l'espèce électroactive est envisagée. Il est vrai que la réduction de cations métalliques au degré d'oxydation zéro leur confère un caractère métallique donc conducteur qui est peut-être susceptible de faciliter un transfert électronique intra-zéolithique. De toute évidence, les analyses contradictoires sur l'électroactivité de certaines espèces intra-zéolithiques fait apparaître qu'il est difficile d'affirmer catégoriquement, malgré la capacité de l'espèce électroactive à diffuser à l'extérieur de la zéolithe, l'exclusivité d'un processus rédox extra-zéolithique.

IV. 3. 2. Processus rédox intra-zéolithique

Le site du transfert électronique est la différence essentielle entre un processus rédox intra-zéolithique et un processus rédox extra-zéolithique. Lors d'un processus intra-zéolithique, l'électron est transféré à une espèce présente au sein de la zéolithe. Ce processus est par conséquent applicable aux espèces prisonnières du système poreux de la zéolithe. Ainsi, l'activité électrochimique des espèces encapsulées — telles les métal–Salen, métallophtalocyanines, métal–bipyridine, métal–phénanthroline et des nickel et cobalt hexacyanoferrates incorporés dans la zéolithe Y (34, 59–74, 99) — a été considérée comme pouvant s'établir selon un processus rédox intra-zéolithique. Malgré la capacité de certaines espèces à pouvoir diffuser hors de la zéolithe, Li et coll. (31–33, 82–85) les considèrent comme pouvant être impliquées dans un processus rédox du type intra-zéolithique. De même, Senaratne et al. (92) et Bessel et Ro-

© 1998 CNRC Canada

lison (87) attribuent l'origine de l'électroactivité de leurs zéolithes chimiquement modifiées par encapsulation de Co-Salen et $(Fe(bpy)_3)^{2+}$ aux complexes immobilisés et associés à la zéolithe mais uniquement situés à la surface de celle-ci. Nous reviendrons en détail sur les travaux de chacun au cours de cette discussion.

On rappelle qu'un processus rédox intra-zéolithique s'établit selon le mécanisme :

$$E_{(z)}^{m+} + ne^- + nC_{(s)}^{+} \Leftrightarrow E_{(z)}^{(m-n)+} + nC_{(z)}^{+}$$

D'après ce mécanisme, deux conditions sont nécessaires pour observer une activité électrochimique : (*i*) un transfert électronique doit pouvoir s'établir entre l'électrode et l'espèce électroactive; (*ii*) un cation doit pouvoir entrer ou sortir de la zéolithe afin de maintenir l'électroneutralité du système.

IV. 3. 2. 1. La compensation de charge : Malgré une espèce intra-zéolithique immobilisée dans le système poreux de la zéolithe, les phénomènes de diffusion associés à un processus rédox intra-zéolithique ont autant d'importance que dans le cas d'un processus rédox extra-zéolithique. En effet, lorsqu'une espèce intra-zéolithique est oxydée ou réduite, la création de charge doit être compensée par l'entrée ou la sortie d'une espèce chargée dans la zéolithe. La zéolithe étant chargée négativement, l'entrée d'un anion dans la zéolithe n'est pas concevable. L'électroneutralité du système est en conséquence maintenue par le mouvement de cations. Ces cations mobiles peuvent être les cations compensateurs de charge de la charpente zéolithique (dans le cas d'une réaction d'oxydation) ou les cations de l'électrolyte support (dans le cas d'une réaction de réduction). Le mouvement de ces cations est indispensable au processus rédox : sans cette mobilité ionique nécessaire pour compenser la charge induite par la réaction de transfert de charge, l'électroactivité du complexe intra-zéolithique est inexistante.

Le transfert électronique étant un processus rapide par rapport au phénomène de compensation de charge, la cinétique d'un processus rédox intra-zéolithique est contrôlée par la mobilité de ces cations. Les phénomènes de diffusion ont été largement débattus lors de l'étude du processus rédox extra-zéolithique et les observations faites sont applicables à la diffusion du cation compensateur de charge lors d'un processus rédox intra-zéolithique. Nous ne reviendrons donc pas sur le sujet. On rappellera simplement que la diffusion des cations mobiles est, entre autres, influencée par leur taille, la nature du solvant, leur localisation dans la zéolithe et la morphologie de l'électrode.

IV. 3. 2. 2. Le transfert électronique : Rarement considéré comme tel, il semble pourtant opportun de faire le distinguo entre le transfert électronique électrode – complexe intra-zéolithique et le transfert électronique complexe intra-zéolithique – complexe intra-zéolithique. Le premier transfert est nécessaire pour obtenir une réponse électrochimique. En l'absence du second, une réponse électrochimique est observée mais elle est faible car seules les espèces présentes dans les cavités les plus proches de l'électrode sont électroactives.

(*a*) *Transfert électrode – complexe intra-zéolithique*. Le caractère isolant de la zéolithe restreint considérablement le transfert électronique entre l'électrode et l'espèce intra-zéolithique. Ce transfert peut s'établir par un contact direct ou par l'intermédiaire d'un médiateur rédox. L'utilisation d'un médiateur rédox est spécifique aux travaux de Li et al. (31–33). Ces travaux sont basés sur le même concept : deux espèces électroactives sont fixées à une zéolithe par un simple échange d'ions. L'une est incorporée dans le réseau poreux de la zéolithe (par exemple un métallocène ou un cation viologène), l'autre est uniquement présente à la surface de la zéolithe car sa taille lui interdit de pénétrer dans la zéolithe (par exemple un métal tris(bipyridyl) ou une métalloporphyrine). L'électron est transféré de l'électrode au complexe intra-zéolithique par l'intermédiaire de l'espèce électroactive fixée à la surface de la zéolithe. Le transfert de l'électron entre ces deux espèces électroactives n'est possible que s'il est thermodynamiquement favorable. En effet, prenons l'exemple de $Ru(bipy)_3^{2+}$ fixé à la surface de la zéolithe Y et $Co(CpCOOCH_3)_2^{+}$ incorporé dans la zéolithe (31). Du fait de leur potentiel rédox respectif, la réduction du cobaltocénium par le complexe de ruthénium est envisageable mais pas la réaction inverse. Mallouk et Li (31) parlent d'un transfert électronique unidirectionnel (ou vectoriel). La possibilité de contrôler le sens du transfert de l'électron laisse présager des applications intéressantes en électrocatalyse ou en photocatalyse. La fixation d'une espèce encombrante à la surface de la zéolithe a également l'avantage d'empêcher un échange rapide des espèces présentes dans la zéolithe avec les cations de l'électrolyte support. Ainsi, la fixation de la tétrakis(*N*-méthyl-4-pyridyl)porphyrine de cobalt à la surface de la zéolithe Y joue non seulement le rôle de médiateur électronique entre l'électrode et le cation méthylviologène intra-zéolithique mais ralentirait aussi le passage de celui-ci en solution (32).

Les travaux de Li et al. (31–33) montrent de manière indéniable la réalité du transfert électronique de l'extérieur de la zéolithe vers l'intérieur des supercages situées à proximité du médiateur rédox. Cependant, dans le cas de l'étude du comportement électrochimique des métallocènes (31, 33), les complexes intra-zéolithiques peuvent diffuser librement dans la zéolithe, du fait de leur taille qui est inférieure à celle des ouvertures des cages de la zéolithe. Dans ce cas, la possible intervention d'un mécanisme de type 1 ne peut être écartée et a pour effet de partager à nouveau les opinions en ce qui concerne le mécanisme électrochimique à considérer.

Un parallèle peut être établi entre les médiateurs rédox utilisés par Mallouk et Li et les particules de graphite utilisées dans la fabrication des électrodes pressées développées au laboratoire (fig. 11). En effet, la poudre de graphite intimement mélangée aux grains de zéolithe sert de conducteur électronique entre la zéolithe et le collecteur de courant (grille métallique). Les électrons peuvent être transférés du collecteur de courant aux espèces encapsulées via les particules de graphite. Il est important de noter que seule la fraction de complexes encapsulés dans les supercages situées à la périphérie des grains de zéolithe est concernée par ce transfert électronique. Par ailleurs, des différences entre les deux types de « conducteurs » d'électrons sont à considérer. Le transfert électronique par l'intermédiaire des particules de graphite n'est pas unidirectionnel car rien n'interdit le passage de l'électron dans les deux sens (oxydation et réduction). De plus, la taille des particules de graphite est plus de

© 1998 CNRC Canada

Fig. 11. Illustration mettant en parallèle le rôle du médiateur rédox et celui de la poudre de graphite dans le mécanisme de transfert électronique.

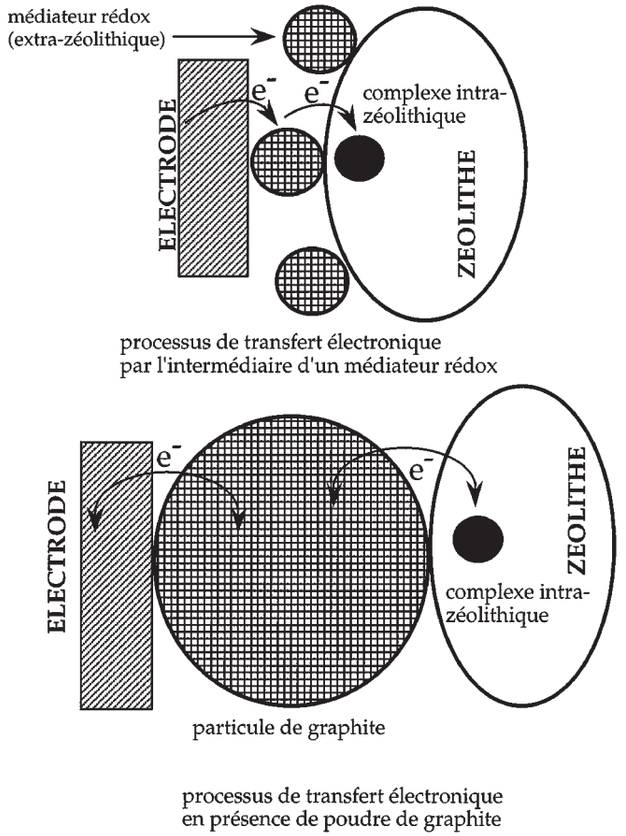

1000 fois supérieure à celle des médiateurs rédox. Par conséquent, le contact entre les espèces intra-zéolithiques et le graphite doit être moins étroit comparé au contact établi à l'échelle moléculaire entre l'espèce intra-zéolithique et le médiateur rédox.

(*b*) *Transfert de charge intervenant dans le cas de complexes encapsulés dans les cavités zéolithiques*. L'encapsulation des complexes à l'intérieur des cavités zéolithiques devrait simplifier l'analyse de leur comportement électrochimique puisque seul le mécanisme de type intra-zéolithique (type 2) peut être avancé pour expliquer les phénomènes observés. Cependant, il n'en est rien et la nature du transfert de charge demeure un sujet très controversé. Quelques publications (66, 70, 87, 92) rendent bien compte des divergences d'avis sur ce sujet. Nous allons développer dans cette partie les arguments avancés par les partisans et les opposants du mécanisme électrochimique de type 2 et nous verrons que, là où certains croient pouvoir mettre en évidence des erreurs d'interprétation d'autres chercheurs, ils ne font que discuter de résultats qui ne sont pas comparables. En effet, la synthèse et les différentes opérations post-synthèse influencent énormément la qualité des produits obtenus et les résultats entre différentes équipes sont parfois peu comparables car les matériaux utilisés sont différents.

Dans le cadre de l'étude des complexes encapsulés dans les zéolithes, de nombreuses publications rendent compte de la possibilité d'utiliser l'électrochimie pour caractériser ces complexes (59–75, 87, 88, 92, 100). Le débat à propos du mécanisme électrochimique est dominé par l'opposition qu'il y a sur plusieurs observations. D'abord, la quantité de complexes pouvant être atteints par électrochimie est rarement supérieure à 1 % de la totalité des complexes présents dans la zéolithe. Ensuite, le comportement électrochimique des espèces encapsulées est parfois très similaire à celui observé pour le complexe en solution.

La faible électroactivité des complexes encapsulés peut s'expliquer par la configuration d'électrode utilisée. En effet, il est clair que seuls les cristaux de zéolithe placés au contact de la grille de platine ou des particules de graphite dispersées au sein de l'électrode pressée sont susceptibles de participer au processus électrochimique. Considérons tout d'abord l'électrode dans son ensemble. Les cristaux de zéolithe se trouvant éloignés de la grille de platine, ou ne se trouvant plus en contact avec les particules de graphite, n'offrent aucun complexe qui soit électroactif. Considérons maintenant les cristaux de zéolithe situés à proximité du conducteur. Trois types de cage contenant le complexe peuvent être considérés dans un cristal de zéolithe : (*i*) les cages localisées à la surface des cristaux, (*ii*) celles situées dans des défauts structuraux et (*iii*) celles présentent dans les profondeurs des cristaux. Les deux premiers types de cages sont a priori accessible par électrochimie puisque rien ne s'oppose au passage du solvant, de l'électrolyte et au transfert électronique. En revanche, le troisième type de cage peut être considéré comme inaccessible par électrochimie pour plusieurs raisons : la présence de complexes volumineux dans les cages situés à la surface des cristaux de zéolithe peut bloquer le passage du solvant et de l'électrolyte, isolant ainsi ces complexes de la solution, de plus, la présence de cages non occupées peut arrêter le processus de transmission électronique entre le collecteur de courant et les complexes encapsulés dans des cages situées dans les profondeurs des cristaux.

En tout état de cause, la voltampérométrie cyclique d'un complexe encapsulé dans la zéolithe Y est fondamentalement différente de celle du même complexe simplement adsorbé à la surface de la zéolithe. La figure 12 montre bien cette différence dans le cas du complexe $[Fe(III)Salen]^+$. Cette différence peut s'expliquer par le fait que dans le cas où le complexe est simplement adsorbé à la surface de la zéolithe, il y a perte du signal électrochimique dès immersion de l'électrode dans la solution électrolytique et ce à cause du passage en solution du complexe adsorbé par « échange ionique » avec le cation de l'électrolyte support.

Pour ce qui est des similitudes parfois rencontrées entre l'activité électrochimique des complexes encapsulés et en solution, nous pouvons avancer l'hypothèse que, bien que la charpente négative des zéolithes soit parfois considérée comme un ligand supplémentaire des complexes cationiques, il est fort possible que les complexes entourés de leurs ligands soient plus stables que les mêmes complexes, avec un ou plusieurs ligands remplacés par les charges négatives de la charpente zéolithique. Cependant, quelques études ont clairement montré que dans certains cas, les interactions entre la charpente de la zéolithe et les complexes intra-zéolithiques pouvaient être mises en avant pour expliquer leur comportement électrochimique. Par exemple, Bedioui et

© 1998 CNRC Canada

Fig. 12. Voltampérogrammes cycliques du complexe Fe(III)Salen adsorbé à la surface de la zéolithe Y (courbe 1) et du complexe Fe(III)Salen encapsulé dans la zéolithe Y (courbe 2) en milieu DMSO + $LiClO_4$, à une électrode composite (vitesse de balayage de potentiel = 10 mV/s), adaptés de la reférence 66.

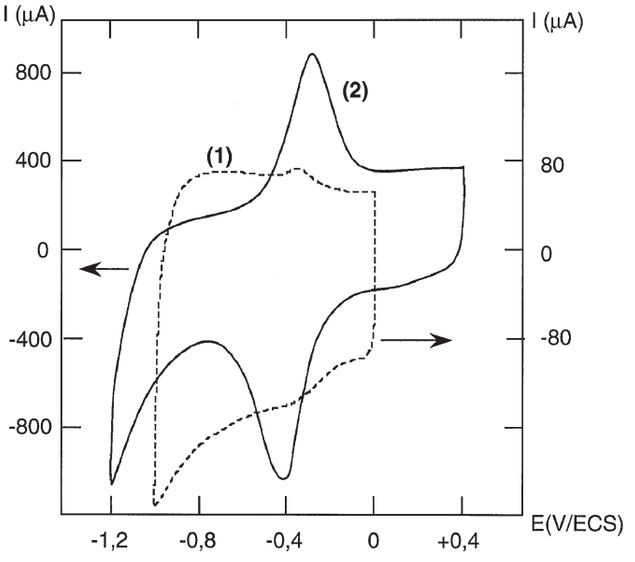

al. (60) ont montré que l'activité électrochimique du complexe CoSalen encapsulé dans la zéolithe NaY montre un pic supplémentaire par rapport à l'étude du complexe en solution. De manière similaire, le système Co(II)/Co(I) est beaucoup mieux défini lors de l'étude électrochimique de perfluorophtalocyanines de cobalt encapsulées que pour le même complexe en solution (64, 66). Les auteurs ont attribué cela à un confinement du complexe au sein de la cavité zéolithique qui empêcherait les phénomènes d'aggrégation observables lorsque le complexe est en solution. En effet, les résultats reportés par Golovin et al. (101) montrent que la dissolution des complexes chloro-substitués de la Co(II)phtalocyanine dans le diméthylformamide conduit à une agrégation des complexes qui induit de nombreuses complications cinétiques ne permettant pas d'observer clairement le système Co(II)/Co(I). Le même comportement a été observé avec le complexe $Cu(II)F_{16}Pc$ qui montre un système Cu(II)/Cu(I) beaucoup mieux défini que pour le complexe en solution, lorsque celui-ci est encapsulé dans la zéolithe NaY.

Il a de plus été montré que le comportement électrochimique du complexe Fe(III)Salen encapsulé dans la zéolithe NaY se distingue de celui du complexe en solution par l'apparition d'un pic supplémentaire pour la réaction rédox Fe(III)/Fe(II) du complexe encapsulé (61). Ce pic peut être attribué à l'existence d'une coordination tétradentate et (ou) bidentate et non plane du ligand Salen au centre métallique fer à l'intérieur des cavités zéolithiques. Ces auteurs ont de plus montré que l'encapsulation du complexe MnSalen dans la zéolithe NaY permet d'éviter la formation du dimère μ-oxo ponté au cours de la réduction Mn(III)/Mn(II), alors que ce dimère se forme en solution. Le volume de la supercage de la zéolithe Y ne permettant pas au dimère du complexe MnSalen d'y tenir, l'électrochimie apporte donc ici une preuve de l'encapsulation du complexe au sein de la zéolithe. Une étude électrochimique similaire a été menée avec le complexe Rh(III)Pc encapsulé dans la zéolithe NaY (72). Ce complexe, connu pour dimériser en solution après la réduction du rhodium au degré d'oxydation II, est stable lorsqu'il est encapsulé dans la zéolithe NaY.

Rolison et coll. (87, 92) ont effectué un certain nombre d'études portant sur l'analyse du comportement électrochimique d'espèces encapsulées dans la zéolithe telles que les complexes CoSalen et $(Fe(bpy)_3)^{2+}$, en utilisant une électrode type « polystyrène » ou « monocouche ». Ils ont focalisé la première partie de leur étude sur la décroissance des intensités de pic observée lorsque plusieurs cycles de potentiel sont effectués avec une électrode contenant le complexe CoSalen encapsulé dans la zéolithe NaY. Lorsque le complexe Co(II)Salen est réduit en Co(I)Salen, il se désorbe de la surface de la zéolithe car il est chargé négativement, provoquant ainsi une perte de matière électroactive à l'électrode et donc une diminution du courant faradique observé. Ils considèrent bien sûr les complexes encapsulés comme non accessibles directement par l'électrochimie. Cette théorie est plausible mais ne corrobore pas les résultats observés par Bedioui et coll. avec des complexes du type $(Co(phen)_3)^{2+}$ (34) ou encore Mn(III)Salen et Fe(III)Salen (66) encapsulés dans la zéolithe NaY. Ces derniers observent, dans certains cas, une diminution des intensités de pics en fonction du nombre de cycles effectués et selon la nature du couple solvant + électrolyte. La figure 13 montre l'évolution des intensités des pics voltampérométrique dans les cas du complexe cationique $Ru(NH_3)_6^{3+}$ fixé par échange d'ion dans la zéolithe Y et étudié dans le DMSO + $LiBF_4$ et dans le cas du complexe Mn(III)Salen encapsulé dans la zéolithe Y et étudié dans l'acétonitrile et le DMSO en présence NBu_4BF_4. La diminution des intensités de pic dans le cas du complexe Mn(III)Salen encapsulé dans la zéolithe Y est, lorsqu'elle existe (dans DMSO), nettement inférieure à ce que Senaratne et al. (92) ont pu mettre en évidence. Bedioui et al. (66) ont interprété cette perte d'électroactivité par la création d'une gêne stérique due à la pénétration du cation de l'électrolyte suite à la réaction rédox à l'intérieur de la supercage de la zéolithe. De plus, la perte d'électroactivité semble liée au nombre de cycles effectués et non au temps d'immersion de l'électrode en solution. Il ressort de ces deux avis opposés que chacun de ces deux commentaires a des raisons d'exister et que l'analyse ne diffère que par la nature des matériaux étudiés. En effet, selon la méthode de synthèse et les procédures post-synthèse choisies, il est possible d'obtenir deux matériaux qui sont finalement peu semblables. Dans le cas des complexes encapsulés, les différences peuvent se situer au niveau du nombre de complexes par supercage, à la présence ou non de cations métalliques non complexés ou de ligands libres ou encore à la présence de complexes non encapsulés à la surface de la zéolithe. De plus, le type d'électrode utilisé peut avoir une influence notable sur la réponse électrochimique observée. Cette hypothèse est confirmée par l'allure des voltammogrammes obtenus par Senaratne et al. (92), radicalement différente de ceux obtenus par Bedioui et al. (66), pour un même complexe mais sur deux configurations d'électrode différentes.

Un point de désaccord important entre les interprétations faites par les différentes équipes travaillant sur le sujet

© 1998 CNRC Canada

Fig. 13. Evolution du rapport I_n / I_1 (n étant le nombre de cycles de balayage de l'électrode et I_n l'intensité du pic voltampérométrique mesurée lors du nième cycle, I_1 étant l'intensité du pic lors du premier cycle de balayage) des intensités du pic anodique du couple Ru(III)/Ru(II) du complexe $Ru(NH_3)_6^{3+}$ fixé par échange d'ion dans la zéolithe Y (courbe 1, milieu DMSO + $LiBF_4$) et du couple Mn(III)/Mn(II) du complexe Mn(III)Salen encapsulé dans la zéolithe Y (courbe 2, milieu acétonitrile + NBu_4BF_4; courbe 3, milieu DMSO + NBu_4BF_4) en fonction du temps dans le cas de cycles récurrents, adapté de la reférence 66.

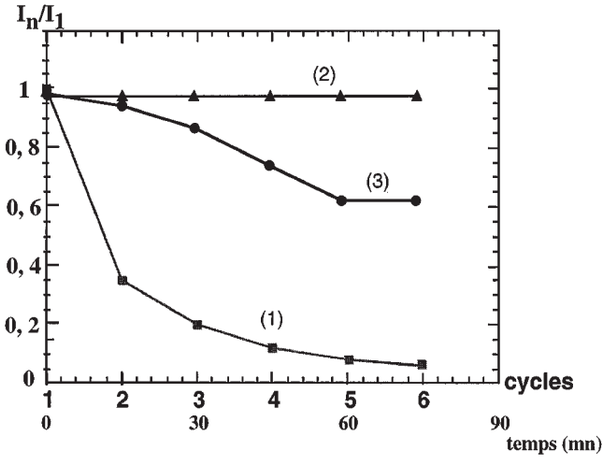

émane de la différence dans la fabrication des électrodes. En effet, la conception des électrodes préssées nécessite une étape dans laquelle le mélange de poudre de graphite et de zéolithe modifiée est pressé sur une grille de platine pendant 2–3 min sous une pression environ 2,5 tonnes/cm^2. D'aprés Rolison et coll. (87, 92, 102), cette étape peut engendrer une perte de cristallinité du matériau, c'est à dire créer des défauts de structure au niveau des supercages contenant les complexes encapsulés. Ainsi, quelle que soient les précautions utilisées pour désorber les complexes non encapsulés, la fabrication de l'électrode engendrerait la formation de complexes extra-zéolithiques qui seraient les seules espèces électroactives. Bessel et Rolison (87) observent par microscopie électronique à balayage une perte de cristallinité notable de la zéolithe lorsque celle-ci est broyée dans un mortier par simple action mécanique (sans pour autant préciser l'ampleur de la force exercée) pendant 10–60 min, alors que Bedioui et al. (72) montrent par diffraction X que le fait de presser la zéolithe pour préparer leur électrode de travail n'endommage pas les cristaux de la zéolithe.

Ainsi, Rolison et al. (87, 92, 102) montrent que le fait d'impartir des forces mécaniques à la zéolithe chimiquement modifiée (par simple broyage dans un mortier) engendre des voltampérogrammes avec des pics plus intenses et mieux définis que ceux obtenus sans broyage ou pression de la zéolithe. Cependant, les intensités développées par ces voltampérogrammes diminuent considérablement au cours du temps, comme nous l'avions souligné auparavant. Les auteurs interpretent l'évolution des voltampérogrammes, en fonction des forces mécaniques imposées à la zéolithe, comme étant le résultat de la déstruction des cristaux de la zéolithe qui offre ainsi la possibilité d'atteindre des complexes situés dans des cages auparavant inaccessibles. L'électroactivité ainsi observée serait celle des seuls complexes présents (à nouveau) à la surface de la zéolithe et dont l'accessibilité est maintenant assurée grâce à la fracture des cristaux de la zéolithe. La diminution rapide des intensités des pics voltampérométriques s'explique alors par la perte de matière électroactive due à son passage en solution. Notons toutefois que même si la préparation des électrodes pressées peut être fortement soupçonnée de conduire à la déstruction locale du réseau de la zéolithe, il n'a pas été reporté dans la littérature une telle évolution des voltampérogramme due à la perte visible du complexe initialement encapsulé (34, 59–75).

Au cours de leurs travaux les plus récents, Bessel et Rolison (87) ont entrepris une étude détaillée des complexes CoSalen et et $(Fe(bpy)_3)^{2+}$ encapsulés dans la zéolithe Y dans le but de mieux faire apparaitre l'effet du traitement mécanique excercé sur la zéolithe, sur la réponse électrochimique. Pour celà, les auteurs ont entrepris l'étude voltampérométrique de leurs zéolithes par la téchnique de l'électrode dispersée. L'analyse des voltampérogrammes cycliques d'une suspension de zéolithe contenant le complexe CoSalen (1 mg/1 mL) sous agitation constante, à une électrode de feutre de carbone vitreux réticulé (1 cm × 1 cm × 2,5 cm) a permis à ces auteurs d'observer deux couples rédox attribués au systèmes Co(III)/Co(II) et Co(II)/Co(I) du CoSalen. Il a été aussi noté qu'aucune évolution des voltampérogrammes cycliques n'avait eu lieu durant plus de 3 h d'expérience, ce qui laisse à penser que la réponse électrochimique observée par cette technique provient du complexe immobile et associé à la zéolithe. Il est important de rappeler ici que la zéolithe n'avait subi aucun traitement mécanique lors de la procédure de son analyse voltampérométrique, ce qui garantie l'intégrité totale de son réseau cristallin. La faible électroactivité mesurée (de l'ordre de 0.07 %) a conduit les auteurs à conclure que seules les espèces immobiles, associées et situées à la limite de la surface de la zéolithe sont électroactives. Cette interprétation est trés proche de celle donnée par Bedioui et al. (66) qui attribuent l'électroactivité observée avec les électrodes pressées à la seule fraction de complexes immobiles et encapsulés (ou associés ou figés) dans les supercages situées à la périphérie des grains de zéolithe au contact du conducteur électronique (fig. 14), comme nous l'avions précisé dans le début de cette section.

Un consensus apparaît cependant lorsqu'il s'agit d'admettre l'existence d'un mécanisme électrochimique dans le cas de l'utilisation de médiateurs rédox (31–33) ou des polymères conducteurs intra-zéolithiques (polyaniline, polypyrrole ou polythiophène) (78, 81) pour assurer le contact entre le collecteur de courant et une espèce fixée à l'intérieur des cavités zéolithiques. Mais le rôle joué par le médiateur rédox ou les polymères conducteurs n'est pas fondamentalement différent de celui joué par les particules de graphite dans les électrodes composites, c'est-à-dire d'assurer la conduction électronique du collecteur de courant (grille de platine) jusqu'aux complexes encapsulés. Cependant, la taille des particules de graphite (de l'ordre de 1 μm) n'est pas comparable à celle des médiateurs rédox (échelle moléculaire, quelques ÅngstrØm) si bien que l'amélioration de la conduction électronique est moins importante dans le cas de l'utilisation des particules de graphite que dans celui

© 1998 CNRC Canada

Fig. 14. Représentation schématique de l'électroactivité des complexes encapsulés en fonction de leur position dans le système microporeux de la zéolithe et dans l'électrode pressée.

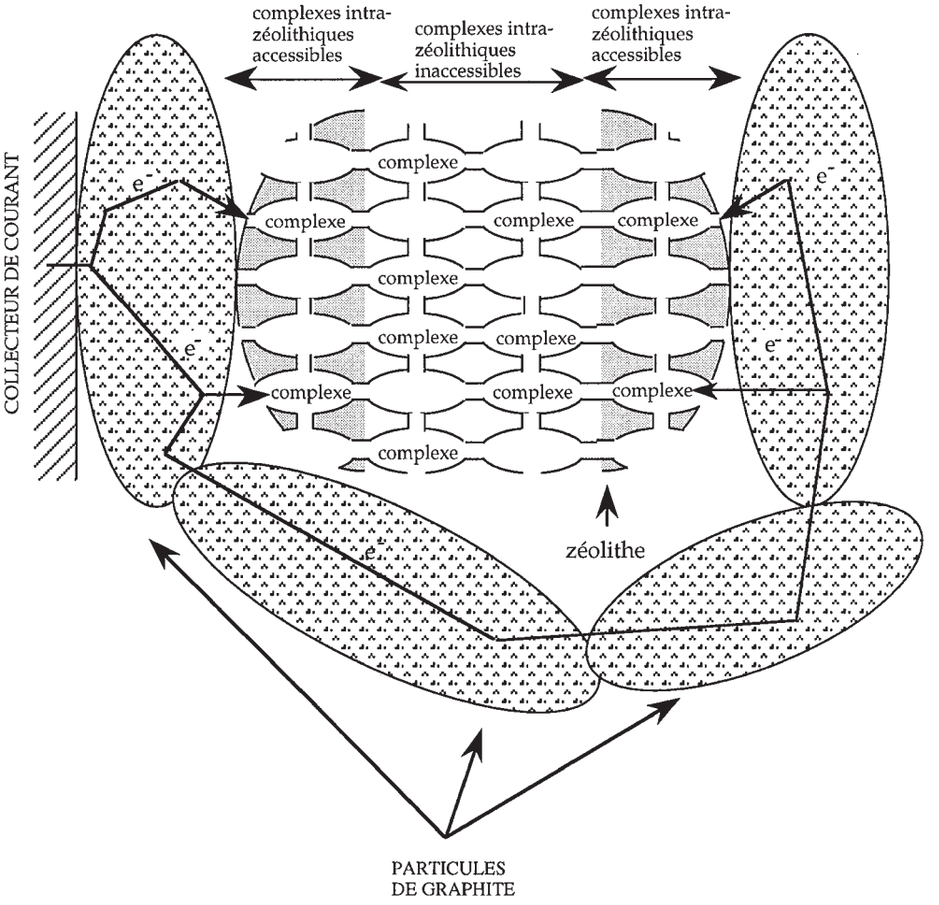

des médiateurs rédox. Dans le but de tenter d'atteindre un plus grand nombre d'espèces encapsulées, il a été développé une zéolithe bi-fonctionnelle contenant un médiateur rédox externe ($((Co(II)(dmbpy)_3)^{2+}$) et une espèce encapsulée ($((Fe(III)Salen)^{+}$) (66). Au cours de la réduction électrochimique Co(II)/Co(I), les espèces Co(I) extra-zéolithiques réduisent les espèces Fe(III) intra-zéolithiques par une réaction rédox, comme indiqué sur la fig. 15. Cette réaction est possible car la différence entre les potentiels standards apparents des couples Co(II)/Co(I) et Fe(III)/Fe(II) est de –700 mV. Le calcul de la quantité de complexes $(Fe(III)Salen)^{+}$ électroactifs suggère une augmentation de 30 % par rapport à ce qui avait été observé lors de l'étude de l'électrode sans médiateur rédox. L'augmentation du nombre de complexes accessibles par voie électrochimique a même été portée à 400 % lors de l'utilisation de particules d'argent électrogénérées au sein de la zéolithe (68).

Tous ces résultats montrent que l'une des principales sources de discorde à propos du mécanisme de transfert de charge provient des différences entre les électrodes de travail utilisées mais aussi et surtout de l'« histoire » des matériaux utilisés. En effet, les études que nous avons présentées utilisent différents échantillons, synthétisés et traités selon des voies diverses. Ainsi, les matériaux finaux sont généralement peu comparables entre eux. Dans les parties consacrées aux autres méthodes d'analyse, nous avons vu que de nombreuses études ont apporté des preuves concernant la localisation intra-zéolithique des complexes encapsulés, mais la preuve la plus évidente est apportée par les résultats obtenus en catalyse. Ils montrent en effet de très importantes différences de réactivité entre les complexes encapsulés et les même complexes simplement adsorbés à la surface de la zéolithe ou dissous en solution (34, 88). Les sélectivités par la taille et la forme des molécules, ainsi que l'accroissement de la stabilité et de l'activité des complexes, sont de bons indicateurs de leur encapsulation.

(*c*) *Transfert complexe intra-zéolithique—complexe intra-zéolithique*. Le transport d'électrons dans les polymères rédox de site rédox en site rédox par un mécanisme de saut d'électrons est un fait établi (103–105). Dans la plupart des cas, le transfert de l'électron nécessite un contact entre les centres rédox. Une certaine mobilité des centres rédox est donc nécessaire et une trop grande rigidité de la matrice peut fortement restreindre le transport électronique. Lorsque les centres rédox sont fixés au polymère par des liaisons covalentes, ils sont incapables de diffuser dans le polymère. Une concentration minimale en centres rédox est dans ce cas requise, concentration au dessous de laquelle les sites électroactifs sont si dilués que leur collision et donc le saut de l'électron est physiquement impossible. Cependant, lorsque

© 1998 CNRC Canada

Fig. 15. (*A*) Principe de fonctionnement de l'électrode composite contenant la zéolithe bifonctionnelle $Co(diméthylbipy)_3^{2+}{}_{surf}$ / $Fe(Salen)_{encap}$ /*Y*. (*B*) Voltampérogramme cyclique de la zéolithe bifonctionnelle en milieu DMSO + $LiClO_4$ (à 10 mV/s), adapté de la reférence 66.

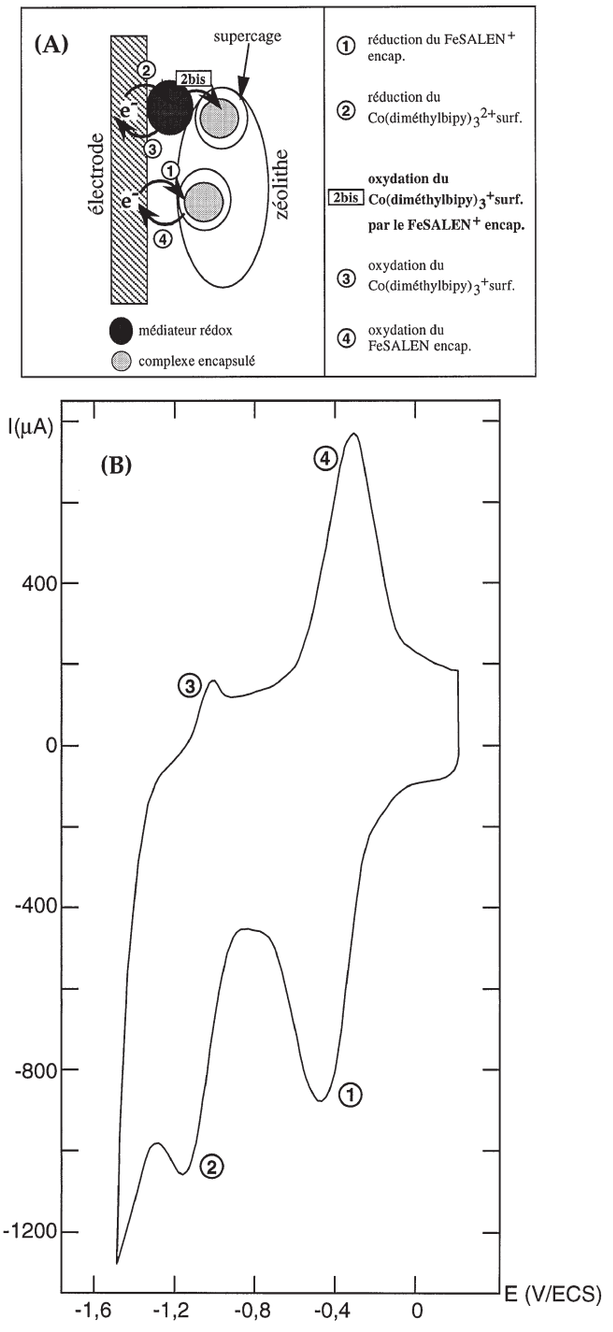

la distance séparant deux centres rédox voisins est supérieure à la somme de leur rayon respectif, un saut d'électron « étendu » peut être considéré. Le modèle théorique établi par Fritsch-Faules et Faulkner (104) montre que deux facteurs ont une influence majeure sur un transfert d'électron « longue-distance » : la concentration des espèces rédox dans le milieu considéré et la distance séparant deux centres rédox. Ils font également intervenir deux paramètres fonction de la structure électronique des centres rédox et de la matrice. Leur modèle est en accord avec les données expérimentales appliquées aux mesures des vitesses de transfert d'électron dans les métalloprotéines.

Le mécanisme de saut d'électron « étendu » ou non est-il transposable aux systèmes intra-zéolithiques? L'étude spectroscopique du complexe $Ru(bpy)_3^{2+}$ encapsulé dans la zéolithe Y montre la nécessité d'un contact direct pour qu'un transfert de charge entre deux complexes puisse avoir lieu (106). Un mécanisme de saut d'électron intra-zéolithique semble donc possible mais il ne peut pas se faire à longue distance, c'est à dire que la présence d'une supercage vide entre deux complexes interrompt la propagation de l'électron. De fait, l'efficacité d'un processus rédox intra-zéolithique sera directement liée à l'efficacité de l'encapsulation. Par ailleurs, les mesures de la conductivité du polypyrrole (longueur des chaînes supérieure à 10 monomères) incorporé dans la zéolithe Y montrent une absence de conduction ($\sigma = 5 \times 10^{-6}\ \Omega^{-1}\ cm^{-1}$). Cette absence de conduction est interprétée par un piégeage des radicaux du polypyrrole (polarons) par les ions de la structure zéolithique (80). Aussi, lors d'un processus électrochimique, les intéractions électrostatiques entre la charpente zéolithique et les espèces électroactives ont certainement une incidence majeure sur le transport de l'électron. Ces interactions seraient-elle susceptibles de placer l'électron à un niveau d'énergie tel que sa propagation lors d'un processus rédox intra-zéolithique serait compromise voire interdite? Selon Li et Mallouk (31), 100 % des cobaltocènes intra-zéolithiques sont électroactifs (en présence de médiateur rédox) ce qui semble démontrer que le transfert électronique entre espèces intra-zéolithiques a bien lieu. Cependant leur calcul de taux d'électroactivité peut être sujet à critique car il est basé sur une quantité de zéolithe succesptible d'être sous-estimée (sur un dépôt d'une épaisseur de 60 µm, 1 µm est considéré dans le processus rédox). De plus, les cobaltocènes sont en quantité faible (environ 3 complexes pour 100 supercages) et libres de circuler dans le système poreux de la zéolithe. Aussi, le transfert électronique peut se produire après migration des cobaltocènes dans les supercages proches de la surface de la zéolithe et donc se limiter à un transfert extra–intra-zéolithe. Li et al. (85) montrent que des ions Ag^+ incorporés dans la zéolithe A sont réduits par un processus intra-zéolithique. Une propagation intra-zéolithique de l'électron semble donc tangible. La formation de clusters intra-zéolithique et le caractère fortement conducteur de l'argent réduit tendent peut-être à faciliter la propagation électronique dans la zéolithe. À noter cependant que selon Baker et al. (41, 93) et Pereira-Ramos et al. (56), la réduction de l'argent intra-zéolithique (dans la zéolithe Y et dans la mordenite) s'opère selon un processus rédox extra-zéolithique.

En définitive, si la possibilité d'un transfert électronique aux espèces intra-zéolithiques présentes dans les supercages situées à la périphérie des grains de zéolithe parait être tout à fait réalisable, et ce malgré les réticences liées à la définition exacte d'une terminologie précise de la part des differents auteurs (30, 66, 70, 87, 88, 91, 92, 100), aucune étude électrochimique ne permet de vérifier catégoriquement que

© 1998 CNRC Canada

le transfert électronique se prolonge entre espèces intra-zéolithiques. L'électroactivité observée lors de l'étude de complexes encapsulés au sein d'une zéolithe se limiterait donc aux complexes en contact direct avec le conducteur électronique (fig. 14). Le consensus vers lequel converge actuellement les différentes équipes travaillant dans ce domaine consiste à dire que l'électroactivité des complexes immobiles, associés à la zéolithe et résidant à la périphérie des pores externes est bien réelle. Il est clair que cette électroactivité est faible et ne concerne qu'une faible proportion de la population totale des espèces encapsulées.

IV.3. 3. Mécanismes électrochimiques intervenant dans le cas de cations métalliques incorporés aux réseaux de tamis moléculaires.

Par analogie avec ce que nous avons vu lors de l'étude des mécanismes électrochimiques intervenant avec les complexes encapsulés, nous pouvons considérer que l'incorporation de cations métalliques au sein du réseau des tamis moléculaires doit aboutir à des mécanismes similaires. En effet, les cations métalliques sont immobilisés au sein de la structure du tamis, ils ne peuvent donc participer qu'à un mécanisme électrochimique de nature intra-zéolithique. Les termes intra- et extra-zéolithique utilisés pour décrire les mécanismes électrochimiques sont conservés dans le cas de l'étude électrochimique des tamis moléculaires. Il y a peu d'études qui portent sur la caractérisation électrochimique des tamis moléculaires modifiés ou de matériaux s'en approchant. Cependant, quelques études électrochimiques de tamis moléculaires modifiées ont été reportées au cours des cinq dernières années.

De Guzman et al. (107) ont été les premiers à étudier l'activité électrochimique d'un tamis moléculaire contenant des cations métalliques de transition. Ils s'agit de tamis moléculaires octaédriques (OMS), ayant la structure todorokite (OMS-1) ou hollandite (OMS-2), contenant des ions Mn(II) ou Cu(II), qu'ils ont étudiés au moyen d'électrodes à pâte de carbone. Leur objectif a été de déterminer si ces ions métalliques sont mobiles et situés dans les tunnels, ou immobiles et donc incorporés au réseau du matériau. Les voltammogrammes obtenus avec OMS-1 montre un couple de pics tandis que ceux obtenus avec OMS-2 ne montrent aucun signal particulier. Ils expliquent la différence entre ces deux matériaux par la présence des ions Mn(II) dans OMS-1 alors qu'ils sont absents dans OMS-2. Des expériences conduites en RPE ont confirmé ces résultats et montré que OMS-2 contient principalement les ions Mn(III) et Mn(IV) qui ne sont pas accessibles par électrochimie dans le domaine de potentiel choisi. Les intensités de pic observées lors de l'étude de Mn–OMS-1 semblent stables alors qu'elles décroissent sensiblement avec le nombre de cycles effectués dans le cas de l'étude de Cu–OMS-1, ce qui permet aux auteurs de localiser les ions Mn(II) à l'intérieur du réseau de OMS-1 alors que les ions Cu(II) semblent occuper une position extra-réseau. Cu–OMS-2 ne montre aucune activité électrochimique particulière, ce qui est certainement dû à une ouverture de canaux trop petite (4,8 Å). D'un point de vue mécanistique, De Guzman et al. expliquent le comportement électrochimique de OMS-1 par un mécanisme intra-zéolithique. Plus précisément, ils expliquent que la conduction peut être assurée par sauts d'électrons entre les sites Mn(II) intra-réseaux. Pour ce qui est des ions Cu(II), extra-réseaux, la comparaison des voltammogrammes effectués avec Cu–OMS-1 (un couple de pics) et à partir d'une solution de Cu(II) (deux couples de pics) semble indiquer que le mécanisme électrochimique est de nature intra-zéolithique.

Venkatathri et al. (108) ont étudié le comportement électrochimique du tamis moléculaire VAPO-5 au moyen d'une électrode à pâte de carbone. L'étude des tamis moléculaires contenant du vanadium est rendue compliquée par les nombreux états d'oxydation et géométries que peut prendre cet élément. De plus, malgré les nombreuses méthodes d'analyse utilisées pour la caractérisation de ce type de matériau, la position intra-réseau du vanadium n'est pas encore clairement démontrée. Les voltammogrammes obtenus par Venkatathri et al. montrent deux couples de pics qu'ils attribuent aux ions vanadium (système V(V)/V(IV)) intra-réseaux situés dans deux environnements différents. Par comparaison avec les analyses effectuées en RPE et le comportement électrochimique des complexes $VO(acac)_2$ (acac = acétylacétonate) et $VO(iso\text{-}OPr_3)$ ($iso\text{-}OPr_3$ = isopropoxyde), les deux systèmes observés semblent dus aux ions vanadium situés en symétrie tétraédrique distordue et pyramide à base carré. Ils observent de plus un pic d'oxydation irréversible situé vers E_{pa} = 0,6 V/ECS, dont l'intensité diminue avec le temps d'immersion de l'électrode en solution. Ils attribuent ce pic à l'oxydation des ions VO^{2+} non incorporés au réseau pendant la synthèse.

Nous avons de notre coté montré (75) qu'il est possible d'observer l'activité électrochimique des ions vanadium situés dans les phases amorphes des échantillons VAPO-5 qui en contiennent, puis celle des ions vanadium situés au niveau du tamis moléculaire après la sédimentation. Ces derniers seraient inobservables dans les premiers temps d'expérience avec les échantillons n'ayant pas subi la sédimentation, car leur accessibilité est moins importante, donc l'activité électrochimique qu'ils engendrent est trop peu intense pour être mesurée. Cette remarque pose à nouveau le problème de la localisation des ions vanadium dans VAPO-5. Sachant que nos résultats d'analyse élémentaire nous ont montré que la quantité de vanadium présente dans les échantillons non calcinés et calcinés n'était que très faiblement supérieure à celle contenue dans les échantillons ayant subit la sédimentation, nous avons été amenés à conclure à une accessibilité beaucoup plus importante des ions vanadium localisés au niveau des phases amorphes. Quant à la localisation des ions vanadium au niveau des parties cristallines du tamis moléculaire, la stabilité des voltammogrammes obtenus après de longs temps d'immersion des électrodes en solution suggère que le vanadium se situe à l'intérieur du réseau du tamis moléculaire (fig. 16). Nous ne pouvons cependant pas exclure un mode d'incorporation des ions vanadium dans le réseau d'AlPO-5 par condensation avec les ions hydroxydes de surface.

Un dernier exemple d'utilisation de l'électrochimie pour la caractérisation des tamis moléculaires chimiquement modifiés a été développé par de Castro-Martins et al. (47, 109). Ils ont étudié le comportement électrochimique du titanosilicate TS-1 au moyen d'une électrode à pâte de carbone. Ils observent un couple de pics qu'ils attribuent au système Ti(IV)/Ti(III) d'ions titane intra-réseaux car la zéolithe ZSM-5 (isostructurale de TS-1) contenant des ions titane

© 1998 CNRC Canada

Fig. 16. Voltampérogrammes cycliques d'une électrode composite contenant VAPO-5 dans H_2O + KBF_4 après 24 h d'immersion en solution (à 10 mV/s). Courbe 1 : VAPO-5 non calciné; courbe 2 : VAPO-5 calciné, adapté de la reférence 75.

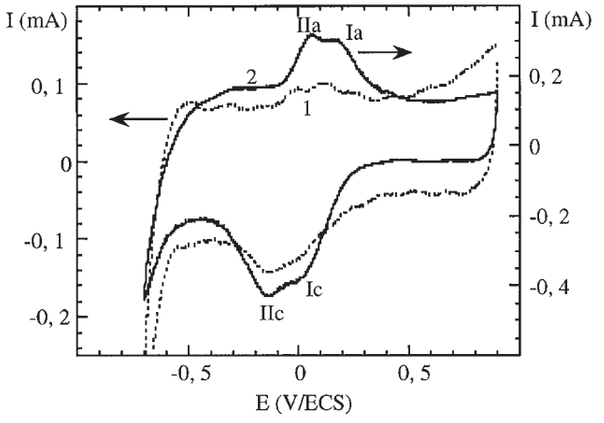

(extra-réseaux) et le composé TiO_2 ne montrent aucune activité électrochimique particulière dans les mêmes conditions. De plus, ils ont montré que le comportement électrochimique de TS-1 est très proche de celui du composé TEOT (tétraéthylorthotitanate), ce qu'ils expliquent par un environnement similaire des ions titane dans les deux matériaux, c'est-à-dire en symétrie tétraédrique. D'après ces auteurs, trois mécanismes électrochimiques sont à considérer :

1. Les ions titane, délogés du centre des tétraèdres TO_4, diffusent vers l'ouverture des canaux du tamis pour y subir le transfert d'électron.

2. Le processus électrochimique ne concerne que les ions titane situés à la frontière entre les grains de tamis et de graphite, à l'interface électrode–solution. Dans ce cas, seuls les ions titane situés à la surface du matériau sont électroactifs.

3. Le processus électrochimique n'est pas limité aux ions titane situés en surface et l'ensemble des ions titane sont impliqués dans le processus rédox. Cette possibilité implique une participation des cations de l'électrolyte pour compenser la charge créée par la réaction rédox.

Les auteurs expliquent que le premier mécanisme peut être infirmé car la diffusion des ions titane vers la solution après de longues périodes d'immersion de l'électrode en solution devrait s'accompagner d'une diminution des intensités des pics. De plus, ils n'ont pas été en mesure de détecter les ions titane en solution. Cependant, ils ne considèrent pas le fait que les ions titane peuvent quitter le tamis moléculaire sans pour autant quitter l'électrode. En revanche, l'utilisation d'un cation d'électrolyte volumineux, tel que le cation TBA^+ qui est exclu des canaux du tamis TS-1, induit la disparition des pics précédemment observés, ce qui s'accorde peu avec un mécanisme de type extra-zéolithique. Pour réfuter le second mécanisme, les auteurs considèrent qu'il n'y a pas de raison pour que les intensités de pic augmentent de manière linéaire avec le temps d'immersion de l'électrode. Cette remarque est discutable quand on sait que l'augmentation des intensités de pic peut être due au mouillage progressif de l'électrode à pâte de carbone par le solvant. La deuxième remarque permettant d'écarter le mécanisme 2 est que la taille des cristaux n'est pas reliée au courant de pic, ce qui signifie que les ions titane situés en surface ne sont pas les seuls à participer au processus électrochimique. Cependant, en se basant sur la trés faible électroactivité de ce matériau (comme unique critère), il est probable que celle-ci ne reflète que l'activité rédox des ions Ti^{4+} tétrahédriques intra-réseau mais situés à la surface du tamis moléculaire (ou à la frontière de celle-ci) sans qu'il y ait propagation électronique à travers tous les sites intra-réseau et intra-zéolithiques (110).

V. Conclusion

Malgré les intenses discussions ayant lieu actuellement concernant la caractérisation électrochimique des zéolithes et des tamis moléculaires, l'ensemble des résultats analysés ici montre tout l'intérêt de l'électrochimie comme méthode d'investigation des complexes de métaux de transition (ou des cations simples) incorporés dans ces structures. Outre sa capacité à caractériser les complexes intra-zéolithiques ou les cations rédox faisant partie intégrante du reseau de certains tamis moléculaires modifiés, l'électrochimie a montré son aptitude à témoigner de l'efficacité de l'incorporation de ces espèces, à détecter la présence de résidus mais aussi à purifier la zéolithe ou le tamis moléculaire en engendrant des phénomènes de désorption. La possibilité d'atteindre des taux d'électroactivité satisfaisants ouvrent la voie à des applications en électrocatalyse. Et dans ce domaine, de par leur structure rigide et parfaitement définie, les zéolithes et les aluminophosphates modifiés sont certainement plus sélectifs par rapport à d'autres structures minérales telles que les argiles. D'autres perspectives d'avenir existent. Ainsi, en photoélectrochimie, l'utilisation de ces matériaux offrent des avantages certains, par exemple en favorisant la séparation des espèces impliquées dans le transfert de charge ou en contrôlant la taille des semi-conducteurs intra-zéolithiques. Par ailleurs, la capacité de la zéolithe à stabiliser les étapes intermédiaires d'un processus réactionnel difficilement observables en solution a été mentionnée. La voltampérométrie peut être une méthode de caractérisation de ces états intermédiaires et permettrait ainsi l'analyse des mécanismes de réaction complexes.

VI. Remerciements

Nous tenons à remercier Dr. Jacques Devynck (Directeur de recherche au CNRS et Directeur du Laboratoire d'électrochimie et de chimie analytique) pour l'intéret qu'il a porté à ce travail et sa collaboration permanente tout au long des recherches que nous avons effectuées sur ce sujet. Nous tenons aussi à remercier Prof. Kenneth J. Balkus, Jr. (Department of Chemistry, University of Texas at Dallas) pour sa collaboration scientifique et son aide précieuse quant à la préparation de certains zéolithes et aluminophosphates chimiquements modifiés. Nous remercions aussi tous les co-auteurs dont les noms apparaissent dans nos travaux cités, ainsi que le Centre national de la recherche scientifique (France) et le National Science Foundation (U.S.A.) pour leur soutien financier.

© 1998 CNRC Canada

VII. Bibliographie

1. J.V. Smith. Chem. Rev. **88**, 149 (1988).
2. D.W. Breck (*Éditeur*). Zeolite molecular sieve. Krieger, Malabar. 1984.
3. R.M. Barrer (*Éditeur*). Zeolites and clay minerals. Academic Press, London. 1978.
4. S.T. Wilson, B.M. Lok, C.A. Messina, T.R. Cannan et E.M. Flanigen. J. Am. Chem. Soc. **104**, 1146 (1982).
5. B.M. Lok, C.A. Messina, R.L. Patton, R.T. Gajek et E.M. Flanigen. J. Am. Chem. Soc. **106**, 6092 (1984).
6. S.T. Wilson et E.M. Flanigen. ACS Symp. Ser. **398**, 329 (1989).
7. M. Gratzel et K. Kalyanasundaram. (*Éditeurs*). Kinetics and catalysis in microheterogeneous systems. Marcel Dekker, New York. 1991.
8. D.C. Bailey et S.H. Langer. Chem. Rev. **81**, 109 (1981).
9. G.A. Ozin et C. Gil. Chem. Rev. **89**, 1749 (1986).
10. T. Bein (*Éditeur*). Supramolecular architecture. ACS Symp. Ser. **499**, American Chemical Society, Washington, D.C. 1992.
11. D.E. De Vos, P.P. Knops-Gerrits, R.F. Parton, B.M. Weckhuysen, P.A. Jacobs et R.A. Schoonheydt. J. Inclusion Phenom. Mol. Recogn. Chem. **21**, 185 (1995).
12. K.J. Balkus, Jr. et A.G. Gabrielov. J. Inclusion Phenom. Mol. Recogn. Chem. **21**, 159 (1995).
13. N. Herron, G.D. Stucky et C.A. Tolman. Inorg. Chim. Acta, **100**, 135 (1985).
14. V.Y. Zakharov et B.V. Romanovsky. Vestn. Mosk. Univ. Ser. 2: Khim. **18**, 142 (1977) (traduction anglaise : Sov. Mosc. Univ. Bull. **32**, 16 (1977)).
15. B.V. Romanovsky, R.E. Mardaleishvili, V.Y. Zakharov et O.M. Zakharova. Vestn. Mosk. Univ. Ser. 2: Khim. **18**, 232 (1977).
16. V.Y. Zakharov et B.V. Romanovsky. Vestn. Mosk. Univ. Ser. 2 Khim. **18**, 348 (1977).
17. V.Y. Zakharov, O.M. Zakharova, B.V. Romanovsky et R.E. Mardaleishvili. React. Kinet. Catal. Lett. **6**, 133 (1977).
18. E.M. Flanigen, B.M. Lok, R.L. Patton et S.T. Wilson. *Dans* New developments in zeolite science and technology. *Édité par* : Y. Murakami, A. Lijima et J.W. Ward. Elsevier, Amsterdam. 1986. p. 103.
19. E.M. Flanigen, R.L. Patton et S.T. Wilson. Stud. Surf. Sci. Catal. **37**, 13 (1988).
20. E. Paes-Mozo, N. Gabruinas, F. Lucaccioni, D.D. Acosta, P. Patrono, A. La Ginestra, P. Ruis et B. Delmon. J. Phys. Chem. **97**, 12819 (1993).
21. B.R. Shaw, K.E. Creasy, C.J. Lanczycki, J.A. Sargeant et M. Tirhado. J. Electrochem. Soc. **135**, 869 (1988).
22. B.R. Shaw et K.E. Creasy. J. Electroanal. Chem. **243**, 209 (1988).
23. C. Senaratne et M.D. Baker. J. Electroanal. Chem. **332**, 357 (1992).
24. M.D. Baker et C. Senaratne. Anal. Chem. **64**, 697 (1992).
25. D.R. Rolison, R.J. Nowak, T.A. Welsh et C.G. Murray. Talanta, **38**, 27 (1991).
26. C. Bing et L. Kryger. Talanta, **43**, 153 (1996).
27. J. Wang et A. Walcarius. J. Electroanal. Chem. **404**, 237 (1996).
28. B. Chen, N.-K Goh et L.-S. Chia. Electrochim. Acta, **42**, 595 (1997).
29. A. Walcarius, T. Barbaise et J. Bessière. Anal. Chim. Acta, **340**, 61 (1997).
30. A. Walcarius. Electroanalysis, **8**, 971 (1996).
31. Z. Li et T.E. Mallouk. J. Phys. Chem. **91**, 643 (1987).
32. Z. Li, C.M. Wang, L. Persaud et T.E. Mallouk. J. Phys. Chem. **92**, 2592 (1988).
33. Z. Li, C. Lai et T.E. Mallouk. Inorg. Chem. **28**, 178 (1989).
34. K. Mesfar, B. Carré, F. Bedioui et J. Devynck. J. Mater. Chem. **3**, 873 (1993).
35. K.E. Creasy et B.R. Shaw. Electrochim. Acta, **33**, 551 (1988).
36. J. Taraszewska, G. Roslonek et W. Darlewski. J. Electroanal. Chem. **371**, 223 (1994).
37. D.R. Rolison, E.A. Hayes et W.E. Rudzinski. J. Phys. Chem. **93**, 5524 (1989).
38. D.R. Rolison et J.Z. Stemple. J. Chem. Soc. Chem. Commun. 25 (1993).
39. A. Walcarius, L. Lambert et E.G. Derouane. Electrochim. Acta, **38**, 2257 (1993).
40. A. Walcarius, L. Lambert et E.G. Derouane. Electrochim. Acta, **38**, 2267 (1993).
41. M.D. Baker, C. Senaratne et J. Zhang. J. Chem. Soc. Faraday Trans. **88**, 3187 (1992).
42. M.D. Baker, C. Senaratne et J. Zhang. J. Phys. Chem. **98**, 1668 (1994).
43. D.R. Rolison. Chem. Rev. **90**, 867 (1990).
44. A.J. Bard et T.E. Mallouk. *Dans* Molecular design of electrode surfaces. *Édité par* R.W. Murray. Wiley, New York. 1992. pp. 271–312.
45. D.R. Rolison. Stud. Surf. Sci. Catal. **85**, 543 (1994).
46. E. Briot et F. Bedioui. Curr. Top. Electrochem. **4**, 87 (1997).
47. S. De Castro-Martins, S. Khouzami, A. Tuel, Y. Ben Taarit, N. El Murr et A. Sellami. J. Electroanal. Chem. **350**, 15 (1993).
48. N. El Murr, M. Kerkeni, A. Sellami et Y. Ben Taarit. J. Electroanal. Chem. **246**, 461 (1988).
49. M.M. Thackeray et J. Coetzer. Solid State Ionics, **6**, 135 (1982).
50. R.M. Barrer et S.D. James. J. Phys. Chem. **64**, 421 (1960).
51. M. Demertzis et N.P. Evmiridis. J. Chem. Soc. Faraday Trans. 1, **82**, 3647 (1986).
52. G. Johansson, L. Risinger et L. Falth. Anal. Chim. Acta, **119**, 25 (1980).
53. M.V. Susic et N. Petranovic. Electrochim. Acta, **23**, 1271 (1978).
54. M.V. Susic. Electrochim. Acta, **24**, 535 (1979).
55. N. Petranovic et M. Susic. Zeolites, **3**, 271 (1983).
56. J.-P. Pereira-Ramos, R. Messina et J. Perichon. J. Electroanal. Chem. **146**, 157 (1983).
57. J.-P. Pereira-Ramos. Thèse de doctorat, Université P. et M. Curie, Paris. 1982.
58. B. De Vismes, F. Bedioui, J. Devynck et C. Bied-Charreton. J. Electroanal. Chem. **187**, 197 (1985).
59. F. Bedioui, E. De Boysson, J. Devynck et K.J. Balkus. J. Chem. Soc. Faraday Trans. **97**, 3831 (1991).
60. F. Bedioui, E. De Boysson, J. Devynck et K.J. Balkus. J. Electroanal. Chem. **315**, 913 (1991).
61. L. Gaillon, N. Sajot, F. Bedioui, J. Devynck et K.J. Balkus. J. Electroanal. Chem. **345**, 157 (1993).
62. L. Gaillon, F. Bedioui, J. Devynck, P. Battioni, L. Barloy et D. Mansuy. J. Electroanal. Chem. **303**, 283 (1991).
63. L. Gaillon, P. Battioni, F. Bedioui et J. Devynck. J. Electroanal. Chem. **347**, 435 (1993).
64. K.J. Balkus, Jr., A.G. Gabrielov, S.L. Bell, F. Bedioui, L. Roué et J. Devynck. Inorg. Chem. **33**, 67 (1994).
65. A.G. Gabrielov, K.J. Balkus, Jr., S.L. Bell, F. Bedioui et J. Devynck. Microporous Mater. **2**, 119 (1994).
66. F. Bedioui, L. Roué, E. Briot, J. Devynck, S. Bell et K.J. Balkus, Jr. J. Electroanal. Chem. **373**, 19 (1994).
67. L. Gaillon, F. Bedioui et J. Devynck. J. Mater. Chem. **4**, 1215 (1994).
68. F. Bedioui, L. Roué, J. Devynck et K.J. Balkus, Jr. J. Electrochem. Soc. **141**, 3049 (1994).
69. F. Bedioui, L. Roué, J. Devynck et K.J. Balkus, Jr. Stud. Surf. Catal. Sci. **84**, 917 (1994).
70. F. Bedioui, J. Devynck et K.J. Balkus, Jr. J. Phys. Chem. **100**, 8607 (1996).

© 1998 CNRC Canada

71. K.J. Balkus, Jr., A.K. Khanmamedova, K.M. Dixon et F. Bedioui. Appl. Catal. **143**, 159 (1996).
72. F. Bedioui, L. Roué, E. Briot, J. Devynck, K.J. Balkus, Jr. et J.F. Diaz. New J. Chem. **20**, 1253 (1996).
73. F. Bedioui, E. Briot, J. Devynck, F. Diaz et K.J. Balkus, Jr. Mater. Res. Soc. Symp. Proc. **431**, 89 (1996).
74. J.F. Diaz, K.J. Balkus, Jr., F. Bedioui, V. Kurshev et L. Kevan. Chem. Mater. **9**, 61 (1997).
75. F. Bedioui, E. Briot, J. Devynck et K.J. Balkus, Jr. Inorg. Chim. Acta, **254**, 151 (1997).
76. H.A. Gemborys et B.R. Shaw. J. Electroanal. Chem. **208**, 95 (1986).
77. C.G. Murray, R.J. Nowak et D.R. Rolison. J. Electroanal. Chem. **164**, 205 (1984).
78. T. Bein et P. Enzel. Angew. Chem. **28**, 1692 (1989).
79. S. Esnouf, F. Beuneu, J. Mory, L. Zuppiroli, P. Enzel et T. Bein. J. Chim. Phys. **89**, 1173 (1992).
80. L. Zuppiroli, F. Beuneu, J. Mory, P. Enzel et T. Bein. Synth. Met. **55–5**7 5081 (1993).
81. C.-G. Wuu et T. Bein. Science, **264**, 1757 (1994).
82. G. Calzaferri, K. Hadener et J Li. J. Chem. Soc. Chem. Commun. 653(1991).
83. J. Li et G. Calzaferri. J. Chem. Soc. Chem. Commun. 1430 (1993).
84. J. Li et G. Calzaferri. J. Electroanal. Chem. **377**, 163 (1994).
85. J. Li, K. Pfanner et G. Calzaferri. J. Phys. Chem. **99**, 2119 (1995).
86. B. De Vismes, F. Bedioui, J. Devynck, C. Bied-Charreton et M Perrée-Fauvet. New J. Chem. **10**, 81 (1986).
87. C.A. Bessel et D.R. Rolison. J. Phys. Chem. **101**, 1148 (1997).
88. C.A. Bessel et D.R. Rolison. J. Am. Chem. Soc. **119**, 12673 (1997).
89. J. Cassidy, W. Breen, E. O'Donoghue et M.E.G. Lyons. Electrochim. Acta, **36**, 383 (1991).
90. J. Sarradin, J.-M. Louvet, R. Messina et J. Périchon. Zeolites, **4**, 157 (1984).
91. A. Walcarius et L. Lamberts. J. Electroanal. Chem. **422**, 77 (1997).
92. C. Senaratne, J. Zhang, M.D. Baker, C.A. Bessel et D.R. Rolison. J. Phys. Chem. **100**, 5849 (1996).
93. M.D. Baker et J. Zhang. J. Phys. Chem. **94**, 8703 (1990).
94. M.D. Baker, J. Zhang et M. McBrien. J. Phys. Chem. **99**, 6635 (1995).
95. R.M. Barrer. J. Inclusion Phenom. **1**, 105 (1983).
96. O. Enea. Electrochim. Acta, **34**, 1647 (1989).
97. C. Iwakura, S. Miyazaki et H. Yoneyama. J. Electroanal. Chem. **246**, 63 (1988).
98. A. Walcarius et L. Lamberts. J. Electroanal. Chem. **422**, 77 (1997).
99. S. Bharathi, K.L.N. Phani, J. Josephh, S. Pitchumani, D. Jeyakumar, G. Prabhakara Rao et S.K. Rangarajan. J. Electroanal. Chem. **334**, 145 (1992).
100. D.R. Rolison, C.A. Bessel, M.D. Baker, C. Senaratne et J. Zhang. J. Phys. Chem. **100**, 8610 (1996).
101. M.N. Golovin, P. Seymour, K. Jayarai, Y. Fu et A.B.P. Lever. Inorg. Chem. **29**, 1719 (1990).
102. C.A. Bessel et D.R. Rolison. Stud. Surf. Sci. Catal. **98**, 114 (1995).
103. N.A. Surridje, J.C. Jernigan, E.F. Dalton, R.P. Buck, M. Watanabe, H. Zhang, M. Pinkerton, T.T. Wooster, M.L. Longmire, J.S. Facci et R.W. Murray. Faraday Discuss. Chem. Soc. **88**, 1 (1989).
104. I. Fritsch-Faules et L.R. Faulkner. J. Electroanal. Chem. **263**, 237 (1989).
105. M. Majda. *Dans* Molecular design of electrode surface. *Édité par* R.W. Murray. Wiley, New York. 1992. pp. 159–206.
106. W. Turbeville, D.S. Robins et P.K. Dutta. J. Phys. Chem. **96**, 5024 (1992).
107. R.N. De Guzman, Y.F. Shen, B.R. Shaw, S.L. Suib et C.L. O'Young. Chem. Mater. **5**, 1395 (1993).
108. N. Venkatathri, M.P. Vinod, K. Vijayamohanan et S. Sivasanker. J. Chem. Soc. Faraday Trans. **92**, 473 (1996).
109. S. de Castro-Martins, A. Tuel et T. Ben Taârit. Zeolites, **14**, 130 (1994).
110. S. de Castro-Martins, A. Tuel, T. Ben Taârit, M.D. Baker et D.R. Rolison. (Zeolite Sci. 1994 : Recent Prog. Discuss.) Stud. Surf. Sci. Catal. **98**, 361 (1995).

© 1998 CNRC Canada

Remarkable kinetic stability of α-thiocarbamoyl substituted 4-methoxybenzyl cations

Robert A. McClelland, Victoria E. Licence, John P. Richard, Kathleen B. Williams, and Shrong-Shi Lin

Abstract: 4-Methoxybenzyl cations bearing α-(*N*,*N*-dimethylcarbamoyl) and α-(*N*,*N*-dimethylthiocarbamoyl) substituents have been generated photochemically upon irradiation of precursors with pentafluorobenzoate or 4-methoxybenzoate leaving groups. The ions have been observed with flash photolysis in 40:60 acetonitrile:water and in 50:50 methanol:water, and rate constants were measured for their decay in solvent alone and for their capture by azide ion. The cations so studied and their lifetimes in 40% acetonitrile are **6**, $ArC^+H\text{-}CONMe_2$, 0.6 μs; **2**, $ArC^+H\text{-}CSNMe_2$, 7 ms; and **4**, $ArC^+(CH_3)\text{-}CSMe_2$, 6 ms, where Ar = 4-$MeOC_6H_4$. The cation **4** reacts with solvent by elimination of a proton from the α-methyl group, and the rate constant for solvent addition must be less than 1 s^{-1}. The $CSNMe_2$ substituted cations are 10^5–10^7-fold longer lived than analogs where the thioamide group has been replaced with an α-methyl. The UV–visible absorption spectra of these two cations also show significant differences from those of typical 4-methoxybenzyl cations. Thus, both the lifetimes and spectra point to a strong interaction of the benzylic centre with the thioamide group.

Key words: flash photolysis, thiocarbamoyl stabilized carbocation, photosolvolysis.

Résumé : L'irradiation de précurseurs appropriés portant des groupes partant pentafluorobenzoate ou 4-méthoxybenzoate permet de générer photochimiquement des cationns 4-méthoxybenzyle portant des substituants α-(*N*,*N*-diméthylcarbamoyle) et α-(*N*,*N*-diméthylthiocarbamoyle). On a observé les ions par photolyse éclair dans des mélanges 40 : 60, acétonitrile : eau et de 50 : 50, méthanol : eau et on a mesuré les constantes de décroissance dans les solvants seuls ainsi que pour leur capture par l'ion azoture. Les cations ainsi étudiés et leurs temps de vie dans l'acétonitrile à 40% sont : **6**, $ArC^+H\text{-}CONMe_2$, 0,6 μs; **2**, $ArC^+H\text{-}CSNMe_2$, 7 ms et **4**, $ArC^+CH_3\text{-}CSNMe_2$, 6 ms dans lesquels Ar = 4-$MeOC_6H_4$. Le cation **4** réagit avec le solvant pour donner une élimination de proton provenant du groupe méthyle en α et la constante de vitesse pour l'addition du solvant doit être inférieure à 1 s^{-1}. Les temps de vie des cations substitués par $CSNMe_2$ sont de 10^5–10^7 fois plus grandes que celles de leurs analogues dans lesquels le groupe thioamide a été remplacé par un α-méthyle. Les spectres d'absorption UV–visible de ces deux cations présentent des différences importantes par rapport à ceux des cations 4-méthoxybenzyles typiques. Les temps de vie et les spectres suggèrent donc tous les deux qu'il existe une forte interaction entre le centre benzylique et le groupe thioamide.

Mots clés : photolyse éclair, carbocation stabilisé par un groupe thiocarbamoyle, photosolvolyse.

[Traduit par la Rédaction]

There have been several recent studies of solvolysis reactions involving carbocations substituted at the C^+ center with a thioamide functional group such as $CSNMe_2$ (1–9). There is good evidence that the reactions do occur by a stepwise $D_N + A_N$ (S_N1) mechanism proceeding via a carbocation intermediate (2, 4, 7). Rate constants for the formation of the α-thioamido substituted cation relative to an analog with α-methyl vary. In some cases the former forms slightly more slowly, in some cases somewhat more quickly, and in some cases considerably more quickly. On the other hand, an α-$CONMe_2$ substituted cation generally forms considerably more slowly than its α-methyl analog.

Less is known about the rate constants for solvent capture of the fully formed cations. The 9-thioamidofluorenyl cation **1** has been claimed as a transient intermediate in a laser flash photolysis experiment in 2,2,2-trifluoroethanol (TFE) (6). There are, however, now serious concerns over the structural assignment in this study, since the chloro precursor that was supposedly employed decomposes instantly when dissolved in TFE (9).

1

Received September 10, 1998.

R.A. McClelland[1] and V.E. Licence. Department of Chemistry, University of Toronto, Toronto, ON M5S 3H6, Canada.
J.P. Richard, K.B. Williams, and S.-S. Lin. Department of Chemistry, State University of New York at Buffalo (SUNY), Buffalo, NY 14260-3000, U.S.A.

[1]Author to whom correspondence may be addressed. Telephone: (416) 978-3592. Fax: (416) 978-3592. E-mail: rmcclell@alchemy.chem.utoronto.ca

© 1998 NRC Canada

Table 1. Rate constants for solvent decay and azide quenching of 4-methoxybenzyl cations 4-$MeOC_6H_4C^+R_1,R_2$ generated by flash photolysis of **7–9**. Experiments at 20°C in 40:60 acetonitrile:water at ionic strength zero and in 50:50 methanol:water at ionic strength 0.5 with $NaClO_4$.

	7 → **6**	**8** → **2**	**9** → **4**
Constant	$CONMe_2$, H	$CSNMe_2$, H	$CSNMe_2$, Me
k_s (40% AN), s^{-1}	(1.6±0.1) × 10^6	(1.5±0.2) × 10^2	(1.8±0.2) × 10^2
k_{az} (40% AN), M^{-1} s^{-1}	(5.4±0.3) × 10^9	(6.3±0.2) × 10^7	Not measured
k_s (50% MeOH), s^{-1}	(8.6±0.4) × 10^6	(2.4±0.1) × 10^2	(2.1±0.1) × 10^2
k_{az} (50% MeOH), M^{-1} s^{-1}	(2.1±0.3) × 10^9	(1.03±0.03) × 10^7	(4.9±0.2) × 10^4
k_{az}:k_s (50% MeOH), M^{-1}	(2.4±0.4) × 10^2	(4.3±0.2) × 10^4	(2.3±0.2) × 10^2
k_{az}:k_s (50% MeOH-sol),[a] M^{-1}	2.1 × 10^2	7 × 10^4	1.8 × 10^2 [b]

[a] Ratio obtained from analysis of products of ground state solvolysis (7).
[b] Solvent reaction is elimination. Azide reaction is sum of elimination and addition.

In a second study, competition kinetics in 50:50 methanol:water revealed that the benzylic derivative **2** has an azide:solvent selectivity k_{az}:k_s of 7 × 10^4 M^{-1} (7). This is 10^4-fold greater than the k_{az}:k_s of 7.2 M^{-1} for the 4-methoxyphenethyl cation **3** in the same solvent (7). With the assumption that the azide combination is a diffusion-limited process (10), so that k_{az} is the same for both cations (~5 × 10^9 M^{-1} s^{-1}), the lifetime ($1/k_s$) of the thioamido-substituted cation is 10 000-fold longer. Unexpected behavior is also seen with α-thioamido, α-methyl substituted cations (4, 7). The cation **4**, for example, reacts with solvent to give exclusively the alkene product derived from elimination of one of the α-protons (7). Elimination even occurs with azide although, with this ion, addition to the C^+ center also occurs. Such behavior contrasts with that of the cumyl cation analog **5**, where only nucleophilic addition is observed (e.g., less than 1% elimination in the reaction with solvent in 50:50 methanol:water) (7).

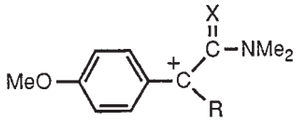

2; X = S, R = H
4; X = S, R = CH_3
6; X = O, R = H

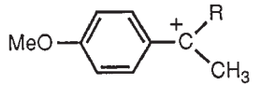

3; R = H
5; R = CH_3

As noted in the original paper (7), the large k_{az}:k_s ratio for **2** leads to concerns about the applicability of the azide clock assumption. The competing elimination/addition with **4** raises this question even more with this system. In consequence, we have performed flash photolysis experiments so as to obtain the absolute rate constants for these cations. The α-amido substituted **6** was included for comparison purposes. It transpires that these cations can be generated from the same precursors employed in the studies of the ground solvolysis. Moreover, the α-thioamido cations are remarkably long-lived.

Results

The substituted benzoates **7–9** were employed as photochemical precursors of the cations **6**, **2**, and **4**, respectively. These esters undergo ground state solvolysis with half-lives of 100 h (**7**), 130 s (**8**), and 5.2 h (**9**) in 50:50 methanol:water at 25°C (7). With **8** this meant that the flash photolysis experiments needed to be carried out immediately after preparation of the solution. It in fact proved possible to prepare the solution and irradiate within 20 s.

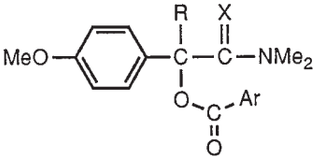

7; R = H, X = O, Ar = C_6F_5
8; R = H, X = S, Ar = C_6F_5
9; R = CH_3, X = S, Ar = 4-$CH_3OC_6H_4$

Flash photolysis spectra obtained with **7–9** in 40% acetonitrile are shown in Fig. 1. The benzoate **7** produces a transient species with λ_{max} around 350 nm, which decays over 5–10 μs to essentially zero OD. The decay is first order, with the same rate constant being obtained across the entire spectrum consistent with the presence of a single transient species. Absorbing species are also observed with **8** and **9**. However, these show no decay up to times as long as 500 μs, the longest time that can be reliably employed with the laser flash photolysis apparatus. Decay is seen, however, using a lamp photolysis apparatus. Like **7**, these decays are first order with the same rate constant throughout the spectrum. The λ_{max} of the transients with **8** and **9** lie in the range 310–325 nm, being slightly higher with **9**. There is, however, some distortion of the spectra, since the thioamido precursors absorb below 310 nm. (Note that these experiments measure a ΔOD, the OD after the laser pulse minus the OD before.) With **9**, there is a second weaker absorption with λ_{max} around 500 nm. This is due to the same transient as the absorbance at lower wavelength, since the decay here has the same rate constant. It can be noted that with **8**, aged solutions that had undergone solvolysis to the alcohol failed to produce any transient.

Azide ion accelerates the decay of all three transients, with linear plots of the observed rate constant versus azide concentration. Values of k_s, the first-order rate constant for decay in solvent alone, and k_{az}, the second-order rate constant for the quenching by azide ion, are given in Table 1. Two solvents were employed, 40:60 acetonitrile:water, and 50:50 methanol:water. The former was chosen to provide comparisons with rate constants measured by flash photolysis for other benzylic cations. The latter was the solvent

© 1998 NRC Canada

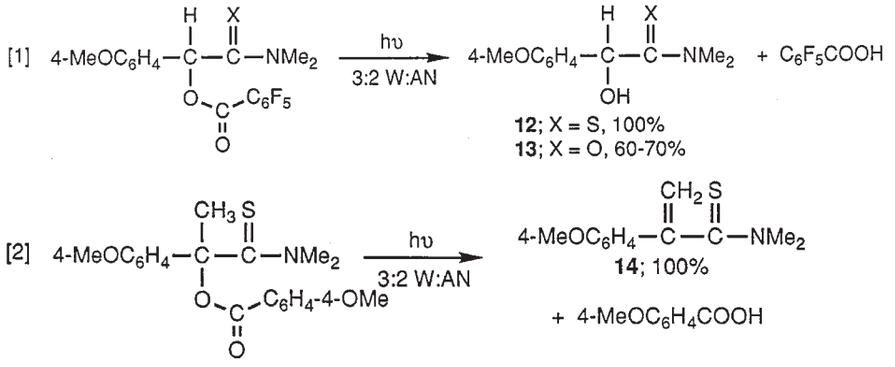

employed in the analysis of the products of the ground state solvolysis of these esters.

The final products of the irradiation were examined in 40% aqueous acetonitrile. These experiments were carried out by preparing a solution of the precursor benzoate of concentration ~100 μM, which was then split in two. One half was irradiated at 254 nm, while the other was kept in the dark under conditions sufficient for complete ground state solvolysis. The HPLC chromatograms of the two were then compared, along with the chromatograms of the authentic products of the ground state hydrolysis.

With **8**, which undergoes a relatively rapid ground state solvolysis, the solvent was cooled to 0°C before addition of the substrate. After substrate addition, half was irradiated at this temperature for 30 s, a time sufficient to remove 95% of the precursor. The other half was warmed to room temperature and allowed to stand for a total time of 1 h. (The half-life at 20°C is 4 min.) The products observed in both the excited state and ground state reactions were the alcohol **10** and pentafluorobenzoic acid (eq. [1]). Based on the relative areas of the peaks (with a small correction for remaining precursor), the yield of the the alcohol in the irradiated solution was 102% of that in ground state. Thus, within experimental error, there was quantitative formation of the same product of the ground state solvolysis.

The same conclusion was reached with **9**. Again, 30 s irradiation was sufficient to photolyze 95% of the precursor. Four hours at 50°C was required for the ground state reaction. The observed products from both were the alkene **12** and 4-methoxybenzoic acid (eq. [2]). The yield of alkene in the irradiated solution was 97% of that of the solvolyzed one.

With **9**, the situation was more complicated. The photolysis was considerably less efficient, 3 min of irradiation for example only reacting 45% of the starting material. A consequence was that the products were not stable, unlike the situation with the two thioamides, but underwent further photochemistry. The solvolysis reaction required overnight at 50°C for completion, and gave the expected alcohol **11** and pentafluorobenzoic acid (eq. [1]). These were also the major products in the irradiated solution, but their yields expressed as a percentage of reacted **7** decreased with increased irradiation time. Based on a three-point extrapolation to zero irradiation, the yield of alcohol is 60–70%. The HPLC chromatogram of the irradiated solution did have other peaks, but these were not identified.

Discussion

Identification of transients as benzylic carbocations

While there is no spectrum of an authentic cation available for comparison, there is good evidence that the transients observed with the three esters **7–9** are cations forming by photoheterolytic cleavage of the α-carbon–oxygen bond. Firstly, the stable products of irradiation are those expected of a photosolvolysis. In the case of the thioamides **8** and **9** in fact, there is a very efficient conversion to exactly the same products obtained in the ground state solvolysis reaction. Secondly, the transients are quenched by azide ion, a typical carbocation trap. More importantly, the absolute rate constants k_{az} and k_s obtained by flash photolysis give selectivities k_{az}:k_s that are essentially the same as those obtained in the ground state solvolysis (7). This comparison was made in 50:50 methanol:water and is shown in Table 1. In the case of the cations **4** and **6**, the flash photolysis ratio is slightly larger but the difference is not outside experimental error. With **2**, the flash photolysis ratio is about two thirds of that obtained in the competition experiment. The latter was, however, obtained with azide ion concentrations in the range 0.5–1.0 mM, where >95% of the products arise from azide trapping (7). This means that the amount of alcohol product being measured is quite small, creating some uncertainty in the final ratio.

Rate constants for addition and elimination in cation 4

The reaction of the cation **4** gives only alkene product in 50:50 methanol:water (7). Thus the decay of this ion observed in the flash photolysis experiments represents the reaction with solvent acting as a base, and the k_s of 210 s^{-1} is equal to k_s(B) of eq. [3]. There is less than 1% of the ether and alcohol products that would arise form nucleophilic addition of solvent. Thus k_s(Nu) < 2 s^{-1}.

With azide ion, both elimination and addition occur. The azide-catalyzed elimination is seen in the observation that the alkene:RN_3 ratio does not approach zero at high concentrations of azide, but plateaus, in fact, with a greater amount of alkene (7). The limiting [alkene]:[RN_3] is 1.69; this is equal to the ratio of rate constants for azide acting as a base and a nucleophile, k_{az}(B):k_{az}(Nu). The quenching that is observed with azide ion in the flash photolysis studies represents the sum of these two processes, i.e., k_{az}(flash photolysis) = k_{az}(B) + k_{az}(Nu). Since the ratio is known from the product analysis, the absolute values of the two can be calculated. Thus k_{az}(B) = 3.1 × 10^4 M^{-1} s^{-1} and k_{az}(Nu) =

© 1998 NRC Canada

Table 2. Lifetimes of 4-methoxybenzyl cations 4-$MeOC_6H_4C^+R_1R_2$ measured by flash photolysis.

R_1	R_2	$(1/k_s)$ in TFE	$(1/k_s)$ in W:AN[a]	Ref.
H	H	0.2 μs		12
H	CH_3	2.5 μs		12
CH_3	CH_3	60 μs	25 ns	12
H	COOMe	6 μs	50 ns	13
H	$CONMe_2$		0.6 μs	This work
H	$CSNMe_2$		7 ms	This work
CH_3	$CSNMe_2$		6 ms (elim.) >1 s (add.)	This work

[a] The lifetimes of carbocations in aqueous acetonitrile solutions (0–60% acetonitrile) do not change by more than 10–20% with changing acetonitrile content (14).

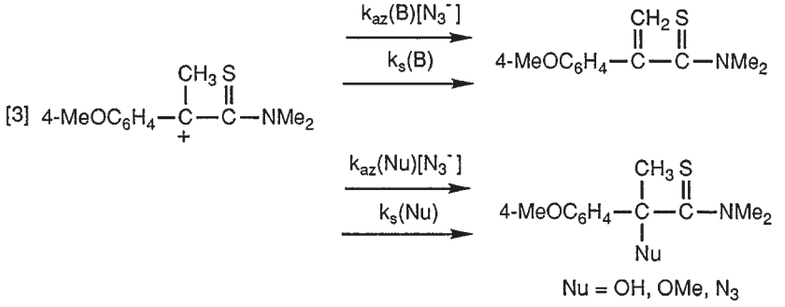

1.8×10^4 M^{-1} s^{-1}. The latter is a remarkably low number for the addition of azide ion to a carbocation. Even the tris(4-methoxyphenyl)methyl cation reacts with k_{az} around 10^7 M^{-1} s^{-1} (11).

It is also worth noting that for stabilized triarylmethyl cations k_{az}:k_s is approximately constant with changing reactivity (11), although the ratio starts to sharply decrease when the azide reaction approaches the diffusion limit. For the cation **2,** where both azide and solvent react as nucleophiles, k_{az}:k_s = 4.5×10^4. If the same ratio were to apply to the nucleophilic reactions of **4**, then k_s(Nu) for this cation would be 0.4 s^{-1}, only 0.2% of the k_s(B) value.

Lifetimes of 4-methoxybenzyl cations

As suspected in the earlier study (7), the assumption of diffusion control for the reactions of azide ion with the cations **2** and **4** is incorrect. The reactions with azide are considerably slower than diffusion, and the lifetimes of these two cations are substantial. A comparison with other 4-methoxybenzylic cations whose rate constants have been directly determined by flash photolysis is presented in Table 2. In the case of the parent 4-methoxybenzyl and the derivative with one α-methyl group, the lifetimes are too short in aqueous solutions for the cations to be studied by ns laser flash photolysis. These cations can, however, be observed in the less nucleophilic TFE.

As was observed previously with an α-COOMe derivative (13), the α-$CONMe_2$ cation **6** examined in this work is longer lived than its α-methyl analog. The differences, however, are not large. The amide is an order of magnitude longer lived than the ester, which in turn is probably about another order of magnitude longer lived in water than the α-methyl derivative (7, 10). These kinetic stabilizations occur in spite of the fact that the α-CO cations are much less thermodynamically stable. Such observations are also made with cations bearing α-CF_3 substituents. Explanations for this behaviour have been proposed in the literature and need not be repeated here (7, 13, 15, 16).

The cations bearing α-$CSNMe_2$ on the other hand are extraordinarily long-lived. The secondary ion **2**, for example, is 10^4 longer lived than its $CONMe_2$ analog and 10^6–10^7 longer lived than the 4-methoxyphenethyl cation. The tertiary **4** is 10^5 longer lived than the 4-methoxycumyl cation. If this comparison involves only solvent addition to the α-C^+ center, this factor rises to 10^7.

There are two possible interactions that could account for the stabilization. One involves a resonance interaction as shown in structure **13b** where the positive charge is delocalized to the sulfur atom. A large fraction of this interaction would be lost in the transition state for solvent capture, leading to an unusually low reactivity (15, 16). The second possibility is the formation of a bridged ion, shown as the resonance structures **13c** and **13d**.

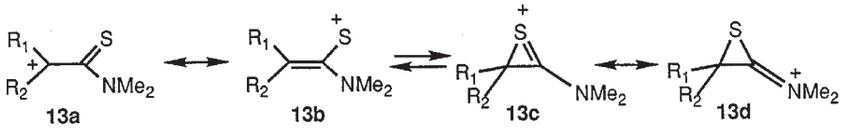

© 1998 NRC Canada

Fig. 1. Flash photolysis spectra obtained on irradiation of **7** (*a*), **8** (*b*), and **9** (*c*) in 40:60 acetonitrile:water. Figure 1(*a*) was obtained with 248 nm laser flash photolysis; Figs. 1(*b*) and 1(*c*) were obtained with lamp flash photolysis. In each figure the uppermost spectrum is the ΔOD measured immediately after the laser or lamp flash, the middle spectrum is the ΔOD at a time corresponding to one half-life of the decay, and the bottom spectrum is the ΔOD at the completion of the decay (6–8 half-lives). The points drawn as full squares in Fig. 1(*b*) were obtained with the laser flash photolysis apparatus, and represent the ΔOD immediately after the laser flash, normalized to the same ΔOD's obtained in the lamp flash photolysis experiment.

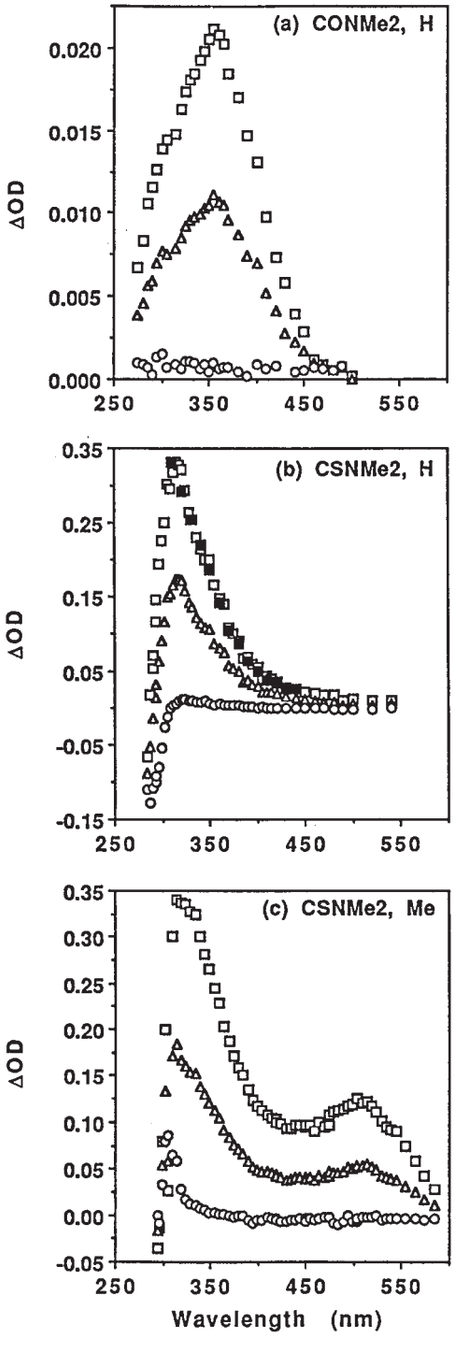

Ab initio calculations have found that an α-thioamido cation where R_1 = H and R_2 = H is stabilized by 35.7 kcal/mol by the first interaction, but a further 47.2 kcal/mol stabilization accompanies conversion to the cyclic structure (17). The cation **13** with R_1 = H and R_2 = 3,5-bis(trifluoromethyl)phenyl reacts predominantly as a closed ion, giving 86% of a product that has arisen from reaction of solvent (acetic acid) at the thioamide carbon (2). The cation **2** of this study, however, reacts to give products of addition at the α-carbon (7). This cation of course has the strongly electron-donating 4-methoxy group, which would favour the open structure, and the contrasting behaviour with the bis-CF_3 cation implies it must be reacting through this form. There is the possibility that the open cation is a minor species in an equilibrium mixture with an unreactive closed form (7). This, however, cannot account for all of the kinetic stabilization. This conclusion is based on the measured k_{az} for **2** in aqueous acetonitrile, which is about 1% of the k_{az} of a diffusion-controlled combination (e.g., the k_{az} for **6**). Providing azide ion reacts with the open cation (as the azide product implies) there must be at least 1% of the open cation in the mixture with the closed one. A percentage less than 1% requires k_{az} to be greater than the encounter limit. This in turn means that k_w for the open cation must still be less than 10^4 s^{-1}. This is still two orders of magnitude lower than the k_w for **6** and 10^4 lower than the value for the α-methyl cation.

The UV–visible spectra observed for the three cations in this study (Fig. 1) are also interesting in the context of the structural issue. The spectrum for the α-amido cation **6** is typical of 4-methoxybenzyl cations. The 4-methoxyphenethyl and 4-methoxycumyl ions, for example, have similarly shaped absorption bands (somewhat narrower) with λ_{max} at 340 and 360 nm, respectively (12), in the same region as **6**. With this cation, therefore, there is no indication of anything highly unusual that could be attributed to a strong interaction with the α-carbonyl group.

This, however, cannot be said for the α-$CSNMe_2$ cations. With **2** the λ_{max} is shifted to a lower wavelength, perhaps not highly unusual for a benzyl cation, but there is a long tailing absorbance, and cation decay is even observed at 550 nm. The methyl cation **4** has a similar λ_{max} at the lower wavelength, and the absorbance at higher λ has now become so pronounced that there is a second band centered around 500 nm. These spectra are clearly different from the spectrum for **6**, and also from those of other benzylic derivatives. It is tempting to ascribe the high-wavelength absorption observed with **4** to increased delocalization, in other words to a strong resonance interaction of the type **13a** ↔ **13b** in an open cation. The same absorption is seen with **2**, but it is much weaker. This suggests the possibility that there is less open cation in this system, although clearly there is still some. Such conclusions are highly speculative, since there are no suitable models that allow unambiguous comparisons to be made. What can certainly be concluded is that the behaviours of the α-$CSNMe_2$ cations are unusual, and this is paralleled in both the absorption spectra and the kinetic stabilities.

Experimental section

The photochemical precursors **7–9** and the solvolysis

© 1998 NRC Canada

products **10–12** were from a previous study (7). Laser flash photolysis experiments involved ca. 20 ns pulses at 248 nm (60–120 mJ / pulse) from a Lumonics excimer laser (KrF) emission. A pulsed Xenon lamp provided monitoring light. After passing through a monochromator, the signal from the photomultiplier tube was digitized and sent to a computer for analysis. Conventional flash photolysis experiments were performed with equipment previously described (18), with the sample being irradiated with a broad-band flash lamp of ca. 100 ms duration.

The products of irradiation were determined by preparing 5 mL of a solution of **7–9** in 40% aqueous acetonitrile of concentration 100 μM. With **8**, the solvent had been cooled to 0°C in an ice bath before the substrate was added. One half (2.5 mL) of these solutions were placed in a UV cuvette, the other 2.5 mL in a capped vial wrapped in tin foil. The former were immediately irradiated at 254 nm in a spinning merry-go-round in a Rayonet reactor, then immediately analyzed by HPLC. The latter solutions were left under such conditions that no precursor remained (see Results), as shown by HPLC. Identical volumes of the irradiated and solvolyzed solutions were injected into a Waters HPLC, eluting with 60:40 water:acetonitrile through a C18 column. Products were identified by comparison with known standards. The yields of the products in the irradiated solutions were calculated from the relative peak areas of the irradiated and solvolyzed solutions.

Acknowledgments

The continued financial support of the Natural Sciences and Engineering Research Council of Canada is gratefully acknowledged.

References

1. F.J. Ablenas, B.E. Georges, M. Maleki, R. Jain, A.C. Hopkinson, and E. Lee-Ruff. Can. J. Chem. **65**, 1800 (1987).
2. X. Creary and T. Aldridge. J. Org. Chem. **53**, 3888 (1988).
3. X. Creary and T. Aldridge. J. Org. Chem. **56**, 4280 (1991).
4. X. Creary, H.N. Hatoum, A. Barton, and T. Aldridge. J. Org. Chem. **57**, 1887 (1992).
5. X. Creary and C. Zhu. J. Am. Chem. Soc. **117**, 5859 (1995).
6. C.S.Q. Lew, D.F. Wong, L.J. Johnston, M. Bertone, A.C. Hopkinson, and E. Lee-Ruff. J. Org. Chem. **61**, 6805 (1996).
7. J.P. Richard, S.-S. Lin, J.M. Buccigross, and T.L. Amyes. J. Am. Chem. Soc. **118**, 12603 (1996).
8. J.P. Richard, S.-S. Lin, and K.B. Williams. J. Org. Chem. **61**, 9033 (1996).
9. X. Creary and J. Tricker. J. Org. Chem. **63**, 4907 (1998).
10. J.P. Richard, M.E. Rothenberg, and W.P. Jencks. J. Am. Chem. Soc. **106**, 1361 (1984).
11. R.A. McClelland, V.M. Kanagasabapathy, N. Banait, and S. Steenken. J. Am. Chem. Soc. **113**, 1009, (1991).
12. R.A. McClelland, C. Chan, F. Cozens, A. Modro, and S. Steenken. Angew. Chem. Int. Ed. Engl. **30**, 1337 (1991).
13. N.P. Schepp and J. Wirz. J. Am. Chem. Soc. **116**, 11749 (1994).
14. R.A. McClelland, V.M. Kanagasabapathy, N. Banait, and S. Steenken. J. Am. Chem. Soc. **111**, 3966 (1989).
15. T.L. Amyes, I.W. Stevens, and J.P. Richard. J. Org. Chem. **58**, 6057 (1993).
16. J.P. Richard. Tetrahedron, **51**, 7981 (1994).
17. M.H. Lien and A.C. Hopkinson. J. Am. Chem. Soc. **110**, 3788 (1988).
18. A.A. Allen, A.J. Kresge, N.P. Schepp, and T.T. Tidwell. Can. J. Chem. **65**, 1719 (1987).

© 1998 NRC Canada

Alumina-assisted reduction of carbonyl compounds with sodium borohydride in hexane

Shigetaka Yakabe, Masao Hirano, and Takashi Morimoto

Abstract: A broad range of aliphatic, alicyclic, and aromatic ketones and aldehydes underwent smooth reduction with a combination of common, inexpensive laboratory reagents, sodium borohydride and chromatographic neutral alumina, in hexane to afford the corresponding alcohols in a selective and high-yielding manner under mild and neutral conditions. The $NaBH_4$-based biphasic system can also successfully be used for the reduction of unsaturated substrates as well as steroidal and highly hindered ketones.

Key words: reduction, carbonyl compounds, sodium borohydride, alumina, alcohols.

Résumé : Beaucoup de cétones aliphatiques, alicycliques et aromatiques et beaucoup d'aldéhydes, peuvent être réduites dans des conditions douces en utilisant une combinaison de réactifs de laboratoires courants et peu coûteux. Par exemple la combinaison: borohydrure de sodium – alumine neutre de pureté chromatographique, dans l'hexane permet d'accéder, de manière sélective et avec des rendements élevés, aux alcools correspondants dans des conditions douces et neutres. On peut également utiliser avec succès le système hétérogène $NaBH_4$–alumine pour réduire, dans les mêmes conditions, les substrats insaturés, le groupe carbonyle des stéroïdes et également les cétones fortement encombrées.

Mots clés : réduction, composés carbonylés, borohydrure de sodium, alumine, alcools.

[Traduit par la Rédaction]

Introduction

The pioneering work of Fetizon's group on the oxidation of various functionalities with silver carbonate supported on Celite (Fetizon's reagent) in 1968 (1) was rapidly followed by rush of extensive investigations into chemistry of supported reagents and catalysts, which were reviewed in journals (2) and more recently in comprehensive books (3). These new, practically attractive reaction systems involve remarkable advantages which cannot be offered by conventional solution-phase counterparts; viz., easy reaction performance, mild conditions, modified or increased agent power, specific product selectivity, improved yield, reduced waste, etc. The last term well fits with the recent trend in environmentally compatible, clean synthesis (4). Thus the use of supported reagents and catalysts has now gained general acceptance and appears to be recognized as a promising strategy in organic synthesis (2, 3).

There have been numbers of procedures available for the preparation of supported reagents (3*a*), among which we have chosen the in situ method on the following two grounds. First, the method can instantly be performed merely by efficient stirring of a heterogeneous mixture of agent(s), substrate, and solid support in an aprotic solvent. Secondly, the method can conveniently be applied to thermally unstable solid agents, such as peroxy acid (Oxone® (5), magnesium monoperoxyphthalate (6)) and oxohalogen acid ($NaClO_2$ (7), $NaBrO_2$ (8), $Ca(OCl)_2$ (9)) derivatives, because thermal drying or activation of supported reagents can be eliminated. Since the agents we have employed are sparingly soluble in the reaction solvents, it is likely that solid supports favorably catalyze the reaction by providing an active site for them, enabling selective and rapid reactions to occur under mild conditions. Although we are mindful of a diversity of methods available for catalytic and stoichiometric reductions (10), the importance of the reaction in organic synthesis and the lack of systematic, extensive studies on this subject using supported sodium borohydride ($NaBH_4$) reagents (11) prompted us to extend TUAT[2] clean synthesis (5–9) to $NaBH_4$ reduction[3] of a wide variety of ketones and aldehydes. We would like to report here some synthetic aspects of $NaBH_4$ reduction by our in situ method using alumina as the solid catalyst (for preliminary results, see ref. 12).

Experimental

Instruments

^{1}H NMR spectra were measured with a JEOL PMX-60, JNM-FX200, or JNM-FX500 spectrometer for solutions in $CDCl_3$ using TMS as an internal standard. Analytical GC was carried out on a Shimadzu GC-14B instrument, equipped

Received May 20, 1998.

S. Yakabe, M. Hirano, and T. Morimoto.[1] Department of Applied Chemistry, Faculty of Technology, Tokyo University of Agriculture and Technology, Koganei, Tokyo 184–8588, Japan.

[1]Author to whom correspondence may be addressed. Telephone and fax: +81-423-88-7033. E-mail: morimoto@cc.tuat.ac.jp

[2]Short for Tokyo University of Agriculture and Technology.

[3]For conventional $NaBH_4$ reductions, see ref. 10, especially the recently published comprehensive review book (10*d*).

© 1998 NRC Canada

with a FID through a 2 m × 5 mm diameter glass column packed with 5% PEG-20M on Chromosorb WAW-DMCS and interfaced with a Shimadzu Chromatopac C-R6A integrator, with temperature programming. Mass spectra were determined on a JEOL SX-102A mass spectrometer which was coupled with a Hewlett Packard GC5890 Series II GC apparatus via a heated capillary column. IR spectra were recorded for thin films (neat) or KBr disks on a JASCO A-100 spectrophotometer. Melting points were determined on a Yanagimoto MP-S3 melting point apparatus and are uncorrected.

Reagents

Hexane was dried ($CaCl_2$), distilled, and stored over molecular sieves. Commercial sodium borohydride (Yoneyama Chemical, Japan) was ground to a fine powder in a dry box and was stored in a desiccator. Ketones and aldehydes to be reduced were available from commercial sources and were used without further purification, the purities of which were checked by GC prior to use. The corresponding alcohols as reference compounds were commercially available. Addition of deionized water (0.02, 0.04, 0.11, 0.2, and 0.3 g) in portions to chromatographic neutral alumina (ICN Biomedical, alumina N, Super I; 1.0 g), which had been predried in an oven at 500°C for 6 h (dry alumina), followed by vigourous shaking of mixtures after every addition for a few minutes until free-flowing powder was obtained, afforded moist aluminas with 2, 4, 10, 17, and 23 wt.% loading of water, respectively, which were immediately employed for the reduction. Acidic and basic aluminas (ICN Biomedical, alumina A and B, respectively, Super I), silica gel (Fuji–Silysia BW-300), florisil (Kishida Chemical), Japanese acid clay (Wako), bentonite (Wako), Montmorillonite K10 (Aldrich), kaolin (Wako), and zeolites A-3 and F-9 (Wako), and calcium oxide (Kokusan Chemical Works) were predried and were then treated with deionized water as described above. Commercial Hammett indicator reagents (3*a*) were used as received.

Reduction procedure

The reduction procedure for benzophenone **1e** was representative. A 30 mL, round-bottom, two-necked flask, equipped with a 1.5 cm long Teflon-coated stirrer bar, a 25 cm long condenser, and a glass gas-inlet tubing connected to an argon-filled balloon was arranged in order to perform the reaction under a dry atmosphere by linking the top of the condenser to a liquid paraffin trap via a flexible silicone rubber tubing. The flask was charged with **1e** (1 mmol, 0.182 g), hexane (10 mL), finely ground $NaBH_4$ (0.4 mmol, 0.151 g), and freshly prepared moist alumina (0.5 g; H_2O content, 10 wt.%) and was then deaerated by passing a gentle stream of dry argon throughout the system. The flask was immersed in an oil bath and was kept at 60°C while efficient stirring of the resultant heterogeneous mixture was continued in order to ensure smooth reduction and to attain reproducible results. After 3 h, the reaction mixture was cooled rapidly to room temperature by external cooling and was then filtered through a sintered glass funnel. The filter cake was washed thoroughly with portions of dry ether (ca. 50 mL). The combined clear solvent was evaporated on a rotary evaporator under a reduced pressure to dryness to give satisfactorily pure (GC, NMR, and TLC) benzhydrol **2e** in 98% yield (0.180 g), based on the starting benzophenone (entry 26 in Table 1): mp 63.2–63.8°C, reported mp 65–67°C (13).

The recovered alumina was washed with portions of deionized water (in total 50 mL) to remove inorganic residues and then oven-dried (500°C, 3 h). After treating with deionized water as above, it was able to be used for repeat runs (Table 2).

The reductions of the other ketones and aldehydes with the $NaBH_4$ – moist alumina system were performed under conditions determined in terms of their reactivities and yields of the corresponding alcohols **2**, followed by the usual work-up as described above, affording **2**. Alcohols thus obtained were fully characterized by spectroscopic comparisons (IR, NMR, and MS) with the commercial authentic samples and were usually of satisfactory purity for a further use, for example, as substrates for the selective oxidation with chemical manganese dioxide in hexane (14).

It is noteworthy that although certain carbonyl compounds and alcohols have only limited solubilities in hexane under the conditions employed, the reductions and the work-ups of the products were achieved without any difficulty. In addition, we also encountered no difficulty upon a large-scale reduction of **1e** (40 mmol), yielding **2e** quantitatively (entry 27 in Table 1). The recovery of acetophenone **1a** and the yield of 1-phenylethanol **2a** in Tables 2 and 3 were determined by GC using biphenyl as an internal standard.

Results and discussion

Sodium borohydride has enjoyed a widespread use as a selective and mild hydride donor for a broad range of functional groups (10). Established procedures of the $NaBH_4$ reduction have been carried out in protic solvents so as to accomplish reasonably rapid reactions, and therefore an aqueous treatment during work-ups of products has been usually required. However, in order to simplify the method, to increase reagent applicability, and to eliminate aqueous wastes, our synthetic approach involves only introduction of an inorganic support material into a slurry of finely pulverized $NaBH_4$ and a carbonyl compound in an aprotic solvent, followed by the efficient stirring of the resultant heterogeneous mixture. The reduction milieu was of close resemble to supported reagent systems (2, 3) and therefore retained the practical advantage of the latter as regards facile product isolation requiring only filtration followed by evaporation of the solvent.

It is frequently observed that efficiency of supported reagents depends strongly on the choice of support materials and the presence of water (3*a*). In fact, we have experienced in the previous studies that these are decisive factors to determine the facility of the reactions, to control selectivity and yield of products (5–9). Thus, effects of supports on the reactivity of a carbonyl compound and the selectivity and the yield of the alcohol were investigated by using acetophenone **1a** as the test substrate (Table 3). The results showed an important role of a support whose absence gave no indication of the reaction in hexane (entry 1). In addition, no appreciable reaction occurred when **1a** and $NaBH_4$ were stirred with commercial or dry alumina (entries 2 and 3, respectively). There have been numbers of reports that a

© 1998 NRC Canada

Table 1. Reduction of carbonyl compounds with $NaBH_4$ and moist alumina.[a]

Entry no.	Carbonyl compound		$NaBH_4$ (mmol)	Temp. (°C)	Time (h)	Al_2O_3 (g)[b]	Yield (%)[c]
19[d]	PhCOMe	**1a**	0.3	40	3	0.5	98
20	$PhCOCH_2Cl$	**1b**	0.3	40	1	0.5	Quant.
21	4-$MeOC_6H_4COMe$	**1c**	1.0	60	3	0.5	Quant.
22	4-ClC_6H_4COMe		0.25	40	3	0.5	95
23	2-$O_2NC_6H_4COMe$		0.3	60	3	0.5	96
24	3-$O_2NC_6H_4COMe$		0.25	40	3	0.5	Quant.
25	4-$O_2NC_6H_4COMe$	**1d**	0.25	40	3	0.5	99
26[d]	PhCOPh	**1e**	0.4	60	3	0.5	98
27[e]	PhCOPh	**1e**	16	60	3	10	Quant.
28	2-Hexanone		0.3	40	3	0.5	95
29	2-Nonanone		0.3	60	3	0.5	98
30	2-Dodecanone		0.5	60	3	0.5	97
31[d]	Hex-5-en-2-one		0.3	40	3	0.5	Quant.
32[d]	Cyclopentanone		0.3	20	1	0.5	97[f]
33[d]	Cyclohexanone	**1f**	0.3	20	1	0.5	92[f]
34[d]	Cycloheptanone		0.3	20	3	0.5	Quant.
35[d]	Cyclooctanone		0.5	30	3	1.0	Quant.
36[d]	Cyclododecanone		0.6	60	3	0.5	98
37[d]	2-Methylcyclohexanone	**1g**	0.4	30	3	1.0	87
38[d]	3-Methylcyclohexanone		0.3	20	1	0.5	93
39[d]	4-Methylcyclohexanone		0.3	20	1	0.5	91
40	3,3,5-Trimethylcyclohexanone		0.3	20	1.5	0.5	99
41	4-Ethylcyclohexanone		0.3	20	1	0.5	Quant.
42[d]	2-*t*-Butylcyclohexanone	**1h**	0.8	40	3	1.5	Quant.
43	4-*t*-Butylcyclohexanone		0.3	20	1	0.5	96
44	2-Cyclohexylcyclohexanone		0.8	40	3	1.5	Quant.
45	4-Cyclohexylcyclohexanone		0.3	20	1	0.5	Quant.
46	Menthone		0.6	40	3	1.5	Quant.
47	Camphor	**1i**	1.2	60	3	1.5	97
48[d]	α-Tetralone		0.5	30	3	1.0	Quant.
49	Cyclohex-2-en-1-one	**1j**	0.4	20	2	0.5	82[f,g]
50[d]	5-α-Cholestan-3-one		0.3	40	3	0.5	96
51	4-Cholesten-3-one		1.0	40	3	1.5	82
52	PhCHO		0.3	40	3	0.5	Quant.
53	4-$MeOC_6H_4CHO$		0.3	40	3	0.5	98
54	4-$O_2NC_6H_4CHO$		0.3	40	3	0.5	96
55	4-NCC_6H_4CHO		0.3	40	3	0.5	95
56	4-$MeOSC_6H_4CHO$		0.3	40	3	0.5	Quant.
57	3,4-O-CH_2-O-C_6H_3CHO	**1k**	0.3	40	3	0.5	Quant.
58	4-$MeO_2CC_6H_4CHO$		0.3	40	3	0.5	99
59	PhCH=CHCHO (*trans*)	**1l**	0.3	40	3	0.5	94
60	Hexanal		0.3	40	3	0.5	92
61	Octanal		0.3	40	3	0.5	93
62	Undecanal		0.3	40	3	0.5	96
63	Geranial	**1m**	0.3	40	3	0.5	94
64	Perillaldehyde		0.3	40	3	0.5	93

[a]Reaction conditions: carbonyl compound **1** 1 mmol, hexane 10 mL.

[b]Moist alumina (H_2O content, 10 wt.%) was used.

[c]Isolated yield of alcohol **2** based on the starting **1**.

[d]Reference 11.

[e]PhCOPh 40 mmol, hexane 50 mL.

[f]GC yield.

[g]Total yield of cyclohex-2-en-1-ol (56.8%) and cyclohexanol (24.7%).

small but definite amount of water is essential for supported reagents to favor their reactions (15) and, in addition, that certain reactions with solid reagents are promoted by the presence of water (16). It is a priori expedient for us to use alumina preloaded with a small amount of water so as to facilitate reactions (5–9). Thus, reactions in the presence of

© 1998 NRC Canada

Table 2. Recycling of alumina in the reduction of acetophenone **1a** with $NaBH_4$ and moist alumina.[a]

	Distribution (%)[b]	
Run	**1a**	**2a**
1[c]	0	100
2	0	100
3	0	100
4	0	100
5	0	100

[a]At 40°C, for 3 h; PhCOMe 1 mmol, $NaBH_4$ 0.3 mmol, hexane 10 mL, moist alumina (H_2O content, 10 wt.%) 0.5 g.

[b]Determined by GC using biphenyl as an internal standard.

[c]Entry 19 in Table 1.

water-treated alumina (moist alumina; water contents 4–17 wt.%) proceeded smoothly, achieved 100% conversion after 1 h, and gave 1-phenylethanol **2a** in quantitative yield (entries 5, 6). Consequently, it is likely that crystal lattice of $NaBH_4$ may be penetrated and then broken up by water to generate highly dispersed active species over a high-surface-area alumina, leading to increse in its accessible sites to proximal carbonyl compound.

Owing to remarkable catalysis of moist alumina in the reduction of **1a**, we looked for other efficient support materials. Comparative study carried out with a number of inorganic solid supports showed that there are appreciable differences in their efficacy (entries 6, 8–18). Clays, zeolites, and calcium oxide exhibited low activity. Aluminas, silica gel, and florisil were found to be superior to the others as solid catalysts. Sodium borohydride is insoluble and the reagent alone has no reducing capability in hexane (e.g., entry 1), and therefore the reduction must take place on support surface. No clear relationship, however, has been found between surface acidities of the supports and their efficiency (3rd column in Table 3). Since this study aimed at elucidating synthetic utility of the $NaBH_4$-based reduction, further information on physicochemical properties of the supports has not been provided; detailed characterization of the support materials and (or) the $NaBH_4$-supported reagents may offer a satisfactory explanation of the results.[4] Of the supports tested, neutral alumina was the support of choice for the present reduction in terms of ease of reaction performace and yield of the alcohol.

Encouraged by the facile and high-yielding formation of 1-phenylethanol from acetophenone, reductions of various types of ketones and aldehydes were then performed in order to examine the scope of this simple procedure (Scheme 1). Reaction conditions (concentration of $NaBH_4$, temperature, time, and quantity of moist alumina) indicated in Table 1 were optimized, under which the reduction reactions were run to 100% conversion. Simple 5–12 membered alicyclic ketones (entries 32–36), aliphatic ketones (entries 28–30), and aldehydes (entries 60–62) having medium to long alkyl chains can be readily reduced to afford the corresponding alcohols in excellent to quantitative yields. That electron-withdrawing group promotes the reduction while electron-donating group exhibits the reverse effect was suggested by the comparison of apparent reactivity of *p*-MeO- **1c** and *p*-NO_2-substituted acetophenone **1d** towards $NaBH_4$, as judged by their conversions under the same conditions (40°C, 3 h; conversions were 58 and 100%, respectively). The reaction was also sensitive to the steric bulk of substituents and (or) their positions on the cyclohexane or benzene ring. For example, independent reactions of cyclohexanone **1f**, 2-methylcyclohexanone **1g**, and 2-*t*-butylcyclohexanone **1h** under the conditions of entry 33 showed that their apparent reactivities decrease as the substituents adjacent to the carbonyls increase in size (conversions of **1f**, **1g**, and **1h** were 100, 78, and 44%, respectively). 2-Cyclohexylcyclohexanone, menthone, and camphor (entries 44, 46, and 47, respectively) also exhibited low reactivities for which higher concentration of $NaBH_4$, higher temperature, and (or) longer reaction period than those used for unhindered substrates were required in order for their reductions to proceed favorably. On the other hand, influence of side-chain α-substituents seems to be less deleterious than that of ring substituents. Indeed, conversions of benzaldehyde, acetophenone **1a**, and benzophenone were found to be 100, 90, and 83%, respectively, at 40°C for 1 h. The relatively small deference in their reactivities may not be explained on steric ground alone. Moreover, it is interesting to note that α-chloroacetophenone **1b**, which has less electron-donating but more bulky chloromethyl group as the α-substituent than methyl group of **1a**, enabled 100% conversion under the same conditions as above. Clearly, **1a** is slightly less reactive than **1b**. It appears therefore that there might be fine balance between steric and electronic factors in determining the reactivities of carbonyl compounds. Combined influence of these factors has also been suggested in the reduction of ketones with $NaBH_4$ in isopropanol (17).

The reductions in Table 1 can be run to 100% conversion in every case and no deactivation was apparent, indicating clearly that free alcohol resulting from the reduction exerts no detrimental effect on the alumina catalysis. No protic acid is added in the present reaction system, and therefore protons (or H_2O) necessary to decompose a boron complex should undoubtedly be provided from adsorbed water (18). Thus, the role of moist alumina is three-fold; it serves as an adsorption site for substrate and $NaBH_4$, a generator of active species from the latter, and a proton (or H_2O) source whose assembly enables $NaBH_4$ to be used as efficient reducing agent in hexane under mild conditions.

The present reduction is chemoselective, tolerating reducible functionalities such as nitro (entries 23–25, 54), cyano (entry 55), sulfinyl (entry 56), and ester groups (entry 58). The anhydrous conditions may favor the reduction of a carbonyl compound having the hydrolytically labile methylenedioxy linkage, **1k**, to produce piperonyl alcohol quantitatively (entry 57). Olefinic double bonds remained intact upon the reduction (entries 31, 51, 59, 63, and 64), except for a conjugated ketone, cyclohex-2-en-1-one **1j**, which underwent competitive 1,2- and 1,4-addition to afford a mixture of cyclohex-2-en-1-ol and cyclohexanol (entry 49). It is noteworthy that the reduction of *trans*-cinnamaldehyde **1l**

[4]Valuable suggestions from referees regarding various aspects of the present supported reagent system are gratefully acknowledged.

© 1998 NRC Canada

Table 3. Reduction of acetophenone **1a** with $NaBH_4$ and various supports.[a]

Entry no.	Support	H_0[b]	Distribution (%)[c]	
			PhCOMe	PhCH(OH)Me
1	Nil		98	0
2	Commercial alumina[d]		93	2
3	Dry alumina[e]		85	1
4	Neutral alumina (2%)[f]		39	60
5	Neutral alumina (4%)[f]		0	Quant.
6	Neutral alumina	+6.8 to +4.8	0	Quant.
7	Neutral alumina (23%)[f]		50	50
8	Acidic alumina	+4.0 to +3.3	3	97
9	Basic alumina	>+9.3	7	93
10	Silica gel BW-300	+4.0 to +3.3	0	Quant.
11	Florisil	+3.3 to +0.8	0	Quant.
12	Japanese acid clay	+0.8 to –3.0	62	38
13	Bentonite	+4.8 to +4.0	37	63
14	Montmorillonite K10	–3.0 to –5.6	17	83
15	Kaoline	+3.3 to +0.8	60	40
16	Zeolite A3	>+9.3	61	39
17	Zeolite F9	+9.3 to +7.1	14	86
18	CaO	>+9.3	36	64

[a]At 40°C, for 1 h; PhCOMe 1 mmol, $NaBH_4$ 1 mmol, hexane 10 mL; 1 g of a support preloaded with 17 wt.% of water was used unless otherwise noted.

[b]Determined by color tests in hexane using Hammett indicators (3*a*).

[c]Determined by GC using biphenyl as an internal standard.

[d]Commercial neutral alumina was used as received.

[e]Predried (500°C, 6 h) neutral alumina was used.

[f]Numbers in parentheses indicate contents of water (wt.%) preloaded on alumina.

Scheme 1.

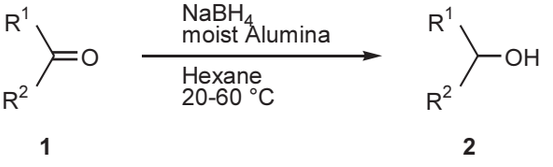

1 **2**

(entry 59) and geranial **1m** (entry 63) proceeded without any loss of the double-bond stereochemistry, giving exclusively *trans*-cinnamyl alcohol and geraniol, respectively, in excellent yields. Usefulness of the present procedure for steroidal ketones is also apparent (entries 50, 51).

About three decades ago the reduction was first reported with the use of independently prepared alumina-supported $NaBH_4$ reagents (19), and some of which are now available from commercial sources (Aldrich, Fluka, etc.). To their disadvantages, impregnation of $NaBH_4$ on supports is required a considerable preparative effort, i.e., a few hours of thorough mixing of alumina and aqueous $NaBH_4$, followed by overnight drying in vacuo (19*d*), and commercial reagents are rather expensive. It is also reported that appreciable amount of $NaBH_4$ decomposed upon the preparation (19*a*, *d*) or during storage of the supported reagent (19*a*), lowering the concentration of available $NaBH_4$, and in the latter case (19*a*), placing serious restriction on its use, since the authors themselves pointed out that a freshly prepared reagent must be employed to attain the best reaction performance. Somewhat surprisingly, the method of Santaniello et al. (19*d*) failed to reduce a highly hindered ketone such as camphor **1i** within a reasonal period of time. Of the carbonyl compounds we examined, it is indeed the least reactive substrate, but can be reduced by our in situ method within 3 h to give borneol in quasi quantitative yield (entry 47). Reductions shown in Table 1 can be readily accomplished with stoichiometric to moderate excess $NaBH_4$ (0.25–1.2 mmol of $NaBH_4$ per mmol of substrate) and can therefore be favorably compared to earlier methods by Hodosan and Serban (19*a*) (1 part of $NaBH_4$ per 2 parts of monoketone) and by Santaniello et al. (19*d*) (2.5–3 mmol of $NaBH_4$ per 1 mmol of substrate), which render the present method more economical. These observations clearly indicate that independent laborious preparation of a supported reagent is not a prerequisite for the efficient $NaBH_4$ reduction in apotic solvent. It can be further emphasized that the present reaction is clean, set-up of reaction and work-up of the product are straightforward, and from economical and environmental points of view, use of hexane as the solvent might be favorable. One additional comment should be made. Although the used alumina can safely be kept in an appropriate container and disposed according to the regional legislation, it is of practical importance to recycle the alumina in order to reduce waste and to increase the reagent utility.[4] Table 2 clearly showed that the alumina regenerated by a simple method (vide experimental section) can successfully be employed for several repeat reductions with no decrease in activity. These advantages coupled with the generality and

© 1998 NRC Canada

economic applicability could make our in situ method an attractive substitute for earlier procedures.

Conclusions

The $NaBH_4$ – moist alumina system is a mild, convenient, and efficient reducing agent, applicable to a wide range of carbonyl compounds under neutral and anhydrous conditions.

Acknowledgment

The authors are indebted to Dr. Masahiro Natsume for the provision of GC–MS facilities and to Mrs. Junko Takizawa for NMR measurements at TUAT.

References

1. (*a*) M. Fetizon and M. Golfier. C. R. Acad. Sci. (Paris) Ser. B, **267**, 900 (1968); (*b*) M. Fetizon, M. Golfier, P. Mourgues, and J.-M. Louis. *In* Organic syntheses by oxidation with metal compounds. *Edited by* W.J. Mijs and C.R.H.I. de Jonge. Plenum Press, New York. 1986. Chap. 10.
2. A. McKillop and D.W. Young. Synthesis, 401 (1979); 481 (1979); G.H. Posner. Angew. Chem. Int. Ed. Engl. **17**, 487 (1978); A. Cornelis and P. Laszlo. Synthesis, 909 (1985).
3. (*a*) J.H. Clark, A.P. Kybett, and D.J. Macquarrie. Supported reagents. Preparation, analysis, and applications. VCH, New York. 1992; (*b*) J.H. Clark. Catalysis of organic reactions by supported inorganic reagents. VCH, New York. 1994; (*c*) K. Smith (*Editor*). Solid supports and catalysts in organic synthesis. Ellis Horwood, Chichester. 1992; (*d*) P. Laszlo (*Editor*). Preparative chemistry using supported reagents. Academic Press, San Diego. 1987; (*e*) M. Balogh and P. Laszlo. Organic chemistry using clays. Springer-Verlag, Berlin. 1993; (*f*) B.K. Hodnett, A.P. Kybett, J.H. Clark, and K. Smith (*Editors*). Supported reagents and catalysts in chemistry. The Royal Society of Chemistry, Cambridge. 1998.
4. J.H. Clark (*Editor*). Chemistry of waste minimization. Chapman and Hall, London. 1995; J.H. Clark and D.J. Macquarrie. Chem. Soc. Rev. 303 (1996).
5. M. Hirano, M. Oose, and T. Morimoto. Chem. Lett. 331 (1991); Bull. Chem. Soc. Jpn. **64**, 1046 (1991); M. Hirano, J. Tomaru, and T. Morimoto. Chem. Lett. 523 (1991); Bull. Chem. Soc. Jpn. **64**, 3752 (1991).
6. M. Hirano, Y. Ueno, and T. Morimoto. Synth. Commun. **25**, 3125 (1995); 3765 (1995).
7. M. Hirano, S. Yakabe, J.H. Clark, and T. Morimoto. J. Chem. Soc. Perkin Trans. 1, 2693 (1996); M. Hirano, S. Yakabe, H. Monobe, J.H. Clark, and T. Morimoto. J. Chem. Soc. Perkin Trans. 1, 3081 (1997); M. Hirano, S. Yakabe, H. Monobe, and T. Morimoto. Can. J. Chem. **75**, 1905 (1997).
8. M. Hirano, H. Kudo, and T. Morimoto. Bull. Chem. Soc. Jpn. **65**, 1744 (1992); **67**, 1492 (1994); T. Morimoto, M. Hirano, K. Iwasaki, and T. Ishikawa. Chem. Lett. 53 (1994); T. Morimoto, M. Hirano, Y. Aikawa, and X. Zhang. J. Chem. Soc. Perkin Trans. 1, 2423 (1988).
9. M. Hirano, S. Yakabe, S. Itoh, J.H. Clark, and T. Morimoto. Synthesis, 1161 (1997).
10. (*a*) H.O. House. *In* Modern synthetic reactions. 2nd ed. W.A. Benjamin, Inc., Calif. 1972. Chap. 2; (*b*) J. March. Advanced organic chemistry. Reactions, mechanisms, and structure. John Wiley & Sons, New York. 1992. 4th ed. Chap. 19. pp. 1206–1223; (*c*) M.B. Smith. Organic synthesis. McGraw–Hill, New York. 1992. Chap. 4. Sect. 4.5.B; (*d*) J. Seyden-Penne; Reductions by the alumino- and borohydrides in organic synthesis. 2nd ed. Wiley–VCH, New York. 1997.
11. J.M. Maud. *In* Solid supports and catalysts in organic synthesis. *Edited by* K. Smith. Ellis Horwood, Chichester. 1992. Chap. 6. p. 181; E. Santaniello. *In* Preparative chemistry using supported reagents. *Edited by* P. Laszlo. Academic Press, San Diego. 1987 Chap. 18, p. 356–357; G. Bram, E. d'Incan, and A. Loupy. Nouv. J. Chim. **6**, 689 (1982).
12 S. Yakabe, M. Hirano, J. H. Clark, and T. Morimoto. J. Chem. Res. Synop. 322 (1998).
13. Dictionary of organic compounds. Chapman and Hall, London. 6th ed. 1996.
14. M. Hirano, S. Yakabe, H. Chikamori, J.H. Clark, and T. Morimoto. J. Chem. Res. Synop. 308 (1998).
15. M. Onaka, K. Sugita, and Y. Izumi. J. Org. Chem. **54**, 1116 (1989); T. Ando, T. Kawate, J. Yamawaki, and T. Hanafusa. Chem. Lett. 935 (1982).
16. L.A. Carpino and A.C. Sau. J. Chem. Soc. Chem. Commun. 514 (1979); M. Tanaka and M. Koyanagi. Synthesis, 973 (1981).
17. H.C. Brown and J. Muzzio. J. Am. Chem. Soc. **88**, 2811 (1966).
18. J.H. Clark, A.P. Kybett, and D.J. Macquarrie. Supported reagents. Preparation, analysis, and applications. VCH, New York. 1992. Chap. 2. Sect. 2.5.2.
19. (*a*) F. Hodosan and N. Serban. Rev. Roum. Chim. **14**, 121 (1969); (*b*) F. Hodosan and V. Ciurdaru. Tetrahedron Lett. 1997 (1971); (*c*) V. Ciurdaru and F. Hodosan. Rev. Roum. Chim. **22**, 1027 (1977); (*d*) E. Santaniello, F. Ponti, and A. Manzocchi. Synthesis, 891 (1978); (*e*) E. Santaniello, C. Farachi, and A. Manzocchi. Synthesis, 912 (1979).

© 1998 NRC Canada

Gas-phase pyrolysis in organic synthesis. Part 2.[1] Novel rearrangement of esters and ethers into aryl ketones

Nouria A. Al-Awadi, Kamini Kaul, and Osman M.E. El-Dusouqui

Abstract: The formate ester of benzoin (**1**) and the methyl ethers of benzoin and anisoin (**2**, **3**) have been converted separately under thermal gas-phase conditions cleanly into 1,2-diarylethanone and have given, respectively, the following Arrhenius log A (s^{-1}) and E_a (kJ mol^{-1}): 10.11 and 132.0, 11.29 and 173.0, and 11.85 and 151.1. A plausible mechanism is suggested to account for these transformations based on the kinetics and products of reaction.

Key words: gas-phase, pyrolysis, kinetics, mechanism, synthesis.

Résumé : Opérant en phase gazeuse thermique, on a transformé proprement l'ester formique de la benzoïne (**1**) ainsi que les éthers méthyliques de la benzoïne et de l'anisoïne (**2** et **3**) en 1,2-diaryléthanones; les valeurs pour le log A d'Arrhenius (s^{-1}) et pour E_a (kJ mol^{-1}) sont respectivement les suivantes: 10,11 et 132,0; 11,29 et 173,0; 11,85 et 151,1. Pour expliquer ces transformations, on suggère un mécanisme plausible qui tient compte de la cinétique et de la nature des produits formés.

Mots clés : phase gazeuse, pyrolyse, cinétiques, mécanisme, synthèse.

[Traduit par la Rédaction]

Introduction

Uncatalyzed gas-phase reactions and heterogeneous processes using benign reagents and catalysts offer valuable alternatives as safe and environmentally friendly technologies in which waste is also reduced or eliminated (2, 3). The former class of reactions has the added advantage of being free of surface and media influence, hence the effects of structure on reactivity and mechanism might be deemed intrinsic.

Taylor (4) has reviewed the gas-phase pyrolysis of allyl esters of formic acid and the vinyl esters of aryl and alkyl carboxylic acids. The major pathways of these reactions lead to the formation of aldehydes and ketones, and to alkene double bonds only when the interconversions are accompanied by the formation of the stable CO_2 and CO molecular species as by-products. Taylor also speculated that when kinetic studies become available, the esters would be found to react more readily than the analogous ethers. In an earlier study, we have analyzed the structural factors which influence the thermal gas-phase reactivity of pyruvic and benzoylformic acids with reference to the elimination reactions of methyl benzoylformate and 3-hydroxy-3-methyl-2-butanone (5). The reactivity of these systems seems to be largely dependent on the magnitude of acidity of the incipient protonic hydrogen fragment. In this communication, we combine kinetic data and analysis of product of reaction with results from earlier relevant studies to elucidate the mechanism of thermal gas-phase conversion of both the aryl formate ester and the aryl methyl ether functionalities into diaryl ketones. This novel functional group transformation is an environmentally friendly chemical process. Cannizzaro-type disporportionation of benzaldehyde has been achieved over solid CaO as catalyst (6). Condensation of benzaldehyde and anisaldehyde, respectively, into benzoin and anisoin using heterogeneous catalysis instead of catalytic KCN is conceivable.

Received April 28, 1998.

N.A. Al-Awadi,[2] K. Kaul, and O.M.E. El-Dusouqui. Department of Chemistry, University of Kuwait, P.O. Box 5969, Safat 13060, Kuwait.

[1] See ref. 1.

[2]Author to whom correspondence may be addressed. Telephone: (+)4811188, ext. 5601. Fax: (+)4816482. E-mail: nouria@kuc01.kuniv.edu.kw

Results and discussion

Kinetics

Rates

Percent (10–20%) pyrolysis at the reaction temperature is used to evaluate the rate constant of reaction on the basis of HPLC retention data. Each recorded rate constant represents an average from at least three kinetic runs which are in agreement to within ± 2%. Rate coefficients were determined at different temperatures of 5–10°C intervals for ≥ 95% reaction. The kinetic measurements of each substrate were followed over a temperature range of 48–51 K, an experimental requirement in thermal gas-phase elimination studies. The reactions were ascertained to be homogeneous and free from surface effects and radical pathways (5, 7). Arrhenius plots of log k versus $1/T$ (K) showed strict linearity up to >90% reaction. A typical plot is shown in the Fig. 1. Kinetic data, Arrhenius parameters, and the rate coefficients of reaction at 600 K are summarized in Table 1. The

 © 1998 NRC Canada

Fig. 1. Arrhenius plot for formate ester of benzoin (**1**).

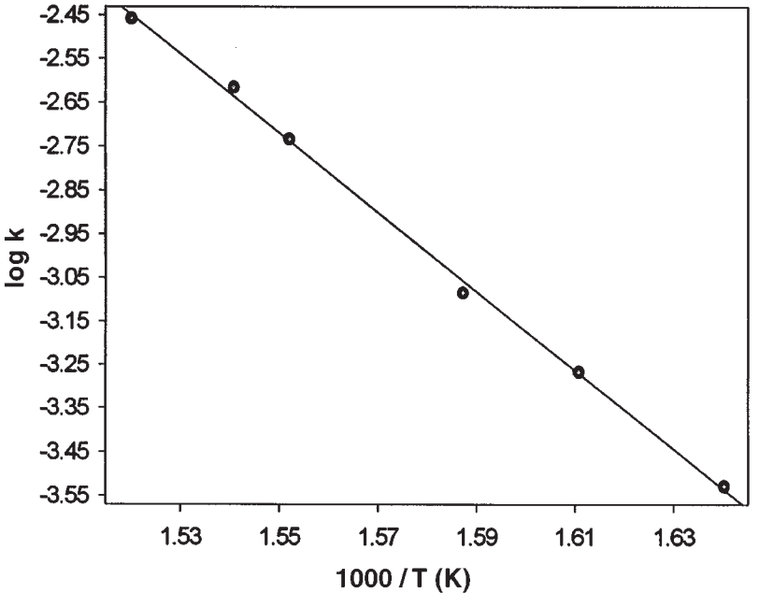

rates at T = 600 K are calculated using the kinetic equation for first-order reactions: log k = log A – E_a/4.575T.

Molecular reactivity

The formate ester of benzoin (**1**) is ca. 250 times more reactive than the analogous methyl ether (**2**). The pathway of the thermal gas-phase elimination reactions of comparable substrates was found to involve a concerted cyclic six-membered transition state (5, 7, 8): Fig. 2.

The same mechanism is suggested to account for the present results. Contribution to reactivity from bond *a* depends on the relative polarity of this bond. Bond *b* exercises its effect via the lability and protophilicity of the π-electrons, and bond *c* contribution to molecular reactivity is a function of the effect of (*Z*) on the acidity of hydrogen (H) and the stability of the incipient fragment containing (*Z*) (4, 5). The structural feature which distinguishes the ester (**1**) from the ether (**2**) is the electron-withdrawing capacity of the formate carbonyl group at *Z* and the stability of its incipient CO_2 fragment.

The reactivity of the anisoin ether (**3**) exceeds that of the benzoin ether (**2**) by a factor of 295. It is possible to rationalize this difference in reactivity in terms of the electron-donating mesomeric effect of the *p*-CH_3O group of the benzene ring on the relative protophilicity of the ketone carbonyl moiety: bond *b* in Fig. 2 (7).

Products and mechanism of reaction

Reaction products

The pyrolysate from each substrate was analyzed using both an online GC–MS and FT-1R pyroprobe techniques. The two ethers (**2**, **3**) and the formate ester (**1**), all gave 1,2-diarylethanone. Besides, the ethers yielded methanal and the ester produced carbon dioxide gas as the other molecular fragments of the thermal gas-phase elimination process.

Fig. 2. Concerted transition state.

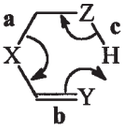

Mechanism

The reaction pathways shown in Scheme 1 are compatible with both the present kinetic results and the products of pyrolysis, and follow earlier findings by us and others (9). The driving force for the pathway of reaction [1] shown in the scheme might be due to the effect that the ester carbonyl group has on the acidity of the incipient H moiety and on the stability of the departing CO_2 fragment. For substrates **2** and **3**, rate-enhancement could be explained in terms of the relative protophilicity of bond *b* which is higher for the *p*-methoxy substituted function of **3** (see reaction [2]).

Experimental

Materials

Synthesis. Benzoin and anisoin

These were prepared in 85 and 44% yield, respectively, following literature procedure (10, 11). For benzoin, 47.5 mL (0.47 mol) of benzaldehyde in 65 mL of 95% ethanol and a solution of about 5 g KCN as catalyst in 50 mL of water were used in the condensation reactions. The quantities used in the preparation of anisoin were 112 g (0.825 mol) anisaldehyde, 150 mL alcohol, 22.4 g KCN, and 90 mL water. Both benzoin and anisoin were recrystallized from alcohol.

*Benzoin formate (**1**)*

A solution of benzoin (2.4 g, 0.1 mol) in 40 mL of 96% formic acid was refluxed for 16 h, and the resulting solution was concentrated under vacuum to yield a semisolid

© 1998 NRC Canada

Table 1. Kinetic data and rate coefficients (10^4 k (s^{-1})) at 600 K for compounds **1**, **2**, and **3**.

Compound	T (K)	10^4 k (s^{-1})	log A (s^{-1})	E_a (kJ mol^{-1})	10^4 k (s^{-1}) (at 600 K)
(1)	502.8	2.44	10.11 ±0.244	132.0 ±2.46	416
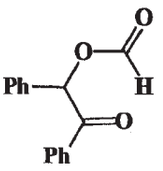	517.5	6.22			
	525.7	9.87			
	529.8	12.2			
	539.3	22.8			
	552.3	41.1			
(2)	609.7	2.97	11.29 ± 0.250	173.0 ±3.04	1.67
	620.8	5.42			
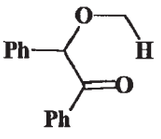	630.0	8.24			
	644.0	18.5			
	649.0	24.2			
	657.8	34.9			
(3)	508.0	2.12	11.85 ±0.252	151.1 ±2.56	492
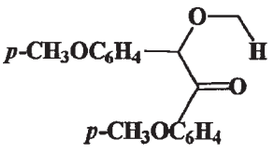	526.0	6.90			
	529.0	8.19			
	537.0	13.18			
	557.0	49.5			

Scheme 1. Pathway for functional groups interconversion.

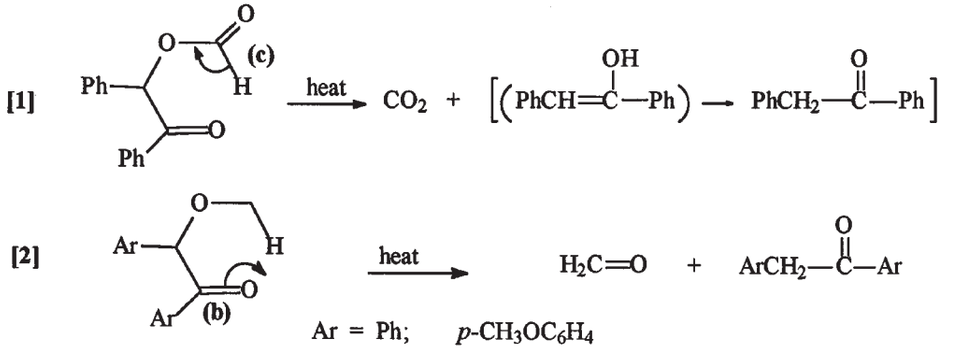

product. The residue was dissolved in 5 mL hot formic acid, and the mixture was cooled and filtered to remove unreacted benzoin. The mother liquor was concentrated under vacuum, and the solid residue was dissolved in ether. Any unreacted benzoin was further removed by filtration. Evaporation of ether gave a pale yellow solid, which was recrystallized repeatedly from petroleum ether to give the pure ester as a cream-coloured solid (12).

Benzoin methyl ether (2)

A solution of benzoin (2.1 g, 0.1 mol) in 140 mL of a mixture of equal volumes of methanol and dioxane was

© 1998 NRC Canada

stirred under reflux at 60–65°C. A steady stream of dry HCl was passed into the solution until saturation (2–3 h). The reaction mixture was then evaporated under vacuum, and the residue was chromotographed using petroleum ether/ethyl acetate (4:1 v/v) as eluent to give the pure ether as a white crystalline solid in 90% yield (13, 14).

*Anisoin methyl ether (**3**)*

The ether prepared from anisoin (2.7 g, 0.1 mol) using the procedure described above also gave a pale yellow compound in 40% yield (13, 15).

Characterization

Melting points were recorded on a Gallenkamp Sanyo melting point apparatus and are uncorrected (12–15). For element analysis, a LECO/CHNS-932 analyzer was used. ^{1}H NMR spectra were obtained on a Bruker AC80 spectrophotometer, and GC–MS spectral data were from a Finnigan Mat INCOSXL spectrometer.

*Benzoin formate (**1**)*: mp 72–73°C; δ_H (80 MHz; DMSO): 7.44–8.08 (5H, m, Ar), 8.18 (1H, s, HCO_{2^-}), 8.53 (1H, s, HC=O). $C_{15}H_{12}O_3$ requires C 75.00, H 5.03%; found: C 75.12, H 5.18%.

*Benzoin methyl ether (**2**)*: mp 46–47°C; δ_H (80 MHz; $CDCl_3$): 3.42 (3H, s, CH_3), 5.47 (1H, s, CH), 7.50 (5H × 2, m, Ar); ν_{max} (cm^{-1}): 1684 (s, CO). $C_{15}H_{14}O_2$ requires C 79.62, H 6.24%; found: C 79.73, H 6.26%.

*Anisoin methyl ether (**3**)*: mp 60–61°C; δ_H (80 MHz; DMSO): 3.70–3.80 (9H, s, $3CH_3$), 5.69 (1H, s, CH), 6.90–8.12 (4H, 2H, 2H, m, Ar); ν_{max} (cm^{-1}): 1682 (s, CO). $C_{17}H_{18}O_4$ requires C 71.32, H 6.30%; found: C 71.51, H 6.60%.

Kinetic procedure and product analysis

Experimental details of both kinetic and reaction product analysis have been described in an earlier communication (16). For the kinetic investigations, a custom-made chemical data pyrolysis system, HPLC (Bio-Rad model 2700), Shimadzu UV-vis detector, Bio-Rad HPLC accessories, and Comark microprocessor and platinum resistance thermometers are used. Analysis of products of reaction were carried out using both a flow technique and an online pyroprobe GC–MS (CDS Analytical Model 2000).

Acknowledgment

The support of Kuwait University through research grant no. SC 086 and use of the facilities of ANALAB and SAF are gratefully acknowledged.

References

1. N.A. Al-Awadi and M.H. Elnagdi. Heteroat. Chem. **8**, 293 (1997).
2. M. Hirano, S. Yakabe, H. Monobe, J.H. Clark, and T. Morimoto. J. Chem. Soc. Perkin Trans. 1, 3081 (1997).
3. (*a*) J.H. Clark, A.P. Kybett, and D.J. Mcqiarrie. Supported reagents: preparation, analysis and applications. VCH, New York. 1992; (*b*) J.H. Clark. Catalysis of organic reactions by supported inorganic reagents. VCH, New York. 1994.
4. R. Taylor. *In* The chemistry of functional groups: supplement B. *Edited by* S. Patai. John Wiley, Chichester. 1979. pp. 876–880.
5. N.A. Al-Awadi and O.M.E. El-Dusouqui. Int. J. Chem. Kinet. **29**, 295 (1997).
6. K. Tanabe. Proc. Int. Congr. Catal. 9th, **5**, 85 (1985).
7. N.A. Al-Awadi, R.F. Al-Bashir, and O.M.E. El-Dusouqui. J. Chem. Soc. Perkin Trans. 2, 579 (1989).
8. N.A. Al-Awadi, R.F. Al-Bashir, and O.M.E. El-Dusouqui. Tetrahedron, **46**, 2903 (1990).
9. K.A. Holbrook. *In* The chemistry of functional groups, supplement B: the chemistry of acid derivatives. *Edited by* S. Patai. John Wiley, Chichester. 1992. pp. 703–745.
10. W.S. Ide and J.S. Buck. Org. React. (NY), **4**, 269, (1948).
11. G. Sumrell, J.I. Stevens, and G.E. Goheen. J. Org. Chem. **22**, 39 (1957).
12. I.M. Lieff, G.F. Wright, and H. Hibbert. J. Am. Chem. Soc. **61**, 865 (1939).
13. R. Quelet and E. Frainnet. Compt. Rend. **236**, 492, (1953).
14. W.G. Dauben, C.F. Hiskey, and M.A. Muhs. J. Am. Chem. Soc. **74**, 2082 (1952).
15. A. Mackenzie and J.D. Pirie. Ber. Dtsch. Chem. Ges. B, **69B**, 861 (1936).
16. N.A. Al-Awadi, M.H. Elnagdi, T. Mathew, I. El-Gamry, and M. Abdel Khalik. Int. J. Chem. Kinet. **28**, 741 (1996).

© 1998 NRC Canada

COMMUNICATION

A computational study on the sources of deuterium secondary kinetic isotope effects in carbocation-forming reactions

Heidi M. Muchall and Nick H. Werstiuk

Abstract: Calculations at the HF-DFT hybrid Becke3LYP level of theory have been undertaken on protonated 2-*exo*- and 2-*endo*-norbornanols as model substrates for 2-*exo*- and 2-*endo*-norbornyl brosylates to explore the source of the experimentally determined deuterium secondary kinetic isotope effects (KIEs). Calculations on protonated alcohols as models reproduce the "normal" behaviour of 2-*endo* substrate **5**. The observed *endo* γ-KIE in the 7-unsubstituted 2-*exo* system **4** is shown to arise from internal return, while those in the 7-chloro substituted 2-*exo* substrates **1** and **2** can be explained with competing 1,3 (6,2)-elimination.

Key words: deuterium secondary kinetic isotope effects, 2-norbornyl cation, Becke3LYP.

Résumé : Utilisant les formes protonées des 2-*exo*- et 2-*endo*-norbornanols comme modèles des brosylates des 2-*exo*- et 2-*endo*-norbornyles, on a effectué des calculs au niveau théorique hybride Becke3LYP HF-DFT afin d'explorer la source des effets isotopiques cinétiques (EIC) secondaires du deutérium observés expérimentalement. Les calculs sur les alcools protonés utilisés comme modèles permettent de reproduire le comportement « normal » du substrat 2-*endo* (**5**). On a démontré que l'EIC-γ *endo* observé dans le système 2-*exo* non substitué en position 7 (**4**) découle d'un retour interne alors que l'on peut expliquer ceux observés avec les substrats 2-*exo* substitués par un chlore en position 7 (**1** et **2**) en invoquant une réaction d'élimination-1,3 (6,2) compétitive.

Mots clés : effets isotopiques cinétiques secondaires du deutérium, cation 2-norbornyle, Becke3LYP.

[Traduit par la Rédaction]

Deuterium secondary kinetic isotope effects (KIEs) have been used for decades to gain information on reaction intermediates and transition states, which forms the basis of widely used structure–reactivity principles. Representative of these studies is the work of Werstiuk et al. on **1-OBs** and **2-OBs** (1) and **3** (2), which was undertaken to probe the degree of C^6-C^1 participation in the cation-forming step of the solvolysis reactions in NaOAc-buffered 80:20 EtOH–H_2O.

Earlier it was shown that *exo*-2-norbornyl brosylate-*exo*-6-*d* (**4-OBs6ex**) and *exo*-2-norbornyl brosylate-*endo*-6-*d* (**4-OBs6en**) exhibit unusually large γ-KIEs (**4-OBs6ex**: 9%, **4-OBs6en**: 11%), and the results were interpreted on the basis of a C^6—C^1 bond assistance in the solvolyses (k_Δ, X = H) (3) (Scheme 1). While *endo*-2-norbornyl brosylate-*exo*-6-*d* (**5-OBs6ex**) did not exhibit a γ-KIE, that of *endo*-2-norbornyl brosylate-*endo*-6-*d* (**5-OBs6en**) was slightly inverse (3%). Similar results were obtained from acetolysis reactions (4). It was reasoned that a strong electron-withdrawing substituent at C^1 or C^7 should reduce the contribution of the k_Δ process (1), as the build up of a partial positive charge on C^1 would become less favourable.

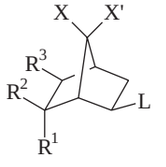

L = OBs, OH_2^+

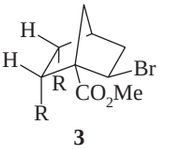

3

R = H, D

	R^1	R^2	R^3	X	X'
1-5ex6ex	H	D	D	Cl	H
2-5ex6ex	H	D	D	H	Cl
1-6en	D	H	H	Cl	H
2-6en	D	H	H	H	Cl

Unexpectedly, γ-KIEs in *anti*- and *syn*-7-chloro-*exo*-2-norbornyl brosylate-*exo*,*exo*-5,6-d_2 (**1-OBs5ex6ex**: 15%, **2-OBs5ex6ex**: 12%) and *anti*- and *syn*-7-chloro-*exo*-2-norbornyl brosylate-*endo*-6-*d* (**1-OBs6en**: 12%, **2-OBs6en**: 13%) were found to be larger than those found for the parent *exo* substrate **4-OBs**. This was interpreted with a combination of ef-

Received October 27, 1998.

H.M. Muchall[1] and N.H. Werstiuk.[1] Department of Chemistry, McMaster University, Hamilton, ON L8S 4M1, Canada.

[1]Authors to whom correspondence may be addressed. Telephone: (905) 525-9140. Fax: (905) 522-2509. E-mail: muchall@mcmaster.ca; werstiuk@mcmaster.ca

© 1998 NRC Canada

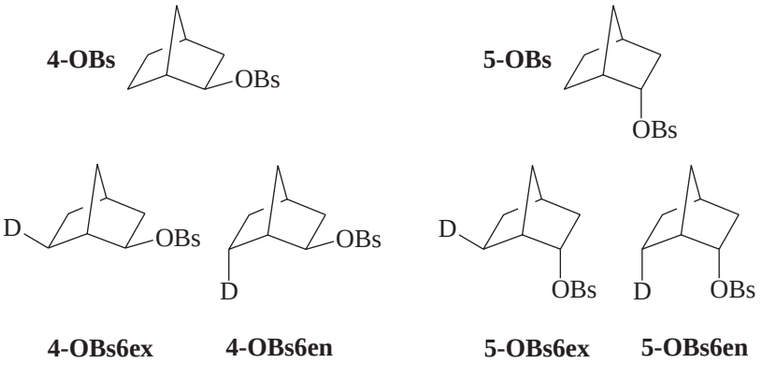

Scheme 1.

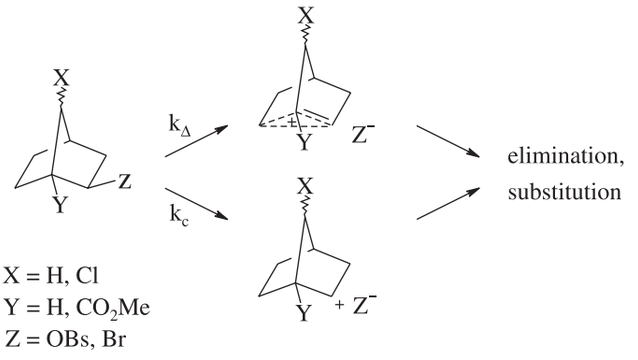

fects instead of a simple C^6—C^1 bond participation (considered were 1,3 elimination, *endo* hydrogen participation, 6,2-hydride shift, and solvent-assisted ionization), yet a final clarification was not achieved (1). Moreover, the unusually large γ-KIE found for bromoester **3** exhibited a solvent-polarity dependence (14% in 0.09 *M* NaOAc buffered 80:20 EtOH–H_2O and 20% in 0.14 *M* NaOAc buffered 80:20 EtOH–H_2O) (2). While the authors (1–4) drew conclusions from the experimental data (KIEs, products) and from analogous reactions, definitive statements could not be made at that time. Today, the full force of quantum chemical calculations can be brought to bear on problems of this type to gain fundamental information not directly accessible experimentally and, as a result, provide definitive solutions (see, for example, ref. 5). In this communication, we report the results of a computational study (using Gaussian 94 (6)) of deuterium secondary KIEs of systems **1**, **2**, **4**, and **5**.

As the brosylate systems are prohibitively large, it was necessary to find a reasonable level of theory as well as suitable model systems for substrates and solvolysis transition states. The problems in describing the 2-norbornyl cation are well known and have been confirmed by a computational study by Schleyer and co-workers (7): the classical 2-norbornyl cation (**7**) is a transition state in the rearrangement from the 2-norpinyl cation (**6**) to the — what so far has been referred to as "nonclassical" — 2-norbornyl cation (**8**); this result was achieved at the MP2(full)/6-31G(d) level of theory that was termed "adequate" because **7** was found not to be a stationary point at the HF/6-31G(d) level. In a more recent paper it is stated that a similar structure for **7** could be calculated using Becke3LYP/6-31G(d) (8). Our excellent experiences with the HF-DFT hybrid theory Becke3LYP (9) for different systems and chemical problems (10) led us to employ the computationally quite inexpensive Becke3LYP/6-31G(d,p) level of theory,[2] the inclusion of polarization functions on the hydrogen atoms being essential for the intended study of deuterium KIEs. We found that the 2-norbornyl cation can be described adequately at this level of theory: transition state **7** exhibits the one desired imaginary frequency (–266.6 cm^{-1}) and an IRC calculation links **7** to **6** and **8**. According to Becke3LYP/6-31G(d,p), **7** lies 13.17 kcal mol^{-1} above **8**,[3] which is in excellent agreement with the 13.64 kcal mol^{-1} found with MP4(sdq,fc)/6-31G (d,p)//MP2 (full)/6-31G(d) (13.1 kcal mol^{-1} with Becke 3LYP/6-311+G(d) (8)) reported by Schleyer and co-workers (7*a*). We therefore carried out geometry optimizations as well as frequency calculations using Becke3LYP/6-31G(d,p).

We assumed[4] that an optimized protonated alcohol is a good model for a reactant with the neutral leaving group water forcing the positive charge onto the hydrocarbon fragment in the transition state for dissociation. To test this approach, we calculated secondary α- and β-KIEs for a "normal" system, cyclopentyl brosylate (**9-OBs**). The KIE is computed as the ratio of the rate constant for the undeuterated (light) species over that for the deuterated (heavy) one. Secondary KIEs were determined with the program MacIEcalc[5] from masses, moments of inertia, and frequencies of light and heavy reactants as well as light and heavy transition states (TS) with the temperature set at 298.15 K if not stated otherwise. As scaling factors for Becke3LYP calculations are very close to 1.0, frequencies were not scaled (11); secondary KIEs do not require correction for a tunneling effect. A transition state for the dissociation of the protonated cyclopentanol could not be located, but computed KIEs using models for the TS, in which the C—O distance in the protonated alcohol is fixed at either 210 or 250 pm, were compared to experimental ones as determined by Stoffer and Christen (12) (KIEs in Table 1). With the 210

[2] See refs. 5*a* and *b*; in these papers, Houk and co-workers conclude that Becke3LYP calculations provide good predictions of KIEs.
[3] Zero-point energy uncorrected total energies are –273.060433 hartrees for **7** and –273.081420 for **8**.
[4] This work was started before ref. 8 was available.
[5] K. Korzekwa, J. Urbauer, D. Kiick, and J. Jones (changes by W.H. Saunders). University of Rochester, Rochester, N.Y.

© 1998 NRC Canada

Table 1. Experimental and calculated α-, β-, and γ-KIEs for **1**, **2**, **4**, **5**, and **9**. Calculations employ the transition state (TS, with C—O distances as given in Fig. 1) and 180, 210, and 310 pm models of the protonated alcohols.

			Model			
	Deuterium position	Expt.[a]	TS	180 pm	210 pm	310 pm
1-5ex6ex	γ,δ	1.150 ± 0.013[b]	1.166		1.082	
1-6en	γ	1.120 ± 0.005[b]	1.064		1.003	
2-5ex6ex	γ,δ	1.119 ± 0.011[b]	1.131[c]		1.045	
2-6en	γ	1.125 ± 0.007[b]	1.028[c]		1.001	
4-6ex	γ	1.09 ± 0.01[d]	1.127	1.015	1.051	1.130
4-6en	γ	1.11 ± 0.01[d]	1.054	0.999	0.998	1.045
4-3en3ex	β,β	1.10[e,f]	1.066[f]	1.037[f]	1.113[f]	1.106[f]
4-5ex6ex	γ,δ	1.09[g]	1.126	1.017	1.053	1.132
5-6ex	γ	1.00 ± 0.02[d,h]	1.015[h]		0.997[h]	
5-6en	γ	0.97 ± 0.01[d,h]	0.949[h]		0.969[h]	
5-2ex	α	1.20[h,i]	1.203[h]		1.144[h]	
5-3en3ex	β,β	1.26[j,k]	1.285[k]		1.141[k]	
5-5ex6ex	γ,δ	1.00[f,k]	1.015[k]		0.993[k]	
9	α	1.187[l]			1.148 (1.238)[m]	
9	β-*cis*	1.153[l]			1.053[n] (1.161)[m,o]	
9	β-*trans*	1.180[l]			1.141[p] (1.206)[m,q]	
9	β[r]	1.888[l]			1.443 (1.959)[m]	

[a]For the brosylates.
[b]Reference 1.
[c]For the 290 pm model.
[d]Reference 3.
[e]Reference 13.
[f]At 317.45 K.
[g]Reference 14.
[h]At 323.15 K.
[i]Reference 15.
[j]Reference 16.
[k]At 338.15 K.
[l]Reference 12.
[m]For the 250 pm model.
[n]From 1.093 and 1.015 for nonequivalent positions 2 and 5.
[o]From 1.039 and 1.297 for nonequivalent positions 2 and 5.
[p]From 1.073 and 1.214 for nonequivalent positions 2 and 5.
[q]From 1.059 and 1.374 for nonequivalent positions 2 and 5.
[r]2,2,5,5-Tetrasubstitution.

pm model, all calculated KIEs for **9** are smaller than the experimental values, while all are slightly too large at 250 pm.

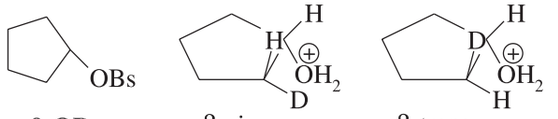

9-OBs β-cis β-trans

These results suggest that the C—O distance in the TS lies between 210 and 250 pm, providing support for our choice of model.

The located transition-state geometries[6] for **4-OH$_2^+$** and **5-OH$_2^+$** resemble those reported (8), and **1-OH$_2^+$TS** is similar to **4-OH$_2^+$TS** (so far we have not been successful in locating the transition state for the *syn*-7-chloro-*exo*-2-norbornyl brosylate (**2**), but a model with the C—O distance at 290 pm was taken as an approximation to **2-OH$_2^+$TS**). The hydrocarbon fragment in each transition state is distinctly unsymmetrical as can be seen from the C^6—C^1 and C^6—C^2 distances given in Fig. 1, and even though the *exo* transition states **1-OH$_2^+$TS** and **4-OH$_2^+$TS** are closer to being symmetrical than the *endo* transition state **5-OH$_2^+$TS**, it is important to note that *all three hydrocarbon cation moieties are classical*, contrary to the interpretation of Schleyer and co-workers (8); a situation that is emphasized in Fig. 1 by means of the highlighted bond for **1-OH$_2^+$TS** and **4-OH$_2^+$TS**. The topology of the charge density of the 2-norbornyl cation that has been moved from C_S symmetry as determined in an atoms in molecules (17) study shows a (3,–1) or bond critical point only between C^6 and C^1, not between C^6 and C^2, and confirms the classical character of every struc-

[6]Zero-point energy uncorrected total energies are –809.111584 (**1-OH$_2^+$**), –809.102719 (**1-OH$_2^+$TS**), –809.129369 (**2-OH$_2^+$**), –349.527681 (**4-OH$_2^+$**), –349.518000 (**4-OH$_2^+$TS**), –349.524206 (**5**), and –349.512550 hartrees (**5-OH$_2^+$TS**).

© 1998 NRC Canada

Fig. 1. Transitions states (TS) for the loss of water from protonated alcohols **1-OH$_2^+$**, **4-OH$_2^+$**, and **5-OH$_2^+$** with C—C and C—O distances in pm. See text for the highlighted bond.

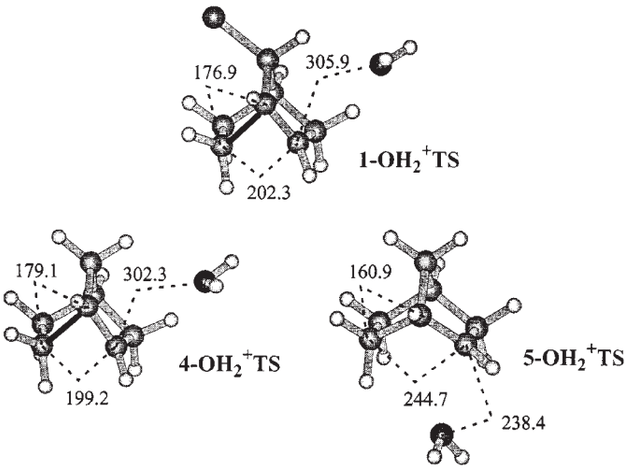

Scheme 2.

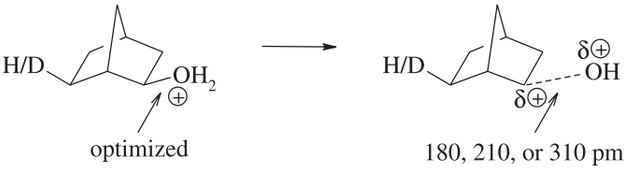

ture but the C_S symmetrical one — *which is a π-complex*, as was suggested earlier by Dewar et al. (18)! A communication reporting these results has been submitted (19).

To gain some further insight into the source of the KIEs, the transition states were also modelled by fixing the C—O bond in the protonated alcohol at an appropriate value (we chose 210 pm) and optimizing the resulting system. These pseudo-transition states, just as the true gas-phase transition states, show one imaginary frequency that has the expected dispositions. Additionally, we performed calculations for 180 and 310 pm C—O distances in **4-OH$_2^+$**. The absolute value of the imaginary frequency is largest for the 210 pm model of **4-OH$_2^+$** (–120.1 cm^{-1}); it is considerably smaller for the 310 pm model (–45.7 cm^{-1}) and for **4-OH$_2^+$TS** (–51.3 cm^{-1}) and nonexistent in the 180 pm model (the lowest frequency is 91.0 cm^{-1}), Scheme 2.

Table 1 gives the computational results and comparisons to experiment for deuterated derivatives of **1**, **2**, **4**, and **5**. Five different KIEs of *endo*-2-norbornyl brosylate (**5-OBs**) can be determined with excellent accuracy in the gas phase when **5-OH$_2^+$TS** is used (entry TS in Table 1). Both normal and inverse KIEs are modelled correctly with only little overestimation. Accordingly, there are no surprises with the 210 pm model of **5**. While the calculated α-effect in **5-OH$_2^+$2ex** and the β-effect in the doubly deuterated **5-OH$_2^+$3en3ex** are slightly too small, as expected due to the 210 pm distance, which is shorter than the one in **5-OH$_2^+$TS** (Fig. 1), the experimentally observed absence of a γ-effect in **5-OBs6ex** and **5-OBs5ex6ex** is confirmed computationally, as is the modest inverse γ-effect in **5-OBs6en**. The situation is more complicated for *exo*-2-norbornyl brosylate (**4-OBs**). With **4-OH$_2^+$TS**, none of the four computed KIEs seems to show a particularly good agreement with experiment, the γ-effect in **4-OBs6ex** and **4-OBs5ex6ex** being overestimated and the β-effect in **4-OBs3en3ex** underestimated. The calculated KIE in **4-OH$_2^+$6en** seems to present the worst case. Using **4-OH$_2^+$TS** it is much too small, and calculations on the 210 pm model even predict the absence of any γ-KIE, whereas experimentally the largest KIE was found for the brosylate (11%) (1). We repeated gas-phase calculations for **4-OH$_2^+$** with C—O distances of 180 and 310 pm. As expected, a C—O distance of 180 pm is too close to the optimized C—O bond length of 163.7 pm and therefore a poor model for a transition state: the γ-effect in **4-OH$_2^+$6ex** is very small, there is no effect for **4-OH$_2^+$6en**. Going to a C—O distance of 310 pm gives rise to a significant γ-KIE in **4-OH$_2^+$6en**. These three TS models allow a step-by-step approach to the geometry change in the hydrocarbon moiety upon ionization and its effects. Figure 2 shows that the 2-norbornyl cation, which is definitely unsymmetrical at 210 pm (with distances C^6—C^1 161.8 pm and C^6—C^2 230.3 pm), is closer to being symmetrical (C^6—C^1 175.2 pm and C^6—C^2 203.7 pm) at a water distance of 310 pm where the distinction between *endo* and *exo* deuterium on C^6 is fading with beginning internal return (the structures given in Fig. 2, with one highlighted bond for the 310 pm model, represent the molecular graphs as determined in an atoms in molecules study (19)). This view finds support in the average KIE of **4-OH$_2^+$6ex** and **4-OH$_2^+$6en**, which equals 1.09 and so represents the experimental value (observed KIEs for **4-OBs6ex** and **4-OBs6en** are identical within experimental error), and also in the early acetolysis study (4), which gives initial KIEs that are in accord with those computed, i.e., a significantly smaller value for **4-OBs6en**: 1.149 ± 0.016 for **4-OBs6ex** and 1.097 ± 0.011 for **4-OBs6en**. For *exo* substrates *anti*-7-chloro **1-OBs** and *syn*-7-chloro **2-OBs**, we calculate *exo* KIEs that agree well with the observed ones whereas the *endo* KIEs, similar to **4-OH$_2^+$6en**, are too small. Yet unlike the case of **4-OBs**, major solvolysis products for

Fig. 2. Gas-phase structures of **4-OH$_2^+$** with the C—O distance at 210 and 310 pm. See text for the highlighted bond.

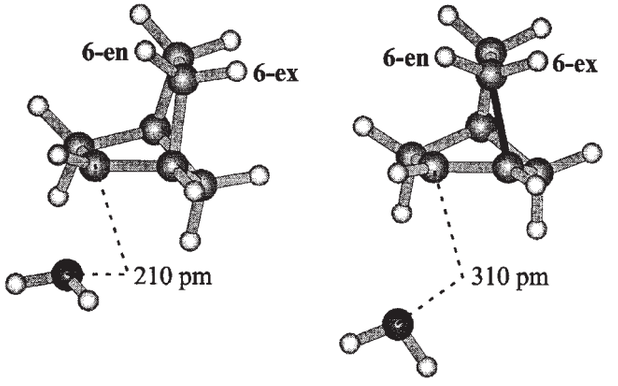

© 1998 NRC Canada

1-OBs6en (13%) and **2-OBs6en** (20%) are the respective chloronortricyclenes formed through a 1,3 (6,2)-elimination with the *endo* deuterium being lost preferentially (close to 80% deuterium loss) (1), and it has been shown in a steady-state treatment of a modified Winstein ion-pair scheme (2) that (and how) the isotope effects for elimination from ion pairs can contribute to k_H/k_D.

In conclusion, deuterium secondary kinetic isotope effects are computed accurately at the Becke3LYP/6-31G(d,p) level of theory when solvolysis transition states are employed. Sources for observed KIEs can be explored and resolved with Becke3LYP calculations.

Acknowledgments

We gratefully acknowledge the grant of cpu time on a CRAY T90 vector computer in the HLRZ Supercomputing Center at the Research Center Jülich, the usage of the IBM SP2 computer at Queen's University granted under the auspices of an IBM Canada – Queen's University collaborative project, as well as the usage of the SGI computing installation in the Geochemistry Labs at McMaster funded by the Natural Sciences and Engineering Research Council of Canada (NSERC). We thank Ms. O. Donini for assistance with operational aspects of parallel Gaussian 94 and NSERC for financial support.

References

1. N.H. Werstiuk, G. Timmins, and F.P. Cappelli. Can. J. Chem. **58**, 1738 (1980).
2. N.H. Werstiuk. Can. J. Chem. **53**, 26 (1975).
3. B.L. Murr, A. Nickon, T.D. Swartz, and N.H. Werstiuk. J. Am. Chem. Soc. **89**, 1730 (1967).
4. J.M. Jerkunica, S. Borčić, and D.E. Sunko. J. Am. Chem. Soc. **89**, 1732 (1967).
5. (*a*) D.A. Singleton, S.R. Merrigan, J. Liu, and K.N. Houk. J. Am. Chem. Soc. **119**, 3385 (1997); (*b*) B.R. Beno, K.N. Houk, and D.A. Singleton. J. Am. Chem. Soc. **118**, 9984 (1996); (*c*) M.M. Davidson, J.M. Guest, J.S. Craw, I.H. Hillier, and M.A. Vincent. J. Chem. Soc. Perkin Trans. 2, 1395 (1997); (*d*) P. Czyryca and P. Paneth. J. Org. Chem. **62**, 7305 (1997).
6. M.J. Frisch, G.W. Trucks, H.B. Schlegel, P.M.W. Gill, B.G. Johnson, M.A. Robb, J.R. Cheeseman, T. Keith, G.A. Petersson, J.A. Montgomery, K. Raghavachari, M.A. Al-Laham, V.G. Zakrzewski, J.V. Ortiz, J.B. Foresman, C.Y. Peng, P.Y. Ayala, W. Chen, M.W. Wong, J.L. Andres, E.S. Replogle, R. Gomperts, R.L. Martin, D.J. Fox, J.S. Binkley, D.J. Defrees, J. Baker, J.P. Stewart, M. Head-Gordon, C. Gonzalez, and J.A. Pople. Gaussian 94, Revision B.3. Gaussian, Inc., Pittsburgh, Pa. 1995.
7. (*a*) S. Sieber, P.v.R. Schleyer, H. Vančik, M. Mesić, and D.E. Sunko. Angew. Chem. Int. Ed. Engl. **32**, 1604 (1993); (*b*) P.v.R. Schleyer and S. Sieber. Angew. Chem. Int. Ed. Engl. **32**, 1606 (1993).
8. P.R. Schreiner, P.v.R. Schleyer, and H.F. Schaefer III. J. Org. Chem. **62**, 4216 (1997).
9. A.D. Becke. J. Chem. Phys. **98**, 5648 (1993); C. Lee, W. Yang, and R.G. Parr. Phys. Rev. B: Condens. Matter, **37**, 785 (1988).
10. (*a*) H.M. Muchall, N.H. Werstiuk, J. Ma, T.T. Tidwell, and K. Sung. Can. J. Chem. **75**, 1851 (1997); (*b*) H.M. Muchall, N.H. Werstiuk, and B. Choudhury. Can. J. Chem. **76**, 221 (1998); (*c*) N.H. Werstiuk, H.M. Muchall, C.D. Roy, J. Ma, and R.S. Brown. Can. J. Chem. **76**, 672 (1998); (*d*) N.H. Werstiuk, H.M. Muchall, J. Ma, and M.T.H. Liu. Can. J. Chem. **76**, 1162 (1998); (*e*) H.M. Muchall, N.H. Werstiuk, J.L. Pitters, and M.S. Workentin. Tetrahedron. In press; (*f*) H.M. Muchall, N.H. Werstiuk, and J. Lessard. J. Mol. Struct. (Theochem). In press.
11. J.B. Foresman and A. Frisch. Exploring chemistry with electronic structure methods. 2nd ed. Gaussian, Inc., Pittsburgh, Pa. 1996.
12. J.O. Stoffer and J.D. Christen. J. Am. Chem. Soc. **92**, 3190 (1970).
13. D.E. Sunko and S. Borčić. Isotope effects in chemical reactions. ACS Monograph 167. *Edited by* C.J. Collins and N.S. Bowman. Van Nostrand Reinhold Company, New York. 1970.
14. S. Borčić, V. Belanić-Lipovac, and D.E. Sunko. Croat. Chem. Acta, **33**, 35 (1961).
15. C.C. Lee and E.W.C. Wong. J. Am. Chem. Soc. **86**, 2752 (1964).
16. J.M. Jerkunica, S. Borčić, and D.E. Sunko. Chem. Commun. 1302 (1967).
17. R.F.W. Bader. Atoms in molecules. A quantum theory. Clarendon Press, Oxford. 1990.
18. (*a*) M.J.S. Dewar and A.P. Marchand. Ann. Rev. Phys. Chem. **16**, 321 (1965); (*b*) M.J.S. Dewar and K.M. Merz, Jr. J. Am. Chem. Soc. **108**, 5634 (1986).
19. N.H. Werstiuk and H.M. Muchall. J. Mol. Struct. (Theochem). In press.

© 1998 NRC Canada

ADDITIONS AND CORRECTIONS/AJOUTS ET CORRECTIONS

Additions and corrections: Skeletal vibrational circular dichroism of a series of bicyclic dilactones: the fingerprint region?

A. Rauk, J.L. McCann, H. Wieser, P. Bour, I.V. Vystorop, Yu.I. El'natanov, and R.G. Kostyanovsky

Ref.: Can. J. Chem. **76**, 717 (1998)

Please note that the name of author I.V. Vystorop was inadvertently omitted from the list of authors. His name and address appear correctly in the box at the bottom of the page.

Additions and corrections: Solubility of fluoranthene in organic nonelectrolyte solvents. Comparison of observed versus predicted values based upon Mobile Order theory

Carmen E. Hernández and William E. Acree, Jr.

Ref.: Can. J. Chem. **76**, 1312 (1998)

The complete title of Table 1 should read "Comparison between experimental fluoranthene mole fraction solubilities and predicted values based upon Mobile Order theory."

The mole fraction solubility of fluoranthene in 4-methyl-2-pentanol was incorrectly listed in Table 1. The listed value contained one too many zeroes. The correct value is $X_A^{sat} = 0.00948$.

Can. J. Chem. Downloaded from www.nrcresearchpress.com by University Town Library of Shenzhen on 09/05/12
For personal use only.

© 1998 NRC Canada

Canadian Journal of Chemistry

Author Index
Volume 76, 1998

Revue canadienne de chimie

Index des auteurs
Volume 76, 1998

Abbady, M.S., 469
Abbotto, A., 765
Abd El Rehim, S.S., 1156
Abraham, M.H., 703
Abu-Eittah, R.H., 1006
Acree, W.E., 1312, 1931
Ahlberg, P., 795
Ahrika, A., 1867
Ahvazi, B.C., 506
Ajji, A., 1491
Alavi, A., 1581
Al-Awadi, N.A., 1922
Allnatt, A.R., 1548
Allnatt, E.L., 1548
Álvarez-Santos, S., 1027
Aly, A.T., 1006
Amin, M.A., 1156
Anacona, J.R., 57
Andrews, M.P., 533, 1717
Andruh, M., 1564
Anklin, C., 546
Annandale, M.T., 873
Anouti, M., 1867
Aquino, M.A.S., 1520
Ardus, J.A., 907
Argyropoulos, D.S., 506, 612, 1606
Armstrong, D.A., 1042
Arnold, D.R., 1238, 1817
Aroca, R., 1730
Artamkina, G.A., 970
Arteca, G.A., 1402
Arvidsson, P.I., 795
Asgari, F., 1606
Auzanneau, F.-I., 1109
Avilov, S.A., 137
Bachand, B., 490
Bader, R.F.W., 284, 973
Badr, M.Z.A., 469
Bain, A.D., 183, 426
Baird, I.R., 1379
Baker, W.E., 884
Bakshi, P.K., 583
Balcom, B.J., 1753
Baldwin, J.E., 806
Banerjee, R., 350
Banton, N.J., 843
Barba, V., 1352
Barclay, K.D., 48
Barclay, L.R.C., 171, 1805
Barnes, C.L., 1371
Barnett, S.M., 158
Baronnet, F., 1875
Barrie, P.J., 960
Bartels, C., 1524
Barthez, J.M., 726
Barton, R.J., 245
Basch, H., 832
Bassett, D.R., 1779
Batchelor, R.J., 1410
Baud, C., 738
Bawagan, A.D.O., 1
Beach, L.J., 1410
Bedioui, F., 1886
Beekman, R.A., 85
Belelie, J.L., 382
Beletskaya, I.P., 970
Bell, R.A., 426
Bell, V., 1530
Bennet, A.J., 431, 1410
Bensebaa, F., 1654
Bensimon, C., 142
Bergens, S.H., 1447
Bernardinelli, G., 205
Bernazzani, P., 1674
Bich, V.T., 1674
Bissada, S., 94
Block, D.A., 1042
Boeré, R.T., 85
Bohme, D.K., 1138
Bolte, M., 1746
Bonev, B.B., 1512
Borecka-Bednarz, B., 1616
Boucher, G.D., 1266
Boudif, A., 1215
Bour, P., 717, 1931
Bowes, C., 1827
Boyd, R.J., 1817
Brazeau, J., 1642
Bree, A.V., 1616
Briois, V., 533
Briot, E., 1886
Brisson, J., 1491
Britten, J.F., 301
Brown, R.J.C., 1581
Brown, R.S., 672
Brownridge, S., 1050, 1220
Bryant, W.S., 1429
Buchanan, G.W., 142
Bui, V.T., 1699
Buncel, E., 873, 884, 896
Bunton, C.A., 946
Burgers, P.C., 335
Butler, I.S., 158, 1365
Cameron, T.S., 583, 1050, 1520
Caplan, J.F., 1520
Carlow, G.R., 1737
Cartier dit Moulin, C., 533
Cassidy, R.M., 194
Castan, P., 205
Caughill, D.I., 1402
Cavallo, L., 1457
Cerrada, E., 1033
Cervera, M., 966
Chénard, Y., 1642
Chandler, W.D., 919
Chapados, C., 1674
Chaudhuri, B., 350
Chen, D., 445
Chen, Q.F., 1437
Cheng, P., 1102
Cheon, K.-S., 896
Chew, W., 48
Chiang, Y., 657
Childs, R.F., 10
Chivers, T., 1093
Choudhury, B., 221, 238
Christensen, M.K., 1109
Chung, E.-K., 729
Cianciosi, S.J., 806
Clarke, C.W., 1119
Cobos, J.C., 1418
Cochran, J.F., 1595
Cohen, S., 828, 1108
Colthurst, M.J., 678
Conner, J.K., 862
Contini, C., 678
Cordes, A.W., 307
Coulthard, I., 1707
Couture, P., 136, 241
Cow, C.N., 301
Cox, R.A., 649, 896

Craig, D.B., 623
Crampton, M.R., 627
Creber, K.A.M., 1699
Cunje, A., 1138
D'Souza, M.J., 751
da Silva Eusébio, M.R., 18
Dahy, A.A., 469
Daley, C.J.A., 1447
Dao, L.H., 1674
Darwish, E.S., 1038
Dass, N.N., 1836
Davie, K., 518
de Athayde Filho, P.F., 869
de la Fuente, I.G., 1418
De, S.K., 199
Degen, S., 1707
Delaviz, Y., 1429
Delmas, G., 1674
Den Auwer, C., 533
Devine, M.A., 356
Dexpert, H., 533
Dhara, M.G., 199
Dheilly, R.M., 1188
di Matteo, M., 770
Dickie, A., 1766
Dicks, A.P., 789
Di Renzo, M., 1668
Doğan, I., 254
Doherty, R.M., 703
Dolphin, D., 1467
Dovichi, N.J., 623
Drake, J.E., 319
Drennan, C.E., 152
Driega, A.B., 142
Drozdova, O.A., 137
Du, X.M., 1717
Dust, J.M., 662
Dutton, D.B., 1064
Duvivier, S., 1210
Edward, J.T., 1294
Einstein, F.W.B., 1410
El-Banna, M.M., 1860
El-Batouti, M.M., 1860
El-Dusouqui, O.M.E., 1922
El-Esawy, M., 1006
El Feninat, F., 1668
El'natanov, Y.I., 717, 1931
Ellis, T.H., 1654, 1668
Elnagdi, M.H., 1038
Erian, A.W., 1038
Eriksson, L.A., 1817
Esteves da Silva, J.C.G., 1197
Fabre, P.L., 205
Facchetti, A., 765
Fafara, A., 265
Falk, M., 48
Fang, Y.-R., 758
Farfán, N., 1352, 1853
Fauconnier, T., 426
Fell, L.M., 1, 335
Feng, D., 635
Fernández, H., 576
Ferreira, M.A., 1197
Ferro, V., 313
Filikov, A.V., 726
Flinn, B.J., 1796
Foroudian, J.J., 946
Francis, R.C., 1064
Frederiksen, L.B., 726
Freedman, T.B., 806
Freeman, G.R., 407, 411
Friesen, R.W., 94
Fry, C.G., 1633
Fyles, T.M., 1015
Gadosy, T.A., 1327
Galloro, J., 1530
Gareyev, R., 765
Garriques, B., 234
Gedye, R.N., 525
Geies, A.A., 469
Ghoneim, N., 1006
Gibson, H.W., 1429
Gill, M.S., 164
Gillit, N.D., 946
Gillman, I.G., 907
Gilson, D.F.R., 1280, 1365
Gimenez, S., 1215
Giumanini, A.G., 1180
Glaser, R., 1371
Glew, D.N., 119
Gomez-Contreras, F., 1174
González, J.A., 1418
González-Lafont, À., 1027
Goodings, J.M., 1437
Goodwin, T.E., 1308
Gracie, K., 464
Grandy, J.K., 1805
Graziano, G., 437
Gregoire, S., 452
Grossman, R.B., 1233
Gudimova, E.N., 137
Guthrie, J.P., 929
Gzouli, K., 937
Haddon, R.C., 307
Hafez, E.A.A., 1038
Haider, J., 862
Haine, A., 1674
Hallé, J.-C., 937
Halls, M.D., 1730
Hansson, M., 795
Haraguchi, M., 989
Harrington, P., 1256
Harris, S.L., 1109
Harrison, P.H.M., 301
Hartman, J.S., 382, 1317
Hassan, H.H., 1156
Hausch, D.L., 806
Havlas, Z., 1274
Hawrylak, B.E., 464, 1266
Hazendonk, P., 426
Heinrich, B., 1595
Heřmánek, S., 1274
Hernández, C.E., 1312, 1931
Hicks, R.G., 307
Hill, M.N.S., 862
Hill, R.T., 1064
Hirano, M., 1916
Holdcroft, S., 1524
Hooper, D.L., 125
Höpfl, H., 1352, 1853
Hopkinson, A.C., 1138
Hore, D., 1648
Horiuchi, K., 1779
Horton, J.H., 1559
Hoveyda, H.R., 414
Hoz, S., 828, 832, 1108
Huang, X., 518
Hubert, C., 234
Hughes, R.J., 152
Huguet, M.-L., 726
Humeres, E., 960
Hunter, D.H., 522
Huntington, A.P., 929
Ibrahim, M.A.M., 1156
Ide, S., 989
Ilnicki, E.I., 1317
Ishihara, K., 62
Ivushkin, V.A., 970
Jacobs, P.W.M., 1540
Jacquier, Y., 738
James, B.R., 1379
Jana, G.H., 297
Jansson, C.M., 1817
Janz, K., 35
Janzen, A.F., 518
Jefferson, E.A., 1284
Jenkins, R.D., 1779
Jiang, Z.-H., 612, 1102
Jimenez, C., 137
Jiménez-Esquivel, B., 1668
Jocys, G., 35
Joly, H.A., 400
Jones, J.R., 726
Kabalka, G.W., 800
Kakkar, A.K., 1766
Kalinin, V.I., 137
Kalinovsky, A.I., 137
Kalita, G., 1836

Kamimura, H., 997
Kanagasooriam, A.J.S.S., 678
Karataş, M., 254
Karunaratne, V., 414, 1467
Kasaai, M.R., 1699
Katritzky, A.R., 635
Kaufman, T.S., 1338
Kaul, K., 1922
Kayser, M.M., 1844
Kazmaier, P.M., 884
Kennedy, C.B., 1753
Kepes, M., 400
Kermis, T.W., 821
Kerr, M.A., 1256
Kesselring, U.W., 553
Keum, S.-R., 896
Kevill, D.N., 751
Khan, A.Z.-Q., 795
Kilway, K.V., 765
Kim, C.-K., 102, 114, 359
Kim, S.S., 836
King, J.F., 164
Kiser, E.J., 147
Klassen, G.A., 48
Kliegel, W., 389, 1082, 1789
Klissurki, D.G., 1361
Knaul, J.Z., 1699
Knop, O., 583
Koh, H.J., 710
Kohda, J., 260
Köhler, K., 1249
Kondo, Y., 62
Koni, S., 254
Kono, M., 265
Kopytko, N., 1875
Kostyanovsky, R.G., 717, 1931
Kou, H.Z., 1102
Kowalewski, M., 1595
Kresge, A.J., 657, 1284
Krom, J.A., 765
Kruus, E., 1654, 1668
Kusaka, H., 498
Kwiatkowski, W., 48
Lacelle, S., 1633
Lafleur, M., 1501
Laguna, M., 1033
Lai, E.P.C., 265
Lai, Z.-g., 758
Lam, R., 1588
Lang, H., 635
Lantos, S.D., 583
Lau, D.Y.K., 546
Lebuis, A.-M., 1827
Leclerc, M., 1571
Lee, D.G., 919
Lee, G.S.H., 1660
Lee, H.W., 710
Lee, I., 710
Lee, J.-W., 710
Lee, S.-M., 729
Lemieux, R.P., 1520
Lessard, R.A., 1746
Letellier, P., 1210
Lewis, M., 1371
Li, N.-S., 800
Liao, D.-Z., 1102
Licence, V.E., 1910
Lim, C.G., 836
Lin, S.-S., 1910
Liu, M.T.H., 851, 1162
Lluch, J.M., 1027
Löbbecke, S., 686
Lock, C.J.L., 426
Logan, J., 1
Loock, B., 1215
Loock, D., 1015
Loroño, M., 57
Loss, T.A.E., 1554
Lotz, B., 1491
Loucks, L.F., 1144
Lowe, J., 1524
Lu, S.-Y., 726
Lynden-Bell, R.M., 1581
Lyon, A.P., 843
Ma, J., 238, 672, 1162
Macartney, D.H., 843
MacDonald, A.C., 292, 1266
MacGillivray, T., 292
Machado, A.A.S.C., 1197
Machin, W.D., 1578
MacKinnon, H.D., 1805
Mahiuddin, S., 1836
Majumdar, K.C., 297
Mak, T.C.W., 546
Malkasian, A., 1766
Mallik, A.K., 199
Manderville, R.A., 662, 907
Manners, I., 371
Manocha, S.K., 245
Mar, A., 1588
Marangoni, D.G., 292, 1266
March, R.E., 452
Marques, A., 770
Marquet, J., 966
Marshall, H., 356
Martell, A.E., 445
Martín, F.J., 284
Maskill, H., 862
Mastikhin, I.V., 1753
Mathurin, J.-C., 452
Matta, C.F., 301
Matthew, L., 1284
McCann, J.L., 274, 717, 1931
McClelland, R.A., 78, 1327, 1910
McDowell, S.A.C., 483
McGarry, P.F., 1474
McIntosh, J.M., 147
McManus, D., 445
McManus, K.A., 1238
McRoberts, C., 522
Meacham, J.M., 1308
Meath, W.J., 483
Mehranpour, A.M, 686
Melanson, R., 1564, 1844
Meldal, M., 1109
Metge, J., 389, 1082
Mihichuk, L.M., 245
Mika, A.M., 10
Miller, J., 869
Miller, J.M., 382
Miller, K., 1144
Mills, A.M., 1588
Minkin, V.I., 776
Minyaev, R.M., 776
Mitchell, K.A.R. 1796
Mitchell, R.H., 546
Mizuno, T., 228
Modro, A.M., 1344
Modro, T.A., 1344
Moffatt, S., 1491
Molina, T.G., 576
Molins, E., 10
Momenteau, M., 1215
Montgomery, C.D., 1060
Moock, K.H., 85
Morimoto, T., 1916
Morin, F.G., 1280
Morneau, A., 10
Morrow, M.R., 1512
Motekaitis, R.J., 445
Mphahlele, M.J., 1344
Muchall, H.M., 221, 238, 672, 1162, 1926
Müller, P., 738
Munro, A.P., 789
Murphy, C.A., 1520
Myland, J.C., 1688
Nagvekar, D.S., 1429
Najafi, S.I., 1717
Nakaguchi, S., 228
Nakayama, K., 62
Natansohn, A., 1648
Navarro, P., 1174
Nemska, S.D., 1361
Nepveu, F., 205
Nichol, H.C., 1805
Nichols, C.J., 414
Nishikawa, J.I., 989

Norton, P.R., 1559
Nunes, M., 960
Oakley, R.T., 307
Oh, I.S., 836
Ohta, K., 228
Oldham, K.B., 1688
Oliveira, C.M.S., 960
Onyszchuk, M., 1827
Orvig, C., 414
Outurquin, F., 937
Pageau, G., 506
Palepu, R., 464
Pardo, M., 1174
Paris, J.L., 1867
Paroli, R.M., 1365
Parvez, M., 85, 533, 1093, 1289
Passmore, J., 1050, 1220
Patrick, B.O., 1616
Paulmier, C., 937
Payne, N.C., 164
Pèpe, G., 1174
Perlikowska, W., 1344
Pestman, M., 862
Pestrin, R., 1530
Pezacki, J.P., 238
Phuong-Nguyen, H., 1674
Pienaar, A., 1344
Piers, W.E., 533, 1249
Pietro, W.J., 1530
Pincock, A., 35
Pincock, J., 35
Pinto, B.M., 1109
Pizzocaro, C., 1746
Plešek, J., 1274
Poirier, R.A., 477
Polsky, B., 265
Ponzo, V.L., 1338
Popik, V.V., 657
Pottie, I.R., 125
Pouet, M.-J., 937
Poulin, S., 1668
Preston, P.N., 1800
Prpic, J., 400
Pugliese, L., 1530
Qi, M., 635
Qin, Z., 1548
Queneudec, M., 1188
Ramek, M., 566
Rang, K., 811
Ranger, M., 1571
Rappoport, Z., 657
Rasmusson, J., 1559
Ratcliffe, C.I., 1660
Rauk, A., 274, 717, 1042, 1289, 1931
Refvik, M.D., 213
Reichardt, C., 686
Reinsborough, V.C., 152
Ren, D., 78, 1327
Ren, H., 751
Rettig, S.J., 389, 414, 1060, 1082, 1379, 1789, 1800
Rey, F., 1197
Rharbi, Y., 1779
Richard, J.P., 1910
Riebe, U., 1789
Riguera, R., 137
Riopelle, R.J., 1389
Ripmeester, J.A., 1660
Ro, S., 114
Robert, J.E., 1867
Robertson, B.E., 245
Robertson, K.N., 583
Robotham, I.A., 627
Rochon, F.D., 1564, 1844
Rochon, P., 1648
Rodriquez, C.F., 1138
Rogers, C.W., 1554
Roig, A., 10
Ross, G.M., 1389
Roué, L., 1886
Roy, C.D., 672
Roy, N., 400
Ruasse, M.-F., 770
Ruelle, P., 553
Rulíšek, L., 1274
Ruttink, P.L.A., 335
Sabbah, R., 18
Sacher, E., 1668
Saied, O., 490
Sales, M., 1344
Samat, A., 1174
Sánchez, M., 1352
Sandström, J., 811
Sanz, A.M., 1174
Saravanamuttu, K., 1717
Saunders, W.H., 821
Sawai, H., 260
Sazonov, P.K., 970
Scaiano, J.C., 1474
Schafer, G., 686
Schäfer, L., 566
Schatte, G., 1050, 1093
Schebesh, K., 382
Scheffer, J.R., 1616
Schepp, N.P., 657
Schiewe, J., 1688
Schwan, A.L., 213
Scott, J.M.W., 643
Sebaibi, Y., 1188
Segstro, E.P., 518
Sella, A., 828, 832, 1108
Selzer, T., 657
Sequinel, L.F., 960
Sham, T.K., 1707
Shamovsky, I.L., 1389
Shapter, J.G., 1559
Shi, Z., 102, 114, 359
Shimizu, K., 1796
Shine, H.J., 695
Shinozuka, K., 260
Shoemaker, J.A.W., 1317
Shuely, W.J., 703
Shurmer, B., 1060
Shustov, G.V., 851
Sierralta, A., 57
Simas, A.M., 869
Skov, K.A., 1379
Smith, M.E., 1308
Smith-Palmer, T., 292
Sorensen, T.S., 1289
Soriyan, O.O., 152
Souchard, J.-P., 205
Stangel, I., 1668
Stathakis, C., 194
Steel, P.J., 635
Stein, A.R., 929
Stephens, A.K.W., 414
Stewart, J.C., 164
Stonik, V.A., 137
Storr, A., 1130, 1800
Stratakis, M., 765
Streitwieser, A., 765
Summers, D., 643
Summers, D.A., 1130
Sun, F., 1289
Sun, S., 301
Sun, X., 1220
Sun, Y., 533
Sutherland, G.W., 1050
Svensson, C., 811
Swaddle, T.W., 183
Swainson, I.P., 1581
Swansburg, S., 35, 1520
Swift, H.R., 789
Szerminski, W.R., 1317
Tabet, J.-C., 452
Tanaka, K.S.E., 431
Tang, F., 1070
Taylor, A.L., 1688
Terlouw, J.K., 335
Terrier, F., 937
Thompson, R.C., 1130
Thomson, B.A., 499
Tian, Z., 147
Tokoroyama, T., 498
Toniutti, N., 1180
Tremblay, L., 1633
Trotter, J., 389, 1082, 1616, 1789, 1800

Trupp, R.J., 1233
Tsuruta, H., 1304
Tsuzuki, H., 989, 997
Tudo, J., 1188
Turmine, M., 1210
Ueda, Y., 228
Um, I.-H., 729
Uzunova, E.L., 1361
Vacheresse, M., 125
Vajda, K.E., 307
Vallazza, E., 183
van Rooyen, P.H., 1344
Van Verth, J.E., 821
VanderNoot, V.A., 265
VanLoon, G.W., 873
Vargas-Baca, I., 1093
Vaughan, K., 125
Veinot, J.G.C., 1530
Verardo, G., 1180
Vernon, M.L., 1540
Verrall, R.E., 25
Viala, C., 205
Vinqvist, M.R., 1805
Vittal, J.J., 522
Vlček, A., 158
Voicu, R., 1654
Vystorop, I.V., 717, 1931
Wails, D., 382
Walker, R.A., 292
Walter, J.A., 48
Wang, D.Z., 765
Wang, G.-L., 1102
Wang, H.-G., 1102
Wang, J.-H., 1144
Wang, Y., 477
Wang, Z., 919
Warkentin, J., 136, 238, 241
Weaver, D.F., 1389
Wee, A.G.H., 1070
Wei, J.B., 525
Weiler, L., 313
Weinberg, N., 102, 114, 359
Wentzell, P.D., 1144
Werstiuk, N.H., 221, 238, 672, 1162, 1926
Westaway, K.C., 758
Wharf, I., 1827
Whiddon, C.R., 946
White, M.A., 1695
Whitehead, M.A., 1766
Whiting, G.S., 703
Wieser, H., 274, 717, 1931
Wiles, J.A., 1447
Williams, A., 678
Williams, D.L.H., 789
Williams, K.B., 1910
Willis, P.A., 1581
Wilson, L.D., 25
Winnik, F.M., 10
Winnik, M.A., 1779
Withers, S.G., 313
Wojtowski, R., 1827
Wolf, M.O., 1554
Wolfe, S., 102, 114, 359
Wong, M.S.O., 678
Wong, P.C., 1796
Woo, T.K., 1457
Wosnick, J.H., 1280
Wu, B.-m., 546
Wu, Z., 1284
Wuest, J.D., 490
Xi, F., 171
Xu, J., 1668
Yakabe, S., 1916
Yam, C.M., 1766
Yamato, T., 989, 997
Yan, S.-P., 1102
Yang, J., 319
Yang, K., 102, 114, 359
Yao, X.-K., 1102
Yavari, M., 1668
Yekta, A., 1779
Yoshimura, Y., 71
Yu, C.-H., 566
Yu, D., 1042
Yu, S., 800
Yuan, Z., 1317
Yuasa, Yoshifumi, 1304
Yuasa, Yoko, 1304
Yuyitung, G., 164
Zakharov, A.N., 955
Zefirov, N.S., 955
Zhang, X.-Z., 1064
Zhao, W., 695
Zhao, Y., 400, 411, 1642
Zhou, X., 1015
Zhou, Y., 884, 1654
Zhu, Y., 836
Zhu, Y.-J., 1707
Ziegler, T., 1457
Ziltener, H., 313
Zinke-Allmang, M., 1737
Ziolo, R.F., 10
Zon, M.A., 576

Canadian Journal of Chemistry

Contents
Volume 76, 1998

Revue canadienne de chimie

Sommaire
Volume 76, 1998

January / Janvier

ARTICLES

A.D.O. Bawagan, L. Fell, and J. Logan Time-resolved structures of electrical discharges in gases: experiment and stochastic model **1**

Françoise M. Winnik, André Morneau, Alicja M. Mika, Ronald F. Childs, Anna Roig, Elies Molins, and Ronald F. Ziolo Polyacrylic acid pore-filled microporous membranes and their use in membrane-mediated synthesis of nanocrystalline ferrihydrite **10**

Raphaël Sabbah et Maria Ermelinda da Silva Eusébio Energétique des liaisons inter- et intramoléculaires dans les trois isomères de l'aminopyridine **18**

Lee D. Wilson and Ronald E. Verrall A ^{1}H NMR study of cyclodextrin – hydrocarbon surfactant inclusion complexes in aqueous solutions **25**

Susan Swansburg, Kristin Janz, Gloria Jocys, Alexandra Pincock, and James Pincock Facial selectivity in the addition of nucleophiles to the radical cations of substituted 2-methyleneadamantanes **35**

Michael Falk, Warren Chew, John A. Walter, Witold Kwiatkowski, Katherine D. Barclay, and Gerald A. Klassen Molecular modelling and NMR studies of the caffeine dimer **48**

Marcos Loroño, J.R. Anacona, and Anibal Sierralta Coriolis coupling constants and inertial defect of B_2F_4 by ab initio calculations and the iterative method **57**

Katsuyuki Nakayama, Yuichi Kondo, and Koji Ishihara A kinetic study of the reactions of dimethyl sulfide bridged tetramethylplatinum(II) and octamethylplatinum(IV) complexes with dimethyl sulfide and bidentate ligands **62**

Yasuki Yoshimura Salt effect on the solubility of *mer*-(+)-tris(L-alaninato)cobalt(III) **71**

Daniel Ren and Robert A. McClelland Carbocation-like reactivity patterns in X′-substituted-4-biphenylylnitrenium ions **78**

Richard A. Beekman, René T. Boeré, Klaus H. Moock, and Masood Parvez Synthesis, electrochemistry, structure, and magnetic susceptibility of 5-*tert*-butyl-1,3-bis-(1,2,3,5-dithiadiazolyl)benzene. Structural effect of the bulky substituent **85**

Richard W. Friesen and Suzanne Bissada Total synthesis of (±)-9-deoxygoniopypyrone. Application of the iodocyclofunctionalization reaction of α-allenic alcohol derivatives **94**

Saul Wolfe, Chan-Kyung Kim, Kiyull Yang, Noham Weinberg, and Zheng Shi Transverse compression and the secondary H/D isotope effects in intramolecular S_N2 methyl-transfer reactions **102**

Saul Wolfe, Zheng Shi, Kiyull Yang, Stephen Ro, Noham Weinberg, and Chan-Kyung Kim Hydration of the carbonyl group. Further evidence for a cooperative mechanism from experimental and theoretical studies of the hydrations of formaldehyde, acetaldehyde, acetone, and cyclohexanone **114**

Donald L. Hooper, Ian R. Pottie, Marc Vacheresse, and Keith Vaughan 1,2-Bis(1-aryl-3-alkyltriazen-3-yl)ethanes and related compounds **125**

ADDITTIONS AND CORRECTIONS / AJOUTS ET CORRECTIONS

Philippe Couture and John Warkentin Chemistry of cyclic aminooxycarbenes **136**

Author Index / Index des auteurs **AI-1**

February / Février

ARTICLES

Sergey A. Avilov, Olga A. Drozdova, Vladimir I. Kalinin, Anatoly I. Kalinovsky, Valentin A. Stonik, Elena N. Gudimova, Ricardo Riguera, and Carlos Jiménez Frondoside C, a new nonholostane triterpene glycoside from the sea cucumber *Cucumaria frondosa*: structure and cytotoxicity of its desulfated derivative **137**

Alex B. Driega, Gerald W. Buchanan, and Corinne Bensimon Synthesis of *cis-p*-dioxano-12-crown-4 and X-ray crystallography of the (1:1) complex with lithium thiocyanate **142**

John M. McIntosh, E. Jay Kiser, and Zhigang Tian The stereochemistry of hippurate alkylation **147**

Catherine E. Drennan, Rachelle J. Hughes, Vincent C. Reinsborough, and Oladega O. Soriyan Rate enhancement of nickel(II) complexation in dilute anionic surfactant solutions **152**

Steven M. Barnett, Antonín Vlček, Jr., and Ian S. Butler Pressure-tuning infrared and Raman spectroscopic study of (2,2′-bipyridine)tetracarbonylchromium(0) **158**

James Frederick King, Gay Yuyitung, Manjinder Singh Gill, Jeffrey Charles Stewart, and Nicholas Charles Payne Stereoelectronic effects in sulfonyl compounds: axial orientation of an *N*-methyl group in a six-membered sultam **164**

Fengde Xi and L. Ross C. Barclay Cooperative antioxidant effects of ascorbate and thiols with di-*tert*-butylcatechol during inhibited peroxidation in solution and in sodium dodecyl sulfate (SDS) micelles **171**

Eva Vallazza, Alex D. Bain, and Thomas W. Swaddle Dynamics of silicate exchange in highly alkaline potassium silicate solutions **183**

Costas Stathakis and Richard M. Cassidy Control of relative migration of small inorganic and organic anions with cyclodextrins in capillary electrophoresis (CE) **194**

Surya K. De, Mrinal G. Dhara, and Asok K. Mallik Synthesis of *trans*-2,3-dimethoxy-3-(phenylamino)flavanones and related compounds **199**

Paule Castan, Christine Viala, Paul-Louis Fabre, Françoise Nepveu, Jean-Pierre Souchard, and Gérald Bernardinelli Crystal structure, spectroscopic and magnetic studies, and antioxidative properties of catena-[diaqua(dihydro-orotato)manganese(II)] **205**

Mitchell D. Refvik and Adrian L. Schwan The reactions of a 1-alkenesulfenate anion with TMS-X reagents; a variable temperature NMR study **213**

Heidi M. Muchall, Nick H. Werstiuk, and Biswajit Choudhury A search for an inexpensive calculational method for the reliable prediction of the first adiabatic and vertical ionization potentials of carbenes. Photoelectron spectra of two stable carbenes **221**

Kiyohisa Ohta, Youko Ueda, Satoshi Nakaguchi, and Takayuki Mizuno Photochemical reduction of CO_2 using Cu-loaded silicate rock powder suspended in water **228**

Cathy Hubert et Bernard Garrigues Influence des ultrasons sur la diastéréosélectivité. Synthèse d'imidazolidine-4-one chirales **234**

COMMUNICATION

H.M. Muchall, N.H. Werstiuk, B. Choudhury, J. Ma, J. Warkentin, and J.P. Pezacki Thermolysis of 2,2-dimethoxy-5,5-dimethyl-Δ^3- 1,3,4-oxadiazoline studied with photoelectron spectroscopy. He(I) photoelectron spectrum of dimethoxycarbene **238**

Author Index / Index des auteurs **AI-1**

March / Mars

ARTICLES

Philippe Couture and John Warkentin A benzo-fused oxapenem from a β-lactam-4-ylidene **241**

Richard J. Barton, Sushil K. Manocha, Beverly E. Robertson, and Lynn M. Mihichuk Synthesis, spectroscopy, and structures of the seven-coordinate complexes $(CH_3)_2AsC(CF_3)=C(CF_3)As(CH_3)_2W(CO)_2I_2P(OC_6H_5)_3$ and $[(CH_3)_2AsC(CF_3)=C(CF_3)As(CH_3)_2]_2W(CO)Br_2$ and spectroscopy of related seven-coordinate complexes **245**

Mehmet Karataş, Serap Koni, and İlknur Doğan Chiral *N*-(*o*-aryl)-thiazolidinediones: synthesis from rhodanines and investigation on rotational enantiomers by NMR spectroscopy **254**

Kazuo Shinozuka, Junya Kohda, and Hiroaki Sawai Oxidation of olefins catalyzed by iron complexes of bleomycin model compounds bearing a hydrophobic or hydrophilic steric factor **260**

Edward P.C. Lai, Ania Fafara, Victoria A. VanderNoot, Mari Kono, and Brandee Polsky Surface plasmon resonance sensors using molecularly imprinted polymers for sorbent assay of theophylline, caffeine, and xanthine **265**

Jennifer L. McCann, Arvi Rauk, and Hal Wieser A conformational study of (1*S*, 2*R*, 5*S*)-(+)-menthol using vibrational circular dichroism spectroscopy **274**

R.F.W. Bader and F.J. Martín Interdeterminancy of basin and surface properties of an open system **284**

Richard A. Walker, Aaron C. MacDonald, Tanya MacGillivray, D. Gerrard Marangoni, and Truis Smith-Palmer A capillary electrophoresis study of the synthesis and stability of 1,2-decanedisulfate, 1-hydroxy-2-decanesulfate, and 2-hydroxy-1-decanesulfate **292**

Krishna C. Majumdar and Gour H. Jana Competitive study of Meisenheimer rearrangement in a substrate tertiary amine with allylic and propargylic moieties **297**

Sengen Sun, James F. Britten, Christopher N. Cow, Chérif F. Matta, and Paul H.M. Harrison The crystal structure of 3,4,7,8-tetramethylglycoluril **301**

A. Wallace Cordes, Robert C. Haddon, Robin G. Hicks, Richard T. Oakley, and Kristen E. Vajda Iodine charge-transfer salts of bis(1,2,3,5-diselenadiazolyl) diradicals; solid-state characterization of the thiophene-bridged derivative $[(Se_2N_2C)C_4H_2S(CN_2Se_2)][I]$ **307**

Vito Ferro, Larry Weiler, Stephen G. Withers, and Herman Ziltener *N*-Glycosyl phosphonamidates: potential transition-state analogue inhibitors of glycopeptidases **313**

John E. Drake and Jincai Yang Synthesis, spectroscopic characterization, and structural studies of organogermanium tri- and monothiocarbonates. Crystal structures of $Me_2Ge[S_2CSEt]_2$, $Ph_3Ge[SCO_2Me]$, $Ph_3Ge[SCO_2(i\text{-}Pr)]$, and $Ph_2Ge[SCO_2Me]_2$ **319**

Lorne M. Fell, Peter C. Burgers, Paul J.A. Ruttink, and Johan K. Terlouw The decarbonylation of ionized β-hydroxypyruvic acid: the hydrogen-bridged radical cation $[CH_2{=}O\cdots H\cdots O{=}C\text{-}OH]^{\bullet+}$ studied by experiment and theory **335**

Beauty Chaudhuri and Rupendranath Banerjee Kinetics and mechanism of hydroxylamine oxidation by $[Fe^{III}_2(\mu\text{-}O)(phen)_4(H_2O)_2]^{4+}$ in aqueous media **350**

COMMUNICATION

Heather Marshall and Marisa A. Devine Precise measurement of fluorescence from uranium taken up in sodium fluoride **356**

ADDITIONS AND CORRECTIONS / AJOUTS ET CORRECTIONS

Saul Wolfe, Chan-Kyung Kim, Kiyull Yang, Noham Weinberg, and Zheng Shi Additions and corrections: Transverse compression and the secondary H/D isotope effects in intramolecular S_N2 methyl-transfer reactions **359**

Author Index / Index des auteurs **AI-1**

April / Avril

ARTICLES

Ian Manners 1997 Canadian Society for Chemistry Award Lecture: Ring-opening polymerization (ROP) of strained metallocenophanes: the discovery and development of a new route to high molecular weight poly(metallocenes) **371**

Jack M. Miller, David Wails, J. Stephen Hartman, Karla Schebesh, and Jennifer L. Belelie Friedel–Crafts catalysis using supported reagents. Synthesis, characterization, and catalytic application of sol–gel-derived silica **382**

Wolfgang Kliegel, Jörg Metge, Steven J. Rettig, and James Trotter Aromatic aldonitrones of 2-(hydroxyamino)benzyl alcohol and their cyclic isomers. Crystal and molecular structures of a 1-hydroxy-1,2-dihydro-4*H*-3,1-benzoxazine, a boron chelate, and its parent nitrone ligand **389**

Helen A. Joly, Maria Kepes, Natalie Roy, and Jason Prpic The reactivity of the high-energy intermediates formed in the reactions of Group 13 metal atoms and aromatic alkenes **400**

Yixing Zhao and Gordon R. Freeman Solvent effects on electrical conductivities of sodium tetraphenylboride in water–methanol, ethanol, and 2-propanol mixed solvents **407**

Yixing Zhao and Gordon R. Freeman Optical absorption spectrum of solvated electrons in pure *tert*-butanol: effect of temperature **411**

H.R. Hoveyda, Veranja Karunaratne, Christopher J. Nichols, Steven J. Rettig, Ashley K.W. Stephens, and Chris Orvig Tripodal trisamides based on nicotinic and picolinic acid derivatives **414**

Theresa Fauconnier, Alex D. Bain, Paul Hazendonk, R.A. Bell, and Colin J.L. Lock Structure and dynamics of azapropazone derivatives studied by crystallography and nuclear magnetic resonance **426**

Kelly S.E. Tanaka and Andrew J. Bennet Synthesis and evaluation of a bicyclic deoxymannojirimycin derivative as a potential glycosidase inhibitor **431**

Giuseppe Graziano Thermodynamics of dissolving gaseous argon in different solvents **437**

Dian Chen, Arthur E. Martell, Ramunas J. Motekaitis, and Derek McManus Syntheses and Fe(II)/Fe(III) equilibria of the new multidentate ligands pyridine-2-phosphonic-6-carboxylic acid and 2,6-pyridinediphosphonic acid for the use of their iron chelates as catalysts for the oxidation of H_2S to S_8 by air **445**

Sébastien Gregoire, Jean-Charles Mathurin, Raymond E. March et Jean-Claude Tabet Étude d'ions négatifs préparés « in situ » dans un piège ionique quadripolaire **452**

Brent Hawrylak, Kim Gracie, and R. Palepu Ultrasonic velocity and volumetric properties of isomeric butanediols plus water systems **464**

M.Z.A. Badr, A.A. Geies, M.S. Abbady, and A.A. Dahy New heterocycles from thienopyridocinnolines **469**

Youliang Wang and Raymond A. Poirier Generalized valence bond study of rotational singlet structures and π bond energies for systems containing C=C, Si=Si, and C=Si double bonds **477**

Sean A.C. McDowell and W.J. Meath Average energy approximations for anisotropic triple-dipole dispersion energy coefficients using three-body interactions involving O_2, NO, CO, N_2, H_2, and the rare gases as tests **483**

Okba Saied, Benoit Bachand, and James D. Wuest Complexes of ketodiesters and related compounds with $TiCl_4$. Attempts to use chelation to promote the simultaneous coordination of ketones by two Lewis acids **490**

ADDITIONS AND CORRECTIONS / AJOUTS ET CORRECTIONS

Takashi Tokoroyama and Hisashi Kusaka Additions and corrections: Folding strain stereocontrol in cyclohexane ring formation by means of an intramolecular ester enolate alkylation reaction **498**

Author Index / Index des auteurs **AI-1**

May / Mai

ARTICLES

Bruce A. Thomson 1997 McBryde Medal Award Lecture: Radio frequency quadrupole ion guides in modern mass spectrometry **499**

Behzad C. Ahvazi, Gerry Pageau, and Dimitris S. Argyropoulos On the formation of diphenylmethane structures in lignin under kraft, EMCC®, and soda pulping conditions **506**

Yimin Sun, Warren E. Piers, and Masood Parvez The solid-state structure of bis(pentafluorophenyl)zinc **513**

Edward Paul Segstro, Kerry Davie, Xiaoling Huang, and Alexander Frank Janzen Cyclic–acyclic equilibrium and selective P—O bond cleavage in 2-hydroxyphenyldiphenyl-phosphinate, $Ph_2P(O)OC_6H_4OH$ **518**

Duncan H. Hunter, Chantelle McRoberts, and Jagadese J. Vittal Bisthiosemicarbazones of 2,4-pentanedione are pyrazolines **522**

R.N. Gedye and J.B. Wei Rate enhancement of organic reactions by microwaves at atmospheric pressure **525**

C. Den Auwer, M.P. Andrews, V. Briois, C. Cartier dit Moulin, and H. Dexpert Structure bifurcation in containerless low-temperature syntheses of solid state niobium chloride compounds from lanthanoid atoms: an X-ray absorption and ab initio EXAFS analysis **533**

Reginald H. Mitchell, Danny Y.K. Lau, Thomas C.W. Mak, Bo-mu Wu, and Clemens Anklin Synthesis of the first [*n*]paracyclophane with an annulene as the aromatic, a necklace-like molecule; NMR, X-ray, and MMX structural comparisons **546**

Paul Ruelle and Ulrich W. Kesselring Solubility prediction of *n*-fatty alcohols and sterols in complexing and non-complexing solvents according to the mobile order theory **553**

Michael Ramek, Ching-Hsing Yu, and Lothar Schäfer Ab initio conformational analysis of the model tripeptide *N*-formyl-L-alanyl-L-alanine amide **566**

Patricia Gabriela Molina, María Alicia Zón, and Héctor Fernández Determination of the acid dissociation constants for some mycotoxins of the *Alternaria alternata* genus **576**

Katherine N. Robertson, Pradip K. Bakshi, Susanne D. Lantos, T. Stanley Cameron, and Osvald Knop Crystal chemistry of tetraradial species. Part 9. The versatile BPh_4^- anion, or how organoammonium H(N) atoms compete for hydrogen bonding **583**

Zhi-Hua Jiang and Dimitris S. Argyropoulos Coupling P-31 NMR with the Mannich reaction for the quantitative analysis of lignin **612**

Douglas B. Craig and Norman J. Dovichi *Escherichia coli* β-galactosidase is heterogeneous with respect to the activity of individual molecules **623**

Author Index / Index des auteurs **AI-1**

June / Juin

This issue is dedicated to Professor Erwin Buncel
Ce tirage est dédié au Professeur Erwin Buncel

ARTICLES

Michael R. Crampton and Ian A. Robotham Kinetic studies of σ-adduct formation and nucleophilic substitution in the reactions of ethyl 2,4,6-trinitrophenyl ether, some phenyl 2,4,6-trinitrophenyl ethers, and phenyl 2,4-dinitronaphthyl ether with aniline in dimethyl sulfoxide **627**

Alan R. Katritzky, Daming Feng, Hengyuan Lang, Ming Qi, and Peter J. Steel Novel syntheses of 4-alkyl-2(5*H*)-thiophenones and 8-phenylimino-1,2,4-triazolo[5,1-*c*]-1,4-thiazines **635**

John M.W. Scott and Danny Summers On the relationship between the rate constants for racemization and isotopic exchange **643**

Robin A. Cox Lactams in sulfuric acid. The mechanism of amide hydrolysis in weak to moderately strong aqueous mineral acid media **649**

Yvonne Chiang, A. Jerry Kresge, Norman P. Schepp, Vladimir V. Popik, Zvi Rappoport, and Tzvia Selzer The acid dissociation constant of triphenylethenethiol, a simple thioenol, and that of its oxygen-enol analog **657**

Julian M. Dust and Richard A. Manderville Carbon versus oxygen nucleophilic selectivity in the reaction of the aryloxide ions, 2,6- and 3,5-di-*tert*-butylphenoxide, with the 2-[(nitro)$_x$aryl]-4,6-dinitrobenzotriazole 1-oxide series of super-electrophiles. Stereoelectronic factors on C-7 Meisenheimer complex formation versus C-1′ S_NAr displacement **662**

N.H. Werstiuk, H.M. Muchall, C.D. Roy, J. Ma, and R.S. Brown A calculational and ultraviolet photoelectron spectroscopic study of distorted amides **672**

Matthew J. Colthurst, Angeline J.S.S. Kanagasooriam, Michael S.O. Wong, Christian Contini, and Andrew Williams α-Effect nucleophiles and azide ion: effective charge studies of displacement reactions at esters **678**

Christian Reichardt, Stefan Löbbecke, Abdol Mohammed Mehranpour, and Gerhard Schäfer Pyridinium *N*-phenoxide betaines and their application to the determination of solvent polarities, XXIV. Syntheses and UV-vis spectroscopic properties of new lipophilic *tert*-butyl- and 1-adamantyl substituted, negatively solvatochromic pyridinium *N*-phenolate betaine dyes **686**

Wenyi Zhao and Henry J. Shine Primary and secondary 5-(alkyloxy)thianthrenium perchlorates. Characterization with ^{1}H NMR spectroscopy, reactions with iodide and bromide ion, and thermal decomposition in solution **695**

Michael H. Abraham, Gary S. Whiting, Wendel J. Shuely, and Ruth M. Doherty The solubility of gases and vapours in ethanol—the connection between gaseous solubility and water–solvent partition **703**

Han Joong Koh, Ji-Won Lee, Hai Whang Lee, and Ikchoon Lee Kinetics and mechanism of the aminolysis of ethyl aryl carbonates in acetonitrile **710**

A. Rauk, J.L. McCann, H. Wieser, P. Bour, I.V. Vystorop, Yu.I. El'natanov, and R.G. Kostyanovsky Skeletal vibrational circular dichroism of a series of bicyclic dilactones: the fingerprint region? **717**

Jean M. Barthez, Anton V. Filikov, Lottie B. Frederiksen, Marie-Loire Huguet, John R. Jones, and Shui-Yu Lu Microwave-enhanced metal- and acid-catalysed hydrogen isotope exchange reactions **726**

Ik-Hwan Um, Eun-Kyung Chung, and So-Mi Lee An unusual ground-state stabilization effect and origins of the α-effect in aminolyses of Y-substituted phenyl X-substituted benzoates **729**

Paul Müller, Corine Baud, and Yvan Jacquier The rhodium(II)-catalyzed aziridination of olefins with {[(4-nitrophenyl)sulfonyl]imino}phenyl-λ^3-iodane **738**

Dennis N. Kevill, Malcolm J. D'Souza, and Haobo Ren Correlation of the rates of solvolysis of arylmethyl *p*-toluenesulfonates: application of the aromatic ring parameter and a discussion of similarity models **751**

Yao-ren Fang, Zhu-gen Lai, and Kenneth Charles Westaway Isotope effects in nucleophilic substitution reactions X. The effect of changing the nucleophilic atom on ion-pairing in an S_N2 reaction **758**

Andrew Streitwieser, Daniel Zerong Wang, Manolis Stratakis, Antonio Facchetti, Roustam Gareyev, Alessandro Abbotto, James A. Krom, and Kathleen V. Kilway Extended lithium ion pair indicator scale in tetrahydrofuran **765**

Antonio Marques, Massimo di Matteo, and Marie-Françoise Ruasse Remarkable efficiency of iron(III) versus manganese(III) tetraphenylporphyrins as catalysts for fast and quantitative oxidation of sulfides into sulfones by hydrogen peroxide **770**

Ruslan M. Minyaev and Vladimir I. Minkin Theoretical study of O→X (S, Se, Te) coordination in organic compounds **776**

Andrew P. Dicks, E. Li, Andrew P. Munro, Helen R. Swift, and D. Lyn H. Williams The reaction of S-nitrosothiols with thiols at high thiol concentration **789**

Per I. Arvidsson, Maria Hansson, Agha Zul-Qarnain Khan, and Per Ahlberg Solvent-induced stereospecific isomerization of an allylic alcohol to a homoallylic alcohol catalyzed by a chiral lithium amide **795**

George W. Kabalka, Su Yu, and Nan-Sheng Li Selective hydroboration of alkenes and alkynes in the presence of aldehydes and ketones **800**

Teresa B. Freedman, Diane L. Hausch, Steven J. Cianciosi, and John E. Baldwin Kinetics of thermal racemization of (2*S*,3*S*)-1-^{13}C-1,2,3-d_3-cyclopropane followed by vibrational circular dichroism spectroscopy **806**

Knut Rang, Jan Sandström, and Christer Svensson The conformational equilibrium of *N*,*N*′-bis[(*S*)-1-phenylethyl]-thiourea and its solvent dependence, studied by NMR and CD spectra and by X-ray crystallography **811**

James E. Van Verth, William H. Saunders, Jr., and Thomas W. Kermis Identity-reaction proton transfers from nitrogen acids yielding localized vs. delocalized conjugate bases. An ab initio study **821**

Ariel Sella, Shmuel Cohen, and Shmaryahu Hoz 1,3-Diphenylsulphonylcyclobutane: an unprecedented case of a higher stability of the *trans* isomer of 1,3-disubstituted cyclobutane **828**

Ariel Sella, Harold Basch, and Shmaryahu Hoz Concerted motion in bicyclobutane **832**

Sung Soo Kim, Yu Zhu, In Seok Oh, and Chang Gyeong Lim Reactions of benzyl methyl substituted-benzyl phosphites with *tert*-butyl hypochlorite: "balanced TS" validating reactivity/selectivity principle **836**

Angela P. Lyon, Nicola J. Banton, and Donal H. Macartney Kinetics of the self-assembly of α-cyclodextrin [2]pseudorotaxanes with polymethylene threads bearing quaternary ammonium and phosphonium end groups **843**

Gennady V. Shustov and Michael T.H. Liu On the possibility of conversion of strained bridgehead alkenes into carbenes via 1,2 hydrogen and 1,2 carbon migrations. A theoretical study of the rearrangements in the adamantene and protoadamantene systems **851**

John K. Conner, Johanna Haider, M.N. Stuart Hill, Howard Maskill, and Monique Pestman The mechanism of solvolysis of 2-adamantyl azoxytosylate: isotopic labelling, medium effect, and attempted deoxygenation studies **862**

Alfredo Mayall Simas, Joseph Miller, and Petrônio Filgueiras de Athayde Filho Are mesoionic compounds aromatic? **869**

Michael T. Annandale, Gary W. vanLoon, and Erwin Buncel Regioselectivity and stereoelectronic effects in the reactions of the dinitroaniline herbicides trifluralin and benefin with nucleophiles **873**

Yuehui Zhou, W.E. Baker, P.M. Kazmaier, and E. Buncel Phenanthroimidazole dimers: structure and free radical reactivity; piezochromism, thermochromism, and photochromism **884**

Robin A. Cox, Kap-Soo Cheon, Sam-Rok Keum, and Erwin Buncel Mechanism of the benzidine disproportionation of (arylhydrazo)pyridines. The reactions of 4-(4-chlorophenylazo)pyridine and -hydrazo)pyridine in acid media **896**

Jason A. Ardus, Ivan G. Gillman, and Richard A. Manderville On the role of copper and iron in DNA cleavage by ochratoxin A. Structure–activity relationships in metal binding and copper-mediated DNA cleavage **907**

Zhao Wang, W. David Chandler, and Donald G. Lee Mechanisms for the oxidation of secondary alcohols by dioxoruthenium(VI) complexes **919**

J. Peter Guthrie, Allan R. Stein, and Anthony P. Huntington Thermodynamics of methanesulfonic acid, methanesulfonyl chloride, and methyl methanesulfonate **929**

François Terrier, Marie-José Pouet, Khalid Gzouli, Jean-Claude Hallé, Francis Outurquin, and Claude Paulmier Carbon–carbon coupling of 4,6-dinitrobenzofuroxan with 3-aminothiophenes: a kinetic and structural study **937**

Clifford A. Bunton, Houshang J. Foroudian, Nicholas D. Gillitt, and Christy R. Whiddon Dephosphorylation and aromatic nucleophilic substitution in nonionic micelles. The importance of substrate location **946**

Nikolai S. Zefirov and Alexandre N. Zakharov Catalysis by topologically anchored metal complexes. Liquid-phase hydroxylation of benzene by H_2O_2 in the presence of zeolite-supported Fe(II) phthalocyanine **955**

Eduardo Humeres, Luiz Fernando Sequinel, Mauricéa Nunes, Célia M.S. Oliveira, and Patrick J. Barrie Kinetic effects induced by cellulose on water-catalyzed reactions. Hydrolysis of 2,4-dinitrophenyl cellulose xanthate and some sugar xanthate ester analogues **960**

Maria Cervera and Jordi Marquet Effects of superoxide anion generated from aromatic radical anions produced in nucleophilic aromatic photosubstitution reactions **966**

COMMUNICATION

Galina A. Artamkina, Petr K. Sazonov, Vasily A. Ivushkin, and Irina P. Beletskaya Formation of *cis*-$[R_f(CO)Re(CO)_4Hal]Na$ complexes as an evidence of halogen–metal exchange between $[Re(CO)_5]Na$ and polyfluorinated aryl and vinyl halides **970**

Author Index / Index des auteurs **AI-1**

July / Juillet

ARTICLES

R.F.W. Bader 1997 Polanyi Award Lecture: Why are there atoms in chemistry? **973**

Takehiko Yamato, Mitsuteru Haraguchi, Jun-Ichi Nishikawa, Seiji Ide, and Hirohisa Tsuzuki Synthesis, conformational studies, and inclusion properties of tris[(2-pyridylmethyl)oxy]hexahomotrioxacalix[3]arenes **989**

Takehiko Yamato, Hideo Kamimura, and Hirohisa Tsuzuki *ipso*-Nitration of *tert*-butyl[*n*.2]metacyclophanes; through-space electronic interactions between two benzene rings **997**

R.H. Abu-Eittah, M. El-Esawy, N. Ghoneim, and A.T. Aly A comparative theoretical study of the electronic structure of some nickel(II) azides, thiocyanates, and isothiocyanates **1006**

T.M. Fyles, D. Loock, and X. Zhou Ion channels based on bis-macrocyclic bolaamphiphiles: effects of hydrophobic substitutions **1015**

Silvia Álvarez-Santos, Àngels González-Lafont, and José M. Lluch Effect of the hydrogen bond network in carbonic anhydrase II zinc binding site. A theoretical study **1027**

Elena Cerrada and Mariano Laguna Heteroleptic gold complexes with 4,5-diselenolate-1,3-dithiole-2-thione ($C_3S_3Se_2^{2-}$, dsit) **1033**

Ayman Wahba Erian, Ebtisam Abdul Aziz Hafez, Elham Sayed Darwish, and Mohamed Hilmy Elnagdi Studies with polyfunctionally substituted heteroaromatics: synthesis of new heterocyclic aromatic amines as potential intermediates for preparation of dyes for thermal diffusion printing **1038**

D.A. Block, D. Yu, D.A. Armstrong, and A. Rauk On the influence of secondary structure on the α-C—H bond dissociation energy of proline residues in proteins: a theoretical study **1042**

Scott Brownridge, T. Stanley Cameron, Jack Passmore, Gabriele Schatte, and George W. Sutherland The preparation, X-ray crystal structure, and spectroscopic characterization of pentafluorophenyl-bis(pentafluorophenylthio)sulfonium hexafluoroarsenate, $[(C_6F_5S)_2SC_6F_5][AsF_6]$ **1050**

Craig D. Montgomery, Steven J. Rettig, and Bryn Shurmer Crystal structure of the spirophosphorane $(OCMe_2C(O)O)_2PH$ **1060**

X.-Z. Zhang, R.C. Francis, D.B. Dutton, and R.T. Hill Decomposition of peracetic acid catalyzed by cobalt(II) and vanadium(V) **1064**

Andrew G.H. Wee and Fuxing Tang Highly diastereoselective synthesis of 1,2-amino alcohols via nucleophilic addition of organocerium reagents to 4- and 5-oxazolidinonecarbaldehydes **1070**

Wolfgang Kliegel, Jörg Metge, Steven J. Rettig, and James Trotter *C*-(2-Hydroxyaryl)-*N*-(2-hydroxyphenylmethyl)nitrones as regioselective bidentate ligands in boron chelate formation. Crystal and molecular structures of a diphenylboron complex and its parent ligand **1082**

Tristram Chivers, Masood Parvez, Ignacio Vargas-Baca, and Gabriele Schatte Conformational isomers of 1,2,5,6-tetrathiocins and the photoisomerization of a 1,2,5,6-tetrathiocin into a 1,2,3,6-tetrathiocin: X-ray structures of $(C_6X_4S_2)_2$ (X = F, Cl) and $C_6F_4SSSC_6F_4S$ **1093**

Hui-Zhong Kou, Dai-Zheng Liao, Peng Cheng, Zong-Hui Jiang, Shi-Ping Yan, Geng-Lin Wang, Xin-Kan Yao, and Hong-Gen Wang A new one-dimensional thiocyanato-bridged bimetallic compound $[Cu(en)_2Mn(NCS)_4(H_2O)_2]_n$. Synthesis, crystal structure, and magnetic properties **1102**

ADDITIONS AND CORRECTIONS / AJOUTS ET CORRECTIONS

Ariel Sella, Shmuel Cohen, and Shmaryahu Hoz Additions and corrections: 1,3-Diphenylsulphonylcyclobutane: an unprecedented case of a higher stability of the *trans* isomer of 1,3-disubstituted cyclobutane **1108**

Author Index / Index des auteurs **AI-1**

August / Août

ARTICLES

France-Isabelle Auzanneau, Mette Knak Christensen, Shannon L. Harris, Morten Meldal, and B. Mario Pinto Synthesis and characterization of polyethylene glycol polyacrylamide copolymer (PEGA) resins containing carbohydrate ligands. Evaluation as supports for affinity chromatography **1109**

Colin W. Clarke and David N. Glew Aqueous nonelectrolyte solutions. Part XV. The deuterium sulfide – deuterium oxide system and the deuterium sulfide D-hydrate **1119**

Alan Storr, David A. Summers, and Robert C. Thompson Transition metal azolates from metallocenes. Part 3: Polymeric manganese(II) and nickel(II) pyrazolates; synthesis, characterization, and magnetochemistry **1130**

Alwin Cunje, Christopher F. Rodriquez, Diethard K. Bohme, and Alan C. Hopkinson Noble gas catalysed 1,2-migrations in N_2H^+ and $N_2CH_3^+$ **1138**

Peter D. Wentzell, Ji-Hong Wang, Leon F. Loucks, and Kelli M. Miller Direct optimization of self-modeling curve resolution: application to the kinetics of the permanganate – oxalic acid reaction **1144**

S.S. Abd El Rehim, Magdy A.M. Ibrahim, Hamdy H. Hassan, and Mohammed A. Amin Electrochemical behaviour of silver in aqueous chromate solutions **1156**

Nick H. Werstiuk, Heidi M. Muchall, Jiagong Ma, and Michael T.H. Liu A study of the vacuum pyrolysis of *para*-substituted diazoacetophenones with He(I) ultraviolet photoelectron spectroscopy **1162**

Ana M. Sanz, Pilar Navarro, Fernando Gomez-Contreras, Mercedes Pardo, Gèrard Pèpe, and André Samat A new diaza heteroaromatic crown of 3,5-disubstituted 1*H*-pyrazole which forms solid dinuclear complexes with lipophilic phenethylamines **1174**

Giancarlo Verardo, Nicoletta Toniutti, and Angelo G. Giumanini Preparation, properties, and reductive alkylation of arylhydrazides **1180**

Rose-Marie Dheilly, Yahya Sebaibi, Joseph Tudo et Michèle Queneudec Importance de la présence de magnésie dans le stockage de la chaux : carbonatation de l'oxyde et de l'hydroxyde de magnésium **1188**

Joaquim C.G. Esteves da Silva, Adélio A.S.C. Machado, Miguel A. Ferreira, and Francisco Rey Method for the differentiation of leaf litter extracts and study of their interaction with Cu(II) by molecular fluorescence **1197**

Stéphane Duvivier, Mireille Turmine et Pierre Letellier Solubilité de la β-cyclodextrine dans les mélanges eau – nitrate d'éthylammonium à 25°C **1210**

Arezki Boudif, Sandrine Gimenez, Bernard Loock, and Michel Momenteau *vic*-Diacrylic ester porphyrins as starting materials for monobenzoporphyrin and *opp*-dibenzoporphyrin syntheses **1215**

Scott Brownridge, Jack Passmore, and Xiaoping Sun The electrophilic substitution reaction of the dithionitronium cation $[SNS]^+$ with benzene **1220**

Author Index / Index des auteurs **AI-1**

September / Septembre

ARTICLES

Robert B. Grossman and Robert J. Trupp The first reagent-controlled asymmetric halolactonizations. Dihydroquinidine–halogen complexes as chiral sources of positive halogen ion **1233**

Donald R. Arnold and Kimberly A. McManus Photochemical nucleophile–olefin combination, aromatic substitution (photo-NOCAS) reaction: methanol, β-myrcene, and 1,4-dicyanobenzene. Intramolecular cyclization of an ene–diene radical cation **1238**

Katrin Köhler and Warren E. Piers Ketone coordination chemistry of the diborane *t*-BuCH=C$[B(C_6F_5)_2]_2$ **1249**

Paul Harrington and Michael A. Kerr The ultra high pressure conjugate addition of indoles to electron-deficient olefins **1256**

Gregory D. Boucher, Aaron C. MacDonald, Brent E. Hawrylak, and D. Gerrard Marangoni A nuclear magnetic resonance investigation of the micellar properties of two-headed surfactant systems: the disodium 4-alkyl-3-sulfonatosuccinates. 1. Equilibrium micellar properties **1266**

Lubomír Rulíšek, Zdeněk Havlas, Stanislav Heřmánek, and Jaromír Plešek Regular polyhedral molecules. P_{20} and its inclusion compounds **1274**

Jordan H. Wosnick, Frederick G. Morin, and Denis F.R. Gilson ^{31}P chemical shift anisotropies of trimethyl- and triphenylphosphine-substituted Group 6 metal pentacarbonyl complexes **1280**

E.A. Jefferson, A.J. Kresge, L. Matthew, and Z. Wu Ketonization of (*Z*)-2-methoxy-1,2-diphenylvinyl alcohol. Quantitative evaluation of the remarkable kinetic stability of this enol **1284**

M. Parvez, A. Rauk, T.S. Sorensen, and F. Sun Structure reassignment of the major isomer from the Diels–Alder reaction of acryloyl chloride and 4,5,6,6a-tetrahydropentalene **1289**

John T. Edward Calculation of octanol–water partition coefficients of organic solutes from their molecular volumes **1294**

Yoshifumi Yuasa, Yoko Yuasa, and Haruki Tsuruta A practical and efficient enantioselective synthesis of (2*S*)-3-(*tert*-butylsulfonyl)-2-benzylpropionic acid, a useful chiral building block for renin inhibitors **1304**

Thomas E. Goodwin, Jennifer M. Meacham, and Mark E. Smith Observations on the stereochemistry of reduction of 2,6-dimethylcyclohexanones **1308**

Carmen E. Hernández and William E. Acree, Jr. Solubility of fluoranthene in organic nonelectrolyte solvents. Comparison of observed versus predicted values based upon Mobile Order theory **1312**

J. Stephen Hartman, Elizabeth I. Ilnicki, James A. W. Shoemaker, Wojciech R. Szerminski, and Zheng Yuan Formation of mixed-ligand fluoroboron cations involving C=N donors. A ^{19}F and ^{11}B NMR study **1317**

Author Index / Index des auteurs **AI-1**

October / Octobre

ARTICLES

Robert A. McClelland, Timothy A. Gadosy, and Daniel Ren 1997 Alfred Bader Award Lecture: Reactivities of arylnitrenium ions with guanine derivatives and other nucleophiles **1327**

Viviana L. Ponzo and Teodoro S. Kaufman Diastereoselective alkoxymethylation of aromatic aldehydes with chiral lithiomethyl ethers. Synthesis of optically active monoprotected glycols **1338**

Agnes M. Modro, Tom A. Modro, Malose J. Mphahlele, Wieslawa Perlikowska, André Pienaar, Marcelo Sales, and Petrus H. van Rooyen Reaction of carbanions generated from arylmethylphosphonates with cyclic enones. Regio- and stereoselectivity of addition **1344**

Herbert Höpfl, Mario Sánchez, Norberto Farfán, and Victor Barba Synthesis and comparative study of three monomeric boronates by spectroscopic methods and X-ray crystallography **1352**

Ellie L. Uzunova, Dimitar G. Klissurski, and Stella D. Nemska Surface studies of nano-dimensional particle size iron–manganese spinel mixed oxides **1361**

Ralph M. Paroli, Denis F.R. Gilson, and Ian S. Butler Spectroscopic and differential scanning calorimetric studies of the phase transitions in oxanorbornane **1365**

Michael Lewis, Charles L. Barnes, and Rainer Glaser The supramolecular architecture of 4-aminoacetophenone (1-(4-fluorophenyl)ethylidene)hydrazone hydrate. Double T-contacts and extremely low-density water layers in a mixed azine **1371**

Ian R. Baird, Steven J. Rettig, Brian R. James, and Kirsten A. Skov Synthesis and characterization of homoleptic ruthenium(II) imidazole complexes, and a carbonyl species derived by CO abstraction from DMF **1379**

Igor L. Shamovsky, Gregory M. Ross, Richard J. Riopelle, and Donald F. Weaver Molecular modelling studies of a nerve growth factor receptor **1389**

Gustavo A. Arteca and Denise I. Caughill Temperature dependence of self-entanglements in protein backbones near the glass-like transition **1402**

Laurence J. Beach, Raymond J. Batchelor, Frederick W.B. Einstein, and Andrew J. Bennet General base-catalyzed hydrolysis and carbonyl-^{18}O exchange of *N*-(4-nitrobenzoyl)pyrrole **1410**

Juan Antonio González, I. García de la Fuente, and J.C. Cobos DISQUAC structure-dependent interaction parameters for mixtures containing *sec*-alkanols and benzene, toluene, or *n*-alkanones **1418**

Harry W. Gibson, Devdatt S. Nagvekar, Yadollah Delaviz, and William S. Bryant Synthesis of a new class of difunctional tetraphenylene crown ethers **1429**

John M. Goodings and QingFeng Chen Chemical kinetics and thermodynamics of tin ionization in H_2-O_2-N_2 flames and the proton affinity of SnO **1437**

Christopher J.A. Daley, Jason A. Wiles, and Steven H. Bergens Application of [Ru((*R*)-BINAP)(MeCN)(1-3:5,6-η-C_8H_{11})](BF_4) as a catalyst precursor for enantioselective hydrogenations **1447**

Luigi Cavallo, Tom K. Woo, and Tom Ziegler A combined QM/MM study of ligand substitution enthalpies in the $L_2Fe(CO)_3$, $RuCpL_2Cl$, and $RuCp^*L_2Cl$ systems **1457**

Veranja Karunaratne and David Dolphin Oxidation of 2-methylpyrroles with perchlorinated iron(III) metalloporphyrin catalysts: a versatile synthesis of symmetric and asymmetric dipyrromethanes **1467**

P.F. McGarry and J.C. Scaiano The absolute kinetics for radical addition and electronic energy transfer to [1.1.1]propellane **1474**

Author Index / Index des auteurs **AI-1**

November / Novembre

Materials Science Special Issue
Numéro spécial sur la science des matériaux

ARTICLES

Sonia Moffatt, Abdellah Ajji, Bernard Lotz, and Josée Brisson Uniaxial deformation of nylon-6 and nylon-11: changes in orientation and crystal phase **1491**

Michel Lafleur Phase behaviour of model stratum corneum lipid mixtures: an infrared spectroscopy investigation **1501**

Boyan B. Bonev and Michael R. Morrow ^{2}H NMR studies of dipalmitoylphosphatidylcholine and dipalmitoylphosphatidylcholine–cholesterol bilayers at high pressure **1512**

Jennifer F. Caplan, Christopher A. Murphy, Susan Swansburg, Robert P. Lemieux, T. Stanley Cameron, and Manuel A.S. Aquino Evidence for room temperature mesomorphism in a mixed-valent diruthenium(II,III) quintapalmitoleate polymer **1520**

Jimmy Lowe, Carl Bartels, and Steven Holdcroft Synthesis and properties of a sterically encumbered poly(thienylene vinylene): poly[*E*-1,2-(4,4′-dihexyl-2,2′-dithienyl)ethylene] **1524**

Jonathan G.C. Veinot, Josie Galloro, Linda Pugliese, Valerie Bell, Robert Pestrin, and William J. Pietro Surface functionalization of cadmium sulfide quantum-confined nanoclusters. 4. Formation and reactivity of an aniline surface quantum dot **1530**

Patrick W.M. Jacobs and Marcia L. Vernon Phonon dispersion and defect energies for rubidium chloride, bromide, iodide, and sulphide **1540**

Ziqiang Qin, Alan R. Allnatt, and E. Loftus Allnatt Computer simulation of time correlation functions and matter transport coefficients for a model order–disorder alloy **1548**

Troy A.E. Loss, Cerrie W. Rogers, and Michael O. Wolf Composite poly(*p*-phenylenevinylene)–Nafion thin films **1554**

J. Hugh Horton, Johann Rasmusson, Joseph G. Shapter, and Peter R. Norton The adsorption of bis(hexafluoroacetylacetonato)zinc(II) on Si(111)-7×7 **1559**

Fernande D. Rochon, Marius Andruh, and Robert Melanson Three-dimensional H-bonded supramolecular complexes. Synthesis and crystal structures of $[Mn(\mu\text{-bpe})(H_2O)_4](ClO_4)_2\cdot 4(bpe)\cdot 2H_2O$ and $[M(\mu\text{-bpe})(bpe)_2(H_2O)_2](ClO_4)_2\cdot bpe\cdot H_2O$, where M = Zn, Ni and bpe = 1,2-bis(4-pyridyl)ethane **1564**

Maxime Ranger and Mario Leclerc Optical and electrical properties of fluorene-based π-conjugated polymers **1571**

William D. Machin A simple method for the generation of negative pressure in liquids **1578**

A. Alavi, R.M. Lynden-Bell, P.A. Willis, I.P. Swainson, and R.J.C. Brown An ab initio and neutron diffraction study of ammonium chloride **1581**

Allison M. Mills, Robert Lam, and Arthur Mar Ternary cobalt germanium pnictides $CoGe_xPn_{1-x}$ (*Pn* = P, As, Sb) and the structure of Co_3Ge_2Sb, an intermetallic compound with stuffed Sb_2 pairs **1588**

B. Heinrich, M. Kowalewski, and J.F. Cochran Engineering of magnetic properties using ultrathin metallic structures prepared by Molecular Beam Epitaxy **1595**

Faraj Asgari and Dimitris S. Argyropoulos Fundamentals of oxygen delignification. Part II. Functional group formation/elimination in residual kraft lignin **1606**

Bozena Borecka-Bednarz, Alan V. Bree, Brian O. Patrick, John R. Scheffer, and James Trotter Second-harmonic generation studies of chiral organic salts **1616**

Luc Tremblay, Serge Lacelle, and Charles G. Fry Characterization of macroscopic disorder in a porous glass with NMR microimaging and scanning electron microscopy **1633**

Julien Brazeau, Yanick Chénard, and Yue Zhao Orientation in stretched polymer-dispersed liquid crystals **1642**

Dennis Hore, Almeria Natansohn, and Paul Rochon Irradiance and temperature dependence of photoinduced orientation in two azobenzene-based polymers **1648**

F. Bensebaa, T.H. Ellis, E. Kruus, R. Voicu, and Y. Zhou The self-assembly of a layered material: metal–alkanethiolate bilayers **1654**

Garry S.H. Lee, Christopher I. Ratcliffe, and John A. Ripmeester A solid state ^{31}P NMR study of the synthesis of phosphorus sulfides from PCl_3 and H_2S in microporous materials **1660**

M. Di Renzo, F. El Feninat, B. Jiménez-Esquivel, S. Poulin, M. Yavari, J. Xu, T.H. Ellis, E. Kruus, E. Sacher, and I. Stangel Adhesion to dentin: studies of surface chemical reactions towards the goal of improved bonding **1668**

P. Bernazzani, V.T. Bich, H. Phuong-Nguyen, A. Haine, C. Chapados, Lê H. Dao, and G. Delmas FTIR analysis of the phase content in low-density polyethylene **1674**

Jan C. Myland, Keith B. Oldham, Jörg Schiewe, and Alicia L. Taylor Electrochemical study of the pore structure of sandstone and similar media **1688**

Mary Anne White Origins of thermodynamic stability of urea:alkane inclusion compounds **1695**

Jonathan Z. Knaul, Mohammad R. Kasaai, V. Tam Bui, and Katherine A.M. Creber Characterization of deacetylated chitosan and chitosan molecular weight review **1699**

I. Coulthard, S. Degen, Y.-J. Zhu, and T.K. Sham Gold nanoclusters reductively deposited on porous silicon: morphology and electronic structures **1707**

Kalaichelvi Saravanamuttu, Xin Min Du, S. Iraj Najafi, and Mark P. Andrews Photoinduced structural relaxation and densification in sol-gel-derived nanocomposite thin films: implications for integrated optics device fabrication **1717**

Mathew D. Halls and Ricardo Aroca Vibrational spectra and structure of tris(8-hydroxyquinoline)aluminum(III) **1730**

G.R. Carlow and M. Zinke-Allmang Initial stages of cobalt-disilicide formation in mesotaxy **1737**

Christine Pizzocaro, Roger A. Lessard, and Michèle Bolte Charge-transfer phenomena in holographic recording material: dichromated poly(acrylic acid) **1746**

Christopher B. Kennedy, Bruce J. Balcom, and Igor V. Mastikhin Three-dimensional magnetic resonance imaging of rigid polymeric materials using single-point ramped imaging with T_1 enhancement (SPRITE) **1753**

Chi Ming Yam, Adam Dickie, Aramice Malkhasian, Ashok K. Kakkar, and M.A. Whitehead Molecular self-assembly of rigid-rod alkynyl chromophores on inorganic oxide surfaces **1766**

Kazunaga Horiuchi, Yahya Rharbi, Ahmad Yekta, Mitchell A. Winnik, Richard D. Jenkins, and David R. Bassett Dissolution behavior in water of a model hydrophobic alkali-swellable emulsion (HASE) polymer with $C_{20}H_{41}$ groups **1779**

Author Index / Index des auteurs **AI-1**

December / Décembre

ARTICLES

Wolfgang Kliegel, Ulf Riebe, Steven J. Rettig, and James Trotter Reaction of ketoximes with aliphatic aldehydes and diphenylborinic acid. Crystal and molecular structure of a diphenylboron chelate derived from the pivaldehyde adduct to cyclohexanone oxime **1789**

K. Shimizu, B.J. Flinn, P.C. Wong, and K.A.R. Mitchell SIMS studies of the effect of H at interfaces formed by oxidized zirconium **1796**

Peter N. Preston, Steven J. Rettig, Alan Storr, and James Trotter Coordination complexes derived from 3,6-di(2-pyridyl)-1,4-dihydro-1,2,4,5-tetrazine (DPDHT). Synthesis and molecular structure of $[(DPT)(GaMe_2)_2]$ **1800**

L. Ross C. Barclay, Jennifer K. Grandy, Heather D. MacKinnon, Heather C. Nichol, and Melinda R. Vinqvist Peroxidations initiated by lignin model compounds: investigating the role of singlet oxygen in photo-yellowing **1805**

Leif A. Eriksson, C. Magnus Jansson, Donald R. Arnold, and Russell J. Boyd Cleavage of neutral alkenes and alkene radical cations; hybrid Hartree–Fock/density functional theory results **1817**

Ivor Wharf, Ryszard Wojtowski, Carol Bowes, Anne-Marie Lebuis, and Mario Onyszchuk Spectroscopic studies of triphenyltin azide and of its adducts with *O*- and *N*-donor ligands; the crystal and molecular structures of triphenyltin azide and of azido(hexamethylphosphoramide)triphenyltin(IV) **1827**

G. Kalita, N.N. Dass, and S. Mahiuddin Mixed anion effect in sodium thiocyanate + sodium thiosulfate + water systems **1836**

Fernande D. Rochon, Robert Melanson, and Margaret M. Kayser Crystal structures of highly stabilized ylides: methyl(3-methoxy,2-methoxycarbonylbenzoyl)triphenylphosphoranylideneacetate and methyl(2-methoxycarbonyl,6-nitrobenzoyl)triphenylphosphoranylideneacetate and the salt methyl(triphenylphosphoranylidene)acetate tetrafluoroborate **1844**

Herbert Höpfl and Norberto Farfán Synthesis and structural characterization of (2′-hydroxyacetophenoneazine)mono(diphenylboron) chelate **1853**

Mohamed M. El-Banna and Mervette M. El-Batouti Temperature dependence of the excess volumes of binary mixtures containing cyclohexane + some higher *n*-alkanes **1860**

A. Ahrika, M. Anouti, J.E. Robert, and J.L. Paris Spectroelectrochemical study of the nucleophilic substitution of diacyl disulfides by 2-nitrophenyl thiolate ions in *N*,*N*-dimethylacetamide **1867**

N. Kopytko et F. Baronnet Valorisation chimique du méthane par plasmas micro-ondes **1875**

Lionel Roué, Emmanuel Briot et Fethi Bedioui Synthèse critique de la caractérisation électrochimique de zéolithes et d'aluminophosphates chimiquement modifiés **1886**

Robert A. McClelland, Victoria E. Licence, John P. Richard, Kathleen B. Williams, and Shrong-Shi Lin Remarkable kinetic stability of α-thiocarbamoyl substituted 4-methoxybenzyl cations **1910**

Shigetaka Yakabe, Masao Hirano, and Takashi Morimoto Alumina-assisted reduction of carbonyl compounds with sodium borohydride in hexane **1916**

Nouria A. Al-Awadi, Kamini Kaul, and Osman M.E. El-Dusouqui Gas-phase pyrolysis in organic synthesis. Part 2. Novel rearrangement of esters and ethers into aryl ketones **1922**

COMMUNICATION

Heidi M. Muchall and Nick H. Werstiuk A computational study on the sources of deuterium secondary kinetic isotope effects in carbocation-forming reactions **1926**

ADDITIONS AND CORRECTIONS / AJOUTS ET CORRECTIONS

A. Rauk, J.L. McCann, H. Wieser, P. Bour, I.V. Vystorop, Yu.I. El'natanov, and R.G. Kostyanovsky Additions and corrections: Skeletal vibrational circular dichroism of a series of bicyclic dilactones: the fingerprint region? **1931**

Carmen E. Hernández and William E. Acree, Jr. Additions and corrections: Solubility of fluoranthene in organic nonelectrolyte solvents. Comparison of observed versus predicted values based upon Mobile Order theory **1931**

Author Index / Index des auteurs **AI-1**

Contents for volume 76 / Sommaire pour volume 76 **C-1**